JOURNAL OF THE ELECTROCHEMICAL SOCIETY

ELECTROCHEMICAL SCIENCE
— AND TECHNOLOGY —

JANUARY
1973

Morphology and Capacity of a Cadmium Electrode

Studies on a Simulated Pore

F. G. Will* and H. J. Hess

Research and Development Center, General Electric Company, Schenectady, New York 12301

ABSTRACT

Conditions in a single pore of a battery plate were simulated by using a cadmium chip of millimeter dimensions covered with an electrolyte film of micron thickness. *In situ* microscopy was applied to study changes in the electrode morphology during charge and discharge. Passivation and increases in particle sizes due to precipitation and electrodeposition of dissolved cadmium species were found to cause profound loss in electrode capacity on repeated charge and discharge.

Cadmium battery plates often exhibit a gradual decrease of their capacity when they are repeatedly charged and discharged (1). A certain part of the "lost" capacity may be regained by changing the conditions of charging and discharging. Another part of the capacity, however, is lost irreversibly. The phenomenon is more pronounced in sealed cells working with a minimum of electrolyte than in flooded, vented cells.

Studies of Cd battery plates with microscopy, x-ray diffraction, and electron microscopy techniques have shown that the decrease of the plate capacity is related, at least in part, to changes in the plate morphology (1-3). Migration of Cd species from the interior of the plate to its surface accompanied by an increase in the size of the particles has been demonstrated. This migration becomes more pronounced as the number of cycles and the rate of charging and discharging increases. Recently it was shown that the loss of capacity on cycling can be substantially reduced by adding certain metal oxides to the battery plate (4).

Numerous studies have dealt with the mechanism of the Cd electrode in bulk solutions of alkali. These studies have established the solubility of Cd as a function of electrolyte concentration and temperature (5-7). No full agreement exists with regard to the nature of the dissolved Cd species. Authors in the past have alternately proposed a dissolution-precipitation (8-14) and a solid-state transport mechanism for the Cd electrode (15-17). Recent results obtained with a ring-disk electrode seem to show that in concentrated alkaline solutions the discharge occurs solely by a dissolution-precipitation mechanism and that both mechanisms enter when charging the electrode (18). The proposed mechanism involves the formation of $Cd(OH)_3^-$ ions as an intermediate species in solution (18-19)

$$Cd + 3\,OH^- \rightleftarrows Cd(OH)_3^- + 2e^- \quad [1]$$

$$Cd(OH)_3^- \rightleftarrows Cd(OH)_2 + OH^- \quad [2]$$

The mechanism of the Cd electrode is complicated by the formation of passivating layers. Certain experimental evidence suggests the formation of CdO films as the cause for passivation (20-21). However, CdO has so far escaped positive identification. The mechanism is further complicated by the formation of several phases of $Cd(OH)_2$ (22-25).

The behavior of battery plates on cycling and the mechanism of Cd electrodes in bulk electrolytes have both been studied. However, a gap exists in our understanding of the effects of repeated charging and discharging on the morphology of smooth Cd electrodes in bulk electrolyte and the mechanisms occurring in porous Cd electrodes such as Cd battery plates. It is apparent that the mechanism of a smooth Cd electrode in bulk electrolyte may differ substantially from the mechanism occurring in the pores of a Cd battery plate. The nonuniform current distribution and changes in the electrolyte concentration in the pores during charging and discharging are expected to give rise to such differences in mechanism. For Cd electrodes covered with electrolyte films of 0.5-2 mm thickness, nonuniform current distribution and changes in the electrolyte concentration during charging and discharging have, in fact, been demonstrated to exist (26).

The present study is aimed at establishing the effect of repeated charging and discharging on the capacity and morphology of Cd electrodes in thin films of alkaline electrolyte. Conditions in a single pore of a battery plate were simulated by using a flat miniature Cd electrode covered with a thin film of electrolyte. Such an electrode may be considered as resulting from unwinding a hollow cylinder of inner diameter equaling the pore diameter (26). With the exception of the nonsignificant electrode width, all dimensions were chosen to approximate those encountered in actual battery plates. The counterelectrode was positioned side-by-side rather than opposite to the test electrode. This resulted in a highly nonuniform current distribution and minimization of electrolyte convection in vast contrast to the usual conditions in bulk electrolyte. The geometry permitted *in situ* microscopic examination of changes in the morphology during charging and discharging. Optical microscopy was supplemented by scanning electron microscopy to identify changes in the morphology during the initial cycles.

* Electrochemical Society Active Member.
Key words: cadmium electrode, capacity loss, morphology, pore simulation.

Experimental

Over-all arrangement.—The film electrolyte experiments were carried out in a cell positioned on the stage of a Leitz Ortholux microscope to allow examining changes in the electrode morphology during charge and discharge. The microscope stage was enclosed in a polyethylene bag, continually flushed with nitrogen, to reduce effects due to the diffusion of oxygen and carbon dioxide into the cell. The carbonate concentration accumulating in the cell during the maximum duration of an experiment was determined by analysis as 0.13 moles of K_2CO_3 per liter of 6*N* KOH.

Electronic instrumentation.—Experiments were carried out under conditions of controlled voltage or controlled current. In the former case, an electronic potentiostat was used to apply potentials with a precision of ±1 mV between the test electrode and the reference electrode. In the latter case, an automatic electronic cycling device was used to apply constant currents between test and counterelectrode. The voltage-time transients under conditions of constant charge and discharge currents were recorded on a Hewlett Packard strip chart recorder. The voltage limits during charge and discharge could be set to various arbitrary values.

Cell design.—The experiments were performed in a Lucite plastic cell of outer dimensions 3 × 3 cm × 0.6 cm thick. A cross section of the cell is shown in Fig. 1. The counterelectrode is contained in a well of dimensions 2 × 2 cm × 0.3 cm deep. It consists of a section of a nickel hydroxide battery plate. The reference electrode is a self-contained hydrogen electrode as described elsewhere (27). It communicates with the electrolyte in the well via a capillary with a 1 mm opening. The opening is located at a distance of 1-2 mm from the test electrode. The latter consists of a copper strip of 1 mm width, 10 mm length, and 0.13 mm thickness. A cadmium oxide layer of dimensions 1 × 1 mm and a few micron thickness is deposited on the end of the copper strip adjoining the well. Shell Epon 828 epoxy resin is used to cement the test electrode into the cell housing in such a way that its upper surface is flush with the top of the Lucite cell housing. A spacer of silicone rubber or polyethylene covers the entire rim of the cell housing except for the 1 × 1 mm layer of cadmium oxide on the copper strip. A glass cover consisting of a microscope slide with 0.25 mm thickness is placed upon the spacer. Thus the spacer thickness determines the thickness of the electrolyte film covering the test electrode.

Electrode preparation.—In all but a few cases, test electrodes were prepared by electrophoretically depositing a cadmium oxide-binder composition on the copper substrate strips. The copper strips were cut from large specimens of electropolished copper foil. The strips were then amalgamated to further reduce the evolution of hydrogen during cathodic experiments. The evolution of even small amounts of hydrogen interferes with the microscopic examinations due to entrapment of bubbles between the test electrode and the glass cover. Electrophoretic deposition resulted in cadmium oxide layers which were even and uniform down to thicknesses of a few microns.

Cadmium oxide-binder compositions were prepared by ball milling a mixture of 12 parts by weight cadmium oxide with 1 part polyvinylidene fluoride and 63 parts dimethyl acetamide (DMA). Thirty parts DMA and 0.3 parts $Cd(NO_3)_2 \times 4H_2O$ were added subsequently. Electrophoretic deposition of cadmium oxide was accomplished at room temperature in a cell containing a platinum anode and the copper substrate foil as the cathode. Typically the application of a voltage of 100V for 20 sec led to a cadmium oxide layer thickness of about 5μ. The porosity and the theoretical capacity of the cadmium oxide layers were calculated from experimental determinations of the film thickness and the weight. Porosities of 46-50% were calculated for cadmium oxide layers of 5-7μ thickness. The theoretical capacity referred to an area of 1 cm² and a thickness of 1μ was calculated as 0.55 A-sec/cm²/μ.

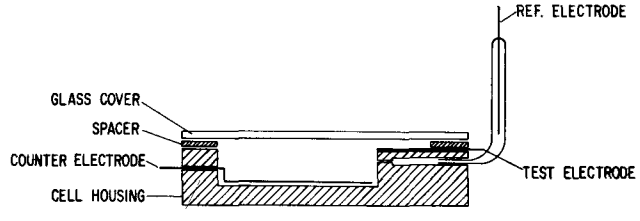

Fig. 1. Cross section of electrolytic cell

Experimental procedure.—After filling the self-contained hydrogen electrode with electrolyte and forming a sufficient amount of hydrogen in the glass capillary, the cell was placed on the microscope stage and the well filled with electrolyte while a reducing potential of −150 mV was applied between the test electrode and the hydrogen reference electrode. The spacer and the glass cover were then placed on the cell housing. With nitrogen flowing through the polyethylene bag, the residual current transient was recorded. When the residual current had decayed to only a few per cent of the cycling currents, typically after 1 hr, the cycling experiments were started. Experimental runs were terminated by using either of two procedures: (*i*) The KOH electrolyte was substantially diluted with distilled water with a constant potential applied, followed by rinsing with water and drying with nitrogen. (*ii*) The cell was disconnected from the electric circuit, the KOH solution immediately discarded, and the cell rinsed with distilled water and dried with nitrogen. No discernible differences in morphology between these two procedures could be detected in micrographs at magnifications up to 20,000X.

Results and Discussion

Effect of cycling on capacity and morphology of CdO films.—Changes in the capacity and morphology of cadmium oxide films during the initial ten cycles in 6*N* KOH were studied in detail, using scanning electron microscopy for increased resolution in addition to the *in situ* microscopic examination. After a given number of cycles, the electrode was removed from the cell, washed, dried, and kept in a dessicator until examined in the scanning electron microscope. A new experiment was always started with a freshly prepared cadmium oxide film. Uniform layers of cadmium oxide on copper strips with thicknesses between 4 and 8μ were prepared by electrophoretic deposition as outlined in the experimental section. The experiments were carried out with a constant electrolyte film thickness of 12.5μ. A variation of the film thickness between 12.5 and 500μ produced no significant changes in the experimental results (27) from those obtained with 12.5μ electrolyte films.

Figure 2 shows the capacity *vs.* the number of cycles for seven different electrodes from the first discharge to the eleventh charge. The first charge, resulting in the reduction of cadmium oxide to cadmium, is always accomplished at a constant potential of −150 mV. A determination of the amount of charge from an integration of the current-time transient is unfeasible because of the simultaneous reduction of oxygen and evolution of hydrogen immediately following the filling of the cell with KOH. Subsequent charges and discharges are performed with a constant current density of 1.4 mA/cm² to cutoff voltages of −200 and 300 mV, respectively. The first discharge results in capacities between 1.4 and 3.1 A-sec/cm². When correction is made for variations in the cadmium oxide film thickness, d_{CdO}, of these electrodes, the discrepancies between the initial capacity values per unit area, C_1/A,

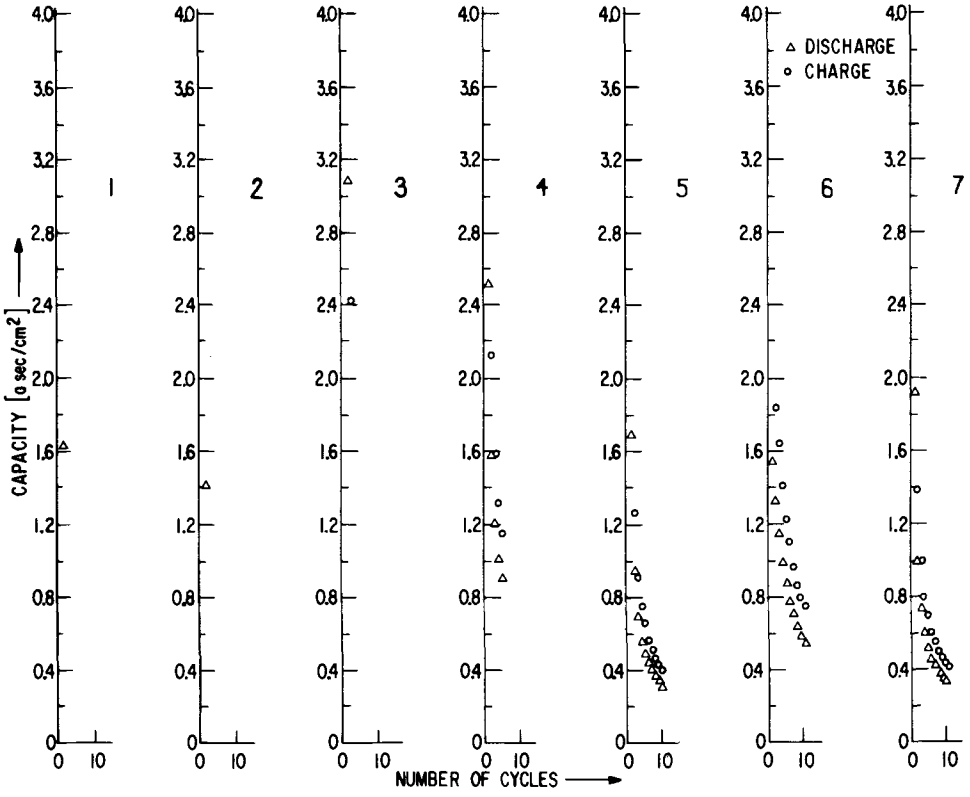

Fig. 2. Capacities of seven different CdO film electrodes *vs.* number of cycles, using a constant 6*N* KOH film thickness of 12.5μ, applying $\pm$1.5 μA/cm^2 between limits 300/—200 mV.

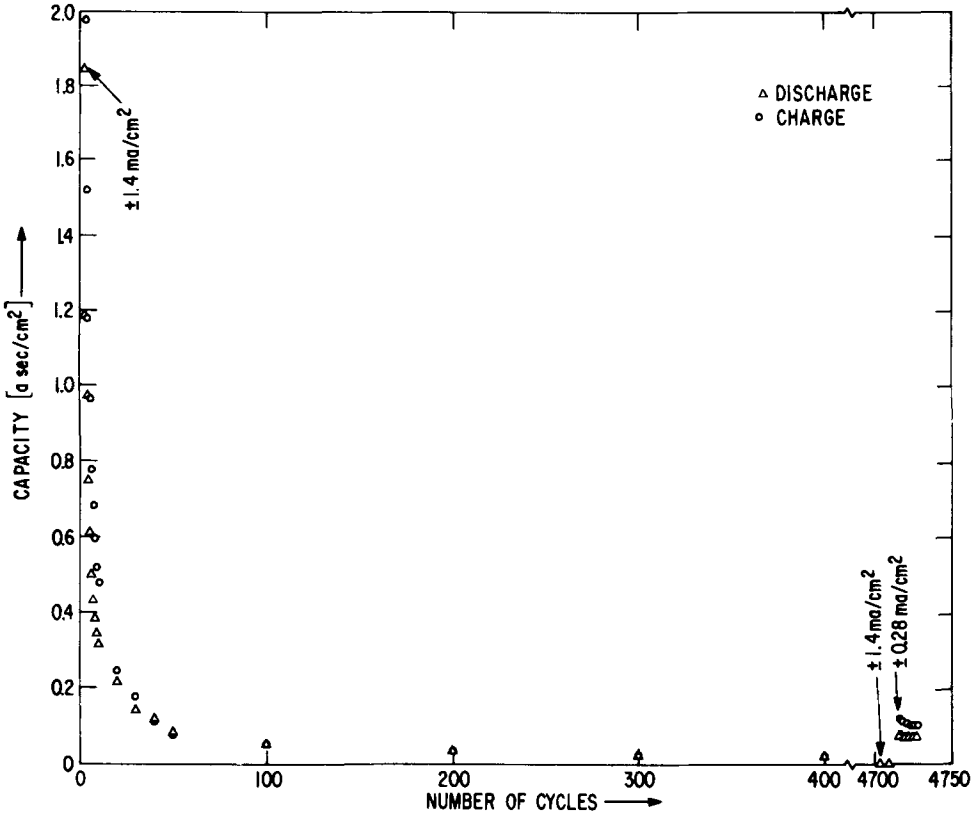

Fig. 3. Capacity of 6μ CdO film electrode (electrode 8) vs. number of cycles, using 12.5μ film of 6*N* KOH and voltage limits 300/—200 mV.

of the seven electrodes are much reduced. Table I presents a summary of the initial capacities per unit area, C_1/A, the capacities referred to 1μ cadmium oxide film thickness and 1 cm^2 area, C_1/Ad_{CdO}, and the ratios of subsequent discharge capacities to the initial capacities, C_n/C_1. The table also shows the ratios of the initial capacities to the theoretical values, C_1/C_{theor} and, in addition to the data obtained on electrodes 1-7 of Fig. 2, data obtained on an eighth electrode which was cycled more than 4000 times (see Fig. 3).

As evidenced by Fig. 2 and Table I, a drastic loss in capacity occurs during the first ten cycles. Typically the capacities decrease to one-third of the initial values within five cycles and to one-fifth within ten cycles. Loss of capacity continues on further cycling, but at a smaller rate, as shown in Fig. 3 for up to 4700 cycles. The shape of the charge and discharge curves remains approximately the same during the initial ten cycles. This is shown in Fig. 4 for the first and tenth cycles. The product of chart speed and time is plotted on the abscissa which is equivalent to the actual length of the curves on the recorder chart. The chart speed during the first cycle was 0.25 in./min as compared to 1 in./min for the tenth cycle. Hence the curves reflect

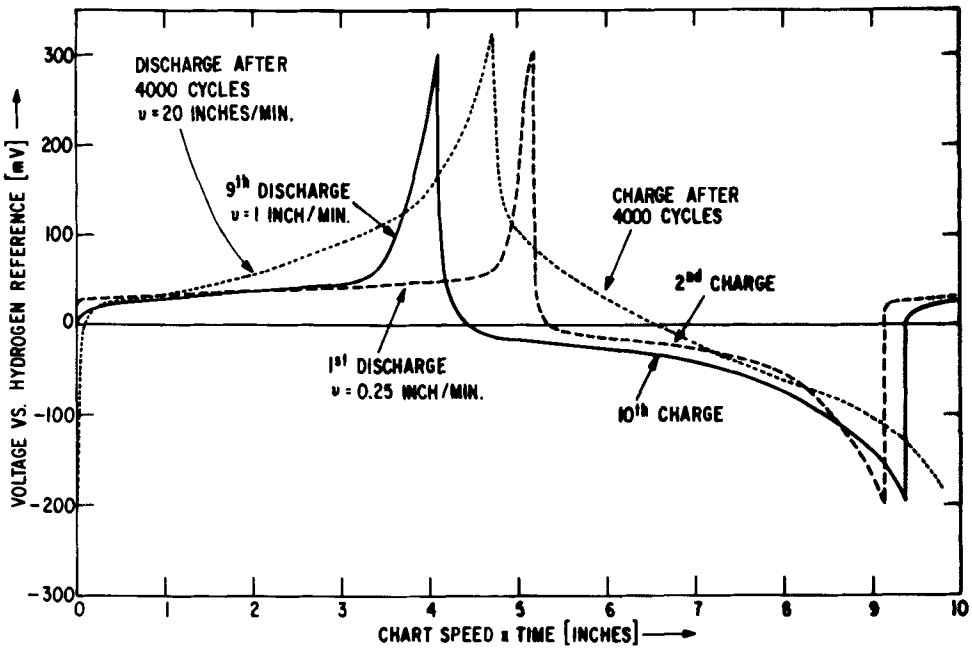

Fig. 4. Recorder traces of discharge and charge curves of electrode 8 after 1, 10, and 4000 cycles, applying ±1.4 mA/cm². Product of chart speed and time (identical to length on recorder chart) is plotted on abscissa.

the large loss of capacity during the first ten cycles as also evidenced by Fig. 3. While the discharge curves for the first and tenth cycles show a pronounced potential arrest near the $Cd/Cd(OH)_2$ equilibrium potential, such a potential arrest is virtually absent in the discharge curve after 4000 cycles, obtained at a chart speed of 20 in./min. The voltage rises continually during the entire discharge which means that higher overvoltages are required for oxidation and reduction of the electrode. This suggests the formation of passivating layers which were apparently not formed to any large extent during the first ten cycles. A different cause for the pronounced loss of capacity during the first ten cycles must therefore exist, and a careful study of the changes in morphology during the first ten cycles was undertaken.

Figure 5 shows an optical micrograph of a cadmium oxide layer in dry condition immediately after electrophoretic deposition, obtained in dark field at a magnification of 220X.[1] Figures 6 and 7 are scanning electron micrographs (SEM) of the same surface obtained at magnifications of 2000X and 10,000X. The layer is uniformly brown, and the SEM's show a large number of well-developed cubic particles of sizes 0.1-1μ. Many of these particles are covered with what appears to be the binder. Exposure of a cadmium oxide layer to a 6*N* KOH film for 10 min on open circuit turns the brown color of the deposit into a bright white color. This is shown in the optical micrograph in Fig. 8. Only a few brown particles remain at the surface after this exposure. The SEM's in Fig. 9 and 10 resolve the changes in the particle shapes caused by the exposure of the electrode to KOH. The formation of a large number of platelets, many of them with hexagonal shapes, is evident. The lateral dimensions lie in the range 3000 to 5000Å. Undoubtedly these particles are β-$Cd(OH)_2$ (25).

Figures 11-13 show the morphology of a surface which results when exposing a cadmium oxide film to

[1] Unless otherwise stated, the following photomicrographs were all obtained in dark field at a magnification of 220X.

Table I. Capacity of cadmium oxide film electrodes during first ten discharges

Electrode No.	1	2	3	4	5	6	7	8
$d_{CdO}[\mu]$*	5	5	8	8	5.5	5	5.5	6
C_1/A[A-sec/cm²]	1.63	1.40	3.08	2.53	1.70	1.56	1.93	1.85
C_1/Ad_{CdO}[A-sec/cm² μ]	0.33	0.28	0.38	0.32	0.31	0.31	0.35	0.31
C_1/C_{theor}	0.60	0.51	0.69	0.58	0.56	0.56	0.64	0.56
C_2/C_1				0.63	0.56	0.86	0.52	0.53
C_5/C_1				0.36	0.29	0.56	0.27	0.33
C_{10}/C_1					0.18	0.35	0.18	0.17

* d_{CdO} = thickness; A = area of cadmium oxide films; C_1, C_2, C_5, C_{10} = capacities during 1., 2., 5. and 10. discharge; C_{theor} = theoretical capacity.

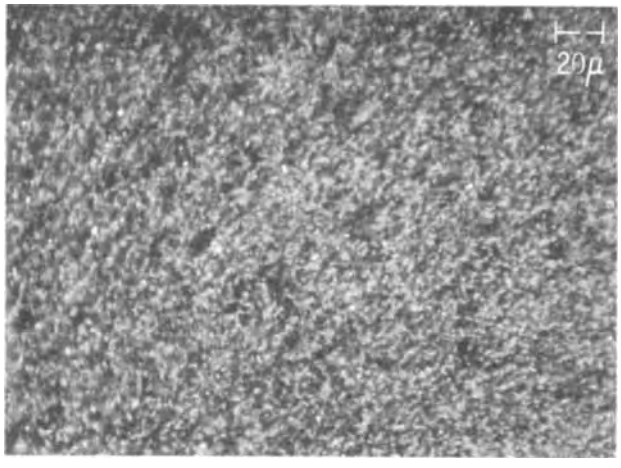

Fig. 5. Optical micrograph of CdO film as deposited by electrophoresis (220X, dark field, dry).

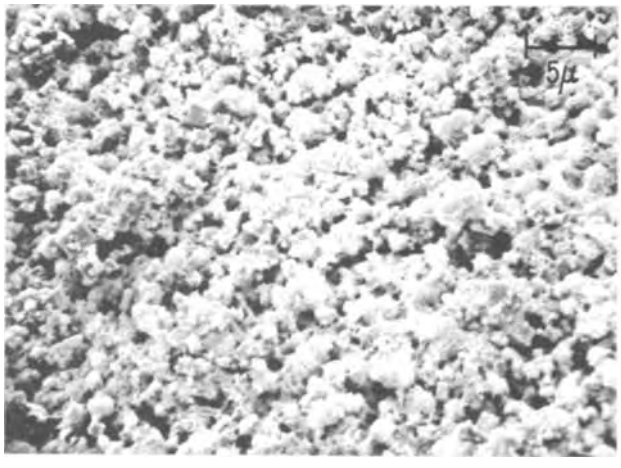

Fig. 6. Scanning electron micrograph (SEM) of same CdO film as Fig. 5 at 2000X.

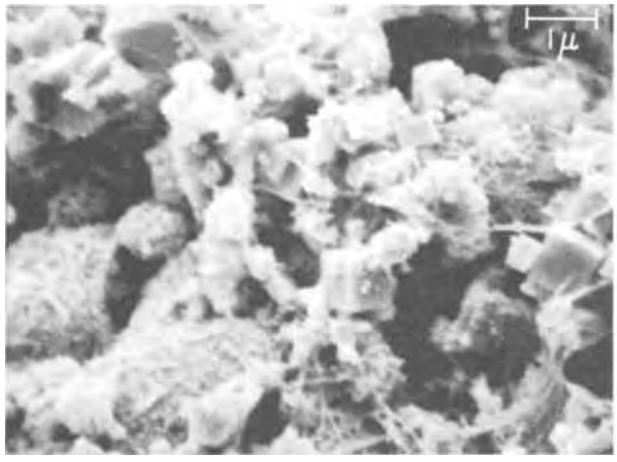

Fig. 7. SEM of same CdO film as Fig. 5 at 10,000X

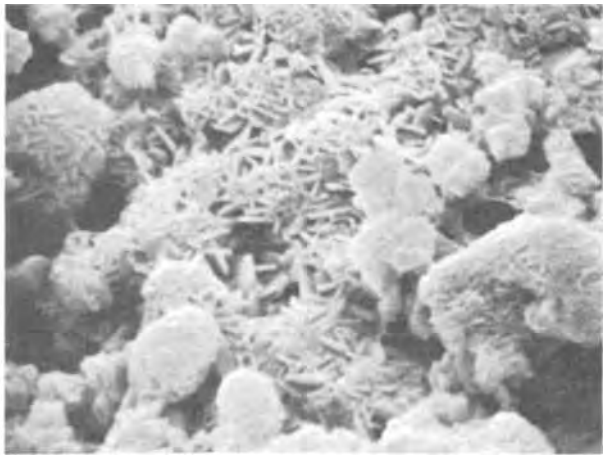

Fig. 10. SEM of same surface as Fig. 8 at 10,000X

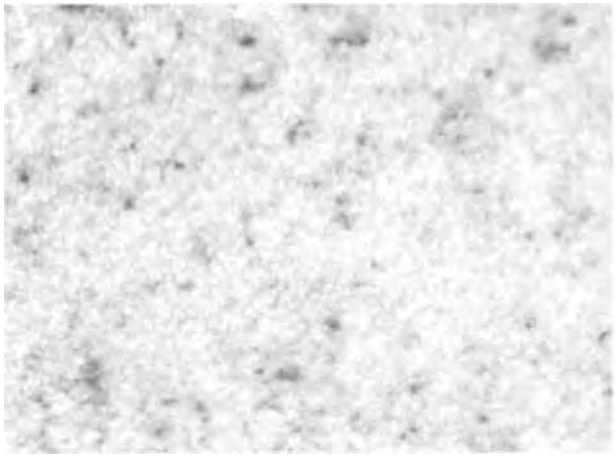

Fig. 8. Optical micrograph of CdO film after exposure to 12.5μ film of 6*N* KOH on open circuit for 10 min (220X, dark field, wet).

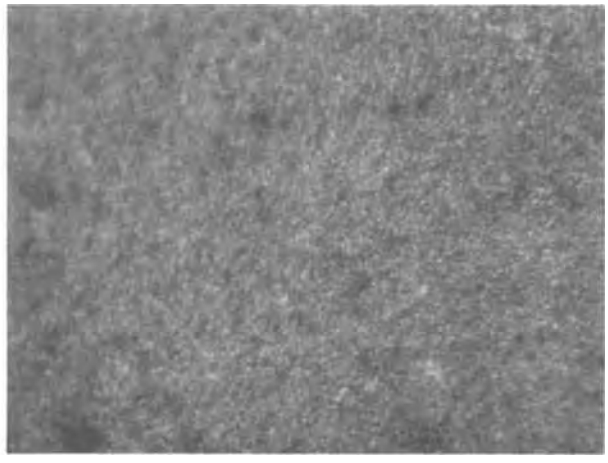

Fig. 11. Optical micrograph of CdO electrode after reducing with −150 mV for 3 hr with 12.5μ film of 6*N* KOH.

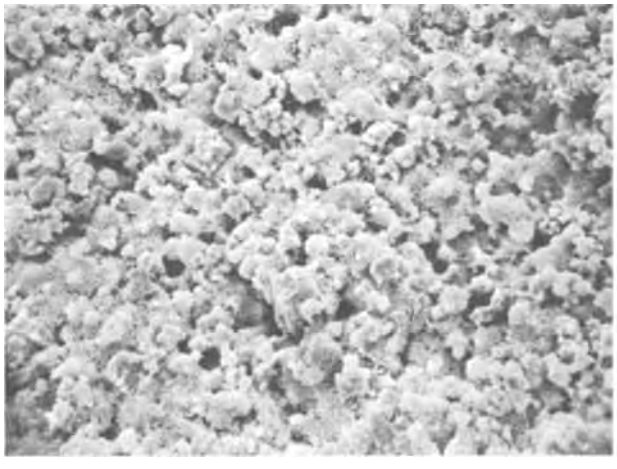

Fig. 9. SEM of same surface as Fig. 8 at 2000X

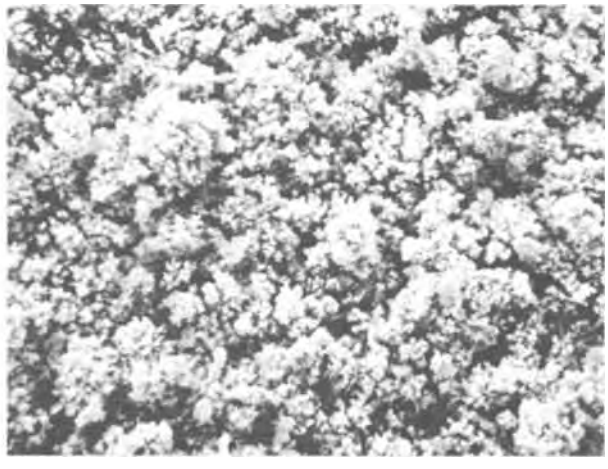

Fig. 12. SEM of same surface as Fig. 11 at 2000X

6*N* KOH with a reducing potential of −150 mV applied for 3 hr. After this reduction, the surface appears uniformly gray in the microscope (Fig. 11). A large number of small, highly reflecting particles are present, but their shapes cannot be resolved in the microscope. The SEM's in Fig. 12 and 13 show that the crystal habit has changed but the particle sizes have not (compare Fig. 6 and 7). The cubic particles in Fig. 7 are no longer visible in Fig. 13. Most of the cadmium particles in Fig. 13 have sizes between 2000 and 3000Å.

During the first discharge, which results in the formation of $Cd(OH)_2$, microscopic examination reveals the formation of dark areas on the surface which ultimately grow together. The distinct darkening of the surface is the only effect of discharge which can be observed in the microscope. Figure 14 shows the surface after complete discharge at a magnification of 220X.

The SEM's in Fig. 15 and 16 show that a large number of well-defined crystals, mostly of sizes 1-2μ, have been formed. The hexagonal shape of these crystals identifies them as β-$Cd(OH)_2$ (25). In addition, a few needle-like crystals, most likely γ-$Cd(OH)_2$ (25), and distinctly shaped particles with sizes one order of

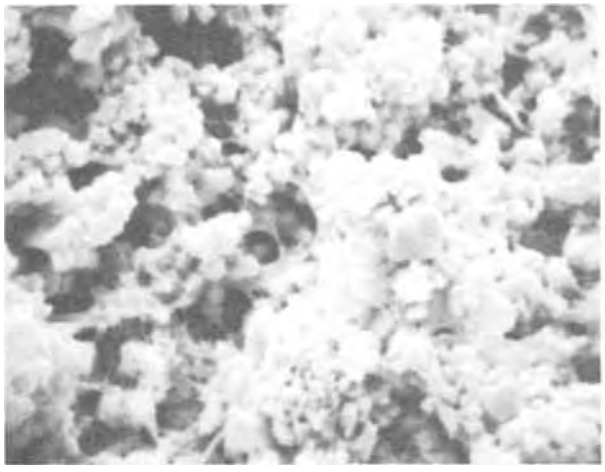

Fig. 13. SEM of same surface as Fig. 11 at 10,000X

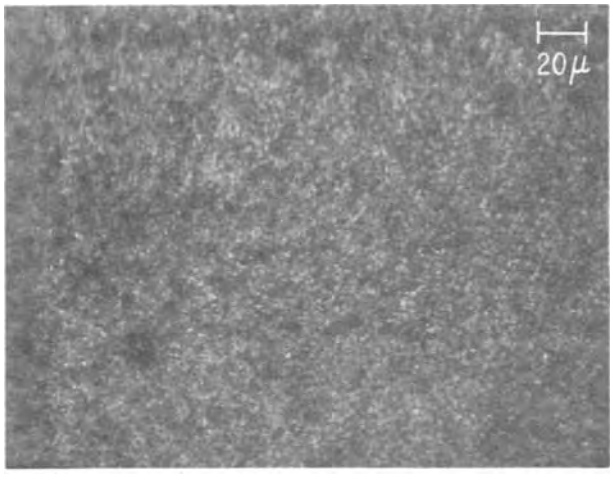

Fig. 14. Optical micrograph of electrode 1 after first discharge with 1.4 mA/cm^2 to 300 mV.

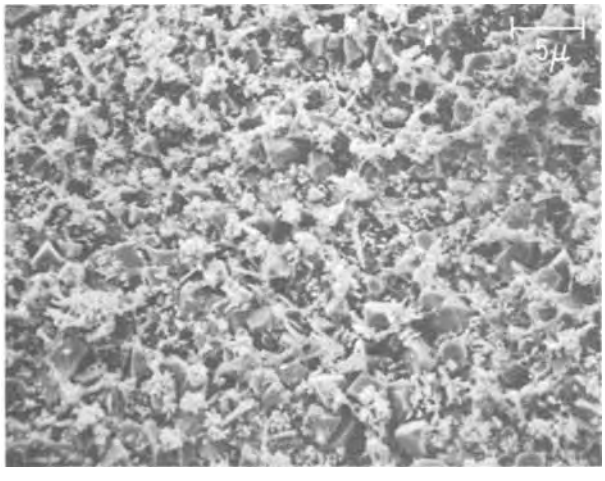

Fig. 15. SEM of electrode 1 at 2000X

magnitude smaller are visible. It is suggested that the crystals of β- and γ-$Cd(OH)_2$ are precipitated from the supersaturated electrolyte and that the small particles are $Cd(OH)_2$ formed by solid-state oxidation of the cadmium particles of identical size as in Fig. 13. The micrographs in Fig. 14-16 were obtained on electrode 1 of Fig. 2 which was removed from the cell on open circuit after discharge at constant current to 300 mV. Electrode 2 in Fig. 2 was removed from the cell after the first discharge, while a potential of 300 mV was being applied. The morphology of this electrode was found to be identical to that of electrode 1.

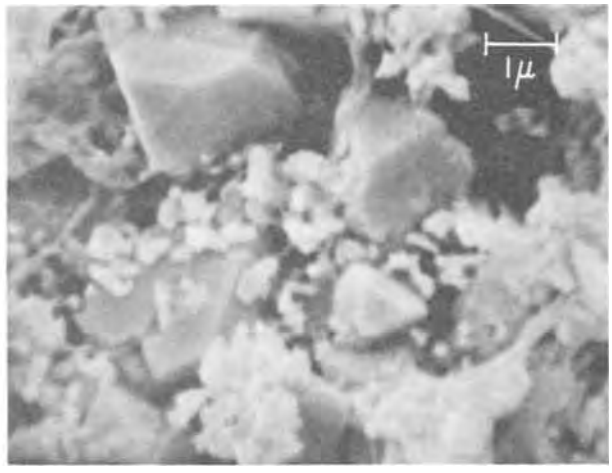

Fig. 16. SEM of electrode 1 at 10,000X

Electrode 3 was removed from the cell after the second charge while a potential of −150 mV was being applied. According to Fig. 2 the second charge leads to a capacity which is 20% smaller than that recovered on the first discharge. Simultaneously the microscope reveals a distinct brightening of the surface, and the particle size appears to have grown (Fig. 17). The SEM's in Fig. 18 and 19 show the formation of whisker-like crystals of lengths up to 10μ and widths up to 1μ. The formation of whisker-like crystals "on charge" has apparently never been described

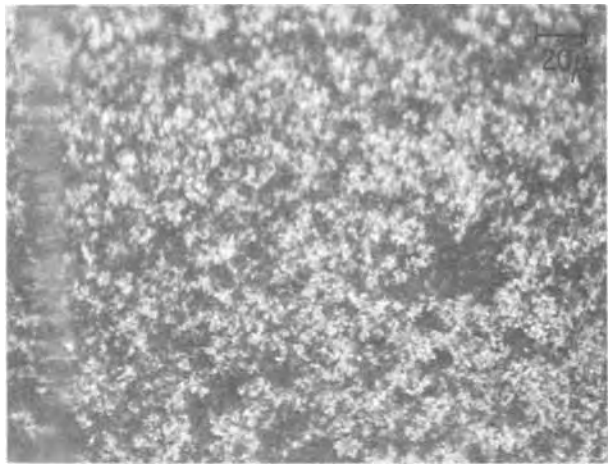

Fig. 17. Optical micrograph of electrode 3 after second charge to −200 mV.

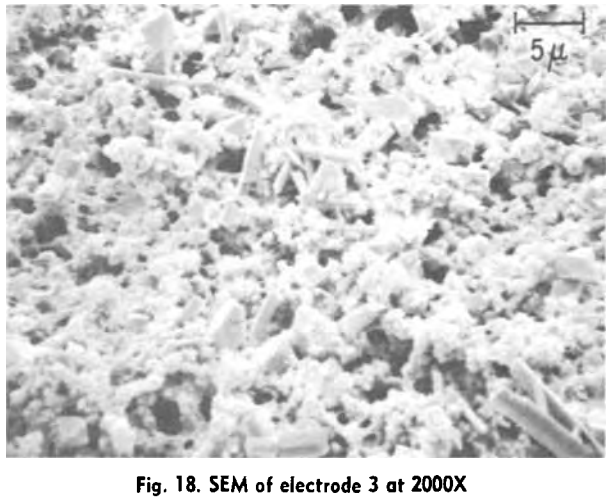

Fig. 18. SEM of electrode 3 at 2000X

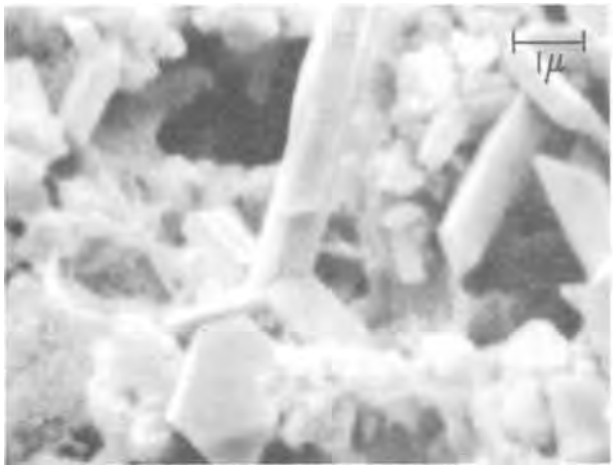

Fig. 19. SEM of electrode 3 at 10,000X

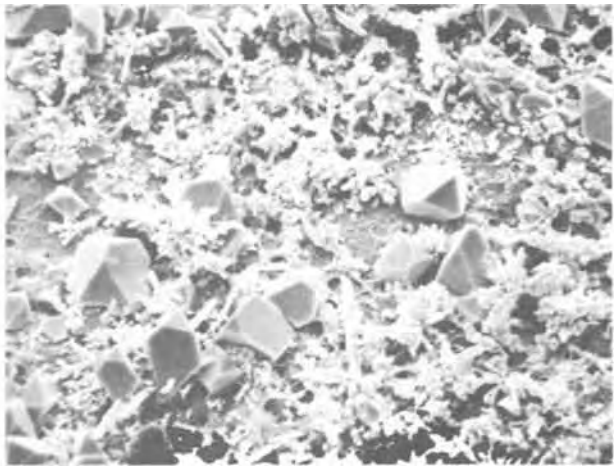

Fig. 21. SEM of electrode 4 at 2000X

before. The nature of these crystals was not identified in the present study. It is also evident from Fig. 18 and 19 that many of the hexagonal particles formed during the first discharge (compare Fig. 6) have remained unchanged during the charge. A great number of the small particles of sizes 2000 to 3000Å have also persisted.

Electrode 4 was removed on open circuit from the cell after completing the fifth discharge to 300 mV. Figure 2 shows that the capacity during five discharges has decreased to 36% of its original value. The photomicrograph in Fig. 20 reveals a coarsening of the surface compared to the appearance of the surface after the first discharge shown in Fig. 14. In the higher resolution of the scanning electron microscope a great number of hexagonal crystals of sizes 2-4μ are clearly visible (Fig. 21 and 22). Needle-like crystals can also be seen in these micrographs. Electrodes 5 and 6 were each cycled ten times. Electrode 5 was removed from the cell on open circuit, electrode 6 after keeping the electrode at 300 mV for 16 hr following the ten cycles. Further coarsening of the surface of electrode 6 is evident from Fig. 23 to 25. Figures 24 and 25 show that the number of well-crystallized particles of sizes 2-4μ have increased compared to Fig. 21 and 22. Extensive oxidation at 300 mV leads to a brownish appearance of the surface, as seen in the microscope, and to a disappearance of many crystals (Fig. 26). At the same time, an erosion of the remaining crystals is evident in Fig. 27 and 28 in that a distinct layer structure of the crystals has developed which was completely absent before the extensive oxidation at 300 mV (Fig. 25). No particular features in the SEM's can

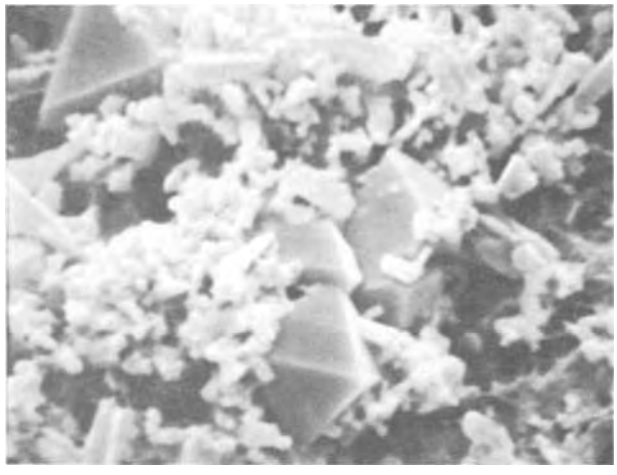

Fig. 22 SEM of electrode 4 at 10,000X

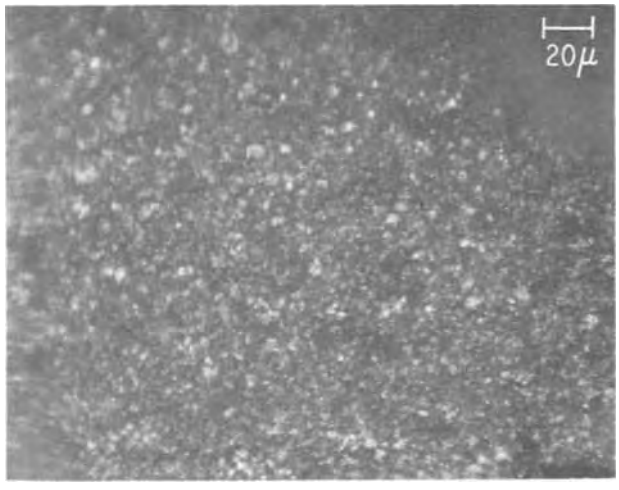

Fig. 23. Optical micrograph of electrode 5 after tenth discharge to 300 mV.

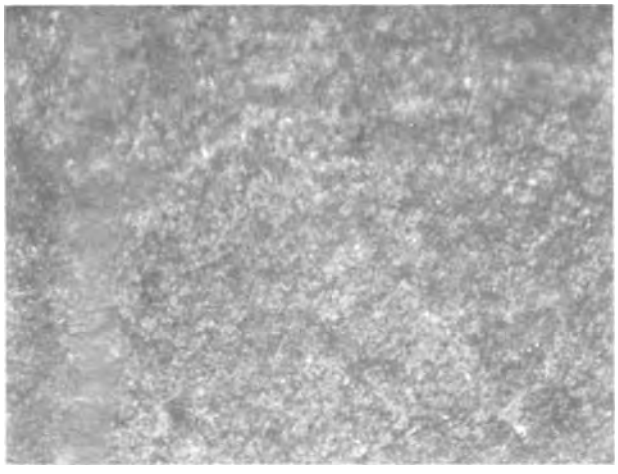

Fig. 20. Optical micrograph of electrode 4 after fifth discharge to 300 mV.

be associated with the brown color clearly observed in the microscope.

Figures 29-31 show the effects of extensive reduction of the electrode. Electrode 7 was kept at −150 mV for 16 hr after the 11th charge. The extensive charging leads to a considerable brightening of the surface (Fig. 29). As evidenced by the SEM's in Fig. 30 and 31, the large crystals formed during the ten preceding cycles (Fig. 16-28) have disappeared. The particles remaining on the surface have much less distinct shapes, and most of them have sizes between 2000 and

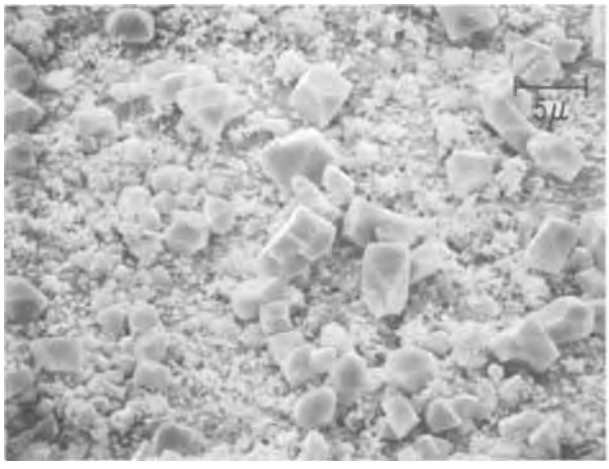

Fig. 24. SEM of electrode 5 at 2000X

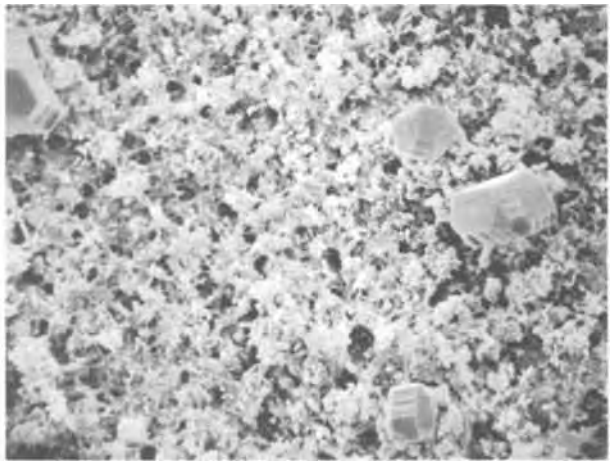

Fig. 27. SEM of electrode 6 at 2000X

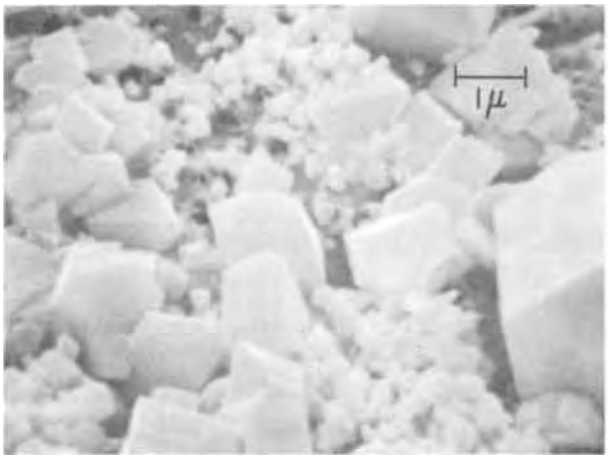

Fig. 25. SEM of electrode 5 at 10,000X

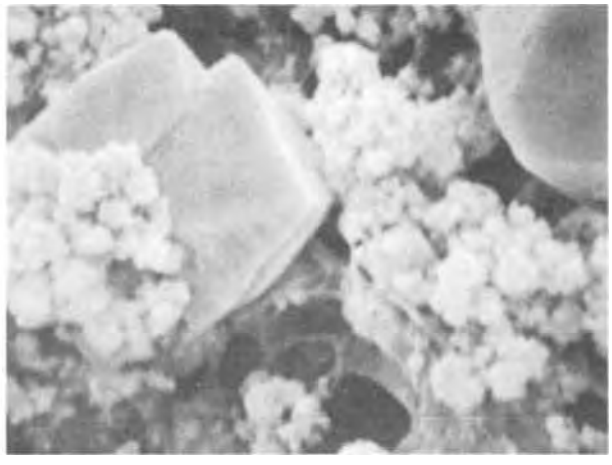

Fig. 28. SEM of electrode 6 at 10,000X

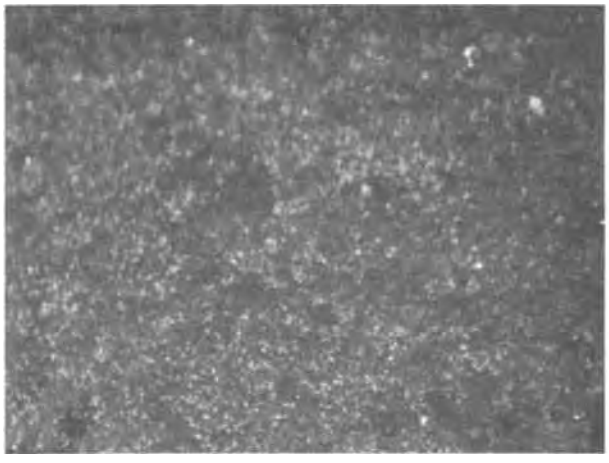

Fig. 26. Optical micrograph of electrode 6 after tenth discharge and anodic polarization at 300 mV for 13 hr.

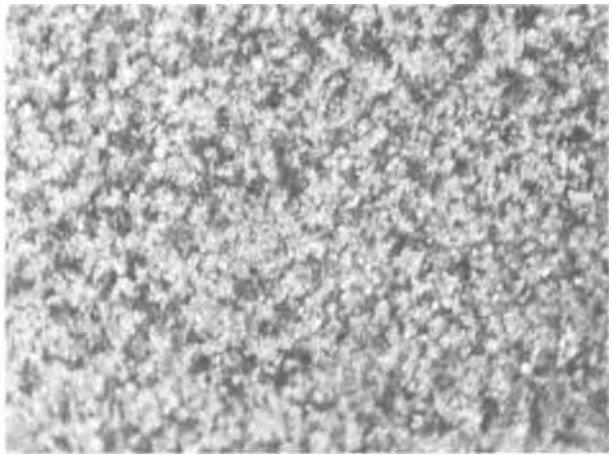

Fig. 29. Optical micrograph of electrode 7 after eleventh charge and cathodic polarization at −150 mV for 16 hr.

3000Å. In fact, the SEM in Fig. 31 looks very similar to that in Fig. 13 which was obtained after the first charge.

Electrode 8 was cycled more than 4000 times with current densities of 0.28 and 1.4 mA/cm^2. Figure 3 shows that the capacity on cycling decreases continually to values as low as 10 mA-sec/cm^2. The micrographs in Fig. 32-34 were obtained after more than 4000 cycles. In this case, the magnification of 220X is sufficient to resolve the shapes of a few very large particles (Fig. 32). The SEM's in Fig. 33 and 34 show the very large crystals which have formed in greater detail. Their sizes range up to 7μ. The hexagonal layer structure already seen in Fig. 27 is strikingly evident in Fig. 34. As in the case of extensive oxidation, the electrode turns brown on extensive cycling.

The initial capacities of electrodes 1 to 8 in Table I amount to between 50 and 70% of the theoretical values and are somewhat lower than the values obtained on pasted battery plates. This is most likely due to the much looser and more porous nature of the layer resulting from electrophoretic deposition as compared

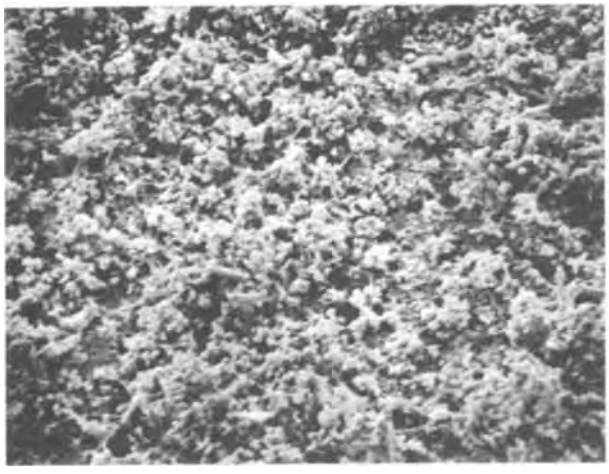

Fig. 30. SEM of electrode 7 at 2000X

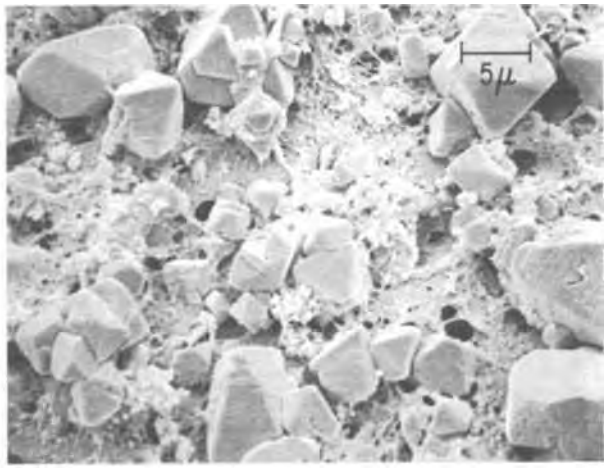

Fig. 33. SEM of electrode 8 at 2000X

Fig. 31. SEM of electrode 7 at 10,000X

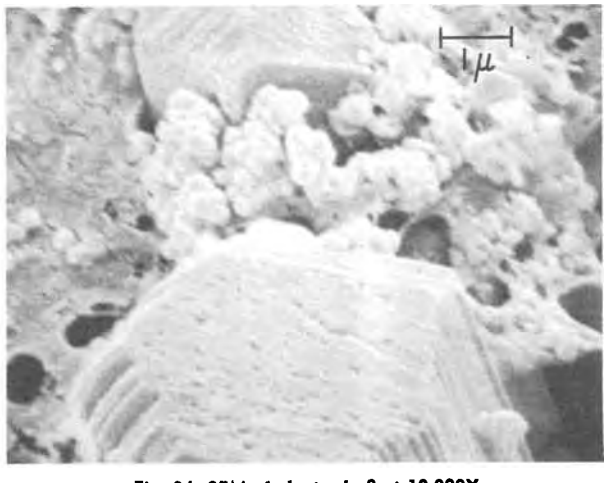

Fig. 34. SEM of electrode 8 at 10,000X

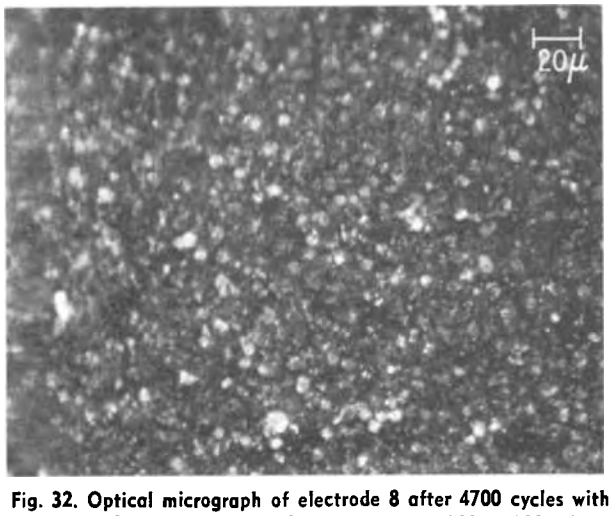

Fig. 32. Optical micrograph of electrode 8 after 4700 cycles with ±1.4 mA/cm^2 and 0.28 mA/cm^2 between limits 300/−200 mV.

to pasting. Loss of contact between the particles and the substrate is thus expected to be a larger problem than with pasted plates and would account for the relatively smaller initial capacities as well as for the more drastic loss of capacity during cycling. The less pronounced loss of capacity during cycling on pasted plates was actually demonstrated. Electrodes prepared by pasting cadmium oxide-binder mixtures of 63μ thickness on copper strips retained 88% of their initial capacity after ten cycles (27).

From the preceding detailed studies of the changes in the morphology during the first ten cycles, it is evident that the pronounced decrease of the capacity during these cycles (compare Fig. 2) is due to the observed formation of large $Cd(OH)_2$ crystals, probably caused by precipitation from the supersaturated KOH film during discharge. The supersaturation is favored by the consumption of hydroxyl ions in the discharge reaction. The lower *p*H, which is expected to result in the KOH film, causes the solubility of cadmium species to decrease. Once formed, many of the larger $Cd(OH)_2$ crystals do not appear to be reduced on continuous cycling (compare Fig. 18) and, hence, do not contribute to the capacity. During periods of extensive reduction, the large $Cd(OH)_2$ crystals seem to dissolve (Fig. 31), and dissolved cadmium species may then be electrodeposited on the test electrode. Dissolution of $Cd(OH)_2$ crystals is favored by the formation of hydroxyl ions during charging, due to the increased solubility of cadmium species at high *p*H. This process leads to a preliminary increase in the capacity up to factors of 3.

Effect of voltage on capacity.—The effect of the magnitude of the (anodic) discharge voltage on the charge capacity and the effect of the magnitude of the (cathodic) charge voltage on the discharge capacity was studied on an electrode with an electrophoretic cadmium oxide film of 3.5μ covered with a KOH film of 12.5μ thickness.

The procedure adopted was as follows: in determining the effect of anodic voltages on the charge capacity, a cathodic voltage of −200 mV was always applied for 20 min between each new measurement. A given

anodic voltage was then applied for 20 min and the capacity determined by applying a cathodic current density of -0.28 mA/cm^2 until a cutoff voltage of -200 mV was obtained. Conversely, the effect of cathodic voltages on the discharge capacity was determined by applying an anodic voltage of 300 mV for 20 min, then applying the cathodic voltage of interest for 20 min followed by applying an anodic current density of 0.28 mA/cm^2 until a cutoff voltage of 300 mV was obtained.

The results of these measurements are shown in Fig. 35. Above anodic voltages of 100 mV, the charge capacity increases linearly with the oxidizing voltage. In contrast, the discharge capacity for voltages more cathodic than -100 mV is independent of the magnitude of the reducing voltage.

The linear dependence of the charge capacity on the magnitude of the discharge voltage was observed previously when performing identical experiments in 0.1*N* KOH bulk electrolyte (27). This behavior had been explained in terms of the formation of passivating films during oxidation and the subsequent transport of ions through these films. In the present case, the original layer consists of individual cadmium oxide particles rather than a continuous cadmium film. Hence, after the first reduction to cadmium, it is appropriate to think in terms of the formation of passivating films around each individual particle. The question regarding the nature of these passivating films must be left open; they may consist of either $Cd(OH)_2$ or CdO. Since their thickness is found to be proportional to the amount of charge applied to the electrode, Fig. 35 signifies that the thickness of the film increases linearly with the voltage across the film. The deviation from the straight-line behavior at voltages between 0 and 100 mV is very likely caused by the increasing penetration of the electrolyte film by the electric field (26). The same phenomenon applies to the discharge capacity as a function of the reducing voltage. The independence of the discharge capacity on the reducing voltage between -100 and -300 mV implies that within the reduction time of 20 min, all reducible particles were in fact reduced with voltages as low as -100 mV while the large $Cd(OH)_2$ particles remain unreduced during short-term reductions. "Reducible" are considered the small particles (compare Fig. 18) in good contact with the substrate surface.

Mechanism for changes in capacity and morphology. —The results in this study are consistent with the following mechanism: on discharge, a solid-state and a dissolution-precipitation mechanism occur simultaneously, both contributing to the measured capacity and the latter leading to the formation of large crystals. The net reactions may be written as

$$Cd + 2\,OH^- \rightleftarrows Cd(OH)_2 + 2e^- \quad \text{(solid state)} \quad [3]$$

$$Cd + 3\,OH^- \rightleftarrows Cd(OH)_3^- + 2e^- \quad \text{(dissolution)} \quad [4a]$$

$$Cd(OH)_3^- \rightleftarrows Cd(OH)_2 + OH^- \quad \text{(precipitation)} \quad [4b]$$

Many of the precipitated particles have poor contact with the substrate. The particles oxidized via solid-state Reaction [3] become surrounded by a layer of cadmium hydroxide which hinders subsequent charge transfer and requires increasing overvoltages. This is evident from those parts of the discharge curves, where the voltage rises steeply with further discharge (compare curve after 4000 cycles in Fig. 4).

On charging, the rate and duration of charging is significant in determining the reaction mechanisms. On short and high-rate charges, the solid-state Reaction [3] (in reverse direction) dominates and explains the observed persistence of the large precipitated $Cd(OH)_2$ crystals. On prolonged and low-rate charges, Reaction [4b] leads to the observed dissolution of $Cd(OH)_2$ crystals. In this case, sufficient time is available for this slow process (18) to occur. The dissolution process is furthermore favored by the increase in pH during charging which raises the solubility of cadmiate ions. The dissolution is followed by the reverse of Reaction [4a] which leads to the electrodeposition of cadmium. In parallel to the dissolution-electrodeposition process, the solid-state reduction of many particles takes place, in particular the smaller ones which are in good contact with the substrate surface. As this process proceeds, the particles become surrounded with a conducting layer of cadmium which facilitates further reduction. This is very likely the reason why charging occurs with smaller overvoltages than discharging.

Cadmiate ions are expected to diffuse and, during discharge, to migrate toward the counterelectrode. Once they have left the small volume of the film electrolyte, very long charging times are required to electrodeposit them on the test electrode. The areas of the test electrode near the electrolyte well are preferred sites for deposition. The observed growth of tree-like structures during prolonged reduction is evidence for this mechanism.

Conclusions

For thin films of concentrated KOH under conditions of highly nonuniform current distribution, simulating

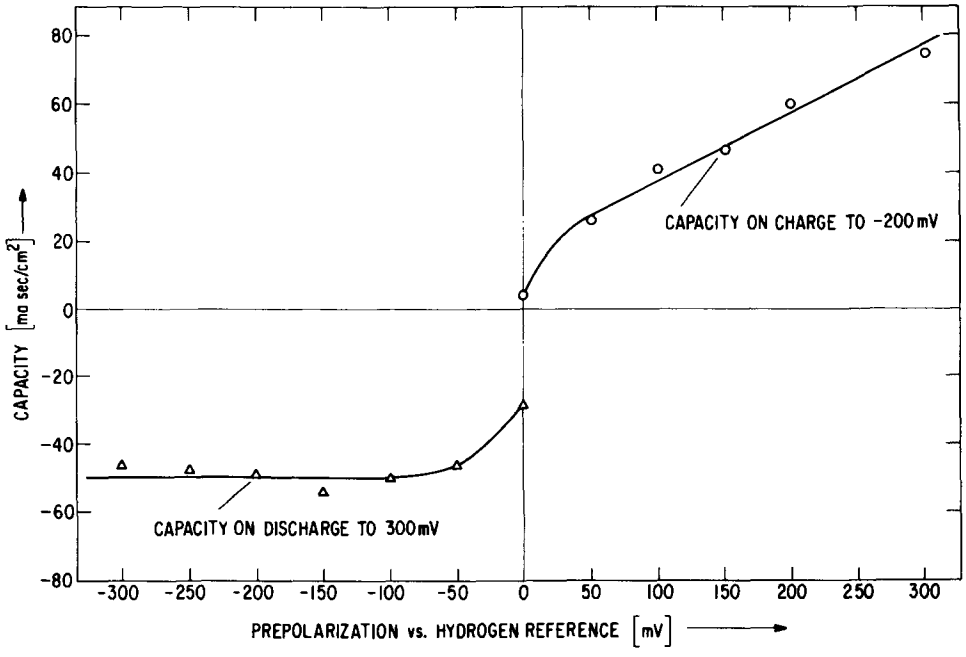

Fig. 35. Charge and discharge of 3.5μ CdO film electrode *vs.* prepolarization, using a 12.5μ film of 6*N* KOH and $\pm$0.28 mA/cm^2.

conditions in a single pore of a cadmium battery plate, we arrive at the following conclusions:

1. The first discharge leads to the recovery of typically 60% of the theoretical capacity, but the capacity decreases steeply during cycling, typically to 12% of the theoretical value in ten cycles. Discharge leads to the formation of large well-behaved crystals of β-$Cd(OH)_2$ and some γ-$Cd(OH)_2$ due to dissolution and subsequent precipitation of soluble cadmium species which is favored by the decreasing pH during discharge.

2. The large crystals do not contribute to the capacity on subsequent cycling and, hence, are responsible for the pronounced loss of capacity observed during the initial cycles.

3. The remaining capacity is due to the charge and discharge of particles of the original size via a solid-state transport mechanism.

4. The formation of passivating films, probably cadmium oxide, is suggested by the appearance of a brown film accompanied by a further decrease of the capacity on continued cycling.

5. Prolonged reduction leads to the dissolution of the $Cd(OH)_2$ crystals due to the increase in pH on charging. Electrodeposition of cadmium leads to increased capacity on subsequent discharge.

6. The method of preparing the electrode may have significant effects on the morphology and capacity. Pasted cadmium oxide electrodes display better coherence between particles than electrophoretic cadmium oxide electrodes and show considerably smaller loss of capacity on cycling.

Acknowledgment

This work was performed under the sponsorship of the NASA-Lewis Research Center, Contract NAS 3-12968.

Manuscript submitted June 12, 1972; revised manuscript received Aug. 21, 1972. This was Paper 68 presented at the Atlantic City, New Jersey, Meeting of the Society, Oct. 4-8, 1970.

Any discussion of this paper will appear in a Discussion Section to be published in the December 1973 JOURNAL.

REFERENCES

1. A. J. Salkind and G. W. Bodamer, "Proceedings 4th Internat. Symp. on Batteries, Brighton, England," p. 55, D. H. Collins, Editor, Pergamon Press (1964).
2. J. P. Harivel, B. Morignat, and J. Migeon, *ibid.*, p. 107.
3. E. Lifshin and J. L. Weininger, *Electrochem. Technol.*, **5**, 5 (1967).
4. O. C. Wagner, *This Journal*, **116**, 693 (1969).
5. R. Scholder and E. Staufenbiel, *Z. Anorg. Chem.*, **247**, 257 (1941).
6. P. E. Lake and J. M. Goodings, *Can. J. Chem.*, **36**, 1089 (1958).
7. R. E. Visco and R. H. Sonner, Electrochem. Soc., Extended Abstracts, Detroit Meeting, Oct. 5-9, 1969, p. 18.
8. K. Huber, *This Journal*, **100**, 376 (1953).
9. K. Huber and S. Stucki, *Helv. Chim. Acta*, **51**, 1343 (1968).
10. P. E. Lake and E. J. Casey, *This Journal*, **105**, 52 (1958).
11. P. E. Lake and E. J. Casey, *ibid.*, **106**, 913 (1959).
12. I. Sanghi, S. Visvanathan, and S. Ananthanarayanan, *Electrochim. Acta*, **3**, 65 (1960).
13. S. Yoshizawa and Z. Takehara, *ibid.*, **5**, 240 (1961).
14. M. A. V. Devanathan and S. Lakshmanan, *ibid.*, **13**, 667 (1968).
15. G. T. Croft, *This Journal*, **106**, 278 (1959).
16. G. T. Croft and D. Tuomi, *ibid.*, **108**, 915 (1961).
17. J. P. G. Farr and N. A. Hampson, *Electrochem. Technol.*, **6**, 10 (1969).
18. Y. Okinaka, *This Journal*, **117**, 289 (1970).
19. P. C. Milner and U. B. Thomas, "Advances in Electrochemistry and Electrochemical Engineering," Vol. 5, C. W. Tobias, Editor, Interscience Publishers, New York (1967).
20. M. W. Breiter and J. L. Weininger, *This Journal*, **113**, 651 (1966).
21. M. W. Breiter and W. Vedder, *Trans. Faraday Soc.*, **63**, 1042 (1967).
22. S. U. Falk, *This Journal*, **107**, 661 (1960).
23. R. D. Armstrong, E. H. Buolt, D. F. Porter, and H. R. Thirsk, *Electrochim. Acta*, **12**, 1245 (1967).
24. F. G. Will, Electrochem. Soc. Extended Abstracts, Detroit Meeting, Oct. 6-9, 1969, p. 62.
25. Y. Okinaka and C. M. Whitehurst, *This Journal*, **117**, 583 (1970).
26. F. G. Will, "Proceedings 6th Intern. Symp. on Batteries, Brighton, England 1968," p. 149, D. H. Collins, Editor, Pergamon Press.
27. F. G. Will and H. J. Hess, Final Report NASA CR-72777, March 15, 1971.

Recent Results on Lead-Calcium Alloys as Grid Materials for Lead-Acid Batteries

G. W. Mao, J. G. Larson, and P. Rao

Gould Inc., Automotive Battery Division, Mendota Heights, Minnesota 55118

ABSTRACT

Pressure cast lead-calcium alloy positive grids for float applications can cause some unexpected service failures due to abnormal growth. Such failures have been interpreted as a result of irregular grain structure and weaker grain boundaries. Since lead-calcium is a precipitation hardening alloy, either heat-treatment or controlled solidification can yield favorable grain size and distribution of Pb_3Ca precipitates in the matrix. The present investigation shows that controlled solidification of pressure cast grids can produce physically sound grids which are corrosion and growth resistant. Differences between industrial and automotive SLI grids cast by gravity and pressure casting techniques are revealed. The effect of casting temperature on the microstructure and anodic corrosion characteristics of lead-calcium alloys ranging from 0.01 to 0.1% calcium content is also presented.

For many years the lead-acid battery industry has manufactured batteries using lead-antimony alloy grids; however, the presence of antimony leads to side reactions that are deleterious to battery performance. To avoid this problem, Bell Laboratories introduced lead-calcium alloy (1). Since then lead-calcium cells have been used exclusively in full-float service. A major drawback of lead-calcium is its unpredictable

Key words: lead-acid battery, lead-calcium grids, corrosion morphology, pressure cast grids.

grid growth behavior. Excessive grid growth occurs in certain plates while other plates within the same cell are practically unaffected. Also, lead-calcium is difficult to cast and weld.

Hardening of a lead-calcium grid does not take place immediately after casting, but occurs later due to aging. Limitations as to the other types of service in which lead-calcium grid battery can be used have not yet been established.

The uniqueness of lead-calcium for a grid alloy lies in its low rate of self-discharge and minimal stand loss. The calcium content of such alloys has always been maintained below 0.10%. Such grids are normally gravity cast, but there is a trend toward pressure casting these grids.

Howard and Willihnganz (2) reported that accelerated testing caused abnormal growth and preferential grain boundary corrosion of pressure cast positive lead-calcium grids with 0.07-0.08% calcium. They related these characteristics to the irregular grain structure and weaker grain boundaries of pressure cast positives.

Townsend (3) revealed that the tensile strength of 0.05-0.09% calcium-lead is sensitive to the cooling rate of the solidifying alloy, and increased with increasing cooling rates. This is a direct consequence of precipitation from a greater degree of supersaturation. In other words, casting conditions would definitely influence the over-all corrosion behavior of the alloy grid, since corrosion behavior is sensitive to precipitate distribution within the matrix.

Pressure casting is accepted in the industry to produce lead-calcium negative grids because negative grids are not subject to the same anodic environment as the positives. Pressure casting is favored because it is economically attractive and is amenable to precise quality control.

In 1967 a program was initiated to obtain acceptable pressure cast lead-calcium positive grids by controlling and optimizing various relevant casting parameters. Fundamental work on the lead-calcium system was simultaneously carried out to establish the influence of composition and casting conditions on over-all corrosion behavior of the alloys. This was necessary to understand and interpret the differences in corrosion and growth behavior of pressure cast and gravity cast grids. The effect of annealing lead-calcium grids has been reported previously (4, 5).

Experimental

Alloy rod corrosion.—Alloy rods 0.63 cm in diameter were gravity cast from a molten metal temperature of 750°F, into a mold maintained at 375° and 500°F respectively. Anodic corrosion of these rods, having various calcium content up to 0.09% was carried out at 2.8V constant potential in 1.115 sp gr H_2SO_4 at room temperature. The corrosion cells were 250 ml Pyrex beakers covered with closely fitted Plexiglas lids. The test rod was mounted in the center of the cover and positioned vertically in the electrolyte. This formed the anode. A pure lead sheet cathode was arranged concentrically 3 cm from the anode. The ratio of initial anode to cathode area was 1:17. Details of similar rod corrosion experiment were described elsewhere (6).

Optimized pressure casting.—A special pressure casting machine was built. With it, various processing variables relevant to the casting operation, such as mold temperature, molten metal temperature, rate and flow path of metal entry into the mold cavity were optimized to yield physically sound grids having relatively large grain size and proper precipitate distribution. For example, industrial battery grids were cast in a cast iron mold where the temperature of both mold halves was controlled. The molten metal entry into the mold was controlled so that it entered at a very low velocity with a minimum amount of turbulence. Vacuum was applied at the end of the mold cavity, directly opposite to the metal entry to minimize air entrapment in the solidifying grids.

Efforts to optimize pressure casting parameters was done only on industrial type grids.

Battery grid corrosion.—Grids having 0.06-0.07% calcium were cast by two different methods, *i.e.*, gravity and pressure casting. Two types of grids were chosen: an industrial type of rectangular design (25.72 cm × 28.41 cm × 0.635 cm) and an automotive SLI type (14.29 cm × 13.49 cm × 0.178 cm).

In addition, 300°-500°F annealing of pressure cast automotive and industrial grids was done. In the case of SLI automotive grids, both pasted and bare grid cells were used; while in industrial grids, only bare grid cells were used.

Corrosion and growth studies on the industrial positives were performed on bare three-plate cells in 1.210 sp gr H_2SO_4. A positive potential of 75 mV above the open circuit (1.185V) was maintained for 60 days at a temperature of 180°F (5). At the end of the test both microstructures and grid dimensional changes were recorded.

Corrosion studies in SLI unpasted grids were performed on 5 plate cells (2 positives/3 negatives) assembled in Plexiglas jars in 1.265 sp gr H_2SO_4 at room temperature. These were anodically corroded at 2.8V for 12 weeks. Similarly, 5 plate (2 positive/3 negative) pasted SLI cells were subjected to 2.6-2.8V constant voltage overcharge. These pasted cells had 25 A-hr capacity based on the 20 hour rate. Every week the cells were discharged at 44A which approximated a 50% depth of discharge. One week was counted as one cycle. The basic objective of these two tests was to accelerate the corrosion of both pasted and bare grids so that their corrosion resistance and growth characteristics could be established.

Experimental Results

Anodic corrosion.—Weight loss of alloy rods due to anodic corrosion at 2.8V constant potential for 60 days is plotted as a function of calcium content for two different casting mold temperatures in Fig. 1. The curve represents the basic trend from duplicated experiments. The weight loss here corresponds to the actual difference in weights of the alloy rods before and after corrosion following removal of all adherent corrosion products.

For the alloys cast in a 375°F mold, the weight loss goes through a minimum between 0.04 and 0.06% calcium. For alloys cast in a 500°F mold, however, the weight loss goes through an extended minima between 0.03 and 0.07% calcium.

The absolute values of corrosion weight loss are of little significance unless they are discussed in conjunction with corroded microstructures, indicating the morphology of corrosion attack. It is the nature of corrosion attack that determines grid growth characteristics and subsequently positive plate life. For this rea-

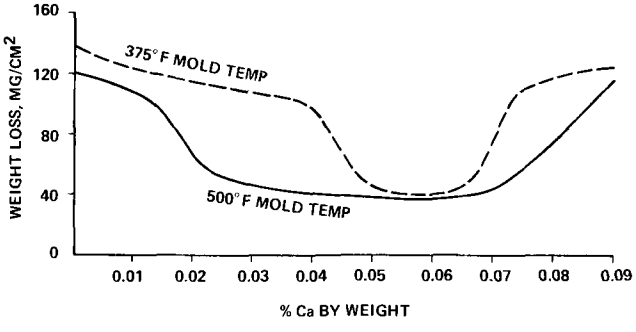

Fig. 1. Effect of casting temperature and calcium content on the anodic corrosion weight losses of gravity cast lead-calcium alloy rods.

son, a thorough evaluation of the microstructures of the various alloys was made.

Microstructures (Fig. 2) indicate that casting in lower temperature molds (375°F), favors the development of irregular grains and serrated grain boundaries for all various calcium alloys. The grain sizes become extremely fine as the calcium content increases beyond 0.06%. Whereas, casting similar alloys in a higher temperature mold (500°F) promotes the development of relatively large, uniform grains characterized by smooth boundaries, irrespective of the calcium content.

For alloys (Fig. 3) cast in a 375°F mold with less than 0.04% calcium, the corrosion penetration is basically intergranular, since the matrix precipitation is small, thus making high energy grain boundaries more vulnerable.

In alloys with 0.04-0.06% calcium, the volume fraction of precipitates is high and most of it is contained in the lead rich matrix and these matrix precipitates control the mode of corrosion. The switch in the mode

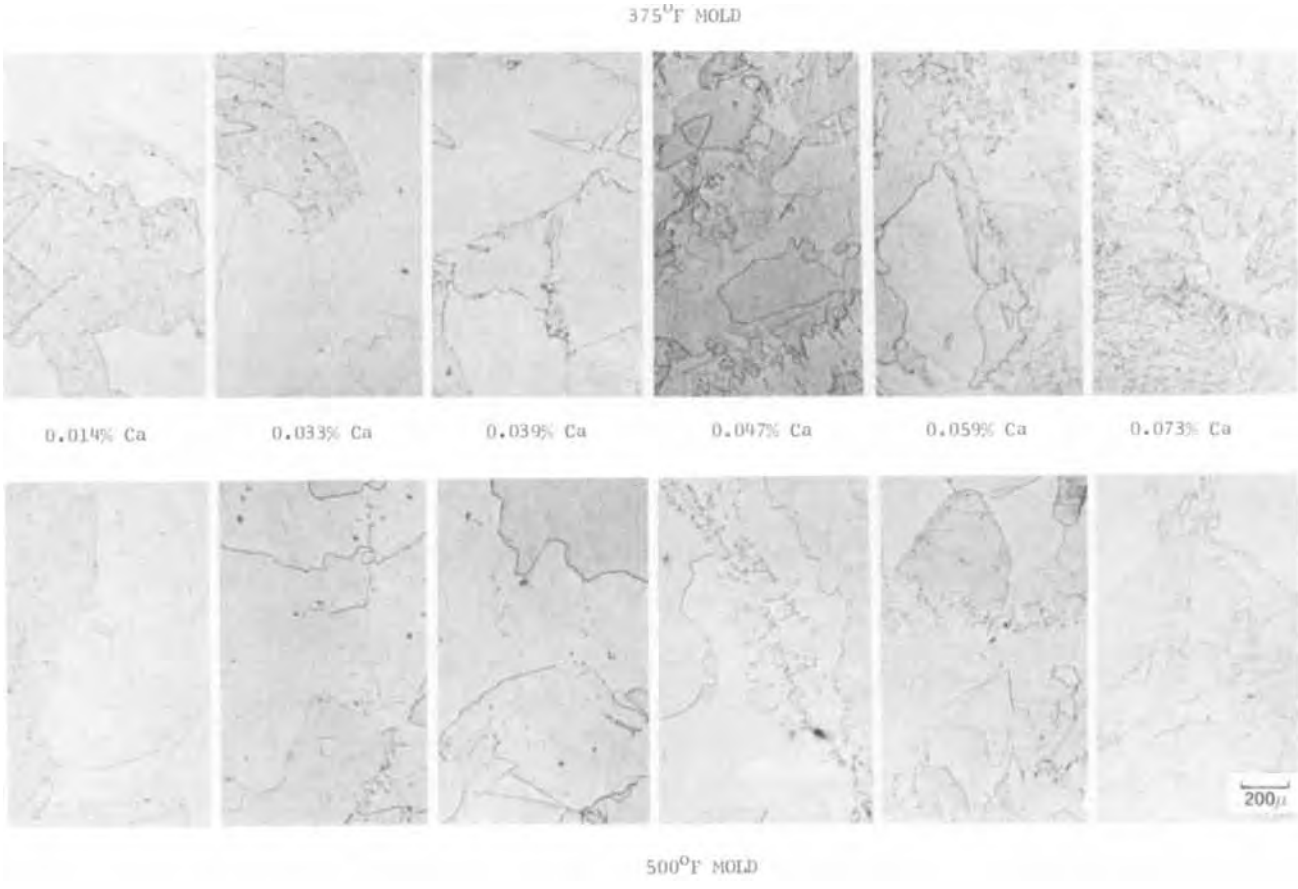

Fig. 2. Effect of casting temperature and calcium content on the microstructures of gravity cast lead-calcium alloy rods

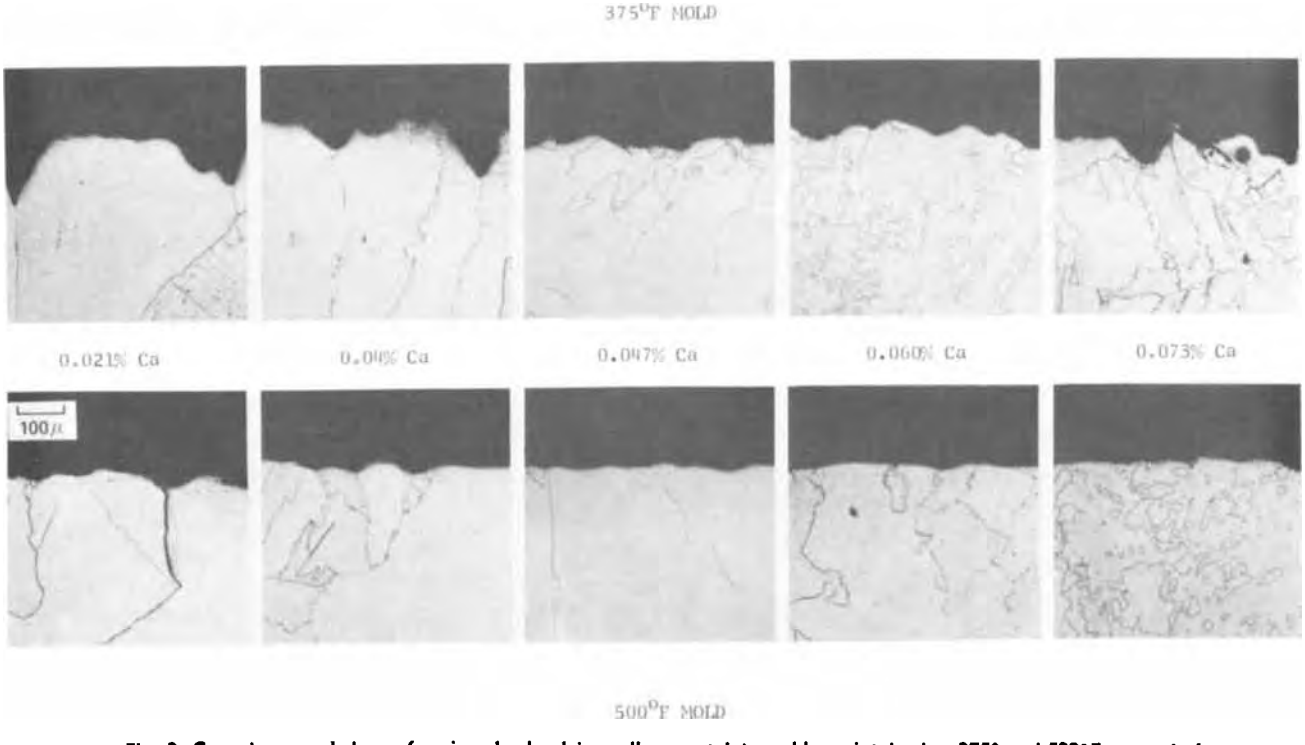

Fig. 3. Corrosion morphology of various lead-calcium alloys cast into molds maintained at 375° and 500°F respectively

of attack from intergranular to a matrix dominated corrosion as the calcium content increases beyond 0.04%, explains the observed minima in corrosion weight loss. However, fine but irregular grain size, together with extensive precipitation in alloys beyond 0.06% calcium combine to permit rapid consumption of grains, and this corrosion process accounts for the higher weight losses.

On the contrary, the range of calcium composition is much wider for alloys that exhibit stable corrosion properties when cast in a 500°F mold. In these alloys, the volume fraction of corrosion active precipitates, and their distribution, control the rates and the mode of corrosion, while the grain boundaries play a secondary role. The basic corrosion process in alloys exhibiting minimal weight losses are similar to the alloys cast in a 375°F mold. More significant than the absolute values of anodic corrosion weight losses, is that alloys cast in a 500°F mold have alloy structures that exhibit remarkable stability to corrosion and thereby deter any tendency for preferential attack as revealed by their corroded microstructures. This characteristic should definitely contribute to improved growth resistance and thereby increase the reliability of grids in float service.

This corrosion behavior has clearly established the necessity for controlling mold temperature while casting lead-calcium grids to obtain grids exhibiting stable corrosion behavior.

Industrial battery grid test.—The grid growth data arising out of accelerated corrosion testing at 180°F are shown in Fig. 4. Only the horizontal growth is compared. Pressure cast grids produced under optimized casting conditions grew at the same rate as the control gravity cast grid. Furthermore, when these pressure cast grids are annealed, the growth rate is slowed further. However, pressure cast grids cast without controlled process conditions show the highest growth rate. Although annealing did slow down the growth rate as shown in Fig. 4 and as shown by Cannone *et al.* (5), it was still slightly higher than the unannealed pressure cast grids produced under optimized conditions.

Macrographs of grid sections taken at various portions of the grid reveal that grids cast under optimized process conditions are physically sound and free of large interconnecting pores and voids (Fig. 5), while the grid cast under unregulated process conditions reveals large voids and a large degree of interconnecting pores (Fig. 6). Macrographs of grid sections taken from a gravity cast grid indicate that they are physically sound, and quite similar to the grid cast under optimized pressure casting conditions. It appears that

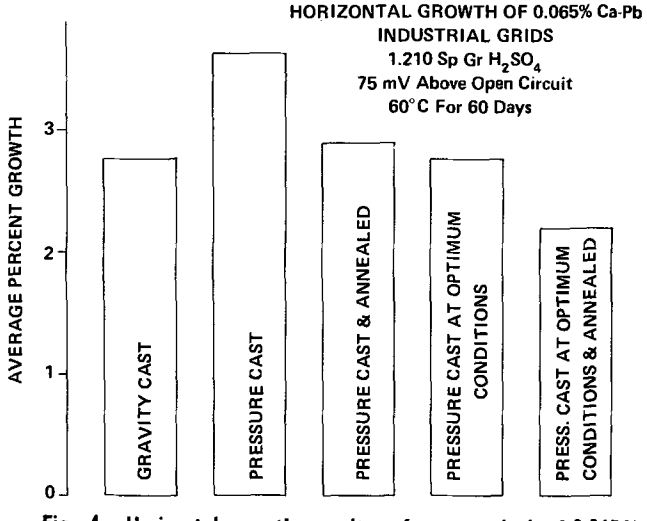

Fig. 4. Horizontal growth results of unpasted lead-0.065% calcium industrial grids. Accelerated growth test.

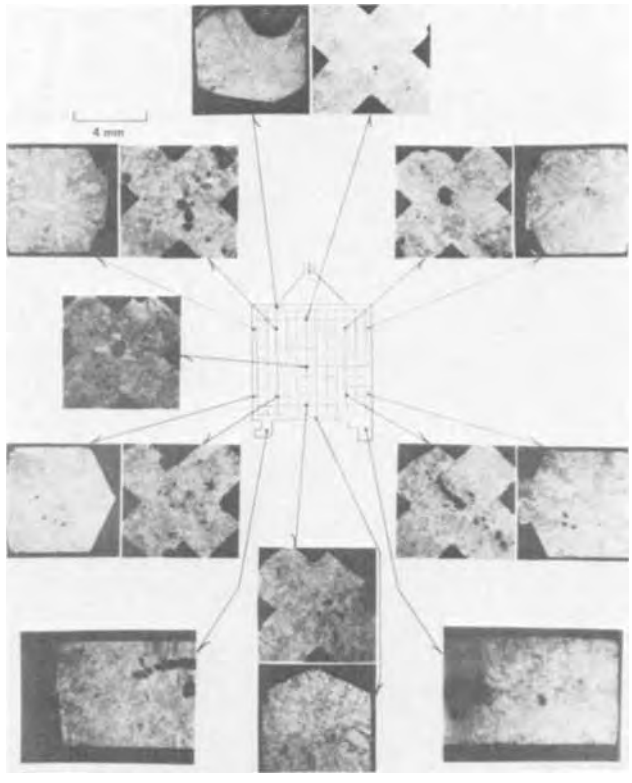

Fig. 5. Macrostructure of various sections of a pressure cast lead-0.065% calcium industrial grid, cast under regulated process conditions.

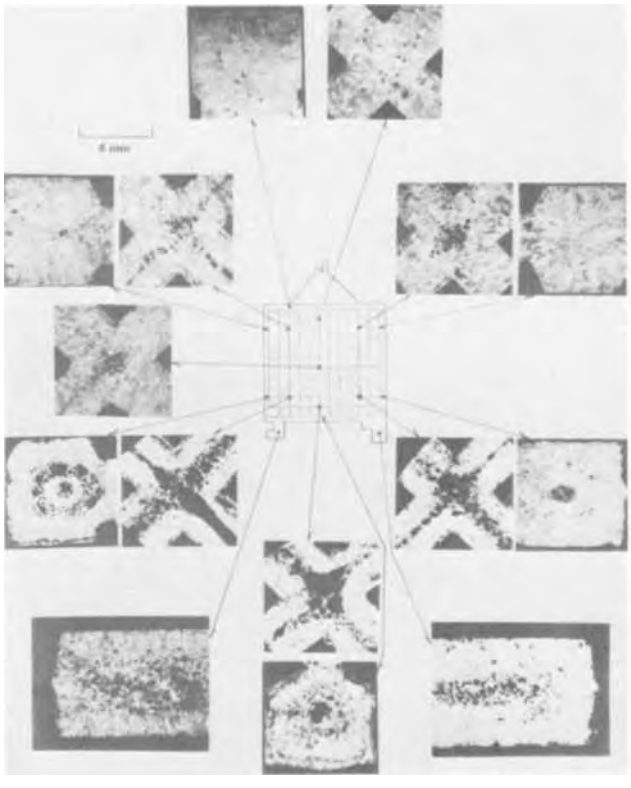

Fig. 6. Macrostructure of various sections of a pressure cast lead, 0.065% calcium industrial grid, cast under normal process conditions.

lack of physical soundness in these pressure cast grids would curtail the strength of grid members and is primarily responsible for their undesirable growth characteristics. Any differences in metallurgical structures arising from the pressure casting will have to play

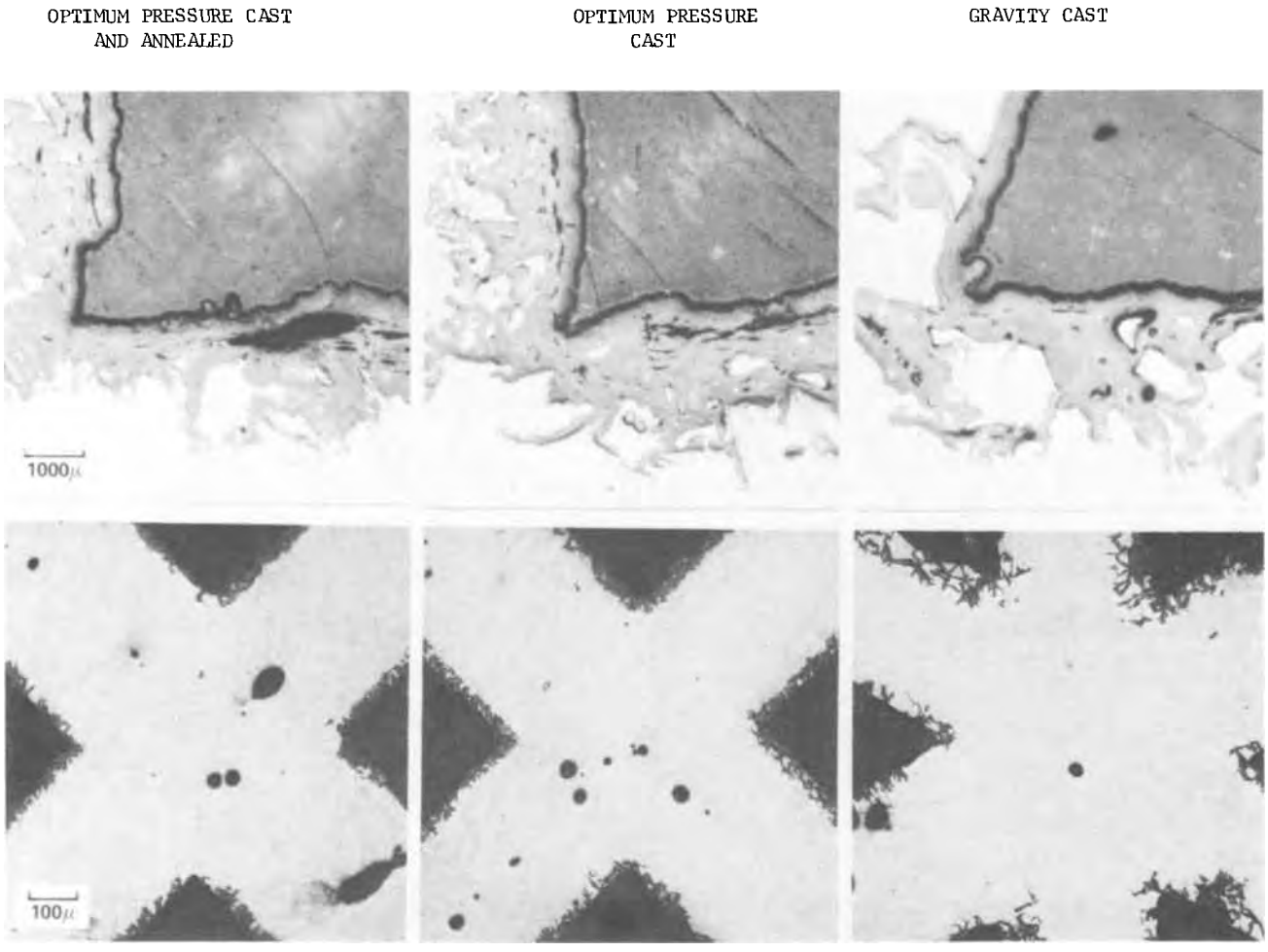

Fig. 7. Corrosion morphology of lead-0.065% calcium industrial grids. Accelerated growth test

a secondary role in its corrosion or its growth characteristics.

The corrosion morphology of these grids strikingly reflects their individual growth characteristics (Fig. 7). In the gravity cast grid, the preferential intergranular type attack is predominant. The grain boundary penetration suggests that since a major portion of the induced stresses are developed in the grain boundary, growth behavior will become unpredictable. Both annealed and unannealed pressure cast grids cast under optimized conditions reveal that the corrosive attack is less severe and more uniform.

Optimized pressure casting conditions are such that substantially faster cooling rates of the solidifying grid alloy, at a defined mold temperature, are achieved than in gravity cast methods, resulting in uniform precipitation of the corrosion active Pb_3Ca precipitates. This reduces the severity of grain boundary corrosion penetration and renders the matrix corrosion more uniform. Both of these factors contribute to slower growth rates.

When pressure cast grids free of internal defects are annealed, it is known that some degree of grain coarsening occurs followed by redistribution of precipitates within the matrix (3). The presence of active precipitates within the grains will favor matrix corrosion over localized grain boundary attack, since grain boundaries are left free of most of the active precipitates. Hence, annealed pressure cast grids exhibit relatively greater stability toward both corrosion and attendant growth.

Automotive battery grid test.—The five plate (25 A-hr) cells were initially put on a 2.6V constant voltage overcharge. But at this test regime, the capacities of the cells during weekly discharges were slowly declining. It was, therefore, decided to give them a 1.0A current boost charge at the seventh cycle. Following this, the cells were put on a 2.8V overcharge instead of 2.6V. The switch was made not only to minimize capacity losses but also to make the overcharge more severe and consequently accelerate grid growth. The weekly discharge capacity has been plotted as a per cent of the original 20 hr rated capacity in Fig. 8. The rapid decline in capacity during cycling of all the lead-calcium cells appears to be related to loss of active material due to shedding. However, all lead-calcium cells, irrespective of the method of grid casting, exhibit nearly identical behavior. The test was terminated after 16 cycles, since most of the cells exhibited steep rises in end-of-charge current values. Localized short circuiting was suspected in these cells and was confirmed

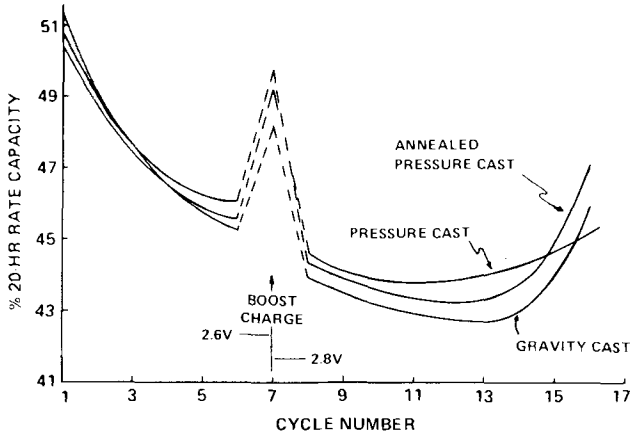

Fig. 8. Constant voltage overcharge performance of automotive lead-calcium cells.

upon examining the positive plates after disassembly of cells.

The unpasted cells consisting of five bare grids (2 positives/3 negatives) were anodically corroded at 2.8V in 1.265 sp gr acid for 12 weeks. This test was started at the middle of a pasted plate overcharge test to supplement the corrosion and growth data of pasted cells. Higher end-of-charge currents in pasted lead-calcium cells over those of similar but unpasted cells become evident (Fig. 9). The similarity in current variations both in pasted and bare grid cells, irrespective of the method of grid casting is to be noted.

The growth data of all the lead-calcium cells, both for pasted and bare grids, are presented in Fig. 10. Pasted and cycled grids show larger growth than their corresponding bare grid counterparts. This is expected on account of the inducement of higher stresses on the underlying grid structure by the active material. Gravity cast grids, both in pasted and bare grid condition show the least growth. Also, the gravity cast grids are characterized by relatively uniform growth. However, in pressure cast and annealed pressure cast grids, excessive growth seems to be occurring only in the lower half of the grid (area away from the casting gate). When cross-sections were examined, the lower part of the grid was having interconnecting pores and large voids. Lack of physical soundness in this region is primarily responsible for the abnormal growth—more so than any metallurgical structural differences arising out of the pressure casting operation. Actually, when these pressure cast grids are annealed, the growth is accelerated (Fig. 10) instead of slowed. Upon annealing, some interconnecting small pores agglomerate and thus create large voids. Since the automotive grid members are relatively thin sections to begin with, the presence of such large internal voids decreases the effective thickness of the grid members to withstand the destructive effects of corrosion and

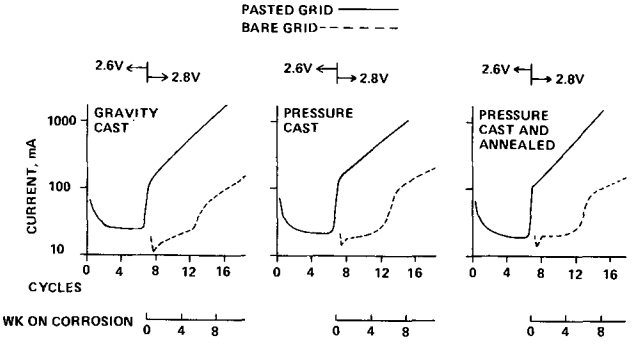

Fig. 9. Current variations during 2.8V constant voltage overcharge of pasted and unpasted lead-calcium cells.

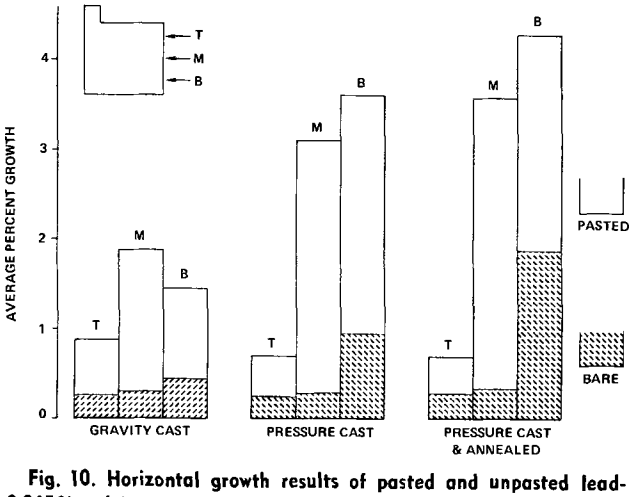

Fig. 10. Horizontal growth results of pasted and unpasted lead-0.065% calcium automotive SLI grids. 2.8V constant voltage overcharge test.

cycling, thereby seriously curtailing both corrosion and growth resistance.

In pressure cast grids, both metal turbulence in the mold cavity and rapid freezing appear to give rise to air entrapment, causing voids in the solidified grid. In the lower half of the grid area, grains are merely in intimate contact, resulting in a probable continuous fissure along the grain boundaries. During corrosion, the greater the volume of PbO_2 liberated in and adjacent to these defects, the greater the internal stress that will act as a wedge to force open the grains. This inevitably leads to expansion of the grid, thus its growth.

Now turning to metallurgical structures, it is seen that larger grains and smooth grain boundaries are characteristic of gravity cast grids while fine grains with serrated boundaries are characteristic of pressure cast grids (Fig. 11). If minimal growth of physically sound gravity cast grids is to be attributed to coarse grains, then it was thought that annealing to coarsen the grains would relieve some of the abnormal growth characteristics of pressure cast grids. Although 500°F annealing of pressure cast automotive grids led to extensive grain coarsening (Fig. 11), annealing did not contribute to any growth resistance in these grids—unlike the physically sound annealed pressure cast industrial grids.

Discussion

One of the earlier papers (2) on anodic corrosion of pressure cast grids relates the abnormal growth to preferential attack and grain boundary slip along solute impoverished zones, particularly adjacent to grain boundaries. It is our thinking that such impoverished zones or "precipitate free zones" do not occur in the lead-calcium alloys. Normally such zones occur in overaged alloys and are characterized by loss of ductility or complete embrittlement of the alloy.

Townsend (3) indicates that in all of the lead-calcium alloys studied, the strength normally increases with increased aging time. Neither we, nor Townsend detect any loss in ductility of aged lead-calcium alloys. Our observations are based on the fact that upon accelerated aging of pressure cast lead —0.06 calcium grids at 140°F for 4 months, no hardness losses were detected. From this it is apparent that changes in metallurgical structure of alloys arising out of aging are not contributing to grid growth.

On the other hand, it has been shown through fundamental corrosion studies on rods that alloy structures exhibiting great stability to preferential attack and growth could be produced by controlling the casting mold temperatures. Similar structural features in industrial battery grids are attained by pressure casting under optimized conditions. This accounts for slower growth rates and better corrosion resistance of the industrial pressure cast grids.

Pressure casting was not optimized during casting of automotive SLI grids, since these grids are short lived in contrast to industrial grids. Lack of physical soundness in pressure cast grids as the primary cause for excessive grid growth is better illustrated by the test results of automotive grids than thicker industrial grids, since here the beneficial effects of annealing are obscured by physical defects. However, structural changes resulting from annealing does contribute to growth resistance even in the presence of internal defects as demonstrated in the pressure cast industrial grids.

In conclusion this study has established that:

1. There is a good correlation between lead-calcium alloy structure and corrosion morphology.
2. Lack of physical soundness in certain regions of pressure cast grids is more responsible for excessive growth than any metallurgical structural differences arising out of pressure casting operation, and particularly as the grid thickness decreases.

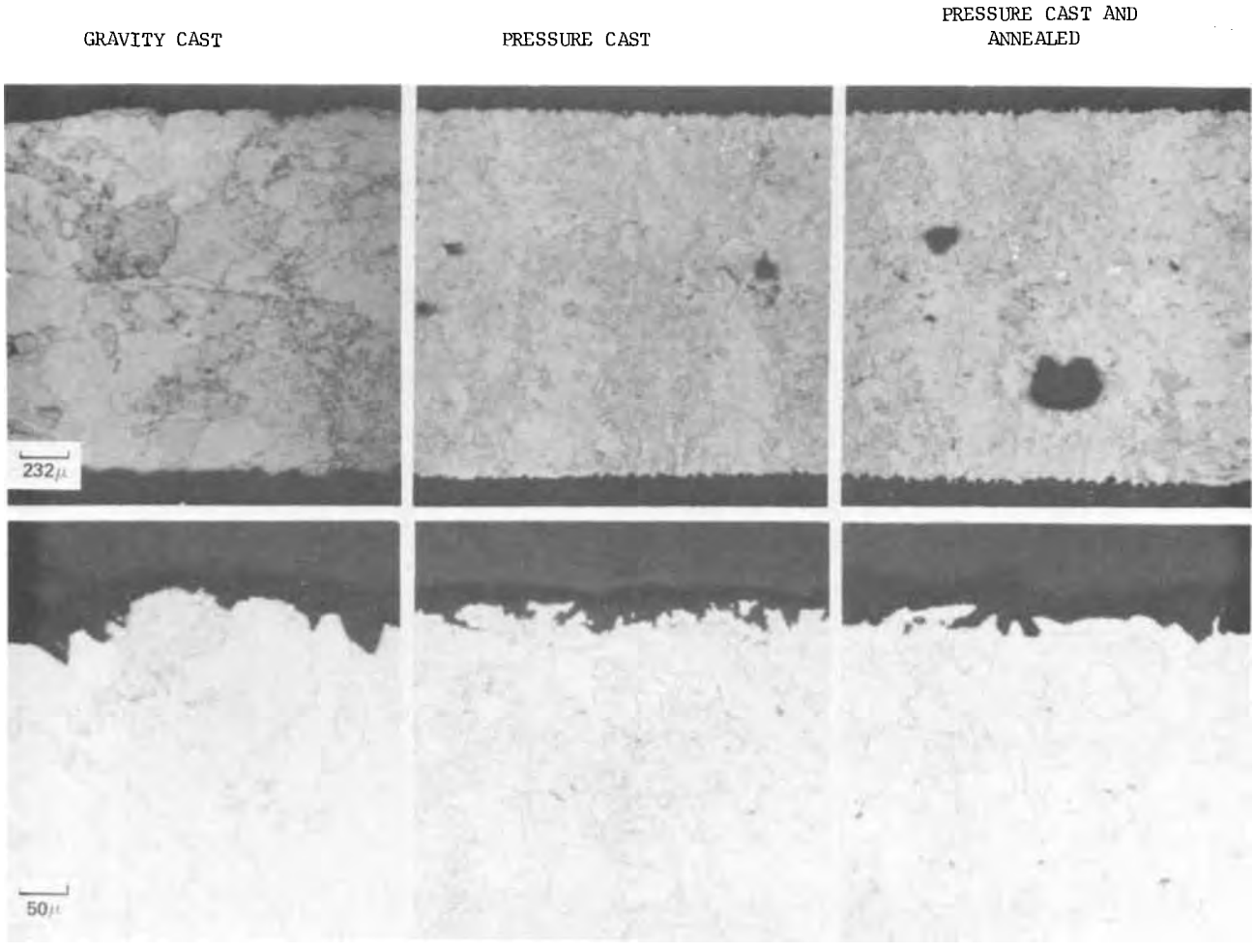

Fig. 11. Corrosion morphology of unposted lead-0.065% calcium automotive SLI grids. 2.8V constant voltage corrosion for 12 weeks

3. Casting conditions are more critical than a particular casting technique to yield acceptable lead —0.065% calcium alloy grids, since this particular step controls both the active precipitate distribution and grain size in the alloy. By casting in a mold held at a relatively higher temperature, lead-calcium alloys containing up to 0.07% calcium can be produced that are characterized by uniform and stable corrosion properties. Such alloys also exhibit good resistance to excessive growth in grids.

4. Under severe constant voltage conditions, even as high as 3.5%, grid growth in automotive SLI grids does not seriously impair either the overcharge life or capacity.

Manuscript submitted April 24, 1972; revised manuscript received Aug. 21, 1972. This was Paper 19 presented at the Cleveland, Ohio, Meeting of the Society, Oct. 3-7, 1971.

Any discussion of this paper will appear in a Discussion Section to be published in the December 1973 JOURNAL.

REFERENCES

1. E. E. Schumacher and G. S. Phipps, *Trans. Electrochem. Soc.*, **68**, 309 (1935).
2. A. M. Howard and E. Willihnganz, *Electrochem. Technol.*, **6**, 370 (1968).
3. A. B. Townsend, Report No. Y-1307, Union-Carbide Nuclear Co., Oak Ridge, Tennessee. U.S. Atomic Energy Commission (1960).
4. G. W. Mao and R. E. Tieder, Paper 365 presented at Electrochem. Soc. Meeting, Montreal, Canada, Oct. 6-11, 1968.
5. A. G. Cannone, D. O. Feder, and R. V. Biagetti, *Bell System Tech. J.*, **49**, 1279 (1970).
6. G. W. Mao and P. Rao, *Brit. Corrosion J.*, **6**, 122 (1971).

Electrochemical Behavior of Germanium in Fused LiCl-KCl Eutectic

Joseph M. Shafir and James A. Plambeck*

Department of Chemistry, University of Alberta, Edmonton, Alberta, Canada

ABSTRACT

The electrode potentials of the Ge(II)/Ge(0) and Ge(IV)/Ge(II) redox couples in fused LiCl-KCl eutectic were found to be −0.792 and −0.665V *vs.* the standard molar platinum reference electrode (SMPE). A voltammetric study of Ge(II) showed that potentials more negative than −0.80V are sufficient for electrodeposition of germanium. Chronopotentiometric reduction of Ge(II) on gold followed the Sand equation and gave evidence of alloy formation. The cell Au-Ge (12 weight per cent Ge, l)/Ge(II) in LiCl-KCl/Ge(s) was studied, and the following parameters were determined for the alloy: $\Delta S°_f = 14.2$ eu, $\Delta G°_f = -1.24$ kcal/mole, $\Delta H°_f = +9.00$ kcal/mole. Optical and scanning electron metallographic studies were made of germanium deposited on a gold substrate.

Literature Review

Attempts to electrodeposit germanium have a long history. Winkler, who discovered the element, electrolyzed aqueous ammoniacal ammonium tartrate solutions of it (1). Further study of the aqueous electrochemical properties of germanium was instigated by the work of Tainton and Clayton (2) who found that small amounts of germanium had a very adverse effect on the electrodeposition of zinc. Several attempts to deposit germanium from aqueous media have since been made, such as those of Hall and Koenig (3) and of Schwarz, Heinrich, and Hollstein (4). A careful study by Fink and Dokras (5) concludes that in any aqueous medium only a thin initial flash of metallic germanium can be obtained. This is followed by hydrogen evolution since the hydrogen overpotential on germanium is low. It is thus necessary to employ nonaqueous media to electrodeposit massive germanium.

Organic baths have been used to electroplate germanium. Of these, the most popular appear to be ethylene glycol and propylene glycol. Fink and Dokras (5) produced thick adherent metal plates from solutions of GeI_4 in ethylene glycol. Solutions of $GeCl_4$ in propylene glycol were used by Szekely (6).

Fused salt media have been employed in the electrowinning of germanium from its oxide. Tressler and Dennis (7) formed metallic germanium by the electrolysis of GeO_2 in molten fluogermanate or cryolite baths. Fink and Dokras (5) employed a fused tetraborate bath to obtain the metal from GeO_2. Barbier-Andrieux (8) did an extensive study of the electrowinning of germanium from germanium dioxide in fused salts such as germanates, borates, silicates, borosilicates, phosphates, and fluorosilicates. Bockris, Diaz, and Green (9) have discussed the production of germanium dendrites by electrolysis of a $Na_2B_4O_7$-GeO_2 melt.

Experimental

Materials.—Reagent grade lithium chloride and potassium chloride (Fisher Scientific Ltd.) were purified as previously described (10). Germanium rod (99.99%) was obtained from A.D. MacKay Inc., New York. The graphite rods used as electrodes were obtained from Union Carbide Corporation, New York (spectroscopic electrodes SPK). Gold used in the thermodynamic study of gold-germanium alloy formation was obtained in bar form from Johnson Matthey and Mallory Ltd., Toronto.

Apparatus.—The apparatus used was similar to that previously described (10-12). The electrodes used for voltammetric scans were made of tungsten wire 5 mm long and 0.5 mm in diameter sealed in uranium glass. Potentials were measured with a Hewlett-Packard Model 3400A digital voltmeter. Voltammetric scans were made with a Metrohm-Polarecord 261 polarograph. Constant potential electrolyses were carried out with a Wenking Model 61RH potentiostat using gold electrodes.

Chronopotentiometric measurements employed a gold foil electrode approximately 0.4 cm^2 in area. The counterelectrode and reference electrode were respectively a carbon rod and a platinum(II)/platinum(0) couple in separate isolation compartments. The constant current was obtained from a Model 6525A d-c power supply (Hewlett-Packard) controlled by appropriate mercury-wetted relay switching circuitry. Traces were recorded on a Model 175A oscilloscope equipped with 1750B and 1781B plug-in units and a 196B camera (Hewlett-Packard), using ASA 3000 Polaroid film.

The gold-germanium alloy [eutectic composition, 12 w/o (weight per cent) germanium (13)] was prepared by placing appropriate amounts of gold and germanium in a quartz boat which had been cleaned by boiling in perchloric acid. The mixture was fused under a flow of argon (dried by passage over magnesium perchlorate) in a Lindberg-Hevi-Duty 54032A furnace in conjunction with a Lindberg-Hevi-Duty 59344 temperature controller. In the thermodynamic study, the alloy was held in a Pyrex cup which was attached to a glass rod. Electrolytic contact with the alloy was made with a tungsten wire sealed in uranium glass. The germanium bar used as a reference electrode was suspended from a platinum wire sealed in a Pyrex tube.

The topography of the germanium deposit on a gold substrate was studied using both optical and scanning electron microscopes: a Carl Zeiss Ultraphot(III) Metallograph, a photographic metallurgical microscope (Carl Zeiss Oberkochen, Wuertt., West Germany), and a Stereoscan S4 scanning electron microscope (Cambridge Scientific Instruments Ltd., Cambridge, England).

Procedure.—The procedure used for carrying out the coulometric oxidations and measurements under argon has been previously described (11, 12). The germanium rod was anodized to give solutions of germanium(II), which could be further oxidized to germanium(IV) at a carbon electrode after the germanium rod had been removed. Measurements of potential were made against a platinum(II)/platinum(0) reference electrode and all potentials given in this paper are with reference to the standard molar platinum electrode (SMPE) (14).

* Electrochemical Society Active Member.

Key words: germanium, germanium-gold alloy, electrodeposition, fused chlorides.

In order to obtain reproducible voltammetric curves, it was found necessary to hold the tungsten microelectrode at positive (chlorine evolution) potential for a few moments before each scan. This was done in the bulk melt. Similar procedures were found necessary to obtain reproducible chronopotentiometric curves. The solutions of Ge(II) were prepared coulometrically. The gold electrode was anodized until all deposits of germanium were removed, *i.e.*, until chlorine evolution just began. It was necessary to carry out this procedure carefully and at low current density (<50 mA/cm^2) to avoid appreciable anodization of gold into solution. The electrode was then momentarily anodized at this potential, the current was shut off, and the compartment stirred by rotation of the flag. Cathodic chronopotentiometric curves were all run 30 sec after cessation of the anodic current.

In the thermodynamic study of gold-germanium alloy formation, which was a study of the cell: Au-Ge alloy/Ge(II) in LiCl-KCl/Ge, the previously prepared LiCl-KCl eutectic was fused and filtered in order to remove any magnesium present, as magnesium ribbon was used in melt preparation. A 0.2M solution of Ge(II) was prepared *in situ* by electrolytic anodization of germanium; the resulting solution was thoroughly stirred after cessation of Ge(II) generation. The solution temperature was monitored with a calibrated Chromel-Alumel thermocouple sheathed in a Pyrex tube. The germanium bar, alloy holder, and thermocouple were placed as close together as possible to minimize thermal gradients. Potential-time measurements were made every 2 hr after a new temperature setting had been made. The experiment was conducted under a static dry argon atmosphere. The thermocouple effect of the electrodes was determined in a separate experiment, and this potential was subtracted from the observed cell potential.

The cross-sectional sample used in the optical microscopic examination was prepared by imbedding a germanium-plated gold specimen edgewise in plastic. The sample was then polished, progressing from a coarse abrasive to a polishing lap using 0.05 μm Al_2O_3 (Linde B). The germanium-plated gold specimen was prepared by electrolytic reduction of solutions of Ge(II) at a constant potential of −0.86V. Germanium(II) solutions were prepared by coulometric oxidation of a germanium bar. Germanium plate thickness was determined with a filar micrometer eyepiece attached to a Tukon Tester (Wilson Mechanical Instrument Company, New York).

Results

Potentiometry.—A total of 27 concentration-potential data points were obtained from four separate coulometric oxidations of the germanium bar electrode at 450° ± 1°C. The concentration of Ge(II) ranged from 0.001 to 0.1M. A plot of electromotive force as a function of the logarithm of coulombs used was linear and had a slope of 0.075 ± 0.006 V/log unit, in agreement with the theoretical value of 0.072 V/log unit expected for a two-electron process at this temperature. The potentials became stable rapidly, usually within 5 min after cessation of the electrolysis and gentle stirring.

The standard potential was calculated in the usual manner (10) and is reported with respect to the appropriate standard platinum electrode on the molar, molal, and mole fraction scales in Table I. The conventions and standard states used in this table have been described elsewhere (14).

Further coulometric oxidation of the germanium(II) solutions at a carbon rod produced visible bubbles at the rod at polarization potentials significantly less than that of chlorine evolution, suggesting the formation of volatile $GeCl_4$ (bp, 84°C). Linear plots of electromotive force against logarithm of concentration ratio could not be obtained or had unreasonably low slopes,

Table I. Standard potentials of germanium couples

Couple	$E°_M$	$E°_M$	$E°_X$	Standard deviation
Ge(II)-Ge(0)	−0.792	−0.792	−0.792	0.008
Ge(IV)-Ge(II)*	−0.665	−0.681	−0.771	−0.002
Ge(IV)-Ge(0)†	−0.728	−0.736	−0.781	−0.008

* Based on a two-electron process.
† Calculated from experimental free energies.

as would be expected if $GeCl_4$ volatilized from the melt. Steady and rapid drifting of the observed potentials in the negative direction also support this interpretation. By taking values as rapidly as possible, this problem could be reduced but not avoided. Using eight points from two runs taken under the best possible conditions and assuming the two-electron oxidation, we calculate standard potentials of −0.664, −0.666, −0.664, −0.667V (Run 1) and −0.666, −0.667, −0.665, −0.663V (Run 2), these values being given in order of increasing generation. The average is −0.626V, standard deviation 0.022V. The systematic deviation is due to loss of $GeCl_4$.

Attempts to cathodize germanium metal into solution were not successful. The only reaction observed was lithium deposition on the germanium, at approximately the standard potential of the Li(I)/Li(0) couple (14).

Voltammetry.—A voltammetric scan of the electrolyte alone indicated a limiting anodic current at about +0.2V (chlorine evolution), a limiting cathodic current at −2.6V (lithium deposition), and a sharp cathodic peak at −0.56 ± 0.05V. This cathodic peak was not due to melt impurities but was highly sensitive to electrode treatment and history. Elimination of the prescan anodization reduced the peak to about 5% of its previous value. This peak is attributed to the reduction of adherent insoluble polymeric chloride films (15) formed when the tungsten microelectrode was anodized in the bulk melt.

Addition of germanium(II) to this melt (by anodization of a germanium rod) produced an additional cathodic wave whose half-wave potential was −0.76V, in reasonable agreement with the standard potential, −0.79V, of the germanium(II)/germanium(0) couple as shown in Fig. 1. The wave height increased with addition of germanium(II) but the relationship was not strictly linear. Curve A in Fig. 1 shows the latter stage in the reduction of the insoluble polymeric chlorides at potentials less than −0.74V, followed by Ge(II) reduction. Curve B represents a voltammetric

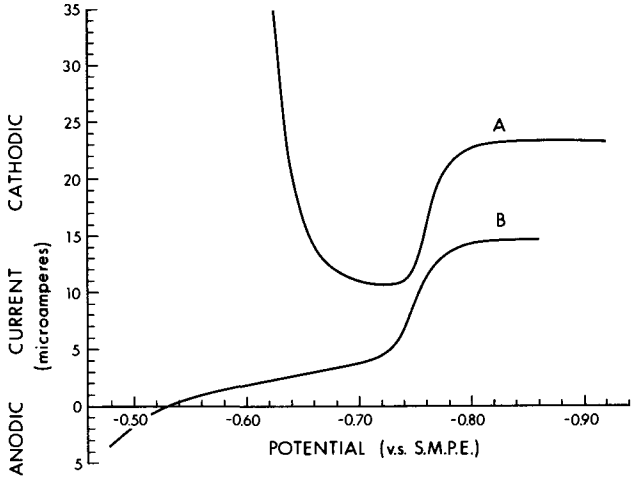

Fig. 1. Voltammetric scans of Ge(II) in fused LiCl-KCl eutectic at 450°C, using a tungsten microelectrode. Curve A was obtained with preanodization of tungsten microelectrode; curve B is a repeated scan, with no preanodization.

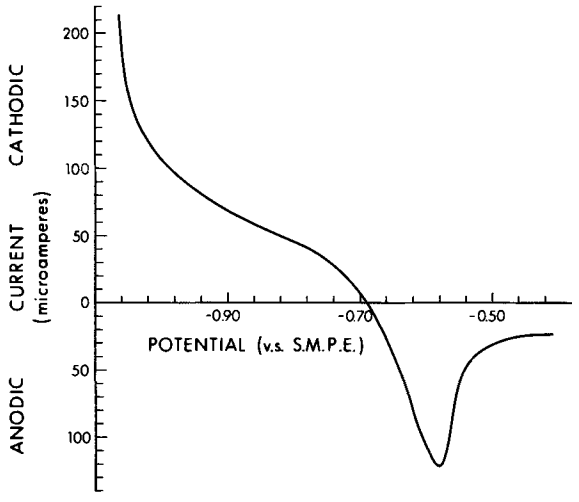

Fig. 2. Anodic voltammogram of electrodeposited germanium on the tungsten microelectrode.

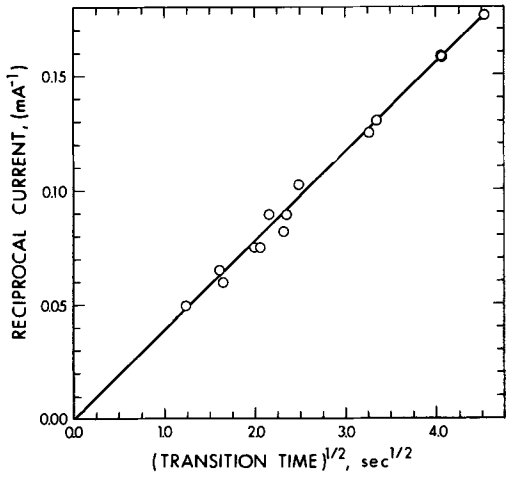

Fig. 4. Plot of reciprocal current vs $\tau^{1/2}$ for the first transition in the chronopotentiometric analysis. Concentration of Ge(II), 7.9 × 10^{-5} mole/cm^3; electrode geometric area 0.4 cm^2.

scan for which the tungsten microelectrode was not preanodized in the bulk melt. When the scan was first made toward more negative potentials, then reversed, an anodic process began to appear at about −0.75V, corresponding to the reoxidation of the deposited germanium (Fig. 2). This study indicates that constant-potential electrodeposition of germanium should be possible at potentials more negative than −0.8V.

Chronopotentiometry.—In order to attempt to observe the behavior of Ge(II) deposition in the melt under constant current electrolysis conditions, a chronopotentiometric study was carried out. Chronopotentiometric curves were run at current densities between 12 and 40 mA/cm^2. A typical curve is shown in Fig. 3. The transition region indicated as B was well-defined in all cases. The transition(s) at C and beyond were poorly defined at low current densities but became more distinct at current densities greater than 25 mA/cm^2. The length of the first transition was taken from the origin, A, to B, although an initial dip close to A was observed on all curves. We now believe that this initial dip is due to formation of surface Au-Ge alloy. The transition B is ascribed to the exhaustion of Ge(II) at the electrode surface in the usual manner. The Sand equation $i\tau^{1/2} = \frac{1}{2}\pi^{1/2} nFAD^{1/2}C$ is obeyed for this process as shown in Fig. 4, and from the data of Table II the diffusion coefficient of Ge(II) was calculated to be 2.2 × 10^{-5} cm^2/sec, in reasonable agreement with values for other divalent ions in this solvent (16).

Using low current densities, and careful observation of the electrode during chronopotentiometry, it was observed that the clean gold electrode took on a bright, mirror-like silver finish soon after cathodic current flow began. With continued electrolysis the finish continually dulled, until after the end of the first transition, B, when massive black deposits began forming. These deposits, unlike the initial finish, did not adhere to the electrode and could be knocked off by gentle stirring.

The data for the transitions observed is given in Table II. Measurement of $E_{\tau/4}$ data was difficult due to the fact that not all chlorine generated in the vicinity of the gold electrode could be removed. This led to varying initial values of potentials. To circumvent this problem, the "true" potential of this point was taken from the chronopotentiogram where the lowest current density was used to anodize the germanium from the gold electrode. All potentials were then measured from this point.

At low current densities (less than 17 mA/cm^2) no transition other than the first could be defined. At higher current densities, other transitions became noticeable, especially a well-defined second one. It has been shown by Berzins and Delahay (17) that the Sand equation for a second transition is given by

$$(\tau_1 + \tau_2)^{1/2} - \tau_1^{1/2} = \pi^{1/2} nFAD^{1/2}C/2i$$

A plot of $1/i$ *vs.* $(\tau_1 + \tau_2)^{1/2} - \tau_1^{1/2}$ was made for the second transition, but it was found that no linear relation existed, and hence the electrode process occurring was not diffusion-controlled. The formation of the black massive germanium deposit noted at the end of the first transition (B in Fig. 2) permits the nonlinearity of the plot $(\tau_1 + \tau_2)^{1/2} - \tau_1^{1/2}$ *vs.* $1/i$ to be ascribed to the rapidly changing electrode area upon

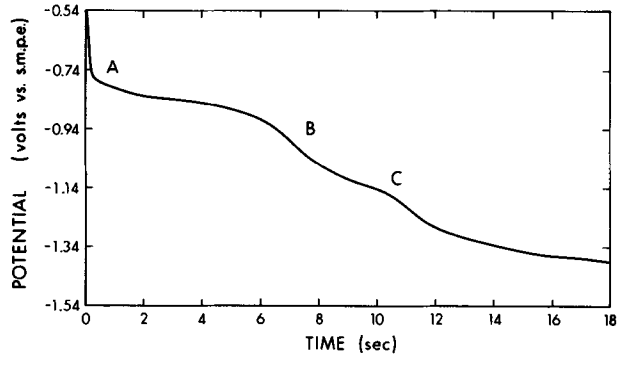

Fig. 3. Chronopotentiogram of 1.0 × 10^{-3} M Ge(II) taken in the fused LiCl-KCl eutectic at 450°C. Current density was 30 mA/cm^2.

Table II. Chronopotentiometric data*

Current (mA)	τ_1 (sec)	$i\tau_1^{1/2}$	τ_2 (sec)	$E_{\tau_1/4}$, V (SMPE)	$E_{\tau_2/4}$, V (SMPE)	$E_{\tau_3/4}$, V (SMPE)
5.67	20.5	25.7	—	−0.71	—	—
6.76	16.5	27.5	—	−0.74	—	—
7.70	11.2	25.8	—	−0.72	—	—
7.99	10.7	26.3	—	−0.74	—	—
9.79	6.2	25.5	6.9†	−0.74	—	—
11.15	4.68	24.2	3.8	−0.74	−1.00	−1.2†
11.35	6.00	27.8	5.2	−0.74	−1.06	−1.4†
12.20	5.40	28.4	2.54	−0.77	−1.03	—
13.25	4.23	27.3	7.4†	−0.77	−1.05	−1.2†
13.26	4.35	27.7	3.68	−0.77	−1.04	—
13.31	4.20	26.8	3.0	−0.80	−1.16	−1.4†
15.46	2.50	24.5	3.4	−0.84	−1.14	—
15.72	3.80	30.6	4.5	−0.80	−1.08	−1.3†
16.78†	5.00	27.6	—	−0.81	—	—
20.21†	1.50	24.8	—	—	—	—

* Concentration of Ge(II), 7.9 × 10^{-5} mole/cm^3. Electrode geometric area 0.4 cm^2. $\tau_{1,2,3}$ refer to first, second, and third transition times. Average value of chronopotentiometric constant $i\tau^{1/2}/C$ is 8(±0.5) × 10^2 A-sec$^{1/2}$ cm mole^{-1}.
† Transition ill-defined.

which the germanium was being deposited. Third transitions were noted at large current densities. These were ill-defined, again probably due to rapid electrode area changes.

Thermodynamics of gold-germanium alloy formation.—The gold-germanium phase diagram has been established (18) and shows simple eutectic formation at 12 w/o germanium. Using this alloy composition, the potential of the cell Au-Ge (12 w/o Ge,l)/Ge(II) in LiCl-KCl/Ge(s) was studied over the temperature range 400°-500°C. A preliminary study of the cell showed that Ge(II) is not stable in the LiCl-KCl melt over extended periods of time when a flow of argon is maintained above the cell assembly; germanium needles grew from the germanium bar and the interior of the upper, cool portion of the apparatus became coated with a white material, presumably $GeCl_4$. It was concluded that Ge(II) disproportionates to Ge(IV) and the metal, *i.e.* $2Ge(II) \rightleftarrows Ge(0) + Ge(IV)$, where Ge(IV) exists as germanium tetrachloride gas. From the standard potentials of the Ge(II)/Ge(0) and Ge(IV)/Ge(II) couples, the equilibrium constant for the disproportionation reaction is calculated to be 1.69×10^{-2} l mol^{-1}. Thus for a 0.02M solution of Ge(II), a concentration of Ge(IV) equal to 7.0×10^{-6}M is required to maintain equilibrium conditions; however, since Ge(IV) is volatile as $GeCl_4$, the disproportionation reaction is slowly forced to the right. To minimize this effect a static argon atmosphere over the cell was necessary; otherwise, the Ge(II) concentration was reduced to the point where reversible potentials were not obtained.

The temperature-potential measurements of the alloy cell are shown in Fig. 5. Data were taken by alternately raising and lowering the temperature; no hysteresis in the cell potential was observed. The cell potential at any given temperature was constant (within 0.1 mV over a 15-min interval). These facts, together with the observation that the equilibrium cell potential recovered its initial value after passage of small amounts of current in either direction through the cell, indicated that the system was reversible. The potential at both the Ge(s) and Au-Ge (12 w/o Ge, l) electrodes is dictated by the concentration of Ge(II) in solution, since the extent of the reaction $2Au + Ge(II) \rightarrow Ge + 2Au(I)$ is small as can be seen from the standard potential of the Au(I)/Au(0) couple, +0.205V (14).

The entropy of alloy formation can be determined from the slope of Fig. 5 and the relationship $\Delta S = n\mathbf{F}(dE/dT)$, where n is the charge on the Ge(II) ion, **F** is Faraday's constant, and dE/dt is the slope of the potential-temperature plot. The standard free energy of alloy formation is directly calculable from the open-circuit potential of the galvanic cell at 450°C ($E°$). The standard enthalpy of alloy formation, $\Delta H°$, is calculable from the free energy and entropy of alloy formation. For the alloy Au-Ge (12 w/o Ge), the following parameters were determined: $\Delta S°_f = 14.2 \pm 0.2$ eu ($dE/dT = 3.07(\pm 0.04) \times 10^{-4}$ V/K); $\Delta G°_f = -1.24 \pm 0.02$ kcal/mole; and $\Delta H°_f = 9.00 \pm 0.10$ kcal/mole. By considering the Nernst equations for the half-cells $Ge(II) + 2e^- \rightarrow Ge$ and $Ge(alloy) \rightarrow Ge(II) + 2e^-$, it can be shown that $E_{cell} = -2.303\ RT/2\mathbf{F} \log a_{Ge(alloy)}$, where $E_{cell} = 26.8 \pm 0.4$ mV (after correction for the thermocouple effect of +9.4 mV) at 723°K and $a_{Ge(alloy)}$ is the activity of germanium in the alloy, which was calculated to be 0.426 ± 0.010. Defining γ as the activity coefficient of germanium in the alloy and X as the mole fraction of germanium in the alloy, then $a_{Ge(alloy)} = \gamma X$ (where $X = 0.270$) gives a value of $\gamma = 1.57 \pm 0.03$. Table III gives a comparison of the thermodynamic properties measured in this work with those of other Au-group(IV) element alloys (19, 20). It should be noted that the interaction between gold and germanium is small as are the interactions between gold and tin and gold and lead. The dip shown at A in Fig. 3 corresponds to a shift of approximately 50 mV in potential. The open-circuit potential corresponding to the standard free energy of gold-germanium alloy formation was found to be 26.8 mV. The gold-germanium composition at A is not exactly known but the 50 mV potential shift at A strongly indicates gold-germanium alloy formation.

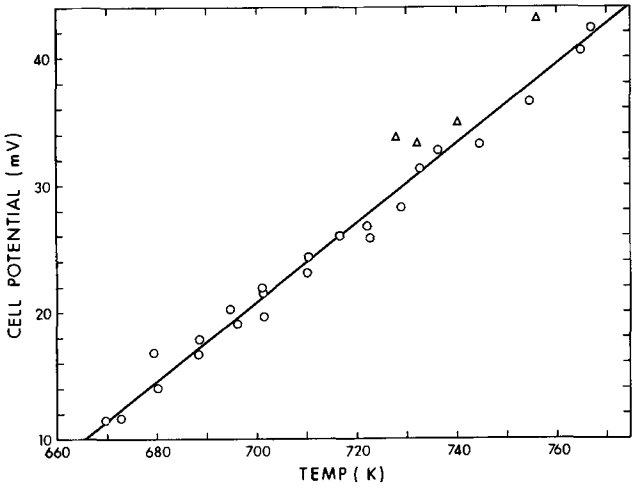

Fig. 5. Plot of potential vs. temperature for the cell Au-Ge (12 w/o Ge,l)/Ge(II) in LiCl-KCl/Ge(s). Nonequilibrium values taken in separate run indicated by triangles.

Using a current density of 50 mA/cm^2 for approximately 3 sec, Ge(II) was plated on to the gold electrode and this plate was then anodized. The $E_{\tau/4}$ for the anodic chronopotentiogram was −0.46V as compared to $E_{\tau/4}$ for the reduction chronopotentiogram which was of the order of −0.84V. The potential of the anodic chronopotentiogram did not rise sharply, *i.e.*, oxidation of germanium was extended over a large period of time. This behavior is also indicative of alloy formation.

Optical metallography of deposited germanium.—Figure 6 is a cross-sectional photomicrograph of germanium deposited onto a gold substrate as previously described. The gold substrate, originally 250 μm in width, was found to be 160 μm wide. The outer layers had a total width of 340 μm. The germanium layer is not pure germanium but is a gold-germanium eutectic as can be discerned by its structure (21) which resembles pearlite. In several regions the germanium had penetrated the gold band so that both outer layers were connected; these connections were blue-gray in color.

Table III. Thermodynamics of gold-metal eutectic alloys, 450°C

Metal	Eutectic composition, mole fraction metal	$\Delta G°_f$, kcal/mole	$\Delta S°$, eu	$\Delta H°_f$, kcal/mole	dE/dT, mV/deg	Activity, metal	Activity coefficient, metal
Ge	0.270	−1.22	14.2	+9.00	0.307	0.423	1.57
Sn	0.294	−7.16*	3.66	−4.51*	0.0795	6.97×10^{-3}*	0.0237*
Pb	0.270	−2.85*	3.78	−0.12*	0.0820	0.137*	0.507*

* Data extrapolated to 450°C.

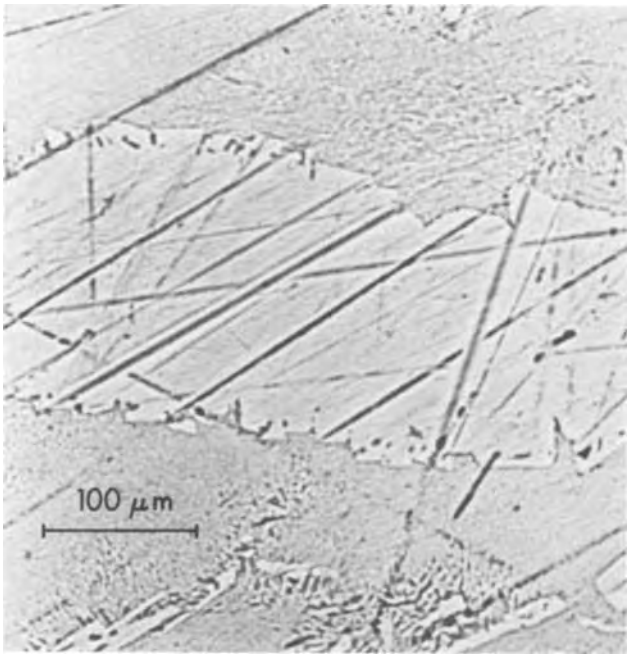

Fig. 6. Photomicrograph of cross section of Ge deposited on gold

Needle-like deposits of germanium were obtained in all experiments utilizing constant potential as the mode of electrodepositing germanium. The needles varied up to 1 cm in length and up to 200 μm in width, and grew from the gold-germanium interface into the solution.

Scanning electron microscopy of deposited germanium.—The samples were obtained either by allowing the sample to slowly cool in the eutectic as the eutectic froze, or by withdrawing the sample from the eutectic melt and cooling it to room temperature. Samples obtained with slow cooling were much smoother than those obtained on rapid cooling. Use of more reducing, *i.e.*, more negative potentials gave rise to rougher surfaces than use of a less reducing potential.

A photomicrograph of a sample obtained by constant-potential electroreduction of a solution of Ge(II) at −0.85V followed by rapid sample cooling showed surface cracks. These cracks produced by the rapid sample cooling were at least 3 μm deep and showed that the gold-germanium deposit was layered.

Conclusion

The oxidation states of germanium stable in the LiCl-KCl melt at 450°C are +2 and +4. The standard reduction potentials of both have been measured. Germanium metal can be electrodeposited from this melt, but the reduction process on gold is complicated by alloy formation. The thermodynamics of this alloy formation have been studied.

Acknowledgment

The authors are grateful to the National Research Council of Canada for support of this research through an Operating Grant (to J.A.P.) and a N.R.C. Scholarship (to J.M.S.), to J. T. Chapman for preliminary work and to the Department of Mining and Metallurgy of the University of Alberta for use of equipment. Taken from the thesis of J. M. Shafir, submitted in partial fulfillment of the requirements for the Ph.D. degree, University of Alberta.

Manuscript submitted June 21, 1972; revised manuscript received Aug. 17, 1972.

Any discussion of this paper will appear in a Discussion Section to be published in the December 1973 JOURNAL.

REFERENCES

1. C. Winkler, *J. Prakt. Chem.*, **34**, 208 (1886).
2. U. C. Tainton and E. T. Clayton, *Trans. Electrochem. Soc.*, **57**, 279 (1930).
3. J. I. Hall and A. E. Koenig, *ibid.*, **65**, 215 (1934).
4. R. Schwarz, F. Heinrich, and E. Hollstein, *Z. Anorg. Allgem. Chem.*, **229**, 146 (1936).
5. C. G. Fink and V. M. Dokras, *This Journal*, **95**, 80 (1949).
6. C. Szekely, *This Journal*, **98**, 318 (1951).
7. K. M. Tressler and L. M. Dennis, *J. Phys. Chem.*, **31**, 1429 (1927).
8. M. J. Barbier-Andrieux, *Ann. Chim. (Paris)*, **10**, 754 (1955).
9. J. O'M. Bockris, J. Diaz, and M. Green, *Electrochim. Acta*, **4**, 362 (1961).
10. J. M. Shafir and J. A. Plambeck, *Can. J. Chem.*, **48**, 2131 (1970).
11. H. A. Laitinen and J. A. Plambeck, *J. Am. Chem. Soc.*, **87**, 1202 (1965).
12. J. A. Plambeck, *Can. J. Chem.*, **46**, 929 (1968).
13. R. I. Jaffee, E. W. McMullen, and B. W. Gonser, *Trans. Electrochem. Soc.*, **89**, 277 (1946).
14. J. A. Plambeck, *J. Chem. Eng. Data*, **12**, 77 (1967).
15. K. E. Johnson and J. R. Mackenzie, *Anal. Chem.*, **41**, 1483 (1969).
16. H. A. Laitinen and W. S. Ferguson, *ibid.*, **29**, 4 (1957).
17. T. Berzins and P. Delahay, *J. Am. Chem. Soc.*, **75**, 4205 (1953).
18. M. Hansen and K. Anderko, "Constitution of Binary Alloys," p. 206, McGraw-Hill Book Co., New York (1958).
19. O. J. Kleppa, *J. Am. Chem. Soc.*, **72**, 3346 (1950).
20. O. J. Kleppa, *ibid.*, **71**, 3275 (1949).
21. R. I. Jaffee, E. M. Smith, and B. W. Gonser, *Trans. AIME*, **161**, 366 (1945).

Intergranular Corrosion of a Ferritic Stainless Steel

R. P. Frankenthal*,[1] and H. W. Pickering*,[2]

United States Steel Corporation, Research Laboratory, Monroeville, Pennsylvania 15146

ABSTRACT

The chromium-depletion theory of intergranular corrosion has been confirmed for a ferritic stainless steel. The potential range over which intergranular attack occurs is limited by the passivation potential of the matrix and that of chromium-free iron. The concentration of chromium in the depleted zone is less than 5% at most grain boundaries and approaches 0% at a few. The width of the depleted zone is less than 1 μm. Under strongly oxidizing conditions another form of intergranular attack occurs in both the sensitized and nonsensitized conditions.

The intergranular corrosion of ferritic stainless steels has been explained by numerous models (1-4). Bäumel (4) suggested that the chromium-depletion theory, proposed by Strauss, Schottky, and Hinnüber (5) in 1930 and by Bain, Aborn, and Rutherford (6) in 1933 for austenitic stainless steels, is also valid for ferritic ones.[3] This theory holds that sensitization to intergranular attack is due to a chromium-depleted zone along the grain boundary resulting from the precipitation of chromium carbide at the boundary; if the chromium concentration of the depleted zone is less than that required to maintain passivity, *i.e. ca.* 13%, preferential dissolution of the depleted zone will occur.

Bond (8) has results for ferritic steels that are consistent with the chromium-depletion theory; but they do not prove it. Also, the extent of depletion, *i.e.*, the chromium concentration and the width of the zone, has yet to be determined for ferritic or austenitic stainless steels.

Cihal and Prazak (9) suggested for austenitic stainless steels, *e.g.*, Fe-18Cr-8Ni, that a chromium-depleted zone should behave electrochemically like an Fe-Ni alloy; the passivation potential of Fe-Cr-Ni alloys becomes more noble with decreasing chromium concentration. Thus the depleted zone should passivate only at potentials more noble than that required to passivate the matrix. Further, preferential attack of the depleted zone should be limited to a potential range between the passivation potential of the matrix (maximum possible chromium content) and the passivation potential of the chromium-free Fe-Ni alloy (minimum possible chromium content). Their (9) experimental evidence is *not* convincing, because much of the intergranular corrosion takes place at a potential at which the matrix is also dissolving, according to their anodic polarization curves. However, Schüller, Schwaab, and Schwenk (10) show that one form of intergranular attack is limited to this potential region.

In this paper the test of Cihal and Prazak (9) is applied to a sensitized ferritic stainless steel and extended to obtain quantitative data on the chromium content of the depleted zone. In addition, the width of the zone is determined by scanning electron microscopy.

Experimental

The principal alloy investigated was a vacuum-melted, hot-rolled[4] Fe-20Cr ferritic alloy with the following analysis in weight per cent (w/o): Cr-20.2; C-0.014; N-0.005; O-0.014; P-0.003; S-0.005; Si-0.014; Mn-<0.005; Ni-<0.03; Cu-<0.01; Mo-<0.01; Al-0.008; Ti < 0.01. Rectangular specimens were machined from a 1.5-cm thick hot-rolled slab. Some specimens were used without further heat-treatment; others were annealed at 1070°K for one week and quenched.

In addition to the above alloy, zone-refined iron and ferritic iron-chromium alloys, containing 4.8, 9.6, and 14 w/o chromium, were used for the determination of the effect of chromium content on the passivation potential. Each of these was hot-rolled, annealed at 1070°K for one week, and quenched.

Two electrolyte solutions were used: 0.5*M* H_2SO_4 (*p*H 0.3) and 0.5*M* NaCl, 0.05*M* H_2SO_4 (*p*H 1.1); they were deaerated with helium. The electrochemical cell and electrical circuit have been described previously (11).

All specimens were polished with an aqueous suspension of 0.3 μm particles of alumina prior to insertion into the cell. The initial applied potential, −0.5V (SHE), was sufficiently cathodic to reduce most of the air-formed oxide film (12). After film reduction the potential was switched to that under study. The current and the potential were monitored continuously. All potentials are reported relative to the standard hydrogen electrode (SHE). All experiments were performed at room temperature, 296°K.

Scanning electron micrographs were taken with a Cambridge Stereoscan microscope; to interpret properly the spatial relationship between the attacked grain boundary and the precipitate decorating the boundary, stereo pairs were obtained.

The Strauss test for susceptibility to intergranular corrosion was performed as follows: the specimen was immersed for two days in a boiling solution of 10% $CuSO_4 \cdot 5H_2O$, 10% H_2SO_4. After the specimen was removed from the solution, washed, and dried, it was lightly polished with an aqueous suspension of 0.05 μm particles of alumina to remove reduced copper and superficial surface attack; the specimen was then examined microscopically. A modified Huey Test (16) was also performed.

Results

During microscopic examination it was observed both for the hot-rolled and for the hot-rolled, annealed Fe-20Cr specimens that most of the grain boundaries were decorated with quasi-continuous sheets of a precipitate. The alloy was dissolved in bromine-methanol solution exposing the precipitate (Fig. 1). Conclusive identification was not possible. X-ray diffraction patterns of the precipitate extracted from hot-rolled specimens were identified as $(Cr,Fe)_7C_3$, while those from hot-rolled, annealed specimens were identified as $(Cr,Fe)_{23}C_6$; however, electron diffraction patterns could not be identified with either carbide.

Steady-state anodic polarization curves were measured for the various hot-rolled, annealed alloys and for annealed iron in the 0.5*M* H_2SO_4 solution. From the potential-current curves (Fig. 2) it is evident that the passivation potential is a strong function of the

* Electrochemical Society Active Member.

[1] Present address: Bell Laboratories, Murray Hill, New Jersey 07974.

[2] Present address: Department of Material Sciences, Pennsylvania State University, University Park, Pennsylvania 16802.

[3] The reader is referred to an excellent review by Wilson (7) for a discussion of other theories of intergranular corrosion in austenitic stainless steels.

[4] A 3-in. ingot is heated to 1500°K; six passes through rolls; reheated; four additional passes.

Key words: chromium, chromium-depletion, iron, passivity.

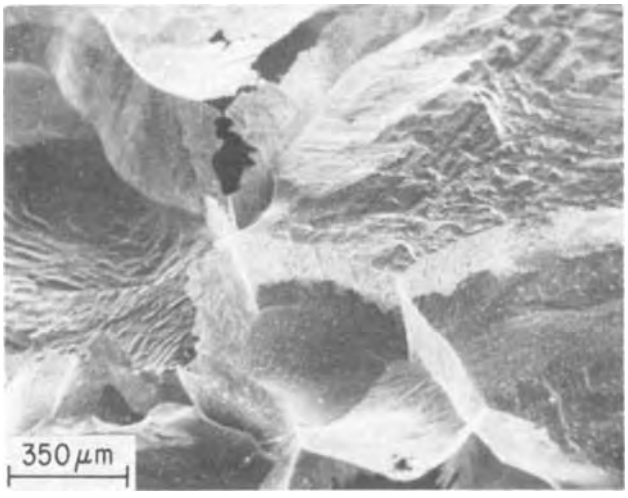

Fig. 1. Alloy has been dissolved in bromine-methanol solution exposing sheet-precipitates along grain boundaries. It can be seen that each side of a grain was bounded by one continuous sheet.

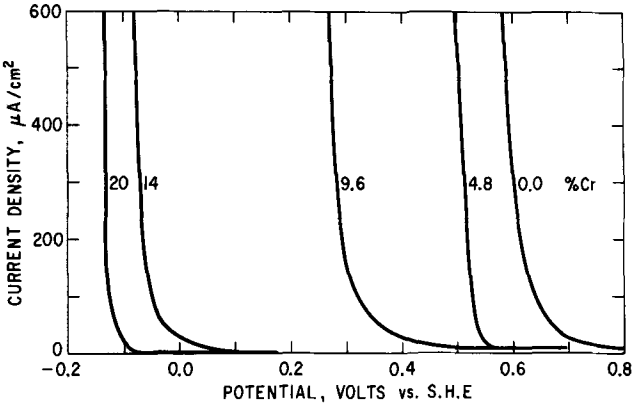

Fig. 2. Anodic polarization curves in the vicinity of the passivation potential for various Fe-Cr alloys in 0.5*M* H_2SO_4.

chromium content of the alloy. The Fe-20Cr alloy in the hot-rolled, annealed condition can be passivated also in the 0.5*M* NaCl, 0.05*M* H_2SO_4 solution, but iron and the Fe-4.8Cr and Fe-9.6Cr alloys cannot be passivated.

The Strauss test showed that the hot-rolled Fe-20 Cr alloy was sensitized, *i.e.*, grain boundary attack occurred, whereas the hot-rolled, annealed one was not. The other Fe-Cr alloys and the iron were not sensitized after annealing. The alloy in the hot-rolled and in the hot-rolled, annealed condition exhibited intergranular attack in the modified Huey Test.

The susceptibility to intergranular attack was also determined potentiostatically in both solutions for the Fe-20Cr alloy in the hot-rolled and in the hot-rolled, annealed conditions. The results are summarized in Table I. For the nonsusceptible specimens the steady-state current density in the potential region of passivity was always less than 1 $\mu A/cm^2$; for the susceptible specimens the current density never was less than about 10 $\mu A/cm^2$. For the latter grain boundary attack

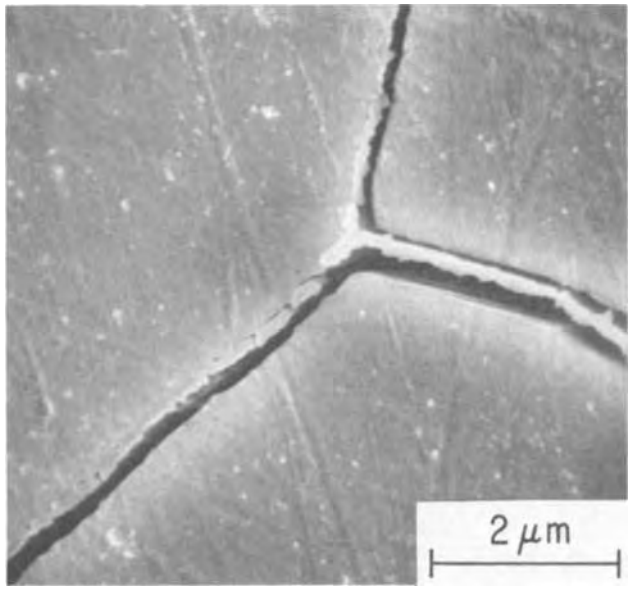

Fig. 3. Scanning electron micrograph of boundaries corroded in 0.5*M* H_2SO_4 at 0.48V. The sheet-precipitates are clearly visible.

could normally be observed in the optical microscope after less than 1 hr; no attack was observed on the former after 24 hr. It is clear that in these experiments the susceptible boundaries never became passivated.

A typical example of grain boundary attack in the H_2SO_4 solution is shown in Fig. 3. The sheet-precipitates are clearly visible; they are never attacked under these experimental conditions. The boundary between the corroded area and the matrix is always smooth, as observed at the specimen surface (Fig. 3). Specimens were held at potential for periods of time up to 24 hr. Measurements on many specimens and many boundaries indicate that the maximum width of the attacked zone is reached within 2 hr. At 0.48V the widest zone observed was 0.7 μm and the narrowest was 0.05 μm.

A typical example of corrosion in the chloride-based solution is shown in Fig. 4 and 5. The attack starts and propagates along grain boundaries; but it also spreads away from the boundaries, forming large pits. The sheet-precipitate is clearly visible in Fig. 5; it is never attacked under these experimental conditions.

Grain boundary attack at high potentials (>1.2V) was not investigated further, except to determine that the matrix and not the precipitate was dissolved.

Discussion

The results confirm the chromium-depletion theory of intergranular corrosion (5, 6), as applied to ferritic stainless steels. The maximum potential at which intergranular attack is observed in the H_2SO_4 solution lies below the passivation potential of iron (Table I, Fig. 2); if the maximum potential were higher than the passivation potential of iron, the chromium-depletion theory would not be applicable (9). Other theories (1-3, 7) are not consistent with these results, inasmuch as they cannot predict the decrease in intergranular attack with increasing potential from 0.48 to 0.58V and the absence of attack at potentials from 0.60 to 1.20V.

Table I. Susceptibility to intergranular corrosion

Electrolyte solution	Thermal history	Potential (V)	Results
0.5*M* H_2SO_4	Hot-rolled & annealed	$-0.05 \leqq E \leqq 1.20$	No intergranular attack
		$E \geqq 1.25$	Intergranular attack
	Hot-rolled	$E \leqq 0.48$	Intergranular attack
		$E = 0.52$	Some intergranular attack
		$E = 0.58$	A few boundaries attacked
		$0.60 \leqq E \leqq 1.20$	No intergranular attack
		$E \geqq 1.25$	Intergranular attack
0.5*M* NaCl, 0.05*M* H_2SO_4	Hot-rolled & annealed	$0.10 \leqq E \leqq 0.60$	No intergranular attack
		$E \geqq 1.00$	Intergranular attack
	Hot-rolled	$E > 0.00$	Intergranular attack

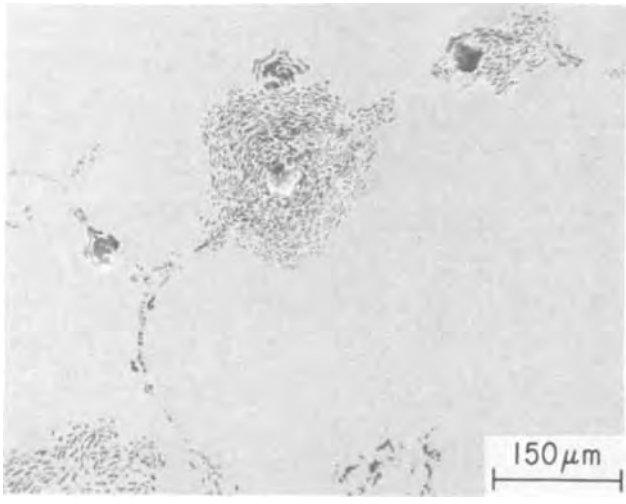

Fig. 4. Scanning electron micrograph showing grain boundary attack in solution containing 0.5M NaCl, 0.05M H_2SO_4. Attack starts at grain boundary but spreads away from the boundary at later stages in chloride-containing solutions.

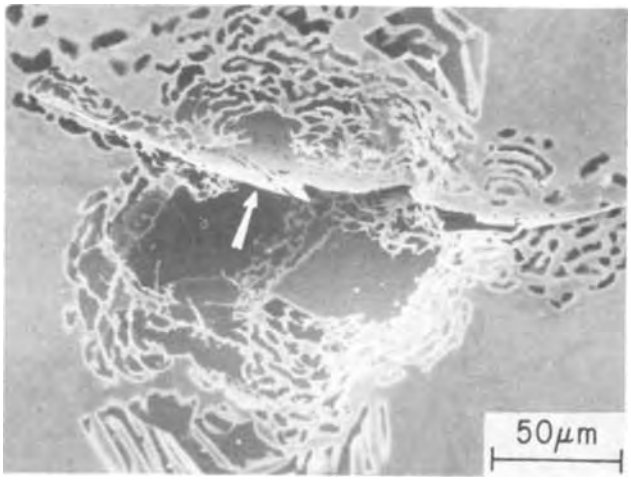

Fig. 5. Scanning electron micrograph showing grain boundary attack and subsequent pitting in solution containing 0.5M NaCl, 0.05M H_2SO_4. Sheet-precipitate (arrow) along grain boundary is clearly visible.

From the results in Table I and in Fig. 2 a lower limit for the chromium concentration of the depleted zone may be obtained. In the H_2SO_4 solution at 0.52V, a potential at which the passivity of the Fe-4.8 Cr alloy begins to decay, most of the grain boundaries were attacked; however, at 0.58V only a few boundaries were attacked and at 0.60V none was attacked. It is concluded that the minimum chromium concentration of the depleted zone is less than 5% for most boundaries; for at least a few boundaries the chromium content must be significantly less than 5% and perhaps approaches 0%. These concentrations represent the lower limit of the gradient from the boundary toward the matrix.

The results of the Strauss test are in agreement with the results of the potentiostatic experiments. The electrode potential of the specimens in the Strauss test is between 0.3 and 0.4V (13); in this potential range ferritic steels, or chromium-depleted zones, with chromium content less than approximately 10% will corrode (Fig. 2).

Since the maximum width (0.7 μm) of the attacked zone across a boundary did not change for corrosion periods from 2 to 24 hr, this width must correspond to that fraction of the depleted zone that dissolves at 0.48V. This width of 0.7 μm is in agreement with the fact that the depleted zone could not be detected by the electron microprobe, which has a beam width of 1 μm. The large variation in the width of the attacked zone, *i.e.*, from 0.05 to 0.7 μm, may indicate that the degree of chromium depletion varies considerably from boundary to boundary, a condition that could have arisen during solidification and cooling of the ingot and could be an effect of the orientation of the grains and of the precipitate.

In the chloride-based solution the grain boundaries of the sensitized alloy are attacked at all potentials, while those of the nonsensitized one are passive over much the same potential range as in H_2SO_4. This is also consistent with the chromium-depletion theory, inasmuch as Fe-20Cr, but not iron, Fe-4.8Cr, or Fe-9.6Cr can be passivated in the chloride-based solution.

The morphology of attack (Fig. 4 and 5) in the chloride-based solution is much different from that in H_2SO_4. This may be explained by the fact that although localized corrosion was initiated as a result of chromium depletion, it propagates in chloride solutions by another mechanism (14, 15) after the depleted zone has been dissolved.

At potentials of 1.25V and higher, intergranular corrosion was observed both in the sensitized and in the nonsensitized alloy, potentiostatically and in the modified Huey Test. This, of course, cannot be explained by the chromium-depletion theory. Aust, Armijo, and Westbrook (16) have suggested that in austenitic stainless steels this may be associated with continuous grain boundary paths either of second-phase or of solute-segregated regions. Their mechanism, however, is relevant only at very high potentials or under strongly oxidizing conditions, such as are rarely encountered in practical situations.

The quasi-continuous sheets of carbide, if indeed they are carbide, decorating grain boundaries (Fig. 1) apparently formed during solidification and cooling of the ingot, as evidenced by the dendritic structure of the sheets. Calculations show that there was sufficient carbon (0.014%) in this alloy with its large grain size (approximately 0.05 cm diameter) for these sheets to be carbide. In any event the sheets are Cr-rich, in view of neighboring Cr-depleted regions, the latter having been identified by the present experimental results.

Conclusions

The chromium-depletion theory of intergranular corrosion has been confirmed for a ferritic stainless steel. A sensitized steel corrodes intergranularly in a potential range limited by the passivation potential of the matrix (corresponding to maximum possible chromium content) and the passivation potential of iron (corresponding to minimum possible chromium content). From a comparison of the anodic polarization curves of Fe-Cr alloys of different chromium content with the potential range over which the extent of intergranular corrosion decreased to none, the minimum concentration of chromium in the depleted zone was established to be less than 5% and at some boundaries to approach 0%. The width of the depleted zone varied from 0.05 to 0.7 μm, as determined from scanning electron micrographs.

At sufficiently high potentials, above the range in which no intergranular corrosion is observed, both the sensitized and the nonsensitized steel exhibited intergranular attack. This attack cannot be due to chromium depletion adjacent to the grain boundary.

Acknowledgments

We thank C. E. Brickner and W. Gundaker for taking the scanning electron micrographs, A. Szirmae and L. Zwell for isolating and identifying the carbides, and S. Barnartt for helpful discussions.

Manuscript submitted May 25, 1972; revised manuscript received Aug. 15, 1972.

Any discussion of this paper will appear in a Discussion Section to be published in the December 1973 JOURNAL.

REFERENCES

1. J. Hochmann, *Rev. Met.*, **48**, 734 (1951).
2. E. Houdremont and W. Tofaute, *Stahl Eisen*, **72**, 539 (1952).
3. R. A. Lula, A. J. Lena, and G. C. Kiefer, *Trans. Am. Soc. Metals*, **46**, 197 (1954).
4. A. Bäumel, *Arch. Eisenhüttenw.*, **34**, 135 (1963).
5. B. Strauss, H. Schottky, and J. Hinnüber, *Z. anorg. allgem. Chem.*, **188**, 309 (1930).
6. E. C. Bain, R. H. Aborn, and J. J. B. Rutherford, *Trans. Am. Soc. Steel Treating*, **21**, 481 (1933).
7. F. G. Wilson, *Brit. Corros. J.*, **6**, 100 (1971).
8. A. P. Bond, *Trans. Met. Soc. AIME*, **245**, 2127 (1969).
9. V. Cihal and M. Prazak, *Hutnicke Listy*, **11**, 225 (1956); *Corrosion*, **16**, 530t (1960).
10. H. J. Schüller, P. Schwaab, and W. Schwenk, *Arch. Eisenhüttenw.*, **33**, 853 (1962).
11. R. P. Frankenthal, *This Journal*, **116**, 580 (1969).
12. R. P. Frankenthal, *ibid*, **114**, 542 (1967).
13. M. A. Streicher, *ibid.*, **106**, 161 (1959).
14. H. W. Pickering and R. P. Frankenthal, *ibid.*, **119**, 1297 (1972).
15. R. P. Frankenthal and H. W. Pickering, *ibid.*, **119**, 1304 (1972).
16. K. T. Aust, J. S. Armijo, and J. H. Westbrook, *Am. Soc. Metals Trans. Quart.*, **59**, 544 (1966).

Structure of Sodium Chloride Films Deposited onto a Leading Edge on Fused Silica

W. Robert Sinclair,* G. W. Kammlott, and R. A. Fastnacht

Bell Telephone Laboratories, Incorporated, Murray Hill, New Jersey 07974

ABSTRACT

Moving mask deposition can considerably affect the structure of evaporated NaCl films on fused silica giving larger grain sizes and enhanced orientation in the plane of the substrate. The dimensions of the mask slit, the substrate temperature, and the speed of the moving mask are important variables. The smaller the width of the slit in the mask the greater the degree of preferred orientation. An intermediate temperature (*ca.* 25°C) gives the largest grain size enhancement and the greatest degree of preferred orientation. The speed of the moving mask must be above the minimum value to achieve these effects. Having once formed an ordered film of small width one can expand the slit width and preserve the orientation.

There have been several studies of the effect on film structure of depositing through a moving mask onto a leading edge. Nowak (1) has reported the preparation of single-crystal films of silicon on amorphous silica at 1150°C by electron beam evaporation. The film was seeded on a bare spot of a silicon wafer and then led over a thermal oxide film while still maintaining the single-crystal arrangement. This maneuver was accomplished using a slotted mask. Unfortunately only the abstract of an oral presentation is available and it is difficult to assess this work especially with respect to experimental details. Another problem posed is the nature of the amorphous silica. This is a film grown from silicon and still attached to the silicon. Distler *et al.* (2) in various papers claim that such films can display a "memory" effect which reproduces the electrical potential at the silicon surface. Thus, if this effect were operative, the evaporated silicon would not have been deposited on a truly amorphous surface. It should be noted, however, that the findings of Distler and his various co-workers have been challenged by Chopra (3).

Braunstein (4) studied the deposition of silicon onto fused silica, single-crystal sapphire, or silicon using a mask system similar to the one indicated in Fig. 1. Braunstein was able to obtain single-crystal silicon on sapphire and on silicon at 1100°C. Films deposited onto fused silica at 1100°C were polycrystalline with very slight indications of preferred orientation. At room temperature, silicon deposited onto fused silica was amorphous whereas use of sapphire at room temperature led to single-crystal films. These films were prepared by vacuum evaporation using rf heating of a carbon crucible, by electron beam evaporation, and by chemical vapor deposition.

In later experiments Braunstein (5) obtained single-crystal films of silicon by evaporating silicon onto a fused silica substrate which had been preclad with gold film and was held at 800°-900°C during evaporation. This experiment was in effect a combination of the V. L. S. technique (6) as used by Nielsen (7) and Filbry and Nielsen (8) with the moving mask technique. Braunstein *et al.* (9) have also reported on this subject.

Clark and Alibozek (10) prepared single-crystal silicon areas by sputtering onto substrates held at 200°C. The substrates were mechanically polished silicon or thermally oxidized silicon (1μ thick). These authors showed that the moving mask substantially improved the orientation. They also sputtered through a moving mask but without the V-shaped fixed mask and obtained a highly oriented film.

These references represent the literature of which the authors are aware on the subject of structural effects resulting from film preparation by deposition through a moving mask system. The general idea of minimizing the number of nuclei by masking is intuitively appealing. The results of Clark and Alibozek

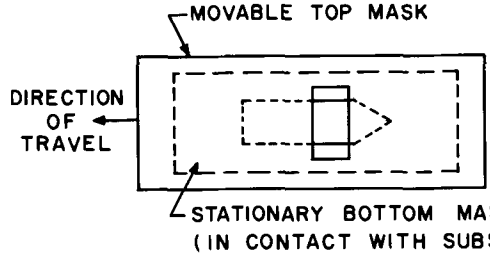

Fig. 1. Typical moving mask assembly used by Braunstein (4) featuring stationary bottom mask in contact with substrate and movable top mask.

* Electrochemical Society Active Member.

Key words: sodium chloride films, moving mask deposition.

are, we feel, inconclusive in demonstrating the efficacy of moving masks per se in that possibilities of changing the film orientation by electric charge effects are also present (11, 12). The experiments of Braunstein and others where silicon was deposited onto a gold film are also open, we feel, to various interpretations. Here the possibility of thermal gradients caused by partially blocking radiation from the evaporation source must be considered.

Despite what we consider to be the inconclusive nature of previous experiments involved with the moving mask concept we have felt there is potential in the idea and that further study is warranted. Our objective in this paper is to present some initial results of a continuing study of the significant parameters involved in moving mask deposition. The ultimate aim of the work is to prepare single-crystal films on nonideal surfaces (*i.e.*, surfaces which are not single crystal and which do not satisfy the often stated requirements of close matching of lattice parameters between film and substrate). The system studied here is sodium chloride on fused silica. Sodium chloride was chosen because such films are easy to deposit and analyze; fused silica because it is in a sense ideally nonideal (*i.e.*, random structure with no grain boundaries) with no complicating features such as exsolution which occurs with some of the more complex glasses on heat-treatment. Because so many variables in thin film work are interrelated it is usually difficult to assess definitively the effects of changing a single parameter. The study presented here is aimed mainly at obtaining some information on the effects of varying substrate temperature and velocity, and varying mask dimensions and shapes.

Experimental Apparatus and Procedures

The apparatus used is depicted schematically in Fig. 2 and 3. Sodium chloride was evaporated downward from a baffled tantalum heater through a double mask system onto the fused silica substrate. In most of our experiments the top mask was fixed and the lower mask and substrate moved together. Keeping the position of the top mask fixed has the advantage of keeping the angle of deposition onto the substrate fixed. We have followed Nowak's (1) terminology and refer to this process as planar edge growth (PEG).

We have used a variety of sizes and shapes of lower masks in geometries similar to that shown in Fig. 1 where the lower mask is in contact with the substrate. We find that with either metal or mica masks the mask edge in contact with the glass substrate acts as a nucleating agent leading to much more random polycrystallinity than in experiments with a mask arrangement as shown in Fig. 3 where the lower mask is not in direct contact with the glass substrate. A straight slit was chosen over the flare type of Fig. 1 to simplify interpretation of the results. Usually, diffraction patterns were obtained only in the region near the end

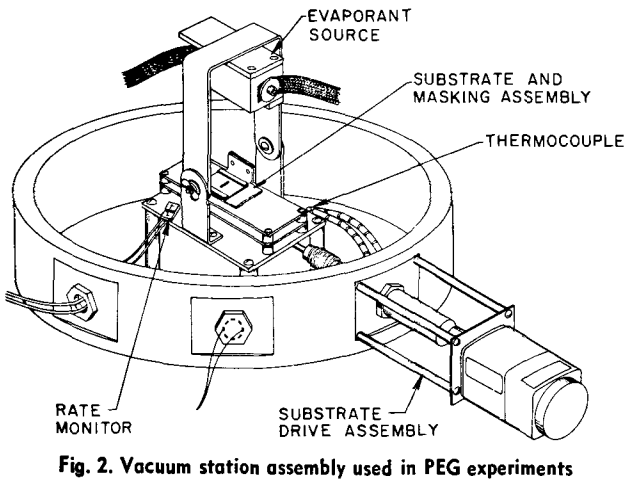

Fig. 2. Vacuum station assembly used in PEG experiments

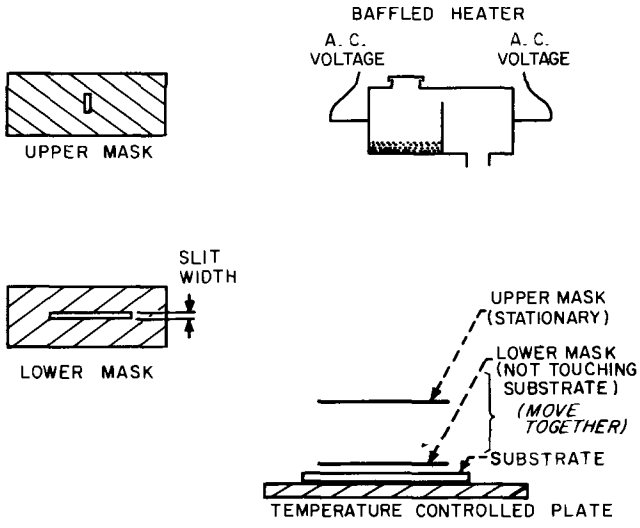

Fig. 3. Detailed drawing of moving mask assembly from Fig. 2 (side view) and diagram of masks usually employed. The slit width labeled on the bottom mask is the dimensional variable referred to in the body of this paper.

of the evaporated line. In other words, we present no information here of how quickly in the deposition process changes occur in the structure of the film but simply what the structure is at the end of the deposition.

The sodium chloride used was from shattered Harshaw single crystals. The substrate was driven by means of a rotating screw powered by a motor outside the vacuum system and equipped with an adjustable gear train. Linear velocities were available in steps from 3.0 cm/min to 3.2×10^{-4} cm/min. The glass slide tested on a metal plate whose temperature could be controlled and measured using an attached thermocouple and associated circuitry. It is the temperature of this metal plate which is referred to herein as the substrate temperature. A conventional vacuum system with an oil diffusion pump was used. The pressure during evaporation was $0.5\text{-}2 \times 10^{-5}$ Torr. The deposition was monitored with a quartz crystal thickness gauge. The rate of deposition was controlled manually. During a run the substrate was moved only after the rate was fixed and stable. Little adjustment was required during a run.

At the conclusion of an experiment the slide was removed, sectioned, and inserted into the electron diffraction apparatus for structure determination by reflection electron diffraction (RED). In some cases the line broadening in these RED patterns was measured to enable estimation of the particle size using the Scherrer equation and the procedure outlined by Bartram (13). It is recognized, of course, that the RED technique samples only the outer surface region of the film and we must specifically assume that the changes in the structure of this outer surface region are symptomatic of similar changes in the bulk of the film.

Results and Discussion

Sodium chloride deposited on glass at room temperature by usual evaporation techniques (*i.e.*, 90° evaporation with no masking) at a rate of 200 Å/min gives a RED pattern indicating no preferred orientation in the plane of the substrate as shown in Fig. 4a. This is in accord with results obtained by Schulz (14) some years ago. The results for substrate temperatures of −100° and +200°C are similar with respect to orientation differing only in the sharpness of the lines.

If now we deposit NaCl films at +200°, 25°, or −100°C using the masking arrangment of Fig. 3 we find that different results can be obtained depending

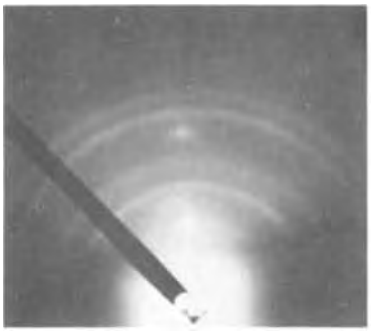

(a) 25°C substrate, no substrate movement.

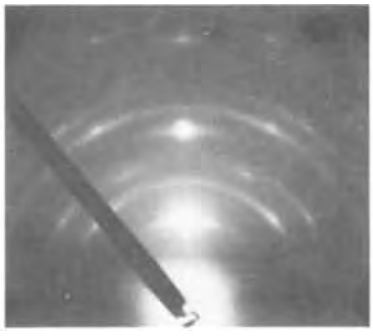

(b) 200°C substrate, 1.5 mm bottom mask slit width, 3 mm/min substrate speed.

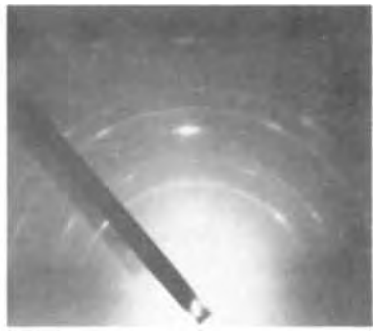

(c) 25°C substrate, 1.5 mm bottom mask slit width, 3 mm/min substrate speed.

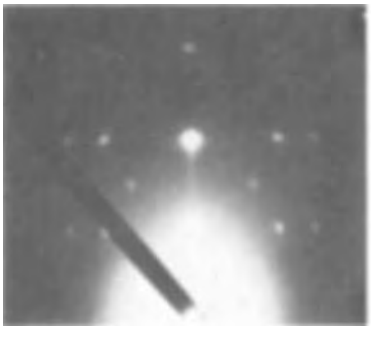

(d) 25°C substrate, 0.05 mm bottom mask slit width, 3 mm/min substrate speed.

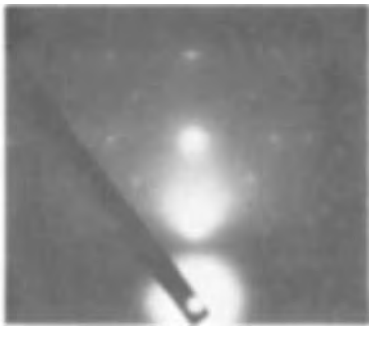

(e) 25°C substrate, bottom mask as shown in Fig. 5, 3 mm/min substrate speed.

Fig. 4. RED patterns obtained from NaCl films prepared in various ways.

on experimental conditions. We shall consider first two variables, substrate temperature and the slit width of the bottom mask, keeping deposition rate (200 Å/min) and substrate velocity (3 mm/min) constant. Inspection of the RED pattern shown in Fig. 4b obtained from a film deposited at 200°C with a bottom mask slit width of 1.5 mm shows that PEG can indeed affect the orientation of the film in the plane of the substrate as judged by the breakdown of some of the RED semicircles in Fig. 4a into arcs. The degree of orientation of the films has been estimated by measuring the angular dispersion of selected reflections. To take a particular example, for the arc going through the point of the 620 reflection one finds angular dispersions of 180°, 20°, and 50° for −100°, 25°, and 200°C, respectively. This maximization of the orientation effect at an intermediate temperature appears to be generally true but is not always as dramatic as the chosen example. Comparison of Fig. 4b and 4c illustrates the effects obtained. Changes are also noted in the particle size as determined from the line broadening. In general, for a given substrate temperature the particle size is increased when the PEG procedure is used with the maximum enhancement achieved at the intermediate temperature, 25°C. For example, for a substrate velocity of 3 mm/min the particle size is *ca.* 40Å at −100°C, *ca.* 60Å at +200°C, and *ca.* 100Å (our upper limit of particle size determination by line broadening using 40 keV electrons) at 25°C. If the PEG procedure were not used the particle sizes would be 25Å or less depending on temperature.

The effect of the slit width of the bottom mask on film structure has been studied at −100°, 25°, and 200°C. In general the RED patterns indicate that orientation in the plane of the substrate is enhanced with decreasing slit width down to slit widths of 0.05 mm at least. At 0.05 mm slit width and a 25°C substrate temperature arcing of the higher order reflections has essentially been replaced by a spot pattern and the arcing of the low index planes is of very low intensity compared with the spot pattern as shown in Fig. 4d. Comparison of Fig. 4c and 4d shows the substantial increase in orientation resulting from decreasing the slit width from 1.5 to 0.05 mm.

In another group of experiments we have investigated the effect of substrate speed. Here temperature was fixed at 25°C, the deposition rate at 200 Å/min, and the slit width of the bottom mask at 1.5 mm. At a speed of 0.48 mm/min or less the film has a random structure in the plane of the substrate yielding RED patterns similar to Fig. 4a. At 3 mm/min an arced pattern is obtained as shown in Fig. 4c. At 30 mm/min some further enhancement of the orientation is obtained. Since the possibility exists that we were seeing here a film thickness effect rather than an effect due to the speed of mask movement, the dimensions of the upper mask opening were changed to increase the film thickness and likewise the substrate was stopped during deposition to allow film build-up on the area to be analyzed. From these experiments it was shown that the film thickness was not the important variable but rather the speed of the substrate during deposition. Schulz also (14) found the structure of NaCl films on glass to be independent of thickness in this thickness range (up to 2000Å) in his non-PEG experiments.

Finally, some experiments were done using a bottom mask as shown in Fig. 5. These differ from Braunstein's (Fig. 1) in that our bottom mask does not touch the substrate and we also have a long narrow section. The specific dimensions are given in the legend of Fig. 5. With NaCl, at least, this added narrow section is significant since without it no preferred orientation is obtained in a PEG experiment. Using the mask of Fig. 5, depositing NaCl onto fused silica at 25°C with a substrate velocity of 3 mm/min a spot pattern as shown in Fig. 4e is obtained which appears to be a mixture of only [020] and [011] oriented crystallites.

In order to correlate these experimental observations we have developed a simple qualitative picture of what processes are operating to give these results. We assume that at the advancing edge of the film

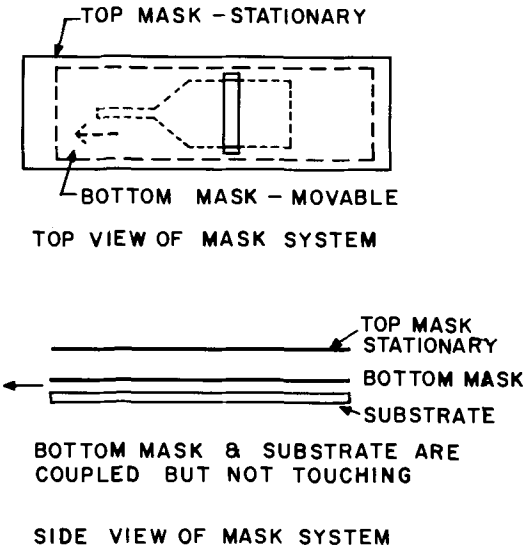

Fig. 5. Top view and side view of mask system used to allow flaring out of deposited film. The narrow neck is 1 mm wide x 10 mm long. The slot flares out at 45° to a final 12.5 mm wide slot.

there are adsorbed single molecules or groups of molecules (*e.g.*, dimers) which do not immediately attach firmly to the substrate but have mobility in the plane of the surface. Those which move away from the advancing film edge have the opportunity to merge with other wandering adgroups, to become firmly attached to the substrate and, to act as nuclei for crystal growth. The slower the advancing film proceeds the greater the opportunity to form randomly oriented nuclei. For a given rate of deposition there should also be mask speeds which would be so great that there would not be a leading edge as such but rather a collection of nucleating sites which would lead to polycrystallinity. This has not been observed as yet. With respect to the effects of temperature on structure noted previously and exemplified on Fig. 4b and 4c we would say that at −100°C there is very little mobility of the admolecules or possibility of reorientation. Therefore, a minimal effect on film structure occurs. Contrariwise, at 200°C we would say that the adgroup mobility is so great that nuclei can be formed in front of the leading edge. An intermediate temperature can be expected to be optimal.

None of this explains the mask width effects noted and we have no satisfying picture of what is happening here. For the moment we shall assume that we are observing a tyranny of large numbers. Certainly the crystallite size is quite small initially and by cutting the width from 1.5 to 0.1 mm we are reducing the number of crystallites competing for growth by a factor of 15 which may be significant.

The remarks of the preceding two paragraphs are admittedly vague and qualitative. This is, however, inevitable when such items as the molecular species being evaporated from this nonequilibrium source, the adgroup mobilities, and the critical size of a nucleus are unknown.

Finally, we would like to remark as to whether these results are in opposition to the general ideas of epitaxy wherein one expects to match substrate symmetry and bond lengths to the symmetry and bond lengths of the film. In our opinion these results do not contradict epitaxial theory. If one can assume that a glass surface is an approximation to an equipotential surface, then the only way that the glass surface can direct the adsorbed NaCl molecule is in a direction perpendicular to the surface. Therefore, by properly manipulating the experiment, we are allowing the sodium chloride to epitax on itself at the leading edge of the film.

Summary

1. Moving mask deposition can considerably affect the structure of evaporated NaCl films on fused silica giving larger grain sizes and enhanced orientation in the plane of the substrate.

2. The dimensions of the mask slit, the substrate temperature, and the speed of the moving mask are important variables. The smaller the width of the slit in the mask the greater the ordering. An intermediate temperature (*ca.* 25°C) gives the largest particle size enhancement and the greatest ordering. The speed of the moving mask must be above a minimum value to achieve these effects.

3. Having once formed an ordered film of small width one can expand the slit width and preserve the orientation.

Manuscript submitted Oct. 4, 1971; revised manuscript received Aug. 9, 1972. This was Paper 18 presented at the Washington, D.C., Meeting of the Society, May 9-13, 1971.

Any discussion of this paper will appear in a Discussion Section to be published in the December 1973 JOURNAL.

REFERENCES

1. W. B. Nowak, *J. Vacuum Sci. Technol.*, **2**, 276 (1965).
2. See *e.g.*, G. I. Distler and Shenyavskaya, *Nature*, **221**, 52 (1969).
3. K. L. Chopra, *Surface Sci.*, **20**, 201 (1970).
4. R. Kikuchi, M. Braunstein, and A. F. Kaspaul, Tech. Report AFML-TR-66-326 (Oct. 1966).
5. R. Kikuchi and M. Braunstein, Tech. Report AFML-TR-67-410 (Dec. 1967).
6. R. S. Wagner and W. C. Ellis, *Appl. Phys. Letters*, **4**, 89 (1964).
7. S. Nielsen, *This Journal*, **112**, 966 (1965).
8. J. D. Filby and S. Nielsen, *ibid.*, **112**, 957 (1965).
9. M. Braunstein, R. R. Henderson, and A. I. Braunstein, *Appl. Phys. Letters*, **12**, 66 (1968).
10. A. H. Clark and R. G. Alibozek, *J. Appl. Phys.*, **39**, 2156 (1968).
11. K. L. Chopra, *ibid.*, **37**, 2249 (1966).
12. W. R. Sinclair and C. J. Calbick, *Appl. Phys. Letters*, **10**, 214 (1967).
13. S. F. Bartram, "Handbook of X-rays," p. 17-6 *et seq.*, E. F. Kaelble, Editor, McGraw-Hill Book Co., New York (1967).
14. L. G. Schulz, *J. Chem. Phys.*, **17**, 1153 (1949).

On the Morphology of Zinc Electrodeposition from Alkaline Solutions

J. O'M. Bockris,*,[1] Z. Nagy,*,[2] and D. Drazic[3]

University of Pennsylvania, Electrochemistry Laboratory, Philadelphia, Pennsylvania 19104

ABSTRACT

The morphology of zinc electrodeposition was investigated from alkaline zincate solutions on single grains of known orientation in polycrystalline zinc electrodes under potentiostatic control. The effect of overpotential, solution composition, and substrate orientation were examined. The deposition morphology was observed with a scanning electron microscope. It was found possible to disrupt the deposition repeatedly for microscopic observation, and then continue deposition. At low overpotential (50 mV) epitaxial layer type growth was observed; the width of the macrosteps increased linearly with time. A theory explaining the linear step widening is proposed, which can also account for the observed effect of substrate orientation. At 100 mV, "boulders" were observed, not all of which were epitaxial with the substrate. They are suggested to be originated by nucleation. The boulder density per cm^2 is first sharply increasing, then slowly decreasing with time. A statistical calculation for this is given, based on the model that large boulders consume the smaller ones. With further deposition a small fraction (*ca.* 0.1%) of the boulders develop into dendrites, their number being limited by the available total current. Experiments were carried out to differentiate between overpotential and current control of morphology; overpotential was found to be the critical variable.

Electrodeposition reactions of metals form a special class of electrochemical reactions, since, in addition to the usual electron transfer processes and surface chemical reactions, the crystallization step has also to be taken into account in the treatment of the kinetics. Investigations of these reactions can be divided in two groups. To obtain knowledge concerning processes on the angstrom-level deposition, the change of surface due to formation of new crystals can be avoided with the use of pulse techniques, and the kinetics and mechanism of the reaction (under the surface conditions of the original substrate) can be investigated. On the micron level, on the other hand, it is just the changes of the surface (morphology) which is itself the subject of research. Recent reviews of both areas are available (1, 2).

The early mechanism of Erdey-Gruz and Volmer (3) consisting of repetitive nucleation and the subsequent spread of steps was not found consistent with the experimental facts. It required a minimum overpotential for deposition (not observed), and also failed to predict a Tafel type current-potential relationship. This difficulty was overcome by the application of Frank's theory of growth (4) to electrocrystallization, which introduced the screw dislocation as an inexhaustible, rotating growth step. This development, and the theory of bunching (5, 6) which explains the formation of macrosteps from atomic steps, were successful in explaining most of the observed epitaxial growth features such as layers, ridges, pyramids, spirals, truncated pyramids, and blocks (7-11). The macrosteps are usually bounded by low energy, high atomic density (low index) planes (12, 13). In spite of the general (but qualitative) success of the dislocation theory, other sources of growth steps should not be neglected. It has been shown (10) that microsteps caused by misorientation of the actual surface from perfect low-index crystal planes can be a major source of growth lines; and the nucleation mechanism has recently been shown to apply to dislocation free surfaces (14, 15), and is also expected to play a part in deposition at high overpotentials (16-17).

Nonepitaxial growth and development of preferred orientation (texture) is much less clearly understood. The two prevailing theories are the nucleation theory [*e.g.*, Ref. (18)] explaining texture by the appearance of nuclei having the smallest energy of formation, and the electrochemical theory (19) based on the different electrochemical growth rate and different electrosorption characteristics of the different crystal planes.

A number of investigations have been made on the morphology of zinc deposition from acidic zinc sulfate solutions. A detailed treatment of deposition habits on single crystals has been reported (20) and the texture of polycrystalline deposits has been examined (21-23). Deposition from alkaline solutions has been studied mainly with respect to dendritic growth (24-33) and only limited observations were made of nondendritic type deposits (24, 25, 30, 32), and texture (33). The degree of mechanistic understanding is small.

A better understanding of the zinc deposition morphology from alkaline solutions is desirable not only because of its relevance to fundamental electrochemistry but also because of the importance of the alkaline zinc/zinc oxide electrodes in high energy density storage batteries. Thus, zinc-air cells (34) are among the most promising electrochemical energy storers for electrical transportation but their development is hindered by a lack of understanding of the electrode processes involved. An angstrom level kinetics and mechanism study was recently reported (35). In the present work the morphological aspects of deposition are discussed.

Experimental

Electrodeposition was carried out onto large-grained zinc electrodes (with known crystallographic orientation of some selected grains) from alkaline zincate solutions, under potentiostatic control. The morphology of the deposit was investigated *in situ* with Nomarski optical microscopy, and after deposition by scanning electron microscopy.

Electrode preparation.—The electrodes were machined from 99.999% pure zinc, into 3 mm diam rods.

* Electrochemical Society Active Member.
[1] Present address: Flinders University, Adelaide, Australia.
[2] Present address: Diamond Shamrock Chemical Company, Painesville, Ohio 44077.
[3] Present address: Faculty of Technology, University of Belgrade, Belgrade, Yugoslavia.

Key words: morphology, zinc, alkaline zincate solutions, layer growth, boulder, dendrites, substrate orientation effect, scanning electron microscopy.

Large grains were grown, after machining, with the following technique. The working surface of the electrode was mechanically polished (180-320-600 silicon carbide papers, followed by 1μ alumina on cloth). The electrode was heat-treated at 330°C for 20 hr under purified nitrogen atmosphere to allow recrystallization and grain-growth to proceed (36), followed by slow (8 hr) cooling. The electrode was finally electropolished in a solution containing 50 volume per cent (v/o) conc. orthophosphoric acid and 50 v/o ethylalcohol (37, 38). The electrode was held in a Teflon holder exposing only the surface to be polished and was positioned horizontally below a flat platinum counterelectrode. The potential was kept below that of gas evolution, which would hinder the polishing process. The polishing was occasionally interrupted and the surface examined for smoothness with a metallurgical microscope equipped with Nomarski interferometry attachment. Polishing times between 2 and 4 hr were usually sufficient to produce a smooth surface.

The grain structure of the electrode surface could be observed with the microscope in polarized light (39); an example is shown in Fig. 1. A large grain was selected on each electrode and its crystallographic orientation was determined by x-ray (Laue back reflection) method (the other areas of the surface were masked by lead foil). All experimental observations were carried out on these selected grains only. The orientation of the selected grain on each electrode used in this study is shown in stereographic projection in Fig. 2.

After this preparation the electrodes were stored in a desiccator. Just before electrodeposition the surface of the electrode was given a final treatment; it was a cathodic reduction, in the cell itself, in zincate free solution (cf. below). This treatment was previously found necessary to produce an oxide film-free surface, on which acceptably reproducible kinetic data could be obtained (35). The surface was characterized by chronopotentiometry (35). Each of the electrodes was used in more than one experiment; between the experiments the electrodes were always electropolished, and before each experiment the surface was reduced.

Solution preparation.—High purity potassium hydroxide-zincate solutions were used which were prepared via potassium and zinc amalgams. The details of the process are given elsewhere (35). Most of the experiments were carried out with solutions containing 2M KOH and 0.1M zincate, in some cases a zincate concentration of 0.02M was used. For the cathodic reduction of the electrodes a similarly prepared 0.1M KOH solution was used.

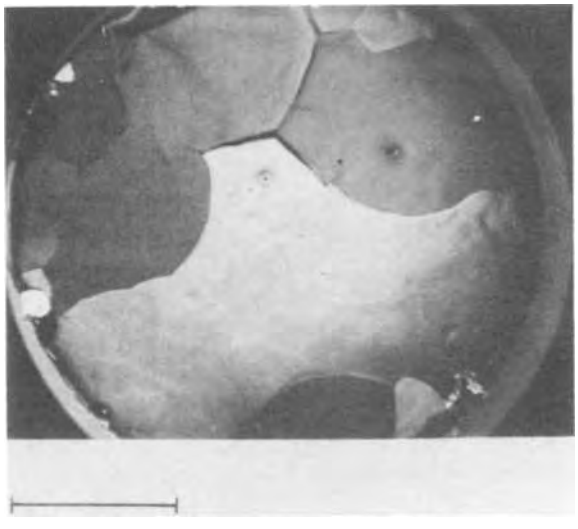

Fig. 1. Electrode No. 2 viewed in polarized light. The mask represents 1 mm.

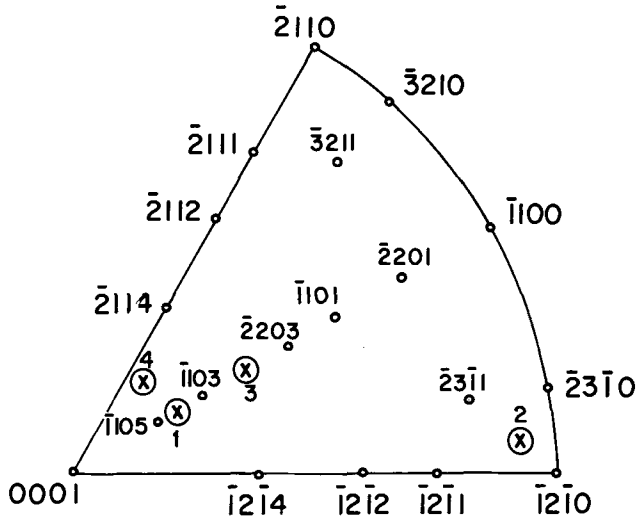

Fig. 2. Crystallographic orientation of selected grains on the electrodes, shown in stereographic projection.

The cell.—A cell was designed to allow *in situ* microscopic observation with short working distance (0.4 mm) objectives. The basic concept of the cell has been reported before (40), and a detailed description of the design is given elsewhere (41). A zinc sheet (7.5×10^{-3} cm thick) was used as a counterelectrode, it was positioned 22.5×10^{-3} cm above the working electrode. The reference electrode was a 1 mm diam zinc wire immersed in the test solution (the purity of all zinc used was at least five 9's). For the cathodic reduction treatment of the electrode an auxiliary platinum counterelectrode was used, placed in the cell outlet.

Deposition techniques.—General procedure.—The cell was assembled on the microscope stage (placing the observation hole of the counterelectrode over the grain to be examined) and was blown free of air by a stream of purified nitrogen. The 0.1M KOH solution was introduced under nitrogen pressure and the working electrode was galvanostatically reduced at a current density of 50 mA/cm^2 for 8 min. The cell was drained under nitrogen atmosphere, then flushed and filled with the test solution. Deposition was carried out potentiostatically (Wenking 61 TR) while the current was continuously recorded on a stripchart recorder. The overpotential was controlled at 50, or 100 mV, and in one experiment at 200 mV. All deposition was carried out at room temperature, from unstirred solutions. After the desired amount of charge was passed (in the range of 0.3-40 C/cm^2) the cell was flushed with distilled water and blown dry with nitrogen. The cell was disassembled and the electrode transferred to a nitrogen-filled desiccator where it was kept until the electron microscopic investigation.

Interrupted deposition.—In a number of tests the deposition was repeatedly interrupted for electron microscopic investigation, and then continued. The same procedure as given above was repeated in each case, including the reduction of the electrode before deposition. Between operations, the electrode was kept and transported in a nitrogen filled desiccator.

Deposition-dissolution-deposition series.—In some cases of the interrupted tests, an anodic dissolution of the deposit was substituted for a cathodic deposition step. The dissolution was carried out galvanostatically, at a current density below that of passivation. In the present test solutions 1.3 mA/cm^2 was found satisfactory.

Observation methods.—Optical in situ observation.—This method of observation of the deposition was carried out using a metallurgical microscope (Zetopan-M,

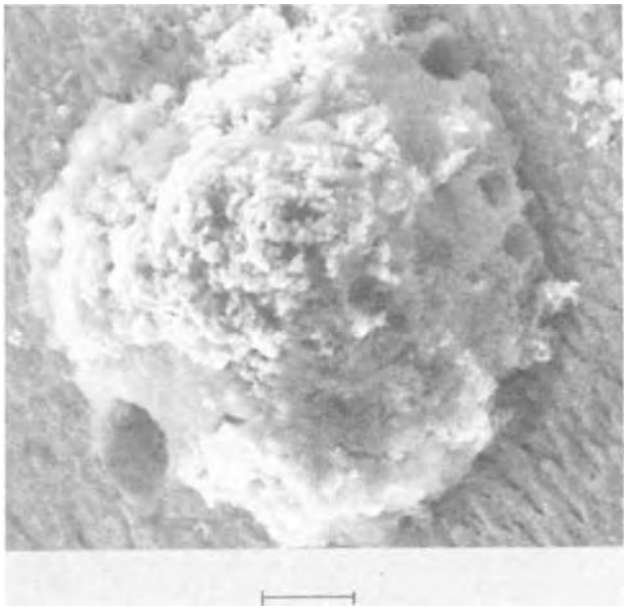

Fig. 3. SEM picture of deposition at 10 mV overpotential. The mark represents 5μ.

Reichart, Austria), equipped with Nomarski interferometry and contrast attachments (42, 43). Periodically pictures were taken of the surface with a Polaroid camera equipped with an electromagnetic shutter and automatic exposure control (Watson, England). The current efficiency of hydrogen evolution is very low in this system (35), and it did not interfere with optical observations.

Electron microscopy.—After the deposition, the electrode surface was investigated with a scanning electron microscope (JSM-U3, JEOLCO, Japan). Pictures were taken at two orientations of the electrode: (*i*) The electrode rod was aligned lengthwise with the optical axis of the electron microscope, or (*ii*) the "c" axis of the grain under investigation was aligned with the optical axis of the electron microscope. In the latter mode, the features of the deposit are expected to appear parallel with each other and be in hexagonal symmetry (120° angles) if the deposit is epitaxial with the substrate; in this case, the orientation of the features could also be determined. Occasionally, stereopair pictures were taken. The electron beam intensity was kept at the minimum value which still allowed good quality observation, to avoid contamination of the surface in the microscope.

Results

General description of the morphology of the deposits.—Detailed tests were carried out at 50, and 100 mV overpotentials, with an additional test at 200 mV; the general morphology of the deposits was different in each case. At 50 mV layers or ridges were found, while at 100 mV the deposit could be best described as consisting of "boulders." At 200 mV, dendritic growth was observed. (During some preliminary experiments mossy growth (27) was observed at 10 mV overpotential, as shown in Fig. 3.) The optical microscopy [with Nomarski interferometry and contrast attachments (42, 43)] did not prove fully successful in this investigation, for the following reasons. The large number of growth features ($\approx 10^7/cm^2$) caused the interferometric patterns to overlap, and the technique was not usable. The interference contrast technique allowed the continuous observation of the deposition *in situ*, but because the scale of the deposit features was close to 1μ, bordering the resolution and depth of focus of the optical system, only an over-all impression of the type of deposition could be obtained but details were not resolvable. The data presented in the following sections are based on electron microscopic observations.

Deposits at 50 mV overpotential from 0.1M zincate solution.—The deposition was of layer (or ridge) type on all electrodes, as shown in Fig. 4. Occasionally

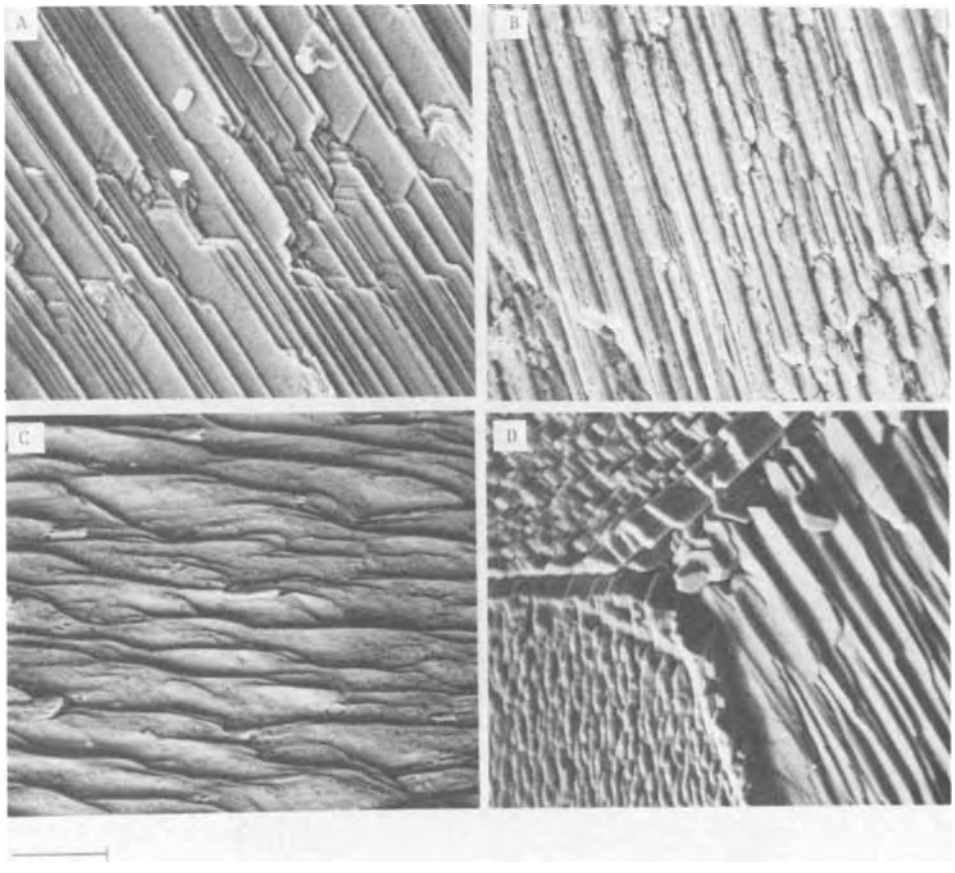

Fig. 4. SEM pictures of deposition at 50 mV. The mark represents 20μ. A, Electrode No. 1, 16.5 C/cm^2; B, electrode No. 3, 11.5 C/cm^2; C, electrode No. 4, 14 C/cm^2; D, electrode No. 1, 20 C/cm^2.

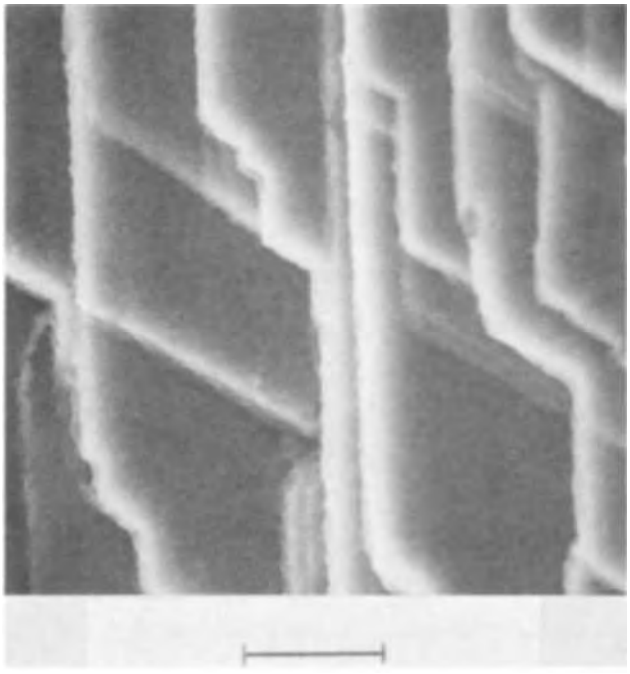

Fig. 5. SEM picture of deposition at 50 mV. The "c" axis of substrate is aligned with the optical axis of microscope. The mark represents 4μ. Electrode No. 1, 16.5 C/cm^2.

boulders appeared on layers, some can be seen on Fig. 4a. At the grain boundaries, a smooth transition existed between the differently oriented layer structures (Fig. 4d). On photographs taken with the "c" axis of the grain aligned with the optical axis of the microscope (Fig. 5) the deposits always appeared as layer type, and were epitaxial with the substrate. The most prominent plane appearing was the (0001), bounded in each case by side surfaces of planes belonging to the $[\bar{1}\bar{1}20]$ zones. If the edges are perpendicular to the layers (*e.g.*, Fig. 6a,b) the bounding planes will be $[\bar{1}100]$. A drawing of the deposition, indicating the orientations, is shown in Fig. 7. Occasionally, the edges were more complex, as shown in Fig. 6c,d, and the orientations could not be determined from the present data; they were presumed to be low order pyramidal faces.

From interrupted deposition studies, a relation between the average layer width and the thickness of the deposit (expressed as C/cm^2) was found, and is shown in Fig. 8.

Deposits at 100 mV overpotential from 0.1M zincate solution.—At this overpotential, the deposit consisted of boulders. The first boulders were observed with the optical microscope after 10-15 sec of deposition, and they appeared in increasing numbers until the surface was completely covered, then their number decreased. The size of the boulders continually increased during the course of the deposition. A typical photograph series is shown in Fig. 9. They first appear to have the shape of a sphere, then turn into irregularly shaped boulders, and finally develop well-oriented crystalline faces during the deposition. At this latter stage, many of them have stepped sides (Fig. 10) and seem to consist of layers. Before they completely cover the surface of the electrode, occasionally a layer-type growth is visible beneath the boulders (Fig. 11, 15a). There is a tendency for the boulders to segregate at grain boundaries of the original substrate (Fig. 15). Photographs, taken with the "c" axis of the crystal aligned with the optical axis of the microscope (Fig. 12), reveal that not all of the boulders are epitaxial with the substrate (note the small misalignment of sides in the circles). The majority of them is epitaxial. These are comprised of layers, parallel to the (0001)

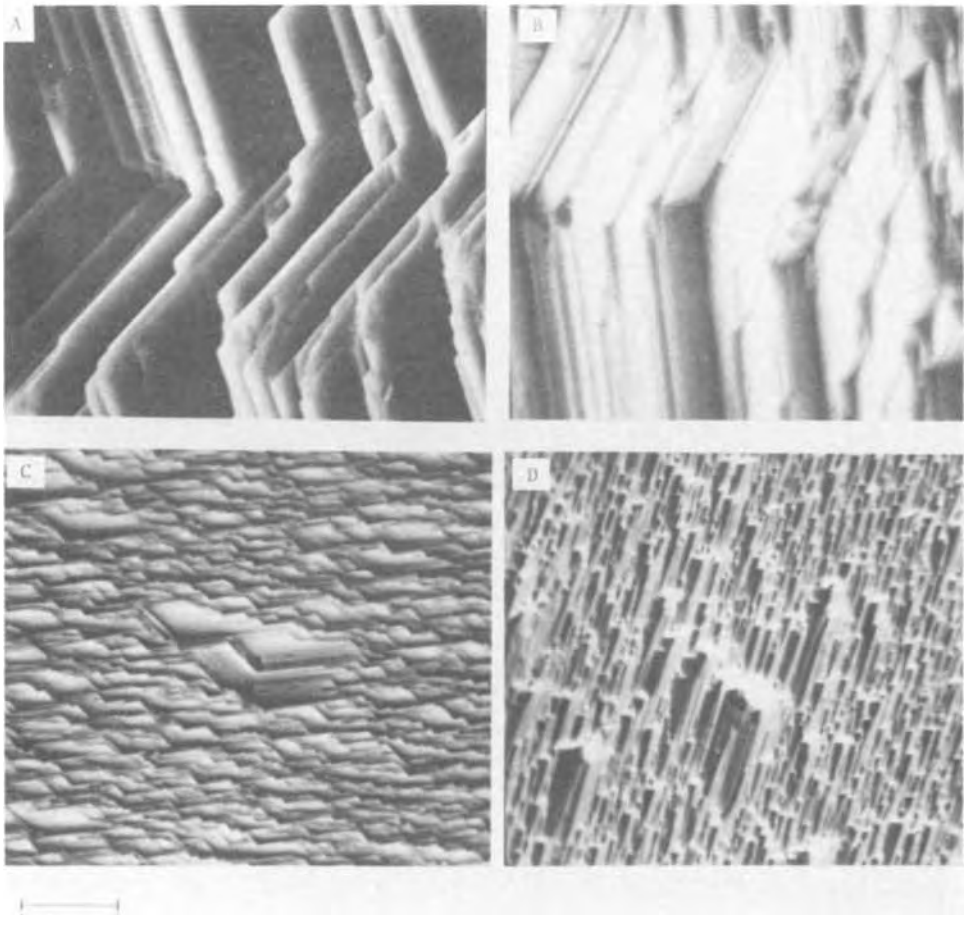

Fig. 6. Effect of observation angle. Electrode No. 4. 50 mV. Mark represents 4μ for A,B, and 10μ for C,D. A,B, (14 C/cm^2); tilt: 32°; B rotated 180° compared to A. C,D, (2.5 C/cm^2); tilt: 36°; C rotated 114° compared to D.

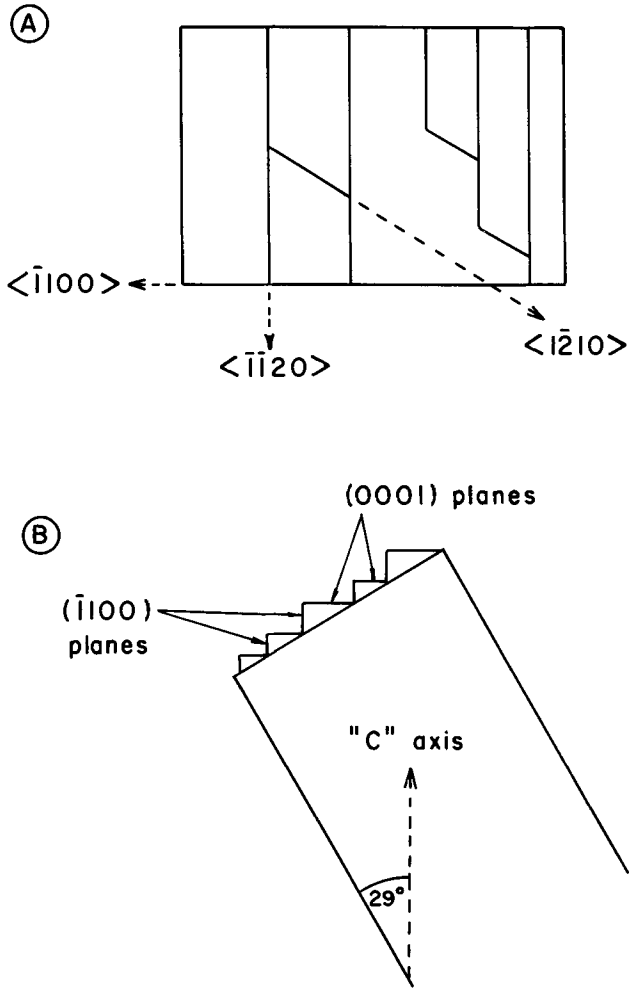

Fig. 7. Schematic representation of deposition shown on Fig. 5. A, Direction of lines; B, cross-sectional view.

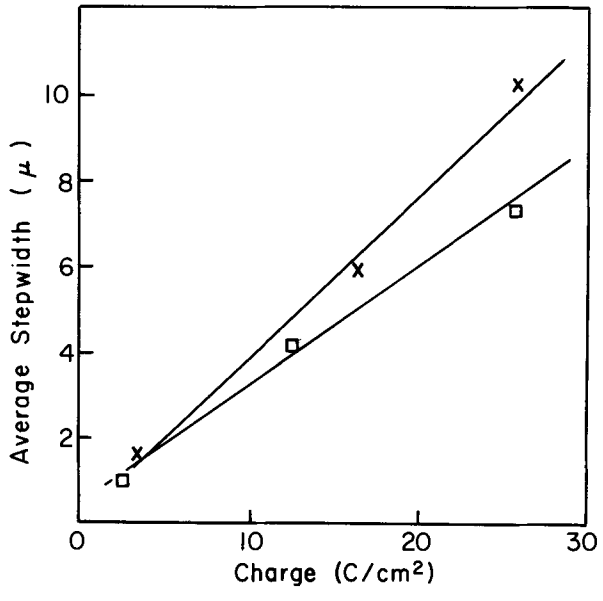

Fig. 8. Dependence of average step width on charge. At 6 mA/cm², 1C is equivalent to 167 sec. x, electrode No. 1; □, electrode No. 3.

plane of the substrate, and are bound by side planes containing lines parallel to the <1̄1̄20> directions.

From the test series with interrupted deposition (*e.g.*, Fig. 9), the variation of average boulder density and size were determined as a function of deposition thickness (C/cm²), and are shown in Fig. 13 and 14. From these data, the charge needed for their formation can be estimated (assuming that the boulders are cubes), and compared to the actual charge density used in the deposition (Table I).

Effect of the crystallographic orientation of the substrate on the morphology of the deposit.—The orientation of the substrate had no effect on the qualitative character of the deposit. At 50 mV, layers were observed on all electrodes, and at 100 mV boulders appeared on every electrode. There were quantitative differences in the number and rate of growth of the features of the deposit. These are shown in Fig. 8, 13, and 14.

Redeposition of dissolved deposit.—The results of one such series (see above), with the depositions carried out at 100 mV overpotential, is shown in a photograph series in Fig. 15.

Deposition from 0.02M zincate solutions.—Limited number of tests were carried out, only to determine the type of deposit at each overpotential. Layers were found at 50, boulders at 100, and dendrites at 200 mV (Fig. 16).

Current-time behavior.—The current, at constant overpotential, was continuously recorded during depositions, a typical current trace is shown on Fig. 17. The average current densities, observed at different overpotentials in different solutions, are given in Table II. At the lower zincate concentration the current was under mass transport control, both at 50, and 100 mV overpotentials. At the higher zincate concentration the current was under mixed activation-mass transport control at 50 mV, and under mass transport control at 100 mV.

Discussion

Comparison of optical and electronoptical observation techniques.—Both techniques have been widely used in electrocrystallization studies (44). Transmission electron microscopy offers a better resolution, but at the price of arduous replication technique, which limits the observation to the end result of a deposition; further, the possibility of recrystallization between deposition and observation is always present. Light microscopy, especially coupled with modern interferometric methods (42, 43), has the advantage that it allows a continuous *in situ* observation of the deposition, its resolution is, however, limited to about 1μ horizontally, and to about 0.02μ vertically; for a structure like the stepped boulders (Fig. 10) where the width of the steps is less than 1μ, it is not applicable. The recent development of the scanning electron

Table I. Data of boulder growth

Electrode No.	Charge deposited (C/cm²)	Average boulder size (μ)	Boulder density per cm² (× 10⁻⁶)	Charge represented by (C/cm²)	% Charge represented by boulders
1	0.4	0.75	5.8	0.053	13
	9.4	3.5	9.7	9.09	97
	18.4	4.5	7.6	15.13	82
2	0.4	1.0	1.1	0.024	6
	1.5	1.0	31	0.67	45
	4.0	1.5	42	3.07	77
	8.5	2.0	29	5.03	59
	20.5	4.0	8.7	12.2	60
	40.0	6.0	3.6	17.0	43
3	0.3	0.75	5.0	0.046	16
	2.8	2.0	25	4.37	156
	9.0	3.0	12	6.80	76
	17.0	4.0	8.3	11.60	68

Table II. Representative current densities

Zincate concentration (mol/liter)	Overpotential (mV)	Current density (mA/cm²)
0.02	50	2.6
0.02	100	2.8
0.02	200	2.9
0.1	50	6
0.1	100	14

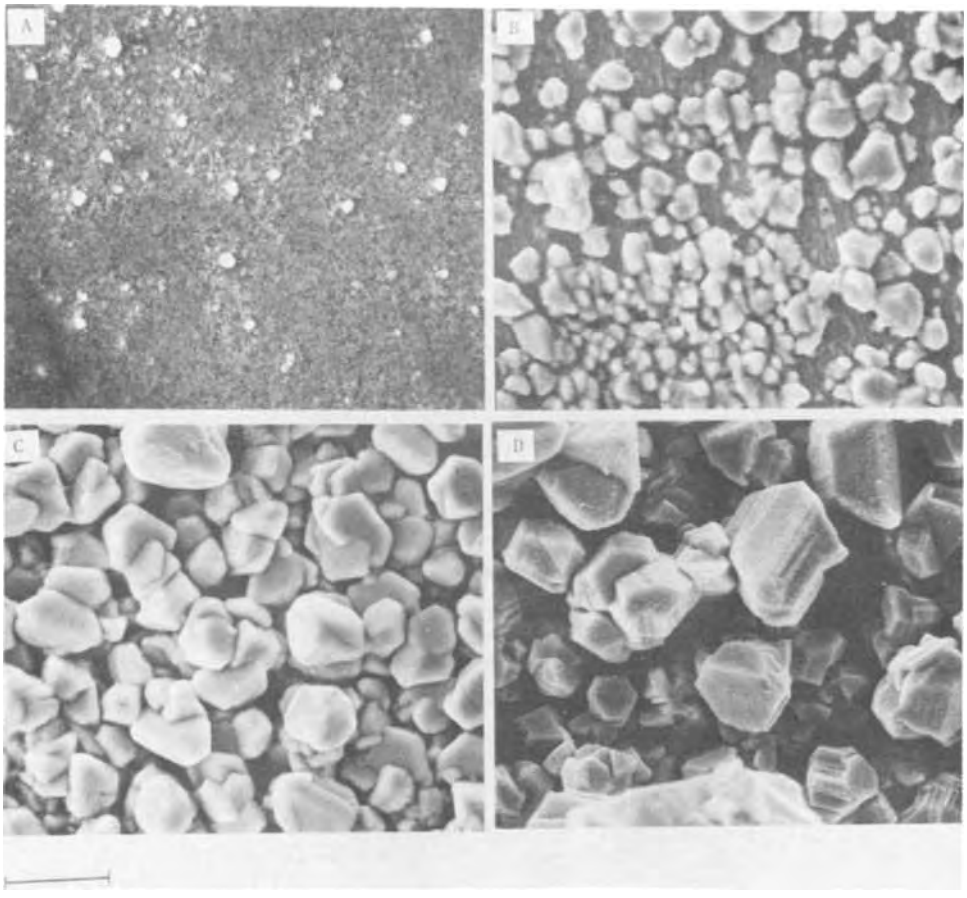

Fig. 9. SEM pictures of deposition at 100 mV as function of charge. Electrode No. 3. The mark represents 5μ. A, 0.3 C/cm^2; B. 2.8 C/cm^2; C, 9 C/cm^2; D, 17 C/cm^2.

microscope allows a compromise between the two methods. A resolution of 0.02μ is possible with direct observation of the surface. Laborious replication is not needed, and since the sample is not destroyed, the deposition can be continued after the microscopic investigation. Therefore, while *in situ* observation is not possible, the deposition can be repeatedly interrupted for observation. A number of questions remains to be answered, however:

(*i*) Does recrystallization take place significantly, after the current had been switched off (especially in the case of high exchange current density processes)?

(*ii*) Does the surface change (*e.g.*, by oxide film formation) in the time between removal from the cell and observation in the microscope?

(*iii*) What is the effect on continued deposition of the interruptions, and electron microscopic investigation?

There can be no generally valid answers to these questions. For the present work the following observations are relevant:

(*i*) At the end of one deposition the light microscope was focused on some clearly visible features at the highest magnification (780×) and the deposit was observed for 15 min after switching off the current. No changes were observed. Since in the actual experiments the cell was drained in less than 30 sec after

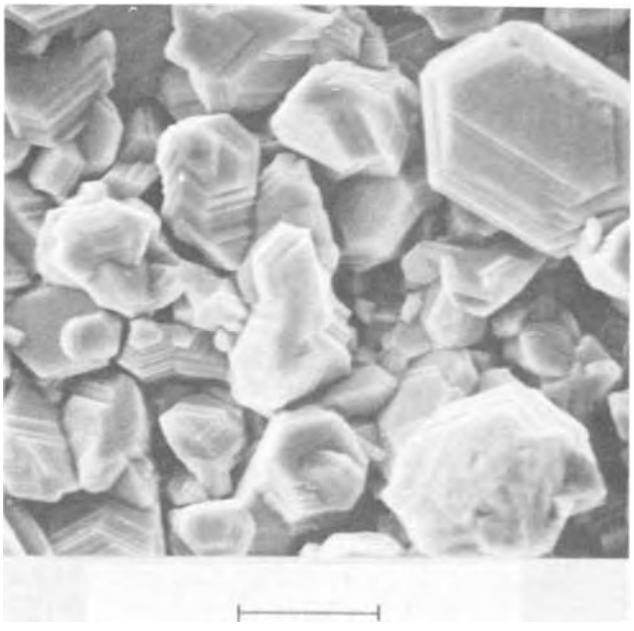

Fig. 10. SEM pictures of deposition at 100 mV. Electrode No. 2. 20.5 C/cm^2. The mark represents 5μ.

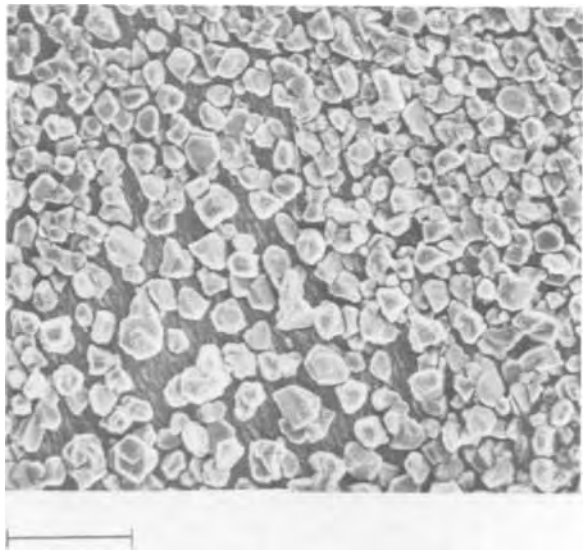

Fig. 11. SEM picture of boulders over layers. Electrode No. 1 100 mV, 9.5 C/cm^2. The mark represents 16μ.

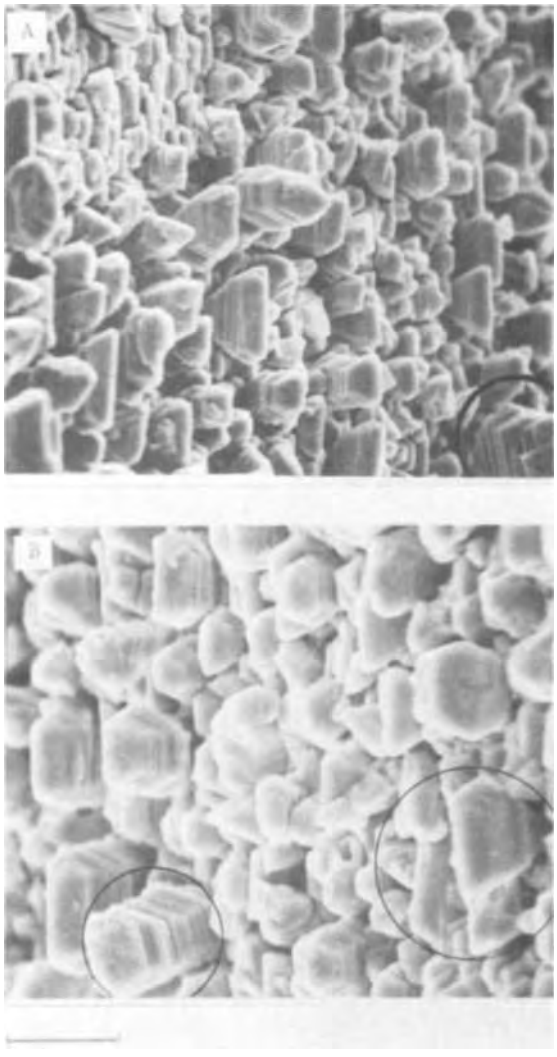

Fig. 12. SEM pictures of deposition at 100 mV. The "c" axis of the substrate is aligned with the optical axis of the microscope. Electrode No. 3. 16 C/cm^2. The mark represents 10μ for A, and 50μ for B.

turning off the potentiostat, recrystallization problems are not expected. The corrosion of the zinc in the test solution is also known to be negligible (35).

(*ii*) The oxidation rate of zinc in dry air at room temperature has been reported (45) as 20×10^{-8} cm/48 hr. Since the electrodes were stored under dry nitrogen, and were exposed to air only for minutes between deposition and microscopic observation, the thin oxide film formed should not affect the observations. This film was then removed before further deposition by cathodic reduction in 0.1M KOH.

(*iii*) Two results obtained here are relevant to the third question. Deposition-dissolution-deposition series (such as shown in Fig. 15) allows the observation of specific boulders as they diminish and grow in size, indicating that they remain active in spite of the interruption and electron microscopic exposure. Furthermore, depositions carried out with numerous interruptions for observation, and ones carried out without any interruption, gave the same morphology at a given coulombs/cm^2 both qualitatively (type of deposition) and quantitatively (number and size of growth features).

Layer growth.—Crystallographic orientation of layers.—Layer growth is a common type of deposit, its appearance is explained by bunching of monoatomic steps into macrosteps (1, 2). This is applicable to the present case.

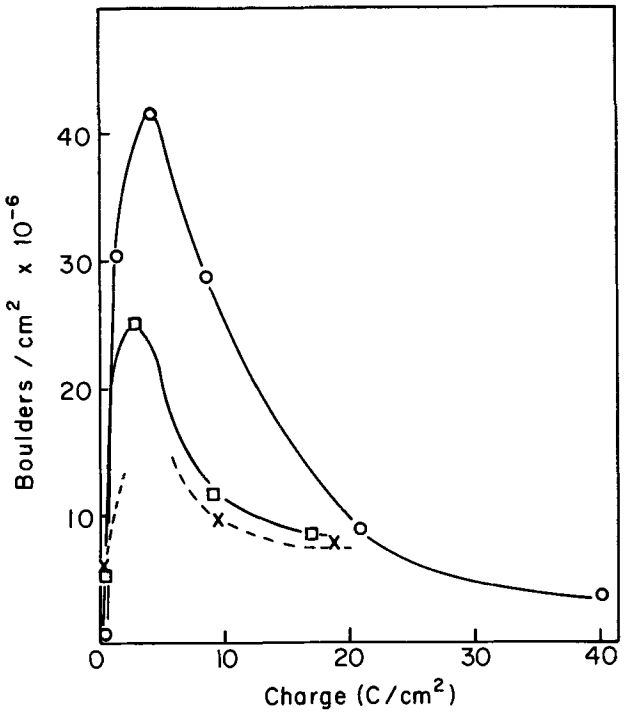

Fig. 13. Boulder density as function of charge. At 14 mA/cm^2, 1C is equivalent to 71 sec. x, electrode No. 1; ○, electrode No. 2; □, electrode No. 3.

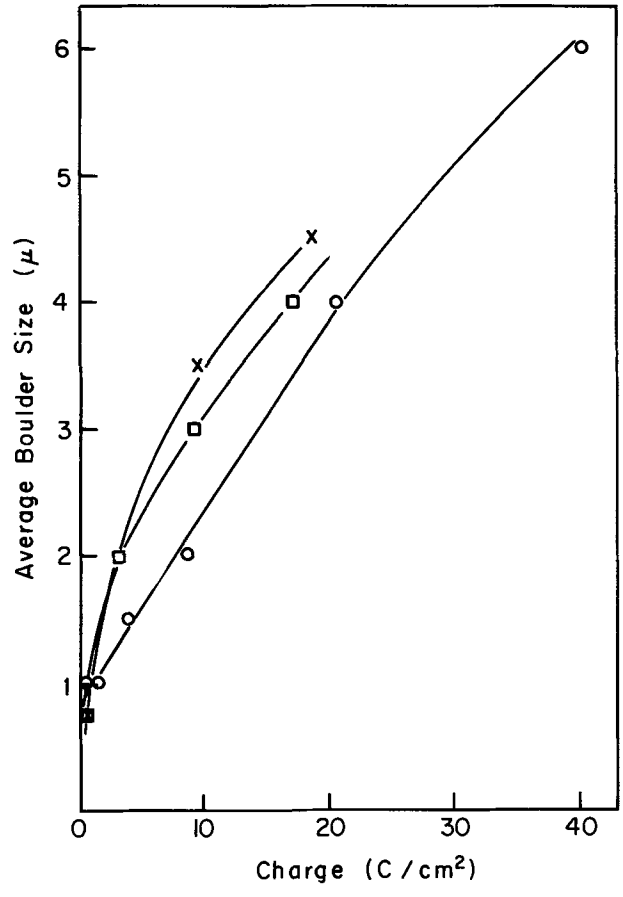

Fig. 14. Average boulder size as function of charge. At 14 mA/cm^2, 1C is equivalent to 71 sec. x. electrode No. 1; ○, electrode No. 2; □, electrode No. 3.

The crystallographic orientation of the layers was the same in all experiments. It should be noted here that the appearance of the layers is similar only when viewed along the <0001> direction, otherwise rather

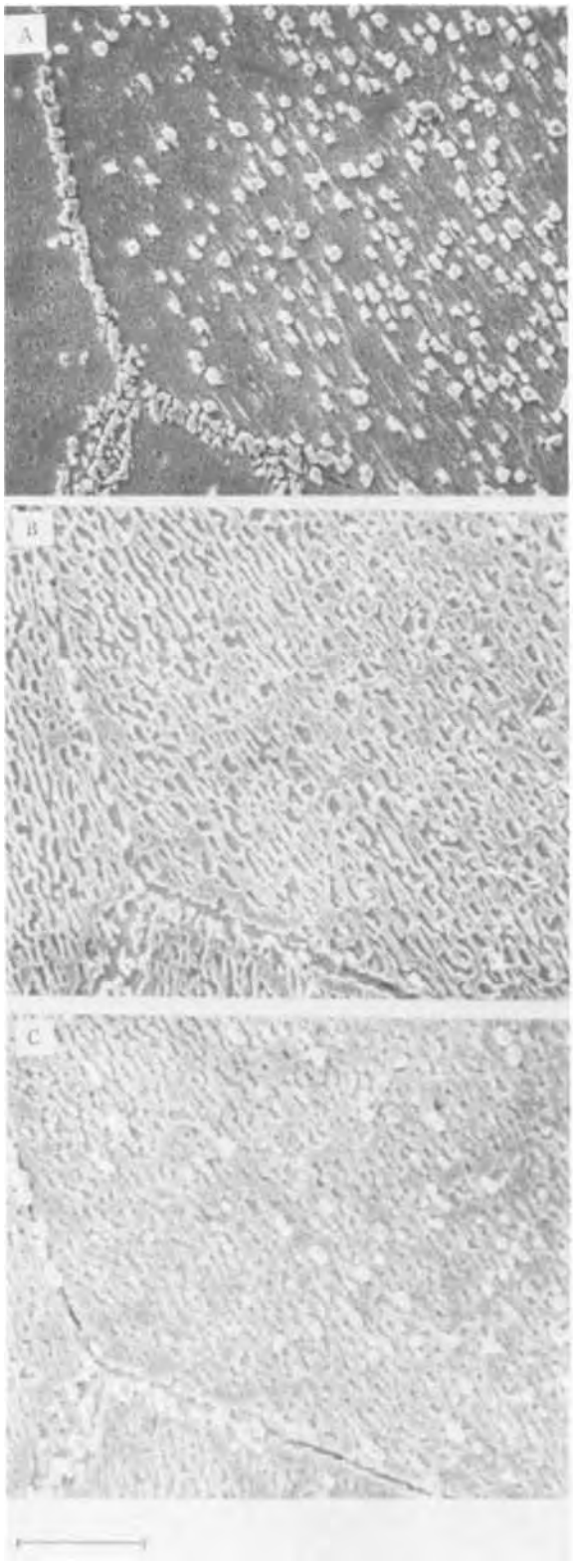

Fig. 15. SEM pictures from a deposition-dissolution-deposition experiment. The mark represents 16μ. A, after deposition of 1.2 C/cm^2; B, after dissolution of 0.3 C/cm^2; C, after further deposition of 1.4 C/cm^2.

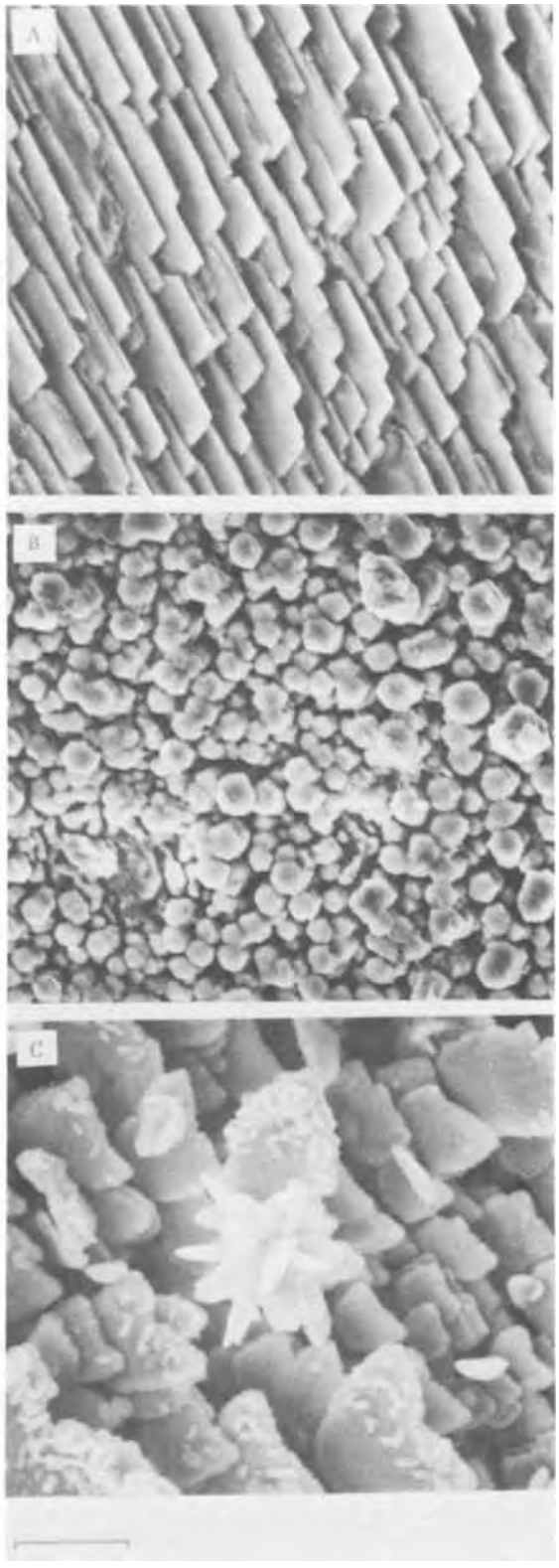

Fig. 16. SEM pictures of depositions from 0.02M zincate solution. Electrode No. 1. The mark represents 10μ. A, 50 mV, 17 C/cm^2; B, 100 mV, 13 C/cm^2; C, 200 mV, 13 C/cm^2.

different ("ridge" or "pencil" type) structures appear as illustrated in the triple grain boundary picture (Fig. 4d). This apparent difference, however, is due to the different orientation of the "c" axis of the grains and the epitaxial deposit with respect to the observation angle. The effect which can be created this way is illustrated in Fig. 6, which shows the same deposits viewed from different angles.

The appearance of the (0001), [$\bar{1}$100], and low order pyramidal planes is expected, based on Bravais's law of crystal growth (13, 46) and Stranski's calculation of equilibrium forms (12). A detailed study of zinc deposition morphology from acidic zinc sulfate solutions (20) has shown similar results. Deposition was carried out on a large number of single crystal faces and the resulting facets were analyzed by optical goniometry: the (0001) plane was the most prominent,

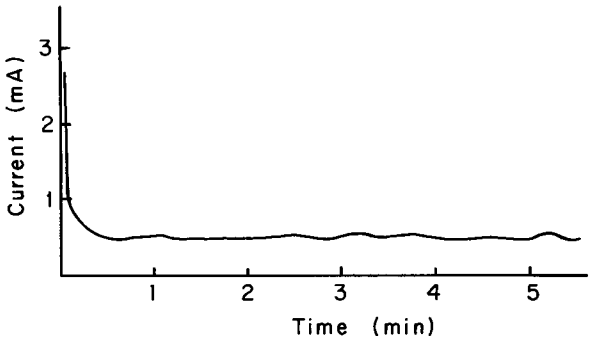

Fig. 17. An example of current-time behavior. Electrode No. 3. 50 mV.

with weaker reflections from the [10$\bar{1}$1] planes, other planes were found only in minor amounts. An analysis revealed that in each case, the most closely packed planes appeared. The appearance of the deposit was described as "layer," "ridge," or "pencil" type, depending on substrate orientation. On this basis, the appearance of hexagonal pyramids would be expected when the substrate is parallel to the basal (0001) plane, and these were indeed observed (24, 30, 32). The appearance of layers has also been reported for depositions from alkaline zincate solutions (24, 25) but their orientation has not been determined.

Mechanism of layer growth.—The sources of steps have been postulated as being dislocations (5). Recently, it has been shown (10) that in the case of copper deposition, on a (100) plane, the source was a slight misorientation of the examined surface from the crystal plane. The results of the present work offer the possibility of differentiating between these sources of steps. A higher index plane can be visualized as being formed of steps bounded by low index planes, and the two electrodes, on which detailed data were obtained on layer growth (Fig. 8), are in such orientation that both surfaces can be represented by steps bounded by (0001) and ($\bar{1}$100) planes only (these are the planes which were found predominant in layer growth), but their tilt with respect of the "c" axis is different. If the sources of steps are the microsteps due to the crystallographic orientation of the substrate, a theory based on this hypothesis should predict the observed differences in step growth (cf., Fig. 8).

The experimental data show a linear increase of step width with time (charge) but the rates are different for the two electrodes. For electrode 1, the rate is 2.2 μ/sec and for 3 it is 1.6 μ/sec. Such a linear widening of steps has been observed before (10), but no theoretical explanation is given in the literature. The following model of step widening is suggested.

Let us assume that at the start of the process the surface is comprised of "n" preliminary steps which are already multiatomic high, 20-30 $\times$ 10^{-8} cm or higher, as shown in Fig. 18. (This assumption will be discussed later.) Metal is being deposited to both surfaces of the steps and they are moving simultaneously outwards and laterally across the surface. Consider first the outward movement only, proceeding with an

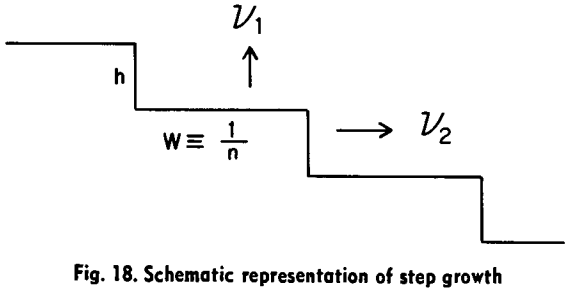

Fig. 18. Schematic representation of step growth

average rate of ν_1 (μ/sec). Step widening will occur if a fraction of the steps ($\rho_1 n$, where $\rho_1 < 1$) will move slower than the average speed ($\delta_1 \nu_1$, where $\delta_1 < 1$).[4] A slow step will be overtaken by a neighboring fast step when

$$\nu_1 t = h + \delta_1 \nu_1 t \qquad [1]$$

or at a time

$$t = \frac{h}{\nu_1(1 - \delta_1)} \qquad [2]$$

It is assumed that at this time the two steps will join and continue to move forwards as one step, thereby eliminating a step. Since there are $\rho_1 n$ such pairs, the rate of decrease of the number of steps can be written as

$$-\left[\frac{dn}{dt}\right]_1 \approx -\left[\frac{\Delta n}{\Delta t}\right]_1 = \frac{\rho_1 n\, \nu_1(1 - \delta_1)}{h} \qquad [3]$$

The total current flowing to the surface will be divided in two parts, one causing the outward, and one causing the lateral growth. Since the exchange current densities of the two growth planes are nearly equal (47) the rate of outward growth, at a total current density of i, can be expressed as

$$\nu_1 = a\, i \frac{w}{h + w} \qquad [4]$$

where a is a constant converting current density to linear growth velocity. Furthermore, the ratio of step width to step height will remain constant during the process, according to the model used[5]

$$\frac{w}{h} = C \qquad [5]$$

Combining [3], [4], and [5] gives the rate of disappearance of steps as

$$-\left[\frac{dn}{dt}\right]_1 = \rho_1(1 - \delta_1)\, a\, i \frac{C}{1/C + 1} n^2 \qquad [6]$$

An exactly analogous treatment can be made for the lateral motion, giving (using index 2 for this case)

$$-\left[\frac{dn}{dt}\right]_2 = \rho_2(1 - \delta_2)\, a\, i \frac{1}{C + 1} n^2 \qquad [7]$$

The total rate of step disappearance is then

$$-\frac{dn}{dt} = -\left\{\left[\frac{dn}{dt}\right]_1 + \left[\frac{dn}{dt}\right]_2\right\} \qquad [8]$$

Combining Eq. [6], [7], and [8] and solving the differential equation gives finally

$$\frac{1}{n} \equiv w = \left[\rho_1(1 - \delta_1)\, a\, i \frac{C}{1/C + 1} + \rho_2(1 - \delta_2)\, a\, i \frac{1}{C + 1}\right] t + w_o \qquad [9]$$

This is the sought relation between step width and time; in agreement with experimental data, the relation is linear. In order to compare the slopes of the lines, a further assumption has to be made. It is assumed that the nature of the processes taking place on the (0001) and ($\bar{1}$100) are similar (they are the first and third most closely packed planes) and therefore $\rho_1 \approx \rho_2$, and $\delta_1 \approx \delta_2$. Equation [9] can then be simplified

$$w = \{\rho(1 - \delta)\, a\, i\} \frac{C(C + 1) + (1/C + 1)}{(1/C + 1)(C + 1)} t + w_o \qquad [10]$$

In the expression for the slope, the parameters in the brackets are the same for electrodes 1 and 3, since

[4] A distribution of propagation rates could result, *e.g.*, from statistical fluctuation of impurity adsorption.

[5] The constancy of this ratio was experimentally observed for copper (10).

the growth faces are (0001) and ($\bar{1}$100) in each case, and the experiments were conducted under identical conditions. The difference in slopes therefore can arise only from the difference in the value of C. This can be obtained with the following argument. The primary steps are produced by the bunching of the monoatomic microsteps originally present on the surface. If one assumes that the microsteps are present due to the crystallographic orientation of the substrate (and not due to dislocations) the value of C is obtained as the cotangent of the angle of inclination of the surface to the "c" axis of the substrate (cf. Fig. 7). This angle is 29° for electrode 1, and 47° for electrode 3. Therefore, the theoretical ratio of the slopes of the lines of Fig. 8 can be calculated as 1.56 (ratio of electrode 1 to electrode 3). The experimental value is 1.35. The agreement is satisfactory, confirming the hypothesis that the origin of the microsteps is indeed the crystallographic orientation, rather than pairs of dislocations. That is, they are present on the surface because, as a high index plane, it consists of monoatomic steps of low index planes [cf. Ref. (1), Fig. 26].

The mechanism of the formation of the "primary" steps from the microsteps has not yet been treated. The kinematic theory is not applicable in the present case. Because of the high angle of inclination of the surface to the "c" axis, the width of the microsteps is only about 1-2 atomic length; the surface can be described rather as an atomically rough surface and not as one containing smooth terraces, as would be needed for the application of the kinematic theory. It is easy to show, however, that the bunching of the microsteps will be energetically favored. The edge energy per atom is always larger than the surface energy, and therefore, the coalescing of microsteps will decrease the total energy of the surface by decreasing the number of edges. It is possible that this occurs during the time the cell is filled with test solution, before the potentiostat is turned on, due to the high exchange current density of the electrode reaction (35).

Boulder growth.—Origin of boulders.—At the higher overpotential (100 mV), the main crystallographic feature of deposition is boulder growth [see also Ref. (25)]. Under the same conditions, dendrites were reported earlier (28, 29), but were observed only after a considerable "initiation time." The present work refers to surfaces formed at times shorter than the initiation time of the dendrites, and therefore dendrite growth was avoided (though occasionally some were observed).[6]

At low coulomb/cm^2 values, a duplex-type deposition was observed: a layer growth, similar to that observed at 50 mV, was partially covered by boulders (Fig. 11, 15a), with most of the deposited material going initially into layers and only about 10% contributing to boulder growth (Table I). At a later time (*ca.* 3 C/cm^2) the boulder growth takes completely over (Fig. 9, and Table I). The appearance of layers can be explained as in the above section. The boulders may be initiated by growth at screw dislocations, or by nucleation. Their appearance from either source could be expected because of the higher overpotentials (as compared with overpotentials associated with layer growth). With increased overpotential, the distance between the turns of a spiral decreases which leads to localized growth as compared to the wide overlapping spirals at low overpotentials, which leads to a uniform growth (1). At the high overpotentials the edge-energy will also be overcome and nucleation becomes a feasible process (1, 16-17). A numerical estimation of the minimum overpotential of nucleation can be made. Such a calculation was carried out earlier for silver (48). Since some of the parameters (equilibrium adion concentration, surface diffusivity of adions) needed for the calculation are not known for zinc, the results reported for silver will be used as a first approximation. It was shown that nucleation becomes possible at an overpotential of little above 100 mV at a step width of 7×10^{-5} cm [cf. Ref. (48), Fig. 8]. In the present experiments, the first boulders were observed after the passage of 0.1-0.2 C/cm^2. If one assumes tthat the step-width relations of Fig. 8 are applicable to 100 mV, and at such low charge, it can be estimated that boulders appeared on steps of 5×10^{-5} cm width, in reasonable agreement with the above theoretical prediction, indicating that nucleation is a possible explanation of boulder growth.

A distinction between the two mechanisms of boulder growth can be obtained from the crystallographic orientation of the boulders relative to the substrate. If growth originates from screw dislocations complete epitaxy is expected, while some deviation from epitaxy can arise if the boulders are nucleated. The preferred orientation of the nucleated boulders will be that of the substrate, since the epitaxial nucleation energy is less than that of the nonepitaxial, but the appearance of some nonepitaxial nuclei can occur. If, therefore, some of the boulders are found, upon determination of their orientation, to be nonepitaxial, this would show that nucleation mechanism was operative. This indeed was the case. The crystallographic orientation of the boulders can be determined from the present data after *ca.* 15 C/cm^2 charge has passed and well developed faces appear. A preferred orientation, epitaxial with the substrate, can be observed with numerous exceptions (Fig. 12). Note the misorientation of the edges of the boulders in the circles on Fig. 12, as compared to the other (epitaxial) boulders.

Nucleation can occur randomly on the surface or at specific sites (*e.g.*, impurities, dislocations). In the deposition-dissolution-deposition experiments (see above) it was attempted to dissolve and renucleate the boulders to differentiate between random and specific sites. No conclusive results were obtained. The preferred nucleation at grain boundaries (Fig. 15), however, indicates specific sites; both impurities and dislocations tend to segregate at grain boundaries. No data are available to allow selection between impurity and dislocation sites.

The change of boulder density with time.—The experimental data are presented on Fig. 13. The following model is suggested. The boulders are nucleated progressively with a constant rate of v(boulders/cm^{2}sec). The boulders are growing under linear diffusion control and therefore, the current into a particular boulder is proportional to its cross-sectional area (this is a good approximation once the surface is nearly covered by the boulders, cf. Table I). As a first approximation the boulders are taken as hemispheres with a radius of r. The current into a boulder is then, at i mA/cm^2 total current density: $r^2\pi i$. If a gives the volume of material deposited, in cm^3/sec, for each mA/cm^2, the change of volume of a boulder with time will be

$$\frac{dV}{dt} = i\,a\,r^2\pi \qquad [11]$$

The volume of a boulder is

$$V = \frac{2\pi}{3} r^3 \qquad [12]$$

and

$$dV = 2\pi\, r^2 dr \qquad [13]$$

Substituting into [11] gives

$$\frac{dr}{dt} = \frac{1}{2}\, i\, a \qquad [14]$$

and

$$r = \frac{1}{2}\, i\, at \qquad [15]$$

[6] At higher potentials dendrites were readily formed at short times (cf. Fig. 16c).

That is, the rate of increase of the radius of the boulder is independent of the size of the boulder, and a small one meeting a larger one will be consumed as shown in Fig. 19. The small boulder will be considered as consumed when the perimeter of the larger one reaches its midpoint. As a boulder is growing it will consume all other ones in its way which are younger than itself (these are continuously nucleating around it with a rate of v), until it reaches a larger one and will be itself consumed. The number of boulders the i^{th} boulder will consume in τ sec as a function of its age (τ) is

$$N'_i = \int_o^\tau v\,\tau\,2\pi r dr \qquad [16]$$

substituting r and dr from [14], and [15], and integrating gives

$$N'_i = \frac{\pi}{6}(i\,a)^2 v\tau^3 \qquad [17]$$

At time t there are boulders with ages ranging from 0 to t (being nucleated at a rate of v), so summarizing over-all boulders gives the number of consumed boulders (N'_{cons}) as a function of time

$$N'_{cons} = \int_o^t v\,N'_i(\tau)\,d\tau = \frac{\pi}{24}(i\,a\,v)^2 t^4 \qquad [18]$$

This expression, however, overestimates the number of boulders consumed because it assumes that all boulders continue to consume others up to time t, but once a boulder is consumed it ceases to consume others. Further, a boulder being at a specific point of the surface will be counted as consumed every time the perimeter of a larger boulder passes that point, but in reality it can be consumed only once.

Correction can be made using Avrami's statistical formula (49, 50), which has been used extensively in electrochemistry for the problem of film formation on electrodes (51). This formula was derived for a specific overlap problem, that of three-dimensionally growing nuclei in a solid-state phase transformation, but it is generally valid for overlap problems. In the phase transformation the volume fraction of the transformed material can be easily calculated knowing the rate of nucleation and the rate of growth of the nucleated grains, but only up to the point when the grains start to overlap. Avrami has shown that when overlap occurs the transformed volume fraction can be calculated as

$$\frac{V_{tr}}{V} = 1 - \exp\left(-\frac{V'_{tr}}{V}\right) \qquad [19]$$

when V_{tr} is the transformed volume, V is the total volume of the solid, and V'_{tr} is the calculated transformed volume neglecting overlap.

The present problem is analogous, and Eq. [19] can be rewritten as

$$\frac{N_{cons}}{N_n} = 1 - \exp\left(-\frac{N'_{cons}}{N_n}\right) \qquad [20]$$

where N_{cons} is the number of boulders consumed in time t, N'_{cons} is the calculated number of boulders consumed in time t, neglecting overlap, and N_n is the total number of boulders nucleated in time t given by

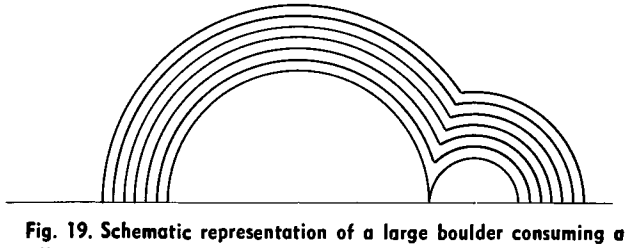

Fig. 19. Schematic representation of a large boulder consuming a smaller one.

$$N_n = v\,t \qquad [21]$$

The number of boulders remaining on the surface (N) will be obtained as

$$N = N_n - N_{cons} = N_n \exp\left(-\frac{N'_{cons}}{N_n}\right) \qquad [22]$$

And combining [22] with [18] and [21] gives the final results

$$N = vt \exp\left(-\frac{\pi}{24} i^2 a^2 v\,t^3\right) \qquad [23]$$

Equation [23] describes the curves of Fig. 13 with a reasonable agreement. It predicts a nearly linear rise, an exponential fall, and a maximum at 5 C/cm^2 (τ = 350 sec) and $N = 34 \times 10^6$ boulders/cm^2 (calculated with $v = 1.4 \times 10^5$ boulders cm^{-2} sec^{-1}, taken from the initial slope of the curves on Fig. 13). This agreement between observed and calculated number of boulders gives support to the suggested model consisting of continuous nucleation, and consumption of the smaller boulders by the larger ones.

Evolution of dendrites from boulders.—Previous work (28) on dendritic growth, carried out under similar experimental conditions, can be connected with the present results. Since deposition at longer times results in densities, the boulders can be assumed to be the dendrite precursors. On the basis of extrapolation of the curves of Fig. 13 to the dendrite initiation time [*ca.* 50 min (28)] one would expect the number of dendrites to be in the order of 10^6/cm^2. Experimentally only about 10^3/cm^2 were observed (28). The critical radius of curvature needed for dendrite growth has been shown for zinc (28) to cover a range of over two orders of magnitude, and therefore differences in the radius of curvature of boulder tips cannot account for this discrepancy. It is suggested here that, under the present experimental conditions, the number of dendrites is controlled by the total current. It has been estimated (28) that the growing dendrite tip draws 1.2 μA, and since the total current is 14 mA/cm^2 (still being controlled by linear diffusion since the height of the boulders is negligible compared to the diffusion layer thickness) the possible maximum number of dendrites is 1.2×10^4/cm^2. Furthermore, the tip current was found to be only a few per cent of the total (28), the rest flowing to the sides of the dendrites and to the substrate, therefore a dendrite density of 10^3/cm^2 is quite reasonable.

In summary: while there are a large number of precursors fulfilling the radius of curvature requirements, only a small fraction ($\approx$0.1%) will develop into dendrites, due to the limitations imposed by the total current. These will be the ones which, being nucleated first, are higher than average and so are able to draw current away from their neighbors.

Qualitatively, similar results were observed by Naybour (25) (though under different experimental conditions), *i.e.*, only a small fraction (less than 1%) of the original nuclei grew into dendrites.

The controlling factor: current or potential?—In theories of electrodeposition (1, 2) it is recognized that overpotential, rather than current density, is the controlling variable of morphology (though sometimes it is assumed that changes in current density cause morphological changes). Experimental indication is lacking, since the two variables change together according to the Butler-Volmer equation, and their effect is not at once separable. In the present work, a possibility arose to obtain experimental evidence by which the effects can be separated. Parts of the data were taken under (or near to) diffusion limiting conditions, where the potential could be increased without considerable coupled increase of the current. By lowering the zincate concentration, it was possible to reach a situation where currents at 50 and 100 mV overpotentials were

essentially the same (Table II). The morphology of the deposits obtained under this condition paralleled exactly that obtained at the high zincate concentration, where the current more than doubled with the increase of overpotential from 50 to 100 mV. The overpotential, not the current density, determined the nature of the deposit.

Acknowledgments

Useful discussions with Drs. A. Damjanovic, A. R. Despic, and G. Razumney are gratefully acknowledged. Our thanks are also due to Mr. R. White for his help and advice during the electronmicroscopic work. Financial assistance for this study was provided by the National Science Foundation under grant NSF-GK-16550; and the A.R.P.A. Program in Materials Science (University of Pennsylvania).

Manuscript submitted Dec. 20, 1971; revised manuscript received Aug. 4, 1972.

Any discussion of this paper will appear in a Discussion Section to be published in the December 1973 JOURNAL.

REFERENCES

1. J. O'M. Bockris and A. Damjanovic, in "Modern Aspects of Electrochemistry," No. 3, Chap. 4, J. O'M. Bockris and B. E. Conway, Editors, Butterworths, Washington (1964).
2. J. O'M. Bockris and A. R. Despic, in "Physical Chemistry," Vol. 9B, Chap. 7, H. Eyring, D. Henderson, and W. Jost, Editors, Academic Press, New York (1970).
3. T. Erdey-Gruz and M. Volmer, *Z. Phys. Chem.*, **A157**, 165 (1931).
4. F. C. Frank, *Discussions Faraday Soc.*, **5**, 48 (1949).
5. N. Cabrera and D. A. Vermilyea, in "Growth and Perfection of Crystals," p. 393, R. H. Doremus, B. W. Roberts, and D. Turnbull, Editors, John Wiley & Sons, New York (1958).
6. F. C. Frank, in "Growth and Perfection of Crystals," p. 411, R. H. Doremus, B. W. Roberts, and D. Turnbull, Editors, John Wiley & Sons, New York (1958).
7. R. Kaischev, E. Budevski, and S. Malinowski, *Z. Phys. Chem.*, **204**, 348 (1955).
8. H. Seiter, H. Fischer, and L. Albert, *Electrochim. Acta*, **2**, 97 (1960).
9. H. J. Pick, G. G. Stoney, and T. B. Vaughn, *ibid.*, **2**, 165 (1960).
10. A. Damjanovic, M. Paunovic, and J. O'M. Bockris, *J. Electroanal. Chem.*, **9**, 93 (1965).
11. A. Damjanovic, T. H. V. Setty, and J. O'M. Bockris, *This Journal*, **113**, 429 (1966).
12. I. N. Stranski, *Discussions Faraday Soc.*, **5**, 13 (1949).
13. C. W. Bunn and H. Emmett, *ibid.*, **5**, 119 (1949).
14. E. Budevski, W. Bostanov, T. Vitanov, Z. Stojnov, A. Kotzeva, and R. Kaischev, *Electrochim. Acta*, **11**, 1697 (1966).
15. R. Kaischev and E. Budevski, *Contemp. Phys.*, **8**, 489 (1967).
16. G. Eichkorn and H. Fischer, *Z. Phys. Chem. N.F.*, **53**, 29 (1967).
17. H. Fischer, *Angew. Chem. Intern. Ed.*, **8**, 108 (1969).
18. N. A. Pangarov, *Electrochim. Acta*, **9**, 721 (1964).
19. A. K. N. Reddy, *J. Electroanal. Chem.*, **6**, 141 (1963).
20. J. M. Keen and J. P. G. Farr, *This Journal*, **109**, 668 (1962).
21. K. M. Gorbunova, O. S. Popova, A. A. Sutyagina, and Yu. M. Polukarov, "Growth of Crystals," Vol. 1, p. 46, A. V. Shubnikov and N. N. Sheftal, Editors, Consultants Bureau, New York (1959).
22. R. Sato, *This Journal*, **106**, 206 (1959).
23. S. Budurov and N. Stoichev, Rost Kristallov, *Akad. Nauk, SSSR, Inst. Kristallogr.*, **5**, 136 (1965).
24. R. W. Powers, *Electrochem. Technol.*, **5**, 429 (1967).
25. R. D. Naybour, *Electrochim. Acta*, **13**, 763 (1968).
26. R. D. Naybour, *This Journal*, **116**, 520 (1969).
27. S. Arouete, K. F. Blurton, and H. G. Oswin, *ibid.*, **116**, 166 (1969).
28. J. W. Diggle, A. R. Despic, and J. O'M. Bockris, *ibid.*, **116**, 1503 (1969).
29. J. W. Diggle and A. Damjanovic, *ibid.*, **117**, 65 (1970).
30. F. Mansfeld and S. Gilman, *ibid.*, **117**, 588 (1970).
31. F. Mansfeld and S. Gilman, *ibid.*, **117**, 1154 (1970).
32. F. Mansfeld and S. Gilman, *ibid.*, **117**, 1521 (1970).
33. S. Higuchi and Y. Miyake, *Denki Kagaku*, **38**, 594 (1970).
34. S. U. Falk and A. J. Salkind, "Alkaline Storage Batteries," John Wiley & Sons, New York (1969).
35. J. O'M. Bockris, Z. Nagy, and A. Damjanovic, *This Journal*, **119**, 285 (1972).
36. G. Brinson and A. J. W. Moore, *J. Inst. Metals*, **79**, 429 (1951).
37. W. J. McG. Tegart, "The Electrolytic and Chemical Polishing of Metals in Research and Industry," Pergamon Press, London (1956).
38. P. A. Jacket, *Met. Rev.*, **1**, (part 2) 157 (1956).
39. G. K. T. Conn and F. J. Bradshaw, Editors, "Polarized Light in Metallography," Academic Press, New York (1952).
40. A. Damjanovic, M. M. Paunovic, and J. O'M. Bockris, *Plating*, **50**, 735 (1963).
41. Z. Nagy and D. Drazic, *Chem. Instr.*, **4**, 53 (1972).
42. G. Nomarski and A. R. Weil, *Rev. Met.*, **52**, 121 (1955).
43. G. LeMehaute, *IBM J. Res. Develop.*, **6**, 262 (1962).
44. J. O'M. Bockris and G. A. Razumney, "Fundamental Aspects of Electrocrystallization," Plenum Press, New York (1967).
45. W. H. J. Vernon, E. I. Akeroyd, and E. G. Stroud, *J. Inst. Met.*, **65**, 301 (1939).
46. H. E. Buckley, "Crystal Growth," John Wiley & Sons, New York (1951).
47. R. F. Ashton and M. T. Hepworth, *Corrosion*, **24**, 50 (1968).
48. A. Damjanovic and J. O'M. Bockris, *This Journal*, **110**, 1035 (1963).
49. M. Avrami, *J. Chem. Phys.*, **7**, 1103 (1939).
50. M. Avrami, *ibid.*, **8**, 212 (1940).
51. M. Fleischman and H. R. Thirsk, in "Advances in Electrochemistry and Electrochemical Engineering," Vol. 3, Chap. 3, P. Delahay and C. W. Tobias, Editors, Interscience, New York (1963).

Measurement of Current and Potential Distribution at Rotating-Disk Electrodes

Barry Miller* **and Maria I. Bellavance**

Bell Telephone Laboratories, Incorporated, Murray Hill, New Jersey 07974

ABSTRACT

Current distribution at the rotating disk electrode has been experimentally evaluated by several techniques including single and double reference probe potential mapping, ring-disk electrode collection efficiency and resistive interaction, interrupter and steady-state resistance measurements, and automatic ohmic compensation methods. Mapping experiments are in quantitative agreement with the predictions of Newman's theory for this system and were further confirmed by resistance determinations and theoretically based correction methods. The implications of the data for various ring-disk and nonsteady-state experiments and also the utility of an approximate approach to estimating the degree of nonuniform current distribution are examined.

The uniform accessibility of the rotating disk electrode (RDE) to mass transfer (1) was implicitly assumed to produce a uniform current density until Newman (2) showed theoretically that there will generally not be a radially independent current distribution because of the solution ohmic potential drop. The shape of the current function *vs.* radial distance and the potential contours in solution depend on the relative interaction of solution ohmic drop, surface and concentration overpotentials across the disk for the given solution, electrode geometry, rotation speed, and electron transfer kinetics. We are concerned in this work with further experimental information on the current distribution at the RDE for testing the theory and its implications for various RDE and rotating ring-disk electrode (RRDE) applications.

Radial nonuniformity of RDE current has been most satisfactorily detected and compared to theory by direct measurement of the thickness distribution of an electrodeposited metal (3, 4). These experiments with copper deposition gave profiles substantiating Newman's theory.

The detection of nonuniform current distribution from reference probe potential or apparent ohmic resistance contours ideally requires measurements close to the RDE itself (2, 5). Angell *et al.* (6) have mapped isopotential contours with a reference electrode for several disk-insulating annular mantle geometries, describing the separation of isopotential lines as qualitatively in accord with Newman's predictions (2, 7). Resistance measurement through current interruption reflects only the value corresponding to a primary current distribution, regardless of that actually obtaining before interruption (8). McIntyre and Peck (9) found interrupter determined resistances independent of current, in support of Newman's conclusion (8).

A quantitative comparison of either interrupter values or potential mapping to theory has not been made at the RDE, to our knowledge. Nor has a test been made of the natural conclusion following from the above that only ohmic measurements made during current flow by appropriately located probes can detect the nature of the prevailing current distribution. Nanis and Kesselman (10) have calculated that the average resistance of the solution between disk and nonpolarizable counterelectrode would be 1.08 times higher for a uniform than a primary current distribution. They imply (10) that this would be detectable from interrupter comparisons of the current for "on" and "off" switching directions.

Albery and Ulstrup (11) suggested that radially increasing as opposed to uniform currents at the disk should be detectable through higher than theoretical collection efficiencies (12) at an RRDE. This expectation has been confirmed (4, 5, 13), although a quantitative interpretation has not yet been given. The comparison of current densities at ring and disk electrodes (sectioned electrodes), when they are independently held at the same potential, similarly affords a test of radial current uniformity (4, 14). Interactions of ring and disk through the ohmic drops from the prevailing currents have been generally disregarded. Ring potentials are shifted only by altering disk current; changes in disk potential without changing steady disk current, as is possible at a disk limiting current, have no effect on the ring potential (15). Potentiometric ring experiments (16) would be sensitive to resistive coupling of ring and disk through the solution and offer a new way to test the effect in the context of Newman's theory.

Several experiments are described in this work. Potential mapping with a single reference probe (6) has been repeated in a manner giving quantitative comparison to Newman's theory. Mapping technique has also been extended to a double probe configuration capable of further refining the detection of nonuniform current distribution. These experiments, in turn, have been correlated to measurements of RRDE collection efficiency. The determination of disk-ring ohmic interactions, comparison of interrupter and current flow resistance measurements, and automatic ohmic compensation techniques based on Newman's theory are also reported. Effects of varying electrode geometry and solution properties along with characterization of the Levich behavior of the electrodes employed are also considered.

The studies were carried out with the Hg_2^{++}/Hg couple in perchloric acid solution. The exchange current of this couple is sufficiently high (17) that concentration overpotential (η_c) becomes the only factor to counteract the primary distribution under all our conditions. Allowing for the reversible case not being the general one, we feel that examining the concentration overpotential-ohmic drop interaction provides a readily manageable and significant test of the theory of overpotential contributions to current uniformity at the disk.

Theoretical

Disk current distribution.—From the calculations of Newman (2), the shape of the full radial current distribution can be approximated [cf. Fig. 2 and 3 of Ref. (2)] if the ratio i/i_{av}[1] at the center of the disk ($r = 0$) is specified. This statement must be qualified to the extent that exceptions exist for which Newman found maxima or other effects in the radial current distribution. For example, such maxima appear in

* Electrochemical Society Active Member.

Key words: rotating disk electrode, current distribution, potential distribution, interrupter measurements, resistance compensation.

[1] Symbols are tabulated following the text.

some cases of Tafel kinetics at appreciable fractions of the limiting current (2).

The quantity $(i/i_{av})_{r=0}$ itself varies only within the limits of 0.5 (primary) to 1.0 (uniform). Albery and Hitchman (13, 18) have presented an approximation to the extended Newman theory by correlating a quantity ρ, the ratio of the ohmic to the dynamic charge transfer plus concentration overpotential resistances, to the Newman parameters J and $\beta\delta$ and thence to the $(i/i_{av})_{r=0}$ obtained from the complete theory (2). The mathematical difficulties of the latter are formidable and no less so for the reversible case. A suitable approximation is distinctly desirable. We have used the ρ method as well as extended computer calculations to obtain a theoretical $(i/i_{av})_{r=0}$ for our comparisons and discuss justifying evidence additional to that presented by Albery and Hitchman (13, 18). We require $(i/i_{av})_{r=0}$ because our experimental design has concentrated on measurements in the axial direction below the disk center where the potential profile is best defined spatially and least sensitive to electrode mantle effects.

We summarize first the parameters of Newman (7) necessary to describe the ohmic drop in solution for the primary current distribution. For the two probe directions experimentally examined here, the axial (z at $r = 0$) and the radial (r at $z = 0$), Newman's quantity ξ is given by z/r_o and $\sqrt{(r/r_o)^2 - 1}$, respectively. The solution of Laplace's equation (7) gives

$$\frac{\Phi}{\Phi_o} = 1 - \frac{2}{\pi}\tan^{-1}\xi \qquad [1]$$

The ohmic resistance of the solution (disk to counter-electrode at $\xi \to \infty$) is

$$R_\infty = \frac{1}{4r_o\kappa} \qquad [2]$$

We define $f = 2/\pi \tan^{-1}\xi = 1 - \Phi/\Phi_o$, a dimensionless probe position. In the case of a primary current distribution f is the fraction of the solution resistance R_∞ sensed from just outside the diffusion layer at the disk to a probe at ξ. The potential from the disk to a probe moved in the axial direction, E_z, will, in primary current theory, have intercepts at f equals 0 and 1 of 0 and IR_∞, respectively.

Apparent deviations of slope and intercept in an E_z-f plot when cell and electrode requirements are satisfied are then attributable to disk overpotentials and to the concurrent change in current distribution. However, even when the current distribution becomes uniform, the slope of the plot will be nearly indistinguishable from the primary case for $\xi > 1$ (beyond about one radius away in the z direction). In the case of Hg/Hg_2^{++} where $\eta_s \cong 0$, the extrapolation of the straight line portion of the E_z-f plot to $f=0$ will give an intercept approximating the concentration overpotential calculated with the average current flowing through the disk.

When two probes ($f_2 > f_1$) with fixed separation are used, the potential ΔE between them in the primary case is given by $(f_2 - f_1)IR_\infty$. If the distance between the probes is greater than r_o, the probe at f_2 should detect little or no deviation from a primary current distribution as a function of z. The potential ΔE for varying Δf may then be translated to an f_1 coordinate by using the quantity $\Delta E + (1 - f_2)IR_\infty$ which represents the ohmic drop between f_1 and a second probe at ∞.

Using subscripts a and c for anodic and cathodic disk current, respectively, the quantity $\Delta E_{a,o}/IR_\infty$, where $\Delta E_{a,o}$ is the value of $\Delta E_a + (1 - f_2)IR_\infty$ extrapolated to $f_1 = 0$, gives a direct measure of the relative increase in resistance equivalent to the $\Phi_o 4\kappa r_o/I$ ordinate in Newman's (2) Fig. 5. This factor ranges from 1.000. (primary) to $4/\pi = 1.273$ in the uniform case, corresponding to the change of $(i/i_{av})_{r=0}$ from 0.500 to 1.000 The cathodic tests were made at the limiting current, where the current distribution should be uniform. Consequently, a second test of the same relative increase is given by a direct comparison of $\Delta E_{c,o}/IR_\infty$ with the value $4/\pi$.

The abscissa of Newman's Fig. 5 is $(i/i_{av})_{r=0}$, and it is here that we have applied the approximate method (13, 18), instead of specifying N, δ, and J and solving the necessary set of simultaneous differential equations. The parameter ρ may be calculated from the ratio of R_∞ to the slope of the IR-free current-potential curve at the specified total current. In the general case, we may differentiate the exponential i-η_s relation, using the form of Newman (Ref. (2), Eq. [27])

$$i = i_o\left(\frac{C_o}{C_\infty}\right)^\gamma\left[\exp\left\{\frac{\alpha n\mathbf{F}}{RT}\eta_s\right\} - \exp\left\{\frac{-\beta n\mathbf{F}}{RT}\eta_s\right\}\right] \qquad [3]$$

A comparison to a full scale calculation can be taken from the $(i/i_{av})_{r=0}$ points of the three radial distribution curves calculated by Marathe and Newman (3) for copper deposition. In this cathodic Tafel case, Eq. [3] can be rewritten as

$$i = -i_o\left(\frac{i_L - i}{i_L}\right)^\gamma\left[\exp\left\{-\frac{\beta n\mathbf{F}}{RT}\eta_s\right\}\right] \qquad [4]$$

and differentiated after solution for η_s to yield

$$\left(\frac{\partial\eta_s}{\partial i}\right) = -\frac{RT}{\beta n\mathbf{F}}\left(\frac{1}{i} + \frac{\gamma}{i_L - i}\right) \qquad [5]$$

Using (3) $\beta = 0.25$, $r_o = 0.25$ cm, $i_L = -65$ mA/cm^2 and respective i_{av} values of 0.194, 0.495, and 0.69 times i_L, we obtain $1/A(\partial\eta_s/\partial i) = 22.84$, 11.48, and 11.3 ohms. R_∞ is given as 19.6 ohms, yielding ρ values of 0.86, 1.71, and 1.74. From a plot of ρ *vs.* $(i/i_{av})_{r=0}$ constructed from the tabulation of Albery and Hitchman (13, 18), we read $(i/i_{av})_{r=0}$ values of 0.875, 0.80, and 0.795 which compare quite exactly to the respective intercepts (3) from the detailed theory of 0.878, 0.802, and 0.793.[2]

The apparent success of the ρ approach in reproducing these values is clear. It is also of interest that the entire radial distribution curves of the two nearly equal $(i/i_{av})_{r=0}$ and ρ values are close to superimposable. However, we have also calculated cases related to the three curves just considered with conditions deliberately shifted to be similar to those earlier referred to from Newman (2) in which calculations show maxima in radial current distribution (and much lower currents at the edge of the disk than one would expect from the ρ value). The calculated cases here involved manipulating some of the parameters (β, N, J) four different ways to keep a given ρ of 4.6 constant with $i_{av}/i_L = 0.9$. The predicted identity of $(i/i_{av})_{r=0}$ from the four calculations with constant ρ was found to show an average deviation of less than 2% from that derived from the ρ value although each radial current curve had a maximum. The magnitude of the deviation depends on the calculational details but seems small enough to suggest that the estimate from ρ remains very good in spite of such further effects (here produced when the surface concentration approaches zero within the disk radius) that modify the full radial curve.

Following through with the ρ calculations applicable to the mercury system, we feel that experimental confirmation substantiates both the general theory and the approximate approach in the limits tested.

For the Hg/Hg_2^{++} case where $\eta_s \cong 0$, only differentiation of the η_c-i curve following from

$$\eta_c = \frac{RT}{2\mathbf{F}}\ln\frac{C_o}{C_\infty} \qquad [6]$$

[2] In the calculation of ρ, t_+ for copper, required by the Newman theory and not specified in Ref. (3), was ignored by us as being accounted for experimentally in i_L and i_{av}. Complete computer calculations following Newman show a change of only 10^{-3} in $(i/i_{av})_{r=0}$ for a t_+ range of 0-0.15.

is necessary. This sequence gives for both anodic and cathodic cases

$$\eta_c = \frac{RT}{2F} \ln\left(\frac{i_L - i}{i_L}\right) \quad [7]$$

and

$$\frac{1}{A}\left(\frac{\partial \eta_c}{\partial i}\right) = \frac{RT}{2FA}\left(\frac{1}{i - i_L}\right) \quad [8]$$

Inspection of Eq. [8] indicates that, for a given i_a, the most uniform situation of current distribution occurs for $i_L = 0$, *i.e.*, anodization into a metal-free solution usually considered when applying the RDE and RRDE to corrosion studies. Naturally, in the anodic case, R_a must still be minimized to keep ρ near zero and $(i/i_{av})_{r=0}$ near 1.

Ring-disk electrode.—Collection efficiency.—If the ring is set to collect Hg_2^{++} by reduction at the limiting current in a Hg_2^{++} containing solution, then for the three conditions of zero, cathodic (−), and anodic (+) current at the disk, i_r will be given by the following

I	i_r
−	$i_{rL} - N_c I$
0	i_{rL}
+	$i_{rL} + N_a I$

In the first case, the disk current, when cathodic and limiting, is expected to be radially uniform and N_c equal to N_t. If the anodic current distribution is also uniform then $N_a = N_c = N_t$; otherwise $N_a > N_c$.

Ring-disk potentials.—Albery, Bruckenstein, and Napp (16) showed that for a ring and disk of metal M, anodization of the disk to M^{+n} while $i_r = 0$ produces a potential between ring and disk

$$E_R^D = \frac{RT}{nF} \ln \frac{N_t}{\beta_t^{2/3}} \quad [9]$$

The expression was confirmed (16) for various I and ω values where ohmic drops were negligible.

Experimental

Apparatus and materials.—The galvanostat-potentiostat (19) and motor control-$\omega^{1/2}$ scanning and modulation circuitry (20) have been described earlier. Potentiometric measurements between disk, ring, and references in appropriate pairs have been made with follower amplifiers or high impedance-floating input digital voltmeter. Interrupter measurements were made with a summing point electronic switch (Burr-Brown 9859) at the control amplifier of the galvanostat configuration (19). Switch resistance was taken into account for current level. A Wavetek 114 function generator was used to turn the switch on and off and simultaneously provide a trigger pulse for a storage oscilloscope (Tektronix 564 with 3A3 and 3B4 plug-ins). The circuitry for the isosurface concentration voltammetry (ISCVA) experiments has been described (20).

The RRDE construction (19) was of gold, amalgamated with mercury before use. The six other electrodes employed were gold disks which were similarly mercury wetted and spun at high speed to remove excess mercury. The configurations of the electrodes are given schematically in Fig. 1 and in detail in Table I. *R* is a cylindrical RRDE of dimensions identical to those used extensively in this laboratory. The other configurations vary from *A*1, a relatively small cylindrical shape, through various mantle designs which conform better to the requirements of hydrodynamic theory (21).[3]

[3] Angell *et al.*, have shown that isopotential contours above the plane of the disk are those expected from electrode geometry. Our maps have concentrated on the axis below the center of the disk where it is expected mantle effects would be the least and where it has been our practice [in the regular cell pictured in Ref. (22)] to place the conventional Luggin capillary. By also obtaining the limiting current behavior of all our electrodes, we have compared both current (Levich) and potential ideality of these reference placements.

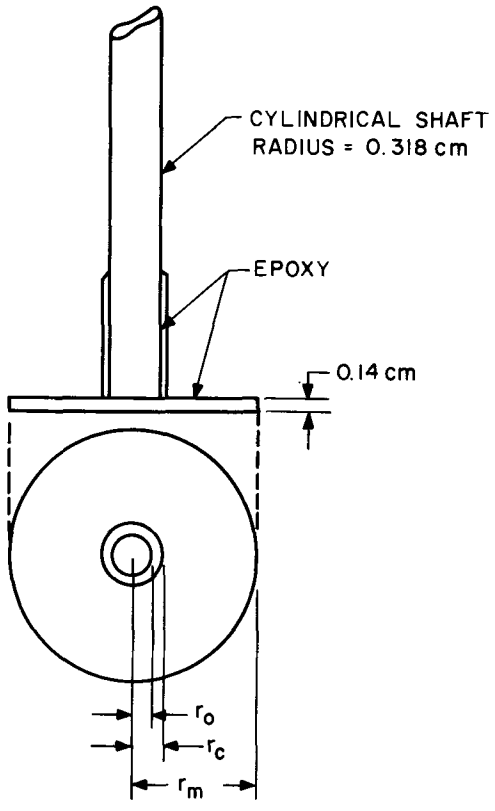

Fig. 1. Electrode configurations

To approach the theoretical requirements of a counterelectrode at infinity with practical dimensions, we employed the arrangement shown in Fig. 2 with a cell based on a three neck, round bottom 1 liter flask and 1 liter cell volumes. The counterelectrode (Hg pool), contacted by a Pt wire, had a minimum surface area of 28 cm^2. The reference probes were gold wires insulated for the last several cm with epoxy and terminating in an amalgamated 0.05 cm tip. Only the nearly planar mercury surface of the wire was exposed. The single probe could either be the upper part of that pictured or a separate single tip electrode.[4] Some experiments, particularly for RRDE measurements, were carried out in the cylindrical J-cell (22) of approximately 250 ml capacity normally used in this laboratory.

Interference with fluid flow by our reference probes is not detectable in limiting current measurements at different probe locations, though these data might not be sensitive to very local effects. Typical values of the diffusion layer thickness are 10^{-3} cm in these

[4] The treatment of Barnartt (23, 24) indicates a minimum distance of 2 × 0.05 = 0.1 cm to which an open end Luggin capillary of 0.05 cm diameter can be brought without affecting the field appreciably under current flow to a large disk ($r_o >> 0.05$ cm). In general, our measurements were begun at about this distance with the metal probes. The double probe (ΔE) experiments, because of the 1.11 cm probe separation, have an additional insensitivity to such shielding effects. Our cumulative experience suggests that shielding was a negligible factor.

Table I. Geometric parameters of electrodes

Electrode	r_o (cm)	r_c (cm)	r_m (cm)
A1	0.148	0.317	—
A2	0.148	—	1.265
B1	0.318	0.377	—
B2	0.318	—	1.252
B3	0.318	—	0.796
C	0.635	—	1.289
R	0.239 ($r_1 = 0.263$, $r_2 = 0.324$)	0.414	—

Note: r_c refers to the insulated cylindrical shaft extending all the way down to the plane of the disk; r_m refers to a case in which the insulated shaft radius << r_m.

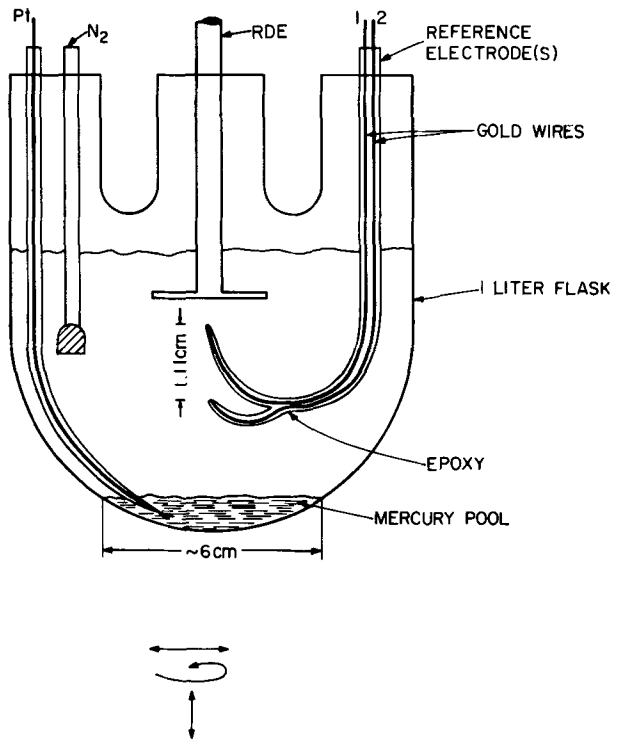

Fig. 2. Cell arrangement. Cell motions in micrometer mount as indicated at bottom.

experiments. Generally, potential comparisons using equal currents of opposite sign which stressed extrapolation of data to the disk surface showed no systematic perturbations attributable to proximity effects on either field or flow.

The cell was mounted in a clamp that was movable by screw adjustments in the three modes indicated in Fig. 2. The disk plane was fixed throughout the experiment, and the reference probes were rigidly set into one neck of the cell. To avoid magnification errors from the round cell walls, the reference probe tip was brought to the disk surface to establish $z = 0.0000$ cm and thereby viewed identically for all z. Cathetometers of 0.0001 cm resolution were employed. Radial mapping in the $z = 0$ plane was not attempted at less than the outer epoxy radius of an electrode to avoid $z > 0$ errors. Full mapping tests were only practical in the z direction. Effects on resistance due to changes in the disk-pool separation during z change were minimal and neglected.

Solutions were prepared from triply distilled water and reagent-grade perchloric acid and mercurous nitrate. All experiments employed an $[H^+]/[Hg_2^{++}]$ ratio required for a supporting electrolyte case, and the presence of nitrate was of no influence. Mercurous solutions were analyzed volumetrically with sodium chloride to a potentiometric end point. Electrodes were polished to a 0.3μ Linde A finish before amalgamation.

Conductivity was measured on a Beckman RC-19 bridge (±0.25%) in a cell of constant 100.6 cm^{-1}. All measurements were made at ambient temperature (23° ± 2°C), with care that conductivity data were taken as near to cell temperature as possible. Potentials were read on digital voltmeters of ≤0.1% full scale accuracy (Hewlett-Packard 3430A and Heath EU-805). Limiting currents were also read digitally.

Automatic ohmic compensation methods to be described were carried out with the analog circuitry shown in Fig. 3. At upper left is the scheme for feedback with a single reference probe. At lower left is the equivalent mode for the double probe potential difference as feedback. Point A is the common connection for either method to the analog correction circuit at right.

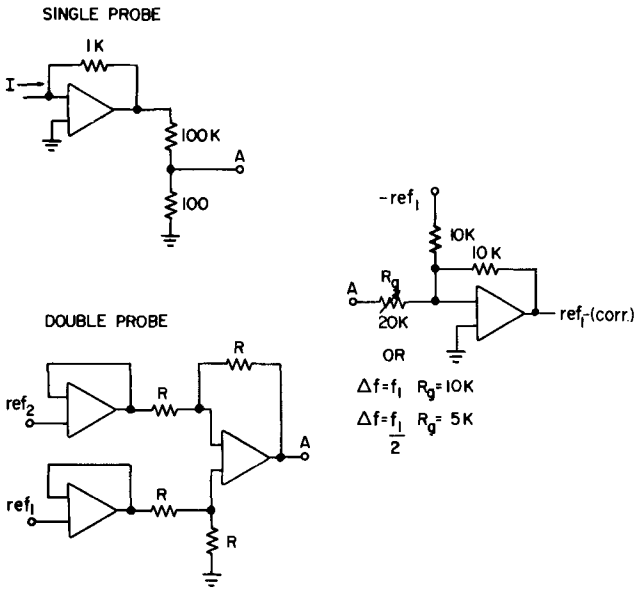

Fig. 3. Automatic ohmic compensation circuitry

Results and Discussion

Levich constant.—Limiting current characterization of the electrodes is shown in Fig. 4 and Table II. Electrodes are grouped in the figure by common disk radius (4 values). Over the speed range to 2500 rpm there is differentiation among mantle designs within a group only at the low end. (At higher speeds than 2500 rpm significant turbulence and air entrapment begin to distort the results, starting with the larger mantles). The ordinate is normalized to unity within each set to show per cent changes readily, but inspection of Table II also reveals that the absolute values of the $i_L/\omega^{1/2}C_\infty$ factor are given to a precision of 1% (standard deviation) including slight differences arising from 1M and 0.2M $HClO_4$ electrolytes.

These data confirm other discussion (25) of the relative insensitivity of the RDE to hydrodynamic ideality of design in the limiting current measurement. For the purposes of this paper we exclude effects on comparative current distribution that might be attributed to such variation. The data are also of practical significance for application of the ISCVA technique

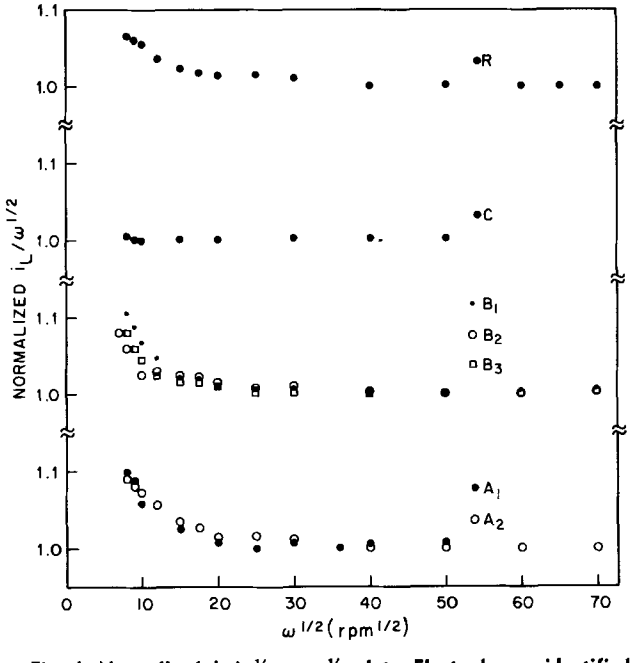

Fig. 4. Normalized $i_L/\omega^{1/2}$ vs. $\omega^{1/2}$ plots. Electrodes as identified in Table I.

Table II. Limiting disk current behavior

Electrode	A, cm²	$I/\omega^{1/2}$, mA-rpm$^{-1/2}$	$10^{-3}\, i_L/\omega^{1/2}\, C_\infty$, mA-cm-rpm$^{-1/2}$-mole^{-1}	Solution
A1	0.0688	0.0140	35.4	I
A2	0.0688	0.0138	34.9	II
B1	0.3177	0.0634	34.8	I
B2	0.3177	0.0630	34.5	II
B3	0.3177	0.0628	34.4	II
C	1.267	1.005	34.5	III
R	0.179	0.0352	34.3	I
I	1M $HClO_4$, 5.74 mM Hg_2^{+2}			
II	0.2M $HClO_4$, 5.74 mM Hg_2^{+2}			
III	1M $HClO_4$, 22.96 mM Hg_2^{+2}			

From these data, the average value of $D_{H_{g_2}}$ +2 in 1M $HClO_4$ at 23° ± 2°C with ν = 0.00863 cm²/sec is 8.2 × 10^{-6} cm²/sec.

(26) in which a constant surface concentration through control of the $I/\omega^{1/2}$ ratio at varying I is assumed. The lowest values of $\omega^{1/2}$ and therefore of current at which this constancy holds correspond to the minimum potential perturbation from equilibrium accessible for the fixed surface concentrations.

Single probe mapping.—Three typical E_z-f plots obtained for varying solution conditions, current direction, ρ parameter, and electrodes are shown in Fig. 5. The data points are well described by theoretical lines drawn between intercepts η_c and $\eta_c + IR_\infty$ calculated from [7] and [2]. The dimensions of the three electrodes restrict the data at low f values. The ρ parameters of 0.57 (*A2*), 1.3 (*B1*), and 4.0 (*B3*) suggest them all to have varyingly nonuniform current distributions. Figure 5 indicates that ohmic compensation with fIR_∞ determined by means of an axial probe at position f and known conductivity ought to give good extrapolation to the values of overpotential at the

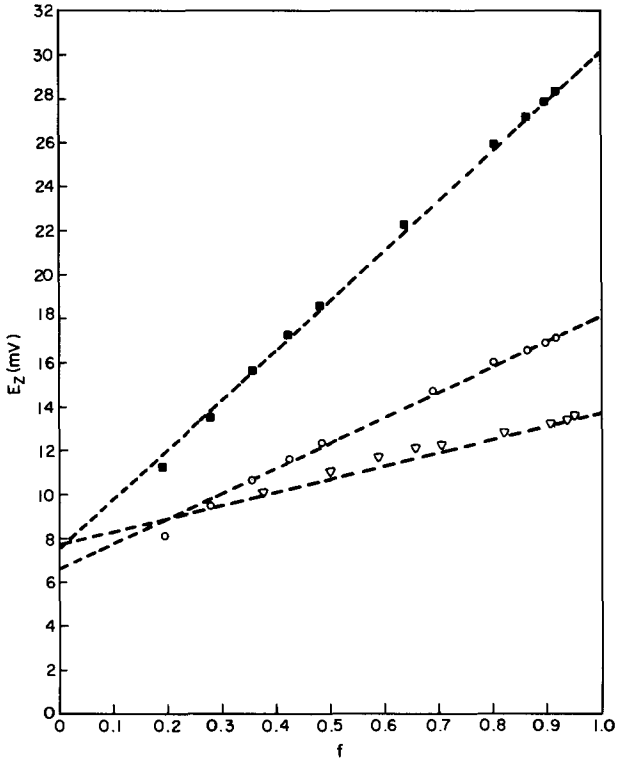

Fig. 5. Single probe potential E_z vs. f.

		I, mA	ρ
▽	*A2*,	−0.25 mA	0.57
○	*B1*,	−1.00 mA	1.3
■	*B3*,	+2.00 mA	4.0

All runs with 0.2M $HClO_4$, 5.74 mM Hg_2^{+2} solution. κ = 0.0692 mhos-cm^{-1}, ω = 1600 rpm. Dashed lines are drawn with slopes of measured IR_∞.

surface calculated assuming the average current across the electrode in spite of the predicted nonuniformity. Further quantitative indication of the actual $(i/i_{av})_{r=0}$ values from probes at low f is not evident with experiments of the limited accuracy of Fig. 5.

Assuming a generally accurate η_c calculation, we have plotted various data including a sample of every one of the electrodes in the form of an f_{exp} *vs.* f correlation in Fig. 6. The estimate of R_z/R_∞ or f_{exp} is calculated from $1 - (E_\infty - E_z)/IR_\infty$ where $E_\infty = IR_\infty + \eta_c$ and η_c is obtained with [7], implicitly assuming $i = i_{av}$ at $r = 0$. The range of parameters covered in Fig. 6 is shown in Table III. The straight line is $f_{exp} = f$. We can conclude from both Fig. 5 and 6 that the agreement between f_{exp} and the geometric f based on z and ξ provides confirmation for all electrode geometries tested of the Newman resistance theory (7) for the RDE.

Measurements in the r direction at $z = 0$ for all the electrodes generally support the conclusions from Fig. 5 and 6. The calculated sum of $\eta_c + fIR_\infty$ is always reproduced within a few mV except for certain cases with the cylindrical designs *A1*, *B1*, and *R*, where the measured values tend to be lower. This conforms to expectation with the reduced insulating region around the disk (6). Also, with the limited range of radial f values accessible due to the mantle starting point, we restrict further quantitative presentation to the axial direction. However, it may also be pointed out that some axial and radial mapping was carried out in the J-cell and, even with the more restricted dimensions involved, the slopes and extrapolations followed very closely the conclusions of the above measurements in the more ideal cell. This holds true also for the automatic compensation techniques to be described.

Double probe potential difference.—In the single probe studies summarized in Fig. 6, a 1-mV error ranges from 2-16% of IR_∞. With the additional η_c uncertainty, it is difficult to achieve resolution sufficient to define the region close to the electrode where changes due to nonuniformity may be detected. The double probe method is, in principle, free of the non-ohmic potentials and contains only the further assumption, now documented in Fig. 5 and 6, that the potential between the second probe at f_2 and ∞ may be calculated from $(1 - f_2)IR_\infty$. The most suitable electrode for detailed study was *C*, with the largest radius, approachable to f_1 of < 0.1 at two probe tip diameters. We thus report only such data for this electrode except for supplementary results from *R* in ring-disk experiments.

Six runs yielding $\Delta E + (1 - f_2)IR_\infty$ *vs.* f_1 plots are shown in Fig. 7, with ρ variation obtained for the single solution through $\omega^{1/2}$ control of i_L. The IR_∞ intercept is obtained with [2] and Ai_L values. The pair of ΔE values shown was taken at each position before the cell was moved. Data were taken for increasing z at least until the decreasing ΔE_c and ΔE_a values were within 0.1 mV. (Further increase of ξ gave ΔE decreasing to essentially zero in accordance with theory.) The plots can be compared directly to the theoretical curve in Fig. 1 of Smyrl and Newman (5).

Extrapolation of the experimental $\Delta E + (1 - f_2)IR_\infty$ to $f_1 = 0$ yielded the necessary $\Delta E_{a,o}$ and $\Delta E_{c,o}$ to

Table III. Experimental and calculated parameters of Fig. 6

Symbol	I, mA	$\lvert Ai_L \rvert$, mA	IR_∞, mV	$\lvert \eta_c \rvert$, mV	ρ
×	3.00	0.71	15.7	21.2	1.51
▼	7.00	2.50	17.2	17.1	1.82
•	2.00	2.47	22.8	7.60	3.96
○	−1.00	2.47	11.4	6.65	1.30
△	1.00	0.55	24.1	13.2	2.91
▽	−0.250	0.55	6.02	7.73	0.57
■	2.00	2.53	22.8	7.46	4.01
□	−1.00	2.53	11.4	6.44	1.35
◇	2.00	1.42	31.4	11.3	4.14
▲	40.0	40.0	50.8	8.90	7.90
◆	0.100	0.026	20.2	20.2	1.98

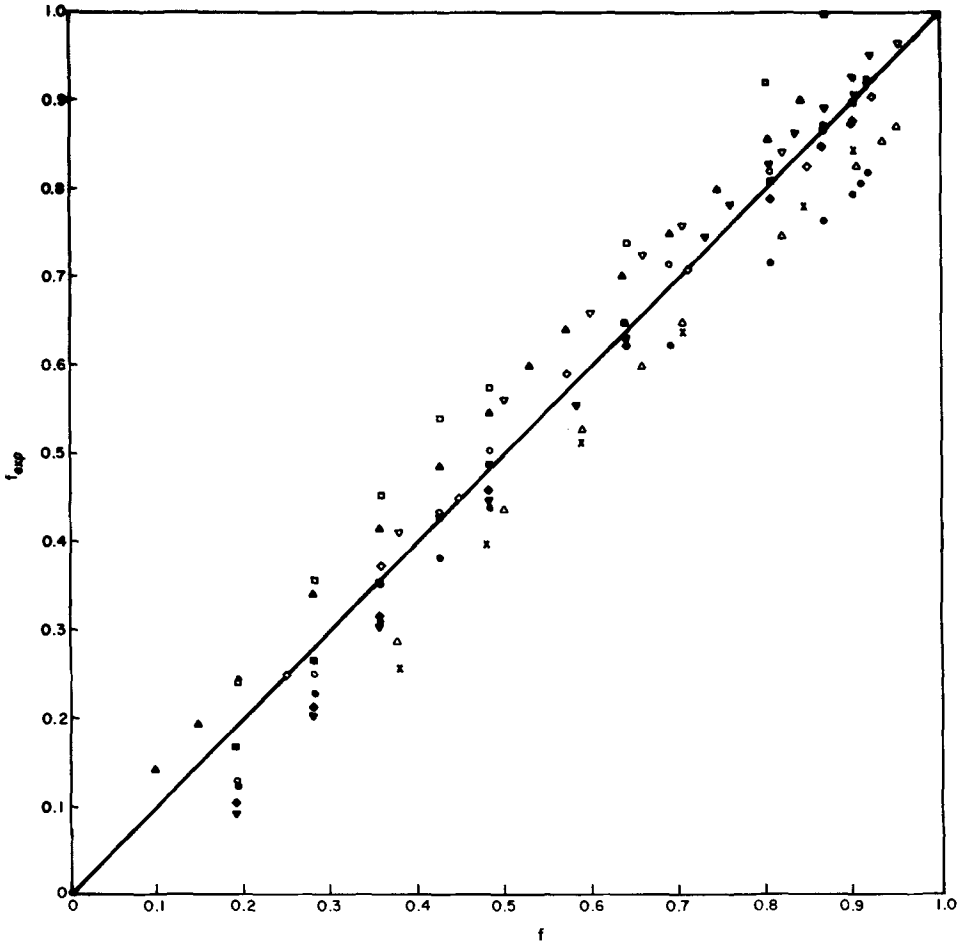

Fig. 6. Experimental f vs. theoretical f. X: *A1*, 1M $HClO_4$ — 5.74 mM Hg_2^{+2}; ▽: *B2*, 1M $HClO_4$ — 5.74 mM Hg_2^{+2}; ●: *B1*, 0.2M $HClO_4$ — 5.74 mM Hg_2^{+2}; ○: *B1*, 0.2M $HClO_4$ — 5.74 mM Hg_2^{+2}; △: *A2*, 0.2M $HClO_4$ — 5.74 mM Hg_2^{+2}; ▽: *A2*, 0.2M $HClO_4$ — 5.74 mM Hg_2^{+2}; ■: *B3*, 0.2M $HClO_4$ — 5.74 mM Hg_2^{+2}; □: *B3*, 0.2M $HClO_4$ — 5.74 mM Hg_2^{+2}; ◇: *R*, 0.2M $HClO_4$ — 5.74 mM Hg_2^{+2}; ▲: *C*, 1M $HClO_4$ — 22.96 mM Hg_2^{+2}; ◆: *B3*, 0.01M $HClO_4$ — 0.0574 mM Hg_2^{+2}. ω = 1600 rpm, all runs. See Table III.

calculate $\Delta E_{a,o}/IR_\infty$ and $\Delta E_{c,o}/IR_\infty$. The intercepts and calculations from Fig. 7 are collected in Table IV along with the ρ_a factors obtained through [2] and [8] and the corresponding $(i/i_{av})_{r=0}$. The six values each of $\Delta E_{c,o}/IR_\infty$ and $\Delta E_{a,o}/IR_\infty$ are used for the ordinates of Fig. 8 points, where the solid line is the theoretical one of Newman's (2) Fig. 5. For each anodic point are plotted two values of $(i/i_{av})_{r=0}$ calculated, respectively, from ρ_a and from a computer program using the extended Newman theory. (The cathodic points all have $(i/i_{av})_{r=0}$ of unity.) The data are in good consonance with the predictions of the theory. The agreement is considered to affirm both the Newman theory and the approximate Albery-Hitchman calculation for the disk center.

Two experiments similar to the above but with ΔE_a and ΔE_c measured as a function of I up to $\pm|Ai_L|$ for two fixed z values are plotted in Fig. 9. Both $\dfrac{\Delta E_c}{\Delta E_a}$ and $\dfrac{\Delta E_c + (1 - f_2)IR_\infty}{\Delta E_a + (1 - f_2)IR_\infty}$ are given in the ordinate *vs.* I/Ai_L. Also shown as abscissa is the ratio $(i_a/i_c)_{r=0}$ corresponding to each point, from ρ calculations as previously. ρ_a at $I = -Ai_L$ is 10.8, giving $(i_a/i_{av})_{r=0} = 0.60$. The ρ_a and ρ_c values become equal as $I \to 0$. The correspondence between the double probe potential ratios and the change in the $(i_a/i_c)_{r=0}$ ratio clearly shows how the shifts in current distribution with current level (δ in the Newman theory) may be detected in this manner. The values of the $\Delta E + (1 - f_2)IR_\infty$ ratios, 1.148 and 1.097, at the fixed f_1 of 0.243 and 0.448, respectively, follow reasonably the predicted 1.194 ratio at $f_1 = 0$ for $(i_a/i_{av})_{r=0} = 0.60$.

Table IV. Experimental and calculated parameters of Fig. 7

ρ_a	Anodic $(i/i_{av})_{r=0}$ From ρ_a	From computer	$\lvert IR_\infty\rvert$, mV	$\Delta E_{a,o}$, mV	$-\Delta E_{c,o}$, mV	$\dfrac{\Delta E_{a,o}}{IR_\infty}$	$\dfrac{\Delta E_{c,o}}{IR_\infty}$
1.91	0.783	0.737	12.3	14.5	15.7	1.179	1.276
2.86	0.733	0.686	18.96	21.7	24.5	1.145	1.292
3.83	0.697	0.653	24.6	27.7	32.1	1.126	1.305
5.80	0.653	0.612	37.3	42.9	47.6	1.150	1.276
7.66	0.627	0.590	49.2	54.5	65.0	1.108	1.321
9.58	0.605	0.575	63.52	68.2	83.0	1.074	1.307

Automatic IR compensation.—Compensation of resistance between the reference probe and disk, assuming the primary current ξ-R_∞ relation, was carried out automatically in two ways with the circuitry of Fig. 3. With a single probe, a cathetometer measurement of z was used to calculate R_z/R_∞ from ξ and then R_z was determined when R_∞ was gained from a conductivity measurement and [2]. The appropriate fraction of current follower output equivalent to a continuous correction IR_z was then fed back and subtracted from the reference potential. The 1K resistor current follower output is divided by 1000, giving a 1 ohm correction modified by the gain of the analog stage, which here can correct for R_z of 0.5 to more than 100 ohms.

The second technique utilized the double probe with known separation and a cathetometer-derived f_1 and thus f_2. ΔE between the probes senses a fraction of IR_∞ equal to Δf. Two convenient analog correction conditions are to set the distance from the disk for $f_1 = \Delta f$ or $f_1 = 2\Delta f$, whence either ΔE or $2\Delta E$ is the correction required for the nearer probe as disk reference. R_∞ determination is not required with double probes.

Both techniques were successfully applied and double probe resistance compensation with the ISCVA technique (20, 26) is shown in Fig. 10, with both linear-time $\omega^{1/2}$ scanning and square wave modulation. In these methods, $I/\omega^{1/2}$ is held constant while I is varied, and the measured E_z is plotted *vs.* I (or *vs.* time, taking data in the steady-state region, for constant $\Delta I/\omega^{1/2}$ under modulation). The $(\partial E_z/\partial I)_c$ or $(\Delta E_z/\Delta I)_c$ outputs corresponding to scan or square

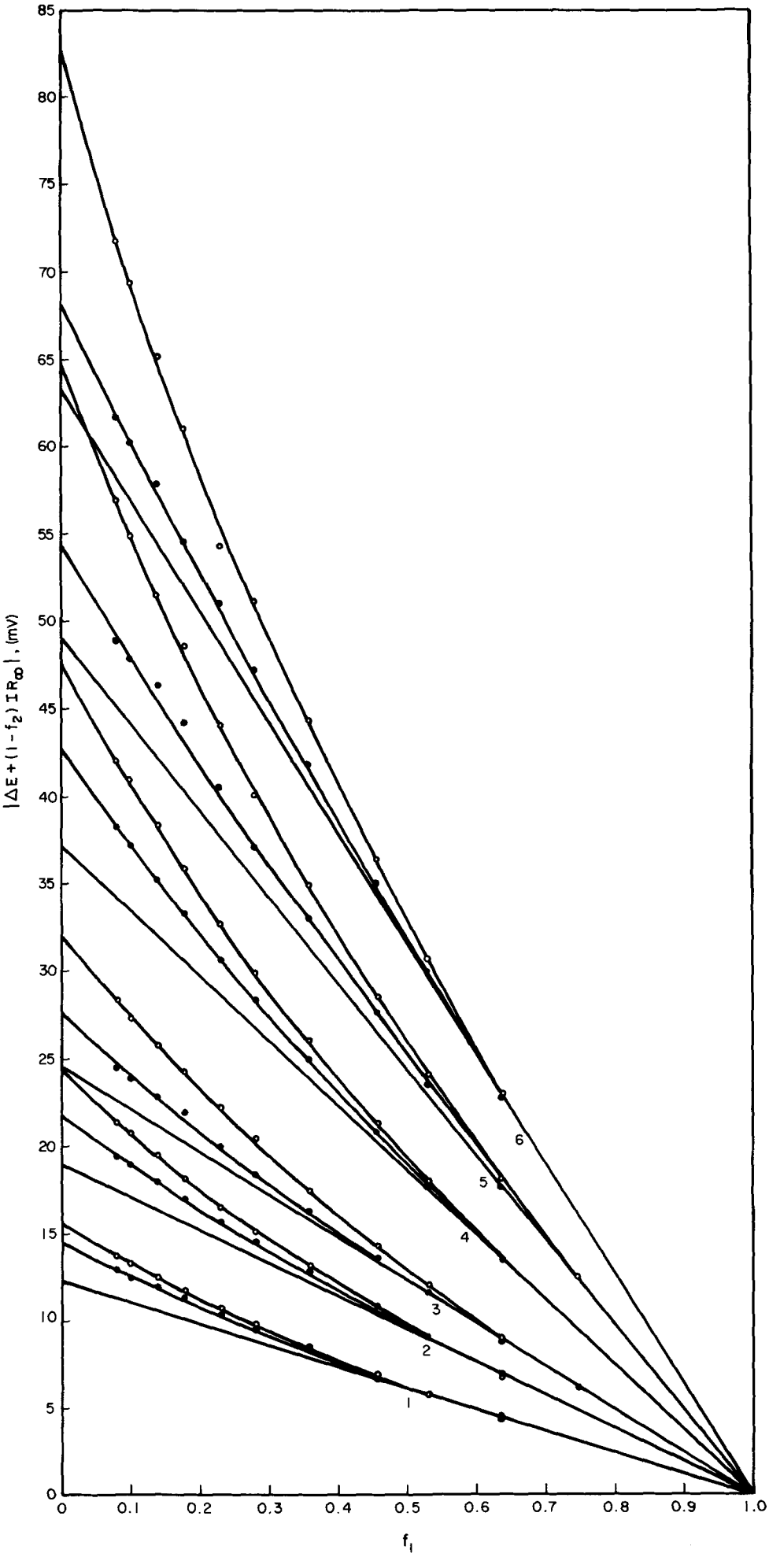

Fig. 7. Double probe $|\Delta E + (1 - f_2)IR_\infty|$ vs. f_1. ○, cathodic (at limiting current) and ●, anodic (at the same magnitude of current). Rotation speed adjusted for desired $I = |Ai_L|$ value. C, 1M $HClO_4$ — 22.96 mM Hg_2^{+2}, $\kappa = 0.320$ mhos-cm^{-1}.

	I,mA	ρ_a
1	−10.0	1.91
2	−14.92	2.95
3	−20.0	3.83
4	−30.3	5.80
5	−40.0	7.66
6	−50.0	9.88

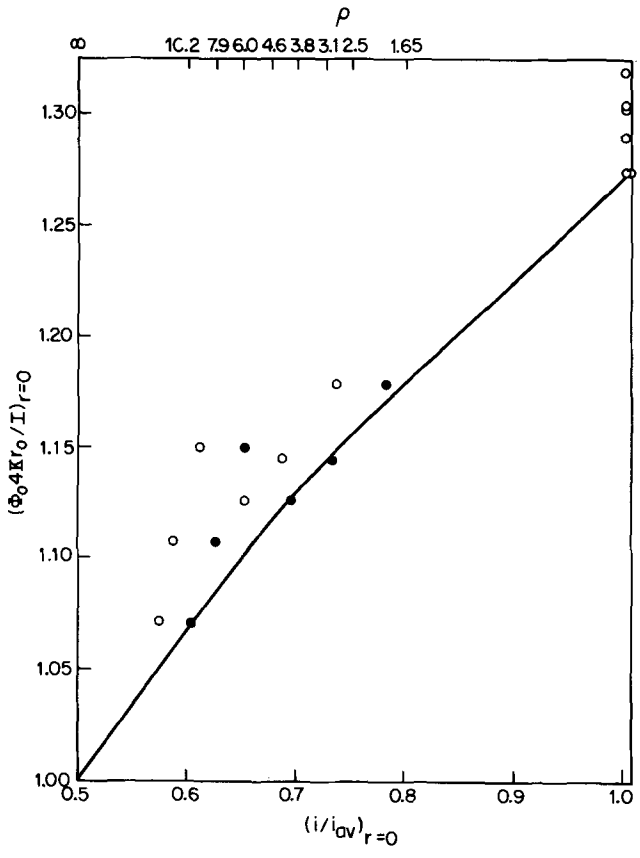

Fig. 8. Experimental values of $\left(\frac{\Phi_0 4\kappa r_0}{I}\right)_{r=0}$ vs. calculated $\left(\frac{i}{i_{av}}\right)_{r=0}$. Abscissa from ρ_a values (●) and from computer calculation after Newman (○), solid line from theoretical plot given by Newman [Fig. 5 of Ref. (2)]. Same data as in Fig. 7 and Table IV.

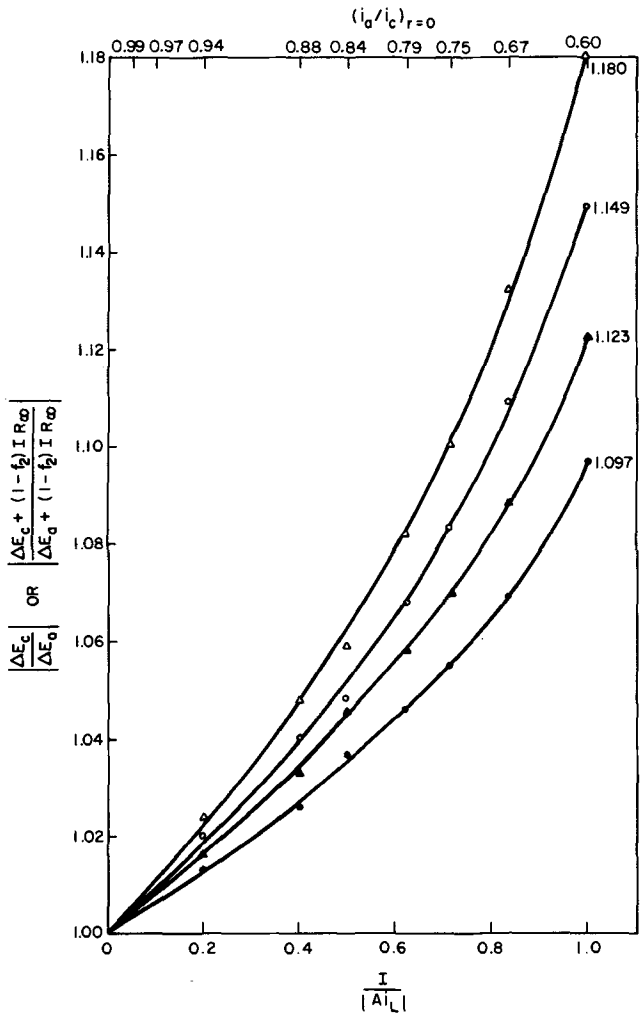

Fig. 9. Ratio of double probe potentials for cathodic and anodic applied current vs. $\frac{I}{|Ai_L|}$.

	zl,cm	f_1
●	0.200	0.448
▲	0.200	
○	0.100	0.243
△	0.100	

● and ○ ordinate $\left|\frac{\Delta E_c}{\Delta E_a}\right|$

▲ and △ ordinate $\left|\frac{\Delta E_c + (1-f_2)IR_\infty}{\Delta E_a + (1-f_2)IR_\infty}\right|$

R, 1M $HClO_4$ — 53.3 mM Hg_2^{+2}, κ = 0.3031 mhos-cm^{-1}. ω adjusted for i_L = −20.0 mA.

wave control are the sum of IR_z and the desired electron transfer resistance, which for the Hg/Hg_2^{++} electrode under the experimental C (5.74 mMC_∞ + 11.4 mM from $I/\omega^{1/2}$) is < 0.02 ohm. This being negligible in comparison to the ohmic resistance to be compensated, about 1.4 ohm, the desired result is an experimental slope or modulation of near zero.

In Fig. 10, traces A and C are the uncompensated slope and $\Delta E/\Delta I$ outputs (measured at 1.42 and 1.35 ohm, respectively) for a setting of $\Delta f = f_1/2$ at the probes. [R_∞ = 2.46 ohms, $2\Delta f$ = 0.586, and $2\Delta f R_\infty$ = 1.44 ohms]. Correction of E_{z1} by $2\Delta E$ (R_g = 5k) gives traces B and D which exhibit the desired compensation. Equivalent results not shown here were obtained by the single probe method.

Ring-disk electrode studies.—Potentiometric measurements.—The mercury disk of R was anodized at various currents into mercury-free 0.2M $HClO_4$, and the potential between ring and disk was measured. The theoretical (IR-free) value (16) of the potential E_R^D from [9] with N_t = 0.366 and $\beta_t^{2/3}$ = 1.108[5] is 14.17 mV. The measured E_R^D up to an I of 5 mA (28 mA/cm²) is given in Fig. 11. Least squares analysis of the line gives an intercept at I = 0 of 14.03 ± 0.05 mV, in satisfactory agreement with theory, and a slope of 6.46 ± 0.02 ohms. Since R_∞ is 14.85 ohms from [2], the indicated values of f and ξ corresponding to the ring as probe are 6.46/14.85 and 0.78, respectively. The radial distance equivalent to this ξ is $\sqrt{[(0.78)^2 + 1]^2 r_0^2}$ = 0.302 cm. The ring radii are 0.263 and 0.324 cm, bracketing this distance.

For the seven points shown in Fig. 11, the ρ values increase with current from 0.11 (nearly uniform current) to 5.8 [$(i/i_{av})_{r=0}$ = 0.67]. In spite of the change in current distribution, a constant ohmic correction factor seems applicable to this experiment. Equation [9] was shown to hold (16) for the Ag/Ag^+ couple independent of I and $\omega^{1/2}$ in 0.1M $HClO_4$, where ohmic drop effects on E_R^D were negligible (I ≤ 30 μA). In the present case, with $\omega^{1/2}$ scanned over wide limits (20-90 $rpm^{1/2}$) at current levels common to Fig. 11, the E_R^D values were constant at each I to ±0.5 mV. The difference between experiment and [9] is still the ohmic drop. No difference in current distribution is expected in the mercury-free solution as a function of $\omega^{1/2}$ since $i_L \cong 0$ at all speeds.

[5] The calculated value (12) of N_t from the gold dimensions is 0.350 and the value consistently found in practice is 0.366 ± 1%. Effects of outward motion of r_0 and r_2 due to the rotating mercury film of less than 2% would account for the difference. This effect tends to cancel in $\beta_t^{2/3}$ where 1.108 was measured and 1.106 calculated.

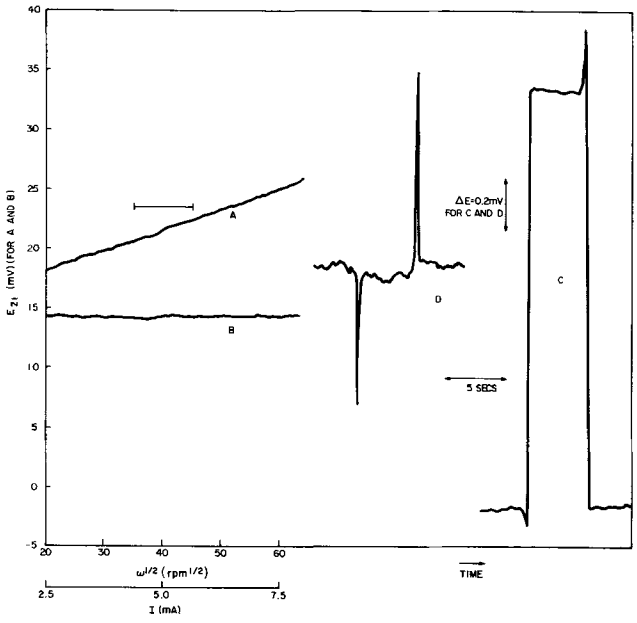

Fig. 10. ISCVA E_{z1} potentials with B2, 1M $HClO_4$ — 5.74 mM Hg_2^{++}, $I/\omega^{1/2} = 0.125$ mA-rpm$^{-1/2}$, $zI = 0.413$ cm, $f_1 = 2\Delta f = 0.586$. Traces A and B vs. I, C and D vs. time. A: uncompensated scan; B: as A, except compensated as in text; C: uncompensated square wave modulation of $\omega^{1/2}$ or I amplitude indicated by horizontal marker above A($\Delta\omega = 45.2 - 35.2$ rpm$^{1/2}$); D: as C, except compensated as in text.

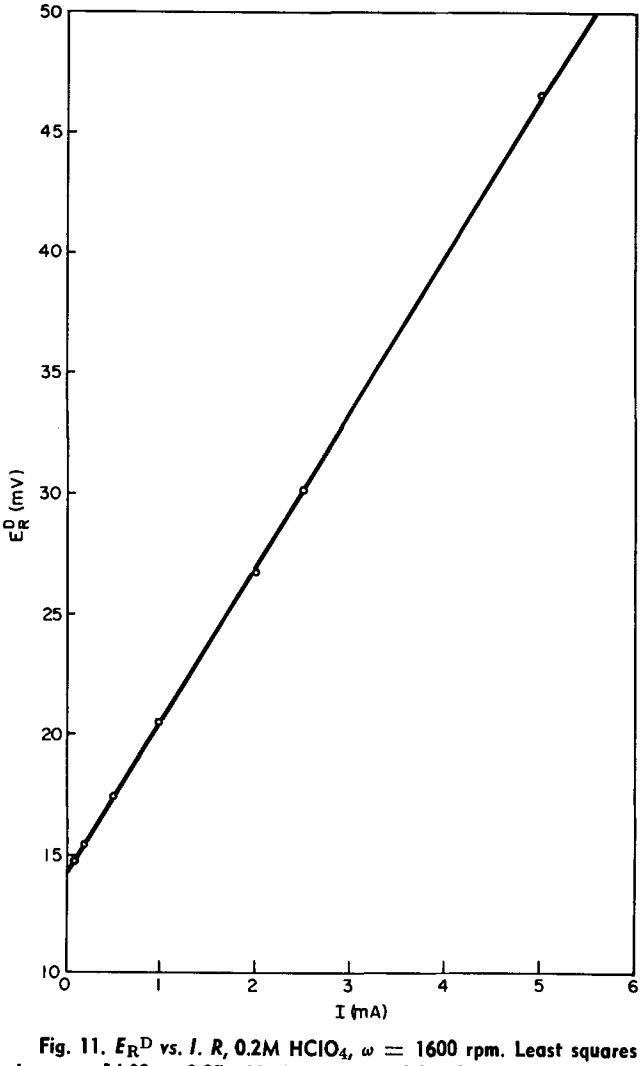

Fig. 11. $E_R{}^D$ vs. I. R, 0.2M $HClO_4$, $\omega = 1600$ rpm. Least squares intercept 14.03 ± 0.05 mV, slope 6.46 ± 0.02 ohm.

With the same system, the potential $E_R{}^{ref}$ was measured over three decades of disk current and therefore of Hg_2^{++} surface concentration. In this one experiment, the probe was a fine-tip Luggin capillary with a saturated calomel reference since the solution was initially mercury-free. The results are the data points (a) in Fig. 12. The reference probe was at an axial ξ of 2, and thus for $R_\infty = 14.85$ ohms, an R_z of 10.5 ohms. In conjunction with the disk-ring resistance from Fig. 11 of 6.50 ohms, this indicates an ohmic drop between ring and reference due to disk current of (10.5-6.5)I. Applying such a correction to 12(a) gives the set of points 12(b). An automatic correction to $E_R{}^{ref}$ is suggested by making R_z equal to the slope of Fig. 11, *i.e.*, $\xi = 0.80$, $z = 0.191$. The best correspondence to a 2.303 $RT/2F$ slope for the upper two decades of disk current was experimentally found at $z = 0.182$ cm. Two sets of data obtained for $E_R{}^{ref}$ for that reference position are shown as (c) in Fig. 12. The line is a theoretical 29.5 mV/decade I plot. Deviations at the lowest currents are mostly due to accumulation of small amounts of Hg_2^{++} in solution from repeated runs.

Reverse effects to those considered above, namely of ring current on $E_D{}^{ref}$, may be readily investigated since the flow pattern is such as not to cause an alteration in the surface concentrations (and Nernst potentials) at the disk by ring processes. $E_D{}^{ref}$ was measured with the axial probe far removed ($f \to 1.0$) and as a function of anodic and cathodic ring current up to 5 mA in Fig. 13. The ring limiting current in the 22.96 mM Hg_2^{++}-1M $HClO_4$ solution was −6.07 mA. The slopes are 1.48 ohm (anodic) and 1.09 ohm (cathodic) in a solution giving $R_\infty = 3.37$ ohms.

The difference in slopes possibly arises from the changing current distributions in cathodic and anodic directions at the ring. Since the ring is not uniformly accessible and tends to infinite current density at the inner edge, overpotential effects will cause a shift of current toward the outer edge. From [8] it is seen that a cathodic current is more effective in contributing polarization resistance than an equal magnitude anodic current. Effects in this direction at the ring make $E_D{}^{ref}$ larger in the anodic case where the current should be relatively higher near the disk-probe axis than for equal cathodic current.

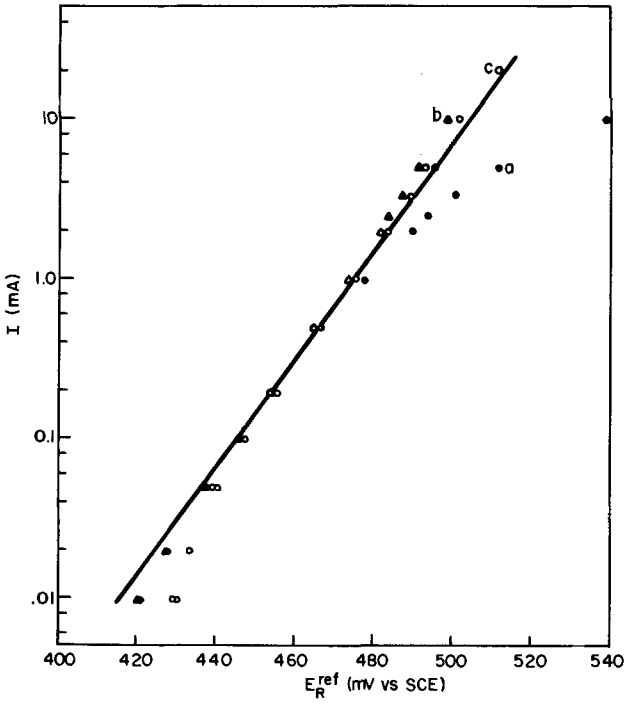

Fig. 12. $E_R{}^{ref}$ vs. log I. R, 0.2M $HClO_4$, saturated calomel reference (ring is positive). $\omega = 1600$ rpm. (a), ● z = 0.478 cm; (b), ▲ a corrected for 4.0 I volt drop; (c), ○ z = 0.182 cm.

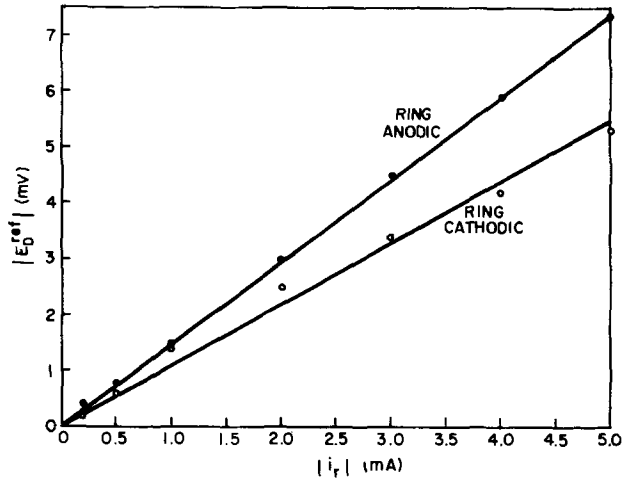

Fig. 13. $|E_D^{ref}|$ vs. $|i_r|$. R, 1M $HClO_4$ — 22.96 mM Hg_2^{+2}, ω = 1600 rpm, z large ($f \rightarrow 1.0$). ●, anodic i_r — least square slope $1.47_5 \pm 0.02$ ohm; ○, cathodic i_r — least square slope 1.09 ± 0.05 ohm.

Coordinated mapping and collection efficiency studies.—Studies were made with electrode R of $\Delta E + (1 - f_2)IR_\infty$ *vs.* f plots and of the values obtained for collection efficiencies N_c and N_a at the same anodic and cathodic currents, $\pm A|i_L|$. The results are summarized in Table V. The value of $(i/i_{av})_{r=0}$ for the anodic case is calculated from ρ and from the three experimental intercepts following the procedure of Fig. 7, except that the extrapolation of the straight portion of the plots was used for IR_∞. The conditions were selected for a high ρ_a and thus a rather nonuniform anodic current. The ratio $N_a/N_c = 1.066$ reflects the higher concentration gradient at the disk edge as sensed in collection efficiency by this particular ring geometry. N_a/N_t determinations for R in mercury-free perchloric acid solutions of various concentrations, as previously done for silver (4), shows a trend with the ρ parameter of about the same level as shown with the current reversal experiment. A combination of these approaches offers a quantitative means to test the relation between disk current distribution, altered systematically, and the resulting collection properties. In the absence of a complete theory, the apparent correlations will not be pursued further here.

Interrupter experiments.—The double probe configuration offers a nearly ideal way to study the transient buildup and decay of the ohmic resistance drop with fast interrupter methods since the changes are not obscured by other sources of potential variation at the disk electrode itself. The total change of ΔE is between zero and the corresponding steady-state values, $I(R_{z2} - R_{z1})$. The latter is what was measured in the double probe mapping experiments and the difference in resistance will be called ΔR here. We wish to compare ΔR to the instantaneous interrupter values for current make and break, $\Delta R'_{on}$ and $\Delta R'_{off}$ (anodic and cathodic), to compare the $\Delta R'$ to the primary distribution prediction of Newman, and to observe the time constant for the change $\Delta R' \leftrightarrow \Delta R$. The previous technique of using $\pm A|i_L|$ to select variable anodic current distribution and a uniform steady-state cathodic current was applied with electronic switching in make and break directions.

The scope pictures have been exactly traced and are shown, for clarity, as the composites for I "on" (Fig. 14) and I "off" (Fig. 15). The four values of $\Delta R'$ determined from the instantaneous change are listed in Table VI. They are within the scope reading error of each other and the theoretical value of 6.7 ohms for the primary resistance R_∞ times $2/\pi$ ($\tan^{-1} \xi_2 - \tan^{-1} \xi_1$), confirming Newman's predictions quantitatively. The steady-state values, ΔR, from the scope pictures compare well to DVM data taken in conjunction and reflect the prevailing current distribution in the manner earlier discussed. For this case $\rho_a = 8.6$ which gives a $(i_a/i_{av})_{r=0}$ of 0.62.

The time constant, τ, of the current decay after the instantaneous drop of the cathodic current in Fig. 15 (time to $1/e$ decrease) is about 120 μsec. The predicted

Table V. Collection efficiency and double probe potential plot data R with $\pm |Ai_L|$ at disk and $E_r = -0.60$ V vs. Hg reference

53.3 mM Hg_2^{+2} — 1M $HClO_4$, ω = 1600 rpm. $N_t = 0.366 \pm 1\%$

	$\rho_c = 0$	$\rho_a = 8.3$	From $\Delta E + (1 - f_2)IR_\infty$ plot and Fig. 8 (ring open circuit)
$(i/i_{av})_{r=0}$	1.00	0.620	0.635

Ai_L, mA	i_r, mA			
−15.15	−11.15	> 5.59	$N_c = 0.369$	$N_a/N_c = 1.066$
0	−16.74			
+15.15	−22.70	> 5.96	$N_a = 0.393$	

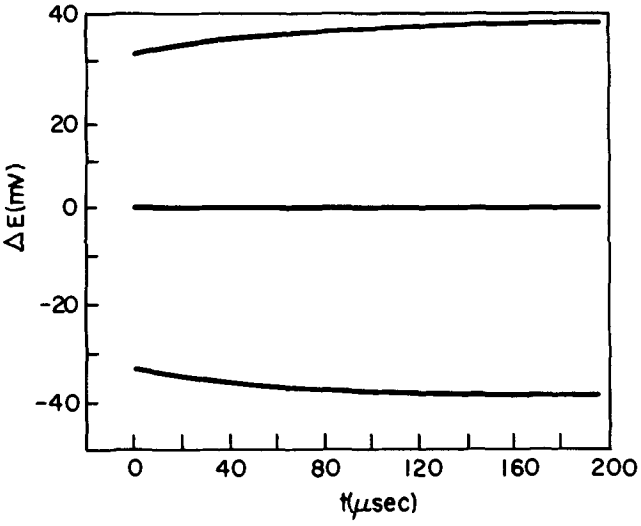

Fig. 14. Interrupter experiments. Double probe potential transient for disk current turned "on". C, 0.1M $HClO_4$ — 4.59 mM Hg_2^{+2}, κ = 0.03565 mhos-cm^{-1}, ω adjusted to give $i_L = -5.00$ mA, $\Delta f = 0.610$. Middle trace: zero current level; lower trace. cathodic current "on" (−5.00 mA); upper trace: anodic current "on" (+5.00 mA).

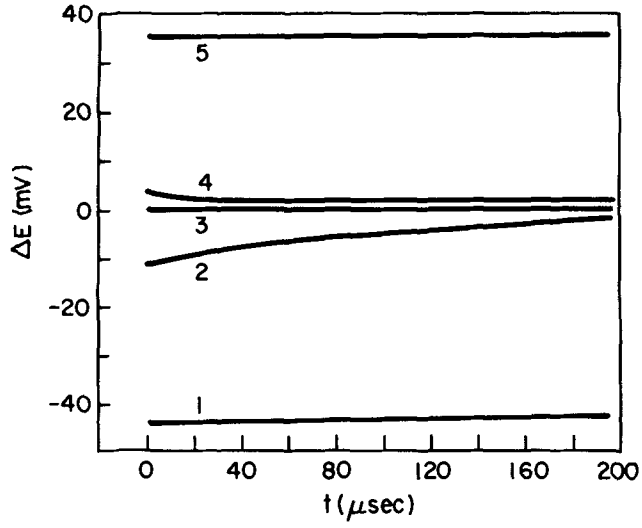

Fig. 15. Interrupter experiments. Double probe potential transient for disk current turned "off." Same electrode and conditions as in Fig. 14. Trace: 1, cathodic current on at steady state; 2, cathodic current "off"; 3, zero current level, all traces; 4. anodic current "off"; 5, anodic current on at steady state.

Table VI. Experimental and theoretical values of resistance from interrupter experiments

	Interrupt				Steady state	
	+ on	+ off	− on	− off	− I	+ I
Ohms, ref. to disk	6.4	6.4	6.5	6.6	8.8 8.7	7.2 (Scope) 7.0 (DVM)
Δf R_∞, ohms	6.7	6.7	6.7	6.7		
Ohms, cell	11.3	11.3	11.5	11.3		

(8)[6] $\iota \cong r_o C_p/4\kappa$, $C_p \cong 28$ μf/cm^2 is reasonable for the ideally polarized surface (limiting current) in 0.1M $HClO_4$.

Also shown in Table VI are the results of interrupter measurements between disk and mercury pool. The four resistances obtained are identical within experimental error. The average value, 11.3_5 ohms, is an experimental measure of R_∞ which, from [2], is 11.0_4 ohms. This is satisfactory confirmation of the geometric assumptions about the cell. However, the suggestion (10) that interrupter data will demonstrate the increased average resistance for uniform current appears incorrect; only the primary R_∞ value will be measured, as follows from Newman (8). The value for uniform current, 1.08 R_∞ (10), is not extractable from the transient data after interruption either, since the polarization and charging processes at the electrodes obscure it.

Interrupter measurements give the correct uncompensated ohmic drop sensed by the reference when current I is flowing in the experimentally limiting case of a steady-state primary current distribution or where the design of cell and electrodes is such that this is coincident with the uniform case. Techniques were employed in this paper which gave good apparent automatic compensation at a RDE in situations where the current distribution was nonuniform. In such cases the interpretation of the resistance corrected potential in terms of electrode processes is not unambiguous. Unfortunately, in the rotating disk system it is not always possible to avoid ohmic drop related nonuniformities even with analytically sized disks and fairly conductive solutions. In the light of the utility of the ρ parameter, which is further documented in this paper, the diagram of Albery and Hitchman (13, 18) correlating the κ, r_o, and $\partial\eta/\partial i$ requirements to keep $\rho \leq 0.1$ (uniform current) deserves special attention, particularly considering the calculational difficulties of employing the full Newman theory (2) in a convenient manner.

Summary

Potential and resistance measurements with well-defined probes have further quantitatively substantiated the Newman theory for current and potential distribution at the RDE. Comparisons of interrupter and steady-state resistance measurements have indicated that transient behavor of the current distribution during the acquisition of the steady state is both a possibly significant experimental factor and another way to detect the nature of the steady-state distribution. For both mapping and resistance methods, the double probe technique is particularly effective. Successful automatic compensation of resistance based on the feedback from precisely located probes through Newman's model is demonstrated, simultaneously corroborating the theory. Observation of nonuniformity of current by potential measurements has been correlated to increases in collection efficiency in a RRDE. The approximate treatment of Newman's theory through the ρ parameter method of Albery and Hitchman is shown throughout this work to be a significant and valid simplification.

[6] A reviewer has informed us of a recent addition of the factor of about 4 to the original equation. The comparison of the limiting current of a fast reaction and ideal polarization is recognized as possibly doubtful.

Acknowledgment

The authors are grateful for many discussions with P. C. Milner, S. Bruckenstein, and J. D. E. McIntyre and to John Newman for generously providing computer programs.

Manuscript submitted June 19, 1972; revised manuscript received Sept. 6, 1972.

Any discussion of this paper will appear in a Discussion Section to be published in the December 1973 JOURNAL.

LIST OF SYMBOLS

A	electrode disk area, cm^2
a,c	subscripts denoting anodic or cathodic directions of current at disk
C_p	differential capacitance, μf/cm^2
C_o	concentration of reactant at electrode surface, mole/cm^3
C_∞	bulk concentration, mole/cm^3
E_R^D	open-circuit potential, disk to ring, V
E_D^{ref}	open-circuit potential, reference to disk, V
E_R^{ref}	open-circuit potential, reference to ring, V
E_r	ring potential (*vs.* reference), V
E_z	single probe potential sensed at z, V
ΔE	double probe potential, V
$\Delta E_{c,o}$, $\Delta E_{a,o}$	extrapolated values of double probe potential to disk surface, V
f	fraction of probe potential sensed at ξ, V
f_{exp}	experimental f
F	Faraday's constant, coulomb/equiv
I	total disk current, A (cathodic current defined as negative, anodic positive)
i	local disk current density, A/cm^2
i_{av}	average disk current density, A/cm^2
i_L	cathodic limiting current density, A/cm^2
i_o	exchange current density, A/cm^2
i_r, i_{rL}	total ring and total ring limiting current, A
J	dimensionless exchange current density [see Ref. (2)]
κ	conductivity of solution, mhos/cm
n	number of electrons transferred per mole of reaction
N	dimensionless limiting current density [see Ref. (2)]
N_t	theoretical collection efficiency
R	universal gas constant, joule/mole-deg
R_z	ohmic resistance, disk to probe at z, ohms
R_∞	ohmic resistance, disk to probe at $z = \infty$, ohms
R_ξ	ohmic resistance, disk to probe at ξ, ohms
r	radial distance (at $z = 0$), cm
r_o	electrode disk radius, cm
r_1	electrode inner ring radius, cm
r_2	electrode outer ring radius, cm
r_c	electrode cylindrical radius, cm
r_m	electrode mantle radius, cm
T	absolute temperature, °K
t_+	transference number of reactant
ω	rotation speed, rpm
z	vertical distance from disk, cm
1,2	identification of nearer probe (1) and farther probe (2)
α,β,γ	kinetic parameters [see Ref. (2)]
β_t	theoretical i_{rL}/Ai_L [see Ref. (12)]
δ	dimensionless average current density [see Ref. (2)]
ξ	rotational elliptic coordinate [see Ref. (7)]
η_c	concentration overpotential, V
η_s	surface overpotential, V
Φ	electrostatic potential, V
Φ_o	external potential extrapolated to electrode surface, V
ρ	ratio of ohmic to total dynamic charge transfer plus concentration overpotential resistances [see Ref. (13) or (18)]

REFERENCES

1. V. G. Levich, "Physicochemical Hydrodynamics," Prentice-Hall, Inc., Englewood Cliffs, N. J. (1962).
2. John Newman, *This Journal*, **113**, 1235 (1966).
3. Vinay Marathe and John Newman, *ibid.*, **116**, 1704 (1969).
4. S. Bruckenstein and B. Miller, *ibid.*, **117**, 1044 (1970).

5. W. H. Smyrl and John Newman, *ibid.*, **119**, 208 (1972).
6. D. H. Angell, T. Dickinson, and R. Greef, *Electrochim. Acta*, **13**, 120 (1968).
7. John Newman, *This Journal*, **113**, 501 (1966).
8. John Newman, *ibid.*, **117**, 507 (1970).
9. J. D. E. McIntyre and W. F. Peck, Jr., *ibid.*, **117**, 747 (1970).
10. L. Nanis and W. Kesselman, *ibid.*, **118**, 454 and 1967 (1971).
11. W. J. Albery and J. Ulstrup, *Electrochim. Acta*, **13**, 281 (1968).
12. W. J. Albery and S. Bruckenstein, *Trans. Faraday Soc.*, **62**, 1920 (1966).
13. W. J. Albery and M. Hitchman, *ibid.*, **67**, 2408 (1971).
14. W. H. Smyrl and John Newman, *This Journal*, **119**, 212 (1972).
15. S. Bruckenstein and B. Miller, Unpublished observations.
16. W. J. Albery, S. Bruckenstein, and D. T. Napp, *Trans. Faraday Soc.*, **62**, 1932 (1966).
17. W. D. Weir and C. G. Enke, *J. Phys. Chem.*, **71**, 280 (1967).
18. W. J. Albery and M. Hitchman, "Ring-Disc Electrodes," Oxford University Press, London (1971).
19. B. Miller, *This Journal*, **116**, 1117 (1969).
20. B. Miller and S. Bruckenstein, *ibid.*, **117**, 1032 (1970).
21. A. C. Riddiford, "Advances in Electrochemistry and Electrochemical Engineering," Vol. 4, P. Delahay, Editor, Interscience, New York (1966).
22. R. H. Sonner, B. Miller, and R. E. Visco, *Anal. Chem.*, **41**, 1498 (1969).
23. S. Barnartt, *This Journal*, **99**, 549 (1952).
24. S. Barnartt, *ibid.*, **108**, 102 (1961).
25. R. N. Adams, "Electrochemistry at Solid Electrodes," Marcel Dekker, Inc., New York (1969).
26. B. Miller, M. I. Bellavance, and S. Bruckenstein, *This Journal*, **118**, 1082 (1971).

Electrocatalysis of Oxygen Reduction by Sodium Tungsten Bronze

I. Surface Characteristics of a Bronze Electrode

J. McHardy*,[1] and J. O'M. Bockris*,[2]

Department of Chemistry, University of Pennsylvania, Philadelphia, Pennsylvania 19104

ABSTRACT

When a metallic crystal of the nonstoichiometric compound sodium tungsten bronze, Na_xWO_3, was used as an oxygen electrode in acidic solution, sodium was lost from the crystal by anodic dissolution, leaving a thin semiconducting layer on the surface. The composition change in the surface layer corresponded to a decrease in x from ~0.7 to ~0.25 for a crystal free of intentional impurities, and from ~0.7 to ~0.05 for a crystal containing traces of platinum. The difference may result from more rapid hole injection in the latter case, associated with the enhanced rate of oxygen reduction observed. The response of the bronze electrode to light revealed a bandgap of ~2 eV and a flatband potential of 0.5-0.6V *vs.* RHE for the semiconducting layer, both apparently independent of platinum content. Donor concentrations in the surface layer determined from $1/C^2$ vs. E (Mott-Schottky) plots were in good agreement with sodium concentrations determined by ion probe mass spectroscopy.

Sodium tungsten bronze, Na_xWO_3, is a nonstoichiometric compound with x a continuous variable from 0 to 1. The compound comprises a WO_3 matrix containing interstitial sodium ions and an equivalent number of quasi-free electrons (1). When x exceeds 0.25, the electrons occupy a conduction band and bestow metallic conductivity on the compound (2). As x increases from 0 to 1, the crystal structure passes through a series of transformations, each representing an increase in symmetry (3). Cubic symmetry in the form of a defect perovskite structure is normally restricted to the composition range $0.4 < x < 1$ but has been extended to considerably lower x values by chemically removing sodium from a crystal initially in the normal cubic composition range (4).

Metallic crystals of sodium tungsten bronze prepared by electrolyzing a molten mixture of Na_2WO_4 and WO_3 were reported to exhibit electrocatalysis for oxygen reduction comparable with platinum (5), but subsequent work demonstrated that the high catalytic activity required the presence of about 100 ppm platinum in the crystals (6). In the course of experiments designed to elucidate the role of platinum in electrocatalysis by Na_xWO_3, it became apparent that the surface of a bronze electrode behaves more like a semiconductor than a metal, and this paper describes an investigation of its semiconducting behavior.

* Electrochemical Society Active Member.

[1] Present address: Pratt and Whitney Aircraft, Middletown, Connecticut 06457.

[2] Present address: The Flinders University, Bedford Park, South Australia 5042, Australia.

Key words: semiconductor electrode, photocurrents, differential capacitance.

Experimental

Preparation of bronze electrodes.—Tungstic oxide obtained from K&K Laboratories was of 99.5% purity. Baker Analyzed sodium tungstate dihydrate was dried for a minimum of 24 hr at 120°C before use.

On the basis of preliminary work, alumina was selected as the crucible material and McDanel ACN high-purity alumina crucibles were used throughout. At first, 40 ml crucibles were used but later on 100 ml crucibles were adopted. The crucible was placed inside a quartz cell which was surmounted by a Pyrex cap and an O-ring seal as described previously (7). Gold wire electrodes (1 mm diameter, 99.99% pure) were sheathed in McDanel high-purity alumina tubes and mounted vertically through the cap of the cell by means of Beckman Teflon tube fittings. Spectroscopic analysis revealed no contamination of the bronze crystals by gold. The cell was heated in a vertical tube furnace (Electro-Applications Inc. No. 620) and the melt temperature maintained at 800° ± 3°C with a Barber Coleman Model 427P Control Unit and a Chromel-Alumel thermocouple in a closed alumina sheath.

Sodium tungstate and tungstic oxide were weighed directly into an alumina crucible which was immediately lowered into the quartz cell. The reagents were fused and allowed at least 4 hr to equilibrate.

A slightly tapered seed crystal about 1.5 × 1.5 × 5 mm cut from a previous crystal with a diamond wheel (Micro-Mech. Inc. Precision Wafering Machine Model WMSA 810) was attached to a gold wire by beating out the tip of the wire into a foil and wrapping it around the wider end of the seed. The seed and a counterelectrode of coiled gold wire were lowered into the melt and allowed a few seconds to warm up.

The constant current employed to grow a crystal was generated by a Dressen Barnes Model 3-150L d-c power supply in series with a Clarostat decade power resistance box. The seed crystal was initially driven anodically at about 10 mA cm^{-2} to clean the surface. The current was then reversed and increased periodically to maintain a cathodic current density of about 5 mA cm^{-2} on the crystal.

The value of x in the bronze crystal increases with the ratio of $[Na^+]$ to $[WO_3]$ in the melt, but the relationship is not a simple one (8). In most cases, the melt composition was 42 m/o (mole per cent) Na_2WO_4: 58 m/o WO_3 and yielded crystals with a sodium content corresponding to $x \sim 0.7$. Electrolysis was continued for about two days and yielded a crystal with (100) faces (cubic morphology) approaching 1 cm on an edge.

Platinum and other impurity elements were introduced into a crystal during its growth by continuous codeposition, a small concentration of the impurity being maintained in the melt by anodic dissolution of the appropriate element. In the case of platinum, for example, the anodic current was divided between the inert (gold) electrode and a 1 cm^2 platinum electrode. The crystal was grown at a fixed total current of 15 mA with a certain fraction of that current passing through the platinum anode. The platinum content of the crystal increased with the fraction of the current passed by the platinum anode, up to a maximum of ~400 ppm at $i_{Pt} = 8$ mA. Attempts to exceed this concentration resulted in a spongy platinum deposit that stifled further crystal growth.

Upon removal from the melt, crystals were allowed to cool in air and were then cleaned of solidified melt with boiling water. Crystals were mounted in Teflon as described previously (9).

Analysis.—Sodium concentrations were determined by measuring the lattice parameter, a, and applying the equation (in angstroms) (10)

$$a = 0.0819x + 3.7846 \quad [1]$$

The lattice parameter of a crystal was measured by the x-ray powder diffraction method using a Phillips Spectrometer and CuKα radiation.

Platinum concentrations were determined by spark emission spectroscopy. Analytical standards were prepared by heating the calculated weight of chloroplatinic acid with a mixture of $3Na_2WO_4$:$2WO_3$:W in nitrogen at 900°C for 2 hr. The ratio of the three reagents was chosen empirically to yield a bronze of x-value close to 0.7 by the reaction (11)

$$\left(\frac{x}{2}\right) Na_2WO_4 + \left(\frac{3-2x}{3}\right) WO_3 + \left(\frac{x}{6}\right) W = Na_xWO_3 \quad [2]$$

The technique had a precision of ±25% and a lower detection limit for Pt of 50 ppm. Other, more precise techniques such as x-ray fluorescence, atomic absorption, and activation analysis suffered from interference by tungsten or sodium.

Optical experiments.—Crystals mounted in Teflon were given a metallographic polish. No special polishing procedure was required until the final stage, when 1μ diamond paste was used instead of alumina. The polishing materials were removed from a crystal by washing it successively in boiling 30% H_2O_2 and boiling conductivity water. The specimen was then mounted in the Teflon assembly (Fluorocarbon Inc. Union Elbow Reducer) shown in Fig. 1.

The test solution was 0.1N $HClO_4$ prepared from reagent grade 70% perchloric acid and conductivity water. The Vycor cell which featured a quartz 50 mm optical window appears in Fig. 2. The reference electrode was the Pd/H electrode, prepared by the method of Fleischmann and Hiddleston (12). Potentials quoted here have been corrected to the scale of a reversible hydrogen reference electrode in the same solution.

A freshly polished specimen was conditioned prior to test by cycling it 20 times between 0.5 and 2.0V at 50 mV sec^{-1}. This procedure was found sufficient to stabilize the current *vs.* potential trace during a sweep. All experiments were performed at room temperature (25° ± 2°C).

The light sources were a series of high-intensity Osram arc lamps operated from a Spectroline Model

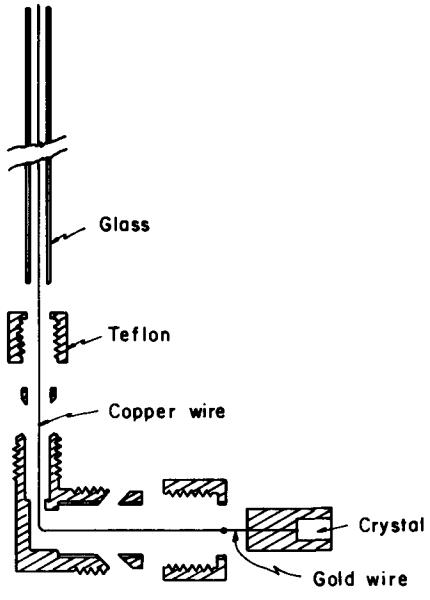

Fig. 1. Teflon and glass crystal mount for optical experiments

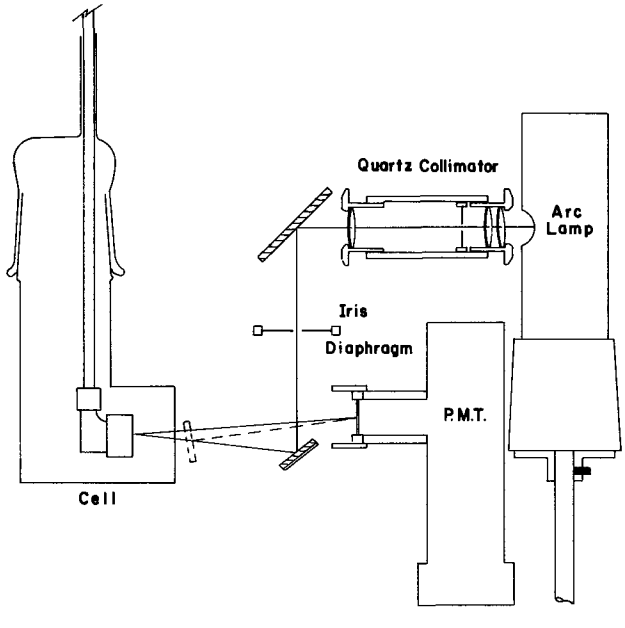

Fig. 2. Apparatus for reflectance spectroscopy

1500 power supply. Each arc lamp put out essentially the line spectrum of a single gaseous element. Monochromatic light was achieved by filtering out all but one line of the spectrum with Spectroline glass filters. The intensity of an arc lamp tended to drift gradually with time, and it was necessary to measure the intensity every few minutes during each experiment. An RCA 1P-21 photomultiplier tube (p.m.t.) in a Schoeffel D-500 housing was used to measure light intensities. The tube was operated at an anode voltage of 500V in conjunction with a Schoeffel Model M-400 photometer. Both the electrochemical experiments and the measurements of light intensity were performed on an optical bench. Preliminary tests showed that for distances greater than about 3 cm a lamp could be treated as a point source of light.

A potassium ferrioxalate chemical actinometer (13) was employed to calibrate the response of the p.m.t. to the two mercury lines at 245 and 365 nm, respectively. The response at other wavelengths was then obtained from the published curve of relative spectral response for this type of p.m.t. (14).

Reflectance spectra were obtained with the arrangement shown in Fig. 2. The weakness of typical reflected intensities necessitated the performance of this part of the work in a dark box. The collimated beam of monochromatic light was reflected into the p.m.t. either by the bronze electrode or by a front surface mirror which was mounted on a hinge so that it could be swung into position in front of the cell window.

Using a triangular voltage sweep generator as the reference input to the potentiostat, the potential of the test electrode was swept at 50 mV sec^{-1} between -1.5 and $+2.0$V. The potential was also applied to the X input of an XY recorder. The intensity of the beam reflected from the electrode surface was measured with the p.m.t. and photometer. A d-c voltage from 0 to 5V put out by the photometer in proportion to the meter reading was applied to the Y input of the XY recorder. The reflected intensity was normalized by comparison with the intensity reflected from the front surface mirror. Absorption by the quartz window and the $HClO_4$ solution was negligible. Potentials were controlled by a Tacussel PIT 20-2 potentiostat and monitored with a Data Technology 350 digital voltmeter. In order to measure the current, the p.d. across a resistor in series with the counterelectrode was fed into a potentiometric electrometer. The output from the null meter of the electrometer was recorded on a 10-in. strip chart recorder to provide a continuous record of the current. A capacitance box in parallel with the measuring resistor could be adjusted from 0 to 200 μf to damp out unwanted oscillations in the recorder trace.

Photocurrents were measured under steady-state potentiostatic conditions. In many cases, the photocurrent was smaller than the dark (background) current and the following procedure was developed to measure it. The voltage signal from the current-measuring resistor was backed off by the potentiometer dials of the electrometer so that the null meter could be set on a more sensitive range (typically corresponding to 10^{-7}A) for a full scale deflection. The recorder could thus register small variations in a relatively large current. The limit of what could be achieved in this way was governed by "a-c noise." To some extent, the a-c noise could be damped out by a suitable choice of capacitance in parallel with the measuring resistor, but RC combinations with time constants larger than 20 sec required too long to register the photocurrent. In practice, the smallest photocurrent that could be accurately measured was about 1% of the dark current.

Capacitance measurements.—Crystals were prepared, polished, mounted in a Fluorocarbon Inc. straight union reducer (9), and stabilized as above. The test solution was 0.1*N* $HClO_4$ prepared from ultrapure acid and triple-distilled water. The solution was prepared and pre-electrolyzed in a closed glass system that included the test cell (15). Prepurified nitrogen was passed through copper turnings heated to 400°C and two columns of molecular sieves (Linde 13X) before being admitted to the test solution.

Differential capacitance was measured as a function of potential by means of galvanostatic charging curves, using the circuit shown in Fig. 3.

Charging curves were obtained by first connecting both the galvanostat and the potentiostat to the cell and then rapidly (10^{-9} sec) opening the circuit between the potentiostat and the counterelectrode by means of the mercury switch. The change in potential produced by the galvanostatic step function (typically 20 mA cm^{-2}) was recorded on a storage oscilloscope. Capacitance was calculated from the initial portion of the trace (<10 μsec) using the equation

$$C = \frac{i}{\frac{dV}{dt}} \qquad [3]$$

The oscilloscope was triggered by the output of the potentiostat which rapidly went into saturation upon disconnection from the cell. Charging curves were obtained every 100 mV, starting from 2.00V and going down.

Ion probe mass spectroscopy.—Specimens for analysis were prepared from unmounted crystals in the following way. Each crystal was metallographically polished on one face, cleaned in isopropanol vapor, rinsed in conductivity water, and suspended in 25 ml of 0.1*N* $HClO_4$ solution so that only the polished face was immersed. The stabilizing procedure described above was applied to each crystal in a fresh sample of solution. The samples of solution were subsequently analyzed for sodium by atomic absorption spectroscopy on a Perkin Elmer Model 300 spectrometer. After stabilizing, a crystal was cut down to yield a polished specimen about 0.7 cm square by 0.25 cm thick. Finally, each specimen was cleaned in isopropanol vapor and rinsed in boiling conductivity water.

Analysis was performed on the CAMECA Ion Analyzer (16). The instrument has the following capabilities: (*i*) mass spectroscopic analysis of an area only a few microns in diameter; (*ii*) the creation of ion images with an optical magnification of 350X; (*iii*) the determination of concentration profiles with depth

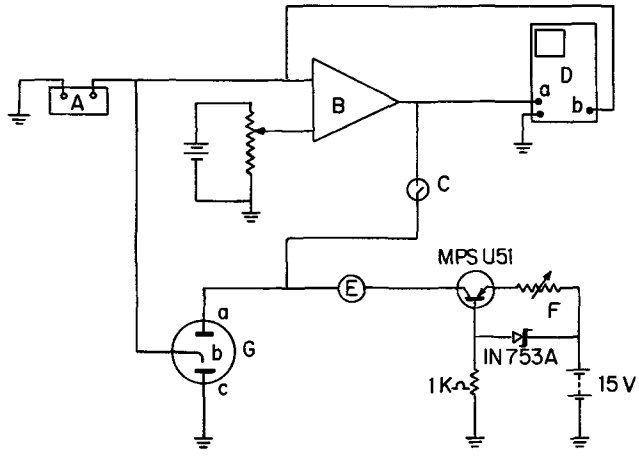

Fig. 3. Circuit for galvanostatic charging curves. A, Data Technology Model 350 digital voltmeter. B, Tacussel Model PIT 20-2 potentiostat. C, Potter and Brumfield mercury wetted relay. D, Tektronix Model 564 storage oscilloscope with 3A7 and 3B3 plug in units; (a) signal input, (b) trigger input. E, Keithley Model 600B electrometer (used as an ammeter). F, Cathodic galvanostat (designed by B.D. Cahan). G, Cell; (a) counterelectrode, (b) reference electrode, (c) working electrode.

of any selected element with a resolution of 50-100Å. Techniques (*i*) and (*ii*) were applied to the study of platinum distribution and that work is covered in Part II of the paper (6). Only the application of technique (*iii*) to the study of sodium distribution is described here.

The mass spectrometer provided a chart of relative intensity (of Na^+ ions in the secondary beam) *vs.* time, corresponding to the sodium concentration of the surface as material was continuously sputtered away. The intensity was calibrated by assuming that the steady value, normally reached within a few seconds, corresponded to the bulk sodium concentration determined from x-ray diffraction data. The penetration was calibrated from the depth of the crater at the end of a "burn" which was measured by Nomarski polarization interferometry (17).

Results

Optical experiments.—Photocurrents were always anodic and depended on wavelength and intensity of the incident light and on electrode potential. The currents did not depend on the history of an electrode or whether the solution was saturated with oxygen or nitrogen.

In all cases, the photocurrents increased in direct proportion to the inverse square of the optical path length (corrected for the refractive index of the solution) between the lamp and the electrode. A typical example appears in Fig. 4. Since the lamp behaved like a point source, the photocurrent was thus a linear function of light intensity. The slope of the line in Fig. 4 corresponds to a quantum yield (ϕ) equal to 1.3% or 0.013 electrons per incident photon.

Typical plots of ϕ *vs.* light frequency at constant electrode potential appear for crystals with and without platinum, respectively, in Fig. 5. Curves drawn through the three points of such curves all extrapolated to $\phi = 0$ at a frequency of $5 \cdot 10^{14}$ sec^{-1}, corresponding to a photon energy of about 2.0 eV.

The variation of ϕ with electrode potential is shown for crystals with and without platinum, respectively, in Fig. 6. The form of the curve was essentially the same in each case, but the value of ϕ at any given potential was lower for the crystal containing platinum.

Results of the reflectance experiments are illustrated by the absorbance *vs.* potential curve in Fig. 7. The curves were similar for all specimens and all frequencies, the absorbance showing no variation except

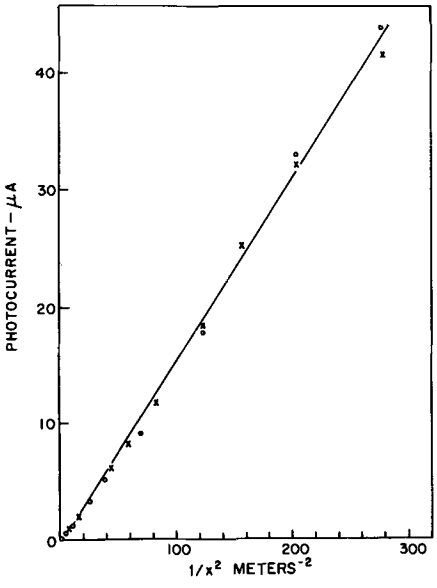

Fig. 4. Variation of photocurrent with inverse square distance from the light source ($E = 1.9V$; $\nu = 11.8 \cdot 10^{14}$ sec^{-1}; Pt = 370 ppm).

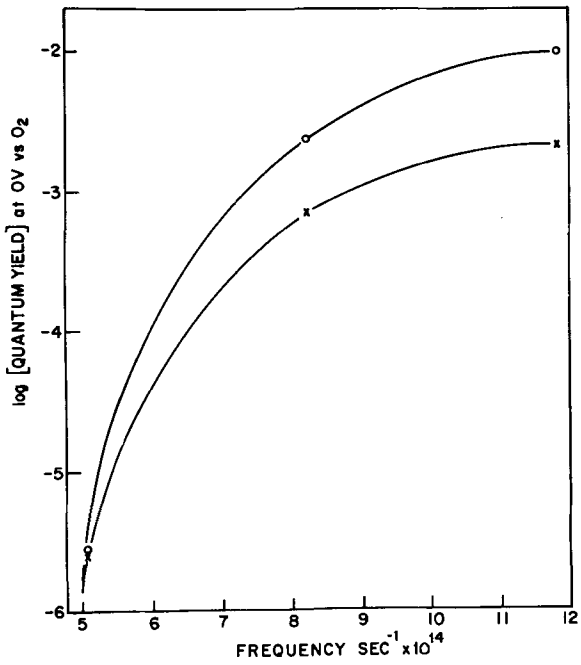

Fig. 5. Variation of quantum yield with frequency: ○ crystal free of Pt; x crystal containing 370 ppm Pt ($E = 1.2V$).

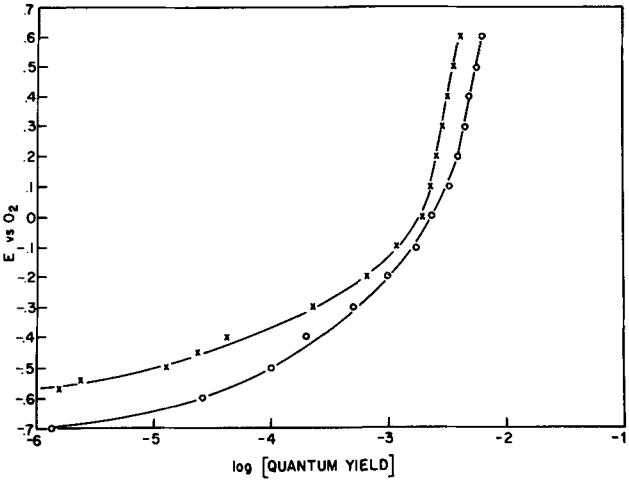

Fig. 6. Variation of quantum yield with electrode potential: ○ crystal free of Pt; x crystal containing 370 ppm Pt ($\nu = 8.2 \cdot 10^{14}$ sec^{-1}).

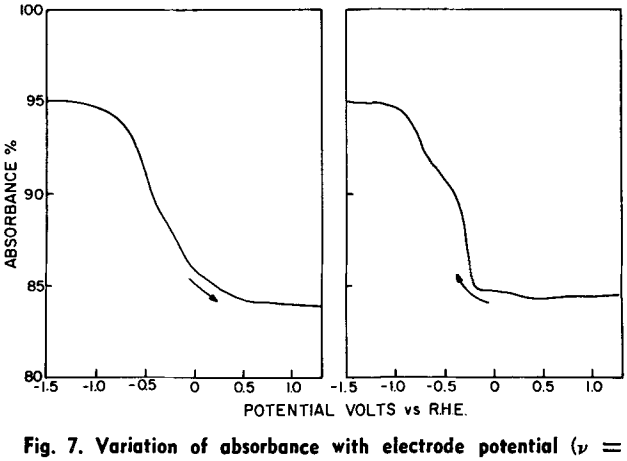

Fig. 7. Variation of absorbance with electrode potential ($\nu = 5 \cdot 10^{14}$ sec^{-1}; Pt = 430 ppm).

in the potential range where color changes have been observed visually (15, 18). The shape of a curve did depend somewhat on the direction in which the poten-

Table I. Average currents and dissolution rates during illumination

	μA	μmoles hr⁻¹
Dark current (I_D)	68	—
Total current (I_T)	113	—
Photocurrent ($I_T - I_D$)	45	—
Sodium dissolution rate	13.4 (calculated)	0.050
Tungsten dissolution rate	—	0.088

(Specimen area 0.3 cm²; Pt content 430 ppm; E = 2.05V; unfiltered Hg arc light.)

tial was changing, an observation suggesting that the color changes result from a solid-state process.

In order to determine what processes were responsible for the photocurrent, the following experiment was performed. Using conditions that favored a large photocurrent illumination was continued for 7.5 hr. Every 2.5 hr a 50-ml sample of the test solution was removed and replaced by 50 ml of the stock solution. The sample was subsequently analyzed for sodium by atomic absorption and for tungsten as the thiocyanate complex by spectrophotometry (19). Results of the experiment expressed as average currents are given in Table I. They show that sodium dissolution accounts for ~30% of the photocurrent at 2.05V.

Capacitance measurements.—At potentials above 1.0V, the differential capacitance of a bronze electrode obeyed the Mott-Schottky equation (20) which may be written (making the usual assumption that the entire Galvani p.d. acts across the space charge region)

$$\frac{1}{C^2} = \frac{8\pi}{eN_D\epsilon}[(E - E_{fb}) - kT/e] \qquad [4]$$

where e is the electronic charge, N_D the donor concentration, ϵ the dielectric constant, and E_{fb} the flatband potential. The slope of a $1/C^2$ *vs.* E plot thus yields the donor concentration, and the intercept yields the flatband potential. Representative plots of $1/C^2$ *vs.* E (Mott-Schottky plots) for crystals with and without platinum, respectively, appear in Fig. 8. A computer least-squares fit of the experimental points from 2.0 through 1.2V was used to determine the slope and intercept of each Mott-Schottky plot, and the results for five crystals appear in Table II.

No data were available on the dielectric constant of Na_xWO_3, so a value for WO_3, derived by Kir'iashkina *et al.* (21), was used. They measured dielectric permittivities of compressed powders as a function of density and obtained a mean value for the ratio of ϵ to ρ (the

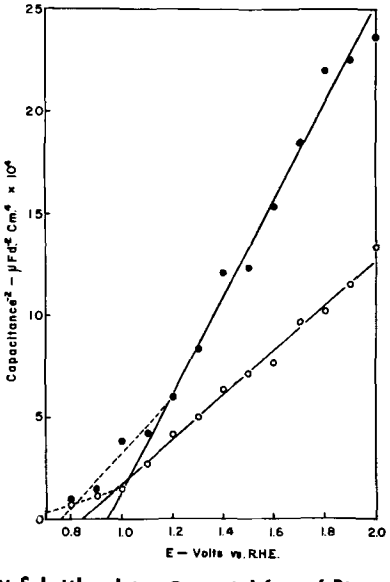

Fig. 8. Mott-Schottky plots: ○ crystal free of Pt; ● crystal containing 290 ppm Pt.

Table II. Donor concentrations calculated from Mott-Schottky plots

Pt content in ppm	Donor concentration, N_D, in cm⁻³	Equivalent x-value
0	2.5×10^{21}	0.14
70	2.3×10^{21}	0.13
120	2.9×10^{21}	0.16
290	1.2×10^{21}	0.06
390	0.8×10^{21}	0.04

density in gram-centimeter⁻³) of 6.93. The density of WO_3 with the cubic bronze structure (estimated by substituting $x = 0$ in Eq. [1]) is 7.2 g-cm⁻³ and hence ϵ is about 50. The presence of sodium undoubtedly alters ϵ, but since the surface layer is so depleted in sodium, the error is probably not serious.

At potentials below 1.0V the differential capacitance of a bronze electrode rose rapidly with decreasing potential, reaching values of several hundred μf-cm⁻² which were too large to permit accurate measurement.

Ion probe mass spectroscopy.—Typical results of sodium concentration *vs.* depth for crystals with and without platinum, respectively, are reproduced in Fig. 9. There was a sodium-depleted surface in both cases but the depleted layer was thinner and much lower in sodium for crystals containing platinum. The initial peak results from chemical enhancement of the sodium emission by adsorbed oxygen (22). The peak height was used to estimate relative sodium concentrations where they were too low to read off the chart. Data calculated from the concentration profiles and the sodium analyses of test solutions are summarized in Table III. The two sets of data agree in general to within half an order of magnitude.

Discussion

Sodium distribution.—Both ion probe analysis of a crystal and atomic adsorption analysis of the solution it was tested in demonstrated that sodium was lost from the surface. The variation of sodium concentration with depth approximated to a step function, where the rising part of the step had a slope dx/dl of about 10^6 cm⁻¹ (Fig. 9). For a platinum-free crystal of $Na_{0.7}WO_3$ the composition of the surface layer after a stabilization treatment corresponded to $x \simeq 0.25$ and its depth was between 500 and 2000Å. For a crystal of the same bulk sodium content but containing platinum, the surface layer had an x value of about 0.05 and a depth between 200 and 400Å.

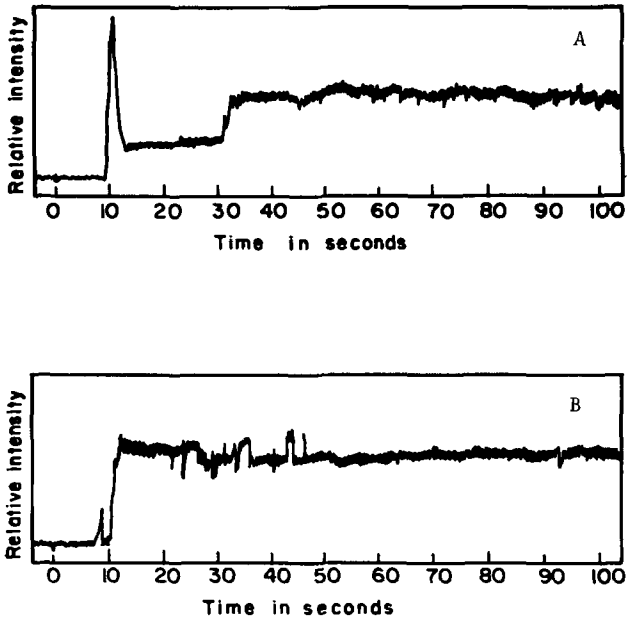

Fig. 9. Sodium concentration profiles: A, crystal free of Pt; B, crystal containing 59 ppm Pt.

Table III. Comparison of ion probe analysis of sodium depleted layers with sodium analysis of the test solutions

Pt content in ppm	Depth of depleted layer in Å	x-Value in depleted layer	Sodium lost in $\mu g\ cm^{-2}$	
			From ion probe results	From analysis of the solution
0	1370	0.26	4.1	8.8
0	460	0.16	1.6 *	2.3
0	480	0.19	1.5 *	
0	460	0.28	1.2	6.0
0	1870	0.30	5.1	4.2
54	—	0.04	—	1.8
59	380	0.03	1.7	3.6
62	270	0.06	1.2	5.7
76	—	0.05	—	28.4
165	—	—	—	7.4

* Two areas were examined on one crystal.

A sodium ion that moves out from the bulk of the crystal to the bulk of the solution must pass through three distinct regions: (*i*) the metal/semiconductor interphase in the crystal, (*ii*) the semiconductor region, and (*iii*) the semiconductor/solution interphase. The passage through each region will have its own rate constant, k_1, k_2, k_3, respectively, and the relative magnitude of the three constants will govern the qualitative form of the sodium concentration profile; some of the possibilities are sketched in Fig. 10. The type of reasoning employed in constructing these hypothetical profiles was as follows. Consider the case $k_3 > k_1,k_2$: this means that passage of sodium through regions (*i*) and (*ii*) is difficult, but that anodic dissolution of sodium out of the surface is easy. Concentration gradients will therefore build up across regions (*i*) and (*ii*) but the concentration of sodium just inside the surface will be vanishingly small.

Comparison of Fig. 9 and 10 reveals that the surface of a Pt-free crystal is characterized by the relation $k_2 > k_1,k_3$, while the surface of a crystal containing Pt is characterized by the relation $k_1 < k_2,k_3$. In both cases, k_1 is small and k_2 is large. The major difference is in the rate constant for the electrochemical step, k_3, and a possible explanation in terms of hole injection is proposed in the next section.

Formation of a semiconducting layer.—Hole injection, i.e., the removal of electrons from the valence band of a semiconductor, is tantamount to the breaking of molecular bonds, and frequently results in oxidative decomposition of the semiconductor (23). In the case of compound semiconductors, decomposition occurs by anodic dissolution of the most electronegative element, *e.g.*, holes generated in a zinc oxide electrode by illumination cause decomposition by the reaction

$$ZnO + 2h^+ \rightarrow Zn^{2+} + \tfrac{1}{2} O_2 \qquad [5]$$

In this example, the holes are created by exciting electrons from the valence band into the conduction band of the semiconductor, but holes may be generated in the dark if highly oxidizing species are present on the semiconductor surface. For example, •OH radicals formed on the surface of gallium phosphide during the reduction of H_2O_2 can be further reduced by reaction with electrons from the valence band (24).

Sodium tungsten bronze is metallic for x values down to 0.25 (2) and no shortage of "holes" exists to limit the initial rate of sodium dissolution. Below $x = 0.25$, however, the material is an n-type semiconductor (4), and holes are scarce. Immersion of metallic Na_xWO_3 in acidic solution will therefore result in a loss of sodium by a corrosion mechanism until x in the surface reaches 0.25

$$Na_xWO_3 \rightarrow Na_{0.25}WO_3 + (x - 0.25)Na^+ + (x - 0.25)e^- \qquad [6]$$

$$H^+ + e^- \rightarrow \tfrac{1}{2} H_2 \qquad [7]$$

Thereafter, further sodium loss from the bronze will be limited by solid-state diffusion. If now a supply of holes is provided, x can fall below 0.25 as sodium is lost by the reaction

$$\frac{1}{x} Na_xWO_3 + h^+ \rightarrow Na^+ + \frac{1}{x} WO_3 \qquad [8]$$

The source of holes may be the excitation of valence electrons into the conduction band by illumination (vide infra), or possibly the reduction of highly oxidizing species on the electrode surface. Such species could be formed as reaction intermediates in the reduction of oxygen to water. Hole injection will then be more rapid into a crystal containing platinum than into one free of platinum because oxygen reduction proceeds thousands of times faster when platinum is present (6). Consequently, the sodium concentration in the surface should fall to lower values for a crystal containing platinum than for one free of platinum.

Properties of the semiconducting layer.—A minimum photon energy of 2 eV was required to produce a

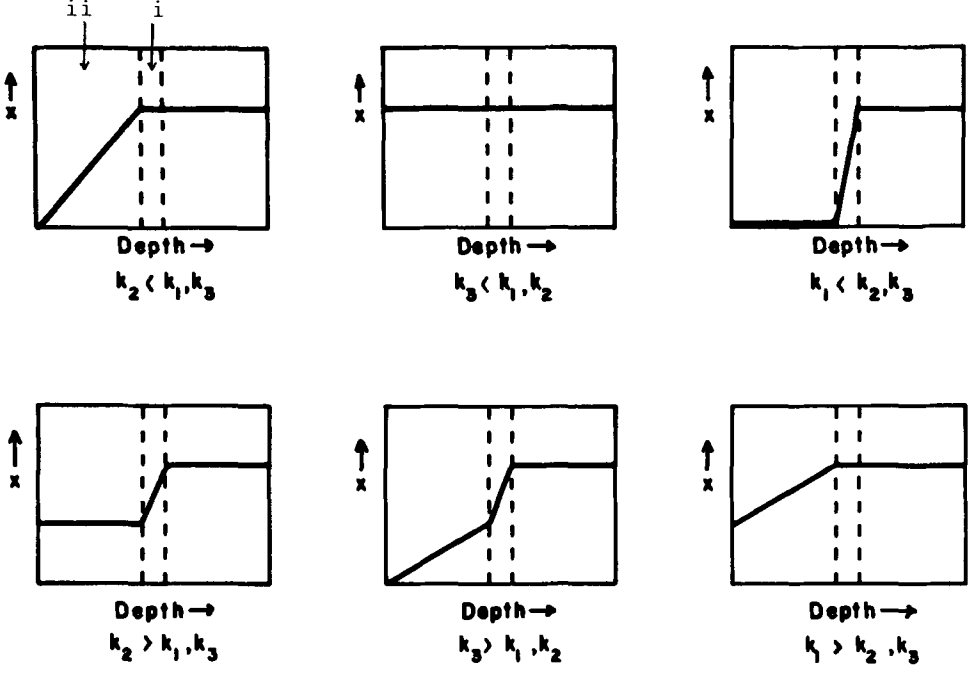

Fig. 10. Hypothetical sodium concentration profiles for various relative diffusion and dissolution rate constants. The ordinate represents x in Na_xWO_3.

photocurrent in a crystal irrespective of platinum content, and this energy threshold undoubtedly corresponded to the bandgap of the semiconductor. By comparison, the bandgap of WO_3, also an n-type semiconductor, is about 2.7 eV (25).

The form of ϕ-E curves (Fig. 6) is qualitatively consistent with the following regime:

(*i*) Electron-hole pairs excited by the incident light are drawn apart by the electrostatic field in the semiconductor.

(*ii*) The electrostatic field will depend on the term $(E - E_{fb})$ where E_{fb} is the flatband potential. When $E = E_{fb}$ the field is zero and recombination is very rapid. Above E_{fb} the concentration of holes in the surface will increase exponentially with $(E - E_{fb})$.

(*iii*) Holes at the surface will participate in electrode reactions at a rate proportional to their concentration. The photocurrent will thus be zero at the flatband potential and then increase exponentially with potential until it approaches the rate at which holes are generated. Thereafter a limiting current will be observed.

The photocurrent on a crystal containing Pt was several times smaller than that on a Pt-free crystal. The difference correlates well with the effect of platinum in lowering the sodium concentration in the surface, and confirms that the photoreaction is sodium dissolution according to Eq. [8]. Above the reversible OER (oxygen evolution reaction) potential, however, the possibility of oxygen evolution by hole capture must be considered

$$2H_2O + 4h^+ \rightarrow O_2 + 4H^+ \qquad [9]$$

The distribution of the photocurrent between reactions [8] and [9] may be estimated for the case of a crystal at 2.05V from the data in Table I. Since sodium dissolution accounted for 30% of the total photocurrent, oxygen evolution by hole capture apparently contributed ~70%. In Fig. 6, ϕ increases threefold between 1.23 and 2.00V. It follows that the photocurrent due to sodium dissolution at 2.05V is equal to the total photocurrent at 1.23V (where Reaction [9] can make no contribution) and therefore that the sodium dissolution rate is independent of potential in this range. Tungsten probably enters the acidic solution as colloidal WO_3 formed when sodium concentrations in the surface drop below the level needed to stabilize the cubic lattice (4) and the structure collapses.

By analogy with Dewald's results on zinc oxide (26), the Mott-Schottky behavior of electrode capacitances at anodic potentials characterizes the bronze surface as a wide bandgap n-type semiconductor, but Mott-Schottky behavior has not previously been reported on such heavily doped material. In spite of this fact, the Mott-Schottky results (Table II) are in reasonable agreement with the results of ion probe analysis (Table III), confirming both the absolute magnitude of the surface x-values and the tendency for x to decrease as platinum is introduced.[3]

The electrode potential at which photocurrents ceased to be manifest on bronze electrodes provides an estimate of the flatband potential E_{fb} of 0.5-0.6V. By contrast, Mott-Schottky plots give E_{fb} as 0.8-0.9V; the discrepancy is discussed below.

Surface redox reactions.—(*i*) *High potentials.*—Discontinuities in Mott-Schottky plots at 1-1.2V (Fig. 8) suggest that a sharp decrease in donor concentration occurs as the potential is raised. This is the reverse of the normal effect, *e.g.*, for WO_3 (27), in which certain donor levels are activated only at high potentials. Furthermore, results to be presented in Part II (6) indicate that the surface of the bronze electrode undergoes a reversible oxidation reaction close to the oxygen electrode potential. The value of E_{fb} obtained by extrapolating Mott-Schottky plots from potentials above 1.2V thus pertains to the "oxidized" bronze surface. The fact that E_{fb} from Mott-Schottky data exceeds E_{fb} from optical data supports the idea of a lower donor concentration at the higher potentials (28).

The reversibility of the surface reaction and its close correspondence with the OER betoken a mechanism in which oxygen atoms in excess of the normal stoichiometry enter and leave the lattice

$$H_2O + nNa_xWO_3 \rightleftarrows 2H^+ + 2e^- + nNa_xWO_{(3+1/n)} \qquad [10]$$

The excess oxygen present at high potentials would lower the apparent donor concentration. Ingold and DeVries (29) found that sodium tungsten bronze can exist with O:W ratios that range from 3 to 3.5, thus the value of n in Eq. [10] could be as low as 2, in which case the reaction would involve one electron transfer per unit cell, or approximately 10^{-4} coulombs cm^{-2} per monolayer of Na_xWO_3.

(*ii*) *Intermediate potentials.*—Unlike the C-E curve of the zinc oxide electrode (30) which levels off at the capacitance of the Helmholtz double layer, the bronze capacitance continued to rise with decreasing potential, reaching several hundred $\mu f\text{-}cm^{-2}$. Such large values signify the presence of a pseudocapacitance, arising from a faradaic adsorption equilibrium. The coverage by adsorbed species, θ, is a function of potential, and since each value of θ corresponds to the accumulation of a certain charge, the variation of θ with potential gives rise to a pseudocapacitance.

Bockris and Kita (31) showed that large capacitances observed on iron electrodes during galvanostatic transients could be explained in terms of the quasi-equilibrium

$$H^+ + e^- \rightleftarrows H_{ads} \qquad [11]$$

Although proton discharge according to Reaction [11] is unlikely to occur at potentials high enough to account for the large capacitances observed, a reaction involving surface polytungstate groups could produce the same effect, *e.g.*

$$\begin{array}{c} | \\ -W-O^- \\ | \end{array} + H^+ \rightleftarrows \begin{array}{c} | \\ -W-OH \\ | \end{array} \qquad [12]$$

Analogous reactions have been advanced to explain the pH dependence of the flatband potential of germanium electrodes (32).

(*iii*) *Low potentials.*—Standard equilibrium potentials according to Pourbaix (33) for redox reactions in the W-O-H system are listed in Table IV. Since all the redox potentials lie close to 0.0V, the color changes undergone by the bronze surface in this region might result from one of these reactions. A further possible reaction, postulated in a similar system by Hobbs and Tseung (34), involves the formation of hydrogen tungsten bronze

$$xH^+ + xe^- + WO_3 \rightleftarrows H_xWO_3 \qquad [13]$$

but Armstrong *et al.* (35) claim that no hydrogen enters the lattice unless the potential is below −0.2V. Both the complex shape of the reflectance *vs.* potential curve (Fig. 7) and the visual detection of several discrete color changes (15, 18) indicate that more than one redox reaction may occur. The color change close

Table IV. Standard equilibrium potentials for the W-O-H system in acid solution (33)

Reaction	E^0 *vs.* NHE in volts at 25°C
$W + 2H_2O \rightarrow WO_2 + 4H^+ + 4e^-$	−0.119-0.059 pH
$2WO_2 + H_2O \rightarrow W_2O_5 + 2H^+ + 2e^-$	−0.031-0.059 pH
$W_2O_5 + H_2O \rightarrow 2WO_3 + 2H^+ + 2e^-$	−0.029-0.059 pH
$W + 3H_2O \rightarrow WO_3 + 6H^+ + 6e$	−0.090-0.059 pH

[3] The surprising success of the Mott-Schottky equation in describing the behavior of highly doped semiconductors may reflect the "exhaustion" of the surface by mobile carriers at potentials where the equation applies.

to 0.0V may result from a reaction such as

$$W^{6+} + e^- \rightleftarrows W^{5+} \quad [14]$$

and color changes at lower potentials may involve hydrogen. The hysteresis in the reflectance curve could mark the latter reaction as being relatively slow.

(iv) Implications for the OER.—The precise identity of each redox reaction undergone by the surface of a bronze electrode between −1.0 and +2.0V *vs.* RHE has not been established, but there are at least three processes involved. At oxygen evolution potentials the surface layer enters a highly oxidized state, perhaps analogous to the pertungstate ion, $W_2O_7^=$. Between the reversible potentials of the OER and the HER, surface groups react with protons in solution, and at lower potentials one or more reactions cause color changes. Unsuccessful attempts elsewhere to detect activity for oxygen reduction by nonsteady-state techniques undoubtedly failed because the OER was masked by reactions involving the substrate. No such difficulties arise under steady-state conditions.

Manuscript submitted May 15, 1972; revised manuscript received Aug. 10, 1972.

Any discussion of this paper will appear in a Discussion Section to be published in the December 1973 JOURNAL.

REFERENCES

1. J. B. Goodenough, *Prog. Solid State Chem.*, **5**, 315 (1971); P. Hagenmuller, *ibid.*, **5**, 86 (1971).
2. H. R. Shanks, P. H. Sidles, and G. C. Danielson, *Advan. Chem.*, **39**, 237 (1963).
3. A. S. Ribnick, B. Post, and E. Banks, *ibid.*, **39**, 247 (1963).
4. W. McNeill and L. E. Conroy, *J. Chem. Phys.*, **36**, 87 (1962).
5. D. B. Sepa, A. Damjanovic, and J. O'M. Bockris, *Electrochim. Acta*, **12**, 746 (1967); A. Damjanovic, D. B. Sepa, and J. O'M. Bockris, *J. Res. Inst. Catalysis*, **16**, 1 (1968).
6. J. O'M. Bockris and J. McHardy, *This Journal*, **120**, 61 (1973).
7. R. A. Fredlein and J. McHardy, *Proc. 24th Annual Power Sources Symp.*, 177 (1970).
8. R. A. Fredlein and A. Damjanovic, *J. Solid State Chem.*, **4**, 94 (1972).
9. Z. Nagy and J. McHardy, *This Journal*, **117**, 1222 (1970).
10. B. W. Brown and E. Banks, *J. Am. Chem. Soc.*, **73**, 5427 (1951).
11. M. E. Straumanis, *ibid.*, **71**, 679 (1949).
12. M. Fleischmann and J. N. Hiddleston, *J. Sci. Inst. (J. Phys. E.), Ser. 2*, **1**, 667 (1968).
13. J. G. Calvert and J. N. Pitts, "Photochemistry," p. 782, John Wiley & Sons, Inc., New York (1967).
14. R.C.A. Technical Manual PT-60, R.C.A., Lancaster, Pa. (1963).
15. J. McHardy, Ph.D. Thesis, Univ. of Pennsylvania (1971).
16. F. W. Karasek, *Research/Development*, **21**, 32 (1970).
17. G. Nomarski and A. R. Weill, *Rev. Met. (Paris)*, **52**, 121 (1955).
18. E. O. Brimm, J. C. Brantley, J. H. Lorenz, and M. H. Jellinek, *J. Am. Chem. Soc.*, **73**, 5427 (1951).
19. F. D. Snell and C. T. Snell, "Colorimetric Methods of Analysis," D. Van Nostrand Co., Inc., New York (1958).
20. V. A. Myamlin and Yu. V. Pleskov, "Electrochemistry of Semiconductors," Plenum Press, New York (1967).
21. Z. I. Kir'iashkina, F. M. Popov, D. L. Bilenko, and V. I. Kiriashkin, *Soviet Phys.-Tech. Phys. (Engl. Transl.)*, **2**, 69 (1967).
22. G. Slodzian and J. F. Hennequin, *C.R. Acad. Sci. Paris, Ser. B.*, **263**, 1246 (1966).
23. H. Gerischer and W. Mindt, *Electrochim. Acta*, **13**, 1329 (1968).
24. H. Gerischer, *Surface Sci.*, **18**, 97 (1969).
25. J. M. Berak and M. J. Sienko, *J. Solid State Chem.*, **2**, 109 (1970).
26. J. F. Dewald, *J. Phys. Chem. Solids*, **14**, 155 (1960).
27. A. M. Baticle, P. Lemasson, F. Perdu, P. Vennereau, and J. Vernieres, *C.R. Acad. Sci. Paris, Ser. B*, **268**, 1203 (1969).
28. J. F. Dewald, *J. Phys. Chem. Solids*, **17**, 334 (1961).
29. J. H. Ingold and R. C. DeVries, *Acta Met.*, **6**, 736 (1958).
30. J. F. Dewald, *Bell Syst. Tech. J.*, **39**, 615 (1960).
31. J. O'M. Bockris and H. Kita, *This Journal*, **108**, 4 (1961).
32. H. Gerischer, "Advances in Electrochemistry," Vol. 1, p. 139, P. Delahay, Editor, Interscience Publishers, Inc., New York (1961).
33. M. Pourbaix, "Atlas d'Equilibres Electrochimiques," p. 281, Gauthier Villars, Paris (1963).
34. B. C. Hobbs and A. C. C. Tseung, *Nature*, **222**, 556 (1969).
35. R. D. Armstrong, A. F. Douglas, and D. E. Williams, *Energy Conversion*, **11**, 7 (1971).

Electrocatalysis of Oxygen Reduction by Sodium Tungsten Bronze

II. The Influence of Traces of Platinum

J. O'M. Bockris*,[1] and J. McHardy*,[2]

Department of Chemistry, University of Pennsylvania, Philadelphia, Pennsylvania 19104

ABSTRACT

The rate of oxygen reduction at a given potential on a sodium tungsten bronze crystal increased by up to four orders of magnitude as platinum was introduced into the crystal and at the maximum platinum concentration achieved (~400 ppm), the rate approached that on metallic platinum. The rate of oxygen reduction increased in proportion to the cube of platinum concentration, C_{Pt}, while the rate of oxygen evolution increased linearly with C_{Pt}. Ion probe mass spectroscopy indicated that the platinum was incorporated preferentially at impurity particles in the bronze but the macroscopic average platinum concentration in a crystal varied little with depth. Assuming that the platinum in a crystal was present in metallic form, its specific activity for oxygen reduction was over 10^3 times that of bulk platinum. The results are consistent with a model in which "spillover" of adsorbed intermediates from platinum to the bronze gives rise to an enhanced rate of oxygen reduction on the platinum.

The work of Sepa *et al.* (1) indicated that crystals of the nonstoichiometric compound sodium tungsten bronze Na_xWO_3 (where x can take any value between 0 and 1) catalyzed the electrochemical reduction of oxygen to water almost as well as platinum which is the best catalyst known for that reaction in acid solution. The finding held the promise of significant progress for both the theory and application of electrocatalysis, and stimulated considerable interest (2). Subsequent work (3) demonstrated that the high catalytic activity observed by Sepa required traces of platinum in the crystals, and this paper describes an investigation of the effect.

Experimental

The distribution of platinum in a crystal was examined by ion probe mass spectroscopy (4). Test solutions were prepared from triple-distilled water and ultrapure acids. Either sulfuric or perchloric acid was used and except for mechanistic work on pH dependence the solution strength was close to 0.1*N*. The purification of gases, the pre-electrolysis of solutions, and the preparation and analysis of bronze electrodes have all been described previously (4). The experiments were performed in a standard three-compartment glass cell (5) thermostated at 25° ± 0.1°C by means of a water jacket. The solution was saturated with oxygen for all tests. Electrochemical measurements were made under steady-state galvanostatic conditions, using the battery and resistor circuit described by Genshaw (6).

The bronze electrode, having been suspended above the solution during pre-electrolysis, was lowered into the solution. An anodic current was applied such that the potential rose to about 2V and when the potential became steady (less than 1 mV min^{-1} drift), its value was recorded. The current was reduced in steps to zero, the steady-state potential being noted each time. A cathodic current of 1 mA cm^{-2} was then applied and a decreasing sequence followed in the same way as for anodic currents. Except where noted, the same results were obtained if currents were started at zero and increased, but steady state at each point generally took longer to reach. Even with the more rapid procedure, the low current points on the cathodic line sometimes required a period of hours to reach steady state.

For a number of electrodes the effects of varying pH and oxygen partial pressure were studied. The pH was varied by starting with strong sulfuric acid in the solution reservoir and successively diluting it with more and more distilled water. The exact pH value was determined after each test by titration against standard KOH solution.

Baker Company calibration mixtures containing 10 and 1% of oxygen, respectively (balance nitrogen), were used to study the effect of oxygen partial pressure on electrode kinetics.

Results

Ion probe analysis.—The polished surface of a crystal seen under low power magnification manifested numerous irregular regions[3] a few microns across which were of lighter color than the matrix. The mass spectrum obtained on a light-colored region in a crystal containing 165 ppm Pt is compared with that of the matrix in Table I. Small differences in intensity for a given ion (*e.g.*, Fe^+) are probably not significant, but the inclusion particle was clearly richer in the elements Al and Pt. In the absence of internal standards, no estimate of relative concentrations of different

[3] As a rough estimate, the regions occupied a total of about 1% of the surface area.

Table I. Major peaks (arbitrary units) in the mass spectra of two regions on a crystal of Na_xWO_3 containing 165 ppm of platinum

Mass No.	Ion	Relative intensity Matrix	Inclusion
16	O^+	4.7	1.5
23	Na^+	>100	>100
25	$NaAl^{2+}$	>100	>100
27	Al^+	2.9	55
39	NaO^+	58	8.8
40	Ca^+	1.26	0.38
43	AlO^+	0.05	1.09
46	Na_2^+	>100	41
52	Cr^+	0.97	0.83
56	Fe^+	1.42	0.82
62	Na_2O^+	>100	39
70	Al_2O^+	0	0.64
86	$Al_2O_2^+$	0	1.32
91	W^{2+}	0.04	0.23
98	Mo^+	0.31	0.76
183	W^+	6.70	12.80
194	Pt^+	0.03*	0.20
195	Pt^+	0.04*	0.25

* Not unequivocally identified because peak height was comparable with background noise.

* Electrochemical Society Active Member.
[1] Present address: The Flinders University, Bedford Park, South Australia 5042, Australia.
[2] Present address: Pratt and Whitney Aircraft, Middletown, Connecticut 06457.
Key words: synergism, spillover, ion probe mass spectroscopy.

Table II. Impurity analysis of a typical sodium tungsten bronze crystal

Element*	ppm
N	≤5
Al	1000
Si	≤5
Cl	5
Ca	40
Ti	20
V	20
Cr	40
Fe	30
Cu	40
Zn	2
As	20
Mo	130
Ta	40

* Concentrations of impurities not listed were <0.5 ppm.

elements is possible, because the intensity of a given peak also depends on such factors as volatility and stability of the ionic species. The quantitative mass spectroscopic analysis of a typical crystal (kindly obtained for us by B. C. Gerstein at Iowa State University) given in Table II shows that the most predominant impurity was aluminum. This impurity undoubtedly originated from the alumina crucible in which crystals were grown, and it is likely that the main component of an inclusion particle was alumina.

Two series of ion images produced by the CAMECA Ion Analyzer are reproduced in Fig. 1. The Pt images which were very weak, almost invariably coincided with Al images. A rare exception is illustrated in Fig. 1a by the Pt image in the center of the photograph. Instead of coinciding with an Al image, it is associated with a bright spot in the W image. The site is probably one where a drop of the Na_2WO_4/WO_3 melt was occluded during crystal growth and then subsequently exposed by polishing. Dark spots in the Na and W images occurred wherever Al images were observed.

Results of the ion probe work thus provide strong evidence that the incorporation of platinum in a crystal occurred preferentially (if not exclusively) at inclusion particles.

Table III. Summary of E-log i data on Na_xWO_3 at 1 atm O_2 pressure, $pH = 1.5$, and 25°C

Noble metal content	$-\log i_{0.9V}$ cathodic	$-\log i_L$[a] cathodic	$-\log i_{1.9V}$ anodic
0	8.7	—	6.0
0	9.3	—	6.1
<50 ppm Pt	8.2	4.6	5.3
55 ppm Pt	7.7	—	5.2
70 ppm Pt	7.6	—	4.7
120 ppm Pt	7.0	5.2	4.7
120 ppm Pt	6.5	—	—
160 ppm Pt	6.6	5.3	5.0
190 ppm Pt	6.2	4.4	4.7
290 ppm Pt	5.7	4.6	4.2
390 ppm Pt	5.4	4.7	4.2
<500 ppm Ir	8.5	—	4.6
<500 ppm Ir	8.0	—	4.0
<500 ppm Rh	8.2	—	4.3
<500 ppm Rh	8.4	—	4.2
<500 ppm Pd	7.5	—	4.9
1100 ppm Pd	6.5	—	3.8
5400 ppm Ag	7.0	—	4.4
8600 ppm Ag	7.4	—	4.5
Pure Pt[b]	5.4	2.7	3.0

[a] i_L = diffusion limited current (estimated). Abnormally low values on crystals containing Pt suggest that only a small fraction of the surface activity catalyzes oxygen reduction.
[b] See Fig. 5.

Electrode kinetics.—No differences were observed whether a crystal was tested "as grown" (suspended in the test solution by the gold wire upon which it was grown) or after mounting in Teflon, grinding, and polishing it (7). The effects of platinum and other impurities on OER (oxygen electrode reaction) kinetics are summarized in Table III. The addition of 390 ppm of platinum improved activity for O_2 reduction by almost four orders of magnitude. The values of log i at $E = 0.9$V and $E = 1.9$V were selected as the criteria for catalytic activity to avoid the long extrapolations of the Tafel regions required in estimating i_0. The catalytic activities for oxygen reduction (0.9V) and oxygen evolution (1.9V) are plotted against log C_{Pt} in Fig. 2; the straight lines drawn through the data points correspond to the empirical equations

$$i_{0.9} \propto (C_{Pt})^3 \quad [1]$$

and

$$i_{1.9} \propto C_{Pt} \quad [2]$$

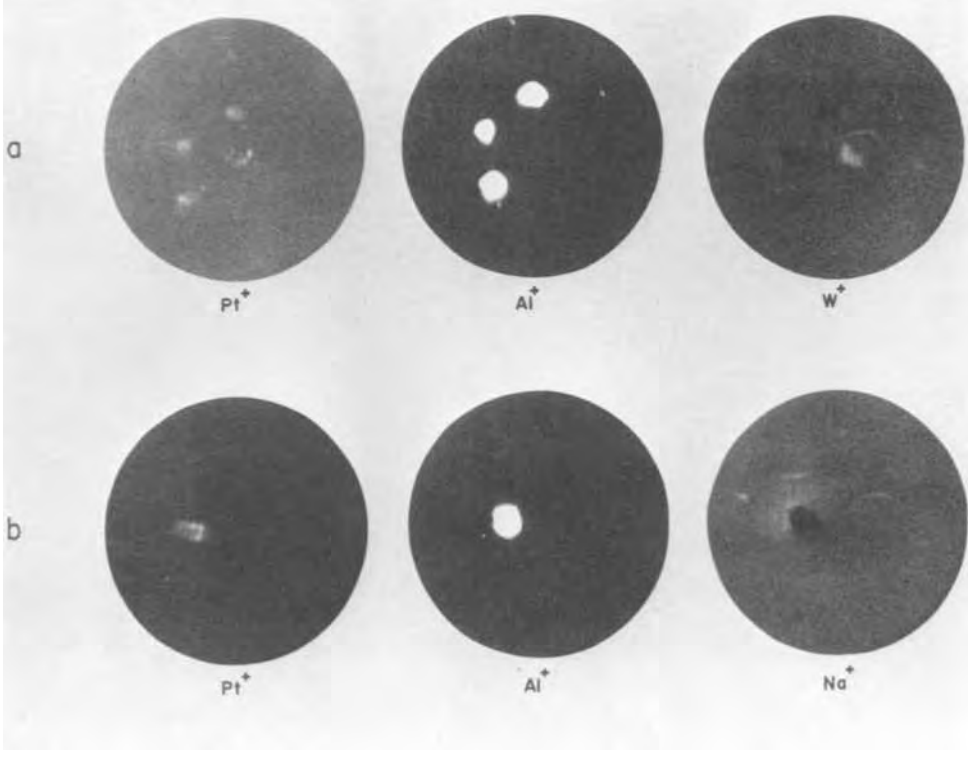

Fig. 1. Ion images of regions 175μ in diameter on two crystals of sodium tungsten bronze. (a) Average Pt content 290 ppm. (b) Average Pt content 390 ppm.

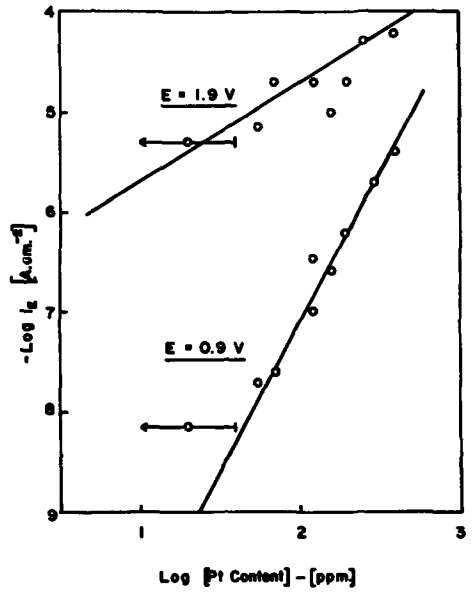

Fig. 2. Log-log plots of catalytic activity vs. Pt concentration for oxygen evolution (1.9V) and oxygen reduction (0.9V), respectively.

Very similar results were obtained when comparisons were made at other potentials.

Of the several impurities tested, only the noble metals improved the catalytic activity of sodium tungsten bronze, and among the noble metals, platinum had the largest effect. From the limited data obtained, the order of merit among the noble metals in this context appeared to follow the relative activities of the pure metals.

Attention is drawn to the column of Table III in which approximate values of diffusion limiting current are compared. The limiting current on a crystal containing platinum is only about 1% of that anticipated for a homogeneous electrode, *e.g.*, solid platinum.

Kinetic parameters with respect to potential, oxygen partial pressure, and *p*H are summarized in Table IV. The anodic reaction order with respect to *p*H is questionable because the anodic Tafel slope tended to increase as the strength of the sulfuric acid decreased. Subsequent work was performed in perchloric acid in case this tendency might reflect a participation of $SO_4^=$ ions in the OER (8), but the Tafel slopes still increased with decreasing acid strength, and the reaction order remained obscure.

In successive tests, the catalytic activity of a crystal for oxygen reduction increased slightly and then leveled off. When the usual anodic treatment was omitted, the initial cathodic performance was extremely poor. Typical cathodic curves showing the difference between initial and final activities appear in Fig. 3. In parallel with the improvement in cathodic activity, the form of the anodic line changed with time as shown in Fig. 4. A departure from linearity occurred at about 10^{-5} A-cm^{-2} on a fresh crystal whereas no such depolarization was observed above 10^{-7} A-cm^{-2}

Table IV. Kinetic parameters for the oxygen electrode reaction on sodium tungsten bronze

Bronze	$\left(\frac{\partial E}{\partial \ln i}\right)_{pH,p_{O_2}}$		$\left(\frac{\partial \log i}{\partial pH}\right)_{E,p_{O_2}}$		$\left(\frac{\partial \log i}{\partial \log p_{O_2}}\right)_{E,pH}$	
	Anodic (b_a)	Cathodic (b_c)	Anodic	Cathodic	Anodic	Cathodic
$Na_{0.7}WO_3$	$\frac{2RT}{F}$	$-\frac{2RT}{F}$	$\frac{1}{2}$	$-\frac{1}{2}$	0	1
$Na_{0.7}WO_3$ (290 ppm Pt)	$\frac{2RT}{F}$	$-\frac{2RT}{F}$	$\frac{1}{2}$	$-\frac{1}{2}$	0	1

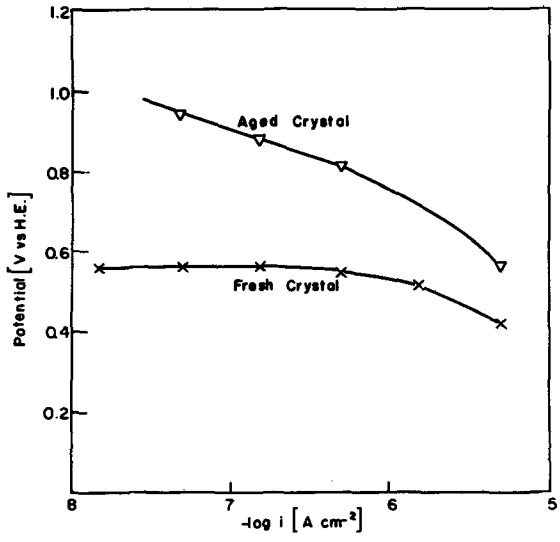

Fig. 3. Effect of aging on cathodic *E*-log *i* behavior

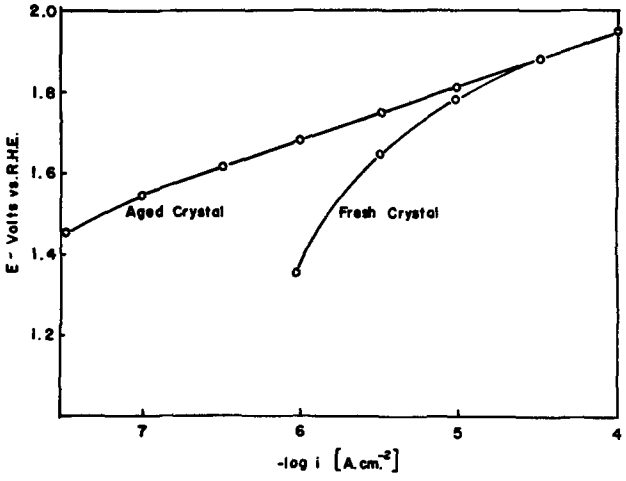

Fig. 4. Effect of aging on anodic *E*-log *i* behavior

on a well-aged crystal. These results fully support the view expressed in Part I (4) that the "aging" of a crystal actually involves anodic dissolution of sodium from the surface. The dissolution rate rapidly diminishes and apparently levels off at about 10^{-7} A-cm^{-2}. The anodic depolarization is unlikely to reflect the oxidation of impurities because no such depolarization was observed on a Pt electrode (Fig. 5).

A phenomenon observed on platinum-free crystals after anodic treatment is illustrated in Fig. 6. When

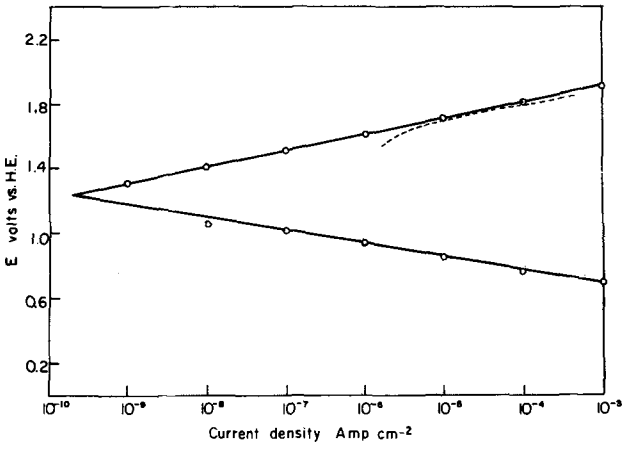

Fig. 5. *E*-log *i* curves for the OER on platinum before (- - - -) and after (———) pre-electrolysis.

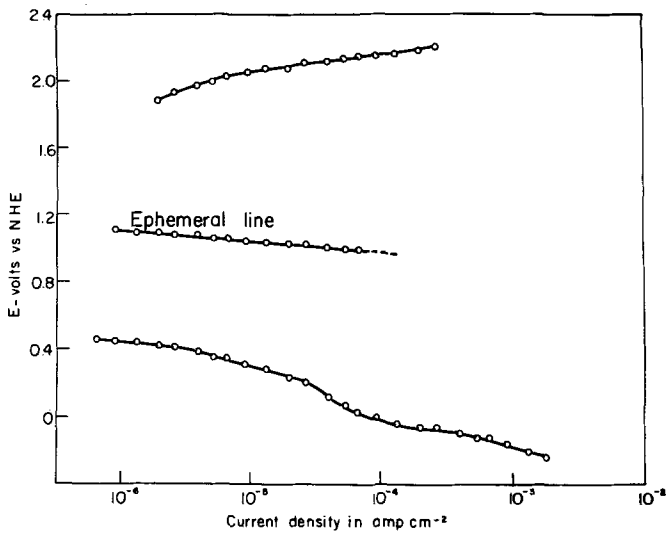

Fig. 6. *E*-log *i* behavior for a crystal free of platinum showing the ephemeral cathodic line obtained after anodic treatment.

the cathodic curve was plotted by starting from zero current and working up, an ephemeral Tafel line that resembled a high i_0 oxygen reduction line was obtained. A finite quantity of electricity, q, was associated with the ephemeral process, and q increased approximately linearly with anodic pretreatment potential as shown in Fig. 7. When a cathodic charge equal to q had passed, the potential at a given current density dropped to a point on the normal cathodic line, and the ephemeral behavior could be reproduced only after further anodic treatment. The reversible oxidation of the bronze surface involved in the ephemeral behavior was discussed in Part I (4). The fact that an ephemeral cathodic line was not observed on crystals containing platinum probably indicates that the cathodic process was too rapid to permit detection by the steady-state techniques employed in this investigation.

Discussion

Mechanism of the oxygen electrode reaction.—The anodic and cathodic parameters in Table IV are not consistent with a single mechanism (7), but they do permit two important deductions. First, the mechanism for each reaction (O_2 evolution and reduction, respectively) is unaltered by the addition of platinum to a crystal. Second, the only type of mechanism for O_2 reduction that can give a Tafel slope of $-2RT/F$ and unit partial pressure dependence is one where the first electron transfer step is rate determining. The evident involvement of hydrogen ions in the rds, albeit a complex one, suggests then that the rds may be the one widely postulated for other electrodes in acid solution (9)

$$O_2 + H^+ + e^- \rightarrow \text{(adsorbed intermediates)} \quad [3]$$

Platinum distribution.—On a macroscopic scale, the distribution of platinum was essentially uniform as evidenced by the fact that mechanical removal of the original surface by grinding and polishing did not alter the catalytic activity (7). On a microscopic scale, however, ion probe analysis revealed that most of the platinum (at least in a crystal of relatively high Pt content) was associated with alumina inclusion particles.

It is not immediately obvious why the platinum in a crystal should concentrate at an inclusion particle. There is no reason, for example, why platinum electrodeposited on the bronze surface should migrate toward alumina, but a qualitative and speculative explanation is possible in terms of colloid chemistry. A colloidal alumina particle, eroded by the melt from the crucible, is likely to acquire a negative charge by the equilibrium

$$Al_2O_3 + WO_4^= \rightleftarrows Al_2O_4^= + WO_3 \quad [4]$$

hence attracting cations to its surface. Platinum ions will be prone to accumulate on the surface because of their (presumably) +4 charge. Colloid particles which settle out onto the growing crystal will be discharged, and the platinum associated with the colloid will be reduced to the metal. The concentration of platinum in the crystal will thus depend on the concentration both of platinum ions and of colloid particles in the melt. Qualitative confirmation of this prediction was obtained recently (10): a bronze crystal grown in a platinum crucible was found to become more active after alumina powder was added to the melt.

Models for the effect of platinum on catalytic activity.—Electronic models.—As a working hypothesis during the experimental phase of the project, the influence of platinum on the catalytic activity of sodium tungsten bronze was attributed to an effect of platinum on electronic levels in the semiconducting surface of the bronze (3). Attempts to construct specific models, however, met with limited success (11). In particular, platinum had no effect on the bandgap or the flatband potential of the semiconducting surface layer (4), a fact that conflicted sharply with the basic requirements of such models. Further evidence against an electronic role for the platinum was the observation that the donor concentration in the surface layer agreed closely with the concentration of sodium (4).

The failure of electronic models, and the results of ion probe analysis, both point to a model in which platinum metal, in some special state, is the active catalyst.

Platinum-centered models.—The first problem facing a platinum-centered model is to explain the remarkable amplification in specific activity of the platinum over that of the bulk metal. If the rate of oxygen reduction on a crystal containing 0.039% Pt were referred to 0.039% of the surface area,[4] the apparent activity would be over 10^3 times that of oxide-free bulk platinum ((Table III).

A trivial model which postulates gross inhomogeneity of the platinum distribution such that the

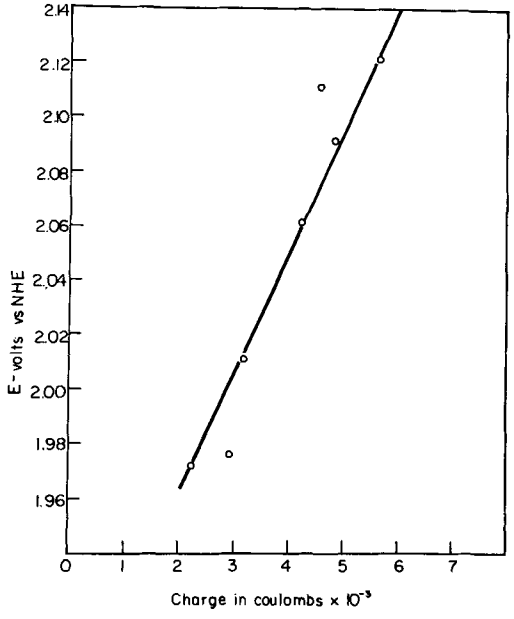

Fig. 7. Charge associated with the ephemeral line as a function of anodic treatment potential.

[4] For a microscopically uniform distribution, a bulk Pt concentration of 0.039 w/o (weight per cent) would correspond to an area concentration of about 0.02% of the surface.

surface of a crystal is enriched in platinum can be discarded on several counts: no change in activity was observed when the original surface was removed by grinding and polishing, and a large area of platinum on the surface is inconsistent with both the distribution observed by ion probe analysis and the low limiting currents for oxygen reduction (Table III).

The next simplest type of model is one that attributes the amplification in catalytic activity to geometrical or crystallographic effects. As no information is available on the size or shape of the platinum particles, the amplification could reflect either a large effective surface area of the platinum resulting from microscopic roughness (or porosity) of the inclusions, or an intrinsic superiority in activity of the platinum particles, resulting perhaps from the predominance of certain crystal faces. This type of model fits most of the experimental observations, but cannot be reconciled with Eq. [1]; the discrepancy will be brought out below.

Synergistic models.—Two models may be proposed in which the enhanced catalysis arises from synergism between the platinum and the matrix; the models are known as "adlineation" and "spillover," respectively. The thesis of adlineation, first advanced in 1928 by Schwab and Pietsch (12), is that the active sites in a two-phase catalyst are the linear boundaries between the phases. An electrochemical example of adlineation appears in the work of Fleischmann *et al.* (13) in which the rate of hydrogen evolution was found to be 10^7 times greater around the edge of a ruthenium film on mercury than on top of the film.

Spillover is a term coined by Boudart (14) to denote surface diffusion of reaction intermediates from a catalyst to its "support." In the present context, adsorbed intermediates produced by Reaction [3] would diffuse from the platinum to the bronze and there undergo further electrochemical reduction to water.

Comparison of prediction from the models with experiment.—If catalysis were due simply to platinum metal, both anodic and cathodic activities should increase linearly with the effective area of platinum. Assuming first that the diameter of the platinum particles remained constant, the number of particles and hence the total area would increase linearly with concentration. At the other extreme, were the number of particles to remain constant, the area would vary as the concentration to the 2/3 power. In the general case, where both the number and size of the particles changed, the area would vary with $(C_{Pt})^u$ where $2/3 \leq u \leq 1$ (15). The simple, platinum-centered type of model can thus account satisfactorily for the dependence of anodic activity on C_{Pt}, but not for the cathodic dependence.

Following the same type of argument as above, the adlineation model would predict a dependence for both anodic and cathodic activities on $(C_{Pt})^v$ where $1/3 \leq v \leq 1$, and is no more able to account for the observed cathodic dependence than was the simpler model. Since the spillover model involves factors other than geometry, it is not subject to the same limitations as the previous models and can be reconciled (vide infra) with a dependence of the activity on $(C_{Pt})^w$ where $w > 1$.

Development of the spillover model.—Enhanced catalytic activity by spillover normally requires that the rds be a reaction involving two adsorbed species. One of the species adsorbs directly onto the support while the other is generated by a reaction on the catalyst and spills over onto the support. The oxygen reduction reaction does not fulfill this requirement, but there is a way in which spillover could affect the rds on platinum (Eq. [3]). At potentials between 0.8 and 1.0V, the adsorption of oxygen species on platinum is governed by the Temkin isotherm (16), whereby the adsorption energy decreases linearly with the fractional coverage, θ. In view of the fact that activation energy for an adsorption step decreases approximately linearly with increasing adsorption energy (17), the rate of Reaction [3] should depend strongly on θ. Spillover of adsorbed species from the platinum to the bronze will result in a lower value of θ on the Pt, and hence an increased velocity of the rds.

Using the data of Wroblowa *et al.* (18) an estimate can be made of the possible increase in rate at a given potential arising from a decrease in θ. The variation of adsorption energy, $-\Delta H_{ads}$, with θ is described by the relation

$$-\Delta H_{ads} = 12(1 - \theta)\,\text{kcal mole}^{-1} \qquad [5]$$

and at 0.9V, θ is about 0.5 (referred to a saturation coverage on Pt of 110 μC-cm^{-2}). If spillover reduces θ to almost zero, the adsorption energy would increase by 6 kcal mole^{-1}. Assuming a Brϕnsted factor of 0.5, the activation energy would thus decrease by 3 kcal mole^{-1}, and the reaction rate would increase by about 150 times.

The spillover model alone cannot therefore explain the observed amplification ($>10^3$) in the catalytic activity of platinum for oxygen reduction, and a combination of spillover with some other model is indicated. Before going on to discuss this possibility, however, it is convenient to consider the catalysis of oxygen evolution.

At potentials above 0.95V, the surface of a platinum electrode is covered with an oxide film (19), and spillover will have relatively little effect on the total coverage by oxygen species, or on reaction rates. A graph of per cent Pt activity *vs.* per cent Pt concentration from the anodic data in Table II is plotted in Fig. 8. Although the data show considerable spread, the graph is essentially linear, as predicted by Eq. [2], and has a slope (activity/concentration) of about 160. The linear dependence indicates that the surface area of platinum particles also increases linearly with concentration. Such a dependence can be obtained only if the diameter of the particles remains constant, and their number increases in direct proportion to concentration (15). The slope is a measure of the amplification in catalytic activity of platinum for oxygen evolution. The amplification may reflect either geometric or crystallographic factors, but the available data do

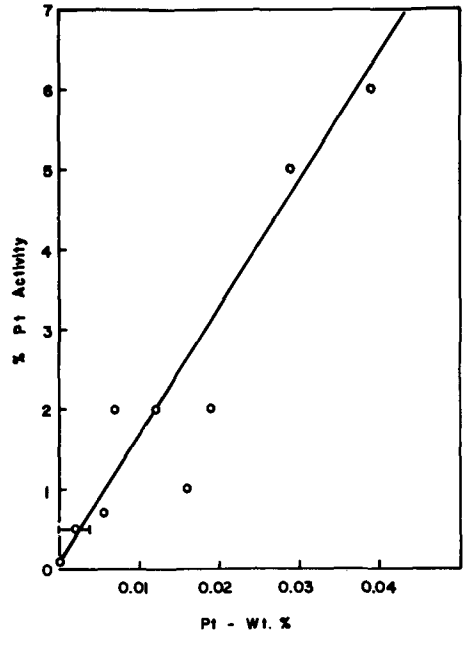

Fig. 8. Linear plot of catalytic activity for oxygen evolution at 1.9V (as a percentage of that for pure platinum) *vs.* Pt concentration.

not distinguish between these possibilities. Whatever the origin of the amplification, it seems reasonable to assume that it will also apply to oxygen reduction. Phenomenologically, the enhanced activity may be discussed in terms of an "effective" area of platinum on the surface of a bronze crystal.

From Fig. 8 the effective platinum surface area for a crystal containing 0.039% (390 ppm) platinum is is about 6% of the total area. The maximum rate of oxygen reduction on the crystal predicted from the spillover model is therefore (6/100) × 150, or about nine times that on an equal area of solid platinum. In point of fact, the cathodic activity of the crystal was somewhat less than that of oxide-free platinum: 4 μA-cm^{-2} at 0.9V compared with about 10 μA-cm^{-2} for platinum under equivalent conditions (9). The difference between predicted and observed activity could result from: (*i*) a decrease in θ that was less than 0.5, or (*ii*) inability of some of the platinum particles to participate in the process of spillover.

If one assumes that the difference arises from (*ii*), it becomes possible to rationalize the observed dependence of cathodic activity on platinum concentration. Consider an inclusion particle as a flat region with a circular boundary, Fig. 9. Since there is no evidence in the literature that oxygen species can spill over from platinum to alumina, only those platinum particles lying in a continuous path to the edge of the inclusion are likely to lose adsorbed oxygen to the bronze surface. All the "active" platinum will thus be located in an annular zone around the edge of the inclusion. If the radius of the inclusion is r, and the average width of the active zone is z, then the fractional area of the platinum particles involved in spillover will be about $2\pi rz/\pi r^2$ or $2z/r$. The area of active platinum, Δ^*, per unit area of crystal will thus be given by

$$\Delta^* = \frac{2z}{r}\Delta \qquad [6]$$

where Δ is the total fraction of the surface occupied by platinum. Now Δ varies linearly with the number of platinum particles and hence with C_{Pt}, but z is a more complex function of these quantities. The width of the active zone depends on the probability that several platinum particles will be in contact with each other. For example, a dependence on $(C_{Pt})^2$ would arise if z were governed by the probability of two particles being in contact. The activity of a crystal, being proportional to the product of Δ and z, would then vary as $(C_{Pt})^3$, as observed in Eq. [1].

A final piece of evidence supporting the spillover model is the finding that anodic dissolution of sodium

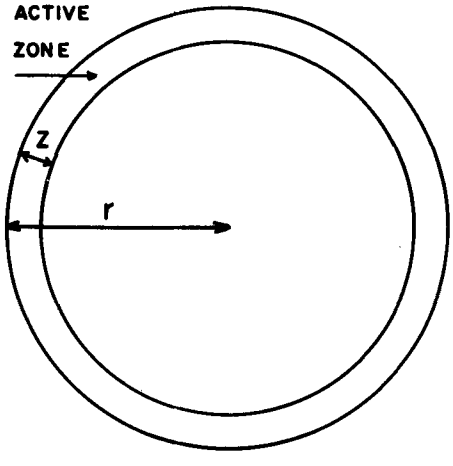

Fig. 9. Schematic diagram of an inclusion particle

out of the surface is enhanced if a crystal contains platinum (4). More rapid hole injection during oxygen reduction was invoked in Part I (4) to explain the effect, and that is precisely what is likely to occur during reduction of the reactive species which spill over from the platinum to the bronze.

Acknowledgments

This work was supported throughout by the United States Army Mobility Equipment R&D Center, Ft. Belvoir, Virginia, which also undertook the spectrographic analysis of our samples. We particularly wish to thank Drs. J. R. Huff and H. C. Egghart of Ft. Belvoir for their sustained interest and help. We are indebted to virtually everybody associated with the Electrochemistry Laboratory over the past five years for stimulating discussions (many relevant to this work), but contributions deserving special note were made by the following: Drs. A. Damjanovic, A. R. Despic, R. A. Fredlein, B. Lovrecek, and K. L. Mittal.

Manuscript submitted May 25, 1972; revised manuscript received Aug. 10, 1972.

Any discussion of this paper will appear in a Discussion Section to be published in the December 1973 JOURNAL.

REFERENCES

1. D. B. Sepa, A. Damjanovic, and J. O'M. Bockris, *Electrochim. Acta*, **12**, 746 (1967); A. Damjanovic, D. B. Sepa, and J. O'M. Bockris, *J. Res. Inst. Catalysis*, **16**, 1 (1968).
2. R. D. Armstrong, A. F. Douglas, and D. E. Williams, *Energy Conversion*, **11**, 7 (1971); B. Broyde, *J. Catalysis*, **10**, 13 (1968); M. A. Cadman, Private communication; J. H. Fishman, J. F. Henry, and S. Tessore, *Electrochim. Acta*, **14**, 1314 (1969); L. W. Neidrach and H. I. Zeliger, *This Journal*, **116**, 152 (1969); M. Voinov and H. Tannenberg, in "From Electrocatalysis to Fuel Cells," p. 101, Univ. of Washington Press, Seattle, Wash. (1972).
3. J. McHardy and J. O'M. Bockris, *ibid.*, p. 109; R. A. Fredlein and J. McHardy, *Proc. 24th Annual Power Sources Symp.*, p. 177 (1970).
4. J. McHardy and J. O'M. Bockris, *This Journal*, **120**, 53 (1973).
5. H. Dahms and J. O'M. Bockris, *ibid.*, **111**, 182 (1964).
6. M. A. Genshaw, Ph.D. Thesis, Univ. of Pennsylvania (1966).
7. J. O'M. Bockris, A. Damjanovic, and J. McHardy, in *Proc. 3rd International Symp. on Fuel Cells*, p. 15, Brussels (1969).
8. M. Breiter, in "Advances in Electrochemistry," Vol. 1, p. 123, P. Delahay, Editor, Interscience Publishers, Inc., New York (1961).
9. A. Damjanovic and V. Brusic, *Electrochim. Acta*, **12**, 615 (1967); A. J. Appleby, *Catal. Rev.*, **4**, 221 (1970).
10. J. McHardy, K. L. Mittal, and J. O'M. Bockris, Final Report, Contract DA 44-009-AMC-469(T), U.S. Army Mobility Equipment R&D Center, Ft. Belvoir, Va., December 1971.
11. J. McHardy, Ph.D. Thesis, Univ. of Pennsylvania (1971).
12. G-M. Schwab and E. Pietsch, *Z. Physik. Chem.*, **B1**, 385 (1928).
13. M. Fleischmann, J. Koryta, and H. R. Thirsk, *Trans. Faraday Soc.*, **63**, 1261 (1967).
14. M. Boudart, M. A. Vannice, and J. E. Benson, *Z. Physik. Chem. N.F.*, **64**, 171 (1969).
15. G. C. Bond, Preprint No. 67, *4th International Congress on Catalysis*, Moscow (1968).
16. A. Damjanovic and M. A. Genshaw, *Electrochim. Acta*, **15**, 1281 (1970).
17. M. G. Evans and M. Polanyi, *Trans. Faraday Soc.*, **34**, 11 (1938).
18. H. Wroblowa, M. L. B. Rao, A. Damjanovic, and J. O'M. Bockris, *J. Electroanal. Chem.*, **15**, 139 (1967).
19. A. K. N. Reddy, M. A. Genshaw, and J. O'M. Bockris, *J. Chem. Phys.*, **43**, 671 (1968).

Electrochemical Generation and Measurement of Sulfide Ion in Molten LiCl-KCl Eutectic

C. H. Liu,[1] A. J. Zielen, and D. M. Gruen

Chemistry Division, Argonne National Laboratory, Argonne, Illinois 60439

ABSTRACT

An electrode composed of the eutectic mixture of nickel sulfide (NiS) and nickel (1:1 mole ratio) has been shown to be useful for coulometrically generating sulfide ion (S^{-2}) in molten lithium chloride-potassium chloride eutectic. A shiny nickel electrode coated with nickel sulfide functions reversibly as an electrode of the second kind for sulfide ion. With this indicator electrode, the solubility product of nickel sulfide in the temperature range 375°-475°C has been determined, and the heat of reaction for the solubility equilibrium $NiS(s) \rightleftarrows Ni(II) + S^{-2}$ has been calculated. The solubility behavior of lithium sulfide in the same temperature range has also been investigated.

There is considerable current interest in the solution chemistry of sulfide ion in molten salt solvents. Thus, the interaction of elemental sulfur with S^{-2} in melts has been the subject of several recent studies (1-3). A variety of species such as S_x^{-2}, S_2^-, and S_3^- have been proposed to account for results of electrochemical and spectroscopic studies of the equilibria involved in the reactions. A key requirement to making further progress in studying the solution chemistry of this system is the development of a method for the preparation of molten salt solutions containing known initial concentrations of S^{-2}. Due to the hygroscopic and corrosive nature of alkali sulfides and the difficulty in their preparation in pure form, the addition of such salts to the melts is neither a satisfactory nor a convenient solution to this problem. In numerous studies, coulometric generation of the chemical species of interest has been shown to be a highly useful technique in molten salts. Bodewig and Plambeck (3) generated S^{-2} by cathodizing a sulfur pool in contact with LiCl-KCl eutectic using a graphite electrode. If a solution of S^{-2} in the absence of sulfur is desired, the electrolytic reduction of a slightly soluble metal sulfide would appear to be a more convenient method.

Furthermore, for measuring the sulfide activity *in situ*, a sulfide indicator electrode is of considerable value. Bodewig and Plambeck reported that the liquid sulfur-sulfide couple showed Nernst behavior for a two-electron process in molten lithium chloride-potassium chloride eutectic and that polysulfides were formed (3). Thompson and Flengas measured the potential of the cell, $Ag/Ag_2S/AgCl/graphite/S(vapor)$, over the temperature range 490°-860°C and observed Nernst behavior (4). The emf of the cell, $Ag(s)/AgI(s)/Ag_2S(s)/S(l)/graphite$, was used to calculate the free energy of formation of silver sulfide by Kiukkola and Wagner (5) and by Reinhold (6). From an experimental point of view, we felt that a metal sulfide-metal electrode system acting as an electrode of the second kind for sulfide would have certain advantages over the other electrode systems described in the literature. Laitinen and Bhatia found that several metal oxide-metal systems showed reversible behavior as electrodes of the second kind toward dissolved oxide in the lithium chloride-potassium chloride eutectic melt at 450°C (7). However, the metal oxides are too soluble for these systems to be generally useful as oxide indicator electrodes.

In the present work, pure NiS and NiS containing an excess of the metal, have been tested as electrode materials for the coulometric generation of S^{-2} in molten lithium chloride-potassium chloride eutectic. Known amounts of S^{-2} can be added coulometrically using the NiS-Ni electrode as a generating electrode. The nickel sulfide-nickel system has been found to be a satisfactory indicator electrode for S^{-2} in this solvent. With the aid of this electrode system, the solubility behavior of nickel sulfide and lithium sulfide over the temperature range 375°-475°C have been studied.

Experimental

Solvent.—The eutectic mixture consisting of 40.9 m/o (mole per cent) potassium chloride and 59.1 m/o lithium chloride was obtained from Anderson Physics Laboratories, Urbana, Illinois. In the preparation of the eutectic, analytical reagents were mixed in the appropriate proportions, vacuum desiccated, melted under dry hydrogen chloride, purged of the hydrogen chloride by repeated flushing with dry argon followed by evacuation, treated with molten lithium which was deposited from the melt on a porous tungsten electrode, filtered through a quartz fritted filter, and sealed under argon.

Apparatus.—Furnace and temperature control.—A massive stainless steel core with a 2¼ in. opening at the top was heated by four 500W Firerod heaters (Watlow Electric Manufacturing Company, St. Louis), two of which were controlled by a Wheelco Capacitrol temperature controller. The core and insulating materials were enclosed in a stainless steel case with cooling furnished by running water through ¼ in. copper tubing welded to the case. By appropriate selection of Variac settings, the melt temperature could be controlled to within 1°C. The furnace was mounted on a sliding base with counterweights so that it could be easily lowered for observation of the electrolytic cell.

Electrolytic cell.—The cell consisted of an outer quartz or Pyrex jacket approximately 14 in. long and 2 in. OD with a 55/30 male joint at the top. Six thermometer adapters (Ace Glass, Inc., Vineland, New Jersey) were sealed to the top of a 55/50 female joint. A vacuum stopcock with Teflon plug sealed to the side of the joint served as an outlet for the argon flow. During an experiment, the male and female joints were sealed with black wax. A flow of dry argon was maintained through an inlet tube provided with a Teflon plug vacuum stopcock. This tube also served as the connection to the vacuum line. All electrodes, a thermocouple tube for monitoring the melt temperature, and the argon inlet were introduced through the thermometer adapters. Tightening nylon bushings against O-rings provided vacuum-tight seals. At the end of an experi-

[1] On sabbatical leave from the Department of Chemistry, Arizona State University, Tempe, Arizona 85281.

Key words: electrochemistry, sulfide ion, molten salts, NiS-Ni electrode.

ment, the cell was opened by melting the wax seal. The LiCl-KCl eutectic was contained in a large quartz beaker. Inserted in the quartz beaker were several smaller compartments consisitng either of quartz tubes with fritted disks, or of beryllia (National Beryllia Corporation, Haskell, New Jersey), thoria or magnesia crucibles (Norton Company, Worcester, Massachusetts). The compartments were heated to 450°C for a few hours, cooled, and kept in a dry N_2 atmosphere. The compartments were weighed before the experiment and with the melt contents after the experiment. In some cases, the melt contents were also determined by argentometric titration of the chloride present (8). Determination of the amount of melt present in each compartment by weighing agrees to 1-2% with determination by argentometric titration provided that the compartment has been washed free of the melt on the outside and redried at 250°C before weighing. The volume of melt present at various temperatures was calculated from the weights determined and the densities of the melt at these temperatures (9).

Electrodes.—Nickel sulfide-nickel eutectic electrodes were made as follows. Sulfur distilled twice from cp reagent under a stream of dry argon, and analytical reagent nickel shot were mixed in a 1:2 g-atom ratio in a quartz reaction tube, evacuated, vented to approximately 200 mm Hg of argon, and sealed. The nickel shot was placed in the middle portion of the tube, which was then horizontally clamped and heated with a Meeker burner. The sulfur was driven with a hand torch back and forth over the heated nickel until the brown vapor completely disappeared. A silvery melt, which is the eutectic mixture of nickel sulfide and nickel with a melting point of 637°C (10), was obtained and was left in a furnace at approximately 750°C for several hours with occasional shaking to insure complete reaction and thorough mixing. After cooling, the silvery product was removed from the reaction tube and cast into rods of about 4 mm OD in quartz tubes after evacuation and venting to argon atmosphere. The rods were then cut into 2 in. lengths and a small hole was drilled ultrasonically at one end. A nickel or platinum wire was then tied securely to each rod through the hole and served as the electrical contact. Before use, each electrode was polished with fine emery paper, washed with detergent, rinsed thoroughly with distilled water, acetone, and trichloroethylene, and vacuum dried. Pure NiS electrodes were made similarly by reacting 1:1 g-atom value of the elements at a temperature of 1000°C.

The platinum and nickel electrodes were made from high purity (at least 99.99%) metal foils or wires in coil form. Analytical reagent copper foils and wires were sometimes used as the auxiliary electrodes.

The reference electrode (8) consisted of a platinum coil immersed in an ~0.01*M*, solution of coulometrically generated Pt(II). For the purpose of correlating results from different experiments, measured potentials were extrapolated to values *vs.* a 1*M* Pt(II)-Pt electrode by the application of the Nernst equation.

Procedures.—The electrolytic cell was assembled in a glove box under dry nitrogen and then placed in the furnace. A rapid flow of argon was maintained while the cell top and the jacket were sealed together with sealing wax and the electrodes were introduced. The system was then evacuated to a pressure of 2-5μ Hg and heated to 400°C. After the melt levels in the compartments had equalized, the system was vented to argon and kept under argon flow. A Pt(II)-Pt reference electrode was then prepared by anodization at a constant current with coulometric measurement of the amount of electricity passed (8). A copper or nickel electrode in a separate compartment served as the auxiliary electrode in all electrolyses.

Two procedures were used to measure the sulfide concentration dependence of the nickel sulfide-nickel electrode potential. A nickel sulfide-nickel eutectic electrode and a shiny nickel electrode were placed in the same compartment. The "eutectic" electrode was cathodized to generate a known amount of S^{-2} and the shiny nickel was anodized slightly to provide some nickel sulfide on the surface. The potential at the nickel electrode was then measured against the Pt(II)-Pt reference. More S^{-2} was generated successively, and the potential was measured after each addition. The solubility of NiS in the melt was negligibly small compared to the analytical concentrations of S^{-2} in these measurements. It turned out that the solubility of Li_2S was relatively low in the eutectic salt melt and equilibration after each period of generation of S^{-2} was quite slow at the higher sulfide concentrations. A better procedure was to generate a large quantity of S^{-2}, let the solution equilibrate for 20-30 min, and measure the final stable potential. Nickel(II) was then coulometrically generated at the nickel electrode (or the eutectic electrode) to precipitate NiS, and the potential was measured after each period of generation. Equilibrium was reached very rapidly at points around the equivalence point of the titration. The current efficiency of the electrode reaction, $NiS + 2e^- \rightleftarrows Ni^0 + S^{-2}$, was checked in three ways. First, the eutectic generating electrodes were weighed before and after the passage of measured amounts of electricity. The weight losses, due to dissolution of S^{-2}, were then compared to the equivalents of electricity passed to determine the n value. Second, melt in the sulfide-containing compartment was dissolved in 0.1*M* NaOH-1*M* NH_3 under nitrogen and titrated argentometrically (11). Third, the S^{-2} generated was potentiometrically titrated *in situ* with Ni(II) coulometrically generated at a nickel electrode; the reverse titration of known amounts of Ni(II) with S^{-2} coulometrically generated at the eutectic electrode was also performed.

To determine the solubility of Li_2S in the eutectic melt in the temperature range 375°-475°C, a large excess of sulfide was generated at the eutectic generating electrode at 500°C. After two or three hours, with occasional stirring by hand using the electrode, the temperature was lowered to 475°C. After allowing 30 min for initial equilibration, the potential at the Ni indicator electrode was measured at 30-min intervals until no shift was observed in three successive measurements. The temperature was then lowered in 25° steps and the potential measurements were repeated. A stable potential was usually reached after 1½ hr of equilibration. Essentially the same potentials were observed when the temperature was raised although a much longer period was required for equilibration. The solubility of Li_2S was then easily calculated from the standard potential of the NiS-Ni electrode system determined at each temperature.

Results and Discussion

The suitability of several materials as containers for S^{-2} in the melt was investigated. Etching of quartz and Pyrex glass in contact with S^{-2} occurred quickly. In the case of thoria crucibles, there was evidence of release of O^{-2} from the container as a result of replacement by S^{-2}. Beryllia and magnesia crucibles were both satisfactory, showing no evidence of attack by S^{-2} over a period of 72 hr. Most of the experimental results reported here were obtained in magnesia crucibles.

Although S^{-2} could be generated by cathodization of the pure NiS electrode the results are not as satisfactory as those obtained with the eutectic electrode.

In the coulometric generation of S^{-2} at the eutectic electrode the electrochemical reaction, $NiS + 2e^- \rightleftarrows Ni^0(s) + S^{-2}$, takes place in the potential range −1.5 to 1.6V *vs.* the 0.01*M* Pt(II) reference electrode. In this potential range the residual current density of the melt at a shiny platinum electrode amounts to 0.05 mA/cm^2 (cathodic). This residual current level, typical

of properly purified melts, must be taken into consideration to account for the amount of S^{-2} generated to an accuracy of better than 1% (12). The *in situ* titration of S^{-2} with coulometrically generated Ni(II) gives very large potential breaks at the equivalence point. Titrations were performed at 25° intervals between 375° and 475°C. Figure 1 represents the titration curves at 375° and 475°C. These titrations and the reverse titration of Ni(II) with coulometrically generated S^{-2} yielded analytical results within 1% of values calculated theoretically. In four replicate determinations of the weight losses of the eutectic electrodes after the passage of measured quantities of electricity in the generation of S^{-2}, n values of 1.86, 1.82, 1.96, and 1.89 were obtained for a theoretical two-electron process. The slightly lower experimental n value is consistent with the expectation that a small amount of the Ni produced would fall off the electrode in the washing process before weighing. Argentometric analysis in ammoniacal solution (11) of the S^{-2} produced yielded a recovery of 96.7% of the theoretical amount. These results show that the reduction of NiS is a two-electron proces yielding S^{-2} and that the current efficiency for the process is essentially 100%.

The potential of the electrode of the second kind, Ni/NiS/S^{-2}, is given by the Nernst equation

$$E = E^\circ_{\text{NiS-Ni}} - \frac{RT}{2F} \ln a_{S^{-2}} \qquad [1]$$

where E is the potential in volts, $E^\circ_{\text{NiS-Ni}}$ is the standard potential, $a_{S^{-2}}$ is the activity of S^{-2}, and R, T, and F have their conventional signficance. Previous reports (8) as well as the present work indicate that activity may be conveniently replaced by concentration for dilute solutions in molten salt solvents. Molarity is used to express concentration in this work. The standard state for a soluble species is unit molarity. For a pure solid, the standard state is defined as its physical state at the operating temperature under 1 atm of pressure and taken as unity. The standard potential of the Pt(II)-Pt system is arbitrarily assigned the value 0.000V and serves as the reference point. $E_{\text{NiS-Ni}}$ is related to $E_{\text{Ni(II)-Ni}}$, the standard potential of the Ni(II)-Ni system through the solubility product of NiS, K_{sp}

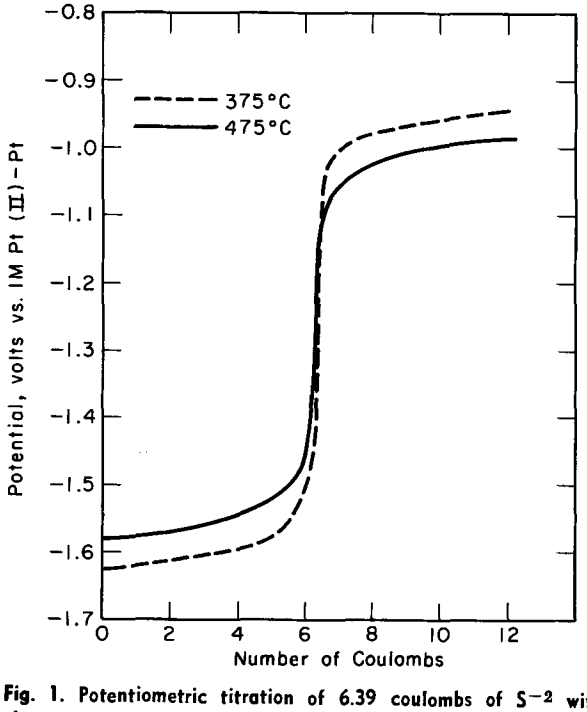

Fig. 1. Potentiometric titration of 6.39 coulombs of S^{-2} with coulometrically generated Ni(II). The weight of eutectic in the compartment was 14.65g.

Table I. Solubility products of NiS at various temperatures

Temperature, °C	$E^\circ_{\text{Ni(II)-Ni}}$, V	$E^\circ_{\text{NiS-Ni}}$, V	pK_{sp}
375	−0.786	−1.783	15.50
400	−0.790	−1.777	14.78
425	−0.794	−1.773	14.12
450	−0.797	−1.768	13.54
475	−0.801	−1.764	12.96

$$E^\circ_{\text{NiS-Ni}} = E^\circ_{\text{Ni(II)-Ni}} + \frac{RT}{2F} \ln K_{sp} \qquad [2]$$

Points on the titration curves in Fig. 1 before the equivalence point can be used to calculate $E^\circ_{\text{NiS-Ni}}$ by extrapolating the S^{-2} concentration to 1M. $E^\circ_{\text{Ni(II)-Ni}}$ can be obtained by extrapolating the Ni^{+2} concentrations to 1M at points on these curves beyond the equivalence point. Similar values of $E^\circ_{\text{NiS-Ni}}$ and $E^\circ_{\text{Ni(II)-Ni}}$ were also obtained in other experiments where Ni^{+2} and S^{-2} were coulometrically generated in separate compartments. In measurements involving Ni(II), both shiny and NiS-coated Ni electrodes were used. These measurements were made in the temperature range 375°-475° in 25° steps and K_{sp} values were calculated from the data with the aid of Eq. [2]. Table I lists the results. The E° value of $E^\circ_{\text{Ni(II)-Ni}}$ obtained at 450° agrees well with that reported previously by Laitinen and Liu (8).

It was found that Eq. [1] was obeyed by the NiS-Ni electrode at the temperatures investigated. Figure 2 presents the results at 450°C from five entirely independent sets of measurements (different symbols) using five different batches of melt. Within each experiment, the theoretical Nernst slope was very well obeyed for measurements at different concentrations. Somewhat larger deviations in $E^\circ_{\text{NiS-Ni}}$ and $E^\circ_{\text{Ni(II)-Ni}}$ were observed from experiment to experiment. The E°'s listed in Table I were obtained by extrapolating all measurements to 1M solutions by applying the theoretical Nernst slope and averaging the results. This procedure was chosen rather than a least squares analysis of all the results from different experiments at each temperature since Nernst behavior was observed for each experiment. The range of $E^\circ_{\text{NiS-Ni}}$ at 450° for 17 measurements in the concentration range 0.0013-0.012M was 9 mV with a standard deviation of 3 mV. For concentrations less than 0.001M positive deviations were observed. $E^\circ_{\text{Ni(II)-Ni}}$ showed a range of 7 mV for 17 measurements, in the concentration range 0.0035-0.067M with a standard deviation of 2 mV at 450°C.

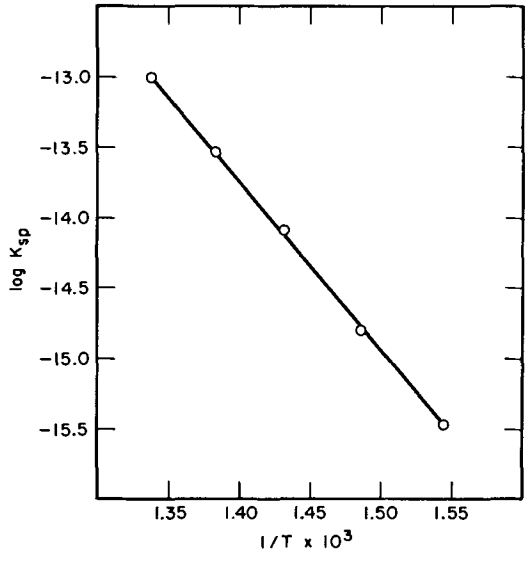

Fig. 2. Temperature dependence of the solubility product of NiS.

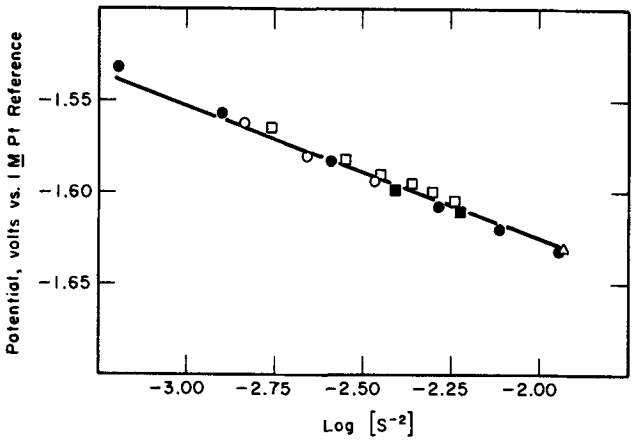

Fig. 3. Nernst plot for the NiS-Ni electrode

Positive deviations occurred below $5 \times 10^{-4}M$. Comparable results were obtained at the other temperatures. The pK_{sp}'s listed in Table I were measured with considerably more precision than the $E°$'s since the difference between $E°_{NiS\text{-}Ni}$ and $E°_{Ni(II)\text{-}Ni}$ from the same experiment was involved in the calculation. The range of pK_{sp} was 0.05 units from the same potential measurements to determine the $E°$'s.

A plot of log K_{sp} *vs.* $1/T$ yields a straight line and is shown in Fig. 3. The heat of reaction for the equilibrium $NiS \rightleftarrows Ni^{+2} + S^{-2}$ can be calculated with the aid of the van't Hoff equation. A value of 55.9 kcal was obtained.

Table II lists the solubility of Li_2S at various temperatures. The solubility was determined by direct potentiometry with the NiS-Ni indicator electrode. The temperature dependence of the solubility is shown in Fig. 4. Considering that deviations of 3-4 mV in the potential measurements have been observed, these results are probably accurate to ±10% which is about the limit of direct potentiometry in molten salts. The solubilities listed in Table II are much lower than the concentration levels examined by Bodewig and Plambeck in their electrochemical investigation of the sulfur-sulfide system (3). Obviously, the interaction of S with S^{-2} increases the solubility immensely. These interactions are, as mentioned previously, very complex and warrant further studies.

Acknowledgment

This work was performed under the auspices of the United States Atomic Energy Commission and the Environmental Protection Agency.

Manuscript submitted Feb. 18, 1972; revised manuscript received July 26, 1972.

Any discussion of this paper will appear in a Discussion Section to be published in the December 1973 JOURNAL.

Table II. Solubility of Li_2S

Temperature, °C	Solubility, moles/liter
375	0.013
400	0.020
425	0.029
450	0.038
475	0.045

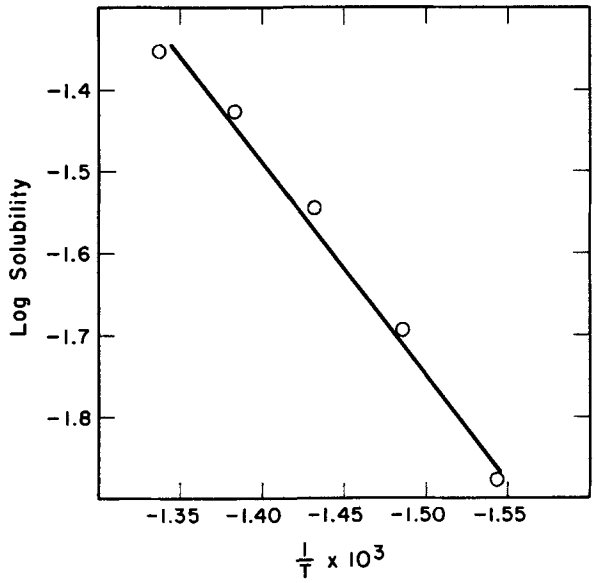

Fig. 4. Temperature dependence of the solubility of Li_2S

SYMBOLS

NiS	nickel sulfide
Ni	nickel
$S_x^=$	polysulfide
S_2^-	supersulfide
S_3^-	trisulfur anion
$S^=$	sulfide
Ag	silver
Ag_2S	silver sulfide
AgCl	silver chloride
NaOH	sodium hydroxide
NH_3	ammonia
M	molarity
$E°$	standard potential
R	gas constant
T	absolute temperature
n	number of electrons
F	faraday
ln	natural logarithm
K_{sp}	solubility product constant
mV	millivolt
kcal	kilocalorie
S	sulfur

REFERENCES

1. W. Giggenbach, *Inorg. Chem.*, **10**, 1308 (1971).
2. D. M. Gruen, R. L. McBeth, and A. J. Zielen, *J. Am. Chem. Soc.*, **93**, 6691 (1971).
3. F. G. Bodewig and J. A. Plambeck, *This Journal*, **116**, 607 (1969).
4. W. T. Thompson and S. N. Flengas, *Can. J. Chem.*, **46**, 1611 (1968).
5. K. Kiukkola and C. Wagner, *This Journal*, **104**, 379 (1957).
6. H. Reinhold, *Z. Electrochem.*, **40**, 361 (1934).
7. H. A. Laitinen and B. B. Bhatia, *This Journal*, **107**, 705 (1960).
8. H. A. Laitinen and C. H. Liu, *J. Am. Chem. Soc.*, **80**, 6701 (1958).
9. B. R. Van Artsdalen and I. S. Yaffe, *J. Phys. Chem.*, **59**, 118 (1955).
10. R. P. Elliott, "Constitution of Binary Alloys, First Supplement," p. 669, McGraw-Hill Book Co., New York (1965).
11. C. H. Liu and S. Shen, *Anal. Chem.*, **36**, 1652 (1964).
12. C. H. Liu and D. M. Gruen, Submitted to *Anal. Chem.*

Transference Number of $NaClO_4$ in Dimethyl Sulfoxide and Dimethyl Sulfite

Alphonzo G. Nelson and Douglas N. Bennion*

Energy and Kinetics Department, School of Engineering and Applied Science, University of California, Los Angeles, California 90024

ABSTRACT

The transference number of Na ions in $NaClO_4$ solutions in dimethyl sulfoxide varied from 0.310 at 0.499M to 0.357 at 0.0750M using the moving boundary method. The transference number of hydrated Cu ions in the following solution varied from 0.280 at 0.223M to 0.326 at 0.0343M. The transference number of Na ions in $NaClO_4$ solutions in dimethyl sulfite was 0.18 at 0.151M. All measurements were at 32°C.

The moving boundary method has been used to measure the transference numbers of $NaClO_4$· and $Cu(ClO_4)_2 \cdot 6H_2O$ in dimethyl sulfoxide and $NaClO_4$ in dimethyl sulfite. The hydrated copper ion was used in the following solution because it formed a stable boundary and made the boundary visible. Attempts to form a stable boundary using $LiClO_4$ in the leading solution were not successful, multiple boundaries being formed.

Use of hydrated copper perchlorate in the following solution required some minor changes in the equations previously presented by Bearman (1) and by Milios and Newman (2). The changes are necessary because the anode chamber is a two-salt system, hydrated and nonhydrated cupric perchlorate, rather than a single-salt as treated in previous analyses. The hydrated cupric perchlorate is the only salt initially in the anode chamber. However, as electrolysis proceeds, it is nonhydrated copper which is produced. A schematic representation showing the various solutions and boundaries is presented in Fig. 1. A third, probably indistinct, boundary will form between the original anolyte solution and the solution being produced at the anode as electrolysis proceeds.

The equation of continuity is valid for any species in the solution

$$\frac{\partial c_i}{\partial t} = \frac{-\partial (c_i v_i)}{\partial x} \qquad [1]$$

The current can be expressed in terms of the fluxes as

$$i = \mathbf{F} \sum_i z_i c_i v_i \qquad [2]$$

The equation of electroneutrality is

$$\sum_i z_i c_i = 0 \qquad [3]$$

Finally, a modified form of the Stefan-Maxwell equation is used to relate diffusive fluxes to chemical potential driving forces

$$c_i \frac{\partial \mu_i}{\partial x} = RT \sum_j \frac{c_i c_j}{c_T D_{ij}} (v_j - v_i) \qquad [4]$$

The definitions of the symbols used are given at end of the paper.

The above equations are solved for the leading solution and following solution in a manner similar to Milios and Newman (2) yielding the equation

$$t_1^o = \frac{\mathbf{F} z_3}{i} \frac{c_3}{c_o} \Bigg|_{x=-\infty} [c_o(v_o - v_b)]_{x=-\infty} \qquad [5]$$

$$t_2^o = \frac{\mathbf{F} z_3}{i} \frac{c_3}{c_o} \Bigg|_{x=\infty} [c_o(v_o - v_b)]_{x=\infty} \qquad [6]$$

or

$$\frac{t_1^o}{t_2^o} = \frac{[c_3/c_o]_{x=-\infty}}{[c_3/c_o]_{x=\infty}} \qquad [7]$$

Equation [7] is the Kohlrausch regulating function. Equation [6] is not used directly. In the above formulation, the notation, $x = -\infty$ refers to a position above the boundary, far enough away from the boundary so that only salt solution A (the leading solution) is present and far enough away from the electrode that $\partial \mu_{13}/\partial x = 0$. Likewise, $x = \infty$ refers to a position far enough below the boundary that μ_{23} is constant with only salt solution B present but still within the Kohlrausch regulated concentration region (see Fig. 1). t_1^o and t_2^o are transference numbers of cations 1 and 2 in leading and following solution, respectively, relative to the solvent, as pointed out by Milios and Newman (2).

In order to calculate the solvent velocity, a material balance is made in the anolyte chamber for a volume between an arbitrary control plane called the solvent plane, x, moving with the solvent velocity, v_o, and the solid electrode interface (see Fig. 1). The rate of change of the volume bounded by the solvent plane and closed electrode, V_o, is

$$\frac{dV_o}{dt} = \frac{d}{dt} \int_{V_o} dV = -v_o A - \frac{IM_e}{z_m \mathbf{F} \rho_e} \qquad [8]$$

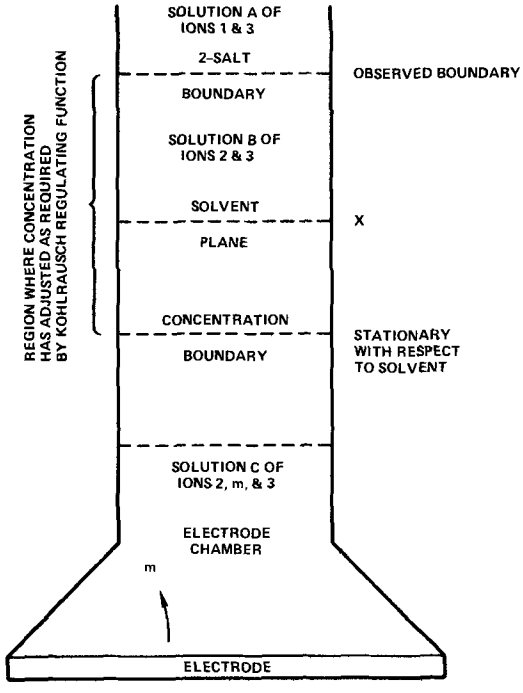

Fig. 1. Closed electrode with electrode material different from positive ionic species originally in solution.

* Electrochemical Society Active Member.

Key words: transference numbers, sodium ions, copper ions, dimethyl sulfoxide, dimethyl sulfite.

where A is the cross-sectional area, I is the total current passing through the electrode (negative for anode), M_e is the atomic weight of the metal anode, ρ_e is the density of the metal electrode. A material balance on the solvent gives

$$\frac{d}{dt}\int_{V_o} c_o dV = 0 \qquad [9]$$

Due to the dissolution of the electrode which produces a species not originally present in the following solution, two different positive ions are present in the following solution, the original one being designated by 2 and the metal ion being designated by m. Material balances on both of these ions yield the following

$$\frac{d}{dt}\int_{V_o} c_2 dV = \frac{It_2^o}{z_2 F} \qquad [10]$$

$$\frac{d}{dt}\int_{V_o} c_m dV = \frac{-I}{z_m F} \qquad [11]$$

It is assumed in this analysis that the boundary of the mixed solution of ion 2 and m never reaches the solvent plane. This assumption is justified in the present study because the distance between the anode and the concentration boundary is relatively large compared to the two-salt boundary movement. Otherwise, Eq. [11] would need to be replaced by the equation

$$\frac{d}{dt}\int_{V_o} c_m dV = \frac{It_m^o}{z_m F} - \frac{I}{z_m F} \qquad [12]$$

Since the solution in the anode chamber is a mixture of two salts, one can assume the density of the two-salt region below the solvent plane is linearly related to the concentration of both salts present.[1]

$$\rho_C = \rho_o + B_B c_{23} + B_m c_{m3} \qquad [13]$$

Here c_{23} is the concentration of the salt composed of ions 2 and 3, and c_{m3} is the concentration of the new salt formed by the metal dissolution, *i.e.*, of ions m and 3.

The exact expression for the density in this region is

$$\rho_C = M_B c_{23} + M_m c_{m3} + M_o c_o \qquad [14]$$

Therefore

$$c_o = c_o^o + b_B c_{23} + b_m c_{m3} \qquad [15]$$

where

$$c_o^o = \rho_o / M_o$$

$$b_B = (B_B - M_B)/M_o$$

$$b_m = (B_m - M_m)/M_o$$

Since $c_{23} = c_2/\nu_2$, and $c_{m3} = c_m/\nu_m$, Eq. [15] becomes

$$c_o = c_o^o + \frac{b_B c_2}{\nu_2} + \frac{b_m c_m}{\nu_m} \qquad [16]$$

Equation [9] then becomes

$$c_o^o \frac{d}{dt}\int_{V_o} dV + \frac{b_B}{\nu_2}\frac{d}{dt}\int_{V_o} c_2 dV + \frac{b_m}{\nu_m}\frac{d}{dt}\int_{V_o} c_m dV = 0 \qquad [17]$$

Substitution of Eq. [8], [10], and [11] with rearrangement yields

$$v_o = \frac{-i}{F}\left[\frac{M_e}{z_m \rho_e} - \frac{b_B t_2^o}{c_o^o \nu_2 z_2} + \frac{b_m}{c_o^o \nu_m z_m}\right] \qquad [18]$$

The expression for v_o, when substituted into Eq. [5] and [6], yields a set of equations which, when solved, give the expression

$$t_2^o = \frac{-c_o^o z_3 c_3}{c_o}\Bigg|_{x=\infty}\left[\frac{Fv_b}{i} + \frac{M_e}{\rho_e z_m} + \frac{b_m}{c_o^o \nu_m z_m}\right] \qquad [19]$$

and by means of the Kohlrausch relation

$$t_1^o = \frac{-c_o^o z_3 c_3}{c_o}\Bigg|_{x=-\infty}\left[\frac{Fv_b}{i} + \frac{M_e}{\rho_e z_m} + \frac{b_m}{c_o^o \nu_m z_m}\right] \qquad [20]$$

These equations are the final expressions needed for the calculation of the transference number from experimental data. When they are compared to the Milios and Newman (2) results, the two sets are seen to differ only in the last term which, in this case, represents the influence of the metal ion produced in the anode chamber being different than the following cation.

Experimental Equipment and Procedures

Solutions.—The solutions used in the present study were prepared from either dimethyl sulfoxide or dimethyl sulfite. The dimethyl sulfoxide was supplied by Crown Zellerbach Company, and the dimethyl sulfite was supplied by Aldrich Chemical Company. Due to the very hygroscopic nature of dimethyl sulfoxide, the water content of as-received dimethyl sulfoxide is on the order of 1076 ppm (3). Two other impurities also present insignificant quantities are dimethyl sulfide (DMS) and dimethyl sulfone ($DMSO_2$) (4). The as-received dimethyl sulfite was also found by Karl Fischer analysis to have a water content of 200 ppm. NMR analysis of the dimethyl sulfite indicated the presence of two major impurities each representing about 0.5% of the total weight, neither of which have been identified (5). The purification of solutions was accomplished by first placing the as-received dimethyl sulfoxide or sulfite in a flask containing Linde 4A molecular sieves. The flask was shaken approximately 3 hr, after which the contents were allowed to stand overnight. The resulting liquid was then centrifuged for 2 hr to remove the last traces of molecular sieve, and then transferred to a distillation column. Dimethyl sulfoxide was distilled at approximately 33 mm Hg pressure and 40°C. The dimethyl sulfite was distilled at 45 mm Hg pressure and 52°C. Karl Fischer titration of the product distillate indicated that the water content had been reduced to 30 ppm for dimethyl sulfoxide and 70 ppm for dimethyl sulfite. NMR analysis run on distilled DMSO indicated that no detectable organic impurities were present. NMR tests on distilled DMSU showed the disappearance of one of the peaks; the other peaks remained unchanged.

The three solutes used in this study were anhydrous purified $NaClO_4$ (City Chemical Corporation), anhydrous $LiClO_4$ (G. F. Smith Chemical Company, purity 97.4%), and reagent grade $Cu(ClO_4)_2 \cdot 6H_2O$ (Aldrich Chemical Company, purity 97-99%). The $NaClO_4$ was recrystallized three times by Yao (3). The salt was dried in vacuum at 70°C for three days; $LiClO_4$ was used as received. A Karl Fischer analysis run on the $LiClO_4$ indicates that approximately 1.74 molecules of water are present for every 10 molecules of salt. The $Cu(ClO_4)_2 \cdot 6H_2O$ was used as received.

Leading and indicator solutions were prepared by weight on a double pan balance (Volmer & Sons, Inc., New Rochelle, New York) inside of an argon filled Dri-Lab inert atmosphere glove box (Vacuum Atmosphere Corporation, Hollywood, California). The Dri-Lab was equipped with a unit through which the argon atmosphere could be continually recirculated for removal of oxygen and water. A Ni-Train unit consisting primarily of a titanium furnace was also provided with the Dri-Lab for the removal of nitrogen. These argon purifying units are capable of maintaining impurity levels between 1 and 5 ppm.

[1] For the copper perchlorate system studied it was found that $\rho_o = 1.093$ g/cm³, $B_B = 0.197$, $B_m = 0.2$ for ρ in grams per cubic centimeter and c_{23} and c_{m3} in mole/liter.

Electrodes.—"Baker Analyzed" copper wire 0.02 in. in diameter (J. T. Baker Chemical Company, purity 99.9%) was the anode. The vertical anode consisted of 24 strands of copper wire looped tightly together. Triple distilled mercury served as the cathode for the $NaClO_4$-$Cu(ClO_4)_2 \cdot 6H_2O$ tests. Contact was made to the mercury by a platinum wire sealed in soft glass.

Apparatus.—Boundaries were formed using a Tiselius cell (Perkin Elmer) with metal support stand and side electrode chambers. The channels of the cell were 0.2 cm thick, 1.5 cm deep, and 7 cm in length. A detailed description of the channel is given elsewhere (6).

In the present study, the boundary was followed by means of a cathetometer (Central Scientific Company), of accuracy ±0.5 mm located outside of the Dri-Lab. The bluish hue of the following cupric solution made it possible to observe directly the boundary formed between the two solutions. The boundary formed was visible down to about 0.03 molar in $Cu(ClO_4)_2 \cdot 6H_2O$, below which visual loss of the boundary occurred along the channel. Timing of the boundary was accomplished by means of antimagnetic stopwatches (Clark Stopwatch Company), of accuracy 0.005 min.

Velocity measurements recorded through a particular cell section are directly converted to volume displacements by multiplication of the cross-sectional area of the channel. The area was found by calibration of the cell with double-distilled water to be 0.3057 ± 0.0055 cm^2.

A Heath Kit regulated power supply (Model number IP-32) in series with a high impedance decade resistance box General Radio Company, was set so that the current remained constant to within ±0.05 mA regardless of the boundary position up the channel. The current readings were read on an ammeter (Simpson Electric Company).

The glass cell parts, electrode chambers, and syringes were cleaned in warm potassium hydroxide followed by dilute chromic acid. Finally, parts were rinsed with distilled water followed by acetone. The electrode chambers and syringes were stored in a vacuum oven at 375°C. The quartz cell was stored in a drawer.

Preparation for a run.—After assembly of the cell in its support stand in air, the apparatus was transferred into the Dri-Lab. Temperature control to ±1°C was accomplished by means of a Full Kontrol heater (Precision Scientific Company), and a temperature regulator (The Chemical Rubber Company, West Germany). These instruments were connected to a control relay box (Precision Scientific Company), mounted outside the Dri-Lab.

The apparatus was filled with solution by first filling the bottom section of the Tiselius cell with the copper perchlorate following solution just up to the flanged joint. A syringe reserved for the copper solution was used. The bottom cell section was then displaced relative to the mid-section so that the bottom was completely full of the following solution. The solution in the left channel was removed by the same syringe reserved for the copper solution. Next, the right side was filled up to the point where the liquid level was even with the right side opening of the top portion of the cell. The anode chamber was then filled until the level in the top cell portion was to the top. A Teflon plug was then inserted into the top carefully so no gas spaces were created. The plug had previously been coated liberally with Dow Corning Silicone grease. After the plug had been inserted, the anode chamber was filled up to the top and the chamber closed off by means of the Teflon stopcock located at the top of the chamber.

The cathode was prepared by inserting the platinum wire into the cathode chamber and then filling the chamber with triple distilled mercury up to the point where the platinum wire was completely submerged. Finally, the chamber and the left channel of the cell were filled with leading solution.

After the apparatus was connected to the electrical circuit, possible solution leakage from channel to channel through the sliding joints was checked. Problems with this type of leakage at the bottom portion during filling of the anode section necessitated this check. If a current was observed, the system was taken apart and the flanged joints recoated with Dow Corning vacuum seal grease and the procedure was started over.

After the leakage test, the potential was switched off and the bottom section of the cell carefully aligned with the middle section forming the sheared boundary. The boundary was given approximately 2 min for stabilization after which the cell was switched into series with the power source.

Operating procedure.—Average boundary velocities were recorded over 10-20 min intervals as the boundary progressed up the channel. When the boundary velocity had reached a constant value, four measurements were taken from which transference numbers were to be calculated. When the boundary had moved up through the top cell flange, the cell circuit was opened and the middle portion of the cell closed off by manipulation of the top and bottom cell sections. This procedure left a column of adjusted following solution closed off from which a sample could be drawn by syringe for later analysis by atomic absorption.

Results

$Na(ClO_4)$ in DMSO.—Stable boundaries were observed with sodium perchlorate as the leading solution and copper perchlorate hexahydrate as indicator and following solution. The data indicated a general trend of high boundary velocities near the starting point with decreasing boundary velocities with progression up the channel until a stable velocity was reached. Figure 2 shows the variation for a typical run. The initial high boundary velocity could have been due to the structure of the channel at the joint or could have been due to initial adjustment of the following solution concentration.

In calculating the transference number of the leading cation, Eq. [20] was used. The calculation of the transference number of the following solution was accomplished by Eq. [19]. The calculated transference numbers are given in Table I.

$NaClO_4$ in DMSU.—The results of a single run made on a 0.1508M solution of $Na(ClO_4)$ in dimethyl sulfite are also given in Table I. The transference number is given without correction for the solvent velocity due to unavailability of density data. The value is substantially lower than sodium ion transference numbers obtained in dimethyl sulfoxide. This suggests that a larger solvation sheath exists around the sodium ion in dimethyl sulfite than in dimethyl sulfoxide.

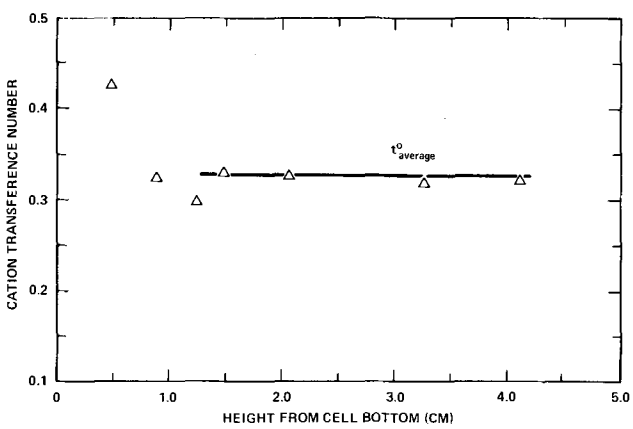

Fig. 2. Transference number at various channel positions for 0.2880M $NaClO_4$ in DMSO.

Table I. Cation transference numbers at 32°C $NaClO_4$ and $Cu(ClO_4)_2 \cdot 6H_2O$ in dimethyl sulfoxide

c $NaClO_4$ mol/l	$t_{Na^+}{}^o$	c $Cu(ClO_4)_2 \cdot 6H_2O$ mol/l	$t_{Cu^{++}}{}^o$	Λ^* $NaClO_4$ mho-cm²/equiv.	$\lambda-$ ClO_4^- mho-cm²/equiv.	Λ^{**} $NaClO_4$ mho-cm²/equiv.	$\lambda-\dagger$ ClO_4^- mho-cm²/equiv.
0.499	0.310	0.223	0.280	22.45	15.49	19.39	13.38
0.402	0.312	0.198	0.298	24.56	16.89	21.29	14.64
0.288	0.328	0.135	0.301	27.10	18.21	23.58	15.84
0.183	0.332	0.082	0.296	29.85	19.94	26.07	17.41
0.150	0.339	0.068	0.304	30.88	20.41	27.00	17.84
0.075	0.357	0.034	0.326	33.87	21.78	29.64	19.06

$NaClO_4$ and $Cu(ClO_4)_2 \cdot 6H_2O$ in dimethyl sulfite

m($NaClO_4$) mol/kg solv.	$t_{Na^+}{}^\ddagger$
0.151	0.182

* Data interpolated from Table II of Yao and Bennion (3) for 32°C.
** Data interpolated from Table II of Yao and Bennion (3) for 25°C.
† Column 2 times column 7 giving estimate of $\lambda-$ at 25°C.
‡ Not corrected for solvent velocity.
Note: The term $b_m/c_o{}^o\ \nu_m\ Z_m$ represented about a 7% correction.

Error analysis—The per cent uncertainty in the calculated transference numbers, for the leading solution, can be attributed to the per cent uncertainty in the measured quantities v_b, I, c_3/c_o, and A. If the error in the boundary velocity, v_b, and cross-sectional area, A, is taken to be the mean deviation of these quantities, the uncertainty in the current, I, taken as the least count of the ammeter, and the uncertainty in the concentration ratio, c_3/c_o, taken to be the uncertainty in the weight of the salt, the total or maximum uncertainty in the transference number can be related to that of the separate quantities as follows

$$\frac{\text{Uncertainty } (t)}{t_{\text{avg}}} = \frac{\text{Uncertainty } (v_b)}{v_{b\ \text{avg}}} + \frac{\text{Uncertainty } (I)}{I_{\text{avg}}} + \frac{\text{Uncertainty } (w)}{w_{\text{avg}}} + \frac{\text{Uncertainty } (A)}{A_{\text{avg}}}$$

The left-hand side is the maximum per cent error of the calculated transference number. Summation of the contributions from each of the right-hand terms gives a maximum uncertainty of 0.7%. A comparison of the calculated per cent errors and the per cent deviation using various readings during a single run of the transference numbers shows that the observed variations are essentially the same as the errors estimated from uncertainties in the individual measured quantities. A more detailed error analysis is given elsewhere (4).

The main contribution to the error in the calculated transference number of the following solution arises from the uncertainty in the measured concentration of the salts. The uncertainty in the measurement of the following solution concentration arises because the actual syringe sample taken from the solution beneath the boundary may have been diluted by the leading solution left at the inner spaces of the flanged joints. Also, in several tests a sample of the following solution was drawn by sticking the syringe through a layer of leading solution. This method was used when the boundary was not run completely up the channel so that a sample of leading solution could also be taken.

Discussion

Della Monica *et al.* (7) have recently published transference number data for $AgClO_4$ in DMSO based on Hittorf cell measurements. They calculated the limiting equivalent conductance for perchlorate ions using two extrapolation techniques. Yao and Bennion (3) extrapolated equivalent conductance data to infinite dilution for $NaClO_4$ in DMSO and determined the limiting equivalent conductance for perchlorate ions based on the assumption that triisoamylbutylammonium ions and tetraphenylboride ions have equal limiting equivalent conductances.

The transference number data determined in this paper have been extrapolated to infinite dilution using the procedure suggested by Longsworth (8)

$$t_+{}^{o\prime} = \frac{t_+{}^o \Lambda'' \beta \sqrt{c}}{\Lambda'' + 2\beta\sqrt{c}} = t_+{}^\infty + bc$$

$$\Lambda'' = \Lambda_o - (\alpha\Lambda_o + 2\beta)\sqrt{c}$$

Using the DMSO properties reported by Yao and Bennion (3) give $\alpha = 0.5041$ and $\beta = 17.55$. The results are shown graphically in Fig. 3. The concentrations used are rather high for such extrapolations. The mean deviation is 0.9%. The limiting equivalent conductance for the perchlorate ion was found using the limiting equivalent conductance reported by Yao and Bennion (3) at 25°C. In this calculation it was assumed the transference number is independent of temperature between 32° and 25°C. Examination of transference number temperature variations as reported by Yao and Bennion (3) indicates that this assumption probably produces an error of about 0.5%. Since this error is less than the extrapolation error, no correction was made.

A comparison of the three determinations of the limiting ionic equivalent conductance for perchlorate ions in DMSO at 25°C is shown in Table II. It appears as if the procedure used by Yao and Bennion (3) gives a slightly high value for $\lambda_-{}^o$. However, the errors in

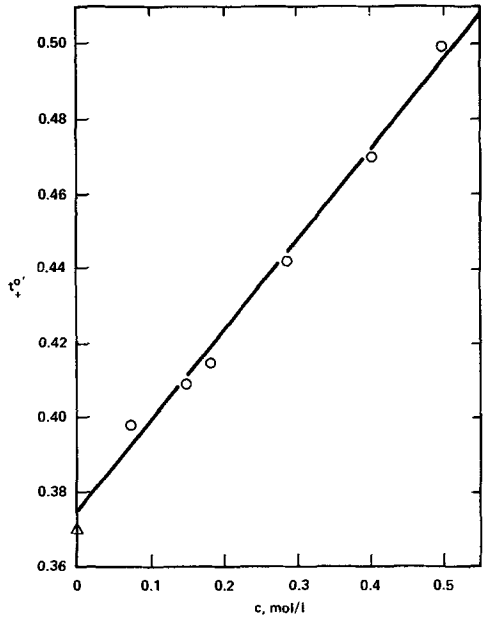

Fig. 3. Extrapolation of transference number data to infinite dilution using Longsworth equation (8). O data this work; △ data of Yao and Bennion (3).

Table II. Limiting equivalent conductance of ClO_4^- in DMSO at 25°C

λ_-^o mho-cm²/equiv.	Reference
24.48*	7
24.42	3
24.24	This work
24.12	7

* Extrapolation procedure very questionable as discussed by Della Monica *et al.* (7).

extrapolating the transference numbers to infinite dilution may account for the discrepancy.

SYMBOLS

A	cross-sectional area of cell channel, cm²
B_B	constant defined in Eq. [13]
B_m	constant defined in Eq. [13]
b_B	defined with Eq. [15]
b_m	defined with Eq. [15]
c_i	concentration of species i, mol/cm³
c_o^o	concentration of pure solvent, mol/cm³
c_T	total solution concentration, mol/cm³
D_{ij}	diffusion coefficient, cm²/sec
$\mathbf{F}$	Faraday's constant, 96,493 coul/equiv.
i	current density, A/cm²
I	current, A
M_i	molecular weight of species i, g/mol
R	universal gas constant, j/mol-deg
t	time, sec
t_i^o	transference number of species i relative to solvent
t_i^∞	transference number of species i at infinite dilution
T	temperature, deg K
V	volume, cm³
v_b	velocity of two-salt boundary, cm/sec
v_i	velocity of species i, cm/sec
x	distance up channel, cm
z_i	charge number of species i
μ_i	electrochemical potential of species i, j/mol
ν_i	number of cations or anions of species i produced by the dissociation of one molecule of parent salt
ρ_e	density of electrode material, g/cm³
ρ_C	density of following solution, g/cm³

Subscripts

o	solvent
1	leading cation
2	following cation
3	common anion
b	two-salt boundary
e	electrode
m	anode metal ion
$x = -\infty$	evaluated in solution A at concentration required by Kohlrausch relation
$x = \infty$	evaluated in solution B at concentration required by Kohlrausch relation
A	salt solution composed of ions 1 and 3
B	salt solution composed of ions 2 and 3
C	salt solution composed of ions 2, 3, and m
+	cation
−	anion

Manuscript submitted Feb. 9, 1972; revised manuscript received Aug. 10, 1972.

Any discussion of this paper will appear in a Discussion Section to be published in the December 1973 JOURNAL.

REFERENCES

1. R. J. Bearman, *J. Chem. Phys.*, **36**, 2432 (1969).
2. P. Milios and J. Newman, *J. Phys. Chem.*, **73**, 298 (1969).
3. N. P. Yao and D. N. Bennion, *This Journal*, **118**, 1097 (1971).
4. W. H. Smyrl, "Properties of Dimethyl Sulfoxide as a Solvent for Inorganic Compounds," Dept of Chem. Engr., Univ. of Calif., Berkeley, NOLC Internal Technical Report (January 1963).
5. N. P. Yao, E. D'Orsay, and D. N. Bennion, *This Journal*, **115**, 999 (1968).
6. A. G. Nelson, "Measurement of Transference Numbers in Nonaqueous Solvents by the Moving Boundary Method," M.S. Thesis, University of California, Los Angeles (June 1971).
7. M. Della Monica, D. Masciopinto, and G. Tessari, *Trans. Faraday Soc.*, **66**, 2872 (1970).
8. L. G. Longsworth, *J. Am. Chem. Soc.*, **54**, 2741 (1932).

Technical Notes

Overpotential Behavior at Pt Cathodes in Stabilized Zirconia Solid Electrolyte Fuel Cells

F. A. Kroger*

Department of Materials Science, University of Southern California, University Park, Los Angeles, California 90007

Etsell and Flengas (1) showed that application of voltages between 0.5 and 2V to cells of the type Pt (porous), Ar + O_2|ZrO_2 − CaO|Pt, O_2 at 700° and 1100°C with the left-hand electrode negative, led to saturated currents. The current was proportional to the oxygen pressure in the argon-oxygen mixture. The authors explained this by assuming that the current was limited by the diffusion of O_2 in the gas phase in the pores of the Pt electrode. For average size pores, this mechanism can be rate limiting only with O_2-inert gas mixtures. With pure O_2, diffusion is replaced by viscous flow, *i.e.*, a wind, which may constitute a limiting step only if the pores have submicron diameters (2); in pure O_2 overpotential was in fact not observed (1).

Experiments by Kleitz (3) and Yanagida *et al.* (4) on similar cells with inert gas-oxygen mixtures with 0.21 atm $\geq p_{O_2} \geq 10^{-4}$ atm at temperatures between 520° and 800°C show a limiting current $\propto p_{O_2}^{1/2}$, believed to be determined by diffusion of oxygen atoms through the platinum near the triple phase boundaries (4); experiments with nonporous foil electrodes at

* Electrochemical Society Active Member.
Key words: fuel cell, solid electrolyte, overpotential, limiting current, Pt cathode, oxygen diffusion.

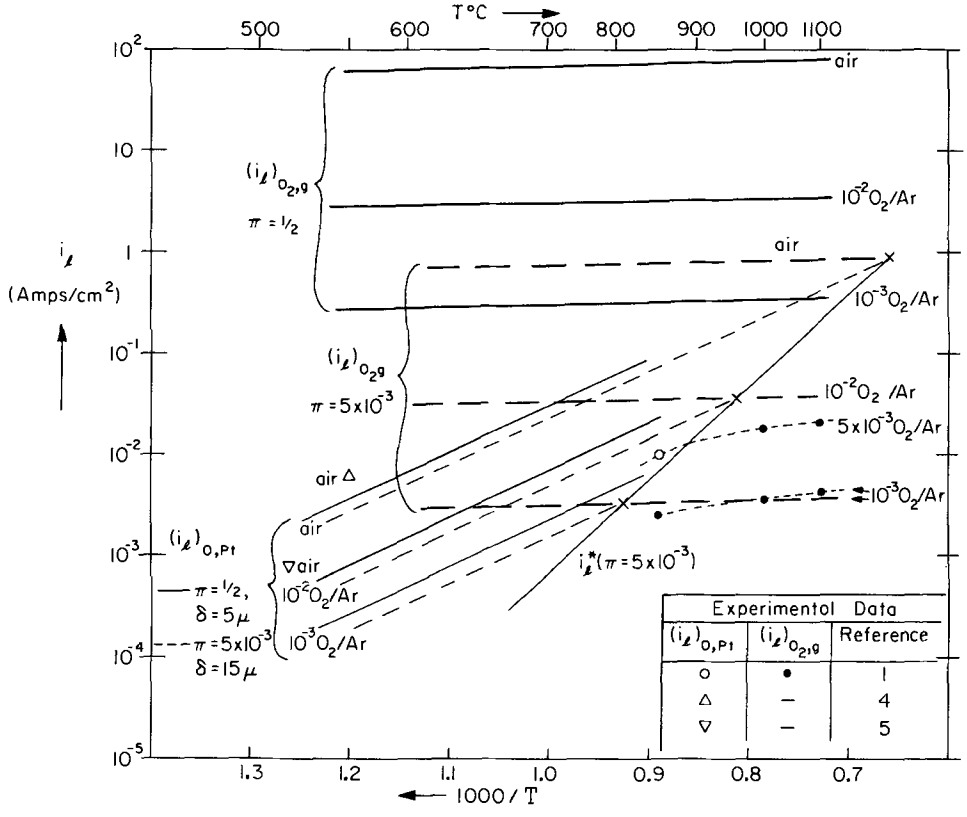

Fig. 1. Comparison of experimental values for the limiting current density with values calculated from Eq. [1] and [2] for three values of pO_2 and two different porosities.

temperatures between 520° and 685°C support this model (5). This mechanism is not limited to O_2-inert gas mixtures, as witnessed by the S-shape of the O_2 curve in Fig. 5 of Brook *et al.* (5).

All authors report rapidly increasing currents at higher voltages, related directly or indirectly to electronic conduction promoted by the increased polarization. As we shall see, the differences in the results at low voltages do not represent a discrepancy, but are due to a change in mechanism with changes in temperature, oxygen pressure, and porosity. Figure 1 shows values as a function of temperature for the current as limited by diffusion of O in Pt and as limited by gas-phase diffusion of O_2, each for various oxygen pressures and for two different porosities. In each case the limits shown in Fig. 1 were calculated from the expressions for the limiting current as given in Ref. (2) and (4)

$$(i_l)_{O_2(g)} = 4\,\mathbf{F}\,c\,D_{O_2(g)}(\pi/tl)\ln(1-x)^{-1}\ \mathrm{A/cm^{-2}} \quad [1]$$

$$(i_l)_{O(Pt)} = 2\,\mathbf{F}\,D_{O(Pt)}\,K\,pO_2^{1/2}\,\Omega/\delta\ \mathrm{A/cm^{-2}} \quad [2]$$

Equation [1] (List of Symbols is at end of note) holds for conditions under which composition changes in the gas outside the porous layer are prevented. If this is not the case, [1] still is valid, but with l and π replaced by $l' = l + \lambda$, and $\bar{\pi}$, respectively, λ being the thickness of the gas layer in which depletion of oxygen has occurred, and $\bar{\pi}$ an effective, average porosity. $\bar{\pi}$ can be estimated as follows. The removal of the oxygen at the pore entrance sets up concentration gradients in the gas outside the pore near the pore entrance. The equiconcentration planes will be approximately spherical close to the pore end, but will become planar at the distance λ from the pore end (Fig. 2a). In a rough treatment we can approximate the flow pattern by one with flat isoconcentration planes inside a cone with 90° top angle with the top at the pore end (Fig. 2b). The particle current of oxygen J_{O_2} through the gas in front of one pore is

$$J_{O_2} = -\frac{1}{RT} D_{O_2} A_x \frac{dpO_2, x}{dx}$$

with A_x the area of a section through the cone at x. If r is the pore radius

$$A_x = \pi^* \{(x + r)^2 - r^2\} = \pi^* x(x + 2r)$$

π^* indicating pi. Under stationary conditions this current is constant, independent of x. Then the oxygen pressure gradient over the gas layer with thickness λ is

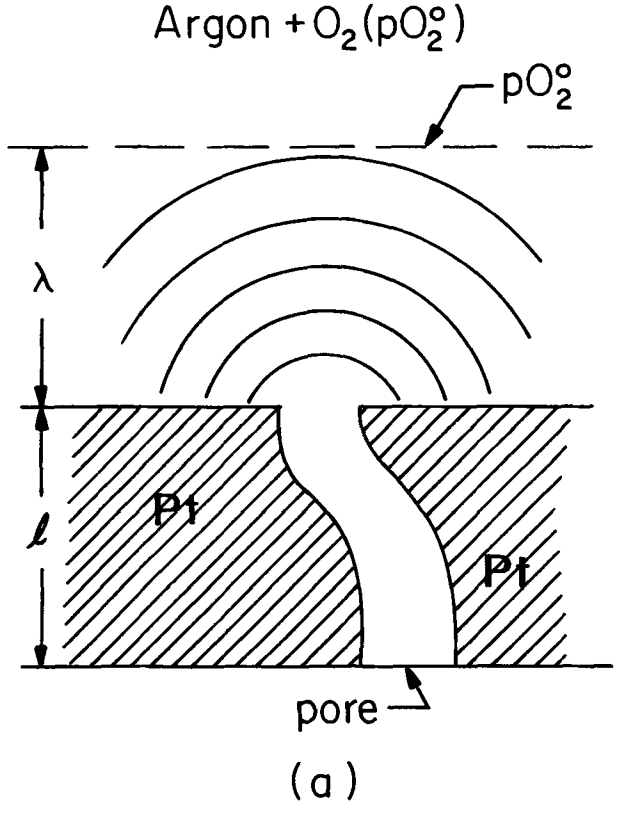

Fig. 2a. A pore in the porous platinum layer and equiconcentration lines for O_2 in the gas outside, near the pore (schematical).

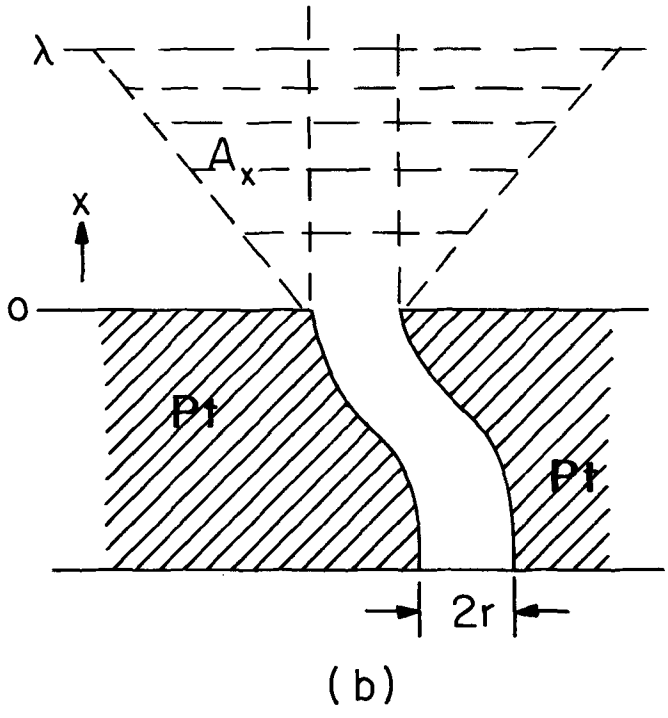

Fig. 2b. Approximate flat isoconcentration lines inside an inverted cone on top of the pore.

$$(\Delta pO_2)_\lambda = -J_{O_2}\frac{RT}{\pi^* D_{O_2}}\int_0^{-1}\frac{dx}{x(x+2r)}$$

Using the tabulated solution for the integral

$$(\Delta pO_2)_\lambda = J_{O_2}\frac{RT}{\pi^* D_{O_2}}\times\frac{1}{2r}\ln\frac{2r+x}{x}\Bigg|_0^\lambda =$$

$$-J_{O_2}\frac{RT}{\pi^* D_{O_2}}\times\frac{1}{2r}\left\{\ln\frac{2r\lambda}{(2r+\lambda)}-1\right\} \qquad [3]$$

The same J_{O_2} can be formulated in terms of a diffusion with a linear gradient through a cylindrical channel with an effective cross section A_e

$$J_{O_2} = -\frac{1}{RT}D_{O_2}A_e\frac{(\Delta pO_2)_\lambda}{\lambda} \qquad [4]$$

For N pores per cm^2 $= \pi/\pi^* r^2$, the effective porosity of the gas layer with thickness λ is $\pi' = NA_e$. Substitution of A_e using [4], and elimination of J_{O_2} with [3], remembering that $\pi = \pi^* r^2 N$

$$\pi'/\pi = 2\lambda/r\left\{\ln\frac{2r\lambda}{2r+\lambda}-1\right\} \qquad [5]$$

The effective average porosity of the combination of the gas layer and the Pt layer, $\bar{\pi}$ is found from

$$(\lambda + tl)/\bar{\pi} = (\lambda/\pi') + (tl/\pi) \qquad [6]$$

The gas layer will only be current limiting in cells in which the Pt layer is very thin.

In constructing Fig. 1, we have used Eq. [1] and [2] with $t \approx 1.5$, $l \approx 100\mu$, $\pi = 5 \times 10^{-3}$, and $\delta = 5$ and 15μ (note that π and δ are related). $D^T{}_{O_2(g)} \propto T^n$ is calculated from $D^{293}{}_{O_2N_2} = 0.22$ cm^2/sec, $D^{293}{}_{O_2,Ar} = 0.20$ cm^2/sec, using for n the average values for the corresponding self-diffusion exponents (6); typical values of n are between 1.66 and 1.81.

In O_2-Ar mixtures D_{O_2} varies from 1.16 cm^2 sec^{-1} at 500°C to 2.55 cm^2 sec^{-1} at 1000°C; for O_2-N_2 the corresponding variation is from 1.19 to 2.56 cm^2 sec^{-1}. According to Ref. (5), $D_{O(Pt,Rh)}K = 2.2 \times 10^{-16}$ exp ($-$ 0.94 eV/kT) g-atom cm^{-1} sec^{-1} atm$^{-1/2}$. The values for pure Pt may be 10 × larger. Recent measurements of $D_{O_2(Pt)}$ and the solubility of O in Pt (7) lead to a completely different expression $D_{O(Pt)}K = (2.4 \pm 0.67)\ 10^{10}$ exp ($-$ 8.45 ± 2.55) ev/kT g-atom cm^{-1} sec^{-1} atm$^{-1/2}$ which gives values for D_OK at 500°C that are 10^{18}-10^{51} smaller than the ones calculated from the expression from Ref. (5) [which are in turn smaller than values reported by Hoare (8)]. We have used the data from Ref. (5). It is obvious that our conclusions would be largely in error should one of the other sets of data prove to be the correct one.

As seen in Fig. 1, the experimental values for i_l in air as determined in Ref. (4, 5) fall close to the curve calculated from [2] for a highly porous layer using reasonable values of the parameters. Since the values of DK used were taken from experiments on nonporous films, the agreement lends support to the assumed model.

The data of Ref. (1) on the other hand, can be represented by [1] with $l \approx 100\mu$ only if we assume a low porosity, $\pi \approx 5 \times 10^{-3}$ with $t = 1.5$, or $\pi = 5 \times 10^{-2}$ with $t = 15$; the observed temperature dependence is, however, slightly larger than the theoretical one. Since Etsell and Flengas describe their Pt layer as a porous one, it seems *a priori*, unlikely that the porosity was so small. We then have to consider the possibility of a larger effective thickness corresponding to depletion of the gas mixture outside the Pt layer. The combination $l' = 1$ mm, $\bar{\pi} = 0.1$, corresponds to $\pi = 2 \times 10^{-2}$; only the combination $\bar{\pi} = 0.5$ and l' as large as 1 cm gives $\pi = 0.2$. Thus it seems that we have to accept a low value for π with probably depletion restricted mainly to the pores.

The difference in the temperature dependence and oxygen pressure dependence contained in [1] and [2] leads to a change in mechanism with a change in temperature and/or pO_2, the change occurring at a pressure $pO_2{}^*$ at a current density $i_l{}^*$ determined by the condition

$(i_l)_{O_2(g)} = (i_l)_{O,Pt} = i_l{}^*$. For $x = pO_2 << 1$, ln $(1 - x) \approx x$ and

$$pO_2{}^* = D_{O(Pt)}K\,\Omega\,tl/2c\,D_{O_2(g)}\pi\delta \qquad [3]$$

$$i_l{}^* = \mathbf{F}\,D^2{}_{O(Pt)}K^2\,\Omega^2\,tl/D_{O_2(g)}\,\delta^2\,\pi c \qquad [4]$$

$i_l{}^* \cdots 1/T$ as drawn in Fig. 1 for $\pi \approx 5 \times 10^{-3}$, separates the field at the right where gas diffusion is rate limiting from the field at the left where diffusion in Pt is rate limiting. The boundary, observable only at low pO_2 and/or low porosity is indicated in the 850°C data of Ref. (1) by a transition from a dependence $\propto pO_2{}^n$ with $n = 1$ at $pO_2 = 10^{-3}$ atm to $n < 1$ at $pO_2 = 5 \times 10^{-3}$ atm. Further work on cathodes for which the structure is better known is necessary to test the various models on variations in other parameters.

Manuscript submitted Feb. 28, 1972; revised manuscript received July 27, 1972.

Any discussion of this paper will appear in a Discussion Section to be published in the December 1973 JOURNAL.

LIST OF SYMBOLS

F	Faraday = 96,493 coulomb/g equiv.
π	porosity = ratio of the contact area gas/ZrO_2 to the total contact area
Ω	fractional contact area Pt/ZrO_2 $\leq (1 - \pi)$
$D_{O_2(g)}$	diffusion coefficient of O_2 in the gas mixture
$D_{O(Pt)}$	diffusion coefficient of O in Pt
K	equilibrium constant of the reaction determining the solubility of oxygen in Pt: 1/2 $O_2(g) \rightarrow O(Pt)$
pO_2	oxygen pressure in the gas mixture
c	molar density of the gas mixture = P/RT
l	total thickness of the Pt layer
δ	effective thickness of the Pt; at high porosity, $\delta \approx$ grain size, at low porosity $\delta \rightarrow l$ for $\pi \rightarrow 0$.

t tortuosity of the pores = average ratio of the actual length of pore channels over the length of the vector connecting its ends

x mole fraction of O_2 in the gas mixture; for a total pressure $P = 1$ atm, $x = pO_2$

REFERENCES

1. T. H. Etsell and S. N. Flengas, *This Journal*, **118**, 1890 (1971).
2. C. S. Tedmon, Jr., H. S. Spacil, and S. P. Mitoff, *ibid.*, **116**, 1170 (1969).
3. M. Kleitz, J. Besson, and C. Deportes, *Rev. Energ. Primaire*, 2, 35 (1966); M. Kleitz, Thesis Université de Grenoble (1968).
4. H. Yanagida, R. J. Brook, and F. A. Kröger, *This Journal*, **117**, 593 (1970).
5. R. J. Brook, W. L. Pelzmann, and F. A. Kröger, *ibid.*, **118**, 185 (1971).
6. Landolt-Börnstein, Tables, Vol. II, Teil 5a, 6th ed., pp. 516, 519.
7. L. R. Velho and R. W. Bartlett, *Metallurg. Trans.*, **3**, 65 (1972).
8. J. P. Hoare, *This Journal*, **116**, 612, 1390 (1969).

Electrochemical Properties of $RbAg_4I_5$ Solid Electrolyte

III. Chargeable Cells

Bruno Scrosati*

Laboratorio di Chimica Fisica ed Elettrochimica, Università di Roma, Rome, Italy

The organic semiconductors commonly known as "charge transfer complexes" (CTC) (1), possess a number of intrinsic properties which make them a very promising class of materials to use as halogen electrodes in solid-state cells. A CTC may be defined (1) as a system involving two components, one acting as electron donor (typically polycyclic aromatic compounds) and the other acting as electron acceptor (typically halogens). The most interesting property of the CTC is that their resistivity remains very low for a wide range of halogen composition (2). This circumstance promises their functioning as halogen electrodes in solid-state batteries. Furthermore, due to their low resistivity, the CTC may be used as electrodes without addition of inert components to assure good electronic conductivity, as is the case of the so far most used cathodes in solid-state cells. This results in immediate specific energy advantages.

In a previous work (3), it has been shown that the CTC, in addition to the above-mentioned advantages, also behave as reversible electrodes in solid-state cells. In particular it has been shown that the iodine-perylene (I_2-P) complex behaves as a reversible electrode in the $RbAg_4I_5$ solid electrolyte cell

$$Ag/RbAg_4I_5/I_2\text{-}P \qquad [1]$$

This reversibility was tested both by micropolarization curves and by the successful charge of the cell

$$Ag/RbAg_4I_5/AgI,P \qquad [2]$$

which is the fully discharged version of cell [1]. The charge process of cell [2] in fact leads to the formation of the I_2-P complex at the positive and the deposition of silver at the negative. The charge-discharge efficiency of cell [2] is very satisfactory, about 70%, as shown in Fig. 1. This is an interesting result since cell [2] may be stored for any desired length of time and activated just before use. The shelf life of this "reserve type" solid-state cell should be therefore very long (3).

The satisfactory behavior of cell [2] suggested further study to improve its technological properties. The results of this study are reported in this work.

Experimental

The electrolyte was prepared in the usual way (4). The positive electrode mixture was formed by mixing silver-iodide and perylene in such a proportion to originate, after a complete AgI to I_2 conversion, an I_2-P complex of 2/3 molar ratio. To reduce interfacial effects (3), to 1 part of this mixture, 3 parts of electrolyte were then added. The cell components were pressed into a single pellet with the following procedure. First a certain amount of powdered zinc (or, alternatively graphite) was slighty pressed in a stainless-steel dye. Then the plunger was raised up and on the top of the zinc pellet was added a moderate amount of electrolyte and pressed at higher pressure. Then the plunger was raised up again and a small amount (typically 0.07g) of the positive electrode mixture was added. The pressure was then raised to about 3000 kg/cm^2 to obtain the final pellet where the electrode materials were uniformly and intimately in contact with the electrolyte. The pellet obtained in this way had a diameter of 1.26 cm and average thickness and weight of 0.2 cm and 0.8g, respectively. The cell was finally assembled into a Teflon container with gold-plated terminals.

The polarization studies were performed by using a silver wire as reference electrode. This was inserted into the electrolyte by heating the wire in order to melt the electrolyte locally. Standard equipment was used to determine current-voltage curves and to register the charge-discharge cycles.

Results and Discussion

Since cell [2] is assembled in the discharge state, it is not strictly necessary to use silver as the negative. Any other material on which silver may deposit a charge can be used as alternative. If this material is inexpensive, as for instance zinc or graphite, the over-all cost of the cell would be reduced. In fact the silver utilized in the discharge would be that obtained from the conversion of silver iodide during charge.

To test this, the cell

$$Zn/RbAg_4I_5/AgI,P \qquad [3]$$

has been assembled. Cell [3] was submitted to 18 hr charge at 0.05 mA. The following discharge, at 0.1 mA,

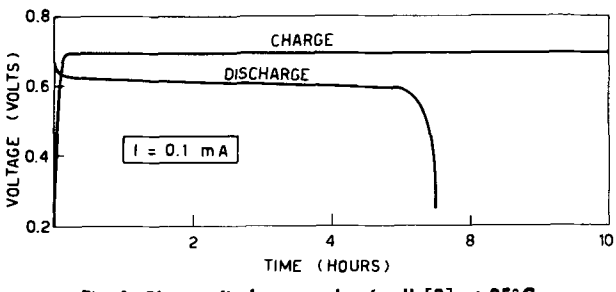

Fig. 1. Charge-discharge cycle of cell [2] at 25°C

* Electrochemical Society Active Member.
Key words: solid electrolyte, chargeable cells.

was satisfactory, giving a utilization (at 0.3V cut off) higher than 50% and being very flat in shape. This cycle is shown in Fig. 2A. In Fig. 2B is shown another cycle realized by charging a cell similar to [3] at 0.1 mA and discharging it at 0.2 mA. This cycle also was satisfactory, giving an efficiency of 53%. These results indicate that cell [3] also is chargeable with a reasonably good discharge efficiency. Figure 3 is a photograph of the positive side of a cell similar to cell [3] charged with a rectangular current collector up to 70% of its complete charge. The black color of the I_2-P complex (3) is evident over the clear color of the original AgI,P mixture. This is a further indication of the chargeability of cell [3].

Figure 4 shows current-voltage curves of the AgI,P electrode used in cell [3] (curve A) and of an electrode similar to the previous one but without AgI in it. In the latter (curve B) appreciable current, obviously due to electrolyte decomposition, flows at potentials ranging from 0.8 to 0.9V. One may therefore exclude electrolyte decomposition during charge of cell [3] if the charging voltage is maintained below 0.8V.

Cell [3] was submitted to continuous charge-discharge cycles which are shown in Fig. 5. Indications of cell deteriorations are evident even at the third cycle. The cell was disconnected and examination under the microscope showed deposition of silver in dendritic form on the negative electrode surface. Scrosati and Butherus (5) have shown that planar silver electrodes behave reversibly at low-current levels. When a considerable amount of charge is passed through the cell, however, one may obtain dendritic deposition of silver at the negative. It has been subsequently shown by Butherus (6) that irreversible degradation on cycling takes place when the cycle

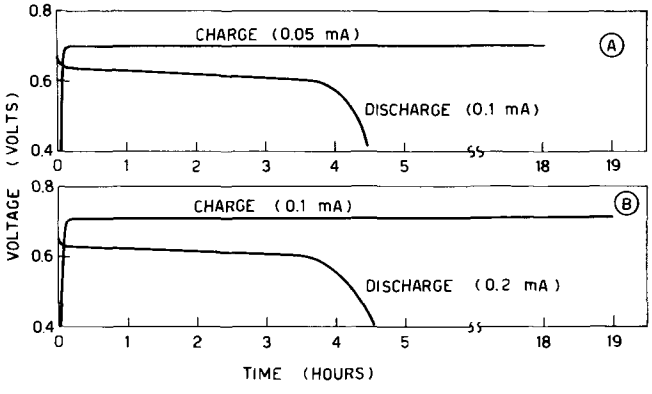

Fig. 2. Charge-discharge cycles of cell [3] at 25°C

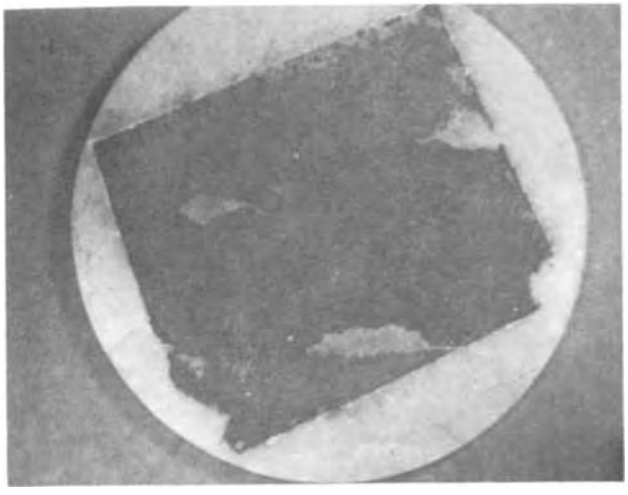

Fig. 3. Microphotograph (6X) of the positive electrode surface of a charged cell [3].

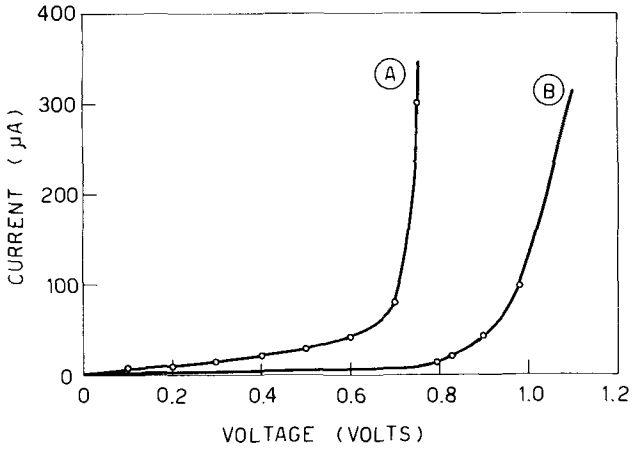

Fig. 4. Current-voltage curves of the AgI, P electrode (curve A) and of the P electrode (curve B) at 25°C. Reference electrode: silver wire.

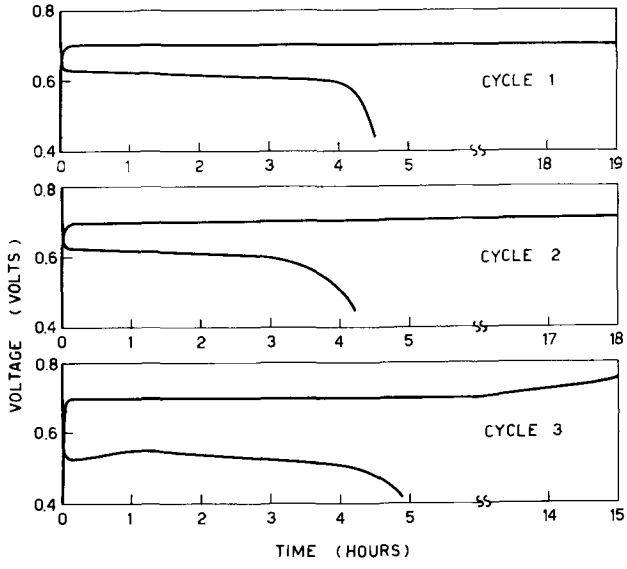

Fig. 5. Continuous charge-discharge cycles of cell [3] at 25°C. Charge current: 0.1 mA; discharge current: 0.2 mA.

regime involves a layer of silver thicker than 0.2μ. This undoubtedly represents the most serious limiting factor to the rechargeability of the $RbAg_4I_5$ cells which has to be limited to shallow cycling regimes only. Under these conditions in fact, Butherus has been able to cycle $RbAg_4I_5$ cells several thousand times (6).

Finally the charge-discharge curve of the cell

$$C/RbAg_4I_5/AgI,P \qquad [4]$$

where zinc has been substituted by graphite as the silver electrode support, is shown in Fig. 6. The charge

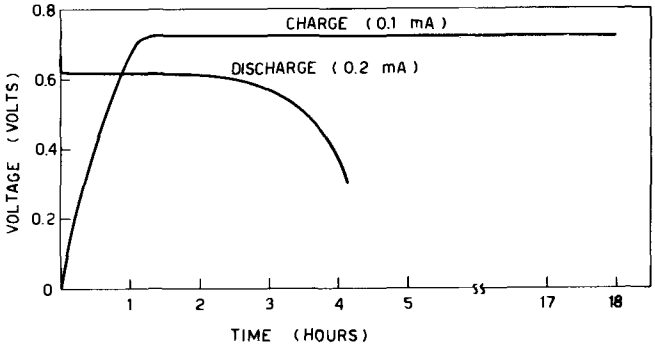

Fig. 6. Charge-discharge cycle of cell [4] at 25°C

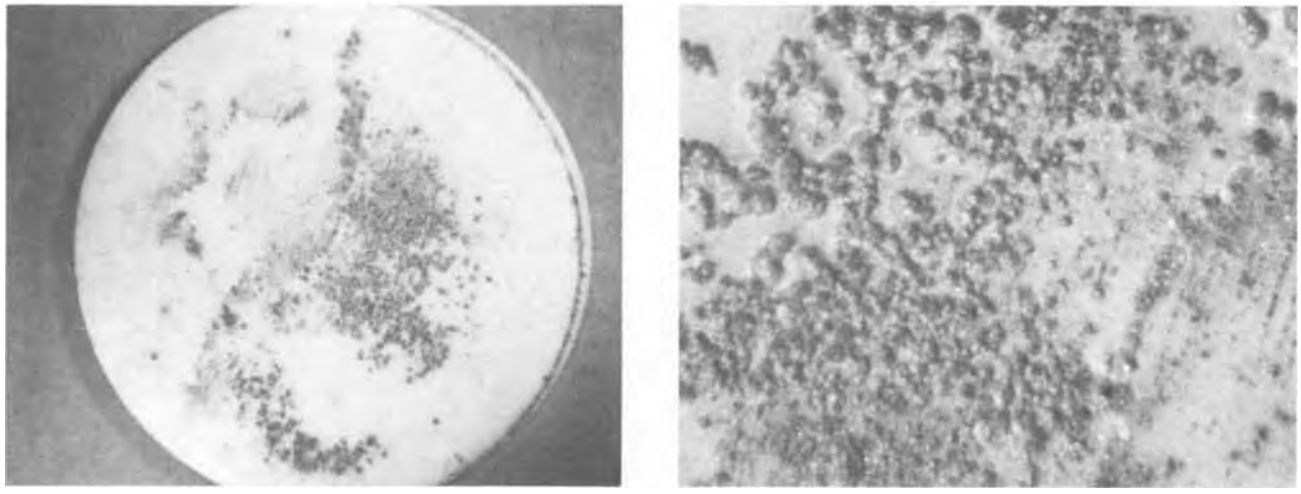

Fig. 7. Microphotographs (6X left and 25X right) of the negative side of a charged cell [4]

voltage rose slowly to a rather high stable value, *i.e.*, 0.72V, and the subsequent discharge gave a utilization of about 40%. A cell similar to [4] was disconnected after charge and microphotographs of its negative side are shown in Fig. 7. Deposition of silver in dendritic form is particularly evident here.

Conclusions

The main purpose of this work is to show that cells having the structure [3] or [4] may be successfully used as "reserve type," reduced-cost solid-state cells. The results of Fig. 2 and 5 indicate that this is indeed the case. Therefore the shelf life of these cells should be very long as might not be the case of primary $RbAg_4I_5$ iodine cells because of the well-known iodine diffusion through the polycrystalline electrolyte (7, 8). It does not seem to be possible, however, to obtain many deep cycles with cells [3] and [4] because of the tendency of silver to deposit in dendritic form, a process which results in a lack of contact points at the electrode-electrolyte surface and, ultimately, in an increase of cell internal resistance. This was also found by Raleigh in his studies on electrodeposition of silver from solid AgBr on various electrodes (9). In fact he reported that Ag electrodeposition onto Pt involves smooth buildup of monolayers while nucleated deposition occurs on graphite, resulting in dendritic growth.

Acknowledgments

The author would like to thank Dr. A. D. Butherus of Bell Telephone Laboratories for his helpful discussions on this study. This work was partially sponsored by the Consiglio Nazionale delle Ricerche (C.N.R.).

Manuscript submitted July 12, 1972; revised manuscript received Sept. 6, 1972.

Any discussion of this paper will appear in a Discussion Section to be published in the December 1973 JOURNAL.

REFERENCES

1. R. Foster, "Organic Charge Transfer Complexes," Academic Press, New York (1969).
2. T. Uchida and H. Akamatu, *Bull. Chem. Soc. Japan*, **34**, 1015 (1961).
3. B. Scrosati, M. Torroni, and A. D. Butherus, "8th International Power Sources Symposium," Brighton, Sussex (1972); Preprint No. 18.
4. B. B. Owens and G. A. Argue, *Science*, **157**, 308 (1967); B. Scrosati, *J. Appl. Chem. Biotechnol.*, **21**, 223 (1971).
5. B. Scrosati and A. D. Butherus, *This Journal*, **119**, 128 (1972).
6. A. D. Butherus, Paper 117 presented at Electrochem. Soc. Meeting, Houston, Texas, May 7-11, 1972.
7. J. E. Oxley and B. B. Owens, in "Power Sources," Vol. 3, p. 535, D. H. Collins, Editor, Pergamon Press, London (1972).
8. R. D. Armstrong, T. Dickinson, H. R. Thirsk, and R. Whitfield, *J. Electroanal. Chem.*, **34**, 47 (1972).
9. D. O. Raleigh, *J. Phys. Chem.*, **71**, 1785 (1967).

Continuous Flow Dielectrophoresis

R. H. Kirchoff and A. Hamdi[1]

Department of Mechanical Engineering, University of Massachusetts, Amherst, Massachusetts 01002

Previous work (1, 2) has established the use of the dielectrophoretic force to separate a solute from its solvent and to perform filtration in a continuous manner. Particles of various materials suspended in liquid dielectrics have been separated in a cell of cylindrical geometry under the action of nonuniform fields (1). Transformer oil has been purified to a breakdown strength of 100 kV/mm in a continuous flow dielectrophoretic cell. Carbon particles of a few tens of Å have been removed (2). Further applications of the dielectrophoretic force may be found in Ref. (7).

In this work, the equation of motion of a particle in a continuous flow dielectrophoretic separator has been solved under certain assumptions. The results have been expressed in terms of dimensionless parameters in order to provide a design curve for such a filter. Based on previous experimental work, limits on the range of the operating parameters of the cell have been indicated.

[1] Present address: Moharem Bey, United Arab Republic.
Key words: dielectrophoresis, deposition.

Analysis

A continuous-flow cylindrically symmetric separator is shown in Fig. 1. The fluid suspension enters at the top with velocity $V_z(r)$; in the presence of the nonuniform field, particles with a dielectric constant greater than that of the fluid will be attracted to the central electrode. The dielectrophoretic force on a particle in a cell of this geometry is given as (3)

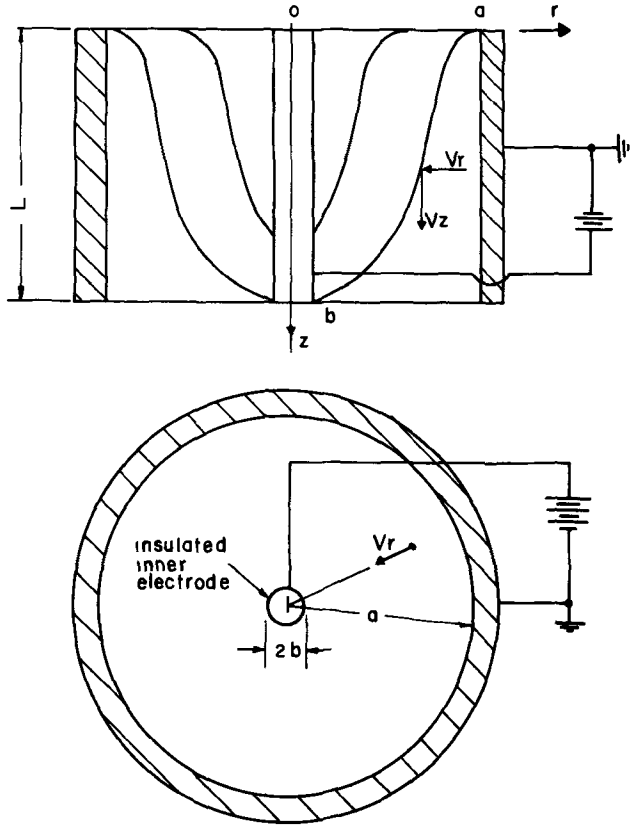

Fig. 1. Cylindrical separation cell

$$\bar{F}_e = -4\pi R^3 \epsilon_0 \frac{K_1(K_2 - K_1)}{(K_2 + 2K_1)} \frac{V_1^2}{r^3\left[\ln\left(\frac{b}{a}\right)\right]^2} \bar{r}_0 \quad [1]$$

where ϵ_0 is the permittivity of free space; r is the distance of the particle from the central axis; R is the radius of the particle; $K_{1,2}$ is the relative dielectric constant of the liquid and the particle, respectively; V_1 is the potential of the inner cylinder; $\bar{r}_0$ is the unit radius vector; and a,b outer and inner cylinder radii, respectively.

The equation of motion for a particle is written under the following assumptions: (*i*) the particle is assumed to be a point mass; (*ii*) the flow is laminar; (*iii*) the particles do not strongly interact; (*iv*) gravitational forces and electrostatic forces are neglected; (*v*) the resistance of a particle is given by Stokes law.

The equation of motion in the r direction may be written as

$$m\frac{dV_r}{dt} = F_e - F_d \quad [2]$$

where m is the particle mass and F_d is the Stokes drag law for a spherical particle $F_d = 6\pi\mu RV_r$. Combining Stokes law with Eq. [1] and [2]

$$\frac{mV_r^2}{6\pi\mu RV_r}\frac{dV_r}{dt} = \left[\frac{4\pi R^3\epsilon_0 V_1^2 K_1(K_2 - K_1)}{r^3\left(\ln\frac{b}{a}\right)^2 6\pi\mu RV_r(K_2 + 2K_1)} - 1\right] V_r^2 \quad [3]$$

Let $P_r = (mV_r^2)/(6\pi\mu RV_r)$ the ratio of the particle kinetic energy to the drag force in the r direction. When P_r is very small, the left side of Eq. [3] may be neglected which is equivalent to ignoring the Newtonian acceleration. This is justified when the inertia force on a particle is much less than the viscous drag force. P_r is a parameter having the dimension of length; it is equal to the distance the particle will travel before coming to rest when launched with velocity V_r into a stationary fluid. For the conditions of the separator in Ref. (1) P_r was found to be on the order of 10^{-13}m. Ignoring the acceleration term and rearranging the equation of motion in the r direction, the particle velocity may be written

$$V_r = 2R^2\epsilon_0 V_1^2 K_1(K_2 - K_1)/3\mu r^3\left(\ln\frac{b}{a}\right)^2(K_2 + 2K_1) \quad [4]$$

The equation of motion in the z direction is

$$m\frac{dV_z}{dt} = 6\pi\mu R(V_z - U) \quad [5]$$

where $U(r)$ is the mean fluid velocity in the annulus. Equation [5] may be rearranged as

$$\frac{mV_z^2}{6\pi\mu RV_z}\frac{dV_z}{dt} = (V_z - U)V_z$$

Let $P_z = mV_z^2/6\pi\mu RV_z$. When P_z is small, the Newtonian acceleration in the z direction may be neglected which implies that the particle velocity and the fluid velocity are identical in the z direction. For the conditions of the separation in Ref. (1) P_z was found to be on the order of 10^{-18}m. For laminar flow in an annulus (4) U is given as

$$U = \left(\frac{1}{4\mu}\right)\left(\frac{\Delta P}{\Delta z}\right)\left(b^2 - r^2 + (a^2 - b^2)\left(\ln\frac{r}{b}\right) \Big/ \ln\left(\frac{a}{b}\right)\right) \quad [6]$$

and the volume flow rate in the annulus is

$$W = \frac{8\pi}{\mu}\left(\frac{\Delta P}{\Delta z}\right)\left(a^4 - b^4 - (a^2 - b^2) \Big/ \left(\ln\frac{a}{b}\right)\right) \quad [7]$$

In the subsequent analysis Eq. [6] and [7] are used together to eliminate $(\Delta P/\Delta z)$.

The optimum length of the dielectrophoretic continuous flow filter is the minimum length for the separation of the axial flowing particle suspension. In Fig. 1 for a particle starting at (O,a) and ending at (L,b) the optimum length is the particle path projection L on the z axis. A similar particle starting at some radius $r < a$ will be collected in some length z less than the optimum length.

To find this optimum length, let $V_z = dz/dt$ and $V_r = -dr/dt$; eliminate the parameter t (time) and integrate along the particle path

$$-\int_o^L dz = K\int_a^b r^3 dr - M\int_a^b r^5 dr + N\int_a^b r^3 \ln(r/b)\,dr \quad [8]$$

K, M, N are constants. Performing the integration

$$L = A\left(A_1\left(\frac{b}{a}\right)^6 - \left(A_2\ln\left(\frac{b}{a}\right) + A_3\right)\left(\frac{b}{a}\right)^4 - A_4\right) \quad [9]$$

where

$$A = \frac{8d^4(\ln d)^3\mu W(K_2 + 2K_1)}{((d^4 - 1)\ln(d) - (d^2 - 1)^2 e_0 V_1^2 R^2 K_1(K_2 - K_1)\pi)}$$
$$A_1 = (d^2/16)b^2$$
$$A_2 = (3(d^2 - 1)/32\ln d)b^2$$
$$A_3 = ((12d^2\ln d - 3d^2 + 3)/(128\ln d))b^2$$
$$A_4 = ((3d^2 - 4d^2\ln d - 3)/(128\ln d))b^2$$
$$d = a/b$$

Substitute the constants A, A_1, A_2, A_3, A_4, and d into Eq. [10] and rearrange to get

$$\frac{LFe}{W_m} = F(d) \quad [10]$$

W_m is a form of mechanical work $W_m = (8/\pi)\mu W(b/R)^2$ having the dimensions of Newton-meters. And Fe is an electric force

$$Fe = \frac{K_1(K_2 - K_1)\epsilon_0 V_1^2}{(K_2 + 2K_1)}$$

having the dimension of Newton. $F(d)$ is a dimensionless shape factor.

$$F(d) = \frac{(\ln d)^2(4d^6 - 1)\ln d - 3(d^5 - d^4 - d^2 + 1)}{128\,((d^4 - 1)\ln d - 3(d^2 - 1)^2)}$$

L is the optimum filter length. Equation [10] is plotted in Fig. 2 which contains all the information necessary to select a filter of optimum length. The bottom line in Fig. 2 is for 100% particle collection. An analysis similar to the foregoing was used to predict the filter length necessary to collect x% of the incoming particles. These results are also indicated on Fig. 2.

By changing the limits of integration on Eq. [8] from O to Z and from a to r the particle path may be generated for 100% particle collection in length L. This particle path is shown in Fig. 3 together with the particle paths for less than 100% collection. Figure 3 is plotted for $d = 10$ only.

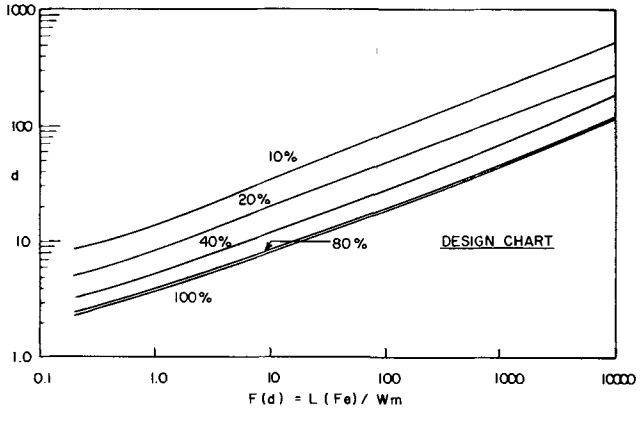

Fig. 2. Design chart

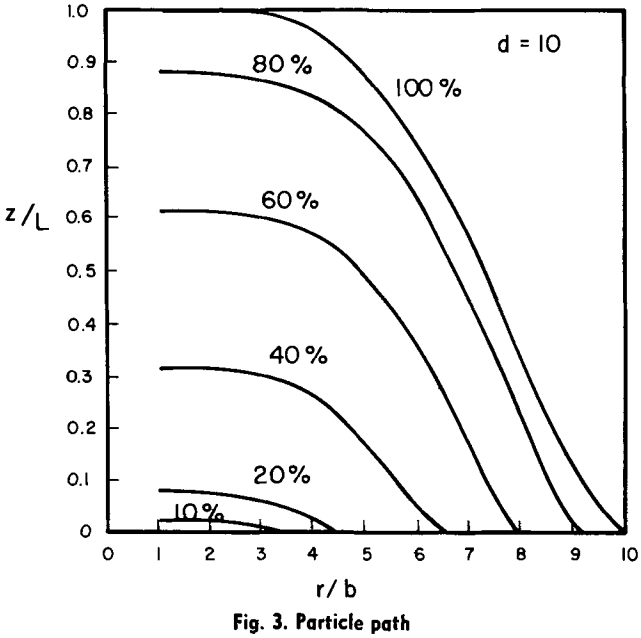

Fig. 3. Particle path

For the conditions of the experiment described in Ref. (1) in which almost 100% separation was observed, the curve of Fig. 2 predicts an optimum filter length from 3 to 12 cm depending on the applied voltage. The actual filter in Ref. (1) was estimated (5) to be about 19 cm in length. This reasonable agreement is taken as sufficient evidence that Eq. [10] can be used to design a continuous flow dielectrophoretic separation cell.

Limitations

There are a number of limitations reported in the literature (1, 2) which place some constraints on the parameters in Eq. [10].

In order to eliminate particle charging and subsequent electrostatic repulsion at the center electrode, that electrode should be coated with Teflon, plastic foam, or another suitable insulating material.

The field strength at the central electrode should be less than 2×10^6 V/m. Greater field strengths have the effect of drastically reduced collection at the central electrode. There is a minimum central electrode voltage of a few hundred volts below which no dielectrophoretic action takes place.

The period of the applied-voltage signal to the electrodes should be much less than the time constant ϵ/δ of the dielectric suspension in order to prevent the decay of free-charge density and the collapse of the nonuniform field in the separation cell.

There is a maximum residence time for which the fluid should remain in the separator. For residence time $t_r = L/V_z$ longer than this maximum, ionic charging of the fluid has been observed to take place with a subsequent decrease in particle collection (6). This time for ionic charging has been given in Ref. (6) as

$$t_s = \frac{\epsilon_0 \rho_1 \rho_2}{\rho_2 - \rho_1}(K_2 - K_1)$$

where ρ_1 and ρ_2 are the resistivities of the liquid and the particles, respectively. In order to avoid ionic charging $t_r < t_s$.

Conclusion

All the parameters involved in the design of a dielectrophoretic separator have been presented on a single dimensionless curve from which optimum filter parameters may be selected. Limitations on these parameters which have been observed in previous experiments have been included for completeness.

Acknowledgment

This work was supported by the National Science Foundation under Grant GK 5569.

Manuscript submitted July 5, 1972; revised manuscript received Aug. 25, 1972.

Any discussion of this paper will appear in a Discussion Section to be published in the December 1973 JOURNAL.

REFERENCES

1. H. A. Pohl and C. E. Plymale, *This Journal*, **107**, 390 (1960).
2. J. A. Kok, J. W. Poll, and C. E. G. Van Vroonhoven, *Appl. Sci. Res.*, **17**, 461 (1967).
3. H. A. Pohl, *J. Appl. Phys.*, **29**, 1182 (1958).
4. J. G. Knudsen and D. L. Katz, "Fluid Dynamics and Heat Transfer," McGraw-Hill Book Co., New York (1958).
5. H. A. Pohl, Private communication.
6. H. A. Pohl, *This Journal*, **107**, 386 (1960).
7. J. N. Castle, "Dielectrophoresis," NTIS Publication No. PB 179533 (1967).

Predicting Current Efficiency of Industrial Aluminum Smelting Cells from Laboratory Measurements

W. E. Haupin*

Aluminum Company of America, Alcoa Research Laboratories, New Kensington, Pennsylvania 15068

Current efficiency tests are costly and difficult to control in industrial cells. On the other hand, current efficiency based on aluminum recovered from laboratory cells is always low. Cammarota and Schlain (1) demonstrated that meaningful current efficiencies can be obtained in laboratory-size cells by using boron nitride for the cell sides and cover, and by correcting for certain metal losses. At the end of each run they found it necessary to: (*i*) cool the cell quickly to avoid continuing losses, (*ii*) analyze the frozen electrolyte for reduced species, and (*iii*) machine away the outer surfaces of the graphite cathode and boron nitride walls and analyze each for reduced species. The aluminum equivalent of the reduced species found by analysis was then included along with the aluminum actually recovered to calculate current efficiency. Unfortunately, liberal use of boron nitride in cell construction made their cell expensive, and machining away part of the surface after each run limited its life.

Thonstad (2) gives an excellent summary of the various sources of current efficiency loss in an aluminum smelter. The corrections made by Cammarota and Schlain were both necessary and valid when one evaluates each loss as a function of cell size, age, and length of run.

Sources of Current Efficiency Loss

The principal current efficiency loss in an aluminum smelting cell results from CO_2 reoxidation of reduced metal species dissolved or suspended in the electrolyte. An activity of metal is maintained in the electrolyte by the following equilibria

$$Al + 3NaF \rightleftarrows AlF_3 + 3Na \quad [1]$$

$$2Al + AlF_3 \rightleftarrows 3AlF \quad [2]$$

NaF, AlF_3, AlF, and Na are present in the electrolyte at less than unit activity. Reduced species subsequently are reoxidized by CO_2 formed at the anode by the following, or similar, reactions

$$3AlF + 3CO_2 \rightarrow Al_2O_3 + 3CO + AlF_3 \quad [3]$$

$$6AlF + 3CO_2 \rightarrow 2Al_2O_3 + 3C + 2AlF_3 \quad [4]$$

$$6Na + 2AlF_3 + 3CO_2 \rightarrow Al_2O_3 + 6NaF + 3CO \quad [5]$$

$$12Na + 4AlF_3 + 3CO_2 \rightarrow 2Al_2O_3 + 12NaF + 3C \quad [6]$$

Although this reoxidation loss may be affected by cell design, it does not appear to be a function of cell size or age. Therefore no correction is required, provided the design factors (anode-cathode distance, gas-retention time, etc.) are adequately simulated.

Some investigators believe vaporization of reduced species from the electrolyte occurs only in laboratory tests. We believe it occurs also in industrial cells but these vapors are reoxidized by air and CO_2. The loss is mainly Na but includes a minor amount of AlF. It is measured by analyzing the condensed fume for reduced species without exposure to air. Its magnitude depends on bath composition, temperature, degree of electrolyte agitation, and gas velocity over the electrolyte. These factors can be measured and made equivalent to conditions present in industrial-cell operation. Velocity of gas leaving the anode at equivalent current densities is less in a small cell than in a large cell because of the increased ratio of area to perimeter. The purge gas, however, can be adjusted to compensate for the velocity difference. Since vaporization loss from an industrial cell is small, a fair degree of equivalence will be adequate.

Some of the metal produced is absorbed by the cell lining in the form of Na, Al_4C_3, and to a lesser extent, Al. This represents a major loss in laboratory cells due to the large surface-to-volume ratio and short period of electrolysis. In industrial cells the lining soon becomes saturated, and the loss through absorption becomes negligible over the major portion of the cell's life. Therefore, in small cells with short periods of operation, absorption loss must be measured and added to the production to make the results comparable to commercial production.

Sodium, Al_4C_3, AlF, and Al that dissolve or disperse in the molten electrolyte represent a considerable part of the total production in runs lasting only a few hours. In industrial operation, however, the metal held by the electrolyte is small compared to total production. Therefore, the Al equivalent of Al_4C_3 and reduced species in the electrolyte must be added to the actual Al produced to make small scale runs comparable to commercial production.

Regardless of how carefully the electrolyte is predried, it still contains moisture after melting. This water is electrolyzed to form H_2 and CO_2 and represents a loss of current efficiency in laboratory cells that would not be present in industrial cells after the first few days. Some loss by water may continue at a low level in industrial cells because a small amount of moisture may be added whenever Al_2O_3 is fed. Loss in current efficiency due to water is evaluated by analyzing the H_2 content of the cell gas and correcting it for H_2 evolved from hydrocarbons from the anode. With prebake anodes, the hydrocarbon correction is dependent on the anode baking temperature, and is usually minor. In the case of Soderberg anodes, it is more significant.

In summary, both electrolyte and cell lining quickly become saturated in the industrial cell and cease to trap additional metal. Therefore, it is valid to measure these losses in a laboratory cell and add their stoichiometric Al equivalent to the Al actually recovered. Further correction may be required for the loss caused by moisture. Other losses parallel industrial experience.

Alternate Cells

Boron nitride absorbs reduced species to a lesser extent than graphite but still has to be sacrificed and analyzed to obtain a correction factor. Therefore, less expensive graphite was used as an alternate since the only penalty was a larger correction. Table I, column 1, shows the results from electrolysis in a graphite container using the cell design illustrated in Fig. 1. In all runs the electrolyte was natural Greeland cryolite plus 6% reagent grade CaF_2, with Alcoa AlF_3 and smelting grade Al_2O_3 added to give the analysis shown in Table I. Use of a gas-collection hood over the anode and a purge gas reduced the residence time of gas produced by the cell, making observation of changes in gas flow and gas composition possible during the run. Ratios

* Electrochemical Society Active Member.

Key words: aluminum production, molten salts, electrolysis, current efficiency.

Table I. Comparison of electrolysis in nickel with electrolysis in graphite

Conditions	Container		
	Graphite	Nickel	Nickel
NaF/AlF_3 wt ratio (start)	1.50	1.50	1.20
NaF/AlF_3 wt ratio (end)	1.43	1.51	1.22
Al_2O_3 (start)	5.50%	6.04%	6.12%
Al_2O_3 (end)	2.81%	2.89%	2.74%
Al_2O_3 (average)	4.15%	4.46%	4.48%
Bath wt (start)	600 g	350 g	350 g
Bath wt (end)	558 g	338 g	336 g
Bath temp °C	980	977	960
Amperes	50	50	50
Minutes	39	25	25
Approx. anode-cathode sep.	25 mm	25 mm	25 mm
A/cm², anode	1.82	2.15	2.15
A/cm², cathode	0.339	0.386	0.386
	% Faraday equivalent		
a. Aluminum recovered	44.6	82.6	90.8
b. Metal vapor loss	2.4	1.9	0.9
c. Al + Na in electrolyte	5.8	1.6	1.0
d. Al_4C_3 in electrolyte	6.7	0.8	1.7
e. Al + Na in graphite	14.8	—	—
f. Al_4C_3 in graphite	10.4	—	—
g. Reoxidized by CO_2	12.5	12.4	5.1
h. H_2 evolved	2.5	0.9	0.5
	% Current efficiency		
Al_2O_3 consumed	84.1	86.1	92.0
a + c + d + e + f + h	84.8	85.9	94.0
100 − b − g	85.1	85.7	94.0

of CO and CO_2 flows to the metered argon flow were determined by gas chromatographic analysis. The gas was also passed through an absorption train similar to that described by Cammarota and Schlain (1), to check the chromatograph and to determine H_2. Argon flow was held proportional to current and, in the examples, equal to the Faraday equivalent for CO_2. Total A-hr were obtained with an electronic integrator.

Items a through f in Table I have been explained under the heading, Source of current efficiency loss. Item g, the aluminum equivalent of metal reoxidized by CO_2 expressed as a per cent of theoretical maximum aluminum production, was calculated

$$g = 50\,CO/(CO + CO_2)$$

where CO = gram mole of CO evolved, CO_2 = gram mole of CO_2 evolved.

Item h, aluminum equivalent of water electrolyzed or metal reoxidized by moisture expressed as a per cent of theoretical maximum aluminum production was calculated

$$h = 100\,W_{H_2}/0.01864I_h$$

where W_{H_2} = grams of H_2 evolved; I_h = ampere hours current passed; 0.01864 = Faraday equivalent of H_2.

Current efficiency by Al_2O_3 consumed expressed as a per cent of theoretical maximum was calculated

$$CE = 100(F_1W_1 - F_2W_2 + A)/0.6340I_h$$

where F_1 = fraction Al_2O_3 in electrolyte at start; F_2 = fraction Al_2O_3 in electrolyte at finish; W_1 = grams of electrolyte at start; W_2 = grams of electrolyte at finish; A = grams of Al_2O_3 added during run, if any; 0.6340 = Faraday equivalent of Al_2O_3.

The item a + c + d + e + f + h is the sum of aluminum recovered plus those losses in a small cell that would have been negligible in a large cell. The item 100 − b − g represents 100% current efficiency minus the two losses measured in a small cell that apply also to an industrial cell.

Although the correction for metal absorbed by the graphite lining was larger than that required by a cell made from BN, the corrected current efficiency was comparable to that obtained in boron nitride cells (1) and also agreed well with industrial practice for similar conditions. If a nonpermeable side lining were available, the lining correction would be eliminated. Since no nonmetallic, impermeable, molten fluoride-resistant material was known, Fe and Ni were tested as containers. Nickel was more resistant to CO_2 oxidation. The cell design for Ni is shown in Fig. 2. Frozen

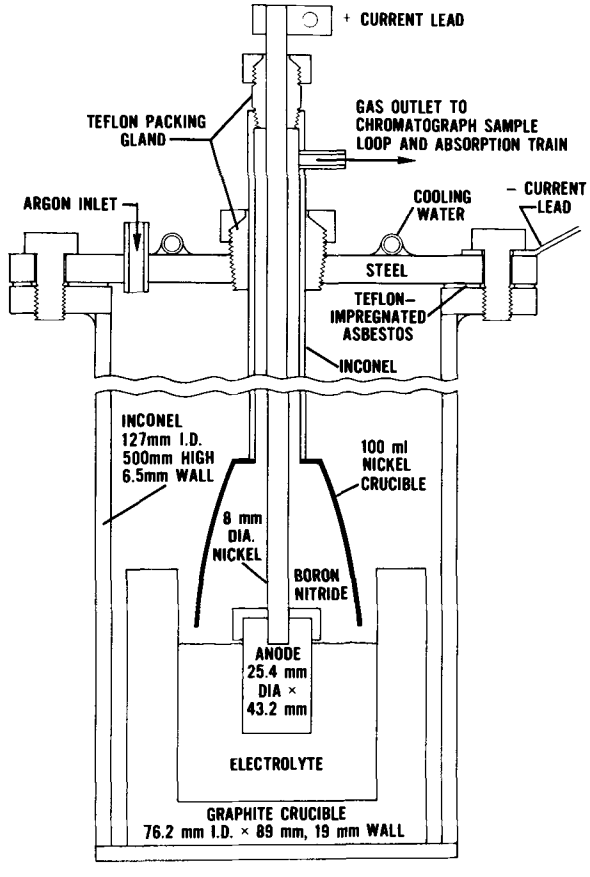

Fig. 1. Cell design for graphite

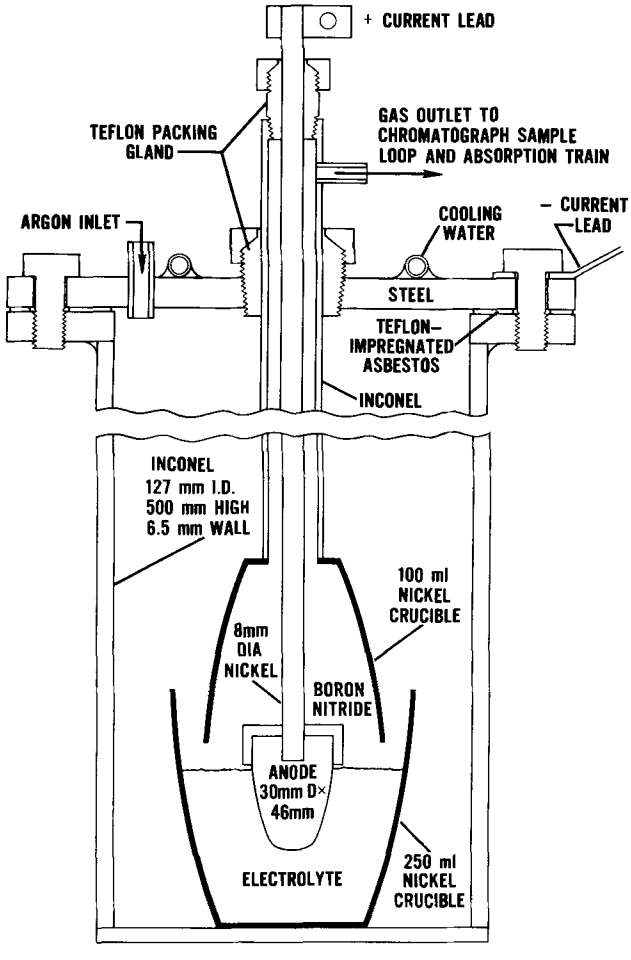

Fig. 2. Cell design for nickel

electrolyte was easily removed after the run by tapping the nickel crucible. Residual electrolyte was removed by immersing the crucible in molten NaCl until it was clean, then removing, cooling and washing it free of NaCl with water. Aluminum production was taken as the weight gain of the nickel crucible.

At first it was feared that this technique reduced the Al activity, and hence produced excessively high current efficiencies. Current efficiencies obtained, however, looked reasonable, and the counter electromotive force measured in this cell was comparable to that of cells with graphite linings, indicating similar Al activities. Cells of Ni, in fact, reached a stable counter electromotive force more quickly than cells of graphite, suggesting that a period of electrolysis was required to establish Na impregnation of the graphite surface before a coating of Al was obtained. It was concluded that Al diffused so slowly into Ni that during electrolysis Al remained on the surface at essentially unit activity. There must be some minimum C.D. below which this is not true, but the level is well below commercial levels. If electrolysis is continued too long, the melting point of the crucible will be lowered excessively by alloying, and it will perforate. This can be avoided by limiting electrolysis to 25 A/hr or less in a 250 ml crucible with a 0.7 mm wall. The results, using nickel crucibles, are shown in Table I, columns 2 and 3. It was still necessary to add the Al equivalent of the reduced species contained in the frozen electrolyte (measured by H_2 evolution) to obtain agreement with industrial current efficiencies. Agreement with industrial practice was better when correlation was based on cathode current density rather than anode current density. The most significant improvement of current efficiency resulted from lowering the NaF/AlF_3 ratio of the electrolyte which also lowers the liquidus temperature allowing a lower operating temperature.

It is believed that water removal by pre-electrolysis below the Al deposition potential, but above the H_2 deposition potential, would be an improvement in technique. Another possible improvement is to add a small measured quantity of Al at the start of electrolysis to quickly establish a metal pad, establish unit Al activity and, if pre-electrolysis is not employed, to remove moisture.

Manuscript submitted May 15, 1972; revised manuscript received July 28, 1972. This was Paper 152 presented at the Houston, Texas, Meeting of the Society, May 7-11, 1972.

Any discussion of this paper will appear in a Discussion Section to be published in the December 1973 JOURNAL.

REFERENCES

1. V. A. Cammarota, Jr. and D. Schlain, *This Journal*, **117**, 282 (1970).
2. J. Thonstad, Tidsskr. Kjemi, *Bergvesen Met.*, (English Translation), **26**, (1966).

Hydrogen Evolution Reaction on Platinum in Liquid Ammonia

C. Lamarre* and A. K. Vijh*

Hydro-Quebec Institute of Research, Varennes, Province of Quebec, Canada

In our recent attempts to synthesize ethylamine by cathodic reduction of an aldimine in liquid ammonia by means of an hypothetical reaction

$$CH_3 - CH{=}NH + 2NH_4^+ + 2e \rightarrow CH_3 - CH_2 - NH_2 + 2NH_3$$

it was observed that the above reduction does not proceed in practice. The reduction of aldimine was attempted on platinum in solutions containing NH_4Cl dissolved in liquid ammonia. For obtaining the general background information on the system, potentiostatic and potentiodynamic polarization studies were conducted on platinum cathodes in (NH_4Cl in NH_3) solutions in several runs, before attempting the actual synthesis in ($CH_3 - CH{=}NH + NH_4Cl + NH_3$) solutions.

The data obtained in the (NH_4Cl in NH_3) solutions are reported here since they reveal some features of the hydrogen evolution reaction (h.e.r.) on platinum in liquid ammonia, a problem on which there is no previous information, it is believed, available in the literature. Since these studies were not conducted with the aim of examining the detailed mechanism of h.e.r., they are necessarily quite brief in nature.

Experimental

The experimental procedures have been described in detail in a recent publication in which anodic behavior of several materials in liquid ammonia (1) was examined. Smooth platinum cathodes were used. A variety of counterelectrodes was tried and the least corroding were found to be those fabricated from pyrolytic carbon. The electrode potentials in the following results refer to the hydrogen electrode in the same solution, *i.e.*, 1g NH_4Cl in 150 ml of liquid ammonia.

Results and Discussion

On cathodization of smooth platinum in (NH_4Cl in NH_3) solutions, hydrogen evolution is observed to occur. In Fig. 1, potentiostatic current-potential relationships, both in the ascending and descending directions of potential, for the h.e.r. are presented. The Tafel slope observed is *ca.* 140 mV and hence roughly equal to $2.3 \times 4\ RT/F$ since $2.3 \times 2\ RT/F$ in this system (−73°C) is 79 mV.

In the potentiodynamic profiles conducted over a wide range of potentials and at a number of sweep rates, no peaks are observed thus indicating that the electrode is not appreciably covered by adsorbed hydrogen during the h.e.r. A typical potentiodynamic profile is shown in Fig. 2.

The hydrogen evolution in this system would occur by means of the over-all reaction

$$2\,NH_4^+ + 2e \rightarrow 2\,NH_3 + H_2 \qquad [1]$$

which may be assumed to proceed via the following elementary steps

$$Pt + NH_4^+ + e \rightarrow Pt - H + NH_3 \qquad [2]$$

followed by

$$Pt - H + NH_4^+ + e \rightarrow Pt + H_2 + NH_3 \qquad [3]$$

or

$$Pt - H + Pt - H \rightarrow 2\,Pt + H_2 \qquad [4]$$

* Electrochemical Society Active Member.

Key words: hydrogen evolution, proton tunneling, liquid ammonia, platinum electrode.

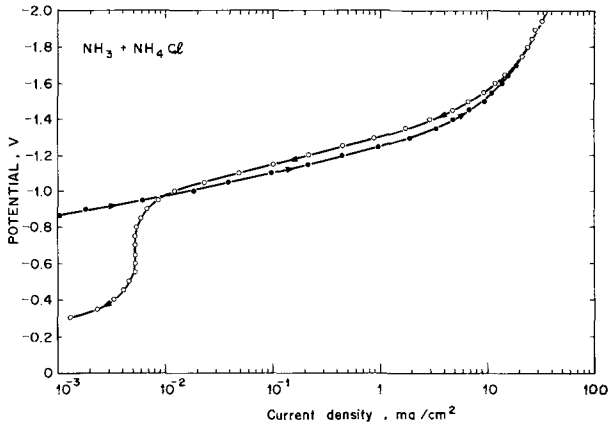

Fig. 1. Potentiostatic, steady-state (point-by-point) current-potential relationships for the electrolytic hydrogen evolution reaction on smooth platinum in (lg NH_4Cl in 150 ml of liquid ammonia). The Tafel slope, both in the ascending and descending direction of potential is *ca.* 140 mV, *i.e.*, 2.3 × 4 *RT/F* at the temperature of the experiments (−73°C).

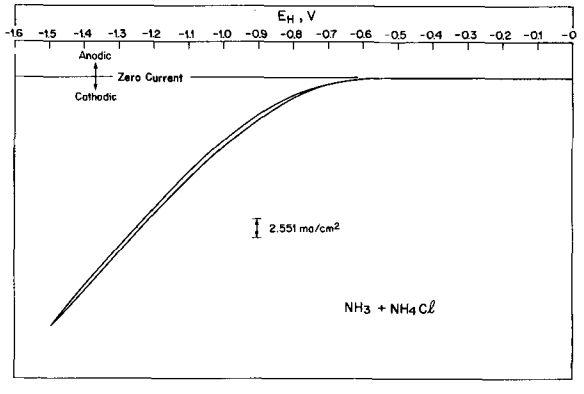

Fig. 2. A typical potentiodynamic profile on platinum in (lg NH_4Cl in 150 ml of liquid ammonia). Absence of any adsorption-desorption peaks may be noted. Sweep rate is 0.15 V sec^{-1}.

Since no electrode coverage is indicated in the potentiodynamic profiles (Fig. 2), the initial discharge step, *i.e.*, reaction [2] above may be deduced as the rate-determining step (rds) on the basis of general electrode-kinetic considerations (2-4). However, the Tafel slope consistent with this suggestion would normally be expected to have a value of 2.3 × 2 *RT/F*, as contrasted to the experimental slope of 2.3 × 4 *RT/F*. The experimentally observed Tafel slope has an anomalously high value in the sense that the usual theoretical procedures (2, 3) always give values equal to or lower than 2.3 × 2 *RT/F*, both under Langmuir and Temkin conditions of adsorption. Several explanations are available in the literature (2, 3) for rationalizing the values of Tafel slopes as high as 2.3 × 4 *RT/F* and some of them are: presence of a solid film on the electrode; potential-dependent adsorption of impurities, which appears unlikely in the present case (though not conclusively excluded) since elaborate care was taken (1) to minimize the presence of impurities in the present system; significant participation of proton tunneling (2, 5). In our case since the experiments were conducted at low temperatures (−73°C) it is possible that proton tunneling plays a significant role. The theoretically predicted Tafel slope for the initial discharge step occurring via a tunneling mechanism, as suggested here, has been derived by Conway (5) to be 2.3 × 4 *RT/F*, *i.e.*, close to the experimental value reported here.

The observed Tafel slope can also arise if filming of the electrode takes place, *e.g.*, by means of a reaction such as

$$Pt + NH_4^+ + e \rightarrow Pt—NH_4 \qquad [2a]$$

Such a filming process is indeed somewhat suggested by the hysteresis in the ascending and descending current-potential relationships in Fig. 1. Here, it is not implied that reaction [2a] is the only process by which filming can occur; in fact any conceivable process leading to a film (*e.g.*, chemisorbed radicals) will result in the enhancement of the 2.3 × 2 *RT/F* slope. For example, reaction [2a] could, at least hypothetically, be followed by a chemical step such as

$$Pt—NH_4 \rightarrow Pt—NH_2 + H_2 \qquad [5]$$

with the filming effect now arising from the chemisorbed $-NH_2$.

It is perhaps relevant to comment further on the significance of Fig. 2. For depicting the complete potentiodynamic profile, as in Fig. 2, over the potential region *ca.* 0.0 to −1.5V, it was necessary to employ low sensitivity on the current scale. In the actual experiments, however, the various regions of the profile were visually examined at high sensitivities in order not to miss any capacitative currents. One is thus quite safe in deducing the lack of appreciable electrode coverage by adsorbed hydrogen under steady-state electrolysis in the present system.

Conclusion

In the hydrogen evolution reaction on smooth platinum in liquid ammonia (at −73°C), a Tafel slope of ca. 2.3 × 4 *RT/F* is observed and an absence of appreciable electrode coverage by adsorbed hydrogen, as deduced from potentiodynamic profiles, is indicated. These results have been concluded to be consistent with a mechanism in which the h.e.r. proceeds with initial discharge step as the rds. The discharge occurs either via a proton tunneling mechanism or, alternatively, it proceeds onto a filmed electrode.

Acknowledgments

The authors thank Mr. R. Jacques for his skillful experimental assistance. Dr. G. Bélanger is thanked for some discussions. The authors are grateful to Dr. P. Lenfant for his interest and encouragement.

Manuscript submitted Jan. 31, 1972; revised manuscript received Aug. 28, 1972.

Any discussion of this paper will appear in a Discussion Section to be published in the December 1973 JOURNAL.

REFERENCES

1. A. K. Vijh, *This Journal*, **119**, 861 (1972).
2. B. E. Conway, "Theory and Principles of Electrode Processes," Ronald (1965).
3. J. O'M. Bockris and A. K. N. Reddy, "Modern Electrochemistry," Vol. 2, Plenum Publishing Corporation, New York (1970).
4. A. K. Vijh and B. E. Conway, *Chem. Rev.*, **67**, 623 (1967).
5. B. E. Conway, *Can. J. Chem.*, **37**, 178 (1959).

Dimensionless Correlation of Mass Transfer in Wire Electroplating Cells of Various Designs

Aladar Tvarusko*

Engineering Research Center, Western Electric Company, Princeton, New Jersey 08540

A large portion of past fluid flow, heat, and mass-transfer studies in and around cylinders was made in simple geometries to facilitate the correlation of the results. Some of the technologically important systems, such as wire electroplating, are usually more complex and difficult to interpret. The purpose of this note is to correlate the diffusion-limited mass-transfer rates measured at a horizontal wire in cells of various designs in terms of dimensionless parameters.

The fluid flow in various wire electroplating cells with axial, normal, radial, or tangential fluid inlets and outlets has been described earlier with details of the cell designs (1). The limiting current densities, I_L, were also measured (2) in these cells as a function of volumetric flow rate, Q, during the reduction of ferricyanide ions in a large excess of supporting electrolyte at a stationary, horizontal, nickel-wire electrode. It was found that (*i*) the fluid velocity and its uniformity near the wire was greatly influenced by the cell design, (*ii*) log I_L increased linearly with log Q in all cells, and (*iii*) the rate of this increase and the magnitude of I_L were cell-design dependent in view of point (*i*).

The I_L values were measured in an alkaline solution of potassium ferro/ferricyanide which is well suited for the measurement of the diffusion-limited mass-transfer rates but not for wire electroplating. These results, however, can be generalized with the help of dimensionless groups containing several variables and thus applied to the electrodeposition of metals on wire. The various dimensionless numbers are very useful for the correlation of experimental data and development of functional relationships, and are widely used in fluid dynamics, heat, and mass-transfer studies.

The flow of fluids in geometrically similar systems is characterized by the Reynolds number, Re which is the ratio of inertia force to the viscous (friction) force. It is given by $\mathrm{Re} = UL^*/\nu$ where U is the average fluid velocity, L^* is a characteristic length of the system (*e.g.*, diameter or length of a body), and ν is the kinematic viscosity of the fluid. The average fluid velocity is given by $U = Q/S$, where S is the free cross-sectional area of the plating chamber normal to the dominant flow direction.

A cursory inspection of the various cells in Fig. 1 [see (1, 2) for details] indicates that the cells are geometrically not similar. This means that the frequently used equivalent dimension will give only a first approximation and the ultimate correlations will have to take into consideration several geometric factors.

The Schmidt number, Sc is widely used in problems of diffusion in flow systems and depends only on the properties of the medium. It is given by $\mathrm{Sc} = \nu/D$ where ν is the kinematic viscosity and D is the molecular diffusivity; Sc is large ($\sim 10^3$) for aqueous solutions.

The mass-transfer rate is characterized by Sherwood number, Sh. For a solution with an excess of supporting electrolyte it is given by $\mathrm{Sh} = I_L L^*/zFDC_o$ where L^* is a characteristic linear dimension, C_o is the bulk solution concentration, and the rest have their usual meanings. It is clear that the I_L values may be obtained from the Sherwood numbers for any concentration in the same or other solution.

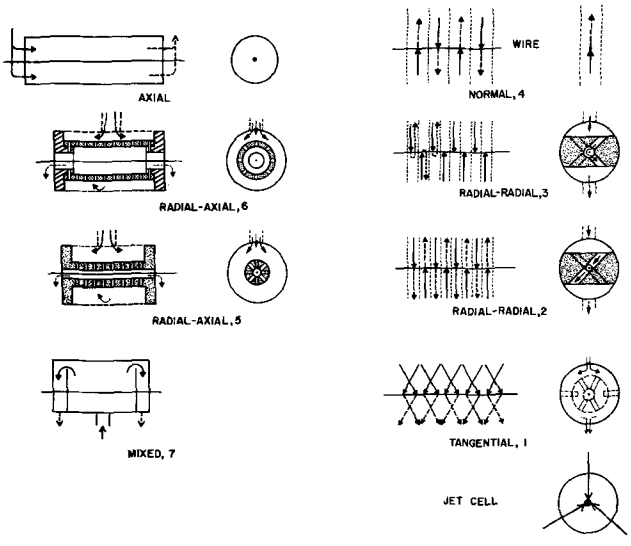

Fig. 1. Schematic illustrations of various cell designs

The diffusion coefficient of the ferricyanide ion, D, and the kinematic viscosity, ν, of the solution were calculated from the equations of Gordon *et al.* (Eq. [30] and Eq. [26], [27], respectively in (3)) to be $D = 6.19 \times 10^{-6}$ cm²/sec and $\nu = 0.0107$ cm²/sec which were used for all calculations. These values compare favorably with the values of Bazan and Arvia (4): $D = 6.84 \times 10^{-6}$ cm²/sec and $\nu = 0.0110$ cm²/sec.

Results and Discussions

The I_L values in simple tubular cells were found to decrease with increasing cell length, L (2). Dimensionless correlations for heat and mass transfer in circular tubes or annuli show that the Sh is a function of Re, Sc, and geometry (5, 6). According to Ross and Wragg (5), log Sh linearly depends on log ($\mathrm{Re} \cdot \mathrm{Sc} \cdot d_e/L$) and the slope of the line is influenced by the nature of the fluid flow and its intercept by the annulus radius ratio. This linear correlation can be clearly seen in Fig. 2 for the axial flow in tubular cells. The slope of the regression line should be either 0.33 for a fully developed laminar flow or 0.50 for a developing laminar flow (5). The slope of the experimental line, B, however, is 0.41 (Table I), which is equidistant from both values indicating the presence of a laminar flow in various stages of development. This is not surprising since the short

Table I. Regression line constants for various cell designs

Flow	Line	$Y = A + BX$ 95% Confidence limits for A	B	R
Axial	—	0.861 ± 0.081	0.410 ± 0.014	0.987
Radial-axial	6	0.91 ± 1.74	0.39 ± 0.27	0.529
Radial-axial	5	0.54 ± 0.23	0.43 ± 0.045	0.987
Mixed	7	0.254 ± 0.007	−0.604 ± 0.016	0.999
Normal	4	−0.167 ± 0.020	−0.510 ± 0.013	0.998
Radial-radial	2	−0.148 ± 0.045	−0.538 ± 0.022	0.995
Radial-radial	3	−0.059 ± 0.037	−0.542 ± 0.021	0.996
Tangential	1	−0.036 ± 0.027	−0.471 ± 0.017	0.997
Jet	—	−1.89 ± 0.50	1.04 ± 0.19	0.940

* Electrochemical Society Active Member.

Key words: mass transfer, influence of fluid flow, cell design, wire electroplating, dimensionless correlation.

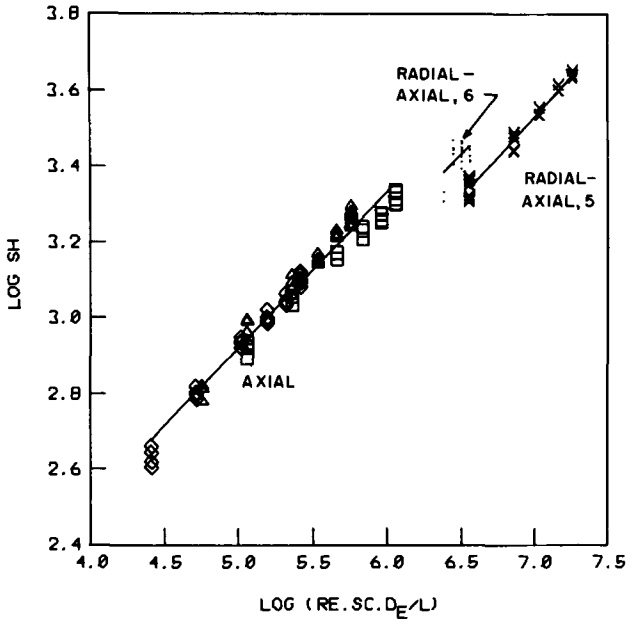

Fig. 2. Mass transfer in axial or predominantly axial-flow (radial inlets, axial outlets) regimes as a function of dimensionless groups containing the Reynolds and Schmidt numbers, the equivalent diameter and length of the tubular cell. The regression line constants are given in Table I.

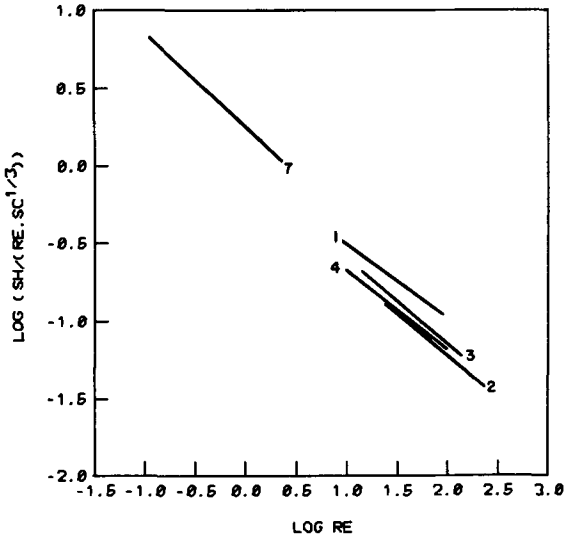

Fig. 3. Correlation of Chilton-Colburn j-factor for mass transfer in cells with normal, radial, or tangential flows. The regression line constants are given in Table I.

doughnut-shaped reservoirs at the fluid entrance and exit are not ideal hydrodynamic entry regions for either case.

In view of the absence of a well-defined flow condition in the tubular cells, the intercept is not expected to correspond to that predicted for either flow. The correlation of Ross and Wragg for a developed laminar flow (Eq. [9] in (5) in logarithmic form) predicts 0.554 for the intercept at our annulus radius ratio of 0.0131 and the experimentally obtained intercept is 0.861. This means that the experimental values are higher by a factor of approximately 2 than those predicted for a developed laminar flow.

A simple circular tube has a well-defined characteristic linear dimension, *e.g.*, length or diameter and the latter is usually preferred for the calculation of Re and Sh. The more complex conduits can be characterized by a number of linear dimensions but their use is cumbersome. Therefore, a simple characteristic linear dimension, the so-called equivalent diameter, d_e is preferred. The choice of the equivalent diameter is critical and must be characteristic for the system. In the case of annulus, d_e simple equals the difference of the outer and inner diameters and this was used in Fig. 2 for the axial flow correlation.

The plating chamber of an electrochemical cell with predominantly axial fluid flow can be considered as a closed conduit and its equivalent diameter can be easily obtained. It is 4 times the hydraulic radius which is the ratio of the cross-sectional area to the wetted perimeter of the plating chamber of constant cross section (7). If the cross section of the horizontal chamber (filled with fluid) is nonuniform, as in the case of the cells with radial inlets and axial outlets (Fig. 1), the volumetric hydraulic radius is used which is defined as the ratio of the volume of free space to the area of wetted surface (7). The results for two cells with radial-axial flow are also shown in Fig. 2 and were obtained using the following data: Line 5—d_e = 1.59 cm, L = 5.28 cm, S = 0.158 cm^2; Line 6—d_e = 1.49 cm, L = 5.26 cm, S = 0.633 cm^2. The correlation for all these axial flow cells is remarkable especially in view of the different designs and simple geometrical characterization.

The mass transfer in cells with dominantly axial flow was treated as that in a conduit of certain diameter and lengths (Fig. 2.) The mass-transfer data for cells with flow normal and radial to the wire surface are correlated separately owing to the nature of the fluid flow and are shown in Fig. 3. The diffusion-limited mass-transfer data are expressed as the Chilton-Colburn j-factor for mass transfer (6) which is the ratio of the Sh to Re · Sc$^{1/3}$ and is widely used in mass-transfer studies. The j-factor is independent of the characteristic length since it is present in both Sh and Re. The j-factor is correlated as a function of Re in which the wire diameter is the characteristic length. Figure 3 reveals that the correlation is remarkable for these cells of various designs.

A comparison of the present results with the available ionic mass-transfer data at large cylindrical electrodes in normal flow (8, 9) reveals that the B-values (Fig. 3, Table I) are similar to those published (−0.44 to −0.58). The coefficients of the exponential term (corresponding to the intercept values in Table I) are within the range of 0.557-0.920 which are similar to those in the literature [0.48 to 1.2 (8, 9)]. In view of the resemblance of the cell with a transverse flow in alternate directions (Line 4) to that used by Rao *et al.* (9), these two results will be compared. In order to account for the observed influence of the wire diameter, they (9) use $\sqrt{dL_E}$ for the characteristic length in Re, where d is the diameter and L_E the length of the electrode. The correlation obtained with this Re for the aforementioned cell is given by j = 1.493 Re$^{-0.51}$ which is comparable to their correlation j = 0.987 Re$^{-0.50}$.

In the case of the jet cell with three slots, the slope of the log I^*_L − log Q is near unity (2) and thus the j-factor − Re correlation would be of little use. The data can be advantageously represented by Sh/Sc$^{1/3}$ = 0.0127 Re$^{1.04}$ where Re is based on the wire diameter. It is interesting to note that Davies and Ting (10) studying the absorption of CO_2 into water jets found the mass-transfer rate to be proportional to Re$^{1.05}$ for turbulent jets exiting from "s" type nozzles with small length to orifice diameter ratio.

Table I shows the numerical values of the regression line intercepts and slopes and the results of the statistical analysis. The linear regression analysis of all data is statistically significant at greater than 99.9% with the exception of Line 6 (>99.0) which is presented for the sake of completeness. The coefficients of correlations are high with the exception of the aforementioned Line 6 and the jet cell with slots which was studied in a narrow range of fluid flows. The following can be said with 95% confidence: (*i*) The slopes are the same for cells with axial or predominantly axial

fluid flow (Fig. 2) and the intercepts are slightly different; (*ii*) For cells with nonaxial flow (Fig. 3) the regression line constants are different and depend on the pattern of the fluid flow. The three subgroups are indicated by the dashed lines. At higher confidence levels the differences would be significantly smaller; and (*iii*) The cell with fluid jets is distinctly different from the other cells in which the wire is surrounded by a large volume of solution.

Conclusion

Mass-transfer results obtained in wire electroplating cells were correlated and generalized with the help of appropriate dimensionless numbers. As a first approximation, the flow regimes in cells of various designs were characterized by Re number and a geometric factor and the correlations are significant. No single correlation has been obtained for the three cell groups of different flow regimes due to the simple representation of complex cell geometries and absence of hydrodynamically well defined fluid flows in the plating chambers. These results, however, can serve as the basis for scale-up and modeling of wire electroplating processes and be directly applied to small scale wire electroplating lines used, *e.g.*, for the electrodeposition of Ni-Fe alloys for magnetic plated wire memories.

Acknowledgment

The author wishes to thank Mr. W. E. Wilson, Jr., for his valuable experimental assistance.

Manuscript submitted Jan. 3, 1972; revised manuscript received July 31, 1972. This was Paper 111 presented at the Cleveland, Ohio, Meeting of the Society, Oct. 3-7, 1971.

Any discussion of this paper will appear in a Discussion Section to be published in the December 1973 JOURNAL.

REFERENCES

1. A. Tvarusko, *Plating*, **58**, 983 (1971).
2. A. Tvarusko, *ibid.*, Accepted for publication.
3. S. L. Gordon, J. S. Newman, and C. W. Tobias, *Ber. Bunsenges. Phys. Chem.*, **70**, 414 (1966).
4. J. C. Bazan and A. J. Arvia, *Electrochim. Acta*, **10**, 1025 (1965).
5. T. K. Ross and A. A. Wragg, *ibid.*, **10**, 1093 (1965).
6. R. B. Bird, W. E. Stewart, and E. N. Lightfoot, "Transport Phenomena," Chapters 13, 21, John Wiley & Sons, New York (1962).
7. J. G. Knudsen and D. L. Katz, "Fluid Dynamics and Heat Transfer," p. 81-82, McGraw-Hill Book Co., New York (1958).
8. P. Grassmann, N. Ibl, and J. Trüb, *Chem.-Ing.-Tech.*, **33**, 529 (1961).
9. K. S. Rao, G. J. V. J. Raju, and C. V. Rao, *Indian J. Technol.*, **6**, 46 (1968).
10. J. T. Davies and S. T. Ting, *Chem. Eng. Sci.*, **22**, 1539 (1967).

JOURNAL OF THE ELECTROCHEMICAL SOCIETY

SOLID-STATE SCIENCE AND TECHNOLOGY

JANUARY 1973

On the Formation of Surface States during Stress Aging of Thermal Si-SiO_2 Interfaces

A. Goetzberger,*,[1] A. D. Lopez, and R. J. Strain*

Bell Telephone Laboratories, Incorporated, Murray Hill, New Jersey 07974

ABSTRACT

Under combined bias and temperature stress, the silicon-silicon dioxide interface is altered by the introduction of more surface states. This effect has been investigated in metal-oxide-semiconductor structures formed by a variety of oxidizing, annealing and metalizing procedures. In most cases, stress of 10^6 V/cm at 300°C caused a surface-state peak to appear in the lower half of the bandgap. The surface-state *vs.* energy curves vary with the oxidation conditions, but they are reproducible when sample preparation is reproduced. The influence of the following parameters was investigated: dry oxygen and steam oxidation, Cr-Au and Al contacts, e-gun and filament evaporation and post-metalization annealing. The surface-state density increases linearly with applied field, and it increases in proportion to the logarithm of time. The nature of the distribution also depends on the annealing procedures, and on the contact metal.

It is well known that fixed positive charge and fast surface states are created in Si-SiO_2 interfaces when negative bias is applied at elevated temperature to the gate electrode of an MOS capacitor (1-4). Deal *et al.* (1), in investigating the kinetics of this process, found that approximately equal amounts of surface charge and surface states are created. Arnold (5), using an IGFET conductance technique, discovered a sharp surface-state peak at 0.32 eV below midgap after negative bias had been applied to the sample at 250°C.

The purpose of the present work was to obtain more detailed information on the nature of stress induced surface states in oxides prepared in various ways. A rapid technique for evaluating surface-state distributions, the quasi-static C-V technique (6, 7) was utilized in these studies. In addition to the changes of surface-state densities, changes of flatband voltage upon aging were investigated.

* Electrochemical Society Active Member.
[1] Permanent address: Institut für Angewandte Festkörperphysik der Fraunhofer-Gesellschaft, 7800 Freiburg 1, BR, Germany.
Key words: reliability, semiconductors, electron insulators.

Preparation of Samples

Metal oxide silicon samples were prepared by twelve different process sequences. Multiple samples were prepared in many cases, so that 23 samples were investigated in total. Most of the samples were made with <100> n-type silicon, although <111> and p-type samples were also tested.

The twelve processes are detailed in Table I. All of the oxides were grown to a thickness of 1000Å, and the first six (Roman I-VI) were prepared in horizontal tube furnaces using standardized, semiproduction conditions. This group includes both steam and dry oxides, and a variety of low-temperature anneals.

Table I. MOS sample preparation

	Oxidation		Anneal			Contact		Anneal		
	Atm	Temp (°C)	Atm	Time	Temp (°C)	Metal (Å)	Source	Atm	Time	Temp (°C)
I	O_2	1100	H_2	30	350	200 Cr / 3000 Au	Filament	—	—	—
II	O_2	1100	—	—	—	2000 Al	e-gun	H_2	30	350
III	O_2	1100	—	—	—	3000 Al	Filament	H_2	30	350
IV	Steam	950	—	—	—	2000 Al	e-gun	H_2	30	350
V	Steam	950	—	—	—	200 Cr / 3000 Au	Filament	—	—	—
VI	O_2	1100	—	—	—	200 Cr / 3000 Au	Filament	—	—	—
HE 1	O_2 (Cold-Wall)	1000	He (Cold-Wall)	30	1000	200 Cr / 3000 Au	Filament	H_2	30	350
HE 2	O_2 (Cold-Wall)	1000	He (Cold-Wall)	30	1000	2000 Al	e-gun	H_2	30	350
H_2-1	O_2 (Cold-Wall)	1000	H_2 (Cold-Wall)	30	1000	200 Cr / 3000 Au	Filament	H_2	30	350
H_2-2	O_2 (Cold-Wall)	1000	H_2 (Cold-Wall)	30	1000	2000 Al	e-gun	H_2	30	350
DI 1	$SiO_2 + Al_2O_3$ (see text)					200 Ti / 2000 Al		N_2	30	350
DI 2	$SiO_2 + Al_2O_3$		N_2	30	1100	200 Ti / 2000 Al		N_2	30	350

The four oxides identified by He and H_2 were grown under laboratory conditions, using a cold-wall system, with an rf heated silicon susceptor and a water-cooled quartz envelope. Perhaps more significantly, all these samples received a high-temperature anneal in either helium or hydrogen.

The final pair of samples (DI 1 and 2) were prepared at Bell Laboratories, Allentown, Pennsylvania. These samples had a two-layer dielectric, 1000Å of steam grown SiO_2 covered by 500Å of pyrolytic Al_2O_3. These films were produced according to the procedures described by Tung and Caffrey (9), and their electrical properties were described by Nigh (10). The two samples differ by the inclusion of a high-temperature inert gas anneal between the silicon oxidation and alumina deposition in the preparation of lot DI 2.

This diverse group of oxides was subjected to the experimental aging evaluations described in the next section.

Procedure for Stress Aging and Evaluation

Fundamentally, the experimental procedure consisted of two steps: accelerated aging of the MOS capacitors under combined electric and thermal stress, and evaluation of changes in interface properties.

Figure 1 shows the apparatus in which the temperature and bias stressing was done. The silicon slices with MOS capacitors were placed on the heated stage and bias was applied to the metalizations with wire probes. For most of the experiment, the standard stress-aging condition was 30 min at 300°C with −10V applied to the field-plate. Not visible in Fig. 1 is the stainless-steel cover which was used over the probe system; during the stressing, this cover was in place and the system was fed a steady flow of line nitrogen.

The evaluation of interface properties included shifts of flatband voltage and changes of the energy distribution of surface-state density. Surface-state density was extracted from plots of the high- and low-frequency C-V curves using a quasi-static (sweep rate between 50 and 100 mV/sec) low-frequency curve and a 1 MHz high-frequency curve on the same capacitor. According to Ref. (6) and (7) those two capacitance values can be used to obtain surface-state density N_{SS}

$$N_{SS} = \left[\frac{C_{LF}}{C_{ox} - C_{LF}} - \frac{C_{HF}}{C_{ox} - C_{HF}}\right] \frac{C_{ox}}{qA}$$

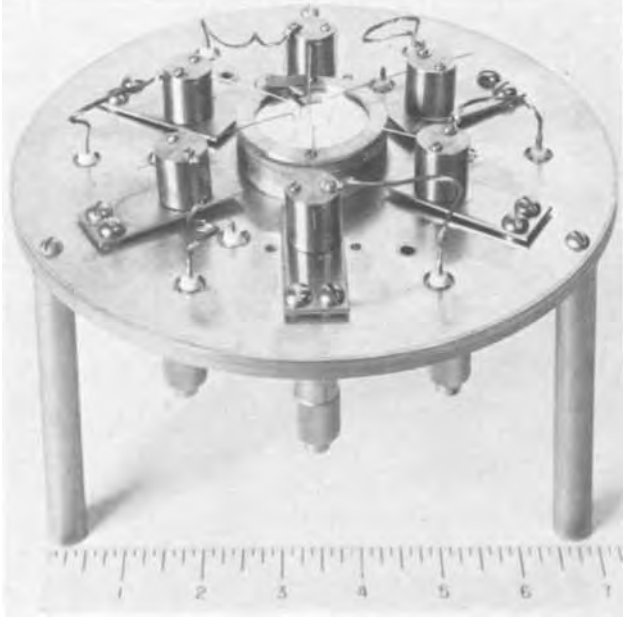

Fig. 1. A photograph of the stress-aging apparatus, with the cover removed to show the heater in the center, and probes mounted on magnets.

where C_{LF} = low frequency capacitance, C_{HF} = high frequency capacitance, C_{ox} = oxide capacitance, A = area of contact, and q = elementary charge. The validity of this equation is limited on one side of the energy gap by the onset of inversion and on the other side by the fact that surface states with short time constants contribute to the high-frequency capacitance. Figure 2 shows a typical group of high- and low-frequency curves, from which surface-state densities have been extracted.

In order to extend the range of the measurement and check consistency of results, stressing for most oxidation conditions was done on n-type as well as p-type samples. The results were in good agreement, as the next section will show.

Surface potential is obtained from the low-frequency curve by integration as described by Berglund (11). The undetermined additive constant was found in one of two ways: The integration was carried from accumulation to inversion and the total integrated surface potential was compared to the bandgap of 1.1 eV. Since the band edges are never quite reached, the total integrated surface potential was lower than 1.1V. The difference between the two was divided by two and added to the measured surface potential. This procedure assumes that the surface potential comes equally close to the band edges in the flat capacitance portions of accumulation and strong inversion. Good agreement was found between this method and another in which a point between flatband and inversion was selected on the high-frequency C-V curve and its surface potential obtained by comparison with the ideal curve. The flatband point per se is not too suitable for this adjustment because at this point some surface states may follow the applied high-frequency signal.

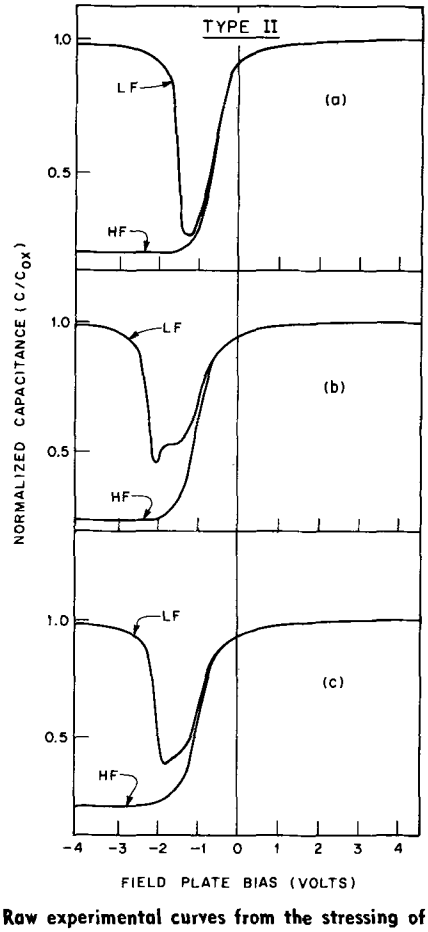

Fig. 2. Raw experimental curves from the stressing of the Type II oxides on n-silicon. The high-frequency curves (HF) are taken at 1 MHz, and the low-frequency curves are taken using the quasi-static technique.

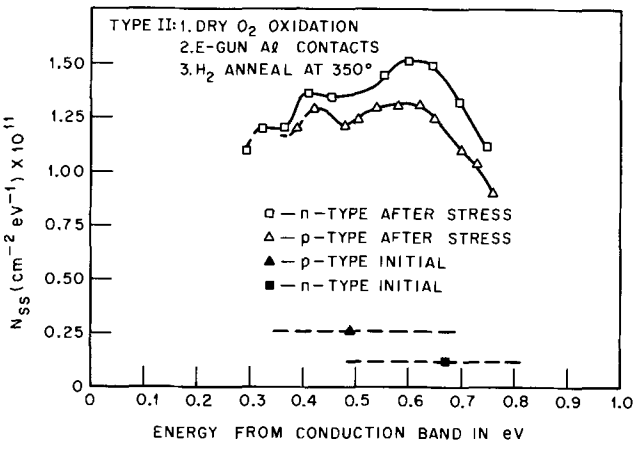

Fig. 3. Surface-state densities calculated from pairs of curves like those shown in Fig. 2. These results pertain to the type II oxide, which is grown dry, then contacted with e-beam evaporated Al, and annealed.

It was found that in the system used for aging the oxides, heat alone affected the oxides under certain conditions. This was particularly true of oxides I, V, and VI, which had Cr-Au contacts; as contacted all these samples had room temperature hysteresis and a relatively high surface-state density. These faults were eliminated by a very brief heating to 300°C in nitrogen. Consequently, all these samples were brought to a standardized initial condition by a short exposure to 300°C in the stressing chamber.

Summary of Results

The most marked feature of the stress aging is the development of a broad, but readily identifiable peak in surface-state density near midgap. This is illustrated by Fig. 3, which shows surface-state densities both before and after stressing for p- and n-type samples of the devices from group II. These curves were calculated from data like that shown in Fig. 2. These particular results show two distinct peaks; this is seen in certain other samples as well, but for the most part the aging will be characterized by the energy and amplitude of the higher peak. Examples of the more prevalent stress induced surface-state distribution, a single peak, are shown in Fig. 4. These distributions were observed after stressing the high-temperature annealed oxides.

Table II gives a summary of the test results on samples I-VI and the two DI samples, and Table III summarizes the tests on the samples prepared and annealed in the cold-wall system. These tables give brief

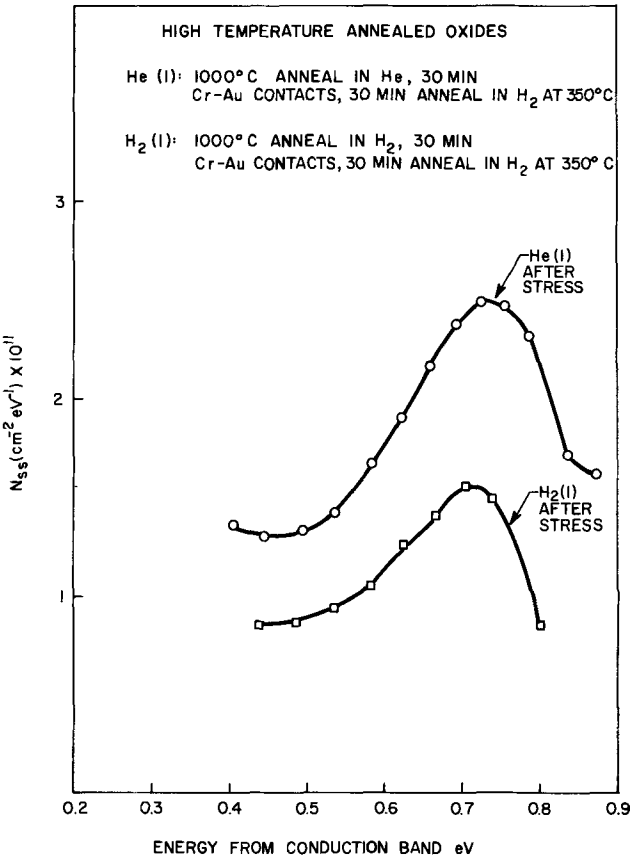

Fig. 4. Experimental surface-state distributions observed after stress aging dry, high-temperature annealed SiO_2. These oxides were annealed at 1000°C in either helium, sample He(1), or hydrogen, sample H_2(1). After contacting with CrAu they got a final anneal at 350° in hydrogen.

summaries of the processing, values for the surface-state densities and flatband voltages before and after stressing, and the apparent center energy of the largest induced surface-state peak. Two regularities are quite apparent when the surface-state data are scrutinized. The first has been observed frequently in the past; the largest increase in surface-state density is correlated with the largest initial density. Figure 5 illustrates this by a plot of final N_{SS} values against initial N_{SS} for all twenty-three test slices. Also shown is the (logarithmic) regression line for this data. The correlation is very good, and the slope is six times larger than the standard deviation about the regression line.

Table II.

Oxidation conditions	No.	Substrate	N_{SS} (cm^{-2}, eV^{-1}) Before stress	N_{SS} (cm^{-2}, eV^{-1}) After stress	Peak of N_{SS} (eV) after stress	Flatband voltage (V) Before stress	Flatband voltage (V) After stress
Type I:							
dry O_2,	I-1	n(100)	5.3×10^{10}	3.1×10^{11}	0.77	−0.40	−0.50
H_2 anneal,	I-2	n(100)	4.6×10^{10}	2.2×10^{11}	0.77	−0.30	−0.40
Cr-Au contacts	I-3	p(100)	9.3×10^{10}	4.5×10^{11}	0.79	−1.50	−1.60
Type II:	II-1	n(100)	1.4×10^{10}	1.5×10^{11}	0.60	−0.50	−0.95
dry O_2,	II-2	n(100)	1.66×10^{10}	1.3×10^{11}	0.60	−0.40	−0.95
e-gun Al,	II-3	p(100)	2.5×10^{10}	1.3×10^{11}	0.60	−1.15	−1.80
H_2 anneal	II-4	p(111)	1.1×10^{11}	4.3×10^{11}	0.59	−3.0	−4.80
Type III:							
dry O_2, fila-	III-1	n(100)	9×10^{10}	1.8×10^{11}	0.60	−0.50	−0.65
Al, H_2 anneal	III-2	p(100)	9×10^{10}	2.3×10^{11}	0.65	−1.75	−1.55
Type IV:	IV-1	n(100)	2.5×10^{10}	3.55×10^{11}	0.47	−0.80	−2.40
steam oxide,	IV-2	n(100)	2×10^{10}	3.1×10^{11}	0.47	−0.80	−2.55
e-gun Al,	IV-3	p(100)	5×10^{10}	3.95×10^{11}	(0.47)	−2.0	−3.80
H_2 anneal	IV-4	p(111)	8×10^{10}	4.2×10^{11}	(0.45)	−3.30	−7.30
Type V:							
steam oxide,	V-1	n(100)	—	6.5×10^{11}	0.71	—	−1.95
Cr-Au contacts	V-2	p(100)	2.4×10^{11}	1.07×10^{12}	0.74	−3.30	−3.80
Type VI:							
dry O_2							
Cr-Au contacts	VI-1	p(100)	1.7×10^{11}	3.2×10^{11}	(0.72)	−0.30	−0.40
Type DI:							
SiO_2-Al_2O_3	DI-1	n(100)	1.8×10^{10}	5.5×10^{10}	0.57	+0.58	+0.40
double layer	DI-2	n(100)	8×10^{9}	2.35×10^{10}	0.57	+0.2	+0.1

Table III. High-temperature annealed dry oxides

Annealing and contacts	Sample	Substrate	N_{SS} (cm^{-2}, eV^{-1}) Before stress	N_{SS} (cm^{-2}, eV^{-1}) After stress	Peak of N_{SS} (eV) after stress	Flatband voltage (V) Before stress	Flatband voltage (V) After stress
He, 1000°C, Cr-Au	He-1	p(100)	4.9×10^{10}	2.51×10^{11}	0.73	−0.66	−0.81
He, 1000°C, e-gun Al	He-2	p(100)	2.4×10^{10}	9.1×10^{10}	0.66	−1.33	−1.0
H_2, 1000°C, Cr-Au	H_2-1	p(100)	6.7×10^{10}	1.57×10^{11}	0.71	−0.70	−0.76
H_2, 1000°C, e-gun Al	H_2-2	p(100)	1.6×10^{10}	7.8×10^{10}	0.62	−1.24	−1.20

The second regularity is less expected. The energies of the peaks fall into distinct groups by metal. Figure 6 illustrates this by presenting the peak locations for all the samples. The energies fall into four groups with the following mean energies: 0.47, 0.57, 0.61, and 0.75 eV. These metal dependences may be related in some way to the contact dependent surface-state densities seen with very thin oxides (12).

Measurements were also made with positive bias, but the surface-state changes were much more modest with positive bias, although increases were observed. This experiment was made more complicated by the existence of positive ion contamination in many of the samples. The consequences of stress and ion drift were separated by lowering the temperature to 90°C and applying negative bias after positive bias stressing at 300°C. Because the ion trapping at the $Si-SiO_2$ interface is very weak (13), the ions could be swept away without affecting the stress results.

Shifts in flatband voltage were also measured, and these results appear in the last two columns of Table II. While these results are more susceptible to ion contamination, there are some fairly clear tendencies in the data. These are illustrated by the histograms of Fig. 7. Although they are superior in most other respects, the samples with electron beam evaporated aluminum contacts, show large and erratic shifts in flatband voltage. This can be attributed to latent damage (14) from the soft x-rays associated with electron impact on the target. Though the x-radiation effects appear to be totally removed by the low-temperature hydrogen anneal, the application of negative bias, temperature stress leads to a "slow trapping" type of instability. On the other hand, there seems to be no latent damage in those samples which were treated at high temperature after oxidation.

A correlation analysis has been done to ascertain the inter-relationship in this experiment between the surface-state creation and the flatband shift. The correlation is very slight, and statistically insignificant.

The surface-state generation has been examined more closely; the voltage and time dependence of surface state density were evaluated using type II oxides (dry thermal oxides with e-beam Al contacts). For the voltage dependence measurements the stressing conditions were 15 min at 300°C, initially unstressed dots receiving stress at various voltages. Typical surface-state distributions are shown in Fig. 8, where a sequence of peaks can be seen emerging near midgap. If the surface-state density in the highest peak is

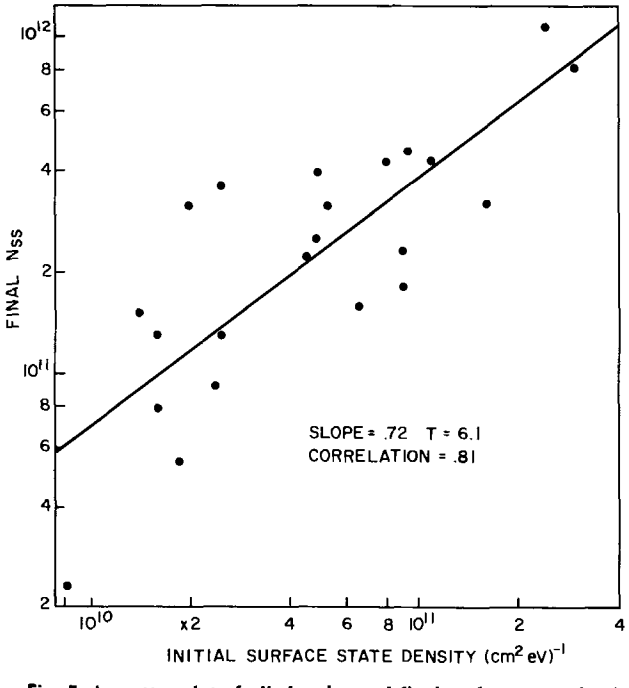

Fig. 5. A scatter plot of all the observed final surface-state densities as a function of the initial surface-state densities, showing the degree of correlation between initial and final values. The logarithmic slope of the best fit line is 0.72, *i.e.*, the rate of increase is slightly sublinear in the initial N_{SS}.

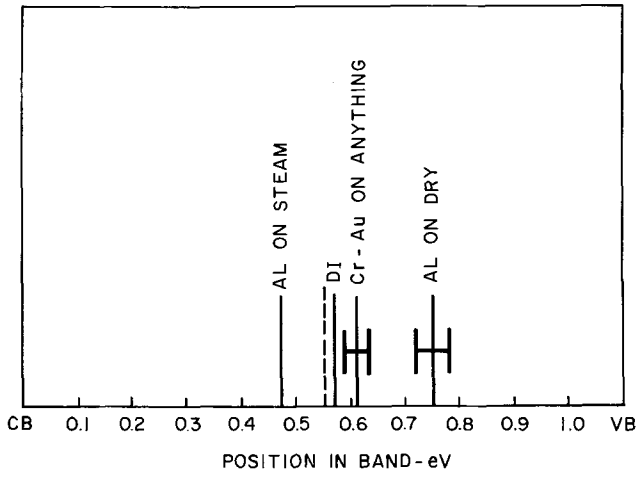

Fig. 6. A diagram showing how the stress induced surface-state peak locations are grouped in the bandgap, according to the processing, particularly metalization.

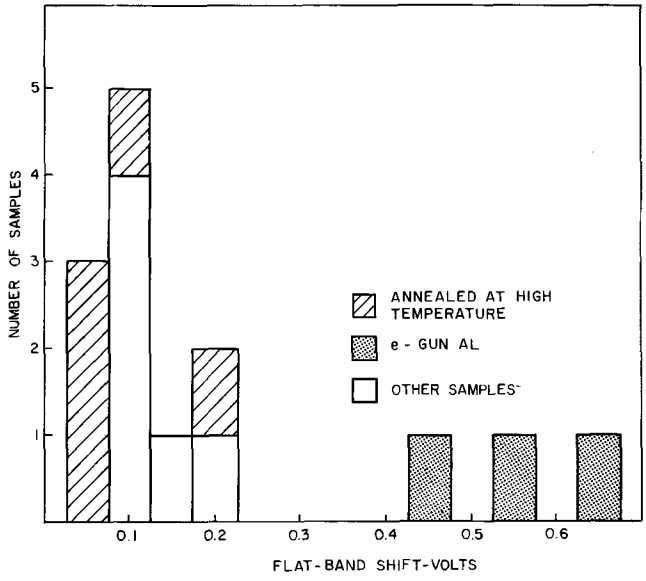

Fig. 7. A histogram showing the grouping of slow-trapping flatband shifts. Note the relative positions of high-temperature annealed oxides, and e-beam evaporated samples.

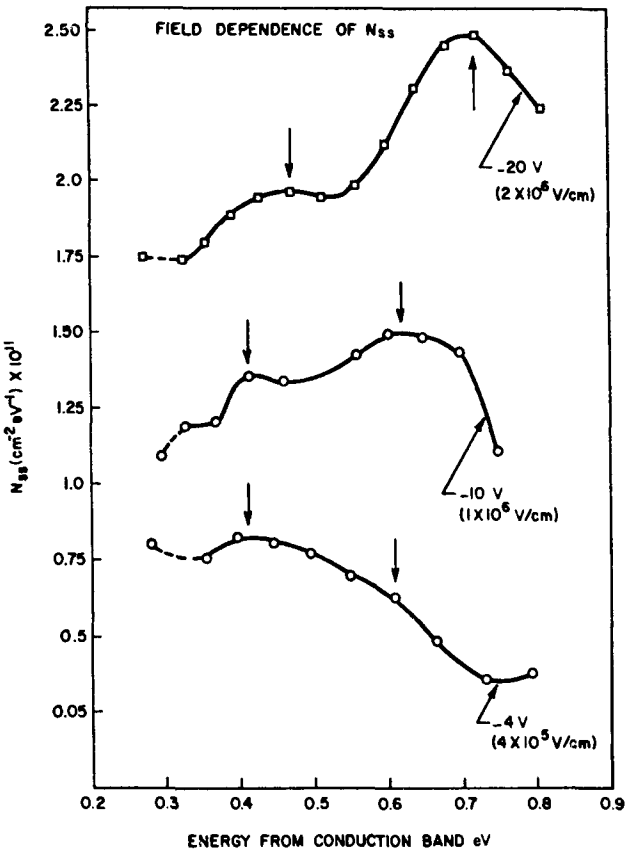

Fig. 8. Experimental surface-state distributions after 15 min of stressing of —4, —10, and —20V. The oxide in this case is the type II dry oxide.

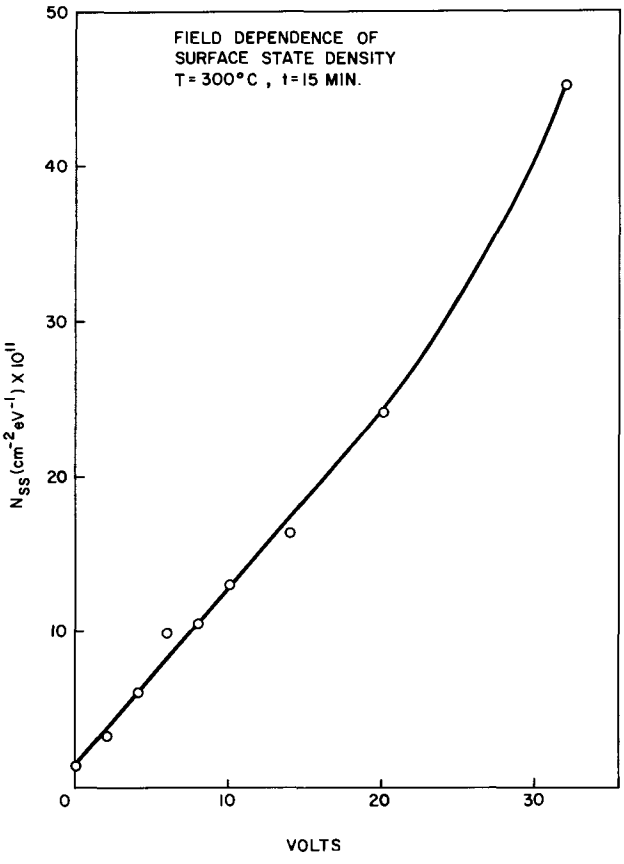

Fig. 9. A curve showing the essentially linear dependence of surface-state densities on stressing voltage. There does not appear to be a threshold for this effect.

plotted against voltage, a linear relationship emerges, as illustrated in Fig. 9.

Walden (15) has shown that the time evolution of charge crossing a barrier because of a high electric field frequently follows a log (t/t_0) law. Following this principle, the increase in surface-state density as a function of time has been plotted in Fig. 10 against the logarithm of time. The log behavior is strongly indicated at both 250° and 300°C. Since the reciprocal of the zero intercept time $(t_0)^{-1}$ carries the field and temperature dependence of the current transport, the intercept times for 250° and 300°C have been used to estimate the activation energy of the process of surface-state formation to be 1.4-1.5 eV.

Discussion of Results

Although a variety of results was obtained in the course of this experiment, the stress-aging behavior of MOS devices prepared in the same way was quite consistent. There are other effects, like disequilibrium during low frequency measurements (16) and gross nonuniformities (17, 18) which can give the appearance of surface-state peaks. These two possibilities can be ruled out; the first because the ramp measurements were made at a sufficiently slow sweep rate to assure equilibrium conditions, and the second because any nonuniformities would have to arise from random defects. Excellent sample-to-sample correlations of surface-state density profiles precluded any explanations based on random nonuniformities. Thus, the results and conclusions in the following paragraphs are all attributed to surface-state effects. The formation of surface states under stress also correlated very well with the initial surface-state density of the interface. During the course of the oxide preparation, several samples had high surface-state densities due to dry oxidation (19) or due to x-irradiation by the electron gun during electrode metalizations. Subsequent to these processes the samples were annealed in hydrogen

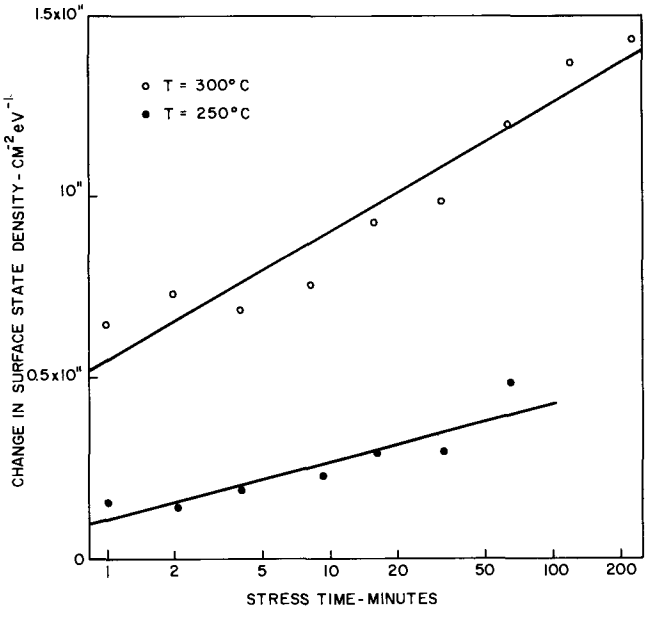

Fig. 10. The time development of surface states under stress at 10^6 V/cm at 250° and 300°C. A best fit log (time) line is shown for each set of points.

at 350°C; this process has been shown to be particularly effective in reducing surface-state densities when aluminum field plates are present (20). Deal *et al.* (21) have shown the annealing is associated with the diffusion of a contact activated species to the interface where it either compensates or annihilates the surface states. The results quoted in Table II indicate surface states are actually annihilated, because the most stable of the oxides I-VI is II, which received both dry oxidation and a large dose of soft x-rays. Had the surface

states created in these two processes merely been compensated, sample II would have been very unstable. It has not been established whether a longer anneal would have eliminated the flatband instability seen in this sample; it is likely that this is a result of residual radiation damage. This example serves to illustrate that the defects responsible for surface states are either chemically or structurally different from those leading to flatband shifts by slow trapping.

Surface-State Distributions

The surface-state distributions for the various types of oxides show distinct features which appear reproducibly in p- and n-type samples prepared in the same way. The structure in the curves and the strong dependence on the details of processing suggest complex processes at the interface. The following observations can be made by inspection of the curves: (*i*) All thermal oxides with one exception develop a surface-state density peak or at least a higher surface-state density in the lower half of the gap. (*ii*) The only exception is type IV which is a steam oxide with e-gun evaporated aluminum. (*iii*) The contact metal influences the position of the induced peak. (*iv*) The dry thermal oxide (type VI) is the only one showing an increase of the surface-state density without distortion of the distribution. (*v*) It can be observed that the p-type samples have a higher surface-state density than the n-type ones. This is in agreement with Ref. (1). (*vi*) <111> samples have the same surface-state distributions as <100> samples. Their flatband change is much more than for <100> as is well known (Table I), but the change of surface-state density is different only for the high quality type II oxide and not for type IV. (*vii*) Double-layer insulator films develop a peak of surface-state density at midgap. (*viii*) In high-temperature annealed oxides the type of contact has more influence than the annealing ambient.

Time Temperature and Field Dependence

The kinetics of surface-state growth during stress are similar to those of surface charge investigated previously. From Fig. 9 we recognized that the peak surface-state density increases linearly with field for fields below 2×10^6 V/cm. This linearity has also been observed for flatband voltage changes in Ref. (1) and (4). Just as in the case of flatband shift, there appears to be no threshold voltage for the effect.

From Fig. 8 it is obvious that the distribution during stressing does not stay the same. Two peaks of surface-state density are observed to emerge at different rates. One which is between 0.4 and 0.5 eV appears to be growing rapidly at lower fields. At higher fields it is outgrown by another peak between 0.6 and 0.8 eV. It should be noted that the same change of the density distribution can also be observed at constant field with increasing time. Therefore, it appears that the two peaks could be independent; one develops rapidly and saturates, and the other develops slowly and continues to high densities.

The energetic positions of the surface-state peaks of Fig. 8 are seen to move to higher energies. This is probably not related to intrinsic properties of surface states, but it arises from the superposition of two independent peaks of changing magnitude.

The logarithmic time dependence observed for the surface-state density increase is very much like that observed by Rossel *et al.* (22) for the field-induced change in threshold voltage in MOS transistors. The behavior was explained quantitatively on the basis of a model involving the tunneling of carriers from the silicon into the oxide. Walden's work has shown that $\log(t)$ charge dependence is common to many other charging processes; all that is required is that the particle current be strongly dependent on the interface field, and that the charged carriers become trapped near the interface, reducing the field. Possible means by which the trapped defects could form surface states include the charge model (23), and a chemical model, which requires an alteration of the chemical bond to form a defect capable of trapping electrons and holes (24).

It is unlikely that the formation of surface states is as simple as the trapping models cited above. If a trapped hole could be associated with each surface state, then a modest change in V_{FB} on n-type samples would be readily explained by the formation of donor-like states near midgap, because these would be neutral under flatband conditions. However, on p-type samples, donor-like states near midgap would be substantially ionized under flatband voltage. While on the average, ΔV_{FB} on the p-type samples is slightly larger than that on n-type, the increase is insufficient to justify an assumption of induced donor-like states; neutral states are more probable.

Evaluation of Oxide Quality

The two parameters most directly related to the quality and stability of an oxide are change of flatband voltage and surface-state density after stress. These two quantities have been combined in a single plot in Fig. 11. The surface-state density after a standard stress of 30 min at 300°C and 10V is plotted against change of flatband voltage due to stress. The best oxides are those closest to the origin. Estimated uncertainty of the points is indicated by circles. It is obvious that the most stable films are the double layer insulators. It is also interesting to note that all the points are in the upper left half of the graph. This means that it is possible to have increase of surface-state density and no change of flatband voltage, but that a change of flatband voltage is always accompanied by an increased surface-state density.

The high-temperature annealed oxides were not included in this graph because they were exclusively p-type, and it was observed that ionic contamination introduced during evaporation influenced their flatband voltages.

The question arises as to why the double layer insulators are so stable. A possible explanation lies in the fact that they were especially well annealed (25). The alumina deposition step involves annealing at 900°C in hydrogen. The importance of this step can be seen by comparing the DI 1 results (Table II) with the high-temperature hydrogen annealed oxide H_2-2 (Table III). Both behave very well during stress. An even better interface in sample DI-2 (Table II) is probably due to the 1100°C N_2 anneal which it received.

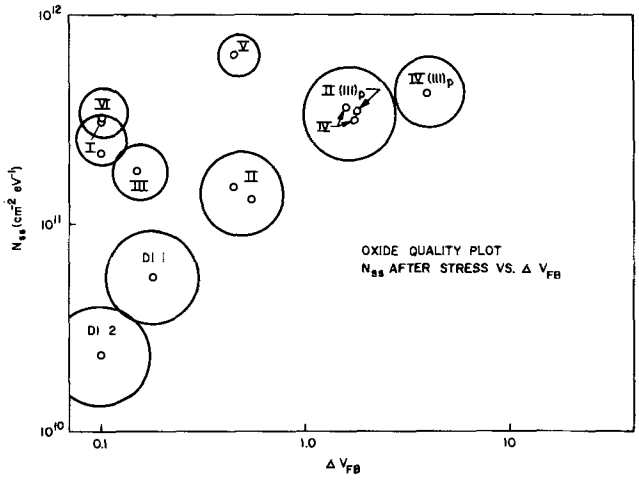

Fig. 11. This diagram summarizes "oxide quality." The oxides are plotted according to their poststress surface-state densities and flatband voltage shifts. The most stable oxides appear in the lower left corner, and the "worst" are diagonally opposite.

Conclusions

This investigation increases our knowledge about the formation of surface states in stressed interfaces. It was shown that the oxidation ambient, nature of metal contacts and postmetalization annealing are of importance for the stressing behavior. The exact physical model of the stress-induced surface states remains uncertain, although some correlation with charge transport across the interface region is likely. Simple charge trapping appears to be unlikely as an explanation for surface states, because the net apparent charge is too small.

The work reported here is strongly indicative both of the processing to use for stable oxides, and of the course of investigation to follow in order to elucidate the aging process.

Acknowledgments

The authors wish to thank M. Kuhn and J. R. Ligenza for valuable discussions and W. Powell for producing the high-temperature annealed oxide samples.

Manuscript submitted June 6, 1972; revised manuscript received Aug. 30, 1972.

Any discussion of this paper will appear in a Discussion Section to be published in the December 1973 JOURNAL.

REFERENCES

1. B. E. Deal, M. Sklar, A. S. Grove, and E. H. Snow, *This Journal*, **114**, 266 (1967).
2. Y. Miura and Y. Matakura, *Jap. J. Appl. Phys.*, **5**, 180 (1966).
3. A. Goetzberger and H. E. Nigh, *Proc. IEEE*, **54**, 1454 (1966).
4. S. R. Hofstein, *Solid-State Electron.*, **10**, 657 (1967).
5. E. Arnold, "International Conference on Properties and Use of MIS Structures," J. Borel, Editor, Grenoble, France, 1969.
6. M. Kuhn, *Solid-State Electron.*, **13**, 873 (1970).
7. R. Castagne, *Compt. Rend. Acad. Sci., Paris*, **267**, 866 (1968).
8. J. A. O'Sullivan, Private communication.
9. S. K. Tung and R. E. Caffrey, *Trans. Met. Soc. AIME*, **233**, 572 (1965).
10. H. E. Nigh, "International Conference on Properties and Use of MIS Structures," J. Borel, Editor, Grenoble, France, 1969.
11. C. N. Berglund, *IEEE Trans. Electron. Devices*, **ED-13**, 701 (1966).
12. S. Karr and W. E. Dahlke, *Appl. Phys. Letters*, **18**, 401 (1971).
13. S. R. Hofstein, *IEEE Trans.*, **ED-13**, 222 (1966).
14. R. H. Dudley and E. F. Labuda, Int. Elect. Device Meeting, Washington, D. C., 1969.
15. R. H. Walden, *J. Appl. Phys.*, **43**, 1178 (1972).
16. M. Kuhn and E. H. Nicollian, *This Journal*, **118**, 370 (1971).
17. T. L. Chu, J. R. Szedon, and G. A. Gruber, *Trans. Met. Soc. AIME*, **242**, 532 (1968).
18. A. D. Lopez and R. J. Strain, *Solid-State Electron.*, To be published.
19. P. V. Gray and D. M. Brown, *Appl. Phys. Letters*, **8**, 31 (1966).
20. P. Balk, Paper 111 presented at Electrochem. Soc. Meeting, Buffalo, N. Y., Oct. 10-14, 1965.
21. P. E. Deal, E. L. MacKenna, and P. C. Castro, *This Journal*, **116**, 997 (1969).
22. P. Rossel, H. Martimot, and D. Esteve, *Solid-State Electron.*, **13**, 425 (1970).
23. A. Goetzberger, V. Heine, and E. H. Nicollian, *Appl. Phys. Letters*, **12**, 95 (1968).
24. C. N. Berglund, Private communication.
25. R. Schmidt, Paper 344 RNP presented at Electrochem. Soc. Meeting, New York, May 4-9, 1969.

Electrolytic Behavior of CaF_2 Crystals under Reducing Conditions

J. W. Hinze*,[1] and J. W. Patterson*

Department of Metallurgy and Engineering Research Institute, Iowa State University, Ames, Iowa 50010

ABSTRACT

Solid CaF_2 was studied from 550° to 800°C with fluorine chemical potentials ranging from Ni,NiF_2 to Ca,CaF_2 coexistence. Measurements of a-c conductivity and galvanic cell emf's lead to the conclusion that the ionic transference number for CaF_2 is essentially unity over the range of conditions studied and hence CaF_2 may be employed as a solid electrolyte therein.

Calcium fluoride has been used extensively (1-4) as the solid electrolyte in galvanic cells designed to determine the free energy of formation of various compounds. These measurements have been undertaken over wide ranges of fluorine activity and temperature without a very certain knowledge as to the limitations of CaF_2 as a solid electrolyte (5, 6). In this connection it is of interest to establish log P_{F_2} — $1/T$ ranges (7, 8) beyond which positive hole and/or excess electron conduction achieves a magnitude equal to or greater than about 1% of the total (ionic plus electronic) conductivity. On the basis of Wagner's theory (9-11) of mixed conduction, many experimental measurement schemes may be devised to shed light on this matter—chief among these are: a-c (total) conductivity determinations (11-13) (as a function of fluorine activity and temperature), open circuit emf measurements (14, 15) and d-c polarization measurements (13, 16-18). "Coulometric titration" variations of the polarization technique have also been developed more recently (19-21).

The need for such studies for CaF_2 has been pointed out previously (5, 6) but none have been reported to date. Wagner (22), however, has used color center migration data by Mollwo (23) in a theoretical analysis to provide an intentionally excessive estimate of the conditions wherein n-type conductivity becomes appreciable in CaF_2. The relationship of Wagner's analysis (22) to the present investigation is developed more fully below.

Previous conductivity *vs.* temperature studies on CaF_2 by Ure (24) and others (25, 26) are not very pertinent in the present context primarily because no efforts were made to establish a well-defined fluorine activity during the experiments. For the present purposes of deducing the electronic contribution to the total conductivity, it is necessary to not

* Electrochemical Society Active Member.
[1] Present address: Systems Research Laboratories, Dayton, Ohio 45440.

Key words: solid electrolytes, calcium fluoride, electronic conductivity, ionic conductivity, ionic transference number, open-circuit emf, oxygen doping.

only fix the fluorine activity in each experiment, but also to fix it at different preselected values (at each temperature) so that the dependence of the total conductivity on fluorine partial pressure P_{F_2} and temperature can be determined. The question as to whether electronic contributions to the total conductivity are significant in CaF_2 has been left virtually unresolved by the previous conductivity studies. A recent study by Matzke (27) of the diffusivity of fluorine in CaF_2 indicates that the electrical conductivity of CaF_2 is due primarily to fluorine ions as Ure had concluded, but again no attempt was made to control the fluorine activity.

In addition to Wagner's analysis (22) previously reported open-circuit emf data provide the most direct evidence that the electrical conductivity of CaF_2 is predominantly ionic over wide ranges of temperature and fluorine partial pressure. Interestingly, the use of CaF_2 in many of these emf studies was justified on the basis of Ure's conductivity study.

The purpose of this paper is to present a-c conductivity and open-circuit emf data which indicate that the transference number for excess electron (n-type) carriers in CaF_2 is negligible even under the most reducing conditions.

Experimental Procedures and Apparatus

Fluorine activities were established by using metal, metal fluoride coexistence electrodes. Standard-free energy of formation data, $\Delta G°_f$, for the various fluorides were used to calculate the fluorine activity which is represented in terms of the effective partial pressure P_{F_2} of fluorine gas. Whenever possible, emf data were used in conjunction with calorimetric data of Rudzitis *et al.* (28) to establish the $\Delta G°_f$ values required. Markin's value (1) of -232.4 ± 0.6 kcal/mole for $\Delta G°_f(MgF_2)$ at 600°C was combined with $\Delta S°_f(MgF_2)$ deduced from standard emf *vs.* temperature plots by Hamer *et al.* (29) to give $\Delta G°_f(MgF_2)$ values over the temperature range from 500° to 850°C. This $\Delta G°_f(MgF_2)$ determination combined with emf measurements reported by Lofgren and McIver (2), Heus and Egan (3), and Rezukhina (4) served to establish $\Delta G°_f$ data for CoF_2, ThF_4, NiF_2, and YF_3 over the temperature range studied. The measurements of Heus and Egan (3) were made only at 600°C; thus, $\Delta S°_f$ values from Hamer *et al.* (29) were combined with these emf's to provide the desired $\Delta G°_f$ values. Experimental open-circuit emf data were not available for Mn,MnF_2 or Ca,CaF_2. Therefore, $\Delta G°_f$ data obtained from Hamer's compilation (29) were used to determine the P_{F_2} values for the Mn,MnF_2 electrode. Data from the JANAF table (30) for $\Delta G°_f(CaF_2)$ were used to determine the P_{F_2} values for Ca,CaF_2 coexistence.

Optical quality, high purity CaF_2 single crystal specimens were used in this study. The 1/8-in. thick specimens were purchased from the Harshaw Chemical Company as optically polished disks cut from a single crystal rod 3/4-in. in diameter with the [111] direction lying along the longitudinal axis of the rod.

The total conductivity of the CaF_2 single crystals was determined from measurements made on a number of symmetrical cells of the type

$$M,MF_n|CaF_2|M,MF_n \qquad \text{[Cell I]}$$

Both coexistence electrodes in this two-probe method are compacts fabricated from the same metal, metal fluoride mixture. The coexistence electrodes: Co,CoF_2; Ni,NiF_2; Mn,MnF_2; Th,ThF_4; Y,YF_3; and Ca,CaF_2 were employed in the a-c conductivity studies from 550° to 800°C. Open-circuit emf measurements were performed on nonsymmetric cells of the type

$$Ca|CaF_2|Th,ThF_4 \qquad \text{[Cell II]}$$

from 400° to 815°C. Encapsulation of the more volatile electrode constituents was achieved by means of graphite and stainless-steel cups pressed against the CaF_2 specimens.

All measurements were performed in purified helium atmospheres. The a-c conductivity measurements were made with the use of a Wayne Kerr transformer ratio arm bridge operated at 1592 Hz while open-circuit emf's were measured with a conventional potentiometer and a high-impedance null detector. The temperature was determined from the emf of a calibrated Pt-Pt 10% Rh thermocouple. Light spring pressure held the electrode|electrolyte|electrode sandwich in place in an alumina cell holder.

Results

The total conductivity *vs.* temperature dependences for the various coexistence electrodes are shown in Fig. 1. These data are replotted as log σ *vs.* log P_{F_2} isotherms in Fig. 2. For comparison, the log σ *vs.* log P_{F_2} isotherms predicted from Wagner's analysis (22) are shown as dashed lines in Fig. 2. The results of three open-circuit emf runs on cell II are shown on Fig. 3 along with the thermodynamic emf (sold line) predicted from $\Delta G°_f$ values for ThF_4 and CaF_2. Also shown on Fig. 3 are the open-circuit emf's (dashed lines) that would result from combining the same thermodynamic $\Delta G°_f$ data with Wagner's analysis (22). The disagreement with Wagner's estimate is not a serious matter primarily because that estimate was intentionally formulated to maximize the magnitude

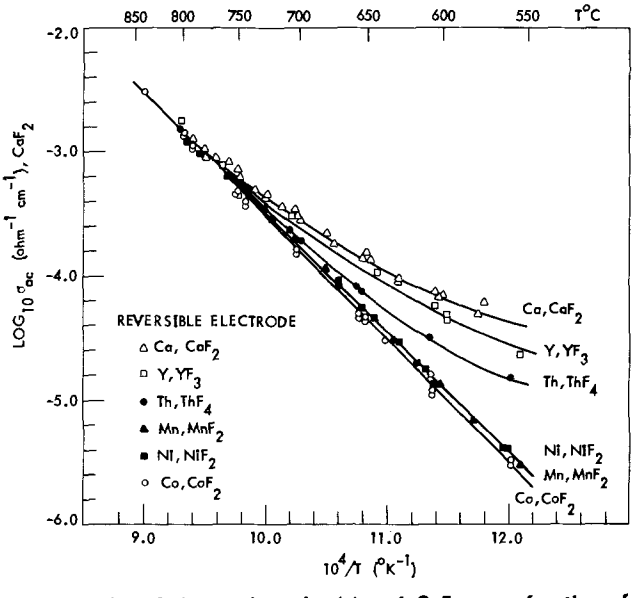

Fig. 1. Plot of the total conductivity of CaF_2 as a function of $1/T$ for a number of reversible electrodes.

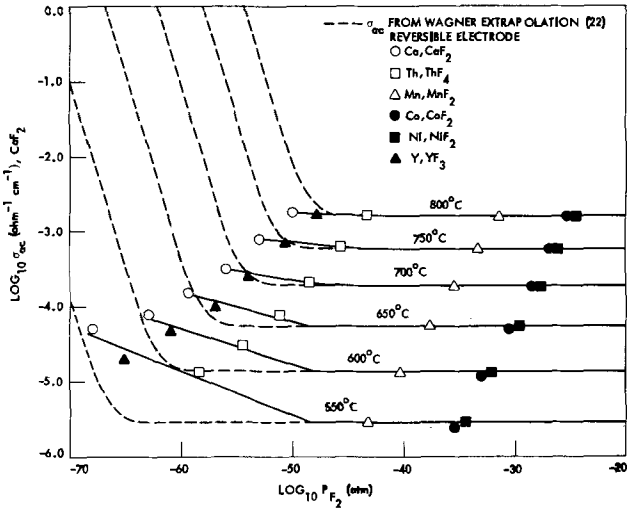

Fig. 2. Total conductivity of CaF_2 as a function of log P_{F_2} for various temperatures.

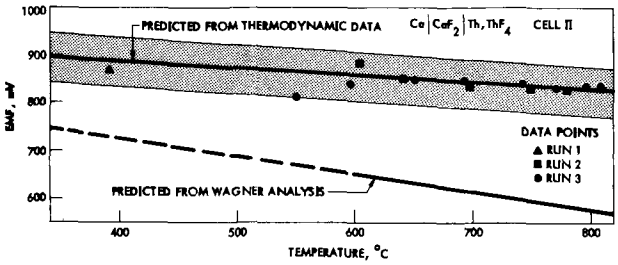

Fig. 3. Open-circuit emf vs. temperature for the cell $Ca|CaF_2|Th,F_4$.

of excess electron conduction in CaF_2 at low fluorine partial pressure.

Discussion

The log σ *vs.* log P_{F_2} data plotted in Fig. 2 do not indicate any rise such as would be expected from the onset of electronic conductivity at very low values of P_{F_2}. The 800°C isotherm remains flat all the way down to Ca,CaF_2 coexistence which is the stability limit of CaF_2. This is indicative of an ionic conductivity which is independent of P_{F_2} and is in accordance with theoretical predictions (22). This isotherm shows no evidence of the n-type conduction which could have occurred.

The gentle rise at the low P_{F_2} end of the lower temperature isotherms is interpreted to be an extrinsic effect and is not associated with the onset of excess electron conductivity. For example, the slope of the 550°C isotherm is only on the order of $-1/16$ and hence is quite removed from the value $-1/2$ which is to be associated with the onset of n-type electronic conduction. Also, the emf *vs.* temperature data of Fig. 3 do not exhibit any large decrease in emf at low temperature. Such a decrease would be expected if the observed conductivity rise were due to some form of electronic conduction. For these reasons the observed conductivity increase is believed to be ionic in nature and is thought to be a contamination effect.

Contamination by cations from the electrodes might appear to be a possible explanation; however, cation diffusivities in CaF_2 are known to be extremely low (24, 31-34), and this tends to rule out the cation contamination possibility. Rather, it is suspected that trace amounts of oxygen from the specimen environment are incorporated into the CaF_2 specimens, thereby augmenting the ionic conductivity. Conductivity and other effects due to oxygen incorporation into CaF_2 crystals have been observed and discussed by previous authors. (24, 35-37).

To supplement the foregoing evidence for the predominant ionic conductivity of CaF_2 under reducing conditions, the emf *vs.* temperature data of Fig. 3 are also offered. The solid line gives the emf that would be predicted for cell II if CaF_2 had an ionic transference number of unity (averaged over the fluorine activity range from Ca,CaF_2 coexistence to Th,ThF_4 coexistence). An uncertainty of ±51 mV in the thermodynamic emf line was obtained by simply adding the uncertainties in all the thermodynamic values used.[1] The measured emf values plotted in Fig. 3 are scattered more or less randomly about the predicted thermodynamic values and fall within the ±51 mV uncertainty band. Thus, within the uncertainty limits of existing thermodynamic data, it appears that the usefulness of undoped CaF_2 as a solid electrolyte extends down to its stability limit over the temperature range 400°-810°C.

Acknowledgments

The authors gratefully acknowledge the financial assistance of the National Science Foundation during the initial phase of this research (research grant GK-1551 and a one-year NSF traineeship).

The major part of this research was conducted by the Engineering Research Institute as part of an Iowa State University Themis Project in Ceramic and Composite Materials, contract No. F33615-68-C-1034.

The authors also wish to acknowledge Mr. Layi Fagbenle, Dr. W. H. Skelton, and Mr. Gary Long for their assistance in the laboratory.

Manuscript received June 22, 1972.

Any discussion of this paper will appear in a Discussion Section to be published in the December 1973 JOURNAL.

[1] The uncertainty for $\Delta G°_f(CaF_2)$ was taken to be the uncertainty in $\Delta H°_f(CaF_2)$ at 298°K which according to the JANAF tables is ±1.5 kcal or ±33 mV. An uncertainty of ±5 mV was reported by Heus and Egan for the cell $Mg,MgF_2|CaF_2|Th,ThF_4$ at 600°C, and Markin gives the uncertainty for $\Delta G°_f(MgF_2)$ at 600°C to be ±0.6 kcal or ±13 mV.

LIST OF SYMBOLS

P_{F_2}	Fluorine partial pressure in atmospheres
$\Delta G°_f$	Standard free energy of formation in cal/mole
$\Delta H°_f$	Standard enthalpy of formation in cal/mole
$\Delta S°_f$	Standard entropy of formation in cal/mole-°K
R	Gas constant
T	Temperature in °K
σ_{ac}	Total conductivity of CaF_2 measured with an a-c bridge

REFERENCES

1. T. L. Markin, in "Electromotive Force Measurements in High Temperature Systems," C. B. Alcock, Editor, p. 91, Proc. of 1967 Symposium, American Elsevier Publishing Co., Inc., New York (1968).
2. N. L. Lofgren and E. J. McIver, United Kingdom Atomic Energy Authority Report 5169 (1966).
3. R. J. Heus and J. J. Egan, *Z. Phys. Chem., N.F.*, **49**, 38 (1966).
4. T. N. Rezukhina and B. S. Pokarev, *J. Chem. Thermodyn.*, **3**, 369 (1971).
5. T. L. Markin, in "Electromotive Force Measurements in High Temperature Systems," C. B. Alcock, Editor, p. 100, Proc. of 1967 Symposium, American Elsevier Publishing Co., Inc., New York (1968).
6. C. Wagner, General Discussion in *Thermodynamics*, **1**, IAEA, 185 (1966).
7. J. W. Patterson, *This Journal*, **118**, 1033 (1971).
8. J. W. Patterson, in "The Physics of Electronic Ceramics," L. L. Hench and D. B. Dove, Editors, p. 131, Marcel Dekker Inc., New York (1971).
9. C. Wagner, *Z. Physik. Chem.*, **B21**, 25 (1933).
10. C. Wagner, Proc. Int. Comm. Electrochem. Thermo. and Kinetics (CITCE), 7th Meeting Lindau, 1955, Butterworth Scientific Publ., London (1957).
11. K. Kiukkola and C. Wagner, *This Journal*, **104**, 373 (1957).
12. M. F. Lasker and R. A. Rapp, *Z. Physik. Chem., N.F.*, **49**, 198 (1966).
13. J. W. Patterson *et al.*, *This Journal*, **114**, 752 (1967).
14. H. Schmalzried, *Z. Elektrochem.*, **66**, 576 (1962).
15. H. Schmalzried, *Z. Physik. Chem., N.F.*, **38**, 87 (1963).
16. J. B. Wagner and C. Wagner, *J. Chem. Phys.*, **26**, 1597 (1957).
17. B. Ilschner, *ibid.*, **28**, 1109 (1958).
18. D. O. Raleigh, *J. Phys. Chem. Solids*, **26**, 329 (1965).
19. J. D. Tretyakov and A. Muan, *This Journal*, **116**, 331 (1969).
20. D. A. J. Swinkels, *ibid.*, **117**, 1267 (1970).
21. T. H. Edsell and S. N. Flengas, *ibid.*, **119**, 1 (1972).
22. C. Wagner, *ibid.*, **115**, 933 (1968).
23. E. Mollwo, Nachrichten von der Gesellshaft der Wissenschaften zu Göttingen, Math. Phys. Kl., N.F., **6**, 79 (1934).
24. R. W. Ure, *J. Chem. Phys.*, **26**, 1363 (1957).
25. W. L. Fielder, NASA Technical Note, D-3816 (1967).
26. W. Bollman *et al.*, *Phys. Status Solidi A*, **2**, 157 (1970).
27. Hj. Matzke, *J. Mater. Sci.*, **5**, 831 (1970).
28. E. Rudzitis *et al.*, *J. Phys. Chem.*, **68**, 2978 (1964).
29. W. Hamer *et al.*, *This Journal*, **112**, 750 (1965).
30. "JANAF Thermochemical Data," Dow Corning Co., Midland, Michigan, June 30, 1971.
31. M. F. Berard, *J. Am. Ceram. Soc.*, **54**, 144 (1971).
32. M. F. Berard, Private communication (1972).
33. Hj. Matzke and R. Lindner, *Z. Naturforsch.*, **19A**, 1178 (1964).

34. M. Baker and A. Taylor, *J. Phys. Chem. Solids*, **30**, 1003 (1969).
35. B. R. Rossing, Thesis, 1966. Dept. of Metallurgy, Massachusetts Institute of Technology, Cambridge, Mass.
36. K. Muto and K. Awazu, *J. Phys. Chem. Solids*, **29**, 1269 (1968).
37. A. D. Franklin *et al.*, *J. Res. Nat. Bur. Std. A*, **71A**, 355 (1967).

Residues Remaining after RF Plasma Photoresist Removal

H. G. Hughes, W. L. Hunter,* and K. Ritchie

Motorola Inc., Semiconductor Products Division, Central Research Laboratories, Phoenix, Arizona 85008

ABSTRACT

A method of photoresist stripping in which oxygen plasma supplies the activation energy necessary for the rapid oxidation of the photoresist has gained widespread use. Oxygen plasma alone, however, does not remove inorganic impurities present in some resists. Recently obtained evidence indicates that interactions between these inorganic impurities and various substrates may result in modification of chemical properties and/or physical characteristics of the substrate surfaces from which the photoresist is removed.

RF oxygen plasma ashing is a method of photoresist removal in which rf energy converts oxygen to an active species which in turn oxidizes the photoresist to volatile products (1). An impediment to the use of oxygen plasma alone is present when photoresists contain inorganic impurities (2) such as tin compounds. This residue is an undesirable contaminant (Fig. 1). Observations suggest that the physical and/or chemical characteristics of the substrate may be altered by the foreign materials.

Results and Discussion

The residue in photoresist "A" was identified from spectrographic analyses as comprising mainly tin compounds. Residues remaining after ashing a 3000Å thick film of photoresist "A" are shown in Fig. 2 and 3. Adhesion of the residue to the SiO_2 substrate tends to increase with longer ash time, greater oxygen flow, and greater rf power. Figure 2 shows that the deposit could be removed by gentle scraping with a tweezer point. Another area of the same wafer is depicted in Fig. 3, following a twofold increase in ash time and rf power. Scraping similar to that used in Fig. 2 produced no observable movement of the residue indicating a marked increase in adhesion.

The adhesion of the residue was further demonstrated by its resistance to ultrasonic cleaning with various reagents (Table I). This seemed to indicate that the residual material was not organic (due to incomplete ashing) nor was it elemental tin. The residue could be removed slowly with hot 20% aqueous KOH and etched off readily with buffered HF, both of which also attack the SiO_2 surface. Hot sulfuric acid, which is used as a reagent in the morin test for tin and tin oxide (3), failed to strip the residue. The residual matter was also not held electrostatically since an ultrasonic aqueous sodium chloride bath did not dislodge the particles.

The form in which tin is present in photoresist "A" is not known with certainty. However, since stannic chloride is often used in the cyclization of natural rubber (4), and would be converted to tin oxide by oxy-

* Electrochemical Society Active Member.
Key words: RF ashing, impure resists, inorganic residue.

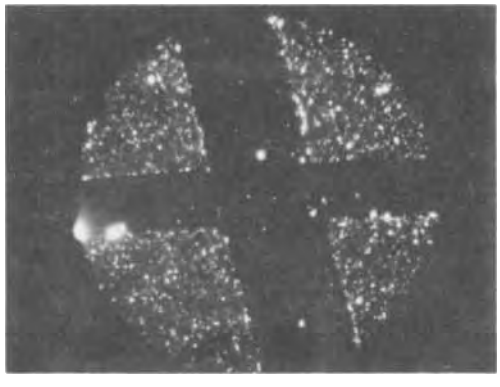

Fig. 2. Mobility of residue on SiO_2 substrate (100X)

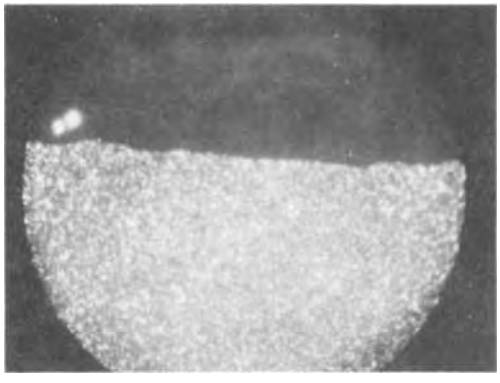

Fig. 1. Inorganics left on SiO_2 substrate after O_2 plasma ash (dark field. 100X).

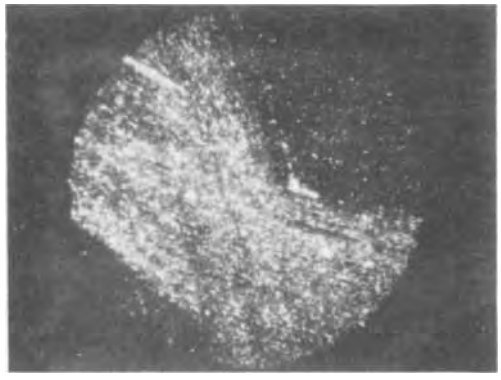

Fig. 3. Immobility of residue on SiO_2 substrate after a twofold increase in ash time and RF power (100X).

Table I. Solvents used for residue removal

Cleaning period (min)	Solvent	Result
15	Hot J-100	Residue
5	Hot A-20	Residue
5	Hot H_2SO_4	Residue
5	Dilute HCl	Residue
5	Dilute H_2SO_4	Residue
2	Hot Chromic Clean	Residue
1	20% KOH at R.T.	Residue
1	20% KOH at 50°C	Residue
5	20% KOH at 75°C	Most residue off
10	20% KOH at 75°C	Residue off

gen plasma, the effect of these compounds on thermal oxide was investigated.

A thermal oxide wafer was dipped in a 1% $SnCl_4 \cdot 5H_2O$-xylene solution. After oxygen plasma ashing for 30 min at 450W and 400 cc O_2/min, the wafer substrate appeared "cracked" in areas (Fig. 4). Although some of the residue could be mechanically dislodged, the "cracked" areas that appeared during ashing could not be removed by scraping with a tweezer point.

No apparent surface effect was noted with the SnO_2-xylene suspension dip. After ashing, most of the tin oxide residue could be wiped clean. However, isolated areas were found which were difficult to dislodge mechanically (Fig. 5). It appears, therefore, that should either of these compounds be present in a photoresist, the surface of the thermal oxide may become altered during oxygen plasma ashing.

Aluminum substrates were also investigated. After ashing, neither light microscopy (dark or light field) nor scanning electron microscopy (Fig. 6a and 6b) could detect any obvious residue or other surface distinction between initially photoresist-covered and bare areas of the same wafer. The presence of residual material was detected chemically, however. Aluminum deposited on silicon oxide was patterned with photoresist "A" and processed in the normal manner. No

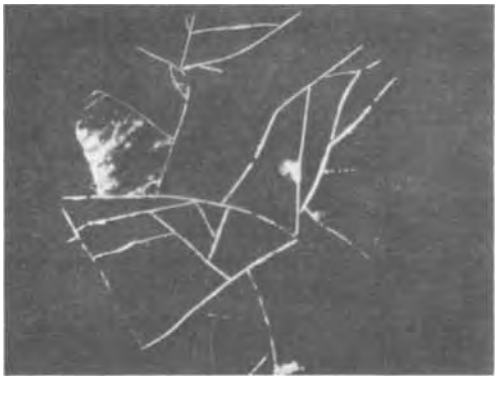

Fig. 4. SiO_2 substrate (dipped in $SnCl_4 \cdot 5H_2O$-xylene solution) after O_2-plasma ash (dark field, 200X).

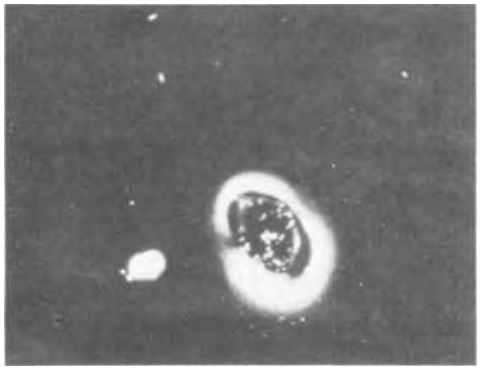

Fig. 5. SiO_2 substrate (dipped in SnO_2-xylene suspension) after ash (dark field, 200X).

Fig. 6a. SEM of aluminum, ashed photoresist side (6500X)

Fig. 6b. SEM of aluminum, ashed nonphotoresist side (6500X)

etching was done prior to resist removal by oxygen plasma. After ashing, the "clean" wafer was placed in a potassium ferricyanide-potassium hydroxide aluminum etchant and a pattern formed even though no photoresist was present (Fig. 7). The residual contaminated areas appeared to etch more slowly. The grid step observed was estimated by Dektak measurement to be 100-200Å deep after 8 sec etch time. Upon further etching the pattern slowly disappeared. It was further noted that when powdered tin or tin oxide was mixed with powdered aluminum metal, the reaction rate of the metal with hydrochloric acid or aluminum etchant increased, whereas on the substrate the tin oxide seemed to form a protective layer on the aluminum oxide surface.

In all cases, photoresist "B" (essentially free of inorganics) was processed along with photoresist "A." No residual material nor detrimental effect was observed (Fig. 8 and 9). Aluminum processed with photoresist "B" followed by ashing did not show any preferential etching.

Conclusion

In conclusion, it is noted that the residual film left from oxygen plasma ashing of photoresist "A" is mainly inorganic material which may be adsorbed or bonded to the oxide surface in various degrees. With aluminum substrates, preferential etching can occur which was not observed on SiO_2 substrates. The contaminants can lead to undesirable effects in subsequent diffusions and passivation.

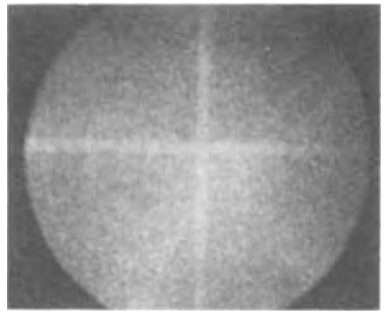

Fig. 7. Aluminum etched after oxygen-plasma ash (100X)

Fig. 8. SiO_2 substrate (processed with photoresist "B") after O_2 plasma ash (dark field, 200X).

Fig. 9. SEM of SiO_2 (processed with photoresist "B") after O_2 plasma ash (650X).

Manuscript submitted Nov. 15, 1971; revised manuscript received Aug. 21, 1972.

Any discussion of this paper will appear in a Discussion Section to be published in the December 1973 JOURNAL.

REFERENCES

1. S. M. Irving, in "Kodak Photoresist Seminar Proceedings," Vol. II, p. 26, 1968.
2. S. A. Harrell, in "Proceedings of the Second Kodak Seminar on Microminiaturization," p. 50, 1966.
3. F. Feigl, "Spot Tests in Organic Analysis," 5th ed., p. 472, Elsevier Publishing Company (1956).
4. M. A. Golub, "Chemical Reactions of Polymers," E. M. Peters, Editor, p. 110, Interscience Publishers, New York (1964).

Impurity Striations in Czochralski Grown Al-Doped Si Single Crystals

B. K. Jindal, V. V. Karelin,[1] and W. A. Tiller

Department of Materials Science and Engineering, Stanford University, Stanford, California 94305

ABSTRACT

Experimental and theoretical studies of interface shapes and striation structures were done on Al-doped Si single crystals. The interface shapes were observed to be complex, variable and with no evidence of a single central facet. Many of the characteristics of the striation structure are similar to those observed by Witt and Gatos, and some additional features are also described. Based on theoretical calculations of variation of Al concentration in the crystal as a function of variations of crystal growth rate, it is deduced that the likely mechanism of interface atomic attachment is by layer motion. Effects of thermal fluctuations and fluid flow are also considered.

Single crystals pulled from alloy melts by the Czochralski method generally exhibit impurity structures (1-7) which are related to fluctuations in the crystal-growth rate (1-5). The present paper deals with some experimental observations of impurity striations in Al-doped Si crystals, and a theoretical assessment of the impurity fluctuations in terms of assumed fluctuations in growth velocity. From these considerations, it seems most reasonable to conclude that the occurrence of the velocity fluctuations is directly related to erratic layer-flow behavior on the interface.

Experimental Procedure

Si single crystals containing 10^{16}-10^{18} Al atoms/cc were grown using a Czochralski-type apparatus from a melt containing 2.5×10^{-1}-2.5×10^{-2} weight per cent (w/o) Al (semiconductor grade Si and 99.999% pure Al). Using (100) seeds, all crystals were pulled at 5 cm/hr at a seed rotation rate of 14 rpm and a crucible rotation rate of -12 rpm (reverse direction). The grown crystals were cut in the middle along the growth axis to expose a (110) plane which was then polished with Linde B abrasive (particle-size, 0.05μ) and the final polish was always performed in a direction perpendicular to the striation direction. Next, the specimens were rinsed with distilled water and chemically polished using CP-4 (5 parts HNO_3, 3 parts CH_3COOH, and 3 parts HF). Etching utilized a CrO_3 solution mixed with HF (1 part 48% HF to 1 part 33% CrO_3 solution) that was prepared immediately prior to use.

Experimental Results

Macroscopic interface shapes.—Typical shapes of the crystal/liquid interface, as revealed by suddenly pulling the crystal out of the melt, are plotted in Fig. 1 and, as revealed by the striation patterns, are shown in Fig. 2. These different shapes are obtained as a result of the different temperature distributions in the furnace. Comparing these shapes with the theoretical work of Kobayashi and Arizumi (8), it is seen that the interface is not always uniformly concave or convex but can assume a complex configuration; the shape in Fig. 1(b) resembles more closely the temperature isotherms in the liquid phase as calculated by Kobayashi and Arizumi (8). The observation that the shape of the interface varies during the growth of a particular crystal leads one to conclude that the microscopic growth rate is not always the same over the entire crystal cross section. Also, a single macroscopic facet in the center is not observable; the absence of a macroscopic facet in Al-doped Si has also been reported by Mil'vidski and Berkova (9).

Striation structure.—The general striation pattern, without magnification, is shown in Fig. 2. Figures 3-5

[1] Present address: Moscow State University, Chemistry Department, Moscow, B-234, U.S.S.R.

Key words: silicon, crystal growth, impurity striations, defects in crystals, Czochralski growth.

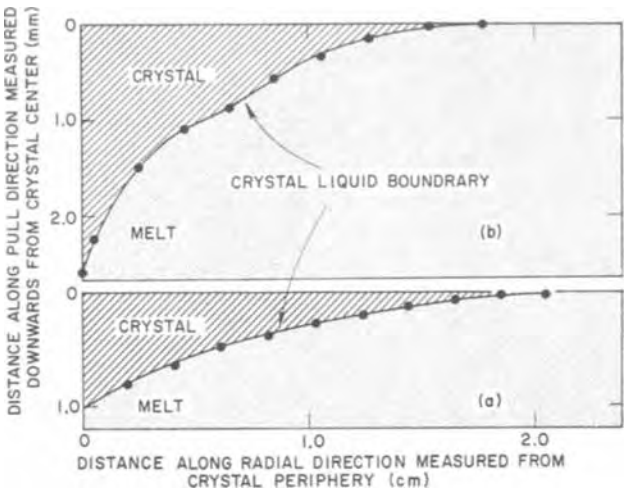

Fig. 1. Typical interface shapes as revealed by rapid pulling of the crystal out of the melt.

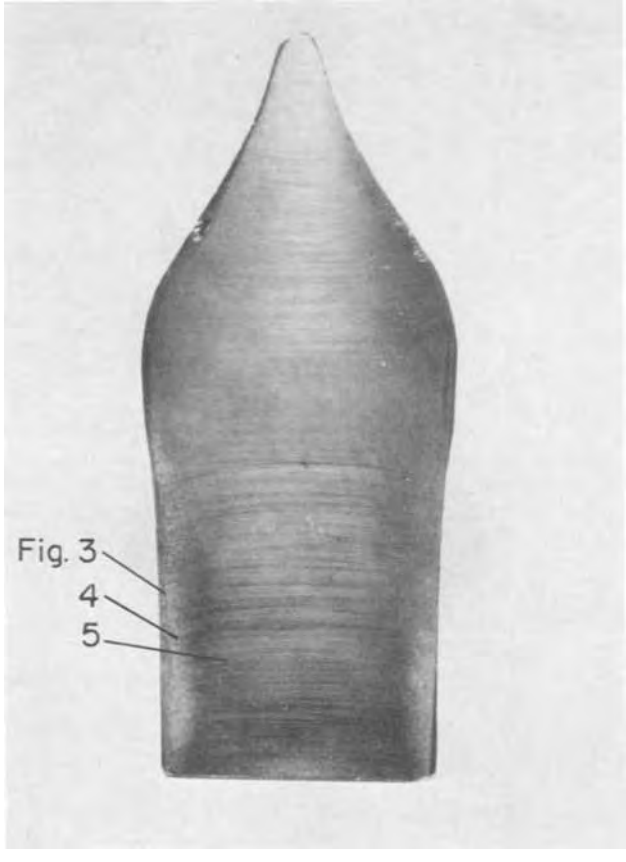

Fig. 2. General striation pattern on (110) plane. Note the change in interface shape from convex in upper part to concave in lower part. Arrows point to regions shown magnified in respective figures. (No magnification.)

show enlarged views of the particular areas marked in Fig. 2. From these figures it is seen that:

(*i*) There is no evidence of a single central facet and the striations appear as straight lines of varying lengths and not necessarily perfectly parallel to each other.

(*ii*) In going from the outer to the central part of the crystal, at a distance of about 2-3 mm from the edge, there is a rapid and discontinuous decrease in striation frequency (Fig. 3, 4). A discontinuity in the structure of both rotational and nonrotational striations has been observed in the growth of InSb crystals, which sometimes appears to be located at the boundary of the central facet with the off-facet region (5). In our case, a discontinuity in striation structure is observed even though there is no evidence of a single central facet.

(*iii*) The striations that extend from the outer into the central part are of variable length and intensity (Fig. 4, 5). Some striations lie entirely within the central part (see Fig. 6). These are also of variable length and intensity. In the central part, the striation frequency shows a slight decrease in going towards the crystal center and is variable along the vertical axis (Fig. 5). The intensity of any one striation is not constant over its entire length; for striations that lie entirely within the central part of the crystal, the intensity is high in the striation's central portion and decreases towards its ends (see Fig. 6).

(*iv*) In lightly doped crystals, the striations are quite difficult to observe. In these crystals, the striation frequency is larger when the crystal diameter is decreasing and smaller when the crystal diameter is increasing (Fig. 7).

Discussion

Since the striations are believed to be caused by a fluctuation in the crystal growth rate, to understand the details of the striation formation mechanisms, let us study the following aspects of the problem: (*i*) effect of crystal growth rate variation on solute incorporation; (*ii*) interfacial atomic attachment mechanisms operating under conditions of required growth rate variations; (*iii*) effect of thermal fluctuations on crystal growth rate; and (*iv*) consequences of fluid motion.

Solute redistribution.—Considering the liquid-solute profile illustrated in Fig. 8, we wish to calculate the variation of solute concentration in the solid associated with a fluctuation in freezing velocity. By this path, we shall determine the necessary velocity fluctuation consistent with the experimentally observed impurity

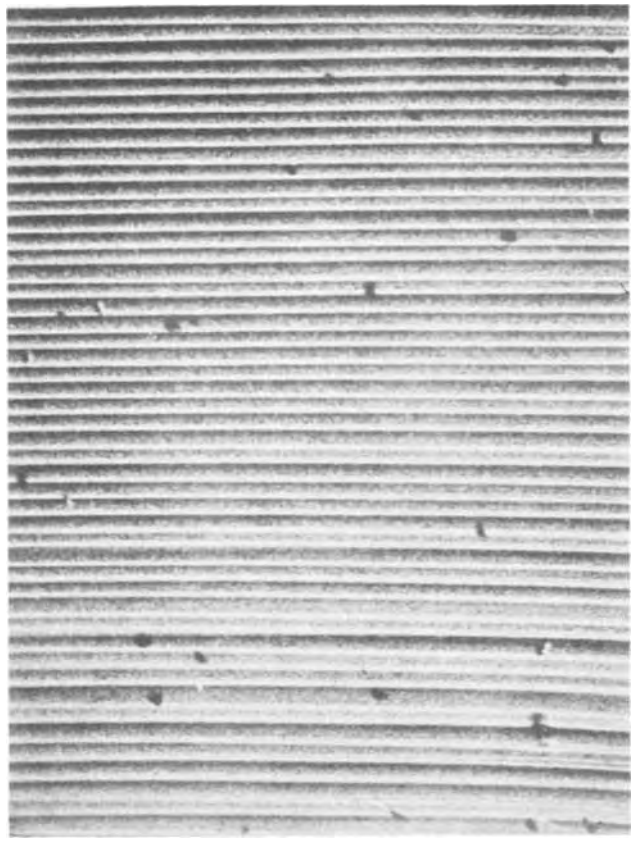

Fig. 3. Striation pattern in the outer regions of the crystal. Many striations end about 2 mm from the edge. Some striations extend deeper into the central part. (Magnification. 100×.)

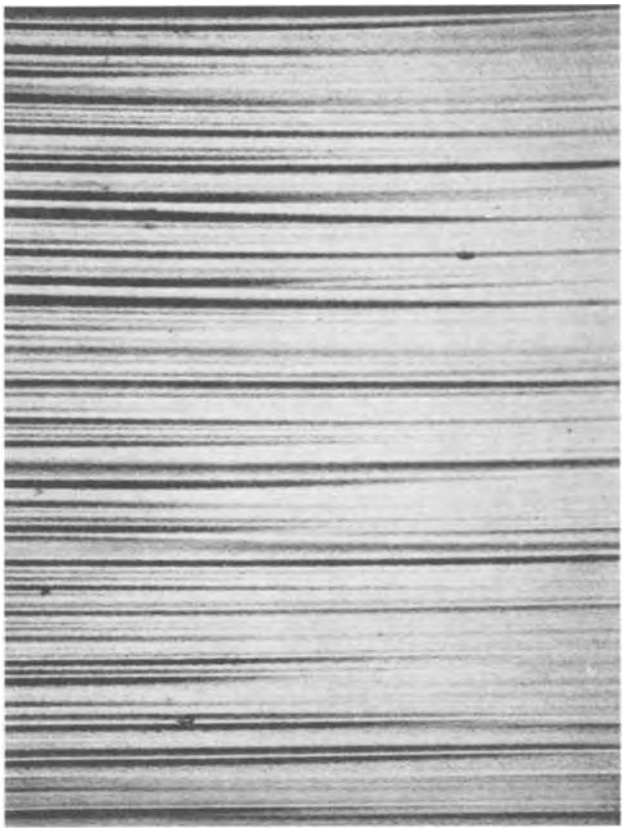

Fig. 4. Striation pattern at the boundary of the outer and central parts. (Magnification, 100×.)

Fig. 5. General striation pattern in the central part of the crystal. (Magnification, 100×.)

fluctuation. Assuming the interface partition coefficient to be equal to the phase diagram partition coefficient k_0, the liquid concentration at the interface,

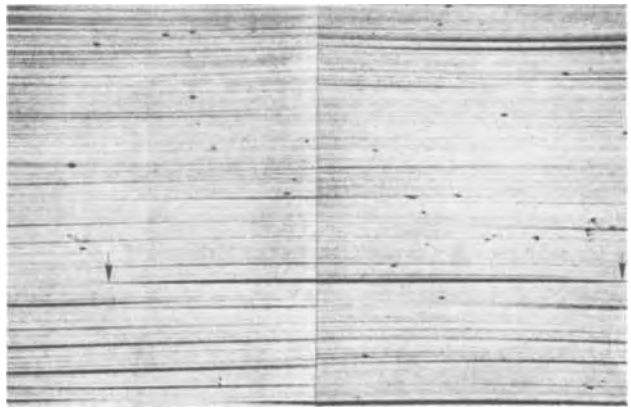

Fig. 6. The striation bounded by arrows lies entirely within the central part. (Distance between arrowheads ≈ 3 mm.)

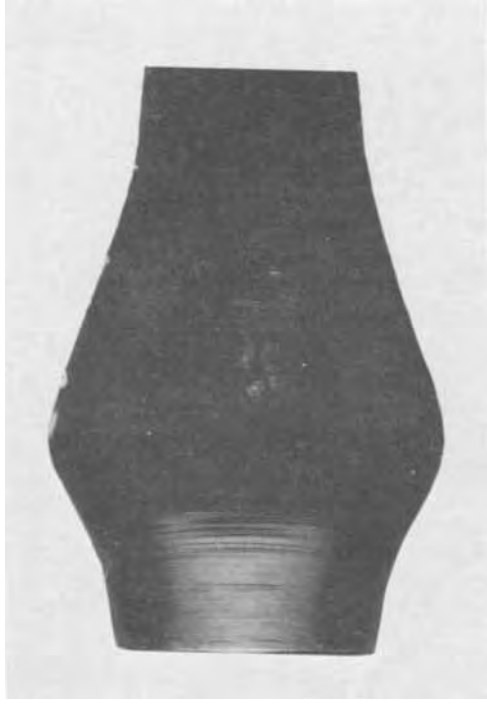

Fig. 7. Striation pattern in a lightly doped crystal. (No magnification.)

$C_L(0)$, is given by

$$C_L(0) = \frac{k}{k_0} C_L(\infty) \qquad [1]$$

where $C_L(\infty)$ is the bulk liquid concentration, and k is the effective solute distribution coefficient given by (10)

$$k = \frac{k_0}{k_0 + (1 - k_0)\, e^{-V\delta c/D}} \qquad [2]$$

where δc is the solute boundary layer thickness and D is the solute diffusion coefficient in the liquid.

We wish now to consider the change in $C_S(x)$ associated with a change in freezing velocity from V to V'. Since $k/k_0 \approx 1.1$, $\delta c \approx 10^{-2}$ cm (11), and the width of a striation is less than 10^{-3} cm in our experiments, for an approximate analysis we may choose $C_L(0) \approx C_L(\infty)$ and use the diffusion only initial transient approximation of Tiller *et al.* (12) to describe $C_S(\xi)$, where ξ is the distance measured from the beginning of the change to V'. In Fig. 9, $C_S(\xi)/C_L(\infty)$ is plotted *vs.* ξ for several values of V' ($V = 1.4 \times 10^{-3}$ cm/sec). Here, we note that a fluctuation of 5-10% in $C_S(\xi)/$

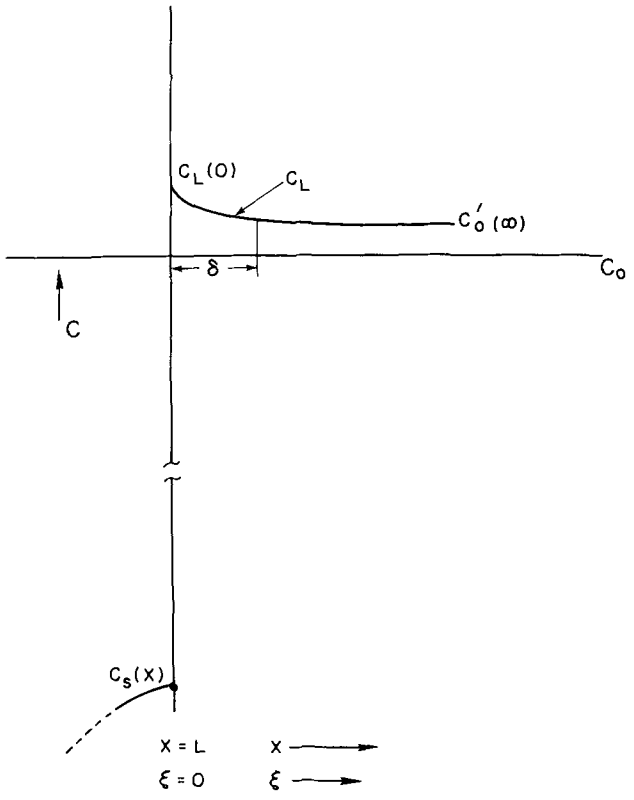

Fig. 8. Schematic of concentration profile in the system after pulling a crystal of length L.

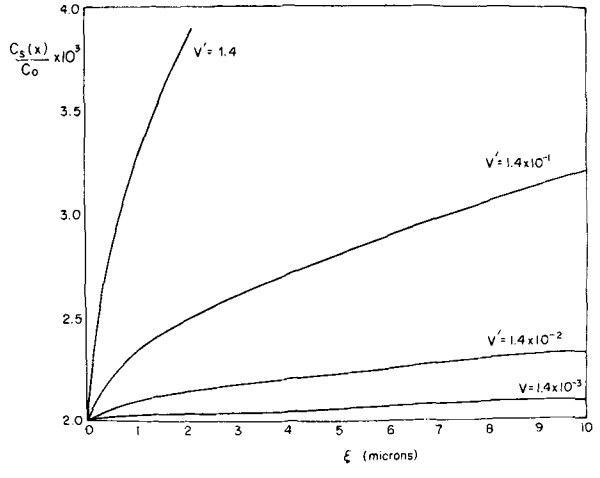

Fig. 9. Effect of variation of growth rate from V to V' on impurity incorporation in the crystal.

$C_L(\infty)$ over a distance of a few microns requires a velocity fluctuation $V'/V \lesssim 10^3$.

Interface attachment.—Since some of the striations are several millimeters in length, it is most likely that to obtain $V'/V \lesssim 10^3$, growth occurs by a layer-flow mechanism at these small driving forces rather than by a uniform attachment mechanism. Consider Fig. 10(a) in which the layers flow across the interface in a very regular way as the position of the freezing point isotherm changes due to steady pulling of the crystal. Suppose that, due to an adsorption event or a temperature fluctuation at the layer edge, the edge cannot continue to flow across the surface. We note that, as illustrated in Fig. 10(b), the layer height increases at e and a zone of supercooling grows at the face f over the region ee'. If, at some later time, the layer edge at e breaks away from its locking point, a multistep height layer will flow across the surface at greater than the average passage velocity. Initially, it will create a

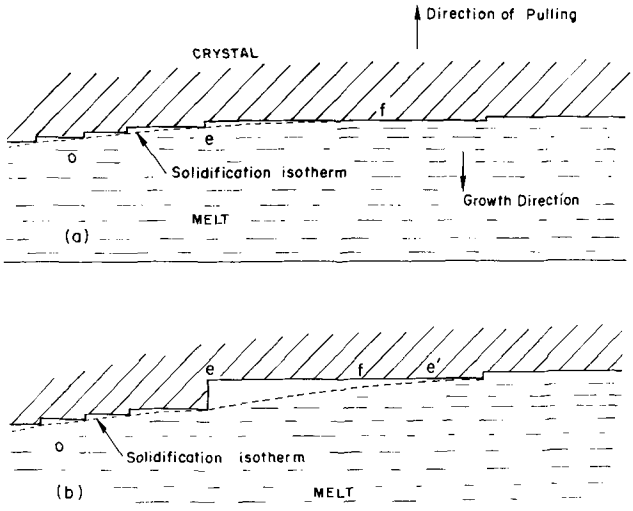

Fig. 10. Schematic representation of interface microstructure and solidification isotherm.

type of initial transient solute distribution which could be from less than a micron to millimeters in length depending on the step height and the passage velocity. It should eventually reach a type of steady-state build-up, and then, as the velocity slows down because of approach to the freezing point isotherm, the solute excess decreases to zero. This is consistent with the type of behavior observed in the present experiments.

Thermal fluctuations.—It is necessary to distinguish between those growth-rate fluctuations which are due to the passage of a thermal fluctuation from the bulk liquid to the interface, and those that are microscopic in nature and originate at the interface during the consumption of a local zone of undercooled liquid. With respect to the thermal fluctuations in the bulk liquid, let us consider a fluctuation of magnitude ΔT and frequency n Hz at a distance δT from the interface, where δT is the thickness of the thermal boundary layer. The temperature fluctuation ΔT_i at the interface due to the above fluctuation in the liquid is given by (13)

$$\Delta T_i = \Delta T \exp\left[\left(-\frac{\pi n}{\alpha_L}\right)^{1/2} \delta T\right] \qquad [3]$$

where α_L is the thermal diffusivity of the liquid. Letting $n = 1$ Hz, $\alpha_L \approx 10^{-1}$ cm^{-1}, $\delta T \approx 0.25$ cm, $\Delta T = 5$°C, we get $\Delta T_i \approx 1$°C. To see the effect of these thermal fluctuations on microscopic growth rate, let us recall that in the previous section the interface was depicted with many more layer edges per unit area in the peripheral section of the crystal than in the central section. Thus in the peripheral section, crystal growth is limited only by layer motion whereas in the central section the growth may have to wait the freeing of a pinned layer edge or the generation of a new one. Since the motion of a layer from an existing layer edge requires much less driving force than the generation of a new edge, therefore fluctuations of $\Delta T_i \approx 1$°C would cause variations of microscopic growth rate more often at the crystal periphery than at the crystal center.

For the case of a temperature fluctuation originating at the interface, if one considers the microscopic zone of a supercooled liquid, it is clear that a layer of solid $\sim 10\mu$ thick could readily form from a layer of liquid 10^{-1} cm thick which is supercooled by a few degrees. The latent heat of this layer of solid is essentially dumped into the remaining zone of liquid eliminating its supercooling. In this case, there is no thermal limitation on the rate at which this heat evolution can occur so that velocity fluctuations of several orders of magnitude could occur via this mechanism. Some of the mechanisms by which thermal fluctuations at the

interface can occur have been discussed by Morizane, Witt, and Gatos (1-5).

Hydrodynamics.—Cochran's (14) exact solution of the hydrodynamic equations for an infinite disk provide the following picture of the fluid motion. Far from the rotating disk, the fluid moves towards the disk, and in a thin layer immediately adjacent to its surface, the liquid acquires a rotating motion. The angular velocity of the fluid increases as the surface of the disk is approached until the angular velocity of the rotating disk is finally attained. In addition, the fluid also acquires a radial velocity under the influence of the centrifugal force. We may expect some divergence from the exact solution due to having a disk of finite radius and due to having a disk that is not flat.

When the diffusion problem was first formulated for the Cochran flow, it was assumed that the solute concentration is only a function of distance from the disk surface and not a function of radius r or the angle ϕ around the disk. However, the distribution of streamlines at a disk surface has been shown to exhibit a spiral pattern (15) such as illustrated in Fig. 11. These streamlines move across the surface, and for a flat untransforming disk, give a constant time-average momentum and solute distribution that is independent of r and ϕ. However, for a transforming interface, such as we have under consideration, we must consider that rotating spiral-shaped oscillations of the momentum and solute boundary layers occur to influence the local growth conditions. In addition, since the spiral arms of the solute distribution are more widely spaced as r increases, the concentration fluctuation that sweeps across the interface like a constitutional supercooling wave is largest at large r.

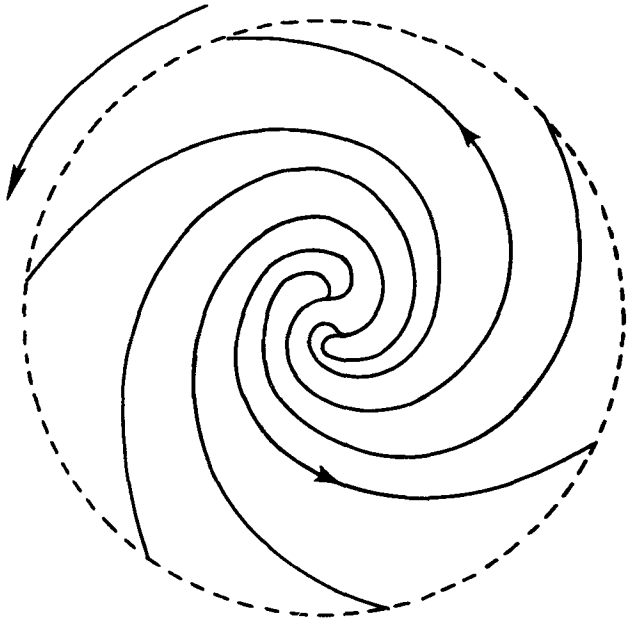

Fig. 11. Spiral streamlines at the surface of a rotating disk

Combining the above with the section on interface attachment, we can expect that the rotating concentration fluctuation acts somewhat like a trigger to release the adsorption-locked layer at point e of the interface (see Fig. 10). Thus, the amount of adsorption-induced undercooling needed before layer movement is stimulated decreases with increasing r so that the striation spacing should be less at larger r. Of course, some allowance must be made for interface shape effects.

The present model suggests that, at decreasing $C_L(\infty)$, the driving force for triggering the layer motion decreases, and if the absorption of a minor constituent is fixed, striations will still occur but will be erratically spaced because of the reduced trigger stimulus. If adsorption also decreases with $C_L(\infty)$, the entire striation effect should disappear. Of course, one should also expect to see some spiral solute patterns even without adsorption for such a postulated streamline pattern. Some of the results of Gatos and Witt (1-5) tend to support this expectation. In addition, for a pure melt, the fluctuations of the momentum-boundary layer will affect the temperature distribution slightly and will give rise to small but regular fluctuations of interface temperature.

Acknowledgment

This work was supported by the U. S. Air Force Office of Scientific Research, Grant No. AFOSR-72-2206.

Manuscript submitted June 12, 1972; revised manuscript received Aug. 18, 1972.

Any discussion of this paper will appear in a Discussion Section to be published in the December 1973 JOURNAL.

REFERENCES

1. K. Morizane, A. F. Witt, and H. C. Gatos, *This Journal*, **113**, 51 (1966).
2. A. F. Witt and H. C. Gatos, *ibid.*, **113**, 808 (1966).
3. K. Morizane, A. F. Witt, and H. C. Gatos, *ibid.*, **114**, 738 (1967).
4. K. Morizane, A. F. Witt, and H. C. Gatos, *ibid.*, **115**, 747 (1968).
5. A. F. Witt and H. C. Gatos, *ibid.*, **115**, 70 (1968).
6. B. Cockayne, *Phil. Mag.*, **XII**, 943 (1965).
7. A. F. Witt and H. C. Gatos, in "Semiconductor Silicon," R. R. Haberecht and E. L. Kern, Editors, The Electrochemical Society Softbound Symposium Series, New York (1969).
8. Nobuyuki Kobayashi and Tetsuya Arizumi, *Japan. J. Appl. Phys.*, **9**, 361 (1970).
9. M. G. Mil'vidski and A. V. Berkova, *Sov. Phys.-Solid State*, **5**, 374 (1963).
10. J. A. Burton, R. C. Prim, and W. P. Slichter, *J. Chem. Phys.*, **21**, 1987 (1953).
11. Hiroshi Koderer, *Japan. J. Appl. Phys.*, **2**, 212 (1963).
12. W. A. Tiller, K. A. Jackson, J. W. Rutter, and B. Chalmers, *Acta Met.*, **1**, 428 (1953).
13. J. J. Kramer and W. A. Tiller, *J. Chem. Phys.*, **37**, 841 (1962).
14. W. G. Cochran, *Proc. Cambridge Phil. Soc.*, **30**, 365 (1934).
15. V. G. Levich, "Physicochemical Hydrodynamics," p. 66, Prentice-Hall, Inc., Englewood Cliffs, N. J. (1962).

Influence of AsH_3, PH_3, and B_2H_6 on the Growth Rate and Resistivity of Polycrystalline Silicon Films Deposited from a SiH_4-H_2 Mixture

F. C. Eversteyn and B. H. Put

Philips Research Laboratories, Eindhoven, Netherlands

ABSTRACT

The deposition rate of polycrystalline silicon from a SiH_4-H_2 mixture is significantly influenced by the addition of AsH_3, PH_3, and B_2H_6. At a deposition temperature of 680°C AsH_3 causes a decrease by a factor of 7, PH_3 causes a decrease by a factor of 2.5, while a two times higher deposition rate is obtained with B_2H_6 addition. Out of these three dopant hydrides AsH_3 and PH_3 do not affect the activation energy of the deposition reaction compared to undoped growth (37 kcal/mole). The Arrhenius plot for the deposition of silicon from a B_2H_6-SiH_4 mixture shows two activation energies: 20 kcal/mole at T = 620°-900°C and 7 kcal/mole below 620°C. The experimentally found minimum values of the resistivity of doped polycrystalline silicon can be explained in terms of solid solubility and carrier mobility. At deposition temperatures below 700°C with and without addition of dopants the polycrystalline silicon surface is mirror-like. Significant differences have, however, been observed by electron microscopy. Compared to undoped growth boron was found to lower the etch rate of the polycrystalline silicon film markedly.

Increasing interest is being shown in the use of polycrystalline silicon in silicon device technology. The application of polycrystalline silicon films is compatible with silicon device processing where polycrystalline silicon is mainly used as gate material in MOS structures (1) (self-aligned gate).

Polycrystalline silicon can be deposited in different ways: by evaporating, by sputtering, and by chemical vapor deposition. Chemical vapor deposition is superior because it permits uniform deposition over oxide steps. To obtain a mirror-like surface, which enables very fine patterns to be etched in it, comparable with those in silicon oxide, the grain size of the polycrystalline silicon film should be as small as possible. DeLuca (2) has found that the grain size of the polycrystalline silicon film decreases with decreasing temperature. However, the deposition rate also decreases with decreasing temperature. At 650°-690°C an acceptable compromise between growth rate and grain size is realized. In this temperature region most polycrystalline silicon films suitable for high resolution I.C. processing are grown.

In the case where polycrystalline silicon is used as the gate material for MOS structures, it may be deposited undoped and subsequently doped by impurity diffusion. In the case where design considerations prohibit high-temperature processing after polycrystalline silicon deposition, doping by codeposition becomes necessary.

The present paper reports on the growth of doped polycrystalline silicon films by codeposition of silicon and either arsenic, phosphorus, and boron from the corresponding hydrides using hydrogen as a carrier gas. In particular the temperature dependence of the growth rate was studied. The effects of deposition temperature and dopant concentration on growth rate and resistivity are discussed.

Experimental

The polycrystalline silicon films were prepared in an uncooled vertical reactor. The substrates were positioned on a circular graphite susceptor coated with pyrographite. A pancake-shaped rf coil was placed on top of the flat-bottomed cylindrical silica bell jar. The distance between the rf coil and the susceptor was about 13 mm. Before deposition the susceptor was coated with silicon. During the deposition process the susceptor was rotated and the gases entered the reactor through a silica injection tube containing slits which were positioned 5 mm above the susceptor. The gas supply unit permitted the injection of any appropriate mixture of palladium-diffused hydrogen, hydrogen containing 5% SiH_4, hydrogen containing 200 ppm B_2H_6, hydrogen with 250 ppm PH_3, and hydrogen with 300 ppm AsH_3. The silane concentration in the reactor was kept below the value where homogeneous gas-phase decomposition occurred (3). The temperature of the silicon slices was measured with an Ircon 600 radiation thermometer corrected for emissivity of silicon and absorption of silica wall (emittance 63%).

The substrates were mechanically polished silicon slices partially covered with silicon oxide. Before each experiment the substrates were cleaned for 15 min in a boiling mixture of 2 parts H_2SO_4 (sp gr 1.84) and 1 part H_2O_2 (30%), rinsed in deionized water, and then spun dry.

The thickness of the polycrystalline silicon film deposited on silicon oxide was measured with a Taylor-Hobson Talysurf after the polycrystalline silicon on silicon oxide had been locally removed. This was done by masking and subsequent etching of the polycrystalline silicon in an etch mixture containing 1 part HF (49%) and 1 part CrO_3 solution (500g CrO_3 in 1000 ml water). At room temperature the etch rate of undoped polycrystalline silicon deposited in the temperature range of 590°-1050°C amounts to 2-5 μm/min, which markedly differs from the etch rate of silicon oxide in this etch mixture which is 0.18 μm/min. The thickness of the polycrystalline silicon film deposited on silicon was determined from the step height between the polycrystalline silicon deposited on silicon and the silicon substrate. For this purpose, near the oxide step present at the substrate surface, the polycrystalline silicon deposited on silicon oxide was locally removed followed by subsequent etching of the underlying silicon oxide with HF.

A big difference in etch rate between silicon oxide and polycrystalline silicon in the above-mentioned etch mixture has also been observed for polycrystalline silicon deposited in the presence of AsH_3 and PH_3. However, polycrystalline silicon films grown in the presence of B_2H_6 show a much lower etch rate of 0.2 μm/min in this etch mixture. For these layers the thickness was measured by beveling (4). The resistivity of the polycrystalline silicon films was determined by using the four-point probe technique.

Key words: polycrystalline silicon, doping, activation energy, thin films, silane.

Results

The growth rate of polycrystalline silicon from a SiH_4-H_2 mixture varies linearly with the SiH_4 concentration. This is also the case when dopants are added. Thereby the thickness increases linearly with deposition time and no induction period has been observed. No difference is found in the deposition rate of polycrystalline silicon on silicon and on silicon oxide. For all experiments the growth is expressed in microns per minute per percentage SiH_4 in the carrier gas, because the experiments have not all been carried out at the same SiH_4 concentration. This normalized value of the growth rate characterizes the deposition rate at a certain temperature since the growth rate varies linearly with the SiH_4 concentration.

The growth rate of undoped polycrystalline silicon at a deposition temperature of 680°C amounts to 0.1 μm/min % SiH_4. The resistivity of these layers is so high that it can be measured only on polycrystalline silicon films over 1.5 μm thick. Values over 500 ohm-cm are obtained. This value does not change on subsequent heat-treatment at 1150°C.

Effect of dopant addition.—When to the SiH_4-H_2 mixture one of the hydrides of As, P, or B is added, the growth rate/% SiH_4 varies as a function of the ratio of dopant atoms at silicon atoms in the gas phase as represented in Fig. 1-3, for a deposition temperature

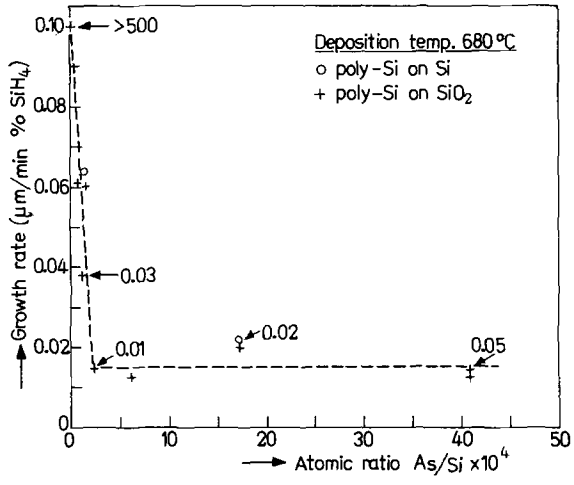

Fig. 1. Influence of addition of AsH_3 on the growth rate and resistivity of polycrystalline silicon deposited at 680°C. The numbers given in this figure represent the values of the resistivity in ohm-cm. $P_{SiH_4} = 0.36 \times 10^{-2}$ atm.

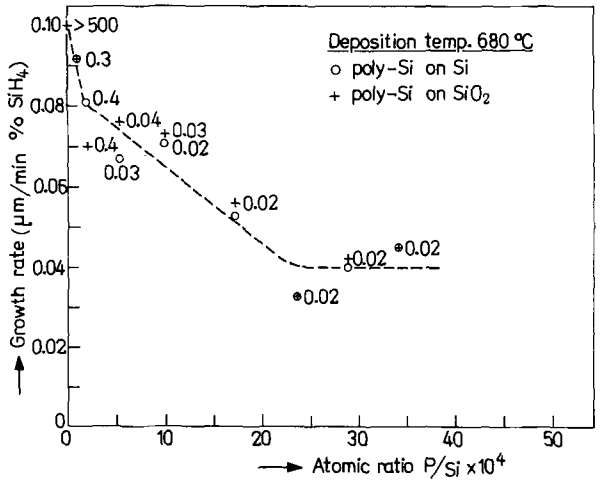

Fig. 2. Influence of PH_3 addition on the growth rate and resistivity of polycrystalline silicon layers deposited at 680°C. The numbers given in this figure represent the values of the resistivity in ohm-cm. $P_{SiH_4} = 0.36 \times 10^{-2}$ atm.

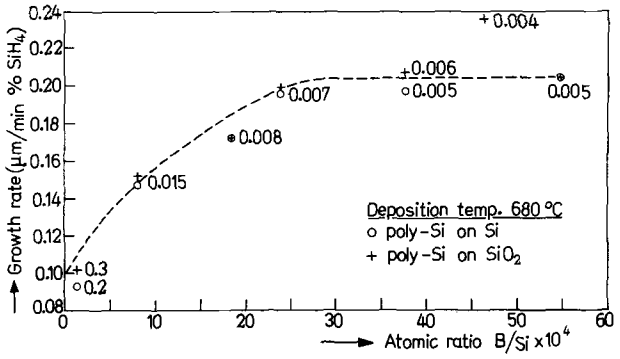

Fig. 3. Influence of B_2H_6 addition on the growth rate and resistivity of polycrystalline silicon layers deposited at 680°C. The numbers in this figure represent the values of the resistivity in ohm-cm. $P_{SiH_4} = 0.36 \times 10^{-2}$ atm.

of 680°C. It turns out that the observed decrease in growth rate compared to undoped growth is the most pronounced for AsH_3 (factor of 7) and less pronounced for PH_3 (factor of 2.5). For B_2H_6 an increase in growth rate by a factor of 2 is found.

The resistivity of the polycrystalline silicon films decreases with dopant addition in that region where dopant addition also influences the deposition rate and remains at a constant level where dopant addition does not influence the growth rate.

The surface quality of the polycrystalline silicon films is not influenced by the addition of dopants. Only at high B_2H_6 concentration ($B/Si > 35 \cdot 10^{-4}$) the surface becomes rough, probably due to the high deposition rate.

Influence of deposition temperature.—For these experiments the atomic ratio of dopant atoms to silicon atoms in the gas phase was chosen in the region where growth rate is practically independent of this value (see Fig. 1-3). Figure 4 gives the results of these experiments.

It appears that for undoped growth the deposition rate is not temperature dependent at temperatures over 830°C. When B_2H_6, PH_3, or AsH_3 are added to the gas stream the temperature at which temperature-dependent growth passes into temperature-independent growth increases. This is most striking for AsH_3. For undoped growth as well as for growth in the presence of AsH_3 and PH_3 the temperature-dependent growth can be described with an activation energy of 37 kcal/mole. For B_2H_6, however, the region of temperature-dependent growth can be divided into two parts: a region from 900°-620°C with an activation energy of

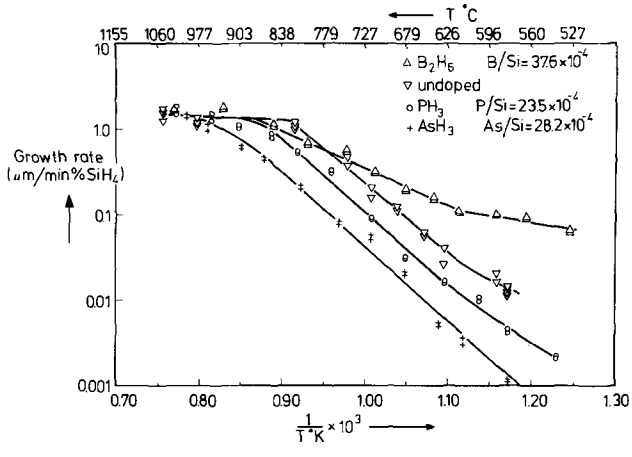

Fig. 4. Influence of deposition temperature on the growth rate of polycrystalline silicon films without and with additional doping of AsH_3, PH_3, and B_2H_6.

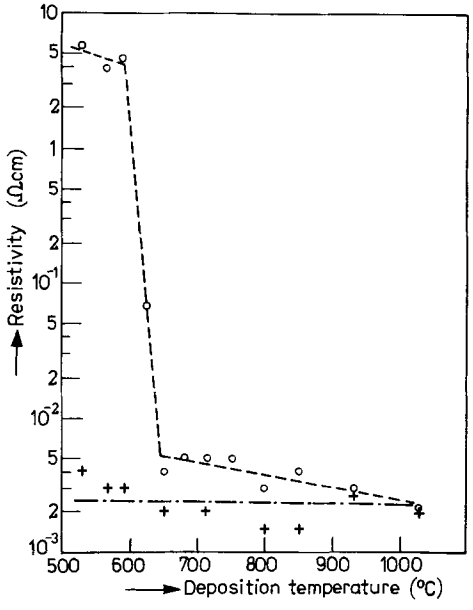

Fig. 5. Resistivity of polycrystalline silicon layers deposited from a SiH_4-H_2 mixture with the addition of B_2H_6 during growth before (O) and after (+) an additional heat-treatment for 30 min at 1150°C in H_2 as a function of deposition temperature. B/Si ratio in the gas phase: 37.6×10^{-4}.

20 kcal/mole and a region below 620°C with an activation energy of 7 kcal/mole. Although less pronounced a lower value of the activation energy below 620°C has also been observed for PH_3 and for undoped growth.

The resistivity of boron-doped polycrystalline silicon films as a function of deposition temperature is given in Fig. 5. The resistivity of as-grown polycrystalline silicon changes significantly at a deposition temperature of 620°C. Below 620°C a much higher value of the resistivity is obtained compared to deposition above 620°C. This difference, however, disappears after an additional heat-treatment for 30 min at 1150°C.

The surface quality of the layers changes with deposition temperature. Below 700°C a mirror-like surface is obtained with and without dopant addition when the deposition rate is kept below 0.07 μm/min. At deposition temperatures over 700°C the surface of the film gradually becomes rough, whether doped or not.

Discussion

In the experiments described in this paper all the substrates were treated before deposition in a boiling mixture of hydrogen peroxide and sulfuric acid followed by a rinsing treatment in deionized water which leaves an oxide film of about 15Å (5) on the silicon substrate. The hydrogen treatment in the reactor before deposition during the warming-up period does not result in an oxide-free silicon surface and a reaction between the oxide present on the silicon slice and the underlying silicon to produce the volatile SiO is not to be expected either (6). This means that no difference in the early stage of deposition on silicon and on silicon oxide should be expected because, in both cases, the silicon is covered with oxide. This was experimentally verified. It has been found by Kramer (7) that the presence of this thin oxide layer between mono- and polycrystalline silicon does not result in a higher contact resistance.

A great influence is observed on the growth rate when dopants (AsH_3, PH_3, B_2H_6) are added to the SiH_4-H_2 mixture from which the deposition of polycrystalline silicon is carried out as represented in Fig. 1-4

Without dopant addition as well as with the addition of AsH_3, the growth rate in the temperature-dependent region can be described with an activation energy of 37 kcal/mole as also has been found by Joyce and Bradley (8) for the growth of undoped silicon. If the deposition rate G is determined by reaction kinetics at the surface of a substrate then according to $G = A \exp(-E/RT)$ (9) the effect of AsH_3 on the deposition rate must be attributed to a decrease of A. The pre-exponential factor A represents the density of nucleation or growth sites and consequently, the effect of arsenic on the growth of polycrystalline silicon appears to be a blocking of the growth sites as also has been concluded by Farrow and Filby (10). A difference in growth mechanism can also be observed from electron micrographs. In Fig. 6 electron micrographs produced with the carbon-carbon replica technique are given for a polycrystalline silicon layer deposited without extra dopant addition and with the addition of AsH_3. Both layers have been deposited at the same deposition temperature and the layer thickness is, in both cases, nearly the same. A clear difference in surface texture is found. In the case of polycrystalline silicon layers deposited without dopant addition a smooth sur-

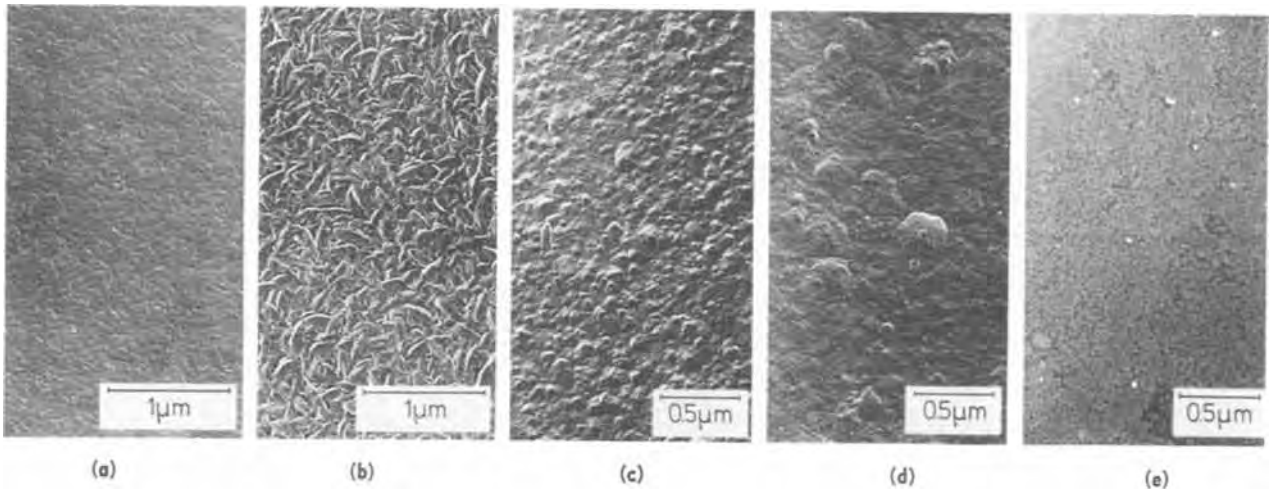

Fig. 6. Carbon-carbon replica electron micrographs of polycrystalline silicon deposited from SiH_4 without additional doping and deposited in the presence of PH_3, AsH_3, and B_2H_6. Substrate: oxidized silicon. a, Without addition of dopants. Layer thickness 0.59 μm; deposition temperature 680°C. b, With AsH_3 addition. As/Si ratio in the gas phase 41×10^{-4}; layer thickness 0.74 μm; deposition temperature 680°C. c, With PH_3 addition. P/Si ratio in the gas phase 34×10^{-4}; layer thickness 0.65 μm; deposition temperature 680°C. d, With B_2H_6 addition. B/Si ratio in the gas phase 54.8×10^{-4}; layer thickness 0.75 μm; deposition temperature 680°C. e, With B_2H_6 addition. B/Si ratio in the gas phase 37.6×10^{-4}; layer thickness 2.15 μm; deposition temperature 530°C.

face is obtained which is not the case when the film is doped with arsenic. Here a faceted growth is observed which confirms the aforementioned blocking action of arsenic on the growth of polycrystalline silicon.

The influence of PH_3 is similar to that of AsH_3. However, the magnitude of the effect is less. While AsH_3 addition causes a decrease in the growth rate by a factor of 7 (see Fig. 1) the maximum effect observed with PH_3 is a decrease by a factor of 2.5 in the growth rate when the deposition temperature in both cases is 680°C (see Fig. 2). The electron micrograph also looks like the one obtained with AsH_3 as regards its surface roughness (see Fig. 6). Only the effect on surface roughness is less than in the case of AsH_3. It should be noted that although polycrystalline silicon layers doped with AsH_3 and PH_3 have a rather rough surface on electron micrographs, the surface looks mirror-like and visually cannot be distinguished from mechanically polished silicon slices.

The addition of B_2H_6 during deposition of polycrystalline silicon causes the opposite effect from that obtained with AsH_3 or PH_3. As given in Fig. 3 at a deposition temperature of 680°C, B_2H_6 addition to the gas stream increases the deposition rate by a factor of 2. By determining the growth rate as a function of deposition temperature, when B_2H_6 is added, we observe a decrease in activation energy compared to undoped growth or doping during growth with PH_3 and AsH_3. In the temperature region of about 620°-900°C the deposition rate of polycrystalline silicon grown in the presence of B_2H_6 can be described with an activation energy of 20 kcal/mole while a much lower value of 7 kcal/mole is found below 620°C.

The change in activation energy compared to undoped growth can be explained by a structural change of the polycrystalline silicon film due to the presence of boron. This is supported by the observation that polycrystalline silicon films deposited in the presence of B_2H_6 show a much lower etch rate (10 times) in a CrO_3-HF solution compared to undoped layers or layers deposited with AsH_3 or PH_3 addition. The experimental result that above and below 620°C another value of the activation energy is found, means that there should be also a change in film structure near this temperature.

The electron micrographs of polycrystalline silicon layers deposited in the presence of B_2H_6 at temperatures of 680° and 530°C are represented in Fig. 6. Compared to polycrystalline silicon deposited in the presence of PH_3 and AsH_3 it is significant that B_2H_6 addition during growth results in a smoother surface texture.

The resistivity of polycrystalline silicon deposited in the presence of AsH_3, PH_3, and B_2H_6 has been given in Fig. 1-3 and 5. It has been observed that at a certain deposition temperature there is a region in which the addition of more dopant in the gas phase gives no decrease in the resistivity of the deposited layer. From the solid solubility data and taking into account the lower value of the mobility in polycrystalline silicon the lowest value of the resistivity can be calculated. The results are given in Tables I and II for polycrystalline silicon deposited between 700° and 1000°C in the presence of PH_3 and B_2H_6. As can be seen from the results given in Table I and II the experimental value of the resistivity is close to the calculated value. This means that the minimum observed value of the resistivity of polycrystalline silicon layers deposited between 700° and 1000°C in the presence of PH_3 or B_2H_6 can be explained with the solid solubility data of P and B in polycrystalline silicon in accordance with the results of Cowher and Sedgwick (16). Below a deposition temperature of 620°C we observe in the case of B_2H_6 addition a sharp increase in resistivity (see Fig. 5). This can be ascribed to a sharp decrease in carrier mobility, as found by Ford (17), due to a change in film structure near this temperature. This effect disappears after an additional heat-treatment for 30 min at 1150°C probably due to a structural change of the polycrystalline silicon film.

Table I. Resistivity of polycrystalline silicon layers deposited from SiH_4 in the presence of B_2H_6

Deposition temp (°C)	Solid solubility (11) (cm^{-3})	μ mono-Si / μ poly-Si (12)	Expected value (ohm-cm)	Experimental value (ohm-cm)
1000	1.8×10^{20}	1.3	1×10^{-3}	1×10^{-3}-2×10^{-3}
900	1.1×10^{20}	1.3	2×10^{-3}	3×10^{-3}-4×10^{-3}
800	5×10^{19}	1.3	3×10^{-3}	3×10^{-3}-4×10^{-3}
700	1.8×10^{19}	1.3	8×10^{-3}	4×10^{-3}-5×10^{-3}

Table II. Resistivity of polycrystalline silicon layers deposited from SiH_4 in the presence of PH_3

Deposition temp (°C)	Solid solubility (cm^{-3})	μ mono-Si / μ poly-Si (16)	Expected value (ohm-cm)	Experimental value (ohm-cm)
1000	10^{21} (13)	7	2×10^{-3}	3×10^{-3}
900	6×10^{20} (13)	7	2.2×10^{-3}	5×10^{-3}
850	4×10^{20} (14)	7	2.6×10^{-3}	5×10^{-3}
800	1.5×10^{20} (15)	7	4.2×10^{-3}	6×10^{-3}

For polycrystalline silicon layers doped during growth with AsH_3 the minimum value of the resistivity cannot be calculated since no data concerning the solid solubility of arsenic in silicon below 1000°C are available. However, postulating that also for arsenic-doped polycrystalline silicon the minimum value of the resistivity can be calculated from solid solubility and mobility, as is the case for B and P, the solid solubility of arsenic in silicon can be calculated from the values of the resistivity at different deposition temperatures. This results in solid solubility values of arsenic in silicon between 700° and 1000°C of 2-5 $\times 10^{19}$ cm^{-3}.

Conclusions

It is shown that at a deposition temperature of 680°C AsH_3 and PH_3 decrease the growth rate of polycrystalline silicon from a SiH_4-H_2 mixture markedly (for AsH_3 and PH_3 a factor of 7 and 2.5, respectively). Compared to undoped growth AsH_3 and PH_3 do not alter the activation energy of the deposition reaction and their effect on deposition rate is attributed to a blocking action of the growth sites. For B_2H_6 at a deposition temperature of 680°C an increase in growth rate by a factor of 2 is found. The activation energy of the decomposition reaction of SiH_4 is decreased by the addition of B_2H_6. This is explained in terms of a change in film structure due to the presence of boron. It thus seems that the polycrystalline silicon layers deposited in the presence of B_2H_6 have a denser structure compared to undoped growth or when grown in the presence of AsH_3 and PH_3.

The resistivity of the polycrystalline silicon films decreases with increasing addition of AsH_3, PH_3, or B_2H_6. The resistivity, however, reaches a minimum value which can be explained in the case of B_2H_6 and PH_3 by the solid solubility of B and P and the carrier mobility in polycrystalline silicon. The resistivity of polycrystalline silicon deposited in the presence of B_2H_6 increases markedly at temperatures below 620°C.

Acknowledgment

The authors wish to thank Mr. J. M. Nieuwenhuizen and Mrs. G. Stienstra for making the electron micrographs and Mr. J. Goorissen for critical review of the manuscript.

Manuscript submitted April 24, 1972; revised manuscript received Aug. 23, 1972. This was RNP213 presented at the Houston Meeting of the Society May 7-11, 1972.

Any discussion of this paper will appear in a Discussion Section to be published in the December 1973 JOURNAL.

REFERENCES

1. L. L. Vadasz, A. S. Grove, T. A. Rowe, and G. E. Moore, IEEE Spectrum, pp. 28-35 (October 1969).
2. R. D. DeLuca, in "Semiconductor Silicon," p. 299, R. R. Haberecht and E. L. Kern, Editors, Electrochemical Society (1970).
3. F. C. Eversteyn, *Philips Res. Repts.*, **26**, 134 (1971).
4. P. A. Schumann, in "Semiconductor Silicon," p. 682, R. R. Haberecht and E. L. Kern, Editors, Electrochemical Soc. (1970).
5. R. C. Henderson, Extended Abstracts Fall Meeting, Electrochemical Society, Cleveland, Oct. 3-7, 1971, Abstract 188.
6. B. A. Joyce and R. R. Bradley, *Phil. Mag.*, **15**, 1167 (1967).
7. R. P. Kramer, Private communication.
8. B. A. Joyce and R. R. Bradley, *This Journal*, **110**, 1235 (1963).
9. J. L. Kenty and J. P. Herth, *Surface Sci.*, **15**, 403 (1969).
10. R. F. C. Farrow and J. D. Filby, *This Journal*, **118**, 149 (1971).
11. G. L. Vick and K. M. Whittle, *ibid.*, **116**, 1142 (1969).
12. T. I. Kamins, *J. Appl. Phys.*, **42**, 4357 (1971).
13. E. Kooi, *This Journal*, **111**, 1383 (1964).
14. F. A. Trumbore, *Bell Systems Tech. J.*, **39**, 205 (1960).
15. N. K. Abrikosov, *Russ. J. Inorg. Chem.*, **7**, 429 (1962).
16. M. E. Cowher and T. O. Sedgwick, Electrochemical Soc. Meeting, Washington, D.C., May 9-13, 1971, Abstract 58.
17. K. D. Ford, R. Thomas, and S. J. Laverty, Electrochemical Soc. Meeting, Cleveland, Oct. 3-7, 1971, Abstract 172.

Arsenic Glass Source Diffusion in Si and SiO_2

M. Ghezzo* and D. M. Brown*

General Electric Corporate Research and Development, Schenectady, New York 12301

ABSTRACT

The diffusion properties of As in Si and SiO_2 using As_2O_3-SiO_2 chemical-vapor deposited glass-diffusion sources made from the oxidation of SiH_4 and AsH_3 are examined. Data on the glass-deposition rate, which decreases rapidly when the molar percentage of AsH_3 in the reactive mixture is greater than 10%, etch rates in buffered HF, and As diffusion data in O_2 and Ar ambients are presented. The As concentration where the glass becomes damaged during diffusion at 1100°C [7 mole per cent (m/o) As_2O_3 in Ar and 3 m/o As_2O_3 in O_2] is also examined.

Doped glass-diffusion sources deposited on heated Si substrates in the presence of O_2 and gaseous hydrides, SiH_4, B_2H_6, and PH_3 have been previously investigated and have been utilized for semiconductor-device manufacturing (1-6). However, most As diffusions until recently have been done using sealed-capsule diffusions with As-doped Si powders (7-9).

Surprisingly, As-doped glasses have not yet received much attention except as a component of the P_2O_5-As_2O_3-SiO_2 ternary glass system discussed by Kato *et al.* (10-11), and the GeO_2-SiO_2-As_2O_3 system utilized by Abe *et al.* (12). As_2O_3-SiO_2 glasses using $AsCl_3$ and SiH_4 (13), or $AsCl_3$ and organosilanes (14-17), have been studied, but very little work has been reported using As_2O_3-SiO_2 glass-diffusion sources formed from the oxidation of SiH_4 and AsH_3. This paper describes the results of such an investigation.

Experimental Techniques

The glasses were deposited on (100) p-type 1 ohm-cm Si wafers at 500°C using SiH_4 and AsH_3, each diluted to 1% in Ar and pure O_2. Argon was used as the buffer gas at a total flow rate of 3200 cc/min. The O_2 flow rate was fixed at 80 cc/min, the 1% SiH_4 at 380 cc/min, and the 1% AsH_3 was varied between 2 and 70 cc/min. The deposition system has been described previously by Brown and Kennicott (6). The thickness of the deposited glasses was 6000 ± 200Å. Both the thickness of these glasses and the thermal oxides used to study As diffusion through SiO_2 were measured ellipsometrically.

Deposition rate.—The glass-deposition rate of As doped SiO_2 *vs.* mole per cent AsH_3 in the reactants, and mole per cent As_2O_3 in the glass, is plotted in Fig. 1 for a substrate temperature of 500°C. The rapid decrease in deposition rate for the higher concentrations is presumably caused by the inhibition of silane pyrolysis by AsH_3 as discussed by Farrow and Filby (18). A more detailed study of this phenomenon as a function of substrate temperature is shown in Fig. 2 which shows the maximum allowable mole per cent AsH_3 curve for observable film deposition (growth rate ≧ 50 Å/min). This feature limits the practical

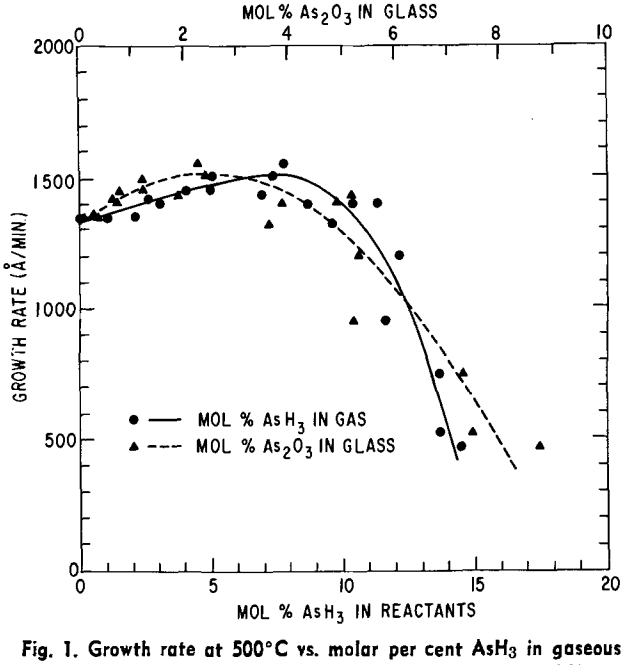

Fig. 1. Growth rate at 500°C vs. molar per cent AsH_3 in gaseous reactants and molar per cent As_2O_3 in glass. Flow rate of 1% argon-diluted mixture of SiH_4 is kept constant at 380 cc/min.

* Electrochemical Society Active Member.

Key words: arsenosilicate glass, diffusion, glass damage, arsine, silicon, silicon oxide.

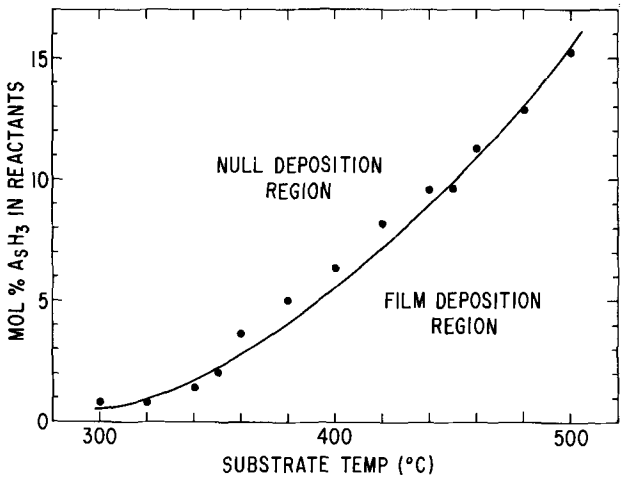

Fig. 2. Maximum molar percentage of AsH_3 in the reactive mixture for obtaining film deposition *vs.* substrate temperature. Flow rate of 1% argon-diluted mixture of SiH_4 is kept constant at 380 cc/min.

attainment of As_2O_3 concentration to about 10 mole per cent (m/o) using this system. Concentrations as high as 20 m/o have been attained using the $AsCl_3/SiH_4/O_2$ system (13).

As_2O_3 concentration.—An *IR* calibration curve for these glasses in terms of glass composition is plotted in Fig. 3. This curve given by Wong and Ghezzo (13) applies equally well to arsenosilicate glasses prepared from oxidation of silane and arsine as it was experimentally verified in some samples. Use of this curve allows a fast and accurate determination of the As_2O_3 concentration in glasses made from different mole per cent AsH_3 in the reactants by measuring the absorption-band peak ratio of the As-O 930 cm^{-1} vibration to the Si-O 1060 cm^{-1} vibration in the glasses as deposited. Besides, Fig. 3 provides experimental information on the correlation between the molar percentage of AsH_3 in the reactants and the molar percentage of As_2O_3 in the glass, appearing roughly

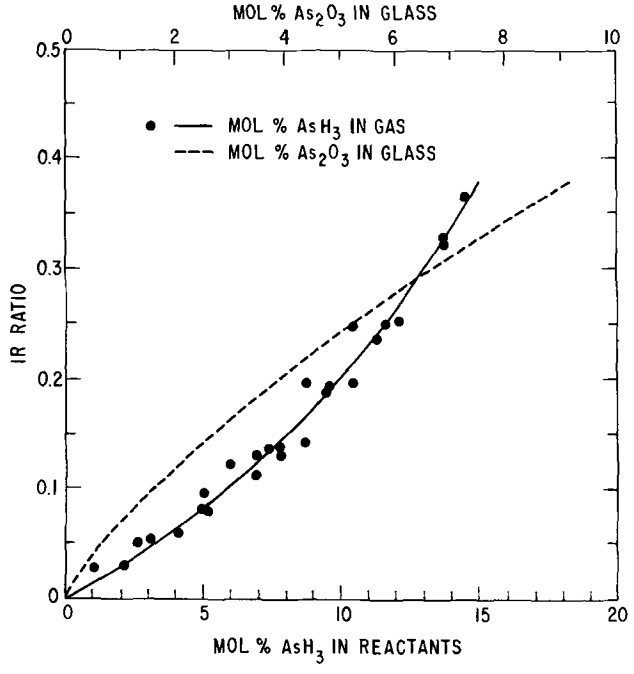

Fig. 3. Ratio of absorbance of the As-O band at 930 cm^{-1} to that of Si-O band at 1060 cm^{-1} of as-deposited arsenosilicate glasses (*IR* ratio) *vs.* molar per cent AsH_3 in gaseous reactants and molar per cent As_2O_3 in glass [after J. Wong and M. Ghezzo, Ref. (13)].

in a 2:1 ratio, as expected according to the molecular formula of these compounds and a complete oxidation of AsH_3 and SiH_4.

Etch rate.—The etch rate in buffered HF after glass densification at 1100°C in argon is plotted *vs.* As concentration in Fig. 4. A nearly two-fold increase in the dissolution rate with increasing As concentration up to 8 m/o As_2O_3 is observed. The rates are comparable to that of undoped SiO_2 and these glasses are therefore easily patterned using standard photoresist techniques.

Glass damage.—N-type glass-diffusion sources are much more susceptible to mechanical damage than the p-type borosilicate glasses for a number of reasons. The phosphosilicate and probably the arsenosilicate glass systems do not form a continuous range of solid solutions like the borosilicate system, as indicated from a comparison of their phase diagrams (19, 20). Hence there is a much greater tendency for phase separation and crystallization especially at high concentrations. These glasses also have a greater tendency to crack or detach from the Si substrate because of a greater degree of thermal mismatch with Si. This problem has been discussed by Arai and Terunuma (17) and studied by Wong (21). Some of these problems probably led to the use of the ternary glass systems used by Kato *et al.* (10) and Abe *et al.* (12).

Glass damage using the type of As glass prepared by the methods described above is observed for high concentrations of As_2O_3 after extensive heating at high temperatures. For instance, after diffusion in Ar the film which is a 7.3 m/o As_2O_3 glass shows clusters of irregular shape as shown in Fig. 5. As the concentration of As_2O_3 is reduced below 7 m/o the occurrence of these randomly scattered damaged regions is avoided completely. It is interesting to compare the nature of this damage and its threshold after heat-treatments at 1100°C in Ar with the damage in As glass films deposited with a different method. Wong and Ghezzo (13) who deposited films from an arsenic trichloride source found that damage starts at much lower concentrations (1 m/o As_2O_3) and appears as circular-interference fringes (Fig. 6) which are due to glass detachment from the substrate. Hence for As glasses the degree and nature of the damage depends on the glass-film preparation method.

The use of O_2 instead of Ar as the diffusion ambient changes the nature of the damage as shown in Fig. 7 where a 3.9 m/o As_2O_3 glass shows isolated crystalline clusters about 40μ in diameter which are at least five times larger than those in Fig. 5. Wherever damage in the glass occurs, associated damage in the underlying Si also occurs. The onset of damage is reduced for diffusion in O_2 at 1100°C to 3 m/o As_2O_3 while in Ar this limit is 7 m/o as stated above. The glass dam-

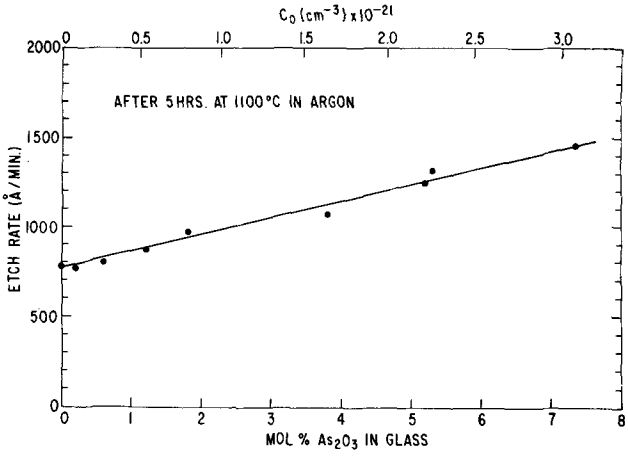

Fig. 4. Etch rate in buffered HF of arsenosilicate glasses after densification in argon at 1100°C, *vs.* molar per cent As_2O_3 and As concentration in the glass.

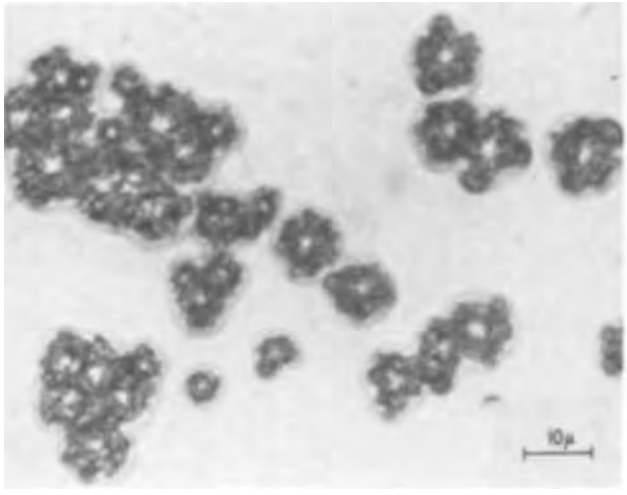

Fig. 5. Micrograph of arsenosilicate glass surface deposited from an arsine source on silicon after heat-treatment in argon at 1100°C for 5 hr. Damage appears in the form of clusters of irregular shape. Mole per cent As_2O_3 in the as-deposited glass is 7.3 (*IR* ratio = 0.32).

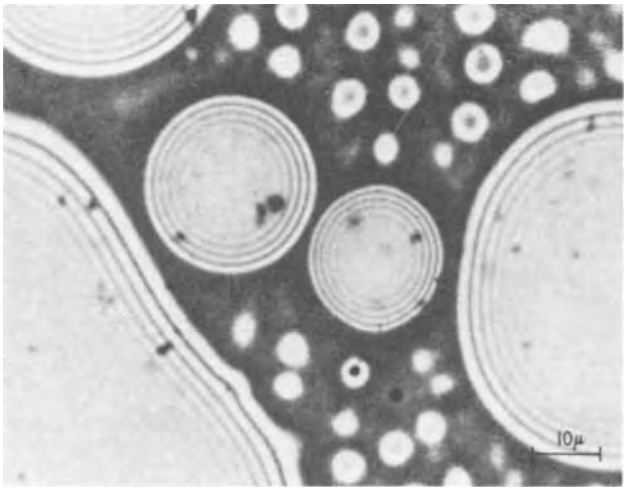

Fig. 6. Micrograph of arsenosilicate glass surface deposited from an arsenic trichloride source on silicon after heat-treatment in argon at 1000°C for 10 min [Ref. (21)]. Damage appears in the form of circular interference fringes due to lifting of the glass film on the substrate. Mole per cent As_2O_3 in the as-deposited glass is 3.6 (*IR* ratio = 0.19).

age region is noted on several of the diffusion data curves that follow.

Diffusion properties.—Arsenic diffusion from these glass sources in Si and through thin SiO_2 layers was done at 1100°C in Ar and O_2. These studies are presented in two groupings: (*i*) diffusion in Ar or O_2 without barrier oxides, and (*ii*) diffusion in Ar or O_2 through barrier oxides. Since As is a slow diffusant in Si, junction depths were about 1μ using a diffusion time of 5 hr at 1100°C. Diffusion through thermal SiO_2 and into bare Si was in most cases measured simultaneously by starting with thermally oxidized wafers, removing the oxide from half of the wafer's surface and then coating the entire wafer with doped glass. Glass damage occurring after diffusion was also monitored, and as discussed previously, generally no glass damage occurs for Ar or O_2 diffusions when the glass contains less than 7 or 3 m/o As_2O_3, respectively.

Diffusion in Si in Ar and O_2 ambients.—Sheet resistance, R_s, and junction depth, x_j, *vs.* mole per cent As_2O_3 in the glass for glass diffusions in Ar on bare Si are shown in Fig. 8. x_j shows essentially no variation with concentration which indicates that the diffusion constant is relatively invariant for the range of surface concentrations covered here (1 to 6 × 10^{19}/cc), as shown in Fig. 9, whose data were obtained from those of Fig. 8 assuming a complementary error-function concentration profile. This method of data reduction is approximate, because the complementary error function does not match the As diffusion profiles in Si (22, 23), but was used here because of the absence of another well-established model. The diffu-

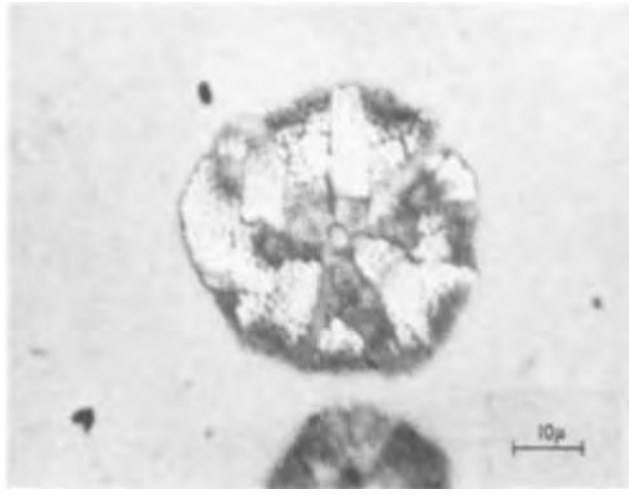

Fig. 7. Micrograph of arsenosilicate glass surface deposited from an arsine source on silicon after heat-treatment in oxygen at 1100°C for 5 hr. Damage appears in the form of individual crystalline clusters with a diameter of about 40μ. Mole per cent As_2O_3 in the as-deposited glass is 3.9 (*IR* ratio = 0.20).

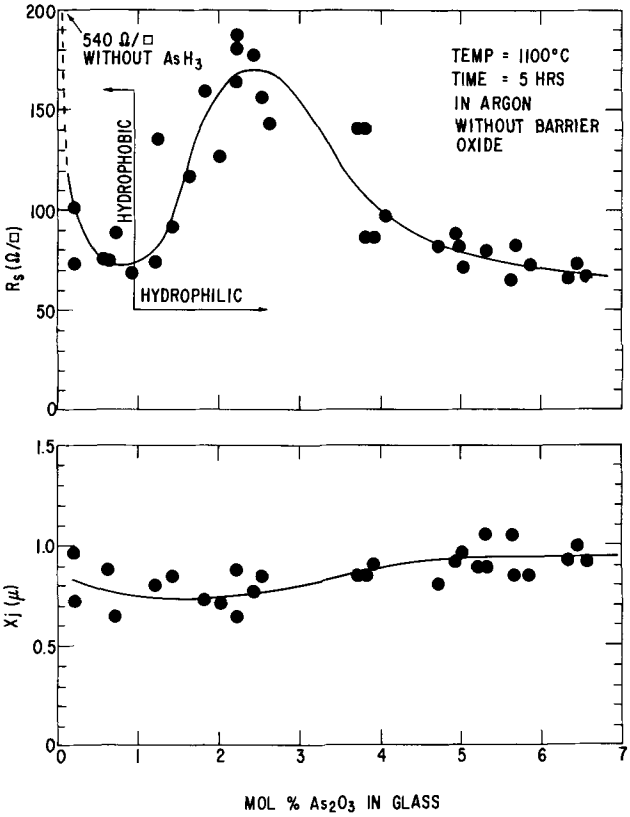

Fig. 8. Sheet resistance, R_s, and junction depth, x_j, of the diffused layers in Si *vs.* molar per cent As_2O_3 in the glass after diffusion in argon for 5 hr at 1100°C with the As-doped glass in contact with Si. After removal of all the glass in HF the silicon surface appears hydrophobic for As_2O_3 concentrations lower than 1 m/o and hydrophilic for higher concentrations.

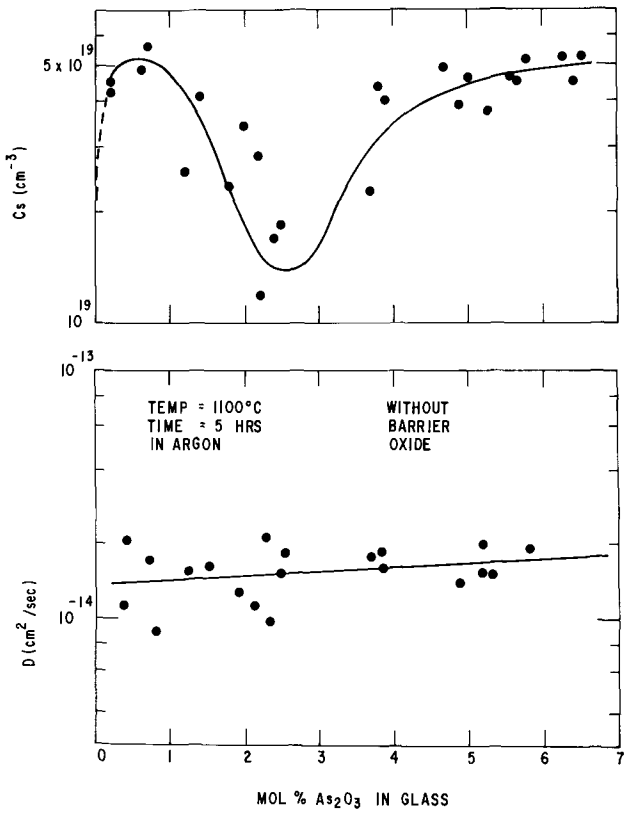

Fig. 9. Surface concentration, C_s, and diffusion coefficient, D, in Si at 1100°C in argon vs. molar per cent As_2O_3 in the glass as computed from the R_s and x_j data of Fig. 8 assuming a complementary error-function diffusion profile.

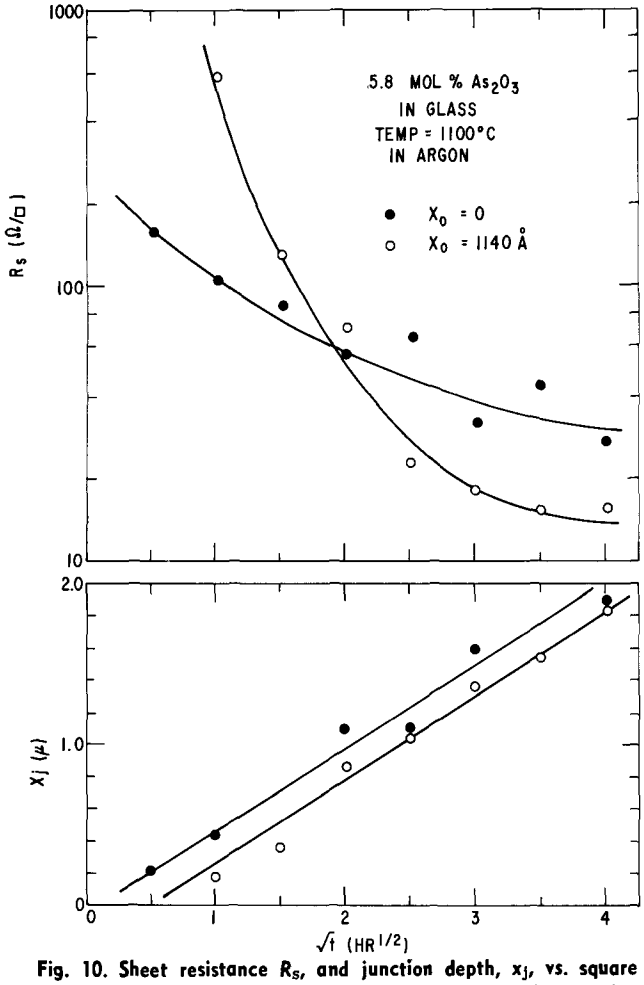

Fig. 10. Sheet resistance R_s, and junction depth, x_j, vs. square root of diffusion time after diffusion in argon at 1100°C from an As-doped glass of 5.8 m/o As_2O_3 in contact with Si ($x_o = 0$) or separated by a barrier thermal oxide of thickness $x_o = 1140$Å.

sion constant shown in Fig. 9 indicates values of 1.5 to 2.0 $\times 10^{-14}$ cm²/sec at 1100°C which are in good agreement with the data of Fuller and Ditzenberger (24) (2.7 $\times 10^{-14}$ cm²/sec), Armstrong (25) (2.0 $\times 10^{-14}$ cm²/sec), Raju *et al.* (26) (1.6 $\times 10^{-14}$ cm²/sec), and Masters and Fairfield (27) (2.4 $\times 10^{-14}$ cm²/sec).

The relative maximum in R_s for glass diffusion on bare Si which occurs for a 2.5 m/o As_2O_3 diffusion source is very surprising. This observation was reproduced several times by repeated experimentation, but we can offer no explanation for its occurrence. Another observation was made on these samples. After diffusion, the Si surface after glass removal in HF was hydrophobic in the region where the As_2O_3 concentration in the glass was <1 m/o but hydrophilic for greater concentrations. The hydrophilic nature of the surfaces that had been diffused using the higher concentrations of As_2O_3 in the glass suggests the presence of an insoluble surface layer. Since the surface concentrations obtained here (Fig. 9) are well below the solid-solubility limit (1.8 $\times 10^{21}$ cm^{-3}) (28) the presence of a second phase like that observed for solid solubility limited boron (29) or phosphorus (30) diffusions is unlikely. This surface layer might be free As, however, which would indicate that for diffusions in argon As is arriving at the Si-glass interface much faster than it can be absorbed by the Si.[1] The formation of an "arsenic-phase layer" was recently reported too by Parekh *et al.* (31) using arsenosilicate glass prepared by thermal decomposition and oxidation of TEOS (tetraethoxysilane) and $AsCl_3$. Plots of junction depth and sheet resistance *vs.* $t^{1/2}$ are given in Fig. 10.

Diffusions done in O_2 instead of Ar show slightly different characteristics. These data are shown in Fig. 11 and 12. Figure 11 gives x_j, R_s, C_s, and D *vs.* As_2O_3 concentration for a 5 hr 1100°C diffusion. In

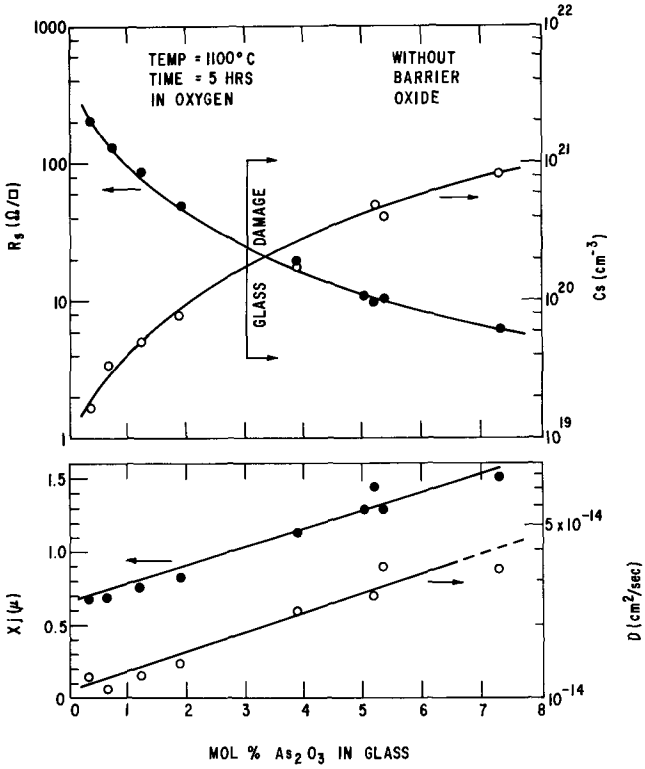

Fig. 11. Sheet resistance, R_s, junction depth, x_j, and computed values of surface concentration, C_s, and diffusion coefficient, D, vs. molar per cent As_2O_3 in the glass after diffusion in oxygen for 5 hr at 1100°C with the As-doped glass in contact with Si. Glass damage occurred for As_2O_3 concentrations higher than 3 m/o.

[1] This layer has also been observed during device fabrication and is not removed by buffered HF. However, it has been removed successfully by the use of ultrasonic cleaning. It should be noted however that the information in Fig 8 shows that this anomalous film can be avoided by using ≤ 1 m/o As_2O_3 glasses without lowering the sheet resistance.

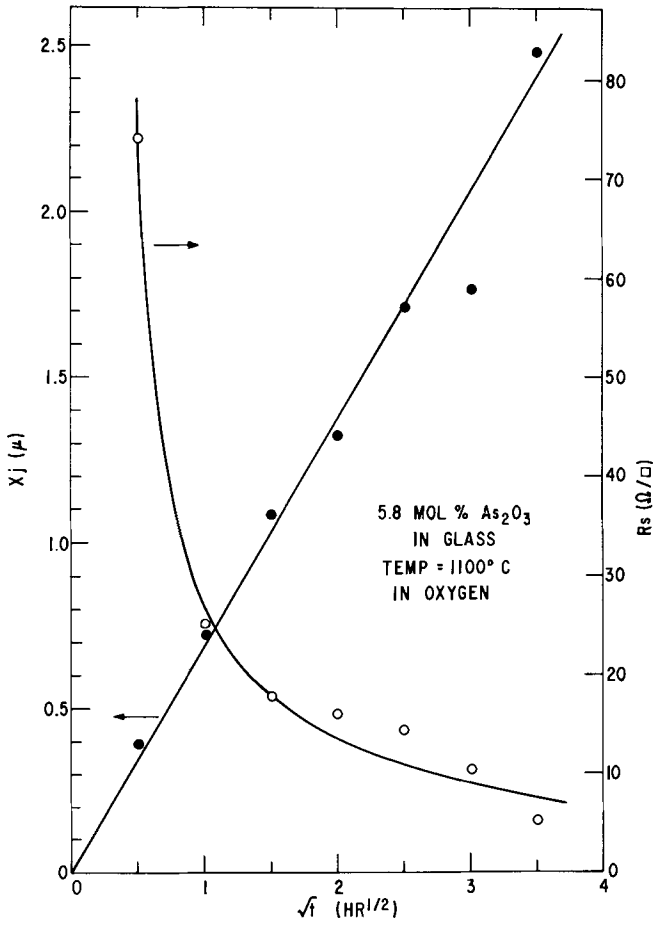

Fig. 12. Sheet resistance, R_s, and junction depth, x_j, vs. square root of diffusion time after diffusion in oxygen at 1100°C from an As-doped glass of 5.8 m/o As_2O_3 in contact with Si.

comparison with Fig. 8, the junction depth in Fig. 11 for low As_2O_3 concentrations is again about 0.7μ but increases to 1.5μ at 7 m/o As_2O_3. Normal monotonic changes in sheet resistance are also shown in Fig. 11 together with surface concentration and diffusion-constant data obtained assuming a complementary error function. An increase in the diffusion constant at 1100°C from 1.0×10^{-14} to 3.5×10^{-14} cm^2/sec in the 10^{19} to 10^{21}/cc surface-concentration range is observed. Finally, Fig. 12 gives the junction depth and sheet resistance *vs.* the square root of diffusion time using a 5.8 m/o glass source.

Diffusion in SiO_2.—Diffusivity of the As carrying species through SiO_2 was studied in the same manner as that used for As diffusions on unoxidized Si. A study of surface concentration *vs.* mole per cent As_2O_3 in the glass was carried out and separate experiments were utilized to determine the diffusivity in SiO_2 using the mathematical model of Sah *et al* (32). Here again an Ar or O_2 ambient was utilized.

Diffusion in SiO_2 in Ar ambient.—Figure 13 plots sheet resistance, surface concentration, and junction depth in the Si after diffusion through 1250Å of thermal SiO_2 *vs.* mole per cent As_2O_3 in the glass. Notice that in this instance the presence of the barrier oxide has removed the nonmonotonic changes in sheet resistance that are observed in Fig. 8. Notice also that the junction depth is only slightly decreased over those values observed in Fig. 8. This indicates that As is a relatively rapid diffuser in SiO_2 for these conditions. Similar behavior is observed in the plot of Fig. 10 where the sheet resistance and junction depth are plotted *vs.* the square root of time using data obtained from experiments utilizing a 5.8% glass and unoxidized and oxidized wafers. The penetration time for 1140Å

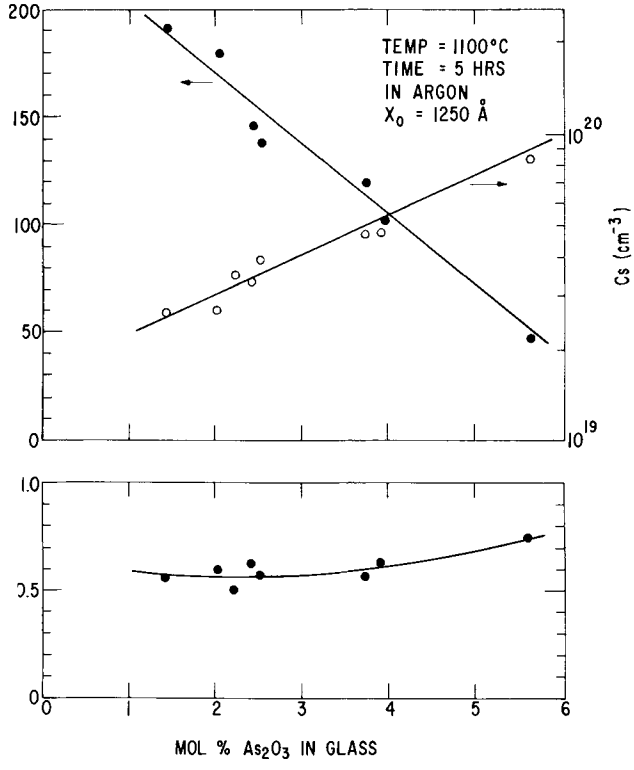

Fig. 13. Sheet resistance, R_s, junction depth, x_j, and computed surface concentration, C_s, vs. molar per cent As_2O_3 in the glass after diffusion in argon for 5 hr at 1100°C through a barrier thermal oxide layer of thickness x_o = 1250Å.

of oxide is only 0.25 hr at 1100°C. Experiments for various barrier oxide thicknesses, Fig. 14, also show the multiple behavior in R_s like that observed in Fig.

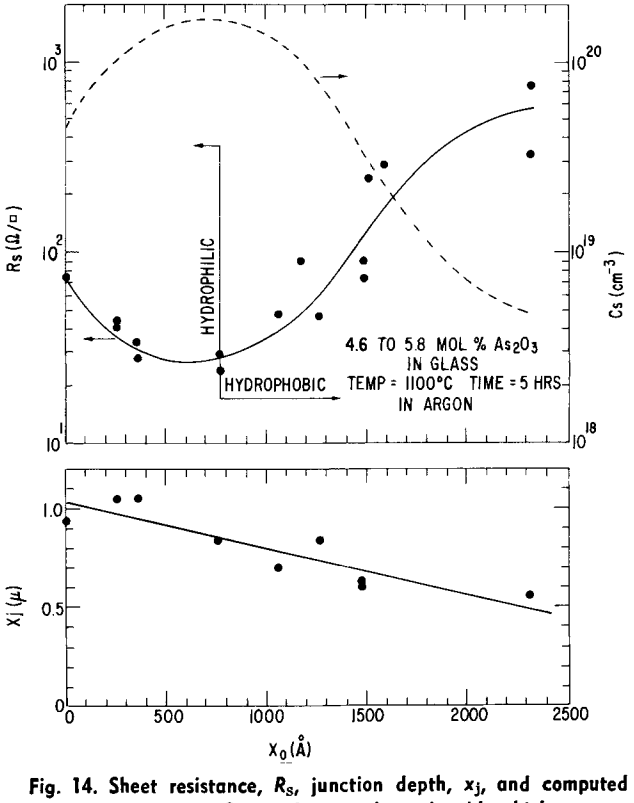

Fig. 14. Sheet resistance, R_s, junction depth, x_j, and computed surface concentration, C_s, vs. barrier thermal oxide thickness, x_o, after diffusion in argon for 5 hr at 1100°C from an As-doped glass of 4.6 to 5.8 m/o As_2O_3. After removal of all the glass in HF, the silicon surface appears hydrophilic for x_o smaller than 800Å and hydrophobic otherwise.

8 where the wafers were not oxidized. A hydrophobic-hydrophilic nature of the surfaces was also observed. Samples with less than 800Å of barrier oxide were found to have hydrophilic surfaces, whereas those above 800Å had hydrophobic surfaces after diffusion and after the glass was removed. This observation agrees with the transition that occurs with increasing As_2O_3 concentration shown in Fig. 8. The decrease of R_s with increasing oxide thickness in the 0-800Å oxide region is another surprising aspect of As glass diffusions. Teshima *et al.* (15) have observed the same phenomenon, and, in addition, recommend the use of barrier oxides to prevent the occurrence of Si surface damage during diffusion. The junction depth data in Fig. 14 were utilized to determine the diffusivity from Sah's (32) mathematical model in the same way that Brown and Kennicott (6) used similar data to determine the diffusivity of B in SiO_2. The diffusivity was determined to be 3.5×10^{-15} cm²/sec at 1100°C in Ar. As indicated in Fig. 13 there is an indication that there might be only a small concentration dependence for glasses containing up to 6 m/o As_2O_3.

Diffusion in SiO_2 in O_2 ambient.—Diffusivity data for As diffusion through barrier oxides when the diffusion is carried out in an O_2 ambient at 1100°C are shown in Fig. 15. These data give a diffusivity of 1.5×10^{-16} cm²/sec, which is smaller than that observed in Ar. This is reasonable since in Ar the diffusion species might be free As whereas in O_2 it most probably would be As_2O_3, since any reduction of As_2O_3 would be inhibited in O_2.

The fact that the glass layers were at least 6000Å thick did not preclude the build-up on Si and continuous doping of an additional 1000Å of glass during diffusion in an oxidizing ambient, with a consequent reduction in junction depth of the diffused layers due to increased thermal oxide masking thickness and movement of the SiO_2-Si boundary. Nevertheless, as the junction-depth reduction is the same for all the wafers, because they were diffused under the same conditions, the slope of x_j *vs.* x_o in Fig. 15 is

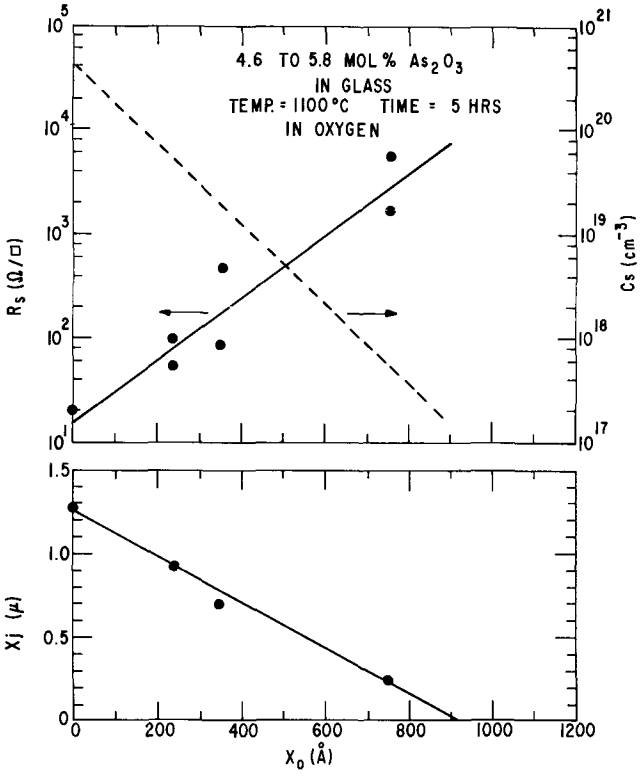

Fig. 15. Sheet resistance, R_s, junction depth, x_j, and computed surface concentration, C_s, *vs.* barrier thermal oxide thickness, x_o, after diffusion in oxygen for 5 hr at 1100°C from an As-doped glass of 4.6 to 5.8 m/o As_2O_3.

not affected by the oxide build-up and therefore this phenomenon can be neglected in the computation of the As diffusivity in SiO_2 in an O_2 ambient.

Summary and Conclusion

Arsenosilicate glass layers deposited at low temperatures (500°C) from Ar diluted mixtures of SiH_4, O_2, and AsH_3 have been investigated as As sources for As diffusion in Si and SiO_2. The film deposition rate decreased sharply for an AsH_3 concentration larger than 10% in the reactive mixture, limiting the molar percentage of As_2O_3 in the glass. Furthermore, as the deposition temperature changed, the highest AsH_3 concentration allowing film deposition changed accordingly in a monotonic relationship, dropping to only 1 m/o AsH_3 at 300°C. Etch rate of the densified films in buffered HF increased with As concentration in the glass becoming 1500 Å/min at 7 m/o As_2O_3, which is nearly twice the etch rate of pure SiO_2 (800 Å/min). Diffusion in Ar from glasses of different As_2O_3 concentrations gave anomalous results for the sheet resistivity of the diffused layers, which after an expected drop with increasing As concentration in the glass source increased again to a relative maximum corresponding to 2.5 m/o As_2O_3 before resuming the negative slope. This phenomenon did not occur in diffusions in an O_2 ambient. Arsenic concentration in the glass was found to be related to the onset of damage in the glass during heat-treatment, which for the diffusion conditions of 5 hr at 1100°C appeared at 7 m/o As_2O_3 in Ar, and at 3 m/o As_2O_3 in O_2. Besides, diffusion in O_2 enhanced the junction depth and the surface concentration of the diffused layers in comparison to similar Ar diffusions with an increase from 1.0 to 1.5μ for x_j, and from 5×10^{19} to 8×10^{20} cm^{-3} for C_s in glasses containing 7 m/o As_2O_3.

Diffusivities of As in SiO_2 were also investigated by means of diffusions at 1100°C in Ar and in O_2 ambients through thermal oxide barriers of different thickness. The results showed that the ambient is very important in determining the As diffusivity in SiO_2, because using the same glass-source composition the diffusivity in Ar was over one order of magnitude higher than in O_2 at 1100°C (3.5×10^{-15} cm²/sec in Ar *vs.* 1.5×10^{-16} cm²/sec in O_2 with a 5.8 m/o As_2O_3 glass source).

Acknowledgments

The authors thank G. Charney and R. Connery for their help in setting up and maintaining the equipment used in these experiments. They also gratefully acknowledge stimulating discussions with many coworkers, particularly M. Garfinkel, A. Tenney, and J. Wong, who contributed some important ideas included in this work.

Manuscript submitted May 5, 1972; revised manuscript received Aug. 25, 1972.

Any discussion of this paper will appear in a Discussion Section to be published in the December 1973 JOURNAL.

REFERENCES

1. A. W. Fisher, J. A. Amick, H. Hyman, and J. Scott, *RCA Rev.*, **29**, 533 (1968).
2. M. L. Barry and P. Olofsen, *This Journal*, **116**, 854 (1969).
3. W. Kern and R. C. Heim, *ibid.*, **117**, 562 (1970).
4. M. L. Barry, *ibid.*, **117**, 1405 (1970).
5. A. Mayer, K. Strater, and D. A. Puotinen, "Manufacturing Techniques for Controlled Deposition and Application of Doped Oxides," Tech. Report AFML-TR-70-191 (1970).
6. D. M. Brown and P. R. Kennicott, *This Journal*, **118**, 293 (1971).
7. W. J. Armstrong and M. C. Duffy, *Electrochem. Technol.*, **4**, 475 (1966).
8. Y. Nakajima, S. Ohkawa, and Y. Fukukawa, Abstract No. 77, p. 189, Electrochem. Soc. Extended Abstracts, Spring Meeting, Washington, D. C., May 9-13, 1971.

9. J. S. Sandhu and J. L. Reuter, *IBM J. Res. Develop.*, **15**, 464 (1971).
10. T. Kato, M. Nakamura, T. Yonezawa, and W. Watanabe, Abstract No. 118, p. 306, Electrochem. Soc. Extended Abstracts, Spring Meeting, Los Angeles, California, May 10-15, 1970.
11. M. Nakamura, T. Kato, T. Yonezawa, M. Watanabe, and S. Takei, Abstract No. 74, p. 181, Electrochem. Soc. Extended Abstracts, Spring Meeting, Washington, D. C. May 9-13, 1971.
12. T. Abe, K. Sato, M. Konaka, and A. Miyazaki, *J. Appl. Phys. (Japan), Suppl.*, **39**, 88 (1970).
13. J. Wong and M. Ghezzo, *This Journal*, **118**, 1540 (1971).
14. D. B. Lee, *Solid-State Electron.*, **10**, 623 (1967).
15. H. Teshima, Y. Tarui, and O. Takeda, *Bull. Electrotech. Lab. (Tokyo)*, **33**, 631 (1969).
16. A. Cuccia, G. Shrank, and G. Queirolo, in "Semiconductor Silicon," R. R. Haberecht and E. L. Kern, Editors, p. 506, The Electrochemical Society, Softbound Symposium Series, New York (1969).
17. E. Arai and Y. Terunuma, *Jap. J. Appl. Phys.*, **9**, 691 (1970).
18. R. F. C. Farrow and J. D. Filby, *This Journal*, **118**, 149 (1971).
19. T. Y. Tien and F. A. Hummel, *J. Am. Ceram. Soc.*, **45**, 422 (1962).
20. T. J. Rockett and W. R. Foster, *ibid.*, **48**, 75 (1965).
21. J. Wong, *This Journal*, **119**, 1080 (1972).
22. Y. Nakajima, S. Ohkawa, and Y. Fukukawa, *Japan. J. Appl. Phys.*, **10**, 162 (1971).
23. T. L. Chiu and H. N. Ghosh, *IBM J. Res. Develop.*, **15**, 472 (1971).
24. C. S. Fuller and J. A. Ditzenberger, *J. Appl. Phys.*, **27**, 544 (1956).
25. W. J. Armstrong, *This Journal*, **109**, 1065 (1962).
26. P. S. Raju, N. R. K. Rao, and E. V. K. Rao, *Indian J. Pure Appl. Phys.*, **2**, 353 (1964).
27. B. J. Masters and J. M. Fairfield, *J. Appl. Phys.*, **40**, 2390 (1969).
28. F. A. Trumbore, *Bell System Tech. J.*, **39**, 205 (1960).
29. K. M. Busen, W. A. Fitzgibbons, and W. K. Tsang, *This Journal*, **115**, 291 (1968).
30. E. Kooi, *ibid.*, **111**, 1383 (1964).
31. P.C. Parekh, D. R. Goldstein, and T. C. Chan, *Solid-State Electron.*, **14**, 281 (1971).
32. C. T. Sah, H. Sello, and D. A. Tremere, *J. Phys. Chem. Solids*, **11**, 288 (1959).

Impurity Atom Transfer during Epitaxial Deposition of Silicon

G. Skelly* and A. C. Adams*

Bell Telephone Laboratories, Incorporated, Murray Hill, New Jersey 07974

ABSTRACT

When epitaxial silicon is deposited on highly doped substrates, impurity atoms transfer from the substrate to the growing epitaxial film. This transfer, usually referred to as autodoping, may establish a lower limit on the dopant concentration in the epitaxial film and may prevent the formation of an abrupt doping profile. We have studied the transfer of arsenic during the deposition of epitaxial silicon by the pyrolysis of silane at a temperature of 1050°C. The amount of autodoping is determined from the flat portion of the doping profile and has been studied as a function of the substrate dopant concentration. The data are interpreted in terms of solid-state diffusion theory by assuming that during deposition the arsenic diffuses to the back of the substrate, evaporates from the back surface, transfers in the gas phase to the front surface, and then is incorporated into the film. Calculations indicate that 0.9% of the arsenic that evaporates from the back surface is deposited into the epitaxial film. Our results show that autodoping is linearly dependent on the substrate doping concentration and becomes significant when the arsenic concentration is greater than 2×10^{18} cm^{-3}. The autodoping can be reduced by a factor of about five by masking the back of the substrate with silicon oxide or by heating the substrate at a high temperature for a few minutes to allow the arsenic near the back surface to evaporate prior to deposition.

Many current silicon device structures require the deposition of lightly doped epitaxial layers over highly doped substrates or over highly doped diffused areas. In these structures, the transfer of dopant from the substrate to the growing epitaxial layer may be an important source of impurities in the epitaxial film. In some cases, this transfer of impurities may even establish a lower limit on the dopant concentration in the epitaxial film and may prevent the formation of an abrupt change in dopant concentration at the film-substrate interface. The dopant transfer that occurs when the epitaxial layer is formed by the hydrogen reduction of silicon tetrachloride or trichlorosilane has been reported (1-8). However, there is no detailed study of the dopant transfer when the layer is deposited by the pyrolysis of silane. In fact, it has been reported that for the silane process the transfer of dopant may not occur (9) or that the transfer can be eliminated by masking the back of the substrate with silicon oxide. (10). We have studied the transfer of dopant during the deposition of epitaxial silicon by the pyrolysis of silane for substrates doped with arsenic. The experimental results are presented and discussed in this paper.

The initial observation of a dopant transfer during epitaxial deposition from silicon tetrachloride was made by Basseches *et al.* (1) who suggested that the impurities were transferred from the back of the substrate wafer. Thomas, Kahng, and Manz (2, 3) reported that the dopant concentration in the epitaxial film decreased with distance from the interface. These authors proposed a model in which the dopant transfers from the substrate surface to the gas phase, mixes with the reactant gases, and is then incorporated into the growing film. A mathematical expression was derived which accounted for the observed impurity profiles. Grossman (4), who used the term "autodoping," derived an expression for the time dependence of the

* Electrochemical Society Active Member.
Key words: autodoping, diffusion, epitaxy, silane, silicon.

epitaxial reaction and suggested that impurities were released during a transient etching of the substrate at the beginning of the deposition. Grove *et al.* (5) studied epitaxial depositions on boron- and antimony-doped substrates, and Abe *et al.* (6) investigated autodoping in layers deposited on arsenic-doped samples. Both groups of authors concluded that the impurity profiles could be accounted for by solid-state diffusion of impurities from the substrate into the epitaxial film; autodoping effects were not required to explain the profile shape. In these previous investigations, the epitaxial layers were deposited by the hydrogen reduction of silicon tetrachloride at temperatures near 1200°C. Joyce, Weaver, and Maule (7) studied dopant transfer during the hydrogen reduction of trichlorosilane at similar temperatures using radiotracer techniques. They concluded that the proposed etch-back mechanism (2-4) was unlikely and that the impurities were transferred from the back of the substrate. They also found that autodoping was not important unless the doping level in the epitaxial layer was less than 5×10^{14} cm^{-3}. Recently, Shepherd (8) has presented a model of autodoping that assumes that impurities evaporate from the back of the substrate into the gas stream and then deposit in the epitaxial film. Gupta and Yee (10), who determined the experimental conditions necessary to obtain abrupt impurity profiles for silane-deposited epitaxial films, found that autodoping could be reduced by growing an oxide on the back of the substrate prior to the deposition.

Most previous workers have inferred the presence or absence of autodoping by comparing the shape of the doping profile with shapes calculated for thermal diffusion of impurities from the substrate into the epitaxial layer. Since it is very difficult to accurately measure and compare profile shapes, most previous studies have not given quantitative information concerning the magnitude of the autodoping effect. In addition, the dopant concentration in the substrate has not been systematically varied in many of the previous studies; consequently, there are few experimental data concerning the dopant transfer as a function of the impurity atom concentration in the substrate. In the work reported in this paper, autodoping is measured from the flat portion of the doping profile rather than from a comparison of profile shapes. In addition, autodoping has been studied for arsenic-doped substrates in which the dopant concentration ranges from 5×10^{14} to 4×10^{19} cm^{-3}.

Experimental

The epitaxial layers have been grown in a single-slice, water-cooled, vertical flow system which is induction heated using a high-purity graphite susceptor. The system has been previously described (11). The substrate, which is 3.1 cm in diameter, is mounted vertically so that the sample is approximately parallel to the gas flow. The epitaxial layers are formed by the pyrolysis of silane at an optical temperature of 1000°C. The actual temperature, obtained by correcting for emissivity and reflection from the quartz reactor walls, is estimated to be 1050°C (12). The silane concentration in the reaction chamber is 0.2%; the carrier gas is hydrogen which has been purified with a palladium diffuser. The gas flow through the reaction chamber is 2.13 l/min; the linear velocity is 1.80 cm/sec. The observed growth rate for these conditions is 0.35 μm/min. Thicknesses of the epitaxial films are typically 4-7 μm. Prior to the deposition, the substrates are cleaned by degreasing with organic solvents followed by a rinse in hydrofluoric acid. Final cleaning is performed in the reaction chamber by an *in situ* etch with 0.1% hydrogen chloride at an actual temperature of 1050°-1100°C. The etch rate is less than 0.02 μm/min. The epitaxial layers are deposited on the (111) or the (100) orientations; no differences between the two orientations have been observed.

Schottky diodes are formed on the epitaxial layers by evaporating gold to form circular dots which are 0.508 mm in diameter and 1000Å thick. The majority carrier concentration in the epitaxial film is determined from measurements on the Schottky diodes using the CIP technique (13, 14) with the modifications reported by Thibault (15). The validity of the Schottky diode and the CIP measurements has been established by also making planar and mesa diodes on some samples and by obtaining capacitance-voltage measurements on the different diodes. The agreement among the different diodes and the different measuring techniques is excellent. Majority carrier concentrations are converted to impurity atom concentrations using the equations reported by Kennedy *et al.* (16, 17).

Results

Typical profiles as measured by the CIP technique on Schottky diodes are shown in Fig. 1. These profiles show the measured majority carrier concentrations and have not been converted to impurity atom concentration (16, 17), thus the actual doping profiles are much sharper than the measured profiles shown in Fig. 1. Except for small changes in the deposition time, the epitaxial layers have been deposited under identical conditions for each sample; the only intentional variable is the substrate doping which is given for each curve. It should be noted that the doping concentration in the epitaxial film is nearly constant with distance from the surface except at the substrate-film interface. This implies that during growth, the dopant is introduced at a nearly constant rate. In these experiments, there is no intentional doping of the epitaxial layer; consequently, the steady-state doping level is a direct measure of the background doping level in the system during a particular experiment. The background impurity concentration is the sum of the impurities in the gases (the silane and the hydrogen) plus the impurities in the system (the gas line, the reactor walls, and the susceptor) plus the impurities from the substrate (the autodoping). Data such as that in Fig. 1 strongly suggest that the background doping level is often established by the im-

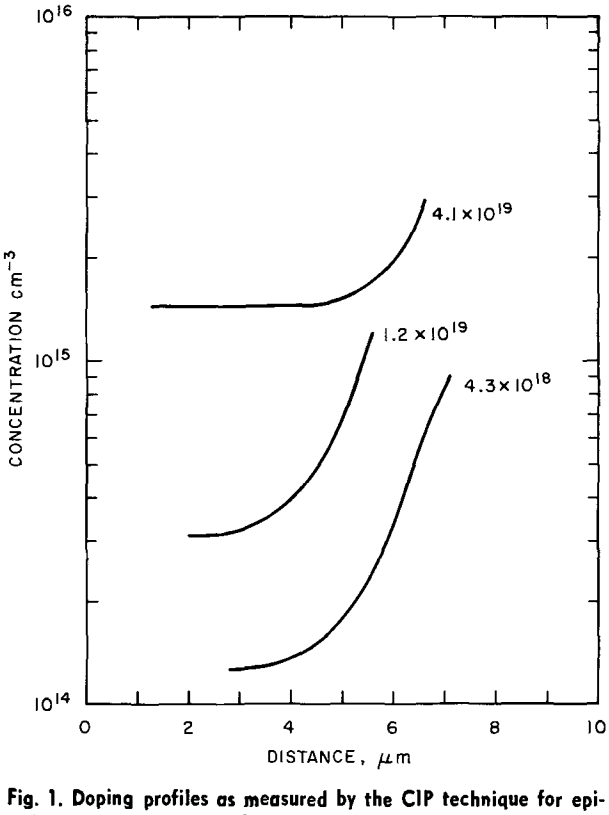

Fig. 1. Doping profiles as measured by the CIP technique for epitaxial layers deposited on three different arsenic-doped substrates.

purities from the substrate; the impurities from the other two sources are negligible. Before this conclusion can be accepted it is necessary to rule out the possibility of random fluctuations in the background doping level that might affect the results.

The absence of fluctuations has been established by correlating the epitaxial dopant concentration with changes in the substrate doping level. When the concentration of arsenic in the substrate is systematically increased or decreased, it is observed that the epitaxial dopant concentration also increases or decreases. When the substrate doping concentration is varied in a random manner, the epitaxial doping still correlates with the substrate doping. Results from such an experiment are shown in Fig. 2 which gives the concentration of dopant in the epitaxial layer for seven consecutive depositions in which the only variable is the arsenic concentration in the substrate (listed on the right in Fig. 2). When the arsenic concentration in the substrate is 5×10^{14}, 8×10^{18}, or 4×10^{19} cm^{-3}, the dopant concentration in the layer on the substrate is 6×10^{13} to 1×10^{14} cm^{-3}, 3×10^{14} cm^{-3}, or 1.5×10^{15} cm^{-3}, respectively. The reproducibility in the epitaxial dopant concentration rules out the possibility of random fluctuation in the background impurity concentration and shows that autodoping often establishes the background doping level.

In general we find that when lightly doped substrates are used and autodoping is not significant, the background doping varies from 5×10^{13} to 1×10^{14} cm^{-3}. This variation probably results from changes in the impurities released from the system since the same gases are used in all the experiments. This variation in the impurities from the system does not change any of our conclusions since the autodoping effects cause the epitaxial layers to be doped at concentrations much higher than this background doping.

The results from several experiments with arsenic-doped substrates are plotted in Fig. 3, which shows the epitaxial doping *vs.* the substrate doping. In each case the dopant concentration in the epitaxial film is measured from the flat portion of the doping profile. The substrate doping is obtained by four-point probe measurements using Irvin's curves to convert resistivity to impurity concentration (18); in some cases this has been checked by measuring the position of the plasma minimum in the infrared reflectance spectrum (19). Again the agreement is excellent. In the experiments shown in Fig. 3, the background doping level (shown

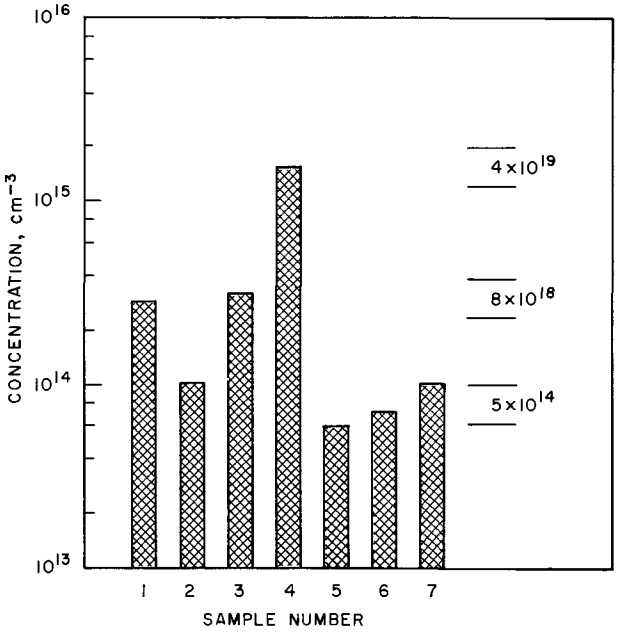

Fig. 2. Epitaxial dopant concentration for seven consecutive depositions on arsenic-doped substrates.

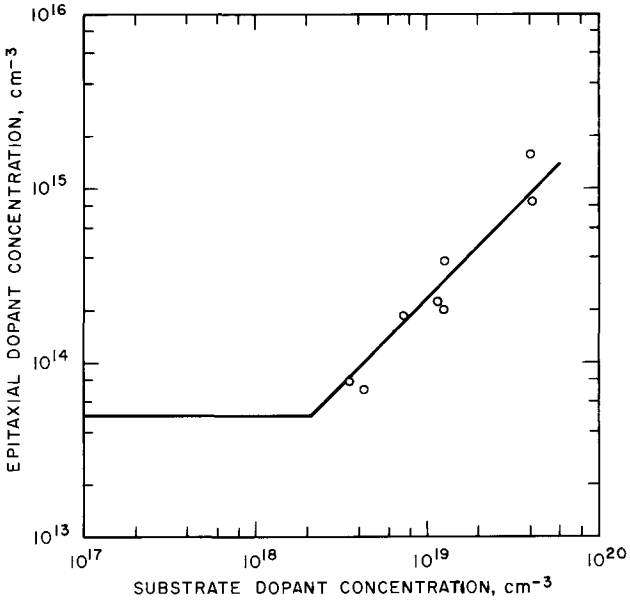

Fig. 3. Epitaxial dopant concentration for arsenic-doped substrates. The background doping level is 5×10^{13} cm^{-3}.

by the horizontal line) has been established to be 5×10^{13} cm^{-3} by depositing on substrates doped to 5×10^{14} cm^{-3}. The sloping line is drawn for the case in which the epitaxial doping is directly proportional to the substrate dopant concentration. The data are consistent with this model. It is clear from this figure that autodoping effects are not significant unless the arsenic concentration in the substrate is greater than 2×10^{18} cm^{-3}.

Several experiments have been performed in an effort to elucidate the autodoping mechanism and to determine if autodoping can be reduced or eliminated. In some experiments a heavily doped epitaxial layer, 3 μm thick, was deposited on a lightly doped substrate. The arsenic concentrations in the epitaxial layer and in the substrate were about 1×10^{19} cm^{-3} and 5×10^{14} cm^{-3}, respectively. The sample was cut in half and an "undoped" epitaxial layer was deposited on the front of one part and on the back of the other part, after the back surface had been polished smooth. When the epitaxial film was deposited on the heavily doped layer, the dopant concentration in the undoped layer was an order of magnitude less than when the undoped epitaxial film was deposited on the original substrate with the heavily doped region at the back. This shows that most of the dopant atoms that are transferred from the substrate to the growing epitaxial layer originate from the back of the substrate as originally suggested by Basseches *et al.* (1). Such a result is reasonable since the back of the substrate is in contact with the hot susceptor and is probably at a higher temperature than the front of the sample so that impurities evaporate from the back at a faster rate than from the front. This result indicates that autodoping will be reduced when the epitaxial layer is deposited over highly doped regions such as in buried layer structures. However, our data do not pertain to the possible lateral transfer of dopant, which may be the dominant mechanism in these structures (20).

The autodoping effect should be reduced or eliminated by masking the back of the substrate with a material which is impervious to the dopant. Epitaxial layers have been deposited on substrates with 15,000Å of steam oxide on the back. In this case the autodoping is reduced by a factor of about five but not eliminated. This agrees with previous reports in which similar results have been presented (7, 10). In these experiments, the arsenic must be transferred through the oxide. This transfer has been demonstrated by Joyce, Weaver, and Maule who measured the transfer of

radioactive arsenic from samples that were completely covered with a thick oxide (7).

The impurity atom distribution across the sample has been determined by measuring Schottky diodes on different parts of the same sample. The results show a slightly higher dopant concentration at the edge than at the center. This effect, which has been observed before (7, 8), has been used to argue that impurities are transferred from the back, over the edges, and toward the center of the sample (7). We have observed differences in dopant concentration between the center and the edge that are about the same as those reported by previous workers (7, 8). However, our differences are not consistent or reproducible; this may result from different gas flow patterns over different areas of the sample.

It is possible that autodoping results from the formation of volatile chlorides of the dopant atoms; the chlorine may come from residual hydrogen chloride that is not removed from the reaction chamber in the time between the vapor etch and the deposition. This possibility has been eliminated by performing experiments in which the epitaxial layers are deposited without the hydrogen chloride vapor etch. There are no significant changes in the doping level in the epitaxial film. This shows that volatile chlorides are not necessary for the transfer of impurities and implies that autodoping results entirely from thermal effects.

Discussion

The experimental data indicate that most of the autodoping originates when impurities are transferred from the back of the sample. This is reasonable since the front of the sample rapidly becomes covered by the growing epitaxial film and diffusion of impurities from the substrate to the front of this film does not normally occur. The condition required to prevent diffusion through the growing film is that the growth rate be much greater than the rate of diffusion, or

$$Gt >> (Dt)^{1/2}$$

where G is the deposition rate, t is the time, and D is the diffusion coefficient. If we consider a growth rate of 0.35 μm/min (5.83×10^{-7} cm/sec) and use the literature value for the diffusion coefficient of arsenic at 1050°C, 2×10^{-14} cm^2/sec (21), then the two terms are equal after a deposition time of 5.9×10^{-2} sec. After 5 sec of growth, Gt is nearly ten times greater than $(Dt)^{1/2}$, showing that for our deposition times the growth rate is much greater than the rate of diffusion and that diffusion through the growing film is negligible.

Our discussion of autodoping considers the case where impurities diffuse from the bulk to the back surface of the sample, evaporate from the back surface, transfer in the gas phase to the front of the sample, and deposit in the growing epitaxial layer. The presence of a gas phase transfer as opposed to surface diffusion has been established since autodoping effects are reported to be much greater in the direction of the gas flow (7, 20). If the rate limiting step in the autodoping process is the rate at which impurities diffuse out of the substrate, then the rate of impurity incorporation in the epitaxial film is proportional to the rate of out-diffusion from the sample and the autodoping effects can be described in terms of solid-state diffusion theory.

Smits and Miller (22) have studied the diffusion of impurities from silicon. They give the following expression for the case in which the impurity concentration in the gas phase is zero and the silicon is initially uniformly doped

$$N(y,z) = N_0 - N_0 \exp(-y^2)\{\exp(y^2)\operatorname{erfc}(y) - \exp[(y+z)^2]\operatorname{erfc}(y+z)\}$$

where

$$y = x/2(Dt)^{1/2}$$

and

$$z = (Dt)^{1/2}K/D$$

The initial impurity concentration in the silicon is N_0; N is the concentration at some time, t, and at some distance from the surface, x; D is the diffusion coefficient; and, K is a first-order rate constant for the evaporation of impurities from the silicon surface. Integrating this expression from $x = 0$ to ∞ and subtracting from the total number of impurity atoms initially present gives the number of impurity atoms which have diffused out of the silicon (22)

$$\overline{N}(t) = 2N_0(Dt)^{1/2}\{\pi^{-1/2} - [1 - \exp(z^2)\operatorname{erfc}(z)]/2z\}$$

Differentiating with respect to time gives the rate at which impurity atoms diffuse out of the substrate

$$R = \frac{d\overline{N}}{dt} = N_0K\exp(z^2)\operatorname{erfc}(z)$$

In the model we are considering, the amount of autodoping is proportional to the out-diffusion rate, R; the proportionality constant is the fraction of impurity atoms that transfer to the growing epitaxial layer. At long times ($z >> 1$), the rate of out-diffusion can be approximated by

$$R \approx N_0(D/\pi t)^{1/2}$$

Under these conditions, the rate of out-diffusion is limited by the rate at which impurities diffuse to the back surface. Our equation for the rate of out-diffusion has the same form as the equation given by Shepherd (8). The difference is in the pre-exponential factor. In our equation this factor is based on an experimentally measured rate constant. In Shepherd's equation, the pre-exponential factor is based on the activity coefficient of the dopant and a gaseous transfer coefficient. Our equations are derived for the case where the impurity concentration in the gas phase is zero. This should not be a serious limitation in a flow system where the gas is continuously removed.

A plot of the calculated rate of out-diffusion *vs.* time is shown in Fig. 4. The value of D (2×10^{-14} cm^2 sec^{-1})

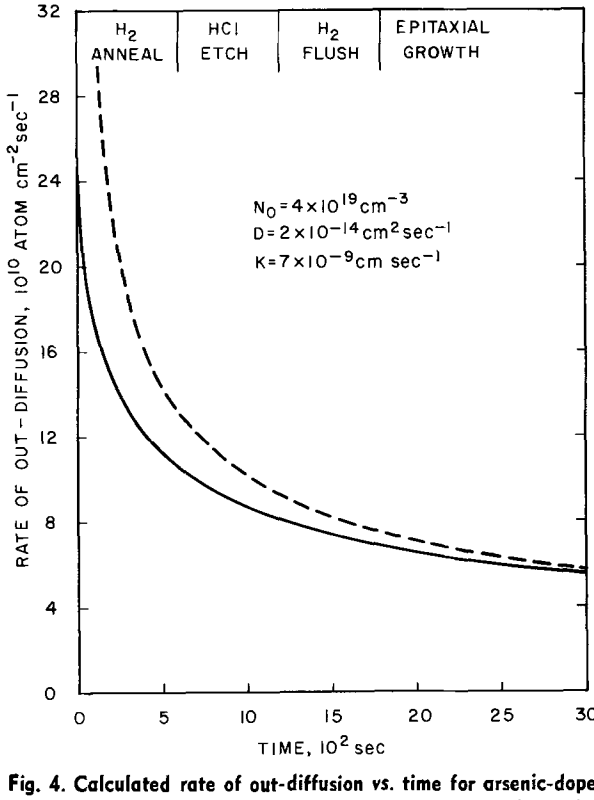

Fig. 4. Calculated rate of out-diffusion *vs.* time for arsenic-doped substrates and for a deposition temperature of 1050°C. The dashed line shows the diffusion-limited case.

has been taken from the data of Masters and Fairfield (21) for a temperature of 1050°C. The value of K (7×10^{-9} cm sec^{-1}) is the value reported by Abe *et al.* (6) at 1250°C corrected for the different temperature by assuming that K has the same temperature dependence as D, as suggested by Lehovec *et al.* (23). The dashed line in Fig. 4 shows the rate of out-diffusion for the diffusion-limited case, which is valid at long times; also shown are the time intervals for the different steps in the epitaxial process. The silicon removed during the hydrogen chloride etch has not been considered in calculating the rate of out-diffusion. Calculated curves for different values of D and K are shown in Fig. 5 and 6. Variations in D do not affect the initial rate; however, they cause a displacement of the curves at long times. This is reasonable since at long times the rate of out-diffusion becomes diffusion limited and is independent of K and proportional to the square root of D. Increasing the value of K only affects the initial part of the rate curve (Fig. 6) since the latter portion is diffusion limited and independent of K. Decreasing the value of K causes the rate of out-diffusion to decrease because the rate of out-diffusion is now limited by the rate of evaporation rather than the rate of diffusion to the surface.

Before discussing our data we briefly consider two additional aspects of this model. First, the fraction of impurity atoms transferred to the epitaxial layer can be determined by combining the measured impurity concentration in the film with the calculated number of impurity atoms that have diffused from the sample. Integration of the rate of out-diffusion between times of 1800 and 2400 sec gives 3.7×10^{13} atoms of arsenic that have diffused from 1 cm^2 of silicon with an initial arsenic concentration of 4×10^{19} cm^{-3} and at a temperature of 1050°C. The epitaxial doping concentration corresponding to this substrate doping is 9.4×10^{14} cm^{-3} (Fig. 3). Thus the number of arsenic atoms per square centimeter of an epitaxial film 3.5 μm thick (corresponding to a deposition rate of 0.35 μm/min and a 10 min deposition time) is 3.3×10^{11} atoms/cm^{-2}. Therefore, only 0.9% of the arsenic that diffuses out of the sample is incorporated in the epitaxial film. Shepherd found that 0.3% of the impurity atoms were transferred (8); however, he was working with much higher gas flows so the lower fraction is not unreasonable.

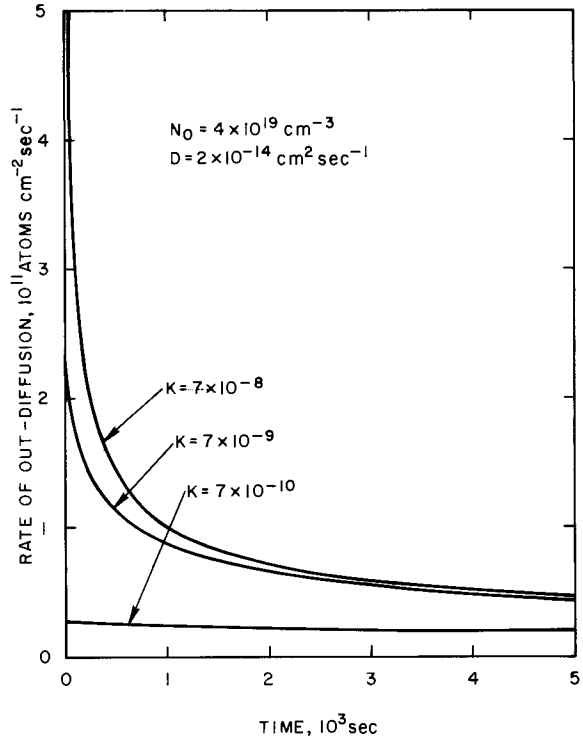

Fig. 6. Calculated rate of out-diffusion *vs.* time for different values of the evaporation rate constant.

The impurity profiles that result from thermal out-diffusion are shown in Fig. 7. It can be seen that the out-diffusion is confined to the region near the surface. Essentially all of the atoms that evaporate from the silicon come from within a few tenths of a micron of the surface. Although the surface concentration may become very low prior to the deposition, this evaporation of impurities from the substrate normally has only a slight effect on the shape of the final substrate-epitaxial film profile as shown by Abe *et al.* (6).

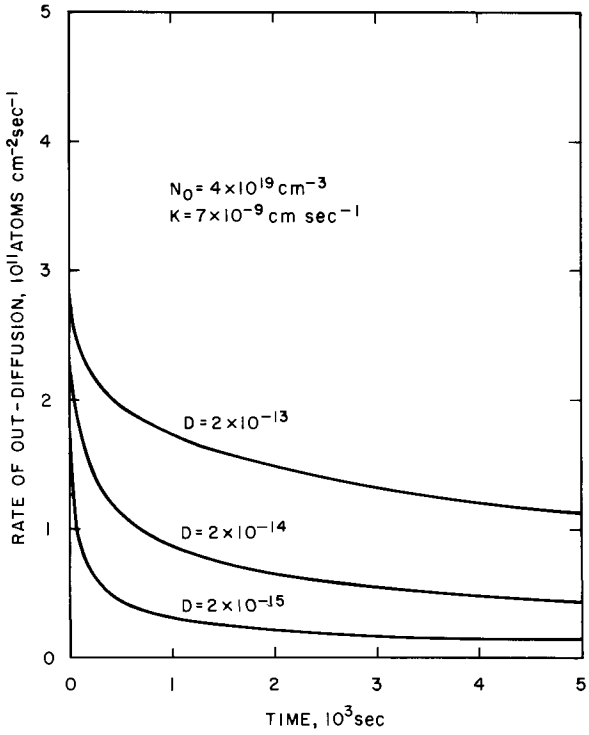

Fig. 5. Calculated rate of out-diffusion *vs.* time for different values of the diffusion coefficient.

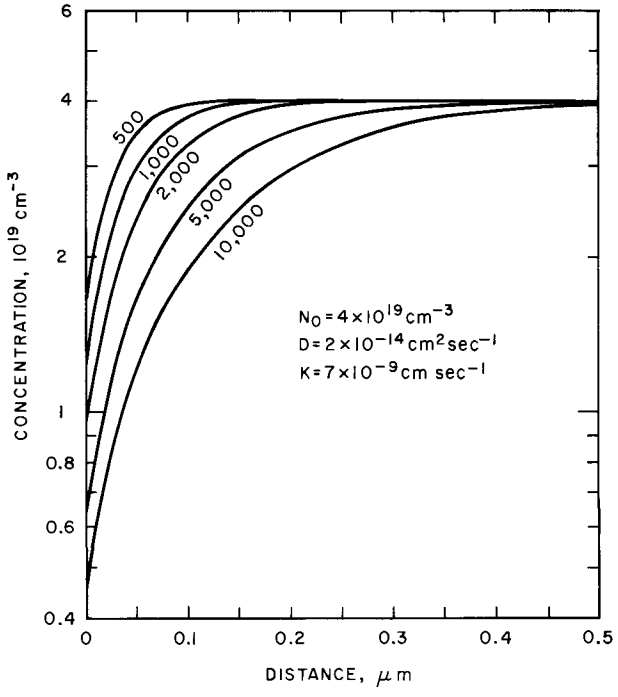

Fig. 7. Calculated substrate doping profiles resulting from evaporation of arsenic at 1050°C. The heating times in seconds are given for each curve.

In the model we are presenting, the rate of out-diffusion is directly proportional to the initial impurity concentration in the silicon substrate. Consequently, the dopant concentration in the epitaxial film should also be proportional to the substrate impurity concentration provided that the fraction of impurity atoms transferred to the epitaxial film is independent of the substrate doping level. Such a linear relationship between the dopant concentration in the epitaxial film and in the substrate is shown in Fig. 3. At very high substrate dopant concentrations, the autodoping may no longer be directly proportional to N_0 because the diffusion coefficient is concentration dependent (21). However, it is obvious that the experimental data approximate a linear relationship. When the substrate doping is less than about 2×10^{18} cm $^{-3}$, the number of arsenic atoms transferred is less than the background dopant concentration and autodoping effects are not observed. Basseches *et al.* (1) found a similar dependence of the epitaxial impurity concentration on the substrate dopant concentration; however, a quantitative relationship was not established.

The shape of the doping profile in regions which are not near the substrate-epitaxial interface is determined by changes in the rate of out-diffusion. From Fig. 4, it can be seen that for depositions between 1800 and 2400 sec, the change in the impurity concentration throughout the epitaxial layer is about 12%. However, part of this change is obscured by the high concentration of impurities that diffuse from the heavily doped substrate into the lightly doped epitaxial layer, and the region near the surface is not measured because of the built-in depletion layer of the Schottky diodes. Thus the total change in dopant concentration that can be observed should be about 5%. Such a small change is consistent with our measured profiles (Fig. 1) and explains the observation that the dopant concentration is nearly independent of thickness. Our model should also apply to the previous reports in the literature where flat doping profiles have been observed (5, 7, 10).

In some experiments we have eliminated the hydrogen chloride etch and the hydrogen flush from the epitaxial deposition procedure and have deposited immediately after a short hydrogen anneal. For these depositions, which typically occurred between times of 180 and 780 sec, the observed dopant concentrations decreased with distance from the interface by a factor of about two. This is consistent with the changes in the rate of out-diffusion as given in Fig. 4. The curves in Fig. 4 show that most of the arsenic escapes prior to the deposition. If we consider a 10-min deposition occurring between times of 1800 and 2400 sec, then only 18% of the arsenic atoms diffuse out of the substrate during the deposition. The remaining 82% diffuse out during the heat-treatments before the deposition and are swept out of the system. This is consistent with the data of Joyce, Weaver, and Maule (7) who found that most of the impurity atom transfer occurs prior to the deposition.

This particular model provides a quantitative explanation for the flat profiles and for the concentration dependence of the autodoping. We now briefly consider a qualitative extension of this model to explain some observations that have been reported in the literature. There are reports of doping profiles resulting from autodoping that are not flat (2, 3). This may result from evaporated impurities being absorbed on the susceptor or the reactor walls prior to deposition and being slowly desorbed during deposition, thus causing a net decrease in the gas phase impurity concentration during deposition. In our experiments we have attempted to minimize these effects by using a small susceptor and by cleaning and coating the susceptor prior to each deposition. Another explanation for the sloping profiles is the possibility of silicon slowly depositing on the back of the sample in addition to the more rapid deposition on the front. If this deposition occurs then the rate of out-diffusion will decrease with time more rapidly than shown in Fig. 4 and the doping profiles will not be flat. A slow deposition on the back of the substrate has recently been observed (24).

A possible method of reducing the autodoping is to heat the sample at high temperature prior to deposition and thus deplete the silicon near the back surface. We have calculated the rate of out-diffusion for substrates with an arsenic concentration of 4×10^{19} cm^{-3} which are heated at 1200°C for 20 min and then heated at 1050°C for 10 min immediately prior to deposition. For these conditions the calculated rate of out-diffusion at the start of the deposition is 1.0×10^{10} atoms/cm^{-2} sec^{-1} as compared to an out-diffusion rate of about 7×10^{10} atoms/cm^{-2} sec^{-1} when the predeposition heat-treatments are performed at 1050°C (Fig. 4). This high-temperature treatment may reduce the autodoping by a factor of seven; however, these calculations assume that D and K have the same temperature dependence and that the temperature changes are abrupt, so that any quantitative interpretation must be considered tentative.

Preliminary data indicate that antimony-doped substrates exhibit less autodoping than arsenic-doped samples. The decreased autodoping may result because the rate of evaporation is less for antimony than for arsenic, since the diffusion coefficients for arsenic and antimony are nearly the same (25). A lower limit for the rate of evaporation of antimony from silicon at 1050°C can be obtained from the data of Grove *et al.* (5), ($K > 1 \times 10^{-10}$ atoms/cm^{-2} sec^{-1}). For small values of K, the rate of out-diffusion can be approximated by N_0K, so that the out-diffusion rate is about 4×10^9 atoms/cm^{-2} sec^{-1} at the lower limit of K. This is an order of magnitude less than the rate for arsenic given in Fig. 4 and may explain the decreased autodoping for antimony-doped samples.

Acknowledgment

We wish to thank M. H. Hanes and L. R. Thibault for their help in making the CIP measurements; T. Misawa and R. A. Moline for making C-V measurements, and R. Lieberman for providing data on the hydrogen chloride etching of silicon.

Manuscript received May 24, 1972.

Any discussion of this paper will appear in a Discussion Section to be published in the December 1973 JOURNAL.

REFERENCES

1. H. Basseches, S. K. Tung, R. C. Manz, and C. O. Thomas, *Met. Semicond. Mater.*, **15**, 69 (1962).
2. C. O. Thomas, D. Kahng, and R. C. Manz, *This Journal*, **109**, 1055 (1962).
3. D. Kahng, C. O. Thomas, and R. R. Manz, *ibid.*, **110**, 394 (1963).
4. J. J. Grossman, *ibid.*, **110**, 1065 (1963).
5. A. S. Grove, A. Roder, and C. T. Sah, *J. Appl. Phys.*, **36**, 802 (1965).
6. T. Abe, K. Sato, Y. Nishi, and N. Oi, *Denki Kagaku*, **35**, 142 (1967).
7. B. A. Joyce, J. C. Weaver, and D. J. Maule, *This Journal*, **112**, 1100 (1965).
8. W. H. Shepherd, *ibid.*, **115**, 652 (1968).
9. S. R. Bhola and A. Mayer, *R C A Rev.*, **24**, 511 (1963).
10. D. C. Gupta and R. Yee, *This Journal*, **116**, 1561 (1969).
11. J. Simpson, A. C. Adams, and M. H. Hanes, in "Silicon Device Processing," C. P. Marsden, Editor, Nat. Bur. Stand. Spec. Publ. 337, p. 87 (1970).
12. F. G. Allen, *J. Appl. Phys.*, **28**, 1510 (1957).
13. J. A. Copeland, *IEEE Trans. Electron Devices*, **ED-16**, 445 (1969).
14. R. R. Spiwak, *IEEE Trans.*, **IM-18**, 197 (1969).
15. L. R. Thibault, Bell Telephone Laboratories, Personal communication, 1968.
16. D. P. Kennedy, P. C. Murley, and W. Kleinfelder, *IBM J. Res. Develop.*, **12**, 399 (1968).
17. D. P. Kennedy and R. R. O'Brien, *ibid.*, **13**, 212 (1969).

18. J. C. Irvin, *Bell System Tech. J.*, **41**, 387 (1962).
19. E. E. Gardner, W. Kappallo, and C. R. Gordon, *Appl. Phys. Letters*, **9**, 432 (1966).
20. H. B. Pogge, D. W. Boss, and E. Ebert, in "Chemical Vapor Deposition," p. 767, J. M. Blocher and J. C. Withers, Editors, The Electrochemical Society, Inc., New York (1970).
21. B. J. Masters and J. M. Fairfield, *J. Appl. Phys.*, **40**, 2390 (1969).
22. F. M. Smits and R. C. Miller, *Phys. Rev.*, **104**, 1242 (1956).
23. K. Lehovec, K. Schoeni, and R. Zuleeg, *J. Appl. Phys.*, **28**, 420 (1957).
24. J. Simpson and R. Lieberman, Bell Telephone Laboratories, Personal communication, 1970.
25. D. L. Kendall and D. B. DeVries, in "Semiconductor Silicon," p. 358, R. R. Haberecht and E. L. Kern, Editors, The Electrochemical Society, Inc., New York (1969).

Effects of Heat-Treatment on Composition of CVD Films: The Case of Binary Arsenosilicate Glasses

J. Wong

General Electric Corporate Research and Development, Schenectady, New York 12301

ABSTRACT

By following the chemical composition and integrated intensity of the combined Si-O and As-O bands in the region 1400-800 cm^{-1} of the infrared as a function of thermal history of CVD (chemical vapor deposition) arsenosilicate films, it is found that structural changes and not composition variations are responsible for the observed shifts in band frequency and maximum absorbance in the resultant heat-treated films. This result indicates that loss of As_2O_3 to the ambient due to out-diffusion from low As_2O_3-content arsenosilicate-glass source (<1 mole per cent (m/o) As_2O_3) may be minimal, if not negligible, in the process of drive-in diffusion of arsenic into silicon at 1000°C and up.

Infrared absorption spectroscopy is a powerful technique for the characterization and structural evaluation of dielectric thin films on silicon (1-14). Aside from its usual ability to identify chemical entities present in the film, it is also capable of furnishing quantitatively chemical compositions of multicomponent films in a nondestructive manner. The latter application has been used to advantage recently to determine nondestructively the composition of as-deposited CVD (chemical vapor deposition) films of binary arsenosilicate (12) and borosilicate (13) in the range 0-20 mole per cent (m/o) As_2O_3 and 0-100 m/o B_2O_3, respectively.

A recent report (15) from this laboratory shows that heat-treatment in an inert argon atmosphere causes quite a marked variation in the vibrational spectra of binary arsenosilicate films vapor deposited on silicon from a one-liquid source SiH_4-$AsCl_3$-O_2-Ar system. The Si-O band at 1060 cm^{-1} shows a positive frequency shift to 1080 cm^{-1} accompanied by an increase in optical density (absorbance) of about 25-30%. The As-O band at 920 cm^{-1} shifts to 930 cm^{-1} and is accompanied by a decrease in optical density. Because of large differences in thermal and evaporation characteristics of the As_2O_3 and SiO_2 end components in this binary system, it is important to establish whether reduction in the As-O band intensity is due to evaporation loss of As_2O_3 to the ambient during heat-treatment at high temperatures, or structure changes within the glassy network without change in composition. The composition variation, or otherwise, of these films is relevant to the understanding of out-diffusion of arsenic species from the glass to the ambient in the process of drive-in diffusion of arsenic for the formation of N^+ diffused layers in silicon.

In an attempt to elucidate the correlation between changes in infrared band intensity and film composition and/or structural variation, the compositions of CVD arsenosilicate films before and after heat-treatment were followed by quantitative chemical analysis.

Key words: CVD films, arsenosilicate, infrared intensity, heat-treatment.

The integrated intensities of the Si-O and As-O vibrational bands in the range 1400-800 cm^{-1} were studied as a function of film thermal history. Spectral variations resulting from chemical treatment of the film in boiling water and conc HCl were also obtained for comparison.

Experimental

Binary arsenosilicate glass films were prepared on silicon wafers by a CVD technique using argon-diluted mixtures of SiH_4-$AsCl_3$-O_2 at 450°C. Details of the deposition procedure and composition determination of as-deposited films from the infrared spectra have been reported elsewhere (12, 15). A Sartorius microbalance sensitive to 20 μg was used to obtain film weights by difference. Film compositions were determined by an x-ray microprobe technique. This technique enables the same film to be analyzed before and after heat-treatment. Films were heat-treated at 800°C for 15 min in Ar (flowing at 1 ft^3 per hr^{-1}) using a conventional horizontal furnace. Infrared spectra were recorded with a Perkin-Elmer 457 double-beam recording spectrophotometer. Scan rates of 400 cm^{-1} per min and 200 cm^{-1} per min were used in the range 4000-2000 cm^{-1} and 2000-250 cm^{-1}, respectively. All spectra were taken at room temperature. The area under the Si-O and As-O vibrational bands in the frequency range 1400-800 cm^{-1} was measured with a calibrated OTT compensating polar planimeter.

Results and Discussion

In Fig. 1, the infrared spectra of a series of arsenosilicate films deposited on silicon wafers are plotted as linear absorbance *vs.* wave number in the range 1400-800 cm^{-1}. The dotted curves are those for the as-deposited films while the solid curves are those for the corresponding films heat-treated in Ar at 800°C for 15 min. It is evident in all cases that upon heat-treatment the Si-O band at 1060 cm^{-1} shows a positive frequency shift of ~20 cm^{-1} accompanied by an increase in absorbance at the band maximum. The As-O band at 920 cm^{-1} also shows a positive frequency

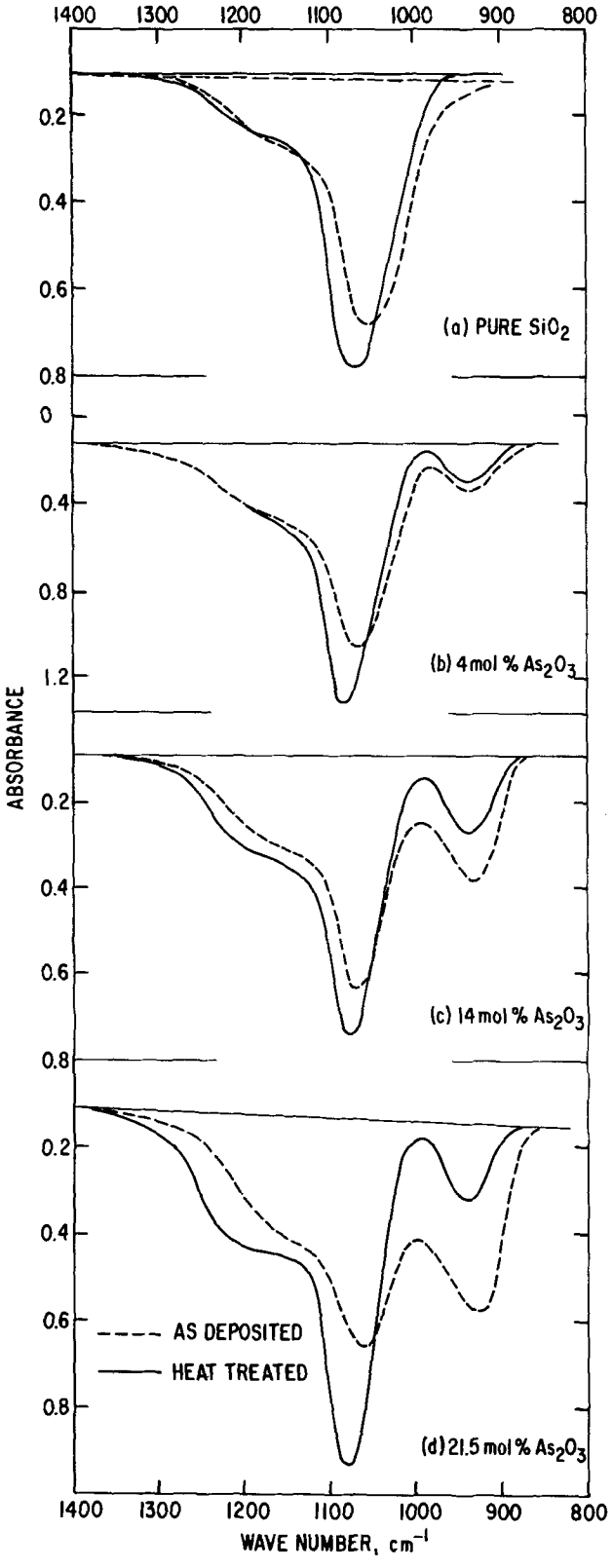

Fig. 1. Infrared spectra of a series of as-deposited and heat-treated arsenosilicate films in the region of the Si-O and As-O stretching vibrations. Heat-treatment: 800°C in Ar for 15 min. Thickness of as-deposited samples: (a) 0.52μ; (b) 0.82μ; (c) 0.70μ; and (d) 0.90μ.

shift of ~10 cm^{-1} but with a decrease in absorbance at the band maximum. Spectral variations of the Si-O band in a pure CVD SiO_2 (Fig. 1a) are similar to those in the binary films.

The total area (see Footnote b under Table I) under each of the absorption curves shown in Fig. 1 is given in Table I. In the binary films (samples 2-4 in

Table I

Sample	Mole per cent As_2O_3[a] (as-deposited)	Total area[b] under absorption bands in the range 1400-800 cm^{-1}: As-deposited	Heat-treated	Chemically treated	Microprobe analysis[e] As/Si atomic ratio: As-deposited	Heat-treated	Estimated error
1	pure SiO_2	73	73				
2	4	146	147		0.08_0	0.08_8	±0.005
3	14	94	94		0.33_4	0.35_1	±0.010
4	21.5	119	117	88[c]	0.56_8	0.53_9	±0.020
5	19.0	89		89[d]			

[a] Determined from the IR spectra of as-deposited films using a previously reported chemical calibration curve (12).

[b] Strictly speaking, the integrated intensity of a band is given by

$$\int_{\text{band}} \alpha(\bar{\nu})\,d\bar{\nu} = \int A(\bar{\nu}) \times \frac{1}{t}\,d\bar{\nu} = \frac{1}{t}\int A(\bar{\nu})\,d\bar{\nu}$$

where $\alpha(\bar{\nu})$ and $A(\bar{\nu})$ are the absorption coefficient and absorbance at frequency $\bar{\nu}$ respectively, and t is the film thickness. The integral $\int A(\bar{\nu})\,d\bar{\nu}$ therefore denotes the area under an absorption band when absorbance is plotted *vs.* wavenumber. Since we are interested primarily in the total absorption of the same film before and after heat-treatment, the term "total area" can be used interchangeably with integrated intensity because t is a common factor.

[c] Films exposed to conc HCl for 20 hr; or to boiling water for 3 min.

[d] Films exposed to 100% R.H. for 670 hr.

[e] High purity silicon and GaAs were used as standards for Si and As.

Table I) there is essentially no change in integrated intensity after heat-treating at 800°C in Ar for 15 min. This suggests that the total Si-O and As-O oscillators in each film remain invariant after heat-treatment and that there is no change in film composition due to volatilization loss of As_2O_3. Furthermore, a film of pyrolytic SiO_2 deposited at 450°C shows no change in integrated intensity (sample 1 in Table I) in the same spectral region after identical heat-treatments. This implies that the shift to higher frequency and narrowing of the half-width of the Si-O band at 1060 cm^{-1} in pyrolytic SiO_2 is merely a manifestation of structural changes in the silica network brought about by thermal annealing (1). Angular reorientation of the Si-O-Si centers (16) and/or further condensation of hydrogen-terminating Si-O chains (17) are possibilities of these structural changes. It is of interest to note that there is no further change in the SiO_2 spectrum upon heat-treatment beyond 800°C in the range 900°-1200°C.

The invariance of integrated intensity of the combined Si-O and As-O bands in the binary films and that of the Si-O band in pure pyrolytic SiO_2 in the range 1400-800 cm^{-1} before and after heat-treatment is informative. This seems to indicate that the observed As-O band in the spectra of as-deposited binary films has a substantial "borrowed" intensity from the Si-O band in the region below 1000 cm^{-1}. This borrowed intensity is reduced when the Si-O band narrows and shifts to higher frequency upon heat-treatment [see Fig. 1(a)]. The decrease in intensity of the As-O band in the heat-treated films appears therefore to be due to a reduction of this borrowed intensity and not to a reduction of As_2O_3 content in the film.

The above conclusion is substantiated by chemical analysis on the same films before and after heat-treatment at 800°C. In Table I, x-ray microprobe data on the same binary films used for the infrared study are given. Film compositions determined by this technique are expressed in terms of the atomic ratio of As/Si. It can be seen that, within instrumental error, there is no change in film composition after heat-treatment. Another series of arsenosilicate films containing 1.8-16.0 m/o As_2O_3 (as-deposited) showed no changes in film weight after heat-treatment for 15 min at 800°C in Ar (Table II).

For completeness, effects on film composition by chemical treatment in various environments have also

Table II. Weights of arsenosilicate films before and after heat-treatment at 800°C in Ar

Sample	Mole per cent As_2O_3 (as-deposited)	Film weight[a] (mg) As-deposited	Heat-treated
5	1.8	1.41	1.41
6	4.5	1.37	1.37
7	8.5	1.67	1.67
8	13.4	1.85	1.85
9	16.0	1.43	1.43

[a] Obtained by subtracting weight of silicon wafer.

been studied. Variations in the infrared absorption in the range 1400-800 cm^{-1} are given in Fig. 2 for films containing about 20 m/o As_2O_3 (as-deposited). Each of these films was separately exposed to a controlled humidity (100% R.H.) at room temperature, treated in boiling water and in conc HCl. The spectral changes in these chemically treated films are qualitatively similar to those that occurred in the heat-treated films

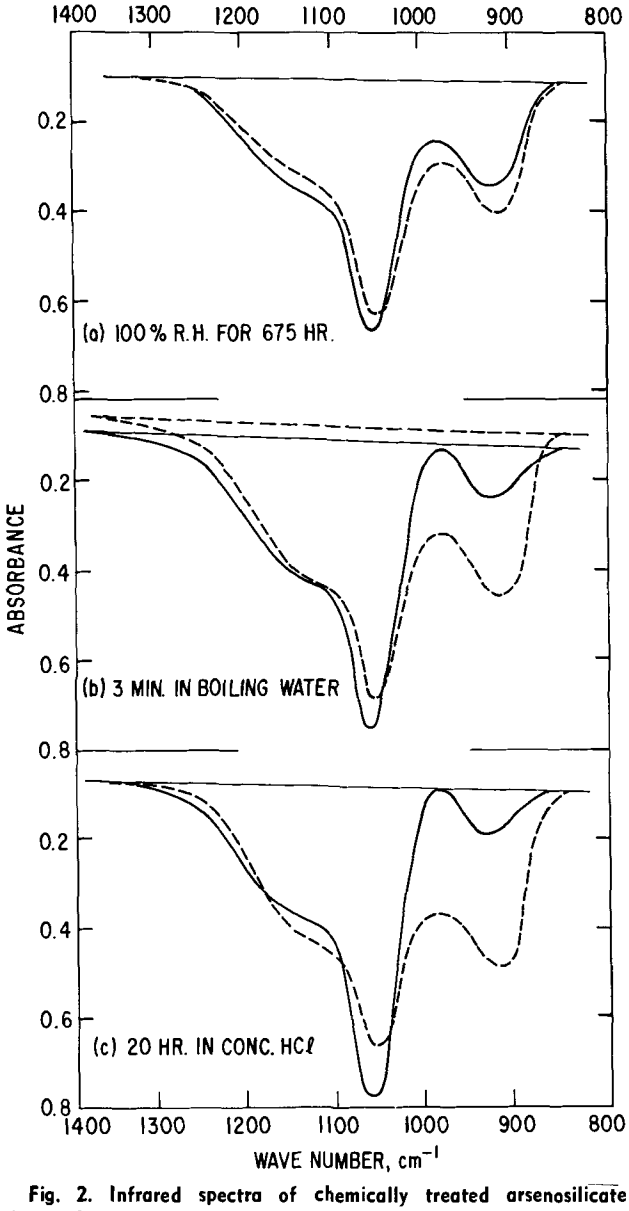

Fig. 2. Infrared spectra of chemically treated arsenosilicate films. The dotted curves represent spectra of the as-deposited films. Film composition (as-deposited): (a) 19 m/o As_2O_3; (b) and (c) 21.5 m/o As_2O_3.

shown in Fig 1. For films treated in boiling water and conc HCl, however, the total area under the combined Si-O and As-O bands decreases by about 25% (Table I) from the "as-deposited" values, showing that there is loss of As_2O_3 in the treated films. This is conceivable in light of the high solubility of As_2O_3 in both water and conc HCl, whereas pure SiO_2 is practically not etchable by either of these reagents. A film exposed to 100% R.H. at room temperature shows no change in integrated intensity implying that there is no leaching of film material by this treatment.

Conclusion

The combined data on infrared integrated intensity, chemical and gravimetric analyses indicate that there is no composition change due to volatilization loss of As_2O_3 at 800°C in Ar from CVD binary arsenosilicate glass films containing as much as 20 m/o As_2O_3. Loss of As_2O_3 to the ambient due to out-diffusion from low As_2O_3-content arsenosilicate glass source (<1 m/o As_2O_3) may be minimal, if not negligible, in the process of drive-in diffusion of arsenic into silicon at 1000°C and up (18). This is no doubt due to a lowering of the As_2O_3 activity (vapor pressure) in low As_2O_3-content mixtures.

Results from chemical treatments show that the combined integrated intensity of overlapping infrared absorption bands intrinsic of the material of interest is a good measure of composition conservation or otherwise in binary systems.

Acknowledgments

Thanks are due to M. Garfinkel for suggesting composition analysis of the films before and after heat-treatment. Useful discussions with J. W. Mitchell are deeply appreciated.

Manuscript submitted Jan. 12, 1972; revised manuscript received Aug. 11, 1972.

Any discussion of this paper will appear in a Discussion Section to be published in the December 1973 JOURNAL.

REFERENCES

1. W. A. Pliskin and H. S. Lehman, *This Journal*, **112**, 1013 (1965).
2. W. A. Pliskin, *Appl. Phys. Letters*, **7**, 158 (1965).
3. R. M. Valletta and W. A. Pliskin, *This Journal*, **114**, 944 (1967).
4. W. A. Pliskin and P. P. Castrucci, *Electrochem. Technol.*, **6**, 85 (1968).
5. W. A. Pliskin, D. R. Kerr, and J. A. Perri, *Phys. Thin Films*, **4**, 257 (1967).
6. J. E. Dial, R. E. Gong, and J. N. Fordemwalt, *This Journal*, **115**, 326 (1968).
7. W. A. Pliskin, R. G. Simmons, and R. P. Esch, in "Thin Film Dielectrics," Frederick Vratny, Editor, p. 524, The Electrochemical Society Softbound Symposium Series, New York (1969).
8. W. Kern and R. C. Heim, *This Journal*, **117**, 568 (1970).
9. N. Nagasima, *Japan. J. Appl. Phys.*, **8**, 879 (1970).
10. E. Arai and Y. Teruma, *ibid.*, **9**, 691 (1970).
11. E. A. Taft, *This Journal*, **118**, 1343 (1971); *ibid.*, **118**, 1985 (1971).
12. J. Wong and M. Ghezzo, *ibid.*, **118**, 1540 (1971).
13. A. S. Tenney, *ibid.*, **118**, 1658 (1971).
14. A. S. Tenney and J. Wong, *J. Chem. Phys.*, **56**, 5516 (1972).
15. J. Wong, *This Journal*, **119**, 1071 (1972).
16. R. C. Mozzi and B. E. Warren, *J. Appl. Cryst.*, **2**, 164 (1969).
17. M. L. Barry, in "Chemical Vapor Deposition, Second International Conference," J. M. Blocher, Jr. and J. C. Withers, Editors, pp. 595-617, The Electrochemical Society Softbound Symposium Series, New York (1970).
18. J. Wong and M. Ghezzo, *This Journal*, **119**, 1413 (1972).

The Growth of Niobium on Perfect and Imperfect Sapphire

J. J. Cuomo* and J. Angilello

IBM Thomas J. Watson Research Center, Yorktown Heights, New York 10598

ABSTRACT

Niobium prepared by rf sputtering has been found to nucleate and grow differently on the basal plane of low dislocation density (chemical vapor deposited) and high dislocation density (Czochralski-grown) sapphire (α-Al_2O_3) wafers. The low dislocation α-Al_2O_3 showed three different orientations related to each other by a threefold axis: (110) Nb//(0001) α-Al_2O_3 and [110] Nb//$\vec{a}_1$, $\vec{a}_2$, $\vec{a}_3$ α-Al_2O_3, while those films grown on more imperfect, high dislocation substrates, generally showed only one orientation: (111) Nb//(0001) α-Al_2O_3 and [110] Nb//[1120] α-Al_2O_3.

The orientation dependence of gold on air-contaminated and uncontaminated sodium chloride has been detailed by Matthews (1). Robbins and Rhodin (2) found a relationship between the maximum number of gold nuclei on MgO and the crystal from which the MgO was cleaved. It was concluded, that the number of gold nuclei depends on the difference in the number of point defects such as impurities in the MgO substrates. In both instances, a correlation between nucleation density and surface defects has been demonstrated. Matthews' work further shows the preference for one orientation to nucleate and another to grow, thus producing a change in orientation and/or crystallinity with nucleation density.

This work reports on the growth of niobium films by rf sputtering technique on the basal planes of "perfect" and "imperfect" sapphire/(α-Al_2O_3) having low and high dislocation densities, respectively. In order to improve the single crystalline quality of niobium on sapphire, CVD sapphire was chosen as a substrate due to its low dislocation density. However, we found the films grown on low dislocation substrates showed three different orientations related to each other by a threefold axis, while those films grown on more imperfect, high dislocation, substrates generally showed only one orientation.

Experimental Procedures

Low dislocation sapphire boules prepared by chemical vapor deposition were purchased from Lexington Laboratories, Lexington, Massachusetts. They were cut into 10 mil thick wafers and polished to a 1 μin. finish by Insaco Corporation, Quakertown, Pennsylvania. High dislocation sapphire wafers were cut and polished by Insaco Corporation from crystals prepared by the Czochralski growth technique. All samples prior to deposition were examined by the x-ray topographic techniques developed by Lang (3, 4) and Schwuttke (5). The orientation of the substrates used in this work were (0001). Niobium was deposited by rf sputtering using the following procedure. The chamber was pumped to 4×10^{-8} mm of Hg and the substrates were then heated to 450°C. Argon was introduced to 15×10^{-3} mm of Hg and the system was presputtered by sputtering niobium onto a shutter for 30 min. The substrates were exposed to the niobium atom flux at a power density of 7.4 W/cm². With the anode target grounded, the niobium accumulation rate was about 10 Å/sec. The substrates and film were examined after deposition by x-ray back-reflection Laue techniques and film orientations were confirmed by x-ray pole figure investigations. Both types of sapphire substrates were deposited on simultaneously; therefore, the conditions for growth were identical. The niobium films used during this investigation were of high quality as indicated by the high resistance ratios (6) and the bulk superconducting properties (7) shown.

* Electrochemical Society Active Member.

Key words: niobium, epitaxy, sapphire, sputtering, nucleation.

Results

Prior to niobium deposition, x-ray topographs were taken of the substrate. Figure 1a shows the topograph of low dislocation, perfect sapphire. The number of dislocation etch pits as revealed by polishing and etching techniques (9) is of the order of 50/cm². Figure 1b is an optical photograph of the pits in one of the highest density areas on the low dislocation wafer. The transmission x-ray topograph of the high

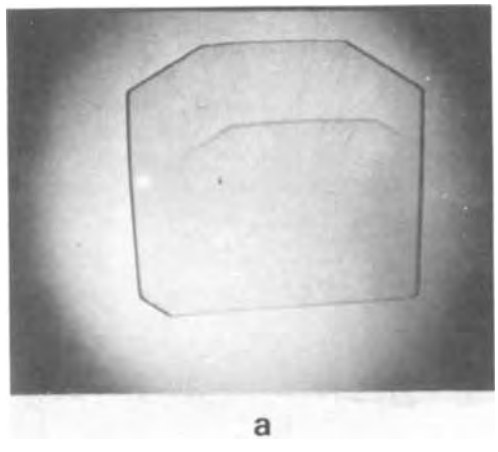

Fig. 1a. Transmission x-ray topograph of low dislocation CVD sapphire (0001). Approx. 4×.

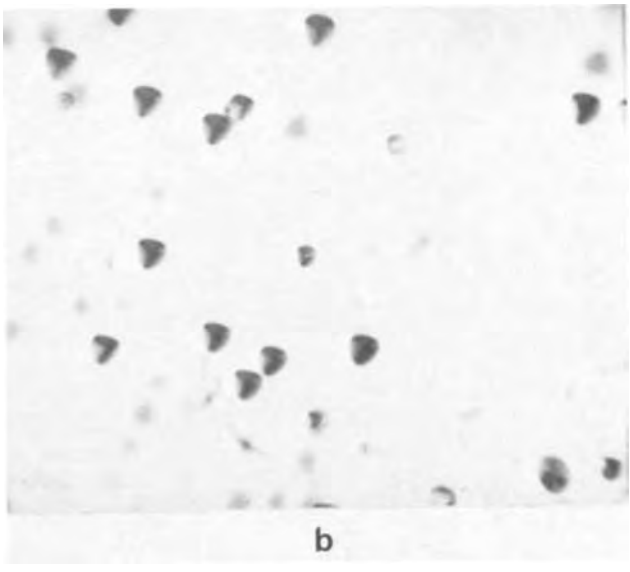

Fig. 1b. Dislocation etch pit pattern of the highest density area on low dislocation CVD sapphire (0001). 78×.

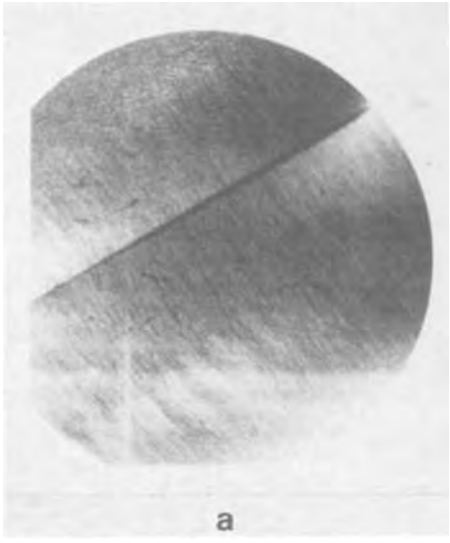

Fig. 2a. Transmission x-ray topograph of high dislocation density Czochralski sapphire (0001). Approx. 3×.

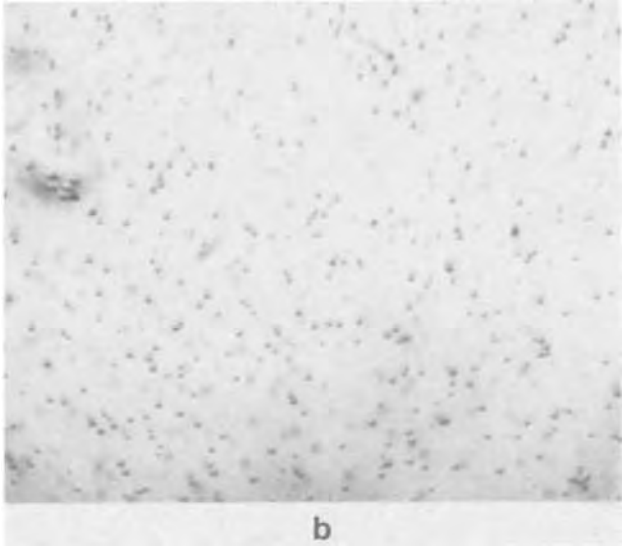

Fig. 2b. Dislocation etch pit pattern of high dislocation Czochralski sapphire (0001). 78×.

dislocation, imperfect sapphire is shown in Fig. 2a. The number of dislocations represented by this topograph, and the pit density shown in Fig. 2b, is of the order of 10^4-10^5/cm^2.

The results of an emission spectrographic analysis of chemical vapor deposited α-Al_2O_3 and Czochralski-grown α-Al_2O_3 are shown in Table I. The impurities found in both materials above the detectable limits were Si and Mg, which were similar for the two types of materials. Verneuil-grown sapphire was also examined and showed about 10 ppm Ti in addition to the other impurities. With the exception of the Ti content and some shallow angle grain boundaries, the Verneuil-grown sapphire showed substantially the same results as the Czochralski-grown sapphire.

Table I. Emission spectrographic analysis of CVD and Czochralski grown α-Al_2O_3

Impurities	CVD α-Al_2O_3 low dislocation, ppm	Czochralski α-Al_2O_3 high dislocation, ppm	Verneuil α-Al_2O_3 high dislocation, ppm
Si	3	3	3
Mg	0.3-1	0.3-1	0.3
Ti	N.D.*	N.D.	10-30

* Not detected.

Approximately 6000Å of niobium was desposited by rf sputtering on both CVD (low dislocation) and Czochralski (high dislocation) substrates. Figures 3a and 3b are x-ray back-reflection Laue photographs of low dislocation, perfect sapphire before and after niobium deposition, respectively. The orientation of the niobium is threefold heteroepitaxial, that is, (110) Nb // (0001) α-Al_2O_3 and [110] Nb // $\vec{a}_1$, $\vec{a}_2$, $\vec{a}_3$ α-Al_2O_3 giving rise to a highly textured polycrystalline film. A schematic depicting the orientation relationship of the niobium on (0001) of α-Al_2O_3 is shown in Fig. 3c. The 120° rotational symmetry of the (110) Nb on the (0001) plane of α-Al_2O_3 accounts for the threefold symmetry shown in the Laue photograph. A lattice overlay for a single set of spots is shown in Fig. 3d. The misfit is calculated to be 1.8% for the $[11\bar{2}0]$ direction.

Figures 4a and 4b are Laue patterns of high dislocation imperfect sapphire before (Fig. 4a) and after

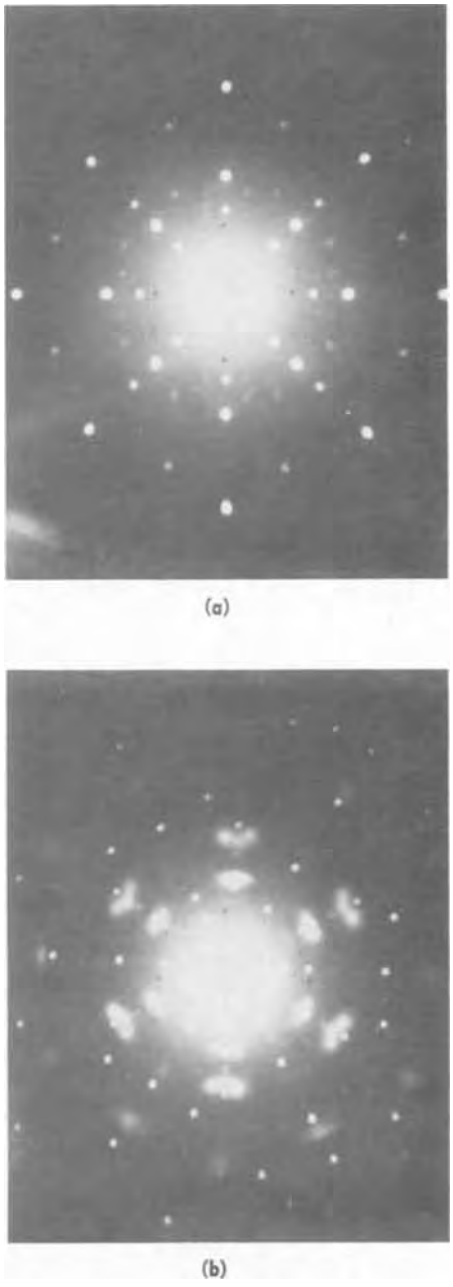

Fig. 3a and b. X-ray back-reflection Laue patterns of the low dislocation CVD sapphire (0001) before and after Nb deposition respectively.

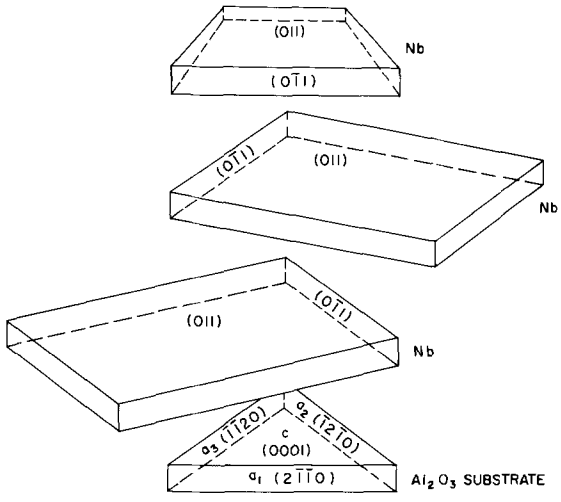

Fig. 3c. Schematic of the orientation of (110) Nb on (0001) α-Al_2O_3.

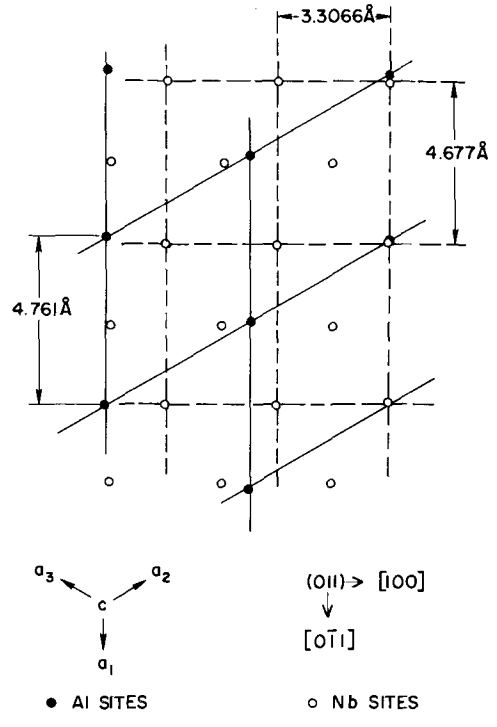

Fig. 3d. Lattice overlay of (110) Nb on (0001) α-Al_2O_3 for one of the orientations.

(Fig. 4b) the niobium deposition. In this case, the niobium is heteroepitaxial and single crystalline with the (111) Nb // (0001) α-Al_2O_3 and the [110] Nb // [11$\bar{2}$0] α-Al_2O_3. In some instances, small quantities of polycrystalline (110) Nb // (0001) α-Al_2O_3 was also found. Figure 4c schematically demonstrates the film substrate relationship and Fig. 4d is the lattice overlay of (111) Nb on (0001) α-Al_2O_3. The lattice misfit between Nb-Nb and Al-Al (8) is 1.8%, the same as in the previous case. It is interesting to note that in both cases the [110] direction of the Nb is parallel to the [11$\bar{2}$0] direction of the α-Al_2O_3 in the plane of the wafer.

Discussion

It is unknown at this time how defects contribute to the difference in nucleation and growth of niobium on the CVD and Czochralski sapphire. The difference in the number of emergence points of dislocations between the two materials would be insufficient to cause the difference in the nucleation and growth observed. Previous discussions (1) have shown that dislocation densities of the order of $10^5/cm^2$ are far below the nucleation density $10^{12}/cm^2$ needed to effect the preference for nucleation of a particular orientation. The result found is related to differences in the nucleation density between (111) and (110), to differences in surface defect concentration and type, and to interfacial surface energy difference between (111) and (110). Indeed, one must consider the orientation with the lowest interfacial surface energy since it will have the highest nucleation density (1).

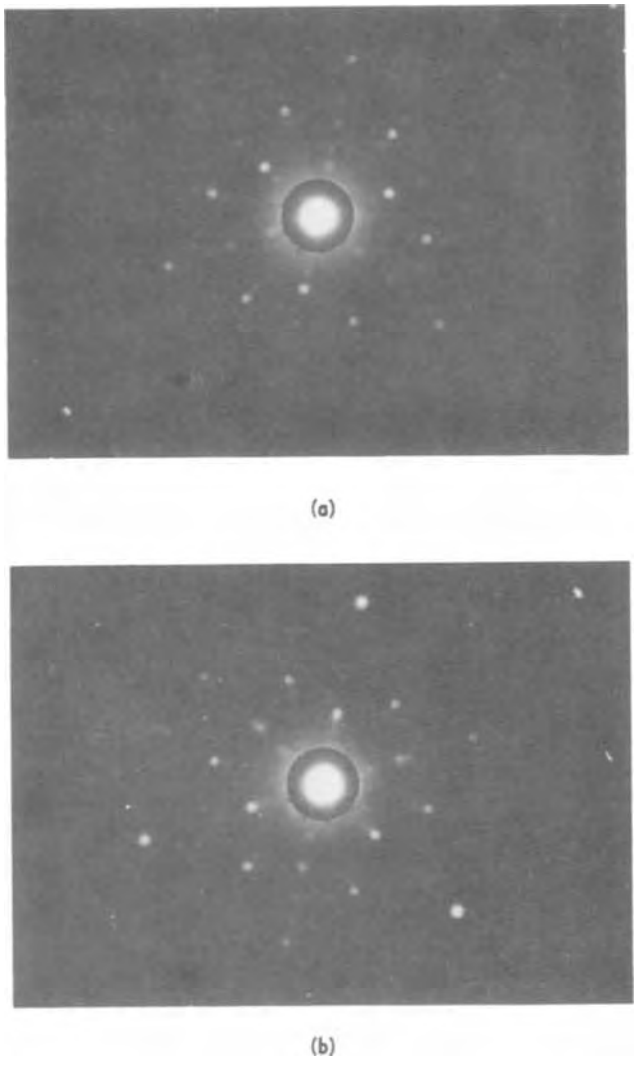

Fig. 4a and b. X-ray back-reflection Laue patterns of Czochralski sapphire (0001) before and after Nb deposition, respectively.

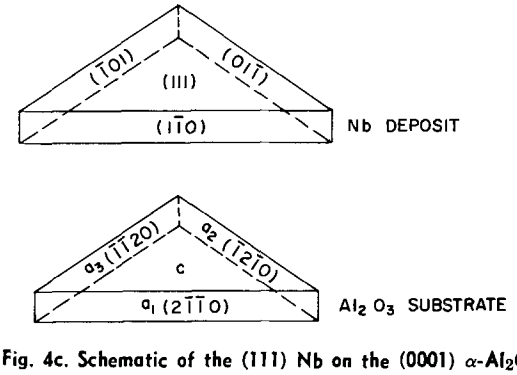

Fig. 4c. Schematic of the (111) Nb on the (0001) α-Al_2O_3

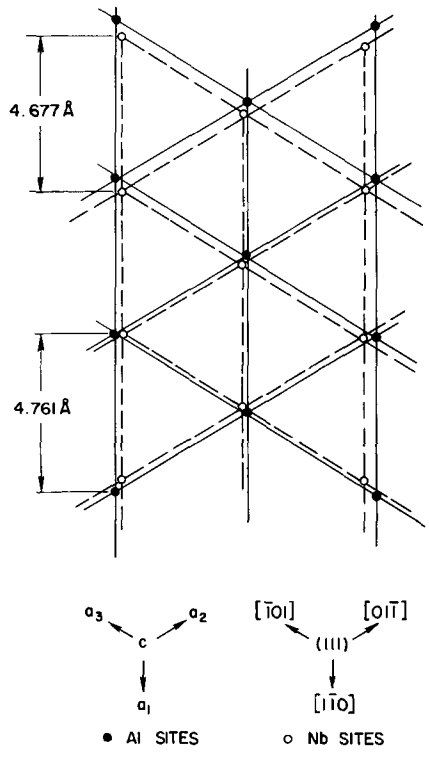

Fig. 4d. Lattice overlay of the (111) Nb on (0001) α-Al_2O_3

Further work is needed to distinguish among the various possibilities in particular studies during the initial stages of growth.

Acknowledgments

The authors acknowledge the helpful contributions of Dr. R. Rosenberg. The helpful discussions with Drs. J. W. Matthews, R. J. Gambino, and A. Segmüller are gratefully acknowledged.

Manuscript submitted Jan. 14, 1972; revised manuscript received June 12, 1972.

Any discussion of this paper will appear in a Discussion Section to be published in the December 1973 JOURNAL.

REFERENCES

1. J. W. Matthews, *Phil. Mag.*, **12**, 1143 (1965).
2. J. L. Robbins, and T. N. Rhodin, *Surface Sci.*, **2**, 346 (1964).
3. A. R. Lang, *J. Appl. Phys.*, **29**, 597 (1958).
4. A. R. Lang, *ibid.*, **30**, 1748 (1959).
5. G. H. Schwuttke, *ibid.*, **36**, 2712 (1965).
6. A. F. Mayadas, R. Laibowitz, and J. J. Cuomo, To be published.
7. R. Laibowitz and J. J. Cuomo, *J. Appl. Phys.*, **41**, 2748 (1970).
8. R. E. Newnham and Y. M. De Haan, *Z. Krist.*, **117**, 235 (1962).
9. W. J. Alford and D. L. Stephens, *J. Am. Ceram. Soc.*, **46** [4] 193 (1963).

On the Anodic Sectioning of Vanadium

II. Studies on Anodic Sectioning

M. R. Arora* and Roger Kelly*

Institute for Materials Research, McMaster University, Hamilton, Ontario, Canada

ABSTRACT

Anodic sectioning can be accomplished with vanadium almost as readily as with Al, Mo, and W, the main problem being the instability of the anodic film. The basic technique consists of forming films in an electrolyte based on acetic acid (as was shown possible by Keil and Salomon) and then removing the films with aqueous KOH. The thickness calibrations were obtained separately for high and low sectioning voltages, the results for high voltages being as follows: total metal removed in units of $\mu g/cm^2$ equal to $5.5 + 0.64 \times$ volts (for voltages ≥ 4); thickness of oxide in units of $\mu g/cm^2$ equal to $2.0 + 1.14 \times$ volts (for voltages ≥ 7.5). Particular attention was paid to extending the calibrations to low sectioning voltages. In the case of the oxide thickness, the approach used can be regarded as an alternative to ellipsometry, being based on a three-step procedure in which a film is formed, 20 or 40-keV Kr^{85} ions are implanted, and the film is stripped with aqueous KOH. The fraction of the Kr^{85} activity which is transmitted can be shown, using amorphous stopping theory, to give direct information on the film thickness. The low-voltage calibrations were as follows: total metal removed in units of $\mu g/cm^2$ equal to $1.0 + 1.78 \times$ volts; thickness of oxide in units of $\mu g/cm^2$ equal to $-5.1 + 2.09 \times$ volts.

A major problem in the use of ion implantation is that a detailed knowledge of the depth distribution of the ions is required. For example, with implanted semiconductors the depth distribution directly determines the junction depth, peak impurity concentration, and the base width (1) and indirectly determines the depth of amorphization (2). A closely related problem is that of determining diffusion profiles under extreme conditions. For example, self-diffusion in the bcc metals Ti, U, V, and Zr is found to have two components (3) and there has therefore been recent interest in extending diffusion measurements with other bcc metals to the lowest possible temperatures (4). In other work there has been concern with near-surface diffusion anomalies which arise (it is assumed) due to Gibbs adsorption, *i.e.*, attraction or repulsion of solute atoms from the surface (5). In all cases, the thicknesses involved are extremely small (0-10,000Å) and sectioning can be difficult.

The most sensitive sectioning technique probably still remains that in which a thin, uniform layer of the specimen is converted electrochemically to an anodic oxide which is subsequently stripped. Layers with thicknesses as low as 15Å can be removed in this

* Electrochemical Society Active Member.

Key words: vanadium, anodization, thin films, depth distributions.

way (6); by contrast, backscattering techniques, which are often regarded as depth probes par excellence, have a resolving power of perhaps 100-200Å with the usual detectors used (7). The only problem with anodic sectioning is that it has been fully perfected for only two metals [(Al (8) and W(6)] and partly perfected for only a further five (Ag, Au, Cu, Nb, and Si). Thus in the latter cases the following faults can be cited:

Ag (9) and Cu (10):	current at fixed voltage remains constant.
Au (11):	current at fixed voltage remains constant and current efficiency is low (~2%).
Nb (12):	dissolution end point (in the sense of the present Fig. 3) is imperfect.
Si (13-15):	current efficiency is low (1-2%); thickness calibration depends on electrolyte.

We have therefore undertaken a continuing study to develop anodic-sectioning techniques for additional metals. A method suitable for Mo has already been described (16), while the present work is concerned with V. Nb and Ta will be discussed in Part III (17).

Actually, there is already a good precedent for anodizing V in view of the work of Keil and Salomon (18, 19) and Keil and Ludwig (20). These authors established what appears to be the only known electrolyte that will permit V to be anodized (see below). In addition, they described the basic electrochemical properties of V, including the facts that the anodization was close to 100% in efficiency, that the anodic current obeyed the expected exponential law, and that the film had a stoichiometry similar to VO_2. The principal contributions of the present work will be seen to lie in the treatment given to stripping and to thickness calibration, neither of which was treated previously (18-20).

Anodic Sectioning of Vanadium

Anodizing step.—The anodic sectioning of V is closely similar to that for Mo (16). Polycrystalline specimens, with dimensions of 15 x 20 x 0.1 mm and with a purity claimed to be 99.98%, were used. They were cleaned using a sequence of petroleum ether, dilute nitric acid, and distilled water and were then anodically sectioned at least 4 times at 50 volts. The electrolyte was the same as that used for Mo (16) and similar to that proposed by Keil and Salomon (19), namely glacial acetic acid such that each liter of solution contained 0.02 moles of $Na_2B_4O_7 \cdot 10H_2O$ and 1.0 mole of additional water. The electrolyte was not protected from air as in the previous work (18-20) and was therefore discarded after 8-10 anodizings or 2 hr, whichever came first. The cathode was either a Pt cylinder with an inside diameter of 2.5 cm or a 2.5 x 2.5 cm Pt square spaced 0.8 to 1.0 cm from the specimen, the choice depending on whether the experiment was concerned with both sides of the specimen (*e.g.*, a gravimetric calibration) or only one side (*e.g.*, a depth distribution). All anodizings were made at 25° ± 1°C with a power supply such that limits to both the current and voltage could be preset (Hewlett-Packard Model 6186B). Voltages refer to the total voltage from anode to cathode.

A crucial step in the anodizing (in those instances where a permanent film was desired) was that in which the specimens were dried in a jet of compressed air immediately after withdrawal from the electrolyte, for without such drying the films were unstable. The instability, as evidenced by changes in the interference colors, set in at about 60 sec, a result similar to that obtained previously with Mo (16). The instability is inherent to the oxides on V and Mo and not to the electrolyte, for films formed on Nb, Ta, or W in this electrolyte have the same high stability as films formed on these metals using aqueous ammonium pentaborate.

Effect of stirring.—Galvanostatic measurements with stirred and unstirred electrolytes showed that stirring affects the rate of film growth such as to lower the voltage-*vs.*-time curves (Fig. 1). Such an effect, which increases with increased stirring and decreased current density, has also been observed with Bi (21) and W (22) and has been explained in terms of the stirring preventing dissolved oxide from accumulating near the surface. All anodizings were therefore carried out in unstirred electrolytes.[1]

Effect of current density.—A second group of experiments was undertaken to explore the nature of the "anodizing end point," *i.e.*, the discontinuity in current which occurs when both current and voltage are preset and which is illustrated in Fig. 2. The object was to see if anodizing under these conditions, which are particularly controllable, was practical; in fact, anodizing with only the current preset [as with Ag (9), Au (11), Cu (10), and Si (13-15)] is not correct with V since, as a result of the low conductivity of the electrolyte, it leads to nonuniform film thicknesses. (The latter result followed by noting the interference colors during the course of an anodizing at 2.0 mA/cm² without voltage limitation.) The results (typical examples are included

[1] An effect of stirring as in Fig. 1 has been confirmed also for Mo. It is therefore important to note that the thickness calibrations of Ref. (16) were made without stirring.

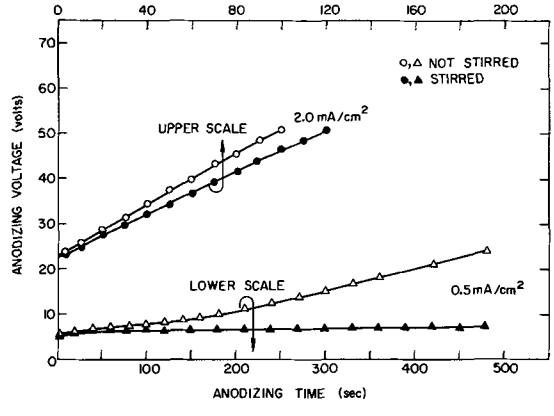

Fig. 1. Effect of stirring on anodization of V. The results show that stirring lowers the voltage-versus-time curves in an undesirable way. The cylindrical cathode was used.

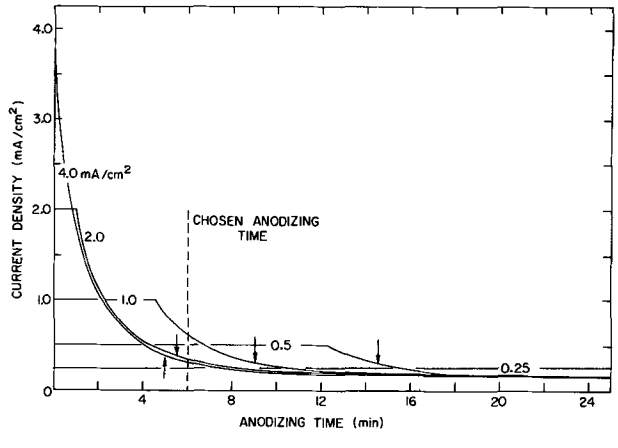

Fig. 2. Effect of initial current density on the anodizing end point. (*i.e.*, current discontinuity) and on the time for the interference colors to become uniform (marked with arrows). The results, which were obtained with a preset voltage of 50 volts, suggest that reproducible sectioning would be obtained with an initial current density of either 2.0 or 4.0 mA/cm² and a time of at least 6 min. The cylindrical cathode was used. The examples given are "typical" of a total of 14 curves.

in Fig. 2) confirmed that initial current densities of 4.0 and 2.0 mA/cm^2 gave excellent anodizing end points, with the value 2.0 mA/cm^2 being chosen for subsequent work.

The lack of an anodizing end point for 0.25 mA/cm^2, which is equivalent to a lack of voltage rise, will be recognized as being in agreement with previous work (19).

Effect of time.—Davies *et al.* (23) found with Si that there was a loss of Si to the electrolyte which was linear in the anodizing time, namely

$$\text{Loss} = 0.04 + 0.017t_{\text{min}}\ \mu\text{g/cm}^2$$

This effect is far more pronounced with V, as can be shown from a series of experiments in which films were formed with a preset current of 2.0 mA/cm^2 and a preset voltage of 50 volts, and were then measured gravimetrically

Anodizing time (min):	6	10	20	30	60
Total metal removed (μg/cm^2):	38.0	43.2	49.5	57.2	80.0
Thickness of oxide (μg/cm^2):	60.0	62.5	64.7	65.5	69.2

There is thus a continuing removal of metal during prolonged anodization at a fixed voltage whereas oxide formation is nearly independent of time. If the oxide thickness is re-expressed in units of μg/cm^2 of metal, an estimate of the metal loss during anodization is obtained

$$\text{Loss (if oxide is } VO_2) = -2 + 0.66t_{\text{min}}\ \mu\text{g/cm}^2$$
$$\text{Loss (if oxide is } V_2O_5) = 0 + 0.69t_{\text{min}}\ \mu\text{g/cm}^2$$

In a further group of experiments it was shown that an anodic film formed with 2.0 mA/cm^2 and 50 volts was uniform, as evidenced from the interference colors, starting at 5.5 min. Results for other initial current densities are marked with arrows in Fig. 2.

These experiments would suggest that a 6 min anodizing time is optimum, since it is short enough to minimize metal loss yet long enough to yield uniform films and to take advantage of the anodizing end point. In summary, the anodizing procedure proposed here thus involves a temperature of 25° ± 1°C, an anode-cathode spacing of 0.8-1.0 cm, conditions in which both current and voltage are preset, no stirring, an initial current density of 2.0 mA/cm^2, a total anodizing time of 6 min, and (when a permanent film is desired) the use of an air jet to dry the specimens. Relaxing any of these conditions will to some extent invalidate the thickness calibrations to be described below.

Stripping step.—Anodic films can be formed with perhaps 20 different elements but in only six cases (Ag, Al, Au, Cu, Mo, and W) is reliable stripping possible. This is because of the problem of the "dissolution end point," such that the reagent used to dissolve the film should not attack the underlying metal. To determine the nature of the dissolution end point with V, specimens were labeled with 30-keV Kr^{85} to a dose of 5 × 10^{15} ions/cm^2 and then anodized; the specimens were now alternately counted and exposed to 0.1% aqueous KOH (Fig. 3). It is seen that the films dissolve in ≤30 sec; the attack on the underlying V, by contrast, occurs at the negligible rate of 0.3 Å/min, as can be deduced by comparing curves as in Fig. 3 (but extended to 25 min) with an integral depth distribution as in Fig. 7, "dashed" (but for 30 keV).

Further experiments showed that also higher KOH concentrations could be used for stripping. For example, the rate of attack on the underlying V was still negligible (about 1.0 Å/min) using saturated KOH.

In a complementary series of experiments, specimens of V were first anodized to 12 volts and only then labeled with 40-keV Kr^{85} and exposed to 1% KOH. The

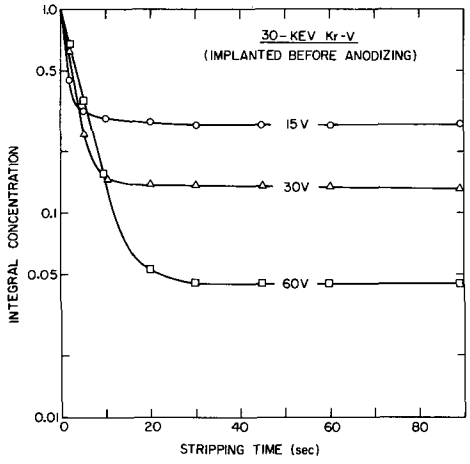

Fig. 3. Dissolution of anodic films on V in 0.1% KOH as inferred by the loss of activity. The activity was introduced prior to anodizing as 5x10^{15} ions/cm^2 of 30-keV Kr^{85}.

object was to determine the extent to which a transmission technique (24) could be used for obtaining depth distributions in the anodic film formed on V. The results (Fig. 4) showed that two problems arose, namely loss of film by sputtering and decreased solubility. They may be summarized as follows:

≤4 × 10^{14} ions/cm^2	sputtering loss unimportant	dissolution time ≤3 min
1 to 4 × 10^{15} ions/cm^2	sputtering loss of ~2 μg/cm^2 [2]	dissolution time ≤11 min
8 to 16 × 10^{15} ions/cm^2	sputtering loss of ~4 μg/cm^2 [2]	dissolution time ~21 min
3.2 × 10^{16} ions/cm^2	sputtering loss undeterminable	film insoluble

It was also shown that the use of saturated KOH gave little or no increase in the dissolution rate. Transmission experiments are thus practicable only for doses of ≤4 × 10^{14} ions/cm^2.

The marked sputtering loss found, which is untypical for an oxide (25), agrees with recent sputtering-coefficient measurements with anodized V (12), while the decreased solubility is undoubtedly related to the result that high-dose bombardment of V_2O_5 or VO_2 leads to preferential oxygen loss and eventual formation of crystalline V_2O_3 (26). Decreased solubilities following

[2] The sputtering loss was estimated by comparing Fig. 4 with a depth-distribution curve constructed using the oxide transmission data of Fig. 8.

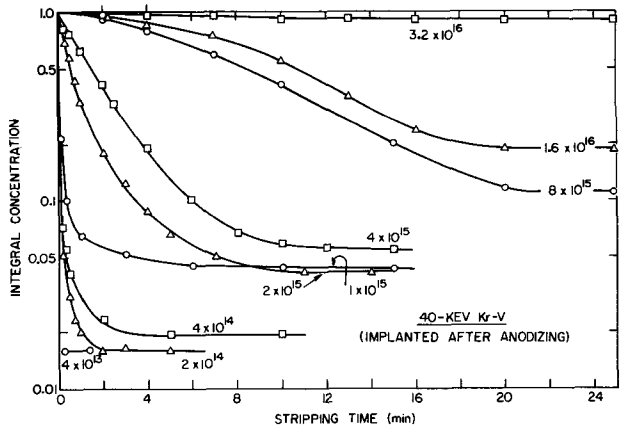

Fig. 4. Dissolution of 12-volt anodic films on V in 1% KOH as inferred by the loss of activity. The activity was introduced following anodization as various doses (indicated in units of ions/cm^2) of 40-keV Kr^{85}.

ion impact have also been confirmed for Nb_2O_5 (12, 17), Ta_2O_5 (17), and WO_3 (12).

Structure of the anodic oxide.—A limited amount of work on the structure of the anodic film formed on V was undertaken using the reflection electron diffraction attachment for a Philips EM-300 microscope. The film as formed was amorphous, and in this respect V thus resembles Al, Mo, Nb, Ta, and W. The amorphous structure was preserved to at least 370°C (10 min), while at 400°-425°C (10 min) crystallization went to completion. By way of comparison, the crystallization temperatures for anodic Nb_2O_5 and Ta_2O_5 are, respectively, 475° and 550°C (27). The temperatures found here for the anodic film on V will be noted to apply to films which were still attached to the metallic substrate and it is likely that, as with Nb and Ta (27), the free oxide would crystallize at perhaps 100°-150°C higher. The diffraction pattern of the crystallization product could be shown (17) to infer the stoichiometry V_6O_{13} (28), a result in quite satisfactory agreement with Keil and Salomon's (19) proposal of VO_2.

Thickness Calibrations

Gravimetric determinations.—The thicknesses of anodic films formed on V at ≥10 volts can, since there is a good dissolution end point (above), be easily determined using the conventional weight-loss method. The results are included in Fig. 5 and 6, and can in addition be represented as follows

Total metal removed (≥4 volts)

$$= 5.5 + 0.64 \times \text{volts } \mu g/cm^2 \text{ of metal} \quad [1]$$

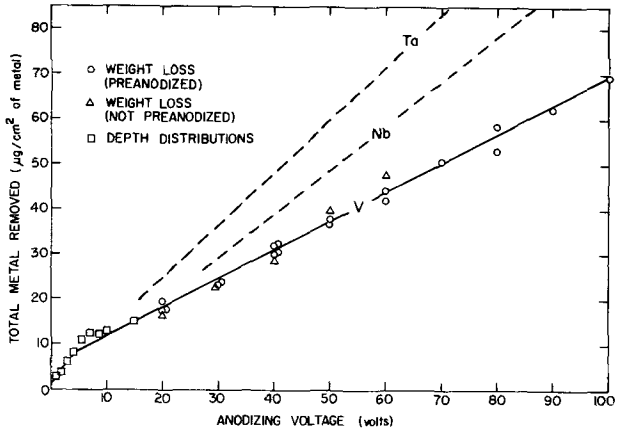

Fig. 5. Total V removed in an anodizing-stripping sequence under the standard conditions as summarized in text. Shown for comparison are the curves for Nb (25) and Ta (29) as deduced indirectly from measurements of oxide-film thickness.

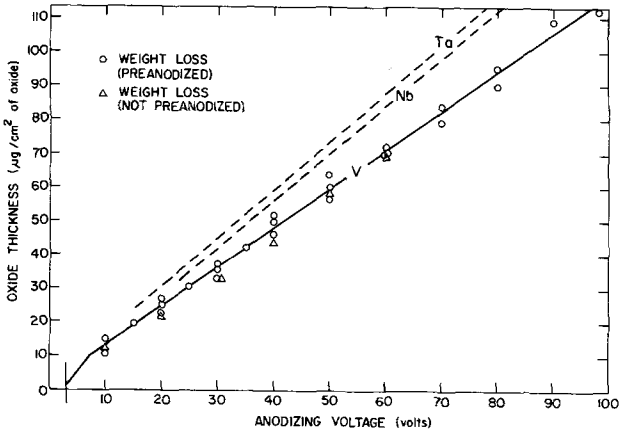

Fig. 6. Thickness of oxide film formed by anodizing (but not stripping) V under the standard conditions of text. Shown for comparison are the curves for Nb (25) and Ta (29). The present work does not establish the behavior between 0 and 3 volts.

Thickness of oxide (≥7.5 volts)

$$= 2.0 + 1.14 \times \text{volts } \mu g/cm^2 \text{ of oxide} \quad [2]$$

These relations are valid only to ~110 volts, as electrical breakdown occurred at higher voltages.

The corresponding curves for Nb (25) and Ta (29) have been included in Fig. 5 and 6 as they serve to emphasize the systematic behavior of the three group 5B metals. Note that the amounts of metal removed (Fig. 5) are, in the cases of Nb and Ta, based on the oxide-film thickness rather than on true anodic sectioning.

Metal-removal thicknesses from depth distributions.—An accurate knowledge of the metal-removal thicknesses for 1-15 volts is essential to a sectioning technique such as is being described here, yet it generally presents serious problems. We will therefore show how it is possible to estimate the metal-removal thicknesses for low voltages as a function of those for higher voltages. The method is related to that used for Mo (16) though with marked improvements.

As a first step, 39 specimens were bombarded with 20-keV Kr^{85} to a dose of 5×10^{15} ions/cm². With 3 specimens the residual activities were determined after repeated 3-volt sectionings. The result was a true depth-distribution curve (Fig. 7, dashed) with depth expressed in units of volts, the curve serving to show that there is no discontinuity in the depth distribution until ~9 volts. With the remaining 36 specimens the residual activities were determined after a single sectioning at various voltages. The resulting curve (Fig. 7, solid), when interpreted in the light of the true depth-distribution curve (Fig. 7, dashed), reveals the following three features about the thickness-voltage calibration: (*i*) the zero-voltage intercept is close to zero, (*ii*) the calibration is "well-behaved" starting at about 1 volt, and (*iii*) there is a discontinuity at 4 ± 0.5 volts.

To get further information, 26 specimens were bombarded under the same conditions as above and the residual activities were determined after repeated sectionings at 1-15 volts. Reference to Fig. 7 (solid) then enabled the metal-removal thicknesses to be expressed as a function of those for higher voltages, with detailed results as in Table I and an analytical expression as follows

Total metal removed ($1 \leq$ volts ≤ 4)

$$= 1.0 + 1.78 \times \text{volts } \mu g/cm^2 \text{ of metal} \quad [3]$$

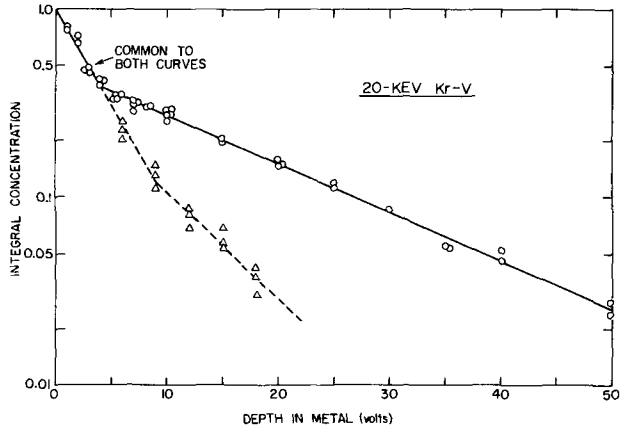

Fig. 7. Integral depth distributions in V for 20-keV Kr^{85} implanted to a dose of 5×10^{15} ions/cm². The depth scale is given in units of the sectioning voltage. Dashed: curve obtained after repeated 3-volt sectionings and which, except for the untypical depth scale, is a true depth distribution. Solid: curve obtained from a series of specimens, each sectioned once at a different voltage. Taken together, these curves demonstrate that there is a discontinuity at 4 ± 0.5 volts in the thickness-voltage calibration.

Table I. Metal-removal thicknesses for low anodizing voltages

Anodizing voltage	Number of sectionings	Residual activity	Thickness in terms of that for a single high-voltage sectioning*	Thickness in $\mu g/cm^2$ assuming the validity of Eq. [1]
1	7	0.139 ± 0.005	(1/7) ($x_{21.4}$)	2.7 ± 0.1
2	5	0.139 ± 0.001	(1/5) ($x_{21.4}$)	3.8 ± 0.0
3	4	0.079 ± 0.007	(1/4) ($x_{30.8}$)	6.3 ± 0.2
4	3	0.080 ± 0.012	(1/3) ($x_{30.6}$)	8.4 ± 0.5
5.5	2	0.108 ± 0.010	(1/2) ($x_{35.4}$)	10.9 ± 0.5
7	2	0.079 ± 0.004	(1/2) ($x_{30.8}$)	12.6 ± 0.3
8.5	2	0.083 ± 0.010	(1/2) ($x_{29.8}$)	12.3 ± 0.7
10	2	0.071 ± 0.002	(1/2) ($x_{32.6}$)	13.2 ± 0.1
15	2	0.048 ± 0.003	(1/2) ($x_{39.2}$)	15.3 ± 0.4

* The nomenclature "$x_{21.4}$" means "metal-removal thickness accomplished in a single sectioning at 21.4 volts."

Oxide-film thicknesses from depth distributions.—A related procedure, based on depth-distributions, has been used for estimating the thicknesses of anodic films formed at low voltages. It is in many respects an alternative to ellipsometry, which could in any case not be used with V due to lack of knowledge of the optical constants. Films were formed at 2-15 volts and the specimens were only then labeled with 20-keV or 40-keV Kr^{85} to a dose of about 1.5×10^{14} ions/cm^2 (higher doses, as shown above, cause a partial sputtering of the films). The Kr^{85} activity was now measured before and after dissolving the films in 1% KOH, with typical results for 40 keV as follows:

voltage:	3	6	9	12	15
fractional transmission of activity:	0.967 ±0.008	0.629 ±0.029	0.170 ±0.003	0.0353 ±0.0019	0.00380 ±0.00010

The basis of the thickness determination lies in recognizing that the fractional activity transmitted through an amorphous film of thickness x is given, according to amorphous stopping theory (30), by

$$C^{\text{int.}}(x) \approx \frac{1}{2}\,\text{erfc}\left[\frac{x - \langle x\rangle}{2^{1/2}(\langle \Delta x^2\rangle)^{1/2}}\right] f(x)$$

$$\equiv \frac{1}{2}\,\text{erfc}\,[A'x - B']$$

Here $C^{\text{int.}}(x)$ stands for integral concentration (*i.e.*, fractional transmission of activity), $\langle x\rangle$ is the mean projected ion range, $\langle \Delta x^2\rangle$ is the mean square projected ion straggling, and $f(x)$ is a factor [see Ref. (31) for its form] which has been here taken as unity. This means that, provided the relation for oxide thickness is of the type

$$x = A + B \cdot \text{volts} \qquad [4]$$

in any voltage interval, the fractional transmission measurements can be plotted to yield straight lines by using the relation

$$\text{erf}^{-1}[1 - 2C^{\text{int.}}(x)] = A'x - B'$$

$$= A' \cdot B \cdot \text{volts} + A' \cdot A - B'$$

where erf^{-1} stands for inverse error function. The results are shown in Fig. 8 and serve to establish (*i*) that the thickness-voltage relationship is "well-behaved" starting at about 3 volts, (*ii*) that there is a discontinuity at 7.5 ± 0.5 volts, and (*iii*) that the slopes are given by

$$\frac{\text{(slope for } \leq 7.5 \text{ volts)}}{\text{(slope for } \geq 7.5 \text{ volts)}} = 1.83 \pm 0.04$$

This along with Eq. (2) is sufficient information to allow the constants A and B in Eq. (4) to be determined at low voltages

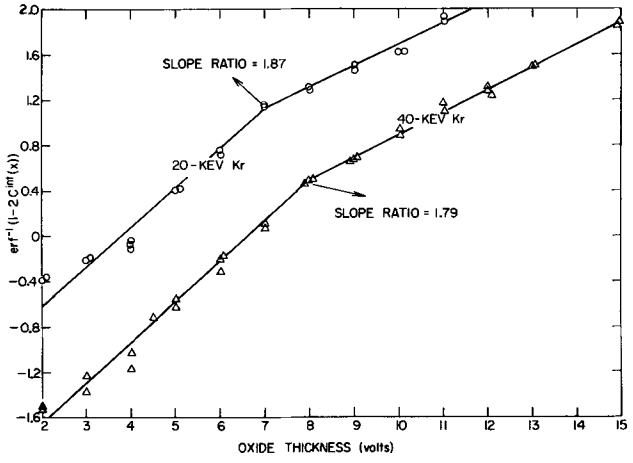

Fig. 8. The quantity $\text{erf}^{-1}\,[1 - 2C^{\text{int.}}(x)]$ vs. oxide thickness, with thickness expressed in units of the anodizing voltage. If the relation for oxide thickness is of the type $x = A + B \cdot$volts, then the slope of such a plot follows as being proportional to B. In the particular case there is evidently a discontinuity in B at 7.5 ± 0.5 volts such that B is larger by 1.83 ±0.04 below this voltage.

Thickness of oxide ($3 \leq$ volts ≤ 7.5)

$$= -5.1 + 2.09 \times \text{volts}\ \mu g/cm^2 \text{ of oxide} \qquad [5]$$

Effect of radiation damage on the calibrations.—All anodizings except those of the section on Metal-removal thicknesses from depth distributions were made with unbombarded specimens. To investigate whether bombardment causes a change in the anodic sectioning of V, 12 specimens were implanted with 10-keV Kr to various doses and were then anodized at 10 or 40 volts. After making suitable corrections for the weight of the implanted Kr, it was found that, to within an uncertainty of about 5%, there was no effect of radiation damage on the behavior of V (Table II).

Such a result is similar to that previously obtained for Mo (16) and Si (23), and is, in fact, probably rather general.

Reproducibility of the calibrations.—With a metal such as V, where anodic films are unstable and where such apparently trivial experimental details as stirring or electrode spacing affect the anodizing behavior, it might be expected that the calibrations would be unreliable. In fact, the experimental scatter was consistently small, having an average of 4% for Fig. 5, 5% for Fig. 6, and 4% for Table I (final column). By comparison, a 5% uncertainty has been claimed for Al (8) and 2% for W (6).

Discussion

The anodic sectioning of V proves to be a far simpler process than might be anticipated. The main problem is the instability of the anodic film, though this can be overcome provided a correct electrolyte is chosen [namely, similar to that of Keil and Salomon (19)] and provided the specimens are dried with an air jet (*i.e.*, in those instances where a permanent film is desired). Vanadium is then found to behave like Al (8), Mo (16), and W (6) in nearly every respect: (*i*) well-defined "anodizing end point," *i.e.*, a sharp discontinuity occurs in the current when both the current and voltage are preset; (*ii*) well-defined "dissolution end

Table II. Effect of radiation damage

Dose of 10-keV Kr (ions/cm^2)	Total metal removed in a 10-volt sectioning ($\mu g/cm^2$)	Total metal removed in a 40-volt sectioning ($\mu g/cm^2$)
zero	14.5 ± 0.1	32.5 ± 0.3
5×10^{15}	14.0 ± 0.1	33.8 ± 0.7
4×10^{16}	14.1 ± 0.1	32.7 ± 0.2
4×10^{17}	13.7 ± 0.3	35.0 ± 0.0

point," i.e., a sharp discontinuity occurs in the rate of dissolution of the specimen when the oxide-metal interface is reached; (*iii*) possibility of removing layers of metal as thin as 50Å, this being the approximate value for a 1-volt sectioning; (*iv*) possibility of using sectioning voltages up to ~110, thence of removing layers of metal with thicknesses up to 1300Å.

Considering the group 5B metals together (i.e., V, Nb, and Ta), perhaps the main similarities in anodizing behavior are that the anodic oxides are amorphous though crystallize in the region of 400°-550°C, and that the extents of metal removal or oxide formation for a given voltage vary systematically (Fig. 5 and 6). Rather different results are obtained with regard to stripping, as the dissolution end point following film formation with conventional electrolytes is of a poor quality with Nb and is virtually nonexistent with Ta (12, 17).

Acknowledgment

This research was supported by grants from the National Research Council, Ottawa, and the Defence Research Board, Ottawa.

Manuscript submitted June 12, 1972; revised manuscript received Aug. 10, 1972.

Any discussion of this paper will appear in a Discussion Section to be published in the December 1973 JOURNAL.

REFERENCES

1. G. Dearnaley, Harwell (U.K.) Report AERE-R 6559 (1970).
2. R. Kelly and Nghi Q. Lam, *Rad. Effects*, **10**, 247 (1971).
3. A. D. LeClaire, in "Diffusion in b.c.c. metals," p. 3, American Soc. for Metals, Metals Park, Ohio (1965).
4. R. E. Pawel and T. S. Lundy, *J. Phys. Chem. Solids*, **26**, 937 (1965).
5. A. J. Mortlock, *J. Australian Inst. Metals*, **14**, 98 (1969).
6. M. McCargo, J. A. Davies, and F. Brown, *Can. J. Phys.*, **41**, 1231 (1963).
7. E. Bφgh, *ibid.*, **46**, 653 (1968).
8. J. A. Davies, J. Friesen, and J. D. McIntyre, *Can. J. Chem.*, **38**, 1526 (1960).
9. Nghi Q. Lam, S. J. Rothman, and L. J. Nowicki, *This Journal*, **119**, 715 (1972).
10. Nghi Q. Lam, S. J. Rothman, and L. J. Nowicki, *ibid.*, **119**, 1344 (1972).
11. J. L. Whitton and J. A. Davies, *ibid.*, **111**, 1347 (1964).
12. Nghi Q. Lam and R. Kelly, To be published. See also N. Q. Lam, Ph.D. thesis, McMaster University, 1971.
13. P. F. Schmidt and W. Michel, *This Journal*, **104**, 230 (1957).
14. L. A. Dubrovskii, V. G. Mel'nik, and L. L. Odynets, *Russ. J. Phys. Chem.*, **36**, 1183 (1962).
15. M. A. Wilkins, Harwell (U.K.) Report AERE-R5875 (1968).
16. M. R. Arora and R. Kelly, *This Journal*, **119**, 270 (1972).
17. M. R. Arora and R. Kelly, To be published.
18. R. G. Keil and R. E. Salomon, *This Journal*, **112**, 643 (1965).
19. R. G. Keil and R. E. Salomon, *ibid.*, **115**, 628 (1968).
20. R. G. Keil and K. Ludwig, *ibid.*, **118**, 864 (1971).
21. I. A. Ammar and M. W. Khalil, *Electrochim. Acta*, **16**, 1379 (1971).
22. I. A. Ammar and R. Salim, *Corrosion Sci.*, **11**, 591 (1971).
23. J. A. Davies, G. C. Ball, F. Brown, and B. Domeij, *Can. J. Phys.*, **42**, 1070 (1964).
24. B. Domeij, F. Brown, J. A. Davies, and M. McCargo, *ibid.*, **42**, 1624 (1964).
25. Nghi Q. Lam and R. Kelly, *ibid.*, **48**, 137 (1970).
26. H. M. Naguib and R. Kelly, *J. Phys. Chem. Sol.*, **33**, 1751 (1972).
27. P. H. G. Draper and J. Harvey, *Acta Met.*, **11**, 873 (1963).
28. F. Théobald, R. Cabala, and J. Bernard, *Compt. Rend. Acad. Sci. Paris*, **266C**, 1534 (1968).
29. D. A. Vermilyea, *Acta Met.*, **1**, 282 (1953).
30. J. B. Sanders, *Can. J. Phys.*, **46**, 455 (1968).
31. I. Reid and R. Kelly, *Rad. Effects*, In press.

Technical Notes

Electron-Microprobe Characterization of Vapor-Grown $InAs_{1-x}P_x$ Layers

James R. Buckmelter and John K. Kennedy

Air Force Cambridge Research Laboratories, Air Force Systems Command, L. G. Hanscom Field, Bedford, Massachusetts 01730

$InAs_{1-x}P_x$ alloys have a broad range of energy gaps which make them potential candidates for infrared detectors in the 0.94 to 3.6μ range (1). These alloys can be tailored to provide peak response at any discrete wavelength within the applicable range by choosing the proper As to P ratio, since the energy gap is a direct function of the composition. $InAs_{1-x}P_x$ alloys can be grown from the melt (2), by liquid phase epitaxy (3), or by vapor-phase deposition (4). Vapor-phase growth offers the advantage of closely controlled growth rates, high purity, orientation, and the ability to vary composition and doping with time. However, compositional analysis of vapor-grown films is difficult because of the generally thin layers, the different composition of the substrate, and the possibly graded layers.

A convenient technique for the analysis of layers as thin as 2500Å is electron-probe microanalysis at low accelerating potentials where the depth of penetration of the electron beam is low (5). The area to be analyzed can also be easily varied from a 1μ diameter spot to any arbitrary size; thus making it possible to focus on grain boundaries, particulates, or large areas. Homogeneity can be rapidly checked by moving various areas of the sample under the electron beam and noting any changes in characteristic x-ray intensity. Homogeneous and pure standards such as InAs, InP, GaAs, GaP, and others, are readily available and suffi-

Key words: microprobe, $InAs_{1-x}P_x$, epitaxy, vapor.

cient since correction procedures for intermediate compounds are reasonably well known (6, 7).

The electron microprobe was utilized to determine the As to P ratio of 24 ungraded $InAs_{1-x}P_x$ epitaxial layers. These layers were deposited on InAs substrates by a vapor-phase growth method similar to that described by Tietjen *et al.* (4). The epitaxial layers were approximately 10μ thick over a substrate area of approximately 1 cm^2. The analyses of these layers were based on the dead-time and background corrected x-ray intensities of the samples compared to standards of InAs or InP. These relative x-ray intensities or "k-ratios" were first calculated for various arbitrary compositions at an electron-beam potential of 10 keV and an x-ray takeoff angle of 52.5° by a computer program (MAGIC IV) (8) which performs all the necessary corrections. The k-ratios were then plotted as a function of composition as in Fig. 1. Several samples were checked for stoichiometry by measuring the k-ratios of all elements present, but once the samples were determined to be stoichiometric, the composition could be defined by measuring the k-ratio of only one element. The pKα line was used since the x-ray intensity of this line was sufficient for counting statistics, yet electron-beam penetration did not exceed 1μ at 10 keV. Those samples with greater than 25 mole per cent (m/o) As were also analyzed for As content. Each sample was analyzed at least twice by counting at 10 places for 40 sec each for every analysis. Background was determined on InAs for pKα and on InP for $AsL\alpha_1$ and this agreed with the background as determined by wavelength scans on InP and one of the alloys. Precision in the worst case for 3 analyses on one sample was 4% of the average measurement, but precision was usually better than 2% of the average measurement. The major limitation on precision was the microscopic surface texture of the material. The uneven surface nature of some samples, especially of the arsenic-rich compositions, made it difficult to focus the sample with the light optics for the crystal spectrometer, leading to a loss of precision (9).

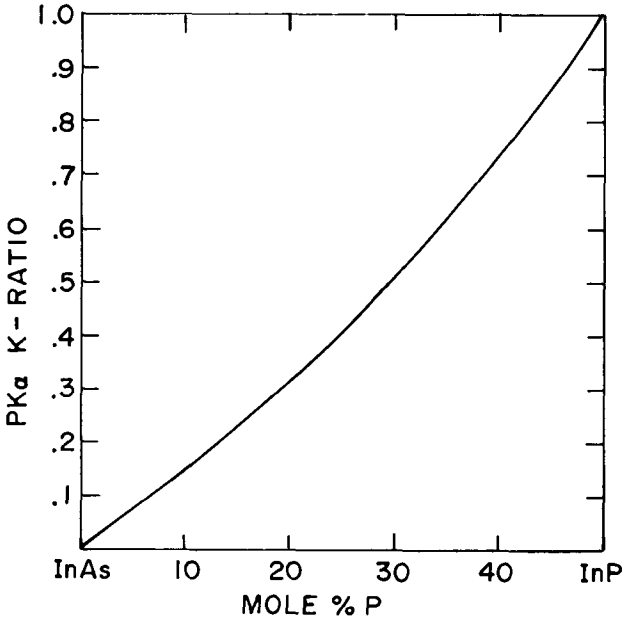

Fig. 1. pKα ratio vs. mole per cent phosphorus for $InAs_{1-x}P_x$ using InP as a standard at 10 keV.

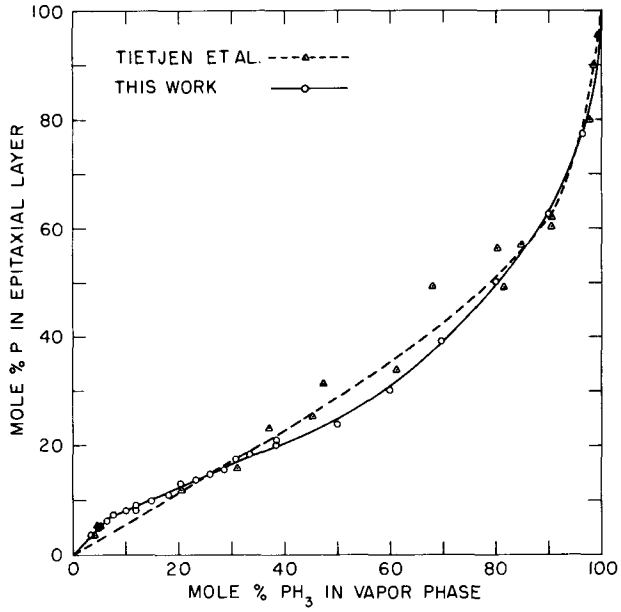

Fig. 2. Dependence of epitaxial phosphorous concentration on concentration of PH_3 in the AsH_3-PH_3 gas mixture.

Figure 2 is a plot of the m/o P measured by this technique *vs.* the m/o PH_3 in the vapor phase as calculated from the gas-flow rates. In this graph only the group V elements of the epitaxial layers and gas mixtures were taken into account for the calculation of mole percentages. Figure 2 agrees with the results reported by Tietjen *et al.*, (4) who used the more tedious destructive method of wet chemical analysis (10) to determine the composition of the epitaxial layers. Thus a direct physical, nondestructive, microprobe analysis technique can be applied to calibrate a vapor-phase growth system capable of producing any desired alloy of $InAs_{1-x}P_x$.

Manuscript submitted May 30, 1972; revised manuscript received Aug. 23, 1972.

Any discussion of this paper will appear in a Discussion Section to be published in the December 1973 JOURNAL.

REFERENCES

1. H. A. Allen and E. W. Mehal, *This Journal*, **117**, 1081 (1970).
2. R. Bowers, J. E. Banerle, and A. J. Comish, *J. Appl. Phys.*, **30**, 1050 (1959).
3. G. A. Antypas and T. O. Yep, *ibid.*, **42**, 3201 (1971).
4. J. J. Tietjen, H. P. Maruska, and R. B. Clough, *This Journal*, **116**, 492 (1969).
5. C. A. Anderson, in "The Electron Microprobe," p. 58, T. D. McKinley, K. F. J. Heinrich, and D. B. Wittry, Editors, John Wiley and Sons, Inc., New York (1965).
6. K. F. J. Heinrich, NBS Technical Note 521, SD Catalog No. C13.46:521 (1970).
7. D. R. Beaman and J. A. Isasi, *Anal. Chem.*, **42**, 1540 (1970).
8. J. W. Colby, Proc. VIth Nat. Conf. on Electron Probe Analysis, p. 17, Pittsburgh, Pa. (1971).
9. K. F. Heinrich, "Advances in X-Ray Analysis," Vol. 11, p. 40, J. B. Newkirk and G. R. Mallett, Editors, Plenum Press, New York (1968).
10. B. L. Goydish, To be published.

The Use of Metalorganics in the Preparation of Semiconductor Materials

V. The Formation of In-Group V Compounds and Alloys

H. M. Manasevit* and W. I. Simpson

Research and Technology Division, North American Rockwell Corporation, Anaheim, California 92803

The feasibility of using various metalorganic-hydride combinations in the preparation of III-V (1-5) and II-VI (6) compounds and alloys has previously been demonstrated in our laboratories. We now wish to report on the extension of the process to the formation of single-crystal films of the In-Group V compounds and alloys.

In 1960 Didchenko and co-workers (7) studied the reaction between trimethylindium (TMI) and PH_3 *in vacuo* and in solution and prepared InP powder by heating a yellow reaction product to 250°-270°C. Harrison and Tompkins in 1962 (8) reacted SbH_3 with TMI at low pressures (2 and 30 mm) and produced crystalline InSb by heating the orange product of their reaction in a sealed tube at 150°-160°C.

However, in our studies, which are directed toward the preparation of epitaxial thin films by chemical vapor deposition (CVD), the source of In was chosen to be triethylindium (TEI), which is a liquid at room temperature (mp −32°C; bp 144°C), rather than trimethylindium, which is a solid at room temperature (mp 88.4°C; bp 135.8°C).

The apparatus used in these studies is essentially similar to the single-temperature-zone vertical reactor apparatus previously described for producing other semiconductor compounds (2). However, because TEI and AsH_3 were found to react at room temperature to form a yellow liquid with low-vapor pressure, the reactor was redesigned to include a side tube near the top of the reactor in order to admit the Group V hydride into the reactor in lines separate from the TEI line. A center tube was also added to the reactor chamber in order to concentrate and direct the reactants toward the substrate. The center-tube configuration seemed to be beneficial for controlling InAs, InP, and $InAs_{1-x}P_x$ growth but optional for preparing $Ga_{1-x}In_xAs$ films. The presence of trimethylgallium (TMG) in the gaseous atmosphere seemed to enhance the uniformity of the deposit as compared with that obtained for pure InAs.

Most of the growth studies were devoted to the formation of InAs and $Ga_{1-x}In_xAs$ on Al_2O_3 and GaAs. Electrical data were obtained for films of these materials. Only a few experiments were performed in preparing the P-containing compounds; these studies were interrupted when the preliminary goal was achieved, *i.e.*, when the feasibility of epitaxy was demonstrated.

The epitaxial growth of the In-Group V compounds and alloys on commercially polished (0001) Al_2O_3 was found to be much more sensitive to the procedures used for substrate surface preparation than is the growth of GaAs on these substrates. The best growth seemed to be achieved on Al_2O_3 substrates which had been cleaned with organic solvents such as trichloroethylene and acetone.

The deposition procedure used most often involved growth in a H_2 atmosphere containing As and/or P produced by decomposing the appropriate hydride(s) (10% in H_2) at the hot pedestal prior to the introduction of TMG and/or TEI into the reactor.

In the preparation of InAs, typical flow rates were as follows; 10% AsH_3-in-H_2, 75-100 cm^3/min; H_2 carrier through the TEI bubbler (at room temperature), 1000 cm^3/min; total H_2 through the reactor, 10 liters/min. These conditions led to InAs growth at rates from 0.04-0.05 μm/min in the reactor with the center-tube configuration. In preparing the $Ga_{1-x}In_xAs$ alloys, the AsH_3-in-H_2 flows were typically 50-75 cm^3/min; the H_2 carrier for the TEI, 1000-1600 cm^3/min; the H_2 through the TMG bubbler (at 0°C), 2-3 cm^3/min; and the total H_2 flow through the reactor, 10 liters/min.

Following deposition, the epitaxial layers were routinely examined by optical microscopy, Laue back-reflection x-ray diffraction, and reflection-electron diffraction (RED). Selected films were analyzed electrically using a Hall-effect "bridge sample" photoetched in the epitaxial layer; inconsistent results were obtained using the van der Pauw (9) technique, perhaps because of inhomogeneities in the films. Optical data were obtained from transmittance scans usually made on polished surfaces with a Beckman DK-1A double-beam recording spectrophotometer. Electron-microprobe techniques were employed to determine the composition of the deposited films. Composition data were obtained by direct comparison of the excited characteristic x-rays of bulk GaAs and InAs with those of the deposited films.

Properties of InAs Films

The electrical properties of 0.5-1.1 μm thick InAs films formed on (0001) Al_2O_3 at 650°C and 700°C had measured resistivity values of 0.003-0.006 ohm-cm, carrier concentrations from 1.4 to 1.6 $\times$ 10^{17} cm^{-3}, and average mobilities from 6,700 to 11,200 cm^2/V-sec. Measurements at 77°K showed only small reductions in carrier concentration and slight increases in mobility, thus indicating relatively poor quality material in these thin films.

The Laue x-ray diffraction pattern reproduced in Fig. 1 was obtained from an InAs film grown directly on (0001) Al_2O_3; upon analysis the pattern was found to be that of (111) InAs growth on (0001) Al_2O_3.

InAs growth studies on the (111) "A" faces, (111) "B" faces, and (100) orientations of polished GaAs substrates and on 15-25 μm thick GaAs films grown on (0001) Al_2O_3 and (111)-oriented $MgAl_2O_4$ wafers indicated the growth rates to be essentially the same on these orientations, as measured on angle-lapped samples. The as-grown films were n-type. Qualitatively, the growths seemed better on (111) GaAs than on (100) GaAs. The surface structure of a (111)-oriented InAs film grown on a (111) GaAs film which had been grown on (0001) Al_2O_3 is shown in the photomicrograph of Fig. 2. Typical (111) crystallographic growth features dominate the surface.

Growth of $Ga_{1-x}In_xAs$ Films

Following the successful achievement of the growth of InAs on Al_2O_3 and on GaAs, studies were begun on producing the $Ga_{1-x}In_xAs$ alloy. All subsequent alloy growth experiments utilized premixing of trimethylgallium (TMG) and TEI to obtain a homogeneous gas mixture prior to mixing with AsH_3.

The electrical properties of some of the better films formed directly on (0001) Al_2O_3 substrates are recorded in Table I. Two different TMG and AsH_3 gas sources were used with the same TEI gas source. Those are reflected in the different carrier concentrations ob-

* Electrochemical Society Active Member.

Key words: crystal growth, heteroepitaxy, films, insulating substrates, chemical vapor deposition.

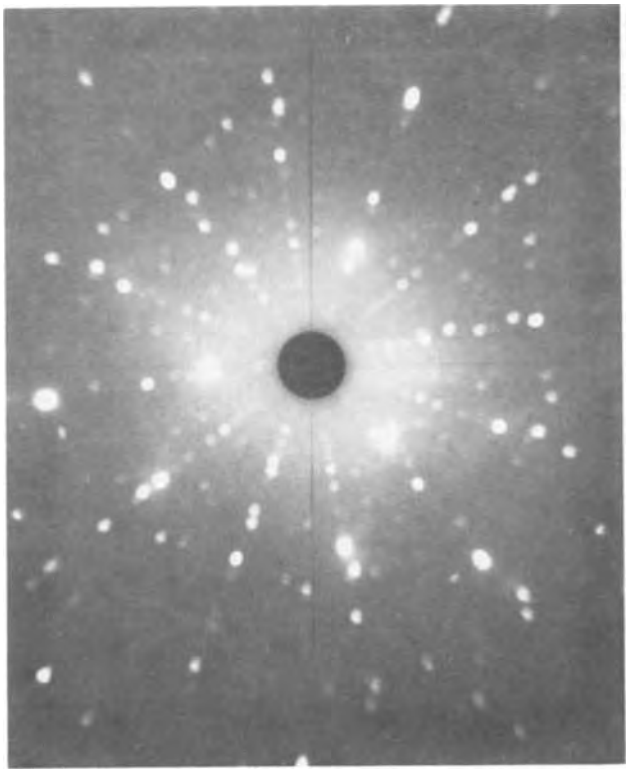

Fig. 1. Laue pattern for (111)InAs/(0001)Al_2O_3 composite

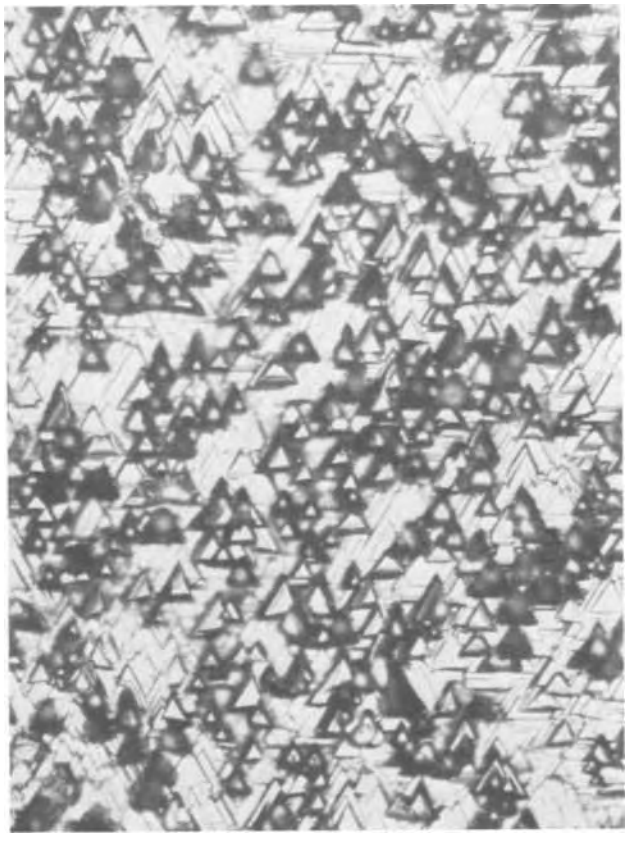

Fig. 2. Surface structure of (111)-oriented InAs film on (111)GaAs/(0001)Al_2O_3.

tained, $\sim 10^{16}$ cm^{-3} and $\sim 10^{17}$ cm^{-3}. The spread in mobilities probably is due to the fact that deposition and substrate-surface conditions were not optimized during this limited study.

The compositions given in Table I are based on electron-microprobe data. The bandgap energies are approximate values based on the location of the absorption edge obtained from optical transmittance curves; these bandgap energy determinations are uncorrected for film-thickness effects or other complications. There was relatively little variation in the composition of the alloy for films grown to various thicknesses on Al_2O_3 under nominally identical growth conditions. The uncorrected bandgap values also reflect the compositional change of the alloy film for the samples listed in the table.

The limited mobility data in Table I suggest 725°C to be a good temperature for growth directly on Al_2O_3, at least for the alloy with $E_g \sim 0.7$ eV. All of the films were grown in the reactor without a central tube. The preferred temperature for growth of the alloy films on Cr-doped (111)GaAs seemed also to be 725°C. An average mobility of 4500 cm^2/V-sec was obtained for an 11.7 μm-thick alloy film ($Eg = 0.68$ eV) at a carrier concentration of 7.6×10^{15} cm^{-3}. For reasons as yet unidentified, the mobilities of epitaxial $Ga_{1-x}In_xAs$ films grown on the "A" and "B" faces of (111)GaAs were lower than those for films formed on (0001)Al_2O_3.

A plot of the bandgap energy *vs.* film composition for the films recorded in Table I and other films grown using a reactor with a center tube is shown in Fig. 3. Values for the room-temperature bandgap energies of GaAs and of InAs are also shown on the graph. For comparison purposes, a dotted line representing a linear dependence of bandgap energy upon film composition between the two binary compounds is also shown. The experimental data obtained on these relatively few alloy films show some scatter and are seen to depart somewhat from the straight line drawn between the bandgap energies for the two pure compounds. They appear to fall along a smooth empirical curve such as has been drawn in the figure.

A similar concave-upward dependence of bandgap upon composition was also observed in the InAs-GaAs system by Abrahams *et al.* (10) using bulk materials, and by Antypas (11), and Wu and Pearson (12), who grew alloy films by liquid-phase epitaxy. Woolley *et al.* (13) obtained an essentially linear variation in energy gap in bulk alloys with composi-

Table I. Properties of $Ga_{1-x}In_xAs$ films grown by CVD on (0001)Al_2O_3 substrates (all films grown in reactor without a central tube)

Deposition temperature (°C)	Film composition	Film thickness (μm)	Growth rate (μm/min)	Bandgap energy[a] (eV)	Resistivity (ohm-cm)	Carrier concentration cm^{-3})	Carrier mobility (cm^2/V-sec)
675	—	4.8	0.08	0.73	6.4×10^{-1}	1.4×10^{16}	690
	—	5.3	0.09	0.72	1.8	5.7×10^{15}	600
700	$Ga_{0.39}In_{0.61}As$	2.6	0.09	0.76	10.4×10^{-3}	1.2×10^{17}	4900
	$Ga_{0.38}In_{0.62}As$	3.9	0.12	0.71	35×10^{-3}	4.1×10^{16}	4300
	$Ga_{0.36}In_{0.64}As$	7.9	0.13	0.64	9.0×10^{-3}	8.8×10^{16}	7900
	—	3.3	0.06	0.81	4.8×10^{-2}	4.2×10^{16}	3100
	—	4.6	0.08	0.76	1.1×10^{-1}	1.2×10^{16}	4450
725	$Ga_{0.33}In_{0.67}As$	7.0	0.11	0.58	5.0×10^{-2}	1.5×10^{16}	8300
	$Ga_{0.29}In_{0.71}As$	9.1	0.15	0.53	7.1×10^{-2}	9.1×10^{15}	9800
	$Ga_{0.84}In_{0.16}As$	5.0	—	1.24	—	—	—

[a] Obtained directly from optical transmittance curve.

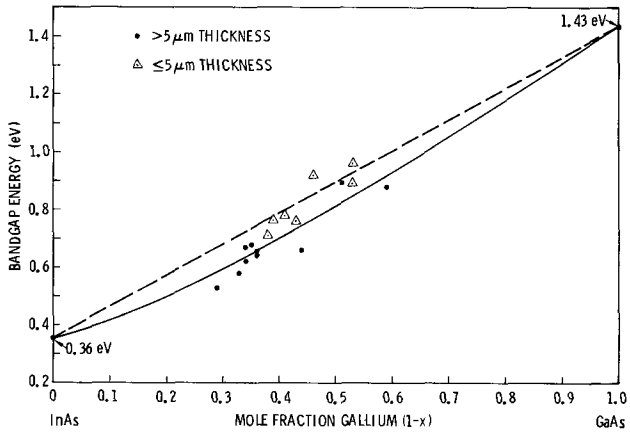

Fig. 3. Band gap energy vs. alloy composition for $Ga_{1-x}In_xAs$ heteroepitaxial films on (0001)Al_2O_3 substrates.

tions up to about 80 mole per cent (m/o) GaAs followed by a more rapid increase up to the gap characteristic of GaAs. Dzhakhutashvili and co-workers (14) determined that the dependence of the energy gap on composition becomes much more linear as the quality of the samples improves.

It has been found experimentally that the method used for establishing optical bandgap energies for $Ga_{1-x}In_xAs$ films, *i.e.*, graphically locating the room-temperature bandgap energy from optical data by selecting the zero-transmittance (maximum absorptance) intercept of the maximum-slope portion of the transmittance curve, is relatively accurate for films ≥ 5 μm in thickness. For thinner films larger intercept energy values result; for example, the bandgap energy for a ~17 μm film was 0.66 eV; a value of 0.77 eV was found when the film was thinned to ~2.5 μm. For this reason, the data points for films of thickness ≤ 5 μm were given reduced weight in establishing the smooth experimental curve drawn in Fig. 3.

Also, since TEI and AsH_3 react at room temperature but TMG and AsH_3 do not (at least no evidence for reaction has been observed during initial mixing), it is also plausible that the early stages of growth involve the formation of a layer of $Ga_{1-x}In_xAs$ of graded composition. Such a layer could result in the observed variation in uncorrected bandgap energies with film thickness.

Growth of InP and $InAs_{1-x}P_x$ Films

As previously indicated, the studies relating to InP and $InAs_{1-x}P_x$ growth have been very limited to date. InP growth was achieved on Al_2O_3 and GaAs by mixing vapors of TEI (H_2 flow was 1000 cm³/min through TEI) and PH_3 (typically 250 cm³/min of the 10% mixture) and decomposing their reaction product at 650°-660°C in a H_2 atmosphere containing excess PH_3. The film of InP on (0001)Al_2O_3 was rather dull appearing, with no distinguishing surface characteristics, but triangular crystallographic structures suggestive of (111) growth did develop on (111)GaAs substrates, and RED did confirm the films to be single crystal at the surface. It was found to be more difficult to control the InP growth on Al_2O_3 than that of InAs, presumably because of the greater instability of InP. The addition of arbitrary amounts of AsH_3 (5-12 cm³/min of the 10% mixture) to the gas stream led to the formation at 660°C of $InAs_{1-x}P_x$ films on Al_2O_3, GaAs, and InAs. Films with bandgaps of 0.5-0.9 eV were grown during this limited study.

Conclusion

The metalorganic-hydride method has been successfully extended to the formation of films of several of the In-Group V compound semiconductors and alloys. InAs, InP, $Ga_{1-x}In_xAs$, and $InAs_{1-x}P_x$ have been grown on insulating and semiconductor substrates using triethylindium, trimethylgallium, AsH_3, and PH_3 as the sources of In, Ga, As, and P, respectively. The versatility of this general process for film formation has again been demonstrated. Certainly further studies in this area are warranted and are in progress in our laboratories.

Acknowledgments

The authors are appreciative of their colleagues who contributed much of the analytical data presented herein: A. C. Thorsen and J. Wendt for the electrical measurements; G. Johnson for the photomicrographs; L. A. Moudy for x-ray evaluation; R. Cunningham for the microprobe data. We especially thank R. P. Ruth for discussions of the subject matter during the course of this work and his review of the manuscript.

This work was supported in part by the Air Force Cambridge Research Laboratories, Air Force Systems Command, Bedford, Massachusetts, under Contract F19628-70-C-0178.

Manuscript submitted April 7, 1972; revised manuscript received Aug. 14, 1972. This was paper 195 RNP presented at the Cleveland Meeting of the Society, October 3-7, 1971.

Any discussion of this paper will appear in a Discussion Section to be published in the December 1973 JOURNAL.

REFERENCES

1. H. M. Manasevit, *Appl. Phys. Letters*, **12**, 156 (1968).
2. H. M. Manasevit and W. I. Simpson, *This Journal*, **116**, 1725 (1969).
3. H. M. Manasevit and A. C. Thorsen, *Met. Trans.*, **1**, 623 (1970).
4. H. M. Manasevit, *This Journal*, **116**, 250C (1969); *ibid.*, **118**, 647 (1971).
5. H. M. Manasevit, F. M. Erdmann, and W. I. Simpson, *ibid.*, **118**, 1864 (1971).
6. H. M. Manasevit and W. I. Simpson, *ibid.*, **117**, 196C (1970); *ibid.*, **118**, 644 (1971).
7. R. Didchenko, J. E. Alix, and R. H. Toeniskoetter, *J. Inorg. Nucl. Chem.*, **14**, 35 (1960).
8. B. C. Harrison and E. H. Tompkins, *Inorg. Chem.*, **1**, 951 (1962).
9. L. J. Van der Pauw, *Philips Tech. Rev.*, **20**, 220 (1959).
10. M. S. Abrahams, R. Braunstein, and F. D. Rosi, *J. Phys. Chem. Solids*, **10**, 204 (1959).
11. G. A. Antypas, *This Journal*, **117**, 1393 (1970).
12. T. Y. Wu and G. L. Pearson, *J. Phys. Chem. Solids*, **33**, 409 (1972).
13. J. C. Woolley, C. M. Gillett, and J. A. Evans, *Proc. Phys. Soc. (London)*, **77**, 700 (1961).
14. T. V. Dzhakhutashvili, A. A. Mirtskhulava, L. G. Sakvarelidze, A. L. Shkol'nik, and M. S. Matinova, *Sov. Phys.-Semicond.*, **5**, 190 (1971).

Vapor-Phase Deposition of Beta-Silicon Carbide on Silicon Substrates

K. Kuroiwa[1] and T. Sugano

Department of Electronic Engineering, Faculty of Engineering, University of Tokyo, Bunkyo-ku, Tokyo, Japan 113

Silicon carbide is one of the semiconductors which have potential application for electron devices that can operate at high temperature and for blue light-emitting diodes. Cubic silicon carbide (β-SiC) crystals have been grown by precipitation from solutions (1-5), chemical vapor deposition (6-9), or by chemical conversion of Si (10-13). The growth of β-SiC by chemical vapor deposition onto Si substrates, or by chemical conversion of Si, can be done at temperatures lower than for the case of α-SiC by sublimation. They are suitable for obtaining SiC crystals with large areas because large Si wafers are commercially available. It is, however, difficult to obtain thick films of β-SiC by chemical conversion of Si.

This note reports our results of vapor-phase deposition of β-SiC by hydrogen reduction of $SiCl_4$ and CCl_4 onto the substrates which had been prepared by chemical conversion of Si.

Substrate Preparation

Substrates were prepared by chemical conversion to β-SiC of Si wafers with (111) orientation, and heated in a mixed gas of CH_4 or CCl_4 and Ar or H_2 at a temperature of 1300°C. β-SiC crystals, obtained by this method, up to around 1000Å thick do not have homogeneous structure. Near the surface of the crystal they have single crystalline structure, but near the interface between β-SiC and Si they have polycrystalline structure, attributable partly to the mismatch of lattice constants (β-SiC: 4.358Å, Si: 5.430Å), and partly to the growth of new β-SiC at the interface between the Si substrate and the previously grown β-SiC by diffusion of carbon through β-SiC layer to the interface (12).

On the β-SiC surface, a mesh-like pattern whose size is up to around 100μ is observed. This pattern seems to have resulted from the growth of β-SiC nuclei on the Si surface and becomes finer with increase of partial pressure of CH_4 or increase of ratio Ar/H_2 in the carrier gas. As the surface pattern becomes finer, the diffraction pattern of electrons reflected from the surface resembles more that of single crystals. This fact shows that the amount of disorder in β-SiC increases as the nuclei grow larger.

Apparatus and Deposition Technique

The substrate was placed upon a SiC-coated graphite pedestal which was heated by rf oscillator in water-cooled 64 mm ID quartz tube. Substrate temperature was measured with an optical pyrometer and corrected for the emissivity of the substrate and the absorption by the reaction tube.

Hydrogen was purified by passing it through a palladium diffuser. Desired mole ratio of tetrachloride gases to hydrogen was achieved by passing hydrogen separately through two saturators held at 0°C which contained $SiCl_4$ and CCl_4, respectively. The normal mole concentration of both $SiCl_4$ and CCl_4 to hydrogen was fixed to 0.1 mole per cent (m/o). The total hydrogen flow was 1-2 l/min. The deposition temperature was between 1300° and 1360°C. The deposition period was in the range of 1-48 hr.

[1] Present address: The Musashino Electrical Communication Laboratory, Nippon Telegraph and Telephone Public Corporation, Tokyo, Japan.

Key words: silicon carbide, vapor deposition, chemical conversion, epitaxial films, nucleus.

Results

Deposition rate.—Figure 1 is a cleaved surface which is perpendicular to the direction of deposition. The thickness of the β-SiC layer of the substrate is negligibly thin as compared with that of the deposited layer. In Fig. 1 the interface between β-SiC and Si is clearly seen, so the thickness of the deposited layer can be seen directly under an optical microscope. But, the layer thickness cannot be determined accurately, firstly because the layer has a very rough surface, and secondly because the layer thickness takes different values from point to point within the same sample. Under the

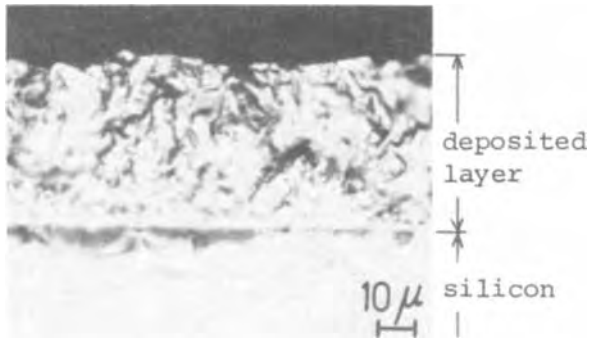

Fig. 1. Cleaved surface of a sample

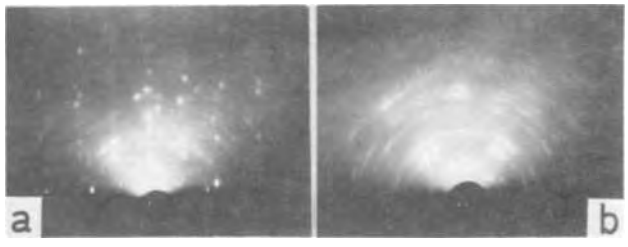

Fig. 2. Effect of concentration of $SiCl_4$ and CCl_4; (a) 0.1 m/o, (b) 0.5 m/o.

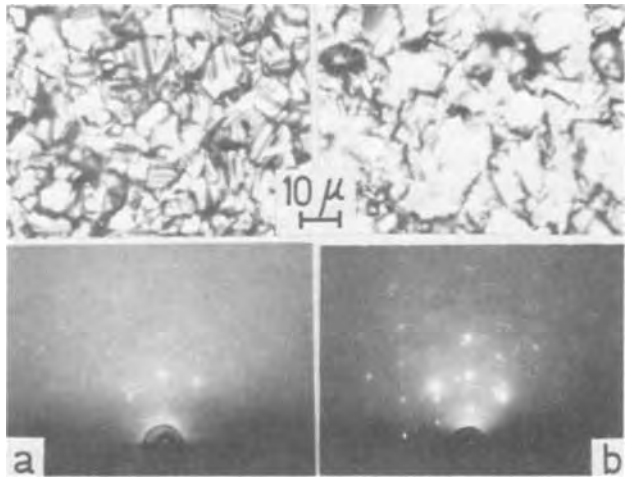

Fig. 3. Effect of preparation period of substrate; substrate orientation (111); preparation temperature 1325°C; CCl_4 concentration 0.2%; preparation period (a) 30 min, (b) 10 min.

Fig. 4. Deposition on silicon; substrate orientation (a) (111), (b) (110), and (c) (100).

condition of the deposition period of 48 hr, a layer up to about 40μ was deposited and the deposition rate was 0.4-1 μ/hr.

Effect of concentration of $SiCl_4$ and CCl_4.—As the concentration of $SiCl_4$ and CCl_4 in hydrogen increases from 0.1 to 0.5%, the polycrystalline character increases in the reflection electron-diffraction pattern of the deposited layer surface. Figure 2 shows the effect of the concentration. As far as electron-diffraction pattern is concerned, the crystalline state of many samples which were deposited under the condition of the concentration of 0.1% seems to be more ordered than that of the substrates.

Effect of preparation period of substrate.—β-SiC layers were deposited simultaneously on several substrates which were prepared under the same conditions except for the preparation period. Figure 3 is a part of the results. As the preparation period of the substrates decreases, grain size of the deposited layer grows larger, and spots in the electron-diffraction pattern grow sharper. β-SiC layers were deposited on the silicon substrate directly as a case of the limit of very short preparation period of the substrate, but this case did not always produce a satisfactory sample.

Deposition on silicon without β-SiC film on the surface.—Figure 4 shows the electron-diffraction patterns of the layers deposited on silicon substrates with (111), (110), and (100) orientations at the same time. The crystalline state of the layer on (100) surface is comparatively better. The deposition on the silicon substrate does not have good reproducibility, and the dependence on substrate orientation cannot be well-defined.

Effect of nucleus size of substrate.—To investigate correlation between the layer feature and the nucleus size of the substrate, β-SiC layers were deposited on two kinds of Si substrates, whose surfaces had been chemically converted to β-SiC. The first is a substrate having fine β-SiC nuclei with high density, and the second is a substrate having large β-SiC nuclei with low density. In Fig. 5, it is shown that the grain size of the deposited layer is in relation to the nucleus size of the substrate, that is, the grain size of the layer on the fine nuclei of the substrate is small, and that on the large nuclei of the substrate is large. But differences between the electron-diffraction patterns of two kinds of samples are not clearly seen.

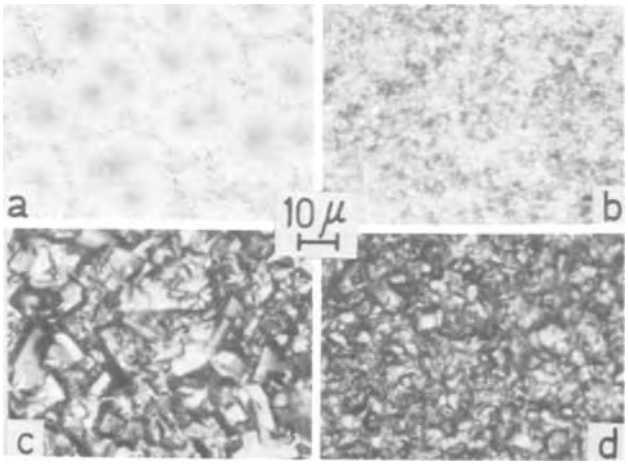

Fig. 5. Effect of nucleus size of substrate; deposition temperature 1320°C; deposition period 40 hr; concentration of $SiCl_4$ and CCl_4 0.1%; (c) deposited layer on (a), (d) deposited layer on (b).

As mentioned above, the electron-diffraction pattern of the deposited layer grows sharply with decrease of the preparation period of the substrate. In this case, if the preparation period of the substrate is very short, the β-SiC film does not cover the silicon surface completely, but nuclei of β-SiC grow like islands. An investigation of the deposited layer on such a substrate shows that the regions upon the nuclei of the substrate have a thicker β-SiC layer than the regions corresponding to the space between the nuclei or silicon surface.

Deposition at temperature of 1550°C.—Substrates were prepared by chemically converting surfaces of Si substrates to β-SiC and by depositing a β-SiC layer of several microns on them. Then the Si part of the substrates was etched off chemically and remaining β-SiC films were used as substrates in the deposition experiments at 1550°C. Oriented pattern of the 1550°C layer is clearly seen when the layer is deposited on the 1300°C substrate whose grain size is large and whose electron-diffraction pattern is sharp. A smooth surface, however, cannot be obtained by elevating the deposition temperature, if the surface of the β-SiC substrate is rough.

Discussion

The surface of the deposited layer is very rough, and the β-SiC layer deposits selectively upon SiC nuclei of the substrate, so that the grain size of the layer corresponds to the nucleus size of the substrate. These results indicate that on the nuclei of the substrate, β-SiC layers deposit selectively with a comparatively rapid deposition rate, but on the regions corresponding to the space between nuclei or silicon surface, β-SiC layers deposit with very low deposition rate, and that the deposited regions are hard to spread sideways. The amount of disorder in β-SiC increases as the nucleus grows large. Therefore, the crystalline state of the regions upon the nuclei of the substrate grows better with the decrease of the preparation period of the substrate. Judging from the electron-diffraction pattern, the crystalline state of grown layers seems to be more ordered than that of substrates. This fact means that well-crystallized regions are thickly deposited and these regions mainly contribute to the electron diffraction.

To obtain a smooth surface, it is necessary to speed up the deposition or to use substrates with uniform β-SiC layers. In order to speed up the deposition, it is necessary to raise the concentration of $SiCl_4$ and CCl_4, or to elevate the deposition temperature. But, if the concentration of $SiCl_4$ and CCl_4 is raised above 0.5%, only a polycrystalline layer is obtained, and the elevation of the deposition temperature above 1414°C melts silicon under the β-SiC substrate. So, it seems difficult to obtain a β-SiC layer of higher quality by this method and uniform SiC substrates must be used to obtain better results.

Acknowledgment

The authors wish to thank Mr. A. Matsumura and Mr. T. Suzuki of Sumitomo Electric Industrial Company for their support of this work.

Manuscript submitted April 3, 1972; revised manuscript received July 31, 1972.

Any discussion of this paper will appear in a Discussion Section to be published in the December 1973 JOURNAL.

REFERENCES

1. W. F. Knippenberg, *Philips Res. Rept.*, **18** 161 (1963).
2. W. F. Knippenberg and G. Verspui, *ibid.*, **21** 113 (1966).
3. W. E. Nelson, F. A. Halden, and A. Rosengreen, *J. Appl. Phys.*, **37**, 333 (1966).
4. P. B. Pickar, Jr., U.S. Pat. 3353914 (1967).
5. R. C. Marshall, *Mater. Res. Bull.*, **4**, S73 (1969).
6. D. M. Jackson, Jr. and R. W. Howard, *Trans. Met. Soc. AIME*, **233**, 468 (1965).
7. V. J. Jennings, A. Sommer, and H. C. Chang, *This Journal*, **113**, 728 (1966).
8. R. B. Campbell and T. L. Chu, *ibid.*, **113** 825 (1966).
9. R. W. Bartlett and R. A. Mueller, *Mater. Res. Bull.*, **4**, S341 (1969).
10. W. G. Spitzer, D. A. Kleinman, and C. J. Frosch, *Phys. Rev.*, **113**, 133 (1959).
11. N. C. Tombs, J. J. Comer, and J. F. Fitzgerald, *Solid-State Electron.*, **8**, 839 (1965).
12. H. Nakashima, T. Sugano, and H. Yanai, *Japan. J. Appl. Phys.*, **5**, 874 (1966).
13. I. H. Khan and R. N. Summergrad, *Appl. Phys. Letters*, **11**, 12 (1967).

Wall Profiles Produced during Photoresist Masked Isotropic Etching

R. G. Brandes

Bell Telephone Laboratories, Incorporated, Murray Hill, New Jersey 07974

and R. H. Dudley

Bell Telephone Laboratories, Incorporated, Allentown, Pennsylvania 18103

Many processes for the definition of patterns in metal and dielectric thin films utilize photolithographic masks and chemical etching. When a second film is to be deposited over a previously etched film, the profile of the etched wall has a strong influence on the ability of the second film to conform (1). The purpose of this paper is to describe two simple idealized models of masked etching which predict the slope of an etched wall as a function of etching time and to present experimental results which test these models.

Most metal or dielectric films of interest in semiconductor or thin-film technologies are either polycrystalline or amorphous. Thus, if chemical composition and physical properties of the films are uniform, the attack by etchants should be isotropic. However, some effects such as limitations in mass transport, variations in mechanical agitation such as in spray etching, local variations in etchant properties with etch depth or time may impose directional nonuniformities in etch rate. Additionally, the adhesion of the particular photoresist used as a mask can influence its ability to protect the surface of the film. The following treatment, though idealized, is intended to provide a simplified base line from which common deviations from ideality such as compositional gradients can be considered.

Two conceptually simple models are considered for the development of wall profiles during isotropic overetching by the immersion technique. In one, the masking material continuously lifts from the film being etched as the etch front proceeds, exposing fresh surface, producing a moving center of curvature, and thus a constant radius of curvature of the etched wall. The second model assumes that the masking film remains intact, fixing the center of the isotropic etching front and producing an increasing radius of curvature. These two models are presented schematically in Fig. 1(a) and 1(b), respectively.

Movable center of curvature model.—Because of the fixed radius of curvature, the shape of the etched wall of the first model would not change with time and would have an average slope of 45° at all times after breakthrough of the etched film.

Key words: etching, masking, photolithography.

Fixed center of curvature model.—The fixed center of the curvature model is shown in Fig. 1(b). A film of thickness, h, is protected by a mask such as a layer of photoresist which contains an opening where etching is desired. Assuming that there is no enhancement or retardation of the etch rate at the mask-film interface and that the rate of etching of the film is completely isotropic, the etch front can be assumed to advance in two dimensions as a circle with center at O, located at

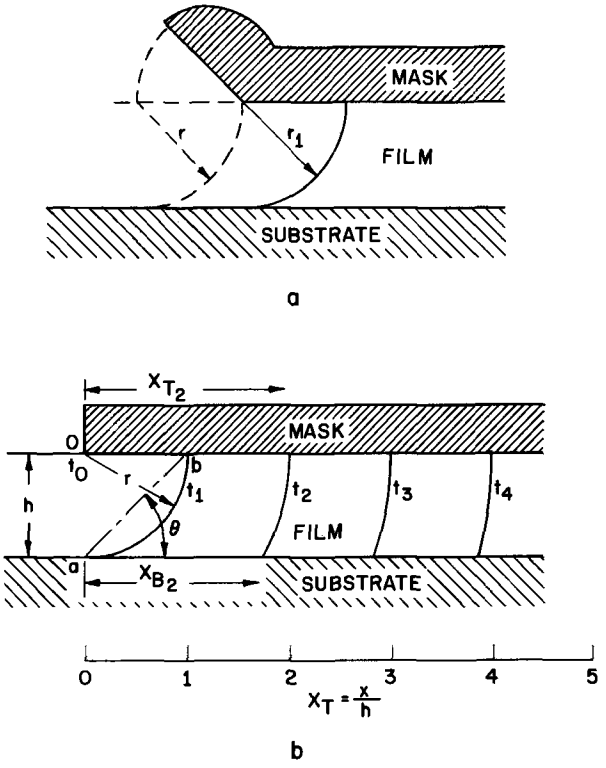

Fig. 1. (a) Schematic model of a wall profile for a movable center of curvature during overetching. (b) Schematic model of a wall profile for a fixed center of curvature during overetching.

Table I.

X_T	θ
1.0	45.0
1.5	69.1
2.0	75.0
3.0	80.3
4.0	82.8
5.0	84.2
6.0	85.2
7.0	85.9
8.0	86.4
9.0	86.8
10.0	87.1

the edge of the resist, and with radius r which is proportional to the time of exposure to the etch. At time t_0, no etching has occurred, and $r = 0$. At time t_1, at the instant of breakthrough, the distance of undercutting of the resist equals the film thickness or h and the average angle (θ) of slope from the horizontal is 45°. As the front advances further and the radius increases, it is evident from Fig. 1(b) that the slope becomes progressively steeper at t_2, t_3, etc.

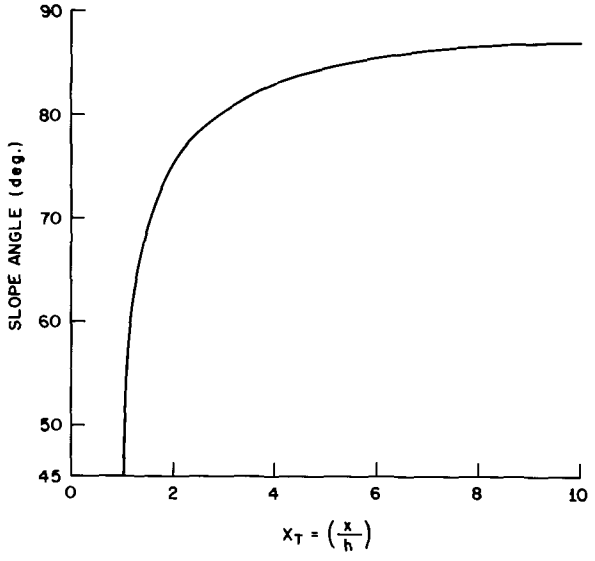

Fig. 2. Plot of $X_T = \left(\frac{x}{h}\right)$ vs. slope angle

Using O as the origin and letting r be the distance of advance of the etching front, the equation for the two dimensional etch front is that of a circle

$$x^2 + y^2 = r^2 \quad [1]$$

It is convenient to normalize all dimensions to the film thickness by dividing them by h, thus

$$X^2 + Y^2 = R^2 \quad [2]$$

where

$$X = \frac{x}{h}$$

$$Y = \frac{y}{h}$$

and

$$R = \frac{r}{h}$$

The points of interest are the intersections of the etch front with the two surfaces of the etched film a and b in Fig. 1(b). At the top surface $Y_T = O$ and $X_T = R$. At the bottom surface

$$Y_B = -1 \text{ and } X_B = (X_T^2 - 1)^{1/2} \quad [3]$$

also

$$\tan\theta = \frac{1}{X_T - X_B} \quad [4]$$

Table I contains the results of calculations of θ for X_T from 1 to 10. These data are plotted in Fig. 2.

Discussion of Fixed Center of Curvature Model

From Fig. 2 of the second idealized model, it is evident that although the slope at breakthrough is 45°, it steepens rapidly as it is etched for longer times. At 1.5 times breakthrough time, the angle approaches 70°; at double the breakthrough time, the angle is 75°. This implies that, in general, etch slopes will be steeper than 45° since nonuniformities in thickness and/or etch rate will necessitate excess etching time to assure complete etching over the entire substrate surface. Thus, the areas first to break through will be subjected to overetching in order to assure that other areas are cleared.

Experimental

A 1¼ in. diameter silicon slice with 6000Å of steam-grown oxide was coated with KMER (1:1) at 12,000

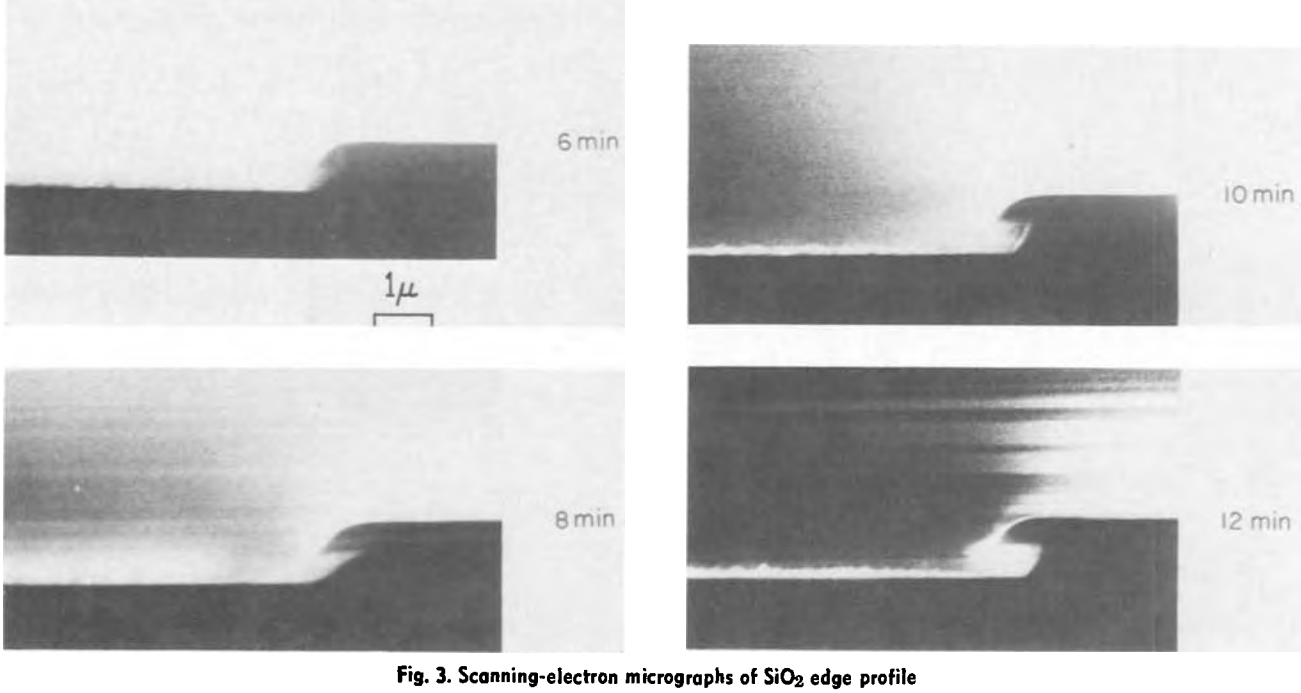

Fig. 3. Scanning-electron micrographs of SiO_2 edge profile

rpm providing a 5000Å resist coating. This resist was exposed to u.v. through an Ealing test array mask (Group II 10-100 cycles/mm patterns) and the image developed. The slice was then quartered. Each quarter was etched for a different length of time by immersion in a commercial buffered HF solution having an SiO_2 etch rate of 1000 Å/min. The etching times were 6, 8, 10, and 12 min; *i.e.*, up to a factor of 2 overetching.

Each quarter slice was then carefully scribed on the back side to break perpendicularly through the 10 cycle/mm bar pattern. These fragments were coated with 500Å of aluminum to avoid charging effects, and then scanned normal to the fracture surface in a Cambridge Stereoscan Electron Microscope following the technique described previously by Brandes and Curran (2).

Results and Conclusions

The etched-edge profiles viewed at 90° and at a magnification of 10,000 times for each of the etching times are presented in Fig. 3. It is evident that the resist did not lift during this experiment and that the edge profile steepened with overetching in qualitative agreement with the fixed center of curvature etching profile model of Fig. 1b. Thus, at least through a factor of 2 overetching, this mechanism is followed during thermal silicon dioxide etching. One may conclude that in etching contact windows, where a gentle edge gradient is desirable to permit uniform metalization, the etching should be carefully controlled to avoid overetching which produces steep walls.

Manuscript submitted July 28, 1972; revised manuscript received Sept. 20, 1972.

Any discussion of this paper will appear in a Discussion Section to be published in the December 1973 JOURNAL.

REFERENCES

1. D. L. Tolliver and C. J. Santoro, *Solid State Tech.*, **14**, 32 (1971).
2. R. G. Brandes and R. K. Curran, *Appl. Opt.*, **10**, 2001 (1971).

Electron Microscopy of Electrolytically Etched Silicon Surfaces

M. J. Hill

Brown Boveri Research Center, CH-5401 Baden, Switzerland

During investigation of the conditions for jet-electrochemical thinning of silicon to prepare transmission-electron microscope (TEM) specimens, heavy etching of the surfaces was observed. Further studies revealed various types of etching when the specimens were examined in the TEM, and in view of the recent interest in electropolishing of n-type silicon (1, 2) and electroetching (3, 5) these etching results are presented here.

The etch figures take the form of holes or tunnels penetrating into the bulk silicon, the form and depth of the tunnels being dependent, among other parameters, on the resistivity ρ of the silicon and the voltage V applied across a simple electrolytic cell. On a much coarser scale electrolytic etching effects have previously been reported in Ge (4) and in Si (1, 3, 5) and also in GaP on the TEM scale (6).

Experimental

The simple electrolytic cell used here is shown in Fig. 1. The specimens were 3 mm diameter disks about 200 μm thick, suitable for the TEM specimen holder. Electroless nickel was deposited on the back surface of the disks and an Au wire bonded to the nickel. The specimens were mounted in the holder with "picein" so that the electrolyte reached only the chemically polished front surface. The cathode was a strip of platinum at a distance of 1 cm from the specimen, and a voltage of between 3 and 100V d.c. was applied across the cell for times of between ½ and 6 min. The electrolyte used throughout these experiments was 1 part 40% HF in 19 parts H_2O, and the silicon was always positively based. The starting material had a dislocation content of less than 3×10^4 cm^{-2} with (111) oriented surfaces, and was either n-type phosphorus-doped of resistivity between 0.1 and 100 ohm-cm or 10 ohm-cm p-type boron-doped. Prior to etching, the specimen surfaces were prepared by fine mechanical polishing followed by chemical polishing to remove at least 30 μm. Before mounting, the specimens were thoroughly cleaned in organic solvents followed by triply distilled water, and before etching they were soaked in the electrolyte for 10 min. During etching the current was usually unstable, and only the maximum and minimum values were recorded. The measured currents varied between 0.5 and 20 mA depending only slightly on voltage and resistivity. Further experiments have shown that there is a very large edge effect with increased etching and presumably increased C.D. within about 0.5 mm of the edge. The observations reported here are from areas within 0.5 mm of the centers of the disks, but it is clear that no value of C.D. can be assigned to the etching process.

After etching, the nickel film was removed and the disks were chemically thinned from the back side using a variation of the standard jet method (7). This gave areas of approximately 100 μm diameter, suitable for examination in the TEM.

Results

The form of the etch figures developed during the anodic etching depended on several parameters includ-

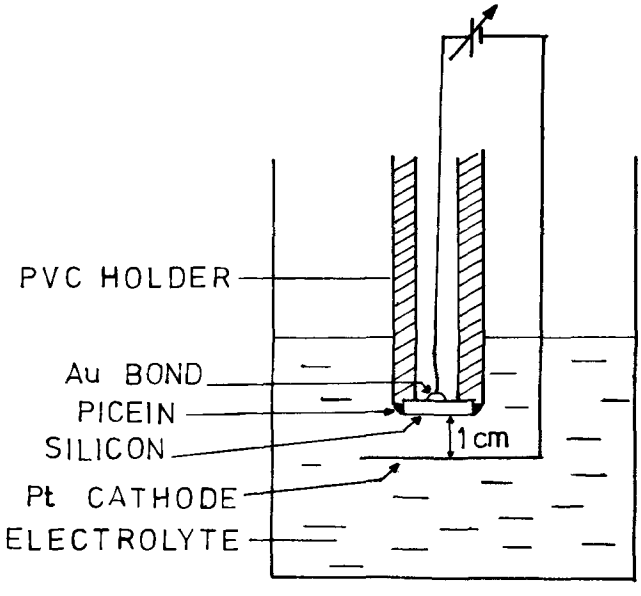

Fig. 1. Schematic of the electrolytic cell

Key words: anodic dissolution, etch channels, silicon, crystal oriented attack.

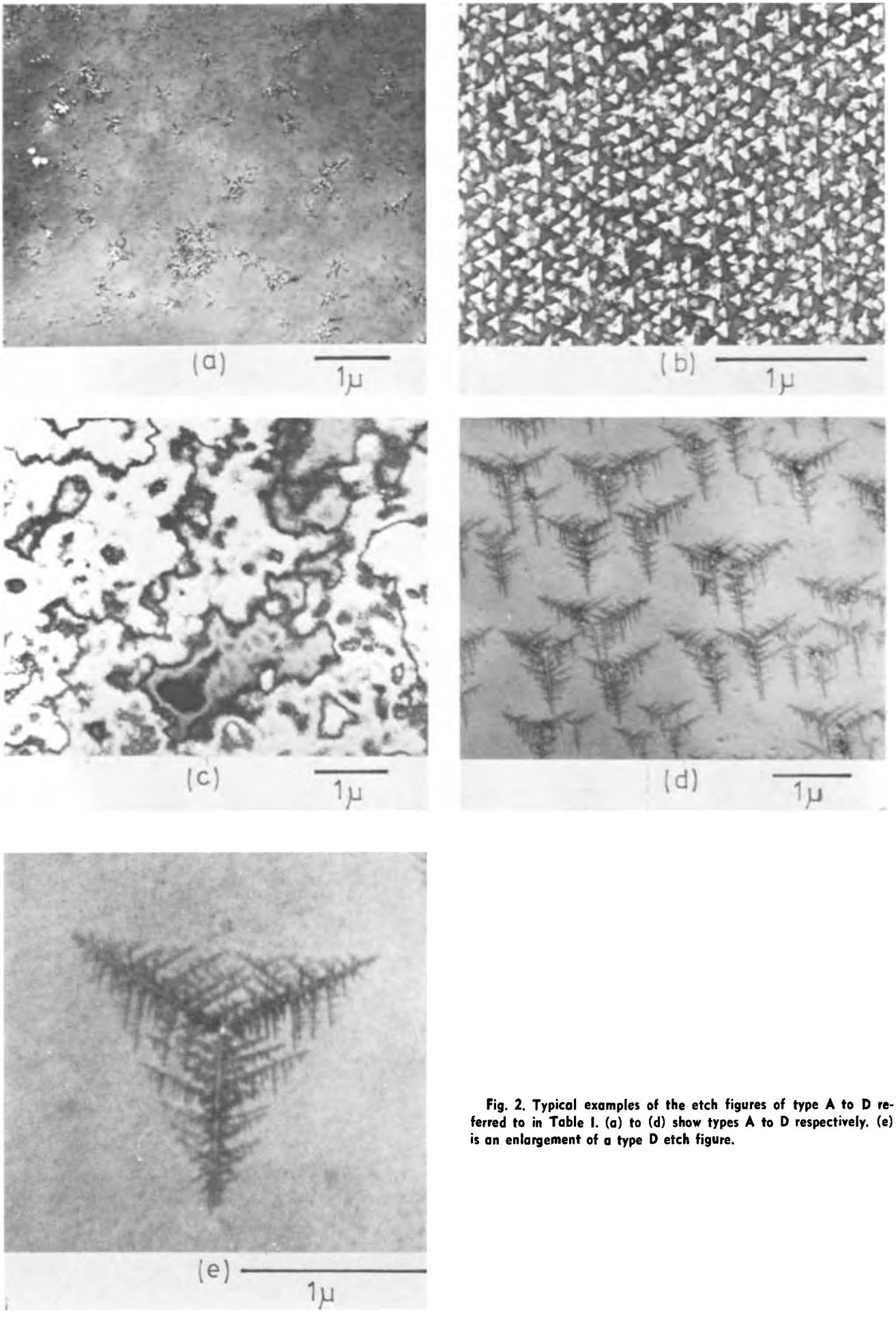

Fig. 2. Typical examples of the etch figures of type A to D referred to in Table I. (a) to (d) show types A to D respectively. (e) is an enlargement of a type D etch figure.

Table I

Resistivity and type	Applied voltage, V					
	3	6	10	20	45	100
0.1 ohm-cm, n	D	D	B	—	—	—
1.2 ohm-cm, n	B, D	A, D	D	E	E	—
10 ohm-cm, n	A	A, B, D	D	D	D	C
100 ohm-cm, n	F	A	A	A	A	E
10 ohm-cm, p	F	F	A	—	—	—

ing resistivity ρ, applied voltage V, and etching time. The transmission-electron microscope observations on specimens of several resistivities are summarized in Table I, where the following symbols are used: A, small rounded tunnels having some directional character; B, sharp triangular etch pits; C, over-all removal of Si, but surface rough on the TEM scale; D, sharp tunnels lying in <100> directions with branches also lying in the same directions; E, surface optically rough with large approximately triangular holes too coarse to study by TEM; and F, no etching detected.

Typical examples of these various Types A to D are shown in Fig. 2(a) to 2(d). Types A and B are both partially developed figures where the voltage was too low to produce the sharp figures of Type D. The exception to this is 0.1 ohm-cm etched at 10V where the triangular holes may well be due to over-all removal of Si competing with the production of Type D figures. Figure 2(c) shows only thickness contours where each fringe corresponds to $\xi_{2\bar{2}0} \simeq 750$Å surface unevenness due to the electropolishing. Figure 2(e) is an enlargement of one sharp star-shaped figure of Type D. Many branches and sub-branches are seen, all lying in <100> directions. This was determined by tilting the specimen 54° in the microscope goniometer stage, until one main arm of the tunnels was parallel to the electron beam. A (100) pole was then also parallel to the electron beam.

Since the etch figures observed in the TEM were always in the form of tunnels where material had been preferentially removed, the contrast was obtained from these by using an approximately 3 or 4 beam-diffracting condition close to the (111) pole. The variations of total specimen thickness through which the electrons pass due to the empty regions inside the sample are then seen as intensity variations relative to the background. In the examples shown here the diffracting conditions were chosen to give dark figures on a lighter background. Stereoscopic pairs of micrographs were taken of several Type D etch figures and the complete three-dimensional tunnel structure could be clearly seen. The depth to which the tunnel networks penetrated below the Si surface was measured from such stereoscopic pictures using a Zeiss Standard Spiegelstereoskop N 2, and for instance in the case of 10 ohm-cm n-type Si etched at 45V for 6 min, this depth was 9500Å ± 500Å. Specimens thicker than about 1 μm are difficult to study in a 100 keV TEM as used here. The depth of the deepest tunnels was proportional to the etching time as expected.

A few samples were etched for much longer times than required for TEM specimens, and these contained a low density of much deeper tunnels similar to those reported previously (5). Metallographic cross sections from these specimens were examined by optical microscopy and the tunnel directions determined by Laue x-ray photographs to be <100> and not <110> as reported in Ref. (3, 5). Uhlir (4) has also reported preferential attack along <100> directions in anodically etched Ge.

In the majority of specimens the distribution of etch figures was apparently random. In some cases, however, this was not so, and one example is shown in Fig. 3 where Type D etch figures are associated with an optically visible scratch caused during mounting.

Fig. 3. An example of nonuniform distribution of etch figures, due to the presence of a surface scratch.

In the few TEM specimens which happened to contain a dislocation, an etch figure formed at the intersection of the dislocation with the surface, but these etch figures were not different from the many others in surrounding dislocation-free areas.

Discussion

At low voltages electrochemical attack at a Si-electrolyte interface is clearly not uniform. Assuming that electrical inhomogeneities do not exist in the electrolyte, then the etching at the interface must be due to inhomogeneities in the silicon. Obviously lattice strain or broken bonds resulting from surface damage provide nucleating sites for attack (Fig. 3) but other smaller crystal defects must be capable of doing this in the absence of grosser defects. We have seen that dislocations are certainly not the cause of the etching figures, as the dislocation density was orders of magnitude smaller than the density of etch figures seen here.

Once the etching has started an explanation for the preferential etching in <100> directions can be found. The (100) type surface has a higher density of free bonds than other planes, and the chemical dissolution rate is known to be proportional to the density of free bonds (8). In the case of electrochemical dissolution it has been pointed out (4) that at a concavity in a surface, the electric field is increased and therefore the necessary dissolution conditions are reached preferentially at such points. Thus a combination of these two factors could provide a feasible explanation for the details of the figures and their voltage dependence.

No attempt has been made here to understand the etching process in detail as has been done previously (9, 10). For instance, only the total voltage across the cell was measured and no reference electrode was used. We may conclude however from the above results that transmission-electron microscopy is a useful method for examining electroetched surfaces of semiconductors, and that if the etching conditions are carefully controlled, then it is likely that useful information concerning the homogeneity of the electrical properties at a silicon-electrolyte interface can be obtained.

Finally it should be mentioned that the jet-electrochemical thinning of Si specimens for the TEM now operates entirely satisfactorily. An electrolyte of 20 ml 40% HF + 8g NaF in 1 liter H_2O is forced through a 0.5 mm diameter jet onto the specimen and 300V is applied between specimen and a tungsten wire in the jet. Strong illumination speeds up the dissolution and is necessary for high resistivity n-type samples. Thinning times vary between 10 and 30 min for specimens of ~400 μm thickness. The method is extremely reliable and controllable producing specimens with more than 100 μm diameter transparent areas every time. The only material which cannot be thinned is Si highly doped with heavy metals, *i.e.*, with very short carrier lifetimes.

Acknowledgments

The author would like to thank Drs. W. Zimmermann and R. Sittig of this laboratory for useful discussions and Mr. A. Frey for much skill and patience with the specimen preparation.

Manuscript submitted July 21, 1972; revised manuscript received Sept. 19, 1972.

Any discussion of this paper will appear in a Discussion Section to be published in the December 1973 JOURNAL.

REFERENCES

1. M. J. J. Theunissen, J. A. Appels, and W. H. C. G. Verkuylen, *This Journal*, **117**, 959 (1970).
2. H. J. A. van Dijk and J. de Jonge, *ibid.*, **117**, 553 (1970).
3. P. H. Bellin and W. K. Zwicker, *J. Appl. Phys.*, **42**, 1216 (1971).
4. A. Uhlir, *Bell System Tech. J.*, **35**, 333 (1956).
5. M. J. J. Theunissen, *This Journal*, **119**, 351 (1972).
6. B. D. Chase and D. B. Holt, *ibid.*, **119**, 314 (1972).
7. G. R. Booker and R. Stickler, *Brit. J. Appl. Phys.*, **13**, 446 (1962).
8. H. C. Gatos and M. C. Lavine, *Progr. Semicond.*, **9**, 1 (1965).
9. R. L. Meek; *This Journal*, **117**, 437 (1971).
10. R. Memming and G. Schwandt; *Surface Sci.*, **4**, 109 (1966).

Brief Communications

Resistivity of Doped Polycrystalline Silicon Films

A. L. Fripp*

Langley Research Center, Hampton, Virginia 23365

and L. H. Slack

Department of Metals and Ceramics, Virginia Polytechnical Institute and State University, Blacksburg, Virginia 23601

Chemical deposition of polycrystalline silicon on oxidized silicon wafers is an important process in the fabrication of silicon gate (1) and shielded silicon gate (2) MOSFET's, two-phase CCD's (3), and dielectrically isolated circuits (4). Silicon has been deposited on oxidized silicon wafers by the pyrolytic decomposition of silane. Diffusion (5), oxidation (6), Hall-effect (7), and preferred orientation (8) investigations have been made on polycrystalline deposits. The resistivity of undoped polycrystalline (9) and amorphous films (10) has been measured. The purpose of this communication is to report the resistivity dependence on the doping concentration in polycrystalline silicon films.

Experimental

The wafers were polished 1 ohm-cm single crystals oriented within 2° of the (111) face. They were oxidized in a quartz tube furnace at 1100°C by the wet-oxidation process. The oxide films were approximately 6000Å thick. To prevent possible errors in measuring resistivity, boron-doped wafers were used for phosphorous deposits and phosphorous-doped wafers were used for boron deposits.

The films were deposited by the pyrolytic decomposition of silane in a horizontal, induction-heated, reactor. The films were doped during deposition by adding either phosphine or diborane, in regulated quantities, to the gas stream. The silane flow rate was 50 cm^3/min and it was mixed with hydrogen to produce an atmosphere of 0.37% by volume of silane.

Data were taken on runs made at temperatures of 1070° and 1170°C for phosphorous-doped films and at 1070°C only for boron-doped films (corrected from optical pyrometer measurements). The wafers were given a 4-min, 1170°C preheat in hydrogen before deposition. The deposition time of 10 min produced a film approximately 7μ thick for the 1070°C runs and approximately 3μ thick for the 1170°C runs. After deposition, and a 1 min flush, the wafers were cooled rapidly in hydrogen.

The standard four-point probe technique was used to measure resistivity. Film thickness was measured by beveling; no staining was necessary since the oxide-silicon interface was quite distinct.

The doping concentration in the polycrystalline films was arrived at by simultaneously depositing an epitaxial layer on a single-crystal substrate. The resistivity of the epitaxial layer was measured and the doping concentration obtained by referring to Irvine's graphs (11). Since both the clean single-crystal and the oxide-coated wafer are at the same temperature and both offer a silicon surface, after the initial deposition, for reacting the doping gas, it is assumed that both will have the same doping concentration within the normal variation of epitaxial depositions.

Results and Discussion

The resistivity as a function of impurity concentration for both polycrystalline and single-crystal films

* Electrochemical Society Active Member.

Key words: polycrystalline silicon, microelectronics, resistivity.

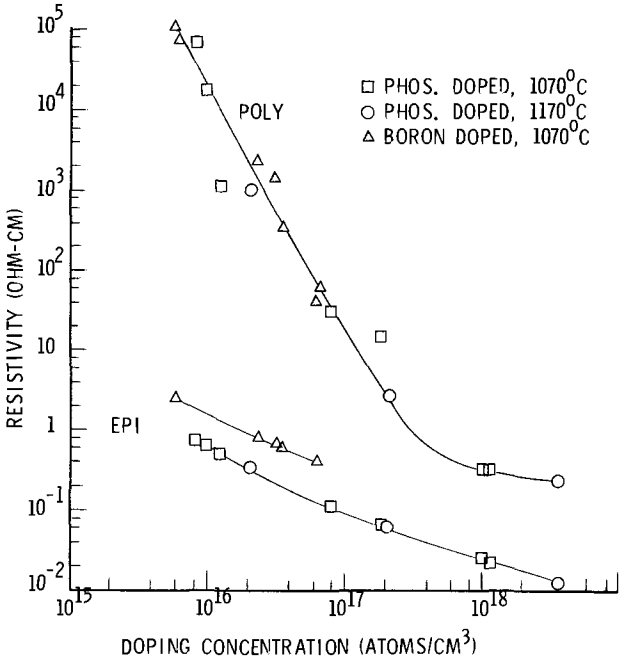

Fig. 1. Resistivity dependence of both single-crystal and polycrystalline silicon on doping concentration.

are shown in Fig. 1. The legend indicates impurity type and temperature of deposition. These data indicate that at concentrations above 10^{17} atoms/cm^3 the concentration dependence of the resistivity substantially decreases and approaches the single-crystal dependence.

The data presently available are insufficient to conclude that the value of concentration dependence in polycrystalline silicon becomes the single-crystal value. However, since resistivities of polycrystalline silicon are not expected to be lower than an equally doped single crystal, such a decrease in doping level dependence would be expected.

The grain boundaries in polycrystalline silicon offer possible sinks for both doping atoms and charge carriers. Carrier trapping in silicon has been discussed by others (7, 12) as being defect-induced, but further work is needed in which the structure of the films is modified and carrier-activation energy, especially in the low doping concentration region, is measured before commencing upon model development.

REFERENCES

1. F. Faggin and T. Klein, *Solid-State Electron.*, **13**, 1125 (1970).
2. H. C. Lin, J. L. Halsor, and P. J. Hayes, *IEEE Trans. Electron Devices*, **ED-19**, 1199 (1972).
3. W. F. Kosonocky, and J. E. Carnes, *IEEE J. Solid-State Circuits*, **SC-6**, 314 (1971).
4. G. L. Schnable, A. F. McKelvey, and J. A. Hastings, *Electrochem. Technol.*, **4**, 57 (1966).
5. T. I. Kamins, J. Manoliu, and R. N. Tucker, *J. Appl. Phys.*, **43**, 83 (1972).
6. T. I. Kamins and E. L. MacKenna, *Metallurgical Trans.*, **2**, 2292 (1971).
7. T. I. Kamins, *J. Appl. Phys.*, **22**, 4357 (1971).
8. A. L. Fripp, R. L. Stermer, and A. Catlin, *This Journal*, **117**, 1569 (1970).
9. J. D. Joseph and T. I. Kamins, *Solid-State Electron.*, **15**, 355 (1972).
10. R. C. Chittick, J. H. Alexander, and H. F. Sterling, *This Journal*, **116**, 77 (1969).
11. J. C. Irvin, *Bell System Tech. J.*, **41**, 387 (1962).
12. D. J. Dumin, *Solid-State Electron.*, **13**, 415 (1970).

Diffusivity Summary of B, Ga, P, As, and Sb in SiO_2

M. Ghezzo* and D. M. Brown*

General Electric Corporate Research and Development, Schenectady, New York 12301

Many investigations have reported data on the diffusivity of semiconductor dopants in SiO_2. However, in many of these papers these data have usually not been considered of primary importance and there was a need for a paper, like this, which summarizes the diffusivities of these impurities in SiO_2.

A difficulty in the earlier and present literature is that the diffusivities of those elements in SiO_2 can be extremely concentration and ambient dependent. B is a fine example of this since its concentration dependence and ambient dependence are definitely marked. In fact, after a preliminary investigation on the oxide-masking properties done by Frosh and Derick (1) the diffusivities of III-V impurities or their carrying species in SiO_2 were determined by many authors using widely different experimental conditions.

The summary of diffusivities in SiO_2 is presented in Table I, which was prepared using the same format of Kendall and DeVries (2) in their tabulation of diffusion coefficients in Si. Whenever the pre-exponential diffusion constant, D_o, the activation energy, Q, or the diffusivities at 1100° and 1200°C were not explicitly given in a reference, the experimental data were fitted to an Arrhenius curve using the least squares method, and the above parameters were derived therefrom. Also included in Table I are the dopant concentrations at which the experiments were performed, the type of source utilized, and the diffusion ambient.

Inspection of Table I shows that the values of the activation energy for B diffusivity in SiO_2 are rather consistent among different investigators and average 3.5 eV, the only exceptions being the values of Thurston *et al.* (3) (2.38 eV) and Schwenker (4) (2.82 eV). The pre-exponential diffusion constant is highly dependent on the boron concentration in the diffusion source, regardless whether it is a vapor or a glass, and increases nearly three orders of magnitude in passing from low to high B concentration diffusions, as apparent from the data of Brown and Kennicott (5) and Schwenker (4). In an earlier work Horiuchi and Yamaguchi (6) reported an increase of the B diffusivity in SiO_2 at 1200°C from 3.2×10^{-16} cm^2/sec to 6.2×10^{-15} cm^2/sec due to an increase of the B_2O_3 vapor pressure, and attributed this phenomenon to a change in the composition of the diffused oxide layer resulting in the formation of a "glassy layer." Similarly Brown and Kennicott (5) referred to B diffusions through SiO_2 from borosilicate glass sources containing more than 18 mole per cent (m/o) B_2O_3 as rapid "melt through SiO_2 diffusions" as explained by relative decreases in viscosity and the B_2O_3-SiO_2 phase diagram (7). Yet oxide masking can still be used in "melt through" diffusions with a borosilicate glass source because the transformation of a thick oxide layer into glass by the "melt through" process is limited by the

* Electrochemical Society Active Member.

Key words: diffusion coefficients, silicon oxide, silicon.

Table I. Diffusivities of Group IIIA and VA elements in SiO_2

Element	Reference	Ref. No.	D_0 (cm^2/sec)	Q (eV)	D(1100°C) (cm^2/sec)	D(1200°C) (cm^2/sec)	C_0 (m/o)	C_s (cm^{-3})	Source	Ambient
Boron	Thurston *et al.*	3	**7.23 × 10^{-6}	**2.38	1.3 × 10^{-14}	5.1 × 10^{-14}	0.001-0.1	1 × 10^{19}-2 × 10^{20}	B_2O_3 vapor	O_2 + N_2
	Horiuchi and Yamaguchi	6	**1.23 × 10^{-4}	3.39	4.6 × 10^{-17}	*3.2 × 10^{-16}	—	6 × 10^{18}	B_2O_3 vapor	Ar
	Horiuchi and Yamaguchi	6	—	—	—	6.2 × 10^{-16}	—	Above 1 × 10^{20}	B_2O_3 vapor	Ar
	Barry and Olofsen	21	*7.38 × 10^{-4}	*3.58	*5.6 × 10^{-17}	*4.3 × 10^{-16}	3.5-7.0	4-8 × 10^{19}	Borosilicate	N_2
	Brown and Kennicott	5	*3.16 × 10^{-4}	*3.53	3.4 × 10^{-17}	*2.6 × 10^{-16}	Below 18	Below 3 × 10^{20}	Borosilicate	— —
	Brown and Kennicott	5	—	—	~2.0 × 10^{-11}	—	Above 18	Above 3 × 10^{20}	Borosilicate	— —
	Schwenker	4	*1.61 × 10^{-5}	*2.82	7.2 × 10^{-16}	*3.6 × 10^{-15}	9.1-9.4	7 × 10^{19}	Borosilicate	Ar
	Schwenker	4	*3.01 × 10^{-2}	*3.56	2.5 × 10^{-15}	*1.9 × 10^{-14}	14.9-15.8	2 × 10^{20}	Borosilicate	Ar + N_2 + H_2O
	Grove *et al.*	8	—	—	—	*7.0 × 10^{-13}	—	—		H_2 + N_2
Gallium	Grove *et al.*	9	*1.04 × 10^{5}	*4.17	5.3 × 10^{-13}	*5.8 × 10^{-10}	—	—	Ga_2O_3 vapor	H_2 +
Phosphorus	Sah *et al.*	13	*5.73 × 10^{-5}	*2.30	2.0 × 10^{-13}	*7.6 × 10^{-13}	—	8 × 10^{19}-1 × 10^{21}	P_2O_5 vapor	N_2
	Allen *et al.*	12	**6.39 × 10^{-11}	**1.27	1.4 × 10^{-15}	2.9 × 10^{-15}	—	3 × 10^{19}-2 × 10^{20}	P_2O_5 vapor	N_2
	Thurston *et al.*	3	**4.72	**4.21	1.7 × 10^{-15}	1.9 × 10^{-14}	3.0	5 × 10^{19}-1 × 10^{20}	P_2O_5 vapor	O_2 + N_2
	Barry	11	*1.86 × 10^{-1}	*4.03	*2.9 × 10^{-16}	*3.0 × 10^{-15}	0.1-3.5	8 × 10^{17}-8 × 10^{19}	Phosphosilicate	N_2
	Hsueh	17	*9.82 × 10	*4.38	*1.2 × 10^{-16}	2.0 × 10^{-15}	—	1-2 × 10^{19}	A_sH_3	O_2 + N_2
Arsenic	Wong and Ghezzo	16	*2.48 × 10^{2}	*4.90	*2.6 × 10^{-16}	*4.4 × 10^{-15}	0.8	1-6 × 10^{19}	Arsenosilicate	Ar
	Wong and Ghezzo	16	*1.63	*4.04	*2.4 × 10^{-15}	*2.4 × 10^{-14}	2.5	—	Arsenosilicate	Ar
	Ghezzo and Brown	18	—	—	3.5 × 10^{-15}	—	5.8	5 × 10^{19}	Arsenosilicate	Ar
	Ghezzo and Brown	18	—	—	1.5 × 10^{-16}	—	5.8	4 × 10^{20}	Arsenosilicate	O_2
Antimony	Thurston *et al.*	3	*1.31 × 10^{10}	*8.75	*9.9 × 10^{-17}	1.5 × 10^{-14}	3.0	5 × 10^{19}	Sb_2O_3 vapor	O_2 + N_2

C_0 = Dopant concentration in the source expressed in mole per cent.
C_s = Surface concentration on silicon after diffusion from the specified source and ambient in absence of oxide barrier.
* = Computed by fitting an Arrhenius curve to the experimental data using the least squares method.
** = Recomputed, because of disagreement with value computed in the reference.

dilution of the B_2O_3 concentration in the glass and further B penetration through the oxide is achieved at a B diffusivity at least two orders of magnitude smaller. Furthermore, three orders of magnitude increase in diffusivity of B in SiO_2 have been reported by Grove *et al.* (8) whenever diffusions are carried out in H_2 ambients. The importance of eliminating H_2 from diffusion ambients whenever B-doped polysilicon gate devices are formed cannot therefore be overemphasized.

The diffusivity of Ga in SiO_2 reported by Grove *et al.* (9) is by far the largest in Table I, assuming a value at 1100°C of 5.2 × 10^{-11} cm^2/sec, which is from 2 to 6 orders of magnitude larger than the diffusivities of B, P, As, or Sb in SiO_2. Besides Ga diffusivity in SiO_2 is higher than in Si [1.7 × 10^{-13} cm^2/sec at 1100°C according to Kurtz *et al.* (10)] preventing the use of SiO_2 as a mask for Ga in device fabrication.

Diffusion constants and activation energies for P diffusions in SiO_2 are widely scattered, the only reasonable agreement existing between the activation energy values computed from the data of Thurston *et al.* (3) (4.21 eV) and Barry (11) (4.03 eV). At 1100°C the diffusivities reported by Allen *et al.* (12) (1.4 × 10^{-15} cm^2/sec) and by Thurston *et al.* (3) (1.7 × 10^{-15} cm^2/sec) for similar surface concentrations of P in Si closely match, but are about five times larger than Barry's value (11) (2.9 × 10^{-16} cm^2/sec) and over two orders of magnitude smaller than the value of Sah *et al.* (13) (2.0 × 10^{-13} cm^2/sec). A justification for this exceedingly high diffusivity reported by Sah *et al.* can be sought in the high P_2O_5 vapor pressure used in these experiments, which resulted in the formation of a glassy compound by reaction of P_2O_5 with the SiO_2 barrier as in the "melt through process" described for boron. Phosphorous glass "melt through" diffusions have also been discussed by Okabe and Tanikawa (14). A comparison with the P diffusivity in Si at 1100°C given by Fuller *et al.* (15) (3.0 × 10^{-13} cm^2/sec) shows that at low P concentrations the P diffusivity in SiO_2 is over two orders of magnitude smaller than in Si, but at high P concentrations the two diffusivities are nearly equal.

Recent investigations of As diffusion through SiO_2 from an arsenosilicate glass source (16) gave results consistent with those previously reported by Hsueh (17). The activation energy is 4.9 eV for low As concentration diffusions and decreases to 4.0 eV with an increase of the As_2O_3 concentration in the arsenosilicate glass source. The smaller increase of As diffusivity with concentration at 1100°C in Ar (from 2.6 × 10^{-16} cm^2/sec to 3.5 × 10^{-15} cm^2/sec) in comparison to B or P suggests that a "melt through process" is unlikely for high concentration As diffusions, considering also the limitation on As_2O_3 percentage in the glass required for avoiding damage. The diffusion ambient affects the As diffusivity in SiO_2, which is drastically reduced in the presence of oxygen as discussed at length by Ghezzo and Brown (18) in a paper on As diffusion properties in Si from arsenosilicate glass sources prepared by simultaneous oxidation of AsH_3 and SiH_4. In any case, As diffusivity in SiO_2 is always smaller than in Si, where at 1100°C in Ar it is close to 1.5-2.0 × 10^{-14} cm^2/sec (19, 20).

The only data available on Sb diffusivities through SiO_2 at different temperatures are given by Thurston *et al.* (3). A computation of the activation energy from these data results in a value of 8.75 eV, which is nearly twice as large than the second highest in Table I (4.9 eV) corresponding to As. Thus a change in diffusion temperature from 1100° to 1200°C corresponds to a very large increase in diffusivities (from 9.9 × 10^{-17} cm^2/sec to 1.5 × 10^{-14} cm^2/sec) and a reduction of the difference between Sb diffusivities in SiO_2 and Si due to the smaller value of the activation energy for Sb diffusion in Si [3.95 eV in Ref. (15)].

Summary

Available diffusivity data on B, Ga, P, As, and Sb in SiO_2 have been summarized and discussed. Agreements and discrepancies in the literature have been pointed out along with the importance of ambient and source conditions. These data have an importance to general device technology and a few examples of this have been pointed out in the text.

Manuscript received Sept. 8, 1972.

Any discussion of this paper will appear in a Discussion Section to be published in the December 1973 JOURNAL.

REFERENCES

1. C. J. Frosch and L. Derick, *This Journal*, **104**, 547 (1957).
2. D. L. Kendall and D. B. DeVries, "Semiconductor Silicon," p. 358, R. R. Haberecht and E. L. Kern, Editors, The Electrochemical Society Softbound Symposium Series, New York (1969).
3. M. O. Thurston, J. C. C. Tsai, and K. D. Kang, "Diffusion of Impurities into Silicon Through an Oxide Layer", Ohio State University Research Foundation, AD-261201, Contract DA-36-039-SC-83874, Final Report, Columbus, Ohio, March 1961.
4. R. O. Schwenker, *This Journal*, **118**, 313 (1971).
5. D. M. Brown and P. R. Kennicott, *ibid.*, **118**, 293 (1971).
6. S. Horiuchi and J. Yamaguchi, *Japan J. Appl. Phys.*, **1**, 314 (1962).
7. T. J. Rockett and W. R. Foster, *J. Am. Ceram. Soc.*, **48**, 75 (1965).
8. A. S. Grove, O. Leistiko, Jr., and C. T. Sah, *J. Appl. Phys.*, **35**, 2695 (1964).
9. A. S. Grove, O. Leistiko, Jr., and C. T. Sah, *J. Phys. Chem. Solids*, **25**, 985 (1964).
10. A. D. Kurtz and C. L. Gravel, *J. Appl. Phys.*, **29**, 1456 (1958).
11. M. L. Barry, *This Journal*, **117**, 1405 (1970).
12. R. B. Allen, H. Bernstein, and A. D. Kurtz, *J. Appl. Phys.*, **31**, 334 (1960).
13. C. T. Sah, H. Sello, and D. A. Tremere, *J. Phys. Chem. Solids*, **11**, 288 (1959).
14. T. Okabe and E. Tanikawa, Proceedings of the 2nd Conference on Solid State Devices, Tokyo (1970).
15. C. S. Fuller and J. A. Ditzenberger, *J. Appl. Phys.*, **27**, 544 (1956).
16. J. Wong and M. Ghezzo, *This Journal*, **119**, 1413 (1972).
17. Y. W. Hsueh, *Electrochem. Technol.*, **6**, 361 (1968).
18. M. Ghezzo and D. M. Brown, *This Journal*, **120**, 110 (1973).
19. P. S. Raju, N. R. K. Rao, and E. V. K. Rao, *Indian J. Pure Appl. Phys.*, **2**, 353 (1964).
20. W. J. Armstrong, *This Journal*, **109**, 1065 (1962).
21. M. L. Barry and P. Olofsen, *ibid.*, **116**, 854 (1969).

JOURNAL OF THE ELECTROCHEMICAL SOCIETY

ELECTROCHEMICAL SCIENCE
— AND TECHNOLOGY —

FEBRUARY
1973

The Hexamethonium-Silver Iodide Reversible Cell

M. De Rossi,* M. L. Berardelli, and G. Fonseca

Istituto di Elettrotecnica, Università di Roma, Rome, Italy

ABSTRACT

The hexamethonium-silver iodide solid-state cell has a highly competitive cost, as compared with those having the $RbAg_4I_5$ as electrolyte. In addition, it seems to possess the characteristic of reversibility and a much less polarizations phenomena at the positive electrode. The results obtained on the cell confirm the property of the hexamethonium-silver iodide as a solid electrolyte.

In a recent paper (1) a new series of compounds of the type $I^- R_3N^+-(CH_2)_n-{}^+NR_3\ I^-$ and in particular the hexane-1,6-bis-trimethylammonium iodide (hexamethonium iodide, $(CH_3)_3N^+-(CH_2)_6-{}^+N(CH_3)_3\ 2I^-$ hereinafter given as $HexI_2$), capable of forming solid electrolytes with AgI and having the peculiar characteristic of high electrical conductivity (comparable to that of compounds of the type M Ag_4I_5 where M = Rb, K, NH_4) has been described. These compounds, as compared with the electrolytes of the type $RbAg_4I_5$, known to date, have a highly competitive cost.

It was, however, necessary to find out whether these new solid electrolytes were suitable for forming a cell; that is if, in addition to the characteristic of a high ionic conductivity, they also had a small amount of electronic conductivity.

In this paper we report the experiments carried out to verify some electric characteristics of these new solid electrolytes and in particular the behavior of the Ag-I_2 electrical cell made with it.

The cell in its essential structure may be represented thus

$$Ag/HexAg_{12}I_{14}/I_2,\ C \qquad [1]$$

Considering the value of the emf and the nature of the end product of the reaction, we believe that the prevailing over-all reaction which takes place in cell [1] is

$$Ag + \tfrac{1}{2}\ I_2 \rightleftharpoons AgI$$

The theoretical value of the emf is 0.688V derived from the thermodynamic free energy of formation of silver iodide.

Experimental

All the chemicals used were reagent grade (Fluka). The solid electrolyte $HexAg_{12}I_{14}$ was prepared according to the method described by De Rossi and co-workers in a previous paper (1). Voltage and current values were determined by a Keithley Model 610 C with high internal impedance (10^{14} ohms). The conductivity measurements were carried out with a 4896 Tinsley conductivity bridge with oscillographic resetting (545 B Tektronix).

The main problems in cell [1] are the contact polarizations which have been reduced, in the present case, by the use of an anodic mixture made of powdered silver and electrolyte and of a cathodic mixture made of powdered graphite, iodine, hexamethonium iodide and electrolyte.

The function of $HexI_2$ in the cathodic mixture is to make addition compounds with iodine in order to prevent reactions by free iodine on the electrolyte when the cell is not operative (2, 3). Iodine is released by $HexI_2$ during discharge and retained during charge.

The actual cell [1] structure is therefore

$$Ag/HexAg_{12}I_{14}/I_2,\ HexI_2,\ C \qquad [2]$$

The cell [2] structure is shown in Fig. 1. The cell consists of a thin silver disk in contact with a silver powder and electrolyte pellet in the ratio of 1:1 (diameter ~ 2.5 cm; thickness ~ 0.1 cm). Another pellet

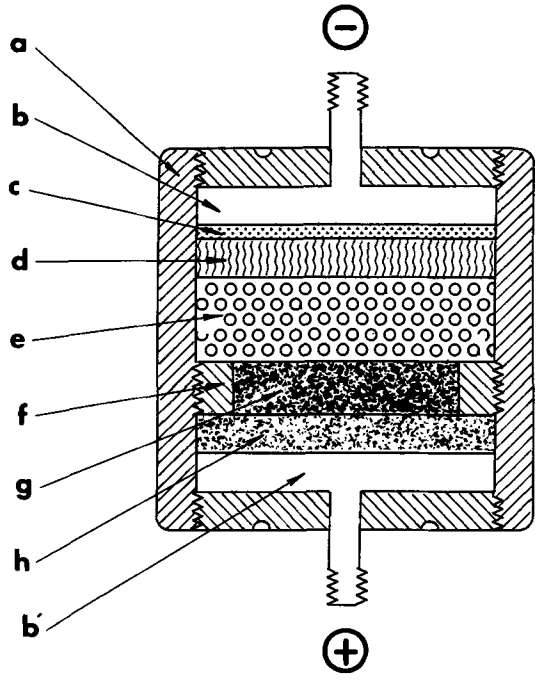

Fig. 1. Cell structure, where a is a polyvinyl-chloride container; b, b' are the external electrical contacts; c a silver disk; d the anodic mixture; e the solid electrolyte; f an insulating ring of PVC; g the cathodic mixture; h the graphite disk.

* Electrochemical Society Active Member.

Key words: solid-state electrochemistry, solid electrolyte, solid-state battery, silver iodide, hexamethonium iodide.

made of the electrolyte alone is compressed on top of this one (diameter ~ 2.5 cm; thickness ~ 0.1 cm). The anode and the electrolyte so formed are put in contact with the cathodic mixture pellet (iodine, $HexI_2$, graphite, and electrolyte in the weight ratio respectively of 2:1:4:7; diameter ~2.2 cm, thickness ~ 0.1 cm). The electrolyte and the cathodic mixture are partially insulated by a polyvinyl-chloride ring in order to prevent possible contacts between the electrodes. A graphite cathode contact terminal electrode is used to complete the cell. The actual weights of the cell components are: 1g of silver powder anode; 1.2g of cathodic mixture; 2.8g of the electrolyte pellet.

Results

The specific conductance of the solid electrolyte has been found to be 0.029 $(ohm \times cm)^{-1}$, the same value as that reported in a previously mentioned paper (1).

The Ag^+ transport number in $HexAg_{12}I_{14}$ at 25°C has been determined by passing a known amount of charge through a cell made of two silver electrodes in contact with a solid electrolyte pellet and comparing the corresponding coulombs with those obtained by measuring the loss in weight of the anode. This method is similar to the one used by Bradley and Greene for the KAg_4I_5 solid electrolyte (4). The transport number of the Ag^+ thus determined is 0.99 ± 0.01, a value that shows how the contribution to the passage of the current within the electrolyte is essentially due to migration of Ag^+ ions alone.

Figure 2 shows a typical current-voltage curve, obtained at 25°C with the electrolyte compressed between two platinum electrodes. The decomposition potential of $HexAg_{12}I_{14}$ is 0.67 ± 0.01V, obtained by back-extrapolating the linear part of the curve.

The OCV of cell [2] is 0.635V at 25°C and its variation with temperature is shown in Fig. 3. The temperature dependence is 0.0002 V/°C in the range −40° to +50°C.

From current-voltage plots at room temperature (Fig. 4) the internal resistance of the cell has been determined at about 15 ohms. Such value is considerably in excess of the resistance due to the pellet alone (about 2 ohms), so that it can be concluded that the remaining internal electric resistance of the cell (about 13 ohms) is due to the effects of contacts to the electrodes.

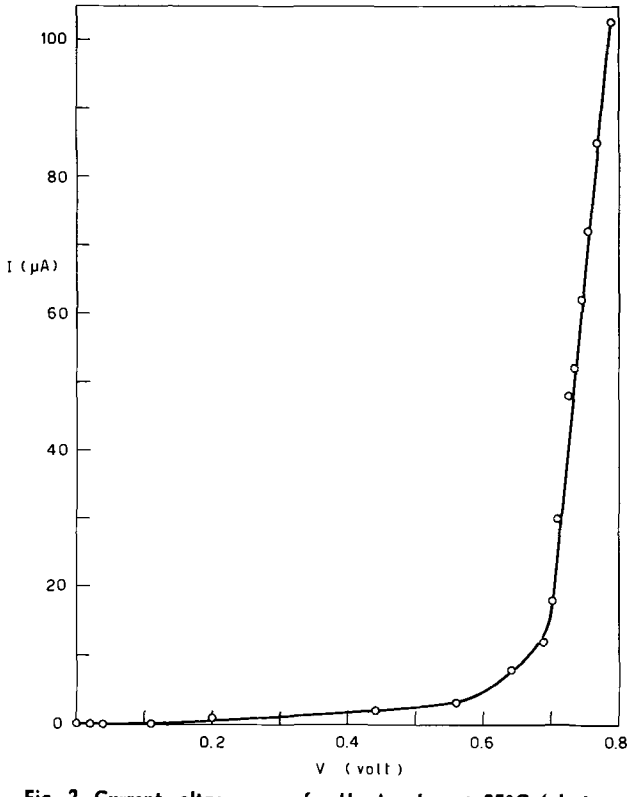

Fig. 2. Current-voltage curve for $HexAg_{12}I_{14}$ at 25°C (platinum electrodes).

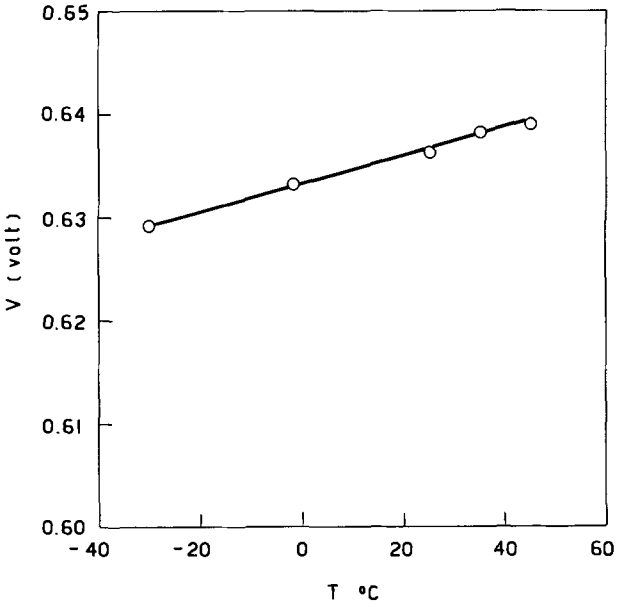

Fig. 3. Temperature dependence of the OCV of cell [2]

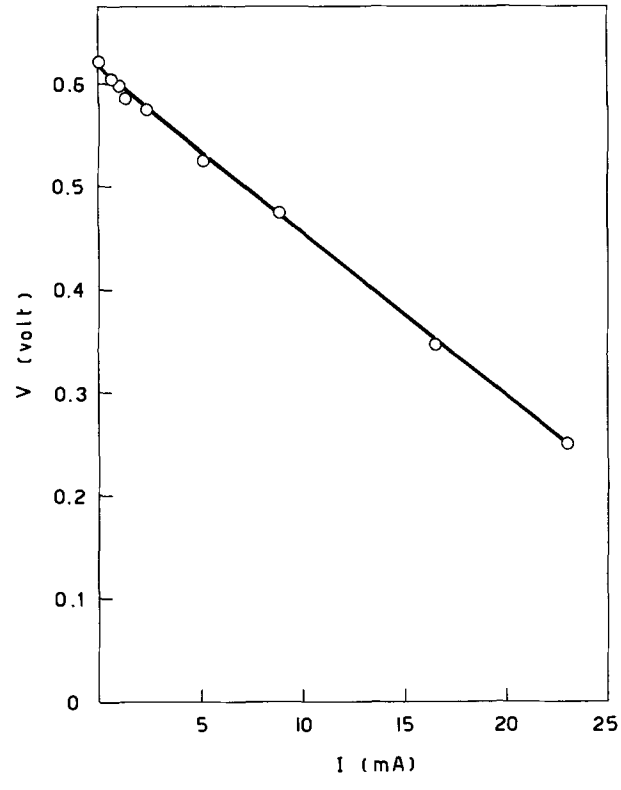

Fig. 4. Current-voltage curves for cell [2] at room temperature

Figure 5 shows typical discharge curves through various loads relating to the component weights as mentioned before; therefore the silver anode efficiency is 10 to 5% from highest intensity discharge rates to the lowest ones.

Figure 6 shows a charge-discharge cycle at 25°C and at a constant current of 0.2 mA.

From the data here reported it can be inferred that the polymethonium-silver iodide compounds (in this case $HexAg_{12}I_{14}$) have a high electrical conductivity almost exclusively ionic. Furthermore, the cell made with it shows reversibility characteristics and can be

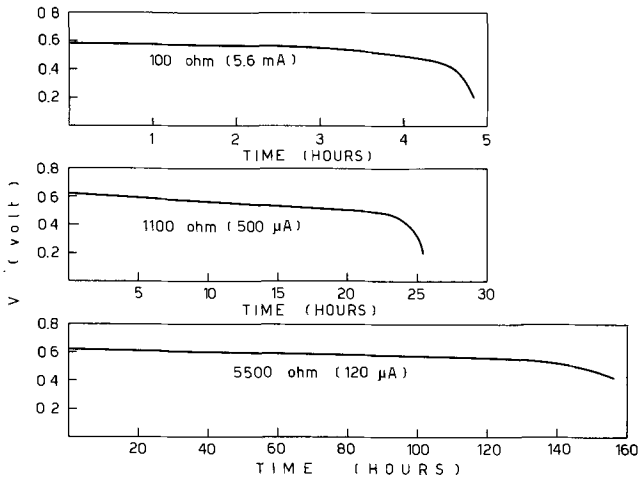

Fig. 5. Typical cell [2] performances at various constant loads at room temperature. As current intensity, an average value is reported.

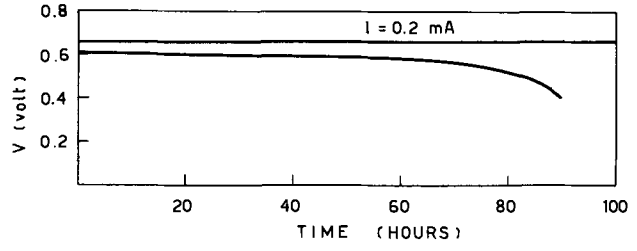

Fig. 6. Charge-discharge cycle of cell [2] at 0.2 mA constant current and at room temperature for efficiency determination.

discharged and charged without apparently altering the efficiency and the state of the operative potential at least within a consistent number of cycles (so far in our experiment 20 complete identical charge and discharge cycles have been carried out).

The capacity output based on iodine has been 90% on the average and that in energy higher than 80% with a value of the average operative voltage of 0.646V in charge and 0.595V in discharge. The stability in the charged state of the cell has been checked at the end of each cycle. The cell in the charged state presents a remarkable stability even after several cycles which in addition to the discharge curves of the cell show the solid electrolyte character of the substance we have studied. Experiments are in progress in order to determine the best weights of the electrode materials and the over-all efficiency of the charge-discharge cycles of the cell.

Summary

A solid-state reversible cell of the type Ag/$HexAg_{12}I_{14}/I_2$, $HexI_2$, C has been developed. The anodic and cathodic contact polarizations have been reduced by the use of a mixture of powdered silver and electrolyte and the use of a suitable mixture of hexamethonium iodide, iodine, graphite and electrolyte, respectively. The cell has an open-circuit voltage of 0.635V at 25°C, an internal resistance of 15 ohms, and is rechargeable with high coulombic efficiency. The above experiments were carried out in order to confirm the property of the $HexAg_{12}I_{14}$ as a solid electrolyte.

Acknowledgment

This work was sponsored by the Consiglio Nazionale delle Ricerche under Contract CNR No. 70.00698/11 115.860.

Manuscript submitted March 24, 1972; revised manuscript received July 17, 1972.

Any discussion of this paper will appear in a Discussion Section to be published in the December 1973 JOURNAL.

REFERENCES

1. M. L. Berardelli, C. Biondi, M. De Rossi, G. Fonseca, and M. Giomini, *This Journal*, **119**, 114 (1972).
2. M. De Rossi, G. Pistoia, and B. Scrosati, *ibid.*, **116**, 1642 (1969).
3. R. Jasinski, "High Energy Batteries," Plenum Press, New York (1967).
4. J. N. Bradley and P. D. Greene, *Trans. Faraday Soc.*, **62**, 2069 (1966).

Current Distribution in the Porous Lead Dioxide Electrode

Daniel Simonsson

Department of Chemical Technology, The Royal Institute of Technology, Stockholm, Sweden

ABSTRACT

A theoretical analysis of initial current distribution in the porous lead dioxide electrode is made by application of the macrohomogeneous model for porous electrodes. The parameters in the model have been determined experimentally for the investigated lead-dioxide battery plates. The theoretical results are in good agreement with experimental determinations by means of electron microprobe analysis of the $PbSO_4$-distribution within partly discharged positive lead-acid plates. The experimental studies of current distribution shows that at high current densities the electrode reaction takes place mainly in the outer layers of the electrode. At low discharge currents, the initial current distribution is uniform while after the first quarter of discharge, the outer layers are more utilized than the inner parts. A mechanism for the passivation of the positive plate in the lead-acid battery is proposed.

The behavior of porous battery electrodes is to a large extent governed by current distribution and reactant depletion. Optimizations of porous electrodes must therefore be based upon some model able to predict how these phenomena influence the discharge behavior. During the last decade various mathematical models have been proposed for the theoretical analysis of electrode reactions in porous media (1-4). While the theoretical work in this field has been extensive, comparatively few applications of these models have, however, been made to practical electrodes. In the case of the practically important lead dioxide electrode, used as positive electrode in the lead-acid cell, theoretical and experimental investigations of current distribution have given contradictory results (5-9).

The purpose of the present paper is to study the current distribution in the porous lead dioxide electrode in solutions of sulfuric acid theoretically and experi-

Key words: lead-acid battery, porous electrode, current distribution.

mentally, and to offer an explanation for the earlier contradictions between theory and experiments.

Choice and Description of Theoretical Model

Various theoretical models have been used to describe the processes in flooded porous electrodes mathematically. Winsel (2) has suggested a model consisting of circular cylindrical pores with constant radius, parallel to each other and perpendicular to the outer surface. Other authors (1) have used a model represented by electrical equivalent circuits. In this way the behavior of the electrode can be simulated with a network of ohmic and charge-transfer resistances.

These two models both have their disadvantages. The first model cannot be used with electrodes of cylindrical shape or with electrodes which must be considered as two-dimensional, since in these cases complications arise concerning the direction of the pores.

The second model has been applied by Euler to some practical electrodes, among them the lead dioxide electrode (6). However, this model makes use of a linearized polarization equation and is thus realistic only for small current densities, while it becomes unrealistic for large current densities where the polarization equation is of exponential type (3, 10). Furthermore it is difficult to include the influence of concentration changes in the electrical model.

Most of the disadvantages of the two mentioned models are eliminated in the so-called continuous or macrohomogeneous model (3, 4). This model disregards the actual geometric detail of the pores and describes the porous electrode as a superposition of two continuous phases, liquid and solid. This model resembles real electrodes when particle and pore dimensions are of the order of micrometer. Under these circumstances the concentration of the electroactive species depends only on time and distance from the outer surface of the electrode.

Because of its mentioned advantages, the macrohomogeneous model will be used in this study. The average pore diameter in the type of lead dioxide plates used in this work was determined by means of mercury porosimetry to 0.3-0.4 μm and the electrodes can therefore be regarded as macrohomogeneous media in accordance with the concepts of the model.

A complete analysis of the discharge behavior of the positive plate in the lead-acid cell requires rather rough approximations concerning the composition of the electrolyte and the basic equations for mass transfer. Furthermore the formation of a passivating reaction product, lead sulfate, in the pores complicates the analysis of the transient behavior. However, an exact analytical solution for the current distribution can easily be obtained in the simplified case of uniform concentration, uniform porosity, and uniform specific surface area, corresponding to the initial moments of discharge. The comparison between theoretical and experimental determinations, which is the primary goal in this work, will therefore be restricted to this special case.

It is easy to show that under these circumstances the current distribution is governed by the following two equations (see Appendix)

$$\bar{i}_2 = \kappa_1\kappa_2 \nabla E/(\kappa_1 + \kappa_2) + \kappa_2 \bar{I}/(\kappa_1 + \kappa_2) \qquad [1]$$

$$\nabla \cdot \bar{i}_2 = Sf(c,E) \qquad [2]$$

The first equation gives the current density, $\bar{i}_2$, in the pore electrolyte as a function of the electrode potential gradient, ∇E and the effective conductivity of the electrode matrix, κ_1, and the pore electrolyte, κ_2.

In the second equation $f(c, E)$ is an electrode kinetic expression of Volmer/Erdey-Gruz type or simply an empirical relation calculated from the polarization curve.

Before the initial current distribution can be calculated from these two equations, the actual values of the parameters appearing in the equations above must be determined by suitable experiments.

Experimental Determination of the Parameters in the Model

The electrodes investigated in this study were positive plates manufactured for use in automobile batteries. These electrodes are manufactured with grids of lead-alloy as current collectors.

To determine actual current distributions from the equations given above, knowledge is required about the parameters κ_1, κ_2 and the rate of the charge transfer process. The actual values of these parameters were determined experimentally for the electrodes under investigation.

Determination of κ_1.—Lead dioxide is a semiconductor with almost metallic conductivity. However, the conductivity of the porous matrix in the electrode depends also on the contact between the particles. A rough estimate of this effective conductivity of the porous lead dioxide was made by simply measuring the voltage drop across a piece of electrode material of known dimensions, when a current of known magnitude was forced through this specimen. For fully charged plates the conductivity was measured by this method to about 5-20 mho/cm. The order of magnitude is in good agreement with an effective resistivity of 0.1 ohm-cm reported by Euler (6).

During discharge the conductivity of the electrode material decreases.

The conductivity measured for fully charged plates is, however, prevailing up to more than 25% of complete discharge and will therefore be sufficient for the analysis of the initial current distribution.

Determination of κ_2.—The effective conductivity of the electrolyte phase in porous electrodes depends on the conductivity of the free electrolyte, the porosity of the electrode, and the tortuosity of the pores. The simplest way to measure this parameter has been described by Euler and Rieder (11). They proposed that the effective resistivity of the electrolyte in the pores could be determined by measuring the electrolyte potential difference between the two sides of the electrode when a direct current passes through the electrolyte in the pores. The potential difference is measured by two reference electrodes with Luggin-capillaries and is corrected for the voltage drop in the free electrolyte. The disadvantage of this simple method is that a certain fraction of the current passes through the solid electrode phase by an anodic electrode reaction on one side of the electrode and a cathodic reaction on the other side. At small currents this fraction is, however, rather small. Romanova and Selitsky (12) determined it to less than 5% for potential differences smaller than 20 mV. A correction for this fraction is not made in this work since the variation of the effective conductivity with different cycles proved to be of much greater magnitude.

A graphical representation of potential difference *vs.* current density yielded a straight line (Fig. 1). The effective conductivity, κ_2, can be calculated from the slope, K, of this line by using the formula

$$\kappa_2 = 2L/K$$

where $2L$ is the thickness of the electrode. The conductivity of 5M H_2SO_4 in the positive plates used in this study was determined to 0.07 $\pm$ 0.01 mho/cm. The great uncertainty is due to variations from cycle to cycle and from electrode to electrode. The measured average of the conductivity is in good agreement with the results of Romanova and Selitsky (12), while it is three times greater than the value reported by Euler (6). The measured effective conductivity is thus only about a tenth of the conductivity of the free electrolyte. This great reduction is probably due to oxygen left in the pores after excess charge. Romanova and Selitsky

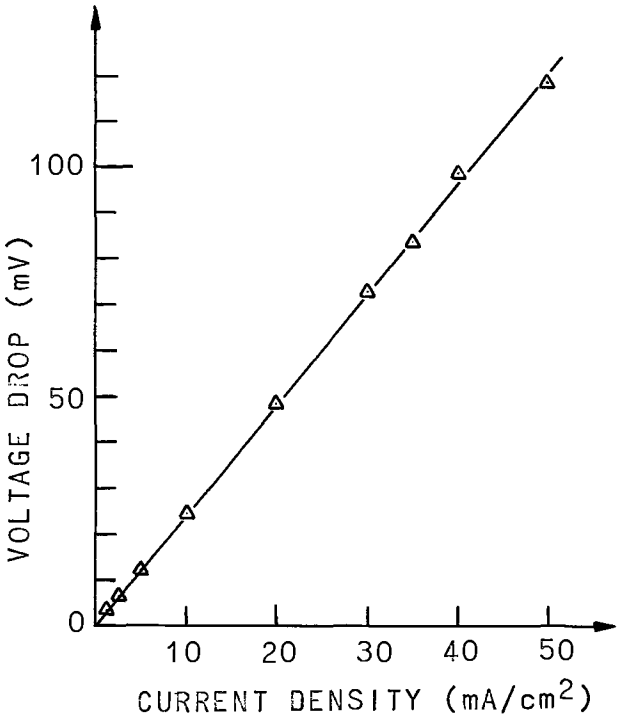

Fig. 1. Voltage drop across a positive lead-acid plate as a function of applied current density in the pore electrolyte.

(12) thus observed a doubling of the conductivity, after the removal of oxygen at reduced pressure.

The Current-Overvoltage Relation for the Lead Dioxide Electrode

There are fairly many reports in literature on the kinetics of the cathodic discharge of the lead dioxide electrode in sulfuric acid

$$PbO_2(s) + 4H^+ + SO_4^{2-} + 2\,e^- \rightleftharpoons PbSO_4(s) + 2H_2O \quad (1)$$

The results are, however, partly divergent and a definite rate equation cannot be found. New experiments were therefore carried out, with the restricted goal to determine the prelogarithmic Tafel coefficient in the region of high overvoltage. The experimental method was galvanostatic discharge of a lead dioxide surface formed by anodic oxidation of a smooth lead sheet (analytical grade from MERCK, Darmstadt) in 5.0M H_2SO_4 (analytical grade in bidistilled water). The electrode was subjected to repeated cycles of charge and discharge to increase the thickness of the lead dioxide layer and consequently decrease the self-discharge of the electrode. The anodic oxidation was carried out with 1.0 mA/cm² for successively increasing times up to 1 hr for the last formation cycles. Care was taken to avoid excess charge leading to flaking of the electrode surface. The self-discharge of the thus formed test electrode was equivalent to a cathodic current of less than 0.01 mA/cm². Microscopic investigations showed, however, that the lead dioxide surface formed in this way was porous, something which is mostly unsuitable in kinetic studies. The thickness of this porous layer is, however, very small (about 0.01 mm), and thus the current distribution in this layer may be expected to be uniform. (This case corresponds to a very low value of the parameter a, appearing in the equation for current distribution in the next section.)

This very thin porous electrode may thus be expected to give lower overvoltages than a smooth lead dioxide electrode but the same Tafel slope at high overvoltages.

As a further control of the Tafel slope, the same experiments were also carried out with a nonporous lead dioxide surface formed by electrodeposition of β-PbO_2 on a smooth (polished) Pt-surface from a solution of $Pb(NO_3)_2$ (10 g/liter) and HNO_3 (15%). The deposition was carried out in 15 min with 3 mA/cm². The deposit was checked by x-ray diffraction to be β-PbO_2.

The galvanostatic discharges were carried out at 20° ± 1°C, and the electrode potential was measured against a mercury-mercurous sulfate reference electrode with a digital voltmeter. The overvoltage was defined as the difference between the maximum, rather constant electrode potential obtained after the initial drop of potential at the beginning of discharge and the equilibrium open-circuit potential. Correction was made for the ohmic potential drop between the surface and the end of the Luggin capillary. The results are illustrated in Fig. 2. The electrode formed by anodic oxidation of a lead surface proved to give much lower overvoltages than the electrode formed by deposition of β-PbO_2 on platinum. This is just what might be expected in consideration of the much larger true surface area for the former electrode. However, the slope of the logarithmic polarization curve was found to be nearly the same for both electrodes, 30 ± 5 mV/decade. From the experimental results above follows that the rate equation for the electrode reaction

$$PbO_2(s) + 4H^+ + SO_4^{2-} + 2e \rightleftarrows PbSO_4(s) + 2H_2O \quad (1)$$

may be written

$$j = -j_o \cdot \exp[-2F\eta/(RT)] \quad [3]$$

for overpotentials between 30 and 90 mV and Eq. [2] may consequently be written

$$\nabla \cdot \bar{i}_2 = -Sj_o \exp[-2F\eta/(RT)] \quad [4]$$

Theoretical Analysis of the Initial Current Distribution

The equations given above can now be applied to the lead dioxide plates under investigation. These electrodes are of grid-type and would therefore require a complicated two-dimensional representation in a coordinate system (Fig. 3).

However, the effective conductivity of the fully charged porous matrix was shown above to be about a hundred times greater than that of the electrolyte in the pores. In comparison to the electrolyte the solid

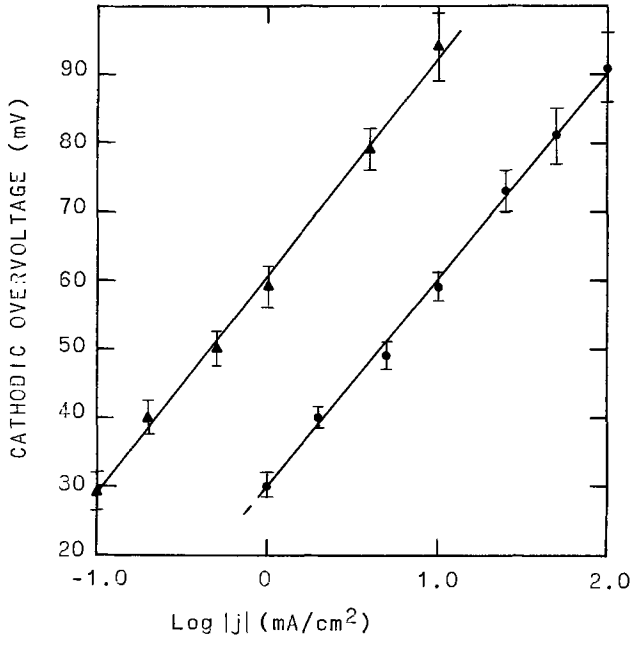

Fig. 2. Tafel plots for lead dioxide electrodes in 5M H_2SO_4. PbO_2 formed by: ●, anodic oxidation of Pb and ▲, electrodeposition of β-PbO_2 on Pt.

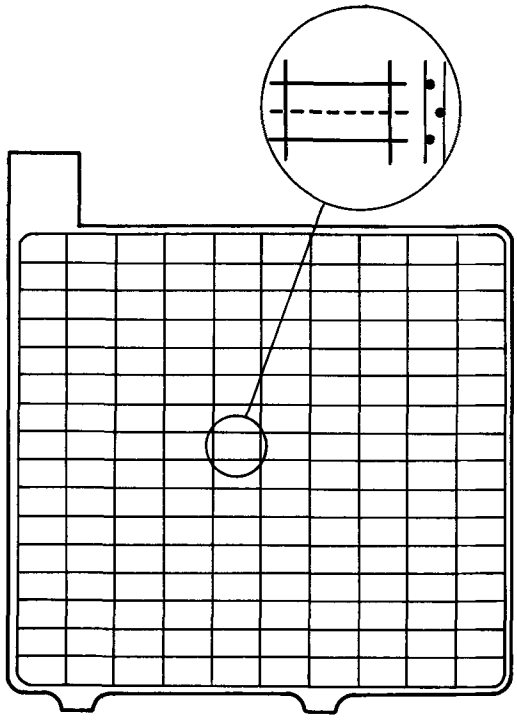

Fig. 3. Porous lead dioxide electrode with grid.

phase can therefore be regarded as an equipotential surface, and the electrode may consequently be regarded as one-dimensional, at least during the first quarter of discharge. The coordinate x is taken $= 0$ at the center of symmetry of the electrode and $= L$ and $-L$ respectively at the two outer surfaces.

Let us now consider the conditions at the first moments of discharge, after the electrolytic double layer has been charged, but before the concentration has changed significantly from its initial uniformity. The current is cathodic, $I < 0$.

Since now

$$\kappa_2 << \kappa_1 \quad \text{and} \quad dE/dx = d\eta/dx$$

Eq. [1] can be written

$$i_2 = \kappa_2 \, (d\eta/dx) \qquad [5]$$

while the rate equation, Eq. [4] can be expressed

$$di_2/dx = -Sj_0 \exp[-2\mathbf{F}\eta/(RT)] \qquad [6]$$

By differentiating Eq. [6] and eliminating $d\eta/dx$, one obtains

$$d^2 i_2/dx^2 + 2\mathbf{F}/(RT\,\kappa_2)\; i_2\, di_2/dx = 0 \qquad [7]$$

To use dimensionless variables instead, the quantities

$$z = x/L, \quad i = i_2/I \quad \text{and} \quad a = -2\mathbf{F}IL/(RT\,\kappa_2)$$

are introduced, whereupon Eq. [7] is transformed into

$$d^2i/dz^2 - ai\, di/dz = 0 \qquad [8]$$

The boundary conditions are then $i = 0$ at $z = 0$ and $i = 1$ at $z = 1$. The solution to this nonlinear differential equation is

$$i = \sqrt{2d/a} \tan (\sqrt{ad/2}\, z) \qquad [9]$$

where $d = di/dz$ at $z = 0$.

A finite current density in the electrode requires that

$$0 < \sqrt{ad/2} < \pi/2$$

The current distribution is obtained by differentiating Eq. [9]

$$di/dz = d \sec^2 (\sqrt{ad/2}\, z) \qquad [10]$$

The value of d is not given for the nonlinear, boundary value problem, Eq. [10] and must therefore be calculated. Putting $z = 1$, $i = 1$ in Eq. [9] gives an equation for d

$$d = a \cot^2 (\sqrt{ad/2})/2$$

from which d can be calculated by means of some numerical method, for example the Newton-Raphson iteration method.

The initial current distribution in a porous PbO_2-electrode at different discharge rates calculated from Eq. [10] is shown in Fig. 4. From the graphs we see that for low current densities (small a), the current distribution is rather uniform, while for higher current densities (increasing a) the electrode reaction takes place mainly near the outer surface of the electrode.

Experimental Investigation of the Initial Current Distribution

To determine the validity of the applied theoretical model, the calculations for the case of constant concentration made above, must be compared with experimental determinations of the initial current distribution. For this purpose there is obviously a need for a practical specification of the concept "initial." In the case of the porous lead dioxide electrode the initial conditions may be regarded as prevailing up to 25% of the total discharge time. There are two arguments for this interpretation: (*i*) The first fourth of the discharge curve is rather flat. (*ii*) Keeping the acid concentration constant by pumping electrolyte through the pores does not produce significant deviations from the normal discharge curve during the first fourth of discharge.

This interpretation allows a direct comparison between the theoretical results in Fig. 4 and the experimental results by Haebler, Panesar, and Voss (9), who measured the distribution of the reaction product, $PbSO_4$ within partly discharged positive lead-acid plates using a scanning x-ray microprobe with sulfur-

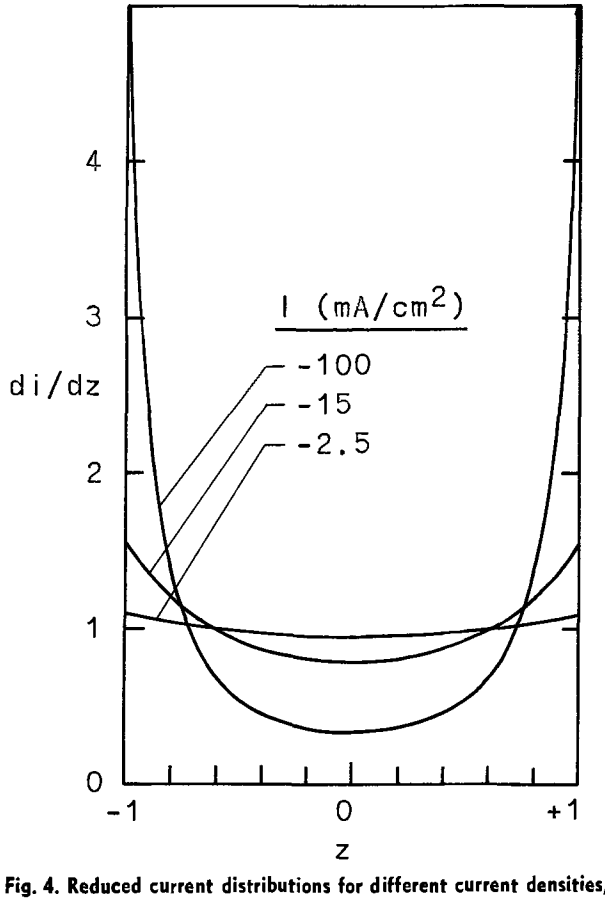

Fig. 4. Reduced current distributions for different current densities, $L = 0.09$ cm, $\kappa_2 = 0.07$ mho/cm.

K_α radiation. These experiments showed that the discharge to $PbSO_4$ in the first fourth of discharge (with -180 mA/cm^2) took place mainly in the interior of the plates. The microprobe analyses made by Bode, Panesar, and Voss (8) gave distribution curves which decreased strikingly near the outer surfaces of the electrode at all discharge rates.

Obviously these experimental results reveal a complete failure of the theoretical predictions. Furthermore the measured distribution curves can hardly be explained at all on the basis of conventional theories of current distribution. This serious contradiction between theory and experiment can, however, also be attributed to some experimental error.

It was thus found necessary in this work to investigate whether the preparation of the specimens for analysis, *i.e.*, soaking of the sulfuric acid in the pores with distilled water, might affect the original distribution of lead sulfate. The underlying idea was that when electrodes containing sulfuric acid of 1-5M are soaked in distilled water, the sulfuric acid concentration at the interface will become very low. The reversible electrode potential will therefore be much lower (up to 100 mV) at the outer surface than in the depth of the pores. This would produce leveling currents resulting in charge of the outer parts of the electrode and discharge of the inner parts. By this process the distribution of sulfate would be shifted to lower values at the interface and higher values in the interior of the electrode. This hypothesis would also explain the strange fall of the distribution curves within a zone of about 0.2 mm depth, observed by Bode *et al.* (8).

Experimental Procedure

The cell used in the experimental investigations consisted of a positive plate of grid-type with dimensions 50 × 50 × 1.8 mm placed symmetrically between two negative (Pb−) plates in 5.0M H_2SO_4. The electrolyte was in great excess to keep the concentration in the bulk almost constant. The potential of the positive plate was recorded against a mercury-mercurous sulfate electrode, and the end of discharge was defined to be at a total overvoltage of 1V. To keep the current load symmetrical on the two sides of the electrode, two different galvanostatic circuits were used, one for each side of the positive electrode and the corresponding counterelectrode. Positive plates were discharged to 25% with -100 mA/cm^2 on each side at 21° ± 1°C. After discharge a portion of the positive plate was soaked in a beaker with periodically renewed distilled water for two days. The plate was dried and a sample from the middle of the plate was subsequently examined using an electron microprobe. The lead sulfate distribution across the electrode was measured by the intensity of the S-K_α-radiation.

To investigate the effect of pretreatment other portions of the electrode were freed from sulfuric acid in another way. The method consisted in moulding a piece of the partly discharged electrode in an epoxy resin, grinding and polishing the cross section of the sample, and then soaking with periodically renewed distilled water for two days. With this method the leveling currents are acting in a direction perpendicular to the cross section of the electrode, thus affecting the absolute height of the distribution curves, but not their form.

Results

The experimental results, Fig. 5, appeared to be dependent on the method of pretreatment. Conventional soaking of the electrode gave a rather uniform distribution of lead sulfate, in accordance with the results obtained by Haebler *et al.* (9). The other method, however, gave a distribution in good agreement with the theoretical prediction. Both methods were checked by analyses of samples from completely charged, electrolyte-filled electrodes, giving low, uniform intensities. These results led to the important conclusion that

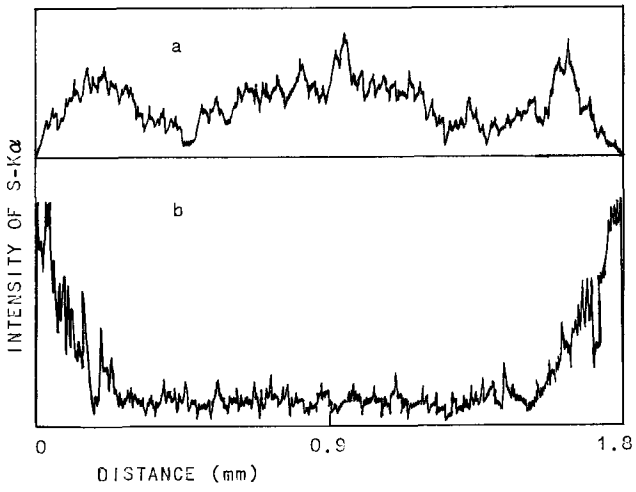

Fig. 5. The dependence of the method of soaking on the obtained distribution curves of sulfur. (a) "Conventional" soaking with H_2O and (b) soaking perpendicular to the cross section.

conventional soaking of the electrode strongly affects the distribution of lead sulfate within the electrode.

The experimental results reported below were therefore obtained with samples soaked with distilled water in the direction perpendicular to the cross section.

The measured distributions of lead sulfate in PbO_2-electrodes discharged with two different current densities to 25% are illustrated in Fig. 6. These curves are in good agreement with the theoretical calculations of initial current distribution (dashed lines).

Changes in current distribution during discharge.— It may be expected that the current distribution undergoes considerable changes during discharge. The

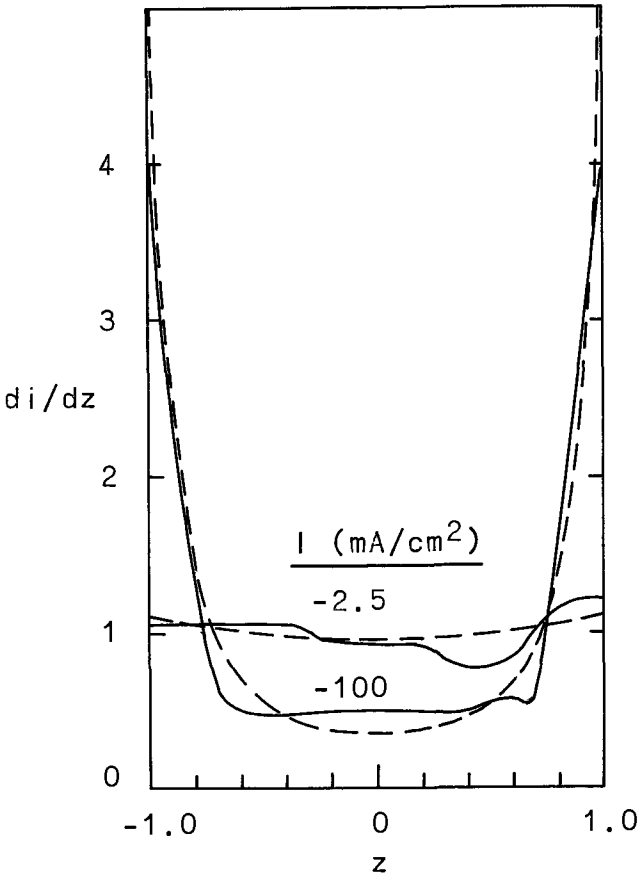

Fig. 6. Reduced current distributions at low- and high-current densities. Comparison between theoretical (dashed lines) and experimental (solid lines) results (L = 0.09 cm, κ_2 = 0.07 mho/cm).

distribution of lead sulfate was therefore measured also at higher degrees of discharge. The results obtained at different discharge rates are illustrated in Fig. 7 and 8.

It is evident from Fig. 7 that in cases of high current densities it is relevant to introduce the concept of a "reaction layer," proceeding from the interfaces of the electrode into the interior parts during discharge. At lower current densities the distribution of lead sulfate is uniform at the beginning of discharge, while the outer parts are somewhat preferred after the first quarter of discharge.

Discussion

The macrohomogeneous model for porous electrodes proves to be a valuable mathematical tool for the prediction of initial current distribution in porous lead dioxide electrodes.

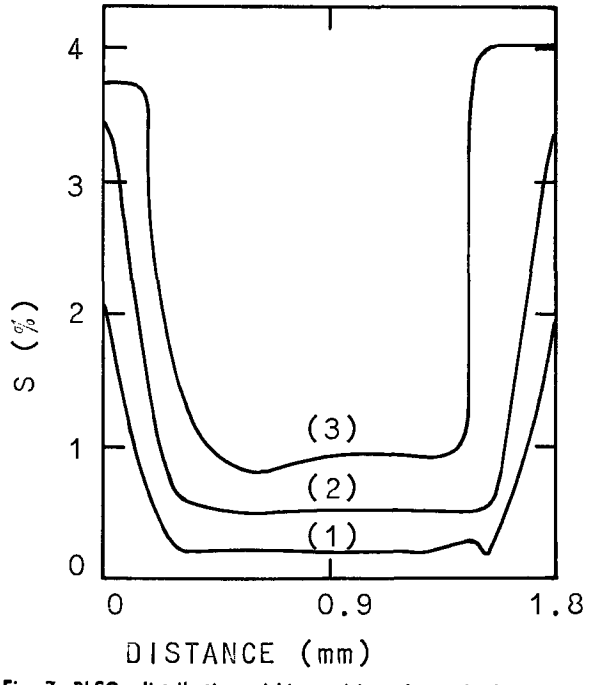

Fig. 7. $PbSO_4$-distribution within positive plates discharged with −100 mA/cm² to: 1, 25%; 2, 50%; and 3, 100%.

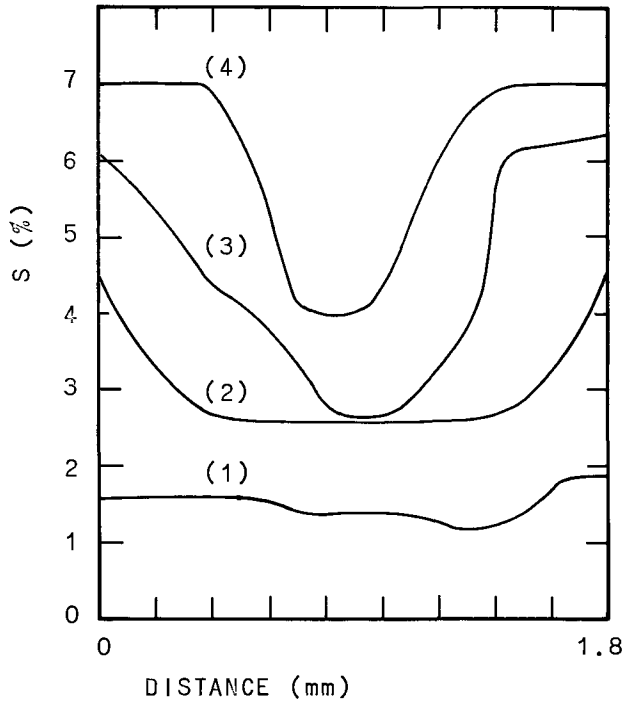

Fig. 8. $PbSO_4$-distribution within positive plates discharged with −2.5 mA/cm² to: 1, 25%; 2, 50%; 3, 75%; and 4, 100%.

The accuracy of the theoretical calculations of initial current distribution is limited by the accuracy with which the input parameters can be experimentally determined. In the present case the greatest uncertainty lies in the determination of the effective conductivity of the electrolyte, which varies considerably (up to 15%) from cycle to cycle and from electrode to electrode.

In this work the electrode kinetics is represented by a Tafel expression. As pointed out by Grens and Tobias (13) such an approximation may be dangerous, since the overvoltage existing over much of the depth of the electrode may be too small to permit the disregarding of the reverse reaction term in the Volmer expression. It is therefore necessary to check that the calculated local overvoltage is everywhere within the range of the validity of the Tafel approximation. In this work the calculated overvoltage profiles were found to be within the Tafel region for the current densities used, although at the smallest current density (2.5 mA/cm²) the electrode interior was operating near the lower limit of this region.

Experimental investigation of the current distribution by means of analysis of the distribution of the reaction product, $PbSO_4$, proved to be successful only under conditions where soaking with distilled water does not produce local concentration cells which redistribute the lead sulfate in the direction perpendicular to the interfaces of the electrode.

The experimental studies of current distribution lead to some important conclusions concerning the mechanism of the passivation of positive plates in lead-acid batteries. At high discharge currents a reaction layer is moving inwards into the electrode due to gradual insulation of the surface by covering lead sulfate crystals. From Fig. 7 it is clear that this reaction layer has not reached the interior parts before the voltage has broken down. Thus, the capacity at high current loads is not limited by a complete passivation of the electrode surface, since there is still active material left in the depth of the electrode. This fact leads to the conclusion that the acid in the depth of the pores is depleted (locally or extensively) during discharge, thus loosing its conductive property. The current can no longer reach the remaining active material in the inner parts, nor be transferred across the electrode surface in the outer parts insulated by lead sulfate crystals, so the voltage consequently breaks down.

At low current densities the total utilization of the active material is higher than at high current densities. However, even at low current densities there still remains active material in the middle of the electrode after the discharge is completed. This is probably due to plugging of the pores.

Acknowledgments

The author wishes to thank Olle Lindström and Torbjörn Nilsson of The Royal Institute of Technology, Stockholm; Karel Micka, J. Heyrovsky Institute of Polarography, Prague, Czechoslovakia; and Alfons Lindholm, AB Tudor, Nol, Sweden, for valuable discussions and support. He is also indebted to Conni Westman, Institute for Metal Research, Stockholm, who performed the electron microprobe measurements.

Manuscript submitted July 13, 1972; revised manuscript received Oct. 9, 1972.

Any discussion of this paper will appear in a Discussion Section to be published in the December 1973 JOURNAL.

LIST OF SYMBOLS

a $\dfrac{-2ILF}{\kappa_2 RT}$

d Integration constant for initial current distribution

E Electrode potential, V
F Faraday's constant, 96 491 As/equivalent
$\bar{i}_1$ Current density in matrix phase, based on overall apparent porous electrode area, A/cm²
$\bar{i}_2$ Current density in electrolyte phase, A/cm²
$\bar{I}$ Total apparent current density applied on one side of the porous electrode, A/cm²
i Dimensionless current, i_2/I
j Local rate of charge transfer, A/cm²
j_o Exchange current density, A/cm²
L Thickness of one symmetric half of the porous electrode, cm
R Universal gas constant, joule/mole-deg.
S Specific active interfacial surface area per unit volume, cm⁻1
T Temperature °K
x Distance coordinate from the symmetry plane of the porous electrode, cm
z Dimensionless distance, x/L
η Overvoltage, V
κ_1 Effective conductivity of the matrix phase, mho/cm
κ_2 Effective conductivity of the electrolyte phase, mho/cm
ϕ_1 Potential of matrix phase, V
ϕ_2 Potential of pore electrolyte, V

APPENDIX

Derivation of Eq. [1] and [2]

The current density in the matrix, $\bar{i}_1$, is given by Ohm's law

$$\bar{i}_1 = -\kappa_1 \nabla \phi_1 \qquad [A\text{-}1]$$

In the case of uniform concentration the current density in the pore electrolyte, $\bar{i}_2$, is also given by Ohm's law

$$\bar{i}_2 = -\kappa_2 \nabla \phi_2 \qquad [A\text{-}2]$$

The conservation of charge requires that the sum of these current densities is equal to the total apparent current density $\bar{I}$

$$\bar{i}_1 + \bar{i}_2 = \bar{I} \qquad [A\text{-}3]$$

The electrode potential is defined as $E = \phi_1 - \phi_2$ and consequently, with Eq. [A-1], [A-2], and [A-3]

$$\bar{i}_2 = \kappa_1\kappa_2 \nabla E/(\kappa_1 + \kappa_2) + \kappa_2\bar{I}/(\kappa_1 + \kappa_2) \qquad [1]$$

Finally, the relation between $\bar{i}_2$ and E is given by the actual electrochemical kinetic expression

$$\nabla \cdot \bar{i}_2 = Sf(c,E) \qquad [2]$$

Equation [2] expresses the rate of the electrode reaction per unit volume of the electrode as proportional to the specific active surface area, S, and to an appropriate expression for the local rate of charge transfer, $f(c, E)$. The appropriate boundary conditions are at the current collector $\bar{i}_2 = 0$ and at the interface of the electrode $\bar{i}_2 = \bar{I}$.

REFERENCES

1. J. Euler and W. Nonnenmacher, *Electrochim. Acta*, **2**, 268 (1960).
2. A. Winsel, *Z. Elektrochem.*, **66**, 287 (1962).
3. J. S. Newman and C. W. Tobias, *This Journal*, **109**, 1183 (1962).
4. K. Micka, *Collection Czech. Chem. Commun.*, **29**, 1998 (1964).
5. W. Stein, Dissertation T.H., Aachen, 1959.
6. K. J. Euler, *Electrochim. Acta*, **13**, 1533 (1968).
7. W. S. Yantschenko and I. A. Selitsky, *Electrotekhnika*, **37**, 34/35 (1966).
8. H. Bode, H. Panesar, and E. Voss, *Chemie Ing.-Techn.*, **41**, 878 (1969).
9. H. Haebler, H. Panesar, and E. Voss, *Electrochim. Acta*, **15**, 1421 (1970).
10. J. Euler and K.-N. Müller, *Electrochim. Acta*, **8**, 949 (1963).
11. J. Euler and E. Rieder, *ETZ-A Bd.*, **85**, H 17 (1964).
12. I. L. Romanova and I. A. Selitsky, *Elektrokhimiya*, **6**, 1776 (1970).
13. E. A. Grens and C. W. Tobias, *Electrochim. Acta*, **10**, 761 (1965).

Monolayer Formation in the Reduction of Nickel and Silver Ions from the LiCl-KCl Eutectic

G. J. Hills,* D. J. Schiffrin,[1] and J. Thompson[2]

Chemistry Department, The University, Southampton, England

ABSTRACT

The deposition of nickel and silver on platinum from the LiCl-KCl eutectic at 400°C has been studied using the chronopotentiometric, cyclic voltammetric, and potential step techniques. An observed predeposition of nickel on platinum was observed to take place at 0.5V anodic to the equilibrium potential between nickel in bulk and the solution of its ions. The predeposition process was studied by an a-c impedance method and delineated as the formation of an adsorbed monolayer. A similar but less well-defined predeposition step was observed with silver at 0.1V anodic to the reversible potential. Notwithstanding the predeposition phenomena, diffusion coefficients for both metal ions were determined by each of the voltammetric techniques and found to be in reasonable agreement with each other and with previously reported values.

Electrode processes involving the deposition of metals from molten salt systems are known to be kinetically very fast, and many previous studies have therefore been concerned mainly with the evaluation of the diffusion coefficient of the metal ions involved (1) employing a variety of voltammetric techniques (2).

In aqueous systems, the deposition of a monolayer of the metal at potentials significantly anodic to that of the bulk deposition has been observed in many instances, *e.g.*, for Tl^+ on silver (3); Cu^{2+} on platinum (4), and Ag^+, Tl^+, and Cu^{2+} on gold (5). The same type of phenomenon has been recognized for many years in the hydrogen evolution reaction on platinum,

* Electrochemical Society Active Member.
[1] I.N.T.I., Libertad 1235, Buenos Aires, Argentina.
[2] Electrochemistry Research Laboratories, School of Chemistry, The University, Newcastle-upon-Tyne, England.

Key words: electrodeposition, molten salts, monolayers, silver, nickel.

where a monolayer of adsorbed hydrogen atoms is a stable precursor to the hydrogen evolution reaction.

Monolayer formation processes in molten salts were briefly considered by Schmidt (6) as part of a study of the deposition of Ag^+, Pb^{2+}, Ni^{2+}, and Cd^{2+} ions on platinum from a LiCl-KCl eutectic melt, using alternating square current pulses.

The purpose of the present work was the study of both monolayer formation and metal deposition processes for Ni^{2+} and Ag^{2+} in a LiCl-KCl eutectic melt at 400°C. The reduction of these ions in this melt has been previously studied using polarographic (7), chronopotentiometric (8), and linear sweep methods (9, 10).

Experimental

LiCl-KCl eutectic (59:41 mole per cent (m/o) melting point, 352°C) was prepared from "Analar" grade KCl and reagent grade KCl, using a purification technique similar to that of Laitinen *et al.* (11). A known weight of eutectic mixture was heated to 200°C overnight in vacuum to remove excess water. This was followed by treatment for several hours with dry HCl gas (B.D.H. 99%) during which period the temperature was gradually increased to above the melting point of the eutectic. HCl was removed by evacuation and replaced by dry nitrogen. Following this dehydration procedure, metal ion impurities were next removed by pre-electrolysis under vacuum for 4 hr at 2.5V, using a stainless steel cathode and a carbon anode. During this time the residual current decreased to 0.1-0.2 mA cm^{-2} and this was assumed to be an acceptable level of reducible impurities. No other test was made for the absence of other impurities. Finally, the melt was filtered through a porosity 4 silica frit directly into a silica pot situated in the bottom of the cell assembly. The filtration unit was removed and the cell head, containing sockets for the reference, working and counter electrodes, Chromel-Alumel thermocouple, and nitrogen bubblers were attached.

A Pt/Pt^{2+} (0.01M) reference electrode was used in the studies of the nickel system, and was prepared by anodizing a Pt wire into a calibrated volume of melt contained in a small compartment separated from the bulk melt by a glass frit. For the silver deposition work, a Ag/Ag^+ (0.01M) reference electrode was employed and prepared in a similar manner. In both cases, a carbon rod counterelectrode was used, also contained in a separate compartment and joined to the bulk melt by a glass frit. Platinum electrodes, both in the form of thin wires and small spheres, were sealed into Pyrex glass after being first cleaned with HCl and annealed at white-red heat for 1 hr using a d-c voltage applied directly across a length of platinum wire.

Silver ions were introduced into the melt by a quantitative anodization of a Ag wire, and nickel was added as anhydrous $NiCl_2$ following the dehydration of $NiCl_2\ 6H_2O$ with dry HCl gas.

Potentiostatically controlled experiments were carried out using a potentiostat (Chemical Electronics, Type 70/2A) in conjunction with a waveform generator (Chemical Electronics, Type R.B.1). Cyclic voltammograms at slow sweep rates were recorded on a Y-T recorder (Bryans) and at high sweep rates on a storage oscilloscope (Tektronix, Type 564). Photographs of the transients were taken with a Polaroid camera (Tektronix, Type C 30). A simple constant current source for the chronopotentiometry measurements consisted of a high-voltage dry battery connected in series with decade resistors; chronopotentiograms were recorded on an oscilloscope (Tektronix, 545B), and photographed with a Thompson-Land polaroid camera.

For the study of the electrode impedance of the nickel system, a potentiostat and phase-sensitive detection system were employed (12, 13). Although the uncompensated resistance was very low (a convenient feature of molten-salt systems), a small amount of positive feedback was employed (12) to render negligible the in-phase component of the current at a potential sufficiently anodic to that of the monolayer formation peak. The a-c signal generator was an oscillator (Associated Instrument Manufacturers, A.I.M., Type P.F.O.) generally operating at 1000 Hz and which provided also the in-phase and quadrature reference channels for the phase-sensitive detector (A.I.M., Type P.S.D. 122) used. The potentiostat was constructed from Philbrick operational amplifiers, and its design will be described elsewhere (14). A block diagram of the measuring circuit is shown in Fig. 1. The potentiostat ensures that a current flows across the interface of magnitude sufficient to force the reference electrode potential to follow the applied a-c signal. We represent the interface as a parallel combination (Fig. 2a), since the potential is the controlled variable, and the current is the measurable quantity. If the current were controlled and the potential measured, then a series combination would be a more convenient representation of the interface. Since the instrument had originally been designed to be used with a dropping mercury electrode (14), the former configuration was employed. The P.S.D. output gives the components of the current both in-phase and in quadrature with the exciting potential. When the uncompensated resistance is zero, the current flowing across the interface is given by

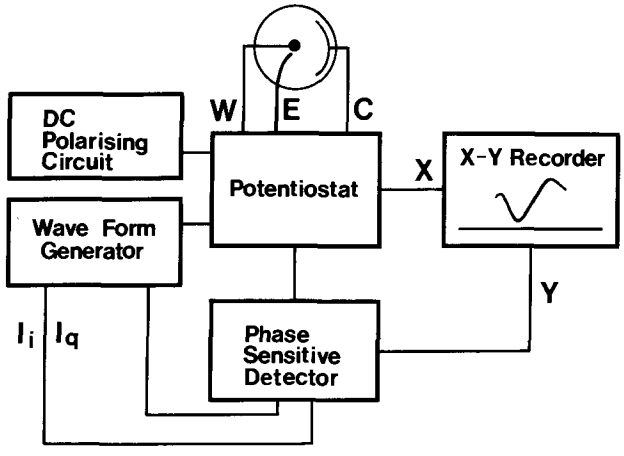

Fig. 1. Block diagram of the potentiostatic-phase detection system used for the impedance measurements. W = working electrode; C = counterelectrode; E = reference electrode; I_i = in-phase reference channel; I_q = quadrature reference channel; X = potential; Y = P.S.D. output.

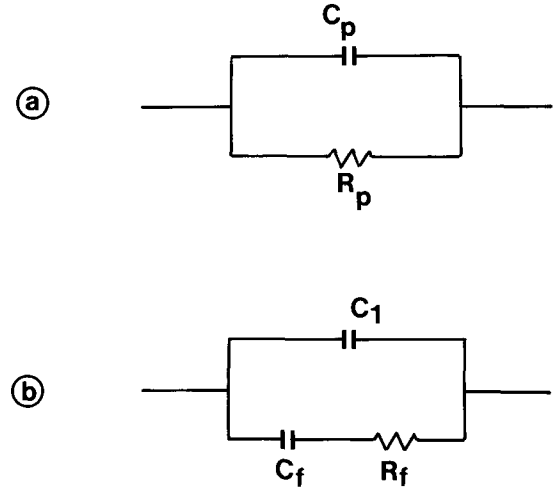

Fig. 2. (a) Parallel components of the interfacial impedance directly measurable by the potentiostatic-phase detection method. (b) Model of the interface for the hydrogen ionization equilibrium [6]; C_1 = double-layer capacitance; C_f = pseudo-capacity, and R_f = charge transfer resistance.

(Fig. 2a)

$$i = V\left(\frac{1}{R_p} + j\omega C_p\right) \quad [1]$$

where V is the applied potential, R_p and C_p are the equivalent parallel interfacial resistance and capacitance, and ω is the angular frequency. The P.S.D. outputs are thus

$$V_q = (GV)\,\omega\,C_p \quad [2]$$

and

$$V_i = (GV)\,\frac{1}{R_p} \quad [3]$$

where V_q and V_i are respectively the quadrature and in-phase potential outputs of the P.S.D., and G is the instrumental gain. For a given a-c signal amplitude, the product (GV) is a constant of the instrument, easily evaluated with a dummy cell made of precision components.

From [2] and [3], it is seen that it is a simple matter to record directly, either on an X-Y recorder or with a data logger, the parallel components of the impedance. This technique has been described here in some detail because of its patent applicability to molten-salt studies and because it involves standard items of equipment. In the present case, C_p and $1/R_p$ were directly recorded on an X-Y recorder at different frequencies.

Results and Discussion

Nickel

Chronopotentiometry.—Chronopotentiograms at several current densities were obtained for the reduction of Ni^{2+} at 400°C at three different concentrations: 6.3, 8.8, and 18.4 mM. A typical transient is shown in Fig. 3. A small transition is noted occurring at potentials ~0.4V anodic to the main reduction wave. The transition time corresponding to the main reduction process is plotted against the reciprocal current in Fig. 4, and the expected linear relationship predicted by the Sand equation (15) is observed, *i.e.*

$$\tau^{1/2} = \frac{z\pi^{1/2}\mathbf{F}AcD^{1/2}}{2i} \quad [4]$$

where z is the number of electrons involved in the reduction, $\mathbf{F}$ is the faraday, A the electrode area, c is the concentration, D the diffusion coefficient, and i the current. From the results presented in Fig. 4, the value of $\tau^{1/2}/Ac$ was found to be constant within 3%, and the calculated diffusions coefficient values are given in Table I.

Table I. Diffusion coefficient of nickel ion, $D_{Ni^{2+}}$, in LiCl-KCl eutectic at 400°C

$c_{Ni^{2+}}$/mM	$10^5\,D_{Ni^{2+}}$/cm² s⁻¹ Cyclic voltammetry	Potential step	Chronopotentiometry	Reference
6.30	0.79	1.10	1.11	This work
8.83	0.76	1.12	1.25	This work
18.35	1.08	1.08	1.20	This work
Mean	0.88 ± 0.14	1.10 ± 0.01	1.18 ± 0.05	This work
8-30	1.26 (450°C)			10
30-50			2.4 (450°C)	6
2.5-15	4.14 (500°C)			7, 8

The transient observed before the main deposition wave, was studied in greater detail by using much lower current densities. Some typical galvanostatic curves are shown in Fig. 5. Stirring of the solution during the recording of the transient was found to have no effect on the transition time or on the shape of the chronopotentiogram for the predeposition step, indicating that this process is not diffusion controlled and that the definition of the transition time in the usual sense cannot be used. For this reason, the transition time was taken as the time for the potential to scan from −0.1 to −0.6V (*vs.* the Pt/Pt^{2+} electrode), in order to evaluate the monolayer charge. These potential limits were chosen so as to exclude both the oxidation of platinum and the deposition of nickel in bulk. These potential limits were also evident from the admittance measurements. Table II shows the calculated monolayer charges (Q_m) at different current densities for the three concentrations studied. The

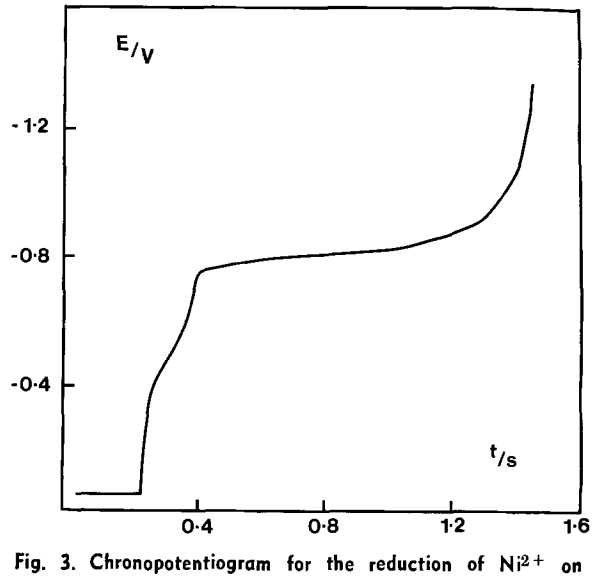

Fig. 3. Chronopotentiogram for the reduction of Ni^{2+} on Pt from a LiCl-KCl molten eutectic. Concentration = 6.3 mM; temperature = 400°C; current density = 3.94 × 10^{-3} A cm^{-2}.

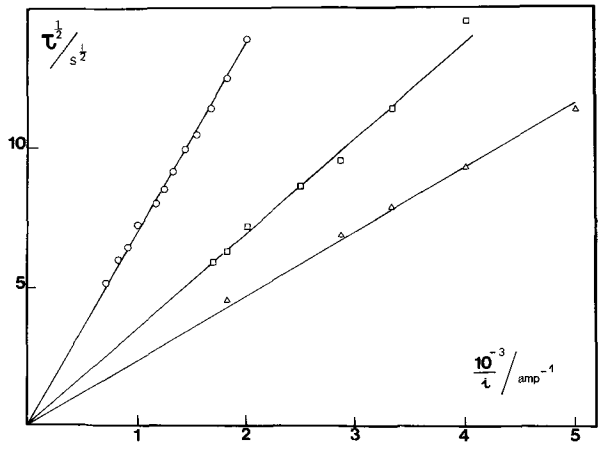

Fig. 4. Test of Sand's equation for the reduction of Ni^{2+} on Pt from a LiCl-KCl molten eutectic. Concentrations: △, 6.3 mM; □, 8.8 mM, and ○, 18.4 mM $NiCl_2$.

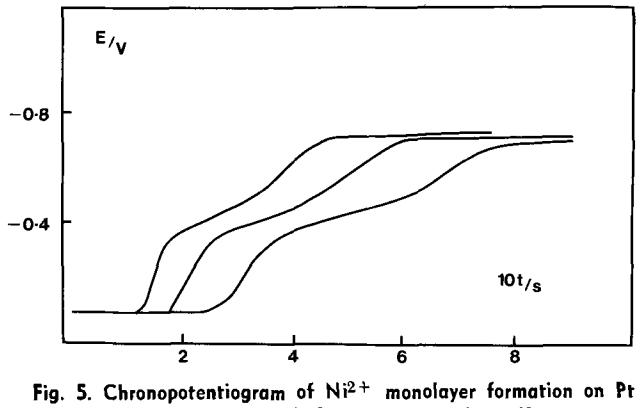

Fig. 5. Chronopotentiogram of Ni^{2+} monolayer formation on Pt from LiCl-KCl eutectic at 400°C. Current densities (from top to bottom) = 2.2; 1.9 and 1.6 × 10^{-3} A/cm^2. Potentials *vs.* a Pt/Pt^{2+} 0.01M reference electrode.

Table II. Monolayer charge (Q_m) for Ni^{2+} in LiCl-KCl eutectic at 400°C obtained from chronopotentiometric transition times

Applied current, $i/\mu A$	Monolayer charge Q_m/μcoulomb cm^{-2}		
	6.3 mM Ni^{+2}	8.8 mM Ni^{2+}	18.4 mM Ni^{2+}
20	740		
30	708	756	710
40	755	725	694
50	788	678	670
60	662	567	567
70	552	615	607
80	630	630	—
100	690	690	646
120	650	650	568
140	630	620	505

Q_m values should be compared with that calculated on the assumption of a close packed layer in which one atom of deposited metal effectively covers a square on the electrode surface of side $2r_a$ (r_a = atomic radius) (16). This is given by

$$Q_m = \frac{ze}{(2r_a)^2} \qquad [5]$$

where e is the electronic charge. Taking $r_a = 1.15$Å for nickel (17), then $Q_m = 606$ μcoulombs cm^{-2}. This value compares reasonably well with the experimental quantity; Q_m results in Table II were calculated from the apparent electrode area of the platinum sphere used without taking surface roughness effects into consideration. Q_m is seen to be fairly independent of both the concentration and the current density which is in support of the formation of a close packed monolayer. There is, however, a definite decrease in Q_m with increasing values of the current density. Several effects might be responsible for this: (*i*) the presence of trace impurities in the melt (notice that the values of the current used here are very low); (*ii*) slowness of the attainment of equilibrium in the last stages of complete coverage, and (*iii*) a certain degree of diffusion of the deposit into the platinum substrate favored by the high temperature at which the experiment is performed. It is not possible from this work to distinguish between these possibilities.

Potential step method.—Potential step transients were recorded for the same three nickel ion concentrations as before. The current-time transient for cylindrical diffusion at short times of electrolysis is given by (15)

$$i = zFADc\left(\frac{1}{\pi^{1/2}D^{1/2}t^{1/2}} + \frac{1}{2r_o}\right) \qquad [6]$$

where r_o is the radius of the wire used. Linear plots of i *vs.* $t^{-1/2}$ were obtained (Fig. 6) having finite extrapolated intercepts at $t = \infty$ in agreement with the predictions of Eq. [6] for the times of electrolysis considered. The diffusion coefficients evaluated from the slopes of Fig. 6 are seen to be in good agreement with the chronopotentiometry results (Table I). However, in any experiment where a wire of finite length is used, the electrode geometry cannot be equated to a semi-infinite cylinder, and the diffusional problem should approach that of a sphere. In this limiting case though, the intercept is twice that of a semi-infinite cylinder and therefore, in any real situation, the intercept should lie somewhere between these two extremes. However, it should be noted that for the 18.35 mM solution a value of D of 1.25×10^{-5} cm^2 sec^{-1} can be calculated from the value of intercept assuming cylindrical diffusion which is in reasonable agreement with the evaluation from the slope.

The formation of a monolayer would be expected to result in a current-time growth transient showing a maximum when the potential is stepped to a value corresponding to monolayer formation. This type of transient is a common occurrence in the electrochemical formation and growth of films (18, 19) and the corresponding theory has been extensively discussed

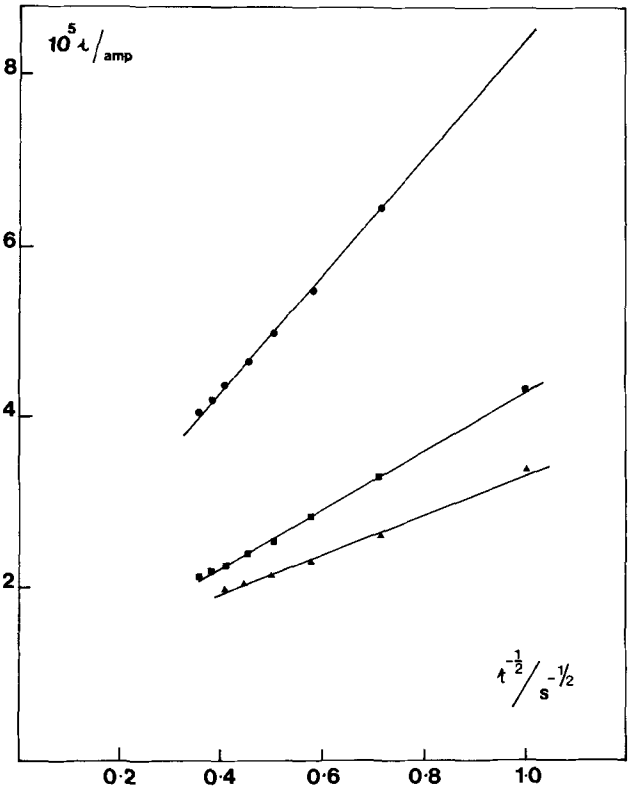

Fig. 6. Potentiostatic current *vs.* (time)$^{-1/2}$ plots for the deposition of Ni^{2+} from the LiCl-KCl eutectic at different concentrations: ▲, 6.3 mM; ■, 8.8 mM; ●, 18.4 mM $NiCl_2$.

(20). However, in the present case, at all the overpotentials studied in the monolayer region, falling transients were observed, even at very short times after pulsing the potential (<100 μsec). It might be concluded that a large number of nuclei are formed at short times, resulting in a limited two dimensional step line propagation growth of patches (20) but no direct evidence of this was observed. There was some indication of a slow attainment of the final equilibrium for times greater than 4 msec, a result in agreement with the lower values of Q_m obtained at high current densities in the galvanostatic study (cf. below, the results from cyclic voltammetry).

Cyclic voltammetry.—Cyclic voltammograms were recorded at different sweep rates between 0.04 and 200 V sec^{-1} for the same concentrations that were used in the chronopotentiometric work. Figures 7a, b, c, and d show typical voltammetric scans for this system at several sweep rates. From the integration of the current, it was found that all the charge deposited in the cathodic sweep was anodically stripped. The sharp anodic dissolution peak is similar to that observed for other systems (3). Here, diffusion control is unlikely to occur, and the current will increase until all the deposited metal is stripped (21). At fast sweep rates, a prepeak corresponding to monolayer formation is observed (see below), at ~0.5V anodic to the main peak, as previously reported (6).

The main cathodic peak potential (E_p) was found to be constant up to sweep rates of 4-8 V sec^{-1}, but an appreciable change was noted at higher sweep rates. It is unlikely that this is caused by the uncompensated resistance between working and reference electrodes. For example, the peak current for the 18.4 mM solution at a sweep rate of 322 V sec^{-1} was 1.76 mA, and the uncompensated resistance of the order of 1 ohm or less, thus introducing an instrumental uncertainty of at most 2 mV. The reason for the change in E_p at high values of v is unclear: little evidence has been found to indicate the existence of a significant nucleation overpotential, as is observed for other systems (22),

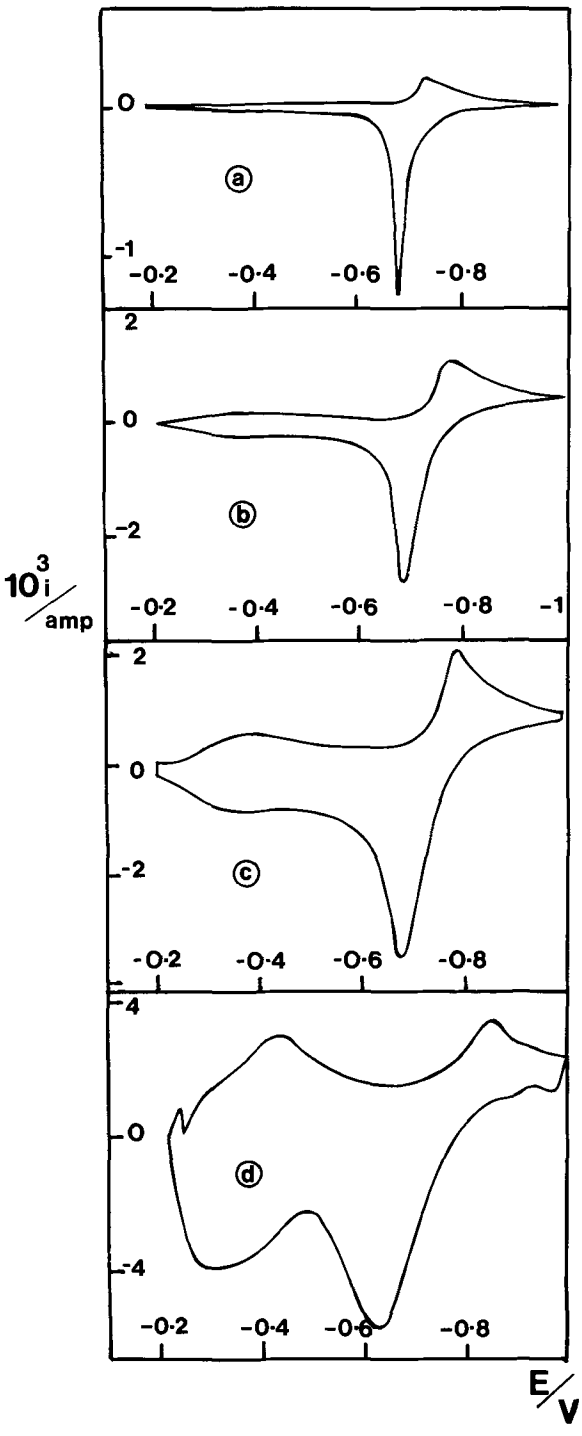

Fig. 7. Cyclic voltammograms of $NiCl_2$ in LiCl-KCl eutectic at 400°C. Concentration = 18.4 mM; electrode area = 0.0105 cm^2. Potentials vs. a Pt/Pt^{2+} (0.01 M) reference electrode: sweep rates: (a) 0.16 V sec^{-1}; (b) 8 V sec^{-1}; (c) 32 V sec^{-1}; (d) 192 V sec^{-1}.

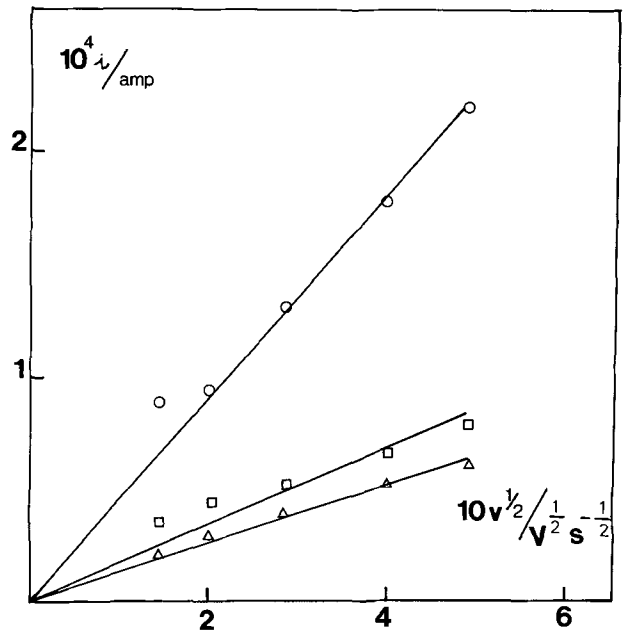

Fig. 8. Cyclic voltammetric peak currents (i_p) vs. (sweep rate)$^{1/2}$ for the reduction of Ni^{2+} on Pt in LiCl-KCl eutectic at 400°C at different concentrations: △, 6.3 mM; □, 8.8 mM; and ○, 18.4 mM $NiCl_2$. Electrode area = 0.0105 cm^2.

although in the galvanostatic transients a very small crystallization overpotential can be seen after the monolayer formation transition time (Fig. 3). Also, no growth region at overpotentials slightly cathodic to the Ni deposition potential was observed. A probable reason for this discrepancy could be the nonuniformity of the deposit.

As predicted by the theory for the reversible deposition of a solid metal (23), the peak current was found to be a linear function of the sweep rate, as shown in Fig. 8. The peak current is given by (23)

$$i_p = \frac{0.610\, z^{3/2} F^{3/2} A\, c\, D^{1/2} v^{1/2}}{R^{1/2} T^{1/2}} \qquad [7]$$

where i_p is the peak current and v the sweep rate. The values of the diffusion coefficients calculated from the slopes in Fig. 8 and Eq. [7], are given in Table I, and are in good agreement with those obtained by the other techniques. A difficulty in this analysis is in the correct subtraction of the capacitance current which can be large; this is particularly important for the high sweep rate scans, which limited the range of values of v that could be used in this analysis.

Figure 9 shows the monolayer region in greater detail. There are two points to notice here: (*i*) the peak current is a linear function of the sweep rate (Fig. 10), as would correspond to a pure capacitative current, and (*ii*) the peak potential is a function of the sweep rate. This would be unexpected if the equivalent circuit corresponding to a monolayer formation could be regarded as an additional pure capacitance in parallel with the double layer. This is considered to be the case in the adsorption of some organic compounds on mercury (15) but it is clearly not true when the adsorption process involves the simultaneous transfer of charge.

The charge deposited between −0.2 and −0.6V obtained by integration of the voltammograms was found

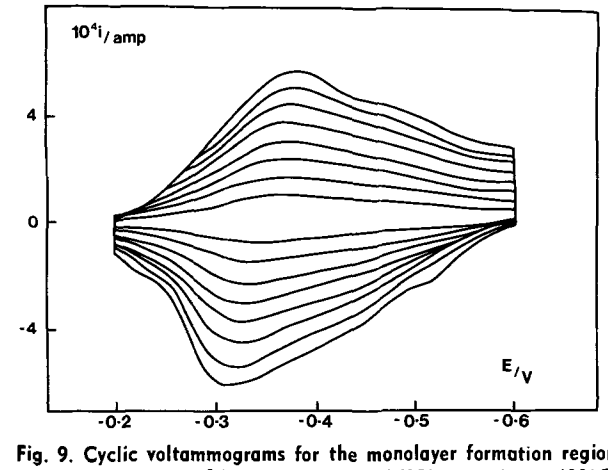

Fig. 9. Cyclic voltammograms for the monolayer formation region in the reduction of Ni^{2+} on Pt in a LiCl-KCl eutectic at 400°C. Sweep rates (from top to bottom) = 8; 16; 24; 32; 40; 48; 56; and 64 V sec^{-1}. Electrode area = 0.0105 cm^2.

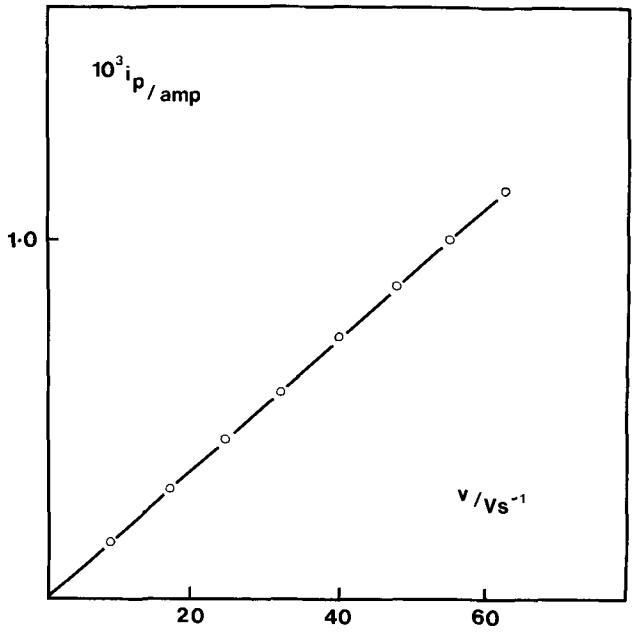

Fig. 10. Peak current as a function of sweep rate for the monolayer formation region in the Ni^{2+} reduction. Electrode area = 0.0105 cm^2.

to be lower than that obtained from chronopotentiometry and some sweep rate dependence of Q_m was noted. Values obtained ranged from 480 to 420 μcoulombs cm^{-2} for sweep rates from 5 to 64 V sec^{-1}. The reason for this difference is not altogether clear, but it should be noted that the cyclic voltammetry results refer to much faster transients than those recorded in the chronopotentiometry experiments, and some of the effects earlier discussed might be responsible for this.

Electrode impedance.—A close correlation can be established between the present case and the hydrogen ionization equilibrium since both involve the same kind of elementary process. In this context, if the equivalent circuit for the hydrogen ionization equilibrium is considered (24) (Fig. 2b), it is easy to see that E_p should now depend on sweep rate [see also Ref. (25)]. Figure 11 shows the parallel components of the interfacial impedance measured at 1000 Hz. The C_p values were found to have a considerable scatter with frequency which was later traced to defects in the phase-shifting system. The in-phase measurements leading to R_p were not affected and it is possible to compare $1/R_p$ with the same quantity for the hydrogen ionization equilibrium calculated from data in the literature (26) (cf. Fig. 12). At infinite frequency $1/R_p$ at the potential of the peak (−0.4V) extrapolates to a value of ~4 ohm^{-1} cm^2 leading to a value of the exchange current of 0.2-0.3 A cm^{-2}. It is an interesting coincidence that the value of the charge transfer resistance is of comparable magnitude in both cases (Fig. 12), especially when it is considered that they correspond to completely different temperatures, solvents, and systems. The results from this work while of only semi-quantitative significance nevertheless show the usefulness of data-acquisition phase-detection techniques. It should be pointed out also, that the difference between the shapes of the voltammetric waves and the admittance results, is due to the different equivalent circuits to which these two methods refer; the latter measures the components of the impedance of the interface taken as a parallel combination, whereas the former measures the over-all electrical response of the actual interface (Fig. 2b, when the solution resistance can be neglected) to a voltage range. The relationship between the two will not be discussed here.

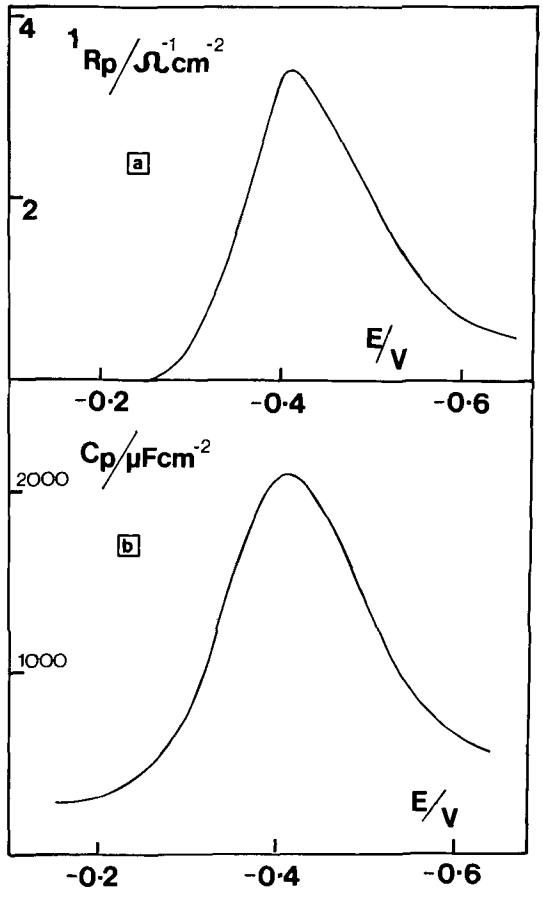

Fig. 11. Parallel components of the electrode impedance for the monolayer formation region for the reduction of Ni^{2+} at 400°C. (a) Parallel conductance and (b) parallel capacitance both determined at 1000 Hz. Electrode area = 0.0105 cm^2. Concentration = 8.4 mM $NiCl_2$. Potentials vs. a Pt/Pt^{2+} 0.01M reference electrode.

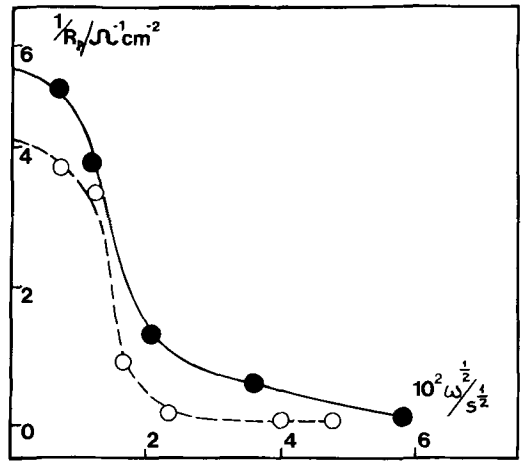

Fig. 12. Frequency dependence of the parallel conductance for the nickel monolayer formation region at −0.4V. ○, Ni^{2+} case; ●, hydrogen ionization (note that different values for $1/R_p$ have been quoted for this case, depending on the surface treatment of the electrode (24)).

Silver

A voltammetric study was also made of the reduction of Ag^+ in the LiCl-KCl eutectic at 400°C. Figure 13a shows a typical transient at slow sweep rates and the presence of a small prepeak is again observed but at a potential less anodic, *i.e.*, ~100 mV to the peak potential corresponding to bulk deposition of Ag^+, than in the case of nickel. At higher sweep rates (Fig. 13b) the close proximity of the prepeak to the main peak is seen to distort the shape of the latter and a quantitative analysis of peak currents at higher sweep

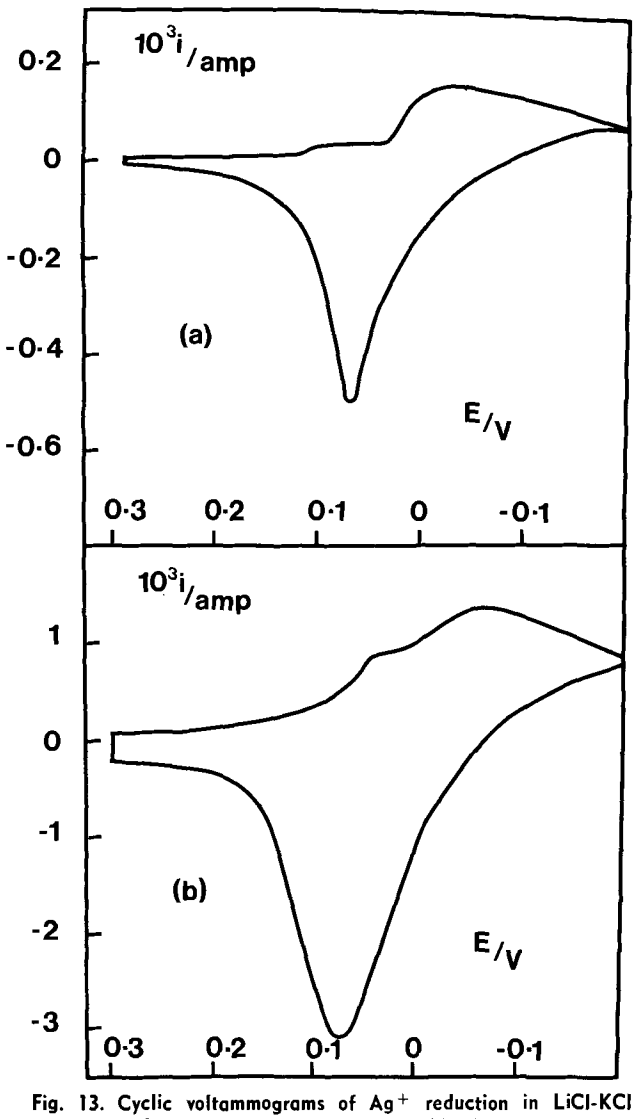

Fig. 13. Cyclic voltammograms of Ag^+ reduction in LiCl-KCl eutectic at 400°C. Concentration = 12.8 mM. Electrode area = 0.0252 cm^2. Potentials *vs.* Ag/Ag^+ (0.01M) reference electrode. (a) Sweep rate = 0.12 V sec^{-1}; (b) sweep rate = 12.0 V sec^{-1}.

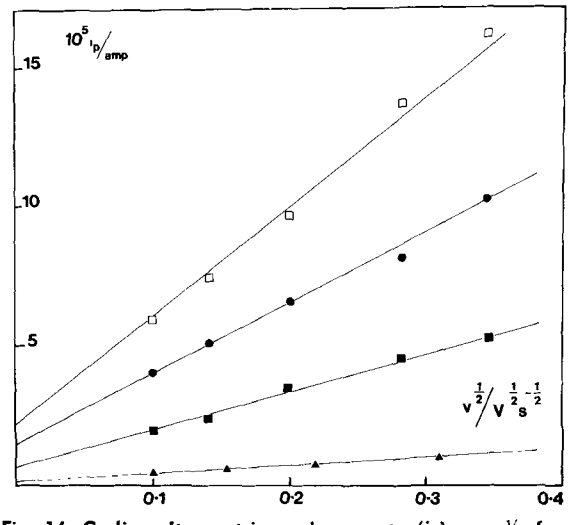

Fig. 14. Cyclic voltammetric peak currents (i_p) *vs.* $v^{1/2}$ for the reduction of Ag^+ on Pt in LiCl-KCl eutectic at 400°C at different concentrations: ▲, 1.06 mM; ■, 4.25 mM; ●, 8.50 mM; □, 12.8 mM. Electrode area = 0.0252 cm^2.

rates is therefore made difficult. Consequently Fig. 14 shows a plot of $i_p v^{1/2}$ only for sweep rates in the range 0.01-0.35 V sec^{-1} where a linear relationship is observed. The intercept on the i_p axis at $v = 0$ is not properly understood but is again probably associated with the prepeak. At these sweep rates the peak potential was found to be independent of sweep rate.

Table III. Diffusion coefficient of silver ion, D_{Ag^+}, in LiCl-KCl eutectic at 400°C

c_{Ag^+}/mM	$10^5 D_{Ag^+}/cm^2\ s^{-1}$ Cyclic voltammetry	Potential step	Chronopotentiometry	Reference
1.06	2.37			
4.25	2.69	3.19	(5.08)	This work
8.50	2.42	2.96	(5.11)	This work
12.76	2.51	3.53	(5.19)	This work
Mean	2.50 ± 0.10	3.23 ± 0.20	(5.13 ± 0.04)	This work
2-50			2.6 (450°C)	27
30-50			3.3 (450°C)	6
—			4.6 (480°C)	8

From the gradients of the i_p *vs.* $v^{1/2}$ plots the diffusion coefficient of Ag^+ was calculated from Eq. [7] at each concentration and is presented in Table III. Potential step current-time transients were recorded from potentials in the region of the prepeak to those cathodic to the main peak. In the potential region of silver predeposition, no growth characteristics corresponding to monolayer formation were observed indicating an instantaneous nucleation process at all available sites on the surface. At potentials cathodic to the bulk deposition step, normal diffusion-controlled transients were obtained giving linear i *vs.* $t^{-1/2}$ plots from which the diffusion coefficient was again calculated using Eq. [6] (Table III).

Chronopotentiometric transients did not exhibit a pretransition since the two steps were insufficiently separated, and hence it was not possible to calculate the charge required for the predeposition step. For this reason also an impedance analysis could not be performed. Diffusion coefficients were calculated from the gradients of linear plots of $\tau^{1/2}$ *vs.* i^{-1} using Eq. [4] and are presented in Table III for three concentrations. Although the values of D_{Ag^+} obtained by each technique at different concentrations are self consistent, Table III shows some discrepancies between the different techniques. While the value of D_{Ag^+} obtained from cyclic voltammetry and the potential step method are in reasonable agreement with other reported values, the chronopotentiometric diffusion coefficient is rather higher. Although it is not possible to quantify the effect of the predeposition the most reasonable explanation in this case, in view of the self consistency of the chronopotentiometric data, is an error in the measurement of effective electrode area. This was also indicated by a separate experiment carried out at 470°C when a value for D_{Ag^+} of 3.87×10^{-5} cm^2 sec^{-1} was obtained. Assuming an approximate value of 4 kcal $mole^{-1}$ for the activation energy of the diffusion process this leads to a value of 3.0×10^{-5} cm^2 sec^{-1} for D_{Ag^+} at 400°C which agrees more closely with the values reported in Table II.

REFERENCES

1. A. D. Graves, G. J. Hills, and D. Inman, in "Advances in Electrochemistry and Electrochemical Engineering," Vol. 4, P. Delahay, Editor, Interscience Publishers, New York, London (1966).
2. G. J. Janz, "Molten Salts Handbook," Academic Press, New York (1967).
3. D. J. Astley, J. A. Harrison, and H. R. Thirsk, *J. Electroanal. Chem.*, **19**, 325 (1968).
4. G. W. Tindall and S. Bruckenstein, *Anal. Chem.*, **40**, 1051 (1968).
5. W. J. Lorenz, I. Moumtzis, and E. Schmidt, *J. Electroanal. Chem.*, **33**, 121 (1971).
6. E. Schmidt, *Electrochim. Acta*, **8**, 23 (1963).
7. P. Drossbach and P. Petrick, *Z. Elektrochem.*, **58**, 95 (1954).
8. Yn. K. Delimarskii and B. F. Markov, "Electrochemistry of Fused Salts," Chapter 8, R. E. Wood, Editor, Sigman Press, Washington, D.C. (1961).

9. G. J. Hills, J. E. Oxley, and D. W. Turner, *Silicates Industriels*, **26**, 559 (1961).
10. W. K. Behl, *This Journal*, **118**, 899 (1971).
11. H. A. Laitinen, W. S. Ferguson, and R. A. Osteryoung, *ibid.*, **104**, 517 (1957).
12. R. de Levie and A. A. Husovsky, *J. Electroanal. Chem.*, **20** 181 (1969).
13. G. J. Hills, D. J. Schiffrin, and T. Solomon, In preparation.
14. T. Solomon, Thesis, Southampton 1972.
15. P. Delahay, "New Instrumental Methods in Electrochemistry," Interscience Publishers, Inc., New York (1965).
16. N. White and F. Lawson, *J. Electroanal. Chem.*, **26**, 113 (1970).
17. L. Pauling, "The Nature of the Chemical Bond," Cornell University Press, Ithaca, N. Y. (1960).
18. M. Fleischmann, K. S. Rajagopalan, and H. R. Thirsk, *Trans. Faraday Soc.*, **59**, 741 (1963).
19. R. D. Armstrong and M. Fleischmann, *Z. Phys. Chemie N.F.*, **52**, 131 (1967).
20. J. A. Harrison and H. R. Thirsk, "Electroanalytical Chemistry, a Series of Advances," Vol. 5, p. 67, A. J. Bard, Editor, Marcel Dekker, Inc., New York (1971).
21. M. M. Nicholson, *J. Am. Chem. Soc.*, **79**, 7 (1957).
22. G. J. Hills, D. J. Schiffrin, and J. Thompson, In preparation.
23. T. Berzins and P. Delahay, *J. Am. Chem. Soc.*, **75**, 555 (1953).
24. A. N. Frumkin, "Advances in Electrochemistry and Electrochemical Engineering," Vol. 3, P. Delahay, Editor, Interscience Publishers, Inc., New York (1963).
25. E. Gileadi and S. Srinivasan, *Electrochim Acta*, **11**, 321 (1966).
26. P. Dolin and B. Ershler, *Acta Physicochim., U.S.S.R.*, **13**, 747 (1940).
27. H. A. Laitinen and W. S. Ferguson, *Anal. Chem.*, **29**, 4 (1957).

Capacitance Measurements on Lithiated Nickel Oxide Electrodes

Dennis M. Tench*,[1] and Ernest Yeager*

Chemistry Department, Case Western Reserve University, Cleveland, Ohio 44106

ABSTRACT

Differential capacitance measurements have been used to study mosaic lithiated nickel oxide electrodes and to obtain information concerning the potential distribution between the space charge region within the semiconductor and the Helmholtz layer in the electrolyte. Plots of $1/C^2$ *vs.* E have been found to exhibit linear behavior over substantial ranges of potentials in accord with the Mott-Schottky treatment. The slopes are somewhat higher than expected from the Li content although they approach the Mott-Schottky values for electrodes prepared with shorter Li doping times. At potentials anodic to 1.0V-0.059(pH)V re SHE the change in electrode potential appears principally across the Helmholtz plane.

The understanding of the electrochemical properties of a semiconductor requires a knowledge of the potential distribution across the interface and the space charge characteristics within the semiconductor. This paper involves the use of capacitance measurements to gain such information for lithiated nickel oxide electrodes.

Nickel oxide is a semiconductor of the mixed valency type usually with p-type conduction occurring by electron transfer between Ni^{+2} and Ni^{+3} states (1). Introduction of univalent cations such as lithium into the lattice at cation sites results in the formation of Ni^{+3} states in a 1:1 ratio to maintain charge neutrality. In a recent review article, Adler (2) has summarized the existing theoretical models for conduction in NiO and has examined their applicability in terms of the available experimental data. Adler concludes that the conduction process probably involves a band structure. The dependence of the Hall mobility on temperature, however, is still in doubt and at the present time the exact nature of this band structure cannot be unambiguously ascertained.

The intrinsic voltammetric behavior of mosaic NiO(Li) electrodes in aqueous solutions has been investigated by Rouse and Weininger (3), Yohe *et al.* (4, 5), and also in this work. This electrode exhibits two voltammetry peaks in both acidic and basic solutions when no easily oxidizable or reducible species are present. These peaks are of considerable importance to the interpretation of the capacitance measurements. In 1.0*N* H_2SO_4 (see Fig. 1), one peak occurs at 0.95V re SHE (peak I) and the other at 1.4V (peak II). Both have a pH dependence of −60 mV/decade over the pH range 0-14 (5). At slow sweep rates (4 V/min) these peaks have been found to be reversible (*i.e.*, anodic and cathodic peak potentials coincide). Even at sweep rates up to 1.0 V/sec, the peak separation is still less than 50 mV (6).

Yohe *et al.* (4) have compared the voltammetry results with the thermodynamic data compiled by Pourbaix (7) and concluded that peaks I and II probably correspond to the oxidation of Ni^{+2} to Ni^{+3} and Ni^{+3} to Ni^{+4}, respectively, coupled with the removal of protons from adjacent oxygen ions. These reactions appear to occur only at the electrode surface since the total charge under both peaks corresponds to less than a monolayer (65%) of the charge for the (100) plane, assuming one electron per Ni^{2+} ion and an idealized (100) surface orientation with no surface roughness. The difficulty of converting all surface Ni^{2+}

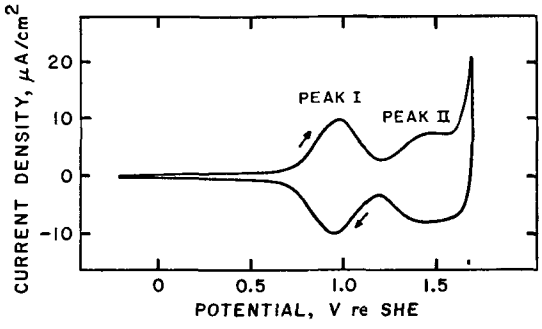

Fig. 1. Linear sweep voltammetry curve at 4.0 V/min for mosaic NiO(0.36 cation % Li) in He-saturated 1.0*N* H_2SO_4 at 25°C. Electrode area: 0.128 cm².

* Electrochemical Society Active Member.
[1] Present address: Fritz Haber Institute, der Max Planck Gesellshaft, West Berlin, Germany.
Key words: nickel oxide, semiconductor electrodes, space-charge effects capacitance measurements.

ions to a higher valency state is not surprising since complete conversion would probably involve very large surface excess charge.

Both Rouse and Weininger (3) and Yohe *et al.* (4, 5) have reported capacitance data for NiO(Li) electrodes in acid sulfate solutions at potentials anodic to the reference reversible hydrogen electrode (RHE). The capacitance passes through a maximum at a potential near that of voltammetry peak I and decreases with increasing frequency in the audio range. This capacitance maximum also was observed in the present work and is presumably related to the faradaic process occurring in this potential region. Neither of the aforementioned authors extended their capacitance measurements to more cathodic potential. Rouse and Weininger (3) observed an appreciable cathodic faradaic current near the reversible hydrogen potential and, therefore, did not extend their capacitance measurements cathodic to this potential. In the work of Yohe *et al.* (4, 5) and also the present study, however, the NiO(Li) electrode was found to remain ideally polarizable even at very cathodic values (*e.g.*, in 1.0*N* H_2SO_4 out to −0.5V re SHE). The hydrogen reduction current observed by Rouse and Weininger was probably due to impurities on or in the electrode, which provided adsorption sites for hydrogen atoms or possibly disturbed the semiconductor space charge layer. These workers used platinum to line the crucibles employed in the doping process (8) at temperatures 1500°-1600°C and it is probable that this procedure resulted in some platinum contamination of the NiO(Li).

Experimental

Electrode fabrication.—Mosaic NiO crystals were prepared by the method of Cech and Alessandrini (9), *i.e.*, hydrolysis of $NiBr_2$ at elevated temperatures with the epitaxial growth of NiO on a (100) facet of single-crystal MgO. Details have been given elsewhere (4, 10). After stripping by dissolving the MgO in 20% H_2SO_4 at 95°C, the NiO was doped by diffusion of lithium at high temperatures (~1500°C) in sealed alumina crucibles containing lithiated NiO powder, using a furnace with alumina walls. The mosaic crystals used for electrodes were rectangular with an area of about 0.1 cm^2 and thickness of 80-150μ.

Electrical contact was made to the rear side of the NiO(Li) electrode in the following way. A thin layer of silver (500-100Å) was evaporated *in vacuo* (<0.5μ Hg) onto the backside of the mosaic crystal at room temperature. The Ag was diffused into the surface by thermal treatment at 960°C in a helium atmosphere. This side of the crystal was then painted with Ag-epoxy resin and an Ag-coated copper wire was attached.

Evidence exists that this procedure yields an ohmic contact. The ferri-ferrocyanide couple was found to exhibit linear plots of ln $[i/(i_d - i)]$ *vs.* E over the anodic branch with the slope and intercept independent of rotation rate using the rotating disk method (i_d = diffusion limiting current density). This constancy of slope and intercept is only possible if there are no appreciable voltage drops within the semiconductor or the electronic contact to the rear surface. Such was not true in the earlier work in the authors' laboratory (5).

The mosaic crystals were molded into Kel-F cylinders so that the electrode surface was flush with the end of the cylinder (6). The lithiated NiO electrodes were then usually cleaned by a dissolution treatment at 0.95V re SHE in helium saturated 1.0*N* H_2SO_4 at 90°C for 30 min. This treatment in most instances had no effect on the intrinsic voltammetry curves in acid solution but for some electrodes it improved the reproducibility of the voltammetry curves.

The chemical analysis of the NiO for Li was carried out by flame spectrophotometry on a 10 mg sample of mosaic NiO(Li) dissolved in azeotropic HCl. The flame spectrophotometric measurements had a relative precision of ±10% and were performed by Union Carbide Corporation (Parma Technical Center, Parma. Ohio).

Electrolytes.—All electrolytes were prepared from doubly recrystallized salts, triply distilled water, and redistilled acid. Before use, each solution was treated overnight with cocoanut charcoal (Barnebey-Cheney) which had been purified with azeotropic HCl in a Soxhlet extractor for at least four weeks. All electrolytes were saturated with helium which was passed through hot copper turnings to remove O_2 and traps containing Linde molecular sieves (3A and 13X) at liquid N_2 temperatures to remove other contaminants.

Electrochemical cell.—The main compartment of the cell (Fig. 2) contained the NiO(Li) working electrode and a mercury pool counterelectrode (12 cm^2 area) in contact with 40-50 ml of electrolyte in this compartment. Separate compartments for the reference electrode and Pt auxiliary counterelectrode were connected to the main compartment through sintered glass plugs. Triply distilled mercury (Bethlehem Apparatus, Inc., Hellertown, Pennsylvania) was used for the internal counterelectrode. A helium atmosphere was maintained inside the cell by bubbling this gas through the solution.

The impedence was measured between the NiO(Li) electrode and the Hg pool counterelectrode, located about 2 cm apart. Since the area of the Hg pool was many times (100-200) larger than that of the NiO(Li) electrodes, its contribution to the total impedance was negligible. The Pt external counterelectrode was used to control the d-c potential of the NiO(Li) electrode.

Electronic equipment.—The a-c impedance between the NiO(Li) electrode and Hg pool counterelectrode was determined with an audio frequency Wheatstone bridge arrangement (6). The balance point was detected by means of a Tektronix Type 543 oscilloscope with a Type 1A7 pre-amp unit. At the null point, the a-c signal across the working and counter (internal) electrodes was always less than 5 mV and usually less than 2 mV. Measurements of the potential difference between the working and reference electrodes were made with a Hewlett-Packard 419A voltmeter.

For some of the impedance measurements the Hg pool counterelectrode was biased to cathodic potentials (using the external counterelectrode) with a Wenking Model 61R potentiostat to eliminate the possibility of anodic dissolution of the Hg counterelectrode under some circumstances. The same results were obtained, however, regardless of whether the Hg pool was biased cathodically or not. Therefore, since potentiostating of the Hg counterelectrode increased the noise level,

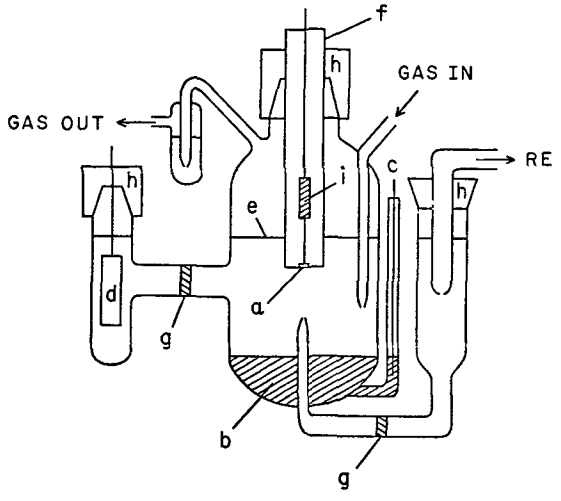

Fig. 2. Pyrex a-c impedance cell. a, NiO(Li) working electrode; b, Hg pool internal counterelectrode; c, Pt wire; d, Pt foil external counterelectrode; e, electrolyte level; f, Teflon enclosed brass tube with concentric Cu wire; g, sintered glass plugs; h, Teflon plugs in standard taper joints; i, spring-cap electrical contact.

it was not used for all of the measurements. Those in 1.0*N* H_2SO_4 were obtained with the Hg pool biased at −1.00V re SHE and the other measurements were made with the Hg pool unbiased. The addition of 10^{-3}M Hg_2SO_4 to the sulfate solutions (*p*H = 2.9) had no effect on the impedance of a NiO(0.21 cation % Li) electrode over the accessible potential range.

Reference electrodes.—In the acidic solutions the Hg/Hg_2SO_4 electrode was used with the same solution as the supporting electrolyte in the cell, whereas a saturated calomel electrode was used in the neutral solution. All potentials are reported relative to the standard hydrogen electrode (SHE).

Experimental Results

The series capacitance at 1 and 20 kHz for a mosaic NiO(0.48 cation % Li) electrode is plotted as a function of electrode potential in Fig. 3 for sulfate solutions of varying pH values. The same trends also were observed at 2 kHz but these curves are not shown because the overlap of points would cause serious complications in the graph. The data in Fig. 3 extend to much more cathodic potentials than those reported heretofore (3-5) for this system. In agreement with the earlier work, the capacitance-potential curves exhibit a peak which is less pronounced at the higher frequency. The frequency dispersion in the present work is less than that observed by earlier workers, however, perhaps because of the nonohmic electrical contact to the NiO(Li) in the earlier work.

The inverse square of the capacitance at various frequencies is plotted *vs.* electrode potential in Fig. 4 for an NiO(Li) electrode in 1.0*N* H_2SO_4. At all frequencies, a straight line is obtained from −0.5 to +0.3V re SHE, and at more anodic potentials the plots deviate from linearity. The slope increases with frequency with relatively little difference between the results at 1 and 2 kHz. Similar behavior has been found also in potassium sulfate solutions of *p*H 2.9 and 6.5 (see Fig. 5 and 6). The intercept with the potential axis does not change with frequency for this NiO(Li) electrode with 0.48 cation % Li but with electrodes containing less lithium, the intercept as well as the slope are frequency dependent (see Fig. 7 and 8). The slope is essentially independent of *p*H in contrast to the earlier findings of Rouse and Weininger (3). The intercept shifts approximately 0.1 V/*p*H.

The lithium concentration dependence of the $1/C^2$ vs. *E* plots is shown in Fig. 9 for 1 kHz. Lower lithium concentrations are not represented because the large frequency dispersion at lower concentrations interferes with such a comparison. Both the slopes and the intercepts are dependent on the lithium concentration.

The addition of 10^{-3}M $ZnSO_4$ or KI to a solution of 0.495M K_2SO_4 + 0.005M H_2SO_4 had no detectable

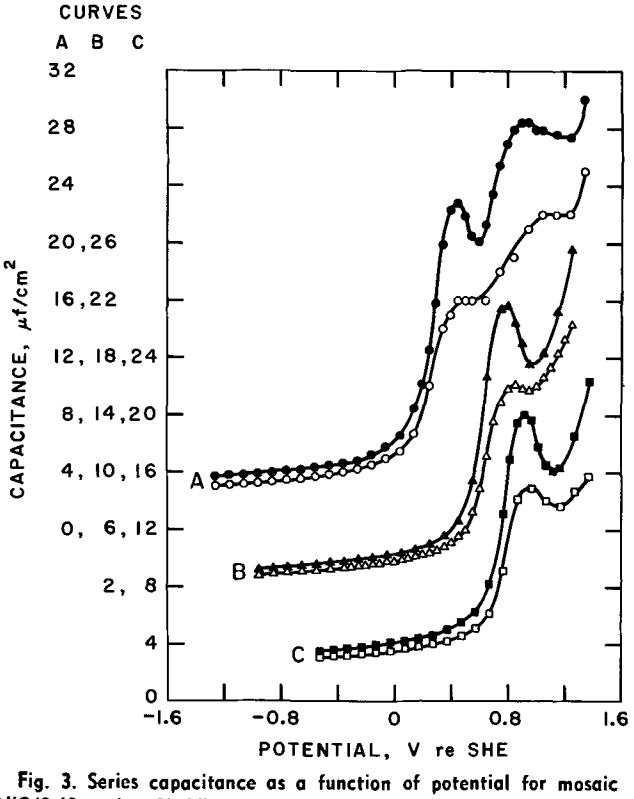

Fig. 3. Series capacitance as a function of potential for mosaic NiO(0.48 cation % Li) in He-saturated sulfate solutions at 25°C. Electrode area: 0.0416 cm². Solid symbols designate the values at 1 kHz and open symbols those at 20 kHz. Circles represent data in 0.50M K_2SO_4 (scale A), triangles in 0.495M K_2SO_4 + 0.005M H_2SO_4 (*p*H = 2.9, scale B), and squares in 1.0*N* H_2SO_4 (scale C).

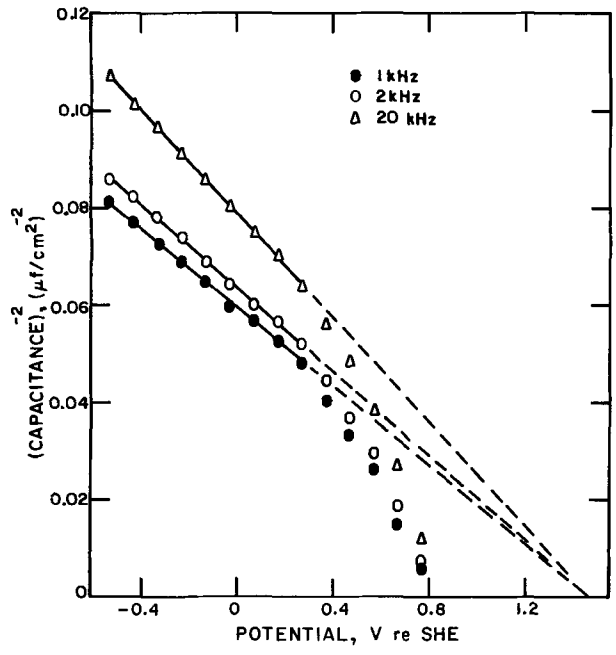

Fig. 4. Plots of $1/C^2$ *vs.* *E* at various frequencies for mosaic NiO(0.48 cation % Li) in He-saturated 1.0*N* H_2SO_4 at 25°C. Electrode area: 0.0416 cm².

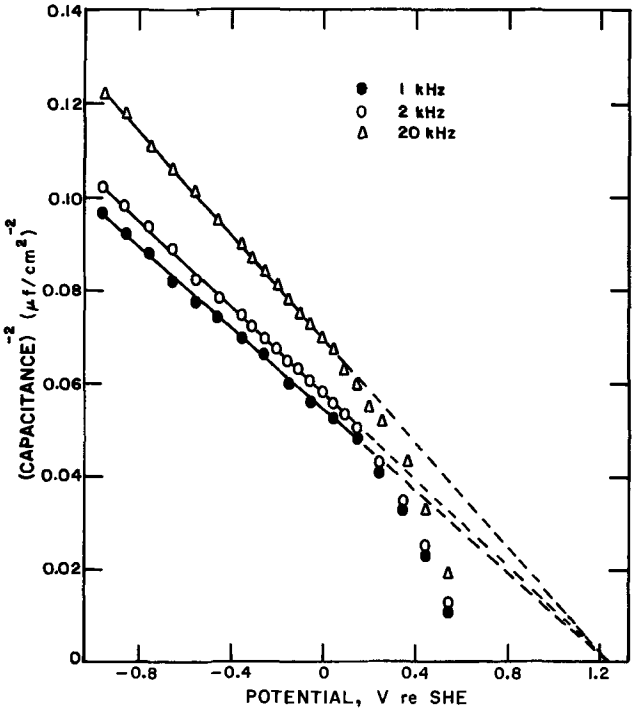

Fig. 5. Plots of $1/C^2$ *vs.* *E* at various frequencies for mosaic NiO(0.48 cation % Li) in He-saturated 0.495M K_2SO_4 + 0.005M H_2SO_4 (*p*H = 2.9) at 25°C. Electrode area. 0.0416 cm².

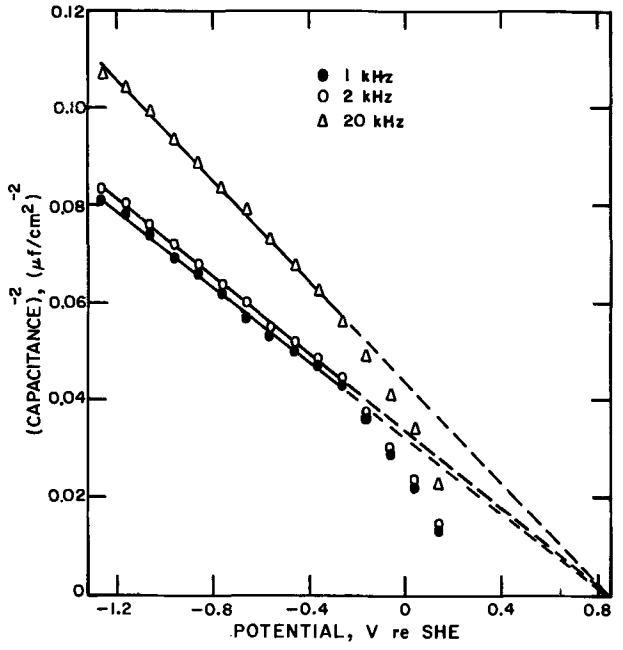

Fig. 6. Plots of $1/C^2$ *vs.* E at various frequencies for mosaic NiO(0.48 cation % Li) in He-saturated 0.50M K_2SO_4 (pH $\simeq$ 6.5) at 25°C. Electrode area: 0.0416 cm^2.

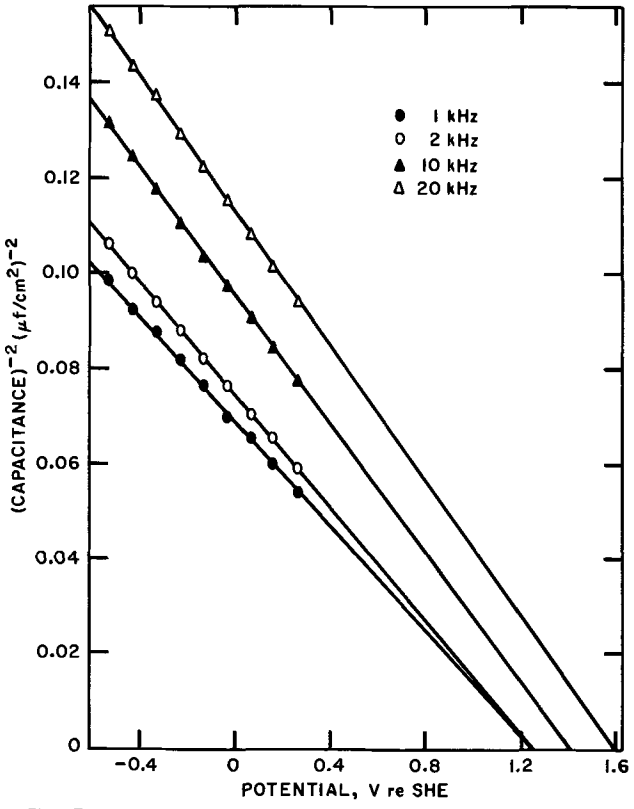

Fig. 7. Plots of $1/C^2$ *vs.* *E* at various frequencies for mosaic NiO(0.36 cation % Li) in He-saturated 1.0*N* H_2SO_4 at 25°C. Electrode area: 0.128 cm^2.

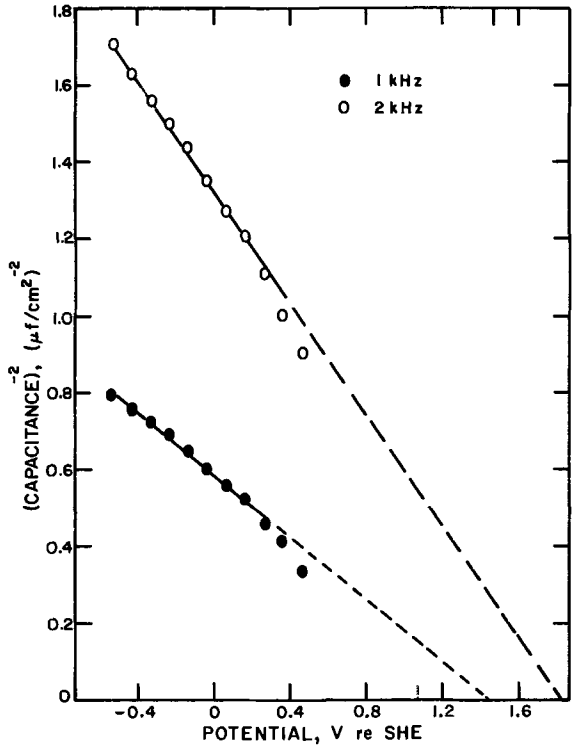

Fig. 8. Plots of $1/C^2$ *vs.* *E* at 1 and 2 kHz for mosaic NiO(0.049 cation % Li) in He-saturated 1.0*N* H_2SO_4 at 25°C. Electrode area: 0.115 cm^2.

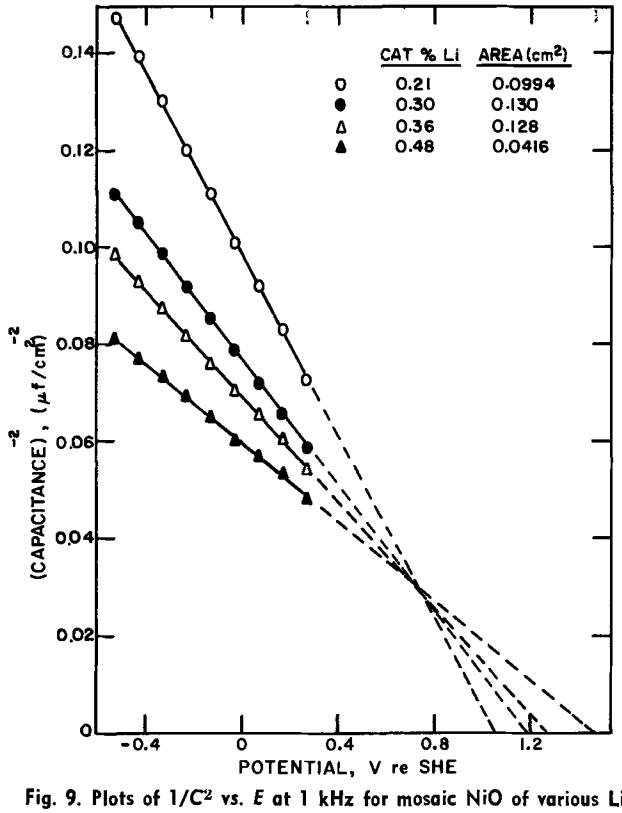

Fig. 9. Plots of $1/C^2$ *vs.* *E* at 1 kHz for mosaic NiO of various Li doping concentrations in He-saturated 1.0*N* H_2SO_4 at 25°C.

effect on the capacitance of a NiO(0.21 cation % Li) electrode in this system over the potential range from 0.95 to 1.25V re SHE. This implies that Zn^{+2} and I^- ions are not strongly specifically adsorbed on the NiO(Li) surface, at least at potentials cathodic to peak I.

The total series resistance was found to decrease with increasing frequency and also slowly with increasing anodic potentials. These trends are illustrated in Table I for a NiO(0.48 cation % Li) electrode in 1.0*N* H_2SO_4. The same general behavior was observed for samples containing less Li except the resistance at a given potential was higher; *e.g.*, 31 ohm-cm^2 at 1 kHz for NiO(0.13 cation % Li) in 1.0*N* H_2SO_4.

On the basis of the cell geometry and the resistivity of the electrolyte, the resistance value of 1.3 ohm-cm^2 listed in Table I for 1.27V and 20 kHz appears to correspond to only the electrolyte resistance. Ohmic drop within the bulk of the electrode phase should

Table I. Series resistance for NiO(0.48 cation % Li) in 1.0N H_2SO_4 as a function of frequency at various potentials re SHE

E (V)	Resistance (ohm-cm²) 1 kHz	2 kHz	20 kHz
−0.53	4.3	2.9	1.5
0.07	4.0	2.8	1.4
0.67	3.6	2.6	1.4
1.27	2.3	1.8	1.3

be negligible for such a high Li concentration and thin electrodes (~100μ). If this series resistance is subtracted from the other resistances listed in Table I, the resistance values so obtained should be associated with the electrode-electrolyte interface provided the metal-oxide rear interface makes no appreciable ohmic contribution to the measurements. The diffuse metal junction used to make electronic contact to the NiO(Li) should eliminate such a contribution. The values of tan δ (δ = phase angle) have been calculated from the capacitance data and the resistance values in Table I after subtracting the resistance of the electrolyte. In the linear range of Fig. 5, tan δ is $8 \pm 1 \times 10^{-2}$ at frequencies of 1 and 2 kHz. The resistance data at 20 kHz are not sufficiently accurate to permit the evaluation of tan δ after subtraction of the electrolyte resistance from the values in Table I.

Rouse and Weininger (3) also observed a decrease of the series resistance with increasing frequency for essentially the same lithium concentrations and potentials, but the resistance values were approximately three times higher than those reported here after correction for electrolyte resistance. The phase factor tan δ also was not constant in their work. The slopes of their plots of $1/C^2$ *vs.* E differed by several fold from those found in the present work and were strongly pH dependent. These differences may be due to nonuniform distribution of lithium, nonohmic electrical contact to the NiO(Li), and/or platinum contamination in the work of Rouse and Weininger. Also, it should be noticed that Rouse and Weininger obtained data only at relatively anodic potentials where, in the present work, large deviations from the Mott-Schottky approximation were found to occur.

Discussion of Results

A simplified equivalent circuit for the semiconductor-electrolyte interface is shown in Fig. 10, where R_B and R_o represent the bulk resistance for the semiconductor and solution, respectively; R_{sc} is the space charge resistance; C_{sc}, C_H, and C_{dl} are the capacitances of the space charge region, Helmholtz layer, and diffuse part of the ionic double layer, respectively; and C_{ss} and R_{ss} are the capacitance and resistance due to surface states. In the present work C_H and C_{dl} are large compared to C_{sc} in the linear $1/C^2$ *vs.* E potential range, and hence do not contribute appreciably to the observed capacitance over this range.

The linear $1/C^2$ *vs.* E behavior observed at more cathodic potentials suggests that an exhaustive depletion layer is involved with the observed differential capacitance corresponding to C_{sc}. In the exhaustive depletion range, C_{sc} is expected to follow the Mott-Schottky equation

$$\frac{1}{C_{sc}^2} = \frac{8\pi}{\epsilon_{sc} e N}\left(E - E_{fb} - \frac{1}{f}\right) \qquad [1]$$

where E is the electrode potential *vs.* a suitable reference, E_{fb} is the flatband potential, ϵ_{sc} is the dielectric constant in the space charge region, N is the concentration of charge carriers, and $f = \mathbf{F}/RT$ where $\mathbf{F}$ is the Faraday constant. The existence of an exhaustive depletion layer is supported by the behavior of various electrochemical couples on NiO(Li) electrodes. Studies of a number of electrochemical processes on such electrodes (4, 6, 11) indicate that oxidation as well as reduction processes do not proceed at appreciable rates at potentials cathodic to voltammetry peak *I* by more than ~0.2V until the onset of H_2 evolution at 0.5V re SHE.

The deviation from linearity in the $1/C^2$ *vs.* E plots at more anodic potentials is probably caused principally by the faradaic capacitive component associated with voltammetry peak *I*.

Possible sources of frequency dispersion.—The frequency dependence of the capacitance data seriously complicates the interpretation of the data. Measurements over a much wider frequency range are needed to establish the nature of this frequency dependence. Possible sources of this frequency dispersion include the following: (*i*) nonuniform a-c distribution on the electrode due to edge effects, (*ii*) impedance contributions from the electrical contact to the rear of the NiO(Li) electrode, (*iii*) grain boundary effects associated with the mosaic nature of the NiO(Li), (*iv*) slow surface states, and (*v*) slow response of some of the charge carriers in the space charge region to the applied alternating potential.

Flat electrodes mounted flush in an insulator exhibit frequency dispersion at audio frequencies as a consequence of nonuniform a-c distribution on the electrode surface. Randin and Yeager (12) have examined such frequency dispersion on pyrolytic graphite electrodes of dimensions and capacitance per square centimeter comparable to those involved with the NiO(Li) electrodes represented in Fig. 4-6. For an electrolytic solution (0.9M NaF) of resistivity close to that involved in Fig. 6 the capacitance was found to decrease by 11% between 1 and 20 kHz because of nonuniform a-c distributions. The decrease in capacitance within the linear $1/C^2$ *vs.* E range in Fig. 6 is comparable. On the other hand, the frequency dispersion is much greater at lower Li concentrations corresponding to smaller capacitances. If only nonuniform current distribution were responsible for the frequency dispersion, it should become less as the capacitance decreases. Thus more than just nonuniform current distribution is involved.

The electrical contact to the rear of the NiO(Li) electrode is not a likely source of frequency dispersion since no appreciable impedance is expected with the diffuse metal junction used in the present work. The kinetic studies cited earlier provide some evidence to support this view for NiO(Li) electrodes with Li concentrations greater than 0.1 cation %. At lower Li concentrations, the contact is probably still ohmic but it is difficult to verify this from the kinetic studies because of appreciable ohmic drop within the bulk of the NiO(Li) electrode.

Grain boundaries and space charge effects associated with these boundries may lead to a complex distributive impedance for the bulk of the NiO(Li) electrodes. This source of frequency dispersion would be expected to become more pronounced at lower lithium concentrations because of the higher resistance component within the bulk of the semiconductor and the greater extent of the space charge regions within the individual grains or crystallites. At high lithium concentrations (>0.1 cation % Li), this source of frequency dispersion is probably not important since the

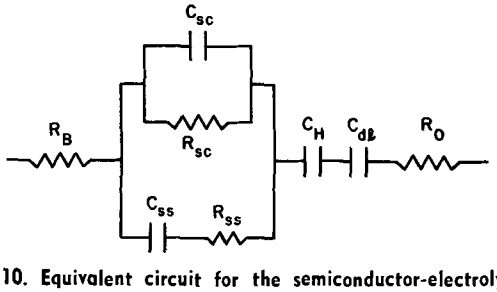

Fig. 10. Equivalent circuit for the semiconductor-electrolyte interface. (Symbols defined in text.)

total resistance loss within the bulk of the NiO(Li) is very low ($<10^{-1}$ ohm-cm^2).

Surface states are expected to contribute substantially to the capacitance over only a relatively limited potential range (*e.g.*, a few tenths of a volt). Further, such states do not contribute appreciably to the observed capacity over the potential range where a linear $1/C^2$ *vs.* E plot is obtained since otherwise such a linear relationship would not be observed. Thus slow surface states are probably not a major source of the frequency dispersion over the linear $1/C^2$ *vs.* E range.

Bosman and Crevecoeur (13) have shown that the activation energy for conduction in NiO(Li) is due primarily to the charge carrier dissociation process and not to the low mobility of the carriers. A slow ionization step can cause frequency dispersion but, in view of the small dissociation energy (0.3 eV), such frequency dispersion would be expected only at frequencies much higher than involved in the present work.

Protons probably penetrate from the solution into the NiO lattice at least a distance large compared to the very thin space charge region involved in the present study. The mobility of protons within the lattice would be much less than that of the Ni^{3+} p-carriers and the trapping energy for protons on oxide ions adjacent to Li^+ cations is probably greater than the dissociation energy of Li^+-Ni^{3+}. Consequently, protons within the lattice may be relatively slow in their response to the a-c field and may cause audio frequency dispersion.

Of these various factors, nonuniform a-c distribution and the slow response of protons in the space charge region of the NiO(Li) seem the most likely sources of the frequency dispersion. If this is correct, the measurements at the lower frequencies should be the more suitable for comparison of the $1/C^2$ *vs.* E slopes with the lithium concentrations. The current distribution should become more uniform at lower frequencies as the interface impedance rather than electrolyte resistance becomes controlling. Furthermore, the lithium concentration corresponds to the sum of the Ni^{3+} carrier plus proton concentrations and only at low frequencies will the full contribution of the protons to the capacitance be realized.

While it would have been desirable to have capacitance data below 1 kHz, this frequency is probably sufficiently low for at least a semiquantitative comparison of the slopes of the $1/C^2$ *vs.* E plots with the lithium concentration for the NiO electrodes containing more than 0.2 cation % Li. These electrodes have quite small frequency dispersion between 1 and 2 kHz.

Mott-Schottky slopes.—In Table II the carrier concentrations (expressed in cation per cent) determined from the Mott-Schottky slopes at 1 kHz are compared with the Li concentrations as determined by flame spectrophotometry. The values obtained from the capacitance data are smaller than those from chemical analysis in every case. Since surface roughness has not been taken into account, the difference may be even somewhat larger. Nonetheless, moderately good agreement is found in Table II for short lithium doping times (< 30 hr) and relatively thin electrodes (*e.g.*, runs 1 and 2). Weininger (8) has determined the doping profile of lithium in mosaic NiO(Li) crystals by flame spectrophotometric analysis of material sand-blasted from the crystal surface. He found that for long doping times (> 25 hr) the surface was less doped than the center of the crystal. It was assumed that this inversion was caused by a depletion of lithium inside the crucible with time, followed by loss of lithium from the mosaic crystal surface. In order to prevent loss of lithium through chemical attack of the alumina doping crucibles by Li_2O vapor, Weininger lined them with platinum metal. This practice was not employed in the present work because of the possibility of contamination of the NiO(Li) surface with platinum. It is probable, therefore, that the surface region of the NiO(Li) used for the present studies was less highly doped than the bulk. This explains why the value of the doping level obtained from the Mott-Schottky slope is smaller than the value determined by chemical analysis.

Table II. Comparison of values for cation % Li determined by a-c impedance in 1.0*N* H_2SO_4 and from flame spectrophotometric analysis for NiO(Li) crystals doped at 1500°C

Run No.	Doping time (hr)	Doping mixture cation % Li	Crystal thickness (μ)	Cation % Li	
				Impedance	Analysis
1	~12	1	80	0.25	0.29
2	30	5	125	0.48	0.55
3	31	10	145	0.30	0.43
4	41	20	90	0.36	0.49
5	41	5	100	0.13	0.29

Mott-Schottky intercept.—The intercept of the $1/C^2$ *vs.* E plot with the potential axis becomes more cathodic as the doping concentration of the electrode decreases (see Fig. 9 but not the plots in Fig. 8 which have a large frequency error). This intercept is expected to depend on the doping concentration when carrier recombination becomes important but to a much less extent than observed. Electrostatic interactions between the charge carriers and surface protons as well as some residual frequency dispersion offer possible explanations for the large dependence of the intercept on doping concentrations. At potentials cathodic to peak I (and to a less extent at anodic potentials), the NiO(Li) surface is covered with a layer of protons (associated with oxygen ions) which tend to repel charge carriers electrostatically in the vicinity of the surface. The thickness of the space charge in the semiconductor becomes smaller (for the same electrode charge) as the doping concentration becomes greater. This results in greater electrostatic repulsion of p-carriers by the adsorbed protons for higher doped samples. Thus it requires more anodic potentials to attain the flatband condition for samples with higher doping concentrations.

From the preceding considerations the intercept with the potential axis should become more anodic at lower *p*H values since the degree of surface protonation should increase. At the intercept, all of the potential drop should be across the Helmholtz plane and hence ideally the potential dependence should be 0.059 V/*p*H unit [see, *e.g.*, Ref. (3)]. The observed dependence from a comparison of Fig. 4-6 is ~0.10 V/*p*H unit.

The determination of the true "flatband" potential for NiO(Li) is complicated by the presence of surface states associated with voltammetry peak I. Extrapolation of $1/C^2$-E plots to potentials anodic to this peak is not valid since the potential distribution is changed by the formation of Ni^{+3} states at the surface. These surface states can compensate much of the charge in the Helmholtz plane as the potential is changed, thus making the effective thickness of the space charge layer smaller. The flatband potential, in this case, is more cathodic than predicted from the Mott-Schottky intercept and probably occurs in the vicinity of peak I.

Potential distribution across the interface.—If the effects of carrier recombination, surface states, and the ionic double layer are neglected, then the potential drop across the Helmholtz layer is given by (14)

$$\phi_s - \phi_2 = \pm \frac{\sqrt{2} d_H \epsilon_{sc}}{f \epsilon_H L_{sc}} [\exp f(\phi_B - \phi_s) - f(\phi_B - \phi_s) - 1]^{1/2} \quad [2]$$

where $\phi_s - \phi_2$ and $\phi_B - \phi_s$ represent the potential drops across the Helmholtz layer and semiconductor space charge layer, respectively, (see Fig. 11); d_H is

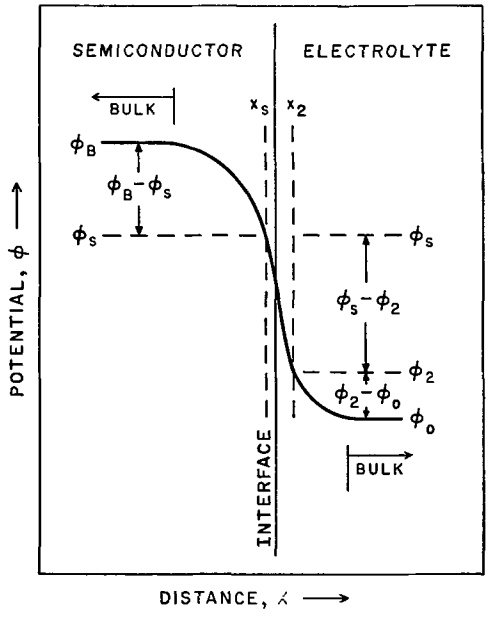

Fig. 11. Potential distribution at the semiconductor-electrolyte interface for a p-type semiconductor with a space charge depletion layer. The distance of closest approach of p-carriers to the surface is taken as the interface and is represented by x_s, whereas, the Helmholtz plane is represented by distance x_2. Inner potentials ϕ_B, ϕ_s, ϕ_2, and ϕ_0 are the values for the bulk of the semiconductor, distance of closest approach of p-carriers to the surface, Helmholtz plane, and bulk of the solution, respectively.

the thickness of the Helmholtz layer, ϵ_H and ϵ_{sc} are the dielectric constants in the Helmholtz layer and space charge region, respectively; and L_{sc} is the Debye length of the space charge region and is given by

$$L_{sc} = \left(\frac{\epsilon_{sc} kT}{4\pi N e^2} \right)^{1/2} \quad [3]$$

The carrier concentration in the NiO(Li) electrode used in the present work is very high (10^{19}-10^{20} carriers/cm^3). Under these circumstances Eq. [2] can only be considered semiquantitative at best. Nonetheless, it is still useful for establishing in what region most of the potential change between the electrode and solution phase should occcr. For a 0.40 cation % Li electrode ($N = 2.4 \times 10^{20}$ carrier/cm^3), the value of L_{sc} is calculated by Eq. [3] to be 2.6Å at 25°C if the dielectric constant in the space charge region is taken to be 12, the same as in the bulk of the semiconductor (15). The value of ϵ_H is assumed to be 6, reflecting the estimate of Bockris (16) for water between the Helmholtz plane and a metal electrode surface. The value of d_H has been taken as 3Å in the absence of specific adsorption. The potential drops in the space charge region and Helmholtz layer, calculated from Eq. [2], are plotted as a function of the rational electrode potential (relative to the flatband potential) in Fig. 12. At potentials anodic to the flatband potential (E_{fb}) most of the change in potential is manifested across the Helmholtz layer. Cathodic to E_{fb}, comparable potential drops occur in the space charge region and the Helmholtz layer with that in the space charge region larger at rational electrode potentials cathodic to about −0.5V.

In the absence of surface states or other mitigating effects, Fig. 12 indicates that only at extremely cathodic potentials (< −2.0V) will most of the potential change occur across the space charge region. Nonetheless, the linearity of the $1/C^2$ *vs.* E plots over a substantial range of potentials indicates that such does occur at much less cathodic potentials. This discrepancy may be caused by the fact that Eq. [2] does not take into account the protonation of the lattice $O^=$ ions at the interface. The $O^=$ ion is a very strong

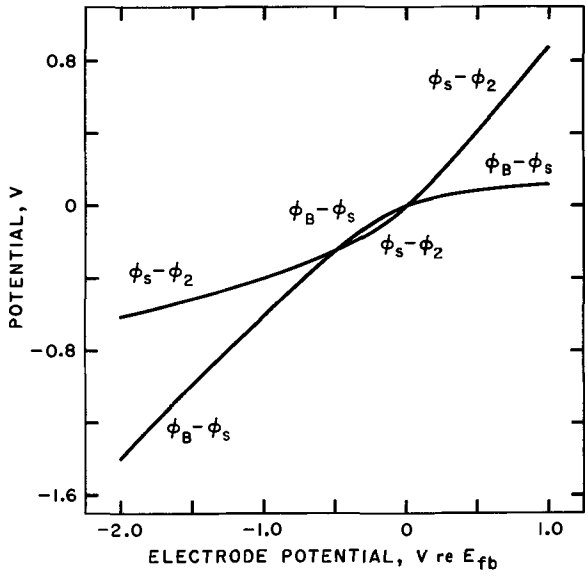

Fig. 12. Potential drops in the space charge region ($\phi_B - \phi_s$) and Helmholtz layer ($\phi_s - \phi_2$) vs. electrode potential (neglecting $\phi_2 - \phi_0$) according to Eq. [4] for NiO(0.40 cation % Li). L_{sc} = 2.6Å; $\epsilon_{sc} = 12$; $d_H = 3$Å; $\epsilon_H = 6$.

base and hence the surface $O^=$ ions of the lattice normally should be protonated. The abnormal surface charge density arising from this adsorption of protons should strongly repel the p carriers (Ni^{3+}) from the surface region and hence increase the fraction of the potential drop across the space charge region. Other specifically adsorbed cations would have a similar effect. Apparently this effect is sufficiently great that an exhaustive depletion layer situation is approached.

Acknowledgments

The authors are pleased to acknowledge the support of this research by the Office of Naval Research. We express appreciation to Dr. C. H. Lee for helpful discussions and to the Union Carbide Technical Center, Parma, Ohio, for help with some aspects of the analytical work.

Manuscript submitted Nov. 22, 1971; revised manuscript received Aug. 29, 1972.

Any discussion of this paper will appear in a Discussion Section to be published in the December 1973 JOURNAL.

REFERENCES

1. J. H. De Boer and E. J. W. Verwey, *Proc. Phys. Soc., (London)*, **A49**, Suppl., 59 (1937).
2. D. Adler, *Solid State Phys.*, **21**, 1 (1968).
3. T. O. Rouse and J. L. Weininger, *This Journal*, **113**, 184 (1966).
4. D. Yohe, A. Riga, R. Greef, and E. Yeager, *Electrochim. Acta*, **13**, 1351 (1968).
5. D. Yohe, E. Yeager, R. Greef, and A. Riga, "Electrochemical Processes on Nickel Oxide," Tech. Report No. 3, Case Western Reserve University, Cleveland, Ohio, U. S. Office of Naval Research, Contract Nonr 1439(09), Project NR 056-451, July 1, 1967.
6. D. M. Tench and E. Yeager, "Electrochemistry of Redox Couples on Lithiated Nickel Oxide Electrodes," Tech. Report No. 28, Case Western Reserve University, Cleveland, Ohio, U. S. Office of Naval Research, Contract N00014-67A-0404-0006, Project NR 359-451, September 15, 1970.
7. M. B. Pourbaix, "Atlas of Electrochemical Equilibria in Aqueous Solutions," Pergamon Press, New York (1966).
8. J. L. Weininger, Private communication.
9. R. Cech and E. Alessandrini, *Am. Soc. Met. Trans. Quart.*, **51**, 150 (1959).
10. A. Riga, R. Greef, and E. B. Yeager, "The Electrochemical and Dissolution Properties of Nickel Oxides," Tech. Report No. 2, Case Western Reserve University, Cleveland, Ohio, U. S. Office of Naval Research, Contract Nonr 1439(09), Project NR 056-451, December 1, 1966.

11. P. Longhi, Unpublished research at Case Western Reserve University, Cleveland, Ohio.
12. J. P. Randin and E. Yeager, *This Journal*, **118**, 711 (1971).
13. A. J. Bosman and C. Crevecoeur, *Phys. Rev.*, **144**, 763 (1966).
14. V. A. Myamlin and Yu. V. Pleskov, "Electrochemistry of Semiconductors," pp. 42-43, Plenum Press, New York (1967); translated (with revisions) from Russian, Nauka Press, Moscow (1965).
15. S. Koide, *J. Phys. Soc. Japan*, **20**, 123 (1965).
16. J. O'M. Bockris and A. K. N. Reddy, "Modern Electrochemistry," Vol. 2, pp. 756-757, Plenum Press, New York (1970).

A Solid-State Reserve Battery

John H. Kennedy,* Fred Chen,* and Ronald C. Miles*

Department of Chemistry University of California, Santa Barbara, California 93106

ABSTRACT

A solid-state reserve battery concept has been demonstrated in which anode/electrolyte and cathode/electrolyte components are separated during storage and pressed together for activation. The concept was shown using the cell Ag/Ag_3SBr/$AuBr_x$ where $x = 2.4 \pm 0.1$. The open-circuit voltage of 0.84V was achieved at a pressure of about 1 psi. Pressures of about 25 psi were required to reach 96% of high-pressure performance during current drain. The cell could store about 10 W-hr/lb of electrical energy.

Until recently, the conventional approach to a long storage life battery has been the "reserve" type in which the battery is kept inactive during storage. The inactive state is normally accomplished by storing the electrolyte separately from the electrodes. With the advent of high current density solid-state batteries using electrolytes of $RbAg_4I_5$ (1), Ag_3SI (2), or $(CH_3)_4NI$:4 AgI (3), a new type of long storage life battery now exists since a solid-state battery can often be kept in its active state for a long period of time.

Our work has focused on still another possibility, a solid-state reserve battery. Many, otherwise acceptable, solid-state batteries cannot be stored for long periods of time because of low level electronic conduction through the electrolyte, either intrinsic or caused by impurities. Self-discharge can also occur by electrode material diffusing through the electrolyte reaching the other electrode and reacting chemically (4). Inactive storage of such batteries makes them feasible for application and could improve storage life of all solid-state batteries. The inactive state is accomplished by forming anode/electrolyte and cathode/electrolyte sections with the electrolyte layers separated during storage. Activation is accomplished (as shown in Fig. 1) by simply pressing the electrolyte layers together under a moderate pressure of a few lb/in.^{2}. This type of reserve battery may be activated and deactivated many times, unlike most conventional reserve batteries.

The silver/gold bromide electrochemical cell was used for demonstrating the reserve battery concept. Gold bromide was chosen since it met the requirements that a cathode material should: (*i*) be highly oxidized, so that the voltage of its reaction with silver will be reasonably high; (*ii*) be unreactive with the electrolyte; (*iii*) support reasonable current densities during battery discharge, and (*iv*) exhibit a low vapor pressure at room temperature. Silver was chosen as the anode since the current was carried by silver ions in the electrolyte.

The theoretical voltage of an Ag/$AuBr_3$ cell is calculated from the following couples using free energies of formation

$$3Ag \rightarrow 3Ag^+ + 3e^- \qquad \text{(anodic reaction)}$$

$$3Ag^+ + AuBr_3 + 3e^- \rightarrow Au + 3AgBr \qquad \text{(cathodic reaction)}$$

with Ag^+ migrating through the electrolyte to the cathode and reacting with Br^- to form AgBr. The over-all cell reaction is

$$3Ag + AuBr_3 \rightarrow Au + 3AgBr \qquad E = 0.91V \quad \text{[Ref. (5)]}$$

A possible reaction taking place simultaneously is

$$Ag + AuBr \rightarrow Au + AgBr \qquad E = 0.83V \quad \text{[Ref. (5)]}$$

The theoretical energy density of an Ag/$AuBr_3$ cell is 43.5 W-hr/lb. In place of $AuBr_3$, $KAuBr_4$ was considered as a cathode material. Its advantage would be a lower vapor pressure, but its theoretical energy density with a silver anode is only 33.8 W-hr/lb. Some of the cathode couples that have been used with silver electrolytes are listed in Table I with their voltages and energy densities.

Silver sulfide bromide was chosen as the solid electrolyte because of its higher decomposition potential than those of silver iodide complex salts (0.84V *vs.* 0.67V) (1, 2, 9).

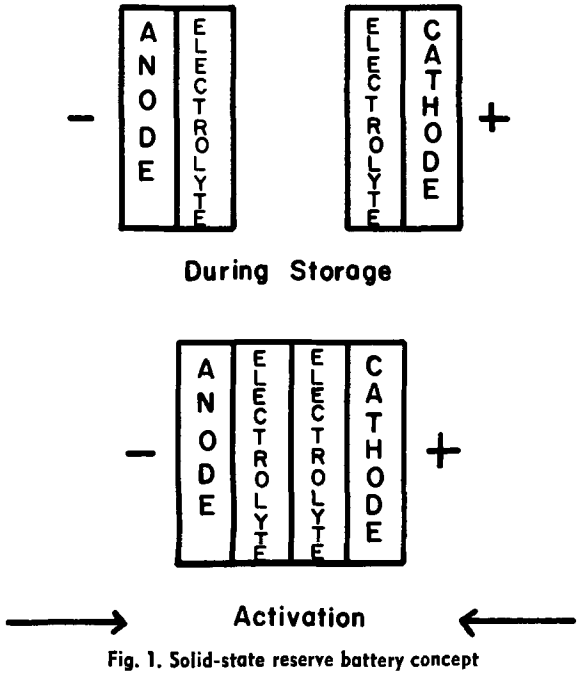

Fig. 1. Solid-state reserve battery concept

* Electrochemical Society Active Member.

Key words: gold bromide, reserve battery, solid-state battery, silver sulfide bromide, solid electrolyte.

Table I. Theoretical voltage and energy density of representative silver/cathode cells

Electrode couples	E° (V)	Energy density (W-hr/lb)	Reference
Ag/Br_2	0.994	64.3	6
$Ag/AuBr_3$	0.91	43.5	Present study
$Ag/KAuBr_4$	0.82	33.8	Present study
Ag/Te	0.217	15.4	1c
Ag/Se	0.265	22.3	1c
Ag/I_2	0.687	35.5	1b, 1c, 7
Ag/RbI_3	0.635	22.6	1a, 8
Ag/CsI_3	0.314	20.4	8
$Ag/I_2 + Rb_2AgI_3$	0.68	33.7	8

Experimental

Gold bromide was prepared by treating gold powder, 99.99% (Wilkinson Company), with excess liquid bromine for 5 days at 60°C. After this period of time, excess unreacted bromine was removed by flowing dry nitrogen through the reaction vessel. Any residual bromine present was removed by evacuating ($<10\mu$ pressure) the reaction vessel for 5 days. The dark brown gold bromide crystals were then ground and stored over silica gel until used. The amount of bromine that reacted with gold was calculated from weight gained by the gold and by weight loss when a known amount of gold bromide was decomposed at 200°C for more than 12 hr. The average nonstoichiometric composition was found to be $AuBr_{2.4\pm0.1}$.

Gold bromide obtained by treating gold powder with liquid bromine at room temperature gave variable gold to bromine ratios ranging from 0.85 to 2.6. In addition to this variability, these samples lost bromine with ease when placed under vacuum. Only gold bromide prepared at elevated temperatures was stable under vacuum.

Silver sulfide bromide was prepared as previously reported (9). Silver powder was obtained from Engelhard Industries. Anhydrous gold tribromide and potassium tetrabromoaurate(III) were obtained from Research Organic/Inorganic Chemicals, Sun Valley, California. Graphite powder was treated with Durite-5143 (Borden Company) in order to make it pressable (10).

The anode/electrolyte and cathode/electrolyte pellets were prepared with a Perkin-Elmer evacuable KBr die (186-0025), 13 mm diameter. As an example of anode/electrolyte pellet preparation: 0.2g of silver and 0.2g of silver sulfide bromide were mixed and then pressed at 6000 psi. On top of the pellet, 0.2g of silver sulfide bromide was added and pressed at 6000 psi and finally a pressure of 60,000 psi was applied to the whole pellet.

An example of cathode/electrolyte pellet preparation is as follows: 0.2g of silver sulfide bromide was pressed at 6000 psi, followed by pressing 0.4g of a gold bromide, silver sulfide bromide, and graphite mixture at 6000 psi, and finally applying a pressure of 60,000 psi to the whole pellet. The gold bromide, silver sulfide bromide, and graphite mixture had an 8:8:1 weight ratio. The exact weight ratio compositions for the cathode mixture were arbitrarily chosen for laboratory convenience although based on other battery studies. The cathode and anode mixtures were mixed with a Crescent Dental Company "Wig-L-Bug" for about a minute before pressing.

To discharge the battery, the anode and cathode components were placed in a plastic jig with graphite current collectors. A representation of the cell is shown in Fig. 2. Test cells were usually 1.6 mm thick, weighed 1.2g, and contained about 120 C of charge based on one electron/bromine atom in the gold bromide. The energy density of a typical test cell with $AuBr_{2.4}$ as cathode material was determined to be 9.7 W-hr/lb based on the cathodic charge and the weight of the electrodes plus electrolyte. With $AuBr_3$ as the cathode material, the energy density of the test cells was determined to be 10.4 W-hr/lb. These energy density values are comparable to the energy densities of other solid-state batteries.

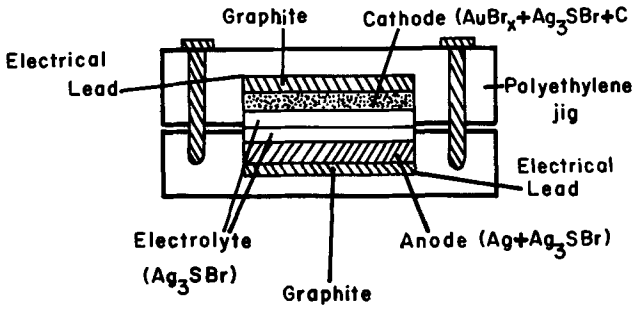

Fig. 2. Schematic diagram of a cell during discharge

X-ray powder diffraction patterns of gold bromide were taken with a Philips x-ray diffraction unit with CuK_α radiation. A Philips Type 52572 scintillation counter with chart recorder was used for x-ray diffractometer measurements.

An Associated Testing Laboratory SW-5101 environmental chamber was used for temperatures other than ambient. A General Radio Incorporated 1650 Impedance Bridge with an 0.5V rms and 1 kHz signal was used for resistance measurements, and General Radio Decade Resistors Type 1433-P were used as resistance loads. The open-circuit voltage and voltage during discharge of the batteries were measured with a Hewlett-Packard VTVM Model 412A. A Hewlett-Packard 7100B strip-chart recorder with 17501 plug-ins was used for recording voltmeter output.

Results and Discussion

Gold bromide.—X-ray diffraction data for commercial anhydrous $AuBr_3$ and $AuBr_{2.4}$ are given in Table II. $AuBr_3$ and $AuBr_{2.4}$ were found to decompose in a very similar way when heated. First, they decomposed into a yellow compound, which according to Campbell (11) was gold monobromide. The yellow compound subsequently decomposed to metallic gold. Both $AuBr_3$ and $AuBr_{2.4}$ were hygroscopic and somewhat soluble in acetone and ethanol.

Ag_3SBr reacted readily with liquid and gaseous bromine, and aqueous HBr:

Table II. X-ray diffraction data for $AuBr_3$ and $AuBr_{2.4}$

d (A)	$AuBr_3$ I/I_o	$AuBr_{2.4}$ I/I_o
8.04	37	9
6.28	7	—
6.06	26	42
5.94	10	12
5.79	44	64
5.71	18	29
5.40	—	7
5.09	35	48
4.64	7	—
4.37	7	—
4.04	9	18
3.96	—	9
3.75	7	7
3.66	15	13
3.52	100	100
3.47	22	19
3.43	—	18
3.36	9	6
3.00	15	8
2.95	16	16
2.90	25	20
2.88	19	—
2.84	15	22
2.80	9	—
2.74	13	9
2.67	9	—
2.62	41	39
2.50	7	7
2.44	7	6
2.41	9	7
2.38	9	—
2.36	21	18
2.34	9	—
2.29	15	15
2.21	13	9

$$Ag_3SBr + Br_2 \rightarrow 3AgBr + S \quad [1]$$

$$Ag_3SBr + 2HBr \rightarrow 3AgBr + H_2S$$

These reactions were exothermic and proceeded readily at room temperature. The decomposition reaction of Ag_3SBr with Br_2 is analogous to the decomposition reaction of Ag_3SI with I_2 (7). However, Ag_3SBr did not react (no decomposition was observed from x-ray diffraction patterns after several months at room temperature) with anhydrous $AuBr_3$ or with $AuBr_{2.4}$.

The crystal structure of $AuBr_3$ has not been reported in the literature, however, $AuBr_3$ has been reported by Burawoy and Gibson (12) to be a dimer

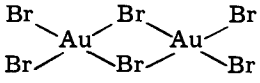

Burroway and Gibson based their results on ebullioscopic measurement in the elevation of bromine's boiling point when a known amount of $AuBr_3$ was dissolved in bromine.

The similarity in properties of $AuBr_{2.4}$ and $AuBr_3$ suggests that $AuBr_{2.4}$ may also be a dimer. The lower ratio of Br:Au may be due to the formation of bromide vacancies (O) such as

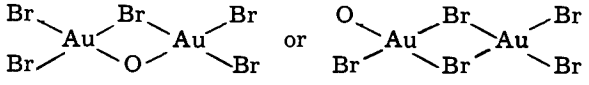

Battery characteristics.—Little pressure was needed to activate the batteries. The relationship between applied pressure, open-circuit voltage, and voltage of a cell with a 50 k-ohm load is shown in Fig. 3. Under high pressure, the open-circuit voltage was 0.84V, about equal to the decomposition potential of the electrolyte, the highest value which can be obtained under equilibrium conditions. As can be seen, at less than 1 psi the open-circuit voltage was over 90% of the cell voltage at high pressure. However, this was not the case when a load was applied to the cell. Even at a pressure of 1 psi the cell voltage under 50 k-ohm load was only 40% that observed under an applied pressure of 1000 psi. The voltage under load rose rapidly above 1 psi, and a pressure of 25 psi was sufficient to activate the battery for current drain (96% of the voltage observed at high pressure). This pressure of about 25 psi needed to activate the battery, *i.e.*, for the cell to have a good electrolyte/electrolyte interface contact, was still much less than the 60,000 psi pressure needed to achieve a good electrode/electrolyte contact (9).

Deactivation of the battery was accomplished by removing the applied pressure. Even cells that were activated with pressures of 2000 psi were deactivated with extreme ease.

Reactivation of a cell required less pressure than in the initial activation. Electrolyte surfaces at the electrolyte/electrolyte interface had been conditioned by the applied pressure during the initial activation and apparently were not damaged during cell deactivation and storage.

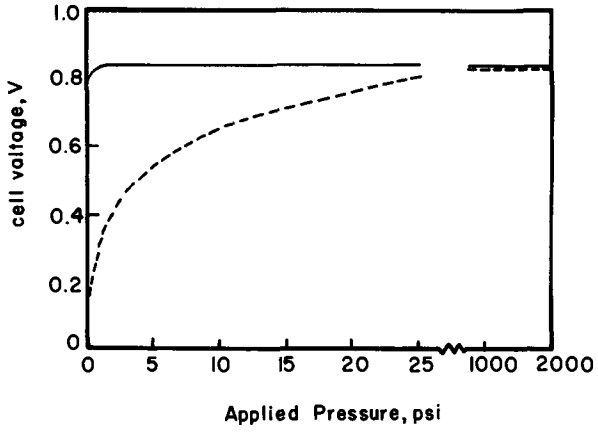

Fig. 3. Cell voltage dependence on applied pressure: (solid line) open-circuit voltage; (broken line) 50 k-ohm load.

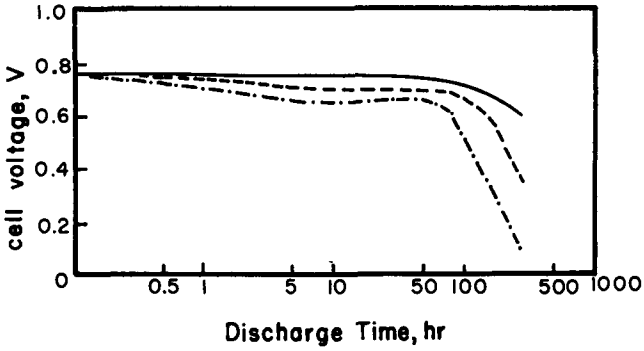

Fig. 4. Discharge curves for Ag + $Ag_3SBr/Ag_3SBr/Ag_3SBr/AuBr_{2.4}$ + Ag_3SBr + C cells under constant load at 0°C. Initial cathode charge was 100C. (—) 33.2 k-ohm, (- -) 20 k-ohm; (· - · -) 10 k-ohm.

The a-c resistances of several batteries are listed in Table III. Usually nonreserve batteries had lower resistances than the reserve batteries by about 2 ohms. This difference in resistance was attributed to the electrolyte/electrolyte interface of the reserve batteries. In general, after a battery had been completely discharged, its resistance increased to about 7000 ohms. The increase in resistance was attributed to the presence of AgBr produced in the cathodic reaction.

Several cells were discharged until their voltages were 0.1V. The per cent battery charge recovered for the cells is listed in Table IV. Four different nonstoichiometric gold bromides were used as cathodes. Best results were obtained with $AuBr_{2.4}$ for which efficiencies of up to 80% were obtained. The per cent of anodic charge that was recovered when the anode was the limiting reactant was above 80%.

The voltages of cells under continuous load discharge at 0°, 21°, and 40°C are shown in Fig. 4-6. Load curves for temperatures between −30° and +40°C are shown in Fig. 7.

Table III. Resistance of solid-state reserve battery cells

Composition of cell	Resistance, ohms
Ag + Ag_3SBr/Ag_3SBr*/Ag_3SBr + $AuBr_{2.4}$ + C	28
Ag + $Ag_3SBr/Ag_3SBr/Ag_3SBr/Ag_3SBr$ + $AuBr_{2.4}$ + C	30
Ag + $Ag_3SBr/Ag_3SBr/Ag_3SBr/Ag_3SBr$ + $AuBr_2$ + C	1200
Ag + $Ag_3SBr/Ag_3SBr/Ag_3SBr/Ag_3SBr$ + $AuBr_3$ + C	90
Ag + $Ag_3SBr/Ag_3SBr/Ag_3SBr/Ag_3SBr$ + $KAuBr_4$ + C	2500

* The amount of Ag_3SBr used for the electrolyte layer of this cell was twice the amount for individual electrolyte layer of the other cells. The total amount of electrolyte used in all cells was the same.

Table IV. Cathode and anode efficiencies of solid-state battery cells

$AuBr_x$ cathode x	Initial charge, C		Cathode utilization %	Anode utilization %
	Cathode	Anode		
0.87	112	225	38.1*	18.9
2.5	155	225	37.9*	26.1
2.0	270	225	47.1	56.4*
2.0	270	225	59.5	71.5*
2.0	108	225	63.2*	30.4
2.0	108	225	55.2*	26.5
2.0	108	225	58.6*	28.1
2.4	243	225	71.1	76.7*
2.4	243	225	69.3	74.6*
2.4	119**	111	78.2	84.0*
2.4	119**	111	80.6	85.4*

* Limiting reactant.
** Cathodes also contained graphite.

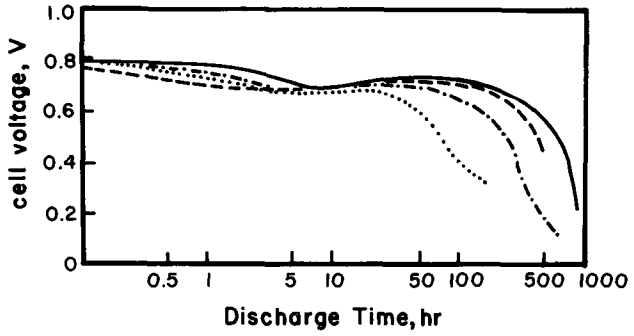

Fig. 5. Discharge curves for Ag + $Ag_3SBr/Ag_3SBr/Ag_3SBr/AuBr_x$ + Ag_3SBr + C cells under constant load at 21°C. Initial cathode charge was 119C. (—) x = 2.4; 20 k-ohm load. (- -) x = 3; 20 k-ohm load. (- · - · -) x = 2.4; 10 k-ohm load. (· · · ·) x = 2; 10 k-ohm load.

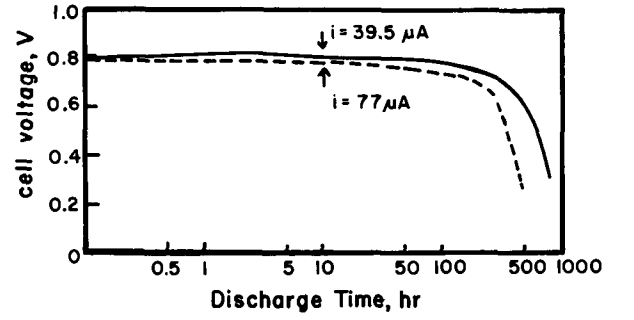

Fig. 6. Discharge curves for Ag + $Ag_3SBr/Ag_3SBr/Ag_3SBr/AuBr_{2.4}$ + Ag_3SBr + C cells under constant load at 40°C. Initial cathode charge was 119C. (Solid line) 20 K ohms; (broken line) 10 K ohms.

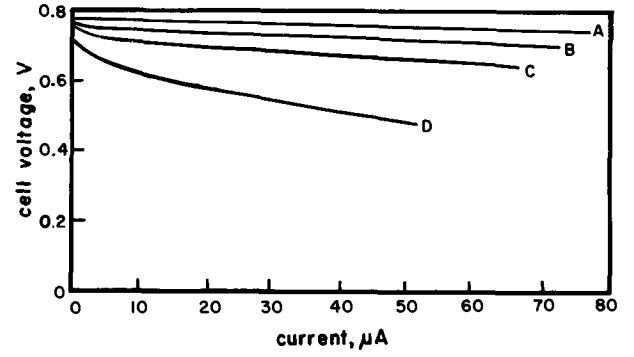

Fig. 7. Load curves for Ag + $Ag_3SBr/Ag_3SBr/Ag_3SBr/AuBr_{2.4}$ + Ag_3SBr + C cell at various temperatures. (A) 40°C; (B) 21°C; (C) 0°C; (D) —30°C. Initial cathode charge was 243C.

Cathodic reaction.—Two mechanisms can be proposed for the cathodic reaction

$$AuBr_x \rightleftarrows AuBr_{x-1} + Br(g)$$
$$\downarrow\ Ag^+ + e^- \longrightarrow AgBr \quad [A]$$

$$AuBr_x + Ag^+ + e^- \rightarrow AuBr_{x-1} + AgBr \quad [B]$$

The first step of mechanism [A] is the formation of gaseous bromine atoms followed by their reaction with silver ions and electrons. In mechanism [B], the cathodic reaction is a solid-state reaction and proceeds whenever there is a silver ion and an electron present at a reaction site.

According to mechanism [A], less stable gold bromides with high vapor pressures should perform better as cathodes than $AuBr_{2.4}$ or $AuBr_3$. However, at room temperature, all gold bromides had about the same average power output. In addition, the per cent cathodic charge recovered with $AuBr_{2.4}$ was significantly more than the other gold bromides (Table IV). Aside from $AuBr_{2.4}$, the poor performance of the other nonstoichiometric gold bromides was due to their instability with the formation of bromine gas, which was lost by diffusion to the atmosphere and by reacting with the electrolyte, reaction [1]. Although the formation of bromine gas with the unstable gold bromides supports the possibility of reaction via mechanism [A]; mechanism [B] must be the predominant cathodic reaction with the more stable gold bromides, considering the amount of charge that was recovered (Table IV), and the fact that $AuBr_{2.4}$ and $AuBr_3$ did not react with Ag_3SBr while the less stable gold bromides did.

The presence of bromide vacancies in the proposed structure of $AuBr_{2.4}$ should facilitate the migration of bromide ions to the reaction sites. An alternative mechanism would be the possible ability of silver ions to migrate into the $AuBr_{2.4}$ because of the bromide ion vacancies. These might explain the better performance of $AuBr_{2.4}$ under load compared to $AuBr_3$ (Fig. 5). In contrast, $KAuBr_4$, a compound without bromide vacancies, behaved poorly as cathode material. In Fig. 8 the voltage of a cell with $KAuBr_4$ as the cathode material is shown as a function of time.

The crystal structure of $KAuBr_4$ has been reported by Cox and Webster (14). They found $AuBr_4^-$ to be planar with the gold ion bonded covalently to four bromides. The passivity of $KAuBr_4$ may be due to the stability of the $AuBr_4^-$ ion in the solid-state since the reaction

$$AuBr_4^- + 3Ag \rightarrow Au + 3AgBr + Br^- \quad E^\circ = 0.79V$$

is thermodynamically favorable in acid solution (5). The passivation of the $KAuBr_4$ cathode took place after all the loosely bound bromide ions initially present at reaction sites were used. The stability of the $AuBr_4^-$ ion structure prevented the formation of any mobile bromide ions, and the absence of bromide vacancies made it difficult for any loosely bound bromide in the bulk to migrate to the reaction sites and form AgBr.

Conclusion

Although the solid-state reserve concept was demonstrated on only one cell system, there is no reason why it could not be applied to any solid-state battery in which electrolyte/electrolyte contact can be made at relatively low applied pressure.

Putting the concept into practice requires an activation technique which will vary with specific application. Single cells can be manually activated and deactivated easily, but batteries require a separator in the electrolyte which can be effectively removed when the battery is activated. One technique which was successful for 4-6 cell batteries was to use compressible plastic spheres positioned in grooves in the electrolyte layers. The applied pressure was sufficient to activate

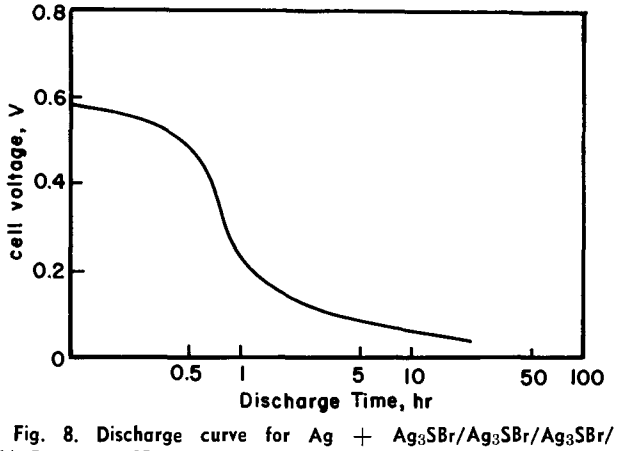

Fig. 8. Discharge curve for Ag + $Ag_3SBr/Ag_3SBr/Ag_3SBr/KAuBr_4$ + Ag_3SBr + C cell under 500 K ohms load at 21°C. Initial cathode charge was 250C.

the battery while the sphere's elasticity was sufficient to deactivate the battery when the applied pressure was removed.

Acknowledgment

The authors acknowledge financial support from PHS Research Grant, No. 1 RO1 APO 1527-01, Office of Air Programs of EPA.

Manuscript submitted July 31, 1972; revised manuscript received Oct. 5, 1972.

Any discussion of this paper will appear in a Discussion Section to be published in the December 1973 JOURNAL.

REFERENCES

1. (a) G. R. Argue, B. B. Owens, and I. Groce, *Proc. Ann. Power Sources Conf.*, **22**, 103 (1968).
(b) M. De Rossi, G. Pistoia, and B. Scrosati, *This Journal*, **116**, 1642 (1969).
(c) T. Takahashi and O. Yamamoto, *ibid.*, **117**, 1 (1970).
(d) T. Takahashi and O. Yamamoto, *ibid.*, **118**, 1051 (1971).
(e) Gould Ionics Inc., Bulletin 218
2. (a) T. Takahashi and O. Yamamoto, *Electrochim. Acta*, **11**, 779 (1966).
(b) T. Takahashi and O. Yamamoto, *ibid.*, **11**, 911 (1966).
3. D. Smyth, C. Tompkins, and S. Ross., *Proc. Ann. Power Sources Conf.*, **24**, 24 (1970).
4. C. C. Liang, *This Journal*, **118**, 894 (1971).
5. W. Latimer, "The Oxidation Potentials of the Elements and their Potentials in Aqueous Solutions," 2nd ed., pp. 342-343, Prentice-Hall, Inc., Englewood Cliffs, N. J. (1952).
6. J. L. Weininger and H. Liebhafsky, U. S. Pat. 2,987,568 (1961).
7. B. B. Owens, G. R. Argue, I. Groce, and L. Hermo, *This Journal*, **116**, 312 (1969).
8. G. R. Argue and B. B. Owens, U. S. Pat. 3,443,997 (1969).
9. J. H. Kennedy and F. Chen, *This Journal*, **116**, 207 (1969).
10. J. H. Kennedy, F. Chen, and J. Willis, *ibid.*, **117**, 263 (1970).
11. F. H. Campbell, *Chemical News*, (1907), 15.
12. A. Burawoy and C. Gibson, *J. Chem. Soc.*, (1935), 217.
13. E. Cox and K. Webster, *J. Chem. Soc.*, (1936), 1635.

On Accelerated Pitting and Crevice Corrosion Tests

Jörgen Degerbeck

Uddeholms Aktiebolag, Hagfors, Sweden

ABSTRACT

Accelerated electrochemical and chemical pitting and crevice corrosion tests have been carried out in order to gauge the validity of the tests in predicting the corrosion resistance of stainless steels in a specific sea-water environment and to determine the relationship between the tests performed. The relationship was investigated by means of regression and correlation analyses. Number of steels investigated, tests performed, and parameters measured were 20, 10, and 20, respectively.

The purpose of this report is to contribute to the recent discussion [*e.g.*, (1-4)] concerning different accelerated pitting corrosion tests, chemical and electrochemical, and their validity in predicting the performance of stainless steels under working conditions in sea-water environment.

Some twenty austenitic and ferritic-austenitic stainless steel grades, standardized and nonstandardized, have been investigated in ten different tests, *i.e.*, field test and accelerated chemical and electrochemical pitting and crevice corrosion tests, and the relationship between the tests has been investigated by means of regression and correlation analysis.

When deciding on a selection of laboratory tests and their evaluation, consideration has been given to their ease and speed of performance as well as their prevalence.

It has not been possible to study the relationship between all combinations of test measurements made for all combinations of steels. Only the relationship found to be of the greatest interest after a rather short initial survey of the results of the corrosion tests has been examined and discussed.

Materials

The material used in the investigation was grouped into the following types: Type 18/9, Type 18/13-3 Mo, Type 18/14-4 Mo, Si-alloyed 18/8 steel, Type 18/20-4 Mo, Type 20/25-Mo-Cu, and ferritic-austenitic stainless steels.

The steels within the different groups were alloyed with more or less varying contents of Ni, Mo, Si, Cu, Ti, Nb, and N. Table I shows the grouping and composition of the different grades.

The test material was taken from sheet and flat bars originating from production and laboratory heats. The production heat material was in the as-delivered condition, *i.e.*, solution heat-treated and pickled, and the laboratory material was solution heat-treated, 1050° and 980°C, for the austenitic and ferritic-austenitic material, respectively, and pickled in the laboratory. The austenitic steels were pickled in an HF/HNO_3 bath and the ferritic-austenitic steels in an HF/H_2SO_4 bath.

As regards the austenitic and ferritic-austenitic steels, the results of the metallographic examination were to a great extent as expected for respective grades and no specimen had a structure that differed from a representative solution-annealed structure for its grade to such an extent that exclusion from the investigation was justified.

Dimensions and surface treatment of the specimens for the different tests: see the section on Experimental and Table II.

Experimental

All corrosion tests performed in this investigation are listed in Table II, regarding type of test, test designation, test duration, test conditions, specimen condition, and measurements made. The tests can be divided into three main groups: field test, test A; electrochemical pitting potential tests, tests B, C, D, E, F; and chemical pitting and crevice corrosion tests, tests G, H, I, K. Within the electrochemical pitting potential test group the differences in test conditions were not very large. This is shown later on. Except for the field test only one test, K, included crevices.

Key words: stainless steel, test methods, pitting, crevice corrosion, sea water.

Table I. Grouping and composition of steels

Group	Grade UHB* stainless	Heat**	Steel No.	Chemical analysis C	Si	Mn	Cr	Ni	Mo	N	Cu	Ti	Nb	S × 10³
18/9	3MM	L	1	0.059	0.47	1.89	18.1	9.2	—	0.065				7
18/13-3Mo	24L	D	2	0.025	0.44	1.84	18.1	12.3	3.2					11
	24LN	D	3	0.030	0.59	1.83	18.6	13.4	2.8	0.20				9
	24LN + Nb	L	4	0.028	0.47	1.83	18.0	13.3	2.7	0.18			0.31	13
	624	D	5	0.048	0.47	1.89	18.0	13.0	2.6				0.56	11
18/14-4Mo	34	D	6	0.046	0.56	1.69	17.5	14.5	4.2					8
	34L	L	7	0.023	0.46	1.74	17.2	14.5	4.3	0.040				17
Si-alloyed 18/8		L	8	0.048	2.1	1.61	18.3	18.1		0.053				9
		L	9	0.027	3.6	1.93	18.2	14.0		0.053				6
		L	10	0.029	3.6	1.94	16.8	15.5	2.3	0.053				9
		L	11	0.020	1.95	1.8	18.4	12.1	—	0.16				3
		L	12	0.020	2.1	1.8	18.2	14.2	2.2	0.18				6
18/20-4Mo		L	13	0.020	0.60	1.93	17.7	24.1	4.3	0.041				15
		L	14	0.020	0.37	1.85	17.7	19.4	4.4	0.14				4
20/25-Mo-Cu	904L	D	15	0.022	0.90	1.80	19.9	25.3	4.7		1.54			11
		D	16	0.031	0.37	0.77	19.2	23.8	2.8		2.2	0.37		14
											Al	O		
Ferritic-austenitic steels	44	L	17	0.082	0.48	0.95	25.1	5.5	1.6	0.071	0.006	0.026		7
		L	18	0.025	1.22	1.37	19.2	4.8	2.8	0.029	0.010	0.010		10
	44L	L	19	0.025	0.48	0.96	25.2	5.1	1.63	0.14	0.004	0.017		9
	44L	L	20	0.030	0.51	0.97	25.1	5.0	1.56	0.16	≈0.014	0.013		13

* UHB = Trade mark of Uddeholms AB.
** D = Production heat, L = laboratory heat.

The electrochemical tests were supposed to give information about the resistance to pitting initiation by measuring the potentiodynamic pitting potential, whereas the field test and the chemical laboratory tests were supposed to give the total effect of resistance to pitting initiation and pit propagation by measuring the number of pits (indicative of resistance to passivity breakdown) and pit depth and weight loss (both to a greater or lesser extent related to propagation resistance). More elaborate measures as "mean value of pit depth" or "percentage attacked crevice area of total crevice area" have not been used.

Before explaining the different tests performed some general information concerning specimen condition and test solution will be given.

An important fact concerning this investigation is that for each grade of steel the laboratory specimens for all the tests were taken from the same piece of sheet or flat bar, *i.e.*, from the field test specimens. The flat surfaces of the specimens, which have in all cases

Table II. Tests performed

Test	Type of test	Test conditions: Corrosive environment	Temp, °C	Duration	Start potential, mV E_{SCE}/time, min	Pol. rate, mV/min	Specimen: Dimension, mm
A	Field	Natural sea water, 1m below the surface, near the shore. Salt: 3.4%, pH: 8.1, O_2: 6.5 mg/l	2-18	One year	—	—	200/100 × 40 × 2
B	Potentiodynamic pitting potential	5% HCl, N_2	30	—	−600/10	20	13 × 13 × 2
C	Potentiodynamic pitting potential	5% HCl, N_2	40	—	−600/10	20	13 × 13 × 2
D	Potentiodynamic pitting potential	5% NaCl, O_2, pH: 6	60	—	Corr. potential/5	10	13 × 13 × 2
E	Potentiodynamic pitting potential	5% NaCl, O_2, pH: 6	60	—	Corr. potential/5	10	13 × 13 × 2
F	Potentiodynamic pitting potential	5% NaCl, N_2, pH: 6	60	—	−1500/5	200 (up to −300 mV E_{SCE})	13 × 13 × 2
G	Chemical pitting	10% $FeCl_3$, pH = 1.3	30	4 hr	−300/15 —	10 —	Approx. 50 × 20 × 2
H	Chemical pitting	0.33 mol/l Al^{3+}, 0.30 mol/l Fe^{3+}, 1.81 mol/l Cl^-, 3.8 mol/l H_2O. Solvent: 50 vol % ethanol, 50 vol % glycerol	22	2 hr	—	—	10 × 10 × 2
I	Chemical pitting and general corrosion	2% HCl 15% HCl	22	140 hr 24 hr	—	—	Approx. 50 × 20 × 2
K	Chemical crevice corrosion	Synthetic sea-water (ASTM-D 1141-52) + 10 g/l $K_3[Fe(CN)_6]$ + 10 g/l $K_4[Fe(CN)_6]$	35	24 hr	—	—	Approx. 50 × 20 × 2

* C = crevice corrosion, P = pitting, G = general corrosion.

been the main or the only test surfaces, have always been parallel to the prior flat surfaces, *i.e.*, the rolled surfaces of the hot rolled sheets or bars.

The specimens were washed and degreased in ethanol.

Passivation treatment was performed in 20% HNO_3 at 40°C for half an hour.

The electrolytes were made from deionized water and reagent grade chemicals.

Deaeration of electrolytes was achieved by bubbling nitrogen through the solution for half an hour prior to the test.

The accuracy of the electrolyte temperature was ±1°C.

The electrochemical experiments were performed by using a Wenking 61 KTR potentiostat.

The specimens for the electrochemical tests, 13 × 13 × 2 mm, were mounted in plastic resin[1] with a single exposed surface, ground, surface treated, and finally masked with plastic resin[1] to a surface of 10 × 10 mm. The test surface was prepared not to get preferential attack at the interface between sample and plastic mount. Still some specimens were attacked at these areas, possibly because of crevices. However, the test results of these specimens were excluded and new tests were performed.

The specimen with its polyethylene-sheathed copper conductor was mounted together with a platinum counterelectrode, a Luggin capillary connected to a saturated calomel reference electrode (SCE), and a gas dispersion tube in the all-glass cell as shown in Fig. 1. One exception to the arrangement shown in Fig. 1 appeared when investigating the pitting potential in 5% HCl, tests B and C. In these cases the test surface was vertical and with the Luggin capillary as close to the specimen as in the "horizontal case," *i.e.* approximately 2 mm.

[1] Scandiplast 9101, Scandinavian Diamond Products, Vipperod, Denmark.

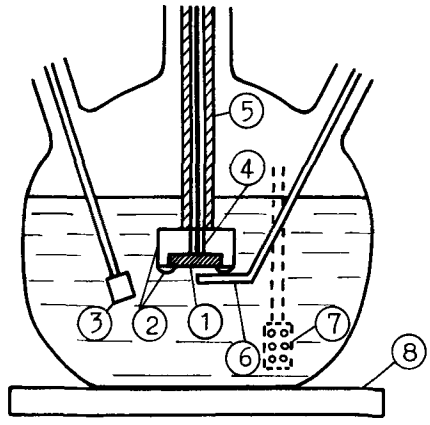

Fig. 1. Electrode assembly for electrochemical investigations. 1, Specimen; 2, plastic mount; 3, platinum counterelectrode; 4, polyethylene-sheathed copper conductor; 5, glass tube; 6, Luggin capillary; 7, gas dispersion tube; 8, hot plate.

The different tests performed were as follows:

Field test, test A.—This test and its results are reported in Ref. (5). A short survey of the experimental procedure is given below.

Plate dimension was: long samples with drilled holes, 18 mm diameter, for suspending the plate speci-

conditions						
Surface treatment	Passivation	Surfaces tested	Number of spec./ trials per grade	Type of corrosion*	Measurements made	Remarks
One flatside ground on 220 paper and the other pickled in HF/HNO_3	HNO_3 20%, 40°C, 0.5 hr	All surfaces	3 occasionally 1	C	Max depth of attack, mm: A_1 Mean number of attacks, ≥0.2 mm per specimen: A_2	Vertical specimens. Crevices steel-steel/PVC. Heavy fouling by sea organisms
Ground on 600 paper	HNO_3 20%, 40°C, 0.5 hr	1 flatside 10 × 10 mm	1	P	Critical anodic current density μA/cm²: B_1 Pitting potential mV E_{SCE}: B_2	Pitting potential: the potential at which the current starts to increase (independent of the current value)
Ground on 600 paper	HNO_3 20%, 40°C, 0.5 hr	1 flatside 10 × 10 mm	1	P	Critical anodic current density μA/cm²: C_1 Pitting potential mV E_{SCE}: C_2	Pitting potential: the potential at which the current starts to increase (independent of the current value)
Ground on 600 paper	HNO_3 20%, 40°C, 0.5 hr	1 flatside 10 × 10 mm	3	P	Pitting potential Mean value mV E_{SCE}: D_1	Pitting potential: the potential at which the current density exceeds 10μA/cm²
Mechanically polished and etched (V2A)	Air, 2 or 3 days	1 flatside 10 × 10 mm	5	P	Pitting potential Min. value: E_1 Mean value: E_2 Max value: E_3	—
Mechanically polished and etched (V2A)	Air, 2 or 3 days	1 flatside 10 × 10 mm	5	P	Pitting potential Min. value: F_1 Mean value: F_2 Max value: F_3	Test, partly according to (1)
Mechanically polished	HNO_3 20%, 40°C, 0.5 hr	All surfaces	1	P	Number of pits per cm² Rolled surfaces: G_1 All surfaces: G_2 Weight loss, g/m²·hr: G_3	—
Mechanically polished	Air, 24 hr	1 flatside	1	P	Number of pits per 0.5 cm²: H_1	Test partly according to (6)
Ground on 150 paper	HNO_3 20%, 40°C, 0.5 hr	All surfaces	2	P and G	Weight loss, g/m²·hr, in 2% HCl: I_1, 15% HCl: I_2	—
Ground on 220 paper	HNO_3 20%, 40°C, 0.5 hr	All surfaces	2 5	C	Relative resistance according to number, depth, and area of attack: K_1 The lower the value the better resistance	Crevices formed through a close clamping of a flat PVC specimen. (20 × 10 × 2 mm, ground on 80 paper) to the steel by rubber bands

mens, 200 × 40 × 2 mm. Short samples without drilled holes, 100 × 40 × 2 mm.

One or, in a few cases, both the flat sides of the pickled samples were ground with 220 paper. All the samples were then passivated in 20% HNO_3 at 40°C for 0.5 hr.

Measurements of surface roughness of the pickled and ground surfaces showed that the ground surfaces on an average were smoother. The average of the roughness value CLA was approximately 1.0 for the pickled surfaces and 0.5 for the ground surfaces.

Two types of specimen were used, single specimen and double specimen. The double specimen consisted of two samples, one long and one short, of the same grade joined by putting two ground flat sides together. The crevice between the ground surfaces was intended to give an idea of the tendency of the steel to crevice corrosion. The two plates were joined together by wire, 1.5 mm diameter in grade UHB[2]) SS 24.

The single sample consisted only of a long specimen.

The test plates were mounted in a frame by specimen holders consisting of two rods, 13 mm diameter, covered with PVC-tubing. The rods were threaded through the drilled holes of the plates and each specimen was fixed on to the specimen holder by middle-pieces made from coarse PVC-tubing. Both the sample holder and the extension casing were manufactured from UHB SS 24, 17/12-3 Mo. The sample holder was placed in the frame so that the longitudinal direction of the samples was vertical.

A description of the samples and their attachment to the specimen holder is given in Fig. 2.

With reference to the crevice geometry it should be pointed out that no more was known for the different crevices than the fact that these had been formed through a close clamping of steel to steel and PVC to steel.

The test station, Bohus-Malmön, is situated on the west coast of Sweden. The raft to which the test frames were fixed was anchored approximately 5m from the shore where the depth is approximately 3m.

The specimens were lowered approximately 1m below the surface and the tests for the austenitic stainless steels lasted from the end of September 1968 to mid-August 1969. The ferritic-austenitic steels were lowered into the sea just after the austenitic steels had been taken up and they were tested almost exactly one year, *i.e.*, they were taken up in mid-August 1970.

[2] Trade mark for Uddeholms Aktiebolag.

Conditions in these coastal waters are: at a depth of less than 5m the salt content varies between 2.2 and 2.8% with a tendency to a higher salt content during the coldest month (February). The pH of the water is approximately 8 and the temperature/time curve reaches a trough of 2°C around February-March and a peak of 18°C around July-August.

After a year's testing the fouling was very heavy. On the whole the test surfaces were completely covered by various sea organisms. The predominant species were balanids,[3] mussles, and algae.

The different grades of steel and surfaces had more or less the same degree of fouling by the various species of sea organisms.

Electrochemical tests, tests B-F.—All of the electrochemical tests performed aimed at investigating the potentiodynamic pitting potential in 5% NaCl or 5% HCl. The critical anodic current density was also investigated in the HCl tests, tests B and C.

The only difference in test condition between these two tests, B and C, was the temperature, 30° and 40°C, respectively.

The potentiodynamic pitting potential in HCl, when scanning in the noble direction with a rate of 20 mV/min from −600 mV E_{SCE}, was defined as the potential in the passive region at which the current starts to increase sharply and not as the potential at which the current density exceeds a certain value; for the NaCl-tests, 10 $\mu A/cm^2$. This is because of the rather varying current density-potential curves in the passive region for the different steels investigated in HCl.

Of the three tests performed in NaCl, D, E, and F, tests D and E differed only in respect to surface treatment, number of trials per grade, and measurements made. See Table II. Otherwise the temperature of the oxygen-saturated NaCl solution was 60°C, and the scanning in the noble direction started at the corrosion potential and at a rate of 10 mV/min for these two tests. Test F, partly performed according to (1), was performed in oxygen-free NaCl solution at a scanning rate of 200 mV/min between −1500 and −300 mV E_{SCE} and 10 mV/min thereafter. At −300 mV E_{SCE} there was a holding time of 15 min. Except from oxygen concentration and electrochemical parameters this test was identical with test E.

Chemical pitting and crevice corrosion tests, tests G-I, K.—Test G was performed in 10% $FeCl_3$, pH 1.3,

[3] Barnacle of the genus Balanus.

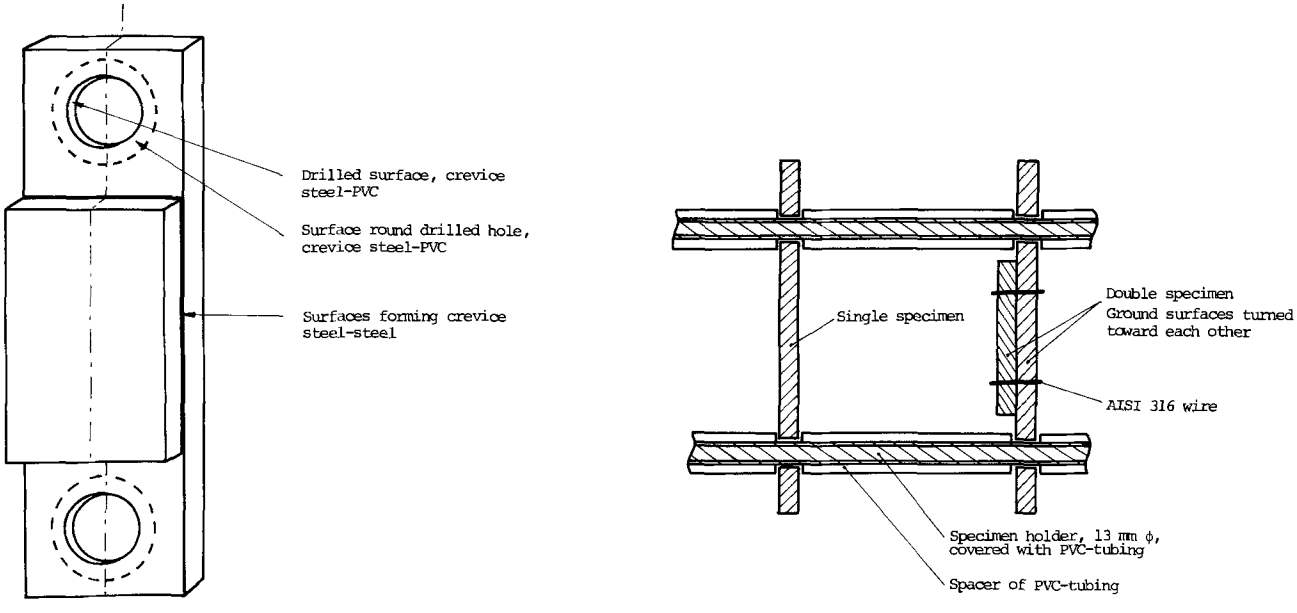

Fig. 2. Mounting of field test specimen; Fig. 2a (right) is double specimen section

at 30°C for 4 hr with one specimen per steel, 50 × 20 × 2 mm, and all surfaces mechanically polished and passivated. Measurements made were number of pits on all surfaces, on rolled surfaces, and weight loss.

Test H was partly performed according to (6). The test media consisted of 0.33 mol Al^{3+}/liter, 0.30 mol Fe^{3+}/liter, 1.81 mol Cl^-/liter, and 3.8 mol H_2O/liter in a solvent of 50% ethanol and 50% glycerol. Solution temperature was 22°C, and test duration 2 hr. The specimen was mounted in plastic resin like the specimens for the electrochemical tests. Thus, one flat side of the specimen was tested. Surface finish was mechanically polished and measurement made was number of pits per unit area.

Test I was performed in 2 and 15% HCl at 22°C with specimens, 50 × 20 × 2 mm, ground on 150 paper and passivated. Test duration for the 2 and 15% HCl solution was 140 and 24 hr, respectively. Total weight loss was measured.

Test K was the only one of the chemical tests which included crevices. These were formed through a close clamping of a flat PVC specimen, 20 × 10 × 2 mm and ground on 80 paper, to one of the flat surfaces of the steel specimen, 50 × 20 × 2 mm and ground on 220 paper, by means of rubber bands. The test was performed in synthetic sea water according to ASTM-D 1141-52 and with 10g $K_3[Fe(CN)_6]$/liter and 10g $K_4[Fe(CN)_6]$/liter added to the water. The temperature was 35°C and the test duration 24 hr.

Measurements made were number of corrosion attacks under the PVC-plate and rubber bands and the relative strength of these attacks. The attacks belonging to the worst ones according to depth and area got the value 3 and those belonging to the intermediate group and the best group, hardly noticeable attacks, got the value 2 and 1, respectively. All attacks on the five tested specimens per investigated steel were divided into these three groups and the number of attacks was multiplied by its group value. Finally these three amounts were added giving the total mark for the steel investigated: *e.g.*, a steel having 3 heavy, 5 medium, and 4 weak attacks got a total mark of $3 \times 3 + 5 \times 2 + 4 \times 1 = 23$.

The regression and correlation analysis was performed in a computer, assuming linear relationship between the different quantities measured. The four ferritic-austenitic steels were excluded from this analysis.

Results and Discussion

The results of the corrosion tests performed are shown in Table III, and those of the regression and correlation analysis, *i.e.*, correlation coefficient (r), intercept, regression coefficient, and standard error of estimate in Table IV.

Field test, test A.—All attacks had taken place on surfaces which during the experiment had formed crevices between steel-PVC tubing and steel-steel and on surfaces covered by balanids, *i.e.*, crevice corrosion. Other surfaces were completely free from local corrosion. The crevice corrosion had taken place mainly round the surface of the drilled holes which had formed a split with the PVC-spacer tubing. Crevice corrosion on the drilled surface itself, crevice steel-PVC, and on the ground surfaces forming a crevice steel-steel was not quite so common.

Normally, the crevice corrosion on the surfaces of the drilled holes covered a comparatively small part of the circumference while the corrosion on the surfaces forming crevice steel-steel was comparatively widespread. In some cases the corrosion on the surfaces of the drilled holes consisted of deep pits in areas with crevice corrosion. Crevice corrosion under fouling organisms, *i.e.*, balanids, took place primarily on the Si-alloyed 18/8 steels.

With regard to maximum depth of attack and number of attacks the following applies to the austenitic stainless steels.

The best group had no attacks with a depth > 0.1 mm. The austenitic steels with Ni contents varying between 13 and 25% and alloyed with Mo combined with N, N plus Si, or Cu were included in this group, *i.e.*, steels 4, 12, 15, and 16.

The second group with few attacks and a maximum depth of corrosion of 0.2-0.4 mm consisted of the 18/8 steels alloyed with Mo combined with N or Si, *i.e.*, steels 3, 10, and 14.

The third group consisted of 18/8 steels alloyed only with Mo and the steel 18/18-2 Si. It should be noted that the steel 18/24-4 Mo is also included in this comparatively poor group, despite its high Ni content. The maximum depth of attack for these steels was between 0.5-1.0 mm. The number of attacks was relatively large. Steels 2, 5, 6, 7, 8, and 13 belonged to this group.

The 18/8 steels without further alloying or alloyed with only Si and/or N were clearly the worst group with maximum depth of attack of 1.5-2 mm and a large number of attacks. Steels 1, 9, and 11 belonged to this group.

The correlation between maximum depth of attack, which is related to propagation resistance, and number of attacks, which is indicative of resistance to passivity breakdown, was rather good, $r = 0.80$.

The well-known beneficial effect of molybdenum as to pitting initiation and propagation [there are certain similarities between the mechanism of formation of pitting and crevice corrosion (7, 8)] and molybdenum combined with nitrogen and/or silicon as to pitting initiation (7, 9-12) is thus clearly shown in this field test, although smaller discrepancies occurred within the groups mentioned, *e.g.*, steel 3 (18/13-3 Mo-N) was somewhat better than steel 14 (18/20-4 Mo-N) with a higher molybdenum content, and steels 6 and 7 with approximately the same composition differed rather widely in respect of maximum depth of attack. One reason for these discrepancies might be that differences in steel structure and composition and distribution of slag inclusions overshadow the effect of minor deviations in steel composition.

This rather good agreement between the field test results and those expected with regard to the composition of the steels and the important fact that the laboratory specimens had been taken out from the field test specimens, *i.e.*, practically the same test surface for all tests performed, make it interesting to let the field test results serve as a reference for the results of the laboratory tests.

It is, however, not quite clear that other sea-water environments, higher temperatures, longer testing times, other evaluation techniques, etc., would have given exactly the same sequence when rating the steels in order of merit.

For more detailed information of the field test results, see (5).

Electrochemical tests.—The scatter, maximum value-minimum value, of the pitting potential results from the tests performed in NaCl was large: mean scatter value of approximately 150 mV.

One contributory explanation of this could be that the specimens, due to their small test area, might or might not expose especially weak points in respect to pitting initiation, *e.g.*, sulfide slag inclusions of dangerous type, *i.e.*, manganese-rich ones. The negative effect of sulfides, especially the duplex and manganese-rich ones as to pitting resistance is clearly shown (13-17).

Although the scatter was large, the results can be regarded as reasonably consistent. This is supported by the good correlation between the tests with large scatter; tests E (5% NaCl, O_2) and F (5% NaCl, N_2).

Table III. Results of corrosion tests

Steel No.	Type analyses	Field test A Calm sea water Max depth of attack A_1	Field test A Calm sea water Number of attacks A_2	Potentiodynamic pitting potential tests B 5% HCl, 30°C I_{Crit}‡ $B_1 \cdot 10^{-3}$	B E_p§ B_2	C 5% HCl, 40°C I_{Crit}‡ $C_1 \cdot 10^{-4}$	C E_p§ C_2	D 5% NaCl, O_2 Ground surface E_p§ D_1	E 5% NaCl, O_2 Etched surface E_p§ Min. E_1	E Mean E_2	Max E_3
1	18/9	1.5	5	†	†	†	†	200	45	103	271
2	18/12-3Mo	1.0	3.5	4	194	1.0	86	225	121	139	173
3	18/13-3Mo-N	0.3	1	2.5	927	0.6	856	770	174	216	320
4	18/13-3Mo-N-Nb	≤0.1*	0	4.2	765	0.9	96	339	144	167	213
5	18/13-3Mo-Nb	1.0	3	5.4	562	0.9	80	248	42	93	110
6	17/14-4Mo	1.0	3	1.4	930	0.2	550	585	112	139	205
7	17/14 4Mo	0.5	3.5	1.9	892	0.4	453	359	230	252	296
8	18/18-2Si	0.8	>10**	52.7	0	14.0	0	246	86	176	445
9	18/14-3.5Si	≈2.0	>10**	77.0	−50	25.0	−90	205	20	50	93
10	17/15-2Mo-3.5Si	0.2	0.5	4.4	952	1.2	40	256	209	331	376
11	18/12-2Si-N	1.4	>10**	61.7	−75	22.0	−80	218	30	55	103
12	18/14-2Mo-2Si-N	≤0.1*	0	3.6	940	1.1	456	283	109	292	398
13	18/24-4Mo	0.8	0.5	1.9	923	0.3	194	425	185	301	364
14	18/20-4Mo-N	0.4	1.5	1.4	926	0.2	938	929	270	303	315
15	20/25-5Mo-1.5Cu	≤0.1*	0	0.6	900	0.2	928	400	270	285	313
16	19/24-3Mo-2Cu-Ti	≤0.1*	0	1.2	938	0.8	180	423	342	835	911
17	25/5-1.5Mo	2.5	3.5	—	—	—	—	287	131	156	207
18	19/5-3Mo-1Si	1.7	3.5	—	—	—	—	225	109	121	156
19	25/5-1.5Mo-N	2.0	2.5	—	—	—	—	723	207	596	875
20	25/5-1.5Mo-N	1.2	7	—	—	—	—	730	203	268	790

* *i.e.* 0.1 in the statistic analysis.
** *i.e.* 10 in the statistic analysis.
† No passivation occurred.
‡ Critical anodic current density, μA/cm².
§ Pitting potential mV E_{SCE}.

Correlation coefficient, r, for minimum, mean, and maximum pitting potential was 0.79, 0.96, and 0.90, respectively.

Out of the three tests performed in NaCl, *i.e.*, tests D, E, and F, not one agreed very well with the field test results if one sees to the mean value of pitting potential and number of attacks on the field-test specimen; r −0.42, −0.55, −0.65, respectively. Test D was least good, probably due to the smaller number of specimens tested.

The correlation between number of attacks and maximum value of pitting potential is still worse: r −0.40 and −0.49 for tests E and F, respectively. The agreement is, however, not too bad when comparing the minimum value of pitting potential with the number of attacks in the field test, r −0.68 and −0.83 for tests E and F, respectively.

The probable reason for the minimum value of pitting potential being more valid than the mean or maximum value of pitting potential is connected to the distribution in the steel of weak points in respect to pitting initiation, *e.g.*, sulfides, and the differences in specimen area used in the field test and the electrochemical tests, respectively. As the area of the electrochemical specimens was much smaller than the crevice area of the field-test specimens and as the smaller the test area the less risk of exposing a weak point belonging to the most dangerous ones, the electrochemical specimen having the lowest pitting potential value ought to correspond better to the crevice surfaces attacked in the field test in respect to weak points than the electrochemical specimens having the highest pitting potential or pitting potentials in the range of mean value.

The tests performed in HCl, tests B and C, agreed very well as far as the critical anodic current density is concerned, r 0.99, and these current density values correlated not too badly with the maximum depth of attack in the field test; r 0.75 and 0.76 for tests B and C, respectively. Both these measured values are to a greater or lesser extent related to propagation resistance.

The correlation between the pitting potential in HCl, according to test B, and number of pits in the field test (both values related to pitting initiation resistance) was good, r −0.91. This is surprising, considering the fact that the pitting potential according to the other HCl test, test C, correlated badly with the number of pits in the field test, r −0.52. The only difference between test B and test C was the temperature, 30° and 40°, respectively.

Having in mind that the tests in HCl were only performed with one specimen per steel, that the highest correlation coefficient related to pitting initiation was achieved with results from the HCl, test B, and that electrochemical tests in HCl give information about propagation resistance, it seems as if HCl is at least as interesting a test solution as NaCl.

The potentiodynamic pitting potential tests performed in HCl and NaCl did not agree very well, r values about 0.5.

Chemical tests.—The results of the accelerated chemical pitting and general corrosion tests did not correspond very well with those of the field test. The correlation coefficients investigated varied between 0.14 and 0.72. Best results were obtained with the ferric-chloride test, but then only with the value "number of pits on rolled surfaces," and the chemical crevice corrosion test K performed in synthetic sea water:

Number of attacks in the field test against relative resistance according to test K, r 0.70.

Maximum depth of attack in the field test against number of pits on rolled surfaces in $FeCl_3$, r 0.67.

Maximum depth of attack in the field test against relative resistance according to test K, r 0.65.

The ferric-chloride test gave some interesting results. When evaluating the results the following was measured: number of pits per square centimeter on rolled surfaces, G_1, number of pits per square centimeter of total surface, G_2, and weight loss, G_3. As mentioned before, G_1 correlated rather well with the results of the field test, while G_2 and G_3 did not. The correlation between G_1 and G_2 was extremely poor, r 0.04, and that

Chemical pitting and crevice corrosion tests									
	F		G			H	I		K
	5% NaCl, N_2		10% $FeCl_3$ at 30°C, pH 1.3			Al^{3+}, Fe^{3+}, and Cl^- in ethanol	HCl		Synthetic sea water
	E_p§		Number of pits per cm^2			and glycerol	Weight loss, $g/m^2 \cdot hr$, in		$K_3/_4[Fe(CN)_6]$
Min.	Mean	Max	Rolled surfaces	All surfaces	Weight loss $g/m^2 \cdot hr$	Number of pits per 0.5 cm^2	2% HCl	15% HCl	Relative resistance
F_1	F_2	F_3	G_1	G_2	G_3	H_1	$I_1 \cdot 10^3$	I_2	K_1
−221	−3	113	3.6	10.2	6.7	1859	673	2.5	25
104	110	138	0.38	18.0	5.1	292	2	2.3	24
146	182	188	0.26	0.61	0.24	259	2	2.5	22
139	149	228	0.25	6.5	0.12	105	1	2.2	13
84	126	145	0.27	45.1	12.8	594	2	3.1	22
188	228	245	0.00	0.51	0.19	117	1	1.2	22
108	195	222	0.67	8.2	1.5	44	3	1.0	13
−93	10	199	0.52	2.6	2.0	375	163	0.74	26
−106	−92	57	5.5	7.3	2.4	440	253	2.7	22
211	254	388	0.00	0.72	0.77	27	343	2.9	12
−200	−124	74	0.52	7.9	1.1	2304	410	3.7	25
63	178	185	0.00	0.10	0.10	33	1	4.2	5
260	291	302	0.27	6.9	0.86	12	4	0.34	6
142	294	304	0.00	0.00	0.19	11	2	0.44	11
253	263	292	0.00	0.00	0.12	5	2	0.24	17
280	976	995	1.9	2.3	0.16	182	3	0.38	3
60	127	136	8.9	12.5	1.3	899	0	37.6	15
79	101	111	8.8	17.2	3.2	1033	3	21.9	20
208	225	280	0.00	0.00	0.00	3	1	36.9	4
308	427	728	0.00	0.00	0.05	407	0	39.6	21

between G_2 and G_3 quite good, r 0.93. Obviously the normally much less pitting-resistant edge surfaces contribute to the poor correlation between G_3, the standard value measured for this type of test, and the results of the field test. It is, however, somewhat surprising that the relative effect of alloying elements, *i.e.*, different steels, on the pitting resistance is not the same for the rolled surfaces and the edge surfaces of the specimen. There are possible reasons for this. One could be that when the flat, elongated slag inclusions, *i.e.*, sulfide slag inclusions, are to a more or less extent dissolved during the passivation treatment in nitric acid, dangerous crevices will be formed on the edge surfaces and not on the flat surfaces. Thus the type, shape, distribution, and number of inclusions could be of much greater importance to the result than the chemical composition of the steel.

The chemical pitting test H, *i.e.*, corrosion in a solution of Al^{3+}, Fe^{3+}, and Cl^- ions in ethanol and glycerol and especially the chemical pitting and general corrosion test I, *i.e.*, corrosion in HCl, seemed to be of little value.

The correspondence between the different accelerated chemical pitting and crevice corrosion tests was poor. None of the calculated correlation coefficient values exceeded 0.55.

Relation between electrochemical and chemical tests.—A comparison of electrochemical and chemical tests shows that the relationship between the two types of test is not very good, r_{max} 0.76.

Some of the more interesting relationships are listed below:

Mean value of pitting potential in NaCl, test E, against relative resistance according to chemical crevice corrosion test K: r −0.76.

Minimum value of pitting potential in NaCl, test E, against relative resistance according to chemical crevice corrosion test K: r −0.69.

Pitting potential in HCl, test B, against number of pits in chemical pitting test H: r − 0.66.

Minimum value of pitting potential in NaCl, test E, against number of pits in chemical pitting test H: r −0.59.

Mean value of pitting potential in NaCl, test E, against weight loss in $FeCl_3$, test G: r −0.38.

Mean value of pitting potential in NaCl, test F, against number of pits on rolled surfaces in $FeCl_3$, test G: r −0.18.

Comparison of tests when rating the steels in order of merit.—As could be expected from the generally poor correlation between the different tests, the sequence when rating the steels in order of merit differs rather widely when comparing the tests.

It seems that the difference in content of alloying elements has to be rather great to achieve a good agreement between the tests. Thus when steels No. 1 (18 Cr-9 Ni), No. 2 (18 Cr-12.5 Ni-3 Mo), No. 7 (17 Cr-14.5 Ni-4.5 Mo), and steel No. 14 (17.5 Cr-19.5 Ni-4.5 Mo-N) are ranked in order of merit according to the different test values measured, the sequence will be the same for 16 out of 20 test values. Those test values which did not agree with the others were I_1, *i.e.*, weight loss in HCl, G_1 and G_2, *i.e.*, number of pits according to the test in $FeCl_3$, and E_3, *i.e.*, maximum value of pitting potential in NaCl.

If another steel with a composition within the range of the composition of the above-mentioned group of steels or with somewhat other content of alloying elements, *e.g.*, silicon and nitrogen, is included in the comparison, problems would arise.

Conclusions

According to the results of this investigation the effect of minor deviations in content of alloying elements in stainless steels on the resistance to localized corrosion in calm natural sea water cannot be evaluated with any degree of certainty by means of the accelerated electrochemical or chemical tests performed.

The agreement between the tests is not acceptable unless the difference in steel composition is at least

Table IV. Results of correlation and regression analysis

Test	Correlation coefficient	Intercept	Regression coefficient	Standard error of estimate
A_1-A_2	0.80	0.30	$1{,}255 \cdot 10^{-4}$	0.36
A_1-B_1	0.75	0.41	$0.2 \cdot 10^{-4}$	0.38
A_1-C_1	0.76	0.42	$0.1 \cdot 10^{-4}$	0.38
A_1-E_2	−0.63	1.17	$-20 \cdot 10^{-4}$	0.47
A_1-F_2	−0.62	0.98	$-15 \cdot 10^{-4}$	0.48
A_1-G_1	0.67	0.48	$2{,}533 \cdot 10^{-4}$	—
A_1-G_2	0.36			
A_1-G_3	0.45			
A_1-I_1	0.56	0.52	$16{,}066 \cdot 10^{-4}$	0.50
A_1-I_2	0.27	0.48	$1{,}208 \cdot 10^{-4}$	0.58
A_1-K_1	0.65	−0.11	$489 \cdot 10^{-4}$	0.46
A_2-B_2	−0.91	8.57	$-85 \cdot 10^{-4}$	1.63
A_2-C_2	−0.52	4.82	$-55 \cdot 10^{-4}$	3.36
A_2-D_1	−0.42	6.01	$-73 \cdot 10^{-4}$	3.48
A_2-E_1	−0.68	7.11	$-261 \cdot 10^{-4}$	2.81
A_2-E_2	−0.55	5.78	$-110 \cdot 10^{-4}$	3.20
A_2-E_3	−0.40	5.54	$-76 \cdot 10^{-4}$	3.52
A_2-F_1	−0.83	4.86	$-194 \cdot 10^{-4}$	2.14
A_2-F_2	−0.65	5.06	$-97 \cdot 10^{-4}$	2.93
A_2-F_3	−0.49	5.33	$-83 \cdot 10^{-4}$	3.35
A_2-G_1	0.50			
A_2-G_2	0.14			
A_2-G_3	0.22			
A_2-K_1	0.70	−2.32	$3{,}308 \cdot 10^{-4}$	2.75
$A_1 \cdot A_2$-E_1	−0.69	10.14	$-419 \cdot 10^{-4}$	4.35
$A_1 \cdot A_2$-E_2	−0.53	7.76	$-166 \cdot 10^{-4}$	5.12
$A_1 \cdot A_2$-E_3	−0.45	8.02	$-135 \cdot 10^{-4}$	5.38
$A_1 \cdot A_2$-F_1	−0.79	6.35	$-291 \cdot 10^{-4}$	3.68
$A_1 \cdot A_2$-F_2	−0.61	6.63	$-145 \cdot 10^{-4}$	4.77
$A_1 \cdot A_2$-F_3	−0.46	7.06	$-125 \cdot 10^{-4}$	5.34
$A_1 \cdot A_2$-G_1	0.72			
$A_1 \cdot A_2$-K_1	0.59	−3.46	$4{,}388 \cdot 10^{-4}$	4.88
B_1-C_1	0.99	$1.04 \cdot 10^{3}$	0.303	$3.17 \cdot 10^{3}$
B_1-E_2	−0.44	$23.6 \cdot 10^{3}$	−60.4	$24.0 \cdot 10^{3}$
B_1-F_2	−0.59	$27.2 \cdot 10^{3}$	−60.5	$21.7 \cdot 10^{3}$
B_1-G_1	0.66	$6.49 \cdot 10^{3}$	$12.0 \cdot 10^{3}$	
B_1-K_1	0.53	$-13.5 \cdot 10^{3}$	$1.75 \cdot 10^{3}$	$22.7 \cdot 10^{3}$
C_1-E_2	−0.44	$9.22 \cdot 10^{4}$	−191	$9.88 \cdot 10^{4}$
C_1-F_2	−0.56	$8.5 \cdot 10^{4}$	−193	$9.13 \cdot 10^{4}$
C_1-K_1	0.50	$-4.3 \cdot 10^{4}$	$5.5 \cdot 10^{3}$	$9.21 \cdot 10^{4}$
D_1-E_2	0.26	313	$2.95 \cdot 10^{-1}$	212
D_1-F_2	0.35	324	$3.04 \cdot 10^{-1}$	205
D_1-K_1	−0.24	491	−6.52	213
E_1-F_1	0.79	109	0.477	61.9
E_1-K_1	−0.69	292	−8.49	72.6
E_2-F_2	0.96	96	0.720	55.6
E_2-G_1	−0.12			
E_2-K_1	−0.76	535	−18.0	152.3
E_3-F_3	0.90	100	0.810	85.9
E_3-K_1	−0.63	568	−15.7	156.2
G_1-B_2	−0.48			
G_1-F_2	−0.18			
G_1-G_2	0.04	0.839	$6.1 \cdot 10^{-3}$	
G_1-K_1	0.23			
G_2-C_2	−0.38			
G_2-E_2	−0.34			
G_2-K_1	0.32			
G_3-C_2	−0.35			
G_3-E_2	−0.38			
G_3-G_2	0.93	$7.0 \cdot 10^{-2}$	0.284	
G_3-K_1	0.45			
H_1-A_1	0.62			
H_1-A_2	0.60			
H_1-$A_1 \cdot A_2$	0.60			
H_1-B_1	0.63			
H_1-B_2	−0.66	925	−0.933	
H_1-E_1	−0.59			
H_1-F_2	−0.47			
H_1-G_1	0.34			
H_1-K_1	0.55			

as great as that between the following steels: 18/9, 18/13-3Mo, 17/15-4.5Mo, and 18/20-4.5Mo-N.

The rather poor correlation between most of the test combinations thus makes it difficult to predict the corrosion resistance in the sea-water environment in question on the basis of just one accelerated test or to relate different tests to each other.

Assuming the results of the field test are representative of the investigated steels in most sea-water environments, the following seems to be true for the accelerated tests performed in regard of their reliability in ranking steels in order of merit for sea-water service:

The electrochemical tests are to be chosen in preference to the chemical tests, when resistance to passivity breakdown is to be investigated.

The minimum value of pitting potential is more reliable than the mean or maximum values.

Pitting potentials obtained in hydrochloric acid are probably more valid than those obtained in sodium chloride.

When investigating the resistance to pitting and crevice corrosion of flat products and tubes in 10% $FeCl_3$ (pH 1, 30°C), it is important that the effect produced on the specimen surfaces perpendicular to the rolled surfaces is excluded from the final evaluation.

Manuscript submitted April 17, 1972; revised manuscript received Aug. 7, 1972.

Any discussion of this paper will appear in a Discussion Section to be published in the December 1973 JOURNAL.

REFERENCES

1. H. P. Leckie, *This Journal*, **117**, 1152 (1970).
2. R. P. Jackson and D. van Rooyen, *Corrosion*, **27**, 203 (1971).
3. B. E. Wilde and E. Williams, *This Journal*, **117**, 775 (1970).
4. B. E. Wilde and E. Williams, *ibid.*, **118**, 1057 (1971).
5. J. Degerbeck, "Proceedings of the 6th Scandinavian Corrosion Congress, Gothenburg 1971," p. 36-1, Ingemar Roos AB, Stockholm (1971).
6. G. Bianchi, A. Cerquetti, F. Mazza, and S. Torchio, *Corrosion Sci.*, **10**, 19 (1970).
7. I. L. Rosenfeld and I. S. Danilow, *Z. Phys. Chem.*, **226**, 257 (1964).
8. J. M. Defranoux, International Nickel. Marine Corrosion Conference in conjunction with the Sea Horse Institute of Harbor Island. Paper No. 3 (Biarritz 1969).
9. O. Steensland, *Anti-Corrosion*, 8 (May 1968).
10. M. A. Streicher, *This Journal*, **103**, 375 (1956).
11. T. N. Rhodin, *Corrosion*, **12**, 465t (1956).
12. G. Riedrich, *Metalltechnik*, **21**, 407 (1942).
13. M. Herthorne, *Corrosion*, **26**, 511 (1970).
14. N. D. Green and B. E. Wilde, *ibid.*, **26**, 533 (1970).
15. L. R. Scharfstein, *Am. Soc. Testing Mater. Spec. Tech. Publ.* No. 418, p. 90 (1967).
16. G. Eklund, *Jernkontorets Ann.*, **155**, 637 (1971).
17. Z. Szklarska-Smialowska *et al.*, *Brit. Corrosion J.*, **5**, 159 (1970).

An Optical Study of the Growth and Oxidation of Nickel Hydroxide Films

M. A. Hopper* and J. L. Ord*

Department of Physics, University of Waterloo, Waterloo, Ontario, Canada

ABSTRACT

The formation and oxidation of nickel hydroxide films under a variety of experimental conditions are studied using *in situ* ellipsometric measurements. Two forms of the hydroxide, which we assume to be the α and β forms reported by other workers, are found. The α- and β-hydroxide layers are both transparent with real refractive indices of 1.52 and 1.46, respectively, at 6328Å. Upon oxidation the two forms of hydroxide convert to different oxides, both of which absorb light. The process involved in the conversion of the β-hydroxide appears to be similar to the process postulated for the charging of the nickel battery electrode.

The complex conversion processes that occur during the charging and discharging of the nickel electrode in a nickel-alkaline battery have been the subject of extensive study over the past fifty years (1). Only recently, however, were some of the details of the mechanism elucidated. In particular x-ray (2, 3) and infrared (4) techniques were applied, with some success, to the determination of the structure and modifications that occur in the solid-state phases involved in the conversion reaction.

Electrochemical investigations of the system are generally performed on nickel electrodes covered with relatively thin films of oxide or hydroxide. The films on the nickel surface are formed using a variety of techniques including deposition of hydroxide from solutions of nickel nitrate (3, 5) and direct oxidation and reduction of the electrode (6, 7). The variation in the behavior reported for the different methods indicates that the properties of the films formed may depend on growth conditions.

In contrast to the extensive studies using ellipsometric methods on the formation of anodic films on nickel in acidic solution (8, 11), only Chernykh and Yakovleva (12, 13) have presented results obtained in strongly basic solution. The present investigation using *in situ* ellipsometric measurements combined with simultaneous studies of the electrical behavior was carried out to determine whether optical techniques could supply additional information on the nature of the process of oxidation of nickel hydroxide in basic solution. This process is of fundamental importance to the understanding of the conversion reactions that occur on charging and discharging the nickel battery electrode. In addition it was hoped that optical methods could determine if the films of nickel hydroxide formed under different conditions showed a similar behavior when oxidized and reduced in basic solution.

Experimental

The self-nulling ellipsometer used in this investigation has been described in detail elsewhere (14). The instrument has a resolution of 0.01° and a typical nulling time of 1 sec for the films formed on nickel in this study. A low-power helium-neon laser is used as the light source for the instrument and all refractive indices reported in this paper are pertinent to its wavelength, 6328Å. All optical measurements were taken with an angle of incidence of 60°. The ellipsometric data were analyzed using a computer program written in BASIC and run on the laboratory HP 2114B computer.

An equilateral hollow glass prism fitted with standard-taper joints for mounting the electrode holder, platinum counterelectrode, mercurous sulfate reference electrode (fitted with a 0.1*N* K_2SO_4 salt bridge), and a gas dispersion tube was used as the electrochemical cell. Argon could be bubbled through the solution but this was not found to have an appreciable effect on the experimental results. All experiments were performed at room temperature (23°).

Single-crystal and polycrystalline samples of nickel were prepared in the form of cylinders and mounted between Teflon washers in the electrode holder. A flat on one side of the cylinder was used as the surface for optical studies. In this configuration approximately 1.2 cm^2 of the metal surface is exposed to the electrolyte. No differences were detected between results obtained with the two types of sample.

Prior to each experiment the nickel surface was chemically polished and then cathodically reduced in the cell to remove any oxide formed on the electrode during the polishing process. In the experiments involving deposition of hydroxide from nickel nitrate solutions, a special procedure was adopted to ensure that the optical readings were disturbed as little as possible after completing the deposition and commencing the oxidation. The method involved draining the cell with the electrode in place, rinsing with distilled water, then adding the solution to be used in the oxidation studies.

The electronic circuitry used with the cell consists of a set of five operational amplifiers, three of which are used to apply constant currents, constant potentials, and linear potential sweeps to the cell. Of the remaining two, one is used in the current-to-voltage converter mode to monitor the cell current and the other as a potential follower.

Results and Discussion

The first experiments were designed to determine the characteristics of the layers formed directly on a nickel substrate by oxidation and reduction in a 5*N* KOH solution. The optical and electrical data obtained on anodically oxidizing the electrode at a current density of 40 $\mu A/cm^2$ followed by cathodic reduction at the same current density are shown in Fig. 1. In the upper section of the figure the polarizer null readings, *P*, are plotted *vs.* the analyzer null readings, *A*. In the lower section of the figure the variation of the potential with time is recorded. The data points start at point A and trace out the curve A-B-C-D-E on oxidation and E-F-G on reduction.

On anodic polarization the optical data show two distinct regions, the section A-B and the section C-D-E. This indicates that layers of different index are formed on the surface in these two regions. On reduction the optical data (E-F) almost retrace the curve C-D-E but the end point of the reduction, point

* Electrochemical Society Active Member.
Key words: ellipsometry, anodic oxidation, nickel.

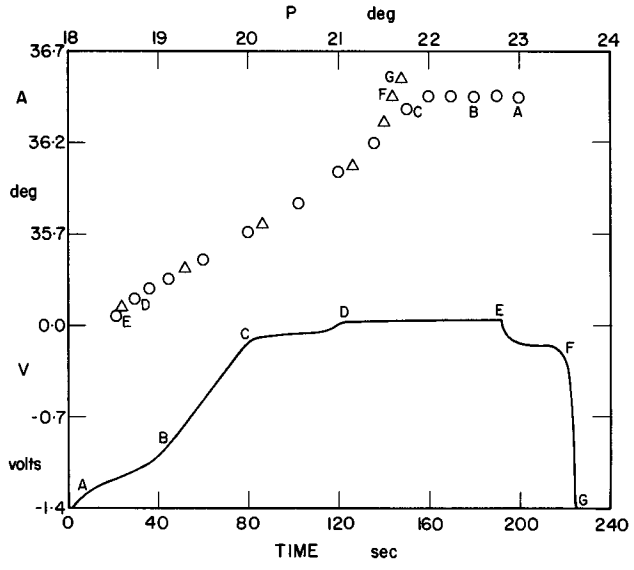

Fig. 1. Anodic oxidation (A-B-C-D-E) and reduction (E-F-G) of nickel at 40 μA/cm^2 in 5*N* KOH.

G, lies at a much lower value of *P* than either points A or B. Further reduction after point G results in no change in the optical data, implying that at this point the surface is covered by a layer of material that cannot be removed by cathodic reduction.

The largest optical changes are observed to occur along CD and EF, corresponding to the plateaus in the potential-time plot. Optical changes of this type are normally interpreted as resulting from growth along CD of a layer of constant index, and removal of the layer along EF. A range of refractive index values can be found which enable the data to be fitted to a process of this type. The values are all complex, indicating that if a film grows along CD it must absorb light. The k values in the complex index, $n - ik$, are on the order of unity for all but the lowest values of n.

Other explanations of the optical data in Fig. 1 are possible. (The major difficulty in interpreting results obtained in ellipsometric studies of thin films is that a unique interpretation of the data is usually impossible.) The charging and discharging of the nickel battery electrode are generally thought to involve conversion between nickel hydroxide and a higher oxide by a mechanism involving proton diffusion (1, 5). Regions CD and EF in Fig. 1 can be fitted to a conversion process, but many parameters can be varied in such a process, and no definite conclusions can be drawn from the fitting.

To decide whether the process is one of layer conversion rather than layer growth and removal, it is necessary to obtain optical data on thicker films. Using thicker films it is possible to determine unique refractive index values for the layers involved, thus permitting a distinction to be drawn between growth and conversion processes.

We found that much thicker layers could be grown on nickel in 5*N* KOH by a process involving prolonged reduction of the electrode combined with repeated cycling between the reduced and oxidized forms of the film. (Prolonged oxidation was found to cause little layer growth.) The optical results obtained using the above procedure to grow thick films are presented in Fig. 2. Points A, E, and G correspond to the same points plotted in Fig. 1. The electrode was subjected to cathodic polarization at 100 μA/cm^2 for a minute followed by anodic oxidation at 40 μA/cm^2 to oxygen evolution, and reduction at this current density until hydrogen evolution begins. This procedure was then repeated with progressively longer periods of cathodic polarization at 100 μA/cm^2. Although ellipsometric readings were recorded continuously during the ex-

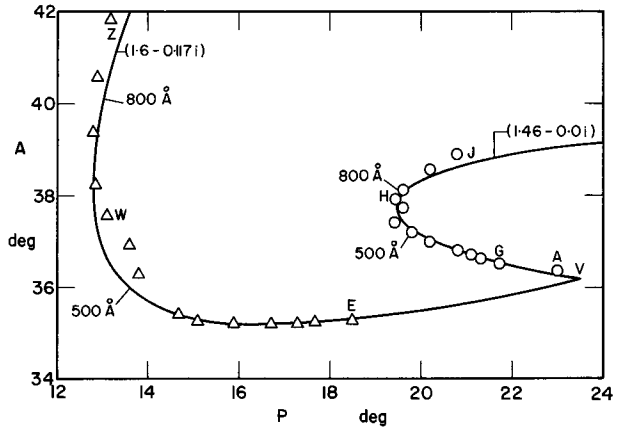

Fig. 2. Optical data on the growth of thick films on a nickel electrode produced by cycling between oxidation (triangles) and reduction (circles) in 5*N* KOH.

periment, only the loci of the optical readings obtained in the fully oxidized state, curve VWZ, and in the state produced on reduction at 40 μA/cm^2, curve VHJ, are plotted in Fig. 2. The data obtained in the reduced state (curve VHJ) are shown fitted to the growth of a film of index 1.46-0.0*i*. The points for the oxidized state (curve VWE) are fitted to the growth of a layer having an index of 1.60-0.117*i*. The value of the refractive index used for the nickel substrate was 2.13-4.31*i*.

The results summarized in Fig. 2 show that the process involved in the oxidation and reduction of a nickel electrode in 5*N* KOH is a conversion from one layer into another of different index, rather than film growth and dissolution. The thickness of both forms increases as the experiment progresses which would indicate that very little film dissolution occurs. Using the values of the refractive index that give the best fit to the locus of the experimental points we find that the thickness of the layer remains almost constant on cycling between the oxidized and reduced forms. For thicknesses greater than 400Å the oxidized layer appears to be thinner than the reduced layer by approximately 10%.

The thin film optical results can be explained by the conversion mechanism using the refractive indices determined from the thick film results. The optical data from Fig. 1 are replotted in Fig. 3 along with theoretical curves for the growth of layers having refractive indices of 1.46-0.0*i* (curve VH) and 1.60-0.117*i* (curve VW) corresponding to the reduced and oxidized forms of the film, respectively. The line shown connecting points D and F is the locus the optical results would take if the process involved uniform growth of a higher oxide film to a thickness of 180Å at the ex-

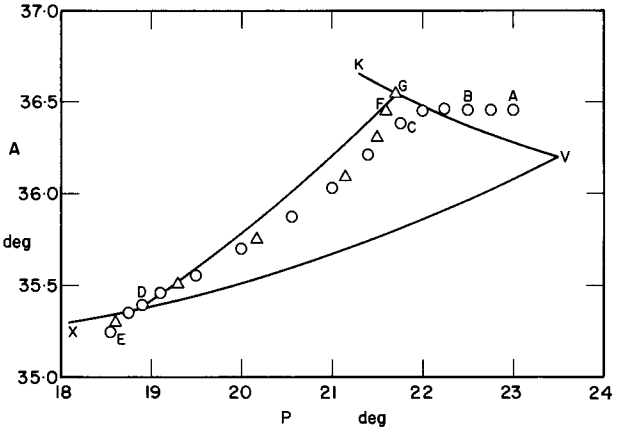

Fig. 3. Optical data from Fig. 1 fitted to the theoretical curves from Fig. 2. G-D is the curve traced out if 180Å of hydroxide are converted to 180Å of oxide.

pense of a layer of hydroxide of initial thickness 180Å and zero final thickness. The experimental data in regions CD and EF fall approximately on this line, indicating that even the first oxidation-reduction cycle involves conversion between layers of nearly equal thickness. The theoretical conversion curve in Fig. 3 is not sensitive to which layer is next to the metal and which is next to the electrolyte. To try and answer this question it is necessary to consider the conversion of a thicker film.

Figure 4 is a plot of the optical data recorded during the oxidation-reduction cycle whose end points are plotted at H and W in Fig. 2. The cycle begins at H with 800Å of hydroxide on the surface, and the data trace out H-C-W on oxidation at 40 μA/cm^2. The thickness of the oxidized film at point W is 730Å. The data trace out W-R-H on reduction at 40 μA/cm^2 to hydrogen evolution. The curves plotted in Fig. 4 are the theoretical loci expected for two models of the conversion process. Curve H-S-W results from a process in which the conversion is initiated at the film-electrolyte interface and proceeds by sweeping the boundary between the oxidized and reduced component layers across the film toward the metal surface. Curve H-B-W results from a similar process initiated at the metal surface and proceeding outward toward the electrolyte.

The data in Fig. 4 fit neither of the plotted processes very closely. Both the oxidation and reduction data exhibit a curvature similar to curve H-B-W over most of the conversion region. The only segment of the data at all similar to curve H-S-W is the final segment of the reduction data. The curvature in the data appears to favor a model for the conversion process which places the hydroxide layer next to the electrolyte and the oxidized layer next to the metal, with the interface between them moving toward the electrolyte on oxidation and toward the metal on reduction. If the data are interpreted as supporting this model, two reasons can be advanced for their poor fit to the model: the presence of a third component not treated in the analysis, and nonuniform progress of the conversion process.

The design of the ellipsometer enables it to detect certain types of nonuniformity in surface films. The stepping-motor drive units produce mechanical vibrations which cannot be damped completely. The vibrations pose no serious problem when uniform films are studied, but with nonuniform films the photomultiplier signal at null has a microphonic component. The recorded data show no evidence of this, but the operator is very conscious of the microphonic signal, having to set the photomultiplier gain and level detector hysteresis to take account of it. The photomultiplier output has a microphonic component across the middle of the conversion regions in Fig. 4, but not at the end

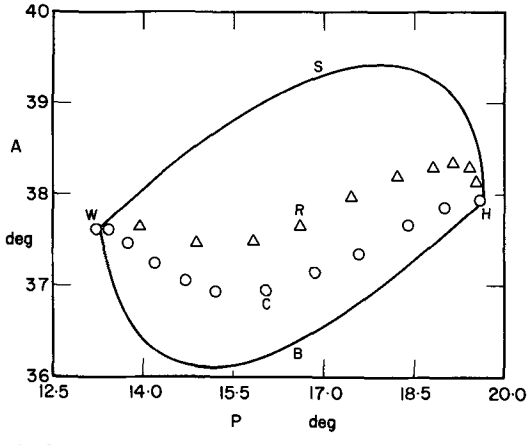

Fig. 4. Conversion of an 800Å film of hydroxide on oxidation (H-C-W, circles) and reduction (W-R-H, triangles) in 5N KOH. The curves represent conversion processes with the higher oxide under (H-B-W) or on top of (H-S-W) the hydroxide film.

points, indicating that during the conversion the surface film is not made up of two component layers of uniform thickness. If the process does not proceed uniformly, no theoretical curve can be calculated for the process, and any conclusions drawn from data obtained during conversion are open to question.

One might expect the oxidation of an anodic oxide film to a higher oxidation state to begin at the interface with the electrolyte, the source of the extra oxygen required. In our experiments we start with a film of hydroxide which can be oxidized without the addition of oxygen from the electrolyte. The hydrogen ions which are also products of the oxidation reaction are thought to migrate to the electrolyte by a diffusion-limited process (1, 5). If this model is valid for the conversion process the oxidation of the hydroxide layer would start at the metal surface and proceed outward toward the electrolyte as the hydrogen ions diffuse out of the film. The interpretation of the data in Fig. 4 as favoring a model with the hydroxide next to the electrolyte and the higher oxide next to the metal, although open to some question, does support a model of this type for the conversion process.

Very similar results to those presented in Fig. 2 were found on applying the same growth procedure to a nickel electrode in 0.2N KOH. This was taken as indicating that the same oxidized and reduced forms occur in this solution as occur in 5N KOH.

Bode *et al.* (3) have shown that nickel hydroxide exists in two forms designated α and β. They state that the α-hydroxide converts into the β-hydroxide on standing in strong KOH solution. In order to determine whether the reduced form of the layer produced in the experiments described above was of the α- or β-form, we next studied the deposition of α-nickel hydroxide films from solutions of nickel nitrate.

The optical data on the growth of α-nickel hydroxide obtained during cathodic deposition at 100 μA/cm^2 are presented in Fig. 5. The film growth starts from point A and traces out the loop A-B-C-D-E as the layer thickens. At point E the optical data have almost returned to the initial conditions, behavior characteristic of a real-index film. Such a film, if grown uniformly, gives cycles of optical data which retrace the initial loop. The data in Fig. 5 retrace the first cycle except at high values of P. We attribute the failure to retrace at high P-values to nonuniformity in the deposition, and fit the data to the curve in the figure for the growth of a film of index 1.52-0.0i. This curve fits the data well up to a thickness of about 1500Å (point C). Each optical cycle represents the deposition of over 3300Å of a film of this index, and we feel that our assumption of film nonuniformity on the second and third cycles is reasonable.

The index of the hydroxide determined in the above experiment is higher than that which we found for the

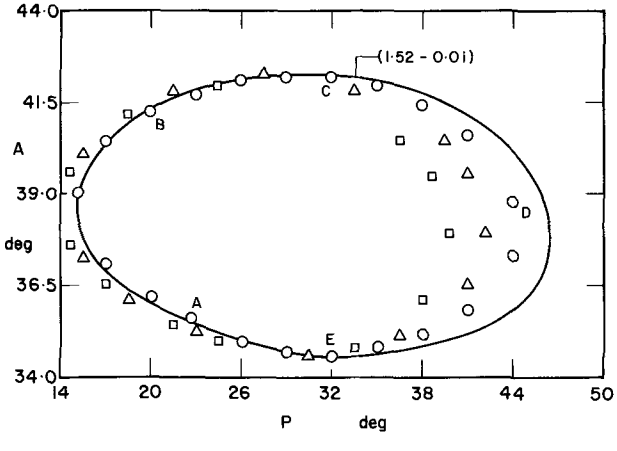

Fig. 5. Three cycles (circles, then triangles, then squares) of optical data on the cathodic deposition of nickel hydroxide onto a nickel substrate from a nickel nitrate solution.

reduced form produced in KOH solutions. This result and the work of Bode *et al.* (3) and MacArthur (5) lead us to assume that the reduced form produced in KOH solution may be identified with the β-hydroxide.

MacArthur (5) has shown that it is possible to oxidize the α-hydroxide to a species called γ-NiOOH in KOH solution, but that repeated cycling between the oxidized and reduced forms is not possible due to the conversion of the α-hydroxide to the β-form. Figure 6 presents the results of an experiment to determine the optical changes that occur on oxidizing α-$Ni(OH)_2$ in 5*N* KOH solution. The small loop A-B-C shows the optical results obtained during the cathodic deposition of approximately 3200Å of α-$Ni(OH)_2$ on the nickel electrode. This curve is shown fitted to the growth of a layer of index 1.52-0.0*i* on a substrate of index 2.12-4.02*i*. The solution of nickel nitrate was then drained from the cell and replaced by a 5*N* KOH solution, without altering the optical alignment of the electrode. On anodic oxidation of the deposited hydroxide at 40 $\mu A/cm^2$ in the KOH solution the optical results trace out the curve D-E-F. Approximately the same path is retraced in the direction F-E-D on reduction of the layer back to the hydroxide form.

Results of experiments similar to that plotted in Fig. 6 but starting with different thicknesses of $Ni(OH)_2$ deposited on the electrode give different values for the refractive index of γ-NiOOH. The real components fall in the range from 1.5 to 2.1 and the imaginary components are all quite significant ranging between 0.4 and 0.8. The variation in the refractive index indicates that the oxidized form is not a homogeneous layer of γ-NiOOH.

The curve D-E-F proved impossible to fit using any relatively simple theoretical model that could describe the conversion process. Following MacArthur (5) and Bode *et al.* (3) we assumed that the conversion is probably from the α-$Ni(OH)_2$ form to γ-NiOOH. Using this model we attempted to fit the observed optical data assuming a two-layer model and allowing uniform conversion of the hydroxide of index 1.52-0.0*i* to the oxidized form both by the formation of an absorbing film on top of and underneath the existing hydroxide. No choice of the thickness conversion ratio for the two forms allows the experimental data to be fitted with this model. In addition, a model assuming that the whole layer converts uniformly from an index corresponding to that of the hydroxide to that of the oxidized form cannot fit the data.

In view of the difficulties described above in determining the refractive index of γ-NiOOH, an alternative method of growing this phase was sought in the hope that this might help determine its optical properties with greater certainty. Guided by the results of experiments we have carried out on nickel electrodes in solutions of different *p*H, we chose a 0.1M sodium borate solution for an attempt at growing γ-NiOOH.

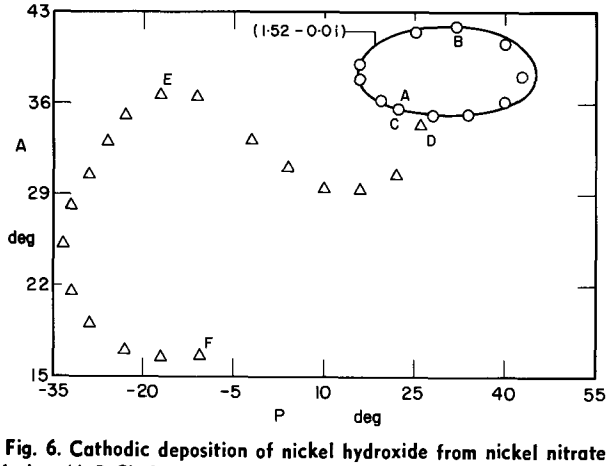

Fig. 6. Cathodic deposition of nickel hydroxide from nickel nitrate solution (A-B-C) followed by anodic oxidation (D-E-F) at 40 $\mu A/cm^2$ in 5*N* KOH.

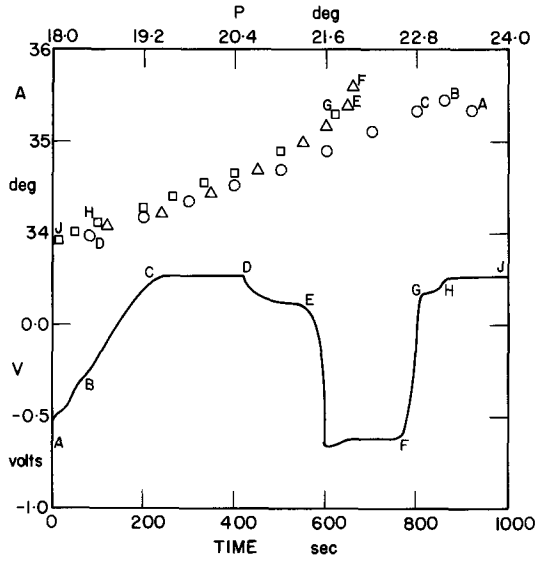

Fig. 7. Anodic oxidation (A-B-C-D, circles), reduction (D-E-F, triangles), and reoxidation (F-G-H-J, squares) of nickel at 20 $\mu A/cm^2$ in 0.1M sodium borate.

The optical and electrical results obtained on oxidizing, at 20 $\mu A/cm^2$, reducing at the same current density and reoxidizing a nickel electrode in 0.1M sodium borate are presented in Fig. 7. The optical results are presented in the upper portion of the figure and the potential-time results in the lower section. The results trace out the curve A-B-C-D on oxidation, D-E-F on reduction, and F-G-H-J on reoxidation. Unlike the oxidation of nickel in 5*N* KOH solution (Fig. 1) there is no evidence of a conversion plateau in the potential-time plot on the first oxidation cycle. The plateau is seen to appear on the first reduction and second oxidation cycles. The lack of a plateau in the potential-time plot for the first oxidation cycle suggests that little $Ni(OH)_2$ forms on the surface in the region A-B-C. In the region C-D a considerable optical change is observed presumably due to the direct formation of an oxide of nickel. On reduction it appears that the oxide is reduced to what is probably a hydroxide. Prolonged reduction does not return the optical results to point A (the "bare" substrate starting point) and it must be concluded that some nonreducible layer remains on the electrode. The second oxidation traces out the curve F-G-H-J and little optical change is observed until point G is reached. A rapid optical change is observed in the region G-H followed by a slower change from H to point J. If anodic polarization is continued after point J optical changes are still observed; these continue for many hours.

Prolonged oxidation of nickel in the sodium borate solution results in the formation of a black film covering the surface. Figure 8 presents the results of an optical experiment on the formation of the thick film by prolonged oxidation. In addition to determining the locus of the optical results for the oxidized film, we reduced the film at intervals during the oxidation to determine the optical properties of the reduced form of this oxide. The curve A-B-C-D in Fig. 8 shows the results obtained for the oxidized species formed in sodium borate, and the curve A-E-F shows the results for the reduced layer. The reduced form is fitted to the growth of a film of index 1.52-0.0*i* on a substrate of index 2.14-4.02*i*. This index is identical to that determined for the film deposited onto nickel from nickel nitrate solutions, and we assume the reduced form of the layer formed in sodium borate to be α-$Ni(OH)_2$. The curve traced out by the oxidized form produced in this solution cannot be fitted to the growth of a uniform layer of constant refractive index. This oxidized layer exhibits optical behavior similar to that of the

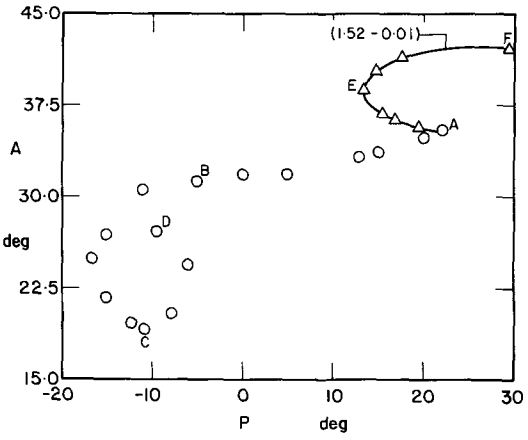

Fig. 8. Optical data on the growth of a thick film (circles for the oxidized form, triangles for the reduced form) produced by extended oxidation of nickel at 40 μA/cm^2 in 0.1M sodium borate.

layer formed by oxidation of the cathodically deposited α-Ni(OH)$_2$, and, although a definite value cannot be determined for the refractive index in either case, we conclude that both films are inhomogeneous layers made up mainly of γ-NiOOH. Curve A-B-C-D in Fig. 8 is produced by the growth of the γ-NiOOH layer in borate electrolyte whereas curve D-E-F in Fig. 6 is produced by conversion of deposited α-Ni(OH)$_2$ to γ-NiOOH.

Conclusions

Using ellipsometric measurements we have shown that two different forms of Ni(OH)$_2$ may be grown on a nickel substrate under appropriate conditions. The α-form, of refractive index 1.52-0.0i, may be grown by cathodic deposition from solutions of nickel nitrate or by reduction of the film produced by prolonged oxidation of a nickel electrode in sodium borate solution. The β-form, of refractive index 1.46-0.0i, may be produced by direct oxidation and reduction of a nickel electrode in concentrated solutions of KOH.

On anodic oxidation the two forms of nickel hydroxide are converted into absorbing films with different refractive indices. The α-Ni(OH)$_2$ converts to an inhomogeneous film which absorbs light strongly, but whose index we are unable to determine. We assume that this layer is composed mainly of γ-NiOOH. The β-Ni(OH)$_2$ converts to a layer of refractive index 1.6-0.11$7i$ which we assume to be β-NiOOH. During conversion of the β-Ni(OH)$_2$ the optical analysis is complicated by nonuniformity in the thicknesses of the component layers, but the data generally favor a model with the β-Ni(OH)$_2$ next to the electrolyte and the β-NiOOH next to the metal.

Our conclusions differ from those reached by Chernykh and Yakovleva (12, 13) in a study of the potentiostatic oxidation of nickel in 2N KOH carried out using a conventional ellipsometer with light of wavelength 5461Å. A comparison of our work with theirs illustrates the problems involved in interpreting thin-film ellipsometric data. They follow the approach which Bockris, Reddy, and Rao (9) used in interpreting optical data obtained in acid electrolyte. In this approach, the surface is assumed to be covered by a single layer whose thickness, real index component, and imaginary index component can all vary with potential. They assume an unspecified value between 2.8 and 3.3 for the real component of the index of the layer formed in 2N KOH, and conclude that (*i*) the layer thickness increases considerably as the potential is raised, and (*ii*) the imaginary index component first decreases then increases due to a change in the nature of the conductivity as the potential is raised. In our analysis of thin-film data, we use refractive index values determined from measurements on thicker films and find that the data fit a process in which one layer converts to another of approximately the same thickness.

Acknowledgment

This work received partial support from the Defence Research Board of Canada under Grant 5480-28.

Manuscript submitted May 9, 1972, revised manuscript received Sept. 27, 1972.

Any discussion of this paper will appear in a Discussion Section to be published in the December 1973 JOURNAL.

REFERENCES

1. S. V. Falk and A. J. Salkind, "Alkaline Storage Batteries," John Wiley & Sons, Inc., New York (1969).
2. S. U. Falk, *This Journal*, **107**, 661 (1960).
3. H. Bode, K. Dehlmelt, and J. Witte, *Electrochim. Acta*, **11**, 1079 (1966).
4. F. P. Kober, *This Journal*, **114**, 215 (1967).
5. D. M. MacArthur, *ibid.*, **117**, 422 (1970).
6. J. L. Weininger and M. W. Breiter, *ibid.*, **111**, 707 (1964).
7. M. A. Sattar and B. E. Conway, *Electrochim. Acta*, **14**, 695 (1969).
8. A. K. N. Reddy, B. Rao, and J. O'M. Bockris, *J. Chem. Phys.*, **42**, 2246 (1965).
9. J. O'M. Bockris, A. K. N. Reddy, and B. Rao, *This Journal*, **113**, 1133 (1966).
10. A. K. N. Reddy and B. Rao, *Can. J. Chem.*, **47**, 2687 (1969).
11. A. K. N. Reddy and B. Rao, *ibid.*, **47**, 2693 (1969).
12. Y. N. Chernykh and A. A. Yakovleva, *Soviet Electrochemistry*, **7**, 510 (1971).
13. Y. K. Chernykh and A. A. Yakovleva, *ibid.*, **7**, 513 (1971).
14. J. L. Ord, *Surface Sci.*, **16**, 155 (1969).

Passivity and Pitting of Al, Ni, Ti, and Stainless Steel in $CH_3OH + H_2SO_4$

Florian Mansfeld*

North American Rockwell Science Center, Thousand Oaks, California 91360

ABSTRACT

The polarization behavior of Ti and Ti alloys, Ni, Al 6061, stainless steel Type 304, Fe, Cu, and Pt has been studied in methanolic solutions containing sulfuric acid. As in solutions of $CH_3OH + HCl + H_2O$, pitting occurs on Ti alloys in solutions of H_2SO_4 in CH_3OH. Addition of 1% H_2O to 0.1*N* H_2SO_4 in CH_3OH leads to a broad region of passivation. Addition of 1% H_2O to 0.1*N* H_2SO_4 in CH_3OH does not effect the polarization curves of nickel in the cathodic region and the region of active dissolution. The water addition leads, however, to passivation on further anodic polarization. Pitting is observed after polarization in the transpassive region. Iron cannot be made passive in 0.1*N* H_2SO_4 in CH_3OH with additions of up to 10% H_2O. Stainless steel is readily passivated in 0.1*N* H_2SO_4 in CH_3OH without addition of water, but pitting is observed after polarization in the transpassive region. Al 6061 suffers from severe pitting when polarized anodically in 0.1*N* H_2SO_4 in CH_3OH free of water additions. Copper shows no active-passive transition in CH_3OH-H_2SO_4 solutions. Experiments with Pt show that methanol is decomposed at potentials higher than +1.0V *vs.* SCE. Contrary to susceptibility in aqueous solutions containing halides, Ti is more susceptible to pitting in CH_3OH containing H_2SO_4 than Al 6061, Ni, and stainless steel 304.

In a previous paper (1), it was shown that water plays a crucial role in determining whether titanium can become passive in solutions of CH_3OH and HCl. In anhydrous solutions Ti could not be passivated even upon anodic polarization. Upon addition of small amounts of water, passivity was observed but pitting occurred at potentials only slightly noble to the corrosion potential. With increasing water content, the pitting potential became more noble. It has also been shown elsewhere that water has a pronounced effect on the stress corrosion cracking (SCC) behavior of Ti alloys (2). Depending on the stress level and the resulting type of failure, water can increase or decrease the rate of crack propagation (3).

The studies concerning the anodic behavior of Ti alloys have now been extended to methanolic solutions containing sulfuric acid. These solutions are of particular interest, since it was shown by Mori and co-workers (4) that SCC of Ti occurs in methanol solutions containing HCl or H_2SO_4. On the other hand, it is usually believed that chloride ions but not sulfate ions cause SCC and a patent has been issued (5) which describes inhibition of SCC of Ti alloys by adding oxyanions such as sulfate to aqueous or methanolic solutions containing chlorides. Studies of passivation characteristics in these solutions are also of interest, since they might indicate whether the oxygen used to form the passive film comes from the sulfate ion as suggested by Evans (6) or from the water molecule.

Since initial experiments with Ti in 0.1*N* H_2SO_4 in CH_3OH provided some rather unusual results, additional experiments were carried out with Ni, Fe, Cu, Al 6061, and stainless steel 304. The results of these investigations are reported in this paper.

Experimental

Unlike the case of methanolic solutions containing HCl, anhydrous solutions of $CH_3OH + H_2SO_4$ cannot be prepared. The solution of 0.1*N* H_2SO_4 in CH_3OH used for most tests contains only 0.04% H_2O, while a solution of 1.0*N* H_2SO_4 in CH_3OH contains 0.4% H_2O as determined by Karl Fischer titration.

Potentiostatic polarization curves were obtained by increasing the potential stepwise every 30 sec in 10, 20, or 40 mV increments; the step height depending on the rate of the anodic or cathodic reaction. In most experiments a cathodic polarization curve was recorded first, the potential was then made more positive, and an anodic curve was recorded. Solutions were either air saturated (but unstirred) or deaerated and stirred by argon. All potentials were measured *vs.* SCE, which was positioned in a separate compartment to avoid contamination of the electrolyte by chloride ions or water. A Luggin capillary was used to minimize the *iR*-drop. After each experiment the electrodes, which were in the form of cylinders, were examined in an optical microscope.

Results

Titanium and Ti alloys.—Polarization curves were obtained for pure Ti (iodide), Ti-75A, and Ti-6Al-4V. No significant differences in the polarization behavior were observed for different alloy compositions. Figure 1 shows polarization curves for pure Ti in 0.1*N* H_2SO_4 in CH_3OH. In the absence of water starting from the corrosion potential, a cathodic polarization curve has been obtained with a Tafel slope of $b_c \approx 0.09$V. This cathodic polarization apparently resulted in reduction of the surface oxide and a lowering of the hydro-

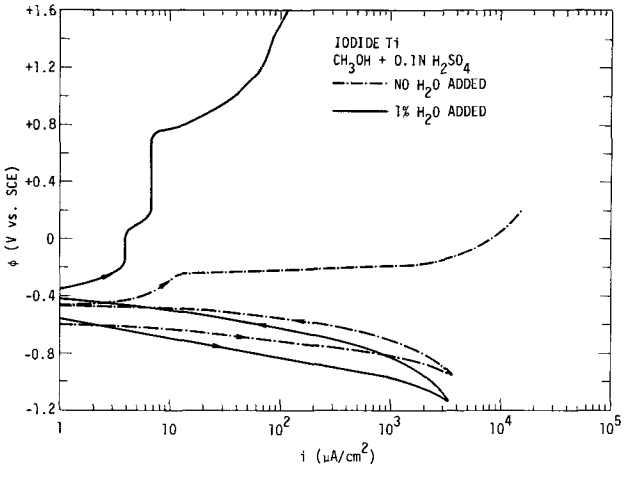

Fig. 1. Potentiostatic polarization curves for pure Ti in 0.1*N* H_2SO_4 in CH_3OH, argon stirred.

* Electrochemical Society Active Member.
Key words: sulfate pitting, active dissolution, anodic and cathodic polarization curves, effect of water additions, photomicrographs.

gen overvoltage as can be seen from the cathodic curve obtained on shifting the potential in the more noble direction. This effect might also result from formation of Ti hydrides which are assumed to have a hydrogen overvoltage lower than oxide covered Ti (16). On the anodic branch of the curve, a short region of passivity can be detected, at about −0.24V *vs.* SCE a sharp increase of the current occurs. Examination of the electrode after the experiment showed that localized attack in the form of pitting had occurred (Fig. 2).

When 1% of water was added to the test solution, the Ti electrode apparently was in the passive state. The anodic current remained small and constant up to about +0.7V (Fig. 1). At higher potentials the current increased steadily, but not as sharply as in water free solutions. These findings are similar to those reported for CH_3OH + HCl (1).

Nickel.—Figure 3 shows the effect of water on the polarization behavior of pure nickel (99.9%) in 0.1*N* H_2SO_4 in CH_3OH. The cathodic branches and the anodic branches of the polarization curves were identical up to +0.2V for solutions with 1% H_2O and without added H_2O. A decrease of the current was observed upon further anodic polarization indicating passivation in the solution containing added water, while only a very small decrease of the current was observed at +0.35V in solutions where no water had been intentionally added. These results show that water has no influence on the kinetics of the hydrogen evolution reaction

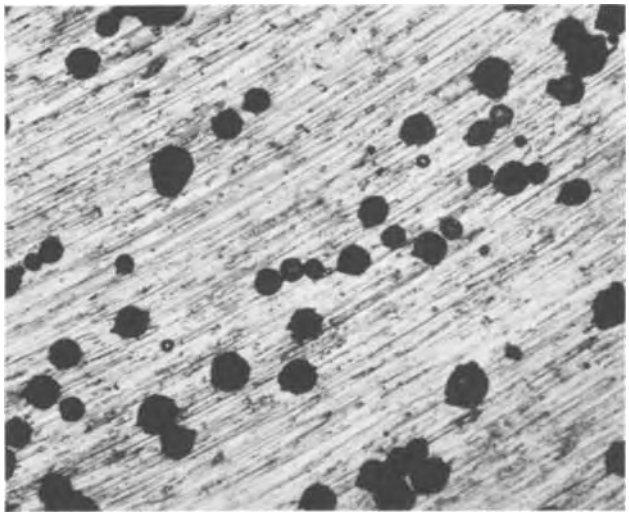

Fig. 2. Pits on surface of Ti after anodic polarization in 0.1*N* H_2SO_4 in CH_3OH without water addition. Magnification approximately 180X.

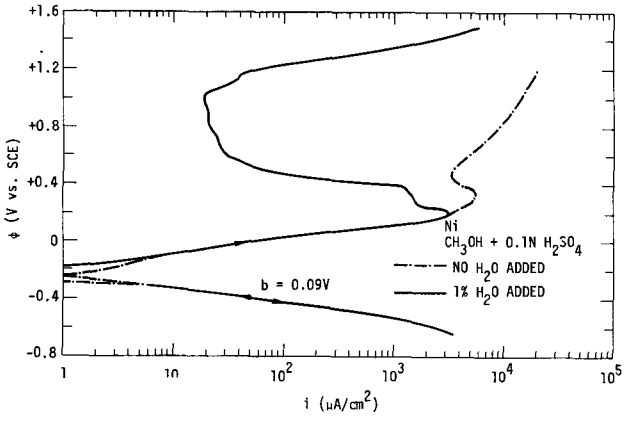

Fig. 3. Potentiostatic polarization curves for nickel in 0.1*N* H_2SO_4 in CH_3OH with and without addition of 1% H_2O, argon stirred.

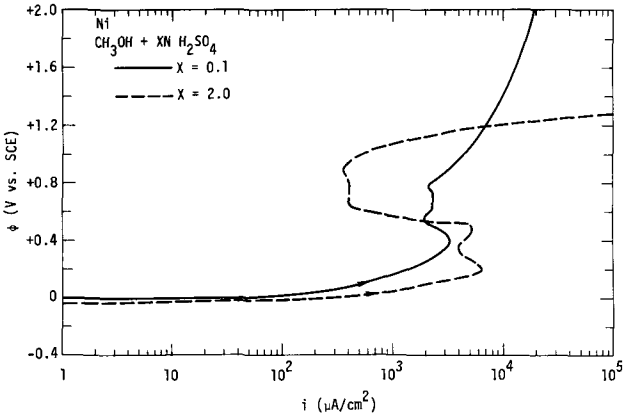

Fig. 4. Potentiostatic polarization curves for nickel in 0.1*N* H_2SO_4 in CH_3OH and 2*N* H_2SO_4 in CH_3OH.

(HER) and on active dissolution. The water plays, however, a decisive role in passivation. Figure 4 shows the effect of H_2SO_4 concentration in methanol. While an increase in acid concentration leads to an increase in the critical current density (C.D.) for passivation, it also leads to a decrease of the passive C.D. The latter effect most likely results from the higher water content inherent in the solution of 2*N* H_2SO_4 in CH_3OH. Pitting of the electrode was observed after the anodic polarization experiments in 2*N* H_2SO_4 in CH_3OH (Fig. 5).

Iron.—The next transition metal studied was pure iron. No passivation occurred in 0.2*N* H_2SO_4 or 2*N* H_2SO_4 in methanol up to a potential of +0.8V *vs.* SCE. The effect of water addition is different than that in the case of Ti or Ni. Additions of water up to 10% did not produce passivation upon anodic polarization, but increased the rate of anodic dissolution reaction (Fig. 6). The corrosion rate of iron in 0.1*N* H_2SO_4 in CH_3OH was very high compared to that of Ti or Ni in the same medium. Using polarization resistance measurements and extrapolation of potentiostatic polarization curves to the corrosion potential, an average corrosion C.D. of 0.32 mA/cm² was measured for iron, which corresponds to 800 mdd (mg/dm² day).

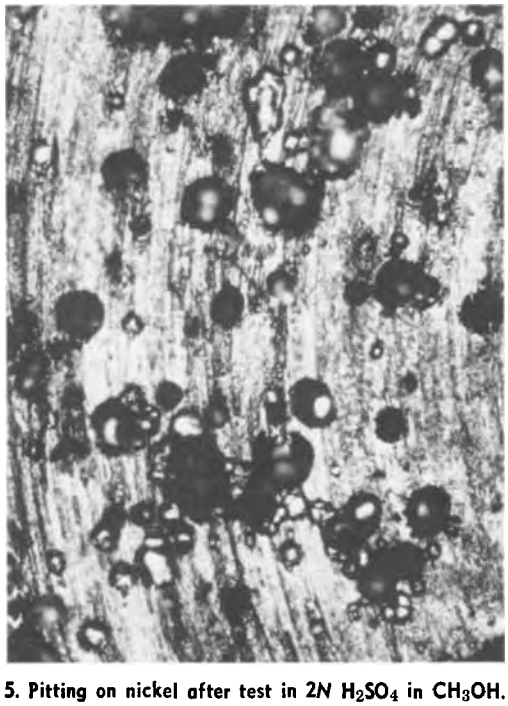

Fig. 5. Pitting on nickel after test in 2*N* H_2SO_4 in CH_3OH. Magnification approximately 180X.

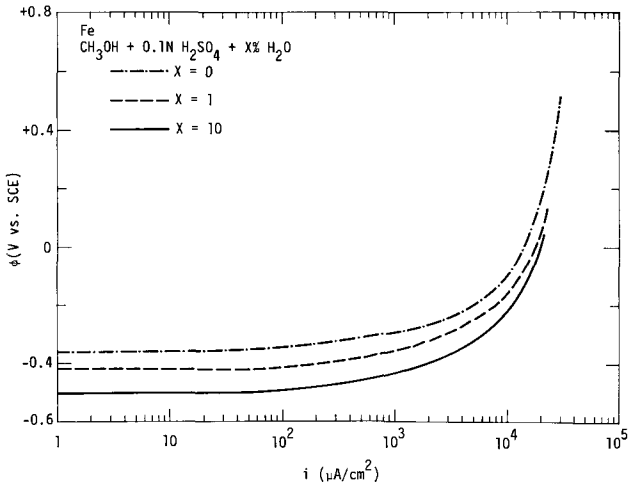

Fig. 6. Potentiostatic polarization curves for Fe in solutions of 0.2*N* H_2SO_4 + X% H_2O (X = 0, 1, or 10) in CH_3OH.

Stainless steel Type 304.—Contrary to iron, stainless steel Type 304 is readily passivated at rather low potentials in 0.1*N* H_2SO_4 (Fig. 7) or 1.0*N* H_2SO_4 in CH_3OH. The active to passive transition in Fig. 7 is only observed after cathodic reduction of the surface film formed in air or in solution. At potentials higher than +1.1V *vs.* SCE a rapid increase of the current was observed. Microscopic observation of the surface of the test specimen showed that pitting had occurred (Fig. 8a). The area around the pits appears to be attacked as shown in Fig. 8b, unlike the results for Ti, Al, and Ni.

Al 6061.—The corrosion rate of Al 6061 in 0.1*N* H_2SO_4 in CH_3OH was low (about 0.2 mdd). The potentiostatic polarization curve is shown in Fig. 9. When the specimen is polarized in the cathodic direction, the current starts to increase continuously with time at potentials more negative than −1.0V. This leads to the loop in the cathodic polarization curve shown in Fig. 9. Upon anodic polarization, the Al alloy is in the passive state up to about 0.0V when the current increases very sharply due to pitting. Gas evolution from the pits is observed under these conditions. Very large pits are observed as shown in Fig. 10. Similar results were obtained in 1.0*N* H_2SO_4 in CH_3OH. The effect of water additions has not yet been studied.

Copper.—The anodic polarization curve for Cu (Fig. 11) was similar to that observed in aqueous H_2SO_4. No active-passive transition was observed up to an applied potential of +2.0V. The anodic current at potentials more noble than about 0.0V *vs.* SCE increased when the solution was stirred by argon, indicating that the anodic process is limited by mass transport in this potential region.

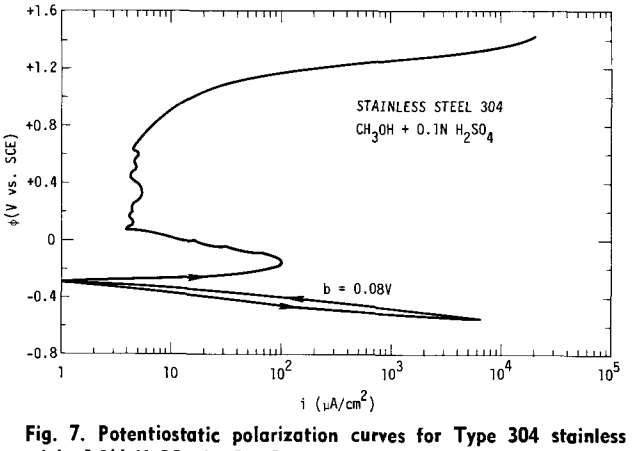

Fig. 7. Potentiostatic polarization curves for Type 304 stainless steel in 0.1*N* H_2SO_4 in CH_3OH, argon stirred.

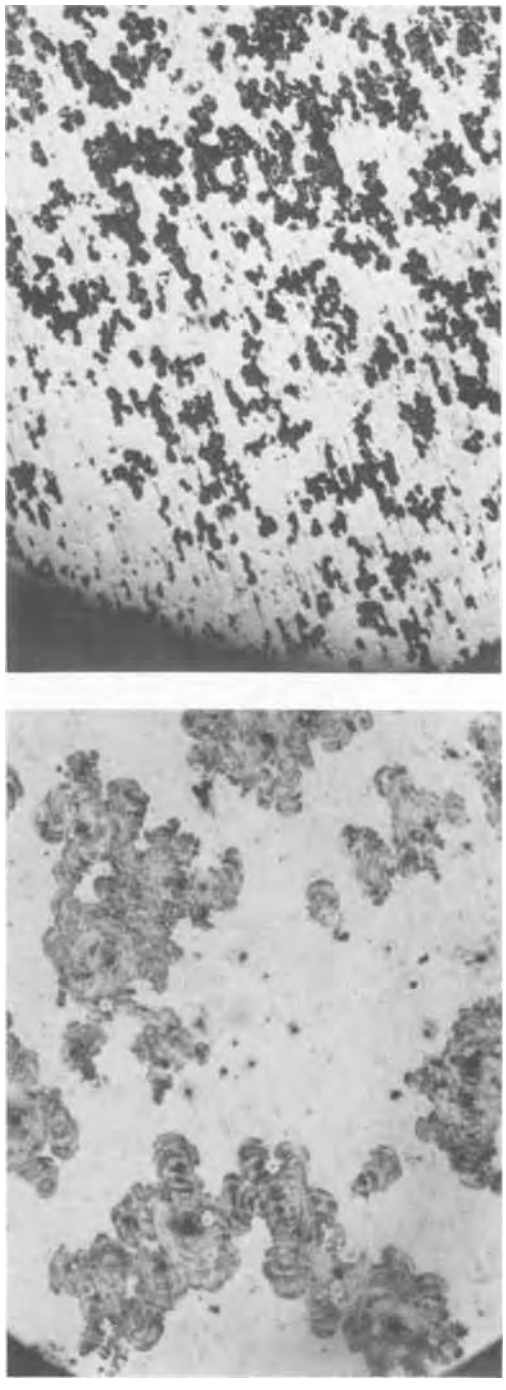

Fig. 8. Pitting on Type 304 stainless steel after anodic polarization in 0.1*N* H_2SO_4 in CH_3OH (Fig. 7). a (top). Magnification approximately 45X. b (bottom). Magnification approximately 180X.

Platinum.—Experiments on platinum were carried out in order to investigate the stability of the electrolyte. Figure 12 shows a polarization curve which was started at −0.8V *vs.* SCE. Tafel behavior with a Tafel slope of b_c = 45 mV is observed over 4 decades, the deviations at higher C.D. are most likely due to uncompensated *iR*-drops. The anodic current remains low up to about +1.0V, from where it increases continuously. This is most likely due to oxidation of methanol as also observed by Stolica on Pt in LiCl-CH_3OH-H_2O solutions (7). No oxygen evolution has been observed on Pt or any other metals studied.

Discussion

Since only potentiostatic polarization curves have been presented here, no conclusions concerning the mechanisms of the hydrogen evolution reaction, passiv-

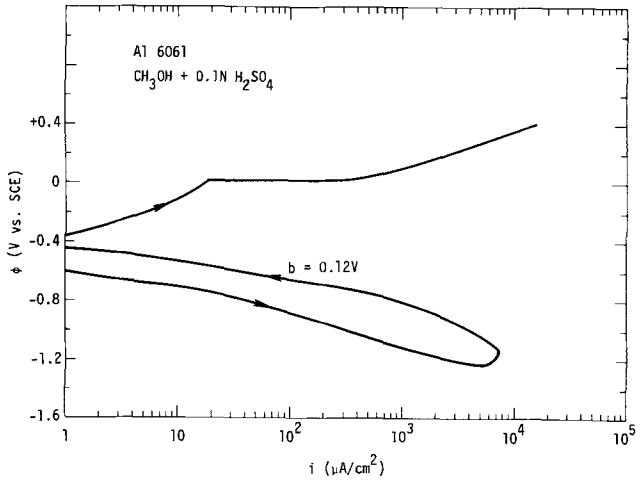

Fig. 9. Potentiostatic polarization curves for Al 6061 in 0.1*N* H_2SO_4 in CH_3OH, argon stirred.

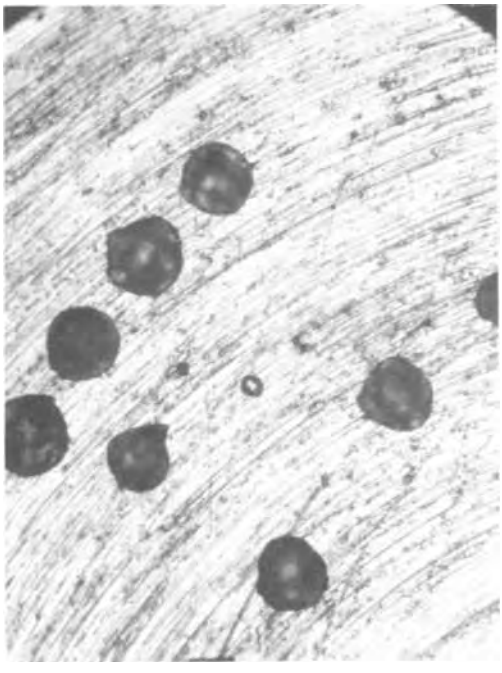

Fig. 10. Pitting on Al 6061 after anodic polarization in 0.1*N* H_2SO_4 in CH_3OH, argon stirred. Magnification approximately 45X.

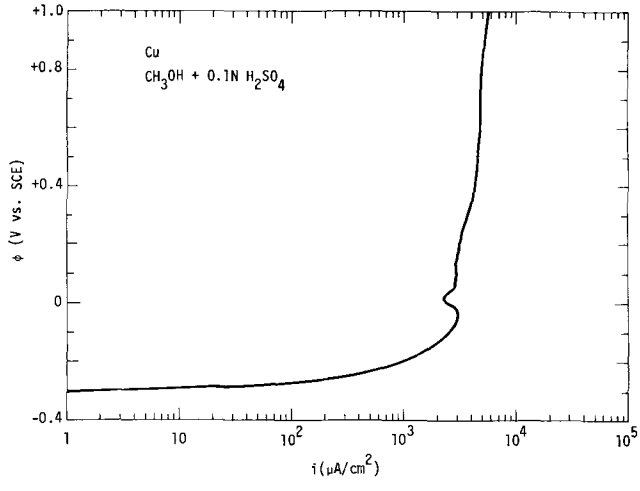

Fig. 11. Potentiostatic polarization curve for Cu in 0.1*N* H_2SO_4 in CH_3OH, deaerated.

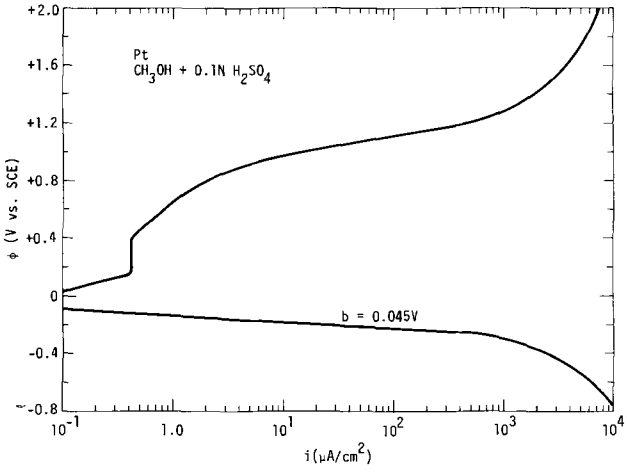

Fig. 12. Potentiostatic polarization curves for Pt in 0.1*N* H_2SO_4 in CH_3OH, argon stirred.

ity, and/or pitting can be drawn. The results obtained here and in Ref. (1) have shown, however, that studies in methanol containing H_2SO_4 or HCl can result in valuable contributions toward a better understanding of basic corrosion reactions.

Effect of water.—In a recent paper (1), it has been shown that for Ti in CH_3OH + HCl the oxygen needed for the formation of the passive film comes from the water molecule. Experiments on Ti in 0.1*N* H_2SO_4 in CH_3OH (Fig. 1) show that water also has a passivating effect in these solutions. It cannot be decided unambiguously whether the small region of passivity observed in 0.1*N* H_2SO_4 in CH_3OH containing about 0.04% H_2O results from adsorption of the oxygen from the sulfate or from the water. By analogy with the results obtained in HCl-CH_3OH solutions and because of the large effect of the addition of 1% H_2O on passivity, it seems logical that the initial step in the passivation reaction on Ti is

$$Ti + H_2O \rightarrow Ti \cdot O_{ads} + 2H^+ + 2e^- \qquad [1]$$

where $Ti \cdot O_{ads}$ represents oxygen adsorbed on Ti.

The results obtained for Ni (Fig. 3) support the assumption that water is responsible for passivation. For iron, on the other hand, no passivation could be observed even with water additions of up to 10% (Fig. 6). Additions of water in fact increased the anodic dissolution current in the potential range studied. A similar behavior was found by Kiss and co-workers (8) for iron in acetic acid containing 0.5M HC_3COONa or 0.5M $HClO_4$. Additions of water in each case accelerated the rate of active dissolution. The authors concluded that in sodium acetate solutions passivation occurs only in the presence of water, while in solutions containing perchloric acid passivation occurred only in the absence of water. For stainless steel 304 it was found in the present study (Fig. 7). that very small amounts of water (about 0.04%) are sufficient for passivation. These results show that many factors determine the ability of a metal to passivate. These may include the electronic structure (14), the relative affinity to oxygen (9), and the characteristics of ion pairs formed in solution (8).

When the results for nickel and iron are compared, it becomes evident that water molecules also have a different effect on the region of active dissolution of these metals. While the rate of the anodic dissolution reaction is not affected by water in the case of nickel (Fig. 3), it increases with increasing water content in the case of iron (Fig. 6). An increase in the acid concentration apparently increases the rate of anodic dissolution of nickel and the critical C.D. for passivation (Fig. 4). In the passive region, the passivating effect of the higher water concentration is stronger

than the activating effect of the higher acid concentration in 2*N* H_2SO_4 in CH_3OH.

Pitting produced by sulfate ions.—It has been observed in this investigation that all metals which undergo passivation also suffer from localized attack in the form of pitting. This is a very surprising result since pitting is usually observed only in the presence of halides, especially chloride ions. Anions like sulfates, nitrates, perchlorates, and chromates have been shown by Uhlig and co-workers to inhibit pitting of iron (10), 18Cr-8Ni stainless steel (11), and Al (12) in aqueous solutions containing halides. Tousek (13) recently pointed out, however, that there is no apparent reason why some of these anions should not lead to pitting. It was shown (13), that under certain conditions pitting can be produced by sulfates on iron and nickel in aqueous acid solutions containing both sulfate and chloride ions. Tousek also mentions briefly that "some sort of pitting corrosion" by sulfate ions occurs in a solution of 2*N* H_2SO_4 and 2% H_2O in CH_3OH resulting in a polarization curve which is similar to that shown in Fig. 4.

Since pitting on nickel and stainless steel is observed at potentials where methanol decomposition occurs ($\phi > 1.0$V) as shown on Pt (Fig. 12), it cannot be concluded solely from the increase of the anodic current that localized attack has occurred. Microscopic observation (Fig. 5 and 8) has confirmed, however, that pitting occurred in both cases. The possibility of reaction between oxidation products of methanol (HCHO, HCOOH) and the passive film has not yet been studied.

It is quite remarkable that Ti, which is so resistant to pitting in aqueous solutions containing halides, is more susceptible to pitting than Al 6061, nickel, and stainless steel in H_2SO_4-CH_3OH. The degree of susceptibility of Ti is similar in H_2SO_4-CH_3OH and HCl-CH_3OH (1). Although this author does not believe that SCC results from a pitting-type attack, there is a striking resemblance in the susceptibility of Ti to pitting and SCC in these solvent systems. This behavior suggests that the nature of the passive film and its rate of formation is different in aqueous solutions (NaCl) and methanolic solutions containing small amounts of water. Recent results by Smith and Mansfeld (15) have shown, however, no differences of film properties in these two media, as measured by ellipsometry.

Acknowledgment

The author thanks D. H. Hern for help in carrying out many of the experiments.

Manuscript submitted June 21, 1972; revised manuscript received Sept. 25, 1972.

Any discussion of this paper will appear in a Discussion Section to be published in the December 1973 JOURNAL.

REFERENCES

1. F. Mansfeld, *This Journal*, **118**, 1412 (1971).
2. F. Mansfeld, Proc. Int. Congress on Stress Corrosion Mechanisms in Ti Alloys, Atlanta, Ga., 1971, NACE.
3. B. S. Hickman, H. L. Marcus, and J. C. Williams, *Ibid.*
4. K. Mori, A. Takamura, and T. Shimose, *Corrosion*, **22**, 29 (1966).
5. U. S. Patent 3,529,928.
6. U. R. Evans, *Electrochim. Acta*, **16**, 1825 (1971).
7. N. D. Stolica, Extended Abstracts, 5th Int. Congress Metallic Corrosion, Tokyo, May 1972, p. 131.
8. L. Kiss, L. DoNgoc, and M. L. Varsányi, *Collection Czech. Chem. Commun.*, **36**, 914 (1971).
9. U. R. Evans, Private communication.
10. S. Matsuda and H. H. Uhlig, *This Journal*, **111**, 156 (1964).
11. H. H. Uhlig and J. R. Gilman, *Z. Phys. Chem.*, **226**, 127 (1964).
12. H. Böhni and H. H. Uhlig, *This Journal*, **116**, 906 (1969).
13. T. Tousek, *Corrosion Sci.*, **12**, 15 (1972).
14. H. H. Uhlig, *Z. Elektrochem.*, **62**, 626 (1958); F. Mansfeld and H. H. Uhlig, *This Journal*, **117**, 427 (1970).
15. T. Smith and F. Mansfeld, *This Journal*, **119**, 663 (1972).
16. R. D. Armstrong, J. A. Harrison, H. R. Thirsk, and R. Whitfield, *ibid.*, **117**, 1003 (1970).

The Interpretation of Impedance Changes on Oxide-Coated Aluminum Produced by Immersion in Inhibitive and Corrosive Aqueous Media

J. A. Richardson[1] and G. C. Wood

Corrosion and Protection Centre,
University of Manchester Institute of Science and Technology, Manchester, England

ABSTRACT

The time dependencies of capacitance and dissipation factor, for aluminum specimens supporting air-formed or anodic films, have been measured at 10^3 Hz during immersion in near-neutral chromate, dichromate, chloride, bromide, iodide, fluoride, and sulfate solutions. Supporting observations have been made using optical microscopy and scanning and conventional electron microscopy. Behavior in chromate and dichromate solutions is interpreted in terms of the healing of "mechanical" flaws originally present in air-formed films and the thinning of anodic films down to a passive film thickness of about 25Å. Results in bromide, iodide, and especially chloride solutions are interpreted in terms of pitting by dissolution of transiently exposed metal at the bases of flaws and subsequent undermining of the surface oxide film, which plays a relatively inert role throughout the process. A quantitative model, describing the effects of pit development from flaws on measured specimen impedances, is presented. Relatively little attack occurs in sulfate solution, whereas in fluoride solution the impedance changes are consistent with rapid removal of the surface oxide film and its replacement by a complex oxyfluoride. The general degree of aggression of the anions toward oxide-coated aluminum increases in the order of dichromate, chromate, sulfate, iodide, bromide, chloride, fluoride.

Pryor and co-workers (1-5) have investigated changes in the dielectric properties of anodic alumina films, immersed in various inhibitive and corrosive media, presenting their data largely in terms of resistivity *vs.* thickness profiles. In terms of the capacitance and dissipation factor of the films, Pryor *et al* have observed the following changes in properties of 240Å barrier-type anodic films, formed in neutral tartrate solution, after exposure to near-neutral M chromate, halide, and sulfate solutions:

1. In chromate solutions the anodic films thinned uniformly down to the passive film thickness, without any evidence of preferential attack. Air-formed films thickened slightly by anodic polarization appeared to have developed crystalline oxide on the outer surface, which affected the impedance characteristics at 10^3 Hz but not at 10^5 Hz.

2. In chloride solution, substantial increases in measured dissipation factor of the films occurred at 10^3 Hz without any accompanying change in capacitance. No such changes were observed at 10^5 Hz, nor was any change in surface topography of the films revealed by electron microscopy in 25 hr.

3. In fluoride solution, immersion for periods of 10-300 min revealed substantial increases in both measured dissipation factor and capacitance at 10^3 Hz, accompanied by the growth of a gross (up to 7000Å) contaminating phase on the metal surface. This phase consisted of nonuniformly distributed crystals of an oxyfluoride.

4. In sulfate solution, little or no change in measured dissipation factor, capacitance, or surface topography occurred in 25 hr.

Pryor *et al.* (1-5) have interpreted their film-thinning in chromate results in terms of a detailed distribution of lattice defect structure through the anodic film, involving four zones. Their data in corrosive solutions have been interpreted as involving ion-exchange processes between the aggressive halide species in solution and oxide ions in the oxide lattice, resulting in the creation of an excessively n-type deficient oxide lattice, and a consequent lowering in ionic resistance of the anodic alumina. The film does not change visibly during an "induction" period while ion penetration occurs, but thereafter localized pitting in the case of chloride, or more general attack in the case of fluoride, is said to establish itself at regions of particularly low ionic resistance. Sulfate ions are not considered able to exchange with oxide ions from the lattice, and thus do not reduce the corrosion resistance of the film.

In contrast, the present paper discusses the changes in impedances of air-formed and anodic aluminas, produced upon immersion in aggressive halide solutions, in terms of a relatively simple model (6, 7) involving both penetration and lateral attack of transiently revealed metal at the bases of pre-existing flaws in the relatively inert surface oxide films. Behavior in inhibitive or less aggressive media, such as chromate and sulfate solutions, is also described in similar terms.

Experimental

Specimens of 99.99% aluminum, of at least 6 cm^2 area, were masked on the edges with Lacomit and were then prepared and coated with air-formed or 240Å anodic films (6). Electropolishing was not used as a prior treatment because of possible complications in the properties of the subsequent films (8).

Impedance-time measurements were made at 10^3 Hz only, because the effects are more pronounced at relatively low frequencies. The data are presented, uncorrected for measuring solution and double layer losses, to permit comparison with earlier results. The inhibitive or corrosive medium in question was used as the measuring electrolyte.

Data for air-formed films were obtained from triplicate specimens of area 0.193 cm^2, which were immersed individually in 80 ml of the nominally stagnant medium, contained in a covered 100 ml beaker at 25°C. A platinum counterelectrode of area 25 cm^2 was inserted into each beaker when required and the dissipation factor and capacitance were recorded. This

[1] Present address: Unilever Research Port Sunlight Laboratory, Port Sunlight, Wirral, Cheshire, England.

Key words: impedance, pitting, aluminum, halide.

approach prevented any alteration to the properties of the air-formed film by washing and drying. Impedance-time data for anodic films were obtained by immersing each of a batch of 30 identical specimens of area 6 cm^2 as for the air-formed films. At appropriate times, triplicate specimens were removed, washed in distilled water, dried, and stopped off to 0.193 cm^2 with tape. Their capacitances and dissipation factors were measured directly in a cell containing the test medium as a measuring electrolyte. Care was taken to select areas for measurement typical of the whole surface. However, for specimens in fluoride solution, measurements were made on triplicate specimens, masked with tape to 0.193 cm^2 prior to immersion as for the air-formed films, thus allowing the very rapid changes in the impedance to be followed.

When dissipation factor and capacitance are plotted as a function of time in certain of the diagrams, scatter bands are sometimes used to give the most representative results. However, the outlines of the scatter bands are themselves individual curves for specimens showing extreme behavior.

Results and Interpretation

Immersion in chromate and dichromate solutions.—Air-formed films.—The capacitance of specimens covered by air-formed films, when immersed in M sodium dichromate solution, adjusted with M chromate solution to *p*H 6.0, (Fig. 1a), or sodium chromate solution, adjusted with M dichromate solution to *p*H 7.0, (Fig. 1b), showed little or no time-dependence, beyond a slight over-all decrease after long immersion periods. Generally, the values for the *p*H 6.0 solution were perhaps slightly lower than the corresponding measurements in the *p*H 7.0 solution. The dissipation factors in both solutions (Fig. 1a and b) were initially irreproducible at about 0.15 ± 15%, exhibited a marked reduction with time, and reached reproducible limiting values of 0.085 ± 0.002 in *p*H 6.0 solution (within 10 hr) and 0.089 ± 0.002 in *p*H 7.0 solution (within 8 hr). The specimen electrode potential trends generally correlated with the dissipation factor changes.

240Å anodic films.—The capacitances and dissipation factors generally exhibited slight but reproducible increases initially in both *p*H 6.0 and 7.0 solutions (Fig. 1c and d). Thereafter, they exhibited sharp, but irreproducible, increases as the film thinned, and the metal-oxide interface was approached. The irreproducibility can be attributed to the differing thinning rates of nominally identical specimens. In the two cases where thinning appears to have proceeded to completion, (Fig. 1c and d), the final capacitance and dissipation factor values were reproducible and comparable to the limiting values obtained for the air-formed films (Fig. 1a and b). The film potential gave trends (6) consistent with the impedance changes, showing itself more sensitive than impedance in sensing changes within flaws in the original film but less sensitive to thickness changes. Replica electron microscopy of partially thinned films showed that the thinning process was not very uniform, particularly when the solution was not replenished frequently.

The measured impedances in Fig. 1c and d therefore showed an apparent dependence on film thickness as the sample thinned, which it did more rapidly in *p*H 7.0 than in *p*H 6.0 solution. However, when such data are corrected for solution and double layer losses (6), the film dissipation factors are thickness-independent.

Immersion in chloride solution.—Air-formed film.—The capacitances of all specimens carrying air-formed films, when immersed in M potassium chloride solution, adjusted to *p*H 6.0 with a few drops of 0.01M hydrochloric acid, showed a slight rise during the early stages of immersion, but remained fairly steady thereafter, displaying a slight tendency to fall in the later stages of immersion (>300 hr) (Fig. 2a). The dissipation factors of all specimens were virtually invariant with time of immersion (Fig. 2a).

The pits visible optically on all specimens, after about 500 hr immersion, were relatively few in number (<1/cm^2), and were relatively small. The pits often showed a definite tendency to be associated with scratch lines in the metal surface. The pits showed no systematic preference for the edges of the specimen. Specimens were not removed for examination during the runs, so it is difficult to say when the pits first appeared.

Anodic film.—The capacitances and dissipation factors of the corresponding specimens with 240Å anodic films were identical to those measured in chromate and dichromate solutions initially (Fig. 2b). After more than 25 hr immersion the impedances were strongly

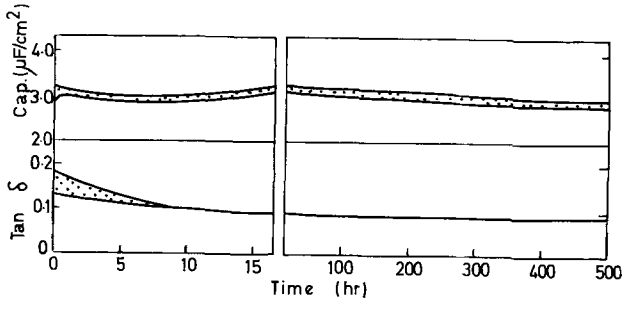

a. Air-formed films in sodium dichromate solution, *p*H 6.0

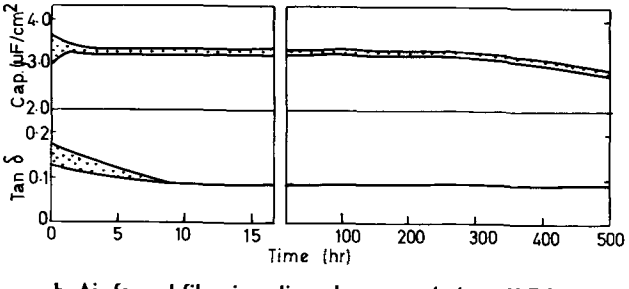

b. Air-formed films in sodium chromate solution, *p*H 7.0

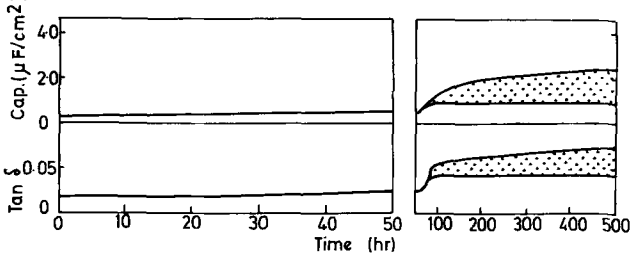

c. 240Å anodic films in sodium dichromate solution, *p*H 6.0

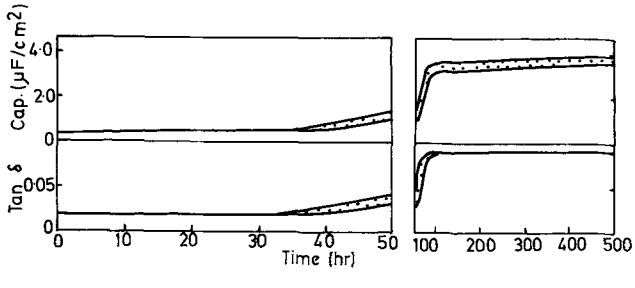

d. 240Å anodic films in sodium chromate solution, *p*H 7.0

Fig. 1. Capacitance and dissipation factor as a function of time

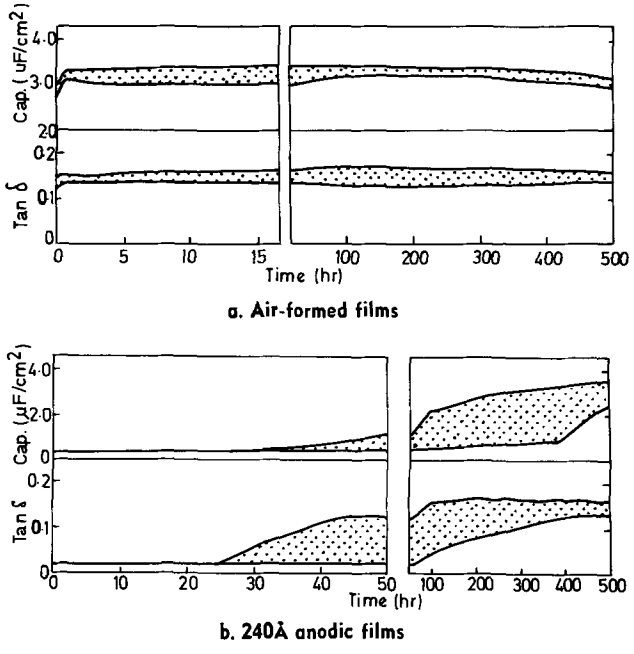

Fig. 2. Capacitance and dissipation factor as a function of time in potassium chloride solution, pH 6.0.

dependent on the degree of breakdown of the surface, and thus on the particular specimen area selected for measurement. Three general types of behavior could be discerned:

1. Specimens without optically visible signs of breakdown generally exhibited virtually identical capacitances and dissipation factors as the as-formed films. Occasionally, however, such a specimen was found to exhibit a slight increase in capacitance, accompanied by a disproportionately larger increase in dissipation factor than that expected from film thinning.

2. Specimens with slight, but visible, signs of breakdown exhibited increases in capacitance, accompanied by disproportionately large increases in dissipation factor.

3. Specimens with relatively severe breakdown (*i.e.*, many pits) showed capacitances and dissipation factors similar to those observed for specimens carrying air-formed films, immersed in potassium chloride solution at pH 6.0.

Referring generally again to Fig. 2b, the initial film breakdown was therefore reflected, if at all, in substantial increases in dissipation factor, with relatively slight increases in capacitance. Thereafter, as breakdown proceeded, the dissipation factors continued to increase toward a value characteristic of the corrosion-affected air-formed film, and breakdown progressively affected the capacitances of the specimens more. Eventually, the capacitance increases "caught up" the increases in dissipation factor, and the net impedance after 500 hr was characteristic of a corrosion-affected, air-formed film for all specimens. For periods up to 80 hr, even though by now all specimens showed signs of breakdown somewhere on their surface, areas of surfaces could be selected for impedance measurements with identical dielectric properties to the as-formed films.

The present results differ from the previous short-term (up to about 17 hr) results of Pryor and co-workers (1-4) on three counts:

(*a*) The impedances of specimens remained unaffected for immersion periods less than 25 hr.

(*b*) Where effects were observed, no specimen underwent the impedance change described by Pryor *et al.*, namely a substantial increase in dissipation factor without any corresponding change in capacitance. Some specimens did, however, almost show this behavior, displaying a substantial increase in dissipation factor accompanied by only slight increases in capacitance.

(*c*) The implication of Pryor *et al.* that immersion in neutral chloride solution causes continuous, and relatively reproducible, increases in the dissipation factors of anodic films contrasts sharply with the present findings. Here, the impedance changes were erratic, grossly irreproducible, and dependent on the test area selected.

All specimens were quite heavily pitted after 500 hr immersion and indeed pits were optically visible on many specimens after more than 33 hr. It is virtually impossible to assess the visible pit density after 500 hr, owing to the great variation from specimen to specimen, and indeed from area to area, on any particular specimen. Generally, more pits were visible on anodized specimens than on specimens carrying air-formed films, although the pits tended to be smaller and showed less preferential association with either scratch lines or specimen edges (7).

Immersion in bromide and iodide solutions.—Air-formed film.—In potassium bromide solution, with pH adjusted to 6.0 with a few drops of 0.01M potassium hydroxide solution, the capacitance, after an initial slight rise, dropped to about 2-2.5 μF/cm^2 over 500 hr, while the dissipation factor remained virtually constant (Fig. 3a). After 500 hr the specimens showed only slight signs of pitting, relative to the chloride-treated specimens. Typically, a central "pit" was surrounded by a "ring" of mounds of corrosion product, which were probably hydrated alumina and below which small pits probably resided. Also, the center surface around the corroded region was covered by a thin film of hydrated alumina, giving rise to interference colors when viewed optically, probably explaining the observed time-dependence of impedance. A fall in capacitance without corresponding change in dissipation factor indicated either over-all film thickening, via some type of field-induced "electrorecrystallization" mechanism, or more likely localized film thickening, resulting from hydrolysis and precipitation of initially soluble corrosion products. Thus, the results for bromide solutions suggest that pitting was much slower than in chloride solutions.

In potassium iodide solution with pH adjusted to 6.0 with a few drops of hydriodic acid (Fig. 3b), the capacitance showed a distinct rise to about 5.5-6.5 μF/cm^2 over 500 hr, with the dissipation factor remaining relatively constant. From the outset, the specimens showed signs of localized brown staining, with the stain "nuclei" developing laterally with time into extensive stained patches. Over-all, the surfaces appeared to suffer general corrosion rather than pitting, consistent with the previous work of Pryor (9). The stains were obviously due to free iodine, and indeed the bulk solution changed color from colorless to straw-yellow over the 500-hr period, so invalidating any direct comparison with the chloride and bromide results. Mounds of hydrated alumina corrosion product were again evident, beneath which were probably pits. The surface appeared to be coated generally with a film of corrosion product, within which cracks and holes were evident. The marked increase in capacitance without any notable increase in dissipation factor points to an increase in real area of the specimen during immersion, as a result of "general" rather than "localized" corrosion.

Anodic film.—During 300 hr in bromide solution, little if any change in the capacitances was evident, except for a slight rise if a pitted area was selected for measurement (Fig. 3c). The dissipation factor, however, tended to rise to values typical of the corrosion-affected, air-formed film after about 25 hr. Indeed, in bromide solutions impedance changes of the Pryor type (1-4) in chloride solutions were evident, namely a distinct rise in dissipation factor without any corre-

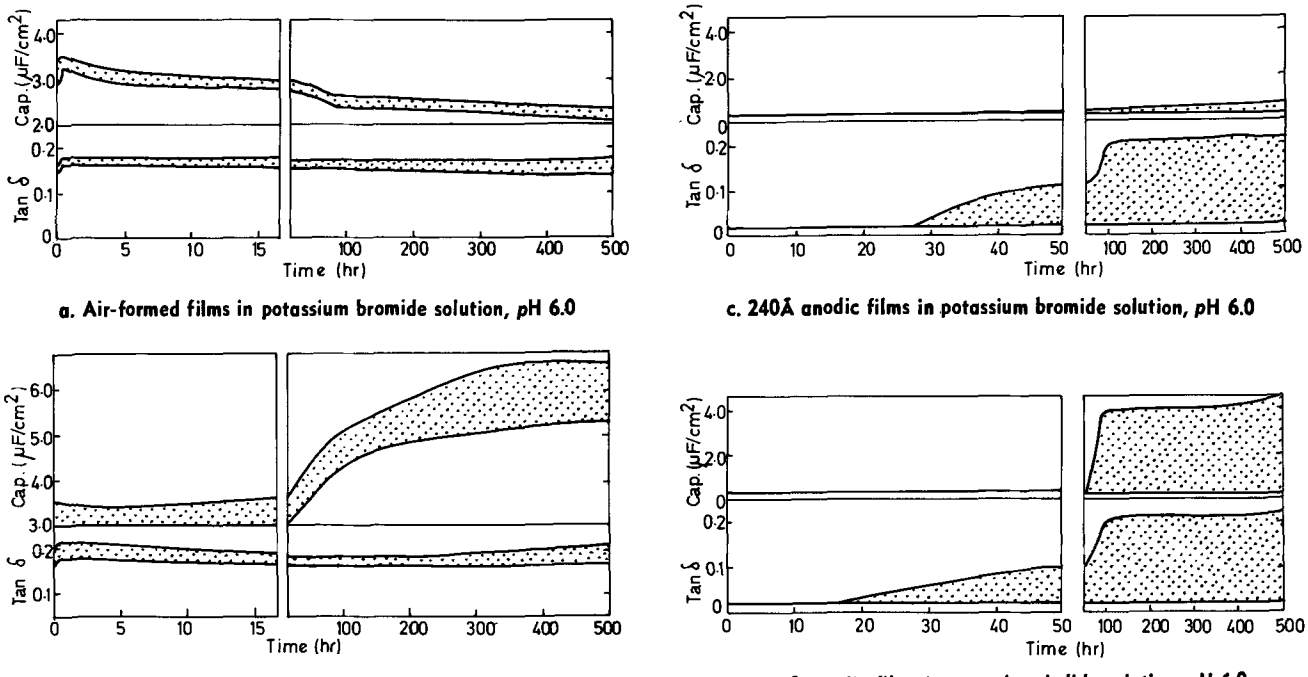

a. Air-formed films in potassium bromide solution, pH 6.0

c. 240Å anodic films in potassium bromide solution, pH 6.0

b. Air-formed films in potassium iodide solution, pH 6.0

d. 240Å anodic films in potassium iodide solution, pH 6.0

Fig. 3. Capacitance and dissipation factor as a function of time

sponding change in capacitance. After 500 hr the specimens were only slightly pitted relative to chloride-treated specimens, and the corrosion was similar to that on surfaces supporting air-formed films.

Capacitance and dissipation factor measurements in iodide were highly dependent on the area selected for measurement. Little iodine staining was evident before about 50-hr immersion, when little or no change in capacitance and only slight increases in dissipation factor were evident. Thereafter, however, as the staining increased, areas of high capacitance and dissipation factor (over stained regions), or low capacitance and dissipation factor (over intact film), could be selected. Even after 500 hr certain areas showed little, if any, impedance change. As with air-formed films, the iodine staining phenomenon commenced at incipient points on the surfaces and spread laterally, rather than in depth. The morphology of attack was much the same as for air-formed films.

Immersion in fluoride solution.—Air-formed film.— Rapid rises in both capacitance and dissipation factor were observed from the very point of immersion in M potassium fluoride solution at pH 8.5 which proved difficult to follow accurately on the a-c bridge. A reliable balance was not possible until after about 30 sec had elapsed, by which time the capacitance and dissipation factor values (Fig. 4a), were both high relative to values for specimens supporting air-formed films in other solutions. Subsequently, both showed drops to minima after 3-4 min. The minimum capacitance value corresponded to an anodic oxide film thickness of about 70Å, although the corresponding measured dissipation factor was much higher than expected for such a film. After about 3-4 min immersion, both the capacitance and particularly the dissipation factor values showed a distinct rise. The dissipation factor gave a maximum of 0.7-0.8 after about 100 min, showing a gradual decline to 0.4 thereafter, during a period of relatively constant capacitance. Corresponding potential measurements (10) exhibited an initial active surge (corresponding to the high capacitance and dissipation factor values), followed by a surge in the noble direction (corresponding to the minimum in capacitance and dissipation factor) before steadying out. Thereafter, the potential tended to move slightly in the active direction.

Replica electron microscopy suggested that, immediately after immersion, a crystalline "film" nucleated at discrete sites, growing in thickness and laterally until, after about 10 min, the entire surface was covered. At this stage, changes in surface morphology were not visible optically. After about 100 min, relatively gross areas of white, flocculent corrosion product appeared on the specimen surfaces, tending to mask the crystalline order of the film beneath. These gradually thickened and spread until, after 40 hr, relatively gross corrosion had obviously occurred.

Anodic film.—Both capacitance and dissipation factor values measured immediately after immersion in fluoride solution agreed very closely with the corresponding values measured in chromate or other halide solutions (Fig. 4b). Thereafter, both parameters showed an ever-rising rate of increase to maximum values, coincident in time with an active peak in corrosion potential (10), after about 6-7 min immersion. As with

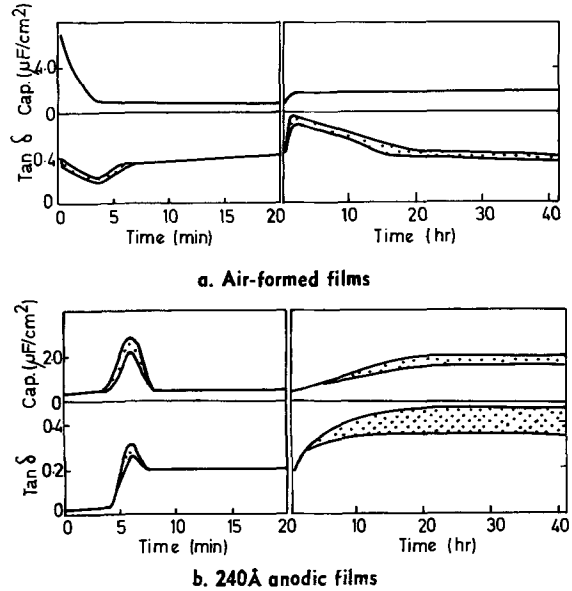

a. Air-formed films

b. 240Å anodic films

Fig. 4. Capacitance and dissipation factor as a function of time in potassium fluoride solution, pH 8.5.

the corrosion potential, the time dependencies of both capacitance and dissipation factor beyond 6-7 min were similar to those for surfaces originally supporting air-formed films, excepting the absence of a peak in the time-dependence of dissipation factor for the surface supporting a 240Å anodic film originally.

Replica electron microscopy and visual observation confirmed similar morphological changes on the surface to those on specimens with air-formed films, although changes perceptible to the naked eye appeared to take longer with the anodized specimens so that, even after 100 min, the "film" consisted almost exclusively of the "crystalline" material. However, the flocculent material gradually aggregated and, after 40 hr, both types of specimen appeared identical, with evidence of gross over-all corrosion.

Immersion in sulfate solution.—Air-formed film.— The capacitance and particularly the dissipation factor values both showed slight drops during the very early stages in M sodium sulfate solution with *p*H adjusted to 6.0 with a few drops of 0.01M sodium hydroxide solution, comparable to behavior in chromate and dichromate solutions (Fig. 1a and b). Both parameters then showed little or no time-dependence throughout a 50-hr immersion period. Subsequently, some general corrosion did occur but this was accompanied by complicated microbiological effects. No changes in the specimens were evident visually or by electron microscopy up to 50 hr. The relative insolubility of sodium fluoride and potassium sulfate in water precluded the use of salts with a common cation for all the experiments.

Anodic film.—The capacitance and dissipation factor, originally at values typical of a 240Å film as initially measured in any other solution, showed little or no increase during about the first 80-hr immersion. Subsequently some more general corrosion of a complicated nature occurred.

Discussion

Impedance models for pitted electrodes.—Before discussing the effects of immersion in the various solutions on the general impedance characteristics, an impedance model is developed for a film containing flaws to cover the case where the flaws are developing into pits, propagating beneath the surface film. Consider an oxide-coated aluminum surface beneath which pits have been developing during natural immersion in an aggressive medium. The specimen is removed, washed and dried, and placed in a measuring cell to determine its impedance. It is assumed in Fig. 5a and the corresponding equivalent circuit in Fig. 5b that the typical pit exhibits crystallographic morphology, that the surface oxide film over its mouth remains intact apart from the original flaw beneath which propagation has occurred, and that, after removal and drying, the pit surface is covered by an air-formed or passive alumina film, 25Å thick (7).

The impedance change produced by immersion in the aggressive medium can be relatively easily calculated. In what follows, it is important to distinguish measured impedance data from corrected data, *i.e.*, measured data to which corrections for solution and double layer losses have been applied. The following corrected data (6) have assumed for the alumina film on the pit surface; C_s (pit) = 3.0 μF/cm^2, R_s (pit) = 4.6 ohm · cm^2, R_p (pit) = 600 ohm · cm^2, and tan δ (pit) = 0.088. It is assumed that the data obtained at 10^5 Hz for a platinum electrode in the measuring solution (6) provide the best available estimate of R_s (flaw), *i.e.*, the resistance of the solution within the flaw, when suitably corrected for the flaw length and area. These data have been treated as follows to provide a predicted measured value of the impedance of a pitted surface, carrying a 240Å film:

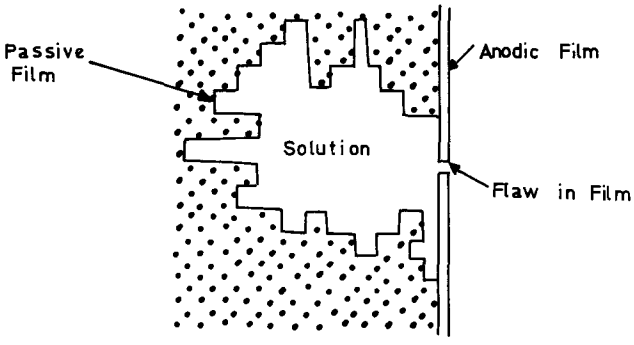

Fig. 5a. Section of model of pit used in impedance calculations

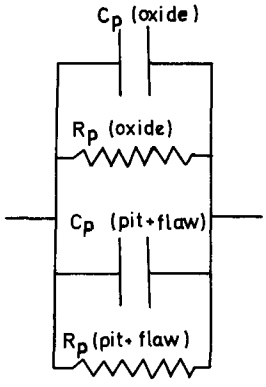

Fig. 5b. Equivalent circuit for pit model shown in Fig. 5a.

1. The value of R_s (pit) is added to R_s (flaw) to give an R_s (pit + flaw) value.

2. From R_s (pit + flaw) and C_s (pit) for the pit surface, a value of tan δ (pit + flaw) can be calculated from the relationship

$$\tan \delta = \frac{1}{\omega R_p C_p} = \omega C_s R_s \qquad [1]$$

3. Corresponding C_p (pit + flaw) and R_p (pit + flaw) values are calculated using the equations

$$\frac{C_p}{C_s} = \frac{1}{1 + \tan^2 \delta} \qquad [2]$$

and

$$\frac{R_p}{R_s} = \frac{\tan^2 \delta + 1}{\tan^2 \delta} \qquad [3]$$

4. R_p (pit + flaw) and C_p (pit + flaw) values are then compounded with R_p (film) and C_p (film) values (*i.e.*, corrected values) for a 240Å film. Thus corrected R_p (pitted film) and C_p (pitted film) values are obtained for a 240Å film containing a pit beneath one of its flaws. From these latter values a corrected tan δ (pitted film) is calculated using relationship [1].

5. Finally the corrected parameters for the pitted film thus obtained are compounded with the R (solution) value for the measuring electrolyte between working and counterelectrodes in the measuring cell, giving predicted measured values of the impedance of the measuring cell, containing a pitted oxide electrode. Against these values the experimental data, such as Fig. 2, may be assessed.

Calculations have been performed for the following systems:

(*a*) A 240Å film containing a single pit/cm^2, variable in surface area in the range 10^{-10}-10^{-1} cm^2, beneath a single flaw, variable in surface area in the range 10^{-10}-10^{-2} cm^2. The predicted measured tan δ and capacitance values for the pitted, filmed surfaces are plotted against pit area in Fig. 6a-g. To put the data in context, an area of 10^{-10} cm^2 is the average area of a typical "residual" flaw in an anodic film (6). Some of the larger areas of flaw are included to illustrate possible effects of larger "mechanical" flaws. Also, a large pit area/flaw area ratio is quite possible in

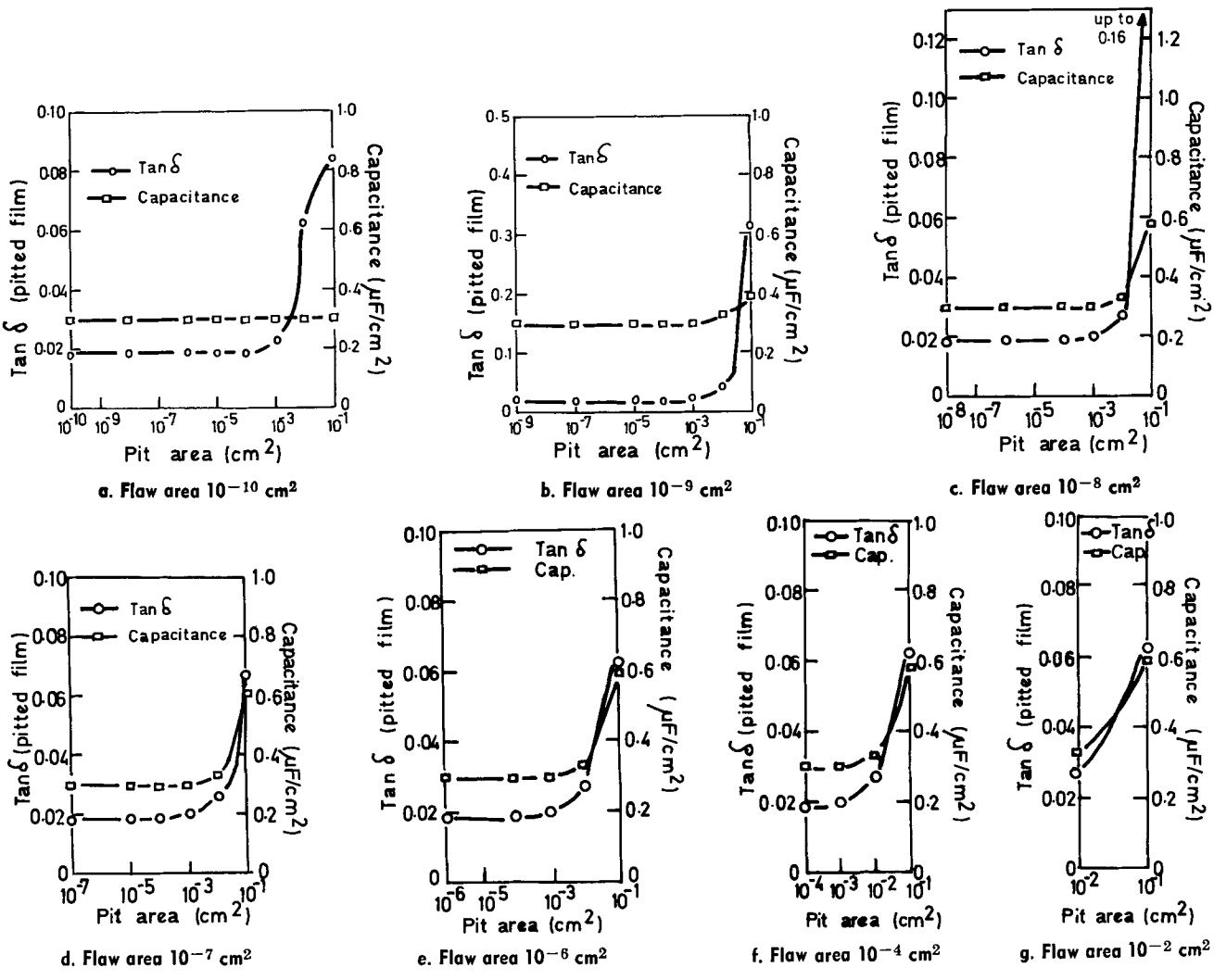

Fig. 6. Calculated effect of pit area beneath flaw on measured capacitance and dissipation factor of a 240Å anodic film

practice, particularly where crystallographic pitting and tunneling are evident.

Closer inspection of Fig. 6a-g shows that the (pit + flaw) combination functions largely as a capacitor at low pit areas (*i.e.*, its impedance resides largely at its base) but, as the pit area/flaw area ratio increases, the combination tends to a more resistive impedance (*i.e.*, the impedance is determined to a greater extent by the resistance of the flaw itself). This manifests itself by changes in tan δ rather than in capacitance. Large increases in tan δ are possible with little or no increase in capacitance occurring.

The (pit + flaw) combination functions as a low-loss capacitance at low flaw areas and as a low-loss, high valued capacitance at high flaw areas, via a medium-valued but high-loss capacitance. Thus, the degree of resistive or capacitative impedance offered by the combination is crucially dependent on the relative pit and flaw areas.

(*b*) A 240Å oxide film containing a variable number of pits/cm² of area 10^{-1} cm² beneath flaws of area 10^{-5} cm². The predicted measured tan δ and capacitance values for the pitted film surface are plotted against pit density in Fig. 7. The capacitance of the pitted film increases linearly with pit density and thus with total pit area, while the measured tan δ value rises steadily at first, leveling out at that value typical of an air-formed film. In more general terms, these calculations show the effect of varying the total area affected/cm² at a constant pit area/flaw area ratio. Thus, they apply whether the pit population density itself increases, or merely the absolute area of an individual pit or pits.

(c) The effect of having a single pit/cm² of variable area beneath a flaw of area 10^{-6} cm² in a 2000Å anodic film. The predicted measured impedance data are plotted as a function of pit area in Fig. 8. Upon comparing the results with those for a 10^{-6} cm² area flaw in a 240Å film (Fig. 6), it is clear that much larger effects are evident for a given pit area/flaw area ratio in the case of the 2000Å film. This means that the effects of a given pit are detected at an earlier stage when the anodic film is thicker.

(d) The effect of having a single pit/cm² of variable area, supporting faradaic processes, beneath a

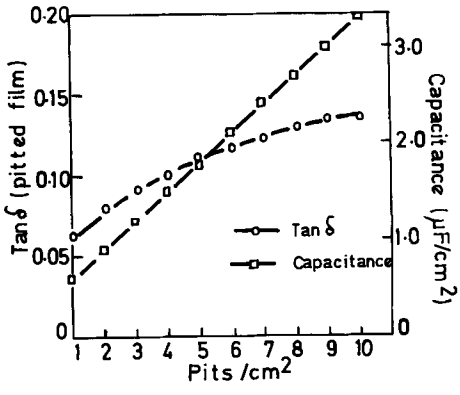

Fig. 7. Calculated effect of pit density on measured capacitance and dissipation factor of a 240Å anodic film, taking the area of the pit beneath the flaw as 10^{-1} cm² and the area of the flaw above the pit as 10^{-5} cm².

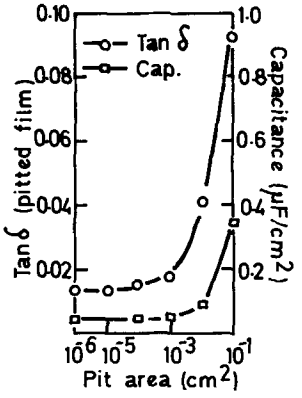

Fig. 8. Calculated effect of pit area beneath flaw, of area 10^{-6} cm², on measured capacitance and dissipation factor of a 2000Å anodic film.

flaw of known area. Data are presented for flaw areas of 10^{-10} cm² and 10^{-6} cm² in Fig. 9a and b, respectively. The appropriate data for faradaic processes are those obtained using a platinum electrode (6).

For small flaws, much the same pattern emerges as with an oxide-coated pit, but the changes in tan δ are

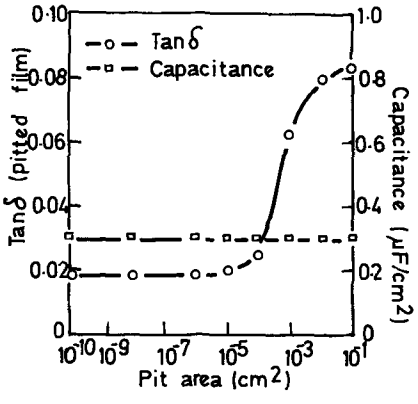

a. Flaw area 10^{-10} cm²

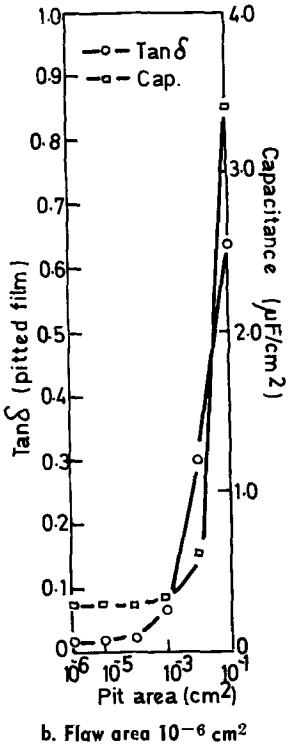

b. Flaw area 10^{-6} cm²

Fig. 9. Calculated effect of pit area beneath flaw on measured capacitance and dissipation factor of a 240Å anodic film, for the case of flaw bases supporting faradaic processes.

evident at much lower pit area/flaw area ratios. Thus, very small pits would give a large increase in tan δ. For larger flaws, massive increases in tan δ and capacitance are observed. Such models with faradaic processes are probably not particularly realistic for aluminum samples which have been removed and dried prior to measurement, nor are they expected to cover large areas of propagating pit surfaces. They are, however, applicable where "bare" metal in pits or at flaw bases is obtained transiently as a result of crack/heal type processes, or possibly when the *p*H has dropped to a very low level in a propagating pit. They could also be more relevant for other metals whose surfaces do not repassivate or oxidize so readily, or where the passive film is removed rapidly in the measuring cell.

Immersion in chromate and dichromate solutions.— There is little doubt that in the case of anodic films, increases in capacitance without corresponding changes in corrected dissipation factor, during immersion in both solutions, resulting from film thinning. For air-formed films, however, substantial decreases in dissipation factor without corresponding changes in capacitance, during the early stages of immersion in both solutions, suggest healing of flaws, rather than film thickness changes. Significantly, the dissipation factors of thinned anodic films, and air-formed films subjected to prolonged immersion in chromate/dichromate solutions, are virtually identical. Immersion, and anodizing, would thus appear to effect the same structural changes in an air-formed film, and the most likely effect of both is considered to be a reduction in initially available flaw area. The latter is perfectly consistent with the slight reduction in capacitance of air-formed films, resulting from immersion in the chromate/dichromate solutions. As the available flaw area reduces, so also does the consequent contribution of double layer or semiconducting oxide capacitance at the flaw bases to the total measured capacitance. The available evidence (6, 11, 12) suggests that there are two types of flaws in surface films, one associated with regularly distributed residual defects in the metal surface, *e.g.*, impurity segregates, inclusions, etc., and the other with less evenly distributed, grosser defects of a more "mechanical" nature, *e.g.*, scratches, rough areas of surface, step edges, etc. Air-formed films contain many more mechanical flaws than anodic films, although all films contain "residual" flaws, the density of which is less dependent on the nature or thickness of the surface film. It is considered that the impedance changes suffered by air-formed films during the early stages of exposure in chromate or dichromate solutions are associated with the healing of largely mechanical flaws.

The mechanical flaws are not persistent bare metal but rather occur by crack-heal type processes upon immersion of the filmed sample. Healing occurs by passivation of the bare metal and partial plugging of the mechanical flaws with alumina. Eventually less crack/heal events occur as stress is relieved. The impure oxides at the bases of residual flaws, although healed by contact with chromate or dichromate solutions, remain largely semi-conducting in character and act as cathodes initially in any electrochemical reactions, although they can in time become sites for corrosion too. There are, of course, a complete range of flaws, incorporating features of the basic mechanical and residual types, giving a complete spectrum of behavior with respect to healing in chromate solution or corrosion in halide solutions. Throughout any sequence of events, the oxide covering the main surface of the electrode, between the flaws, is considered to play a relatively inert role, functioning largely as an insulator (7). This is particularly true for anodic films but would also apply to any films produced by overall thickening of air-formed films in the corrosive solution.

Heine and Pryor (5) thickened the passive film on aluminum to around 40Å by anodizing in chromate solution and then obtained resistivity profiles through the thickened film at 10^3 and 10^5 Hz by making impedance measurements during thinning in chromate solution, pH 7.0. Their measurements indicated that the outer regions of the thickened film exhibit a higher resistance at 10^5 Hz than a thermal film of the same thickness but a remarkably lower resistance at 10^3 Hz. Following the theory of their earlier papers (2-5) they attributed the low "ionic" resistance of the thickened passive film at 10^3 Hz to the formation of crystalline γ-Al_2O_3 of very low ionic resistance at the oxide-electrolyte interface, and the high "electronic" resistance at 10^5 Hz to the inclusion of some protons in the passive film.

Their interpretation is open to two major criticisms:

1. Only slight thickening of a passive film by anodizing would heal many weak spots present in the original film. Even if weak spots are considered to be absent, it does not follow that the structure of the anodic film would reflect the properties of the pre-existing passive or air-formed film.

2. The resistance-thickness profiles are uncorrected for solution and double layer losses, whereas substantial correction to the measured profiles is required for 40Å films at both 10^5 and 10^3 Hz (6). It is doubtful whether any significant contribution from the oxide is sensed at all at 10^5 Hz, in view of the large contribution of the resistance of the measuring solution to the total measured impedance at that frequency (>95%).

Immersion in chloride solution.—On the basis of the strong evidence for flaws presented elsewhere (6, 10-12), and the morphological evidence from scanning electron microscopy (7), pitting is considered to initiate at the bases of flaws in the surface oxide film. Mechanical flaws are considered to support anodic attack more readily than residual flaws, which are predominantly cathodic in nature, at least initially. Once bare metal is exposed, albeit transiently, the metal either repassivates, as in chromate or dichromate solutions, or active dissolution of the exposed area commences as suggested for chloride solutions. Thus, pitting attack is considered to proceed from the very point of immersion in the chloride solution, as is further evidenced by potential measurements (10, 13, 14). Pitting then proceeds by a process of undermining of the relatively inert surface oxide film.

Thus, a surface supporting an anodic film exhibits the following changes in impedance, upon exposure to a pitting environment:

1. Initially there is no measurable effect but the first changes become evident in the measured tan δ value as the active pit areas increase, and the impedances of (pit + flaw) combinations are determined by the flaw dimensions in the surface film over the pit mouth.

2. As the pits increase in size, and the surface films over their mouths becomes less intact due to rupture etc., the impedance of the pitted film tends to become more capacitative, and the latter value rises.

3. As the pits become still larger, and the overlying surface film less intact, the impedance of the specimen is "seen" merely in the pits themselves, and the latter "short-out" the remainder of the anodic film. At this stage, the specimen shows characteristics typical of a corrosion-affected air-formed film and indeed, on heavily pitted surfaces, the capacitance of the specimen might well exceed that characteristic of the geometric area.

All three phenomena described above are realized in practice, and are preferred to alternative explanations of the phenomena such as field-induced anion ingress (16) or anion exchange (1-4). Further changes observed are scarcely due to over-all thinning of the oxide film on the surface, particularly as Khan (15) has shown that the thickness of unpitted oxide does not change, even upon prolonged exposure to neutral chloride solutions.

Rather, the observations of Pryor *et al.* (1-4) constitute a special case of the more general trends in impedance variation demonstrated here. They represent the measured effects of tiny, largely resistive (pit + flaw) combinations on the impedance of an apparently unpitted, anodized specimen. Furthermore, the correlation between impedance data from etched and electron microscopical data for electropolished surfaces, invoked by Pryor *et al.*, are not considered valid for two reasons:

(*a*) Films stripped from pitted surfaces at the relatively early stage, and examined by transmission electron microscopy, would not be expected to show any signs of pitting, in view of their being undermined rather than dissolved during pitting.

(*b*) Electropolished aluminum (10) or stainless steel (17) surfaces are known to possess somewhat different pitting characteristics from etched or mechanically polished surfaces.

In an attempt to simulate the conditions considered to prevail during the experiments of Pryor *et al.* (1-4), a specimen supporting a 240Å anodic film was scratched minutely with a razor blade, thus rupturing the surface film. The film was then thinned in chromate solution, pH 7.0, and the variation in measured capacitance and dissipation factor with time during thinning is shown in Fig. 10a. These data are replotted in the form of average resistivity as a function of thickness in Fig. 10b. During the early stages of film thinning, healing of the base of the mechanical rupture in the film occurs simultaneously, giving an initial decrease in measured dissipation factor, associated with an increase in measured capacitance. A comparison of the data of Fig. 10b with those of Heine, Keir, and Pryor (4) points strongly to the presence of small mechanical flaws (*i.e.*, pits) in the anodized surface, rather than an anion-exchanged film.

Finally, to establish the validity of the present model further, an anodized surface was subjected to galvanostatic polarization for a sequence of consecutive time intervals at 1 μA/cm^2. The measured capacitance and dissipation factor are shown as a function of charge

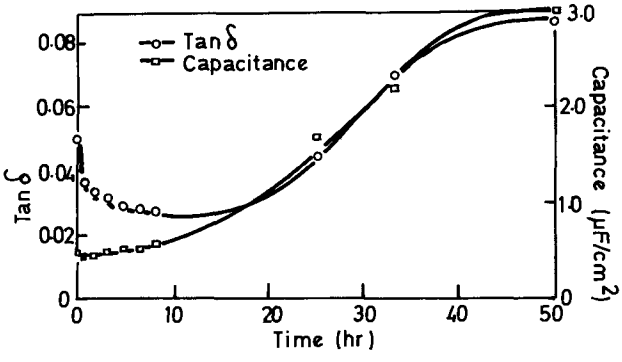

Fig. 10a. Capacitance and dissipation factor of a scratched 240Å anodic film as a function of time, in sodium chromate solution at pH 7.0.

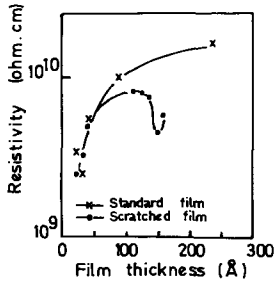

Fig. 10b. Data of Fig. 10a, replotted as resistivity as a function of film thickness.

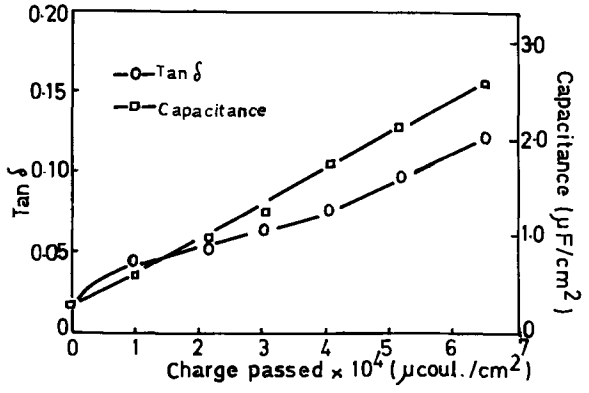

Fig. 10c. Variation of impedance of a 240Å anodic film with extent of pitting, due to galvanostatic polarization in potassium chloride solution, pH 6.0.

passed (an approximate measure of the degree of pitting of the surface) in Fig. 10c. Comparison of Fig. 7 and 10c yields good evidence for the proposed model.

Immersion in bromide and iodide solutions.—Generally, the considerations of the previous section apply. Under conditions of "natural" immersion, there is little doubt that the case of breakdown of oxide-coated aluminum proceeds in the order

$$Cl^- > Br^- > I^-$$

Not surprisingly, therefore, the bromide results reflect in general the early stages of breakdown of air-formed and anodic aluminas, in the former case localized film thickening rather than increased specimen area due to pitting being observed in the capacitance, and in the latter the type of impedance changes described by Pryor *et al.* for chloride solution, and associated with tiny pits beneath flaws in the anodic film. A complicating feature of breakdown in iodide solutions is that they are known to oxidize spontaneously in the presence of dissolved oxygen to liberate free iodine (18), according to the reaction

$$4I^- + O_2 + 2H_2O = 2I_2 + 4\,OH^-$$

The liberated iodine, rather than the iodide ion itself, appears to be the cause for the "anomalously" high corrosion rates observed for aluminum in iodine solutions [see also Ref. (9)]. Probably the iodine attacks the basis metal, rather than the surface oxide film itself, in view of the extensive use of alcoholic iodine for stripping alumina films.

Immersion in fluoride solution.—The surface oxide once again plays a relatively inert role throughout the corrosion initiation process. Attack commences at flaws in the existing surface film and rapidly spreads laterally beneath the original film, completely undermining it and removing it from the metal surface. Attack is extremely rapid and is supported by hydrogen evolution (20), even in relatively neutral solutions. The original surface film is completely replaced on the metal surface by an insoluble crystalline film, which appears to consist of a complex aluminum oxyfluoride (1, 2, 19), within a few minutes of immersion. The latter film then determines entirely the subsequent behavior of the specimen, and the nature of the initial oxide film soon becomes irrelevant. The corrosion rate is so fast because of the ability of the fluoride ion, unlike any of the other aggressive species considered, to complex aluminum, giving a series of well-defined complex salts with fluoride ions that range from AlF^{2+} to AlF_6^{3-} (21).

The proposed mechanism is considered consistent with the data of Fig. 4. The capacitance and dissipation factor in Fig. 4b measured immediately after immersion in fluoride solution, are a function of the presence of still partially intact original oxide film on the metal surface. As attack proceeds, the area of contact of the original oxide film with the surface decreases, and the corresponding area of the newly formed oxyfluoride film increases. Thus, the capacitance and dissipation factor increase, reflecting at their extreme values complete removal of the original surface film and the presence of a very thin layer of crystalline oxyfluoride film on the metal surface. The time required to reach the extreme values is longer for the anodic film (Fig. 4b) because of the smaller number of flaws at which attack can commence. As time proceeds beyond that required for complete removal of the original surface film (about 20 sec for air-formed films, 6-7 min for 240Å anodic films), the new surface film thickens to its limiting value. The capacitance and dissipation factor are then a function of the dielectric properties of the crystalline material and both decrease to limiting values as the film thickens. Later, corrosion would be expected to proceed at flaws, intercrystalline regions, etc., in the new surface film, and the longer-term processes of hydrolysis, deposition of hydrolyzed products, local pH changes, etc., to establish themselves, with consequently less reproducible effects on the capacitances and dissipation factors.

In an attempt to provide supporting evidence for the proposed theory 240Å anodic films were stripped from aluminum surfaces and immersed in fluoride solutions. Transmission electron microscopy revealed little or no change in structure or degree of intactness of the film for periods of immersion up to 10 min. Certainly no crystallization of the film was evident, nor any gross thinning. Thereafter, the film tended to disintegrate into small fragments, and presumably ultimately to dissolve in the fluoride solution.

It is therefore difficult to explain the drastic changes which occur in oxide-coated aluminum electrodes, during the very early stages of immersion, merely on the basis of chemical "modification" and "contamination" of the surface oxide film, involving extensive anion exchange between fluoride ions and the surface oxide ions (1, 2). Furthermore, the previous workers do not appear to have detected or reported these very significant initial changes in both capacitance and dissipation factor. Nor are the present results consistent with other studies, in which it was concluded that direct solution of the surface film is responsible for the initiation of corrosion in fluoride solutions (20).

Immersion in sulfate solutions.—Ignoring the complicated, apparently microbiological, corrosion in the late stages, it is evident that sulfate solution does not cause rapid corrosion of aluminum for long periods because no significant changes in dielectric properties or film appearance can be detected. Presumably the anion permits passivation at the bases of mechanical flaws, or else the rate of attack is too low to be detected.

Conclusions

1. In chromate and dichromate solutions, mechanical flaws originally present in air-formed films tend to be healed and anodic films are thinned to the passive film thickness. Little attack is detected in sulfate solution until after long periods.

2. In chloride solution, and to a lesser extent bromide and iodide solutions, pitting commences rapidly by preferential dissolution of metal transiently exposed at flaw bases in air-formed or anodic films. Undermining of the relatively inert surface film occurs. Good agreement is obtained between measured impedance data and values developed from a model in which pits develop from flaws.

3. In fluoride solution, the oxide film is removed, apparently largely by undermining, and is replaced by a complex oxyfluoride.

4. The general degree of aggression of the anions in the order dichromate, chromate, sulfate, iodide, bromide, chloride, fluoride, although complications occur

with sulfate after long periods and with iodide as a result of the release of free iodine.

Acknowledgments

The authors are indebted to Professor T. K. Ross for his interest and provision of facilities and to Dr. M. J. Pryor and colleagues, Dr. A. J. Brock, Mr. J. N. Wanklyn, Dr. P. J. Harrop, and Mr. W. H. Sutton for interesting discussions and valuable suggestions at various stages of the work.

Manuscript submitted July 23, 1972; revised manuscript received Oct. 6, 1972.

Any discussion of this paper will appear in a Discussion Section to be published in the December 1973 JOURNAL.

REFERENCES

1. J. J. McMullen and M. J. Pryor, Proc. 1st Int. Congress on Metallic Corrosion, p. 52, Butterworths, London (1961).
2. A. F. Beck, M. A. Heine, D. S. Keir, D. van Rooyen, and M. J. Pryor, *Corrosion Sci.*, **2**, 133 (1962).
3. M. A. Heine and M. J. Pryor, *This Journal*, **110** 1205 (1963).
4. M. A. Heine, D. S. Keir, and M. J. Pryor, *ibid.*, **112**, 24 (1965).
5. M. A. Heine and M. J. Pryor, *ibid.*, **114**, 1001 (1967).
6. J. A. Richardson, Ph.D. Thesis, University of Manchester, 1969.
7. J. A. Richardson and G. C. Wood, *Corrosion Sci.*, **10**, 313 (1970).
8. A. F. Beck, M. A. Heine, E. J. Caule, and M. J. Pryor, *ibid.*, **7**, 1 (1967).
9. M. J. Pryor, *Z. Elektrochem.*, **62**, 782 (1958).
10. J. A. Richardson, W. H. Sutton, and G. C. Wood, *Thin Solid Films*, In press.
11. G. C. Wood, W. H. Sutton, J. A. Richardson, T. K. N. Riley, and A. C. Malherbe, Paper presented at Williamsburg Conference on Localized Corrosion, NACE, In press.
12. W. H. Sutton, Ph.D. Thesis, University of Manchester, 1971.
13. T. Hagyard and W. B. Earl, *This Journal*, **114**, 694 (1967).
14. T. Hagyard and J. R. Williams, *Trans. Faraday Soc.*, **57**, 2283 (1961).
15. I. H. Khan, DIC Thesis, University of London, 1966.
16. T. P. Hoar, D. C. Mears, and G. P. Rothwell, *Corrosion Sci.*, **5**, 279 (1965).
17. R. P. Frankenthal, *ibid.*, **8**, 491 (1968).
18. F. A. Cotton and G. Wilkinson, "Advanced Inorganic Chemistry," p. 446, Interscience, London (1962).
19. N. Katoh, *Corrosion Sci.*, **8**, 423 (1968).
20. K. F. Lorking and J. E. O. Mayne, *Brit. Corrosion J.*, **1**, 181 (1966).
21. "Stability Constants, Part II: Inorganic Ligands," pp. 92, 105, London Chemical Society (1958).

Cathode-Overpotential and Electrosorption Effects of Additives Containing Divalent Sulfur

R. O. Loutfy[1] and A. J. Sukava*

Chemistry Department, University of Western Ontario, London, Ontario, Canada

ABSTRACT

The cathode-overpotential and electrosorption effects during electrodeposition of copper of some simple compounds containing divalent sulfur (thiols, thioacids, and mercaptoacids), under galvanostatic conditions at current densities up to 20 mA-cm^{-2}, show a behavior consistent with the simple blocking theory, according to which overpotential increments arise directly from increased true current density due to additive adsorption. The calculated free energies of adsorption indicate a net repulsive interaction between adsorbed particles and a strong specific interaction between the sulfur-containing functional group and the copper surface. The adsorption behavior of the monofunctional thiols and thioacids agrees to a first approximation with the simple Traube's rule prediction for homologous series. The bifunctional mercaptoacids, with functional groups at terminal carbons, show an alternation in adsorbability with increasing length of hydrocarbon chain, indicating that the relative adsorbability is enhanced by an odd number of carbon atoms in the molecule. The *cis*-configuration in such cases presumably results in specific adsorption of both functional groups. Adsorption free energy contributions of the structural units of the additive molecules were estimated.

Previous reports (1-3) have indicated that the cathode-overpotential effects during electrodeposition of copper of low molecular weight monocarboxylic acids can be understood in terms of simple adsorption and blocking theory. The assumption is made that the only significant effect of such additives at low surface coverages, and under galvanostatic conditions, is to increase the true current density by blocking part of the electrode surface. This has the effect of increasing the charge-transfer overpotential when the electrodeposition conditions fall in the Tafel region, *i.e.*, when charge transfer is rate controlling. The free energy of adsorption is regarded as the sum of separate contributions by the carboxyl and methylene groups in the additive molecule (after correcting for lateral interaction).

The present report deals with overpotential increments caused by the more strongly adsorbed sulfur compounds of correspondingly simple monofunctional and bifunctional structure. Short-chain thiols, thioacids, and mercaptoacids were used to compare behavior with that of monocarboxylic acids, and also as a further test of the blocking theory. Three consecutive and homologous members of each series of compounds were chosen for study, with the number of carbons varying from two to four in each case.

Experimental

The experimental procedure, with cathode overpotentials measured under galvanostatic conditions by a Luggin-probe technique, was the same as described

* Electrochemical Society Active Member.
[1] Present address: University of Guelph, Guelph, Ontario, Canada.
Key words: adsorption, homologous additives, repulsive interaction, free energy.

previously (2), except that special precautions were employed in preparing the solutions. The sulfur-containing compounds were found to form precipitates with the copper sulfate electrolyte if they were added in pure form. To prevent this precipitation, the additives were introduced in dilute form by dissolving the requisite amount in the triply distilled water that was used in preparing the solutions. All compounds were obtained commercially except thiobutyric acid, which was prepared in this laboratory. The product was distilled twice and a fraction was collected to agree with literature specifications (4). All other additives were redistilled before use.

Copper anodes with a relatively large surface area were used to prevent any possible oxidation of the sulfur compounds during electrolysis. This was accomplished by using copper wire coiled in a spiral. Copper wire cathodes, about 2 mm in diameter, were used in all cases. These were cleaned before each experiment by a dip in 50% nitric acid followed by a thorough rinse with distilled water.

Steady-state cathode overpotential measurements were made at 25° ± 0.1°C and without stirring the solutions, *i.e.*, allowing only free convection at the cathode. Measurements made at various current densities up to 20 mA-cm^{-2} showed that the Tafel region occurred with nonacidified 0.5M copper sulfate solution (see next section) at current densities greater than about 14 mA-cm^{-2}. Accordingly, the 20 mA-cm^{-2} current density for which data are reported falls in the Tafel region. At this current density, the steady-state cathode surface is polycrystalline, characteristic of the electrolyte composition and the temperature.

Results

The three thioacids, thioacetic (TAA), thiopropionic (TPA), and thiobutyric (TBA), and also mercaptoacetic acid (MAA), showed a distinctly different behavior from most organic additives in that they caused a depolarization, *i.e.*, a decrease in cathode overpotential, during electrodeposition of copper from acidified copper sulfate solution (0.5M $CuSO_4$ and 1.0M H_2SO_4). [This depolarization by mercaptoacetic acid has been noted before (5)]. However, all of these compounds behaved as normal polarizers, *i.e.*, they increased the cathode overpotential, if the electrodeposition was carried out from neutral copper sulfate solution containing no added sulfuric acid. On the other hand, the three thiols, ethanthiol (ET), propanthiol (PT), and butanthiol (BT), and the other two mercaptoacids, β-mercaptopropionic (MPA) and γ-mercaptobutyric (MBA), caused only an increase in cathode overpotential whether the solution was acidified or not. It was found as well that the overpotential increments with the latter group of compounds were essentially independent of the sulfuric acid concentration, depending only on the nature and concentration of the additive at a given current density and temperature. Accordingly, the present report is based on data obtained with nonacidified 0.5M copper sulfate solution in which all the thiols, thioacids, and mercaptoacids caused the cathode overpotential to increase. The overpotential increments shown in Fig. 1-3 were obtained from steady-state total overpotentials reproducible to ±5%, at an apparent current density of 20 mA-cm^{-2}, at 25° ± 0.1°C, and with free convection at the cathode. These increments were obtained by subtracting from the total overpotential with additive present the total overpotential (50 ± 2 mV) obtained under the same experimental conditions with neutral additive-free 0.5M copper sulfate solution.

As the data indicate, the overpotential increased with increased concentration of additive in every case. The monofunctional thiols and thioacids caused a regular increase in overpotential with increasing length of carbon chain, while the bifunctional mercaptoacids showed evidence of alternation in relative effectiveness

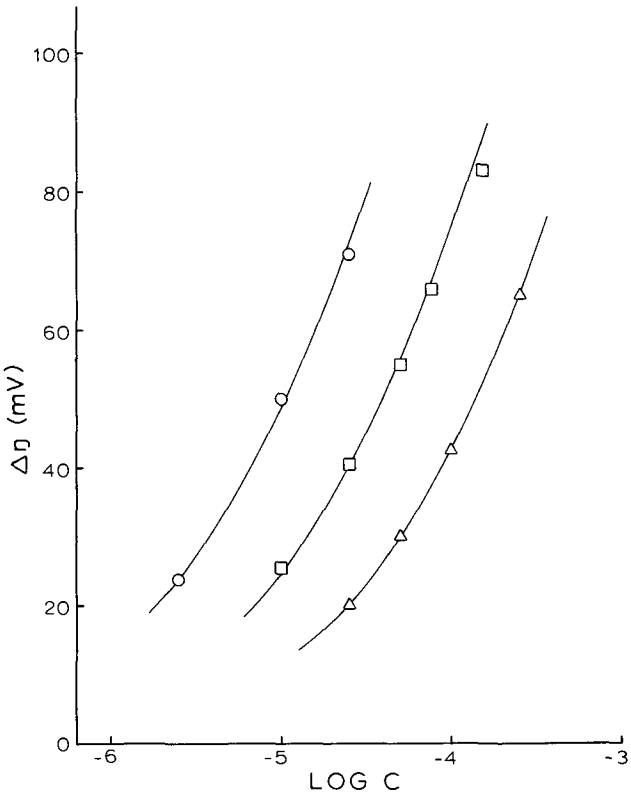

Fig. 1. Overpotential increment *vs.* logarithm of concentration, thiols: △, ET; □, PT; ○, BT.

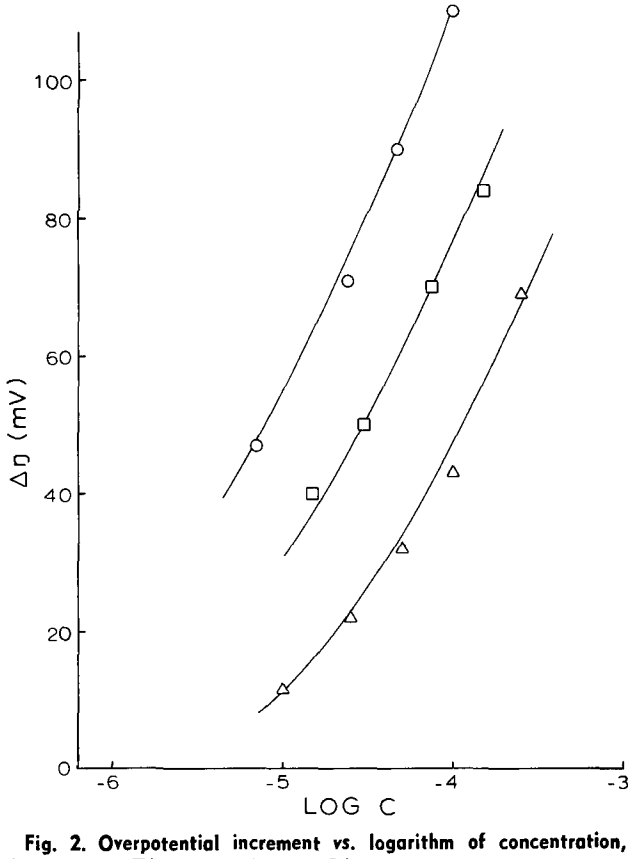

Fig. 2. Overpotential increment *vs.* logarithm of concentration, thioacids: △, TAA; □, TPA; ○, TBA.

with increasing number of carbon atoms in the molecule. A similar alternation has been observed with straight-chain dicarboxylic acids with the carboxyl groups at terminal carbons (6), indicating that bifunctional compounds in such a homologous series containing an odd number of carbon atoms are more effective

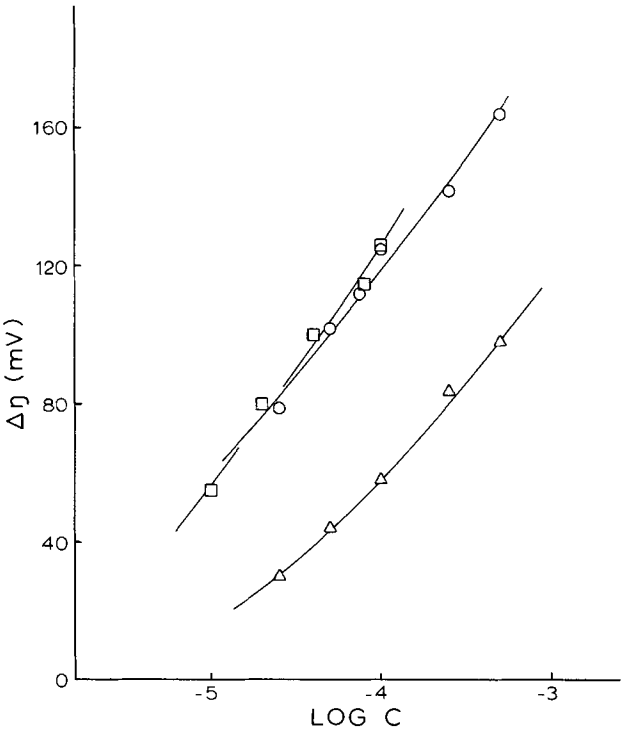

Fig. 3. Overpotential increment *vs.* logarithm of concentration, mercaptoacids: △, MAA; □, MPA; ○, MBA.

in increasing the cathode overpotential than those with an even number. This is particularly noticeable in the data for β-mercaptopropionic and γ-mercaptobutyric acids in Fig. 3.

Discussion

Methylene group adsorption and Traube's rule.— When the overpotential-increment and additive-concentration data are plotted in the form $\Delta\eta$ *vs.* log C as in Fig. 1-3, it is seen that the monofunctional thiols and thioacids behave in much the same manner as the normal monocarboxylic acids discussed previously (2). To a first approximation, and within the accuracy of the data, the $\Delta\eta$ *vs.* log C curves in Fig. 1 and 2 are parallel, indicating that Traube's rule is obeyed in the adsorption of these homologous compounds on a copper cathode. Therefore, assuming this parallelism to be correct,[2] an equation can be written by means of which the adsorption free-energy contribution of each methylene group in such molecules can be calculated directly from appropriate additive concentrations. This is done as described in Ref. (2), *i.e.*, by subtracting Eq. [5] in that reference for any two additives in a homologous series at a given overpotential increment. Accordingly, one can write for additives 1 and 2 in such a series, the simple equation

$$(x_2 - x_1)\Delta G^\circ_{CH_2} = RT \log(C_2/C_1) \qquad [1]$$

where $\Delta G^\circ_{CH_2}$ is the standard free energy of adsorption of each methylene group, including the terminal methyl, x_i is the number of methylene groups present in the molecule of additive i, and C_i is the concentration of i corresponding to a given $\Delta\eta$. Application of Eq. [1] to the data in Fig. 1 and 2 gives the value of $\Delta G^\circ_{CH_2}$ for the thiols and for the thioacids as about −760 and −790 cal/mole, respectively, which, considering the accuracy of the data, are in reasonably good agreement with the value −704 cal/mole found for monocarboxylic acids (2).

[2] It should be noted that the $\Delta\eta$ *vs.* log C curves would be expected to deviate from parallelism if the adsorbability of the methylene group is sufficiently sensitive to the change in cathode potential represented by $\Delta\eta$. The experimental data in this study are not sufficiently accurate to give conclusive evidence of such an effect.

The $\Delta\eta$ *vs.* log C curves for the mercaptoacids in Fig. 3 show that a greater, or enhanced, relative adsorbability occurs when the two functional groups at terminal carbons in such molecules are in *cis*-configuration, as they are in β-mercaptopropionic acid. This suggests that a simultaneous specific adsorption of both functional groups probably takes place, in contrast to compounds like mercaptoacetic and γ-mercaptobutyric acids in which the terminal functional groups are in *trans*-configuration, and in which these groups can therefore be expected to be more or less incapable of similar simultaneous specific attachment to the surface. It is interesting to note that if this interpretation is at least approximately correct, and if the adsorptive capabilities of the same structural units in MAA and MBA molecules are at least nearly the same, then the over-all adsorbabilities of these two compounds as indicated in Fig. 3 would be expected to differ primarily because of their difference by two methylene groups. Accordingly, in view of the approximate parallelism of the corresponding $\Delta\eta$ *vs.* log C curves in Fig. 3, Eq. [1] can be applied at any arbitrary $\Delta\eta$ to give the adsorption free energy contribution per methylene group. The value found is −710 cal/mole, which, once again, is in good agreement with the values found for thiols, thioacids, and monocarboxylic acids.

Calculation of standard free energy of adsorption.— If the blocking equation (7, 1, 2)

$$\theta = 1 - \exp(-\Delta\eta/b) \qquad [2]$$

can be applied to the data obtained for the divalent sulfur compounds in the present study, then the surface coverage θ can be calculated from the overpotential increment $\Delta\eta$ and the Tafel slope b (b was approximately 52 mV in these experiments). Then, in turn, the over-all standard free energy of adsorption can be calculated if an appropriate adsorption isotherm can be chosen. In previous work with homologous monocarboxylic acids (2), use was made of a modified version of the Bockris-Swinkels isotherm (8)

$$\frac{\theta}{(1-\theta)^n} \cdot \frac{\{\theta + n(1-\theta)\}^{n-1}}{n^n} = \frac{C}{55.5} \exp(-\Delta G^\circ_a/RT) \qquad [3]$$

in which a coverage-dependent parameter $g(\theta)$ was included by writing

$$\Delta G^\circ_a = \Delta G^\circ_p + x\ \Delta G^\circ_{CH_2} + g(\theta) \qquad [4]$$

where ΔG°_p is the standard free energy of adsorption of the polar functional group, $\Delta G^\circ_{CH_2}$ the free energy contribution of each methylene group, x the number of methylene groups present, and $g(\theta)$ a coverage-dependent apparent standard free energy attributable to lateral interaction between adsorbed molecules (2, 3, 9). Any potential dependence of the free energy of adsorption is considered in Eq. [4] to be incorporated primarily in the term ΔG°_p (3), since, to a first approximation, $\Delta G^\circ_{CH_2}$ can be considered sufficiently insensitive to potential change to the extent that the parallelism of the $\Delta\eta$ *vs.* log C curves such as those in Fig. 1 is correct. This means that ΔG°_p in [4] is coverage-dependent, along with $g(\theta)$, because the cathode potential (viz., $\Delta\eta$) is directly dependent on coverage under galvanostatic conditions.

Application of Eq. [2] and [3] to the sulfur compounds in the present study gave the results shown in Fig. 4 for ethanthiol, thioacetic acid, and mercaptoacetic acid. Free energy values were calculated at various coverages, taking the solvent displacement number as 2 since the projected cross-sectional area of these molecules can be expected to be nearly the same as for monocarboxylic acids (2). Free energy values were then calculated as well for $n = 1$, to give

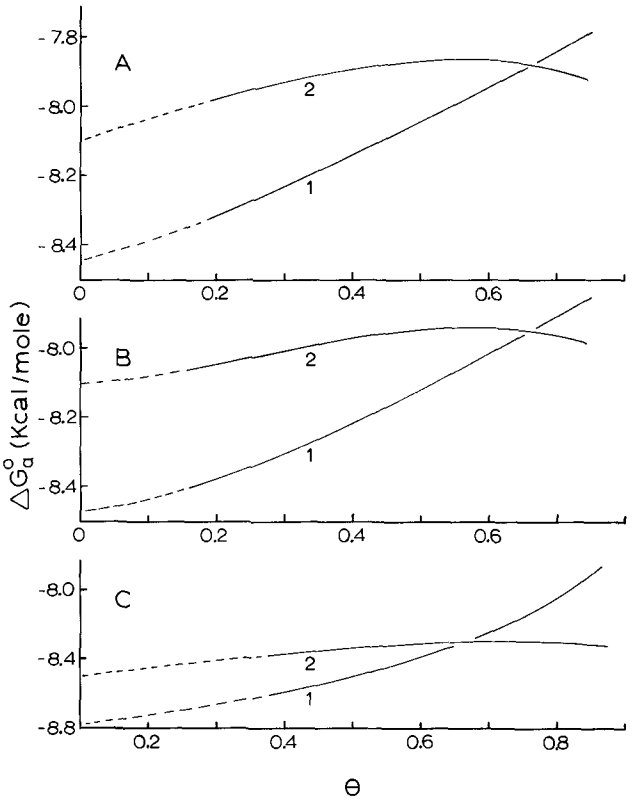

Fig. 4. Adsorption free energy vs. coverage: A, ET; B, TAA; C, MAA; 1, $n = 1$; 2, $n = 2$.

a comparison with what amounts essentially to use of the Frumkin isotherm (10)

$$\frac{\theta}{1-\theta} = \frac{C}{55.5} \exp\left[\frac{-\Delta G^{\circ}_{a}}{RT} + 2a\theta\right]$$

in which the interaction term $2a\theta$ corresponds to our $-g(\theta)/RT$. The two separate curves for each compound are shown in Fig. 4.

An important observation arising from Fig. 4 is that thiols, thioacids, and mercaptoacids undergo a net repulsive interaction when they are adsorbed on copper from neutral solution. The magnitude of the potential dependence of ΔG°_{p} has not been determined, but if it can be assumed that lateral interaction is the dominant influence in causing the coverage dependence of ΔG°_{a} as calculated from Eq. [3], then $g(\theta)$ in [4] will be opposite in sign to ΔG°_{p} and $\Delta G^{\circ}_{CH_2}$ for the sulfur compounds used. This is in contrast to the net attractive interaction found in the adsorption of monocarboxylic acids from acidified copper sulfate solution (2), where $g(\theta)$ has the same sign as ΔG°_{p} and $\Delta G^{\circ}_{CH_2}$.

Mutual lateral repulsion between adsorbed particles is easily understood, and can in fact be expected, in the case of thioacetic and mercaptoacetic acids in neutral solution. These compounds, in view of their acid ionization constants which are 4.7×10^{-4} and 4×10^{-4}, respectively, (4), will occur primarily in ionic form in the neutral copper sulfate solution and at the concentrations used in our experiments. Accordingly, a dominant ion-ion repulsion can be expected in the adsorbed phase. The free energies of adsorption of the functional groups in these compounds, *i.e.*, ΔG°_{p} in Eq. [4], should therefore be considered as applying to the anionic rather than the molecular form (see estimated values below). On the other hand, the much lower acidity of ethanthiol, for which $K = 2.5 \times 10^{-11}$ (4), means that the dissolved species at our experimental concentrations is primarily the molecular form[3] and so the net repulsive interaction as seen in Fig. 4 might be speculatively attributed perhaps to parallel orientation of dipoles, as would be the case if the molecules were adsorbed with the dipoles perpendicular to the surface. This point, admittedly, requires further study and clarification.

The rough extrapolations in Fig. 4 give estimates of ΔG°_{a} at zero coverage. These in turn give estimates of the limiting zero-coverage value of ΔG°_{p} in Eq. [4] since $\Delta G^{\circ}_{CH_2}$ is known from Eq. [1] and since $g(\theta)$ approaches zero as θ approaches zero. The ΔG°_{p}-values obtained correspond to the cathode-potential state (3) at which the overpotential is experimentally fixed at 50 ± 2 mV, the value found for the additive-free neutral copper sulfate solution at the experimental current density and temperature. The roughly approximate values for $n = 2$ are, in cal/mole: —SH, —6580; —COS^-, —7300; and HS----COO^-, —7740. For $n = 1$ they are: —SH, —6930; —COS^-, —7660; and HS----COO^-, —8090. The magnitudes of the free energies are indicative of physical adsorption forces. They indicate as well a relatively strong interaction between the functional groups in these additives and the copper surface.

Due to some uncertainties, no satisfactory explanation can be offered at present for the apparent maximum and the subsequent downward trend with increasing coverage in the curves for $n = 2$ in Fig. 4. Further study is required to examine not only the reliability of the experimental data but also the possible extent to which the blocking theory, Eq. [2], is inapplicable to charged adsorbates as in the present case (see below). In addition, information is required on the coverage (potential) dependence of ΔG°_{p}. Certainly, this kind of change from repulsive to attractive interaction would not be expected with thioacetic and mercaptoacetic acids if lateral interaction remains the dominant influence in the coverage dependence of adsorbability. These compounds are about 85 and 75% ionized, respectively, at the concentrations corresponding to the maxima in the curves in Fig. 4, and, accordingly, ion-ion repulsion would be expected to continue as a dominant effect in the adsorbed phase. Change in orientation of ethanthiol molecules might occur to account for a change in the nature of the interaction, but speculation of this kind is scarcely justified with present data.

Real and apparent surface coverage.—Ionic adsorbates such as the thioacids and mercaptoacids used in the present study can be expected to affect the surface activity of Cu^{2+} ions within the charge field of the adsorbate particles. The resulting effect on the true charge-transfer current density over uncovered portions of the cathode surface in such instances will mean that application of the blocking theory to galvanostatic overpotential increments will give surface coverages that are apparent rather than real. The adsorption free energies estimated for these compounds in this work should therefore be regarded as apparent to the extent that the adsorbate charge is important.

Acknowledgment

Financial support for this work from the National Research Council, Ottawa, is gratefully acknowledged.

Manuscript submitted July 3, 1972; revised manuscript received Sept. 11, 1972.

Any discussion of this paper will appear in a Discussion Section to be published in the December 1973 JOURNAL.

REFERENCES

1. A. K. P. Chu and A. J. Sukava, *This Journal*, **116**, 1188 (1969).
2. R. O. Loutfy and A. J. Sukava, *ibid.*, **118**, 216 (1971).
3. R. S. Salter, P. Seto, and A. J. Sukava, *ibid.*, **119**, 852 (1972).
4. E. E. Reid, "Organic Chemistry of Bivalent Sulfur," Chemical Publishing Co., Inc., New York (1958).

[3] Ethanthiol would be only about 0.3% ionized at 2.5×10^{-5} mole/liter, the lowest concentration used in this study.

5. A. J. Sukava and C. A. Winkler, *Can. J. Chem.*, **34**, 128 (1956).
6. R. O. Loutfy, Ph.D. Thesis, University of Western Ontario (1971).
7. R. S. Hansen and B. H. Clampitt, *J. Phys. Chem.*, **58**, 908 (1954).
8. J. O'M. Bockris and D. A. L. Swinkels, *This Journal*, **111**, 736 (1964).
9. B. E. Conway, "Theory and Principles of Electrode Processes," Chap. 5, Ronald Press (1965).
10. B. B. Damaskin, O. A. Petrii, and V. V. Batrakov, "Adsorption of Organic Compounds on Electrodes," English Translation, Plenum Press, New York (1971).

Cathodic Reduction Pathways of Haloaromatics

III. Halonitrobenzenes

Robert F. Nelson* and A. K. Carpenter
Department of Chemistry, University of Idaho, Moscow, Idaho 83843

and Eddie T. Seo*
TRW Systems Group, TRW, Inc., Redondo Beach, California 90278

ABSTRACT

All of the monohalogenated nitrobenzenes have been studied in nonaqueous media using various electrochemical and spectroscopic methods. A mechanism involving halide elimination and hydrogen atom abstraction from the solvent to form nitrobenzene was verified by deuteration experiments employing electron paramagnetic resonance measurements. In addition to formation of nitrobenzene, azoxybenzenes and nitrobiphenyls could be generated under different experimental conditions. Possible electrosynthesis studies are also proposed based on these data.

Several years ago, Holleck and Becher noted anomalous polarographic waves in the reduction of *p*-bromo- and *p*-iodonitrobenzene (1). Earlier, Maki and Geske had also observed anomalous behavior with *p*-iodonitrobenzene and had been unable to obtain an electron paramagnetic resonance (EPR) spectrum for the reduced compound (2). Subsequently, several pathways were proposed for the electrochemical reduction of monohalogenated nitrobenzenes in nonaqueous media (3-7). Except for minor differences, they all entailed an over-all transfer of three electrons and the expulsion of a halide ion after the first electron transfer. Nitrobenzene anion radical was identified as the final product.

More recently, alternate pathways have been suggested based on data showing clearly that the over-all process involves two electrons and not three as previously proposed. This possibility was initially proposed by Seo and Nelson (8) and expanded upon by Lawless and Hawley (9). Basically, the electrode process was found to involve an initial one-electron reduction to the halonitrobenzene anion radical; the ensuing decomposition reaction consists of a loss of halide ion and extraction of a hydrogen atom from the electrochemical medium (8, 9), not necessarily in that order. The halogen elimination step has been proposed to be a reversible equilibrium process (9). Further studies are reported herein concerning the source of the abstracted hydrogen atoms and alternate reaction pathways of the intermediate nitrophenyl radicals.

Experimental

Chronoamperometric and chronopotentiometric measurements were made by using a transistorized version of a multipurpose instrument designed for experiments in electrochemistry (10). Data were recorded on a Hewlett-Packard Model 7035A X-Y plotter; short-time data were displayed on a Tektronix Type 535A oscilloscope with Type "D" plug-in unit and photographed. Controlled-potential electrolyses were carried out using a Wenking 61RH potentiostat and associated instrumentation (11).

The purification of the solvents, acetonitrile (AN), N,N-dimethylformamide (DMF), and propylene carbonate (PC), has been described (12, 13); benzonitrile was vacuum distilled and stored over Linde 4A molecular sieves. The supporting electrolyte was tetraethylammonium perchlorate (TEAP). Electrochemical cell design and electrodes have been described (12). All the halogenated nitrobenzenes were obtained from commercial sources and purified through recrystallization or distillation. Deuterated acetonitrile (99%) and deuterium oxide (99.9%) were obtained from Bio-Rad Laboratories and U.S. Nuclear Corporation.

The electron paramagnetic resonance studies were carried out using a Varian Associates Model E-3 spectrometer. *In situ* electrolyses in the microwave cavity were carried out at a platinum-gauze working electrode. The electrolysis cell for use in the solution compartment of a Cary Instrument Model 14 spectrophotometer has been described (14).

Results and Discussion

Electrochemical studies.—The data from cyclic voltammetry, chronoamperometry, and chronopotentiometry experiments carried out with all the isomeric halonitrobenzenes are summarized in Table I. The half-peak potentials, $E_{p/2}$, are in reasonable agreement with reported values obtained in AN at platinum (9) and DMF at a mercury working electrode (5, 7); some differences are to be anticipated from solvent and electrode effects due to the influence of chemical reactions associated with the electron-transfer processes (15). From the $i_p v^{-1/2} C^{-1}$, $it^{1/2} C^{-1}$, and $i\tau^{1/2} C^{-1}$ data, one can estimate the number of electrons involved in the first reduction step relative to nitrobenzene, a reversible one-electron redox process under the conditions of our experiments (16, 17). Note that the peak current and the chronoamperometric and chronopotentiometric quotient for most of the halonitrobenzenes approximate those of nitrobenzene. Also, cyclic voltammograms of these compounds show peak current ratios (cathodic to anodic) that are close to unity. The data indicate that these nitrobenzenes undergo a reversible (in an electrochemical sense) one-electron reduction to form their respective anion radicals. Verification is provided by EPR spectra obtained for these compounds by *in situ* electrolysis experiments; the spectra are readily interpretable in terms of the primary halonitrobenzene anion radicals (2, 3, 7, 16, 18, 19); slight variations in hyperfine splittings are attributable to solvent effects.

The other halonitrobenzenes exhibit electrochemical behavior that differs from that of nitrobenzene; for

* Electrochemical Society Active Member.
Key words: halonitrobenzenes, halide elimination, hydrogen abstraction, radical anions, deuteration.

Table I. Electrochemical data for halonitrobenzenes

No.	R	$-E_{p/2}$,[a] V *vs.* SCE	$i_p v^{-1/2} C^{-1}$,[b] μA V$^{-1/2}$ sec$^{1/2}$ mF^{-1}	$it^{1/2} C^{-1}$,[c] μA sec$^{1/2}$ mF^{-1}	$i\tau^{1/2} C^{-1}$,[d] μA sec$^{1/2}$ mF^{-1}	k,[e] sec^{-1}
1	o-F	1.10	256	65.0	106[f]	0.004[g]
2	*m*-F	1.13	248	64.0	107	0.002[g]
3	*p*-F	1.13	248	64.0	106	0.003[g]
4	o-Cl	1.10	248	63.0[h]	108[f]	0.009
5	*m*-Cl	1.04	240	60.0	103[f]	0.003[g]
6	*p*-Cl	1.06	259	63.5[h]	108[f]	0.006
7	o-Br	1.15[i]	442-488[j]	126[k]	212[k]	20.0
8	*m*-Br	1.00	232	58.0	102[f]	0.005
9	*p*-Br	1.03	232-248[j]	60.5[h]	100[f]	0.012
10	o-I	1.13[i]	449-465[j]	127[k]	203[k]	>100
11	*m*-I	1.02[i]	232-263	63.0[h]	102[f]	0.057
12	*p*-I	1.04[i]	248-294[j]	61.0[h]	105[f]	0.64
13	H	1.14	267	65.0	110	—

[a] Measured in AN/0.1F TEAP, Pt working electrode.
[b] Measured at scan rates from 0.033 to 0.33 V sec^{-1}.
[c] Chronoamperometric data obtained from current-time curves (pen and ink).
[d] Chronopotentiometric data obtained from potential-time curves (pen and ink).
[e] First-order rate constants for halonitrobenzene decomposition. Values cited are ±20%.
[f] Increases with decreasing current density.
[g] Too slow to be measured in AN. Data obtained in PC/0.2F TEAP.
[h] Increases slowly with time.
[i] Potential is shifted by the chemical reactions; $E_{p/2}$ varies with scan rate.
[j] Increases with decreasing scan rate.
[k] Limiting two-electron value.

example, the value for the peak current function, $i_p v^{-1/2} C^{-1}$, increases with decreasing scan rate. Such behavior can be ascribed to an ECE (electrochemical-chemical-electrochemical) mechanism where the intermediate step (chemical reaction) is relatively slow (20).

The $i_p v^{-1/2} C^{-1}$ values for o-bromo- and o-iodonitrobenzenes are almost twice that for a one-electron process. This result is characteristic of a fast ECE process (the chemical reaction essentially goes to completion during the time span of the measurement) where both electrochemical steps involve a one-electron transfer. Both electrochemical steps occur at nearly the same potential or, in a reduction, the second occurs at less negative potential. The significance of these peak current data is that a total of two electrons are involved in the over-all process. Previously reported mechanisms required three electrons in the over-all reductions. The two-electron data from cyclic voltammetry are supported by exhaustive controlled-potential electrolysis. The major product is nitrobenzene anion radical.

In Fig. 1, the chronopotentiometric quotient, $i\tau^{1/2} C^{-1}$, is plotted as a function of current. The figure graphically illustrates the variations in chronopotentiometric behavior. All the compounds except o-iodonitrobenzene exhibit or approach one-electron reduction behavior at short transition times (high currents); the one-electron reduction corresponds to the first electrochemical step, the first "E" of the ECE process. The figure provides a qualitative picture of the relative stabilities of the intermediate reduction product (halonitrobenzene anion radical). The more stable the intermediate, the lower the current at which one-electron behavior is attained.

The data are consistent with the ECE mechanism previously proposed (8, 9) in which the halonitrobenzene undergoes (*i*) electrochemical reduction to its anion radical, followed by (*ii*) elimination of halogen and formation of nitrobenzene, and (*iii*) electrochemical reduction of the resulting nitrobenzene to its anion radical. Identification of the latter anion radical by EPR leaves no doubt as to its formation; this was done for all the isomers, although for several of the derivatives (1-6, 8) rather prolonged electrolysis was necessitated.

Controlled-potential electrolyses were carried out with the three iodonitrobenzenes because these compounds undergo very rapid elimination reactions, therefore permitting easier product analysis. None of the electrochemical or spectroscopic techniques detected the presence of any organic compound other than nitrobenzene and its anion radical as final product at low concentrations (10^{-3} M or less) of parent halo-

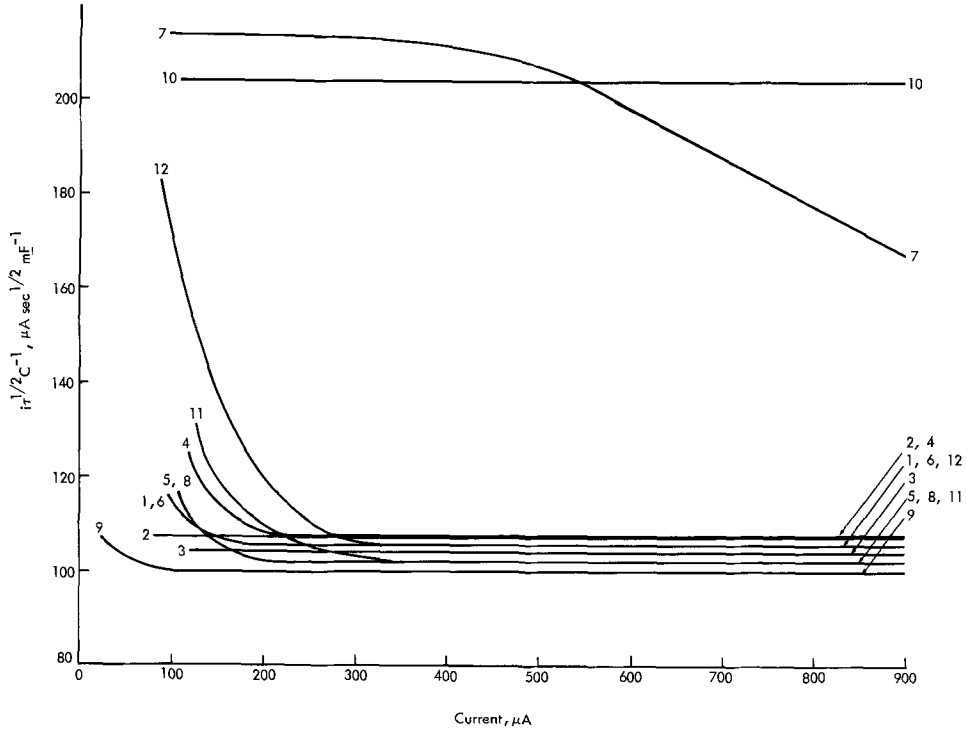

Fig. 1. Chronopotentiometric data taken from potential-time curves. Numbers correspond to those in Table I. Individually plotted points have been omitted to avoid confusion. Electrode area, 0.234 cm^2.

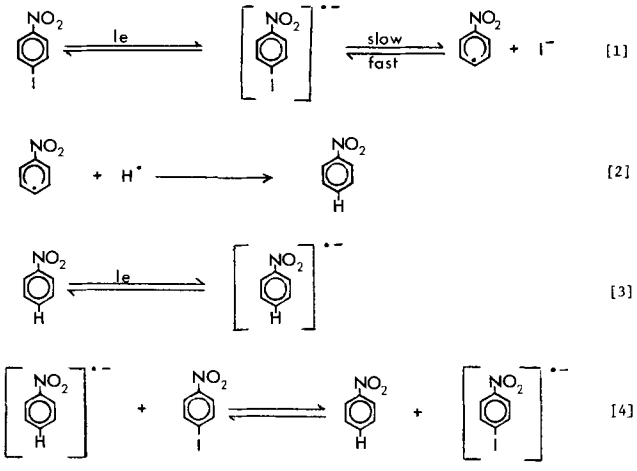

nitrobenzene. Neither isolation and analysis of products nor thin-layer chromatography of the electrolyte solution after exhaustive electrolysis indicated compounds other than starting materials and nitrobenzene.

The proposed mechanism is as shown in Eq. [1]-[4] above for *p*-iodonitrobenzene; all the halonitrobenzenes have similar reduction behavior.

The equilibrium in Eq. [1] has been inferred from more recent studies involving the coupling of anions with electrolytically generated nitrophenyl radicals (22) and is still debatable. In addition, the order of halogen elimination and hydrogen atom abstraction has not been unequivocally established, but it is clear that this process is a first-order ECE process with the chemical step involving decomposition of the halonitrobenzene anion radical and each electron transfer process being one-electron in nature. The rate constants for the intermediate decomposition reaction were measured with chronoamperometric data using digital simulation working curves (22, 23). Although the chemical redox process shown in Eq. [4] is of some importance in these systems based on the redox potentials of nitrobenzene and the halo derivatives, the working curve for the K = $^0/_0$ case was used. This case neglects the effects of any ECC (electrochemical-chemical redox-chemical) complications such as in Eq. [4] and considers the process as a pure ECE. The rate constants obtained are given in Table I; the values are ±20% for the very fast and very slow reactions, with better precision for the intermediate rates. Since the effect of the ECC "nuance" is not being accounted for, the absolute values of the rate constants are not completely valid; however, relative rates in the series can be examined with a good deal of confidence. In addition, these data cannot be compared directly with those of Hawley and co-workers since their rate measurements were done in the presence of added halide (9), or in DMF as solvent (24). The anion radicals of all three fluoronitrobenzenes and *m*-chloronitrobenzene have decomposition rates that are too slow to be measured in acetonitrile before convection sets in (10-12 sec). These compounds were studied in the more viscous solvent propylene carbonate. There is certainly a solvent effect on the rate constant values (9), but since the *k*'s for these compounds are only reported to one significant figure this is not considered a serious problem. The decomposition rate for the *o*-iodonitrobenzene system, on the other hand, is too rapid to be followed potentiostatically. Studies using rotating-disk electrode techniques for the determination were unsuccessful due to fouling of the disk by electrolysis products.

The data correlate nicely with the chronopotentiometric curves in Fig. 1. In terms of isomers, the rate constants follow the order, $k_m < k_p < k_o$; in terms of the halogen substituent, they follow the order, $k_F < k_{Cl} < k_{Br} < k_I$. For chloro-and fluoronitrobenzenes, the respective *ortho*- and *para*-isomers exhibit comparable decomposition rates, with the *ortho*-isomer having a slightly greater rate because of steric effects. However, the ratio of rate constants, k_o/k_p, increases substantially with the bromo and iodo isomers.

EPR studies.—A series of EPR experiments were devised in order to determine the source of the abstracted hydrogen atoms. When the various halonitrobenzenes are electrolyzed *in situ* in the EPR spectrometer cavity, nitrobenzene anion radical appears after varying electrolysis times. For the more stable halonitrobenzene anions, several hours are required before nitrobenzene anion radical is observed. For species with intermediate primary radical stability, one obtains mixed spectra representing the halonitrobenzene anion radical and a gradually increasing amount of nitrobenzene anion radical. Prolonged electrolysis leads to a spectrum of only the latter radical. When elimination is rapid, only the nitrobenzene anion radical spectrum is seen. Figure 2 shows a typical spectrum resulting from *o*-iodonitrobenzene reduction. The resolution is not outstanding, but the spectrum is undoubtedly that of nitrobenzene anion radical.

To determine if the loss of halide followed by hydrogen abstraction from water (or vice versa) represented the proper mechanism, experiments were carried out in which several of the halonitrobenzenes were electrolyzed in acetonitrile containing small amounts of deuterium oxide. If deuterium abstraction by a nitrophenyl radical occurred, deuterium would be incorporated into the nitrobenzene molecule and the EPR spectrum of the secondary anion radical would be different from that of nitrobenzene anion radical. A proton (I = ½) gives a doublet EPR splitting, whereas a deuterium (I = 1) in the same substituent position gives rise to a triplet with a coupling constant about 1/6th that of the proton. Therefore, if a deuterium were incorporated into the position of the eliminated halogen, a spectrum for deuterated nitrobenzene anion radical should result. Figure 3 shows the spectrum obtained from *m*-iodonitrobenzene in AN containing 1% deuterium oxide by volume. The amount of deuterium oxide is far in excess of the amount of water present in purified AN. Smaller amounts (0.1 to 1%) of D_2O gave similar results. Although a solvent effect results from the presence of deuterium oxide, changing the coupling constants slightly, the spectrum obtained is that of nitrobenzene anion radical; deuterium is not incorporated. Identical results were obtained for o- and *p*-iodonitrobenzenes.

Electrolysis of the three iodonitrobenzenes in perdeuteroacetonitrile, CD_3CN, led to spectra that could not be interpreted in terms of nitrobenzene anion radical. Figure 4 shows the spectrum obtained from electrolysis of *m*-iodonitrobenzene in CD_3CN; the spectrum is different from that of nitrobenzene anion radical and can be interpreted as that of *m*-deuteronitrobenzene anion radical. Similar results were obtained for the o- and *p*-iodonitrobenzenes in CD_3CN. In all cases, experimental spectra agreed with computer-plotted curves; over-modulated spectra were

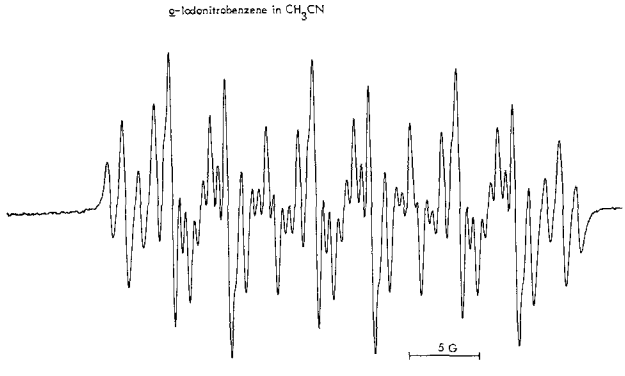

Fig. 2. EPR spectrum obtained from *in situ* electrolysis of o-iodonitrobenzene (1.0 x 10^{-3}*F*) in AN/0.1*F* TEAP at a platinum gauze electrode.

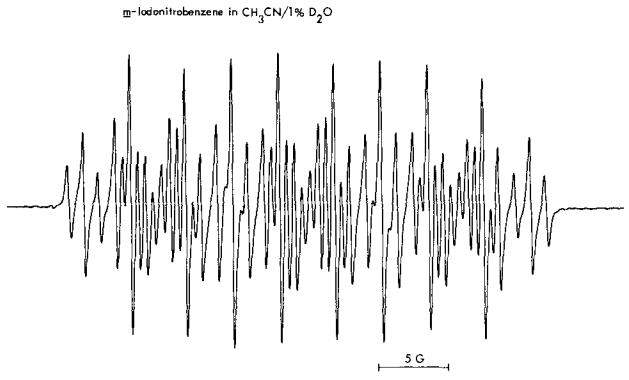

Fig. 3. EPR spectrum obtained from *in situ* electrolysis of *m*-iodonitrobenzene (1.0 x 10^{-3}*F*) in AN/0.1*F* TEAP containing 1 volume per cent D_2O. This is the secondary radical spectrum obtained at a platinum gauze electrode. The parent radical spectrum is observed first, but it is slowly replaced by the spectrum shown in the figure.

identical with those of Ward obtained from authentic deuteronitrobenzenes (25).

Electrolysis of nitrobenzene in CD_3CN produced only nitrobenzene anion radical, thus excluding rapid exchange of deuterium between the solvent and some nitrobenzene species.

Electrosynthesis considerations.—It was mentioned earlier that the only product detected in these systems is nitrobenzene; in fact, this is true only under very limited conditions, namely AN/TEAP with concentrations of halonitrobenzene at or below the millimolar level. As the concentration is increased the yield of nitrobenzene diminishes markedly and the system becomes more complicated. Since the nitrophenyl radical is a possible intermediate in these systems it was anticipated that at higher concentrations of halonitrobenzene one might observe coupling to form 4,4′-dinitrobiphenyl. In fact, the presence of 4,4′-dinitrobiphenyl was verified early in the electrolysis at these concentration levels (10^{-3}M) by its characteristic radical EPR and visible absorption spectra (purple radical). However, when 10^{-2} and 10^{-1}M solutions of *p*-iodonitrobenzene in AN/TEAP were exhaustively electrolyzed no 4,4′-dinitrobiphenyl could be isolated, although the color of the solutions suggested its presence early in the electrolysis. This is partially explained by the observation that electrolysis of authentic samples of 4,4′-dinitrobiphenyl produced a variety of color changes and it was apparent that the system was not completely reversible; in the time scale of a mass electrolysis any 4,4′-dinitrobiphenyl formed could decompose and thus not be isolated.

In an attempt to remove the source of hydrogen atoms and force generation of the dinitrobiphenyl, several electrolyses were run in benzonitrile/$NaClO_4$ solutions. Benzonitrile is a very poor solvent for electrosynthesis studies, primarily because it is so difficult to remove after electrolysis. The EPR spectra run on these solutions indicated the presence of a radical other than that of nitrobenzene; a great deal of fine structure was present on a spectrum consisting basically of a 3 × 3 × 3 pattern. It was suspected that the intermediate nitrophenyl radical was attacking the benzonitrile to form a substituted nitrocyanobiphenyl; although the EPR spectrum was rich in fine structure, it could not be sufficiently resolved for interpretation. This type of reaction pathway had been previously speculated upon in the electrochemical reduction of *o*-halonitrobenzenes (9) and is in keeping with reports of the propensity of nitrophenyl radicals for aromatic systems (26).

In an effort to verify this pathway by generating a known compound, *p*-iodonitrobenzene was electrolyzed in 50:50 mole per cent AN/benzene. Preliminary EPR and cyclic voltammetric studies indicated that, in fact, 4-nitrobiphenyl was being formed in appreciable amounts in millimolar solutions; spectral and electrochemical data were positively matched with an authentic sample of 4-nitrobiphenyl. Controlled-potential electrolyses of 10^{-2}M solutions yielded a 20% yield of the 4-nitrobiphenyl from *p*-iodonitrobenzene. The same process was also verified by EPR when *p*-iodonitrobenzene was electrolyzed in MeCN/toluene. Thus, this appears to be a rather general reaction pathway in which the intermediate nitrophenyl radical attacks substituted benzenes to form the corresponding nitrobiphenyls. Further studies are in progress to maximize yields in these systems and define the types of products that can be formed by this method.

It had been noted in early studies on these systems that in cases where the halogen did not appear to eliminate under electrochemical conditions nitrobenzene was formed by further reduction of the halonitrobenzene anion radical (3). This has been further verified by Lawless and Hawley, who reduced *p*-bromonitrobenzene in DMF/TEAP and found that at −2.0V dilute solutions (10^{-3}M) yielded appreciable amounts of nitrobenzene (27). In AN/TEAP, however, *p*-bromonitrobenzene yields nitrobenzene anion radical upon prolonged electrolysis past the first reduction wave (verified by EPR) as shown in Fig. 5. Exhaustive electrolysis of dilute solutions of *p*-bromonitrobenzene at −2.0V in AN/TEAP also yields nitrobenzene as the primary product, but as the concentration of the halonitrobenzene is increased to 10^{-2}M and above the presence of another product becomes increasingly prominent. Comparison of *IR* spectra, melting points, and cyclic voltammetric curves of the electrolysis product with an authentic sample showed it to be 4,4′-dibromoazoxybenzene, formed in a second-order process. This is obviously a multi-electron process and no attempt was made to investigate the mechanism. In addition, the yield of the azoxybenzene is contingent upon the applied potential and n-value, but is typically about 50-60%. These conditions were not tried with any other halonitrobenzenes, but it is likely that the same pathway will apply to any of the systems where the halogen elimination rate is slow.

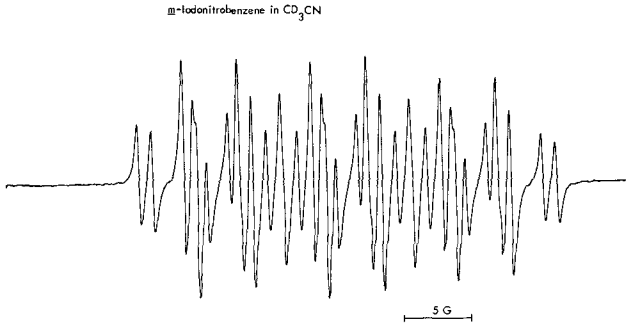

Fig. 4. EPR spectrum obtained from *in situ* electrolysis of *m*-iodonitrobenzene (1.0 x 10^{-3}*F*) in CD_3CN/0.1*F* TEAP at a platinum gauze electrode.

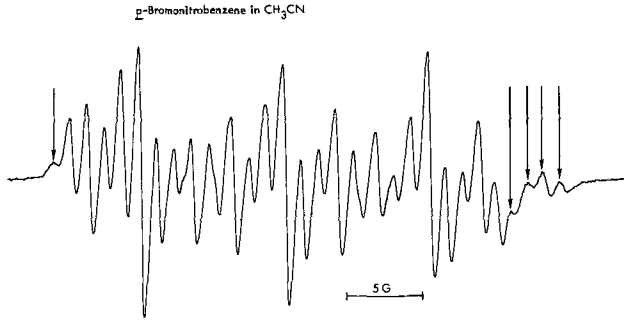

Fig. 5. EPR spectrum obtained from *in situ* electrolysis of *p*-bromonitrobenzene (1.0 x 10^{-3}*F*) in AN/0.1*F* TEAP at a platinum gauze electrode. Spectrum was recorded after 45 min electrolysis at −1.2V. The arrowed lines are due to nitrobenzene anion radical; the spectra are asymmetrical due to different g-values.

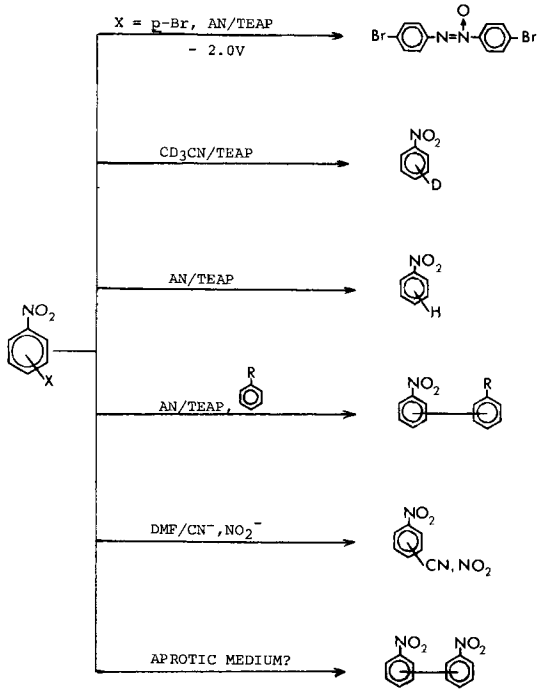

Fig. 6. Products obtained or potentially obtainable from halonitrobenzenes on a synthesis scale.

It has also been shown previously (24) that anions such as CN^- and NO_2^- can be added to the intermediate nitrophenyl radicals to form substituted nitrobenzenes. This type of reaction was not attempted on a synthesis scale, but studies are now in progress toward this end.

Attempts to generate appreciable yields of 4,4'- and 2,2'-dinitrobiphenyls from the corresponding halonitrobenzenes have been singularly unsuccessful. In order to do this, one would have to work in a solvent with a very low hydrogen atom availability (such as liquid SO_2) to avoid nitrobenzene formation. However, at concentrations suitable to electrosynthesis work, the competing reaction of azoxybenzene formation may become significant. Since the dinitrobiphenyls can also be synthesized in high yields by simple Ullmann reactions involving the chloronitrobenzenes this does not appear to be a promising electrosynthesis area.

From the viewpoint of synthesis studies, then, the halonitrobenzenes appear to be well suited to obtaining different products under variable electrolysis conditions. The products obtained, or potentially obtainable on a synthesis scale, are summarized in Fig. 6. Studies are now in progress to improve the yields in these systems and extend the range of products that can be obtained.

Acknowledgment

The authors are grateful to Dr. R. W. Fish for many helpful discussions and to J. F. Ambrose, S. J. Kinsey, and G. Manning for technical assistance. This study was supported through the Petroleum Research Fund (Grant No. 1039-G3), the Independent Research and Development Program of TRW Systems Group, TRW Inc., and NSF Grant No. GP-31199. Special thanks are also due to Dr. R. N. Adams and Dr. D. E. Smith for their support and encouragement.

Manuscript submitted July 12, 1972; revised manuscript received Sept. 15, 1972. This was Paper 207 presented at the Boston Meeting of the Society, May 5-9, 1968.

Any discussion of this paper will appear in a Discussion Section to be published in the December 1973 JOURNAL.

REFERENCES

1. L. Holleck and D. Becher, *J. Electroanal. Chem.*, **4**, 321 (1962).
2. A. H. Maki and D. H. Geske, *J. Am. Chem. Soc.*, **83**, 1852 (1961).
3. T. Fujinaga, Y. Deguchi, and K. Umemoto, *Bull. Chem. Soc. Japan*, **37**, 822 (1964).
4. T. Fujinaga, T. Arai, and C. Kitazawa, *Nippon Kagaku Zasshi*, **85**, 811 (1964).
5. T. Fujinaga, T. Arai, and K. Umemoto, 17th CITCE Meeting, Tokyo, September 1966, Abs. No. B 214.
6. T. Fujinaga, K. Izutsu, K. Umemoto, T. Arai, and K. Takaoka, *Nippon Kagaku Zasshi*, **89**, 105 (1968).
7. T. Kitagawa, T. P. Layloff, and R. N. Adams, *Anal. Chem.*, **35** 1086 (1963).
8. (a) E. T. Seo and R. F. Nelson, 133rd National ECS Meeting, Boston, May 1968, Abstract 207; (b) R. F. Fogle, E. T. Seo, and H. P. Silverman, "Voltammetric Studies on Non-aqueous Systems," Final Report on Contract DA-28-043-AMC-02464(E), December 1967, AD 668936.
9. J. G. Lawless and M. D. Hawley, *J. Electroanal. Chem.*, **21**, 365 (1969).
10. M. D. Hawley, Private communication.
11. P. Peterson, A. K. Carpenter, and R. F. Nelson, *J. Electroanal. Chem.*, **27**, 1 (1970).
12. E. T. Seo, R. F. Nelson, J. M. Fritsch, L. S. Marcoux, D. W. Leedy, and R. N. Adams, *J. Am. Chem. Soc.*, **88**, 3498 (1966).
13. R. F. Nelson and R. N. Adams, *J. Electroanal. Chem.*, **13**, 184 (1967).
14. J. F. Ambrose, M. S. Thesis, Sacramento State College, 1968.
15. R. S. Nicholson and I. Shain, *Anal. Chem.*, **36**, 706 (1964).
16. D. H. Geske and A. H. Maki, *J. Am. Chem. Soc.*, **82**, 2671 (1960).
17. B. Kastening, *Electrochim. Acta*, **9**, 241 (1964).
18. P. B. Ayscough, F. P. Sargent, and R. Wilson, *J. Chem. Soc.*, **1963**, 5418.
19. P. L. Kolker and W. A. Waters, *ibid.*, **1964**, 1136.
20. R. S. Nicholson and I. Shain, *Anal. Chem.*, **37**, 178 (1965).
21. D. E. Bartak, W. C. Danen, and M. D. Hawley, *J. Org. Chem.*, **35**, 1206 (1970).
22. M. D. Hawley and S. W. Feldberg, *J. Phys. Chem.*, **70**, 3459 (1966).
23. R. N. Adams, M. D. Hawley, and S. W. Feldberg, *ibid.*, **71**, 851 (1967).
24. W. C. Danen, T. T. Kensler, J. G. Lawless, M. F. Marcus, and M. D. Hawley, *ibid.*, **73**, 4389 (1969).
25. R. Ward, *J. Chem. Phys.*, **30**, 852 (1959).
26. R. Ito, T. Migita, N. Morikawa, and O. Simamura, *Tetrahedron*, **21**, 955 (1965).
27. J. G. Lawless and M. D. Hawley, *J. Electroanal. Chem.*, **23**, APP. 1 (1969).

Electrolytic Preparation of Vanadium from Vanadium Carbide

K. P. V. Lei, R. E. Campbell, and T. A. Sullivan

United States Department of the Interior, Bureau of Mines, Boulder City Metallurgy Research Laboratory, Boulder City, Nevada 89005

ABSTRACT

The preparation of vanadium by molten-salt electrolysis of a commercial vanadium carbide (VC) containing 84% vanadium was investigated. An electrolytic process was developed for the extraction of vanadium from VC in an LiCl-NaCl-VCl_2 electrolyte contained in a helium-atmosphere cell at 650°C. The effects of electrolyte composition, vanadium depletion of the VC, and cathode current densities on the process, as well as the effects on the quality of vanadium products, were determined. Vanadium of 99% purity was prepared with an 85% recovery of vanadium and a cathode current efficiency of 70%. The vanadium contained approximately 0.60% oxygen and had a 100 Rockwell B hardness. High-purity, ductile vanadium was prepared from the VC by electrorefining the extraction products in a separate cell or by combining the extraction and electrorefining processes in a single cell. In the combined process, the vanadium was first extracted from the VC and deposited on a cylindrical electrode; this vanadium was then electrorefined and deposited on a central cathode rod. Both methods yielded vanadium of 99.9% purity with 35-40 Rockwell B hardness. With limited tests in the combined process, 58% recovery of ductile vanadium from the VC was achieved.

Ductile vanadium (1-7) and vanadium with purity higher than 99.9% (8-12) have been prepared from various materials containing vanadium. A starting material for the production of vanadium is vanadium carbide, which is produced commercially for use as a replacement for ferrovanadium in the steel industry. The preparation of a vanadium carbon alloy from vanadium oxides for use as a steel additive was investigated by Downing and Merkert (13). Current commercial production of vanadium carbide is of the VC-type. This carbide contains approximately 14% carbon and 84% vanadium, with iron, nitrogen, and oxygen as the chief impurities.

A molten-salt electrolytic process was developed by the Bureau of Mines to extract and prepare ductile vanadium having a purity ranging from 98 to 99.6% from a commercial V_2C-type carbide containing 10% carbon, 85% vanadium, and 5% of other elements, including chromium, iron, and oxygen (14). Electrolytic efficiency in the process decreased as the anode composition changed from V_2C to VC as a result of the vanadium extraction. When metallic impurities such as chromium and iron were present in V_2C, they contaminated the vanadium product. Low electrolysis efficiency as well as deterioration in product quality also occurred in the electrorefining of vanadium prepared by carbothermic reduction of V_2O_5 (15). This was attributed to the change of anode composition from a carbide phase rich in vanadium to a VC phase. The successful preparation of vanadium from vanadium-carbon alloys was dependent on the development of an efficient process for treating VC-type carbide.

The phase diagram of the vanadium-carbon system (16) indicates that the carbon-saturated VC-type carbide is $VC_{0.88}$. Extraction of vanadium from the carbide should be feasible since it will not increase the carbon content of the $VC_{0.88}$ phase. The reaction and free energy change (17) are

$$VC_{0.88} \rightarrow V + 0.88C, \quad \text{and} \quad \Delta F^\circ_{1000^\circ K} = +23 \text{ kcal} \quad [1]$$

The energy requirement for the reaction to proceed is furnished by electrolysis.

Experimental

Vanadium was prepared by electrolysis of VC in a helium-atmosphere, electrolytic cell shown in Fig. 1. The cell consisted essentially of a lock, a slide valve, and an electrolyte chamber. The chamber was constructed of Hastelloy, 1.3-cm thick, 15-cm ID, 76-cm high, and equipped with a graphite liner encased by a molybdenum crucible. The slide valve provided a gas-tight seal between the chamber and the lock. The lock was used to cool the vanadium deposit. The cathode was a 1.1-cm diam molybdenum rod.

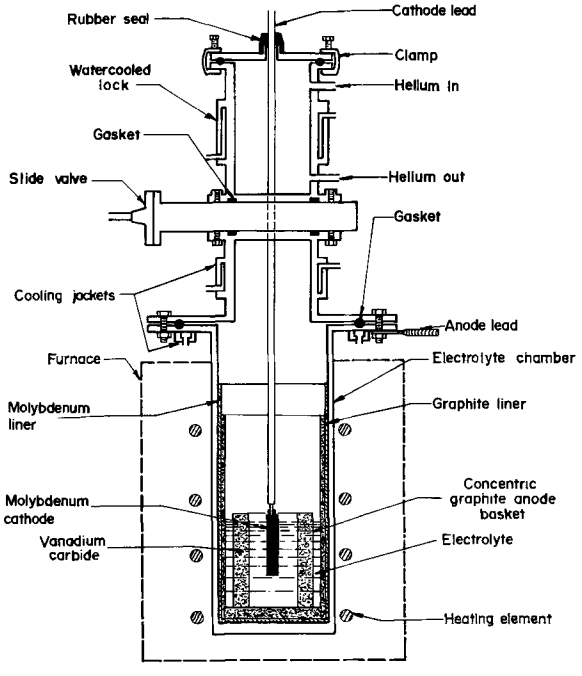

Fig. 1. Schematic diagram of the electrolytic cell

The vanadium carbide, in the form of 1.9 × 1.3-cm briquettes, was supplied by the Union Carbide Corporation. It was crushed into chunks of minus 3-, plus 4-mesh size and charged into a concentric graphite basket, 11.5-cm OD, 9-cm ID, and 30-cm high. The anode assembly was placed in the bottom of the graphite liner. Table I shows the analysis of the vanadium

Table I. Analysis of VC, %

Combined C	Free C	Fe	N	O	V
14.02	0.16	0.05	0.04	1.45	84.25

Key words: vanadium, vanadium carbide, electrolysis, preparation, molten-salts.

carbide. The chief impurities in the carbide were iron and oxygen, totaling 1.5%; minor metallic impurities were aluminum and chromium. The major component was identified by its x-ray diffraction pattern as VC.

The electrolytes were composed of VCl_2 dissolved into molten mixtures of alkali chlorides, and alkaline-earth chlorides with alkali chlorides, and VBr_2 dissolved in a molten mixture of NaBr and KBr. Vanadium dichloride and bromide were formed by direct chlorination and bromination of vanadium at 750°C into the respective molten salt mixtures in separate cell chambers (7, 18). The solid electrolyte was transferred to the electrolytic cell, heated to 400°C in a 0.01 Torr vacuum, and then melted under a helium atmosphere. Approximately 7-9 kg of the electrolyte were used in the cell.

The direct current for electrolysis was furnished by a 15V, 30A constant voltage power supply, and by a 15V, 150A full-wave selenium rectifier with variable output. The electrolytic reaction for the preparation of vanadium by electrolysis of VC, with X representing the chlorine or bromine atom, was as follows

$$\text{Anode: } VC + 2X^- \rightarrow VX_2 + C + 2e^- \quad [2]$$

$$\text{Cathode: } VX_2 + 2e^- \rightarrow V + 2X^- \quad [3]$$

On completion of 60 A-hr of electrolysis, the deposit was withdrawn from the electrolyte and cooled to room temperature (25°C) in the lock. The slide valve was closed and the deposit removed. A new cathode was attached and placed in the lock; the lock was then evacuated and filled with helium. The slide valve was opened and the cathode lowered into the electrolyte for starting another deposition. A test in this report refers to the preparation of a single electrolytic deposition of vanadium on the cathode; a series refers to all depositions made with a single charge of the VC material, varying from 1-3 kg; and the term cathode current density refers to initial cathode current density.

The vanadium deposit was immersed for 12 hr in a 2% hydrochloric acid solution to leach out most of the electrolyte. The vanadium was stripped from the cathode, washed with water, then acetone, and dried at 75°C. Previous vanadium research (7, 14) indicated that the minus 80-mesh vanadium fraction of such deposits contained a higher proportion of impurity elements; therefore, the cathode product was sized by screening into plus and minus 80-mesh fractions.

The carbon in the vanadium carbide remained in the anode basket as a skeleton form of the original briquette. The carbon was removed from the cell upon removal of the anode basket at the completion of a series.

Results

Electrolyte composition.—Although an average of 81% vanadium recovery was achieved in the electrolysis of a V_2C carbide in a $BaCl_2$-KCl-NaCl-VCl_2 electrolyte at 670°C (14), electrolysis of VC in the same electrolyte yielded only a 50% vanadium recovery. Low recoveries were also obtained with the use of other electrolytes: 17% in a KCl-LiCl-VCl_2 at 620°C; 21% in an $MgCl_2$-KCl-$CaCl_2$-VCl_2 at 720°C; and 44% in a KBr-NaBr-VBr_2 at 700°C. Increased recoveries of vanadium were obtained in the electrolysis of VC in electrolytes composed of a mixture of NaCl and VCl_2 with other alkali chlorides. These electrolytes contained, in weight per cent (w/o): (*i*) 90 NaCl, 10 VCl_2; (*ii*) 51 KCl, 39 NaCl, 10 VCl_2; (*iii*) 50 CsCl, 40 NaCl, 10 VCl_2; and (*iv*) 45 LiCl, 45 NaCl, 10 VCl_2.

The effects of these electrolytes on the extraction process are compared in Table II. A series of tests was performed with each electrolyte, using 1.5-2.0 kg of VC. Potentials ranging from 0.1-0.6V, and initial cathode current densities from 460-4600 A/dm² were used for electrolyses. Each series was terminated when cathode current efficiencies of individual tests dropped below 30%. The data in Table II show that the LiCl-NaCl-VCl_2 electrolyte was superior to the other electrolytes with respect to lower operating temperature, better vanadium recovery, and a larger yield of plus 80-mesh vanadium. Although cathode current efficiencies of 70 and 72% were obtained in the KCl-NaCl-VCl_2 and NaCl-VCl_2 electrolytes, respectively, the yield of plus 80-mesh vanadium was lower compared with that in the LiCl-NaCl-VCl_2 electrolyte. With the exception of a low operating temperature, the CsCl-NaCl-VCl_2 electrolyte was not as efficient as the other electrolytes.

Table II. Effect of electrolytes on the electrolysis of VC

	Electrolyte*			
	NaCl	KCl-NaCl	CsCl-NaCl	LiCl-NaCl
Temperature, °C	780	750	720	650
Vanadium recovery, %	91	83	72	93
Plus 80-mesh vanadium, %	32	36	24	50
Minus 80-mesh vanadium, %	68	64	76	50
Cathode current efficiency, %	72	70	46	60

* All electrolytes contained 10 w/o VCl_2.

The average analyses of all the plus 80-mesh and minus 80-mesh products prepared in each electrolyte are shown in Table III. The chief impurities in the product were iron and oxygen. Higher iron contamination occurred in the products prepared in the NaCl-VCl_2 and KCl-NaCl-VCl_2 electrolytes. The advantage of employing a low-temperature electrolyte for the preparation of vanadium was indicated by the lower carbon and oxygen contents of the products produced from the LiCl-NaCl-VCl_2 electrolyte. The products from the latter electrolyte were >99% vanadium, whereas those prepared with other electrolytes were approximately 98% pure.

Vanadium depletion.—The effect of increasing extraction of vanadium from VC on the electrolytic process and the quality of vanadium products was determined in two separate series of tests with the LiCl-NaCl-VCl_2 electrolyte, using 1.4 and 2.6 kg of VC. Each deposit in the series was made with a constant-current electrolysis of 20A, corresponding to an initial cathode current density of 3200 A/dm². Each series was terminated when approximately 90% of the vanadium had been removed from the anode. Figures 2 and 3 show the effects of vanadium extraction on potential, cathode current efficiency, the yield of plus 80-mesh vanadium, and the dragout of electrolyte with deposits. The potential required for maintaining a constant-current electrolysis varied slightly with the extraction of vanadium. The cathode current efficiency, production of plus 80-mesh vanadium, and metal-to-salt drag-out ratio of deposits decreased with increasing extraction of vanadium from the VC. When the quantity of VC was increased, the efficiency of the electrolytic process improved and resulted in lower potential requirements, better cathode current efficiency, higher yield of plus 80-mesh vanadium, and less electrolytic drag-out. Figure 4 shows vanadium

Table III. Analyses of vanadium products prepared with various electrolytes, %

	Electrolyte*			
	NaCl	KCl-NaCl	CsCl-NaCl	LiCl-NaCl
Carbon	0.12	0.02	0.04	0.01
Iron	0.20	0.22	0.07	0.08
Nitrogen	0.01	0.01	0.01	0.01
Oxygen	1.07	0.96	0.98	0.56
Vanadium	98.50	98.20	98.32	99.22

* All electrolytes contained 10 w/o VCl_2.

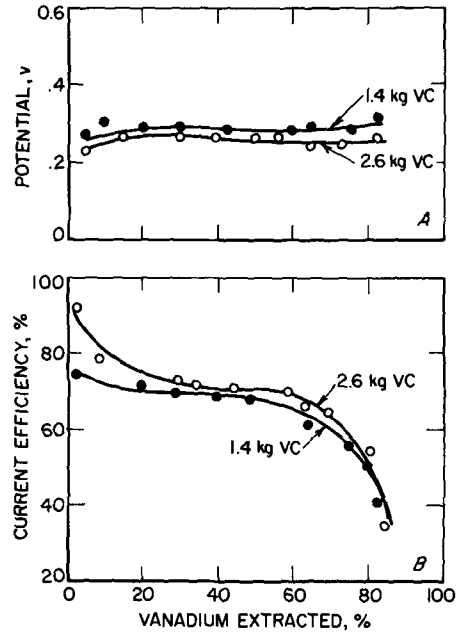

Fig. 2. Effect of vanadium extraction on (A) potential and (B) cathode current efficiency.

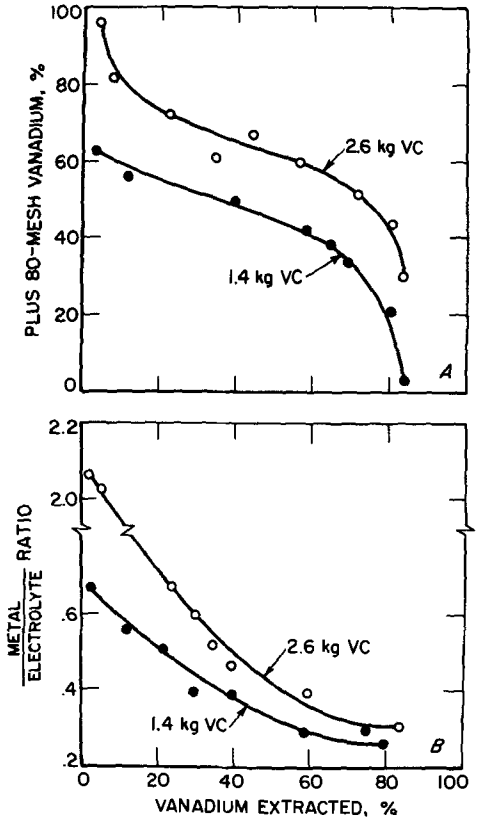

Fig. 3. Effect of vanadium extraction on (A) yield of plus 80-mesh vanadium and (B) metal-to-electrolyte drag-out ratio.

deposits prepared at 5 and 90% vanadium extraction from 1.4 kg of VC.

The purity of the vanadium prepared by electrolysis of VC was governed by its iron and oxygen contents. Figure 5 shows the variations of iron and oxygen content of the vanadium with vanadium extraction. The VC contained 0.05% iron and 1.45% oxygen. Contamination of the vanadium products by these impurities was highest in the first 20% of vanadium extracted and lowest between 21 and 75%, then increased gradually with increasing depletion of vanadium from the VC anode. The best quality vanadium was produced in the middle of the extraction tests. An increase in the initial quantity of VC available for electrolysis lowered both the iron and oxygen content in the vanadium products. The average iron and oxygen content of all products was 0.12 and 0.70%, respectively, for the extraction of the 1.4 kg charge, and 0.07 and 0.58%, respectively, for extraction of the 2.6 kg charge.

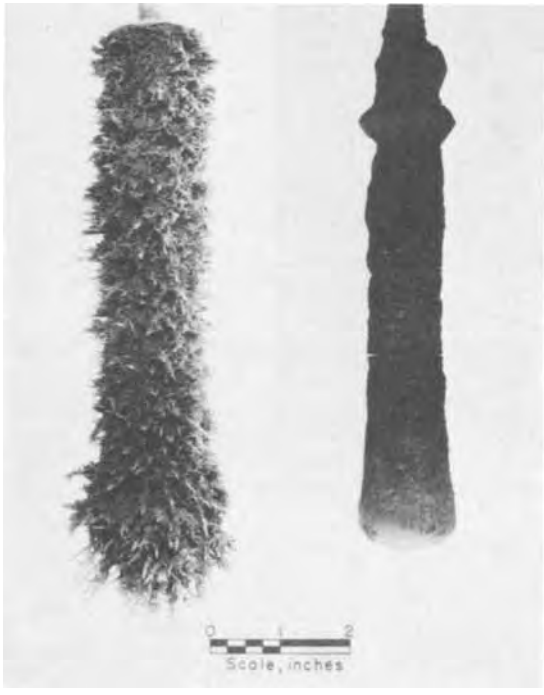

Fig. 4. Vanadium deposits prepared at (left) 5% and (right) 95% vanadium extraction.

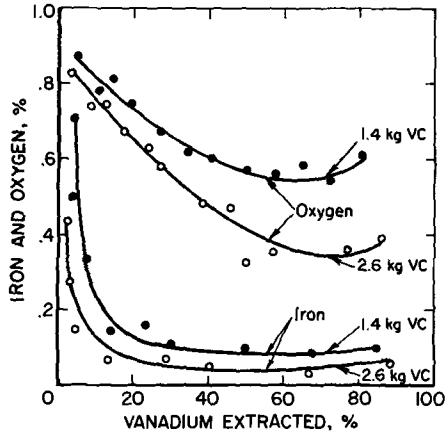

Fig. 5. Variation of iron and oxygen contents of vanadium with vanadium extraction.

Cathode current densities.—The use of various cathode current densities for the electrolyses of VC affected the cathode current efficiencies and yield of plus 80-mesh vanadium, as illustrated in Fig. 6. The values in the graphs were the average values obtained in each series of electrolyses conducted with currents of 5, 15, 20, 25, and 35A in the LiCl-NaCl-VCl_2 electrolyte. Each series was terminated after approximately 85% of the vanadium had been extracted from 1 kg VC. The cathode current efficiencies increased with cathode current densities from 990-3100 A/dm^2, reached a maximum at 3200 A/dm^2, and decreased thereafter with cathode current densities greater than 3300 A/dm^2. The yield of plus 80-mesh vanadium products was relatively constant with cathode current densities ranging from 930 to 3700 A/dm^2, then increased with increasing cathode current densities.

The plus 80- and minus 80-mesh products prepared in each of the series were similar in quality. The plus

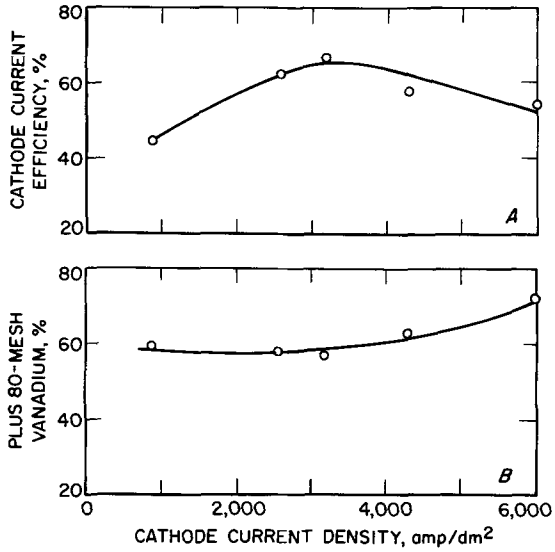

Fig. 6. Variation of (A) cathode current efficiency and (B) yield of plus 80-mesh vanadium with cathode current density.

80-mesh products were 99.2% vanadium, and the minus 80-mesh products were 98.8% pure vanadium. The quality of vanadium prepared with cathode current densities higher than 3700 A/dm² was slightly better than with lower cathode current densities, because larger quantities of plus 80-mesh vanadium were produced with the high cathode-current densities.

Optimum parameters for electrolyses.—The preparation of vanadium by electrolysis of VC was conducted in an LiCl-NaCl-VCl_2 electrolyte at 650°C, using the operating data show in Table IV. The optimum parameters had been determined in preceding tests. Eighty-five per cent of the vanadium was extracted from the VC. The average drag-out ratio of metal-to-electrolyte in the deposits was 0.6-1.0. The quality of the vanadium is shown in Table V. The process yielded an average of 99% vanadium by reducing the carbon, nitrogen, and oxygen contents of the VC. The vanadium was not ductile.

High-purity, ductile vanadium from VC.—High-purity, ductile vanadium was prepared from VC by electrorefining the extraction products in a separate cell or by combining the extraction and electrorefining processes in a single cell. In the first procedure, vanadium deposits which were obtained by electrolysis of VC in an LiCl-NaCl-VCl_2 electrolyte were electrorefined in a KCl-LiCl-VCl_2 electrolyte at 620°C. Electrolyte was not leached from the deposit prior to electrorefining. Previous research (9) showed that a mixture of KCl, LiCl, and VCl_2 was the best suited electrolyte for electrorefining vanadium. Figure 7 compares an extracted vanadium deposit with an electrorefined deposit. The extracted deposit was made with a cathode current density of 4600 A/dm² from VC in which 87% of the vanadium had been removed. The refined deposit was made with a cathode current density of 1300 A/dm². In the extraction 60 A-hr of electrolysis was used and in the electrorefining 32 A-hr of electrolysis was used. The extracted deposit contained approximately 35-40g of vanadium, which was refined to yield 29g of pure metal. Typical analysis of the extracted and refined vanadium is shown in Table VI. Electrorefining reduced the carbon, iron, nitrogen, and oxygen contents of the extracted products and produced 99.9% plus vanadium with a 35 Rockwell B hardness.

Table IV. Operating data, electrolysis of VC in an LiCl-NaCl-VCl_2 electrolyte

Number of tests	49
Potential, V	0.2-0.3
Current, A	20-25
Cathode current density, A/dm²	3200-3700
Electrolysis, A-hr	2960
Vanadium carbide added, kg	2.74
Vanadium deposited, kg	1.97
Plus 80-mesh vanadium, %	68
Minus 80-mesh vanadium, %	32
Cathode current efficiency, %	70

Table V. Analysis of vanadium prepared by electrolysis of VC, %

	Vanadium products	
	Plus 80-mesh	Minus 80-mesh
Carbon	0.008	0.02
Iron	0.05	0.10
Nitrogen	0.002	0.002
Oxygen	0.45	0.84
Vanadium	99.42	98.74
Hardness, R_B	95	100

Fig. 7. Extracted vanadium deposit (right) and refined vanadium deposit (left).

In the combined process, the vanadium was first extracted from the VC and deposited on the inside of a cylindrical electrode; this vanadium was then electrorefined and deposited on a central cathode rod. Figure 8 shows the cylindrical electrode which was made of molybdenum sheet 0.08-cm thick, 13-cm OD, and 56-cm high. One end of the electrode was attached to a nickel flange, and a molybdenum cup was loosely fitted over the other end. The function of the cup was to prevent the extracted vanadium deposits from falling to the cell bottom and to permit the electrolyte to enter the center of the cylinder. This assembly was installed between the flanges of the chamber and the slide valve of the molybdenum-lined electrolytic cell. The VC was contained in a perforated graphite tube, 5.5 cm diam × 32 cm long, which was suspended in the center of the cylindrical electrode. Extractions were made with potentials of 0.2-1.2V, currents of 23-90A, and 1500-2300 A-hr to deposit the vanadium on the cylindrical electrode. The VC anode container was removed and replaced with a 1.1 cm diam molybdenum rod. Electrorefining of the extracted vanadium was made with a potential of 0.08V, a current of 10A, and 70 A-hr of electrolysis to deposit purified vanadium on the molybdenum rod. Optimum operating parameters were not determined in the combined process. Limited tests showed that the process was capable of producing 400g of refined vanadium from 850g of VC. Typical refined vanadium deposit from the combined process is shown in Fig. 9. The drag-out ratio of metal-to-electrolyte in

Table VI. Analysis of extracted and refined vanadium, %

	Vanadium, extracted	Vanadium, refined
Carbon	0.05	0.001
Iron	0.10	0.03
Nitrogen	0.002	0.001
Oxygen	0.98	0.01
Vanadium	98.72	99.92
Hardness, R_B	—	35

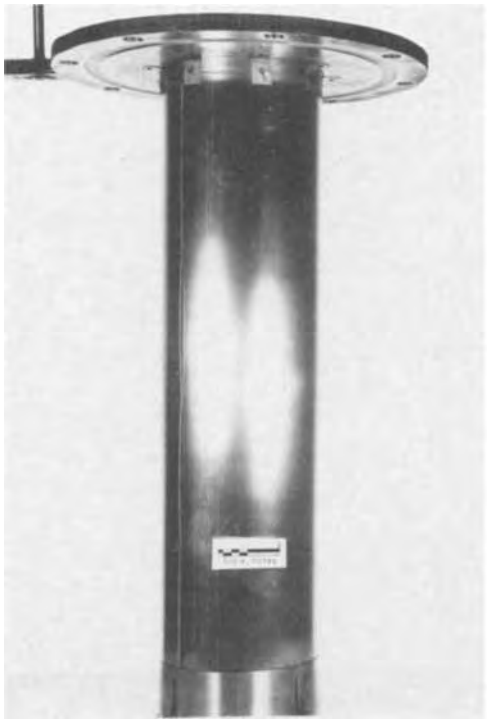

Fig. 8. Cylindrical molybdenum electrode

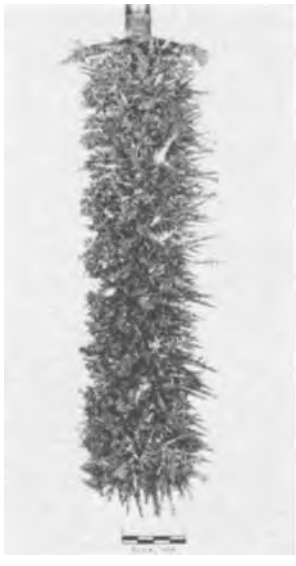

Fig. 9. Refined vanadium deposit

the deposit was 3 to 1. Analysis of the vanadium is presented in Table VII. In essence, the two-cycle electrolyses of VC in this combined process produced a ductile vanadium of approximately 99.9% purity in a single-cell system.

Table VII. Analysis of vanadium from the combined process, %

Carbon	<0.005
Iron	0.006
Nitrogen	0.0006
Oxygen	0.02
Vanadium	99.86
Hardness, R_B	40

Conclusions

The preparation of vanadium by molten-salt electrolysis of a commercial vanadium carbide was demonstrated in a helium-atmosphere electrolytic cell. An LiCl, NaCl, and VCl_2 molten salt mixture was the best electrolyte tested for the preparation. A process was developed for the extraction of 99% pure vanadium by electrolysis of VC with cathode current densities from 3200-3700 A/dm^2 in an LiCl-NaCl-VCl_2 electrolyte at 650°C. The vanadium recovery at the cathode was 85% with 70% current efficiency.

High-purity, ductile vanadium was prepared from the VC by electrorefining the vanadium deposits from the extraction process in a separate cell or by combining the extraction and electrorefining processes in a single cell. Both procedures yielded vanadium of 99.9% purity with 35-40 Rockwell B hardness.

Manuscript submitted March 23, 1972; revised manuscript received Aug. 14, 1972.

Any discussion of this paper will appear in a Discussion Section to be published in the December 1973 JOURNAL.

REFERENCES

1. J. W. Marden and M. N. Rich, *Ind. Eng. Chem.*, **19**, 786 (1927).
2. E. E. Van Arkel, "Reine Metalle," J. Springer, Berlin, Germany (1939).
3. R. J. McKechnie and A. N. Seybolt, *This Journal*, **97**, 311 (1950).
4. A. Yu Polyakov, Brutcher Trans. No. 4376 from *Primenenie Vakuuma Met., Akad. Nauk SSSR, Inst. Met. Tr. Sovesch.*, Moscow, p. 147 (1958).
5. F. R. Cattoir and D. H. Baker, Jr., *U.S. Bur. Mines, Rept. Invest.* 5630 (1960).
6. F. E. Block, R. R. Brown, and M. J. Ferrante, *U.S. Bur. Mines Rept. Invest.* 5722 (1961).
7. K. P. V. Lei, F. R. Cattoir, and T. A. Sullivan, *U.S. Bur. Mines Rept. of Invest.* 6972 (1967).
8. O. N. Carlson, F. A. Schmidt, and W. E. Krupp, *J. Metals*, **18**, 320 (1966).
9. K. P. V. Lei and T. A. Sullivan, *U.S. Bur. Mines Rept. Invest.* 7036 (1967).
10. M. J. Ferrante, F. E. Block, and J. L. Schaller, *U.S. Bur. Mines Rept. Invest.* 7145 (1968).
11. C. T. Wang, E. F. Baroch, S. A. Worcester, and Y. S. Shen, *Met. Trans.*, **1**, 1683 (1970).
12. H. A. Beale and R. J. Arsenault, *ibid.*, **1**, 3355 (1970).
13. J. H. Downing and R. F. Merkert, French Pat. 1,422,683, Nov. 15, 1965.
14. K. P. V. Lei and T. A. Sullivan, *U.S. Bur. Mines Rept. Invest*, 7484 (1971).
15. K. P. V. Lei and T. A. Sullivan, *Met. Trans.*, **2**, 2312 (1971).
16. E. Rudy, St. Wendisch, and C. E. Brukl, *Planseeber. Pulvermet.*, **16**, 3 (1968).
17. A. D. Mah, *U.S. Bur. Mines Rept. Invest.* 6177 (1963).
18. T. A. Sullivan and F. R. Cattoir, *U.S. Bur. Mines Rept. Invest.* 6631 (1965).

Thermal Behavior of a Plasma-Heated Tungsten Probe in the Presence of Tungsten Vapor

Paul Meubus

Chemical Engineering Department, Université du Québec à Chicoutimi, Chicoutimi, Province of Quebec, Canada

ABSTRACT

A tungsten metal probe is heated in an argon plasma containing variable amounts of tungsten vapor. It is observed that the metal surface temperature substantially decreases when the vapor concentration increases in the gas. All other conditions being equal, the difference residing in the presence of metal vapor in the plasma, the introduction of about 0.7% vapor in the argon gas decreases the probe surface temperature by 18%, while the presence of 8% metal vapor decreases the surface temperature by 28%, the gas temperature around the probe surface being respectively 9000 and 10,000°K. An equation is found, showing the probe temperature variations in terms of the total tungsten particle concentration as well as the gas temperature immediately around the probe. A possible explanation is given for the phenomena observed which involves the existence of a protective shield of tungsten atoms and ions in equilibrium along the saturation vapor curve for tungsten. Also, the presence of solid condensed particles around the probe, with relatively low thermionic work function, may provide a protective, positively charged shield against positive ion bombardment of the probe. This interpretation is supported, to a certain extent, by the equation found.

Thermal protection of solid surfaces submitted to very high temperatures has been extensively studied, especially in view of atmospheric re-entry problems associated with ballistic missiles and also for the protection of jet propulsive devices, turbine blades, etc. Ablation effects have been studied by Slattery (1) and others, while ceramics and refractory oxide coatings have been made the object of considerable work (2).

Also, heat exchange phenomena occurring in the presence of corona discharges (3), as well as heat effects around anodes in arc discharges, have been studied (4). However, the case of the thermal protection for a refractory metal exposed to very high temperatures (plasma gas), by means of a metal vapor of low vapor pressure at elevated temperature, does not seem to have been considered.

In the present work, a tungsten probe is used, one end of which is cooled at a constant rate while the other extremity is plunged in an argon plasma. The plasma gas temperature around the probe is obtained by a spectroscopic method using the intensity emission ratio of argon lines 4158.6Å and 4259.4Å as described in a previous article (5). The solid surface temperature is recorded by pyrometric observations and the validity of this method, which could be altered by the presence of a continuum emission from argon, has been controlled and found acceptable, using a method described elsewhere (6).

Tungsten vapor is supplied to the gas stream issuing from the plasma torch by means of a second tungsten probe exposed to the plasma flame and positioned between the gun outlet and the experimental probe previously described. The metal vapor is then released at a rate which is controlled by the gas temperature and by the relative position of the experimental probe. Also, the rate of cooling water used for avoiding rapid destruction of the probe may be used as a parameter for changing the amount of tungsten vapor present in the main argon gas. Finally a plasma may be obtained with variable amounts of tungsten vapor, it being possible to change the temperature of the gas surrounding the experimental tungsten probe. As the resulting gas flows around the experimental probe, the relationship between metal vapor concentration and probe surface temperature can be studied. Using the argon plasma, identical situations are compared, except for the presence of tungsten vapor at different concentration levels.

The purpose of this study is to examine the possibility of using metal evaporation techniques in order to provide thermal protection to vital equipment parts submitted to very high temperatures, in isolated conditions when heat sinks are not available. Pieces of metal adequately positioned could supply the necessary protective vapor component.

Key words: heat protection by means of metal vapor, heat protection at very high temperatures, heat transfer in high-temperature gas-metal vapor mixtures, heat protection by thermionic emission from high-temperature particles.

Theory

Determination of tungsten vapor concentration around the experimental probe.—Referring to Fig. 1, consider an argon plasma jet P of cylindrical symmetry and the tungsten cylindrical probes R_1 and R_2 described in the section on Apparatus and Mode of Operation. The amount of tungsten vapor in the main argon stream is obtained by evaporation from probe R_1 and the temperature T_S of the probe surface S is modified by either changing the probe position along the plasma axis or by varying the power supplied to the plasma jet.

Average radial spectral readings are made, immediately above the tungsten surface S, for the experimental probe R_2. In this way, average intensities are recorded for argon lines 4158.6 and 4259.4Å. The ratio of these intensities, after correction for absorption and sensitivity variation, leads to the knowledge of an average gas temperature above S. The temperature being known, one can now proceed to the determination of tungsten vapor concentration around the probe R_2 when the choice is made of a suitable tungsten emission line. In the case of the present study, the atomic excitation emission at 4008.8Å for tungsten is used.

Generally speaking, the absolute emission intensity for a given transition leading to an emission at frequency ν and temperature T, modified for absorption by a factor L, is given by

for tungsten

$$I_W = \frac{L_W A_W g_W h_{\nu W} n_W e^{-E_W/kT}}{Z_W(T)} \qquad [1]$$

for argon

$$I_{Ar} = \frac{L_{Ar} A_{Ar} g_{Ar} h_{\nu Ar} n_{Ar} e^{-E_{Ar}/kT}}{Z_{Ar}(T)} \qquad [2]$$

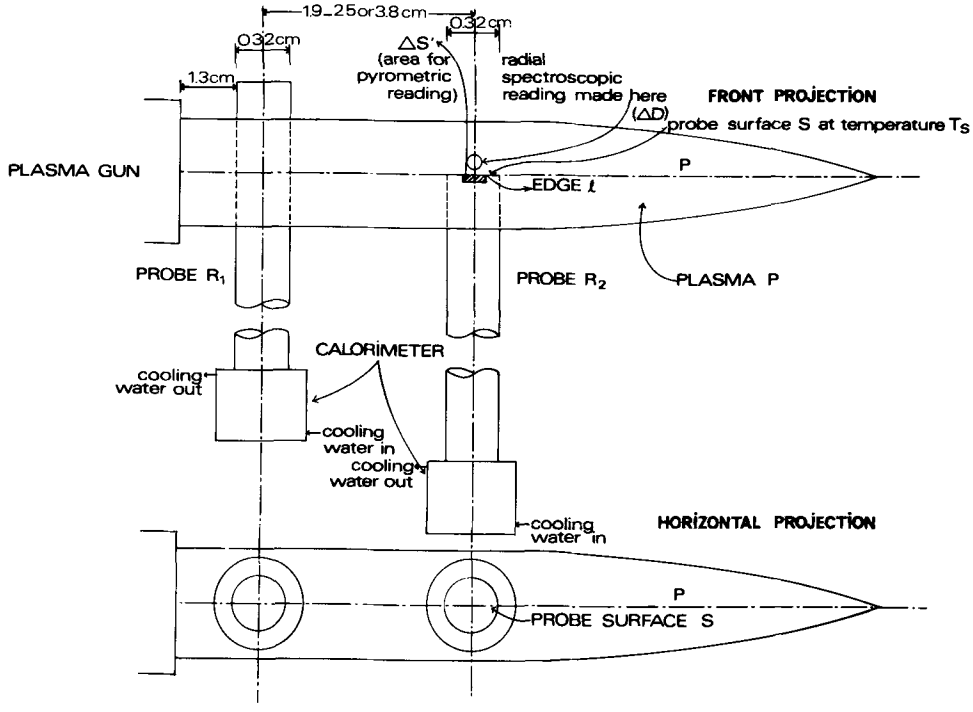

Fig. 1. View of the plasma, tungsten vapor source, and experimental probe.

Dividing [1] by [2] and affecting the results by indices 1 and 2 so as to describe two distinct temperature situations one obtains

$$\left(\frac{I_W}{I_{Ar}}\right)_1 = \frac{Z_{Ar}(T_1) L_W A_W g_W \nu_W}{Z_W(T_1) L_{Ar} A_{Ar} g_{Ar} \nu_{Ar}} \left(\frac{n_W}{n_{Ar}}\right)_1 e^{-\frac{1}{kT_1}(E_W - E_{Ar})} \quad [3]$$

$$\left(\frac{I_W}{I_{Ar}}\right)_2 = \frac{Z_{Ar}(T_2) L_W A_W g_W \nu_W}{Z_W(T_2) L_{Ar} A_{Ar} g_{Ar} \nu_{Ar}} \left(\frac{n_W}{n_{Ar}}\right)_2 e^{-\frac{1}{kT_2}(E_W - E_{Ar})} \quad [4]$$

When ν_W and ν_{Ar} are close enough and I_W comparable in intensity to I_{Ar}, then $L_W \approx L_{Ar}$ and division of [3] by [4] results in the following expression

$$(n_W)_2 = (n_W)_1 \frac{(n_{Ar})_2 (I_W)_2 (I_{Ar})_1 Z_{Ar}(T_1) Z_W(T_2)}{(n_{Ar})_1 (I_W)_1 (I_{Ar})_2 Z_{Ar}(T_2) Z_W(T_1)} e^{\frac{E_W - E_{Ar}}{k}\left(\frac{1}{T_2} - \frac{1}{T_1}\right)} \quad [5]$$

Then, if one value for n_W can be ascertained, the concentration of tungsten neutral atoms n_W can be obtained from Eq. [5] for a set of experimental conditions, where temperature and tungsten total atom concentration are varied, provided $(n_{Ar})_2$ is known. It is to be noted that neither transition probabilities nor absolute spectral emission intensity values have to be known.

The following equations may be written:

1. Saha constant at temperature T for the system $W \rightarrow W^+ + e$

$$K_W = \frac{(n_e)(n_{W+})}{n_W} = 2\frac{Z_{W+}(T)}{Z_W(T)} \left(\frac{2\pi m_e kT}{h^2}\right)^{3/2} e^{-\frac{7.98}{kT}} \quad [6]$$

2. Saha constant at temperature T for the system $Ar \rightarrow Ar^+ + e$

$$K_{Ar} = \frac{(n_{Ar+})(n_e)}{n_{Ar}} = 2\frac{Z_{Ar+}(T)}{Z_{Ar}(T)} \left(\frac{2\pi m_e kT}{h^2}\right)^{3/2} e^{-\frac{15.76}{kT}} \quad [7]$$

3. Total number of particles at temperature T

$$K = (n_{Ar}) + (n_{Ar+}) + (n_W) + (n_{W+}) + n_e = \frac{P}{kT} \quad [8]$$

P being the pressure of operation.

4. Conservation of charge

$$n_{Ar+} + n_{W+} = n_e \quad [9]$$

if the assumption is made of negligible second ionization, which is quite valid in the considered study.

5. Dropping index 2 in Eq. [5], n_W can be obtained provided $n_{Ar}/(n_{Ar})_1$ is known. As a first evaluation, n_{Ar} can be calculated using Eq. [7], [8], and [9] written for argon only. As a result, a first approximation of n_W is available.

From Eq. [6] to [9] together with the value at hand for n_W, one can write

$$[n_W(K_{Ar} - K_W) - KK_{Ar}]\, n^2_{W+} + 2K_W K_{Ar} n_W n_{W+} + K^2_W n^2_W = 0 \quad [10]$$

Solving [10] for n_{W+} (discarding the negative root), the total number of tungsten particles n_{W_T} can be written

$$n_W + n_{W+} = n_{W_T} \quad [11]$$

From the knowledge of n_W and n_{W+}, together with Eq. [6], [7], and [8], a value of n_{Ar} should be found which is identical to the assumed one and an iteration method is applied until this requirement is fulfilled. In this way, a final value is obtained for n_{W_T} in the plasma gas mixture.

Energy dissipation around the experimental probe.— Referring to Fig. 2 which shows the sublimation and vapor equilibrium curve for tungsten, point B is representative of a situation in the plasma above the solid surface S at temperature $(T_S)_B$, the corresponding gas temperature being T_B and the total tungsten particles concentration $(n_{W_T})_B$. Since the flow conditions are turbulent, $(T_S)_B$ and $(n_{W_T})_B$ may be considered as

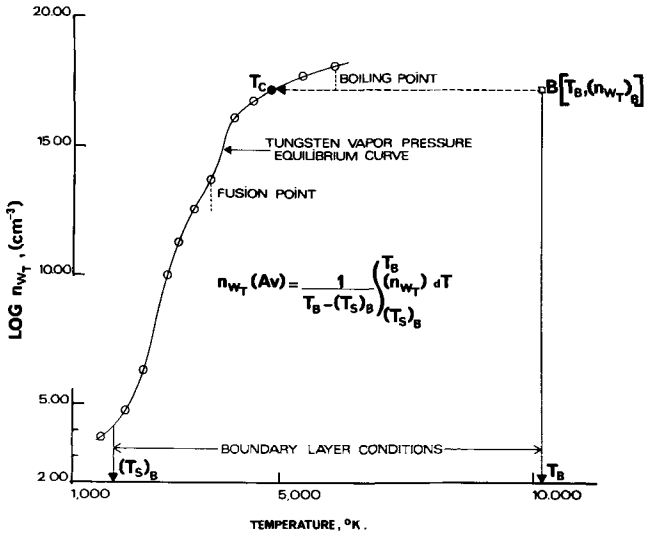

Fig. 2. Vapor and sublimation equilibrium curve for tungsten. Definition of an average value, for the total number of tungsten particles n_{W_T}(Avg) in the boundary layer, for a given concentration $(n_{W_T})_B$ of total tungsten particles in the main gas stream.

the upper limit conditions for, respectively, the temperature and tungsten concentration in the boundary layer adjacent to the surface S. Within this layer, $(n_{W_T})_B$ remains constant while temperature is decreasing until the equilibrium curve is met. Then tungsten vapor starts condensing and solidifying if equilibrium conditions are met.

An average value for n_{W_T} within the boundary layer may be written

$$n_{W_T}(\text{Avg}) = \frac{1}{T_B - (T_S)_B}\int_{(T_S)_B}^{T_B} n_{W_T}\,dT \quad [12]$$

Considering the situation within the boundary layer gas metal vapor, the collision frequency of argon and tungsten particles will depend on n_{W_T} and on the cross section for unlike particles. When momentum is transferred from argon to tungsten atoms, the latter are either repelled out of the boundary layer or condensed when entering a region of lower temperature. Thus, a possible means for avoiding direct heat transfer with the surface S is available. Assuming a maxwellian velocity distribution (which is approximate because of the presence of ions and species of different kinds), the collision frequency for unlike particles, at a given temperature, should be for one argon particle

$$N_{Ar\text{-}W} = \pi n_{W_T} d^2_{Ar\text{-}W}(\bar{v}^2_{Ar} + \bar{v}^2_W)^{1/2} \quad [13]$$

The thermal velocity $\bar{v}_W$ is equal to $\bar{v}_{Ar}\sqrt{m_{Ar}/m_W}$ so that Eq. [13] can be written

$$N_{Ar\text{-}W} = 1.12\pi n_{W_T} d^2_{Ar\text{-}W}\bar{v}_{Ar} \quad [14]$$

When argon particles only are present, the collision frequency is

$$N_{Ar} = 1.41\pi(n_{Ar} + n_{W_T})d^2_{Ar}\bar{v}_{Ar} \quad [15]$$

Taking into account that $d_{Ar} = 1.82$Å and $d_{Ar\text{-}W} = 1.62$Å, then the per cent collision with tungsten particles is of the order of 7% for a 10% tungsten concentration. The collisions between unlike atoms of the considered kind lead ultimately, as already mentioned, to momentum transfer to solid tungsten particles, as well as to ionic recombination, both effects adding up to avoid direct heat transfer with the probe surface.

Also, thermionic emission may possibly contribute to the thermal protection of the tungsten surface S. Considering a solid particle formed by tungsten vapor condensation, the current emission per unit surface is given by the Richardson equation

$$j = UT^2e^{-\phi/kT} \quad [16]$$

where j is the current emission per unit surface, while U and ϕ are, respectively, a constant and the thermionic work function for the considered emissive material. In the case of tungsten Eq. [16] becomes

$$j = 60.2T^2e^{-4.52/kT} \quad [17]$$

If the electrons escaping from the tungsten surface are assumed to take initially the average velocity corresponding to the surface temperature, then the electron concentration at the surface may be obtained from

$$n_{es} = j/e\bar{v}_e \quad [18]$$

and electrons will evaporate from the solid when $n_{es} > n_e$, where n_e is the electron concentration around the particle, leaving a positively charged surface which can play the role of a protective shield for the probe submitted to ion bombardment. This aspect is considered in the section on Results and Discussion.

Apparatus and Mode of Operation

The power supply, control panels, and plasma torch used have been described elsewhere (5). Referring to Fig. 3, the torch generates a plasma of cylindrical symmetry and is enclosed in a chamber C provided with quartz windows for spectroscopic observations. The

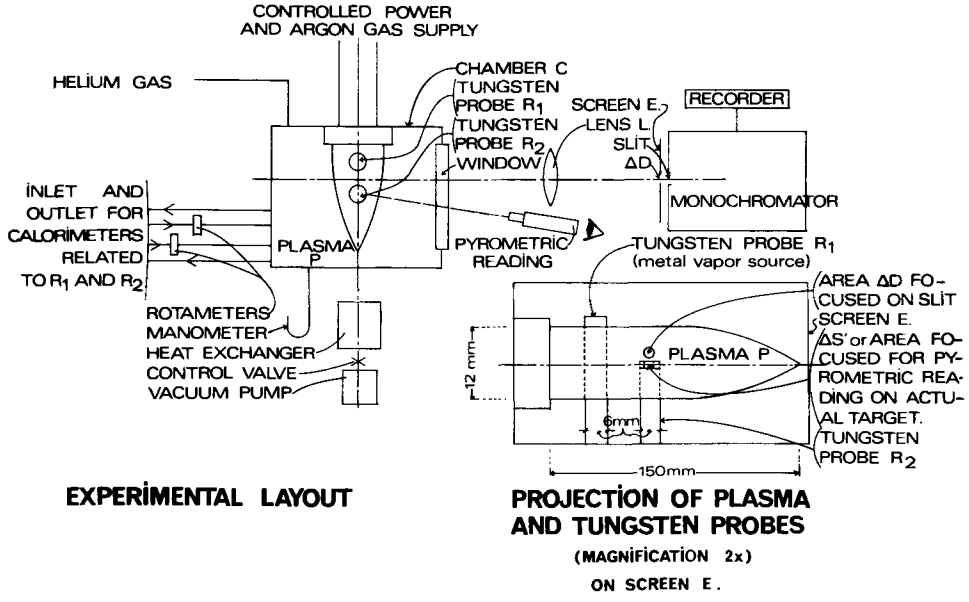

Fig. 3. Layout of the experimental set-up used, with a view of the plasma and probe projection on the monochromator screen E.

chamber is connected to a helium gas supply as well as to a vacuum pump so that it can be scavenged and filled with helium prior to operation.

Referring to Fig. 1, two tungsten probes R_1 and R_2, made of cylindrical rods 3.8 cm long and 0.32 cm diameter, are mounted on calorimeters and installed in such a way that the vertical plane of symmetry of the plasma contains the probe axes. Also, the position of rod R_2 is adjusted so that its upper horizontal surface S contains the axis of symmetry of plasma P. The probe R_1 is positioned across the flame and near the plasma gun outlet as indicated in Fig. 1. This probe is used to supply variable amounts of tungsten vapor to the main gas stream.

Highly turbulent conditions allow a rapid mixing of the metal vapor and plasma gas as may be concluded from relative tungsten vapor average concentration measurements along the plasma axis, in the downstream direction. Probes R_1 and R_2 are cooled at a constant cooling water flow rate in order to avoid rapid destruction and also to maintain identical conditions during the whole set of experiments. The water flow rates are 600 cm^3/min for R_1 and 80 cm^3/min for R_2.

The plasma is operated at 760 mm Hg and various power levels, varying between 4.5 and 6.5 kW, and the argon mass flow rate is kept constant at 500 g/hr for all the experiments made. For a given power input, R_2 is adjusted at three positions along the plasma axis, respectively, at 1.9, 2.5, and 3.1 cm from the probe R_1 which remains in a fixed position at 1.9 cm from the plasma gun nozzle. The geometrical conditions already stated are respected in all cases. As a result, various gas temperature conditions around R_2 may be obtained while the metal vapor concentration is also varied.

A screen E (Fig. 3) is placed in front of a monochromator (Jarrell-Ash 75-150), close to the slit plane, and a magnifying lens L projects an image of the plasma and probes on screen E. Prior to the experiments, rods R_1 and R_2 are adjusted in the plasma vertical plane of symmetry. Position along the plasma axis and adjustment of height are made from outside the chamber and can accurately be adjusted by viewing the image projection on screen E. Transverse and vertical motions of chamber C allow a given radial line in the plasma to be focused on the slit and spectroscopically analyzed. Spectrograms are recorded immediately above the surface S of probe R_2, at ΔD (Fig. 1 and Fig. 3), whose actual size is 1.25 mm in diameter (magnified two times on screen E) and through which a radial average spectrogram is taken.

In this way, intensities are recorded for neutral argon lines 4158.6 and 4259.4Å and for an atomic excitation line for tungsten at 4008.8Å. The wavelength proximity for these lines as well as the comparable magnitude of their intensity in many cases, validates the assumption that total absorption is similar for all the considered lines. An example of recorded spectrogram is given in Fig. 4. The argon lines 4259.4 and 4158.6Å are used for the gas temperature determination, while the 4158.6Å line is used as a reference line for tungsten concentration determinations by means of tungsten line 4008.8Å.

Pyrometric readings (Leeds and Northrup 8131F instrument) are made on $\Delta S'$ (Fig. 1) near the edge 1 of surface S and the observed temperature is considered as equal to the temperature existing on the probe surface S. The validity of the pyrometric reading, which could possibly record solid surface and gas continuum emissions at high gas temperatures, has been verified by using a method described elsewhere (6).

Results and Comments

Varying the heating conditions for probe R_1 as well as the position of probe R_2 resulted in the obtaining of a set of spectroscopic data for transverse readings just above the probe R_2, an example of which is given on Fig. 4. Also, pyrometric readings were taken in order to obtain the associated surface temperature T_S. Considering Eq. [5], the partition functions for atomic and ionized tungsten between 1500 and 11,000°K were calculated using energy levels from Ref. (7) and the correction for ionization potential lowering (8) was found negligible for the electron concentrations met in all the experiments made. The partition function values are found in Table I. For argon, the partition functions, within the useful temperature range, were available in the literature. The energy transition for the 4008.8Å emission was found equal to 3.10 eV.

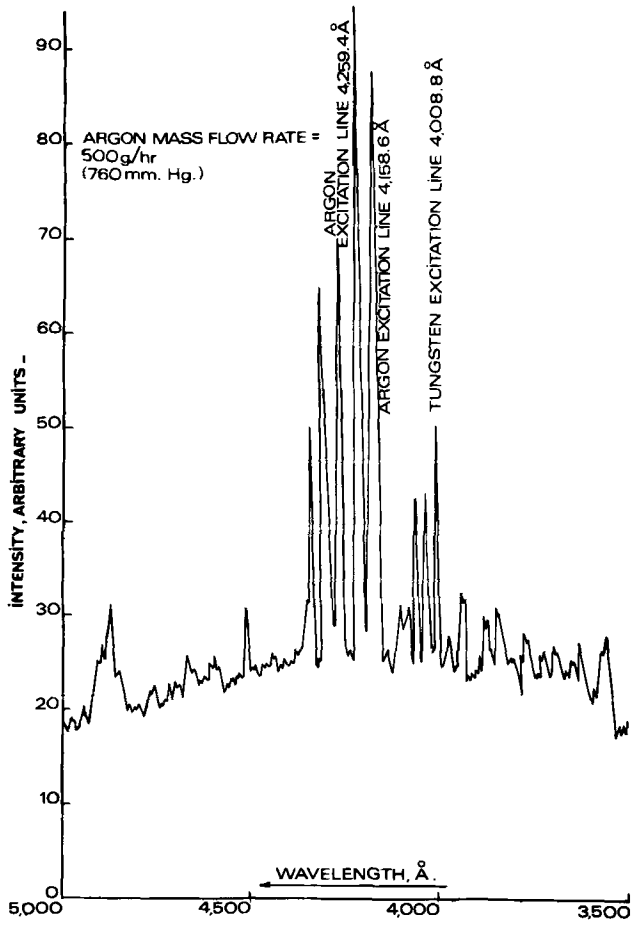

Fig. 4. Example of spectrogram taken immediately above the experimental probe surface and showing the 4259.4 and 4158.6Å lines for argon and 4008.8Å for tungsten.

The reference conditions identified by index 1 in Eq. [5] were taken at 6600°K. The argon line 4158.6Å was taken for defining $(I_{Ar})_1$ and more generally $(I_{Ar})_n$. Then, in order to evaluate $(n_W)_2$ or $(n_W)_n$, an evaluation of $(n_W)_1$ was made. From the projection of probe R_1 on screen E (Fig. 3) and measurement of an average temperature for the area exposed to plasma P, it could be found that a tungsten area of 3.22 cm^2, at a temperature of 3500°K, was available for tungsten evaporation in the argon main stream flowing at a rate

Table I. Partition functions calculated for atomic and ionized tungsten between 1500° and 11,000°K

Temperature, °K	Partition function: Atomic tungsten, Z_W	Partition function: Singly ionized tungsten, Z_{W^+}
1,500	2.60	13.40
2,000	3.53	14.40
3,000	6.20	16.90
4,000	9.35	20.12
5,000	12.78	23.60
6,000	16.77	28.10
7,000	21.92	32.90
8,000	27.38	38.35
9,000	34.20	44.00
10,000	42.26	50.30
11,000	52.20	56.60

of 500 g/hr. The vapor pressure at 3500°K is equal to 7.52 dynes/cm² (9) so that the total number of tungsten particles, n_{W_T}, in the gas stream above 3500°K can be calculated, assuming rapid evaporation equilibrium attainment. $(n_{W_T})_1$ was found equal to 2.13×10^{14} particles/cm³. Application of Eq. [10] and [11], with n_{W_T} being known instead of n_W, and using the iteration method already described, led to the value $(n_W)_1 = 1.30 \times 10^{13}$, the values of K_{Ar}, K_W, and K being represented on Fig. 5.

With this result at hand, all intensity measurements, at different temperatures, of the tungsten line 4008.8Å could be replaced by concentration values n_{W_T} from which total tungsten particle concentrations n_{W_T} could be determined in the argon stream.

The parameters used for describing the probe surface temperature T_S were the gas temperature T_B and an average $n_{W_T}(Avg)$ value for the tungsten particles in the so-called boundary layer, as defined in Eq. [12]. The results obtained for the experiments made are shown in Table II which includes the gas temperature T_B immediately above the probe surface and the corresponding average concentration $n_{W_T}(Avg)$ as well as the surface temperature T_S.

To obtain $n_{W_T}(Avg)$, it was necessary to determine, for tungsten, the sublimation curve obtained from data in Ref. (10), while the vapor equilibrium curve was calculated by means of Kistiakowsky's (11) equation for nonpolar substances

$$\Delta H_T = 8.75T + 1.987T \ln T \qquad [19]$$

together with the Clausius-Clapeyron equation for small temperature ranges

$$\ln \frac{(n_{W_T})_a}{(n_{W_T})_b} = -\frac{\Delta Ha,b}{1.987}\left(\frac{1}{T_a} - \frac{1}{T_b}\right) \qquad [20]$$

The complete equilibrium curve is shown in Fig. 2.

The variation of T_S with respect to $n_{W_T}(Avg)$ for different constant values of T_B appears on Fig. 6 while

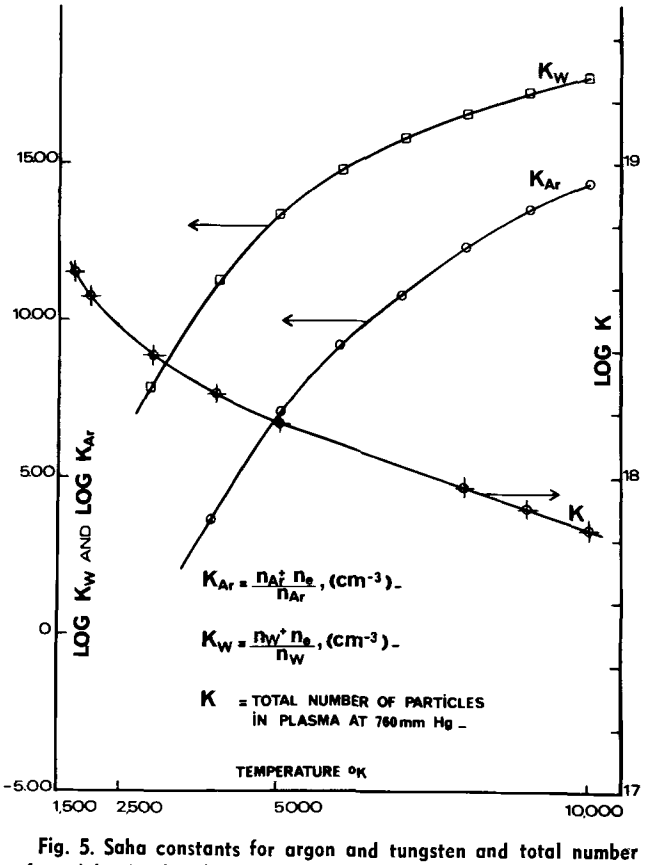

Fig. 5. Saha constants for argon and tungsten and total number of particles in the plasma, for different temperatures at a pressure of 760 mm Hg.

Table II. Effect of tungsten vapor on probe surface temperature

Test No.	Probe surface temperature, T_S, °K	Gas temperature above probe, T_B, °K	Tungsten particle concentration in gas stream around probe, atoms/cm³, $(n_{W_T})_B$	Average tungsten concentration in "boundary layer," atoms/cm³, $n_{W_T}(Avg)$
1	2100	8,000	3.3×10^{15}	2.3×10^{15}
2	2080	6,800	8.4×10^{14}	5.8×10^{14}
3	2040	7,600	1.4×10^{14}	7.0×10^{14}
4	1750	9,800	1.4×10^{17}	8.6×10^{10}
5	1750	10,200	1.6×10^{17}	7.1×10^{17}
6	2000	8,700	8.8×10^{15}	6.0×10^{15}
7	2050	8,000	1.1×10^{15}	7.7×10^{14}
8	1920	10,000	8.4×10^{16}	5.9×10^{16}
9	1950	6,400	1.7×10^{14}	2.5×10^{14}
10	1850	6,300	1.6×10^{14}	9.4×10^{13}
11	2120	9,500	9.1×10^{16}	5.6×10^{16}
12	2040	8,400	5.6×10^{15}	4.0×10^{15}
13	2050	6,500	9.3×10^{25}	6.5×10^{15}
14	2000	8,700	1.4×10^{15}	9.0×10^{14}
15	2120	7,700	2.0×10^{16}	6.0×10^{15}
16	2120	7,700	1.3×10^{15}	9.1×10^{14}
17	1850	10,000	1.5×10^{17}	1.0×10^{17}
18	1900	6,700	0	0
19	1900	7,200	0	0
20	2100	6,900	0	0
21	2300	7,700	0	0
22	2400	8,300	0	0
23	2300	8,600	0	0
24	2200	7,600	0	0
25	2400	7,700	0	0
26	2400	9,000	0	0
27	2500	10,000	0	0

the derived rate of variation $\partial T_S/\partial T_B$ is shown on Fig. 7 as a function of log $n_{W_T}(Avg)$. It can be seen that, up to a value for $n_{W_T}(Avg)$ of approximately $n_{W_T}(Avg) = 1.5 \times 10^{15}$ particles and for temperatures T_B be-

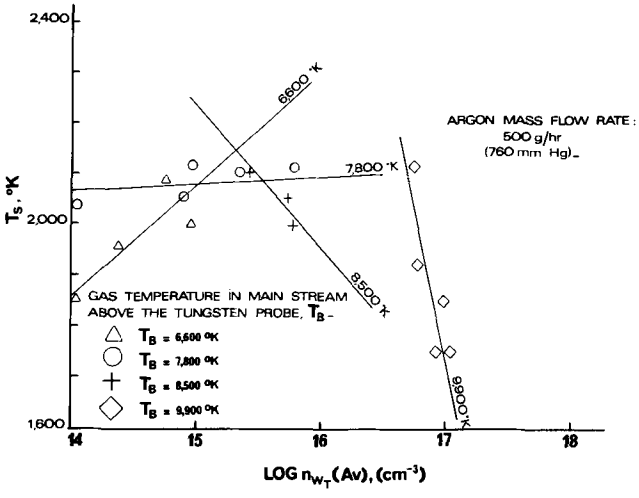

Fig. 6. Probe surface temperature T_S as a function of the average number of total tungsten particle concentration (log) in the boundary layer, for different main gas stream temperatures, T_B, above the probe.

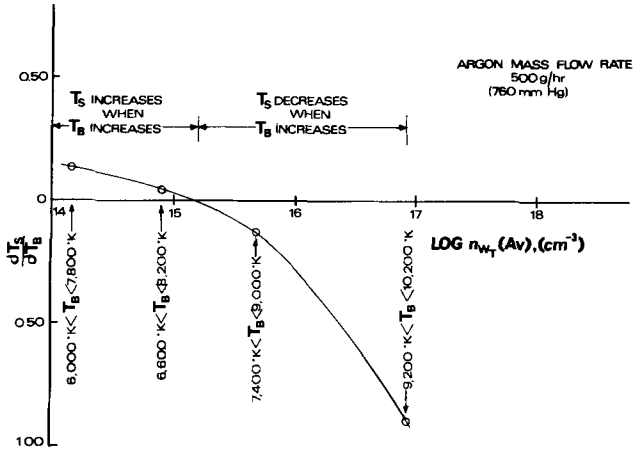

Fig. 7. Rate of variation $\left(\frac{\partial T_S}{\partial T_B}\right)$ as a function of log $n_{W_T}(Avg)$

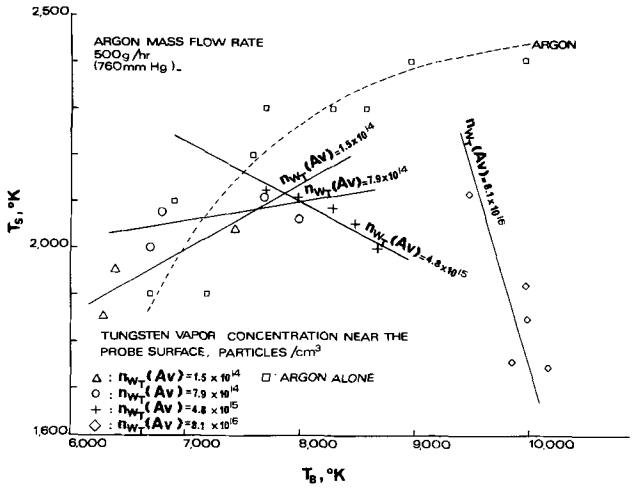

Fig. 8. Probe surface temperature, T_S, as a function of the main gas stream temperature, T_B, above the probe, for different values of the average number of total tungsten particle concentration in the boundary layer.

tween 6600° and 8200°K, the probe surface temperature T_S increases with T_B. For $n_{WT}(Avg) > 1.5 \times 10^{15}$ and temperatures higher than approximately 7000°K, T_S decreases when T_B increases. Figure 8 shows the variation of T_S as a function of T_B for different constant values of $n_{WT}(Avg)$. On the same figure, the variation of T_S against T_B is shown when argon only is present and it can be seen that T_S does increase continuously when T_B increases up to 10,000°K, T_S increasing well beyond the maximum attained by this temperature when tungsten vapor is present. At 9000°K, the presence of about 5×10^{15} tungsten particles per cubic centimeter, or 0.7% tungsten in the gas mixture, decreases the probe surface temperature by 18%, all other conditions being equal.

Figure 9 shows the variation of the rate of change $(\partial T_S/\partial \log n_{WT}(Avg))$ as a function of $\log n_{WT}(Avg)$, the trend being similar to the one already observed. T_S goes through a maximum when $n_{WT}(Avg)$ increases and then starts decreasing, the rate of decrease being higher when the temperature increases. Finally, T_S goes through a maximum for $n_{WT}(Avg) = 1.5 \times 10^{15}$ and $T_B = 7800$°K.

From Fig. 6 and 8, it may be deduced that

$$T_S = f_1(n_{WT}(Avg))\,T_B + f_2(n_{WT}(Avg)) \quad [21]$$

$$T_S = f_3(T_B)\log n_{WT}(Avg) + f_4(T_B) \quad [22]$$

from which

$$\frac{\partial^2 T_S}{\partial T_B\,\partial \log n_{WT}(Avg)} = \frac{df_1(n_{WT}(Avg))}{d\log n_{WT}(Avg)} \quad [23]$$

and

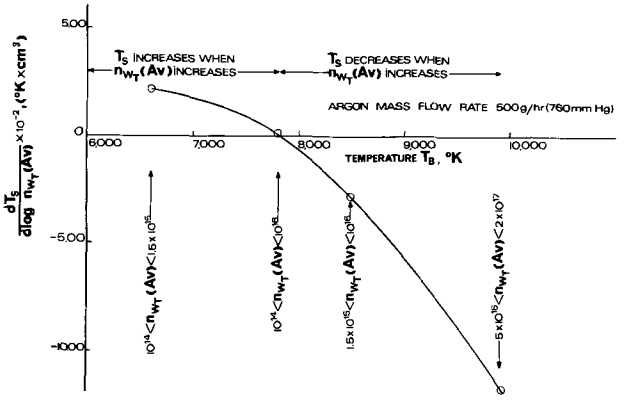

Fig. 9. Rate of variation $\left(\frac{\partial T_S}{\partial \log n_{WT}(Avg)}\right)$ as a function of T_B

$$\frac{\partial^2 T_S}{\partial T_B\,\partial \log n_{WT}(Avg)} = \frac{df_3(T_B)}{dT_B} \quad [24]$$

so that

$$\frac{df_1(n_{WT}(Avg))}{d\log n_{WT}(Avg)} = \frac{df_3(T_B)}{dT_B} = a \quad [25], [26]$$

where a is a constant.

As a result

$$T_S = (a\log n_{WT}(Avg) + b)T_B + f_2(n_{WT}(Avg)) \quad [27]$$

$$T_S = (aT_B + b_1)\log n_{WT}(Avg) + f_4(T_B) \quad [28]$$

From the identity of Eq. [27] and [28], one can write

$$T_S = aT_B \log n_{WT}(Avg) + b_1 \log n_{WT}(Avg) + bT_B \quad [29]$$

Using the experimental data available, it can be found that

$$T_S = -0.0217T_B \log n_{WT}(Avg) + 127.9 \log n_{WT}(Avg) + 0.340T_B \quad [30]$$

Table III shows experimental values for T_S and the corresponding values calculated from Eq. [30], together with the deviation from the predicted mean, this deviation being included between maxima of −8.2 and 9.5% from the predicted mean, the average deviations being +4.2 and −4.4%.

Considering the possible thermionic effects from solid tungsten particles, the electronic concentration n_{es} has been calculated from Eq. [18] for a point temperature around 3500°K in the boundary layer. Table IV shows, for these temperatures, the electron equilibrium concentration n_e in the gaseous phase at a point L, together with n_{es}, the ratio n_{es}/n_e, n_{WT}, and T_B. It can be seen that n_{es} is at least two orders of magnitude higher than n_e, so that it may be expected that positively charged solid particles are present around the surface probe, thus yielding a protective shield against ion bombardment. The importance of the shield depends, of course, on the total number of particles having condensed at point L, or $[(n_{WT})_B - (n_{WT})_L]$, which for all practical purposes is equal to $(n_{WT})_B$. In Table IV, n_{es}/n_e measures the trend toward formation of positively charged solid particles while $(n_{WT})_B$ is a measure of the total thermionic effect per unit gas volume, assuming constant average particle dimension in all cases.

Finally, the right-hand side member of Eq. [30] is made up of two expressions which may be briefly analyzed.

$$(a) \qquad F_1 = -0.0217T_B \log n_{WT}(Avg) \quad [31]$$

The function F_1 accounts for the momentum and thermionic effects already described in the section on Theory and is essentially related to the concentration

Table III. Deviation between experimental value and predicted value from Eq. [30] for probe surface temperature, T_S

Test No.	Probe surface temperature, T_S, °K: Experimental	Probe surface temperature, T_S, °K: Calculated from Eq. [30]	Deviation, °K	Deviation, %
1	2100	2027	79	3.9
2	2080	2037	48	2.4
3	2040	2078	−28	−1.4
4	1750	1910	−156	−8.2
5	1750	1887	−132	−7.0
6	2000	2018	−12	−0.6
7	2050	2050	+8	+0.4
8	1920	1912	+15	+0.5
9	1950	2029	−74	−3.6
10	1850	2025	−171	−8.4
11	2120	1943	+184	+9.5
12	2040	2017	+29	+1.4
13	2050	2005	+51	+2.5
14	2000	2030	−25	−1.2
15	2120	1993	+129	+6.5
16	2120	2041	+86	+4.2
17	1850	1895	−40	−1.2

Table IV. Parameters n_{es}/n_e and $(nW_T)_B$ defining possible thermionic effects

Test No.	Point temperature in boundary layer, T_L, °K	n_{es}, electrons/cm³ at point L	n_e, electrons/cm³ at point L	$\frac{n_{es}}{n_e}$	$(nW_T)_B$ or approx. concentration of condensed tungsten particles at L, particles/cm³	Probe surface temperature, T_S, °K	Main stream gas temperature, T_B, °K
1	3600	2.0×10^{14}	6.5×10^{11}	3.1×10^{2}	3.3×10^{15}	2100	8,000
2	3400	1.0×10^{14}	9.6×10^{10}	1.4×10^{3}	8.4×10^{14}	2080	6,800
3	3500	1.6×10^{14}	2.5×10^{11}	6.5×10^{2}	1.4×10^{14}	2040	7,600
4	3600	2.0×10^{14}	5.8×10^{11}	3.5×10^{2}	1.4×10^{17}	1750	9,800
5	3400	1.0×10^{14}	1.8×10^{11}	5.6×10^{2}	1.6×10^{17}	1750	10,200
6	3600	2.0×10^{14}	8.3×10^{11}	2.4×10^{2}	8.8×10^{15}	2000	8,700
7	3500	1.6×10^{14}	3.2×10^{11}	5.0×10^{2}	1.1×10^{15}	2050	8,000
8	3600	2.0×10^{14}	6.6×10^{11}	3.0×10^{2}	8.4×10^{16}	1920	10,000
9	3500	1.6×10^{14}	3.4×10^{11}	4.7×10^{2}	1.7×10^{14}	1950	6,400
10	3400	1.0×10^{14}	1.3×10^{11}	8.0×10^{2}	1.6×10^{14}	1850	6,300
11	3600	2.0×10^{14}	1.1×10^{12}	1.8×10^{2}	9.1×10^{16}	2120	9,500
12	3300	7.0×10^{13}	4.7×10^{10}	1.5×10^{3}	5.0×10^{15}	2050	8,400
13	3600	2.0×10^{14}	1.1×10^{12}	1.8×10^{2}	9.3×10^{15}	2050	8,500
14	3500	1.6×10^{14}	4.2×10^{11}	4.0×10^{2}	1.4×10^{16}	2120	6,700
15	3500	1.6×10^{14}	3.7×10^{11}	4.3×10^{2}	2.0×10^{16}	2120	7,700
16	3500	1.6×10^{14}	3.3×10^{11}	4.9×10^{2}	1.0×10^{17}	2120	7,700

$n_{WT}(\text{Avg})$ in the boundary layer. If $n_{WT}(\text{Avg})$ is high, then the number of solid particles should also be high, thus increasing the thermionic protective effects described. But this effect should increase with an increase of ion content in the medium, which is a function of T_B and this justifies the presence of T_B in F_1.

$$(b) \qquad F_2 = 127.9 \log n_{WT}(\text{Avg}) + 0.340 T_B \qquad [32]$$

or

$$F_2 = \log[n_{WT}(\text{Avg})]^{127.9}\,[2.19]^{T_B}$$

Equation [32] implies an increase of heat exchange with the probe and consequently an increase of T_S, all other conditions being equal. This is, of course, related to an increase in transfer effects normally expected when the gas temperature increases. Larger heat transfer rates may also be the result of a thermal conductivity increase with temperature for partially ionized argon (12). Obviously, Eq. [32] is valid only for a temperature range such that 6000°K $< T_B <$ 10,000°K, which has been used in the present investigation.

The probe surface temperature T_S has been determined by means of pyrometric measurements so that an error of ±2% may be expected, which is well within the maximum (around 2400°K) and minimum (around 1700°K) temperatures recorded. The gas temperature should bear an error of ±5% which is normally expected for spectroscopic measurements made in this experiment. This does not essentially affect the conclusions of the present study.

Conclusions

The surface temperature of a tungsten probe heated by an argon plasma has been investigated in the presence of a metal vapor (tungsten) mixed in the plasma gas. The gas temperature near the tungsten surface was varied between 6000° and 10,000°K while the total tungsten atom and ion concentration varied between 10^{14} and 10^{17} particles/cm³ (at 760 mm Hg) or roughly 0.01 and 7% of the plasma gas. Similar tests have been conducted with the argon plasma alone.

Starting from 6000°K, the probe surface temperature goes through a maximum when the metal vapor concentration is about 1.5×10^{15} particles/cm³ (approximately 0.2%) and the gas temperature around 7800°K. At 9000°K, the presence of 5×10^{15} tungsten particles/cm³ decreases the surface temperature by 18% when the latter is compared with identical conditions employing argon alone. It is concluded that the presence of tungsten vapor contributes to a form of thermal protection. The reasons for this behavior are attributed to the formation of solid condensed particles which absorb energy, favor recombination effects, and may build up a protective layer of positively charged solid particles by means of a thermionic effect.

Acknowledgment

The author is indebted to the National Research Council of Canada and the authorities of the University of Quebec at Chicoutimi, Province of Quebec (Canada), for their financial help. The assistance of Messrs. G. Touzot and J. Bresse, of this university, for the computer program is acknowledged with appreciation.

Manuscript submitted April 13, 1972; revised manuscript received Sept. 11, 1972. This was Paper 88 presented at the Miami Beach, Florida, Meeting of the Society, Oct. 8-13, 1972.

Any discussion of this paper will appear in a Discussion Section to be published in the December 1973 JOURNAL.

NOMENCLATURE

A	transition probability, sec^{-1}
a	constant in Eq. [25] to [29], cm^3
Å	angstroms
b	constant in Eq. [27] and [29], dimensionless
b_1	constant in Eq. [28] and [29], °K-cm^3
d_{Ar}	diameter of argon atom, Å
d_W	diameter of tungsten atom, Å
$d_{Ar\text{-}W}$	average diameter $(d_{Ar} + d_W)/2$ defining the cross section of the sphere of influence for unlike collisions between argon and tungsten particles, Å
e	symbol for electron or base of naperian logarithms
E	excitation energy level or ionization potential, eV
f_1, f_2	functions of $n_{WT}(\text{Avg})$ in Eq. [21]
f_3, f_4	functions of T_B in Eq. [22]
F_1, F_2	functions of $n_{WT}(\text{Avg})$ and T_B in Eq. [31] and [32]
g	statistical weight
h	Planck's constant, 6.624×10^{-27} erg-sec
I	total spectral emissive power emitted per unit volume and unit frequency
j	thermionic current emission, A/cm^2
k	Boltzmann's constant, 1.380×10^{-16} erg/°K
K	total concentration of particles in plasma, cm^{-3}
K_{Ar}	Saha equilibrium constant for argon, cm^{-3}
K_W	Saha equilibrium constant for tungsten, cm^{-3}
L	combined geometrical and spectral absorption constant in Eq. [1] and [2]
m	mass of particle, g
n	concentration, particles/cm^3
n_{es}	concentration of thermionic electrons corresponding to the emitting surface temperature, electrons/cm^3
N	collision frequency, sec^{-1}
p	plasma pressure, dynes/cm^2
T	temperature, °K
U	constant in Richardson's thermionic current equation ($U = 60.2$ A/cm^2-°K^2)
v	average speed for particles, or $\sqrt{8kT/\pi m_e}$
$Z(T)$	partition function written as a function of temperature
ϕ	thermionic work function, eV
ν	spectral emission frequency, sec^{-1}
ΔH_T	enthalpy of vaporization at T(°K), cal/g-mole
$\Delta H_{a,b}$	average enthalpy of vaporization between temperatures T_a and T_b, cal/g-mole

Subscripts
Ar pertaining to argon
a, b pertaining to different temperatures
Ar-W identifies the cross section of the sphere of influence for unlike collisions between argon and tungsten particles, or average atomic diameter $(d_{Ar} + dw)/2$
B situation in the plasma main stream, immediately above the probe surfaces
e pertaining to electrons
L particular points in the plasma
S pertaining to the probe surface
T total
W pertaining to tungsten
1, 2 related to distinct situations in the plasma

Superscript
+ first ionization

Abbreviations
ln naperian logarithms
log decimal logarithms
Avg or Av average

REFERENCES

1. I. C. Slattery and E. Tagliaferri, *Nucl. Sci. Abstr.*, **21** (19), 34-406 (1967).
2. I. R. Hague *et al.*, "Refractory Ceramics of Interest in Aerospace Structural Applications," Technical Report No. ASD-TDR-63-4102, AF Materials Laboratory, Research and Technology Division, Wright Patterson Air Force Base (October 1963).
3. M. E. Franke, Winter Annual Meeting of the AIME, Paper No. 68-WA/HT-9, New York (Dec. 5, 1968).
4. K. T. Shih *et al.*, *AIAA J.*, **6**, 1482 (1968).
5. P. Meubus and M. Fortin, *Can. J. Chem. Eng.*, **49**, 797 (1971).
6. P. Meubus, *Chem. Eng. Sci.*, To be published.
7. C. E. Moore, "Atomic Energy Levels," NBS 467, National Bureau of Standards, Washington, D. C. (1949).
8. H. R. Griem, "Plasma Spectroscopy," p. 143, McGraw-Hill Book Co., New York (1964).
9. Handbook of Chemistry and Physics, 41st Edition, Chemical Rubber Publishing Co., Cleveland (1960).
10. *Ibid.*
11. J. M. Smith and H. C. Van Ness, "Introduction to Chemical Engineering Thermodynamics," 2nd Ed., McGraw-Hill Book Co., New York (1959).
12. A. Kanzawa and I. Kimura, *AIAA J.*, **5**, 1315 (1967).

Solvent Equilibria of $AlCl_3$-NaCl Melts

L. G. Boxall,* H. L. Jones, and R. A. Osteryoung*

Department of Chemistry, Colorado State University, Fort Collins, Colorado 80521

ABSTRACT

The solvent acid-base properties of $AlCl_3$-NaCl melts containing 50-70 mole per cent $AlCl_3$ at temperatures of 175°-355°C are fully described by the use of three equilibrium constants

$$2AlCl_{3(l)} = Al_2Cl_{6(l)} \qquad K_0$$
$$AlCl_4^- + AlCl_3 = Al_2Cl_7^- \qquad K_2$$
$$2AlCl_4^- = Al_2Cl_7^- + Cl^- \qquad K_M$$

At 175°C the K values on the mole fraction scale are 2.86×10^7, 2.4×10^4, and 1.06×10^{-7}, respectively. The ΔH and ΔS values for each equilibrium were found to be temperature independent and calculated values for previously unreported formation constants for the liquid $NaAlCl_4$, $NaAl_2Cl_7$, and Al_2Cl_6 species are reported. Emf data for the aluminum electrode

$$AlCl_4^- + 3e^- = Al\downarrow + 4Cl^-$$

determined as a function of the mole per cent $AlCl_3$, are used to evaluate the equilibrium constants. In the calculations it was necessary to use a variable $AlCl_4^-$ activity coefficient when the mole per cent $AlCl_3$ exceeded 50%. An experimental nondestructive *in situ* procedure for the determination of the exact composition and pCl of any melt is described. This procedure is essential when working in volatile melts.

The $AlCl_3$-NaCl melt can be considered as an acid-base system in which an acid is defined as a chloride ion acceptor and a base is defined as a chloride ion donor. The dissociation of the melt into Na^+ and $AlCl_4^-$ ions leads to an equilibrium involving $AlCl_4^-$

$$\underset{\text{Base}}{2AlCl_4^-} = \underset{\text{Acid}}{Al_2Cl_7^-} + Cl^- \qquad [1]$$

The electrode reaction at an aluminum reference electrode in these melts can be written as

$$AlCl_4^- + 3e^- = Al\downarrow + 4Cl^- \qquad [2]$$

and the electrode potential is given by

$$E = E^o - \frac{RT}{3F} \ln \frac{(a_{Cl^-})^4}{(a_{AlCl_4^-})} \qquad [3]$$

Several other electrode reactions can be written for this electrode; however, the inclusion of the appropriate equilibrium constants in the E^o term will reduce them to the simpler form given above (1). The $AlCl_4^-$ activity is approximately constant in the composition region near 50 m/o (mole per cent) $AlCl_3$; hence, in this region the aluminum electrode becomes a pCl electrode. The term mole per cent $AlCl_3$ throughout this paper refers to the over-all melt composition expressed in terms of the relative number of moles of $AlCl_3$ and NaCl. The amount of true chemical species in the melt is referred to as mole fractions. Several groups of workers have demonstrated that the response of an aluminum electrode to a change in pCl in the equimolar melt can be as large as 300 mV for a change in the mole per cent $AlCl_3$ from 50.0 to 50.4 (1-3). This response becomes less pronounced in the $AlCl_3$ or NaCl rich melts, *i.e.*, the mole per cent $AlCl_3$ is $>$ 50.2% or $<$ 49.8%, respectively. This behavior is analogous to the pH behavior in an aqueous strong acid-base titration.

The high volatility of the $AlCl_3$ inhibits the preparation of a melt of accurately known composition and a reference electrode with a known potential. The po-

* Electrochemical Society Active Member.

Key words: fused salts, $AlCl_3$-NaCl melt, aluminum electrode, acid-base melts.

tential of an aluminum reference electrode in a melt saturated with NaCl (*ca.* 49.7 m/o $AlCl_3$ at 175°C) is extremely slow to stabilize and temperature dependent. The exact reason for the slow equilibration is unknown; however, a slow rate of dissolution of NaCl is suspected.

The purpose of this work was to calculate, at several temperatures, the thermodynamic constants required to completely describe the $AlCl_3$-NaCl melt over a composition range from the NaCl saturated melt to the 70 m/o $AlCl_3$ melt. The design of our electrochemical cell could not contain the high $AlCl_3$ vapor pressure which is present over melts containing more than about 70 m/o $AlCl_3$. The NaCl-rich melts are initially titrated by the electrical anodization of aluminum into the melt and then by the addition of solid $AlCl_3$. A mathematical procedure is developed which enables one to accurately determine the composition of the melt, as well as to adjust the composition of the melt to any desired value.

Experimental Section

Dried Fluka (A.G., anhydrous, iron free) aluminum chloride and Fluka (A.G.) sodium chloride were quantitatively weighed out into a Pyrex cell in a nitrogen-filled dry box. The details of the cell and the electrolysis purification procedure are described elsewhere (4). The final melt (*ca.* 50:50 m/o) was completely colorless and exhibited no irregularities in the current-voltage curves using a microtungsten indicator electrode. A large tungsten counterelectrode and an aluminum reference electrode compartment were then sealed into the cell by means of machined Teflon. A second 10-mm fritted compartment, which was changed for each trial, was used to isolate the aluminum electrode under examination from the rest of the system. The working aluminum electrode (99.999% purity) served both as a source of aluminum for the electrical titration portion of the experiment and as one-half of the aluminum concentration cell potentiometric measurement.

The $AlCl_3$ concentration in the working compartment was increased to about 51 m/o in small increments by constant current anodization. The potential of the working aluminum electrode *vs.* the arbitrary aluminum reference electrode was recorded after each increment in the $AlCl_3$ concentration. Above 51 m/o $AlCl_3$, small weighed amounts of $AlCl_3$ were added until the melt contained *ca.* 70 m/o $AlCl_3$. Cyclic voltammetry showed no appreciable change in the melt's impurity level after these additions. The melt was weighed after solidification to determine the exact amount of melt in the working compartment. No hysteresis in the equilibrium potentials was observed when the $AlCl_3$ mole per cent in the melt was cycled several times between 49.9 and 50.5 by the electrical addition or removal of aluminum. The potential of the aluminum electrode reached a constant value within 2 min after each addition of aluminum and remained constant for up to 10 hr (±0.5 mV). At high $AlCl_3$ concentrations (>65 m/o), there was a slow downward drift in the potential due to the diffusion of the $AlCl_3$ through the frit and the increased volatility of the melt.

A proportional thermoelectric controller was used to control the temperature of the melt to ±0.5°C. The temperature was measured using a Chromel-Alumel Pyrex-sheathed thermocouple and an L&N potentiometer. The precision of the L&N Student Potentiometer was better than ±0.1 mV compared to a precision voltage source.

Results

The following electrochemical cell was used to determine the equilibrium constants for the $AlCl_3$-NaCl system

$$Al/AlCl_3(C_{ref}),\ NaCl/\text{Fritted Pyrex}/AlCl_3(C),\ NaCl/Al \quad [4]$$

where C_{ref} is a constant but unknown reference electrode system. For the same reasons as those outlined by Torsi and Mamantov (2), the liquid junction potential across the Pyrex frit may be neglected in all of the calculations. Only the Na^+ ion needs to be considered in the theoretical calculation of the liquid junction potential since its mobility is much larger than that of the bulky anions in the melt. The Na^+ concentration in the 50 m/o $AlCl_3$ melt is about double that in the 66 m/o $AlCl_3$ melt. A Na^+ concentration profile of this magnitude in nitrate melts produces a junction potential of about 1 mV (5), hence neglecting the junction potential appears to be justified. Then from Eq. [3] the potential for cell [4] is given by

$$E = \frac{RT}{3F} \ln \left[\frac{(a_{AlCl_4^-})}{(a_{AlCl_4^-})_{ref}} \right] + \frac{4RT}{3F} \ln \left[\frac{(a_{Cl^-})_{ref}}{(a_{Cl^-})} \right] \quad [5]$$

It has been shown that the mole fraction activity coefficient for ions in melts remains constant provided that N, the mole fraction, remains below 0.1 (6). For regular solutions, γ_N may be expressed as

$$RT \ln (\gamma_N) = W_T(1 - N)^2 \quad [6]$$

where W_T is the work constant at temperature T. It has been shown experimentally that Eq. [6] is valid for multicomponent melts, as well as the simple binary melts (5). In our system the $AlCl_4^-$ concentration traverses the 1.0-0.1 mole fraction region and a γ value for the $AlCl_4^-$ species must be considered in all the calculations. (Although the $Al_2Cl_7^-$ mole fraction reaches a maximum value of approximately 0.7 in the 66.6 m/o $AlCl_3$ melt, the inclusion of any significant γ value for the $Al_2Cl_7^-$ species in the calculation produced a parabolic deviation between the calculated curve and the experimental curve in the 55-65 m/o $AlCl_3$ region. The best least squares fit to the experimental data was obtained by the use of only the $AlCl_4^-$ γ variation.) Equation [5] can now be simplified to

$$E = \frac{RT}{3F} \ln \left[\frac{\gamma(N_{AlCl_4^-})}{\gamma_{ref}(N_{AlCl_4^-})_{ref}} \right] + \frac{4RT}{3F} \ln \left[\frac{(N_{Cl^-})_{ref}}{(N_{Cl^-})} \right] \quad [7]$$

Other workers (1-3) have postulated that the $AlCl_3$-NaCl melts contain the following species

$AlCl_3$	$AlCl_4^-$	Na^+
Al_2Cl_6	$Al_2Cl_7^-$	Cl^-
	$Al_3Cl_{10}^-$	

Since the $Al_3Cl_{10}^-$ anion exists only in melts of very rich $AlCl_3$ content, we found its inclusion unnecessary for our system calculations. The following set of thermodynamic equilibria were used to interrelate these species in the various melts

$$2AlCl_{3(l)} = Al_2Cl_{6(l)} \qquad K_o \qquad [8]$$

$$AlCl_4^- + AlCl_3 = Al_2Cl_7^- \qquad K_2 \qquad [9]$$

$$2AlCl_4^- = Al_2Cl_7^- + Cl^- \qquad K_M \qquad [10]$$

The K_o values were calculated from vapor pressure data utilizing the procedure outlined by King *et al.* (3). The K_M value was determined from the "S" portion of the titration curve (49.7-51.0 m/o $AlCl_3$) and the K_2 value from the $AlCl_3$-rich portion of the curve (51-70 m/o $AlCl_3$). The K_M determination is almost independent of the initial estimate for the K_2 value, whereas the K_2 determination is moderately dependent upon the K_M value. Iterative procedures involving the K_M determination followed by the K_2 (and W_T) determination were repeated several times to give the best least squares fit to the experimental data.

The mathematical procedure outlined in Appendix I is used to calculate the composition of the melt at each

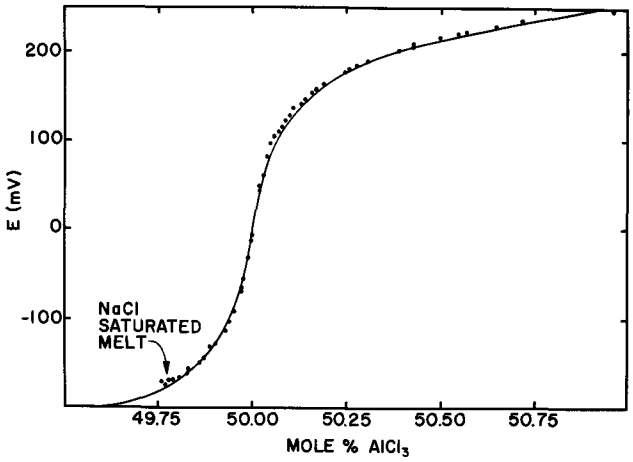

Fig. 1. Comparison of experimental and calculated aluminum electrode potential in a $AlCl_3$-NaCl melt at 175° ± 0.5°C as a function of melt composition (49.75 ≤ m/o $AlCl_3$ ≤ 51).

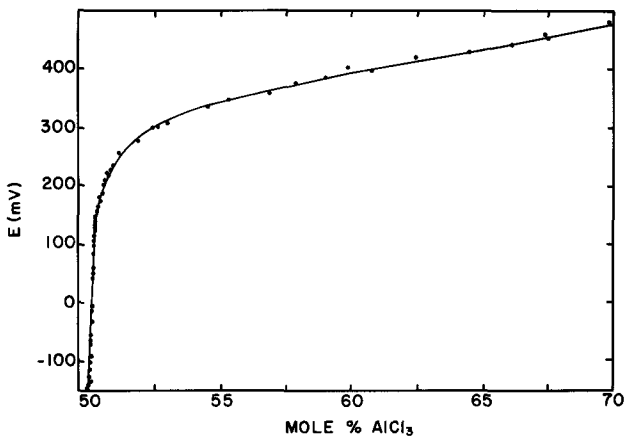

Fig. 2. Comparison of experimental and calculated aluminum electrode potential in a $AlCl_3$-NaCl melt at 175° ± 0.5°C as a function of melt composition (49.75 ≤ m/o $AlCl_3$ ≤ 70%).

experimental point along the electrical titration curve. The mathematical procedure given in Appendix II is now used to obtain a K_M value which gives a minimum least squares deviation between the calculated and experimental aluminum electrode potentials. A final K_M value is obtained by taking the average of the K_M values determined from at least four independent experiments. The data from all the independent experiments are combined by adjusting the potentials to one common reference electrode, *i.e.*, Al in a $NaAlCl_4$ (50:50) melt. The set of combined data in conjunction with the procedure given in Appendix III is used to calculate least square values for K_2 and W_T. Since the original K_M determination relied, to a small degree, on the estimated K_2 and W_T values, the entire computation was repeated until changes in the calculated K_M and K_2 values between two successive iterations were all $<0.1\%$.

The calculated curve for the "S" portion of the titration curve is compared to the experimental data in Fig. 1 and the fit for the entire composition range is given in Fig. 2. A portion of the final computer printout for all the data at 175°C is given in Appendix IV. The final results for all of the measurements are summarized in Table I along with a comparison with the K_M values reported by Torsi and Mamantov (2).

The temperature dependence of W_T is larger in this melt than that observed in other melts (6). This may be due in part to structural changes in the melt with temperature (Fig. 6) which may not be present in simpler melts. The relatively large error in the determination of W_T would also account for much of this apparent temperature dependency. The decrease in the W_T value with increasing temperatures is consistent with observed behavior in other melts (6).

The changes in entropy and enthalpy for the reactions [8], [9], and [10] were calculated using the relationship

$$\Delta G^\circ = -RT \ln K \qquad [11]$$

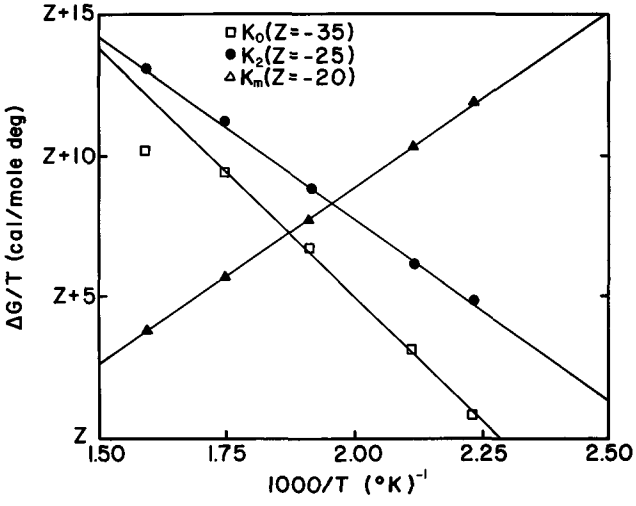

Fig. 3. Gibbs-Helmholtz plots for the determination of ΔH for the equilibria indicated; K_0 ($2AlCl_3 \rightleftarrows Al_2Cl_6$), K_2 ($AlCl_4^- + AlCl_3 \rightleftarrows Al_2Cl_7^-$), and K_M ($2AlCl_4^- \rightleftarrows Al_2Cl_7^- + Cl^-$).

and the Gibbs-Helmholtz equations

$$\Delta S = -\left(\frac{\partial \Delta G}{\partial T}\right)_P \qquad [12]$$

and

$$\Delta H = 1000\left(\frac{\partial(\Delta G/T)}{\partial(1000/T)}\right)_P \qquad [13]$$

The appropriate plots are given in Fig. 3 and the results are summarized in Table II. Cubic equations were used to fit the JANAF temperature dependency of the thermodynamic data (7) for NaCl, $AlCl_3$, and $NaAlCl_4$. The values given for the solid $NaAlCl_4$ in the JANAF Tables are estimates based on the data for solid $KAlCl_4$. No heats of fusion were given for the tetra-

Table I. Mole fraction equilibrium constants for the $AlCl_3$-NaCl melt

Temperature (°C ± 0.5°)	175	200	250	300	355
K_0 [calcd, Ref. (3)]	2.86×10^7	9.40×10^6	1.49×10^6	3.85×10^5	2.72×10^5
K_2	2.4×10^4	1.3×10^4	3.4×10^3	1.0×10^3	4.0×10^{2a}
Error in K_2	$\pm 0.1 \times 10^4$	$\pm 0.1 \times 10^4$	$\pm 0.2 \times 10^3$	$\pm 0.2 \times 10^3$	$\pm 0.2 \times 10^{2a}$
K_M	1.06×10^{-7}	2.23×10^{-7}	8.55×10^{-7}	2.37×10^{-6}	5.83×10^{-6}
Error in K_M	$\pm 0.2 \times 10^{-8}$	$\pm 0.2 \times 10^{-8}$	$\pm 0.3 \times 10^{-8}$	$\pm 3 \times 10^{-8}$	$\pm 5 \times 10^{-8}$
K_M [Ref. (2)]	7.9×10^{-8}	—	5.0×10^{-7}	2.06×10^{-6}	5.0×10^{-6b}
W_T (cal mole^{-1})[d]	1400	1400	700	0	0[a]
E_{SD} (mV)[c]	2.9	3.7	1.9	2.9	3.2

[a] Estimated value.
[b] Value for 350°C.
[c] Standard deviation in E.
[d] ±100 cal mole^{-1}.

Table II. Thermodynamic constants for $AlCl_3$-NaCl equilibria, 175°-355°C

Reaction (liquid states)	$\Delta H°$ (kcal mole^{-1})	$\Delta S°$ (cal mole^{-1} deg^{-1})	$\Delta G°$ at 200°C (kcal mole^{-1})
$2AlCl_3 = Al_2Cl_6$	-17.66 ± 0.005	-5.2 ± 0.8	-15.2 ± 0.4
$NaAlCl_4 + AlCl_3 = NaAl_2Cl_7$	-13.00 ± 0.005	-8.9 ± 0.6	-8.8 ± 0.3
$2NaAlCl_4 = NaCl + NaAl_2Cl_7$	12.54 ± 0.005	-4.1 ± 0.3	14.5 ± 0.1
$NaCl + AlCl_3 = NaAlCl_4$	-25.54 ± 0.005	-4.8 ± 0.5	-23.3 ± 0.2

Table III. Temperature dependence of the formation constants for the species in the $AlCl_3$-NaCl melt, 175°-355°C

Species (liquid state)	Constant[c]	$X = a + bT \times 10^{-2} + cT^2 \times 10^{-4} + dT^3 \times 10^{-6}$[d] a	b	c	d	Error
Al[a]	$\Delta H_f°$	1.37	0.300	−0.023	0.06	±0.2[b]
	$S°$	−3.08	5.493	−0.647	3.32	±0.1[b]
Na[a]	$\Delta H_f°$	0	0	0	0	±0.1[b]
	$S°$	1.57	5.979	−0.741	3.83	±0.1[b]
Cl[a]	$\Delta H_f°$	28.59	0.101	0.004	−0.04	±0.01[b]
	$S°$	31.64	3.683	−0.419	2.11	±0.01[b]
NaCl[a]	$\Delta H_f°$	−82.08	−6.600	1.327	−8.61	±0.2[b]
	$S°$	5.46	7.972	−0.857	4.22	±0.1[b]
$AlCl_3$[a]	$\Delta H_f°$	−166.42	2.327	−0.252	1.65	±0.2[b]
	$S°$	−2.25	20.39	−2.259	10.9	±0.1[b]
$NaAlCl_4$	$\Delta H_f°$	−274.00	−4.273	1.075	−8.99	±0.4
	$S°$	−1.60	28.36	−3.116	5.87	±0.6
$NaAl_2Cl_7$	$\Delta H_f°$	−453.46	−1.946	0.823	−9.37	±0.6
	$S°$	−12.72	48.75	−5.375	6.52	±0.8
Al_2Cl_6	$\Delta H_f°$	−350.50	4.654	−0.505	3.30	±0.3
	$S°$	−9.67	40.78	−4.518	21.8	±1.0

[a] Obtained from JANAF Tables.
[b] Estimated.
[c] $\Delta H_f°$ in kcal mole^{-1}; $S°$ in cal mole^{-1} deg^{-1}.
[d] T in °K.

chloroaluminate salts. The interpolated JANAF values and the reaction values given in Table II enabled us to calculate energies of formation for all the species in the $AlCl_3$-NaCl melt. The temperature dependencies of these thermodynamic values are given in Table III.

Discussion

The aluminum electrode is the reference electrode most extensively used in the published electrochemical studies on melts containing aluminum chloride. This electrode offers the advantage of a potential which is stable with respect to time and simplicity of construction and operation. The major disadvantage is the dependence on the melt composition as illustrated in Fig. 1 and 2. Fortunately, the major portion of the published work has been carried out in the 2:1 $AlCl_3$-NaCl melt in which the aluminum electrode is relatively insensitive to small changes in the $AlCl_3$ concentration. In a 2:1 melt, a 25 mV change in potential corresponds to a change of 100 mg of $AlCl_3$ per gram of melt. Since the melts are usually prepared by mixing given amounts of NaCl and $AlCl_3$, the high vapor pressure of the $AlCl_3$ during the fusion process and the uncertainties in the weights of the salts, due to moisture and/or impurities, prevent the accurate preparation of a precisely equimolar melt. In order to obtain a reproducible 1:1 melt (±10 mV reliability in the reference electrode), the weights must be accurate to at least 20 ppm with no volatilization of the $AlCl_3$. This procedure is equivalent to attempting to dissolve solid NaOH in concentrated HCl to produce a pH 7.0 ± 0.1 solution. Our experience indicates that during the purification procedure, enough $AlCl_3$ is lost to produce a melt having a composition of approximately 49.8 m/o $AlCl_3$ and a reference potential of *ca.* 169 and 160 mV *vs.* an aluminum reference in the 1:1 melt at 175° and 200°C, respectively. Increasing the temperature beyond 250°C results in additional loss of a small amount of $AlCl_3$ (*ca.* 0.25 m/o).

The use of an aluminum electrode in a NaCl saturated melt [*ca.* 49.75 m/o $AlCl_3$ (2)] is unattractive due to a slow NaCl solubility equilibrium. In addition, the melt composition is temperature dependent [49.75% at 175°C, 49.3% at 300°C (2)].

With the E_{50} program (Appendix I), an accurate nondestructive determination of the exact composition of the melt in the working electrode compartment can be performed. The ease and accuracy of the aluminum electrolysis addition method enables the adjustment of the melt composition to any desired value within the 50 m/o region. However, at higher $AlCl_3$ concentrations it is necessary to use the less accurate and less convenient method of solid $AlCl_3$ addition. The printout from the E_{50} program directly predicts the electrolysis time required to obtain an equimolar melt by the addition or removal of aluminum.

The K values determined in this work at 175°C are compared with the previously published values in Table IV. All of the new K values are flanked by the published values which contain errors of at least twice those quoted for our values. The computational methods used here permit a better than ±4 mV theoretical fit to the experimental emf data. The simpler procedure used by Mamantov (2) gives a reasonable fit for only the equimolar region (±1%) and generates a 190 mV error in the 2:1 melt. King (3) uses two semiempirical equations to fit the emf data (±12 mV) over the concentration ranges of 51-71 m/o $AlCl_3$ and 49.8-50.4 m/o $AlCl_3$. The concentration range of 50.4-51 m/o $AlCl_3$ is not covered by King's semiempirical equations and there appears to be a definite deviation between the fitted curve and the experimental data at the higher $AlCl_3$ concentrations. Even though King

Table IV. Mole fraction equilibrium constants for the $AlCl_3$-NaCl system, 175°C

Source	K_0[a]	K_2[b]	K_3[c]	K_M[d]	W_T[e] (cal mole^{-1})
This work	2.86×10^{7}[f]	$(2.4 \pm 0.1)10^{4}$	0[g]	$(10.6 \pm 0.2)10^{-8}$	1400
Tremillon, Ref. (1)	—	∞[g]	0[g]	$(13.3 \pm 1.5)10^{-8}$[h]	0[g]
Mamantov, Ref. (2)	—	∞[g]	0[g]	$(8.0 \pm 1.8)10^{-8}$	0[g]
King, Ref. (3)	2.9×10^{7}[f]	2.5×10^{4}	$\leq 10^{3}$	7.77×10^{-8}[i]	0[g]
		$(5.5 \pm 0.5)10^{4}$[j]			
		$(1.5 \pm 0.3)10^{4}$[j]			

[a] Equilibrium constant for $2AlCl_3 = Al_2Cl_6$.
[b] Equilibrium constant for $AlCl_3 + AlCl_4^- = Al_2Cl_7^-$.
[c] Equilibrium constant for $AlCl_3 + Al_2Cl_7^- = Al_3Cl_{10}^-$.
[d] Equilibrium constant for $2AlCl_4^- = Cl^- + Al_2Cl_7^-$.
[e] From the equation $RT \ln(\gamma AlCl_4^-) = W(1 - N_{AlCl_4^-})^2$.
[f] Calculated from the JANAF Tables.
[g] Defined.
[h] Converted from the molal concentration scale.
[i] Calculated from Mamantov's data [Ref. (2)].
[j] Calculated by King from vapor pressures.

gives an upper bound for K_3, he does not use it in his calculations. We observed an identical trend in our fit until we included the activity coefficient term for $AlCl_4^-$ species. Species composition diagrams constructed using the first part of the K_M program (Appendix II) are presented in Fig. 4 and 5. These diagrams are similar to King's (3) except that they show far greater detail in the equimolar region. Figure 5 shows that Mamantov's two assumptions (that the $AlCl_4^-$ concentration remains constant and that the melt contains no neutral aluminum chloride) were incorrect, as he suggests at the end of the paper (2). His assumptions were reasonable for the equimolar region but not for the $AlCl_3$-rich melts. This is borne out by the increasing deviation between his calculated emf values and the experimental values. The K_M values determined by Mamantov are equal to *ca.* 70% of our values over the entire experimental temperature range (Table I). Possibly at higher $AlCl_3$ concentrations (>70%), it may be necessary to acknowledge the presence of $Al_3Cl_{10}^-$ species as suggested from Raman work (8).

The melt composition temperature dependencies for both the 1:1 and 2:1 melts are illustrated in Fig. 6. As would be expected, both the NaCl and the Al_2Cl_6 species become more predominant with an increase in temperature. For the reaction

$$AlCl_3 + NaAlCl_4 = NaAl_2Cl_7 \qquad [14]$$

the free energy becomes positive at about 325°C, whereas for the reaction

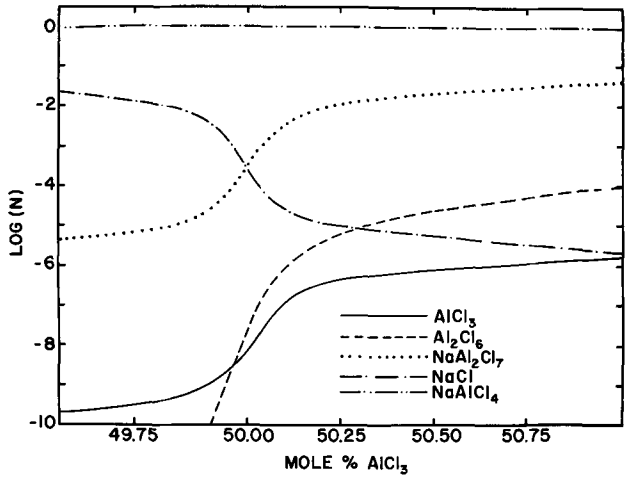

Fig. 4. Mole fraction of the species in the chloroaluminate melt at 175° ± 0.5°C as a function of the net $AlCl_3$-NaCl ratio (49.75 ≤ m/o $AlCl_3$ ≤ 51).

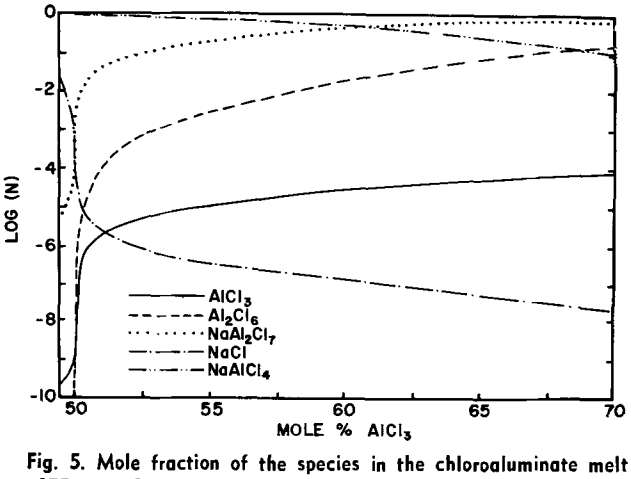

Fig. 5. Mole fraction of the species in the chloroaluminate melt at 175° ± 0.5°C as a function of the net $AlCl_3$-NaCl ratio (49.75 ≤ m/o $AlCl_3$ ≤ 70).

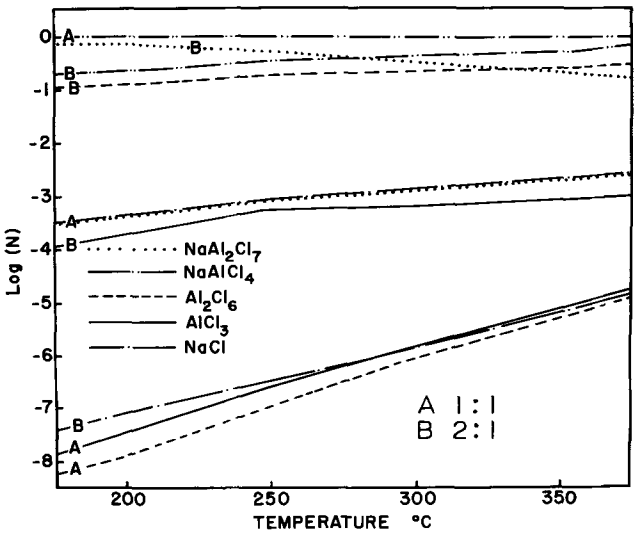

Fig. 6. Temperature variation of the composition of the 1:1 and 2:1 $AlCl_3$-NaCl melts.

$$AlCl_3 + NaCl = NaAlCl_4 \qquad [15]$$

ΔG remains negative until about 480°C. The useful temperature range for the equimolar melt is *ca.* 150°-500°C, but for the 2:1 melt it is 115°-500°C, where the lower temperature limits are literature melting points (14). The magnitude and temperature dependency of the γ values are in accord with that observed for other fused salt systems (5).

The heat of fusion for $NaAlCl_4$ is estimated to be 3.6 kcal $mole^{-1}$ from the entropy values. In the JANAF Tables, the $\Delta H°$ values for solid $NaAlCl_4$ (which were estimated from the $KAlCl_4$ values) appear to be about 10 kcal $mole^{-1}$ too positive. Previously unreported thermodynamic values for the liquid $NaAlCl_4$, $NaAl_2Cl_7$, and Al_2Cl_6 species are summarized in Table III.

The ability to vary the concentration of the chloride ion and the $AlCl_3$ species over four or five orders of magnitude provides a powerful tool to study various equilibria in these melts. Aluminum chloride melts are used in many organic reactions (9) and organic radical cations are stabilized in these melts (10). The acid-base character of amines can be easily studied by the variation of the pCl of the melt. Hames and Plambeck (11) report that the monovalent Cd and Hg species are stabilized by the 2:1 $AlCl_3$-alkali metal chloride melt. Our investigations show that this is not the case in the equimolar melts (4). It appears that the stabilization of these lower valency states is directly related to the acidity of the melt, *i.e.*, the concentration of the $AlCl_3$ and Al_2Cl_6 species. The presence of these low valency states complicates the interpretation of electrochemical results and causes unstable potentials (11). The main disadvantage of the equimolar system is that it is a completely unbuffered system which complicates any dynamic measurement. It may be possible to buffer this system by the addition of a weak acid or base such as $ZnCl_2$ or an organic chloride.

Numerous other inorganic salts (*e.g.*, $SbCl_3$, $FeCl_2$, $SnCl_4$) have vapor pressures high enough to produce the same uncertainty in melt composition as observed in the $AlCl_3$ melt. Workers in these melts must be aware of these problems and how they can affect the concentration of ions analogous to the Cl^- and $AlCl_3$ species. Bauer *et al.* (12) have investigated the $SbCl_3$ melts containing $AlCl_3$ and KCl in which $SbCl_3$ acts as a base

$$SbCl_3 = SbCl_2^+ + Cl^- \qquad [16]$$

$$K = [SbCl_2^+][Cl^-] = 1.2 \times 10^{-10} \quad \text{(mole fraction scale)} \qquad [17]$$

However, they assume that $AlCl_4^-$ exhibits no chloride ion donor or acceptor property. The K values for the $AlCl_4^-$ system indicate that the amount of Cl^- ion originating from the $AlCl_4^-$ would be *ca.* 1000 fold greater than that from the $SbCl_3$. Fortunately, the concentrations used and the accuracy claimed for their measurements minimize the seriousness of this oversight.

The experimental techniques and mathematical procedures developed here elucidate many of the properties and difficulties encountered in the use of the $AlCl_3$-NaCl melt. The ability to determine the exact melt composition by a nondestructive means, as well as to adjust the acidity of the melt to any desired value, makes this melt useful as a high temperature system in which to study numerous organic and inorganic reactions. In addition, the characteristic ability of this melt to dissolve most of the refractory metal oxides will greatly facilitate the quantitative analysis of those oxides (13). These techniques should be applicable to other acid-base fused salt systems.

Acknowledgments

This work was supported by the Air Force Office of Scientific Research under Grant No. AFOSR-71-1995. The computer used in this work was purchased, in part, by funds from an N.S.F. Equipment Grant No. GP-18219. The National Research Council of Canada provided a postdoctoral fellowship for L. G. Boxall. We would also like to acknowledge helpful discussions with Lowell King, G. Dana Brabson, A. A. Fanin, and D. W. Seegmiller, of the United States Air Force Academy.

Manuscript submitted April 5, 1972; revised manuscript received Aug. 1, 1972.

Any discussion of this paper will appear in a Discussion Section to be published in the December 1973 JOURNAL.

APPENDIX I

The following symbols are used throughout the mathematical derivations to differentiate between the number of moles and the mole fraction of a given species (see List of Symbols).

$$n_{NaCl} = \text{number of moles of NaCl} \quad \text{[A-I-1]}$$

$$[NaCl] = N = \text{mole fraction of NaCl} \quad \text{[A-I-2]}$$

In the equation

$$[NaCl] = \frac{(n_{NaCl})_i}{T_i} \quad \text{[A-I-3]}$$

T_i equals the total number of moles in the i^{th} composition of the system. The two neutral forms of $AlCl_3$ in the melt are interrelated by Eq. [8], hence

$$\frac{(n_{Al_2Cl_6})_i}{(n_{AlCl_3})_i^2} = \frac{K_0}{T_i} \quad \text{[A-I-4]}$$

The total amount of neutral aluminum chloride expressed in terms of $AlCl_3$ is given by the equation

$$TN_i = 2(n_{Al_2Cl_6})_i + (n_{AlCl_3})_i \quad \text{[A-I-5]}$$

Equation [9] relates the amount of $AlCl_3$ to the ionic species according to

$$(n_{AlCl_3})_i = \frac{(n_{Al_2Cl_7^-})_i T_i}{(n_{AlCl_4^-})_i K_2} \quad \text{[A-I-6]}$$

From Eq. [A-I-4], [A-I-5], and [A-I-6]

$$TN_i = \left\{ \frac{2K_0 (n_{Al_2Cl_7^-})_i}{K_2 (n_{AlCl_4^-})_i} + 1 \right\} \left\{ \frac{(n_{Al_2Cl_7^-})_i T_i}{K_2 (n_{AlCl_4^-})_i} \right\} \quad \text{[A-I-7]}$$

The number of moles of $AlCl_3$ and Al_2Cl_6 are, respectively

$$(n_{AlCl_3})_i = \frac{-1 + \sqrt{1 + 8K_0 TN_i / T_i}}{4K_0 / T_i} \quad \text{[A-I-8]}$$

and

$$(n_{Al_2Cl_6})_i = D_i = \tfrac{1}{2}\{TN_i - (n_{AlCl_3})_i\} \quad \text{[A-I-9]}$$

The chloride ratio between two different melt compositions, 1 and i, can be calculated from Nernst (Eq. [7]). Let E_1 be the potential of the aluminum electrode in melt composition 1 *vs.* a reference electrode and E_i the aluminum electrode potential in melt composition i *vs.* the same reference electrode.

In the 50 m/o $AlCl_3$ region (±1%), the activity coefficient for $AlCl_4^-$ ion can be considered to be unity and Eq. [7] can be rearranged to

$$R_i = \frac{(n_{Cl^-})_i}{(n_{Cl^-})_1} = \frac{T_i}{T_1} \exp \left\{ \left[E_1 - E_i - \frac{RT}{3F} \ln \left\{ \frac{(n_{AlCl_4^-})_1 T_i}{(n_{AlCl_4^-})_i T_1} \right\} \right] \frac{3F}{4RT} \right\} \quad \text{[A-I-10]}$$

In order to simplify the calculations, all of the experimental data are normalized with respect to 1 mole of $NaAlCl_4$ plus QT moles $AlCl_3$. The electrolysis data are normalized by dividing the electrolysis time by a factor calculated by dividing the initial weight of the melt by (191.8 + QT (133.4)) where QT is the excess $AlCl_3$ in the original melt. In diagram [A-I-12], E_0 represents the original melt in the normalization procedure. During the first iteration QT is assumed to be zero since it is not known; however, in each successive iteration, the calculated QT value is used in the normalization procedure at the beginning of each iteration. If $3Q_i$ faradays of anodic electrical current are passed through the cell, the following will occur

$$3NaCl + Al - 3e^- \xrightarrow{Q_i} AlCl_3 + 3Na^+\uparrow \quad \text{[A-I-11]}$$

with $3Q_i$ moles of Na^+ ions leaving the fritted compartment. The mobility of the sodium ion is sufficiently greater than any of the other ions in the system to permit the assumption that it is the only current carrier in the system. The net result of the electrolysis is then the gain of Q_i moles of $AlCl_3$ and the loss of $3Q_i$ moles of NaCl from the half cell.

The computation procedure can be more easily understood by the use of the following potential-composition diagram

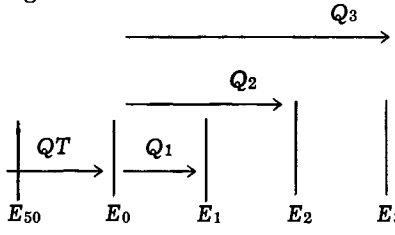

[A-I-12]

Experimentally, three potentials, E_1, E_2, and E_3, separated by two electrolysis periods, Q_2 and $Q_3 - Q_2$, are required for each determination of QT and E_{50}. At any E_i the melt's over-all composition can be expressed as

$$(1 - 3Q_i)NaCl + (1 + QT + Q_i)AlCl_3 \quad \text{[A-I-13]}$$

and the chemical reactions required to produce an equilibrium condition are

$$Cl^- + AlCl_3 \xrightarrow{A_i} AlCl_4^- \quad \text{[A-I-14]}$$

$$Cl^- + 2AlCl_3 \xrightarrow{J_1} Al_2Cl_7^- \quad \text{[A-I-15]}$$

$$2AlCl_3 \xrightarrow{D_i} Al_2Cl_6 \quad \text{[A-I-16]}$$

The total number of moles in the system are

$$T_i = 2 + QT - 2Q_i - A_i - 2J_i - D_i \quad \text{[A-I-17]}$$

where

$$(n_{AlCl_4^-})_i = A_i \quad \text{[A-I-18]}$$

$$(n_{Al_2Cl_7^-})_i = J_i \quad \text{[A-I-19]}$$

$$(n_{Cl^-})_i = 1 - A_i - J_i - 3Q_i \quad \text{[A-I-20]}$$

$$TN_i = 1 + QT + Q_i - A_i - 2J_i \quad \text{[A-I-21]}$$

$$TN_i = \left[\frac{2K_0 J_i}{K_2 A_i} + 1 \right] \left[\frac{J_i T_i}{K_2 A_i} \right] \quad \text{[A-I-22]}$$

since

$$A_i = 1 + QT + Q_i - 2J_i - TN_i \quad \text{[A-I-23]}$$

therefore

$$(n_{Cl^-})_i = J_i + TN_i - 4Q_i - QT \quad \text{[A-I-24]}$$

Using the equilibrium expression for Eq. [10] and Eq. [A-I-10], [A-I-18], [A-I-19], [A-I-23], and [A-I-24], the ionic species in the melt are interrelated by the expressions

$$\frac{(J_1)(J_1 + TN_1 - QT)}{(A_1)^2} = \frac{(J_i)(R_i)(J_1 + TN_1 - QT)}{(A_i)^2} \quad \text{[A-I-25]}$$

$$J_i = \frac{J_1(A_i)^2}{R_i(A_1)^2} = S_i J_1 \quad \text{[A-I-26]}$$

Combining Eq [A-I-10], [A-I-24], [A-I-26], and solving for QT gives

$$QT = \frac{J_1(R_i - S_i) + R_i TN_1 - TN_i + 4Q_i - 4Q_1R_i}{(R_i - 1)} \quad \text{[A-I-27]}$$

and

$$J_1 = \frac{(R_3 - 1)(TN_1R_2 - TN_2 + 4(Q_2 - R_2Q_1)) - (R_2 - 1)(TN_1R_3 - TN_3 + 4(Q_3 - R_3Q_1))}{(R_2 - 1)(R_3 - S_3) - (R_3 - 1)(R_2 - S_2)} \quad \text{[A-I-28]}$$

In melts containing 50 m/o $AlCl_3$ or less the concentrations of the neutral species are at least four orders of magnitude smaller than those of the ionic species and can be neglected. The procedure outlined above has limited usage in the NaCl-rich portion of the titration since it becomes necessary to find small differences between large numbers.

In order to obtain an equimolar melt from a NaCl-rich melt the required amount of aluminum to be added to the melt by electrolysis is

$$Q_{50} = \frac{-QT}{4} \quad \text{[A-I-29]}$$

The ionic concentrations in the equimolar melt would be

$$T_{50} = 1 + \frac{3}{4}QT \quad \text{[A-I-30]}$$

$$TN_{50} = 0 \quad \text{[A-I-31]}$$

$$J_{50} = \frac{(1 - \frac{3}{4}QT)(-2K_m + \sqrt{K_m})}{1 - 4K_m} \quad \text{[A-I-32]}$$

$$[AlCl_4^-] = (1 + \tfrac{3}{4}QT - 2J_{50})/T_{50} = A_{50}/T_{50} \quad \text{[A-I-33]}$$

$$[Al_2Cl_7^-] = J_{50}/T_{50} \quad \text{[A-I-34]}$$

$$[Cl^-] = J_{50}/T_{50} \quad \text{[A-I-35]}$$

and the aluminum electrode potential, E_{50}, *vs.* the reference electrode is

$$E_{50} = E_1 - \frac{RT}{3F}\ln\left\{\frac{A_1}{A_{50}}\left(\frac{T_1}{T_{50}}\right)^3\left(\frac{J_{50}}{(n_{Cl^-})_1}\right)^4\right\} \quad \text{[A-I-36]}$$

$$(n_{Cl^-})_1 = \frac{K_m A_1^2}{J_1} \quad \text{[A-I-37]}$$

The procedure above (Eq. [A-I-13] to [A-I-27]) indicates that if at least two of the data points are in the NaCl-rich portion of the titration curve an alternate procedure must be used [*i.e.*, the over-all number of moles of $NaCl(1 - 3Q_i)$ exceeds the over-all number of moles of $AlCl_3(1 + QT + Q_i)$].

In this case only reaction [A-I-14] needs to be considered and the following equations result

$$A_i = 1 + QT + Q_i \quad \text{[A-I-38]}$$

$$(n_{Cl^-})_i = -QT - 4Q_i \quad \text{[A-I-39]}$$

$$Ti = 1 - 3Q_i \quad \text{[A-I-40]}$$

$$R_i = \frac{QT + 4Q_i}{QT + 4Q_1} \quad \text{[A-I-41]}$$

$$QT = \frac{4(Q_i - R_iQ_1)}{R_i - 1} \quad \text{[A-I-42]}$$

$$J_1 = \frac{-K_m(A_1)^2}{QT + 4Q_1} \quad \text{[A-I-43]}$$

The location of the data points on the titration curve dictated which set of equations, [A-I-13] to [A-I-27], for the $AlCl_3$-rich portion and [A-I-38] to [A-I-43] for the NaCl-rich portion was used. An iterative procedure was repeated utilizing the appropriate set of equations until the change in J_1 became less than 0.01% of the previous J_1 value. Once this was accomplished, the QT and E_{50} values were added to their respective summations in order to provide average values at the end of the experimental data.

The final computer program input requires the temperature, the weight of the melt, the current used in the electrolysis, and estimates for the three equilibrium constants. The experimental data consists of pairs of points, the observed emf, and the cumulative electrolysis time in minutes. Every possible combination of three points is used to calculate the best average values for the entire data set. On the first pass, only every fourth combination is used to arrive at an estimate for the final E_{50} and QT values. In the second pass, every combination is used; however, if the results for a combination differ by more than 20% from the estimated values, they are not included in the final averaging procedure. The final results are printed out in terms of the observed emf and the required electrolysis time to obtain the equimolar melt. Since this procedure relies more on the shape of the curve than the exact values of the equilibrium constants, usually iteration of two or three times utilizing the K values determined in Appendices II and III was sufficient to obtain invariant values (±0.1%). The calculation of the melt composition at each of the data points is now possible.

These calculations were originally programmed in Focal-12 and then as an assembly program for a PDP-12 digital computer.

APPENDIX II

The calculations used to calculate the concentration of the various species in the $AlCl_3$-NaCl melt at any given $AlCl_3$:NaCl ratio are based on the equations

$$1NaAlCl_4 + QT\ AlCl_3\ (moles) \quad \text{[A-II-1]}$$

$$AlCl_3 + AlCl_4^- \xrightarrow{L} Al_2Cl_7^- \quad \text{[A-II-2]}$$

$$2AlCl_4^- \xrightarrow{J} Cl^- + Al_2Cl_7^- \quad \text{[A-II-3]}$$

$$2AlCl_3 \xrightarrow{D} Al_2Cl_6 \quad \text{[A-II-4]}$$

The total number of moles, T, and the total number of moles of neutral aluminum chloride, TN, expressed in terms of $AlCl_3$, are

$$T = 1 + QT - L - D \quad \text{[A-II-5]}$$

$$TN = QT - L \quad \text{[A-II-6]}$$

The amounts of the various species in the melt at equilibrium are

$$(n_{AlCl_4^-}) = 1 - L - 2J \quad \text{[A-II-7]}$$

$$(n_{Al_2Cl_7^-}) = L + J \quad \text{[A-II-8]}$$

$$(n_{Cl^-}) = J \quad \text{[A-II-9]}$$

$$(n_{AlCl_3}) = QT - L - 2D \quad \text{[A-II-10]}$$

$$(n_{Al_2Cl_6}) = D \quad \text{[A-II-11]}$$

From the $NaAlCl_4$ dissociation equilibrium [10] and the definitions

$$M = L - 4K_M\{L - 1\} \quad \text{[A-II-12]}$$

$$N = 4K_M\{L - 1\}^2\{1 - 4K_M\} \quad \text{[A-II-13]}$$

the value of J is given by

$$J = \frac{-M + \sqrt{M^2 + N}}{2 - 8K_M} \qquad \text{[A-II-14]}$$

The subtraction round-off error in the calculation of the $Al_2Cl_7^-$ concentration is avoided by the use of the dissociation equilibrium [10]. Equations [A-I-7] and [A-II-6] are then used to calculate the total amount of unreacted neutral aluminum chloride and to approximate L, respectively. This is repeated until the change in L between two successive iterations is <0.01% of L.

If N/M^2 is less than 0.001 (*i.e.*, in melts containing more than 50.8% $AlCl_3$), all the significance of the N term in the square root term is lost. Therefore, in these aluminum-chloride-rich melts, a different set of equations is required to maintain significance in the calculations. In this instance, J is approximately zero and its contribution in Eq. [A-II-7] and [A-II-8] can be neglected. The value for L must be between 0 and 1, and the mole amounts of the major species are given in Eq. [A-I-8], [A-I-9], and

$$(n_{AlCl_4^-}) = 1 - L \qquad \text{[A-II-15]}$$

$$(n_{Al_2Cl_7^-}) = L \qquad \text{[A-II-16]}$$

The equilibrium constant K_2 is used to set up an equation which can be solved for L in order to minimize the error Z.

$$Z = K_2 - \frac{4LK_0}{\{1 - L\}\{-1 + \sqrt{1 + 8K_0\,TN/T}\}} \qquad \text{[A-II-17]}$$

$$0 \leq L < 1 \qquad \text{[A-II-18]}$$

The J value is given by

$$J = \frac{K_M\{1 - L\}^2}{L} \qquad \text{[A-II-19]}$$

Finally, the concentrations of the neutral aluminum chloride species are calculated from Eq. [A-I-8] and [A-I-9].

The calculation of the aluminum electrode potential is achieved by first calculating the species compositions for the equimolar melt ($QT = 0$), then the composition of melt in question and substituting these values into Eq. [7].

The change in the $AlCl_4^-$ activity coefficient is compensated for in all the calculations wherever $[AlCl_4^-]$ appears by multiplying all the $[AlCl_4^-]_i$ values by γ_i

$$\gamma_i = \exp\left(\frac{W_T}{RT}\left[1 - \frac{n_{AlCl_4^-}}{T_i}\right]^2\right) \qquad \text{[A-II-20]}$$

γ_i is unity for melts containing less than 51 m/o $AlCl_3$; therefore, there is no need to consider it in the K_M calculations.

The data for the S portion of the titration curve ($49.7 \leq$ m/o $AlCl_3 \leq 51$) are used to obtain the best K_M and E_{50} values. These two parameters are adjusted according to the average deviations between the calculated and the experimental emf values (E_C and E_E, respectively, until a minimum standard deviation in E is obtained. The experimental error in the melt composition determination necessitates the use of the perpendicular distance between the experimental curve and the calculated curve, particularly in the 50 m/o region. The perpendicular distance automatically weights the variable which has the largest effect in the calculated error and prevents an over-adjustment in the QT values in the steep portion of the titration curve. This perpendicular value is obtained by multiplying the vertical value $(E_C - E_E)_i$ by a weight factor, WF_i, to obtain the correct error value, ER_i. For D data points, the correction applied to E_{50} in each iteration is

$$E_{50} = E_{50} - \frac{\sum_{i=1}^{D} ER_i}{D} \qquad \text{[A-II-21]}$$

and for K_M

$$K_M = K_M \exp\left\{\frac{8 \times 2.303}{D} \times \left[\sum_{i=1}^{D} \frac{(E_{Ci} - E_{50})ER_i}{|E_{Ci} - E_{50}|}\right]\right\} \qquad \text{[A-II-22]}$$

where

$$ER_i = (E_{Ci} - E_{Ei})WF_i \qquad \text{[A-II-23]}$$

$$FQT = |50 - \text{m/o } AlCl_3| \qquad \text{[A-II-24]}$$

$$WF_i = 1, \text{ if } FQT > 0.289 \qquad \text{[A-II-25]}$$

otherwise

$$WF_i = 18.637(FQT)^3 - 19.888(FQT)^2 + 6.8227(FQT) + 0.1817 \qquad \text{[A-II-26]}$$

The standard deviation in E, E_{SD}, is given by

$$E_{SD} = \sqrt{\frac{\sum_{i=1}^{D} (ER_i)^2}{(D - 1)}} \qquad \text{[A-II-27]}$$

APPENDIX III

The calculated E_{Ci} and ER_i values are determined by the same procedure as outlined in Appendix II. The K_M and E_{50} values are kept constant and the K_2 value is varied to obtain a minimum standard deviation between the observed and calculated potentials. The adjustment to K_2 at the end of each iteration is given by

$$K_2 = K_2 \exp\left\{\frac{8 \times 2.303}{D}\left[\sum_{i=1}^{D} ER_i\right]\right\} \qquad \text{[A-III-1]}$$

The W value for the activity coefficient calculation is then varied manually by units of 100 cal mole^{-1} until an over-all minimum in the standard deviations is realized.

APPENDIX IV

Partial Computer Printout from K2FIT Program (Data for $AlCl_3$-NaCl System at 175°C)

KO = 2.865E7
K2 = 2.38E4
KM = 10.61E-8
TEMP = 175
W = 1400
E1:1 = 0.0

EMF	% $AlCl_3$
−158.9	49.83
−147.3	49.86
−127.9	49.90

... 60 additional points

Calculated Results

E (mV)	Deviation in E (mV)	% $AlCl_3$	$\gamma AlCl_4^-$
−156.5	+2.4	49.83	1.00
−146.6	+0.7	49.86	1.00
−129.4	−1.4	49.90	1.00
− 53.2	+0.8	49.98	1.00
+ 53.3	+5.7	50.02	1.00
+124.5	+0.6	50.09	1.00
+177.5	+0.4	50.25	1.00
+282.5	+2.1	51.71	1.01
+299.9	−1.9	52.29	1.01
+416.4	−4.8	62.35	1.73
+484.9	+1.9	69.90	3.35

... 52 additional points
S.D. in E = 2.92 mV K2 = 2.36E + 04

LIST OF SYMBOLS

K_i	equilibrium constant for the ith chemical reaction
E	electromotive force
R	gas constant
T	temperature in degrees Kelvin
F	Faraday constant
a_i	thermodynamic activity of the ith species
γ_N	activity coefficient on the mole fraction scale
N_i	mole fraction of the ith species

W_T work constant at temperature T
G Gibbs free energy
S entropy
H enthalpy
n_i the number of ith species
$[i] = N_i$ = mole fraction of ith species
T_i total number of moles in the ith melt composition
TN_i total number of moles of nonionic $AlCl_3$ in the ith melt composition
D_i number of moles of Al_2Cl_6 in the ith melt composition
QT number of moles of $AlCl_3$ in excess equimolar $AlCl_3$-NaCl melt in the initial melt at the beginning of the experiment
R_i ratio of the number of moles of Cl^- in the ith melt composition to that in the composition designated as 1
Q_i the number of moles of Al^{3+} added electrically to the melt to change its composition from its initial value to that of the ith composition
E_i the emf of an aluminum electrode in the melt after Q_i moles of Al^{3+} have been added
E_{50} the emf of the aluminum electrode in an equimolar melt
A_i, J_i the number of moles reacting according to the given reaction to reach equilibrium in the ith melt composition
S_i the ratio between $Al_2Cl_7^-$ concentrations in the ith and 1 melt compositions
Q_{50} number of moles of Al^{3+} to be added in order to reach the equimolar composition
D, J, L the number of moles reacting in a given melt composition
M defined by Eq. [A-II-12]
N defined by Eq. [A-II-13]
Z defined by Eq. [A-II-17]
WF_i the weight factor to be applied to the error in the calculated fit of the ith data point
ER_i weighted error in the calculated fit of the ith data point

REFERENCES

1. B. Tremillon and G. Letisse, *J. Electroanal. Chem.*, **17,** 371 (1968).
2. G. Torsi and G. Mamantov, *Inorg. Chem.*, **10,** 1900 (1971).
3. A. A. Fannin, Jr., L. A. King, and D. W. Seegmiller, *This Journal*, **119,** 801 (1972).
4. L. G. Boxall, H. L. Jones, and R. A. Osteryoung, In preparation (for submission to *J. Electroanal. Chem.*).
5. L. G. Boxall, Ph.D. Thesis, University of Saskatchewan, Regina Campus, Regina, Saskatchewan, Canada, 1970.
6. L. G. Boxall and K. E. Johnson, *Trans. Faraday Soc.*, **67,** 1433 (1971).
7. D. R. Stull, H. Prophet, *et al.*, Editors, "JANAF Thermochemical Tables," 2nd ed., NSRDS-NBS37, June 1971.
8. G. Torsi, G. Mamantov, and G. Begun, *Inorg. Nucl. Chem. Letters*, **6,** 553 (1970).
9. H. L. Jones and R. A. Osteryoung, To be published in "Molten Salt Chemistry," G. Mamantov, G. P. Smith, and J. Braunstein, Editors, Plenum Press, New York.
10. H. L. Jones, L. G. Boxall, and R. A. Osteryoung, *J. Electroanal. Chem.*, **38,** 476 (1972).
11. D. A. Hames and J. A. Plambeck, *Can. J. Chem.*, **46,** 1727 (1968).
12. D. Bauer, J. P. Beck, and P. Texier, *Collection Czech. Chem. Commun.*, **36,** 940 (1971).
13. R. Gut, *Helv. Chim. Acta*, **108,** 830 (1960).
14. J. Giner and G. Hollek, (Tyco Laboratories, Inc.), "Aluminum Chlorine Battery," Report to NASA, September 1969, Contract No. NAS-12-688.

The Kinetics of Chlorine Evolution and Reduction on Titanium-Supported Metal Oxides Especially RuO_2 and IrO_2

A. T. Kuhn and C. J. Mortimer

Department of Chemistry and Applied Chemistry, University of Salford, Salford, Lancashire, England

ABSTRACT

Current-voltage curves were determined on precious metal oxide-coated titanium electrodes under conditions relevant to the chlor-alkali industry. Electrodes in which the oxide coating was of a base metal or only partly of a precious metal were also studied. Clear electrocatalytic effects were found, though in general, linear Tafel behavior was not observed. A possible explanation for the lack of linear Tafel plots in terms of a semiconducting oxide coating was suggested.

Recently there has been a growing interest in the electrochemical behavior of metal oxide films on a passive metal support such as titanium (1-6) following the introduction of electrodes using RuO_2 films into the chlor-alkali industry. Claims have been made that such films are semiconductive in nature (1, 2) but this is at variance with much conductivity data on RuO_2 (7, 8). To elucidate the role of the oxide film, the kinetics of chlorine evolution, and in some cases reduction, have been studied on thermally deposited films of RuO_2, IrO_2, their mixtures with TiO_2, and on films of TiO_2 with other metal oxides. There are clear electrocatalytic effects dependent on the nature of the oxides. Some of the data in both anodic and cathodic directions may suggest specifically semiconducting properties. Whereas work is still continuing, it is felt appropriate to present some of the data obtained to date as this presents a significantly different picture to the only other study (9) yet published.

Key words: semiconducting electrodes, chloralkali anodes, electrocatalysis.

Experimental Procedure

Instrumentation.—The anodic polarization measurements were carried out galvanostatically. This was permissible as no cases of passivation have been observed. The current was provided by a transistorized galvanostat capable of providing currents from 10 μA to 1A.

Since the current densities on different electrodes varied from 1 μA to 10 A $\cdot$ cm^{-2} various arrangements were used for eliminating the ohmic component of the steady-state measured overvoltage. For current densities up to 10^{-1} A $\cdot$ cm^{-2} a conventional Luggin

capillary was used (tip diam ca. 0.5 mm). Where necessary ohmic correction was applied by interrupting the current with a Hg reed switch (ERG HA/W) and recording the potential decay transient in the usual manner on a storage oscilloscope (Hewlett-Packard 141A). This technique was, however, inadequate at the higher current densities since the very active nature of the electrodes and the relatively high resistivity of sodium chloride solutions means that the correction to be applied becomes large in comparison with the value of η_{act}. Moreover, since the capacitance of the electrodes was not high in comparison with their activity, the initial rate of decay is large when such a transient is measured (for a typical capacitance of ca. 100 $\mu F \cdot cm^{-2}$, and a current density of 10 $A \cdot cm^{-2}$, $dV/dt = 10^5\ V \cdot sec^{-1}$). Such a rate of change cannot be followed by a fine Luggin capillary because the time constant of the capillary is included in the reference electrode-working electrode measuring circuit. A coarse capillary is therefore necessary (tip diam ca. 1 mm) and this must be placed at least 2 mm from the surface to avoid shielding effects. The result is now that the sensitivity of the oscilloscope when used in the conventional manner must be low to avoid overloading the amplifier with the total steady-state overvoltage. For this reason the oscilloscope input was switched, as suggested by Flinn (10), with a field effect transistor (FET) switch and a unity gain operational amplifier as a buffer, the latter capable of following $10^7\ V \cdot sec^{-1}$, in the reference circuit. Both the FET and the oscilloscope were triggered by the rise in potential across the galvanostat when this was open-circuited. All leads to the cell were kept as short as possible, and the leads in the current carrying working electrode counterelectrode circuit were twisted together to reduce ringing caused by stray inductances in the current carrying circuit. Substitution of a graphite counterelectrode for a Pt one changed the nature of the ringing from a damped oscillation to a critically damped decay which was more difficult to separate, presumably due to the higher resistance in the circuit. With this circuit the value of η_{act} could be read directly from the oscilloscope and was independent of the position of the Luggin, even when this was at distances of 1 cm. Measurement of the overvoltage by this technique does not necessarily separate potentials in the oxide film from those in the solution since the decay of the potential in the oxide film will also be associated with a R.C. time constant. In view of the high capacitance of anodic films on Ti (16) it is likely that potentials in the film are included in the measured overvoltages. Further work is being carried out in an attempt to clarify this point. Faita and Fiori (9), in a similar study, used the method of short circuiting the working electrode to the counterelectrode rather than open circuiting them. Whereas this will reduce stray capacitances to a minimum, the value of the ohmic overpotential recorded will be in error since the current will be in error because the current will not decay to zero, but rather take up some value in the other direction. It is simple to show that

$$\eta_{apparent} = \eta \cdot \frac{(1 + \text{final cell voltage})}{\text{initial cell voltage}}$$

where initial and final refer to the instant preceding and following the short circuiting. Thus the value of the ohmic drop measured will be a function of the cell resistance and the nature of the counterelectrode.

Cell.—The cell design was similar to that used previously in this laboratory (11). The electrolyte was maintained saturated with chlorine, and was slowly flowed through the cell to prevent any build-up of chlorate. The counterelectrode was of such a size that the main reaction occurring on it was chlorine reduction. The addition of a tap at the top of the Pt/Cl_2 reference compartment enabled electrolyte to be drawn up into the reference compartment from the main body of the cell and held there in a Cl_2-saturated state. All connections, taps etc., in contact with the electrolyte were of glass or PTFE and greaseless.

Trial runs on a rotating disk electrode showed that the only effect of rotation was to displace the η *vs.* log i curve to slightly lower values of log i, indicating a slightly greater surface area available on the rotating electrode. Individual measurements of η_{act} were also slightly more reproducible. However it was felt that in view of the number of electrodes studied, the advantage to be obtained was too small. In runs on stationary electrodes the lowest value of η_{act} measured consecutively at a given current density was taken as the value most representative of the bare surface.

Chemicals.—Brines were made up from GPR grade NaCl. No change in the polarization curves was found from those in an initial experiment using Analar grade NaCl. Chlorine was commercial grade from a cylinder.

Electrodes.—The electrodes were prepared from commercial CP titanium. Plate electrodes were spot welded onto Ti wire supports. All electrodes were etched in 10% oxalic acid at 100°C for 30 min to provide a key for the coating. Coatings were applied by brush and from solutions of precious metal chlorides in propanol, and anhyd. $TiCl_4$ or $Ti(OEt_4)$ in propanol. In applying multilayer coatings the individual layers were fired in air at 400°C for 5 min and the whole electrode for a definite period after that (usually 6 hr). The area of the electrode was defined by covering the support with heat shrinkable PTFE (Raychem Ltd.). In this manner, with 1 mm wire, electrodes down to 0.05 cm^2 can readily be obtained.

Results

Since most of the patent literature (1-6) refers to oxide coatings based on mixtures of RuO_2 and/or TiO_2; coatings of RuO_2 and IrO_2 alone were investigated to define the base from which to study other coatings.

Ruthenium oxide.—Two series of electrodes were prepared to investigate both the effect of the firing time and the coating thickness for RuO_2 coatings. Series (*i*) electrodes (No. 1-4) were coated with 6 coats of 0.4M $RuCl_3$ in propanol fired at 400°C for 1, 5, 20, and 50 hr respectively. Series (*ii*) electrodes (No. 5-8) were coated with 2, 4, 6, and 8 coats of $RuCl_3$ as before and fired at 400°C for 20 hr.

There was no systematic variation in the activity of electrodes 1-4, and only a marginal increase in activity of electrodes 5-8 in that order. A typical polarization curve is shown in Fig. 1 for 5M brine at 20°C.

The curve in Fig. 1 is seen to have two regions, a curved section below $\eta = 85$ mV and a Tafel line of 95 mV/dec. slope above that. Analysis shows that the curved section is longer than would be expected from a mechanism in which the forward and reverse reactions were controlled by a slope of $2RT/F$, without any change of mechanism above the reversible poten-

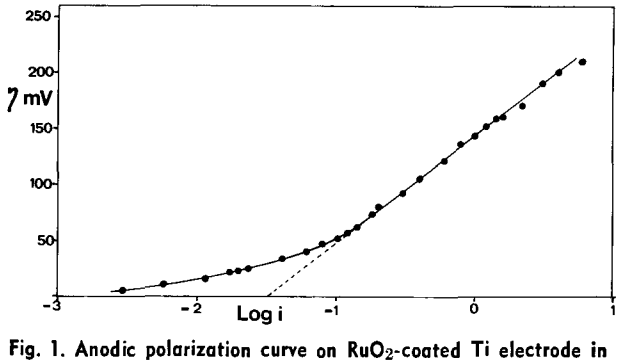

Fig. 1. Anodic polarization curve on RuO_2-coated Ti electrode in Cl_2 sat. 5M NaCl, 20°C. Current density in this and all subsequent figures is given in $A \cdot cm^{-2}$.

tial. This is confirmed by the fact that the calculation of the exchange current on similar electrodes (see below) from the value of the transfer resistance (r_t) in the linear portion of the η *vs.* i plot

$$i_o = \frac{RT}{n\mathbf{F} \cdot r_t}$$

gives a value of log $i_o = -2.2 \pm 0.5$. A tangent drawn from this point to the curve has a gradient of about $RT/2\mathbf{F}$. For the eight electrodes studied the value of the Tafel slope was 108 ± 12 mV/dec. and the value of log $i_o = -1.41 \pm 2$. The reproducibility of the polarization curve on any given electrode is of the order of slope ±5 mV and log $i_o \pm 0.15$.

The behavior of such electrodes at different temperatures in 5M brine is shown in Fig. 2. It is seen that the $2RT/\mathbf{F}$ slope moves to higher values of i_o as expected and that the potential at which it starts rises from about 60 mV at 20°C to 80 mV at 80°C. Measurements of log i_o from the near equilibrium transfer resistance show that this varies very little with temperature, which is consistent with the change in potential at which the $2RT/\mathbf{F}$ slope becomes rate controlling.

Attempts to study such electrodes at progressively more and more dilute brine strengths encounter a problem in so far as these electrodes catalyze the formation of chlorate to a greater extent than a platinum electrode. Thus as the brine becomes more dilute the rest potential, with respect to the reversible Cl^-/Cl_2 electrode on Pt, becomes more cathodic owing to the spontaneous reactions

$$6HClO + 3H_2O \rightarrow 3/2\ O_2 + 4Cl^- + 2ClO_3^- + 12H^+ + 6e^-$$

and

$$2e^- + Cl_2 \rightarrow 2Cl^-$$

Bubbles of oxygen can be seen rising from the electrode at the rest potential in chlorine-saturated 0.1M brine. These reactions account for the position of the curves in Fig. 3.

Current efficiency measurements to be published elsewhere (18) show that the amount of current going to O_2 is *ca.* 4% in 1M brine over the current range of Fig. 3, and 8% in 0.4M brine, before diffusion limitation of Cl^- sets in. In 0.1M brine diffusion limitation of Cl^- occurs at current densities above 0.8 A cm^{-2}. With respect to a RuO_2 counterelectrode

$$\frac{di}{d(Cl^-)\eta} = 0 \quad \text{for } 5M > [Cl^-] > 0.5M \text{ and } i < 100\ mA \cdot cm^{-2}$$

Figure 4 shows the temperature variation of the overpotential in 1M brine. It is seen that at low brine temperatures the overvoltages at current densities > 0.1 A · cm^2 are much higher in 1M brine than in 5M brine, but that at 80°C there is no significant difference.

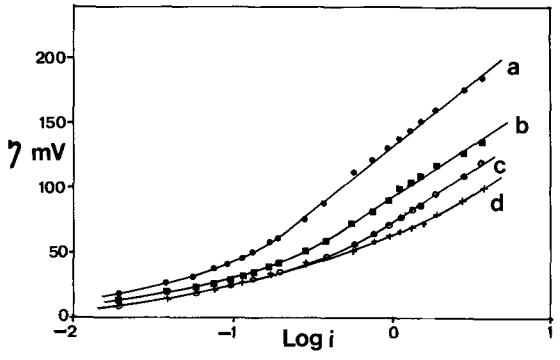

Fig. 2. Anodic polarization curves on RuO_2-coated Ti in Cl_2 sat. 5M NaCl at (a) 20°C, (b) 40°C, (c) 60°C, (d) 80°C.

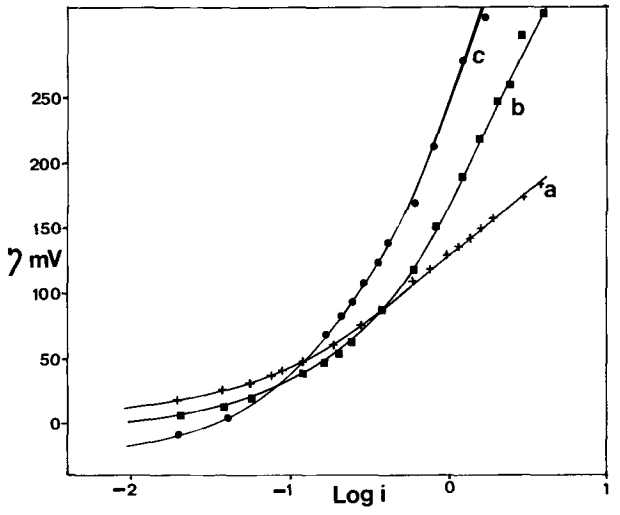

Fig. 3. Anodic polarization curves on RuO_2-coated Ti in Cl_2 sat. brines. (a) 5M, (b) 1M, (c) 0.1M.

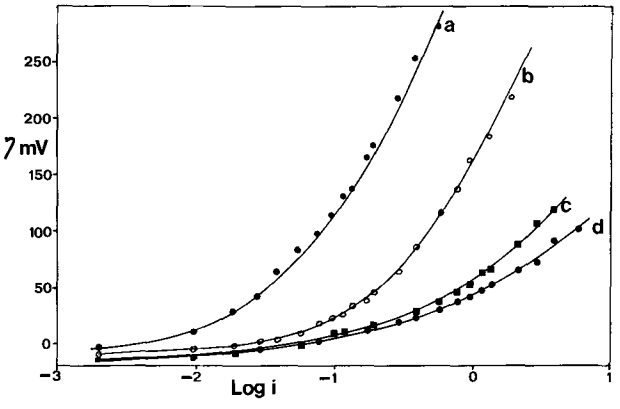

Fig. 4. Anodic polarization curves on RuO_2-coated Ti in Cl_2 sat. 1M NaCl at (a) 20°C, (b) 40°C, (c) 60°C, (d) 80°C.

Iridium oxide.—Figure 5 shows the polarization curve of an electrode coated with IrO_2 in 5M NaCl at 20°C. Such an electrode is black. It is interesting to note that this polarization curve may be compared directly with that for bright Ir which also exhibits a slope of $2RT/\mathbf{F}$. From this it can be concluded that the roughness factor of such electrodes is about 70× that of a bright electrode. Such a comparison cannot be made for Ru since Ru metal becomes coated with a thick coat of RuO_2 when chlorine is evolved on it (17). It is of interest that if the electrode is reduced to Ir with hydrogen at about 500°C the resultant polarization curve is identical to that in Fig. 5, as is the polarization curve of an IrO_2 coating on Ir reduced as above.

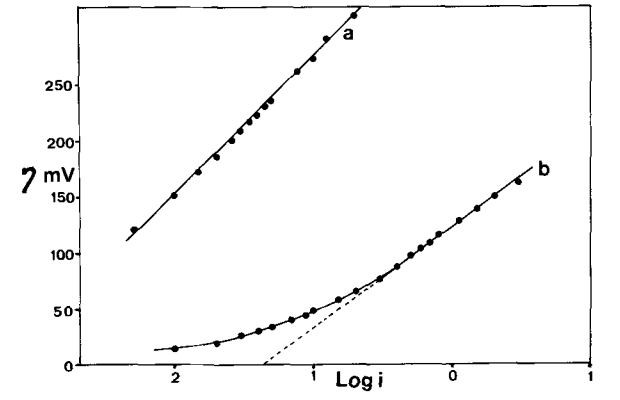

Fig. 5. Anodic polarization curves on (a) bright Ir and (b) IrO_2-coated Ti in Cl_2 sat. 5M NaCl at 20°C.

Mixed oxides.—Since much of the technical data have been concerned with mixed oxides it was decided to investigate coatings with different ratios of $(Ru/Ti)O_2$. A comparison of their activity using i_o derived from the transfer resistance near $\eta = 0$ gave results depicted in Fig. 6. It is to be noticed that with a Ru content greater than about 40 mole per cent (m/o) there is no significant change in the value of i_o. Also, that whereas a rise in temperature increases i_o on the electrodes poor in RuO_2, it has an insignificant effect with RuO_2 concentrations greater than 15-20 m/o RuO_2. However, when the whole polarization curves are plotted the picture is somewhat different (Fig. 7). It is to be noticed that there seems to be a current limiting phenomenon on the electrodes containing TiO_2 and they no longer exhibit the 120 mV slope. The difference between the polarization curves for pure RuO_2 and the mixtures with RuO_2 20% become much less with increasing temperature (Fig. 8). To investigate whether the effect was caused by the film resistance electrodes were prepared with TiO_2 coatings (8 coats) both over and under RuO_2 coatings (3 coats). It was found that placing the TiO_2 underneath resulted in an electrode with the activity of a pure RuO_2 coating. Thus simple resistance of these films would seem to be discounted. The result of placing the TiO_2 on top was rather surprising in that the result was as active as an electrode containing about 20% Ru. Presumably considerable diffusion must have taken place during the firing (20 hr at 400°C). Similar results were found for electrodes of IrO_2 and TiO_2.

In order to investigate a wider range of oxides a series of coatings were prepared containing 90 m/o Ti and 10% of the second metal. These were compared with RuO_2 and TiO_2 coatings (Fig. 9). It is interesting to note the current densities on thermally deposited

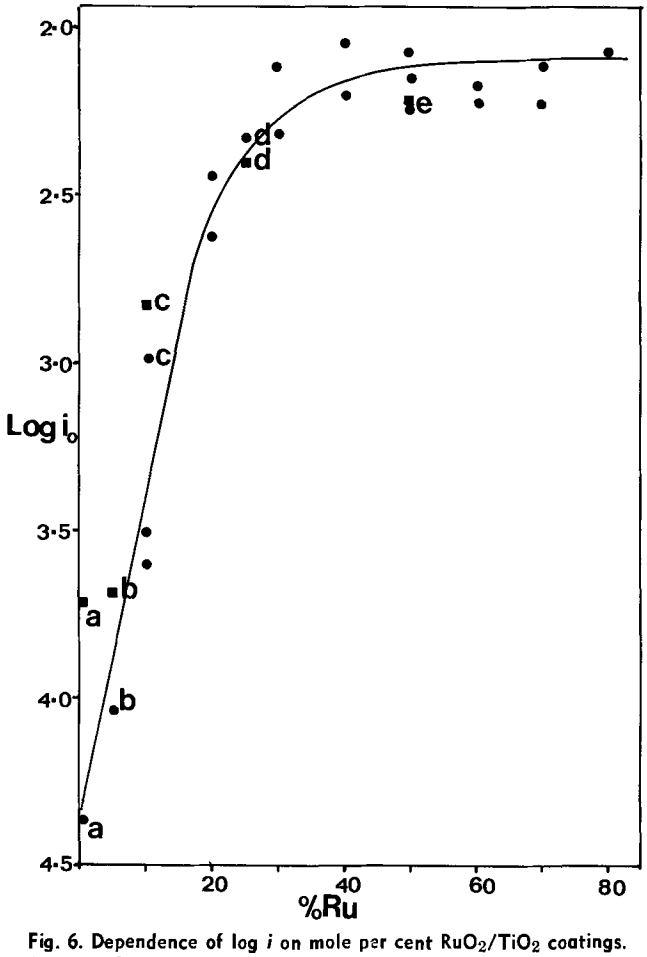

Fig. 6. Dependence of log i on mole per cent RuO_2/TiO_2 coatings. Values at 20°C. Values at 60°C (a-e refer to electrodes on which temperature variations were studied).

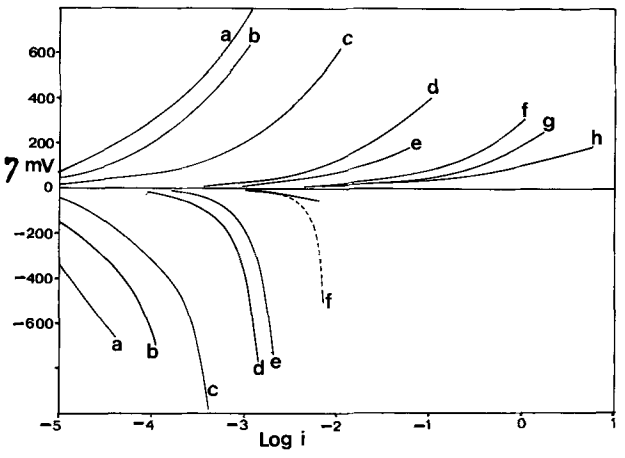

Fig. 7. Anodic and cathodic polarization curves in Cl_2 sat. 5M NaCl at 20°C for electrodes coated with RuO_2/TiO_2 mixtures. (a) 0, (b) 0.1, (c) 0.5, (d) 1.0, (e) 5, (f) 20, (g) 80, (h) 100 m/o RuO_2. In the cathodic direction – – – indicates the diffusion limited current on electrode (f) and —— the curve when vigorously stirred.

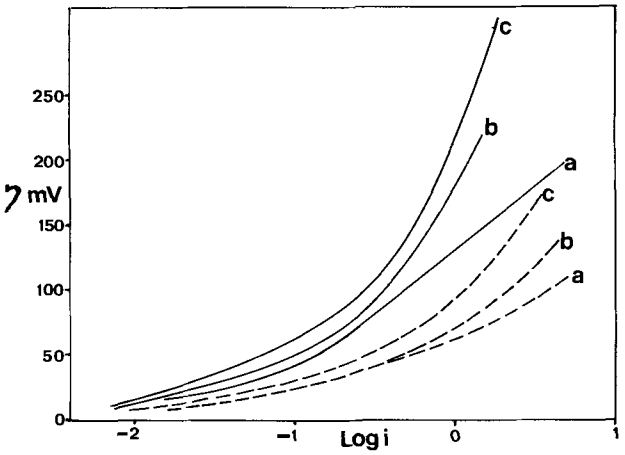

Fig. 8. Anodic polarization curves in Cl_2 sat. 5M NaCl —— at 20°C and – – – at 80°C for RuO_2/TiO_2 coated electrodes. (a) 100, (b) 80, (c) 40 m/o RuO_2.

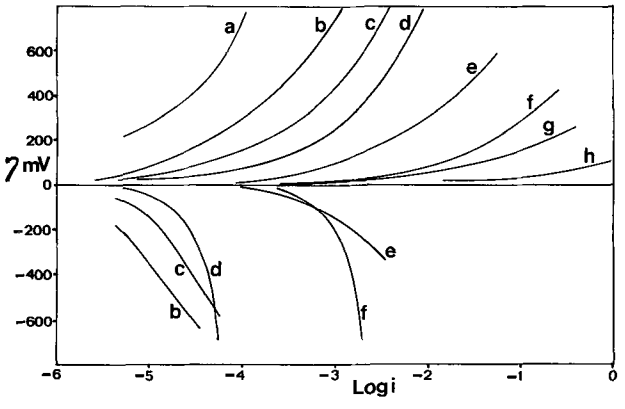

Fig. 9. Anodic and cathodic polarization curves in Cl_2 sat. 5M NaCl at 20°C. Electrodes coated with oxides containing (mole per cent cation) (a) 10% Pt, 90% Ti; (b) 100% Ti; (c) 10% Co, 90% Ti; (d) 10% Cr, 90% Ti; (e) 10% Pt, 90% Ti; (f) 10% Ru, 90% Ti; (g) 10% Ir, 90% Ti; (h) 100% Ru or Ir.

TiO_2 films. On anodically formed TiO_2 films the current densities are very much smaller.

Cathodic polarization curves.—Although the cathodic chlorine reduction curves on these electrodes are limited by chlorine diffusion in the case of the active electrodes, the less active electrodes show behavior which is difficult to explain on any simple basis (Fig. 8-10). There is, on electrodes containing up to 10%

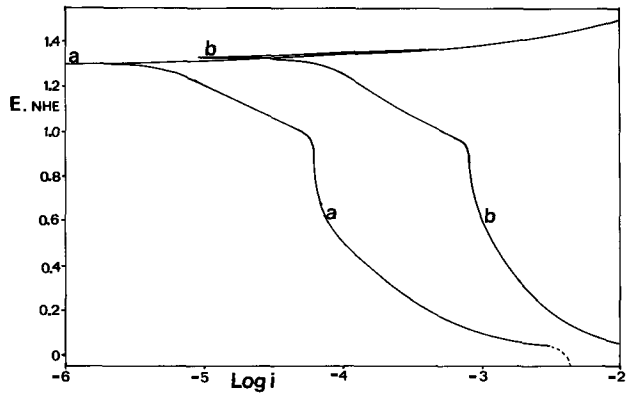

Fig. 10. Anodic and cathodic polarization curves in 5M NaCl at 20°C for an electrode coated with (0.5% Ru 99.5% Ti) oxide (a) in a solution purged with 1/20 atm Cl_2 in N_2 and (b) in Cl_2 sat. solution.

RuO_2, a definite current limitation in the cathodic sense; that this is not diffusion limited is demonstrated both by the diffusion limited curve (f) on Fig. 7, and by the fact that such curves are insensitive to stirring. Working with an electrolyte maintained at 1/20 atm by Cl_2 by means of a stream of Cl_2/N_2 it is seen that the order of reaction on one of these electrodes is almost unity (0.8) at constant E, for values of E between 1.3 and 0.6V NHE.

Introduction of tri- and penta-valent impurities into the oxide layer to alter the semiconducting properties of the film only complicates the polarization curve, and both sets of impurities increase the activity in the anodic sense (Fig. 11).

Discussion

Although there are still many problems in defining the activity of these electrodes with any accuracy since the activity of various batches can vary considerably, especially with electrodes containing only a few per cent of the platinum metal, a general picture has emerged. Only the pure IrO_2 and RuO_2 coatings show any Tafel behavior and then only in 5M brine. In general the activity of the electrodes in the cathodic direction is considerably less than in the anodic direction, but Fig. 9 shows interesting variations in this effect amongst different metal oxide mixtures.

As with any electrode a basic problem is the surface roughness. Trassati (12) asserts that this is not greater than that of the underlying metal, but our results on Ir would seem to contradict this, and would suggest a

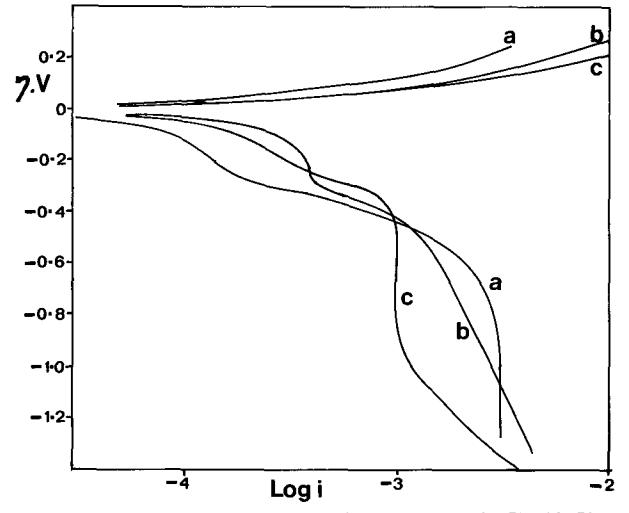

Fig. 11. Anodic and cathodic polarization curves in 5M NaCl at 20°C for electrodes coated with (a) (1% Ru, 99% Ti) oxide (b) (1% Ru, 5% Al, 94% Ti) oxide (c) (1% Ru, 5% Sb, 94% Ti) oxide.

surface roughness of the order of 70× that of bright Ir. A krypton BET that was done on *ca.* 10 cm^2 of RuO_2 coating on a Ti rod gave the surface roughness as 240. This would seem to be in good agreement if every surface atom is considered to be a krypton site, but only 1/3 of them sites for chlorine evolution on the Ir or Ru atoms, assuming that the stoichiometry of this solid extends to the surface.

A second problem concerns the electrical nature of the surface. Whereas both RuO_2 and IrO_2 in the pure crystalline state are metallic conductors due to overlap of the inner d-band electrons the situation for the RuO_2 films is rather different. Fletcher *et al.* (13) found that RuO_2 powder prepared by dehydration of precipitated RuO_2 at 650°C takes up water on exposure to air. The resistivity of the hydrate is about 0.3 ohm-cm when compressed to 40% theoretical density, as compared with 6×10^{-3} ohm-cm for the dry powder at 50% theoretical density. (The resistivity of the pure RuO_2 is 3.5×10^{-5} ohm-cm) (7, 8, 12). These values for the resistivity will not produce any simple ohmic resistance in a film of 1-2 μm thick but do suggest that the films must be classed as semiconductors, and it would be reasonable to assume semiconductors as a n-type. A further confirmation of this hypothesis is that the conductivity of RuO_2 films on silica is sensitive to the firing temperature and has a positive temperature coefficient (14). As the proportion of TiO_2 is increased, moreover, it would be expected that the resistivity would increase. The polarization curves can thus be accounted for by the fact that in a semiconductor there will be a diffuse double layer of charge in the solid. The potential across the layer will increase as the number of carriers in the semiconductor decreases in much the same manner as in dilute electrolytes owing to the depletion of carriers in the layer. The potential across this layer is not separable from that across the Helmholtz double layer since it is also associated with capacitance. For a n-type semiconductor this potential will increase as the electrode becomes more anodic and the increasing charge on the Helmholtz layer, and the increasing number of surface states deplete the interface of charge carriers.

The behavior of pure RuO_2 and IrO_2 can be accounted for by assuming that their conductivity is still high enough to exhibit essentially metallic behavior. This would explain the identical nature of the polarization curves on a layer of black IrO_2 and that on the same oxide when it has been reduced, and is presumably only covered with a monolayer of oxide.

The fact that a thick film of coherent oxide grows on Ru (17) when chlorine is evolved on it suggests that the oxide may have a lower conductivity when grown in this manner.

In the more dilute brines where there will be an increasing tendency to absorb oxygen or hydroxyl ions on the surface, the additional number of surface states may account for the change in behavior of RuO_2 to that observed on the less active electrodes in 5M brine.

The behavior of the RuO_2/TiO_2 mixtures can be divided into two types. When RuO_2 is greater than 20% the difference in activity from that on pure RuO_2 is slight at low current densities. On increasing the current density an additional overpotenital is found, which is greater the greater the concentration of TiO_2. However, this latter overpotential decreases on raising the temperature. This is what would be expected if this potential were located in the film since raising the temperature will increase the number of charge carriers. On these electrodes the effect of temperature on the low density region is slight as on the pure RuO_2 electrode, and one can assume the overpotential in this region to be in the Helmholtz layer. On the inactive electrodes $RuO_2 < 5\%$ the effect of temperature on their activity is marked even at low current densities (Fig. 6). On these electrodes the major part of the

overpotential observed may lie in the film, and is thus decreased with increasing temperature.

Industrially it is known that electrodes such as those may fail by oxide growth at the Ti/coating interface if used at too high an overpotential which would also suggest potentials in the film.

The fact that the film seems to have rectifying characteristics in the cathodic direction may be due to the shift from a mechanism in which electrons are being donated to the conduction band, to one in which they are being accepted by the valence band (15), but such a hypothesis is extremely tentative.

Trasatti has studied the amount of charge involved in charging and discharging a RuO_2 coating in $HClO_4$, obtaining values of "q" the charge-to-change electrode potential from 1.54 to 0.3V between 20-90 mC. This charge depended linearly on the thickness of the films and it was suggested that this represents some change in the bulk of the film. Such charging, involving between 2-7% of the Ru atoms in the crystal might also account for the cathodic behavior observed by changing the stoichiometry of the oxide and therefore its conductivity from one type to another, as the amount of Ru^{III} increases.

Generally, similar results have been noted on anodic TiO_2 films where the capacitance of thick films may be greater than the double layer capacity and increases with the thickness of the film (16). In the latter study the capacitance was decreased by cathodic polarization apparently by protonation of the film. However, the film could be restored by anodic polarization without any apparent change in the film thickness. We have noted a general tendency for films to become less active when taken to high anodic potentials, this activity is restored by cathodic polarization without any apparent permanent damage. Changes in the proton content of the film and thus the Ru^{III}/Ru^{IV} balance as envisaged by Trasatti might account for this.

The difference between this work and that of Faita and Fiori (9) can, we believe, be explained as follows: (*i*) the method for ohmic correction that they used may have affected their results especially at low current densities, (*ii*) they worked in a cell that was not saturated with chlorine, but had a steam of N_2 flowing over the top, presumably to protect the rotating disk mechanism. This means that the readings at the lower current densities will be referred to a more cathodic reversible potential than the reading at higher current densities. Such a curve may be seen in the anodic direction in Fig. 10, and would suggest a Tafel slope of about $RT/2\mathbf{F}$ over at least two decades of current. It is otherwise difficult to explain why their electrodes should have such high overpotentials in comparison with generally similar electrodes in this study at low current densities, *i.e.*, 50 mV *vs.* 5 mV at 1 mA · cm^{-2} in 5M NaCl at 20°C.

Acknowledgment

One of us (C.J.M.) wishes to thank the SRC for their support in the form of a CAPS grant.

Manuscript submitted May 22, 1972; revised manuscript received Aug. 21, 1972.

Any discussion of this paper will appear in a Discussion Section to be published in the December 1973 JOURNAL.

REFERENCES

1. South African Pat. 68/7371 and 68/7482 (1968).
2. German Pat. 2,021,422 (1969).
3. German Pat. 2,014,746 (1970).
4. German Pat. 1,915,951 (1970).
5. British Pat. 1,206,863 (1970).
6. French Pat. 1,583,370 (1970).
7. W. F. Ryden and A. W. Lawson, *Phys. Rev.*, **1B**, 1495 (1970).
8. D. B. Rogers, R. D. Shannon, A. W. Sleight, and J. L. Gilson, *Inorg. Chem.*, **8**, 841 (1969).
9. G. Faita and G. Fiori, *J. Applied Electrochem.*, **2**, 31 (1972).
10. D. R. Flinn, M. Rosen, S. Schuldiner, and J. D. Fahey, *This Journal*, **117**, 79 (1970).
11. A. T. Kuhn and P. M. Wright, *J. Electroanal. Chem.*, In press.
12. S. Trasatti and G. Buzzanca, *ibid.*, **29**, App. 1-5, (1971).
13. J. M. Fletcher, W. E. Gardner, B. F. Greenfield, M. Holdoway, and M. Rand, *J. Chem. Soc.*, (**A**), 653 (1968).
14. G. Bianchi, *J. Applied Electrochem.*, **1**, 231 (1971).
15. H. Gerischer in "The Surface Chemistry of Metals and Semiconductors," H. C. Gatos, Editor, p. 177, John Wiley and Sons, New York (1959).
16. J. S. Leach, *This Journal*, **110**, 680 (1963).
17. A. T. Kuhn and P. M. Wright, In course of publication).
18. A. T. Kuhn and C. J. Mortimer, *J. Applied Electrochem.*, **2**, 283 (1972).

The Piezogalvanic Effect

Gerald D. Mitchell* and Charles Feldman

Applied Physics Laboratory, The Johns Hopkins University, Silver Spring, Maryland 20910

and Robert T. Foley*

Chemistry Department, The American University, Washington, D. C. 20016

ABSTRACT

The "piezogalvanic effect" is an electrical response produced by the application of an asymmetric external force to a symmetrical solid electrolyte cell. An experimental study of this effect in a solid ionic conductor has been conducted. Parameters controlling the effect were found to be fabrication procedures, electrodes, and stress produced by the applied force. Tests demonstrated that the effect was present under both static and cyclic conditions. Observations lead to the conclusion that the piezogalvanic effect is established by an interfacial (faradaic) process rather than any process associated solely with the mechanical and physical properties of either the electrolyte or the electrode.

When a unidirectional force is applied to one face of a symmetrical solid electrolyte cell such as Ag/AgI/Ag a potential is generated and a current flows in an external circuit connecting the two electrodes. This pressure-induced potential in solid electrolytes was reported by Mrgudich (1) in an experimental study and a theoretical explanation was put forward by Hunger (2) in terms of the defect structure of the

* Electrochemical Society Active Member.
Key words: piezogalvanic effect, solid electrolyte cycling test.

solid electrolyte (AgI). We have termed this effect the "piezogalvanic effect." This refers to the potential difference and the accompanying flow of current induced by unsymmetrical stress on the electrodes of a galvanic cell. This definition is applicable to galvanic cells employing liquid and solid electrolytes.

The effect of stress on electrodes in aqueous solutions has been studied by a number of investigators (3-24) and the effect of stress on ionic conduction in crystals has also been considered (25-32). New observations on stress-induced effects in solid electrolytes should, of course, be related to these prior studies.

In this report, experiments that (*i*) evaluate fabrication parameters, (*ii*) determine the sign and magnitude of the potential and current, and (*iii*) assert the reproducibility of the signal obtained in solid electrolyte cells are described. A second paper will deal with the theoretical interpretation of the effect.

Experimental

Cell construction.—The cell under investigation consists of a Ag electrode, a AgI electrolyte, and another Ag electrode. The electrodes were made from pressed Ag powder or vacuum-deposited Ag metal. The AgI used in this study was obtained commercially and purified in our laboratory except where otherwise indicated. "Purified" AgI from Fisher Scientific Company was washed several times with hot deionized water and dried at 125°C for 24 hr. Ag electrodes were prepared from different types of material, precipitated Ag powder, Ag paste, and "liquid" Ag, a viscous suspension of finely divided Ag in organic solvents. All electrode materials were used without any further purification or treatment. Pressing of powders was accomplished with a 24-ton hydraulic press with an evacuable die 1¼ in. in diameter.

A number of techniques for fabricating the cells were explored: (*i*) pressing of individual layers of Ag and AgI powder and subsequent assembly of the three pressed disks, (*ii*) consecutively compacting the three individual layers followed by pressing of the complete cell, (*iii*) method (*ii*) except that the die was heated to about 120°C during pressing, (*iv*) vacuum deposition of Ag onto pressed AgI, (*v*) cementing of prepressed Ag electrodes onto the pressed AgI disk with conductive Ag filled epoxy resin, and (*vi*) painting and subsequent firing of Ag paste and/or "liquid" Ag onto a pressed AgI disk.

Methods (*ii*) and (*iv*) were most successful and used for studies reported here. In a preliminary study, the influence of "forming pressure" was evaluated. No significant advantage was observed with using a hot die [method (*iii*)]. A typical cell prepared by method (*ii*) contained 10g of AgI and 3g of Ag powder for each electrode. The complete cell measured 3.1 cm in diameter and 2.3 mm thick. A typical cell prepared by method (*iv*) contained 10g of AgI and vacuum-deposited electrodes 4000Å thick. Thin Ag wires were soldered to the electrodes with indium for electrical measurements.

Cell Testing

Static measurements.—The cell was mounted on the base plate of a John Chatillon and Sons Model HTC press as pictured in Fig. 1. The cell was placed on a recessed lip 2.3 mm in width. Force was applied through a Plexiglas rod. A Brown and Sharpe deflection gauge with a deflection sensitivity of 2×10^{-4} cm/division was mounted in contact with the sample 5.6 mm from the point of application of the force (Fig. 2). No strain measurements or calculations were made; only deflection data were used. The open-circuit voltage and the resistance of the cells were measured. Cell voltages were measured with a high impedance Keithley Model 610 electrometer.

A typical voltage-time response that describes the time frame of the effect is shown in Fig. 3. The measurement was performed by loading the cell with a 2-kg force and then dropping a 1-kg weight on a plate attached to the top of the test apparatus. This technique of preloading the cell was only used in this particular measurement in order to avoid possible lag in the apparatus. The voltage rises to a peak at about 1 min after dropping the weight and then decays to

Fig. 1. Test apparatus

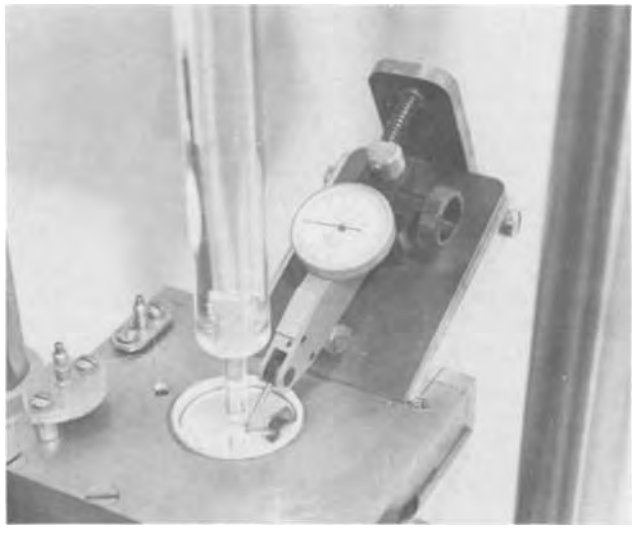

Fig. 2. Close-up view of test apparatus

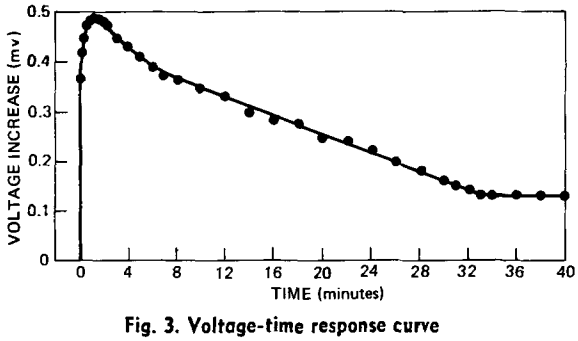

Fig. 3. Voltage-time response curve

a new equilibrium under constant load in approximately 40 min. The peak or maximum voltage is used in all data presented in this work.

Electrical resistances given in this report, except where noted, were measured on a ESI Model 250 DA impedance bridge operated at 1 kHz frequency. In several experiments the resistance under cyclic stress, the dynamic resistance, was measured by observing the resistance necessary to reduce the cell voltage to one-half the open-circuit value. The dynamic resistance was measured at a frequency of less than 1 Hz.

The temperature dependence of the piezogalvanic potential and cell resistance was measured over the range of 24°-212°C. Cells were mounted in an oven and stress was applied through the top of the oven by means of weights.

Cyclic Testing

"Cyclic testing" similar to that reported by Mrgudich (1) was conducted in order to evaluate the mechanical behavior and reversible character of cells over an extended period of time. The apparatus used for the cyclic testing is shown in Fig. 4. The cell was mounted on a cold-rolled steel bar (1 x 17 x 0.045 in.). The motors housed in boxes were Gleason Avery synchronous 30 rpm right-hand rotation motors. A Hewlett-Packard Model 7100B strip chart recorder (Model 17501A plug-in units) with a voltage range of 1.0 mV full scale recorded the piezogalvanic potential change. The one most successful technique for attaching cells to the oscillating steel bar consisted of attaching the cells directly to the bar by a nonconducting epoxy resin. The samples were tested by continued oscillation for a period between 200-300 hr without interruption.

Results

Evaluation of cell preparation methods.—The influence of forming pressure on the following properties was evaluated: (*a*) density of pressed electrolyte, (*b*) breaking force of the cell, (*c*) piezogalvanic signal at a 3 kg (arbitrary) load, and (*d*) maximum piezogalvanic signal at the breaking load.

Table I summarizes these electrical and mechanical properties of the cell with two types of electrodes, vacuum-deposited and pressed Ag powder. Samples with deposited electrodes and with AgI pressed with a force of 22 tons/in.^{2} show the maximum voltage response. For cells with deposited electrodes the maximum voltage output due to an applied force and the force needed to break the cell increased with forming pressure. Cells prepared using pressed electrodes showed essentially no change in the voltage response as a function of forming pressure. Cells so prepared exhibited higher breaking forces than cells prepared with deposited electrodes due to the greater amount of material (Ag) incorporated into the cell.

Table I. Summary of the electrical and mechanical properties of cells with varying types of electrodes

Sample No.	Type of electrode	Forming pressure (tons)	Per cent single crystal density	Voltage change under a 3 kg force (mV)	Breaking force (kg)	Voltage change at breaking point (mV)
AgI-1	Deposited	1	88.2	0.55	4.00	0.68
AgI-2	Deposited	4	95.2	1.70	3.75	2.40
AgI-3	Deposited	8	97.2	1.40	5.00	2.80
AgI-4	Deposited	12	98.6	1.84	5.50	3.41
AgI-5	Deposited	16	99.3	1.52	5.00	2.56
AgI-6	Deposited	20	98.8	1.85	9.50	5.00
AgI-7	Deposited	22	99.3	1.85	10.50	4.60
AgI-8	Pressed	1		0.20	6.50	1.25
AgI-9	Pressed	4		0.05	15.50	0.63
AgI-10	Pressed	8		0.09	13.25	0.41
AgI-11	Pressed	12		0.10	16.00	0.53
AgI-12	Pressed	16		0.06	16.50	0.41
AgI-13	Pressed	20		0.13	18.00	0.69
AgI-14	Pressed	22		0.07	20.00	0.57

The density of the compacted AgI was measured as a function of forming pressure using cells prepared with 10g of AgI and with vacuum-deposited electrodes. The density of the pressed electrolyte asymptotically approaches the theoretical with increased forming pressure. A maximum density of 5.64 g · cm^{-3} equivalent to 99.3% of the single crystal density for AgI (33) was achieved.

Dependence of Signal on Deflection and Force

Cells with varying amounts of AgI electrolyte were constructed using deposited Ag electrodes. The test stand and deflection gauge shown in Fig. 1 were used to determine the peak voltage response as a function of applied force and deflection of the cells. A potential difference is developed across the cell during fabrication. This potential difference is referred to here as the bias voltage. The bias voltage associated with the cells tested ranged from a few tenths of a millivolt to as much as 10 mV. All voltage changes reported have been normalized for the existing bias voltage. Figures 5 and 6 show the piezogalvanic response for cells of varying thicknesses of electrolyte material. In Fig. 5 there is a linearity between voltage response and deflection. In the thicker cells, the curves are offset from zero but exhibit the same slope, that is, 1.8 mV/μ. This offset is attributed to a portion of the applied force

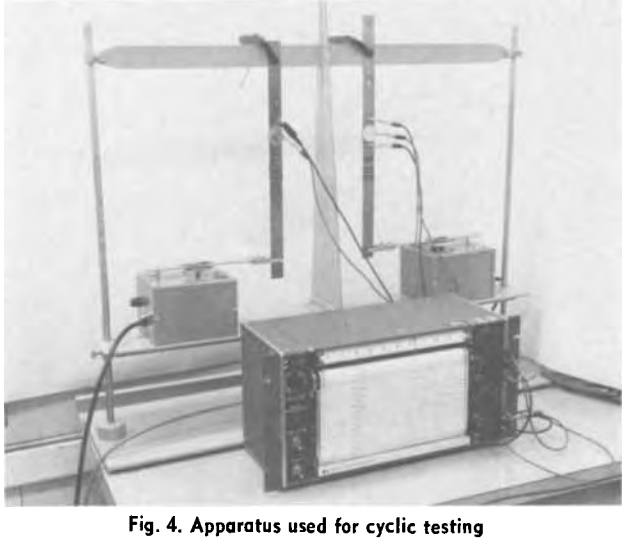

Fig. 4. Apparatus used for cyclic testing

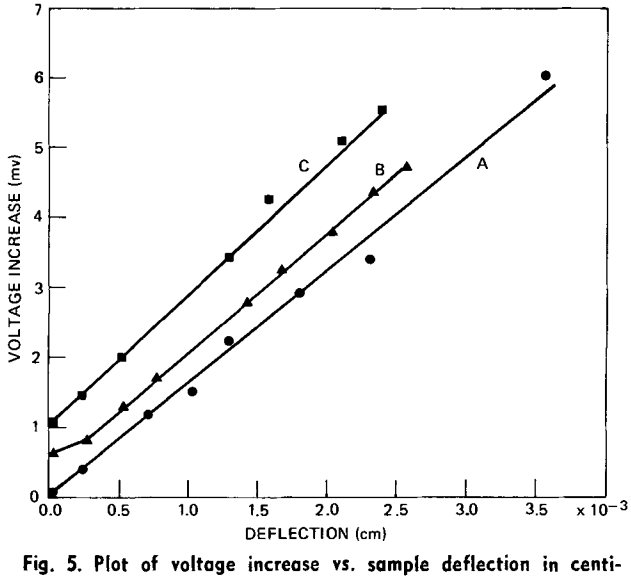

Fig. 5. Plot of voltage increase vs. sample deflection in centimeters. Curve A, cell thickness 1.50 mm; bias voltage + 1.10 mV. Curve B, cell thickness 3.20 mm; bias voltage + 2.00 mV. Curve C, cell thickness 2.40 mm; bias voltage — 0.30 mV.

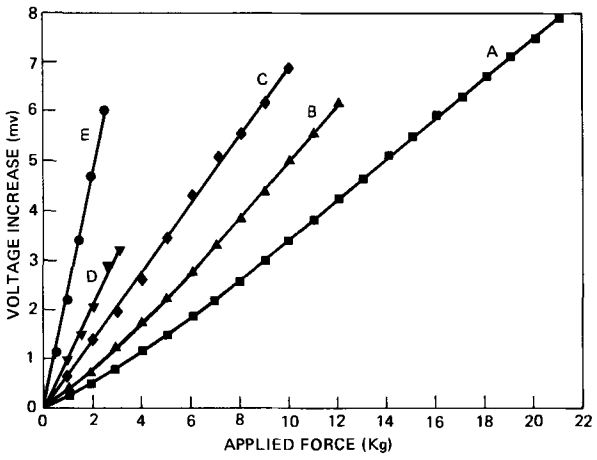

Fig. 6. Plot of voltage increase vs. applied force for cells of various thickness. Curve A, cell thickness 4.20 mm; bias voltage −3.15 mV. Curve B, cell thickness 3.20 mm; bias voltage + 2.00 mV. Curve C, cell thickness 2.40 mm; bias voltage − 0.30 mV. Curve D, cell thickness 1.85 mm; bias voltage + 1.30 mV. Curve E, cell thickness 1.50 mm; bias voltage + 1.10 mV.

going into compressing the electrolyte rather than bending the entire cell. Figure 6 demonstrates linearity of voltage response as a function of applied force for cells of varied thickness. The sensitivity or slope for Fig. 6 is greatest for the thinner sample. For example, a cell 4.2 mm thick shows a slope of 0.50 mV/kg, while a cell of 1.5 mm exhibits 2.5 mV/kg.

Temperature dependence of conductivity and voltage response.—The electrical conductivity and the voltage response of cells was measured over the range 24°-212°C. AgI (99.999% pure) from Semi-Element Corporation was used as the electrolyte and the electrodes were vacuum-deposited. Arrhenius-type plots are shown in Fig. 7 from which activation energies may be estimated.

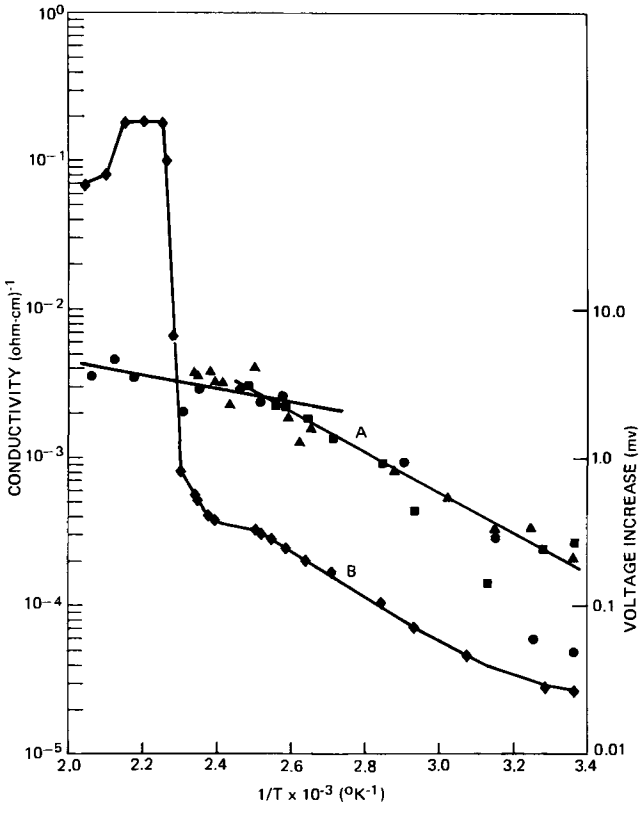

Fig. 7. Temperature dependence of conductivity and piezogalvanic voltage. Curve A, plot of voltage increase vs. 1/temperature. Curve B, plot of conductivity vs. 1/temperature.

The activation energy for the conduction process, ΔE^*_c is calculated from

$$\sigma = \sigma_0 e^{\frac{-\Delta E^*_c}{RT}}$$

where σ is the conductivity and σ_0 is an experimentally determined constant (34). The rapid change in the slope of the curve at about 150°C is due to the $\beta \rightarrow \alpha$ phase transition of AgI. Using the slope of the curve from 100° to 147°C, an activation energy of 15.5 kcal was calculated. This agrees with the activation energy of 15.7 kcal reported in the literature for conduction in β-AgI over the temperature range of 20°-146°C (35).

The activation energy for the piezogalvanic potential, ΔE^*_p was calculated from

$$\Delta V = \Delta V_0 e^{\frac{-\Delta E^*_p}{RT}}$$

where ΔV is the piezogalvanic potential at temperature T and ΔV_0 is a constant. The activation energy derived from the low temperature data (from 24° to 100°C) is 13.4 kcal. Above about 100°C the process becomes almost temperature independent with an activation energy of less than 1 kcal. From Fig. 7 it is evident that there is no corresponding increase in piezogalvanic signal above 150°C to correlate with the $\beta \rightarrow \alpha$ phase transition.

Cyclic behavior of cells.—Cells were tested for extended periods of time with stresses exerted in a cyclic manner with the apparatus shown in Fig. 4. A typical trace from a recording is shown in Fig. 8. In this experiment the cell was mounted 12.7 cm, and the drive attachment, 35.5 cm from the point of attachment. The amplitude of the bar swing was 3.8 cm. The symmetry of the voltage oscillation is evident from this curve as is the linearity of the effect with stress. During the testing period of over 200 hr, no appreciable change in open-circuit voltage output occurred. The dynamic resistance of the cells were also measured and determined to be approximately 200 ohms.

Cells with dissimilar electrodes.—Cells were prepared with the following configurations

Ag/AgI/Ni and Ag/AgI/Au

Forces were applied to the Ag and Ni (or Au) electrode side of the sample by the apparatus shown in

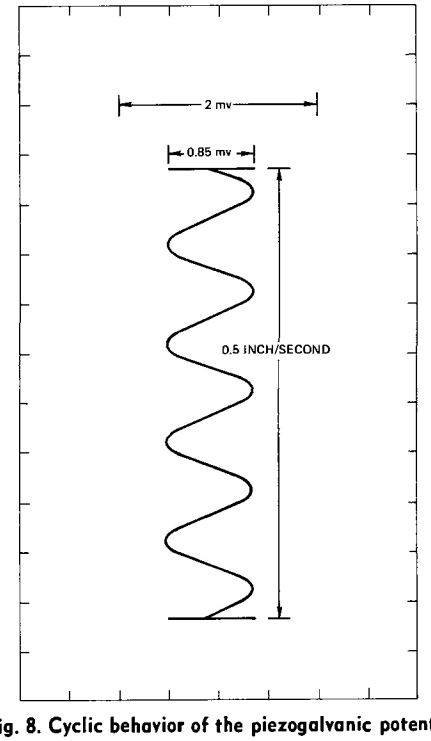

Fig. 8. Cyclic behavior of the piezogalvanic potential

Table II. Piezogalvanic effect with cell of dissimilar electrodes

	Force (kg)	(mV)	(mV)
		$\Delta V_{Ag(stressed)}$	$\Delta V_{Ni(stressed}$
Sample No. 1 Ag/Ni (formed at 22 tons)	1	0.60	0.20
	2	1.40	0.60
	3	1.95	1.10
		$\Delta V_{Ag(stressed)}$	$\Delta V_{Au(stressed}$
Sample No. 2 Ag/Au (formed at 20 tons)	1	0.50	0.10
	2	1.35	0.20
	3	1.15	0.40

Fig. 1. Table II shows the behavior of these cells with applied forces up to 3 kg.

The behavior of the cells depended on the electrode receiving the applied force. Changes in voltage were consistently larger when the Ag electrode received the applied force rather than the Ni or Au electrode.

Discussion

The progress in understanding the piezogalvanic effect has been hampered by a lack of quantitative information with respect to the parameters determining the magnitude of the effect (both voltage and current). This research was intended to correct that situation and from these experiments it is possible to make certain observations.

In the literature describing potential-stress experiments in aqueous solutions two types of effects have been reported. The first has been that of the transient type wherein a transient voltage peaks and decays in times less than 1 sec after the electrode is plastically strained. Such an effect has been reported by Funk *et al.* (9). The second type described by Fryxell and Nachtrieb (12) consists of a "stable and reversible" voltage response persisting for many minutes after plastic strain. The effects reported in this study are in the second category. On sudden loading the voltage rises rapidly to a peak in about a minute and decays over an extended period of time up to 1 hr.

The magnitude of the piezogalvanic effect depends on the method of preparation and the mechanical properties of the cell. It is of particular interest that the voltage signal is determined in a significant way by the type of electrode. Cells constructed with vacuum-deposited electrodes yield voltage signals greater by an order of magnitude than those prepared with pressed powder electrodes. This would tend to make unrealistic a theoretical explanation based only in terms of the electrolyte.

A systematic study of the dependence of the signal on deflection and force showed that the effect is linear with force. Sensitivity, in terms of millivolts per kilogram loading, is a function of cell thickness. Sensitivity in terms of millivolts per micron deflection, however, is independent of cell thickness. Equal changes in electrode deflection, regardless of sample thickness, produced equal piezogalvanic voltages. (The slopes of the curves in Fig. 5 are essentially equal.) Cells containing thicker electrolytes appear less sensitive than ones containing thinner electrolytes because more force is required to achieve the same deflection change. This implies that electrode and/or interface stress plays a major role in the effect.

The temperature dependence of the piezogalvanic voltage change when compared with the temperature dependence of conductivity yields two significant conclusions. The conductivity in solid AgI increases when the beta form is transformed into the alpha form at 146°C. However, a corresponding increase in piezogalvanic voltage is not observed. Thus, the piezogalvanic effect is not determined by the conductivity of the solid ionic conductor. The dynamic resistance of the cell is larger than the cell (AgI) resistance. These resistances were measured at different frequencies. The frequency dependency of resistance should provide a significant clue to the theoretical basis of the effect and for that reason is now under investigation.

The activation energies for both the conduction process and the piezogalvanic effect appear to be similar at low temperatures. The energies are such as to suggest a diffusion process as the rate limiting process. However, above 100°C the piezogalvanic effect shows a very low activation energy and apparently processes that limit the rate at the lower temperature do not occur at the higher temperature.

The cyclic tests demonstrate that the effect is reversible. On this basis it is difficult to attribute the effect entirely to the composition of the electrolyte. Hunger (2) has proposed that the source of the piezogalvanic effect resides in the crystal lattice itself. According to Hunger's mechanism, the mechanical force produces edge dislocations. The impurities within the crystal exist as impurity-ion-cation vacancy complexes. The movement of edge dislocations breaks up these complexes and produces point defects (cation vacancies) which increase the mobility of silver ions. To our knowledge there is no evidence for such a process being reversible. Rather, it would be expected that the defects would tend to coalesce or migrate to the surface. The similarity of the piezogalvanic effect obtained with liquid and solid electrolytes also provides evidence against attributing the effect to crystal structure. On the other hand, an interfacial process would be reversible.

Cells fabricated with electrodes other than Ag indicated that the magnitude of the signal is related to an electrode couple, *i.e.*

$$Ag = Ag^+ + e^-$$

in the case where the Ag electrode in contact with the AgI electrolyte receives the force. This suggests a faradaic process with current passing through an interface. If the source of the piezogalvanic effect was entirely in the solid ionic conductor, the magnitude of the signal should be independent of the nature of the metal electrode. Such is not the case.

These observations lead us to conclude that the piezogalvanic effect is established by an interfacial (faradaic) process rather than any process associated solely with the mechanical and physical properties of either the electrolyte or the electrode.

Acknowledgments

The authors gratefully acknowledge the support of the Naval Air Systems Command, Contract N00017-72-6-4401, Task A160, and also Mr. Kenneth Hoggarth for his assistance in vacuum depositing the electrodes. This paper is based in part on the dissertation submitted by G. D. Mitchell in partial fulfillment of requirements for the PhD degree in Chemistry to the American University, 1971.

Manuscript submitted June 16, 1972; revised manuscript received Sept. 14, 1972.

Any discussion of this paper will appear in a Discussion Section to be published in the December 1973 JOURNAL.

REFERENCES

1. J. N. Mrgudich, 21st Annual Proceedings Power Sources Conference (1967).
2. H. F. Hunger, U.S. Army Electronics Command, Fort Monmouth, New Jersey, Technical Report ECOM-3360 (1970).
3. T. W. Richards and G. E. Behr, *Z. Physik. Chem.*, **58**, 301 (1907).
4. W. H. Walker and C. Dill, *Trans. Faraday Soc.*, **11**, 153 (1907).
5. L. Giulott, *Nuovo Cimento*, **13**, 320 (1936).
6. H. Endo and S. Kanazawa, *Sci. Rept. Tohoku Imp. Univ.*, **20**, 124 (1931).
7. U. R. Evans and M. T. Simnad, *Proc. Roy. Soc.*, **188A**, 372 (1947).
8. L. V. Nikitin and V. G. Sochevanov, *Mettallografiya*, **1**, 23 (1935).

9. A. G. Funk, J. C. Giddings, C. J. Christensen, and H. Eyring, *J. Phys. Chem.*, **61**, 1179 (1957).
10. W. Spring, *Bull. Classe Sci., Acad. Roy. Belg.*, 1066 (1903).
11. G. Tammann and C. Wilson, *Z. Anorg. Chem.*, **173**, 156 (1928).
12. R. E. Fryxell and N. H. Nachtrieb, *This Journal*, **99**, 495 (1952).
13. R. S. Dudley, R. Elliott, W. H. McFadden, and L. W. Shemitt, *J. Chem. Phys.*, **23**, 585 (1955).
14. K. Nobe, E. Baum, and W. F. Seyer, *This Journal*, **108**, 97 (1971).
15. L. R. Gautam and J. B. Jha, *Proc. Ind. Acad. Sci.*, 108 (1953).
16. W. Thompson, *Trans. Roy. Soc. (London)*, **146**, 649 (1856).
17. M. J. Druyvesteyn, *Physica*, **17**, 748 (1951).
18. G. C. Kuczynski, *Phys. Rev.*, **94**, 61 (1954).
19. A. G. Funk, J. C. Giddings, C. J. Christensen, and H. Eyring, *Proc. Natl. Acad. Sci.*, May (1957).
20. G. Gouy, *J. Physique*, **9**, 457 (1910).
21. D. L. Chapman, *Phil. Mag.*, **25**, 475 (1913).
22. O. Stern, *Z. Electrochem.*, **30**, 508 (1924).
23. R. J. Friauf, *J. Chem. Phys.*, **22**, 1329 (1954).
24. T. B. Grimley and N. F. Mott, *Discussions Faraday Soc.*, **1**, 3 (1947).
25. D. O. Raleigh, *J. Phys. Chem.*, **70**, 689 (1966).
26. F. B. Fishback and A. J. Nowick, *Phys. Rev.*, **99**, 1333 (1955).
27. S. Amelinckx, J. Bennick, and G. Remaut, *J. Phys. Chem. Solids*, **11**, 170 (1959).
28. R. L. Sproull, *Phil. Mag.*, **5**, 815 (1960).
29. C. Henrickx and J. Van Cakenberghe, *Applied Phys. Letters*, **1**, 15 (1962).
30. J. D. Eshelby, C. W. A. Nowey, and P. L. Pratt, *Phil. Mag.*, **3**, 75 (1958).
31. N. Weber and M. Goldstein, Jr., *Chem. Phys.*, **41**, 2898 (1964).
32. R. J. Charles, *This Journal*, **116**, 1514 (1969).
33. "Handbook of Chemistry and Physics," 49th Edition, (1968-1969).
34. "American Institute of Physics Handbook," second edition, pp. 9-66, McGraw-Hill, New York (1963).
35. R. F. Lindner, *J. Physik, Chem. (Frankfurt)*, **9**, 304 (1965).

Electrogenerated Chemiluminescence

XI. Electrochemistry and Electrogenerated Chemiluminescence in Scintillator Dye Melts

Csaba P. Keszthelyi* and Allen J. Bard**

Department of Chemistry, The University of Texas at Austin, Austin, Texas 78712

ABSTRACT

Melts of scintillator compounds which are solid at room temperature, such as 2,5-diphenyloxazole (PPO) and 2,5-diphenyloxadiazole (PPD) containing several quaternary ammonium salts as supporting electrolytes, were examined as solvents for electrochemical and electrogenerated chemiluminescence (ECL) studies. Although the resistance of these solutions was high, cyclic voltammetry of 9,10-diphenylanthracene and rubrene in PPO showed the production of stable radical anions and cations for both compounds, and the ECL emission was essentially the same as the fluorescence emission of these compounds in PPO. ECL of rubrene was also observed in molten phenanthrene, PPD, thianthrene, and p-terphenyl, as well as in mixtures of PPO with 1- or 2-methylnaphthalene.

There has been much interest in recent years in the application of nonaqueous solvents in electrochemistry (1). Many of these solvents have the advantage of rather wide potential limits before the solvent itself or the supporting electrolyte undergoes reduction or oxidation at an inert electrode; these solvents are also often less likely to react with electrogenerated species. Most solvents employed are liquid at room temperature [*e.g.*, N,N-dimethylformamide (DMF), acetonitrile (ACN)] while several liquefy at low temperatures (SO_2, NH_3). Only a few studies of organic systems have employed as solvents compounds which are solid at room temperature; these include dimethylsulfone (mp 127°C) (1, 2), molten ethylammonium chloride (3), and the $AlCl_3$-KCl molten salt system (4). Recent studies involving aprotic solvents include electrogenerated chemiluminescence (ECL) of aromatic compounds, where electrogenerated radical anions ($R^{\cdot -}$) and radical cations ($R'^{\cdot +}$) react to form excited state species

$$R^{\cdot -} + R'^{\cdot +} \rightarrow R^* + R' \text{ or } R'^* + R \qquad [1]$$

We have recently reported on the ECL of the scintillator material 2,5-diphenyl-1,3,4-oxadiazole (PPD) with thianthrene in acetonitrile solutions (5) and also on the ECL of several other scintillator materials, including 2,5-diphenyloxazole (PPO), 2,5-diphenylfuran (PPF), and p-terphenyl (PTP) (6).

Because PPO has a low melting point (70°C), we thought it of interest to investigate the ECL of molten PPO itself, using a quaternary ammonium salt as a supporting electrolyte. We had additional reason to investigate ECL in molten PPO itself, because, although the ECL of PPO in nonaqueous solvents is of a very unsatisfactory nature (6), showing low intensity, unstable spectral distribution of the emitted light and poor stability of the electrogenerated cation radicals, we have also found that the presence of a 10-fold molar excess of PPO with respect to DPA increases the DPA ECL intensity when only $DPA^{\cdot +}$ and $DPA^{\cdot -}$ are electrogenerated in an ACN-0.1M TBAP solution. In the course of these studies we also investigated PPO and related compounds as solvents for electrochemical and ECL studies of other organic species. Although molten scintillator compounds have been used as nuclear reactor coolants (7), to our knowledge they have not been used previously as solvents for electrochemical or spectroscopic studies.

* Electrochemical Society Student Member.
** Electrochemical Society Active Member.
Key words: nonaqueous solvents, elevated temperature, luminescence, spectroscopy, scintillators, cyclic voltammetry, chemiluminescence.

Experimental

Chemicals.—Scintillation grade 2,5-diphenyloxazole (PPO) was obtained from Aldrich Chemical Company and from Nuclear Equipment Chemical Corporation (NEC). Phenanthrene, 98+%, obtained from Aldrich, was purified by four recrystallizations alternately using spectroscopic grade methanol and hexane. A portion of this purified sample was vacuum sublimed with no detectable improvement in the phenanthrene sample. Thianthrene (TH) was obtained from Aldrich, and it was used without further purification after its properties were compared with specially purified thianthrene samples (5). The p-terphenyl (PTP), scintillation grade, was supplied by NEC. Scintillation grade 2,5-diphenyl-1,3,4-oxadiazole (PPD), rubrene (puriss), and one of the 9,10-diphenylanthracene (DPA) samples were obtained from Aldrich. A second sample of DPA was obtained from City Chemical Corporation. The 1- and 2-methylnaphthalene were obtained from Aldrich, and together with the scintillation grade compounds, they were used without further purification after no electrochemical or fluorescent impurities could be detected. Because vacuum sublimation actually leads to considerable decomposition of rubrene and DPA, that technique was abandoned in favor of recrystallization from spectrograde hexane. Several experiments were conducted using as-received rubrene or DPA and there was no observable difference between these results and data obtained using samples purified by recrystallization from spectrograde hexane. Tetraphenylporphin (TPP) was obtained from Mad River Chemical Company and was used without furthur purification. Tetra-n-butylammonium perchlorate (TBAP), tetraethylammonium perchlorate (TEAP), tetramethylammonium perchlorate (TMAP), tetra-n-butylammonium fluoborate ($TBABF_4$), and tetramethylammonium fluoborate ($TMABF_4$), all polarographic grade, were obtained from Southwestern Analytical Chemicals, Inc., and used without further purification; they were dried for 48 hr at 90°C in a vacuum oven and stored in a desiccator over anhydrone. In most experiments TBAP was used as a supporting electrolyte, although all other supporting electrolytes (except those containing chloride anion) behaved satisfactorily in molten PPO.

Apparatus.—For preliminary and spectroscopic experiments a cell having a detachable Pyrex or quartz ground glass bottom compartment, a central electrode compartment, and a vacuum adapter (8) was used; when luminescence was a result of optical excitation, the central section housing the electrodes was removed, so that the possibility of interference with the right angle excitation process could be eliminated. The cell used in most ECL experiments is shown in Fig. 1 (a silver wire reference electrode, similar in size and position to the platinum working and auxiliary electrodes, is not shown in the drawing). Through a vacuum adapter the cell can readily be evacuated to 10^{-6} Torr when empty due to the absence of the more numerous ground glass joints used in usual cell construction. Since the solvent-supporting electrolyte system is solid at room temperature, the usual freeze-pump-thaw deaeration procedure is replaced by a pump-melt-freeze (PMF) cycle; the pressure over the ECL mixtures was reduced to $<10^{-5}$ Torr by several PMF cycles. We have previously reported (9) that a silver wire was an acceptable reference electrode in the case of dimethylformamide-TBAI solutions; the use of a silver reference electrode in molten salt electrochemistry has also been described (10). The applied potential or current was controlled using a PAR Model 170 Electrochemistry System (Princeton Applied Research Corporation) which could be linked with a Wavetek Model 114-G function generator for fast electrogeneration. The ECL emission was detected using an Aminco-Bowman spectrophotofluorometer (SPF) in conjunction with a Hamamatsu TV Corporation R-456 photomultiplier tube (PMT) which is required for spectral measurements extending beyond 580 nm. To detect the very low intensity ECL of TPP the SPF was modified to allow operation of the PMT at 1100V d.c. rather than at the original 700V d.c. The ECL cell was placed in a temperature-controlled cell compartment (Aminco-Bowman part No. 4-8262) and hot water was circulated using a Labline-controlled temperature bath. In the case of phenanthrene it was found necessary to boost the heating rate obtained from the constant temperature bath by using a heating tape powered by an auto transformer, around the constant temperature cell compartment in addition to the hot water. The signal from the SPF was fed either into a Moseley 7005A X-Y recorder, or to a Tektronix storage oscilloscope equipped with a Polaroid camera. An alternate heating arrangement, mainly used for electrochemistry and visual observation of ECL, involved use of a small Pyrex bath filled with water or mineral oil, and heated with an immersed Nichrome coil. In a typical experiment the constant temperature bath and the controlled temperature cell compartment of the SPF are heated to reach the desired temperature (commonly 95°-97°C for the Labline bath and 75°-80°C for the cell compartment heated by the circulating hot water) while the clean cell is evacuated on a vacuum line to a pressure less than 10^{-6} Torr. The solid compounds are next introduced (usually 1.000g PPO, 0.100g TBAP, and 10.0 mg DPA or rubrene), and the cell is evacuated again. Several PMF cycles are carried out before the cell is permanently sealed using a natural gas-oxygen torch. Cells so prepared remain in an apparently contamination-free state for as long as 18 months as attested by essentially identical electrochemical and ECL results obtained at various time intervals. The stability of the silver wire reference electrode in these systems appeared very satisfactory.

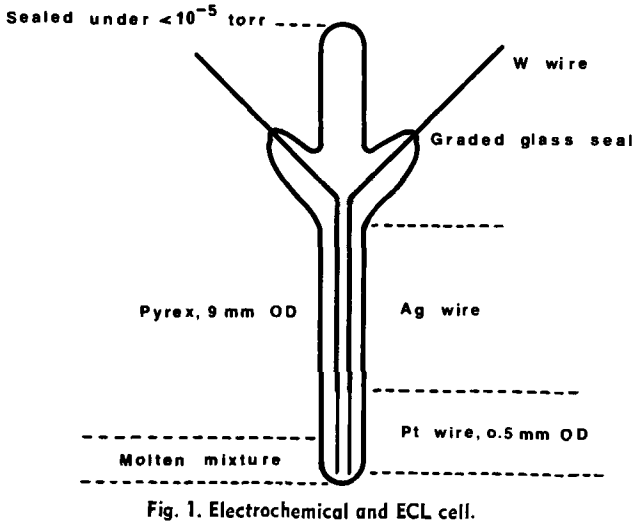

Fig. 1. Electrochemical and ECL cell.

Results and Discussion

Electrochemistry of the melts.—In selecting a solvent for electrochemical work, it is necessary that the potential limits of the solvent-supporting electrolyte system, *i.e.*, the potentials at which the electrode-solvent system shows reduction and oxidation, are wide enough to encompass the potential region of interest. The potentials at which several of the scintillator compounds and solutes of interest reduce and oxidize in ACN solutions containing 0.1M TBAP are shown in Fig. 2. (The structures of these compounds and other compounds that are discussed in this work are shown in Fig. 3.) These potentials suggest that the pure scintilator compounds, such as PPO and PPD, will have sufficiently wide potential ranges to be useful solvent systems. Some of the more useful molten solvents and their approximate potential ranges are given in Table I.

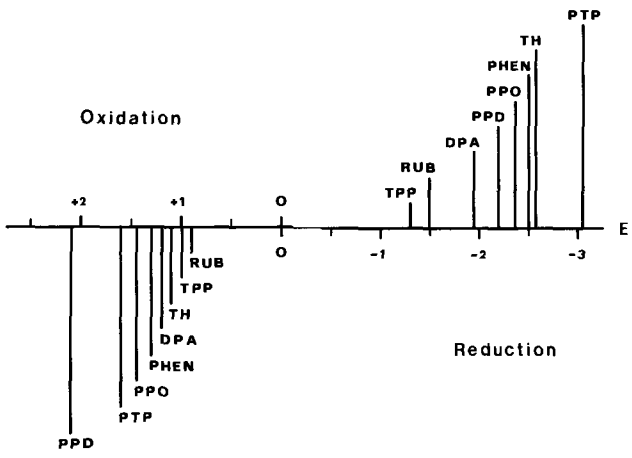

Fig. 2. Oxidation-reduction potentials of scintillator dyes and solutes. Electrochemistry in solutions of 0.1M TBAP in CH_3CN at a platinum electrode *vs.* a Ag wire reference electrode (except for PTP which was reduced in propylene carbonate-0.1M TBAP). The oxidation and reduction limits of DMF and ACN *vs.* the Ag reference electrode are +1.7 to −2.8 (DMF) and +2.3 to −2.9 (ACN-TBAP).

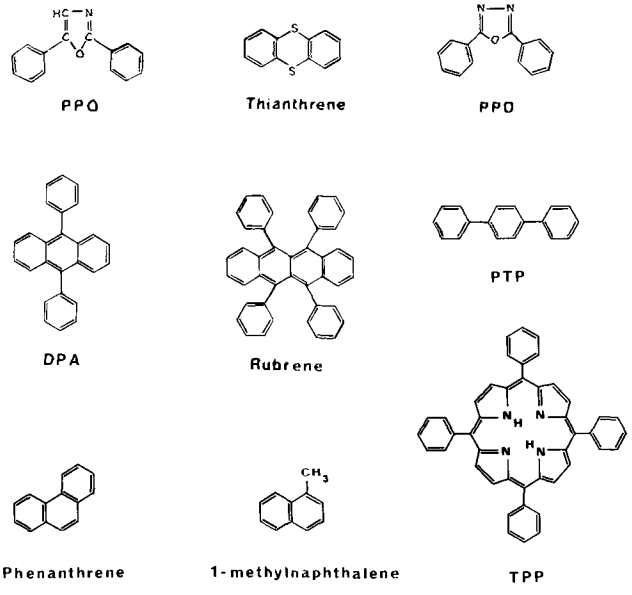

Fig. 3. Structural formulas. Accepted abbreviations (11) are used where possible in naming the compounds.

In ECL experiments attempted in the molten scintillator solvent systems without added solutes other than supporting electrolytes (*e.g.*, Table II, 5 and 18), no light emission was observed.

Electrochemistry of rubrene and DPA in melts.—The melts could be employed as solvents for the aromatic hydrocarbons rubrene and DPA conventionally used in ECL studies. Typical cyclic voltammograms in molten PPO-TBAP are shown in Fig. 4 and 5. These voltammograms are similar in shape to those found in DMF and ACN and show that the radical anion and cation of rubrene and DPA are stable in PPO under these

Table I. Some of the molten solvents used and their useful potential ranges

Solvent (MP)	Electrolyte	Oxidation-reduction limit (V *vs.* Ag reference electrode)
PPO (70-72)	TBAP	+1.5/−2.2
PPD (140-141)	TBAP	+1.8/−2.0
TH (154-6)	TBAP	+1.1/−2.4
TBAP (217-8)	—	+2.8/−3.0
PHEN (100-1)	TBAP	+1.4/−2.2

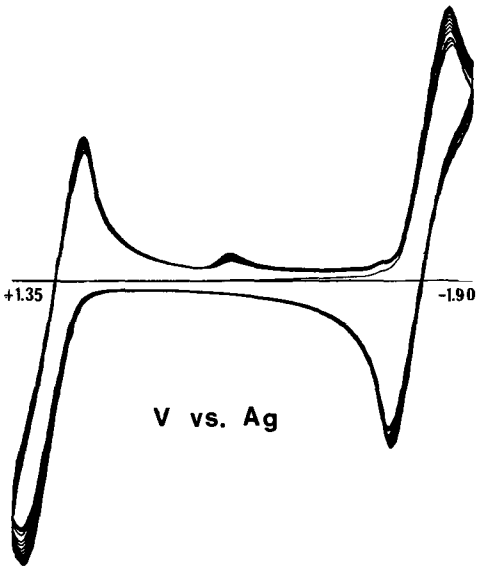

Fig. 4. Cyclic voltammogram of rubrene in molten PPO-TBAP. Sweep rate was 100 mV/sec; rubrene concentration was 3 mM.

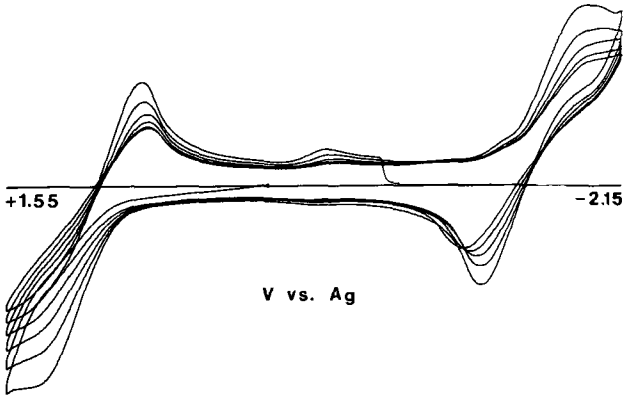

Fig. 5. Cyclic voltammogram of 9,10-diphenylanthracene in molten PPO-TBAP. Sweep rate was 100 mV/sec; DPA concentration was 3 mM.

conditions. The differences of the peak potentials of the forward and reversal waves are larger than those for nernstian electrode reactions at these temperatures (*e.g.*, for rubrene reduction $E_{pc} - E_{pa} = 400$ mV (exp); compared to 67 mV [theoretical]). However, the resistance of these solutions is high so that uncompensated resistance effects are probable. The cyclic voltammograms all show an increase in peak currents under continuous cycling (which is opposite to the usual behavior observed for multiple scans) as well as a decrease in the separation of the forward and reversal E_p-values. This effect may be caused by some kind of filming of the platinum wire electrode in molten PPO, a film which is being removed under continuous cycling, accompanied by an increase in the active area on the electrode. It is also possible that the stable electrogenerated cations and anions make a contribution to the total ionic population of the solution, especially in the vicinity of the electrode and decrease the uncompensated iR.

The relatively high resistance of these molten solutions was evidenced by very high uncompensated iR losses; for example, when currents as low as 200 μA were passed, the full iR compensation of the PAR had to be applied.

ECL in molten solvents.—The major effort in this research was directed toward a study of ECL in the molten systems. Important requirements in observing ECL are that the excited state species formed by the radical ion annihilation reaction [1], are not quenched

to a large extent by the solvent molecules and that the solvent does not absorb the emitted radiation. To investigate these effects a study of the fluorescence of the solvent PPO, and of solutions of rubrene and DPA in PPO was undertaken. The fluorescence spectrum obtained in molten PPO itself, shown in Fig. 6, consists of a single peak shifted to the red with respect to PPO emission obtained in dilute solutions at 3800 nm. In cyclohexane solutions upon change of the PPO concentration from 0.1 to 25 g/liter, the fluorescence emission peak decreases in height and broadens toward the red region of the spectrum (11); this broadening, which is usually attributed to excimer formation, is not found in the pure PPO melt. The attenuation of certain wavelengths of the emission beam in traversing the *ca.* 6 mm of molten PPO from the center of the cuvette where excitation occurs may also be a factor. It is also possible that the observed fluorescence is caused by a trace impurity in the PPO, although the shape of the fluorescence emission spectrum is independent of excitation wavelength from 2800-3800 nm. Both DPA and rubrene exhibit fluorescence spectra in PPO (Fig. 7 and 8) which are very similar to those seen for these compounds in dilute solutions of ACN.

When the platinum working electrode in a molten PPO-TBAP solution containing either DPA or rubrene is pulsed between potentials where $R^{-\bullet}$ and $R^{+\bullet}$ are formed ECL results; typical ECL emission spectra for pulse lengths of 0.05-1 sec are shown in Fig. 9 and 10. The ECL spectra are virtually the same as the fluorescence spectra in PPO and hence, nearly the same as the ECL spectra in ACN and DMF, so that there is no evidence for interaction between the PPO and the excited states. Neither is there a temperature effect on the ECL spectra for DPA or rubrene in PPO as compared to ECL in ACN or DMF, although there is a small shift of the rubrene ECL peak toward the red. The emitted ECL light was very steady with time on repeated cycling for both rubrene (Fig. 11a) and DPA (Fig. 11b), showing stability of the radical ion species in this medium. Experiments involving other supporting electrolytes ($TBABF_4$, TEAP, TMAP) in PPO and other scintillator melts (PPD, PTP, TH, PHEN) are shown in Table II. We also tried molten supporting electrolytes (*e.g.*, TBAP, TBACl) themselves as solvents. The electrochemical behavior of rubrene and

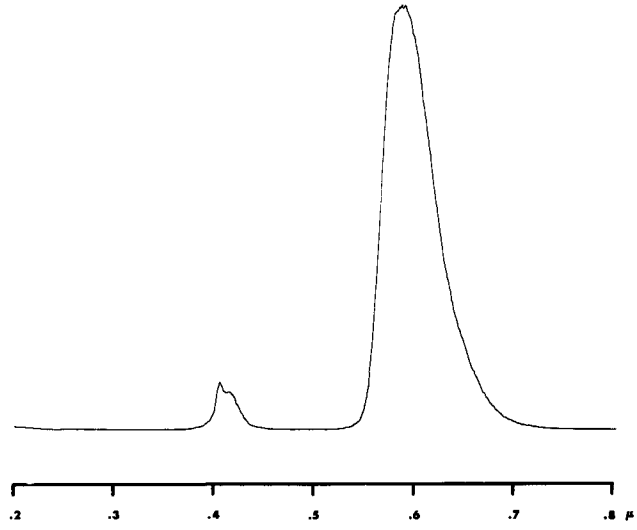

Fig. 8. Fluorescence spectrum of rubrene in molten PPO. Rubrene concentration was 3 mM; peak at 0.40μ represents scatter of λ excitation.

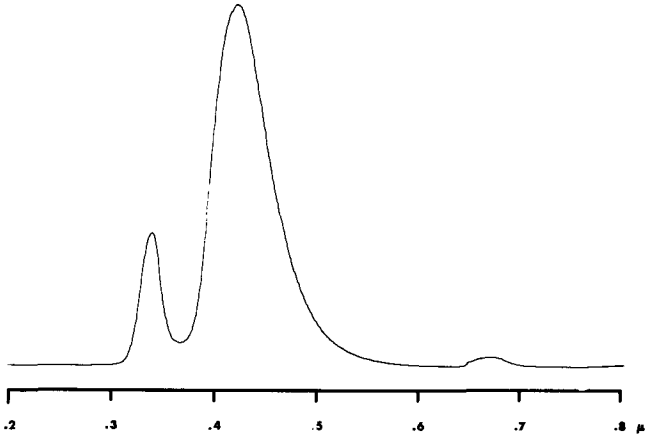

Fig 6. Fluorescence spectrum of molten PPO. Peak at 0.34μ represents scatter of λ excitation.

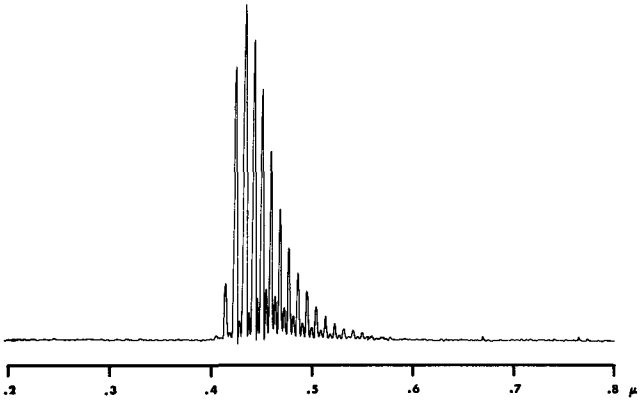

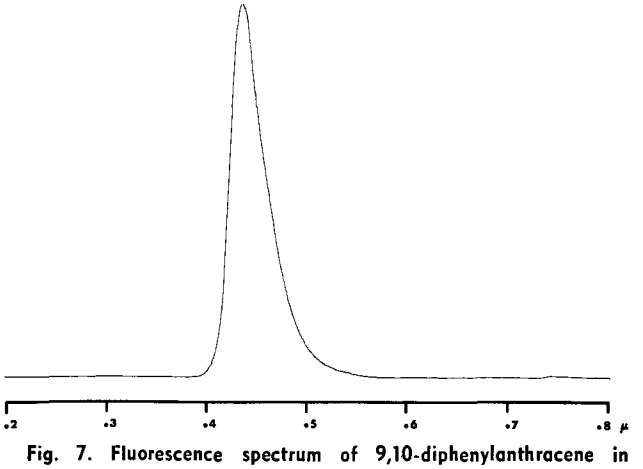

Fig. 7. Fluorescence spectrum of 9,10-diphenylanthracene in molten PPO. DPA concentration was 3 mM; λ excitation = 400 nm.

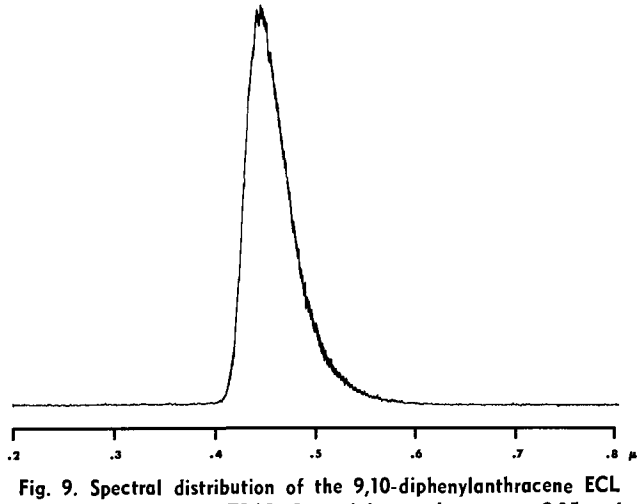

Fig. 9. Spectral distribution of the 9,10-diphenylanthracene ECL emission in molten PPO-TBAP. Potential steps between −2.15 and +1.55 (V *vs.* Ag reference electrode) at 0.5 Hz (top) and 5 Hz (bottom); DPA concentration was 3 mM.

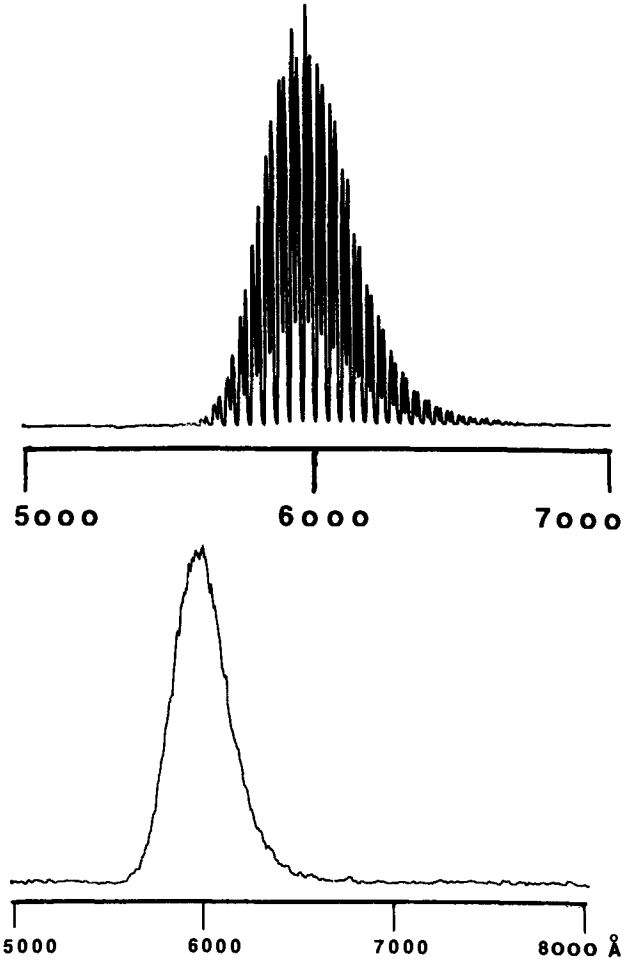

Fig. 10. Spectral distribution of the rubrene ECL emission in molten PPO-TBAP. Rubrene concentration was 3 mM. Top: voltage pulses with +4.00/−2.50 limits at 1 Hz; bottom: potential steps between −1.90 and +1.40 (*V vs.* Ag reference electrode) at 10 Hz.

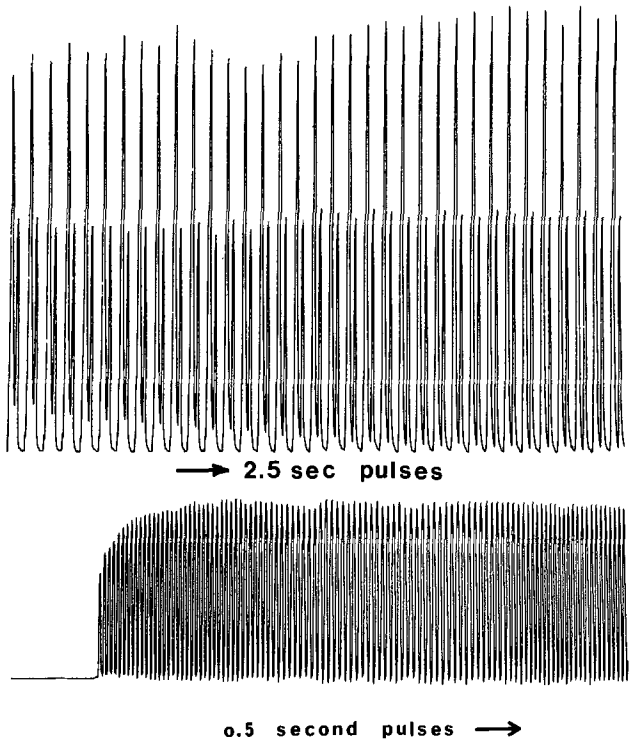

Fig. 11. Intensity-time characteristics of the rubrene (*a*, top) and 9,10-diphenylanthracene (*b*, bottom) ECL emission at the wavelength of spectral maximum in molten PPO-TBAP.

DPA in these was generally unsatisfactory and no ECL was observed with them. In molten TBAP the cyclic voltammetric behavior of both DPA and rubrene was characterized by irreversible waves and unstable radical ions. In molten TBACl the reduction of DPA shows reversible cyclic voltammetric behavior at −1.4V *vs.* Ag reference electrode; the oxidation background limit of TBACl occurs at +1.5V *vs.* Ag reference electrode, so that oxidation of DPA or rubrene to the cation radical cannot be observed. As shown in Table II, all of the following molten scintillator-TBAP-rubrene systems produced ECL: PPD, TH, PHEN, and PTP. Not all compounds with seemingly acceptable properties were usable, however; N,N-diphenylformamide, for example, was found to be unsuitable to observe rubrene ECL. Also, the PPD^{-}/TH^{+} pair, which has good ECL characteristics in ACN-TBAP (5), was found to yield no detectable luminescence in molten PPO-TBAP. No luminescence was observed in binary PPO-TBAP, PPD-TBAP, TH-TBAP, or PHEN-TBAP under any conditions in the absence of DPA or rubrene.

In some experiments "pre-annihilation" ECL was observed for PPO-TBAP solutions containing rubrene or DPA, when the potential was stepped to one where the anion (or cation) radical was produced and then stepped to potentials insufficient to produce the oppositely charged species. For example, when rubrene cation radical was produced first, light could be detected when the electrode was stepped back to potentials more negative than −1.0V *vs.* Ag, although rubrene anion radical is not produced until −1.7V. Similar pre-annihilation effects were found for initial production of rubrene anion and DPA ion radicals. Some unusual effects on the pre-annihilation ECL, such as the variation of the ECL intensity with applied potentials that are still short of the foot of the wave, similar to what we have found in the case of thianthrene pre-annihilation ECL (5), may also involve nonuniform current densities and uncompensated iR effects in these highly resistive media.

As seen from experiments 23 and 24 in Table II, the addition of 25% by weight of 1- or 2-methylnaphthalene to the PPO-TBAP solution resulted in an approximately two-fold increase in rubrene ECL emission compared to PPO solutions not containing methylnaphthalene. We have noticed similar increases in ECL intensities upon addition of less polar solvents, such as benzene or toluene, to ACN solutions (6). A systematic investigation of the effect of solvent on ECL efficiency is currently under way.

Although the experiments described using the usual three-electrode, potential step, technique are most appropriate for obtaining electrochemical data, ECL can also be produced in the two-electrode mode, employing voltage or current steps. In fact in some circumstances, particularly at higher frequencies or when reaction products can cause shifts in the potential of the silver wire reference electrode, the two electrode mode, with the voltage span adjusted empirically to give maximum light output and the applied program an asymmetric square wave with the potentiostat reference and auxiliary leads connected together, can produce larger light intensities than the three-electrode mode. In practical devices employing ECL, the two-electrode mode would, of course, be preferred.

Although this work was not concerned with the construction of ECL devices, some possible applications of molten scintillator systems can be mentioned. The melting point of these compounds, or of their mixtures, is constant within a few degrees centigrade, and a range from room temperature to over 200°C can be covered by varying the composition. The ohmic resistance of a frozen mixture is very high while the melts have a much lower resistance (less than 1000 ohms in the cells used here) so that a circuit incorporating one or several of these mixtures can behave as a temperature sensing device. Addition of DPA or rubrene to

Table II. Summary of electrogenerated chemiluminescence experiments

No.	Solvent[a]	Electrolyte	Solute(s)[b]	Temperature[c] (°C)	Experimental conditions[d]	Results and remarks[e]
1	TBAP	—	—	220	CV; potential steps; voltage pulses	No luminescence detected
2	TBAP	—	RUB	220	CV; potential steps; voltage pulses	No luminescence; unstable RUB cation & anion
3	TBAP	—	DPA	220	CV; potential steps; voltage pulses	No luminescence; unstable DPA cation & anion
4	TBACl	—	DPA	80	CV; potential steps	No luminescence; stable DPA-, TBACl unsuitable for DPA+
5	PPO	TBAP	—	80	Potential steps; voltage pulses	No luminescence
6	PPO	TBAP	RUB	80	CV	Stable R^+ and R^-
7	PPO	TBAP	RUB	80	Potential steps	RUB ECL detected
8	PPO	TBAP	RUB	80	Voltage pulses	RUB ECL, brighter than above
9	PPO	TBAP	RUB	80	Voltage pulses (sine wave) at 60 cps	RUB ECL for 30 days continuous, intensity fell
10	PPO	$TBABF_4$	RUB	80	Voltage pulses	RUB ECL
11	PPO	$TMABF_4$	RUB	80	Voltage pulses	RUB ECL
12	PPO	TEAP	RUB	80	Voltage pulses	RUB ECL
13	PPO	TMAP	RUB	80	Voltage pulses	RUB ECL
14	PPO	TBAP	TH & PPD	80	Potential steps	No luminescence
15	PPO	TBAP	DPA	80	CV; potential steps; voltage pulses	Stable R^+ & R^-; DPA ECL;[g] DPA ECL
16	PPO/PPD	TBAP	RUB	115	Voltage pulses	RUB ECL
17	PPO/PTP	TBAP	RUB	95	Voltage pulses	RUB ECL
18	TH	TBAP	—	150	CV; potential steps	No luminescence
19	TH	TBAP	PPD	150	Potential steps	No luminescence
20	PHEN	TBAP	RUB	100	Voltage pulses	RUB ECL[f]
21	PPD	TBAP	RUB	140	Voltage pulses	RUB ECL
22	PTP	TBAP	RUB	220	Voltage pulses	RUB ECL
23	PPO/1-methylnaphthalene	TBAP	RUB	80	Potential steps; voltage pulses	RUB ECL; brighter than using PPO alone
24	PPO/2-methylnaphthalene	TBAP	RUB	80	Potential steps; voltage pulses	RUB ECL; brighter than using PPO alone
25	N,N-diphenylformamide	TBAP	RUB	80	Voltage pulses	No luminescence
26	PPO	TBAP	TPP	80	CV; potential steps; voltage pulses	TPP ECL of very low intensity

[a] The typical ratio of solvent to electrolyte to solute was 100:10:1, resulting in solutions approximately 5 mM in solute. When a mixed solvent was used, the component added to PPO was approximately 25% by weight.
[b] RUB = rubrene; DPA = 9,10-diphenylanthracene.
[c] Estimated sample temperatures in the vicinity of the electrode. The bath temperature was considerably higher than these values, *e.g.*, in the case of molten TBAP the bath had to be higher than 235°C to prevent solidification of the sample in the vicinity of the electrode. Since the electrodes are good heat conductors, the temperature in the vicinity of the electrode is lower than that of the rest of the ECL solution.
[d] Voltage pulses: two electrode mode of electrogeneration (see text); CV: cyclic voltammetric experiment; potential steps; three electrode mode; potential is stepped between first reduction and first oxidation process.
[e] Visual observations in case of high-temperature experiments by the dark adapted eye.
[f] Molten phenanthrene was found to sublime excessively in the ECL cell during experiments.
[g] DPA ECL in PPO is approximately twice as intense as that obtained in ACN under similar conditions.

these mixtures would also result in the emission of light upon melting when a cyclic signal is applied to the electrode and this process is a reversible one following the solid-liquid phase transitions.

Acknowledgment

We thank Dr. W. V. Childs for his helpful discussions. This work was supported by the U.S. Army Research Office-Durham.

Manuscript received July 11, 1972. This was Paper 101 presented at the Houston Meeting of the Society, May 7-11, 1972.

Any discussion of this paper will appear in a Discussion Section to be published in the December 1973 JOURNAL.

REFERENCES

1. C. K. Mann and K. K. Barnes, "Electrochemical Reactions in Nonaqueous Solvents," M. Dekker, New York (1970).
2. B. Bry and B. Tremillon, *J. Electroanal. Chem.*, **30**, 457 (1971).
3. G. Picard and J. Vedel, *Bull Soc. Chim. France*, **1969**, 2557.
4. M. Fleischmann and D. Pletcher, *J. Electroanal. Chem.*, **25**, 447 (1970).
5. C. P. Keszthelyi, H. Tachikawa, and A. J. Bard, *J. Am. Chem. Soc.*, **94**, 1522 (1972).
6. C. P. Keszthelyi and A. J. Bard, Paper 14, San Antonio American Chemical Society Regional Meeting, 1971.
7. W. W. West, U.S. Atomic Energy Comm. AECU-4295 (1959).
8. N. E. Tokel, C. P. Keszthelyi, and A. J. Bard, *J. Am. Chem. Soc.*, **94**, 4872 (1972).
9. W. V. Childs, J. T. Maloy, C. P. Keszthelyi, and A. J. Bard, *This Journal*, **118**, 874 (1971).
10. H. Bloom, "The Chemistry of Molten Salts," p. 167, Benjamin (1967).
11. I. B. Berlman, "Handbook of Fluorescence Spectra of Organic Molecules," Second Edition, p. 294, Academic Press (1971).

Kinetics of Iron Deposition on a Rotating Platinum Disk Electrode

A. A. El Miligy, F. Hilbert, and W. J. Lorenz*

Institute of Physical Chemistry and Electrochemistry, University of Karlsruhe, Karlsruhe, Germany

ABSTRACT

The kinetics of iron deposition from acid solutions under steady-state conditions have been studied using a rotating platinum disk electrode. The data obtained in the pH range between 1.8 and 3.8 can be explained on the basis of two reaction mechanisms. The noncatalyzed mechanism is applicable at pH $\leq$ 2.4, while the catalyzed one is applicable at pH $\geq$ 3.3. In between there is a transition from one mechanism to the other. Measurements of electrochemical reaction order as a function of the pH indicate the existence of the catalyzed mechanism at pH $\geq$ 3.3. In this pH-range the ferrous ion discharge takes place in the charge transfer region of the HER and consequently the pH at the electrode surface is the same as in the bulk of the solution. At pH $<$ 2.4 such measurement shows that the pH at the electrode surface is different from that in the bulk of the solution. This is attributed to the fact that the ferrous ion discharge takes place at the onset of the transfer controlled region of the HER. These results are in good agreement with an earlier investigation on the iron deposition on a rotating gold disk electrode.

The kinetics of iron dissolution and deposition are of considerable interest. Consistency, however, of obtained results and hence offered reaction mechanism remained a subject of controversy. The reasons for this inconsistency and an experimental method for its avoidance have been offered and carried out (1, 2). Gold in the form of a rotating disk electrode (RDE) was used in the cathodic iron deposition investigation (2). It is suitable as a working electrode for such cathodic studies because of low value for the exchange current of the hydrogen evolution reaction (HER), which constitutes a big hindrance in such studies. Also on gold the iron deposition takes place in the Tafel range of the HER. Consequently the hydrogen ion concentration will be the same at the electrode surface as that in the bulk of the solution. This is very important because the kinetics of iron deposition is a function of the pH at the electrode surface.

Taking this dependence into consideration the kinetic data obtained on gold showed the existence of two reaction mechanisms. The noncatalyzed mechanism, first proposed by Bockris *et al.* (3), takes place in a pH range between 1.8-2.4 and the catalyzed one, initially proposed by Heusler *et al.* (4), between pH 3.3-3.8.

Beyond pH = 3.8, the hydrolysis products will interfere and below pH = 1.8, the HER is dominating to a great extent. The agreement between the kinetic data obtained on gold experimentally and those calculated theoretically is good.

Another feature in such studies may then arise when using platinum as a working electrode. One reason is that the exchange current of the HER on platinum is relatively high compared to that on gold and, second, the iron deposition will probably take place in the diffusion-controlled range of the HER. Consequently there will be an overlap between the activated-controlled iron deposition and the diffusion-controlled discharge of protons and HSO_4^--ions (5). This will lead to a pH difference between the electrode surface and the bulk of the solution. An insight in the characteristics of the iron deposition under such conditions may then be obtained.

Experimental

Solutions, cell, apparatus, and experimental procedure have been described in detail earlier (2). It remains here to mention that the working electrode is a rotating disk of platinum having a radius of 0.375 cm. The rotating speed was 4140 rpm. Evaluation of the results has been carried out only for the steady state, the current densities are referred to square centimeter and the potentials to normal hydrogen electrode. All experiments were carried out at 25°C.

The partial current densities for iron deposition were estimated by potentiostatic anodic stripping method, which is described elsewhere (2). The anodic stripping potential is 100-150 mV more positive then the corrosion potential. In this range practically the whole current is used for the anodic dissolution of iron, because the stripping potential is more negative than the equilibrium potential of the H_2/H^+-electrode in the same solution. This was confirmed by spectroscopic measurements.

Results

Figure 1 shows the behavior of the measured total current density, $i_{-,\,\text{total}}$, as a function of the electrode potential, ϵ, for different pH values of the solution between 1.8-3.8. It can be seen that there are three types of behavior. The first is represented by curves 1, 2, and 3 for solution pH = 1.8, 2.08, and 2.4, respectively, where the curves show at the beginning a gradual increase of the C.D. with potential. The second type is represented by the curves 4, 5, and 6 for solution pH = 3.3, 3.5, and 3.8, respectively, where the curves show at first an almost linear behavior followed by a sudden rise in C.D. before reaching a kind of plateau. The third type, represented by curves 7 and 8 for pH = 2.77 and 2.96, shows a behavior lying between the first two types. Here the curves show a gradual increase in C.D. over larger period of potential than the first group and the rise to the plateau is not as sudden as in the second one. As will be seen later, this rise is attributed to an increase in the absolute value of the partial current density (P.C.D.) of iron, $i_{-,\,Fe^{++}}$, as compared to that of hydrogen, $i_{-,\,H^+}$. It may also be noticed on Fig. 1 that at the very beginning of all the curves where $i_{-,\,Fe^{++}} \ll i_{-,\,H^+}$, a correlation between the HER and the pH of the solution may be observed, *i.e.*, $i_{-,\,\text{total}}$ decreases when the pH of the solution increases.

The P.C.D.'s for the discharge of iron and hydrogen were calculated using the results obtained from the potentiostatic anodic stripping method described in detail elsewhere (2).

* Electrochemical Society Active Member.

Key words: corrosion, iron deposition, charge transfer mechanism of iron, platinum substrate, rotating disk electrode.

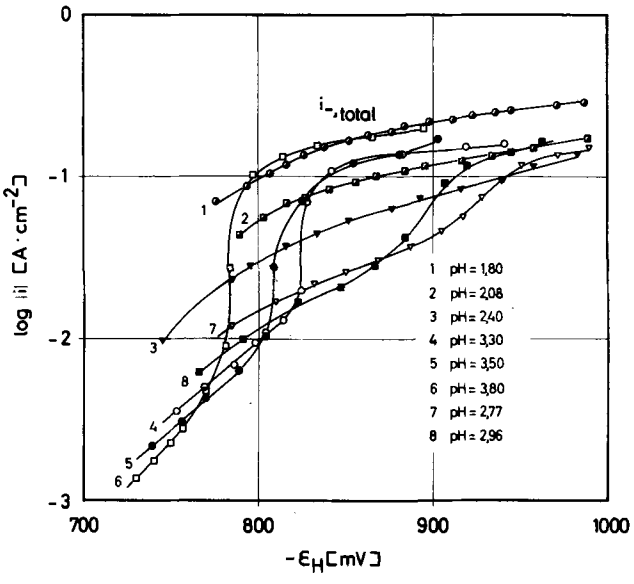

Fig. 1. Total current density-potential curves under potentiostatic steady-state conditions depending on the pH. Electrolyte: 0.1M $FeSO_4$ + 0.875M Na_2SO_4. Curve 1, pH = 1.8; curve 2, pH = 2.08; curve 3, pH = 2.4; curve 4, pH = 3.30; curve 5, pH = 3.5; curve 6, pH = 3.80; curve 7, pH = 2.77; curve 8, pH = 2.96 (T = 298°K).

Figure 2 shows the P.C.D.-potential curves $i_{-,Fe^{++}}$ and i_{-,H^+} *vs.* ϵ obtained from curves 1, 2, and 3 of Fig. 1. The charge transfer controlled iron deposition, as represented by Tafel lines, lies at the onset of the diffusion-controlled range of the HER, which means that the pH at the electrode surface is a function of the electrode potential and not equal to that in the bulk of the solution. The Tafel lines have a slope of $b_{-,Fe^{++}} = -85 \pm 3$ mV. The experimental results seem to show an increase of the P.C.D. of iron with the pH of the solution in the range of transport controlled HER. Possibly this effect is due to a powdery deposition of the metal (6). The resulting roughness of the electrode surface will lead to turbulent flow of the solution and hence an increase of the limiting diffusion current density (L.D.C.D.).

The P.C.D.'s $i_{-,Fe^{++}}$ and i_{-,H^+} obtained from curves 4, 5, and 6 of Fig. 1 are shown in Fig. 3. Here, as in the case of gold as a RDE discussed elsewhere, the ferrous ion discharge takes place mainly in the charge transfer controlled range of the HER. The slope of the Tafel lines of the HER has the expected value of $b_{-,H^+} = -115 \pm 5$ mV (7) whereas that for the ferrous ion discharge shows a value of $b_{-,Fe^{++}} = -36 \pm 4$ mV in agreement with earlier results obtained on gold (2). The sudden rise of the $i_{-,Fe^{++}}$ is due to nonstability of the pH at the electrode surface when the L.D.C.D. for the HER is reached. The scattering of the results for the HER in the L.D.C.D. region may be attributed to this behavior and possibly also the above-mentioned increase of roughness of the electrode surface. Contrary to the above-mentioned case for pH < 2.4 in Fig. 2, the deviation of the L.D.C.D. for iron discharge lies within the experimental error. Here, however, there is a decrease in the magnitude of L.D.C.D. with increasing negative potential. This behavior, which may be correlated to electron tunneling from the electrode surface and thereby decreasing the iron yield, is discussed thoroughly elsewhere (6, 8).

Figure 4 shows the P.C.D.'s obtained from curves 7 and 8 from Fig. 1. The slope of the Tafel line is $b_{-,Fe^{++}} = -56$ mV and -76 mV, respectively. It shows a systematic change between the two mentioned ranges. The change of $i_{-,Fe^{++}}$ from charge transfer to diffusion control takes place gradually and the magnitude of L.D.C.D. for the ferrous ion agrees satisfactorily with those from Fig. 3.

Figure 5 shows the logarithm of the partial current densities $i_{-,Fe^{++}}$ as a function of the pH of the solution at constant electrode potentials. From the slope one can get the electrochemical reaction orders related to the pH.

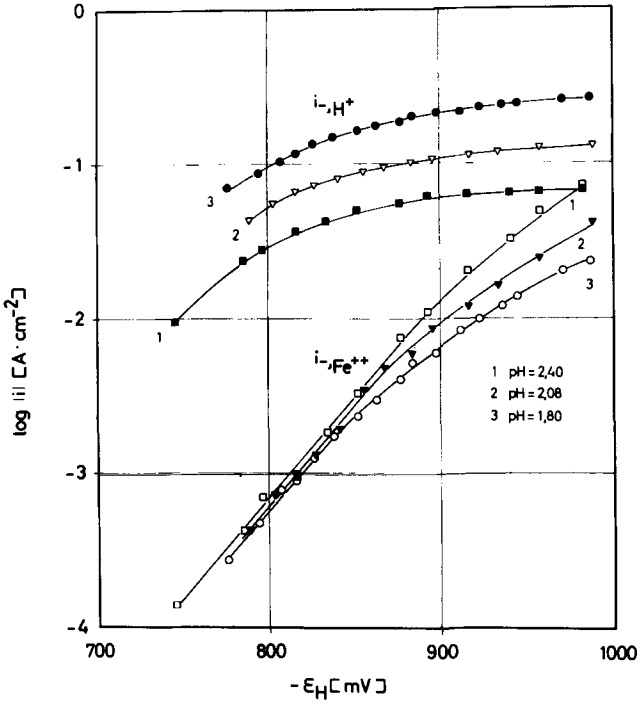

Fig. 2. Partial current density-potential curves under potentiostatic steady-state conditions depending on the pH. Electrolyte: 0.1M $FeSO_4$ + 0.875M Na_2SO_4. pH = 1.8. 2.08. 2.4 (T = 298°K)

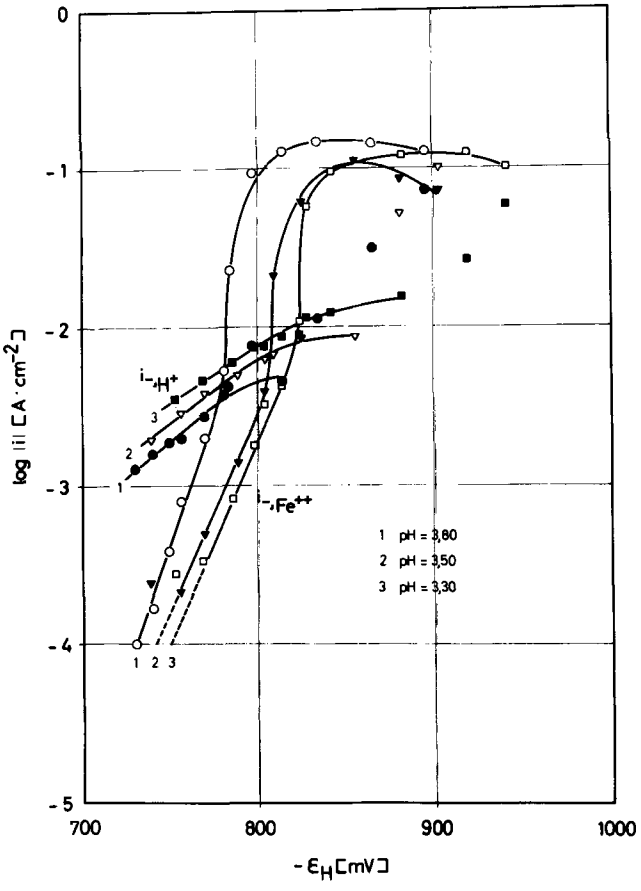

Fig. 3. Partial current density-potential curves under potentiostatic steady-state conditions depending on the pH. Electrolyte: 0.1M $FeSO_4$ + 0.875M Na_2SO_4. pH = 3.30, 3.5, 3.8 (T = 298°K).

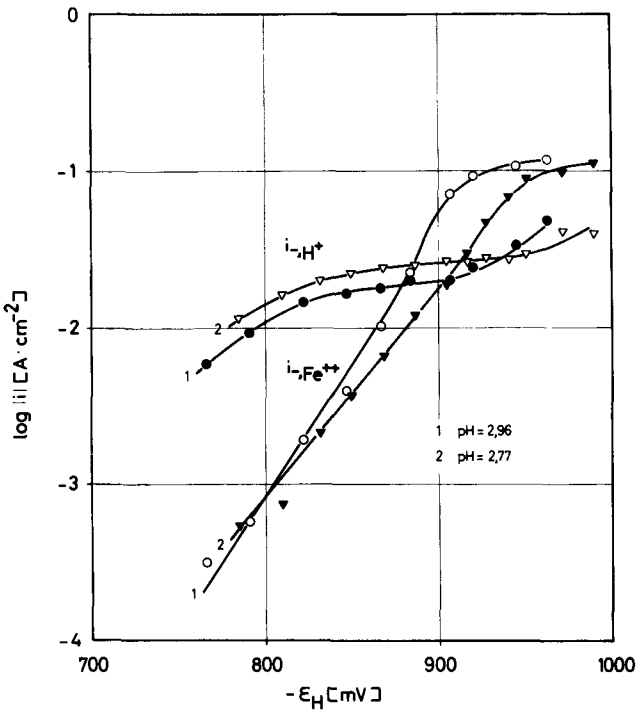

Fig 4. Partial current density-potential curves under potentiostatic steady-state conditions depending on the pH. Electrolyte: 0.1M $FeSO_4$ + 0.875M Na_2SO_4. pH = 2.77, 2.96 (T = 298°K).

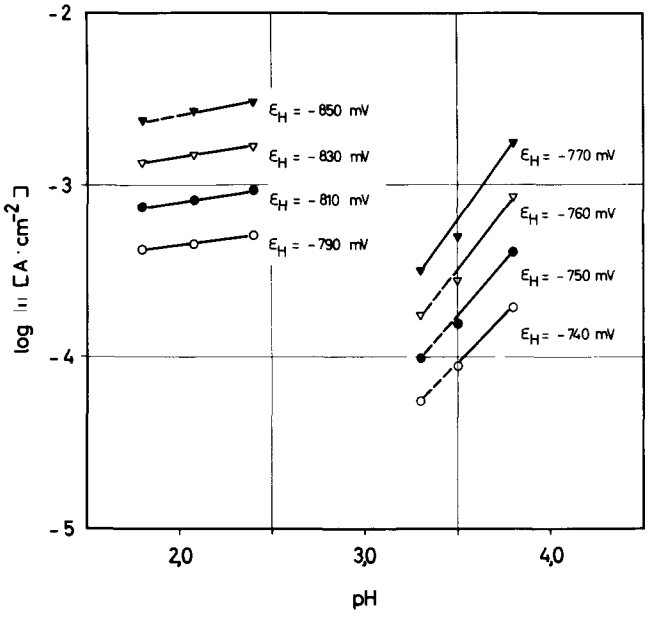

Fig. 5. Partial current densities $i_{-,Fe^{++}}$ as a function of pH for determination of the electrochemical reaction order of iron deposition related to pH. Electrolyte: 0.1M $FeSO_4$ + 0.875M Na_2SO_4 (T = 298°K).

For pH > 3.3, the value for $n_{-,pH} = 1.4 \pm 0.2$. For pH < 2.4 $n_{-,pH}$ has a value which deviates from zero in the positive direction, but is, however, too small to be determined accurately (about 0.17).

Discussion

It has been shown in Fig. 2 that for pH < 2.4, the ferrous ion discharge takes place at the onset of the L.D.C.D. of the HER. Consequently the concentration of protons in the double layer is decreasing, *i.e.*, the pH at the electrode surface is not constant, which must be taken into consideration in derivation of the kinetic equation.

The noncatalyzed mechanism (3) is given by the following sequence

$$Fe^{++}{}_{aq} + H_2O \rightleftharpoons FeOH^+ + H^+ \quad [1]$$

$$FeOH^+ + e^- \rightleftharpoons (FeOH)_{ads} \quad [2]$$

$$(FeOH)_{ads} + H^+ + e^- \rightleftharpoons Fe + H_2O \quad [3]$$

Steps [1] and [3] are fast reactions while step [2] is a slow one and hence the RDS. The current density-overvoltage relation for this mechanism is given by (1, 2)

$$i_{Fe^{++}} = 2\, i_{0,2} \left[\frac{A}{B} \exp\left(\frac{(1+\alpha_2)F\eta}{RT} \right) - C \exp\left(-\frac{(1-\alpha_2)F\eta}{RT} \right) \right] \quad [4]$$

where η is the total overvoltage.

The expressions for A, B, and C are

$$A = \frac{a_{Fe}}{\bar{a}_{Fe}} \cdot \frac{a_{H_2O}}{\bar{a}_{H_2O}}, \quad B = \frac{a_{H^+}}{\bar{a}_{H^+}}, \quad C = \frac{a_{FeOH^+}}{\bar{a}_{FeOH^+}}$$

The expression C can be replaced by the following terms according to the chemical equilibrium [1]

$$C = \frac{a_{Fe^{++}}}{\bar{a}_{Fe^{++}}} \cdot \frac{a_{H_2O}}{\bar{a}_{H_2O}} \cdot \frac{\bar{a}_{H^+}}{a_{H^+}} = D \cdot \frac{1}{B} \quad [5]$$

Under the condition[1]

$$a_i = \bar{a}_i$$

i.e., A, B, C, $D = 1$ then the overvoltage is only charge transfer overvoltage ($\eta = \eta_t$)

$$i_{Fe^{++}} = 2\, i_{0,2} \left[\exp\left(\frac{(1+\alpha_2)F\eta_t}{RT} \right) - \exp\left(-\frac{(1-\alpha_2)F\eta_t}{RT} \right) \right] \quad [6]$$

From Eq. [6] the Tafel slope for the cathodic process ($\eta << 0$) can be obtained

$$b_{-,Fe^{++}} = \left(\frac{\partial \eta_t}{\partial \log/i_{-,Fe^{++}}/} \right)_{a_i = \bar{a}_i} = -\frac{2.303\,RT}{(1-\alpha_2)F} = -118.3\ \text{mV} \quad [7]$$

with $\alpha_2 = 0.5$ and $T = 298$°K.

From Eq. [4] the electrochemical reaction orders related to the pH or to the activity of Fe^{++}-ions can be derived

$$n_{-,pH} = \left(\frac{\partial \log/i_{-,Fe^{++}}/}{\partial\, pH} \right)_{a_i,\,\epsilon} = +1 \quad [8]$$

$$n_{-,Fe^{++}} = \left(\frac{\partial \log/i_{-,Fe^{++}}/}{\partial \log a_{Fe^{++}}} \right)_{a_i,\,\epsilon} = +1 \quad [9]$$

Under the conditions

$$a_{Fe} = \bar{a}_{Fe}$$

$$a_{H_2O} = \bar{a}_{H_2O}$$

$$a_{Fe^{++}} = \bar{a}_{Fe^{++}}$$

$$a_{H^+} \neq \bar{a}_{H^+}$$

from Eq. [4] follows

$$i_{Fe^{++}} = 2\, i_{0,2} \left[\frac{1}{B} \exp\left(\frac{(1+\alpha_2)F\eta}{RT} \right) - \frac{1}{B} \exp\left(-\frac{(1-\alpha_2)F\eta}{RT} \right) \right] \quad [10]$$

[1] $\bar{a}_i$ = equilibrium activity of the species i at $\epsilon = \epsilon_0$.

The current density-overvoltage relation for the cathodic process ($\eta << 0$) is given by

$$i_{-,Fe^{++}} \cong -2\, i_{0,2} \cdot \frac{1}{B} \cdot \exp\left(-\frac{(1-\alpha_2)\mathbf{F}\eta}{RT}\right) \quad [11]$$

or

$$\eta = \frac{RT}{(1-\alpha_2)\mathbf{F}} (\ln 2\, i_{0,2} - \ln/i_{-,Fe^{++}}/ - \ln B) \quad [12]$$

For $a_{H^+} = \bar{a}_{H^+}$, *i.e.*, $B = 1$, it follows $\eta = \eta_t$ and from Eq. [12] the same Tafel slope as in Eq. [7] is obtained.

On the other hand for $B \neq 1$ the Tafel slope will be derived from Eq. [12] as follows

$$\left(\frac{\partial \log/i_{-,Fe^{++}}/}{\partial \eta}\right)_{a_i} = \frac{1}{b_-} = -\frac{(1-\alpha_2)\mathbf{F}}{2.303\,RT} - \left(\frac{\partial \log B}{\partial \eta}\right)_{a_i} \quad [13]$$

This will be the case, if the simultaneous HER is controlled by charge transfer and diffusion.

For the HER

$$H^+ + e^- \rightleftharpoons \frac{1}{2} H_2 \quad [14]$$

the current density-overvoltage relation for the cathodic process ($\eta << 0$) is given by

$$i_{-,H^+} \cong i_{0,H} \cdot B \exp\left(-\frac{(1-\alpha_H)\cdot \mathbf{F}\eta}{RT}\right) \quad [15]$$

or

$$\eta = \frac{RT}{(1-\alpha_H)\mathbf{F}} (\ln i_{0,H} - \ln/i_{-,H^+}/ + \ln B) \quad [16]$$

Only in a certain overvoltage range, where $B \neq 1$, *i.e.*, $\eta = \eta_t + \eta_d$ for the HER, then Eq. [13] shows that $b_{-,Fe^{++}}$ will be changed. Considering only the overpotential range for which $i_{-,H^+} = i_{-,L.D.C.,H^+} =$ constant the variation of B is given by

$$\left(\frac{\partial \log B}{\partial \eta}\right)_{a_i} = \frac{(1-\alpha_H)\mathbf{F}}{2.303\,RT} \quad [17]$$

Substituting Eq. [17] in Eq. [13] one gets the Tafel slope of the iron deposition reaction in this overvoltage range

$$b_{-,Fe^{++}} = -\frac{2.303\,RT}{(1-\alpha_2)\mathbf{F}} - \frac{2.303\,RT}{(1-\alpha_H)\mathbf{F}} \quad [18]$$

For $\alpha_\alpha = \alpha_H = 0.5$ and $T = 298°K$ then $b_{-,Fe^{++}} = -59.2$ mV.

The experimental results for pH < 2.4 showed that the measured range of the curves lies just at the onset of the diffusion-controlled range of the HER. Consequently, the contribution from the second term on the right side of Eq. [13] will be relatively small compared to the case when the L.D.C.D. of the HER is fully reached. Therefore the measured slope, $b_{-,Fe^{++}} = -85 \pm 3$ mV of the Tafel lines is between the calculated above, $b_{-,Fe^{++}} = -60$ mV and that for charge transfer controlled HER, $b_{-,Fe^{++}} = -120$ mV (2). Also the fact that the determination of the electrochemical reaction order $n_{-,pH}$ in this pH range is rather difficult may be considered as a confirmation for the difference between the electrode surface pH and that in the bulk of the solution.

The catalyzed reaction mechanism which is supposed to explain the results of pH > 3.3 is given by (1, 2)

$$Fe^{++}{}_{aq} + H_2O \rightleftharpoons FeOH^+ + H^+ \quad [1]$$

$$[Fe(FeOH)] + FeOH^+ + 2e^- \rightleftharpoons [Fe(FeOH)] + Fe + OH^- \quad [19]$$

and the parallel reaction to [19]

$$Fe + FeOH^+ + e^- \rightleftharpoons [Fe(FeOH)] \quad [20]$$

The current density-overvoltage equation under steady-state conditions for this mechanism, taking into consideration that step [19] is the RDS is given by (1, 2)

$$i_{Fe^{++}} = i_{0,19}\left[\frac{a_K}{\bar{a}_K} \cdot \frac{A}{B} \cdot \exp\left(\frac{2\alpha_{19}\mathbf{F}\eta}{RT}\right) - \frac{a_K}{\bar{a}_K} \cdot C \exp\left(-\frac{2(1-\alpha_{19})\mathbf{F}\eta}{RT}\right)\right] \quad [21]$$

with K = [Fe(FeOH)].

For $\eta << 0$ one can write

$$i_{-,Fe^{++}} \cong -i_{0,19} \cdot \frac{a_K}{\bar{a}_K} \cdot C \exp\left(-\frac{2(1-\alpha_{19})\mathbf{F}\eta}{RT}\right) \quad [22]$$

Under steady-state conditions

$$\frac{da_K}{dt} = -\frac{i_{20}}{z_{20}\cdot \mathbf{F}} = 0 \quad [23]$$

The expression for i_{20} is

$$i_{20} = i_{0,20}\left[\frac{a_K}{\bar{a}_K} \exp\left(\frac{\alpha_{20}\mathbf{F}\eta}{RT}\right) - \frac{a_{Fe}}{\bar{a}_{Fe}} \cdot C \cdot \exp\left(-\frac{(1-\alpha_{20})\mathbf{F}\eta}{RT}\right)\right] \quad [24]$$

From Eq. [23] and [24] using [5] one can write

$$\frac{a_K}{\bar{a}_K} = \frac{D}{B} \cdot \frac{a_{Fe}}{\bar{a}_{Fe}} \exp\left(-\frac{\mathbf{F}\eta}{RT}\right) \quad [25]$$

Substituting [25] into [22] one gets

$$i_{-,Fe^{++}} \cong -i_{0,19} \cdot \frac{a_{Fe}}{\bar{a}_{Fe}} \cdot \left(\frac{D}{B}\right)^2 \cdot \exp\left(-\frac{[1+2(1-\alpha_{19})]\mathbf{F}\eta}{RT}\right) \quad [26]$$

From [26] one derives the following kinetic data

$$b_{-,Fe^{++}} = \left(\frac{\partial \eta_t}{\partial \log |i_{-,Fe^{++}}|}\right)_{a_i = \bar{a}_i} = -\frac{2.303\,RT}{[1+2(1-\alpha_{19})]\mathbf{F}} = -29.6 \text{ mV} \quad [27]$$

with $\alpha_{19} = 0.5$ and T = 298°K, furthermore

$$n_{-,pH} = \left(\frac{\partial \log |i_{-,Fe^{++}}|}{\partial\, pH}\right)_{a_i,\epsilon} = +2 \quad [28]$$

$$n_{-,Fe^{++}} = \left(\frac{\partial \log |i_{-,Fe^{++}}|}{\partial \log a_{Fe^{++}}}\right)_{a_i,\epsilon} = +2 \quad [29]$$

Following the same procedure as above in the case of the pH at the electrode surface not being constant, for the Tafel slope $b_{-,Fe^{++}} = -20$ mV when putting $\alpha_{19} = \alpha_H = 0.5$ at $T = 298°K$. Assuming, however, that the pH is constant at the electrode surface, which is the case when the ferrous ion discharge takes place in the charge transfer controlled range of the HER, then the Tafel slope according to Eq. [27] is found.

The agreement is satisfactory between the measured Tafel slopes and the calculated value based on the last assumption. From Fig. 5 follows an electrochemical reaction order related to the pH of $n_{-,pH} = +1.4 \pm 0.2$. This value is not in good agreement with the calculated one according to Eq. [28]. The deviation is possibly due to the fact, that the absolute value of measured slope for the Tafel lines is somewhat higher than the theoretical one, which may be attributed to an $\alpha_{19} \neq 0.5$. However, the experimental value $n_{-,pH}$ is not

equal to one, which may then correspond to the non-catalyzed mechanism. Therefore the measured Tafel slopes as well as the determined electrochemical reaction order related to the pH indicate the existence of the catalyzed mechanism.

Conclusions

The comparison between the results obtained in this work and those in the previous one (2) shows

1. The substrate of the working electrode (gold or platinum) has obviously no influence on the mechanisms of the iron deposition reactions themselves.
2. On the contrary the substrate influences the HER, because the exchange current density of the hydrogen electrode is much greater on platinum than on gold or iron. Therefore in the case of platinum electrode at pH < 2,4 the HER is partially controlled by diffusion in the potential range of iron deposition.
3. Consequently the simultaneous deposition of iron and evolution of hydrogen lead in the case of platinum at pH < 2.4 to an increase of pH at the electrode surface. This does not change the iron deposition mechanism, however, the measurable electrochemical kinetic data will be changed.
4. Under our measuring technique (2) in the case of platinum at pH < 2.4 the electrode coverage with iron is apparently incomplete under steady-state conditions. The measured iron efficiency values are very small in this range, *i.e.*, $|i_{-,Fe^{++}}| << |i_{-,H^{++}}|$.

Acknowledgment

The authors are indebted to Mrs. Burger for helping in the experimental work. They also acknowledge gratefully substantial financial support by the Deutsche Forschungsgemeinschaft and the Bundeswirtschaftsministerium of the BRD.

Manuscript submitted Nov. 29, 1971; revised manuscript received Aug. 1, 1972.

Any discussion of this paper will appear in a Discussion Section to be published in the December 1973 JOURNAL.

REFERENCES

1. F. Hilbert, Y. Miyoshi, G. Eichkorn, and W. J. Lorenz, *This Journal*, **118**, 1919 (1971).
2. F. Hilbert, Y. Miyoshi, G. Eichkorn, and W. J. Lorenz, *ibid.*, **118**, 1927 (1971).
3. J. O'M. Bockris, D. Drazic, and A. R. Despic, *Electrochim. Acta*, **4**, 325 (1961).
4. K. F. Bonhoeffer and K. E. Heusler, *Z. Phys. Chem. NF.*, **8**, 390 (1956); K. E. Heusler, Habilitationsschrift TH Stuttgart (1966).
5. Y. Miyoshi and W. J. Lorenz, *Ber. Bunsenges, Phys. Chem.*, **74**, 412 (1970).
6. F. Hilbert and N. A. Darwish, *Monatsh. Chem.*, **102**, 498 (1971).
7. K. J. Vetter, "Electrochemical Kinetics," Academic Press, New York, London (1967).
8. F. Hilbert, A. A. El. Miligy, and W. J. Lorenz, "Electron Tunneling and Cathodic Metal Deposition," Lecture, 1st International Summer School on Quantum Mechanical Aspects of Electrochemistry, Ohrid/Yugoslavia, 1971.

Technical Notes

The Triangular Voltage Sweep Method for Determining Double-Layer Capacity of Porous Electrodes

Part I. Theory

L. G. Austin*,[1] and E. G. Gagnon*,[2]

Material Sciences Department, The Pennsylvania State University, University Park, Pennsylvania 16802

Scientific analysis of the behavior of porous battery electrodes is greatly aided by a knowledge of the electrochemically active area of the electrode. The measurement of double-layer capacity in concentrated electrolytes is the most direct measurement of the electrode area in contact with electrolyte. If the double-layer capacity of an electrode is compared to that of a known, smooth area of the same material, a relative measure of area is obtained. The capacitance per unit area (1) for clean negatively charged metal surfaces is 15-20 $\mu F/cm^2$, and for positively charged surfaces is 30-40 $\mu F/cm^2$. In general, this comparison is best made under the same conditions of electrolyte concentration, voltage, temperature, etc. However, a major problem in the measurement of double-layer capacity for porous electrodes is the effect of distributed capacity. Ohmic resistance in electrolyte in the pores has the effect of making it easier for the mouth of the pore to charge, or discharge, while the back of the pore lags behind (2). Another problem is to eliminate or allow for faradaic current, which is often caused by processes which are complex and difficult to describe mathematically, such as the removal of impurities at an electrode or the adsorption of species present in the electrolyte.

A number of cases have been treated by Posey and Morozumi (3), but they do not treat the case of linear or triangular voltage sweep in the presence of a significant external *IR* drop. It will be shown that this is a particularly useful technique since it enables an approximate correction to be made for faradaic current. Johnson and Newman (4) have formulated general

* Electrochemical Society Active Member.
[1] Present address: Department of Chemical Engineering, The University of Natal, Durban, Republic of South Africa.
[2] Present address: Electrochemistry Department, Research Laboratories, General Motors Corporation, Warren, Michigan 48090.
Key words: double-layer capacity, porous electrodes, voltammetry.

mass and current balances, but the equations are too complex to be of use for simple double-layer capacity measurement; when reduced for the case considered here, their expressions lead to our starting equation.

Physical Model and Assumptions

Consider the physical situation illustrated in Fig. 1, where a Luggin capillary is positioned a distance, d, from the surface of a porous electrode having a thickness, L. Only one face of the electrode is exposed to the electrolyte to ensure uniform current through the face. It is assumed that the porous system is so highly interlinked that the concentration of species dissolved in the electrolyte flooding the pores of the electrode is constant over plane x in the electrode. Similarly, the electrode potential is constant over plane x. It is further assumed that the potential gradients are one-dimensional (along x), which is true when the thickness, L, of the electrode is much greater than the pore diameters (10 to 20 times). It is assumed that the electronic conductivity of the electrode material is large compared to the ionic conductivity of the electrolyte within the pores, so that the absolute potential of the electrode material is constant along x. The electrolyte is assumed to be concentrated, so that diffuse double-layer effects are negligible. In the absence of faradaic current, there are no changes of concentration of species along x. These assumptions are reasonable for many cases of practical interest.

Theory

The differential equation (2, 3) governing the distribution of potential in one-dimensional porous electrodes with the above assumptions is given by

$$\partial V(x,t)/\partial t = (L/\rho C)\,(\partial^2 V(x,t)/\partial x^2) \qquad [1]$$

L is the thickness of the electrode (cm); ρ is the effective resistance of the electrolyte in the porous system of the electrode (ohm-cm); C is the double-layer capacity per unit external, plane area of electrode (farads/cm^2); $V(x,t)$ is electrode-electrolyte potential at position x (volts). (If the true double-layer per unit surface area is c, and the specific surface area is a, then $C = caL$.) At $t > 0$, the current density through the face at L is i, and $i = i(L,t) = (1/\rho)[\partial V(x,t)/\partial x]_{x=L}$.

When a linearly increasing voltage is applied from rest conditions, the initial condition is $V(x,0) =$ constant $= V_0$, and the boundary condition is $V_m = kt + V_0$. The resistance, R_e, between test electrode and reference tip includes that of the electrolyte between the face of the electrode and the tip (see Fig. 1), and $V_s = V_m - iR_eA$, where A is the plane area of the electrode. Then

$$i = (1/\rho)[\partial V(x,t)/\partial x]_{x=L} = (V_m - V_s)/R_eA$$

or

$$[\partial V(x,t)/\partial x]_{x=L} + h(V_s - V_m) = 0$$

where

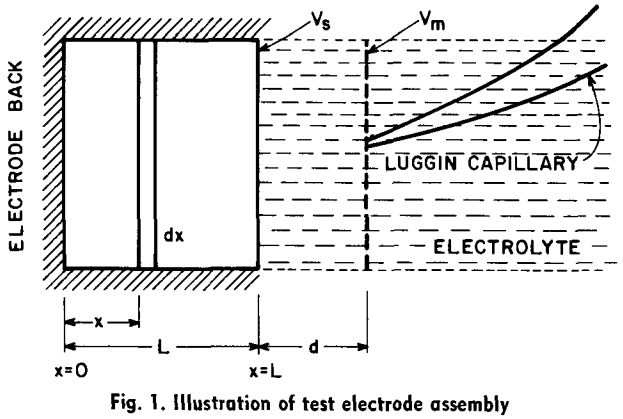

Fig. 1. Illustration of test electrode assembly

$$h = \rho/R_eA \qquad [2]$$

The effective specific resistance is $\rho = \lambda\rho_{free}$, where λ is the labyrinth factor. If R_e is due mainly to the electrolyte path of length d between test-Luggin tip, $R_eA = \rho_{free}d$, and $h = \lambda/d$.

The solution of Eq. [1] for these conditions (5) is

$$V(x,t) - V_0 = kt - \frac{k[h(L^2 - x^2) + 2L]}{2h(L/\rho C)} + \frac{2hk}{(L/\rho C)}\sum_{n=1}^{\infty}\frac{\exp(-tL\alpha_n^2/\rho C)\cos\alpha_n x}{\alpha_n^2[(h^2 + \alpha_n^2)L + h]\cos\alpha_n L} \qquad [3]$$

where α_n values are the positive roots of $\alpha_n\tan(\alpha_n L) = h$. Hence

$$i = i(L,t) = \beta kC \qquad [4]$$

where

$$\beta = 1 - \sum_{n=1}^{\infty}\exp\left(-\frac{t}{\rho CL}m_n^2\right)\cdot\left[\frac{2\psi^2}{m_n^2[\psi^2 + m_n^2 + \psi]}\right] \qquad [4a]$$

with

$$m_n = L\alpha_n$$
$$m_n\tan m_n = \psi$$
$$\psi = Lh = L\rho/R_eA$$

The values of β *vs.* $t/\rho CL$ as a function of ψ (calculated by digital computation) are given in Fig. 2. It is readily shown (6) that Eq. [4] reduces to the well-known result

$$i = kC[1 - \exp(-t/R_eC)] \qquad [5]$$

for ψ small, that is, a very thin electrode and to

$$i = kC - \frac{8kC}{\pi^2}\sum_{n=0}^{\infty}\frac{(-1)^n}{(2n+1)^2}\cdot\exp\left(\frac{-(2n+1)^2}{4}\pi^2\frac{t}{\rho CL}\right)\left(\sin\left(\frac{2n+1}{2}\right)\pi\right) \qquad [6]$$

for ψ large, that is, R_e small, the case similarly treated by Posey and Morozumi (3).

If the direction of voltage scan is sharply reversed at some voltage, that is, a triangular voltage pulse is used, the general solution to the following voltage-distance-time curve is complex (7), and is obtained from

$$V_m(t_1) - V(x,t) = u(x,t) + w(x,t)$$

where $V_m(t_1)$ is the controlled potential at the Luggin tip at the time t_1 of voltage reversal, t is time measured from t_1 and

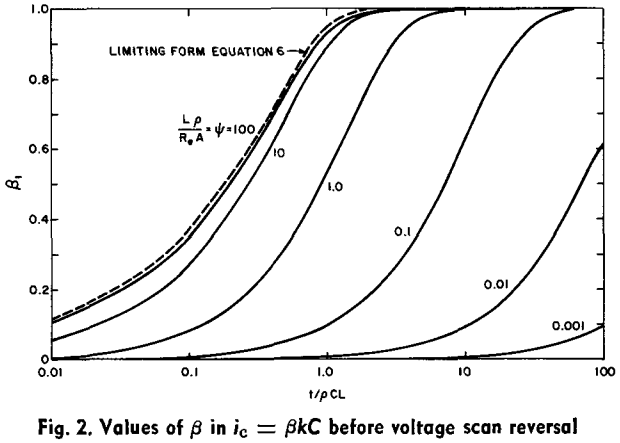

Fig. 2. Values of β in $i_c = \beta kC$ before voltage scan reversal

$$w(x,t) = kt - \frac{k[h(L^2 - x^2) + 2L]}{2h(L/\rho C)} + \frac{2hk}{(L/\rho C)} \sum_{n=1}^{\infty} \frac{\exp(-tL\alpha_n^2/\rho C)\cos \alpha_n x}{\alpha_n^2[(h^2 + \alpha_n^2)L + h]\cos \alpha_n L}$$

$$u(x,t) = 2 \sum_{n=1}^{\infty} \exp(-k\alpha_n^2 t) \cdot \frac{h^2 + \alpha_n^2}{(\alpha_n^2 + h^2)L + h} \cos \alpha_n x \int_0^L f(x)\cos \alpha_n x dx$$

with

$$f(x) = V_m(t_1) - V(x,t_1) = (kt_1 + V_0) - V(x,t_1) = \frac{k[h(L^2 - x^2) + 2L]}{2h(L/\rho C)} - \frac{2hk}{(L/\rho C)} \sum_{n=1}^{\infty} \frac{\exp(-tL\alpha_n^2/\rho C)\cos \alpha_n x}{\alpha_n^2[(h^2 + \alpha_n^2)L + h]\cos \alpha_n L}$$

This general solution is considerably simplified when the initial voltage sweep is maintained long enough for the summation term in Eq. [3] to become negligible ($\beta \rightarrow 1$), giving the voltage distribution through the electrode at time t_1 as

$$f(x) = \frac{k[h(L^2 - x^2) + 2L]}{2h(L/\rho C)}$$

Then, it can be shown that

$$i = i(L,t) = \gamma kC \qquad [7]$$

$$\gamma = \beta_1 - \beta_2$$

where β_1 is obtained from Eq. [4a] and

$$\beta_2 = \sum_{n=1}^{\infty} \exp\left(-m_n^2 \frac{t}{\rho CL}\right)\left(\frac{\psi^2 + m_n^2}{m_n^2 + \psi^2 + \psi}\right) \cdot \left(\frac{2}{m_n^2}\right) \sin^2 m_n \qquad [7a]$$

The limits for long time are $\beta_1 = 1$, $\beta_2 = 0$, and for zero time, $\beta_1 = 0$, $\beta_2 = 1$; so after voltage gradient reversal the current goes from kC at $t = 0$ to $-kC$ at long time. Values for γ are shown in Fig. 3, again as a function of $t/\rho CL$ and ψ.

Discussion

Figure 4 illustrates a typical set of values. It is clear that in the absence of faradaic current it is easy to determine C from an experimental result of this form, using the constant values of i. In addition, by matching the experimental values of β *vs.* time against the theoretical results of Fig. 2, it is possible to estimate the best value of the unknown, ρ. Then, since

$$\rho = \rho_{free}\lambda \qquad [8]$$

the labyrinth factor λ can be calculated. Alternatively, knowing rough estimates of the parameters it is possible from Fig. 2 to estimate the time at which β tends to one, t_1 say, and hence determine the sweep rate necessary to obtain C from constant i values for a given voltage excursion, ΔV

$$k = \Delta V/t_1 \qquad [9]$$

Part II of this paper will show that there is good agreement between theory and experiment, in the absence of faradaic current.

On the other hand, it is commonly observed that the current does not always reach a truly horizontal value (Fig. 5) due to faradaic current which increases as the voltage scans from the zero-current starting point. Such faradaic current rarely behaves as if an ideal faradaic resistance were present. This makes it impossible to determine C from a horizontal portion, just as it would be impossible to determine it from a galvanostatic test which did not give a linear V-t curve after some time. However, the triangular voltage sweep enables an estimate of C to be made, as follows.

At the point at which the voltage gradient reverses, the faradaic current is about the same before and just after the reversal. Thus, if i_f is not too large compared to i_c

$$i_1 = i_f + kC$$
$$i_2 \approx (-\gamma)kC - i_f$$

and

$$i_1 + i_2 \approx kC(1 - \gamma) \qquad [10]$$

from which C can be estimated by a trial and error matching of the experimental results with the theoretical values. A trial estimate of C is made as shown in Fig. 5, and by comparing the results with Fig. 2 a value of ψ can also be estimated. Assuming that a small faradaic current does not change Fig. 3 much, the

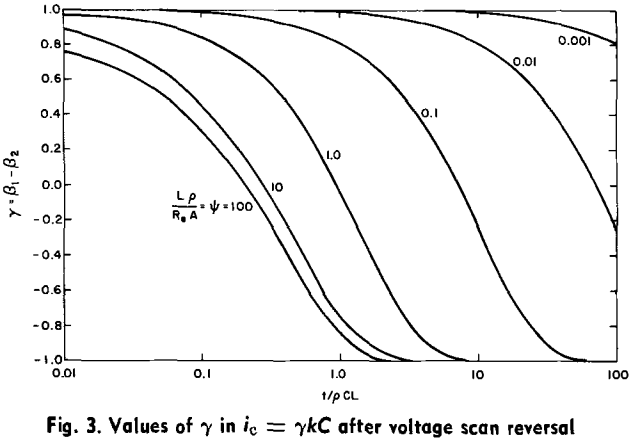

Fig. 3. Values of γ in $i_c = \gamma kC$ after voltage scan reversal

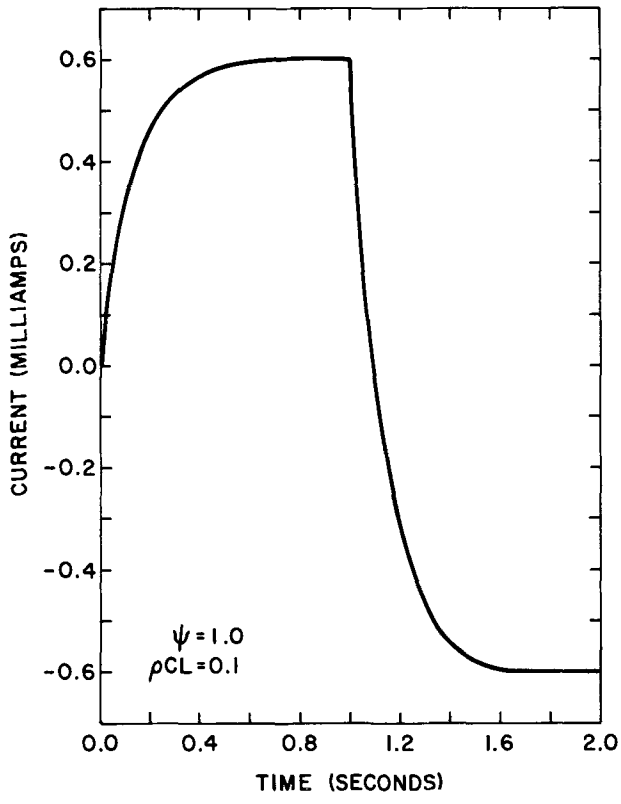

Fig. 4. Example of variation of capacitive current with time [$A = 0.3$ cm^2, $L = 0.05$, $\lambda = 2$, $d = 0.1$ cm, $\rho_{free} = 20$ ohm cm, $C = 0.05$ farads/cm^2, $k = 40$ mV/sec.

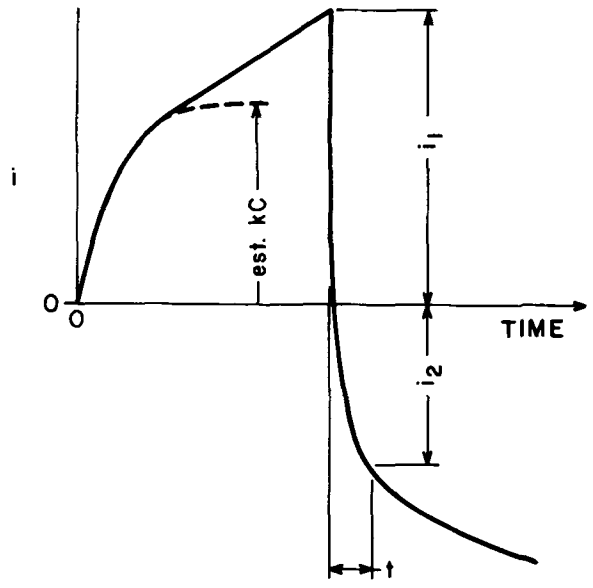

Fig. 5. Illustration of i/t result for triangular voltage sweep in presence of faradaic current.

value of γ at t_2 is estimated, and a second estimate of C made using Eq. [10], and so on.

It will be shown in a later publication that these techniques work well when the faradaic current at the point of reversal is not too large compared to the capacitive current. Often this can be achieved experimentally by keeping the voltage excursions small. It will not, of course, eliminate a reversible pseudocapacity due to a reversible build-up/removal of species on the surface, $S + R^+ + e^- \rightleftarrows S[R]$, since faradaic current due to a reversible process of this kind will reverse as the voltage gradient reverses.

Acknowledgment

We gratefully acknowledge the financial support of the National Science Foundation for this work.

Manuscript submitted July 25, 1972; revised manuscript received Oct. 10, 1972.

Any discussion of this paper will appear in a Discussion Section to be published in the December 1973 JOURNAL.

REFERENCES

1. A. N. Frumkin, in "Advances in Electrochemistry and Electrochemical Engineering," Vol. 1, P. Delahay, Editor, p. 65, Interscience Publishers, Inc., New York (1961).
2. L. G. Austin, Fuel Cells, NASA SP-120, Washington, D. C. (1967).
3. F. A. Posey and T. Morozumi, *This Journal*, **113**, 177 (1966).
4. A. M. Johnson and J. Newman, *ibid.*, **118**, 510 (1971).
5. H. S. Carslaw and J. C. Jaeger, "Conduction of Heat in Solids," p. 127, 2nd ed., Oxford University Press (1959).
6. E. G. Gagnon, Ph.D. Thesis, The Pennsylvania State University, University Park, Pa. (1970); and HDL-065-4, Contract No. DAAG 39-67-C-0065, U.S. Army Materiel Command, Harry Diamond Laboratories, Washington, D. C. (1971).
7. H. S. Carslaw and J. C. Jaeger, "Conduction of Heat in Solids," p. 120, 2nd ed., Oxford University Press (1959).

Influence of Steric Effects upon Redox Potentials of Cyanine Dyes

Tadaaki Tani

Research Laboratories, Ashigara, Fuji Photo Film Company, Minami-ashigara, Kanagawa, Japan

In earlier reports (1, 2) it has been indicated that the lowest vacant electronic energy levels ϵ_{lv} and the highest occupied ones ϵ_{ho} of simple cyanine dyes calculated by Hückel-approximation molecular orbital (HMO) method can be related to their reduction potentials E_{red}, oxidation potentials E_{ox}, excitation energies E_{ex} by the following equations

$$\epsilon_{lv} = -E_{red} + C \quad [1]$$

$$\epsilon_{ho} = -E_{ox} + C' \quad [2]$$

$$\epsilon_{lv} - \epsilon_{ho} = E_{ex} = \frac{hc}{\lambda_{max}} \quad [3]$$

where λ_{max} is the wavelength of maximum absorption of a dye, and C and C' are electrochemical constants.

Although some steric effects are thought to exist in monomethine cyanine dyes, they are not amenable to the HMO treatment (1). In this paper, rather strict comparison has been made between the calculated and experimental values of simple cyanine dyes with various methine chain lengths in terms of Eq. [1]-[3], in order to obtain knowledge of the influence of steric effects upon the electronic structures of the cyanine dyes. The cyanine dyes studied are as follows

Key words: steric effect, redox potential, cyanine dye.

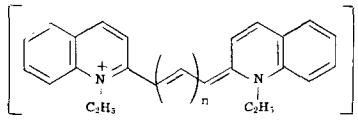

n = 0; 2,2′-quinocyanine ($2Q_0$)
n = 1; 2,2′-quinocarbocyanine ($2Q_1$)
n = 2; 2,2′-quinodicarbocyanine ($2Q_2$)
n = 3; 2,2′-quinotricarbocyanine ($2Q_3$)

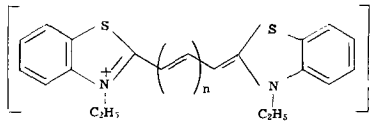

n = 0; thiacyanine (S_0)
n = 1; thiacarbocyanine (S_1)
n = 2; thiadicarbocyanine (S_2)
n = 3; thiatricarbocyanine (S_3)
n = 4; thiatetracarbocyanine (S_4)
n = 5; thiapentacarbocyanine (S_5)

The experimental and calculated values of these dyes were already reported (1-5).

Figure 1 shows the relations between reduction potentials and the lowest vacant electronic energy levels, and between oxidation potentials and the highest occupied levels of these dyes. As shown in this figure, the

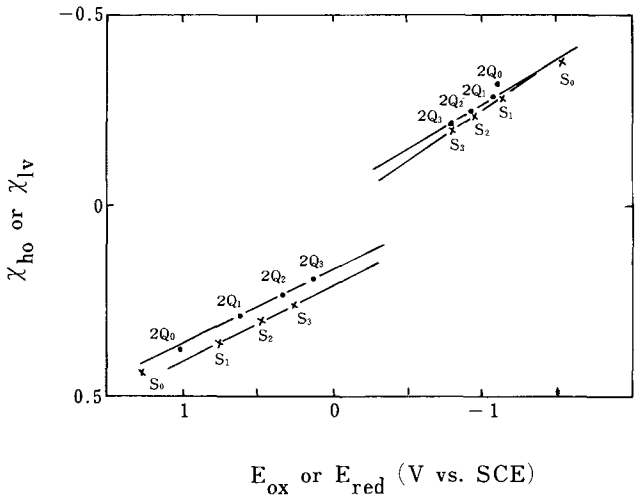

Fig. 1. The relation between the calculated electronic-energy levels and the observed redox potentials of simple cyanine dyes. χ_{ho} and χ_{lv} are $(\epsilon_{ho} - \alpha)/\beta$ and $(\epsilon_{lv} - \alpha)/\beta$, respectively.

observed reduction potential of 2,2′-quinocyanine is more positive, and that of thiacyanine is more negative than expected by the HMO method. On the other hand, the observed oxidation potential of 2,2′-quinocyanine is more negative, and that of thiacyanine is more positive than expected by the HMO method.

Figure 2 shows the relation of the observed excitation energies with the magnitude of the calculated energy gap between the lowest vacant and the highest occupied electronic energy levels of these dyes. The observed excitation energy of 2,2′-quinocyanine is

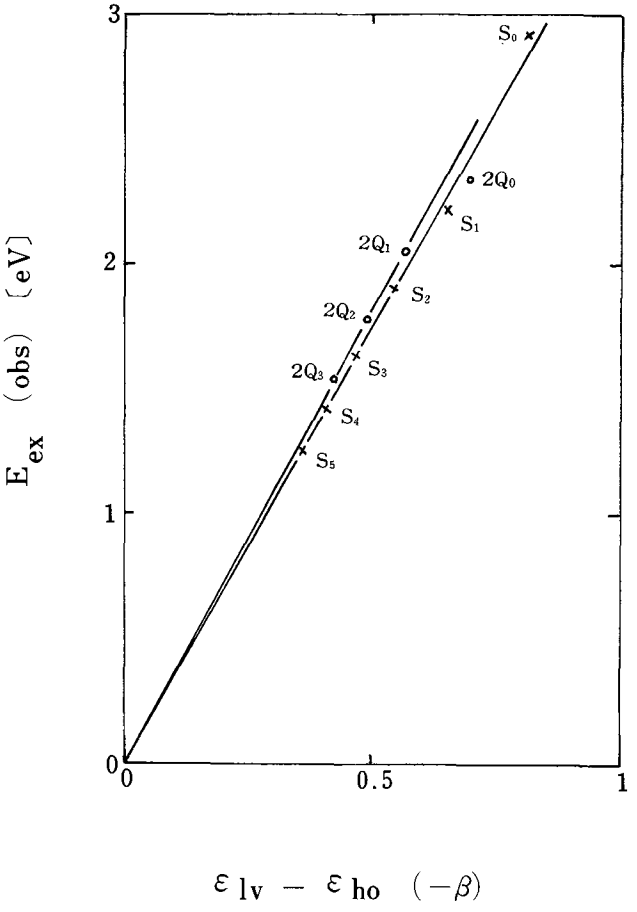

Fig. 2. The relation between the observed excitation energies and the magnitude of the calculated energy gap between the lowest vacant and the highest occupied electronic-energy levels of simple cyanine dyes.

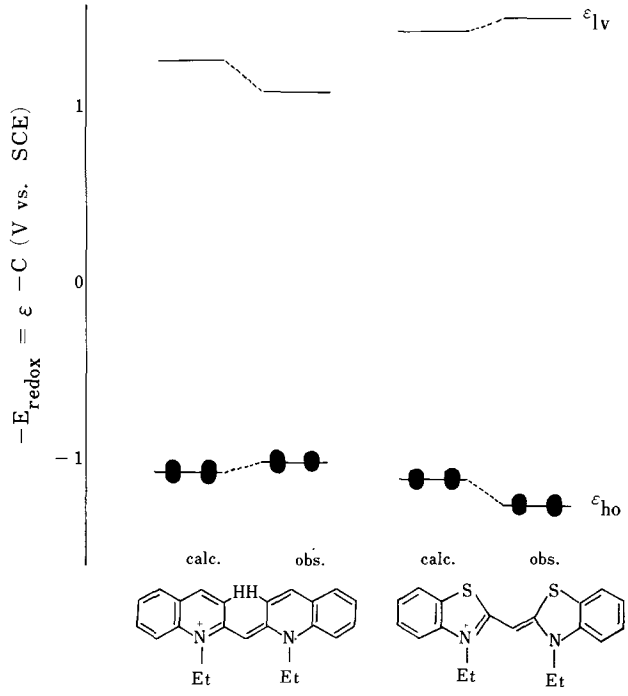

Fig. 3. The electronic-energy level diagram of 2,2′-quinocyanine and thiacyanine calculated by the HMO method and estimated by the experimental data, in terms of redox potentials.

smaller, and that of thiacyanine is larger than expected by the HMO method. This result is thought consistent with the results shown in Fig. 1, under the light of Eq. [1]-[3].

These results are thought to suggest the existence of some steric effects in 2,2′-quinocyanine and thiacyanine. Figure 3 shows the electronic-energy levels of these dyes given by the HMO calculation and their reported redox (reduction and oxidation) potentials. It is thought that the calculated electronic-energy levels correspond to those of the dyes in the absence of the steric effects, and the energy levels estimated from the experimental data correspond to those in the presence of the steric effects.

According to the x-ray diffraction analysis by Dammeier and Hoppe (6), and by Nakatsu and co-workers (7), a 2,2′-quinocyanine molecule is nonplanar, owing to its intramolecular steric hindrance (the hindrance between hydrogen atoms at 3 and 3′ positions). Since the highest occupied level was bonding, and the lowest vacant one was antibonding, according to the HMO method, the nonplanarity of this dye is expected to cause the unstabilization of its highest occupied level, and to cause its stabilization of the lowest vacant one. This view is consistent with the results shown in Fig. 1-3.

According to Nakatsu and co-workers (8), a thiacyanine molecule is planar, and the distance between sulfur atoms in the molecule is 2.994Å, being smaller than the sum of the van der Waals' radii of two sulfur atoms (*ca.* 3.7Å). This fact suggests the existence of the interaction of electronic orbitals between two sulfur atoms in the molecule. Since it was suggested from the HMO method that the molecular orbital interaction between the two sulfur atoms in the molecule was bonding at the highest occupied level, and antibonding at the lowest vacant one, the interaction is thought to cause the stabilization of the highest occupied level, and to cause the unstabilization of the lowest vacant one. This view is consistent with the results shown in Fig. 1-3.

Manuscript received June 26, 1972.

Any discussion of this paper will appear in a Discussion Section to be published in the December 1973 JOURNAL.

REFERENCES
1. T. Tani and S. Kikuchi, *Phot. Sci. Eng.*, **11**, 129 (1967).
2. T. Tani, K. Honda, and S. Kikuchi, *J. Electrochem. Soc. Japan*, **37**, 17 (1969).
3. A. Stanienda, *Z. Wiss. Photo.*, **59**, 76 (1965).
4. A. Stanienda, *Naturwissenschaften*, **47**, 353 (1960).
5. A. Stanienda, *Z. Physik. Chem. N. F.*, **33**, 170 (1962).
6. B. Dammeier and W. Hoppe, *Acta Cryst.*, **B27**, 2364 (1971).
7. H. Yoshioka and K. Nakatsu, *Chem. Phys. Letters*, **11**, 255 (1971).
8. K. Nakatsu, H. Yoshioka, and T. Aoki, *Chemistry Letters*, 339 (1972).

The Error in Measurements of Electrode Kinetics Caused by Nonuniform Ohmic-Potential Drop to a Disk Electrode

William H. Tiedemann*

Energy and Kinetics Department, School of Engineering and Applied Science, University of California, Los Angeles, California 90024

John Newman*

Inorganic Materials Research Division, Lawrence Berkeley Laboratory, and Department of Chemical Engineering, University of California, Berkeley, California 94720

and Douglas N. Bennion*

Energy and Kinetics Department, School of Engineering and Applied Science, University of California, Los Angeles, California 90024

Newman, in his treatment of the current distribution on a rotating disk electrode (1,2), has implied that the nonuniform ohmic, potential drop will lead to errors in the determination of kinetic parameters unless special corrections are applied. Because the error will be relatively larger for high exchange-current densities and low solution conductivities, linear electrode kinetics have been chosen to assess the magnitude of the effect. The complexity of the results is simplified by restricting the analysis to the same geometry—a disk electrode of radius r_0 in a large insulating plane, with the counterelectrode at infinity—and ignoring concentration variations. The apparent surface overpotential is taken to be that measured by a reference electrode, with the ohmic-potential drop being determined by interruption of the current. Three particular reference-electrode positions are used to illustrate the effect. The results are qualitatively applicable for other electrode geometries afflicted with a similar nonuniform ohmic potential drop.

Analysis

The potential in solution outside the doublelayer, in the absence of concentration variations, satisfies Laplace's equation

$$\frac{\partial}{\partial \xi}\left[(1+\xi^2)\frac{\partial \Phi}{\partial \xi} \right] + \frac{\partial}{\partial \eta}\left[(1-\eta^2)\frac{\partial \Phi}{\partial \eta} \right] = 0 \quad [1]$$

where the rotational elliptic coordinates η and ξ are related to cylindrical coordinates r and z by

$$z = r_0 \xi \eta \qquad r = r_0[(1+\xi^2)(1-\eta^2)]^{1/2} \quad [2]$$

[see Ref (3)]. The boundary conditions adopted for the disk electrode are (1)

$$\frac{\partial \Phi}{\partial \eta} = 0 \text{ at } \eta = 0 \text{ (on the insulating plane)}$$

$$\Phi = 0 \text{ as } \xi \to \infty \text{ (far from the disk)} \quad [3]$$

Φ well behaved at $\eta = 1$ (on the axis of the disk)

The solution to Eq. [1] satisfying boundary conditions [3] can be expressed as (1)

$$\Phi = \frac{RT}{\mathbf{F}} \sum_{n=0}^{\infty} B_n P_{2n}(\eta) M_{2n}(\xi) \quad [4]$$

where $P_{2n}(\eta)$ is the Legendre polynomial of order $2n$ and $M_{2n}(\xi)$ is a Legendre function with known properties (1).

For sufficiently small current densities (linear polarization), the relationship between the surface overpotential and the local current density is

$$i(r) = i_0(\alpha_a + \alpha_c)\frac{\mathbf{F}}{RT}\eta_s = -\kappa_\infty \frac{\partial \Phi}{\partial z} \text{ at } z = 0,\ r < r_0 \quad [5]$$

where $i(r)$ refers to the local current density, η_s refers to the local surface overpotential (which is characteristic of the local current density) and $i_0(\alpha_a + \alpha_c)\mathbf{F}/RT$ relates to the local kinetics of the faradaic reaction, taken here to be linear. The local surface overpotential is given by

$$\eta_s = V - \Phi(r,0) \quad [6]$$

where V is the electrode potential (assumed to be uniform) and $\Phi(r,0)$ is the potential in the solution just outside the double layer.

The overpotential measured experimentally usually contains an ohmic contribution which must be removed by either a numerical calculation (1,3) or use of an interrupter technique (4). Newman (5) has shown that the ohmic potential measured by the interrupter technique corresponds to an average potential characteristic of the primary current distribution. A nonuniformly charged double-layer is associated with a nonuniform ohmic-potential drop during the passage of current. Immediately after the current is interrupted, the double layer remains charged, and the potential just outside the double-layer changes by a uniform amount over the entire surface of the disk

$$V' - \Phi'(r,0) = V - \Phi(r,0) \quad [7]$$

where primes denote quantities after interruption. The potential at an arbitrary point in the solution is

* Electrochemical Society Active Member.
[1] Present address: Globe-Union, Incorporated Milwaukee Wisconsin 53201.
Key words: ohmic-potential drop, electrode kinetics, disk electrode, current distribution.

$$\Phi'(r,z) = \Phi(r,z) - \bar{\Phi}(r,z) \quad [8]$$

where $\bar{\Phi}(r,z)$ represents the local ohmic drop associated with the primary distribution for the same current. The surface overpotential as measured by the current interrupter method with the reference electrode at r,z can be written as

$$\eta_{s,app} = V - \Phi(r,z) - \bar{\Phi}(r,0) + \bar{\Phi}(r,z) \quad [9]$$

It is assumed that one who does not take into account the nonuniform current distribution would calculate an apparent exchange current density, $i_{o,app}$ with the linear polarization expression based on the average current density and apparent surface overpotential

$$i_{avg} = i_{o,app}(\alpha_a + \alpha_c)\frac{\mathbf{F}}{RT}\eta_{s,app} \quad [10]$$

The difference between Eq. [5] and [10] is a consequence of the nonuniform ohmic drop to the disk electrode which is unavoidably contained in Eq. [10]. Substitution of Eq. [4] and [9] into Eq. [10] gives an expression for the error one might expect in the exchange current density

$$i_o/i_{o,app} = \frac{\pi J}{4}\left[\frac{4\kappa_\infty r_o V}{I} - 1 - \sum_{n=1}^{\infty}\frac{B_n}{B_o}P_{2n}(\eta)M_{2n}(\xi)\right] \quad [11]$$

where

$$J = (\alpha_a + \alpha_c)\frac{\mathbf{F}r_o i_o}{RT\kappa_\infty}$$

$$B_o = \frac{\mathbf{F}}{RT}\frac{I}{4\kappa_\infty r_o}$$

and the B_n values have been determined in Ref. (1). Equation [11] is valid for any arbitrary position of the reference electrode.

Let us now examine three special cases. With the reference electrode at infinity, Eq. [11] can be expressed as

$$i_o/i_{o,app} = \frac{\pi J}{4}\left[\frac{4\kappa_\infty r_o V}{I} - 1\right] \quad [12]$$

With the reference electrode adjacent to the work electrode

$$i_o/i_{o,app} = i(r)/i_{avg} \quad [13]$$

a general result applicable to other geometries as well. Placing the reference electrode close to the working electrode decreases the ohmic-potential drop, but it also permits the extremes in the error for the exchange-current density. Near the center, $i(r)$ has its smallest value, and the error can be expressed as

$$i_o/i_{o,app} = \frac{\pi J}{4}\left[\frac{4\kappa_\infty r_o V}{I} - \sum_{n=0}^{\infty}\frac{B_n}{B_o}\right] \quad [14]$$

Near the edge, $i(r)$ has its largest value, and

$$i_o/i_{o,app} = \frac{\pi J}{4}\left[\frac{4\kappa_\infty r_o V}{I} - \sum_{n=0}^{\infty}\frac{B_n}{B_o}P_{2n}(0)\right] \quad [15]$$

With the reference electrode farther from the surface, the error can actually be expected to lie between these extremes. Figure 1 contains the numerical results of the error in the exchange-current density for several positions of the reference electrode as a function of the dimensionless exchange-current density J. For the values of J considered, the error in i_o can range from -50 to more than 300%.

Discussion and Conclusions

The most important result of the paper is that serious errors in the measurement of electrode kinetic parameters (*i.e.*, i_o) can result from an electrode which is characterized by a nonuniform current distribution. The magnitude of this error depends on the position of the reference electrode relative to the working electrode. For the cases shown in Fig. 1, the errors associated with nonuniform current distribution are smallest when the reference electrode is located far from the disk. However, decreasing the error in this manner increases the ohmic drop which must be compensated for by an interrupter technique. Under certain experimental conditions, the compensated ohmic potential can be as large as 90% of the total measured overpotential, with a consequent decrease in the accuracy of the surface overpotential. There are cell designs (6, 7) which provide a uniform primary current distribution over the surface of the electrode and at the same time position the reference electrode in the plane of the working electrode in such a manner as not to disturb the local current distribution. Also, the use of a spherical electrode, as pointed out by Newman (2), can be used to eliminate current distribution problems.

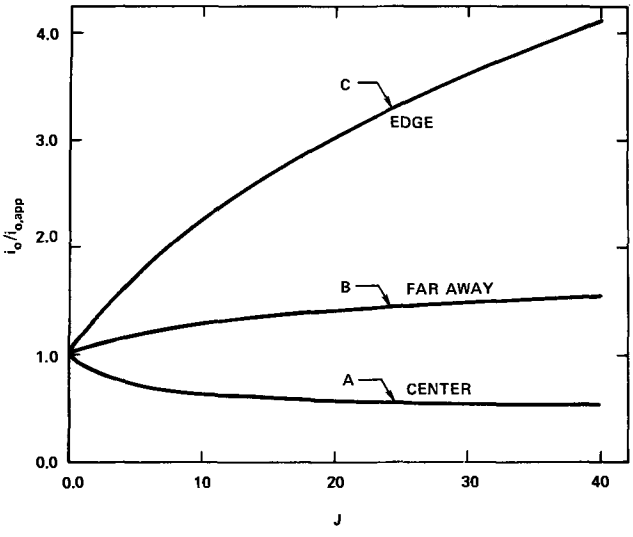

Fig. 1. Correction in i_o determination for linear polarization for various positions of the reference electrode relative to the disk electrode. Curve A approaches 0.5 for large J, while curve C approaches infinity.

A second result of this work is that for the reference electrode positions shown in Fig. 1, one needs only to measure the value of J for the system in question to assess the degree of error in i_o. For other reference electrode positions, Eq. [11] can be evaluated to assess the error in i_o. The results in this paper can be used qualitatively to assess the error for configurations other than the disk electrode. Equation [13] can be used on any electrode system provided that $i(r)$ is known.

Acknowledgment

This work was supported by Naval Air Systems Command under contract N00019-71-C-0342 and by the United States Atomic Energy Commission.

Manuscript received June 30, 1972.

Any discussion of this paper will appear in a Discussion Section to be published in the December 1973 JOURNAL.

LIST OF SYMBOLS

B_n	coefficients in series for potential
$\mathbf{F}$	Faraday's constant, coulomb/equiv
i	normal current density at electrode surface, A/cm^2
i_o	exchange current density, A/cm^2
$i_{o,app}$	apparent exchange current density, A/cm^2
i_{avg}	average current density, A/cm^2
I	total current to the disk, A
J	dimensionless exchange current density (see Eq. [11])
M_{2n}	a Legendre function

P_{2n} Legendre polynomial of order $2n$
r radial coordinate, cm
r_o radius of disk, cm
R universal gas constant, joule/mole-deg
T absolute temperature, °K
V potential of metal disk electrode, V
z normal distance from disk, cm
z_i charge number of species i
α_a, α_c parameters in kinetic expression (see Eq. [5])
η elliptic coordinate (see Eq. [2])
η_s surface overpotential, V
$\eta_{s,app}$ apparent surface overpotential, V
κ_∞ conductivity of bulk solution, mho-cm^{-1}
ξ elliptic coordinate (see Eq. [10])
Φ electrostatic potential, V
$\overline{\Phi}$ ohmic drop, V

REFERENCES

1. John Newman, *This Journal*, **113**, 1235 (1966).
2. John Newman, *Ind. Eng. Chem.*, 4, **60**, 12 (1968).
3. John Newman, *This Journal*, **113**, 501 (1966).
4. J. D. E. McIntyre and W. F. Peck, Jr., *ibid.*, **117**, 747 (1970).
5. John Newman, *ibid.*, **117**, 507 (1970).
6. B. D. Cahan, F. Nagy, and M. A. Genshaw, *ibid.*, **119**, 64 (1972).
7. William Tiedemann, Ph.D. Thesis, University of California, Los Angeles, October, 1971.

JOURNAL OF THE ELECTROCHEMICAL SOCIETY

SOLID-STATE SCIENCE AND TECHNOLOGY

FEBRUARY 1973

High-Temperature Dielectric Behavior of TiO_2(Rutile)

M. A. Seitz, R. T. McSweeney, and W. M. Hirthe

Metallurgy and Materials Science, College of Engineering, Marquette University, Milwaukee, Wisconsin 53233

ABSTRACT

The dielectric behavior of "a" and "c" orientation single crystals of TiO_2 (rutile) was investigated as a function of frequency, from 100 Hz to 500 kHz, and temperature, over the interval from 500° to 1000°C. The a-c conductivity at low applied voltages was found to be due to electronic carriers throughout the frequency and temperature range studied. The dielectric polarization processes occurring in this material were found to depend on the temperature and frequency ranges being investigated. At frequencies above 10^5 Hz, electronic and lattice polarization was found to predominate throughout the temperature interval investigated. The lower frequency data could be rationalized on the basis of a space-charge polarization model involving mobile point defects, which are blocked or partially blocked at the electrodes, and electronic carriers, which are able to pass through the electrode. At temperatures below 750°C, the "c" orientation specimens were found to exhibit an anomalous behavior that was felt to be the result of a thin barrier layer in the vicinity of the specimen electrodes.

The rutile crystalline modification of TiO_2 is a representative metal oxide of commercial importance which is also of interest from a research standpoint. Various high- and low-temperature measurements including conductivity (1-6), weight change (7, 8), thermoelectric power (3, 4), diffusion (9-11), transient conductivity (12-14), Hall effect (15-20), and dielectric measurements (21-26) have been made for the purpose of elucidating its defect structure and physical properties.

High-temperature measurements (1-8) have qualitatively confirmed the presence of nonstoichiometric defects resulting in n-type behavior, although the species, concentration, and ionization states are still somewhat in doubt.

Previous dielectric measurements (21-26) on rutile have been restricted to relatively low temperatures. Most of this work has been performed at room temperature after heat-treatment at elevated temperatures in either an oxidizing or reducing atmosphere. Dielectric dispersion and relaxation have been observed at room temperature by several investigators, but their data does not agree, and a consistent model has not been determined. The experiments of von Hippel *et al.* (24) are an exception in that they were performed at temperatures up to 500°C. This temperature, however, is still less than one-fourth the melting point of rutile, and impurities and quenched-in defects could play a major role in controlling the behavior.

To avoid the inconsistencies evident in the low-temperature investigations of rutile, dielectric measurements were performed at as high a temperature as feasible using a technique developed in our laboratories. Under these conditions the nonequilibrium conditions noted in the literature could be minimized or possibly avoided. Analysis of high-temperature data should lead to information about the defect structure and its role in controlling the dielectric behavior.

Key words: dielectric behavior, TiO_2 (rutile), polarization.

Experimental Procedure

In our early attempts to measure high-temperature dielectric behavior, it was noted that the specimen conductance, G_{sp}, exhibits a much stronger temperature dependence than the specimen capacitance, C_{sp}. This results in a dissipation factor which increases significantly with increasing temperature. For rutile, tan δ approached 10^3 to 10^4 at 1000°C and, therefore, a special technique had to be developed to perform the dielectric measurements. This substitution technique, where corrections are made for parasitic capacitances and inductances associated with the system, was the subject of a previous paper (27). With this technique the capacitance of specimens having a total resistance of greater than 100 ohms and a dissipation factor less than 10^4 can be measured to ±15%. For mid-range frequencies (1-50 kHz) the error is less than ±5%.

Single crystal titanium dioxide boules purchased from the National Lead Company (see Table I) were oriented to within ±2° of the "a" or "c" axis by the Laue back reflection x-ray technique. Specimens ranging in thickness from 0.23 to 0.6 cm and in surface area from 0.4 to 0.7 cm^2 were cut from boule slices. The surface area to thickness ratio ranged from 0.5 to 1 cm. All surfaces were mechanically polished with No. 600 grit silicon carbide or boron carbide to remove irregularities and to provide reproducible surface conditions. Three to five coats of Engelhard liquid bright platinum paint No. 05 were applied to the plane parallel surfaces perpendicular to the orientation direction and baked at 500°C between each application. An additional three to five coats of Engelhard fluxed platinum paste No. 6082 were applied to the surfaces and baked at 850°C between applications. Care was taken to use thin coats of paint and paste and to heat the specimen slowly so that the layers would not bubble or crack. When the resistance between any pair of points on the contact surface was

Table I. Mass spectrographic analysis of boule of TiO_2 obtained from National Lead Company (ppmw)

Element		Element	
Li	<0.01	Pd	<0.1
Be	<0.003	Ag	<0.06
B	0.02	Cd	<6.0
C (a)	1.0	In	<0.1
N (a)	0.2	Sn	<0.1
O	major	Sb	<0.07
F	<0.06	Te	<0.1
Na	(b)	I	<0.04
Mg	<0.3	Cs	<0.04
Al	0.1	Ba	<0.06
Si	<0.6	La	<0.05
P	<0.1	Ce	<1.0
S	<0.6	Pr	<0.5
Cl	1.0	Nd	<3.0
K	1.0	Sm	<0.2
Ca	0.5	Eu	<0.1
Sc	<0.02	Gd	<0.2
Ti	major	Tb	<0.6
V	<0.2	Dy	<0.2
Cr	<0.6	Ho	<0.06
Mn	<0.2	Er	<0.2
Fe	0.6	Tm	<0.06
Co	<0.2	Yb	<0.2
Ni	0.2	Lu	<0.06
Cu	<4.0	Hf	<0.2
Zn	<2.0	Ta	≦0.4
Ga	<0.04	W	<0.2
Ge	<0.1	Re	<0.1
As	<0.02	Os	<0.1
Se	<3.0	Ir	<0.1
Br	<0.06	Pt	<0.3
Rb	<0.05	Au	(c)
Sr	<0.04	Hg	<0.3
Y	<0.03	Tl	<0.1
Zr	<0.06	Pb	<1.0
Nb	<0.1	Bi	<0.3
Mo	<0.2	Th	<0.1
Ru	<0.1	U	<1.0
Rh	<0.03		

reduced to less than 1 ohm, the platinum paste applications were terminated and the specimen placed into the holder shown in Fig. 1.

The specimen was allowed to equilibrate at temperature in various partial pressures of oxygen provided by oxygen-argon tank mixtures. Equilibrium was assumed when the capacitance and resistance changes over a several hour period were less than those due to the variation in temperature. Measurements of the capacitance and resistance were made at selected frequencies in the range 100 Hz to 500 kHz. The specimen temperature was increased or decreased at approximately 50°C intervals and the above procedure repeated.

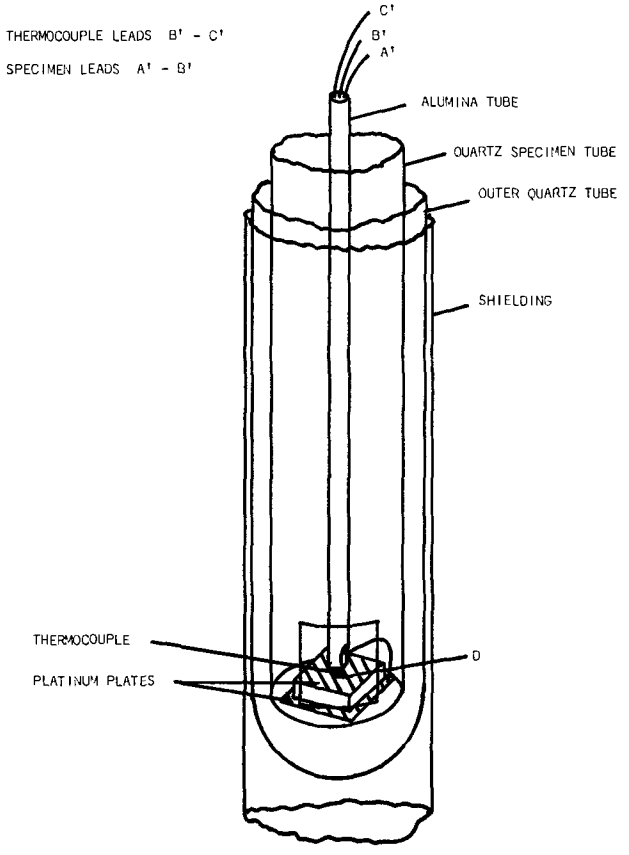

Fig. 1. Specimen holder

Results and Discussion

Isothermal dielectric measurements were performed in the range 100 Hz to 500 kHz over the interval 500°-1000°C at several oxygen partial pressures. The apparent dielectric constant, K', as a function of frequency for "a" and "c" orientations is shown in Fig. 2 and 3, respectively. No dispersion in conductivity was noted over the ranges of frequency and temperature investigated; consequently, isothermal conductivity *vs.* frequency data were not included. From Fig. 2 and 3 it can be seen that the large apparent dielectric constant evident at low frequencies decreases monotonically with increasing frequency over the entire range. At high frequencies a constant value of K' is approached, K'_∞, which is independent of temperature. The decrease in K' with frequency followed the relationship $K' \alpha \omega^{-x}$ where x is 5/4 ± 1/4. A maximum static dielectric constant, K_s, was not obtained since the dielectric constant continues to increase with decreasing frequency.

Figures 4 and 5 show the dependence of K' on reciprocal absolute temperature for "a" and "c" orientations, respectively. The linear segments of these plots suggest that the apparent dielectric constant is controlled by a thermally activated process. For the "a" orientation at low frequencies, K' followed the relationship $K' \alpha \exp(-E/RT)$ over the temperature range investigated. In contrast to this, K' for the "c" orientation exhibited a negative temperature dependence in the range 500° to approximately 750°C followed by a positive temperature dependence at higher temperatures.

Two probe a-c (1 kHz) and d-c ($I_{dc} < 15$ μA) conductivities *vs.* the reciprocal of absolute temperature for the "a" and "c" orientations are shown in Fig. 6

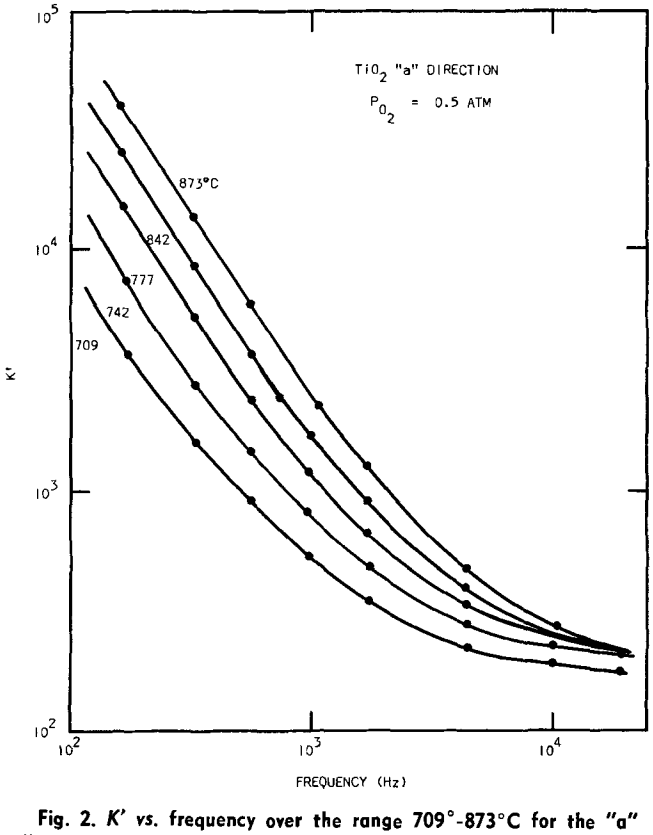

Fig. 2. K' *vs.* frequency over the range 709°-873°C for the "a" direction and $P_{O_2} = 0.5$ atm.

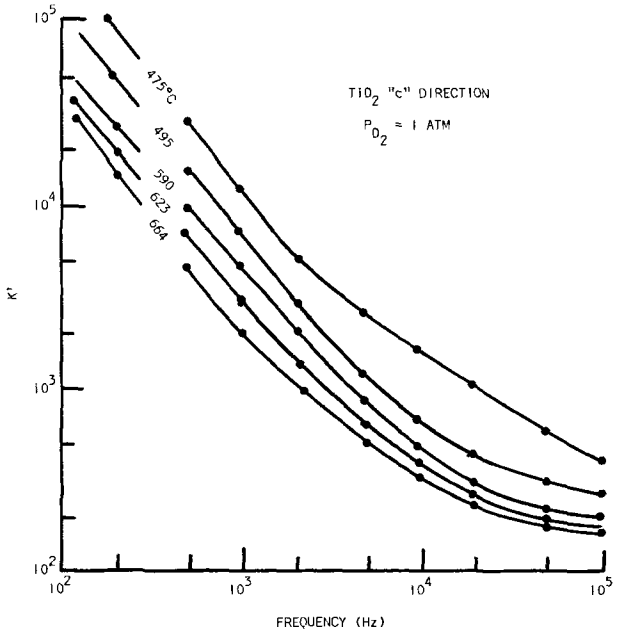

Fig. 3a. K' vs. frequency over the range 664°-475°C for the "c" direction and $P_{O_2} = 1$ atm.

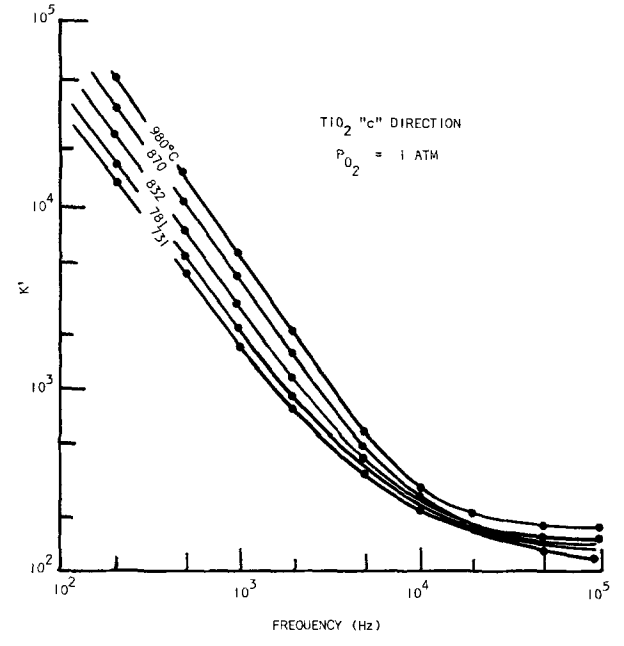

Fig. 3b. K' vs. frequency over the range 730°-980°C for the "c" direction and $P_{O_2} = 1$ atm.

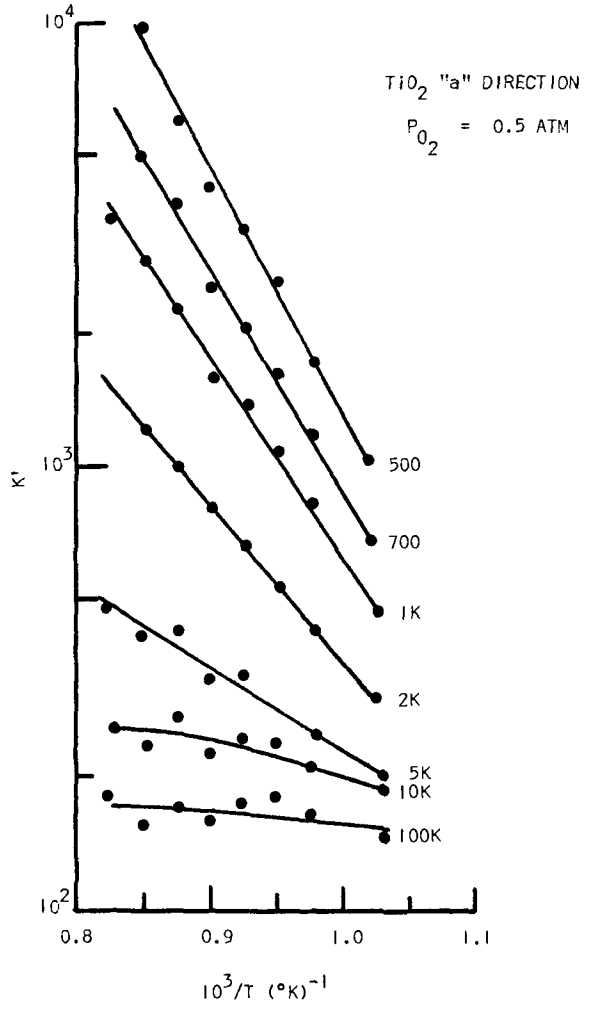

Fig. 4. The logarithm of K' vs. $1/T$ over the range 500-100,000 Hz for the "a" direction and $P_{O_2} = 0.5$ atm.

and 7, respectively. The a-c and d-c conductivities for the "a" orientation were identical and exhibited an exponential temperature dependence with an activation energy of 1.6 ± 0.2 eV. The "c" orientation behaved in a similar manner at temperatures above 750°C, but below this temperature the a-c conductivity approached a constant value, whereas the d-c conductivity exhibited an exponential temperature dependence. Therefore, at temperatures below 750°C the conductivity is frequency dependent. These conductivity data were reproducible to within ±2% upon thermal cycling except for the "c" orientation data below 750°C which was dependent on history.

The conductivity and dielectric constant were dependent on oxygen partial pressure over the range 1-10^{-5} atm at 950°C. They were proportional to $P_{O_2}{}^{-1/n}$ where n was approximately equal to 6. This oxygen partial pressure dependence was not evident at lower temperatures. This would indicate that either quenched-in nonstoichiometric defects or impurities controlled the conductivity behavior of TiO_2 at lower temperatures. The former seems more attractive due to the agreement of the conductivity data with previous measurements (6). Partial pressure studies were not continued because the platinum contacts degraded with further reduction of the specimen. The values of dielectric constant and a-c conductivity did not exhibit a dependence on the magnitude of the applied a-c field at less than 50 V/cm. The dissipation factor calculated from these data are shown in Fig. 8 and 9. It is observed that tan δ is very large, and also that tan δ_{max} is a strong function of temperature.

An understanding of the high-temperature dielectric behavior of TiO_2 may be obtained from the data presented in Fig. 2-9. The exponentially dependent a-c and d-c conductivities are in good agreement with four-probe d-c conductivities reported in the literature (6), and this indicates that the platinum contacts acted in an ohmic fashion. The imaginary part of the dielectric constant, K'', was always much greater than the real part, K', which suggests that the dielectric losses were associated with electronic conduction rather than relaxation processes.

The variation of K' with frequency and temperature at elevated temperatures indicates that similar polarization processes are responsible for the dielectric behavior in the "a" and "c" orientations.

Electronic and atomic polarization mechanisms are active in rutile at all temperatures and frequencies of this investigation. The frequency and temperature independent dielectric constant, K'_∞, at high frequencies is controlled by atomic and electronic polarization processes. The high-frequency dielectric constants, K'_∞,

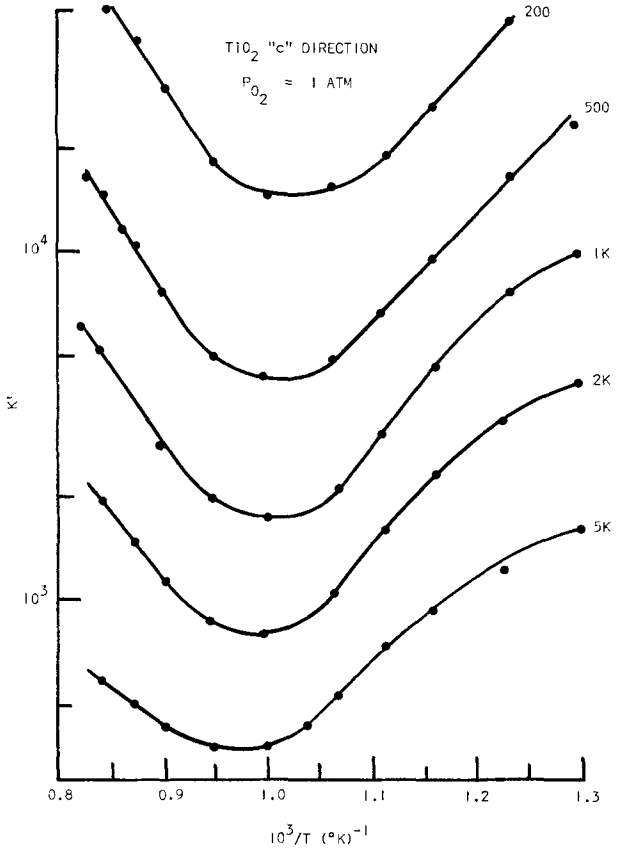

Fig. 5. The logarithm of K' vs. $1/T$ over the range 200-5000 Hz for the "c" direction and $P_{O_2} = 1$ atm.

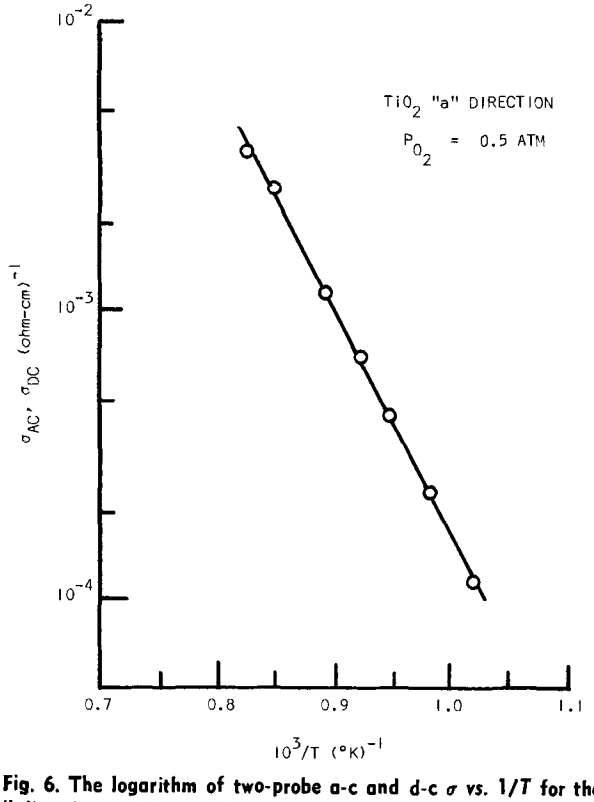

Fig. 6. The logarithm of two-probe a-c and d-c σ vs. $1/T$ for the "a" direction and $P_{O_2} = 0.5$ atm.

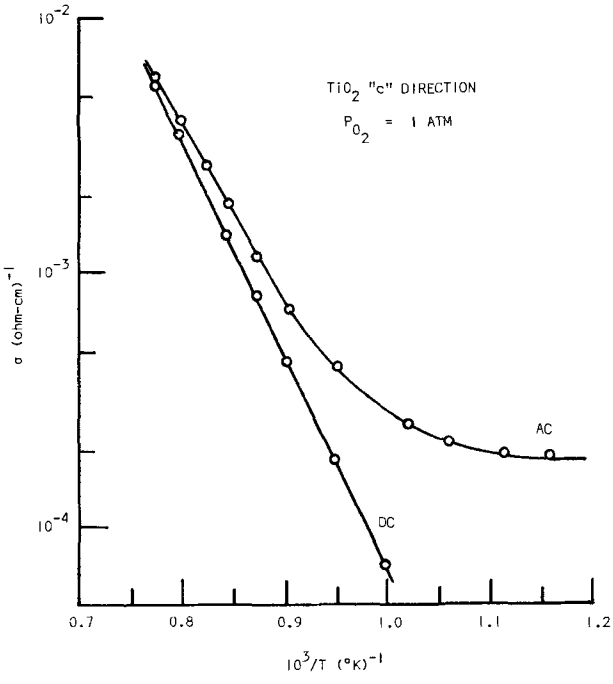

Fig. 7. The logarithm of two-probe a-c and d-c σ vs. $1/T$ for the "c" direction and $P_{O_2} = 1$ atm.

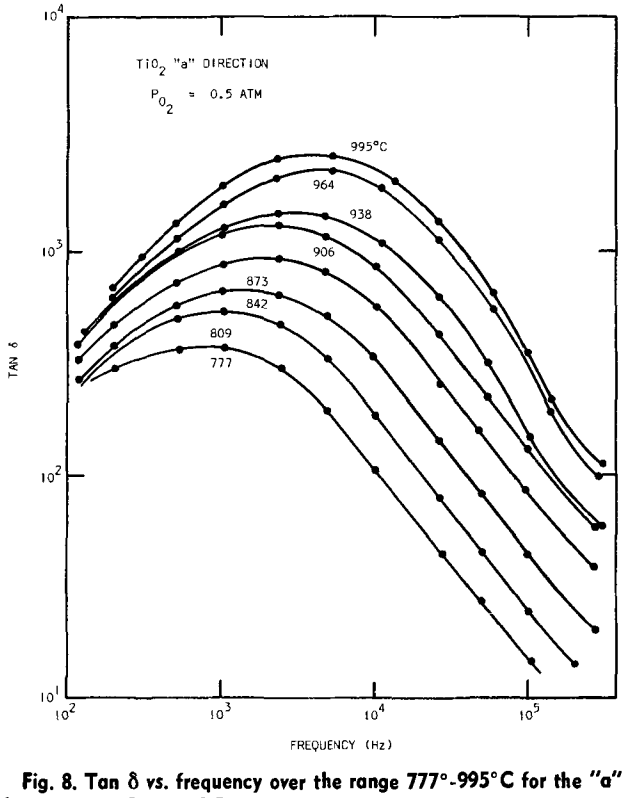

Fig. 8. Tan δ vs. frequency over the range 777°-995°C for the "a" direction and $P_{O_2} = 0.5$ atm.

reported by Parker (28) at 1 MHz and 300°C were 170 in the "c" direction and 86 in the "a" direction. These values compare well with the high-frequency data of this study. The low-frequency data of this investigation were analyzed in terms of barrier layer and space-charge polarization models in addition to the constant contribution expected from electronic and atomic polarization processes.

Various interfacial barrier layer models have been considered by Volger (29), and others (30, 31). Only two of the special cases considered by Volger could explain the large values of K' observed in this investigation. In these limiting cases the dielectric constant of the barrier layer, K'_1, and the bulk material, K'_2, are assumed to be identical. The large apparent dielectric constants are shown to result from resistivity and resistance differences between the barrier layers and the bulk of the specimen. When both the resistivity of the interfacial material, ρ_1, and the barrier layer resistance, $\rho_1 d_1/A$, are much larger than that of the bulk,

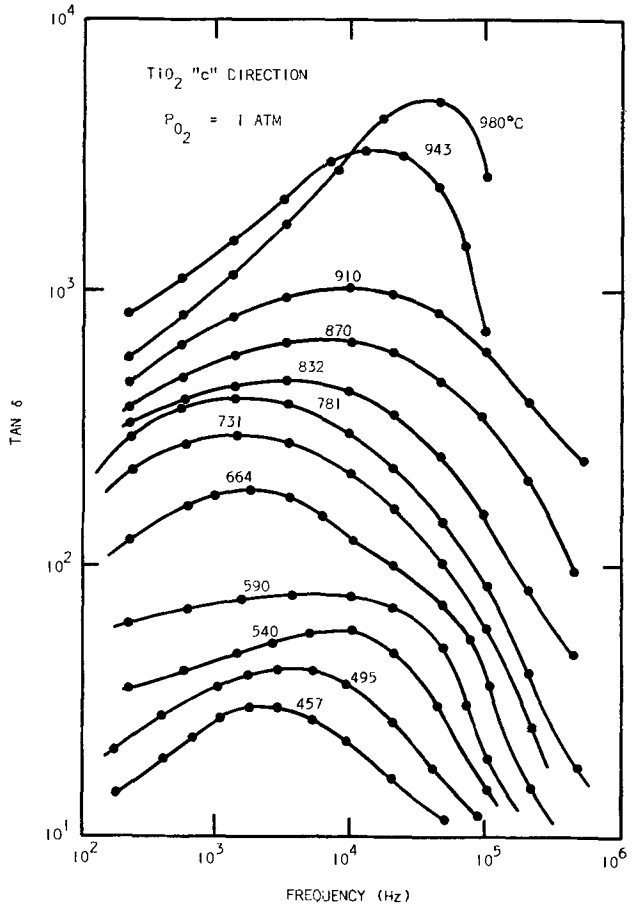

Fig. 9. Tan δ vs. frequency over the range 457°-980°C for the "c" direction and $P_{O2} = 1$ atm.

i.e., $\rho_1^2 d_1 >> \rho_2^2 d_2$ and $\rho_1 d_1 >> \rho_2 d_2$, the ratio of the static to the bulk dielectric constant equals the ratio of the bulk thickness, d_2, to the barrier thickness, d_1, *i.e.*

$$\frac{K'_s}{K'_\infty} = \frac{d_2}{d_1} \qquad [1]$$

In this case a large dispersion in conductivity is also predicted.

In the second model, the resistivity of the interfacial material, ρ_1, is assumed to be much larger than that of the bulk, ρ_2, *i.e.*, $\rho_1^2 d_1 >> \rho_2^2 d_2$, but the barrier layer resistance is negligible when compared with the bulk resistance, *i.e.*, $\rho_1 d_1 << \rho_2 d_2$. The ratio of the static to the bulk dielectric constant equals the ratio of the interfacial to bulk resistivities, *i.e.*

$$\frac{K'_s}{K'_\infty} \simeq \frac{\rho_1^2 d_1}{\rho_2^2 d_2} \qquad [2]$$

A conductivity dispersion is not predicted for this situation.

Space-charge processes can also lead to significant polarization as the result of the motion of electronic or atomic point defects in an initially homogeneous material. In order to have space-charge polarization, two requirements must be fulfilled. Charge-carrying species must be mobile and blocked or partially blocked from passing through the specimen electrodes. These charge-carrying species could be electronic defects, in which case they would be blocked at the electrodes by non-ohmic processes; or atomic defects, for which electrode porosity and slow rates of chemical reaction would result in charge-carrier blocking.

Jaffe (32), Friauf (33), Macdonald (34-36), and Beaumont and Jacobs (37) have developed theoretical relationships describing the effect of space-charge polarization on the conductivity and dielectric constant. Three basic models have been developed, one of these involves a single mobile charge-carrying species which is blocked or partially blocked at the specimen electrodes (37). The others (32-36) deal with two mobile charge-carrying species of opposite sign, where either both or only one of the charged species are blocked or partially blocked at the electrodes. The single-carrier model requires a dispersion in the conductivity, which was not observed, while the second case does not appropriately describe the observed frequency dispersion. The last case is deemed the most appropriate when considering the high temperature dielectric behavior of TiO_2 and will be expanded here.

The model as presented by Friauf involving two charge-carrying species one of which is blocked at the specimen electrodes can readily be applied to the observations for TiO_2. Negatively charged species are assumed to pass through the electrodes while positively charged species are blocked at the electrodes. The equivalent parallel circuit capacitance, C, and resistance, R, per unit area of the specimen can be expressed as a function of frequency, ω, as

$$-\Delta\left[\frac{1}{R}\right] = \omega C = \frac{e\mu_n c_o}{\sqrt{2}\,L^2}\left[\frac{D_n + D_p}{2D_n}\right]^{1/2}\left[\frac{D_p}{\omega}\right]^{1/2} \qquad [3]$$

Here, D_n and D_p are, respectively, the diffusion coefficients of the negative and positive charge-carrying species of charge e, c_o is the equilibrium concentration of defects, $2L$ is the specimen thickness, and μ_n is the mobility of the negative species. It is to be noted that Eq. [3] was derived for a case where both charge-carrying species have approximately the same mobility. For TiO_2, however, the negative charge-carrying species are assumed to be electrons which would have a much larger diffusion coefficient than the positively charged species which are assumed to be positive ions. Using the inequality, $D_n >> D_p$, the Einstein equation

$$\frac{\mu_n}{D_n} = \frac{e}{kT} \qquad [4]$$

along with the relationship

$$C = \frac{K'\epsilon_o}{2L} \qquad [5]$$

Eq. [3] reduced to

$$K' \simeq \frac{e^2 c_o}{\epsilon_o L k T}\left[\frac{D_p}{\omega}\right]^{3/2} \qquad [6]$$

Here, K' is the effective dielectric constant and ϵ_o is the permittivity of free space.

The high-temperature ($T > 750$°C) dielectric behavior found for TiO_2 could not be rationalized using the concept of a thin barrier layer having a resistivity and resistance greater than that of the bulk material. Although Eq. [1] does predict a large dispersion in K', no associated dispersion in conductivity was observed.

A model involving a thin barrier layer, which has a resistivity greater than and resistance less than the bulk material, also, does not seem to explain the data. First, it is noted that K' does not approach a constant value, K'_s, at low frequencies as predicted by Eq. [2]. Neither did K' obey the Debye-type dispersion as predicted by Volger (29). In addition, the increase in the dissipation factor with increasing temperature, shown in Fig. 8 and 9, is not in agreement with this limiting case of the barrier layer model. According to Volger, the maximum value of tan δ is dependent only upon the relative thicknesses of the bulk and barrier layers. A further argument discounting this barrier layer model will be presented when the low temperature dielectric data for the "c" orientation is discussed.

The high-temperature dielectric behavior of TiO_2 seems to be best described by a space-charge polarization model involving two charge-carrying species of opposite sign. Here, electrons are assumed to be the

negatively charged species and are able to freely pass through the electrodes, while ionic point defects are taken to be the positively charged species which are blocked or partially blocked at the specimen electrodes.

According to Eq. [6] the effective dielectric constant should vary as $\omega^{-3/2}$ at high temperature and low frequency where ion migration can predominate the polarization processes in TiO_2. At higher frequencies diffusion distances would be shorter and atomic and electronic polarization mechanisms would predominate. This qualitatively agrees with what is observed in Fig. 2 and 3b. The conductivity as observed in Fig. 6 and 7 would not necessarily vary with frequency as described in Eq. [3] due to the large electronic contribution in TiO_2. It is noted that K' varies with $\omega^{-5/4\pm1/4}$ as opposed to that predicted by Eq. [6]. This could be due to some degree of electronic depolarization, unequal charge-carrier mobilities, or the fact that the electrodes do not totally block the positively charged species. The degree of charge-carrier blocking would depend upon the nature of the diffusing species, electrode material, and electrode reactions occurring in the specimen. If decomposition reactions of the type [$TiO_2 \rightleftarrows Ti_i + O_2(g)$] and [$Ti_L + O_2(g) \rightleftarrows TiO_2$] occurred at the specimen electrodes then only partial blocking would result.

The diffusion coefficient of the positive charge-carrying species could be calculated from Eq. [6] if its concentration were known. Since the nature of the migrating point defect is unknown, a quantitative evaluation of D_p using Eq. [6] is not possible. If the mobile point defect were assumed to be an interstitial impurity or a quenched-in interstitial nonstoichiometric defect, an activation energy of motion of 0.5 eV would be obtained from the variation of K' with temperature. This value of energy is consistent with the values found for interstitial diffusion of Li^{+1} and B^{+3} in TiO_2 (9, 10). The calculated energy of motion would be significantly less than 0.5 eV if a defect-formation energy were to be included in this calculation (4, 6). This would seem unreasonable in light of the previously reported diffusion results.

Thus, the dielectric behavior of rutile at elevated temperatures (*i.e.*, from 500° to 1050°C for the "a" orientation and 700° to 1050°C for the "c" orientation) can be rationalized using the concept of field-enhanced atomistic migration and space-charge polarization. It should be noted that although the type of defects (*i.e.*, monovalent, ionic defects existing in equal concentrations) which were assumed to be responsible for the space charge polarization in Friauf's analysis are not equivalent to the types of defects expected in rutile (*i.e.*, electrons and polyvalent positively charged ionic defects existing in unequal concentrations), the frequency and temperature trends exhibited by the data are still in reasonable qualitative agreement with theory.

However, the dielectric behavior of the "c" orientation specimens below approximately 750°C did not follow all the previously mentioned trends. Although K' increased with decreasing frequency, the low-frequency values decreased with increasing temperature. The apparent a-c conductivity became frequency dependent and temperature independent below 750°C as is seen in Fig. 7. The d-c conductivity, however, was found to maintain the same exponential dependence that existed in the higher temperature region.

These data seem to indicate that, at lower temperatures, a barrier layer process as described by Eq. [2] exists, *i.e.*, $\rho_1 >> \rho_2$ and $R_1 >> R_2$. However, as the temperature is increased, the resistivity of the barrier layer decreases until the conditions laid out for Eq. [2] are met, *i.e.*, $\rho_1 > \rho_2$ and $R_1 \simeq R_2$. Upon further increase in temperature ρ_1 approaches ρ_2 and the barrier layer disappears completely. It should be noted that the subsequent increase of K' at higher temperatures could, thus, not be accounted for on the basis of barrier-layer polarization.

The high frequency or bulk conductivity in the "c" direction seems to be controlled by impurities at temperatures below about 750°C, while the d-c or barrier-layer conductivity followed a similar behavior as observed at higher temperatures. It has been observed that for TiO_2 a n to p transition, due to departures from stoichiometry, occurs in this oxygen partial pressure and temperature range (4). Thus, acceptor centers might lead to compensation at the external face of the specimen. This would not occur in the interior of the specimen due to limited diffusion at low temperatures.

The general behavior seen at low temperatures in the "c" orientation was not observed in the "a" direction. Several factors might contribute to this difference. First, the a-c data in the "a" direction was not taken at as low a temperature due to the strong history dependence found in this data for the "c" direction. It is also noted that although the "a" and "c" orientation specimens were cut from the same boule, their absolute conductivities and, also, impurity concentration might differ. Finally, it has been reported that diffusion occurs in the "c" direction more readily than in the "a" direction (38, 39). Therefore, any barrier layers that might form due to compensation at low temperatures for the "a" orientation would be quite thin and might not be observed in the measurements, *i.e.*, $\rho_1 > \rho_2$ but $R_1 << R_2$.

A further explanation for the existence of a barrier layer at low temperature might involve a Schottky barrier (40). The low-temperature data reported here were very dependent on history and, therefore, further experimentation in this region did not seem pertinent to this investigation.

The effects of biasing were studied at 800°C using the three electrode configuration with platinum electrodes shown in Fig. 10. It was generally noted that upon biasing, the a-c conductivity and capacitance at low frequency increased between the middle and negative electrodes of the specimen, while the reverse occurred between the middle and positive electrodes. These observations are consistent with the multiprobe transient conductivity studies of Blumenthal *et al.* (39). These results were interpreted in terms of positive ions migrating to the negative end and carrying along their associated electronic charge. Thus the increase in capacitance observed in this study could be associated with a larger ion concentration in the vicinity of the negative electrode while the increase in conductivity would be due to the larger electron concentration in this vicinity.

Along with the above observations, volt-ampere characteristics using various values of constant current were recorded between various probe pairs as

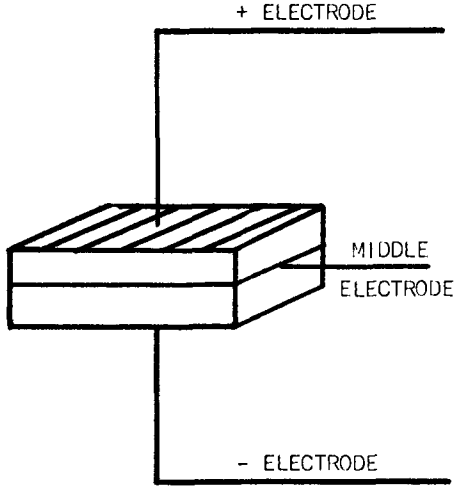

Fig. 10. The three-probe d-c configuration.

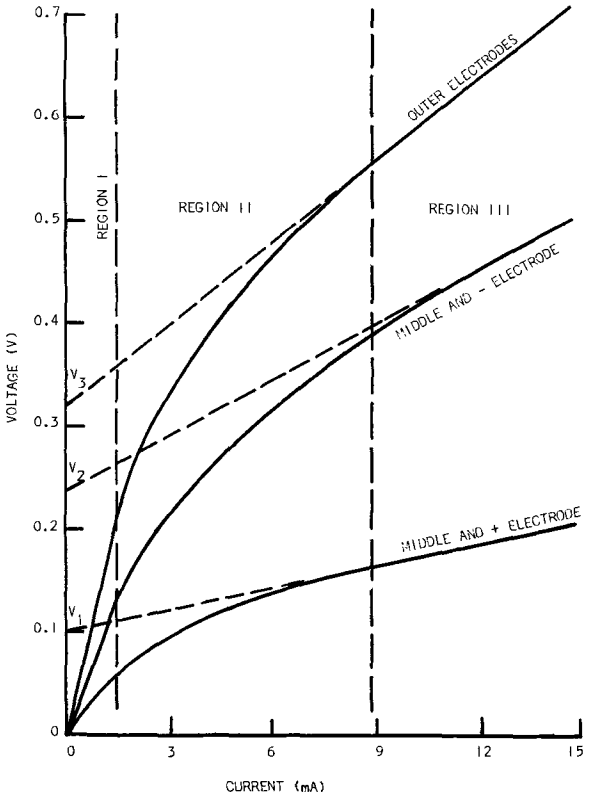

Fig. 11. The three-probe voltage vs. current d-c data.

shown in Fig. 11. These results, although very history dependent, provide a qualitative interpretation consistent with the previously discussed dielectric behavior. It is noted that the data can be characterized by three distinct regions. In region I Ohm's law was obeyed and the incremental d-c resistance, $\Delta V/\Delta I$, was approximately equal to the a-c resistance. At higher currents and/or fields, a nonohmic region exists, *i.e.*, $I \propto V^n$. In region III the current is a linear function of voltage; however, the incremental d-c resistance, $\Delta V/\Delta I$, was much smaller than the a-c resistance in this region which was equal to the incremental d-c resistance in region I. These data are similar to previously reported nonohmic studies for TiO_2 (12).

These results can also be interpreted in terms of moving point defects. In region I the current is most probably due to electron motion only and therefore, if no barrier layers were present, one would expect identical ohmic behavior for both a-c and d-c conductivity studies. The nonohmic behavior of the type depicted in region II was interpreted by Greener and Whitmore (12) as being due to space-charge-limited currents. However, their interpretation required that the mobility of electrons in TiO_2 be the order of 10^5 $cm^2/V\text{-}sec$, which is much greater than the measured values of 10^{-1} $cm^2/V\text{-}sec$ (18). The behavior observed in region II might also be interpreted as resulting from a combination of both electron and ion currents. In this region the field impressed across the sample, and the surface concentration of defects could be of such a magnitude that the decomposition reactions ($TiO_2 \rightleftarrows Ti_i + O_2(g)$) and ($Ti_L + O_2(g) \rightleftarrows TiO_2$) could be driven at the anode and cathode, respectively. Thus, the electrodes would not be totally blocking to the flow of ions as was assumed in the interpretation of the aforementioned dielectric studies, *i.e.*, a Faradaic type component of current would exist (41, 42). Region III might then be interpreted as the result of electron and ion flow. The voltage intercepts obtained upon extrapolating region III to $I = 0$ would be a measure of the decomposition potential required to drive the electrode chemical reactions. Further qualitative interpretation of this data would seem fruitless due to the strong history dependence encountered.

Mitoff and Charles (43) have invoked the concept of a Warburg (44) impedance to rationalize the magnitude of capacitance and its dispersion which they observed in beta alumina, soda-lime glasses, and single crystals of sodium chloride. The arguments presented by these authors were explored with respect to the results observed for TiO_2 at elevated temperatures. Mitoff and Charles pointed out that, if the space charge polarization model is to be valid, the magnitude of the measured capacitance, C_{sp}, should lead to a reasonable Debye length. The maximum value of capacitance and the Debye length, L_D, can be related by the equation

$$C_{spmax} = \frac{K'_\infty \epsilon_0 A}{L_D} \qquad [7]$$

Here, A is the area of the specimen, ϵ_0 is the permittivity of free space, and K'_∞ is the high-frequency relative dielectric constant. The largest value of specimen capacitance, C_{spmax}, observed for TiO_2 in this study was approximately 0.5 μf. Using the appropriate values of $K'_\infty \simeq 100$, $A = 1$ cm^2 and $\epsilon_0 = 8.85 \times 10^{-12}$ Fcm^{-1}, a value of $L_D \simeq 2 \times 10^{-5}$ cm results. This Debye length is reasonable and also suggests that the space-charge polarization model is appropriate at elevated temperature for TiO_2.

If a Warburg impedance is to be present, then electrode reactions of the type $M^+ + e \rightleftarrows M^o$ would have to occur in the vicinity of the electrodes, *i.e.*, a Faradaic current would have to exist (41, 42, 44). The interpretation of the results of Fig. 11 suggests that appreciable electrode reaction or Faradaic current does not exist until a critical voltage or surface concentration of defects is reached. Therefore at the low voltages used in the dielectric measurements, it is expected that the Warburg impedance would not be an important contribution to the dielectric dispersions observed.

Conclusions

The dielectric behavior of TiO_2 (rutile) can be rationalized on the basis of electronic and lattice polarization mechanisms at frequencies above 10^5 Hz. In the frequency interval 10^2-10^5 Hz, dielectric polarization for the "a" orientation and the "c" orientation above 750°C can be rationalized on the basis of a space-charge polarization model. Here, electrons, the negatively charged mobile species, were assumed to pass through the electrodes, while positively charged mobile ionic point defects were assumed to be blocked at the electrodes. The nature of the mobile ionic point defects could not be determined, however, their activation energy for motion was of the order of 0.5 eV. At temperatures below 750°C, the dielectric polarization processes occurring in the "c" orientation specimens seem to be controlled by a thin-barrier layer.

The measured a-c conductivity data agreed with four-probe d-c conductivity data reported in the literature, where electrons were assumed to be the charge carrying species. The d-c volt-ampere characteristics for a "c" orientation specimen of TiO_2 at 800°C were recorded. Three regions were noted in this curve. At low currents, Ohm's law was obeyed and the conductivity was, again, in agreement with previously reported results. At intermediate currents, a nonohmic behavior was observed, while at higher current values a second Ohm's law region appeared. The conductivity calculated for the latter region was found to be higher than that for the low-current region. The conductivity at low currents can be ascribed to electronic carriers. The larger conductivity found in the second Ohm's law region can be rationalized on the basis of a Faradaic process or a decomposition reaction leading to an ionic contribution to the conductivity.

Acknowledgment

The authors gratefully acknowledge the support of the Aerospace Research Laboratories, Office of Aerospace Research, United States Air Force, Contract No. AF33615-68-C-1355.

Manuscript submitted Feb. 1, 1972; revised manuscript received Sept. 11, 1972. This was Paper 114 presented at the Detroit, Michigan Meeting of the Society, Oct. 5-9, 1969.

Any discussion of this paper will appear in a Discussion Section to be published in the December 1973 JOURNAL.

REFERENCES

1. M. D. Earle, *Phys. Rev.*, **61**, 56 (1942).
2. D. C. Cronemeyer, *ibid.*, **87**, 876 (1952).
3. J. Rudolph, *NaturF.*, **14a**, 727 (1959).
4. J. Yahia, *Phys. Rev.*, **130**, 1711 (1963); J. Yahia, *Bull. Am. Ceram. Soc.*, **1**, 221 (1962).
5. E. H. Greener, F. J. Barone, and W. M. Hirthe, *J. Am. Ceram. Soc.*, **48**, 623 (1965).
6. R. N. Blumenthal, J. Baukus, and W. M. Hirthe, *This Journal*, **114**, 172 (1967); R. N. Blumenthal, J. Coburn, J. Baukus, and W. M. Hirthe, *J. Phys. Chem. Solids*, **27**, 643 (1966).
7. P. Kofstad, *J. Less Common Metals*, **13**, 106 (1968).
8. K. S. Forland, *Acta Chem. Scand.*, **18**, 1267 (1964).
9. V. N. Bogomolov, *Fiz. Tverd. Tela*, **5**, 2011 (1963).
10. O. W. Johnson, *Phys. Rev.*, **136**, A284 (1964).
11. R. Haul and G. Dumbgen, *J. Phys. Chem. Solids*, **26**, 1 (1965).
12. E. H. Greener and D. H. Whitmore, *J. Appl. Phys.*, **32**, 1320 (1960).
13. F. Cardon, *Phys. Status Solidi*, **8**, 1415 (1963).
14. H. B. Whitehurst, J. J. Morrison, F. L. English, B. M. Warmkessel, and C. J. Kevane, *J. Phys. Chem. Solids*, **28**, 861 (1967).
15. J. H. Becker and W. R. Hosler, *J. Phys. Soc. Japan, Suppl.*, **18**, 152 (1963).
16. G. A. Acket and J. Volger, *Physica*, 1680 (1966).
17. V. N. Bogomolov, E. K. Kudinov, and Y. A. Firsov, *Fiz. Tverd. Tela*, **9**, 3175 (1967).
18. I. Bransky and D. S. Tannhauser, *Solid State Commun.*, **7**, 245 (1969).
19. R. N. Blumenthal, J. C. Kirk, Jr., and W. M. Hirthe, *J. Phys. Chem. Solids*, **28**, 1077 (1966).
20. R. G. Breckenridge and W. R. Hosler, *Phys. Rev.*, **91**, 793 (1953).
21. J. Van Keymeulen, *Naturwissenschaften*, **45**, 56 (1958).
22. R. A. Parker and J. H. Wasilik, *Phys. Rev.*, **120**, 1631 (1960).
23. L. E. Hollander, Jr. and P. L. Castro, *J. Appl. Phys.*, **33**, 3421 (1962).
24. A. von Hippel, J. Kalnajs, and W. B. Westphal, *Phys. Chem. Solids*, **23**, 779 (1962).
25. J. M. Wimmer, Masters Thesis, Marquette University (1963).
26. K. G. Strivastava, *Physica*, **28**, 368 (1962).
27. M. A. Seitz, R. T. McSweeney, and W. M. Hirthe, *Rev. Sci. Instr.*, **40**, 826 (1969).
28. R. A. Parker, *Phys. Rev.*, **124**, 1719 (1961).
29. J. Volger, in "Progress in Semiconductors," Vol. 4, pp. 206-263, A. F. Gibson, Editor, John Wiley and Sons, New York (1960).
30. D. Miliotis and D. N. Yoon, *J. Phys. Chem. Solids*, **30**, 1241 (1969).
31. D. F. Gibbs and B. W. Jones, *J. Phys. D: Appl. Phys.*, **3**, 157 (1970).
32. G. Jaffe, *Phys. Rev.*, **85**, 354 (1952).
33. R. J. Friauf, *J. Chem. Phys.*, **22**, 1329 (1954).
34. J. R. Macdonald, *Phys. Rev.*, **92**, 4 (1953).
35. J. R. Macdonald, *J. Chem. Phys.*, **54**, 2026 (1971).
36. J. R. Macdonald, *J. Electroanal. Chem.*, **32**, 317 (1971).
37. J. H. Beaumont and P. W. Jacobs, *J. Phys. Chem. Solids*, **28**, 657 (1967).
38. J. L. Steele and E. R. McCartney, *Nature*, **222**, 79 (1969).
39. R. N. Blumenthal, W. M. Hirthe, and B. A. Pinz, in "Anisotropy in Single-Crystal Refractory Compounds," Vol. 2, pp. 137-150, F. W. Vahldiek and S. A. Mersal, Editors, Plenum Press, New York (1968).
40. J. G. Simmons, G. S. Nadkarni, and M. C. Lancastes, *J. Appl. Phys.*, **41**, 538 (1970); J. Maserjian and C. A. Mead, *J. Phys. Chem. Solids*, **28**, 1971 (1967).
41. D. C. Grahame, *This Journal*, **99**, 370C (1952).
42. J. R. Macdonald, *Trans. Faraday Soc.*, **66**, 943 (1970).
43. S. P. Mitoff and R. J. Charles, *J. Appl. Phys.*, **43**, 927 (1972).
44. E. Warburg, *Ann. Phys.*, **6**, 125 (1901).

Charge Trapping in Polymers

D. K. Davies and P. J. Lock

Electrical Research Association, Leatherhead, United Kingdom

ABSTRACT

An investigation is described of the role of unsaturated groups in the molecular structure on charge trapping in synthetic polymers. An attempt has also been made to quantify the effect on carrier migration of doping these materials with halogens. Using a surface charge decay technique carrier mobility has been determined *in vacuo* for a number of synthetic polymers and also for both high- and low-density polyethylenes doped with halogens. These data are presented together with an account of concurrent measurements of optical absorption in the same materials. The data indicate a tendency for "pure polymers" with known higher unsaturation content to exhibit a lower carrier mobility. Increased mobility was observed with either bromine or iodine impregnation of polyethylene. The optical data show that the iodine enters the polymer as neutral molecules most of which emerge under atmospheric conditions. The remainder, however, form charge exchange complexes at unsaturation sites in the polymer. The role of complexes in carrier transport is discussed.

The charge storage property of insulating materials—as exemplified in the electret—is becoming of widespread technological importance from microphones (6; and references therein) to prostheses (1). The elucidation of the underlying charge injection and carrier migration processes in synthetic polymers is vital to the future utility of these materials in almost any capacity.

Modern experimental techniques are yielding increasingly more definitive models of the basic mechanisms. It has been shown (3, 7) that carrier mobility

Key words: polymers, carrier mobility, conduction.

in low conductivity polymers is extremely small, the carriers being predominantly located in traps. Carrier migration is described by a hopping process. Recently published data (2) indicate that both polymer crystallinity and molecular symmetry significantly affect the electret stability, that is, charge trapping, and further, that phenyl and unsaturated groups in the molecular structure can form traps. Previous work (4) has also shown that carrier mobility in these materials may be greatly increased by impregnating the polymer with iodine. This effect has been interpreted by postulating charge exchange complex formation in the polymer, the complexes effectively reducing trapping effects by "handing-on" the carriers. A charge exchange complex in the present context means an interaction between two species, the strength of which lies between a full chemical bond and a small orbital overlap.

The present paper describes an investigation of the role of unsaturated groups in carrier trapping and an attempt to quantify the effects of doping on the transport mechanism. Using a surface-charge decay technique, carrier mobility has been determined *in vacuo* for a number of synthetic polymers and also for both high-density (HDPE) and low-density (LDPE) polyethylenes impregnated with halogens. An account of concurrent measurements of optical absorption in the same materials is also presented.

The experimental results show a tendency for carriers in polymers with known higher unsaturation content to exhibit a lower mobility. Carriers in polymethylene have a significantly higher mobility than in either HDPE or LDPE but the mobility extrapolated to room temperature is still 3½ orders of magnitude lower than that observed for octacosane ($C_{28}H_{58}$).

Mobility increases were observed with both LDPE and HDPE doped with either bromine or iodine, the affect being greater with the latter impregnant. Spectrophotometric measurements in the u.v./visible show that iodine enters the polymer as neutral iodine molecules some of which form charge exchange complexes with the polymer. Absorption measurements in the infrared range show that the complexes are associated with sites of unsaturation yielding a picture consistent with the data obtained for the "pure" polymers.

It is concluded from these mobility and optical absorption data that carrier trapping is associated, at least in part, with unsaturated sites in the polymer. The earlier conclusion that the enhanced mobility produced by doping results from charge exchange formation is confirmed and the carrier transport model is elaborated.

Experimental Techniques

Mobility determination.—The method of determining carrier mobility in low conductivity polymers has been described previously (Davies, 1967). A surface charge is injected into the free surface of the polymer specimen mounted on the flat top of an earthed, temperature-controlled cell. The specimen is maintained at a fixed temperature and the remanent charge on the surface is determined, using a calibrated probe technique, at intervals appropriate to the rate of dissipation. The mobility is calculated directly from these charge density data and the measurements repeated at several temperatures.

Specimen preparation.—Specimens of all the "pure" materials examined were cut from sheet samples. The specimens were washed with isopropanol and fixed onto the cell using Eccobond 59C electrically conducting adhesive. No significant differences were observed in the results obtained from specimens mounted in this way from those obtained with specimens relaxed onto the cell as was done in previous experiments.

Halogen-doped materials were obtained by maintaining samples in the halogen vapor at elevated temperatures. The actual temperature was significant only in determining the rate of halogen absorption, a value around 60°C being usually employed. Doped specimens were subsequently cut, washed, and mounted as described earlier.

Optical absorption measurements.—The optical absorption spectra of all the materials investigated were obtained in both the u.v./visible and infrared ranges using Beckman DB-GT and Grubb-Parsons Spectromaster spectrophotometers, respectively.

Experimental Results

"Pure" polymers.—Carrier mobility has been determined for HDPE, LDPE, octacosane, polymethylene, and polypropylene. The experimental values of mobility in some of these materials are plotted against inverse of absolute temperature in Fig. 1. Despite considerable scatter in the data there are significant differences in the mobilities. It was concluded previously that the mobility in HDPE was smaller than that in LDPE owing to the greater crystallinity of the former. Some doubt has been cast on this conclusion by observation of a density change from 0.96 to 0.98 in a sample of HDPE held at 120°C *in vacuo* for some days with no apparent change in mobility.

It is known that HDPE contains some 1.5-2 terminal unsaturated groups per 1000 carbon atoms; each chain being terminated by 1 vinyl and 1 methyl group. In LDPE the density is about an order of magnitude less although this material also contains significant numbers of pendant unsaturated groups. Both polymethylene and polypropylene, which should virtually contain no such groups, exhibit a higher mobility. It may be concluded, therefore, that the terminal vinyl group contributes significantly to the trapping. That the vinyl group only contributes to the over-all carrier impedance is underlined by the observation that the mobility in polymethylene extrapolated to room temperature is still some 3½ orders of magnitude smaller than that in octacosane.

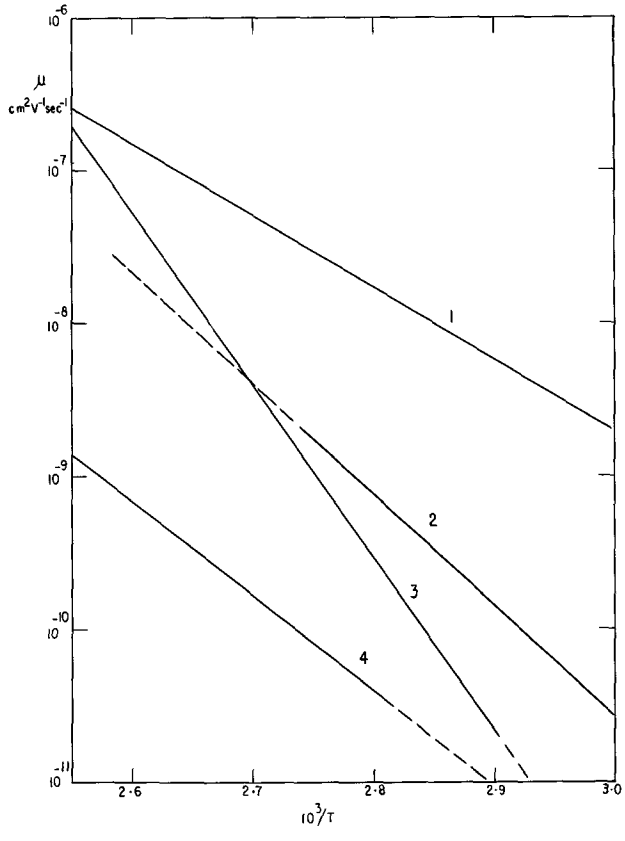

Fig. 1. Average values of carrier mobility obtained for 1 polymethylene, 2 LDPE (XDG33), 3 polypropylene, 4 HDPE (Rigidex 50), plotted against the inverse of absolute temperature.

Table I

Material	μ_0	W (eV)
Polymethylene	1.2×10^5	0.91
WNC18 } LDPE	2.8×10^5	0.99
XDG33 } LDPE	2.4×10^{11}	1.45
'Rigidex' 50 } HDPE	1.3×10^7	1.24
'Rigidex' 002.47 } HDPE	1.1×10^{18}	1.72
Polypropylene	1.0×10^{22}	2.23

Hopping carrier transport may be described by the expression, $\mu = \mu_0 \exp(-W/kT)$, where W, k, and T are the activation energy, Boltzmann constant, and absolute temperature, respectively. The values of μ_0 and W calculated from the experimental data are given in Table I.

In the simple "hopping" model the constant $\mu_0 = e/kT\ \nu/N^{2/3}$, where N is the trap density, e the electron charge, and ν a lattice vibration frequency. Using conventional values for these parameters, the value of μ_0 obtained for polypropylene yields a trap density of less than 1 cm^{-3}. Clearly this is unacceptable and hence the simple model is not valid. Examination of the values of W and μ_0 shows an interdependence in these parameters, *i.e.*, $\mu_0 = fn\ (W)$. This compensation affect is familiar for organic semiconductors (5). This could indicate a consistent transport mechanism for all polymers with the hop distance being related to the height of the potential barrier. Clarification of this effect, however, must await more extensive data.

Doped polymers.—Mobility increases were observed with both LDPE and HDPE doped with either bromine or iodine. The values of mobility obtained with doped HDPE ("Rigidex" 50) are plotted against the inverse of absolute temperature in Fig. 2, together with the data for the "pure" polymer. Clearly iodine has the greater effect.

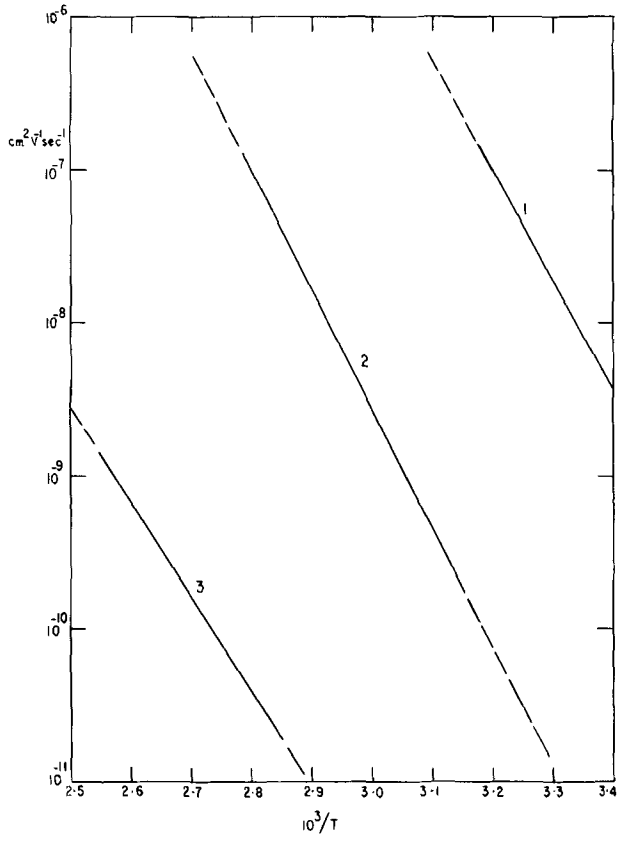

Fig. 2. Average values of carrier mobility obtained for 1 HDPE (Rigidex 50) doped with iodine, 2 HDPE (Rigidex 50) doped with bromine, and 3 HDPE (Rigidex 50), plotted against the inverse of absolute temperature.

Typically LDPE takes up 3-4% of iodine w/w, (weight for weight) this being reduced to an equilibrium 1% weight increase on standing in air or on evacuating. The corresponding figures for HDPE are 2.5% and 1.5-2%, respectively. The color changes which occur during this desorption show an interesting effect when examined spectrophotometrically. Figure 3 shows typical optical absorption traces in the u.v. visible obtained with iodine-doped HDPE, trace 1 being obtained immediately after doping and trace 2 with the same specimen after standing some 30 min in air. The absorption peak centered on 515 nm, which decreases with time (cf. traces 1 and 2), is attributed to molecular iodine which has a broad absorption band centered around 520 nm. This indicates that the iodine diffuses into the polyethylene as neutral molecules—most of which re-emerge on standing in air. The other band centered around 270 nm, which is permanent, is interpreted as charge exchange complex formation between iodine and the polymer.

Optical absorption data in the infrared range obtained with the same materials are presented in Fig. 4. Trace (a) shows the spectrum in the 8-13 μm range for the "pure" HDPE, the absorption peaks at about 11 μm (910 cm^{-1}) and 10 μm (993 cm^{-1}) being conventionally assigned to vibrations of the terminal double bond groups, $-CH = CH_2$ (vinyl group). Traces (b) and (c) exhibit the effect of introducing iodine, the latter trace being obtained after a longer "soak" in the iodine vapor. The double bond group vibrations are reduced and eventually disappear while two new peaks are generated at 9.3 μm (1079 cm^{-1}) and 12.3 μm (812 cm^{-1}). This is interpreted as indicating that the complexes are formed in association with the terminal double bond groups.

Bromination is also associated with the vinyl groups, similar changes being observed in the polyethylene infrared spectrum. Witenhafer and Koenig (8), who brominated crystals of "Marlex" 6050, observed reductions in the vinyl band intensities and concluded that these unsaturated groups lay largely outside the crystal lattice.

The uptake of iodine is roughly equivalent to the unsaturation concentration in HDPE. It is found that the original mobility characteristics of the "pure" polymer can be measured on dissolving an iodine-doped specimen in xylene and recasting a film. This confirms that the iodine forms loosely coupled complexes with HDPE rather than react chemically forming a new species. In LDPE, however, the bond appears much stronger since the iodine-doped material is insoluble in xylene.

Conclusions

It is concluded from these experimental data that the terminal vinyl groups contribute significantly to carrier trapping in polyethylene. The earlier model of trapping being associated with the crystalline/amorphous interface is reaffirmed, since the vinyl groups lie outside the crystalline regions. The halogens clearly associate with the double bonds in the terminal groups. Their effect on the carrier mobility is envisaged as releasing a "hole" into relatively unimpeded motion along the molecule chain, this lying largely within a crystalline structure.

This is a "discrete" model, the trapping effects discussed contributing only to the over-all carrier impedance. The "continuum" implied by a compensation effect, where trapping characteristics of all polymers are identical—the individual properties of each material being defined by an interrelated activation energy and hop distance—is intriguing. Within the latter context, the model currently presented appears as a defect property of the materials. Further investigations of this compensation effect are indicated, the data allowing interpretation of the presently somewhat nebulous parameter, μ_0.

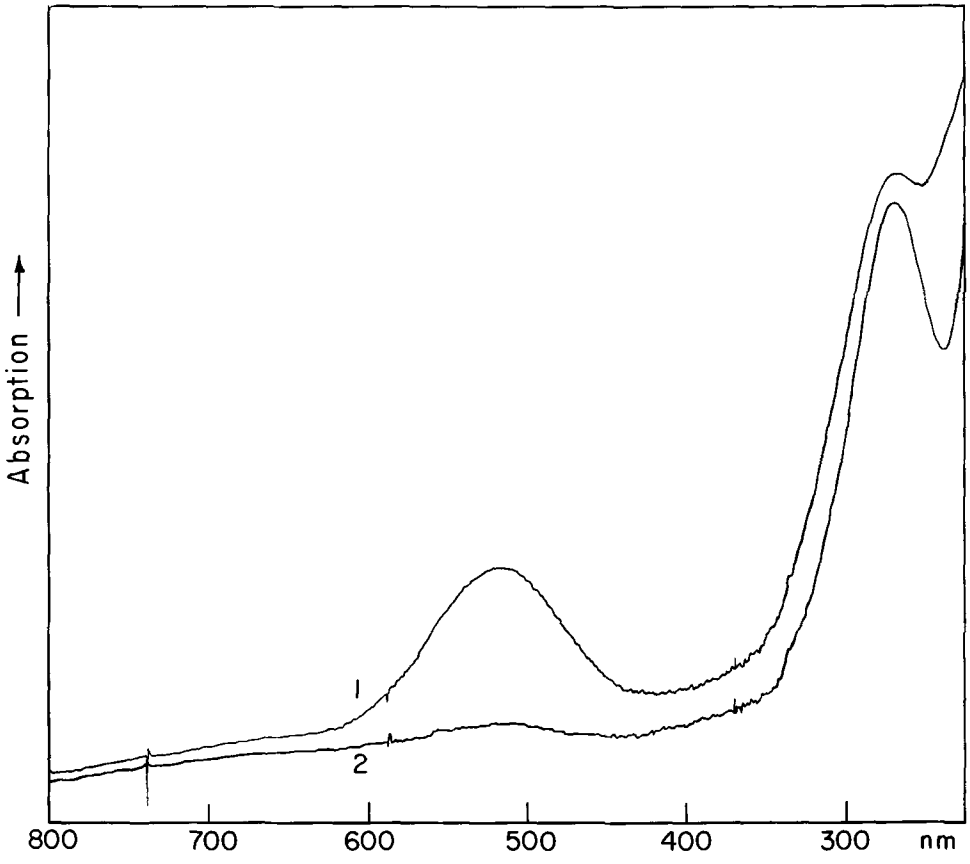

Fig. 3. U.V./visible absorption spectra of iodine-doped polyethylene: 1, immediately after doping; 2, after standing for 30 min in air.

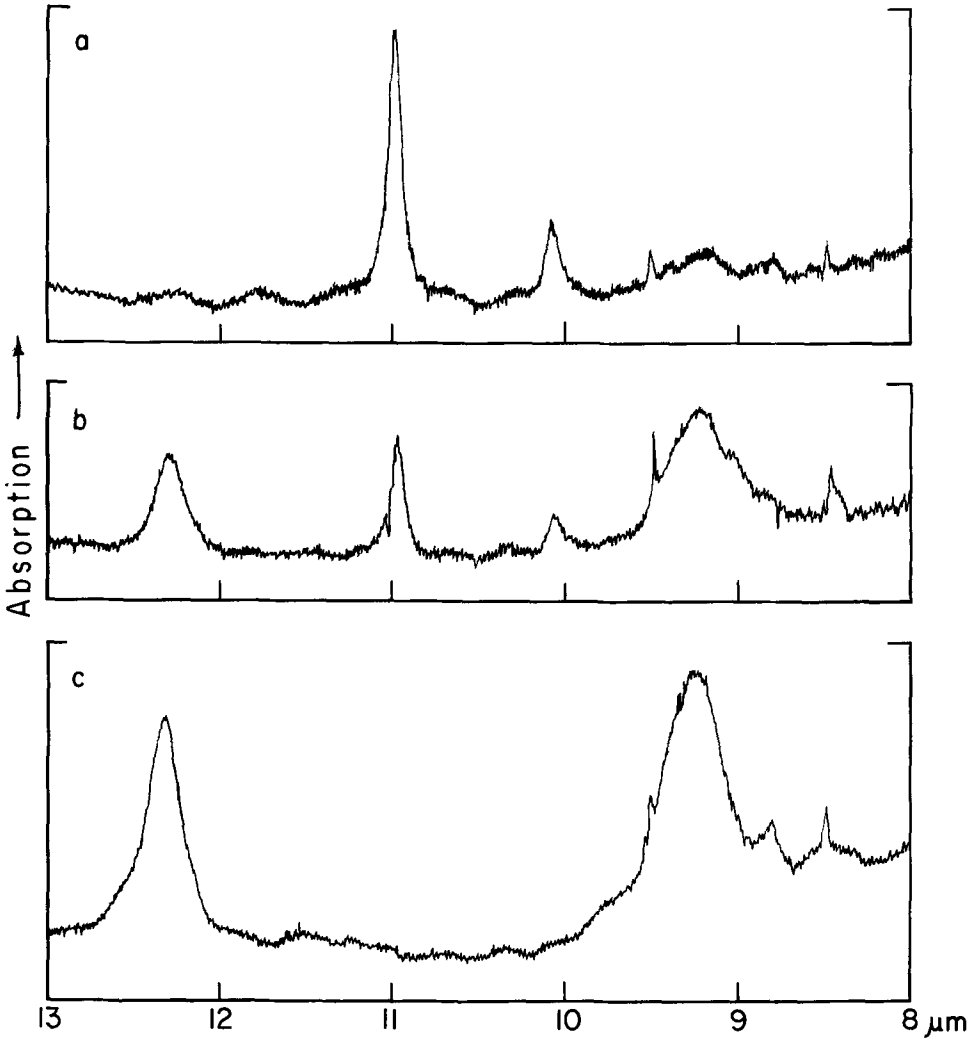

Fig. 4. Infrared absorption spectra of polyethylene: a, undoped; b, iodine-doped; and c, after longer soak in iodine.

Acknowledgment

The authors thank the sponsors of this investigation for permission to publish this material.

Manuscript received July 31, 1972. This was Paper 117 presented at the Miami Beach, Florida, Meeting of the Society, Oct. 8-13, 1972.

Any discussion of this paper will appear in a Discussion Section to be published in the December 1973 JOURNAL.

REFERENCES

1. H. G. Clark, L. D. Ikenberry, and R. G. Mason, in "Clean Surfaces," G. Goldfinger, Editor, pp. 45-76, Marcel Dekker, Inc., New York (1970).
2. R. A. Creswell, M. M. Perlman, and M. A. Kabayama, in "Dielectric Properties of Polymers," F. E. Karasz, Editor, pp. 295-312, Plenum Publishing Corp., New York (1972).
3. D. K. Davies, "Static Electrification," IPPS Conf. Ser. No. 4, pp. 29-36 (1967).
4. D. K. Davies, *J. Phys. D. Appl. Phys.*, **5**, 162 (1972).
5. D. D. Eley, A. S. Fawcett, and M. R. Willis, *Trans. Faraday Soc.*, **64**, 1513 (1968).
6. B. Gross, *Endeavour*, **30**, 115 (1971).
7. E. H. Martin and J. Hirsch, *J. Non-Cryst. Solids*, **4**, 133 (1970).
8. D. E. Witenhafer and J. L. Koenig, *J. Polymer Sci. A-2*, **7**, 1279 (1969).

Polymethyl Methacrylate as an Electron Sensitive Resist

R. A. Harris[1]

Electrical Engineering Laboratories, University of Manchester, Manchester, M13 9PL, England

ABSTRACT

The effect of the molecular-weight distribution of polymethyl methacrylate on its performance as a resist material for electron beam exposure is investigated with the aid of gel-permeation chromatography. The solubility of PMMA in a developer comprising a 3:1 ratio of isopropyl alcohol to methyl isobutyl ketone is determined, and the need for post-development washing of substrates in isopropyl alcohol is shown to be due, in part, to the liberation of insoluble polymer molecules from the film during development. Removal of very high molecular weight molecules, which are dominant in determining intrinsic viscosity, is found to lend considerable improvement to the rate of dissolution of PMMA in solvents, ease of filtration, and quality of spin-coated films. The optimum molecular-weight distribution is determined as being one which contains very few molecules with weights below about 50,000 or above a few hundred thousand. The preparation of PMMA with such a distribution by fractionation is outlined, and 10% concentrations of the resulting fractions are found to dissolve in methyl isobutyl ketone at 21°C in 2-3 min. The effectiveness of fractionated PMMA as a resist against chemical etchants is also found to be considerably better than that of broadly distributed polymers. Baking of films prior to exposure is considered with regard to its effects on substrate adhesion, molecular-weight distribution, and the rate at which films dissolve in solvents. Preliminary results on the use of polymer hydrolysis as a method of improving adhesion of the polymer to substrates are reported, an order of magnitude improvement being easily achieved.

Electron beams are being used increasingly as a means of fabricating microelectronic devices (1). The use of conventional photoresists for electron-beam exposure has been investigated and their resolution shown to be limited (2, 3). However, several polymers which can be used as positive-acting resists have been described by Haller *et al.* (4), and one, polymethyl methacrylate (PMMA) has been shown to be well suited to electron-beam exposure. The polymer is currently in general use as an electron resist and several papers describing its use for the fabrication of devices with submicron linewidths have been published during recent years, of which Ref. (5-7) are typical.

The effect of radiation on polymers, including PMMA, has been described by Charlesby (8) and an investigation of the effects of electron irradiation on PMMA has been reported by Shultz *et al.* (9). Ku and Scala (10) have discussed the effect of electron beams on polymers which can act either as positive or as negative resists and have shown that the molecular-weight distribution of a polymer is an important factor in determining its performance as a resist material.

This paper describes the effect of the molecular-weight distribution of PMMA on its performance as an electron resist. Preliminary results on the use of hydrolysis as a method of improving adhesion are also reported.

[1] Present address: GEC Ltd., Hirst Research Centre, Wembley, Middlesex, HA 9 7PP, England.

Key words: molecular weight, adhesion, polymer, methacrylate, resist.

Method of Investigation

Molecular-weight distribution analysis by gel-permeation chromatography (GPC) has been used for all results reported in this paper and values are limited in accuracy to about ±10% by errors inherent in GPC. However all the results are self-consistent and good for comparison. Values for the number-averaged molecular weights M_n, weight-averaged molecular weights M_w, and weight distribution of molecular weights were obtained by computer analysis of the chromatographs using the procedure described by Pickett *et al.* (11).

Degradation and Development

The use of PMMA as a positive-acting resist is based on two effects: (*i*) degradation on exposure to an electron beam and (*ii*) removal of the exposed areas using a developer based on the principle of soluble fraction. When PMMA is exposed by an electron beam with an exposure charge density in the region of 5×10^{-5} to 5×10^{-4} coulombs/cm^2, random scission of the molecular chains occurs and the average molecular weight decreases. The exact exposure range depends on a number of factors of which the most significant is electron-beam accelerating voltage (3, 7). At high-charge den-

sities crosslinking is predominant and the exposed areas are insoluble.

Development of the resist is achieved by using a poor solvent which will dissolve away molecules of low molecular weight but leave unaffected those of high molecular weight. Such a solvent can be obtained by mixing together a liquid which is a good solvent for any molecular weight of the polymer with one which will not dissolve even the very low molecular weights. For PMMA a developer comprising isopropyl alcohol (IPA) as nonsolvent and methyl isobutyl ketone (MIBK) as solvent is frequently used, and Hatzakis (7) has referred to a solution comprising 1 part MIBK and 3 parts IPA as being "standard developer," the development time being 1½-2 min at 21°C.

Charlesby (8) and Saito (12) have shown that the distribution of the molecular weights in a degraded polymer is largely independent of the initial distribution if the number of scissions is large. This is the case for PMMA when exposed with typical charge densities and Ku and Scala (10) have calculated the most probable distribution for exposed PMMA and shown that a value of a few thousand for M_n is to be expected.

The integral molecular-weight distribution of a 0.5 μm thick film of PMMA exposed at 10 kV with 10^{-4} coulomb/cm^2, as determined by GPC, is shown in Fig. 1 together with the distribution of the unexposed polymer. The degraded polymer sample was obtained by exposure of 625 separated millimeter square areas on each of 20 substrates, this number being necessary to obtain a sufficient weight of polymer for GPC analysis (5-10 mg). Separation from the unexposed material was achieved by developing the films for 1½ min at 21°C in standard developer and then soaking in IPA for 5 min, following the procedure outlined by Hatzakis. The polymer extracted by the two solutions was then combined to form the sample for analysis. To prevent thermal degradation during exposure each substrate was coated with 1 μm of aluminum to ensure rapid heat dissipation (13). Industrial polymers often contain plasticizers and copolymers and to ensure that pure PMMA was used the original polymer was prepared by polymerization of monomer methyl methacrylate using benzoyl peroxide as catalyst.

The value of M_n for the degraded polymer, determined by analysis of the GPC data, is 2400 and the value of 3600 calculated following the method of Ku and Scala shows that the theoretical calculation can be regarded as providing a good order of magnitude estimate of the peak of the distribution of the degraded polymer. Figure 2 shows the theoretical integral distribution of the degraded polymer; comparison with curve B in Fig. 1 shows moderately good agreement. The main error in the calculation arises from the assumption of a uniform rate of loss of energy of an elec-

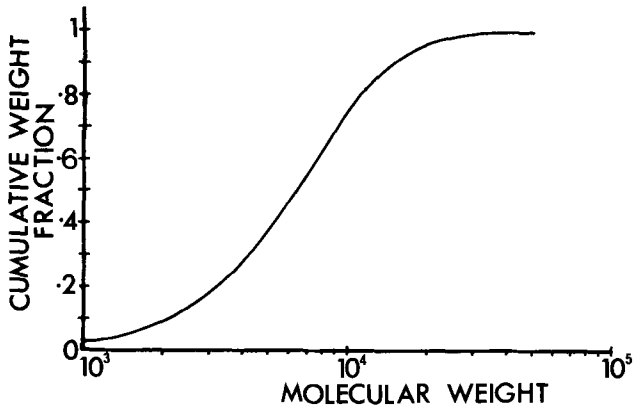

Fig. 2. Theoretical molecular-weight distribution of a 0.5 μm thick film of polymethyl methacrylate exposed at 10 kV with 10^{-4} coulomb/cm^2. (Initial M_n = 563,000; final M_n = 3600).

tron passing through the film. The actual rate of loss increases rapidly with depth (14) and accounts for the rather broad GPC distribution which has a dispersity of 3.4 compared with a dispersity of 2 for the most probable distribution. A significant feature of the degraded distribution is that it extends to molecular weights in excess of 50,000. Although molecules of this weight have been extracted from the film by the development procedure it does not necessarily follow that they are readily soluble in developer. This point will be discussed more fully in a later paragraph.

Due to the Gaussian cross-sectional density distribution of an electron beam and scattering in the polymer film the number of scissions in the molecules at the edges of exposed areas falls gradually to zero (14). Therefore at these edges a range of molecular weights exists of which only some are soluble in developer; furthermore, not all of the soluble molecules are removed by the developer since some will be held in place by neighboring high molecular-weight molecules. Figure 3 shows the GPC distributions of the PMMA remaining on the substrates after development. Distribution A is the polymer removed by spraying the substrates with chloroform, which is a good solvent for all molecular weights. This procedure did not remove all of the polymer from the substrates and distribution B shows the remaining polymer removed by prolonged soaking in chloroform. Spraying the substrates served to remove the most readily soluble PMMA and distribution A is largely comprised of those scission fragments not removed by developer, whereas distribution B mainly consists of unexposed polymer.

Distribution A shows that scission fragments with molecular weights between the initial and degraded

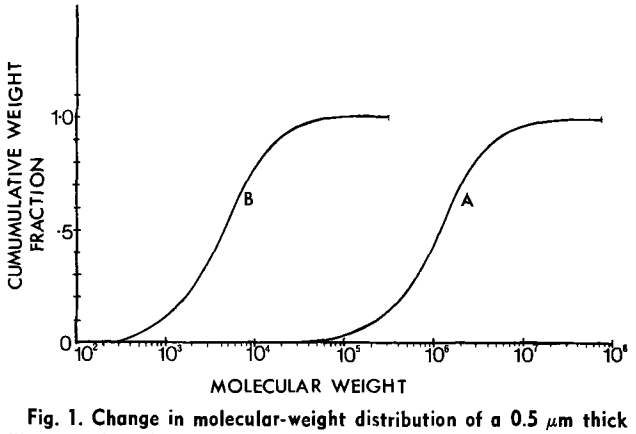

Fig. 1. Change in molecular-weight distribution of a 0.5 μm thick film of polymethyl methacrylate due to an electron dose of 10^{-4} coulomb/cm^2 at 10 kV. A—Distribution before exposure (M_n = 5.63 × 10^5; M_w = 2.26 × 10^6); B—distribution of exposed polymer removed by standard developer (M_n = 2370; M_w = 8160).

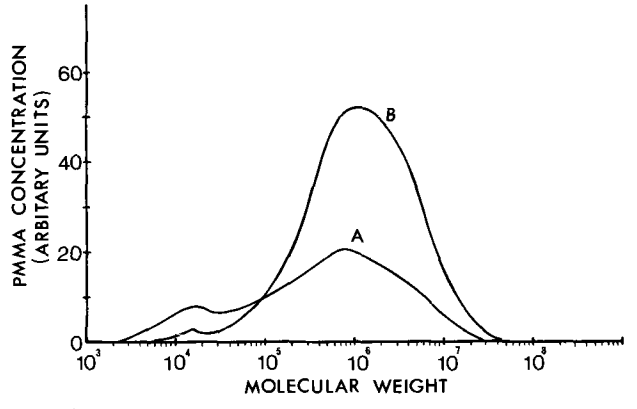

Fig. 3. Concentration of polymethyl methacrylate remaining on the substrates after development as a function of molecular weight. A—Polymer removed by spraying with chloroform (M_n = 5.6 × 10^4; M_w = 1.32 × 10^6); B—remaining polymer removed by soaking in chloroform (M_n = 2.47 × 10^5; M_w = 2.04 × 10^6).

PMMA distribution peaks are generated. These will mainly consist of the insoluble scission fragments formed round the edges of the exposed areas. Small peaks occur at a molecular weight of about 15,000 in both distributions. This value is well within the range extracted by the developer and corresponds to soluble scission fragments trapped by higher molecular-weight molecules. Few of the very low molecular-weight molecules are retained in this way since most are not directly adjacent to the bulk of the insoluble polymer.

To investigate the solubility in standard developer PMMA with a range of molecular weights extending from 2,000-110,000 with a peak at 25,000 was prepared by fractionation, as described below. 0.5g of this polymer was completely dissolved in 500 ml of standard developer by heating the solution to 50°C. The solution was then allowed to cool over a period of 24 hr to the normal development temperature of 21°C. During this time insoluble molecules were precipitated onto the walls of the flask. The solution containing the soluble fraction was decanted off and the PMMA precipitated by addition of excess methyl alcohol (nonsolvent).

Figure 4 shows the integral molecular-weight distributions of the soluble and insoluble fractions together with the distribution of the initial polymer. Although 50% of the initial polymer consists of molecules with weights above 25,000 these comprise only 30% of the soluble fraction, indicating that they are not fully soluble in the solution. The peak of the molecular-weight distribution of the soluble fraction occurs at 20,000 and molecular weights above this must therefore gradually decrease in solubility with complete insolubility of weights above about 65,000.

The molecules with molecular weights above about 50,000, which are extracted from the exposed resist by the development process, must, as suggested earlier, have a very low solubility in developer and are probably washed away as insoluble particles. However, Fig. 3 indicates that many low solubility molecules remain on the substrate and their removal will therefore still be in progress when the substrate is withdrawn from the developer. The presence of this material must in part account for the need to wash substrates in a nonsolvent, usually isopropyl alcohol, after development and before drying. Such a procedure serves to remove any loose insoluble material before it can become reattached to either the remaining film or the substrate.

Molecular-Weight Distribution

Table I lists GPC data on typical PMMA molecular-weight distributions. The polymers designated C1, C2, and C3 correspond to three of the most commonly used commercial forms of powdered PMMA in Britain. PMMA in sheet form has not been considered because

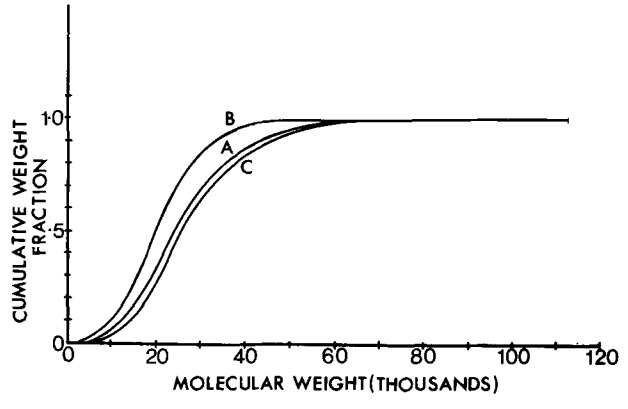

Fig. 4. Integral molecular-weight distribution indicating the solubility of polymethyl methacrylate in standard developer. A—Initial polymer (M_n = 21,500; M_w = 27,000); B—soluble fraction (M_n = 17,500; M_w = 21,000); C—insoluble fraction (M_n = 23,800; M_w = 28,800).

Table I. Typical molecular-weight distribution data for polymethyl methacrylate[a]

Polymer	M_n	M_w	Molecular weight range	Percentage weight of polymer with molecular weight <20,000
C1	35	71	1-1,000	17.3
C2	127	415	2-6,900	2.3
C3	304	1064	6-17,000	0.6
L1	191	516	15-17,000	0.5
L2	563	2257	18-75,000	0.008

[a] Molecular weights in thousands.

it takes appreciably longer to dissolve. Polymers L1 and L2 were prepared in this laboratory using benzoyl peroxide as catalyst; L2 is the undegraded polymer used for the experiment on degradation described above. The percentage weight of each polymer with molecular weights below 20,000 provides an indication of the amount of each polymer that is readily soluble in standard developer at 21°C.

PMMA with only a small percentage weight of molecules soluble in developer will not exhibit pinhole formation during development because the molecules will be held in place by the much larger number of insoluble high molecular-weight molecules. However C1 is unsuitable for use as a resist and C2 was found to form pinholes when developed, especially in films of less than 3000Å thickness.

To avoid pinhole formation in thin films due to low molecular-weight material it is necessary to use polymer C3, L1, or L2. However, these all contain molecules of a very high molecular weight which are dominant in determining the intrinsic viscosity and solubility of the polymers in any solvent. The intrinsic viscosity η is related to the molecular weight M by $\eta = KM^a$ where K and a are constants for any one solvent and temperature (for methyl ethyl ketone at 25°C $K = 6.8 \times 10^{-5}$ and $a = 0.72$).

Methyl ethyl ketone or methyl isobutyl ketone are suitable as solvents for PMMA when preparing a solution for spin-coating, although of the two MIBK is to be preferred since it evaporates more slowly during the coating process. However, the intrinsic viscosities of C3, L1, and L2 in MIBK are very high and they are very difficult to dissolve, prolonged heating and stirring being required (typically 12 hr). The high intrinsic viscosities also result in the thickness of spin-coated films being nonuniform and nonrepeatable. The polymers dissolve more readily in MEK and film quality is better but is limited by the faster evaporation rate of the solvent. Polymers C1 and C2 dissolve in MIBK in about 12 hr if left standing at room temperature and both produce a good quality of film on substrates.

Using the five types of PMMA, tests were made on undeveloped films of various thickness to examine the variation of etch resistance and adhesion with molecular-weight distribution. These showed that decreasing M_n corresponds to better adhesion and a more prolonged resistance to etchants. This is to be expected because of the better spin-coating characteristics of lower molecular-weight polymers.

The optimum molecular-weight distribution of PMMA for use as an electron resist must therefore be a compromise between two conflicting requirements. Increasing the molecular weight reduces pinholes generated during development and improves edge definition, but causes a decrease in over-all etch resistance, adhesion, and film quality. Furthermore, the polymer becomes harder to dissolve and the resist difficult to filter. The best molecular-weight distribution of PMMA for use as a resist must therefore be one which has a narrow molecular-weight range with a sharp cutoff at both low and high molecular weights.

An optimum distribution is one containing little or no molecules with weights below 40,000-50,000 or above a few hundred thousand and would ideally be monodisperse (*i.e.*, $M_w/M_n = 1$). However, the most probable distribution for PMMA is a Poisson distribution with a dispersity of 2, although there are polymerization processes which can produce nearly monodisperse distributions (15). The most readily available and the most simply polymerized forms of PMMA have a dispersity equal to or greater than 2, as can be seen from Table I, and narrow distributions are in general more conveniently obtained by fractionation.

To investigate the performance of PMMA with narrow distributions as resist, 20g of polymer C1 was fractionated to remove the high molecular-weight material and then refractionated into the five fractions whose distribution data is given in Table II. The PMMA was dissolved in 2 liters of toluene and fractionated by a combination of nonsolvent addition and cooling, with 40°-60°C petroleum ether as nonsolvent. For each fractionation the solution was initially raised to a temperature sufficient to dissolve the PMMA fully (40°-55°C) and then cooled to 25°C over a 24 hr period, after which the precipitated fraction was removed.

A low starting concentration is necessary in order to obtain narrow fractions, and because of this it is difficult to fractionate quantities of PMMA in excess of 20g on a laboratory scale since the final volume is often about 10 liters. To obtain fractions of a usable quantity the initial polymer must therefore be one whose distribution contains a large percentage weight of molecular weights in the region of the desired fraction. Of the polymers listed in Table I only C1 is suitable in this respect but because of its large content of low molecular weights, significant quantities have appeared in all the fractions. Fractions 4 and 5 contain too much of this material to be useful; however, further fractionation of fractions 1, 2, and 3 can be used to remove most of the low molecular-weight material from them.

An investigation of the performance of these fractions as resists confirmed the trends found with unfractionated polymers with respect to adhesion, etch resistance, and resolution. All fractions produced films of a very high quality, well in excess of all types of unfractionated PMMA. Furthermore, all fractions were readily soluble in MIBK; for example 10% concentrations of fraction 1 could be dissolved at room temperature in 2-3 min. The solutions were also easily filtered. This considerable improvement in film quality, solubility, and ease of filtration, associated with the reduction in intrinsic viscosity, is sufficient to make the use of fractionated PMMA highly advantageous. In addition, some improvement in adhesion is attained and further fractionation to remove most of the low molecular-weight molecules eliminates pinhole formation during development and produces a resist with very good etch resistance and edge resolution.

Table II. Molecular-weight distribution data for fractionated polymethyl methacrylate

Fraction number	M_n	M_w	Molecular weight range	Percentage weight of polymer with molecular weight <20,000	Weight fraction (g)
1	61	91	4-650	5	4.92
2	43	62	4-346	13	3.33
3	38	51	2-346	12	3.46
4	29	41	2-346	27	2.13
5	21	27	2-113	37	1.84
Residue	15	19	1-68	76	1.04

[a] Molecular weights are in thousands.

Baking

Baking films at 170°C for 20-30 min before exposure is generally used as a means of improving adhesion. At this temperature, which is well in excess of the glass-transition temperature of PMMA (typically T_g = 100°-110°C), the polymer exhibits a rubber-like elasticity and molecules are able to slide over each other enabling strains generated during the coating process to be released.

The ease with which the molecules slide increases with temperature. Films must be heated to at least 160°C before the polymer is sufficiently soft to allow solvent remaining in the film after the coating process to be released (16). At temperatures above 190°C the rate of thermal degradation of PMMA becomes appreciable and 170°C therefore allows for solvent evaporation with a minimum of thermal degradation. GPC analysis of films baked at 170°C for 30 min shows the amount of degradation is insignificant.

Baking films removes solvent, water, or monomer present in the polymer. This raises the glass-transition temperature, makes films harder and more brittle at temperatures below T_g, and reduces the surface area to weight ratio. A reduction in the rate of dissolution of the films in solvents results, and it is possible to use a developer with a higher solvent to nonsolvent ratio without increasing pinhole formation. Hatzakis (7) has described the use of 100% MIBK as a developer for films baked at 170° for at least 1 hr.

Adhesion

Failures of PMMA resist in etch baths are mainly due to the polymer film lifting off the substrate because of poor adhesion. Even when baked the adhesion is still relatively poor and any improvement would lead to a reduction in resist failure in etch baths. It should be noted, however, that the adhesion is adequate for the lift-off metalization technique (4, 7); indeed an improvement in adhesion might be detrimental to the process.

To compare adhesion of different PMMA samples a technique used by Long (17) with purified photoresists was adopted. Films are placed in an ultrasonic water bath, preheated to 60°C, and examined for evidence of lifting at regular time intervals. Films of all types of PMMA listed in Table I and II were tested in this way and the increase of adhesion with decreasing M_n was established. After 15 min about 50% of each film of polymer type L2 had lifted off glass substrates, but only 5% of each film of polymer type F5. However, Long reported photoresists which showed no lifting after 45 min after which time all types of PMMA film were almost completely stripped.

Photoresists generally contain molecules with localized regions of high polarity; in particular hydroxyl groups are often present (18). The latter form hydrogen bonds with the substrate and thereby considerably increase molecular, and hence resist, adhesion. However PMMA, which has the structure

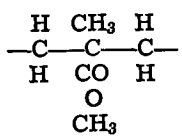

contains no hydroxyl groups. Furthermore, the molecules have very little polarity, and Van Der Waals forces between them and the substrate are therefore very weak. This absence of any strong bonding between the molecules and the substrate accounts for the relatively poor adhesion of PMMA.

The adhesion can be improved by introducing a number of hydroxyl groups onto each molecule by hydrolysis. To investigate the effect of PMMA hydrolysis on adhesion, two samples of polymer of type F1 in Table II were hydrolyzed, one by acid hydrolysis using the procedure described by Robertson and Har-

wood (19), and the other by base hydrolysis following the method of Bains and Bevington (20). The adhesion of these two polymer samples was then compared with that of the initial polymer using the technique already described. The acid-hydrolyzed sample showed no significant improvement in adhesion, but films of the base-hydrolyzed polymer showed no signs of lifting after ultrasonic agitation for periods in excess of 2 hr. This represents more than an order of magnitude improvement in adhesion and it may be concluded that hydrolysis is a powerful method for improving adhesion.

The resist sensitivity and resolution were found to be unchanged by hydrolysis but etch resistance was considerably improved. The reason for the failure of the acid-hydrolyzed films was found to be due to the presence of insoluble submicron particles generated during hydrolysis. More careful control of the process might eliminate this problem; alternatively, one of the many other methods described in the literature could be tried.

Conclusions

A general indication of the effect of the molecular-weight distribution of PMMA on its performance as an electron resist has been given. It has been shown that a developer comprising 3 parts isopropyl alcohol to 1 part methyl isobutyl ketone used at 21°C will readily dissolve molecules with weights below 20,000, and that over 90% of polymer molecules exposed at 10 kV with a dose of 10^{-4} coulomb/cm have molecular weights below this value. However, a small quantity of molecules with weights of up to about 65,000 are dissolved by the developer and 1% of the molecules removed by the development process were found to have weights above 50,000, with some in excess of 100,000. Therefore, to avoid pinhole formation during development it is essential to use PMMA which has a very low percentage of molecules with weights below 20,000, and preferably very few below 50,000.

It has also been shown that the removal of very high molecular-weight molecules, which are dominant in determining intrinsic viscosity in solution, produces PMMA with properties which considerably enhance its performance as a resist. It has therefore been concluded that the optimum distribution of PMMA for use as a resist is one which contains little or no molecules with weights below about 50,000 or above about 600,000, and the preparation of such a distribution by polymer fractionation has been outlined.

Optimizing the molecular-weight distribution has been found to considerably improve the rate of PMMA dissolution in solvent, ease of resist filtration, film quality, and etch resistance. It has also been established that hydrolysis can provide a means by which the adhesion of PMMA to a substrate is considerably improved. It is therefore suggested that hydrolyzed PMMA with an optimized molecular-weight distribution provides a material which can be used as a very high quality electron resist. For use with the lift-off technique the use of resist which has not been hydrolyzed may be preferred.

Acknowledgments

The author wishes to thank Dr. C. Booth and Mr. R. L. Bartosiewicz for supplying the GPC data-analysis program and for many helpful discussions. Thanks are also extended to Dr. D. Machin for his help with polymer fractionation and hydrolysis, and to Mr. D. Roy for his technical assistance.

Manuscript submitted Aug. 28, 1972; revised manuscript received Oct. 16, 1972.

Any discussion of this paper will appear in a Discussion Section to be published in the December 1973 JOURNAL.

REFERENCES

1. S. J. Angello, *IEEE, Trans. Electron Devices,* **ED17,** 442 (1970).
2. R. F. M. Thornley and T. Sun, *This Journal,* **112,** 1151 (1965).
3. M. Hatzakis, *ibid.,* **116,** 1033 (1969).
4. I. Haller, M. Hatzakis, and R. Srinivasan, *IBM J. Res. Develop.,* **12,** 251 (1968).
5. R. F. M. Thornley, M. Hatzakis, and V. A. Dhaka, *IEEE, Trans. Electron Devices,* **ED17,** 961 (1970).
6. E. D. Wolf, L. O. Bauer, R. W. Bower, H. L. Garvin, and C. R. Buckley, *ibid.,* **ED17,** 446 (1970).
7. M. Hatzakis and A. N. Broers, "Electron-Beam Techniques for Fabricating Fine Metal Lines," in IEEE 11th Symposium on Electron, Ion and Laser Beam Technology, p. 337, San Francisco Press, Inc., San Francisco (1971).
8. A. Charlesby, "Atomic Radiation and Polymers," Pergamon Press, New York (1960).
9. A. R. Shultz, P. I. Roth, and G. B. Rothman, *J. Polymer Sci.,* **22,** 495 (1956).
10. H. Y. Ku and L. C. Scala, *This Journal,* **116,** 980 (1969).
11. H. E. Pickett, M. J. R. Cantow, and J. F. Johnson, *J. Polymer Sci., Part C,* **21,** 67 (1968).
12. O. Saito, *J. Phys. Soc. Japan,* **13,** 198 (1958).
13. G. S. Almasi, J. Blair, R. E. Ogilvie, and R. J. Schwartz, *J. Appl. Phys.,* **36,** 1848 (1965).
14. R. J. Hawryluk and H. I. Smith, Paper 128 presented at Electrochem. Soc. Meeting, Houston, Texas, May 7-11, 1972.
15. T. J. R. Weakley, R. J. P. Williams, and J. D. Wilson, *J. Chem. Soc.,* **73,** 3963 (1960).
16. N. Grassie, "Chemistry of High Polymer Degradation Processes," Butterworths, London (1956).
17. M. L. Long, "Quantitative Evaluation of a Photoresist," in Proc. Kodak Seminar on Microminiaturization, p. 60 (1970).
18. D. H. Gittelman, "Improved Techniques of Photoresist Processing," in Proc. Kodak Seminar on Microminiaturization, p. 37 (1970).
19. A. B. Robertson and H. J. Harwood, *Polymer Preprints,* **12,** 620 (1971).
20. F. C. Baines and J. C. Bevington, *J. Polymer Sci., Part A-1,* **6,** 2433 (1968).

Annealing Activation Energies of Sputtered Ge Films

S. Mardix and D. K. Paul

University of Rhode Island, Electrical Engineering Department, Kingston, Rhode Island 02881

ABSTRACT

Ge films were sputtered on water-cooled substrates. Conductivity was measured during isothermal and step-annealing experiments. These measurements indicate that activation energies for annealing increase from about 0.9-1.4 eV. A linear relationship was found between the activation energy for annealing and the change of conductivity at a certain reference temperature. The results are discussed and a mechanism is suggested in which a transformation from microcrystallinity to randomly disordered networks occurs in the low-temperature annealing mode.

Associated with annealing of amorphous Ge films is a decrease in conductivity, which can be lowered by a few orders of magnitude from its initial value (1-3). Si, Te, and SiC behave in a similar manner (3-5). Although there is evidence that this phenomenon is related to an atomic reorientation process, the mechanism involved in the annealing of the conductivity is still not quite understood. Activation energies of annealing can give some insight to the process taking place during annealing, and conversely models suggested for this process should predict the values found for the activation energies. Annealing activation energies for Ge evaporated films were found by Longini and Pansino to be in the range of 0.1 eV (6). This low-activation energy is compatible with a process involving slight reorientation of atoms in the amorphous films. Mogab and Kingery (5) found for SiC films the range of activation energies for annealing to be 0.4-2.3 eV. This led the authors to the conclusion that a variety, and perhaps a continuum, of defect types or configurations are present in their films.

It is not clear from the research noted above whether there is a basic difference between the rearrangement processes in Ge and SiC, or the low range of activation energies found for Ge is just a part of a wider spectrum similar to the situation for SiC. In this paper we attempt to resolve this question and report the results of annealing activation energy measurements of Ge amorphous sputtered films. The results are discussed on the basis of an analysis introduced by Primak (7).

Experimental

The samples were prepared by rf-sputtering of intrinsic Ge on water-cooled glass or quartz substrates. The sputtering took place in an atmosphere of 4 mTorr argon at a rate of 360 Å/min. The temperature of the film during sputtering was about 40°C. The final thickness of the films was measured by an interferometric technique or calculated from *IR* interference fringes. The thickness was around 1.5 μm for the different samples. The films appear smooth and shiny under a Normarsky-interference Zeiss microscope; x-ray diffraction photographs of the films were taken and do not show any indication of crystallinity. The optical constants near the absorption edge were calculated, using a method proposed by Baldini *et al.* (8). These are plotted in Fig. 1 together with the values found by Dash and Newman (9) for Ge crystals, and those of Clark (10) and Donovan *et al.* (11) for amorphous Ge.

From the above results we conclude that our films are amorphous. This is common for films deposited at or below room temperature (12). The conductivity during annealing was measured between previously sputtered Mo electrodes using a lock-in amplifier. In order to form the Mo electrodes a tungsten ribbon of about 0.7 mm wide was placed on top of the glass substrate. The sputtered Mo formed two electrodes, the thickness of which was about 0.8 μm. As some of the Mo was sputtered under the edges of the ribbon, they were tapered towards the gap which was about 0.5 mm wide. The contacts between the Ge layer (about 1 cm wide) and Mo electrodes were found to be ohmic before and after annealing. No cracks or other irregularities could be detected in the contact regions. Some of the specimens were annealed in an He atmosphere while others were immersed in silicon oil during annealing. No appreciable difference was found in the general behavior of the conductivity changes during annealing. If there are differences, they are small in comparison to the conductivity changes due to annealing. As some crystallization might occur even at low temperatures (13) we did not exceed 220°C at any stage of annealing, thus reducing the possibility of effects due to partial crystallization.

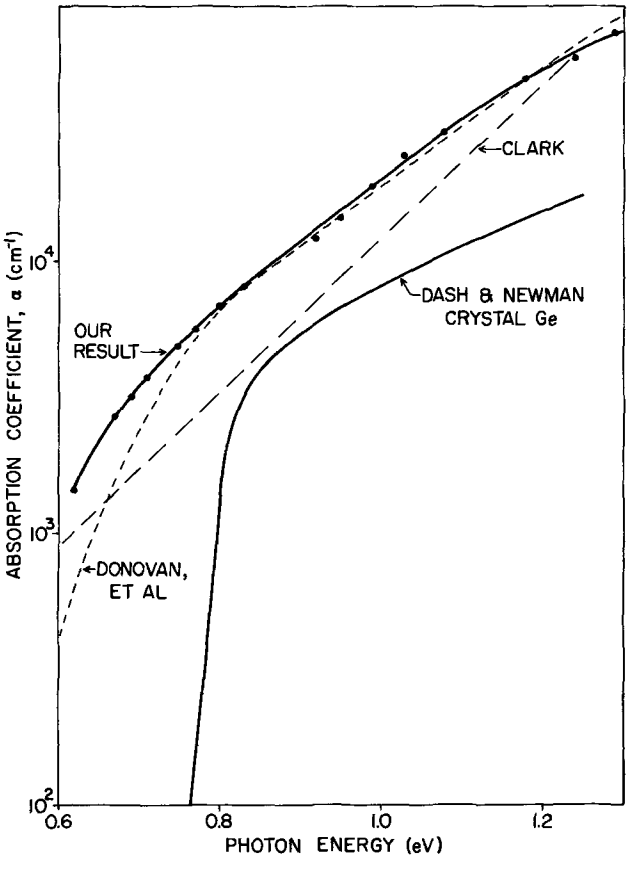

Fig. 1. Absorption constant of our sputtered Ge films before annealing. Curves of absorption constant of crystalline Ge reported by Dash and Newman (9), and those for amorphous Ge found by Clark (10) and Donovan et al. (11) are given for comparison.

Key words: annealing, amorphous, germanium, activation-energy, film.

Theoretical Considerations

The calculations involved in evaluating the activation energies and the discussion of the results are based on the theory reviewed and developed by Primak (7).

We assume that the conductivity is a property that is proportional to the concentration of the possible kinetic processes that take place during annealing. The conductivity σ is a function of time for isothermal annealing and is given by

$$\sigma(t) = \int_0^\infty s_0(\epsilon)\, \theta_n(\epsilon,t)\, d\epsilon \qquad [1]$$

where t is the time measured from the beginning of the annealing; ϵ is the activation energy; $s_0(\epsilon)$ is the conductivity distribution function (the spectrum) at $t = 0$; θ_n is termed the "characteristic isothermal-annealing function" and is given by

$$\theta_n = [1 - (1-n)Bte^{-\epsilon/kT}]^{1/(1-n)} \qquad [2]$$

where n is the order of reaction; B is a quantity having the dimension of frequency and may depend on ϵ; k is Boltzmann's constant; T is the absolute temperature.

According to Primak (7), the dependence of B on ϵ can be neglected for a broad activation spectrum; the measured activation energy E_a is approximately equal to the energy ϵ_0 at the inflection point of θ_n and is given by[1]

$$E_a \cong \epsilon_0 \cong kT \ln (Bt) \qquad [3]$$

also

$$\frac{d\sigma}{dt} \cong -s_0(\epsilon_0)\frac{d\epsilon_0}{dt} \qquad [4]$$

putting $x = \ln t$ we have from [3] and [4]

$$\frac{d\sigma}{dx} = -kT\, s_0(\epsilon_0) \qquad [5]$$

The characteristic activation energies of annealing can be measured by the step-annealing procedure. The rate of annealing R_1 is measured at the end of an isothermal-annealing experiment at temperature T_1. The temperature is raised rapidly to T_2, starting a new isothermal-annealing process with a rate of annealing R_2. Accordingly, ϵ_0 is given approximately by

$$\epsilon_0 \cong k\frac{T_1T_2}{T_2 - T_1}\ln\frac{R_2}{R_1} \qquad [6]$$

Results and Discussion

Isothermal-annealing curves for a number of specimens are given in Fig. 2. These specimens were annealed in different atmospheres and temperatures. In Fig. 2 $1/kT\ (\sigma/\sigma_0)$ is plotted against log t (σ_0 is the conductivity value at $t = 0$).[2]

It is seen that the slopes of all curves start with small values and after annealing reach a constant value which is almost the same for all of them. According to Eq. [5], the slopes of the curves in Fig. 2 should be proportional to the initial conductivity-distribution function at the characteristic activation energy ϵ_0. This means that the initial distribution function $s_0(\epsilon)$ has very small values up to a certain value of ϵ, then rises to a constant value and remains constant in the range of activation energies scanned by ϵ_0.

The activation energies for annealing were evaluated by the step-annealing method using Eq. [6]. The conductivity data for sample 35 are given in Fig. 3, and the calculated values of the activation energies E_a after each step of annealing are plotted in Fig. 4 against the change in conductivity $(\sigma_0 - \sigma)$ at the reference temperature of 84.3°C. Here σ_0 refers to the conductivity at the beginning of the first step of the step-annealing experiment.

The activation energy E_a is seen to increase approximately linearly with the change in conductivity. From Eq. [4] one gets for an isothermal-annealing process

$$\frac{d\sigma}{d\epsilon_0} \cong -s_0(\epsilon_0) \qquad [7]$$

This relation holds for each step of the step-annealing

[1] This is because the processes having activation energies around ϵ_0 make the maximum contribution to the change of conductivity.

[2] As the value of σ is temperature dependent, σ_0 is used here as a normalization factor for comparing isothermal annealings at different temperatures. Thus σ/σ_0 is, to a good approximation, independent of temperature for a certain state of annealing of the specimen. More accurately, if we start from two identical specimens and anneal them at two different temperatures (for different time lengths) so that both reach the same characteristic activation energy, we assume that both have the same value of σ/σ_0; σ and σ_0 are measured for each specimen at its annealing temperature.

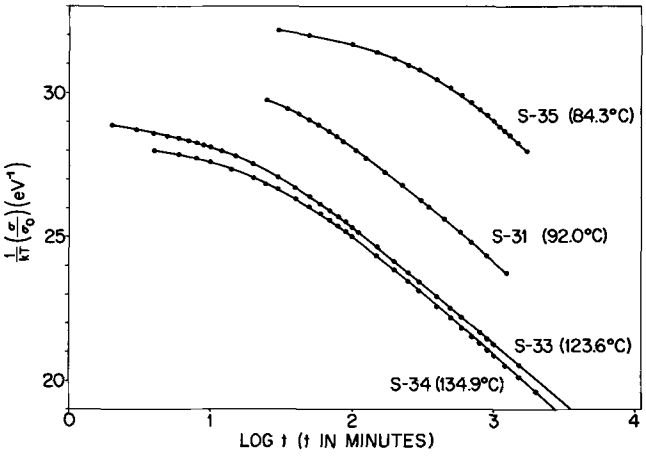

Fig. 2. Isothermal-annealing curves of normalized conductivity vs. log time for specimens S-31, annealed in an He atmosphere, S-33 annealed in transformer oil, and S-34 and S-35 annealed in silicon oil. Temperatures of annealing are given in the figure.

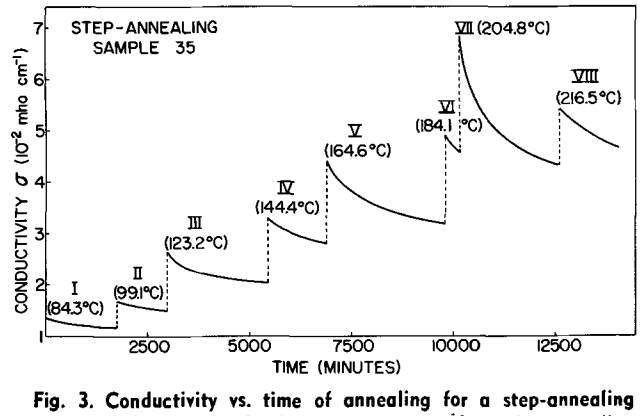

Fig. 3. Conductivity vs. time of annealing for a step-annealing experiment of S-35. Conductivities are measured at the annealing temperatures; these are indicated in the figure.

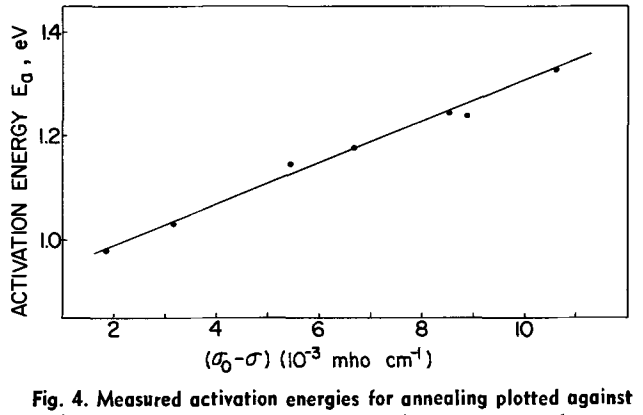

Fig. 4. Measured activation energies for annealing plotted against the change in conductivity at 84.3°C during a step-annealing experiment.

procedure. In accordance with the assumption on which the step-annealing procedure is based, there are no changes in the spectrum taking place while the temperature is raised between the steps, so that Eq. [7] holds also for a step-annealing procedure.[3] The linear relationship found in Fig. 4 follows from Eq. [7] if $s_0(\epsilon)$ is constant throughout the range of activation energies that ϵ_0 acquires during the experiment. From the first and last steps of annealing, we get a value of about 0.9 eV for the initial activation energy and about 1.4 eV for the final value. The data of Fig. 3 are replotted in Fig. 5 to give $1/kT$ (σ/σ_0) as a function of log t, with $t = 0$ for the beginning of each step of annealing. The curves of Fig. 5 are similar to those for the different specimens given in Fig. 2, which is in accord with the assumption that $s_0(\epsilon)$ is constant in the given energy range. It is to be noted that putting $t = 0$ in the beginning of each step is equivalent to taking the initial distribution function as that reached at the end of the former step. This new distribution function is different from $s_0(\epsilon)$ mainly in its low energy part. Instead of a constant value, it will now have an increasing one. This accounts for the fact that the curves in Fig. 5 reach their linear part only after some annealing took place. We plotted the activation energies calculated from the step-annealing experiment (Fig. 3) against the absolute temperature[4] (Fig. 6). According to Primak (7) a consequence of Eq. [3] is that such a plot would be linear for a constant spectrum. Thus Fig. 6 gives further support to the claim that $s_0(\epsilon)$ is constant.

[3] We neglect the change of shape of the rising part of the spectrum in the successive steps.

[4] The temperature associated with each activation energy is taken as the average of the annealing temperatures of the two steps from which the activation energy is calculated.

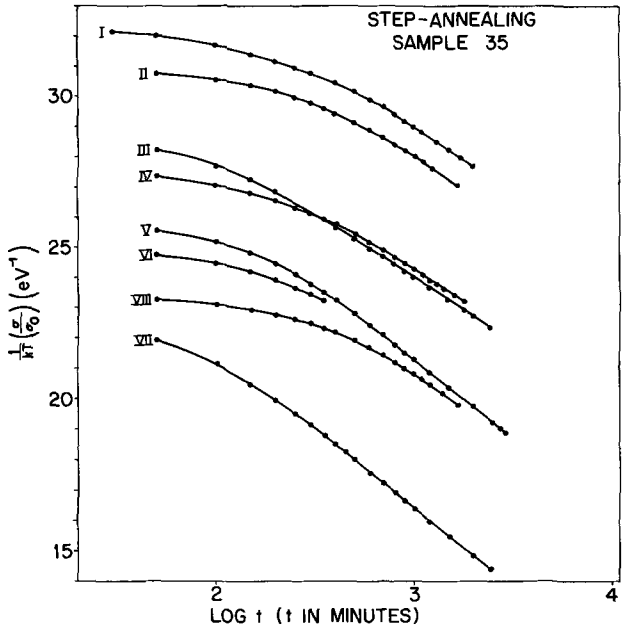

Fig. 5. Normalized conductivity data for step-annealing experiment of S-35, where $t = 0$ for each step. Annealing temperatures for the various steps are given in Fig. 3.

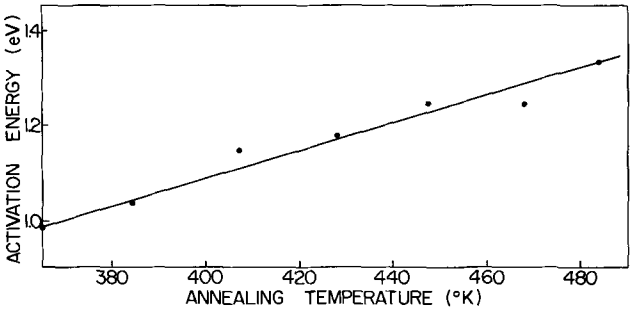

Fig. 6. Activation energy vs. absolute annealing temperature for the step-annealing of sample S-35.

From step-annealing experiments the value of the frequency factor (B in Eq. [2]) can be evaluated (7). Values of B calculated from the data of the different steps of annealing of sample S-35 given in Fig. 3 fall in the range 3×10^8 to 3×10^9 sec^{-1}, with no apparent correlation to the temperature of annealing or activation energy.

The continuous increase of the characteristic activation energy and the corresponding decrease in conductivity indicate that (*i*) the process of annealing in the range of temperatures investigated remained essentially the same during the various stages of annealing, and (*ii*) the annealing mode characterized by a sharp irreversible increase in conductivity was not reached.

The results given demonstrate that the behavior of the annealing process in the beginning, in contrast to the behavior after a long time of annealing, is essentially dependent on the history of the sample. Another consequence is that the term "properly annealed" at a given temperature occasionally used in the literature has a doubtful meaning as to the state of annealing of the sample, as long as the falling part of $s_0(\epsilon)$ is not reached. The fact that no annealing seems to take place after a certain time of annealing at a given temperature, might be due to the almost linear dependence of σ on log t which changes slowly with time. However, it does not have an asymptotic value characteristic of the annealing temperature. The same reasoning applies also to the evaluation of σ from a plot of σ *vs.* t. It is suggested that in addition to other information given about a specimen annealed for a long time, the value of the characteristic activation energy should also be used to characterize the state of annealing of the sample.

The discrepancy between our results and those of Longini and Pansino (6) who found a range of activation energies around 0.1 eV, may be due to the fact that their specimens were evaporated on a liquid-nitrogen cooled substrate. Thus, the specimens were in an early stage of annealing with ϵ_0 at very low energies. If the samples were not annealed for a sufficiently long time, then low values of calculated activation energies are expected.

The activation energies found with annealing range from about 0.9-1.4 eV and presumably extend to higher values. This range is within that found by Mogab and Kingery for SiC (5), namely 0.4-2.3 eV which might be an indication that a similar mechanism of annealing operates in both materials.

The high values of the characteristic activation energy indicates that the mechanism of low-temperature annealing is not restricted to a slight "reordering diffusion process" as suggested by Longini and Pansino (6). It seems that the reordering process involves groups of atoms.

In a recent paper (14) Rudee and Howie present evidence for the microcrystalline structure of amorphous Ge in contrast to the random network structure (15). According to Rudee and Howie, Ge amorphous films consist of hexagonal microcrystallites of about 14A. As the cubic phase is the stable one at low temperatures and pressures, a stabilizing force is necessary for the existence of the hexagonal phase. This force is provided by the grain-boundary surface tension.

We suggest that the low-temperature annealing process is associated with the collapse of the hexagonal microcrystallites. Thermal agitation can reduce momentarily the distances of atoms on both sides of a grain boundary, thus reducing the surface energy of the microcrystallite. If this energy falls below a certain value, the atoms of the microcrystallite will rearrange. As the microcrystallite is surrounded by randomly oriented neighbors, it will not necessarily transform

into the cubic structure but rather to a random network with a large percentage of second nearest neighbors in or near cubic positions. In this rearrangement, the rebonding of dangling bonds present in the grain boundary is easily conceived. During annealing, islands of random networks are created in the film. The high-temperature annealing process is associated with the recrystallization of the random networks to cubic crystallites. The activation energies measured are thus the activation energies initiating the rearrangement process described. These activation energies will depend on the microcrystallite's size and neighbors and as such are expected to fall in a broad spectrum. High-activation energies are quite reasonable for this mechanism. The decrease in the number of unpaired electrons found experimentally (16, 17) is also explained. The diffraction pattern is not expected to change much during annealing as the new arrangement is also a random one, in accord with experimental results (6).

An experiment similar to that of Rudee and Howie (14) on films in different stages of annealing might confirm or disprove our model. As the annealing behavior of Si and SiC resembles that of Ge, it is possible that a similar mechanism of annealing is operative also in these materials.

Summary

Activation energies for annealing of Ge films were found to be about 0.9 eV after sputtering at room temperature and to increase up to 1.4 eV after annealing. This range is similar to that found for SiC and can be explained by a distribution of the annealing processes in activation energy. A rearrangement mechanism is suggested for the low-temperature annealing mode wherein a microcrystalline structure is transformed into groups of random networks.

Acknowledgments

The authors wish to thank Dr. S. Nudelman for critically reading the manuscript.

This work was sponsored by Project Themis, Contract No. DAAB07-69-C-0420.

Manuscript submitted Aug. 10, 1972; revised manuscript received Sept. 29, 1972.

Any discussion of this paper will appear in a Discussion Section to be published in the December 1973 JOURNAL.

REFERENCES

1. R. Grigorovici, N. Croitoru, A. Devenyi, and E. Teleman, *Proc. Int. Conf. Phys. Semicond.*, 7th, p. 423, Paris (1964).
2. P. A. Walley and A. K. Jonscher, *Thin Solid Films*, **1**, 367 (1968).
3. R. Grigorovici, *Mater. Res. Bull.*, **3**, 13 (1968).
4. H. Keller and J. Stuke, *Phys. Status Solidi*, **8**, 831 (1965).
5. C. J. Mogab and W. D. Kingery, *J. Appl. Phys.*, **39**, 3640 (1968).
6. R. L. Longini and S. R. Pansino, *ibid.*, **40**, 2653 (1969).
7. W. Primak, *Phys. Rev.*, **100**, 1677 (1955).
8. G. Baldini and L. Rigaldi, *J. Opt. Soc. Am.*, **60**, 495 (1970).
9. W. C. Dash and R. Newman, *Phys. Rev.*, **99**, 1151 (1955).
10. A. H. Clark, *ibid.*, **154**, 750 (1967).
11. T. M. Donovan, W. F. Spicer, J. M. Bennett, and G. J. Asheley, *ibid.*, **B2**, 397 (1970).
12. K. L. Chopra and S. K. Bahl, *ibid.*, **B1**, 2545 (1970).
13. F. Oki, Y. Ogawa, and Y. Fujiki, *Japan. J. Appl. Phys.*, **8**, 1056 (1969).
14. M. L. Rudee and A. Howie, *Phil. Mag.*, **25**, 1001 (1972).
15. R. Grigorovici and R. Manaila, *J. Non-Crystalline Solids*, **1**, 371 (1969).
16. M. H. Brodsky and R. S. Title, *Phys. Rev. Letters*, **23**, 581 (1969).
17. M. H. Brodsky, R. S. Title, K. Weiser, and G. D. Pettit, *Phys. Rev.*, **B1**, 2632 (1970).

Ce^{3+} Activated $Y_3Al_5O_{12}$ and Some of Its Solid Solutions

T. Y. Tien,* E. F. Gibbons, R. G. DeLosh, P. J. Zacmanidis, D. E. Smith, and H. L. Stadler*

Scientific Research Staff, Ford Motor Company, Dearborn, Michigan 48121

ABSTRACT

The systems $Y_{3-x}Ce_xAl_5O_{12}$, $Y_{3-x}Ce_xAl_{5-z}Ga_zO_{12}$, and $Y_{3-x-z}Gd_zCe_xAl_5O_{12}$ were studied. It was found that the solid solubility of Ce^{3+} in $Y_3Al_5O_{12}$ varies with the atmosphere during firing. Only 2 mole per cent (m/o) of Ce^{3+} can be dissolved in the yttrium aluminum garnet in air while almost 6% Ce^{3+} enters the garnet lattice when fired at 1450°C under a hydrogen atmosphere. Complete solid solutions were observed in the systems $Y_3Al_5O_{12}$-$Gd_3Al_5O_{12}$ and $Y_3Al_5O_{12}$-$Y_3Ga_5O_{12}$. The cathodoluminescence emission-peak position of the Ce^{3+} ion in $Y_3Al_5O_{12}$ host shifted to a longer wavelength while the latttice parameter of the solid solution expanded when Gd^{3+} ions were substituted for Y^{3+}. On the other hand, the emission-peak position shifted to a shorter wavelength when the garnet host contained Ga^{3+} ions in the Al^{3+} position. The lattice parameter of the solid solution increased with Ga concentration.

Ce^{3+} activated phosphors are known to have very short decay times. Most of the Ce^{3+} activated phosphors show a blue or nearly ultraviolet emission band; however in the yttrium aluminum garnet host a yellow band was reported by Blasse *et al.* (1).

In $Y_3Al_5O_{12}$ the ionic radius similarity between Y^{3+} and Ce^{3+} suggests that the Ce^{3+} activator ions will occupy the Y^{3+} sites. Blasse *et al.* (1) reported that 10 atomic per cent (a/o) of Ce^{3+} could be accommodated in the $Y_3Al_5O_{12}$ solid solution and no difference in luminescent properties were observed whether the material was fired in air, oxygen, nitrogen, or hydrogen. No study of different activator concentrations has been reported. Holloway and Kestigan (2) prepared single crystals of yttrium aluminum garnet solid solutions containing La^{3+}, Lu^{3+}, or Gd^{3+} presumably in the Y^{3+} sites and Ga^{3+} in the Al^{3+} site. All these single crystals were actviated with Ce^{3+} of unknown concentration. It was found that the Ce^{3+} emission peak under cathode-ray excitation shifted in these

* Electrochemical Society Active Member.
Key words: luminescence, phosphors, rare earth activation.

solid solutions. Substitution by larger ions in the Y^{3+} site shifted the emission peak to a longer wavelength while larger ions in the Al^{3+} sites shifted the emission peak to a shorter wavelength.

Because of a specific application in this laboratory, the luminescence characteristics of the Ce^{3+} activated Y_3AlO_{12} at different activator concentrations and the effect of the solid-solution compositions were studied.

Experimental

All compositions used in the study were prepared using the coprecipitation method. All starting materials used were 99.9% pure or better. Mixtures of 0.4*N* metallic nitrate solution in the determined cation ratio were added to 0.4*N* NH_4OH solution. The final compositions were checked with x-ray fluorescence, comparing with standard mixtures of known concentration. The *p*H value of the final solutions were always kept at a value slightly higher than 9. For the compositions containing Ga^{3+} the *p*H was kept at the value at which the Ga^{3+} has its lowest solubility. The precipitates were then filtered and dried without washing. The dried powder was fired in an alumina crucible in a tube furnace with flowing gas at 300 ml per min. The gases used were nitrogen, hydrogen, or dry air. The fired samples were analyzed by x-ray diffraction. Cu $K\alpha$ radiation with a graphite diffracted beam monochrometer was used on a Norelco diffractometer. The diffractometer was operated at a scanning rate of ⅛° 2θ per min for lattice parameter determination. The peak positions of the (116), (120), (128), (152), (176), and (180) diffraction lines were measured and results were plotted *vs.* $\cos^2\theta$ and extrapolated to 180° The indexing of the garnet lattice was taken from the ASTM card index.

The cathodoluminescence (C.L.) data were obtained in a demountable electron-beam gun system operated at 3 kV. Samples were mounted at the focal point of an optical system which then refocused the emitted light on the entrance slit of a ¾m Czerny-Turner spectrometer. The output from a photomultiplier (P.M.) tube, located at the exit slit of the spectrometer, was amplified by means of a synchronous detector and displayed on an x-y recorder. The required periodic signal for the P.M. tube was obtained by applying a 13 Hz square wave to the horizontal deflection plates of the electron-beam gun, thus providing a 50% excitation duty cycle on the sample. The same square-wave generator provided the reference signal for the synchronous detector.

The excitation spectra were taken in a system utilizing a xenon light source focused through a mechanical light chopper onto the entrance slit of a ¾m spectrometer. The emission from the sample, coming from the exit slit, was recorded by means of a photomultiplier tube, the output of which was amplified by means of a synchronous detector and displayed on an x-y recorder. Appropriate filters were used in front of the sample and the P.M. tube and the spectra shown were corrected for system response.

Results

(*i*) $Y_3Al_5O_{12}$:Ce. The solid solubility of Ce^{3+} in $Y_3Al_5O_{12}$ depends on the atmosphere in which the powder was fired. At 1450°C in hydrogen, 6 m/o of Ce^{3+} can be accommodated in the $Y_3Al_5O_{12}$ lattice. At higher cerium concentrations, the perovskite phase, $CeAlO_3$, appears together with the garnet $Y_3Al_5O_{12}$. The lattice parameter increased with increasing Ce^{3+} concentration as shown in Fig. 1. At 1450°C in air, the solid solubility is only 2 m/o. At higher cerium concentration, the CeO_2 phase was observed. However, within the solid-solubility limit, the cerium ions exist in the trivalent state because identical emission spectra were observed for the samples fired in air and in hydrogen for the composition containing 2% cerium.

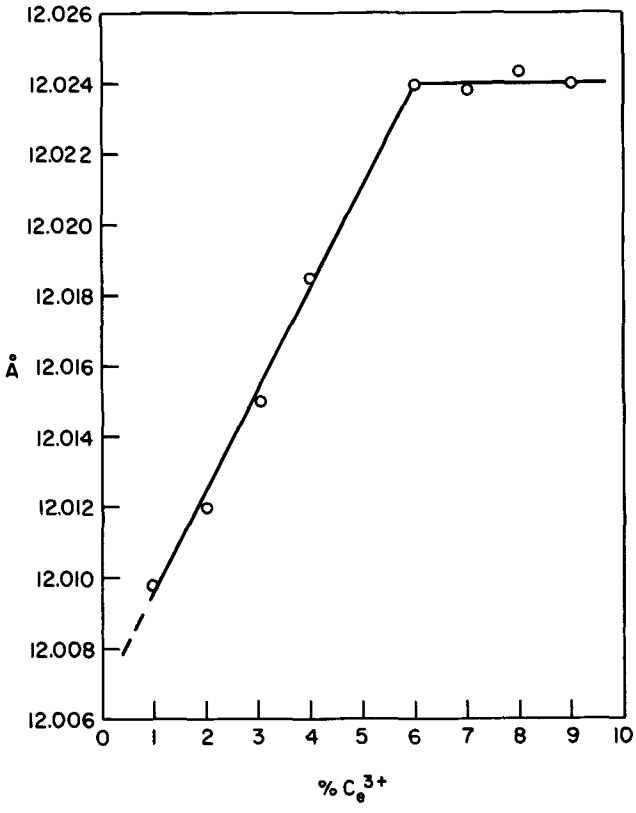

Fig. 1. Ce^{3+} concentration *vs.* lattice parameter for $Y_3Al_5O_{12}$:Ce^{3+}

The general shape of the excitation and emission spectra of the Ce^3 activated yttrium aluminum garnet are given in Fig. 2. The emission peak position under C.L. excitation shifted to a higher wavelength at higher Ce^{3+} concentration as shown in Fig. 3.

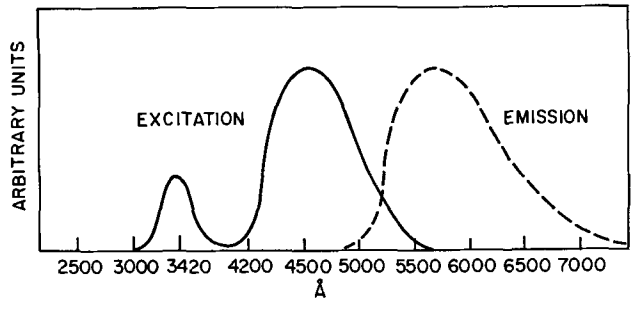

Fig. 2. Excitation and emission spectra for $Y_3Al_5O_{12}$:Ce^{3+}

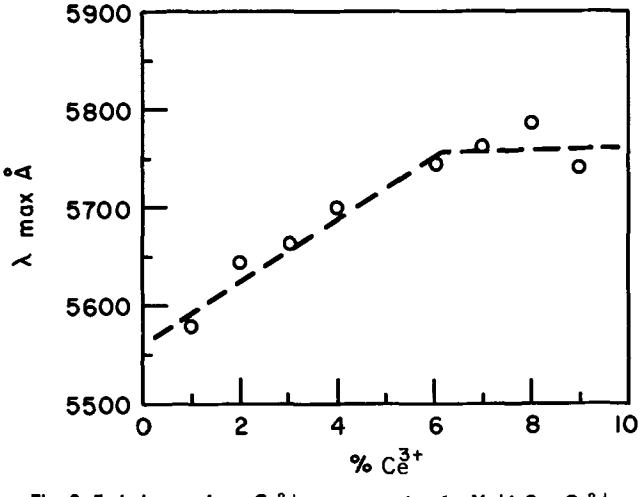

Fig. 3. Emission peak *vs.* Ce^{3+} concentration for $Y_3Al_5O_{12}$:Ce^{3+}

The electronic transition in Ce^{3+} has been assigned by Blasse *et al.* (1) as a 5d → 4f transition and the two peaks in the excitation band are attributed to the splitting of the 5d levels of the Ce^{3+}. The dependence of the low energy excitation-peak position on Ce concentration in $Y_3Al_5O_{12}$:Ce is shown in Fig. 4. The high-energy peak (at about 3470Å) does not shift appreciably as the Ce^{3+} concentration increases.

Decay times were measured with C.L. and u.v. excitations. It was found that the decay has 1/*e* time of about 70 nsec for C.L. excitation and about 50 nsec for u.v. excitation. The u.v. excitation decay curve is very nearly exponential; however the C.L. excitation decay curve is highly nonexponential, exhibiting a tail which differs considerably depending on the firing method used in the phosphor preparations. A detailed discussion will be published separately.

(*ii*) The systems $Y_3Al_5O_{12}$ and $Gd_3Al_5O_{12}$ are known to crystallize in the garnet structure (3). The compositions in the system were fired at 1450°C in hydrogen and furnace cooled. All compositions contained 2 m/o of Ce^{3+}. The lattice parameter data are given in Fig. 5. As shown in this figure, a complete series of solid solution was observed with the lattice parameter increasing from 12.017Å for $Y_3Al_5O_{12}$:Ce to 12.12Å for the compound $Gd_3Al_5O_{12}$:Ce. As expected, the emission peak of the Ce^{3+} under C.L. excitation shifted to a longer wavelength. The results are shown in Fig. 6. The intensity of the emission decreased with increasing Gd^{3+} concentration. The excitation spectra of the $(Y, Gd)_3Al_5O_{12}$:Ce are the same shape as that shown in Fig. 2 with the low energy peak position shift given in Fig. 7. Again, the shift of the high energy peak position was not appreciable.

(*iii*) The system $Y_3Al_{5-x}Ga_xO_{12}$:Ce. Complete solid solution in this system with 2 m/o Ce^{3+} was observed. The lattice parameter data are shown in Fig. 8. The lattice parameter increases from 12.01Å for the composition $Y_3Al_5O_{12}$:2 m/o Ce to 12.29Å for the composition $Y_3Ga_5O_{12}$:2 m/o Ce. Figure 9 shows that the emission peak positions of these solid solutions under C.L. excitation are shifted to a shorter wavelength as the Ga^{3+} concentration increases until the composition

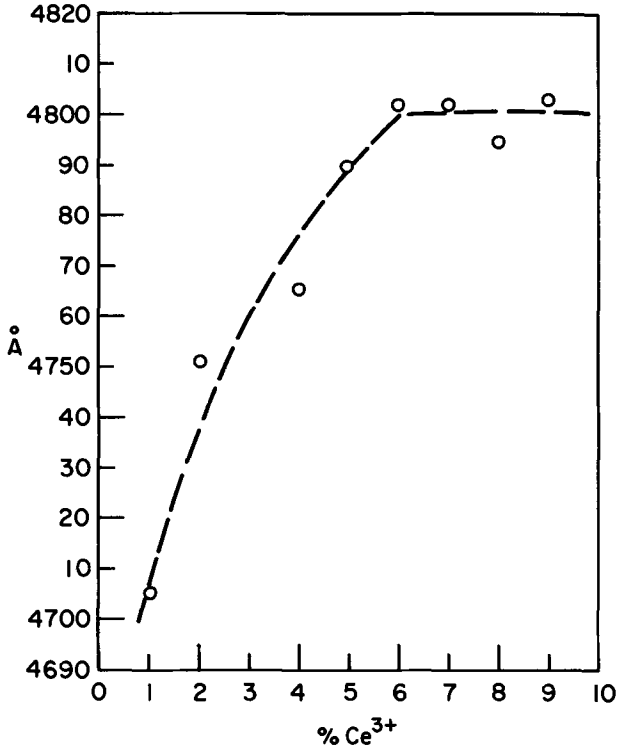

Fig. 4. Excitation-peak position vs. Ce^{3+} concentration for $Y_3Al_5O_{12}$:Ce^{3+}

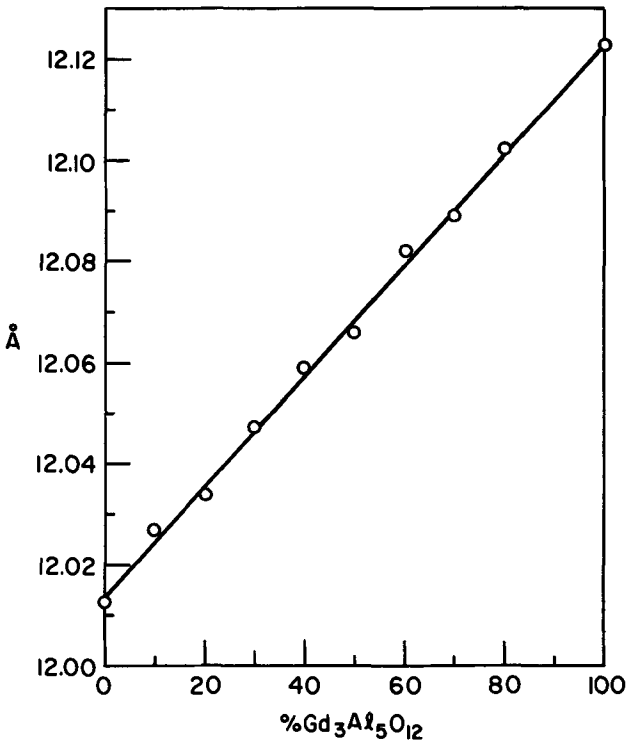

Fig. 5. $Y_3Al_5O_{12}$-$Gd_3Al_5O_{12}$ lattice parameters

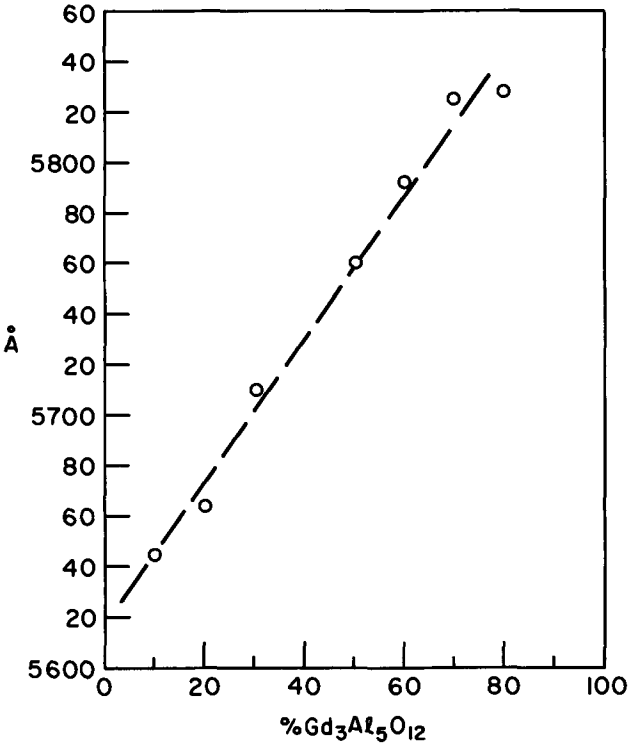

Fig. 6. Emission peak vs. Gd concentration for $Y_{3-x}Gd_xAl_5O_{12}$: Ce^{3+}

containing 40 m/o Ga is reached. Beyond 40% Ga, the emission-peak position remained at a constant wavelength even though the lattice parameter kept increasing. In the garnet structure, there are two different Al^{3+} sites (3). Forty per cent of the sites are six-fold coordinated and the other 60% are four-fold. It is therefore assumed that the Ga^{3+} preferentially occupies the six-fold site until all such sites are filled, and that the emission-peak position is only affected by the substitution of the Ga^{3+} in the six-fold site. The low energy excitation-peak position as a function of the Ga^{3+} concentration is given in Fig. 10. It is observed that the

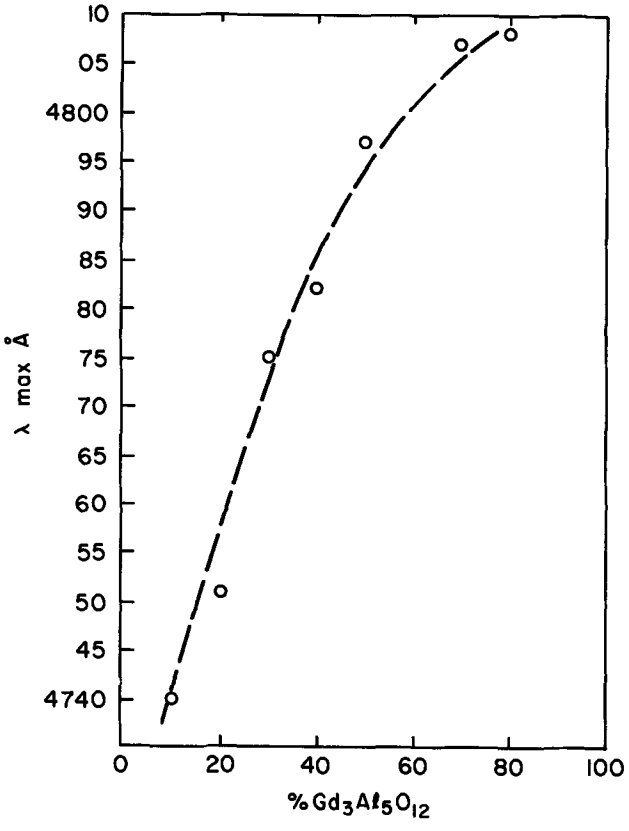

Fig. 7. Excitation peak vs. Gd concentration for $Y_{3-x}Gd_xAl_5O_{12}$:Ce^{3+}

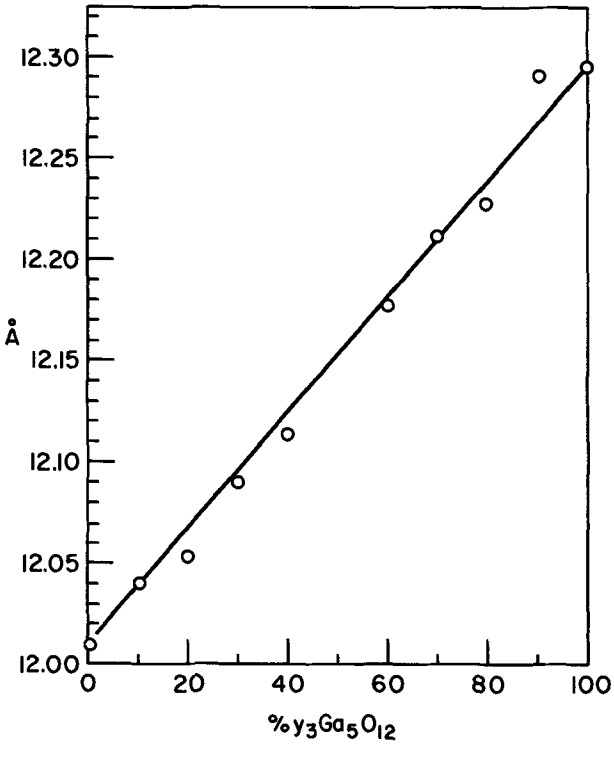

Fig. 8. $Y_3Al_5O_{12}$-$Y_3Ga_5O_{12}$ lattice parameter

break in the curve occurs at the same composition as in Fig. 9.

Summary

It has been shown that the solubility of Ce^{3+} in $Y_3Al_5O_{12}$ is highly dependent on the firing atmosphere, increasing from 2-6% when the atmosphere is changed from oxidizing to reducing. Also, the Ce^{3+} emission and excitation peaks show a continuous shift with increasing Ce^{3+} concentration.

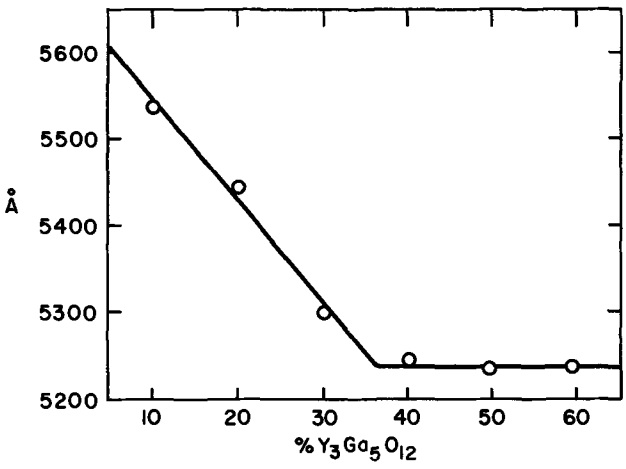

Fig. 9. Emission peak vs. Ga concentration for $Y_3Al_{5-x}Ga_xO_{12}$:Ce

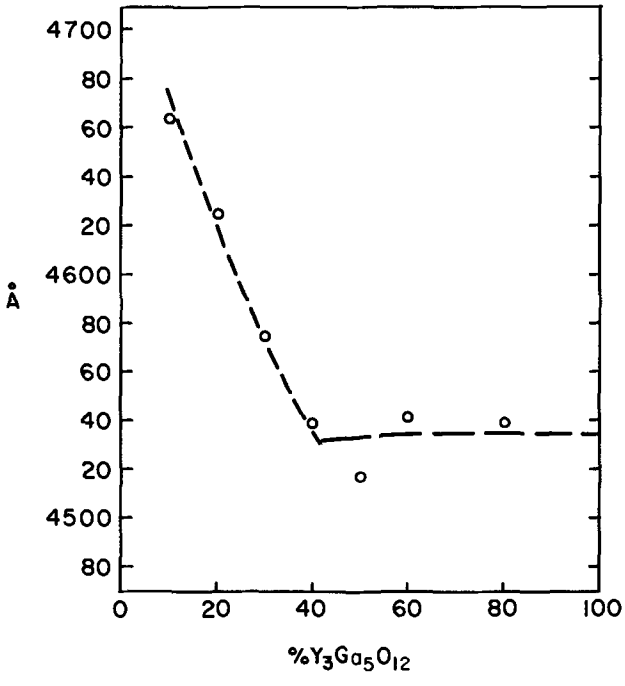

Fig. 10. Excitation peaks vs. Ga concentration for $Y_3Al_{5-x}Ga_x$ O_{12}:Ce

These peak positions are also influenced by the substitution of Gd^{3+} for Y^{3+} and Ga^{3+} for Al^{3+}. The Gd^{3+} substitution moves the Ce^{3+} emission peak to longer wavelengths while the Ga^{3+} substitution moves the emission peak to shorter wavelengths. The latter effect appears to arise only from the influence of Ga^{3+} in six-fold coordinated sites.

Acknowledgment

The authors wish to thank Carol Kelly and John Larson for their help on x-ray diffraction and x-ray fluorescence work.

Manuscript submitted July 12, 1972; revised manuscript received Oct. 9, 1972.

Any discussion of this paper will appear in a Discussion Section to be published in the December 1973 JOURNAL.

REFERENCES

1. G. Blasse and A. Bril, *Appl. Phys. Letters*, **11**, 53 (1967).
2. W. W. Holloway, Jr., and M. Kestigian, *J. Opt. Soc. Am.*, **59**, 60 (1969).
3. R. W. G. Wyckoff, "Crystal Structures," Interscience Publishers, Inc., New York (1968).

A High-Gain Light-Intensifying Device Incorporating a Fiber-Optic X-Ray Intensifying Faceplate

Kenneth L. Reifsnider and Jesse J. Brown, Jr.*

College of Engineering, Virginia Polytechnic Institute and State University, Blacksburg, Virginia 24061

ABSTRACT

The results of initial attempts to apply a new concept to the development of an x-ray sensitive image-intensifying device are reported. The new device consists of an x-ray sensitive fiber-optic faceplate which converts x-ray photons into visible light. The fiber-optic fluorescent plate replaces the powder-fluorescent screen common to such techniques, with a subsequent improvement in resolution and in the per cent of absorbed incident radiation. The resolution and x-ray stopping power of the fluorescent fiber-optic plate are not coupled as is the case for powder-fluorescent screens. A resolution of 28 line pairs per millimeter (lp/mm) is demonstrated in the present work.

A number of time-resolved x-ray systems have been developed in the past and have recently been reviewed by Green (1). It appears that the multiple-stage, image-intensifier system coupled to a fluorescent screen is the most sensitive to x-rays and at present is the "only truly instantaneous system" (1). This type of system, which includes commercial medical radiographic devices, uses a powder-fluorescent screen which requires a trade-off between intensity (enhanced by thick screens) and resolution (enhanced by thin screens).

The present work reports the successful removal of the polycrystalline fluorescent screen restrictions by replacing it with a fluorescent fiber-optic bundle. The resolution of the bundle is determined by the fiber size and is independent of the thickness of the screen. The resolution and sensitivity of the system are essentially "de-coupled."

Related Literature

X-ray detection system.—The development of suitable equipment to achieve a time-resolved display of x-ray diffraction images such as to allow immediate viewing (or recording) has been along three basic lines, all of which involve electro-optical devices and convert an x-ray photon image to a more intense image in the visible spectrum. The first of these methods involves a raster device which is itself sensitive to x-ray photons, *e.g.*, a silicon diode array vidicon or lead oxide vidicon so called Plumbicon (2-4). These devices are relatively insensitive to x-rays but the resolution can be very good, of the order of 15μ.

A second line of development has resulted in the use of raster tubes which are not x-ray sensitive, but are made so by coupling with a fluorescent screen which converts x-rays to visible light at low intensity. Tubes such as the SEC vidicon, or the orthacon with a single state intensifier added in front, are used to process and display the image on a monitor (5, 6). Such devices usually have less resolution (of the order of 30-50μ) and medium sensitivity to x-rays.

The most sensitive of all types of systems (and the only truly time-resolved systems) use a high-gain optical image intensifier tube coupled to a fluorescent screen which converts x-rays to visible light as in the raster systems (7-9). The resolution is limited by the fluorescent screen that converts the x-rays.

Radiographic sensitizing screen.—The majority of current x-ray image conversion systems rely upon a phosphor to detect and convert x-ray photons to blue-violet-ultraviolet wavelengths, with the quality and detail of the image limited by the quality and construction of the sensitizing screen. The most common sensitizing screen is the powder (polycrystalline) screen which is prepared by mixing an x-ray sensitive phosphor with a suitable binder and spreading the mixture on a thin x-ray transparent substrate. By design, the thickness of the phosphor layer upon drying is of the order of 100-300μ, which is arrived at by balancing light output and resolution. Typical x-ray generating machines emit radiation whose effective energy range is 30-70 keV. In order to maximize light output, one would like to absorb nearly 100% of the incident x-ray beam. This would require a bed of phosphor up to 1 in. thick, but this thickness is prohibitive because scattering of the light (by reflection, refraction, dispersion, and absorption) emitted by the phosphor as it passes through the bed limits resolution. In the case of $CaWO_4$, a 100-300μ thick layer represents a compromise. The resolution of about 10 line pairs per millimeter (lp/mm) and the amount of incident x-ray energy absorbed by the phosphor is 10-20%. Moreover, the energy efficiency, *i.e.*, per cent of energy absorbed which is actually converted to visible radiation, of $CaWO_4$ is about 3%, which gives an over-all efficiency for the system of only 0.3-0.6%. It is also noteworthy that there are other secondary factors that contribute to resolution and light output such as phosphor efficiency and particle size of the phosphor.

Other inorganic phosphors used in sensitizing screens include lead-activated barium sulfate, and silver or copper-activated zinc (or zinc-cadmium) sulfide. These phosphors have high mass-absorption coefficients, their blue-violet-ultraviolet emissions and energy efficiencies ranging from 3% for $CaWO_4$ to about 20% for ZnS:Ag. (These numbers, however, can be misleading because the ability to absorb x-rays is strongly dependent upon the energy of the x-rays and varies greatly from phosphor to phosphor. Calcium tungstate, for example, has an absorption band at about 70 keV and is a markedly poorer absorber at lower energies.)

A 1961 patent (10) advanced a phosphor-binder combination designed to reduce the internal scatter of the emitted radiation by the use of thallium-activated alkali iodides in aluminum stearate binders. This, together with the minimized internal scatter of the luminescence permitting thicker screens) enabled exposure time reductions of four over comparable $CaWO_4$ screens.

In recent years considerable interest has been directed towards rare earth-activated phosphors (11, 12). Of special interest are matrices activated by ions which allow 5*d* to 4*f* electronic transitions such as the blue emitting Ce^{3+} and divalent rare earth ions. The emis-

* Electrochemical Society Active Member.

Key words: phosphors, x-ray sensitizing screen, fiber-optic, light-intensification, radiography.

sions from these ions are broad band with fairly short lifetimes (decay times of a fraction of a microsecond).

Because the scattering of light is one factor responsible for the resolution limit in polycrystalline screens, single-phase materials such as the single crystal and the thick film are attractive. There are, however, basically two problems inherent in these screens. Firstly, the production of luminescent single crystals suitable for screens is very costly. Secondly, these screens also have a resolution dependency on thickness. This can be seen when one considers the excitation mechanism (Fig. 1). The volume of phosphor excited by each x-ray photon is dependent upon the range of the secondary electrons (13) which in turn are related proportionally to the energy of the incident x-ray photon (14). For example, a 35 keV x-ray might produce a channel about 3μ long and 0.9μ in diameter in ZnS (13). The luminescent flux density from such an emission channel will be considerably higher in the forward and reverse directions than radially because of the fiber alignment. However, as the thickness of the screen increases from the 3μ level, dispersion of the emitted light will result. Although this provides an improvement over the polycrystalline case, realistic single phase screens 300-500μ thick still possess an unsatisfactory inherent resolution limit.

The fiber-optic sensitizing screens, the third type of sensitizing screen and the type advanced in this paper, is constructed from small (20μ diameter) luminescent glass fibers. The fibers are clad with a low refractive index glass, and pressed together under mild heating to form bundles with hexagonal cross sections of about 5 mm diameter. These rods can subsequently be pressed together in a similar fashion in any practical thickness. Slices ½-1 in. thick are then cut from these rods, which in turn are ground and polished, and one side receives a reflector coating. The result is a fluorescent fiber-optic faceplate that can be used as an x-ray sensitizing screen, (Fig. 2).

This idea was first described by Hilton and Squire (15) where they pointed out some of the advantages of a fiber-optic sensitizing screen. In essence, improved resolution is a result of the channeling (light piping) effect of the fibers. The excitation channel in a sense is the limiting parameter on the resolution. However, this limit is 3-4μ for a 35 keV x-ray photon, and a screen made from fibers this small would provide resolution capabilities beyond the statistical limit of most existing intensifying systems. Not only is the resolution improved by the fiber-optic screen, but it is independent of screen thickness. This results from the high transmission of light by the glass. Most significant is the fact that the sensitizing screen can be made sufficiently thick to absorb all of the incident x-ray photons with only small losses in resolution.

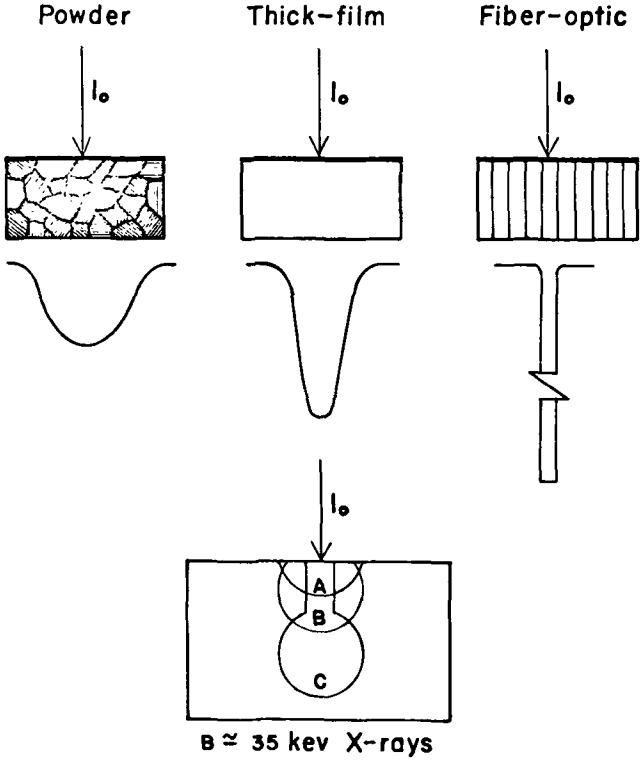

Fig. 1. Schematic of the emission-intensity distributions from three types of x-ray sensitizing screens (top) and of the excitation channel formed by the incident x-ray photons (bottom).

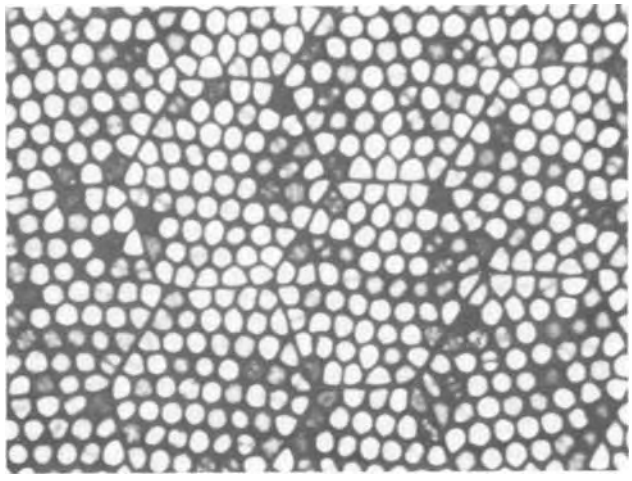

Fig. 2. Optical photograph of fluorescent faceplate. (Average fiber diameter approximately 15μ.)

Experimental Apparatus and Procedure

Image intensification was provided by a modified RCA 8606 three-stage cascaded optical image intensifier tube. The tube is electrostatically focused and has a magnification of 1:1. Details of the operation of the tube and the manner in which it is incorporated into a time-resolved x-ray diffraction or radiographic device have been described previously [see Ref. (16)]. The input and output faceplates of the image-intensifier tube are fiber-optic bundles which are flat on the exterior ends. In order to convert the x-ray image into a visible light image for intensification, an x-ray fluorescent fiber-optic faceplate was mounted in direct contact with the input fiber-optic bundle of the image-intensifier tube. The image intensifier tube used for the present work increased the luminous flux of the visible light image produced by the fluorescent fiber-optic screen by a gain of about 77,200. The on-center measured resolution of the tube itself was 36 lp/mm with a peripheral value of 30 lp/mm. The tube had a useful cathode diameter of 37.5 mm.

The results shown in the following section were obtained by direct photographic recording of the image which was displayed at the rear of the intensifying tube. Various commercial x-ray fluorescent fiber-optic faceplates were used which ranged in thickness from 2 to 10 mm, and in diameter from 1 to 3 cm. The individual glass fibers in the fiber-optic faceplates were about 7μ in diameter and were placed on approximately 15μ centers. The spacing of the individual fibers sometimes varied up to as much as 25μ. At the corners of these hexagonal bundles there are disturbances in the fiber spacing of up to 60μ. Such a screen should have the ability to resolve details spaced apart by between 20 and 25μ, *i.e.*, it should be capable of a resolution of between 40 and 50 lp/mm.

If the resolution of the x-ray fluorescent fiber-optic faceplate is taken to be 45 lp/mm and the resolution of the image tube is taken to be 36 lp/mm, then the resolution of the image system consisting of those two components used in tandem should be about 28 lp/mm.

Such a system would be expected to resolve detail spaced apart by slightly less than 35μ.

Experimental Results

A series of tests was run to determine the feasibility of the new concept in the time-resolved x-ray devices described above. The objectives of these tests were to determine the resolution and sensitivity of the best available device at this point of development, since those characteristics are the most critical to applications of the method.

In order to check the resolution of the system accurately, several different types of tests were conducted. The most straightforward type of resolution test is provided by radiographic examination of wire meshes. The results of such a test are shown in Fig. 3. The wires in the screen were 51μ in diameter and spaced apart by 74μ. Therefore, the resolution illustrated by Fig. 3 is between 20 and 25 lp/mm. No wire mesh screen was available to test the exact value of 28 lp/mm predicted in the previous section. A Cu target at 20 kV and a few milliamperes was used to obtain the picture.

A second test of resolution was made in connection with the application of time-resolved x-ray radiography to the study of dynamic-material response in our laboratory. For such tests, it is useful to have a time history of the chronology, duration, and general character of the breakage of reinforcing fibers in the interior of opaque reinforced materials. Such a breakage is shown in Fig. 4. The white horizontal region is the section of the specimen which was radiographed. The two dark vertical lines in the radiographed section are "shadows" of two reinforcing fibers. The reinforcing fiber on the right is broken as indicated by the small white horizontal bar in the vertical shadow. A fiber-optic fluorescent screen was used to make the photograph shown in Fig. 4a, and a powder-fluorescent screen used to make the photograph shown in Fig. 4b. It should be emphasized that both images were displayed on the rear of the image-intensifying tube with sufficient intensity to be recorded on cine film at standard framing rates (30 frames/sec). The reinforcing fibers were 1 mm diameter tungsten wires embedded in a matrix of aluminum. The specimens were plate-shaped, so that the thickness through which the x-rays were passing was 1.56 mm. Figure 4b is the best previous radiograph of the breakage obtained using a fluorescent-powder screen in contact with the input fiber-optic bundle of the image-intensifying tube used in the present work as described in Ref. (16). The radiograph in Fig. 4a, taken at 30 kV and 15 mA, shows a distinct improvement in general clarity. This is to be expected since the resolution in Fig. 4a is about three times that of the powder screen in Fig. 4b. This increase in resolution is of critical importance to this application, since it is useful to examine the breakage of much smaller fibers than those shown in Fig. 4.

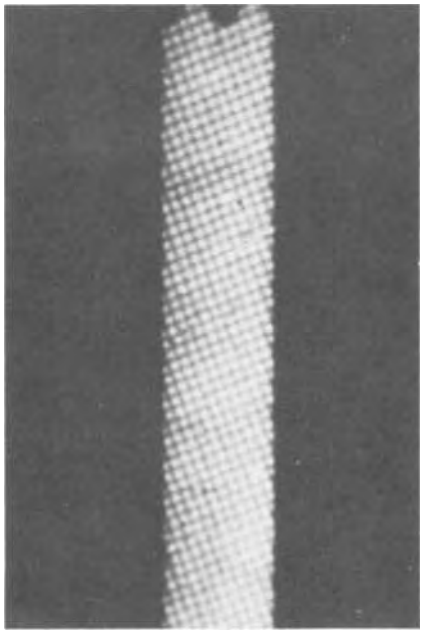

Fig. 3. Radiograph of wire mesh showing about 20-25 lp/mm resolution taken using a fluorescent fiber-optic x-ray sensitive faceplate (X20).

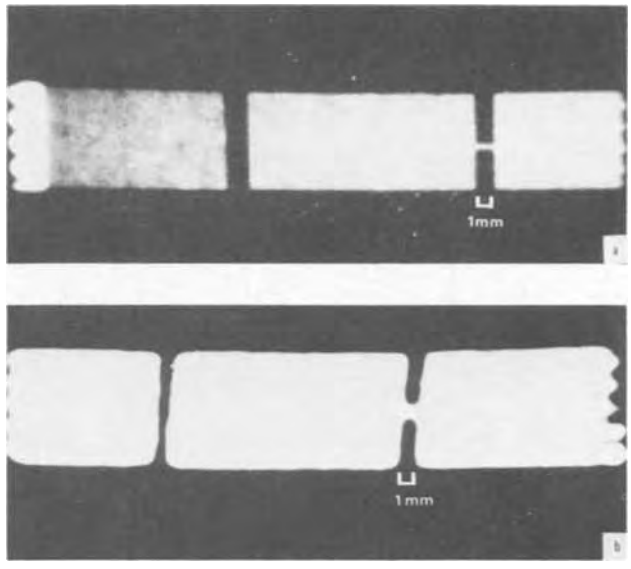

Fig. 4. Radiograph of 0.2 mm break in one of two adjacent fibers in a metal matrix composite tensile specimen, (a) taken using fluorescent fiber-optic faceplate (X20), (b) best previous radiograph taken using a powder screen (X14).

In an effort to compare resolution of the present system with that of another system previously reported, a third test was conducted. A chip of the same silicon-crystal integrated circuit used by Rozgonyi, *et al.* to demonstrate the resolution of their silicon-diode array camera in Ref. (2) was kindly supplied by the author of that paper. An optical photograph of part of that integrated circuit is shown in Fig. 5a. On the basis of our previous discussion, it would be expected that the present system should resolve the 38μ strips with 76μ spacing quite clearly. In the area where the strips double in number so that the spacing between strips drops to 19μ, delineation of that detail would require greater than 30 lp/mm. Hence, we would not expect these areas to be clearly delineated by the present system. Figure 5b shows a radiograph of the silicon chip made with the present device. The x-ray focal spot size was 0.4 $\times$ 0.4 mm at a distance of 40 cm from the chip. As expected, the 38μ strips are quite distinct, but the detail in the area of double strips cannot be clearly discerned. It should be mentioned that visual observation of this pattern as displayed on the rear of the image-intensifying tube using a microscope revealed that the 19μ spacings of the 38μ strips could, in fact, be clearly observed and counted. However, the extreme criticality of focus requirements for the cameras available to the authors, which magnified the image to a much lesser degree, served to prevent perfect recording of that detail. At any rate, the resolution of the present system is at least as high as the value predicted in the previous section. Considerable care was taken to mount the incident x-ray collimator and fluorescent fiber-optic faceplate almost in contact with opposite sides of the silicon chip so as to insure a 1:1 comparison between dimensions observed on the optical photograph and those displayed on the radiographic pattern.

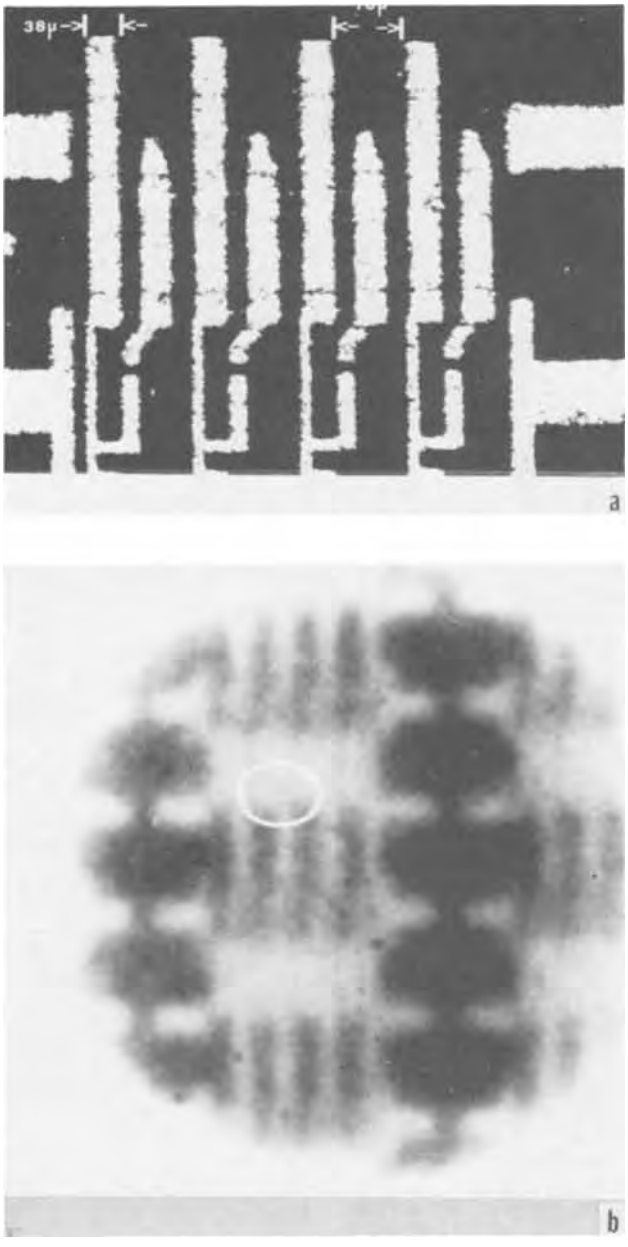

Fig. 5. Optical photograph (a), and x-ray radiograph (b), of silicon integrated circuit [same crystal as used by Rozgonyi *et al.*, see Ref. (3)]. Radiograph was made using fluorescent fiber-optic x-ray sensitive faceplate.

While questions of resolution can be settled by radiographic techniques, the questions of sensitivity are more easily examined by attempting to study various x-ray diffraction patterns. The sensitivity of the present device has not yet been optimized, and is the subject of present development efforts. Using the 900 VA x-ray source available to the author, it was impossible to display instantaneously x-ray topographs. Since the image on the image-intensifying tube used in the present system cannot be intensified by integrating the input over various time periods as has been done by various other investigators, no x-ray topographs could be recorded. However, Laue patterns of various types were recorded using smaller x-ray target-to-specimen distances and less collimation than is needed for topographic work. An example of a recorded diffraction spot is provided in Fig. 6. Only one diffraction spot was recorded, since the most sensitive fluorescent fiber-optic screen available was only 1 cm in diameter. The crystal which produced the diffraction was 1.56 mm thick 5 nines aluminum, and the pattern recorded was obtained using a standard Laue transmission

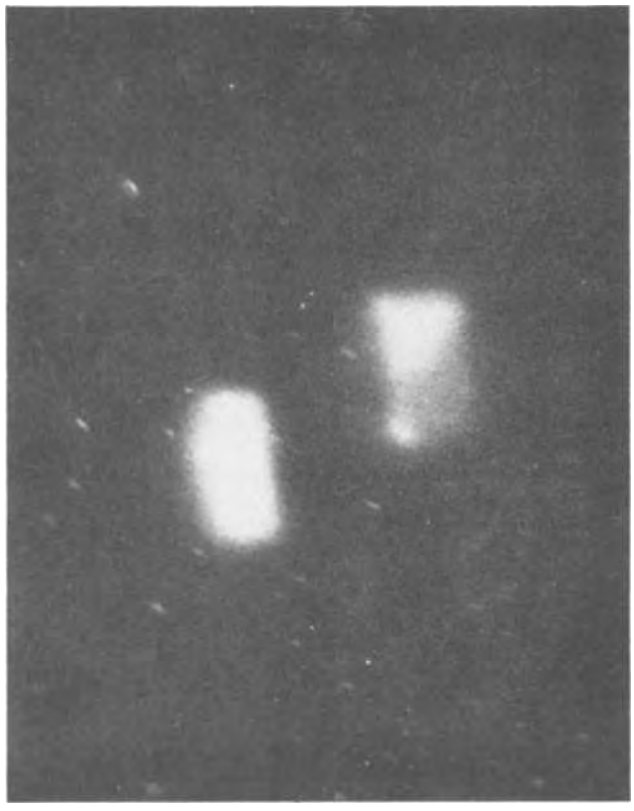

Fig. 6. Laue diffraction spot (on the right) and transmitted direct beam from a 1.56 mm thick aluminum single crystal shown on a photograph made using a fluorescent fiber-optic screen. (40 kV 20 mA, 20 sec exposure on ASA 150 film from back of image intensifying tube) (X10).

arrangement. The x-ray target-to-specimen distance was 12 cm and the final collimater size was 1 mm × 0.5 mm. The x-ray tube was operated at 40 kV and 20 mA. More complete Laue patterns with ellipses which can be analyzed for orientation purposes have been obtained using somewhat less collimation. Interestingly enough, observation of Fig. 6 reveals that the diffraction spot shows distinct intensity variations and represents, in some sense, a topograph of that area of the aluminum crystal. The real significance of the photograph in Fig. 6, however, is to provide evidence of the sensitivity of the present method. Even at this point in development, the conversion efficiency of the fiber-optic x-ray fluorescent faceplates is sufficient to provide instantaneous time-resolved recording of very weak x-ray diffraction patterns. It is estimated that the present low value of conversion efficiency for the fiber-optic screens results in a sensitivity to x-rays which is about one order of magnitude less than that of the same system operating with a fluorescent-powder screen having about 10 lp/mm resolution as described in Ref. (16).

Discussion

The successful application of a radically new type of x-ray sensitive fluorescent screen which converts x-rays to visible light is described. The new screen differs from previous types in that the visible light image is created and conducted by fluorescent glass fibers which are assembled in a bundle in a standard manner to form a fiber-optic plate. In the present work, the fiber-optic x-ray fluorescent plate was placed in direct contact with the fiber-optic bundle which formed the faceplate of the input end of an image-intensifier tube. The resulting system has a resolution of about 28 lp/mm and a sensitivity sufficient for truly instantaneous recording of x-ray radiographic and diffraction images. The sensitivity of the present device is

about one order of magnitude less than the best previously reported system (16). The brightest fiber-optic fluorescent faceplate used in the present work was found to emit 11.4% of the white light intensity of a Dupont Cronex Lightning Special powder-fluorescent screen with identical incident x-ray flux.

While sensitivity is still being optimized, the fact that we have recorded transmission x-ray diffraction patterns through 1.56 mm thick aluminum single crystals at 800 VA indicates that even now the system has better sensitivity than many other available time-resolved systems. However, it should be noted that, with development, the present system has the potential of being much more sensitive to x-rays than any system using a fluorescent-powder screen. Equally important is the fact that the present system also has the potential to reach the theoretical limitation on resolution imposed by statistical variations in the x-ray flux incident on the system. These potentialities come about because of the additional absorption of the fiber-optic screen. If the conversion efficiency of the glass fibers can be increased to a point where they are just half as efficient in converting x-ray photons to visible light, the fiber-optic screen would then be twice as sensitive to x-rays as a powder screen with even 10 lp/mm which absorbs, at most, 25% of the x-rays incident upon it. There is every reason to believe that glass fibers with conversion efficiencies at least that high can be developed. If such sensitivity is obtained, the quantum statistical variations in the incident x-ray beam will be the limiting factor on image formation. This limitation is determined by the theoretical signal-to-noise ratio which can be obtained for a given detail spacing with a specified number of photon events in the picture element area (17). No amount of intensification by subsequent image systems will exceed this limit. The theoretical high-contrast resolution limit for x-ray intensities common to applications discussed in the present work is about 35 lp/mm [see Ref. (11)]. A fiber-optic fluorescent faceplate with a resolution which exceeds this value could easily be constructed.

The per cent of incident x-ray photons absorbed, and the conversion efficiency of the fiber-optic fluorescent screen are of equal importance in the face of statistical fluctuations in the incident image to resolution arguments. If it is assumed that the variation in the incident x-ray photon flux with time is given by a Poisson distribution (as is commonly done), then the photoemission (output) of the fluorescent layer can be characterized by a signal-to-noise ratio (SNR) given by the following expression, $SNR = (\eta \times \bar{n})^{1/2}$, where η is the conversion efficiency of the fluorescent fibers (defined as the probability that an optical photon will be emitted when an x-ray photon strikes) and $\bar{n}$ is the average number of x-ray photons which strike the fluorescent fibers per unit time. The conversion efficiency consists of two parts, the percentage of incident photons stopped (or absorbed) by the fibers times the quantum efficiency of converting the absorbed x-ray photons into visible light photons.

The system reported here is presently being used to monitor fiber breakage in fiber-composite reinforced specimens during continuous testing radiographically, and to record the changes in diffraction patterns during continuous deformation of aluminum single crystals.

Acknowledgments

The authors would like to thank G. P. Rozgonyi for the silicon crystal used in some of the present work. They would also like to thank Kenneth McCauley and Robert Davis for their assistance in constructing the equipment and carrying out the tests. Further thanks goes to Pat Blackley for typing this manuscript.

This work was supported in part by grant number GK-4741 from the National Science Foundation.

Manuscript submitted Sept. 30, 1971; revised manuscript received Sept. 25, 1972. This was Papers 155 and 156 presented at the Cleveland, Ohio, Meeting of the Society, Oct. 3-7, 1971.

Any discussion of this paper will appear in a Discussion Section to be published in the December 1973 JOURNAL.

REFERENCES

1. R. E. Green, Jr., "Dynamic X-ray Diffraction Systems," Transactions, "Advances in X-ray Analysis," Denver (1970).
2. G. A. Rozgonyi, S. E. Haszko, and J. L. Statile, *Appl. Phys. Letters*, **16**, 443 (1970).
3. A. N. Chester, and F. B. Koch, in "Advances in X-ray Analysis", C. S. Barrett, J. B. Newkirk, and G. R. Mallett, Editors, Vol. 12, pp. 165-173, Plenum Press, New York (1969).
4. J. Chikawa and I. Fujimoto, *Appl. Phys. Letters*, **13**, 387 (1968).
5. J. Ball and T. C. Furnas, Jr., "Dynamic Display of X-ray Patterns," 19th Annual Denver X-ray Conference: Applications of X-ray Analysis, Denver, Colorado, August (1970).
6. E. S. Meieran, J. K. Landre, and S. O'Hara, *Appl. Phys. Letters*, **14**, 368 (1969).
7. A. R. Lang and K. Reifsnider, *ibid.*, **15**, 258 (1969).
8. K. Reifsnider and R. E. Green, Jr., *Rev. Sci. Instr.*, **39**, 1651 (1968).
9. A. Bril, in "Absolute Efficiencies of Phosphors with Ultraviolet and Cathode-Ray Excitation, Luminescence of Organic and Inorganic Materials," H. P. Kallman and G. M. Spruce, Editors, John Wiley and Sons, Inc., New York (1962).
10. M. Ter-Pogossian, U.S. Pat. 2,968,725 (1961).
11. S. Z. Toma and F. N. Sheaffer, U.S. Pat. 3,527,710 (1970).
12. R. A. Buchanan and K. A. Wickersheim, *IEEE, Trans. Nucl. Sci.*, 95 (1970).
13. D. Curie, "Luminescence in Crystals," John Wiley and Sons, Inc., New York (1960).
14. H. Kallman and J. Dresner, *Phys. Rev.*, **114**, 71 (1959).
15. J. L. Hilton and R. K. Squire, U.S. Pat. 3,225,193 (1961).
16. K. Reifsnider, *J. Soc. Motion Picture Television Eng.*, **80**, 18 (1970).
17. L. E. Flory, *Ann. N. Y. Acad. Sci.*, **157**, 38 (1969).

Measurement of Si Epitaxial Thickness Using a Michelson Interferometer

Paul F. Cox and Arnold F. Stalder*

Texas Instruments Incorporated, Corporate Research and Engineering, Dallas, Texas 75222

ABSTRACT

A system has been designed to measure the thickness of silicon epitaxial material using a scanning Michelson interferometer rather than a conventional dispersive *IR* spectrometer. The sampling capacity of this system with a 5-6 sec sampling time exceeds that of several dispersive instruments. The long-term precision on a single machine (3σ) is $\pm$ (0.05 μm + 0.005t), where t is the film thickness. Computer processing of the reflection interferogram from an epitaxial wafer provides film thickness data by a Fourier transform method. This method is shown to be mathematically equivalent to the method used for dispersion spectrometers as given by ASTM procedure F95-68T. The two measurements are in agreement within the published interlaboratory precision of the ASTM method: $\pm$ (0.25 μm + 0.025t) for P-type material and $\pm$ (0.25 + 0.005t) for N-type. The lack of moving mechanical parts in the interferometer system contributes to making this type of instrument very reliable. Down time due to system failure has been minimal, and two systems have been in operation a total of over 4 machine years.

Silicon and germanium have been commonly used in semiconductor device fabrication. Recent developments in the optoelectronics area have introduced new materials such as GaAs, GaP, and GaAsP. Epitaxial structures have been used with all of these materials. Effective use of this type of material requires knowledge of the epitaxial layer thickness as well as the electrical properties of the material. The system described in this paper was intended for use with silicon epitaxial material, although the same method could easily be applied to other materials.

Kane and Larrabee (1) have described several ways to measure silicon epitaxial film thickness. One type of destructive determination involves angle lapping and staining the material. If a selective stain is chosen, the layer thickness can be determined with a calibrated microscope, or an interference microscope. Another method involves the use of an etch solution that etches selectively along crystal defects and exposes the source of stacking faults. In epitaxial material a great number of faults will originate at the layer-substrate interface, and the size of the etch pits associated with these may be used to determine the layer thickness.

The substrates generally used for epitaxial layer growth are quite heavily doped, with resistivities on the order of 0.005-0.020 ohm-cm. The layer material is much less heavily doped. The presence of high doping levels in the substrate causes an abrupt change in the optical properties of the material at the layer-substrate interface, in the infrared region of the spectrum. This change in the extinction coefficient caused by free carrier absorption is only apparent at long wavelengths in the infrared, and is difficult to observe at wavelengths less than 10 μm. The change in the optical properties of the epitaxial material at the interface permits nondestructive optical interference methods to be used for film thickness measurements. Ellipsometry at 54.6 μm has been employed by Hilton and Jones (2). Despite the potential of ellipsometry, the lack of a strong monochromatic radiation source in the long wavelength *IR* region has limited its use to laboratory experiments.

The method most commonly employed to measure epitaxial thickness has been *IR* interferometry using the reflection interference spectrum obtained on an *IR* spectrometer. This method was reviewed recently by Severin (3) and has been exploited extensively during the last 10 years (4-10). A standardized procedure based on *IR* interference has been adopted by the American Society for Testing Materials (11).

Even though *IR* interferometric measurements have done a great deal to simplify the measurement of epitaxial films, a few disadvantages do exist where a large number of samples must be measured routinely. The time required for a manually operated instrument and the simplest data processing is approximately 1 min per sample. Even a commercial system using a computer coupled scanning spectrometer requires 30 sec to measure one sample.[1] The time is determined by that required to scan the spectrum. However, coupling 4 spectrometers to the computer allows a very good measuring rate of 8 samples/min to be attained.

One problem not alleviated by computer data processing is that of mechanical wear caused by repeated rapid cycling of the spectrometer mechanism. Ten years of experience at the authors' company coupled with the information obtained from others in the semiconductor industry indicate that this is a very serious problem. Even the best commercial spectrometers suffer a great deal of down time after extended use, in spite of extensive maintenance programs.

The advantages of using the nondestructive *IR* interferometric technique can be retained while virtually eliminating the problem of mechanical wear and long sampling time if the data are collected with a scanning Michelson interferometer. The data handling with this system requires Fourier analysis to extract all of the available spectral information, but if an automated system using a small computer is desired this is no handicap. The only moving part in the scanning Michelson interferometer is the translation drive on the scanning mirror. In the case of one commercial interferometer, this is composed of the solenoid drive mechanism from an audio speaker and has proven to be very reliable under normal operating conditions.[2] The spectral resolution of the least expensive scanning Michelson systems capable of reasonable scanning rates is very low, around 20-40 cm^{-1}, but for the epitaxial thickness measurement this is no drawback. The optical system in a Michelson interferometer offers two advantages over a conventional dispersive system which greatly enhance the signal/noise ratio and allow

* Electrochemical Society Active Member.
Key words: silicon, epitaxial, film thickness, interferometer.

[1] Beckman Data Processor System, Model 565151, using a modified Beckman IR-20 spectrometer.
[2] Digilab, Inc., Model 196TC.

the data to be collected very quickly (12-14). Since no restrictive slit mechanism is required and a reasonably wide angular aperture can be used without impairing performance, the radiation throughput of the system is quite large. In addition, Fellgets multiplex advantage is applicable. All wavelengths are viewed simultaneously by the detector, and in a detector noise limited system this multiplexing of the spectrum will greatly improve the signal/noise ratio.

A complete system for the measurement of epitaxial layer thickness utilizing a scanning Michelson has been developed in this laboratory. A similar system has subsequently been marketed commercially.[3]

Application of the Michelson Interferometer to Epitaxial Measurements

A schematic of the optical system used for *IR* interferometry with a Michelson interferometer is shown in Fig. 1. The single beam incident upon the sample is split into beams A and B upon reflection from the epitaxial sample. Beam B is out of phase with A by an amount Δ, due to the path through the layer and phase shifts upon reflection at both surface and layer-substrate interfaces. The beam splitter (M_3) in the interferometer splits each beam into two equal amplitude components. These go to either the fixed mirror (M_1) or the scanning mirror (M_2) where they are reflected back to the beam splitter. The beams recombine at this point and travel to the detector (D). The scanning mirror translates about the point at which the two paths in the interferometer are of equal length. The scanning range of the mirror must be able to introduce a phase difference between the two legs of the interferometer that exceeds the phase difference Δ introduced by the sample. Since each beam traverses a leg of the interferometer twice, it means that the mirror must travel a distance that introduces a phase shift of $\pm\Delta/2$, in order to be useful in making an epitaxial measurement. The maximum sample thickness that can be measured is determined by the limits of the mirror travel. The range can be extended on some instruments by adjusting the mirrors so that the scanning is done only on one side of the equal path position, thus doubling the useful thickness range for a given scanning distance.

An example of an interferogram produced by a system such as that described in Fig. 1 is shown in Fig. 2. The a-c signal intensity is plotted *vs.* the phase shift introduced by the scanning mirror. The phase shift is related to mirror movement by the relationship

$$\text{phase shift} = \frac{2\pi x}{\lambda} = 2\pi\nu x \qquad [1]$$

where x is the optical path difference in the interferometer, λ is the wavelength of the radiation, and $\nu = 1/\lambda$. A maximum signal occurs at the point where the phase shift for most wavelengths is zero. This would occur where $x = 0$, if no distortion were present in the signal. Signal distortion has caused the asymmetry in the interferogram shown in Fig. 2. The satellite peaks occur where the phase shift introduced by the interferometer is $\pm\Delta$, and cancels that introduced by the sample. Beams A_2 and B_1 combine to produce a satellite at $+\Delta$, and A_1 and B_1 produce the peak at $-\Delta$.

[3] Digilab, Inc. Film Thickness Gauge.

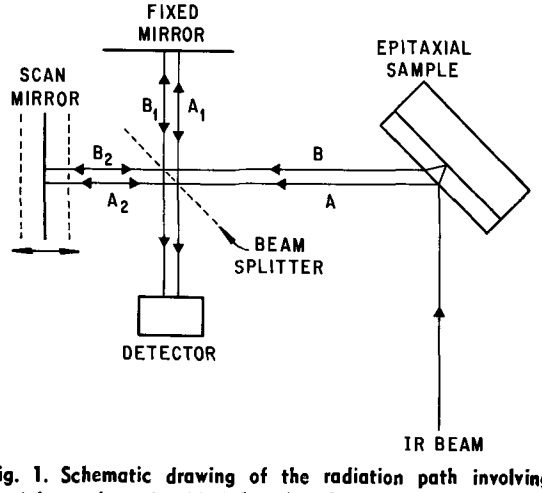

Fig. 1. Schematic drawing of the radiation path involving an epitaxial sample and a Michelson interferometer.

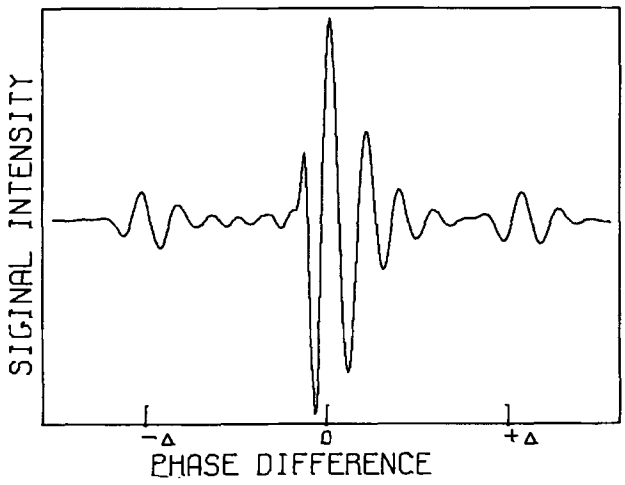

Fig. 2. Unprocessed interferogram of reflection from a 12.5 μm epitaxial film.

The mirror position at any point in a scan can be accurately determined, and hence locating the satellites relative to the central peak will yield a measured value of Δ. If the phase shifts introduced upon reflection at the surface and layer-substrate interfaces were the same, the film thickness could be derived from the simple equation

$$t = \frac{\Delta}{2n_1 \cos\theta} \qquad [2]$$

where n_1 is the refractive index of the film, t the film thickness, and θ the angle of refraction.

For epitaxial semiconductor material a phase shift correction is necessary to obtain an accurate film thickness measurement. The phase shift at the layer-substrate interface for silicon epitaxial material and the general method for correcting the thickness measurement made with a dispersion spectrometer have been published (9, 11). Thickness measurements using an interferometric spectrometer must also include a similar correction for reflection phase shifts to obtain accurate measurements and to be compatible with existing measurement techniques.

Experimental

The epitaxial film thickness monitor constructed at Texas Instruments was called the EPILOG system. A block diagram of the EPILOG system is shown in Fig. 3. Data collection was handled by the optical unit, which included the source, source optics, and Michelson interferometer. The amplified signal was converted to digital data and stored in a computer memory. The film thickness extracted from the data was presented on a digital readout or printed by a typewriter or strip printer.

The development of the EPILOG system has so far resulted in two systems. The second system, EPILOG II, surpassed the first model in performance and only this system will be described in detail. Data from both systems, however, will be shown later to demonstrate the improvements obtained with the more advanced system. A third model, EPILOG III, using a more compact and faster computer[4] is currently under con-

[4] Texas Instruments Model 960A.

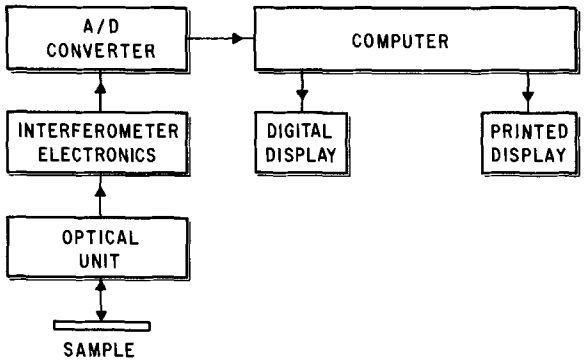

Fig. 3. Block diagram of EPILOG system

struction, but will be essentially the same in all performance parameters as EPILOG II, the only exception being in that a faster computation in EPILOG III might slightly shorten the sampling time.

The optical schematic for the second system is shown in Fig. 4. In this case a 1:1 image of the globar was formed on the sample surface, with no prefiltering of the radiation. The radiation reflected from the sample was partially collimated before being sent into the interferometer. The interferometer used was again the Block 196TC. The image of the globar on the sample was about ¼ × ¾ in. Provisions were made to reduce this to ¼ × ½ in. for profiling the thickness over a large slice. The data processing in this case was handled by a Texas Instruments Model 861 process control computer, with a 24 bit, 8K memory, and hardware arithmetic. The additional computational capability permitted a fairly sophisticated calculation of the film thickness, using a Fourier transform technique. The details of this computation will be described in the next section. Film thickness was displayed on a digital display, with the option of a permanent record on a strip printer. In this system the interferometer scanned 4 times per second and the number of scans averaged before data processing was 16. The computation time varied somewhat from one slice to another, depending on the film thickness, but the average time required to measure a film thickness was ~6 sec.

The reliability of both systems has been excellent. The Michelson interferometer heads which are kept under a dry nitrogen purge have caused no down time at all. The EPILOG I system was put into extensive use in June of 1969, and EPILOG II in July of 1970. Both are currently still in use.

Fourier Transform Analysis

The computer used for the EPILOG II system permitted the use of a sophisticated data analysis. The method developed utilized the Cooley-Tukey (16) fast Fourier transform (FFT) algorithm and can be shown to be mathematically equivalent to the ASTM procedure.

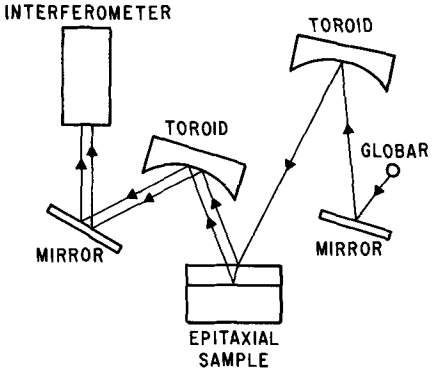

Fig. 4. Source and collection optics for EPILOG II

When a single beam of radiation enters a Michelson interferometer, the signal at the detector is a function of the frequency distribution of the radiation, $A(\nu)$, and the phase difference between the components which are separated and recombined in the interferometer. This signal intensity can be expressed by

$$I(x) \sum_{\nu} A(\nu) \cos(2\pi\nu x) \quad [3]$$

where x is the optical path difference between the two rays in the interferometer and ν is the optical frequency, $1/\lambda$.

For the system shown schematically in Fig. 1, the radiation entering the Michelson interferometer consists of two beams, differing in phase by an amount Δ. The signal intensity at the detector in this case is given by

$$I(x) = \sum_{\nu} (A(\nu) + B(\nu)) \cos(2\pi\nu x) + \sum_{\nu} 2\sqrt{A(\nu)\,B(\nu)} \cos(2\pi\nu x \pm \Delta) \quad [4]$$

where $A(\nu)$ and $B(\nu)$ are the frequency distributions of the radiation reflected at the first surface and layer-substrate interface, respectively. The first term in the summation produces the center feature shown in the interferogram in Fig. 2. The satellites shown at phase shift of $\pm\Delta$ in Fig. 2 are generated by the second term in Eq. [4]. Equations [3] and [4] imply that the interferogram should be symmetrical about $x = 0$; the data shown in Fig. 2 obviously are not. Some of the asymmetry can be attributed to imperfect compensation in the interferometer optical system but most is the result of distortions in the detector electronics at the high-scan velocities used. The distortions are most apparent at high-signal frequencies, which are generated by shorter wavelength radiation. An optical filter was used on the EPILOG I system to remove most of these high-frequency components and permit accurate identification of features in the interferogram with a minimum of computation.

In the EPILOG II system it was desired to include the shorter wavelength radiation in the analysis to permit the measurement of thinner samples. In this case it was necessary to remove the distortions seen in Fig. 2 prior to data analysis. The properties of the Fourier transform can be easily utilized to remove these phase distortions and generate an idealized, symmetrical interferogram. The original interferogram consisted of 1024 data words collected at 1.0 μm increments of interferometer path difference. The Fourier transform of this raw interferogram yielded a complex function of ν.

$$I(x) = \sum_{\nu} (N(\nu) + iM(\nu))\, e^{-2\pi i\nu x} \quad [5]$$

These complex coefficients occur because there is no wavelength-independent content in the distorted interferogram. These complex coefficients were then replaced by the real amplitude of the vector they represent. The transformed interferogram was apodized to remove contributions from wavelengths shorter than 8 μm since no information of the epitaxial layer thickness can be obtained in this spectral region. The reverse transform on the real, apodized coefficients yielded a symmetric, filtered interferogram. The data used to generate Fig. 2 is shown again in Fig. 5 after symmetrization and filtering. While most of the data analysis time was spent in this step, the time required was more than offset by improved signal/noise ratio and hence reduced sampling time. Since the interferogram was then symmetrical and contained no contributions from wavelengths shorter than 8 μm, it could at that point be described by a single sided interferogram

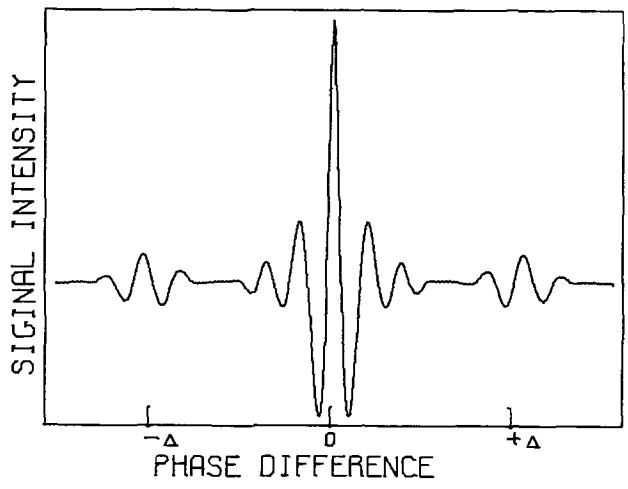

Fig. 5. Symmetrized interferogram from a 12.5 μm epitaxial film

of 128 points; each point corresponding to 4 μm increments of interferometer path difference.

The accurate analysis of the reflection interferogram depends critically on the isolation of the satellite fringes from the central fringe. All of the information concerning the epitaxial layer thickness is contained in the satellite fringes, and their complete characterization is very important. The sample used to generate the interferograms in Fig. 1 and 5 had a 12.5 μm epitaxial layer, and the central and satellite fringes were well separated. The satellite fringes can be easily isolated and identified in this case. However, samples with thinner epitaxial layers will exhibit satellite fringes shifted toward the central fringe, and when the layer becomes thin enough the three fringes will merge and location of the satellites will be impossible without further data manipulation. This merging of the fringes occurs with film thicknesses less than 8 μm. Extraction of film thickness information for thin samples can only be carried out after the contribution of the central fringe is removed from the interferogram.

The central fringe is composed of radiation reflected from both the first surface and the epitaxial layer-substrate interfaces. The amplitude and wavelength distribution of the central fringe depend on the optical constants of the epitaxial layer and the substrate and hence on the impurity type and resistivity in both areas. It has been found that the central fringe of a wide variety of samples can be approximated by a linear combination of the reflection interferogram from a clean high-resistivity silicon slice and an average of the central fringes of thick samples previously measured on the system. In this case thick samples are defined as having a layer thicker than 10 μm. The coefficients for the linear combination are chosen so that after subtraction from the sample interferogram the signal amplitude at the zero mirror displacement position and at a wavelength of 8 μm are both zero. The amplitude at 8 μm is determined from the Fourier transform of the interferogram. The residual noise left in the center of the interferogram after this subtraction is very small relative to the satellite amplitude. The satellites can be easily located after this subtraction step, and samples as thin as 0.6 μm have been analyzed reliably. For samples thinner than 0.6 μm the satellites themselves overlap at the center of the interferogram, and they cannot be separated by any computations currently in use in this system. Physically, at this point the optical thickness of layer is less than ½ the wavelength of the observing radiation and no strong interference effects can be characterized.

The mathematical representation of a single satellite can be given by

$$I(x)_{SAT} = \sum_{\nu} 2\sqrt{A(\nu)\,B(\nu)}\cos(2\pi\nu x - \Delta) \quad [6]$$

The term Δ can be expanded to

$$\Delta = \phi_{01} - \phi_{12} + 2\pi\nu n_1 t\cos\theta \quad [7]$$

where $\phi_{01} = \pi$ is the phase shift at the air-layer interface, ϕ_{12} is the phase shift at the layer-substrate interface, n_1 is the refractive index of the layer, t the film thickness, and θ the angle of refraction.

Both ϕ_{12} and $B(\nu)$ are functions of the optical constants of the substrate, n_2 and k_2, where these are the real and imaginary parts of the refractive index. At this point the mathematical representation of the satellite can be better expressed in complex notation as

$$I(x)_{SAT} = \sum_{\nu} G(n_1, n_2, k_2, \nu)\,H(n_1, t, \theta) \quad [8]$$

where

$$G(n_1, n_2, k_2, \nu) = 2\sqrt{A(\nu)\,B(\nu)}\,e^{-i(\phi_{01} - \phi_{12})} \quad [9]$$

and

$$H(n_1, t, \theta) = e^{-2\pi i(x - n_1 t\cos\theta)} \quad [10]$$

The function G will determine the shape of the satellite; it is independent of film thickness but dependent on the optical constants of the substrate. The function H will determine the location of the satellite as determined by the film thickness and refractive index, but it is independent of the substrate parameters. In Fig. 6 the change in satellite shape with substrate material is shown for both P- and N-type material. This demonstrates the effect of the function G. In Fig. 7 the thickness independence of the satellite shape, again expected from the function G in Eq. [8], is demonstrated. The data shown in Fig. 6 and 7 are measured data, after symmetrization of the interferogram and central fringe removal.

The satellites shown in Fig. 6 and 7 are quite asymmetric for the most part. This asymmetry made it impossible to use any single feature of a satellite to define its location. The asymmetry in this case was due to the phase-shift difference between the surface and layer-substrate reflections rather than the measurement system as discussed previously. The phase shift correction factors have been calculated and published, and can be used when the substrate type and resistivity are known (9, 11).

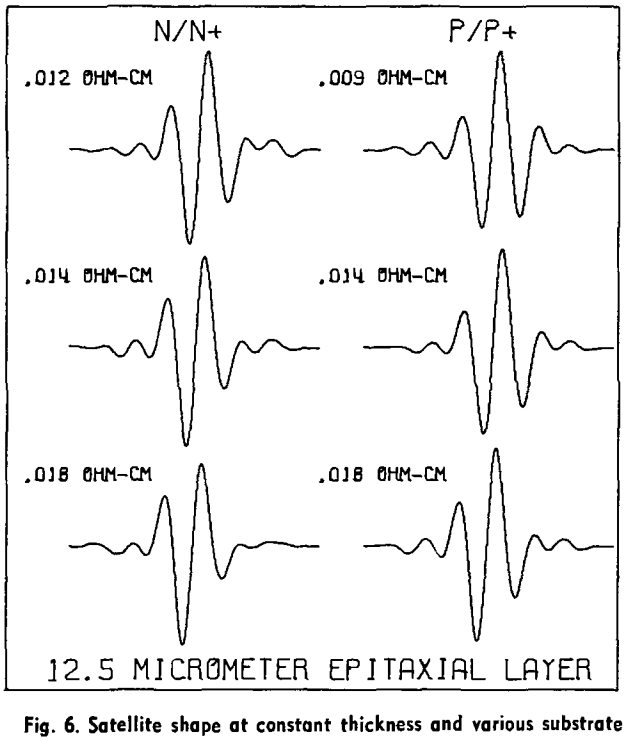

Fig. 6. Satellite shape at constant thickness and various substrate resistivities.

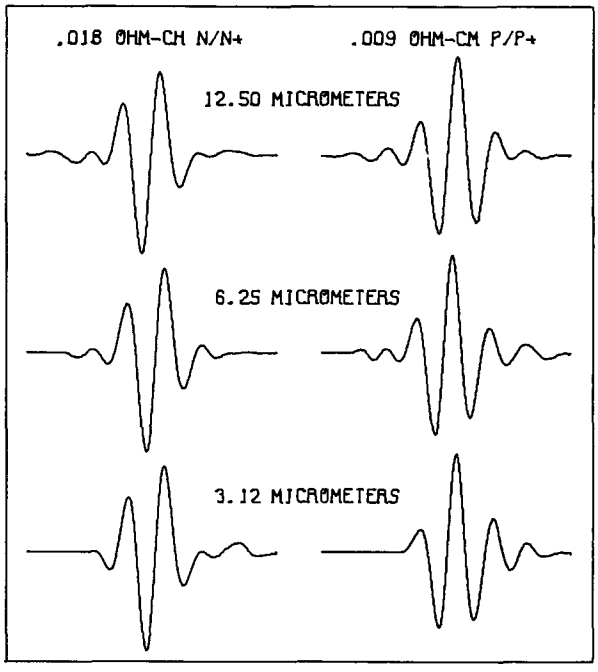

Fig. 7. Satellite shape for various thicknesses and constant substrate resistivity.

Using these published values for ϕ_{12}, we can define a function P, such that

$$P(x) = \sum_{\nu} e^{+i(\phi_{01}-\phi_{12})} \quad [11]$$

The convolution of $P(x)$ with $I(x)_{SAT}$ will yield

$$P(x) * I(x)_{SAT} = \sum_{\nu} 2\sqrt{A(\nu)\,B(\nu)}\; e^{-2\pi i\nu(x-n_1 t\cos\theta)} \quad [12]$$

This function, $P(x) * I(x)_{SAT}$, is symmetric with its maximum at

$$x_{max} = n_1 t \cos\theta \quad [13]$$

The effect of the convolution is shown in Fig. 8, with measured data of both P- and N-types. The location of the satellites was then easily accomplished by locating the point of maximum signal intensity. This location was used to derive the film thickness from Eq. [13]

$$t = \frac{x_{max}}{n_1 \cos\theta} \quad [14]$$

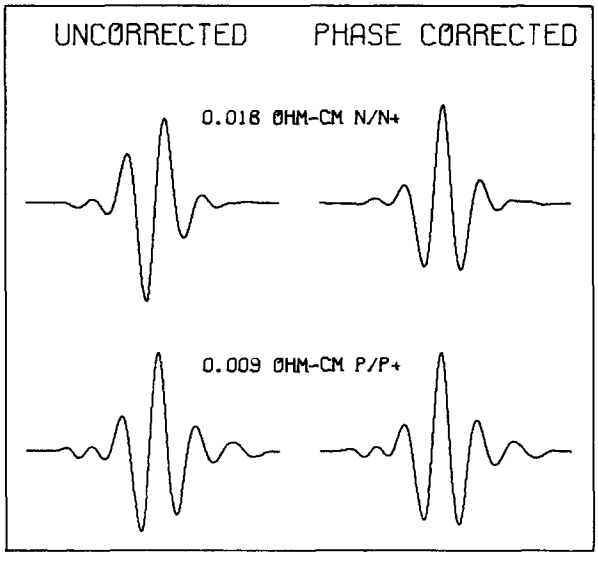

Fig. 8. Satellite shape after convolution.

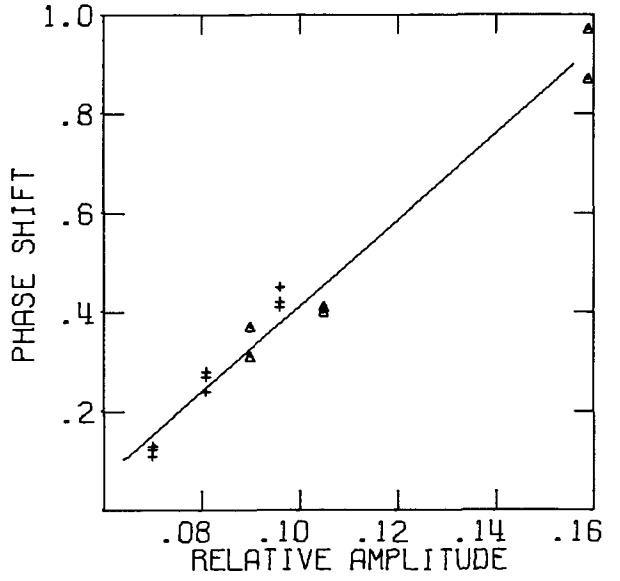

Fig. 9. Correction of layer-substrate phase shift with satellite amplitude.

For routine measurements, it is not desirable to require that the operator enter the type of resistivity of each sample. In many cases, the operator may only know the type and a resistivity range for a given lot of epitaxial samples. It was found that an excellent correlation exists between the relative amplitude of the reflection from the layer-substrate interface at a given wavelength and the calculated phase shift (9) at that wavelength. A plot of this empirical correlation at 16 μm is shown in Fig. 9. These data include both P- and N-type material, so that neither type nor resistivity need be entered by the operator. This empirical estimation of the reflection phase shift is now used on all routine measurements with the EPILOG systems.

Results and Conclusions

The use of a scanning Michelson interferometer to measure epitaxial film thickness is simply a modification of standard *IR* interferometry. An evaluation of the method can best be made by comparing the results from an EPILOG type system with those obtained using ASTM procedure F95-68T. To expedite this comparison a set of samples including both P- and N-type material was collected. The reflectance spectra were obtained on a Perkin-Elmer 221 spectrometer with KBr optics, and film thicknesses calculated according to the ASTM procedure. In Table I the ASTM thicknesses are compared with those obtained on both EPILOG systems. The term $|\delta|$ is the magnitude of the difference between an ASTM and EPILOG measurement. The interlaboratory precisions (3σ) given for the ASTM procedure are $\pm(0.25\ \mu m + 0.025t)$ for P-type material and $\pm(0.25\ \mu m + 0.005t)$ for N-type. The

Table I. Comparison of epitaxial film thickness measurements

Sample Resistivity/Type	ASTM (μm)	EPI I (μm)	$\lvert\delta\rvert$ (μm)	EPI II (μm)	$\lvert\delta\rvert$ (μm)
0.006 ohm-cm/PP+	24.16	24.10	0.06	24.23	0.07
0.006 ohm-cm/PP+	12.07	12.12	0.05	12.01	0.06
0.006 ohm-cm/PP+	5.89	5.77	0.12	5.82	0.07
0.006 ohm-cm/PP+	3.05	3.05	0.00	2.82	0.23
0.018 ohm-cm/PP+	24.77	24.92	0.15	25.15	0.38
0.018 ohm-cm/PP+	12.24	12.22	0.02	12.22	0.02
0.018 ohm-cm/PP+	5.72	5.69	0.03	5.82	0.10
0.018 ohm-cm/PP+	3.12	3.20	0.08	3.07	0.05
0.009 ohm-cm/NN+	25.91	26.09	0.18	26.04	0.13
0.009 ohm-cm/NN+	12.14	12.04	0.10	12.04	0.10
0.009 ohm-cm/NN+	6.27	6.35	0.08	6.32	0.05
0.009 ohm-cm/NN+	3.48	3.58	0.10	3.51	0.03
0.018 ohm-cm/NN+	24.71	24.87	0.16	24.84	0.13
0.018 ohm-cm/NN+	12.50	12.60	0.10	12.70	0.20
0.018 ohm-cm/NN+	6.38	6.30	0.08	6.32	0.06
0.018 ohm-cm/NN+	3.71	3.56	0.15	3.61	0.10

Table II

	IR	EPILOG I	EPILOG II
Thickness range	1.0-100 μm	30-70.0 μm	0.75-70.0 μm
Sampling time	30 sec-15 min	5 sec	6 sec
Precision (3σ)	$\pm$ (0.25 μm + 0.025t)	$\pm$ (0.15 μm + 0.015t)	$\pm$ (0.05 μm + 0.005t)
Profiling capability	yes	no	yes

numbers obtained with both EPILOG systems fall within this range. The precisions obtained with the two EPILOG systems were somewhat better than the interlaboratory precision for the ASTM method. Repeated measurements on a set of four P-type samples over a period of several months yielded 3σ precisions of $\pm(0.15 + 0.015t)$ for EPILOG I and $\pm(0.05 + 0.005t)$ for EPILOG II.

The computational procedure used with the EPILOG systems was actually mathematically equivalent to the ASTM calculation, with the exception of the empirical determination of the phase shift correction.

Some of the important features of the EPILOG systems are compared to the standard *IR* method in Table II. The upper thickness limit is determined by the available resolution in the *IR* technique. In an interferometer the resolution is limited by the available mirror travel. Hence the upper limit for the EPILOG system is less than that of a good *IR* spectrometer, although it is of no practical importance since little material thicker than 70 μm is used in device fabrication. The shortest sampling time for an *IR* spectrometer is probably available in the Beckman system, although a manually scanned system followed by a full ASTM calculation would probably take about 15 min. This accounts for the wide range of sample times shown for the IR technique in Table II.

In summary, it appears that a computer data processing station coupled to a scanning Michelson interferometer can provide rapid and accurate epitaxial film thickness measurements. Where the sample volume can justify the initial equipment investment, the improvement in hardware reliability and measurement speed is well worthwhile. The precision that arises out of computer data processing exceeds that possible with the standard ASTM procedure carried out manually.

Acknowledgment

The authors wish to thank Jack Whichard for his invaluable services in the design and construction of the EPILOG systems.

Manuscript submitted May 18, 1972; revised manuscript received Oct. 2, 1972.

Any discussion of this paper will appear in a Discussion Section to be published in the December 1973 JOURNAL.

REFERENCES

1. P. F. Kane and G. B. Larrabee, "Characterization of Semiconductor Materials," pp. 224-230, McGraw-Hill Book Co., New York (1970).
2. A. R. Hilton and C. E. Jones, *This Journal*, **113**, 472 (1966).
3. P. J. Severin, *Appl. Optics*, **9**, 2381 (1970).
4. W. G. Spitzer and M. Tanenbaum, *J. Appl. Phys.*, **32**, 744 (1961).
5. M. P. Albert and J. F. Combs, *This Journal*, **109**, 709 (1962).
6. P. A. Schumann, Jr. and R. P. Phillips, *IBM Tech. Report*, TR 22.182 (1965).
7. T. Abe and T. Kato, *Japan. J. Appl. Phys.*, **4**, 742 (1965).
8. K. Sato, Y. Ishikawa, and K. Sugawara, *Solid-State Electron.*, **9**, 771 (1966).
9. P. A. Schumann, Jr., R. P. Phillips, and P. J. Olshefski, *This Journal*, **113**, 368 (1966).
10. P. A. Schumann, Jr., *ibid.*, **116**, 409 (1969).
11. American Society for Testing Materials, F95-68T (1968).
12. Horlick, *Appl. Spectroscopy*, **22**, 617 (1968).
13. S. T. Dunn and C. T. Foskett, "Industrial Research," p. 36, Feb. 1971.
14. L. Mertz, *App. Optics*, **10**, 386 (1971).
15. Digilab, Inc., Silver Spring, Maryland.
16. J. W. Cooley and J. W. Tukey, *Math. of Comput.*, **19**, 297 (1965).

Photoresist Cleaning

F. P. Laming[1] and R. E. Straile

Bell Laboratories, Murray Hill, New Jersey 07981

ABSTRACT

Filtration and centrifugation methods for cleaning KTFR and KMER photoresists have been quantitatively compared using a light-scattering technique to monitor both processes. It was found that material of a given purity can always be prepared more easily by centrifugation. In particular, KMER, comparable in purity to KTFR, can readily be prepared without adjusting resist viscosity prior to centrifugation, though centrifuging times are reduced by dilution of the material. Typically, centrifugation for 25,000 g-hr produces good quality KMER from 1:1 material. Centrifuged KMER is capable of resolving better than 1μ lines. Because of the superior adhesion of KMER, compared to KTFR, it should prove useful in applications where high resolution is required.

Photoresist cleanliness is a major factor influencing the resolution of the photolithographic process. Clearly, the presence of large particles of polymeric material or foreign matter will result in severe degradation of the developed image. The most common method of reducing particulate contamination of the resist is filtration immediately prior to application. Naturally the efficiency of this cleaning method depends on the ease of filtration, which, in some cases, can prove a major obstacle. Undiluted Kodak Thin Film Resist (KTFR), for example, can only be conveniently filtered through a 14μ filter, or through a 1.2μ filter if diluted 1:1. Filtration is even more difficult for Kodak Metal Etch Resist, and is virtually impossible with undiluted material;

[1] Present address: IBM Corporation, East Fishkill Facility, Hopewell Junction, New York 12533.

Key words: nephelometry, photolithography, filtration.

therefore, unpurified KMER is not used for high-resolution work in spite of its greater adhesion (1) as compared to KTFR and consequent potential for high-resolving power. A somewhat complex purification procedure to prepare usable KMER was developed a few years ago by Harrel of Texas Instruments (2).

In this work we describe a quantitative comparison between filtration and centrifugation techniques for cleaning both KTFR and KMER. The cleanliness of the resists was determined and monitored during the course of cleaning by measuring the intensity of light scattered from the solutions. Light scattered in this way is primarily a function of particle size and concentration; contributions from the solvent are relatively small and could be ignored. Since cleaning of the resist is largely a matter of eliminating pre-crosslinked material and particles of foreign matter, light scattering is, thus, a good measure of resist cleanliness.

The truth of this proposal can readily be ascertained from Fig. 1, where scattering-filtration data are compared for old and new samples of KTFR. Presumably the difference between the curves results from the fact that the old sample contains thermally cross-linked material.

Experimental

The light scattering apparatus has been described in detail elsewhere (3). In this work a He/Ne laser operating at 6328Å was used as a light source and scattering measured at a fixed angle of 90°. All scattering intensities were normalized against the intensity measured at the same angle for pure xylene. The standard was measured before and after each resist measurement.

Filtration is normally performed immediately prior to resist application, using syringe-mounted filters operated by hand. This was not a practical solution here because we wished to use fine porosity filters and to filter relatively large volumes. We, therefore, designed a filter holder capable of operating to pressures of 500 psi. Nitrogen was used as the pressurizing gas, and solutions were filtered directly into a glass-scattering cell having three windows positioned at 0°, 90°, and 180° to the incident light.

For centrifugation we used a small centrifuge capable of producing 1300g at the center of 50 ml centrifuge cells. Initially we used conventional glass tubes, the material subsequently being transferred to the filtration-scattering cell for monitoring purposes. This method resulted in spurious readings because the solutions were unavoidably disturbed during transfer so that centrifuged residue reappeared in suspension. This problem was overcome by using the specially designed centrifuge-scattering cells illustrated in Fig. 2. The three quartz windows were mounted from the inside and supported by shoulders to withstand the centrifugal pressure; the body of each cell was machined from aluminum, anodized, and dyed black to reduce internal reflections. In operation each cell was filled to at least one centimeter above the top edges of the windows in order to reduce reflections from the liquid-air interface. Covers were used to minimize evaporation.

Results

Because filtration of resists through fine porosity filters is virtually impossible even at high pressure, each resist was diluted to 5% of its original concentration for these experiments. This diluted material was then filtered sequentially through seven filters varying in pore size from 3-0.05μ; scattering intensity was determined after each filtration step. Figure 1 shows the results of such an experiment for one sample tested immediately after receipt from the manufacturer, and for another after three years of storage. The difference between the two is readily apparent and is clearly due to presence of thermally cross-linked material in the old sample. Notice that after filtration through a 0.8μ filter, however, there remained little difference between the two samples.

The filtration curve for KMER is shown in Fig. 3, together with scattering data from the centrifugation experiment. Again, these results were obtained from 5% solutions, but here the limiting filter size was 0.2μ, through which KMER passed only with great difficulty even at a pressure of 500 psi. The curves clearly demonstrate that the resist cleanliness, attained only with difficulty by filtration, is attained in ½ hr and with ease by centrifugation.

A similar result is obtained when filtration and centrifugation are compared for KTFR, as in Fig. 4. Again, the centrifuged material seems to equal in cleanliness that obtained with greater time and difficulty by filtration.

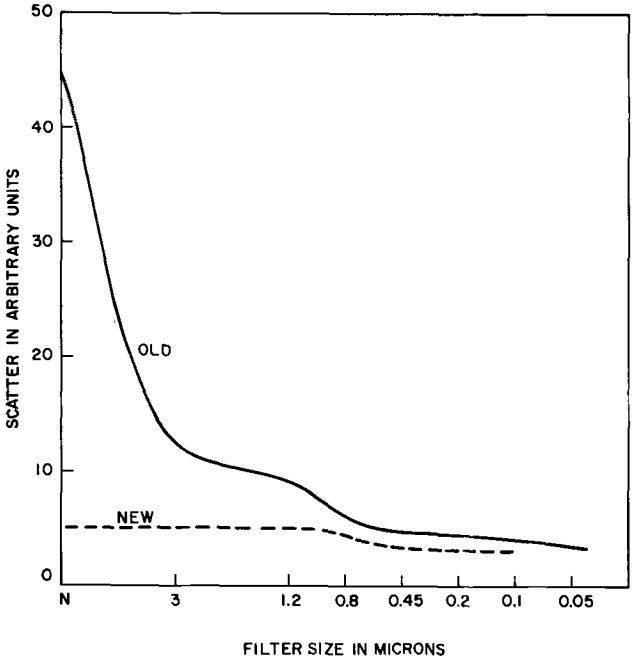

Fig. 1. Scattering data from KTFR 5% filtration

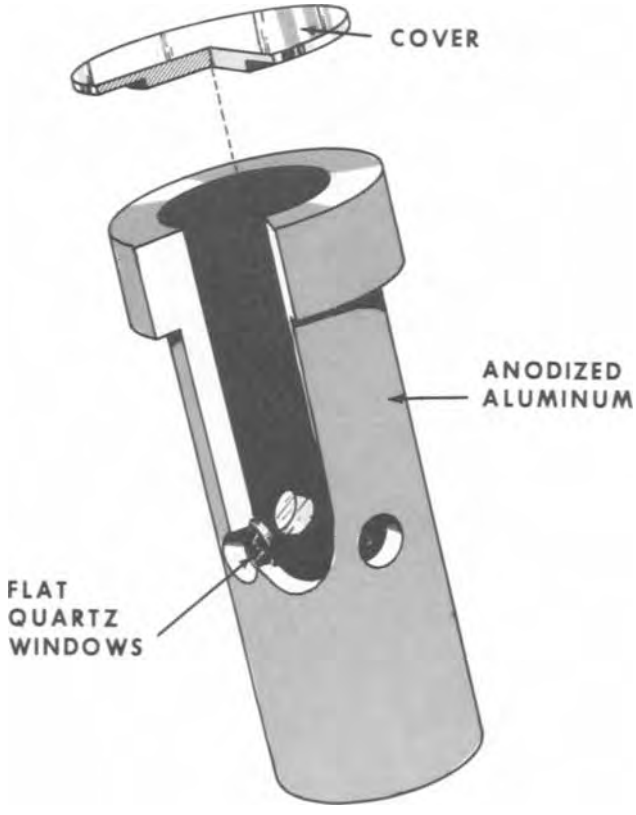

Fig. 2. Centrifuge-scattering cell

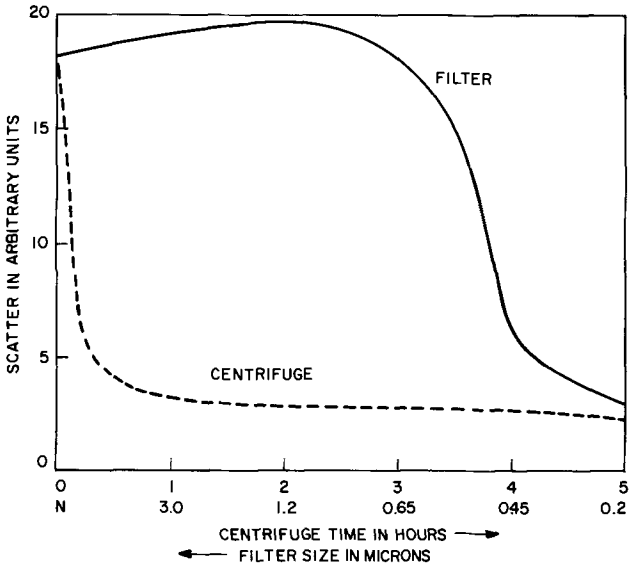

Fig. 3. Comparison of scattering from filtration and centrifugation of 5% KMER.

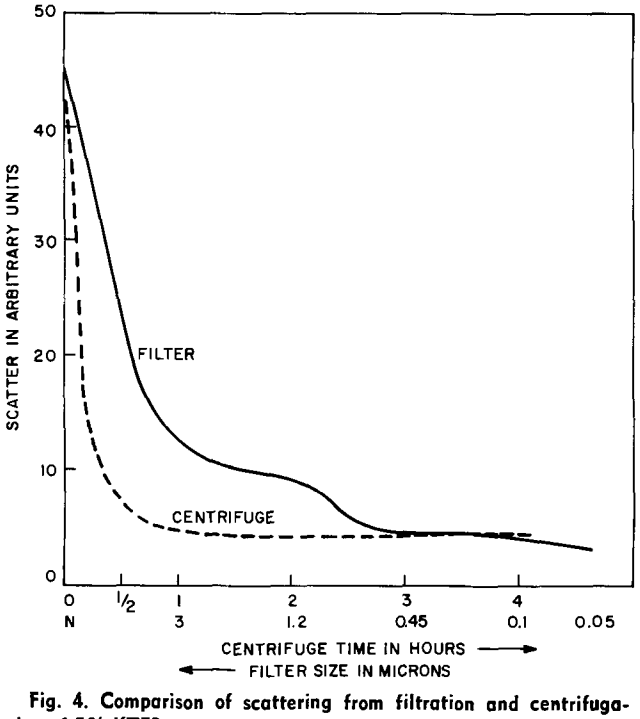

Fig. 4. Comparison of scattering from filtration and centrifugation of 5% KTFR.

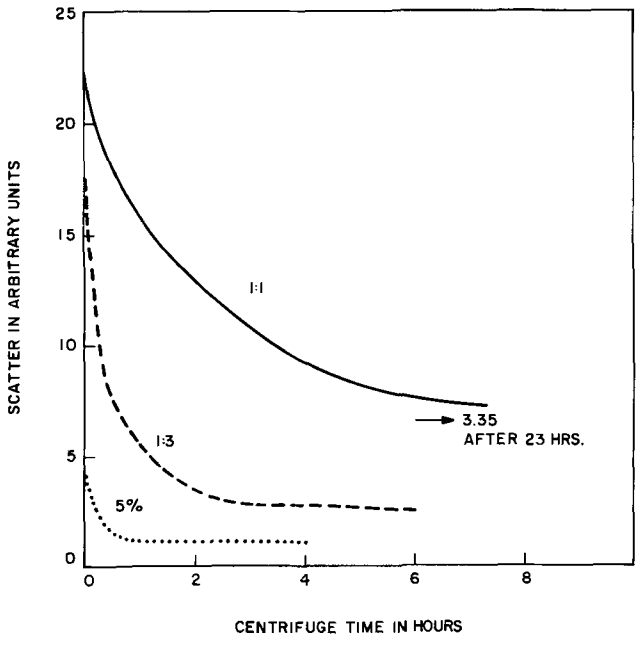

Fig. 5. KTFR centrifugation rates

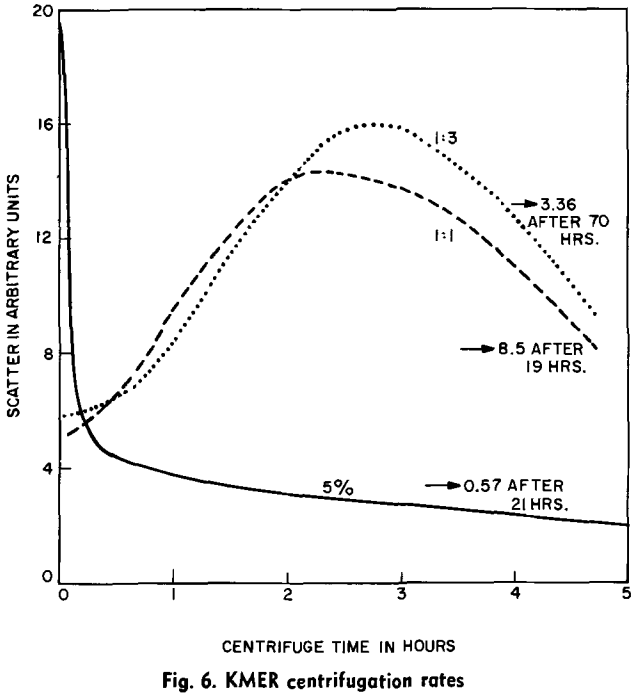

Fig. 6. KMER centrifugation rates

So far we have described cleaning procedures which would result in material which could not be used directly for photolithography because the solutions are too dilute. In practice it is more usual to use material which has been diluted to only 25 or 50% of the supplied concentration. The greater solids content and higher viscosities of such solutions would then result in both centrifugation and filtration being more difficult. Dilute resist solutions can be returned without degradation to their original concentrations by vacuum distillation, but this procedure would be inconvenient to accomplish in production. An alternative solution is to use brute force methods to clean the resists at their normal concentrations. For KTFR, as has been previously described, filtration can be used in this way with moderate success, but for KMER filtration at high-concentration levels is impossible. In both cases, however, centrifugation of the more concentrated material produces excellent results; though naturally longer times are required for the higher viscosities.

Scattering curves for centrifuged samples of various concentrations of KTFR and KMER are shown in Fig. 5 and 6, respectively. The maxima observed in the KMER curves result from multiple scattering; the material is so dirty that both the incident-scattering beam and the scattered light are severely attenuated prior to purification, so that an apparent increase in scattering intensity is observed at first as the resist is purified. A similar, but less pronounced, maximum can be seen in the KMER data of Fig. 3. It is apparent that the cleaning process is still progressing even at these high viscosities. In fact, the curves level off at virtually the same degree of cleanliness, taking into account the difference in particle concentration and therefore final scattering intensities at different dilutions. Thus, a scattering intensity of 0.57 from a 5% solution of KMER after 21 hr centrifuging would be equivalent to an intensity of 5.7 from 1:1 solution, providing scattering is directly proportional to concentration. In fact, the 1:1 KMER solution had a scattering value of 8.5 after 19 hr centrifuging.

The solids content of solutions used in these studies were determined by evaporation of weighed samples

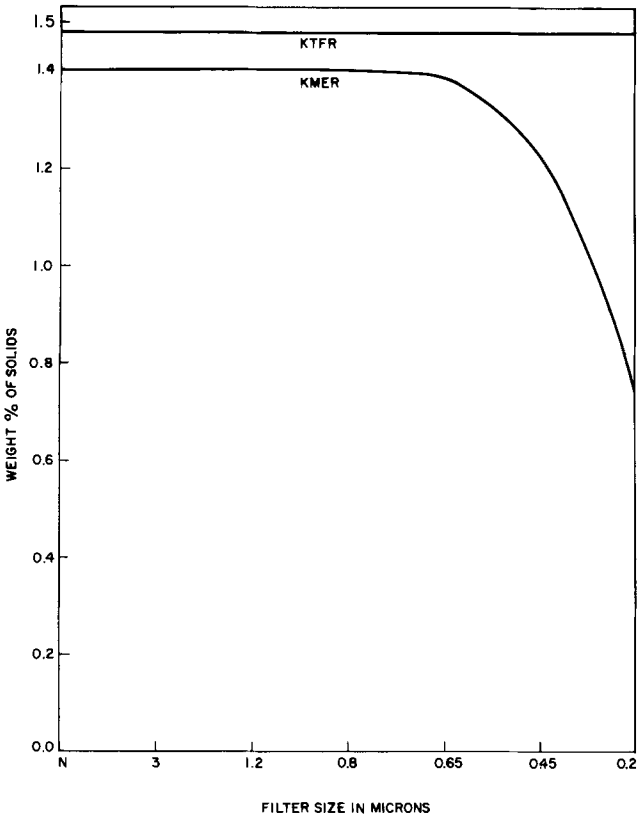

Fig. 7. Variation of solids content of KMER and KTFR during filtration of 5% solutions.

in small aluminum containers. The effect of filtration on solids content of 5% solutions of KMER and KTFR is illustrated in Fig. 7. The nonfiltered values shown here correspond to weight per cent (w/o) solids content in the undiluted solutions of 28.0 for KMER and 29.6 for KTFR. The manufacturer gives values in the range of 24.7-27.3 for KMER and 27.2-28.8 for KTFR. Filtration does not seem to affect the solids content of KTFR, and this is confirmed by the scattering data of Fig. 1 (for the new sample). Apparently there are not many particles larger than 0.2μ in crude KTFR. The solids curve for KMER is also in good agreement with scattering data (see Fig. 3) and suggests that a considerable proportion of this material consists of particles sized in the range 0.2-0.65μ. The weight per cent solids content of KMER after filtering through the 0.2μ filter has been reduced to 11.6 (computed for the initial concentration). Such a reduction might be expected to have an adverse effect on adhesion; however, our measurements indicate that centrifugated KMER is superior in adhesion to KTFR by a factor of approximately 2. We have also demonstrated that the purified KMER is at least capable of matching KTFR for pattern generation. Clean 1μ lines have been resolved.

Conclusion

We have demonstrated that light scattering can be used as an effective monitor of photoresist cleanliness. The technique was used to follow in detail, and to compare, filtration and centrifugation procedures for cleaning both KMER and KTFR.

Results are most significant for KMER which is impossible to clean effectively by filtration but which can be easily and effectively cleaned by centrifugation. The material may be centrifuged at the same dilution at which it would normally be employed, *e.g.*, KMER diluted 1:1 would require centrifuging for approximately 25,000 g-hr.

We recommend the use of centrifuge cleaned KMER in all applications where KTFR would normally be used for high-resolution work.

Manuscript submitted June 16, 1972; revised manuscript received Sept. 25, 1972.

Any discussion of this paper will appear in a Discussion Section to be published in the December 1973 JOURNAL.

REFERENCES

1. R. O. Lussow, *This Journal*, **115**, 660 (1968).
2. S. A. Harrel, "2nd Kodak Seminar on Microminiaturization," Eastman Kodak (1966).
3. F. P. Laming and R. E. Straile, *This Journal*, **12**, 1745 (1972).

Optical Properties of Silicon Nitride

Herbert R. Philipp

General Electric Research and Development Center, Schenectady, New York 12301

ABSTRACT

The optical properties of silicon nitride layers formed by the pyrolysis of a mixture of SiH_4 and NH_3 are presented. These results are used together with published data for SiO_x materials to formulate a bonding model for SiN_x and SiO_xN_y which quantitatively describes their optical characteristics. The basic units of this structure are Si tetrahedra of the type $Si\text{-}(Si_xO_yN_z)$ in which the distribution of atoms for all possible $x + y + z = 4$ is statistical for any given atom ratio.

The use of silicon nitride films in semiconductor technology has prompted a number of investigations concerning their electrical and chemical characteristics (1, 2). The optical properties of this material, on the other hand, are relatively unknown. This is due in part to the fact that the spectral region where these layers absorb light strongly is in the vacuum ultraviolet, and this wavelength range is not accessible with conventional measuring equipment. In addition there is no theory for this absorption and thus such data, even if available, would appear to have little analytical value.

Key words: reflection spectra, optical constants, silicon oxynitride, bonding model.

In a recent paper (3) we presented and discussed the optical properties of noncrystalline SiO_x materials for $x = 0 \rightarrow 2$. The data could best be interpreted by assuming the bonding to be of the type $Si\text{-}(Si_yO_{4-y})$ where the four atoms bonded to each Si are determined by statistics for any given atom ratio. We related the presence of Si-Si and Si-O bonds in these materials with certain rather general optical characteristics. In

addition we were able to correlate the presence of like bonds of the dimension of a Si-(Si_4) and Si-(O_4) tetrahedron with more specific optical structure which shows up in the data and which is a prominent and distinguishing feature of the curves for amorphous silicon and quartz, respectively, in bulk. This point of view had not been considered previously.

The present investigation (4) was undertaken in the expectation that the simple concepts outlined above might prove useful in the discussion and comparison of silicon nitride films made under various conditions and having different stoichiometries. By evaluating those optical characteristics particular to Si-N bonds and utilizing our knowledge of the properties of Si-Si and Si-O bonds, we may be able to account for the optical effects which show up in silicon nitride layers containing excess Si (5, 6) or new atom constituents such as oxygen (1). Thus the position of the absorption threshold or the value of the index of refraction could have quantitative significance in characterizing such materials.

To test this approach, the optical properties of silicon nitride must first be documented. This is the main task of the present paper. It is accomplished by analyzing a variety of data including that obtained from reflectance and transmission studies and by utilizing the Kramers-Kronig relations (7) to find a consistent set of optical parameters for the range of photon energies where silicon nitride absorbs strongly. For completeness, photoelectric data were also obtained which enables the electron affinity to be estimated (8).

The material selected for this study is noncrystalline silicon nitride formed on silicon or quartz substrates at 1000°C by reaction of a gaseous mixture of silane and ammonia in the ratio 1 to 40,000 (1). Such layers have a stoichiometry very near to that of crystalline Si_3N_4 yet possess at most only short range atomic ordering (2). Thus we are able to relate the properties we find to a rather localized environment of Si-N bonds. This feature is essential to the discussion of SiO_xN_y materials which we envision as made up of a network of Si atoms tetrahedrally bonded to other Si, N, or O atoms where the distribution of different Si-($Si_xO_yN_z$) tetrahedra for all possible $x + y + z = 4$ is statistically determined for any given atom ratio.[1] We will show that this model (3) is vastly superior in explaining the observed optical properties than the one generally considered (9) which treats such materials as mixtures of Si, Si_3N_4, and SiO_2 compounds. We shall use data obtained on chemical vapor deposited samples of SiO_xN_y prepared as above but with the addition of NO gas (1) to help support this conclusion.

Procedures and Results

The optical properties of any material may be described by the complex frequency dependent dielectric constant $\epsilon = \epsilon_1 + i\epsilon_2$ which in turn is related to the optical constants n and k by $\epsilon_1 = n^2 - k^2$ and $\epsilon_2 = 2nk$ (10). The extinction coefficient k describes the attenuation of the electromagnetic wave as it traverses the material. It is simply related to the absorption coefficient by $\alpha = 4\pi k/\lambda$ where λ is the wavelength of the light in vacuum. The real part of the index of refraction n has particular significance in the region of optical transparency where it describes the propagation velocity of the light wave. These parameters can be evaluated from transmission and reflectance studies which take into account interference effects and the presence of a substrate (11).

In the present study reflectance data were obtained from silicon nitride layers on polished silicon substrates (*i*) in the region 6 to 24 eV where this material is opaque and (*ii*) in the region 1 to 6 eV where these layers are transparent and the position and magnitude of interference minima enable n and hence the reflectance R for silicon nitride to be evaluated.[2] The experimental procedures used here have been described previously (10, 12). The uncertainty in the smooth curve of reflectance shown in Fig. 1 is estimated to be less than 5% in the region 1-10 eV and possibly larger at higher energies. From this curve initial values of n and k were computed in the range 1-24 eV using the Kramers-Kronig relation

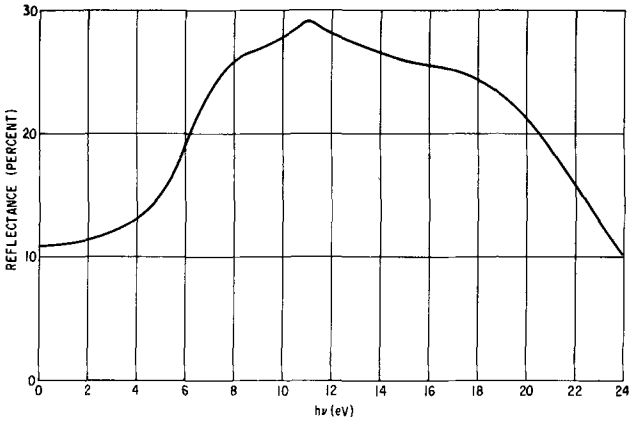

Fig. 1. The spectral dependence of the reflectance of silicon nitride.

$$\theta(\omega_0) = \frac{1}{2\pi}\int_0^\infty \frac{d\ln R(\omega)}{d\omega} \ln\left|\frac{\omega+\omega_0}{\omega-\omega_0}\right| d\omega \quad [1]$$

which connects

$$R = |r|^2 = \frac{(n-1)^2 + k^2}{(n+1)^2 + k^2} \quad \text{and} \quad \tan\theta = \frac{-2k}{n^2 + k^2 - 1} \quad [2]$$

where $r = (n - ik - 1)/(n - ik + 1) = |r|e^{i\theta}$. This procedure is described in more detail elsewhere (13).

Transmission data were obtained in the range 4-8 eV for silicon nitride layers of various thicknesses on quartz substrates to independently and more accurately evaluate k in this energy span. For absorption coefficients greater than 10^3 cm^{-1} these results are reasonably precise (±5%) and are presented in the curve for absorption given in Fig. 4 below. These values were used to correct those obtained above and a second Kramers-Kronig analysis was performed using

$$n(\omega_0) = 1 + \frac{\lambda(\omega_0)}{4\pi^2}\int_0^\infty \frac{d\alpha(\omega)}{d\omega} \ln\left|\frac{\omega+\omega_0}{\omega-\omega_0}\right| d\omega \quad [3]$$

to again compute n (and thus R) for the region 1-24 eV (7). These procedures were repeated until a set of values for n and k were obtained which best agreed with the experimental reflectance and transmission measurements and were consistent with both Kramers-Kronig causality relations. The results for ϵ_1 and ϵ_2 are shown in Fig. 2. More detailed graphs of the index of refraction and absorption coefficient for selected energy ranges are presented in Fig. 3 and 4.

Photoelectric data were obtained for silicon nitride layers on silicon substrates using sealed-off vacuum tubes with LiF windows.[3] The techniques employed here have been described previously (8). The photoelectric yield curve is plotted in Fig. 5.

Transmission and index of refraction data were obtained on a series of films, 6000Å thick, on quartz substrates prepared in the manner previously described but with the addition of various amounts of NO gas to the silane and ammonia mixture (1). This intro-

[1] The numbers x and y used to denote a range of stoichiometry in SiO_x, SiN_x, and SiO_xN_y materials are not related to the integers x, y, and z which describe possible tetrahedra types.

[2] The n and k values of the silicon substrate used in this determination were taken from H. R. Philipp and E. A. Taft, *Phys. Rev.*, 120, 37 (1960).

[3] These samples were exposed to the atmosphere prior to mounting in the tube. The surfaces are thus not uniquely characterized, and the results should be considered approximate.

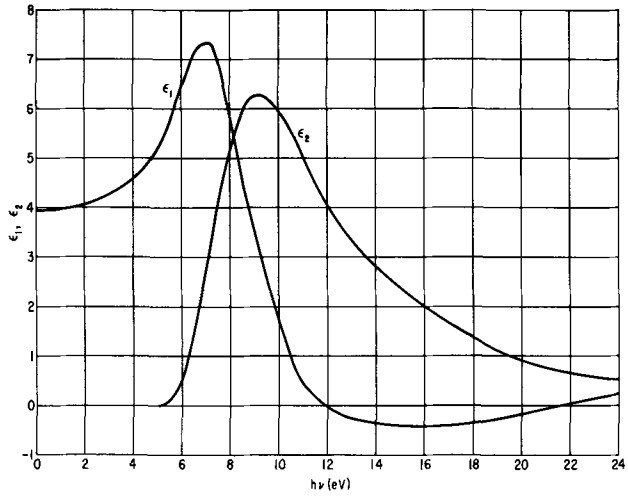

Fig. 2. The spectral dependence of the real and imaginary parts of the dielectric constant, ϵ_1 and ϵ_2, for silicon nitride.

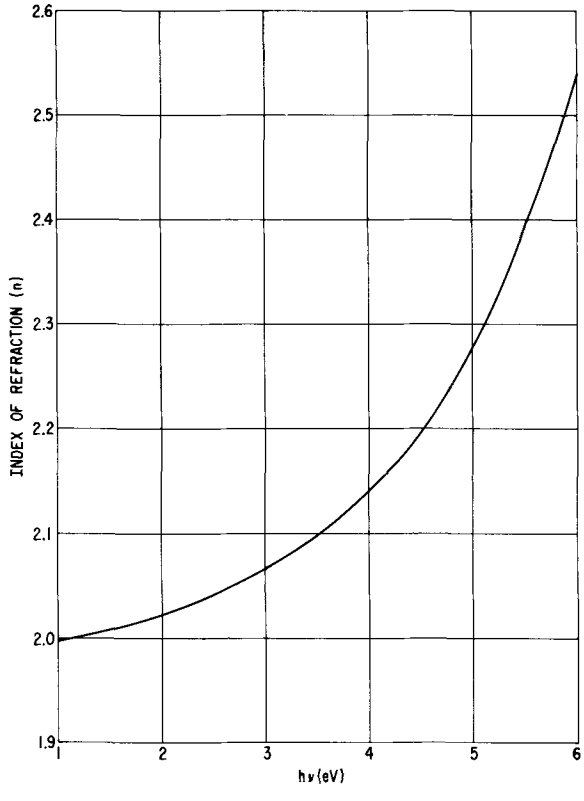

Fig. 3. The spectral dependence of the real part of the index of refraction, *n*, for silicon nitride.

duces oxygen into the material and forms silicon oxynitride, SiO_xN_y. The photon energy at which the transmission is 10% and the index of refraction for light of wavelength 6000Å are shown in Fig. 6 as a function of the per cent of injected NO gas. The amount of oxygen introduced into the films by this process appears to saturate with increasing NO percentage at a lower value than expected. We do not understand this effect since the "pyrolytic" decomposition of silane and NO gas alone produce layers of SiO_2 which do not absorb within the energy scale of Fig. 6 and have an index of about 1.45. It could be an experimental artifact due to the particular way the gases are introduced in the apparatus employed or to some unknown or premature chemical reaction taking place somewhere in the sample chamber. The situation, however, does not affect the results or the discussion below in any known way.

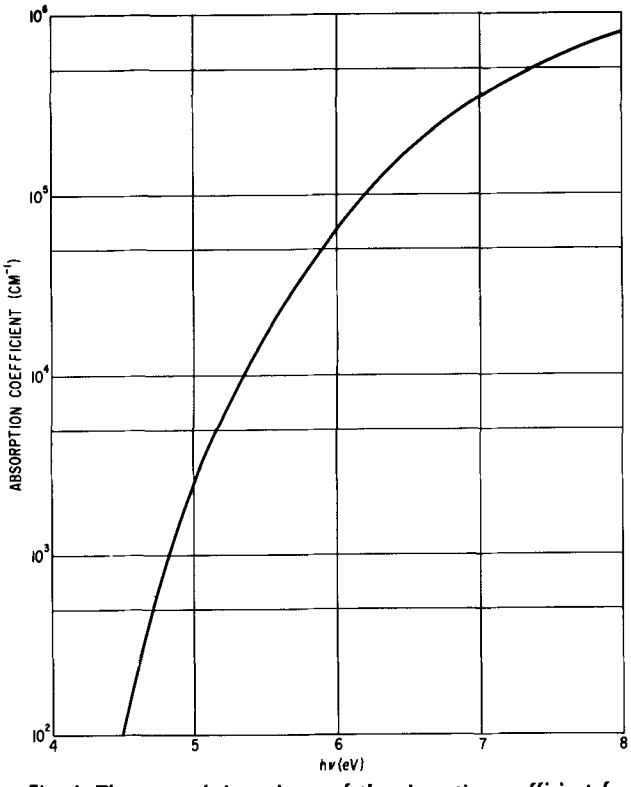

Fig. 4. The spectral dependence of the absorption coefficient for silicon nitride.

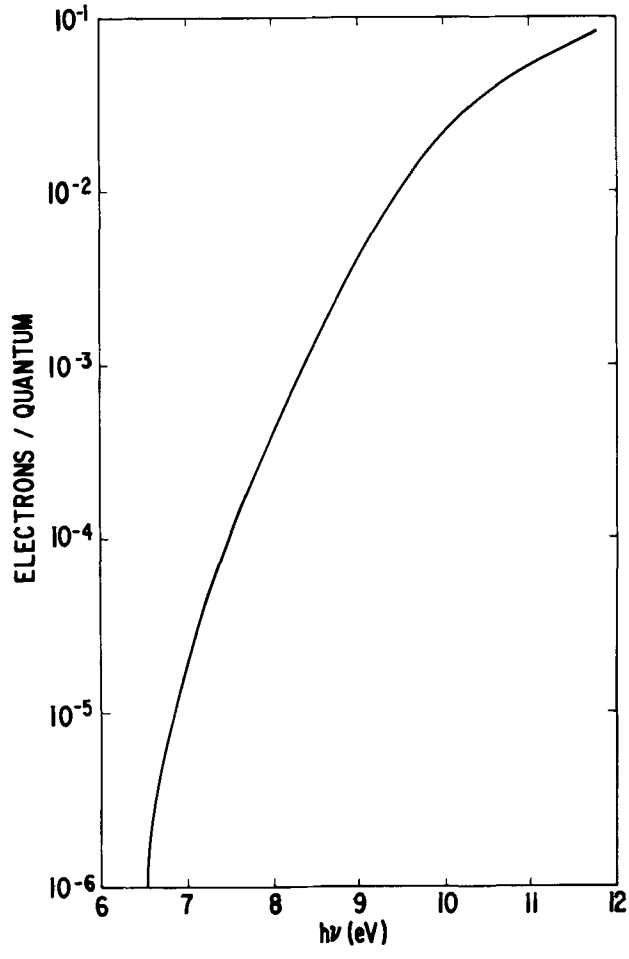

Fig. 5. The spectral dependence of the photoelectric yield for silicon nitride.

Discussion

We shall take the point of view that the fundamental bonding unit in materials like SiN_x and SiO_xN_y is the

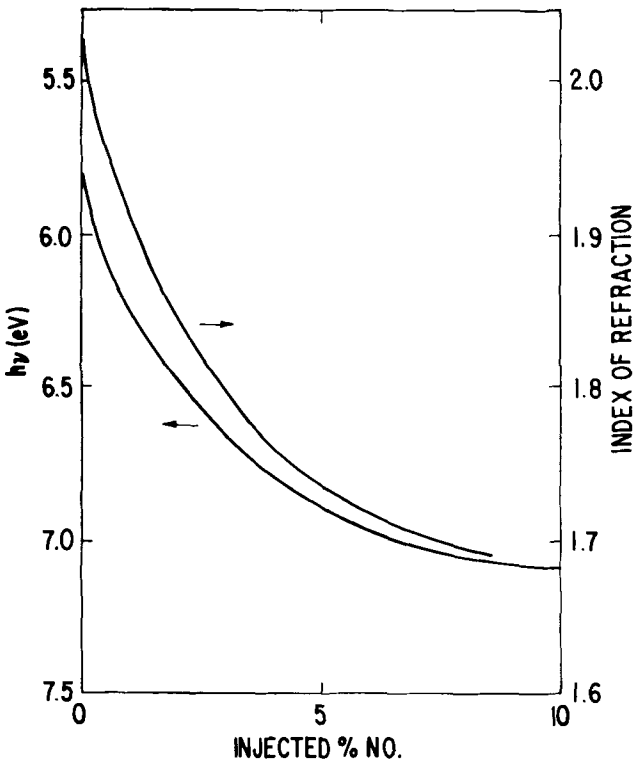

Fig. 6. The index of refraction and the photon energy at which the transmission is 10% for SiO_xN_y films as a function of the per cent of NO gas used in forming the film.

Si tetrahedron and that the atom constituents form bonds with Si on a statistical basis with no dominant rules of selection.[4] That is, for any given atom ratio, the numbers of each kind of atom in the network of Si-($Si_xO_yN_z$) tetrahedra for all possible $x + y + z = 4$ are determined by chance and O-O, N-N, and N-O bonds are assumed not to occur. This is called the random bonding model. The amount of each constituent present in these materials depends on the method of fabrication and in our case on the types of gases present and their pressures, sample temperature, etc. This complicated aspect of the problem is beyond the scope of this discussion. We will make the reasonable assumption, however, that where the amount of silane in the gas mixture is extremely small, there is no excess Si present and we must only consider Si-(O_yN_{4-y}) tetrahedra in this network. In the absence of NO gas in the mixture and for arbitrary silane to ammonia ratios we obviously only consider Si-(Si_yN_{4-y}) tetrahedra.

An entirely different point of view is taken in the analysis of x-ray and electron scattering experiments where these materials are considered to be mixtures of "pure compounds" (9). They claim SiN_x is composed of 10 to 20Å particles of Si and Si_3N_4 and SiO is really a mixture of Si and SiO_2. It should be pointed out, however, that the experimental radial distribution functions from which these results are deduced can be equally well explained using our model (3) provided we make the very reasonable assumption, which is actually inherent in this model, that the individual bond distances are about the same as in the pure materials. The argument is that in such non-ordered systems each scattering event can be considered independently of all others and thus the contribution from one Si-N bond is the same whether this silicon is bonded to other nitrogens as in a Si-(NN_3) tetrahedral grouping or to other silicons as in Si-(NSi_3) or to some random distribution of atoms as in Si-(Si_yN_{4-y}). The radial distribution function counts only the number of atom pairs of each particular kind and in most cases this number would be the same for both the mixture and random bonding model. Differences would actually exist in the radial distribution function calculated for the two models which might distinguish between them, however, this would require a more precise analysis than has been heretofore attempted.

More significantly however, the mixture model fails in several important aspects. It is difficult to cite a mechanism for the growth of such particles especially in materials made at relatively low temperature as in glow discharge deposition apparatus. In addition this model is not able to explain the optical properties and other basic characteristics of these materials. Particles 10-20Å in diameter should exhibit the same optical properties as materials in bulk. Thus the position of infrared bands, the threshold for intrinsic absorption, etc., should essentially stay fixed as the composition is varied since this is the consequence of the existence of these particles. Actually these "markers" and others vary smoothly and continuously with changes in composition (1, 6). The magnitude of these absorptions (or, for example, the value of the dielectric constant) should vary linearly with the amount of each component in the mixture while in reality they are often observed to be grossly nonlinear. We thus conclude that the atom species are blended on a finer scale such that these properties cannot be accounted for by the simple addition of bulk, pure compound characteristics.

We found (3) that data for SiO_x materials could best be interpreted where this blending is on an atomic scale. This result was achieved by postulating there was some reasonable size to a grouping of Si-Si or Si-O bonds which would indeed have the essential optical properties of these bonds in bulk. We calculated the density of such clusters, which had the dimension of a Si-(Si_4) and Si-(O_4) tetrahedra respectively, on the basis of our random bonding scheme and found that the magnitude of the absorption near threshold (and thus its apparent position) and the position and intensity of a prominent absorption peak at much higher energy could be correlated with this density. The same reasoning should apply to SiN_x and SiO_xN_y. We will demonstrate below that data for the latter material shown in Fig. 6 are consistent with the random bonding model and the assumption that a group of Si-N bonds the size of a Si-(N_4) tetrahedra has approximately the optical properties of $SiN_{4/3}$ in bulk. The results of Fig. 6 cannot be explained on the basis of the mixture model.

The optical properties of the tetrahedral bonding arrangements considered in our model are difficult to predict. We can, however, make use of certain sum rules on ϵ_2, which are completely general and valid for any arbitrary system (10) to help clarify various aspects of their expected behavior. The first of these

$$\left(\frac{2\pi^2 N e^2}{m}\right) n_{\text{eff}} = \int_0^{\omega_0} \omega\, \epsilon_2(\omega)\, d\omega \qquad [4]$$

is for n_{eff}, the effective number of electrons per atom or molecule of density N contributing to the optical properties in the energy range to $\hbar\omega_0 = E_0$. Thus according to Eq. [4] the electrons of importance in the bonding of these tetrahedra contribute a definite amount to the integral of $\omega\epsilon_2$ although we cannot off hand specify the energy range involved except for the case where these electrons or bonds are considered in bulk and this equation can be evaluated experimentally.[5] For silicon (3) this integral saturates near

[4] The use of the word tetrahedron or tetrahedral here and below is not meant to imply any particular angle between bonds but simply a coordination number of 4. Such tetrahedra might well be greatly distorted in these materials. We also recognize that the bond energies are different and that the formation of some bonds may be "easier" than others.

[5] In this discussion and elsewhere we consider individual bonds (for example a Si-N bond) to possess "optical properties." We do not mean to imply by this that absorption processes are governed by some particular mechanism or are localized to this degree but rather that through Eq. [4] a definite $\epsilon_2(\omega)$ exists for these bonding electrons. In a similar way a Si tetrahedron can be thought of as having optical properties as do bulk samples which contain many bonds.

4 electrons per atom or 2 electrons per Si-Si bond at 16 eV with most of the contribution occurring in the region 3 to 10 eV. For quartz this integral reaches 8 electrons per SiO_2 molecule or 2 electrons per Si-O bond at ~24 eV with the largest contribution being in the region 12-20 eV. These are the characteristics of electrons in a collection of similar bonds of minimum size corresponding to that of a Si-(Si_4) or Si-(O_4) tetrahedra respectively. Each of these would contribute 8 electrons per tetrahedral unit to the integral of Eq. [4] for energies to ~24 eV. The integrated contribution should also be 8 electrons per unit for mixed tetrahedra, Si-(Si_yO_{4-y}) although the spectral dependence can no longer be precisely specified. A Si-Si bond in a mixed tetrahedron has a higher threshold for absorption (ϵ_2) than a Si-Si bond in Si-(Si_4) and the contribution to n_{eff} occurs mainly in the 4-10 eV range rather than between 3 and 6 eV as in silicon (3). On the other hand, an Si-O bond in a mixed tetrahedra appears to absorb in nearly the same energy span as an Si-O bond in Si-(O_4) although it does not have the sharp features associated with absorption in quartz. Unfortunately, the theoretical framework for any analysis of this behavior is entirely lacking and the most we can present is an empirical picture based on experimental observations.

The second sum rule

$$\epsilon_{0,\text{eff}} = 1 + \left(\frac{2}{n}\right)\int_0^{\omega_0} \omega^{-1}\epsilon_2(\omega)\,d\omega \qquad [5]$$

is for $\epsilon_{0,\text{eff}}$, the contribution to the dielectric constant associated with optical absorption in the energy range to $E_0 = \hbar\omega_0$. This formula describes the effect on ϵ_0 of changes in material density or in the spectral dependence of absorption (possibly associated with variations in composition or methods of preparation, etc.). We shall use Eq. [5] to estimate the composition of the SiO_xN_y material described in Fig. 6. The curve of ϵ_2 for silicon nitride shown in Fig. 2 has a broad maximum near 9 eV and falls off slowly at higher energies decreasing below 1 above 19 eV. The ϵ_2 curve for SiO_2 (3) has a sharp maximum at 10 eV and a similar fall off at higher energies decreasing below 1 above 19 eV. Although the threshold energy for absorption in these materials is different, as will be discussed further below, we note that the main absorption for groupings of both Si-N and Si-O bonds is relegated to the same energy region and has roughly the same spectral shape. If we now make the reasonable assumption that electrons associated with individual Si-N bonds in Si-(O_yN_{4-y}) tetrahedra contribute to an absorption spectrum having these same gross characteristics, which, as mentioned earlier appears to be the case for individual Si-O bonds, then ϵ_2 for SiO_xN_y would depend linearly on the density of Si-O and Si-N bonds present. Thus from Eq. [5] we should have simply $\epsilon_{SiO_xN_y} = f_{SiO_2}\epsilon_{SiO_2} + f_{SiN_{4/3}}\epsilon_{SiN_{4/3}}$ where $f_{SiO_2} + f_{SiN_{4/3}} = 1$ are the equivalent fractions of the material (based on the density of Si-N and Si-O bonds present) which are SiO_2 and $SiN_{4/3}$ respectively. That is, the dielectric constant is a linear function of composition and the index data, $\epsilon_0 = n^2_0$, of Fig. 6 can be used to approximate the composition of our SiO_xN_y material. Knowing this we can calculate the distribution of the five possible tetrahedron types, Si-(O_yN_{4-y}) for y = 0-4, assuming the atoms to be statistically placed.[6]

The absorption of SiO_xN_y should be lower in magnitude than that of $SiN_{4/3}$ in the region of the threshold of absorption in $SiN_{4/3}$, 4.5-5.5 eV, by an amount equal to or greater than the ratio of the density of Si-N bonds in the two materials. This is due to the fact that in SiO_xN_y, Si-N bonds are replaced by Si-O bonds which contribute to absorption only at much higher energy. If absorption processes in these materials are localized to an essentially atomic basis, that is, if the optical characteristics of single Si-N bonds are independent of their environment, then the absorption in SiO_xN_y should be lower than that for $SiN_{4/3}$ by exactly the Si-N bond density ratio. In this case the mixture model would describe these optical properties even though clusters of "pure material" 10-20Å in extent were not present. However we found in our work on SiO_x (3), that absorption processes are not atomically localized but rather extend to a larger unit of the dimension of a silicon tetrahedron and that within this dimension some averaging of possible single bond optical properties takes place. If this is also valid for SiO_xN_y then we would expect that the threshold absorption characteristics of Si-(N_xO_{4-x}) tetrahedra would be progressively shifted to higher energy as the number of oxygen bonds is increased, attaining the characteristics of quartz, with an absorption threshold near 9 eV, when all the bonds are to oxygen as for Si-(O_4) tetrahedra. Thus the absorption in macroscopic SiO_xN_y in the region 4.5-5.5 eV compared to that for $SiN_{4/3}$ would be given by the relative density of Si-(N_4) tetrahedra in the materials and for higher energies would decrease from this ratio as tetrahedra containing oxygen atoms commence their contribution to the optical absorption. At still higher energy, near and above 11 eV, the Si-N bond contribution in all tetrahedra should be closely the same, as discussed previously in connection with Eq. [5]. Since Si-O and Si-N bond absorption are also comparable here, the absorption of all SiO_xN_y materials should be roughly the same at these energies.

We can test the above reasoning using the data of Fig. 6 and 7. We find from Fig. 6 that a SiO_xN_y layer

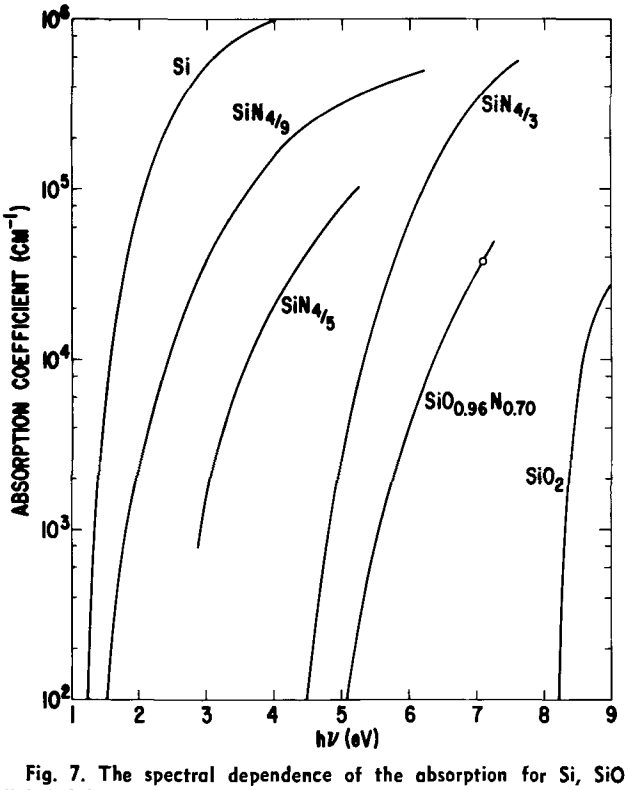

Fig. 7. The spectral dependence of the absorption for Si, SiO (labeled $SiN_{4/9}$), $SiO_{1.5}$ (labeled $SiN_{4/5}$), and SiO_2 obtained from Ref. (3). The basis for relabeling the curves for SiO and $SiO_{1.5}$ is given in the text. The curve for $SiN_{4/3}$ is obtained from Fig. 4. The data point for $SiO_{0.96}N_{0.70}$ and the extension of this curve to lower energies is described in the text.

[6] The ratio of density to formula weight is proportional to the number of atoms corresponding to this formula present in a unit volume of the material. If this quantity determined for $SiN_{4/3}$ and SiO_2 is multiplied by the fraction of the unknown material which is $SiN_{4/3}$ and SiO_2 respectively, as calculated from the dielectric constant, the composition can be determined. Each $SiN_{4/3}$ and each SiO_2 formula unit present contribute 4 Si-N and 4 Si-O bonds respectively to the material. Since these are the only bonds considered here, their probabilities of formation may be found and thus the distribution of tetrahedron types simply calculated.

formed at 10% injected NO has an index of 1.68 ($\epsilon_0 = 2.82$) and an absorption coefficient of 4×10^4 cm^{-1} at 7.09 eV. This point is indicated by the circle in Fig. 7. From the index we estimate[6] the composition to be $SiO_{0.96}N_{0.70}$ and the probability of forming a Si-N bond to be 0.52. Thus the fraction of tetrahedra which are Si-(N_4) is 0.073. This value is slightly smaller than the experimental ratio of absorption at 7.09 eV which, according to Fig. 7, is ~0.1. Unfortunately the data of Fig. 6 are for relatively thin samples. For this large a value of absorption coefficient and for an energy far from threshold (4.5 eV), the experimental ratio should be lower than that calculated since absorption due to Si-N bonds in mixed atom tetrahedra may be contributing. We can extend the curve for $SiO_{0.96}N_{0.70}$ to lower energies by assuming that the ratio of absorption in this material compared to that in $SiN_{4/3}$ is proportionally the same for corresponding values of absorption coefficient as that of SiO compared to Si where for SiO the probability of a Si-Si bond is 0.5. This extrapolation is shown in Fig. 7 and we note that in the region of $\alpha = 10^2$ to 10^3 cm^{-1}, this curve is lower than the one for $SiN_{4/3}$ by the ratio ~0.04. It is this value which should be compared to the calculated one of 0.073. The agreement is very good considering the simplicity of the analysis. We thus conclude that SiO_xN_y is not a simple mixture of SiO_2 and Si_3N_4 particles but rather the atoms are blended on an atomic scale and like bonds of the dimension of a Si-(N_4) tetrahedra have the same optical properties as these bonds in bulk.

In discussing SiN_x we shall assume that Si-Si bonds have the same properties in SiN_x as in SiO_x. That is we assume that for energies below ~5 eV all the absorption is due to the presence of Si-Si bonds and that this absorption is not appreciably influenced by the existence of Si-N compared to Si-O bonds nearby. Thus, neglecting density changes, the absorption curve for $SiN_{4/9}$ should be identical to that of SiO since the probability of a Si-Si bond in each case is ½. The curve for $SiN_{4/5}$ should be identical to that of $SiO_{1.5}$ where the probability of a Si-Si bond is ¼. These curves are drawn in Fig. 7 using the results of (3). It should also be noted that the dielectric constant of SiN_x is not a linear function of the "equivalent" amount of Si and Si_3N_4 present. This is due to the fact that as the number of Si-Si bonds increases not only does the absorption (ϵ_2) increase, but it occurs at lower energy and each of these factors contribute to ϵ_0 according to Eq. [5]. Thus we might expect $\epsilon_{SiN_x} = (1 - 3x/4)^n\epsilon_{Si} + (3x/4)\epsilon_{Si_3N_4}$ where $n \sim 2$, is the number used for SiO_x.

Finally, we can utilize the absorption and photoelectric data to estimate the electron affinity of $SiN_{4/3}$. The photoelectric threshold fixes the valence band relative to the vacuum level and the optical absorption edge corresponds to the valence-conduction band separation. The difference is the electron affinity which for $SiN_{4/3}$ is ~2 eV. However, in the absence of a quantitative theory which assigns a unique threshold energy to the valence band photoemission data and to the optical absorption data, this value is an estimate.

The point of view taken in the above discussion is an obvious oversimplification of the complex factors which control the bonding and optical absorption processes in these materials. It is hoped that this approach has some analytical value in classifying substances like SiN_x and SiO_xN_y. There are a number of other experiments, in addition to those employed here, which would help clarify the bonding in these materials. These include the measurement and analysis of infrared bands for various SiN_x and SiO_xN_y compositions and new work of a more precise nature concerning the measurement and interpretation of x-ray and electron scattering experiments. It should also be emphasized that at the present time there is no theoretical framework for the discussion of these materials. It is further hoped that this paper will stimulate this important and much needed activity.

Manuscript submitted Jan. 14, 1972; revised manuscript received Sept. 25, 1972.

Any discussion of this paper will appear in a Discussion Section to be published in the December 1973 JOURNAL.

REFERENCES

1. D. M. Brown, P. V. Gray, F. K. Heumann, H. R. Philipp, and E. A. Taft, *This Journal*, **115**, 311 (1968).
2. See for example, J. R. Yeargan and H. L. Taylor, *ibid.*, **115**, 273 (1968); B. E. Deal, P. J. Fleming, and P. L. Castro, *ibid.*, **115**, 300 (1968).
3. H. R. Philipp, *J. Phys. Chem. Solids*, **32**, 1935 (1971).
4. H. R. Philipp, Paper 155 presented at Electrochem. Soc. Meeting, Philadelphia, Oct. 9-14, 1966.
5. V. Y. Doo and D. R. Nichols, Paper 146, presented at Electrochem. Soc. Meeting, Philadelphia, Oct. 9-14, 1966; L. F. Cordes, *Appl. Phys. Letters*, **11**, 383 (1967).
6. E. A. Taft, *This Journal*, **118**, 1341 (1971).
7. H. R. Philipp and H. Ehrenreich, *J. Appl. Phys.*, **35**, 1416 (1964).
8. E. A. Taft and H. R. Philipp, *J. Phys. Chem. Solids*, **3**, 1 (1957).
9. S. C. H. Lin and M. Joshi, *This Journal*, **116**, 1740 (1969); M. V. Coleman and D. J. D. Thomas, *Phys. Status Solidi*, **22**, 593 (1967); *ibid.*, **25**, 241 (1968).
10. H. R. Philipp and H. Ehrenreich, *Phys. Rev.*, **129**, 1550 (1963).
11. O. S. Heavens, "Optical Properties of Thin Solid Films," Butterworths Scientific Publications, London (1955).
12. H. R. Philipp and E. A. Taft, *Phys. Rev.*, **113**, 1002 (1959).
13. H. R. Philipp and E. A. Taft, *ibid.*, **136**, A1445 (1964).

Tin Solvent Activity Equations for Cu-Sb-Sn Liquid Alloys by Stirred H-Cell EMF Measurements

Don A. Griffiths, Jeffrey Braithwaite, Leo W. Beckstead

Department of Mining, Metallurgy, and Fuels Engineering, University of Utah, Salt Lake City, Utah 84112

and Guy R. B. Elliott*

Los Alamos Scientific Laboratory, University of California, Los Alamos, New Mexico 87544

ABSTRACT

EMF measurements have been made on Cu-Sn, Sb-Sn, and Cu-Sb-Sn molten alloys using molten $SnCl_2$ electrolyte in stirred H-cells. Deviations from the approach to the slope of Raoult's law by emf and vapor pressure data in dilute metallic solutions are discussed. In this case the deviations can be ascribed to a need to correct for reaction between $SnCl_2$ and Cu, although known corrections do not account for similar deviations in all cases. Effects of liquid structuring are discussed in relation to the solution activity equations. A heat of formation of $SnCl_2$ of ~ -81 kcal/mole (as selected elsewhere) is supported. Solute-solute interactions between Sb and Cu have little effect on the tin activity. Possible fine structure in Sb-Sn solutions as suggested by earlier work is not supported.

Many solution theories describe activities, logarithms of activity coefficients, freezing points, heats of mixing, etc., by mathematical-power series involving the solute composition. A single set of constants is assumed to apply over a broad range of solution compositions, and one constant is assumed to be obtainable by extrapolating the measurements to infinite dilution.

Especially for molten alloys (but also for some aqueous electrolytes (1, 2), *e.g.*, divalent sulfates) precise measurements now show that solutions often behave contrary to the assumptions of the theories. For one thing, as pointed out elsewhere (3), in most cases the published activities are not consistent with the constant evaluated at infinite dilution. Also, instead of demonstrating slowly varying behavior, the alloys frequently show sharp changes of behavior; often a two-term power series with one set of constants will apply over a few per cent in composition, and then abruptly (within one tenth of a per cent in composition) a new set of constants will be needed. Furthermore, there can be liquid-phase nucleation problems. Sometimes a phase is observed for many days in metastable equilibrium at a composition beyond its region of true stability.

We use the term "structural complexity" to describe the abruptly changing behavior and metastability. Such complexity has been demonstrated by vapor-pressure studies, calorimetry, emf work, viscosity behavior, solution densities, electrical conductivities, metallography on quenched alloys, and x-ray studies. References to this work can be found elsewhere (3, 4).

In spite of numerous failures, the theories work very well in some cases. When tin is used as the reactive solvent in Sb-Sn (5), Ag-Sn (5, 6), and Au-Sn (5, 6) solutions as measured by emf with molten $SnCl_2$ electrolyte, the calculated activities fall very close to regular solution behavior with its asymptotic approach to the slope of Raoult's law. This relationship holds even though structural complexity is definitely shown in the Au-Sn data (6). For cadmium solutions, using molten salt emf techniques (7-9), the measurements for Ni-Cd, Au-Cd, and Pd-Cd all indicate very nearly the same limiting slope, and this limiting slope can be brought into Raoult's law by assuming corrections for Cd_2^{++} formed by the reaction of Cd^{++} with cadmium (7). Ag-Cd and Cu-Cd behaviors (9) are also perhaps consistent with regular solution theory if other corrections are applied to the data.

In view of the conflicts in detail between the earlier theories and the structural complexity, it becomes important to understand why the older theories worked as well as they did. As discussed earlier (3, 4) part of the answer seems to lie with trends of entropy and enthalpy which pass closely through the complexity; in effect, the complexity often can be treated as a "fine structure" which is imposed on the general thermodynamic trends. Thus, the earlier theories (though simplistic) often can give a good description of the solution behavior although the exact behavior may be quite different (*e.g.*, a constant evaluated as zero at infinite dilution may be far from zero at finite concentrations).

Because so many of the earlier measurements were either imprecise or widely spaced in composition, they cannot answer the question of whether the detailed behavior was approaching Raoult's law asymptotically. Therefore the present detailed emf work with Cu-Sb-Sn alloys was undertaken to examine (*i*) the solvent behavior in two-component alloys and (*ii*) the effect of interactions between solute atoms upon the solvent behavior in three-component systems.

Earlier emf studies with Cu-Sn solutions (10) had shown a shift of relationship between solvent activity and composition at $\sim$0.07 mole fraction of copper, and metallographic studies of very rapidly quenched specimens (11) showed that the shift of behavior was associated with an equilibrium two-liquid region. Thus another purpose (*iii*) was to examine the effect of antimony on the shift of behavior. Regarding the Sb-Sn solutions, the earlier work [(5), as will be plotted later] seemed to indicate structural complexity. Finally, the possibility of important interactions between different kinds of solute atoms in molten alloys has been emphasized recently, *e.g.*, in Ref. (12-14).

Equipment and Procedures

The usual stirred H-cell procedures [*e.g.*, (6-8, 10)] were followed. Reagent grade copper and antimony were used without further purification. Molten reagent grade tin was washed with boiling $SnCl_2$. Reagent grade $SnCl_2$ hydrate was dried, then vaporized in vacuum 3 times (including once in contact with molten tin). The cell volume was used to estimate closely how much $SnCl_2$ was added. Argon was condensed in liquid nitrogen, frozen by evaporative cooling, then distilled

* Electrochemical Society Active Member.

Key words: activity, structure, interactions, Raoult, enthalpy.

Table I. Emf-composition relationships for Cu-Sn, Sb-Sn, and Cu-Sb-Sn alloys

No.	Components Sn (g)	Cu (g)	Sb (g)	T°K	EMF (μV)
Run 1					
1	46.0010	0.2499		661.4	268.3[a]
2		0.4850		662.6	515.3
3		0.7623		662.2	793.2
4		1.0228		661.6	1044.3
5		1.2942		661.1	1299.8
6		1.4328		661.7	1428.8
7		1.5678		662.0	1548.2
8		1.7106		661.6	1678.0
9		1.8571		661.0	1804.8
10		2.0058		660.1	1933.5
11		2.1442		662.9	2050.1
12		2.4345		663.1	2290.0

[a] Run 1 readings are 2.7 μV less than the measured values to correct for tin *vs.* tin original bias.

Run 2					
1	46.0005		0.2391	662.6	142.0[b]
2			0.4904	662.5	296.0
3			0.6951	663.2	420.7
4			0.9470	663.1	570.4
5			1.1128	663.2	672.0
6			1.2686	663.2	767.7
7			1.5217	663.0	921.0
8		0.2524		661.9	1181.2
9		0.4928		662.3	1420.5
10		0.7688		662.8	1691.3
11		1.0240		662.4	1929.7
12		1.2919		662.0	2177.2
13		1.4315		661.9	2302.8
14		1.7089		662.6	2541.4
15		1.8548		662.4	2661.5
16		2.0037		662.6	2790.0
17		2.1401		662.3	2904.0
18		2.4299		663.0	3139.2
19		2.7164		662.9	3361.7

[b] Run 2 readings are 157.3 μV less than the measured values to correct for the bias.

into the H-cell. Tin and $SnCl_2$ were melted together in the cell before solute was added. The H-cell had three legs: (*i*) tin reference, (*ii*) weighed tin to which weighed copper would be added, and (*iii*) weighed tin to which weighed antimony and then weighed copper would be added. All solute additions were introduced *in situ* from sidearms on the cell.

Results and Comments

Table I gives the results of the emf measurements. Figure 1 shows a simple activity-mole fraction plot, based on a calculation of activity using $n = 2$ in $\Delta F = -nF\mathcal{E}$, and on mole fractions from the metals added.

Figure 2 uses the more sensitive plot of $(\log \gamma_{Sn})/N_{Cu}$ *vs.* N_{Cu}. Linearity on this plot corresponds with the equation

$$\log \gamma_{Sn} = \alpha_1 N_{Cu} + \alpha_2 N_{Cu}^2 \quad [1]$$

α_1 is zero only if the intercept is (0,0). As calculated then, the intercept is nonzero. [Elliott and Lemons (6)

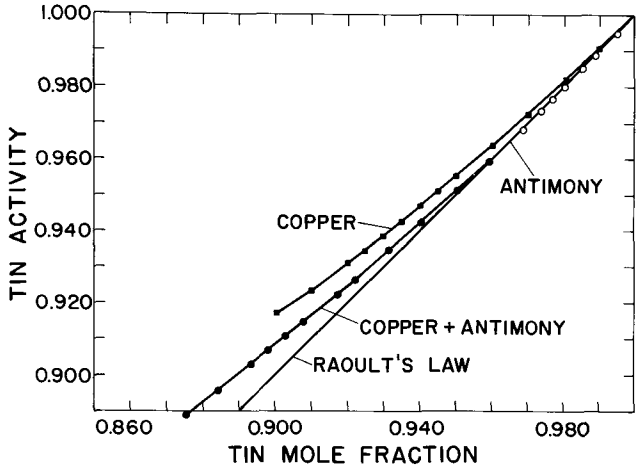

Fig. 1. Tin "activity-mole fraction" relationships for Cu-Sn, Sb-Sn, and Cu-Sb-Sn molten alloys. (See text about calculations.)

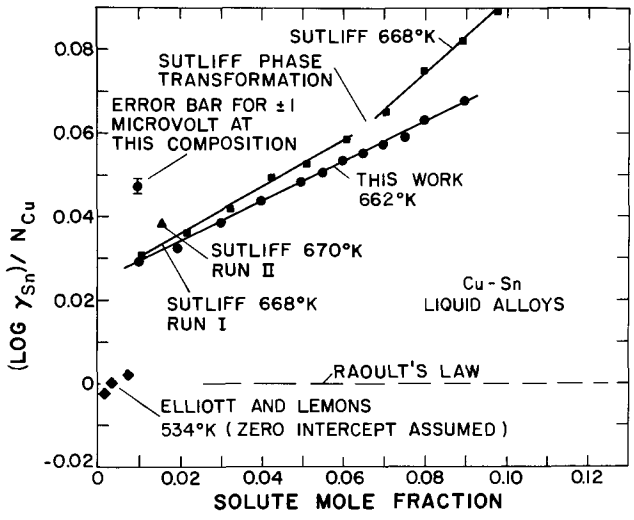

Fig. 2. γ-function plot for Cu-Sn molten alloys. (See text about calculations.)

were not justified in assuming that their limiting slope lay on Raoult's law.] Agreement with Sutliff *et al.* (10) is excellent in the most dilute solutions, but there are small differences in the slope of the line, and finally, the phase change observed by Sutliff *et al.* is not observed in the present results. (The error bar for ± 1 μV is shown in Fig. 2 for the composition indicated. By the right end of the figure, $\pm$ 1 μV is smaller than the data points.)

Figure 3 shows the present Cu-Sn, Sb-Sn, and Cu-Sb-Sn data with the latter system plotted in two ways, *i.e.*, $(\log \gamma_{Sn})/(N_{Cu} + N_{Sb})$ or $(\log \gamma_{Sn})/N_{Cu}$ *vs.* the solute mole fraction. The latter plot superimposes the Cu-Sn and Cu-Sb-Sn data.

Discussion

Superposition of the Cu-Sn and Cu-Sb-Sn plots in Fig. 3 shows that the tin activity is not strongly influenced by mixed solute-solute interactions. This behavior was not necessarily to be expected in view of the mixed solute interactions in three-component alloys, as already mentioned (12-14).

The large bias subtracted in Run 2 appears not to have affected the measurements significantly. Although any large bias is undesirable, the worst uncertainty arises from the bias if a temperature coefficient is taken. Fortunately in this case it was not necessary to take a temperature coefficient.

We do not have thermodynamic data for an accurate calculation of the reactions Cu + 1/2 $SnCl_2$ =

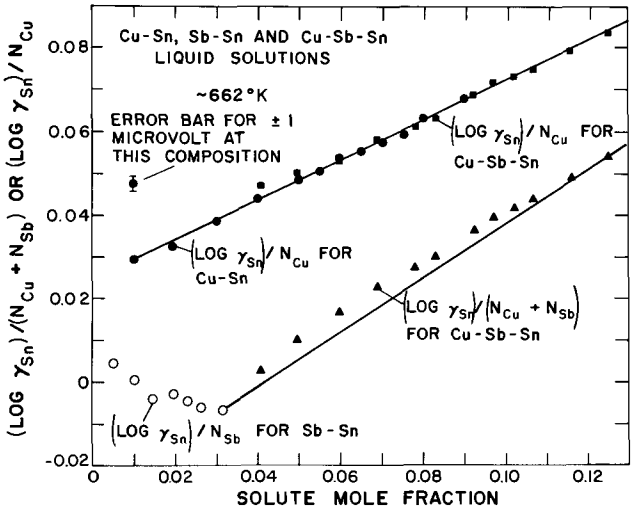

Fig. 3. γ-function plots for Cu-Sn and Cu-Sb-Sn molten alloys. (See text about calculations.)

CuCl + 1/2 Sn and 1/3 Sb + 1/2 $SnCl_2$ = 1/3 $SbCl_3$ + 1/2 Sn. We can, however, roughly predict the extent of these reactions using data from Brewer *et al.* (15).

For the Sb, the exchange reaction should be trivial. $\Delta H°_{298}$ data for the formation of CuCl and $SnCl_2$ are given as −32.6 and −81.1 kcal/mole, and one can use 9.8 and 29 eu for $(\Delta F - \Delta H°_{298})/T$ in the salt melt. Then by assuming unit activity coefficients in the melts, one would predict about 0.025 for the mole fraction distribution ratio of the copper between the molten salt and the alloy.

The distribution ratio would lead to ~2.5% removal of the alloy copper, and it would produce a similar dilution of the $SnCl_2$. These dilution effects would lead one to anticipate about a 5% apparent deviation from the limiting Raoult's law slope. In fact, this apparent intercept is $(\log \gamma_{Sn})/N_{Cu} \approx 0.025$, or the deviation is (0.025) (2.303) (100) ≈ 5.8%.

Thus one can, in this case, account for the whole deviation from the apparent limiting Raoult's law slope as being due to reaction between copper and $SnCl_2$. Such a reaction would also account for the difference in slope between our data and Sutliff's; the proportions of Sn and $SnCl_2$ were not identical in the two cases. (This is a very sensitive plot, and the absolute agreement between our data and Sutliff's is good. For example, at $N_{Cu} = 0.01$ the difference is ~1 μV.)

With reservations one can turn this argument around the other way also. Accepting as a tentative generalization for tin solutions that the tin activities closely approach a Raoult's law slope at these dilutions (in spite of the structuring), and accepting the unit activity coefficients as not in gross error, then Brewer's choice of −81.1 kcal/mole for $SnCl_2$ seems good (15). This value did need confirmation (and still needs further confirmation); it was a value which was included in the original paper (15) which offered estimates and values from meager data in order to present a comprehensive whole; it was not certain enough, however, to include in the tables in "Thermodynamics" (16) which were limited to well-established values.

The plot of $(\log \gamma_{Sn})/(N_{Cu} + N_{Sb})$ is not applicable in this case (Fig. 3) because only the Cu is being extracted into the $SnCl_2$. The Sb is necessary on the abscissa however.

In this case we did not see the phase transformation observed by Sutliff *et al.* at $N_{Cu} \approx 0.07$ and seen (11) in metallographic studies of very rapidly quenched alloys at $N_{Cu} \approx 0.07$. Nucleation of the second phase can be difficult, and liquid metastability can be persistent, as was shown by Sutliff *et al.* We do not consider that there is any contradiction between our results and those of the others.

This phase metastability clouds the issue of the effect of the antimony on the Cu-Sn phase transformation. We did not see the transformation with Sb present, but we do not know if the dilute phase was extended stably or metastably with the added Sb.

Figure 4 compares the present Sb-Sn data with those of Yanko, Drake, and Hovorka (5). The rise at the left of this plot in the earlier data suggested the possibility of fine structure in the Sb-Sn system, and their data at other temperatures showed the same trends. Our results, however, seem to rule out fine structure in this case; there is no indication of a change of behavior of a different slope where the lines of earlier data were lost.

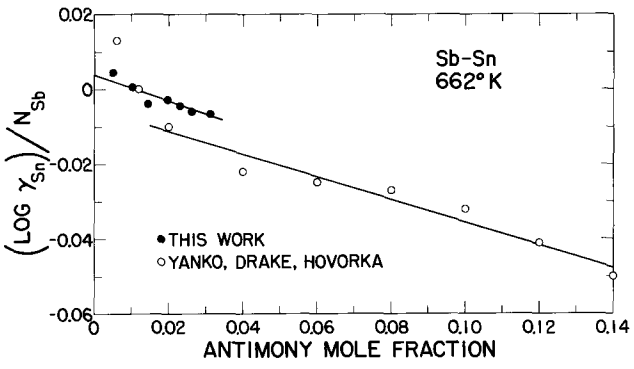

Fig. 4. Comparison of the present and earlier data for Sb-Sn solution emf's. No fine structure is indicated for $N_{Sb} < 0.02$ in the present case.

Summary

In spite of other evidence for structural complexity, the molten Cu-Sn solutions appear to lie very close to regular solution behavior. By comparison with other work, extensive metastability in Cu-Sn solutions is demonstrated. Sb-Sn solutions showed no structural complexity. Interactions between Sb and Cu atoms do not influence the solvent tin activity.

Acknowledgment

Work supported in part by the U.S. Atomic Energy Commission.

Manuscript submitted June 12, 1972; revised manuscript received Sept. 20, 1972. This was Paper 144 presented at the Houston, Texas, Meeting of the Society, May 7-12, 1972.

Any discussion of this paper will appear in a Discussion Section to be published in the December 1973 JOURNAL.

REFERENCES

1. G. R. B. Elliott, Los Alamos Scientific Laboratory Report, LA-3891, 1968.
2. D. R. Conant, Los Alamos Scientific Laboratory Report, LA-4428, 1970.
3. G. R. B. Elliott, D. R. Conant, B. L. Houseman, H. S. Swofford, Jr., P. L. Robinson, and C. E. Holley, in "Advances in High Temperature Chemistry," L. Eyring, Editor, **3**, 87, Academic Press, New York (1971).
4. P. L. Robinson and G. R. B. Elliott, *High Temp. Sci.*, **4**, 1 (1972).
5. J. A. Yanko, A. E. Drake, and F. Hovorka, *Trans. Electrochem. Soc.*, **89**, 357 (1946).
6. G. R. B. Elliott and J. F. Lemons, *This Journal*, **114**, 935 (1967).
7. D. R. Conant, *J. Chem. Eng. Data*, **16**, 430 (1971).
8. B. L. Houseman and G. R. B. Elliott, *This Journal*, **116**, 1363 (1969).
9. G. R. B. Elliott, D. R. Conant, H. S. Swofford, Jr., B. L. Houseman, and J. F. Lemons, Los Alamos Scientific Laboratory Report, LA-DC-11606 (Preliminary Draft), 1969.
10. K. E. Sutliff, B. R. Ruhlander, S. L. Pohlman, J. S. Jackson, and G. R. B. Elliott, Unpublished.
11. D. N. Hopkins and G. R. B. Elliott, Unpublished.
12. P. J. Spencer and M. J. Pool, *AIME Trans.*, **242**, 291 (1968).
13. R. L. Louvet, J. V. Gluck, and R. D. Pehlke, *AIME Trans.*, **242**, 2369 (1968).
14. L. F. Kozin and R. Sh. Nigmetova, *Russ. J. Phys. Chem.*, **41** 1152 (1967).
15. L. Brewer, L. Bromley, P. W. Gilles, and N. L. Lofgren, in "National Nuclear Energy Series," Vol. 19b, pp. 104-115, McGraw-Hill Book Co., New York (1950).
16. L. Brewer and K. S. Pitzer, 2nd ed., Revision of G. N. Lewis and M. Randall, "Thermodynamics," McGraw-Hill Book Co., New York (1961).

Oxygen Diffusion in Liquid Gallium and Indium

K. A. Klinedinst and D. A. Stevenson*

Department of Materials Science, Stanford University, Stanford, California 94305

ABSTRACT

A potentiostatic electrochemical technique was used to determine the diffusion coefficients of oxygen in liquid Ga and In, for temperatures between 750° and 950°C. The oxygen diffused radially outward in cylindrical samples contained in the bottoms of yttria-doped thoria and calcia-stabilized zirconia electrolyte tubes. The experimental results are expressed by the following equations

$$D_O(\text{Ga}) = (3.68 \pm 0.42)(10^{-3}) \exp\left(\frac{-8.37 \pm 0.25}{RT}\right) \text{cm}^2/\text{sec}$$

$$D_O(\text{In}) = (8.22 \pm 1.87)(10^{-4}) \exp\left(\frac{-12.6 \pm 0.5}{RT}\right) \text{cm}^2/\text{sec}$$

The large observed difference between the magnitudes of $D_O(\text{Ga})$ and $D_O(\text{In})$ is not predicted by current theories of impurity diffusion.

Relatively few investigations of the diffusion of oxygen in liquid metals have been reported in the literature, particularly in systems in which the oxygen solubility is low. There is, however, both fundamental and practical interest in such systems. There is interest in diffusion phenomena as a basis for models concerning the structure and transport properties of liquids. Furthermore, in the use of liquid metals as coolant materials or as solvents in the growth of semiconducting thin films by liquid epitaxial methods, the role of oxygen in the melt is important. In the present study, the diffusion coefficients of oxygen in liquid Ga and in liquid In were determined using a potentiostatic electrochemical technique.

Studies of the diffusion coefficients of oxygen in both solid and liquid metals have been reported in which potentiostatic techniques were employed with calcia-stabilized ziconia (CSZ) as the solid oxide electrolyte. Rickert and Steiner (1) reported measurements of the diffusion coefficient of oxygen in solid silver, and Pastorek and Rapp (2) reported measurements of the diffusion of oxygen in solid copper. In both of these studies, a linear cell geometry was used. Rickert and El Miligy (3) determined the diffusion coefficients of oxygen in liquid silver and copper, using a cylindrical cell geometry. The metals used in all of these studies possess relatively high oxygen solubilities and form oxides with relatively high decomposition pressures. As a consequence, the ranges of oxygen chemical potential encountered in the diffusion studies were within the electrolytic domain of CSZ [ZrO_2 containing 7.5 weight per cent (w/o) CaO] (4).

The metals Ga and In form quite stable oxides, and in particular the decomposition pressures of β-Ga_2O_3 at temperatures of interest in this study are close to the lower electrolytic domain boundary for the CSZ electrolyte (5). Therefore, a sufficiently broad range of oxygen activity for a study of the diffusion of oxygen in liquid Ga would involve oxygen partial pressures outside of the electrolytic domain of CSZ. As a consequence, yttria-doped thoria (YDT) (ThO_2 containing 7.0 w/o Y_2O_3), whose electrolytic domain encompasses much lower oxygen partial pressures than does that of CSZ (4), was used as the electrolyte in this work. However, CSZ was used in some of the experiments with liquid In samples.

Experimental

The electrochemical cell used in this work, shown in Fig. 1, was similar to that described in a previous article (5). Vacuum-tight YDT and CSZ tubes, containing 7.0 w/o Y_3O_3 and 7.5 w/o CaO, respectively, were obtained from the Zirconium Corporation of America. The tubes were about 46 cm long and were closed on one end. The outer diameter of the tubes was about 0.95 cm, and the wall thickness was about 0.045 cm. The inner diameter of the tubes varied from 0.689 to 0.722 cm. The tubes were always helium leak-checked before and after every experiment. Gallium and indium of 99.999% purity were purchased from Eagle-Picher Industries, Incorporated, and Cominco American, respectively. The liquid metal was melted in the bottom of the electrolyte tube and formed a cylindrical column about 10 cm high. A porous platinum electrode (made from Englehard unfluxed platinum paste, No. 6926) extended from the bottom of the electrolyte tube to a height of about 10 cm, to coincide with the height of the column of liquid metal. Electrical contact with the

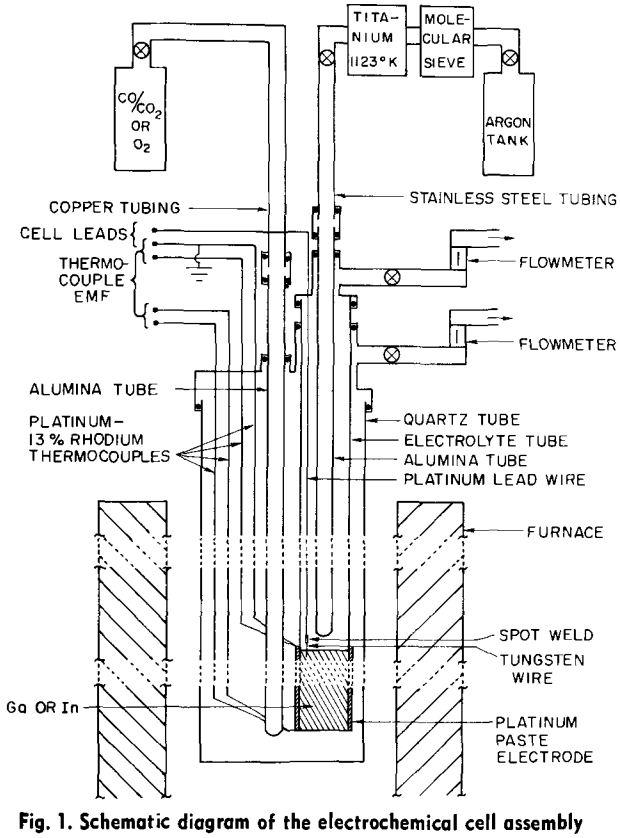

Fig. 1. Schematic diagram of the electrochemical cell assembly

* Electrochemical Society Active Member.

Key words: oxygen diffusion, impurity diffusion in liquid metals, gallium, indium.

liquid metal was made using a short piece of tungsten wire spot-welded to the platinum lead wire.

Two platinum-13% rhodium thermocouples were attached to the extremities of the platinum electrode and were used to determine the sample temperature and the temperature gradient along the column of liquid metal. The cell was heated with a Marshall resistance-heated furnace, 61 cm long with a 5 cm bore. Temperature control of ±1°C was achieved using a Barber-Colman Model 357A Digiset null balance controller. The thermocouple potentials were measured using a Leeds and Northrup K-3 potentiometer and a Leeds and Northrup 9834 null detector. External shunt resistors were used to adjust the furnace temperature profile to produce a temperature gradient of about 1°C along the length of the liquid metal sample with the hotter region on top in order to eliminate possible thermal convection (6). The platinum side of one of the two thermocouples was used to carry the cell current while the other thermocouple was being used to measure the cell temperature.

Argon gas, purified by passing through a column of activated Linde 4A molecular sieve and a column of titanium metal sponge heated to 850°C, was slowly flowed through an alumina tube and over the surface of the liquid metal (to prevent contamination of the metal by gaseous oxygen). Using an oxygen gauge with a YDT electrolyte and porous platinum electrodes, the oxygen content of the argon was determined to be about 10^{-25} atm.

In most experiments, the reference oxygen partial pressures were established with a high purity CO-CO_2 gas mixture, prepared by Liquid Carbonic, Incorporated. The CO-CO_2 mixture was flowed through an alumina tube and over the porous platinum electrode at a rate of 5-10 cc/min. The ratio of the partial pressure of CO_2 to that of CO, determined by I_2O_5 analysis of several different samples of the gas mixture, was 12.50. In some experiments, pure oxygen was used as the reference gas as described below. The oxygen, obtained from Liquid Carbonic, Incorporated, was maintained at a pressure of one atmosphere. It was purified by passing through an Englehard Deoxo gas purifier and a column of activated Linde 4A molecular sieve.

A schematic diagram of the electrical circuit used in the potentiostatic measurements is given in Fig. 2. Constant voltages were provided by the output of a Lambda Model LA50-03B regulated power supply. The output voltage could be instantaneously changed by the use of a calibrated decade resistor wired into the output circuit of the power supply. Voltages were accurately measured with the K-3 potentiometer and null detector. Currents were measured using a Keithley 602 electrometer and were recorded as a function of time with a Hewlett-Packard Model 7101B strip chart recorder.

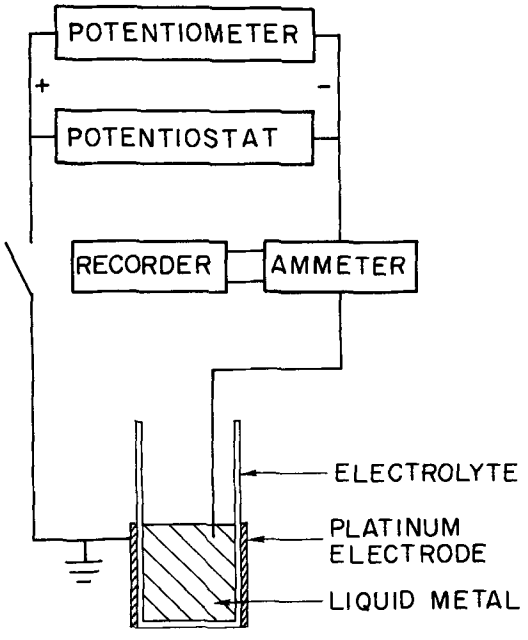

Fig. 2. Schematic diagram of the circuit for potentiostatic measurements.

In a typical experiment, a weighed amount of solid gallium or indium was placed in the bottom of an electrolyte tube. The cell was then assembled in the furnace, and the tube was alternately evacuated and filled with the purified argon gas. The cell temperature was slowly raised to between 850° and 900°C. With the reference gas flowing over the platinum electrode and the argon flowing over the surface of the liquid metal, an emf was applied to the cell so that the oxygen activity in the metal was reduced to a value several orders of magnitude lower than that corresponding to the equilibrium between the metal and its most stable oxide (in order to insure that any residual oxide was dissolved). This deoxygenation was continued for at least 12 hr and until the cell current had reached a value of about 10^{-5}A.

The cell temperature was then adjusted to the desired value and an emf was applied to the cell, corresponding to an oxygen activity in the metal slightly lower than that at which the most stable oxide of the metal forms. After the cell had equilibrated at this temperature and applied emf value, the emf was instantaneously changed to a value corresponding to an oxygen activity in the metal between 10^{-2} and 10^{-4} times the equilibrium value. Oxygen then diffused out of the metal, and the diffusion-limited current was measured and recorded as a function of time. An analysis of the time dependence of the current, for long times, resulted in the determination of D_O in the metal at the cell temperature. An equilibration time of at least 3 hr was allowed between consecutive out-diffusion runs.

Out-diffusion experiments, with either gallium or indium as the liquid metal, were performed using YDT as the electrolyte with the CO-CO_2 reference gas mixture. In addition, some experiments were performed, with indium as the liquid metal, in which CSZ was the electrolyte and either the CO-CO_2 mixture or pure O_2 served to fix the reference oxygen partial pressure. The CO-CO_2 reference gas mixture was used with the YDT electrolyte, rather than a metal-metal oxide mixture, in order to avoid possible errors resulting from anodic polarization.

Calculations

Values of the oxygen partial pressures in equilibrium with the CO-CO_2 gas mixture, $p(O_2,CO\text{-}CO_2)$, were calculated from the data of Wicks and Block (7) and are listed in Table I for temperatures between 750° and 950°C. The authors have previously determined the oxygen partial pressures in equilibrium with Ga and In and their most stable oxides, $p(O_2,Ga\text{-}\beta\text{-}Ga_2O_3)$ and $p(O_2,In\text{-}In_2O_3,In_2O)$, respectively (5, 8). These values are also listed in the table.

The Nernst equation expresses the relationship between the emf applied to the electrochemical cell, the reference oxygen partial pressure, and the activity of atomic oxygen in the liquid metal

Table I. Equilibrium oxygen partial pressures

T(°C)	log[p(O₂, CO-CO₂) (atm)]	log[p(O₂, Ga-β-Ga₂O₃) (atm)]	log[p(O₂, In-In₂O₃,In₂O) (atm)]
750	−17.53	−25.75	−20.14
800	−16.19	−24.02	−18.67
850	−14.96	−22.48	−17.58
900	−13.84	−21.10	−16.70
950	−12.81	−19.79	−15.82

$$\text{emf} = \frac{RT}{2F} \ln \frac{p(O_2,\text{ref})^{1/2}}{a_O(M)} \quad [1]$$

Here, $p(O_{2,ref})$ is the reference oxygen partial pressure [$p(O_2,CO\text{-}CO_2)$ or 1.00 atm, corresponding to the $CO\text{-}CO_2$ gas mixture and pure O_2, respectively], $a_O(M)$ is the activity of atomic oxygen in the liquid metal M, R is the ideal gas constant, $\mathbf{F}$ is the Faraday constant, and T is the absolute temperature. In the limiting case of a saturated solution of O in Ga or In, the following identities hold

$$a_O(Ga)_{satn} = p(O_2,Ga\text{-}\beta\text{-}Ga_2O_3)^{1/2} \quad [2a]$$

$$a_O(In)_{satn} = p(O_2,In\text{-}In_2O_3,In_2O)^{1/2} \quad [2b]$$

Radial diffusion in a cylindrical sample can be treated as if the sample were of infinite length if the ratio of the sample length to its radius is large enough to cause the distortions in the diffusion flux *vs.* time curve (resulting from end effects) to be negligible. It was assumed that this was the case in the present work, since the sample length was about thirty times larger than the sample radius.

The mathematical solution of the diffusion equation for radial diffusion in an infinitely long cylinder has been reviewed by Rickert and El Miligy (3). The diffusion equation in cylindrical coordinates

$$\frac{\partial C}{\partial t} = \frac{1}{r}\frac{\partial}{\partial r}\left(rD_O\frac{\partial C}{\partial r}\right) \quad [3]$$

must be solved for the following potentiostatic boundary conditions

$$\begin{aligned} C &= C_o \quad 0 < r < a \quad \text{for } t = 0 \\ C &= 0 \qquad r = a \qquad \text{for } t > 0 \end{aligned} \quad [4]$$

Here, C is the concentration of dissolved oxygen, D_O is the diffusion coefficient of oxygen in the liquid metal, C_o is the initial concentration of dissolved oxygen (assumed to be uniform), r is the radial coordinate, a is the sample radius, and t is the time.

For sufficiently long times, the solution of the diffusion equation can be expressed as (3, 9)

$$\frac{M_t}{M_\infty} = 1 - \frac{4}{\alpha_1^2}\exp\left(-\frac{\alpha_1^2 D_O t}{a^2}\right) \quad [5]$$

where M_t is the amount of oxygen that has diffused out of the cylinder in time t and is given by

$$M_t = \frac{1}{2F}\int_o^t I dt \quad [6]$$

M_∞ is the amount of oxygen that has diffused out of the cylinder in the limit of infinite time (equal to the total amount of dissolved oxygen) and α_1 is the first root of the Bessel function of zero order (having the numerical value, 2.405), and I is the cell current.

Differentiation of Eq. [5] with respect to t results in the following expression for I as a function of t

$$I = \frac{8F D_O M_\infty}{a^2}\exp\left(\frac{-\alpha_1^2 D_O t}{a^2}\right) \quad [7]$$

Thus the value of D_O can be calculated from the slope of a plot of log I *vs.* t. It should be noted that the cylindrical cell geometry allows the determination of D_O without a prior knowledge of the initial equilibrium concentration of oxygen in the liquid metal (*i.e.*, without knowing the activity coefficient for dissolved oxygen as a function of temperature).

An important test of the above solution may be achieved by using a series of potential changes to initiate the out-diffusion process. Assuming that the step change in potential is large enough to approximate the second boundary condition, the calculated value of D_O should be independent of the actual magnitude of the potential change. If the calculated D_O values appear to be functions of the magnitude of the potential step (for sufficiently large steps), then it is probably safe to conclude that the I *vs.* t curve is at least partly determined by some process other than the diffusion of oxygen in the liquid metal.

Results and Discussion

Potentiostatic experiments, in which the YDT electrolyte was used and the $CO\text{-}CO_2$ mixture served as the reference gas, were performed on samples of liquid Ga, for temperatures between 750° and 950°C. For sufficiently long times, the plots of log I *vs.* t were linear to a good approximation. A typical log I *vs.* t plot is shown in Fig. 3. Values of $D_O(Ga)$, calculated from the slopes of such plots, were independent of the size of the potential step used to initiate the out-diffusion process (for steps corresponding to out-diffusion interfacial activities between 5×10^{-2} and 5×10^{-3} times the equilibrium activities).

The initial equilibrium activities used were usually slightly smaller than the saturation values as given by Eq. [2a] and Table I. However, as expected for diffusion of a very dilute solute, changes in the initial oxygen activities were found not to affect the calculated $D_O(Ga)$ values.

Assuming that the temperature dependence of $D_O(Ga)$ can be expressed by an equation of the form

$$D_O(M) = A\exp(-E/RT) \quad [8]$$

a least-squares analysis of the data resulted in the following analytical representation for the diffusion coefficient of oxygen in liquid Ga

$$D_O(Ga) = (3.68 \pm 0.42)(10^{-3}) \exp\left(\frac{-8.37 \pm 0.25}{RT}\right) \text{cm}^2/\text{sec} \quad [9]$$

$$1023 < T < 1223\ K$$

The indicated uncertainties correspond to two standard deviations, and the activation energy is given in units of kcal/mole.

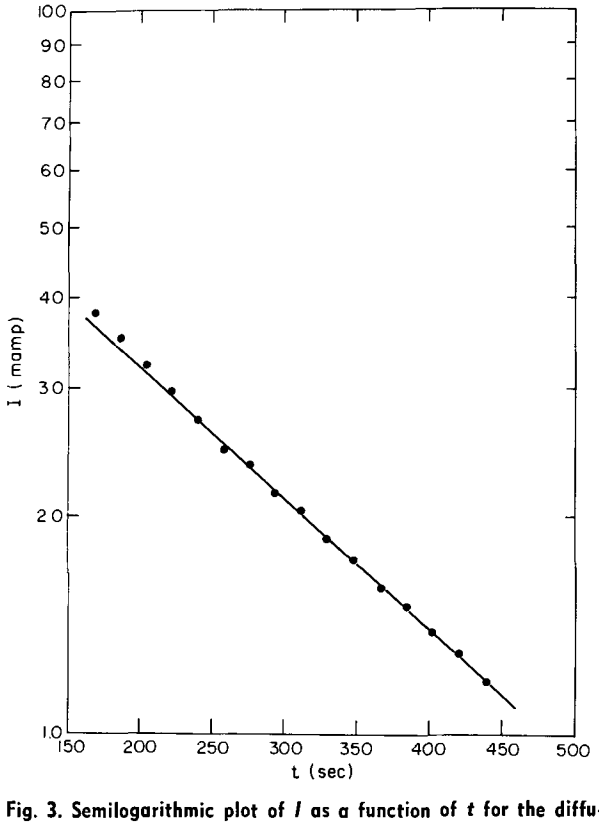

Fig. 3. Semilogarithmic plot of I as a function of t for the diffusion of oxygen in liquid gallium at 850°C.

Similar potentiostatic experiments were performed on samples of liquid In, using the YDT electrolyte and the CO-CO_2 reference gas mixture. The equilibrium activities used were slightly smaller than the saturation values given by Eq. [2b] and Table I. As in the case of diffusion in liquid Ga, the plots of log I *vs.* t were linear for long enough times. A typical log I *vs.* t plot is shown in Fig. 4. As seen from the figure, the slopes of these plots and the derived values of $D_O(In)$ were much smaller than the corresponding quantities for diffusion in liquid Ga.

Additional experiments were performed with liquid In, using CSZ as the electrolyte and either CO-CO_2 or O_2 as the reference gas. The resulting values of $D_O(In)$ were in agreement with the values obtained in the experiments with YDT as the electrolyte.

In all of the experiments with liquid In, $D_O(In)$ values were found to be independent of the magnitude of the potential step used to initiate out-diffusion, for steps corresponding to out-diffusion interfacial oxygen activities between 5×10^{-2} and 5×10^{-3} times the initial equilibrium activities.

The temperature dependence of $D_O(In)$ can be represented by the following expression obtained from a least-squares analysis of the experimental values

$$D_O(In) = (8.22 \pm 1.87)(10^{-4}) \exp\left(\frac{-12.6 \pm 0.5}{RT}\right) \text{cm}^2/\text{sec} \quad [10]$$

$$1023 < T < 1223\ K$$

The indicated uncertainties correspond to two standard deviations, and the activation energy is expressed in units of kcal/mole. The larger uncertainties in $D_O(In)$, as compared with $D_O(Ga)$, resulted primarily from the difficulties encountered in obtaining the diffusion coefficient from the much smaller slopes of the log I *vs.* t plots.

In Fig. 5, $D_O(Ga)$ and $D_O(In)$ are plotted semilogarithmically as a function of $1/T$. The points shown are those given by Eq. [9] and [10], and the error bars indicate two standard deviations. The figure shows clearly the large difference between the rates of diffusion of oxygen in liquid Ga and in liquid In. This result is not predicted by any of the current theories of impurity diffusion in liquid metals.

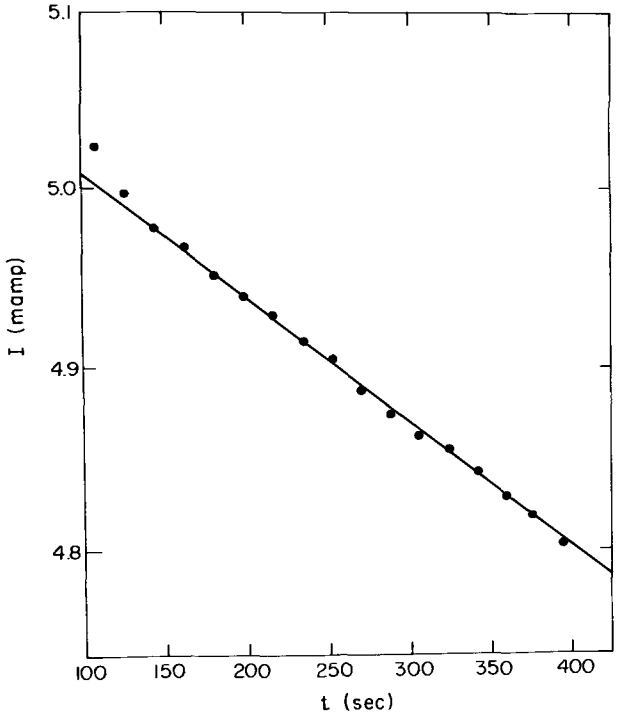

Fig. 4. Semilogarithmic plot of I as a function of t for the diffusion of oxygen in liquid indium at 850°C.

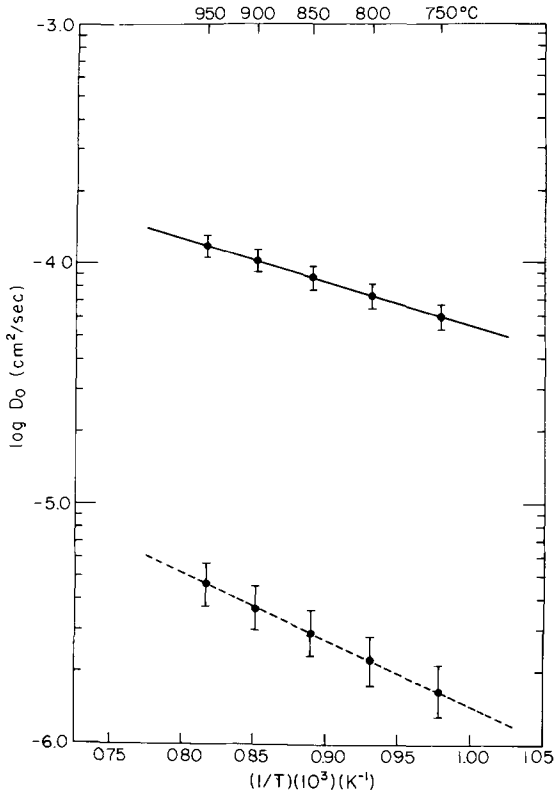

Fig. 5. Diffusion coefficients of oxygen in liquid metals as a function of temperature, plotted as log D_O *vs.* $1/T$. ———, O diffusion in Ga; - - - -, O diffusion in In.

The most important theories of diffusion have recently been critically reviewed (10). What emerged from this review was the fact that almost all of the theories assume that the diffusing atoms and solvent atoms can be treated as noninteracting hard spheres. This assumption may be acceptable for the derivation of self-diffusion coefficients. However, these theories should not be expected to accurately estimate diffusion coefficients in systems such as Ga-O and In-O, where strong interatomic potentials are present (as evidenced by the formation of quite stable oxides).

The factors leading to the large difference between the measured diffusion coefficients of oxygen in Ga and In are not known. However, some insight might be gained by investigating the diffusion of oxygen in liquid Ga-In alloys, as a function of temperature and composition. To the best of our knowledge, the diffusion of an impurity atom in a binary metallic alloy system has never been studied by an electrochemical technique, as a function of alloy composition. In a recent investigation, it was found that the Ga-In system is nearly regular (11). Also, heats of mixing have been shown to be small (amounting to about 275 cal/mole for an equimolar mixture) (12, 13). The relative thermochemical simplicity of this system should increase the chances of such a study producing useful insights into the nature of impurity diffusion in liquid metals.

In order to successfully observe diffusion-limited currents in potentiostatic experiments, it is necessary to use an electrolyte with a sufficiently low internal resistivity. Since CSZ has often been used in such experiments, a comparison of the ionic conductivity of YDT with that of CSZ was sought. Such a comparison has been made by other investigators (14), using samples they prepared containing the same amounts of Y_2O_3 and CaO as those used in this work. It was shown that the ionic conductivity of CSZ is only about three or four times that of YDT, for tem-

peratures between 800° and 1000°C. This fact, and the fact that the D_O(In) values obtained in this work using both CSZ and YDT as the electrolyte were in agreement, indicates that YDT can be safely used as a replacement for CSZ in such measurements.

However, it was found in the course of our experiments that most of the YDT tubes obtained from the Zirconium Corporation of America could not be used. The internal resistivity of the tubes was much higher than expected, as evidenced by the fact that the magnitude of I, for a particular value of t, was roughly proportional to the emf applied to the cell. Further, the log I *vs.* t plots were not linear for these tubes.

In an effort to explain these observations, electron microscope and electron microprobe analyses of the high resistivity YDT tubes were carried out. It was found that the tube surfaces were partially covered with needle-shaped crystallites of Y_2O_3, indicating that a partial segregation of the electrolyte constituents had occurred, probably during the firing process. Since the ionic conductivity of the oxide electrolytes varies significantly with the concentration of the dopant, such segregation would be expected to result in conductivities lower than those observed in the absence of segregation.

Summary

A potentiostatic electrochemical technique was used to determine the diffusion coefficients of oxygen in liquid Ga and In, for temperatures between 750° and 950°C. The oxygen diffused radially outward in cylindrical samples contained in the bottoms of YDT and CSZ electrolyte tubes. The experimental results can be expressed by the following equations

$$D_O(\text{Ga}) = (3.68 \pm 0.42)(10^{-3}) \exp\left(\frac{-8.37 \pm 0.25}{RT}\right) \text{cm}^2/\text{sec}$$

$$D_O(\text{In}) = (8.22 \pm 1.87)(10^{-4}) \exp\left(\frac{-12.6 \pm 0.5}{RT}\right) \text{cm}^2/\text{sec}$$

$$1023 < T < 1223\ K$$

The large observed difference between the magnitudes of D_O(Ga) and D_O(In) is not predicted by current theories of impurity diffusion. A study of the diffusion of oxygen in liquid Ga-In alloys, as a function of alloy composition and temperature, might lead to some insight into the nature of oxygen impurity diffusion in liquid metals.

Acknowledgments

This research was supported by the Advanced Research Projects Agency through the Center for Materials Research at Stanford University.

Manuscript submitted May 25, 1972; revised manuscript received Oct. 9, 1972.

Any discussion of this paper will appear in a Discussion Section to be published in the December 1973 JOURNAL.

REFERENCES

1. H. Rickert and R. Steiner, *Z. Phys. Chem. N. F.*, **49**, 127 (1966).
2. R. L. Pastorek and R. A. Rapp, *Trans. Met. Soc. AIME*, **245**, 1711 (1969).
3. H. Rickert and A. A. El Miligy, *Z. Metallkde.*, **59**, 635 (1968).
4. J. W. Patterson, *This Journal*, **118**, 1033 (1971).
5. K. A. Klinedinst and D. A. Stevenson, *J. Chem. Thermody.*, **4**, 565 (1972).
6. J. D. Verhoeven, *Trans. Met. Soc. AIME*, **242**, 1937 (1968).
7. C. E. Wicks and F. E. Block, Bur. of Mines Bull. 605, U. S. Govt. Printing Office, Washington, p. 29 (1963).
8. K. A. Klinedinst and D. A. Stevenson, *J. Chem. Thermody.*, To be published.
9. J. Crank, "The Mathematics of Diffusion," p. 66, Oxford, London (1957).
10. J. B. Edwards, E. E. Hucke, and J. J. Martin, *Met. Rev.*, **13**, No. 120 (1968).
11. K. A. Klinedinst, M. V. Rao, and D. A. Stevenson, *This Journal*, **119**, 1261 (1972).
12. J. P. Bros, R. Castanet, and M. Laffitte, *Compt. Rend.*, **264**, 1804 (1967).
13. B. Predel and D. W. Stein, *J. Less-Common Metals*, **18**, 49 (1969).
14. J. W. Patterson, E. C. Bogren, and R. A. Rapp, *This Journal*, **114**, 752 (1967).

Brief Communications

Residual Chlorine in O_2:HCl Grown SiO_2

Ronald L. Meek*

Bell Telephone Laboratories, Incorporated, Murray Hill, New Jersey 07974

Workers in a number of laboratories (1-4) have found that inclusion of small amounts of chlorine-bearing species (Cl_2, HCl, or C_2HCl_3) in the oxidizing ambient (O_2 or H_2O) used for thermal oxidation of silicon results in improved oxide properties. In particular, sodium, or other positive fixed charge, appears to be reduced, and, perhaps more important, the stability of the oxide to bias-temperature stress aging is improved. In order to understand these effects as well as effects on the oxidation kinetics it is useful to know the amount and distribution of chlorine incorporated into the oxide. In this note, results of direct measurement of the chlorine distribution by He^+ ion scattering are reported.

For these experiments 1000Å thick silica films were grown at 1100°C in 1% HCl in O_2 on <111> phosphorus-doped 10 ohm-cm silicon wafers which had been precleaned using a procedure involving NH_4OH and H_2O_2 (5). For control purposes, oxides were also grown at 1100°C in pure dry oxygen.

The chlorine distribution in the oxide was determined by measuring the energy spectrum of backscattered 2 MeV He^+ ions. The Rutherford backscattering technique (6-8) for chemical analysis is now widely used and here only a brief discussion will be necessary.

* Electrochemical Society Active Member.
Key words: silicon oxidation, silica, ion scattering, chlorine in silica.

For energetic ions undergoing Rutherford scattering from a target atom the scattering yield per unit solid angle is given by

$$\frac{dn}{d\Omega} = \frac{n_o N b^2}{16} \sin^{-4}\left(\frac{\theta_c}{2}\right) \quad [1]$$

where

$$b = \frac{Z_1 Z_2 e^2}{\frac{1}{2}\left(\frac{M_1 M_2}{M_1 + M_2}\right) V^2} \quad [2]$$

Z_1 and Z_2 are the atomic numbers of incident particle and target atom, M_1 and M_2 are the respective masses, and θ_c is the center of mass-scattering angle. e is the electronic charge, V is the velocity of the incident ion, n_o is the number of incident ions, and N is the number of target atoms cm^{-2}. The center of mass and laboratory scattering angles are related by

$$\sin(\theta_c - \theta_L) = \frac{M_1}{M_2} \sin\theta_L \quad [3]$$

Since the scattering is elastic, ions scattered from a target atom of given mass at a given θ_L have a characteristic energy, E, given by

$$\frac{E}{E_o} = \frac{M_1^2}{(M_1 + M_2)^2} \left\{ \cos\theta_L + \left(\frac{M_2^2}{M_1^2} - \sin^2\theta_L\right)^{1/2} \right\}^2 \quad [4]$$

where E_o is the ion energy before the scattering event.

For scattering from target atoms of given mass distributed in a substrate, the energy scale may be converted to a depth scale by use of the kinematic energy loss and the specific energy loss rate in the material; namely

$$\Delta t = \Delta E \left\{ \left(\frac{dE}{dx}\right)_{E_{in}} \left(\frac{E_{out}}{E_{in}}\right) + \left(\frac{dE}{dx}\right)_{E_{out}} \frac{1}{|\cos\theta_L|} \right\}^{-1} \quad [5]$$

which relates the energy shift ΔE to thickness increment Δt.

In these experiments a beam of 2 MeV He^+ ions collimated to ~0.05° through two Ta collimators 1 mm in diameter about 2m apart was used. The backscattered He ions were detected at $\theta_L = 177°$ in a 50 mm^2 surface-barrier detector having an energy resolution of 16 keV. This energy resolution corresponds to a depth resolution of about 200Å. Secondary electron suppression and pile-up rejection electronics were used. Samples were surrounded by a baffle cooled to liquid nitrogen temperature and were mounted in a two-axis goniometer. The scattering chamber was maintained at 10^{-6} Torr and the He ion fluence was typically 10^{16} cm^{-2}.

Typical backscattered ion spectra from an as-grown oxide, oriented with the crystal silicon substrate in a random and a <110> axial channeling direction, are shown in Fig. 1. The arrows labeled O and Si denote the energy of ions scattered from oxygen and silicon at the surface. The arrows labeled Cl denote the range of energies for ions scattered from chlorine in the oxide film. For this sample the total chlorine concentration is 5.4 $(10)^{14}$ cm^{-2}, and varies from sample to sample in the range 5-7 $(10)^{14}$ cm^{-2}. Spectra from control wafers show only a few isolated counts in the energy region corresponding to scattering from chlorine.

The oxide thickness, 1000Å, can be checked using the width of the silicon and oxygen peaks corresponding to scattering from the oxide and in this way accurately position the end points for the depth scale corresponding to chlorine in the oxide. Thus we can invert the

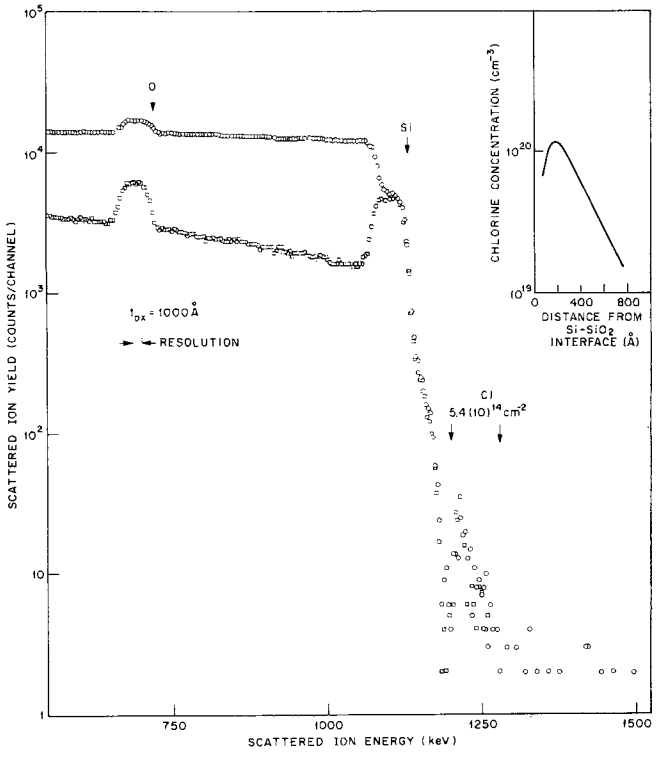

Fig. 1. Backscattered ion spectrum for 2 MeV He ions scattered from a O_2:HCl grown silicon dioxide film on silicon. Ion yield (as counts per channel) vs. ion energy.

observed scattered ion yield from chlorine to a volume distribution for chlorine in the oxide. In doing this one must be cognizant of the fact that chlorine has two abundant isotopes, ^{35}Cl (75.5%) and ^{37}Cl (24.5%). Scattered ions from the two at the same depth are separated in energy by 32 keV. The chlorine concentration in the oxide is given in the insert to Fig. 1. The distribution is always found to be peaked at about 200 ± 100Å from the silicon-silica interface at a level of about 10^{20} cm^{-3}, and drops below 10^{19} cm^{-3} at 500-800Å from the interface. It should also be noted that impurities heavier than chlorine are absent in both pure O_2 and O_2:HCl oxides. The sensitivity for detection of heavier species is about 10^{13} cm^{-2} for mass numbers near Cu, and about 10^{12} cm^{-2} for mass numbers near Au.

If a given wafer is annealed at 1100°C in argon to improve MOS properties, no change in the chlorine distribution is observed. Also, oxides have been bias-temperature stressed at 200° and 300°C with a voltage on the field plate (Al or Au) corresponding to $\pm 10^6$ Vcm^{-1}. Again no shift in the chlorine distribution is observed. However, it does appear that bombardment with 10^{14} cm^{-2} 1 keV Ar^+ can shift the chlorine since in that case we find all of both chlorine isotopes within 200Å of the silicon-silica interface. This latter observation is of significance to the interpretation of impurity profiles in insulating films which are obtained by progressively sputtering away the film since several impurity species, apparently including Cl, are known to become mobilized.

Finally, it is noted that Kriegler (9) recently found from radiotracer Na^{22} studies that the ions in HCl oxides still migrated to the vicinity of the silicon-silicon dioxide interface, but had no effect on the surface potential, presumably because they became neutralized through some interaction with the chlorine containing species. In fact, after drifting to the interface, the Na^{22} distribution was found to be peaked at 200Å from the interface, dropping off by an order of magnitude at the interface and about 500Å from the interface.

Manuscript submitted Aug. 11, 1972; revised manuscript received *ca.* Oct. 23, 1972.

Any discussion of this paper will appear in a Discussion Section to be published in the December 1973 JOURNAL.

REFERENCES

1. E. MacKenna, V. Rodriguez, and P. Kodama, Paper 146 presented at Electrochem. Soc. Meeting, Atlantic City, New Jersey, October 4-8, 1970.
2. P. H. Robinson and F. P. Heiman, *This Journal*, **118**, 141 (1971).
3. M. C. Chen and J. W. Miles, *ibid.*, **119**, 223 (1972).
4. R. J. Kriegler, Y. C. Cheng, and D. R. Colton, *ibid.*, **119**, 388 (1972).
5. W. Kern and D. A. Puotinen, *RCA Rev.*, **31**, 187 (1970).
6. J. A. Davies, J. Denhartog, L. Eriksson, and J. W. Mayer, *Can. J. Phys.*, **45**, 4053 (1967).
7. E. Bøgh, *ibid.*, **46**, 653 (1968).
8. O. Meyer, J. Gyulai, and J. W. Mayer, *Surface Sci.*, **22**, 263 (1970).
9. R. J. Kriegler, *Appl. Phys. Letters*, **20**, 449 (1972).

Procedure for Polishing PbS and $PbS_{1-x}Se_x$

G. A. Ferrante, M. C. Lavine, T. C. Harman, and J. P. Donnelly

Lincoln Laboratory, Massachusetts Institute of Technology, Lexington, Massachusetts 02173

For the fabrication of quality p-n junction diodes in PbS and $PbS_{1-x}Se_x$, an etchant which leaves a smooth, undamaged, film-free surface is necessary. The etchant procedures (1-4) previously reported in the literature were found to either badly pit the surface or to leave an insoluble film. Using the etchant technique described below, smooth, damage-free clean surfaces have been obtained, and high quality photodiodes in PbS and $PbS_{0.58}Se_{0.42}$ have been fabricated (5).

Key words: PbS, $PbS_{1-x}Se_x$, polishing, etching, IV-VI compounds.

The PbS and $PbS_{1-x}Se_x$ crystals used in these experiments were grown by the Bridgman method. Both p and n-type crystals, appropriately annealed in either a chalcogenide or metal -rich atmosphere, were used. For example, the p-type PbS crystals were annealed in a sulfur-rich PbS atmosphere for 7 days at 700°C and an additional 7 days at 500°C. They had a p-type

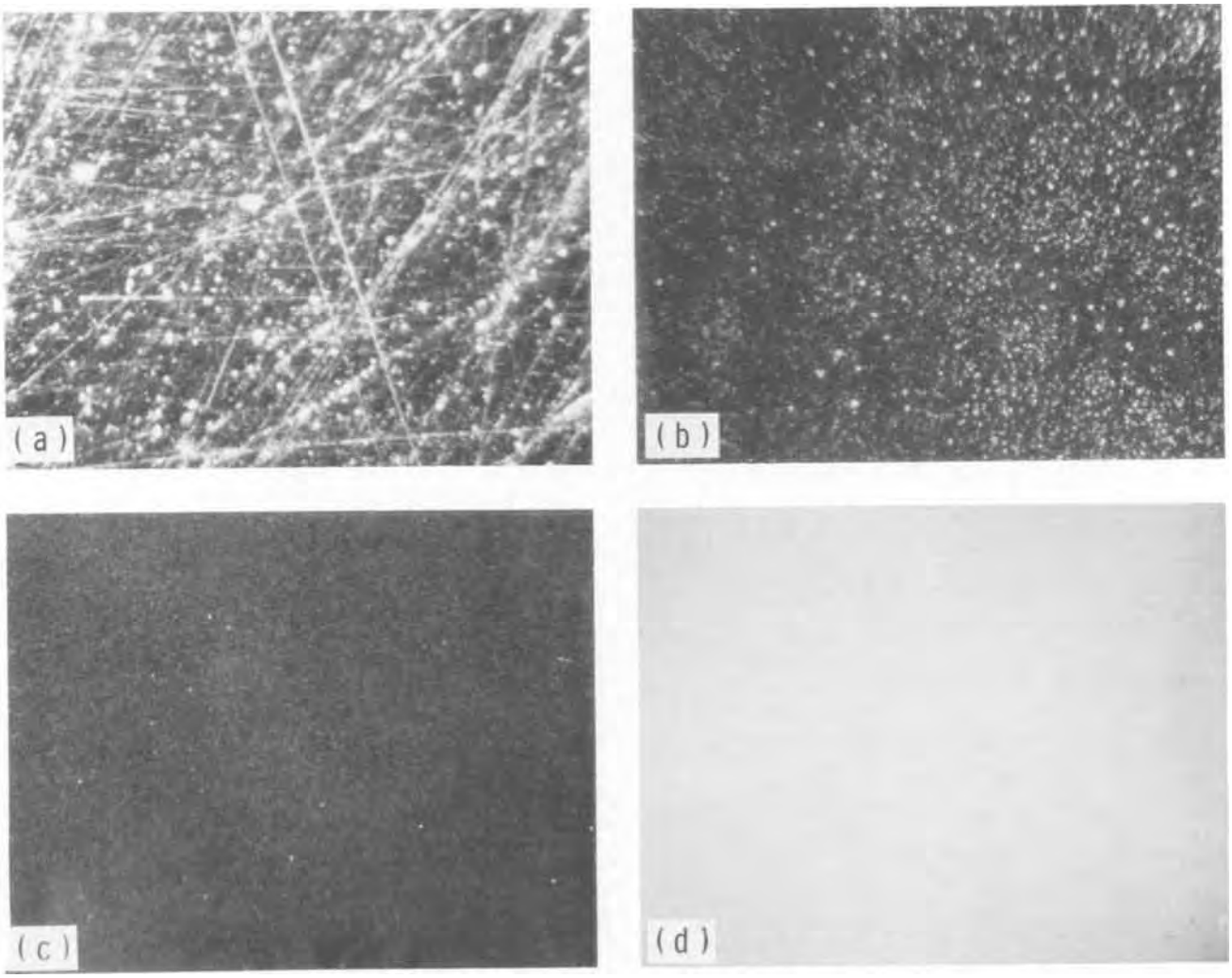

Fig. 1. PbS sample: (a) after lapping with 0.1 μm grit, showing scratches and particles, dark field, 300×; (b) after etching for 15 min in aqua regia at 40°C and rinsing in distilled water showing sulfur particles in film, dark field, 300×; (c) after rinsing in CS_2, CCL_4, and absolute CH_3OH, dark field, 300×; and (d) as in (c), bright field, 300×. Results for PbS_xSe_{1-x} are similar.

carrier concentration of 3×10^{18} cm^{-3} and a mobility of 9000 cm^2/V-sec at 77°K. The etch-pit density of these crystals was about $10^7/cm^2$.

Slices were cut using a 5 mil wire saw. Both unoriented and (100) oriented slices were used. After slicing, approximately 25 μm was removed from each side of the sample by polishing with 2 μm grit. An additional 5 μm was then removed by using 0.1 μm alumina.

Each sample was then etched in a solution of aqua regia (3 parts HCl, 1 part HNO_3) heated to between 35° and 45°C. During etching the aqua regia was vigorously agitated using a Teflon-coated magnetic stirring bar. The sample being etched was held close to the stirring bar but away from the center of rotation using a pair of Teflon-coated tweezers. The agitation close to the sample was found important to minimize film formation. The etch rate was found to be 7 μm per minute at 35°C and 10 μm per minute at 45°C. About 150 μm was removed from each side of the sample during etching. This appears to be more than sufficient to remove any surface damage introduced by lapping and sawing. On removal from the aqua regia the sample was rinsed in a stream of distilled water to dislodge any film formed during etching. The sample was then rinsed in carbon disulfide for $\approx$30 sec to remove any residual sulfur film or specks that were left on the surface. Following the carbon disulfide rinse the sample was further rinsed sequentially in carbon tetrachloride, methanol, and finally deionized water. The surface of each sample was then examined under a metallurgical microscope. If necessary, the above procedure was repeated. Dislocation etch measurements indicate that no additional bulk strain was introduced by holding the samples with the Teflon tweezers.

Figure 1 is a series of photomicrographs showing the surface of a p-type PbS sample after lapping, after etching for 15 min at 40°C in aqua regia, and after cleaning in carbon disulfide, carbon tetrachloride, and absolute methanol. As can be seen, the final surface is polished with a roughness of the order of 0.1 μm. Similar results have been obtained on n-type material. These surfaces have been found suitable for fabricating shallow p-n junction diodes by ion implantation (5).

Acknowledgment

This work was sponsored by the Department of the Air Force.

Manuscript submitted Aug. 21, 1972; revised manuscript received Sept. 28, 1972.

Any discussion of this paper will appear in a Discussion Section to be published in the December 1973 JOURNAL.

REFERENCES

1. M. K. Norr, "Polishes and Etches for Tin Telluride, Lead Sulfide, Lead Selenide, and Lead Telluride," NOLTR 63-156, U. S. Naval Ordnance Laboratory, White Oak, Maryland (1963).
2. R. F. Brebrick and W. W. Scanlon, *J. Chem. Phys.*, **27**, 607 (1957).
3. A. A. Urusovskaya, R. Tyaagaradzhan, and M. V. Klassen-Neklyudova, *Sov. Phys.-Cryst.*, **8**, 501 (1964).
4. M. K. Norr, "Polishes and Etches for Tin Telluride, Lead Sulfide, Lead Selenide, and Lead Telluride: Supplement," NOLTR 66-32, U. S. Naval Ordnance Laboratory, White Oak, Maryland (1966).
5. J. P. Donnelly, T. C. Harman, and A. G. Foyt, To be published.

JOURNAL OF THE ELECTROCHEMICAL SOCIETY

ELECTROCHEMICAL SCIENCE AND TECHNOLOGY

MARCH 1973

Leak Rates in Sealed Cells

H. A. Frank* and A. A. Uchiyama*

Jet Propulsion Laboratory, Pasadena, California 91103

ABSTRACT

Water vapor loss rates were determined from simulated and imperfectly sealed alkaline cells in the vacuum environment. The observed rates were found to be in agreement with a semi-empirical equation employed in vacuum technology. Results thereby give support for using this equation for the prediction of loss rates of battery gases and vapors to the aerospace environment. On this basis it was shown how the equation can be applied to the solution of many heretofore unresolved questions regarding leaks in batteries. Among these are the maximum permissible leak size consistent with a given cell life or conversely the maximum life consistent with a given leak size. It was also shown that loss rates of these cells in the terrestrial environment are several orders of magnitude less than the corresponding loss rates in the aerospace environment.

At the present time there is no reliable method for establishing whether a sealed cell is sufficiently leak tight such that it can operate unattended and effectively for a prescribed period of time (1). The phenolphthalein leak test (2) is purely qualitative and gives no indication whatsoever of the magnitude of the leak or its effect on cell life. The vacuum-type "helium" leak test and the "rate of pressure rise" test (3) do give some measure of the size of a leak but, as above, neither of these tests indicate what effect the leak will have on cell life. What is clearly needed to resolve this problem are two additional sets of information. The first is the relationship between leak size, as measured by one of the above or other techniques, and loss rate of leakable components. The second is the relationship between the loss of these components and the cell's electrical characteristics.

The lack of this type of information is explained by the apparent lack of a need for it in the past. This, in turn, is attributed to the fact that leaks have not heretofore represented the primary limitation to cell life. Rather, the life of these cells has been limited by the prior occurrence of degrading chemical and electrochemical phenomena such as dendrite growth, passivation, slumping, and separator degradation.

During the past several years progress has been made in delaying the onset and also reducing the severity of degradative phenomena in sealed cells. As a result it is now quite possible that the life of some of these cells may now very well be limited by leaks rather than the other phenomena. In this regard some models of the nickel-cadmium cell have been shown to exhibit satisfactory electrochemical performance for over ten years. On this basis then, the leakage studies take on renewed importance in that they may very well determine the degree of improvement that may be obtained in ultimate life expectancy and the reliability of a cell, especially during the latter stages of its electrochemical life. This information is needed in many applications of sealed cells, such as in aerospace applications, wherein reliability and life are of prime concern.

* Electrochemical Society Active Member.

Key words: leaks, sealed cells.

This paper deals with the former of the above leakage problems, which is the loss rate of the leakable gases and vapors and primarily for the condition of the aerospace or vacuum environment. The primary objective is to test the applicability of a previously developed mass-transfer equation for the prediction of loss rates under these conditions. Having established this point it will then be possible to determine the cumulative loss of each component based on the known or measured leak size as indicated above. The major emphasis is on a test of the equation for the transport of water vapor in that: (*a*) this compound is one of the key leakable components in this type of cell, (*b*) the transport of water vapor has not heretofore received much study under the conditions as described herein, and (c) the equation has already been shown to be applicable to the transport of other leakable gases, H_2 and O_2, under similar conditions as described herein.

The equation of concern was originally derived by Guthrie and Wakerling in 1949 and was later modified by Ochert and Steckelmacher in 1951 (4, 5). As shown below, it gives the mass flow or leak rate, Q, of a gas through a small hole with a diameter D and length L. The gas pressure on one side of the hole is given by P and the pressure on the other side is zero or a hard vacuum. The terms k_1 through k_4 are constants dependent on temperature and the physical properties of the gas including viscosity and molecular weight

$$QL = k_1D^4P^2 + k_2D^3P + k_3D^2 \ln (1 + k_4DP) \quad [1]$$

Heretofore, Eq. [1] has been used primarily for its intended application which has been in the study of leaks in high vacuum systems. Therein it has proved useful in design of variable and fixed leaks for calibration purposes and for estimating leak rates of gases, including H_2 and O_2, other than those for which a leak has been calibrated.

The following section describes experimental studies aimed at confirming the applicability of Eq. [1] for the prediction of water vapor leak rates from alkaline cells to the vacuum environment. The studies were carried out in simulated alkaline cells and over a wide range of the indicated parameters, including hole

length and diameter as well as electrolyte concentration and temperature, both of which affect water vapor pressure.

Experimental

A schematic diagram of the simulated cell assemblies is given in Fig. 1. These consisted of small glass containers each of which was equipped with a fill tube, a leak assembly, and two vent pipes which communicated with an adjacent cold trap and vacuum manifold line through a three-way stopcock. One of these tubes was used for degassing the electrolyte and the other for transmitting the water vapor which passed through the leak assembly. The leak assemblies consisted of 1.0 cm sections of 0.635 cm diameter stainless steel tubes of which one end was attached to the glass container by a Kovar seal and the other end was sealed off with stainless steel disks of various thicknesses and with holes of accurately known size in their centers. The disks and their holes were prepared either by machining a disk from stainless sheet stock and then laser drilling a hole in its center or by slicing segments of special tubing which had been drawn previously on small diameter wires. The former method was employed for thin disks with small holes and the latter method was employed for thicker disks and somewhat larger holes. In either case the disks were electron beam-welded to the tubes and the complete assemblies were helium leak checked after temporarily blocking off the holes.

The first step in a leak rate determination consisted of connecting the assembly to the manifold of a vacuum system and then partially filling the container with KOH solution of known concentration. The solution was then degassed in the frozen state by placing a Dewar of liquid nitrogen around the container followed by turning the three-way valve to open the degas tube to the vacuum. The Dewar was then removed and the solution allowed to melt; on reaching room temperature, the complete assembly was removed and accurately weighed on an analytical balance. The assembly was then reinstalled on the vacuum system and a run was initiated by turning the three-way valve to open the leak assembly to the vacuum. After a given period of time, which was accurately measured with a stop watch, the run was terminated by removing the assembly from the vacuum and weighing it once again on an analytical balance. Water loss rate was then calculated on the basis of the observed weight loss and the elapsed time. Time under test was selected to be sufficient to obtain a measurable and accurate weight loss of at least 50 mg but yet not so long as to cause a change in the KOH concentration of more than a small fraction of 1%. On this basis the test times ranged from several minutes for the larger sized holes to several hours for the smaller sized holes. The *pH* of water condensed in the adjacent cold trap was measured periodically to insure that there was no KOH entrainment in the evolved vapors. The runs at low and high temperature were carried out in a similar manner to the above but in a bell jar vacuum assembly located in an environmental chamber.

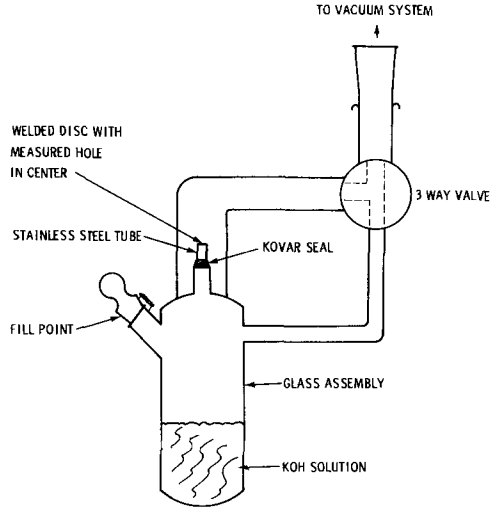

Fig. 1. Schematic diagram of simulated alkaline cell containing known leak size.

Table I. Summary of experimental and theoretical water loss rates

Diam (cm)	Length (cm)	Conc (% KOH)	Temp (°C)	Experimental loss rate (g/hr)	Theoretical loss rate (g/hr)
0.0150	0.051	30	20	0.0612	0.1110
0.0150	0.127	30	20	0.0350	0.0480
0.0150	0.254	30	20	0.0185	0.0229
0.0150	0.254	30	20	0.0185	0.0229
0.0150	0.254	40	20	0.0060	0.0090
0.0150	0.254	45	20	0.0043	0.0048
0.0150	0.254	30	0	0.0005	0.0008
0.0150	0.254	30	20	0.0185	0.0229
0.0150	0.254	30	50	0.1910	0.3410
0.0011	0.025	30	20	0.0003	0.0002
0.0019	0.025	30	20	0.0008	0.0006
0.0051	0.025	30	20	0.0033	0.0051
0.0102	0.025	30	20	0.0353	0.0443

Test Results

Table I gives a summary of the experimentally determined water loss rates in terms of grams/hour for the indicated values of the parameters. Also shown therein are the corresponding theoretical water loss rates, in the same units, obtained by substituting the appropriate values in Eq. [1]. Figures 2 through 5 give graphical representations of these rates as a function of each of the parameters. The water loss rates in these figures are expressed in terms of grams/year to facilitate subsequent battery life estimates. The effect of hole length on loss rate is given in Fig. 2 for the case of a hole diameter of 0.015 cm and with 30% KOH at 20°C. The effect of electrolyte concentration on loss rate is given in Fig. 3 for the case of hole length and diameter of 0.254 cm and 0.015 cm, respectively, and at 20°C. The effect of temperature on loss rate is given in Fig. 4 for the case of hole length and diameter of 0.254 cm and 0.015 cm, respectively, and with 30% KOH. The effect of hole diameter on loss rate is given in Fig. 5 for the case of hole length of 0.025 cm and with 30% KOH at 20°C. The *pH* of condensed vapor samples was found to be in the range of 6 to 7 so that there was little if any KOH entrainment.

Discussion

Examination of Fig. 2 through 5 reveals good correspondence between the experimentally determined

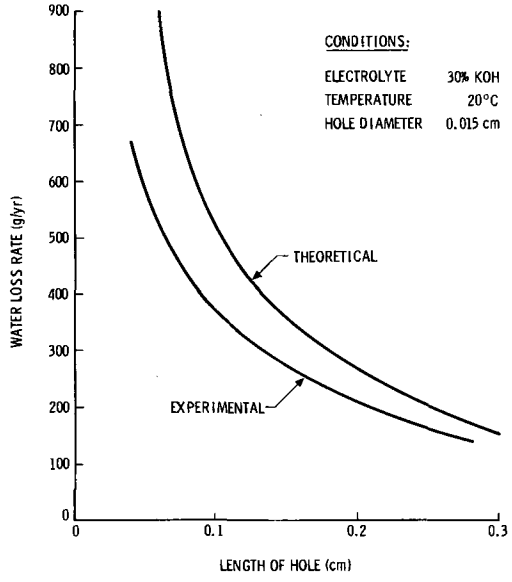

Fig. 2. Effect of hole length on water vapor loss rate

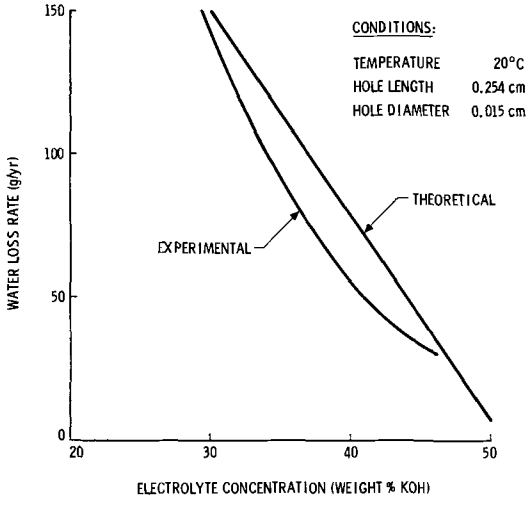

Fig. 3. Effect of electrolyte concentration on water vapor loss rate

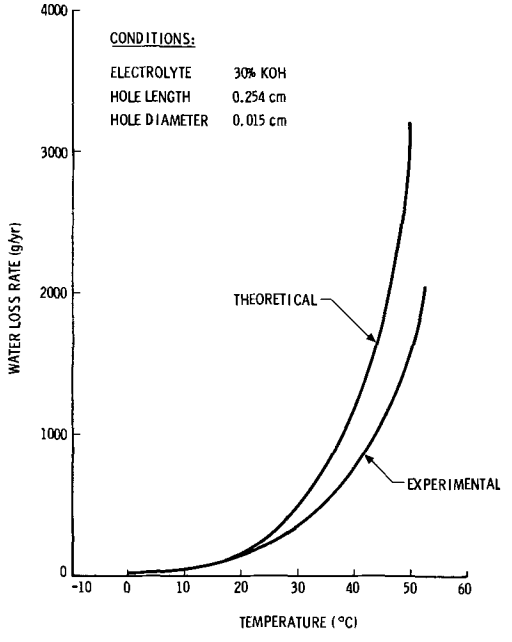

Fig. 4. Effect of temperature on water vapor loss rate

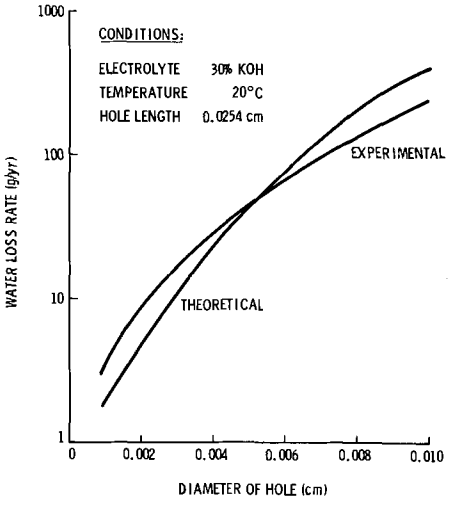

Fig. 5. Effect of hole diameter on water vapor loss rate

water loss rates and those predicted by Eq. [1]. Values of the experimental and theoretical rates are noted to correspond within a factor of two, and usually much less, over the complete range of each parameter. Figure 2 indicates that the experimental water loss rate is inversely proportional to length of the hole in accord with Eq. [1] and there is good agreement in the actual magnitude of the experimental and theoretical water loss rates especially for hole lengths greater than 0.1 cm. Figure 3 reveals that the loss rate declines in an essentially linear manner with increase in KOH concentration. This trend is in accord with theory in that vapor pressure is known to decrease in an essentially linear manner with KOH concentration in this range (6) and furthermore that loss rate is proportional to the first power of pressure under these conditions. The latter follows from the fact that under the given conditions the flow is of the molecular type and the rate is primarily dependent on the second term in Eq. [1] (5). There is also good agreement in the magnitude of the experimental and theoretical water loss rates over the indicated range of KOH concentration. Figure 4 reveals that the loss rate increases sharply with increase in temperature. This is in accord with theory in that vapor pressure, and hence loss rate, is known to be an exponential function of temperature. Good agreement is noted in the magnitude of the experimental and theoretical water loss rates, at least at temperatures below 30°C. Figure 5 reveals that the loss rate also increases sharply with increase in hole diameter. Detailed examination of this curve indicates that the loss rate is approximately proportional to the third power of diameter. This trend is in accord with theory in that molecular flow again predominates under these conditions and the rate is therefore primarily dependent on the magnitude of the second term in Eq. [1] (5). With much larger diameter holes the flow will be of the viscous type and the rate will be primarily dependent on the magnitude of the first term in Eq. [1]. Under these conditions the rate will be proportional to the fourth power of the diameter.

Having established applicability of Eq. [1] to the prediction of instantaneous water loss rates, it will now be applied to the problem of determining cumulative water loss of imperfectly sealed cells as a function of time in the aerospace environment. This problem is quite straightforward and involves integration of the instantaneous rates, taking into account the variation in rate with time due to the changing electrolyte concentration and hence vapor pressure driving force. The process is most conveniently carried out by integrating the losses over assumed short intervals of time wherein concentration and vapor pressure, and hence loss rate, remain relatively constant.

As an example of the above the cumulative water loss of a 20 A-hr aerospace Ni-Cd cell was calculated for each of three different assumed leak sizes. The leaks were assumed to consist of small holes located in the cell's stainless steel cover with assumed thickness of 0.076 cm (0.030 in). To simplify the numerical calculations it was decided to define the leak size in terms of the hole diameter rather than the more commonly employed helium leak rate. Either of these characteristics would have been sufficient, however, in that they are mutually dependent for a given hole length as shown by Eq. [1]. The diameters which were selected for this example were 0.001, 0.003, and 0.010 cm (10, 30, and 100μ respectively). On the basis of Eq. [1] the corresponding helium leak rates are calculated to be 1.3×10^{-3}, 6.6×10^{-2}, and 6.6 cm^3 atm He/sec, respectively. Initial electrolyte content was arbitrarily taken as 80 cm^3 of 30% KOH. This electrolyte level may perhaps be somewhat high for cells of this type, but is at least within a workable range. Results shown in Fig. 6 reveal a marked difference in the cumulative losses for the relatively narrow range of hole diameters. For example, the time required for loss of 20g of water is noted to increase from 2.0×10^{-1} yr to 3.5×10^{2} yr as the diameter is decreased from 100 to 10μ. Although not shown in Fig. 6 it was also determined that the corresponding time for a loss of 20g with a 1.0μ hole is 4.0×10^{5} yr. By way of this example, it has thus been shown how Eq. [1] can be applied to the determination

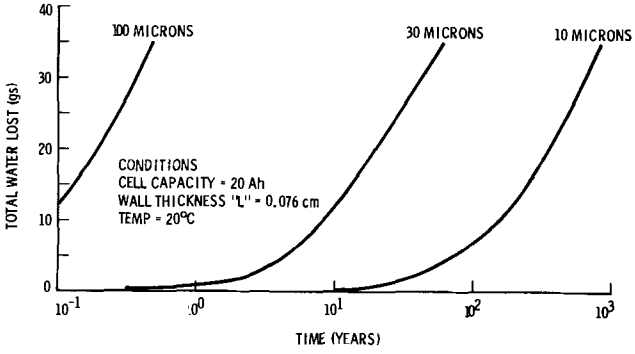

Fig. 6. Predicted cumulative water loss of a typical 20 A-hr aerospace Ni-Cd cell in the space environment.

of cumulative losses over a wide range of leak sizes and operating conditions.

The cumulative loss results, such as above, are directly applicable to the problem of predicting maximum permissible life of a cell with a known leak size or conversely the maximum leak size for a given cell life. All that is necessary to know, as described above, is the relationship between cumulative loss and cell performance. This latter relationship may, as shown in a subsequent paper (7), be derived analytically but is best obtained by experimental data on actual cells. Figure 7 presents such data for an actual Ni-Cd cell which is similar to the one described in the above example. Capacity of this cell was 20 A-hr, as in the above example, and its electrolyte consisted of 66 cm^3 of 33.8% KOH, which is not too different than in the above example. Wall thickness, 0.076 cm, was the same in both examples. Curve A gives the initial discharge characteristics of this cell in the as-received condition. Curves B, C, and D give the discharge characteristics after having removed the indicated amounts of water by venting the cell and exposing it to vacuum. Results indicate a gradual decline in capacity with water loss to about 20g as shown by curve C, where the cell can deliver about 75% of its initial capacity. Thereafter, the results indicate a sharp decline in capacity with water loss to about 28g as shown by curve D, where the cell has essentially lost all of its capacity. Based on these performance results in Fig. 7 and the cumulative loss results in Fig. 6, it is now possible to arrive at quantitative estimates to the above questions. For example, if it is known that this cell has a 30μ hole in its case it can be shown by Fig. 6 and 7 that its maximum life will be approximately 12 years in a space environment if it is to deliver at least 75% of its initial capacity. Alternatively, it could be stated that the maximum permissible leak size would be 30μ if the cell is expected to retain at least 75% of its capacity for 12 years. By way of this example it has been shown

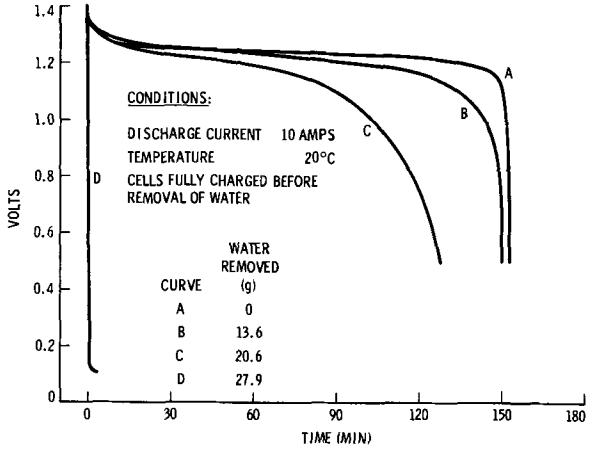

Fig. 7. Effect of water loss on output of typical 20 A-hr aerospace type Ni-Cd cell.

how the previously developed relationships may be employed to determine maximum cell leak size consistent with a specified performance level and life.

The above life estimates apply only to the indicated 20 A-hr Ni-Cd cell. Extrapolation of the procedures to the solution of life estimates for other types and sizes of cells is possible. These extrapolations must consider the pertinent differences in these cells which affect loss rate, *i.e.*, cell dimensions and initial electrolyte content and concentration.

Finally, it is worthwhile to briefly examine the analogous expression to Eq. [1] which describes the rate of water loss to the terrestrial rather than the space environment. This will give some basis for judging the severity of leaks in aerospace cells which may be subjected to long periods of storage before use or in cells which are intended for commercial or industrial use. The pertinent equation, which accounts for the inhibiting effects of air, is given (8)

$$QL = k_5 A P_t (P_1 - P_2/P_m) \qquad [2]$$

In Eq. [2] the terms Q and L again refer to the water loss rate and length of leakage path as in Eq. [1], P_t represents the total system pressure which in this case is 1.0 atm, and P_1 represents the vapor pressure of water inside the cell which can, of course, be determined with known temperature and electrolyte concentration. P_2 represents the vapor pressure of water in the surrounding air which can be determined with the known temperature and relative humidity. P_m is the logarithmic mean pressure of the water vapor which can be determined directly with known values of P_1 and P_2. Finally, the factor k_5 is a constant which can be determined from known values of the diffusion coefficient of water in air, the gas constant, and the temperature.

The magnitudes of the leak sizes predicted by Eq. [2] are found to be appreciably lower than those predicted by Eq. [1] for the same size leakage path. For example, the predicted water loss rate from a cell with 30% KOH at 20°C and with hole diameter of 100μ and length of 0.1 cm is calculated to be 4.6×10^{-2} g/yr to the terrestrial environment with 0% relative humidity and $1.0 \times 10^{+2}$ g/yr, or over three orders of magnitude more, to the aerospace environment. In actual practice the rate predicted by Eq. [2] may be somewhat high due to the existence of normally higher relative humidity than the above and also the impediment to flow that will most likely result from carbonate formation in the hole. On this basis, then, it may be concluded that water loss rates in the terrestrial environment are several orders of magnitude less than those in the space environment and hence maximum permissible leak sizes or operating lives of imperfectly sealed cells will be appreciably higher in the terrestrial than the space environment.

Conclusions

It has been shown that a previously developed mass transfer equation is applicable to the problem of predicting loss rates of leakable gases and vapors from imperfectly sealed alkaline cells in the vacuum environment. Experimental confirmation of this point was demonstrated for the case of water vapor loss from simulated alkaline cells in a vacuum chamber. On this basis it was shown how the equation can be used to obtain quantitative estimates to many heretofore unresolvable questions regarding maximum permissible leak size and life of such cells in the aerospace environment. Finally, it was shown that the loss rate from a cell with a given size leak will be several orders of magnitude less in the terrestrial environment than in the aerospace environment.

Acknowledgments

This paper presents the results of one phase of research carried out at the Jet Propulsion Laboratory, California Institute of Technology under Contract No.

NAS 7-100, sponsored by The National Aeronautics and Space Administration.

Manuscript submitted June 12, 1972; revised manuscript received Sept. 25, 1972. This was Paper 32 presented at the Cleveland Meeting of the Society, Oct. 3-7, 1971.

Any discussion of this paper will appear in a Discussion Section to be published in the December 1973 JOURNAL.

SYMBOLS

A	cross sectional area of leakage path, cm^2
D	diameter of leakage path, μ
k_1 to k_4	constants in Eq. [1]
k_5	constant in Eq. [2]
L	length of leakage path, cm
P	vapor pressure of water inside cell in Eq. [1], mm Hg
P_1	vapor pressure of water inside cell in Eq [2], mm Hg
P_2	vapor pressure of water outside cell in Eq. [2], mm Hg
P_m	log mean vapor pressure of water in Eq. [2], mm Hg
P_t	total pressure in Eq. [2], mm Hg
Q	water vapor loss rate, g/yr

REFERENCES

1. See., for example (*a*) W. R. Scott, "A Study of The State-of-The-Art of Hemetic Seals for Secondary Alkaline Spacecraft Cells," Final Report Contract NAS 5-10432, TRW Report 09299-6601-R0-00, Redondo Beach, Calif. (1968); (*b*) A. Fleischer, "Batteries, Primary and Secondary," Paper submitted to Interagency Power Group under Contract NASr-191, Power Information Center (1964).
2. P. Bauer, "Batteries for Space Power Systems," NASA SP-172, p. 42, U. S. Government Printing Office, Washington, D. C. (1968).
3. W. Jakobi *et al.*, "Research and Development Program on Sealed Nickel-Cadmium Cells for Space Use," Final Report, Contract No. NAS 5-1045, Gould-National Batteries Inc., Minneapolis, Minn. (1963).
4. A. Guthrie and R. K. Wakerling, "Vacuum Equipment and Techniques," pp. 190-194, McGraw-Hill Book Co., New York (1949).
5. N. Ochert and W. Steckelmacher, *Brit J. Appl. Phys.*, 2, 332 (1951).
6. N. A. Lange, "Handbook of Chemistry," Revised 10th ed., p. 1871, McGraw-Hill Book Co., New York (1966).
7. H. A. Frank, Unpublished results to be submitted to *This Journal*.
8. T. K. Sherwood and R. L. Pigford, "Absorption and Extraction," 2nd ed., p. 6, McGraw-Hill Book Co., New York (1952).

The Electrochemistry of Iron in 1M Lithium Hydroxide Solution at 22° and 200°C

Digby D. Macdonald[1] and D. Owen

Research Chemistry Branch, Whiteshell Nuclear Research Establishment, Atomic Energy of Canada Limited, Pinawa, Manitoba, Canada

ABSTRACT

The electrochemical behavior of iron in 1M LiOH solution at 22° and 200°C has been investigated using cyclic voltammetry, galvanostatic charging, and steady-state polarization techniques. At 22°C the data are consistent with the initial formation of Fe_3O_4 and $Fe(OH)_2$ on the surface followed by the oxidation of iron to γ-Fe_2O_3 or $Fe(OH)_3$. The anodic behavior of iron at 200°C can be explained by the following processes

$$Fe + 3\,OH^- \rightarrow HFeO_2^- + H_2O + 2e^- \quad [1]$$

$$3Fe + 8\,OH^- \rightarrow Fe_3O_4 + 4H_2O + 8e^- \quad [2]$$

$$3HFeO_2^- \rightarrow Fe_3O_4 + H_2O + OH^- + 2e^- \quad [3]$$

$$Li^+ + HFeO_2^- \rightarrow LiFeO_2 + H^+ + e^- \quad [4]$$

where process [1] accounts for active dissolution of iron, [2] for the direct formation of the base oxide layer from the metal, and [3] and [4] for the nucleation and growth of the "upper-layer" oxide crystals.

The behavior of iron and carbon steel in hydroxide solutions at temperatures greater than 100°C is of practical interest to the electrical energy producing industries, since many of the nuclear and fossil fueled power stations employ dilute hydroxide solutions as heat transport media. Lithium hydroxide is the most commonly used alkalizing agent in nuclear reactors, since lithium gives rise to fewer radiation problems than other alkali ions. The use of lithium hydroxide has also been suggested by Bloom (1) as a means of avoiding boiler pitting due to localized concentration of the feed water alkali. This alkalizing agent is of fundamental interest, since a number of studies (1-4) have suggested that the corrosion mechanism of mild steel in LiOH solution at elevated temperatures is distinctly different from that in NaOH under the same conditions.

The present study was undertaken to define more clearly the electrochemical behavior of iron and carbon steel in lithium hydroxide solution at 22° and 200°C. The electrochemical techniques used include cyclic voltammetry, which is a convenient method of "mapping" the general behavior of solid electrodes (5-9), and the more conventional potentiostatic and galvanostatic methods for studying active to passive transitions. The electrochemical studies were supplemented by detailed examination of the oxide films formed on iron and carbon steel surfaces using scanning electron microscopy.

Experimental

Electrochemical studies.—The high-temperature electrochemical cell used for polarization studies of iron

[1] Present address: Department of Chemistry, Victoria University of Wellington, Wellington, New Zealand.

Key words: electrochemistry, autoclave, corrosion, lithium hydroxide, iron.

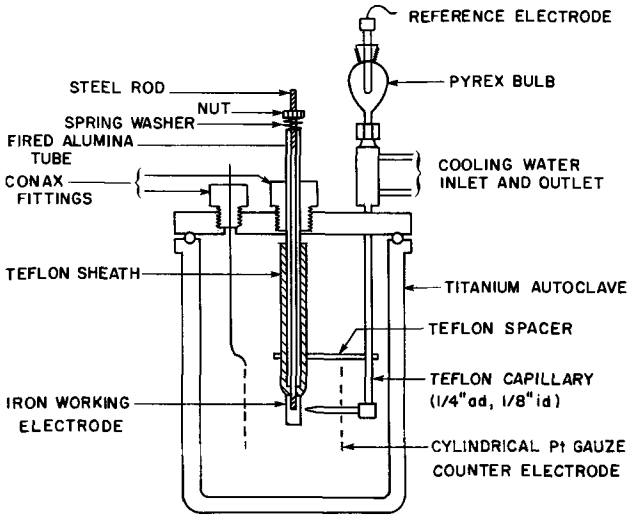

Fig. 1. High-temperature electrochemical cell

in 1M LiOH at 22° and 200°C is shown in Fig. 1. The pressure vessel was constructed from titanium and used without a liner. Analysis of the autoclave contents by atomic absorption spectroscopy after polarization runs lasting up to 10 days failed to detect any titanium in solution (*i.e.* < 0.5 ppm). The working electrode was insulated from the autoclave body by a fired alumina tube. In order to avoid contamination of the solution by aluminate ions, direct contact between the alumina tube and the alkali solution was prevented by a Teflon sleeve. The working electrode assembly was made pressure tight by compressing the spring washers at the top of the alumina tube.

The autoclave was heated by an a-c furnace coupled to an automatic controller which allowed temperature to be regulated to ± 1°C. Since the working electrode was grounded via the potentiostat, it was necessary to isolate the autoclave and furnace from ground and from the rest of the system.

The reference electrode assembly used is shown in Fig. 2. A porous asbestos plug was employed to maintain electrolyte contact between the autoclave contents and the external reference electrode which was maintained at room temperature. By carefully adjusting the compression nut the rate of flow of solution across the pressure drop (~ 250 psig at 200°C) could be reduced to less than 1 ml/week. Initial experiments showed that interruption of the electrolyte column frequently occurred and resulted in the loss of potentiostatic control. The interruptions were attributed to vapor bubble formation in the Teflon capillary, especially at the low pressure side of the system. This

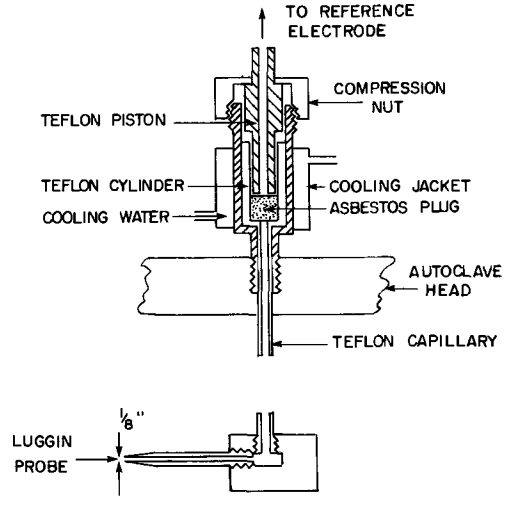

Fig. 2. High-temperature reference electrode bridge

problem was eliminated by cooling the asbestos plug and by inserting asbestos string into the Teflon capillary to act as a wick. The tip of the Luggin probe was held 1 mm from the surface of the working electrode by a Teflon spacer. All potential measurements were made with reference to a $Hg/Hg_2SO_4/K_2SO_4$ (sat.) electrode. This reference electrode was chosen in preference to the more conventional calomel system to eliminate possible diffusion of chloride ions into the autoclave. Chloride ions are known to affect the electrochemical behavior of metals in hydroxide solutions at elevated temperatures (10, 11).

Potentiostatic and cyclic voltammetry studies were performed using an electronic potentiostat coupled to a motor potentiometer. Potentials were measured with a high impedance electrometer and the polarization curves were recorded on an x-y recorder. Galvanostatic experiments were performed using a d-c constant current power supply.

Corrosion studies.—A series of experiments were performed in which 2.54 cm diameter carbon steel disks were rotated in 1M lithium hydroxide solution at 200°C for one to four days. The apparatus consisted of an autoclave and heater assembly similar to that described in the previous section. The autoclave head was fitted with a pressure-tight gland and stirrer connected via a belt-pulley arrangement to a constant speed motor. The disk was rotated at 43.5 rad sec^{-1} (415 rpm) in all experiments. This velocity corresponds to a maximum Reynold's number (Eq. [A] of ~ 7×10^3

$$Re = \frac{\omega r^2}{\nu} \qquad [A]$$

where ω is the rotational velocity, ν the kinematic viscosity (taken as 1×10^{-2} cm^2 sec^{-1}), and r is the radius of the disk. This value is well below the lower limit for transition to turbulent flow (12) and the corrosion process occurs in the laminar flow regime.

In order to eliminate possible precipitation of corrosion products on the metal surface during cool-down, the solution was removed from the autoclave at 200°C via a cooling coil. The disks were then rotated in the vapor space for a brief time to remove any adhering liquid. After cooling, the disks were removed and examined using scanning electron microscopy. Surface charging effects were alleviated by evaporating a film of gold onto the corroded surface prior to microscopic examination.

Materials.—Iron electrodes, 0.635 cm in diameter and 1.27 cm long, were machined from commercially pure material. Spectrographic analysis revealed the following impurities in ppm: C 20, Cu 75, Mn 18, and Ni 80. The area exposed to solution (2.85 cm^2) was polished on a lathe with No. 600 grit silicon carbide paper. The iron electrodes were degreased with acetone immediately before exposure to the solution. A number of experiments were performed with vacuum annealed electrodes (670°C for 24 hr) which were etch-cleaned in 5M HNO_3 before polarization. Unless otherwise noted the electrochemical work reported here refers to the abraded electrodes.

Carbon steel disks, 2.54 cm in diameter and 0.635 cm thick, were machined from commercially available material. Spectrographic analysis revealed the following major constituents (besides iron) in weight per cent: C 0.3, Ni 0.09, Cr 0.1, Sn 0.015, Mo 0.1, Al 0.034, Cu 0.11, Mn 0.75, and Si 0.33. The surface was abraded as described above and washed with acetone and distilled water immediately before commencing an experiment.

Lithium hydroxide solutions were prepared from reagent grade lithium hydroxide monohydrate and doubly distilled water. The alkalinity of each solution was checked by titrating to neutrality with standard hydrochloric acid. All solutions were purged *in situ* with pure nitrogen (99.999%) or hydrogen (99.99%)

gas before the start of each experiment. No specific effects of either gas were noted.

Results

General.—At room temperature (22° ± 1°C) an iron electrode in contact with 1M LiOH spontaneously adopted a corrosion potential of −750 to −800 mV *vs.* the $Hg/Hg_2SO_4/K_2SO_4$ (sat.) reference electrode used in this work. During heat-up (~ 3°C/min) the potential at first changed slowly until the temperature reached ~ 100°C, and then rapidly to −1420 ± 10 mV at ~ 125°C. No further change in potential with temperature was noted during the rest of the heat-up period. The electrode maintained this potential for a certain time and then changed to a stable corrosion potential of −1250 mV. The time taken from the end of the heat-up period until the electrode adopted the stable corrosion potential was found to be highly dependent on the previous history of the autoclave. If the interior walls of the autoclave were freshly sand-blasted this transition frequently took several days to occur. However, if the autoclave walls were covered with a layer of iron oxide from previous runs the transition would occur in a few minutes.

A scanning electron micrograph of the oxide film formed on carbon steel in 1M LiOH at 200°C for 24 hr is shown in Fig. 3. The film is similar to that reported previously by others (13, 14) and consists of two layers: a base layer with little apparent structure at a magnification of 1200X and an upper layer of octahedral crystals. The highly developed crystallographic faces suggest growth from solution as suggested by Castle and Mann (15) and Moore and Jones (16). Similar films were formed on iron electrodes exposed to the same oxidizing conditions and at the stable corrosion potential of ~1250 mV. Further, the morphology of the oxide film did not depend on whether or not the solution was removed from the autoclave prior to cooling. This discounts the possibility that deposition of corrosion products during cool-down contributes to the observed morphology. If the corroding surface was removed from the solution before the potential decayed from −1420 to −1250 mV, only a single layer film was formed which was similar to the base layer shown in Fig. 3. High magnification showed that this layer consisted of small (< 200Å) cubic particles separated by deep channels extending well below the surface. Field *et al.* (17) found that the base layer formed on carbon steel surfaces in 15% NaOH at 315°C had a porosity of 10-15% and that the oxide grains ranged in size from 250 to 5000Å.

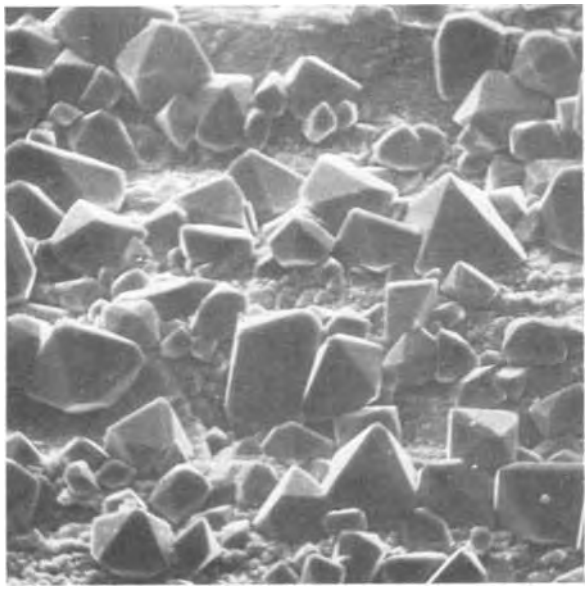

Fig. 3. Oxide film formed at −1250 mV on carbon steel in 1M LiOH at 200°C for 24 hr (×900).

Electrochemistry. — *Cyclic voltammetry.* — Cyclic voltammetry traces for iron electrodes in 1M LiOH at 22° and 200°C are shown in Fig. 4 and 5, respectively. In both cases the potentials at which peaks occur on the anodic and cathodic sweeps were highly reproducible. However, the current passed at any given potential was not very reproducible from run to run and particularly so for the low temperature experiments. It was found that reproducibility improved by first briefly holding the potential of the electrode well into the hydrogen evolution region in order to reduce oxides which form spontaneously on the metal surface. A similar procedure was used by Asakura and Nobe (18) in a recent potential sweep study of iron in 1M KOH at room temperature. In the present work at 22°C the electrode was held at −1800 mV for 10 min prior to sweeping the potential of the electrode to oxygen evolution and back. At 200°C the electrode was held at −1700 mV for 2 min prior to sweeping; the shorter time and lower potential being dictated by the greatly increased rate of hydrogen evolution at the higher temperature. The sweep behavior was not affected by further increasing the potential cathodically nor by holding the potential for longer times.

Double layer capacities (C_{dl}) for metal electrodes in aqueous solutions are usually less than 100 $\mu F/cm^2$ (19). Thus, for an area (A) of 2.85 cm^2 and a sweep rate of 0.0139 V/sec (*i.e.*, 50 V/hr) the nonfaradaic contribution $[C_{dl}A(dE/dt)]$ to the total current should not exceed 4×10^{-6}A. This is several orders

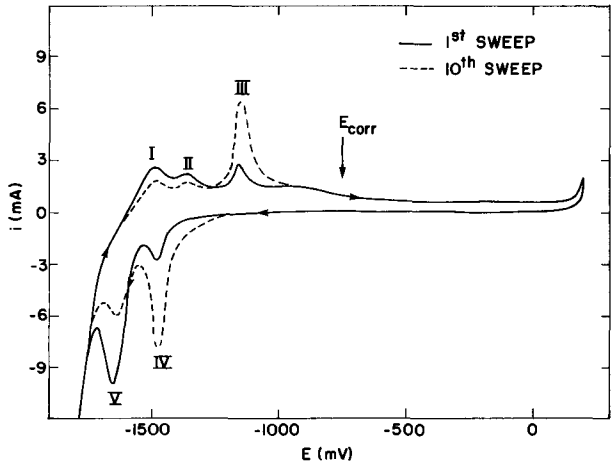

Fig. 4. Cyclic voltammetry of iron in 1M LiOH at 22°C, dE/dt = 50 V/hr.

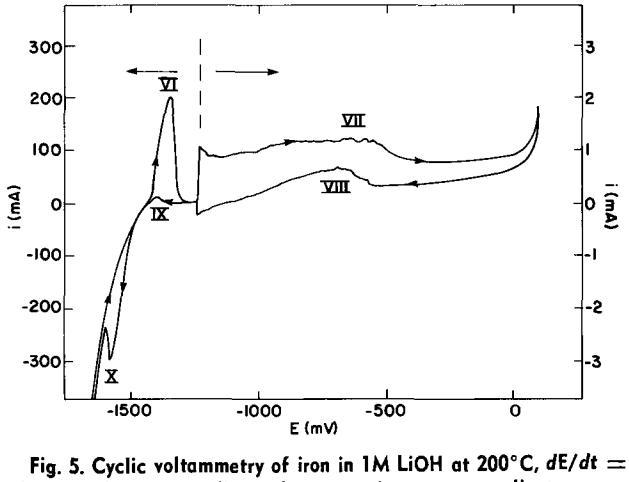

Fig. 5. Cyclic voltammetry of iron in 1M LiOH at 200°C, dE/dt = 50 V/hr. The arrows indicate the appropriate current ordinates.

of magnitude less than the observed current (Fig. 4) and can be ignored. Thus the observed current arises almost entirely from charge transfer for processes which occur at the metal surface.

As seen in Fig. 4, iron exhibits five clearly defined peaks on cyclic sweeping between hydrogen evolution and oxygen evolution at 22°C. Three peaks (I, II, and III) occur on anodic sweeping and two (IV and V) on the reverse cathodic sweep. The current/voltage traces show that on repetitive sweeping the charge consumed at peaks I, II, and V decreases while that consumed at peaks III and IV increases. Further, if the sweep is reversed after each anodic peak (Fig. 6) then both peaks I and II result in a single reduction process at −1650 mV (*i.e.*, peak V). However, if the sweep is reversed after peak III both peaks IV and V occur on the cathodic sweep. Annealed electrodes gave similar results, except peak I was greatly reduced in size relative to peak II and peaks II and V showed little variation on repetitive sweeping.

The cyclic voltammetry behavior of iron in 1M LiOH at 200°C is illustrated in Fig. 5. These experiments tended to be more reproducible than those at 22°C. This probably reflects enhancement of rate processes due to the higher temperature. The electrochemical behavior of iron at 200°C is markedly different from that at 22°C. At 200°C a single, large peak (VI) occurs at −1360 mV on anodic sweeping followed by a broad peak (VII) from −1250 to −500 mV which is characterized by erratic current fluctuations. On the reverse sweep from oxygen evolution the current/voltage trace tends to follow the anodic sweep, including a region of current fluctuations (VIII) and a small anodic "loop" (IX) close to the potential at which peak VI occurs. Further cathodic sweeping results in a large reduction peak (X) at −1600 mV. If the anodic sweep is reversed immediately after peak VI the reduction peak (X) still occurred at −1600 mV. Multiple sweeps resulted in a slight decrease in peak current (< 10%) for peaks VI and X on the second and third sweeps. Further cycling produced super-imposable traces. Finally, the existence of anodic peaks on the reverse sweep (*i.e.*, peaks VIII and IX) are indicative of reactivation processes involving charge transfer reactions which produce ionic products. It is interesting to note that Bignold (6) could find no evidence for similar processes on iron in 0.1-10M NaOH at temperatures between 200° and 250°C.

Cyclic voltammetry studies were carried out at 22° and 200°C using sweep rates of 20, 50, 60, and 150 V/hr. At both temperatures the peak currents were found to increase markedly with sweep rate as has been observed for other systems at 25°C (9, 18). Unfortunately, the peak currents were not sufficiently reproducible at room temperature to allow a quantitative determination of the functional dependence of peak current on sweep rate. At 200°C, however, reproducibility was sufficiently good that this functional dependence could be ascertained and it was found that the peak currents for peaks VI and X were proportional to the square root of the sweep rate. The same functional dependence has also been observed during room temperature studies of iron in 1M KOH (18) and polycrystalline lead in sodium hydroxide solution (9) and indicates that the charge transfer process is mass transport controlled, probably through the diffusion of hydroxyl ions to the metal surface. Finally, it was found that at both 22° and 200°C the potential differences between conjugate oxidation/reduction peaks increased significantly with sweep rate. This indicates that the charge transfer processes occurring on the electrode surface are not very reversible (20).

Galvanostatic charging studies.—Anodic and cathodic charging curves for iron in 1M LiOH at 22° and 200°C are shown in Fig. 7 and 8, respectively. Initial surface treatment consisted of polarizing the electrode cath-

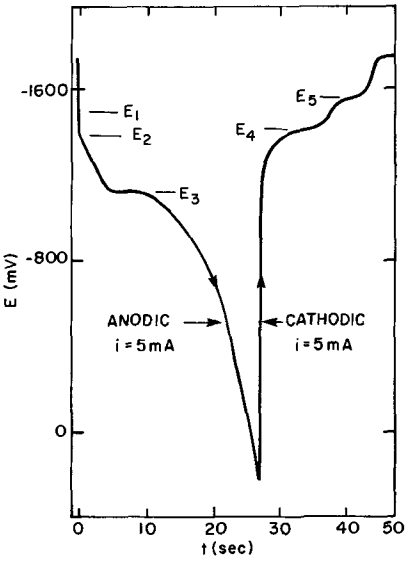

Fig. 7. Galvanostatic charging curve for iron in 1M LiOH at 22°C and at a current of 5 mA. The electrode was polarized cathodically at 5 mA for 2 min prior to anodic charging.

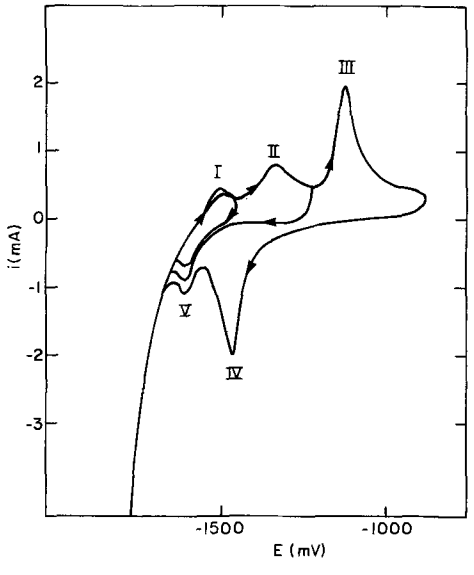

Fig. 6. Cyclic voltammetry of iron in 1M LiOH at 22°C, dE/dt = 50 V/hr. The sweeps were reversed at −1450, −1230, and −880 mV.

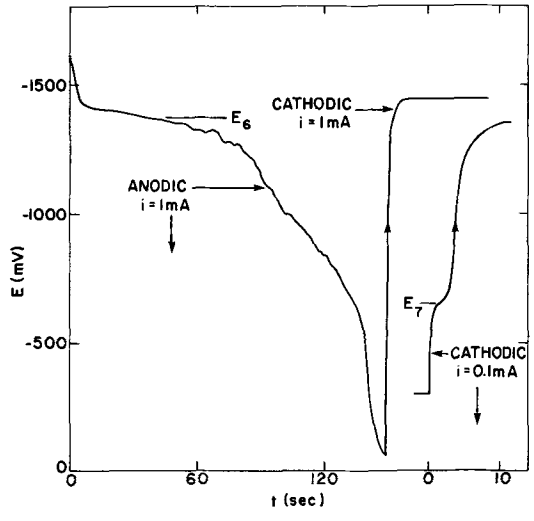

Fig. 8. Galvanostatic charging curves for iron in 1M LiOH at 200°C. The electrode was polarized cathodically at 100 mA for 2 min prior to anodic charging.

odically until the potential remained constant. The current was then reversed and the potential recorded as a function of time. When the potential had reached a preselected value (usually at oxygen evolution) the current was again reversed and the potential recorded on the cathodic sweep. In a few experiments the sequence described above was repeated over a number of cycles (usually five).

Two clearly defined potential arrests were observed on both anodic (E_2 and E_3) and cathodic (E_4 and E_5) sweeps at 22°C (Fig. 7). Improved time resolution indicated the existence of an additional arrest (E_1) at about −1500 mV during anodic polarization. The potentials at which the arrests occur on galvanostatic charging are close to the peak potentials observed in the cyclic voltammetry studies (Fig. 4). This suggests that both the potential arrests and current peaks reflect the same electrochemical processes at the metal surface. Additional support for this hypothesis is gained from cyclic charging studies in which it was found that the charge consumed during the arrests at E_3 and E_4 increased, while that at E_5 decreased, on successive cycling. This is precisely the behavior of the corresponding peaks in cyclic voltammetry (Fig. 4).

The galvanostatic charging curves for iron in 1M LiOH at 200°C are illustrated in Fig. 8. On anodic polarization the potential changes rapidly to −1420 ± 10 mV followed by an arrest (E_6) which extends to about −1300 mV. The latter stages of this arrest are characterized by the onset of erratic potential fluctuations. These potential fluctuations continued as the potential of the electrode drifted to −600 mV. The potential then changed rapidly to oxygen evolution. On cathodic polarization from oxygen evolution the potential changed rapidly to −1450 mV with a brief arrest (E_7) at −650 mV. This arrest is shown more clearly by a cathodic transient at 0.1 mA obtained by first polarizing the electrode anodically at this current for 2 min. Again, there is a close correspondence between the galvanostatic charging behavior and cyclic voltammetry. Thus, the arrest E_6 observed on anodic charging occurs at the same potential as peak VI during the anodic sweep shown in Fig. 5. Further, the region of potential instability shown in Fig. 8 corresponds closely with the region of current instability exhibited during cyclic voltammetry. This is expected in view of the interdependence of current and potential.

Steady-state polarization studies.—Galvanostatic and potentiostatic polarization curves for iron in 1M LiOH at 200°C are presented in Fig. 9. Polarization experiments from the stable corrosion potential at −1250 mV were carried out as follows: the electrode was first held potentiostatically at −1700 mV for 10 min to reduce any oxide on the metal surface and to provide a reproducible initial state. The potentiostat was then turned off and the potential allowed to decay for a preselected time before determining the current/voltage curve for the electrode. The potential first decayed rapidly to −1420 ± 10 mV and held this value for a time which depended on the previous history of the autoclave as described earlier. This was followed by a rapid decay to −1250 mV. The polarization curves were obtained by increasing the current (galvanostatic) or potential (potentiostatic) in increments of 0.05 mA or 50 mV, respectively, every 2 min. In both experiments it was found that the potential and current, respectively, changed only very slightly after 2 min at each setting. Thus, the polarization experiments were performed under very nearly steady-state conditions. Potentiostatic polarizations were carried out 1, 19, and 47 hr after cathodic pretreatment of the electrode. No reproducible dependence of the current/voltage curves on the time between initial cathodic treatment and the start of polarization was noted (Fig. 9). Galvanostatic polarization from −1250 mV was performed 1 hr after cathodic pretreatment of the electrode. Both the potentiostatic and galvanostatic polarization experiments initiated at −1250 mV exhibit a typical active to passive transition at −600 mV, *i.e.*, the same potential as the small arrest (E_7) on cathodic charging. Further, the active region exhibited considerable fluctuations in current and potential and this phenomenon became more pronounced as the potential approached −600 mV. This is precisely the potential region where similar fluctuations are exhibited in cyclic voltammetry and anodic charging studies.

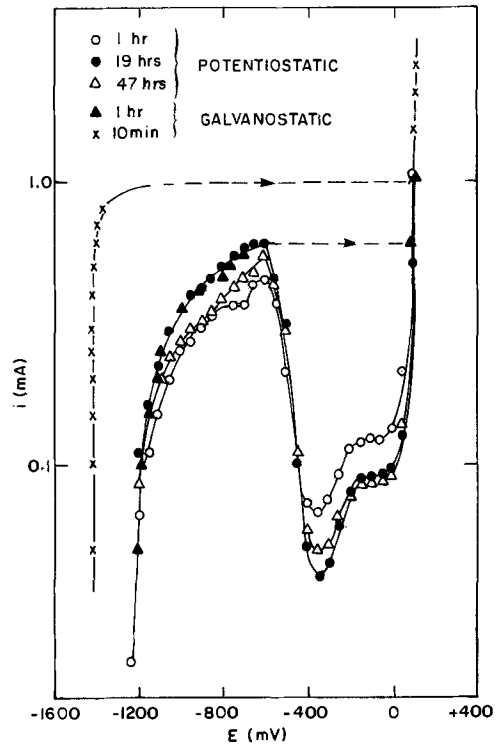

Fig. 9. Steady-state galvanostatic and potentiostatic polarization curves for iron in 1M LiOH at 200°C.

Galvanostatic polarization from the metastable corrosion potential of −1420 ± 10 mV was carried out 10 min after cathodic pretreatment of the electrode. The potential at first changed very slowly until the current was increased to 1 mA. At this point the potential drifted rapidly to oxygen evolution. An attempt was made to obtain a potentiostatic polarization curve from −1420 mV. However, at any potential between −1420 and −1250 mV the current decreased continuously to very small values and no steady-state potentiostatic curve could be obtained in this region.

Discussion

Room temperature study.—A number of previous studies on the behavior of iron in alkaline solution at room temperature have been reported (18, 21-26). Attempts have been made to identify the surface oxides using x-ray and electron diffraction (22-25) and electrochemical methods (18, 21, 26), principally by comparing potential arrests obtained on galvanostatic charging with equilibrium potentials calculated from thermodynamic data (27). These studies have reported the existence of $Fe(OH)_2$, Fe_3O_4, γ-Fe_2O_3, and γ-$Fe_2O_3 \cdot H_2O$ on iron surfaces which have been exposed to highly alkaline solutions.

The cyclic voltammetry and galvanostatic charging studies reported here show that two charge transfer processes occur on iron in 1M LiOH at 22°C between hydrogen and oxygen evolution. Further, the dependence of peak potential on sweep rate, and the large potential differences between the anodic and cathodic peaks, suggests that the charge transfer processes are

quite irreversible and significant overpotentials are required to oxidize or reduce the compounds on the metal surface. Since overpotentials are not included in equilibrium potentials calculated from thermodynamic data there is every reason to expect that experimentally observed potential arrests in charging studies or current peaks in cyclic voltammetry will differ from the calculated values. However, the overpotential ($E - E_o$), where E_o is the equilibrium potential, is positive and negative for anodic and cathodic processes, respectively. Thus, the conjugate oxidation/reduction processes must satisfy the following inequality

$$E_a > E_o > E_c \qquad [B]$$

where E_a and E_c are the potentials at which the potential arrests or current peaks occur on oxidation and reduction.

The first charge transfer process, which gives rise to peaks I and V, is probably the oxidation of iron to $Fe(OH)_2$

$$Fe + 2\,OH^- = Fe(OH)_2 + 2e^- \qquad [1]$$

The equilibrium potential for this reaction at pH = 4 is −1490 mV which satisfies inequality [B] since E_a and E_c are −1470 and −1650 mV, respectively. The $Fe(OH)_2$ is then oxidized to magnetite (reaction [2]) resulting in peak II

$$3Fe(OH)_2 + 2\,OH^- = Fe_3O_4 + 4H_2O + 2e^- \qquad [2]$$

The equilibrium potential for this reaction is −1640 mV which suggests that considerable overpotential is required for the forward process, *i.e.*, reaction [2] represents a highly irreversible process. The above scheme accounts for the similar response of peaks I and II (consecutive reactions) to repetitive sweeping and is consistent with previous findings that $Fe(OH)_2$ (26) or both $Fe(OH)_2$ and Fe_3O_4 (22) are the initial oxidation products formed on iron in alkaline solution at room temperature.

The third charge transfer process results in peaks III and IV at −1150 mV (E_a) and −1480 mV (E_c), respectively. Further, the charge consumed at these peaks increased on repetitive sweeping, while that consumed at peaks I, II, and III decreased. This indicates that the products initially formed on the surface at peaks I and II are not major precursors for the oxidation which takes place at peak III, *i.e.*, the charge transfer processes responsible for peaks I and II and for peak III occur in parallel and not consecutively as is apparently the case for peaks I and II. Thus, it is reasonable to conclude that peak III arises from the direct oxidation of metallic iron. Electron diffraction (23-25) studies have indicated that γ-Fe_2O_3 forms spontaneously on iron in alkaline solution. The equilibrium potential for reaction [3]

$$2Fe + 6\,OH^- = \gamma\text{-}Fe_2O_3 + 3H_2O + 6e^- \qquad [3]$$

was calculated from the free energy data of Wicks and Block (28) and found to be 1450 mV. This value barely satisfies Eq. [B]. However, reactions [1]-[3] all consume hydroxyl ions. Thus, the concentration of OH^- close to the electrode surface will be less than in the bulk solution and the equilibrium potential for reaction [3] will become more positive by 59 mV/pH unit (27). Alternatively, peaks III and IV may be due to the formation of ferric hydroxide, $Fe(OH)_3$, at the metal surface

$$Fe + 3\,OH^- = Fe(OH)_3 + 3e^- \qquad [4]$$

Reaction [4] has an equilibrium potential at pH = 14 of −1380 mV (27) which therefore satisfies Eq. [B]. The ferric hydroxide may then transform to γ-Fe_2O_3 during or prior to electron diffraction examination (29)

$$2Fe(OH)_3 = \gamma\text{-}Fe_2O_3 + 3H_2O \qquad [5]$$

Since no crystalline phase of ferric hydroxide appears to exist (30), it would not be detected on the electrode surface by diffraction techniques.

High-temperature study.—The electrochemical studies reported here on the behavior of iron in 1M LiOH at 200°C demonstrate that iron will adopt one of two corrosion potentials depending on the previous history of the autoclave. With a "clean" autoclave the iron electrode adopts a corrosion potential of −1420 ± 10 mV. However as soon as the autoclave walls become covered with iron oxide the corrosion potential drops suddenly to −1250 mV. The galvanostatic and potentiostatic polarization studies reported in this work show that iron corrodes in an active mode at both corrosion potentials. The sudden drop in potential from −1420 to −1250 mV appears to coincide with the nucleation and growth of octahedral crystals on the base oxide layer on the metal surface.

Thermodynamic calculations (31) show that the stable ionic species in alkaline solutions at 200°C is the dihypoferrite ion, $HFeO_2^-$, and it seems reasonable to assume that the anodic reactions in the active corrosion states at −1420 and −1250 mV involve this species. Further, previous studies (4, 17, 32) have shown that the oxide formed on iron and carbon steel under similar conditions is magnetite, Fe_3O_4, with the possible inclusion of a small amount of $LiFeO_2$ (4). We have found that both Fe_3O_4 and $LiFeO_2$ crystals nucleate and grow on platinum in 1M LiOH at 285°C in the presence of a corroding carbon steel surface (33). These crystals were found to have a similar morphology to the crystals which form the "upper layer" on the corroded steel surface. Accordingly, the following set of reactions is proposed to account for the anodic and corrosion behavior of iron and carbon steel in 1M LiOH solution at elevated temperatures

$$Fe + 3\,OH^- \rightarrow HFeO_2^- + H_2O + 2e^- \qquad [6]$$

$$3Fe + 8\,OH^- \rightarrow Fe_3O_4 + 4H_2O + 8e^- \qquad [7]$$

$$3HFeO_2^- \rightarrow Fe_3O_4 + H_2O + OH^- + 2e^- \qquad [8]$$

$$Li^+ + HFeO_2^- \rightarrow LiFeO_2 + H^+ + e^- \qquad [9]$$

Townsend (31) has recently shown that as the potential of iron is increased anodically it becomes thermodynamically possible for reactions [6], [7], and [8] to occur in the order listed above.

On galvanostatic polarization from −1420 mV iron first dissolves as the ion $HFeO_2^-$ with the concurrent formation of magnetite on the surface by the direct oxidation of the metal according to reaction [7]. The oxide layer produced corresponds to the base film observed by scanning electron microscopy. The proposed origin of the layer is consistent with the previous observation (13, 17) that the film is formed by the metal/oxide interface receding into the metal phase. Marker experiments (13, 17) have shown that this oxide layer is formed with zero volume change from the original metal. Since the number of iron atoms per unit volume is less in magnetite than in metallic iron the excess iron must leave the oxide. This occurs by dissolution of iron through pores in the oxide layer according to reaction [6]. Further galvanostatic polarization from −1420 mV (Fig. 9) causes increased blocking of the metal surface by magnetite and the potential of the electrode shifts slightly in the anodic direction. At a total current of about 1 mA reactions [6] and [7] are no longer able to consume the charge being forced across the interface and the potential shifts rapidly to oxygen evolution at + 100 mV. The gradual blocking of the freely corroding surface by magnetite is supported by the potential behavior of the electrode during arrest E_6 on anodic charge (Fig. 8). Thus, at the start of the arrest (−1430 mV) the potential increases smoothly but as the amount of charge passed increases the potential becomes unstable. Since the potential is determined partly by the

current density due to reaction [6], fluctuation in the area available for free dissolution due to the increasing formation of magnetite on the surface would produce the observed fluctuations in potential.

The processes described above also account for the active dissolution behavior on polarizing the electrode from the stable corrosion potential of −1250 mV. However, the electrode surface is now essentially covered with magnetite and free dissolution of metal is restricted to intergranular pores in the base oxide film. Thus, the potential fluctuations exhibited on anodic charging (Fig. 8) from −1430 to −1250 mV continue to −600 mV and the erratic current fluctuations observed on potentiostatic polarization (Fig. 9) occur over the same range of potential. Since the porosity of the base film is now quite low [10-15% (17)], the current density due to free dissolution will be high. This leads to the concentration overpotential effects exhibited by both the potentiostatic and galvanostatic curves above a total current of 0.1 mA (Fig. 9). Further polarization results in an active to passive transition at −600 mV after which the potential on galvanostatic polarization drifts rapidly to oxygen evolution and the current on potentiostatic polarization drops sharply to less than 0.1 mA. Although no clearly defined potential arrest occurs at −600 mV on anodic charging (Fig. 8), a small one does exist at −650 mV on cathodic charging from the passive state at 0.1 mA. The amount of charge passed during this arrest is small and probably much less than is required to convert all of the oxide on the metal surface to another oxidation state. However, in order to passivate the electrode it would only be necessary to produce an oxide [possibly α-Fe_2O_3 or a lithium iron spinel oxide (4)] impervious to free dissolution at the base of the pores and the amount of charge required would be small. It is interesting to note that the total charge consumed on oxidizing the electrode is considerably greater than that required to reduce it back to the original potential (Fig. 8). The difference in charge is accounted for by dissolution since the product of this process (reaction [6]) diffuses away from the electrode surface and will not be reduced on cathodic polarization.

The shift in corrosion potential from −1420 to −1250 mV, which appears to coincide with nucleation and growth of the octahedral crystals on the base layer, can be accounted for by electrocrystallization of $HFeO_2^-$ to form Fe_3O_4 and $LiFeO_2$ (*i.e.*, reactions [8] and [9], respectively) exerting partial control over the corrosion potential. Evidence for the nucleating and growth of these crystals from solution has been assembled by Castle *et al.* (15, 34). Additional evidence has been obtained in this laboratory (33) including the observation of growth steps (Fig. 10) on the faces of crystals grown on iron and carbon steel in 1M LiOH at 200°C. The potential dependence of the origin of the octahedral crystals was illustrated experimentally by potentiostating an iron electrode at −1400 mV for 24 hr at 200°C. Examination of the surface did not reveal any "upper layer" oxide crystals even though the conditions chosen were such that nucleation would have occurred in a few minutes on open circuit. Instead, a single layer of oxide was formed and was considerably thicker than the base layer produced on free corrosion. However, the potential was controlled slightly anodic to the metastable corrosion potential at −1420 ± 10 mV and a small anodic current (~ 0.02 mA) was passed for the duration of the experiment. The increased thickness of the oxide layer probably results from the partial consumption of this charge by reaction [7].

Finally, we have observed that if the corrosion tests are performed in a "clean" autoclave a single layer oxide film is first produced but as soon as the autoclave walls become covered with corrosion products then octahedral crystals nucleate on the base oxide

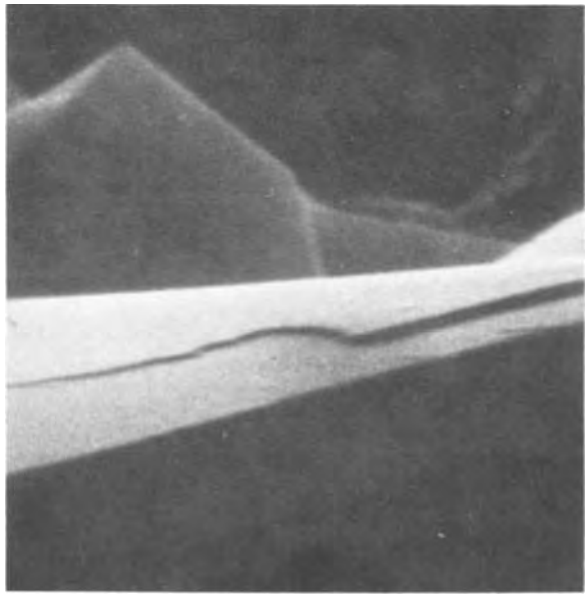

Fig. 10. Growth step on the face of an "upper layer" octahedral crystal grown on carbon steel in 1M LiOH at 200°C for 24 hr (×18,000).

layer and the corrosion potential shifts from −1420 to −1250 mV. This suggests the existence of a source/sink relationship between the corroding electrode and the autoclave walls. Thus, when a freshly cleaned autoclave is used the flux of $HFeO_2^-$ from the electrode to the autoclave walls is sufficiently large that the concentration of this species at the base layer/solution interface does not exceed the value necessary to nucleate the octahedral crystals. However, when the autoclave walls become covered with corrosion products the sink for $HFeO_2^-$ no longer exists and the concentration of this species in the bulk solution quickly increases to the value necessary for nucleation on the corroding surface. However, iron metal is thermodynamically less stable than magnetite (and most likely $LiFeO_2$) so the concentration of $HFeO_2^-$ derived from reaction [6] at the electrode surface will be greater than the equilibrium values for reactions [8] and [9]. At this point the nucleation and growth of the octahedral crystals on the corroding surface becomes thermodynamically possible.

Manuscript submitted April 24, 1972; revised manuscript received Sept. 18, 1972.

Any discussion of this paper will appear in a Discussion Section to be published in the December 1973 JOURNAL.

REFERENCES

1. M. C. Bloom, W. A. Fraser, and M. Krulfeld, *Corrosion*, **8**, 401t (1962).
2. M. C. Bloom, M. Krulfeld, and W. A. Fraser, *ibid.*, **19**, 327t (1963).
3. O. Asai and N. Kawashima, Extended Abstracts, 4th Int. Conf. on Metallic Corrosion, Amsterdam, 1969, National Association of Corrosion Engineers, Houston, Texas, p. 126 (1969).
4. R. L. Jones and E. W. Steinkuller, *Corrosion*, **27**, 353 (1971).
5. M. W. Breiter, *J. Phys. Chem.*, **69**, 901 (1965).
6. G. J. Bignold, *Corrosion Sci.*, **12**, 145 (1972).
7. E. Brauer and B. Teusdier, *Z. Physik. Chem. Frankfurt*, **65**, 216 (1969).
8. J. S. Mayell and W. A. Barber, *This Journal*, **116**, 1333 (1969).
9. J. P. Carr and N. A. Hampson, ibid., **118**, 1262 (1971).
10. J. Postlethwaite, *Electrochim. Acta*, **12**, 333 (1967).
11. D. de. Jones and H. C. Masterton, *Advances in Corrosion Sci. Technol.*, **1**, 1 (1970).
12. V. G. Levich, "Physicochemical Hydrodynamics," Prentice-Hall, Inc., Englewood Cliffs, N. J. (1962).

13. E. C. Potter and G. M. W. Mann, Proc. 1st. Inter. Conf. on Metallic Corr., London, p. 417 (1961).
14. J. B. Moore, Jr. and R. L. Jones, *This Journal*, **116**, 1080 (1969).
15. J. E. Castle and G. M. W. Mann, *Corrosion Sci.*, **6**, 253 (1966).
16. J. B. Moore, Jr. and R. L. Jones, *This Journal*, **115**, 576 (1968).
17. E. M. Field, R. C. Stanley, A. M. Adams, and D. R. Holmes, Proc. 2nd Inter. Conf. on Metallic Corr., New York, p. 829 (1963).
18. S. Asakura and K. Nobe, *This Journal*, **118**, 536 (1971).
19. D. C. Grahame, *Chem. Rev.*, **41**, 441 (1947).
20. P. Delahay, "New Instrumental Methods in Electrochemistry," Interscience Publishers Inc., New York (1954).
21. A. M. Sukhotin and K. M. Kartashova, *Corrosion Sci.*, **5**, 393 (1965).
22. A. J. Salkind, C. N. Venuto, and S. U. Falk, *This Journal*, **111**, 493 (1964).
23. J. E. O. Mayne, J. W. Menter, and M. J. Pryor, *J. Chem. Soc.*, **1950**, 3229.
24. J. E. O. Mayne and J. W. Menter, *ibid.*, **1954**, 99.
25. C. L. Foley, J. Kruger, and C. J. Brechtoldt, *This Journal*, **114**, 994 (1967).
26. B. Kabanov, R. Burstein, and A. Frumkin, *Discussions Faraday Soc.*, **1**, 259 (1947).
27. M. Pourbaix, "Atlas of Electrochemical Equilibria," Pergamon Press, London (1964).
28. C. E. Wicks and F. E. Block, U. S. Bur. Mines, Bull. 605 (1963).
29. T. V. Solenko, M. M. Gol'dman, and E. U. Daulbaev, *Tr. Inst. Met. i Obogashch., Akad. Nauk Kaz. SSR*, **16**, 40 (1966); Chem. Abstr. 66:119346v.
30. J. D. Bernal, D. R. Dasgupta, and A. L. Mackay, *Clay Minerals Bull.*, **4**, 15 (1959).
31. H. E. Townsend, *Corrosion Sci.*, **10**, 343 (1970).
32. R. L. Jones, L. W. Strattan, and E. D. Osgood, *Corrosion*, **26**, 399 (1970).
33. D. D. Macdonald and T. E. Rummery, Submitted to *Corrosion Sci.* (1973).
34. J. E. Castle and H. G. Masterson, *Corrosion Sci.*, **6**, 93 (1966).

Measurement of Zincate Permeation in a Polyethylene Battery Separator with Controlled External Hydrodynamic Conditions

Mitchell Litt, Leonard Nanis,* and Joseph L.-P. Chen[1]

Department of Chemical Engineering, School of Engineering and Applied Science, University of Pennsylvania, Philadelphia, Pennsylvania 19104

ABSTRACT

A rotating disk geometry has been used to characterize solution-side transport resistance in measurements of zincate permeation in Ag-Zn battery separator material. The apparent diffusivity of zincate was 1.2×10^{-7} cm^2 sec^{-1} at 25°C in a polyethylene, acrylic acid grafted and divinylbenzene cross-linked membrane, and was independent of zincate concentration up to 0.57M ZnO in 40% KOH. In the temperature range 11°-27°C, the activation energy for diffusion of zincate in the membrane is 6.1 kcal/mol.

The alkaline silver-zinc secondary battery is of considerable interest for space and other applications because of its potentially high energy output per unit weight and volume. Broader application of this battery has been limited because of limited cycle life. Development of a battery separator which will improve the performance and life of alkaline cells has been and continues to be the focus of concerted efforts in polymer science, in both formulation and production of new materials.

The characterization of separator performance includes the important factor of permeability of the membrane to electrolyte ion constituents. The permeability, in turn, reflects the diffusivity of ionic species through the membrane matrix and any interaction between permeant and membrane. In conjunction with measurements such as electrical conductivity and porosity determination, the effective ionic diffusivity can ultimately be used to correlate membrane microstructure and battery performance. Measurement of membrane permeability requires knowledge of permeant ion concentration at both sides of the membrane in the membrane phase, as well as the flux through the membrane, from which effective diffusivity can be calculated from knowledge of membrane thickness. Unfortunately, these membrane concentrations are not available from direct measurement, and concentration in the bulk solution on either side of the membrane are used, requiring an accounting of transport resistance effects caused by depletion of diffusant in a solution-side boundary layer adjacent to the membrane surface. For the usual two-compartment arrangement, the membrane is properly considered as a transport resistance in series with two solution-side film resistances. Clearly, the ideal situation is one in which the solution-side resistances are negligible in comparison with the diffusion rate control provided by the membrane. Unless this is known *a priori*, however, considerable error may be introduced by neglecting the boundary layer resistances, particularly in the very viscous solutions characteristic of battery electrolytes. Furthermore, as the goal of more permeable separator materials is approached, the effect of boundary layer resistances becomes increasingly important.

Techniques for the measurement of the diffusion of electrolyte constituents through membranes have been discussed by Harris, Dirkse, and Lander in separate chapters of a compilation of screening methods for alkaline silver-zinc battery separators (1). Each of the three methods for diffusion measurements considers essentially a two-compartment cell separated by the membrane. Two of the three arrangements provided for rapid stirring on the dilute side with no stirring in the concentrated solution compartment, while the third method provided for no stirring whatever. The lack of definition of the mass transport conditions in the liquid immediately adjacent to the membrane is undesirable, since the truly fundamental parameter of importance is the apparent diffusivity of a particular ion in the separator. Stirring, *per se*, cannot be assumed to remove the liquid resistances, unless repeated runs at several stirring rates show no effect

* Electrochemical Society Active Member.
[1] Present address: Westinghouse Electric Corporation, Pittsburgh, Pennsylvania 15200.
Key words: zincate, diffusivity, permeation, membrane, rotating disk, mass transfer resistance.

on ion flux. A classical technique in chemical engineering to determine such parameters is the Wilson plot (2), which is usually found in the heat transfer literature. An application of this method to membrane permeability was made by Leonard and Bluemle (3) for artificial kidney dialysis membranes. Their data showed that even with rapid stirring in aqueous solution, the boundary layer resistances were not negligible. To our knowledge, no application of this technique to battery membranes has been made. The method requires quite lengthy determinations, since repeated runs at many stirring rates must be made. Furthermore, in order to properly characterize membrane behavior, the apparent diffusivity should be measured over a temperature range in order to obtain an estimate for the activation energy. By comparison of such membrane results with the free liquid diffusivity and activation energy, valuable insights may be derived concerning the nature of ion-membrane chemical interaction, if any.

A second approach, which has been used in the present investigation, is to adopt a configuration for the permeation cell in which the boundary layer resistances are known *a priori* or measured in a separate experiment. The membrane permeability can then be calculated by subtracting the solution-side resistances from the over-all resistance which includes the membrane. The geometry used here is that of a membrane which rotates at a fixed speed while simultaneously serving as a divider between two compartments. For this rotating disk geometry, the film resistance may be computed from a knowledge of the membrane disk radius, the rotational speed, and the solution viscosity. In addition, the free liquid diffusivity of the ion should be known. Using such an apparatus, we have investigated the permeation of zincate ion in 40% KOH solution through a polyethylene membrane. The membrane material, designated as SWRI-GX, was manufactured by the Southwest Research Institute for the Jet Propulsion Laboratory. It is polyethylene, grafted with acrylic acid, and cross-linked with divinylbenzene.

Experimental

Permeation cell.—The apparatus has been adopted from that used by Litt and Smith (4) to study sodium chloride permeation through ion-exchange membranes. In a preliminary study, Smith (5), using a "membrane" of solid benzoic acid, showed that the rotating membrane seal conformed quite closely to the prediction of mass transfer theory for this geometry, after making suitable allowance for edge effects. The technique was successful in separating boundary layer from membrane resistances and in determining interactions between membrane and diffusant from temperature determinations.

For the present study of zincate ion permeation in polyethylene, the two-compartment cell with rotating membrane used by Smith and Litt (4) was modified slightly for compatibility with concentrated caustic solutions. The apparatus is shown in cross section in Fig. 1. The membrane support is machined of polymethyl methacrylate (Lucite) with a removable center section (B and B') which holds the membrane (A). A Lucite ring (C) screws flush against the surface of B to clamp the membrane tightly, so that the exposed diameter of membrane is exactly 1 in. An "O" ring seals the membrane against leaks. An aluminum ring gear (D), machined from a standard timing belt gear, is glued with epoxy to the outer surface of the membrane holder. The gear was first coated with Kymar, an alkali-impervious vinylidene fluoride resin, to protect the gear in case of leaks.

The membrane holder seals to the faces of the Lucite support (E) with neoprene "O" rings (F). During runs, the "O" rings are lubricated with Dow Corning FS1281 lubricant to provide smooth rotation. Dow Corning 111 lubricant was used as sealer for the plastic components. Pressure of the rotating membrane against the "O" rings is provided by a fixed ring (G). Two Lucite chambers with volumes of 259 (H) and 295 (J) ml, respectively, form the solution compartments, which are held to the center support (E) with flanges and gaskets. Each compartment is internally jacketed (not shown) for temperature control of the bulk electrolyte by water pumped from a constant temperature bath. A separate jacket adjacent to the "O" ring seal was used to maintain constant temperature and to remove frictional heat in the vicinity of the membrane (not shown). Each electrolyte compartment was also provided with a nylon stirrer (K) to maintain bulk concentration constant when taking samples and adding electrolyte. The main rotor assembly was turned by a variable speed 0-3600 Servotek motor and Boston gear 25:1 speed reducer coupled to the ring gear (D) by a timing belt. With this apparatus, speeds up to 25 rpm could be maintained with smooth operation, with temperatures maintained constant to ±0.5°C. Chromel-Alumel thermocouples were used to monitor temperature, using a Keithley Model 160 digital voltmeter.

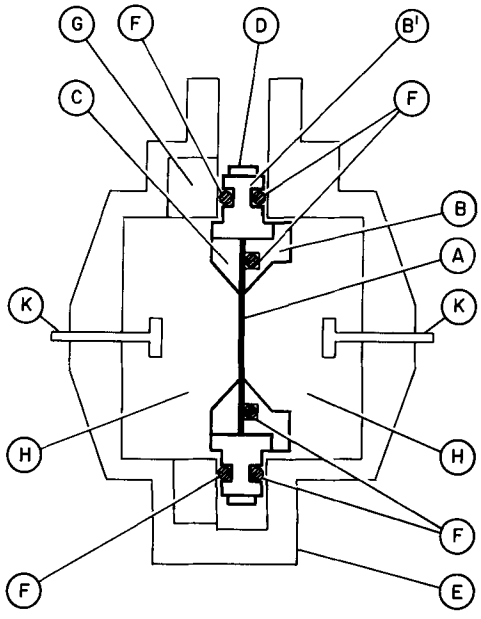

Fig. 1. Schematic arrangement of rotating permeation cell

Procedure.—Membranes were presoaked in 40% KOH solution for 24 hr prior to use. After clamping of the membrane in the holder (B), both chambers were filled with 40% KOH, and the membrane was set to rotate at a speed of 21.5 rpm. An impulse response technique for step changes in the concentrated solution compartment was used to decrease the number of separate runs needed to evaluate a given membrane. The permeation of zincate into the dilute compartment was monitored by analysis of discrete samples removed at regular intervals. At the start of a typical run, a step change of zinc concentration was introduced into the concentrated compartment (H, henceforth called compartment 1) by withdrawing a 100 ml sample of solution and simultaneously replacing the same volume of 0.8M ZnO in 40% KOH. The stirrers (K) were activated for 1 min to promote uniform mixing.

For a given concentration in compartment 1, permeation was allowed to proceed for 30 min. Samples of 1 ml were taken from compartment 2 at 2-min intervals (started from zero time) in the first 6 min and and then at intervals of 5 min for the rest of the run. One milliliter of 40% KOH was replaced for each sample removed from compartment 2 to maintain a constant chamber volume. At the end of 30 min, a second concentration step in compartment 1 was accomplished by removal of a 100 ml volume rapidly followed by replacement with another 100 ml volume of 0.8M ZnO-40% KOH to provide a second step rapid change. A third step was similarly accomplished.

Samples (1 ml) were also taken from compartment 1 in order to monitor the step change of concentration. For each temperature studied, permeabilities were examined for the three zincate concentration steps in a single run, provided that no leakage had occurred and that the continuously monitored temperature was in control within ±0.5°C from the set value. The absence of leaks was verified at the end of a run by the absence of coloration in compartment 2 following the addition of a few drops of methylene blue to side 1. The step changes in side 1 and resulting changes in compartment 2 are shown in Fig. 2 for a typical run at 21.5°C.

Zincate analysis.—A Varian AA-120 atomic absorption spectrophotometer was used for analysis of zinc concentration. For calibration with known concentrations and for use with actual samples, a neutralization procedure was followed to prevent attack of the titanium burner slit by hot alkali. The 1 ml samples were added to 19 ml of 2.4% nitric acid and were well mixed, neutralizing the alkali and reducing the viscosity of the resulting solution, thus avoiding attack and clogging of the AA-120 burner slit. The 20-fold dilution of the zinc was still well within the sensitivity of the analysis. To further reduce analytical error, at least three aliquots of the diluted sample were sprayed into the machine consecutively, with the absorption signal monitored continuously on a strip-chart recorder. The average value of the three readings was then used to determine Zn concentration by comparison with a standard calibration curve. A new calibration was prepared for each series of determinations to compensate for changes in lamp and flame conditions. Calibration curves of absorption *vs.* concentration were linear, facilitating interpolation.

Measurement of membrane thickness.—The wet membrane thickness is of importance in determining the steady-state concentration gradient and thus the permeation flux. A simple microscope method was used to determine the thickness of a wet, swollen membrane without actual contact. A piece of optically flat glass marked with black ink on both sides was used to calibrate the microscope height measurement. By focusing the microscope on the bottom and top surfaces of the glass plate, a scale reading was measured corresponding to the thickness of the glass plate (measured by micrometer to 0.0001 in.). At a magnification of 262.5, ten scale divisions of the height adjustment corresponded to 0.001 in. The dry membrane thickness was measured by micrometer to be 0.0011 in. To measure the thickness of the wet membrane, the microscope was focused alternately on the top surface of the supporting glass plate and on the top surface of the wet membrane placed on the glass plate. The scale difference so obtained indicated that the wet (40% KOH) thickness of the wet membrane was 0.00204 in. at 25°C. The polyethylene GX material is reported to have a typical wet thickness of 0.0014 in. when measured by contacting methods which may cause compression of the wet membrane. Accordingly, the present computations of diffusivity are based on the optically determined wet thickness as a truly representative parameter.

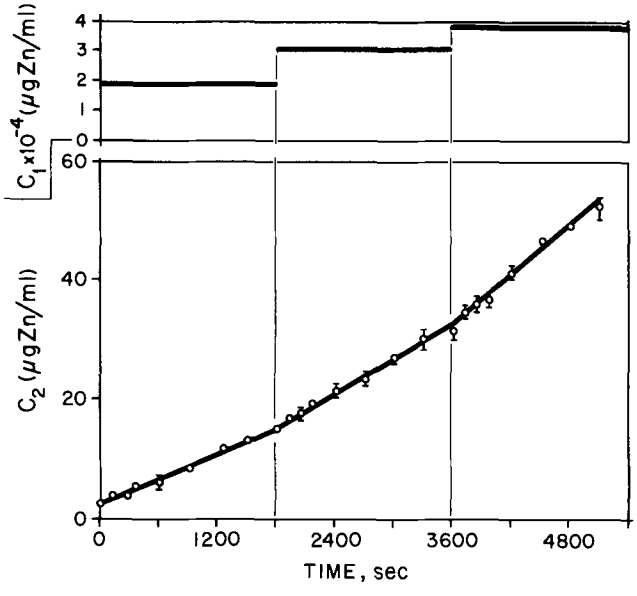

Fig. 2. Concentration *vs.* time for permeation at 21.5°C

In order to determine any effect of zincate concentration on wet thickness, measurements were made on membranes soaked for at least 24 hr at 25°C in 0.2M ZnO-40% KOH, 0.4M ZnO-40% KOH, and 0.6M ZnO-40% KOH. No change in the thickness of the membrane was detected over this concentration range. This result is fortunate, since it implies that there will be no unequal expansion of a membrane which has a concentration gradient of zincate ion during active permeation in the apparatus. Also, the thickness of both the dry and the wet membrane does not measurably change with temperature, as determined at 16°, 25°, and 28°C.

Results

In general, if two well-mixed chambers with the concentration of a permeant species in the first compartment much greater than that in the second compartment are separated by a membrane, the concentration of permeant in the second chamber will increase with time. After an initial unsteady-state period during which the concentration gradient within the membrane is established, a steady-state, or rather, pseudosteady-state period will ensue and last as long as the concentration in the first chamber is much greater than that in the second. This was found to be the case in all runs, as indicated by a linear increase of side 2 zincate concentration with time. Therefore, depletion of side 1 is of no concern. The maximum concentration of zincate in side 2 at the end of a run is still three orders of magnitude less than the concentration in side 1, so that virtually constant boundary conditions at either side of the membrane are assured. Thus, the rate of change of zincate in the second chamber (side 2) is given by

$$\frac{V_2 dc_2}{dt} = KA(c_1 - c_2) \qquad [1]$$

where c_1 = zincate concentration, mol cm^{-3}, in chamber with volume V_1 (side 1); c_2 = zincate concentration, mol cm^{-3}, in chamber with volume V_2 (side 2); K = over-all permeability, including resistance of membrane and boundary layers on either side, cm sec^{-1}; and A = membrane area, cm^2. The factor K includes the effective diffusivity and wet thickness plus similar terms for the solution resistances. No detailed information is needed for the actual zincate concentration just at the membrane surfaces. Since the flux is identical through each region, *i.e.*, boundary layer in side 1, membrane and side 2 boundary layer, Eq. [1] considers the net driving force as the concentration difference ($c_1 - c_2$) across the three transport resistance regions in series. Equation [1] may be further simplified, because $c_2 << c_1$ at all times and for all experiments reported here. Also, dc_2/dt is essentially constant, so that Eq. [1] becomes, solving for K

$$K = \frac{V_2 \dfrac{dc_2}{dt}}{Ac_{10}} \qquad [2]$$

where c_{10} is the concentration in compartment 1 after introduction of the step, and dc_2/dt is obtained as the slope of a regression line fitted to the data, after correcting for the volume changes involved in taking samples. Correlation coefficients for the slopes were all better than 0.99, indicating excellent fit. Values of K for the three different temperatures and concentrations

Table I. Membrane transport parameters

T, °C	$c_{10} \times 10^{-4}$,* μg Zn/ml	$K \times 10^5$, cm/sec	$K_m \times 10^5$,** cm/sec	D_m,† cm²/sec × 10^8
11	2.45	1.321 ± 0.016‡	1.405	7.28
17	1.845	1.953 ± 0.041	2.149	11.15
17	2.793	1.739 ± 0.043	1.889	9.80
17	3.52	2.077 ± 0.089	2.295	11.90
21.5	1.868	1.929 ± 0.073	2.114	11.05
21.5	3.06	1.706 ± 0.073	1.850	9.60
21.5	3.75	1.880 ± 0.173	2.058	10.80
27	1.868	2.376 ± 0.066	2.653	13.85
27	3.06	2.338 ± 0.250	2.618	13.60

* A concentration of 2.45 × 10^4 μg Zn/ml corresponds to 0.375M ZnO.
** K_m = Permeation coefficient of zincate through membrane.
† D_m = Diffusion coefficient of zincate through membrane.
‡ Range calculated for 95% confidence limits of slope of regression line.

of zincate are given in Table I. A separate membrane sample was used for each temperature.

Calculation of membrane permeability.—The overall coefficient K in Eq. [2] is related to the membrane permeability by the relation

$$1/K = 1/K_m + 1/K_{b1} + 1/K_{b2} \quad [3]$$

where K_m is the membrane permeability and K_b is the mass transfer coefficient in the boundary layer on either side of the membrane.

The rotating disk system has permitted theoretical prediction of the mass transfer coefficient, K_b, in the fluid adjacent to the membrane, if the dimensions of the system, rotational speed of the disk, and fluid properties are known (5). The mass transfer correlation is given in terms of the dimensionless Reynolds, Sherwood, and Schmidt numbers as

$$Sh = 0.544\ Re^{1/2}\ Sc^{1/3} \quad [4]$$

where $Sh = K_b r/D$; $Re = r^2\omega/\nu$; $Sc = \nu/D$; K_b = mass transfer coefficient through the boundary layer, cm sec^{-1}; r = radius, cm; D = diffusivity of zincate in liquid, cm² sec^{-1}; ω = rotational speed, sec^{-1}; and ν = kinematic viscosity, cm² sec^{-1}.

The numerical coefficient 0.544 in Eq. [4] differs slightly from that for a rotating disk in an infinite medium (0.662) because of edge effects, and is based on the work of Smith (5).

In order to precalculate the mass transfer coefficient, K_b, for zincate in the boundary layer, the following property values were used. The density and viscosity of the KOH-H_2O system at temperatures of 25° and 75°C have been reported by Klochko and Godneva (6). Dirkse (7) has reported the density and viscosity of saturated solutions of ZnO in aqueous KOH at 25°C. Using these sparse data for the properties of ZnO/KOH-H_2O solutions, and assuming that the density and viscosity vary linearly with the content of zinc in the aqueous KOH solution and, further, that they do not change very much in the temperature range of 11°-27°C, it is possible to apply Eq. [4]. For obtaining K_b from the Sherwood number, the value of 5.3 × 10^{-6} cm² sec^{-1} for the diffusivity of zincate ion was used as found by Lu (8) using a rotating disk method with 0.25M ZnO-23.4% KOH at 23°C. The value 5.1 × 10^{-6} cm² sec^{-1} at 25°C is used for the present calculation of the mass transfer coefficient by adjusting Lu's result for the viscosity of the 40% KOH solution. For the temperature range 11°-27°C and for the three zincate step concentrations up to 0.57M ZnO in 40% KOH, solution density was essentially constant, ranging from 1.42 to 1.45 g cm^{-3} depending on temperature and zincate concentration. Likewise, the kinematic viscosity was estimated to range from 0.0307 cm² sec^{-1} at 17°C for 0.27M ZnO in 40% KOH to 0.0344 cm² sec^{-1} at 0.57M ZnO in 40% KOH. Because Eq. [4] involves fractional powers of the Schmidt and Reynolds numbers, the variations in properties such as viscosity and density over the range of temperature and zincate concentrations studied are not greatly significant. Accordingly, the term $Re^{1/2}$ varies from 10.7 (at 11°C, 0.27M ZnO) to 10.2 (at 27°C, 0.57M ZnO). The term $Sc^{1/3}$ varies from 18.4 to 19.0 in the same range. At the rotational speed of 21.5 rpm, the Sherwood number varies even less in this range, from 107 to 105, and the side 1 mass transfer coefficient is taken for all computations as an average value of 4.27 × 10^{-4} cm sec^{-1}. The mass transfer coefficients in side 2 do not vary because the concentration of zinc is so small that the transport properties of 40% KOH were used to compute a value of 4.5 × 10^{-4} cm sec^{-1} for K_{b2}. Although the approximations used here are rough, they are justified given the sparsity of property data, since the values of the solution-side coefficients are roughly twenty times greater than the over-all permeability, so that small errors in K_{b1} and K_{b2} will not greatly influence the calculated values of K_m.

Calculation of membrane permeability.—The permeation coefficient of the membrane can be calculated from the measured over-all permeation coefficient and the mass transfer coefficients (K_{b1} and K_{b2}) through the boundary layers by using Eq. [3]. In the present study, the correction for the liquid boundary layers is a non-negligible 10%. The effective diffusivity can be calculated, therefore, by multiplying the membrane permeation coefficient by the wet membrane thickness. It is understood that the resulting values of effective diffusivity include not only the actual diffusivity of permeant in the membrane matrix, but also any effect of distribution or partition coefficient between the free solution phase concentration and the membrane phase concentration. If such an effect is large, one might expect to find a large dependence of K_m on zincate concentration. Average values of the effective diffusion coefficients for each temperature are shown in the last column of Table I to be on the order of 10^{-7} cm² sec^{-1}. The diffusivity of zincate ion in the membrane is less than the free liquid diffusivity by a factor of about twenty.

Although there is considerable scatter in the results, which is most probably due to using a different membrane sample for each temperature, it is clear that diffusivity of zincate in the membrane increases with increasing temperature, but appears to be independent of zincate concentration over the range used. From the data, the best value of diffusivity activation energy is 6 ± 3 kcal/mol (p = 0.05). Because of the wide confidence interval, no definite statement can be made about permeant-membrane interaction, since the value straddles the range for free liquid diffusivities, and more definite statements will have to await compilation of additional data. If it can be assumed that no permeant-membrane interaction takes place, the reduction in diffusivity can be attributed to reduced area for permeation, or to average pore lengths being increased due to tortuosity in the membrane, or both. A tortuosity factor of 2 would indicate a ten-fold reduction in free permeation cross section, which is of the same order of magnitude reported by Smith (5) for polyethylene and ion exchange membranes. There are no independent data on tortuosity or pore size for the membrane used in this study with which to compare these results. Such data would be extremely useful and will be obtained in future studies.

Summary and Discussion

Effective diffusion coefficients of zincate ion through an acrylic acid grafted and divinylbenzene cross-linked polyethylene membrane in 40% KOH solution were determined as a function of temperature with various zincate concentration gradients across the membrane by using an impulse-response technique on a rotating disk system. This technique permits determination of the diffusion coefficient in a suitably short time on the order of 30 min once the equipment is assembled. Extremely useful features of the method are (*i*) the abil-

ity to precalculate the solution-side transfer resistance, (*ii*) the capability of studying concentration effects for the same membrane, and (*iii*) the capability of studying the same membrane at various temperatures. These features are helpful in characterizing the quality of battery separator material.

There is a scarcity of polyethylene membrane permeation data against which to compare the present results. Lander (1) has determined the permeation rate of zincate ion in 45% KOH solution through a low density polyethylene membrane grafted with acrylic acid at room temperature by using a stationary diffusion cell. From the data, an average permeation coefficient of 2.4×10^{-6} cm sec^{-1} is calculated. This value is about ten times smaller than the present results but is not strictly comparable, since (*i*) the material studied by Lander was cross-linked first and then grafted, and (*ii*) no stirring was provided on side 1. A closer comparison may be made with data obtained by Adams and Harlowe (9) for the typical SWRI produced GX polyethylene used in the present study. They used an arrangement similar to that of Lander (1) but included stirring for both side 1 and side 2 (10). Using the wet thickness reported by Adams and Harlowe (1.4 mil) with their measured (25°C) permeation rate of 2.39×10^{-6} mol cm^{-2} sec^{-1}, the effective diffusivity is 2.2×10^{-8} cm^2 sec^{-1}. Using their permeation rate with the present optically determined wet thickness (2.04 mil), the effective diffusivity is 3.2×10^{-8} cm^2 sec^{-1}, about one-fourth of that reported here, interpolating from the data in Table I for 25°C. This discrepancy may be due partly to solution-side resistances which could not be completely eliminated in the apparatus of Adams and Harlowe. It is unlikely to account for the entire difference, since such a large solution-side resistance in their study would imply a large (1 cm) film thickness, which is improbable given that some stirring is reported to have taken place. The remaining difference is no doubt due to variations in material, even if prepared in a similar manner. Adams and Harlowe report large differences in zincate permeability with small changes in amount of grafting and cross-linking agents, so that differences of the order of magnitude noted would not be unusual.

It is clear, however, that attention should be directed to improved characterization of the solution-side resistances. The presently used disk arrangement has, in addition to known values of K_{b1} and K_{b2}, the advantage of uniform accessibility or constant boundary layer thickness (constant K) over the entire membrane surface (5). Other types of flow cells may also be used to predetermine K_b based on known mass transport geometries such as unidirectional flow in a flat channel past a flat plate (11). Local variations in K_b such as the greater-than-average value at the leading (upstream) edge of a sheet membrane are a minor penalty compared with the great advantage of predictability of K_b.

Acknowledgment

This work was performed for the Jet Propulsion Laboratories, California Institute of Technology, sponsored by the National Aeronautics and Space Administration under Contract NAS7-100. Helpful discussions with Dr. Ralph Lutwack, JPL, are gratefully acknowledged.

Manuscript submitted July 24, 1972; revised manuscript received Oct. 17, 1972.

Any discussion of this paper will appear in a Discussion Section to be published in the December 1973 JOURNAL.

REFERENCES

1. J. E. Cooper and A. Fleischer, Editors, "Characteristics of Separators for Alkaline Silver Oxide Zinc Secondary Batteries," (1965), AD-447301; (a) E. L. Harris, p. 93; (b) T. P. Dirkse, p. 103; (c) J. J. Lander, p. 115.
2. E. E. Wilson, *Trans. Am. Soc. Mech. Engrs.*, **37**, 47 (1915).
3. E. F. Leonard and L. W. Bluemle, *Trans. Am. Soc. Artificial Internal Organs*, **8**, 182 (1962).
4. M. Litt and W. G. Smith, *Science*, **160**, 201 (1968).
5. W. G. Smith, Ph.D. Dissertation, University of Pennsylvania, 1968.
6. M. Klochko and M. Godneva, *Russ. J. Inorg. Chem.*, **4**, 964 (1959).
7. T. P. Dirkse, *This Journal*, **106**, 154 (1959).
8. C. Lu, M.S. Thesis, University of Pennsylvania, 1970.
9. L. M. Adams and W. W. Harlowe, Jr., Southwest Research Institute Final Report, Jet Propulsion Laboratory Contract No. 951718, Proj. No. 01-2015-01, April 1970.
10. L. M. Adams, Personal communication.
11. R. P. deFilippi and R. L. Goldsmith, in "Membrane Science and Technology," p. 33, J. E. Flinn, Editor, Plenum Press, New York (1970).

Phase Equilibria in Lithium-Chalcogen Systems

III. Lithium-Tellurium

P. T. Cunningham, S. A. Johnson, and E. J. Cairns*

Argonne National Laboratory, Chemical Engineering Division, Argonne, Illinois 60439

ABSTRACT

The equilibrium phase diagram of the lithium-tellurium phase system has been investigated. Eutectic points occur at 179.9°C and greater than 99.0 atomic per cent (a/o) lithium, 448.5°C and 35.7 a/o lithium, and 423.1°C and 10.5 a/o lithium. Two intermediate phases, Li_2Te and $LiTe_3$, are present having melting points of 1204.5° and 459.9°C, respectively.

The interest in lithium-chalcogen phase equilibria resulting from development work on high-specific-power, high-specific-energy secondary cells has been outlined in the two previous papers of this series (1, 2). The lithium/tellurium couple is not usually considered as a candidate for such cells because of the weight of tellurium, but the possible use of tellurium as an additive to selenium or sulfur cathodes (3) and the desirability of completing study of the phase equilibria in the lithium-chalcogen series led us to investigate this system.

The lithium-tellurium phase diagram has not been previously reported. The intermediate phase Li_2Te has been prepared in liquid ammonia (4) and by directly combining stoichiometric quantities of the elements in a BeO crucible at 950°C (5). Li_2Te has an antifluorite

* Electrochemical Society Active Member.
Key words: lithium, tellurium, phase equilibria, cathode.

structure with a lattice constant of 6.517 (4). The free energy of formation of Li_2Te at 798°K has been determined by emf measurements to be −77.9 kcal/mol (6).

Experimental

Materials.—The tellurium used was a special high-purity semiconductor grade (99.999+%) obtained from American Smelting and Refining Company, South Plainfield, New Jersey. The lithium was high-purity reactor grade (99.98%) obtained from the Foote Mineral Company, Philadelphia, Pennsylvania. Both elements were used without further purification. Li_2Te was prepared in 1-10g batches using the method previously described for Li_2Se (1) except that the lithium was placed in a tungsten crucible and the final reaction temperature was 650°C. The Li_2Te obtained was generally a light gray color but a large amount was also formed as light yellow translucent crystals. The x-ray powder patterns produced by this material were very sharp and agreed with previously reported data for Li_2Te (4). $LiTe_3$, an intermediate phase found in this study, was prepared in a purified-helium-atmosphere glove box (7) by direct addition of stoichiometric amounts of lithium to molten tellurium contained in a tungsten crucible. The reaction is quite violent and lithium must be added in very small quantities. Samples of various compositions used in subsequent experiments were prepared by mixing Li_2Te with the appropriate terminal phase. Samples were contained in quartz, tungsten, niobium, and graphite depending on the sample composition and maximum temperature of the experiment.

Apparatus and Procedures.—Most of the data were obtained using thermal analysis (heating and cooling curves) and differential thermal analysis (DTA). The apparatus and the procedures used for calibration and data collection have been previously described (1).

A platinum-wound resistance furnace was used in determining the melting point of Li_2Te. The sample was placed in a tungsten crucible and could be observed at temperature with a small telescope and suitable optics. The temperature was measured with a calibrated optical pyrometer at the instant when the sample was observed to melt.

Chemical analysis of selected samples was used to verify composition. In most cases, lithium was analyzed by flame photometry and tellurium was obtained by difference. Check analyses, in which tellurium was also determined by standard gravimetric methods, confirmed the accuracy of this procedure (±5% of the lithium weight). X-ray diffraction powder photographs were obtained for a number of samples of various compositions and thermal histories using a 114.6 mm Debye-Scherrer camera with CuKα radiation. Density measurements were made on samples of $LiTe_3$ using a Beckman Model 930 air-comparison pycnometer operated inside a helium-atmosphere glove box.

Results and Discussion

The presence of the intermediate phase $LiTe_3$, which had been tentatively reported by Foster *et al.* (8), has been confirmed. X-ray powder patterns obtained on a sample of $LiTe_3$ prepared by direct combination of the elements are consistent with a body-centered-cubic structure with a lattice constant of 6.162Å. The strongest lines of the Li_2Te pattern appeared very faintly in the pattern produced by the $LiTe_3$ sample and chemical analysis showed the lithium content to be 26.3 ± 1.0 a/o. The density of the sample, as measured with the air-comparison pycnometer, was found to be 5.29 ± 0.25 g/cm^3, which is in good agreement with the calculated density of $LiTe_3$ (5.531 g/cm^3) based on the x-ray data. Powder patterns were obtained for a number of other samples having a variety of compositions and thermal histories. In all cases, the observed lines could be fully explained by Li_2Te, $LiTe_3$ and the terminal phases.

Thermal analysis results are presented in Table I. The tellurium-rich samples had a strong tendency to undercool and vigorous stirring was required to obtain reproducible results for the heating and cooling curves. Composition changes in the sample due to vaporization losses from the open sample crucibles did not appear to be a problem. Chemical analysis of numerous samples indicated that the over-all compositions listed in Table I are accurate to ±0.5 a/o. The DTA temperatures tabulated were all taken from the intersection of the base-line extension and the leading slope of the peak on the heating cycle. Accurate determination of the liquidus crossings was generally not possible from the DTA curves.

The thermal data for samples of over-all composition on the lithium-rich side of Li_2Te indicate a eutectic point at 179.9° ± 0.1°C and more than 99.0 a/o lithium. This temperature is 0.6°C below the lithium melting point and well outside the estimated uncertainty of these measurements. Thermal effects were observed using DTA at 812° ± 5.0°C for three samples with composition between 91 and 80 a/o lithium. It is tentatively suggested that these effects are due to a monotectic reaction taking place at 812°C but the possibility that they are caused by a tellurium-niobium corrosion product has not been ruled out.

The melting point of Li_2Te was observed to be 1208°C using DTA and 1201°C in the resistance furnace with visual observation of melting. The agreement of the two methods is considered satisfactory considering the difficulties associated with accurate high-temperature measurements. The melting point of Li_2Te is taken to be 1204.5° ± 7°C.

Thermal effects observed for samples of over-all composition between Li_2Te and tellurium appear to be completely consistent with the phase relations shown in Fig. 1. The eutectic point between Li_2Te and $LiTe_3$ occurs at 448.5° ± 1.2°C and 35.7 ± 1.0 a/o lithium whereas the eutectic point between $LiTe_3$ and tellurium occurs at 423.1° ± 0.7°C and 10.5 ± 1.0 a/o lithium. The melting point of $LiTe_3$ is found to be 459.9° ± 0.7°C and that of tellurium 449.8° ± 0.3°C.

The stable intermediate phase $LiTe_3$ contrasts sharply with the extensive miscibility gaps observed for the chalcogen-rich regions of the lithium-sulfur

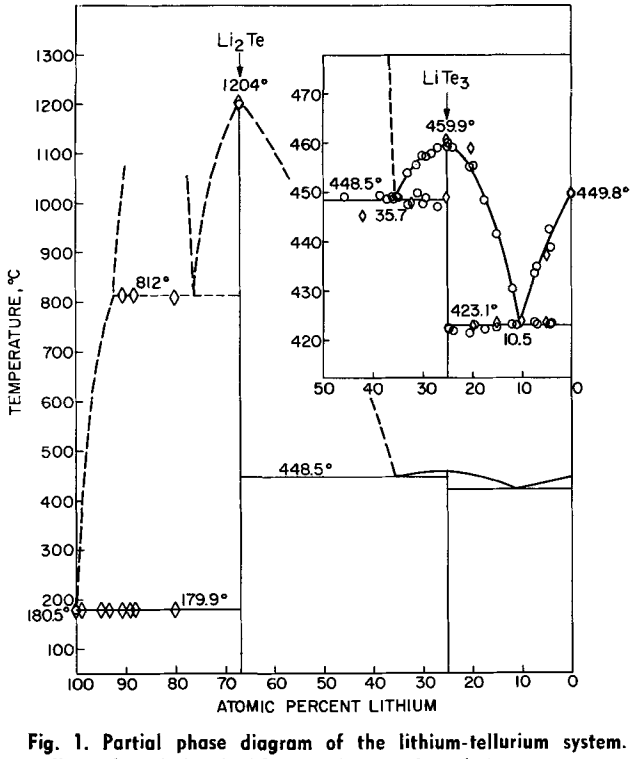

Fig. 1. Partial phase diagram of the lithium-tellurium system. ○, Thermal analysis; ◇ differential thermal analysis.

Table I. Summary of thermal analysis data on the lithium-tellurium system

Over-all composition, a/o Li in Te	Method[a]	Container material	Maximum temperature (°C)	Temperature of thermal effects (°C)						
100.0 (Li)	TA	W	220							180.5
100.0 (Li)	DTA	Nb	230							180.5
100.0 (Li)	DTA	W	270							180.2
98.9	DTA	W	325							179.8
94.9	DTA	W	825							179.9
93.7	DTA	Nb	860							178.0[b]
90.6	DTA	Nb	860		814					179.9
89.0	DTA	W	815							179.9
88.2	DTA	Nb	860		814					178.0[b]
80.0	DTA	Nb	865		809[c]					180.0[b]
66.7 (Li_2Te)	Visual	W	1300	1201						
66.7 (Li_2Te)	DTA	Nb	1245	1208						
46.1	DTA	W	810				449.2			
42.0	DTA	graphite	675				445.0			
38.4	TA	quartz	500				449.5			
37.2	TA	quartz	580				448.6			
36.3	TA	quartz	470				449.2			
35.8	TA	quartz	495				449.1			
35.8	TA	quartz	495				448.7			
35.1	TA	quartz	500				449.3			
34.9	TA	quartz	550				449.0			
33.1	TA	quartz	495			454.0	447.5			
32.1	DTA	graphite	475				448.0			
31.0	TA	quartz	550			455.6	450.0			
29.8	TA	quartz	600			457.6	447.5			
29.4	TA	quartz	495			457.5	449.0			
27.9	TA	quartz	505			458.0				
26.9	TA	quartz	515			459.3	447.0			
25.0	DTA	graphite	480			461.0	449.0[c]			
25.0	TA	quartz	495			459.2				
25.0	TA	quartz	510			459.2			422.4[c]	
25.0	TA	quartz	485			460.1			422.5[c]	
23.8	TA	quartz	425			459.0			422.0	
20.4	TA	quartz	495			455.2			421.5	
20.0	DTA	graphite	475			459.0			423.0	
19.7	TA	quartz	480			455.5			423.3	
17.5	TA	quartz	505					448.5	422.3	
15.1	TA	quartz	505					441.6	422.7	
15.0	DTA	Nb	480						423.7	
12.0	TA	quartz	540					430.7	423.3	
11.2	TA	quartz	500						423.4	
10.0	DTA	Nb	480						424.2	
7.4	TA	quartz	465					433.7	423.8	
7.0	TA	quartz	435					435.0	423.4	
5.0	DTA	Nb	475					437.4	423.9	
5.0	DTA	graphite	475						423.8	
4.5	TA	quartz	485					443.5	423.2	
4.1	TA	quartz	505					439.0	423.6	
0.0 (Te)	DTA	Nb	475			450.0				
0.0 (Te)	DTA	graphite	480			449.8				
0.0 (Te)	TA	quartz	505			449.5				

[a] The methods used were heating or cooling curves, (TA), where the temperatures reported are those of thermal arrests or breaks; and differential thermal analysis (DTA), where reported temperatures are those of the intersection.
[b] These temperatures are inaccurate because of rapid heating and are reported for completeness only.
[c] Very weak effects.

(2) and lithium-selenium (1) systems. This trend is similar to that observed for the sodium-chalcogen systems for which a miscibility gap on the sulfur-rich side of the sodium-sulfur system (9) gives way to a peritectically melting $NaSe_3$ phase for the sodium-selenium system (10) and finally to the eutectic form with the congruently melting $NaTe_3$ in the sodium-tellurium system (10). The existence of other stable chalcogen-rich phases in the sodium series confuses the analogy somewhat. That the decreasing tendency for the formation of polymeric species with increasing atomic number in the chalcogens is a significant factor in the trends pointed out above is an interesting possibility. The use of additives that inhibit polymer formation to the cathode of lithium-selenium and lithium-sulfur cells may eliminate the immiscibility and thereby improve mass transfer in the cathodes of these cells.

Acknowledgments

The authors wish to acknowledge Dr. C. E. Johnson and Dr. M. S. Foster who initiated this work and carried out early experiments. X-ray analysis was performed by Mr. R. Shablaske and chemical analyses were carried out by Mr. Z. Tomczuk and Mrs. R. Hanna. The encouragement and support of Dr. R. C. Vogel and Dr. A. D. Tevebaugh is appreciated. This work was performed under the auspices of the United States Atomic Energy Commission.

Manuscript received Oct. 16, 1972.

Any discussion of this paper will appear in a Discussion Section to be published in the December 1973 JOURNAL.

REFERENCES

1. P. T. Cunningham, S. A. Johnson, and E. J. Cairns, *This Journal*, **118**, 1941 (1971).
2. P. T. Cunningham, S. A. Johnson, and E. J. Cairns, *ibid.*, **119**, 1448 (1972).
3. E. C. Gay, W. J. Walsh, J. D. Arntzen, and E. J. Cairns, "Proc. 7th Intersociety Energy Conversion Engineering Conference," American Chemical Society, Washington, D. C., In press.
4. E. Zinth, A. Harden, and B. Dauth, *Z. Elektrochem.*, **40**, 588 (1934).
5. D. M. Gruen, R. L. McBeth, M. S. Foster, and C. E. Crouthamel, *J. Phys. Chem.*, **70**, 472 (1966).
6. M. S. Foster and C. C. Liu, *ibid.*, **70**, 950 (1966).
7. C. E. Johnson, M. S. Foster, and M. L. Kyle, *Nucl. Appli.*, **3**, 563 (1967).
8. M. S. Foster, C. E. Johnson, K. A. Davis, J. Peck, and R. Schablaske, USAEC report ANL-7575, p. 141 (1969).
9. N. K. Gupta and R. P. Tischer, *This Journal*, **119**, 1033 (1972).
10. M. Hansen and K. Anderko, "Constitution of Binary Alloys," 2nd ed., McGraw-Hill Book Co., Inc., New York (1958).

Ion Selectivity and Diffusion Potentials in Corrosion Layers

$PbSO_4$ Films on Pb in H_2SO_4

P. Ruetschi*

Leclanché S.A., Yverdon, Switzerland

ABSTRACT

The behavior of $PbSO_4$ corrosion layers on Pb in H_2SO_4 solutions is shown to resemble that of perm-selective $PbSO_4$ precipitation membranes, prepared by interdiffusion of Pb^{+2} ions and SO_4^{-2} ions into cellophane foil. Diffusion potentials in these precipitation membranes follow, over a wide pH-range, the equation

$$\Delta\psi_d = (RT/F) \ln (a_{H+1})/(a_{H+2})$$

and can reach values of several hundred mV. The lower limit of that electrode potential range where PbO (and/or α-PbO_2) forms in the interior of the corrosion film, underneath a perm-selective $PbSO_4$ layer, that is, -0.4V (or $+0.5$V) *vs.* Hg/Hg_2SO_4, can be predicted theoretically in a proper manner by taking into account the diffusion potential in the film.

Diffusion Potentials

Anodic corrosion films on Pb in aqueous H_2SO_4 exhibit, when formed within a certain potential range, a characteristic multi-phase structure. Such films then consist in their exterior part (against the solution) of a layer of $PbSO_4$ and in their interior part of tetragonal PbO and/or α-PbO_2 (1-10). The limits of the electrode potential range where PbO, and/or α-PbO_2, is found to be present underneath a protecting $PbSO_4$ layer have been fairly well established experimentally by means of x-ray and electron diffraction. PbO occurs above -0.40V and α-PbO_2 above $+0.50$V *vs.* Hg/Hg_2SO_4 (that is above $+0.25$ and $+1.15$V *vs.* STP H_2, respectively). These limits depend somewhat on H_2SO_4 concentration, temperature, and length of anodizing treatment. Basic lead sulfates may be present along with tetr. PbO. Below -0.40V *vs.* Hg/Hg_2SO_4 the anodic deposit is no longer multi-phased, but consists largely of $PbSO_4$. Above $+0.50$V *vs.* Hg/Hg_2SO_4, the interior part is composed of mixed material PbO-α-PbO_2, above 1.1V of α-PbO_2. Above 1.1V the exterior part consists of β-PbO_2 instead of $PbSO_4$.

Electrode potential measurements during (interrupted) anodization (11, 12) and during depassivation, or cathodic stripping, (3, 4, 6-8, 10, 13, 14) have also been used in the past to obtain diagnostic information on the types of corrosion products present in anodic films on Pb. For meaningful studies of this sort it is imperative to exclude carefully any oxygen from the cell, to work with highly purified solutions, and to employ voltage recording equipment of very large input impedance (4, 13). As discussed in this paper, the interpretation of any experimentally observed potential arrests in galvanostatic or depassivation studies, or of current peaks in potentiodynamic experiments (15) and their correct assignment to specific corrosion products, requires the consideration of possible membrane diffusion potentials existing in the corrosion film.

PbO is thermodynamically stable only above a certain pH, the stability limit depending on the concentration of SO_4^{-2} ions (4, 16). The presence of PbO in the interior of corrosion films means that it is protected against the H_2SO_4 solution by a layer of $PbSO_4$, practically impermeable to H_2SO_4. As the $PbSO_4$ film builds up in thickness, the following equilibria successively determine the *p*H in the interior of the film (16).

$$\begin{aligned}
H_2SO_4 &= SO_4^{-2} + 2H^+ \\
Pb^{+2} + SO_4^{-2} &= PbSO_4 \\
\log a_{Pb^{+2}} + \log a_{SO_4^{-2}} &= -7.8 \\
PbSO_4 + 2H_2O &= HPbO_2^- + 3H^+ + SO_4^{-2} \\
\log a_{HPbO_2^-} + \log a_{SO_4^{-2}} &= -36.0 + 3\,pH \\
pH &= 12.0 + (1/3) \log a_{HPbO_2^-} + (1/3) \log a_{SO_4^{-2}}
\end{aligned} \qquad [1]$$

$$\begin{aligned}
2Pb^{+2} + SO_4^{-2} + H_2O &= PbO\,PbSO_4 + 2H^+ \\
2 \log a_{Pb^{+2}} + \log a_{SO_4^{-2}} &= 1.0 - 2\,pH \\
PbO\,PbSO_4 + 3H_2O &= 2HPbO_2^- + 4H^+ + SO_4^{-2} \\
2 \log a_{HPbO_2^-} + \log a_{SO_4^{-2}} &= -55.2 + 4\,pH \\
pH &= 13.8 + (1/2) \log a_{HPbO_2^-} + (1/4) \log a_{SO_4^{-2}}
\end{aligned} \qquad [2]$$

$$\begin{aligned}
4Pb^{+2} + SO_4^{-2} + 4H_2O &= 3PbO\,PbSO_4\,H_2O + 6H^+ \\
4 \log a_{Pb^{+2}} + \log a_{SO_4} &= 21.2 - 6\,pH \\
3PbO\,PbSO_4\,H_2O + 4H_2O &= 4HPbO_2^- + 6H^+ + SO_4^{-2} \\
4 \log a_{HPbO_2^-} + \log a_{SO_4^{-2}} &= -91.2 + 6\,pH \\
pH &= 15.2 + (2/3) \log a_{HPbO_2^-} + (1/6) \log a_{SO_4^{-2}}
\end{aligned} \qquad [3]$$

$$\begin{aligned}
5Pb^{+2} + 7H_2O &= 5PbO\,2H_2O + 10\,H^+ \\
\log a_{Pb^{+2}} &= 12.6 - 2\,pH \\
5PbO\,2H_2O + 3H_2O &= 5HPbO_2^- + 5H^+ \\
\log a_{HPbO_2^-} &= -15.5 + 1\,pH \\
pH &= 15.5 + \log a_{HPbO_2^-}
\end{aligned} \qquad [4]$$

Individual $PbSO_4$ crystals in the outer layer have dimensions in the order of 0.1 to 10 μm, (6, 7, 9, 10, 14, 17-21). The layers become impermeable to SO_4^{-2} and HSO_4^- when they have reached a thickness of 1 to several μm. The pores are then practically closed. The same behavior is observed with AgCl films on Ag (22). Further corrosion of Pb then occurs by dissociation of H_2O underneath the $PbSO_4$ layer, precipitation of the anodically generated Pb^{+2} in form of PbO, and migration of the H^+ ions away from the electrode interface. The potential-determining couple Pb/PbO is thus exposed to a basic environment.

Under these conditions one would theoretically expect the existence of a considerable diffusion potential across the outer $PbSO_4$ layer, this latter exhibiting the characteristics of a precipitation membrane with pronounced ion selectivity (23). It appears that diffusion

* Electrochemical Society Active Member.

Key words: anodization, corrosion, diffusion potential, lead-acid battery, lead.

potentials in corrosion films have received little attention hitherto.

Generally, membrane potentials due to concentration differences between opposite sides may, at vanishing matrix charge and vanishing current, be expressed by (24)

$$\Delta\psi_d = -(RT/F) \int_1^2 \sum_n (t_i/Z_i)\, d \ln a_i \qquad [5]$$

where

t_i = transport number
Z_i = valency
a_i = activity of ions of type i

Equation [5] follows from the condition of equilibrium for those ions i for which the membrane is permeable. If the completely formed $PbSO_4$ membrane becomes essentially nonpermeable to SO_4^{-2}, HSO_4^-, and Pb^{+2} ions, so that the diffusion potential ψ_d arises entirely from the H^+, or OH^- ion concentration difference, one derives with $(a_{H+}) \cdot (a_{OH-}) = \text{const}$

$$\Delta\psi_d = (RT/F) \ln (a_{H+})_1/(a_{H+})_2 \qquad [6]$$

At 25°C the diffusion potential amounts thus to 59.16 mV per unit of pH difference.

In the interior of a corrosion film containing PbO, the pH can be expected to reach a value of 9.34, corresponding to equal activities of Pb^{+2} and $HPbO_2^-$ (25, 26). With a pH of 0 in the H_2SO_4 bulk solution, the diffusion potential would then amount to 553 mV (Fig. 1).

When the electrode potential of the Pb/PbO interface in the interior of the film, exposed to the local pH of 9.34, is being measured experimentally by means of a Hg/Hg_2SO_4 reference electrode, located, *e.g.*, in 0.1M H_2SO_4 bulk solution of pH 1, the diffusion potential is included in the measured value. For an experimentally measured potential of, *e.g.*, −0.500V, the actual, local potential for the Pb/PbO interface in the interior of the corrosion layer would be −0.993V *vs.* Hg/Hg_2SO_4.

Measurements with $BaSO_4$ and $PbSO_4$ Precipitation Membranes

In the light of the foregoing, it appeared of interest to simulate corrosion film behavior on lead with artificially prepared precipitation membranes.

Huber (22) had been able to separate corrosion films of Al_2O_3 on Al, and of AgCl on Ag, from the substrate and to measure Donnan equilibrium potentials of such isolated anodic membranes, inserted between two electrolyte compartments of different concentration. However, such measurements are difficult to carry out experimentally. Easier to handle are precipitation membranes in cellophane, as studied by Hirsch-Ayalon (27), and Honig and Hengst (28). These authors found $BaSO_4$ membranes to be highly ion-selective, being nonpermeable for Ba^{+2}, SO_4^{-2} and HSO_4^- ions, but permeable for H^+, OH^-, and H_2O. The two-compartment cell used in the present study (Fig. 2) consisted of 2 precisely machined Teflon blocks, clamped together by 8 threaded bolts. The electrolyte cavity in each block had a volume of 50 cm^3, the horizontal connecting bore had a diameter of 15 mm. The cellophane membrane, du Pont 193 PUDO, (thickness 12 μm) was sealed tightly between the two compartments by means of a Neoprene O-ring.

The precipitation membranes were formed by filling compartment I with 0.1M H_2SO_4, compartment II with 0.1M $Ba(ClO_4)_2$ for $BaSO_4$ membranes, and with 0.1M $Pb(ClO_4)_2$ for $PbSO_4$ membranes. A minimum time of 24 hr was allowed to complete the precipitation in the membrane. Thereafter the forming solutions were carefully removed through suction by means of evacuation pipes, and the solutions to be studied were then introduced into the cell. After insertion of the reference electrodes, which had previously been equilibrated during at least 24 hr with the corresponding solutions, the potentials were read and the measurements continued for several hours. Reference electrodes were Hg/Hg_2SO_4 in H_2SO_4 solutions, and Hg/HgO in sat. $Ba(OH)_2$ solutions (29). In those experiments where the pH was varied systematically by dilution, a H^+/H_2 reference was employed.

Figures 3 and 4 show electron micrographs of a $PbSO_4$ membrane. To prepare the membrane for electron microscopy, it was washed quickly in distilled water, dried in air, coated on the side to be studied with a carbon film, then shadowed with chromium (Balzers high-vacuum equipment).

The carbon layer was reinforced with paraffin and the cellophane subsequently dissolved with Schweizer's reagent during 24 hr. After watering, the paraffin-reinforced carbon layer was collected onto a copper screen carrier, whereupon the paraffin was removed by chloroform vapor extraction. Pictures were taken with a Siemens electron microscope at 60 kV.

From Fig. 3, showing the side exposed originally to the $Pb(ClO_4)_2$ solution, it is apparent that the $PbSO_4$ crystals resemble in morphology those found in corrosion films (20, 21). They exhibit primarily the diamond-shaped basal pinacoid. The humps in the sur-

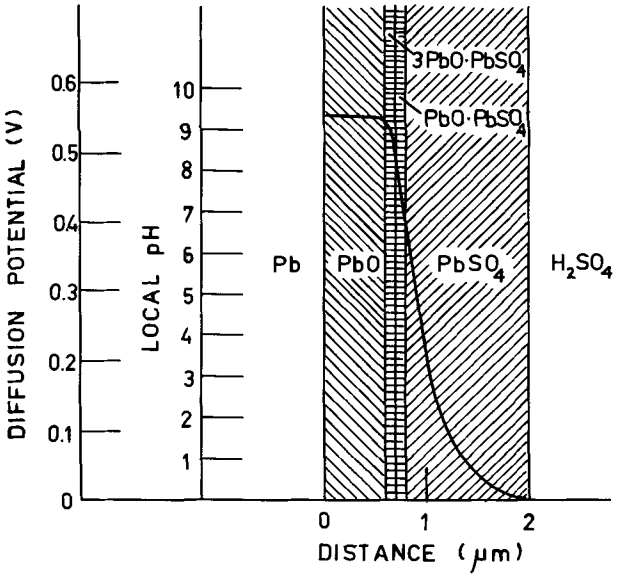

Fig. 1. Schematic representation of the diffusion potential in a multiphase corrosion layer on lead.

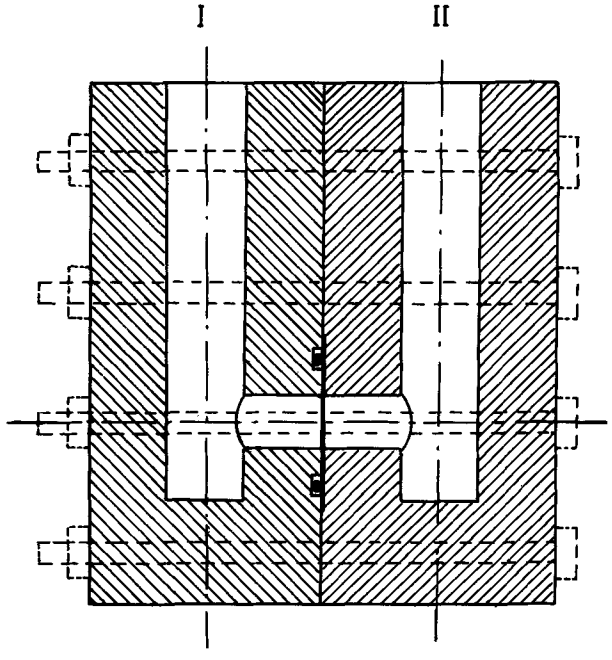

Fig. 2. Electrolytic cell for membrane-potential measurements.

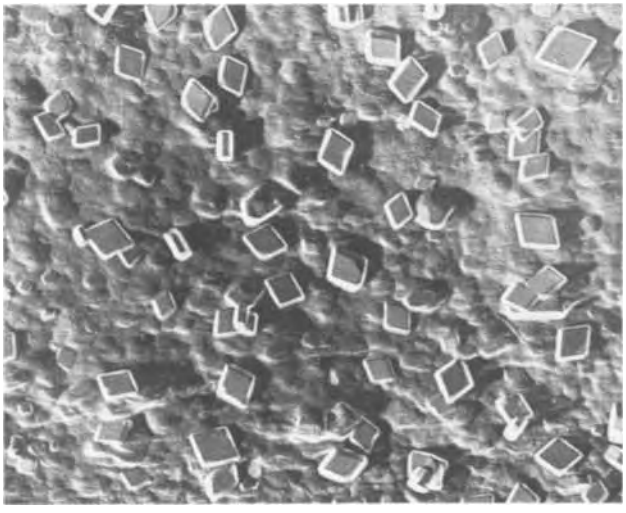

Fig. 3. Electron micrograph of $PbSO_4$ precipitation membrane. Side against $Pb(ClO_4)_2$ forming solution. Magnification: 40,000×.

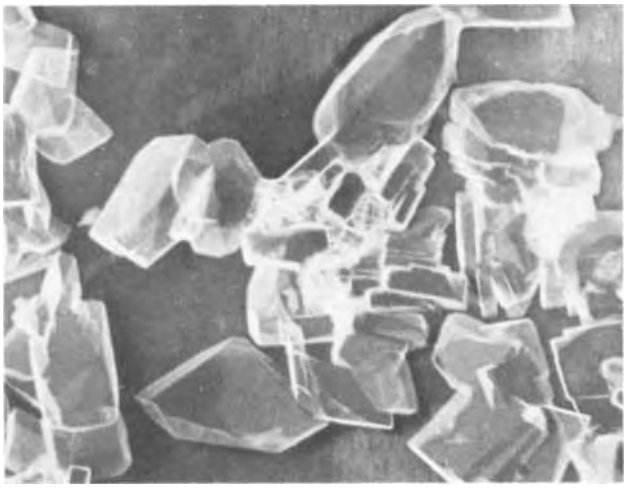

Fig. 4. Electron micrograph of $PbSO_4$ precipitation membrane. Side against H_2SO_4 forming solution. Magnification: 40,000×.

face are due to $PbSO_4$ crystals which had developed just below the surface in the cellophane membrane. On the H_2SO_4-side (Fig. 4) the $PbSO_4$ crystals are much larger and the cellophane surface appears smooth. This indicates that SO_4^{-2} ions diffuse more rapidly than Pb^{+2} ions during formation of the precipitation membrane.

Figure 5 refers to results obtained with a $BaSO_4$ membrane. For this series of measurements compartment I was filled with 0.1M H_2SO_4, equipped with a Hg/Hg_2SO_4 reference, compartment II was filled with successively diluted solutions of H_2SO_4, and finally with increasingly concentrated solutions of $Ba(OH)_2$, and was equipped with a H^+/H_2 reference electrode.

The measured potential difference (curve A) between the two electrodes remained invariant at $-0.735V \pm 5$ mV, irrespective of the pH in compartment II. Theoretically, the H^+/H_2 potential should have decreased by 59.16 mV per pH unit, as indicated by the line B. The pH dependence of the H^+/H_2 electrode was therefore exactly compensated by the pH dependence of the diffusion potential in the membrane, the latter following Eq. [6] over a very wide pH range. Similar results were obtained with $PbSO_4$ membranes for the pH range 0-5.

In the presence of foreign ions, such as ClO_4^- or K^+, the measured potential difference is no longer independent of pH in compartment II. The results of Fig. 6 were obtained by again filling compartment I with 0.1M H_2SO_4. In compartment II the pH was varied systematically by diluting 1M $HClO_4$ with 0.1M $Ba(ClO_4)_2$ or by diluting $Ba(OH)_2$ sat. + 0.1M $Ba(ClO_4)_2$ with 0.1M $Ba(ClO_4)_2$. The diffusion potential is decreased in proportion to the relative importance of the transport number of ClO_4^-.

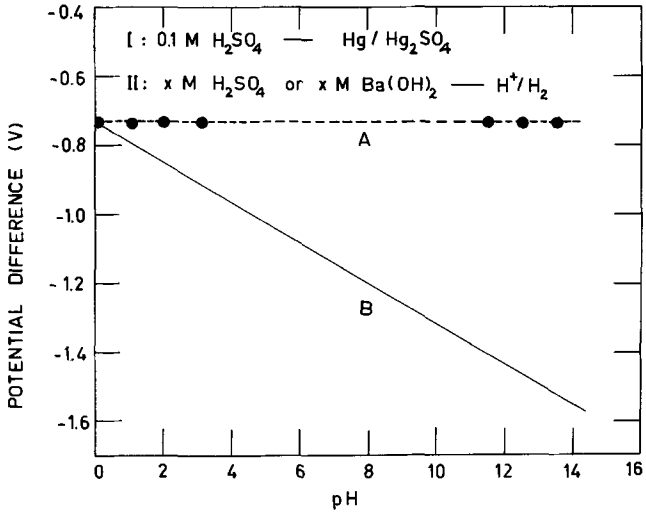

Fig. 5. Electrode potential of a H^+/H_2 electrode in solutions of varying pH (compartment II) against a Hg/Hg_2SO_4 electrode in 0.1M H_2SO_4 (compartment I). $BaSO_4$-membrane.

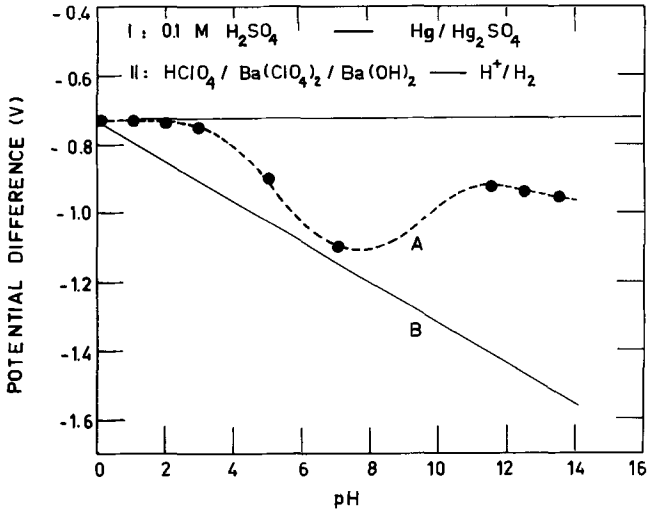

Fig. 6. Electrode potential of a H^+/H_2 electrode in solutions of varying pH containing ClO_4^- anions (compartment II) against a Hg/Hg_2SO_4 electrode in 0.1M H_2SO_4 (compartment I). $BaSO_4$-membrane.

Figure 7 illustrates the influence of K^+ ions on the membrane potential. Here, compartment I was filled with $Ba(OH)_2$ sat. and was equipped with a Hg/HgO reference electrode (29). The pH in compartment II was varied by diluting 1M H_2SO_4 + 0.1M K_2SO_4 with 0.1M K_2SO_4 or by diluting 1M KOH + 0.1M K_2SO_4 with 0.1M K_2SO_4. As in the case of the ClO_4^- anion, the influence of the transference number of the K^+ cation is most pronounced around pH 7 where the concentrations of H^+ or OH^- ions are smallest.

In conclusion, one can state that $BaSO_4$ and $PbSO_4$ precipitation membranes are highly selective, being nonpermeable for SO_4^{-2}, HSO_4^-, and Ba^{+2}, or Pb^{+2}, but being permeable for H^+, OH^-, and at least partly permeable for ClO_4^- and K^+.

The results confirm that very large diffusion potentials (over 700 mV) can indeed exist over prolonged time periods (several days or weeks) in precipitation membranes. An analog behavior can be expected for $PbSO_4$ corrosion films on Pb.

In order to carry the analogy to a corroding electrode as far as possible, the cell of Fig. 2 was used to mea-

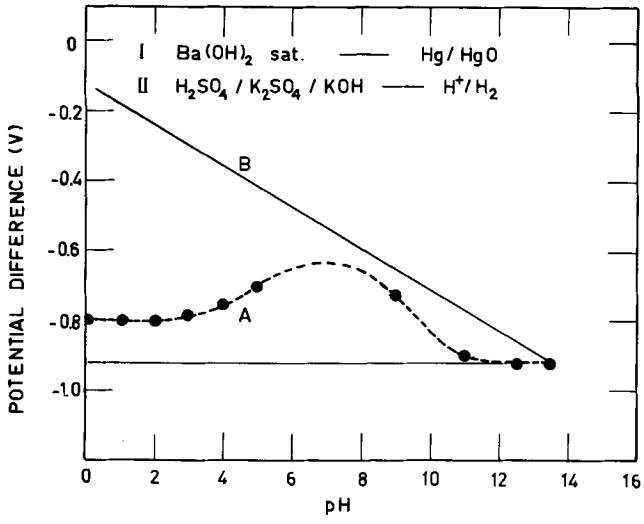

Fig. 7. Electrode potential of a H^+/H_2 electrode in solutions of different pH containing K^+ cations (compartment II) against a Hg/HgO electrode in $Ba(OH)_2$ sat. solution (compartment I). $BaSO_4$-membrane.

sure directly the potential difference of the following system

Pb/PbO	$Ba(OH)_2$ sat. + PbO sat. pH 13.2	$PbSO_4$ – $BaSO_4$ membrane	H_2SO_4 0.1M pH 1	Hg_2SO_4/Hg

The pH of a sat. $Ba(OH)_2$ solution (pH ~ 13.2) is of course considerably higher than the value expected in the interior of corrosion films containing PbO(pH 9.34). However, the $Ba(OH)_2$ sat. + PbO sat. electrolyte provided the desirable conductivity for reproducible measurements and contained, as required for the build-up of a maximum diffusion potential, beside OH^- only nonpermeating ions. The effect of the increased pH on the Pb/PbO potential was compensated by a correspondingly larger diffusion potential in the membrane. Indeed, the measured voltage of the above system, −0.49V, was very close to the experimental value for the depassivation plateau at −0.50V of a corroding Pb electrode in 0.1M H_2SO_4 (4). Using Eq. [6] for the diffusion potential, (13.2 − 1) × 59.16 mV, one calculates theoretically for the above system, with the value of 0.676V for the Hg/Hg_2SO_4 electrode in 0.1M H_2SO_4 *vs.* STP H_2 (4), and with the standard potential of 0.260V for Pb/PbO the following voltage

$$E = 0.260 - (13.2 \times 0.05916) + (13.2 - 1) \times 0.05916 - 0.676 = -0.48V$$

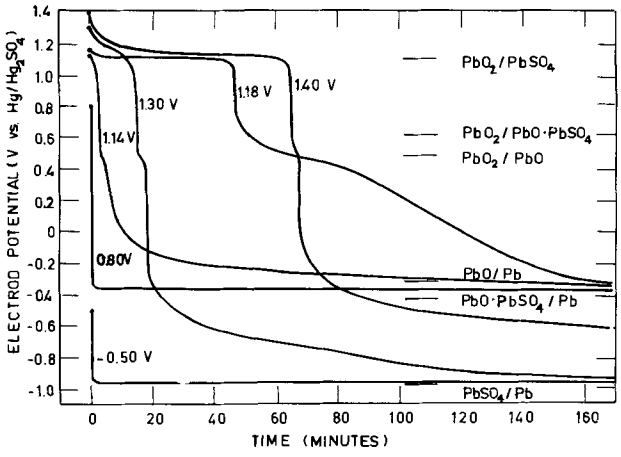

Fig. 8. Self-depassivation of lead electrodes after potentiostatic anodization at different potentials (−0.5, +0.8, +1.14, +1.18, +1.30, and +1.40V *vs.* Hg/Hg_2SO_4) for 24 hr in 4.2M H_2SO_4.

Interpretation of Depassivation Potential Plateaus

Lead electrodes, anodized in H_2SO_4 at different constant potentials and then put on open circuit, show during depassivation on open circuit at least 4 characteristic plateaus (3, 4, 7-9, 14). Typical voltage-time curves on open circuit are reproduced from Ref. (4) in Fig. 8.

Taking into account the diffusion potential in the corrosion film, these plateaus may now be interpreted and assigned to electrochemical processes in an unambiguous manner. The interpretation given earlier (4) must be qualified as being valid only in the absence of diffusion potentials.

Plateau potentials may be computed theoretically by calculating the reversible potential of the presumed potential-determining couple (*e.g.*, PbO/Pb) at the local pH in the interior of the film, using the proper pH-potential-dependence, and then adding the diffusion potential in the $PbSO_4$ film (this is the product of the pH difference across the film with 59.16 mV).

In order to express the potential against the Hg/Hg_2SO_4 electrode one must subtract the potential difference between the STP H_2 electrode at pH 0 and the Hg/Hg_2SO_4 electrode in the corresponding H_2SO_4 solution. For 4.2M H_2SO_4, pH 0.48, this amounts to 0.620V (4).

Table I presents calculations made on this basis for experiments in 4.20M H_2SO_4. The formulation of Bode and Voss (16) was retained for the basic sulfates and for hydrated lead oxide. Using PbO instead of 5 PbO ·

Table I.

Plateau	Experimental plateau potential *vs.* Hg/Hg_2SO_4 (V)	Electrode reaction [see Ref. (4), Table II]	pH at potential determining site	Film diffusion potential (V)	Calculated plateau potential *vs.* Hg/Hg_2SO_4 (V)
I	1.12	$PbO_2 + SO_4^{-2} + 4H^+ + 2e^- = PbSO_4 + 2H_2O$ $E = 1.685 - 0.1182\ pH + 0.0295 \log a_{SO_4^{-2}}$	−0.48 (4.2M H_2SO_4)	0	1.120
II	~0.50	$2PbO_2 + SO_4^{-2} + 6H^+ + 4e^- = PbO{\cdot}PbSO_4 + 3H_2O$ $E = 1.422 - 0.0886\ pH + 0.0147 \log a_{SO_4^{-2}}$	6.35* ($\log a_{SO_4^{-2}} = -3.9$)	0.405	0.588
		$5PbO_2 + 10H^+ + 10e^- = 5PbO{\cdot}2H_2O + 3H_2O$ $E = 1.070 - 0.0591\ pH$	9.34**	0.586	0.478
III	−0.38	$5PbO{\cdot}2H_2O + 10H^+ + 10e^- = 5Pb + 7H_2O$ $E = 0.260 - 0.0591\ pH$	9.34**	0.586	−0.332
		$PbO{\cdot}PbSO_4 + 2H^+ + 4e^- = 2Pb + SO_4^{-2} + H_2O$ $E = -0.099 - 0.0295\ pH - 0.0148 \log a_{SO_4^{-2}}$	6.35* ($\log a_{SO_4^{-2}} = -3.9$)	0.405	−0.443
IV	−0.96	$PbSO_4 + 2e^- = Pb + SO_4^{-2}$ $E = -0.356 - 0.0295 \log a_{SO_4^{-2}}$	−0.48 (4.2M H_2SO_4)	0	−0.970

* Equilibrium value for coexistence of $PbSO_4$ and $PbO{\cdot}PbSO_4$, at a sulfate activity corresponding to the solubility product of $PbSO_4$ ($a_{SO_4^{-2}} = a_{Pb^{+2}} = 10^{-3.9}$).

** Equilibrium value for PbO ($a_{Pb^{+2}} = a_{HPbO_2^-}$).

$2H_2O$ the calculated values remain practically unchanged.

Excellent agreement exists between observed and calculated plateau potentials. During depassivation of an electrode with PbO_2 film, the following stages are successively reached. First a sulfate layer starts to form on the PbO_2 film by a self-discharge mechanism described earlier (4, 30, 31), while the electrode potential is determined by the $PbO_2/PbSO_4$ couple. As the sulfate layer increases in thickness, the pH in the interior rises abruptly due to hindered H_2SO_4 diffusion. The self-discharge of PbO_2 proceeding rapidly at this point, the electrode passes then quickly through the sequence of potential-determining couples: (*i*) $PbO_2/PbO \cdot PbSO_4$, (*ii*) $PbO_2/3PbO \cdot PbSO_4 \cdot H_2O$, (*iii*) PbO_2/PbO. (In Table I only the first and the last of the plateau potentials are calculated since the second falls in-between the two others). At the potential of the PbO/Pb couple it can remain for a considerable time, depending only on the diffusion of H_2SO_4 into the film. Finally, when the PbO is (completely) sulfated, the potential decreases to the value of the $PbSO_4/Pb$ couple. In Fig. 8 it is apparent that for thin-corrosion films (1.30 and 1.40V) the amount of $PbSO_4$ formed during self-discharge is insufficient to protect properly the region of high pH in the interior, and the plateau at −0.4V is absent. Although some α-PbO_2 is apparently formed in the film, as predicted theoretically, at potentials as low as +0.5V *vs.* Hg/Hg_2SO_4 (8), it does not seem to be potential-determining, possibly because sufficient PbO remains in contact with the underlying Pb at all times.

It had been pointed out by different authors (3, 6-8, 12, 14) that the depassivation plateau at −0.4V *vs.* Hg/Hg_2SO_4 (+0.25V *vs.* H_2) coincides with the value one would expect theoretically for Pb/PbO at pH of about 0. However, at this low pH, PbO is unstable, and at a high pH its theoretical potential is lower than the experimentally observed value. This dilemma had led earlier to the suggestion that the plateau at −0.4V was due to the PbO_2/PbO couple in alkaline solution (4). Now, taking account of the diffusion potential in the film, the coincidence of the experimental plateau with the hypothetical Pb/PbO potential at pH 0 is readily explained.

Since, for the couple

$$PbO + 2H^+ + 2e^- = Pb + H_2O \qquad [7]$$

$$E = 0.260 - 0.05916\,pH^1 \text{ (vs. STP } H_2)$$

and for the diffusion potential in the film, when the pH in the solution is 0

$$\Delta\psi_d = +0.05916\,pH^1 \qquad [8]$$

the externally measured value becomes

$$E_{exp} = E + \Delta\psi_d = 0.260\text{V (vs. STP } H_2) \qquad [9]$$

corresponding to the Pb/PbO value at pH 0.

It is to be noted that the cancellation of the pH dependence of the potential-determining couple is only complete if the potential of this latter varies with 0.05916V per pH unit (as *e.g.* in [7]). For potential-determining couples with different pH-dependence, (see Table I), the experimentally measured potential cannot then be expected to be close to the standard potential.

Cathodic Stripping

During cathodic stripping of corrosion films on Pb, one observes characteristic potential plateaus (4), corresponding to those obtained during self-depassivation. The plateaus are, however, displaced in the cathodic direction. The plateau at −0.4V, *e.g.*, due to the PbO/Pb couple may thus be found at −0.8V *vs.* Hg/Hg_2SO_4. Using the data of Ref. (4) and the present theory on diffusion potentials in corrosion films, the multi-phase structure of the films, after potentiostatic anodization in 4.2M H_2SO_4 during 24 hr, can be represented schematically as shown in Fig. 9. This illustration differs from an earlier model (4), in that α-PbO_2 may now be expected to be present in the film only above +0.5V *vs.* Hg/Hg_2SO_4 and that below this voltage the inner layer consists essentially of PbO, in agreement with (8) and (9).

Interpretation of Potentiodynamic Studies

The diffusion potential in the corrosion film is also of importance for the assignment of current peaks to specific electrode couples during linear anodic and cathodic potential sweep. In fact, a reduction peak, observed at −0.8V *vs.* Hg/Hg_2SO_4, that is slightly above the $PbSO_4/Pb$ peak (15), should, on the basis of the present theory, be attributed to the reduction of PbO to Pb at pH 9.34 and not to the reduction of α-PbO_2 to PbO.

Implications with Respect to Lead-Acid Storage Battery Technology

Plate formation.—Unformed, cured battery plates, made with a paste of PbO, Pb, and H_2SO_4, show in 1M H_2SO_4 a potential of about −0.6V *vs.* Hg/Hg_2SO_4. This means that the potential is about 350 mV above the theoretical value for the $Pb/PbSO_4$ couple. Upon formation at low current the potential of the negative plates may remain for a considerable length of time above the expected value (−0.97V *vs.* Hg/Hg_2SO_4) while the potential of the positive plates may stay several hundred mV below the value of the $PbO_2/PbSO_4$ couple, (+1.1V *vs.* Hg/Hg_2SO_4). This behavior, which is illustrated in Fig. 10, may readily be explained by the fact that the interior of the plates stays, during the initial hours of formation, in an alkaline condition, due to the presence of PbO (pH 9.34). A surface film of $PbSO_4$ prevents the acid from penetrating into the plate. In this way Pb in the negative plate and PbO_2 in the positive plate are formed under alkaline conditions, where the potential is higher, or lower, respectively. For the same reason, a high proportion of α-PbO_2 is found in the positive plate (13, 30-35).

From Table I it may be seen that 5 PbO · 2 H_2O could theoretically be oxidized to PbO_2 already at 0.478V *vs.* Hg/Hg_2SO_4, and 5 PbO · 2 H_2O could be reduced to Pb already at −0.332V *vs.* Hg/Hg_2SO_4. In a solution of pH 9.34 the formation voltage is only 0.81V. In acid solution one has at $a_{SO_4^{-2}} = 1$ and pH 0 a formation volt-

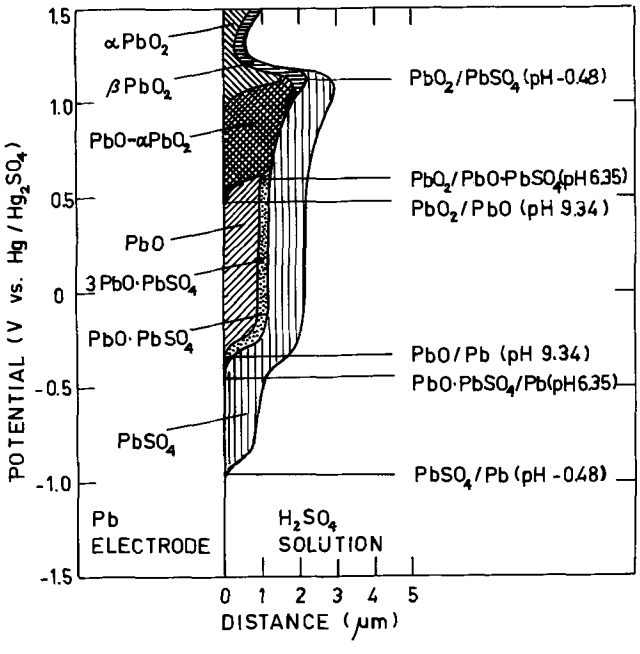

Fig. 9. Schematic representation of the multi-phase corrosion layer at different electrode potentials. (Layers formed during 24 hr at constant potential in 4.2M H_2SO_4).

[1] Local pH in the interior of the corrosion film.

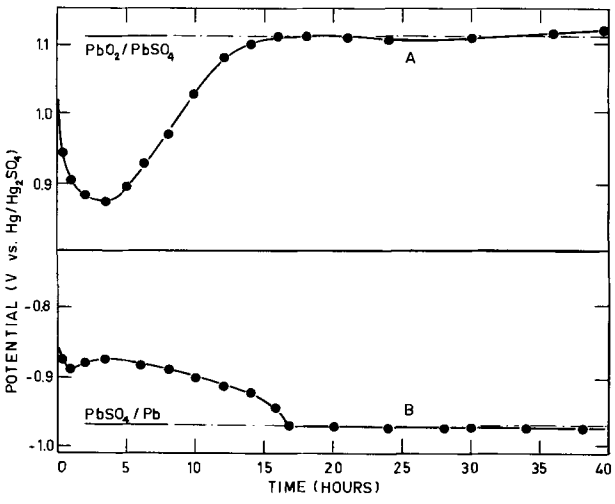

Fig. 10. Potential of positive (A) and negative (B) storage battery plates (12 A-hr) during initial, very low-rate formation (200 mA) in 2.2M H_2SO_4.

age of

$$2\,PbSO_4 + 2H_2O = Pb + PbO_2 + 2H_2SO_4$$

$$E = 2.041V$$

since the energy of the sulfation process

$$PbO + H_2SO_4 = PbSO_4 + H_2O \quad \Delta G = -28\ \text{kcal}$$

$$\Delta E = 0.61V$$

must be added to each electrode.

Grid corrosion on open circuit.—If positive storage battery plates are stored in a partly or completely discharged condition, a relatively high *p*H can develop underneath the $PbSO_4$ films on the grids. Self-discharge of positive plates due to reaction between PbO_2 in the active material and Pb in the grid (30, 31) is then highly accelerated. It should be noted that the present discussion has been limited to Sb-free grids. On Pb-Sb alloys, the sulfate films are probably less dense, due to the higher solubility of the basic Sb-sulfates. The $PbSO_4$ layers may then be less permselective, the diffusion potentials possibly somewhat decreased, and α-PbO_2 would be able to form even at lower potentials than +0.5V *vs.* Hg/Hg_2SO_4. It would be of interest to measure experimentally diffusion potentials in mixed $PbSO_4$ — $(SbO)_2 \cdot SO_4$ precipitation membranes.

Acknowledgment

The author is indebted to Professors Dr. Huber, Dr. Giovanoli, and Dr. Schmidt of the Institute of Physical Chemistry of the University of Berne for electron microscopy and valuable discussions on this subject.

Manuscript submitted Aug. 28, 1972; revised manuscript received Nov. 8, 1972.

Any discussion of this paper will appear in a Discussion Section to be published in the December 1973 JOURNAL.

REFERENCES

1. E. F. Wolf and C. F. Bonilla, *Trans. Electrochem. Soc.*, **79**, 307 (1941).
2. J. J. Lander, *This Journal*, **98**, 213, 220 (1951); **103**, 1 (1956).
3. J. Burbank, *ibid.*, **103**, 87 (1956); **104**, 693 (1957); **106**, 369 (1959).
4. P. Ruetschi and R. T. Angstadt, *ibid.*, **111**, 1323 (1964).
5. L. M. Levinzon, I. A. Aguf, and M. A. Dasoyan, *J. Appl. Chem. USSR*, **39**, 556 (1966).
6. D. Pavlov, *Ber. Bunsenges. Phys. Chem.*, **71**, 398 (1967).
7. D. Pavlov, *Electrochim. Acta*, **13**, 2051 (1968).
8. D. Pavlov, C. N. Poulieff, E. Klaja, and N. Iordanov, *This Journal*, **116**, 316 (1969).
9. D. Pavlov and N. Iordanov, *ibid.*, **117**, 1103 (1970).
10. D. Pavlov and R. Popova, *Electrochim. Acta*, **15**, 1483 (1970).
11. K. Nagel, R. Ohse, and E. Lange, *Z. Elektrochem.*, **61**, 795 (1957).
12. R. Ohse, *Werkstoffe Korrosion*, **11**, 220 (1960).
13. P. Ruetschi and B. D. Cahan, *This Journal*, **104**, 406 (1957); **105**, 369 (1958); **106**, 543 (1959).
14. W. Feitknecht, *Z. Elektrochem.*, **62**, 795 (1958).
15. H. S. Panesar, in "Power Sources 3," p. 79, D. H. Collins, Editor, Oriel Press (1971).
16. H. Bode and E. Voss, *Electrochim. Acta*, **1**, 318 (1959).
17. A. I. Astakhov, F. S. Vaisberg, and B. N. Kabanov, *Dokl. Akad. Nauk. USSR*, **154**, 1414 (1964).
18. R. Grauer, P. Wehr, and H. J. Engell, *Werkstoffe Korrosion*, **20**, 94 (1969).
19. T. Chiku and K. Nakajima, *This Journal*, **118**, 1395 (1971).
20. J. Burbank, *ibid.*, **118**, 525 (1971).
21. J. Burbank in "Power Sources 3," p. 13, D. H. Collins, Editor, Oriel Press (1971).
22. K. Huber, *Z. Elektrochem.*, **59**, 693 (1955).
23. R. Grauer, *Chimia*, **24**, 269 (1970).
24. T. Thorell, *Proc. Soc. Exp. Biol. Med.*, **33**, 282 (1935); *Trans. Faraday Soc.*, **33**, 1053, 1086 (1937); K. H. Meyer and J. F. Sievers, *Helv. Chim. Acta*, **19**, 649 (1936); Th. Overbek, *Progr. Biophys. Biophys. Chem.*, **6**, 57 (1956); R. Schlögl, "Stofftransport in Membranen," *Fortschr. Phys. Chem.*, **9**, Steinkopf, Darmstadt (1964).
25. M. Pourbaix, "Atlas d'Equilibres Electrochimiques," p. 487, Gauthier Villars, Paris (1963).
26. P. Chartier, Thèse, p. 62, Université de Strasbourg (1968).
27. P. Hirsch-Ayalon, *Electrochim. Acta*, **10**, 773 (1965).
28. E. P. Honig and J. H. Th. Hengst, *ibid.*, **15**, 491 (1970); **17**, 75 (1972).
29. D. J. G. Ives and G. J. Janz, "Reference Electrodes," pp. 336, 404, Academic Press, New York (1961).
30. P. Ruetschi and R. T. Angstadt, *This Journal*, **105**, 555 (1958).
31. P. Ruetschi, J. Sklarchuck, and R. T. Angstadt, *Electrochim. Acta*, **8**, 333 (1963).
32. J. Burbank and E. J. Ritchie, *This Journal*, **116**, 125 (1969); **117**, 299 (1970).
33. W. O. Butler, C. J. Venuto, and D. V. Wisler, *ibid.*, **117**, 1339 (1970).
34. A. C. Simon, C. P. Wales, and S. M. Caulder, *ibid.*, **117**, 987 (1970).
35. D. Pavlov, G. Papazov, and V. Iliev, *ibid.*, **119**, 8 (1972).

The Anodic Oxidation of Several Rare Earth Metals in Sodium Aluminate Solution

Leonard Gruss* and Thomas Mackus

Pitman-Dunn Laboratories, Frankford Arsenal, Philadelphia, Pennsylvania 19137

ABSTRACT

Samarium, europium, gadolinium, yttrium, dysprosium, holmium, erbium, and ytterbium metal rods (99.9% pure) were anodized in a 0.1*N* solution of sodium aluminate (15°C) at constant current density of 0.16 A/cm^2. Anodic barrier film effects and dielectric breakdown (sparking) were observed with all of the metal-electrolyte combinations investigated. Powder x-ray diffraction patterns and diffuse reflectance spectra in the near u.v. to visible range were obtained for the anodic oxidation products. The anodic spark reaction process produced perovskite structured coatings on the lower atomic number samarium, europium, and gadolinium metals. Mixtures of perovskite and garnet structured coatings were produced on the higher atomic number dysprosium, holmium, erbium, and ytterbium metals including yttrium.

A variety of aluminate compounds having different structures are formed when the rare earth sesquioxides and/or Y_2O_3 react with Al_2O_3. The two most common varieties are the perovskite (1:1) and garnet (3:5) structures. Many ABO_3 compounds containing the rare earths and small trivalent ions such as aluminum have been the subject of intensive and detailed studies. The ABO_3 compounds containing lanthanum closely resemble an ideal perovskite structure but those compounds containing smaller rare earths form a distorted perovskite. Keith and Roy (1) studied the 1:1 aluminates of lanthanum through samarium and classified them as perovskites with $LaAlO_3$ being nearly cubic. Goldschmidt *et al.* (2) first prepared $YAlO_3$ and considered it to have the perovskite structure. However, on the basis of substantial differences in optical and powder x-ray diffraction data, Keith and Roy (1) classified this compound as having a distorted perovskite structure. Geller and Bala (3) and Bertaut and Forrat (4) carried out an extensive investigation of the ABO_3 rare earth compounds. They considered all these compounds to be of the perovskite type having an orthorhombic distorted structure.

Yoder and Keith (5) unexpectedly synthesized the first rare earth aluminate (3:5) garnet. They investigated the extent of the substitution of $Y^{+3} + Al^{+3}$ for $Mn^{+2} + Si^{+4}$ in the garnet $Mn_3Al_2(SiO_4)_3$. A garnet having a formula $Y_3Al_2(AlO_4)_3$ was produced corresponding to complete substitution of the Y^{+3} and Al^{+3} ion. In terms of molar composition the formula $Y_3Al_2(AlO_4)_3$ corresponds to $3Y_2O_3 \cdot 5Al_2O_3$. Bertaut and Forrat (4) prepared aluminum garnets only with rare earths smaller than samarium but no studies were made with europium compounds. They showed that gadolinium, dysprosium, yttrium, and erbium garnets can be produced. Warshaw and Roy (6) and Schneider *et al.* (7) agree that aluminum garnets can be formed with the smallest rare earths between thulium and lutetium but no aluminum garnets are formed with europium and gadolinium. $NdAlO_3$ to $DyAlO_3$, $YAlO_3$, $TbAlO_3$ (8) single crystals were prepared from various flux compositions in some cases by slow cooling and in others by evaporation of the flux at constant temperatures. It is noted that $YbAlO_3$ thus prepared (8) coexists with the garnet phase, $Yb_3Al_5O_{12}$. The usual procedure for the preparation of polycrystalline aluminum perovskites or garnets involves firing a rare earth oxide with aluminum oxide at temperatures over 1000°C. This investigation was undertaken to study the preparation, structure, and composition of rare earth aluminates by the anodic spark reaction of rare earth metals in sodium aluminate solution.

The phenomena of anodic sparking has been observed by many investigators and was described in detail in the work of Guntherschulze and Betz (9). The effect appears when the voltage across an anodic barrier film is raised to a point where film thickness can no longer increase uniformly and any small increase in voltage results in a large increase in current. The excess current is carried by scintillations, hence, dielectric breakdown. The anodic spark reaction has been utilized for the protection of light metals, *i.e.*, magnesium by the HAE (10) and Cr-22 (11) processes. In the HAE and Cr-22 process, a hard adherent layer containing a mixture of refractory magnesium compounds is deposited on the magnesium surface. The solution in the HAE process which contains OH^-, PO_4^{-3}, F^-, AlO_2^-, and MnO_4^{-2} ions produces an alkaline coating whereas the Cr-22 solution which contains CrO_4^{-2}, HPO_4^{-2}, and F^- ions produces a nonalkaline coating. Cadmium niobate (12) was prepared by anodic sparking of cadmium in potassium niobate solution. Anodic spark reactions were made with a variety of metals (13) in sodium aluminate, sodium tungstate, and sodium silicate solutions. The principal spark reaction products were α-Al_2O_3 and spinels, *i.e.*, $MgAl_2O_4$ with aluminate solutions, monoclinic WO_3 with tungstate solutions, and crystalline silicates or metals dispersed in amorphous material with silicate solutions. Cadmium sulfide was also synthesized by the anodic spark reaction of cadmium in $Na_2S \cdot 9H_2O$ solutions (14).

Although many studies have been made with the rare earths, electrochemical studies of the rare earth metals have been limited. In 1963, Greene and Lee (15) studied the electrochemical characteristics of the rare earth metals in dilute phosphoric acid solution up to 4V in the noble direction. He found anodic polarization curves of the rare earth metals to be typical of metals which form oxide barrier films at their interfaces, *i.e.*, aluminum, zirconium, and tantalum. Most recently, Heller *et al.* (16-18) studied cathodic and solution electroluminescence of trivalent rare earth ions. Solutions of inorganic cations in phosphorus oxychloride electroluminesce when a direct current is passed through the liquids. The electroluminescence originates at the surface of the cathode.

Experimental

The rare earth metals in rod form were mounted in tight-fitting Teflon sleeves. These sleeves serve to mask the anode at the air-electrolyte interface and to fix the area for anodization. Prior to anodization the

* Electrochemical Society Active Member.

Key words: rare earth metals, rare earth aluminates, anodic oxidation, anodic spark reaction.

metals were polished with a series of silicon carbide abrasive papers down to a 3/0 emery and finally with microcut polishing paper (GRIT=600 soft) and washed with absolute ethanol. Samarium, europium, gadolinium, yttrium, dysprosium, holmium, erbium, and ytterbium metal rods (99.9% pure) were anodized in a 0.1*N* solution of reagent grade sodium aluminate. A current density of 0.16 A/cm^2 was employed in all reactions. The reaction cell was thermostated at 14.5° ± 0.5°C. The cell was equipped with a magnetic stirrer and a platinum cathode whose area was at least equal to the anode surface area in all experiments.

The voltages were monitored by an Electronic Measurements constant current power supply and a Hewlett-Packard 410c voltmeter and recorded on a Speedomax strip chart recorder.

The analyses of the anodic spark reaction products were performed on the insoluble material which was ejected from the anode surface during the spark reaction. X-ray diffraction patterns were obtained on all samples using a Debye-Scherrer 114.59 mm camera (Norelco) and a Norelco basic x-ray diffraction unit employing nickel filtered copper K_α radiation. The results of powder x-ray diffraction analysis on the anodic products are shown in Table I.

Diffuse reflectance spectra between 220-700 mμ were obtained for the anodic spark products using a Cary Model 14 Spectrophotometer equipped with a Model 1411 diffuse reflectance (ring collector) accessory.

Results

Anodic barrier film effects and dielectric breakdown were observed with all of the rare earth metal-electrolyte combinations investigated. The composite voltage-time curves for the anodic reactions of seven rare earth metals and yttrium, in sodium aluminate solution, are shown in Fig. 1. The curves of Sm, Gd, Y, Dy, Ho, and Er are typical of metals which form oxide-barrier films at their interfaces, *i.e.*, Al, Ta, and Zr. Steeply rising slopes are evident occurring within the first 15-20 sec of anodization corresponding to the growth of thin transparent insulating films. In the regions of the steeply rising slope up to the point of dielectric breakdown yttrium apparently divides the curves (except europium) of the low and high atomic number rare earth metals.

Most studies were made with erbium metal and in the initial stages of the anodic reaction up to 20V, the very rapid rise of voltage is accompanied by a film which exhibits a sequence of interference colors corresponding to increases in thickness. As the anodic film increases in thickness the 20V film which is gray-white has the tendency to become cloudy although an iridescence can be seen at 500V.

Yb and Eu have the tendency of deviating from the trends which exist with the other rare earths, *i.e.*, atomic volumes, melting points, densities, etc. A similar effect was noted with the voltage-time curves. The curves are somewhat typical of valve metals except that a much longer period of time was required to achieve dielectric breakdown. An unusual effect was noted with europium in the $NaAlO_2$ solution. Europium being very reactive, reacted to form a bulky lime-green coating during polishing, water rinsing, and during immersion in the $NaAlO_2$ solution just prior to anodization. As current was passed through the cell, the voltage rose slowly with time. This was followed by a rapid rise in voltage to about 75V. At this point, a shoulder formed representing a slow rise in voltage with time. At about 100V an anodic reaction occurred which is somewhat typical of those metals which form oxide-barrier films at their interfaces. Although europium is very reactive in sodium aluminate solution it appears to undergo two anodic reactions evidently forming two separate barrier films. The final spark reaction coating formed on the europium surface prevents reaction of the europium metal with either water or sodium aluminate solution.

Table I. The anodic spark reaction products of the rare earth metals when anodized in sodium aluminate solution

Metal	Products
Samarium	$SmAlO_3$
Europium	$EuAlO_3$
Gadolinium	$GdAlO_3$
Yttrium	$YAlO_3$
	$Y_3Al_5O_{12}$
Dysprosium	$DyAlO_3$
	$Dy_3Al_5O_{12}$
Holmium	$HoAlO_3$
	$Ho_3Al_5O_{12}$
Erbium	$ErAlO_3$
	$Er_3Al_5O_{12}$
Ytterbium	$YbAlO_3$
	$Yb_3Al_5O_{12}$

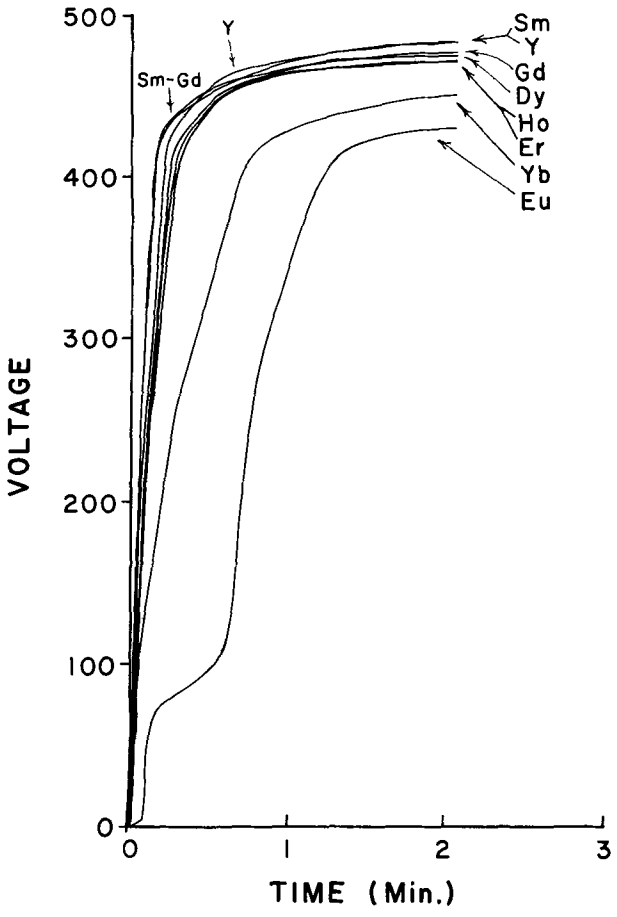

Fig. 1. The composite voltage-time curves for a variety of rare earth metals and yttrium anodized in 0.1*N* $NaAlO_2$ solution.

Electroluminescence was observed with all of the metal-electrolyte combinations investigated except with europium. The electroluminescence appeared over the entire anodic film at voltages below the spark potential and was present with spark discharges at 400V. The color of the electroluminescence varied from one rare earth metal to another but no color variations were noted with increases in voltage.

The appearance of sparking was noted with all of the rare earth metals including yttrium. The sparks were as described by Guntherschulze (9) increasing in size and becoming less mobile as the voltage increased toward the maximum. The potentials at initial and highly energetic sparking and the final potentials are given in Table II. The final potentials were obtained from the constant current density experiments performed manually after 30 min of anodization. The voltages at which highly energetic sparking became apparent for each rare earth metal were taken at the base of the knee of the curve at the point of deviation from linearity. Since small highly mobile scintillations precede the highly energetic sparks the change in slope

Table II. The potentials for initial and highly energetic sparking and the final anodization potentials for rare earth metals anodized in sodium aluminate solution

Metal	Potential (volts)		
	Initial sparking	Highly energetic sparking	Final
Samarium	271	423	555
Europium	203	385	502
Gadolinium	263	423	550
Yttrium	251	422	555
Dysprosium	250	415	543
Holmium	220	413	543
Erbium	183	412	550
Ytterbium	175	407	555

prior to the knee of the curve was taken as the point where scintillations begin.

The very strong adherent anode coatings display striking colors characteristic of the individual rare earth cations under the influence of visible light. The colors are best described in Table III. These coatings were very hard and had the appearance of fired ceramics.

The anodic spark reaction process produced perovskite coatings (see Table I) on the lower atomic number samarium, europium, and gadolinium metals. Mixtures of perovskite and garnet coatings were produced on the higher atomic number rare earth metals including yttrium. These results show the component(s) of the spark reaction products are derived from the anion constituent of the electrolyte. It is possible that noncrystalline compounds may also be present but are unaccounted for by x-ray diffraction analysis. In some patterns, *i.e.*, ytterbium products, a few extraneous and weak lines were present. Since only a few lines are left unaccounted for, it is very difficult to assign them to a definite compound. These lines, however, do not correspond to ytterbium sesquioxide.

Diffuse reflectance spectra in the near uv to visible range were obtained for the spark reaction products. The reflectance spectra for europium, holmium, and ytterbium products are shown in Fig. 2. In these regions of the spectrum the sharp absorption peaks characteristic of the rare earth ion were observed. These peaks are intra f-f transitions of predominantly electric dipole character (19) resulting from spin-orbit interactions and to a lesser extent due to the extent of the crystalline field. For the samarium, europium, and gadolinium products the spectra contained slightly displaced peaks from the corresponding peaks of similar sesquioxides. In addition, in the region of strong optical absorption only a single absorption edge was observed for the perovskite products, indicative of a single compound. The spectra for yttrium, dysprosium, holmium, erbium, and ytterbium products in addition to the slightly shifted peaks contained some extra peaks when compared to the corresponding sesquioxides. The observed spectra in the region of strong optical absorption for the perovskite-garnet products is suggestive of the existence of two absorption peaks as is found in a mechanical mixture. This data apparently confirms the results of the x-ray diffraction study that single compounds exist in the anodic products of the lower atomic number rare earth metals and mixtures exist in the anodic products of the higher atomic number rare earth metals when these metals are anodized in sodium aluminate solutions. In addition, many of the peak intensities of the perovskite and perovskite-garnet products increase and/or decrease from similar peaks found in the sesquioxides.

Table III. Color description of the anodic coatings deposited on the rare earth metals by the anodic spark process

Metal	Color
Samarium	Dark tan-brown
Europium	Light yellow-green tint
Gadolinium	Light tan
Yttrium	Tan
Dysprosium	Light tan
Holmium	Salmon
Erbium	Pink (orange-purple tints)
Ytterbium	Yellow (with pale green)

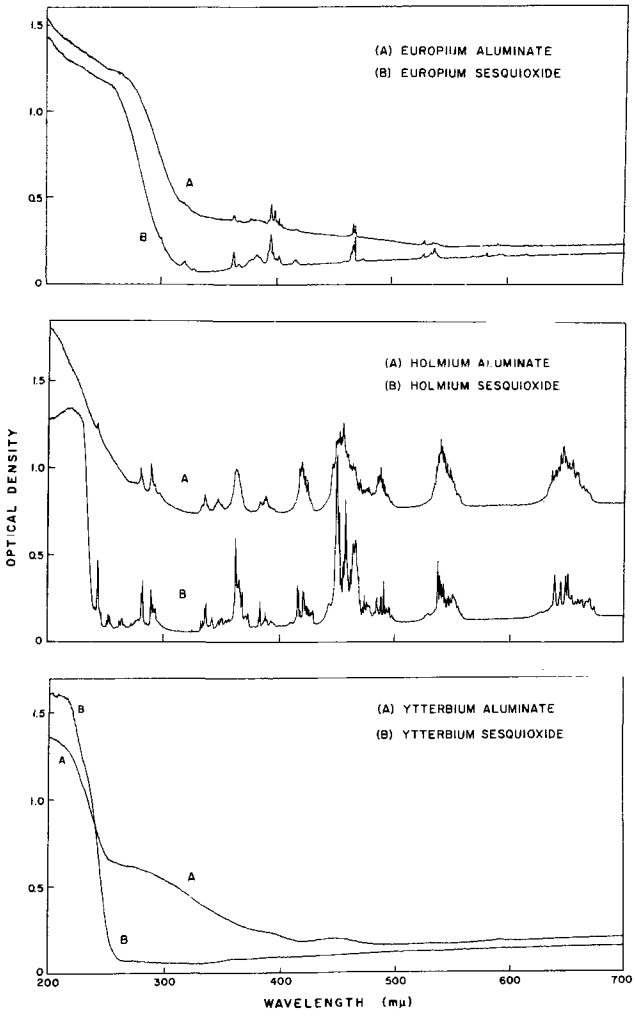

Fig. 2. Comparison of the diffuse reflectance spectra of the spark reaction products of europium, holmium, and ytterbium metals with the reflectance spectra of the sesquioxides of these metals, respectively.

Discussion

When a rare earth ion such as Yb^{+3} is added to a rare earth sesquioxide lattice, *i.e.*, Er_2O_3, no interactions take place between the erbium and ytterbium cations in the solid solutions (20). The electrostatic field generated by the Yb^{+3} ion in the erbium oxide lattice has no effect on the erbium ion. In other words, the erbium ion when in the ground state is completely independent of the ytterbium ion. However, when Al^{+3} is added to a rare earth sesquioxide lattice the tightly bound f electron levels are no longer shielded from the changes in the electrostatic field produced by the addition of Al^{+3} to the rare earth oxide lattice. This was observed in the diffuse reflectance spectra of the rare earth aluminates where the f-f transition absorption peaks were shifted. In addition, there are variations in the occupancy of the levels as indicated by the increases and/or decreases in some of the peak intensities. Where mixtures occurred as with perovskite-garnet products the extra peaks as mentioned under results are merely the absorption peaks of two compounds some of which are superimposed upon each other and others are shifted when compared to the rare earth oxide absorption peaks.

We note in Table II that both the initial spark potential and highly energetic spark potentials decrease with a decrease in size of the rare earth metal atom. Europium is an exception but the general trend is ap-

parent. This decrease in the spark potentials from Sm to Yb is similar to the decreasing values for the standard oxidation potentials of the rare earths described by the equation (21)

$$RE(s) \rightleftarrows RE^{+3}(aq) + 3e^-$$

The high values of the standard oxidation potentials which are in accord with their electropositive character places yttrium metal between gadolinium and dysprosium metals. The values of both the initial and highly energetic spark potentials also place yttrium metal between gadolinium and dysprosium. The chemistries of the rare earths (22) in the +3 oxidation state are nearly identical although slight quantitative differences exist varying systematically from lanthanum through lutetium with yttrium being placed approximately between dysprosium and holmium.

X-ray diffraction analyses showed that the anode metal was found chemically combined in the crystalline spark reaction products forming stable perovskite or perovskite-garnet rare earth compounds (Table I). This was true with all rare earth metals studied. Anodization studies of erbium metal at a voltage (150V) below the spark potential revealed the existence of two coatings. The outer coating was a white opaque glassy material identified by x-ray diffraction to be β-$Al_2O_3 \cdot 3H_2O$. The inner portion of the anode coating is pink erbium oxide produced by oxidation of the erbium anode. Continuation of anodization into the sparking region produces a series of glassy pink beads at each spark site in the white coating. These pinkish beads were identified by x-ray diffraction as the products given in Table I for erbium. Further continuation of sparking (30 min) produces on the anode surface the final pinkish colored products described in Table III.

The growth mechanism which apparently accounts for the compositions of the anodic coatings formed in sodium aluminate solution is similar to that reported by McNeill and Gruss (23) who studied anodic film growth by anion deposition in sodium aluminate solution. The present study showed that erbium metal and presumably the other rare earth metals and yttrium form a film of oxide of the anode metal prior to the deposition of the anion constituent. The metal oxide film is apparently the anodic barrier film which is common to anodes such as Al, Ta, and Zr which exhibit strong tendencies to form such barrier films in most electrolytes. This, of course, is followed by accumulation and precipitation of the anion constituent on the anode surface that is β-$Al_2O_3 \cdot 3H_2O$. At this point it is uncertain whether the barrier film remains as the metal oxide initially formed or has been modified by the deposition of the anion constituent. Upon precipitation of the anion constituent on the anode surface sparking induces the interaction of the metal oxide film and the precipitated anion constituent. It is uncertain whether the metal-oxidation and/or anion deposition reactions continue when sparking commences. However, since spark reaction products are ejected from the anode surface followed by healing at the site of ejection, it is believed that both reactions continue. In addition to the reactions described, there are undoubtedly other anodic phenomena occurring simultaneously at the anode.

The crystalline spark products obtained from the anodic reactions of Sm, Eu, Gd, Y, Dy, Ho, Er, and Yb metals in 0.1*N* sodium aluminate solution are quite similar to the solid solutions produced by Schneider *et al.* (7). In the study of Schneider *et al.* equimolar amounts of Sm_2O_3, Eu_2O_3, Gd_2O_3, Y_2O_3, Dy_2O_3, Ho_2O_3, Er_2O_3, and Yb_2O_3 were respectively mixed with Al_2O_3, pressed into pellets, and fired in an atmosphere using a program controlled furnace at 1650°C for 6 hr. Equilibrium was attained when x-ray patterns of a specimen showed no change with successive heat-treatments. Perovskite structures of $SmAlO_3$, $EuAlO_3$, and $GdAlO_3$ were produced for equimolar compositions heated to 1650°C for 6 hr. These results were also obtained by Geller and Bala (3). Perovskite and garnet mixtures having the general formulas of $(RE)AlO_3$ and $(RE)_3Al_5O_{12}$ (RE = rare earth) respectively were produced for dysprosium, holmium, yttrium, and erbium. Only garnets were produced with ytterbium. Most of these mixtures also contained an unknown or c-type oxide. Garton and Wanklyn (8) in their work with the rare earth aluminates reported that $YbAlO_3$ prepared coexisted with the garnet phase which is comparable to our results (see Table I).

The lattice parameter of the $Yb_3Al_5O_{12}$ garnet which we prepared by the anodic spark reaction was calculated to be 11.8962Å. This value is in agreement with the trend demonstrated by Bertaut and Forrat (4) showing decreasing lattice parameter values in going from gadolinium to erbium.

Manuscript submitted Sept. 5, 1972; revised manuscript received Oct. 27, 1972. This was Paper 15 presented at the Houston, Texas, Meeting of the Society, May 7-11, 1972.

Any discussion of this paper will appear in a Discussion Section to be published in the December 1973 JOURNAL.

REFERENCES

1. M. L. Keith and Rustum Roy, *Am. Mineralogist*, **39**, 1 (1954).
2. V. M. Goldschmidt, T. Barth, G. Lunde, and W. Zachariasen, Geochemische Verteilungsgesetze der Elemente, VII. Skrifter Norske Videnskap-Akad. Oslo, I. Mat. Naturv. Kl., No. 2 (1926).
3. S. Geller and V. B. Balla, *Acta Cryst.*, **9**, 1019 (1956).
4. F. Bertaut and F. Forrat, *Compt. Rend.*, **243**, 1219 (1956).
5. H. S. Yoder and M. L. Keith, *Am. Mineralogist*, **36**, 519 (1951).
6. I. Warshaw and Rustum Roy, *Am. Ceram. Soc. Bull.*, **38**, 169 (1959).
7. S. J. Schneider, R. S. Roth, and J. L. Waring, *J. Res. Nat. Bur. Std. A.*, **65A**, 845 (1961).
8. G. Garton and B. M. Wanklyn, *J. Cryst. Growth*, **1**, 164 (1967).
9. A. Guntherschulze and H. Betz, *Z. Physik.*, **78**, 196 (1932).
10. H. A. Evangelides, U. S. Pat. 2,723,952 (1955).
11. W. McNeill and R. Wick, *This Journal*, **104**, 356 (1957).
12. W. McNeill, *ibid.*, **105**, 544 (1958).
13. L. L. Gruss and W. McNeill, *Electrochem. Technol.*, **1**, 283 (1963).
14. W. McNeill, L. L. Gruss, and D. G. Husted, *This Journal*, **112**, 713 (1965).
15. N. Greene and L. Lee, *U. S. At. Energy Comm.*, TID-18697 (1963).
16. A. Heller, K. W. French, and P. O. Haugsjaa, *Chem. Phys. Letters*, **10**, 127 (1971).
17. P. O. Haugsjaa, A. Heller, and K. W. French, *ibid.*, **10**, 130 (1971).
18. A. Heller, K. W. French, and P. O. Haugsjaa, *J. Chem. Phys.*, **56**, 2368 (1972).
19. B. G. Wybourne, "Spectroscopic Properties of Rare Earths," p. 205, Interscience, New York, (1965).
20. Leonard Gruss and Robert E. Salomon, *J. Phys. Chem.*, **74**, 3969 (1970).
21. W. M. Latimer, "The Oxidation States of the Elements and Their Potentials in Aqueous Solutions," 2nd ed., Chap. 20, Prentice-Hall, New York (1952).
22. F. A. Cotton and G. Wilkinson, "Advanced Inorganic Chemistry," p. 882, Interscience, New York (1962).
23. W. McNeill and L. Gruss, *This Journal*, **110**, 853 (1963).

pH Optimization Studies on a Basic Ammoniacal Citrate Ni-Fe Plating Solution for Use in Plated Wire Memory Production

R. L. Barauskas* and A. E. Guttensohn

GTE Automatic Electric Laboratories Incorporated, Northlake, Illinois 60164

ABSTRACT

Plated wire was produced from a basic ammoniacal citrate Ni-Fe plating solution. The solution pH and solution aging characteristics were investigated *vs.* plated wire material, device, and memory properties. An optimum operating range of this solution was found to be between pH = 8.4 and 8.6. A group of equations was developed which accurately predicted both the device and the memory characteristics of the plated wire from only the materials data and solution pH.

The electrodeposition of zero magnetostrictive Ni-Fe alloys for plated wire memory applications has been successfully accomplished with either acid or basic Ni-Fe electrolyte solutions (1, 2). Both solution types were also tried in our laboratories. A preference was found after extensive experimentation with both. The basic ammoniacal citrate solution was found more acceptable for the following reasons: (*i*) The evaporation rate of deionized water from the Ni-Fe baths was lower for the basic bath which was operated between 18°-24°C than for the acid sulfate baths which were operated between 45°-50°C. The advantage of the lower evaporation rate is that the concentration level of the various ionic species present in the bath is more stable with time. (*ii*) After a two-day "age in" the oxidation of Fe^{++} to Fe^{+++} in the basic solution is complete. In the case of the acid sulfate solutions, the oxidation aging is a continuing process which necessitates daily bath analysis and appropriate additions. After two days only pH adjustments have to be made to the basic solution. This is accomplished by additions of NH_4OH. The Ni and Fe levels in the basic solution are monitored every two weeks and maintained by additions of nickel and iron(III) citrate. By using this technique we were able to maintain a bath for two and one-half years. (*iii*) No stress relievers were necessary. (*iv*) Bath analysis and maintenance are simpler which result in lower costs for bath upkeep.

In the process of working with the basic bath as described in Stephen's patent (2), it was found that concentration changes and Ni-Fe ratio changes were required in order to produce zero magnetostrictive films with our plating line (3). The 5 to 1 Ni-Fe ratio which Stephen proposes had to be changed to 9 to 1 because of our solution flow rates and cell currents. Also the suggested pH range of 9.2-9.25 at our operating conditions and the new concentration levels produced some undesirable plated wire device and memory properties. Therefore, it became of interest to characterize fully, for the conditions of use, the basic ammoniacal citrate Ni-Fe plating solution in terms of the material, device, and memory properties of the plated wire. The characterization led to a new and more stable pH operating range and the development of a group of equations which allowed us to predict the device and memory properties of the annealed plated wire from only the materials and pH data. Results from these equations were spot checked with an off-line memory tester. Agreement was close enough to allow us to eliminate an on-line memory test screening station and replace it with a few simple off-line materials tests. A very simple on-line device test setup which displayed e_{out} *vs.* I_w (see Fig. 1) was also used to aid in wire screening. By using these equations and the on-line device test setup we were able to screen out wires or wire lots which were unworthy of any off-line memory testing.

* Electrochemical Society Active Member.
Key words: electrodeposition, alloys permalloy, Ni-Fe films, plated wire, pH.

Experimental Procedure

The basic plating line setup uses Lexan and Lucite plating cells with various exposure lengths and solution flow rates. Our plating line consisted of the following steps (3): an anodic electroclean solution (Enbond 160) operated at 70°C and 6.5 A/dm²; a 5% H_2SO_4 solution operated at 65°C; an anodic electropolish solution consisting of 2 to 1 parts by volume phosphoric acid to glycerin operated at 55°C and 8 A/dm²; a 50% methanol water rinse operated at room temperature; a pyrophosphate dip consisting of 540 g/liter of Unichrome S-13 in water operated at pH = 9, and room ambient; a cathodic pyrophosphate copper strike consisting of 540 g/liter of Unichrome S-12 in water operated at pH = 9, room ambient and 20 A/dm²; a cathodic bright acid sulfate copper plate consisting of 655g $CuSO_4 \cdot 5H_2O$, 107 ml conc H_2SO_4, 15 ml UBAC No. 1 brightener, enough HCl to make the total chloride ion concentration 30 mg/liter, and deionized water to make the total volume 3000 ml, operated at room ambient and 50 A/dm²; an anodic etch consisting of 2 to 1 parts by volume phosphoric acid to water operated at room ambient and 40 A/dm²; four identical NiFe plating cells operated between 18°-20°C with a flow rate of 1.5-2 liters/min and a current density of 10 A/dm²; a deionized water rinse cell; an on-line annealer which was operated between 225°-325°C with a nitrogen gas atmosphere; and a limited on-line device test station. All plating cells were followed by a water rinse cell except electropolish, pyrophosphate, and NiFe cells. The specifics on the geometry of each of our plating cells is proprietary.

Seven plated wire lots, each containing 120 pieces of 9-in. long plated wire, were made at seven different values within the pH range of 8.23-9.61 of the basic ammoniacal citrate NiFe plating solution. The resultant NiFe plate was then evaluated for material, device, and memory characteristics (see Fig. 1). In all, twenty-two characteristics were evaluated. The materials characteristics included H_c, H_k, skew, dispersion, hysteresis of the Belson trace, film thickness as calculated from the hard axis sense voltage output for a sinusoidal drive field large enough to completely saturate the film in the hard axis direction, and alloy composition in terms of torsional strain sensitivity. The device characteristics included output, uniformity of output as σ/output, where σ is the standard deviation of sampled outputs from a 9-in. long piece of plated wire, time duration of the output, initial switching, intermediate switching, final switching, output symmetry, switching symmetry, I_{Hc}, maximum

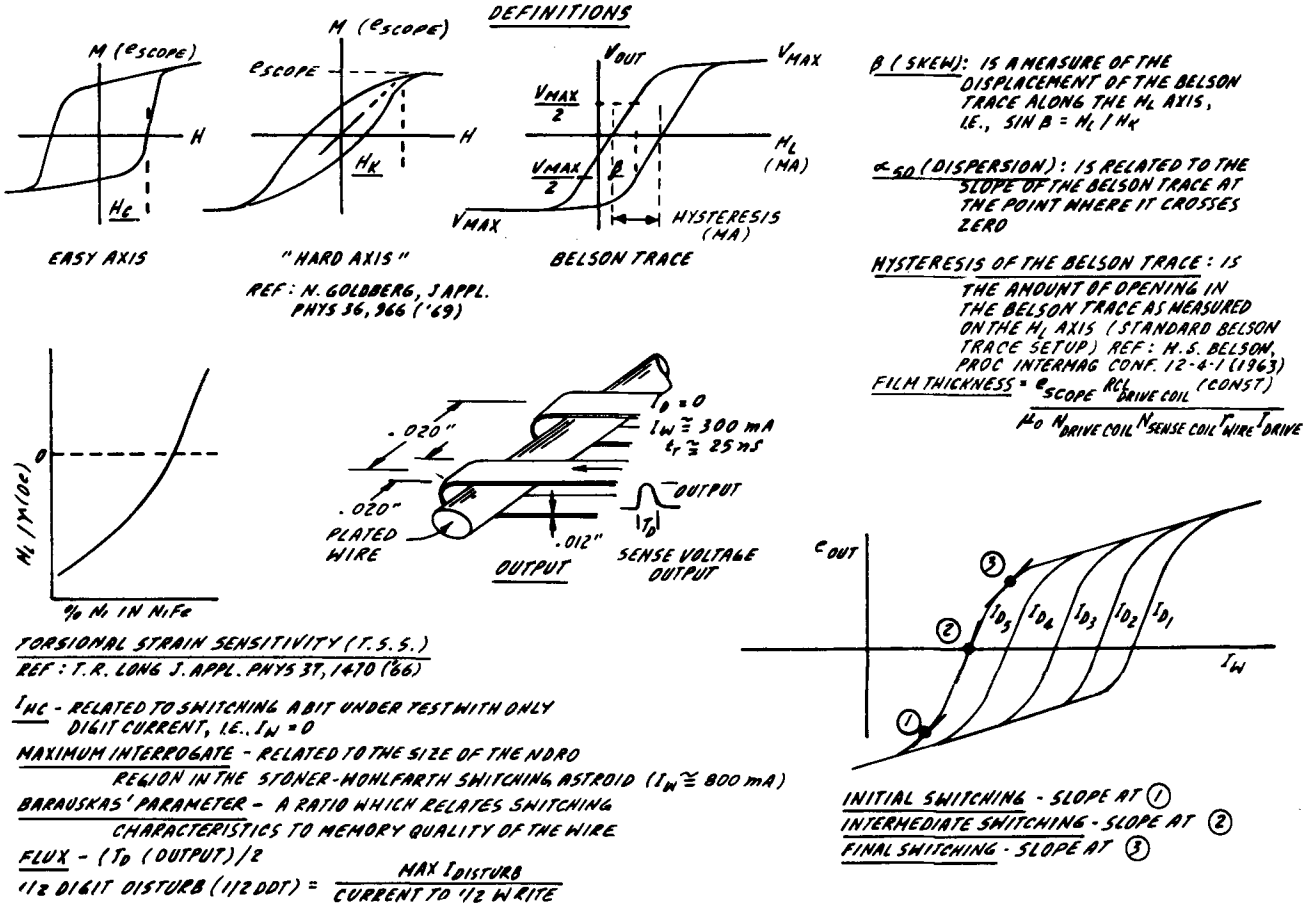

Fig. 1. Definition of terms

interrogate, flux, flux/film thickness, output, film thickness, and Barauskas' parameter. Barauskas' parameter is a quotient of two digit currents. The numerator is the digit current which when combined with a word current of 600 mA causes the output from the plated wire to be reduced by ½ of its fully switched value. The denominator is the digit current which when combined with zero word current produces 0.9 of the fully switched output value. It was verified that wires with smaller Barauskas' parameter values had a better chance of passing the half-digit disturb creep related memory test than those with larger values. The single memory characteristic which was tested was half-digit disturb. Previous work showed that some characteristics, even though they varied significantly, produced little or no effect on the memory quality of the wire. These characteristics are termed noncritical. The remaining characteristics were critical and are referred to as such: skew, dispersion, H_k, uniformity of output, I_{Hc}, maximum interrogate, initial switching, Barauskas' parameter, and half-digit disturb. These were further broken down into three groups of three with the last three characteristics being the most critical to the functioning of the wire as a memory element, the middle three being less critical, and the first three being the least critical.

The ammoniacal citrate plating solution (Ni/Fe = 9) contained the following; Part 1: 900g of $NiCO_3$, 1504g of $(NH_4)_2HC_6H_5O_7$ (ammonium citrate), and 1250g of $HOC(CH_2CO_2H)_2CO_2H \cdot H_2O$ (citric acid monohydrate) diluted to 11 liters with deionized water; Part 2: 49.5g of iron dust, 223.3g of $(NH_4)_2HC_6H_5O_7$ (ammonium citrate), and 191.6g of $HOC(CH_2CO_2H)_2CO_2H \cdot H_2O$ (citric acid monohydrate) diluted to 5.5 liters with deionized water.

Results and Discussion

The aging mechanism of this ammoniacal citrate nickel-iron plating solution was investigated. Upon mixing, all iron is in the ferrous (Fe^{++}) state and oxidation to the ferric (Fe^{+++}) state starts immediately (see Fig. 2). When the solution is brought up in pH by additions of NH_4OH this oxidation takes place more rapidly. Data in Fig. 2 were taken immediately after the NH_4OH addition. As the $2Fe^{++} + H_2O + \frac{1}{2} O_2 \rightarrow 2Fe^{+++} + 2(OH)^-$ reaction neared completion, both film thickness and output increased and the magnetic properties approached those characteristic of wires plated from a used or aged ammoniacal citrate nickel-iron plating solution. The Fe^{++} was monitored hourly by titration. The reaction took two days to reach completion. Wires were taken hourly and materials tested. It was found that as Fe^{++} decreased, both output and thickness increased. The rate of Fe^{++} oxidation to Fe^{+++} when the solution was agitated (about 1.5 liters/min flow) was an order of

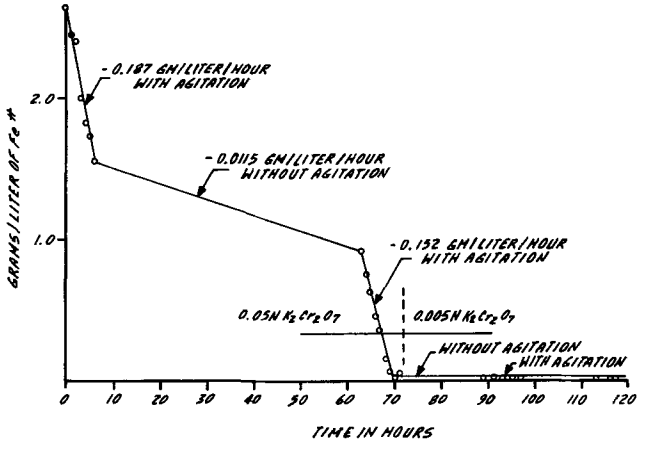

Fig. 2. Grams/liter of Fe^{++} vs. time for ammoniacal citrate nickel-iron plating solution. Solution temperature +16°. Fe^{++} determined by the dichromate method.

magnitude greater than that for the nonagitated state (see Fig. 2). The increased oxidation rate is due to the larger surface area of solution exposed to the atmosphere when the solution is agitated. The iron plates out from some Fe^{+++} complex rather than from a complex of Fe^{++}. The effective magnetic thickness tells us when the solution is ready for plating. When the effective magnetic plating thickness reaches 0.8 μm at standard operating conditions, the solution is then producing wire characteristic of an aged solution. This oxidation aging process can be avoided by using ferric citrate.

The efficiency study of the ammoniacal citrate nickel-iron plating bath was done under the following conditions: nickel to iron ratio was 9, the nickel-iron solution temperature was 17°C, the pH of the solution was 9.2, the cathode was the beryllium copper wire, the current density was 9.873 A/dm^2, the anode was a platinum helix, the flow rate of the solution was 1.6 liters/min, four 1-inch cells were used, the wire speed was 3 in./min, and the annealing temperature was 225°C.

Thickness measurements were made using a B-H loop tracer which measures integrated voltage output from the film *vs.* drive field (see Fig. 1). From these film thickness measurements we were able to determine efficiency of the plating solution.

The resulting efficiency of the basic ammoniacal citrate NiFe solution was calculated to be 30.6%.

In making plated wire it was found that in order for the wire to work as a memory element, the materials and device parameters had to assume certain values. Thus we were able to predict good memory properties with a high probability using just materials and device testing results. Barauskas' parameter correlates highly with the half-digit disturb test (95% confidence level). If Barauskas' parameter was 40 or less, there was then a high confidence that the wire had good memory properties (passing, or nearly so).

An arbitrary value of 100 or less for Barauskas' parameter, (anything over 100 was failing), was used to define testworthy wire. These testworthy wires were found to have predictable properties, while untestworthy wires (those which failed Barauskas' parameter) were found to have nonpredictable properties and were not worth device and/or off-line memory testing.

We then constructed a matrix of materials, device, and memory parameters using 49 lots of wire, including both testworthy and untestworthy wires. Using regression analyses between highly correlating parameters, we defined values of all other parameters in terms of just passing Barauskas' parameter with a value of 100 or less (testworthy wires) and having a value of 40 or less for Barauskas' parameter (memory value). The results are given in Table I.

To get the most out of our data, we developed equations to predict device and memory characteristics from materials data. Since the extensive device and off-line memory tests are time consuming, wire lots can be screened for this testing by the quick materials and on-line device tests. The one qualification that had to be imposed was that only testworthy wires (with Barauskas' parameter less than 100) could be used to predict device and memory values with any accuracy using the developed equations. From these equations one can tell that a wire is untestworthy, but one cannot characterize it, so that in this case the equations can be used to screen but cannot be used to predict values. The testworthy wires followed the equations closely.

The development of the equations was straightforward, but assessing their worth was time consuming. Initially, we had the 28 testworthy lots in a matrix and ran correlations among the device, materials, and memory characteristics. After making sure that the correlation was linear by running a scatter diagram, we picked the highest correlation between a materials and memory/device characteristic and ran a regression analysis for the particular materials and memory device characteristic. We picked the next highest correlation and repeated the procedure until we had all of the device and memory parameters in terms of material parameters. We then compared values for the device and memory characteristics using the developed equations and the actual values obtained when they were tested. Most of the equations were found to be unsatisfactory. The highest correlating parameters were fairly close. Our hope to keep the equations simple was gone. We then ran a multiple regression with each device and memory parameter against all five of the materials parameters to get equations of the form: $y = a_1x_1 + a_2x_2 \ldots + a_nx_n + b$. These were found to be quite satisfactory except in one case, half-digit disturb. We did a multiple regression analysis for half-digit disturb in terms of both materials and device parameters. The equation which resulted was found to be useful. Therefore, if one had only materials parameters, one could calculate the device parameters and then use these values in the equation for half-digit disturb.

The last refinement of the equations was the addition of a process parameter, namely NiFe solution pH, to the matrix. This refinement came after we had seen that lots run at pH's significantly different from 8.5 (our operating pH) were not as close in their calculated to actual values as those run at a pH of 8.5. To make these equations useful for the range of pH's studied we ran multiple regressions with each memory and device parameter against all five materials parameters and pH (for the half-digit disturb materials parameters, pH and device parameters were included). Upon comparing the multiple regressions, we found that for some device and memory characteristics, adding pH to the equation did not produce an increase

Table I. Regression analyses

(Refer to Fig. 1)

Parameter	Testworthy wire value	Memory value
Initial switching	≧0.74	≧0.95
Maximum interrogate	≧560 mA	≧830 mA
Hysteresis	≦20 mA	≦11 mA
H_k	≦7.4 oe	≦5.7 oe
I_{H_c}	≦195 mA	≦155 mA
Dispersion	≦25 mA	≦19 mA
Current to half write	≦76 mA	≦48 mA
Output	≧15 mV	≧20 mV
H_c	≦6.1 oe	≦4.5 oe
Maximum current to disturb	≧31 mA	≧28 mA
Thickness	0.83-0.87 μm	0.83-0.87 μm
Uniformity	≦10%	≦5%
Composition	±0.5 mA/deg. off ZMC	±0.5 mA/deg. off ZMC
Skew	0 ± 0.5 mA	0 ± 0.5 mA
Output/thickness	17 mV/μm	24 mV/μm

Table II. Equations developed

Initial switching	−0.051 H_k − 0.0066 hysteresis + 0.0015 dispersion − 0.0126 pH + 0.038 H_c + 1.203
Current to half-switch	−9.03 H_k − 0.435 hysteresis + 2.13 dispersion + 19.69 pH + 18.93 H_c − 154.3
Output	1.12 H_k − 0.31 hysteresis − 0.373 dispersion − 6.18 pH − 2.41 H_c + 82.58
Barauskas' parameter	19.07 H_k + 1.92 hysteresis − 0.836 dispersion + 1.53 pH − 11.26 H_c − 37.35
Maximum interrogate	−192.14 H_k − 19.97 hysteresis + 1.1 dispersion + 84.7 pH + 194.4 H_c + 382.6
I_{H_c}	−11.03 H_k + 1.14 hysteresis + 0.55 dispersion + 13.7 pH + 32.9 H_c − 74.2
Maximum current to disturb	8.23 H_k − 0.9 hysteresis − 0.85 dispersion + 12.1 H_c − 70.6
Half-digit disturb	−0.0066 Barauskas'* + 0.00048 I_{H_c}* + 0.235 H_k + 0.00002 maximum interrogate* + 0.014 hysteresis − 0.031 dispersion + 0.57 initial switching* − 0.119 pH − 0.0175 H_c + 0.0035 TSS − 0.00076

* The * parameters can either be actual or calculated values. TSS is torsional strain sensitivity.

in accuracy of the equation. The final equations are listed in Table II.

Figures 3-14 show the material and device characteristics from the 49 wire lots (seven lots at each of seven different pH levels between 8.23 and 9.61 pH units) plotted *vs.* pH. From these data the operating range of 8.39 to 8.5 was defined, since more threshold values were passed in this range than in any other.

To show the usefulness of the equations developed to predict device and memory characteristics from materials parameters, we have graphed both actual and predicted values of the device and memory parameters for the pH mapping, (see Fig. 7-14).

Since only on-line annealing was done and no long-term aging studies were performed on the plated

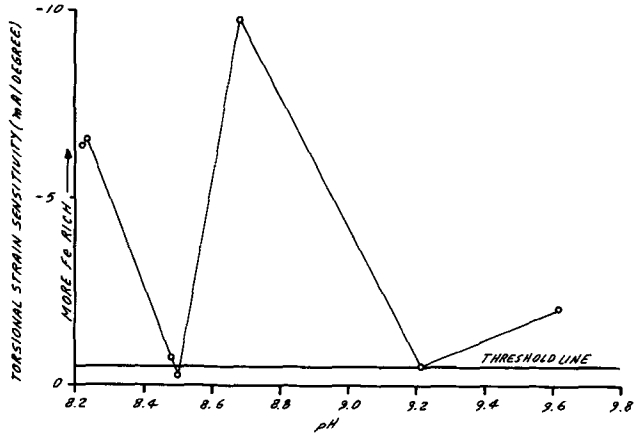

Fig. 3. Torsional strain sensitivity *vs.* pH for citrate Ni-Fe plating solution wires. ○ = Observed.

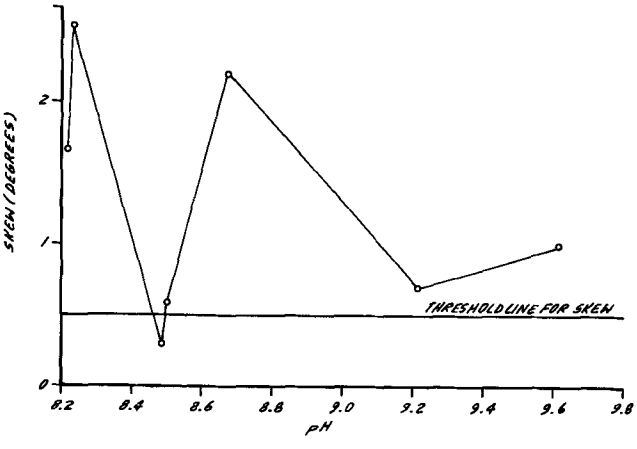

Fig. 4. Skew *vs.* pH for citrate Ni-Fe plating solution wires. ○ = Observed.

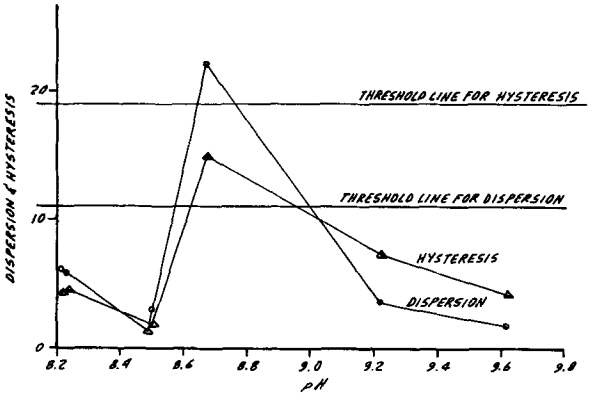

Fig. 5. Dispersion and hysteresis *vs.* pH for citrate Ni-Fe plating solution wires. ○ = Observed dispersion, △ = observed hysteresis.

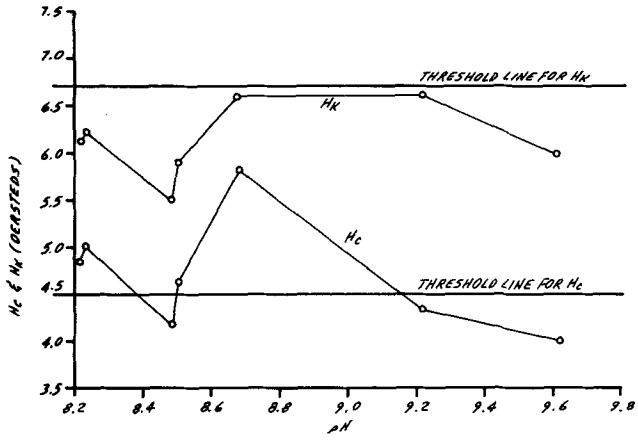

Fig. 6. H_c and H_k *vs.* pH for citrate Ni-Fe plating solution wires. ○ = Observed.

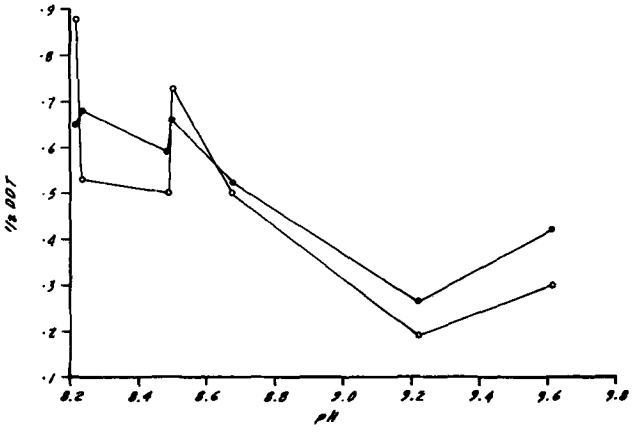

Fig. 7. ½ Digit disturb *vs.* pH for citrate Ni-Fe plating solution wires. ○ = Observed, ● = calculated.

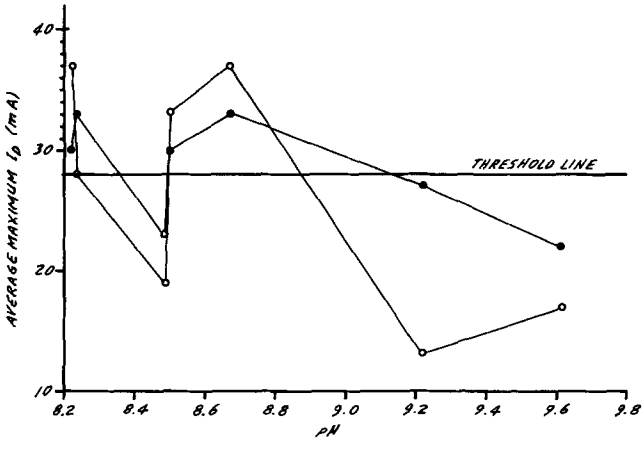

Fig. 8. Average maximum I_D *vs.* pH for citrate Ni-Fe plating solution wire. ○ = Observed, ● = calculated.

wires produced from this basic ammoniacal citrate bath, it is difficult to say anything quantitative about radial or circumferential compositional gradients in our wires. However, others have found that the first roughly 1200-1500Å of plate is very iron rich, usually 40-60% instead of 20% Fe (4, 5). If these gradients do in fact exist in our wires (6), we feel that they could be eliminated by changes in the NiFe solution flow pattern around the wire and/or by the superposition of an a-c current on the d-c NiFe plating current (7).

Conclusion

The usual 9.2-9.25 pH range for the basic ammoniacal citrate Ni-Fe plating solution has been found

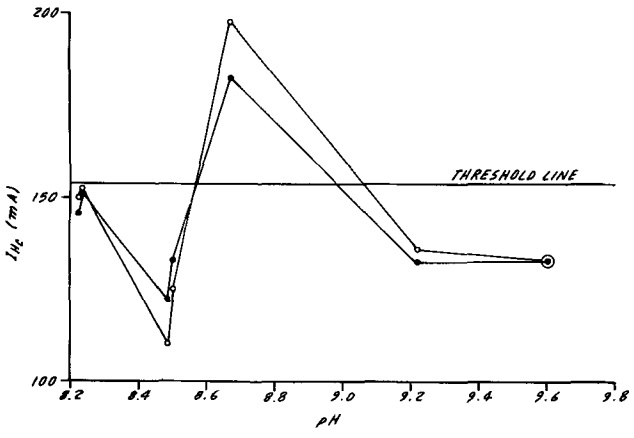

Fig. 9. I_{Hc} vs. pH for citrate Ni-Fe plating solution wires. ○ = Observed, ● = calculated.

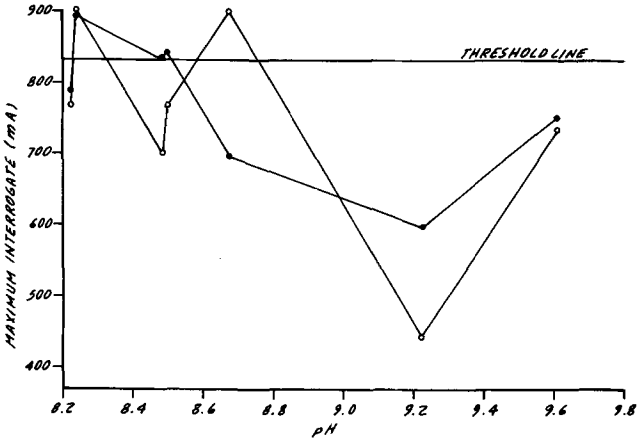

Fig. 10. Maximum interrogate vs. pH for citrate Ni-Fe plating solution wires. ○ = Observed, ● = calculated.

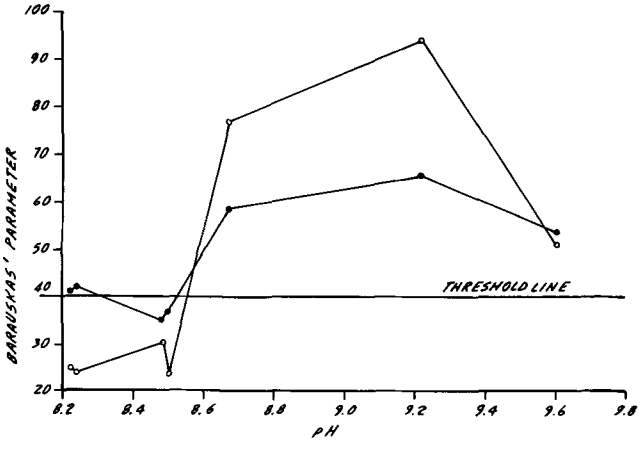

Fig. 11. Barauskas' parameter vs. pH for citrate Ni-Fe plating solution wires. ○ = Observed, ● = calculated.

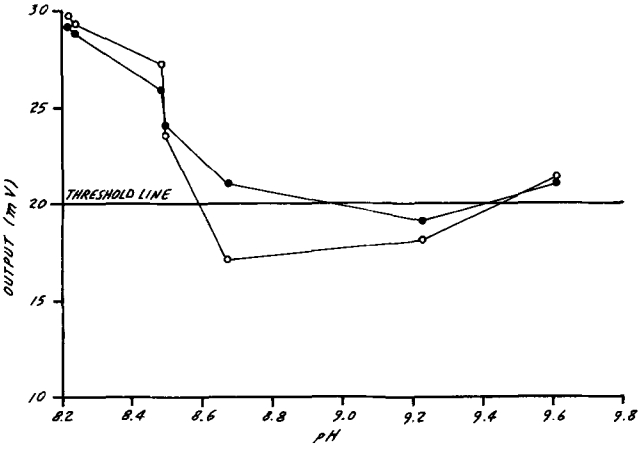

Fig. 12. Output vs. pH for citrate Ni-Fe plating solution wires. ○ = Observed, ● = calculated.

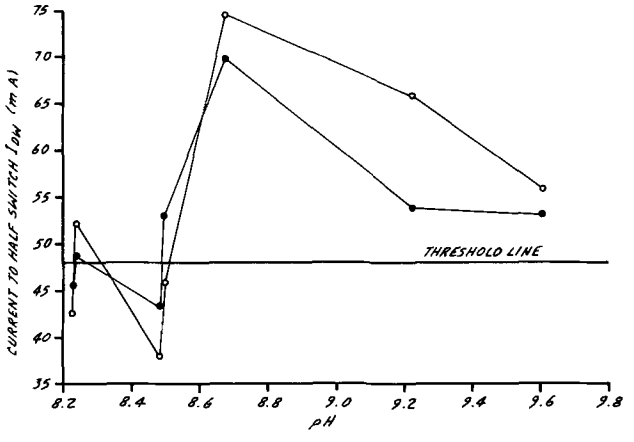

Fig. 13. Current to half switch I_{DW} vs. pH for citrate Ni-Fe plating solution wires. ○ = Observed, ● = calculated.

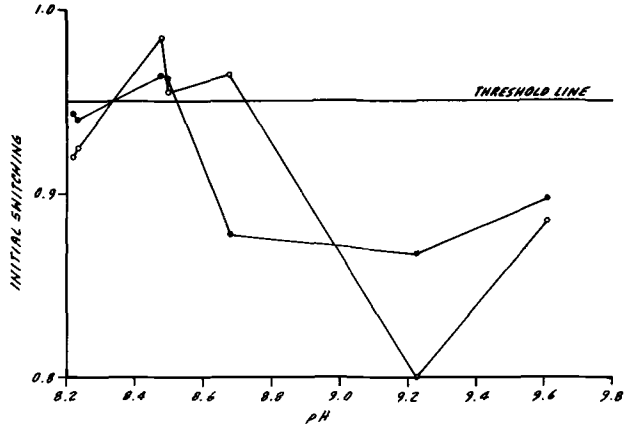

Fig. 14. Initial switching vs. pH for citrate Ni-Fe plating solution wires. ○ = Observed, ● = calculated.

less acceptable for producing memory quality plated wire than the 8.39-8.5 pH range (solution Ni Fe = 9).

For this particular plating solution a group of equations was developed which accurately predicted the resultant device and memory characteristics of annealed plated wire from the materials and pH data alone. This approach proved to be a valuable time saver prior to off-line memory testing as it served as a very effective screener of good, bad, and marginal quality memory wires. Studies to note changes in the developed equations brought about by wire aging and a combined a-c to d-c plating current had been planned but to date have not been accomplished.

Acknowledgments

The authors wish to acknowledge the help of E. P. Bulan, all of the members of the plated wire efforts at our laboratories, and especially Doctors R. F. Janninck and M. E. Dempsey for their suggestions and encouragements during the course of this study. Also special thanks to Hernando Corredor for drawing the figures.

Manuscript submitted June 19, 1972; revised manuscript received Sept. 27, 1972. This was Paper 106 presented at the Cleveland Meeting of the Society, Oct. 3-7, 1971.

Any discussion of this paper will appear in a Discussion Section to be published in the December 1973 JOURNAL.

REFERENCES
1. T. R. Long, *J. Appl. Phys.*, **31**, 1235 (1960).
2. J. H. Stephen, British Pat. 925,144.
3. R. L. Barauskas and A. E. Guttensohn, *GTE Automatic Electric Tech. J.*, **11**, 346 (October 1969).
4. H. Dahms, *Electrochem. Technol.*, **4**, 530 (Nov.-Dec. 1966).
5. W. D. Doyle, *J. Appl. Phys.*, **38**, 1441 (1967).
6. J. S. Mathias and G. A. Fedde, *IEEE Trans-Magnetics*, **MAG-5**, 728 (1969).
7. Z. Kovac, *This Journal*, **118**, 51 (1971).

Anodic Oxidation of N,N,N'-Triphenyl-o-Phenylenediamine

Peter Berkenkotter[1] and Robert F. Nelson*

Department of Chemistry, University of Idaho, Moscow, Idaho 83843

ABSTRACT

The anodic oxidation of N,N,N'-triphenyl-o-phenylenediamine in acetonitrile at platinum leads to 5,10-dihydro-5,10-diphenylphenazine in near quantitative yields *via* an intramolecular cyclization reaction. This reaction is the key intermediate step in the formation of dihydrophenazines from substituted diphenylamines. Selection rules are presented for these reactions defining the structural requirements and electrolysis conditions necessary.

The oxidative cyclization process of certain substituted diphenylamines to form the corresponding dihydrophenazines has been known for some time. This reaction was first effected chemically by Wieland using either permanganate or lead dioxide (1, 2). Recently, a number of investigators have studied the electrochemical oxidation of a series of substituted diphenylamines and have found that in some cases this same pathway is followed. This possibility was first suggested by Němec and co-workers (3) for di-*p*-tolylamine and later verified for a number of 4,4'-disubstituted diphenylamine derivatives (4). Subsequent studies of Cauquis and co-workers have further established the validity of this process in diphenylamine systems (5, 6). Thus, there is little doubt that the over-all process is as shown below

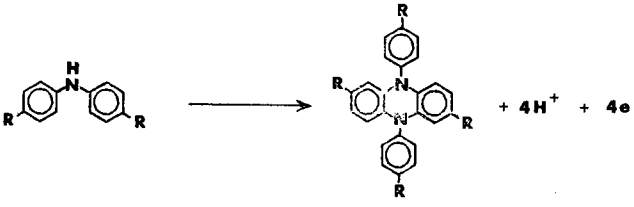

The detailed mechanism is still somewhat in doubt; this communication is intended to identify the intermediate in this remarkable reaction and provide a set of selection rules for formation of dihydrophenazines.

Experimental

The N,N,N'-triphenyl-o-phenylenediamine (TPOPD) was prepared by the method of Welzel (7), mp 94.5°-95° (lit. 93°). Acetonitrile (MeCN) was purified by drying for several days over CaH_2, followed by distillation twice from P_4O_{10}; for the distillations, only the middle 60% fraction was retained. The tetraethylammonium perchlorate (TEAP) was prepared from tetraethylammonium hydroxide and perchloric acid, followed by recrystallization four times from water. The instrumentation and electrodes used were standard and all potentials reported are *vs.* an aqueous SCE. An authentic sample of 5,10-dihydro-5,10-diphenylphenazine (DPPZ) was donated by Professor Henry Gilman.

Preparative electrolysis of TPOPD.—The TPOPD (84 mg) was dissolved in MeCN/0.1F TEAP (200 ml) in a commercial two-compartment Sargent electrolysis vessel; the working electrode was a platinum gauze and the auxiliary a carbon rod. At a cell potential of +1.3V the electrode process yielded an n-value of 4.1 ± 0.1 Faradays/mole of TPOPD. The oxidation process required roughly 40 min for completion (1% of initial current) and was followed by re-reduction at −0.7V to convert the product to the neutral form and electrolyze away protons generated in the coupling reaction. The solvent was evaporated, (room temperature) and the residue was extracted with benzene. This was combined with a small amount of product scraped off the working electrode and the whole was chromatographed on Woelm neutral alumina with benzene and recrystallized from benzene/petroleum ether, mp 286°-287° [lit. 283°-285° (8)]. Cyclic voltammetric curves established the absence of any parent material following electrolysis and the isolated yield was 74 mg (88%).

Results and Discussion

In Fig. 1, cyclic voltammetric curves are shown for a millimolar solution of TPOPD before and after exhaustive electrolysis. There is some distortion of the TPOPD curves at different scan rates due to adsorption

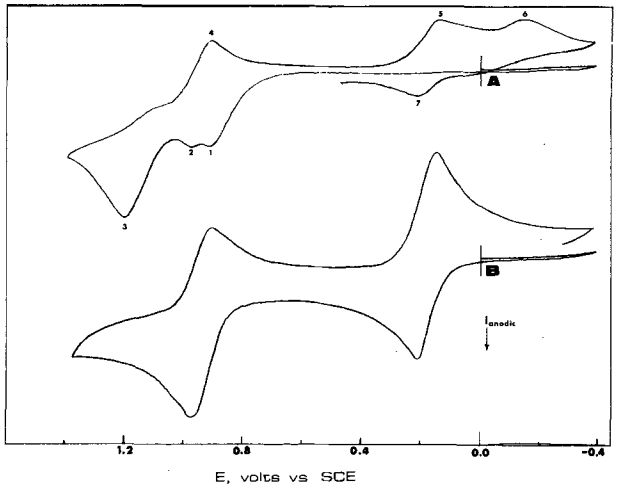

Fig. 1. Curve A: Cyclic voltammogram of 1.2 X 10^{-3}F TPOPD in MeCN/TEAP Pt button working electrode, scan rate = 0.5 V/sec. Curve B: Cyclic voltammogram of the same solution following controlled-potential exhaustive electrolysis at +1.3V, scan rate = 0.1 V/sec.

* Electrochemical Society Active Member.
[1] Present address: Department of Chemistry, Ohio State University, Columbus, Ohio 43200.
Key words: diphenylamines, dihydrophenazines, N,N,N'-triphenyl-o-phenylenediamine, anodic cyclization.

of the various species involved, but the data shown are representative. Wave 1 is the primary oxidation of the parent TPOPD to the cation radical; the radical is moderately stable. At a sweep rate of 2 V/sec and a reversal potential of +1.0V this wave is completely reversible. Waves 2, 4, 5, and 7 are due to the DPPZ, as can be seen in curve B, a scan of the solution following exhaustive electrolysis; curve B is identical to the cyclic voltammogram of an authentic sample of DPPZ. Wave 3 is most likely the TPOPD cation-dication wave (its height decreases markedly with decreasing scan rate), although this must be considered as speculative. Wave 6 is due to the reduction of protons released in the coupling reaction.

Chronoamperometric data confirm the coulometric n-value of four electrons per TPOPD molecule. Although some details of the oxidation process have not been delineated, the mechanism can be depicted as the following

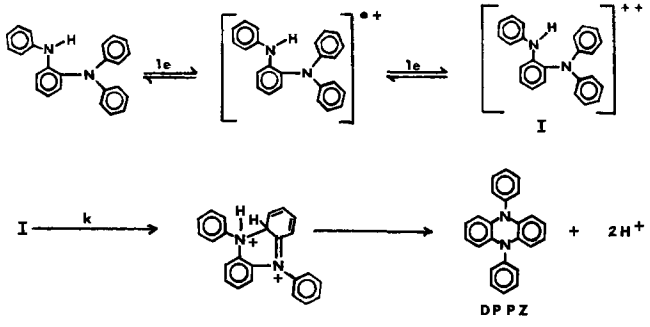

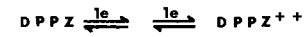

Note that the cyclization is depicted as occurring in the dication state; however, in Fig. 1, curve A it can be seen that some DPPZ is present following the initial oxidation process, *i.e.*, following generation of the cation radical. If the cyclization reaction does take place through the dication, then the possibility of rapid disproportionation of the cation radical to parent and dication must be considered. This is not unlikely, since the parent-cation and cation-dication waves are only separated by about 250 mV. Another possibility is cyclization of the cation radical and subsequent oxidation of this species to generate the DPPZ. Both of these mechanisms are tenable, but it would be difficult indeed to distinguish between them at this time. It is also possible, as shown, that some oxidation of the TPOPD cation occurs at the potential where DPPZ shows up in curve A; upon formation of the dication there would be an immediate cyclization to the DPPZ. Chemical intuition suggests a cyclization from the dication, but all of the above pathways must be considered plausible at this time.

This cyclization reaction going through a TPOPD-like intermediate is not at all general for all diphenylamines; in fact, there are several stringent structural limitations to its facilitation. As can be seen, TPOPD could be generated from diphenylamine (DPA) by N-*ortho* intermolecular coupling. However, previous studies of the electrolytic oxidation of DPA in MeCN have not cited the formation of DPPZ (4, 9,10), although in the presence of bases some N-ring coupling has been cited (10). It could be argued that since DPPZ is not obtained from DPA under standard electrolytic conditions the cyclization reaction of TPOPD to DPPZ cannot strictly be analogized to the formation of substituted DPPZ's from the corresponding diphenylamines. However, inspection of the reaction pathway shows that the substituent positions are relatively remote from the cyclization site and so their effect would only be upon the rate of cyclization. In addition, it is difficult to propose another likely intermediate in place of substituted TPOPD's for the diphenylamine systems; an intermediate is almost a certainty, since it is not likely that the diphenylamine-dihydrophenazine pathway would go by a single concerted reaction. Further spectroscopic studies are under way to search for TPOPD-type intermediates in anodic oxidations of 4,4'-disubstituted DPA's in order to obtain quantitative kinetic data.

Interestingly, this reaction does not occur with 2-aminodiphenylamine (N-phenyl-o-phenylenediamine) (9, 11), although it has been noted for a series of polyfluorinated 2-aminodiphenylamines (12, 13). It was noted in these latter systems that a necessary condition for cyclization was a fluorine *ortho* to the NH group in the ring not containing the amino function (12); the dihydrophenazine derivatives were oxidized on to the corresponding phenazines since the nitrogens were not protected. It seems to be generally true that the nitrogens must be heavily substituted as in TPOPD in order to prevent decomposition of the dihydrophenazines once they are formed.

An extensive study of substituted diphenylamines (4) has revealed that the following selection rules apply to the formation of the dihydrophenazines by electrolytic oxidation of substituted diphenylamines in MeCN:

1. Both *para* ring positions must be substituted.
2. The *para* substituent must not eliminate; if this occurs *para-para* benzidines form (as with 4,4'-dibromodiphenylamine).
3. The *para* substituent must be strongly electron donating, neutral, or weakly electron withdrawing; substituents such as nitro and cyano inhibit formation of the corresponding dihydrophenazine.
4. The amine nitrogen must not be alkylated or arylated.
5. The yields in these reactions on a preparative scale are increased substantially by electrolyzing at low current densities.

These points will be considered more fully in a later publication (14), but they are presented here to provide background information for consideration of the decomposition pathway of TPOPD.

The reaction pathway for 4,4'-disubstituted diphenylamines, then, is as shown below

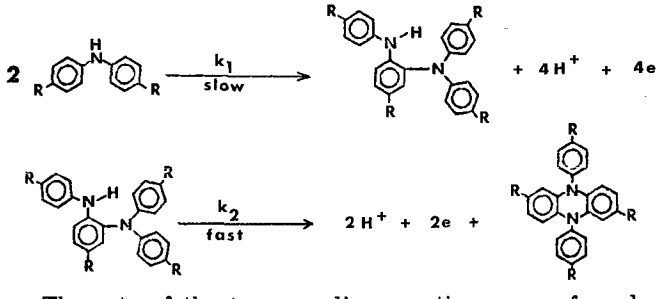

The rate of the two coupling reactions are inferred from electrochemical data on TPOPD and substituted diphenylamines. According to this scheme, these systems should exhibit second-order kinetics and the rate constants should be easily measurable (the "fast" rate constant in the second reaction is actually quite slow, estimated at about 1-10 sec^{-1} from cyclic voltammograms for TPOPD).

The system is obviously complex, but it is unique in that two discrete steps are involved and both reactions are slow compared to many electrochemical processes.

Acknowledgments

Financial support for this study was provided by NSF grants GP-20606 and GP-31199. The support and encouragement of Drs. R. N. Adams and D. E. Smith are gratefully acknowledged.

Manuscript submitted July 31, 1972; revised manuscript received Oct. 17, 1972. This was Paper 116 presented in part at the Washington, D.C., Meeting of the Society, May 9-13, 1971.

Any discussion of this paper will appear in a Discussion Section to be published in the December 1973 JOURNAL.

REFERENCES

1. H. Wieland, *Ber.*, **41**, 3478 (1908).
2. H. Wieland and H. Lecher, *ibid.*, **45**, 2600 (1912).
3. V. Dvořák, I. Němec, and J. Zýka, *Microchem. J.*, **12**, 99 (1967).
4. P. Berkenkotter and R. F. Nelson, Paper 116 presented at Electrochemical Society Meeting, Washington, D. C., May 9-13, 1971.
5. G. Cauquis, H. Delhomme, and D. Serve, *Tetrahedron Letters*, 4113, 4649 (1971).
6. G. Cauquis, H. Delhomme, and D. Serve, *ibid.*, 1965 (1972).
7. P. Welzel, *Chem. Ber.*, **103**, 1318 (1970).
8. H. Gilman and J. J. Dietrich, *J. Am. Chem. Soc.*, **79**, 6178 (1957).
9. R. F. Nelson, Ph.D. Thesis, Kansas University, 1966.
10. G. Cauquis, J. Cognard, and D. Serve, *Tetrahedron Letters*, 4645 (1971).
11. P. Berkenkotter and R. F. Nelson, Unpublished data.
12. A. G. Hudson, A. E. Pedler, and J. C. Tatlow, *Tetrahedron Letters*, 2143 (1968).
13. A. G. Hudson, M. L. Jenkins, A. E. Pedler, and J. C. Tatlow, *Tetrahedron*, **26**, 5781 (1970).
14. P. Berkenkotter and R. F. Nelson, In preparation.

Electrochemical Behavior of Blood Coagulation Factors

Prothrombin and Thrombin

L. Duic,*[1] S. Srinivasan,* and P. N. Sawyer

Electrochemical and Biophysical Laboratories of the Vascular Surgical Services, Department of Surgery, State University of New York, Downstate Medical Center, Brooklyn, New York 11203

ABSTRACT

Cyclic voltammetry was used to investigate the electrochemical behavior of prothrombin (blood coagulation Factor II) and thrombin, its product in the blood coagulation sequence. The results show that these proteins undergo adsorption and charge transfer reactions at the platinum electrode-sodium chloride solution interface. The electrochemical conversion of prothrombin to thrombin at constant anodic potentials was attempted. Preliminary results indicate the possibility of intermediate electrochemical steps in the over-all blood coagulation reaction.

Heart disease is the number one killer in the United States. The heart attack is the end result; thrombosis is the real cause of the heart attack. Thrombosis may be defined as the formation of a solid or semisolid mass from constituents of blood anywhere within the heart or blood vessels during life (1). A mass formed from the constituents of blood *in vitro* or within the cardiovascular system after death is a clot (1). The thrombosis reaction is catalyzed (*i*) at a site of injury in blood vessels, (*ii*) in atherosclerotic vessels, or (*iii*) in vascular and heart valve prostheses.

The evidence accumulated within the last two decades suggests that thrombosis at the blood vessel wall or prosthetic material-blood involves intermediate steps which are electrochemical in origin (2-8). The data published to date have shown the importance of the surface charge (and/or potential across the solid-electrolyte interface) of blood vessel wall as well as of prosthetic materials in inhibiting or catalyzing blood clotting and/or thrombosis. Positively charged surfaces initiate thrombosis, while clean uniformly negatively charged surfaces inhibit thrombosis. In addition, a number of papers have been published describing the effect of electrolysis of blood and plasma in both *in vitro* and *in vivo* systems. While the work of our group and of several other workers gives evidence for the accelerated coagulation of electrolyzed plasma or blood (7-13), there are other authors who have presented work which gives somewhat conflicting results (14-16). Blood as well as plasma are far too complex systems to investigate the electrochemical phenomena taking place in the over-all thrombosis reaction, or in general in blood coagulation.

The International Committee on Blood Clotting Factors has recognized thirteen blood coagulation factors, most of which are involved in the over-all blood coagulation sequence (17). They are designated by Roman numerals from I to XIII. The most common synonyms for these factors are given in Table I. The final step in the coagulation sequence is the conversion of fibrinogen to fibrin. The cellular elements (erythrocytes, leukocytes, and platelets) are linked by this fibrous structure in a blood clot or thrombus deposit. The fibrinogen-fibrin conversion reaction is catalyzed by the enzyme thrombin. Thrombin, in turn, is formed from the blood coagulation factor prothrombin. There are two distinctive mechanisms by which the prothrombin-thrombin conversion occurs. In the intrinsic mechanism, only the constituents of blood are involved. The extrinsic mechanism occurs outside the vascular tree and requires tissue factors. The two pathways (18) are represented in Table II.

Since the prothrombin-thrombin conversion is an essential step in the over-all blood coagulation sequence, the electrochemical behavior of both these factors was determined in the present study. Prothrombin was first isolated from bovine prothrombin

Table I. Roman numeral designation and most common synonyms for blood coagulation factors (1)

Roman numeral designation	Most common synomym
Factor I	Fibrinogen
Factor II	Prothrombin
Factor III	Tissue thromboplastin
Factor IV	Calcium ions
Factor V	Proaccelerin
Factor VI	Not assigned
Factor VII	Proconvertion
Factor VIII	Antihemophilic factor
Factor IX	Christmas factor
Factor X	Stuart factor
Factor XI	Plasma thromboplastin antecedent
Factor XII	Hageman factor
Factor XIII	Fibrin stabilizing factor

* Electrochemical Society Active Member.
[1] Present address: Institute of Electrochemistry, Faculty of Technology, University of Zagreb, Zagreb, Yugoslavia.
Key words: adsorption, blood coagulation, charge transfer, clotting time, cyclic voltammetry, prothrombin, thrombin, thrombosis.

Table II. Intrinsic and extrinsic pathways in blood coagulation

Intrinsic*	Extrinsic†
$XII \xrightarrow{\text{contact}} XII_a$	$II + VII + IV \longrightarrow$ Active product 1
$XI \xrightarrow{XII_a} XI_a$	Active product 1 + $X \longrightarrow X_a$
$XI \xrightarrow{XI_a} IX_a$	X_a + phospholipid + $IV \longrightarrow$ Active product 2
$IX_a + VIII$ + phospholipid + $IV \longrightarrow$ Complex A	Active product 2 + $V + IV \longrightarrow$ Prothrombin activator
$X \xrightarrow{\text{Complex A}} X_a$	Prothrombin activator + Prothrombin + $IV \xrightarrow{\text{Thrombin}}$ Thrombin
$X_a + V$ + phospholipid + $IV \xrightarrow{\text{Complex B}}$ Complex B	Fibrinogen $\xrightarrow{\text{Thrombin}}$ Fibrin
Prothrombin $\xrightarrow{\text{Thrombin}}$ Thrombin	
Fibrinogen $\xrightarrow{\text{Thrombin}}$ Fibrin	

* From A. C. Hemker and M. J. P. Kahn, *Nature*, 215, 1201 (1967).
†From R. Biggs and R. G. Macfarlane, "Human Blood Coagulation and Its Disorders," Blackwell, Oxford (1962).

by Seegers *et al.* (19). The concentration of prothrombin in bovine plasma is 0.1-0.15 mg/ml. Human and bovine prothrombin are similar in most respects. The molecular weight of purified prothrombin is 68,000-68,500. The main contaminants in prothrombin preparations are Factors VII, IX, and X. These activities can be removed by chromatography on DEAE cellulose. The molecular weight of bovine prothrombin complex (*i.e.*, prothrombin containing Factors VII, IX, and X activities) is 70,500. Bovine prothrombin complex is ellipsoidal, of length 119Å, and width 34Å. It contains 526 amino-acid residues. The amino-acid composition of bovine prothrombin is given in Table III. The molecular weight of the amino-acid fraction in bovine prothrombin is 58,800. Subtracting this value from the molecular weight of purified thrombin, a value of about 8000 is arrived at for the molecular weight of the carbohydrate fraction in prothrombin. This represents about 11.2% by weight. It is made up as follows: galactose 3.03%, mannose 1.53%, fucose 0.09%, hexosamine 2.3%, and sialic acid 4.2%. In 8 molar urea, 8 moles of disulfide were found per mole of bovine prothrombin. The N-terminal amino acid in prothrombin is alanine. Two C-terminal amino acids, tyrosine and glycine, were found in nonchromatographed and on IRC-chromatrographed bovine prothrombin complex.

Thrombin can be obtained from prothrombin in different ways. Its molecular weight is 33,700. The length of the molecule is 84Å and its width is 30Å. Its amino-acid composition is listed in Table III. Bovine thrombin contains 258 amino-acid residues, corresponding to a molecular weight for this fraction of 28,400. There are 2.15 moles of disulfide per mole of thrombin. It has two N-terminal amino acids, isoleucine and threonine. The total carbohydrate content of thrombin, 9.68%, is made up as follows: galactose 2.34%, mannose 1.17%, fucose 0.07%, hexosamine 2.2%, and sialic acid 3.9%. The physicochemical evidence indicates that thrombin has

Table III. Amino-acid composition of bovine prothrombin and thrombin (1)

Amino acid	Ratio of appearance using methionine as reference	
	Prothrombin	Thrombin
Aspartic acid	9.0	7.0
Threonine	5.0	3.2
Serine	6.2	3.5
Glutamic acid	12.8	7.2
Proline	5.8	3.5
Glycine	8.3	5.2
Alanine	6.0	3.0
Cystine/2	2.0	1.5
Valine	6.2	4.0
Methionine	1.0	1.0
Isoleucine	3.3	2.7
Leucine	7.6	6.0
Tyrosine	4.2	2.5
Phenylalanine	3.8	2.5
Lysine	5.8	4.5
Histidine	1.6	1.3
Arginine	8.2	4.5
Tryptophan	1.8	1.5

half the molecular weight of prothrombin. It has been hypothesized that the other half of prothrombin is composed of autoprothrombin III (inactive Factor X). More recent investigations suggest that prothrombin might be a dimer of two thrombin molecules (17).

One method of obtaining information concerning the possible participation of electrochemical reactions in thrombosis is to determine the electrochemical behavior of blood coagulation factors at metal-solution interfaces. These relatively simple studies on the individual factors should indicate whether they are subject to electrosorption, and whether they undergo charge transfer processes. Electrosorption of some blood proteins and their structural subunits (amino acids and peptides) have been previously investigated (20-22). Electrochemical polymerization of fibrinogen (Factor I) yields a product quite similar to the enzymatically produced fibrin (23).

Cyclic voltammetry appears to be a convenient screening technique to give at least a qualitative picture of the electrochemical behavior of proteins. In the present work, the electrochemical activities of prothrombin and thrombin were ascertained from such studies on a platinum electrode in 0.154*N* sodium chloride solutions containing one of these proteins. The biological activity of the electrochemically treated product, particularly with prothrombin, was determined. In addition, the possibility of electrochemical conversion of prothrombin to a thrombin-like product was investigated.

Cyclic Voltammetric Studies on Prothrombin and Thrombin

Experimental

It is well known that siliconization greatly enhances the clotting times of blood in glass tubes. Hageman factor (Factor XII) is activated in unsiliconized glassware. It is not certain whether prothrombin is activated in unsiliconized glassware. For this reason, experiments were carried out in both siliconized and nonsiliconized three-compartment glass cells. Siliconization was carried out using standard procedures with General Electric Dri-Film No. 9987. A smooth platinum wire, 1 cm^2 of geometric area, served as the test electrode. The test electrode was placed in the central compartment. In the side compartments, separated from the central one by closed stopcocks, the Pt-counter and reference electrodes (SCE) were placed. The physiological concentration of sodium chloride (0.154*N* NaCl) was used as the supporting electrolyte. All the experiments were carried out in an open air atmosphere so as to avoid denaturation of proteins which occurs in an inert atmosphere.

Voltammetric studies were carried out with a three-electrode potentiostatic circuit, using a Wenking Model 61R potentiostat and Elron Model CHF-1 signal generator which provides potential variation for cyclic single and multiple scans with a choice of different scan rates (from 10^{-2} to 10^2 V/sec). The potential of the test electrode was checked using a Keithley electro-

meter (610B). Voltammograms were recorded for lower scan rates in a Hewlett Packard Model 7001AM X-Y recorder, and for higher scan rates on a Tektronix oscilloscope Model 564 with plug in units Model No. 3A3 for the horizontal and 2A63 for the vertical axes.

Bovine prothrombin (obtained from "Sigma"[2]) was studied at two concentrations (0.1 and 1 unit/ml). Three concentrations of bovine thrombin (obtained from "Upjohn") were investigated (1, 10, and 100 NIH units/ml).[3]

Results and Discussion

Adsorption and charge transfer reactions of prothrombin.—Voltammograms were first recorded in the supporting electrolyte. The change in transient was recorded immediately after introducing the desired amount of protein. Figure 1 shows the immediate change in *I-V* transient after prothrombin was introduced into the supporting electrolyte making the bulk concentration of prothrombin 0.1 unit/ml.[4] Hydrogen peaks are suppressed, the current in the platinum oxide formation region is lowered, and the area representing platinum oxide reduction is reduced. Experiments were repeated at least three times and the reproducibility in current at any potential is within 10%. This is also the case with peak potentials. The change in voltammogram can be attributed to the blocking of the electrode surface by adsorption of added species, reducing the electrode area available for the hydrogen adsorption and desorption processes and for platinum oxide formation. During subsequent cycling, a further decrease in the area representing oxide reduction was recorded. This behavior was observed at both concentrations, 0.1 and 1 unit/ml. At the higher concentration (1 unit/ml), however, a further change in the voltammogram was observed with continuous cycling. In saline solution containing no prothrombin, there was no change in the shape of the voltammogram with repeated cycling over long periods of time (> 48 hr). Thus, the changes observed in the voltammogram when prothrombin is present in solutions do indeed correspond to processes other than electrode surface processes. The voltammogram recorded after 10 min of continuous cycling at 50 mV/sec shows the development of new peaks. There is no trace of a platinum oxide reduction peak, but a new cathodic peak is recorded at more positive potentials (+200 mV *vs.* SCE). There is also a significant change in the hydrogen region. New peaks develop giving rise to much higher peak currents than can be attributed to hydrogen peaks, the difference approaching one order of magnitude after 60 min of cycling. From the values of the peak currents (Fig. 2), it is clear that some Faradaic process is taking place. From the voltammogram recorded at this stage, it appears that at least two electrode reactions are taking place; one at positive and the other at negative potentials.

It was of interest to determine the interdependence of electrode reactions and the potentials at which the electrode reactions are triggered. With continuous cycling in the positive potential region (*vs.* SCE) for an additional 30 min, and then returning to the usual scan, the peak currents showed a slight increase, but without any major change (Fig. 3). By limiting scanning only to the negative potential region, the peak currents displayed an immediate decrease. It therefore appears that the species participating in the electrode reaction at negative potentials is the product of the reaction, the reactant (prothrombin) undergoes in the

[2] According to specifications from the company, the total content of Factors VII, IX, and X is less than 0.01 units per unit of prothrombin.

[3] The amount of prothrombin expressed as 1 unit is the amount of prothrombin present in 1 ml of normal human blood, *i.e.*, the physiological concentration of prothrombin. Concentration units for thrombin cannot be based on physiological concentrations since thrombin is not normally present in blood. Therefore 1 NIH unit of thrombin is not directly comparable to one unit of prothrombin. 1 NIH unit is the amount of thrombin which clots fibrinogen at 37°C in 15 sec. Empirically 1 unit of prothrombin can be compared to 100 NIH units of thrombin (24).

[4] The IUPAC sign convention is followed, *i.e.*, anodic currents are positive, potentials anodic with respect to the potential of the reference electrode are positive, and vice versa. The opposite convention is adopted in most polarographic texts.

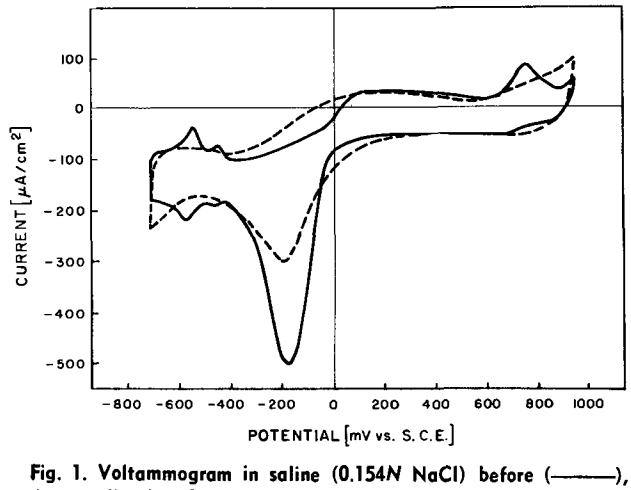

Fig. 1. Voltammogram in saline (0.154*N* NaCl) before (———), and immediately after (- - - -) the addition of prothrombin (0.1 unit /ml) at a scan rate of 50 mV/sec.

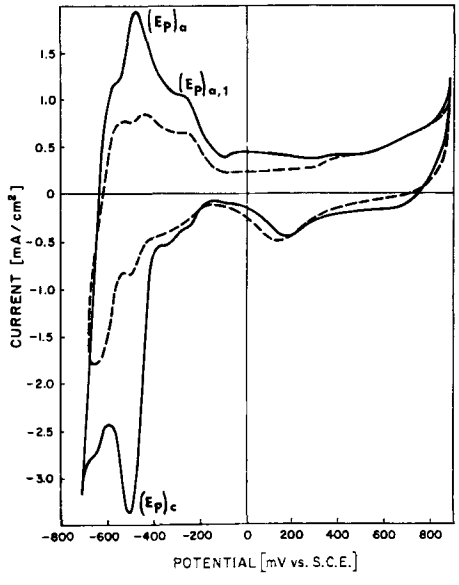

Fig. 2. Voltammogram for prothrombin (1 unit/ml) after prolonged scanning: 10 min (- - - -), 60 min (———) at a scan rate of 50 mV/sec.

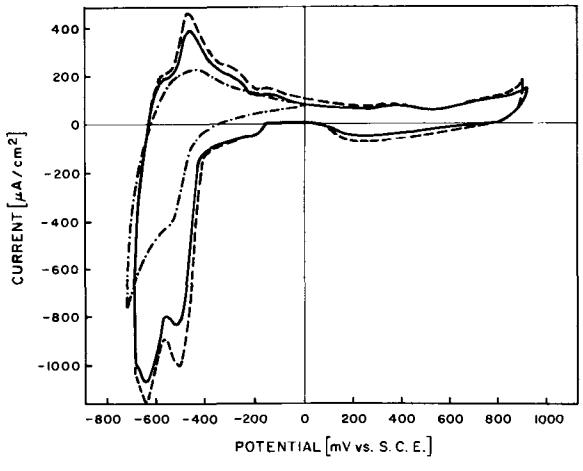

Fig. 3. Effect of limiting potential scan to only positive and to only negative potential range: normal scanning region (———), after 30 min scanning only in anodic (- - - -), and after 30 min scanning only in cathodic (—·—·—·) potential range at a scan rate of 50 mV/sec.

positive potential region where, possibly, an intermediate is formed. Thus the reaction taking place at positive potentials is a necessary step for the electrode reaction at negative potentials.

To evaluate the nature of reactions recorded in voltammograms, the scan rate was altered from 50 mV/sec, which was generally used throughout the study, to lower and higher values in the range from 10 mV/sec to 2 V/sec. Although the difference in potentials of cathodic and anodic peaks (ΔE_p) for lower scan rates is 57 mV (a criterion for the reversible charge transfer), the shift of both peak potentials, $(E_p)c$ and $(E_p)a$, with the change in scan rate, indicates a departure from the reversible behavior, *i.e.*, the degree of irreversibility increases with the increase in scan rate.

The shift of E_p *vs.* logarithm of scan rate (v) gives a slope of 30 mV per tenfold change in scan rate for both cathodic and anodic peaks in the negative potential region (Fig. 4). The criterion for the irreversible charge transfer reaction, $dE_p/d \log v = 30/\alpha n$, thus gives the value $\alpha n = 1$, where α is the charge transfer coefficient and n is the number of electrons participating in the charge transfer reaction (25).

The values of the peak currents also change with the change in scan rate. The ratio of anodic to cathodic peak currents (i_a/i_c) increases with log v (Fig. 5) but never approaches unity. The fact that the ratio i_a/i_c gives lower values at lower scan rates and increases with the increase of scan rate might indicate that a chemical reaction is interfering with charge transfer (26, 27). If it is assumed that the chemical reactions are slow compared to charge transfer reactions, the observed effects on the ratio of peak current at higher scan rates are understandable.

The poorly pronounced post peak $(E_p)a,1$ (Fig. 2) following the anodic charge transfer in the negative potential region shows the behavior expected for a strongly adsorbed reactant, *i.e.*, increases with the increase in scan rate and diminishes at lower scan rates (27). However, additional studies would be necessary for the evaluation of this peak as well as for the other peaks appearing in the voltammogram.

Adsorption and charge transfer reactions of thrombin.—A similar study was undertaken with thrombin. Figure 6 shows that adsorption takes place immediately after the introduction of thrombin into the supporting electrolyte, at concentrations as low as 1 NIH unit/ml. At a first glance, the *I-V* transient resembles that with prothrombin.[5] Studies at low and intermediate concentrations of thrombin (1 and 10 NIH units/ml) showed no significant changes in the voltammograms with continuous cycling. At a high concentration (100 NIH units/ml) continuous cycling resulted in new peaks. Although resembling the shape of the voltammograms recorded for prothrombin, the peaks recorded in the negative potential region are at more negative potentials for the same scan rate than is the case with prothrombin. Only the resultant cathodic peak at positive potential appears to be close to the potential of the peak (200 mV/SCE) with prothrombin (Fig. 7).

The influence of restricting the potential scan only to the cathodic or anodic part is similar to that observed with prothrombin. Figure 8 represents the change in voltammogram after 30 min of scanning in the positive

[5] Cyclic voltammetric studies have been conducted on some other blood coagulation factors as well (fibrinogen, Factors, V, VIII, and IX). The voltammograms, their time responses, variations with scan rates are quite specific for each of the factors investigated.

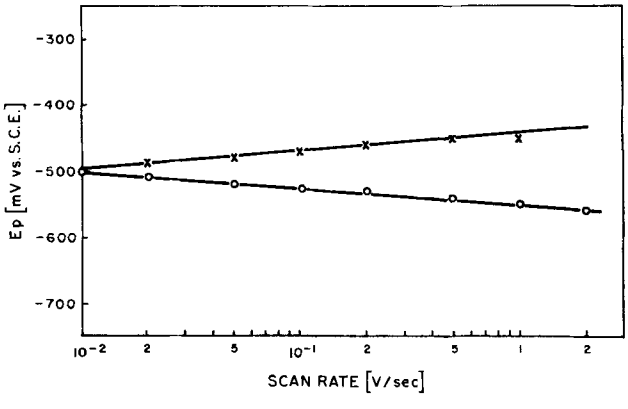

Fig. 4. Peak potential (E_p) as a function of scan rate for the solution containing prothrombin (1 unit/ml).

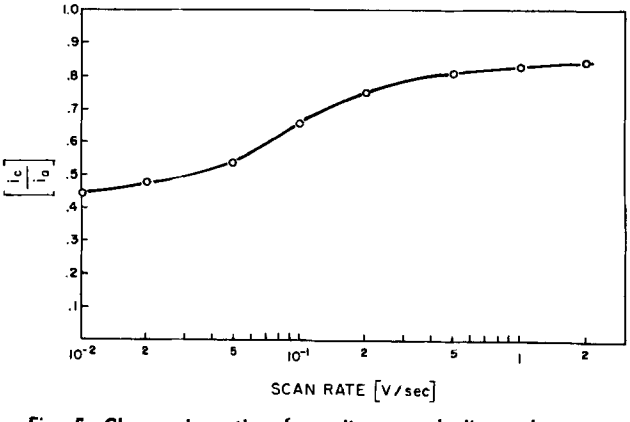

Fig. 5. Change in ratio of anodic to cathodic peak currents i_a/i_c with the change in scan rate for the solution containing prothrombin (1 unit/ml).

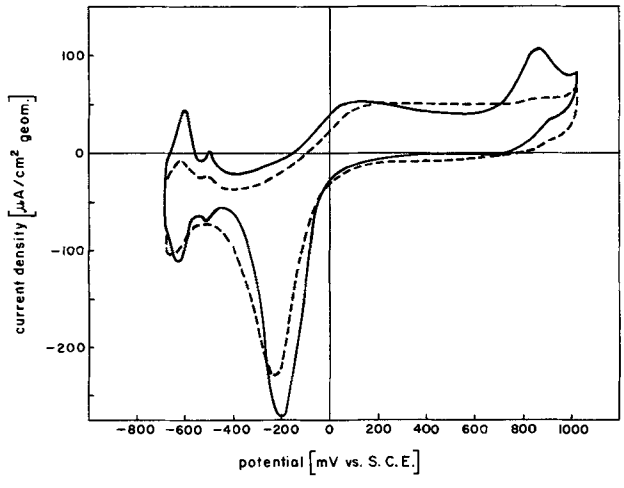

Fig. 6. Voltammogram before (———) and immediately after (- - - -) the addition of thrombin (1 NIH unit/ml) to saline.

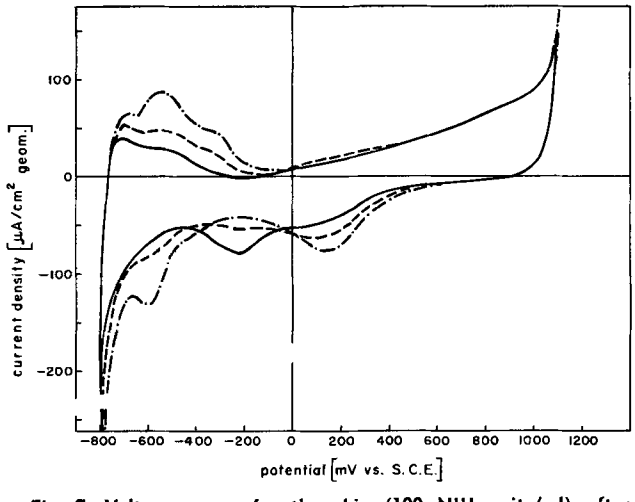

Fig. 7. Voltammogram for thrombin (100 NIH units/ml) after 20 min (———), 60 min (- - - -), and 180 min (—·—·—·) of scanning at a scan rate of 50 mV/sec.

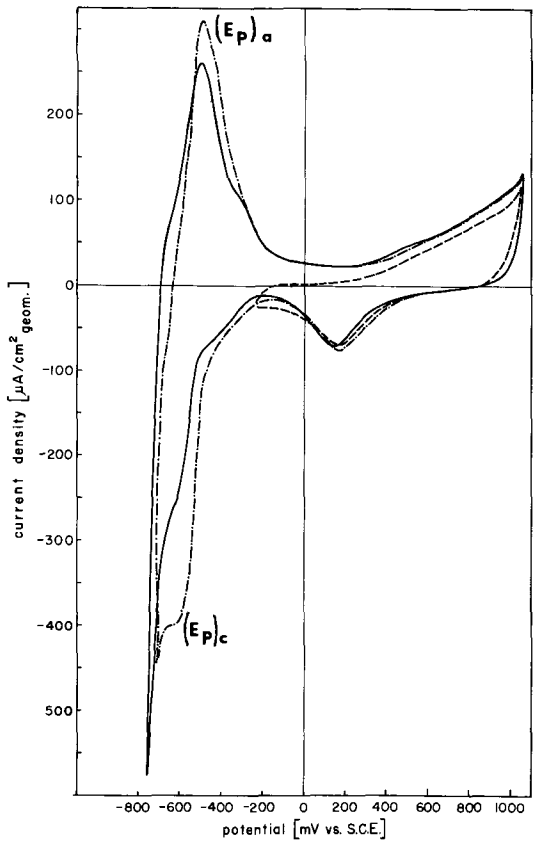

Fig. 8. Effect of scanning in anodic potential region (- - - -) for thrombin (100 NIH units/ml): after 6 hr of scanning over the usual potential range (———), after 30 min scanning in anodic region (—·—·—·).

potential region, the peak currents increase; Figure 9 shows the change during the scan at negative potentials which resulted in a rapid decrease in peak currents.

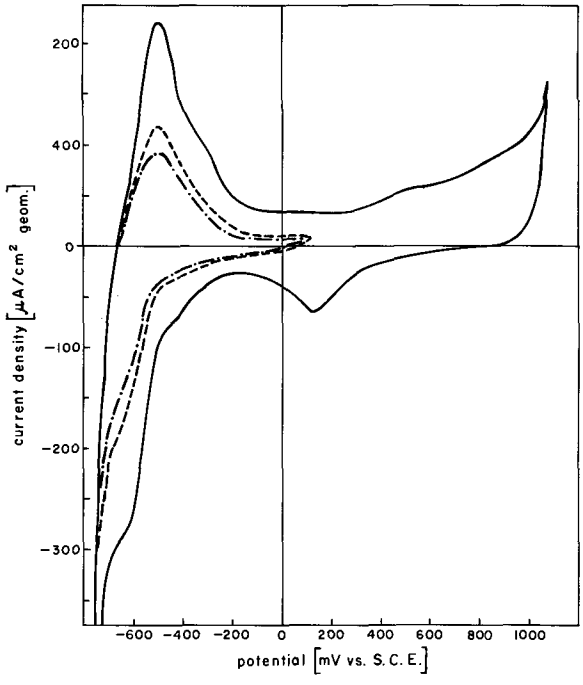

Fig. 9. Effect of scanning at cathodic potentials for thrombin (100 NIH units/ml): after 5 hr of scanning over the usual potential range (———), after 10 min scanning at negative potential range (- - - -), and after 20 min scanning over the negative potential range (—·—·—·).

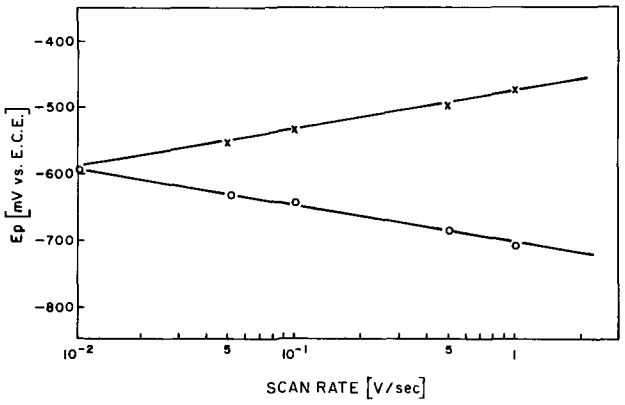

Fig. 10. Peak potential (E_p) as a function of scan rate for the solution containing thrombin (100 NIH units/ml).

The shift of the peak potential (E_p) with the logarithm of scan rate gives a slope of 60 mV per tenfold change in the scan rate (Fig. 10). This gives an αn value of 0.5. Speculating that the charge transfer coefficient α might be of the same value for these two proteins (prothrombin and thrombin), it appears that the number of electrons involved in the charge transfer process in the case of prothrombin is twice the number of electrons involved in case of thrombin.

The ratio of anodic to cathodic peak currents (i_a/i_c), Table IV, shows that the charge transfer reaction is complicated by some chemical reaction. The ratio gives values lower than unity throughout the applied rates of scan, although there is a steady increase with increase in scan rate.

Some conclusions from the cyclic voltammetric studies.—Although the results presented in this work are essentially of qualitative value and additional research is necessary to understand the mechanism of the reactions involving prothrombin and thrombin, the present studies reveal that both proteins take part in adsorption and charge transfer processes. At the lower concentrations, adsorption effects predominate, while at higher concentrations, the rates of charge transfer reactions are significant. The product of the charge transfer reaction at anodic potentials takes part in a further charge transfer reaction at negative potentials.

Some additional studies have been performed in an attempt to obtain information on the possible electrochemical transformation of prothrombin to thrombin.

Electrochemical Conversion of Prothrombin to Thrombin?

One of the simplest methods of determining whether electrochemical activation causes a prothrombin-thrombin conversion is to check whether there is any change in the hematological activity after the electrochemical treatment. After the cyclic voltammetry experiment, the effects of the solution samples on the clotting time of blood were determined. The tests showed a decrease in clotting time and hence a reduction in prothrombin activity but did not reveal significant increases in thrombin activity. The explanation for such a result might be that the conversion of prothrombin into thrombin was in minute quantities and as such could not be detected, or that the conversion was not complete. Biochemical studies on prothrombin show that the first stage of prothrombin conversion yields three different species, one of which plays the

Table IV. Effect of scan rate on the ratio of anodic to cathodic peak currents $(i_p)a/(i_p)c$ with thrombin

Scan rate, V/sec	$(i_p)a/(i_p)c$
10^{-2}	0.63
5×10^{-2}	0.76
10^{-1}	0.78

role of an inhibitor in the further conversion of two additional species to thrombin (19). In accordance with this, the electrochemical conversion of prothrombin could have stopped at the intermediates and thus did not reach complete conversion to thrombin.

In an alternate study, solutions containing prothrombin were exposed to electrodes maintained at constant anodic potentials. The same cell and supporting electrolyte, as in previous experiments, were used. A platinized platinum electrode was used as the working electrode; its potential was maintained at one of several values from +500 to 1200 mV/SCE. Prothrombin was at a concentration of 0.1 unit/ml, and a fresh solution was prepared for each potential applied. The test on the clotting time of fibrinogen was carried out with the samples of prothrombin that were taken after 15 min of maintaining the electrode at a constant potential. Table V shows a decrease in clotting times of fibrinogen with samples being exposed to higher anodic potentials. The pH of each of the solutions was measured. It was found that the pH decreased with increase of the potential because solutions were not buffered. However, the shorter clotting time obtained for the solutions exposed to higher anodic potentials cannot be attributed to the change in pH, since a lower pH inhibits the clotting activity of thrombin (28). Thus, one may conclude that during electrolysis at constant anodic potentials a product with thrombin-like activity was formed. The formation of this material is increasingly favored at more positive potentials. Since thrombin is the only one of the proteins present that causes clotting, these results indicate that the product formed is thrombin and that electrochemical reactions are involved in the conversion of prothrombin to thrombin. It is necessary to elucidate further the electrochemical path of prothrombin to thrombin conversion by identifying the intermediates or products of the electrochemical reactions.

Acknowledgments

The research this publication is based upon was performed pursuant to contract No. PH 43-68-75 from the National Heart and Lung Institute, National Institute of Health, Public Health Service, Department of Health, Education and Welfare. The authors express their deep gratitude to Dr. Glen Stoner and Miss W. L. Walker of the University of Virginia, Charlottesville, for assistance in the experiments to determine the effect of electrochemically activated prothrombin on the clotting time of fibrinogen. Helpful discussions with and suggestions from Drs. N. Ramasamy and J. S. Keates of our laboratories are gratefully acknowledged.

Manuscript submitted Feb. 25, 1972; revised manuscript received Sept. 27, 1972. This was Paper 133 presented at the Washington, D. C., Meeting of the Society, May 9-13, 1971.

Any discussion of this paper will appear in a Discussion Section to be published in the December 1973 JOURNAL.

Table V. Effects of prothrombin electrolyzed for 15 min at constant anodic potentials on clotting time of fibrinogen at 22°C

Potential of Pt electrode, mV/SCE	pH	Clotting time of fibrinogen, hr
500	6.1	45
600		45
700	5.6	27
800		27
900	5.4	25
1000		25
1100	4.3	9.5
1200		9.5
Control	6.2	45

REFERENCES

1. S. Wessler, and W. E. Stehbens, Thrombosis, Chap. XI in "Thrombosis and Bleeding Disorders," N. U. Bang, F. K. Beller, E. Deutsch, and E. F. Mammen, Editors, George Thieme Verlag, Stuttgart (1971).
2. P. N. Sawyer, and S. Srinivasan, *Am. J. Surg.*, **114**, 42 (1967).
3. P. S. Chopra, S. Srinivasan, T. Lucas, and P. N. Sawyer, *Nature*, **215**, 1494 (1967).
4. J. C. Brown, S. M. Lavelle, and P. N. Sawyer, *Thromb. Diath. Haemorrhag.*, **21**, 325 (1969).
5. E. Gileadi, S. Srinivasan, and P. N. Sawyer, *J. Electroanal. Chem.*, **21**, 6 (1969).
6. S. Srinivasan and P. N. Sawyer, *J. Colloid Interface Sci.*, **32**, 455 (1970).
7. P. N. Sawyer, and J. W. Pate, *Surg.*, **34**, 491 (1953).
8. J. C. Lamb, J. P. Isaacs, W. L. Bloom, and D. S. Harner, *Am. J. Physiol.*, **208**, 1006 (1965).
9. P. N. Sawyer, and B. Deutch, *Am. J. Physiol.*, **187**, 473 (1956).
10. P. N. Sawyer, C. Dennis, and S. A. Wesolowski, *Ann. Surg.*, **154**, 556 (1961).
11. S. I. Schwartz, *Surg. Gyn. Obs.*, **113**, 324 (1961).
12. R. D. Williams, and L. C. Carey, *Ann. Surg.*, **149**, 381 (1959).
13. R. R. Bradham, *Surg. Gyn. Obs.*, **113**, 324 (1961).
14. A. Naumovski, and A. Dejanov, in "Biophysical Mechanism in Vascular Hemostasis and Intravascular Thrombosis," P. N. Sawyer, Editor, Appleton-Century Crofts, New York (1965).
15. D. B. Matthews, *Ann. N. Y. Acad. Sci.*, **77**, 146 (1968).
16. D. B. Matthews, and A. Catlin, *This Journal*, **114**, 221 (1967).
17. Ref. 1, Chap. 1.
18. E. W. Salzman and A. Britten, "Hemorrhage and Thrombosis," Little Brown and Co., Boston (1965).
19. W. Seegers, in "Blood Clotting Enzymology," Chap. 1, W. Seegers, Editor, Academic Press, New York (1967).
20. D. B. Matthews, *J. Biomed. Res.*, **3**, 475 (1969).
21. G. E. Stoner, *ibid.*, **3**, 655 (1969).
22. G. E. Stoner, and S. Srinivasan, *J. Phys. Chem.*, **74**, 1088 (1970).
23. G. E. Stoner and L. Walker, *J. Biomed. Res.*, **3**, 645 (1969).
24. L. Vroman, Private communication.
25. R. S. Nicholson and I. Shain, *Anal. Chem.*, **39**, 706 (1964).
26. R. H. Wopschall and I. Shain, *ibid.*, **39**, 1535 (1967).
27. R. H. Wopschall and I. Shain, *ibid.*, **39**, 1514 (1967).
28. B. Blomback, Chap. 4 in Ref. 19.

Electrochemical Behavior of Blood Coagulation Factors

Fibrinogen

N. Ramasamy,* M. Ranganathan,[1] L. Duic,*[2] S. Srinivasan,* and P. N. Sawyer

Electrochemical and Biophysical Laboratories of the Vascular Surgical Services, Department of Surgery, State University of New York, Downstate Medical Center, Brooklyn, New York 11203

ABSTRACT

The adsorption and charge transfer reactions of fibrinogen, one of the blood coagulation factors, have been investigated using ellipsometric, potentiodynamic, and steady-state potentiostatic methods. The protein is adsorbed on platinum over a wide potential range (−600 to +800 mV *vs.* SCE) even at very low concentrations. Steady-state potentiostatic studies show that it is involved in anodic and cathodic charge transfer reactions. Adsorption plays a prominent role in the development of potentiokinetic peaks and in their shifts with scan rate variation. The observed charge transfer reactions of this protein throw new light on the correlations between blood compatibility of metallic materials and their spontaneous potentials in blood.

Fibrinogen plays a crucial role in blood clotting and in thrombosis. It is one of the thirteen blood coagulation factors (Table I) recognized by the International Committee on Blood Coagulation Factors (1). Many of the proteins involved in the blood coagulation sequence are activated before they take part in the blood coagulating scheme (2). Fibrinogen is present at a concentration of about 3 mg/ml in blood, while some of the other blood coagulation factors are present only in trace amounts (3). The polymerization of fibrinogen to fibrin is the last of the series of intermediate steps in thrombosis and in blood clotting. The fibrin strands trap blood cells and other particles in blood leading to thrombus formation. The terminal conversion of fibrinogen to fibrin is one of the most fundamental steps in thrombosis. The preceding steps, leading to the formation of the fibrin in the normal intact vascular system, have been elucidated. In the intrinsic pathway (4) the cascade process starts with activation of Hageman factor and involves various other proteins in sequential steps. The fibrinogen-fibrin conversion reaction is catalyzed by the enzyme thrombin. This is not present in circulating blood but is formed from the precursor prothrombin. The prothrombin-thrombin conversion can also take place by the extrinsic pathway (5) without the surface activation of Hageman factor. The two pathways for blood coagulation are represented in Table II. Irrespective of the type of activation, the last two steps of the blood coagulation scheme are the same, *i.e.*, conversion of prothrombin to thrombin and the polymerization of fibrinogen to fibrin by thrombin.

Table I. Roman numeral designation and most common synonyms for blood coagulation factors (1)

Roman numeral designation	Most common synomym
Factor I	Fibrinogen
Factor II	Prothrombin
Factor III	Tissue thromboplastin
Factor IV	Calcium ions
Factor V	Proaccelerin
Factor VI	Not assigned
Factor VII	Proconvertion
Factor VIII	Antihemophilic factor
Factor IX	Christmas factor
Factor X	Stuart factor
Factor XI	Plasma thromboplastin antecedent
Factor XII	Hageman factor
Factor XIII	Fibrin stabilizing factor

The reactions leading to thrombosis are in general catalyzed by materials used in cardiovascular implants. Metals, alloys, and insulator materials have been used in the fabrication of heart valves and other vascular prostheses (6). The presence of the foreign material provides a new interface with blood, and this can cause or induce thrombus formation. Studies in this laboratory on blood compatibility of prosthetic materials have shown that insulators with a uniform negative surface charge in contact with blood are nonthrombogenic, while those with a positive surface or with a nonuniform surface charge almost invariably induce thrombus formation (7). Metals which register spontaneous negative potentials in normal saline with reference to NHE are thrombo-resistant. Noble metals

* Electrochemical Society Active Member.
[1] Present address: Indian Institute of Science, Bangalore, India.
[2] Present address. Institute of Electrochemistry, Faculty of Technology, University of Zagreb, Zagreb, Yugoslavia.
Key words: adsorption, charge transfer, blood coagulation, blood proteins, fibrinogen, ellipsometry, potential sweep.

Table II. Intrinsic and extrinsic pathways in blood coagulation

Intrinsic*	Extrinsic†
$XII \xrightarrow{contact} XII_a$	$II + VII + IV \longrightarrow$ Active product 1
$XI \xrightarrow{XII_a} XI_a$	Active product 1 + $X \longrightarrow X_a$
$IX \xrightarrow{XI_a} IX_a$	X_a + phospholipid + $IV \longrightarrow$ Active product 2
IX_a + VIII + phospholipid + $IV \longrightarrow$ Complex A	Active product 2 + V + $IV \longrightarrow$ Prothrombin activator
$X \xrightarrow{Complex\ A} X_a$	Prothrombin activator + Prothrombin + $IV \xrightarrow{Thrombin}$ Thrombin
X_a + V + phospholipid + $IV \xrightarrow{Complex\ B}$ Complex B	Fibrinogen $\xrightarrow{Thrombin}$ Fibrin
Prothrombin $\xrightarrow{Thrombin}$ Thrombin	
Fibrinogen $\xrightarrow{Thrombin}$ Fibrin	

* From Ref. (4).
† From Ref. (5).

that develop positive potentials in blood are thrombogenic (8). When blood or plasma comes in contact with electronic conductors, only two basic reactions can occur, namely, adsorption and charge transfer. Most of the proteins are large molecular weight organic compounds containing multiple functional groups with a number of benzene rings (*e.g.*, tryptophan residues in fibrinogen). They may be expected to be adsorbed on the metal surface over a wide potential range. Since plasma or whole blood contains, in addition to the blood coagulation factors, albumins and globulins it cannot be used to investigate the electroactivity of individual blood proteins. Purified individual blood coagulation factors, dissolved in saline (0.154M NaCl), have been used in some basic investigations.

The blood proteins are very difficult to purify, especially to remove completely the extraneous blood coagulation factors. Even in the purest preparations available, trace amounts of other proteins are present as contaminants. The fibrinogen used for the investigation is free of plasminogen and plasmin but contains trace amounts of fibrin stabilizing factor and Factor VIII. Because of the difficulty of isolation and extreme lability of some of these proteins, (*e.g.*, Factors V, VIII) very little is known about the structural aspects like the amino-acid content, amino-acid sequence, etc. Fibrinogen, however, is a well-characterized protein. It has a molecular weight of 300,000. It is a globular-type protein with about 3% carbohydrate content. Irrespective of the source, *i.e.*, human, bovine, or canine, fibrinogen has similar composition and molecular weight. The molecule contains about 18 amino acids of which glycine, lysine, tyrosine tryptophan, and arginine are a few. A large number of molecules of each of these amino acids are present per molecule of fibrinogen. For example, bovine fibrinogen contains in addition to other amino acids, 60 tryptophan, 55 lysine, and 84 tyrosine residues per molecule. Fibrinogen is believed to exist as a dimer with about 28 disulfide links in the molecule. Human fibrinogen was used in the present work.

Thrombin, generated from its precursor prothrombin through the complex series of conversions acts on fibrinogen, polymerizing it to fibrin. The protein has a proteolytic effect on fibrinogen which is highly specific at four peptide bonds in fibrinogen. The sequence of steps leading to the final formation of a stable fibrin clot and the type and structure of *fibrinopeptides* released during this reaction have been elucidated (9).

The results of ellipsometry at constant potentials, steady-state potentiostatic and potentiodynamic methods employed in an investigation of the adsorption and charge transfer reactions of fibrinogen, are reported in the present communication.

Experimental

Purity and Source of Fibrinogen

Fibrinogen used for these investigations was prepared from human plasma[3] (10) by a modification of glycine precipitation procedure of Kazal *et al.* (11). It is 97% clottable and is free from plasminogen and plasmin but contains trace amounts of fibrin stabilizing Factor VIII. Ultra-centrifugal analysis gives a main peak comprising 95% of total area with apparent sedimentation coefficient of 5.8×10^{-13} and a smaller peak of 5% area with sedimentation coefficient of 3.5×10^{-13}.

Experimental Methods

Ellipsometric studies.—The potential dependent adsorption of fibrinogen was determined using this method. Since fibrinogen is one of the most strongly adsorbed peptides, it is possible to use very small concentrations of the protein. The three concentrations used were 0.07, 0.03, and 0.007 mg/ml of fibrinogen in normal saline (0.154M NaCl). The lowest concentration corresponds to 1/400 of physiologic concentration of the protein in normal human blood.

Experiments were carried out with a Rudolph Model No. 436-200E ellipsometer which uses the mercury green line as the source and has the quarter wave plate after metallic reflection. The angle of incidence was adjusted for 75° and the azimuth of the retardation plate was fixed at 135°. Only orientations of the polarizer and analyzer were varied during measurements. The reflecting surface was a glass slide sputtered with platinum (10,000Å thick) over tantalum oxide base (3000 Å thick). The electrical circuit consisted of a potentiostat, a silver-silver chloride reference electrode, a platinum foil counterelectrode, and the test electrode (the platinum sputtered glass slide). The potential of the electrode was initially set at −500 mV/Ag-AgCl reference electrode. The settings of the polarizer and analyzer were adjusted for minimum transmission and the readings were noted. Two sets of readings were taken in two different zones. These correspond with a blank set before the addition of the protein. The potential was varied in steps of 100 mV from −500 to +500 mV/Ag-AgCl. At each potential the "blank" readings were taken 15 min after impressing the potential. The protein was added and a similar set of readings were taken under similar conditions for each potential setting from −500 to +500 mV/Ag-AgCl. During the period of 15 min, the variation of photointensity was recorded with a Honeywell Recorder (Electronic No. 194). The measurements were made for three concentrations of the protein in solution.

Potentiostatic studies.—In the potentiostatic study, a platinum foil of 1 cm^2 apparent area was used as the test electrode. As in the previous case, the potentials were varied in steps of 100 mV from −800 to +1000 mV/SCE. The steady-state current passing through the system was measured 15 min after impressing the potential. A blank reading was taken with pure saline solution for the entire potential range. The experiment was repeated following addition of protein. Three concentrations of the protein were studied, 0.007, 0.07, and 3 mg/ml in physiologic saline (0.154M). The highest concentration corresponds to the physiologic concentration of the protein in blood. The experiments were carried out in air-saturated solutions because the proteins undergo denaturation during the process of deaeration by bubbling N_2. One experiment was conducted with deaerated saline solution to which fibrinogen was added (concentration of 0.07 mg/ml of the protein).

Potentiodynamic studies.—The equipment for the potentiodynamic study consisted of a potential sweep generator (Elron Model CHF1), a potentiostat (Wenking Model 61TR), and an X-Y recorder (Hewlett-Packard Model 700 AM). Platinum electrodes were used; a calomel reference electrode was employed. The potential range scanned was from −800 to +1050 mV/SCE. The scan rate was varied from 10 to 300 mV/sec. Multiple sweeps were employed; it was observed that the sweeping must be continued for at least an hour to reach a steady state.

Three concentrations of the protein were used, 0.007, 0.07, and 3 mg/ml in saline. At each concentration, the system was swept at a constant rate of 50 mV/sec for an hour, so as to develop a reproducible voltammogram shape. To determine the shift of peak potential with scan rate, the scan rates were varied from the 10-300 mV/sec. At each scan rate, sweeping was continued for the necessary time to obtain a constant shape of the voltammogram. The peak currents and corresponding potentials were noted as a function of scan rate for the two higher concentrations of the protein.

Results

Ellipsometric Studies

Under the conditions of the ellipsometer geometry indicated, the shift in analyzer settings is, to a first

[3] The purified protein was obtained from Dr. Glen Stoner and Miss Louise Walker of the Department of Materials Science at the University of Virginia, Charlottesville.

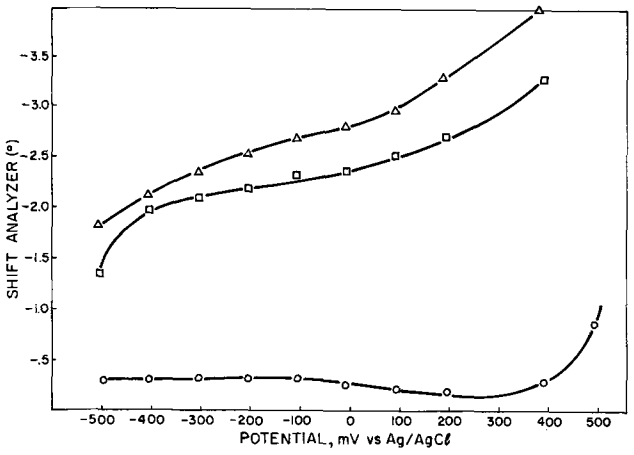

Fig. 1. Change in ellipsometer analyzer setting (a measure of adsorption) as a function of potential for three concentrations of fibrinogen in solutions; 0.07 (▲), 0.03 (□), and 0.007 (○) mg/ml.

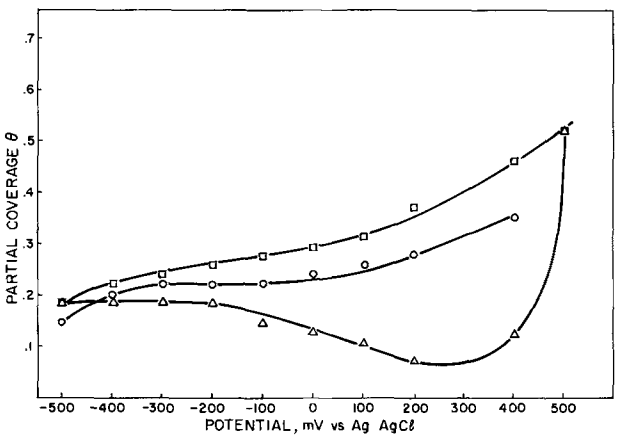

Fig. 2. Coverage-potential relation deduced from ellipsometry for three concentrations of fibrinogen in solution: 0.07 (□), 0.03 (○), and 0.007 (△) mg/ml.

approximation, proportional to the film thickness. Hence the analyzer setting was plotted as a function of potential. The curves for the different concentrations of the protein are shown in Fig. 1.

The plots of the shift of analyzer settings as a function of potential indicate that for all the concentrations of the protein there is an increase of coverage as one passes over from cathodic to anodic potentials. The variation of thickness is not so marked for the lowest concentration. Not only is the variation with potential much less for this concentration but there also appears to be a minimum in the analyzer setting-potential curve.

To obtain more quantitative results, the amplitude and phase changes were deduced from the changes in the polarizer and analyzer settings. For the particular ellipsometer geometry, from a consideration of the Poincare spherical representation, it is seen that the amplitude (Δ) and phase (ψ) are related to the two azimuths by

$$\Delta = 2A - 270 \text{ and } \psi = P \quad [1]$$

The changes in the amplitudes and phases from the corresponding values in pure saline are given by

$$\delta\Delta = \Delta - \Delta_0 = \delta\, 2A \quad [2]$$

$$\delta\psi = \psi - \psi_0 = \delta P \quad [3]$$

where A and P are the analyzer and the polarizer azimuths. The angle of incidence was corrected for refraction at the air-glass and glass-solution interfaces. Knowing the wavelength of light used, the optical constants for platinum, (5461Å and $n = 2.450$ and $k = 3.460$) and the refractive index for fibrinogen, ($n = 1.600$) assuming it to be nonabsorbing (12), the computer was programmed to give a set of Δ's and ψ's for a range of refractive indices of the film for each probable thickness of the film. The fibrinogen molecule is made up of three globules of diameter 50-60Å and has a length of about 500-700Å. Thus, a search for the closest fit of the experimental and computed values of the Δ's and ψ's was made over the thickness range indicated. The closest fit for the Δ's and ψ's gave the refractive index n_f of the film. Assuming the refractive index of the fibrinogen (n_f) to be 1.600 and the refractive index of the surrounding medium, saline (n_s), to be 1.3317 the coverage θ of the protein on the surface was deduced from the empirical relation (13)

$$n_f = \theta n_p + (1 - \theta) n_s \quad [4]$$

The coverage was calculated for each potential for all the concentrations of the protein. The coverage-potential ($\theta - E$) relations, observed for the three different concentrations of protein, are shown in Fig. 2. It is observed that the $\theta - E$ behavior is not very different from the plot of analyzer setting as a function of potential. The essential features are the same.

Potentiostatic Studies

The i-E curves[4] for the three concentrations of fibrinogen in aerated saline are shown in Fig 3-5. The curve of fibrinogen at a concentration of 0.07 mg/ml in deaerated saline is shown in Fig. 6.

Potentiodynamic Studies

The voltammogram[4] on a platinum electrode in normal saline and with the protein in solution at a concentration of 0.007 mg/ml are represented in Fig. 7. The two reversible hydrogen peaks and the platinum oxide reduction peak are clearly visible in normal saline, Fig. 7, curve 1. The addition of fibrinogen completely eliminates the hydrogen peaks developed at the anodic and cathodic scans, Fig. 7 curve 2. The platinum oxide reduction peak, however, is still observable. For the higher concentration of fibrinogen, 0.07 mg/ml (Fig. 8), one clearly sees the distinct de-

[4] The IUPAC sign convention, i.e., anodic currents are positive, potentials anodic with respect to potential of reference electrode are positive, and vice versa, is adopted in this paper.

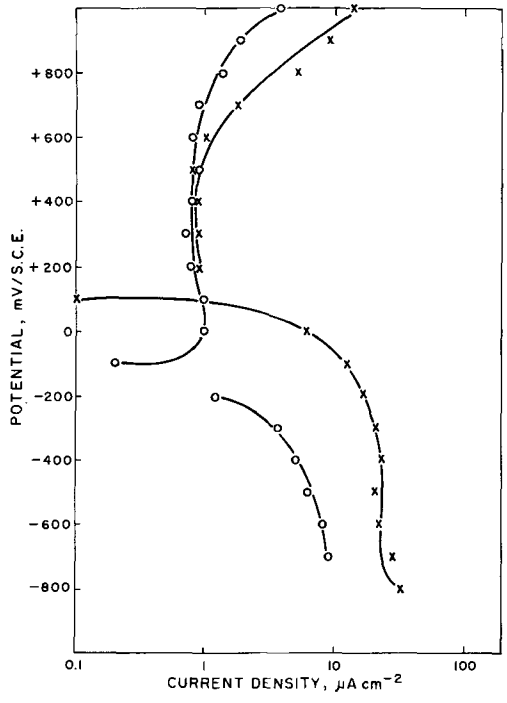

Fig. 3. Steady-state potentiostatic current density (i)-potential (E) relations in aerated saline (X) and in aerated saline containing 0.007 mg/ml of fibrinogen (○).

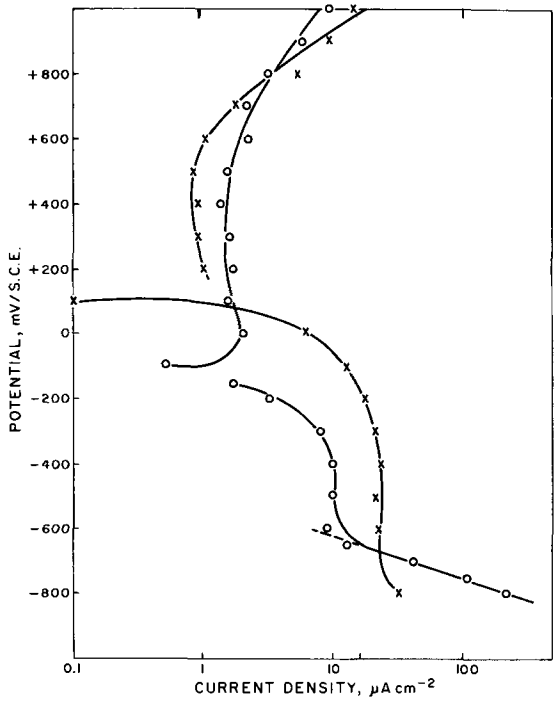

Fig. 4. Steady-state potentiostatic current density (*i*)-potential (*E*) relations in aerated saline (X) and in aerated saline containing 0.07 mg/ml of fibrinogen (○).

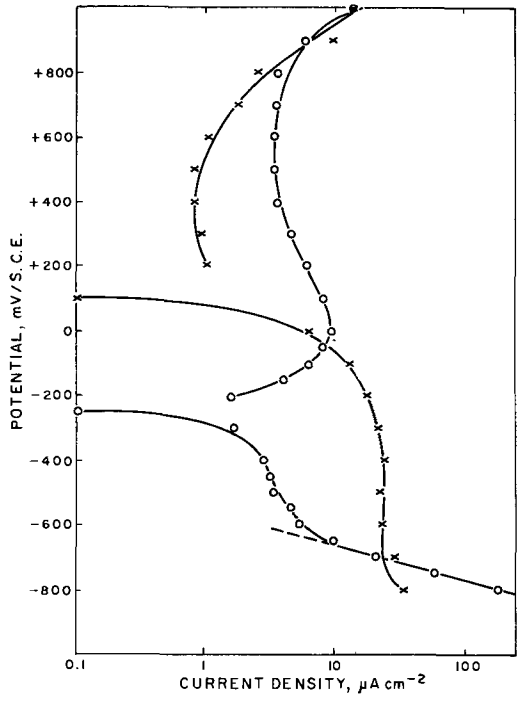

Fig. 5. Steady-state potentiostatic current density (*i*)-potential (*E*) relations in aerated saline (X) and in aerated saline containing 3 mg/ml of fibrinogen (○).

velopment of a new peak on the anodic scan at about −620 mV/SCE. There is a high current peak on the cathodic scan at about −800 mV/SCE. But this is not properly developed at all sweep rates, perhaps because the currents are so high that the cell resistance limitations come into play. Thus, in some fast scan rates one observes only a flattened portion of the curve in the highly cathodic region of the voltammogram. These voltammograms were recorded at a scan rate of 50 mV/sec. At the physiologic concentration (3 mg/ml) (Fig. 9), the peak on the anodic scan is more pronounced with higher peak current and also there is a small but distinct hump at +20 mV/SCE on the cathodic scan. These two peaks are also visible for

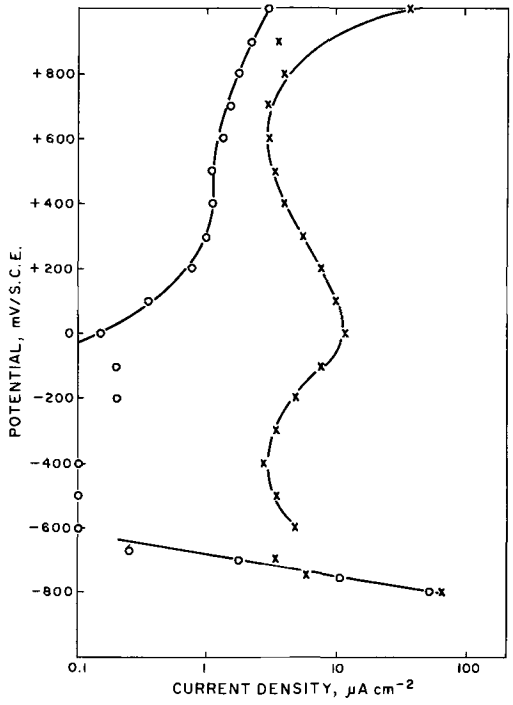

Fig. 6. Steady-state potentiostatic current density (*i*)-potential (*E*) relations in deaerated saline (X) and in deaerated saline containing 0.07 mg/ml of fibrinogen (○).

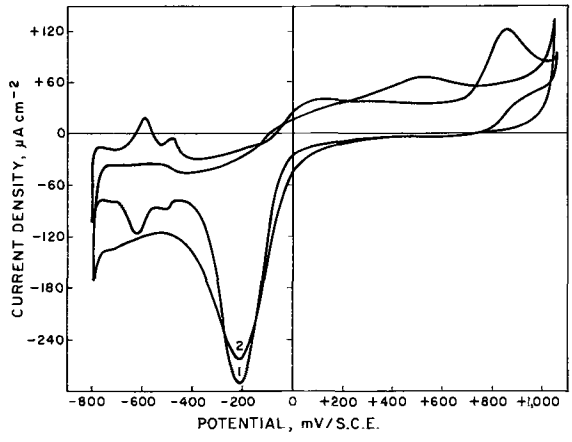

Fig. 7. Voltammograms in saline 1, before and 2, after additions of fibrinogen (0.007 mg/ml) at a scan rate of 50 mV/sec.

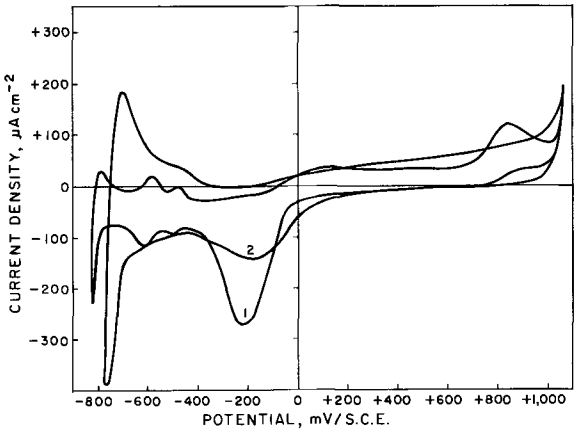

Fig. 8. Voltammograms in saline 1, before and 2, after addition of fibrinogen (0.07 mg/ml) of fibrinogen at a scan rate of 50 mV/sec.

lower concentrations of fibrinogen at faster scan rates. The effect of cycling time on the development of peaks and the attainment of steady state is shown in Fig. 10. The slow but complete elimination of the oxide

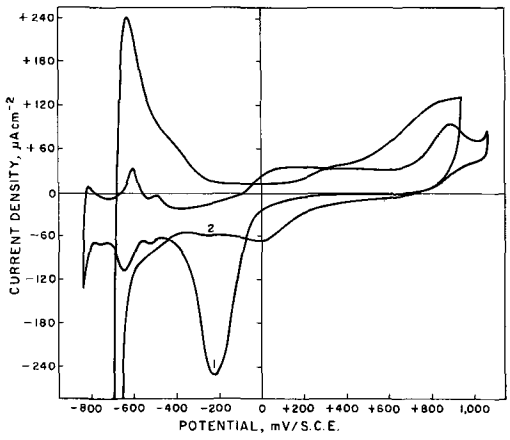

Fig. 9. Voltammograms in saline 1, before and 2, after addition of fibrinogen (3 mg/ml) at a scan rate of 50 mV/sec.

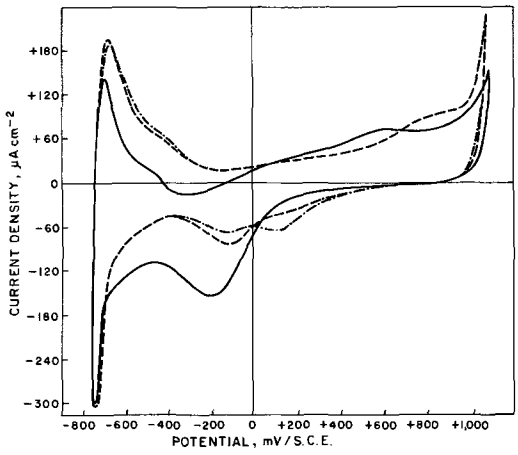

Fig. 10. Voltammograms in saline containing fibrinogen (0.07 mg/ml) with prolonged scanning: 5 min (————); 10 min (- - - -); 120 min (—·—·—·) after fibrinogen addition.

reduction peak and its replacement by a new peak at +100 mV are clearly seen in this case.

Since the potentiodynamic technique is applied to the study of high molecular weight compounds with a number of functional groups, it is worthwhile indicating the specificity and reproducibility of voltammograms observed with some blood proteins. Six blood coagulation factors have been investigated so far, *i.e.*, fibrinogen, prothrombin, thrombin, Factors V, VIII, and IX. The potentials (E_p) at which peaks develop, their peak currents (i_p), the variation of E_p and i_p with scan rates (v), the dependence of i_p/v and $i_p/v^{1/2}$ on concentrations are clearly distinct for each one of the proteins. Hence, it is believed that the method is specific to the type of protein under study. Many replications have been made for each of the proteins, using samples from different lots and the variation in peak current is about 10%, while the shift of peak potential (ΔE_p) with scan rate also shows about the same deviation. From a hematological standpoint even though these proteins are complex molecules, only some specific peptide links are probably involved in the blood coagulation scheme. It is likely that in electrochemical studies as well, only some specific sites are active. These may or may not be the same ones attacked enzymatically. The present studies, however, are not sufficient to localize the active sites in the molecule. The observed activity does not appear to be due to that of contaminants, because these are present in very low concentrations ($\approx$1%), and it is unlikely that they can give rise to the recorded currents.

Discussion

Potential Dependent Adsorption of Fibrinogen on Platinum

The adsorption behavior of the protein and its dependence on potential are revealed by ellipsometric (Fig. 2) and steady-state potentiostatic studies (Fig. 3-6). The coverage-potential curve passes through a minimum at +300 mV/SCE for a concentration of 0.007 mg/ml of the protein. The evidence from this study is not sufficient to indicate any desorption at this potential range for that particular concentration. At higher concentrations the coverage steadily increases with increasing anodic potential. This agrees with the surface excess-potential behavior of fibrinogen in electrocapillary measurements (14).

At low concentrations of the protein in solution, steady-state potentiostatic studies also show that the decrease in current over the entire potential range is probably due to the fact that fibrinogen is adsorbed over a wide potential range from −600 to +800 mV/SCE (Fig. 3). However, one cannot exclude other possible causes such as modification of the double layer structure or interaction of the proteins with the reactants. With increase of concentration, charge transfer reactions seem to take place at highly cathodic and over a wide range of anodic potentials (Fig. 4, 5).

The potentiodynamic investigations also indicate the influence of adsorption on the development of peaks. Unlike with the other methods, the presence of adsorption is not explicitly revealed here. In potentiodynamic studies, the presence of adsorption is shown by the development of pre- or post-peaks in addition to charge transfer peaks. Such peaks are not developed for this protein and thus there is no direct evidence for the presence of adsorption. Some of the quantitative diagnostic criteria to establish the role of adsorption have been applied (15). Two of these are (*i*) the study of the variation of the peak current functions i_p/v and $i_p/v^{1/2}$ (v is the scan rate and i_p is the peak current at that scan rate) with scan rate. If adsorption is present, the former is constant while the latter steadily increases; and (*ii*) determination of concentration dependence. If adsorption is present, i_p/c will increase with decrease of concentration, c, at the same scan rate. The results are shown in Tables III-V. It is seen that for both concentrations investigated, the anodic peak II and the cathodic peak obey both these criteria while the anodic peak I shows an increase of i_p/c with decrease of c.

Table III. Dependence of peak current function on scan rate, concentration of fibrinogen 3 mg/ml

Scan rate (v), V/sec (× 10^{-3})	Anodic peak I i_p*/v (× 10^{-4})	Anodic peak I $i_p/v^{1/2}$ (× 10^{2})	Anodic peak II i_p/v (× 10^{-4})	Anodic peak II $i_p/v^{1/2}$ (× 10^{-2})	Cathodic peak i_p/v (× 10^{-4})	Cathodic peak $i_p/v^{1/2}$ (× 10^{-2})
10	99	99	—	—	—	—
20	59.5	85	—	—	—	—
40	44.5	67.5	12.5	25	16.5	33
70	41	64	16	42	16.6	44
100	33	104	15.2	48	15.5	49
200	27	119	15.4	69	10.5	47
300	23	125	16	872	10	54.5
400	—	—	16	102	10	65

* Peak current i_p is in A-cm^{-2}.

Table IV. Dependence of peak current function on scan rate, concentration of fibrinogen 0.07 mg/ml

Scan rate (v), V/sec (× 10^{-3})	Anodic peak I i_p*/v (× 10^{-4})	Anodic peak I $i_p/v^{1/2}$ (× 10^{-2})	Anodic peak II i_p/v (× 10^{-4})	Anodic peak II $i_p/v^{1/2}$ (× 10^{-2})	Cathodic peak i_p/v (× 10^{-4})	Cathodic peak $i_p/v^{1/2}$ (× 10^{-2})
10	160	160	—	—	—	—
25	74.5	118	—	—	—	—
50	39	87	13.5	30	11	24
75	28.4	77	12	33	12	33
100	20	64	12	38	13.5	42.5
250	13.2	65	11.4	57	11.4	59

* i_p is in A-cm^{-2}.

Table V. Variation of peak current (i_p) with concentration of fibrinogen

Scan rate, mV/sec	Peak	i_p*/c for Concentrations (c in mg/ml) of 3.0	0.07	0.007
10	Anodic peak I	33	2300	—
50	Anodic peak I	59	2800	5150
100	Anodic peak I	110	2860	—
50	Anodic peak II	17	950	2860
100	Anodic peak II	51	286	—
300	Anodic peak II	160	4070	—
50	Cathodic peak	22	770	—
100	Cathodic peak	52	1930	—
300	Cathodic peak	100	4070	—

* i_p is in A-cm^{-2}.

Charge Transfer Reactions of Fibrinogen at the Platinum-Saline Interface

Information regarding the charge transfer reactions of the protein is obtained from steady-state potentiostatic and potentiodynamic studies. The i-E curves for three concentrations of the protein (Fig. 3-5) indicate that at the lowest concentration, only adsorption reactions predominate over the entire potential range because the currents in the solutions with protein are always less than that in normal saline. But if the concentration of fibrinogen is increased (Fig. 4, fibrinogen concentration of 0.07 mg/ml), distinct changes are observed at cathodic potential (more cathodic than −600 mV/SCE). There is a steep increase of cathodic currents by more than one order of magnitude over the corresponding values for blank saline solution. Ellipsometric study shows that the coverage θ decreases with increase of cathodic potential. The increase of cathodic current at potentials more negative than −700 mV/SCE cannot be explained on the basis of desorption alone. Either the protein is taking part in a direct charge transfer reaction or the hydrogen evolution reaction on the platinum substrate is catalyzed by fibrinogen.

To determine whether the protein is directly involved in an electron transfer reaction across the metal-solution interface at these potentials or hydrogenation of the molecule by the discharged hydrogen occurs, the steady-state potentiostatic studies were carried out in deaerated saline with the addition of fibrinogen. The results are presented in Fig. 6. Even though the behavior of the protein on the anodic side is very different from the one observed for the same concentration in air-saturated solution (Fig. 4), the cathodic currents below −600 mV/SCE are almost identical in pure saline and in saline containing the protein at the same potential. In aerated solutions of saline, the dissolved oxygen in the system causes depolarization and hence the cathodic currents do not increase steeply at the extreme cathodic potential. From the behavior in deaerated saline, it appears that the protein undergoes an electrolytic hydrogenation reaction at the metal-solution interface. This type of electrolytic hydrogenation of organic molecules has been reported earlier (16). This is the first time in which a physiologically important blood protein has been shown to take part in such a type of reaction. From a knowledge of the structure of the fibrinogen molecule, the present findings are not surprising. Even assuming in a crude way that the cathodic process does not lead to decomposition of the molecule as a result of the reduction process, the reaction can be accounted for due to the presence of a large number of tryptophan residues. It is probable that these are hydrogenated. It is also likely that the sulfhydryl groups in the molecule may be hydrogenated. At present, the type of product formed as a result of the reaction is based only on speculation. Detailed amino-acid, N- and C-terminal assays, and gel electrophoresis studies on the reduced product have to be carried out to characterize the product formed at these highly cathodic potentials. At physiologic concentration of the protein, not only at highly cathodic potentials but also at anodic potentials, fibrinogen is involved in electron transfer reactions (Fig. 5). This increase of anodic current from about −100 mV/SCE is visible even at the lower concentration (0.07 mg/ml, Fig. 4) but is more marked at the higher concentration (3 mg/ml) of protein. This indicates that fibrinogen undergoes an anodic charge transfer reaction. This anodic reaction seems to take place over a wide range of potentials from −100 to 900 mV/SCE. It was shown previously that fibrinogen undergoes electropolymerization to fibrin in the region from −200 to +100 mV/SCE (17). This conclusion was arrived at by showing that the electron micrographs of the anodic product and of the enzymatically formed fibrin by addition of thrombin to fibrinogen were quite similar. Also in the potential range investigated, *i.e.*, −200 to +100 mV/SCE, the log current was observed to vary linearly with potential. The present work shows that the electropolymerization reaction probably takes place over a much extended region of anodic potentials up to +900 mV/SCE. At anodic potentials above +900 mV, the anodic current is nearly the same as in pure saline probably due to the influence of the oxide formation reaction and the desorption of the protein at such high potentials.

The results of potentiodynamic studies for the three concentrations of the protein show that it takes part in at least three charge transfer reactions. The complete elimination of the reversible hydrogen peaks, the suppression of the oxide reduction peak at all but the lowest concentration of the protein, and the development of new peaks at distinctly different potentials are seen in Fig. 8 and 9. The figures indicate the shape of the voltammogram at a scan rate of 50 mV/sec. The anodic peak I appears at −620 mV/SCE and anodic peak II at −400 mV/SCE, while the cathodic peak is developed at about 0 mV/SCE. The pronounced anodic peak I at the more cathodic potential masks the next peak (anodic peak II) and it is more easily discernible at faster scan rates. On the anodic scan, at potentials more cathodic to −600 mV/SCE, there is a steep increase of current and the peak at this potential region is not properly developed. At faster scan rates, one observes a truncation over a 100-mV region. It is interesting to note that the position of the peak appears to be exactly at the same potential where the second hydrogen reduction peak is observed for normal saline without protein addition.

In the light of the information obtained from ellipsometric and potentiostatic studies, an examination of the voltammograms indicates the involvement of the protein in electrochemical reactions both at extreme cathodic and over a wide range of anodic potentials. Adsorption effects predominate in the intermediate potentials. But the voltammograms do not explicitly indicate these charge transfer reactions by any pronounced peak or even a hump in the cathodic or anodic scans. The cathodic reaction is, however, indicated by the large increase of current in the highly negative regions. The recording of this in the voltammogram is vitiated by external factors like cell resistance and instrument limitation. The currents from −100 to +1000 mV/SCE in the anodic scan, suggests the occurrence of an anodic charge transfer reaction, although no peaks are visible in this region. The three clearly visible peaks (anodic peaks I and II and cathodic peak) are probably due to reactions of the products of the charge transfer reactions visible in the steady-state potentiostatic measurements. Thus, it appears that the results of the potentiodynamic study complement those from potentiostatic measurements.

The effect of scan rate variation was investigated for the two concentrations of fibrinogen in which the development of peaks is distinct (concentrations 3 and 0.07 mg/ml). Several of the diagnostic criteria developed by Nicholson *et al.* (15) for stationary electrode polarography have been applied to this case, leading to some valuable conclusions regarding the nature of these reactions, the role of adsorption, and reversibil-

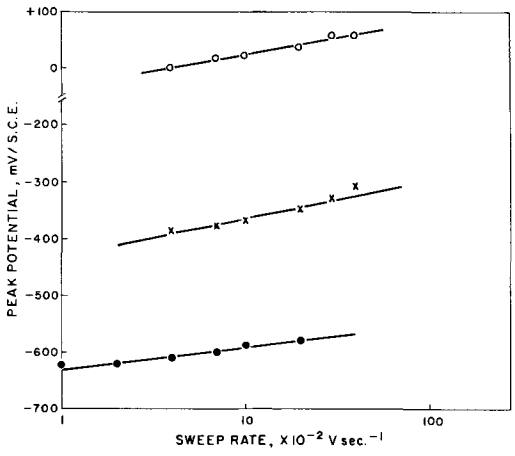

Fig. 11. Peak potentials as a function of scan rate: anodic peak I (●), anodic peak II (X), and cathodic peak (○).

ity. The shifts of peak potential as a function of scan rate for anodic peaks and the cathodic peak are shown in Fig. 11. The anodic peak I has a shift of 30 mV/decade of scan rate, while the second anodic peak and the cathodic peak have a shift of 60 mV for a tenfold increase of scan rate. The variation of the peak potentials with scan rate and the nonoccurrence of corresponding cathodic peaks show that the reactions are probably irreversible. The other criterion of total irreversibility, *i.e.*, the peak current function ($i_p/v^{1/2}$) being independent of the scan rate is not fulfilled by these peaks (Tables III and IV). Normally, the variation of peak potential with scan rate and the current function dependence are both to be considered for determining reversibility of the reaction. It is likely that complications may arise due to the adsorption of the reactant and perhaps the product. The development of pre- or post-peaks which readily characterize adsorption is not clear in this case. Even the anodic peak II cannot be considered as a post-peak as it shows a distinctly different shift of peak potential with scan rate (Fig. 11). As discussed earlier, the application of quantitative methods for determining the presence of adsorption shows the three charge transfer reactions to be also associated with adsorption processes. No attempt is made to calculate the number of electrons involved in the charge transfer reactions indicated by the three peaks due to the complexity of the system.

Correlation Between Electroactivity of Fibrinogen and Blood Compatibility of Materials

It is now necessary to examine the results in the light of some of clinical findings with materials used for cardiovascular prostheses. The observation that fibrinogen is adsorbed on the surface over a wide range of potentials (potentiostatic and ellipsometric study) is fully corroborated with earlier research in the field. Irrespective of the type of material, insulators, or metallic conductors, it is well known that fibrinogen is one of the first proteins to be adsorbed on to the surface (18). Fibrinogen adsorption seems to be the first step even during platelet retention studies in glass bead columns (19). Electrocapillary and capacity data also confirm its strong adsorption as found in the present work (20). The involvement of fibrinogen in anodic and cathodic reactions at the metal-solution interface seems to throw new light on the behavior of metallic prosthetic materials. It is generally known (21) that among metallic materials, noble metals, *i.e.*, those that develop a spontaneous positive potential in saline with respect to the NHE are thrombogenic, while the corrodible base metals are nonthrombogenic. The metallic materials so far experimented with can be classified under three headings, (A), thrombogenic, (B) fairly thromboresistant, and (C) highly thromboresistant. Copper, silver, gold, and platinum belong to class A; stellites and other cobalt-chrome alloys, some types of stainless steels to class B; and pure aluminum and its alloys and magnesium to class C. A cursory examination of their rest potentials in saline shows that class A metals have their spontaneous potentials in the thrombogenic range. If it is assumed that the primary reaction in thrombosis is the formation of a fibrin clot at the interface and the prime material for this fibrin clot formation is fibrinogen, the importance of the potentiostatic studies and their bearing on the data of thrombogenicity of metals becomes clear. The predominantly thrombogenic metals fall in the potential zone in which electropolymerization is most likely to occur. The metals of class B fall in the middle range of potentials where fibrin formation does not appear to occur but only adsorption of the protein predominates. In this region, for some of the materials, kinetic factors may play a role in leading to thrombus formation. Thus, surface roughness, contamination, and similar problems may induce thrombosis as has been observed (22). In the case of metals which belong to class C, their potentials are so highly negative that either there is complete desorption of fibrinogen or it may undergo a cathodic charge transfer reaction. Thus for aluminum the rest potential in saline is −800 mV/SCE. This falls in the zone where the cathodic reduction of fibrinogen possibly takes place. Probably the cathodic product acts as an inhibitor in the over-all thrombosis reaction. It was also observed that blood treated with aluminum powder shows a longer clotting time than controls (23).

To support the above qualitative conclusions on a solid quantitative biological footing, it is necessary to conduct hematological correlations of these findings. It is necessary to compare N-terminal assays of the electrolytically formed fibrin and the naturally formed fibrin. Similarly on the cathodic side, it is necessary to determine the influence of the cathodically formed product on the normal plasma clotting times. Such studies should yield useful information to the clinicians in addition to providing an insight on the mechanism of electropolymerization and fibrinolysis.

Conclusions

Investigations of the electrochemical reactions of one of the most important blood coagulation factors, fibrinogen, by using some of the well-known electrochemical and optical tools yield interesting information. The molecule is adsorbed on the metal surface over a wide potential range even at a very low concentration of the protein. The presence of adsorption is shown by ellipsometric, potentiodynamic, and potentiostatic methods. This confirms the previous observations that this protein adsorbs on most surfaces from plasma solutions.

The results of the potential sweep study are rather interesting. The investigations do not shed any new light on the charge transfer reactions, as revealed by the potentiostatic method, but show the occurrence of at least three charge transfer reactions at different potentials in the anodic and cathodic scans. These seem to be due to the products of the two primary reactions (shown by potentiostatic method) taking part in subsequent charge transfer reactions. All these reactions have significant adsorption contributions and the shift of peak potentials with scan rate leads to a crude guess about the number of electrons in the reactions. However, due to the absence of more sophisticated information, no quantitative conclusions can be drawn from the present results on this and on the type of adsorption.

The material undergoes both anodic and cathodic charge transfer reactions at the metal-solution interface. The cathodic reaction occurs at highly negative potentials beyond −600 mV/SCE, while the anodic reaction seems to take place over a wide potential range. The anodic reaction has been studied earlier and its product shown to be identical electron microscopically to enzymatically formed fibrin by the action of thrombin (17). The present work shows that this reaction takes place over an extended potential region.

The results of the potentiostatic study throws new light on the blood compatibility of metallic prosthetic materials. They explain the previously known fact that the spontaneous potential of the metal in saline is an important criterion in assessing its blood compatibility. The extreme thromboresistant property of metals with highly cathodic potentials in saline seems to be due to the involvement of the protein in some cathodic reaction at the interface and the product of this reaction may have an inhibitory effect on thrombus deposition. Correlative experiments are essential to prove that similar reactions occur in biological systems.

Acknowledgment

The authors thank the Medical Devices Applications Program, Division of the National Heart and Lung Institute, National Institute of Health for award of Contract No. PH 43-68-75 to carry out this work. Thanks are also due to Dr. L. Vroman of the Veterans Administration Hospital, Brooklyn, for permission to use the ellipsometer; Dr. P. J. Boddy of Bell Telephone Laboratories, for platinum sputtered slides; Dr. W. Paik, of the University of Pennsylvania, for helpful discussions in processing ellipsometric data; and Dr. G. E. Stoner, of the University of Virginia, for providing purified fibrinogen and for helpful discussions and suggestions.

Manuscript submitted March 1, 1972; revised manuscript received Sept. 27, 1972. This was Paper 132 presented at the Washington, D. C., Meeting of the Society, May 9-13, 1971.

Any discussion of this paper will appear in a Discussion Section to be published in the December 1973 JOURNAL.

REFERENCES

1. N. U. Bang *et al.*, Editors, "Thrombosis and Bleeding Disorders," Chap. 1, Academic Press, New York (1971).
2. F. N. Eldin, "Blood Coagulation Simplified," Chap. 1, Appleton Century Crofts (1971).
3. J. F. Foulton, "Text Book of Physiology," 16th edition, Chap. 28, W. B. Saunders Co., (1951).
4. A. C. Hemker and M. J. P. Kahn, *Nature*, **215**, 1201 (1967).
5. R. Biggs and R. G. Macfarlane, "Human Blood Coagulation and Its Disorders," Blackwell, Oxford (1962).
6. P. N. Sawyer, Editor, "Biophysical Mechanisms in Vascular Homeostasis and Intravascular Thrombosis," Appleton Century Crofts (1965).
7. S. Srinivasan and P. N. Sawyer, *J. Colloid. Inter. Sci.*, **32**, 456 (1970).
8. S. Srinivasan and P. N. Sawyer, "Advances in Biomedical Engineering and Medical Physics," Vol. 3, Chap. 14, Interscience Publishers, Inc., New York (1970).
9. N. U. Bang *et al.*, Editors, "Thrombosis and Bleeding Disorders," Chap. VI, Academic Press, New York (1971).
10. L. Walker and A. Catlin, *Thromb. Diath. Haemorrhag.*, **26**, 99 (1971).
11. L. A. Kazal S. Amsel, O. P. Miller, and L. M. Tocantins, *Proc. Soc. Expt. Biol. Med.*, **113**, 989 (1963).
12. Y. C. Chiw and M. A. Genshaw, *J. Phys. Chem.*, **73**, 357 (1969).
13. L. Vroman, Private communication.
14. G. E. Stoner, *J. Biomed. Mat. Res.*, **3**, 655 (1969).
15. R. S. Nicholson and I. Shain, *Anal. Chem.*, **39**, (3), 1514 (1967).
16. S. H. Langer and H. P. Landi, *J. Am. Chem. Soc.*, **86**, 4964 (1964).
17. G. E. Stoner and L. Walker, *J. Biomed. Mat. Res.*, **3**, 43 (1969).
18. L. Vroman and A. L. Adams, *ibid.*, **3**, 43 (1969).
19. E. Gugler and E. F. Lusher, *Thromb. Diath. Haemorrhag.*, **14**, 361 (1969).
20. G. E. Stoner and S. Srinivasan, *J. Phys. Chem.*, **74**, 1088 (1970).
21. P. S. Chopra, S. Srinivasan, T. R. Lucas, and P. N. Sawyer, *Nature*, **215**, 1494 (1967).
22. L. A. Brewer, Editor, "Proc. Second Nat. Conf. on Prosthetic Heart Valves," Los Angeles, Calif., May 30-June 1, Charles C. Thomas, Publication (1969).
23. P. N. Sawyer and S. Srinivasan, Unpublished results.

A New Technique for First-Drop Polarography

E. Kirowa-Eisner, N. Tshernikovski, and U. Eisner

Institute of Chemistry, Tel-Aviv University, Ramat-Aviv, Israel

ABSTRACT

A new instrument for automatic "first-drop" polarography is described. The advantages of this system are shown in the evaluation of kinetic parameters of an electrode reaction. A detailed description of the operation of the instrument is presented.

It is well known that in spite of the stirring effect caused by the falling of the mercury drops, successive drops grow into a solution whose concentration differs from that to which the first drop at any particular potential is exposed. Depletion of the diffusion layer and accumulation of intermediates near the electrode surface may alter the character of the layer adjacent to the drop and cause a change in the current-time characteristics.

Advantages of first-drop measurements were demonstrated by the Czechoslovak School of Polarography. First-drop measurements were achieved with the use of horizontal or tilted capillaries (1). Other devices were constructed by Hans *et al.* (2) and by Němec (3).

Despite its advantages mainly in kinetic studies of electrochemical processes, the technique has not been generally adopted for routine work by electrochemists.

Key words: polarography, instrumentation, electrode kinetics.

In a recent paper by Kirowa-Eisner and Gileadi (4) a first-drop technique was used for the elucidation of the electroreduction of glycol aldehyde (GA). In these experiments the potential was kept at a less negative value where no electrochemical process took place and was then stepped up to a value corresponding to the plateau just as a drop fell. In this way measurements were conducted on what electrochemically constitutes a first drop.

The present work describes an instrument which enables one to carry out first-drop polarography conveniently and automatically. Its advantages are demonstrated with the use of some electrochemical processes.

Experimental

Polarograms were recorded on a Yokogawa recorder Type 3046. Fast transients were recorded on a Tektronix Type 564 storage oscilloscope. Lifetime of the

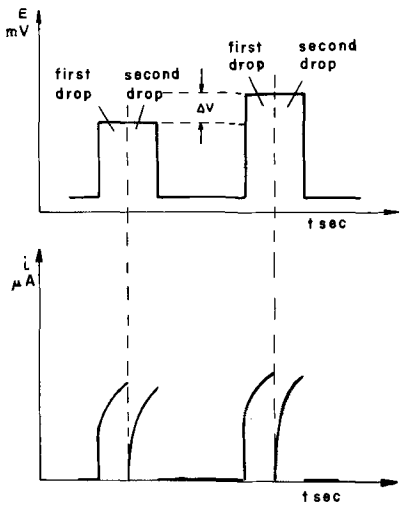

Fig. 1. Potential wave form and respective current of the polarographic unit.

drops was determined by a Radiometer Drop Lifetimer Type DLT1, currents were measured with the aid of a home-made current follower. Cell and electrodes were Radiometer, Copenhagen.

Method of operation of the instrument.—General.— The initial potential is set at some value at which no electrochemical process occurs. The potential is kept at this value for a predetermined number of drops and is then stepped synchronically with the enforced fall of the next drop, to the desired value. The potential is held constant, again for a predetermined number of drops, and then changed back to the initial value. (Fig. 1).

The final potential may be kept at a certain value thus permitting the recording of the current to be repeated as many times as desired.

In a different mode of operation the potential can be kept at the final value indefinitely. The instrument can also operate as a regular staircase generator for polarographic measurements. In that case, its main feature is the fact that the potential does not change during the lifetime of the drop. A delay in the application of the pulse for a predetermined time enables application of the potential toward the end of the drop life. A time sampler constructed in this laboratory connected to the present generator enables the operation of the instrument in a "Tast" mode. This mode of operation and the use of the instrument for solid/electrode voltammetry will be discussed in subsequent papers. The generator also can be used for the construction of electrocapillary curves. Results will be reported later.

Description of the instrument and its operation.—The instrument comprises three main parts: (*i*) central control unit, (*ii*), counter and digital-to-analog converter (D/A), and (*iii*) output stage

The control unit.—The central control unit (CCU) controls the functioning of the instrument. It contains a delay and a trigger unit which synchronizes the operation of the instrument with the lifetime of the drop. The unit is activated by an external pulse obtained from a drop dislodger (in this work the drop life timer manufactured by Radiometer was used). Each drop is counted by one of two counters. One counts a certain predetermined number of drops, m (1-9), to which the initial voltage is applied. The second counts another predetermined number, n (1-9), of drops to which the working voltage is applied. The values of m and n are chosen independently by "4-bit" digital comparators to which the counters are connected.

The comparators control the state of a "flip-flop" circuit. The latter chooses which of the two counters will get the trigger pulses. It also controls the output stage.

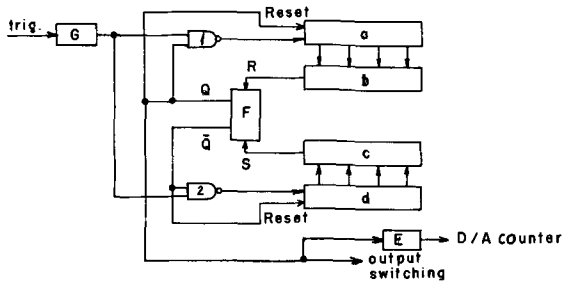

Fig. 2. Block diagram of the control unit. a, Counter n; b, comperator n; c, comperator m; d, counter m; e, delay; f, flip flop; g, delay.

Theory of operation.—At the outset the flip-flop circuit is in its zero state, $Q=0$, $\overline{Q}=1$ (Fig. 2). Gate 1 is open and gate 2 is closed. The trigger pulses will be counted by the m counter until the number in the counter equals m. At this point the m comparator will change the state of the flip-flop, $Q=1$, $\overline{Q}=0$. Gate 2 is then opened, gate 1 is closed, and the m counter is reset to zero. The trigger pulses are counted by the n counter up to a value n. At this point the flip-flop will return to its initial state and the n counter is reset to zero. At the end of each flip-flop cycle a pulse is sent to the D/A counter which is advanced by one. The role of the delay is to ensure that the advance will occur while the output is already at the initial voltage. The flip-flop connects the D/A while the n counter is on and the m counter is off. The D/A is disconnected when the m counter is on and the n counter is off.

The D/A unit (Fig. 3).—The counter is a 9-bit binary counter which is made of an 8-bit counter and a 1-bit counter. This arrangement permits one to obtain 512 pulses with a voltage difference of ΔV between two successive pulses or 256 pulses with a voltage difference of $2\Delta V$. In this work a ΔV of 2.5 mV was chosen. (If a larger potential is desired, ΔV may be increased up to 5 mV in the output stage.) The nine binary outputs of the counter are connected through nine Nand gates to the D/A electronic switches. The second inputs of all the gates are connected to the flip-flop in the control unit.

When the m counter is on, a "zero" appears on this line and all the gates will be in the "high state" which opens all the switches. When the n counter is on, a "1" will appear on the line and the outputs of the gates will depend on the number contained in the 9-bit counter. This number will be translated to an analog current value by the switches and resistor network.

The output stage (Fig. 4).—The output stage comprises two operational amplifiers. The first is fed by two sources: (*i*) The current output from the D/A. This current will be either zero or proportional to the number of measuring cycles passed, depending on the state of the control unit. (*ii*) A second source supplies the initial voltage which will be applied to the electrodes

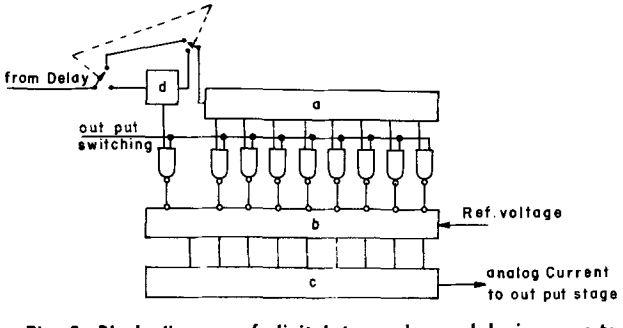

Fig. 3. Block diagram of digital to analog and logic converter (D/A unit). a, 8-bit counter; b, D/A switches; c, R, 2R resistor network; d, 1-bit counter.

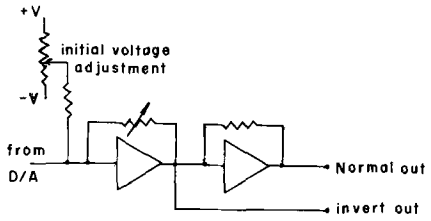

Fig. 4. Block diagram of output stage

in the m state. A second amplifier acts as an inverter enabling one to obtain pulses of reversed polarities.

Results and Discussion

The behavior of the first and subsequent drops are demonstrated for a few cases.

Diffusion-controlled process.—The system selected was Cd^{+2} in KCl.

1. The current at the beginning of the drop life is different in the first drop from that in subsequent drops (Fig. 5). At the end of the drop life (2-4 sec) the currents differ by less than 2%.

2. A "true" first drop is obtained only when three or more drops are released at the potential where no faradaic current flows (Fig. 6).

3. The log i *vs.* log t plot for the first drop is linear with a slope of 0.17 for a time less than 1 sec (drop life about 4 sec) (Fig. 7). This value differs from the slope of 0.19 obtained by others (5). The reason is that under the conditions in our experiment (measurements were carried out at the early stages of drop growth) the spherical correction is smaller and the value of the slope approaches 1/6 as is expected for linear diffusion.

The reproducibility of the current/time curves is excellent (better than 0.1%). Thus a log i/log t plot (during drop growth) is proposed as a method to determine whether or not a process is diffusion controlled. This method is faster and more accurate than the evaluation of the dependence of current on the height of the mercury column or the dependence of current on the drop time (maintaining the same height of mercury column and using different drop times by enforced fall of the drops).

Temperature effect.—As the temperature is lowered the diffusion coefficient decreases, slowing down the equalization of concentrations and one might expect greater differences between the first and subsequent drops than at higher temperatures. This difference, which is not very pronounced, can be seen from Fig. 8.

Analytical aspects.—First-drop polarography for diffusion-controlled processes has no advantage over classical polarography for routine polarographic analysis since calibration curves are generally used.

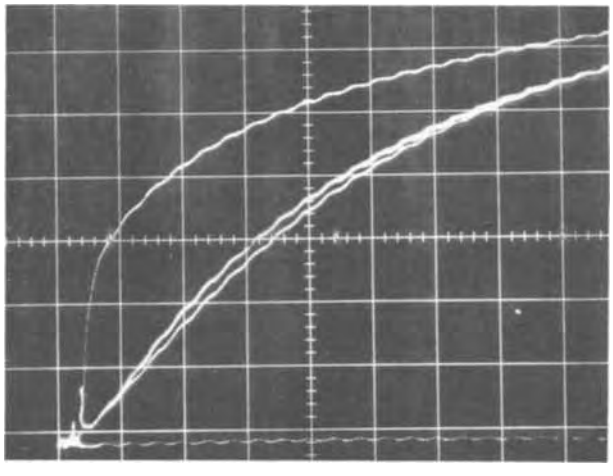

Fig. 5. First, second, and third drop. τ = 4 sec, 3 mM Cd^{++}, 1M KCl, h = 40 cm. X axis = 50 msec/cm, Y axis = 2.1 μA/cm, temperature = 4°C.

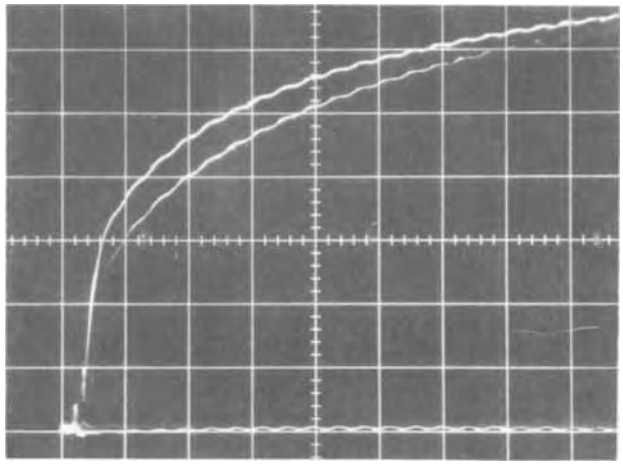

Fig. 6. Effect of the number of the drops at initial potential on the first drop. Upper curve, three drops at initial potential; lower curve, one drop at initial potential; other conditions as for Fig. 5.

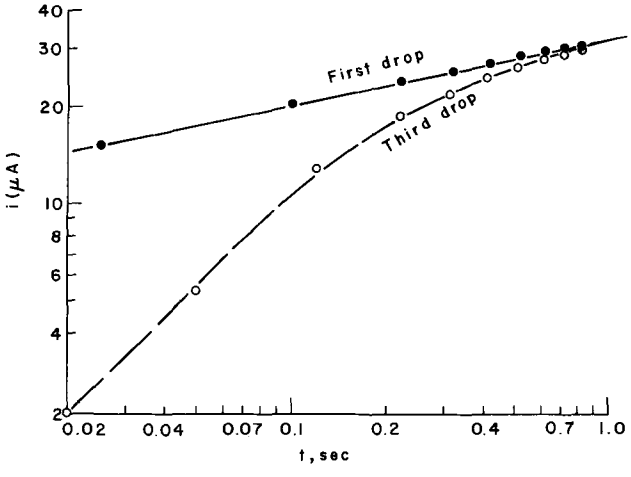

Fig. 7. Log i-log t dependence for first and third drops. 3 mM Cd^{++} in 1M KCl.

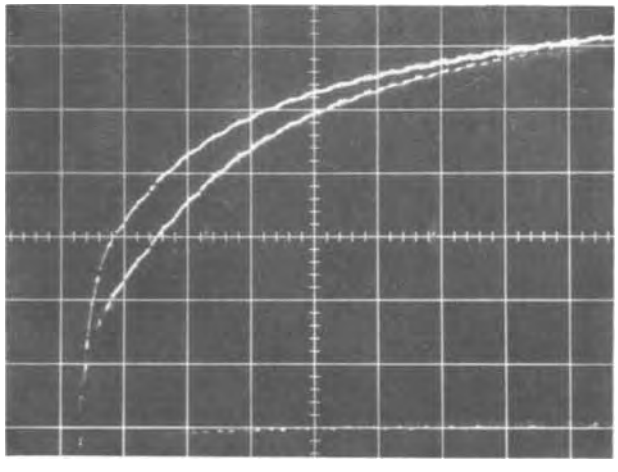

Fig. 8. Same as Fig. 6 but at 25°C and current density (Y axis) 3.1 μA/cm.

Kinetic processes.—The reduction of glycol aldehyde (GA) is presented as an example of a kinetic process. The general reduction scheme is

$$GA_{hydrated} \xrightarrow{k} GA \qquad \text{(base catalyzed process} \quad [1]$$

$$GA + 2e + H_2O \rightarrow AA + 2\,OH^- \qquad \text{(AA acetaldehyde)} \quad [2]$$

The detailed mechanism was studied by Kirowa-Eisner and Gileadi (4).

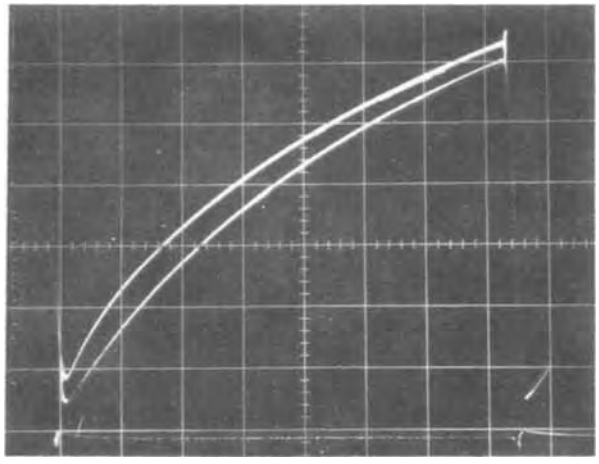

Fig. 9. First drop and second drop current-time curves throughout the drop life (4 sec) for GA. pH = 12.7. (Distortion of the curve at the beginning of the drop life is caused by an external capacitor connected in parallel with the resistor at the output stage for elimination of "noise.")

The curve of the limiting current as a function of pH has a maximum at pH = 12.7.

This pH was chosen for the experiments described below. The supporting electrolyte was $LiClO_4$ and the pH was adjusted by the addition of LiOH. As the potential is applied and the current-time curves are recorded, the accumulation of OH^- near the electrode surface results in an increase in pH which suppresses the limiting current of the subsequent drops. The current for the first drop is higher throughout the drop life (Fig. 9). When the pH of the solution is 11.5, the i-t curves for the first and subsequent drops are essentially the same. Depletion of GA in the vicinity of the electrode causes a decrease in the current, but this is compensated by the increase in pH. Thus the determination of the kinetic parameters of a reaction must be carried out on the first drop.

The rate constant for the chemical step in the reduction of GA was determined by Koutecky's method with the use of i-t curves (4).

The difference in the behavior of i-t curves will be most pronounced for catalytic processes

$$A + e \rightarrow B$$

$$B + c \rightarrow A$$

Accumulation of reaction products which affect the kinetics of the over-all process at the electrode surface will result in a large difference between the i-t curves of first and subsequent drops.

i-E curves.—The calculation of the Tafel slope $(\partial E/\partial \log i)$ for electrochemical processes is essential for the evaluation of the mechanism of the process. First-drop polarography is most convenient in this respect. The potential is stepped automatically in the desired step heights. The potential is constant during the life of the drop as opposed to the case of classical polarography where it changes linearly with time during the drop life. Figure 10 presents a Tafel slope for formaldehyde.

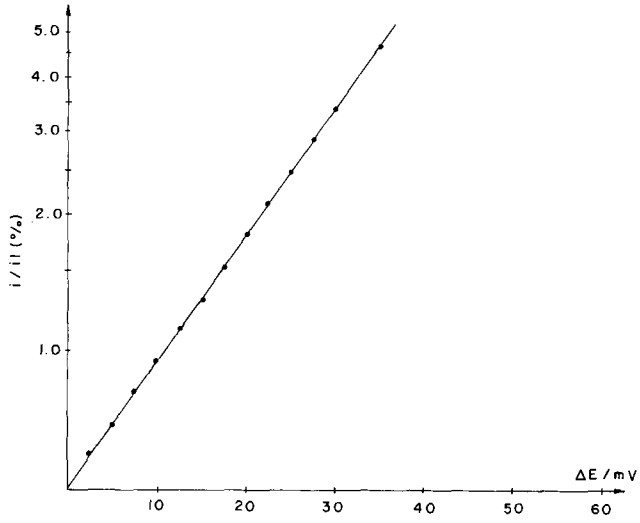

Fig. 10. Tafel plot for formaldehyde

Conclusions

The instrument described herein is a useful and convenient tool for the elucidation of the character of electrode reactions. It enables automatic measurements on first drops, thus avoiding the changes in the current-time curves which stem from depletion of reactants or accumulation of intermediates near the electrode surface. It is, furthermore, most suitable for evaluation of the kinetic parameters of kinetic, catalytic, or adsorption processes. It is versatile, dependable, and simple to operate.

Acknowledgment

The authors thank Mr. Y. Kliger for carrying out the design of the details and building of the instrument.

Manuscript submitted Aug. 10, 1972; revised manuscript received Oct. 18, 1972.

Any discussion of this paper will appear in a Discussion Section to be published in the December 1973 JOURNAL.

REFERENCES

1. I. Smoler, *Coll. Czech. Chem. Comm.*, **19**, 238 (1954).
2. W. Hans, W. Henne, and F. Meurer, *Z. Elektrochem.*, **58**, 836 (1954).
3. L. Němec and I. Smoler, *Chem. Listy*, **51**, 1958 (1957).
4. E. Kirowa-Eisner and E. Gileadi, *J. Electroanal. Chem.*, **38**, 191 (1972).
5. J. Herovsky and J. Kuta, "Principles of Polarography," Academic Press, New York (1966), and references therein.

Electrode Filming in Ring Substituted Anilines

Keith B. Prater*

Department of Chemistry, University of Texas at El Paso, El Paso, Texas 79968

ABSTRACT

The study of the electrode filming behavior of a series of ring substituted anilines has indicated that filming occurs only in those compounds containing several doubly activated ring positions. This leads to the conclusion that the films arise due to multiple ring-ring coupling.

Electrode filming is one of the banes of the electrochemist's existence. All too often, an interesting compound is electrolyzed and found to yield an insoluble material which rapidly coats the electrode and renders it nonconducting. Such filming makes obtaining electrochemical data difficult at best, and usually necessitates the use of very rapid transient methods in which the data are (hopefully) collected before significant filming has occurred. More often, however, the compound is simply set aside and some more well-behaved compound is studied.

It is generally assumed that these films are polymeric materials, but, to the author's knowledge, no one has considered the problem of why some compounds form such films and others do not. This paper reports the results of a survey of the filming properties of a series of ring substituted anilines and suggests that these results are understandable on the basis of the effects of the substituents on the activities of various ring positions.

Experimental

All solutions were prepared from acetonitrile which had been stored over CaH_2 and then triply distilled from P_4O_{10}. The solutions were 0.1*M* in tetraethylammonium perchlorate. The ring substituted anilines were obtained from Eastman-Kodak and were used as received. The N,N-dimethylated anisidines were prepared from the corresponding anisidines by methylation with trimethylphosphate (1). Solutions were *ca.* $10^{-3}M$ in the anilines. The working electrode was a platinum wire and the reference electrode was a silver wire. The potentiostat and voltage scanner were of standard design.

Results and Discussion

The results which were obtained for a series of ring substituted anilines are summarized in Table I. There was little difficulty in separating these compounds into the two categories shown in Table I on the basis of their cyclic voltammograms. Those compounds which were classed as nonfilming exhibited cyclics similar to that of *o*-anisidine as shown in Fig. 1. After stirring the solution, a second cyclic could be obtained which differed in peak height from the first by less than 2% and in peak potential by less than 30 mV.

Those compounds which were classified as filming exhibited behavior similar to that of *m*-aminophenol shown in Fig. 2. The first cyclic on a clean electrode was characterized by a broad, rounded peak and a rapid decrease in current after switching the direction of potential scan. After stirring the solution, the second cyclic yielded a peak height significantly smaller than before and the peak potential was shifted by several hundred millivolts. After wiping the electrode, a third cyclic was obtained. In general, the peak height for this third cyclic was much less than had been observed on the clean electrode, but the peak potential was close to that obtained on the clean electrode. It should be pointed out that examples of less severe filming were also observed.

The obvious observation to be made from Table I is that filming occurs only when the substituent group is electron donating and *meta* to the amine group. An electron donating group *ortho* to the amine does not cause filming, nor does an electron withdrawing group ($-NO_2$) in either position. The difference between these two groups of compounds is that, since electron donating groups (including $-NH_2$) activate the ring

* Electrochemical Society Active Member.
Key words: filming, substituted anilines.

Table I. Filming behavior of ring substituted anilines

Nonfilming	Filming
o-NH_2	*m*-NH_2
o-OH	*m*-OH
o-OCH_3	*m*-OCH_3
o-Cl	*m*-Cl (slight)
o-NO_2	
m-NO_2	

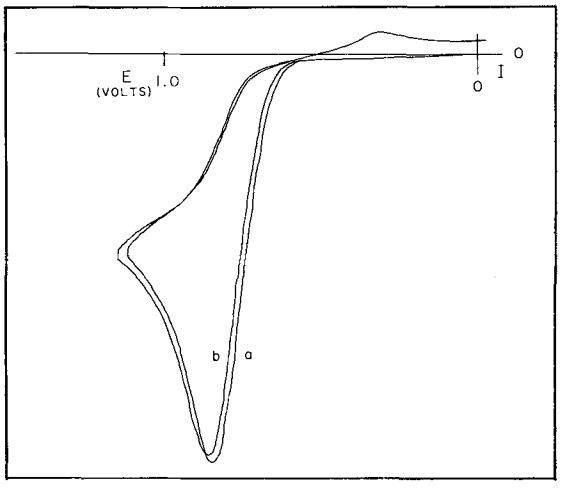

Fig. 1. Cyclic voltammogram of *o*-anisidine in acetonitrile. a. Clean electrode; b, after stirring solution.

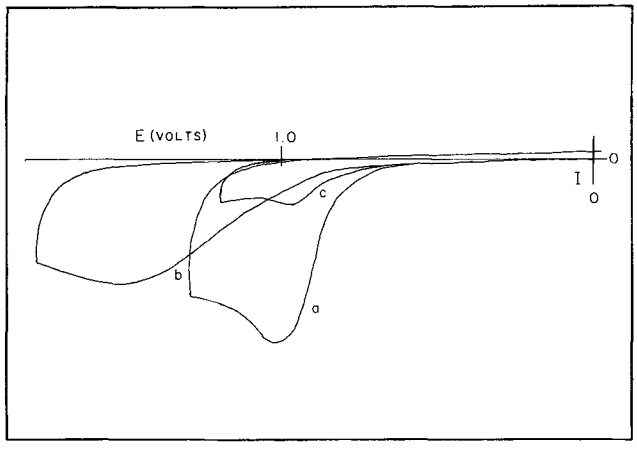

Fig. 2. Cyclic voltammogram of *m*-aminophenol in acetonitrile. a. Clean electrode; b. after stirring solution; c. after wiping electrode.

to electrophilic attack at the positions *ortho* and *para* to the substituent itself, a compound having two electron donating groups *meta* to one another will have three ring positions which are doubly activated (see Fig. 3), whereas, if the two electron donating groups are *ortho* to one another, there are no doubly activated positions. The presence of an electron withdrawing group anywhere on the ring would be expected to decrease the susceptibility toward electrophilic attack.

From these arguments, one would conclude that the mechanism of the formation of the films involves multiple electrophylic attack, probably by electrogenerated cation radicals, on such an activated ring yielding a polymeric material containing units such as is shown in Fig. 4.

In addition to the compounds listed above, the N,N-dimethylated *o*- and *m*-anisidines were investigated. As expected, the *ortho* isomer showed no signs of filming. The *meta* isomer was observed to film, but much less than the corresponding anisidine; less even than *m*-chloroaniline. This result could be taken as evidence that coupling through the amine nitrogen is important in the filming process. Coupling through nitrogen is well known in the oxidation of aniline (2). It hardly seems likely, though, that the amine nitrogen would be further activated by the *meta* substitution of an electron donating group. A more palatable explanation is that the N-methyl groups interfere sterically with attack on the positions *ortho* to the amine group and thus deter polymer formation. This is consistent with the fact that little *ortho-para* or *ortho-ortho* benzidine is formed when N,N-dimethylaniline is oxidized electrolytically (3) even though MO calculations indicate only slight differences between the electron densities at the *ortho* and *para* positions in dimethylaniline (1).

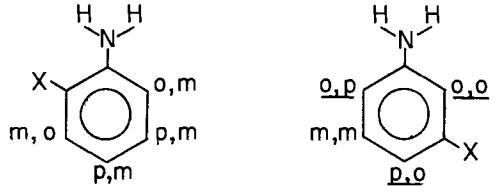

Fig. 3. Activation of the ring by *ortho* and *meta* substitution of electron-donating Group X.

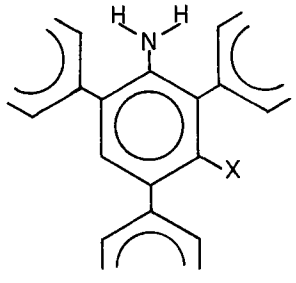

Fig. 4. Supposed polymer unit

Conclusion

This work strongly suggests that electrode filming in ring substituted anilines is due to the formation of polymeric material resulting from multiple electrophilic attack on molecules having several doubly activated ring positions. This immediately suggests several other studies including quantitative correlation of filming with electron densities from MO calculations, tracer studies to prove that the polymers arise due to ring-ring coupling and to measure the extent of this coupling, and the extension of such studies to other types of compounds.

Acknowledgments

The author wishes to thank the Robert A. Welch Foundation for support of this work.

Manuscript submitted Sept. 1, 1972; revised manuscript received Oct. 18, 1972.

Any discussion of this paper will appear in a Discussion Section to be published in the December 1973 JOURNAL.

REFERENCES

1. A. Zweig, J. E. Lancaster, M. T. Neglia, and W. H. Jura, *J. Am. Chem. Soc.*, **86**, 4130 (1964).
2. D. M. Mohilner, R. N. Adams, and W. J. Argersinger, *ibid.*, **84**, 3618 (1962).
3. R. Hand and R. F. Nelson, *This Journal* **117**, 1353 (1970).

Electroreduction of Vanadium(V) in the Presence and Absence of Chlorite Ion

Ronald L. Birke* and Thomas D. Santa Cruz

Department of Chemistry, University of South Florida, Tampa, Florida 33620

ABSTRACT

Polarographic and voltammetric *i vs. E* curves have been used to study the electroreduction of ammonium metavanadate solutions in 1*F* NH_3, 1*F* NH_4Cl at dropping and hanging drop mercury electrodes. Polarographic experiments were also made in the same media with EDTA added. When chlorite ion is present in these systems, a catalytic current is manifested. In the absence of EDTA, the catalytic current process appears to involve an equilibrium reaction of the product of the electrode reaction. In the presence of EDTA, a normal catalytic current is found. The mechanisms of these processes are discussed and rate constants are measured. The average homogeneous rate constant calculated for the proposed electrode mechanism is 2×10^5 liter/mole-sec without EDTA and 9×10^4 liter/mole-sec in 0.1*F* EDTA.

The electroreduction of vanadium(V) on mercury electrodes in alkaline media has been studied with polarographic methods by several workers (1-3). There has been some confusion in the literature concerning the polarographic behavior of V(V) in ammonia, ammonium chloride media. Lingane (2) found that a $1.58 \times 10^{-3}F$ solution of ammonium metavanadate in 1*F* NH_3, 1*F* NH_4Cl exhibited two closely spaced waves with a 3:1 ratio of wave heights. His interpretation was that the first wave is due to the reduction of V(V)

* Electrochemical Society Active Member.
Key words: electroreduction, vanadium, mercury electrode.

to V(IV) and that the second wave is due to the reduction of V(IV) to V(II). Schmidt and Reilley (4) found that sodium vanadate in 1*F* NH_4Cl, 6*F* NH_3 shows a single wave up to concentrations of about $5 \times 10^{-4}F$ and at higher concentrations a double wave appears. The first wave is not a function of total [V(V)], whereas the total wave height is directly proportional to this concentration. Their interpretation of the double wave is that the first wave is caused by an inhibited electrode reaction where the product of the initial reduction forms a film of vanadium hydroxide of lower oxidation state on the electrode surface and presents a barrier to further reduction until the potential is made more negative.

Baumann (5) has observed the same inhibition effect with vanadium(V) concentrations above $5 \times 10^{-4}M$ in 1*F* NH_3, 1*F* NH_4Cl medium. It is somewhat surprising that often quoted tables of polarographic half-wave potentials (6) still list the first wave in this system as the V(V) to V(IV) reduction process and give a diffusion current constant for the first wave. Since the ammoniacal medium is convenient for analytical determination of trace quantities of vanadium (7, 8), it is important to emphasize that only the plateau on the second wave corresponds to a diffusion controlled process.

Recently Jedral and Galus (9, 10) studied V(V) in 2-8*F* NH_3 and 0.1*F* $NaClO_4$ solutions. Their slow sweep voltammetric and chronopotentiometric experiments give additional evidence of film formation at higher [V(V)] which inhibits the electroreduction. They propose a mechanism in which V(V) is irreversibly reduced and forms a monolayer of $V(OH)_2$, which is blocking, and at more negative potentials a thick dense film of $V(OH)_2$ can be formed on the monolayer. The formation of the latter film is the process occurring on the second wave or peak of the *i vs. E* curve, and the first peak or wave is due solely to the inhibited irreversible electrode reaction.

We have investigated the voltammetric behavior of the electroreduction of V(V) at concentrations above and below $5 \times 10^{-4}F$ in the 1*F* NH_3, 1*F* NH_4Cl buffer. This treatment was undertaken because it was felt that $V(OH)_3$ may also be involved in the mechanism since $V(OH)_3$ is more insoluble than $V(OH)_2$. In addition, we have studied the polarographic catalytic current produced when chlorite, ClO_2^-, is added to the medium in the presence and absence of ethylenediammine tetraacetic acid (EDTA). Baumann (5) has observed the catalytic process with NO_2^- in the V(V) system in the 1*F* NH_3, 1*F* NH_4Cl buffer. We had previously (11) studied the oxidation kinetics of several ferrous complexes and cuprous amine with ClO_2^- in 1*F* NH_3, 1*F* NH_4Cl by the catalytic current method, and so it was natural to extend the treatment to the vanadium system.

Experimental

The instrumental setup used for polarographic and controlled potential coulometry has been described previously (11). In the present experiments a Hewlett Packard 7100B strip chart with disk integrator was used for integrations. Single and multiple cycle cyclic voltammetry was accomplished using a Wenking 68 FR 0.5 potentiostat, a Chemtrix Model 800 waveform generator, and a Hewlett Packard 7004B X-Y recorder. The electrolysis cell in this work was a Metrohm water-jacketed vessel (EA 874 and 876) with the microburette hanging mercury drop apparatus (E 410). For some experiments, a low resistance amalgamated Pt tip electrode was used to hang a mercury drop extruded from the microburette. A gas train for purifying nitrogen over copper at 350°-400°C was used in all measurements. The reference electrode in every case was a Metrohm saturated calomel electrode, SCE. Experimentally determined residual currents were subtracted from all measured polarographic currents in the catalytic current study.

All reagents used were analytical reagent grade purity. The sodium chlorite was purified by a procedure already described (11). A vanadium(V) stock solution was made up from ammonium metavanadate, NH_4VO_3, by dissolving the salt in 1.0*F* NH_3, 1.0*F* NH_4Cl. The stock solution was standardized by reduction with ferrous solution, oxidation of excess ferrous with persulfate solution, and titration of the V(IV) with $KMnO_4$. Chlorite solutions were made up determinately.

Error limits for slopes of plots are rough estimates and those for rate parameters are the standard deviations for the indicated number of measurements.

Results and Discussion

Polarography and coulometry of NH_4VO_3 in 1F NH_3, 1F NH_4Cl.—In order to interpret the kinetic data for the catalytic current produced by the chlorite oxidation of a vanadium species of lower oxidation state, it is necessary to consider the polarographic reduction of V(V) species in ammoniacal media in the absence of chlorite. The polarographic current-potential curves at concentrations above 0.5 millimolar [V(V)] in ammoniacal buffer exhibit two waves. At 0.50, 1.0, and 2.0 millimolar [V(V)], the ratio of total wave height to the first wave height is 2.0:1, 2.4:1, and 3.0:1, respectively, with $E_{1/2}$ nearly the same for each concentration. Clearly, the changing ratio of the wave heights is not proportional to the number of electrons transferred. If the concentration is increased to around 5 millimolar the current time curves in the potential region from −0.94 to −1.3V *vs.* SCE show a drastic decrease over the drop life indicating an adsorption process.

A controlled potential electrolysis, cpe, at a Hg pool electrode at −1.3V *vs.* SCE showed the number of electrons exchanged as 2.05 and 2.02, indicating a V(V) → V(III) process. Jedral and Galus (9) established that a V(II) electrode product reacts with V(V) in ammoniacal media to produce a V(III) species so that cpe does not establish the product of the electrode reaction Assuming $D = 5 \times 10^{-6}$ cm²/sec Jedral and Galus (9) calculate $n = 3$ in a voltammetric experiment. Calculations of n at −1.4V *vs.* SCE on the polarographic diffusion current plateau are ambiguous because a value of $n = 2.96$ is found for a 1.00 millimolar V(V) using the above value of D whereas a value closer to two is found at lower concentrations. This apparent dependence of n on concentration results because of a nonlinear relationship between i_d and V(V) concentration (5). Thin layer voltammetry (9) in 6*F* NH_3, 0.5*F* $NaClO_4$ indicates that electrode reaction product is a V(II) species. A similar process is most likely occurring in the 1*F* NH_3, 1*F* NH_4Cl buffer.

A number of interesting phenomena occur upon cpe of NH_4VO_3 at a large Hg pool electrode at −1.3V *vs.* SCE. The experiment was performed with a DME placed in the electrolysis cell for recording *i vs. E* curves, and stirring was achieved with a Teflon stirring bar on the Hg pool surface. The solution turns yellowish-brown as electrolysis proceeds and becomes very cloudy indicating colloid formation. An *i vs. E* curve taken with the DME directly after the cpe (Fig. 1) shows a residual current from +1.0V *vs.* SCE where Hg is oxidized to −0.8V *vs.* SCE where hydrogen is reduced. This *i vs. E* behavior appears to be caused by a passivating film on the Hg surface which is rather amazing in its blocking of Hg oxidation. There is some passivation of a DME in the pure supporting electrolyte buffer, but nothing like that when colloidal V(III) is present. The decrease in hydrogen overvoltage is most likely due to a catalytic process involving the reduction of a hydrogen ion located on the film. Both the potential which corresponds to oxidation of Hg and that which corresponds to reduction of hydrogen become more negative with time after reduction.

An additional experiment was performed on the colloidal solution of V(III) obtained by cpe. A solution of 0.625×10^{-2} millimoles of ClO_2^- was added to 2.50×10^{-2} millimoles of V(III). The solution cleared

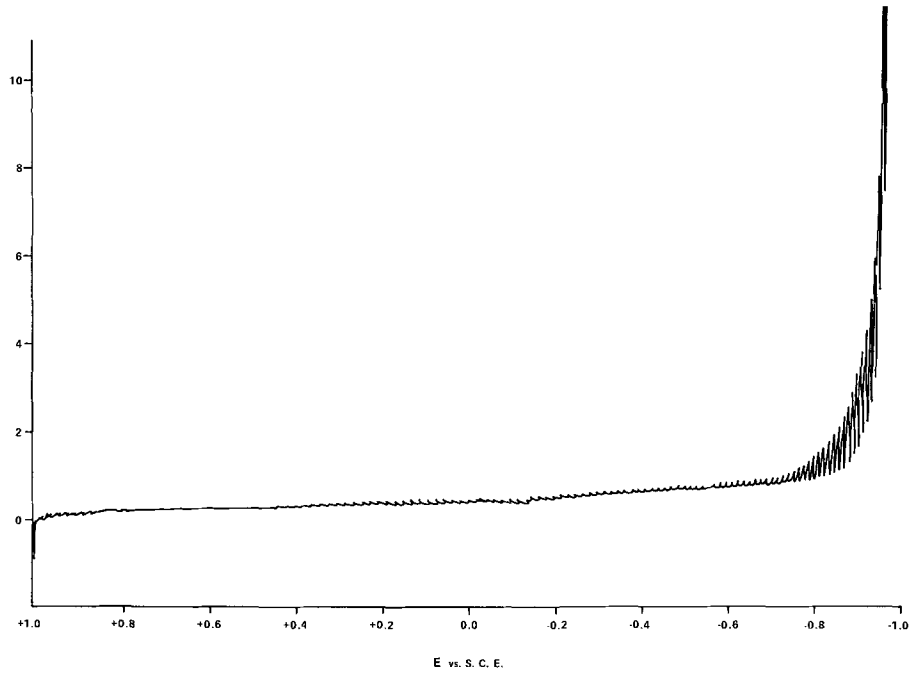

Fig. 1. Polarogram run on 50.0 ml of a 5.00 x $10^{-4}F$ NH_4VO_3 in 1.0F of NH_3, 1.0F NH_4Cl after controlled potential reduction at —1.30V vs. SCE.

up immediately and a polarogram run on this solution was very irreversible, but had an $E_{1/2}$ of —0.68V compared to —1.1V *vs.* SCE for the original 5 × $10^{-4}F$ NH_4VO_3 solution before electrolysis. The positive shift in $E_{1/2}$ after oxidation is evidence of the production of a V(IV) species since V(IV) → V(II) is more reversible than V(V) → V(IV) (9). A calculation using i_d showed that n was approximately 2, which is another indication that a 1:4 ratio of ClO_2^- to V(III) gives a V(IV) species.

Polarography and coulometry of NH_4VO_3 in 0.1F EDTA, 1F NH_3, 1F NH_4Cl.—In the presence of 0.1F EDTA, the *i vs. E* curves of NH_4VO_3 in 1F NH_3, 1F NH_4Cl show a morphology quite different from the curves observed in the pure supporting electrolyte buffer. The polarography of the V(V)-EDTA system was originally investigated by Pecsok and Juvet (18). These workers describe the number of waves in the *i vs. E* curve changing from 2 to 1 as the *p*H is varied from 9.0 to 10.0. Figure 2 shows that the V(V)-EDTA system in 1F NH_3, 1F NH_4Cl has three discernable polarographic waves. The experimental determined *p*H is 9.44. The first wave begins from the potential of Hg oxidation. The second and the third waves are irreversible with $E_{1/2}$ *vs.* SCE of —1.01V and —1.29V respectively. The $E_{1/2}$ of the third wave corresponds to the $E_{1/2}$ found by Pecsok and Juvet (18) for the V(III) to V(II) electrode process. The second wave appears as an irreversible prewave on the polarograms given by Pecsok and Juvet for the V(V)-EDTA system and was not reported by them as a separate wave. These authors, however, do discuss this prewave as the V(IV) to V(III) reduction and the "main wave" as the V(III) to V(II) reduction in the polarogram of V(IV)-EDTA solution at *p*H = 9.54.

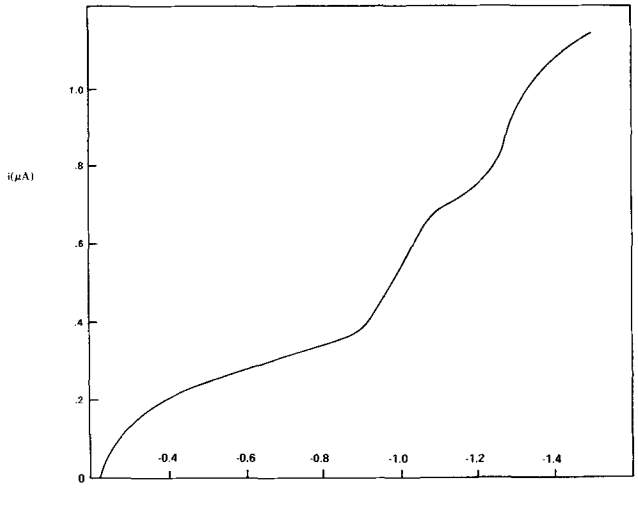

Fig. 2. Polarogram of 1.02 x $10^{-4}F$ NH_4VO_3 in 1.0F NH_3, 1.0F NH_4Cl, and 0.10F EDTA. T = 25°C, m = 1.627 mg/sec.

When the height of the Hg column is raised to 73 cm, a maximum develops on the rising portion of the third wave. The peak of the maximum drops at —1.43V *vs.* SCE and is followed by a sharp dip in the curve which then rises to a current level slightly higher than the peak of the maximum. Addition of Triton X-100 results in complete disappearance of the peak on the third wave but a fourth wave now appears with $E_{1/2}$ at about —1.6V *vs.* SCE. A plot of log *i vs.* log *h*, where *h* is the Hg column height, was obtained over the range of 32.8 to 72.8 cm. In the absence of maximum suppressor, the log-log plot gave coefficients of 0.44, 0.53, and 0.70 for currents on the plateau of waves one to three, respectively. Since $i \propto h^{0.50}$ for pure diffusion control, the plateau currents on the first two waves are close to diffusion controlled. The fact that the coefficient is high for the third wave might be due to the contribution of the maximum current. However when *i vs. h* was studied in the presence of 0.001% Triton X-100 the current was proportional to $h^{0.41}$, $h^{0.43}$, and $h^{0.98}$ for the three waves, respectively. The coefficient in the case of the third wave suggests an adsorption process, however, this may be due to the effect of maximum suppressor.

Coulometry at a large Hg pool electrode was carried out on the V(V)-EDTA system. A blank correction was made on each determination and the electrolysis stopped when the current reached that of the electrolyzed blank. When the potential was controlled at —0.70V *vs.* SCE and 1.936 × 10^{-2} millimoles of V(V) added, the number of coulombs found was 1.968 giving an n = 1.05. On moving the potential to —1.1V *vs.* SCE on the plateau of the second wave, 370 millicoulombs were found for 1.936 × 10^{-3} millimoles of V(V) giving an n = 1.98. Controlled potential reduction at —1.40V vs. SCE was not possible since a catalytic hydrogen wave moved positive during electrolysis and the current did not decay. This wave is most likely the fourth wave which appears when Triton X-100 is added.

At the pH of our buffer the solution composition is a mixture of the VO_2EDTA^{3-} complex and polyvanadates (19). The log formation constants (19, 20) of $VEDTA^{2-}$, $VEDTA^{1-}$, $VOEDTA^{2-}$, and VO_2EDTA^{3-} are 12.7, 25.9, 18.4, and 18.1, respectively, indicating that all vanadium species are complexed. At concentrations of V(V) larger than $10^{-3}F$, the *i vs. t* curves do not show the decrease with time which is present when EDTA is absent. Complexation undoubtedly prevents the inhibited electrode process which occurs when EDTA is not present.

The ratio of the total wave height of the third wave to the second wave is 1.50 ± 1.5% for three concentrations in the range $5 \times 10^{-5}F$ to $2 \times 10^{-4}F$. The coulometry shows that the process occurring on the plateau of the second wave is the reduction of V(V) to V(III), *i.e.*, a two-electron transfer. The ratio of wave heights then indicates that a V(II) species is formed on the third wave. Thus the assignment of stepwise reduction processes V(V) to V(IV), V(IV) to V(III), and V(III) to V(II) can be made for the three waves. The actual species involved in the electrode reactions have not been determined. In fact, the first wave may be due to Hg $EDTA^{2-}$ produced by oxidation of Hg by NH_4VO_3.

Cyclic voltammetry of NH_4VO_3 in 1F NH_3, 1F NH_4Cl. —Figure 3 is a cyclic voltammogram of $1.00 \times 10^{-3}F$ NH_4VO_3 in 1F NH_3, F NH_4Cl. The hanging mercury drop area was 0.0491 cm^2 and the scan rate was 0.0278 V/sec. There are two cathodic peaks at $E^c_{p1} = -1.05V$ and $E^c_{p2} = -1.21V$ and a sharp anodic peak at −0.39V *vs.* SCE. The two cathodic peaks correspond to the two waves in polarographic scans. The sharpness of the second cathodic peak and the anodic peak indicate that a surface film is being electrolyzed in both cases. If the sweep is stopped at −1.0V *vs.* SCE and held for 60 sec and then continued, Fig. 4 is obtained. The peak current on the second cathodic peak is now 22.5 μA as compared with 15.0 μA when the sweep was not stopped. The anodic peak current has also increased from 17.1 to 31.0 μA. The large increase in current can be explained assuming that V(III) hydroxide film is the

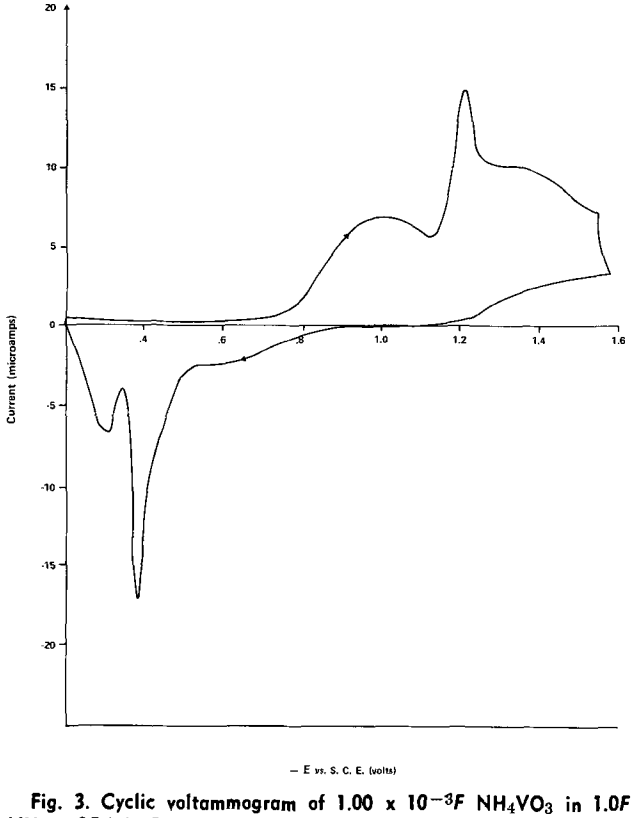

Fig. 3. Cyclic voltammogram of 1.00 x $10^{-3}F$ NH_4VO_3 in 1.0F NH_3, 1.0F NH_4Cl. Scan rate of 0.0278 V/sec and hanging mercury drop area is 0.0491 cm^2.

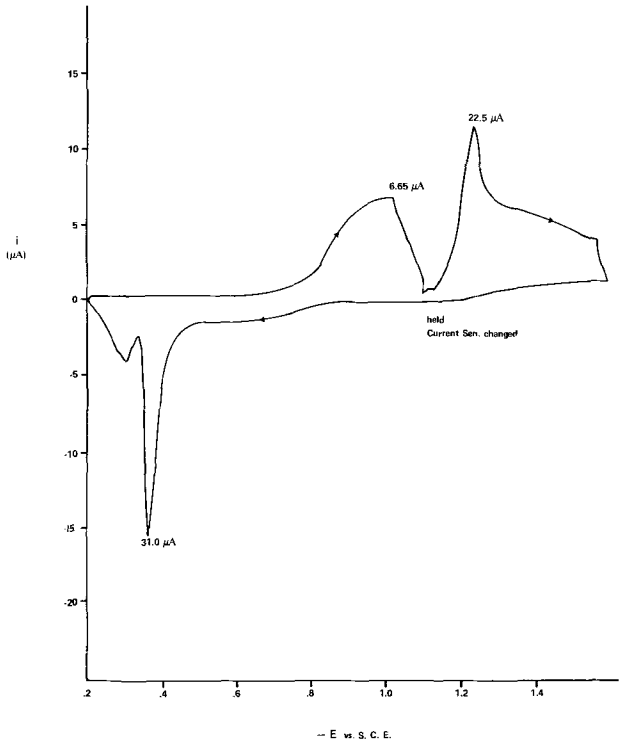

Fig. 4. Cyclic voltammogram of 1.00 x $10^{-3}F$ NH_4VO_3 in 1.0F NH_3, 1.0F NH_4Cl where the scan is held at −1.1V vs. SCE for 60 sec and then continued. Scan rate is 0.0278 V/sec and hanging mercury drop area is 0.0491 cm^2. The current sensitivity was changed after the holding period to 10 μA/in.

reduction product at −1.0V *vs.* SCE. When the sweep is started again the surface quantity of V(III) hydroxide is reduced to V(II) hydroxide giving the sharp cathodic peak. Results of Garrels (12) show that the log solubility product constant is −15.4 for $V(OH)_2$ and −34.4 for $V(OH)_3$ and that at $pH = 9.0$ and a potential of −1.24V *vs.* SCE the $V(OH)_3$ is the stable solid. At a potential of *ca.* −1.3V *vs.* SCE and *pH 9.0*, the $V(OH)_2$ becomes the stable solid. Thus the cyclic voltammetry curves are in agreement with thermodynamics in regard to the formation of surface layers of both (III) and (II) oxidation states. As we shall see, this is only the case at V(V) concentrations larger than $5 \times 10^{-4}F$. The existence of a $V(OH)_3$ species which is blocking is also in agreement with the controlled potential experiment in which a V(III) species passivated a dropping electrode over a large potential region.

The fact that the electrode reaction is inhibited by film formation is confirmed (Fig. 5) by a scan on a single hanging drop from −0.8V to −1.5V *vs.* SCE. The first cathodic peak disappears on the second cathodic scan indicating that the film (which has not been oxidized off) inhibits the electrode reduction in the potential region −0.9V to −1.2V. A very similar curve is obtained if the scan is stopped at −1.1V, held for 10 sec, returned to the initial potential and then rescanned through the second peak. These results indicate that both $V(OH)_2$ and $V(OH)_3$ are blocking in the potential region −0.9V to −1.2V *vs.* SCE.

Another experiment performed on the hanging drop electrode was to scan the potential from −0.6V *vs.* SCE to −1.1V *vs.* SCE and hold the potential constant for various lengths of time. The scan was then continued and the peak currents on the second wave were plotted as a function of holding time (Fig. 6). A set of such runs was made on an individual drop which was cleaned between each run by cyclic scanning in the anodic direction before the normal cathodic scan. The reproducibility of identical experiments made under these conditions was very good. The curve obtained (Fig. 6) tends to reach a constant value of peak cur-

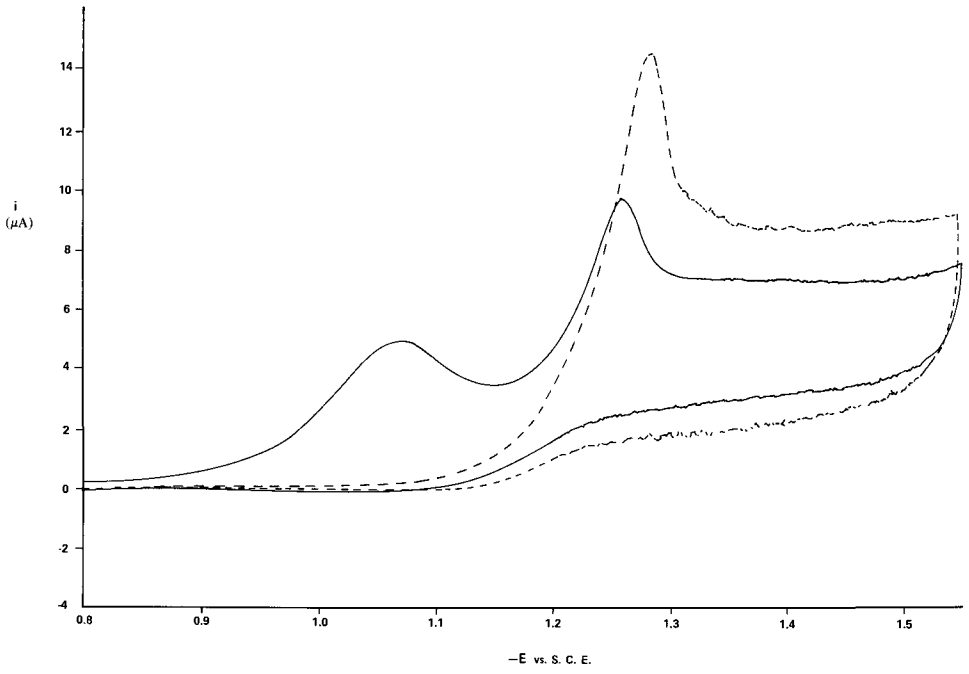

Fig. 5. Effect of repetitive voltammetric scan on 1.00 x $10^{-3}F$ NH_4VO_3 solution in ammoniacal buffer. Hanging drop area is 0.0491 cm^2 and voltage scan rate 0.0149 V/sec.

rent indicating that there is a monolayer of $V(OH)_3$ plated out in agreement with the results of Jedral and Galus (10).

The features of cyclic voltammetry curves change as the concentration of V(V) is lowered. At a concentration of $4.5 \times 10^{-4}F$, there is a single peak at *ca.* —1.2V *vs.* SCE which does not disappear on cyclic scanning but does shift in a cathodic direction on repeated cycles. The peak current is proportional to the 0.55 power of scan rate which is close to the 0.50 value for a diffusion controlled process. At $1.0 \times 10^{-4}F$ V(V) concentration, there is no shift on repeated cycling indicating that at or below this concentration adsorption on the electrode surface is negligible.

Polarographic catalytic current.—In the presence of ClO_2^-, there is a large increase in the polarographic current (in a potential region where the ClO_2^- is not reduced) of a solution of NH_4VO_3 in 1*F* buffer as compared to the current in the absence of ClO_2^-. Under these conditions the limiting current is constant to ±0.5% as a function of mercury column height from 30 to 90 cm. Both of these facts indicate a catalytic current process with a fast regeneration reaction.

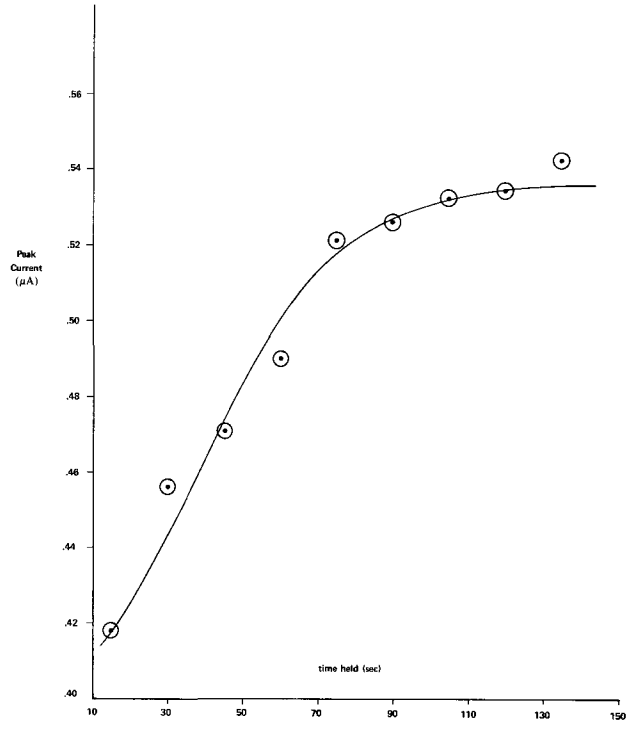

Fig. 6. Peak current as a function of time held at —1.1V *vs.* SCE. NH_4VO_3 is 1.00 x $10^{-3}F$ in ammoniacal buffer, hanging mercury drop area 0.0491 cm^2 and scan rate 0.140 V/sec.

Table I gives data for the instantaneous limiting current as a function of $[ClO_2^-]$. Since $E_{1/2}$ for the ClO_2^- polarographic wave is —1.5V *vs.* SCE, it is necessary to keep $[ClO_2^-]$ values low in order to reduce its reduction current to a minimum in the region of the catalytic wave. The value of $[ClO_2^-]$ was always equal to or less than $10^{-3}F$. A plot of log *i* *vs.* log $[ClO_2^-]$ at a total vanadium concentration of $2.0 \times 10^{-5}F$ has a slope of 0.58 ± 0.08 illustrating reaction which is first order in ClO_2^- since $i \propto [ClO_2^-]^{1/2}$ for this case (13). In addition, the table shows that at $2.00 \times 10^{-5}F$ the values of $i/[ClO_2^-]^{1/2}$ have a 6% deviation from the average value and at $5.00 \times 10^{-5}F$ V(V) there is only a 1.5% deviation from the average value. These data certainly show that *i* is proportional to $[ClO_2^-]^{1/2}$ as is predicted for a catalytic process.

A normal polarographic catalytic process should show values of catalytic limiting current divided by the diffusion current measured in the absence of the catalytic mechanism that are independent of vanadium concentration. This is definitely not the case for this system since values of i/i_d decrease as the total vanadium concentration increases as can be seen in Table II. The diffusion current i_d was measured with mass flow rate $m = 1.63$ mg/sec and drop time $\tau = 7.50$ sec, and it is directly proportional to [V(V)] in the concentration range of interest. The value i^*_d is a value of diffusion current converted to capillary characteristics of the particular catalytic current, *i*. The data in Table II were taken with $[ClO_2^-] = 1.00 \times 10^{-3}M$ and $E = -1.25$V *vs.* SCE. A log-log plot of *i* *vs.*

Table I. Catalytic current of NH_4VO_3 as a function of chlorite concentration[a]

[V(V)]	$[ClO_2^-]$	i(mA)	$i/\sqrt{[ClO_2^-]}$
2.00×10^{-5}	2.00×10^{-4}	0.72	0.52×10^2
2.00×10^{-5}	5.00×10^{-4}	1.39	0.62×10^2
2.00×10^{-5}	1.00×10^{-3}	1.82	0.58×10^2
5.00×10^{-5}	5.00×10^{-4}	2.26	1.01×10^2
5.00×10^{-5}	1.0×10^{-3}	3.22	1.04×10^2

[a] These data were taken at a temperature of 27°C, mass flow rate *m*, of 1.07 mg/sec, drop time τ of 5.88 sec, and E = —1.25V *vs.* SCE.

Table II. Limiting current data for NH_4VO_3 in 1.00 x 10^{-3} M chlorite

[V(V)]	$i(\mu A)$	m	τ	$m^{2/3}\tau^{1/6}$	i_d[a]	i_d^*	i/i_d^*
2.00 x 10^{-5}	1.82	1.07	5.88	1.41	0.160	0.115	15.8
2.73 x 10^{-5}	2.40	1.89	1.83	1.69	0.220	0.191	12.6
5.00 x 10^{-5}	3.22	1.07	5.88	1.41	0.400	0.289	11.1
5.46 x 10^{-5}	3.54	1.89	1.83	1.69	0.440	0.382	9.27
9.09 x 10^{-5}	5.75	1.89	1.83	1.69	0.733	0.669	8.89
1.00 x 10^{-4}	4.90	1.07	5.88	1.41	0.812	0.587	8.34

[a] i_d calculated from a calibration curve where m = 1.63 mg/sec, τ = 7.50 sec, E = −1.25V *vs.* SCE.

[V(V)] at [ClO_2^-] = 1.0 × $10^{-3}M$ has a slope significantly less than unity. A slope of one would be expected for a reaction first order in the vanadium species which is oxidized in the catalytic process.

A catalytic current is also found in a V(V) solution of ClO_2^- in 1*F* buffer when 0.1*F* EDTA is added. In this case the values of i/i_d are independent of V(V) concentration as can be seen from Table III. Thus the mechanism of the electrode process in the presence of 0.1*F* EDTA is the normal catalytic process.

It is possible to derive a current expression for a catalytic process which has the properties of the trend in data of Table II. The mechanism upon which this current expression is based is the situation where the product of the electrode reaction dimerizes (14). If it is considered that monomer and dimer are in a mobile equilibrium and both react with ClO_2^-, the current expression (14) for a mechanism with two regeneration reactions, one first order in monomer and ClO_2^-, the other first order in dimer and ClO_2^- is

$$i = n\mathbf{F}qf(a_o)\,[\alpha b^* k_1 D_a]^{1/2}\,H(u) \qquad [1]$$

with

$$f(a_o) = a_o\left[1 + \frac{8D_eKa_o}{3D_a} + \frac{2k_2Ka_o}{3k_1} + \frac{2k_2D_eK^2a_o^2}{k_1D_a}\right]^{1/2}$$

and

$$a_o = \frac{D_a}{4KD_e}\left[\left(1 + \frac{8D_eD_cKc^*}{D_a^2}\right)^{1/2} - 1\right]$$

where n is the number of electrons transferred per species in the electrode reaction, **F** is the Faraday constant, q is the electrode area, α is a stoichiometric coefficient, k_1 and k_2 are the homogeneous rate constants for the monomer species A and the dimer E, respectively. C stands for the electrode reactant and B for chlorite. The lower case letters represent the concentration of species; thus $K = e/a^2$ is the dimerization constant. Starred lower case letters represent bulk concentrations with b^* = [ClO_2^-]; the D_i's are the diffusion coefficients of the i-th species, and a_o is the concentration of A at the electrode surface under limiting current conditions. The factor $H(u)$ in Eq. [1] depends on the deviation from pseudo first-order conditions and a very accurate approximation for this factor (15) is

$$H(u) = \tfrac{1}{2}\left[1 + \left(1 - \frac{1.504\,n_b i}{\alpha n i'_d}\right)^{1/2}\right] \qquad [2]$$

where

$$i'_d = n_b\mathbf{F}qb^*\sqrt{\frac{7D_b}{3\pi\tau}}$$

Table III. Data and rate constant calculations for $VEDTA^{2-}$ oxidation

[V(V)]	$i(\mu A)$	$i_d(\mu A)$	i/i_d	$H(u)$	k
1.02 x 10^{-5}	1.6	0.085	18.8	0.965	7.91 x 10^3
5.10 x 10^{-5}	5.6	0.30	18.6	0.864	9.57 x 10^4
6.12 x 10^{-5}	7.2	0.38	18.9	0.814	11.1 x 10^4
8.16 x 10^{-5}	8.1	0.50	16.2	0.783	8.84 x 10^4

Equation [1] can be put in a more useful form by dividing it through by the diffusion current in the absence of ClO_2^-

$$i_d = n_c\mathbf{F}qc^*\sqrt{\frac{7D_c}{3\pi\tau}}$$

giving

$$\frac{i}{i_d} = \frac{n}{n_c}\,1.160\,(k_1b^*\alpha\tau D_a/D_c)^{1/2}\,(f(a_o)/c^*)H(u) \qquad [3]$$

This equation along with Eq. [2] can be used to calculate rate constants if the values of K and the D_i's are known.

The function $f(a_o)$ takes limiting forms as the value of K goes to zero and to infinity. Thus in the limit as

$$K \to 0, f(a_o) \to \frac{D_c}{D_a}c^*$$

since

$$a_o \to \frac{D_c}{D_a}c^*$$

and as

$$K \to \infty, f(a_o) \to \left(\frac{k_2D_c^2}{k_1\,2D_eD_a}\right)^{1/2}c^*$$

since

$$a_o \to \left(\frac{D_cc^*}{2D_e}\right)^{1/2}$$

Thus, both limiting cases yield i/i_d expressions which are independent of c*. It is only for the case when K is large and $k_1 >> k_2$ that i/i_d is a function of c* and decreases with increasing c*. For this case Eq. [3] becomes

$$\frac{i}{i_d} = \frac{n}{n_c}\,1.160\,\sqrt{k_1b^*\alpha\tau}\left(\frac{8D_c}{9D_eK}\right)^{1/4}\frac{H(u)}{c^{*1/4}} \qquad [4]$$

Equation [4] predicts that if the mechanism is occurring, a log i/i_d *vs.* log c* plot will have a slope of −0.25. Such a plot for the data in Table II gives a slope of −0.37. Since Eq. [4] is an approximation of Eq. [3] for particular conditions which may not exactly hold, the experimental result is considered in good enough agreement with the theory to support the conclusion that the mechanism involves an aggregation (dimerization) equilibrium of the reduced form of the electroactive species.

Mechanism and rate constant calculation.—In order to calculate a rate constant for the ClO_2^- oxidation, the mechanism of the catalytic electrode process must be known. A value of $n_c = 3$ indicating a V(II) species as the product of the electrode reaction in the absence of adsorption is most consistent with the data. An independent value of the diffusion coefficient has not been determined making the calculation of $n_c = 3$ from diffusion current somewhat unsatisfactory. However, the thermodynamic data already cited indicate that at voltages more negative than −1.3V *vs.* SCE a V(II) hydroxy species should be formed. In an earlier paper (14), we concluded that a V(III) species was being oxidized. This conclusion was based on the controlled potential data which showed a two equivalent reduction; however, the reaction between V(II) and V(V) leads to this stoichiometry even if V(II) is formed at the electrode. The oxidation experiment with ClO_2^- shows that a V(IV) species is the product of the homogeneous oxidation so that in the catalytic current Eq. [1], $n = 2$.

The following proposed mechanism for the catalytic process is based on the above conclusions concerning oxidation states and a dimerization equilibrium where only the monomer is oxidized.

$$V(V) + 3e \xrightarrow{k_e} V(II)$$

$$2V(II) \rightleftarrows V_2(II)$$

$$2H_2O + 2V(II) + ClO_2^- \xrightarrow{k_1} 2V(IV) + Cl^- + 4\,OH^-$$

$$V(IV) + 2e \xrightarrow{k_e} V(II)$$

The reactions

$$V(II) + V(IV) \rightarrow 2V(III)$$

$$2V(II) + V(V) \rightarrow 3V(III)$$

will most likely take place outside the reaction layer and therefore are not considered to effect the mechanism. A similar electrode process without dimerization has been proposed for the catalytic reduction of NO_2^- in the same V(V) system (5).

In order to calculate a homogeneous rate constant a value of K for the equilibrium constant must be used. A very rough value of K can be found from the data by finding the smallest value of K necessary to give the c* dependence of Eq. [4]. In this way, a value of $K = 7 \times 10^5$ is found. Also we make the not too unreasonable assumption that $D_a = D_c$ and assume spherical symmetry so that $D_e/D_a = 0.8$. With the above values of K and D_i's, $n_c = 3$, $n = 2$, and $\alpha = 2$, a value for the homogeneous rate constant can be calculated using Eq. [3] and a value of $H(u)$ from Eq. [2]. Since we assume $k_1 >> k_2$ only the first two terms of the $f(a_o)$ function are retained in the calculation. The values of k_1 are given in Table IV along with k values calculated for the usual catalytic mechanism where $f(a_o)/c^* = 1$. The average value of k is $4.0 \pm 2.2 \times 10^4$ liter/mole-sec while the average value of k_1 is found to be $2.2 \pm 1.1 \times 10^5$ liter/mole-sec. The value of 2×10^5 liter/mole-sec of course is only a lower bound to the actual value of the rate constant which depends on $K^{1/4}$.

When the solution is 0.1F in EDTA, there is no need to postulate an aggregation equilibrium involving a lower oxidation state of vanadium since the value of i/i_d is independent of c*. The effect of the EDTA is no doubt to complex the lower oxidation states of the vanadium central ion reducing the hydrolytic and aggregation equilibrium. The catalytic process is found to take place on the third wave which means that it is the V(II)-EDTA species which is being oxidized by the ClO_2^-. Table III gives the data and the values of k calculated. The $[ClO_2^-]$ was 1.00×10^{-3} M, $\tau = 3.64$ sec, and the measurement was made at $E = -1.40$V *vs.* SCE. The average value of the rate constant is $9.4 \pm 0.7 \times 10^4$ liter/mole-sec which shows better precision than in the absence of EDTA.

The fact that the rate constants for homogeneous oxidation of a V(II) species by ClO_2^- are about the same in the presence and absence of EDTA is consistent with the proposed mechanism involving dimerization in the absence of EDTA. The latter rate constant was calculated with an assumed value of K that would only give a lower bound to the true rate constant. However, since both rate constants are found to be very similar, if we assume an identical oxidation step the value of K used in the calculation must be of an order of magnitude close to the true equilibrium constant. Of course, the two rate constants in question can only be approximately compared since they refer to different vanadium species as reactants in the oxidation.

Table IV. Rate constant calculations for V(II) oxidation

c*	b*	i/i_d*	$H(u)$	$f(a_o)/c^*$	k	k_1
2.00×10^{-5}	2.00×10^{-4}	6.25	0.89	0.49	3.5×10^4	1.4×10^5
2.00×10^{-5}	5.00×10^{-4}	12.2	0.92	0.49	5.0×10^4	2.7×10^5
2.00×10^{-5}	1.00×10^{-3}	15.8	0.94	0.49	4.0×10^4	1.7×10^5
2.73×10^{-5}	1.00×10^{-3}	12.6	0.94	0.44	8.2×10^4	4.1×10^5
5.00×10^{-5}	5.00×10^{-4}	7.8	0.86	0.40	2.4×10^4	1.5×10^5
5.00×10^{-5}	1.00×10^{-3}	11.1	0.91	0.40	2.1×10^4	1.3×10^5
5.46×10^{-5}	1.00×10^{-3}	9.27	0.91	0.40	4.9×10^4	3.0×10^5
9.09×10^{-5}	1.00×10^{-3}	8.59	0.85	0.36	4.7×10^4	3.6×10^5
1.00×10^{-4}	1.00×10^{-3}	8.34	0.84	0.34	1.4×10^4	1.12×10^6

Table V. Kinetic data for the oxidation of complexes by chlorite

Complex	k_{av} ($T = 27.0°$) liter/mole-sec	Reference
$Fe(II)(Tar)_n^z$	$6.2 \pm 0.2 \times 10^4$	(11)
$Fe(II)(Cit)_n^z$	$6.3 \pm 0.5 \times 10^4$	(11)
$Fe\ EDTA^{2-}$	$3.0 \pm 0.3 \times 10^4$	(11)
$Fe(CN)_6^{4-}$	too small to est.	(11)
$Cr(NH_3)_5(OH)^+$	$1.6 \pm 0.2 \times 10^4$	(15)
$Cr(EDTA)(H_2O)^{2-}$	$1.8 \pm 0.4 \times 10^3$	(16)
$V(II)(OH)_n(NH_3)_y^z$	$2.2 \pm 1.1 \times 10^5$	This work
$VEDTA^{2-}$	$9.4 \pm 0.7 \times 10^4$	This work
$Cu(NH_3)_2^+$	44.0 ± 3.7	(11)

Rate constants for the oxidation of various complexes by ClO_2^- are compared in Table V. The rate constant for the $Cr(NH_3)_5OH^{2+}$ was calculated from the data given in an earlier publication (15). The data for the chromium system in the presence of EDTA has not been presented (16). The rate constant in this case is an order of magnitude smaller than that found in the absence of EDTA. From the table it can be seen that the high spin metal complexes of Fe(II) and Cr(II) which are substitution labile show fast oxidation kinetics. The low spin substitution inert complex $Fe(CN)_6^{4-}$ does not have a catalytic polarographic current with ClO_2^- and uv-vis spectroscopy shows the reaction is very slow. This reaction is thermodynamically favored and it must be concluded that both fast inner-sphere substitution and outer-sphere electron transfer do not operate in this case.

In an earlier paper (11), it was suggested that a general mechanism for ClO_2^- oxidation of metal complexes involved inner-sphere substitution. However, V(II) which shows fast kinetics is a d^3 ion and somewhat substitution inert (17). If inner-sphere substitution were rate controlling V(II) complexes should be oxidized much slower than Cr(II) complexes which is not the case. A possible rate determining step for V(II) oxidation may be an outer-sphere atom transfer of an oxygen atom in a two electron change.

The complexes with rate constants from 10^3-10^5 liter/mole-sec and their oxidation products will have H_2O molecules in their coordination sphere, and it is highly possible that oxidation by ClO_2^- in these cases involves either outer-sphere oxygen atom transfer or O^- ion transfer. Such a mechanism remains to be experimentally verified. However, what has been established is that ClO_2^- shows fast oxidation kinetics with a wide variety of metal complexes of the first transition series.

Acknowledgment

The support of the National Institutes of Health (5 ROI AM14298) is gratefully acknowledged. Also, the authors wish to acknowledge W. F. Marzluff, Jr., who made some of the preliminary polarographic measurements at Harvard University.

Manuscript submitted Sept. 1, 1972; revised manuscript received Nov. 10, 1972.

Any discussion of this paper will appear in a Discussion Section to be published in the December 1973 JOURNAL.

REFERENCES

1. M. V. Stackelberg, P. Klinger, W. Koch, and E. Krath, *Forschungsberichte Tech. Mitt. Krupp. Essen*, **2**, 59 (1939).
2. J. Lingane, *J. Am. Chem. Soc.*, **67**, 182 (1945).
3. I. Filipović, Z. Hahl, Z. Gašparac, and V. Klemenčić, *ibid.*, **76**, 2074 (1954).
4. R. W. Schmidt and C. N. Reilley, *ibid.*, **80**, 2087 (1958).
5. F. Baumann, *J. Electroanal. Chem.*, **6**, 245, (1963).
6. L. Meites, "Polarographic Techniques," 2nd ed., p. 627, John Wiley and Sons, Inc., New York (1965).
7. G. B. Jones, *Anal. Chim. Acta*, **17**, 258 (1957).
8. C. Dragulescu and M. Pirlen, *J. Anal. Chem. USSR*, **27**, 1148 (1967).

9. T. Jedral and Z. Galus, *Rocz. Chem.*, **44**, 1517 (1970).
10. T. Jedral and Z. Galus, *ibid.*, **44**, 2015 (1970).
11. R. L. Birke and W. F. Marzluff, Jr., *J. Am. Chem. Soc.*, **91**, 3481 (1969).
12. R. M. Garrels; *Am. Mineralogist*, **38**, 1251 (1953).
13. J. Heyrovsky and J. Kuta, "Principles of Polarography," pp. 382, 452, Academic Press, New York (1966).
14. R. L. Birke, *J. Electroanal. Chem.*, **22**, 319 (1969).
15. R. L. Birke and W. F. Marzluff, Jr., *J. Electroanal. Chem.*, **17**, 1 (1968).
16. R. L. Birke and W. F. Marzluff, Jr., Unpublished data (1968).
17. F. Basolo and R. G. Pearson, "Mechanisms of Inorganic Reactions," 2nd ed., p. 482, John Wiley and Sons, Inc., New York (1967).
18. R. L. Pecsok and R. S. Juvet, *J. Am. Chem. Soc.*, **75**, 1202 (1953).
19. A. Ringbom, S. Siitonen, and B. Skrifvars, *Acta Chem. Scand.*, **11**, 10 (1957).
20. G. Schwarzenbach and J. Sandera, *Helv. Chim. Acta*, **36**, 1089 (1953).

Thermoelectric Powers and Transported Entropies in Aqueous Hydrochloric Acid

Arthur D. Payton,* Bruce H. Boyd, C. Michael Houck, Edward H. Temple, and Albert H. Zimmerman

Chemistry Department, Willamette University, Salem, Oregon 97301

ABSTRACT

The initial thermoelectric power (TEP) has been determined for hydrogen electrodes in aqueous HCl solutions as a function of molality from 0.002 to 0.6 mol/kg and as a function of temperature for a 10° gradient at mean temperatures of 20°, 25°, and 30°C. For each mean temperature the TEP's are analyzed by fitting the data to an equation with three constants. At rounded molalities, the TEP's that were obtained from the 25° equation have been combined with known values for the heat of transport of HCl in order to determine a single-ion property, the transported entropy of the hydrogen ion. By extrapolation the standard value of this property has been determined as 5.42 ± 0.16 eu, which is in agreement with literature values.

In order to determine the concentration dependence of transported entropies of ions in aqueous electrolytes over a wide range of concentration, we decided to measure initial thermoelectric powers (TEP) as a function of molality from 0.002 to 0.6 mol/kg. In addition, we wanted to determine the concentration dependence of initial TEP's at several mean temperatures, since there is a lack of data on temperature-dependent experiments related to thermal diffusion in solutions. Aqueous HCl with hydrogen electrodes was chosen as the system to be investigated because the electrodes are excellent in terms of reproducibility and because auxiliary data on HCl are readily available. Although we have measured these emf's at mean temperatures of 20°, 25°, and 30°C, we could determine the transported entropy $\overline{\overline{S_i}}$ at 25° only, due to a lack of data for heats of transport at other temperatures.

In an electrolytic solution, $\overline{\overline{S_i}}$ is the entropy carried along by the ion to which the electrodes are reversible. It is made up of the sum of the partial molal entropy S_i and the entropy of transport $\hat{S}_i$. The latter quantity is equal to the heat of transport $\hat{Q}_i$ divided by the Kelvin temperature T. One fascinating aspect of $\overline{\overline{S_i}}$ is that it represents a single-ion property that is not based on an arbitrary convention (1). For example, this is not the case when dealing with individual ionic activity coefficients, ionic heats of transport, and partial molal ionic entropies. For individual ionic heats of transport, the molar heat of transport $\hat{Q}$ is usually split into its ionic contributions using the convention (2) that $\hat{Q}^0_{Cl^-} = 0$ or $\hat{Q}_{Cl^-}\ (m = 0.01) = 0$. The superscript zero on the heat of transport indicates the value at infinite dilution and m the molality. For partial molal ionic entropies S^0 of neutral salts are broken up using the convention that $S^0_{H^+} = 0.0$ (3), −5.5 (4), or −5.1 eu (5), in which the superscript indicates the standard value (1 eu = 43.36 μV **F**/K = 1 cal/K = 4.184 J/K).

It turns out that data of such quality as we obtained for HCl with hydrogen electrodes are not needed in order to calculate transported entropies because the concentration dependence of the heat of transport is not known that precisely. However, the initial TEP's themselves should prove valuable in elucidating the concentration dependence of related quantities in thermocells.

For aqueous HCl the heat of transport may be obtained from the Soret coefficient by means of the formula (2)

$$\hat{Q}_{HCl} = 2\sigma RT^2\,[1 + (\partial \ln \gamma_\pm / \partial \ln m)] \qquad [1]$$

in which $\gamma_\pm$ is the mean molal ionic activity coefficient, $R = 8.31434$ J K^{-1}mol^{-1}, $T = 298.15$K, and 1 cal = 4.184 J. The expression $[1 + \partial \ln \gamma_\pm / \partial \ln m]$ is usually called the "thermodynamic term." The Soret coefficient σ is defined as $(-1/m)(\delta m/\delta T)$ at the steady state (Soret equilibrium) (1). This convention makes σ algebraically positive for the normal Soret effect (salts diffusing thermally from hot to cold) and avoids the attendant confusion in comparisons of values of Soret coefficients. In place of Eq. [1], Breck, Cadenhead, and Hammerli (6) measured $\hat{Q}$ directly by obtaining both the initial and final thermoelectric powers of an aqueous HCl thermocell with quinhydrone electrodes, before thermal diffusion had commenced, and at the steady state, respectively. They used the formula

$$\mathbf{F}(\epsilon_0 - \epsilon_\infty) = \tfrac{1}{2}(\hat{S}_Q - \hat{S}_{H_2Q}) + (t_{Cl^-})(\hat{Q}_{HCl}/T) \qquad [2]$$

in which t_{Cl^-} is the transference number, and $(\epsilon_0 - \epsilon_\infty)$ is the difference between the initial and final thermo-

* Electrochemical Society Active Member.

Key words: entropy of transport, heat of transport, hydrogen electrodes, single-ion property, Soret coefficient, temperature gradient, thermal diffusion.

electric powers. They assumed that one-half the difference of entropies of transport between quinone (Q) and hydroquinone (H_2Q) is small and estimated its value to be 0.05 eu at all molalities.

By use of Eq. [3] we corrected all observed emf's so that the hydrogen pressure in both the hot and cold electrode compartments was 760 Torr (= 1 atm = 101325 N/m^2). The barometric-pressure- and vapor-pressure-correction factor was given by

$$k = \frac{RT_U}{2F} \ln \frac{BP - P_U + \Delta P_U}{760} - \frac{RT_L}{2F} \ln \frac{BP - P_L + \Delta P_L}{760} \quad [3]$$

in which R = 8.31434 J/mol K, $\mathbf{F}$ = 96487 C/equiv, BP is the barometric pressure in Torr, and T_U and T_L are the upper and lower temperatures. Here P_U and P_L are the vapor pressures of pure water and ΔP_U and ΔP_L are the solvent vapor-pressure lowerings at the upper and lower temperatures, respectively. At m = 0.1 mol/kg, this correction was approximately −200, −265, and −350 μV for runs at 15°/25°, 20°/30°, and 25°/35°C, respectively. This correction was added to the emf before division by the temperature difference ΔT to obtain the TEP. For the vapor pressure of pure water, we used the constants given in Lange's Handbook (7) for Antoine's equation

$$\log P \text{ (in Torr)} = 8.10765 - \frac{1750.286}{(T - 38.15)} \quad [4a]$$

At 25°C, the fractional vapor-pressure lowering was calculated by

$$(\Delta P/P) = 10^{-4}m(272.144 + 271.016m - 225.760m^2) \quad [4b]$$

derived from vapor-pressure lowering data given in Ref. (8). At 25°C and the highest molality (*ca.* 0.6m) valid for Eq. [4b], the fractional vapor-pressure lowering was calculated to be 0.021. This increased the value of k by 5.2 μV, compared with the value obtained from Eq. [3] by neglecting ΔP_U and ΔP_L. This correction, although small, was not ignored.

In our calculation of the TEP, we have considered neither the increase in hydrogen pressure due to the depth of the bubblers below the surface of the solution nor the nonideality of hydrogen gas, mentioned by Hills and Ives (9).

We found the function $\sqrt{m}/(1 + \sqrt{m})$ suitable for the abscissa of graphs of our results. At nine rounded values of this function we determined $\bar{\bar{S}}_{H^+}$ from our values of the TEP and from Breck, Cadenhead, and Hammerli's (6) values of $\hat{Q}_{HCl}$ using the formula

$$\bar{\bar{S}}_{H^+} = \tfrac{1}{2}S^0_{H_2} - \bar{\bar{S}}_e + (t_{Cl^-})(\hat{Q}_{HCl}/T) - \mathbf{F}(TEP) \quad [5]$$

in which $S^0_{H_2}$ = 31.21 eu, the standard value of the entropy of hydrogen gas (3), and $\bar{\bar{S}}_e$ (Pt) = 0.104 eu (10), the transported entropy of the electron in the nonisothermal part of the platinum. After we corrected these values for the mass-action term, using Eq. [6]

$$\bar{\bar{S}}_{H^+} \text{ (mod 1)} = \bar{\bar{S}}_{H^+} + R \ln m \quad [6]$$

they still showed a trend. However, we obtained nearly constant values by including the mean molal ionic activity coefficient and its temperature derivative, according to Eq. [7]

$$\bar{\bar{S}}_{H^+} \text{ (mod 2)} = \bar{\bar{S}}_{H^+} \text{ (mod 1)} + R \ln \gamma_{\pm} + RT \frac{\partial \ln \gamma_{\pm}}{\partial T} \quad [7]$$

as has been derived by deBethune and Daley (11) [cf. Eq. 10 of Ref. (11)].

We also determined the concentration dependence of the TEP at mean temperatures of 20°, 25°, and 30° by fitting the data to an equation of the form

$$Y = A - B\sqrt{m}/(1 + \sqrt{m}) + Cm \quad [8]$$

in which Y is defined by Eq. [9a]

$$Y = TEP - (R/\mathbf{F}) \ln m \quad [9a]$$

Here TEP is $(1/\Delta T)$ times the observed emf corrected for barometric pressure and vapor pressure according to Eq. [9b]

$$TEP = \frac{\text{emf(obs)} + k}{\Delta T} \quad [9b]$$

Other workers (1, 6) have used Eq. [8] without the Cm term in their critical evaluation of the nonideal behavior. Preliminary graphs of the TEP *vs.* log m were not sensitive enough to evaluate our data, although at lower molalities the data approached the limiting slope of $(R/\mathbf{F})\ln 10$.

Experimental

Electrical apparatus.—To measure the emf's, a L&N Type K-3 potentiometer was used with the revised circuit for measurement of high-resistance emf's. In this circuit the Ayrton shunt of the potentiometer is shorted out and the unknown emf is put in series with the detector. For null detection a Boonton sensitive d-c meter No. 95A (input resistance 10 megohm) was used. Standardization was accomplished with the normal circuit and a guarded constant voltage supply (Dynage Model No. 505A) and a plug-in standard cell (Dynage Model No. LVB-1).

Temperatures.—Temperatures were measured at 20°, 25°, and 30° by means of a Brooklyn Thermometer Company thermometer graduated in 0.01° (range 19°-34°). Since some of the temperatures were outside this range, a 2- or 4-junction copper-constantan thermocouple was used to determine the other temperature (20°/30° = 1615 μV *vs.* a 4-junction table (12) value of 1628 μV). We used 803 μV for the 2-junction thermocouple for 15°/25°, 811.5 μV for 20°/30°, and 819 μV for 25°/35°. The two water thermostats were regulated by Bronwell thermoregulator-circulators, which maintained the temperatures to ±0.01°.

The bath temperatures were always within ±0.1° of 15°, 20°, 25°, 30°, or 35°C. Although the mean temperature for a run was known to 0.01°, it could vary by up to 0.1° from the values 20°, 25°, or 30°. Antoine's equation (Eq. [4a]) was used in the temperature range 14.9°-35.1° for the vapor pressure of pure water. Use of Eq. [4a] avoided the need for five different sets of constants for linear interpolation within 0.1° of the five bath temperatures. A deviation of 0.10° from 25.00° for the mean temperature would cause TEP or Y to change by 0.2 μV/K, which is well within our experimental error of ±2 μV/K. This change was calculated from the temperature derivative of the TEP as given in the next section (dY/dT = 2 μV/K).

For one of the 20°/30° runs, the temperature of the solution in the hot side of the cell was found to be less than 0.01° lower than the bath temperature. Since ambient temperature was *ca.* 25°C, density instability causing convection in the solution would have reduced the solution temperature even farther below that of the bath. Therefore, the effect of convection was neglected, and we equate our bath temperature to that of the solution.

One run was performed using a 6° temperature difference, instead of 10°. The result of this run was not significantly different from our usual 10° runs, although the precision was not as good. Use of a temperature difference, which is less than 10° in order to avoid errors due to the temperature dependence of the TEP, is probably unnecessary (13). Thus we identify our TEP as the true TEP at the mean temperature of the run.

Electrodes.—Each hydrogen electrode was constructed by welding a 1 cm^2 (0.002 in. thick) piece of platinum to a length (*ca.* 80 cm) of No. 27 platinum wire with an oxygen-gas flame. The length of wire was then sealed in a 3-mm OD, soft glass tubing. This length of external wire allowed us to be certain that the temperature gradient of the metallic connector was in platinum, rather than in the copper part of the lead that was connected to the potentiometer. Platinum black was deposited on the electrode by reduction of a 2% platinic chloride solution that contained 0.02% lead acetate (9). The electrolysis was carried out for a few minutes at a current density of 80 mA/cm^2, until the deposit appeared uniformly black. It was not necessary to reverse the current periodically as some authors recommend.

Chemicals.—Ultra-pure (99.9998% pure, Airco) hydrogen gas was further purified by a "de-oxo" cartridge (J. T. Baker Company), which was attached directly to the regulator. The gas was then bubbled through deionized water to saturate it with water vapor before it entered the solution in the cell. Reagent grade HCl was used to make stock solutions, which were then diluted to the desired concentrations with deionized water. Titrations were carried out on the solution that was removed from the cell following a successful run, when the concentration was above 0.02*N*. For more dilute solutions the concentration was taken as that calculated from dilution of the standardized stock solution. One run was performed using HCl purified by distilling the constant-boiling azeotrope, but the result of the run was not noticeably different from the other runs.

Cell and bubblers.—The cell was W shaped, with each compartment being 35 mm diam by 40 cm tall. The compartments were connected with 12-mm OD Pyrex tubing to which was sealed a side arm and Teflon stopcock. The solutions in the compartments could then be drawn together by gentle suction, thus avoiding the stopcock. The design of an H-shaped cell (14) had been discarded because of the possibility of convection in the solution causing an error in the temperature difference. Treating our cell as a conductivity cell, we determined the cell constant to be 200 cm^{-1}. Two electrodes and a bubbler tube were inserted into a rubber stopper, which was sealed into the 34-mm diam end of a 34/45 standard taper joint. Apiezon W was used for the sealing of the electrodes, bubbler tube, and stopper. One of these assembled female joints was placed on top of each side of the W-shaped cell. The solution was never allowed to come in contact with the lightly greased joint (Apiezon N), since the grease was on the outside.

Procedure.—To remove oxygen, prepurified nitrogen was bubbled through the saturator and cell solution for 15 min, with the solution in each cell half separated. Then hydrogen was bubbled for another 15 min, before the solutions were drawn together. Usually the emf became steady within 15-30 min after the solutions were drawn together. The emf was then recorded. In some of the runs this waiting period had to be extended to 1-2 hr until "things settled down." The nonsteady results could usually be explained as being caused by an empty saturator, not waiting long enough for equilibration of the electrodes in the solution, or an extra gas-escape hole. Freshly platinized electrodes sometimes caused erratic results. For concentrations above 0.05*N* the electrodes had to be presoaked in a solution of that concentration for 20 hr before the run. At concentrations below 0.05*N* the electrodes were merely placed in deionized water prior to use in the cell. With each pair of electrodes, two readings were taken, first with the current in the forward direction and then in the reverse direction. The more dilute the solution was, the larger was the difference between forward and reverse readings. This is due to the resistance of the solution being comparable to the input impedance of the null detector (15). To eliminate any asymmetry in the electrodes, bubblers, or solution, the bubblers were disconnected, the cell physically reversed, and bubbling started again. Four readings were again taken, making a total of eight in all. A slight difference in concentration between the solutions in each cell compartment would show up as a large difference in emf: a 0.1% difference in molalities causing an estimated 50 μV difference in the two emf readings. It was found very important to have only one escape outlet in the stopper for the hydrogen gas. Atmospheric gases outside the cell tended to flow in through any other opening and thus change the partial pressure of hydrogen above the solution. If the single escape hole were covered temporarily, this could also be observed as a change in the emf of the thermocell.

Results and Discussion

Thermoelectric powers.—In all runs the polarity of the thermocell was such that the hot electrode was positive, except for the three most dilute runs at 15°/25°. Our results are summarized in Fig. 1, in which curves are shown for the function $Y = TEP - (R/F) \ln m$ at mean temperatures of 20° (lower curve), 25° (middle), and 30° (upper). Each of our actual data points is represented by a rectangle. The width of each rectangle is twice as large as the estimated error of ±0.1 in the molality function $100\sqrt{m}/(1 + \sqrt{m})$, whereas the height of the rectangle approximates the estimated error of ±2 $\mu V/K$ (0.046 eu). Approximately 10% of our runs were not within our estimated limits of precision and were not retained in the final data analysis. The curve shown for each set of rectangles was fitted by nonlinear least squares to an equation of the form of Eq. [8]. The constants are given in Table I. From the three values for the A constant at the three mean temperatures, we determined the temperature coefficient of Y° (the limiting value at infinite dilution) to be 2.19 $\mu V/K^2$.

Transported entropies at 25°C.—We used Eq. [5] to calculate the transported entropy of the hydrogen ion $\bar{\bar{S}}_{H^+}$ at nine rounded values of the molality function $100\sqrt{m}/(1 + \sqrt{m})$. Details of this calculation are found in columns 1 to 5 of Table II.

The transported entropy of the counter ion $\bar{\bar{S}}_{Cl^-}$ may also be calculated, if one first determines $\gamma_\pm$, S_{HCl}, and $\bar{\bar{S}}_{HCl}$ at the nine molalities. The mean molal ionic activity coefficients were calculated by Eq. [10] from Harned and Owen (17)

Table I. Results and constants based on the three-constant equation (Eq. [8]) for Y as a function of molality

Mean temperature, °C	Molality range, mol/kg	n, number of runs	Standard error,[a] $\mu V/K$	A	B	C
20	0.0016-0.61	50	1.01	510.33 ± 0.39[b]	88.02 ± 3.16	14.76 ± 2.64
25	0.0019-0.56	46	1.10	521.37 ± 0.52	101.68 ± 3.91	20.03 ± 3.14
30	0.0024-0.55	51	1.27	532.24 ± 0.57	118.30 ± 4.43	19.59 ± 3.50

[a] $(\text{Standard error})^2 = [Y(\text{obs}) - Y(\text{calc})]^2/(n - 3)$, summed over all n data points.
[b] The errors indicated for each of the nine constants are termed standard errors, and were calculated by the method of Deming (16).

Table II. Calculation of transported entropies

$\frac{100\sqrt{m}}{(1+\sqrt{m})}$	m, mol/kg	t_{Cl^-}[a]	$\hat{Q}_{HCl}$,[b] cal/mol	Y,[c] μV/K	$\bar{\bar{S}}_{H^+}$,[d] eu	S_{HCl},[e] eu	$\bar{\bar{S}}_{HCl}$,[f] eu	$\bar{\bar{S}}_{Cl^-}$,[g] eu	$\bar{\bar{S}}_{H^+}$,[h] (mod 1), eu	$\bar{\bar{S}}_{H^+}$,[i] (mod 2), eu	$\bar{\bar{S}}_{Cl^-}$,[j] (mod 1), eu	$\bar{\bar{S}}_{Cl^-}$,[k] (mod 2), eu
5	0.00277	0.1767	3090	516.4	17.12	36.92	47.29	30.16	5.42	5.25	18.46	18.29
10	0.0125	0.1742	3010	511.4	14.20	31.31	41.40	27.20	5.47	5.13	18.47	18.13
15	0.0311	0.1716	3030	506.7	12.44	27.94	38.11	25.66	5.55	5.06	18.77	18.28
20	0.0625	0.1694	3160	502.6	11.22	25.47	36.07	24.85	5.71	5.07	19.34	18.70
25	0.111	0.1673	3360	498.2	10.27	23.48	34.75	24.49	5.90	5.11	20.12	19.33
30	0.184	0.1654	3605	494.6	9.46	21.75	33.65	24.40	6.09	5.16	21.03	20.10
35	0.290	0.1636	3880	491.6	8.75	20.21	33.23	24.48	6.29	5.23	22.02	20.96
40	0.444	0.1620	4170	489.6	8.09	18.78	32.77	24.68	6.48	5.29	23.07	21.88
45	0.670	0.1607	4480	489.0	7.43	17.42	32.44	25.02	6.63	5.30	24.22	22.89

[a] Obtained by least-squares analysis of transference numbers in Ref. (17), p. 723.
[b] Calculated from Eq. [2]; interpolated values from Ref. (6).
[c] Values from Eq. [8] and Table I.
[d] From Eq. [5].
[e] From Eq. [12].
[f] From Eq. [13].
[g] From Eq. [13] (column 7 minus column 5 of Table II).
[h] From Eq. [6].
[i] From Eq. [7].
[j] Analogous to Eq. [6].
[k] Analogous to Eq. [7].

Table III. Constants for determination of mean molal ionic activity coefficients and molarity of HCl using Eq. [10] and [11]

Mean temperature, °C	$-\mathfrak{S}^{\mu}$	A'[a]	B[b]	D[b]	a[b]	b[b]
20	0.5033	1.414	0.1312	0.0063	0.9982	0.01805
25	0.5075_5	1.418_5	0.1292	0.0061	0.9972	0.01817
30	0.5129_5	1.423	0.1272	0.0060	0.9958	0.01822

[a] Determined by averaging values from Ref. (17) and from Ref. (23) (with $\mathring{a}$ = 4.33Å).
[b] From Ref. (17).

$$\log \gamma_{\pm} = \frac{-\mathfrak{S}\sqrt{c}}{1 + A'\sqrt{c}} + Bc + Dc^2 - \log(1 + 0.03604m) \quad [10]$$

The molarity c is given by

$$c/m = a - bm \quad [11]$$

The constants for Eq. [10] and [11] are shown in Table III. Comparison of the values for $\gamma_{\pm}$ determined from Eq. [10] with literature values (18) at ten rounded molalities in the range 0.001-1.0 mol/kg yielded an excellent average error of 0.0005. After calculating $\gamma_{\pm}$, we next obtained the partial molal entropy of HCl at the nine rounded values of the molality function by a formula similar to that of Haase, Hoch, and Schönert (19)

$$S_{HCl} = S^0_{HCl} - 2R \ln m - 2R \ln \gamma_{\pm(25)} - \frac{2RT[\gamma_{\pm(30)} - \gamma_{\pm(20)}]}{10\,\gamma_{\pm(25)}} \quad [12]$$

in which T = 298.15K and S^0_{HCl} = 13.17 eu (3). By use of Eq. [13]

$$\bar{\bar{S}}_{H^+} + \bar{\bar{S}}_{Cl^-} = \bar{\bar{S}}_{HCl} = S_{HCl} + (\hat{Q}_{HCl}/T) \quad [13]$$

we obtained $\bar{\bar{S}}_{Cl^-}$. The results of these calculations are given in columns 7, 8, and 9 of Table II.

Earlier, it was suspected (6, 11) that the transported entropies, after correction for the mass-action term (R ln m), would vary only slightly with molality. Since our results did not confirm this, we added two additional (negative) terms to $\bar{\bar{S}}_{H^+}$ (mod 1) to obtain the quantity $\bar{\bar{S}}_{H^+}$ (mod 2), according to Eq. [7]. Column 13 of Table II shows the results of a similar calculation to obtain $\bar{\bar{S}}_{Cl^-}$ (mod 2). These values are not as nearly

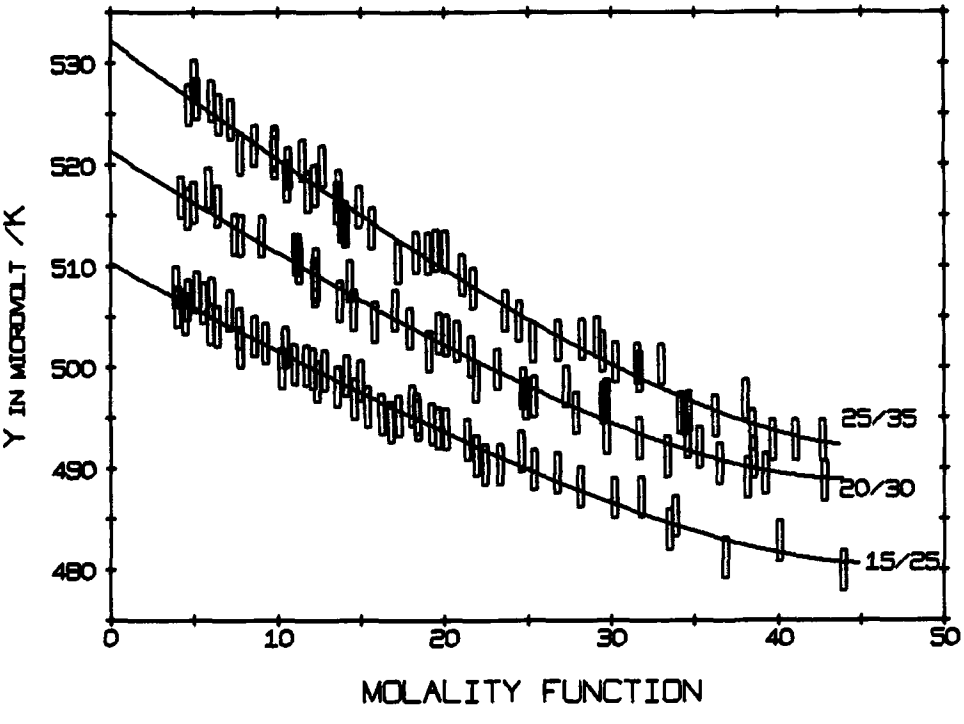

Fig. 1. Function $Y = TEP - (R/F)$ ln m vs. the molality function, $100\sqrt{m}/(1 + \sqrt{m})$. The three curves have been fitted by least-squares analysis according to Eq. [8] with values of constants from Table I. The mean temperatures are: 20° (lower curve), 25° (middle), and 30°C (upper curve).

constant as those for $\bar{\bar{S}}_{H^+}$ (mod 2) in column 11.

Error analysis for transported entropies.—The dominant contribution to the error in both $\bar{\bar{S}}_{H^+}$ and $\bar{\bar{S}}_{H^+}$ (mod 1), calculated from Eq. [5] and [6], respectively, comes from the third term on the right-hand side of Eq. [5], *viz.*, $(t_{Cl^-})(\hat{Q}_{HCl}/T)$. This contribution was determined from Eq. [2]. An error of ±5 μV/K for $(\epsilon_0 - \epsilon_\infty)$ in Eq. [2] corresponds to ±0.69 eu in the entropy of transport of HCl, or ±210 cal/mol in $\hat{Q}_{HCl}$ (6). Our estimate of ±2 μV/K in the TEP yields an additional contribution of ±0.046 eu for the error in both $\bar{\bar{S}}_{H^+}$ and $\bar{\bar{S}}_{H^+}$ (mod 1). Thus the total error comes out to be ±0.16 eu for both transported entropies.

In calculating S_{HCl} at 25°C we used the mean molal ionic activity coeffiecient $\gamma_\pm$ at 20°, 25°, and 30°. An error of ±0.002 in $\gamma_\pm$ leads to ±0.4 eu for the error in S_{HCl}, calculated by Eq. [12]. This error then contributes to the error in both $\bar{\bar{S}}_{Cl^-}$ and $\bar{\bar{S}}_{Cl^-}$ (mod 1).

Although we calculated $\bar{\bar{S}}_{Cl^-}$ (mod 1) from Eq. [12] and [13], we estimated its error from an equation analogous to Eq. [6]. An error of ±2 μV/K in the TEP leads to ±0.046 eu for the error in **F** (*TEP*). The final significant term in the error of $\bar{\bar{S}}_{Cl^-}$ (mod 1) is $(t_{H^+})(\hat{Q}_{HCl}/T)$, although it does not appear explicitly in our calculation of $\bar{\bar{S}}_{Cl^-}$ (mod 1). Because of the occurrence of this term, rather than $(t_{Cl^-})(\hat{Q}_{HCl}/T)$ as in Eq. [6], this term contributes ±0.63 eu to the error in both $\bar{\bar{S}}_{Cl^-}$ and $\bar{\bar{S}}_{Cl^-}$ (mod 1). For these quantities the total error is then ±1.08 eu.

This error may be contrasted with a slightly smaller value of ±0.9 eu for the error in $\bar{\bar{S}}_{Cl^-}$ (mod 2), resulting from the three sources just mentioned. However, this time, the error contribution from the terms in the activity coefficients is only ±0.2 eu instead of ±0.4 eu. The smaller value results from cancellation of terms in going from $\bar{\bar{S}}_{Cl^-}$ (mod 1) to $\bar{\bar{S}}_{Cl^-}$ (mod 2).

Comparison of results with other values.—From extrapolations to infinite dilution of $\bar{\bar{S}}_{H^+}$ (mod 1) and $\bar{\bar{S}}_{H^+}$ (mod 2) of Table II, we determined $\bar{\bar{S}}^0_{H^+}$ as 5.42 ± 0.16 eu. This value compares well with the value of 5.12 eu of Breck, Cadenhead, and Hammerli (6), which was determined using quinhydrone electrodes in aqueous HCl. Our result for $\bar{\bar{S}}^0_{H^+}$ is in agreement with the value 5.27 eu of deBethune and Daley (11), which was determined from thermocells with calomel electrodes.

By extrapolation of $\bar{\bar{S}}_{Cl^-}$ (mod 1) and $\bar{\bar{S}}_{Cl^-}$ (mod 2) of Table II to infinite dilution, we found $\bar{\bar{S}}^0_{Cl^-}$ to be 18.6 ± 1.0 eu. This is in excellent agreement with the value 18.69 eu for $\bar{\bar{S}}^0_{Cl^-}$, as determined by deBethune and Daley (11) using calomel electrodes. It also compares well with the value 19.1 eu of Haase, Hoch, and Schönert (19), obtained using silver-silver chloride electrodes. Our values are also in agreement with those of Agar (1) and Temkin and Khoroshin (10).

A comparison may also be made of our TEP with the work of Goyan (20). He measured the initial emf of a hydrogen-electrode thermocell containing 0.01*M* HCl, and obtained 1.41 mV for ΔT = 9.90K. For this result the two temperatures were centered at 25°C and the warm electrode was positive. We used a typical value of $k = -264$ μV in Eq. [9b] and obtained *TEP* = 115.8 μV/K for Goyan's result. Our value of 115.77 μV/K, calculated from Eq. [8] for 20°/30°C and for m = 0.01003 mol/kg, is in excellent agreement with this value.

At m = 0.1003 mol/kg, our values of Y calculated from Eq. [8] and the constants from Table I are 490.66, 498.94, and 505.78 μV/K at mean temperatures of 20°, 25°, and 30°C, respectively. From these values dY/dT is calculated to be +1.656 and +1.368 μV/K². These temperature derivatives compare favorably with those of Fales and Mudge (21), as calculated by deBethune, Licht, and Swendeman (22). Their value for the temperature derivative of the TEP of a thermocell at m = 0.1003 mol/kg and 25°, using hydrogen electrodes and a saturated KCl salt bridge, was 1.287 μV/K². Considering the different experimental conditions and that our bridge was 0.1*m* HCl, while Fales and Mudge used a saturated KCl salt bridge, this is excellent agreement indeed.

SYMBOLS

A	intercept in Eq. [8] for Y as a function of molality
A'	constant in first term of Eq. [10]
a	constant in first term of Eq. [11], for the molarity to molality ratio
$\mathring{a}$	mean distance of approach for HCl (= 4.33 angstroms)
B	coefficient of the $\sqrt{m}/(1+\sqrt{m})$-term in Eq. [8]
B	constant in linear term of Eq. [10]
b	constant in linear term of Eq. [11]
BP	barometric pressure (corrected to 0°C), Torr, (1 atm = 760 Torr = 101325 newton meter^{-2})
C	coefficient in linear term of Eq. [8]
c	molarity, mols of solute per liter of solution
D	constant in quadratic term of Eq. [10]
emf(obs)	the observed electromotive force of a thermocell, μV
F	Faraday constant, 96487 coulomb/equiv
k	correction factor for barometric and vapor pressure, μV, calculated from Eq. [3], used in Eq. [9b]
m	molality, mols of solute per kilogram of solvent
Molality Function	$= 100\sqrt{m}/(1+\sqrt{m})$
N	normality, mols of H^+ ions per liter of solution
P_U, P_L	vapor pressure of pure water at temperatures T_U and T_L, respectively
$\hat{Q}_i$	heat of transport of a salt or ion, cal/mol, defined by Eq. [2] (1 cal = 4.184 Joule)
R	gas constant, 8.31434 J mol^{-1} K^{-1}, 1.987175 eu mol^{-1}
S_i	molal entropy, partial molal entropy of a salt or ion, eu mol^{-1}, cal mol^{-1} K^{-1}
S^0_i	standard value of S_i
$\bar{\bar{S}}_i$	transported entropy of an ion or salt, eu mol^{-1}
$\bar{\bar{S}}^0_i$	transported entropy of an ion in the hypothetical standard state with m = 1 mol/kg
$\hat{S}_i$	entropy of transport of a salt, eu mol^{-1}
$\bar{\bar{S}}_i$(mod 1), $\bar{\bar{S}}_i$(mod 2)	"modified" transported entropies of an ion, eu mol^{-1}, defined by Eq. [6] and [7], respectively
T	Kelvin temperature, K
t_i	Hittorf transference (transport) number of an ion
T_U, T_L	upper and lower thermostat temperatures, °C
TEP	initial thermoelectric power, μV/K, defined by Eq. [9b]
Y	thermoelectric power corrected for the mass-action term, defined by Eq. [9a], μV/K
Y^0	the value of Y at infinite dilution, μV/K
$\gamma_{\pm(25)}$	mean molal ionic activity coefficient at 25°C
ΔP	solvent vapor pressure lowering, in Eq. [4b]
ΔP_U, ΔP_L	solvent vapor pressure lowering at T_U and T_L, respectively, Torr
ΔT	temperature difference between thermostats, K
ϵ_0, ϵ_∞	initial and final thermoelectric power of a thermocell, respectively, μV/K
σ	Soret coefficient, K^{-1}, $= (-1/m)(\delta m/\delta T)$ at the steady state (= Soret equilibrium)
$\mathfrak{S}$	constant in first term of Eq. [10]

Acknowledgment

We are indebted to Professor J. N. Agar of the University of Cambridge for his numerous suggestions and helpful discussions during the course of the project. We are also indebted to Professor A. J. deBethune of Boston College for his critical review of the manuscript and for suggesting the comparison of our result for dY/dT with that of Fales and Mudge. We gratefully acknowledge support from several sources: two grants from Research Corporation, a grant from the Petroleum Research Fund of the American Chemical Society, and several undergraduate-research-participation grants to Willamette University from the National Science Foundation. Finally, we are thankful for the work of earlier students on the project: Norman P. Hunter, James E. Price, Kenneth D. Rost, Richard W. Harper, and Robert W. Smith.

Manuscript received March 13, 1972.

Any discussion of this paper will appear in a Discussion Section to be published in the December 1973 JOURNAL.

REFERENCES

1. J. N. Agar in "Advances in Electrochemistry and Electrochemical Engineering," Vol. 3, Chap. 2, P. Delahay, Editor, Interscience Publishers, New York (1963).
2. J. N. Agar and J. C. R. Turner, *Proc. Roy. Soc., Ser. A*, **255**, 37 (1960).
3. W. M. Latimer, "The Oxidation States of the Elements and Their Potentials in Aqueous Solution," 2nd ed., Prentice-Hall, Inc., Englewood Cliffs, N. J. (1952).
4. R. W. Gurney, "Ionic Processes in Solution," pp. 172-184, McGraw-Hill Book Co., New York (1953).
5. T. Ikeda, *J. Chem. Phys.*, **43**, 3412 (1965).
6. W. G. Breck, G. Cadenhead, and M. Hammerli, *Trans. Faraday Soc.*, **61**, 37 (1965).
7. N. A. Lange, Editor, "Handbook of Chemistry," 10th ed., p. 1438, McGraw-Hill Book Co., New York (1961).
8. "International Critical Tables," 1st ed., Vol. 3, p. 293, McGraw-Hill Book Co., New York (1928).
9. G. J. Hills and D. J. G. Ives in "Reference Electrodes," Chap. 2, D. J. G. Ives and G. J. Janz, Editors, Academic Press, Inc., New York (1961).
10. M. H. Temkin and A. B. Khoroshin, *Zh. Fiz. Khim.*, **26**, 500, 773 (1952).
11. A. J. deBethune and H. O. Daley, *This Journal*, **116**, 1395 (1969).
12. "Reference Tables for Thermocouples," *Natl. Bur. Std. Circ. 561*, p. 35, U.S. Government Printing Office, Washington, D. C. (1955).
13. Ref (1), p. 73.
14. T. Ikeda and H. Kimura, *J. Phys. Chem.*, **69**, 41 (1965).
15. H. V. Malmstadt and C. G. Enke, "Electronics for Scientists," p. 265, W. A. Benjamin, Inc., New York (1963).
16. W. E. Deming, "Statistical Adjustment of Data," pp. 27, 226-230, Dover Publications, Inc., New York (1943).
17. H. S. Harned and B. B. Owen, "The Physical Chemistry of Electrolytic Solutions," 3rd Ed., p. 469, Reinhold Publishing Corp., New York (1958).
18. Ref (17), p. 466.
19. R. Haase, K. Hoch, and H. Schönert, *Z. phys. Chem.* (Frankfurt), **27**, 421 (1961).
20. F. M. Goyan, Ph.D. Thesis, University of California, Berkeley (1937).
21. H. A. Fales and W. A. Mudge, *J. Am. Chem. Soc.*, **42**, 2434 (1920).
22. A. J. deBethune, T. S. Licht, and N. Swendeman, *This Journal*, **106**, 66 (1959).
23. R. Parsons, "Handbook of Electrochemical Constants," p. 13, Butterworths Scientific Publications, Ltd., London (1959).

Technical Notes

Kinetics of Anodic Oxide Growth on Sodium Tungsten Bronzes

Jean-Paul Randin*

Hydro Quebec Institute of Research, Varennes, Province of Quebec, Canada

Sodium tungsten bronzes have been proposed as electrocatalysts for the oxygen reduction reaction. Their electrocatalytic activity has been the subject of numerous studies (1-8) but the oxide-growth kinetics on this material have not been reported. This aspect of the electrochemical stability of the bronzes is of crucial importance if the material is to be used in a practical device such as a fuel cell or a battery. In such devices, high anodic transients may arise in the course of utilization which can give rise to anodic oxide growth, and hence change the initial properties of the electrocatalyst. The present note reports on the oxide-growth kinetics on sodium tungsten bronzes.

Experimental

The sodium tungsten bronzes were prepared by electrolyses of fused mixtures of sodium tungstate and tungsten trioxide in an alumina crucible (Coors). Analytical reagent grade Na_2WO_4 and H_2WO_4 (Baker Company) were used without further purification. Both reagents were previously dried at 200°C. Gold wires, 99.99% purity, were used as anode and cathode in the crystal preparation where no platinum was included. A platinum sheet, 99.99% purity, was used as anode in electrolyses in which platinum incorporation was sought. The concentration of platinum in the melt was therefore maintained by anodic dissolution of the metal. Galvanostatic depositions were performed at 720°-800°C with current densities between 20 and 50 $mA \cdot cm^{-2}$, applied current being altered appropriately during the growth. Large clusters of adherent crystals were obtained at the cathode. The cleaning procedure consisted of alternate boiling in dilute sodium hydroxide and triply distilled water.

The sodium content in the cubic tungsten bronzes was determined by x-ray measurements of the lattice parameters using Brown and Banks relation between the lattice parameter and the sodium content (9). The value of x in the cubic Na_xWO_3 varied from 0.58 to 0.88 as the melt composition was changed from 10 to 50 mole per cent (m/o) WO_3.

Crystals of sodium tungsten bronze were mounted in electrodes by compression moulding within a Kel-F holder, according to the method described by Yohe *et al.* (10). The apparent surface area of the electrodes used in the present study were about 0.2 cm^2 each. All

* Electrochemical Society Active Member.

Key words: sodium tungsten bronze, oxide growth, anodic oxide.

data are given with respect to the apparent surface area of the electrode. Prior to the electrochemical measurements, the bronze electrode was mechanically polished using different grades of alumina (Buehler Limited) down to 0.3μ.

An all-glass, three-compartment cell was used for the galvanostatic charging experiments. The a-c impedance of the electrode-electrolyte interface was measured in a cell of the type described by Tench and Yeager (11). This cell has three compartments, which contain the sodium tungsten bronze electrode and a Hg pool counterelectrode (internal counterelectrode used only for the a-c impedance measurements) spectroscopic grade graphite auxiliary counterelectrode (external counterelectrode), and the Hg/Hg_2SO_4 reference electrode, respectively.

All the potentials have been measured with respect to a Hg/Hg_2SO_4 reference electrode but all the results reported in the present study are given in V *vs.* NHE.

Helium was used to deaerate the solutions and to maintain an inert atmosphere inside the cells. The gas was purified by passing it through a train, which included a BTS catalyst (BASF, Ludwigshafen-am-Rhein, Germany) maintained at 180°C to remove oxygen and CO, and Linde Type 3A and 13X molecular sieves to remove other impurities.

The 1*N* sulfuric acid solutions were prepared by diluting H_2SO_4 Ultrex (J. T. Baker Chemical) in deionized and doubly distilled water, both distillations being over alkaline permanganate.

Constant current d-c power supply (Hewlett-Packard, Model 6177B) was used for the charging curves. The measurements of the equivalent series capacitances and resistances were carried out at 23°C with an a-c Wheatstone bridge and a d-c polarization circuit. The bridge was checked with standard resistance and capacitance components and found to contribute a negligible error in the experimental conditions used in this study. The a-c voltage applied to the cell did not exceed a few millivolts.

Results

The general behavior of sodium tungsten bronze during galvanostatic anodic charging is shown in Fig. 1. In order to improve the reproducibility of the results, galvanostatic charging curves were recorded after mechanical polishing and cathodic prepolarization at 13 mA · cm^{-2} for 200 sec. An arrest is obtained below 1V *vs.* NHE, the detailed analysis of which will be presented in a future publication. At about 2.3V *vs.* NHE, oxygen evolution is visible at the surface of the electrode. At low charging currents (typically 5 mA/cm^{-2}), this potential remains almost constant over a long period of time. When the charging current was greater than 5 mA · cm^{-2}, the voltage increased rapidly following a period during which it remained constant at about 2.3V. This transition time is shorter the higher the applied current density. At a still higher current density, a voltage buildup as high as 40V is reached during anodization, which is an indication that some electrically limiting layer is formed on the surface.

The repetition of the anodic charging experiment at high current density, preceded by a short prereduction at 13 mA · cm^{-2} for 200 sec, gives rise to a curve slightly different from the first one performed on a fresh electrode surface. The irreproducibility between the first galvanostatic charging curve and the following one may mean that the reduction of the layer formed at high anodic current has not been removed or reduced up to the initial state.

The rotation of the electrode has no significant effect on the potential-time measurements. The electrode was rotated at low speed (1000 rpm) to help remove the oxygen bubbles from the bronzes surface.

The relations between the electrode potential and the time during anodization at different constant current densities are reported in Fig. 2. A logarithmic growth law is indicated.

The impedance measurements of the sodium tungsten bronze/electrolyte interface have been made on an electrode previously anodized for 1 hr at 21 mA · cm^{-2}. Capacitance values between 4 and 6 $\mu f \cdot cm^{-2}$ have been recorded at potentials between 2.7 and 1.0V *vs.* NHE. The capacitance values increase as the potential decreases, whereas the series resistance decreases with the applied potential. The Mott-Schottky plot calculated from a typical capacitance curve obtained in going from high anodic potentials towards more cathodic potentials is reported in Fig. 3. Two linear regions are indicated, which suggest a change in the surface composition at potentials close to 1V. This change occurs only on highly anodized electrode surfaces. The same measurements performed on a nonoxidized surface give only one straight line, whose intersection with the potential axis gives the same flatband potential as that observed at low potentials on the anodized electrode.

The linear section in the most anodic potential region of the Mott-Schottky plot gives a flatband potential of about 0V *vs.* NHE and a slope of 1.22×10^{-2} $\mu f^{-2} \cdot cm^4 \cdot V^{-1}$, from which a n_D value of 2.6×10^{20} carriers · cm^{-3} is calculated. The x value in Na_xWO_3 deduced from the latter donor concentration is 0.015 assuming that: (*i*) the donors are all sodium

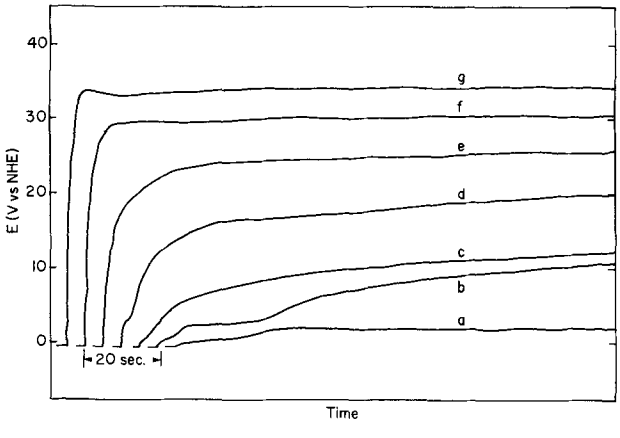

Fig. 1. Effect of current density on anodic charging curves for a sodium tungsten bronze ($x = 0.65$) electrode in helium saturated 1*N* H_2SO_4 at 23°C. Electrode polished before each measurement and reduced at 13 mA · cm^{-2} for 200 sec. Curve a, 4.25; b, 8.50; c, 12.8; d, 29.8; e, 59.6; f, 119; g, 183 mA · cm^{-2}.

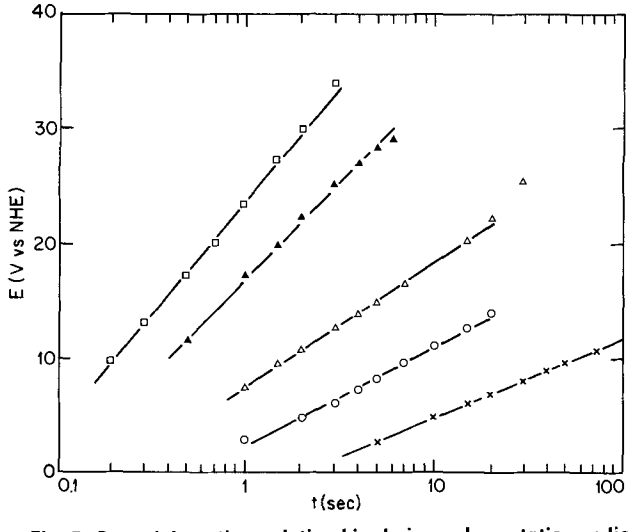

Fig. 2. Potential *vs.* time relationship during galvanostatic anodic oxide growth on a sodium tungsten bronze ($x = 0.65$) electrode in helium saturated 1*N* H_2SO_4 at 23°C; same measurements as in Fig. 1. x, 12.8; ○, 29.8; △, 59.6; ▲, 119; □, 183 mA · cm^{-2}.

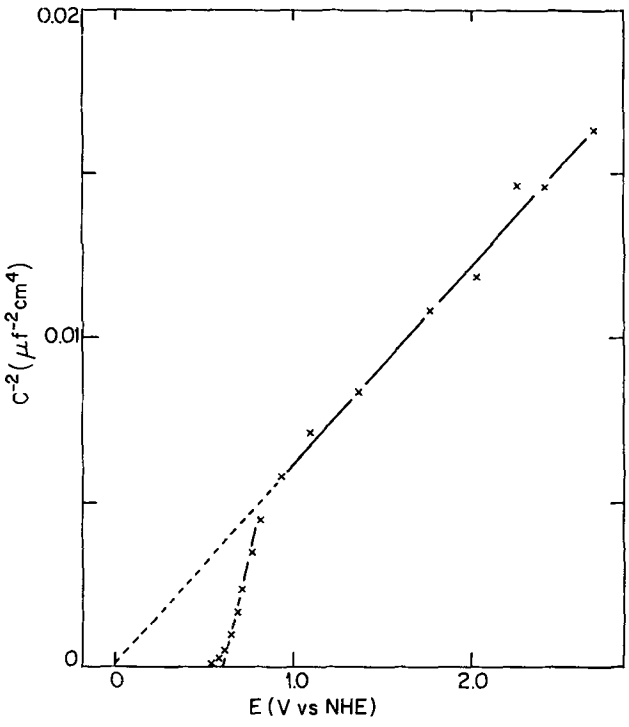

Fig. 3. Mott-Schottky plot for the sodium tungsten bronze ($x = 0.65$) following anodic oxidation at 21 mA · cm^{-2} for 1 hr in helium saturated 1N H_2SO_4 at 23°C. A-C impedance measurements for the determination of capacitance values performed at 1000 Hz.

atoms and that (*ii*) the dielectric constant, ϵ, of the bronze is 50. The only available data from which the dielectric constant of sodium tungsten bronze can be estimated is found in a paper by Kir'iashkina *et al.* (12), who quote a value for the ratio ϵ/ρ as 6.95 for WO_3. From the density, ρ, for WO_3 with the cubic tungsten bronze structure being about 7.2 g · cm^{-3}, it can be deduced that $\epsilon \simeq 50$.

The small linear section in the less anodic potential regions of the Mott-Schottky plot gives a flatband potential of 0.6V *vs.* NHE and a slope of 2.5×10^{-2} $\mu f^{-2} \cdot cm^4 \cdot V^{-1}$, which corresponds to a n_D value of 1.25×10^{20} carriers · cm^{-3} and a x value (in Na_xWO_3) of 0.007, with the same assumptions as previously.

The effect of the x value in Na_xWO_3, ranging from 0.58 to 0.88, and the platinum concentration from 2 up to 1200 ppm, has been studied. No significant effect of these two parameters has been found on the general shape of the galvanostatic charging curves. The effect of the x value and the platinum concentration on the oxide growth-kinetics (curve E *vs.* log time) has been found to be within the experimental errors of the measurements.

Discussion

The increase in voltage up to about 40V for high applied currents, the logarithmic-growth law, and the a-c impedance measurements suggest that the electrically limiting layer formed on the bronze surface is most likely an oxide. A similar oxide growth has been observed on valve metals, including tungsten (13-14).

A logarithmic law is generally observed for the oxide growth of both semiconducting and conducting oxides. The rate of growth of a semiconducting oxide is expressed by the following equation (15-16)

$$L = \frac{\epsilon kT}{4\pi \rho e^2 L_1} \ln Kt \qquad [1]$$

where L is the thickness of the oxide, t is the time, ϵ is the dielectric constant, ρ is the density of trapped electrons (or holes) in the oxide; e is the electronic charge, L_1 the thickness of the total space charge, K is a constant $= B/c \exp(-e\psi/kT) \exp(e\chi^\circ/kT) \exp(e C_1/kT)$, in which B and c are constants, ψ is the work function of the metal being oxidized, χ is the applied voltage across the metal-oxide interface, χ° is the potential drop that would hypothetically exist if the oxide thickness were zero, and $C_1 = -4\pi \rho e^2 L_1/\epsilon$.

The rate of growth of a conducting oxide may be expressed by the following equation (15)

$$L = \frac{RT}{b} \ln t + \frac{RT}{b} \ln \frac{RTA}{b} - \frac{\Delta G^*_o}{b} + \frac{cFE}{b} \qquad [2]$$

where A, b, c are constants, ΔG^*_o is the standard free energy of activation for the oxide growth, R, the gas constant, T, the temperature, and E, the electric field. At constant field, the growth follows a logarithmic law.

A direct proportionality between thickness and potential has been frequently observed [see, for example, Ref. (17, 18)], particularly with the valve metals (15). Assuming such a dependence in the case under study, Fig. 2 shows that the anodic oxide growth on sodium tungsten bronze follows a logarithmic law. The a-c impedance measurements from which linear Mott-Schottky plots have been calculated suggest the presence of a semiconducting oxide, rather than a conducting one.

The exact nature of the oxide grown at the surface of the sodium tungsten bronze during anodization is not known. However, some interesting features of the present work may be outlined even though the following discussion is somewhat speculative.

It has been mentioned above that the repetition of the anodic charging experiment at high current density, preceded by a reduction period gives rise to a curve different from the first one measured on a freshly polished electrode surface. This behavior suggests an irreversible change of the electrode surface after anodization. The analysis of the arrest measured at low potentials also suggests a change in the surface composition after prolonged anodization of the electrode (19). The change in surface behavior has also been noticed by McHardy (8) and attributed to a sodium depletion reaction. The same author (8) confirmed by ion-probe analysis of an aged crystal that sodium was lost from the bronze surface. The sodium depletion reaction may be written as

$$Na_xWO_3 \rightarrow Na_yWO_3 + (x - y)Na^+ + (x - y)e^- \qquad [3]$$

The first process taking place during anodization of the sodium tungsten bronze electrode is believed to be the sodium depletion of the surface layer. Reaction [3] is confirmed by the a-c impedance measurements which give a very small value of y in Na_yWO_3, *i.e.*, smaller than 0.02.

In the calculations of the x values of the surface layer from the a-c impedance measurements, it has been assumed that the only donor is the sodium atoms. This assumption is justified at x values greater than 0.25 since bronzes with such a composition are known to have one free electron per metal atom in the host lattice (20). A different mechanism of conduction is operative below 0.25, however. For a single crystal of sodium tungsten bronze of composition $Na_{0.025}$ WO_3 semiconductor-type behavior has been established (21). The equivalent x values, calculated from the a-c measurements using the assumption that the only donor is the sodium atoms, give very low values. Moreover, the calculations have been made using the capacitance values with respect to the apparent surface area of the bronze electrode. If the ratio of the true to the apparent area (not measured) could be taken into account the equivalent x values would drop still further by the square of this ratio (probably at least 25 times). At the very low values of x calculated from the a-c impedance data the sodium atom is most likely not the only donor.

A second possible oxide growth reaction on the sodium tungsten bronze whose surface has previously

been depleted in sodium may be as follows

$$WO_3 + z\,H_2O \rightleftharpoons WO_{(3+z)} + 2z\,H^+ + 2z\,e^- \quad [4]$$

A negative ionic charge carrier is injected into the surface layer of the oxide with adjustment of the electron concentration. The oxide growth on sodium tungsten bronze is therefore analogous to the change of valence observed in the surface region of nickel or silver oxide electrodes on anodic charging (22-24).

Following the preceding discussion, it can be assumed that the a-c impedance measurements are carried out on a bronze electrode whose surface layer is almost completely depleted of sodium. These impedance measurements (Fig. 3) suggest that the surface composition changes with the applied potential since both the slope and the potential at the intersection with the y-axis change with the applied potential. The linear section of the Mott-Schottky plot in the low potential region is observed only over a small range of potential (0.2V) and the capacitance values in this potential range are too high (16-35 μf per apparent cm^2) to be associated only with a space-charge capacitance. The data calculated from the low potential section of the Mott-Schottky plot, therefore, should be interpreted very carefully. In particular the flatband potential determined from the intersection of the potential axis with the extrapolated Mott-Schottky plot shifts from about 0 to 0.6V *vs.* NHE in going from the high to the low potential region. This fact is difficult to explain solely by a change in the oxide stoichiometry according to Reaction [4]. On the contrary, the change in carrier concentration from 2 to 1 $\times$ 10^{20} cm^{-3} observed in going from highly anodic potentials to cathodic potentials can be attributed to a variation of the stoichiometry of the oxide. At high anodic potentials the oxide is less stoichiometric (oxygen-excess, *i.e.*, high values of z) and consequently, has a higher carrier concentration. On reaching less anodic potentials, the oxide becomes more stoichiometric (small values of z) and has a lower donor concentration.

The growth rate of the oxide has not been found to depend significantly on the x value, even if the density of trapped electrons in the oxide is contained in Eq. [1]. This may be attributed to the fact that the oxide growth (Reaction [4]) occurs on a sodium depleted surface layer. In these conditions, the composition of the oxide formed at the bronze surface is not believed to depend significantly on the bulk composition.

Acknowledgments

Grateful acknowledgment is made to Dr. A. K. Vijh for numerous critical discussions and suggestions throughout the course of this study. The author thanks Mr. R. Bellemare for his assistance in the experimental work and Dr. P. Lenfant for his interest and encouragement.

Manuscript submitted Aug. 28, 1972; revised manuscript received Oct. 30, 1972.

Any discussion of this paper will appear in a Discussion Section to be published in the December 1973 JOURNAL.

REFERENCES

1. D. B. Sepa, A. Damjanovic, and J. O'M. Bockris, *Electrochim Acta*, **12**, 746 (1967).
2. A. Damjanovic, D. Sepa, and J. O'M. Bockris, *J. Res. Inst. Catalysis, Hokkaido Univ.*, **16**, 1 (1968).
3. B. Broyde, *J. Catalysis*, **10**, 13 (1968).
4. J. M. Fishman, J. F. Henry, and S. Tessore, *Electrochim. Acta*, **14**, 1314 (1969).
5. J. O'M. Bockris, A. Damjanovic, and J. McHardy, Proc. "3rd Int. Symp. Fuel Cells, Brussels, Belgium, June 16-20, 1969," p. 15, Press. Acad. Européennes, Brussels (1969).
6. R. A. Fredlein and J. McHardy, "24th Power Sources Symp.," p. 175, P.S.C. Pub. Committee, Red Bank, N. J. (1970).
7. R. D. Armstrong, A. F. Douglas, and D. E. Williams, *Energy Conversion*, **11**, 7 (1971).
8. J. McHardy, Ph.D. Thesis, University of Pennsylvania, Philadelphia (1972).
9. B. W. Brown and E. Banks, *J. Am. Chem. Soc.*, **76**, 963 (1954).
10. D. Yohe, E. Yeager, R. Greef, and A. Riga, "Electrochemical Processes on Nickel Oxide", Tech. Report No. 3, Case Western Reserve University, Cleveland, Ohio, U.S. Office of Naval Research, Contract No. 1439 (09); project N.R. 056-451, July 1, 1967.
11. D. M. Tench and E. Yeager, "Electrochemistry of Redox Couples on Litiated Nickel Oxide Electrodes" Tech. Report No. 28, Case Western Reserve University, Cleve'and, Ohio, U.S. Office of Naval Research, Contract N00014-67A-0404-006, Project NR 359-451, September 15, 1970.
12. Z. I. Kir'iashkina, F. M. Popov, D. N. Bilenko, and V. I. Kir'iashkina, *Soviet Phys.-Tech. Phys.*, **2**, 69 (1957).
13. I. A. Ammar and R. Salim, *Corrosion Sci.*, **11**, 591 (1971).
14. I. A. Ammar and R. Salim, *Werkstoffe Korrosion*, **23**, 161 (1972).
15. M. A. Genshaw, in "Electrosorption," E. Gileadi, Editor, p. 73, Plenum Press, New York (1967).
16. E. H. Uhlig, *Acta Met.*, **4**, 541 (1956).
17. A. C. Makrides, *This Journal*, **113**, 1158 (1966).
18. K. J. Vetter and J. W. Schultze, *J. Electroanal. Chem.*, **34**, 131 (1972).
19. J. P. Randin, A. K. Vijh, and A. B. Chughtai, In preparation.
20. P. G. Dickens and M. S. Whittingham, *Quart. Rev.*, **22**, 30 (1968).
21. W. McNeill and L. E. Conroy, *J. Chem. Phys.*, **36**, 87 (1962).
22. J. P. Hoare, "The Electrochemistry of Oxygen," Chapter VII, Interscience Publishers, New York (1968).
23. N. A. Hampson, J. B. Lee, and J. R. Morley, *Electrochim. Acta*, **16**, 637 (1971).
24. M. A. Sattar and B. E. Conway, *ibid.*, **14**, 695 (1969).

Electrical Conductivity for Aluminum Cell Electrolyte between 950°-1025°C by Regression Equation

G. Choudhary

Department of Chemistry, Alabama A. & M. University, Normal, Alabama 35762

The electrical conductivity of molten cryolitic systems is of considerable importance to the aluminum industry. The electrolyte of aluminum reduction cells consists of a molten mixture of cryolite and alumina with occasional additions of salts such as CaF_2, MgF_2, LiF, NaCl, and Li_3AlF_6 to the system. The object of this note is to correlate the effect of the components and the temperature of the cryolitic systems with a view to predicting the electrical conductivity of the electrolyte under the situations normally encountered

Key words: electrical conductivity, cryolitic systems, aluminum extraction, regression equation.

been depleted in sodium may be as follows

$$WO_3 + z\,H_2O \rightleftharpoons WO_{(3+z)} + 2z\,H^+ + 2z\,e^- \quad [4]$$

A negative ionic charge carrier is injected into the surface layer of the oxide with adjustment of the electron concentration. The oxide growth on sodium tungsten bronze is therefore analogous to the change of valence observed in the surface region of nickel or silver oxide electrodes on anodic charging (22-24).

Following the preceding discussion, it can be assumed that the a-c impedance measurements are carried out on a bronze electrode whose surface layer is almost completely depleted of sodium. These impedance measurements (Fig. 3) suggest that the surface composition changes with the applied potential since both the slope and the potential at the intersection with the y-axis change with the applied potential. The linear section of the Mott-Schottky plot in the low potential region is observed only over a small range of potential (0.2V) and the capacitance values in this potential range are too high (16-35 μf per apparent cm^2) to be associated only with a space-charge capacitance. The data calculated from the low potential section of the Mott-Schottky plot, therefore, should be interpreted very carefully. In particular the flatband potential determined from the intersection of the potential axis with the extrapolated Mott-Schottky plot shifts from about 0 to 0.6V *vs.* NHE in going from the high to the low potential region. This fact is difficult to explain solely by a change in the oxide stoichiometry according to Reaction [4]. On the contrary, the change in carrier concentration from 2 to 1 $\times$ 10^{20} cm^{-3} observed in going from highly anodic potentials to cathodic potentials can be attributed to a variation of the stoichiometry of the oxide. At high anodic potentials the oxide is less stoichiometric (oxygen-excess, *i.e.*, high values of z) and consequently, has a higher carrier concentration. On reaching less anodic potentials, the oxide becomes more stoichiometric (small values of z) and has a lower donor concentration.

The growth rate of the oxide has not been found to depend significantly on the x value, even if the density of trapped electrons in the oxide is contained in Eq. [1]. This may be attributed to the fact that the oxide growth (Reaction [4]) occurs on a sodium depleted surface layer. In these conditions, the composition of the oxide formed at the bronze surface is not believed to depend significantly on the bulk composition.

Acknowledgments

Grateful acknowledgment is made to Dr. A. K. Vijh for numerous critical discussions and suggestions throughout the course of this study. The author thanks Mr. R. Bellemare for his assistance in the experimental work and Dr. P. Lenfant for his interest and encouragement.

Manuscript submitted Aug. 28, 1972; revised manuscript received Oct. 30, 1972.

Any discussion of this paper will appear in a Discussion Section to be published in the December 1973 JOURNAL.

REFERENCES

1. D. B. Sepa, A. Damjanovic, and J. O'M. Bockris, *Electrochim Acta*, **12**, 746 (1967).
2. A. Damjanovic, D. Sepa, and J. O'M. Bockris, *J. Res. Inst. Catalysis, Hokkaido Univ.*, **16**, 1 (1968).
3. B. Broyde, *J. Catalysis*, **10**, 13 (1968).
4. J. M. Fishman, J. F. Henry, and S. Tessore, *Electrochim. Acta*, **14**, 1314 (1969).
5. J. O'M. Bockris, A. Damjanovic, and J. McHardy, Proc. "3rd Int. Symp. Fuel Cells, Brussels, Belgium, June 16-20, 1969," p. 15, Press. Acad. Européennes, Brussels (1969).
6. R. A. Fredlein and J. McHardy, "24th Power Sources Symp.," p. 175, P.S.C. Pub. Committee, Red Bank, N. J. (1970).
7. R. D. Armstrong, A. F. Douglas, and D. E. Williams, *Energy Conversion*, **11**, 7 (1971).
8. J. McHardy, Ph.D. Thesis, University of Pennsylvania, Philadelphia (1972).
9. B. W. Brown and E. Banks, *J. Am. Chem. Soc.*, **76**, 963 (1954).
10. D. Yohe, E. Yeager, R. Greef, and A. Riga, "Electrochemical Processes on Nickel Oxide", Tech. Report No. 3, Case Western Reserve University, Cleveland, Ohio, U.S. Office of Naval Research, Contract No. 1439 (09); project N.R. 056-451, July 1, 1967.
11. D. M. Tench and E. Yeager, "Electrochemistry of Redox Couples on Litiated Nickel Oxide Electrodes" Tech. Report No. 28, Case Western Reserve University, Cleve'and, Ohio, U.S. Office of Naval Research, Contract N00014-67A-0404-006, Project NR 359-451, September 15, 1970.
12. Z. I. Kir'iashkina, F. M. Popov, D. N. Bilenko, and V. I. Kir'iashkina, *Soviet Phys.-Tech. Phys.*, **2**, 69 (1957).
13. I. A. Ammar and R. Salim, *Corrosion Sci.*, **11**, 591 (1971).
14. I. A. Ammar and R. Salim, *Werkstoffe Korrosion*, **23**, 161 (1972).
15. M. A. Genshaw, in "Electrosorption," E. Gileadi, Editor, p. 73, Plenum Press, New York (1967).
16. E. H. Uhlig, *Acta Met.*, **4**, 541 (1956).
17. A. C. Makrides, *This Journal*, **113**, 1158 (1966).
18. K. J. Vetter and J. W. Schultze, *J. Electroanal. Chem.*, **34**, 131 (1972).
19. J. P. Randin, A. K. Vijh, and A. B. Chughtai, In preparation.
20. P. G. Dickens and M. S. Whittingham, *Quart. Rev.*, **22**, 30 (1968).
21. W. McNeill and L. E. Conroy, *J. Chem. Phys.*, **36**, 87 (1962).
22. J. P. Hoare, "The Electrochemistry of Oxygen," Chapter VII, Interscience Publishers, New York (1968).
23. N. A. Hampson, J. B. Lee, and J. R. Morley, *Electrochim. Acta*, **16**, 637 (1971).
24. M. A. Sattar and B. E. Conway, *ibid.*, **14**, 695 (1969).

Electrical Conductivity for Aluminum Cell Electrolyte between 950°-1025°C by Regression Equation

G. Choudhary

Department of Chemistry, Alabama A. & M. University, Normal, Alabama 35762

The electrical conductivity of molten cryolitic systems is of considerable importance to the aluminum industry. The electrolyte of aluminum reduction cells consists of a molten mixture of cryolite and alumina with occasional additions of salts such as CaF_2, MgF_2, LiF, NaCl, and Li_3AlF_6 to the system. The object of this note is to correlate the effect of the components and the temperature of the cryolitic systems with a view to predicting the electrical conductivity of the electrolyte under the situations normally encountered

Key words: electrical conductivity, cryolitic systems, aluminum extraction, regression equation.

Table I. Sources of the preferred specific conductivity vs. temperature investigations for cryolitic systems

Cryolic system (molten)	Temp. range of observations, °C	Investigator(s)	Reference
Na_3AlF_6-CaF_2, AlF_3, LiF, MgF_2, NaCl, Li_3AlF_6 (binaries)	1000	Grjotheim and Matiasovsky	(1)
Na_3AlF_6 (Uniary)	1000-1060	Matiasovsky *et al.*	(2)
Na_3AlF_6-Al_2O_3	1000	Matiasovsky *et al.*	(2)
Na_3AlF_6-bath-weight ratio	1000	Frank and Foster	(3)
Na_3AlF_6-bath-weight ratio-MgF_2	940-1080	Belyaev *et al.*	(4)
Na_3AlF_6-Al_2O_3-CaF_2	980-1020	Yim and Feinleib	(5)
Na_3AlF_6-Al_2O_3-MgF_2	1070	Belyaev *et al.*	(6)
Na_3AlF_6-Al_2O_3-NaCl	1000	Matiasovsky *et al.*	(2)
Na_3AlF_6-Al_2O_3-LiF	1000	Matiasovsky *et al.*	(7)
Na_3AlF_6-Al_2O_3-Li_3AlF_6	1000	Matiasovsky *et al.*	(7)
Na_3AlF_6-AlF_3-LiF	1000	Belyaev *et al.*	(8)
Na_3AlF_6-AlF_3-NaCl	1070	Belyaev *et al.*	(9)
Na_3AlF_6-AlF_3-MgF_2	1000	Belyaev *et al.*	(8)
Na_3AlF_6-CaF_2-MgF_2	1000	Belyaev *et al.*	(8)
Na_3AlF_6-MgF_2-AlF_3	1000	Belyaev *et al.*	(8)
Na_3AlF_6-NaCl-AlF_3	1070	Vakhobov *et al.*	(9)
Na_3AlF_6-AlF_3-LiF	1000	Belyaev *et al.*	(8)
Na_3AlF_6-Al_2O_3-AlF_3-NaCl	1000	Matiasovsky *et al.*	(1)
Na_3AlF_6-AlF_3-MgF_2-CaF_2	1000	Belyaev *et al.*	(8)
Na_3AlF_6-Al_2O_3-AlF_3-MgF_2-CaF_2	1000	Belyaev *et al.*	(8)
Na_3AlF_6-Al_2O_3-CaF_2-MgF_2-LiF	1000	Vakhobov *et al.*	(10)

in the aluminum industry, *i.e.*, salt additions 0-10 weight per cent (w/o); weight ratio of NaF/AlF_3 1.1-1.5, and the temperature range 950°-1025°C.

Experimental investigations of the specific electrical conductivity of molten cryolite with additives have been carried out by numerous observers in the last three decades. The author feels that due to the development of more sophisticated methodology of measurements, only the data from the investigations during the last 15 years are sufficiently reliable to be cited. Table I summarizes the references for preferred specific conductivity-temperature diagrams as selected from such investigations. During the choice of these data, particular emphasis has been placed on cells, electrode material, design of measuring bridges, and the technique of measurement. The results of these preferred conductivity-temperature diagrams have also been examined from the point of view of validity, consistency, and accuracy.

The temperature dependence of the electrical conductivity of molten salts of predominantly ionic character has been given by Bloom and Heymann (11) in the form of a basic Arrhenius type of equation

$$k = A_k \exp(-E/RT) \quad [1]$$

where k = specific conductivity, $ohm^{-1}\ cm^{-1}$; A_k = coefficient related to the chemical composition of the melt; E = activation energy of conductance; T = temperature of the melt, in °K; R = universal gas constant, 8.3143 J $mol^{-1}\ K^{-1}$ = 1.987 cal $mol^{-1}\ K^{-1}$.

Morrissey (12) suggested that the coefficients in conductivity-temperature Eq. [1] can be rearranged to render it advantageous to practical cryolitic systems. The parameters required for computing the coefficients can be chosen from the ones commonly encountered in systems of alumina reduction cells. In the present work, the contemplated condition has been met by development of an equation in the form

$$\ln k = A_0 + A_1X_1 + A_2X_2 + A_3X_3 + A_4X_4 + A_5X_5 + A_6X_6 + A_7X_7 + A_8/T \quad [2]$$

where A_0, A_1, A_2, etc. are constants and X's are X_1 = w/o Al_2O_3; X_2 = w/o CaF_2; X_3 = w/o MgF_2; X_4 = w/o LiF; X_5 = w/o Li_3AlF_6; X_6 = w/o NaCl; X_7 = bath-weight ratio: NaF/AlF_3; T = bath temperature, K. The expression of composition in weight per cent and ratio of weights has been chosen because these measures are in conformity with the normal practices in industry.

The unknown constants of Eq [2] were determined by a multiple "least squares" regression program performed by an 1130 IBM computer. A total of 305 electrical conductivity values, covering the composition range normally used in cells for aluminum production, as extracted from the preferred conductivity-temperature diagrams from the references given in Table I, and some taken from the direct measurements of Richards (13) in a 10 kA aluminum reduction cell, yielded the coefficients for the equation as given in the following electrical conductivity equation

$$\ln k = 2.0156 - 0.0207X_1 - 0.0050X_2 - 0.0166X_3 + 0.0178X_4 + 0.0077X_5 + 0.0063X_6 + 0.4349X_7 - 2068.4/T \quad [3]$$

The regression program yielded the square of the multiple correlation coefficient (R^2) of 0.3744 which predicts the error in correlation, thus indicating that

Table II. Comparison of the calculated electrical conductivities of cryolitic bath vs. the observed values
(References for $k_{obs.}$ are shown in parenthesis)

Bath additives, w/o						NaF/AlF_3		$k_{obs.}$,	$k_{calc.}$ from Eq. [3],	
Al_2O_3	CaF_2	MgF_2	LiF	Li_3AlF_6	NaCl	weight ratio	Temp, °C	$ohm^{-1}\ cm^{-1}$	$ohm^{-1}\ cm^{-1}$	% error
						1.50	1000	2.82 (2)	2.84	+0.7
						1.29	1000	2.56 (3)	2.59	+1.2
						1.16	1000	2.44 (3)	2.45	+0.4
						1.25	1010	2.69 (5)	2.58	−4.1
						1.50	1020	2.94 (2)	3.02	+2.9
7.0				4.0		1.50	1000	2.47 (7)	2.57	+2.5
2.0					3.0	1.50	1000	2.87 (2)	2.76	−3.3
5.0					7.0	1.50	1000	2.76 (2)	2.68	−3.1
5.0	10.0	3.0				1.38	1000	2.20 (8)	2.19	−0.1
9.0						1.50	1000	2.41(2)	2.36	−2.4
10.0				2.0		1.50	1000	2.35 (7)	2.34	−0.3
1.5						1.50	978	2.76 (13)	2.67	−3.1
3.0	8.0					1.50	980	2.43 (5)	2.50	+3.0
5.0	2.0	6.0				1.38	1000	2.20 (8)	2.17	−1.3
5.0	9.0	1.0				1.38	1000	2.25 (8)	2.28	+1.3
					4.0	1.35	1000	2.66 (7)	2.73	+2.5
10.0			10.0			1.50	1000	2.35 (7)	2.44	+4.0
6.0				3.0		1.50	1000	2.51 (7)	2.56	+2.2
			7.0			1.35	1000	3.01 (8)	3.02	+0.1
5.0	3.0	3.0	1.0			1.35	1000	2.42 (10)	2.35	+3.0
2.0					2.0	1.50	1000	2.85 (8)	2.76	−3.3
2.0						1.50	1020	2.84 (13)	2.79	−1.7
2.5	7.9					1.41	992	2.44 (13)	2.47	+1.1
5.0					9.0	1.45	1000	2.75 (8)	2.65	−3.6
5.0	5.0	5.0				1.38	1000	2.20 (8)	2.18	−1.1
5.0					1.0	1.38	1000	2.55 (1)	2.45	−4.0
			3.0			1.50	1000	2.88 (1)	2.99	+4.0
3.1						1.49	1018	2.80 (13)	2.71	−3.2
5.3	7.9					1.42	988	2.32 (13)	2.32	0.0
8.0						1.50	1020	2.53 (13)	2.47	−2.5
2.0				5.0		1.50	1000	2.91 (7)	2.83	−2.7
				7.0		1.50	1000	2.97 (1)	2.99	+0.7
8.0	3.5	4.7				1.27	970	1.92 (4)	1.89	−1.1
1.0	8.0					1.50	980	2.55 (5)	2.60	+2.1
			10.0			1.35	1000	3.14 (9)	3.18	+1.2
			2.0			1.35	1000	2.80 (9)	2.75	−1.6

37.4% of the variation in the dependent variable (ln k) is due to the influence of the independent variables. The value of R (0.6119) indicates a fair closeness to a good fit (14) to the "least squares" plane. The mean deviation from the observed values of the electrical conductivity is 0.1144 ohm^{-1} cm^{-1} which is 4% of the accepted value (15) of 2.82 ohm^{-1} cm^{-1} for pure cryolite ($3NaF \cdot AlF_3$) at 1000°C. Table II shows a comparison of some 36 representative electrical conductivity values as calculated from Eq. [3] with those observed by different investigators, from the total population of 305 experimental points used to develop Eq. [3].

Since the electrical conductivity equation covers a broad range of compositions of practical cryolitic systems, it can be recommended for use in alumina reduction cells within the ranges of temperature and chemical composition specified above and illustrated in Table II.

Acknowledgments

This work was done in the Reduction Research Division of Reynolds Metals Company, Sheffield, Alabama.

I wish to thank Mr. W. E. Watts and Dr. N. E. Richards of the Reduction Research Division of Reynolds Metals Company for programming the computations and for assistance while revising the manuscript, respectively. Permission of Reynolds Metals Company to publish this work is gratefully acknowledged.

Manuscript submitted Aug. 3, 1971; revised manuscript received Nov. 16, 1972.

Any discussion of this paper will appear in a Discussion Section to be published in the December 1973 JOURNAL.

REFERENCES

1. K. Grjotheim, M. Malinovsky, and K. Matiasovsky, *J. Metals*, 28 (1969).
2. K. Matiasovsky, M. Malinovsky, and S. Ordzovsky, *This Journal*, **111**, 973 (1964).
3. W. B. Frank and L. M. Foster, *J. Phys. Chem.*, **64**, 310 (1960).
4. A. I. Belyaev and Ye. A. Zhemchuzhina, *Tsvetn. Metal.*, **1**, 58 (1960).
5. E. W. Yim and M. Feinleib, *This Journal*, **104**, 622 (1957).
6. E. Bataslavik and A. I. Belyaev, *Zh. Neorgan. Khim.*, **3**, 1044 (1958).
7. K. Matisovsky, V. Danek, and M. Malinovsky, *This Journal*, **116**, 1381 (1969).
8. A. I. Belyaev, "Electrolit Aluminievikh. Vann," Metallurgical Press, Moscow (1961).
9. A. V. Vakhobov and A. I. Belyaev, in "Fizicheskaya Khimia Rasplavlnnykh Solei," edited by The Institute of General and Inorganic Chemistry of the Soviet Academy of Sciences, Metallurgizdat, Moscow (1965).
10. A. V. Vakhobov and A. I. Belyaev, *Russ. Met. Mining*, **4**, 55 (1964).
11. H. Bloom and E. Heymann, *Proc. Roy. Soc. (London)*, **A188**, 392 (1947).
12. H. A. Morrissey, Reynolds Metals Company Internal Report (1963).
13. N. E. Richards, S. Gjerstad, T. J. Johnston, and J. O. Cook, Reynolds Metals Company, Sheffield, Alabama, Internal Report (1967).
14. W. Joseph Dixon, "Introduction to Statistical Analysis," Chapter 11, McGraw-Hill, New York (1969).
15. G. Choudhary, Reynolds Metals Company, Sheffield, Alabama, Internal Report (1971).

Polarographic Behavior of MoO_3 in Butyrolactone Solutions

Luigi Campanella and Gianfranco Pistoia

Instituto di Chimica Analitica and Instituto di Chimica Fisica, Universtà, Rome, Italy

Molybdenum trioxide has been shown (1) to be a suitable positive electrode in a nonaqueous secondary battery based on butyrolactone (BL) as solvent

$$Li/LiAlCl_4 - BL/MoO_3, C \qquad [1]$$

The reduction of MoO_3 in a cell [1] is more complicated than the simple reduction to lower oxides (Mo_2O_5, MoO_2), as evidenced by thermodynamic considerations, and the electrolyte seems able to participate in some way in the process occurring at the positive electrode.

With the aims of elucidating some aspects of these processes, a polarographic study of the cathodic behavior of MoO_3 dissolved in some BL solutions has been performed. Furthermore, through coulometric analysis the number of electrons involved in the reduction process has been determined, by means of which the cathodic efficiency of cell [1] can be calculated.

Experimental

Apparatus.—Polarographic curves have been obtained with an AMEL Model 461 polarograph using a stationary Pt working electrode *vs.* a saturated calomel electrode (SCE), connected to the working electrode half cell by means of a KNO_3 agar bridge, suitably probe shaped in order to reduce the ohmic drop due to the solution. The potential scanning rate (from 0 to negative values) was 0.1 V/min. All the polarographic curves were reproducible within about 5%.

Key words: nonaqueous batteries, MoO_3, lithium.

Techniques.—The saturated solutions of MoO_3 in butyrolactone were prepared by equilibrating an excess of MoO_3 in stirred BL and then by filtering under vacuum. The concentration of MoO_3 was determined by spectrophotometric analysis for molybdenum and was of the order of $10^{-4}M$. The solvent used for the equilibration also contained the supporting electrolyte. Four different electrolytes at concentration $10^{-2}M$ were employed: $LiAlCl_4$, $NaBF_4$, $LiClO_4$, LiCl. Their influences on the solubility of MoO_3 was small. The solutions to be polarographed were deoxygenated with pure N_2. All the manipulations and measurements were performed in a dry box under a dry argon atmosphere, so that the water content can be reasonably assumed not higher than 10 ppm.

Materials.—BL was purified by fractional-vacuum distillation. In this way, according to Foley and Bogar (2), a product containing less than 10 ppm organic impurities and water can be obtained. Commercial high purity $NaBF_4$ and LiCl were dried under vacuum without further purification. Dry $LiClO_4$ was obtained by melting under vacuum the anhydrous commercial product. $LiAlCl_4$ was prepared according to the method described by Rao (3).

Results and Discussion

The reduction behavior of MoO_3 is affected by the supporting electrolyte, the number of involved electrons alone being always the same. In fact, by coulometric analysis, all the reduction processes are found

to involve two electrons, that is, reduction proceeds from Mo(VI) to Mo(IV). The cathodic efficiency was calculated to be 66% for cell [1] at 1 mA/cm^2 current density of discharge (1).

In $LiAlCl_4$ and $NaBF_4$ a quasi reversible ($\alpha = 0.9$) reduction wave was only observed with $E_{1/2} = -1.04$V (*vs.* SCE). The adopted reversibility criteria were based on the logarithmic analysis, on the values of the temperature coefficient of the wave height (di_d/dT, where i_d is limiting current, and T is temperature) and half-wave potential ($dE_{1/2}/dT$), and on ($E_{3/4} - E_{1/4}$) values.

In LiCl two waves were observed, the first of which was irreversible, having $E_{1/2} = -0.32$V (*vs.* SCE) and the second quasi reversible ($\alpha = 0.9$) with $E_{1/2} = -1.02$V (*vs.* SCE).

In $LiClO_4$ one wave is observed characterized by $\alpha = 0.5$ and $E_{1/2} = -0.36$V (*vs.* SCE).

The experimental results can be explained by considering the possibility that molybdenum is made complex by the anion of the supporting electrolyte. So when $LiClO_4$ is used as the supporting electrolyte, the reduction wave of free molybdenum is observed, whereas when $LiAlCl_4$ and $NaBF_4$ are used only the complex molybdenum wave is recorded. In LiCl, both the reductions, *i.e.*, of complex and free molybdenum, were evidenced.

The fact that the reduction is reversible for the complex and irreversible for the free molybdenum accounts for the experimental evidence that a Li/$LiClO_4$-BL/MoO_3, C battery cannot be cycled.

Chloride ions are well-known, strong, complexing agents for molybdenum (4). The fact that in $LiAlCl_4$ (and $NaBF_4$) the wave of free molybdenum is not observed while it is still recorded in LiCl is in agreement with the expected greater concentration of Cl^- in the former electrolyte, due to the presence of $AlCl_3$. This assumption is also sustained by the following considerations. Because of the high-charge density of Li^+ and Cl^-, a strong association occurs on LiCl, as shown for instance by the low conductivity of the solutions of LiCl in cyclic esters, such as propylencarbonate (PC) and BL (5, 6). In PC the association constant of LiCl was found to be 557, while $LiClO_4$ is not associated (7). The same behavior is expected in BL which is characterized by a lower dielectric constant. A very low association, if any, must therefore also be foreseen for $LiAlCl_4$ both in PC and BL because of the reduced interaction between Li^+ and the large anion $AlCl_4^-$. Moreover, the equilibrium $AlCl_4^- \rightleftarrows AlCl_3 + Cl^-$ will be present; in PC and BL this equilibrium will be shifted to the right following the fact that the Lewis acid $AlCl_3$ is strongly coordinated by the negative dipole of the solvent (7). This coordination produces ions such as $Al(PC)_n^{3+}$ and $AlCl_4^-$ and this latter can further yield other Cl^- ions. The problem can be analogously discussed in the case of $NaBF_4$, on the basis of the similarity between the anions $AlCl_4^-$ and BF_4^-

Due to the fact that MoO_3 is sparingly soluble in $LiAlCl_4$-BL (5.10^{-4}M at 18°C), a positive electrode based on this oxide would show considerable polarization for discharge current densities of 1-2 mA/cm^2 (1), if it had previously to dissolve and form complexes with the electrolyte. Thus it is probable that MoO_3 discharges initially as such to Mo(IV) (probably in a complex form); by charging, Mo(VI), in a complex and sparingly soluble form, could be generated, and subsequently cycled.

The hypothesis seems to be confirmed by the fact that the micropolarization test previously reported (1) gives a straight line (the cathodic side on the prolongation of the anodic one) without any appreciable hysteresis, only after three or four polarization cycles.

Acknowledgment

Work carried out with the aid of Italian C.N.R.

Manuscript submitted June 14, 1972; revised manuscript received Oct. 30, 1972.

Any discussion of this paper will appear in a Discussion Section to be published in the December 1973 JOURNAL.

REFERENCES

1. L. Campanella and G. Pistoia, *This Journal*, **118**, 1905 (1971).
2. R. Foley and F. Bogar, Report N.5, NGR 09-003-005 (April 1967).
3. M. Rao, *This Journal*, **114**, 13 (1967).
4. J. C. Bailar, "The Chemistry of Coordination Compounds," p. 15, Reinhold Publishing Corporation, New York (1956).
5. R. Jasinski, "High Energy Batteries," Plenum Press, New York (1967).
6. R. Jasinski in "Advances in Electrochemistry and Electrochemical Engineering," P. Delahay, Editor, Vol. VIII, Wiley Interscience, New York (1971).
7. L. Mukherjee and D. Boden, *J. Phys. Chem.*, **73**, 3965 (1969).

Brief Communications

On the Nature of Films over Corrosion Pits in Stainless Steel

J. Yahalom[1]

Technion-Israel Institute of Technology, Haifa, Israel

and L. K. Ives and J. Kruger*

National Bureau of Standards, Washington, D. C. 20234

There is evidence that the presence of thin films over corrosion pits in stainless steel plays an important role in pit development. Rosenfeld and Danilov (1) have observed covered pits in several austenitic stainless steels; destroying the covering film led to the deactivation of the pit. Isaacs (2) made similar observations on 304 stainless steel, but found that after a sufficient length of time disrupting the film did not necessarily

* Electrochemical Society Active Member.
[1] Guest Worker at National Bureau of Standards, Washington, D. C. 20234, 1970-1971.
Key words: Fe-Cr alloys, passive films, scanning electron microscopy, transmission electron microscopy, x-ray analysis.

to involve two electrons, that is, reduction proceeds from Mo(VI) to Mo(IV). The cathodic efficiency was calculated to be 66% for cell [1] at 1 mA/cm^2 current density of discharge (1).

In $LiAlCl_4$ and $NaBF_4$ a quasi reversible ($\alpha = 0.9$) reduction wave was only observed with $E_{1/2} = -1.04$V (*vs.* SCE). The adopted reversibility criteria were based on the logarithmic analysis, on the values of the temperature coefficient of the wave height (di_d/dT, where i_d is limiting current, and T is temperature) and half-wave potential ($dE_{1/2}/dT$), and on ($E_{3/4} - E_{1/4}$) values.

In LiCl two waves were observed, the first of which was irreversible, having $E_{1/2} = -0.32$V (*vs.* SCE) and the second quasi reversible ($\alpha = 0.9$) with $E_{1/2} = -1.02$V (*vs.* SCE).

In $LiClO_4$ one wave is observed characterized by $\alpha = 0.5$ and $E_{1/2} = -0.36$V (*vs.* SCE).

The experimental results can be explained by considering the possibility that molybdenum is made complex by the anion of the supporting electrolyte. So when $LiClO_4$ is used as the supporting electrolyte, the reduction wave of free molybdenum is observed, whereas when $LiAlCl_4$ and $NaBF_4$ are used only the complex molybdenum wave is recorded. In LiCl, both the reductions, *i.e.*, of complex and free molybdenum, were evidenced.

The fact that the reduction is reversible for the complex and irreversible for the free molybdenum accounts for the experimental evidence that a Li/$LiClO_4$-BL/MoO_3, C battery cannot be cycled.

Chloride ions are well-known, strong, complexing agents for molybdenum (4). The fact that in $LiAlCl_4$ (and $NaBF_4$) the wave of free molybdenum is not observed while it is still recorded in LiCl is in agreement with the expected greater concentration of Cl^- in the former electrolyte, due to the presence of $AlCl_3$. This assumption is also sustained by the following considerations. Because of the high-charge density of Li^+ and Cl^-, a strong association occurs on LiCl, as shown for instance by the low conductivity of the solutions of LiCl in cyclic esters, such as propylencarbonate (PC) and BL (5, 6). In PC the association constant of LiCl was found to be 557, while $LiClO_4$ is not associated (7). The same behavior is expected in BL which is characterized by a lower dielectric constant. A very low association, if any, must therefore also be foreseen for $LiAlCl_4$ both in PC and BL because of the reduced interaction between Li^+ and the large anion $AlCl_4^-$. Moreover, the equilibrium $AlCl_4^- \rightleftarrows AlCl_3 + Cl^-$ will be present; in PC and BL this equilibrium will be shifted to the right following the fact that the Lewis acid $AlCl_3$ is strongly coordinated by the negative dipole of the solvent (7). This coordination produces ions such as $Al(PC)_n^{3+}$ and $AlCl_4^-$ and this latter can further yield other Cl^- ions. The problem can be analogously discussed in the case of $NaBF_4$, on the basis of the similarity between the anions $AlCl_4^-$ and BF_4^-

Due to the fact that MoO_3 is sparingly soluble in $LiAlCl_4$-BL (5.10^{-4}M at 18°C), a positive electrode based on this oxide would show considerable polarization for discharge current densities of 1-2 mA/cm^2 (1), if it had previously to dissolve and form complexes with the electrolyte. Thus it is probable that MoO_3 discharges initially as such to Mo(IV) (probably in a complex form); by charging, Mo(VI), in a complex and sparingly soluble form, could be generated, and subsequently cycled.

The hypothesis seems to be confirmed by the fact that the micropolarization test previously reported (1) gives a straight line (the cathodic side on the prolongation of the anodic one) without any appreciable hysteresis, only after three or four polarization cycles.

Acknowledgment

Work carried out with the aid of Italian C.N.R.

Manuscript submitted June 14, 1972; revised manuscript received Oct. 30, 1972.

Any discussion of this paper will appear in a Discussion Section to be published in the December 1973 JOURNAL.

REFERENCES

1. L. Campanella and G. Pistoia, *This Journal*, **118**, 1905 (1971).
2. R. Foley and F. Bogar, Report N.5, NGR 09-003-005 (April 1967).
3. M. Rao, *This Journal*, **114**, 13 (1967).
4. J. C. Bailar, "The Chemistry of Coordination Compounds," p. 15, Reinhold Publishing Corporation, New York (1956).
5. R. Jasinski, "High Energy Batteries," Plenum Press, New York (1967).
6. R. Jasinski in "Advances in Electrochemistry and Electrochemical Engineering," P. Delahay, Editor, Vol. VIII, Wiley Interscience, New York (1971).
7. L. Mukherjee and D. Boden, *J. Phys. Chem.*, **73**, 3965 (1969).

Brief Communications

On the Nature of Films over Corrosion Pits in Stainless Steel

J. Yahalom[1]

Technion-Israel Institute of Technology, Haifa, Israel

and L. K. Ives and J. Kruger*

National Bureau of Standards, Washington, D. C. 20234

There is evidence that the presence of thin films over corrosion pits in stainless steel plays an important role in pit development. Rosenfeld and Danilov (1) have observed covered pits in several austenitic stainless steels; destroying the covering film led to the deactivation of the pit. Isaacs (2) made similar observations on 304 stainless steel, but found that after a sufficient length of time disrupting the film did not necessarily

* Electrochemical Society Active Member.
[1] Guest Worker at National Bureau of Standards, Washington, D. C. 20234, 1970-1971.
Key words: Fe-Cr alloys, passive films, scanning electron microscopy, transmission electron microscopy, x-ray analysis.

lead to a cessation of pit growth. In both of these investigations the covering films were referred to as being exposed passive film material that originally existed on the metal surface. However, the composition and structure of the films were not described or compared in any way with those of the passive film. It was the purpose of the present investigation to examine such films found over pits in ferritic and austenitic stainless steels by means of transmission electron microscopy (TEM) and scanning electron microscopy (SEM). In addition, the SEM was equipped with an energy dispersive x-ray detector making it possible to obtain a semiquantitative analysis of the chemical composition of the films for elements above 11 in atomic number.

In order to prepare the films for study by the above methods, a technique was used which was similar to that employed by Yahalom and Weisshauss (3) in a recent investigation of pitting in nickel. When pits were allowed to penetrate very thin rolled-sheet specimens, they found that films remained stretched over the resultant holes. These films were amenable to study by TEM.

Experimental

The materials consisted of a series of high purity ferritic Fe-Cr alloys containing approximately 5, 12, and 19 weight per cent (w/o) Cr [analysis given in Ref. (5)] and two commercial austenitic stainless steels, AISI 304 and 316. Annealed thin-sheet specimens of each alloy were electropolished in a perchloric acid-glacial acetic acid solution to obtain regions thin enough for TEM examination.

The samples were then passivated in an N_2 gas-purged, aqueous solution of 3% ammonium tartrate at the potentials shown in Table I. The potentials were chosen to be above the values usually considered to be critical to initiate pitting (4). An NaCl (or NaBr) solution was then introduced yielding the Cl^- (or Br^-) ion concentrations indicated in Table I. Anodic polarization was continued until the specimens were visibly perforated by pitting.

Results and Discussion

When a pit perforated a foil, a film was typically observed to remain over the resultant hole (Fig. 1). On TEM examination the films were often found to consist, not of a single film, but of two overlapping films usually with entrapped particles or corrosion products (Fig. 1). One film (the back surface film) was the passive film which was exposed when the pit penetrated the foil to produce a hole. The other film (the front surface film) had its origin on the surface at which the pit initiated. An example of a pit with the front surface film visible is shown in Fig. 2. From observations of the broken edges of films their individual thicknesses were estimated to be on the order of 50Å.

Electron diffraction patterns from films over pits in the austenitic 304 and 316 alloys consisted of four or five very broad and diffuse rings, suggesting an amorphous structure. Corresponding TEM images at high magnification showed a fine grain-like morphology on the order of 20Å. Front and back surface films did not appear to be significantly different. Images of films from the ferritic alloys were similar to those from the austenitic alloys. However, the ferritic alloy films produced distinct diffraction spots which, in the case of the 12 and 19% alloys, were present together with diffuse rings. The spot patterns were usually quite symmetrical in appearance, suggesting a single-crystal structure. But, on studying dark field images of the films, it was found that the spots were produced by very small crystallites and that different sets of crystallites, crystallographically oriented with respect to one another, were responsible for the different diffraction spots. Similar diffraction patterns were obtained from the passive films on the metal foil surface, indicating that by this measure the passive film and films over pits were the same. It was not possible to determine the crystal structure of the films on the basis of the electron diffraction results because of the limited number of diffraction spots present and relatively large scatter in the measured values. McBee and Kruger (5) have studied passive films produced in 1*N* H_2SO_4 on the same series of ferritic alloys and found that oxides with a spinel structure were present.

Semiquantitative analyses of the compositions of films from the 12% Cr, 304, and 316 alloys were ob-

Table I. Conditions for pitting

Alloy	Halide ion conc.	Anodic polarization potential (mV SCE)
Fe-5% Cr	0.1*N* Cl^-	+300
Fe-12%	0.1*N* Cl^-	+300
Fe-19%	0.2*N* Cl^-	+700
304	0.1*N* Cl^-	+400
316	1.0*N* Cl^-	+425
316	0.3*N* Br^-	+700

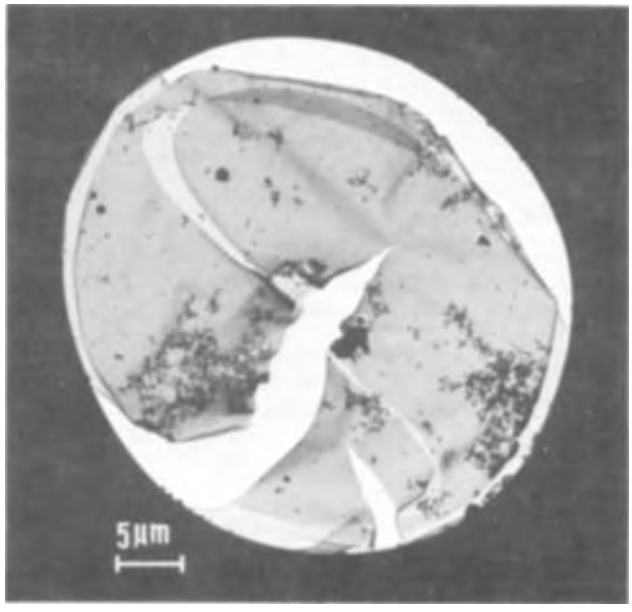

Fig. 1. Transmission electron micrograph of film covering hole left by corrosion pit in 316 stainless steel. Two overlapping films are present. Corroding solution contained 0.3M NaBr.

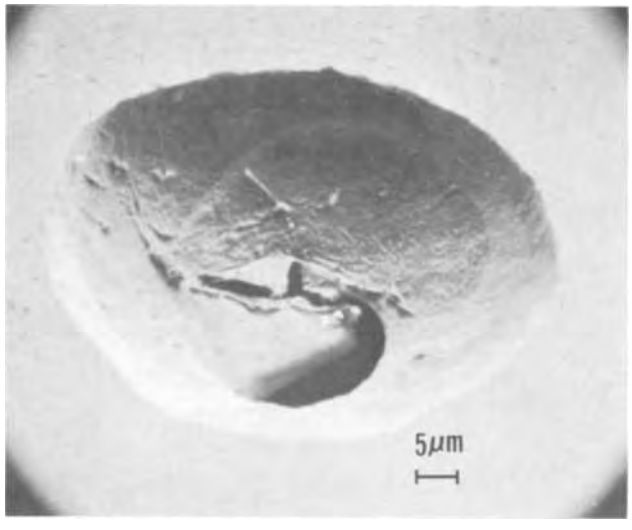

Fig. 2. Scanning electron micrograph of pit in 316 stainless steel corroded in 0.3M NaBr. A film has collapsed to the inside surface of the pit (dark area) and extends across the hole where the pit has penetrated the metal foil.

tained by utilizing energy dispersive x-ray analysis facilities attached to the SEM. To avoid spurious x-ray signals from the metal, the films were cemented to thin tungsten wires and pulled from the foil pits. Films were not successfully extracted from the 5% and 19% Cr alloys. For the films studied, the ratio of Cr to Fe ranged from approximately 2:1 to 5:1 or more, which is considerably larger than the corresponding alloy composition ratio. A large scatter in results did not permit a meaningful quantitative comparison among films from different alloys to be made. Among the other elements found, chlorine was usually detected in films from alloys corroded in solutions containing that element. However, bromine was not detected in films from the 316 stainless steel corroded in a solution containing NaBr. Molybdenum was detected in the 316 films, but nickel was not detected in the 304 or 316 films.

In conclusion, thin films that covered corrosion pits in a series of ferritic Fe-Cr alloys and two commercial stainless steels, 304 and 316, were studied by means of TEM and SEM. Corrosion pits completely penetrated the foils leaving holes that were covered by two overlapping films—one from the entrant opening of the pit and the other exposed when the pit penetrated the back surface of the thin foil sample. The two films appeared comparable in microstructure and produced similar electron diffraction patterns. Since the back surface film did not enter into the pitting process and was the passive film exposed when penetration occurred, these observations indicate that films covering the entrant openings of pits were originally passive film. This is further supported by the fact that electron diffraction results from passive films and films covering pits are similar.

Manuscript received Oct. 30, 1972.

Any discussion of this paper will appear in a Discussion Section to be published in the December 1973 JOURNAL.

REFERENCES

1. I. L. Rosenfeld and I. S. Danilov, Proc. Third Intern. Cong. Metallic Corrosion, Moscow, 1966, Vol. I, p. 139.
2. H. S. Isaacs, The U. R. Evans International Conference on Localized Corrosion, Williamsburg, Va., 1971, In press.
3. J. Yahalom and I. Weisshauss, The U. R. Evans International Conference on Localized Corrosion, Williamsburg, Va., 1971, In press.
4. J. M. Kolotyrkin, *Corrosion*, **19**, 261t (1963).
5. C. L. McBee and J. Kruger, *Electrochemica Acta*, **17**, 1337 (1972).

Studies on Ignition Characteristics and Combustion Mechanism of Magnesium in a Chlorine Atmosphere

K. Elguindi and H. Sullivan

Department of Mechanical Engineering, University of Waterloo, Waterloo, Ontario, Canada

and D. R. Spink*

Department of Chemical Engineering, University of Waterloo, Waterloo, Ontario, Canada

The present study was carried out as a basic investigation of the mechanism and kinetics of the reduction reaction between metal halides and magnesium. Examples of metal halides reduced commercially with magnesium include zirconium tetrachloride, titanium tetrachloride, hafnium tetrachloride, and uranium tetrafluoride. Later studies of the zirconium or titanium tetrachloride-magnesium reaction with magnesium as the fuel burning in an atmosphere of zirconium or titanium tetrachloride are planned.

No data could be found in the literature on the ignition and combustion of magnesium in chlorine or other single halide atmospheres. Extensive data are available (1-5, 9, 10) on magnesium ignition and combustion in several other gases; these investigations were carried out relative to propulsion and aerospace applications.

Although ignition and combustion of magnesium in chlorine differs basically from that of magnesium in other gaseous oxidizers, the fundamental approaches used in carrying out the studies are essentially the same. Theoretical studies and experimental work in combustion laboratories have shown that magnesium burns in the vapor phase under certain oxygen partial pressures when an inert gas is used as a diluent (1). This work is concerned with the fundamental investigation of ignition and combustion of magnesium metal in a chlorine atmosphere.

* Electrochemical Society Active Member.
Key words: combustion, magnesium, chlorine, ignition, reaction, mechanism.

Experimental Techniques and Procedures

Two approaches were employed to carry out the present investigations. In the first tests, attempts were made to ignite magnesium ribbons by passing electrical current though the sample. In these tests combustion could not be sustained. The samples merely heated up until local melting broke the ribbon and interrupted the heating current. It was concluded from these tests that the ignition temperature of magnesium in chlorine atmospheres is above the melting point of magnesium, 650°C. In oxygen atmospheres, magnesium ignites below its melting point (2).

In the second series of tests, induction heating was used to ignite magnesium particles. Induction heating provides predominantly surface heating that emphasizes pre-ignition oxidation as would be found in practice in reduction reactors. Magnesium particles of sizes ranging from 1-5 mm were placed on the surface of a pure calcium oxide bed in a Pyrex glass chamber situated within the work coil of the induction furnace. The gas within the chamber consisted of chlorine or a mixture of chlorine and inert gas (argon or helium).

In addition to visual observations, high speed, colored motion pictures and flame spectra were obtained. Tests were made at pressures up to 1500 Torr with compositions ranging from pure chlorine to almost pure diluent gas.

Ignition temperature measurement.—A Chromel-Alumel thermocouple with a 1/16 in. OD stainless steel

shield was used for the temperature measurements. The temperature was recorded using a 2-channel temperature module, Model 17502A, made by Hewlett Packard Company.

The magnesium sample was mounted on the tip of the thermocouple but supported by a 2.0 cm diameter ceramic disk that was in turn supported by the stainless steel thermocouple shield. The sample and the associated thermocouple were placed in a Pyrex glass tube which was positioned exactly at the center of the work coil of the induction furnace. In these experiments 100% Cl_2 at 500 and 760 Torr were used.

Results and Discussion

Ignition phenomenon of magnesium in chlorine.—In the experiments carried out under different conditions of pressure and concentration of chlorine in the total oxidizing gas mixture, the magnesium particle was observed to ignite only after complete melting as indicated by the formation of a spherical droplet of metal.

In a chlorine atmosphere it was observed that the magnesium formed a thin chloride layer on its surface prior to ignition, similar to the oxide formed in combustion in an oxygen atmosphere. Although the sample was initially cleaned in dilute hydrochloric acid, a very thin oxide layer was always present due to exposure to air. Thus it was concluded that the layer formed on the sample before ignition was a mixture of magnesium oxide and magnesium chloride. However, positive identification by specific analytic techniques has not been undertaken.

Flashing or sparking from the metal surface was observed just before ignition took place for those cases where relatively low pressures of the chlorine-inert gas mixture was used *i.e.*, < 760 Torr total pressure. This phenomenon may be related to a pressure build-up of magnesium vapor beneath the coating on the particle, although in no instance did the vapor pressure of magnesium equal the pressure in the container. Following flashing, the entire sample was almost instantaneously engulfed in flame. As the total pressure was increased (to 1000-1500 Torr), the ignition process became more violent and usually the sample ignited so explosively that unreacted magnesium droplets spattered on the walls of the vessel. This was apparently related to the protective qualities of the coating formed on the sample surface. Just prior to ignition, fissures appeared in the molten coating on the magnesium which likely relates to the surface tension of the coating *vis-à-vis* the vapor pressure of the magnesium. This observation, coupled with the fact that magnesium melts at 650°C and that magnesium chloride melts at 712°C, provided visual evidence that the ignition temperature was greater than either of these temperatures. The high speed, colored movies of the ignition sequence were used for most of the visual observations.

Measurement of ignition temperature.—Ignition occurred above the melting point of both the magnesium and magnesium chloride in all the runs carried out in this part of the work and under all the conditions of the experiments. This was an important observation for it supported an explanation accounting for the failure of the resistance heating tests to provide combustion, namely, that the ignition of magnesium in chlorine took place above the melting point of the magnesium.

Ignition, for the most part, occurred within a temperature range of 850° to 1100°C as indicated below. Several variables seemed to have an important influence on the ignition temperature:

1. Heating rate: the ignition temperature was observed to decrease from approximately 980° to 860°C as the heating rate increased from approximately 50° to 100°C/sec. This is not in agreement with what was concluded by Mellor (2) in his experimental work involving the ignition of magnesium cylinders (2.38 cm diam by 3.8 cm length) and magnesium wafers (3.28 cm diam by 1.59 mm thick) in oxygen atmospheres in an induction furnace in which he stated that any dependence on the heating rate was slight. It is possible that sample size might be responsible for some of these observed differences plus the fact that MgO films are rigid and porous and therefore might be less effective with increasing thickness than an impervious film such as that formed by $MgCl_2$. In the present work where relatively slow heating was employed, occasionally ignition of the sample did not occur below 1000°C. Possibly, at the high heating rates, some temperature lag could have distorted the observed results, but not by more than 40°C (See below). Upon heating the magnesium specimens the thermocouple indicated the melting point of magnesium to be at or slightly below the accepted value of 650°C; the faster the heating rate, the lower the melting point indication. Some samples, after heating to temperatures of approximately 900°C without ignition, exhibited freezing point arrests at exactly 650°C on cooling.

2. Sample size: The ignition temperature increased generally as the sample size decreased. Two sizes, however, were used in these experiments, 3 and 5 mm cubes. The 5 mm size gave an average ignition temperature of 900°C, while the 3 mm size gave an average of 950°C. This, however, seems to be a very small effect under the present experimental conditions. The work of Cassel and Liebman (6), and Mellor's work (2) showed this same effect in more detail over a wide range of sizes in other gases.

3. Total gas pressure: The ignition temperature was found to be somewhat dependent on pressure, increasing from approximately 850° to 980°C with an increase in pressure from 500 to 760 Torr under constant heating rates.

In the ignition runs conducted at high-heat-up rates, it was impossible to detect the ignition temperature within 20°-40°C, and this temperature range combined with an observed melting point lag of approximately 10°C gave an uncertainty of as much as 50°C in the ignition temperature.

Because the ignition temperature could be varied considerably by the heat-up rate, further work was abandoned in this area. The most significant result of this phase of the investigation was that $T_{ign} >> 650$°C.

Effect of ambient pressure.—One of the more interesting factors influencing ignition was the total pressure of chlorine used. A series of experiments were carried out at ambient pressures of 300, 500, 760, and 1000 Torr, all other experimental conditions being held constant. Thus a constant partial pressure ratio of chlorine to argon of 2:1, constant particle size of magnesium (3 mm cubes), and constant heating rates were maintained throughout the experiments.

At comparatively high pressures (760 and 1000 Torr), it took a longer time to ignite the samples than at 500 Torr. Thus, at the higher pressure, higher ignition temperatures could be expected and accordingly were measured at 500 and 760 Torr as reported earlier, *i.e.*, the ignition temperature was 850°C at 500 Torr and 980°C at 760 Torr.

In several experiments, slow heating of the magnesium led to great difficulty in igniting the sample; some samples were held for several minutes at temperatures well above 1000°C without ignition. Under these conditions, the vapor pressure of the magnesium approached the total pressure in the vessel. This was thought to be due to the greater protection offered by a thicker chloride (-oxide) layer formed on the surface of the molten magnesium during the slower heat-up period.

It was shown that an increase of the partial pressure of chlorine up to a certain limit would speed up the ignition process, while an increase in the total pressure at constant chlorine content retarded the ignition process.

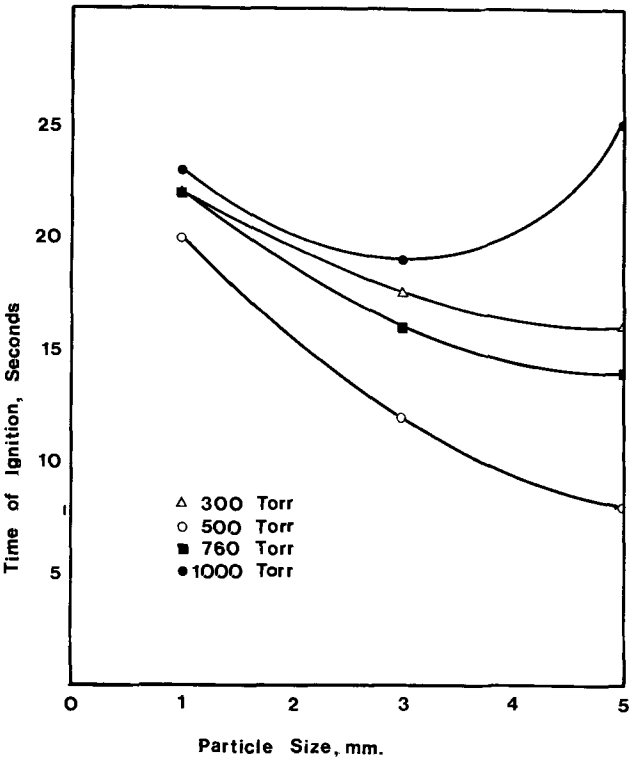

Fig. 1. Variation in time of ignition with particle size and chlorine pressure.

Effect of sample size on the time required for ignition.—Magnesium of 1, 3, and 5 mm sizes were ignited in 100% chlorine at pressures of 300, 500, 760, and 1000 Torr. Each run was repeated three times and the results averaged. Time of ignition was taken from the start of power input to the induction coil to the ignition point. The experimental results are shown in Fig. 1.

From Fig. 1, it can be observed that for the constant pressure experiments, the ignition time for small particles was longer. This could be indicative of a higher ignition temperature on one hand or a slower induction heating of smaller particles with smaller surface area on the other hand.

The sample surface to volume ratio used in the present work were 6, 2, and 1.33 mm^{-1} corresponding to 1, 3, and 5 mm cubes, respectively. Thus, the surface to volume ratio used in this work may be compared to the larger particle sizes that Mellor used in his experiments. Mellor (2) studied the ignition characteristics of magnesium in oxygen and CO_2 gases and found that by merely changing the sample surface area to volume ratio, the ignition temperature reverses its dependence on pressure. The present work does not show this relationship (see Fig. 1), if it is assumed that the observed relationship between time of ignition and ignition temperature is valid.

Spectrographic observations and chemical reaction mechanism.—Spectrography can be used as a tool to investigate the combustion reaction and further, to postulate the reaction mechanism. Emission spectra of the flame of magnesium burning in chlorine gas were recorded at different pressures and chlorine concentrations. Spectra were recorded for flames with 30-100 volume per cent (v/o) Cl_2 in the gaseous oxidizer mixture of chlorine and helium, and 500-1000 Torr total pressure.

Spectral features of MgCl were observed resulting from the $^2\pi$-$^3\Sigma$ transition at 3780, 3775, and 3770Å. Also, the magnesium singlet at 4571.15Å as well as other magnesium lines at 5167 and 5183Å, were recorded.

In addition, other lines and bands were recorded as impurities in the flame. The two Na lines at 5889.95 and 5895.22Å and the Ca line at 4227.73Å were observed. Identification of the atomic and molecular spectra was carried out with the aid of tables (7).

The existence of magnesium lines in the spectrum proved the existence of magnesium atoms in the vapor phase in the flame.

The presence of MgCl in the flame indicates that MgCl in the vapor phase is most probably an intermediate product in the combustion reaction.

From the spectrographic results, the steps of the reaction mechanism have been postulated as follows

$$Mg_{(c)} \rightarrow Mg_{(l)} \rightarrow Mg_{(v)} \quad [1]$$

The following reactions then occur in the vapor phase

$$Mg + Cl_2 \rightarrow MgCl + Cl \quad [2]$$

$$Mg + Cl \rightarrow MgCl \quad [3]$$

$$MgCl + Cl_2 \rightarrow MgCl_2 + Cl \quad [4]$$

$$MgCl + Cl \rightarrow MgCl_2 \quad [5]$$

The dichloride vapor then condenses rapidly and exothermically as follows

$$MgCl_{2(v)} = MgCl_{2(c)} \quad [6]$$

$$\Delta H = -32.7 \text{ kcal (11)}$$

The over-all reaction can thus be written

$$Mg_{(c)} + Cl_2 = MgCl_{2(c)}$$

$$\Delta H = -153.2 \text{ kcal at } 298°K \text{ (11)}$$

Summary and Conclusions

Visual observations, spectroscopy, and high-speed photography were the main tools used in this study. The work may be summarized by the following points.

1. Individual magnesium particles were observed to ignite only after they had melted and formed droplets with a thin protective oxide-chloride coating covering their surface.

2. The ignition temperature of magnesium in chlorine was measured at 760 and at 500 Torr and was found to be in the range of approximately 850°-1100°C depending on the conditions of the experiment.

3. Under most conditions there was flashing from the metal surface just before ignition took place; this could be indicative of point ignition through the protective chloride layer but where the vapor pressure of magnesium was not sufficient to sustain a flame.

4. Up to the point of ignition, heat was continuously supplied to each droplet by the induction furnace. The temperature and vapor pressure of the magnesium metal within the droplet rose gradually until ignition, after which a stable flame was established. Thus magnesium burns in chlorine by a vapor-phase diffusion phenomena in a manner similar to that of magnesium in oxygen as discussed by Coffin (8), Brzustowski and Glassman (1), and Sullivan (10). In all cases in oxygen-containing atmospheres, magnesium ignites before melting occurs which indicates that the oxide-coating on magnesium metal is porous and possibly quite rigid below the melting point of magnesium thereby facilitating diffusion of magnesium vapor from the hot magnesium surface. Magnesium vapor could also escape through faults in the oxide film.

5. Studies of the physical phenomena of combustion of magnesium in chlorine were carried out in the pressure range of 100-1500 Torr. Experimental investigations indicated that magnesium vapor plays the major role in initiating the reaction.

6. A chemical combustion mechanism of magnesium in chlorine was suggested on the basis of the experimental results. Flame spectra revealed that both MgCl bands and magnesium lines were present. The presence of MgCl in the flame suggested that MgCl is an intermediate product in the combustion reaction whereas the presence of magnesium lines indicated the presence of magnesium vapor.

The study carried out in the present work has shed some light on the problem of igniting magnesium in chlorine. It is felt that further studies of the structure of the flame on the basis of flame models in the literature may be important. Except for the ignition temperature measurements carried out in this work, the study was mainly qualitative.

Acknowledgments

The authors gratefully acknowledge financial support from the National Research Council of Canada.

Manuscript submitted March 6, 1972; revised manuscript received Oct. 8, 1972.

Any discussion of this paper will appear in a Discussion Section to be published in the December 1973 JOURNAL.

REFERENCES

1. T. A. Brzustowski and I. Glassman in "Heterogeneous Combustion," H. G. Woolfhardt, I. Glassman, and L. Green, Jr., Editors, Academic Press, New York (1964).
2. A. M. Mellor, Ph.D. Thesis, Princeton University (1967).
3. A. M. Mellor and I. Glassman, in "Heterogeneous Combustion," H. G. Woolfhard, I. Glassman, and L. Green, Jr., Editors, pp. 159-176, Academic Press, New York (1964).
4. R. A. Rhein, *Astonaut. Acta*, **11**, 322, 327 (1965).
5. J. T. Bryant and N. J. Sippel, *J. Spacecraft Rockets*, **8**, 192-93 (1971).
6. H. M. Cassel and I. I. Liebman, *Combustion Flame*, **7**, 79-81 (1963).
7. R. Pearse and A. Gaydon, "The Identification of Molecular Spectra," Chapman and Hall Ltd., London (1963).
8. K. Coffin, in 5th Symposium (International) on Combustion, Reinhold, New York (1955).
9. G. H. Markstein, *AIAA Journal*, **1**, 550-562 (1963).
10. H. F. Sullivan, Ph.D. Thesis, Princeton University (1969).
11. C. E. Wicks and F. E. Block, Bulletin 605, U.S. Bureau of Mines, U.S. Government Printing Office (1963).

JOURNAL OF THE ELECTROCHEMICAL SOCIETY

SOLID-STATE SCIENCE AND TECHNOLOGY

MARCH 1973

Kinetics and Morphological Development of the Oxide Scale on Iron at 800°C in Oxygen at 2.5×10^{-3} to 3.0×10^{-1} Torr Pressure

A. G. Goursat and W. W. Smeltzer*

Department of Metallurgy and Materials Science, McMaster University, Hamilton, Ontario, Canada

ABSTRACT

A thermogravimetric technique was employed to investigate the oxidation of iron in oxygen over the pressure range 2.5×10^{-3}-3.0×10^{-1} Torr at 800°C. The oxidation curves exhibited distinct intervals of linear kinetics followed by transitions to intervals of parabolic kinetics during exposures extending to 125 min. Linear kinetics governed the growth of uniformly thick wustite scales; the linear rate constants showed a proportional dependence on oxygen pressure due to reaction control by a phase boundary reaction involving nondissociative adsorption of oxygen. The sticking coefficient of oxygen on wustite was equal to 0.067. Parabolic kinetics governed growth of wustite-magnetite scales containing magnetite as outermost layers. The values of the parabolic rate constants were independent of oxygen pressure since scale growth was directly dependent on the iron vacancy gradient in wustite established by the oxygen activities at the Fe/FeO and FeO/Fe_3O_4 interfaces.

Several investigations have been carried out to determine the influence of oxygen pressure on the oxidation properties of iron at temperatures in the range 200°-550°C (1-6). The early oxidation stage involves processes for nucleation and growth of magnetite. Growth of hematite on a developed magnetite layer or separation of this layer from the metal leads to a decrease in the oxidation rate. Detailed information is not available, however, on iron oxidation properties at temperatures sufficiently high for formation of wustite as a scale constituent (7-12). Nucleation and growth of wustite occur in the early stage of the reaction at temperatures exceeding 600°C, growth of wustite as a layer being controlled during exposures of short duration by an oxide/gas phase boundary reaction. Growth of a wustite scale at long exposures or the growth of a multilayer scale containing wustite, magnetite, and hematite is associated with diffusional processes. Iron diffuses through wustite and magnetite, while both iron and oxygen may diffuse through hematite (13-15).

Large discrepancies occur among results reported for the influence of oxygen pressure on the form of the oxidation curve obeyed and the magnitudes of the reaction rates at temperatures in the range 600°-1000°C. The results obtained at low pressures appear to be strongly affected by the iron purity and different transport limiting factors depending on the experimental conditions (16). We have therefore systematically investigated the oxidation of high-purity iron in oxygen atmospheres at pressures ranging from 2.5×10^{-3} to 3.0×10^{-1} Torr at 800°C.

Experimental

Iron, 99.999 w/o (weight per cent) pure, was exposed to research-grade oxygen, <25 ppm impurities, in an assembly containing a continuously recording microbalance. Impurity contents of the iron are recorded in Table I.

Iron specimens were prepared by cutting disks, 0.3-1 mm thick, from the received, 1 cm diameter rod. All surfaces of these disks were subjected to abrasion on silicon carbide papers, a wax lap impregnated with 15μ alumina, and a final polish on cloths impregnated with 6 and 1μ diamond pastes using kerosene as lubricant. They were then electropolished in a 5% perchloric acid-glacial acetic acid solution and washed in distilled water and acetone. Finally the specimens were sealed in quartz tubes containing high-purity argon and annealed for 18 hr at 800°C. The metal grain size varied from 0.03 to 0.3 mm which corresponds to ASTM grain size No. 5. Before an oxidation test, an annealed specimen was resubjected to electropolishing and washing.

The thermogravimetric assembly is schematically illustrated in Fig. 1. Weight gains of specimens were determined within ±1 μg by the Cahn R. G. microbalance. The pressures of oxygen at the entrance and exit of the reaction tube were measured by Pirani gauges. These measurements were used to calculate the pressure over the exposed metal specimen assuming a linear gradient. During an experiment, oxygen was leaked from the supply tank and continuously allowed to flow through the reaction tube by means of the open Pyrex tube to the vacuum pump. A specimen was ex-

Table I. Spectrochemical analysis of high-purity iron (in ppm)

Al	Cd	Cr	Co	Cu	Mg	Mn	Mo	Si	Ti	V
Tr	Nd	Tr	Nd	10	30	Tr	Tr	30	Tr	Tr

Tr = trace.
Nd = not detected.

* Electrochemical Society Active Member.
Key words: iron oxidation, wustite-magnetite scales.

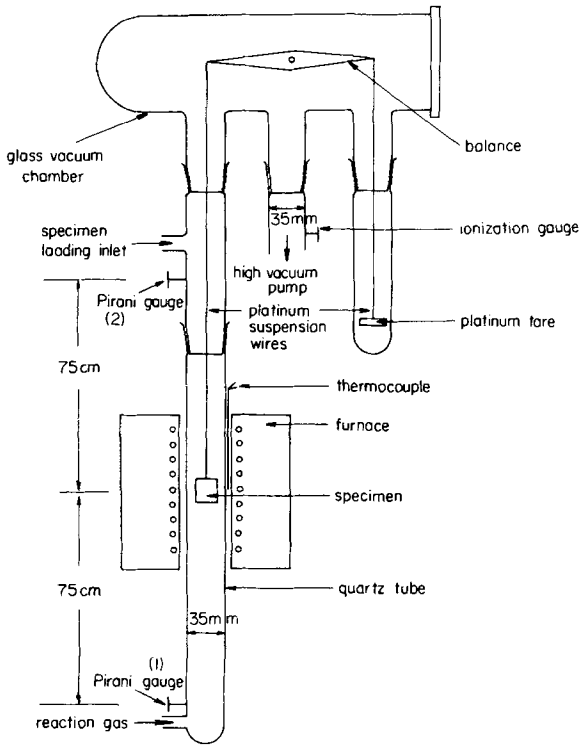

Fig. 1. Assembly containing a Cahn continuously recording R. G. microbalance. The oxygen pressure is determined by Pirani gauges at positions (1) and (2).

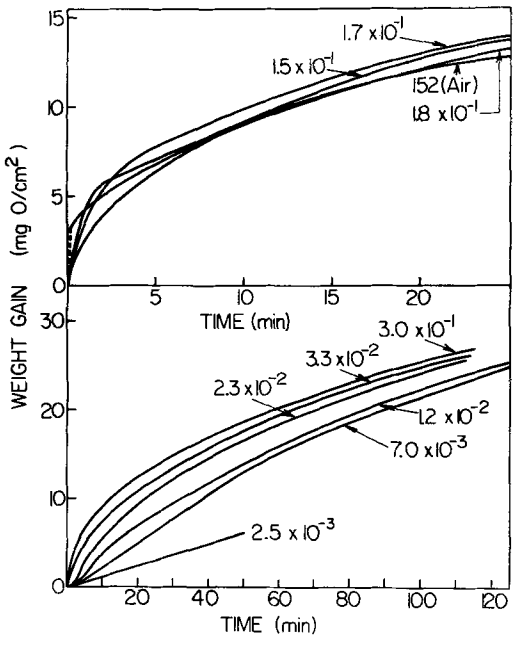

Fig. 2. Oxidation curves for iron exposed at 800°C to oxygen over the pressure range 2.5×10^{-3}-3.0×10^{-1} Torr for periods up to 125 min. A curve is also given for oxidation in dry air at 1 atm pressure.

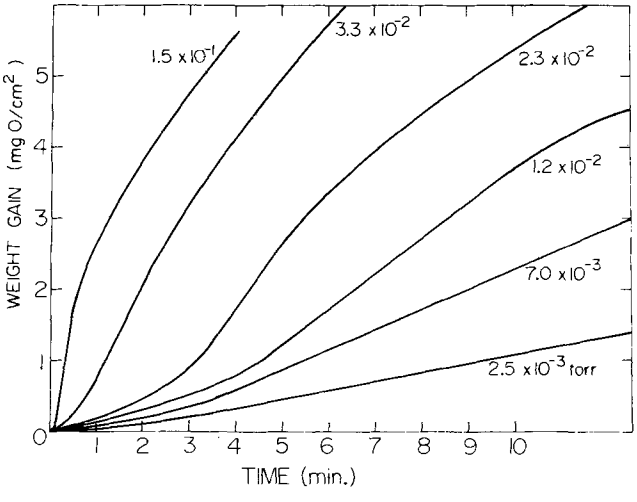

Fig. 3. Oxidation curves for iron exposed at 800°C to oxygen over the pressure range 2.5×10^{-3}-3.0×10^{-1} Torr for periods of 10 min.

posed to a vacuum of 3×10^{-6} Torr for 10 min for stabilization of the temperature upon raising the heated furnace around the reaction tube. The temperature was controlled to ±2°C. Up to 3 min were required to establish the constant pressure gradient upon admission of oxygen. A test was terminated by simultaneously lowering the furnace and evacuating the assembly.

Oxidized specimens for microscopic examination were mounted in room-setting epoxy resin and metallographically polished as described above. An ethyl alcohol solution containing 5% concentrated hydrochloric acid was used as an etchant to distinguish wustite from magnetite. Identification of the oxide constituents was carried out by reflection x-ray examinations using Cu-Kα irradiation with a graphite monochrometer and the preferred orientation of wustite in a scale determined by reflecting Mo-Kα x-ray irradiation from the surface of a rotating specimen. Morphological features of the scales were determined by optical and scanning electron microscopy.

Results

The oxidation curves at pressures from 2.5×10^{-3} to 3.0×10^{-1} Torr are shown in Fig. 2 and 3 as weight change (mg O/cm^2) *vs.* time (min) for periods up to 125 min (1 mg O/cm^2 = 7.2μ FeO). The curves of the weight change were constructed using the original dimensions of a specimen. Five runs at 1.2×10^{-1} Torr were reproducible within ±5%. A typical curve exhibited initially a region wherein the reaction rate continually increased, followed by a region of linear reaction behavior and finally by a region of continually decreasing rate. Considering Fig. 2 and 3, the effect of oxygen pressure on reaction behavior is important particularly during the first hour of exposure.

It was found that small wustite crystals developed over a thin base film, their shape and population being dependent on the orientations of the underlying metal grains. These crystals grew laterally and vertically to a uniformly thick layer during the initial period of continually increasing oxidation rate before onset of linear kinetics. An example of the distribution of these crystals is shown in Fig. 4. The composition and structure of the base oxide film have not yet been determined (7).

The metal was covered by a uniformly thick wustite scale during the period of linear reaction kinetics and a subsequent part of the interval described by the continuously decreasing rate. A cross-section of this type of scale is presented in Fig. 5. As illustrated by the micrograph in Fig. 6, quenching of the scales which contained large 10-100μ wustite grains, did not lead by disproportionation to observable amounts of magnetite. Magnetite was also not detected by reflection x-ray examinations nor by scanning electron microscopy observations at a magnification of X1000. These latter observations, as shown by the micrograph in Fig. 7, demonstrated that a scale developed by lateral and vertical growth of wustite platelets.

Wustite grains in the scales also exhibited a preferred texture. Examination of a scale 10μ thick showed a strong preferred orientation of the (311) wustite face parallel to the metal surface. Five thicker scales approximately 50μ thick showed the (110), (100), and (311) faces of wustite lying in decreasing order of parallel orientation with the metal surface.

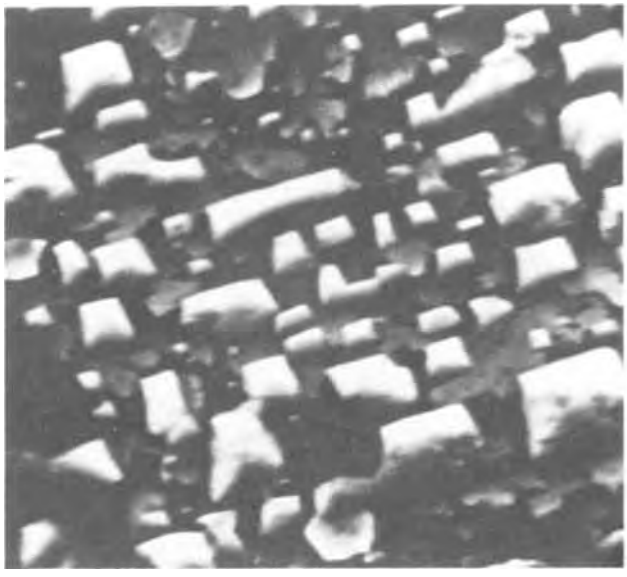

Fig. 4. Scanning electron micrograph of wustite crystals on iron after an exposure for 3 min in oxygen at 2.5×10^{-3} Torr (X3265).

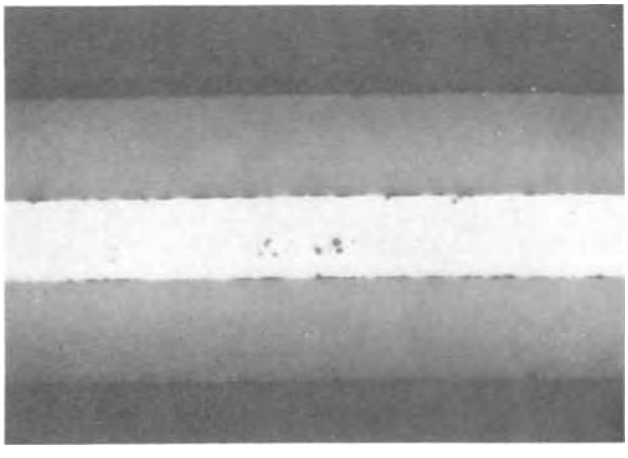

Fig. 5. Cross section of the wustite scale on iron exposed for 30 min in oxygen at 2.5×10^{-2} Torr (X110).

Fig. 6. Cross section of the etched wustite scale shown in Fig. 5 (X300).

Magnetite was nucleated and it grew to cover the wustite layer in the early period of decreasing oxidation rate which became of shorter duration with increasing oxygen pressure. Using the scanning electron microscope, it was definitely established that the wustite layer was completely covered by magnetite during the first 60 min at pressures in the range 7×10^{-3}-3.3×10^{-2} Torr and within the first 10 min at pressures greater than 0.15 Torr. Figure 8 shows an area from a wustite scale over which magnetite has commenced to grow, while Fig. 9 shows the magnetite crystals in a complete layer at a more advanced stage. Apparently magnetite preferentially formed at ledges on the wustite surface. The grains in a fully developed magnetite layer exhibited ledges and flat surfaces and they appeared to be smaller than the underlying wustite grains. The magnetite layer never did exceed 5% of a scale. This type of scale, as illustrated by the micrograph in Fig. 10, exhibited copious magnetite precipitation in the outermost regions of the underlying wustite layer upon its quenching to room temperature. Nevertheless, hematite was never detected in any of the x-ray diffraction patterns of scales formed to oxygen pressures of 3.0×10^{-1} Torr.

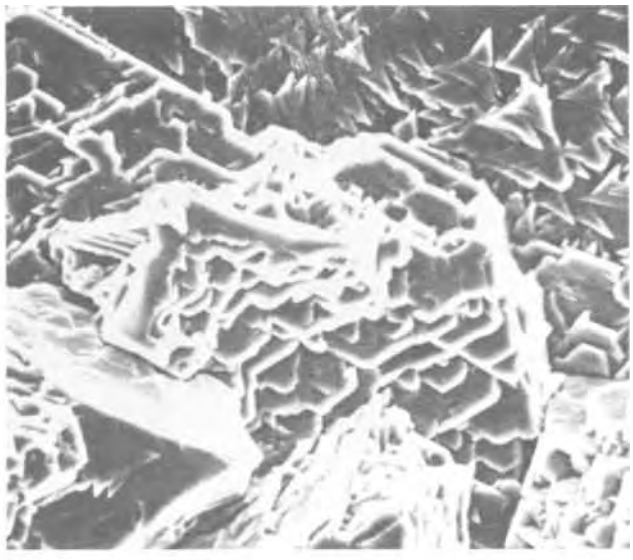

Fig. 7. Scanning electron micrograph of the surface of a wustite scale forming on iron exposed for 20 min in oxygen at 4×10^{-2} Torr (X800).

Fig. 8. Scanning electron micrograph of scale surface showing partial coverage of wustite by magnetite (X440). Exposure: 30 min in oxygen at 3.0×10^{-2} Torr. The micrograph shows the partial coverage of the underlying large wustite crystals by an outermost layer consisting of small magnetite crystals.

Fig. 9. Scanning electron micrograph of the magnetite layer formed on wustite (X885). Exposure: 120 min in oxygen at 3.0×10^{-1} Torr.

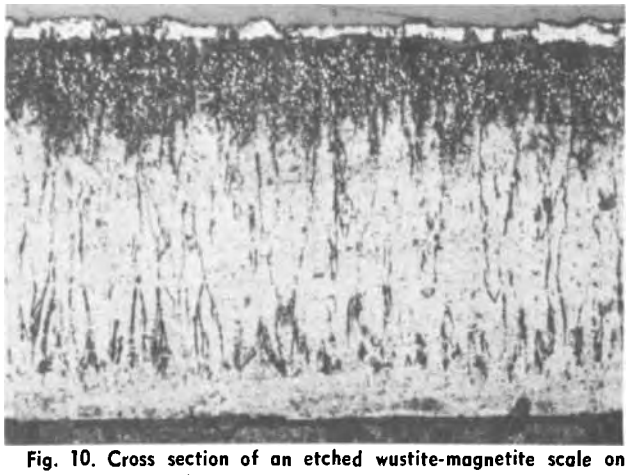

Fig. 10. Cross section of an etched wustite-magnetite scale on iron exposed for 170 min in oxygen at 3.0×10^{-1} Torr (X290). The outermost layer and the precipitates in the outer region of the wustite layer are composed of magnetite.

Discussion

The dissociation pressures of wustite, magnetite, and hematite at 800°C are 1.01×10^{-16}, 2.21×10^{-15}, and 3.96×10^{-7} atm, respectively (17, 18). Formation of these oxides is therefore thermodynamically feasible under the experimental conditions chosen. The present results have shown, however, that the two lower oxides only formed under kinetic conditions in oxygen at pressures ranging from 2.5×10^{-3} to 3×10^{-1} Torr for exposures up to 125 min. The oxidation curves exhibited initially an increasing rate followed by a transition to a constant rate which transformed to a decreasing rate. Magnetite nucleated and grew during the early intervals of this latter stage to cover the wustite surface. Although this curve has not been observed before for the oxidation of iron in oxygen, it exhibits the same form as the curve obtained when iron is oxidized in a carbon dioxide atmosphere (19-21).

Charbonnier *et al.* (22) investigated the growth of wustite in the early exposure stages of increasing oxidation rate by employing oxygen pressures ranging from 10^{-6} to 10^{-4} Torr at temperatures in the range 750°-950°C. They were able to demonstrate that wustite crystals expanded over a thin base oxide film, the shape and population of the crystals being dependent upon the metal crystallographic orientation. These crystals had grown to form a uniform layer upon onset of linear kinetics. Our observations confirm these findings and they show that a uniform textured wustite scale subsequently grows during periods of constant and decreasing oxidation rates.

A scale consisting of a wustite or of wustite and magnetite layers grows by means of outward diffusion of iron via vacancies to react with oxygen. It is appropriate, accordingly, to correlate those regions of an oxidation curve exhibiting constant and continuously decreasing reaction rates with mechanisms for linear and parabolic kinetics. The linear kinetics, Fig. 2 and 3, are strongly dependent on oxygen pressure and it can be shown that scale growth is determined by a phase boundary reaction for adsorption and incorporation of oxygen into wustite. On the other hand, the regions of decreasing oxidation rate show a much smaller oxygen pressure dependence. Since this dependence is confined to intermediate times, the decreasing rate at long exposures can be shown to determine the parabolic growth of a scale comprised of wustite and magnetite layers.

Values of the linear oxidation constants, K_L, at pressures in the range $2.5 \times 10^{-3} - 3.3 \times 10^{-2}$ Torr were obtained from the linear sections of the oxidation curves in Fig. 2 and 3. They are plotted *vs.* pressure in Fig. 11. Since they show a proportional dependence on pressure, the expression

$$K_L = \alpha (K_L)_{theor} = \alpha P_{O_2} / (2\pi m k T)^{1/2} \qquad [1]$$

is used to calculate the fraction of impinging oxygen molecules, α, incorporated into wustite. $(K_L)_{theor}$ represents the rate constant assuming that all impinging molecules react, k is Boltzmann's constant, m is the mass of an oxygen molecule, and T is the temperature in °K. The calculated values, Table II, demonstrate that the fraction of impinging molecules adsorbed is only 6.7% and independent of pressure. These results are consistent with the conclusion that the rate-controlling step during linear kinetics involves a non-dissociative oxygen adsorption mechanism.

The oxidation curves have been plotted in parabolic form in Fig. 12. A typical curve exhibits a transition from linear to parabolic kinetics. It is to be noted that the periods for this transition decrease with increasing pressure. Above 1.5×10^{-1} Torr, the transition also occurs at progressively smaller weight gains with increasing pressure presumably due to more rapid nucleation and growth of magnetite. Results are also included for oxidation in dry air in order to show that the rate of parabolic scaling remains pressure independent up to approximately 1 atm. This behavior is

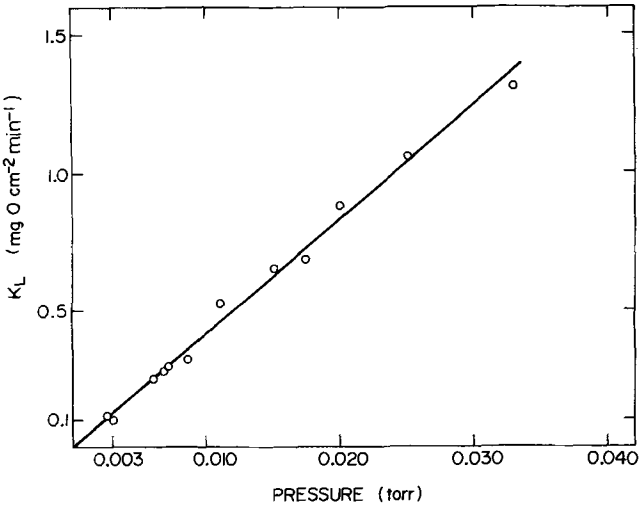

Fig. 11. Plot of the linear oxidation constant for wustite formation on iron *vs.* oxygen pressure over the range 2.5×10^{-3}-3.3×10^{-2} Torr.

Table II. Sticking coefficient, $\alpha = K_L/(K_L)_{theor}$, for oxygen on wustite at 800°C

Pressure × 10^3 (Torr)	α
2.5	0.077
2.9	0.058
3	0.055
6	0.069
6.8	0.067
7	0.067
7	0.068
8.5	0.062
12	0.079
17.4	0.065
23	0.067
25.2	0.063
33	0.066

Average value: $\alpha = 0.067 \pm 0.012$

precisely shown by the plot in Fig. 13 for the values of the parabolic constant *vs.* pressure. The values from this investigation lie in agreement to a previously determined value for zone-refined iron. They are also

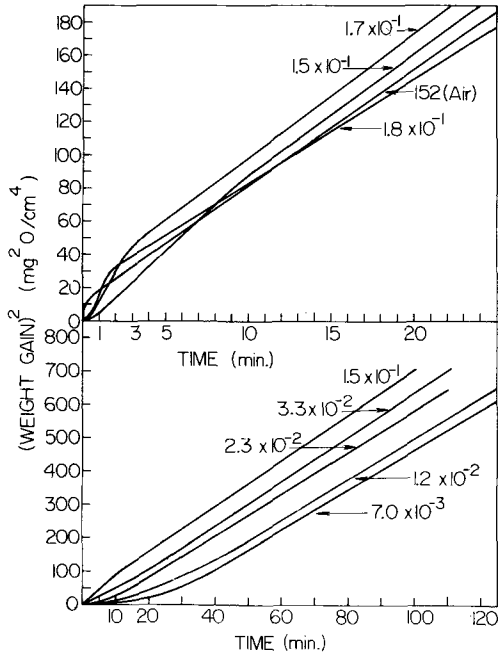

Fig. 12. Oxidation curves plotted in parabolic form: (weight gain/unit area)² vs. time.

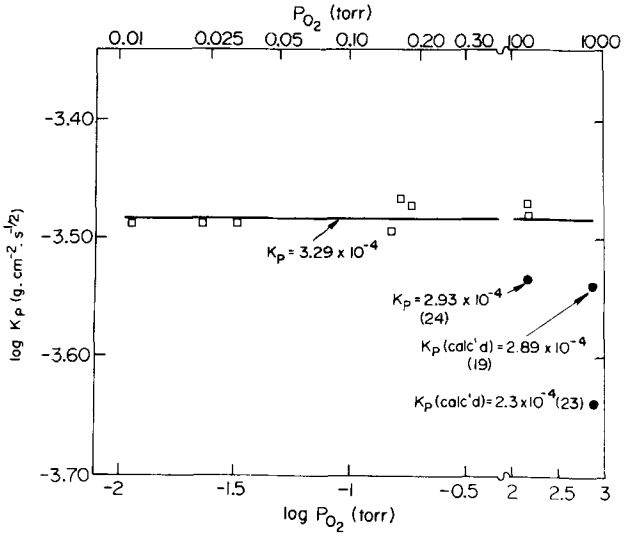

Fig. 13. Plot of the parabolic oxidation constants vs. oxygen pressure. The references are designated by the numbers in brackets.

equal to calculated values, within the accuracy of the calculation, using independent iron diffusivity measurements in wustite in the equation derived from the Wagner theory for parabolic scale growth (19, 23). All these values are equal irrespective of oxygen pressure because wustite accounts for at least 95% of the scale thickness. The flux of iron for growth of the scale is then directly related to the iron vacancy concentration gradient in wustite established by the oxygen activities at the Fe/FeO and FeO/Fe_3O_4 interfaces (19, 23).

Conclusions

Iron exposed to oxygen in the pressure range 2.5×10^{-3}-3×10^{-1} Torr exhibits initially an increasing oxidation rate followed by a stage of linear kinetics before onset of parabolic kinetics. The first oxidation stage is associated with the growth of wustite crystals over an oxide base film while linear kinetics govern the growth of a uniformly thick wustite scale. This scale exhibits a textured structure containing the (110), (100), and (311) faces of wustite in the predominant parallel orientations with the metal surface. The magnitude of the linear rate constant was proportionally dependent on pressure due to reaction control by nondissociative oxygen adsorption; the sticking coefficient of oxygen was 0.067. Parabolic kinetics, which were not dependent on oxygen pressure, governed growth of duplex scales containing layers of wustite and magnetite for exposures up to 125 min. Magnetite comprised less than 5% of scale thickness. Values of the parabolic constant at low pressures were equal to those at pressures near 1 atm because the iron flux for scale growth was directly related to the iron vacancy concentration gradient in wustite established by the oxygen activities at the Fe/FeO and FeO/Fe_3O_4 interfaces.

Acknowledgments

This research was carried out by A. G. Goursat in partial fulfillment of the requirements for award of the Master of Science degree in Materials Science from McMaster University. The authors were indebted to G. R. Wallwork for helpful discussion. Financial support was given by the National Research Council of Canada.

Manuscript submitted July 3, 1972; revised manuscript received Nov. 2, 1972.

Any discussion of this paper will appear in a Discussion Section to be published in the December 1973 JOURNAL.

REFERENCES

1. W. E. Boggs, R. H. Kachik, and G. E. Pelissier, *This Journal*, **112**, 539 (1965).
2. W. E. Boggs, R. H. Kachik, and G. E. Pelissier, *ibid.*, **114**, 32 (1967).
3. M. J. Graham and M. Cohen, *ibid.*, **116**, 1430 (1969).
4. D. Caplan, M. J. Graham, and M. Cohen, *Corrosion Sci.*, **10**, 1 (1970).
5. R. J. Hussey and M. Cohen, *ibid.*, **11**, 699 (1971).
6. R. J. Hussey and M. Cohen, *ibid.*, **11**, 713 (1971).
7. J. C. Charbonnier and J. Bardolle, *Mem. Sci. Rev. Met.*, **65**, 423 (1968).
8. H. Pfeiffer and C. Laubmeyer, *Z. Electrochem.*, **59**, 575 (1955).
9. N. G. Schmahl, H. Baumann, and H. Schenck, *Arch. Eisenhuttenw.*, **29**, 147 (1958).
10. N. G. Schmahl, H. Küpperbusch, and H. Schenck, *ibid.*, **34**, 115 (1963).
11. A. Rahmel and H. J. Engell, *ibid.*, **30**, 743 (1959).
12. P. Belin, *Corrosion Anti-Corrosion*, **7**, 384 (1959); **8**, 96 (1960); **8**, 140 (1960).
13. M. H. Davies, M. T. Simnad, and C. E. Birchenall, *Trans. AIME*, **191**, 889 (1951); **197**, 1250 (1953).
14. R. Linder, *Arkiv Kemi*, **4**, 481 (1952).
15. W. C. Hagel, *Trans. AIME*, **236**, 179 (1966).
16. A. G. Goursat, These Doct. Chimie Physique, Poitiers (1970).
17. G. G. Charette and S. N. Flengas, *This Journal*, **115**, 756 (1968).
18. P. E. C. Bryant and W. W. Smeltzer, *ibid.*, **118**, 1405 (1969).

19. W. W. Smeltzer, *Acta Met.*, **8**, 377 (1960).
20. F. S. Petitt and J. B. Wagner, Jr., *ibid.*, **12**, 35 (1964).
21. M. Hoogewys, J. Paidassi, and R. Darras, *Compt. Rend. Acad. Sci., Ser. C*, **271**, 97 (1970).
22. J. C. Charbonnier, J. Bardolle, and D. Mollimard, *Metallurgie*, **7**, 107 (1967).
23. L. Himmel, R. F. Mehl, and C. E. Birchenall, *Trans. AIME*, **197**, 827 (1953).
24. J. Paidassi, *Rev. Met.*, **LIV**, 569 (1957).

Charge Formation Characteristics of Epoxy Resin Electrets

P. K. C. Pillai and Malti Goel

Indian Institute of Technology, New Delhi-29, India

ABSTRACT

Charge storage properties of epoxy resin are investigated in this paper. Thermoelectrets of the resin are prepared by external thermal and electrical treatment and resultant surface charges are measured for one month. Initial heterocharges are observed on both the surfaces of thick sample, but a charge reversal takes place on anode surface depending upon the conditions of polarization such as polarizing field, polarizing temperature, and polarizing time. For thin foil electrets, positive surface charges are observed on both the sides. Permanent charges of both thick and thin electrets are positive, on both the surfaces, suggesting hole conduction in this resin. Optical absorption studies have been used as an experimental tool to detect the changes taking place during polarization.

Epoxidation of olefins was first reported in early 1900. First, epoxy resin from Bisphenol was isolated by Schlack in 1933 in Germany. This is used in casting adhesive. Charge-storage phenomena in epoxy resin which is a mixture of diglycidyl ether of Bisphenol A (DGEBA resin) and polyamine has been investigated by studying its thermoelectret properties. Thermoelectrets are permanently polarized dielectrics, which were first prepared by Equchi (1) from carnauba wax. Most of the work on thermoelectrets has been done on waxes and their mixtures. Recently, some plastic materials were used for electret preparation and studied for their stability (2-6). Resins were used for formation of thermoelectrets for the first time by Mikola (7). Those electrets were found to retain charges and showed peculiar characteristics.

The resin used in present investigation is supplied by Ciba of India Limited. Its electret-forming properties have not been studied so far. Electret effect is investigated, since this resin is widely used for insulation in electrical instruments and as a binder in some electret-forming materials. Molded sheets of epoxy resin were prepared and cut into slabs of 0.1 cm thickness and were used for electret preparation. Thin foils were also developed and used for the investigation. Heterocharges or homocharges are observed depending upon conditions of polarization.

The structure of DGEBA resin is given below

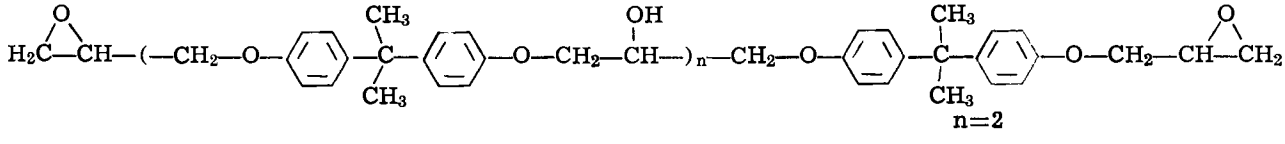

Experimental

Samples with two different thicknesses were used for polarization by thermal and electrical treatment. One was 0.1 cm thick sheet cut from a molded block and another was 0.007 cm thick prepared in thin foil form. Resin was molded in block form by mixing the hardener 7% in volume in DGEBA resin at casting temperature of 60°C. The mixture was put into an aluminum casting and heated to 100°C at the rate of 1°C/hr. It was kept at 100°C for 4-5 hr and later brought down to room temperature at a rate of 1°C/hr. Annealing was done for 15 hr at 120°C. The breakdown voltage of this molded substance was found to be 23 kV/cm at room temperature. A slab of dimensions 1 cm × 1 cm × 0.1 cm was cut and kept in between aluminum electrodes and pressed tightly with the help of screws. The whole assembly was kept inside an electric oven, the temperature of which can be adjusted up to 240°C.

The sample was heated to a desirable temperature and an electric field through a high-voltage stabilizer was applied to it for 2 hr at constant temperature and for another 2 hr during its cooling to room temperature. The electric field was switched off at room temperature and resultant surface charges of thermoelectret so formed, were measured with the help of Keithley solid-state electrometer 610C, which can measure charge down to 10^{-13} coulombs. The charge measurements were then carried out after definite time intervals for approximately 1 month. Electrets were kept short circuited by wrapping in aluminum foil in desiccated conditions between successive measurements. The ultraviolet and visible spectra of polarized and unpolarized foil were taken from Unicam SP500 spectrophotometer.

Results and Discussion

Electrets of 0.1 cm thickness show heterocharges on both sides of the electret surface initially. These charges first decay very rapidly and then regain a constant value after some time, which finally decays slowly to zero. Isothermal surface charge decay of electrets prepared by 10 kV/cm at 140° and 200°C are shown in Fig. 1. Charge reversal is observed on the anode surface in 4 days for an electret prepared at 140°C and in 9 days for an electret prepared at 200°C. The final charges on both the surfaces are positive. Observation of initial heterocharge and its subsequent reversal to homocharge indicates the presence of volume polarization in the polarized samples.

The initial values of surface charges as a function of polarizing field are shown in Fig. 2. At 10 kV/cm maximum charge is observed. As the field strength increases further, the magnitude of charge is reduced.

Key words: epoxy resin, thermoelectret, heterocharge, homocharge.

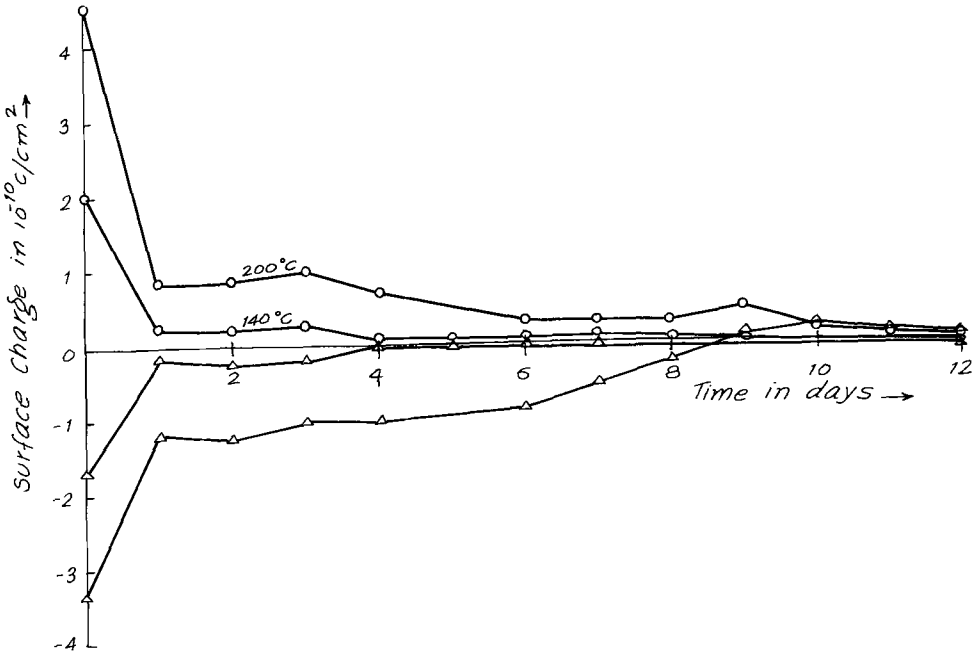

Fig. 1. Surface charge decay of electrets of thickness 0.1 cm prepared at 10 kV/cm at different temperatures in 4 hr polarizing time.

This reduction in initial heterocharge is due to the increased homocharge component at higher fields. The initial charges of electrets prepared at different temperatures is shown in Fig. 3. These surface charges are shown to increase with increasing polarization temperature. The polarizing temperature thus enhances the volume polarization. The electrical resistance of the resin decreases with increasing temperature.

Dependence of surface charge on polarizing time is shown in Fig. 4. The best electret of this material is formed in 4 hr when the sample is prepared at 10 kV/cm. By increasing polarization time, electret properties are found to deteriorate.

In the case of thin foil electrets, positive-surface charges are only observed on both the surfaces, and no charge reversal takes place. The magnitude of positive charge is found to be greater on the anode surface than on the cathode surface. The charges decay initially for 2-3 days, than rebuild up to a high value, again decay slowly, and finally become constant. It is found that the magnitude of surface charge as well as the time taken in acquiring the maximum build-up of charge after polarization depend upon the polarizing field. The initial surface charge as a function of applied voltages for 0.007 cm thick foil polarized at 140°C in 4 hr are shown in Fig. 5. There exists an optimum value of polarization field in this case also, at which maxi-

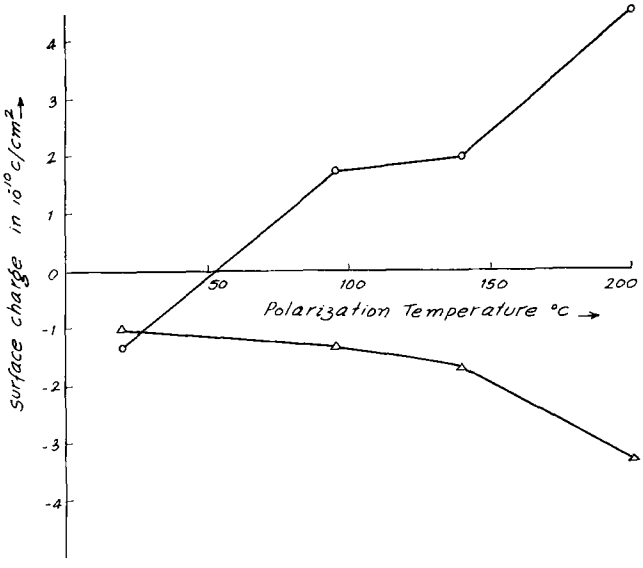

Fig. 3. Surface charge as a function of polarizing temperature prepared at 10 kV/cm in 4 hr polarizing time (thickness 0.1 cm).

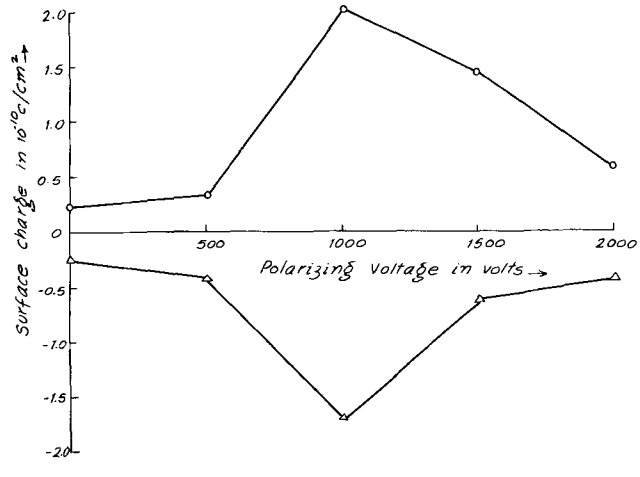

Fig. 2. Surface charge as a function of polarizing voltages prepared at 140°C in 4 hr polarizing time (thickness 0.1 cm).

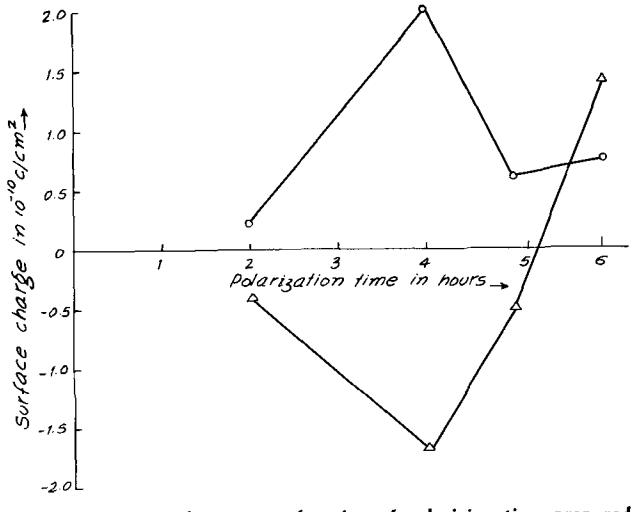

Fig. 4. Surface charge as a function of polarizing time prepared at 10 kV/cm and 140°C (thickness 0.1 cm).

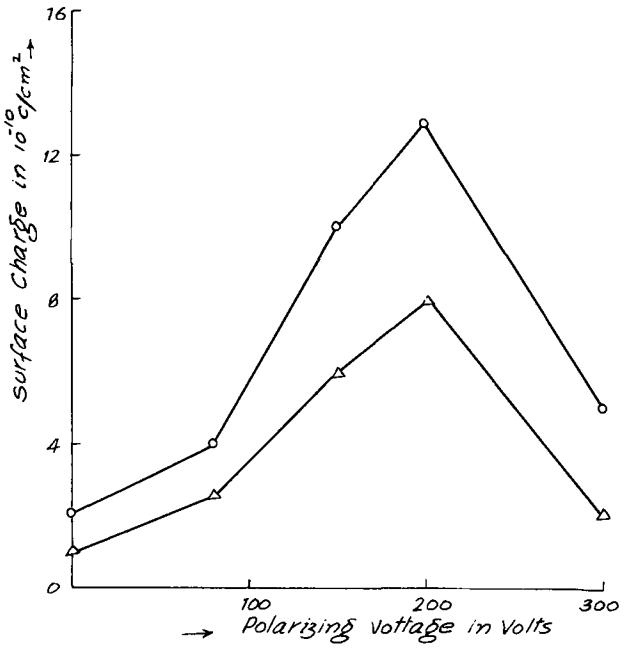

Fig. 5. Surface charge as a function of polarizing voltage prepared at 140°C in 4 hr (thickness 0.007 cm). △, cathode; ○, anode.

mum polarization is obtained. Assuming that the effective surface charge of an electret is given as

$$\sigma_{eff} = \eta - P$$

η is the component due to homocharge formation which may arise because of transfer of charge from electrode-electret gap, molding, and stripping charge.

P is the component due to heterocharge formation, which may be due to dipole alignment, trapping of charge, and interfacial polarization.

The observed surface charge will depend on which of the two components is predominant at a given time. Bisphenol A is a complex molecule and therefore a multiple process of polarization can be expected in this material. In its molecular structure a number of permanent dipoles are present, which orient and align themselves in the direction of applied electric field. In addition space charge trapping and bulk trapping of charge are also taking place (8). Dipole relaxations, ionic and electronic movements are responsible for the charge reversal. Final charges on both the surfaces are positive in this case indicating that holes and positive ions are more predominantly trapped, while in other electret forming plastic materials (6, 9) predominance of electron conduction has been observed.

The optical absorption studies have been carried out in ultraviolet and visible range of spectrum for this resin. The absorption spectra of an unpolarized 0.007 cm thick sample are taken in the wavelength range 200-700 mμ as shown in Fig. 6a. A sample of 0.007 cm thickness is polarized at 140°C by a field strength of 20 kV/cm and its spectral characteristics are shown in Fig. 6c. Absorption spectrum of another sample heated to the polarization temperature of 140°C in the absence of electric field is also shown in Fig. 6b. It is found that an unpolarized sample shows a broad transmission in the wavelength range 300 to 700 mμ. On heating the absorption is increased and in wavelength range 300-340 mμ there is no transmission. This change is contributing to molding and stripping charges observed during surface charge measurements. However, it was found that these surface charges decay quickly. On polarization the absorption is further increased as well as visible opacity of the sample is increased. This increased absorption is due to certain changes taking place in the structure particularly the —OH— group of Bisphenol A. A more quantitative description is yet to be suggested.

Summary and Conclusions

1. Charge storage takes place in epoxy resin when it is heated under electrical stress. This charge is retained approximately for 15 days in thick sample and for 1 month in thin foil.

2. There exists an optimum value of polarization field polarization temperature and polarization time for getting the maximum polarization in case of this epoxy resin.

3. The charge reversal on anode surface takes place from initial heterocharge to final homocharge depending upon conditions of polarization. Permanent heterocharges are only observed on cathode surface.

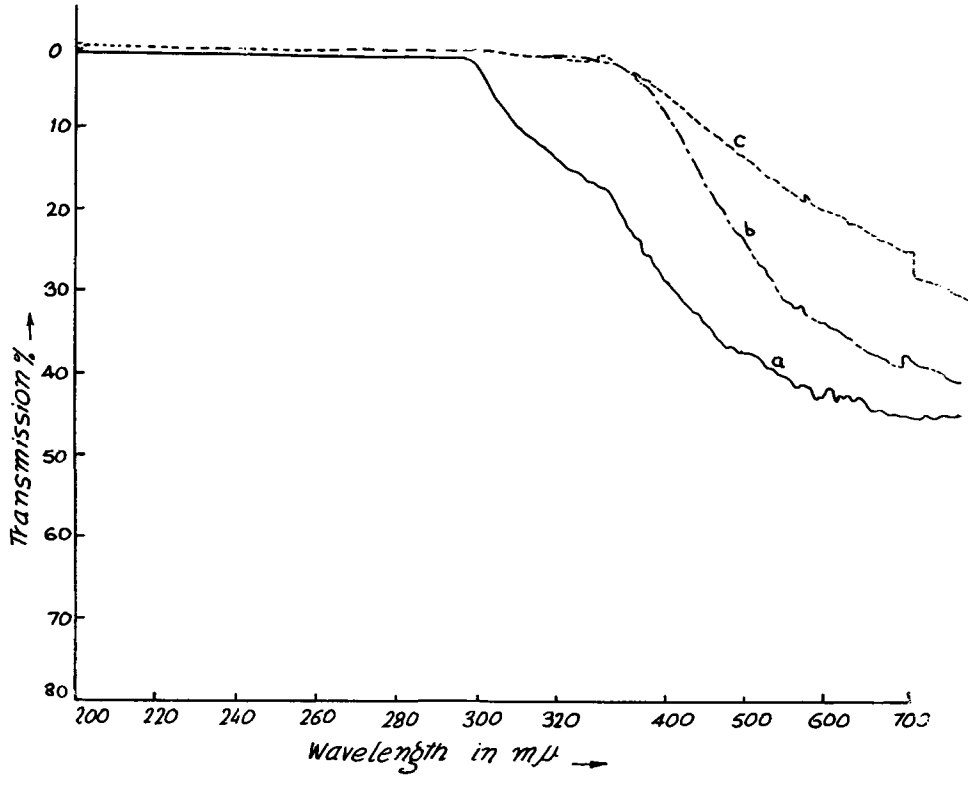

Fig. 6. The ultraviolet and visible absorption spectra of epoxy resin foil of thickness 0.007 cm before and after polarization. a, —— unpolarized; b, —·—·— heated to 140°C; c, - - - - - polarized at 20 kV/cm and 140°C.

4. The final charge of resin electrets is always positive indicating that positive carrier is more predominantly trapped in this resin.
5. The optical studies in the ultraviolet and visible region show the structural changes taking place in the polarized sample.

Acknowledgment

The authors are thankful to Prof. K. L. Chopra and Prof. M. S. Sodha, Department of Physics, I.I.T., Delhi, for the encouragement given to them during the course of these investigations. The financial aid given by the C.S.I.R., Government of India is also gratefully acknowledged.

Manuscript submitted May 1, 1972; revised manuscript received Sept. 14, 1972.

Any discussion of this paper will appear in a Discussion Section to be published in the December 1973 JOURNAL.

REFERENCES

1. M. Equchi, *Phil. Mag.*, **49**, 178 (1925).
2. R. A. Creswell and M. M. Perlman, *J. Appl. Phys.*, **41**, 2365 (1970).
3. R. A. Creswell, M. M. Perlman, and M. A. Kabayama, "Dielectric Properties of Polymers," Plenum Press, New York (1972).
4. G. M. Sessler and J. E. West, *This Journal*, **115**, 836 (1968).
5. P. K. C. Pillai, K. K. Jain, and V. K. Jain, *Phys. Status Solidi*, **6**, K121 (1971).
6. P. K. C. Pillai and Malti Goel, *J. App. Phys.*, To be published.
7. S. Mikola, *Z. Physik*, **32**, 476 (1925).
8. B. Gross, Proc. Conf. on Stat. Elect., Paper 4, p. 33 (1971).
9. P. K. C. Pillai and Malti Goel, Unpublished.

Transport Numbers of Metal and Oxygen during the Anodic Oxidation of Tantalum

J. P. S. Pringle*

Chalk River Nuclear Laboratories, Atomic Energy of Canada Limited, Chalk River, Ontario, Canada

ABSTRACT

An oxide film on a metal surface will thicken only if metal, or oxygen, or both, migrate across it. The relative magnitude of the metal and oxygen migrations can be determined using markers, and the possible results are reviewed for the ideal case of a homogeneous oxide grown to uniform thickness on a plane metal surface. Such experiments require markers that are both inert and immobile; criteria are developed to establish that these requirements have been met. Experimentally, it has been shown that the anodic oxidation of tantalum is a system close to the ideal, and that the radioisotope of a noble gas is a good approximation for the required marker. Radioactive noble gases were implanted by means of a mass separator into thin films of anodic tantalum oxide, and the transport numbers of the tantalum and oxygen measured after thickening by further anodization. The transport numbers were found to be 0.243 and 0.757, respectively, for anodizing conditions of 1 mA/cm^2 at 25°C in 0.1M H_2SO_4. The noble gas concentration profiles were observed to broaden on further anodizing, and this was interpreted as being due to the simultaneous movement of tantalum and oxygen atoms during the charge transfer event.

The oxidation of metals is frequently a rather complex process, and so the fundamentals are best studied in a system that is as simple as possible. The anodic oxidation of tantalum meets this requirement admirably, for it requires little apparatus, can be performed at room temperature, and gives a highly uniform and homogeneous oxide all over the metal surface. Furthermore, the rate of oxidation can be controlled by the applied current, and its extent by the applied voltage.

The anodic oxidation of tantalum has been studied many times, mostly by means of electrical measurements on the current-voltage relationship. These have established the over-all kinetics of the process, and have shown that the current passes through the oxide via the migration of ionic species; they have, however, provided no information on the nature of these species or their migrations. In particular, they have been unable to determine how much of the current is carried by tantalum migrating toward the oxide/electrolyte interface, and how much by oxygen migrating in the opposite direction.

The marker experiments reported here were designed to investigate this problem, using the techniques reported elsewhere (1-3).

* Electrochemical Society Active Member.
Key words: tantalum, anodic oxidation, markers, transport number, oxidation mechanism.

Principle of Marker Experiments

Possible mechanisms for oxide growth.—Under normal conditions, almost all metal surfaces are covered with a thin film of oxide. The oxidation system is one, therefore, in which the two reactants, metal and oxygen, are separated by a layer of their product. If further reaction is to take place, so that the product layer becomes thicker, either metal or oxygen or both must be transported across the existing film. There are then five possibilities.

I. The metal alone migrates, and the reaction to form new oxide occurs only at the oxide/oxygen interface.

II. The oxygen alone migrates, so that the new oxide is formed only at the metal/oxide interface.

III. When both metal and oxygen migrate, these two mechanisms could occur together, so that new oxide would be formed at both interfaces.

IV. When both the metal and oxygen migrate, however, the new oxide does not have to be formed at the interfaces; it could be formed within the existing oxide through the transport of material from each side.

V. Since mechanisms III and IV are not mutually exclusive, the new oxide could be formed both within the existing oxide and at the interfaces.

Other metal and oxygen migrations, not leading to oxide formation, could occur simultaneously with any

of the above. Thus oxygen could be transported to the metal/oxide interface, and there dissolve in the metal instead of combining with it to form new oxide. Similarly, migrating metal atoms could, by crossing the oxide/oxygen interface, be lost to the environment.

Identification of the possible mechanisms.—In the discussion that follows, an ideal oxide is assumed; one that is homogeneous, of uniform thickness, and grown on a plane metal surface. It is also assumed that no oxygen dissolves in the metal and that no metal atoms are lost to the environment.

The five mechanisms can be distinguished if it is possible to identify a particular plane in the oxide parallel to the two interfaces; that is, if the plane can be labeled with a marker. The position of the marker after further oxidation then provides a measure of the fresh oxide laid down on either side of the reference plane. An experiment of this kind is sufficient to distinguish mechanisms I and II, but the remaining possibilities can only be distinguished by labeling a series of reference planes so that the marker takes up a distribution in the oxide. The possible results of such an experiment, assuming that the marker is normally distributed about the middle of the initial oxide, are illustrated in Fig. 1.

For metal migration alone (I), the marker position relative to the metal/oxide interface remains unchanged, since no new oxide is formed between it and the metal surface. Accordingly, the marker becomes deeply buried in the oxide. Similar argument shows that the marker position will remain unchanged relative to the oxide/oxygen interface if oxygen alone moves (II). When both move, so that the new oxide is formed only at the interfaces (III), the marker will be found somewhere in the middle of the final oxide, its exact position depending on the relative amount of oxide formed at each interface. In all three mechanisms, the distribution of the marker about its mean position remains unchanged; it will change only if new oxide is being formed within the marked layer, as in mechanisms IV and V.

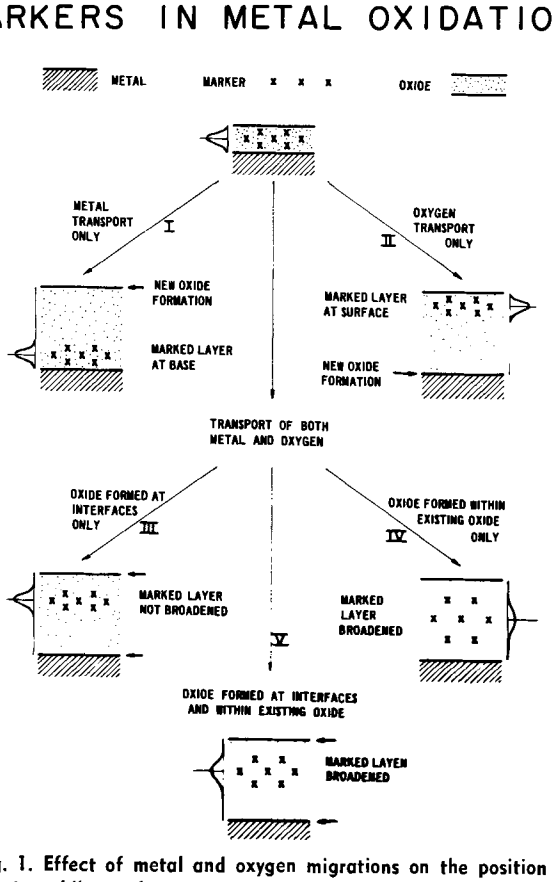

Fig. 1. Effect of metal and oxygen migrations on the position of inert, immobile markers in an oxide film. Roman numerals index the five possible mechanisms discussed in the text, and the resulting marker profiles are shown at the side of each diagram.

In mechanism IV the distribution will broaden, the nature of the broadening depending on where the new oxide is being formed. If the oxide is homogeneous, it is reasonable to assume that the new oxide will be laid down uniformly throughout the existing oxide; the marker would then maintain the same relative position in the oxide, and the same relative profile across it. A combination of III with this form of IV would also lead to profile broadening, but in this case, (V), both the relative position and the relative profile would change as the oxidation progressed.

It must be emphasized at this point that these marker experiments can only determine how much of the new oxide is being formed by metal and/or oxygen migration; they cannot determine how the individual atoms migrate. They cannot distinguish, for example, whether oxygen migrates across the oxide by some process of diffusion, or whether, having crossed the oxide/oxygen interface, it then migrates in one jump to some point at or near the metal/oxide interface. To distinguish between these possibilities, a marker for oxygen itself is required; experiments of this kind have been reported elsewhere [see (4) and the references cited therein].

Criteria for selection of suitable markers.—The first requirement for any marker is that it should not interfere with the oxidation process; that is, it should be inert. Since the mere presence of a marker is enough to perturb the oxide in its immediate vicinity, some interference is inevitable. The best that can be done, therefore, is to reduce the number and size of the markers as much as possible.

The second requirement is that the marker shall be immobile. The position of a marker after oxidation can be interpreted in two ways.

Hypothesis A: The marker is immobile, and its position is determined entirely by the migration of metal and oxygen around it.

Hypothesis B: The marker is not immobile, and its position is determined by its own migration as well as that of the metal and oxygen around it.

If only the position of the marker is known, these hypotheses cannot be distinguished from one another. Since A is a much more rigorous condition than B, the latter is, at first sight, much more likely. And if B is correct, then the relative mobilities of metal and oxygen cannot be determined from the experiment. It is therefore essential that the marker be immobile, and the prime difficulty with any marker experiment lies in establishing this fact.

Evidence for the mobility can be obtained by measuring the marker profile, and by studying the changes in this profile as the oxidation proceeds. The profile must broaden if the marker migrates, due to statistical fluctuations in the distance traveled by individual particles. The absence of such broadening is conclusive proof that the marker is immobile, but its presence is not certain evidence for migration, since the profile could broaden for other reasons; through the formation of new oxide within the existing oxide, for example. If the profile broadens, then, the immobility of the markers is still in doubt.

The doubt can be resolved by noting that any truly inert, immobile marker will behave in exactly the same way as any other truly inert, immobile marker. If two markers are incorporated with exactly the same initial distribution, and they are in fact truly inert and immobile, then (*a*) they will finish up at exactly the same position in the final oxide, and either (*b*) (*i*) their concentration profiles will not broaden at all, or (*ii*) they will broaden by exactly the same amount.

Measurement of transport numbers in anodic oxidation.—To define a measure for the relative migration of metal and oxygen, consider a reference plane in the oxide, parallel to the two interfaces. The formation of

new oxide between this plane and the oxide/electrolyte interface can only occur if metal atoms are transported outward across it; similarly, oxygen atoms must cross in the opposite direction to form new oxide between it and the metal surface. If the total amount of new oxide is proportional to the charge passed during anodization, the amount of new oxide formed on each side of the reference plane is proportional to the fraction of the charge carried by the migrating metal and oxygen atoms. In other words, the fraction of the new oxide formed on either side of the reference plane is proportional to the transport numbers of the metal (t_m) and oxygen (t_o) across it.

The position of an inert, immobile marker in the final oxide is thus determined by the transport numbers of the metal and oxygen across the plane in which it is located. Accordingly, the position of the marker provides a measure of the transport numbers. The preceding discussions can then be recast in terms of transport numbers, so that criterion (*a*) for the immobility of the markers becomes (*a*) the transport numbers measured by the different markers must be exactly the same.

The characteristics of the five mechanisms then become:

I. Metal migration only: $t_m = 1$, $t_o = 0$ for all planes in the oxide film.

II. Oxygen migration only: $t_m = 0$, $t_o = 1$ for all planes in oxide film.

III. Metal and oxygen migration with the new oxide being formed only at the interfaces: $t_m < 1$, $t_o < 1$, with t_m and t_o constant for all planes in the oxide film. This follows since the flux of, say, oxygen atoms crossing the oxygen/oxide interface must equal that arriving at the oxide/metal interface.

IV. Metal and oxygen migration with the new oxide being formed uniformly within the existing oxide: $t_m = 1$, $t_o = 0$ at the metal/oxide interface and $t_m = 0$, $t_o = 1$ at the oxide/oxygen interface. The transport numbers vary monotonically between these limits in such a way that, for a plane at a distance x from the metal/oxide interface

$$(t_m)_x = (h - x)/h$$
$$(t_o)_x = x/h \qquad [1]$$

where h is the oxide thickness.

Suppose that the oxide thickens by an amount Δh, and that x increases by an amount Δx. Then from the definition of transport number

$$(t_o)_x = \Delta x/\Delta h \qquad [2]$$

Combining [1] and [2]

$$(t_o)_x = (x + \Delta x)/(h + \Delta h) = (t_o)_{x+\Delta x} \qquad [3]$$

so that the transport number across the given reference plane remains constant with increasing oxide thickness. The transport numbers observed in a marker experiment would then be determined solely by the position of the marker within the initial oxide, and would remain constant as the oxide thickness increased.

V. Metal and oxygen migration with new oxide being formed both at the interfaces and within the existing oxide: at the metal/oxide interface $t'_m < 1$ and $t'_o < 1$, while at the oxide/oxygen interface $t''_o < 1$ and $t''_m < 1$; within the oxide, $t'_m > t_m > t''_m$ and $t'_o < t_o < t''_o$ in the same way as IV so that

$$(t_m)_x = t'_m - (t'_m - t''_m) \cdot (x/h)$$
$$(t_o)_x = t'_o + (t''_o - t'_o) \cdot (x/h) \qquad [4]$$

A combination of [4] with [2] will show that $(t_o)_{x+\Delta x}$ cannot, except fortuitously, be the same as $(t_o)_x$; that is, the transport numbers across a given plane will vary as anodization proceeds. In this case, therefore, the measured transport numbers would be a function of both the position (x/h) of the marker within the initial oxide, and of the increasing oxide thickness h.

If new oxide is being formed within the existing oxide, the transport numbers of the metal and oxygen must change by equal and opposite amounts at the planes where it is being formed; the rate of formation at plane x is, in fact, proportional to dt_o/dx ($= -dt_m/dx$). When the transport numbers across two neighboring planes are identical, $dt_o/dx = 0$ between them; since no new oxide is being formed, the planes remain the same distance apart. Markers located on two such planes will also remain the same distance apart, and so there will be no broadening of the marker profile. These conditions obtain in mechanisms I, II, and III, since $dt_o/dx = 0$ for all planes within the oxide.

In mechanism IV, however

$$dt_o/dx = 1/h \qquad [5]$$

and in mechanism V

$$dt_o/dx = (t''_o - t'_o)/h \qquad [6]$$

It can then be shown that the breadth of the marker profile will be proportional to h in mechanism IV, and to $h_i + (t''_o - t'_o)(h - h_i)$ in mechanism V, where h_i is the initial thickness of the oxide film.

Transport number measurements using at least two marker species can thus establish whether the markers are immobile, and if so, where the new oxide is being formed. These concepts have been applied experimentally to a study of the anodic oxidation of tantalum.

Marker Experiments in Anodic Oxidation of Tantalum

Ideality of anodic tantalum oxide.—The preceding discussion has been based on the assumption that the oxide is ideal, and so the application of its conclusions to a real system is only as good as the approximation to ideality. For anodic tantalum oxide, the approximation is indeed excellent. All available evidence [see (1) and the references cited therein] suggests that anodic tantalum oxide is very highly homogeneous when formed in dilute aqueous electrolytes. The only irregularities are those resulting from impurities in the underlying tantalum or from fragments of crystalline oxide, but these occupy a minute fraction of the surface area (1, 3). Furthermore, the thickness uniformity is maintained during anodization and the underlying tantalum surface is smoothed (1). No significant amount of tantalum is found in the electrolyte after anodizing (5), and internal friction measurements (6) show that the diffusion of oxygen in tantalum is negligible at room temperature.

Choice of markers.—As already noted, the requirement that the marker be inert cannot be met absolutely; the best that can be done is to use markers that are as small and as few as possible. Obviously, the smallest possible marker is a single atom, and this feature has been provided in both this and previous work (5, 7) by using noble gases. Radioactive isotopes simplify the problem of detection and diminish the number of atoms required; ^{41}Ar, ^{79}Kr, ^{125}Xe, and ^{222}Rn were used as markers in the present experiments. Nevertheless, it is still questionable whether the radioactive noble gases are completely inert.

Apart from ^{222}Rn, obtained from the Radium Chemical Company of New York, the isotopes were all prepared by (n, γ) reactions on the stable precursors. They were then implanted in the oxide by means of a mass separator, whose use for this purpose has been described elsewhere (2, 8). The implantation of a radioisotope is normally accompanied by the implantation of a much larger number of the neighboring stable isotopes (2), and so the total fluence is determined almost exclusively by the latter. Beam current measurements, or counting data in the case of ^{222}Rn, showed that the implanted fluences were about 10^{13} ions/cm^2 for Ar and Kr, 10^{12} ions/cm^2 for Xe, and 10^{11} ions/cm^2 for ^{222}Rn.

The implantations were performed at low energy, so that the noble gas atoms were concentrated in the region immediately adjacent to the oxide surface; thus nearly 99% of the $^{125}Xe^+$ implanted at 5 keV came to rest in the first 80Å of oxide (3). Anodic tantalum oxide has a density of 8.03 (9), and so, assuming it is stoichiometric Ta_2O_5, it can be calculated that each angstrom contains 7.63×10^{14} tantalum and oxygen atoms/cm^2. The implantation of 10^{12} ions/cm^2 of $^{124}Xe^+$ and $^{126}Xe^+$ then produces a maximum concentration of 262 xenon atoms per million matrix atoms, while activity measurements show that the maximum concentration of the radioactive ^{125}Xe is less than 8 atoms per million.

Such concentrations are minute, particularly when compared to the 1700 atoms per million of sulfur impurity incorporated from the 0.1M H_2SO_4 electrolyte (10). The latter has no detectable effect on the properties of the oxide (1), and so it would seem reasonable to suppose that the noble gases would behave likewise. Evidence for this has been presented elsewhere (2), where it has been shown that implantation fluences up to 10^{13} ions/cm^2 have no detectable effect on the anodic oxidation or on the oxide dissolution rate. Since the noble gases are implanted, they must come to rest at the end of a damage trail; no effect that could be attributed to radiation damage has been detected (2). All in all, therefore, radioactive noble gas markers behave as though they were effectively inert.

Previous arguments (5) supporting the immobility of noble gas markers can be summarized as follows. Of all the possible atomic markers, the noble gases are the least likely to exist as charged species in the oxide matrix, and hence are the least likely to move under the influence of the strong electric field present during anodization. The heavier gases, at least, should be very much larger than the tantalum and oxygen atoms surrounding them, and should therefore diffuse more slowly; evidence was presented to show that they did not thermally diffuse in the static oxide. Probabilistic arguments of this kind are, however, unsatisfactory; in particular, no evidence could be cited to support the neutrality of the noble gases within the oxide, and no evidence could be cited to support the absence of diffusion in the growing oxide.

The application of criterion (*a*) to results already obtained with ^{125}Xe (5) and ^{222}Rn (11) tends to support the immobility of these markers. In these experiments, the noble gas atoms were implanted at 5 keV (^{125}Xe) and 6 keV (^{222}Rn) into chemically polished tantalum, which is now known to be covered with a layer of thermal oxide some 30Å thick (12); from the range studies reported elsewhere (3), therefore, half the noble gas was implanted in this oxide and half in the underlying metal. The specimens were then anodized, and the position of the noble gas within the final oxide determined by β-ray spectroscopy (13) for ^{125}Xe and by α-ray spectroscopy (14) for ^{222}Rn. The measured values of t_0 were 0.71 ± 0.03 and $0.74 \pm 0.02_5$, respectively, which agree within experimental error; criterion (*a*) is thus satisfied. No test under criterion (*b*) is possible, since β-ray spectroscopy provides no information at all on the concentration profile, while α-ray spectroscopy is insensitive to small changes. The latter did, however, show that all the ^{222}Rn finished up in approximately the same place, and hence that the ^{222}Rn implanted in the metal behaved in the same way as that implanted in the oxide.

What was required, therefore, was an accurate method for measuring the noble gas concentration profiles, so that both criteria could be used to establish their immobility. Such a method is provided by the sectioning technique discussed in previous papers (1-3).

Experimental Procedure

Data collection.—Tantalum coupons, $3.5 \times 1.0 \times 0.037$ cm^3 were cut from sheet supplied by the Fansteel Metallurgical Company, and a 0.05 cm diameter tantalum wire spot welded on one corner to provide electrical contact. The coupons were cleaned, chemically polished, and dipped in concentrated HF almost saturated with NH_4F to remove any film left by the chemical polish (1, 15). They were then anodized, normally to a thickness of about 880Å, and wrapped in household aluminum foil, leaving the middle 2.0×0.4 cm^2 of one face exposed. Radioactive noble gas ions were implanted into the exposed portion at an energy of 2 keV (^{41}Ar) or 5 keV (^{79}Kr, ^{125}Xe, and ^{222}Rn), and the coupons reanodized to the final thickness, normally 3000Å. All anodizations were performed at 1 mA/cm^2 in 0.1M H_2SO_4 at 25°C, using a constant current apparatus devised by Walker (16). Integrated concentration profiles, as illustrated in Fig. 2, were obtained by means of the procedure elsewhere described (3).

The initial thickness was standardized at 880Å as this was close to the bottom of the continuously measurable range (1). Low implantation energies were chosen to obtain the best compromise between a narrow profile and a complete normal distribution (3); the former enabled small changes in the breadth to be detected, while the latter made for more accurate analysis of the concentration profiles. To make the transport number measurements as precise as possible, it was necessary to anodize to a large final thickness. When the initial thickness was 880Å and the final thickness 3000Å, the noble gas was found with a normally distributed profile at about 2450Å from the metal/oxide interface (Fig. 2).

Analysis of concentration profiles using normal distributions.—The PDP-5 program used to process the counting data in the previous paper (3) was replaced by an improved version written for a CDC G-20 computer. This corrected the N observed counts, $I = 1,2,.....N$, for counter dead time, background, and decay, and expressed the results as percentages, $Y(I)$, of the initial count; it also calculated the corresponding standard error, $EY(I)$, from the square root of the observed counts. The oxide thickness remaining, $X(I)$, was computed in angstroms by interpolation from the calibration in (1); its standard error, $EX(I)$, was taken as 0.067 times the difference between the two "kick" wavelengths (1), rather than 1.8Å as in (3). The quantities $X(I)$, $Y(I)$, $EX(I)$, and $EY(I)$ were then printed

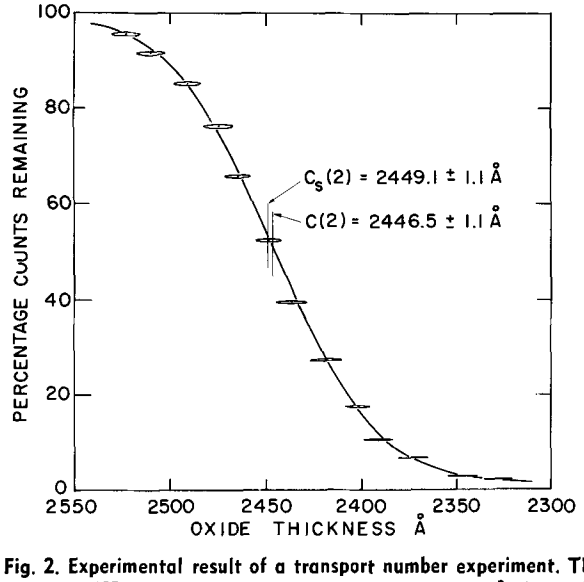

Fig. 2. Experimental result of a transport number experiment. The marker was ^{125}Xe implanted at 5 keV into an oxide 885Å thick, the oxide being subsequently reanodized to 3024Å. On sectioning, the integrated profile shown was obtained; 95% confidence limits have been drawn around each experimental point. The smooth curve is an error function complement, which on differentiation gives the normal distribution describing the concentration profile itself. The significance of C(2) and $C_s(2)$ is discussed in the text.

out, plotted out as in Fig. 2, and punched out on IBM cards for subsequent analysis by the fitting programs.

The purpose of the analysis was to compare the concentration profiles of the noble gases before and after the anodization event. To that end, the experimental data were analyzed for two parameters; one defining the noble gas position, and the other its dispersion about that position. The initial range profiles could be adequately fitted by a normal distribution (3), in which the mode defined the position and the standard deviation the dispersion. Fortunately, the concentration profiles after anodization could also be fitted by a normal distribution, and so the parameters before and after were directly comparable.

The experimental data describe the integrated concentration profile, and so the function least squares fitted (3) was the integrated normal distribution

$$\mathrm{YFIT}(I) = \frac{C(1)}{2} \cdot \mathrm{erfc}\left(\frac{\mathrm{XFIT}(I) - C(2)}{\sqrt{2} \cdot C(3)}\right) + B \qquad [7]$$

where $C(1)$ is a normalizing factor, approximately equal to $Y(1)$; $C(2)$ is the mode of the distribution, and $C(3)$ its standard deviation; $\mathrm{XFIT}(I)$ and $\mathrm{YFIT}(I)$ are the fitted values of $X(I)$ and $Y(I)$, respectively; and B is a background correction.

Since the noble gases were implanted at low energy, the background correction needed was that for the 40 keV neutral tail (3), which has the form

$$B = \frac{C(4)}{2} \cdot \mathrm{erfc}\left(\frac{\mathrm{XFIT}(I) - C(2) - (r_{40} - r)}{\sqrt{2} \cdot \sqrt{(\sigma_{40})^2 + (C(3))^2 - \sigma_i^2)}}\right) \qquad [8]$$

where $C(4)$ is a normalizing factor, similar to $C(1)$; r_{40} is the modal range and σ_{40} is the standard deviation of the noble gas implanted at 40 keV; r is the modal range, and σ_i the standard deviation at the implanted energy.

Values for r_{40}, σ_{40}, r, and σ_i were obtained from the range studies reported in the previous paper (3), and best values for the four parameters $C(1)$, $C(2)$, $C(3)$, and $C(4)$ computed from the fit.

The form of the final concentration profile is determined by the action of the broadening process on the initial profile. Since both initial and final concentration profiles can be analyzed as normal distributions, it follows that the broadening process must also give rise to a normal distribution. Accordingly, the final standard deviation $C(3)$ can be expressed as the sum of components

$$(C(3))^2 = \sigma_i^2 + \sigma_{bn}^2 \qquad [9]$$

where σ_{bn} is the standard deviation associated with the broadening.

Correction for truncation of initial range profiles.— Although the final concentration profiles could all be adequately fitted by a normal distribution, it is nonetheless certain that this cannot be the correct description. As discussed elsewhere (3), the initial range profiles are probably not normal distributions, but can be treated within experimental error as though they are. In any event, they are not complete normal distributions because they are truncated by the oxide surface. Normal broadening of a truncated normal distribution leads , as in Fig. 3, to a final profile that is almost, but not quite, normal; the departure from normality will increase with increased truncation and decrease with increased broadening. Experimentally, the truncation was less and the broadening more than that for the sample illustrated, and so the departure from normality was actually very small. Nevertheless, it was significant for the experimental accuracy achieved here, and therefore had to be taken into account.

The most striking feature of Fig. 3 is that the mode of the fitted normal distribution does not coincide with the mode of the initial distribution. As the broadening increases, it corresponds more and more to the initial

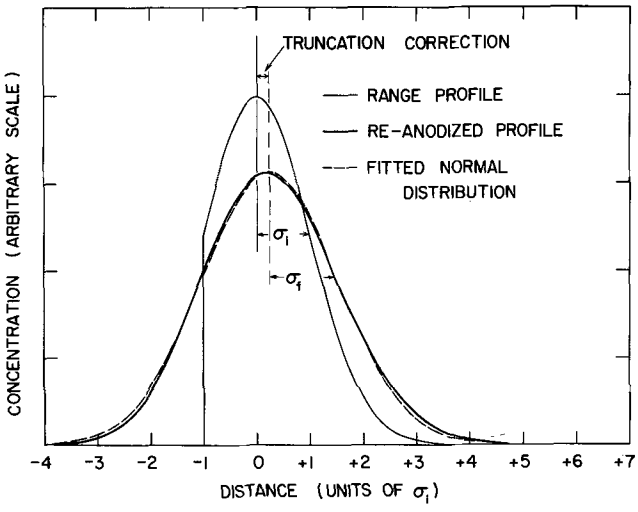

Fig. 3. Relationship between the initial truncated range profile, the same profile broadened after further anodizing, and the corresponding fitted normal distribution. The mode of the fitted normal distribution does not coincide with the mode of the initial profile, and so a truncation correction is required. In the example shown, the standard deviation associated with the broadening, σ_b, was taken equal to σ_i.

mean rather than the mode. The parameter $C(2)$ is therefore in error, and hence $C(3)$ is also in error. An attempt to define the correct mathematical function led to an integral that could not be evaluated analytically, and so the function was simulated numerically by the procedure illustrated in Fig. 4.

The initial concentration profile was divided into elements of equal width, and then simulated by the equivalent histogram shown in the top section of Fig. 4. An initial profile in the form of a line element was assumed to broaden to a normal distribution, and this too was simulated by the equivalent histogram shown in the center section. By summing the broadened histograms for each element in the initial histogram, the final profile could be obtained as illustrated at the bottom of the figure. Despite the crudeness of the ex-

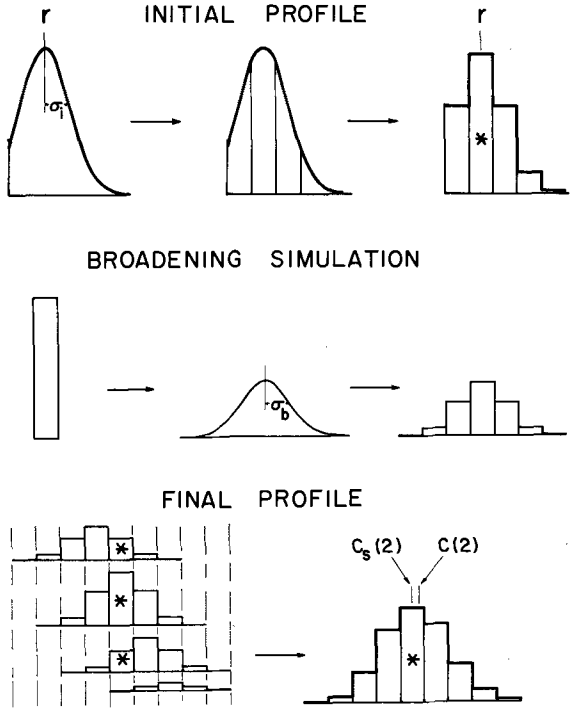

Fig. 4. Simulation of the broadening for a truncated normal distribution. The * indicates the element corresponding to the original mode.

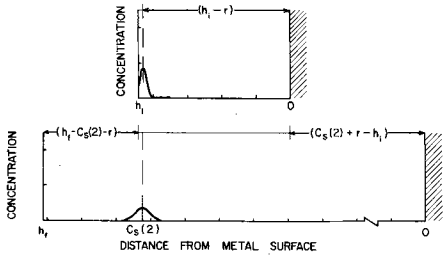

Fig. 5. Diagram illustrating the position of a noble gas marker before (above) and after (below) further anodization, and the quantities required for the calculation of transport number.

ample, the final histogram is obviously close to a normal distribution, and the shift in the mode is readily apparent. For the purpose of computation, the initial profile was split up into elements 1Å wide; the reanodized profile in Fig. 3 is an example of the results, computed with a standard deviation for broadening, σ_b, equal to $\sigma_i = 10$Å.

By summing the elements of the final histogram in succession, starting, in Fig. 4, from the right-hand end, the integrated concentration profile can be obtained. The shape of this is determined by the relative magnitudes of r, σ_i, and σ_b; the first two are known from the range measurements while σ_b is a parameter, $C_s(3)$, that must be fitted. To make a least squares fit through the experimental points, a normalizing factor, $C_s(1)$, is required as before for matching to the $Y(I)$, and a positioning factor, $C_s(2)$, for matching to the $X(I)$. The positioning factor here corresponds exactly to the mode of the initial profile, and so no truncation correction is needed. Finally, a background correction for the neutral tail, involving the adjustable parameter, $C_s(4)$, was made in the same way as before, using a slightly modified version of Eq. [8]. The least squares fitting procedure was then applied to obtain best estimates for $C_s(1)$, $C_s(2)$, $C_s(3)$, and $C_s(4)$, together with their errors. It should be noted that while $C_s(1)$, $C_s(2)$, and $C_s(4)$ are essentially the same as $C(1)$, $C(2)$, and $C(4)$, $C_s(3)$ is not the same as $C(3)$; the former is the standard deviation for the broadening alone, and thus corresponds to σ_{bn} in Eq. [9].

The experimental data were fitted by both the integrated normal distribution and the simulated distribution to see which gave the better fit. No distinction was possible, however, since the fitting probabilities determined from the χ-square test were virtually identical. All fits, except one for ^{222}Rn, were acceptable; that is, $p(\chi^2)_{N-4}$ was greater than 0.025 (3).

Calculation of transport numbers and their errors.—Assuming that the noble gases are ideal markers, the parameter $C_s(2)$ provides a measure of the transport numbers. Writing h_i for the initial oxide thickness and h_f for the final oxide thickness, it can be shown, as in Fig. 5, that the oxide thickness formed outside the marked layer due to tantalum migration is $h_f - C_s(2) - r$. Similarly, the thickness formed underneath the marked layer due to oxygen migration is $C_s(2) + r - h_i$. The transport numbers for the tantalum, t_m, and oxygen, t_o, are therefore

$$t_m = (h_f - C_s(2) - r)/(h_f - h_i)$$
$$t_o = (C_s(2) + r - h_i)/(h_f - h_i) \quad [10]$$

and the standard error in each of these ratios is

$$\epsilon_t = \sqrt{[(C_s(2) + r - h_i)^2 \cdot (\epsilon(h_f))^2 + (h_f - C_s(2) - r)^2 \cdot (\epsilon(h_i))^2 + (h_f - h_i)^2 \cdot (\epsilon(C_s(2) + r))^2]/(h_f - h_i)^2} \quad [11]$$

where

$$\epsilon(h_f) = \sqrt{[(0.00144h_f)^2 + EHF^2]}$$
$$\epsilon(h_i) = \sqrt{[(0.00144h_i)^2 + EHI^2]}$$
$$\epsilon(C_s(2) + r) = \sqrt{[(0.00144C_s(2))^2 + (EC_s(2))^2 + ERA^2]}$$

and EHF is the measured random error in h_f, EHI the measured random error in h_i, $EC_s(2)$ the computed error in $C_s(2)$, and ERA is the computed error in r obtained from previous work (3).

The first term in the errors $\epsilon(h_f)$, $\epsilon(h_i)$, and $\epsilon(C_s(2) + r)$ is, in effect, a systematic error due to uncertainty in the exact value for the refractive index; the factor of 0.00144 is calculated (1) from data by Young. These systematic errors are not independent of one another, but have been treated in the derivation of Eq. [11] as though they are: ϵ_t is therefore somewhat of an overestimate.

Results

Experiments were performed with the radioactive isotopes ^{41}Ar, ^{79}Kr, ^{125}Xe, and ^{222}Rn and the results are listed in Tables I, II, and III. The experiments with radon must be considered less reliable than the others for reasons which are unknown (3).

Error in transport number measurements.—Tables I and II show that the fluctuations in the measured transport numbers are generally consistent with the standard errors calculated from [11].

Variation of transport number with noble gas position in initial oxide.—Mechanisms IV and V require such variation; mechanisms I, II, and III do not. This was studied by implanting 5 keV ^{125}Xe into various thicknesses of initial oxide. Since the xenon was always implanted to the same depth, varying the initial oxide thickness was equivalent to varying its relative position within the oxide. Examination of Tables I and II shows that the transport numbers did not vary significantly with initial position of the noble gas.

Variation of transport number with increasing oxide thickness on reanodization.— Mechanism V predicts such variation while none of the others do. Table I shows that no variation was observed.

Table I. Variation of σ_b and t_o with $(h_f - h_i)$

Anodic tantalum oxide implanted with 5 keV ^{125}Xe (r = 30.0 ± 2.0A, σ_i = 20.2 ± 0.7A) and reanodized at 1 mA/cm² and 25°C in 0.1M H_2SO_4. Data obtained by least squares fit of a truncated normal distribution that had been broadened by the procedure in Fig. 4 using elements 1A wide; fits acceptable if $p(\chi^2)_{N-4} > 0.025$ (3). All thickness measurements have been rounded to the nearest angstrom, which is why they do not sum properly. Standard errors quoted.

Final thickness, h_f (Å)	Initial thickness, h_i (Å)	Incremental thickness, $(h_f - h_i)$ (Å)	Standard deviation for broadening, σ_b (Å)	Transport number for oxygen, t_o	Points used in fit, N	Chi-square probability, $p(\chi^2)_{N-4}$
1007	881	125	—	$0.73_5 \pm 0.02_5$[a]	14	0.465[a]
1112	875	237	9.6 ±1.4	$0.73_2 \pm 0.01_4$	14	0.651
1326	882	443	13.5 ± 3.2	0.750 ± 0.008	13	0.140
1758	884	874	26.1 ± 0.7	0.746 ± 0.004	17	0.510
2211	880	1330	29.6 ± 1.6	0.741 ± 0.003	17	0.042
2666	887	1779	35.7 ± 1.3	0.752 ± 0.003	13	0.526
3023	885	2139	38.4 ± 1.5	0.746 ± 0.003	12	0.945
3536	885	2651	41.8 ± 2.9	0.747 ± 0.002	13	0.422
4092[b]	221	3872	51.7 ± 0.7	0.752 ± 0.002	17	0.948

[a] Fitted by integrated normal distribution as the final standard deviation was less than the initial.
[b] Anodized in 0.01M KI, since this thickness cannot be attained in 0.1M H_2SO_4.

Table II. Variation of σ_b and t_o with noble gas used

The experimental conditions were exactly the same as those for Table I

Final thickness, h_f(Å)	Initial thickness, h_i(Å)	Incremental thickness, $(h_f - h_i)$(Å)	Standard deviation for broadening, σ_b(Å)	Transport number for oxygen, t_o	Points used in fit, N	Chi-square probability, $p(\chi^2)_{N-4}$
		^{41}Ar implanted at 2 keV; $r = 15.2 \pm 3.2$Å, $\sigma_i = 20.2 \pm 1.3$Å[a]				
3024	881	2134	54.7 ± 0.4	0.740 ± 0.003	19	0.995
3019	880	2139	55.8 ± 0.3	0.742 ± 0.003	19	1.000
		^{79}Kr implanted at 5 keV; $r = 27.2 \pm 2.0$Å,[b] $\sigma_i = 22.0 \pm 0.6$Å				
3020	895	2125	46.4 ± 1.2	0.744 ± 0.003	14	0.905
3019	894	2125	46.2 ± 1.3	0.742 ± 0.003	14	0.774
		^{125}Xe implanted at 5 keV; $r = 30.0 \pm 2.0$Å, $\sigma_i = 20.2 \pm 0.7$Å				
2378	373	2005	37.5 ± 0.6	0.745 ± 0.002	12	0.887
2377	377	2000	36.0 ± 0.6	0.748 ± 0.002	12	0.763
3024[c]	885	2139	38.4 ± 1.4	0.746 ± 0.003	12	0.945
3026	885	2141	38.9 ± 1.0	0.746 ± 0.003	13	0.987
3023[d]	905	2118	37.2 ± 0.6	0.746 ± 0.003	15	0.826
		^{222}Rn implanted at 5 keV; $r = 36.5 \pm 1.9$Å,[e] $\sigma_i = 18.0 \pm 0.4$Å				
2016	220	1796	35.1 ± 1.5	0.749 ± 0.002	12	0.000
2895	223	2672	42.5 ± 0.5	0.747 ± 0.002	12	0.355
3802	221	3581	43.8 ± 0.9	0.750 ± 0.002	13	0.472

[a] Parameters quoted are for 2 keV ^{42}K (3).
[b] Range very small compared to results quoted in (3); measured in same implantation as that used for the reanodization experiments.
[c] Illustrated in Fig. 2.
[d] Specimen originally anodized to 2031Å and then stripped back to 885Å in order to remove the layer containing sulfur species (9).
[e] Range unusually large; reason not known (3).

Variation of profile broadening with increasing oxide thickness on reanodization.—Mechanisms I, II, and III predict no broadening, IV that the breadth of the marker profile will vary as h_f, and V that the increase in the profile breadth will vary as $(h_f - h_i)$.

Table I shows that there is a broadening, but that it is definitely not proportional to h_f. To find out if the increase was proportional to $(h_f - h_i)$, the last eight samples of Table I were fitted to an equation of the form

$$(C(3) - \sigma_i) = c \cdot (h_f - h_i) \qquad [12]$$

where $C(3)$ is used in place of $C_s(3)$ because it is the observed breadth of the profile that is being tested. The proportionality constant, c, was found to be 0.0095 ±0.004, but $p(\chi^2)_7$ was far less than 0.001; the fit was therefore unacceptable. Accordingly, the broadening is not proportional to $(h_f - h_i)$ either.

The same samples were, however, successfully fitted by an equation of the form

$$C_s(3) = \beta \cdot \sqrt{(h_f - h_i)} \qquad [13]$$

with $\beta = 0.835 \pm 0.011$, and $p(\chi^2)_7 = 0.135$; the latter is well above the 0.025 rejection level (3).

Variation of transport number with noble gas used.—If the noble gases are truly immobile, then, by criterion (*a*), the transport numbers measured with the different gases should be identical. The data in Tables II and III, however, suggested that there was a slight variation. To find out whether this variation was significant, the statistical *t* test was applied as follows. Assuming that there were no significant differences between the individual variances for t_o, a pooled estimate for the variance was obtained from

$$S^2_{t_o} = \sum_I [(n_I - 1) \cdot S^2_I] / [\sum_I n_I - 3] = (0.00127)^2 \qquad [14]$$

Table III. Summary of the positioning, t_o, and broadening, β, parameters for the noble gases

Values of t_o are arithmetic means of the data in Table II, quoted with the standard deviation about those means; β and its extrinsic error are obtained from least squares fits of $\sigma_b = \beta \cdot \sqrt{(h_f - h_i)}$ to the same data. All fits were acceptable; i.e., $p(\chi^2)_{N-1} > 0.025$.

Noble gas	t_o	β
^{41}Ar	0.7413 ± 0.0017	1.196 ± 0.013
^{79}Kr	0.7432 ± 0.0011	1.005 ± 0.003
^{125}Xe	0.7461 ± 0.0012	0.821 ± 0.007

where I = Ar, Kr, Xe; n_I are the number of measurements with each gas and S^2_I are the individual variances. Three test values τ were then formed by

$$\tau_{I,J} = (t_{oI} - t_{oJ}) / [S_{t_o} \cdot \sqrt{(1/n_I + 1/n_J)}] \qquad [15]$$

where I, J = Ar, Kr, Xe and I ≠ J. The probability, $p(\tau_{I,J})_F$, of obtaining a value of τ as great or greater than $\tau_{I,J}$ was then computed for $F = n_1 + n_J - 2$ degrees of freedom, and found to be

$$p(\tau_{Ar,Kr})_2 = 0.139$$
$$p(\tau_{Kr,Xe})_5 = 0.020$$
$$p(\tau_{Xe,Ar})_5 = 0.003 \qquad [16]$$

Since both the second and the third probability is less than the acceptance level of 0.05 for a one tailed test, the differences between argon and xenon, and krypton and xenon, are statistically significant.

Variation of profile broadening with noble gas used.—If the noble gases are truly immobile, then, by criterion (*b*), their profiles should either not broaden at all, or they should all broaden equally. Tables II and III show that although they all broaden, they do not do so equally.

Discussion

The results obtained, therefore, are consistent with none of the mechanisms presented earlier, and the noble gases do not meet the criteria for immobile markers. They must therefore be mobile, and the nature of their mobility must be elucidated before the oxidation mechanism can be discussed.

Characteristics of profile broadening.—Two features of the broadening process have been established experimentally. First, the broadening can be described in terms of a normal distribution, and second, the standard deviation for the increase in the profile breadth, σ_b or $C_s(3)$, is proportional to $\sqrt{(h_f - h_i)}$. Since more than one broadening process may occur, σ_b can be expressed in terms of its components by

$$\sigma_b^2 = \sum_{j=1}^{n} \sigma_j^2 \qquad [17]$$

where σ_j is the standard deviation associated with the *j*th process. Because of the squared dependence, the value of σ_b is determined mainly by the magnitude of the largest σ_j, and so this must also vary as $\sqrt{(h_f - h_i)}$.

In fact, the broadening must be due to at least two processes. Measurement of the concentration profiles by means of the sectioning technique involves the removal of thin oxide layers, and inevitably these will not be completely uniform. If nonuniform layers are being removed, the measured profile will be broader than the real one. This type of broadening must occur to some extent, but it is obviously not the dominant process; for if it were, the noble gas profiles would all broaden equally. The nature of the nonuniformities has been studied in a previous paper (1), where it was shown that they are so small as to be effectively negligible for the measurement of concentration profiles. The observed broadening must, therefore, be due to some other process, or group of processes, that depends on the nature of the noble gas itself.

Interpretation of profile broadening.—If the noble gases are mobile, they must be undergoing some form of diffusion. This would account very well for the dependence on $\sqrt{(h_f - h_i)}$, and for the normalcy of the profile broadening. The dependence on $\sqrt{h_f - h_i}$ shows that the diffusion takes place only during anodization, thus confirming that thermal diffusion in the static oxide is negligible (5). Such diffusion could occur in at least three ways, as illustrated in Fig. 6.

(i). The noble gas atoms could be forced to diffuse under the influence of the applied field because they are charged. Since they differ in size and mass, and presumably also in degree of ionization, they may be expected to diffuse at substantially different rates. They would therefore finish up at markedly different positions in the final oxide, and so the transport numbers actually measured would depend on the noble gas used.

As a first approximation, one may assume that noble gas ions diffuse in the same way as the tantalum and oxygen ions. The first question is whether the latter jump from one lattice site to the next, or whether they jump several lattice sites at a time. Evidence presented in the next paper (4) will show that the oxygen ions, at least, jump a distance corresponding to not much more than one interoxygen distance; no evidence is presently available on the migration of the tantalum ions.

The proposed model, then, is that shown schematically at the top of Fig. 6. Here the charge transfer event is the movement of an individual ion from one lattice site to the next as space becomes available, and so the migration of tantalum and/or oxygen ions is balanced by a flow of vacancies in the opposite direction. The concepts of "vacancy" and "lattice site" are rather difficult to define in an amorphous solid such as anodic tantalum oxide, but the usual concepts will serve as a basis for the present discussion.

Some rather simple arguments can be used to predict the profile broadening that would result from such

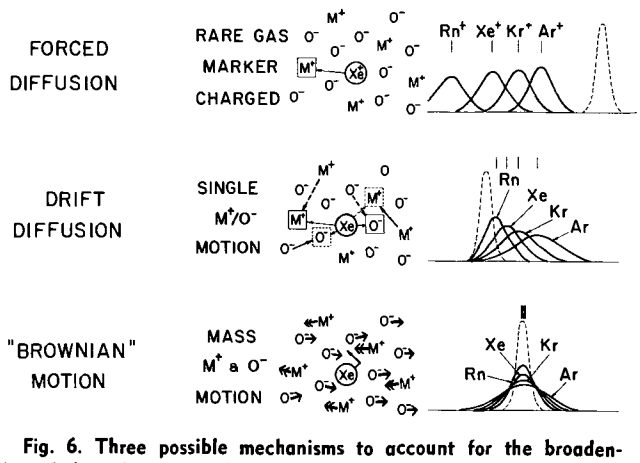

Fig. 6. Three possible mechanisms to account for the broadening of the noble gas profiles on further anodizing. The applied field is such that the metal atoms migrate to the left, oxygen to the right.

diffusion. In discussing the "high field approximation" for the motion of an ion in anodic oxide, Young (17) noted that the most probable jumps would be those in directions close to the axis of the field, and in the forward direction; the probability of a jump in a backward direction, against the field, would be remote. The concentration of the jumps around the forward axis of the field would mean that if the jump distance was a, the average distance jumped along this axis would also be close to a, and hence almost constant from jump to jump. For simplicity, it may be assumed that the jump distance along the axis of the field is constant and equal to a.

Under these conditions, the mean distance diffused by the noble gas atoms will be $a \cdot n$, where n is the mean number of jumps made. The constancy of the transport numbers in Table I requires that the distance diffused, d, be proportional to the thickness added during anodization, so that

$$d = k \cdot (h_f - h_i) = a \cdot n \qquad [18]$$

where k is a constant of proportionality. The root mean square deviation about this mean will be equal to the square root of the sum of the variances in n and a; the latter is of course zero since a has been assumed constant. For a series of uncorrelated jumps, n follows a Poisson distribution with mean and variance both equal to n; if n is large, the Poisson distribution approximates to a normal one. The standard deviation for the normally distributed profile broadening, σ_b, can then be equated with the root mean square deviation in the distance traveled, so that

$$\sigma_b = a \cdot \sqrt{n} \qquad [19]$$

provided n is large. Substituting [18] into [19]

$$\sigma_b = \sqrt{(a \cdot k)} \cdot \sqrt{(h_f - h_i)} \qquad [20]$$

so that σ_b has the observed dependence on $(h_f - h_i)$.

Combining [18] and [19] for two different gases, say argon and xenon, gives

$$d_{Ar} - d_{Xe} = (\sigma^2_{Ar} - \sigma^2_{Xe})/a \qquad [21]$$

since the proposed mechanism requires that a be the same for all gases. The left-hand side of this equation is equivalent to $-(t_o(Ar) - t_o(Xe)) \cdot (h_f - h_i)$; substituting [13] into the right-hand side, and eliminating $(h_f - h_i)$ gives

$$-(t_o(Ar) - t_o(Xe)) = (\beta^2_{Ar} - \beta^2_{Xe})/a \qquad [22]$$

in which the only quantity not determined experimentally is a. When the values listed in Table III are substituted into this equation, a is found to be 160Å, which is an absurd result for the model chosen. To put it another way, if a is to be the expected interatomic distance of about 3Å, Eq. [22] requires that either $|t_o(Ar) - t_o(Xe)|$ be about 0.25, or that β^2_{Ar} be nearly equal to β^2_{Xe}; both possibilities are far outside the experimental error in the results. The noble gases do not therefore move by jumping one interatomic distance at a time.

The possibility remains that they might move more than one interatomic distance at a time; for example, they might actually move 160Å at a time. Given the values for σ_b in Tables I and II, it follows from [19] that n would be considerably less than unity in all cases. Few of the noble gas atoms would therefore move, and they would form a satellite normal distribution 160Å to one side of the original range profile. Similar arguments can be advanced to eliminate other distances.

In deriving [22], it was assumed that the jumps were all in the same direction, and that they were all of equal length. Neither of these assumptions is strictly true, but small departures therefrom will not affect the conclusions reached. Large departures mean that the physical picture of the motion is not as presented;

any other form of forced diffusion seems much less probable. Accordingly, forced diffusion can be eliminated as a possibility.

(*ii*). The noble gas atoms could diffuse via a vacancy mechanism even if they were uncharged. If they are to diffuse at all, they must be capable of jumping into neighboring vacancies, and if they are uncharged, it seems reasonable to suppose they would jump with equal probability in all directions. In making their jumps, however, the noble gas atoms would have to compete for oxygen vacancies with neighboring oxygen ions, and the latter, being charged, would have a marked preference for jumping downfield. The noble gas atoms would therefore tend to jump in the same direction because, as indicated in the middle of Fig. 6, there would be less oxygen competition for the vacancy labeled by the solid square than for that labeled with the pecked square. Similar arguments can be applied to the metal vacancies, and so the net movement of the noble gas atoms would be determined by a combination of the two processes.

The charge transfer event is therefore the same as before, and the noble gas atoms can be regarded as drifting along in the wake of the moving ions, instead of racing with them. Except in the event that the drifts in the two directions are equal, there will be a net motion of the noble gas atoms in one direction or the other. Movement of the different noble gases will depend as before on their size and mass, and so the measured transport numbers will again depend on the noble gas used.

For the drifts in both directions to be equal, the ratio of the probabilities for jumping into tantalum and oxygen vacancies must be equal to the inverse ratio of the corresponding jump distances. Such a cancellation would be highly unlikely for even one gas, and would be impossible for four. The noble gases would almost certainly jump into one kind of vacancy alone, and then only if it was immediately downfield. The mathematics would thus be the same as for forced diffusion, and so the same conclusion applies; it, too, must be rejected.

(*iii*). A third possibility for the diffusion of the noble gas atoms arises if charge is transported through the oxide by the simultaneous movement of a group of atoms. In this model, illustrated at the bottom of Fig. 6, each moving atom carries a fraction of the charge a fraction of a "lattice spacing" in such a way that the total effect is equivalent to one charged atom jumping one "lattice spacing." Both tantalum and oxygen take part in this process, so that the lattice loses its rigidity during the charge transfer event. A noble gas atom situated in the middle of a group of moving tantalum and oxygen atoms must collide with them, and will therefore be subjected to a form of Brownian motion.

True Brownian motion occurs when a particle undergoes a series of displacements, the displacements being of random length and direction. Mathematically, the process can be described as a random walk, whose properties are well known (18). The mean position of such particles remains unchanged, but their dispersion about that mean position increases in proportion to the square root of the time; the concentration profile therefore broadens, and the broadening follows a normal form. Furthermore, it can be shown that the broadening should be approximately proportional to the square root of the reciprocal of the particle radius; that is, the concentration profile of the smallest particles should broaden most. This has been confirmed experimentally for colloidal particles in water (18).

The most familiar illustration of Brownian motion is that discovered by Brown himself; pollen grains suspended in water undergo continual random displacements due to fluctuations in the number of water molecules striking them from each direction. The proposal here, then, is that noble gas atoms embedded in anodic Ta_2O_5 undergo similar displacements during anodization, due to collisions with the moving tantalum and oxygen atoms. At constant current, the increase in the oxide thickness, $(h_f - h_i)$, is directly proportional to the anodization time; since the profile broadening is observed experimentally to be proportional to $\sqrt{(h_f - h_i)}$, it is also proportional to the square root of the time, as required. Furthermore, the profile of the smallest and lightest gas, ^{41}Ar, shows the greatest degree of broadening, again as required.

There is, however, one important difference between ordinary Brownian motion and that postulated here. Water molecules striking the pollen grains have a truly random motion of their own, and so the pollen particles may be expected to behave likewise. In the anodic oxide, however, the motion of the tantalum and oxygen atoms will be largely aligned with the axis of the electric field, the tantalum ions jumping toward the oxide/electrolyte interface, while the oxygen ions jump in the opposite direction. Under these conditions, the noble gas displacements can hardly be random; the inevitable consequence would be a small net motion superimposed on the random component. Once again, therefore, the transport numbers actually measured would depend on the noble gas used.

The magnitude of this net migration is impossible to predict, but since it is a consequence of the broadening process, it would presumably be very small. If so, the differences between the various noble gases would also be very small, as observed experimentally. Calculations based on the data in Table III show that the difference between the argon and xenon positions is 9.6 ± 3.8Å after reanodization by 2000Å, whereas the corresponding difference in the standard deviations is 16.8 ± 0.5Å.

The broadening of the noble gas concentration profiles on further anodizing is therefore attributed to a form of Brownian motion.

Validity of noble gases as inert, immobile markers.—If this Brownian motion hypothesis is true, no markers will be immobile during anodic oxidation of tantalum. All will be subjected to this form of Brownian motion, and so all will have a net migration imposed on their random fluctuations. As the markers get bigger and heavier, the fluctuations will decrease, and hence the magnitude of the net migrations will also decrease. The differences in migration rate will therefore decrease until they are no longer experimentally detectable as differences in the measured transport numbers. At this point, the markers will behave as though they were effectively immobile; but they may by then be so large that they are no longer effectively inert. That is, their geometric interference with the oxidation system may be so great that the final position of the marker depends not on its migration, but on its size. Results by Sachs (19) appear to illustrate this phenomenon experimentally.

In these circumstances, therefore, no truly inert, immobile marker for the system exists. The best that can be done is to find that set of markers that obeys criteria (*a*) and (*b*) most closely. Noble gas markers do obey these criteria rather closely, but it is uncertain, in the absence of comparable information on other possible markers, whether they obey the most closely.

Best estimates for transport numbers.—The data in Table III can be corrected for marker migration by assuming that the distance migrated is directly proportional to the standard deviation for the broadening. It is then possible to extrapolate the β *vs.* t_o data to $\beta = 0$, and hence calculate t_o for a noble gas marker that undergoes no broadening at all; that is, one which undergoes no Brownian motion, and is therefore truly immobile.

Three points are insufficient for a satisfactory least squares fit to a straight line, but graphical extrapolation gave $t_o = 0.757$, with a standard error that may be estimated as about 0.003. This can be taken as the best estimate for the transport number of oxygen in anodic tantalum oxide under the conditions stated;

25°C, 1 mA/cm², 0.1M H_2SO_4 electrolyte, and reanodization to add approximately 2000Å. The transport number of the metal is therefore 0.243 ± 0.003.

Transport mechanism in anodic tantalum oxide.—If the broadening of the marker profiles can be accounted for entirely on the basis of Brownian motion, mechanisms IV and V in Fig. 1 must be eliminated. Since the transport numbers are not 1 and 0, mechanisms I and II must also be eliminated. Accordingly, the transport mechanism is best described by III, in which the new oxide is formed at the metal/oxide and oxide/electrolyte interfaces only.

Conclusions

1. A marker used for measuring transport numbers during the oxidation of a metal must be both immobile and inert. Any inert immobile marker will behave in exactly the same way as any other inert immobile marker.
2. This definition has been used to test the suitability of the radioactive noble gas markers, ^{41}Ar, ^{79}Kr, ^{125}Xe, and ^{22}Rn during the anodic oxidation of tantalum. Although these markers are effectively inert, they are not immobile.
3. Their small mobility has been attributed to a form of Brownian motion resulting from collisions with migrating tantalum and oxygen atoms.
4. This necessarily requires that both tantalum and oxygen migrate during the anodic oxidation, and that these migrations occur simultaneously.
5. The oxide thickens through the formation of new oxide at the metal/oxide and oxide/electrolyte interfaces only.
6. Best estimates for the transport numbers of the tantalum and oxygen are 0.243 ± 0.003 and 0.757 ± 0.003, respectively, for anodizing conditions of 25°C, 1 mA/cm², 0.1M H_2SO_4 electrolyte, and 2000Å thickness of oxide added.

The significance of these conclusions will be discussed in a later paper.

Acknowledgments

Grateful thanks are due to D. Hall, C. Sitter, J. Tole, and O. Westcott for implantations with the mass separator, to D. Phillips for assistance with the experiments, and to J. A. Davies, T. A. Eastwood, J. A. L. Robertson, and J. L. Whitton for comments on the manuscript.

Manuscript submitted March 9, 1972; revised manuscript received Oct. 30, 1972.

Any discussion of this paper will appear in a Discussion Section to be published in the December 1973 JOURNAL.

REFERENCES

1. J. P. S. Pringle, *This Journal*, **119**, 482 (1972).
2. J. P. S. Pringle, "The Effect of Ion Implantation on Certain Properties of Anodic Tantalum Oxide," To be submitted to *This Journal*.
3. J. P. S. Pringle, "Range Profiles for Ions Implanted into Anodic Tantalum Oxide," To be submitted to *This Journal*.
4. J. P. S. Pringle, "The Migration of Oxygen during the Anodic Oxidation of Tantalum," To be submitted to *This Journal*.
5. J. A. Davies, B. Domeij, J. P. S. Pringle, and F. Brown, *This Journal*, **112**, 675 (1965).
6. R. W. Powers and M. V. Doyle, *J. Appl. Phys.*, **30**, 514 (1959).
7. J. L. Whitton, *This Journal*, **115**, 58 (1968).
8. J. A. Davies, F. Brown, and M. McCargo, *Can. J. Phys.*, **41**, 829 (1963).
9. A. J. Schrijner and A. Middelhoek, *This Journal*, **111**, 1167 (1964).
10. J. J. Randall, Jr., W. J. Bernard, and R. R. Wilkinson, *Electrochim. Acta*, **10**, 183 (1965).
11. J. A. Davies and B. Domeij, *This Journal*, **110**, 849 (1963).
12. J. Siejka, J. P. Nadai, and G. Amsel, *ibid.*, **118**, 727 (1971).
13. R. L. Graham, F. Brown, J. A. Davies, and J. P. S. Pringle, *Can. J. Phys.*, **41**, 1686 (1963).
14. B. Domeij, I. Bergstrom, J. A. Davies, and J. Uhler, *J. Arkiv. Fysik.*, **24**, 399 (1963).
15. B. Maurel, D. Dieumegard, and G. Amsel, Electrochemical Society Meeting, Cleveland, Oct. 3-7, 1971, Abstract 88.
16. D. Walker, Atomic Energy of Canada Ltd., Report AECL 2502 (1965).
17. L. Young, "Anodic Oxide Films," Academic Press, New York (1961).
18. M. H. Jacobs, "Diffusion Processes," Springer Verlag, Berlin (1967).
19. K. Sachs, *Metallurgia*, **54**, 11 (1956).

Gallium Arsenide Surface Film Evaluation by Ellipsometry and Its Effect on Schottky Barriers

A. C. Adams* and B. R. Pruniaux

Bell Telephone Laboratories, Incorporated, Murray Hill, New Jersey 07974

ABSTRACT

To evaluate polishing and cleaning methods for gallium arsenide, the surface film thickness is estimated by ellipsometry. For measurements made at a wavelength of 5461Å, a refractive index of 1.9 is assumed for the film, and an extinction coefficient of 0.304 is assumed for the gallium arsenide. The film thickness is found to be correlated with the cleaning method and a simple and effective cleaning procedure is proposed. The refractive index and the extinction coefficient measured at wavelengths of 4375 and 5461Å for gallium arsenide samples prepared by three commonly used polishing techniques are the same as those of freshly grown epitaxial gallium arsenide. For clean samples the thickness of the surface film increases when the gallium arsenide is exposed to air until a final thickness of about 30Å is reached after a few days. Experimental data describing the behavior of Schottky diodes on differently prepared surfaces are presented. The barrier height increases by 0.07 eV when the thickness of the film increases from 8.5 to 16Å. The reverse bias current-voltage characteristics are explained by existing interfacial layer theories. The annealing of aluminum oxide films on gallium arsenide is also reported.

The use of ellipsometry to study the chemical processing of silicon wafers has been previously described (1, 2). Because the ellipsometric measurements are rapid, nondestructive, and very sensitive to small changes in the sample surface, this technique is ideally suited for studying the surfaces which result after polishing and cleaning of semiconductiors (2). In this paper, we describe the use of ellipsometry to study and evaluate the polishing and cleaning of gallium arsenide. In addition, results on the use of ellipsometry to study thick, nonabsorbing films on gallium arsenide substrates and the behavior of Schottky diodes on differently prepared gallium arsenide surfaces are presented.

Experimental

The experimental data have been obtained with a Gaertner Model L119 ellipsometer. The light source is a 150W xenon arc lamp which is used with a Schoeffel quartz prism monochromator. A photomultiplier is used as the detector. The light source, monochromator, and ellipsometer are mounted on a metal table to reduce vibration and eliminate errors due to misalignment of the components. The measurements are made in a dark, laminar flow clean booth. The dark room is necessary to prevent spurious results due to stray light entering the detector. The clean atmosphere prevents particulate contamination of the samples during the measurements. All ellipsometric measurements have been made at an angle of incidence of 70.00° using radiation with a wavelength of 4375 or 5461Å. At both wavelengths, extinction is measured at two settings of the polarizer and analyzer (zones 1 and 3) (3), and psi and delta are calculated from these settings using the equations for nonideal compensators (4).

The samples are n-type gallium arsenide with a (100) orientation and a carrier concentration of about 1×10^{18} cm^{-3}. The Schottky diode measurements are made on epitaxial gallium arsenide deposited by the arsenic trichloride transport process; the epitaxial layers have a (100) orientation and a carrier concentration near 5×10^{15} cm^{-3}. The Schottky diodes have been formed by evaporating a gold-germanium compound [12 atomic per cent (a/o) Ge] or pure gold at a substrate temperature of 100°C to give a metal film 3000Å thick.

* Electrochemical Society Active Member.

Key words: cleaning, dielectric films, interfacial layer, oxidation, semiconductor devices.

Procedure

The model used to interpret the ellipsometric data assumes that the substrate, which has a complex refractive index, n_2-ik_2, is covered by a nonabsorbing film that is characterized by a real refractive index, n_1, and a thickness, d. It is further assumed that n_1 is independent of the film thickness, and that the substrate-film and film-air interfaces are flat and parallel. There are four variables in this model, n_2, k_2, n_1, and d. Because the ellipsometer measures only two quantities, psi and delta, both of which may be functions of all four variables, it is necessary to independently measure the values for two of these variables before the remaining two can be calculated from the ellipsometric data. We have taken values for k_2 and n_1 from the literature and have calculated the real part of the gallium arsenide refractive index, n_2, and the film thickness, d, from the ellipsometric measurements. For measurements made at a wavelength of 5461Å, the values of k_2 and n_1 are 0.304 and 1.9, respectively. The value of k is taken from the review by Seraphin and Bennett (5) and the recent paper by Lukes (6). The film on a gallium arsenide sample which has been exposed to air is reported to be gallium oxide (7, 8) with a refractive index of 1.9 (9) or 1.8 (10, 11).

The real part of the refractive index of the gallium arsenide, n_2, and the thickness of the film, d, are obtained from the measured values of psi and delta using the curves in Fig. 1. These curves, which show the values of psi and delta for values of n_2 between 4.01 and 4.15 and for values of d between 0 and 50Å, have been calculated using the computer program written by Cox (12). The experimental points are typical data for gallium arsenide samples polished and cleaned using the methods reported in this paper. The errors caused by using $n_1 = 1.90$ and $k_2 = 0.304$ are given in Table I. If the film refractive index is between 1.50 and 2.50 and the gallium arsenide extinction coefficient is between 0.25 and 0.35, the errors caused by assuming $n_1 = 1.90$ and $k_2 = 0.304$ are less than 0.4 and 23% for n_2 and d, respectively. Although this per cent error in d is large, the absolute error in the film thickness is still less than 4.5Å. Furthermore, this is a systematic error so that differences in film thickness can still be precisely measured.

The optical constants of the gallium arsenide surfaces have also been measured at a wavelength of 4375Å. The values of psi and delta measured at 4375Å are corrected for the presence of the surface

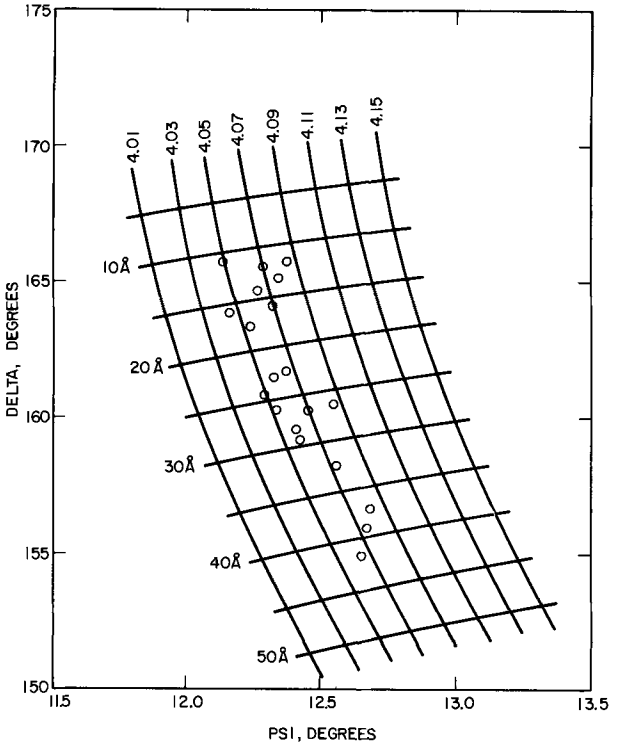

Fig. 1. Delta *vs.* psi for gallium arsenide refractive indices, n_2, from 4.01 to 4.15 and for film thickness, d, from 0 to 50Å. The curves are calculated for $k_2 = 0.304$, $n_1 = 1.90$, $\lambda = 5461$Å, and $\phi = 70.00°$.

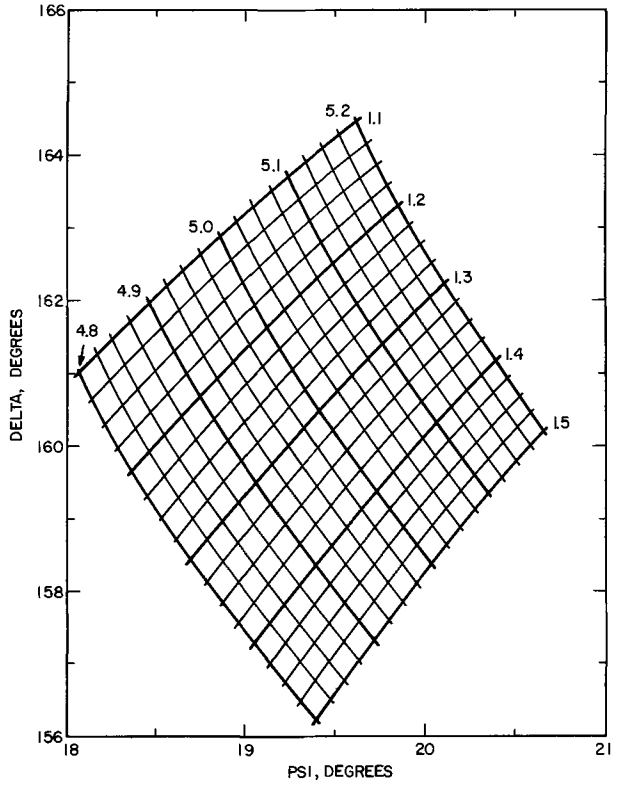

Fig. 2. Delta *vs.* psi for refractive indices, n_2 from 4.8 to 5.2 and for extinction coefficients, k_2, from 1.1 to 1.5. The curves are calculated for a film-free sample ($d = 0$) and $\phi = 70.00°$.

film using exact ellipsometric equations (13). The complex refractive index, n_2-ik_2, at a wavelength of 4375Å is determined from the corrected values of psi and delta using Fig. 2. This figure shows the values of psi and delta that would result from measurements made on clean surfaces with the real part of the refractive index between 4.8 and 5.2 and the imaginary part between 1.1 and 1.5.

The values for n_2 and k_2 obtained from Fig. 2 depend on the correction of the experimental values of psi and delta for the presence of the surface film. The magnitudes of the possible errors in n_2 and k_2 are given in Table II. The calculations presented in Table I indicate a possible error of less than 5Å in the film thickness. An uncertainty of this magnitude in the film thickness may cause an error of about 1% in the value for n_2 and about 10% error in the value for k_2.

Results

Polishing.—Values for d and n_2, which are obtained from Fig. 1, and for n_2 and k_2, which are obtained from Fig. 2, are given in Table III. Data are given for three polishing procedures and for freshly grown epitaxial samples. Each entry is an average of at least four separate experiments. Optical constants are not reported for samples polished by the hydrogen peroxide-ammonium hydroxide process because the computational procedure is not valid for samples with film thicknesses greater than about 50Å.

The values for n_2 and k_2 nearly agree with the values reported in the literature [n_2 equals 4.09 at 5461Å (5); k_2 equals 1.42 at 4375Å (5); n_2 is near a

Table I. Possible errors in n_2 and d caused by assuming values of 1.90 and 0.304 for n_1 and k_2 (calculated for $d = 20$Å, $n_2 = 4.050$, $\lambda = 5461$Å, and $\phi = 70.00°$)

n_1[a]	k_2[a]	n_2	d
1.50	0.304	4.054	17.0
1.75	0.304	4.052	19.0
2.00	0.304	4.049	20.0
2.25	0.304	4.042	19.0
2.50	0.304	4.035	18.0
1.90	0.250	4.041	15.5
1.90	0.275	4.045	17.0
1.90	0.304	4.050	20.0
1.90	0.325	4.054	22.0
1.90	0.350	4.060	23.5

[a] The tabulated values of n_1 and k_2 are used to calculate values for Ψ and Δ. Values for n_2 and d are obtained from the calculated values of Ψ and Δ using Fig. 1 which assumes that n_1 and k_2 are 1.90 and 0.304. The error is obtained by noting the deviation of n_2 and d from 4.050 and 20Å.

Table II. Possible errors in n_2 and k_2 caused by errors in the film thickness

Assumed film thickness, Å	n_2	k_2	Per cent error[a] n_2	k_2
5	4.890	1.52	4.12	26.6
10	4.965	1.42	2.65	18.3
15	5.035	1.31	1.27	9.2
20	5.100	1.20	0.00	0.0
25	5.145	1.08	0.88	10.0

[a] Values of Ψ and Δ were calculated for $n_1 = 1.90$, $d = 20$Å, $n_2 = 5.10$, and $k_2 = 1.20$. Values for n_2 and k_2 were then obtained from Fig. 2 after correcting Ψ and Δ for surface film with the different assumed thicknesses.

Table III. Gallium arsenide refractive index and the film thickness for different polishing techniques

Surface preparation	d[a]	n_2[a]	n_2[b]	k_2[b]
"Syton"-Br_2[c]	23.6	4.066	5.096	1.178
Br_2-methanol[d]	27.3	4.052	5.078	1.223
H_2O_2-NH_4OH[e]	73.6	—	—	—
Epitaxial deposit	11.0	4.050	5.073	1.215

[a] Determined from measurements made at 5461Å using Fig. 1.
[b] Determined from measurements made at 4375Å using Fig. 2.
[c] Syton is produced by the Monsanto Chemical Company; the polishing solution contains 5.7 ml bromine and 100 ml methanol in 1 liter of "Syton." The polishing rate is 10 μm/hr.
[d] Samples are polished with a 0.00916M solution of bromine in methanol. The polishing rate is approximately 1 μm/min.
[e] The samples are polished with a solution containing 1.41 ml of ammonium hydroxide in 1 liter of 30% hydrogen peroxide. The polishing rate is approximately 10 μm/hr.

maximum at 4375Å and is greater than 4.93 (5)]. There is no significant difference in the values of the optical constants for the different surface preparations. This agrees with previous work which reports that the optical constants of gallium arsenide are independent of the polishing technique (14) and that "Syton" polished samples have the same reflectance properties as epitaxially deposited samples (15).

The differences in the film thicknesses for the different polishing procedures should not be considered characteristic of the polishing process since these films can be easily removed by slight changes in the final cleaning. The cleanest surfaces have been observed in freshly grown epitaxial layers which have films that are 8-12Å thick. However, when gallium arsenide is exposed to air, the film thickness increases with time so that these thicknesses are strongly dependent on the time between the epitaxial deposition and the ellipsometric measurement. For our measurements, the epitaxial samples have been exposed to air for less than 10 min. The film that results from the H_2O_2-NH_4OH polish can be easily removed with hydrochloric acid. When the films are removed from the samples polished by the H_2O_2-NH_4OH technique, the optical constants of the resulting surfaces are the same as those reported in Table III. Except for the difference in film thickness, the ellipsometric data show that there are no differences in the surfaces produced by the three polishing methods. Furthermore, the surfaces obtained by these techniques are optically similar to the surface of an epitaxial layer.

Cleaning.—The results from several experiments to determine changes in film thickness when gallium arsenide samples are immersed in various solvents are reported in Table IV. The numbers give the film thickness in angstroms for samples immersed in the given reagent for times from 0 to 24 hr. In general, the film can dissolve giving a decrease in film thickness or the gallium arsenide can react with the reagents to produce a thicker film. The organic solvents listed in Table IV have only slight effects on the film thickness, even when the samples are immersed in the solvents for 24 hr. The film thickness is also only slightly affected when gallium arsenide is immersed in water for 5 min; however, the film thickness increases to about 100Å after 1 hr. This indicates that the gallium arsenide reacts with the water to form an insoluble film on the surface. The original films on the polished gallium arsenide samples partially dissolve in concentrated hydrochloric acid or sulfuric acid. For both reagents, the film thickness is reduced to 12 to 13Å after a 5 min treatment. However, thicker films form when the gallium arsenide remains in the sulfuric acid for 24 hr; consequently, long contact times with sulfuric acid should be avoided. Finally, hydrofluoric acid and phosphoric acid both form a reaction product on the sample surface. In the case of hydrofluoric acid, this reaction is severe since the surfaces often become stained after 1 hr.

Table IV. Film thickness for gallium arsenide samples immersed in different solvents

Reagent	Film thickness, Å 0 min	5 min	1 hr	24 hr
Trichloroethylene	25	36	33	28
Acetone	26	25	24	27
Methanol	30	23	23	25
Ethanol	27	26	28	27
Isopropanol	25	23	23	24
Chloroform	27	27	27	27
Water	25	22	101	—
Hydrochloric acid[a,d]	24	12	16	28
Hydrochloric acid[b,d]	27	13	—	—
Sulfuric acid[a,d]	28	12	27	206
Phosphoric acid[a,d]	30	28	32	42
Hydrofluoric acid[a,d]	17	22	230[c]	—

[a] 30 sec water rinse.
[b] 30 sec methanol rinse.
[c] Surface was stained.
[d] Acids are concentrated reagent grade.

The thicknesses reported in Table IV are calculated by assuming that the film refractive index is 1.90. This assumption is justified if the film is gallium oxide; however, other film compositions are likely for many of the reagents (gallium hydroxide, fluoride, sulfate, or phosphate are obvious possibilities, but many other compositions are also possible). However, as shown in Table I, the error in the film thickness is less than 3Å when the film refractive index is between 1.5 and 2.5. Consequently, it is believed that the thicknesses in Table IV are accurate in spite of the variation in film composition.

The data in Table IV indicate that a suitable cleaning procedure for gallium arsenide consists of rinsing the sample in organic solvents to remove possible organic contamination followed by rinsing in hydrochloric acid and then rinsing in water or preferably methanol. We have found that this procedure gives surfaces with 12-14Å of film. We have also attempted to use this cleaning procedure with hydrofluoric acid substituted for the hydrochloric acid rinse. In this case, the film thickness ranged from 18 to 40Å with most of the films being about 35Å thick. This result is consistent with the data in Table IV which shows that films form on the surface when gallium arsenide is treated with hydrofluoric acid.

We have also examined a sample after it has been heated in vacuum for 1 hr at 420°C at a pressure of 10^{-6} Torr. The film thickness decreased from 27.5 to 23.5Å, indicating that heating in vacuum under these conditions does not produce effective cleaning of the sample.

The film thickness increases when clean gallium arsenide samples are exposed to air. Data from two "Syton" polished samples cleaned with concentrated hydrochloric acid and rinsed with methanol are given in Fig. 3. As in the case of silicon and germanium (1), the thickness is a logarithmic function of time over much of the growth period. The slope of the curve is 7.2Å/decade which compares with 6.8 and 8.1Å/decade for silicon and germanium, respectively (1). After several days, a limiting thickness of about 30Å is reached.

Schottky diodes.—Data from Schottky diode experiments are given in Fig. 4-7. The samples are all n-type epitaxial layers with carriers concentrations of about 5×10^{15} cm^{-3} grown on n^+ substrates with a (100) orientation. The forward current-voltage characteristics for diodes made by evaporating a gold-germanium alloy on two parts of the same sample are shown in Fig. 4. Schottky diodes were made on E599A immediately after the epitaxial deposition; no cleaning

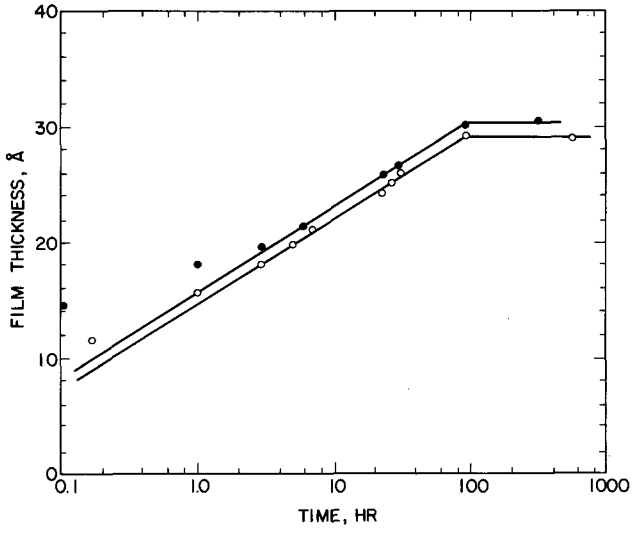

Fig. 3. Film thickness vs. log time for clean gallium arsenide samples exposed to air. The open circles are for the (111) orientation; the closed circles are for the (100) orientation.

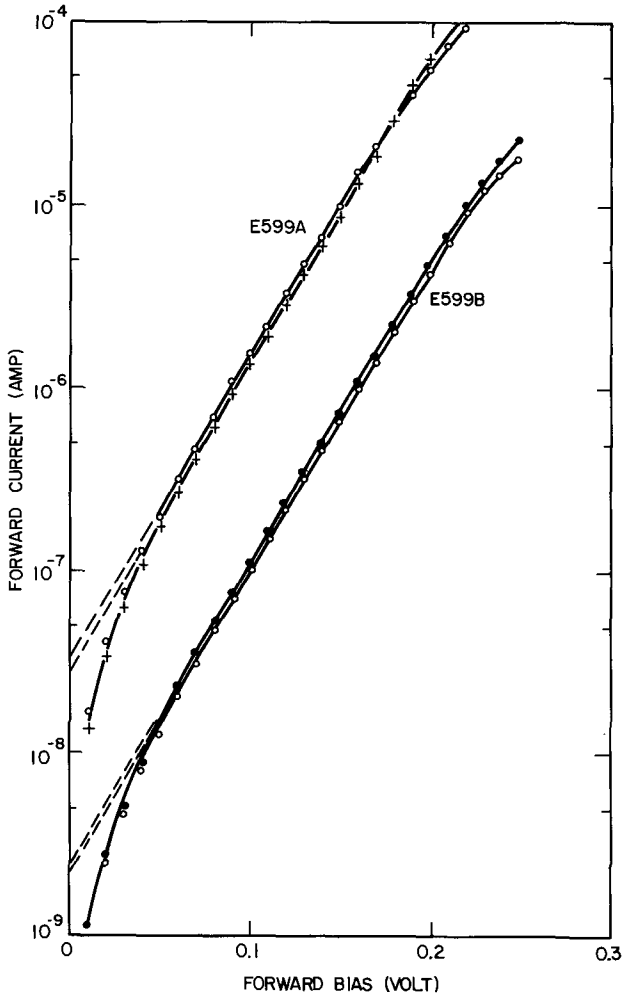

Fig. 4. Forward bias I-V characteristics of Schottky diodes deposited on two differently cleaned gallium arsenide surfaces.

of the sample was performed and a surface film 8.5Å thick was measured by ellipsometry. However, the part of the sample designated E599B was etched in bromine-methanol solution and given a "pre-epitaxy" cleaning before making the diodes, and the remaining surface film was 16Å thick. The curves show data for two diodes on each sample. The forward characteristics for both samples follow the classical thermionic emission law

$$J_f = J_s \exp\left(\frac{qV}{nkT}\right)$$

with the n factor very close to one ($n \approx 1.01$). The electronic barrier height, calculated by extrapolating the current to zero bias, is 0.58 eV for the freshly grown epitaxy and is 0.65 eV for the cleaned sample.

The reverse characteristics given in Fig. 5, are even more interesting. As in the case of the forward bias, the current for the freshly grown surface is about ten times higher than for the treated surface. Also for both samples, log J_r is proportional to the square root to the voltage (Fig. 6), as expected from the interfacial transition layer theory (16, 17). According to this theory, the slopes of the curves in Fig. 6 are given by

$$\text{slope} = \frac{\alpha}{kT}\left(\frac{2eN_D}{\epsilon_s}\right)$$

where N_D is the donor concentration, ϵ_s is the semiconductor dielectric constant, and α is a proportionality constant that depends on the thickness and dielectric constant of the surface film and on the surface states density and dielectric constant of the semiconductor. The values of α, obtained from the slopes of

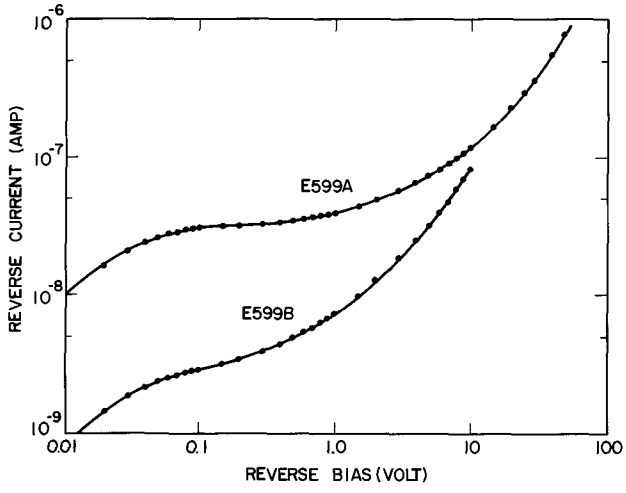

Fig. 5. Reverse bias I-V characteristics of the same Schottky diodes as in Fig. 4.

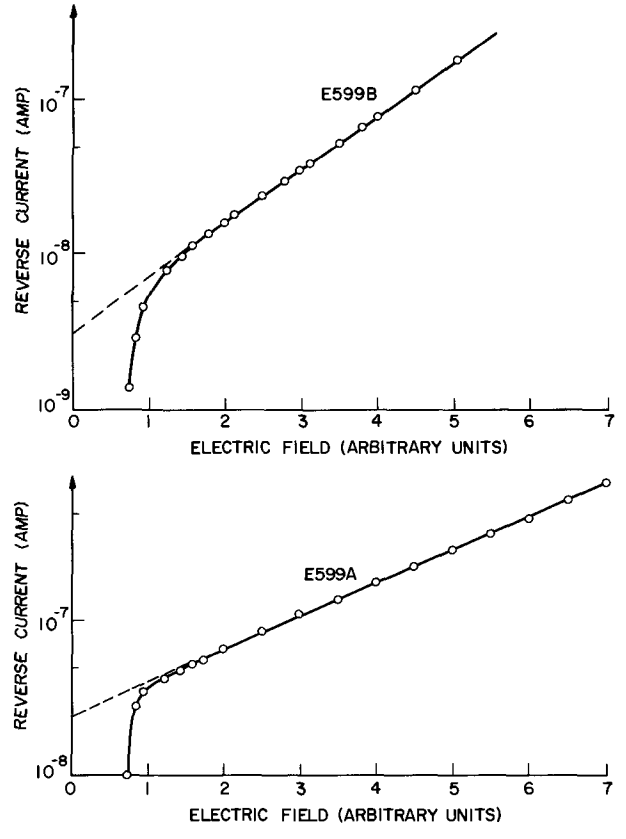

Fig. 6. Log reverse current vs. the square root of the reverse voltage for the same Schottky diodes as in Fig. 4.

the curves in Fig. 6 are 34 and 55Å for E599A and E599B, respectively.

The effects of surface preparation on the reverse characteristics of the Schottky diodes are further illustrated in Fig. 7. This figure shows the reverse current-voltage characteristics for diodes made on six pieces of the same sample; each piece having been subjected to a different cleaning or storage procedure. The particular procedure used, the film thickness as determined by ellipsometry, and the proportionality constant, α, are listed in Table V. The reported film thicknesses are average values for samples which have been given the same treatments as listed in Table V. As the film thickness increases, the value of α increases and the reverse current decreases. The reverse current reaches a minimum for samples 4 and 5 with film thicknesses of 35-45Å and with values of α near 55Å. A further increase in film thickness causes the reverse current to increase and α cannot be measured be-

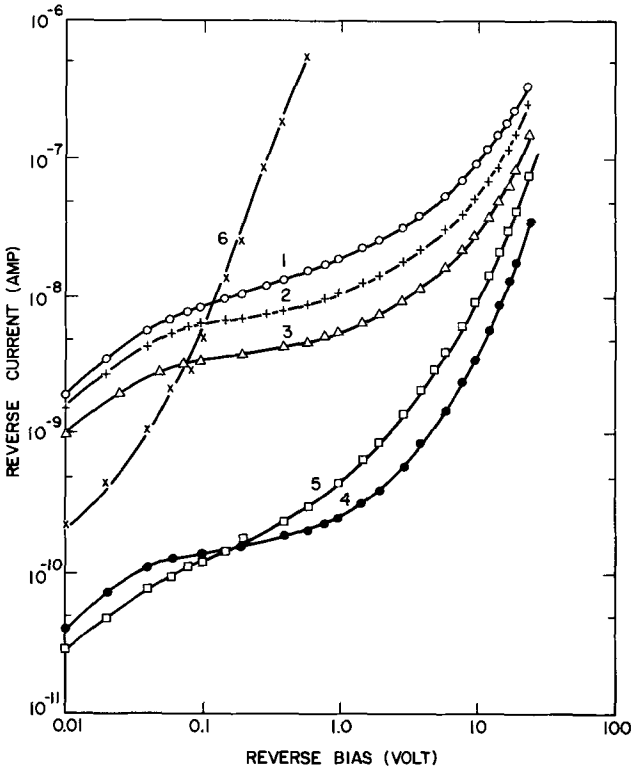

Fig. 7. Reverse bias I-V characteristics of Schottky diodes on parts of the same sample cleaned by different procedures.

cause log J_r is no longer proportional to the square root of the voltage.

These experiments indicate that the electronic barrier height is a function of the thickness of the interfacial film between the metal and the semiconductor. This subject will be discussed in another paper. These experiments also indicate a correlation between the film thickness and the reverse bias proportionality constant, α.

According to the interfacial layer theory (17), the proportionality factor is related to the film thickness by

$$\alpha = \frac{\epsilon_s}{\epsilon_i/d_i + 2qD_s}$$

where ϵ_i and d_i are the dielectric constant and the thickness of the film, D_s is the density of surface states, and q is the electronic charge. The values of α as a function of d_i are plotted in Fig. 8 using D_s as a parameter and assuming $\epsilon_i = \epsilon_o$. The theory is successful in predicting the magnitude of α and also the variation of α with film thickness. From this curve a mean density of surface states of 5×10^{12} cm^{-2} eV^{-1} is

Table V. Film thickness and proportionality constant, α, for Schottky diodes on gallium arsenide

Sample No.	Surface preparation	Film thickness, Å	Alpha, Å
6	No cleaning	57	Not measureable
5	"Pre-epitaxy" cleaning,[b] stored in "Cobehn"[c]	44	57
4	Acetone rinse	34	52 57[a]
3	"Pre-epitaxy" cleaning[b]	16	37
2	"Pre-epitaxy" cleaning,[b] stored in hydrogen	12	34
1	"Evaporation" cleaning[d]	11	30

[a] Measurements made on two samples.
[b] Samples are heated in acetone, Cobehn, and then methanol; cleaned with hydrochloric acid and rinsed with methanol; etched with dilute sulfuric acid and rinsed with methanol; stored in methanol.
[c] Cobehn is produced by Cobehn, Incorporated, Fairfield, New Jersey.
[d] Samples are heated in trichlorethylene and then in ethanol; dipped in hydrofluoric acid; dried with nitrogen.

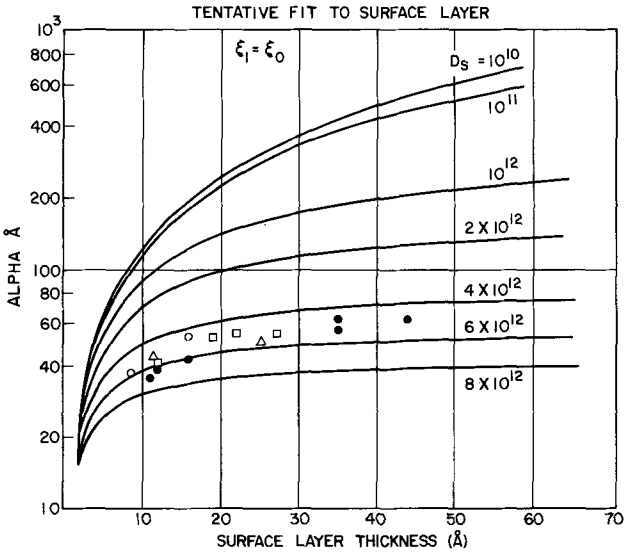

Fig. 8. Comparison between experimental and theoretical values of the reverse bias proportionality factor, α, as a function of film thickness with the surface-states density, D_s, expressed in cm^{-2} eV^{-1}.

deduced. The scatter of the data may be due to different cleaning procedures leaving films of slightly different chemical composition and giving a different dielectric constant and different density of states at the semiconductor surface. Still, these results strongly support the interfacial layer theory.

Thick films.—The use of ellipsometry to measure the thickness and refractive index of thick transparent films is well established (18). The method is based on the fact that for a given substrate psi and delta are determined by the refractive index and thickness of the film. Plots of delta *vs.* psi for films of constant refractive index and increasing thickness are given in Fig. 9. The curves are the loci of points generated by increasing the film thickness while keeping the film refractive index constant. Curves are shown for refractive indices between 1.1 and 3.5; curves of constant phase shift, δ, are shown as dashed lines. The phase shift is related to the film thickness by

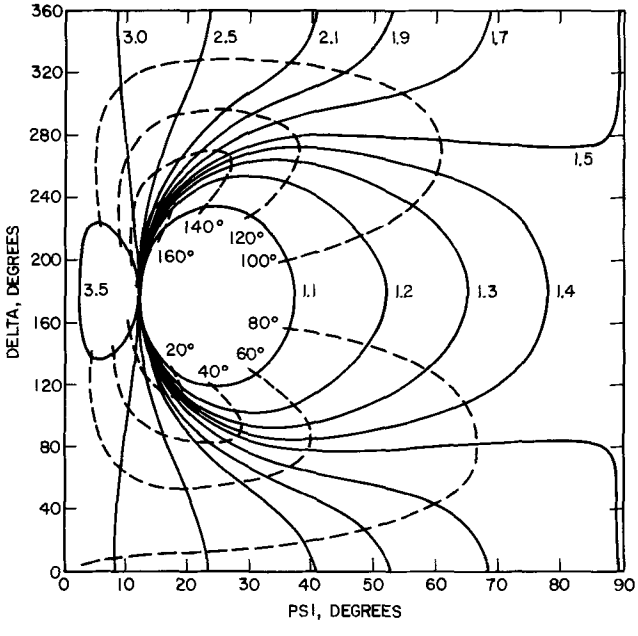

Fig. 9. Delta *vs.* psi for transparent films with refractive indices, n_1, between 1.1 and 3.5 on gallium arsenide substrates. The curves are calculated for $n_2 = 4.050$, $k_2 = 0.304$, $\lambda = 5461$Å, and $\phi = 70.00°$.

$$\delta = \frac{360}{\lambda} d(n_1^2 - \sin^2 \phi)^{1/2}$$

where λ is the vacuum wavelength of the incident light, d is the film thickness, n_1 is the film refractive index, and ϕ is the angle of incidence. The curves in Fig. 9 are quite similar to the curves given by Zaininger and Revesz (19). The differences are due to the slightly different values used for the optical constants of the gallium arsenide substrate.

The curves for all values of the film refractive index pass through a common origin. Consequently, the refractive index of the film cannot be determined if the film thickness is such as to give a value of δ near 0° or 180°. The most accurate values for the film refractive index are obtained when δ is near 90°.

We have made measurements to determine the thickness and refractive index of aluminum oxide films formed by the reactive evaporation of aluminum in a water vapor atmosphere (20) onto gallium arsenide substrates. The results for annealed samples are given in Table VI. The values of δ are all near 90°, thus we expect high precision in the values for the film thickness and the refractive index. The thicknesses as measured by the Talysurf and the ellipsometer fall within the uncertainty of the Talysurf measurement for samples which have been annealed. The refractive indices of the annealed samples increase with annealing time and annealing temperature. This is the expected trend if the films are losing water during the annealing. The reported refractive indices at 5892Å for $Al_2O_3 \cdot 3H_2O$, $Al_2O_3 \cdot H_2O$, and Al_2O_3 are 1.58, 1.62, and 1.77, respectively (21). The slightly anomalous values for the refractive index and the thickness of unannealed samples are not completely understood. The freshly deposited films may contain small amounts of elemental aluminum which cause the film to be absorbing. Since our analysis of the data assumes that the film is nonabsorbing, the reported values for the refractive index and the thickness will be in error if free aluminum is present. The aluminum may be converted to aluminum oxide by reaction with water during the annealing.

Discussion and Summary

The ellipsometric data from the polished samples have been interpreted in terms of a simple optical model in which the values for the real part of the refractive index of the gallium arsenide and the thickness of the surface film are obtained by assuming that the film refractive index is 1.9 and that the complex part of the gallium arsenide refractive index is 0.304. The optical constants at a wavelength of 4375Å have been calculated by correcting the ellipsometric data at this wavelength for the presence of the surface film. The values of these optical constants have been used to investigate the polishing of the gallium arsenide. The ellipsometric technique is expected to be sensitive to variations in the gallium arsenide surfaces because the light penetrates only a very small distance into the sample. Thus the optical constants are measured for gallium arsenide at or near the surface rather than for the bulk gallium arsenide. The penetration depth can be defined as

$$D = \lambda/4\pi k_2$$

where λ is the vacuum wavelength of light and k_2 is the imaginary part of the gallium arsenide refractive index (22). The penetration depth will be smallest when the imaginary part of the complex refractive index is at a maximum. For gallium arsenide, a maximum occurs near 3900Å (5). The penetration depths, calculated using the optical constants in Table III, are 1430 and 290Å for wavelengths of 5461 and 4375Å, respectively. The optical constants reported in Table III show no significant variation with different polishing techniques, indicating that the surfaces are the same for the three different surface preparations, at least for penetration depths of 300Å. This similarity is not surprising since the three polishing methods are all based on the chemical etching of the surface. If a mechanical polishing technique had been used, differences in the optical properties of the surface might be observed (23, 24).

The optical constants reported in Table III are in good agreement with the values reported in the literature (5, 7, 11). However, the value of n_2 at 5461Å is higher than the value reported by Zaininger and Revesz ($n_2 = 3.923$) who also used ellipsometric measurements (19). The difference may result because of different surface preparations on different crystallographic orientations. Zaininger and Revesz made measurements on the (110) orientation; they state that the $(\bar{1}\bar{1}\bar{1})$ and (100) orientations give slightly different results, but no data are reported. This possible difference should be studied in more detail.

Cleaning techniques have been evaluated by measuring the thickness of the surface film. On this basis, the cleanest surface observed has about 8Å of film. This is nearly the same thickness that is reported for etched gallium arsenide (19) and probably represents between one and two monolayers of oxide. This film slowly grows due to air oxidation and reaches a maximum thickness of 30Å.

Alfano has also evaluated the cleaning of gallium arsenide by ellipsometry (25). However, he used the value of delta as a measure of the cleaning rather than actually calculating the film thickness. It is impossible to compare his data with ours because his angle of incidence is not specified.

The Schottky diode measurements indicate that the reverse current-voltage characteristics are very sensitive to surface preparation. In addition, there is a correlation between the thickness of the film that remains after the different surface treatments and the alpha factor obtained from the slope of log J_r *vs.* the square root of the voltage. Such a correlation is predicted by the interfacial transition layer model (16, 17).

Finally, the use of ellipsometry to measure the thickness and the refractive index of deposited transparent films on gallium arsenide substrates has been demonstrated. High precision in these measurements can be obtained by suitably choosing the thickness and the angle of incidence so that the phase shift, δ, is near 90°. This technique should be particularly useful in the future for studying the properties of insulating films on gallium arsenide.

Table VI. Film thickness and refractive index for aluminum oxide films on gallium arsenide

Annealing treatment	Delta, δ	Refractive index	Film thickness, Å Ellipsometry	Talysurf
As deposited	114.8	1.610	3420	3000
500°C, 1 hr	85.8	1.571	3210	3300
600°C, 1 hr	93.9	1.590	3250	3230
700°C, 1 hr	110.0	1.720	3050	—
500°C, 2 hr	92.0	1.579	3250	3230
500°C, 64 hr	88.9	1.586	3200	—
600°C, 3 hr	97.3	1.627	3170	—
As deposited	109.0	1.583	5580	5000
850°C, 2 min	85.5	1.677	4870	—

Acknowledgment

We wish to thank R. H. Kaiser for making several ellipsometry measurements; R. O. Miller, G. D. Cravello, and W. M. Urban for polishing and cleaning many samples; W. A. Johnson for preparing the epitaxial gallium arsenide; and J. Simpson, T. J. Riley, A. U. MacRae, and R. M. Ryder for several helpful discussions and for reviewing the paper.

Manuscript submitted Jan. 1, 1972; revised manuscript received Nov. 1, 1972.

Any discussion of this paper will appear in a Discussion Section to be published in the December 1973 JOURNAL.

REFERENCES
1. R. J. Archer, *This Journal*, **104**, 619 (1957).
2. A. C. Adams and R. H. Kaiser, Abs. 134, p. 343, Electrochem. Soc. Extended Abstracts, Spring Meeting, Los Angeles, May 10-15, 1970.
3. F. L. McCrackin, E. Passaglia, R. Stromberg, and H. L. Steiberg, *J. Res. Nat. Bur. Std.*, **67A**, 363 (1963).
4. R. J. Archer and C. V. Shank, *J. Opt. Soc. Am.*, **57**, 191 (1967).
5. B. O. Seraphin and H. E. Bennett in "Semiconductors and Semimetals," Vol. 3, R. K. Willardson and A. C. Beer, Editors, pp. 518-523, Academic Press, New York (1967).
6. F. Lukes, *Optik*, **31**, 83 (1970).
7. C. E. E. Stewart, *Solid-State Electron.*, **10**, 1199 (1967).
8. H. T. Minden, *This Journal*, **109**, 733 (1962).
9. A. W. Laubengayer and H. R. Engle, *J. Am. Chem. Soc.*, **61**, 1210 (1939).
10. O. A. Weinreich, *J. Appl. Phys.*, **37**, 2924 (1966).
11. C. J. Dell'Oca, G. Yan, and L. Young, *This Journal*, **118**, 89 (1971).
12. R. E. Cox, *Appl. Opt.*, **3**, 1188 (1964).
13. D. K. Burge and H. E. Bennett, *J. Opt. Soc. Am.*, **54**, 1428 (1964).
14. R. E. Morrison, *Phys. Rev.*, **124**, 1314 (1961)
15. D. D. Sell and A. U. MacRae, *J. Appl. Phys.*, **41**, 4929 (1970).
16. M. P. Lepselter and J. M. Andrews, in "Ohmic Contacts to Semiconductors," B. Schwartz, Editor, p. 159, the Electrochemical Society Softbound Symposium Series, New York, (1969).
17. A. M. Cowley and S. M. Sze, *J. Appl. Phys.*, **36**, 3212 (1965).
18. R. J. Archer, *J. Opt. Soc. Am.*, **52**, 970 (1962).
19. K. H. Zaininger and A. G. Revesz, *J. Phys. (Paris)*, **25**, 208 (1964).
20. E. Ferrieu and B. Pruniaux, *This Journal*, **116**, 1008 (1969).
21. "Handbook of Chemistry and Physics," 47th ed., p. B-150, Chemical Rubber Publishing Co., Cleveland, Ohio (1966).
22. M. Born and E. Wolf, "Principles of Optics," 3rd ed., p. 614, Pergamon Press, New York (1965).
23. M. P. Lisitsa, V. N. Malinko, E. V. Pidlisnyi, and G. G. Tsebulya, *Surface Sci.*, **11**, 411 (1968).
24. B. Tuck, *Phys. Status Solidi*, **36**, 285 (1969).
25. R. R. Alfano, *Solid-State Electron.*, **11**, 789 (1968).

The Effect of Dislocation Density on the Diffusion of Gold in Thin Silicon Slices

F. A. Huntley[1] and A. F. W. Willoughby

Engineering Materials Laboratories, The University, Southampton, United Kingdom

ABSTRACT

The effect of dislocation density on the diffusion of gold in thin silicon slices has been investigated. Precision grinding together with γ-scintillation counting was used to measure concentration profiles of ^{198}Au diffused, over a temperature range 900°-1200°C, into thin slices of both high-and low-dislocation density silicon crystals. U-shaped gold concentration profiles as observed by previous workers were obtained in all cases. Significant differences were observed between diffusion profiles in slices which had different initial dislocation content, but had undergone identical diffusion processing. This effect of dislocation density on gold diffusion is strong evidence to support the dissociative mechanism for gold diffusion in silicon. The differences between diffusion profiles in high- and low-dislocation density material are interpreted by means of a model in which vacancy generation occurs at climbing grown-in dislocations, but it is concluded that this may not be the only process determining the rate of gold uptake in thin slices.

Considerable interest has been shown in recent years in the diffusion of gold in silicon. This interest has arisen both from the needs of silicon device technology, and from the general scientific need to try to fill the many gaps in our knowledge of point defects and impurity diffusion in silicon.

Evidence that gold diffuses in silicon by the dissociative mechanism, first developed by Frank and Turnbull (1) for copper diffusion in germanium, was provided by the studies of Wilcox and LaChappelle (2). The dissociative mechanism involves the fast interstitial diffusion of the element in question accompanied by the transition of interstitial atoms into substitutional sites by annihilating lattice vacancies. Since this should cause the vacancy concentration to drop and hence may cause vacancy generation at dislocations and other lattice defects, the evidence that the diffusion of copper in germanium is highly sensitive to the dislocation density (1) is perhaps the strongest evidence in support of the dissociative mechanism in this case. However, unambiguous evidence on this point has not yet been published for gold diffusion in silicon, although there is evidence that gold diffusion causes vacancy generation at grown-in dislocations (3, 4). A study of the effect of dislocation density on gold diffusion in silicon is thus an essential experiment to test the validity of the dissociative mechanism for this system, and offers the possibility of gathering information about lattice vacancies in silicon.

There are two previous reports, by Yoshida and Saito (5) and Lambert (16), of experiments to determine the effect of dislocation density on gold diffusion in silicon. In neither of these studies were gold concentration profiles measured. Yoshida and Saito (5) measured average diffused gold concentration in slices of silicon crystals grown by four different techniques which they called float zoned (FZ), float-zoned defect free (FZDF), pulled (CZ), and pulled-defect free (CZDF). Small differences were seen between central concentrations of gold, which was diffused into slices of the four different materials for the same times and at the same temperatures. However, differences were also seen between central concentrations of gold, in slices of the same material but of different thicknesses, diffused for the same time at the same temperature. This suggests that the gold profiles in the central parts of at least some of the specimens used to determine

[1] Present address: Institut für Physik, Max-Planck-Institut für Metallforschung, 7 Stuttgart 1, Azenbergstr. 12, Germany.
Key words: dislocation density, vacancy generation, nonequilibrium dissociative diffusion.

the gold concentrations were not flat, as had been assumed on the basis of the work of Martin *et al.* (7) and Sprokel and Fairfield (8). Differences in the gold concentrations, due to the different defect structures of the specimens, might therefore have been masked by apparent concentration differences due to concentration gradients. Lambert (6) has obtained a limited number of results from experiments similar to those to be described here. However, as in the work of Yoshida and Saito, only average gold concentrations were measured, by counting large parts of the specimens after neutron activation.

The experiments reported here are an attempt to determine the effect of initial dislocation density on profiles of gold diffused into silicon, and were designed to test the results of a previously published theory (9) in which vacancy generation during gold diffusion was assumed to take place at jogs on climbing dislocations.

Methods

Disk-shaped slices of between 400 and 480 μm thick and 2.5 cm in diameter were cut from two silicon crystals. Both crystals were N-type, phosphorous-doped, (111) orientation, and of resistivity between 6 and 10 ohm-cm. One crystal had been grown by the float-zone process and had a fairly high dislocation density (EPD $\simeq 10^4$ cm^{-2}). The other crystal was of the Mon-X type (Monsanto Chemicals Limited) and had been grown by a process that yields crystals with a low oxygen content (as for FZ crystals) but with a near zero density of grown-in dislocations as measured by etch-pit techniques, and x-ray topography. The FZ slices were lapped flat on both sides, and then polished on one face with a combined chemical/mechanical polish. In order to preserve their initial perfection the slices of Mon-X crystals were not lapped after sawing, but were heavily etched, removing about 25 μm from each face. One face was then polished by a combined chemical/mechanical tehnique. X-ray topographs of such as-polished slices indicated that the perfection of the starting crystal had been well preserved.

A thin film diffusion source of ^{198}Au, a few hundred Angstroms thick, was vacuum evaporated on the unpolished face of the slices. The ^{198}Au was obtained by the thermal neutron activation of spectroscopically pure metallic gold (the irradiation was carried out at the Isotope Production Unit, A.E.R.E., Harwell). For diffusion, the slices were taken directly from the evaporator and placed horizontally on a flat quartz boat, with the gold-evaporated side underneath, and diffused in a horizontal, open-tube furnace. After diffusion, the slices were quenched by removing them rapidly from the furnace into a quartz transfer tube. A flow of dry nitrogen was maintained over the slices during diffusion and quenching.

As a precaution against possible edge effects, a disk of about 1 cm diameter was cut from the center of each slice for the determination of the gold concentration profile. This disk was mounted on the plug of a microgrinding jig for the lapping of the polished face of the specimen. This face was aligned parallel to the lapping surface by an optical interference technique by using the micrometer adjustments on the jig feet. Successive sections of between 1 and 20 μm thick were then lapped from the specimen, starting at the polished front face, and proceeding through the specimen, towards the rear face on which the gold diffusion source had been evaporated. The grindings were collected and assayed for ^{198}Au using γ-scintillation counting. Careful cleaning of the jig and specimen was necessary between the cutting of each section in order to prevent cross contamination. The thicknesses of the removed layers were measured directly to an accuracy of $\pm$ 0.25 μm using an inductance probe, taking the back surface of the grinding jig plug as a reference surface for each measurement.

In order to determine the specific activity of the ^{198}Au, a known weight of the gold from each irradiation was dissolved in aqua regia. The specific activity was calculated from the scintillation count-rates of suitably diluted aliquots of this solution.

The gold concentration in each section was then computed from the section thickness, the specimen area, the scintillation counter data and the specific activity of the ^{198}Au. Concentration profiles were then plotted from these data.

The only data in which large errors are suspected are those obtained within 50 μm of the rear (gold-deposited) surface of each slice, where concentrations apparently exceeded the maximum solubility limit. The high concentrations are thought to be largely an artifact of the sectioning technique. When the remaining specimen had a thickness of only about 50 μm the mechanical lapping process began to cause chipping round the periphery of the slice. Consequent contamination of the removed section with part of the evaporated gold film from the rear of the slice apparently caused erroneously high gold concentrations to be measured.

Results

In order to make a comparison of gold diffusion in thin slices of different dislocation content, slices of both FZ and Mon-X crystals (high- and low-dislocation density respectively) were gold diffused for approximately 10, 40, 100, and 400 min at each of four temperatures, 900°, 1000°, 1100°, and 1200°C. The families of concentration profiles are shown in Fig. 1 to 8. Both before and after diffusion the defect structure of the slices was investigated using both x-ray topography, and infrared microscopy following copper decoration. Figure 9 shows an x-ray topograph of a FZ slice after gold diffusion, revealing a density of $\rho \simeq 3 \times 10^4$ cm^{-2} of dislocations fairly uniformly dis-

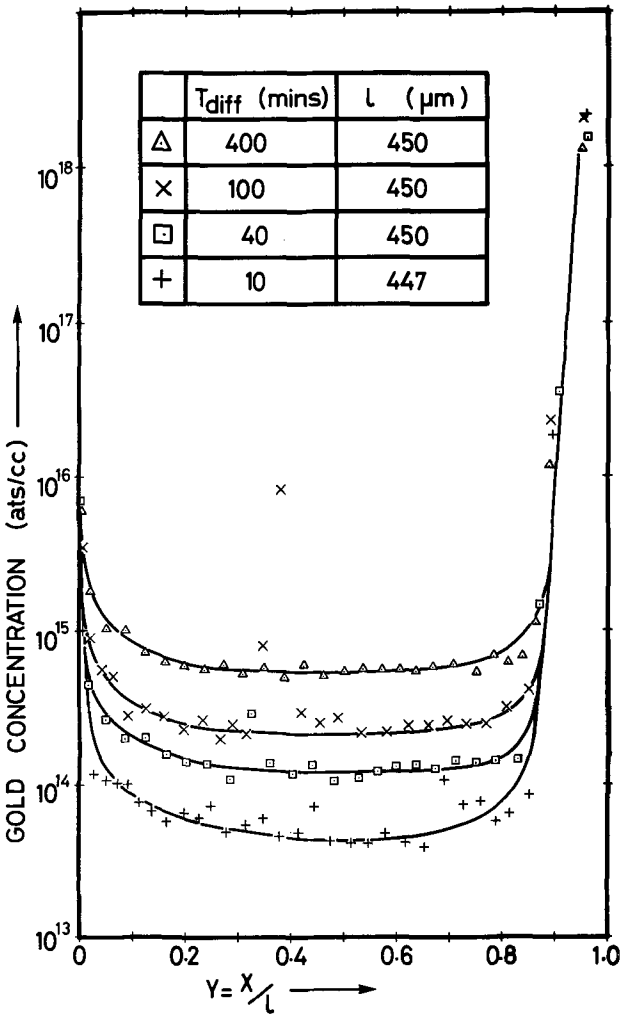

Fig. 1. Concentration profiles of gold diffused into FZ silicon slices at 900°C.

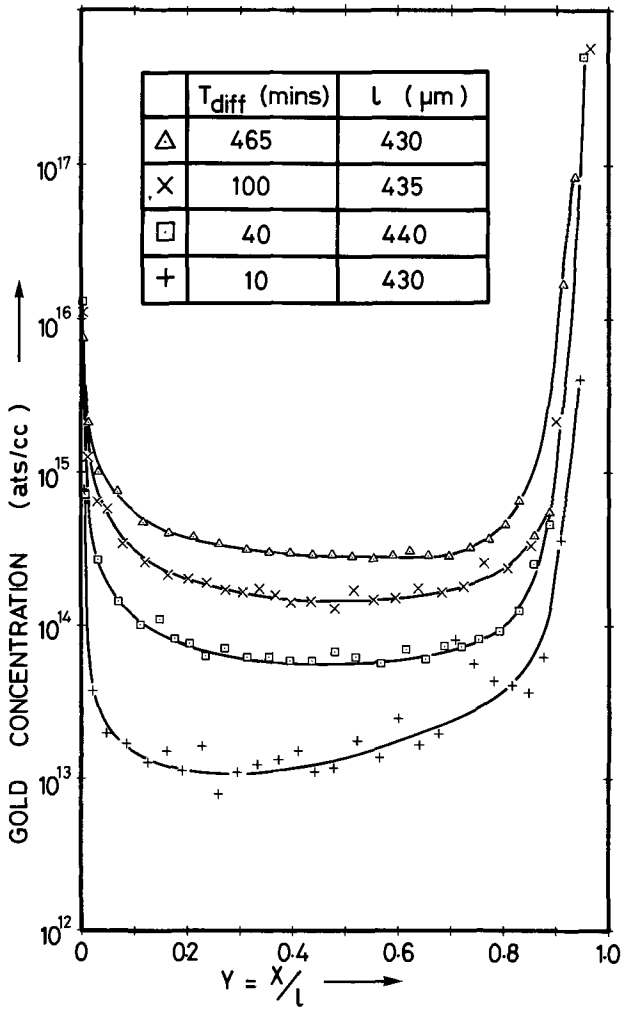

Fig. 2. Concentration profiles of gold diffused into Mon-X silicon slices at 900°C.

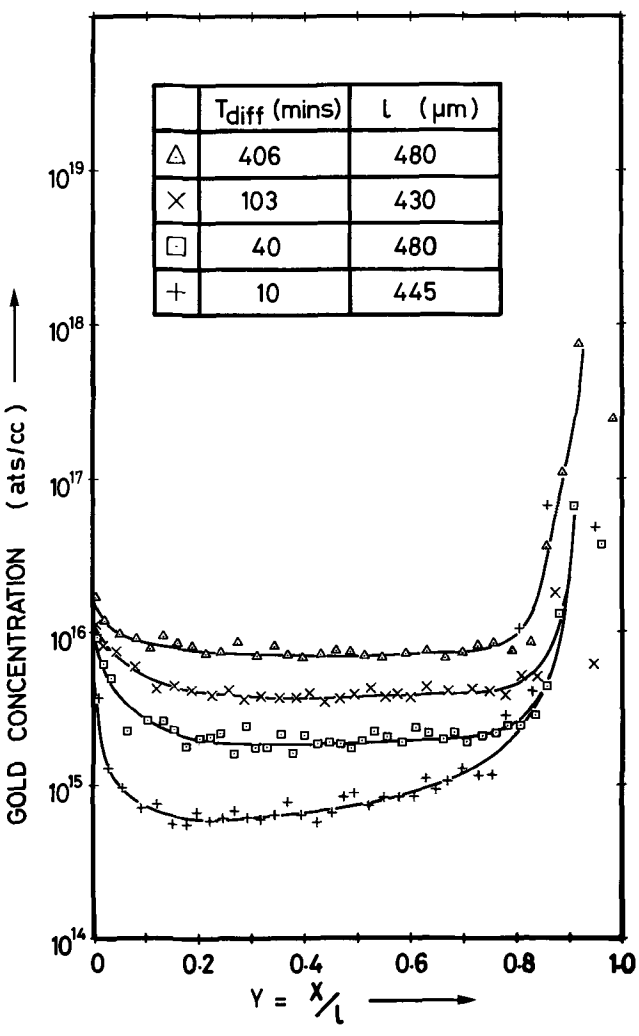

Fig. 3. Concentration profiles of gold diffused into FZ silicon slices at 1000°C.

tributed in the slice, and showing no evidence of gross climb of the grown in dislocations, such as helix formation, etc. No difference was obvious between topographs of FZ slices taken before and after gold diffusion. X-ray topographs of the Mon-X slices both before and after gold diffusion were featureless. However, Sirtl etching of the Mon-X slices before gold diffusion revealed roughly spiral striations of etch-pits. After copper diffusion (15 min at 1000°C) both topography and infrared microscopy revealed copper precipitates with the same striated distribution as the etch-pits (Fig. 10). Similar results have been presented by de Kock (10), who suggested that the cause of the etch-pits and the sites of nucleation of the copper precipitates were vacancy clusters, perhaps stabilized by complexing with oxygen atoms. After gold diffusion, changes in the form of the copper precipitates were observed, as discussed below.

The form of the thin slice profiles.—Despite differences in the profiles for the two types of material which are discussed below, the profiles shown in Fig. 1 to 8 are all U-shaped and are similar to those seen by previous workers (7, 8) and to the theoretical profiles obtained in our earlier work (9). This over-all U shape has been discussed in a previous paper by the present authors (11), in which it was pointed out that the rise, or "tip-up" in gold concentration at the surface towards which the gold was diffused, as well as that on which the gold was deposited, had been observed under a variety of conditions (7, 8, 12-14). Earlier work of the authors (11) has shown that, while rapid surface diffusion of gold on silicon certainly does take place on polished or lapped silicon surfaces, surface diffusion is likely to be only a contributory cause of this front surface "tip-up" phenomenon in oxidized silicon slices. Assuming that gold diffuses by the dissociative mechanism, the following three types of process could lead to a "tip-up":

(*i*) A near surface effect over a region much less than 1 μm from the surface. In this group are surface reactions, absorption effects, interface effects (at Si/SiO_2 interface). Concentrations of gold, in "tip-up" regions in this category, may exceed the solid solubility limit.

(*ii*) A bulk effect extending a few tens of microns from the surface, caused by vacancy diffusion from the surface in regions saturated with interstitial gold. Gold concentrations in these cases should not exceed the solid solubility limit.

(*iii*) A bulk effect in regions not saturated with interstitial gold, caused by the true dissociative diffusion of vacancies and gold from the crystal surface. In this case the gold would be transported to the front surface solely by surface diffusion. Concentrations of gold in the "tip-up" regions caused by this effect should not exceed the solid solubility limit.

In the present investigation unoxidized slices were used and it is thus impossible to rule out conclusively mechanism (*iii*), as a contributory cause of the "tip-up" extending over tens of microns. Whether (*iii*) or (*ii*) is dominant depends on whether interstitial diffusion produces saturation before or after surface diffusion produces an effective source on the front surface. The data available at present is inadequate to make a clear conclusion on this point. In the case of profiles obtained for diffusion in thick (1 cm) silicon specimens, however, which also show a "tip-up" near the

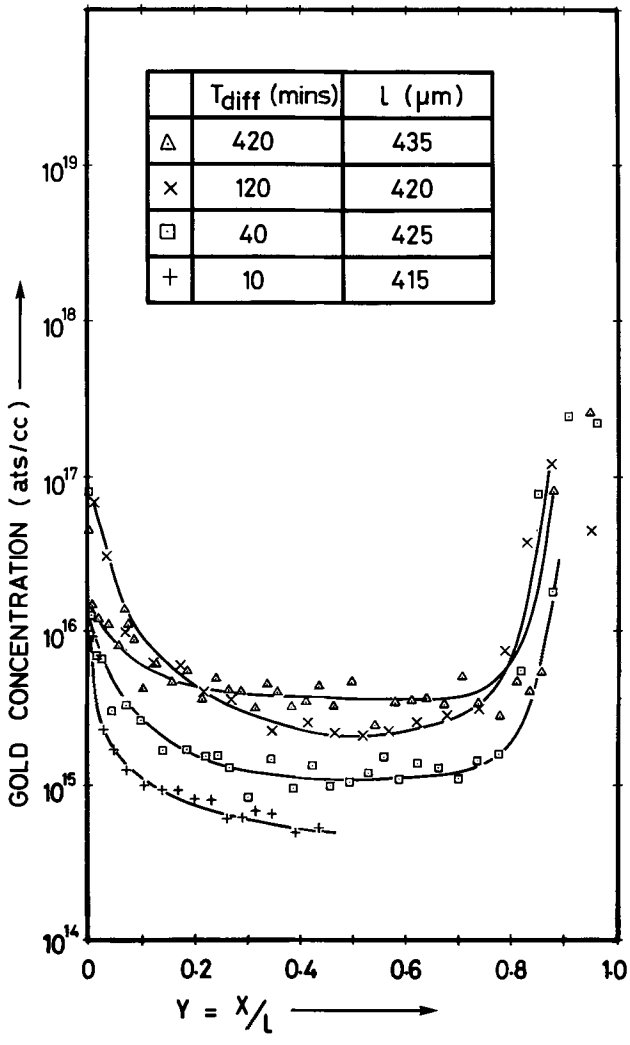

Fig. 4. Concentration profiles of gold diffused into Mon-X silicon slices at 1000°C.

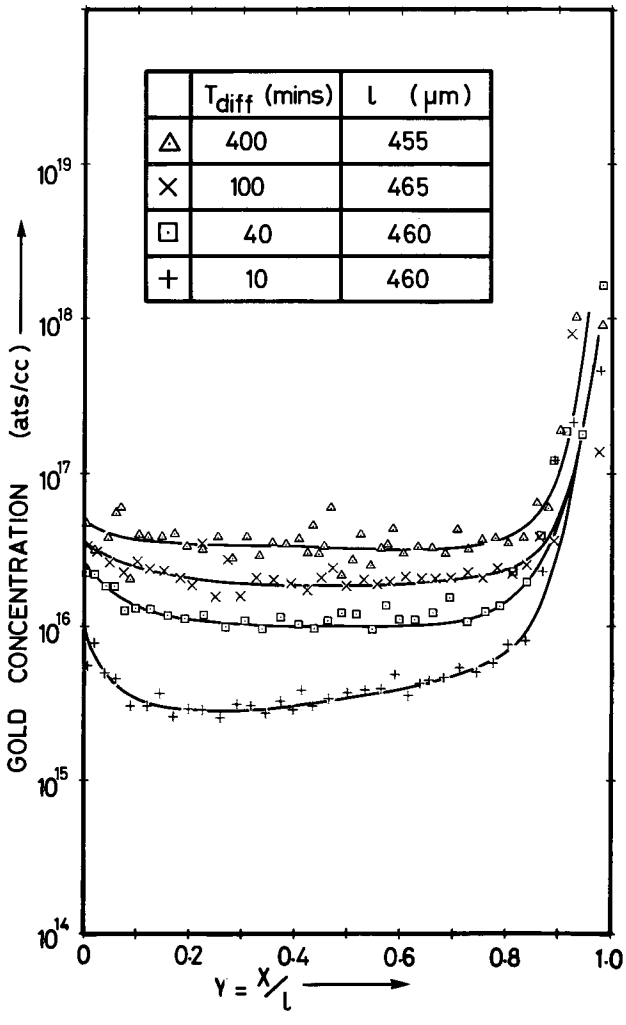

Fig. 5. Concentration profiles of gold diffused into FZ silicon slices at 1100°C.

front surface (15), the rise is thought to be due primarily to surface diffusion, since the conditions used make it unlikely that full saturation with interstitial gold occurred.

The effect of dislocation density on the profile shape.—Although an over-all U-shape of the profiles was found in all cases, there were noticeable differences in the profile shapes for the two types of crystal. The Mon-X profiles were consistently more rounded than the FZ profiles, which had very flat central regions, as may be seen by comparing, for example, Fig. 5 and 6.

These differences can be explained qualitatively on the dissociative diffusion model assuming that, in most cases, the slices are saturated with interstitial gold more rapidly than with the vacancies, and hence that the gold concentration is controlled primarily by the vacancy concentration. (This assumption is obviously not good in all cases, and will be discussed further below.) If vacancy generation from climbing dislocations occurs in the center of the FZ slices, the vacancies diffusing from the surface will make a smaller relative contribution to the total vacancy concentration in this material than in the low dislocation density Mon-X material [cf. Fig. 1 and 2 in Ref. (9)]. Thus the deeper vacancy diffusion profiles in the Mon-X slices will lead, on this model, to more rounded gold diffusion profiles than in the FZ slices.

The second feature of the profiles worthy of note is that some of the profiles for the shortest diffusion times (10 min) are not flat, but show a gradient away from the diffusion source. Again assuming that interstitial gold diffusion is more rapid than vacancy diffusion, this can be understood if the diffusion time is too short to enable $C_i \rightarrow C_i'$ throughout the whole sample. This enables an estimate to be made for D_1 if

$$\sqrt{D_1 \cdot t} \simeq l \quad \text{(the slice thickness)}$$

For $t = 10$ min, $l = 450$ μm, a value of $D_1 = 3 \times 10^{-6}$ cm²/sec is obtained, which agrees well with that determined experimentally by Wilcox and LaChappelle (2) over the temperature range 900°-1200°C, and thus reinforces this interpretation. The fact that the concentration gradient in the central region was predominantly seen only in the FZ specimens can be explained by the interstitial to substitutional gold reaction not proceeding so fast towards the substitutional species in the Mon-X, as in the FZ material, due to the lower vacancy generation rate in the more perfect crystal. The rate of conversion of interstitial to substitutional gold might thus be expected to be slower in the Mon-X material, and saturation with interstitial gold to occur faster than in the FZ material, thus removing the gradient.

Effect of dislocation density on central gold concentrations.—Figure 11 compares gold concentration profiles in slices of Mon-X and float-zoned crystals, diffused at 900°, 1000°, and 1100°C for 40 min. At all three temperatures the central concentration in the float-zoned slices was higher than in the Mon-X slices. Lambert (6) has recently observed an effect of the same direction and similar magnitude for diffusion at 835°C, and although average gold concentrations in parts of the slices were measured, rather than concentration profiles, as in the present work, these results are strong confirmation of the present trends. These consistently observed effects of dislocation density, the first direct studies of this parameter to be re-

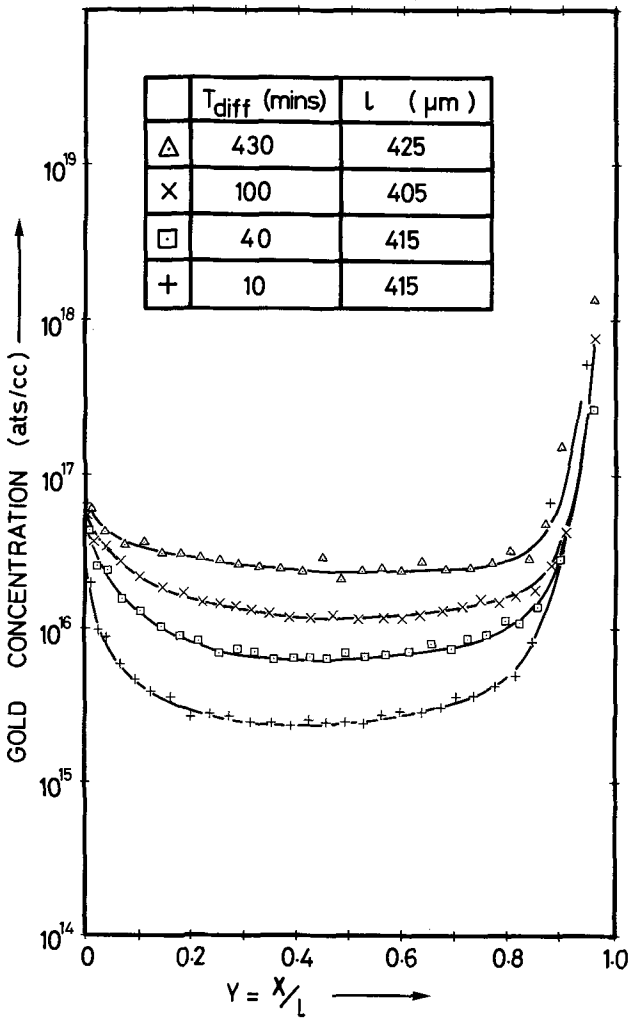

Fig. 6. Concentration profiles of gold diffused into Mon-X silicon slices at 1100°C.

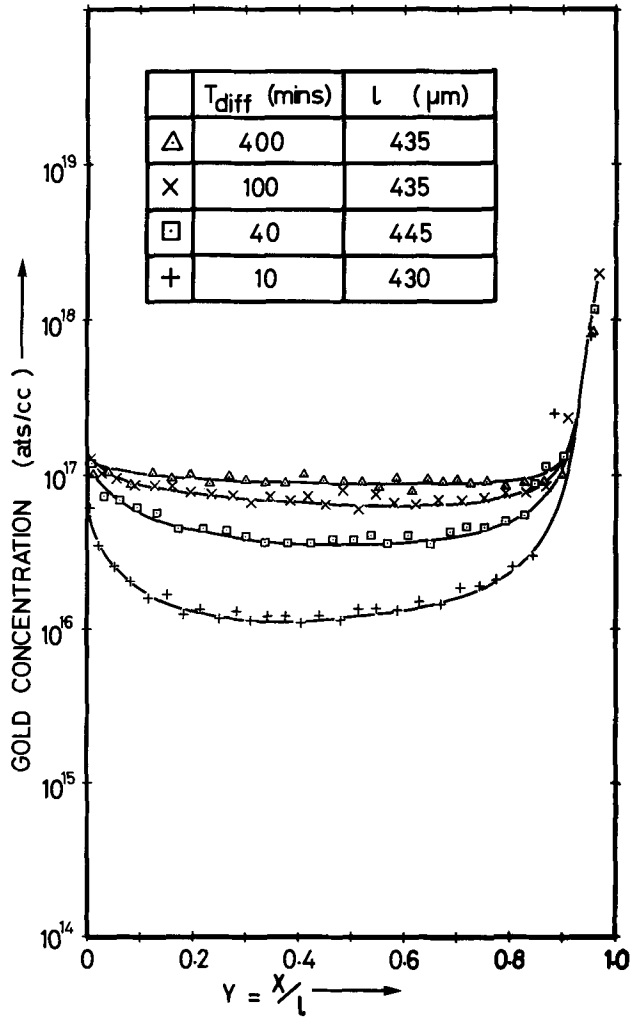

Fig. 7. Concentration profiles of gold diffused into FZ silicon slices at 1200°C.

ported, confirm qualitatively the predictions of the previously described dislocation climb model (9). The results provide strong evidence of the involvement of dislocations in gold diffusion in silicon, and strongly support the contention that gold diffuses in silicon by the dissociative mechanism.

Central gold concentration time dependence.—The central gold concentrations in slices of the two types of material, over the temperature range 900°-1200°C, are plotted as a function of time from 10 to 400 min in Fig. 12. As discussed above, the concentration in the float-zoned material was higher than in the Mon-X material in all cases, except for the two longer diffusion times at 1200°C. In these latter cases the solubility limit was apparently being approached, showing a saturation effect as seen in Fig. 7 and 8. The solubility limit is not likely to be a function of the dislocation density.

Two lines, labelled K and G, having the same slope as two families of theoretical solutions [in the regime unaffected by approach to the solubility limit or to zero concentration (9)], are also shown in Fig. 12 to allow comparison with the observed time dependences. The curve labelled K was obtained using the previously published dislocation climb model (9) which, assuming again that interstitial saturation occurred rapidly compared with vacancy diffusion, led to the following expression for the time dependence of the central gold concentration

$$C_s = C_s' \{1 - \exp(-2Kt)\}^{1/2} \qquad [1]$$

[The notation of this expression has been changed from the nondimensional form used in the earlier work (9) to the dimensional form used by Lambert (6), for ease of comparison.] The parameter K has the units (time)$^{-1}$ and is a function of the dislocation density of the crystal as

$$K = \frac{D^{sd}{}_{1v} \cdot L_j \cdot \rho}{b^2 \cdot (C_s' + C_v')} \qquad [2]$$

where $D^{sd}{}_{1v}$ is the self-diffusion coefficient by a vacancy mechanism, L_j is the jog line density on the dislocations, ρ is the dislocation density, b is the dislocation Burgers vector magnitude, and C_s' and C_v' are the solubility limits of substitutional gold and vacancies respectively.

The previous theoretical work (9) showed that the time dependence of the central concentration under conditions of zero generation rate would be quite different from Eq. [1]. As discussed below however, it is extremely unlikely that the Mon-X material contained absolutely zero vacancy generating defects, and its behavior would thus be expected to conform to Eq. [1], as observed.

The curve labelled G was obtained on the empirical model of Sturge (16) which assumed that vacancy generating sources in the bulk obeyed first-order kinetics, unlike dislocations. This gave a time dependence of the form

$$C_s = C_s' \{1 - \exp(-g't)\} \qquad [3]$$

Comparing the experimental and theoretical curves in Fig. 12 it can be seen that the experimental curves have gradients which lie closer to that of the K curve than to that of the G curve, as do those of Lambert (6) and Sprokel and Fairfield (8) shown in Fig. 13,

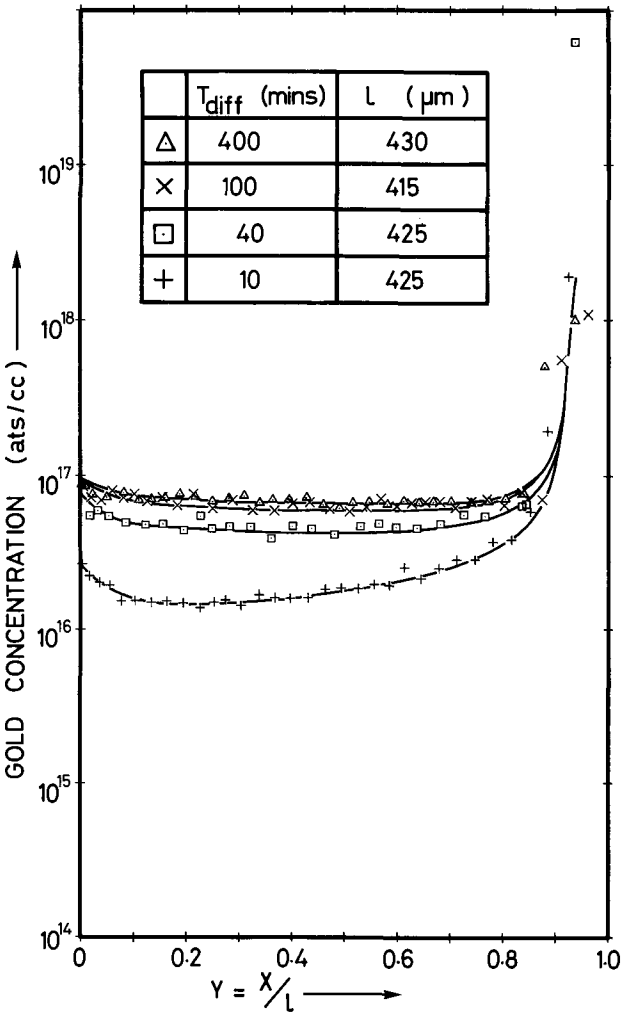

Fig. 8. Concentration profiles of gold diffused into Mon-X silicon slices at 1200°C.

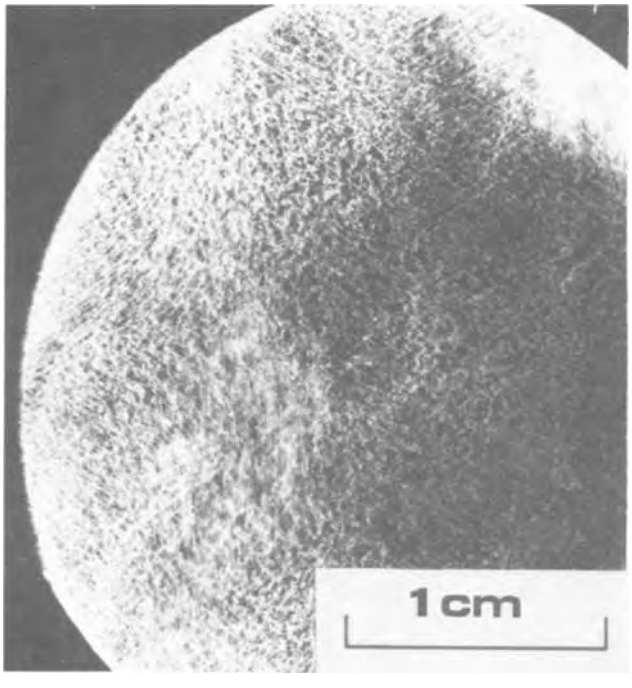

Fig. 9. Transmission x-ray topograph (220 reflection) of an as-polished FZ silicon slice.

thus supporting the vacancy generation model proposed in the earlier work (9). The range of values shown for the results obtained in this work at the

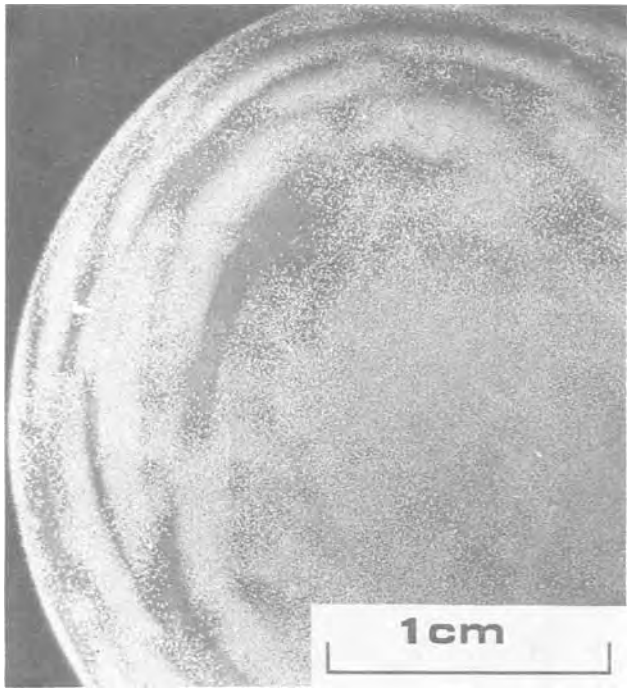

Fig. 10. Transmission x-ray topograph (220 reflection) of an Mon-X silicon slice after copper decoration (15 min diffusion at 1000°C).

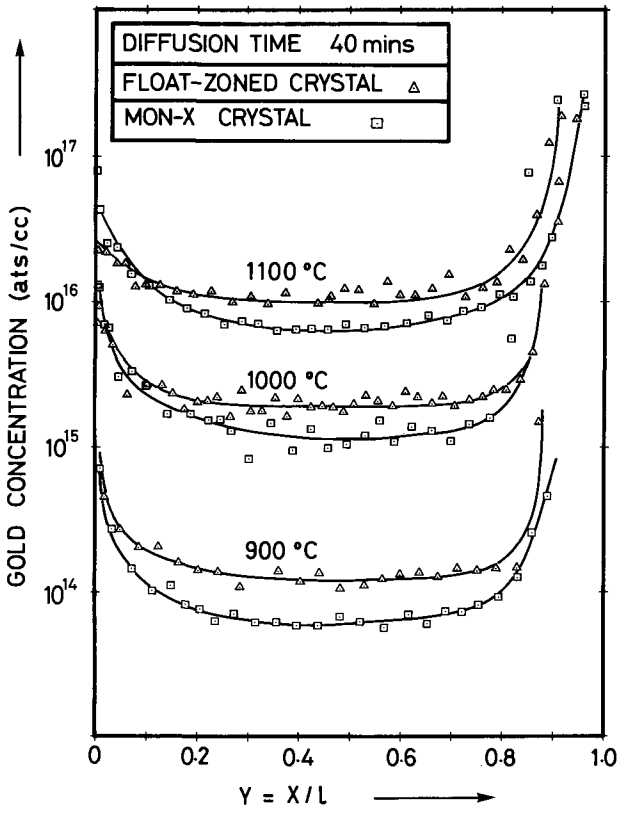

Fig. 11. Concentration profiles of gold diffused into slices of both FZ and Mon-X silicon, at 900°, 1000°, and 1100°C.

shortest diffusion time, indicates the presence of concentration gradients in the central region. At very short diffusion times the slope of the central concentration curve can be expected to increase due to local equilibrium not being established in the $I + V \rightleftharpoons S$ reaction. It can be shown (28) that if the rate of increase of the central concentration is limited by the reaction rate of the $I \rightarrow S$ transition, the slope of the central concentration VS time curve should approach

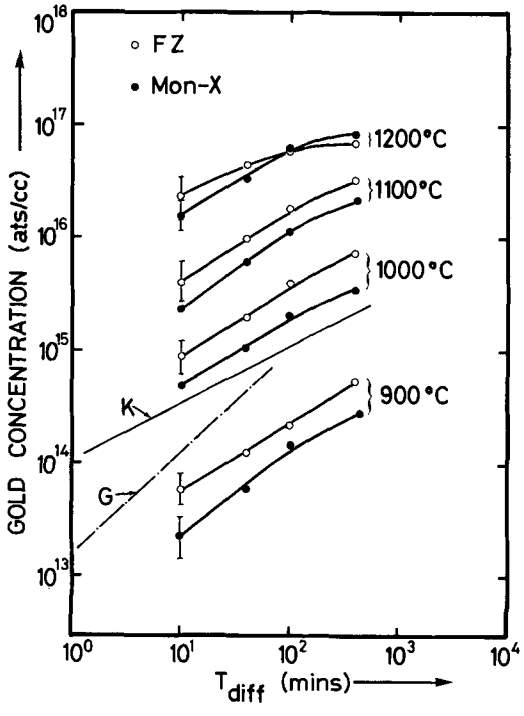

Fig. 12. Gold concentration at the center of diffused slices as a function of time, temperature, and material type.

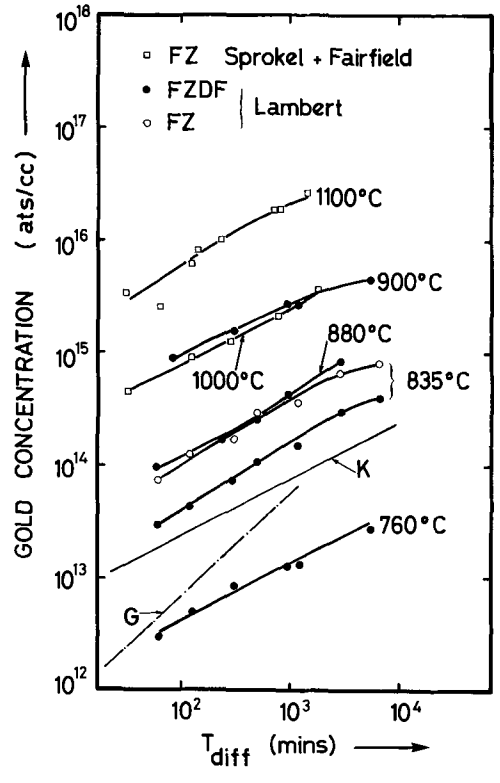

Fig. 13. Central concentration time dependence as determined by Lambert (6) and Sprokel and Fairfield (8).

that of the G curve. This might cause concentrations in slices diffused for short times to be low in general, as well as containing concentration gradients as explained above.

Quantitative test of dislocation climb model.—Substituting the measured dependence of C_s on time into Eq. [1], together with gold solubility limits (18) for C_s', enables values of K for each temperature and material type to be calculated which are shown in Fig. 14.

At a given temperature, Eq. [2] shows that K should be directly proportional to the dislocation density (assuming similar distributions of Burgers vectors, and jog densities in both materials). Figure 14 shows that the K values for the FZ material are a factor of 2 to 6 greater than those for the Mon-X material. The ratio of K values thus implies a similar ratio between the dislocation densities, *i.e.*, much smaller than the ratio of dislocation densities of 10^4:~1 observed by x-ray topography before and after gold diffusion. This difference between the central concentrations found in the high- and low-dislocation density materials was thus consistently smaller for all diffusion temperatures than that anticipated from the measured dislocation density difference. It is to be expected, however, that a large proportion of grown-in dislocations do not act as efficient vacancy generators due to interactions with impurities initiated during the high temperature crystal growth process. This was confirmed by the x-ray topography study which revealed ltitle evidence of gross dislocation climb after gold diffusion.

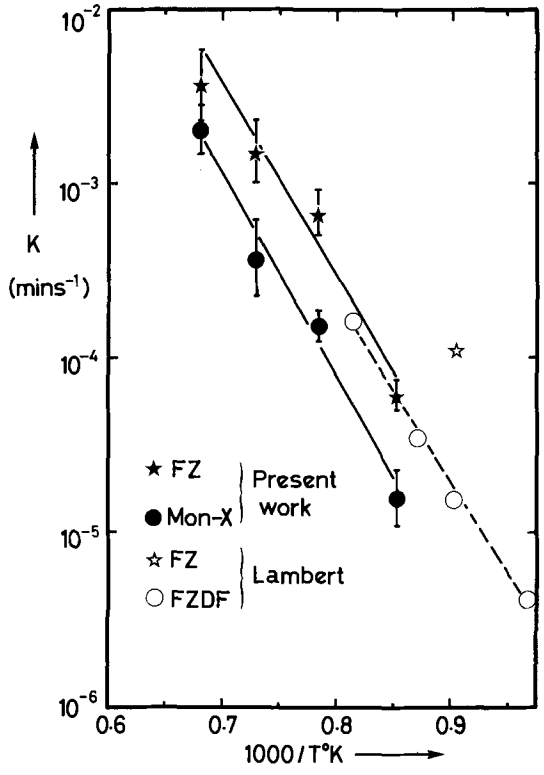

Fig. 14. Temperature dependence of vacancy generation parameter K, as a function of material type.

While the ratio of K values for the two types of material can be thus closely related to the differences in dislocation density, the absolute magnitude of the K values calculated are more difficult to explain, as pointed out (9), and discussed (19, 20), previously. Substituting the measured values of K in Eq. [2] lead to values of jog spacing of less than 10Å which is much smaller than might be expected using simple calculations of jog activation energies, albeit in this nonequilibrium situation. Although the value of $D^{sd}{}_{1v}$ used in this calculation is subject to much uncertainty, the true value cannot be higher than the self-diffusion coefficient measured by tracer methods; and the jog line density calculated using a lower value would be even more unreasonable. It therefore remains to explain a high apparent vacancy generation rate in all samples, upon which the effect of grown-in dislocations is apparently superimposed. Possible explanations of this apparently high background generation rate are discussed further below.

Temperature dependence of thin slice diffusion.—Figure 14 shows the calculated values of K plotted against temperature for both types of material used in this work and that of Lambert (6). Both material types indicate a distinct activation energy of about 2.11 eV

in the temperature range of the measurements, although there appears to be a discrepancy between the absolute values of K determined in this work, and by Lambert (6). If reliable values of the activation energy for self-diffusion by a vacancy mechanism were available [there is considerable doubt as to whether the dominant self-diffusion process in silicon is a monovacancy mechanism (21)] these measured activation energies could be used to test the model further, by calculating jog formation energies. At present it is sufficient to note that the activation of the vacancy generation process appears to be well established [by both the current work and that of Lambert (6)] at about 2.11 eV, and that this is not inconsistent with a dislocation climb process.

Discussion

In this work small but significant differences in the diffusion behavior of gold have been found between two silicon crystals having different dislocation content. It must first be discussed whether these differences in diffusion behavior are associated with the differences in dislocation content, or whether other differences, such as concentrations of trace elements (or even of original gold content) could have been responsible. While alternative explanations seem unlikely even on a theoretical basis, perhaps the strongest argument against such alternatives is the remarkable agreement between the present work and that of Lambert (6) since it is extremely unlikely that both studies would have used crystals with identical trace element concentrations.

Perhaps the most severe handicap in interpreting the results of this work has been the lack of data concerning self-diffusion mechanisms and the properties of native defects in silicon. It has been seen that, even for qualitative explanations of dislocation density effects, the relative diffusion rates of vacancies and interstitial gold atoms really need to be known. It must be pointed out, therefore, that the more quantitative explanations suggested in this paper are very tentative, and await firm data on vacancy diffusion and concentrations for conclusive tests of the models.

With these reservations it can be concluded that the positive effects of dislocation density afford strong evidence in favor of the dissociative mechanism for gold diffusion in silicon. It has been seen, however, that certain quantitative correlations with a dislocation climb model are not fully satisfactory. It is possible that the climb model assumed previously (9) is not appropriate to this particular nonequilibrium situation. Even with the assumption that it is appropriate, an explanation is needed for the apparent high vacancy generation rate.

The possibility that vacancy generation at dislocations in the bulk is only a secondary rate-determining process cannot be ruled out, and the primary process might be one of a number of other processes, *e.g.*, vacancy diffusion from bulk sources, interstitial-substitutional gold transition etc. The time-dependence behavior would appear to rule out the latter interpretation, but all alternatives cannot be dismissed.

Since the rapid penetration of the dissociative impurity cannot be ascribed to dislocation-pipe diffusion [the necessary flux per dislocation appears to be unreasonably high, see Frank and Turnbull (1)] it seems unlikely that the measured dislocation-density effect is due to pipe diffusion. Further, a much more dramatic difference than has been observed would be expected between the diffusion profiles in the two materials, if dislocation pipe diffusion played a significant role. While it has been concluded from this work that there must be a significant concentration of vacancy generation sources in the Mon-X material, there is certainly no dislocation network running through the whole specimen thickness as in the FZ material. Since there can, therefore, be no pipe diffusion in the Mon-X material, if pipe diffusion does take place in the FZ specimens a stronger asymmetry in the FZ profiles would be expected, as well as a greater difference in absolute magnitude of the diffusion profiles in the two materials. Such an effect was not observed, and hence dislocation pipe diffusion can be dismissed.

The only comprehensive interpretation in terms of dislocations alone must assume the presence of a large density of dislocations which were not detected by x-ray topography. As discussed above, there was some indirect evidence for defects in the Mon-X material, which have been suggested to be vacancy clusters (10), formed perhaps during the post-growth cooling of low dislocation density silicon crystals (22) due to the lack of vacancy sinks in the bulk.

It has been proposed that, during the high-temperature anneals, vacancy clusters collapse to form extrinsic stacking faults surrounded by sessile dislocation loops. Such defects have been reported (23-26) in silicon which has been diffused with gold or platinum. In each case it has been proposed that the observed loops, up to a few hundred microns in diameter, have arisen as a result of the growth of similar, but much smaller loops. Diffraction contrast studies, and double crystal topographs of the stacking faults indicate that they are extrinsic (23, 26), *i.e.*, will grow if they emit vacancies. The growth of such loops is therefore consistent with the demand for vacancies caused by dissociative diffusion.

It thus seems possible that the effect of initial dislocation density is apparently so small because significant vacancy generation takes place at dislocation loops, as described above. In addition to the direct evidence obtained by Iizuka (23), the present copper decoration studies also imply that copper precipitation nucleation sites are influenced by gold diffusion and are thus involved in the gold diffusion process. The copper precipitates observed in Mon-X slices before gold diffusion were in the form of complete, or partial six-point stars, as have been previously observed by other workers [for example Dale (27), and by Fiermans and Vennik (28-30)]. An example of the complete star shape can be seen in Fig. 15 (labelled 1). In fact Fig. 15 is a micrograph of precipitates in gold diffused Mon-X. The other two precipitates (labelled 2 and 3) in this figure are examples of types found only after gold diffusion, and which have a more shadowy planar form than the star precipitates. The precipitate labelled 2 would appear to be a derivative of the star form, while the precipitate labelled 3 appears to be more like a hexagonal loop. This evidence

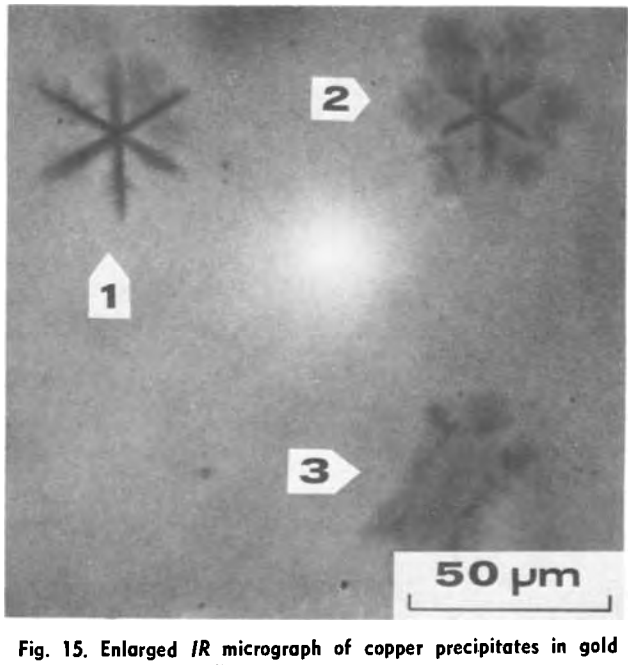

Fig. 15. Enlarged *IR* micrograph of copper precipitates in gold diffused Mon-X silicon slice.

is, however, highly indirect, as there is no evidence that the geometry of the observed copper precipitates bears any fixed relationship to the structure of the nucleating defect.

Against this dislocation loop model it must be pointed out that no evidence for such loops was seen in float-zoned material, and since the equivalent dislocation density in the loops must be greater than the grown-in density it seems surprising that no loops were seen by x-ray topography after gold diffusion. At present, therefore, vacancy generation at climbing dislocations cannot be conclusively established as the only rate-determining process. Detailed explanation awaits more data on intrinsic defects in silicon and on the interaction of impurities with dislocations and point defects.

Conclusions

1. The dislocation density of thin silicon slices affects both the profile shape and the concentration of gold diffused from one face.
2. This small but significant effect of dislocation density on gold diffusion is strong evidence to support the dissociative mechanism for gold diffusion in silicon.
3. The differences between diffusion profiles in high and low dislocation density material are satisfactorily explained by a model in which vacancy generation occurs at climbing dislocations.
4. Vacancy generation at climbing grown-in dislocations is not the only process determining the rate of gold uptake in the thin slices studied in this work. Other processes, such as the growth of diffusion-induced loops, are suggested to account for the results.

Acknowledgments

This work was carried out under a C.V.D. contract and is published by permission of the Ministry of Defence (Navy Department), whose financial support is gratefully acknowledged. Thanks are also due to Dr. J. L. Lambert of A.E.G.-Telefunken, Frankfurt a.M., for a preprint of his results. We further wish to thank S. R. C. for a grant to one of us (F.A.H.) and Professor R. L. Bell for provision of laboratory facilities. We are most grateful to Dr. J. D. Filby, (R. R. E. Malvern) for the x-ray topographs presented in this work, and also for helpful discussions throughout this project. Thanks are also expressed to Dr. R. F. Peart (Plessey Company, Caswell) for assistance with design of the precision grinding jig.

Manuscript received Sept. 6, 1972. This was Paper 174 presented at the Cleveland, Ohio, Meeting of the Society, Oct. 3-7, 1971.

Any discussion of this paper will appear in a Discussion Section to be published in the December 1973 JOURNAL.

REFERENCES

1. F. C. Frank and D. Turnbull, *Phys. Rev.*, **104**, 617 (1956).
2. W. R. Wilcox and T. J. Chappelle, *J. Appl. Phys.*, **35**, 240 (1964).
3. W. C. Dash, *ibid.*, **31**, 2275 (1960).
4. L. S. Milevskii, *Soviet Phys. Solid State*, **4**, 1792 (1963).
5. M. Yoshida and K. Saito, *Japan. J. Appl. Phys.*, **9**, 1217 (1970).
6. J. L. Lambert, Paper 81 presented at Electrochem. Soc. Meeting, Washington, D. C., May 9-13, 1971.
7. J. Martin, E. Haas, and K. Raithel, *Solid-State Electron.*, **9**, 83 (1966).
8. G. J. Sprokel and J. M. Fairfield, *This Journal*, **112**, 200 (1965).
9. F. A. Huntley and A. F. W. Willoughby, *Solid-State Electron.*, **13**, 1231 (1970).
10. A. J. R. De Kock, *Appl. Phys. Letters*, **16**, 100 (1970).
11. F. A. Huntley and A. F. W. Willoughby, *Solid-State Electron.*, **14**, 641 (1971).
12. C. J. Slabinski, Ph.D. Thesis, Case Western Reserve University (1969).
13. J. W. Adamic and J. E. McNamara, Paper 149 presented at Electrochem. Soc. Meeting, New York, Sept. 29-30, Oct. 1-3, 1963.
14. S. D. Brotherton, *J. Appl. Phys.*, **42**, 2085 (1971).
15. F. A. Huntley and A. F. W. Willoughby, To be published.
16. M. D. Sturge, *Proc. Phys. Soc. (London)*, **73**, 297 (1959).
17. S. D. Brotherton, Private communication.
18. W. M. Bullis and F. J. Streiter, *J. Appl. Phys.*, **39**, 314 (1968).
19. J. L. Lambert, *Phys. Status Solidi (a)*, **4**, K33 (1971).
20. F. A. Huntley and A. F. W. Willoughby, *ibid.*, **5**, K213 (1971).
21. A. Seeger and K. P. Chik, *ibid.*, **29**, 455 (1968).
22. W. C. Dash, *J. Appl. Phys.*, **30**, 459 (1959).
23. T. Iizuka, *Japan. J. Appl. Phys.*, **4**, 1018 (1966).
24. V. A. Phillips and W. C. Dash, *J. Appl. Phys.*, **33**, 568 (1962).
25. Y. Tokamaru and M. Kikuchi, *Japan. J. Appl. Phys.*, **5**, 847 (1966).
26. O. Brummer and M. Hofmann, *Phys. Status Solidi (a)*, **5**, 199 (1971).
27. J. R. Dale, in "Semiconductor Silicon," R. R. Haberecht and E. L. Kern, Editors, p. 622, The Electrochemical Society Softbound Symposium Series, New York (1969).
28. L. Fiermans and J. Vennik, *Phys. Status Solidi*, **12**, 277 (1965).
29. L. Fiermans and J. Vennik, *ibid.*, **21**, 627 (1967).
30. L. Fiermans and J. Vennik, *ibid.*, **22**, 463 (1967).

Conduction Mechanisms in Very Thin Silicon Nitride Films

Juan H. Sanchez-Lassise

Department of Electrical Engineering, University of Puerto Rico, Mayaguez, Puerto Rico 00708

and J. R. Yeargan

Department of Electrical Engineering, University of Arkansas, Fayetteville, Arkansas 72701

ABSTRACT

The steady-state d-c conduction properties of silicon nitride films in the range of 50-100Å are reported. The nitride films were formed by vapor deposition on degenerate silicon substrates using the silane-ammonia reaction. The temperature, thickness, and field dependence of current indicates that a transition in current mechanisms occurs at a film thickness of approximately 80Å. Below this film thickness, the current is characterized by low temperature dependence and large thickness dependence. At film thickness above this value, the current is proportional to $\exp[\beta V^{1/2}]$.

Due to their importance in the semiconductor industry, the electrical and physical properties of thin-film insulators have received considerable attention in the literature. Extensive studies have been made concerning the electrical characteristics (mostly conduction properties) of these insulators. Previous works have established that current in thin insulating films is due to either a thermal or a tunneling mechanism which can be further divided into a bulk-limited, or an electrode-limited process.

In the case where the insulator is very thin, *i.e.*, less than 50Å, several authors have found direct tunneling to be the dominant conduction mechanism either for MIM (1, 2) or MIS (3, 4) devices. For films above 200-300Å thick, it has been found (5, 6) that the conduction mechanism is a Poole-Frenkel emission at high fields and temperatures. However, the range of thicknesses between 50 and 200Å has not received much attention in the literature. At some thickness in this range, a transition from a bulk-controlled to an electrode-controlled mechanism occurs. The purpose of this work has been to study this transition in a vapor-deposited film of silicon nitride.

Experimental Procedure

The silicon nitride films were deposited by chemical vapor deposition techniques (7) on degenerate p- and n-type silicon substrates. The substrates were polished, cleaned, degreased, and etched in concentrated HF prior to deposition of the films. A deposition rate of 40-60Å/min was used with a silane to ammonia ratio of 10-100 cm^3/min in 500 cm^3/min of hydrogen at a temperature of 650°C. After deposition, aluminum dots of 2 mm diameter were deposited on the silicon nitride film at a vacuum of 6×10^{-6} Torr. The devices were completed by depositing aluminum on the opposite face of the substrates.

Current *vs.* voltage measurements were made with a Keithley Model 602 electrometer and a Darcy Model DM-440 digital voltmeter. The thickness of the films was measured by the capacitance method. Current *vs.* temperature measurements were taken by immersing a test fixture with the sample on it into a Dewar flask filled with liquid air (77°K). A Chromel-Alumel thermocouple measured the temperature.

Experimental Results

The current *vs.* voltage characteristics of a MIS sample which is 94Å thick are shown in Fig. 1. The positive and negative signs indicate the potential of the metal relative to the substrate. This plot shows the typical behavior of p- and n-devices thicker than 90Å. The linear characteristic indicates that $\log I \propto \beta V^{1/2}$ where β is a constant. Figure 2 shows a $\log I$ *vs.* $1/T$ plot for a device of 110Å thick which also exhibits this linear behavior on a Schottky plot. Note here the strong temperature dependence of the current at room temperature.

Other workers (5, 6) report that Poole-Frenkel emission is the dominant current mechanism in silicon nitride films at room temperature. However, this type of emission does not show a polarity effect (as in Fig. 1) because it occurs from impurity centers deep within the insulator. This polarity effect, which the Poole-Frenkel model alone cannot explain, is accounted for by noting that there is always a thin layer of SiO_2 on a silicon surface. Optical measurements (7) have shown that on a freshly etched surface of silicon, an oxide layer of 15-20Å thick is formed in about 2 min of exposure to the atmosphere. After the samples used in this work were chemically etched, they were exposed to the atmosphere for about 5 min. Capacitance measurements on devices reported here indicate an oxide thickness varying from 35 to 45Å. This SiO_2 film

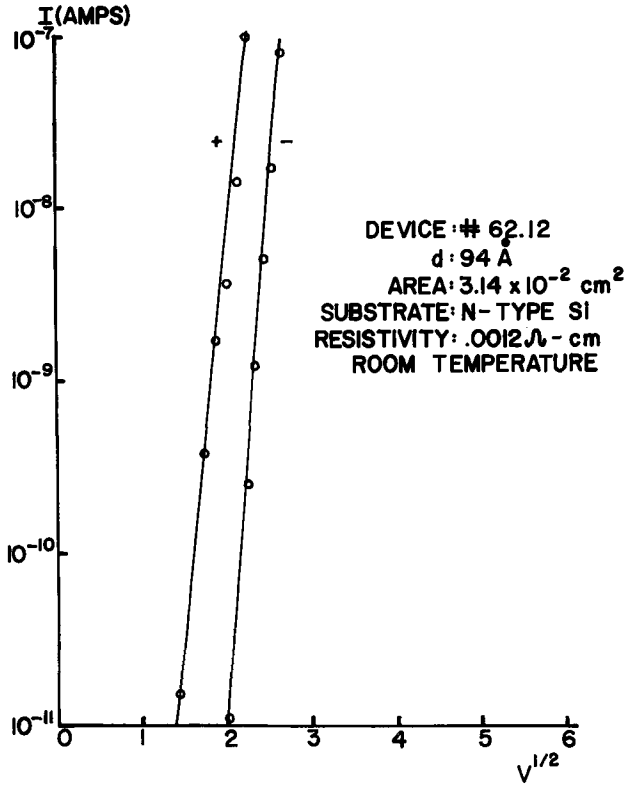

Fig. 1. Current-voltage characteristics of MIS device with 94Å film thickness and n-type substrate.

Key words: steady state, thin films, silicon nitride.

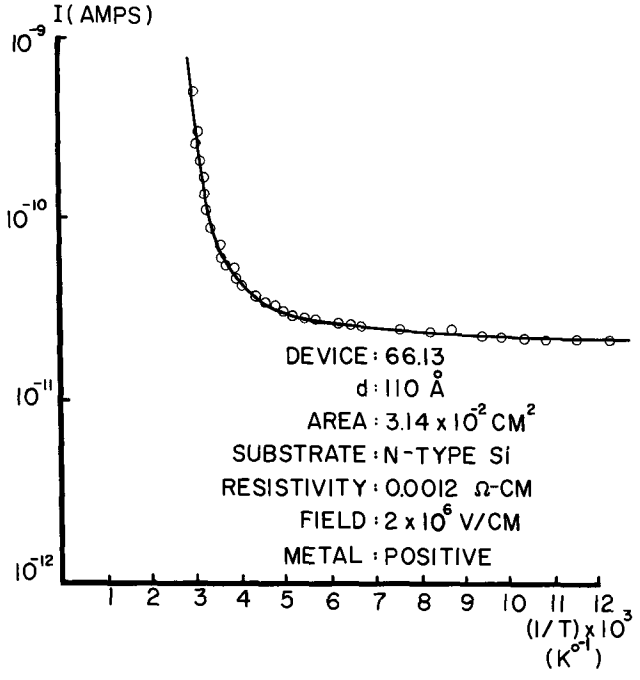

Fig. 2. Current-temperature plot for a n-type substrate device which exhibits linear I-V behavior on a Schottky plot.

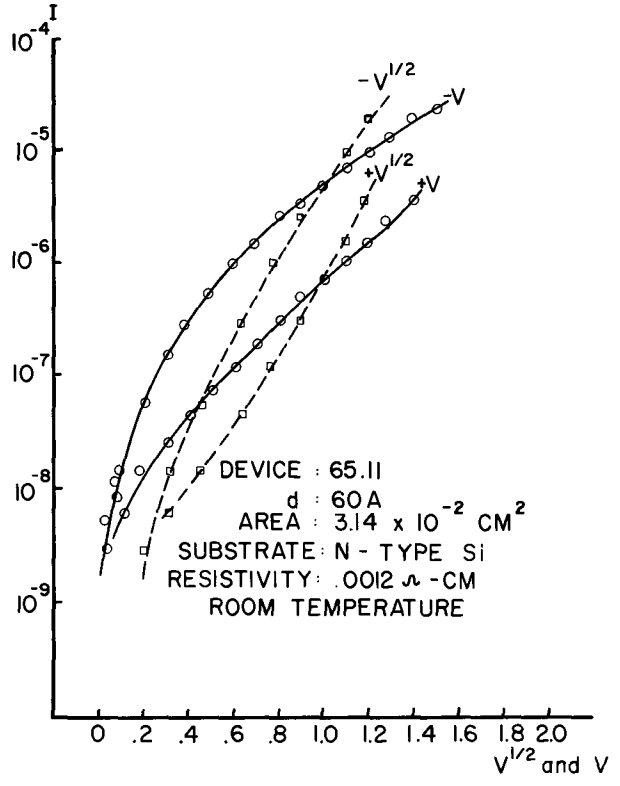

Fig. 3. Log I vs. V and log I vs. V½ curves showing nonlinear characteristics and higher current densities of films below approximately 80Å.

modifies the conduction process from a Poole-Frenkel mechanism to a combination of Poole-Frenkel for the nitride and tunneling through the oxide (9).

Frohman-Bentchkowsky and Lenzlinger (9) studied a similar case with thicker nitride films for which they calculated theoretical current *vs.* voltage characteristics using the two mechanisms mentioned above. Their curves, although for thicker films, are similar to that shown in Fig. 1.

All samples with behavior similar to Fig. 1 exhibit linear behavior up to breakdown. At breakdown, the current shows transient instabilities first, then increases several orders of magnitude. Reducing the field at the onset of the transient behavior prevents the increase in current, but the original characteristics are not recovered.

The current is time dependent, and starts decreasing from the moment the field is applied. A period of 10-15 min is necessary for the current to reach its final value after each increment in voltage. This effect is reduced at liquid-air temperatures.

The samples with film thickness between 60-80Å show different behavior. In Fig. 3, which is typical of this range, conduction starts with a field of the order of 10^3 V/cm, while in devices similar to that of Fig. 1, it starts near 10^6 V/cm. In devices with 60Å films, the current is about three orders of magnitude greater for the same applied field than in devices with 80Å films, as a comparison between Fig. 3 and 4 shows. Such thickness dependence is indicative of a tunneling mechanism (10).

In Fig. 4, the curve corresponding to negative voltages is smooth, while that corresponding to positive voltages shows structures due to the effect of the semiconductor bandgap.

Figure 5 shows the current *vs.* temperature characteristics of an 80Å MIS device. Note here the small variation of current with temperature which is another characteristic of a tunneling mechanism.

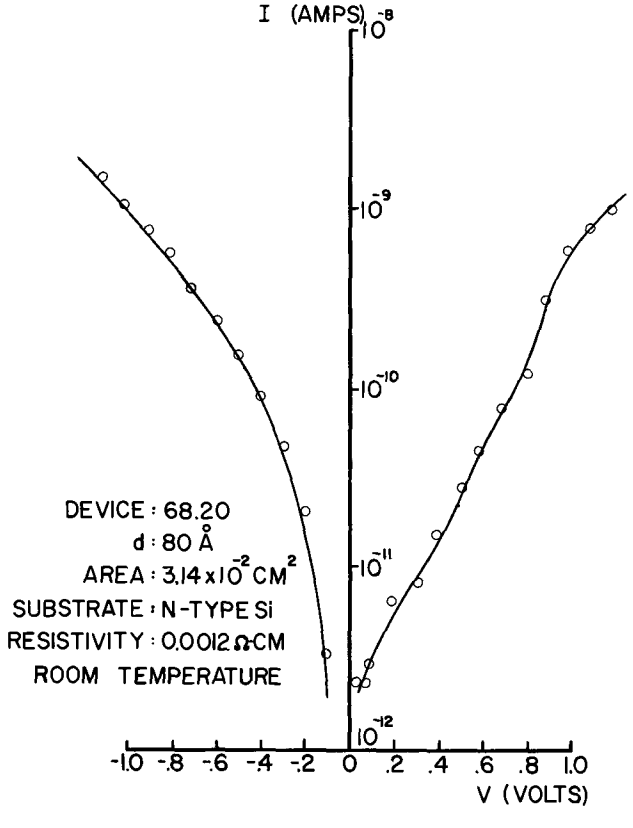

Fig. 4. Current-voltage characteristics of 80Å n-type substrate MIS device which exhibits tunneling.

Conclusion

An analysis of the current *vs.* voltage and temperature characteristics of MNS devices leads us to the conclusion that we have observed a transition of current mechanisms in thin silicon nitride films. For the thicker films, the logarithm of the current is proportional to $\beta V^{1/2}$ over several decades of current, and the current is very temperature dependent at room temperature. This indicates that the emission mechanism is a type of field-assisted, thermal ionization of electrons into the conduction band of the insulator. The polarity effect is due to a thin (40Å) SiO_2 film between the nitride and the semiconductor.

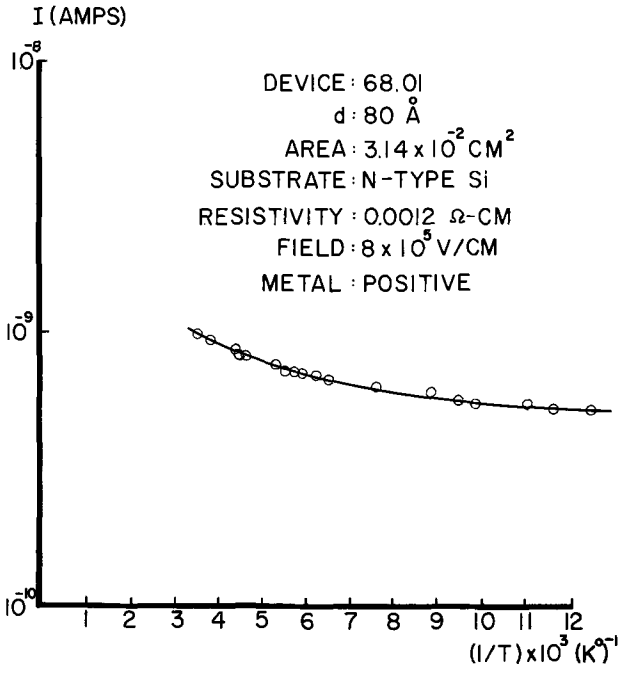

Fig. 5. Current-temperature plot for a n-type substrate device which exhibits tunneling.

At thicknesses below 80Å, the current is due to direct tunneling from metal to semiconductor as shown by the small temperature and large thickness dependence of the current. We were unable to observe both mechanisms on the same device due to the large difference in the field at which both occur.

Manuscript submitted April 18, 1972; revised manuscript received Nov. 10, 1972.

Any discussion of this paper will appear in a Discussion Section to be published in the December 1973 JOURNAL.

REFERENCES

1. R. Stratton, *J. Phys. Chem. Solids*, **23**, 1177 (1962).
2. T. E. Hartman and J. Chivian, *Phys. Rev.*, **134**, A1094 (1964).
3. W. E. Dahlke and S. M. Sze, *Solid-State Electron.*, **10**, 865 (1967).
4. J. Shewchun, A. Waxman, and G. Warfield, *Solid-State Electron.*, **10**, 1187 (1967).
5. S. M. Sze, *J. Appl. Phys.*, **38**, 2951 (1967).
6. J. R. Yeargan and H. L. Taylor, *This Journal*, **115**, 273 (1968).
7. D. E. Cullen, E. L. Wolf, and W. D. Compton, *Phys. Rev. B.*, **2**, 3157 (1970).
8. M. Lenzlinger and E. H. Snow, *J. Appl. Phys.* **40**, 278 (1969).
9. D. Frohman-Bentchkowsky and M. Lenzlinger, *ibid.*, **40** (1964).
10. E. Burstein and S. Lundquist, "Tunneling Phenomena in Solids," Plenum Press, New York (1969).

Transfer of Mobile Ions from Aqueous Solutions to the Silicon Dioxide Surface

S. I. Raider,* L. V. Gregor,* and R. Flitsch

IBM System Products Division, East Fishkill Laboratory, Hopewell Junction, New York 12533

ABSTRACT

The transfer of mobile ions to the SiO_2 surface was investigated by immersing thermally oxidized Si wafers in aqueous solutions containing Na^+ and/or H^+ ions. The number of mobile charges at the SiO_2 surface was determined by electrical measurements on MOS capacitors and the number of Na^+ ions was determined by flame photometry. For deionized H_2O and acid solutions, there is essentially no transfer of mobile charge to the SiO_2 surface. For neutral NaCl solutions, the number of mobile charges transferred is proportional to the Na^+ concentration in solution, and comparable to the number of transferred Na^+ ions. For acidified NaCl solutions, the number of transferred Na^+ ions is comparable to the number of neutral solutions with the same Na^+ concentration; the number of mobile charges is initially much smaller, but slowly increases. These observations are interpreted in terms of the kinetics of cationic adsorption from aqueous solutions at the SiO_2 surface. It is proposed that mobile Na^+ ions are physically or chemically adsorbed directly on an oxide surface, whereas immobile Na ions are adsorbed on an acid-covered oxide surface.

Mobile ions in SiO_2 films can cause semiconductor-device instabilities at concentrations of about 10^{11} singly charged ions/cm^2. This concentration of ions is at, or below, the limit of detection of most available analytical techniques. As a result of the difficulties present in direct identification of the mobile ions, their identities were previously deduced from the nature of the contaminating source. Metal-oxide-semiconductor (MOS) structures were used to study ionic conduction in SiO_2 films. Results from SiO_2 contamination experiments, radiotracer experiments, and electrical measurements were interpreted to show that either alkali ions (1-3) or H^+ ions (4-6) from H_2O, C_2H_5OH (7), and other organics are mobile in SiO_2 films.

In the present investigation, the number of mobile charges transferred to the SiO_2 surface from various contaminating aqueous solutions was determined by electrical measurements on MOS structures and compared with the number of transferred Na^+ ions determined by flame photometry. The mobile ionic species has been identified and experimental results are discussed in terms of adsorption at the SiO_2 surface from the aqueous contaminating solutions.

Experimental

Sample preparation and electrical measurements.— Si wafers (1.25 in. diameter, p-type, 2 ohm-cm, <100>, chem-mech polished) were cleaned in solutions of

* Electrochemical Society Active Member.

Key words: SiO_2 thin films, mobile ions, Na^+ ions, H^+ ions, surface adsorption, MOS, SiO_2-electrolyte interface.

NH_4OH-H_2O_2, HCl-H_2O_2, and HF, then oxidized. An O_2-steam-O_2 oxidation cycle was used at 970°C to grow SiO_2 films 5700Å thick. Some experiments were performed after removing about 200Å of the oxide surface in dilute (1:25) HF and then hydrolyzing in deionized (D.I.) H_2O to form silanol groups. Thinner oxide films were also grown in dry O_2 at 1000°C. Oxides 1000Å thick grown on n-type Si wafers were used for contamination experiments with 1*N* H_2SO_4.

Reagent or electronic grade chemicals were used for contamination experiments. Solutions for contamination of the SiO_2 surfaces were prepared by diluting concentrated solutions with deionized H_2O. Flame photometric analyses showed that the deionized H_2O contained less than 0.3 ppb Na^+ ions. The concentrated HNO_3 and HCl acids each contained about 0.5 ppm Na^+. The starting NaCl or NaOH solutions were prepared by standard volumetric procedures, and Na^+ ion concentrations were determined by flame photometric measurements. Acid or alkali concentrations were determined by acid-base titrations. Contaminating solutions containing both Na^+ and H^+ ions were prepared by combining 45 ml of the Na^+ solution with 5 ml of an acid of appropriate concentration. The solutions were stored in plastic bottles and transferred using only cleaned plastic beakers and plastic graduated cylinders. Contaminations of SiO_2 at elevated temperatures were carried out with Teflon beakers. Quartz beakers were used for the studies in which wafers were ultrasonically agitated during the contamination step.

The SiO_2 surface was contaminated by immersing the wafer, SiO_2 surface up, in a plastic beaker containing 50 ml of the contaminating solution. Generally, this process was carried out at room temperature (22° ± 2°C) for 5 min with no agitation of the solution, but in some experiments, periods of 15 sec, 4 hr, or 4 days were employed. After contamination, the wafers were removed from the beakers and blown dry with warmed, filtered N_2 gas. No H_2O rinse was used after the wafers were contaminated. Control wafers were prepared omitting the contamination step.

Clean Al electrodes (0.05 cm diameter, 5000Å thick) were deposited on the SiO_2 surface through metal masks by electron-gun evaporation. Blanket Al electrodes were deposited on the backside of the Si wafer to improve the electrical contact when testing. The wafers were then annealed at 400°C for 20 min in N_2. In some experiments, Au instead of Al electrodes were evaporated onto the oxide surface.

The electrical MOS measurements to determine the total number of mobile charges per unit area (Q/q) were performed at 250°C with d-c fields of 0.7 MV/cm for biasing. The number (Q/q) was determined from capacitance-voltage measurements (8) by obtaining the difference in flatband voltages before and after biasing MOS structures for 5 min. For $\geq 10^{13}$ mobile charges/cm^2, the charge-time (Q-t) technique (9) was used to make a direct measurement of the total mobile charge when the MOS structures were thermally biased. Four or more MOS structures were examined on each wafer for a particular contamination experiment.

Several lots of oxides were grown over an extended period of time during which the described experiments were conducted. Mobile-charge levels in control samples of these oxides varied from 0.4-2.8 × 10^{11}/cm^2. However, the scatter in this background mobile-charge level for oxides obtained from any particular oxidation lot was generally $<10^{11}$/cm^2. Negligible mobile-ion contamination occurs during Al metallization since thin oxides grown in dry O_2 contained $\leq 5 \times 10^{10}$ mobile charges/cm^2 after Al electrode depositions. Oxides used for a related group of contamination experiments were grown in a single lot. Immersion of the oxide for 5 min in deionized H_2O frequently reduced the mobile charge below that of a nonrinsed control wafer.

Flame photometric determination of Na^+ ions.[1]—The number of Na^+ ions present at an oxide surface was measured by flame photometry. About 200Å of the SiO_2 surface of a wafer was etched away with 15 drops of diluted (1:20) ultrapure (0.5 ppb Na^+)HF. The etch solution was transferred to a clean disposable plastic beaker. The wafer surface was then rinsed with deionized H_2O. The rinse H_2O was also transferred to the disposable beaker, giving a total of about 2 ml of solution. The total number of Na^+ ions was obtained from the solution weight and the Na^+ concentration measured with the flame photometer. The detection limit for Na^+ ions was about 1 ppb by weight or 0.001 μg/ml of solution. When possible, lower Na^+ levels were determined after solvent evaporation to increase the Na^+ concentration of the solution. To facilitate comparisons with the results of electrical measurements, the flame photometric data are expressed as the total number of Na^+ ions per unit area of oxide surface. For example, a weight of 0.1 μg of Na from the wafer surface is equivalent to 3.3 × 10^{14} Na/cm^2.

Results

Total mobile charge transferred to SiO_2 from contaminating aqueous solutions.—Deionized H_2O.—To determine whether deionized H_2O introduces mobile charge to the oxide, wafers were immersed into H_2O for varying times and temperatures, after which the mobile charge was found by C-V measurements. The data from these experiments are given in Table I. These results, which are contrary to those of Hofstein (4) and in agreement with that of Yurash and Deal (10), indicate that SiO_2 immersion into deionized H_2O does not increase the number of mobile charges at SiO_2 surfaces.

Acid solutions.—Both HCl and HNO_3 solutions were used for contamination studies over a wide range of acid concentrations. In Fig. 1, the mobile charge present at the SiO_2 surface after immersion in HCl solutions for 5 min at 22°C is shown as a function of H^+ ion concentration. Similar results were obtained after SiO_2 immersion into HNO_3 solutions and a 1*N* H_2SO_4 solution. Essentially, no mobile charge is transferred to the oxides from these acids despite the large number of H^+ ions present at the oxide surface in solution.

Solutions containing Na^+ ions.—The effects of NaCl contamination of SiO_2 surfaces from neutral aqueous solutions on the total mobile charge for an immersion time of 5 min at 22°C are shown in Fig. 1. The number of mobile charges present at the SiO_2 surface is proportional to the Na^+ ion concentration in the neutral NaCl solutions. Similar results were obtained after SiO_2 immersion into NaCl solutions at 22°C. In Table II, the number of mobile charges present at the oxide surface is given as a function of Na^+ concentration for four different immersion times at 22°C. The rate of adsorption of mobile ions is a function of Na^+ con-

[1] Although flame photometry does not distinguish between Na atoms and Na^+ ions, for convenience we shall refer to the species detected by this technique as the Na^+ ion, since in general the Na present at SiO_2 surfaces is in ionic form.

Table I. Effect of deionized H_2O on total mobile charge at SiO_2 surfaces

	Immersion time	$Q/q \times 10^{-11}$ (cm^{-2})
D.I. H_2O 22°C	1 min	1.4
	5 min	0.9-1.1
	10 min	1.0-1.1
	20 min	1.1-1.6
	1 day	0.5-0.7
	T°C	
	22	0.9-1.1
D.I. H_2O	50	0.7-1.4
Immersion time = 5 min	80	1.1-1.3
Control		1.7

D.I. $H_2O \geq 14$ megohm-cm.
Na^+ in $H_2O \leq 0.3$ ppb (flame photometry).

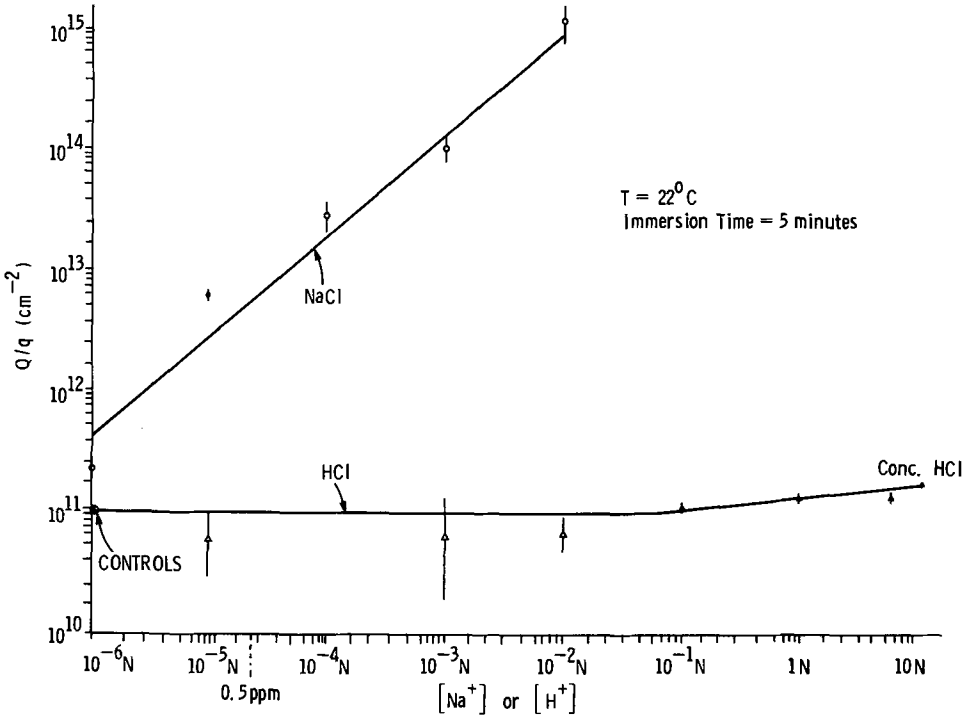

Fig. 1. Total mobile charge at SiO_2 surfaces after immersion in aqueous HCl and neutral NaCl solutions, plotted as a function of the concentration of H^+ and Na^+ ions in solution, respectively.

centration and initially is rapid but decreases with increasing time of immersion. When the temperature of the contaminating NaCl solution was increased from 22° to 70°C, the number of mobile charges transferred to SiO_2 was increased (Table III).

Figure 1 shows that a neutral NaCl solution, with 0.5 ppm of Na^+ ions ($2.2 \times 10^{-5}N$), transferred between 10^{12}-10^{13} mobile charges/cm² to the oxide surfaces after an immersion time of 5 min at 22°C. Concentrated HCl and HNO_3, which also contained 0.5 ppm of Na^+ ions, transferred only about 10^{11} mobile charges/cm² to SiO_2 under the same conditions. This difference indicates that there is a relationship between the concentration of H^+ ions in NaCl solutions and the transfer of mobile charge to the oxide surface. A number of experiments were performed to examine this relationship.

Wafers were contaminated by immersion into acidified (1*N* HCl) NaCl solutions at 22°C for varying periods of time. In Fig. 2 the number of mobile charges present at the oxide surface is plotted as a function of Na^+ concentration for three different immersion times and compared with transfer from neutral NaCl solutions for a 5 min contamination period. During immersion for 5 min no mobile charges were transferred to the oxide from the acidic solutions until the Na^+ ion concentration reached $10^{-2}N$. As the time of wafer immersion is increased, the number of mobile charges transferred to the oxide surface is also increased. After immersing wafers for 4 days in acidified NaCl solutions, the numbers of mobile charges transferred to the oxides appear to be approaching the values obtained with neutral contaminating solutions with the same Na^+ concentrations. These results indicate that in aqueous NaCl contaminating solutions, which are 1*N* with respect to HCl, the rate of mobile charge transfer to the oxide surfaces is decreased in comparison with neutral contaminating solutions.

The number of mobile charges present at the SiO_2 surface after immersion into aqueous NaCl solutions at 22°C was also measured as a function of acid concentration in the solutions. The time of wafer immersion was kept constant at 5 min.

The data from these experiments, which are plotted in Fig. 3, show that as the H^+ ion concentration is decreased, *i.e.*, as the pH is increased, the number of mobile charges transferred to the oxide is increased. Considerable scatter in mobile-charge data was obtained for oxides immersed into NaCl solutions acidified with HCl at concentrations between $10^{-2}N$ and $10^{-5}N$. These results fall between those of $10^{-1}N$ HCl and neutral solutions (D.I. H_2O) and are illustrated as a cross-hatched region in Fig. 3. At pH values greater than 7, solutions of NaOH, rather than NaCl, were used for contamination of the oxides. For Na^+ concentrations of $10^{-5}N$ and above, the number of mobile charges transferred in 5 min was greater for the NaOH solutions than for the neutral NaCl solutions. When the acidified NaCl solutions were ultrasonically agitated, or when the temperatures of the solutions were elevated during the contamination step, the numbers of mobile charges transferred to the oxide increased. Data showing these results are given in Table III.

Some of the room temperature contamination experiments with solutions containing Na^+ and H^+ were repeated with 500Å oxides grown in dry O_2. The results were the same as those obtained for thick oxides.

Table II. Total mobile charge at SiO_2 surfaces as a function of immersion time in neutral aqueous solutions

Contaminating solution	$Q/q \times 10^{-11}$ (cm⁻²) ~15 sec	5 min	4 hr
Control	0.6-0.8	0.9-1.1	0.7-0.8
$10^{-4}N$ NaCl	72-110	140-370	290-540
$10^{-3}N$ NaCl	360-430	750-1,200	1,400-2,500
$10^{-2}N$ NaCl	2,800-3,300	6,700-16,000	12,000-21,000

$T = 22°C$.

Table III. Effect of ultrasonic agitation (U.A.) and elevated temperatures of contaminating solutions on mobile charge transfer to SiO_2

Contaminating solution	$Q/q \times 10^{-11}$ (cm⁻²) U.A. 22°C	No U.A. 22°C	No U.A. 45°C	No U.A. 70°C
$10^{-3}N$ NaCl	—	750-1200	—	2800-4100
$10^{-3}N$ NaCl + 1*N* HCl	—	1.3-1.6	580-830	1800-3300
$10^{-3}N$ NaCl + 0.1*N* HNO_3	27-41	0.5	100-370	120-560
$10^{-4}N$ NaCl	—	140-370	—	340-2100
$10^{-4}N$ NaCl + 0.1*N* HNO_3	2.2-14.7	0.8-0.9	21-44	27-75

Immersion time = 5 min.
— no measurement performed.

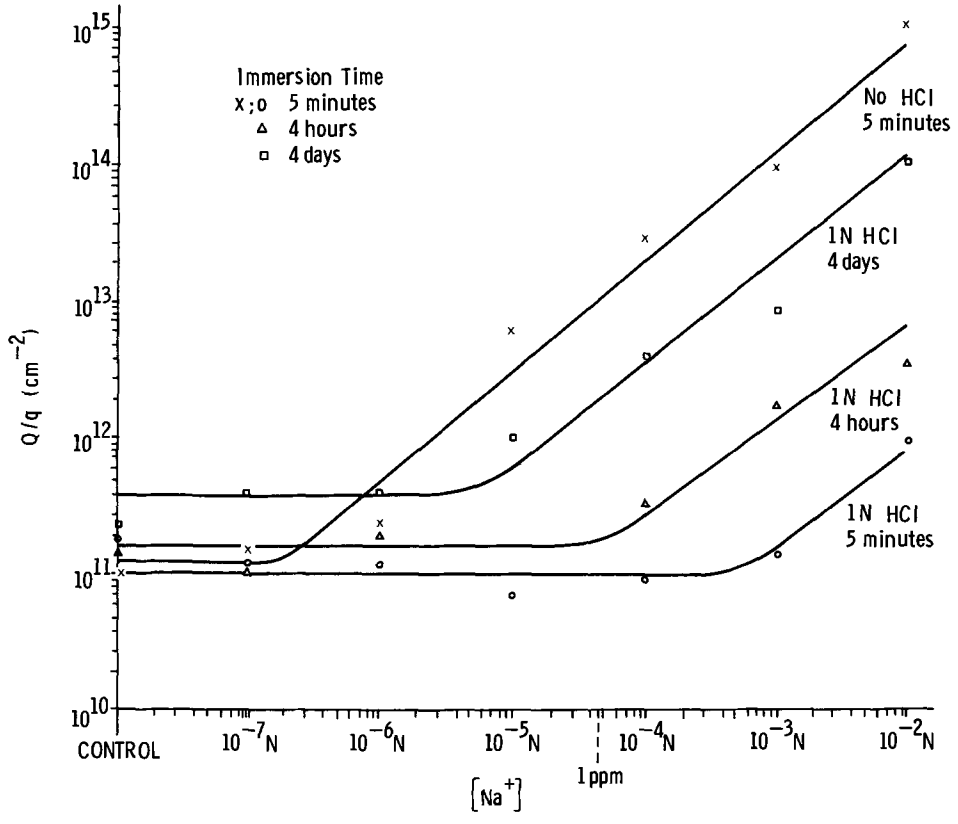

Fig. 2. Total mobile charge at SiO_2 surfaces after immersion in aqueous NaCl solutions, plotted against Na^+ concentration in solution, for neutral solutions (from Fig. 1), and for solutions acidified with 1*N* HCl.

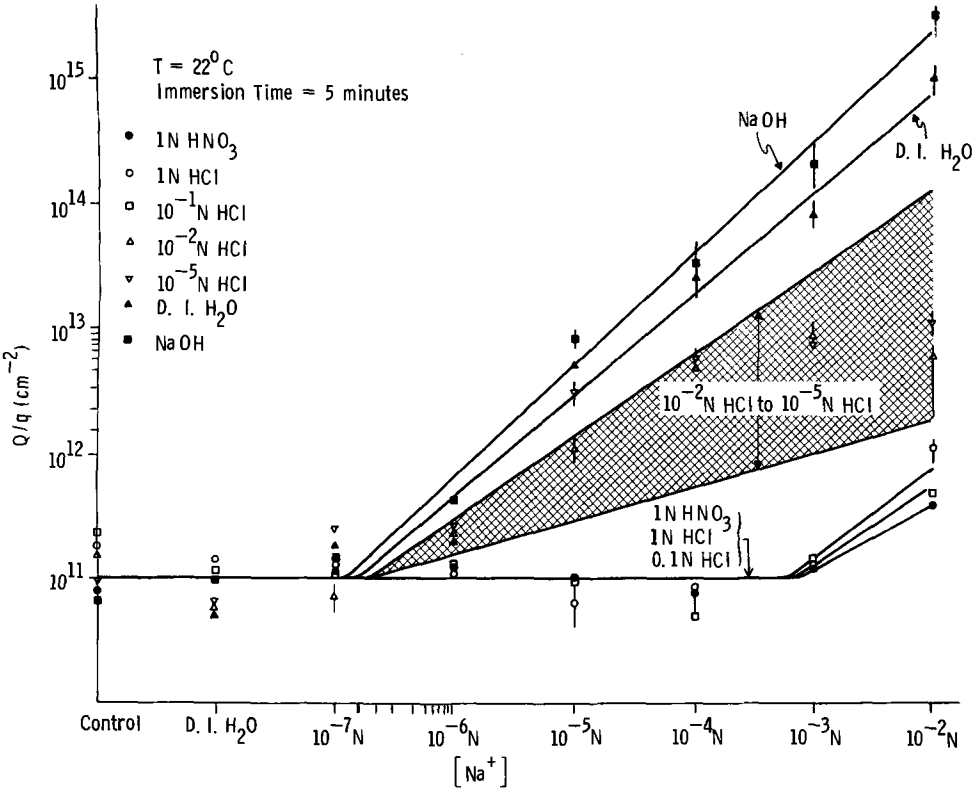

Fig. 3. Total mobile charge at SiO_2 surfaces after immersion in aqueous NaCl solutions, plotted as a function of Na^+, H^+, and OH^- concentrations in solution.

Similar results in reducing mobile charge transfer to the SiO_2 were obtained when 1000Å films (n-Si, <100>, 2 ohm-cm, oxidized in dry O_2) were contaminated by NaCl solutions acidified with 1*N* H_2SO_4. The same effect of acid in reducing mobile ion transfer to SiO_2 was obtained using Au rather than Al electrodes.

Additional experiments were performed to determine whether the SiO_2 surface could be pretreated with acid to prevent transfer of mobile charge. Immersion of the wafers in acidic solutions was followed either by immersion in neutral NaCl solutions, or by evaporation of NaCl onto the oxide surface. In both cases the acid treatments did not prevent mobile-charge transfer to the oxide surfaces. Annealing the oxides in forming gas (H_2:N_2 = 1:9) at 400°C for 20 min prior to immersion into neutral NaCl solutions also failed to reduce the number of mobile charges transferred to the oxides. The reduction in the rate at which mobile charges are transferred to SiO_2 from aqueous solution clearly requires both H^+ and Na^+ ions to be present in the same solution. The removal of mobile charges from SiO_2 surfaces intentionally contaminated with Na^+ ions was also studied. Initially, wafers were immersed into neutral $10^{-2}N$ NaCl solutions for 5 min at 22°C. After drying the wafers with warmed N_2 gas, these contaminated oxides were then

Table IV. Removal of mobile charge from contaminated oxides by rinsing

Contamination pretreatment	Rinse solution[a]	$Q/q \times 10^{-11}$ (cm^{-2})
None (control)	None	0.7-1.1
$10^{-2}N$ NaCl	None	6,700-16,000
$10^{-2}N$ NaCl	D.I. H_2O	3.1-5.9
$10^{-2}N$ NaCl	$0.1N$ HNO_3	0.5-1.3
$10^{-2}N$ NaCl	$1N$ HNO_3	0.6-2.2
$10^{-2}N$ NaCl	Conc. HNO_3	10-13
$10^{-2}N$ NaCl	$0.1N$ HCl	1.6-2.5
$10^{-2}N$ NaCl	$1N$ HCl	3.1-7.7
$10^{-2}N$ NaCl	Conc. HCl	22-27

[a] $T = 22°C$.
Immersion time = 5 min (with ultrasonic agitation).

immersed into 50 ml of ultrasonically agitated solutions containing different concentrations of HNO_3. Mobile-charge drift data, shown in Table IV, indicate that a $0.1N$ HNO_3 solution was the most effective for removal of mobile charge from the SiO_2 surface. Similar results of experiments using HCl are also given in Table IV.

Total number of Na^+ ions present at the SiO_2 surface after immersion in contaminating aqueous solutions.— Flame photometry was used to determine the number of Na^+ ions[1] present at oxide surfaces which had been (*i*) immersed into neutral NaCl solutions, (*ii*) immersed into acidified ($1N$ HNO_3) NaCl solutions, or (*iii*) immersed into acidified ($1N$ HNO_3) NaCl solutions and subsequently metalized with Al. In all cases the immersion time was 5 min at 22°C. The results of these analyses are given in Table V where they are compared with results from electrical measurements of mobile charge present on the oxide after the same treatment. For SiO_2 surfaces immersed in neutral NaCl solutions, the total number of Na^+ ions determined by flame photometry is comparable to the number of mobile charges found electrically. However, there is no agreement between these two measurements when the contaminating solution is acidified. In this case, the electrical measurements show that mobile charges were not transferred to the oxide, whereas the flame photometric analysis indicated that Na^+ ions were present at the oxide surface. After Al deposition, the total number of Na^+ ions measured by flame photometry decreased by a small amount but remained orders of magnitude larger than the number of mobile charges found electrically. This decrease in total Na^+ ions after Al deposition was the result of scattering of Na^+ ions by the Al evaporated onto the oxides. In order to avoid the scattering of Na^+ ions, control wafers for flame photometric analyses had to be metalized in the absence of oxides contaminated with NaCl. (Control wafers for electrical measurements of mobile charge were metalized in the presence of oxides contaminated with NaCl. This did not affect the mobile charge level.)

Discussion

The mobile ions transferred to SiO_2 from the different aqueous solutions are identified in the first part of this discussion. In the second part, the effects of H^+ (or OH^-) ions in solution on mobile ion adsorption onto SiO_2 surfaces are considered. A qualitative model is proposed which distinguishes between the mobile and immobile Na transferred to SiO_2 surfaces from aqueous solutions.

Identification of mobile ions transferred to SiO_2.— Negligible mobile charge is transferred to SiO_2 when it is immersed in Na-free solutions containing varying concentrations of HCl (Fig. 1) or HNO_3, or in solutions of $1N$ H_2SO_4, a less volatile acid than HCl or HNO_3. Similar results were obtained with other inorganic [H_2O (10), NH_4OH (11)] or organic [ethanol (7), trichloroethylene (10), acetone (11), i-propanol (11)] reagents containing hydrogen but free of alkali ions. In addition, tritium incorporated in tritiated steam-grown oxides does not drift in an electric field (12). Thus it appears that H in SiO_2 is immobile at typical applied fields used for oxide stability studies.

Appreciable quantities of mobile charge are transferred to SiO_2 from neutral aqueous NaCl (or NaI) solutions. The number of mobile charges is proportional to the Na^+ ion concentrations in these solutions and is approximately equal to the number of transferred Na^+ ions (measured by flame photometry). The polarity (Al+) of the applied bias used to stress the MOS capacitors is consistent with cationic drift. Since the solvent, H_2O, does not transfer mobile charge to the SiO_2, these results show that the transferred mobile charges are Na^+ ions. The difference between Na and H transport in SiO_2 in response to an electric field may be related to a difference in polarizability of the bonds formed. However, when comparing the mobility of Na and H in the present work, it must be kept in mind that no direct evidence was obtained for the presence of H^+ ions on an SiO_2 surface after acidic solution contamination and MOS capacitor fabrication.

Experimental data are given in Fig. 3 for the number of mobile ions present at the SiO_2 surface after immersion into contaminating solutions containing both Na^+ and H^+ ions. Under those conditions in which some charge transfer to SiO_2 is observed, the number of mobile ions increases with an increase in concentration of Na^+ ions and a decrease in concentration of the acid. The mobile ions transferred from the acidified solutions are apparently Na^+ rather than H^+ ions.

The flame photometry results show that the number of Na^+ ions transferred from acidic ($1N$ HNO_3) NaCl solutions to SiO_2 is similar to the number transferred from neutral NaCl solutions (Table V). However, the MOS measurements show that relatively few mobile ions are transferred to SiO_2 from these acidic solutions. Thus Na^+ ions present at the Al/SiO_2 interface can be either mobile or immobile when an MOS capacitor

Table V. Number of Na^+ ions (flame photometry) and mobile charges (MOS measurements) at SiO_2 surfaces after immersion in aqueous solutions

Contaminating solution	Na^+ ions (cm^{-2})				Mobile charge (cm^{-2})
	Without Al		With Al		
	Run 1	Run 2	Run 1	Run 2	
Neutral solutions					
$10^{-2}N$ NaCl	3.3×10^{14}	2.5×10^{15}	—	—	$5.9\text{-}8.9 \times 10^{14}$
$10^{-3}N$ NaCl	5.2×10^{13}	3.4×10^{14}	—	—	$3.0\text{-}8.3 \times 10^{13}$
$10^{-4}N$ NaCl	1.3×10^{13}	5×10^{12}	—	—	$1.4\text{-}3.7 \times 10^{13}$
$10^{-5}N$ NaCl	$<3 \times 10^{12}$	$<3 \times 10^{12}$	—	—	$3.1\text{-}12.3 \times 10^{12}$
Acidified ($1N$ HNO_3) solutions					
$10^{-2}N$ NaCl	4.3×10^{15}	6.3×10^{14}	1.8×10^{14}	2.5×10^{14}	$1\text{-}7 \times 10^{11}$
$10^{-3}N$ NaCl	9.0×10^{12}	1.3×10^{13}	4.2×10^{13}	1.2×10^{13}	$\leq 10^{11}$
$10^{-4}N$ NaCl	$<3 \times 10^{12}$	$<3 \times 10^{12}$	—	—	$\leq 10^{11}$

$T = 22°C$.
Immersion time = 5 min.
— no measurement performed.

is stressed in an electric field at an elevated temperature.

Adsorption at the SiO_2 surface.—To explain the behavior of Na^+ ions at the SiO_2 surface, we propose that these ions are mobile if in solution they are adsorbed directly on this surface, but are immobile if they are separated from the surface by a layer of adsorbed acid molecules.

A SiO_2 surface provides approximately 10^{15} sites/cm^2 for cation adsorption. The surface of an untreated thermally grown film consists of siloxane (Si-O-Si) groups, and adsorbed Na^+ ions deposited on such a surface by evaporation are mobile (2). If a thermally grown film is etched with HF and then immersed into H_2O the surface consists of silanol (SiOH) groups. Our experiments show that Na^+ ions transferred to this surface from neutral aqueous solutions are mobile. Thus Na^+ ions adsorbed directly on the SiO_2 surface are mobile whether they are physically adsorbed at siloxane sites or chemically bound (SiO^-Na^+) at silanol sites. This conclusion is consistent with our observation that Na^+ ions are mobile on the surface obtained when a thermally grown SiO_2 film is immersed directly in H_2O without prior etching in HF; in this case the relative numbers of siloxane and silanol groups are not well established.

For contamination of the SiO_2 surface by neutral aqueous NaCl solutions, identifying the mobile-charge carriers as directly adsorbed Na^+ ions permits a straightforward interpretation of the observed dependence of the number of mobile charges on the immersion time (Table II) and on the Na^+ ion concentration in solution (Table II and Fig. 1). The increase in mobile charge with time is due to the increase in the number of adsorbed Na^+ ions as this number approaches the equilibrium value determined by the concentration of Na^+ ions in solution. The rate of approach to equilibrium, which increases with increasing temperature (Table III), is probably determined by the rates at which Na^+ ions diffuse through the solution and are adsorbed and desorbed at the oxide surface. After any fixed immersion time, the number of adsorbed Na^+ ions increases with increasing Na^+ ion concentration in solution and causes a corresponding increase in the number of mobile charges.

Strong acids in alkali-free aqueous solutions modify SiO_2 surfaces by inhibiting dissociation of silanol groups and by becoming contact adsorbed (13) at the siloxane or silanol oxygen atoms, *i.e.*, at the cationic adsorption sites. Anions from solution are subsequently adsorbed to form a layer of acid molecules hydrogen-bonded to the SiO_2 surface. A 1:1 complex between SiO_2 (in solution) and HCl has been reported by Sadek (14).

If a SiO_2 surface is immersed in an aqueous solution containing both H^+ and Na^+ ions, the two types of ions will compete for the cationic adsorption sites. Because of their higher mobility in H_2O, the H^+ ions tend to be more rapidly adsorbed than the Na^+ ions. Electrokinetic and H^+ ion adsorption studies on quartz and other oxides have indicated that H^+ ions are potential-determining (13); they rapidly modify surface charge and become contact absorbed on an oxide surface in the presence of Na^+ or other cations (13, 16, 17).

For contaminating solutions with sufficiently large H^+:Na^+ ion ratios, the number of mobile charges transferred to the SiO_2 surface is initially very small (Fig. 2) even though the number of adsorbed Na^+ ions is appreciable (Table V). This observation can be explained by assuming that in this case H^+ ions are initially adsorbed on practically all the adsorption sites on the SiO_2 surface, an acid layer which completely covers the surface is then formed by adsorption of anions from the solution, and Na^+ ions from the solution are adsorbed on the acid layer. Finally, the model assumes that the order of anion and Na^+ ion adsorption from solution is retained during MOS capacitor fabrication and that Na^+ ions adsorbed on a layer of anions are immobile, so that they cannot be detected by MOS drift measurements.

The proposed immobility of Na^+ ions adsorbed on an acid layer probably results because the drift of these ions toward the SiO_2 surface in an electric field is sterically hindered by the adjacent sheet of large anions. Alternatively, the Na^+ ions might be trapped either in the metal deposited to form the MOS structure or at the metal-oxide interface, since the flame photometric data indicate that Na scattering and entrapment occur during metal deposition. However it is not apparent how this explanation could account for the proposed difference in mobility between Na^+ ions adsorbed on an intermediate acid layer and those adsorbed directly on the SiO_2 surface. Furthermore, Na^+ ions from acid solutions are immobile in MOS structures made with Au electrodes. Since this element is less likely than Al to react with SiO_2, this observation suggests that the metal layer does not play a critical role in immobilizing the Na^+ ions.

Even for contaminating solutions that are sufficiently acidic to make the initial transfer of mobile charge to the SiO_2 surface very small, the number of mobile charges increases appreciably with increasing immersion time (Fig. 2). According to our model, this observation shows that at equilibrium an appreciable fraction of the adsorption sites on the SiO_2 surface in these solutions is occupied by Na^+ ions. The increase in mobile charge occurs as equilibrium is approached by the desorption of initially adsorbed, immobile H^+ ions and their replacement by Na^+ ions that are mobile because they are adsorbed directly on the SiO_2 surface. This exchange process is strongly accelerated by raising the temperature and by ultrasonic agitation (Table III).

Decreasing the H^+ ion concentration in acidified NaCl contaminating solutions increases the amount of mobile charge transferred to the SiO_2 surface during immersion for 5 min (Fig. 3). This change is due to the increased transfer of directly adsorbed, mobile Na^+ ions which is made possible by decreasing the competition of H^+ ions for the adsorption sites on the SiO_2 surface.

Summary

Alkali-free aqueous solutions containing H^+ ions do not transfer mobile charges to thermally grown SiO_2 films. In oxide contaminations with neutral NaCl solutions, the number of mobile charges transferred to SiO_2 was proportional to the Na^+ ion concentration in the contaminating solution and approximately equal to the total number of Na^+ ions determined by flame photometry. The rate of mobile-charge transfer to SiO_2 was reduced by adding H^+ ions to the contaminating solution and increased by adding OH^- ions. To explain these observations, it is proposed that Na ions are mobile if they are adsorbed from solution directly on the SiO_2 surface but are immobile if they are separated from the surface by a layer of adsorbed acid molecules. The kinetics of competing H^+ and Na^+ ion adsorption and exchange on the oxide surface determine the rate of mobile Na^+ ion transfer to SiO_2.

Acknowledgments

The authors wish to thank F. W. Anderson, T. W. Hickmott, D. R. Kerr, D. L. Klein, and W. A. Pliskin for their helpful comments and E. F. Roginsky for his technical assistance. The recommendations of A. J. Strauss, Electronics Divisional Editor, are gratefully acknowledged.

Manuscript submitted Oct. 2, 1970; revised manuscript received Oct. 26, 1972. This was Paper 363RNP presented at Electrochem. Soc. Meeting, Los Angeles, Calif., May 10-15, 1970.

Any discussion of this paper will appear in a Discussion Section to be published in the December 1973 JOURNAL.

REFERENCES
1. E. Snow, A. S. Grove, B. E. Deal, and C. T. Sah, *J. Appl. Phys.*, **36**, 1664 (1965).
2. J. S. Logan and D. R. Kerr, Paper presented at the 1965 Solid State Devices Res. Conf., Princeton, N. J.
3. E. Yon, W. H. Ko, and A. B. Kuper, *IEEE Trans. Electron Devices*, **ED-13**, 276 (1966).
4. S. R. Hofstein, *ibid.*, **ED-13**, 222 (1966).
5. S. R. Hofstein, *ibid.*, **ED-14**, 749 (1967).
6. R. Sunshine, Late News Paper presented at the 5th Annual Symp. on the Physics of Failure in Electronics, Columbus, Ohio, November 1966.
7. S. I. Raider and R. Flitsch, *This Journal*, **118**, 1011 (1971).
8. A. S. Grove, B. E. Deal, E. Snow, and C. T. Sah, *Solid-State Electron.*, **8**, 145 (1965).
9. D. R. Kerr, Abstract No. 14 presented at Electrochem. Soc. Meeting, Cleveland, Ohio, May 1-6, 1966.
10. B. Yurash and B. E. Deal, *This Journal*, **115**, 1191 (1968).
11. Unpublished results.
12. P. J. Burkhardt, *This Journal*, **114**, 196 (1967).
13. A. M. Gaudin and D. N. Fuerstenau, *Mining Eng.*, **7**, 66 (1955).
14. H. Sadek, *J. Indian Chem. Soc.*, **29**, 507 (1952).
15. R. K. Iler, "The Colloid Chemistry of Silica and Silicates," Cornell University Press, Ithaca (1955).
16. H. C. Li and P. L. DeBruyn, *Surface Sci.*, **5**, 203 (1966).
17. G. Y. Onoda, Jr. and P. L. DeBruyn, *ibid.*, **4**, 48 (1966).
18. G. A. Mills and S. G. Hindin, *J. Am. Chem. Soc.*, **72**, 5543 (1950).
19. D. L. Dugger, J. H. Stanton, B. N. Irby, B. L. McConnell, W. W. Cummings, and R. W. Maatman, *J. Phys. Chem.*, **68**, 757 (1964).
20. L. H. Allen and E. Matijevic, *J. Colloid and Interface Sci.*, **31**, 289 (1969).

Striations Due to Compositional Variations in Czochralski-Grown $(Pb_{1-x}Sn_x)_{1-y}Te_y$

J. R. Burke, J. D. Jensen, and Bland Houston

Naval Ordnance Laboratory, Silver Spring, Maryland 20910

ABSTRACT

Compositional striations in $(Pb_{1-x}Sn_x)_{1-y}Te_y$ crystals grown by the Czochralski technique in two different laboratories have been revealed by application of Norr's electroetch. The striations appear as contours which delineate the prevailing growth interface. In crystals from both laboratories, the spacing of the contours is much too large and not sufficiently periodic to be accounted for by rotational effects. The nonrotational origin of the striations was confirmed by the observation that their intensity and spacing were not changed by stopping the rotation during growth. Electron-probe microanalysis studies show that x varies by as much as 0.01 over distances of the order of 100 μm in the direction normal to the striations.

Solid solutions of $(Pb_{1-x}Sn_x)_{1-y}Te_y$ are known to exist in the face-centered cubic structure for $0 \leq x \leq 1$ and for $0.50 \leq y \leq 0.51$ approximately (the exact limits of y depend on x). Each composition thus far investigated is a direct-gap semiconductor with conduction and valence-band extrema at or near the L-points of the Brillouin zone. Considerable interest centers on this system from both a basic and device point of view, because (*i*) the bandgap is a strong function of x, and (*ii*) this gap can be made arbitrarily small by the proper choice of x. In this paper we will present some of the metallurgical properties of single crystals grown by the Czochralski technique, and briefly mention the results of Shubnikov-de Haas experiments which appear to be influenced by this method of growth.

Crystal Growth and Surface Preparation

Most of our studies were carried out on material grown by the Electronic Materials Division of Bell and Howell Company (hereafter referred to as BH) (1). Some material recently grown at our laboratory has also been examined. BH provided either complete as-pulled single crystals, or single crystal slices that had been annealed to alter their properties. The crystals were in general pulled in a <111> direction at 8 mm/hr with a seed rotation rate of 10 rpm. Because of the high vapor pressure of $(Pb_{1-x}Sn_x)_{1-y}Te_y$, B_2O_3 was used to encapsulate the melt. The slices were cut out with a wire saw and lapped to a thickness of about 0.75 mm before annealing.

Key words: striations, crystal growth and characterization, compound semiconductors, $(Pb_{1-x}Sn_x)_{1-y}Te_y$, electropolishing, alloys.

As-pulled crystals of $(Pb_{1-x}Sn_x)_{1-y}Te_y$ are characterized by hole concentrations of the order of 10^{19} cm^{-3} produced by deviations from $y = \frac{1}{2}$. In order to obtain lower hole concentrations, the slices were annealed in evacuated ampoules in the presence of a two-phase ingot with the same x, but with $y < 0.5$. Equilibration with the ingot takes place through the vapor phase. This is a well-established procedure for the lead chalcogenides and the $(Pb_{1-x}Sn_x)_{1-y}Te_y$ alloys (2, 3).

To prepare a specimen for metallographic examination, the following steps were applied to one of its surfaces: (*i*) rough grinding on 600 grit SiC paper with flowing water as a lubricant until about 60 μm of material was removed; (*ii*) fine grinding on nylon cloth with Buehler's 6 μm Metadi diamond paste and Metadi fluid as a lubricant for twice as long as necessary to remove the scratches from step (*i*); (*iii*) polishing on Buehler's Microcloth using ¼ μm diamond paste and Metadi fluid for twice as long as necessary to remove the scratches from step (*ii*); and (*iv*) electropolishing and electroetching using the solution and procedures developed by Norr (4). The electropolishing times varied from about 2-10 min. The striations were formed during this period, and usually 2 min were sufficient for them to be easily observable. This stage was followed by an electroetch for 15 sec to see if pits could be developed.

Although Norr's solution was designed for preparation of PbTe surfaces and is not effective on SnTe, we have found that the electropolishing procedure gives high polishes on $(Pb_{1-x}Sn_x)_{1-y}Te_y$ surfaces for x as large as 0.30, and some polishing for $x = 0.60$. The

polishing action, and the degree to which the striations develop, do not depend strongly on the crystallographic orientation of the surface. The electroetching procedure did not produce etch pits consistently, even on {100} surfaces and for x as small as 0.13.

Results of Etching Studies

$(Pb_{0.70}Sn_{0.30})_{1-y}Te_y$.—Figure 1 shows a prepared (001) plane of a slice cut out of a [111]-grown BH single crystal with $x = 0.30$. The slice is about 0.75 mm thick, and prior to our preparation had been annealed by BH at 583°C for 44 days. A well-defined pattern of striations is apparent. They are always visible to the naked eye in fluorescent room light (note the low magnification in Fig. 1). Since the effectiveness of the electroetching technique decreases with increasing Sn content, it was suspected that the striations are caused by variations in x. This has been confirmed by the results of electron probe microanalysis.

The side of this slice after electroetching is shown in Fig. 2. The normal to the striations makes an angle of about 55° with the [001] direction. Thus the striations lie approximately in {111} planes perpendicular to the [111]-growth direction.

Figure 3 is an interference pattern showing the relief of the surface in Fig. 1. It was formed by placing this surface in contact with a 50% transmitting aluminum coating on an optical flat, and using the Hg 546.0 nm line for illumination. The hills (or valleys) are about 100 μm apart. There is a shift of approximately one fringe between a hill and a valley, corresponding to a height difference of about ¼ μm.

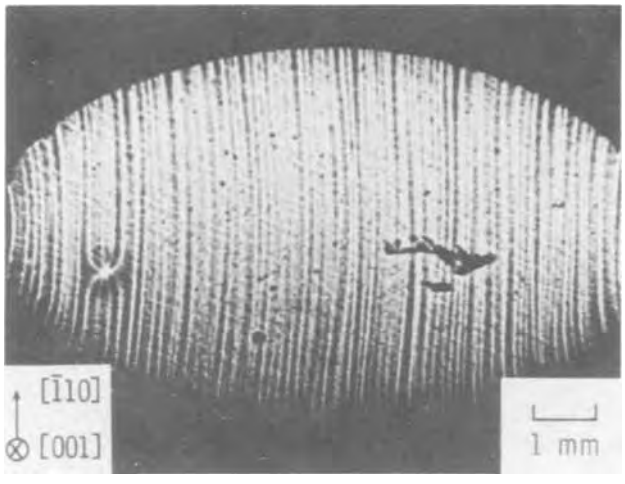

Fig. 1. (001) plane of a single-crystal slice of $(Pb_{0.70}Sn_{0.30})_{1-y}Te_y$ after electroetching.

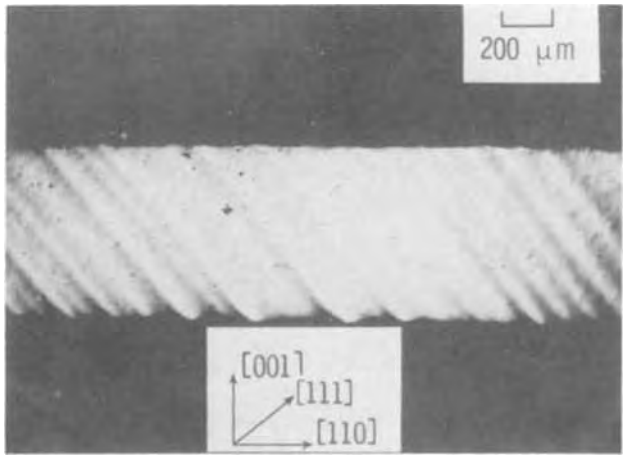

Fig. 2. (110) surface of the $(Pb_{0.70}Sn_{0.30})_{1-y}Te_y$ slice

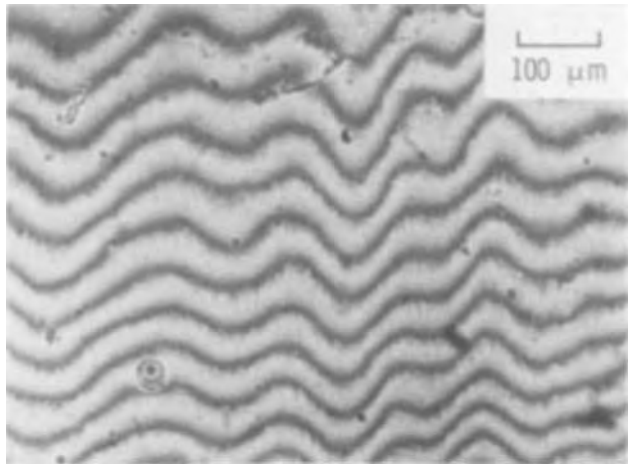

Fig. 3. Interference pattern showing the relief of the surface shown in Fig. 1.

$(Pb_{0.40}Sn_{0.60})_{1-y}Te_y$.—Figure 4 shows a prepared (001) plane of a slice cut out of a [111]-grown BH single crystal with $x = 0.60$. The slice is approximately 0.75 mm thick, and prior to our preparation had been annealed by BH at 500°C for 49 days, 452°C for 17 days, and 405°C for 46 days. In addition to striations, scratches remaining from preparation steps (*i-iii*) are also present. As mentioned above, the electropolishing rate for this material was significantly reduced due to the large amount of tin present. As a consequence the electropolishing time in step (*iv*) was extended to 10 min. Figure 5 is a magnified view of an area near the center of the upper edge of the slice. Figure 6 is an interference pattern obtained by the method described above. The microscope was slightly defocused so that both the striations and the interference pattern could be seen and compared. Higher magnification shows that there is a shift of about four fringes between a hill and valley, which corresponds to a height difference of about 1 μm. This is a factor of 4 greater than the corresponding difference on the $x = 0.30$ slice, but the electropolishing time was also about 5 times longer. This suggests the possibility that the rates of preferential etching are independent of average composition.

Further studies.—Our laboratory has recently initiated a study of the growth of $(Pb_{1-x}Sn_x)_{1-y}Te_y$ crystals by the Czochralski technique. Figure 7 shows a crystal that was pulled at 8 mm/hr using a crucible rotation rate of 10 rpm. It is not single but composed of large single crystal sections. Prior to preparation,

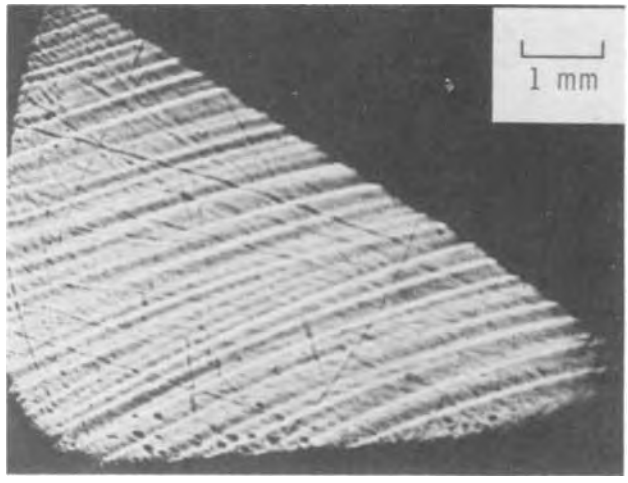

Fig. 4. (001) plane of a single-crystal slice of $(Pb_{0.40}Sn_{0.60})_{1-y}Te_y$ after electroetching.

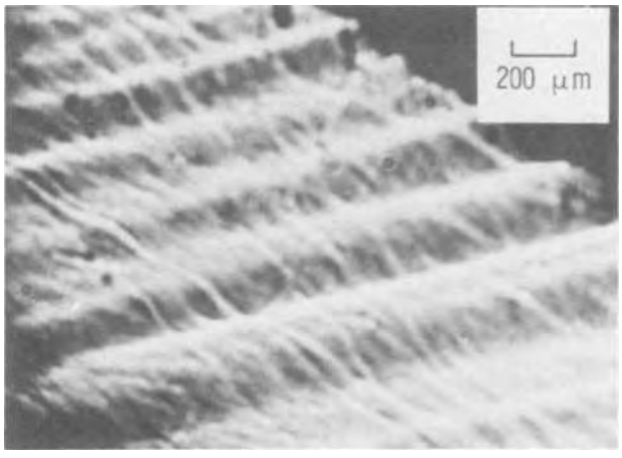

Fig. 5. Magnified view of an area near the center of the upper edge of the surface shown in Fig. 4.

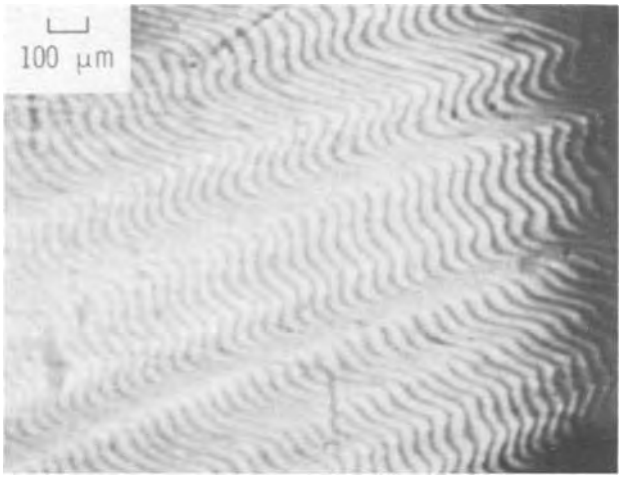

Fig. 6. Interference pattern for part of the surface shown in Fig. 4. Defocusing the microscope slightly revealed both the striations and the interference fringes.

the plane shown was arbitrarily selected by grinding parallel to the growth direction, which is vertical in the figure. The starting composition of the melt was $x = 0.35$, $y = 0.50$. The striations were revealed by the surface preparation previously described. Crystals pulled at the same rate, but with seed rotation instead of crucible rotation, show essentially the same pattern. In addition to the regular striations common to the BH material, there is a superimposed mosaic structure in Fig. 7 near the end of the crystal that was last to grow. This may have been the result of constitutional supercooling caused by an excessive growth rate.

Striations in doped semiconductor crystals pulled from the melt have been studied extensively (6). Both rotational and nonrotational striations are observed. The former are shown to be precisely periodic and caused by rotation of the crystal in a melt in which the temperature gradient is asymmetric, relative to the axis of rotation. Nonrotational striations are known to be caused by destabilizing thermal gradients. The periodicity of rotational striations calculated from the pull rate and rotation rate (6) used to grow our crystals and those of BH is 13 μm, an order of magnitude smaller than the spacing between the observed striations. The nonrotational origin of the striations in our material was confirmed by stopping the rotation during growth. Their intensity and spacing were found to remain unchanged relative to those obtained during rotation.

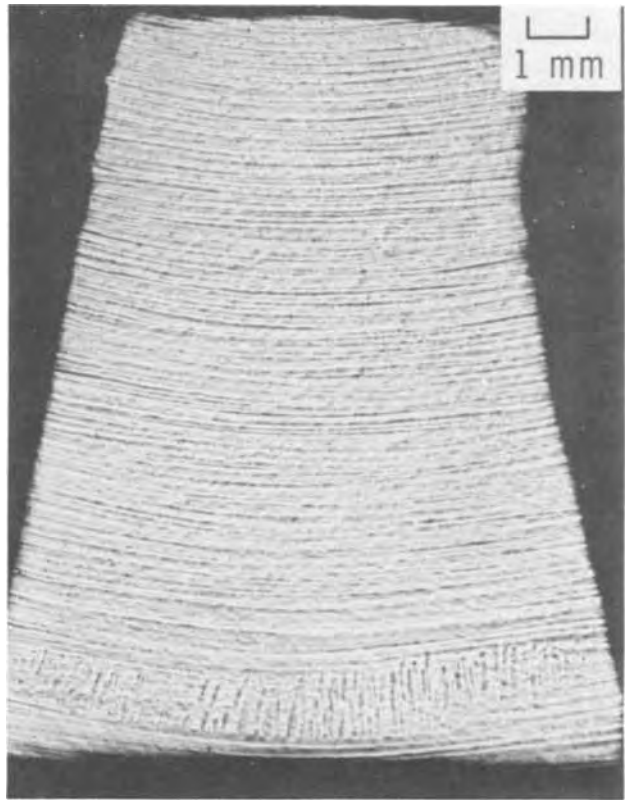

Fig. 7. Electroetched plane of a $(Pb_{1-x}Sn_x)_{1-y}$ Te_y crystal pulled at this laboratory. The plane is parallel to the growth direction, which is vertical in this figure.

Electron-Probe Microanalysis

In order to determine the compositional changes causing the striations, a section of the slice shown in Fig. 1 was submitted to the National Bureau of Standards for electron-probe microanalysis. Figure 8 shows part of this section after microanalysis was completed. The illumination and exposure time were adjusted so that both the striations and the spots made by the electron beam would be visible in the photograph. The spots are due to surface contamination by hydrocarbons broken down by the 20 keV electron beam. It was found that if the beam were scanned over a spot 5 × 4 μm, a target current of 50 nA could be used without damaging the sample. This was checked by repeating measurements at the same point several times. Higher current densities, *e.g.*, 100 nA and a 1μm diameter spot, caused melting.

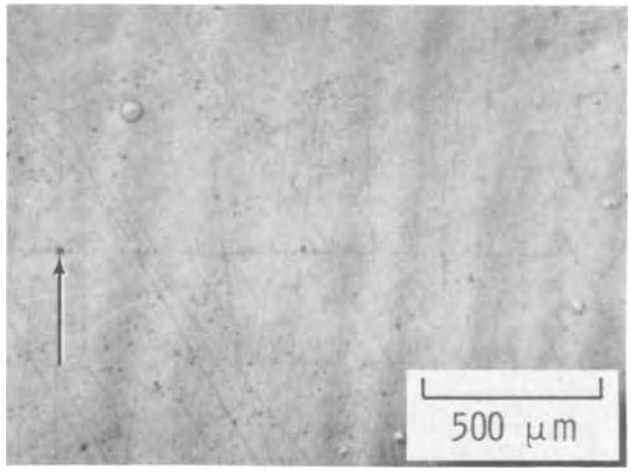

Fig. 8. Section of the surface shown in Fig. 1 that was used for electron-probe microanalysis.

Measurements were made at 20 μm intervals over a distance of 1200 μm beginning at the sixth spot to the right of the large square spot indicated by the arrow. Under microscopic examination, the positions of the spots could be correlated with features of the striations and compared to the results of the microanalysis. Correlation with the microanalysis of a number of detailed features of the striations not apparent in Fig. 8 was possible. As anticipated, it was clear that the hills were associated with excess tin and the valleys with excess lead.

Figure 9 shows the atomic fraction of each element at all the measured points. The x-ray intensities for all three elements were simultaneously measured with a three-spectrometer ARL microprobe having a take-off angle of 52.5°. LiF crystals were used for analysis of Sn L_α and Te L_α lines while an RAP crystal was used for analysis of the Pb M_α (second order) line. These data were then corrected for x-ray absorption, atomic number effects, and secondary fluorescence. Since only relative changes were of interest, the specimen itself was used as a standard for the three elements. The average of all counts for each element was taken as the standard intensity for that element, and the corresponding chemical composition was assumed to be $(Pb_{0.70}Sn_{0.30})_{0.50}Te_{0.50}$. The Pb and Sn concentrations in this formula were determined at BH from Vegard's law which has been verified for this system (5). These compositions were also checked at our laboratory by the same method.

Neglecting for the moment monotonic changes as a function of position, there is a good correlation between the minima in the Pb fraction and the maxima in the Sn fraction. The largest changes in x are about 0.01. The differences between the atomic fractions of Sn in the peaks and valleys are significantly outside the corresponding $\pm 3\sigma$ ranges, and the decrease in the atomic fraction of Sn is in general much larger than

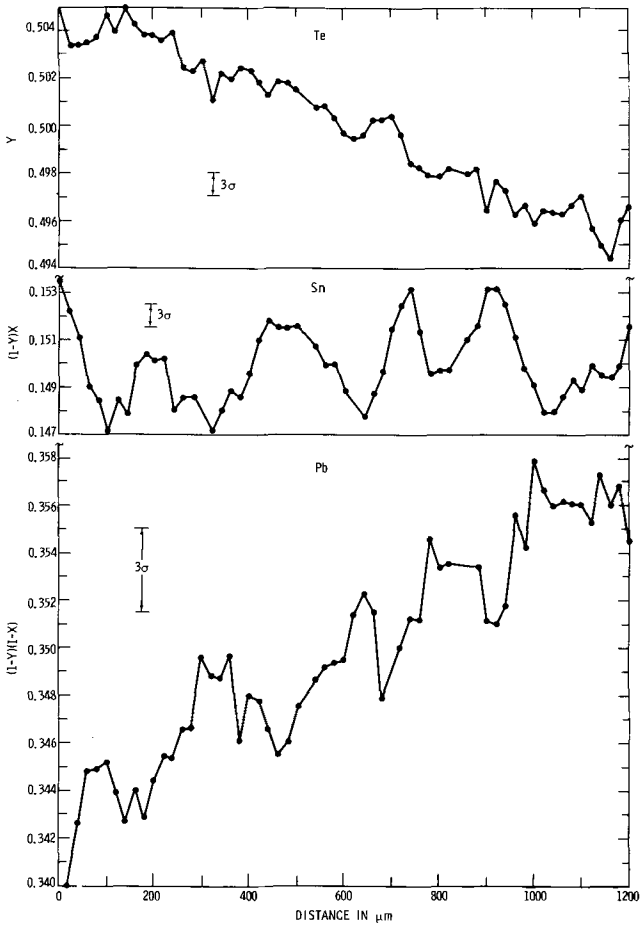

Fig. 9. Atomic fractions of Te, Sn, and Pb as a function of position on the surface shown in Fig. 8.

that forced by the corresponding increase in the atomic fraction of Pb. The fluctuations in the atomic fractions of Pb and Te are comparable to $\pm 3\sigma$. The large σ for Pb is due to the use of the second order M_α line and to a large background. However, the correlation of the Sn and Pb results suggests that the latter are significant.

The monotonic changes in the atomic fractions shown in Fig. 9 were observed in the raw data for the x-ray intensities. They are surprising because this specimen was taken from a slice in which the metal and Te concentrations should have been homogenized by annealing (2, 3). From a linear least squares fit to the Te data, the decrease in y over 1200 μm is 0.01. Although the width of the solidus field has not been established for the alloy $x = 0.30$, this change in y is much larger than the solidus field width for example of the alloy $x = 0.27$ (3). The change in the hole concentration corresponding to a change in y of 0.01 would be about 6×10^{20} cm^{-3} (assuming one carrier per extra atom). To check this, we made Hall coefficient measurements on a sample taken from the microanalyzed specimen. The sample was cut so that it included the spots shown in Fig. 8, and also so that its long dimension lay parallel to the gradient indicated by the microanalysis. Measurements were made at several points along the length of the sample. The results at 300° and 77°K are given in Table I along with the hole concentration $1/R_{77°K}e$. The hole concentration is essentially uniform, and as anticipated, any variation is much less than required if the measured change in the atomic fractions is assumed to come from a change in composition of the alloy phase. Unless there is an error in the electron-probe microanalysis, these measurements suggest that electrically inactive precipitates are present.

Shubnikov-de Haas Measurements

Studies of the Shubnikov-de Haas effect in Czochralski-grown $(Pb_{1-x}Sn_x)_{1-y}Te_y$ alloys (7) suggest that this particular transport phenomenon is very sensitive to the presence of striations. The Shubnikov-de Haas effect, which appears as oscillations in the resistivity as a function of applied magnetic field, is used to study the geometry of the Fermi surface. The number of component frequencies in the oscillations is normally determined by the complexity of this surface. In addition to those frequencies which can be identified with Fermi surface geometry, we have found that extra frequencies are present in each alloy thus far examined. These are the BH alloys with $x = 0.13$, 0.19, and 0.30 (7), and one sample with $x = 0.24$ taken from a crystal grown at our laboratory. Shubnikov-de Haas oscillations observed in nonstriated Bridgman-grown alloys having similar compositions (8) do not exhibit extra frequencies. We believe that variations in carrier concentration are the cause of the extra frequencies in the Czochralski crystals, but a correlation with the detailed nature of the striations has not been established.

Acknowledgments

The cooperation of Dr. D. W. Ernst and Dr. G. F. Hoff of the materials preparation group at this labora-

Table I. Hall coefficient R and hole concentration $1/R_{77°K}e$ of a sample taken from the microanalyzed specimen. The distance d of the Hall probes from one end of the sample is measured in the direction of the compositional gradient. Sample dimensions are 0.61 mm x 0.82 mm x 4.34 mm.

d, mm	R(300°K), cm³/C	R(77°K), cm³/C	$1/R_{77°K}e$, cm^{-3}
0.974	6.19	4.76	1.31×10^{18}
1.341	6.21	4.43	1.41×10^{18}
2.117	6.39	4.63	1.35×10^{18}
2.708	6.24	4.65	1.34×10^{18}
3.400	6.43	4.66	1.34×10^{18}

tory enabled us to observe the effects of changes in growth conditions on the striations. The efforts of Mr. R. L. Myklebust of the Spectrochemical Analysis Section, Analytical Chemistry Division, National Bureau of Standards, who carried out the electron-probe microanalysis, are greatly appreciated. Finally, we wish to thank the Electronic Materials Division of Bell and Howell Company for the material which they provided. In particular we are indebted to Mr. J. W. Wagner for many helpful discussions.

This work was supported by the Naval Ordnance Laboratory Independent Research Fund and by the Naval Air Systems Command under Task A310310B/292A/2R02103002.

Manuscript submitted Feb. 2, 1972; revised manuscript received Oct. 24, 1972.

Any discussion of this paper will appear in a Discussion Section to be published in the December 1973 JOURNAL.

REFERENCES

1. J. W. Wagner and R. K. Willardson, *Trans. AIME*, **242**, 366 (1968).
2. R. F. Brebrick, *J. Phys. Chem. Solids*, **32**, 551 (1971).
3. A. R. Calawa, T. C. Harman, M. Finn, and P. Youtz, *Trans. AIME*, **242**, 374 (1968).
4. M. K. Norr, *This Journal*, **109**, 433 (1962).
5. R. F. Bis and J. R. Dixon, *J. Appl. Phys.*, **40**, 1918 (1969).
6. A. F. Witt and H. C. Gatos, *This Journal*, **113**, 808 (1966); K. Morizane, A. Witt, and H. C. Gatos, *ibid.*, **114**, 738 (1967); K. M. Kim, A. F. Witt, and H. C. Gatos, *ibid.*, **119**, 1218 (1972).
7. J. R. Burke, J. D. Jensen, and B. Houston in "The Physics of Semimetals and Narrow-Gap Semiconductors," D. L. Carter and R. T. Bate, Editors, p. 393, Pergamon Press, New York (1971).
8. John Melngailis, T. C. Harman, J. G. Mavroides, and J. O. Dimmock, *Phys. Rev.*, **B3**, 370 (1971).

Studies of Electret Effects on Polyvinyl Chloride in a Vacuum

P. K. C. Pillai, Kamlesh Jain, and V. K. Jain[1]

Department of Physics, Indian Institute of Technology, New Delhi-29, India

ABSTRACT

Details of an apparatus for the fabrication and measurement of the surface charge of an electret in a vacuum is reported in this paper. The apparatus is useful in the preparation and preservation of the polarized sample under controlled conditions of humidity, temperature, and pressure. The effect of the polarizing field on the formation and characteristics of PVC(SR_{11}) foil electrets under vacuum conditions are investigated systematically. These investigations confirm that a polarizing field is necessary to obtain permanent polarization in electrets. Charge reversal was also obtained at low polarizing fields under vacuum conditions.

The investigation of dielectric properties has provided an important tool for the understanding of the structure of matter. Permanent polarization (1, 2) will occur when the electric field is applied to an insulator at an elevated temperature and has solidified the displaced positive and negative charges in opposite directions. To explain the electret effect more adequately, Pillai and Jain (3, 4) have added the contribution due to the molding and stripping charges to the net effective surface charge calculated by Peich and Handerek (5).

In the study of the electret effect, the measurement of the surface charge is of great importance due to its large number of applications (6). Gubkin *et al.* (7), and later on Pillai and Jain (8), have reviewed the various techniques for the measurement of the charge and they (8) have also developed a simple and accurate induction method for the charge measurement. In 1949 Gross (9, 10) employed the dissectible capacitor method for the polarization and measurement of electrets. Recently Palia (11) has studied electrets under different pressures and found that the charge of the electret decreased as the pressure was reduced from 760 to 10^{-2} Torr.

Extensive studies have been made on electrets of various dielectrics in the form of slabs. But from the practical point of view foil electrets are more important. In this article results obtained from PVC (SR_{11})[2] foil electrets prepared under vacuum conditions have been reported. For this purpose, an apparatus was designed and fabricated in which electrets could be made and the surface charge measured, in vacuum, without removing the sample from the assembly. The apparatus is quite useful for studying the effect of different ambient conditions on the formation and characteristics of electrets.

[1] Present address: Evaluation Group, Solid-State Physics Laboratory, Lucknow Road, Delhi-7, India.

Key words: dielectrics, electrostatics.

[2] Polyvinyl chloride PVC(SR_{11}) manufactured by Sri Ram Vinyl and Chemical Industries, Kota, India.

Apparatus

The gadget for the polarization and measurement of surface charge of foil electrets was enclosed in a glass chamber as shown in Fig. 1 (point 1). An unpolarized sample was kept in the cavity of a mica holder (point 2, Fig. 1) which was screwed to a brass piece. This assembly was supported with a horizontal glass rod (point 3, Fig. 1). One surface of the sample was in contact with a metallic circular disk (point 4, Fig. 1), 2.5 cm in diameter and of 1 mm thickness, which was supported with a collar (point 5, Fig. 1) and could be moved upward and downward by a rod (point 6, Fig. 1) which passed through a vacuum seal. The vacuum seal was fixed at the center of a 23 cm^2 brass plate of 1 cm thickness. The motion of the lower electrode was restricted to 7 mm in the vertical direction from the horizontal axis of the glass rod (point 3, Fig. 1). The upper electrode (point 7, Fig. 1), of area ½ cm^2, was attached at the end of a movable glass tube (point 8, Fig. 1). The upper portion of the glass tube contained wax and particles of soft iron so that the electrode could be lifted by passing a current through the solenoid. Good contact between the upper electrode and the surface of the dielectric was obtained due to the weight of the electrode system. The sample can be rotated from outside about its horizontal axis without disturbing the vacuum in order to measure the surface charge on both sides of the sample. The rubber tube (point 13, Fig. 1) was connected to the rotary and an oil-diffusion pump, and a vacuum of the order of 10^{-4} Torr was obtained in the glass chamber.

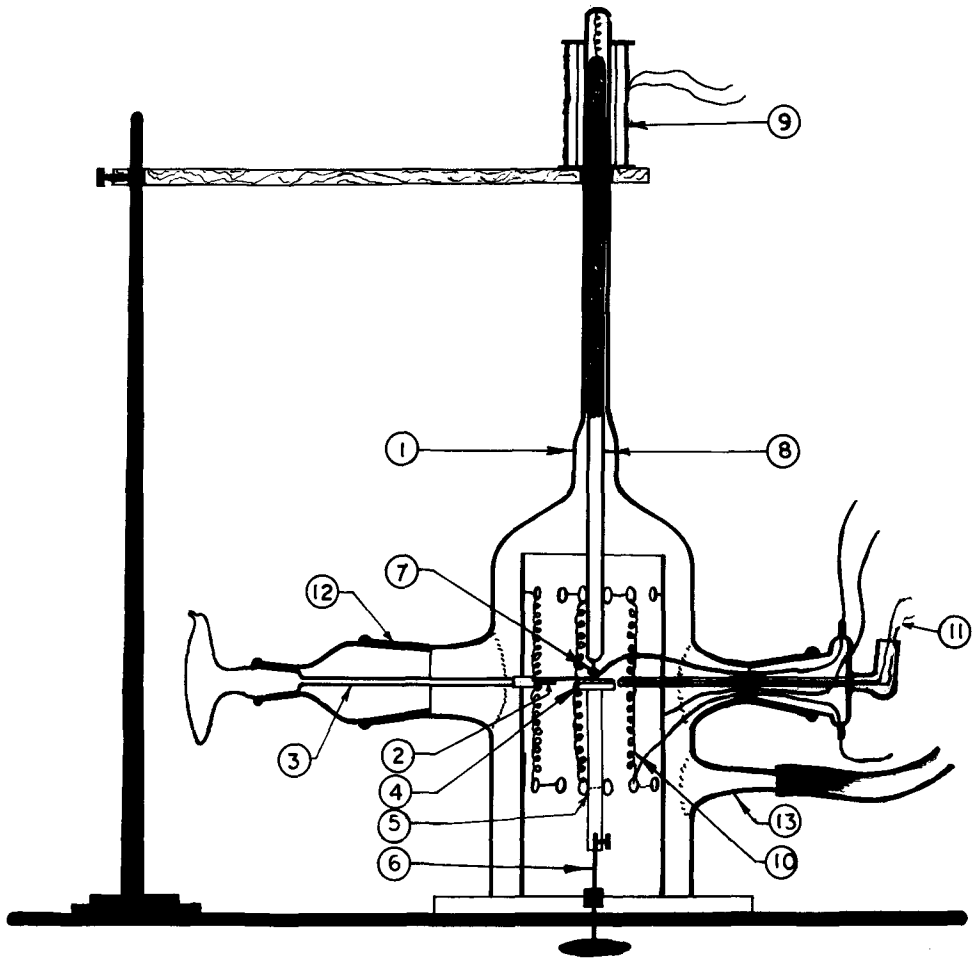

Fig. 1. (1) Glass chomber; (2) mica sheet; (3) glass rod; (4) circular brass disk; (5) collar; (6) vacucm seal; (7) upper brass electrode; (8) glass tube; (9) electromagnetic coil; (10) heating system; (11) Cu-constantan thermocouple; (12) ground joint; and (13) rubber tube.

A glass cylinder with a heating coil was placed inside the glass chamber around the electrodes (point 10, Fig. 1). The tip of the copper-constantan thermocouple (point 11, Fig. 1) was fixed just near the electrodes to measure the temperature. The upper and lower electrodes were used for the polarization as well as for the surface-charge measurements. All the metallic parts of the system were connected to the ground to obtain good electrostatic shielding. The measurements of the surface charge on both sides were taken by the induction technique with the help of an EA810A electrometer amplifier (12) supplied by the Electronic Corporation of India Limited.

Experimental

A solution of polyvinyl chloride (SR_{11}) was made in tetrahydrofuran (Reidal make) and poured in a petri dish with a flat bottom. It was kept in a dust-free chamber at 35°C for about 15 hr to form a thin transparent PVC foil. Samples of size 4 × 4 × 0.04 cm were cut from this foil for polarization studies. Each sample was polarized at 95°C for 3 hr inside the vacuum chamber. After polarization, the samples were kept in the same vacuum chamber throughout the period of investigation. After each measurement, the sample was short-circuited and preserved (13) in the same vacuum chamber for further studies.

Results

In order to see the effect of a polarizing field on the characteristics of foil electrets, especially when it is prepared under vacuum conditions, a series of samples were polarized under different field strengths ranging from 1.25 kV/cm to 2.75 kV/cm. The decay characteristics of these samples were studied for about a month and the results are shown graphically in Fig. 2 and 3.

Another sample was prepared under identical conditions but without the application of the forming field. A relatively smaller amount of charge was obtained on both faces of this sample [Fig. 2 (1A)] which decayed to zero after a few days. This clearly shows that it was merely a surface phenomena due to the close contact between the dielectric and the insulator (14, 15). However, this helps in increasing the magnitude of the initial heterocharge of the samples prepared with polarizing fields. This investigation thus confirms that a

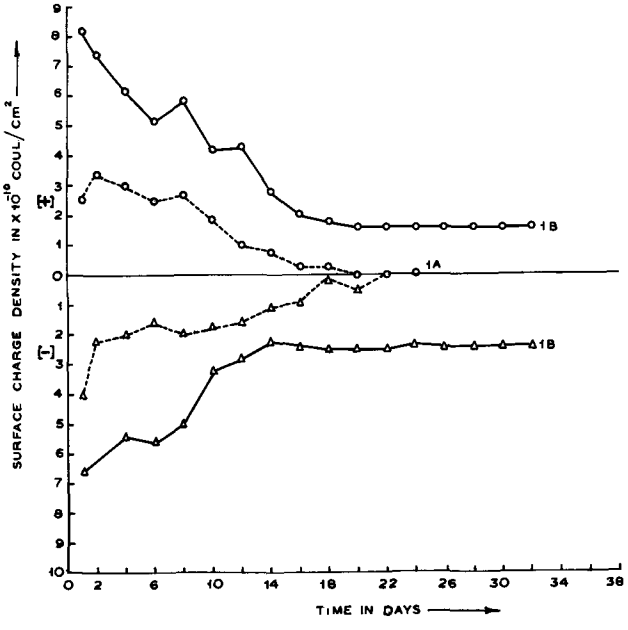

Fig. 2. Surface-charge density plotted as a function of time for PVC(SR_{11}) electret formed in 3 hr polarizing time at a polarizing temperature of 95°C. Curve (A), zero polarizing field; Curve (B), 1.25 kV/cm polarizing field

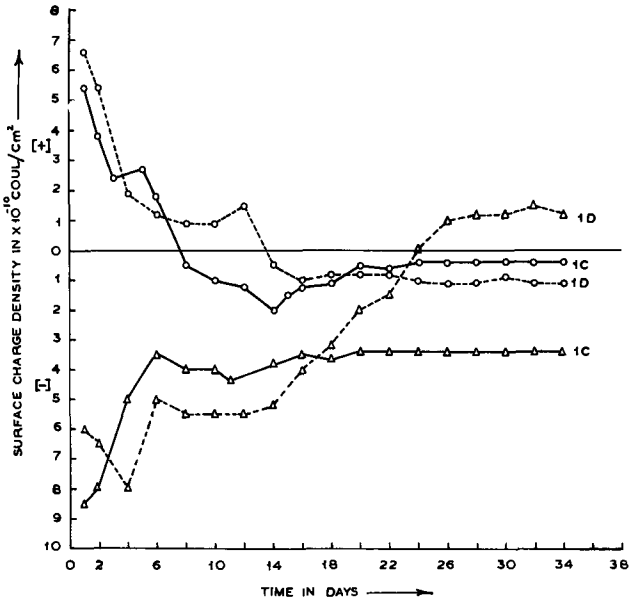

Fig. 3. Surface-charge density plotted as a function of time for PVC(SR_{11}) electret formed in 3 hr polarizing time at a polarizing temperature of 95°C. Curve (C), 2.00 kV/cm polarizing field; Curve (D), 2.75 kV/cm polarizing field

polarizing field is necessary to obtain a permanent polarization.

The samples prepared with 1.25 kV/cm and 2.0 kV/cm [Fig. 2(1B) and 3(1C)] show the presence of the heterocharge on both sides of the sample. But the cathode face of the sample prepared with 2.0 kV/cm [Fig. 3(1C)] shows a reversal from heterocharge to homocharge. By increasing the polarizing field up to 2.75 kV/cm [Fig. 3(1D)] the heterocharge on both faces reverses to a permanent homocharge. The results of this investigation confirm the electret behavior obtained by Gross (9) and Gemant (16) for the reversal from hetero to homocharge.

Discussion

The presence of heterocharge can be explained on the basis of the two-charge theory established by Gross (9) which has been accepted by most of the recent workers in this field. For an electret there are two charge distributions of opposite polarity. One of them is a surface charge, of the same polarity as that of the adjacent forming electrodes, which is generally known as an homocharge. The other is due to the internal polarizations, which produce a net surface charge opposite to that of the forming electrode, and is known as an heterocharge. If a real surface charge predominates over the charge due to volume polarization, the resultant charge will be an homocharge, and vice versa.

Gross (17, 18), and later on Gubkin (19) and Matsionashvili (20), have also given the phenomenological theories to discuss a similar type of results.

It is possible that when a high field is applied in the molten sample, the dipoles are oriented in the direction of the field, and these oriented dipoles in turn attracted the excessive ions of opposite polarity from the bulk of the material, which will be stuck to the surface when the sample is solidified. From the study of thermal degradation of polyvinyl chloride, it was found (21-23) that the weakest C-Cl bond will be ruptured at a higher temperature. This was followed by an abstraction of an hydrogen atom from an adjacent carbon and formation of a double bond in the chain. This will increase the polarizability of the polymer. The difference of polarity reversal on the cathode and anode surfaces might then be explained by the different mobilities of the two types of ions, especially above the glass-transition temperature (80°C) of the material. Above this glass-transition temperature, the conduction in PVC is ionic (24) and these ions in turn will be collected near the surfaces of the sample due to the attraction of the dipoles.

The measured net effective surface charge is the algebraic sum of the heterocharge and homocharge. When the electret is short-circuited the field within the sample becomes negligibly small. And the heterocharge decays only due to thermal motions, while the homocharge remains relatively constant causing the observed reversal in polarity of the net surface charge.

The presence of the homocharge includes two more factors; one is due to the spray of ions from the electrode on the surface of the dielectric, and the other is due to the breakdown of air inside the chamber. It also includes stripping and molding charges (3, 4) as there is close contact between the dielectric and the electrode. But the contribution due to the air breakdown, in this case, must be considerably smaller as the samples were prepared in vacuum conditions.

Acknowledgments

The authors are grateful to Professors K. L. Chopra, S. C. Jain, and M. S. Sodha for the encouragement given to them during the course of this investigation. They are also grateful to Dr. R. K. Jain for experimental help.

Manuscript submitted Feb. 2, 1972; revised manuscript received Aug. 7, 1972.

Any discussion of this paper will appear in a Discussion Section to be published in the December 1973 JOURNAL.

REFERENCES

1. R. J. Meakins, *Progr. Dielectrics*, **3**, 151 (1961).
2. C. P. Smith, "Dielectric Behavior and Structure," McGraw-Hill Book Co., New York (1955).
3. P. K. C. Pillai and V. K. Jain, *J. Appl. Phys.*, **40**, 3487 (1969).
4. P. K. C. Pillai, V. K. Jain, and G. K. Vij, *This Journal*, **116**, 836 (1969).
5. T. Peich and J. Handerek, *Phys. Status Solidi*, **9**, 361 (1965).
6. G. M. Sessler and J. E. West, in "Electrets and Related Electrostatic Charge Storage Phenomena," L. M. Baxt and M. M. Perlman, Editors, p. 134, The Electrochemical Society Softbound Symposium Series, New York (1967); C. W. Reedyk, *ibid.*, p. 104; V. A. J. Carbaugh, *ibid.*, p. 100.
7. A. N. Gubkin, V. S. Mitronins, and V. F. Sergienko, *Instr. Exp. Tech.*, **1**, 63 (1959).
8. P. K. C. Pillai and V. K. Jain, *J. Sci. Ind. Res. (India)*, **29**, 270 (1970).
9. B. Gross, *J. Chem. Phys.*, **17**, 866 (1949).
10. B. Gross, *Am. J. Phys.*, **12**, 324 (1944); **12**, 329 (1944).
11. F. L. Palia and A. Catlin, *J. Chem. Phys.*, **52**, 3651 (1970).
12. P. K. C. Pillai, Kamlesh Jain, and V. K. Jain, *Il Nuovo Cimento (B)*, **3**, 225 (1971).
13. H. Frei and G. Groetzinger, *Z. Physik*, **37**, 720 (1936); G. Groetzinger, *ibid.*, **37**, 589 (1936); M. M. Perlman, *J. App. Phys.*, **31**, 356 (1960).
14. D. K. Davies, "Proceedings of Phys and the Physical Society London (1961) on Static Electrification, Ed. A. C. Stickland, pp. 29; I. I. Incluet and E. P. Wituschek, *ibid.*, p. 37; R. C. Cunningham and D. J. Montgomery, *J. Textile Res.*, **28**, 971 (1958); O. O. Vanostenberg and D. J. Montgomery, *ibid.*, **28**, 22 (1958); P. E. Wagner, *J. Appl. Phys.*, **27**, 1300 (1956).
15. P. K. C. Pillai, Kamlesh Jain, and V. K. Jain, *Phys. Letters (A)*, **34**, 403 (1971).
16. A. Gemant, *Direct Current*, **1**, 145 (1953).
17. B. Gross, *Brit. J. Appl. Phys.*, **1**, 259 (1950).
18. B. Gross, *Phys. Rev.*, **66**, 26 (1944); B. Gross and L. F. Denard, *ibid.*, **67**, 253 (1945).
19. A. N. Gubkin, *Zh. Tekhn. Fiz.*, **27**, 1954 (1957); [*Soviet Phys.-Tech. Phys.*, **2**, 1813 (1957)].
20. A. N. Gubkin and V. N. Matsionashvili, *Fiz. Tverd. Tela*, **4**, 1196 (1962); [*Soviet Phys.-Solid State*, **4**, 878 (1962)].
21. P. K. C. Pillai and V. K. Jain, *J. Phys. D: App. Phys.*, **3**, 829 (1970).
22. N. Grassie, *Trans. Faraday Soc.*, **48**, 379 (1952).
23. P. K. C. Pillai, Kamlesh Jain, and V. K. Jain, *Phys. Status Solidi (A)*, **13**, 341 (1972).
24. M. Kosaki, K. Sugiyama, and M. Ieda, *J. Appl. Phys.*, **42**, 3388 (1971).

Evaluation of $HgCl_2$ as a Transport Agent for ZnO

M. Shiloh and J. Gutman

Soreq Nuclear Research Centre, Yavne, Israel

ABSTRACT

The chemical vapor transport of ZnO by $HgCl_2$ in a closed ampoule was evaluated experimentally and theoretically. A diffusion-controlled mechanism does not explain the experimental results, except for the prediction of the correct order of magnitude, which might indicate that diffusion is an important rate-determining step. The experiments were performed in the temperature range, 1160°-1260°K; a total pressure range, 0.1-3 atm; and with temperature gradients of 70°C and 100°C Above a total pressure of 1.5 atm the measured transport rate increases more slowly (with increasing total pressure) than the calculated rate based on a diffusion mechanism. Computer calculated curves of the relationships between the source and crystallization chamber temperatures, the total pressure, and the partial pressure difference of $ZnCl_2$ in the two chambers, can serve as a guide for future experiments. Single crystals of ZnO, average size 4 × 2 × 2 mm, were grown under the conditions studied in the present work.

In previous studies on the growth of single crystals of ZnO (1), $HgCl_2$ was found to be a promising transport agent. In this system $ZnCl_2$ is responsible for the transport process, in contrast to transport via Zn vapor, which is formed when NH_4Cl is used as a transport agent. The different transport mechanisms of these two agents were taken into account in selecting the one used to grow doped single crystals of ZnO (2).

In the present work the ZnO-$HgCl_2$ system is evaluated by comparing experimental results with calculated thermodynamic quantities, in a closed system. A quantitative evaluation of the growth of ZnO in an open system by the reaction mixture Zn-H_2O, was published recently by Reisman (3).

Experimental

The experimental procedure was similar to that described in a previous publication (1). A set of sealed ampoules, each containing about 5g ZnO and different quantities of $HgCl_2$, were placed in a horizontal tube furnace with the desired temperature gradient between the source chamber and the crystallization chamber.

The ZnO powder (B.D.H. Analar) was calcined at 1000°C before use, in order to eliminate traces of carbonate and hydroxide. The ZnO was heated in the ampoule at 350°C and 10^{-6} mm Hg before sealing. The upper part of the ampoule was cooled with wet cotton to prevent the loss of sublimed $HgCl_2$.

Results and Discussion

The data obtained from two sets of experiments, where the source temperature was the same but the temperature gradients differed (70° and 100°C), are given in Table I.

The average dimensions of the crystals obtained were 4 × 2 × 2 mm. Some of the crystals are shown in Fig. 1.

In order to correlate the results with an assumed diffusion-controlled transport mechanism, the partial pressures of the molecules, which are responsible for the transport effect, have to be computed.

Key words: ZnO single crystals, chemical vapor transport, thermodynamics of the ZnO-$HgCl_2$ system.

Fig. 1. Single crystals of ZnO grown with $HgCl_2$ as a transport agent.

The following equilibrium was assumed for this system

$$ZnO(s) + HgCl_2(g) \overset{K_p}{\rightleftharpoons} ZnCl_2(g) + Hg(g) + \tfrac{1}{2}O_2(g) \quad [1]$$

The function $\Delta F_{(T)}$ for the equilibrium given in Eq. [1] was derived, from available thermodynamic data (5, 6), by combining the individual $\Delta F_{(T)}$ functions given in Table II for the following equilibria

Table I. Transport data of ZnO in closed ampoules with different concentrations of $HgCl_2$

Source chamber	T_1 = 1260°K						T_1 = 1260°K							
Crystallization chamber	T_2 = 1160°K						T_2 = 1190°K							
Diffusion path	ID = 1.0 cm						ID = 1.25 cm							
	Length = 5.0 cm						Length = 3.7 cm							
	Time: 334 hr						Time: 376 hr							
Initial concentration of $HgCl_2$ [mg/cm³]	0.76	1.14	1.52	1.95	2.29	3.56	0.11	0.47	0.79	1.10	1.62	2.31	2.86	3.40
Rate of transport of ZnO ($T_1 \rightarrow T_2$) [mg/h]	2.4	4.8	5.5	5.6	5.9	6.3	2.64	3.05	4.70	5.20	8.43	9.72	9.96	9.95

Table II. Standard free energy of reaction ($\Delta F°_{(T)} = A + B\,T \log T + CT$)

Reaction	$\Delta F°$ in cal A	B	C	Temp. range, °K	Ref.
$ZnO(s) \rightleftharpoons Zn(g) + \frac{1}{2}O_2(g)$	115,400	10.35	−82.36	1170-2000	(6)
$Zn(g) + Cl_2(g) \rightleftharpoons ZnCl_2(g)$	−93,800	−9.44	38.6	1180-1800	(6)
$HgCl_2(g) \rightleftharpoons Hg(g) + Cl_2(g)$	46,500	—	−23.5	630-1500	(5)

$$\begin{aligned} ZnO(s) &\rightleftharpoons Zn(g) + \tfrac{1}{2}O_2(g) \\ Zn(g) + Cl_2(g) &\rightleftharpoons ZnCl_2(g) \\ HgCl_2(g) &\rightleftharpoons Hg(g) + Cl_2(g) \\ \hline ZnO(s) + HgCl_2(g) &\rightleftharpoons ZnCl_2(g) + Hg(g) + \tfrac{1}{2}O_2(g) \end{aligned}$$

The resulting value of $\Delta F_{(T)}$ for reaction [1] is

$$\Delta F_{(T)} = 68{,}100 + 0.91T \log T - 67.26T \text{ [cal/mole]} \quad [2]$$

The equilibrium constant of Eq. [1] can be expressed by

$$K_p = \frac{P_{ZnCl_2}{}^{2.5}}{P_{HgCl_2}} \quad [3]$$

where P_{ZnCl_2} and P_{HgCl_2} are the equilibrium partial pressures of the corresponding halides. The total equilibrium pressure, in a closed system, is given by

$$P_T = P_{HgCl_2} + 2.5P_{ZnCl_2} \quad [4]$$

Using Eq. [2], [3], [4] and the relation

$$\Delta F = -RT \ln K_p \quad [5]$$

one obtains the following relation for P_{ZnCl_2}, P_T, and T

$$\ln \frac{P_{ZnCl_2}{}^{2.5}}{P_T - 2.5P_{ZnCl_2}} = \frac{1}{R}\left[-\frac{68{,}100}{T} - 0.91 \log T + 67.26\right] \quad [6]$$

Assuming a closed ampoule of volume $2V$ (liter) half of which (V) is at T_1 and half at T_2, ($T_1 > T_2$), with an abrupt temperature gradient between them; an expression is derived to relate the initial amount of $HgCl_2$ m (g) placed in the ampoule, to the equilibrium total pressure, and the equilibrium partial pressures of $ZnCl_2$ at T_1 and T_2 (designated P_1 and P_2, respectively). The experimental temperature gradient changed gradually along 10 mm between the two regions.

The initial pressure of $HgCl_2$, P_i, is expressed by

$$P_i = P_{HgCl_2} + P_{ZnCl_2} \quad [7]$$

which, on substitution from Eq. [4] gives

$$P_i = P_T - 1.5P_{ZnCl_2} \quad [8]$$

Using the ideal gas law, inserting the corresponding values of the gas constant (0.082 liter atm), the molecular weight of $HgCl_2$ (271.5) and Eq. [8] for P_i, one obtains

$$m = 3309V\left[\frac{P_T - 1.5P_1}{T_1} + \frac{P_T - 1.5P_2}{T_2}\right] \quad [9]$$

Using a computer program, values of P_{ZnCl_2} at T_1 and T_2 (P_1 and P_2, respectively) were calculated by Eq. [6] for a given set of values of P_T. From these sets of values Fig. 3 and 4 were constructed, using the parameter ΔP_{ZnCl_2} defined as the partial pressure difference of $ZnCl_2$ between the two temperatures ($P_1 - P_2$).

The initial amount of $HgCl_2$, m, is calculated by Eq. [9] for given values of P_T and the corresponding values of P_1 and P_2, calculated by Eq. [6]. The initial concentration of $HgCl_2$ is given by

$$C_i = \frac{m}{2VM} \times 10^3 \left[\frac{\text{micromoles}}{\text{c.c.}}\right] \quad [10]$$

where M is the molecular weight of $HgCl_2$.

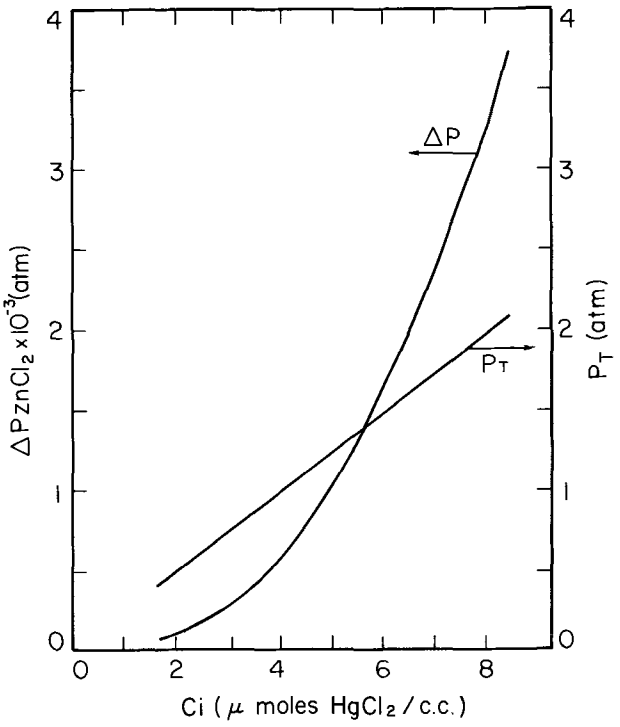

Fig. 2. The partial pressure difference of $ZnCl_2$ and the total pressure as a function of the concentration of $HgCl_2$ in a closed ampoule. $T_1 = 1260°K$; $T_2 = 1200°K$; $V_1 = V_2 = 0.006$ liter (V_1 and V_2 are the volumes of the ampoule at T_1 and T_2, respectively).

For constant values of V, T_1, and T_2 in the range of temperatures and temperature gradients given in Fig. 2-4, the values of ΔP_{ZnCl_2} are small compared with P_1, P_2, or P_T and therefore there is a linear relationship between m, or C_i, and P_T.

Figure 2 shows the effect of increasing the initial concentration, C_i, of $HgCl_2$ (or the initial pressure) with a constant temperature difference between the two chambers of the ampoule (having equal volumes of 6 cm³, $V_1 = V_2$, at T_1 and T_2, respectively). It is seen that ΔP_{ZnCl_2} increases more rapidly than P_T.

Figure 3 shows the dependence of ΔP_{ZnCl_2} on the total pressure and source temperature (T_1), for a constant temperature gradient ($T_1 - T_2 = 100°C$) between the source and crystallization chambers. It is seen that by lowering the source temperature, keeping P_T constant, ΔP_{ZnCl_2} is increased. At the same time ΔP changes more slowly with P_T at lower source temperatures. Figure 4, constructed from the same data, shows the family of curves of ΔP as a function of the source chamber temperature, at various values of P_T. At higher total pressure the maximum value of ΔP shifts to a higher source temperature.

A comparison of the experimental transport rate results with calculated curves, as a function of total pressure, is seen in Fig. 5. For the calculations diffusion-controlled transport was assumed, and the following equation was used (4)

$$R' = \frac{\Delta P_{ZnCl_2}}{P_T}\overline{T}^{0.8}\frac{A}{L}14.65 \text{ (mg ZnO/h)} \quad [11]$$

where $\overline{T}$ is the average temperature between the source and crystallization chambers, A is the cross-section area of the ampoule in the diffusion path, and L is the diffusion-path length. (The data are given in Table I.) In order to eliminate the geometrical factor, the rate values given in Fig. 5 were normalized to 1 cm² cross-section area and 1 cm of diffusion path length

$$R = R'\frac{L}{A} \text{ (mg ZnO/h cm)} \quad [12]$$

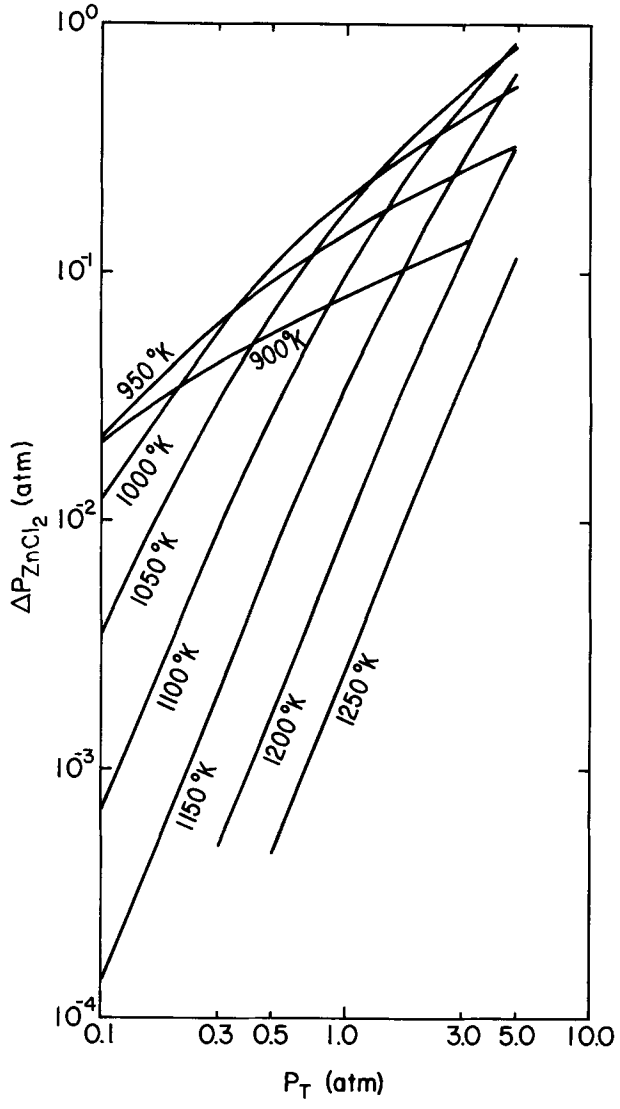

Fig. 3. The partial pressure difference of $ZnCl_2$ as a function of the total pressure at different source temperatures. $V_1 = V_2 = 0.006$ liter; $T_1 - T_2 = 100°C$.

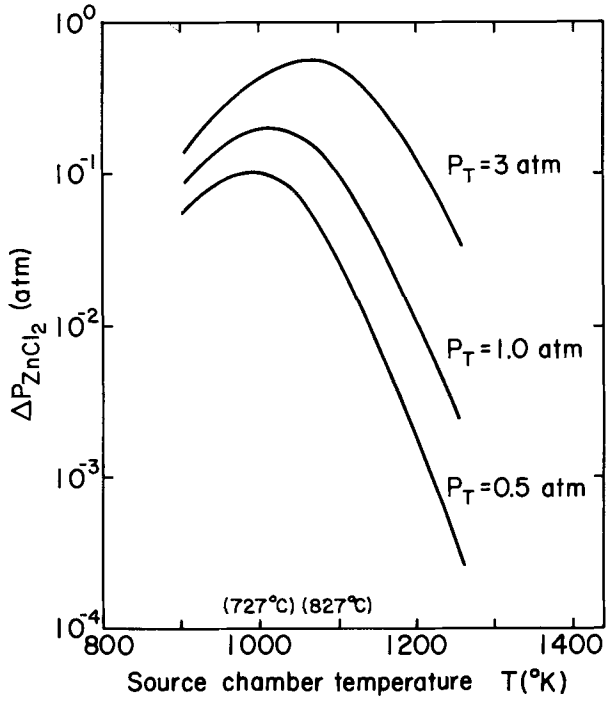

Fig. 4. The partial pressure difference of $ZnCl_2$ as a function of the source temperature, at different total pressures. $V_1 = V_2 = 0.006$ liter; $T_1 - T_2 = 100°C$.

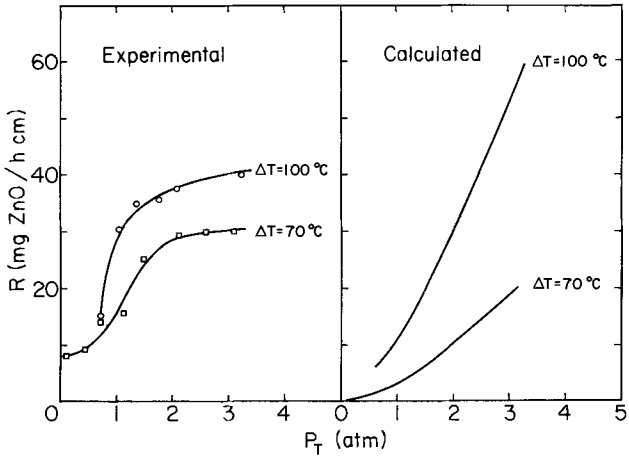

Fig. 5. The transport rate of ZnO as a function of the total pressure. Transport agent, $HgCl_2$; source temperature, 1260°K. (The data are normalized for a transport path of 1 cm^2 cross-sectional area and 1 cm diffusion length).

The calculated curves are in good agreement with the experimental results only in the lower P_T range, below 1.5 atm. A diffusion-controlled transport mechanism and the assumptions made in the derivation (4) of Eq. [4] probably oversimplify the actual mechanism. Figure 3 shows that, with the temperature profiles used in the present work, ΔP (and hence the transport rate) will increase more slowly with P_T only at much higher values of P_T (above the range studied in this work). One should note that the calculated curves are very sensitive to the numerical values of the coefficients in Eq. [2], which were derived from experimental data (5, 6).

The slower change of R at higher pressures might show the heterogeneous reaction to be the rate-determining step at this range.

Figures 2-4, which present the computer calculated values of ΔP_{ZnCl_2} as a function of the various parameters, are very useful as a guide when searching for the appropriate crystal growing conditions. One can estimate the effect of various experimental parameters on ΔP_{ZnCl_2} and hence on decreasing as increasing the growth rate in order to control the nucleation.

The effect of an additional equilibrium, the decomposition of ZnO, was also calculated

$$ZnO(s) \rightleftharpoons Zn(g) + \tfrac{1}{2}O_2(g) \qquad [13]$$

The temperature dependence of the partial pressure of the Zn vapor is given by (7)

$$\log P_{Zn} = \frac{-16{,}173}{T} + 7.24 \qquad [14]$$

From this relation it was found that at the highest temperature used in the present work (1260°K), the partial pressure of Zn is about 10^{-6} atm. This will significantly affect the transport rate of ZnO only at a low total pressure, below 0.1 atm.

Acknowledgment

This work was performed under the sponsorship of the U. S. Department of Commerce, National Bureau of Standards, Washington, D. C. 20234.

Manuscript submitted May 18, 1972; revised manuscript received Oct. 30, 1972.

Any discussion of this paper will appear in a Discussion Section to be published in the December 1973 JOURNAL.

REFERENCES

1. M. Shiloh and J. Gutman, *J. Crystal Growth*, **11**, 105 (1971).

2. M. Shiloh and J. Gutman, To be published.
3. A. Reisman, *This Journal*, **118**, 1479 (1971).
4. H. Schafer, "Chemical Transport Reactions," pp. 22-25, Academic Press, New York (1964).
5. J. Villa, *Soc. Chem. Ind. (London)*, **69**, (Suppl. No. 1) S9 (1959).
6. O. Kubaschowski, E. LL. Evans, and C. B. Alcock, "Table E Metallurgical Thermochemistry," 4th ed., Pergamon Press, Oxford (1967).
7. M. J. N. Pourbaix and C. Ronive-Bouté, *Discussions Faraday Soc.*, **4**, 223 (1948).

Preparation and Properties of II-Ln_2-S_4 Ternary Sulfides

W. M. Yim,* A. K. Fan,[1] and E. J. Stofko

RCA Laboratories, David Sarnoff Research Center, Princeton, New Jersey 08540

ABSTRACT

Some 50 ternary sulfides of the type II-Ln_2-S_4 were explored, where II = (Zn, Cd, Mg, and Ca) and Ln = (Sc, Y, La, Ce, Pr, Nd, Sm, Gd, Tb, Dy, Ho, Er, Tm, Yb, and Lu). The structure of the compounds, if they were formed, was investigated with x-ray diffraction techniques using primarily the materials synthesized in powder form. Single crystals were subsequently grown from the powders for several compounds including $ZnSc_2S_4$ and $CdSc_2S_4$ which were found to have bandgaps of 2.1 and 2.3 eV, respectively, at room temperature. Doping with a variety of impurities provided conducting n-type specimens for both $ZnSc_2S_4$ and $CdSc_2S_4$, and for the latter p-type specimens were also obtained. Weak cathodoluminescence was observed from several compounds including $CaCe_2S_4$ with a green-yellow and $ZnLu_2S_4$ with a blue-green emission color.

Many ternary compounds of the type IIB-III_2-VI_4 (Group IIB element = Zn,Cd,Hg; Group III element = Al,Ga,In; Group VI element = S,Se,) have been synthesized previously (1-3) and some of their electronic properties investigated (4). In contrast, relatively little work has been done on compounds of the similar type II-Ln_2-VI_4 (II = Zn,Cd,Mg,Ca; Ln = Sc, Y, or a rare earth) (5-7). Information is especially lacking regarding the single-crystal growth and the electrical and optical properties of such compounds.

We have explored some 50 II-Ln_2-S_4 compounds which included many of the ternary sulfides involving Ca and Mg, in addition to all of those involving Zn and Cd, with Sc and Y and all but two rare-earth elements (Eu and Pm). The majority of the sulfides was first synthesized in the form of powders, with which we made x-ray determination of the structure and also made visual examination of the luminescence color under cathode-ray excitation. Several compounds, particularly $ZnSc_2S_4$ and $CdSc_2S_4$, were subsequently prepared in the form of single-crystal platelets, on which we measured the optical bandgaps and electrical conductivities. The results show that many of these ternary sulfides have bandgaps in the visible region (*e.g.*, 2.1 and 2.3 eV, respectively, for $ZnSc_2S_4$ and $CdSc_2S_4$), and that electrically conducting specimens could be obtained by doping with suitable impurities.

Materials Preparation

Powders of Zn-Ln_2-S_4, Cd-Ln_2-S_4, Ca-Ln_2-S_4, and Mg-Ln_2-S_4 were synthesized in flowing CS_2 with He carrier gas at temperatures between 1000° and 1200°C, using the apparatus shown schematically in Fig. 1. The general reaction scheme was as follows

$$\begin{matrix} \text{II-S} \\ \text{or} \\ \text{II-CO}_3 \end{matrix} + \begin{matrix} \text{Ln}_2\text{-S}_3 \\ \text{or} \\ \text{Ln}_2\text{-O}_3 \end{matrix} \rightarrow \text{II-Ln}_2\text{-S}_4$$

The carbonates were used for the ternary compounds containing Ca or Mg, and for those containing Zn or Cd the reactant binary sulfides were ZnS or CdS powders. The starting Ln_2-S_3 were obtained by the reaction of corresponding sesquioxides Ln_2-O_3 with CS_2. The stoichiometric proportions of these reactant powders were ground, mixed, and reacted again in CS_2 for total periods ranging generally between 3 and 6 hr until x-ray powder patterns showed the product was a homogeneous, single-phase material, or until no further change occurred in the x-ray patterns upon longer reaction times.

Crystal growth of the II-Ln_2-S_4 compounds was investigated by closed-tube chemical transport at average temperatures of 1000°-1100°C with temperature gradients ranging between 5° and 50°C, using the powders synthesized as above. Single-crystal platelets as large as 5 mm on an edge with thickness ranging up to 200 μm were successfully grown for $ZnSc_2S_4$ and $CdSc_2S_4$, and crystals of smaller sizes were also obtained for $ZnTm_2S_4$ and $ZnLu_2S_4$; while for the remainder of the II-Ln_2-S_4 compounds investigated, only polycrystalline material resulted. Single crystallinity was manifest in the Laue back-reflection patterns with well-defined diffraction spots shown, for example, in Fig. 2 for a (111) $ZnSc_2S_4$ single crystal. It is worthy of note that among the two transport gases used (I_2 and HCl), HCl was found to give crystals of larger dimensions. In general, the crystal growth was made difficult by reactions with quartz of Ca, Mg, as well as the majority of the rare-earth elements. Emission spectrographic analysis showed that the grown

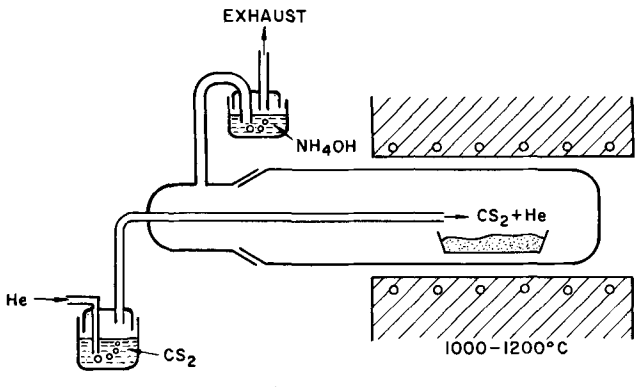

Fig. 1. CS_2 reaction apparatus

* Electrochemical Society Active Member.
[1] Pre-Doctoral ARPA Summer Working Visitor from Brown University; present address: University of Texas, Austin, Texas.
Key words: rare-earth ternary sulfides, crystal structure, bandgap, doping, cathodoluminescence.

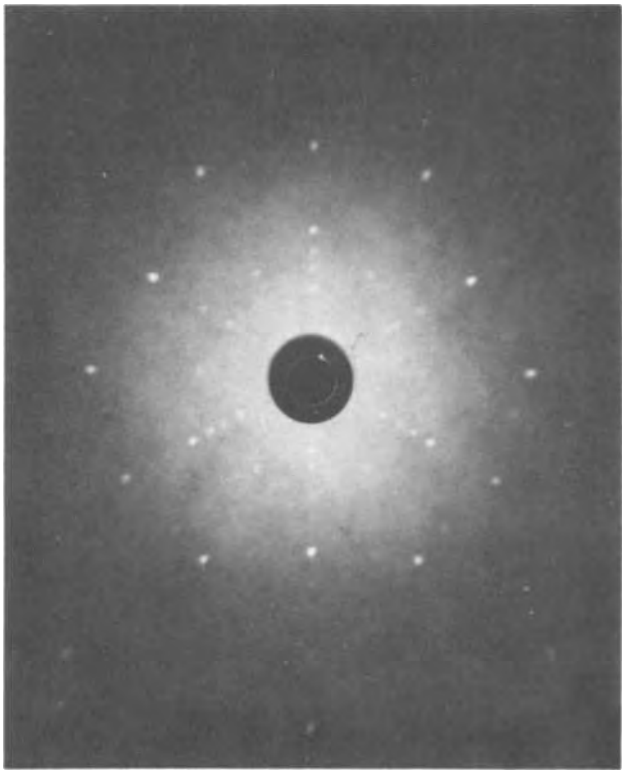

Fig. 2. X-ray Laue back-reflection pattern of a (111)-oriented $ZnSc_2S_4$ single crystal.

crystals contained sometimes as much as 1000 ppm Si, probably from the quartz growth ampoule used.

Crystal Structure

Tables I-IV list crystal structures determined by x-ray analyses (powder diffraction or Weissenberg techniques) of the majority of the 15 possible compounds in each group of Zn-Ln_2-S_4, Cd-Ln_2-S_4, Ca-Ln_2-S_4, and Mg-Ln_2-S_4, respectively, where Ln = Sc,Y,La,Ce,Pr,Nd,Sm,Gd,Tb,Dy,Ho,Er,Tm,Yb, and Lu. For the first three groups we have attempted to synthesize all the 15 possible combinations, but for the Mg-Ln_2-S_4 group we explored only two possibilities ($MgSc_2S_4$ and MgY_2S_4). Those listed with ? marks denote the case where no stoichiometric compounds were found (in which case x-ray patterns usually showed mixtures of unreacted starting compounds), or the observed structures were too complex to be readily identified. In Ca-Ln_2-S_4 (Ln = Ho through Lu) the crystal structures were not analyzed but were all isomorphous (noncubic), probably with an orthorhombic structure reported previously for these compounds (6). The present lattice constants are generally in good agreement with previous values, as seen in Tables I-III.

The crystal structure data are summarized in Fig. 3, which conveniently shows general relationship between the lattice constants of cubic compounds (spinel or Th_3P_4 type) and the ionic radii of Ln elements (8). While we will not attempt to analyze these data in any quantitative manner, the following generalization emerges from an inspection of Fig. 3. The spinel structure is favored for the Ln elements with small ionic radii—this is true for compounds involving Zn (0.74Å), Cd (0.97Å), and Mg (0.65Å). The Th_3P_4 structure is favored for the Ln elements of large ionic radii, particularly in the compounds containing Ca (0.99Å), while for the Ln of intermediate radii an orthorhombic structure exists. The lattice parameters for the cubic forms as well as for the orthorhombic form, generally decrease with decreasing ionic radii of the Ln elements. This trend holds true whether covalent or metallic radii, instead of the ionic radii, are used.

Optical Bandgap

Optical absorption measurements were made at 300°K with single-crystal platelets, whenever available, using a Cary Model No. 14 double-beam spectrophotometer. The measurements were also made on some of the compounds obtained originally in powder form, after cold-pressing these powders mixed in KBr binder. Although the absorption edges obtained for the KBr-pressed specimens were not sharp, approximate values of the bandgap could be derived from the observed edges. These values ranged from 1.8 eV for $CdEr_2S_4$ to 3.1 eV for $ZnDy_2S_4$, and the largest bandgap value observed for the present II-Ln_2-S_4 compounds was 3.7 eV for $ZnLu_2S_4$, as listed in Tables I, II, and IV.

Somewhat more detailed analyses of the optical absorption data were made on $ZnSc_2S_4$ and $CdSc_2S_4$ with (111)-oriented single-crystal platelets, 25-200 μm thick. The optical absorption coefficient α was calculated, neglecting reflection, as $\alpha = (1/t) \ln (I_0/I)$, where t is the thickness, and I_0 and I are the initial and trans-

Table I. Zn-Ln_2-S_4 Compounds

Possible compounds	Structure: This work, Type	Structure: This work, a_0 (Å)	Structure: Previous work, Ref.	Structure: Previous work, a_0 (Å)	Bandgap[a] (eV)	Cathodolumin.[b]	Remarks
$ZnSc_2S_4$	Spinel	10.483	S[c] (7)	10.478	2.1	none	E_g of Sc[d]
ZnY_2S_4	?[e]	—	—	—	—	blue-green	—
$ZnLa_2S_4$	?	—	—	—	—	brown	—
$ZnCe_2S_4$	?	—	—	—	—	y-green	—
$ZnPr_2S_4$	?	—	—	—	—	blue	—
$ZnNd_2S_4$	?	—	—	—	—	none	—
$ZnSm_2S_4$	?	—	—	—	—	blue	—
$ZnGd_2S_4$	?	—	—	—	—	none	—
$ZnTb_2S_4$	?	—	—	—	—	none	—
$ZnDy_2S_4$	?	—	—	—	~3.1	dark blue	E_g of KBr-p[f]
$ZnHo_2S_4$	?	—	—	—	—	none	—
$ZnEr_2S_4$	?	—	—	—	—	none	—
$ZnTm_2S_4$	Orthor.	a = 7.734 b = 13.227 c = 6.263	—	—	3.6	none	E_g of SC
$ZnYb_2S_4$	Orthor.	—	O[g] (7)	—	~2.5	none	E_g of KBr-p
$ZnLu_2S_4$	Orthor.	a = 7.658 b = 13.183 c = 6.246	O (7)	—	3.7	blue-green	E_g of SC

[a] Room temperature.
[b] Room temperature, visual examination, no intentional impurities added, cathodoluminescence could be due to unreacted starting materials.
[c] Spinel structure, cubic.
[d] Single crystal.
[e] X-ray patterns are either for mixtures of the starting materials or are very complex.
[f] KBr-pressed pellet.
[g] Orthorhombic, MnY_2S_4 type.

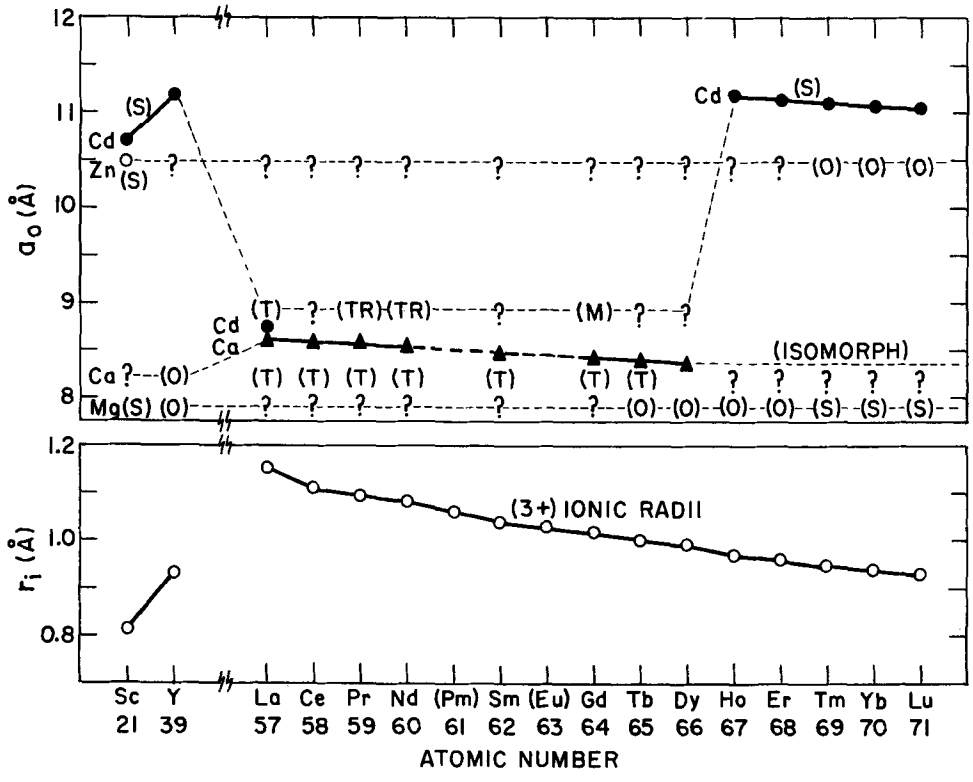

Fig. 3. Crystal structures and lattice constants of Zn-Ln_2-S_4 (○), Cd-Ln_2-S_4(●), Ca-Ln_2-S_4(▲), and Mg-Ln_2-S_4. (S): spinel, (T): Th_3P_4, (O): orthorhombic, (TR): trigonal, (M): monoclinic, and (?): no compound formed or unknown structure. Lower graph shows known 3+ ionic radii of Sc, Y, and the rare earths [Ref. (8)]. In the upper graph, dashed lines (- - - -) are used merely for the purpose of grouping together the individual group of II-Ln_2-S_4 having the same Group II element; while the heavy lines connecting data points represent actual variations in the lattice constants of cubic-form (spinel and Th_3P_4 type) II-Ln_2-S_4 sulfides.

mitted intensities, respectively. In all cases, weakly energy-dependent, low-background absorption was subtracted from the measured absorption in calculating the α values.

In Fig. 4 and 5 are shown the dependence of α upon wavelength λ for $ZnSc_2S_4$ and $CdSc_2S_4$ (111) single crystals, respectively, at 300°K. The fundamental absorption edge is seen to occur near 6000Å for the former and near 5300Å for the latter, corresponding to a bandgap of 2.1 eV for $ZnSc_2S_4$ and 2.3 eV for $CdSc_2S_4$. These data are consistent with the observed transparent red to yellow colors of the respective samples.

It is known that the absorption coefficient in the fundamental absorption edge region obeys, in general, a power law of the form $\alpha \propto (h\nu - E_g)^n$, where $h\nu$ is the photon energy and E_g is the bandgap. The exponent n for a direct bandgap is ½ if the electronic transitions are that of the allowed case, and for the forbidden case it is 3/2; for an indirect gap the n is 2 and 3, respectively, for the allowed and forbidden transitions (9). We have attempted to fit the present α to the various power laws; however, the results were inconclusive, although for both $ZnSc_2S_4$ and $CdSc_2S_4$ the direct-bandgap $\alpha \propto (h\nu - E_g)^{1/2}$ relation provided a somewhat better fit for the experimental points than did the other power dependences. It is perhaps worth mentioning in this regard that calculations of the band structure of spinel-type semiconductors have been attempted previously (10); however, only the valence band levels at the Γ points could be deduced with any certainty, leaving lower symmetry points such as X or L uncertain, with the results that unambiguous determination of the type of the fundamental bandgap was not possible.

From the interference fringes obesrved with thin specimens, the refractive index in the wavelength region of 1-2 μm was calculated to be 1.56 for $ZnSc_2S_4$ and 2.39 for $CdSc_2S_4$. Thus the dielectric constant of the former is less than that of the latter, indicating that $ZnSc_2S_4$ is probably more ionic than $CdSc_2S_4$.

Doping Behavior and Electrical Properties

As-grown, undoped II-Ln_2-S_4 compounds investigated were all high resistivity, and consequently their conductivity type could not be determined. Efforts to

Table II. Cd-Ln_2-S_4 Compounds

Possible compounds	Structure: This work Type	Structure: This work a_o (A)	Structure: Previous work Ref.	Structure: Previous work a_o (A)	Bandgap[a] (eV)	Cathodolumin.[b]	Remarks
$CdSc_2S_4$	Spinel	10.733	S[c] (6)	—	2.3	brown	E_g of SC[d]
$Cd_2Y_2S_4$	Spinel	11.172	S (5)	11.196	—	brown	—
$CdLa_2S_4$	Th_3P_4	8.7033	T[h] (6)	—	~2.6	weak green	E_g of KBr-p[f]
$CdCe_2S_4$	?[e]	—	T (6)	—	—	none	—
$CdPr_2S_4$	Trigonal	—	T (6)	—	~2.1	none	E_g of KBr-p
$CdNd_2S_4$	Trigonal	a = 4.6 b = 8.0	T (6)	—	—	none	—
$CdSm_2S_4$	?	—	T (6)	—	—	none	—
$CdGd_2S_4$	Monocl.[i]	—	T (6)	—	—	—	—
$CdTb_2S_4$	?	—	T (6)	—	—	—	—
$CdDy_2S_4$	?	—	T (6)	—	~2.5	none	E_g of KBr-p
$CdHo_2S_4$	Spinel	11.1674	S (6)	11.168	—	dark red	—
$CdEr_2S_4$	Spinel	11.1347	S (6)	11.136	~1.8	none	E_g of KBr-p
$CdTm_2S_4$	Spinel	11.09	S (5)	11.092	~2.4	none	E_g of KBr-p
$CdYb_2S_4$	Spinel	11.0684	S (6)	11.068	~2.5	none	E_g of KBr-p
$CdLu_2S_4$	Spinel	11.045	S (6) O[g] (7)	11.036	—	dark orange	—

[h] Thorium phosphide structure, cubic.
[i] Monoclinic.
For other abbreviations, see Table I.

Table III. Ca-Ln_2-S_4 Compounds

Possible compounds	Structure: This work Type	This work a_0 (A)	Previous work Ref.	Previous work a_0 (A)	Bandgap[a] (eV)	Cathodolumin.[b]	Remarks
$CaSc_2S_4$	?[e]	—	? (6)	—	—	—	—
CaY_2S_4	Orthor.	—	O[j] (6)	a = 12.98 b = 13.11 c = 3.88	—	—	—
$CaLa_2S_4$	Th_3P_4	8.66	T[h] (6)	8.687	—	—	—
$CaCe_2S_4$	Th_3P_4	8.616	T (6)	8.615	—	green-y	—
$CaPr_2S_4$	Th_3P_4	8.572	T (6)	8.578	—	none	—
$CaNd_2S_4$	Th_3P_4	8.534	T (6)	8.533	—	none	—
$CaSm_2S_4$	Th_3P_4	8.473	T (6)	8.472	—	none	—
$CaGd_2S_4$	Th_3P_4	8.42	T (6)	8.423	—	none	—
$CaTb_2S_4$	Th_3P_4	8.402	T (6)	8.400	—	none	—
$CaDy_2S_4$	Th_3P_4	8.38	T (6)	8.376	—	none	—
$CaHo_2S_4$	?	—	O (6)	a = 12.90 b = 13.04 c = 3.86	—	none	noncubic
$CaEr_2S_4$	?	—	O (6)	a = 12.87 b = 13.01 c = 3.85	—	none	&
$CaTm_2S_4$	?	—	O (6)	a = 12.85 b = 12.98 c = 3.84	—	none	all
$CaYb_2S_4$	?	—	O (6)	a = 12.82 b = 12.95 c = 3.83	—	none	
$CaLu_2S_4$	?	—	O (6)	a = 12.82 b = 12.95 c = 3.83	—	dark y	isomorphous

[j] The lattice parameters given here are for the Yb_2S_4-type orthorhomic structure, which is the more stable form at low temperatures. The stable form at high temperatures is the MnY_2S_4-type orthorhombic structure, but the lattice parameters are nearly the same as that of the Yb_2S_4-type; see a review article by Flahaut cited in Ref. (6). The only exception is CaY_2S_4 for which the low-temperature form is the Th_3P_4-type cubic. The temperature range of the phase transformation for the above-mentioned compounds is between 900° and 1200°C.
For other abbreviations, see Table I.

Table IV. Mg-Ln_2-S_4 Compounds

Possible compounds	Structure: This work Type	This work a_0 (A)	Previous work Ref.	Previous work a_0 (A)	Bandgap[a] (eV)	Cathodolumin.[b]	Remarks
$MgSc_2S_4$	Spinel	—	S[c] (6)	10.627	~3	none	E_g of KBr-p[f]
MgY_2S_4	Orthor.	—	O[g] (6)	a = 12.60 b = 12.73 c = 3.77	—	—	—
$MgLa_2S_4$	not made	—	? (6)	—	—	—	—
$MgCe_2S_4$	not made	—	? (6)	—	—	—	—
$MgPr_2S_4$	not made	—	? (6)	—	—	—	—
$MgNd_2S_4$	not made	—	? (6)	—	—	—	—
$MgSm_2S_4$	not made	—	? (6)	—	—	—	—
$MgGd_2S_4$	not made	—	? (6)	—	—	—	—
$MgTb_2S_4$	not made	—	O (6)	a = 12.62 b = 12.74 c = 3.78	—	—	—
$MgDy_2S_4$	not made	—	O (6)	a = 12.59 b = 12.70 c = 3.77	—	—	—
$MgHo_2S_4$	not made	—	O (6)	a = 12.54 b = 12.66 c = 3.76	—	—	—
$MgEr_2S_4$	not made	—	O (6)	a = 12.51 b = 12.63 c = 3.74	—	—	—
$MgTm_2S_4$	not made	—	S (6)	10.958	—	—	—
$MgYb_2S_4$	not made	—	S (6)	10.957	—	—	—
$MgLu_2S_4$	not made	—	S (6)	10.949	—	—	—

For abbreviations, see Table I.

dope these materials low resistivity were concentrated on $ZnSc_2S_4$ and $CdSc_2S_4$, since single crystals of relatively large dimensions were readily grown for them.

It is probable that both $ZnSc_2S_4$ and $CdSc_2S_4$ have the normal spinel structure, in which the Group II element (Zn or Cd) occupies the tetrahedral sites and the Group III element (Sc) occupies the octahedral sites. On the basis of valence consideration assuming a simple substitution of elements at various lattice sites, possible p-type dopants are the elements in Groups I, II, IV, and V, and several divalent transition metals; possible n-type dopants are the elements in Groups III and IV, and several trivalent transition metals. In addition, a consideration must be given to the relative size of the doping ion and the host lattice ion to be substituted by it. Of a large number of the possible dopants, we selected 17, and these were incorporated into $ZnSc_2S_4$ and $CdSc_2S_4$ during growth by closed-tube chemical transport in the concentration range 200-5000 ppm, as shown in Table V.

The results of Hall effect measurements[2] on doped crystals in Table V show that Ga, Ag, or Cr doping provided n-type materials for $ZnSc_2S_4$ with carrier concentrations in the 10^{17}-10^{18}/cm^3 range. N-type materials having carrier concentrations of 10^{14}-10^{15}/cm^3 were also obtained for $CdSc_2S_4$ by doping with Ga or Li. To date, p-type material was obtained only for $CdSc_2S_4$ by doping with Cr, which gave a hole concentration of 10^{12}/cm^3. Hall mobilities for both the n-type and p-type materials ranged up to ~40 cm^2/V · sec.

It appears from these results that Ag and Li are interstitial donors since if they are substitutional impurities, they would have acted as acceptors; on the

[2] Ohmic contacts were made with alloys of Zn-In and Cd-In, respectively, for $ZnSc_2S_4$ and $CdSc_2S_4$.

Table V. Doping experiment of $ZnSc_2S_4$ and $CdSc_2S_4$

Material	Dopant			Electrical prop. at 300°K				Remarks
	Element	Group	Conc. (ppm)*	Cond. type	ρ (ohm·cm)	n (cm^{-3})	μ ($cm^2/V \cdot sec$)	
$ZnSc_2S_4$	Cu	I	Strong	—	High	—	—	All crystals prepared by closed-tube chemical transport.
	Ag	I	5000	n	7.1×10^{-1}	1.2×10^{18}	7.6	
	Li	I	Trace	—	—	—	—	—
	Na	I	—	—	—	—	—	Very small crystals mixed with Al_2O_3 from alumina boat.
	Be	II	1000	—	—	—	—	No crystal.
	Mg	II	5000	—	High	—	—	—
	Ga	III	500	n	2.53	8×10^{17}	3	—
	Cr	VI	200	n	3.1×10^{-1}	5×10^{17}	40	—
$CdSc_2S_4$	Cu	I	1000	—	—	—	—	No crystal.
	Ag	I	Strong	—	4.5×10^{6}	—	—	—
	Li	I	Trace	n	1.1×10^{3}	1.4×10^{14}	41	—
	Na	I	—	—	—	—	—	Very small crystals mixed with Al_2O_3 from alumina boat.
	Be	II	300	—	—	—	—	—
	Mg	II	3000	—	2.5×10^{8}	—	—	—
	Ca	II	1000	—	—	—	—	—
	Al	III	300	—	3.2×10^{7}	—	—	—
	Ga	III	1000	n	4.5×10^{2}	2.8×10^{15}	4.9	—
	In	III	1000	—	—	—	—	—
	Ge	IV	Trace	—	—	—	—	—
	Sn	IV	500	—	1.8×10^{7}	—	—	—
	Pb	IV	500	—	8.3×10^{7}	—	—	—
	As	V	Strong	—	—	—	—	—
	P	V	Strong	—	4.8×10^{7}	—	—	—
	Cr	VI	Strong	p	7×10^{4}	2×10^{13}	43	—
	Ni	VIII	Strong	—	—	—	—	—

* ppm by weight, determined by emission spectroscopic analysis; "strong" denotes the case of impurity concentration $>10^4$ ppm, and "trace" denotes the case of impurity concentration <1 ppm.

other hand, it appears that Ga is a substitutional donor for the tetrahedral sites. The behavior of Cr is somewhat puzzling in that it acted as an acceptor in $CdSc_2S_4$, but for $ZnSc_2S_4$ it acted as a donor. Halogens apparently do not provide conducting n-type specimens, since all the materials were grown in a halogen atmosphere and they were high resistivity. Group IV elements also appear to be ineffective dopants since as-grown crystals containing a large amount of Si, as well as those crystals intentionally doped with Ge, Sn, and Pb, were all high resistivity. Since Ga doped both $ZnSc_2S_4$ and $CdSc_2S_4$ n-type, we attempted to grow n-type crystals of these compounds from Ga solutions by slowly cooling the melts from about 1200°C. However, only GaS crystals resulted, and thus the solution growth technique appears unsuitable, at least with the Ga solvent.

Observations on Cathodoluminescence

On all powder specimens synthesized without intentional doping, we have made visual examinations of the luminescence color emanating under a cathode-ray excitation. The emission color ranged from a brownish red to a blue, as listed in Tables I-IV. Of the speci-

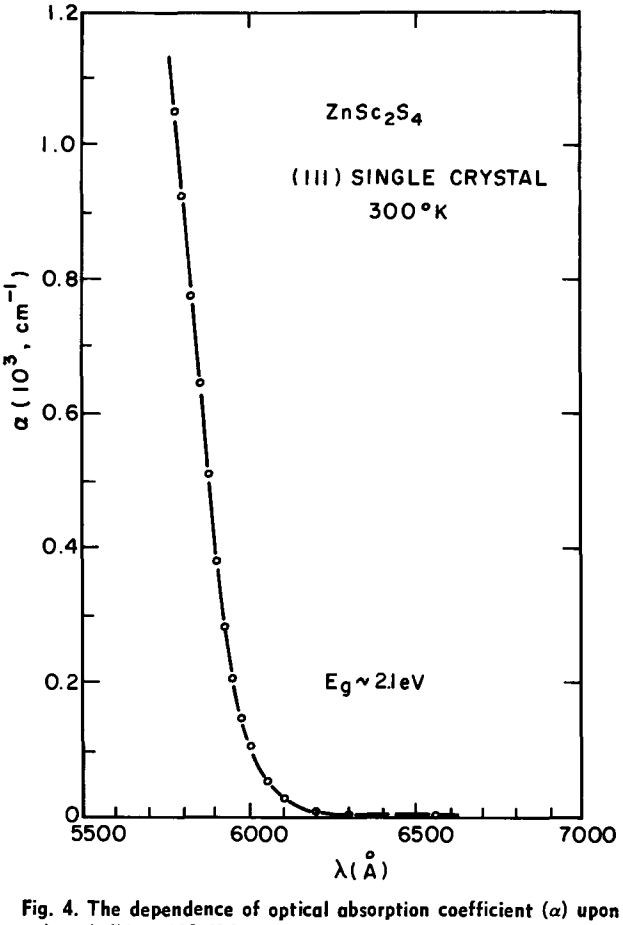

Fig. 4. The dependence of optical absorption coefficient (α) upon wavelength (λ) at 300°K for (111) single-crystal $ZnSc_2S_4$.

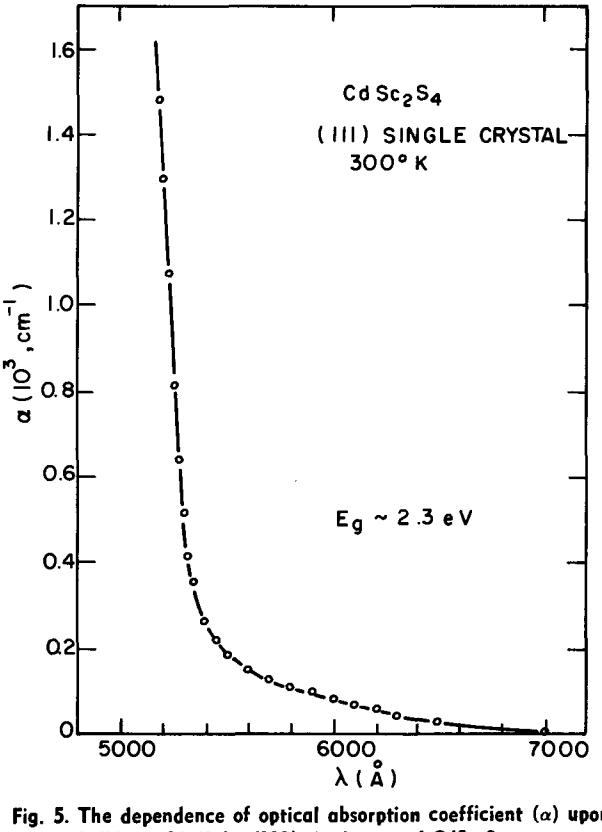

Fig. 5. The dependence of optical absorption coefficient (α) upon wavelength (λ) at 300°K for (111) single-crystal $CdSc_2S_4$.

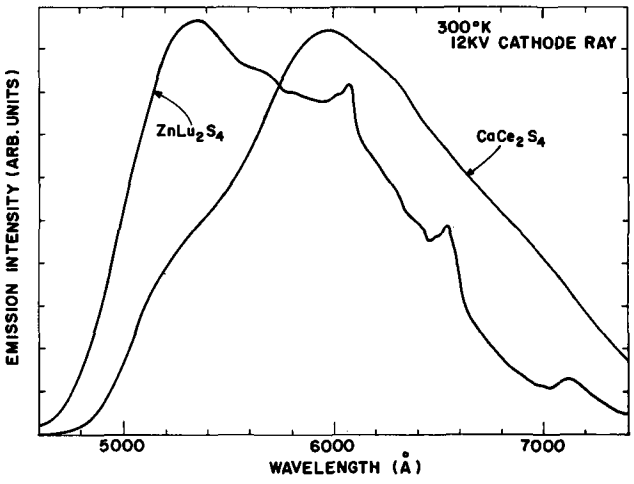

Fig. 6. Spectral distribution of cathodoluminescence with 12-kV excitation for $ZnLu_2S_4$ and $CaCe_2S_4$ at room temperature.

mens which showed a visible cathodoluminescence, virtually all exhibited less-than bandgap emissions (judging from the emission colors) and thus appeared to involve recombination at deep levels of unknown nature. For $CaCe_2S_4$ and $ZnLu_2S_4$ showing a yellow to green emission which is of practical importance as phosphors, we measured the emission spectral distribution with a 12-kV excitation at room temperature, shown in Fig. 6. The observed cathodoluminescence for both materials was quite weak, and so no quantitative measurements were made to determine the emission efficiency. It would be interesting, however, to try to activate these phosphors with suitable impurity additions, since the emission colors observed were in the visible spectral range.

Acknowledgments

We wish to thank H. L. Pinch and P. N. Yocom for communicating to us their early results on synthesis of several compounds reported in this paper. We are also indebted to J. Gerber for spectral distribution measurements. The research herein reported was made possible by the support of the Advanced Research Projects Agency under Order No. 1034, through the U.S. Army Electronics Command, Fort Monmouth, New Jersey, under Contract No. DAAB07-70-C-0155.

Manuscript submitted June 14, 1972; revised manuscript received Nov. 3, 1972.

Any discussion of this paper will appear in a Discussion Section to be published in the December 1973 JOURNAL.

REFERENCES

1. H. Hahn and W. Klingler, *Z. Anorg. Allgem. Chem.*, **263**, 177 (1950).
2. H. Hahn, G. Frank, W. Klingler, A. Störger, and G. Störger, *ibid.*, **279**, 241 (1955).
3. R. Nitsche, H. U. Bölsterli, and M. Lichtensteiger, *Phys. Chem. Solids*, **21**, 199 (1961); R. Nitsche, *Fortschr. Mineral.*, **44**, 231 (1967).
4. J. A. Beun, R. Nitsche, and M. Lichtensteiger, *Physica*, **26**, 647 (1960); *ibid.*, **27**, 448 (1961); and L. Krausbauer, R. Nitsche, and P. Wild, *ibid.*, **31**, 113 (1965).
5. L. Suchow and N. R. Stemple, *This Journal*, **111**, 191 (1964).
6. J. Flahaut, M. Guittard, M. Patrie, M. P. Pardo, S. M. Golabi, and L. Domange, *Acta Cryst.*, **19**, 14 (1965); J. Flahaut, in "Progress in the Science and Technology of the Rare Earths," Vol. 3, L. Eyring, Editor, Pergamon Press, New York (1968).
7. R. E. Tressler, Ph.D. Thesis, Pennsylvania State University, September (1967).
8. L. Pauling, "The Nature of the Chemical Bond", 3rd ed., Cornell University Press, Ithaca (1960).
9. See for example, T. P. McLean, in "Progress in Semiconductors," Vol. 5, A. F. Gibson, Editor, John Wiley and Sons, Inc., New York (1960).
10. W. Rehwald, *Phys. Rev.*, **155**, 861 (1967).

Silicon Oxynitride Films from the $NO-NH_3-SiH_4$ Reaction

Myron J. Rand* and James F. Roberts

Bell Telephone Laboratories, Incorporated, Allentown, Pennsylvania 18103

ABSTRACT

Silicon oxynitride films from the $NO-NH_3-SiH_4$ reaction in nitrogen at 850°C are clear, adherent, amorphous dielectrics whose composition may be varied over the entire range between SiO_2 and Si_3N_4 by controlling the NH_3/NO ratio employed. The refractive index is a convenient and accurate measure of the composition. Over much of the nitrogen-rich range, the Si content is about 2% lower than stoichiometric, and the hypothesis is made that one nitrogen in three is bonded to only two other skeletal atoms instead of three, and that some of these nitrogens bear bonded hydrogen. The N-H groups are believed to play a role similar to that of O-H in silicas. Compositions near Si_2ON_2 are highly resistant to ionizing radiation under bias, and are excellent Na^+ barriers at 300°C and 10^6 V/cm. However, they are not better barriers to Na^+ thermal diffusion at 600°C than SiO_2. With appropriate pre- and post-deposition chemical treatments, oxynitride films give low Si surface charge and small nonionic shifts in flatband voltage with bias-temperature aging. Other properties investigated for various compositions include etch rate, i.r. spectrum, film stress, and cathodoluminescence spectra. Films from the $NO-SiH_4$ and $NO-NH_3-SiH_4$ processes are compared.

Silicon oxynitride (SiON), as used here, implies no definite stoichiometry, and means an amorphous polymer of silicon, oxygen, and nitrogen in varying amounts. It is not a mixture or codeposit of SiO_2 and Si_3N_4. Nevertheless these may be considered the extremes of its composition range in the sense that many of the properties of a SiON are consistent with its position along the composition scale between oxide and nitride. SiON films are of interest in device fab-

* Electrochemical Society Active Member.

Key words: silicon oxynitride, thin films, dielectric films, silane, nitric oxide.

rication to the extent that they retain the favorable features of either SiO_2 or Si_3N_4 while minimizing their drawbacks. Among the properties in which the two differ significantly are etch rate, reaction with moisture, resistance to sodium ion drift and diffusion, refractive index, and MIS capacitor behavior (Si surface-state density, charge injection from the contacts, high-field conductivity, dielectric constant, etc.).

In addition to the possibilities for trade-offs in properties, SiON becomes of interest for the case where oxide and nitride are both unsatisfactory but in opposing directions. Two examples have already been reported (1-3). Grown or deposited SiO_2 on Si is under compressive stress, while Si_3N_4 is under even greater tensile stress. It is possible to tailor a SiON film ($SiO_{1.75}N_{0.25}$) which will leave film and substrate stress-free. Another application of the principle is the response to ionizing radiation under electrical bias, where SiO_2 accumulates a positive charge and Si_3N_4 preferentially traps electrons. IGFETS in particular, and bipolar devices to a lesser degree, are thus susceptible to degradation. Si_2ON_2 (*i.e.*, SiON of about 1.77 refractive index) insulating films in MIS structures are insensitive to absorbed doses of 10^7-10^8 rad of ^{60}Co-γ's, and Si_2ON_2-passivated npn transistors require 30 times the radiation dose of those with SiO_2 for the same h_{FE} degradation (3).

The chemical-vapor deposition of SiON films from silane and nitric oxide in nitrogen carrier has already been described (4). The SiON composition is controlled by the reactant ratio, with low NO/SiH_4 ratios giving a deposit richer in nitrogen. NO (which is thermally stable) was chosen because whatever happens during the reaction, probably a free-radical chain mechanism, the nitrogen must go along with oxygen if the N—O bond is not broken, or an active nitrogen moiety must be generated if the bond is broken. In either case some nitrogen should be incorporated into the deposit. But if either N_2O or NO_2 is used as the oxidant, oxygen is liberated upon heating, or can be easily abstracted by attack by silane, silyl radicals, or atomic hydrogen. At any rate, the product of these reactions is essentially SiO_2 only.

The NO-SiH_4 process is not capable of covering the entire range between SiO_2 and Si_3N_4. At $NO/SiH_4 = 1$ the film composition is near $Si_3O_3N_2$; further lowering the reactant ratio results in codeposition of Si, because there is not enough oxidant to combine with all the thermally decomposing silane. There are various ways to reach the nitride-rich SiON composition, most of which involve ammonia and an oxidant competing for the silane. Thermodynamically the oxidation reaction is favored, so that an amount of oxidant so small as to be difficult to control often produces a product with more oxygen than nitrogen. In fact, from the physical properties reported by some investigators for pyrolytic silicon nitride, it is likely that their system contained enough oxygen or moisture to produce a SiON instead. The purest commercially available ammonia, Matheson Gas Products "Ultra High Purity," may require bleeding many liters from the tank before it will yield uncontaminated silicon nitride, as diagnosed by etch rate. We consider that Si_3N_4 deposited at 850°-900°C should have a buffered HF etch rate of 11 ± 2 Å/min at 25°C.

The systems which have been used to produce the full range of SiON film compositions include SiH_4-N_2O-NH_3 (5), SiH_4-CO_2-H_2-NH_3 (6), SiH_4-O_2-NH_3 (6, 7), SiH_4-NO-NH_3 (8), $SiCl_4$-CO_2-NH_3 (9), and rf reactive sputtering in $N_2 + N_2O$ (10), or $N_2 + O_2$ (11) mixtures. In most of these, film composition was not known accurately, although usually it was inferred from refractive index or spectra. Evaluation was mostly concerned with electrical properties. Some products obviously contain excess silicon. Studying these papers it is again evident that NO is the most controllable oxidant, and the work of Brown *et al.* (8) has the most data on the nitride-rich SiON's. Their deposition was at 1000°C, in ammonia at high flow rates, with no carrier gas diluent.

In this paper, SiON films produced by the SiH_4-NO-NH_3 reaction are examined critically, particularly in the nitride-rich region inaccessible to the NO-SiH_4 reaction. Deposition temperature was usually 850°C, in nitrogen ambient with $<8\%$ NH_3 (usually much less). This is a summary report, abstracting and generalizing results, since at this writing about 200 samples have been studied.

Experimental

Depositions were done in a vertical fused silica tube with a bulged section containing a graphite (preferably) or silicon cylindrical pedestal heated inductively at 3 MHz. Substrates were usually 1 in. diameter polished Si wafers of a thickness, type, and resistivity appropriate for the tests to be performed. Reactant gases entered through a jet on the axis of the tube at the top; the coaxial jet was important for thickness uniformity. Film thickness was monitored during growth using the device of Roberts (12).

Tank silane was supplied at 3% in nitrogen, NO as 4% in nitrogen, and ammonia was ultrahigh purity grade (5-9's min.); all were from Matheson Gas Products. Stainless-steel tubing was used throughout. The NO was introduced into the carrier nitrogen stream first and shut off last. The silane and ammonia streams were mixed, and deposition time began with introduction of this mixture into the gas manifold. Total gas flow through the deposition chamber was 1-3 liter/min, a linear velocity of about 3 cm/sec. Reaction appears to be confined to the close vicinity of the heated pedestal, since the reactor remains quite clean for many runs.

SiON film composition was determined using the electron-beam microprobe (13), making twelve analyses per sample; nitrogen was by difference. Refractive index was measured ellipsometrically at 546 nm. Infrared transmission spectra 4000-250 cm^{-1} were taken using high resistivity, thick Si substrates polished on both sides, with a bare substrate in the reference beam. Film-thickness measurements were made by constant angle reflection interference spectra (14), using reference standards measured by ellipsometry and multiple-beam interferometry. Average film stress was measured by deposition on a thin, optically flat, elastic Si beam and observing the curvature interferometrically (15). Cathodoluminescence was investigated in the apparatus described by Mitchell (16), at 7 kV and 1 μA beam current, over the 200-600 nm range. MIS capacitors for studying various electrical properties were made by filament evaporation of 20 mil diameter Al field plates through a mask, and also Al back contacts on the Si. The quasi static technique (17) was used to determine interface-state densities. Procedures in studying sodium ion diffusion strongly influence results of the experiments, and will be described later in the appropriate section.

Results

All SiON films made from SiH_4-NO-NH_3 are clear, smooth, and tightly adherent. Electron diffraction shows no ordering >20Å (estimate).

Composition.—In Fig. 1, which is part of a three-component diagram, electron-microprobe analyses of various SiON films are plotted. All the points are from the SiH_4-NO-NH_3 system, which evidently can produce any composition between SiO_2 and Si_3N_4. In the oxygen-rich end, the points lie on the SiO_2-Si_3N_4 tieline up to a composition of $Si_3O_3N_2$. This happens to be about the limit of the SiH_4-NO process (4), and is also a composition for which some evidence for compound formation has been reported (9). Beyond this point the analyses fall slightly below the tieline, and average ~2% Si low all the way to Si_3N_4. The accuracy of the probe analysis is $\pm 2\%$, but the statistics and distribution of the results suggest a systematic slight

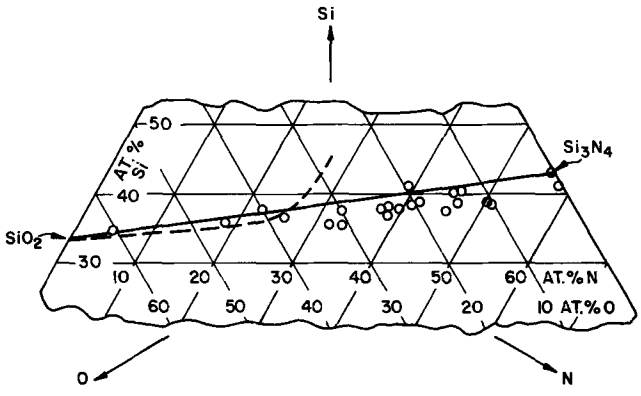

Fig. 1. Microprobe analyses of SiON from the SiH_4-NO-NH_3 reaction. The tieline (solid) represents stoichiometric oxynitride and the dotted line the compositions accessible to the NO-SiH_4 reaction. All the points are analyses of films from the NO-NH_3-SiH_4 reaction.

Si deficiency from the expected oxynitride stoichiometry. It will be shown below that SiON's of apparently the same composition made by the two oxynitride processes do indeed differ in certain properties.

SiON compositions known at this writing to have properties of interest for device applications are located in the ternary diagram in Fig. 2. These have all been reported earlier (1-4).

Preparation of a desired composition.—The concentrations of the three reactants were varied independently in many experiments, but the NH_3/SiH_4 ratio was always >20, to avoid any possibility of Si codeposition. The film-deposition rate depends solely on the SiH_4 concentration (see Fig. 3). The film composition, on the other hand, is governed by the NH_3/NO ratio. In Fig. 4, the refractive index is plotted *vs.* this ratio; note that the abscissa scale is logarithmic. Figures 3 and 4 are both for 850°C deposition, and will probably change somewhat with the deposition equipment used. The silane concentrations used in the runs of Fig. 4 vary over a factor of four. The scatter in the data is much reduced if a given SiH_4 concentration is selected. With all reactant concentrations fixed, the reproducibility of the refractive index has consistently been ±0.01.

The close correlation between the refractive index and composition is shown in Fig. 5, where all the data points are from the SiH_4-NO-NH_3 reaction. The abscissa may be considered the atomic fraction of the oxygen of SiO_2 which has been replaced by nitrogen in proceeding along the SiON composition scale. The NO-SiH_4 process, as shown, follows the same curve

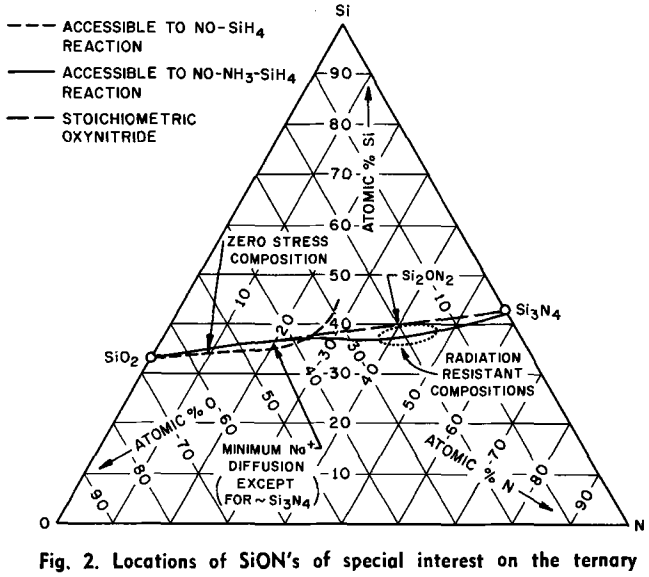

Fig. 2. Locations of SiON's of special interest on the ternary composition diagram.

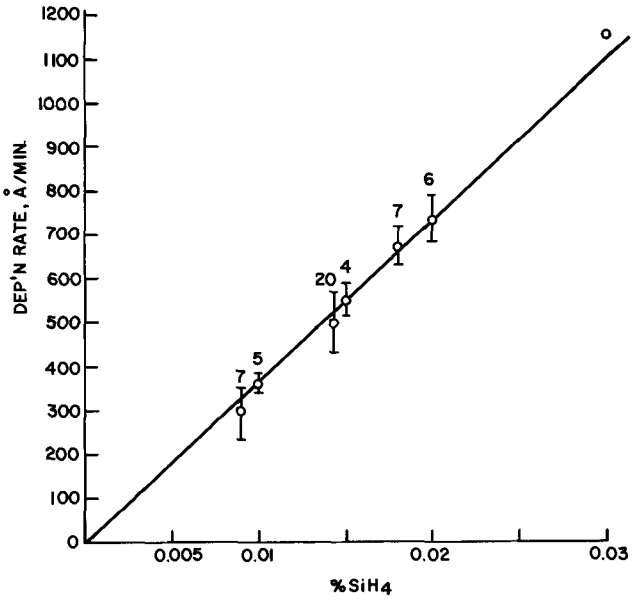

Fig. 3. Dependence of the deposition rate on silane concentration. The number of runs at each concentration is shown. The NH_3:NO ratio varies over a range of 10^3.

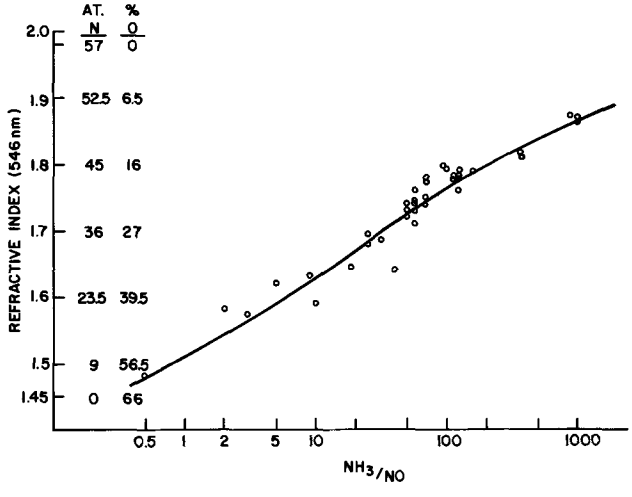

Fig. 4. Control of film composition by the NH_3:NO ratio. Per cent SiH_4 = 0.01-0.04.

until the film becomes Si rich and n shoots up. Although we suspect differences in structure of SiON's of the same analysis made by the two processes, the refractive index is apparently insensitive to any such differences.

Spectrum.—The variation in infrared absorption maximum with film composition is shown in Fig. 6. This is the strongest argument for calling SiON an "inorganic copolymer" rather than a "codeposit" or "mixture," since separate bands for Si-O and Si-N stretching do not appear, but instead only a broadened band in some intermediate position indicative of the composition. This is the result obtained for SiON made by any process, vacuum or pyrolytic. The bending vibration at lower frequency behaves the same way, progressing gradually from the 450 cm^{-1} of SiO_2 to the 485 cm^{-1} of Si_3N_4 as the composition changes.

The curve for the NO-SiH_4 process SiON (Fig. 6) is slightly different, but it lies well outside the uncertainty of the probe analysis. Thus here there is a detectable structural difference between supposedly identical SiON's.

Figure 6 also shows the danger of judging silicon nitride purity by infrared spectrum. The film can have an O/N ratio up to 0.2 and still have an absorption maximum at the same wavelength as pyrolytic Si_3N_4.

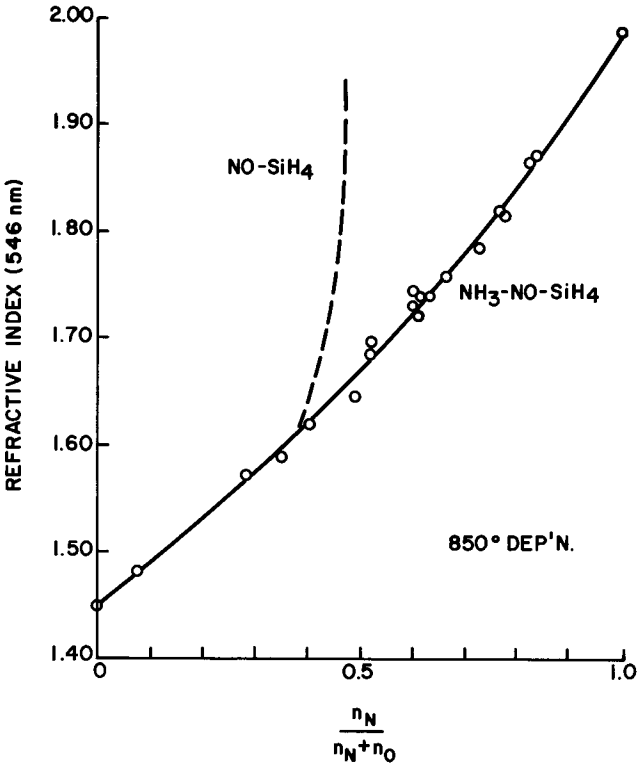

Fig. 5. Refractive index as a function of composition

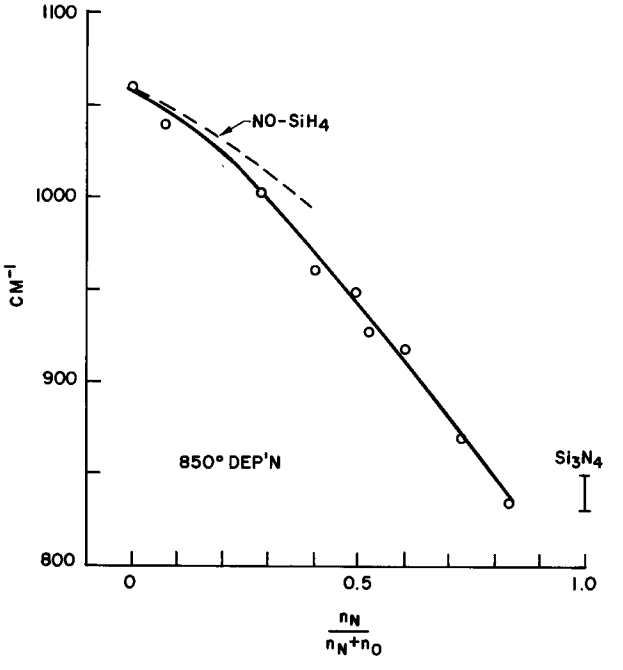

Fig. 6. The infrared absorption maxima of SiON's of various composition.

In addition to the skeletal vibrations given above, all SiH_4-NO-NH_3 SiON's show weak absorption at 3360-3390 cm^{-1}, and weak, very broad absorption at ~1200 cm^{-1}. No absorption at the O-H or Si-H stretching frequencies has been seen.

Etch rate.—Figure 7 shows the variation of buffered HF (7:1) etch rate with SiON composition. The etch rate decreases smoothly over a factor of $\sim 10^2$ from oxide to nitride. Unlike examination by i.r. spectrum, the etch rate is able to detect slight oxygen contamination in Si_3N_4. The difference in etch rate at $n \sim 1.6$ for SiON's from the two processes (more than a factor of two) reinforces the belief that there are fundamental differences between these SiON's. Etch rate is

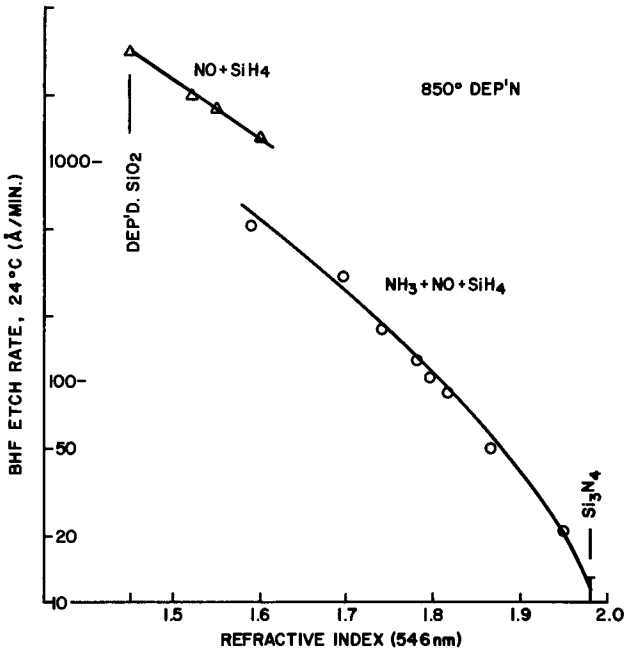

Fig. 7. The buffered HF etch rate of SiON's. Note that the ordinate is logarithmic.

evidently a sensitive indicator of structural strain, as it is with various kinds of SiO_2.

H_3PO_4 (180°C) etch rates have not been determined except at $n = 1.77$, where the rate is 110 Å/min. The rate undoubtedly decreases with increasing oxygen content.

Film stress.—The average stress in films of SiON on Si is shown in Fig. 8. Like Si_3N_4 itself, nitride-rich SiON is under high tension, and there is no drift with time. The failure of the curves for the two processes to join smoothly can only provide further evidence of a fundamental structural difference in the two SiON's. Note also that although NO-SiH_4 process SiON is under much less stress, nevertheless it etches more rapidly (Fig. 7). Mechanical stress, at least in films

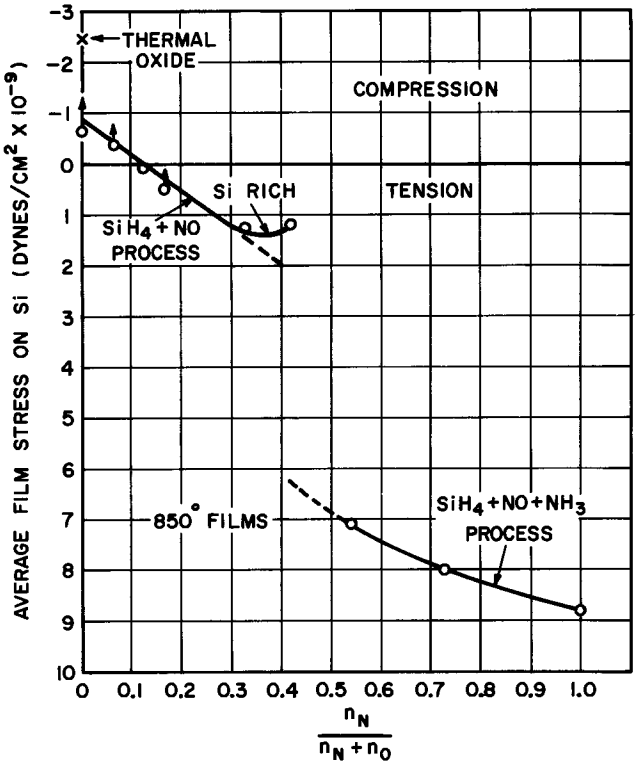

Fig. 8. Average film stress on Si of SiON's from the two processes

deposited at high temperatures, can hardly be a major factor in etch rate, and probably is not a reliable clue to bond strain in the film structure.

Sodium ion diffusion.—NaCl containing $^{22}NaCl$ was evaporated in a vacuum furnace onto the surface of slices coated with 2500-3400Å of SiON. The outer ⅛ in. was covered by Al masks. About a monolayer was deposited and uniformity of deposition was checked by autoradiography. To minimize evaporation losses the slices were paired face to face, horizontally, and diffused for 22 hr at 600°C in forming gas. Excess NaCl was rinsed off, and the back side of the wafers was also etched, although this precaution removed very little of the radioactivity. The samples were etched in steps and the remaining activity of the surfaces measured using a scintillation counter and a Baird-Atomic Model 530 spectrometer, counting the 0.51 MeV annihilation radiation gammas.

With a thin, depletable film source diffusing into a semi-infinite body as a model, and neglecting the absorption of the energetic gammas by the film, the residual activity I as a function of penetration depth x and diffusion time t is written (24)

$$I(x, t) = I_0[1 - \text{erf}(x/2\sqrt{Dt})]$$

where D is the diffusion coefficient (cm²/sec). At $x = 0$, at the surface, $I(0, t) = I_0$. This will be taken to be the initial intensity after diffusion and rinsing off excess.

Then

$$\frac{I}{I_0} = 1 - \text{erf}(x/2\sqrt{Dt})$$

$$= 1 - \text{erf}\, q$$

so that if there is a single diffusion process, and $D \neq f(t, \text{conc.})$, a plot of q *vs.* x gives a straight line passing through the origin of slope $\frac{1}{2}\sqrt{Dt}$, from which $D = x^2/4tq^2$ may be extracted. Note that in this plot a high q corresponds to a low residual activity, *i.e.*, a steep slope indicates a good sodium barrier. Fifty per cent of original activity corresponds to $q = 0.48$, and 10% to $q = 1.16$.

While this model is successful at high temperatures in vitreous silica (25), it is of questionable applicability at <700°C in thermally grown silica. It assumes a single-diffusion mechanism, a completely depletable source, no built-in electrical field, no diffusant reaching the far side of the medium, enough $^{23}Na^+$ or other cationic impurity present to exchange with the $^{22}Na^+$ to preserve over-all electroneutrality, etc. Probably none of these is true, and indeed experimentally a U-shaped sodium profile is found, with anomalously high Na^+ concentration at both film interfaces (26). Little has been reported on sodium diffusion profiles in deposited insulator films; it is not known whether they behave like bulk materials and follow the "residual activity" model outlined above.

Figure 9 is a q *vs.* x plot for SiON's of various compositions, etching and counting until about a third of the original film thickness has been etched away. The plots are not linear, and have a definite tendency to be steeper in the first 200Å, *i.e.*, as with grown silica, there is Na^+ holdup at the surface. These SiON's are not particularly good Na^+ barriers; none is as good as the best SiON ($n \sim 1.58$) from the NO-SiH_4 process, and some are not as good as freshly grown steam oxide. That the best is $n = 1.87$ might be predicted for a sample so close to pure nitride. Next best, however, are those compositions of $n \sim 1.6$, just what was found in the NO-SiH_4 system. Compositions of $n = 1.7$-1.8 are distinctly inferior, indicating no direct correlation between Na^+ barrier properties and nitrogen content or radiation resistance. And $n = 1.48$, which is essentially 850°C deposited oxide, is uniformly permeated with Na^+ throughout its thickness, which is hardly surprising.

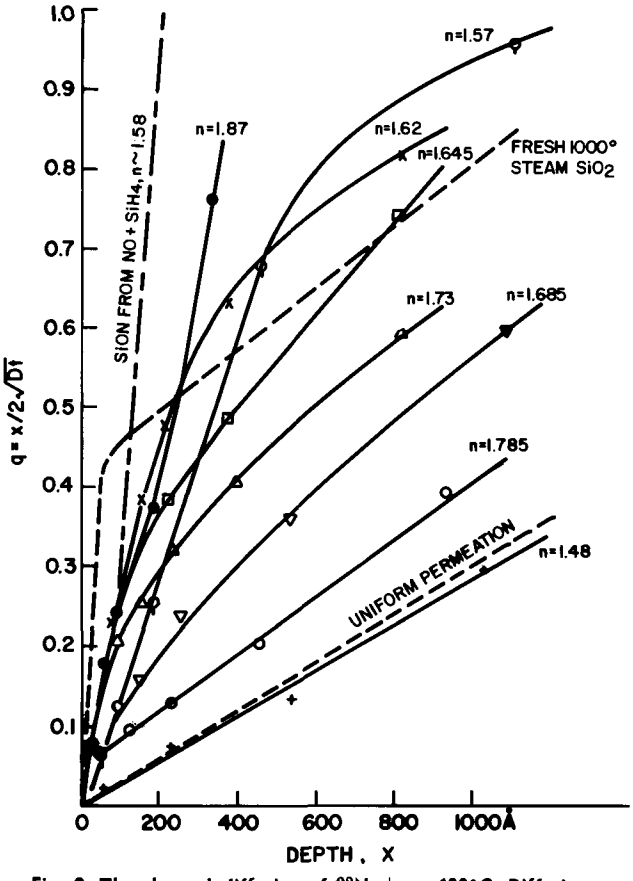

Fig. 9. The thermal diffusion of $^{22}Na^+$ at 600°C. Diffusion was for 22 hr in forming gas.

Autoradiographs of the samples after diffusion often show small "hot spots" surrounded by a depletion zone, or, less often, the exact reverse. The pattern of these spots was usually replicated in the other wafer of the diffusion sandwich; also, the pattern was still present after etching away a third of the film. There is a strong suspicion that there are certain areas of the surface which for some reason attract and tightly hold Na^+. Upon heating to 600°C, nearby Na^+ migrates rapidly over the surface to these sinks, and subsequently diffuses into the film, here as elsewhere.

Sodium ion drift under bias has been investigated mostly for radiation-hard SiON's *i.e.*, $n \sim 1.77$. This is a region of poor resistance to diffusion at 600°C; nevertheless, no unequivocal example of ionic drift under B-T aging at ≤300°C has been found. In other experiments, $^{22}Na^+$ contaminated SiON surfaces were covered by evaporated Al electrodes and attempts were made to drift in the sodium for 2 hr at 160°C and 1.6×10^6 V/cm. After removal of the Al and rinsing the surfaces no radioactivity remained, indicating no penetration into the film. Such tests emphasize a discrepancy between high-temperature diffusion and drift under B-T aging conditions; evidently the diffusion mechanisms can be markedly different.

Radiation resistance; cathodoluminescence spectra.—The remarkable resistance of compositions near Si_2ON_2 ($n \sim 1.77$) to ionizing radiation up to the megarad range has already been reported (2, 3), and will be summarized here only very briefly. The buildup of positive space charge in SiO_2 under irradiation is caused by hole-trapping, while the corresponding electrons, more mobile, drift out under bias. Apparently Si_2ON_2 has an approximate balance of deep traps for both holes and electrons, and an abundance of recombination centers. Under irradiation there is no bias instability at $<3 \times 10^5$ V/cm for negative bias (above which there is negative charge injection by the metal contact) and $<1.5 \times 10^6$ V/cm for positive bias. Interface-state density, after a hydrogen post-

deposition bake, is ~8 × 10^{10}/cm²-eV near midgap and rises only to ~10^{11} after irradiation with bias. Both bipolar and IGFET devices have been fabricated with SiON as the sole insulator, and much improved radiation resistance over devices using SiO_2 has been demonstrated.

Cathodoluminescence spectra have been taken on a series of six samples ranging from deposited oxide through SiON to deposited nitride. In Fig. 10 the light output of the various compositions is shown at two wavelengths: the C peak, 450 nm, which is the major output in SiO_2 films, and the B peak, ~365 nm, which is present in steam-grown oxide but not in dry O_2 oxide (16). The C peak is the strongest seen in deposited oxide (SiH_4 + NO), but it is weaker than in steam oxide, which is in turn weaker than in dry oxide. Figure 10 shows that as soon as nitrogen is introduced into the film the light output drops, and the B peak becomes the major one. Luminescence is at a minimum at $n = 1.77$, the radiation-resistant composition. At a high n it rises again, but silicon nitride gives essentially no signal. One additional findng to be kept in mind in studying Fig. 10 is that the electron-beam radiation annihilates the B peak in a few seconds, and it takes 1 min to sweep the spectrum from 200 to 600 nm.

Electrical properties.—Most of the electrical evaluation of SiON has been on films of $n = 1.72$-1.80, the radiation-resistant composition. In general, there are no surprises; SiON has properties intermediate between those of SiO_2 and Si_3N_4. For example, the 1 MHz dielectric constants for 850°C deposited materials are: SiO_2 ($n = 1.46$), 3.8; SiON ($n = 1.78$), 6.4; Si_3N_4 ($n = 1.98$), 8.0. Again, SiON shows roughly one order of magnitude higher d-c conductivity than SiO_2, but not the high quasi-stable, nonohmic conductivity of Si_3N_4 at > 10^6 V/cm.

For MIS evaluation, 2500-3000Å SiON was deposited on ~5 ohm-cm n- and p-type epitaxial Si layers on <0.01 ohm-cm <111> substrates. When the silicon was cleaned in the conventional way, *i.e.*, with a procedure in which the last steps are HF, water rinse, and spin dry, the fixed charge N_{FC} was 2-3 × 10^{12}/cm², the n-type invariably giving the lower figure. The interface-state density N_{ss} was very high, probably in the high 10^{12}/cm²-eV range.

Because of the persistently high N_{FC}, the aging behavior of SiON on HF treated Si was not studied in detail. The C-V curve is, however, fairly stable, and can be scanned repeatedly to ±2 × 10^6 V/cm with shifts of less than 0.5V, in contrast to the large "hysteresis loops" usually seen with silicon nitride. Holding the sample at 300°C for 24 hr with no bias does not affect the curve.

Deposition of SiON over ~100Å of thermal silica, results in more useful MIS properties. N_{FC} is now ~6 × 10^{11} (on n-type) to 10^{12} (on p-type). N_{ss} is still high, but may be reduced to ~2 × 10^{10}/cm²-eV near midgap by several hours of hydrogen bake at 500°C. These samples of SiON over thin silica have been aged at 300°C and ~1.6 × 10^6 V/cm for 24-64 hr. Slow drifts of V_{FB} of 3-4V in the nonionic direction occurred. Intervening silica layers >100Å do not further reduce N_{FC}. On the few samples of <100> Si tried, N_{FC} was somewhat lower.

The most useful procedure of all for control of SiON MIS properties is treatment of the Si before deposition with a mixture of aqueous ammonia and hydrogen peroxide. This procedure, first used to influence N_{FC} of reactively sputtered SiO_2 (29), works equally well on all CVD insulators we have tried (SiO_2, SiON, Si_3N_4). Its effect is to reduce measured V_{FB}, to an extent apparently determined by the pH of the solution. HNO_3-H_2O_2 has little effect, but NH_4OH-H_2O_2 of pH = 9 reduces N_{FC} by ~2 × 10^{12}. In other words, V_{FB}'s of the order of −20 for 2000Å films can be shifted to zero or even a few volts positive. After the peroxide treatment, N_{ss} is still high, but again a 500°C H_2 bake for several hours reduces it to <10^{11} near midgap, and without effect on the N_{FC} shift. Bias-temperature aging for 24 hr at 300°C and 10^6 V/cm typically produces a slow drift in the nonionic direction of ~3V (ΔN_{FC} ~5 × 10^{11}/cm²) which is proportional to log time. Quite probably a sizable part of this represents the development of higher N_{ss}.

No bias drifts in the ionic direction have been observed on any SiON sample, with the exception of one which had received a 900°C H_2 bake. This latter treatment was abandoned as soon as it was discovered that N_{ss} could be reduced, albeit more slowly, at 500°C without introducing protonic instability.

Representative MIS results are summarized in Fig. 11.

Discussion

The SiH_4-NO-NH_3 system evidently will produce good amorphous insulating films whose composition may be controlled readily and may be varied anywhere between SiO_2 and Si_3N_4. Over the range SiO_2 to about $Si_3O_3N_2$ ($n \sim 1.62$) the even simpler NO-SiH_4 process will serve, and no advantage is known for adding NH_3 to make these compositions. NH_3 is essential for the nitrogen-rich end of the scale. However, microprobe analyses, spectra, etch rates, and stress

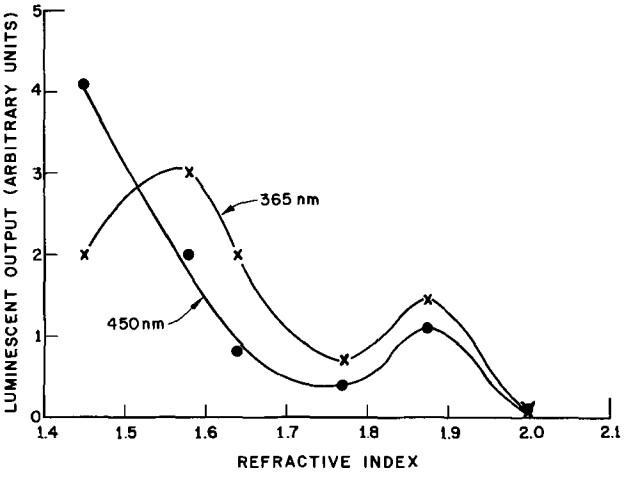

Fig. 10. Cathodoluminescence of SiON's from the SiH_4-NO-NH_3 system; 7 kV electrons.

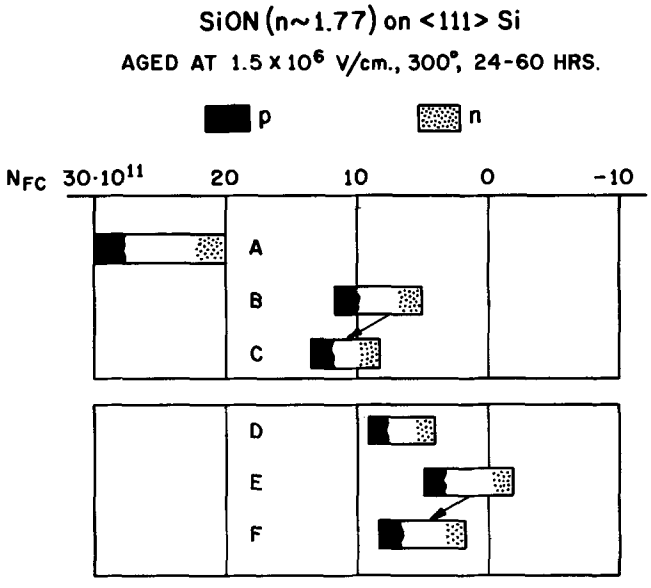

Fig. 11. Summary of typical MIS behavior. A = as deposited on Si with cleaning procedure ending with aqueous HF, rinse, and dry. B = deposited over 100Å of thermal silica. C = B, after negative bias-temperature aging. D = as deposited on Si with cleaning procedure ending with 4% aqueous H_2O_2 + NH_3, pH = 8. E = same, pH = 9. F = E, after negative bias-temperature aging.

determinations all provide evidence that these latter SiON's are not exactly Si^{+4}, O^{-2}, N^{-3} polymers, that their properties reflect this departure, and that there is a significant difference in bonding structure in the products of the two CVD reactions. The discontinuities in the etch rate and film-stress curves are particularly noticeable.

We propose that in SiON's made with ammonia roughly one nitrogen in three is bonded to only two other atoms (Si or O) instead of three. Some or all these "divalent" nitrogens may also have hydrogen atoms attached. This hydrogen would not be detected by the electron probe and would have scarcely any effect on the weight per cent of each component determined.

The probe could hardly distinguish between $Si_{1.85}ON_2$ [38 atomic per cent (a/o) Si] and $Si_{1.85}ON_2H_{0.7}$, but some of their properties may be quite different. The presence of bound hydrogen in pyrolytic silicon nitride was pointed out by Watanabe (18), and a trace of N-H in SiON has also been reported (8). The source of the hydrogen is undoubtedly the ammonia; SiON's from NO-SiH_4 show at the most only traces of OH or NH stretching vibrations in the i.r. spectrum. The refractive index curve is the same for SiON's made with or without ammonia, but sensitivity would be poor because of the low atomic refraction of hydrogen.

The infrared spectrum can detect differences not only in the skeletal vibrations but in the weak 3360-90 cm^{-1} and 1200 cm^{-1} absorptions. These are consistent with the presence of —N(H)—. Marchand *et al.* (19), reporting the spectra of organosilazanes, $R_3SiNHSiR_3$, give 3350-3380 cm^{-1} for ν (NH) and 1176-1179 cm^{-1} for γ (NH). Similarly, when NH_3 adsorbs on SiO_2, new bands at 3400 and 3320 cm^{-1} are attributed to asymmetric and symmetric N-H stretching (20). Pyrolytic Si_3N_4 invariably shows 3330-3350 cm^{-1} and 1200 cm^{-1}, strongest where the most ammonia was used in preparation, with parallel intensity changes, and much diminished by 1100°C baking (21). Si_3N_4 made in a d-c plasma has neither absorption. One note of caution in the picture is that SiO_2 also has a broad, weak absorption at 1200 cm^{-1} (22) which is probably a combination band. Nevertheless, the case remains strong for N-H binding in pyrolytic Si_3N_4 and SiON's made using ammonia. And these groups may well act as efficient electron traps, exactly as the OH sites of hydroxylated silica are believed to do (23).

It is likely that SiON's have some N-O bonding, but this vibration can have a very wide range of frequencies (30), and could easily be either inconspicuous or hidden among the combined Si-O and Si-N absorptions. Finally, the absence of detectable Si-H absorption does not mean no Si-H bonds; thermally grown silicas do not show Si-H in conventional transmission measurements either, but it is present at $\sim 5 \times 10^{19}/cm^3$ (31).

Structure and local stoichiometric anomalies very likely influence diffusion of sodium ion at 600°C also, but speculation on mechanism must await more detailed study; even the case for SiO_2 is not understood at this temperature, since it appears to follow a combination of at least two mechanisms (24). Although SiON is a deposited film, and therefore not formed by the diffusion of charged species through the growing film, the Na^+ profile follows no simple model. Like thermal silica, there is surface holdup, as though there were a surface zone in which the diffusion coefficient was considerably lower. The $n = 1.48$ sample, which is virtually a deposited oxide, is an exception; it is so permeable that after 22 hr the Na^+ is uniformly distributed throughout its thickness. The fact that the $n \sim 1.6$ SiON is the best barrier, regardless of which process is used, is mysterious, especially since that from NO + SiH_4 is much better than that from the process including NH_3.

Concern about the thermal diffusion of Na^+ through SiON becomes academic, however, in the face of its impermeability to bias-aided Na^+ drift at 300°C, a condition of greater pertinence to device operation. At least at $n = 1.7$-1.8, no test has shown any net ionic drift at all, or any penetration of radiosodium. The barrier lowering by the field is more than enough to compensate for the difference in temperatures in the two tests if the same diffusion mechanism were involved. We conclude that two different trapping centers for Na^+ may exist, or that ion charge neutralization phenomena may be quite different with bias-aided drift. At any rate, it seems there is no necessary correlation between a thermal diffusion test and B-T aging behavior of the film on Si; the latter should be a better approximation to real use. We believe that SiON's of substantial nitrogen content are good sodium barriers under conditions pertinent to device testing and operation.

Autoradiograph hot spots are not believed to be decorated pinholes, or areas of different composition, since electron-microprobe analyses (twelve per sample, analyzing a 2μ spot) have never shown such anomalies. SiON MIS capacitors seldom break down or show other evidence of weak spots in the dielectric. Pure Si_3N_4 also shows hot spots, although often they are removed by 100Å or so of etching. Hot spots are sometimes seen even in carefully prepared steam-grown silica. Finally there is the observation that these concentrations of sodium glass etch more slowly than the surrounding film. We think the evidence is best explained by areas of inchoate crystallinity of the film. Sodium ion would accelerate this devitrification.

The cathodoluminescence experiments have added some provocative data to that already known for silica, but the structural features responsible for behavior under irradiation are still unknown. In thermal silica the B peak (365 nm) emanates mostly from the outer part of the film and is destroyed by continued exposure; the larger C peak (450 nm) is concentrated near the Si-SiO_2 interface, its intensity varies inversely with the OH content, it is created by radiation, and is associated with positive space charge buildup (16). We can now add that as soon as nitrogen is introduced (or is it N-H?) the B peak begins to predominate over the C peak, and at the radiation-resistant composition both are at a minimum. While a large number of recombination centers are required for our picture of radiation hardness, this recombination is without luminescence, at least in the 200-600 nm range. Finally, silicon nitride itself gives practically no luminescent signal. An atom-scale model accounting for all these phenomena has yet to be proposed.

The high surface charge observed when SiON is deposited on conventionally cleaned Si is common for vapor-deposited insulators, especially silica, in the absence of special pre- or post-deposition treatments. The difference in N_{FC} with substrate type has been seen also in deposited silica (27) and Al_2O_3 (28); since the V_{FB} difference is several volts as against a work function difference of 0.6V, it is not understood.

The ammoniacal H_2O_2 treatment of the silicon before deposition yields more attractive properties, *i.e.*, low N_{FC} and, with hydrogen baking, $N_{ss} < 10^{11}$. Whatever the mechanism, the treatment acts as though it introduces into the native Si oxide negative charge which survives the 850°C deposition conditions. This oxide, typically ~10Å thick on a freshly cleaned surface, is not significantly thickened by the peroxide treatment; ellipsometer measurements have shown increases of only 2-3Å. Furthermore, the N_{FC} difference between Si types is preserved: both types shift the same amount.

The potential uses of SiON films evolve directly from the properties they possess that other insulators do not. So far SiON of $n \sim 1.76$ is unmatched for resistance to ionizing radiation under bias. The stress-free composition would be useful for unusually thick films, or thinned down or otherwise fragile substrates. SiON deposited on HF cleaned Si, with its stable, high negative V_{FB}, may be useful as insulator in closely spaced diode arrays, as in the Picturephone® camera tube. SiON, $n = 1.7$-1.8, on surface-treated Si, looks promising as a B-T stable, HF etchable, deposited insulator highly resistant to Na^+ drift, with low, and adjustable, surface charge and low fast state densities. Finally, the close adjustment and control of composition available at any stage during deposition permits adjustment of etch rate, and thus the contour of a window. If one wanted a steep-sided or even vertical window, say, for very precise delineation of diffusion or ion implantation, he could use slow-etching, high-nitrogen SiON graded down to silica, and etch with HF. A more common profile, a beveled-edge window for metalization, could be etched out with oxygen-rich SiON over silica, or N-rich SiON graded down into O-rich SiON and using H_3PO_4 etch. Such shapes can be cut with present technology, for example using deposited silica over thermal silica, but an extra operation is usually required, or an extra photoresist step if the profile is terraced. The resistance of oxynitride to Na^+ drift is a further bonus.

Conclusion

Silane, nitric oxide, and ammonia, diluted with nitrogen, react at the surface of a substrate at ~850°C to chemically vapor deposit a clear, adherent, thin-film insulator which is a Si, O, N polymer containing also some H bound to the N. The O:N ratio of this material is readily controllable over the entire range between SiO_2 and Si_3N_4. Its H content is believed to make this oxynitride somewhat different in structure from that from the NO-SiH_4 reaction, and this difference is detectable in several of its properties. Oxynitride composition may be most easily inferred from the refractive index. The composition near Si_2ON_2, $n \sim 1.76$, has been most carefully studied, since this film is radiation hard, a barrier to Na^+ drift under bias, and quite stable to bias-temperature aging as an MIS dielectric. For good characteristics in the latter test the silicon substrate must be pretreated with ammoniacal H_2O_2; then the V_{FB} will be close to zero, and the interface-state density $<10^{11}/cm^2$-eV after hydrogen baking. These treatments do not degrade any of the other properties of the SiON.

Acknowledgments

We acknowledge many helpful discussions with Paul F. Schmidt on the MIS properties of SiON. Much of the sodium drift data are his. The cathodoluminescence measurements were done by J. P. Mitchell of the Whippany, New Jersey, laboratories. Electron-microprobe analyses were done by D. R. Wonsidler.

Manuscript submitted May 22, 1972; revised manuscript received Oct. 20, 1972. This was paper 89 presented at the Washington, D.C., Meeting of the Society, May 9-13, 1971.

Any discussion of this paper will appear in a Discussion Section to be published in the December 1973 JOURNAL.

REFERENCES

1. C. M. Drum and M. J. Rand, *J. Appl. Phys.*, **39**, 4458 (1968).
2. P. F. Schmidt, M. J. Rand, J. P. Mitchell, and J. D. Ashner, *IEEE Trans. Nucl. Sci.*, **NS-16 (6)**, 211 (1969).
3. P. F. Schmidt and J. D. Ashner, *ibid.*, **NS-17 (6)**, 11 (1970).
4. M. J. Rand, U.S. Patent 3,558,348 (1971); *This Journal*, **115**, 194C (1968).
5. N. C. Tombs, F. A. Sewall, Jr., and J. J. Comer, *ibid.*, **116**, 862 (1969); N. C. Tombs, U.S. Patent 3,422,321 (1969).
6. Ferranti, Limited, Annual Report on Research Project RP1-55, AD 827049 (1967).
7. T. L. Chu, J. R. Szedon, and C. H. Lee, *This Journal*, **115**, 318 (1968).
8. D. M. Brown, P. V. Gray, F. K. Heumann, H. R. Philipp, and E. A. Taft, *ibid.*, **115**, 311 (1968); F. K. Heumann, D. M. Brown, and E. Mets, *ibid.*, **115**, 99 (1968).
9. Y. I. Kol'tsov, N. G. Kol'tsov, G. I. Zhuravlev, and I. V. Korobov, *Izv. Akad. Nauk SSSR, Neorgan. Materialy*, **7**, 521 (1971).
10. R. I. Frank and W. L. Moberg, *This Journal*, **117**, 524 (1970).
11. S. M. Hu and L. V. Gregor, *This Journal*, **114**, 826 (1967).
12. J. F. Roberts, C. A. Clark, and A. C. Dumbri, *Rev. Sci. Instr.*, **41**, 247 (1970).
13. J. W. Colby, *Advan. X-Ray Anal.*, **11**, 287 (1968).
14. E. A. Corl and H. Wimpfheimer, *Solid-State Electron.*, **7**, 755 (1964); F. Reizman, *J. Appl. Phys.*, **36**, 3804 (1965).
15. C. M. Drum, *Rev. Sci. Instr.*, **40**, 853 (1969).
16. J. P. Mitchell, "Radiation Effects on Interceptor Electronics," Vol. II of report on Weapon Effects Studies for Advanced Ballistic Missile Defense Agency under Contract DAHC-60-69-C-0008, Bell Telephone Laboratories (1970).
17. M. Kuhn, *Solid-State Electron.*, **13**, 873 (1970).
18. Y. Watanabe, *Japan. J. Appl. Phys.*, **7**, 960 (1968).
19. A. Marchand, M. Forel, F. Metras, and J. Valade, *J. Chim. Phys.*, **61**, 343 (1964).
20. M. L. Hair, "Infrared Spectroscopy in Surface Chemistry," p. 102, Marcel Dekker, Inc., New York (1967).
21. M. J. Rand, Unpublished results.
22. J. Bock and G-J. Su, *J. Am. Ceram. Soc.*, **53**, 69 (1970).
23. W. Ehrenberg, V. B. Gutan, and L. K. Vodopyanov, *Brit. J. Appl. Phys.*, **17**, 63 (1966).
24. G. H. Frischat and H. J. Oel, *Z. Angew. Phys.*, **20**, 195 (1966); G. H. Frischat, *J. Am. Ceram. Soc.*, **51**, 528 (1968).
25. G. H. Frischat, *Phys. Chem. Glasses*, **11**, 25 (1970); *Z. Angew. Phys.*, **25**, 163 (1968); *Glastech. Ber.*, **42**, 351 (1969).
26. See, for example, G. L. Holmberg, A. B. Kuper, and F. D. Miraldi, *This Journal*, **117**, 677 (1970); F. M. Fowkes and T. E. Burgess, *Surface Sci.*, **13**, 184 (1969); J. F. Osborne, G. B. Larrabee, and V. Harrap, *Anal. Chem.*, **39**, 1144 (1967).
27. M. J. Rand, Unpublished work.
28. L. P. Adda, Private communication.
29. S. Iwauchi and T. Tanaka, *Japan. J. Appl. Phys.*, **7**, 1193 (1968).
30. See, for example, K. Nakamoto, "Infrared Spectra of Inorganic and Coordination Compounds," p. 298, John Wiley & Sons, New York (1963).
31. K. H. Beckmann and N. J. Harrick, *This Journal*, **118**, 614 (1971).

Preparation of Vacuum-Deposited Films of Rubidium Silver Iodide

John H. Kennedy,* Fred Chen,* and James Hunter

Department of Chemistry, University of California, Santa Barbara, California 93106

ABSTRACT

Vacuum-deposited thin films of $RbAg_4I_5$ have been prepared exhibiting conductivities of 0.25 ohm-cm^{-1} at 25°C and an activation energy of 2.3 kcal/mole. The purest films of $RbAg_4I_5$ were produced when the evaporation source composition was 83-85 mole per cent (m/o) AgI.

Electrolytic cells were prepared of the type $Ag/RbAg_4I_5/Au$ and were studied by cyclic voltammetry with a silver reference electrode and as coulometers. Cells could be cycled electrochemically over 1000 times, but coalescence of $RbAg_4I_5$ films eventually led to loss of e ctrode contact. Degradation was accelerated when the cells were exposed to humid air.

Techniques for vacuum deposition of thin films have advanced greatly in recent years as evidenced by extensive reviews on the subject by Behrndt (1) and Neugebauer (2). Although the characteristics of metallic films such as gold and silver are well known, films of materials which can serve as solid electrolytes have not been extensively investigated. Silver halide thin films have been prepared (3), and a thin-film electrolytic coulometer using AgBr as the electrolyte has been reported (4). It is a natural extension of this work to attempt the preparation of $RbAg_4I_5$ films, although this complex compound owes its stability to its crystal lattice, and therefore, evaporation could lead to decomposition. Takahashi *et al.* (5) have reported the existence of $RbAg_4I_5$ films, but we report here additional details on the preparation and electrochemical properties of $RbAg_4I_5$ thin films.

Experimental

Preparation of $RbAg_4I_5$ evaporation source material.—A RbI (Alfa Inorganics) and AgI powder mixture [83-85 mole per cent (m/o) AgI] was placed in an alumina crucible, and the crucible was placed inside a three-neck flask. AgI was obtained from precipitation by mixing together aqueous solutions of 1M $AgNO_3$ and 1M KI. The three-neck flask was flushed with dry nitrogen gas for several minutes and then evacuated ($<40\mu$ pressure). While under vacuum the mixture was heated at a rate of 10°C/min, until it reached 450°C. The mixture melt had an orange color at 450°C. After heating at 450°C for about 1 hr and after bubbling had stopped, the sample was cooled slowly, and a light yellow solid was obtained. The source material was not removed from the crucible since the same crucible was used during vacuum evaporation. The crucible and source material were stored over silica gel until used.

Preparation of $RbAg_4I_5$ films.—The alumina crucible with the $RbAg_4I_5$ source material was placed inside a tungsten crucible heater. The pressure of the chamber was then lowered to about 1×10^{-6} Torr. The temperature of the sample was increased slowly until it started to melt around 250°C. Ten minutes after the source material had completely melted, the source temperature was increased to 350°C at a rate of 5°C/min. Bubbling by the melt usually stopped within 5 min, and the temperature of the melt was then increased to 500°C. The shutter protecting the substrate from spattering was removed and deposition on the substrate proceeded. The pressure of the chamber during deposition was about 4×10^{-4} Torr, and the average deposition rate was about 1.6×10^3 Å/min.

* Electrochemical Society Active Member.

Key words: rubidium silver iodide, thin films, coulometers, vacuum deposition, solid electrolyte conductivity.

Preparation of thin-film electrolytic cells.—The configuration of the electrolytic cells has already been described in a previous paper (4). A metallic film, usually gold, was deposited first on a clean glass slide. The gold film was about 1000Å thick. The electrolyte film was deposited next with a thickness of 80,000-200,000Å. Finally, another metallic film, about 1000Å thick, was deposited on top of the electrolyte film. If a silver film was used as the second metallic film of the cells, care was taken to ensure that the deposition chamber was perfectly clean before depositing silver, otherwise the deposited silver film was tarnished quite readily by any residual oxidizing gas in the evaporation chamber.

Electrolytic cells with a Ag reference electrode were prepared in the same manner, but instead of using the electrolyte mask of 12 cells per slide, a 6 double-cell electrolyte mask was used. The reference electrode was prepared by electroplating one of the two gold electrodes in the cell with 15 or more monolayers of silver.

Vacuum deposition equipment.—Fairchild Instruments vacuum deposition equipment was used to prepare all thin films. The lowest pressure obtainable with this equipment was 1×10^{-7} Torr. A high nickel content, stainless steel sheet was wrapped around the interior of the bell jar, and a dry ice-acetone trap was installed between the diffusion and mechanical pumps. The substrate was located about 12 in. above the evaporation source material while a stainless steel shutter was placed about 8 in. above the source. A Sloan Technology Corporation Ommi II system, with a deposition monitor and an SCR power controller, was used to monitor (*i*) the initiation of evaporation, (*ii*) the approximate film thickness during deposition, and (*iii*) the rate of deposition.

X-ray diffraction equipment.—X-ray diffraction studies were made with a Philips Electronics x-ray diffraction unit with CuK_α radiation. A Philips 52572 scintillation counter with chart recorder was used for the x-ray diffractometer measurements.

Electrochemical equipment.—A General Radio Incorporated 1650A impedance bridge with a 0.5V rms, 1 kHz a-c signal was used for resistance measurements. A Wavetek voltage-controlled generator was attached to the impedance bridge for resistance measurements at frequencies other than 1 kHz. A Harrison 6112A d-c power supply was used for residual current determinations. A Beckman Instruments Electroscan 30 was used for cyclic voltammetry. A Bissett-Berman Corporation E-Cell Digital Coulometer was used for constant current-charging of cells and for those experiments designated as constant current readouts. A Bissett-Berman Corporation EDR-300 E-Cell Digital Coulometer was used for pulse charge and dis-

Table I. Calculated vapor pressures of AgI and RbI

T °C	p_{RbI} (Torr)	p_{AgI} (Torr)
425	1.8×10^{-4}	6.3×10^{-5}
450	3.6×10^{-4}	1.6×10^{-4}
475	1.1×10^{-3}	3.8×10^{-4}
500	2.6×10^{-3}	8.6×10^{-4}
525	5.6×10^{-3}	1.8×10^{-3}
550	1.1×10^{-2}	3.8×10^{-3}

charge of cells. The unit was modified to deliver pulses of 1 μcoulomb in place of the normal 100 μcoulombs. Two Hewlett-Packard 412A VTVM's attached to a Hewlett-Packard 7100B strip-chart recorder with 17501 plug-ins were used for measuring the potentials of the cell electrodes *vs.* a reference during the charge and strip cycles.

An Associated Testing Laboratories SW-5101 environmental chamber was used for temperatures other than ambient.

Results and Discussion

Evaporation of AgI and RbI mixtures.—Since $RbAg_4I_5$ owes its stability to crystal-lattice energy, and especially an entropy effect from the random distribution of silver ions, evaporation should lead to a mixture of RbI and AgI. The preparation of $RbAg_4I_5$ films will depend on the ability of RbI and AgI vapors to condense on a substrate in this crystalline form. Obviously, it is imperative that the condensing vapors maintain a stoichiometric ratio of 4AgI:RbI. It is more important to consider the condensation process stoichiometry than the stoichiometry of the source material. Appropriate source composition can be calculated from the vapor pressures of AgI and RbI.

The approximate vapor pressures for RbI and AgI in the temperature range used for vacuum deposition of $RbAg_4I_5$ can be calculated by extrapolating the equation (6)

$$\log_{10} p = (-0.2185\, A/T) + B$$

where T is temperature (°K), and A and B are constants. For RbI between 748° and 1304°C, $A = 38{,}072.3$ and $B = 8.174712$. For AgI between 820° and 1506°C, $A = 37{,}340.1$ and $B = 7.48857$. The calculated vapor pressures for RbI and AgI between the evaporation temperatures of 425° and 550°C are given in Table I.

Assuming ideal behavior for the vapor mixture of both evaporants, a 90-93 m/o of AgI in the AgI + RbI melt is needed in order to obtain an initial vapor pressure ratio of 1:4 (p_{RbI}/p_{AgI}) in the 425°-550°C temperature range. However, with the evaporation of 4AgI for every RbI, the melt would rapidly become richer in AgI, and excess AgI might start depositing on the substrate. When an initial 4AgI:RbI melt composition was used, an initial vapor pressure was obtained which was rich in RbI. The films produced in this way, although containing primarily $RbAg_4I_5$, had very low conductivity. To compromise between an initial excess of RbI, or a later excess of AgI, melt compositions between 83 and 85 m/o AgI were chosen which resulted in a slight initial excess of RbI, but did not lead to a large excess of AgI later in the deposition.

X-ray diffraction data for $RbAg_4I_5$ films are given in Table II. Several features of the $RbAg_4I_5$ films can be noted from the data: (*i*) the tendency for the $RbAg_4I_5$ films to deposit initially on gold along their (110) planes; (*ii*) the preferred orientation along the (110) plane increased with increasing substrate temperature at least up to 70°C; (*iii*) the films reoriented toward their (110) planes by annealing them at 150°C; (*iv*) randomness in orientation increased with increasing film thickness; and (*v*) no diffraction peaks corresponding to RbI, Rb_2AgI_3, and AgI were observed.

Takahashi *et al.* (5) have reported x-ray diffraction results for $RbAg_4I_5$ films deposited on glass between 25° and 152°C. Unfortunately they did not report the intensity, if any was observed, of the peak at 11.3° corresponding to the (110) plane. They did report that x-ray diffraction patterns of films deposited at 101°C or higher showed a peak around 24.5°, and the intensity of this peak increased with increasing substrate temperature. However, this peak can be assigned to Rb_2AgI_3 (5).

Although it has been reported that $RbAg_4I_5$ decomposes slowly into AgI and Rb_2AgI_3 in the presence of humidity at temperatures below 27°C, x-ray diffraction lines corresponding to AgI and Rb_2AgI_3 were not detected for films deposited at 20°C. The detection limit for x-ray diffraction is about 1%, so that traces of AgI and Rb_2AgI_3 could still be present. It is very likely that they were indeed present since electrolytic cells deposited at 20°C usually had resistances 100 times higher than those deposited at 35°C.

Electrochemical characteristics.—The resistances of Ag/$RbAg_4I_5$/Au and Au/$RbAg_4I_5$/Au thin-film cells were found to be frequency dependent as shown in Fig. 1. Some of this frequency dependence and high resistances, compared to pressed powder samples, can be attributed to the existence of silver iodide (or gold iodide) at the interface of the electrode that was on top of the $RbAg_4I_5$ film. During the deposition of $RbAg_4I_5$, some of the AgI in the source boat decomposed liberating iodine gas, and part of the iodine gas might have been trapped at the $RbAg_4I_5$ film surface which could then react with the electrode material forming the iodides. The decomposition of silver halides during evaporation with liberation of halogen gas has also been observed by Vouros (3); and tarnish of the electrode deposited on top of $RbAg_4I_5$ samples has been observed by Breitweiser (7) and Scrosati (8).

The conductivity of our $RbAg_4I_5$ films was determined by using a variation of Takahashi's method. Our cell consisted of 12 equally spaced gold electrodes with a $RbAg_4I_5$ film of known thickness deposited at 40°C on top. A plot of the resistance between two gold electrodes *vs.* electrode separation distance is

Table II. X-ray diffraction data for $RbAg_4I_5$ films

Sample designation	(1)	(2)	(3)	(4)	(5)	(6)	(7)	(8)	(9)
Substrate	gold	gold	gold	gold	gold	gold	gold	gold	powder
Film thickness, kA	1.25	8.3	20	8.3	2.5	5.2	5.2	100	
Deposition temperature, °C	20	20	20	20	70	70	70	40	
Special conditions				Sample (2) annealed at 150°C for 20 hr			Sample (6) annealed at 150°C for 6 hr		Reference material
(hkl) planes I/I_o									
(110)	100	99	36	100	100	100	100	31	w
(221)	47	65	39	53	52	38	31	40	ms
(310)	—	—	2	—	—	—	2	8	vw
(311)	62	100	100	48	—	53	44	100	s
(222)	15	20	17	9	10	8	7	9	w
(411, 330)	10	14	21	—	7	8	4	20	w
(332)	12	10	10	3	—	6	4	7	w
(422)	10	10	12	8	—	6	4	7	mw
(430)	12	29	18	27	12	31	24	18	mw
(510, 431)	20	33	47	27	—	20	14	48	s
(511, 333)	—	4	6	—	—	—	—	5	vw
(520, 432)	12	25	22	16	—	11	9	19	m
(521)	—	16	16	7	7	6	4	17	mw
(441)	5	12	6	13	5	17	14	6	w
(522, 441)	5	10	6	9	7	7	6	6	w

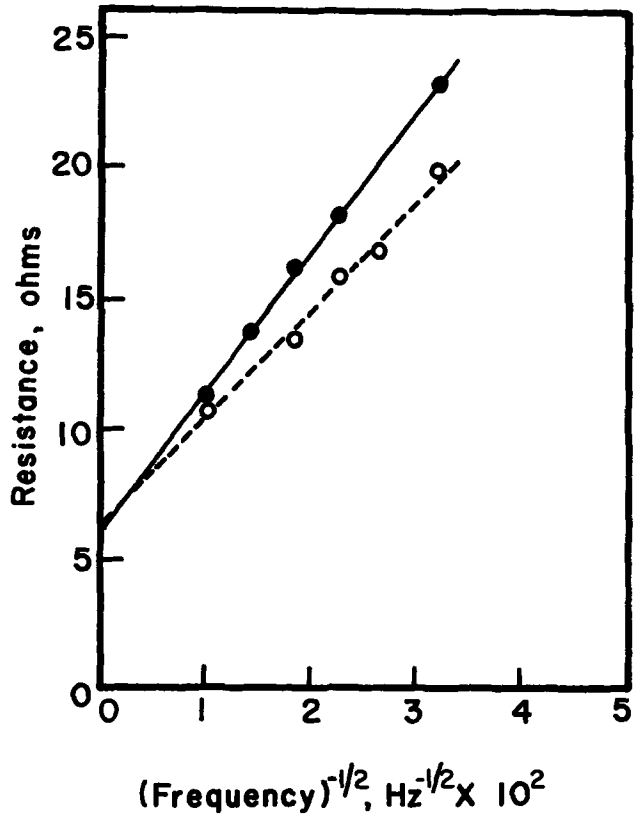

Fig. 1. Frequency dependence of $RbAg_4I_5$ thin-film resistance. ○, Au/$RbAg_4I_5$/Au; ●, Ag/$RbAg_4I_5$/Au.

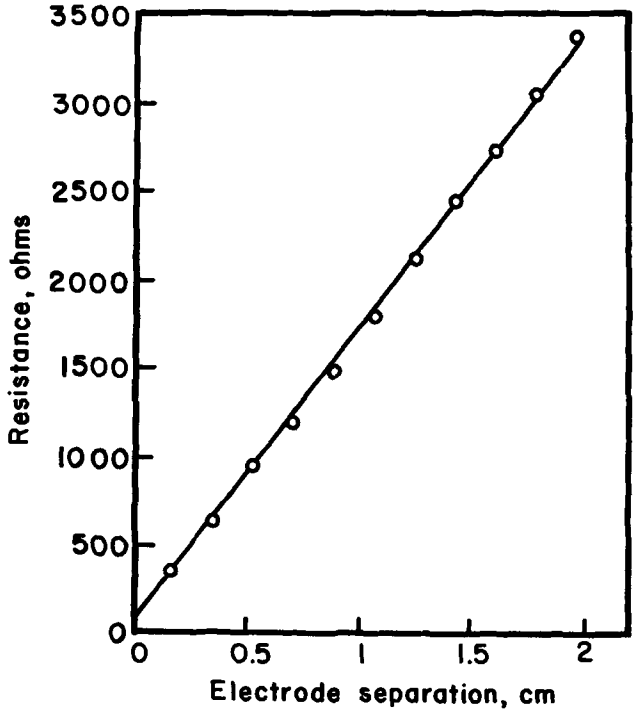

Fig. 2. Resistance of Au/$RbAg_4I_5$/Au thin-film cell as a function of electrode separation. Area of electrolyte path (film width × film thickness) is 2.67 x 10^{-3} cm^2.

shown in Fig. 2. In this way, no effects due to the top surface of the $RbAg_4I_5$ were encountered. The conductivity was calculated from the slope and found to be 0.25 ohm-cm^{-1}. This conductivity value is slightly higher than the value of 0.2 ohm-cm^{-1} reported by Takahashi (5) for films deposited at 25°C and compares closely with the conductivity of polycrystalline $RbAg_4I_5$ of 0.26 ohm-cm^{-1} (9). The measured resistance between two gold electrodes was also

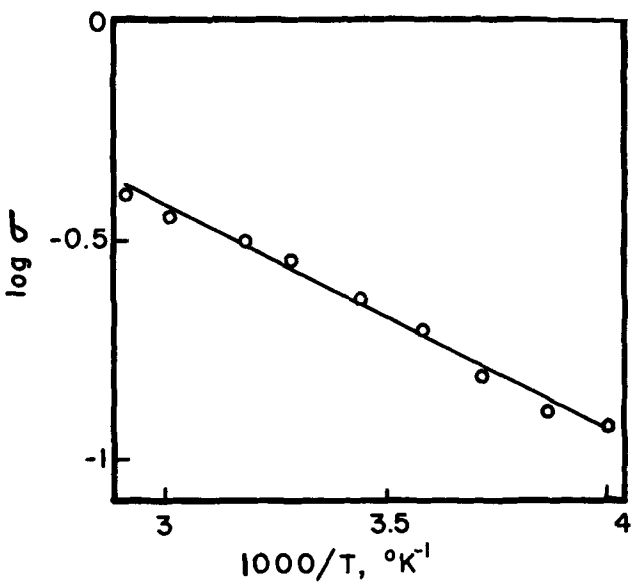

Fig. 3. Temperature dependence of $RbAg_4I_5$ thin-film conductivity determined from slope of Fig. 2.

found to be somewhat frequency dependent. However, by plotting the measured resistances as a function of electrode separation and assuming that the frequency dependency had about the same effect on all measured resistances, the portion of the resistance that was frequency dependent would only affect the intercept and not the slope.

The conductivity of $RbAg_4I_5$ films as a function of temperature is shown in Fig. 3. The activation energy for conduction was 2.3 kcal/mole. This value is about 0.6 kcal/mole higher than the activation energy reported for polycrystalline $RbAg_4I_5$ (9), but only 0.3 kcal/mole higher than the activation energy for Ag^+ tracer diffusion in $RbAg_4I_5$ (10).

Blocking electrode studies with the Ag/$RbAg_4I_5$/Au cells gave residual currents of <1 nA between 0.2 and 0.6V. Assuming that all the residual current was due to electronic current, the electronic conductivity calculated with Wagner's equation (11) was $<4 \times 10^{-10}$ ohm-cm^{-1}. Oxley (12) has reported that the electronic conductivity for polycrystalline $RbAg_4I_5$ to be $<10^{-11}$ ohm-cm^{-1}.

As with pressed powder samples (13), $RbAg_4I_5$ films were found to be sensitive to humidity. The resistance of film cells increased from a few ohms to over 1,000,000 ohms in less than 7 days when exposed to room atmosphere. The increase in cell resistance could be decreased by storing the cells over silica gel between 30° and 35°C. Even so, there was an initial increase of a few ohms during the first couple of days of storage as shown in Fig. 4. This increase in cell resistance can be attributed to coalescence of the $RbAg_4I_5$ film which made it lose contact with the electrode films. Usually, the base electrode film became detached from the glass slide when the $RbAg_4I_5$ film had completely coalesced. The initial film crystallites were less than 4μ in diameter, while some of the coalesced crystals were about 600μ long and 200μ wide with an undefined shape. Figure 5a is a photomicrograph (250X) of a $RbAg_4I_5$ film 150,000Å thick over glass and kept in the normal laboratory environment, taken 3 days after it was deposited, and it shows that coalescence had occurred at several points. Figure 5b is another photomicrograph (250X) which shows complete coalescence for a film 7 days old. As can be observed, the coalesced crystals' grain boundaries are very well defined.

Owens and Argue (13) reported that traces of AgI and Rb_2AgI_3 present in powdered $RbAg_4I_5$ samples can be eliminated by annealing $RbAg_4I_5$ pressed pellets at 160°C for several hours. However, during an-

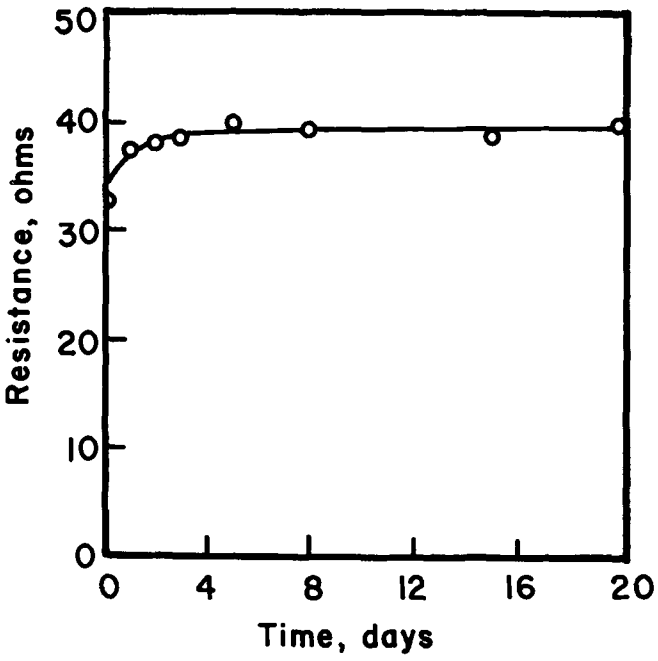

Fig. 4. Dependence of $Au/RbAg_4I_5/Au$ thin-film cell resistance (1 kHz) on storage time.

nealing of film cells at 160°C for several hours the gold electrode lost contact with the glass slide. The loss of contact was probably due to differences in thermal expansion between the gold film, the $RbAg_4I_5$ film, and the glass slide.

Cyclic voltammetry.—Cyclic voltammetry was used to examine the electrode reactions that took place on the gold electrode. The potential of the gold electrode was measured *vs.* a silver reference electrode. In general, one cathodic peak near 0.0V and two small anodic peaks near 0.05 and 0.2V were observed during the forward scan before the final cutoff, Fig. 6. Similar voltammograms were obtained during the succeeding cycles.

An initial applied potential of 0.0V *vs.* the Ag reference electrode caused a cathodic current from Ag^+ reduction since the silver activity at the gold electrode was lower than at the silver electrode. The anodic peak near 0.05V can be attributed to the oxidation of Ag which had been plated on the gold while the current was cathodic. The anodic peak near 0.2V was attributed to the oxidation of some trace impurity such as oxide or sulfide ions at the gold surface.

The final cutoff peak near 0.67V can be attributed to any of the reactions describing the oxidation of gold *vs.* iodide such as

Reaction	Potential calculated from $\Delta G°_f$
$RbAg_4I_5 \rightarrow RbI + 3AgI + Ag^+ + \frac{1}{2}I_2 + e^-$	$E° = 0.729$ *vs.* Ag
$2RbAg_4I_5 + Au \rightarrow Rb_2AgI_3 + 6AgI + Ag^+ + AuI + e^-$	$E° = 0.642$ *vs.* Ag
$RbAg_4I_5 + 4Au \rightarrow RbI + 4Ag^+ + 4AuI + 4e^-$	$E° = 0.665$ *vs.* Ag

It was interesting to note that the final cutoff peak started to rise around 0.45V. This was an important factor in selecting the voltage of 0.45V as the cutoff potential for timing with $RbAg_4I_5$ coulometers. Hull and Pilla (14) reported that iodine started to be liberated in AgI systems with platinum electrodes at 0.46V. During the reverse scan a small cathodic current was observed around 0.2V which can be attributed to reduction of iodine still present at the gold electrode.

Coulometry.—Coulometry of $Ag/RbAg_4I_5/Au$ cells was studied by techniques described previously (4). Accuracy of $RbAg_4I_5$ thin-film cell coulometers was determined for charges of 20-2500 μcoulombs. The results are tabulated in Table III. For constant current readouts, the cutoff voltage was 0.45V. The average error was the average of ten determinations. In general, higher deviations from the average error were observed for the first two determinations. The larger errors for the first few determinations have been attributed to the diffusion of silver along the grain boundaries into the gold electrodes (4).

The use of pulsing techniques during charge and strip cycles did not improve the timing accuracy of the coulometers, Table IIIb, but errors were not greater on initial determinations. A discussion of the pulsing technique has been made in a previous publication (4).

Pulsing techniques were also used to determine the charge storage capabilities of $RbAg_4I_5$ thin-film cells. A charge of 500-1000 μcoulombs was plated on the gold and allowed to stand for several days before stripping. Figure 7 shows that there was rapid loss of about 80 μcoulombs of charge during the first day, and then little additional loss. This can be explained again by the migration of silver into the gold electrode along the gold electrode grain boundaries with the gold electrode eventually becoming saturated. A similar

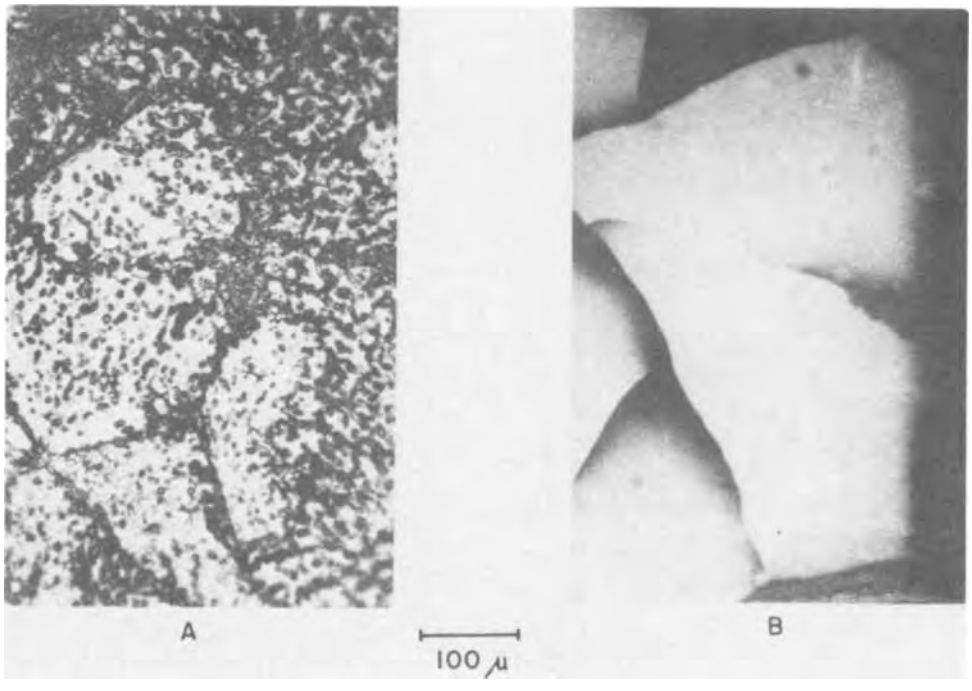

Fig. 5. Coalescence of $RbAg_4I_5$ films. (A) 150,000Å on glass after 3 days (250×); (B) 150,000Å on glass after 7 days (250×).

Table III. Timing accuracy for $RbAg_4I_5$ thin-film coulometers at 35°C

A. Constant current readout	Charge time, sec							
	20		50		100		250	
Current, μA	Avg error, %	Std dev, %	Avg error, %	Std dev, %	Avg error, %	Std dev, %	Avg error, %	Std dev, %
1.0	+28.4	0.5	+14.8	0.5	+7.9	0.7	+3.4	1.0
3.6	+1.0	0.4	+0.7	0.4	+0.3	0.1	+0.2	0.1
10.0	+0.5	0.1	+0.1	0.1	−0.1	0.1	−0.3	0.3

B. Pulse readout	Charge, μcoulombs							
	100		250		500		1000	
	Avg error, %	Std dev, %	Avg error, %	Std dev, %	Avg error, %	Std dev, %	Avg error, %	Std dev, %
	−4.0	0.8	−2.0	0.9	−0.7	0.2	−0.7	0.4

saturation value was found for AgBr thin-film cells. It was not surprising that the saturation values for both types of thin-film cells were about the same since they had essentially the same type of gold electrode.

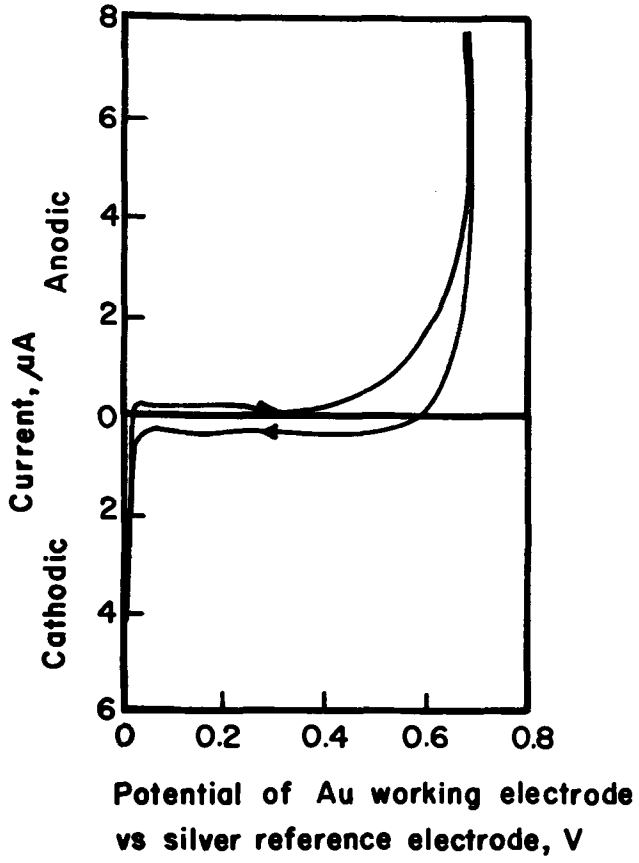

Fig. 6. Cyclic voltammogram of $RbAg_4I_5$ cell. Scan rate, 2 mV/sec

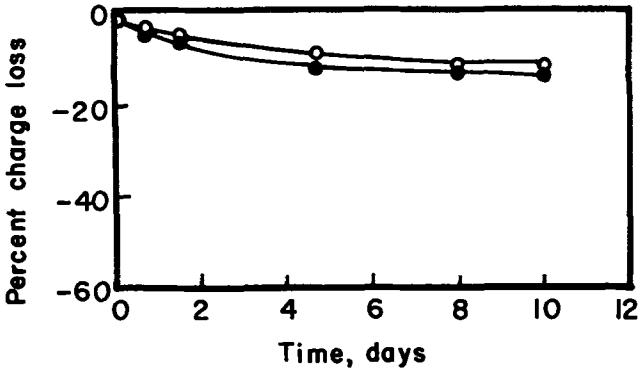

Fig. 7. Charge loss with storage of $RbAg_4I_5$ thin-film coulometers. Initial charge: ●, 500 μcoulombs; ○, 1000 μcoulombs.

Life of the cells was reasonably long considering the close electrode spacing. Some of the cells were cycled continuously with 200 μcoulombs of charge for more than 1000 cycles with no apparent damage. However, the cell life was limited by the coalescence of $RbAg_4I_5$ which can destroy the contact between the gold electrode and the $RbAg_4I_5$ film. Keeping the cells in a dry atmosphere is necessary if the cells are to be used for more than a few days.

Acknowledgment

The authors acknowledge financial support from PHS Research Grant, No. 1 R01 APO 1527-01, Office of Air Programs of EPA.

Manuscript submitted Aug. 28, 1972; revised manuscript received Nov. 16, 1972.

Any discussion of this paper will appear in a Discussion Section to be published in the December 1973 JOURNAL.

REFERENCES

1. K. H. Behrndt, "Techniques of Metal Research," Vol. 1, R. H. Bunshah, Editor, p. 1191, Interscience Publishers, Inc., New York (1968).
2. C. A. Neugebauer, "Proceedings Third International Vacuum Congress," Vol. 1, p. 29, Pergamon Press, New York (1966).
3. a) P. Vouros and J. I. Masters, *This Journal*, **116**, 880 (1969).
   b) J. I. Masters, P. Vouros, and P. Clune, U.S. Pat. 3,575,715, (1971).
   c) D. W. Pashley, *Proc. Phys. Soc.*, **65**, 33 (1952).
   d) J. F. Hamilton and L. E. Brady, *Surface Sci.*, **23**, 389 (1970).
   e) F. E. Swindells and W. R. Lanier, U.S. Pat. 3,547,700, (1970).
4. J. H. Kennedy and F. Chen, *This Journal*, **118**, 1043 (1971).
5. T. Takahashi, O. Yamamoto, and S. Ikeda, *J. Electrochem. Soc. Japan*, **44**, 796 (1971).
6. R. C. Weast, Editor, "Handbook of Chemistry and Physics," 52nd ed., p. D-171, Chemical Rubber Co., Cleveland (1971).
7. G. Breitweiser, Personal communication.
8. B. Scrosati, G. Germano, and G. Pistoia, *This Journal*, **118**, 86 (1971).
9. B. B. Owens and G. R. Argue, *ibid.*, **117**, 898 (1970).
10. G. G. Bentle, *J. Appl. Phys.*, **39**, 4036 (1968).
11. C. Wagner, *Z. Elektrochem.*, **60**, 4 (1956).
12. J. E. Oxley and B. B. Owens, "Power Sources 3: Res. Develop. Non-Mech. Elec. Power Sources, Proc. Int. Symp., 7th," 535 (1971).
13. G. R. Argue and B. B. Owens, *Science*, **157**, 308 (1967).
14. M. Hull and A. Pilla, *This Journal*, **118**, 72 (1971).

JOURNAL OF THE ELECTROCHEMICAL SOCIETY

ELECTROCHEMICAL SCIENCE AND TECHNOLOGY

APRIL 1973

The Anodic Dissolution of Copper in Flowing Sodium Chloride Solutions Between 25° and 175°C

A. L. Bacarella and J. C. Griess, Jr.*

Reactor Chemistry Division, Oak Ridge National Laboratory, Oak Ridge, Tennessee 37830

ABSTRACT

The anodic dissolution of copper in chloride solutions was studied under laboratory conditions up to 101°C and up to 175°C in a specially designed cell that could be flanged into a pump loop. Under all conditions the anodic polarization curves demonstrated Tafel behavior with slopes equal to 2.3 RT/F. The anodic process was under diffusion control with the primary dissolution product being $CuCl_2^-$; no evidence of solid corrosion products was found at the highest current densities employed. The anodic process was independent of pH and between 0.124 to 1.24M Cl^- depended on the square of the chloride ion concentration. Loop experiments showed that under fixed conditions the current density was proportional to the 0.8 power of flow velocity. A simple kinetic expression based on the Nernst equation and Fick's first law was derived which was in excellent agreement with the experimental results.

Copper and its alloys find extensive use in sea water, and over the years a great wealth of empirical data concerning the corrosion of these materials has accumulated. However there have been relatively few systematic studies of corrosion mechanisms of copper or its alloys in chloride media. Of those that have been reported most were conducted at temperatures below 100°C.

Lal and Thirsk (1) appear to have been the first to demonstrate that the anodic dissolution of copper in sodium chloride solutions exhibits pure concentration polarization and from 17° to 60°C showed that the anodic Tafel slope was equal to 2.3 RT/F. Hurlen (2) also showed the anodic polarization of copper to be under diffusion control. In addition he showed that the potential (E) at constant anodic current varied with chloride concentration according to the relationship

$$\frac{dE}{d \log (Cl^-)} = 2 \left(\frac{2.3\,RT}{F} \right)$$

at chloride concentrations up to about 1M but at higher chloride levels the coefficient was 3 rather than 2. Boden (3) carried out anodic polarizations of copper in sodium chloride solutions from 30° to 140°C. He observed Tafel slopes of approximately 60 mV/decade in the temperature range of 30°-100°C but at higher temperatures the slopes were 140-160 mV/decade. North and Pryor (4) exposed copper specimens to boiling 0.5M NaCl and concluded from their results that Cu_2O formed as a direct anodic corrosion product. More recently Taylor (5) using a ring-disk electrode demonstrated that copper anodically dissolves in 0.5M NaCl only by the generation of soluble cuprous ions over the range of 2.5 to 900 $\mu A/cm^2$. This latter result is consistent with the data of Lal and Thirsk (1) and Hurlen (2) since concentration polarization would not occur if Cu_2O were a direct corrosion product. Thermodynamic considerations at 25°C such as the solubility product of Cu_2O (6), the standard potential for the formation of Cu_2O (15), and the stability constant of the $CuCl_2^-$ complex ion (7) also indicate that in the range of the corrosion potentials of copper in sodium chloride solutions the *in situ* formation of Cu_2O should not occur.

In many distillation-type desalting plants copper alloys are exposed to salt-water solutions well above 100°C, and although their performance is generally satisfactory little is known about their corrosion mechanisms at higher temperatures. While pure copper is seldom used in desalting applications, an understanding of the mechanism of copper corrosion is essential if the mechanism of the corrosion of copper alloys is to be obtained. This paper presents the results of an electrochemical study of the kinetics of the anodic dissolution of copper. The results presented here duplicate to a minor extent the work of Lal and Thirsk (1) and Hurlen (2) but extend the temperature range to 175°C and include studies in flowing streams. In addition our analysis of the data has resulted in the derivation of a simple kinetic expression which is applicable over the entire temperature range.

Experimental

Electrochemical studies were conducted in two different types of cells: conventional laboratory glass cells and a cell mounted in a recirculating pump loop which was constructed of Hastelloy C. In the glass cell temperatures up to atmospheric boiling were investigated and in the loop temperatures were as high as 175°C. Zone-refined copper was used in the laboratory studies whereas standard electrical-conductor grade copper was used in the loop study. In the zone-refined material all metallic impurities were below the level of detection by emission spectrographic analysis. Based on the same method of analysis the electrical-conductor grade copper contained 300 ppm

* Electrochemical Society Active Member.

Key words: copper dissolution kinetics, high-temperature polarization curves, $CuCl_2^-$ ion, anodic concentration polarization, high-temperature polarization cell.

Ag, 90 ppm Fe, and 40 ppm Ni as the major impurities. In the studies described here no detectable difference between the two materials was apparent.

All solutions were prepared from reagent grade chemicals without further purification. In the laboratory studies the chemicals were dissolved in triply distilled water and for the loop studies deionized water with a specific resistivity of $> 10^6$ ohm-cm was the solvent. Again the quality of the solvent made no apparent difference. Solutions were saturated with the appropriate gas by sparging for several hours before use. In these systems the corrosion of copper is proportional to the oxygen concentration, but, since most of our measurements were made at potentials well above the corrosion potential, removal of the last traces of oxygen was not essential.

Both constant current and constant potential polarizations were carried out. All measurements were taken at steady state which was generally achieved within relatively few minutes after changing either the current or potential. An electronic potentiostat designed and built at Oak Ridge National Laboratory and an Anotrol Model 4700 potentiostat were used in these studies. Both instruments also included provisions for galvanostatic operation. In all cases currents were measured as potential drops across precision resistors with Keithley Model 600A battery-operated electrometers, the outputs of which were recorded with Hewlett-Packard Model 7100B dual channel recorders.

Some of the laboratory studies were carried out in a Pyrex glass cell similar to that described by Kelly (8). In these cases temperature control was ± 0.1°C of the specified value. However most of the laboratory experiments were performed in a 3-liter flask which had ground glass necks for admission of a test electrode, a polarizing electrode, a Haber-Luggin capillary probe, a tube for gas entry, a mercury thermoregulator, and a condenser. The condenser was equipped with a water-bubbler trap to prevent back diffusion of atmospheric oxygen. Heat was applied with an electric mantle activated by the mercury thermoregulator through an electronic relay assembly. In this larger flask temperatures were usually within a degree of the specified value. With both cells the potential of the test electrode was measured with reference to a saturated calomel electrode (SCE) in an external compartment at room temperature (~ 29°C) connected to the cell via the Haber-Luggin capillary. The test specimens were cut from 0.65 cm diameter rod stock and were 0.65-0.95 cm long. In both glass cells the electrodes were mounted on conventional Teflon holders and either platinum or graphite served as the polarizing electrode. Gentle stirring was provided by means of a magnetic stirrer in the bottom of the cell.

Polarizations in the Hastelloy C pump loop were carried out in a cell mounted in a bypass line of the loop. Figure 1 is a schematic drawing of the cell which consisted of a 1½-in. diameter schedule 80 titanium pipe with six welded fittings through which the electrodes were inserted. A heavy-walled Teflon tube with a 1-cm diameter flow channel fitted snugly inside the pipe section. The ends of the pipe and the caps (also titanium) were threaded, and flat Teflon gaskets prevented leakage between the liner and the caps. The cell was mounted in the bypass line with flanges (not shown in Fig. 1) attached to the caps.

Figure 2 shows the manner in which a specimen was mounted in the cell. The Teflon liner was drilled and threaded as shown and Teflon seal B was inserted. This seal was permanently bonded to the liner with Chemgrip (Chemplast Inc., Wayne, New Jersey). The specimen was pushed through the opening, and Teflon seal A was then slid over the specimen. Tightening the gland nut sealed the specimen in the vicinity of the junction of the two seals. The four graphite polarizing electrodes were mounted in nearly the same manner. The diameter of the graphite was 0.64 cm, and the ends were shaped so that they could be mounted flush with the inner surface of the Teflon liner. In contrast to the specimen mount, the liner was threaded throughout its thickness as was the graphite. Both the graphite and the lower Teflon seal were permanently bonded to the liner. Threaded into the short length of graphite was a 3-mm diameter copper wire so that the remainder of the assembly was identical to that shown in Fig. 2. During polarizations, the four graphite electrodes were connected in parallel. The reference electrode was in an external vessel and was connected to the cell by a salt bridge as described by Bacarella and Sutton (9). The end of the salt bridge extended into the flow channel and ended a short distance (1-2 mm) from the specimen. At the current densities used no IR corrections were necessary.

The specimens used in the loop were made from 3.2-mm diameter rods which were coated with epoxy cement (Epoxi-Patch, Hysol Division, Dexter Corporation, Olean, New York), and enclosed in a Teflon tube. The end of the rod to be inserted into the cell was ground flat so that the exposed surface area of the specimen was its cross sectional area, 0.08 cm^2. The surface of the test electrode was essentially flush with the Teflon liner.

The loop was constructed of Hastelloy C and a 25 gpm Hastelloy C pump driven by a variable speed motor circulated the solution. In these studies the flow rate of solution past the specimen was either 122 or 244 cm/sec (4 or 8 ft/sec). In all loop tests the solution was 1M NaCl with a *p*H between 6.3 and 7.0. The total volume of solution in the loop was 3.7 liters, and this was refreshed at the rate of 1 l/hr by means of a pulse pump and letdown valve. Loop pressure was maintained at about 200 psig in most cases. Heat was applied to the loop by electric heaters on the pipe

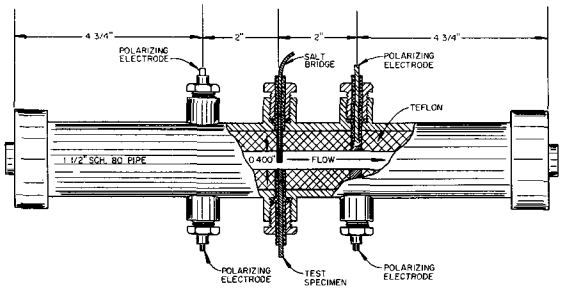

Fig. 1. Schematic drawing of the polarization cell used in high-temperature flowing solutions.

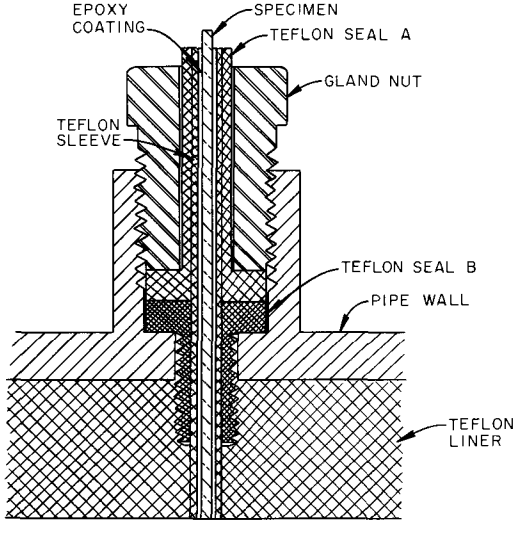

Fig. 2. Method of mounting test specimens in high-temperature polarization cell.

walls and the desired temperature was maintained within ± 2°C by a pneumatic controller operated from a thermocouple upstream from the cell.

In both the loop and laboratory experiments polarization curves were obtained by proceeding stepwise from the open-circuit potential in an anodic direction. However, reversing the polarization sequence retraced the same curve.

Experimental Results

A typical polarization curve for copper in deaerated 1.24M NaCl at 30°C is shown in Fig. 3. The anodic process consists of the oxidation of copper and has a Tafel slope of 60 mV/decade which corresponds to 2.3 *RT/F*. In this particular case the cathodic curve represents primarily the reduction of water to hydrogen, but at low current densities some reduction process which appeared to be diffusion limited can be detected. A future communication will discuss the cathodic behavior of copper in chloride solutions.

Anodic polarization curves obtained with zone-refined copper at different temperatures are shown in Fig. 4. All of these were obtained in 1.24M NaCl using glass equipment under conditions of constant stirring and moderate sparging with H_2 gas. In this figure

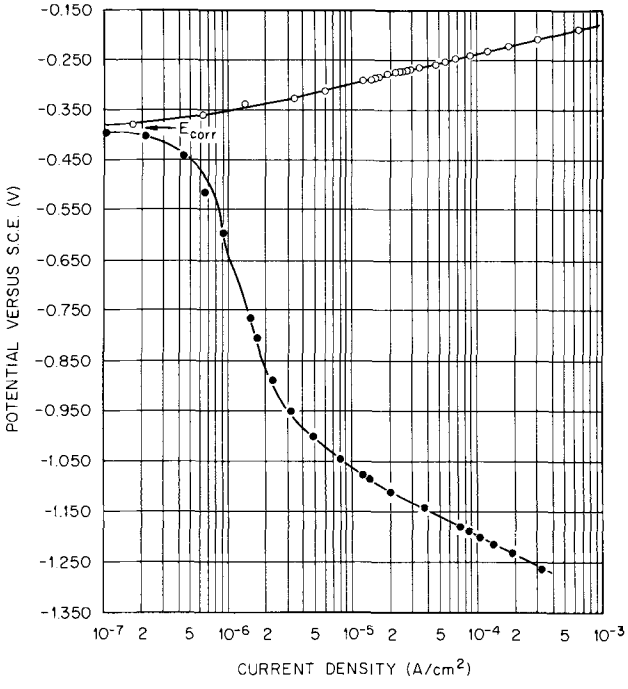

Fig. 3. Electrochemical polarization of copper in deaerated 1.24M NaCl at 30°C, pH = 5.4.

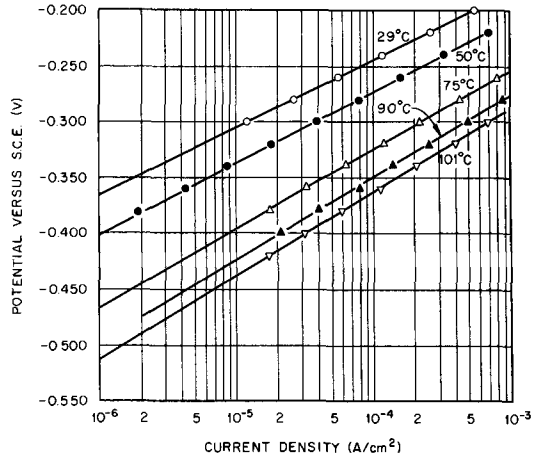

Fig. 4. Anodic polarization of copper in deaerated 1.24M NaCl at different temperatures.

only experimental data in the Tafel region are shown. Polarizations near the corrosion potential were difficult to interpret because contributions from unknown cathodic processes were included. For this reason corrosion potentials at a given temperature were not always reproducible. On the other hand, under constant conditions the polarization curves in the Tafel region were very reproducible and the slopes were equal to 2.3 *RT/F*.

Figure 5 shows anodic polarization curves obtained in 1.24M HCl (*p*H = 0.04) at 29° and 101°C. The dashed lines are those obtained in 1.24M NaCl (from Fig. 4). At 29°C the curve at *p*H = 6.4 is displaced about 13 mV in the anodic direction from the curve at *p*H = 0.04. At a fixed potential an increased dissolution rate in the acid solution might be inferred from these results, but the increase is only apparent and represents the difference in liquid junction potentials ($E_{j2} - E_{j1}$) where E_{j1} is the 1.24M NaCl || sat. KCl junction and E_{j2} is the 1.24M HCl || sat. KCl junction, both at 29°. Using the Henderson equation (10) these junction potentials were estimated to be about 14 mV for E_{j2} and about 1 mV for E_{j1} which accounts for the observed difference between the two curves and shows that the anodic dissolution process is independent of *p*H.

At 101°C the curve obtained at a *p*H of 6.4 is displaced anodically about 28 mV from the one at a *p*H 0.04. At the higher temperature thermal as well as liquid junction potentials existed in both cases. In all experiments described in this report the reference electrode (SCE) was located in a separate vessel at 29°C and was connected to the cell by a salt bridge filled with the particular test solution, so that the temperature of the liquid junction was always constant regardless of the cell temperature. Assuming the anodic dissolution rate to be independent of *p*H at 101°C as it was at 29°C, the difference between the thermal potentials for 1.24M NaCl and 1.24M HCl, both with a thermal gradient of 72°C, is approximately 15 mV. The data presented by Ikeda *et al.* (11) show that thermal potentials are much greater for HCl than for NaCl and most of the 15 mV difference must be due to the thermal potential developed in the 1.24M HCl bridge. Other polarization curves (not shown) were obtained in 1.24M Cl^- at *p*H = 2.8. In these cases the curves were usually within a few millivolts of those obtained in 1.24M NaCl (*p*H = 6.4) under the same conditions indicating that both liquid and thermal junction potentials were less significant than in the 1.24M HCl and within the range of experimental error. Thus in the treatment of the data both junction potentials were ignored except in the 1.24M HCl solution.

Figure 6 shows anodic polarization curves obtained over a greater temperature range in the pump loop. The electrolyte was 1.0M NaCl at a *p*H of 6.3 and the solution flowed past the specimen at either 122 or 244 cm/sec. The procedure consisted of obtaining the

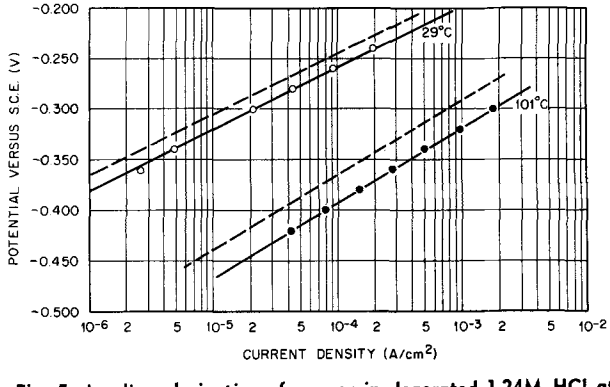

Fig. 5. Anodic polarization of copper in deaerated 1.24M HCl at 29° and 101°C. (The dashed lines are those shown in Fig. 4 for 1.24M NaCl at the same temperatures.)

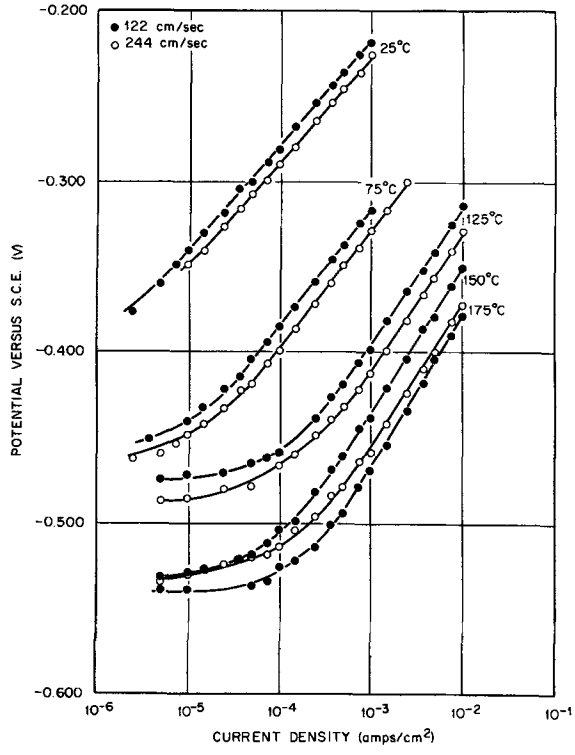

Fig. 6. Anodic polarization curves obtained with copper in flowing deaerated 1.0M NaCl.

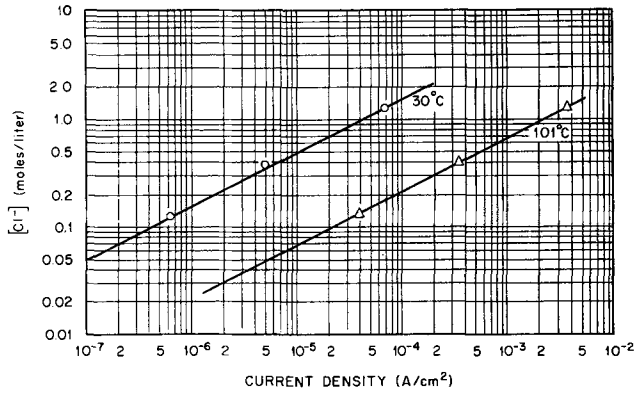

Fig. 7. Anodic current densities at $E = -0.250$V *vs.* SCE as a function of chloride ion concentration at 30° and 101°C.

curve at the lowest temperature and the lower flow rate, then disconnecting the cell and increasing the flow rate. After the electrode reached a steady-state open-circuit potential, the curve at the higher flow rate was obtained. The temperature was then raised to the next higher level and the procedure was repeated. Thus all of the curves shown in Fig. 6 were obtained with the same electrode without removing it from the loop. At the highest temperature it was not possible to control the temperature at 8 ft/sec in the existing experimental equipment.

Another specimen was run under conditions identical to the previous run except that the only curve obtained at 244 cm/sec was at 75°C. The agreement between the two specimens was excellent as illustrated in Table I, where the coefficients of the equations for the anodic Tafel lines are shown for both specimens. These values were obtained from least squares analyses of the data points in the Tafel region. At the 95% confidence level all Tafel slopes (A in Table I) were within ± 2% of the reported values. It is evident from the table that the slopes of the Tafel lines are very close to 2.3 RT/F (0.059, 0.069, 0.079, 0.084, and 0.089 V/decade at 25°, 75°, 125°, 150°, and 175°C, respectively).

Although the slopes of the lines at the same temperature were nearly the same at 122 and 244 cm/sec (turbulent flow in both cases), there were slight differences. Hence a determination of the increase in current on going from 122 to 244 cm/sec depends slightly on the potential. At an arbitrarily chosen potential of −0.400V *vs.* SCE the ratios of current at 244 cm/sec to that at 122 cm/sec are 1.5, 1.7, 1.5, and 1.8 at 25°, 75°, 125°, and 150°C, respectively (Fig. 6), and 1.9 for the duplicate specimen at 75°C. The average of these values is 1.7. Since in turbulent flow the Reynolds number (Re) is directly proportional to velocity at a given temperature, the current increased as $Re^{0.8}$.

Other experiments in the loop showed that the reproducibility of the data with regard to the relative positions of the anodic polarization curves at different temperatures was very good, but the absolute values from specimen to specimen varied by as much as 10 to 15 mV. As the data in Fig. 6 clearly indicate the anodic process is diffusion controlled, and slight variations in mounting the specimen in the loop with resultant variation in fluid turbulence probably accounted for the slight differences observed in the curves for different specimens.

The effect of chloride ion concentration on the anodic dissolution current density of copper is shown in Fig. 7. The temperature was either 30° or 101°C, the electrolyte was neutral, deaerated sodium chloride at concentrations of 0.124, 0.372, and 1.24M, and the electrode potential was −0.250V *vs.* SCE. These data were obtained in glass equipment under constant stirring conditions. The slope of the line through the data points, $d \log i/d \log (Cl^-)$, is 2.0 indicating that copper dissolves as the $CuCl_2^-$ ion.

The value of the standard redox potential for the half reaction

$$Cu + 2Cl^- = CuCl_2^- + e$$

is −0.050V *vs.* SCE at 25°C (12), but its temperature coefficient was not available. Similarly activities of the ions involved are not known. In order to determine the temperature coefficient the following experiment was performed at 30° and 101°C. A copper electrode was anodically polarized at a low constant current in deaerated 1.24M NaCl for various lengths of time, and after each interval the open-circuit potential of the copper electrode was measured. From the coulombs of current passed and the volume of solution the con-

Table I. Coefficients for the equations of the Tafel lines, $E = A \log i + B$, for the polarization curves shown in Fig. 6 and for similar curves obtained with a duplicate specimen under the same conditions

	Tafel slope (A)				Intercept (B)			
	122 cm/sec		244 cm/sec		122 cm/sec		244 cm/sec	
Temp, °C	Fig. 6	Duplicate	Fig. 6	Duplicate	Fig. 6	Duplicate	Fig. 6	Duplicate
25	0.062	0.063	0.062		−0.032	−0.032	−0.042	
75	0.067	0.070	0.069	0.070	−0.114	−0.099	−0.121	−0.120
125	0.081	0.077	0.082		−0.154	−0.175	−0.165	
150	0.085	0.087*	0.082		−0.182	−0.206*	−0.209	
175	0.089				−0.200			

* Actual temperature was 156°C.

Table II. Apparent E^0 values for the half cell reaction $Cu + 2Cl^- = CuCl_2^- + e^-$ obtained in 1.24M NaCl at 30° and 101°C

Temperature, °C	$(CuCl_2^-)$, M	Potential, V vs. SCE	Apparent E^0, V vs. SCE
30	3.17×10^{-5}	−0.319	−0.038
30	9.43×10^{-5}	−0.293	−0.040
30	2.71×10^{-4}	−0.268	−0.043
101	2.61×10^{-5}	−0.424	−0.071
101	5.51×10^{-5}	−0.400	−0.071
101	1.05×10^{-4}	−0.380	−0.072
101	1.98×10^{-4}	−0.360	−0.072

centration of $CuCl_2^-$ was calculated. Using the Nernst equation, apparent E^0 values were calculated using concentrations instead of activities. Table II shows the results obtained at both temperatures.

Reasonably constant values of E^0 were obtained, averaging −0.040V *vs.* SCE at 30°C and −0.071V at 101°C. Assuming that the ratio of activity coefficients of $CuCl_2^-$ and Cl^- does not change significantly with temperature, $dE^0/dT = -0.4$ mV/deg; this value was used in all subsequent calculations.

Discussion

Our results, as well as those of other investigators, show that the anodic dissolution of copper in chloride solutions is diffusion rather than activation controlled. The reactions of importance are

$$Cu + 2Cl^- = (CuCl_2^-)_i + e^- \quad [1]$$

and

$$(CuCl_2^-)_i \xrightarrow{\text{rds}} (CuCl_2^-)_s \quad [2]$$

where the subscripts i and s refer to concentrations at the copper-solution interface and bulk solution, respectively. The rate determining step [2] is the diffusion transport of $CuCl_2^-$ from the interface to the bulk solution. The first step [1], the oxidation of Cu to $CuCl_2^-$ is assumed to be in equilibrium for which the Nernst equation

$$E = E^0 + \frac{RT}{\mathbf{F}} \ln \frac{(CuCl_2^-)_i}{(Cl^-)^2} \quad [3]$$

is applicable and from which $(CuCl_2^-)_i$ is obtained

$$(CuCl_2^-)_i = (Cl^-)^2 \exp \frac{\mathbf{F}(E - E^0)}{RT} \quad [4]$$

Substituting $(CuCl_2^-)_i$ into the rate-determining diffusion transport equation (Fick's first law)

$$i = \frac{z\mathbf{F}D\,(CuCl_2^-)_i}{\delta} \quad [5]$$

leads to the rate expression

$$i = \frac{z\mathbf{F}D}{\delta} (Cl^-)^2 \exp \frac{\mathbf{F}(E - E^0)}{RT} \quad [6]$$

In Eq. [6] z, the charge on the species undergoing mass transport $(CuCl_2^-)$, is 1; D is the diffusion coefficient for $CuCl_2^-$ (cm^2/sec); δ is the diffusion layer thickness (cm), and the concentration of $(CuCl_2^-)_i$ is much greater than $(CuCl_2^-)_s$ and is expressed in moles/cm^3. Since the diffusion coefficient is temperature dependent

$$D = D_0 \exp \frac{-\Delta H_D^*}{RT} \quad [7]$$

Equation [6] can be rewritten to include the apparent activation energy for diffusion transport, ΔH_D^*

$$i = \frac{z\mathbf{F}D_0}{\delta} (Cl^-)^2 \exp \frac{-\Delta H_D^*}{RT} \exp \frac{\mathbf{F}(E - E^0)}{RT} \quad [8]$$

In the above expression, E^0, the standard redox potential for Eq. [1] is temperature dependent. Defining overvoltage, η, as $E - E^0$ and expressing Eq. [8] in logarithmic form yields

$$\log i = \log \frac{z\mathbf{F}D_0}{\delta} + 2 \log (Cl^-) - \frac{\Delta H_D^*}{2.3\,RT} + \frac{\mathbf{F}\eta}{2.3\,RT} \quad [9]$$

From this equation the functional dependence of the current ($\log i$) on overvoltage, chloride ion concentration, and temperature is obtained

$$\left(\frac{\partial \log i}{\partial \eta}\right)_{T,Cl^-} = \frac{\mathbf{F}}{2.3\,RT} \quad [10]$$

$$\left(\frac{\partial \log i}{\partial \log (Cl^-)}\right)_{T,\eta} = 2.0 \quad [11]$$

$$-2.3R \left[\frac{\partial \log i}{\partial \frac{1}{T}}\right]_{Cl^-,\eta} = \Delta H^* = \Delta H_D^* - \mathbf{F}\eta \quad [12]$$

The validity of Eq. [10], the inverse Tafel slope, is shown by the data in Fig. 4-6 and Table I up to 175°C. Lal and Thirsk (1) showed a similar result up to 60°C, and Hurlen's data (2) at 25°C were consistent with this relationship. The validity of Eq. [11] is demonstrated by Fig. 7 which agrees with the results of Hurlen (2). Although Lal and Thirsk (1) also investigated the dependence of the anodic process on chloride ion concentration, their concern was with the effect of chloride concentration on the deposition of CuCl on the electrode surface.

Equation [12] relates the temperature dependence of the anodic process to the apparent activation energy of diffusion transport and the electrical work, $\mathbf{F}\eta$. Inherent in Eq. [12] is the assumption that the diffusion layer thickness, δ, is independent of temperature. In the case of the laboratory studies no estimate of the effect of temperature on δ could be made, and δ was assumed to be constant. In the case of the loop experiments the hydrodynamic conditions were better defined and the effect of temperature on δ could be approximated. At either 122 or 244 cm/sec the solution was highly turbulent and for such conditions it has been shown (13) that

$$\delta \propto Re^{-0.9}\,Pr^{-1/3} \quad [13]$$

where Re is the Reynolds number (the product of the diameter of the flow channel and the velocity divided by the kinematic viscosity) and Pr is the Prandtl number (the kinematic viscosity divided by the diffusion coefficient of $CuCl_2^-$ in this case). The average of our data indicated that the current density depended on the 0.8 power of Re which is in reasonable agreement with Eq. [13] since the current density is inversely proportional to δ. The values of all the terms involved in Eq. [13] are known (14) as a function of temperature except the diffusion coefficient for $CuCl_2^-$. Table III shows the values of the Reynolds and Prandtl numbers under the test conditions at 122 cm/sec, and the value of $Re^{-0.9}\,Pr^{-1/3}$ assuming the diffusion coefficient of $CuCl_2^-$ is 10^{-5} cm^2/sec at 25°C and at assumed activation energies of 3.5, 4.5, and 5.5

Table III. Values of Reynolds and Prandtl numbers and the product $(Re^{-0.9}\,Pr^{-1/3})$ using an assumed value of 10^{-5} cm^2/sec for the diffusion coefficient of $CuCl_2^-$ at 25°C and activation energies of 3.5, 4.5, and 5.5 kcal/mole

Temp, °C	Reynolds No.* × 10^{-4}	Prandtl No. × 10^3	$(Re^{-0.9}\,Pr^{-1/3} \times 10^5)$* 3.5 kcal	4.5 kcal	5.5 kcal
25	1.21	9.63D^{-1}	2.14	2.14	2.14
75	2.72	4.28D^{-1}	1.80	1.95	2.11
125	4.43	2.63D^{-1}	1.78	1.94	2.24
150	5.20	2.24D^{-1}	1.68	1.98	2.34
175	5.70	2.04D^{-1}	1.72	2.08	2.51

* At a velocity of 122 cm/sec.

kcal/mole. Under these conditions δ is not very sensitive to temperature at all of the assumed activation energies but the minimum spread over the temperature range is at an activation energy of 4.5 kcal/mole. Based on the above analysis δ was considered independent of temperature in the treatment of the data obtained from the loop.

Figure 8 is a plot of the log of the dissolution rate (A/cm^2) *vs.* the reciprocal temperature (°K^{-1}) for the data presented in Table I. The upper three curves were obtained at a constant η of −0.450V whereas the lower three were obtained at $\eta = 0$. E^0 is −0.050V *vs.* SCE at 25°C and dE^0/dT, was assumed to be −0.4 mV/deg over the entire temperature range. The current densities were determined from the equations for the Tafel lines, $E = \eta + E^0 = A \log i + B$ with the values of A and B taken from Table I. From the least squares slopes of the upper three curves apparent activation energies of 14.6, 15.4, and 15.0 kcal/mole were calculated for two experiments at 122 cm/sec and the one at 244 cm/sec, respectively. The agreement among these three sets of data is excellent.

It is obvious from Eq. [12] that the above activation energies are composed of the electrical work, $\mathbf{F}\eta$, and the activation energy for diffusion transport of $CuCl_2^-$. The electrical work at $\eta = -0.450$V is equivalent to −10.4 kcal/mole (23.05 kcal/mole·volt × −0.450 volt) which when subtracted from the above values results in apparent activation energies of 4.2, 5.0, and 4.6 kcal/mole for the diffusion process. The same result should be obtained from similar plots at $\eta = 0$, that is at the standard redox potential. The lower three curves shown in Fig. 8 were obtained in this manner, and from the slopes obtained by least squares analyses apparent activation energies of 6.2, 5.1, and 7.0 kcal/mole were obtained. These latter values are subject to greater error than the former values because of the larger extrapolations of the polarization curves. This is reflected in the relatively large scatter of the data points around the lower three curves in Fig. 8.

Figure 9 shows similar plots of the data obtained from the laboratory studies at pH values of 0.04, 2.8, and 6.4 (Fig. 4 and 5). The current densities were determined at $\eta = -0.450$V and $\eta = 0$ in the same way as for the loop data, and δ was assumed to be independent of temperature. At a pH of 0.04 only two temperatures were studied, 30° and 101°C. At 101°C a correction of 15 mV was made because of the thermal potential as previously discussed, and at both temperatures a liquid junction potential correction of 13 mV was applied. A single line is drawn through all the points at each overvoltage. The slope of the top curve ($\eta = -0.450$V) corresponds to an activation energy of 14.7 kcal/mole; subtracting 10.4 kcal/mole ($\mathbf{F}\eta$) results in an activation energy of 4.3 kcal/mole for the diffusion transport of $CuCl_2^-$. The apparent activation energy obtained from the slope of the lower curve ($\eta = 0$) is 4.3 kcal/mole.

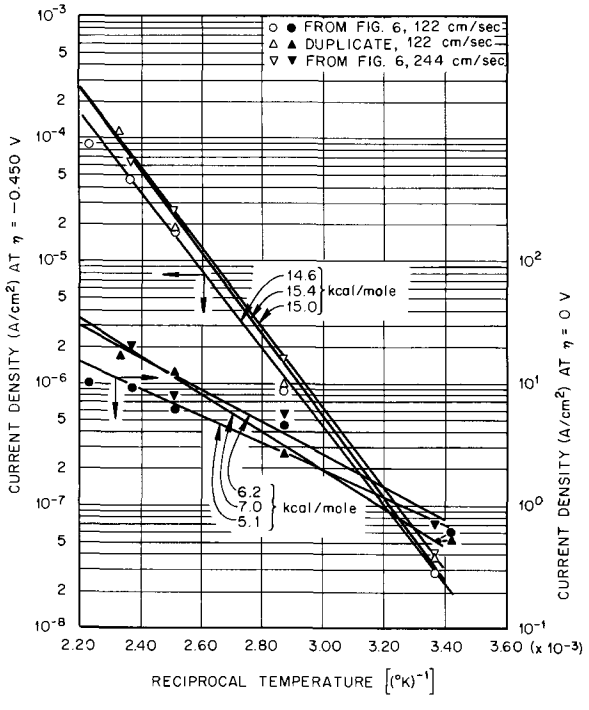

Fig. 8. Arrhenius-type plot showing the temperature dependence of current density at $\eta = -0.450$V and 0V based on data obtained from loop experiments.

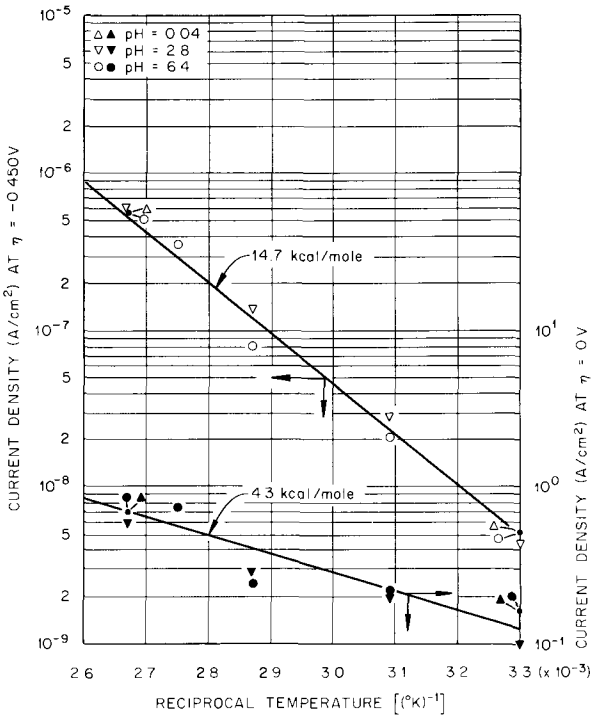

Fig. 9. Arrhenius-type plots showing the temperature dependence of current density at $\eta = -0.450$V and 0V based on data obtained under laboratory conditions.

Figures 8 and 9 show the consistency of the data from the loop and laboratory experiments. At $\eta = -0.450$V the average apparent activation energy for the anodic dissolution of copper (both loop and laboratory data) was 14.9 kcal/mole. Subtracting the electrical work results in an apparent activation energy for diffusion transport of $CuCl_2^-$ of 4.5 kcal/mole which is a reasonable value; a higher average value of 5.7 kcal/mole was obtained at $\eta = 0$, but this value is less reliable because of the large extrapolations involved. Considering the assumptions made, such as the absence of junction potential (except as noted), the constancy of the temperature coefficient of E^0 and the temperature independence of δ, and considering the standard errors inherent in obtaining polarization data, the agreement between the results and the proposed kinetic expressions is excellent.

Although the mechanism postulated above indicates $CuCl_2^-$ as the primary corrosion product, unreported data obtained by us have shown that thin films of Cu_2O developed on copper specimens exposed to flowing deaerated neutral sodium chloride solutions at 100°C and above. A similar observation has been reported in static tests (4). In view of the mechanism postulated the reason for the presence of Cu_2O on the freely corroding copper may be explained as follows.

The standard potential for the reaction

$$Cu_2O + H_2O + 2e = 2Cu + 2\,OH^-$$

is −0.602V *vs.* SCE at 25°C and the temperature coefficient is −0.445 mV/deg (15). Thus at 100°C in

neutral solution the potential of formation of Cu_2O is -0.117V *vs.* SCE. In deaerated sodium chloride solution the corrosion potential is well below this value. Therefore Cu_2O could not be a primary corrosion product under these conditions.

A possible explanation for the presence of Cu_2O is hydrolysis of $CuCl_2^-$ within the diffusion layer. The equilibrium constant for the reaction

$$CuCl_2^- = Cu^+ + 2Cl^-$$

is 2.8×10^{-6} at 25°C (7), and the solubility product of Cu_2O is 1.25×10^{-15} at the same temperature (6). Using Fick's first law (Eq. [5]) and assuming a corrosion rate of 10 miles per year (mpy) it can be shown that Cu_2O should begin to precipitate at a *p*H of about 9.2 in 1M NaCl. In the above calculation δ and D for $CuCl_2^-$ were assumed to be 3×10^{-3} cm and 10^{-5} cm^2/sec, respectively. No evidence of Cu_2O was observed in the polarization experiments at current densities considerably greater than that corresponding to 10 mpy, but this observation was made on an electrode on which the cathodic processes were suppressed. On a freely corroding copper surface both anodic and cathodic processes occur and both $CuCl_2^-$ and OH^- are produced at equivalent concentrations. Using the same assumptions as above and $D_{OH^-} = 5 \times 10^{-5}$ cm^2/sec, it can be shown that at a corrosion rate of 20 mpy the product of Cu^+ and OH^- at the specimen-solution interface would be approximately equal to the solubility product of Cu_2O. Thus even at 25°C the appearance of Cu_2O on corrosion specimens could occur if the corrosion rate is as high as 20 mpy. If either the dissociation constant for $CuCl_2^-$ becomes larger or the solubility product of Cu_2O becomes smaller as the temperature increases, Cu_2O could appear at correspondingly lower corrosion rates. Unfortunately values of both constants are not known at temperatures other than 25°C.

Summary

The anodic dissolution of copper in 1M chloride solution proceeded by the formation of $CuCl_2^-$ at temperatures as high as 175°C, the highest temperature investigated. Anodic polarization curves demonstrated Tafel behavior with slopes equal to 2.3 RT/F. The anodic process was under diffusion rather than activation control, and at chloride concentrations between 0.124 and 1.24M depended on the square of the chloride ion concentration. Within the range of current densities investigated the process was independent of *p*H. At a fixed anodic potential in the Tafel region with other conditions constant, the dissolution rate (current density) increased as about the 0.8 power of the Reynolds number. Using Fick's first law and the Nernst equation a simple kinetic expression was derived which was in agreement with experimental results.

Acknowledgment

The authors would like to acknowledge J. F. Winesette and A. L. Sutton for help in conducting the experiments and to Dr. R. E. Meyer for useful discussion concerning interpretation of the data. This work was sponsored by the Office of Saline Water, United States Department of the Interior and the Atomic Energy Commission under contract with Union Carbide Corporation.

Manuscript received July 14, 1972; revised manuscript received Nov. 8, 1972.

Any discussion of this paper will appear in a Discussion Section to be published in the December 1973 JOURNAL.

REFERENCES

1. H. Lal and H. R. Thirsk, *J. Chem. Soc.*, 2638 (1953).
2. T. Hurlen, *Acta Chem. Scand*, **15**, 1231, 1239 (1961).
3. P. J. Boden, *Corrosion Sci.*, **11**, 353 (1971).
4. R. F. North and M. J. Pryor, *ibid.*, **10**, 297 (1970).
5. A. H. Taylor, *This Journal*, **118**, 854 (1971).
6. W. Feitknecht, *Helv. Chim. Acta*, **27**, 771 (1945).
7. M. J. Pourbaix, "Thermodynamics of Dilute Aqueous Solutions," p. 68, Edward Arnold and Co., London (1949).
8. E. J. Kelly, *This Journal*, **112**, 124 (1965).
9. A. L. Bacarella and A. L. Sutton, *This Journal*, **112**, 546 (1965).
10. S. Glasstone, "Textbook of Physical Chemistry," p. 943, D. Van Nostrand Co., New York (1946).
11. T. Ikeda and H. Kimura, *J. Phys. Chem.*, **69**, 41 (1965).
12. M. J. Pourbaix, *op. cit.*, p. 69.
13. K. J. Vetter, "Electrochemical Kinetics Theoretical and Experimental Aspects," p. 191, Academic Press, New York (1967).
14. A. E. Duckler, L. C. Elliott, and A. L. Farber, "Distillation Plant Data Book," prepared for Office of Saline Water. Available from Superintendent of Government Documents, Washington, D. C.
15. A. J. de Bethune and N. A. Swendeman Loud, "Standard Aqueous Electrode Potentials and Temperature Coefficients at 25°C," Clifford A. Hampel, Skokie, Ill.

Effect of Tempering on the Anodic Polarization Behavior of an 11 Cr-12 Ni Martensitic Stainless Steel

K. G. Moerschel[1] and A. Tvarusko*

Engineering Research Center, Western Electric Company, Princeton, New Jersey 08540

and G. Krauss

Metallurgy and Materials Science Department, Lehigh University, Bethlehem, Pennsylvania 18015

ABSTRACT

Anodic polarization measurements in 1*N* H_2SO_4 and in 1*N* H_2SO_4-0.1*N* NaCl were made on an 11 Cr-12 Ni martensitic stainless steel in the as-rolled, as-quenched, and quenched and tempered conditions. Structural changes on tempering between 100° and 600°C were evaluated by hardness measurements, light metallography, and transmission electron microscopy. The basic shape of the anodic polarization curves was not significantly affected by cold work (75% reduction) or by the carbide precipitation, recovery and recrystallization which occurred on tempering. The critical potential for pitting was unaffected by tempering and chloride addition. The primary passivation potential became more active on tempering above 300°C for 1 hr. A 600°C temper, accompanied by significant recrystallization, resulted in severe transpassive region pitting when the steel was polarized in the presence of Cl^-.

The anodic polarization behavior of austenitic stainless steels has been extensively evaluated by anodic polarization techniques (1-6). The anodic polarization behavior of tempered martensitic stainless steels, on the other hand, has received little attention, although some studies have been made to correlate microstructure and corrosion in quenched and tempered plain carbon steels (7) and quenched and tempered stainless (30% Cr) irons (8). For these two types of alloys, the corrosion rates passed through a maximum as tempering temperature increased, presumably as a result of the development of a critical dispersion of carbide particles.

This paper presents an evaluation of the effects of heat-treatment on the structure and anodic polarization behavior of a low-carbon martensitic stainless steel. Emphasis was placed on the evaluation of the microstructure and fine-structure changes produced by systematically tempering an as-quenched lath martensite to higher temperatures. The structural changes were then correlated with the anodic polarization behavior.

Experimental

The chemical analysis of the vacuum induction-melted martensitic stainless steel used in this investigation is given in Table I. Final heat-treatment was accomplished by annealing a 0.1-in. thick strip at 982°C for 10 min in an air atmosphere and by subsequent air cooling. After annealing, approximately 0.008 in. was removed from each surface by grinding. The strip was then pickled and cold rolled to 0.020 in., a nominal reduction of 75%. All samples were prepared by annealing at 1037°C for ½ hr in an argon atmosphere and then water quenching. Tempering treatments were performed in an argon atmosphere for 1 hr at the specified temperature.

Samples for light microscopy were heat-treated and then mounted in epoxy. The samples were mechanically polished through a 0.3 μm alumina slurry and etched in a solution of 5g $FeCl_3$, 50 ml conc HCl, and 10 ml water to reveal the general microstructure. Electrolytic etching in a 10% oxalic acid solution was used to reveal carbide precipitation. Current densities of approximately 1 A/cm² provided good etching characteristics.

Table I. Composition of the 11 Cr-12 Ni steel in per cent

C	Mn	P	S	Si	Cr	Ni	N
0.015	0.005	0.008	0.002	0.005	11.40	12.28	0.007

Samples for electron microscopy were prethinned electrolytically to about 80 μm in a 20:1 solution of acetic-perchloric acids. The thin foils were prepared by the Bollman technique (9) in a chromic-acetic acid solution. The resultant foils were mounted in copper grids and stored in ethyl alcohol prior to examination in an electron microscope operating at 100 kV.

The diamond pyramid hardness readings were taken on the metallographic samples with a Vickers microhardness machine at an applied load of 300g.

The potentiodynamic polarization experiments were performed using standard equipment and techniques. The potential of the anode was linearly varied by a potentiostat and a motor-driven potentiometer. The potential of the anode was measured against a saturated calomel electrode (SCE) with an electrometer. The current flowing through the cell was measured as a voltage drop across a 100-ohm resistor by a logarithmic converter (dynamic range of 10^6:1). The outputs of the logarithmic converter and electrometer were recorded on an x-y recorder.

The polarization cell was similar to those used by others (10, 11). Two bright platinum sheets (each 29 cm²) served as counterelectrodes and were symmetrically positioned on each side of the sheet sample. The 2 cm² stainless steel samples were abraded through 600 paper, pickled in a 10% conc HCl-2% conc HF (by volume) solution at 60°C, and rinsed in distilled water. The sample was mechanically mounted such that the solution was only in contact with the sample material. Prior to the start of polarization, the solutions were deaerated by bubbling nitrogen gas. The commercial prepurified nitrogen was further purified by passing it through a hot (500°C) copper trap. After 3 hr, the sample was inserted in the electrolyte and bubbling was continued for 10 min. Subsequently, the nitrogen

* Electrochemical Society Active Member.
[1] Present address: Allentown Works, Western Electric Company, Allentown, Pennsylvania 18103.
Key words: stainless steel, anodic polarization, heat-treatment, microstructure, pitting.

was bypassed to the cell atmosphere and the potential sweep was initiated.

The solutions were prepared from distilled water and reagent grade H_2SO_4 and NaCl. Solutions of 1*N* H_2SO_4 and 1*N* H_2SO_4-0.1*N* NaCl were used for the polarization studies of each sample. The measurements were made in a constant temperature water bath at 25° ± 0.2°C.

Results

Effect of sweep rate.—The effect of sweep rate variation on the polarization curves was evaluated with samples tempered at 500°C. Results for samples immersed in a solution of 1*N* H_2SO_4-0.1*N* NaCl are shown in Fig. 1. The critical anodic current density, I_c, *i.e.*, the maximum current density attained prior to the start of the formation of a passive film, increased with faster sweep rates. The primary passivation potential, E_{pp}, defined as the potential at the critical anodic current density, was slightly more noble at higher sweep rates. The critical potential, V_c, defined as the potential above which the passive film begins to break down, was more pronounced and distinguishable at lower sweep rates. The transpassive region, where dissolution rate increases with increasing potential, has been attributed to a breakdown of the passive film at very positive potentials. In view of these and other results (12), the 10 mV/min sweep rate was used for all subsequent polarization studies.

Microstructure.—The microstructure of the 11 Cr-12 Ni stainless steel after quenching from 1037°C consisted of lath-type martensitic units which formed parallel to one another in a limited number of orientations. Within the parent austenite grain structure (ASTM grain size of 5), regions consisting of parallel laths of martensite of different orientations formed and could be identified by their etching differences. The martensitic structure is clearly visible in the transmission electron micrograph shown in Fig. 2. The boundaries between the individual martensite plates are well defined and the contrast effects within the plates are due to the high dislocation densities associated with this type of martensite (13). No x-ray or electron diffraction evidence was found for retained austenite in the as-quenched samples.

Tempering treatments below 400°C produced no observable differences in the microstructures of samples etched with either $FeCl_3$-HCl or oxalic acid solutions. The first evidence of carbide precipitation at prior austenite grain boundaries was observed after tempering at 400°C. The former austenite grain boundaries serve as preferred nucleation sites for the precipitation of carbides and localized attack by oxalic acid occurred at these areas. Transmission electron

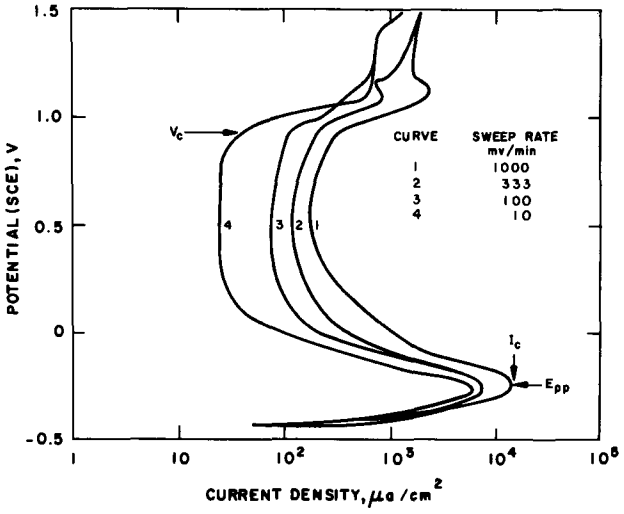

Fig. 1. Effect of sweep rate on polarization of a sample, tempered at 500°C in 1*N* H_2SO_4-0.1*N* NaCl.

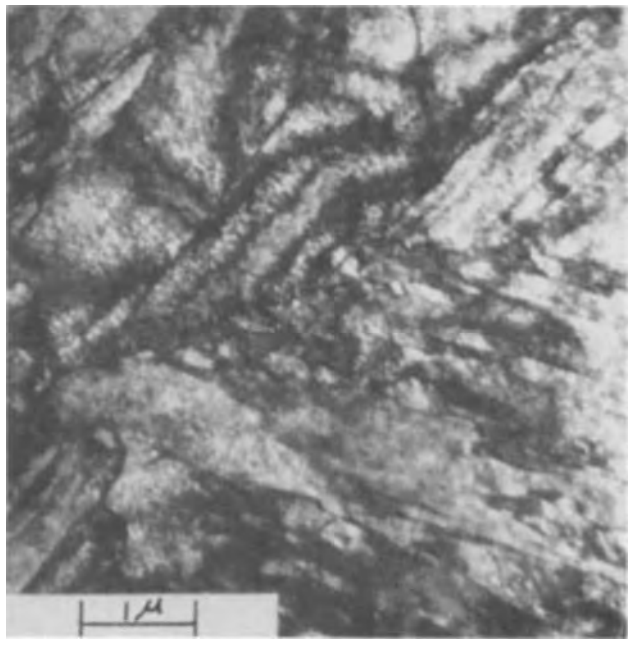

Fig. 2. Martensite plates and fine structure in as-quenched sample. Transmission electron micrograph. 13,600×.

microscopy showed that two types of carbide distributions were present in the samples tempered at 500°C. Carbides were present at the lath boundaries of the martensite, and as parallel arrays in areas that no longer showed a typical lath structure. Examples of the latter type of carbide distribution are shown in Fig. 3. The strong contrast from the parallel features was the only microstructural evidence obtained for the presence of carbides. Figure 4 shows reduced dislocation densities and some areas where equiaxed

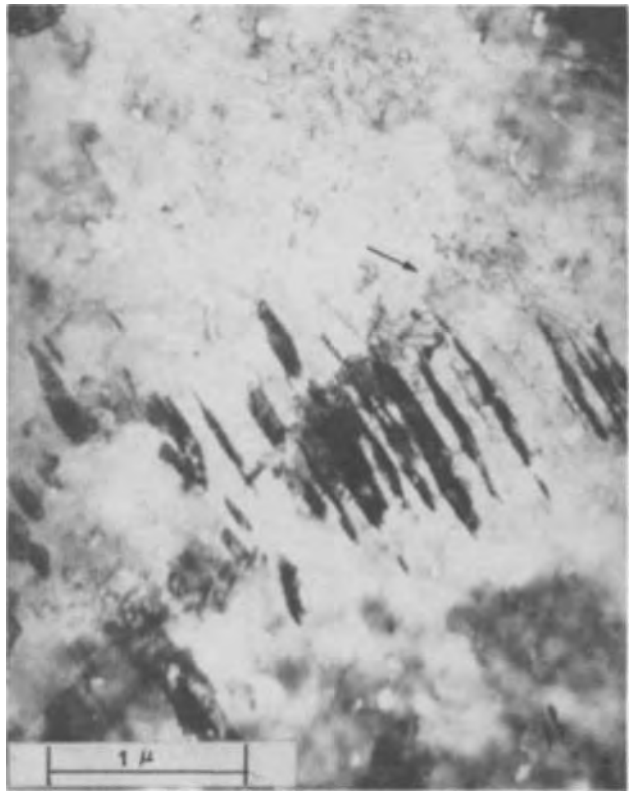

Fig. 3. Fine structure within a martensite plate. Sample tempered at 500°C. Note the low density of dislocations, low angle boundary (arrow), and carbide distribution. Transmission electron micrograph. 24,500×.

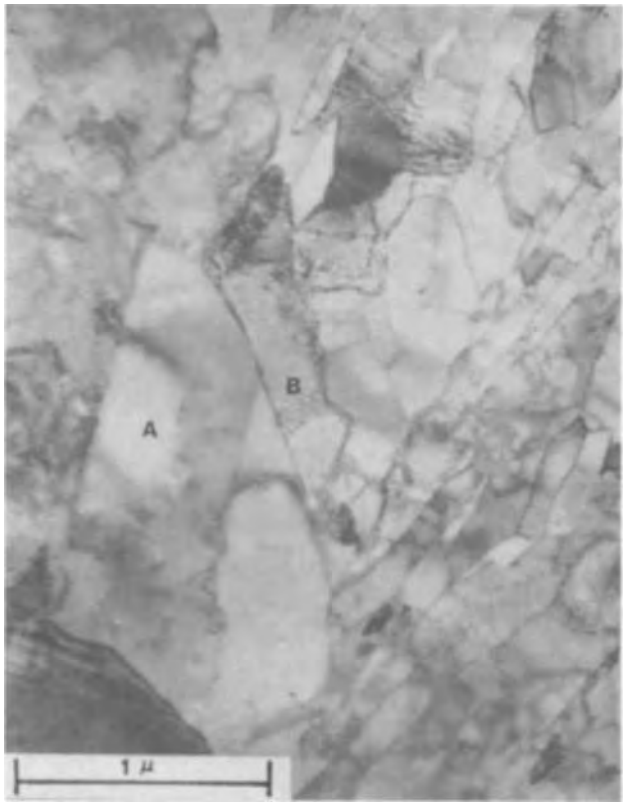

Fig. 4. Partially recrystallized microstructure of sample tempered at 600°C. Note the large equiaxed ferrite grain (A) and the subboundary (B). Transmission electron micrograph. 32,000×.

ferrite grains have replaced the laths of the as-quenched martensite after a 600°C temper. Partial recrystallization has obviously occurred.

Hardness measurements.—Tempering above 200°C produced an increase in the hardness of the alloy as shown in Fig. 5. At 300°C, large variations in the microhardness readings were observed, possibly because of the localized nature of the tempering processes discussed in the previous section. Some areas may have experienced carbide precipitation while other areas may have undergone appreciable recovery. As tempering was accelerated by higher temperatures, the structural changes became more uniformly distributed and the variation in the hardness readings decreased. The fact that the hardness increases to a maximum after tempering between 400° and 500°C strongly supports the structural evidence for carbide precipitation presented in the previous section. Recovery and recrystallization processes that lower the dislocation density and replace the fine laths of martensite with a coarser, equiaxed grain structure would tend to lower the hardness, not increase it. This is conclusive evidence that carbide precipitation occurred on tempering.

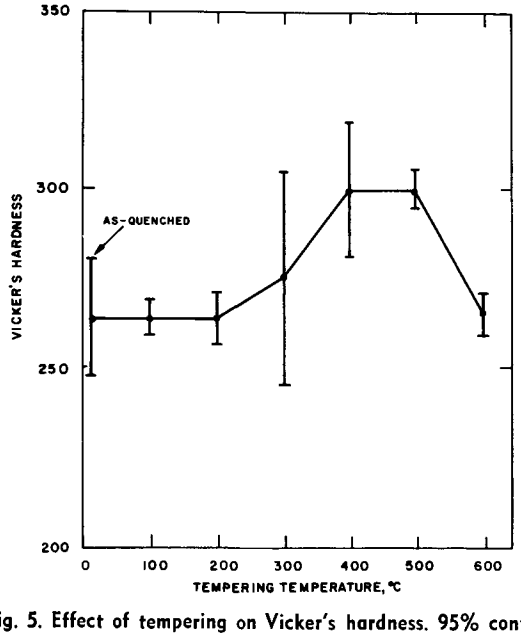

Fig. 5. Effect of tempering on Vicker's hardness. 95% confidence limits on measurements are shown. The as-rolled hardness was 342 ± 6.7.

Table II. Summary of anodic polarization results

Treatment	1N H_2SO_4		1N H_2SO_4-0.1N NaCl	
	I_c, mA/cm²	E_{pp}, V (SCE)	I_c, mA/cm²	E_{pp}, V (SCE)
As-rolled	3.0	−0.30	7.0	−0.26
As-quenched	2.5	−0.30	13.0	−0.28
100°C temper	3.2	−0.30	10.0	−0.26
300°C temper	2.2	−0.30	10.0	−0.28
500°C temper	2.3	−0.32	5.3	−0.26
600°C temper	20.0	−0.34	16.0	−0.30

Anodic polarization measurements.—The numerical data for the polarization studies conducted in 1N H_2SO_4 and 1N H_2SO_4-0.1N NaCl solutions are summarized in Table II. Data obtained from reproducibility experiments showed a limit of error of ±0.01V and ±0.1 mA/cm² for E_{pp} and I_c, respectively.

In the 1N H_2SO_4 solution, the polarization behavior of the as-rolled sample was not significantly different from that of the as-quenched sample. The polarization parameters were virtually identical for the as-quenched sample and the as-rolled sample. Figure 6 shows the polarization curves for the two extreme cases, *i.e.*, as-quenched and quenched and tempered at 600°C. From these two curves it is evident that tempering has no effect on the critical potential when polarization is conducted in 1N H_2SO_4; however, the other two parameters, I_c and E_{pp}, were definitely affected by tempering. It is evident from Fig. 6 and Table II that the primary passivation potential became slightly more active on tempering about 300°C. A significant increase in I_c was noted when the steel was tempered at 600°C where I_c increased almost tenfold.

In all samples, the addition of Cl^- influenced I_c, E_{pp}, and V_c to a greater extent than tempering did. Figures 7 and 8 show the effect of Cl^- additions on the polarization behavior of the as-quenched sample and the quenched and tempered (600°C) sample, respectively. It is obvious that chloride additions increased I_c in untempered samples or samples tempered at temperatures less than 500°C. Chloride additions also ennobled E_{pp}; however, the critical potential V_c was unaffected by chloride additions.

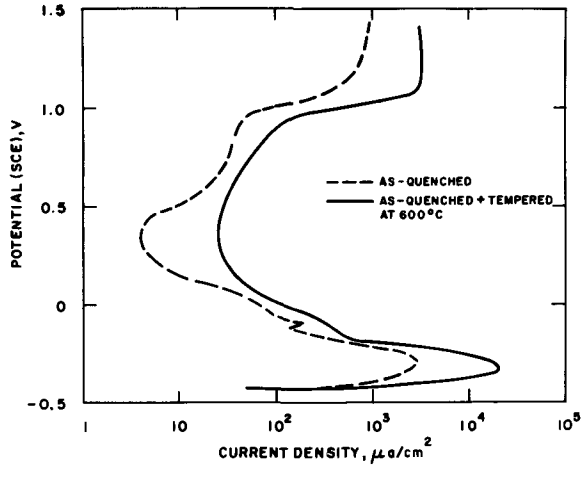

Fig. 6. Polarization curves of as-quenched and quenched and tempered (600°C) samples in 1N H_2SO_4.

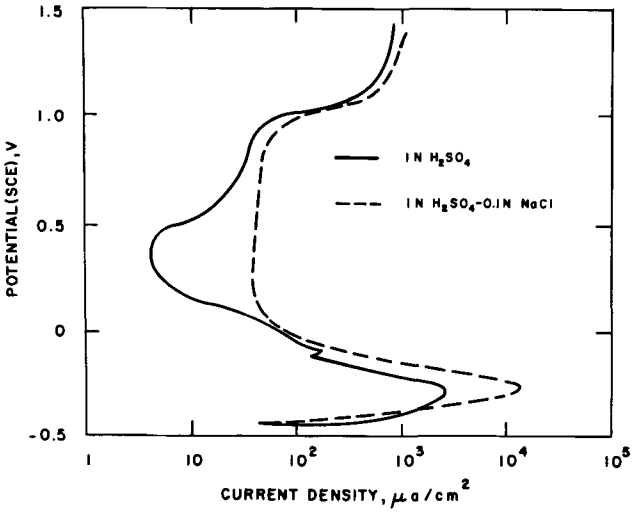

Fig. 7. Polarization curves of as-quenched samples in the presence and absence of Cl^-.

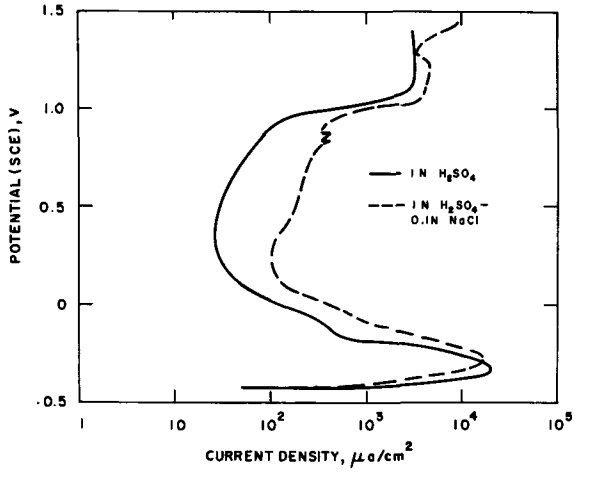

Fig. 8. Polarization curves of samples, tempered at 600°C, in the presence and absence of Cl^-.

Comparison of Fig. 7 and 8 shows that tempering to 600°C did not affect V_c, regardless of which solution was used. The behavior of I_c and E_{pp} (in the presence of Cl^-) was somewhat erratic at intermediate tempering temperatures. Nevertheless, the 600°C sample had the most active value of E_{pp}.

When the 600°C samples were polarized in the 1*N* H_2SO_4-0.1*N* NaCl solution, numerous pits formed in the transpassive region. The pits ranged in size up to 0.5 mm and were randomly distributed on the sample surface. Some pits also formed in the passive region at a potential of approximately 0.8V. Current fluctuations were associated with this pit formation. A repeat of this experiment with a different 600°C sample yielded similar results except that passive region pitting and its associated current fluctuation occurred at 0.4V as opposed to 0.8V mentioned above. The initiation of pitting during polarization in the passive region evidently involves a temporary and localized breakdown of passivity which is not reproducible from sample to sample. A small bridge of metal was observed to span one of pits which formed during polarization in the passive region. Apparently the pit was repassivated before the bridge had time to dissolve. The fact that this bridge remained after polarization suggests that the pit did not serve as a nucleus for future transpassive region pitting. Bond and Lizlovs (14) experienced the same phenomenon in their investigation and associated the repassivated pits with small regions of considerable composition differences from the bulk composition; that after these regions are removed the pits are too small to propagate at the potential in question.

Discussion

The aforementioned results obtained with an 11 Cr-12 Ni stainless steel show that a relationship exists between polarization behavior and microstructural changes caused by tempering. The observed net changes in E_{pp} and particularly I_c are indeed significant because of the excellent reproducibility of these parameters ($\pm$0.01V for E_{pp} and $\pm$0.1 mA/cm^2 for I_c). The parameters E_{pp} and I_c did not vary in a systematic fashion with tempering temperature in the presence of Cl^-. Since the general effect of tempering may have been obscured by the Cl^- addition, the polarization behavior of samples in 1*N* H_2SO_4 will be discussed first.

Some microstructural changes, especially carbide precipitation, were observed in the alloy on tempering above 300°C. Precipitates serve as cathodic sites and have been shown, in general, to enhance corrosion of carbon steel and austenitic stainless steels in aqueous media (1, 3, 15-18). It is reasonable to assume that this induced heterogeneity will cause specific changes in the polarization behavior since microstructural changes affect corrosion behavior and corrosion behavior can be correlated with anodic polarization behavior (1, 3, 4, 14, 19).

The microstructural results have shown that precipitation of carbides began to occur at and above a 300°C temper. The primary passivation potential, however, was not significantly affected until the metal was tempered above 400°C. This precipitation was followed by a change in E_{pp} in the active direction for samples tempered at 500°C. No other parameters exhibited a significant change until tempering was carried out at 600°C. Then the critical anodic current density increased almost tenfold. It was found that the only difference between the 500° and the 600°C samples was the extensive recrystallization occurring at 600°C. The heterogeneity created by recrystallization of varying degrees in adjacent areas may have been responsible for the observed increase in I_c. None of the tempered samples exhibited pitting or a change in the critical potential.

It is interesting to note that the polarization behavior of the as-rolled sample differed little from that of the as-quenched sample in 1*N* H_2SO_4. Perhaps this similarity in behavior is due to the high concentration of dislocations produced by both cold working and the martensite shear-type transformation. Further, Straumanis and Wang (20) have shown that cold working per se does not enhance the corrosion rate of aluminum.

According to Foroulis and Uhlig (18), cold working had little or no effect on the corrosion rate of zone-refined iron in HCl solutions. They concluded that galvanic cells are formed only when cold working causes the precipitation of a second phase, a change in the crystal orientation, or the segregation of impurities at imperfections. The energy imparted to the zone-refined iron by cold working was too small to account thermodynamically for the change in corrosion behavior. In view of these observations, it is not surprising that the polarization characteristics of the stainless steel used in this investigation were hardly affected by cold work because only a minimal amount of carbide precipitation or impurity segregation could have occurred during cold rolling of the sample.

The only pitting experienced in this study occurred on samples which were tempered at 600°C and polarized in the presence of chloride ions. This result suggests that either the recrystallization, which occurred, induced the pitting or a critical size and/or dispersion of carbide particles served as nucleation sites for transpassive and passive region pitting. However, the latter seems unlikely because no carbide particles were observed in the transmission electron micrographs taken of samples tempered at 600°C. The higher temperature

treatments probably resulted in the solution of carbide precipitates.

Manuscript submitted May 15, 1972; revised manuscript received Aug. 31, 1972.

Any discussion of this paper will appear in a Discussion Section to be published in the December 1973 JOURNAL.

REFERENCES

1. M. A. Streicher, *This Journal*, **103**, 375 (1956).
2. J. Horvath and H. H. Uhlig, *ibid.*, **115**, 791 (1968).
3. N. D. Tomashov, G. P. Chernova, and O. N. Marcova, *Corrosion*, **20**, 166 (1964).
4. N. D. Greene and G. Judd, *ibid.*, **21**, 15 (1965).
5. H. P. Leckie and H. H. Uhlig, *This Journal*, **113**, 1262 (1966).
6. G. M. Schmid and N. Hackerman, *ibid.*, **108**, 741 (1961).
7. E. Heyn and D. Bauer, *J. Iron Steel Inst.*, **79**, 109 (1909).
8. J. H. G. Monypenney, "Stainless Iron and Steel," 2nd ed., Chapman and Hall, London (1931).
9. W. Bollman, *Phys. Rev.*, **103**, 1588 (1956).
10. M. E. Komp and H. E. Trout, *Corrosion*, **24**, 11 (1968).
11. H. H. Uhlig and G. E. Woodside, *J. Phys. Chem.*, **57**, 280 (1953).
12. N. D. Greene and R. B. Leonard, *Electrochim. Acta*, **9**, 45 (1964).
13. J. F. Breedis, *Trans. AIME*, **20**, 1583 (1964).
14. A. P. Bond and E. A. Lizlovs, *This Journal*, **115**, 1130 (1968).
15. K. J. Aust, J. S. Armijo, and J. G. Westbrook, *Trans. ASM*, **59**, 544 (1966).
16. R. W. Manuel, *Corrosion*, **3**, 415 (1947).
17. H. T. Shirley, *J. Iron Steel Inst.*, **174**, 242 (1953).
18. Z. A. Foroulis and H. H. Uhlig, *This Journal*, **111**, 522 (1954).
19. H. P. Leckie, *ibid.*, **117**, 1152 (1970).
20. M. E. Straumanis and Y. N. Wang, *Corrosion*, **12**, 39 (1956).

A Soft X-Ray Study of the Near Surface Composition of Cu30Zn Alloy during Simultaneous Dissolution of Its Components

J. E. Holliday[1] and H. W. Pickering*[,2]

Edgar C. Bain Laboratory for Fundamental Research,
United States Steel Corporation, Research Center, Monroeville, Pennsylvania 15146

ABSTRACT

For certain conditions, alloys composed of metals of different nobility anodically dissolve without noticeable preferential dissolution of the less noble metal (simultaneous dissolution). In principle, an induction period of disproportionate dissolution of the less noble metal should precede simultaneous (nonselective) dissolution. In the present paper, the existence of the induction period is demonstrated by soft x-ray spectroscopy of the alloy surface. Results are presented for anodically polarized Cu-30 atomic per cent Zn in an acidic sulfate solution. Analyses of the Cu $L_{II,III}$, Zn $L_{II,III}$, and oxygen K band spectra of these specimens for several accelerating voltages (corresponding to different depths into the alloy ranging up from 10^2Å) show that the amount of elemental copper in the surface layer increases during an initial period of dissolution. It is concluded that Cu-enrichment of the surface is a necessary condition for simultaneous dissolution of the alloy. A model of simultaneous dissolution is presented which incorporates Cu-enrichment and a diffusion field in a shallow, alloy layer at the surface.

In prior investigations (1-4) it was found that when one component of an alloy undergoes quasi-stationary preferential dissolution in an electrolyte, *i.e.*, when parting of the alloy occurs, the surface and subsurface atom layers enrich in the more noble metal and the surface area greatly increases. Preferential dissolution is expected and is well known to occur in alloys in which the standard potentials, E°, of the components differ greatly (by many times RT/F). Yet for certain conditions simultaneous (nonselective) dissolution[3] of these alloys is the commonly observed stationary mode of dissolution.

In a recent study (5) of brass-acidic sulfate systems it was found that the stationary mode of dissolution (simultaneous or preferential) is mainly determined by the Zn content of the brass and the electrode potential. The boundaries are not sharp. Preferential dissolution more readily occurs at the less noble potentials and in the Zn-rich brasses, and the converse is true for simultaneous dissolution.

In principle, dissolution of brass by the simultaneous mode should be preceded by an induction period of preferential zinc dissolution in view of the difference in nobility of copper and zinc; simultaneous dissolution would then occur when a certain level of enrichment of copper is reached in the surface, and possibly subsurface, atomic layers.

Some data for α-brass [Cu-30 a/o (atomic per cent) Zn] in acidic sulfate solutions are available which support this view. It was found by chemical analysis of the electrolyte that during an induction period a disproportionate amount of Zn dissolves prior to the attainment of steady-state simultaneous dissolution; the "excess" copper on the surface amounts to $\lesssim 10^2$ atom layers (5, 6).

Further studies are needed of alloys undergoing simultaneous dissolution in order to determine the

* Electrochemical Society Active Member.
[1] Present address: Research Laboratory, McDonnell Douglas Corporation, St. Louis, Missouri 63166.
[2] Present address: Metallurgy Section, Department of Material Sciences, The Pennsylvania State University, University Park, Pennsylvania 16802.
Key words: alloy dissolution, corrosion, surface enrichment, partial currents.
[3] Simultaneous dissolution is defined as when all components of an alloy dissolve at rates proportional to their mole fraction in the alloy; *e.g.*, the rates of dissolution of Cu and Zn in mol cm^{-2} sec^{-1} from a single-phase Cu-30 a/o Zn alloy would be in the ratio of 7:3 for the formation of divalent Cu and Zn ions.

composition of the surface and the state (metallic or oxidized) and spatial distribution of the residual (more noble) component. In the present paper, a soft x-ray technique is described which enables (*a*) a determination of the composition of the surface region from the first several atom layers to a depth of several hundred atom layers of the alloy and (*b*) the identity and measurement of the relative amounts of oxides on the surface.

The effect of alloy composition and of oxide formation on the shape and wavelength of characteristic soft x-ray emission bands (electron transition from the valence band to vacancies in inner atomic core levels) from the elements, as well as the experimental techniques for measuring these bands, has recently been reviewed (7). When a metal or compound is bombarded with electrons of energy up to 3 kV, soft x-rays originating near the surface are emitted; the depth from which the x-rays come decreases with decreasing electron energy (decreasing accelerating voltage).

For copper and zinc, the L_{II} and L_{III} bands (4s + 3d → 2p transitions) occur in the soft x-ray region (Cu L_{III} at 13.3Å, Zn L_{III} at 12.2Å). The L_{II} band is a (4s + 3d → 2p $J_{1/2}$) transition and the L_{III} band is a (4s + 3d → 2p $J_{3/2}$) transition. The spectra, each consisting of both bands for copper and for zinc, are usually designated Cu $L_{II,III}$ and Zn $L_{II,III}$, respectively.

Since the copper and the zinc emission band intensities from Cu-Zn alloys are a function of alloy composition as shown by Curry and co-workers (8), a variation in composition as a function of distance from the surface of an alloy can be determined from the soft x-ray emission bands by varying the accelerating voltage. This is so since the x-rays come from closer to the surface as one reduces the accelerating voltage. This method differs from that of Curry and co-workers (8) in that their data were obtained at constant voltage in accord with the use of specimens of different bulk composition. In measuring a series of alloys, there will always be the possibility of various instrumental changes from one specimen to another. This can be overcome by comparing the ratio of the peak intensities of the components of binary alloy specimens, *e.g.*, the ratio of the peak intensities of the Cu L_{III} and Zn L_{III} bands of a Cu-Zn alloy.

If a thin oxide is present on the surface, some further change in the Cu L_{III}/Zn L_{III} ratio may occur as a result of a difference in the ratio of the components in the oxide from that in the alloy. The effect of oxide on the intensity ratio is usually easily distinguishable from an alloy composition effect for the following reasons: the structure of the emission band is different for the metallic and ionic states, and the L_{II}/L_{III} intensity ratios are much higher for metal in the oxidized than in the elemental form.

In the present experiments, the Cu L_{III}/Zn L_{III} ratio should increase over that of the undissolved sample if copper accumulates on the surface during dissolution. The Cu L_{III}/Zn L_{III} ratio should increase at a decreasing rate as a function of dissolution time, corresponding to a thickening of the Cu-rich layer at an ever slower rate in the approach to a steady-state thickness; the ratio eventually should level off at a high-value characteristic of the (average) composition of the layer at steady-state simultaneous dissolution; and at all times the ratio should be a decreasing function of the accelerating voltage.

Experimental Procedure

Data were obtained for α-brass containing 30 a/o Zn (Cu30Zn) provided by American Smelting and Refining Company. The alloy was homogenized at 873°K for 60 hr in an evacuated capsule, rolled to 0.015 cm and annealed in vacuum at 873°K for 20 hr. Rectangular specimens were cut with an area of ~7 cm^2, and the specimens were then given a final anneal in vacuum at 873°K.

Surface preparation of the specimens consisted of dry mechanical polishing. Wet polishing was avoided since it was found from the ratio of the Cu L_{III} and Zn L_{III} intensities that the surface was Cu-rich after normal mechanical polishing using aqueous suspensions of alumina; this is described further in the Results section. Specimens to be used in the controlled potential runs, therefore, were only given a dry polish consisting of 600 and 3/0 emery paper, and contact with all liquids prior to anodic dissolution was carefully avoided following the 873°K anneal.

The closed Pyrex cell contained a platinum counter-electrode and a mercury-mercurous sulfate reference electrode. The electrolyte, 1*N* Na_2SO_4-0.01*N* H_2SO_4 of pH 2, was made from reagent grade chemicals and doubly distilled water. Prepurified helium was continuously passed through the electrolyte to remove oxygen. All runs were at room temperature (297°K). All potentials are on the standard hydrogen scale.

The specimen was inserted in the cell at a set potential in the potential region of steady-state, simultaneous dissolution (0.20-0.30V) (5, 6). After dissolution at the control potential, it was withdrawn from the cell, rinsed in distilled water and in methanol, and air-dried. This procedure avoided any redeposition of copper during anodic dissolution. The potential range 0.20-0.27 corresponds approximately to the Tafel region for pure copper in acidic sulfate solution. The specimen was then stored in a desiccator prior to the soft x-ray analyses.

Some changes in composition of the uppermost surface layer are inevitable during drying, exposure to air, and exposure to low pressures in the soft x-ray apparatus. Waters of hydration, hydroxides, and oxides will be removed or undergo changes in structure. As a result, only changes in the amount of the more firmly bound oxygen will be measurable by the soft x-ray technique. It is also possible that between the time the specimen is removed from the cell and then washed, copper ions in the adhering solution may deposit if the open-circuit potential is less noble than the copper potential. This will provide an added increment of copper to the surface, the amount of which is independent of the time of dissolution and, therefore, distinguishable from copper enrichment which occurs during the constant potential dissolution experiment.

Enrichment of copper in the first 10^2 atom layers was examined by the change in ratio of the Cu L_{III} and Zn L_{III} x-ray intensities as a function of accelerating voltage of the incident electrons. The depth from which the emission spectra mainly come is about 100Å at 1.5 kV and increases to several hundred angstroms at the higher accelerating voltages, as roughly estimated from other experiments where metal layers of known thickness and density were examined (9, 10). The intensity distribution of the oxygen K (O K) and Cu $L_{II,III}$ and Zn $L_{II,III}$ band spectra of the anodically dissolved specimens showed with which alloying element the oxygen is bonded, and the intensity of the O K band shows changes in the amount of oxide as a function of dissolution time. The O K, Cu $L_{II,III}$, and Zn $L_{II,III}$ band spectra were measured using a blazed grating analyzer with 3600 grooves/mm in a spectrometer with a 50 cm radius of curvature and a flow proportional counter as detector (11). Undissolved α-brass, zinc, and copper specimens were used as standards. The main source of contamination is the residual vapors, such as hydrocarbons and CO, which may be cracked by the electron beam; some carbon, therefore, may accumulate on the specimen surface. Carbon contamination has been reduced by using ion pumping and a cold finger around the specimen (7). A monolayer or so of carbon on the specimen surface is not expected to affect significantly the metal emission bands, and any influence it may have on oxygen bonding at the specimen surface could be revealed in the oxygen K spectra.

Results

Metal emission spectra.—The single-phase Cu30Zn specimens were dissolved at $E = 0.24$V for times of 0.5, 3, 5, 15, and 60 min. Simultaneous dissolution for this alloy-electrolyte system at $E = 0.24$V is obtained in less than 1 hr and sometimes as early as 10 min, according to chemical analyses of the electrolyte (5). Prior to simultaneous dissolution a disproportionate fraction of Zn^{2+} ions enter the electrolyte; the concomitant copper build-up amounts to $\lesssim 10^2$ atom layers (5, 6). A steady-state current is obtained at or soon after the onset of simultaneous dissolution; both the copper and zinc currents are higher in the initial period (5, 6). The steady-state current at $E = 0.24$V in the present experiments was about 0.05 mA cm^{-2}.

Typical metal emission spectra are shown in Fig. 1. These copper and zinc spectra are from the undissolved (standard) Cu30Zn specimen. For the undissolved Cu30Zn specimens the Cu L_{III}/Zn L_{III} ratio is about 2.6 ($t = 0$ in Fig. 2) at all accelerating voltages, except at the lowest voltage of 1.5 kV for which the ratio is larger. Similarly the Cu L_{III}/Zn L_{III} ratio for the pure elements at $t = 0$ did not vary significantly except at 1.5 kV. One possible explanation for the larger Cu L_{III}/Zn L_{III} ratio at 1.5 kV is the closer proximity of the zinc excitation potential (1.023 kV) to the 1.5 kV accelerating voltage than is the copper excitation potential (0.922 kV).

After anodic dissolution at $E = 0.24$V (time > 0 in Fig. 2) higher Cu L_{III}/Zn L_{III} ratios are obtained. The greatest increase in the ratio as a function of time of dissolution occurs at the lowest voltage corresponding to the shallowest depth of x-ray emission, whereas a rather small change occurs at 4 kV. The ratio eventually levels off and then decreases slightly. The Cu L_{III}/Zn L_{III} ratio was determined at 2, 3, and 4 kV and found to be characteristic of the elemental, rather than oxidized, form of copper. The absolute intensities

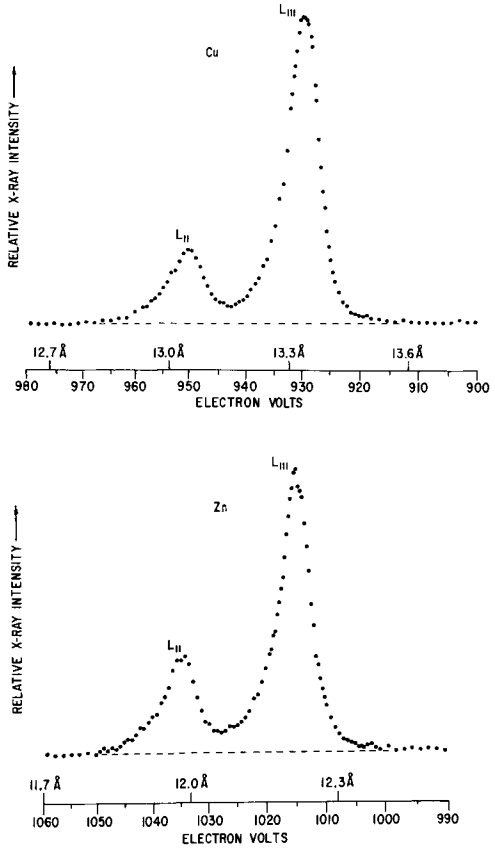

Fig. 1. Cu $L_{II,III}$ and Zn $L_{II,III}$ emission band spectra from an undissolved (standard) Cu30Zn specimen at an accelerating voltage of 4 kV.

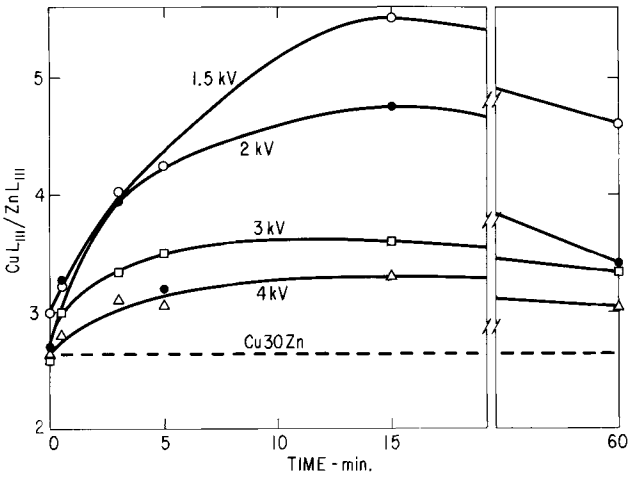

Fig. 2. Cu L_{III}/Zn L_{III} ratio as a function of dissolution time for different accelerating voltages.

of the Cu L_{III} and Zn L_{III} bands go through a maximum as a function of dissolution time; by 1 hr the intensity of the Cu L_{III} band is somewhat higher and that of the Zn L_{III} band somewhat lower than their respective initial values.

Another series of Cu30Zn specimens was dissolved at $E = 0.22$V for times of 5, 15, 40, 60, and 360 min. Simultaneous dissolution is attained after 10^2 min, at this potential according to chemical analysis of the electrolyte (5). The steady-state current at $E = 0.22$V is $\lesssim 5$ μA cm^{-2}. The Cu L_{III}/Zn L_{III} ratios were determined for these specimens at accelerating voltages of 1.5, 2, 3, 4, and 5 kV. A plot of these data is similar to that in Fig. 2. The ratios at the lower voltages were always higher after dissolution and tended to increase and go through maxima prior to leveling off at the longest times of 60 and 360 min.

The surfaces of the specimens polarized at $E = 0.22$ and 0.24V retain their bright, metallic luster. Scanning electron microscopy examinations of similarly polarized Cu30Zn specimens (6) show that a faceted (etched) structure, not unlike that observed for pure metals in the Tafel region (12, 13), develops, *i.e.*, the extent of surface roughening is relatively minor, being comparable to that of a heavily etched pure metal; this is in counterdistinction to the profuse surface roughening which occurs during quasi-stationary preferential dissolution (1-4), and which is expected in principle when diffusion in the alloy is rate controlling (14, 15).

Wet mechanical polishing also causes an increase in the Cu L_{III}/Zn L_{III} ratio of otherwise unreacted specimens. Comparison of the Cu L_{III}/Zn L_{III} ratios as a function of accelerating voltage for a Cu30Zn specimen given a wet (aqueous suspension of alumina) mechanical polish with those for another specimen which was prepared by the aforedescribed dry polishing technique showed that for the wet-polished specimen the copper content was significantly higher in the near-surface region. Comparison of these ratios with those obtained from pure zinc and copper samples showed that the surface of the dry-polished Cu30Zn specimen was characteristic of the bulk alloy composition.

Oxygen emission spectra.—The oxygen K emission band was obtained for the anodically dissolved Cu30Zn specimens described above and in addition for specimens dissolved at $E = 0.23$ and 0.30V (Fig. 3). At $E = 0.22$, 0.23, and 0.24V the O K band is the same as that from pure zinc oxide. The amount of oxide on the surfaces of these anodically dissolved α-brass specimens is small (estimated at a few monolayers), does not increase with dissolution time, and is actually less ($\lesssim 50\%$) than that present on the specimen prior to dissolution. At $E = 0.30$V films are observed to form

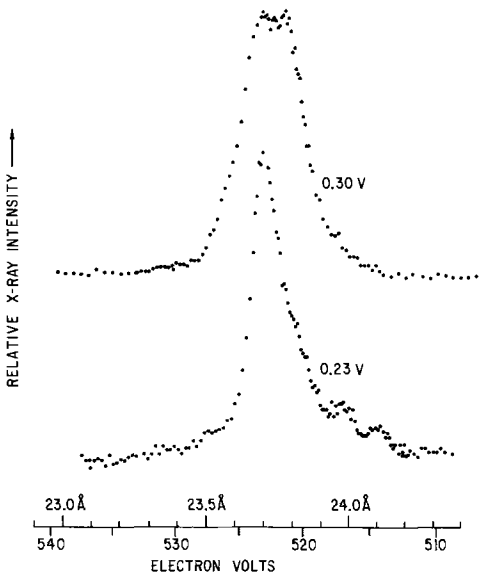

Fig. 3. Oxygen K band spectra for Cu30Zn specimens showing oxygen bonded (a) with zinc atoms after dissolution at $E = 0.23$V (3 kV accelerating voltage) and (b) with copper atoms for $E = 0.30$V (4 kV).

on the specimen during dissolution, in agreement with other studies (5). For these specimens the O K band was that of pure copper oxide, as shown in Fig. 3. This result shows that copper on the surface is converted to copper oxide only at relatively high dissolution potentials. The O K band intensity which indicates oxygen content was much greater on these specimens than on those polarized at the lower potentials.

Discussion

Soft x-ray results.—The Cu $L_{II,III}$, Zn $L_{II,III}$, and O K band spectra of the anodically polarized specimens are all consistent with a build-up during dissolution of the elemental copper content at the surface. This is most directly indicated by the increase after dissolution of the Cu L_{III}/Zn L_{III} ratio (Fig. 2). The O K band spectra and the L_{II}/L_{III} ratios rule out an oxide effect since the former shows that the oxygen content of the surface is less after dissolution at $E = 0.22$ and 0.24V, and the latter are characteristic of copper and zinc in their elemental forms. The slight decrease of the Cu L_{III}/Zn L_{III} ratio observed in the later dissolution periods at the lower accelerating voltages for both the $E = 0.22$ and the 0.24V runs (Fig. 2) is not an expected composition effect, and may be related to area change or to cold work introduced by the surface preparation.

The large increase of the Cu L_{III}/Zn L_{III} ratio during the early dissolution periods at the lower accelerating voltages (Fig. 2) indicates a rather sizable increase of the copper content in the surface region. The depth of the zone of copper enrichment is estimated to be of the order of 10^2Å. The distribution of copper in this zone is unknown. The soft x-ray data are consistent both with a zone where the composition *vs.* distance profile is the same along all normals to the surface, and with a zone involving patches of original alloy and pure copper.

Enrichment model of simultaneous dissolution.—A satisfactory model of simultaneous dissolution must take into account the induction period during which the surface enriches in the more noble metal, and the presence of this enriched layer during simultaneous dissolution. The salient points may be understood without calculations as follows. Let the alloy dissolve at a constant current density, as may be provided by a galvanostatic external circuit. At the start of dissolution of a brass of uniform composition, the rate of preferential zinc dissolution is highest; thereafter the rate decreases as the surface coverage by copper atoms increases.

Let us assume for the moment that interdiffusion of the components in a shallow region of alloy next to the surface does not occur. Then a simplified description of the alternatives is as follows:

(*a*) In the absence of surface diffusion, copper and zinc atoms at kinks alternatively enter the solution without any enrichment of the more noble component.

(*b*) When copper atoms at kinks do not enter the solution, Zn atoms may pass from the uppermost lattice plane into the solution so that this lattice plane attains finally a very loose structure. Furthermore, zinc atoms in the next lattice plane may pass into the solution and so forth. In parallel, sidewise motions of surface copper atoms may occur so that two dimensional patches of copper are formed. Before these patches grow together by supply of copper from underlying lattice planes and form a complete "blocking layer," however, simultaneous passage of zinc and copper atoms into the solution may occur.

Next, let us assume that interdiffusion of the components in a shallow region of alloy next to the surface can occur because of an increase in the vacancy concentration. As in the case of quasi-stationary preferential dissolution (1), vacancies may be formed by zinc dissolution from terrace sites in view of the high overpotential for zinc dissolution. In this event, zinc atoms migrate to the surface from subsurface positions (and copper atoms migrate into the alloy), Fig. 4. Briefly the diffusive flux of zinc to the surface controls the extent of preferential dissolution; this flux is, therefore, inversely proportional to the depth, δ, of the interdiffusion layer. However, since the surface recedes by dissolution of copper and zinc atoms, the interdiffusion depth and flux of zinc to the surface reach steady-state values (the onset of simultaneous dissolution); *i.e.*, the "front" of the interdiffusion layer moves into the alloy at a decreasing rate until this rate equals that at which the surface recedes. The velocity of the front does not decrease further since this would lead to a decrease in the diffusion distance, which would be countered by disproportionate zinc dissolution until the two velocities were again equal. The rates of diffusion and dissolution therefore determine the steady-state thickness of the interdiffusion layer and the time to reach steady-state simultaneous dissolution.

The electrode potential initially assumes a value sufficient for zinc dissolution but below that of cop-

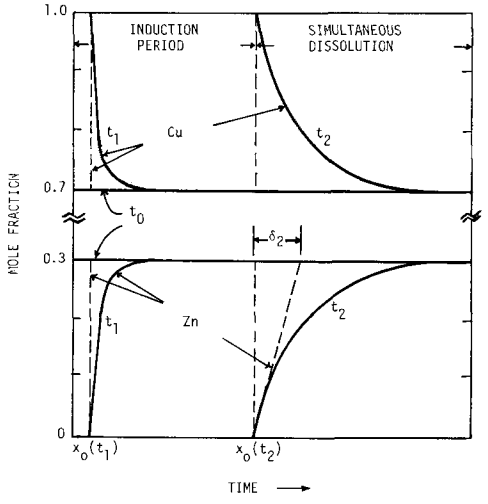

Fig. 4. Schematic illustration of the zinc and copper concentration profiles in the approach to and during simultaneous dissolution. The effective thickness, δ, of the depletion zone increases during the induction period and is constant thereafter (simultaneous dissolution).

per dissolution. However, as the flux of zinc to the surface decreases the potential assumes a more positive value so that anodic dissolution of copper, in addition to that of zinc, becomes thermodynamically possible. The overpotential of copper dissolution is relatively low. Thus copper dissolution is not retarded by some slow step once the electrode potential is only slightly more positive than the copper equilibrium value.

If the specimen is dissolved at a constant potential in the region of copper and zinc dissolution (as in experiments in this paper), instead of at constant current, the aforementioned description needs some modification as follows. At the start of dissolution copper, as well as zinc, dissolves. As in the case of constant current conditions, though, disproportionate zinc dissolution occurs initially because of the difference in nobility of copper and zinc, and decreases as the availability of zinc at the surface decreases until the ratio of Zn/Cu entering the solution becomes equal to the ratio of Zn/Cu in the bulk alloy (simultaneous dissolution).

One may calculate the zinc concentration profile next to the surface, the flux of zinc to the surface, and the depth of interdiffusion when the alloy/electrolyte interface moves at a steady rate in the following way according to Wagner (16). Assume a planar surface, although this is not quite true since faceting of the surface occurs during the induction period, and one-dimensional diffusion normal to the surface. Furthermore assume that the interdiffusion coefficient in the alloy is not extremely low. This latter assumption is realistic only in a shallow surface region, and then only if excess monovacancies and/or divacancies are present by virtue of their formation at the surface.

Let the alloy dissolve with a constant current density, i, in which case the alloy/electrolyte interface recedes at a steady rate. Thus for x equal to the distance from the original position of the interface and x_o equal to the instantaneous position of the interface, one has the following situation (16)

$t = 0$: electrolyte | alloy ($x = 0$)

$t > 0$: electrolyte | alloy ($x = x_o = ut$)

The position of the interface as a function of time is given by

$$x_o = ut = \frac{i}{2\mathbf{F}} V_m t \qquad [1]$$

in which V_m is the molar volume of the alloy and $\mathbf{F}$ is the Faraday constant. The factor 2 is valid for dissolution of copper and zinc as divalent cations.

Since copper is much more noble than zinc, the mole fraction of zinc, N_{Zn}, is assumed to virtually vanish at the surface, $x = x_o$

$$N_{Zn} = 0 \text{ at } x = x_o = ut \qquad [2]$$

For an interdiffusion coefficient independent of composition, D, Fick's second law reads

$$\frac{\partial N_{Zn}}{\partial t} = D \frac{\partial^2 N_{Zn}}{\partial x^2} \text{ at } x > x_o \text{ or } x > ut \qquad [3]$$

Assuming a uniform mole fraction of zinc at $t = 0$, one has

$$N_{Zn} = N_{Zn}^o \text{ at } t = 0,\ x > 0 \qquad [4]$$

Equations [2] through [4] are satisfied by

$$N_{Zn} = N_{Zn}^o \left\{ 1 - \tfrac{1}{2} \exp\left(-\frac{ux - u^2t}{D} \right) \cdot \operatorname{erfc}\left[\frac{x}{2(Dt)^{1/2}} - \frac{ut^{1/2}}{D^{1/2}} \right] - \tfrac{1}{2} \operatorname{erfc} \frac{x}{2(Dt)^{1/2}} \right\} \text{ at } x > ut \qquad [5a]$$

For $t >> Du^{-2}$, *i.e.*, $x_o >> Du^{-1}$, Eq. [5a] becomes

$$N_{Zn} \cong N^o_{Zn}\left[1 - \exp\left(-\frac{ux - u^2t}{D} \right) \right] = N^o_{Zn}\left[1 - \exp\left(-\frac{u(x - x_o)}{D} \right) \right] \text{ at } x > x_o = ut \qquad [5b]$$

According to Eq. [5b] a constant zinc concentration profile moves in the x direction as is illustrated in Fig. 4.

The amount of zinc dissolved per unit area at time t is

$$\frac{n_{Zn}}{A} = \frac{x_o N^o_{Zn}}{V_m} + \frac{1}{V_m} \int_{x_o}^{\infty} (N^o_{Zn} - N_{Zn})\, dx \qquad [6]$$

Substituting Eq. [5b] and [1] into Eq. [6] gives

$$\frac{n_{Zn}}{A} = \frac{ut\, N^o_{Zn}}{V_m} + \frac{N^o_{Zn}}{V_m} \int_{x_o}^{\infty} \exp\left(-\frac{u(x - x_o)}{D} \right) dx = \frac{ut\, N^o_{Zn}}{V_m} + \frac{N^o_{Zn}}{V_m} \cdot \frac{D}{u} \text{ if } x_o >> Du^{-1} \qquad [7]$$

The second term on the right side of Eq. [7] may be called "excess" zinc dissolved, $\Delta n_{Zn}/A$, due to diffusion of zinc to the electrolyte/alloy interface. Thus

$$\frac{\Delta n_{Zn}}{A} = \frac{N^o_{Zn}}{V_m} \cdot \frac{D}{u} \qquad [8]$$

Furthermore, one may define an effective thickness δ of the depletion zone in the alloy

$$\delta = \frac{N^o_{Zn}}{(\partial N_{Zn}/\partial x)_{x=x_o}} = \frac{D}{u} \qquad [9]$$

In the above reported experiments, $i = 5 \times 10^{-5}$ A cm^{-2} at $E = 0.24$V. Hence, for $V_m = 7.1$ cm^3 mol^{-1}, Eq. [1] yields $u = 1.8 \times 10^{-9}$ cm sec^{-1}.

If D is as low as 10^{-16} cm^2 sec^{-1} or even less, and surface roughening does not occur, Eq. [9] yields a value of δ which is of the order of, or less than, an atomic radius. For this condition, the foregoing calculation has no physical significance. One obtains a value of δ from Eq. [9] or $\Delta n_{Zn}/A$ from Eq. [8] which is relevant only if D is much greater than 10^{-16} cm^2 sec^{-1} possibly due to the presence of excess mono- or divacancies (1).

If surface roughening has taken place, the stationary rate of movement of local regions of the interface has to be calculated upon introduction of the true current density in Eq. [1]. Since for a rough surface the true current density is less than the apparent current density (calculated as the quotient of current and the geometrical surface area), lower values of u are obtained. Thus, lower values of D in Eq. [9] yield a value of δ which has physical significance.

Since the situation is complex, the above calculation of the amount of excess zinc dissolved via diffusion to the electrolyte/alloy interface has been presented only in order to show how one may understand qualitatively that zinc initially is dissolved preferentially, and that, thereafter, there is enrichment of copper in an alloy layer next to the surface when (simultaneous) dissolution continues under quasi-stationary conditions.

Conclusions

Soft x-ray data of the surface region of Cu30Zn alloy specimens show an induction period of disproportionate zinc dissolution prior to the attainment of steady-state simultaneous (nonselective) dissolution of the alloy. The Cu $L_{II,III}$, Zn $L_{II,III}$, and oxygen K band spectra indicate the presence of excess elemental copper in the surface region. These spectra show that the copper content and depth of Cu-enrichment increases in the initial period, and that the average

thickness of the layer at steady state is on the order of 10^{-6} cm. Since the polarization conditions are such that steady-state simultaneous dissolution is eventually obtained, it is deduced that a Cu-rich surface layer is a necessary condition for simultaneous dissolution of Cu30Zn. The oxygen K band spectra show that the amount of bound oxygen on the surface decreases during the first dissolution period and then holds constant during subsequent dissolution periods at $E = 0.24$V, and that this oxygen is bound to zinc ions.

These data show the utility of soft x-ray spectroscopy for the investigation of alloying effects which occur very near the surface.

The Cu $L_{II,III}$ and Zn $L_{II,III}$ band spectra show that the usual mechanical polishing methods involving aqueous suspensions of alumina leave the surface of Cu30Zn alloy enriched in copper. Dry mechanical polishing methods are, therefore, recommended for the attainment of a more nearly uniform composition between the bulk and surface.

A model of simultaneous dissolution is presented. It shows how zinc may initially be dissolved preferentially. Then, simultaneous dissolution occurs in the presence of a Cu-rich alloy surface layer.

Acknowledgments

We gratefully acknowledge the contributions of P. J. Byrne who prepared and anodically polarized the specimens, and of W. A. Hester who assisted with the soft x-ray investigations, and the helpful comments of Professor Carl Wagner of the Max-Planck-Institut für Biophysikalische Chemie.

Manuscript submitted May 16, 1972; revised manuscript received Nov. 22, 1972. This was Paper 43 presented at the Miami Beach Meeting of the Society, Oct. 8-13, 1972.

Any discussion of this paper will appear in a Discussion Section to be published in the December 1973 JOURNAL.

REFERENCES

1. H. W. Pickering and C. Wagner, *This Journal*, **114**, 698 (1967).
2. H. W. Pickering, *ibid.*, **115**, 143 (1968); **117**, 8 (1970).
3. H. W. Pickering, *ibid.*, **115**, 690 (1968).
4. C. Wagner, *ibid.*, **116**, 343 (1969).
5. H. W. Pickering and P. J. Byrne, *ibid.*, **116**, 1492 (1969).
6. H. W. Pickering and P. J. Byrne, To be submitted to *This Journal*.
7. J. E. Holliday, in "Techniques of Metals Research," Vol. 3, Part I, Chap. 9, R. F. Bunshah, Editor, John Wiley & Sons, Inc., New York (1970).
8. J. Clift, C. Curry, and B. J. Thompson, *Phil. Mag.*, **8**, 593, 639 (1963).
9. J. E. Holliday, "Advances in X-ray Analysis," Vol. 14, p. 243, C. S. Barrett, J. B. Newkirk, and C. O. Rund, Editors, Plenum Press, New York (1971).
10. J. E. Holliday, Unpublished data.
11. J. E. Holliday, in "Soft X-ray Band Spectra and Electronic Structure of Metals and Materials," p. 101, D. J. Fabian, Editor, Academic Press, New York (1968).
12. S. Barnartt, *This Journal*, **119**, 812 (1972).
13. R. P. Frankenthal and H. W. Pickering, *ibid.*, **119**, 1304 (1972).
14. C. Wagner, *ibid.*, **103**, 571 (1956).
15. J. D. Harrison and C. Wagner, *Acta Met.*, **7**, 722 (1959).
16. C. Wagner, Private communication.

Surface Characterization of Sensitized and Activated Teflon

N. Feldstein* and J. A. Weiner

RCA Corporation, David Sarnoff Research Center, Princeton, New Jersey 08540

ABSTRACT

A tin sensitizer solution has been developed which is useful with hydrophobic surfaces. Based on radiochemical tracer adsorption measurements and conventional analytical techniques, a chemical characterization of the surface was made following the sensitization and activation steps. Quantitative results relating to the surface concentrations of active components [tin (II), tin(IV), and palladium] have been established. The surface concentration ratio of tin(II) and tin(IV) was found to be about 3:1. It was also demonstrated that the tin(II)-palladium(II) redox reaction is of low efficiency.

In the plating of dielectric substrates, a pretreatment of the substrate is essential in order to effectively deposit metals by the electroless plating technique. Of the various procedures used commercially in meeting the above requirements, a two-step immersion sequence in acidic stannous chloride solution followed by an acidic palladium chloride solution is commonly used. In general, the first bath is referred to as the "sensitizer" solution while the second solution is the "activator." The net result of this sequence is the formation of finely divided palladium nuclei which initiate the autocatalytic plating process (1, 2). The formation of the palladium metal nuclei has been proposed to be due to a redox reaction (3-5) taking place between the stannous ions adsorbed on the surface and the palladium ions in the activating solution.

The following simplified reactions probably account for some of the chemical and physical changes taking place during the sensitization and activation sequence:

1. Sensitization through stannous adsorption

$$S^* + Sn^{+2}\,(aq) \rightarrow S^* \cdot Sn^{+2}\,(ad)$$

2. Activation through a galvanic replacement

$$S^* \cdot Sn^{+2}\,(ad) + Pd^{+2}\,(aq) \rightarrow S^* \cdot Pd\,(ad) + Sn^{+4}$$

where S* refers to the dielectric substrate, and (ad) refers to an adsorbed state. Although the above process is widely used commercially, little data has been reported as to the efficiency of the reaction and the role of the substrate in such reaction.

In recent publications (6-12) it has been demonstrated that the effectiveness of conventional tin sensitizer solutions ($SnCl_2$/HCl) may be altered through proper bath modification. Specifically, the incorporation of aged stannic chloride solutions was found to provide the improvements in performance. During the aging process, a colloidal compound of tin(IV) was

* Electrochemical Society Active Member.
Key words: sensitizer, electroless plating, tin-113.

formed. The colloidal compound is believed to be β-stannic acid. It was also found (6) that the aged stannic chloride solution may be either added to conventional tin sensitizers or used in a separate step prior to the immersion in conventional tin sensitizers. In either case, identical results were obtained, both with respect to the uniformity of metallic coverage, and by an examination of the resulting surface by contact angle measurements (10). This improvement was of special significance in the case of hydrophobic substrates. Based on the tendency for the interaction between tin(II) and tin(IV), a model has been proposed (11) which accounts for the mechanism of sensitization using the improved sensitizer. In the proposed model (11), it was suggested that the sensitization process is a two-step sequence of adsorption of the aged tin(IV) component, followed by the adsorption of the tin(II) component. The adsorbed tin(IV) component provides a path for the adsorption of tin(II). The new path is based on the chemical interaction of tin(II) and tin(IV) (11). This sequence takes place whether the aged tin(IV) and tin(II) are present together or are used separately.

The choice of Teflon substrates was made in view of its great degree of hydrophobicity (10). It is also believed that the results of the current investigation would be applicable to other hydrophobic substrates (*e.g.*, photoresists) as was demonstrated in the previous work on contact angle measurements (10).

In the current work, analytical examination of the surface under varied conditions was undertaken. This work was carried out to provide verification of the proposed mechanisms (11) and to establish some quantitative values related to the concentrations of active components on the treated surfaces in the course of the sensitization and activation sequence.

Experimental Procedures

Tracer solutions.—Preparation and calibration.—The tracer (tin-113) solution of $SnCl_4$ was obtained from Amersham/Searle Corporation, Chicago, Illinois. The supplier's specification for this material was: chemical form, $SnCl_4$ in 6.3*N* HCl; volume, 2.1 ml; and solids content, 0.181 mg Sn/ml.

The tracer solution (2.1 ml) was transferred to a 100 ml volumetric flask using a freshly prepared 0.51M $SnCl_4$ solution as the transfer agent. After bringing to 100 ml volume, the final concentration was 0.50M $SnCl_4$. No appreciable effect on solution characteristics was encountered due to the slight addition of acid. This solution was allowed to age for about one week before use.

Two milliliters of the $SnCl_4$ tracer stock solution were diluted to 100 ml. Duplicate 2 ml aliquots were removed, placed into individual 1 dram screw-top glass vials and counted in a 2 × 2 in. NaI (Tl) well-type crystal coupled to a multi-channel analyzer. The average count rate of the two standards was adjusted by the appropriate dilution factor to determine the activity of the stock solution. It was found that the activity of the 100 ml tagged stock solution was 6.50×10^6 counts/min/ml. As the stock solution was 0.50M with respect to the tin(IV), the equivalent counts/min/mole of tin(IV) is 1.3×10^{10}.

The tracer (tin-113) solution of $SnCl_2$ was obtained from the same supplier as above. The supplier's specification of this material was: chemical form, $SnCl_2$ in 6*N* HCl; volume, 0.38 ml; and solids content, 1.32 mg Sn/ml.

The tracer solution was transferred to a 25 ml volumetric flask and brought to volume with 0.47M HCl. One milliliter of this stock solution was added to a 50 ml portion of $SnCl_2$/HCl solution for each 0.065 mole/liter $SnCl_2$ present in the 50 ml portion. The hydrochloric acid was held fixed at 0.47 molar.

A technique similar to that described for the tin(IV) tracer calibration was used to determine the activity of the 25 ml stock solution. An activity of 1.17×10^7 counts/min/ml was found. This activity level corresponds to 3.6×10^9 counts/min/mole of tin(II).

Substrate preparation and treatment.—The substrates used throughout the radiochemical measurements were Teflon rods 4 × 0.65 cm. The rods were cleaned in a mild alkaline soap solution, rinsed well in deionized water, and then vapor degreased with Freon TF®. The rods were immersed to a constant depth of 2 cm in a volume of 50 ml of the sensitizer solution. This constant depth immersion was done so that counting rates could be correlated to a solution of known tin-113 activity, which had a height of 2 cm, in order to provide identical counting geometries (area of 4.5 cm^2) in all cases.

Sample counting.—Counting was done on a Packard Model 116 multichannel analyzer in channels 1 through 49 (10 to 490 keV). Background radiations were low and subtracted from the measured values. Each sample was counted for 30 min, and the results are presented on a count/min basis. Prior to counting, the sensitized samples were stored for 24 hr to allow for a complete ingrowth of the In^{113m} daughter from the deposited Sn^{113}, as well as to allow the decay of any co-deposited In^{113m}. Counting of the same samples immediately after the sensitization step showed no In^{113m} peak. The following decay scheme (13) is provided representing the radiochemical characteristics of Sn^{113}.

$$Sn^{113} \xrightarrow[t_{1/2} = 118 \text{ days}]{\text{IT}} Sn^{113m} \xrightarrow[t_{1/2} = 20 \text{ min}]{\text{EC}}$$

$$In^{113m} \xrightarrow[t_{1/2} = 100 \text{ min}]{\text{IT} \cdot \gamma} In^{113}$$

where EC = electron capture: a mode of decay involving capture of an orbital electron by its nucleus; IT = isomeric transition: the decay of a nuclide to an isomeric nuclide by gamma radiation and/or internal conversion electron transition; and γ = gamma radiation of $In^{113m} \rightarrow In^{113}$ with a peak at 392 keV. In all counting experiments, at least two runs were made per composition used. The duplicate runs showed good agreement, well within ±10%.

Chemicals and solution.—All chemicals used throughout were reagent grade; the hydrochloric and nitric acids used were electronic grade. The water used was deionized and then distilled.

Etching and analysis of surface concentrations.—In this phase of the investigation, Teflon spheres were used. The spheres used were 0.094 ± 0.001 in. in diameter and supplied by Orange Products, Inc., Chatham, New Jersey. In all cases 2000 spheres were used, providing a surface area of about 360 cm^2. Following the cleaning procedure described above, these substrates were sensitized and activated in a standard fashion.

For estimating the palladium surface concentration, etching was done in both concentrated HCl and in 1:1 HCl/HNO_3. A colorimetric technique (14) was employed in estimating the reclaimed palladium. In order to estimate the surface chloride concentration following the sensitization step, the sensitized surfaces were etched in concentrated nitric acid, and the chloride was determined by nephelometry.

Results and Discussion

In investigating the interaction between tin(II) and tin(IV), Browne *et al.* (15) studied the kinetics of exchange using a radiochemical tracer technique. The tin(II) and tin(IV) were separated by the selective precipitation of Cs_2SnCl_6 by the addition of a CsCl solution. This technique, however, is applicable only in high concentrations of hydrochloric acid and is not within the range of typical sensitizing solutions. In 10.0F hydrochloric acid, the authors (15) found that the rate of thermal homogeneous exchange reaction (between 0° and 25°C) is given by

$$R = (\text{Sn II})(\text{Sn IV}) \times 4.5 \times 10^{7} \times \exp(-10{,}800/RT) \text{ liter mole}^{-1}\text{ min}^{-1}$$

Furthermore, at 25°C, the rate constants in 9.0, 10.0, and 11.0F hydrochloric acid were found to be 0.38, 0.55, and 0.73 liter mole^{-1} min^{-1}, respectively.

In view of these findings (15), and the lack of knowledge of the exchange rate for solutions having less than 1.0F hydrochloric acid (typical acid concentrations present in sensitizer formulations), the sensitization sequence for the current work was modified to provide additional information. The over-all sensitization process was carried out in two consecutive steps (6, 10), each followed by deionized water rinsing (at room temperature for 1 min): (*i*) immersion in aged stannic chloride solution with added sodium chloride and (*ii*) immersion in conventional sensitizer ($SnCl_2$/HCl). This approach was previously found (6) to give equivalent results in comparison to a sensitization process in which the stannous and stannic components coexist in the same media. By adopting this procedure, the problem of homogenous exchange between tin(II) and tin(IV) was eliminated. The incorporation of sodium chloride was made in view of the further improvement in the wetting of hydrophobic surfaces as demonstrated previously (6, 10).

Table I provides the results of the radiochemical measurements. As stated previously, these values correspond to the average of duplicate runs. In Table IA, the effect is demonstrated of varied concentration of aged stannic chloride on the surface concentration adsorbed. Examination of the results reveals no major variations although the stannic concentration is varied over a five-fold concentration range. Table IA indicates that the adsorbed stannic species (β-stannic acid) was adsorbed onto the Teflon surface to a final surface concentration which was essentially independent of bulk concentration. From the values of Table IA, an average surface activity of 521 counts/min was obtained. This value corresponds to a stannic activity of 4.0×10^{-2} μmole/substrate or 0.89×10^{-2} μmole/cm^2 tin(IV).

Table IB shows the net surface activity after immersion in a fixed stannous chloride/hydrochloric acid solution for substrates which were previously immersed in varied concentrations of aged stannic chloride solutions. Once again, little change is noted as the stannic concentration was varied over a tenfold range. Over this range, an average value of 419 ± 9 counts/min was found.

Based on the average results of Tables IA and IB, there is about a 20% loss in surface activity of tin(IV) following the immersion in stannous chloride/hydrochloric acid solution.

In order to determine the effect(s) associated with varied immersion times in the aged stannic chloride solution, the results of Table IC are provided. From the values of Table IC, it appears that for immersion times of about 1 min or greater in $SnCl_4$ solution, the surface activity of tin(IV) is constant at a value of about 410 counts/min. This value is in excellent agreement with the average results of Table IB (419 ± 9 counts/min).

In Table ID, the net surface activity of tin(IV) is shown following an immersion in acidic stannous chloride solutions of fixed hydrochloric acid content, but variable stannous chloride contents. Over a four-fold concentration range of tin(II), an average value of 381 ± 34 counts/min was obtained, in good agreement with the averages of Tables IB and IC. This result suggests that the fraction of surface material [tin(IV)] desorbed during a 1-min immersion in acidic stannous solution is independent of the stannous content of the solution.

It is interesting to note that a 1-min immersion in a solution containing 0.47M HCl (without $SnCl_2$) resulted in a surface activity [for tin(IV)] of about 200 counts/min. In fact, de-wetting of the Teflon surface takes place in the hydrochloric acid within a few minutes. By contrast, immersion in the same hydrochloric acid media with $SnCl_2$ (*e.g.*, 0.13M) did not produce any de-wetting of the surface after several hours.

In another experiment, the sequence of immersion and timing were identical, but tagged stannous chloride solutions were employed rather than tagged stannic solution. As seen from the results of Table IE, the surface activity of the stannous ion was independent of the bulk concentration used and had an average value of 314 ± 19. This corresponds to a surface concentration of 8.9×10^{-2} μmole/substrate or 2.0×10^{-2} μmole/cm^2 of tin(II). It should also be noted that extended immersion (15 min in the acidic stannous chloride solution) did not change the surface concentration of the adsorbed stannous component. From the average values of Tables IB, IC, and ID, a mean surface activity of 387 ± 29 was found for the tin(IV) after brief immersion (1 min) in acidic tin(II) solutions. From these results, the ratio of tin(IV) to tin(II) was approximately 1:3.

In Fig. 1 the net surface activity for tin(IV) as a function of immersion time in a $SnCl_2$/HCl solution is shown. Although there was an initial decrease in the surface concentration of tin(IV), after about 5 min an equilibrium value was achieved, in the range of 350 ± 25 counts/min/substrate.

This slight desorption of the tin(IV) may be due to either of the following factors operating singly or in combination: (*i*) desorption and/or dissolution of the β-stannic oxide in the acid media (*ii*) desorption due to the replacement of adsorbed stannic component by the stannous ion. Based on the current results it would seem that the possible replacement of adsorbed tin(IV) by tin(II) does not take place to any appreciable extent; instead, the desorption of tin(IV) is

Table I. Radiochemical adsorption measurements

Experiment	Aged $SnCl_4$ solution* Concentration (moles/liter × 100)	Aged $SnCl_4$ solution* Immersion time (min)	$SnCl_2$ solution** Concentration (moles/liter × 10)	$SnCl_2$ solution** Immersion time (min)	Counts/min Sn(IV)	Counts/min Sn(II)
A	0.50	1.0	—	—	564	—
	1.0	1.0	—	—	520	—
	2.5	1.0	—	—	480	—
B	0.50	1.0	1.3	1.0	415	—
	2.5	1.0	1.3	1.0	409	—
	5.0	1.0	1.3	1.0	433	—
C	2.5	0.25	1.3	1.0	347	—
	2.5	1.0	1.3	1.0	408	—
	2.5	5.0	1.3	1.0	411	—
D	2.5	1.0	0.65	1.0	360	—
	2.5	1.0	1.3	1.0	409	—
	2.5	1.0	1.9	1.0	304	—
	2.5	1.0	2.6	1.0	372	—
E	2.5	1.0	1.3	1.0	—	305
	2.5	1.0	1.9	1.0	—	351
	2.5	1.0	2.6	1.0	—	300
	2.5	1.0	1.3	15.0	—	298

* All solutions contained 3M NaCl.
** All solutions contained 4.8×10^{-1}M HCl.

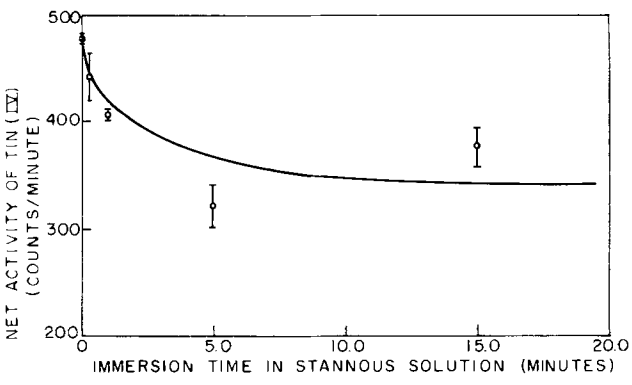

Fig. 1. Surface activity of tin(IV) vs. immersion time in stannous solution.

probably due to the acidic nature of the media and the chloride present. Yet it should be apparent that in a $SnCl_2$/HCl solution an equilibrium state is reached after which no further desorption of the adsorbed tin(IV) component takes place. This stabilization of the surface suggests that either a highly preferred configuration is established comprised of tin(II) and tin(IV), or a subsequent reaction on the surface might have taken place forming a product which is insoluble in the media. In this preferred configuration there is a fixed molar ratio between the stannous and the stannic components. Hence, at equilibrium, which is established (Fig. 1) after about 5.0 min of immersion, the following are the surface concentrations for the tin components

$$\text{Tin(II)} - 20 \times 10^{-3}\ \mu\text{mole/cm}^2$$

$$\text{or } 1.2 \times 10^{16}\ \text{atoms/cm}^2$$

$$\text{Tin(IV)} - 6.0 \times 10^{-3}\ \mu\text{mole/cm}^2$$

$$\text{or } 0.36 \times 10^{16}\ \text{atoms/cm}^2$$

This corresponds to a ratio of about 1 tin(IV) to 3.3 tin(II) existing in the mixed adsorbed layer. This configuration is quite stable and does not seem to change over a period of several hours.

Table II provides a summary of the changes in the surface concentrations of tin(IV) at each stage in the cycle.

Although in the current work the measurements were obtained using the aforementioned technique of consecutive immersion in stannic and stannous solutions, one experiment was conducted using a mixed solution of tin(II) and tin(IV). The solution used was composed of 4.7×10^{-1}M HCl, 1.3×10^{-1}M $SnCl_2$, and $SnCl_4$ varied from 1.5×10^{-3} to 1.5×10^{-1}M. Tagged $SnCl_4$ was incorporated into a 0.5M $SnCl_4$ stock solution which was aged and then used to prepare the mixed tin(II)-tin(IV) solutions.

Radiochemical measurements revealed a surface concentration which was independent of the bulk concentration of tin(IV). The surface concentration found was approximately 4×10^{-3} μmole/cm^2 tin(IV). It is interesting to note that this value agrees fairly well with the surface concentration of tin(IV) found under equilibrium conditions (6×10^{-3} μmole/cm^2) using the two-step sequence. This may indicate that little homogenous exchange between tin(II) and tin(IV) takes place under the conditions employed. This conclusion is consistent with the reported (15) trend of a lower homogenous rate of exchange with decreased acidity. Also, these results reinforce the previous proposal (11) that an identical over-all mechanism takes place regardless of whether the aged stannic component is used with conventional sensitizers or is used as a separate immersion step prior to conventional sensitization.

From the equilibrium concentration data for tin(II) and tin(IV), it would seem that both the adsorbed tin(II) as well as the tin(IV) colloid must be of several monolayers in thickness, since a monolayer is generally 10^{15} atoms/cm^2.

It was also found that the surface activity (tin(II)) of sensitized Teflon was not changed by subsequent immersion in a $PdCl_2$ solution (1.0 g/l $PdCl_2$ + 1.0 ml/l conc HCl). This trend was demonstrated using different types of sensitization [one using combined tin(II) and tin(IV) and the other using tin(IV) followed by tin(II)] procedures. The per cent change in surface activity of tin(II) was below 5%, well within the accepted 90% confidence level.

Analysis for the chloride content following the sensitization sequence revealed a chloride level of less than 3×10^{-2} μmole/cm^2. This upper limit is due to the limitation in the nephelometric method of analysis used. Based on this result, the actual role of the chloride ions in the sensitized film is not understood and requires additional investigation. However, its use in the media has provided improved wetting performance (10).

Etching and analysis of the palladium following the activation step has resulted in surface concentrations in the range of about 2×10^{-3} to 4.5×10^{-3} μmole/cm^2. These values correspond to about 10-25% of the surface concentration of tin(II). It would thus seem that the proposed redox exchange reaction between tin(II) and Pd(II) takes place only to a limited extent. This observation, while it may be puzzling at first, is not surprising since the sensitized surface [composed of tin(IV) and tin(II)] was shown to be a highly preferred configuration which does not change with time. It should be pointed out that the extent of oxidation-reduction observed for the present system does not necessarily apply to other sensitizer media. In fact, Cohen *et al.* (4, 5) have suggested that in conventional sensitizers there is a complete exchange between tin(II) and Pd(II) using Kapton as the substrate. More recently, P. F. J. v.d. Boom *et al.* (16) have shown that no replacement of tin(II) by Pd(II) takes place using soda-lime glass as the substrate.

Table II. Net radiochemical adsorption after each step* in the cycle

Step	Average counts/min for tin(IV)
After immersion in aged stannic solution**	521
After immersion in stannous solution***	419
After 1-min immersion in palladium chloride solution (2.8×10^{-3}M $PdCl_2$ and 6×10^{-3}M HCl)	413

* In all cases, 1-min immersion time was used.
** Average of results of Table IA.
*** Average of results of Table IB.

Conclusions

The present investigation, using radioactive tin-113, has provided quantitative results for the adsorption of aged tin(IV) and tin(II), the findings of which support the proposed model for this system (11). Moreover, it has been demonstrated that prior to the activation step, the surface concentration ratio of tin(II) to tin(IV) is about 3:1. Although the exact surface configuration and bonding is not known, the resulting sensitized film is highly stable, probably due to the chemical interaction of the aged stannic component with the stannous ions. As was found previously (10), the aged stannic component may be used as a distinct immersion step prior to the immersion in conventional sensitizers or be combined with the conventional sensitizer into one solution. In either case, the surface concentration for the aged tin(IV) component was found to be nearly the same.

From a practical consideration of the current system, it has been demonstrated that the surface concentration of active components is fairly independent of variations in immersion times, concentrations of aged tin(IV), and concentrations of tin(II). This permits industrial processes to be operated with wide margins in sensitizer make-up.

It would also seem doubtful whether the redox reaction between tin(II) and palladium(II) does occur. As there has not been a significant decrease in surface activity (using tagged tin(II)) after the activation step, it is possible that either (*i*) the redox reaction does not take place and the palladium is adsorbed in an ionic state, or (*ii*) the redox reaction takes place resulting in tin(IV) which is insoluble in the activator solution. Moreover, if the redox reaction does take place, its efficiency is, at best, 25%.

In view of the wide range of per cent efficiencies reported for the tin(II)/palladium(II) redox reaction, future work in this field should provide greater consideration of the sensitization system and the role played by the substrate. It is believed that future improvements in the sensitization of dielectric substrates

will further result in improved properties of thin films deposited by chemical plating techniques.

Acknowledgments

The writers wish to thank P. Blumberg and R. J. Lagomarsino of LeDoux and Company for their assistance in the radiochemical measurements, B. L. Goydish for technical assistance in the palladium analysis, and G. L. Schnable and R. Williams for useful suggestions and the reviewing of this manuscript.

Manuscript submitted June 15, 1972; revised manuscript received Nov. 30, 1972. This was Paper 218 presented at the Miami Beach, Florida, Meeting of the Society, Oct. 8-13, 1972.

Any discussion of this paper will appear in a Discussion Section to be published in the December 1973 JOURNAL.

REFERENCES

1. J. P. Marton and M. Schlesinger, *This Journal*, **115**, 16, (1968).
2. R. Sard, *ibid.*, **117**, 864 (1970).
3. W. Goldie, "Metallic Coatings of Plastics," Vol. 1, Chap. 5, Electrochemical Publications Limited, Hatch End, Middlesex, England (1968).
4. R. L. Cohen, J. F. D'Amico, and K. W. West, *This Journal*, **118**, 2042 (1971).
5. R. L. Cohen and K. W. West, *ibid.*, **119**, 433 (1972).
6. N. Feldstein and J. A. Weiner, *Plating*, **59**, 140 (1972).
7. Staff Editor, *Chem. Eng. News*, Feb. 21, p. 17 (1972).
8. Staff Editor, *Elec. Packaging and Production*, **12**, 16, April (1972).
9. Staff Editor, *Ind. Finishing*, p. 112, May (1972).
10. N. Feldstein and J. A. Weiner, *This Journal*, **119**, 668 (1972).
11. N. Feldstein, J. A. Weiner, and G. L. Schnable, *ibid.*, **119** 1486 (1972).
12. N. Feldstein and T. S. Lancsek, U.S. Pat. 3,667,527, issued May 30, 1972.
13. U.S. Department of Health, Education and Welfare, Public Health Services, "Radiological Health Handbook," 1960 edition, p. 311.
14. K. L. Cheng and B. L. Goydish, *Microchem. J.*, **10**, 158 (1966).
15. C. I. Browne, R. P. Craig, and N. Davidson, *J. Am. Chem. Soc.*, **73**, 1946 (1951).
16. P. F. J. v.d. Boom and C. H. deMinjer, Private communication (1972).

The Influence of Anions on the Structure of Porous Anodic Al_2O_3 Films Grown in Alkaline Electrolytes

P. Neufeld and H. O. Ali

Polytechnic of the South Bank, London SE1 OAA, England

ABSTRACT

Porous, anodic Al_2O_3 films have been grown in a variety of alkaline electrolytes. At elevated temperatures film growth beyond the normal barrier thickness and the development of a well-defined pore structure is not uncommon, but only borate solutions have been found to support the growth of films of a thickness comparable to commercial acid anodizing processes.

A transition from porous film growth to electropolishing has been observed in the case of citrate solutions.

The significance of the results is discussed in relation to present theories of acid anodizing.

Some electrolyte solutions such as ammonium tartrate and boric acid-borax mixtures support the growth of thin barrier films of anodic oxide on aluminum. Others, such as sulfuric and chromic acids support the growth of thick, porous films, while electropolishing may occur in others such as phosphoric acid-butyl alcohol (1). The simplest classification of these electrolytes has been in terms of their solvent ability, barrier electrolytes having the least dissolving power on the oxide film. It has long been evident that solubility alone does not explain all the variations of behavior shown by anodized aluminum, and the nature of the anions present has been shown to be important as well as the *p*H. Kissin (2) and Murphy (3) suggested that only di- or trivalent acids would support porous film growth, though evidence for the growth of such films in sulfamic acid ($NH_2\ SO_3H$) is found in the work of La Vecchia (4).

The growth of thick porous Al_2O_3 anodic films has traditionally always been carried out in acid electrolytes. Thus theories of film growth have assigned importance to the role of the hydrogen ion. Hoar and Yahalom (5) suggested that proton entry against the field could reduce the film resistance and lead to increased current flow, Joule heating, and pore initiation. Brock and Wood (6), however, reported heavy hydration and lowering of resistance for films grown in alkaline-tartrate solutions. These ideas may be harmonized to some extent by considering, as did O'Sullivan and Wood (7), that mobile protons in the film would be likely to be included in OH^- ions. Thus structural modifications due to proton entry in acid electrolytes may not substantially differ from those produced by hydroxylation in alkalies.

Recent work by Leach and Neufeld (8) and Neufeld and Ali (9, 10) has shown that thick, porous, anodic films may be grown in hot alkaline solutions containing borate ions. Heating is essential; if the dissolving power of the electrolyte is increased simply by raising the *p*H, pitting attack is induced. Active participation by the anions in the anodizing electrolyte is thus a major factor in the growth of porous films in alkaline electrolytes. The present work describes a study of the effect of a variety of anions in porous anodic Al_2O growth in alkaline solutions at temperatures above ambient.

Key words: aluminum, anodizing, alkaline, anions.

Experimental Techniques

Material.—The material used was 99.99% purity aluminum sheet, about 0.3 mm thick. Flag-shaped specimens were cut, 1 cm^2 in size, with a long narrow "flag pole" which was used for handling and making electrical contact.

The specimens were cleaned and degreased in trichloroethylene vapor. They were then chemically polished in Phosbrite 159 at 105°C, rinsed in distilled water at 65°C, desmutted in 50/50 nitric acid, and then rinsed in cold distilled water.

Electrolytes.—The electrolytes used were prepared from research-grade reagents and distilled water. The various solutions used are tabulated as follows:

Electrolyte	Composition (weight/volume per cent)
Sodium tetra-borate (borax)	5
Ammonia solution (sp gr 0.88)	8.8 (10% by volume)
Sodium meta-silicate	5
Sodium carbonate	5
Potassium sodium tartrate	5
Sodium citrate	2

Anodizing was carried out in a 1 liter Pyrex beaker immersed in a thermostatic water bath which enabled the temperature to be controlled within ±0.5°C.

Electrical control.—The power source used had an automatic switchover from a controlled current to a controlled voltage operation, enabling the anodizing sequence to be as follows:

(*i*) Film growth was started at a constant applied current until a preset cell voltage was reached.

(*ii*) Anodizing was then continued at this constant voltage, the current flow being monitored using a potentiometric recorder.

Microscopy.—For transmission-electron microscopy, very thin oxide films were grown for short times varying from 3 to 60 sec. These films, being fragile, required a special handling technique. Before dissolving away the metal (using 5% iodine methanol solution) the oxide on one side of the specimen was backed with a thin layer of cellulose acetate deposited from a 5% solution in acetone. An abrasive paper (emery paper) was used to make a small window, about 3 mm in diameter, on the other side of the specimen, until the underlying metal was exposed. A special apparatus (11) was used for dissolving away the exposed metal without affecting the plastic backing on the other side of the specimen.

Carbon was then vacuum-deposited onto the exposed oxide surface to provide mechanical support when the plastic was dissolved later.

The doubly supported oxide was then removed from the surrounding metal and placed in a folding electron-microscope grid. The plastic backing was dissolved away by submerging the grid in acetone for about 2 hr. After drying, the specimen was ready for microscopical examination. These thin specimens were also examined by electron diffraction to find out if there were any evidence of crystallinity.

The electron microscope used was an A.E.I. E.M.6.G. Vacuum-deposition was done using an A.E.I. 12 in. vacuum-coating unit.

Results

When the electrolytes were used at room temperature, the current density (for constant voltage anodizing) sharply increased and then dropped to very low values; this indicates the formation of barrier films only. With appropriate *p*H and temperature adjustments, all these electrolytes (except the silicates) were found to support porous film formation; however, only borates allowed the growth of thick anodic films (up to 15μ in an electrolyte of *p*H 10 used at 70°C) (2). The shapes of the current-time curves obtained during anodizing in 5% borax solution (*p*H 10 at 70°C) are generally similar to those recorded during sulfuric and chromic acid anodizing (Fig. 1). This form of current-time curve is diagnostic of porous film growth, following an initial barrier-film formation. Pore formation is confirmed by electron-optical examination of very thin films (Fig. 2). The pore structure showed a development with time in the early stages of growth. The general trend is for a fine structure of many small

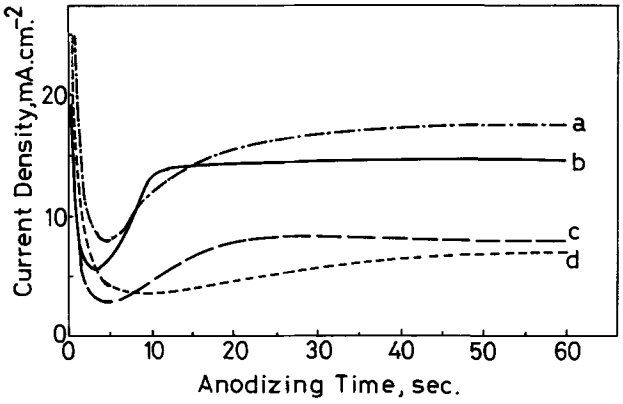

Fig. 1. Current-time curves for different electrolytes. Curves a and c for 5% borax solution (*p*H 10, at 70°C) at 50 and 20V, respectively; b for 15% by volume sulfuric acid at 20°C and 10V; d for 10% chromic acid at 40°C and 30V.

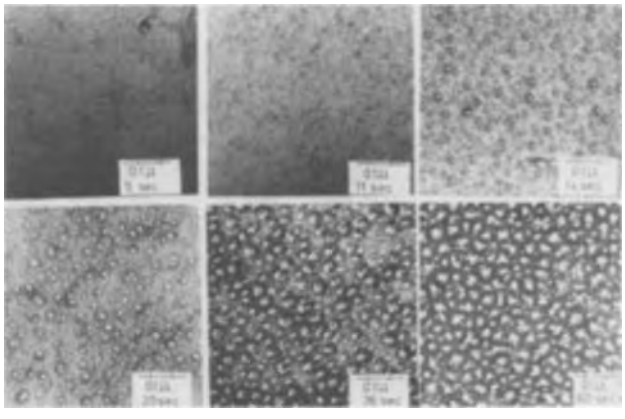

Fig. 2. Transmission electron micrographs of specimens anodized in 5% borax, *p*H 10, at 20V and 70°C.

pores to develop into a coarser one with fewer but larger pores.

The anion in the alkaline electrolyte seems to have very marked effects on both the electrical characteristics during anodic film growth, and the final film structure. Thus on anodizing in a 5% weight/volume sodium metasilicate solution (*p*H 12.5) at 70°C and 50V, only a barrier film was obtained. The current density observed was in the region of 0.3 mA/cm^2 (Fig. 3) which is high for reported leakage currents. When the *p*H was increased to about 13.5 by adding 2 g/liter solid sodium hydroxide, the current density increased to about 0.7 mA/cm^2 (Fig. 3), but the resulting oxide was still mostly a barrier-type film, with very few isolated tiny pores (Fig. 4 III).

When anodizing was carried out in a solution of 5% weight/volume potassium-sodium tartrate + 2 g/liter solid sodium hydroxide (*p*H 12.5) at 70°C and 50V, the current-time curve was indicative of porous film formation. After the initial surge (Fig. 3) the current dropped and then steeply rose to a value of 35 mA/cm^2 within 3 sec. The structure of the film obtained after anodizing for 15 sec showed channels about 15.0-20.0 nm wide (Fig. 4 II). After 1 min of anodizing, pores having diameters of the order 15.0-20.0 nm were more apparent although some channels can still be seen.

The current-time curve obtained during anodizing in the 8.8% weight/volume ammonia solution (*p*H 11.3) at 70°C and 50V (Fig. 3) did not show a rise after the initial drop to a value of 8-10 mA/cm^2. Few irregular pores were initially obtained, but after 10 min of anodizing these were replaced by large and more regular ones (Fig. 4 I).

During anodizing in 5% weight/volume sodium carbonate solution (*p*H 11.7), at 60°C and 50V, the current density dropped to about 50-60 mA/cm^2 (Fig. 3) and

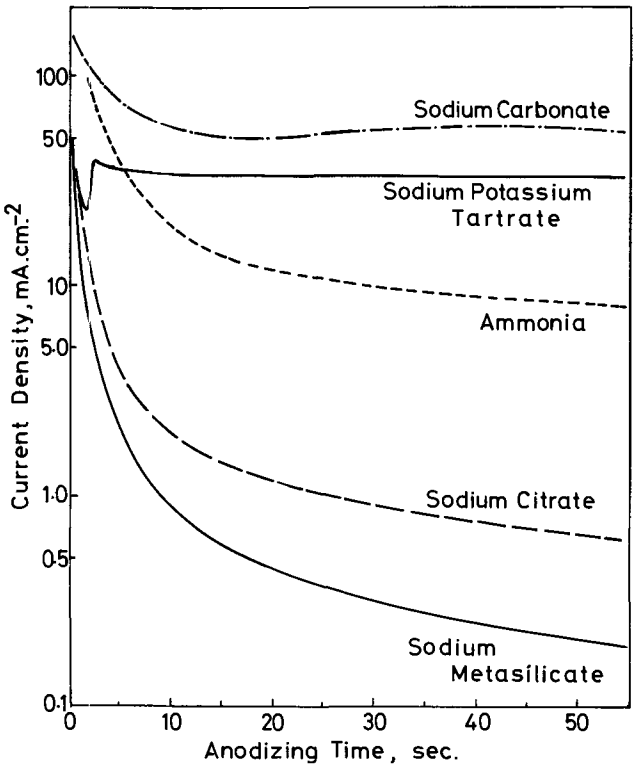

Fig. 3. Effect of anion on current density

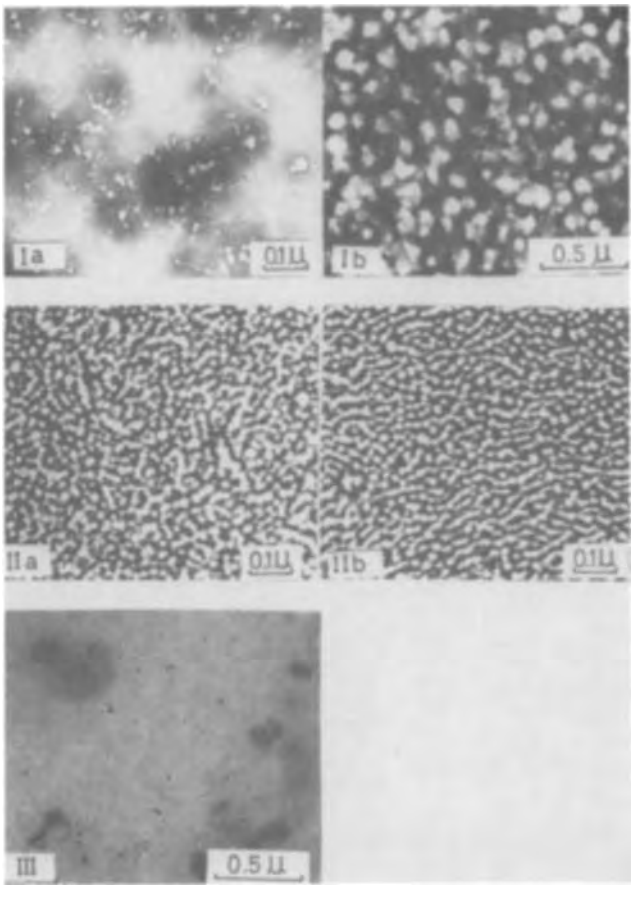

Fig. 4. Electron micrographs of specimens anodized at 50V and 70°C in: I. 10% by volume ammonia solution for (a) 30 sec, (b) 10 min; II. 5% weight/volume sodium potassium tartrate + 0.2% weight/volume sodium hydroxide for (a) 15 sec, (b) 1 min; III. 5% weight/volume sodium metasilicate + 0.2% weight/volume sodium hydroxide for 30 sec.

the resulting structure was porous, with the pores showing large variations in size and distribution (Fig. 5).

On anodizing in a 2% weight/volume sodium citrate solution of pH 8.0, at 70°C and 50V, for 1 min, only a barrier film is formed (Fig. 6), although the current density observed was about 0.6 mA/cm² which is relatively high for nonporous films (Fig. 3). On prolonged anodizing, the current density showed a slow rise to about 0.7 mA/cm² (after 30 min of anodizing) indicating pore formation, which is indeed confirmed by electron microscopy (Fig. 6). On adding 1 g/liter of solid sodium hydroxide to the citrate solution (pH 12.5) a porous structure developed more quickly (Fig. 7b).

With an increasing sodium hydroxide content, which increases the dissolving power of the electrolyte, larger pores were obtained (Fig. 7c). An extreme example was when 10 g/liter sodium hydroxide were added. The current density increased to about 1 A/cm² (Fig. 8), and the specimen was highly polished after anodizing. The stripped oxide showed a cellular structure under the electron microscope (Fig. 7d). The visual contrast was very poor; the significance of this is discussed later. In the case where 2 g/liter sodium hydroxide was added, the film grown for 1 min was similar to that grown for 30 min (Fig. 7e and f), which shows that no considerable thickening had taken place, and probably a terminal thickness had been reached.

All the thin, anodic, oxide films obtained in the alkaline electrolytes were examined by electron diffraction and gave broad diffuse rings; there was no indication of crystallinity.

Discussion

Electrolyte temperature.—It is significant that at normal ambient temperatures no films grown in alka-

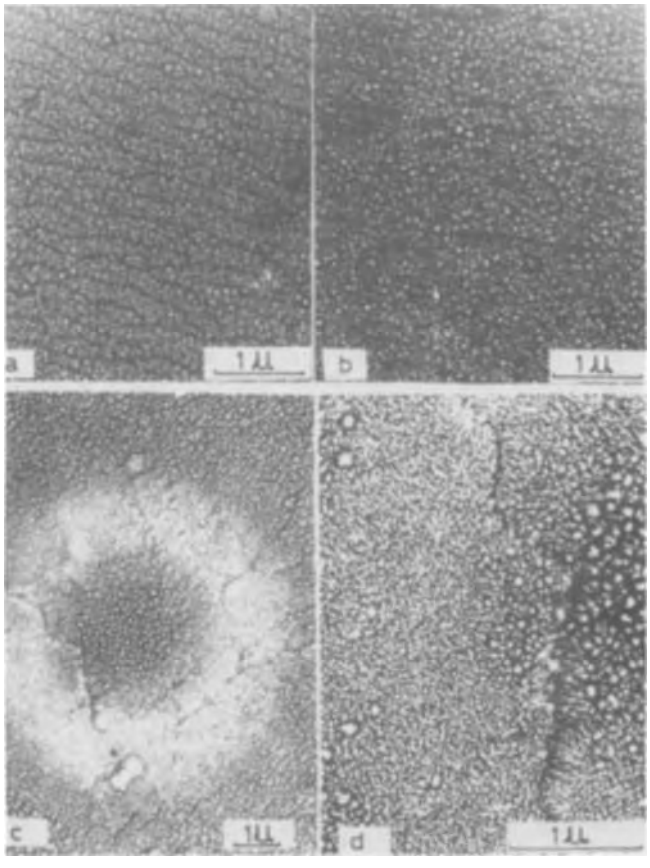

Fig. 5. Electron micrographs of specimens anodized in a 5% weight/volume sodium carbonate solution at 50V and 60°C: (a) anodized for 15 sec; (b) 30 sec; (c) different region in specimen (a); and (d) magnified portion of (c).

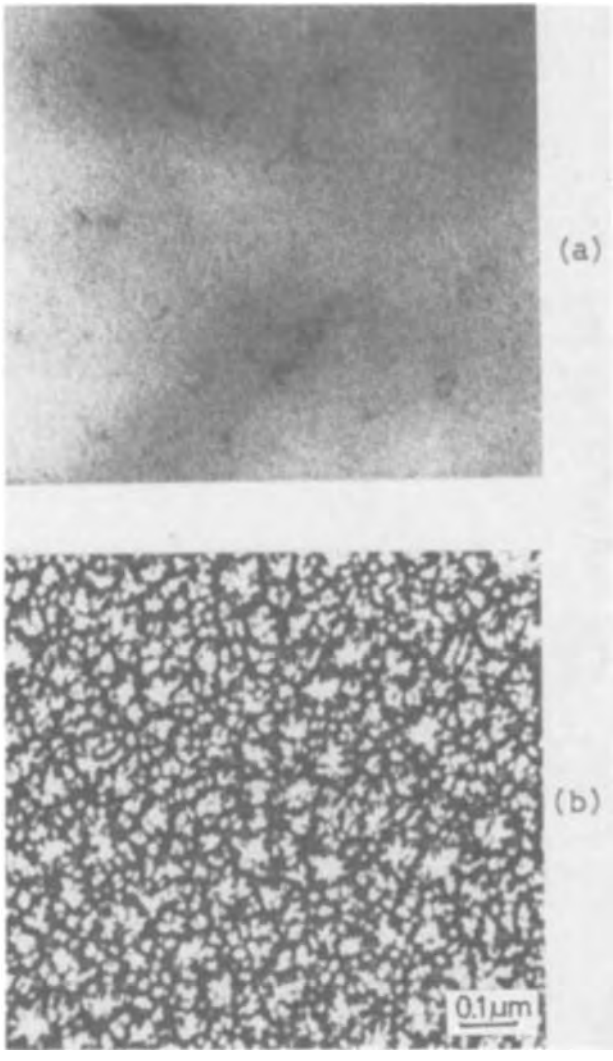

Fig. 6. Electron micrographs of specimens anodized in 2% weight/volume sodium citrate solution (pH 8) at 70°C and 50V: (a) anodized for 1 min; (b) anodized for 30 min.

line electrolytes have been observed to develop a well-defined pore structure. A faint irregular texture may be observed in most barrier films, but this does not develop further. This implies that preferential dissolution does not occur at surface sites, and hence that the chemical dissolving power due to the OH^- ion concentration is not the controlling factor in pore development.

Pore development is observed when the temperature is raised. This leads to the conclusion that the changes which produce pore formation occur due to adsorption or absorption of ionic species (anions in alkaline solutions) by the oxide film. Electrolytes which operate when cold, such as sulfuric, phosphoric, and oxide acids, are known to incorporate significant concentrations of anions in the oxide (12-14). It must be assumed that under alkaline conditions sufficient modification of film properties by anions can only take place at temperatures above ambient.

Pore initiation.—The results obtained throw further light on the earliest stages of pore formation. All workers are agreed that the initial pore structure is much finer than that which supports continued film thickening. The earliest texture has been described as consisting of micropores (8) or as small, thicker (or more opaque) "islands" (7). Figure 4 (II and III) shows both types of feature to be present on the same specimen. (This is less clearly visible in Fig. 4 III.)

Irregularity in structural modification can only be ascribed to irregularity in the original structure, hence

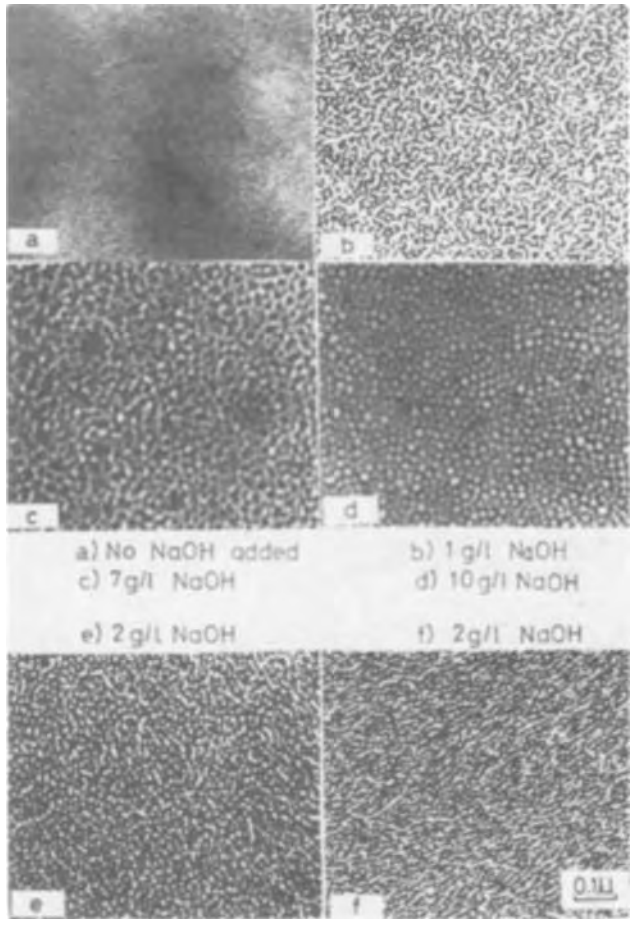

Fig. 7. Electron micrographs of specimens anodized at 50V and 70°C in a sodium citrate solution containing various amounts of NaOH. a, b, c, and d anodized for 1 min, e for 30 sec, and f for 30 min.

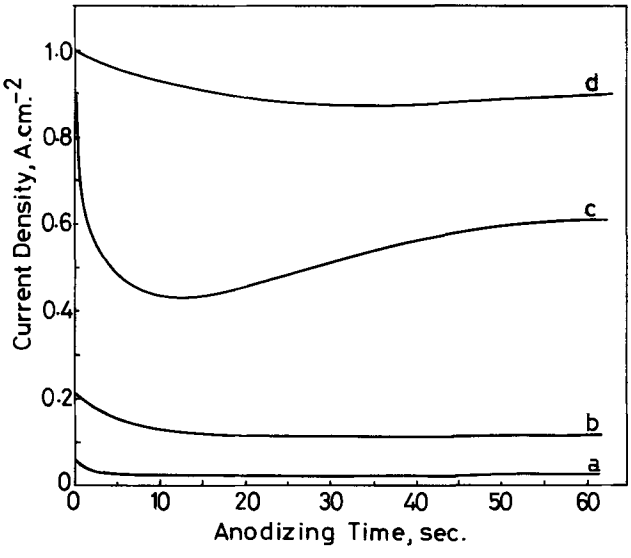

Fig. 8. Effect of sodium hydroxide content on current density. Anodizing carried out in a 2% weight/volume sodium citrate solution containing: (a) 1 g/liter, (b) 4 g/liter, (c) 7 g/liter, and (d) 10 g/liter NaOH, and used at 50V and 70°C.

the initial barrier film cannot be regarded as amorphous but must consist of crystallites. We believe that the less dense regions in electron micrographs of textured barrier films represent regions of hydration or hydroxylation and possibly also penetration by other anions as proposed by Murphy and Michelson (15) and

O'Sullivan *et al.* (16). Where a micrograph shows dense "islands" these may not represent regions of local growth, as proposed by O'Sullivan and Wood (17) but rather crystallites entirely surrounded by modified "grain boundary" regions. Where "pores" are seen, this represents modification only at "triple points," while a structure as seen in Fig. 4 II represents an intermediate stage where modification has extended from triple points along some, but not all, grain boundaries. The crystallite size as revealed by electron micrographs (10) is generally in the range 2.5-5.0 nm which is too small to give well-defined diffraction patterns.

Field-assisted dissolution.—The earliest development of texture in barrier films may be observed even with films which do not develop large pores later on (Fig. 4 II). Thus the effect of anions in modifying the pore structure and film growth is operative on the next stage of pore development which involves the concentration of current through the film in local regions and field-assisted dissolution in these same locations. O'Sullivan and Wood (7) considered a mechanism which would give stoichiometric oxide dissolution at a pore base. This is unnecessary, since under irreversible conditions, oxyanions could not simultaneously be moving into the electrolyte to give dissolution and into the oxide to support further oxidation. Recent tracer measurements by Amsel and Siejka (17) support the view that oxygen in the lattice will not pass into the electrolyte during field-assisted dissolution. This leads to the conclusion that only metal ion dissolution needs to be considered in the mechanism of field-assisted dissolution.

Under acidic conditions a metal ion which has entered the electrolyte will be solvated as a cation and will move away from the interface by diffusion and migration. Under alkaline conditions the metal will be solvated as an anion and migration will oppose diffusion. The concentration of aluminate ions will thus tend to be very high near the surface and will impede further dissolution. Since it has been shown that experimental results favor an interpretation of the influence of anions in terms of modification of oxide properties during field-assisted dissolution, it may be concluded that this effect is produced by adsorption of anions at the pore base. Any adsorption (which would be favored at metal-ion sites on the surface) will displace hydroxyl ions and provide a more favorable environment for dissolving metal to traverse the double layer in the form of cations. All the anions studied, except for silicate, show some development of pore structure; in the latter case there is evidence that a resistant alumino-silicate may form (18). The outstanding effect of the borate ion is not reflected in a particularly high boron content of the anodic film (19), and must be ascribed to adsorption. Borates are well known as corrosion inhibitors for aluminum and it can be assumed that borax inhibits pore-wall dissolution while permitting field-assisted cation escape at the pore base.

Oxygen entry.—During porous film growth, oxyanions must enter the film and migrate under the influence of the field so as to contribute to the formation of new Al_2O_3 at or near the metal-oxide interface; only in this way can growth of oxide in between pore locations be explained. It is likely, in view of the substantial evidence for hydration of the anodic film (20), that OH^- ions would be more mobile than O^{2-} ions (7). In the case of acid electrolytes the oxygen contributing to fresh oxide growth must derive from H_2O molecules (17) and the *p*H of the solution at the pore base would tend to decrease. In alkaline solutions there is an abundance of OH^- ions and the simplest mechanism that can be proposed is one of direct entry of hydroxyl ions into the lattice under the influence of the field. It may be mentioned that the mechanism of field-assisted dissolution proposed by O'Sullivan and Wood (7) can be modified by assuming that a single proton would attach to a surface oxygen anion, which would then become more mobile and re-enter the oxide bulk. This is more likely than the acquiring of a second proton and dispersal into the solution as a water molecule.

Pore angle and terminal thickness.—In the cases where the electrolyte did not support the growth of a very thick porous film (all alkaline electrolytes used except borate), it may be suggested that field-assisted dissolution at the pore base is weak, and that relatively fast chemical dissolution occurs at the pore walls. Thus the terminal thickness is established rapidly. When the pore-wall dissolution is not relatively fast (in the case of borates) long pores and thick, anodic films are obtained.

It has been proposed (21, 22) that chemical dissolution of the pore wall during film thickening leads to a truncated pore structure. The maximum or terminal anodic film thickness is reached when the pore-mouth diameter becomes equal to the diameter of the cell containing it (Fig. 9). This would be expected to occur earlier when the dissolving power of the electrolyte is increased (*e.g.*, when sodium hydroxide is added to a sodium citrate bath). Apparently the terminal thickness is reached after only 30 sec of anodizing, since the film does not thicken enough to obstruct the electron beam even after 30 min of anodizing (Fig. 7e and f). Now consider two adjacent pores in an oxide film which has reached its terminal thickness (Fig. 9). When dissolution is not very severe (*i.e.*, 1 g/liter sodium hydroxide added), the pore would be expected to have a slightly slanting wall (small ϕ Fig. 9a). On increasing the dissolving power of the electrolyte (*i.e.*, add 10 g/liter sodium hydroxide), faster dissolution of the pore wall takes place resulting in a more slanting wall (large ϕ) and a relatively thin film (Fig. 9c).

Electron micrographs (Fig. 7b, c, and d) confirm this effect of increased ϕ and reduced film thickness. When ϕ is relatively small, the wedge-shaped oxide film between two neighboring pores obstructs the elec-

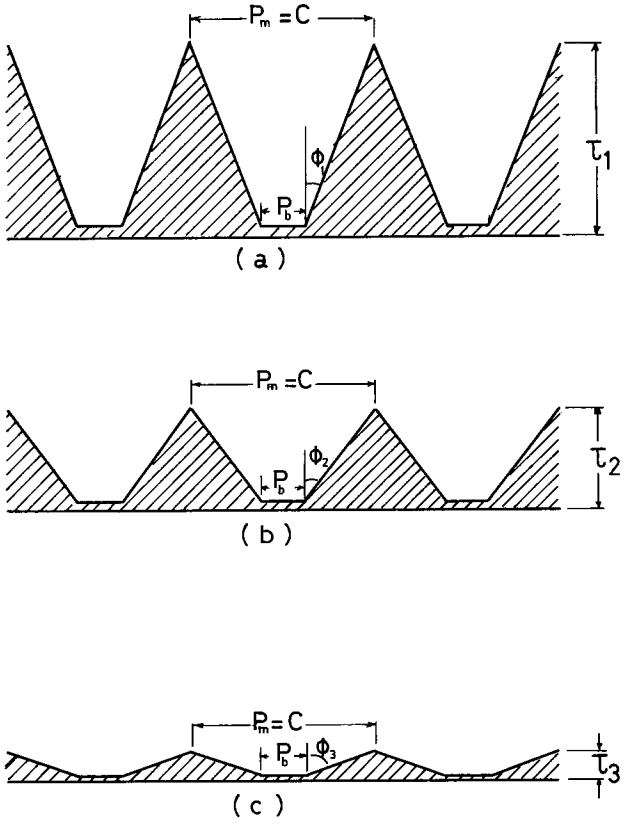

Fig. 9. Film dissolution leading to polishing. P_b, pore base diameter; P_m, pore mouth diameter; C, cell size (diameter); ϕ pore wall slant; τ terminal film thickness.

tron beam substantially. This oxide appears as very dark areas surrounding the light pores, producing a strong contrast. As ϕ increases, the thickness of the oxide wedge decreases, and the contrast drops drastically. This was the case when the sodium hydroxide content in the citrate bath was increased to 10 g/liter. The contrast is essentially due to the difference in thickness of the oxide wedge and that of the barrier film. The thickness of the latter, under the conditions used, was in the region of 5 to 15 nm. Significantly, this extreme barrier film thinning (0.1-0.3 nm/V^{-1}) (19) was reflected in the very high current density (about 1 A/cm^2) which passed during the process (Fig. 8).

It seems likely that the observed electropolishing of aluminum is a form of porous type anodizing, where the angle ϕ approaches 90°.

Conclusions

The results reported support the view derived from Murphy and Michelson (15) that as-formed anodic Al_2O_3 consists of crystallites which become surrounded by hydrated regions. The early stages of pore initiation show features consistent with increased current flow and field-assisted dissolution at these modified regions.

While increasing the pH of alkaline electrolytes does not necessarily produce well-defined, porous, oxide growth, the raising of the electrolyte temperature will induce such growth in electrolytes containing a variety of anions. Thus the action of the anions in supporting and modifying porous film growth is operative on the film properties rather than on dissolved species.

The powerful effect of the anion in altering the morphology and thickness of porous Al_2O_3 films grown in alkaline electrolytes may be tentatively explained in terms of the relative effects of adsorption on the rates of field-assisted dissolution and pore-wall dissolution. Only borate has been found to support film growth beyond a few microns and only metasilicate has been found to inhibit pore formation altogether.

The transition from porous oxide growth to electropolishing has been observed in the case of citrate solutions. The change is not due to a fundamental alteration in film structure, but rather to an increase in pore-wall dissolution at increasing pH.

Acknowledgments

The authors are indebted to Mr. G. Isserlis for the provision of laboratory facilities and for encouraging this study. This paper described part of the work carried out for the Ph.D. degree of the University of London (H.O.A.).

Manuscript submitted Sept. 8, 1972; revised manuscript received Nov. 13, 1972.

Any discussion of this paper will appear in a Discussion Section to be published in the December 1973 JOURNAL.

REFERENCES

1. M. Gy Hollo, *Acta Met.*, **4**, 265 (1960).
2. G. H. Kissin, *ASTM Special Tech. Publ.*, **388**, 34 (1965).
3. J. F. Murphy, *Plating*, **54**, 1241 (1967).
4. A. La Vecchia, G. Piazzesi, and F. Siniscalco, *Electrochim. Metal.*, **2**, 71 (1967).
5. T. P. Hoar and J. Yahalom, *This Journal*, **110**, 614 (1963).
6. A. J. Brock and G. C. Wood, *Electrochim. Acta*, **12**, 395 (1967).
7. J. P. O'Sullivan and G. C. Wood, *Proc. Roy. Soc. (London), Series A*, **317**, 511 (1970).
8. J. S. L. Leach and P. Neufeld, *Corrosion Sci.*, **9**, 413 (1969).
9. P. Neufeld and H. O. Ali, *Trans. Inst. Metal Finishing*, **47**, 171 (1969).
10. P. Neufeld and H. O. Ali, *ibid.*, **48**, 175 (1970).
11. H. O. Ali and P. Neufeld, *J. Phys. E. Scient. Instrum.*, **3**, 747 (1970).
12. G. A. Dorsey, *Plating*, **57**, 1117 (1970).
13. F. Liechti and W. D. Treadwell, *Helv. Chim. Acta.*, **30**, 1204 (1947).
14. R. C. Plumb, *This Journal*, **105**, 498 (1958).
15. J. F. Murphy and C. E. Michelson, *Proc. Conf. Anodising Aluminum*, pp. 83-95, University of Nottingham (1962).
16. J. P. O'Sullivan, J. A. Hockey, and G. C. Wood, *Trans. Faraday Soc.*, **65**, 535 (1969).
17. G. Amsel and J. Siejka, Communicated at a meeting on "Fundamental Aspects of Ion Movement in Anodic Films," University of Nottingham (1972).
18. B. A. Wilson, *Corrosion Sci.*, **11**, 527 (1971).
19. H. O. Ali El-Awad, Ph.D. Thesis, University of London (1972).
20. G. A. Dorsey, *Plating*, **56**, 180 (1969).
21. L. A. Cosgrove, *J. Phys. Chem.*, **60**, 385 (1956).
22. G. Poalini, M. Masaero, F. Sacchi, and M. Pagenelli, *This Journal*, **112**, 32 (1965).

Pulse Electroplating of Silver-Tin Alloys and the Formation of Ag_3Sn

Henry Leidheiser, Jr.* and A. R. P. Ghuman

Center for Surface and Coatings Research, Lehigh University, Bethlehem, Pennsylvania 18015

ABSTRACT

Silver-tin alloys were electrodeposited at 50° by pulse plating from a bath containing AgCN 0.020M; $K_2SnO_3 \cdot 3H_2O$ 0.375M; KCN 1.40M; and KOH 1.25M. The major variables studied were pulse cycle and current density. In the current density range of 1.5-3 A/dm^2 with pulse on-times of 5-100 msec and off-times of 50-200 msec, the major constituent in the deposit was the intermetallic compound Ag_3Sn. Several experimental conditions were determined in which the elemental tin and silver contents were small. The Ag_3Sn coatings showed excellent integrity at thicknesses up to 2×10^{-3} cm and were highly ductile. The tarnish resistance of the Ag_3Sn coatings was superior to that of pure silver.

The work reported herein represents a continuing interest in the formation of intermetallic compounds during corrosion and electrodeposition (1-5). Illustrative of this interest a method was given recently for the preparation of Ag_3Sn coatings (5). This method was based on the observation that in stirred solutions the deposit composition was constant over a range of current densities and could be controlled by using spe-

* Electrochemical Society Active Member.

Key words: electrodeposition, intermetallic, silver, tin.

cific silver and tin concentrations. Concentrations of dissolved silver and tin in the plating bath which yielded a 3:1 atomic ratio of silver and tin in the deposit crystallized as Ag_3Sn.

The chief disadvantage of the method was the fact that the deposit tended to become dendritic and noncompact in nature for thicknesses in excess of 1.5×10^{-3} cm. Presumably deposition was occurring near the limiting current density for silver deposition with the consequent difficulty of maintaining a relatively uniform growth rate over the entire surface. It appeared that pulse plating offered a means for circumventing this difficulty. The purpose of this study is therefore to explore pulse plating as a technique for forming useful Ag_3Sn electrodeposits.

Experimental

All deposits were made from a solution containing AgCN, 0.020M; $K_2SnO_3 \cdot 3H_2O$, 0.375M; KOH, 1.25M; and KCN, 1.40M. The bath was stirred during deposition and the temperature of the bath was maintained at 50° by a thermostated water bath. In the majority of cases copper substrates were used, but in several cases steel substrates were used. The counterelectrode was graphite.

The pulsing unit was similar to that developed by Avila and Brown (6). The minimum pulse width obtainable was of the order of 1.5 msec, but the minimum pulse width used in these studies was 5 msec. The current pulses were essentially square wave in character with a very slight decrease in current over the on-time period.

X-ray diffraction examinations of the deposits were made on unstripped coatings using conventional electronic recording of the diffraction lines.

The composition of the deposits was obtained from electron microprobe measurements using both static beam and scanning beam techniques. The data were corrected for absorption and fluorescence effects using a computer program. Inadequacies in the analytical method are apparent from the fact that the sum of the calculated tin and silver contents was always less than 100%, generally being 97-98%.

Results

Effect of pulse cycle.—Important data are summarized in Fig. 1-4 for pulse on-times of 5-100 msec, pulse off-times of 5 to 200 msec, and current densities of 0.8 to 3.25 A/dm². It should be noted that the data are given in terms of the intensity of the strongest line in the x-ray diffraction pattern for the three constituents of interest, silver, tin and Ag_3Sn. Preferred orientation of the constituents was fortunately not a complication as shown by the fact that the relative intensities of the lines for each constituent were always in approximately the same ratios. Changes in the concentration of each constituent can be determined qualitatively as a function of experimental variables, but no conclusions can be drawn from these data alone concerning the relative amounts of each constituent present in the deposit.

The generalizations can be made that at fixed current density, the concentration of elemental silver in

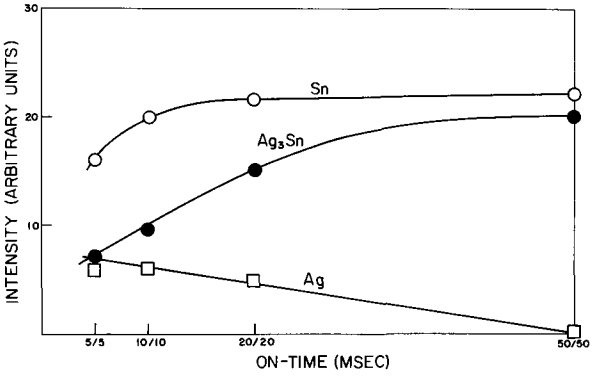

Fig. 1. Changes in Ag_3Sn, elemental silver, and elemental tin content in the electrodeposit as a function of pulse cycle with equal on- and off-times. Current density = 2.26 A/dm². The ordinate represents the intensity of the strongest line in the x-ray diffraction pattern.

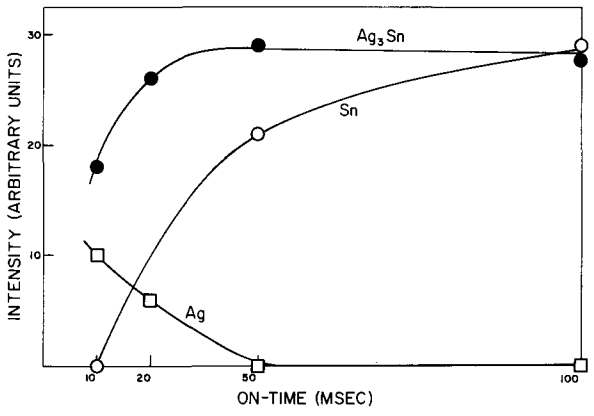

Fig. 2. Changes in Ag_3Sn, elemental silver, and elemental tin content in the electrodeposit as a function of on-time. The off-time is constant and equal to 100 msec. Current density = 3 A/dm². The ordinate represents the intensity of the strongest line in the x-ray diffraction pattern.

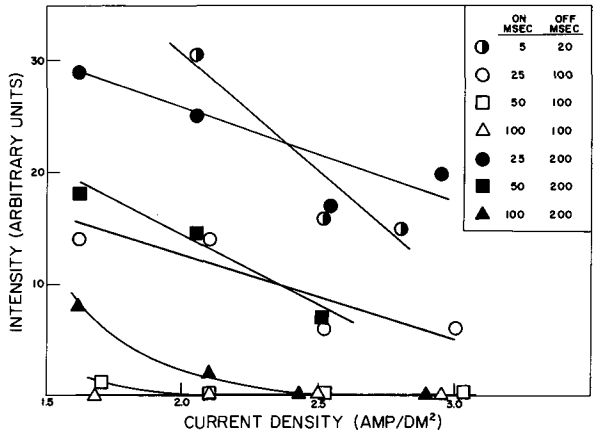

Fig. 3. Change in elemental silver content of the electrodeposit as a function of current density for various on-off cycles. The ordinate represents the intensity of the strongest line in the x-ray diffraction pattern of silver.

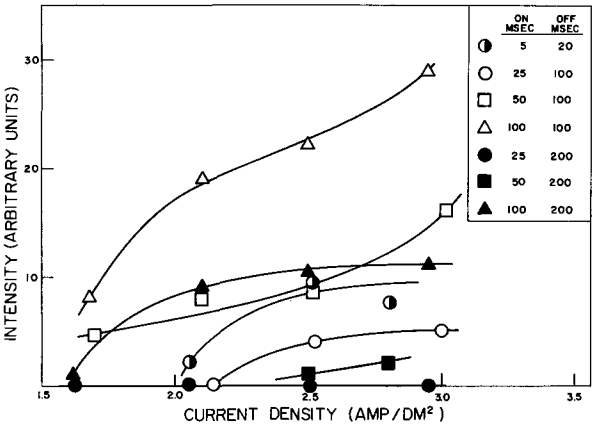

Fig. 4. Change in the tin content of the electrodeposit as a function of current density for various on-off cycles. The ordinate represents the intensity of the strongest line in the x-ray diffraction pattern of tin.

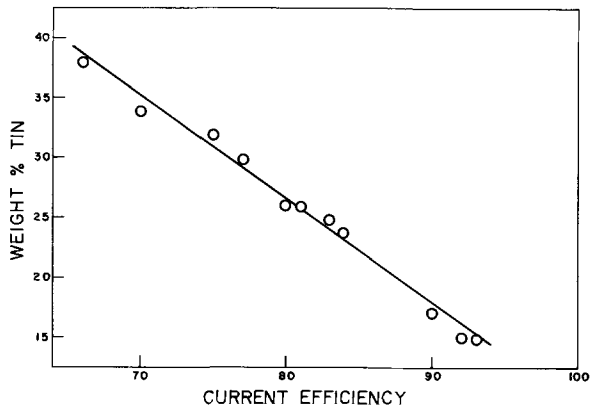

Fig. 5. Current efficiency for the electrodeposition of silver-tin alloys as a function of the composition of the deposit.

the deposit decreases with increase in the on-time and the concentration of elemental tin in the deposit increases with increase in on-time. For fixed on-off cycles, the amount of elemental silver in the deposit decreases with increase in current density and the amount of elemental tin in the deposit increases with increase in current density. The current density required to maximize the amount of Ag_3Sn in the deposit is a function of the on-off cycle utilized.

Current efficiency.—Current efficiencies were calculated from the composition of the deposit as obtained from microprobe measurements and under the assumption that tin was reduced from the tetravalent state and silver from the monovalent state. Representative data from eleven different experiments are plotted in Fig. 5. It will be noted that the current efficiency is a linear function of the weight per cent of tin in the deposit. At the composition corresponding to that of Ag_3Sn [27 weight per cent (w/o) tin] the current efficiency was 80%. The data summarized in Fig. 5 are consistent with the conclusion that silver is deposited in excess of 100% current efficiency and tin is deposited at approximately 15% current efficiency.

Homogeneity of deposits.—The cross sections of many of the deposits were examined by electron microprobe and by scanning microscopy. In the case of compositions approximating Ag_3Sn the composition was uniform throughout the thickness and the distribution of the two metals was homogeneous. X-ray images of a 20μ thick deposit formed at a current density of 2.1 A/dm^2 with an on-time of 100 msec and an off-time of 200 msec are given in Fig. 6a and 6b. This deposit had a composition approximating Ag_3Sn but x-ray diffraction analysis showed the presence of small amounts of elemental silver and elemental tin. Both the silver and the tin x-ray images indicated homogeneity, but the tin x-ray image was much more sensitive to small compositional differences in neighboring regions.

Mechanical properties of the deposits.—Knoop hardness measurements were made on cross sections of eleven deposits. Results are summarized in Fig. 7. The hardness of deposits containing approximately 100% Ag_3Sn were intermediate to those containing excess silver and those containing excess tin.

Deposits generally were made on steel substrates without an intermediate strike of silver. Occasionally such deposits exhibited poor adherence and could be peeled from the substrate with relative ease. The isolated deposit was extremely ductile and could be bent back and forth without fracture.

Deposits could be polished to high luster with no difficulty.

Tarnish resistance.—The tarnish resistance of the electrodeposited coatings relative to that of electrodeposited silver was determined by exposure of metallographically polished and buffed samples to a gaseous environment containing 1% H_2S-1% SO_2-98% air at room temperature. The samples containing Ag_3Sn with minimal amounts of excess silver or tin and those containing excess tin exhibited tarnish resistance superior to that of silver and to the Ag_3Sn deposits containing excess silver. The intermetallic deposit discolored to a yellow or tan while a pure silver electrodeposit became dark blue to black in the same time interval. Quantitative information on the rate of tarnish film growth was not obtained.

Discussion

This study has shown that pulse plating is a very effective technique for the electrodeposition of silver-tin alloys of fixed composition. It is a particularly effective technique for the preparation of high quality Ag_3Sn coatings with minimal amounts of elemental silver and tin. Experimental conditions which lead to the maximum Ag_3Sn content, as determined by x-ray diffraction analysis, are summarized in Table I.

The question arises as to why pulse plating is so effective in forming the intermetallic compound Ag_3Sn. As shown by Girard (7) pulse plating is more effective in maintaining a uniform composition over the thickness of the deposit than is d-c plating. Our microprobe studies confirm that the composition is very uniform over the thickness of the deposit (see Fig. 6a and 6b). Thus, it is to be expected that once the experimental

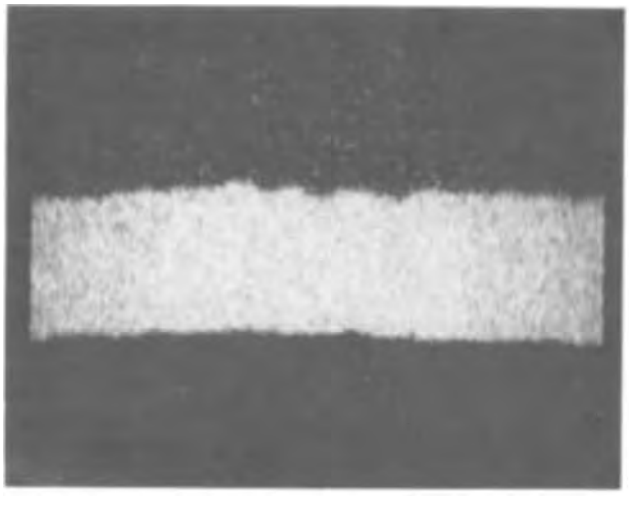

Fig. 6a. Silver x-ray image of 2 x 10^{-3} cm thick deposit formed at 2.1 A/dm^2 with a pulse cycle of 100 msec on-time and 200 msec off-time. (1000×)

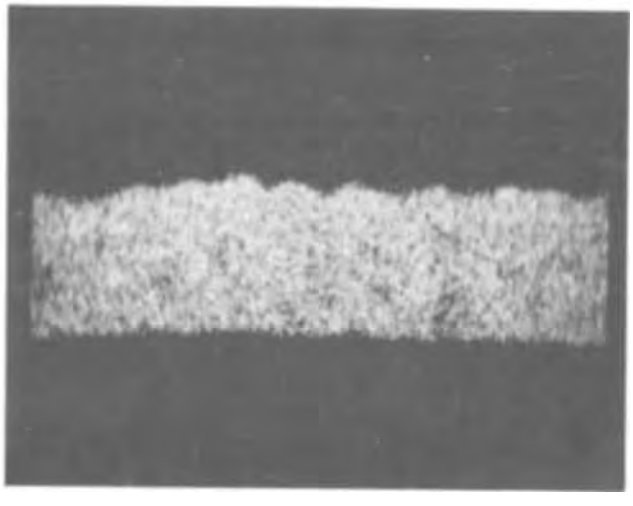

Fig. 6b. Tin x-ray image of 2 x 10^{-3} cm thick deposit formed at 2.1 A/dm^2 with a pulse cycle of 100 msec on-time and 200 msec off-time. (1000×)

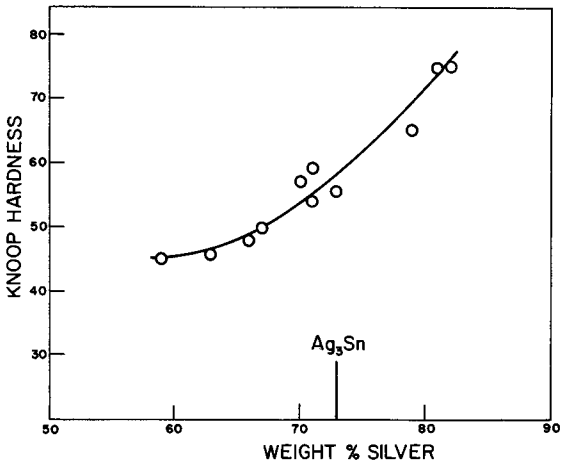

Fig. 7. Knoop hardness of deposits as a function of composition.

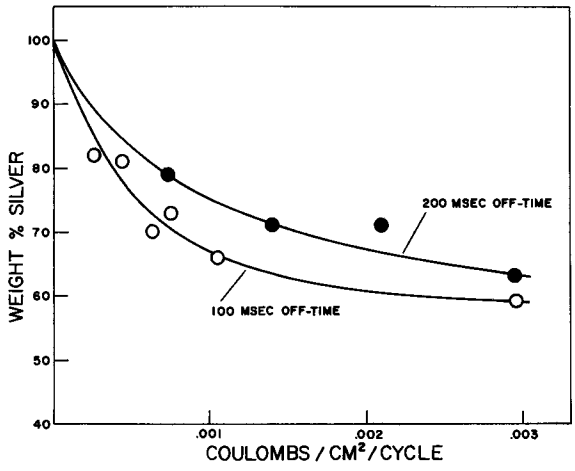

Fig. 8. Composition of the deposit as a function of the coulombs passed during one cycle.

conditions are known for depositing silver and tin in a 3:1 atomic ratio, this composition will be maintained over the thickness of the deposit during the deposition time.

Cheh (8) has calculated the limiting current density for pulse plating as a function of pulse cycle and the ratio of (on-time)/(total pulse cycle time). The majority of our experiments were carried out under conditions where the limiting current density under pulse plating is very similar to that for d-c plating. For example, with an on-time of 50 msec and an off-time of 100 msec, extrapolation of Cheh's curves give a limiting current density under pulse plating not greatly different than that for d-c plating.

Figure 5 indicated that there is a linear relationship between the composition of the deposit and the current efficiency. If the curve is extrapolated to 0% tin in the deposit, the calculated current efficiency for silver deposition is approximately 109%. The most likely explanation for this excess current efficiency is that during the off-time there is a metal replacement reaction between electrodeposited metallic tin and silver ions which diffuse to the surface during the off-time.

The importance of the off-time in controlling the composition of the deposit is demonstrated by Fig. 8. In all cases the weight per cent of silver in the deposit is greater for a 200 msec off-time than for a 100 msec off-time at equivalent coulombs passed during the cycle. Two reasons for this result are proposed. First, the longer off-time allows greater replenishment of silver complex ions in the cathode film. Second, the longer off-time allows greater reaction of metallic tin in the surface of the deposit with ionic silver in the adjoining liquid. The relative magnitude of these two effects is unknown.

Pulse-plated silver-tin alloys, and particularly those with a composition approximating Ag_3Sn, show promise as decorative coatings since the tarnish resistance is greater than that of pure silver. The deposits are ductile, can be polished to high luster and have a pleasing appearance.

Table I. Optimum current density for maximum Ag_3Sn content and minimal metallic silver and metallic tin content in deposit

On-time msec	Off-time msec	Current density at which metallic silver and metallic tin contents are minimal A/dm^2
5	20	*ca.* 2.8
25	100	*ca.* 3
50	100	1.6
100	100	1.5
25	200	3.5 (crude estimate)
50	200	2.8
100	200	1.8

Manuscript submitted Aug. 4, 1972; revised manuscript received Dec. 7, 1972. This was Paper 200 presented at the Miami Beach, Florida, Meeting of the Society, Oct. 8-13, 1972.

Any discussion of this paper will appear in a Discussion Section to be published in the December 1973 JOURNAL.

REFERENCES

1. T. G. Carver and H. Leidheiser, Jr., Abstracts, XVIIIth International Congr. Pure and Appl. Chem., Montreal, No. B3-46, 199 (1961).
2. W. R. Buck, III and H. Leidheiser, Jr., *Nature*, **204**, 177 (1964).
3. W. R. Buck, III and H. Leidheiser, Jr., *This Journal*, **112**, 243 (1965).
4. H. Leidheiser, Jr. and J. Sachdev, *ibid.*, **117**, 1523 (1970).
5. H. Leidheiser, Jr. and A. R. P. Ghuman, *Nature Phys. Science*, **236**, 48 (1972).
6. A. J. Avila and M. J. Brown, *Plating*, **57**, 1105 (1970).
7. R. Girard, "Electrodeposition of Thin Magnetic Films," French Atomic Energy Commission, Grenoble Center of Nuclear Studies, June 10, 1965.
8. H. Y. Cheh, *This Journal*, **118**, 551 (1971).

Diffusion Coefficients and Kinetic Parameters in Copper Sulfate Electrolytes and in Copper Fluoborate Electrolytes Containing Organic Addition Agents

Carmen J. Milora

Western Electric Company, Incorporated, North Andover, Massachusetts 01845

and John F. Henrickson

Western Electric Company, Incorporated, Greensboro, North Carolina 27407

and Walter C. Hahn

Lehigh University, Bethlehem, Pennsylvania 18015

ABSTRACT

Measured limiting currents i_L for the deposition of copper on a platinum rotated disk electrode (RDE) were used to calculate the diffusion coefficients of copper ions in high-purity aqueous copper sulfate and copper fluoborate electrolytes. The diffusion coefficient in a 0.100M $CuSO_4$/1.0M H_2SO_4 electrolyte was found to be $5.23 \pm 0.13 \times 10^{-6}$ cm²/sec, while the diffusion coefficient in a 0.072M $Cu(BF_4)_2$/1.0M HBF_4 electrolyte was found to be $9.88 \pm 0.05 \times 10^{-6}$ cm²/sec. The values of i_L were found to be directly proportional to the square root of the disk rotational rate ω, as predicted by theory. Consistent correlations between the kinetic parameters controlling copper depositions and the concentration of addition agents were found for copper fluoborate electrolytes containing Cubath Hy,[1] thiourea, and gelatin. Generally both the transfer coefficients (α_c) and the exchange current densities (i_o) were found to decrease with increasing concentrations of additives, in accord with the hypothesis that additives retard primary charge transfer and the rate of copper deposition. Anomalous results were obtained at a thiourea concentration of 3.3×10^{-2} g/liter and at a gelatin concentration of 3.2×10^{-2} g/liter.

The purpose of this work was to investigate the deposition of copper from a copper fluoborate/fluoboric acid electrolyte and from fluoborate solutions containing various leveling/brightening agents known to be effective in copper sulfate solutions. Emphasis was placed on obtaining the diffusion coefficient for Cu^{++} ions in the pure solution, and in correlating changes in the kinetic parameters α_c and i_o with the concentration of various additives employed. For comparative purposes the values for $D_{Cu^{++}}$, α_c, and i_o were obtained using a pure copper sulfate/sulfuric acid electrolyte.

Experimental

The apparatus used is depicted schematically in Fig. 1. A time swept cathode/reference potential (2500 mV/min) was generated through a potentiostat circuit consisting of a motor potentiometer (ramp generator), operational amplifier (OA), and electrometer to feed back the reference potential. Cell current was monitored by a current-sensing resistor and continuously recorded on a strip chart recorder along with the potential of the reference electrode. With this equipment the cathode potential could be linearly increased from ~0V *vs.* reference.

The platinum rotated disk cathode[2] was cleaned prior to each experiment by a chromic acid/HCl sequence with multiple rinses. An experimental check of the actual cathode area using published (1) diffusion coefficient data for a $AgNO_3/KNO_3$ electrolyte agreed within 1% with the calculated geometric area. The electrolyte contained 8.379×10^{-4} m/liter of $AgNO_3$ and 0.2 m/liter of KNO_3 and had a kinematic viscosity of 0.874 centistokes measured at 25.0°C.

The reference electrode was fabricated from 99.999% pure OFHC copper wire coiled in a burette containing the test solution and connected to the electrolysis cell by a capillary tube. The capillary was drawn to a tip diameter of ~0.2 mm, and the tip was located in the plane of the RDE as near to the electrode as was possible. The electrolysis cell was immersed in a water bath (not shown on Fig. 1) maintained at 25.0° ± 0.2°C. Nitrogen gas was bubbled through the cell prior to all runs, and a positive nitrogen pressure was maintained over the solution during experiments.

All electrolytes were prepared using triply distilled water. Special care was taken to purify the solutions

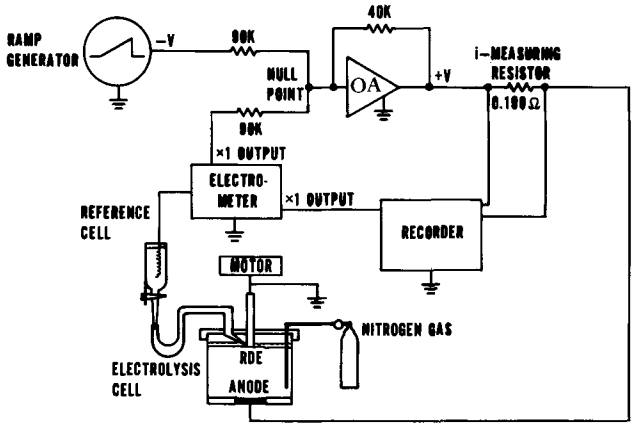

Fig. 1. Diagram of electrochemical cell and supporting electrical equipment.

Key words: rotating disk, thioruea, gelatin, Cubath.

[1] Proprietary leveling agent marketed by the Sel Rex Company, Nutley, New Jersey.

[2] Manufactured by the Pine Instrument Company, Grove City, Pennsylvania.

by H_2O_2 and carbon treatments and by pre-electrolysis at ~10 mA/cm² for about 15 hr. The Cu^{++} concentration of the fluoborate electrolyte was determined to be 0.072 moles/liter by atomic absorption spectroscopy, and the kinematic viscosity of the electrolyte was 0.876 centistokes at 25.0°C. Titrations with EDTA established the Cu^{++} concentration as 0.100 moles/liter in the sulfate electrolyte, while measurements at 25.0°C resulted in a value of 1.041 centistokes for the kinematic viscosity. The fluoborate solution contained 1.0 moles/liter of fluoboric acid and the sulfate solution contained 1.0 moles/liter of sulfuric acid. All physical properties were measured after the solutions were purified and pre-electrolyzed.

Procedure

Determination of the limiting current for copper deposition was conducted with approximately 450 ml of test solution that had been purged with nitrogen gas for 45 min minimum. After purging, the potential of the RDE was adjusted to +50 mV relative to the reference electrode and held at that value for 60 sec. The cathode potential was then forced to negative values at a sweep rate of 2500 mV/min. Electrolysis was continued until the limiting deposition current was exceeded (as evidenced by the abrupt slope increase of the i-E curve), an operation which required about 30 sec.

The kinetic parameters α_c and i_o were evaluated from that portion of the i-E curve corresponding to the Tafel region ($\eta < -50$ mV) (2). To obtain usable curves for analysis, the plating procedure was modified from that used in determining the limiting currents. Prior to the determination of the i-E relationship for the test solution, the platinum RDE was copper plated at ~2 mA/cm² for 5 min to effectively transform the platinum electrode to a copper electrode. (The potential difference between the copper plated RDE and the copper reference electrode was measured as −3.9 mV). The RDE was then swept to negative potentials at 250 mV/min until a current corresponding to ~0.1 i_L was reached. All kinetic parameter experiments were performed at 900 rpm.

Regressions of i_L on $\omega^{1/2}$ and log i on $-\eta_A$ were performed using a computer CALL/360 STATPACK[3] statistical package.

Results and Discussion

The diffusion coefficient of copper ions.—The diffusion coefficients of Cu^{++} ions in the solutions studied were calculated from the slopes of the i_L *vs.* $\omega^{1/2}$ relationship derived by Levich (3), according to the following equation

$$i_L = 0.62\, n\, \mathbf{F}\, A\, D^{2/3}\, \upsilon^{-1/6}\, C_B\, \omega^{1/2} \qquad [1]$$

A family of curves representing experiments using the 0.072 molar copper fluoborate electrolyte is shown in Fig. 2. Results of the regressions of i_L on $\omega^{1/2}$ along with the values of D_{CU++} calculated from the regression slopes are shown on Fig. 3 and contained in Table I. The regressions included a minimum of five

[3] Provided by Service Bureau Corporation, Philadelphia, Pennsylvania.

Table I. Regression parameters and calculated diffusion coefficients for the Cu^{++} ion from electrolysis of copper sulfate and fluoborate electrolytes

Electrolyte	Regression coefficient, b, mA-sec$^{1/2}$/cm²	Regression intercept, a, mA/cm²	Correlation coefficient	$D_{Cu^{++}} \times 10^6$, cm²/sec
$CuSO_4$*	7.70	4.75	0.99	5.23 ± 0.13
$Cu(BF_4)_2$**	8.79	5.45	0.99	9.88 ± 0.05

* 0.100M $CuSO_4$/1.0M H_2SO_4.
** 0.072M $Cu(BF_4)_2$/1.0M HBF_4.

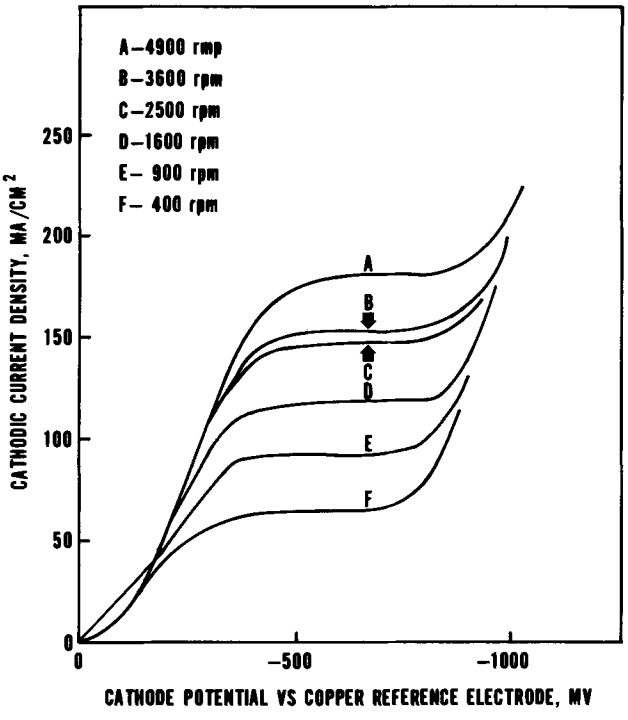

Fig. 2. Polarization curves for a 0.072M $Cu(BF_4)_2$/1.0M HBF_4 electrolyte at a platinum RDE.

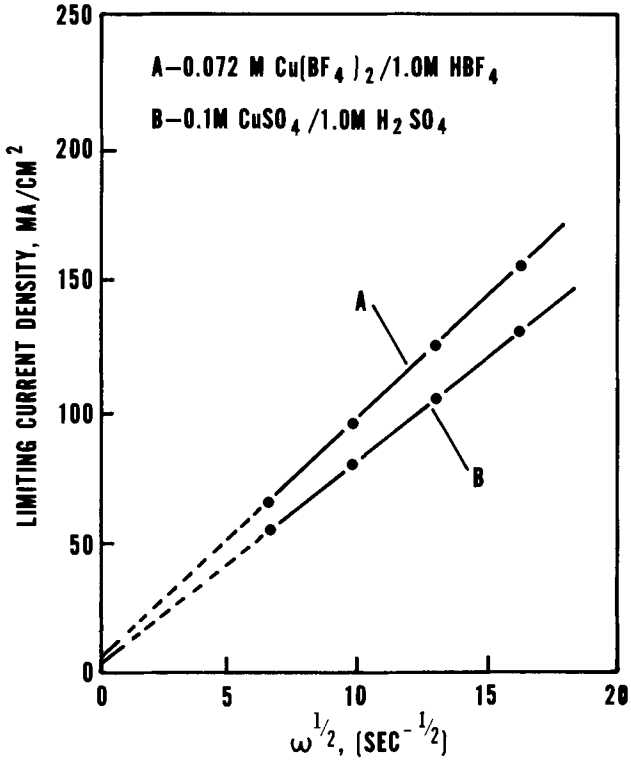

Fig. 3. Regression lines describing i_L *vs.* $\omega^{1/2}$ behavior for copper fluoborate and copper sulfate solutions electrolyzed at a RDE.

i_L values at 400, 900, 1600, and 2500 rpm. Rotation rates >2500 rpm produced turbulent fluid flow at the surface of the disk (4). The area of the cathode was taken as 0.453 cm², the concentration of Cu^{++} ions was 0.072 molar in the fluoborate electrolytes and 0.100 molar in the sulfate electrolyte, and n was taken as 2. In both instances the i_L values were directly proportional to $\omega^{1/2}$ and obeyed an equation of the following form:

$$i_L = a + b\, \omega^{1/2}$$

where a and b were positive numbers. The small values of a have no physical significance and are probably due to anomalous experimental effects discussed by Adams (1) and Riddiford (5).

The diffusion coefficient for the Cu^{++} ion in the 0.100M $CuSO_4$/1.0M H_2SO_4 electrolyte was found to be 5.23 ± 0.13 × 10^{-6} cm^2/sec at 25.0°C. Because the deposition of copper from acidified solutions has been repeatedly used in recent years as an indicator reaction for the determination of mass transfer coefficients, comparisons of the value obtained in this work with values obtained by other experimenters was easily accomplished. The diffusion coefficient calculated in this work showed good agreement with reported values obtained in similar $CuSO_4/H_2SO_4$ electrolytes, as shown in Table II.

These results lend credibility to the accuracy of the basic RDE technique employed in this investigation. Bearing in mind that the diffusion coefficient obtained in the copper fluoborate electrolyte was 9.88 ± 0.05 × 10^{-6} cm^2/sec at 25.0°C and that the techniques used for both sulfate and fluoborate electrolytes were identical, one must conclude that the observed difference in diffusivities is a real and accurate effect of the different electrolytes employed. No sound explanation of the cause of the difference in diffusivities can be formulated at this time.

The kinetic parameters governing copper deposition.—The kinetic parameters of deposition can be determined from examination of the current-potential characteristics of the electrolyte, which can be described by the following equation (2)

$$i = i_o \left[\exp \frac{-\alpha_c \eta_A F}{RT} - \exp \frac{\alpha_a \eta_A F}{RT}\right] \quad [2]$$

If η_A is more negative than about 50 mV, the second term in the brackets of Eq. [2] can be neglected, and taking logarithms yields

$$\eta_A = \frac{RT}{\alpha_c F} \ln i_o - \frac{RT}{\alpha_c F} \ln i \quad [3]$$

The kinetic parameters α_c and i_o can be obtained from the slope and intercept, respectively, of a plot of η_A *vs.* ln i. The effect of addition agents on copper deposition should be embodied in the resulting kinetic parameters for the process.

Because of the procedure used in this work, it was more convenient to prepare curves of log i *vs.* $-\eta_A$ for determination of α_c and i_o. The slope of the log i *vs.* $-\eta_A$ curve equals $\alpha_c/0.060$ at 25.0°C, while the intercept at $\eta_A = 0$ yields log i_o directly. Values for $-\eta_A$ could be estimated to ± 1 mV accuracy. Regressions of log i on $-\eta_A$ contained data from 10 duplicate runs for the pure copper sulfate electrolyte, 7 duplicate runs for the pure fluoborate electrolyte and for each concentration of Cubath Hy and thiourea in copper fluoborate, and 5 duplicate runs for gelatin in copper fluoborate. Results are shown on Fig. 4 and 5 and listed in Table III.

The regression analysis performed on the log $i/-\eta_A$ data for the 0.100M $CuSO_4$/1.0M H_2SO_4 solution produced values of 0.35 for α_c and 1.09 mA/cm^2 for i_o. The value for α_c is considerably smaller than the value of 0.59 obtained by Johnson and Turner (2) for a 1.0M $CuSO_4$/1.0M H_2SO_4 solution, the values of 0.47-0.51 obtained by Hayashi and co-workers (9) for a 0.5M $CuSO_4$ solution containing either 0.25M or 1.0M H_2SO_4, and the values of 0.41, 0.45, and 0.49 reported by Radovici and Vass (10) for copper deposition from electrolytes containing 0.05M, 0.25M, and 0.50M $CuSO_4$, respectively, (1.0M H_2SO_4). The exchange current density could not be compared directly with literature values because of differences in the Cu^{++} concen-

Table II. Reported values of D_{Cu++} for copper sulfate solutions

$D_{Cu^{++}} \times 10^6$, cm^2/sec	Method of determination	Reference	$CuSO_4$ Molarity	H_2SO_4 Molarity	Temperature, °C
5.2	i_L at rotating cylinder	6	0.07	1.50	25.5
6.2	i_L for a flowing fluid in a tubular electrode	7	0.10	1.47	25.0
5.9	i_L at a plane vertical electrode in a still solution	8	0.10	1.51	23.7

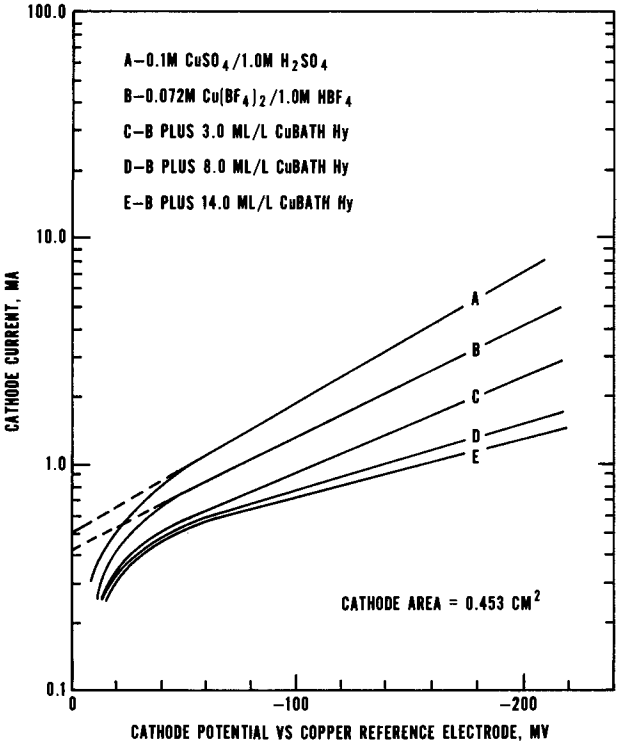

Fig. 4. The cathode potential-current relation for a 0.1M $CuSO_4$/1.0M H_2SO_4 electrolyte and a 0.072M $Cu(BF_4)_2$/1.0M HBF_4 electrolyte with and without Cubath Hy.

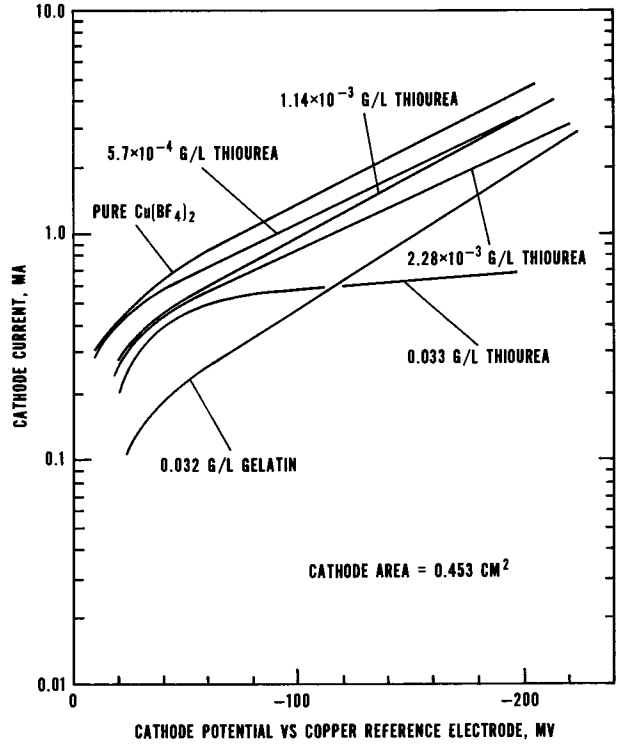

Fig. 5. The effect of thiourea and gelatin concentrations on the cathode potential-current relation for copper plating in a 0.072M $Cu(BF_4)_2$/1.0M HBF_4 electrolyte.

Table III. Summary of α_c and i_o results for the reduction of Cu^{++} ions from aqueous fluoborate and sulfate electrolytes

Electrolyte	Slope, current decade/mV	Standard error of the estimate, mA/cm²	α_c	i_o, mA/cm²
$CuSO_4$	5.88×10^{-3}	0.133	0.35	1.09
$Cu(BF_4)_2$**	5.06×10^{-3}	0.088	0.30	0.91
$Cu(BF_4)_2$** Plus ...				
5.70×10^{-4} g/liter thiourea	4.59×10^{-3}	0.373	0.27	0.84
1.14×10^{-3} g/liter thiourea	5.34×10^{-3}	0.108	0.32	0.60
2.28×10^{-3} g/liter thiourea	4.55×10^{-3}	0.088	0.27	0.66
3.30×10^{-2} g/liter thiourea	0.78×10^{-3}	0.055	0.05	1.04
3.20×10^{-2} g/liter gelatin	6.28×10^{-3}	0.062	0.37	0.24
3.0 ml/liter Cubath Hy	4.18×10^{-3}	0.046	0.25	0.79
8.0 ml/liter Cubath Hy	3.05×10^{-3}	0.040	0.18	0.84
14 ml/liter Cubath Hy	2.61×10^{-3}	0.029	0.15	0.88

* 0.100M $CuSO_4$/1.0M H_2SO_4.
** 0.072M $Cu(BF_4)_2$/1.0M HBF_4.

tration between published work and this work. However, using the following equation presented by Laitinen (11)

$$i_o = n\,\mathbf{F}\,K_s\,C_{Cu^{++}}{}^{\alpha_c} \qquad [4]$$

where K_s (cm/sec) is the heterogeneous rate constant for the deposition reaction and other symbols have their previously designated meanings, modifications of the i_o value obtained in this work corresponding to the different Cu^{++} concentrations reported in the literature could be made, so that the various values could be compared. Results of this analysis are contained in Table IV. A larger value of α_c would have resulted in closer agreement among published values and the one obtained experimentally from the 0.100M $CuSO_4$ electrolyte.

The values of α_c and i_o derived from the fluoborate electrolytes could not be compared with any published values, for no experimental data have been published. However, no significant difference existed between $\alpha_c = 0.30$ and $i_o = 0.91$ mA/cm² obtained from the additive-free fluoborate electrolyte and the corresponding values from the sulfate electrolyte. Correction of i_o to correspond to a Cu^{++} concentration of 0.100M resulted in a value of 1.02 mA/cm² which is close to the 1.09 mA/cm² obtained from the $CuSO_4$ solution.

Results using additions of Cubath Hy to the pure copper fluoborate electrolyte have been presented in Table III. Generally, they were consistent with what was expected, *i.e.*, increasing concentrations of Cubath Hy produced lower values of α_c and i_o than were obtained with the pure electrolyte. The transfer coefficient was found to be more sensitive to changes in Cubath Hy concentration than was the exchange current density. For example, α_c decreased from 0.30 to 0.25 to 0.18 to 0.15 as the additive concentration increased from 0 to 3.0 to 8.0 to 14 ml/liter, respectively. Because the Cubath Hy additive was proprietary and of unknown composition, no analyses could be formulated.

Table IV. Comparison of modified values of i_o (modified to compensate for different Cu^{++} ion concentrations) from 0.1M $CuSO_4$ with reported values at different Cu^{++} ion concentrations

$CuSO_4$ Molarity	H_2SO_4 Molarity	i_o, mA/cm² Published values (Reference)	i_o, mA/cm² This work	i_o, mA/cm² This work adjusted per Eq. [4]
0.10	1.0	None	1.09	1.09
0.25	0.1	1-2 (12)	1.09	1.50
0.50	1.0	2.5-3.6 (9)	1.09	1.92
1.00	1.0	3.0 (2)	1.09	2.46

The effect of thiourea on copper deposition from the fluoborate electrolyte was less well-behaved than was the effect of Cubath Hy. The transfer coefficient for copper plating remained fairly constant as the concentration of thiourea was increased to 2.28×10^{-3} g/liter; however, at a thiourea concentration of 3.30×10^{-2} g/liter the transfer coefficient changed abruptly to a value of 0.05. On the other hand, the exchange current density was found to decrease to a value of ~0.6 mA/cm² as the thiourea concentration was increased to 2.28×10^{-3} g/liter, and then to abruptly increase to 1.04 mA/cm² at a concentration of 3.30×10^{-2} g/liter. Johnson and Turner (2) saw a similar trend in α_c with increasing thiourea concentrations in a sulfate electrolyte, *i.e.*, α_c decreased from 0.59 to 0.20 with the addition of 3×10^{-2} g/liter of thiourea to the electrolyte. The corresponding exchange current density increased from ~3 mA/cm² (additive-free electrolyte) to ~10 mA/cm² at a thiourea concentration of ~10^{-4} g/liter, and then it gradually decreased with increasing thiourea to the original value at 3×10^{-2} g/liter of thiourea. It is noteworthy that i_o reverted to the original values for both electrolytes at about the same thiourea concentrations. The contrary behaviors at the intermediate concentrations is unexplainable.

It is interesting to note that the concentration of thiourea that resulted in the 0.05 value for α_c was very near that concentration found to produce discontinuous copper electroplates in previously conducted leveling ability experiments (4). It was possible that the cathode efficiency for copper plating in that work was far less than that for the pure copper fluoborate electrolyte (as evidenced by the absence of plated copper from most of the cathode surface). This suggests that thiourea could have complexed cuprous ions as they were formed to prevent complete reduction to metallic copper. Also, it is possible that only a small percentage of the applied overpotential was being utilized to deposit copper, and that much of the applied overpotential could have been used to reduce thiourea to products that "poisoned" the cathode surface to copper deposition

With the addition of 3.2×10^{-2} g/liter of gelatin to the copper fluoborate electrolyte the transfer coefficient increased to 0.37 and the exchange current density decreased to 0.24 mA/cm², compared to values obtained from the pure electrolyte. A similar decrease in the exchange current density had been observed by Johnson and Turner (2). With the addition of 3×10^{-3} g/liter of gelatin to their $CuSO_4$ test solution, they observed a tenfold reduction in i_o from the value of ~3 mA/cm² obtained in their additive-free solution.

Acknowledgments

The authors would like to thank Mr. Robert E. Visco for his continuing interest and valuable suggestions during the course of this work.

Manuscript submitted March 13, 1972; revised manuscript received Nov. 20, 1972.

Any discussion of this paper will appear in a Discussion Section to be published in the December 1973 JOURNAL.

LIST OF SYMBOLS

A	Electrode area (cm²)
C_B	Concentration of electroactive species in the bulk of the solution (moles/liter)
C_{Cu++}	Concentration of copper ions (moles/liter)
D	Diffusion coefficient of electroactive species (cm²/sec)
D_{Cu++}	Diffusion coefficient of copper ions in aqueous electrolytes (cm²/sec)
E	Potential of an electrode (V)
$\mathbf{F}$	Faraday's constant (coulombs/equivalent)
i	Current density (A/cm²)
i_o	Exchange current density (A/cm²)
i_L	Limiting current (A)
K_s	Heterogeneous rate constant for metal deposition (cm/sec)

n	Number of electrons transferred in a reaction
R	Gas constant (joules/mole °K)
RDE	Rotated disk electrode
T	Temperature (°K)
α_a	Anodic transfer coefficient
α_c	Cathodic transfer coefficient
η_A	Activaiton overpotential (V)
υ	Kinematic viscosity (cm^2/sec)
ω	Angular velocity (sec^{-1})
Ω	Resistance (ohms)

REFERENCES

1. R. N. Adams, "Electrochemistry at Solid Electrodes," pp. 90, 91, 223, Marcel Dekker, New York (1969).
2. D. R. Turner and G. R. Johnson, *This Journal*, **109**, 799, 801, 802 (1962).
3. V. G. Levich, "Physicochemical Hydrodynamics," p. 296, Prentice-Hall, Englewood Cliffs, New Jersey (1962).
4. C. J. Milora, M.S. Thesis, pp. 89, 128, Lehigh University, Bethlehem, Pennsylvania (1971).
5. A. C. Riddiford, "Advances in Electrochemistry and Electrochemical Engineering," Vol. 4, pp. 76, 77, Interscience Publishers, New York (1966).
6. D. J. Robinson and D. R. Gabe, *Trans. Inst. Metal Fin.*, **48**, 40 (1970).
7. J. C. Bazan and A. J. Arvia, *Electrochim. Acta*, **9**, 23 (1964).
8. C. R. Wilke, M. Eisenberg, and C. W. Tobias, *This Journal*, **100**, 517 (1953).
9. T. Hayashi, S. Higuchi, H. Kinoshita, and T. Ishida, *J. Electrochem. Soc. Japan*, **37**, 70 (1969).
10. O. Radovici and C. Vass, *Revue Roumaine de Chimie*, **12**, 1184 (1967).
11. H. A. Laitinen, "Chemical Analysis," p. 308, McGraw-Hill Book Company, Inc., New York, N.Y. (1960).
12. A. Damjanovic, T. H. V. Setty, and J. O'M. Bockris, *This Journal*, **113**, 435 (1966).

The Low Potential Oxidation of Ethanol on Bright Platinum

A. R. Blake

The Electricity Council Research Centre, Capenhurst, Chester CHI 6ES, England

A. T. Kuhn

Department of Chemistry, University of Salford, Salford M5 4WT, Lancashire, England

and J. G. Sunderland

The Electricity Council Research Centre, Capenhurst, Chester CHI 6ES, England

ABSTRACT

The adsorption and oxidation of ethanol has been studied in 1*N* H_2SO_4 on bright platinum. Adsorption of two species, one cathodically desorbable, the other nondesorbable, has been found over the potential region 0.05-0.8V. The reaction rate is independent of *p*H at constant overpotential and the reaction is first order in ethanol, at low concentrations, tending toward zero order at high concentrations. The *i-V* curve shows current inhibition above about 0.6V. Possible reaction schemes are discussed in the light of the findings.

The mechanism of the oxidation of ethanol at platinum electrodes has been the subject of attention during recent years (1-4). Probably the most significant studies are those of Rightmire *et al.* (2) and Frumkin (3). Rightmire *et al.* (2) used quasi-steady-state methods (slow potentiodynamic sweeps) coupled with chemical product analysis to investigate the reaction in the potential range up to 0.8V. They proposed a mechanism which involved an electrochemical rate-limiting step preceded by a chemisorption/oxidation step, viz.

$$CH_3 \cdot CH_2 \cdot OH \rightarrow CH_3 \cdot \overset{*}{C}HOH + H^+ + \epsilon$$

and

$$CH_3 \cdot CHOH \rightarrow CH_3 \cdot CHO + H^+ + \epsilon$$

Frumkin (3) carried out similar studies with the addition of experiments in which potential changes, following open-circuit decay from more anodic potentials, were made. Among the products found on analysis were ethane and methane. From these results Frumkin deduced that the initial chemisorption step is rate determining. In addition, slow charging curves demonstrated that the chemisorbed species oxidized at a rate two orders of magnitude lower than did ethanol itself and therefore was regarded as a "poison" rather than an adsorbed intermediate in the over-all reaction. Franklin (4) in his studies showed that the rate was first order in ethanol at concentrations <0.3M but tended toward zero order above this.

In contrast to methanol (5, 6) except where formaldehyde is formed only under unusual conditions (7), and hydrocarbons (8-11) where carbon dioxide and water are formed as sole oxidation products, ethanol (2) and higher alcohols (12) are only partially oxidized to the corresponding aldehydes. It is this fact that makes the reaction an interesting one.

In the present work the studies have been extended to examine the nature of the adsorbate in terms of cathodically desorbable and nondesorbable species in the potential range 0.05-0.9V.

Two distinct species have been identified and their role in the over-all reaction is discussed.

Key words: ethanol, oxidation, adsorbate.

Experimental

Equipment.—The electrochemical cell used has been described previously (13). Potential profiles and potential sweeps were obtained from a pulse generator designed in these laboratories, the signal being fed into a Chemical Electronics 1.6A valve potentiostat. The *i-t* transients were displayed on a Tektronix 502A dual beam oscilloscope and photographed. The oscilloscope was operated in a triggered time-base mode at the beginning of the potential ramp or step of interest.

The *i-t* transient was displayed on the upper beam and the potential ramp or step on the lower beam of the oscilloscope. All measurements were made at 30°C.

Test electrode.—This consisted of a 0.0254 cm diameter platinum wire (Johnson-Matthey) which was first cleaned in hot 1:1 v/v (volume/volume) HNO_3/H_2SO_4 followed by washing with distilled water, and was then annealed in a hydrogen atmosphere at 700°C for 7 hr. The electrode was then sealed into Pyrex glass, a heat sink being used to conduct the heat away from the exposed wire, and the electrode again heated to 450°C in a hydrogen atmosphere for 8 hr, and allowed to cool in hydrogen until required. The exposed geometric area of the electrode was 0.075 cm^2 and the hydrogen deposition charge from 0.4V was 24.2 $\mu C\text{-}cm^{-2}$. This indicated a roughness factor of *ca.* 1.5 if 210 $\mu C\text{-}cm^{-2}$ was taken as the charge for hydrogen deposition (14).

All charges are reported on the basis of the true electrode area based on hydrogen deposition measurements and all potentials are referred to the hydrogen electrode in the same electrolyte. No correction to the potentials was necessary in the presence of ethanol.

Electrolyte.—In all the studies, 1*N* sulfuric acid was used and was prepared by dilution of B.D.H. Aristar grade with triply distilled water. Pre-electrolysis for 48-72 hr at 0.48V was carried out in all experiments, vigorous argon gas stirring was applied during this period. The pre-electrolysis electrode was raised into the gas space. Variation of greater than 10% in the anodic or cathodic charges after 5-min adsorption at 0.4V, with respect to the charges corresponding to adsorption for 10 millisec were rejected. Argon purge gas was Air Products prepurified grade.

Reactants.—Ethanol was B.D.H. Aristar grade and was used without further purification. Ethanol was introduced into the cell through Teflon tubing which had been previously cleaned with 1:1 v/v HNO_3/H_2SO_4 followed by copious washing with triply distilled water and finally dried by purging with argon for two days. The ethanol was introduced into a vessel where it was purged with argon for 1 hr before the required volume was transferred to the cell via the Teflon tubing. A similar procedure was followed for the introduction of the ethanol into the anolyte presaturator. The concentration of ethanol used in the adsorption experiments was 0.1M.

Determination of current/voltage relationships.—A gas/ethanol stirred system was again employed, the results being obtained by setting the potential and then waiting until a steady current was attained before the next potential was set. A constant argon purge was maintained during the determination of the *i-V* curve so that acetaldehyde did not build up to any significant extent and itself become oxidized to acetic acid (2, 15). The *i-V* curve was obtained at four temperatures, and two concentrations at 30°C.

pH effect.—The reference electrode was a bubbling hydrogen electrode placed in the same electrolyte as the anode. The ethanol concentration was 0.1M. The base electrolyte was 1*N* potassium sulfate and the pH monitored using a Pye Dynacap. The pH's studied were 2.0, 3.5, 6.1, 7.4, 9.8, and 11.3. Steady-state *i-V* curves were recorded. Stirring of the anolyte was achieved by means of an argon gas purge.

Concentration effect.—For these determinations 1*N* H_2SO_4 was used. Ethanol concentration was varied from 0.02 to 5M. The results presented were obtained with the aid of cyclic voltammetry, with a sweep rate of 0.048 $V\text{-}sec^{-1}$.

Results

In the pH experiments the current values at constant overpotential showed poor correlation, nevertheless it was clear that $(d \log i/dpH)_\eta \simeq 0$.

Concentration effect.—The variation of the logarithm of the current as a function of the logarithm of the concentration, over the range 0.02-5.0M ethanol, is shown in Fig. 1 for 0.55V, within the approximate Tafel region. It may be seen that the rate starts off first order in ethanol, but approaches zero order as the concentration increases above about 0.5M. This was also observed by Franklin (4). Steady-state measurements also verified this and over the potential range 0.55-0.9V a similar concentration dependence was observed.

Current-potential relationship.—The steady-state *i-V* curves for the oxidation of 1M ethanol on bright platinum at a series of temperatures are shown in Fig. 2 and for comparison 0.1M ethanol at 30°C is also shown. There is a linear Tafel region below about 0.6V followed by the appearance of a passivation region, which occurs below the potential at which significant amounts of chemisorbed oxygen have been detected by optical (16, 17) or electrochemical techniques (18, 19). The oxidation reaction is not therefore inhibited by chemisorbed oxygen in this region in the manner previously reported (10).

Characterization of adsorbate.—The data obtained, using the method described below, enable the coverage of the electrode by adsorbate to be characterized in a number of ways. Thus, the total coverage may be expressed as Q_{ox} (the amount of oxidizable material) or as θ^{org}, in which the adsorbate is defined in terms of the fraction of the electrode it covers. The results, expressed in either way, may be subdivided in terms of adsorbate which can be desorbed at cathodic poten-

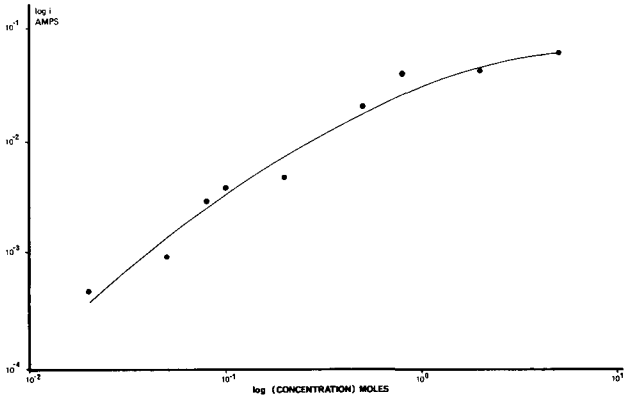

Fig. 1. Variation of the logarithm of reaction rate as a function of the logarithm of ethanol concentration.

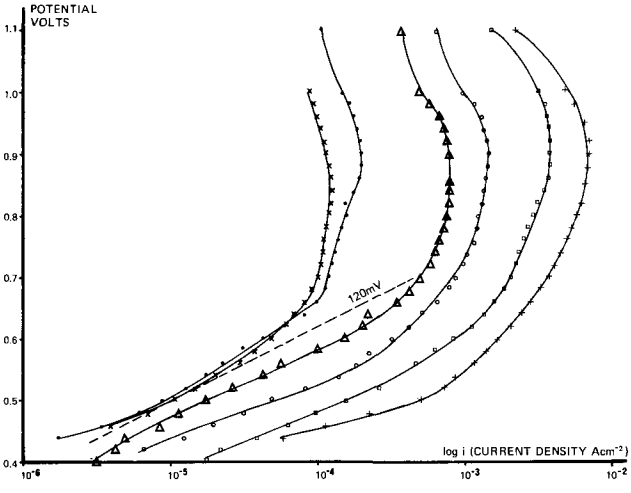

Fig. 2. *i-V* for ethanol oxidation on bright platinum in 1*N* H_2SO_4 at several temperatures. x 0.1M C_2H_5OH, 30°C; ● 1.0M C_2H_5OH, 0°C; △ 1.0M C_2H_5OH, 15°C; ○ 1.0M C_2H_5OH, 30°C; □ 1.0M, C_2H_5OH, 45°C; + 1.0M C_2H_5OH, 60°C.

tials (type I) and that which cannot (type II). Furthermore, by use of Q_{ox}, *i.e.*, θ_{anodic} data, the quantity N_e may be defined, which is the number of electrons required to oxidize the adsorbate expressed on a "per site" basis.

The anodic charge Q_{ox}^{total}, was shown to be independent of the sweep rate over the range 140-1040 V-sec^{-1} for adsorption times 500 millisec to 100 sec at 0.4V. It was noted, however, from the shape of the charging curve that the transient was not identical to the argon blank although the charge under the curves were identical; this is probably attributable to a double layer effect. A sweep rate of 200 V-sec^{-1} was used for routine measurements. Potential sequence shown in Fig. 3A was used to obtain the anodic data. In the estimation of the charge corresponding to electrode coverage, Q_H^{total}, a sweep rate of 250 V-sec^{-1} was employed; no desorption of adsorbed ethanol at this sweep rate being observed. Potential sequence shown in Fig. 3A was again used.

In addition to the total charges, Q^{total}, determined using sequence 3A, the charges corresponding to the oxidation of cathodically nondesorbable material (designated type II) were obtained using potential sequence shown in Fig. 3B. The desorbable material (designated type I) was then obtained by difference. In addition to this, charges corresponding to hydrogen deposition after hydrocarbon adsorption (Q_H^{org}) and subsequent cathodic desorption (Q_H^{nondes}) were obtained (using the same potential sequence).

Figures 4 and 5 show the anodic and cathodic charge data after adsorption to equilibrium coverage. This was typically obtained after 600 sec, although it should be noted that at 0.05 and 0.1V equilibrium coverage may not necessarily have been achieved. The increase in cathodic charge with time, corresponding to type I and type II species at several potentials are shown in Fig. 6. Behavior was similar in the case of the anodic data, closely following the cathodic pattern of adsorption. It may be seen from Fig. 4 and 5 that for potentials below 0.3V type II species predominate, while at 0.3V and above type I species predominate. Type I species release significantly more electrons per site than the type II material.

The charges corresponding to type II observed above 0.7V may indicate the presence of adsorbed oxide due to the nature of the electrode pretreatment used in estimating the electrode coverage data.

Above 0.5-0.6V the electron per site values were observed to fall to fractional values if resolution of the

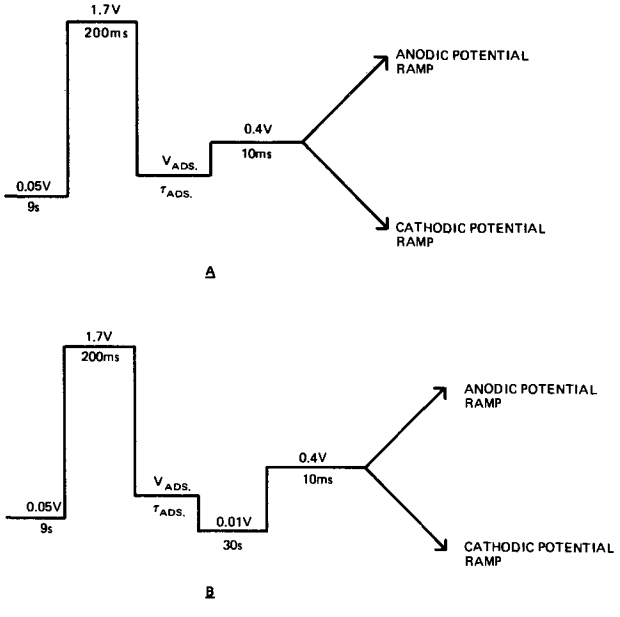

Fig. 3. Potential profiles used in the estimation of the adsorbed species; quiescent state during the above sequences.

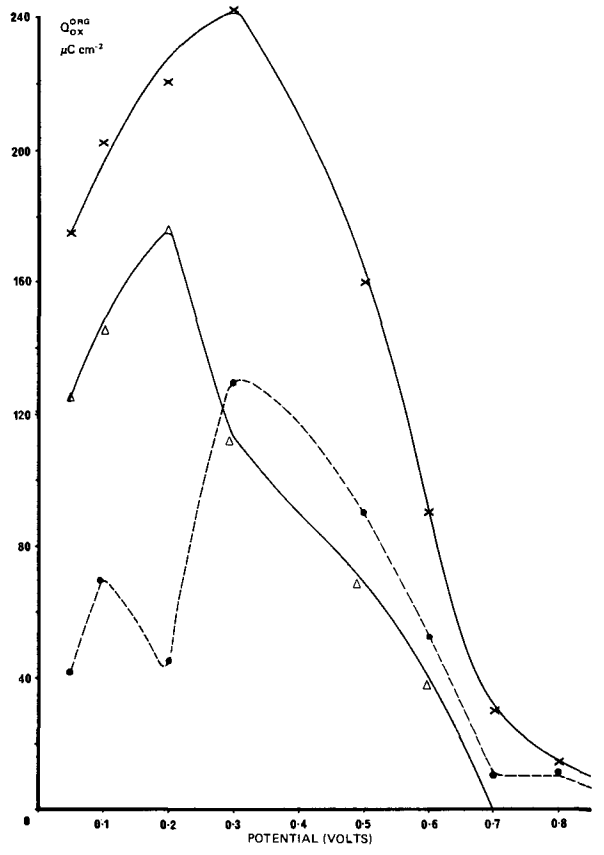

Fig. 4. Anodic charge data as a function of potential. x Total charge; - - - charge corresponding to desorbable species type I; △ charge corresponding to nondesorbable species type II.

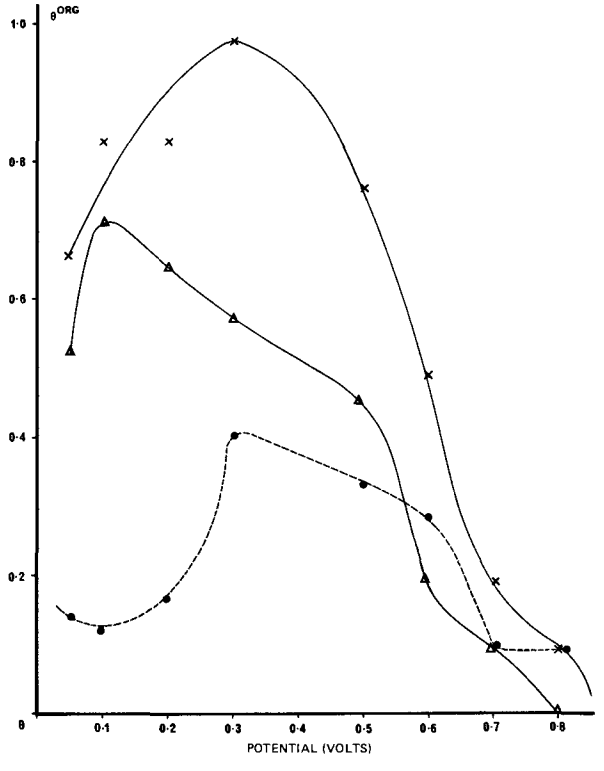

Fig. 5. Coverage data as a function of potential. x Total coverage; — coverage with desorbable species, type I; △ coverage with nondesorbable species type II.

two adsorbed species was attempted. The value of the electrons per site for type I and type II species are shown in Table I.

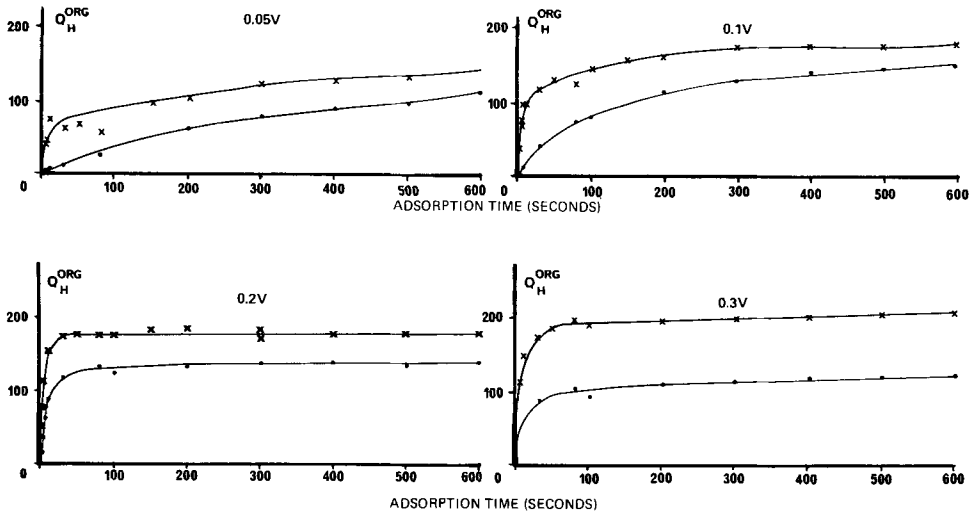

Fig. 6. Cathodic charge data as a function of adsorption time. x Total charge; ● cathodically nondesorbable type II.

Discussion

There is little controversy regarding the over-all oxidation mechanism of ethanol. It is agreed by all authors that the major product of the oxidation process is acetaldehyde. Any acetic acid or carbon dioxide reported arise from conditions where significant quantities of acetaldehyde have been allowed to build up and separate studies on the oxidation of acetaldehyde (15) confirm this.

The incidence of ethane or methane as detectable products derived from ethanol arises when the electrode is taken (or decays on open circuit) to potentials where adsorbed hydrogen is present, and on this evidence, Frumkin postulated that the adsorbate consisted partially at least of CH_{ads} fragments, the result of cracking. The data presented here seek to verify the presence of such adsorbed fragments.

Steady-state current-voltage data.—The results shown in Fig. 2 are in accord with Frumkin (3) where the experimental conditions make comparison possible, *i.e.*, the Tafel slopes below 0.6V are similar, 90-110 mV. They disagree, however, with Rightmire (2) who obtained a rectilinear Tafel slope of 110 mV which extended up to about 0.75V. It is perhaps better appreciated now than formerly that nonsteady-state data has little significance and referring to Fig. 6 it will be seen that, over the period of 5 min during which Rightmire's sweeps (0.45-0.95V) were carried out, the amount of adsorbate and the ratio of the two components could change, and Tafel slopes so obtained are dependent on the sweep rate.

pH effects.—Regarding the poor correlation referred to in the results it should be noted that the possibility exists that aldehydic condensation or polymerization of the product, acetaldehyde, can occur which may explain the observed behavior. Conclusions similar to this were made by Liang (4) on the basis of the lack of charge linearity as a function of scanning frequency in solutions of high pH.

Nature of the adsorbate.—It is seen from Fig. 4 and 5 that the total charges for ethanol follow the characteristic bell-shaped isotherm typical of most hydrocarbons. Unusually high coverages of ethanol are measurable, however, at potentials as cathodic as 0.05V, where $\theta_{ethanol} = 0.67$ for an adsorption time of 10 min and is still rising. At this potential $\theta_H = 0.9$ in the absence of ethanol (20). This indicates, in general terms, formation of a much more strongly bound adsorbate than is the case with hydrocarbons. At 0V, however, electrode coverage with ethanol is zero.

Table I. Variation of electrons per site with potential

Potential	Type I species	Type II species
0.05	1.4	1.14
0.1	2.8	1.0
0.2	1.3	1.3
0.3	1.5	0.94
0.5	1.3	0.6
0.6	0.9	0.93

The electron per site values remain reasonably constant for the type II species, releasing $1.1 \pm 0.2e$ per site on oxidation at potentials 0.7V. The type I also remains constant yielding a somewhat higher value at most potentials. At 0.1V, however, a more highly reduced species (type I) is noted at adsorption times >50 sec, releasing *ca.* 2.8*e* per site. This is reflected in Fig. 4 and 5 where it is seen that adsorption maxima (anodic) and minima (cathodic) occur. This suggests that, at 0.1V pre-adsorbed hydrogen affects the mode of adsorption of ethanol.

From Fig. 4 and 5 it may be seen that the two adsorbed species are potential dependent, type II falling to zero coverage at 0.6-0.8V and type I at a slightly higher potential. The *e* values required for the oxidation of adsorbed ethanol, acetaldehyde, and acetic acid are significantly higher than those observed in this work. It is unlikely that these molecules in their uncracked states, contribute significantly to the adsorbate and it is, therefore, likely that the adsorbed species are in part cracked products of the parent molecule. This postulate is necessary to explain the observation that a nondesorbable species occurs, and to explain the higher *e* per site values noted for the type I species.

Kinetics of oxidation.—The following experimental facts need to be explained in any reaction sequence which is considered.

1. The rate of oxidation is substantially independent of pH (with the reference electrode in the same solution).
2. The reaction order with respect to ethanol over the initial concentration range (<0.5M) is first order but approaches zero order as the concentration of ethanol is increased.
3. The slope of the Tafel line progressively increases, except at potentials <0.6V where 90-110 mV is observed.
4. The coverage with adsorbed species decreases as the potential is increased from 0.3 → 0.7V.

Previously, Rightmire (2) proposed a reaction sequence in which the second electron transfer was rate determining although no quantitative analysis was presented, particularly with respect to the effect of pH or concentration. The reaction scheme proposed was

$$C_2H_5OH + M \rightarrow C_2H_5OM + H^+ + e \quad [1]$$

$$C_2H_5OM \rightarrow CH_3CHO + H^+ + e + M \quad [2]$$

Piersma and Gileadi (21) derived kinetic equations assuming that Eq. [1] was in pre-equilibrium, but were

unable to explain the reported experimental facts (4, 22) concerning the effects of concentration and pH.

Reaction schemes as shown below can be envisaged to summarize the possible reaction pathways

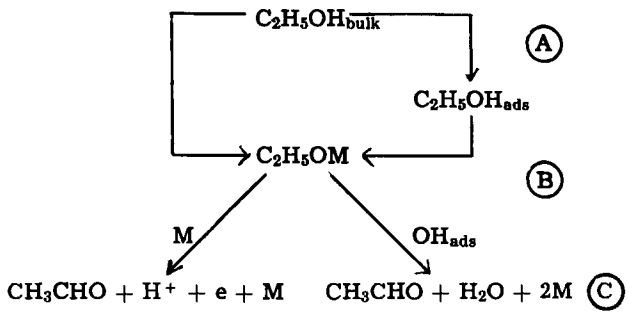

where A → B proceeds either directly or via an associative adsorption step.

B → C proceeds either via a second dehydrogenation step or via reaction with OH.

The main mechanistic possibilities are summarized above with the understanding that, as in so many electro-organic reactions, the simultaneous formation of a "poison" can slow any of the above reactions.

Two distinct types of mechanism are suggested.

(*a*) The first type involves dehydrogenation

$$C_2H_5OH + \text{free surface} \rightarrow C_2H_5OM + MH \quad [3]$$

$$MH \xrightarrow{\text{fast}} H^+ + M + e \quad [4]$$

$$C_2H_5OM \rightarrow CH_3CHO + M + H^+ + e \quad [5]$$

where Rightmire has suggested that [5] is rate determining

However, the question arises whether ethanol as reacting species is that to be found in the bulk solution or whether it is physically adsorbed. In the latter case in order to obtain agreement with our experimental results it would be necessary to postulate that such physically adsorbed ethanol, even present at appreciable coverage, is undetectable by the transient methods used here. In addition, it is necessary to explain why the reaction is not diffusion controlled, the rate under all conditions being many times smaller than the limiting current. The rate of this reaction would therefore be determined by the concentration of surface physically adsorbed ethanol and free surface. This mechanism would, however, give the observed parabolic or similar current voltage curve.

The observed first-order concentration in ethanol tending to zero order, which holds over the entire potential range studied here, can only be interpreted on the basis of a Langmuir or a Temkin-Frumkin (23, 24) isotherm applied to the physically adsorbed but undetectable ethanol.

A second mechanism which involves bare metal may be expressed by the following reaction sequence.

$$C_2H_5OH + M \xrightarrow{\text{slow}} C_2H_5OM + H^+ + e \quad [6]$$

$$C_2H_5OM \xrightarrow{\text{fast}} CH_3 \cdot CHO + H^+ + e + M \quad [7]$$

For Eq. [6] the rate equation can be expressed in Langmuir terms, viz.

$$v_{10} = k_{10}C_{C_2H_5OH}(1 - \theta_T)\exp\frac{\beta VF}{RT} \quad [8]$$

where θ_T is the total coverage with adsorbed species, the other terms having their usual significance.

This predicts a Tafel slope of 120 mV, which is close to that observed below 0.7V. This reaction scheme as it stands, however, does not explain all the observed experimental facts, particularly the progressively increasing slope and the observed reaction order. Both these shortcomings can be overcome if a surface poison derived from ethanol is postulated.

The simplest case involves a "poison" produced by an electrochemical mechanism

$$C_2H_5OH \rightleftharpoons \text{"poison"} + H^+ + e \quad [9]$$

$$\text{coverage} = \theta_P$$

In this hypothetical reaction sequence it must be assumed that the rate of removal of "poison" balances its formation in order that a "pseudo steady-state" is attained, the coverage potential dependence of the "poison" resulting in the increasing slope. Consider, therefore

$$\frac{\theta_p}{1 - \theta_T} = k_9 C_{C_2H_5OH}\exp\frac{VF}{RT} \quad [10]$$

If $\theta_T \equiv \theta_p$ then

$$\theta_p = \frac{k_9 C_{C_2H_5OH}\exp\frac{VF}{RT}}{1 + k_9 C_{C_2H_5OH}\exp\frac{VF}{RT}} \quad [11]$$

Substituting for $\theta_T \equiv \theta_p$ in [8] then

$$v_{10} = k_{10}C_{C_2H_5OH}\left[1 - \frac{k_9 C_{C_2H_5OH}\exp\frac{VF}{RT}}{1 + k_9 C_{C_2H_5OH}\exp\frac{VF}{RT}}\right]\exp\frac{\beta VF}{RT} \quad [12]$$

At low coverages with "poison" a Tafel slope of $2RT/F$ is predicted but as the potential increases and coverage with "poison" becomes important the slope observed will increase and eventually in the limit when $k_9 >> 1$ the slope will become $-2RT/F$, *i.e.*, inhibition (25-27) will be observed.

The variation of the rate with pH could be due to the formation of a "poison" which may explain the differences observed by Franklin (4); and in this present work, in passing from acid to alkaline electrolytes.

If the reaction order (25) is defined as $(d \ln i/d \ln C_{C_2H_5OH})_{V,pH}$ then using Eq. [8] and [9] the required reaction order is predicted. This analysis in combination with the experimental results could explain the experimental facts. It must be emphasized, however, that no "poison" has been detected in the adsorption studies, although a similar concept has been suggested by Brummer for formic acid oxidation (28). It is interesting that during experiments to examine time-effects at 0.65V the region where a sharp reduction in the oxidation rate occurred corresponded to the time where coverage with adsorbed ethanol became almost constant (Fig. 7). This suggests that ethanol predominantly undergoes oxidation on free surface [*cf.* Gilman (29)]. It is suggested, therefore, that competition for the active sites will be important.

(*b*) The second mechanism is similar to that widely accepted for a variety of anodic organic oxidations on platinum electrodes (10). Water is oxidized to form a species such as an OH radical which reacts on the surface with associatively adsorbed organic

$$C_2H_5OH_{bulk} \rightarrow C_2H_5OH_{ads} \quad [13]$$

$$H_2O \rightarrow H^+ + e + OH_{ads} \quad [14]$$

$$C_2H_5OH_{ads} + OH_{ads} \rightarrow C_2H_5OM + H_2O \quad [15]$$

$$C_2H_5OM \rightarrow CH_3CHO + H^+ + e + M \quad [16]$$

In the case of ethylene (10) which can be regarded as being strongly adsorbed, negative pressure effects support the hypothesis that increasing coverages with ethylene reduces the over-all reaction rate by reducing

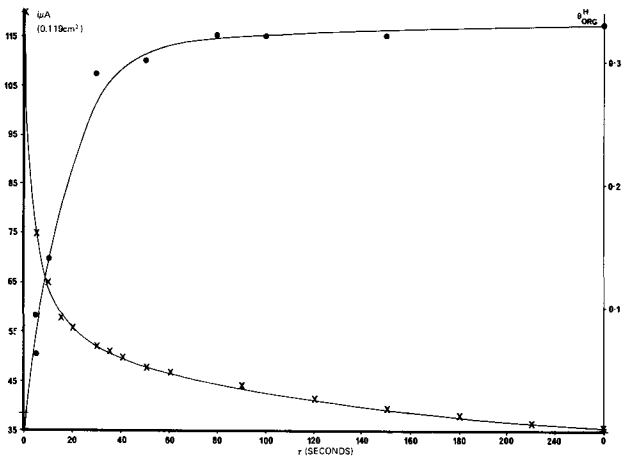

Fig. 7. Variation of ethanol coverage and oxidation current as a function of reaction time.

the coverage of the hydroxyl radicals. For a weakly adsorbed species such inhibition would not play such a dominant role and first-order reaction kinetics in organic at low concentration tending at higher concentrations to zero order would be expected. Such a mechanism then can explain the reaction order in ethanol. The apparent absence of adsorbate at higher potentials where the reaction is proceeding at a considerable rate can be explained on the same grounds as those used by Bockris *et al.* for the hydroxyl radical, namely, that although the concentration is small the rate per adsorbed molecule is extremely high. On this assumption step [14] might be considered to be rate determining and the observed i-V behavior could then be interpreted in terms of ever decreasing amounts of adsorbate. Similar arguments to those postulated by Bockris *et al.* (10) can be invoked to explain the pH effect observed here. One further observation is possibly relevant in considering Eq. [14]; if this mechanism is rate determining then a Tafel slope of $2RT/\mathbf{F}$ would be expected and indeed, if at each potential, the observed current is normalized to unit coverage of organic using the data shown in Fig. 5 a Tafel slope of $2RT/\mathbf{F}$ is obtained up to about 0.7V, beyond which values of θ are too small to be relied upon. This would suggest that OH_{ads} might be involved in the rate determining step. The normalized results are shown in Table II and in Fig. 2.

Another possibility is one in which ethanol is dissociatively chemisorbed and reacts with hydroxyl radicals according to Eq. [15] with Eq. [13] and [14] in pre-equilibrium. This reaction sequence results in a Tafel slope (Langmuir adsorption) at low coverage with hydroxyl species of $RT/2\mathbf{F}$ leading to a limiting slope as the coverage with hydroxyl species increases. This reaction sequence could explain the pH and concentration effects.

Table II. Normalized results

Potential	Deviation factor required to achieve slope of 120 mV	Relative reduction in $\theta^{H}_{ads\ total}$ with potential
0.50	0	0
0.55	1.1	1.18
0.60	1.52	1.57
0.65	2.58	2.46
0.7	4.9	4.0

Conclusions

Ethanol has been shown to adsorb on bright platinum over the potential region 0.05-0.8V, the adsorbate in general comprising a cathodically desorbable and nondesorbable species. These species give N_e values of 1.2 ± 0.3 and 1.1 ± 0.2 between 0.05V and 0.5-0.6V, respectively. A third species, cathodically desorbable, is indicated at long adsorption times at 0.1V and releases 2.8 electrons per site. Above 0.5-0.6V fractional N_e values are noted.

Two distinct mechanisms have been considered, dehydrogenation and reaction involving hydroxyl radicals. No single reaction scheme appears capable of explaining the observed current-voltage behavior although the role of free-surface seems important, indicating the possible formation of a "poison."

Manuscript submitted July 18, 1972; revised manuscript received Nov. 21, 1972.

Any discussion of this paper will appear in a Discussion Section to be published in the December 1973 JOURNAL.

REFERENCES

1. G. A. Bogdanovskii and A. I. Shlygin, *Zh. Fiz. Khim.*, **31**, 2428 (1957).
2. R. A. Rightmire, R. L. Rowland, D. L. Boos, and D. L. Beals, *This Journal*, **111**, 242 (1964).
3. B. I. Podlovchenko, O. A. Petry, A. N. Frumkin, and Hira Lal, *J. Electroanal. Chem.*, **11**, 12 (1966).
4. C. Liang and T. C. Franklin, *Electrochim. Acta*, **9**, 517 (1964).
5. M. W. Breiter and S. Gilman, *This Journal*, **109**, 622, 1099 (1962).
6. M. J. Schlatter, "Fuel Cells," Vol. II, G. J. Young, Editor, Reinhold Publishing Co., New York (1963).
7. T. P. Pavela, *Ann. Acad. Sci. Fennicae*, Ser. A II, 59, 1 (1954).
8. H. Binder, A. Köhling, H. Krupp, K. Richter, and G. Sandstede, *This Journal*, **112**, 355 (1965).
9. R. Thacker, *Electrochem. Technol.*, **3**, 312 (1965).
10. H. Wroblowa, B. J. Pierzma, and J. O'M. Bockris, *J. Electroanal. Chem.*, **6**, 401 (1963).
11. J. O'M. Bockris, H. Wroblowa, E. Gileadi, and B. J. Pierzma, *Trans. Faraday Soc.*, **61** (11), 2531 (1965).
12. K. Elbs and O. Brunner, *Z. Electrochem.*, **6**, 608 (1900).
13. A. R. Blake, A. T. Kuhn, and J. G. Sunderland, *This Journal*, **119**, 1027 (1972).
14. S. B. Brummer, J. I. Ford, and M. J. Turner, *J. Phys. Chem.*, **69**, 3424 (1965).
15. M. Hollnagel and M. Lohse, *Z. Physik Chem.*, 232, 237 (1966).
16. R. Greef, *J. Chem. Phys.*, **51**, 3143 (1969).
17. A. N. Reddy, M. A. Genshaw, and J. O'M. Bockris, *ibid.*, **50**, 671 (1968); **51**, 3149 (1969).
18. S. Gilman, *Electrochim. Acta*, **9**, 1025 (1964).
19. P. Stonehart, H. A. Kozlowska, and B. E. Conway, *Proc. Roy. Soc.*, A310, 541 (1969).
20. M. W. Breiter, *Trans. Faraday Soc.*, **61**, 749 (1965).
21. E. Gileadi and B. J. Pierzma in, "Modern Aspects of Electrochemistry," Vol. 4, J. O'M. Bockris, Editor, Butterworths, London (1966).
22. V. S. Bagotsky and Y. B. Vasliyev, *Electrochim. Acta*, **9**, 869 (1964).
23. A. N. Frumkin, *Z. Physik. Chem.*, **116**, 466 (1925).
24. B. E. Conway and E. Gileadi, *Trans. Faraday Soc.*, **58**, 2493 (1962).
25. B. E. Conway "Theory and Principles of Electrode Processes," Ronald Press, New York (1964).
26. B. E. Conway in, "Modern Aspects of Electrochemistry," No. 3, J. O'M. Bockris and B. E. Conway, Editors, Butterworths (1964).
27. D. Gilroy and B. E. Conway, *J. Phys. Chem.* **69**, 1259 (1965).
28. A. H. Taylor, R. D. Pearce, and S. B. Brummer, *Trans. Faraday Soc.*, **67**, 801 (1971).
29. S. Gilman in, "Hydrocarbon Fuel Cell Technology," B. S. Baker, Editor, Academic Press (1965).

The Coexistence of Conductivity and Persistent Electrical Polarization in Polyelectrolyte Membranes

Charles Linder

Montefiore Hospital, Bronx, New York 10467

and Irving F. Miller*,[1]

Polytechnic Institute of Brooklyn, New York 11201

ABSTRACT

Persistent electrical polarization (heterocharged electret formation) and electrical conduction have been found to be compatible in polymer membranes consisting of mixtures of sodium polystyrenesulfonate and various polar polymer matrices. This compatibility is apparently the result of the fact that the mechanisms for these two phenomena are quite different. While the mechanism for conduction is probably electronic in this system, the persistent polarization is probably the result of microscopic displacement of some sodium ions from their fixed sulfonate sites and stabilization of these ions in new sites by interaction with surrounding molecules.

The phenomenon of persistent electrical polarization in materials has been of interest for many years. The phenomenon was first conceived as an electrical analog of a magnet by Heaviside (1) in 1885 and was first experimentally demonstrated by Eguchi (2) in 1922 in studies involving carnauba wax. It has been postulated that such polarization phenomena underlie many biological processes (3-5) and, indeed, the phenomenon has been used in such commercial devices as microphones, electrophotography, electrometers, etc. (6-8).

In spite of the fact that persistent electrical polarization phenomena seem to appear in such a wide variety of places, these phenomena are not too well understood. Since most of the early experimental studies were made with carnauba wax, most of the theoretical work has gone into a phenomenological description of the nature of the process in carnauba wax and the dynamics of its decay (6, 9, 10). As a result of this, most workers in the field still consider the phenomenon to take place essentially in dielectrics of a parallel plate condenser system (11).

Based on our present understanding, two different types of phenomena can be distinguished. When polarization is established by charging electrodes and when the sign of the charge on the surface of the material is the same as the charge on the adjacent electrode, the material is referred to as a homocharged electret. When the charge on the surface is opposite to the charge of the adjacent electrode, the material is referred to as a heterocharged electret (2, 10). Since the rates of formation and decay of homocharged electrets and heterocharged electrets are quite different, it is possible to distinguish between them in the same material.

Studies of homocharged electrets (12-14) indicate that they are formed essentially by absorption of charges by dielectric breakdown of the gas in a space between electrode and dielectric. On the other hand, heterocharged electrets have been shown to involve volume polarization (15) and have been shown to decay by mechanisms of dielectric relaxation (4, 11). In most cases, it is not known whether such heterocharge formation is due to dipole orientation, ion displacement, electron trapping, or some combination of these. Most studies of heterocharged electrets have involved electrical insulators and workers have postulated their formation to involve electron trapping (16) in some cases, or ion displacement of ionic impurities in other cases involving insulating plastics (17). In spite of the fact that a report has appeared in which large amounts of persistent heterocharged polarization was observed in a polyelectrolyte-polyethylene membrane that was a good electrical conductor (19) most workers in the field still state unequivocally that conductivity and electret formation are not compatible and that the electret phenomenon only becomes important when the resistance of the material increases. In fact, however, the incompatibility of electret formation and conductivity has been demonstrated only in insulators and mostly for homocharges.

It is the purpose of this report to present some results on heterocharge formation and conductivity in well-characterized polyelectrolyte-polar polymer membranes in which the polyelectrolyte is incorporated into the polar polymer matrix over a range of concentrations.

Experimental

Polyelectrolyte membranes were prepared with sodium polystyrenesulfonate (PSSNa) in a polar polymer matrix consisting either of poly(vinyl alcohol) (PVA), polyacrylamide (PAC), or polyvinylpyrrolidone (PVP). All polymers used were linear polymers and were purified by standard techniques typically involving dialysis against distilled water.

Membranes were formed by mixing appropriate amounts of the PSSNa and the particular matrix studied in distilled water and casting on a plate of polystyrene, or by pouring into a polystyrene petri dish approximately 44 mm in diameter. The water was then allowed to evaporate in a dust-free environment to form the membrane approximately 0.05 mm thick and the membranes were then preconditioned for 24 hr in a vacuum at 60°C to drive off most of the remaining water. The electrets were formed and characterized in a temperature-controlled vacuum oven able to maintain a controlled temperature to within ±0.2°C in the range 35°-98°C. The electrodes as well as the chamber were machined of naval bronze, and the electrode surfaces were coated with Aquadag (an aqueous carbon suspension from the Anderson Colloids Company) to reduce corrosion of the electrodes and subsequent membrane contamination.

In an experiment, the membrane was placed between the electrodes, the chamber was closed, and a vacuum was established. The chamber was brought to the desired charging temperature and the material was polarized by placing a battery in series with the membrane-electrode system for an arbitrary time, usually 90 min. During the charging cycle and subsequently during the stabilization and discharging cycle, the

* Electrochemical Society Active Member.
[1] Present address: University of Illinois at Chicago Circle, Chicago, Illinois 60680.
Key words: electrets, membranes, conductivity, polarization.

current flowing across the membrane was monitored with a model 610-C Keithley Electrometer. After a fixed time of charging, the system was cooled to room temperature at about 5°C per min while maintaining the charging field intact. As in the formation cycle, the membrane current and temperature were recorded throughout.

At room temperature the voltage was removed and the discharge current measured. The discharge current, consisting of free capacitor charge and dielectric absorption not frozen in, decayed exponentially by about 3 orders of magnitude over the 90 min in which the decay current was monitored.

To measure the amount of charge frozen in, the membranes were reheated to 10°C above the temperature of polarization at the rate of 2°C per min. The depolarization current was measured during the heating process and for an additional time required for the current to decay at least 1.5 orders of magnitude from its peak value at the elevated temperature. The measured current integrated over the time of measurement was taken as the amount of frozen polarization per unit area of the membrane. In all depolarization measurements, the currents flowed in the opposite direction from the charging currents, thus indicating heterocharge formation with no sign of homocharge.

The membrane conductivity was calculated from the polarization currents measured at the end of the polarization period before cooling. The reported values are, therefore, for the fully polarized membrane electret. Further details of the experimental techniques utilized may be found in Ref. (20).

All data points presented represent an average of at least 3 separate experiments, with a reproducibility of ±10%.

Results

Figure 1 presents the results obtained for both persistent polarization and conductivity for PSSNa-PVA membranes polarized at 76°C and a charging field of approximately 4.5 kV/cm for 90 min. Although there is a significant difference in the shape of the two curves, the main point to be noted is that both persistent polarization (in this case heterocharge formation) and membrane conductivity increase together. Results for the PSSNa-PVA system were also obtained under a wide variety of other operating conditions of temperature and polarization field. Figure 1 is typical of the results obtained.

Figures 2 and 3 represent typical results obtained for the PSSNa-PAC system and the PSSNa-PVP system, respectively, under the same conditions, namely, 76°C and a field of approximately 4.5 kV/cm for 90 min to achieve polarization. Again, it must be noted that although the shapes of the curves vary considerably, the general trend is that polarization and membrane conductivity increase together.

It might be noted from Fig. 1-3 that there is a significant change in shape for the curves as one increases the PSSNa concentration beyond a mole fraction of about 0.3. A detailed analysis of the shape of these curves has been presented elsewhere (21) and will not be repeated here. However, in summary, what seems to be involved is an indication that the chief mechanism for heterocharge electret formation involves interactions between the polarizable groups on the PSSNa and adjacent molecules. At low concentrations of PSSNa, the predominant interaction is between a PSSNa group and adjacent matrix molecules. At higher concentrations of PSSNa, the predominant interaction involves two or more adjacent PSSNa groups. Since the nature of the interaction between PSSNa and the matrix group is quite different when the matrix is PVA or PAC or PVP, the variation in shape from Fig. 1-3 can be explained on this basis. It may be noted that at higher PSSNa concentrations all three systems approach a common behavior.

An estimate of the stability of the electret presented in Fig. 1-3 can be made by taking the ratio of the total stored charge to the discharging current just prior to

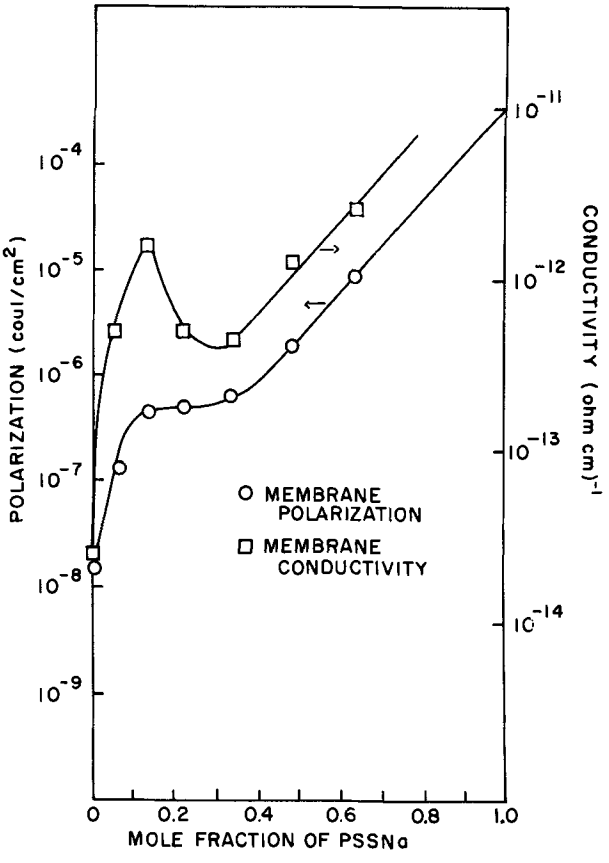

Fig. 1. Membrane polarization and conductivity vs. mole fraction of PSSNa in PVA. Polarization was at 76°C and 4.5 kV/cm for 90 min.

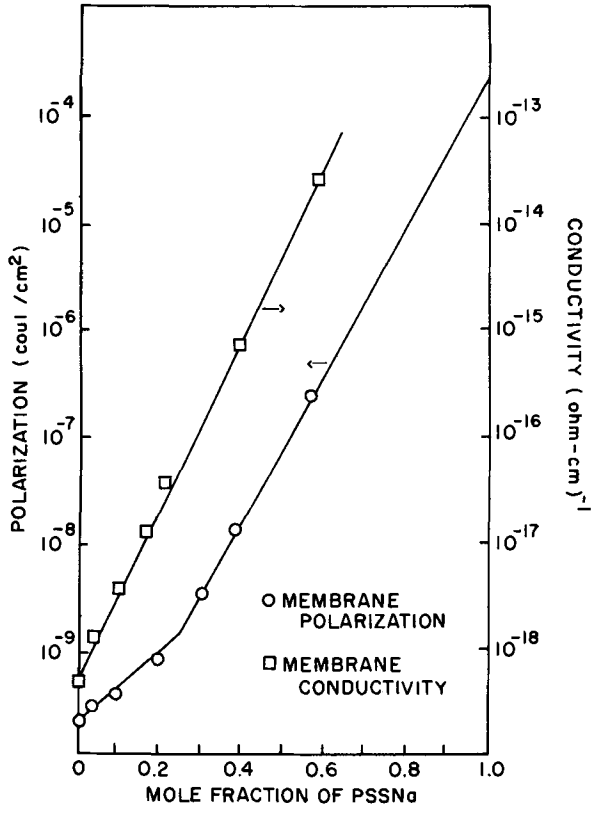

Fig. 2. Membrane polarization and conductivity vs. mole fraction of PSSNa in PAC. Polarization was at 76°C and 4.5 kV/cm for 90 min.

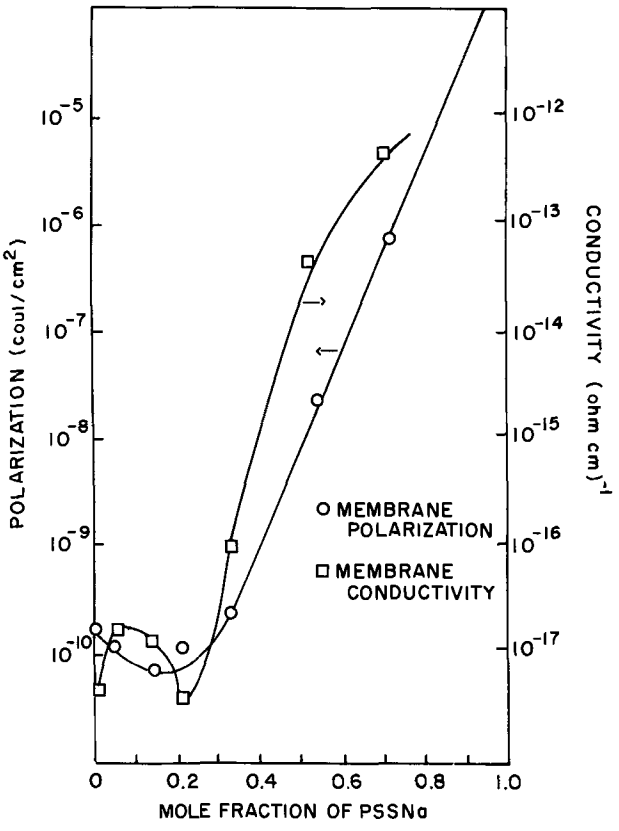

Fig. 3. Membrane polarization and conductivity vs. mole fraction of PSSNa in PVP. Polarization was at 76°C and 4.5 kV/cm for 90 min.

thermal depolarization. Since the discharging current decreases with time, this ratio will be an estimate of the lower limit of the time it would take totally to discharge the electret at room temperature. Estimates of membrane stability calculated in this way are presented in Table I. From Table I it should be noted that an increase in membrane conductivity does not necessarily decrease the apparent stability of the electret and in many cases actually increases the stability. In order to explain such results, one is forced to the conclusion that the mechanism of conduction and persistent polarization must be different. In particular, space charge formation via conduction currents as a mechanism for the persistent polarization observed is essentially ruled out.

Figures 4 and 5 represent results obtained for the amount of persistent polarization and the membrane

Table I. Estimates of electret stability

PVA matrix	
Mole fraction of PSSNa	Stability × 10^{-5} (sec)
0	18.4
0.059	19.6
0.130	9.54
0.218	15.0
0.330	19.0
0.480	30.7
0.630	19.2
PAC matrix	
Mole fraction of PSSNa	Stability × 10^{-5} (sec)
0	14.9
0.034	46.0
0.10	8.50
0.152	11.2
0.20	16.5
0.30	18.7
0.387	26.5
0.565	37.9
PVP matrix	
Mole fraction of PSSNa	Stability × 10^{-4} (sec)
0	12.1
0.046	2.55
0.140	1.2
0.210	1.74
0.330	0.50
0.520	4.10
0.710	29.0

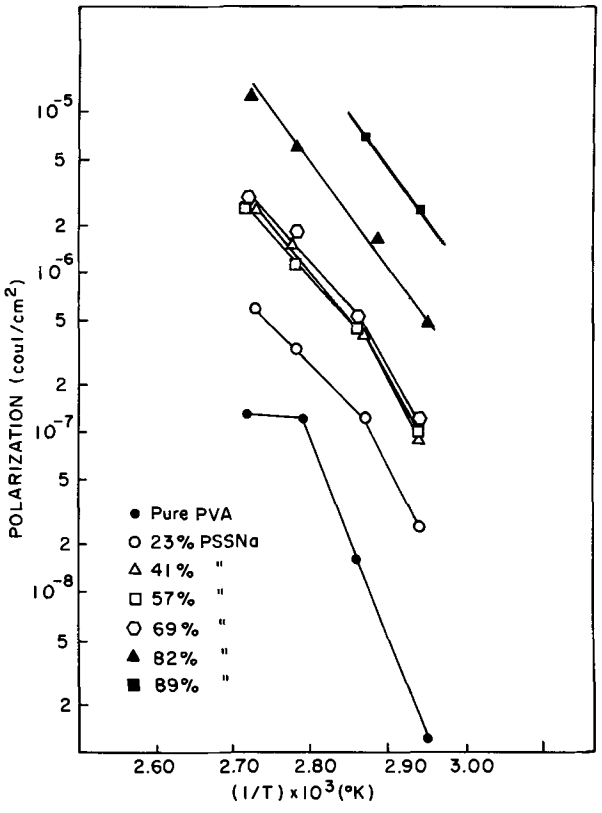

Fig. 4. Polarization vs. temperature of polarization in PSSNa-PVA membranes.

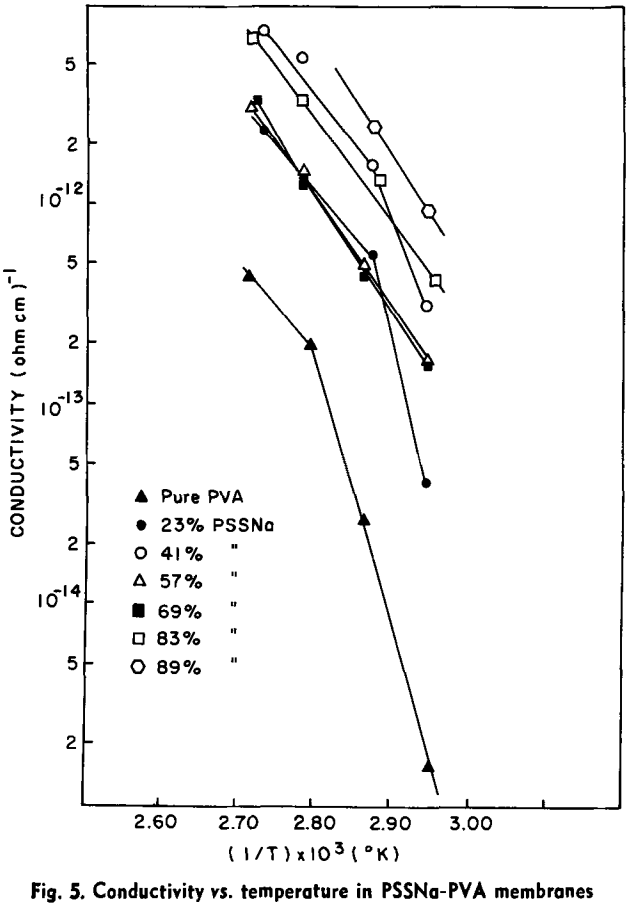

Fig. 5. Conductivity vs. temperature in PSSNa-PVA membranes

conductivity, respectively, for a series of PSSNa-PVA membranes of varying composition at different temperatures between 66° and 94°C. The amount of persistent polarization and the membrane conductivity are both seen to increase substantially as the temperature is increased. The break seen in the curves for both polarization and conductivity correspond to the glass transition temperature of the system, known to be in the neighborhood of 86°C. Above the glass transition temperature, T_g, the free volume for long-range correlation of segmental movement is considerably greater than below T_g and a different mechanism of response to an external force is possible. This change in response mechanism shows up as a change in slope on Fig. 4 and 5. The slope on Fig. 4 and 5 can be thought of as a "heat of polarization" and a "heat of conductivity," respectively, by analogy to the van't Hoff equation, in which a standard "heat of reaction" is determined from the temperature dependence of a chemical equilibrium constant. It should be noted that above T_g there is a strong similarity between the calculated heats for conduction and polarization in PSSNa-PVA membranes. The calculated heats are 24.5 ± 1.4 kcal/mole, and 26.2 ± 1.1 kcal/mole for the conduction and polarization processes, respectively, above T_g. The similarities between the two heats indicate a similarity in the thermal response of the material to the two phenomena. It should be noted that such a similarity does not exist below T_g where the calculated heat for conduction is considerably higher than that for polarization.

Discussion

From the results obtained in this study, it is clear that the nature of the heterocharge in these polyelectrolyte membranes is that of a volume polarization rather than space charge formation. Clearly, space charge formation is incompatible with a conductive membrane system. In addition, it was observed that the position of the peak of the thermal depolarization curve (current *vs.* time) was found to be independent of applied field intensity for a constant heating rate for nearly all the membranes studied. This would be expected for homogeneous volume polarization but not space charge formation (22). Since the membranes were found to obey Ohm's law throughout the voltage range studied, with no rectification, and since all the experiments were performed in vacuum, it is likely that the conduction mechanism is electronic. Therefore, the persistent polarization mechanism must involve a volume polarization in the vacuum independent of the electronic conduction current.

Clearly, different mechanisms must be postulated for the polarization process and the conduction process although each mechanism must be dependent on the same property of the material. If the conduction phenomenon is electronic, the important factors are the concentration of electrons and their mobility (6). Increasing the concentration of PSSNa increases the polarity of the material as characterized by an increase in the dielectric constant. The higher the dielectric constant, the easier it is to ionize electrons from sites or valence bands into other sites further down the field or into the conduction band, respectively. Electron injection from the electrodes is also facilitated if the dielectric is highly polar. Besides increasing the number of electrons participating in the conduction process, an increase in PSSNa concentration also increases the electron mobility. If the conduction process is that of electron hopping, then a higher density of sites (which are postulated to be PSSNa monomer units) would decrease the distance between hops and thus increase mobility. If the process is via a conduction band mechanism, the width of the band is increased at a higher density of polar sites because there is a more efficient overlapping of the electrostatic fields from one site to another.

In the polarization process, on the other hand, the electrostatic units are postulated to be ensembles of sodium sulfonate groups of the PSSNa monomer. Under an electric field these structures would form larger dipole structures in the general direction of the field by ionizing the Na^+ ion to a neighboring site. The higher the concentration of PSSNa, the larger is the dielectric constant and, thus, the easier it would be to ionize the Na^+ ion from its parent sulfonate group. An increase in PSSNa concentration also increases the number of sites available to receive the Na^+ ion and, thus, the stability of the final electret structure. In this model it is presumed that matrix molecules also participate in stabilizing the electret structure. A detailed presentation of this model is presented in Ref. (21). Thus, polarization is characterized by the formation of electrostatic structures with the direction of the applied electric field and which could form additional conductive pathways for electron conductivity. The possibility of polarization producing conductive channels through the membrane could explain why the conductivity of some membranes increases with time (see Fig. 6).

Since both the conduction and polarization process depend on the local electrostatic fields in the same way, and since the concentration of PSSNa as well as the thermal energy content of the system (that is, the temperature) affect these fields, one should also expect that polarization and conductivity increase with PSSNa concentration and the observation that the heat for both of these processes is similar in a given temperature range is to be expected.

Conclusions

Experimental results obtained on a series of PSSNa-polar polymer membranes have demonstrated that persistent polarization (heterocharged electret formation) and electrical conduction are compatible in the same system. This compatibility is apparently the result of the fact that the mechanisms for persistent polarization and electrical conduction are different. Although the mechanism for electrical conduction is probably electronic in this system, the mechanism for heterocharge electret formation probably involves microscopic displacement of some sodium ions from their fixed sulfonate sites and stabilization of these ions in new sites by interaction with surrounding molecules. Historically, persistent polarization and electrical conduction in the same system have been thought to be incompatible. However, this conclusion was formed as a result of studies on simple insulator systems. Clearly, the mechanisms of electrical conduction and charge storage in such simple systems should be differ-

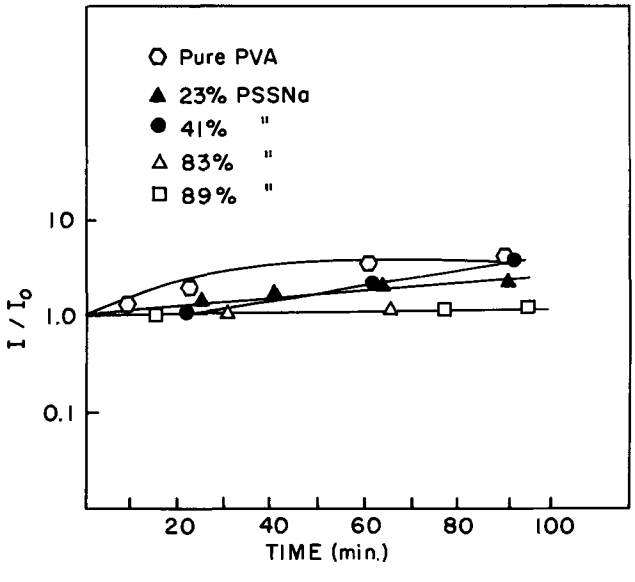

Fig. 6. Relative change in polarization current *vs.* time of polarization for PSSNa-PVA membranes.

ent than the mechanisms for such phenomena in semiconductors, complex biological systems, or the system studied in the work presented herein. The main conclusion of this work, therefore, must lie in the inappropriateness of assuming a basic incompatibility of persistent polarization and conduction, in general, from results obtained on studies only of simple insulator systems.

Acknowledgment

This work is based on part of a thesis submitted by Charles Linder in partial fulfillment of the requirements for the Ph.D. degree in Polymer Chemistry at the Polytechnic Institute of Brooklyn. The work was partially supported by a grant from the National Institutes of Health under grant no. GM-12013.

Manuscript submitted May 4, 1972; revised manuscript received Oct. 16, 1972.

Any discussion of this paper will appear in a Discussion Section to be published in the December 1973 JOURNAL.

REFERENCES

1. O. Heaviside, "Electrical Papers," Vol. 1, p. 488, Macmillan and Co., London, England (1892).
2. M. Eguchi, *Japan J. Phys.*, **1**, 10 (1922).
3. L. Y. Wei, *Bull. Math. Biophys.*, **31**, 39 (1969).
4. H. C. Berg, *Biophys. J.*, **8**, 1051 (1968).
5. E. C. Hughes, Private communication.
6. V. M. Fridkin and I. S. Zheludev, "Photoelectrets and the Electrophotographic Process," Consultants Bureau, New York (1960).
7. V. A. J. Carbaub, *Electrochem. Technol.*, **6**, 3 (1968).
8. H. R. Anderson, E. A. Bartkus, and J. A. Reynolds, *IBM J. Res. Develop.*, **15**, 140 (1971).
9. M. M. Perlman and J. L. Mennier, *J. Appl. Phys.*, **36**, 420 (1965).
10. F. Gutmann, *Rev. Mod. Phys.*, **20**, 457 (1948).
11. B. Gross, "Charge Storage in Solid Dielectrics," Elsevier Publishing Co., Amsterdam (1964).
12. J. R. Beeler, J. D. Stranathan, and G. G. Wiseman, *J. Chem. Phys.*, **32**, 442 (1960).
13. R. A. Draughn and A. Catlin in, "Electrets and Related Electrostatic Charge Storage Phenomena," M. M. Perlman and L. M. Baxt, Editors, The Electrochemical Society, Softbound Symposium Series, New York (1967).
14. M. M. Perlman and C. W. Reedyk, in "Electrets and Related Electrostatic Charge Storage Phenomena," M. M. Perlman and L. M. Baxt, Editors, The Electrochemical Society Softbound Symposium Series, New York (1967).
15. B. Gross and R. J. DeMoraes, *J. Chem. Phys.*, **37**, 710 (1962).
16. R. Gerson and J. H. Rohrbaugh, *ibid.*, **23**, 238 (1955).
17. M. L. Miller, *J. Poly. Sci., Part A-2*, **4**, 685 (1966).
18. D. K. Donald, in "Electrets and Related Electrostatic Charge Storage Phenomena," M. M. Perlman and L. M. Baxt, Editors, The Electrochemical Society Softbound Symposium Series, New York (1967).
19. Z. Urban and R. Wallace, *This Journal*, **115**, 518 (1968).
20. C. Linder, "Persistent Electrical Polarization in Polyelectrolyte Membranes," Ph.D. Thesis, Polytechnic Institute of Brooklyn, New York (1972).
21. C. Linder and I. F. Miller, *J. Phys. Chem.*, **76**, 3434 (1972).
22. T. Nedetzka, M. Reichle, A. Mayer, and H. Vogel, *ibid.*, **74**, 2652 (1970).

Generative and Stabilizing Processes in Tin-Palladium Sols and Palladium Sol Sensitizers

R. L. Cohen and K. W. West

Bell Telephone Laboratories, Murray Hill, New Jersey 07974

ABSTRACT

An extensive study of sol systems produced by the reduction of solvated Pd by Sn^{2+} is presented. We show that the reaction is initiated by the formation of a polynuclear Sn-Pd complex, which is autoreductive, yielding sol particles of a Sn-Pd alloy core with a stabilizing layer of Sn^{2+} ions. The role of the Sn^{2+} stabilizing layer in controlling particle size is discussed in detail. We apply the knowledge of these systems to understand similar processes occurring in commercial Pd sol systems used for sensitizing insulating surfaces for electroless plating. The chemistry of the sensitizing layer generated by these systems has also been studied. The sol sedimentation rate has been studied by centrifugation. Most of the investigation has been carried out via Mössbauer spectroscopy; precise isomer shift parameters for a number of Sn-Pd compounds are reported.

Electroless plating to metalize insulating substrates generally requires a preliminary treatment of the surface to make it catalytic (also called "active" or "sensitive") to initiate the deposition of metal from the electroless bath. An overview of the approaches used has been given by Goldie (1). For many years, the most common preparation process was a two-stage treatment, in which the surface was immersed first in a dilute stannous chloride solution, and then in a dilute palladium chloride solution. We have recently reported (2, 3) a detailed description of the chemical processes and reactions of the two-step process, based on the results of Mössbauer spectroscopy measurements on the tin compounds and complexes formed.

Key words: sensitization, colloids, tin chemistry, palladium chemistry, Mössbauer spectroscopy.

More recently, a number of proprietary systems achieving "sensitization" with only a single-stage treatment have become available. The advantage of the single-stage system goes beyond the elimination of one bath; it makes possible the elimination of intermediate washes, re-racking, and drag-in problems. A number of proprietary[1] single-stage sensitizers are available; all involve tin and palladium. Two of the systems (4, 5) are stated to be Pd sols stabilized by a "protective colloid." These systems are somewhat similar involving mixtures of Sn^{2+} and Pd^{2+} ions, HCl, and water; the concentrations and order of addition are varied. Tetravalent tin may be also added to

[1] The proprietary single-stage sensitizers referred to are the Shipley Corporation 6F sensitizer (4), the MacDermid Corporation Metex PTH 9070 sensitizer (5), and the Dynachem Corporation Activator 101 and 120.

improve wetting of hydrophobic substrates. The evidence is that the palladium colloid coats the substrate in the treatment process, and subsequently is the active agent that nucleates deposition from the electroless bath.

This paper reports the results of measurements by Sn^{119} Mössbauer spectroscopy on the tin components used in the palladium colloid, and an investigation of the colloid formation and stabilization. Special emphasis is placed on the way the colloid-forming reactions determine the properties of the resultant sol. We also discuss the results of Mössbauer measurements on the sensitizing layers themselves. An additional experiment on centrifugation of the commercial sensitizer systems has also been performed to give some idea of the particle size distribution.

The patents describing preparation of two of the one-component systems discuss procedures which are similar in outline, but different in detail. Rather than following analytically each of these "recipes," we have performed a series of experiments which establish the basic chemical stages characterizing the over-all process. The preparation procedures of the individual patents can then be viewed in the light of the findings we present.

This paper deals with a number of very different aspects of the Sn-Pd sol system, and we have modified the normal order of presentation to maintain clarity. We begin with a brief description of the experimental techniques used for the Mössbauer spectroscopy measurements, and a discussion of the interpretation of the spectra obtained. The next section of the paper discusses the formation and identification of a tin-palladium complex which is critical to the colloid formation process. This is followed by a description of the colloid formation as the complex decomposes, and characterization of the components of the colloid from its Mössbauer spectra. In the last third of the paper, the knowledge of the tin-palladium colloid system is used to understand the "recipes" described in the patents for the commercial sol systems and the chemistry of the sensitizing layer deposited on the dielectric. In the last part of the paper, the relation between solution chemistry and particle size in the colloid is also discussed.

Mössbauer Spectroscopy

Experimental techniques and interpretation of spectra.—The experimental techniques used are essentially those discussed in Ref. (2) and (3), and are standard for tin Mössbauer spectroscopy. The source consisted of about 8 mCi of Sn^{119m} in the form of $BaSnO_3$, and was kept at liquid nitrogen temperature.[2] Absorbers were made by freezing the solutions in liquid nitrogen in plastic capsules about 8 mm deep.[3] These capsules were stored and the measurements were made at liquid nitrogen temperatures. A standard transmission-geometry Mössbauer spectrometer was used, with the source being moved by an electromagnetic drive system (8). Data were taken using time-mode up-down multiscaling in a multichannel analyzer, and the figures shown here are traced from the analyzer plotter output. Least squares analysis of the data, and "spectrum stripping" to reveal minor spectral components more clearly, were done as described in the text and figure captions.

Both the systematics and details of the interpretation of Sn^{119} Mössbauer spectra have been extensively discussed in various reviews (9, 10). Only a few different types of tin-containing compounds are involved in this study, and it is possible to identify them, and thus to use the spectra for analysis, by comparison with "standards" of known composition. For convenience, the isomer shifts and quadrupole splittings determined have been listed in Table I. The major features which repeatedly appear, and will be important for the interpretation of the data, are:[4]

1. Sn^{2+} ions, OH^- or Cl^- complexed, give a doublet in the absorption spectrum, centered near +3.6 mm/sec (Fig. 1A).
2. Sn^{4+} ions, bare or complexed, give a broad absorption line (Fig. 1B), near zero velocity.
3. Sn-Pd alloys (11)[5] give a singlet or barely resolved doublet, at about 1.5-2 mm/sec (depending on the Sn-Pd ratio, see Fig. 1C and 1D and Table I).

In all of the results, of course, the spectra are those of the Sn^{119} component of the compound; the chemical state of the palladium can only be inferred from its connection with the tin.

Table I. Isomer shift and quadrupole splitting (in mm/sec) for Sn^{119} in materials studied here

	Material	Isomer shift[a]	Quadrupole splitting[a]
Alloys[b]	$Sn_{0.05}Pd_{0.95}$	1.55	—
	$Sn_{0.09}Pd_{0.91}$	1.53	—
	$Sn_{0.14}Pd_{0.86}$	1.57	—
Intermetallics[f]	Pd_3Sn	1.87	—
	Pd_2Sn	1.62	0.73
	PdSn	2.01	0.62
	$SnO_2 \cdot nH_2O$	0.00	0.55
Frozen solutions	Sn^{2+} in 30% HCl[c]	3.56	1.13
	Sn^{4+} in 30% HCl[c]	0.32	0.43
	Pd(II) · 3Sn(II) complex in 30% HCl	1.42	1.98 ± 0.02
	"PdSn" complex[d]	1.37	2.21 ± 0.05

[a] Quoted with respect to $BaSnO_3$ at 78°K; all absorbers were at 78°K during the measurement. Error ±0.04 mm/sec.
[b] Isomer shift differences among these alloys are significant, but may simply reflect clustering phenomena in these disordered alloys.
[c] These materials contain a number of different complexes; the parameters quoted simply describe a "best fit" of a doublet of the data, and do not characterize any particular complex.
[d] From Ref. (15), extracted as the tetramethylammonium salt. (Isomer shift value converted assuming that the isomer shift of α-tin is 2.00 mm/sec with respect to $BaSnO_3$.)
[e] Obtained by least squares fitting doublets to unresolved broad lines. Estimated accuracy ±0.2 mm/sec, except for Pd(II) · 3Sn(II).
[f] These data are in fair agreement with those of Ref. (11) insofar as it is possible to compare them.

Results and Discussion

Complex formation.—The first part of the experimental work reported here was successful in elucidating the details of the formation of the Pd colloid, and the intermediate reactions. These results are very closely connected with the formation of a Sn-Pd complex. The literature contains a number of reports of tin-palladium complexes, discussing the theoretical and structural chemistry (12, 15),[6] of this system as well as the applications (12, 14, 16). Briefly summarizing, the addition of Sn^{2+} to HCl solutions containing small quantities of Pd^{2+} ions results in the formation of a series of highly colored complexes, which are unstable (14). These are variously reported as being red, brown, yellow-green, and bluish green, depending on the concentration of various species and the solution age. So far as we know, no crystal structure determination on a solid derivative of the Pd-Sn complexes has been performed, and the structures shown in the research articles are either conjectural or based on analogy with similar transition metal complexes.

We investigated the complex by combining two solutions:

[2] The isomer shift of this source with respect to a high-purity $BaSnO_3$ absorber at 78°K was less than 0.01 mm/sec. We are greatly indebted to Dr. P. K. Gallagher of this laboratory for supplying this material.
[3] We have recently discussed the necessity of having glass-forming systems if "frozen solution" Mössbauer spectroscopy experiments are used to characterize the liquid phase (6). In the systems studied here, the presence of 30% (or more) HCl in the solutions served as the glass-forming agent (7). We were able to verify the effectiveness of the glass-forming process both by visual observation of the solutions during freezing and auxiliary experiments with added glycerol as a glass-forming agent.
[4] The major complexing reactions for Sn^{2+} and Sn^{4+} in HCl solutions have been summarized in Ref. (3).
[5] We have also made Sn-Pd alloys and several Pd-Sn intermetallics in our laboratory, and the spectra of these materials are shown in Fig. 1. Values shown in Table I come from measurements on materials made by us.
[6] Baranovskii *et al.* (15) give quadrupole splitting and isomer shift values for a complex which they identify as $(PdCl_2(SnCl_3)_2)^{2-}$, extracted from HCl with hexyl alcohol and as tetramethylammonium salts.

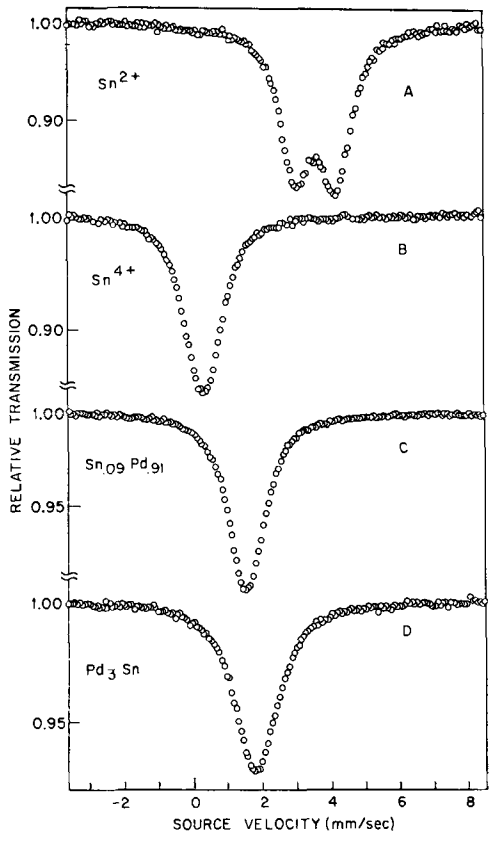

Fig. 1. Mössbauer spectra of pure phases of some tin species encountered in the solutions studied; for comparison with data in other figures. A and B, spectra of Sn^{2+} and Sn^{4+}, respectively, complexed ions dissolved in 4M HCl. C and D, spectra of $Sn_{0.09}Pd_{0.91}$ alloy and Pd_3Sn.

Pd soln.	100 mg	$PdCl_2$ (Fisher)
(11 mM	10 ml	37% HCl (reagent grade)
in Pd^{2+})	20 ml	H_2O (distilled)
Sn soln.	Amount given in text	$SnCl_2$ (purified to remove Sn^{4+})
	1 ml	37% HCl
	2 ml	H_2O (distilled)

The solutions were made slightly above room temperature and cooled to ~0°C (see below); they were maintained under nitrogen gas at all times to prevent oxidation. The Pd solution had a pale orange color; the Sn solution was essentially colorless. These two solutions were combined with rapid stirring, and an intense reddish-brown color formed instantly.

Figure 2A shows the Mössbauer spectrum of a sample of the mixture taken and frozen within 10 sec after combining the Sn and Pd solutions. The most obvious feature of that spectrum is that the doublet characteristic of SnCl complexes (Fig. 1A) is not visible; it has been replaced by another doublet, which our results show arises from the red-brown Sn-Pd complex in HCl. We have explored a range of Sn-Pd ratios and find that for Sn/Pd < 3, all of the tin is immediately complexed to produce the spectrum of Fig. 2A, while for Sn/Pd > 3, additional components which can be identified as arising from SnCl complexes (as in Fig. 1A), appear. Thus each Pd ion complexes three Sn ions, and we conclude that the stoichiometry of the Sn-Pd complex is Pd(II) · 3Sn(II). We abbreviate the dissolved complex as $(Pd\text{-}Sn)_c$ below. This is consistent with the results of Batley and Bailar (12) who suggest $(PdCl)(SnCl_3)_3^{2-}$ for the structure of the complex precipitated (from an HCl-methanol solution) using tetraphenylarsonium chloride.

Colloid generation.—The Pd colloid begins to form immediately after the complex is made, and we found it necessary to cool the Pd solution (as mentioned above) to make the reaction proceed slowly enough to

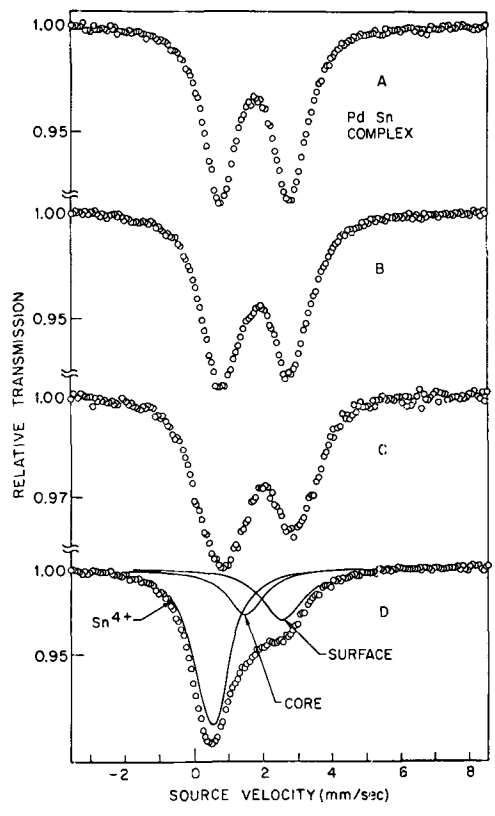

Fig. 2. Spectra of Sn-Pd complex solutions (Sn/Pd ratio 2:1) at (A) 0.2 min, (B) 6 min, (C) 30 min, (D) 120 min after mixing. The doublet in (A) is due to the Sn-Pd complex. This decomposes with time, producing complexed Sn^{4+} due to the redox reaction, Sn-Pd alloy, a small amount of dissolved Sn^{2+}, and a line which we attribute to a protective Sn^{2+} layer surrounding the Pd-Sn sol particles.

be monitored conveniently. As shown in the Mössbauer spectra (Fig. 2), the spectrum of the complex is gradually replaced by three new components. These are identifiable (with the help of subsidiary experiments) as (*a*) dissolved complexed Sn^{4+}, (*b*) the tin protective layer, and (*c*) Sn in Pd-Sn alloy. While it is difficult to resolve the line arising from the alloy from that of the dissolved Sn^{4+}, the colloid can be separated (see below) either by coagulation or centrifugation. It is the spectra of separated materials that allow the identification of the particulate phase as Sn-Pd alloy.

Neglecting for the moment the Sn component in the alloy, this decomposition to produce the Pd colloid would be expected to result from

$$(Pd\text{-}Sn)_c \rightarrow Pd_{metal} + Sn^{4+} + 2Sn^{2+} \qquad [1]$$

During this decomposition process, the red-brown color of the solution changes to a muddy grayish-brown, and then eventually to gray, corresponding to the destruction of the complex. This autoreduction of the Sn-Pd complex is probably the cause for the disappearance of color with time in the use of the Sn-Pd complex test (14) for trace amounts of Pd.

It is instructive to consider four different ratios of Sn/Pd describing the process. For Sn/Pd = 1, the divalent tin is consumed in reducing the palladium, and the spectrum shows only lines attributable to dissolved Sn^{4+} and Sn-Pd alloy. There is no line attributable to stabilizing Sn^{2+} visible in the spectrum, and the sol is in fact unstable and coagulates rapidly.

For Sn/Pd = 2, not all of the Pd is immediately complexed, since the stoichiometry of the complex is Pd:3Sn. As the redox reaction [1] occurs, some Sn^{2+} is returned to the solution, where it is immediately complexed by the remaining Pd. Some Sn^{2+}, however, remains attached to the Pd metal. This Pd metal can

become a nucleus for growth by attaching other Pd metal-tin clusters, and can grow until the Pd core is completely surrounded by Sn^{2+} ions. At this point the growth ceases. This model provides (*i*) a mechanism for particle growth, and (*ii*) a mechanism for terminating the growth and preventing coagulation. Note that if, after the complex-reduction process is complete, the colloidal particles are not completely surrounded by Sn^{2+} ions, they will agglomerate. This process decreases the surface:volume ratio until the amount of Sn^{2+} present is enough to coat the remaining particles.

In the Centrifugation section at the end of the paper we discuss the effects of the amount of available Sn^{2+} in controlling the colloid particle size. The spectra of Fig. 2 show clearly that the complex decomposes completely, leaving (dissolved) Sn^{4+}, a tin-palladium alloy phase, and a third component, which we identify below as the Sn^{2+} stabilizing layer. For the ratio Sn/Pd = 2, there is just enough divalent tin to reduce the Pd and stabilize the colloid; no dissolved Sn^{2+} is observed after the reaction is complete.

For Sn/Pd = 3, all the tin and palladium are immediately complexed; the spectra again show the Sn-Pd alloy phase, Sn^{4+}, and the tin stabilizing layer, but show additional lines, arising from dissolved Sn^{2+}, after the complex has decomposed.

For Sn/Pd > 3, all the Pd is initially complexed, and dissolved Sn^{2+} is observed in the spectrum at all times. Figure 3A shows an example of such a solution, in which a substantial amount of dissolved Sn^{2+} is present after the decomposition is complete.

Visual observations of the color change of the solution show that the decomposition of the complex (as monitored by the disappearance of the red-brown color) is very much slower in tin-rich solutions than in the mixture used for Fig. 2. This has been confirmed by Mössbauer spectroscopy of the frozen solutions.

This probably results from two phenomena. First, the presence of excess dissolved Sn^{2+} forces reaction [1] to the left, increasing the amount of complex at equilibrium. (This residual complex may provide the brownish color in the commercial sol sensitizers.) Second, if large amounts of Sn^{2+} are dissolved, they will immediately coat and passivate fresh sol particles which could otherwise act as nucleation centers for the accretion of additional Pd metal and as catalytic centers for the Pd reduction reaction. At a constant Sn/Pd ratio, the rate of decomposition of the complex was not noticeably affected by increasing the starting concentration by a factor of four over that described above.

We have not been able to determine in detail the chemical mechanism that incorporates the tin in the colloid, but a number of redox reactions involving $(Pd\text{-}Sn)_c \rightarrow (Sn\text{-}Pd)_{alloy} + 2Sn^{4+}$ would be possible.

Composition of solid phase.—One preparation patent (5) states that the Pd colloid is stabilized by a "protective colloid" of Sn^{2+} ions. This picture is supported by the fact that if the solution containing the colloid is allowed to oxidize by contact with air, the particles suddenly coagulate and precipitate just as a Mössbauer spectrum of the frozen bath shows that all the dissolved Sn^{2+} ions in the bath have been oxidized to Sn^{4+}. This coagulation is characteristic of all of the commercial systems. Figure 3 shows spectra taken during this air-oxidation process; lines from the dissolved (Cl^- complexed) Sn^{2+} ions are seen to decrease while the Sn^{4+} line grows in intensity. Just before precipitation, (Fig. 3C), no dissolved Sn^{2+} is visible, but another Sn^{2+} line is visible. We attribute this line to the protective Sn^{2+} layer on the sol particles. This interpretation is supported by the fact that we observe this line only in the colloidal suspensions, and that it disappears just as the colloid coagulates. This, plus the fact that no ionic Sn compound composed of the available ions has a line in the position observed, provides strong evidence that the tin ions involved are at the colloid surface. A likely configuration for such a layer could be for $(SnCl_3)^-$ complexes (which were originally components of the Sn-Pd complex) to be bonded to the Pd-Sn alloy core via Sn-Pd bonds, with the Cl^- ions on the outside.

After coagulation, the supernatant contains only Sn^{4+} ions, while the coagulated solid phase consists of Sn-Pd alloy, plus a small quantity of Sn^{4+} ions. Spectra of these materials are shown in Fig. 4.

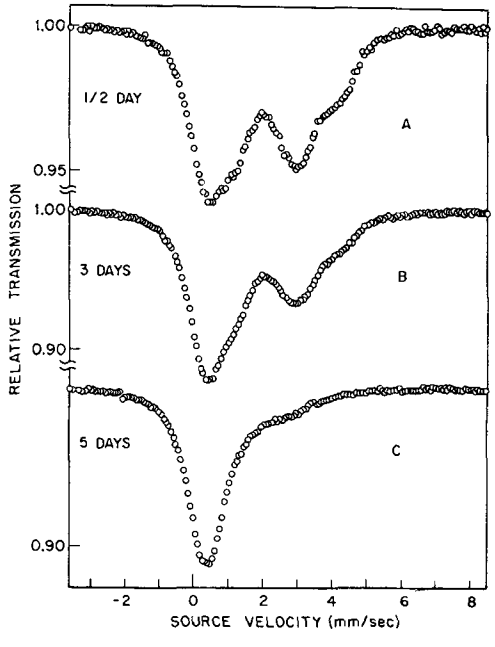

Fig. 3. Spectra showing air oxidation of Sn-Pd sol, made as described in text, but with Sn-Pd ratio of 6:1. The bath was aged at room temperature in an open beaker; (A) ½ day, (B) 3 days, (C) 5 days after Sn-Pd mixing. Initially, most of the Sn^{2+} is complexed in the HCl solution (compare Fig. 1A), and it tends to hide the line originating from the protective Sn^{2+}. As the dissolved Sn^{2+} ions are progressively oxidized, the Sn^{4+} line grows and begins to hide the Sn-Pd alloy line although the latter does remain constant in intensity. Note the line at ~3 mm/sec, due to the Sn protective layer. Coagulation occurred a few hours after sample (C) was taken.

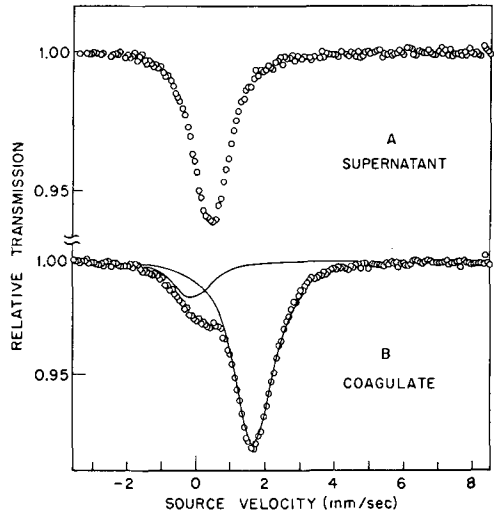

Fig. 4. Spectra of (A) supernatant and (B) coagulated precipitate (washed with H_2O) immediately after coagulation of the colloid following air oxidation of Pd sol used in Fig. 2. Note that no Sn^{2+} ions remain in solution, and that the Sn^{2+} line which we have ascribed to the stabilizing tin layer is no longer present. The Sn^{4+} line visible in the precipitate is characteristic of the $SnO_2 \cdot nH_2O$ family of compounds and results primarily from precipitation during the H_2O wash. Coagulates washed with HCl have relatively little Sn^{4+}.

It is possible to observe the particulate phase much more clearly in colloids in which it has been concentrated by centrifugation. Figure 5A shows such a spectrum, and its resolution (17)[7] into Pd-Sn alloy and the stabilizing Sn^{2+} layer. Instead of washing the centrifuged material to remove traces of electrolyte containing dissolved Sn^{2+} and Sn^{4+} ions, we have taken spectra of the supernatant and subtracted a small fraction of the supernatant spectrum from the spectrum of the sedimented material. In this way, we could eliminate the lines due to dissolved tin ions without coagulating or otherwise changing the colloid in the process of making the absorber. Centrifugation did not coagulate the colloidal particles; they would redisperse spontaneously after standing for a few days. All of the measurements on the commercial sensitizers were done using the undiluted "stock solution" concentration, as supplied by the manufacturers.

Spectra such as those in Fig. 5A allow accurate determinations of line positions of the various components, and least squares fitting has shown small variations in isomer shift and line width for both the core and stabilizing layer components. Isomer shift values for the "Sn-Pd alloy" cores have been found to be up to 0.15 mm/sec less than values for the metallurgically prepared alloys shown at the top of Table I. This is very likely due to the lattice contraction occurring in very small particles.

[7] We have previously written a brief report (17) of the analysis of the particulate phase of these sols.

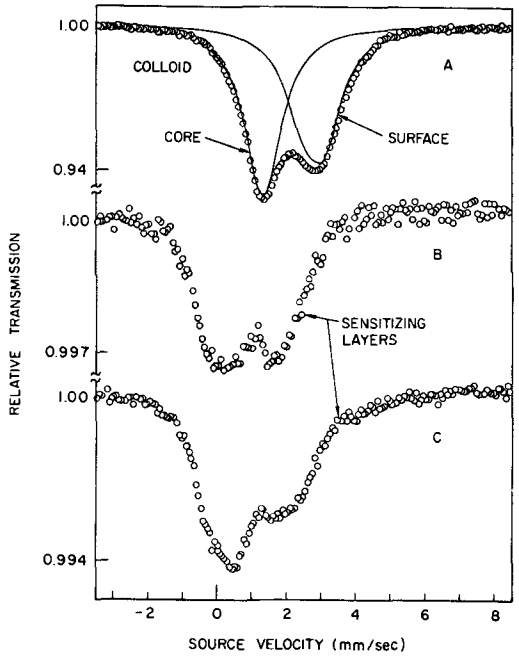

Fig. 5. Spectrum of sol particles (A), concentrated by centrifuging. This shows clearly the two lines which we attribute to the Pd-Sn alloy cores of the sol particles, and the broader line we ascribe to the stabilizing layer. This sample, made with a Sn/Pd ratio of 3, had finer particle size than the solutions shown in Fig. 6, and would be expected to have a relatively large amount of tin in the stabilizing layer, (*i.e.*, the smaller sol particles should have a large surface to volume ratio). Spectra of sensitizing layers (B and C) deposited on Kapton foil using MacDermid Metex PTH 9070 in accordance with the standard MacDermid dilution instructions. The (B) sample (688 layers) was rinsed with 0.5M HBF_4 as an "accelerator" (5) and then with water after sensitization; (C) (456 layers) was rinsed in water. The additional spectral intensity in (C) just to the right of the Pd-Sn alloy peak could very well arise from the mixed-valence (Sn^{2+} and Sn^{4+}) colloid shown in Fig. 6A of Ref. (3) (that material was produced by increasing the pH of a solution of Sn^{2+} and Sn^{4+} in HCl), or could be (3) $SnO \cdot 2H_2O$. Thus, the role of the accelerator is to remove the divalent tin so that it is not precipitated when the pH is raised during the wash step (see footnote 4). We were able to verify that the fluoborate ion is a complex former with Sn^{2+} in the concentrations used here.

Mössbauer measurements in very fine supported gold sols have already demonstrated the existence of this effect (18) and have shown that the observed isomer shift is the same as would be expected if the decrease of the lattice constant were produced by hydrostatic pressure (19). In the case of the Sn-Pd alloys, experiments on the variation of the isomer shift with (pressure-induced) lattice contraction have already been performed (20). The decrease in the lattice constant in Pd-Sn alloy under pressure decreases (20) the electronic density at the tin nucleus; this would produce a smaller isomer shift under lattice contraction, which is what we observe. Using the results of Ref. (20), we can estimate that the change in isomer shift we observe in the smallest sol particles corresponds to a contraction that would be produced by pressures of 100-200 kbar. Such high pressures are in line with previous observations on gold sol particles of comparable size (21).

X-ray measurements were made to determine the lattice constant and structure of the coagulated sol particles. These showed a pattern with only very broad lines, due to compositional inhomogeneities, small particle size, or strain. The lattice constant was appropriate for an alloy containing about 16% Sn in Pd, near the solid solubility limit.

Small variations in the isomer shift and line width of the Sn^{2+} stabilizing layer would be expected to arise from changes in the site (on the Pd-Sn core) to which the stabilizing tin was bound.

We also observed a small increase in isomer shift of the sol particle phase upon coagulation, and some precipitates actually had slightly larger isomer shifts than the Sn-Pd alloy. This probably arose from the incorporation of some of the Sn^{2+} stabilizing ions into the outer layers of the sol particle; as can be seen from Table I, all of the intermetallics containing more than 15 atomic per cent tin had larger isomer shifts than the Sn-Pd alloy.

Extension of Results to Commercial Sensitizer Systems

The results reported above are based on studies of solutions which differ in various ways from those sold commercially, and we have attempted to verify that the mechanisms that we describe are valid for those solutions. We have done this both by ultracentrifuging (which concentrates the particulate phase without coagulation) and by coagulating samples of the proprietary baths to concentrate the solid phase, and taking spectra of the precipitates. For the 6F and 9070 sensitizers, the colloid spectra were very similar to those of Fig. 5A, with minor differences attributable to different proportions between the Pd-Sn alloy and stabilizing Sn^{2+} components, and some uncertainty arising from the background subtractions as described above. The supernatant after centrifuging always appeared to be a simple mixture of dissolved Sn^{2+} and Sn^{4+} ions, as in Fig. 1A and 1B. This confirms the generalization of our results to the commercial systems described in Ref. (4) and (5).

We have also studied the reactions occurring in Sn-Pd solutions in concentrated (*i.e.*, 37%) HCl, and have found that the Mössbauer spectrum of the Sn-Pd complex produced is identical to that shown in Fig. 2A; this is good evidence that the complexes are identical. Although complex formation in the concentrated HCl is essentially instantaneous, the autoreduction reaction [1] is slower, and is still further slowed if a large excess of Sn^{2+} is present. Judging from the color of the solution, however, most of the complex has decomposed within 24 hr at room temperature. The sol produced from a tin-rich solution also contains a higher concentration of tin in the alloy, with the isomer shift of the coagulated particles approximately that of Pd_3Sn. No other attempt was made to stabilize the complex.

Sensitization Mechanism

The information above is consistent with the over-all picture [discussed, *e.g.*, in Ref. (4) and (5)] that sensitization occurs via the adsorption of Pd particles on the surface, and that the Pd alloy is the active agent in catalyzing deposition from the electroless solution. The detailed information above on the colloid composition and stabilization may lead to some additional understanding of the adhesion process, and we have supplemented studies of the baths with measurements of the sensitizing layer on a plastic surface.

Figure 5 shows Mössbauer spectra of many layers of Kapton[R] plastic film, sensitized with a commercial bath, given various rinse treatments, and dried in nitrogen. The surfaces were checked with a standard copper electroless solution to verify that sensitization had indeed occurred. The use of the "accelerator" wash dramatically increased the catalytic activity of the surface. The spectra are somewhat different from those of the sol particles; a strong line characteristic of stannic hydroxide appears, and the line (attributed in Fig. 5A to the stabilizing Sn^{2+}) is no longer present. Lines due to dissolved Sn ions are, of course, absent.

The differences can be readily explained on the basis of what is known about the chemistry of these colloids. When the substrate is immersed in the sensitizing bath, in addition to the adsorption of the sol particles, there will be some oxidation of the Sn^{2+} by oxygen adsorbed on the substrate and by dissolved oxygen in the solution used for surface pretreatment. (Note that the amount of Sn^{2+} deposited corresponds to only $\approx$ 1 monolayer, assuming uniform coverage, so that only very small amounts of dissolved oxygen suffice to produce this oxidation.) The chemical reaction at the interface could possibly promote stronger adhesion of the colloid particles since ionic, rather than van der Waals bonding, would then be operative.

Centrifugation Experiments

As a corollary to the Mössbauer experiments, samples of the concentrated commercial sensitizer formulations were centrifuged to determine qualitatively their particle size and size distributions. The results of those experiments are shown in Fig. 6, as photographs of the vials after centrifugation. The variation of optical density of the samples gives some indication of the particle size distribution. Note that for all the commercial formulations shown, the top layer of the vial is essentially colorless, indicating that the smallest particle size with substantial population is $\sim$ >10Å diameter.[8] However, the well-known Stokes-law breakdown is significant in this size range, and, more important, there is probably a large shell of Cl^- ions complexing the tin protective layer, and this would greatly decrease the effective density of the particle. Thus, the lower end of the colloidal particle size distribution is probably about 20Å in diameter.

Earlier in the paper we discussed the limitation of particle growth by the stabilizing layer of Sn^{2+}, and control of particle size by this mechanism. In the model presented, particles would grow and agglomerate until they were covered by a layer of Sn^{2+} ions [probably as $(SnCl_3)^-$ complexes], after which growth would stop. We have performed a critical test of this model, as follows: tin-palladium sols were made (starting with 100 mg $PdCl_2$ in 10 ml + 20 ml H_2O) using Sn/Pd ratios of 1.2, 1.5, 2 and 2.5 and 3. The complex was allowed to decompose at room temperature under nitrogen gas, to avoid oxidation. After the decomposition was complete (12 hr), some additional Sn^{2+} (Sn/Pd = 1) was added to decrease the sensitivity of the solutions to oxidation, and the mixtures were centrifuged. The results, in Fig. 7, show graphically that the smaller the amount of excess Sn^{2+} present when the sol was forming, the larger the particles grew before they were stabilized. This is exactly what the model would have predicted.

This approach can also be used to understand the differences in particle size distribution between the Shipley 6F and MacDermid 9070 sensitizer solutions. The Shipley process (4) generates the sol by mixing the Pd solution into a solution containing a large excess of Sn^{2+}. This should provide the finest possible

[8] We assume that Sn-Pd alloy has a density of 10 g/cc and that the viscosity of the electrolyte (at ~15°C) is the same as that of water at 20°C. Uncertainties arising from the presence of the shell of solvating ions are far larger than these approximations. Electron micrographs of the sol particles in the commercial systems show spherical particles, typically ~100Å in diameter (22).

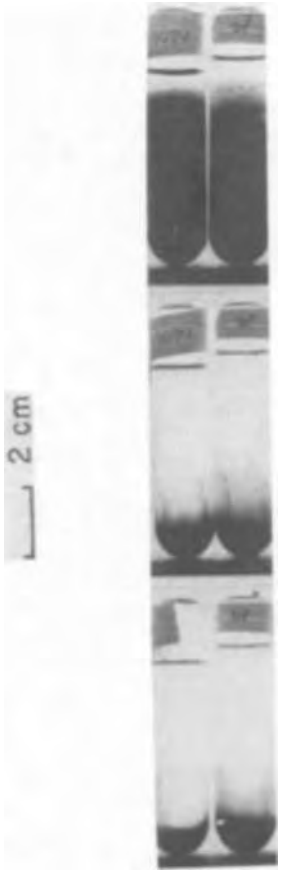

Fig. 6. Photographs of vials containing commercial sensitizers after centrifugation at 110,000G at 15°C. Centrifuging times are (from top) 4, 21, and 29 hr; samples are (from left) MacDermid 9070 and Shipley 6F.

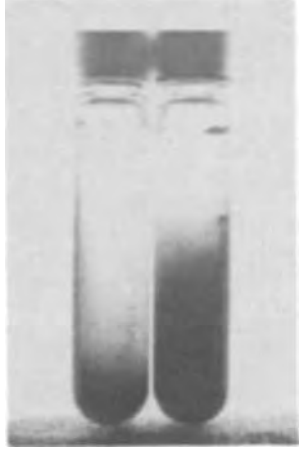

Fig. 7. Photographs of centrifuged Sn-Pd sols, made as described in text. With Sn/Pd = 1.5 and 1.8, coagulation occurred spontaneously within a few hours. The photograph shows sols with Sn/Pd = 2, left, and Sn/Pd = 2.5, right. An additional experiment with Sn/Pd = 3 (not shown) produced still finer particles. The decrease in particle size with increasing Sn/Pd ratio supports the picture of sol formation and particle stabilization given in the text. Centrifugation conditions were 15 hr at 110,000G. Note that the sedimentation rate for the left vial is essentially the same as that of the MacDermid colloid (Fig. 6), which is also generated with Sn/Pd = 2.

particle size, as the sol particles are quickly covered by Sn^{2+} from the solution, but should not provide especially uniform particle size. In Fig. 6, the 6F material is seen to have both the finest particle size and a relatively gradual tailing off of the top of the sedimented column, symptomatic of a range of small particle sizes. The MacDermid process (5), on the other hand generates the sol with a Sn/Pd ratio of 2, and then adds stabilizing tin after the sol has formed. The result should be somewhat larger sol particles than those made by the Shipley process, but particles of a more uniform size limit. The centrifuging results in Fig. 6 confirm this; the upper level of the sedimenting column is relatively sharp for the 9070 bath.

Thus, particle size analysis of the commercial sensitizers, and our own experiments with particle size control, provide strong confirmation of our mechanism of particle size control in these colloid systems.

Summary and Conclusions

We have defined a number of processes in the Pd-Sn sol system:

1. The sol-generating reaction is initiated by the formation of a Pd-Sn complex.
2. The stoichiometry of the complex has been determined to be Pd(II) · 3Sn(II).
3. The complex is unstable and autoreductive, yielding a Sn-Pd alloy.
4. The sol particle size is determined by a layer of Sn^{2+}, which limits further growth.
5. The model developed here correctly predicts relative colloid particle size, both in our test solutions and in the commercial sensitizing baths.
6. The chemical processes occurring in the adhesion of the colloid to the sensitized surface have been described.
7. Chemical changes due to air oxidation of the bath have been described.
8. The colloid sedimentation rate has been determined.

Acknowledgments

We are greatly indebted to the personnel of the Shipley, MacDermid, and Photocircuits companies for supplying samples of their sensitizers and their willingness to furnish technical information. Samples of the Kapton^{R} film used for sensitization were supplied to us by the du Pont Company. We would like to acknowledge discussions with D. Dinella and his staff, and with H. Cole, who first brought the existence of these sensitizer systems to our attention. The centrifuging experiments were performed using the ultracentrifuge of the Biophysics Research Department. The x-ray lattice constant measurements were performed by A. R. Storm.

Manuscript submitted June 15, 1972; revised manuscript received Nov. 20, 1972.

Any discussion of this paper will appear in a Discussion Section to be published in the December 1973 JOURNAL.

REFERENCES

1. W. Goldie, "Metallic Coating of Plastics," Vol. I, p. 39ff, Electrochemical Publications Limited, Middlesex (1968).
2. R. L. Cohen, J. F. D'Amico, and K. W. West, *This Journal*, **118**, 2042 (1971).
3. R. L. Cohen and K. W. West, *ibid.*, **119**, 433 (1972).
4. See C. R. Shipley, Jr., U.S. Pat. 3,011,920 (1961).
5. See E. D. D'Ottavio, U.S. Pat. 3,532,518 (1970).
6. R. L. Cohen and K. W. West, *Chem. Phys. Letters*, **13**, 482 (1972).
7. G. Vuillard, *Ann. Chim.*, **2**, 233 (1957).
8. R. L. Cohen, *Rev. Sci. Instr.*, **37**, 260, 957 (1966).
9. R. H. Herber, in "Progress in Inorganic Chemistry," Vol. 8, p. 1, F. A. Cotton, Editor, John Wiley & Sons, Inc., New York (1967).
10. J. D. Donaldson, in "Progress in Inorganic Chemistry," Vol. 8, p. 287, F. A. Cotton, Editor, John Wiley & Sons, Inc., New York (1967).
11. N. S. Ibraimov and R. N. Kuz'min, *Soviet Phys. (JETP)*, **21**, 70 (1965); and D. K. Snediker, in "Mössbauer Effect Methodology," Vol. 2, p. 161, I. J. Gruverman, Editor, Plenum Press, New York (1966).
12. G. E. Batley and J. C. Bailar, Jr., *Inorg. Chem. Letters*, **4**, 577 (1968).
13. M. A. Khattak and R. J. Magee, *Chem. Commum.*, **1965**, 400.
14. G. H. Ayres and J. H. Alsop II, *Anal. Chem.*, **31**, 1135 (1959).
15. V. I. Baranovskii, V. P. Sergeev, and B. E. Dzevitskii, *Soviet Phys. (Doklady)*, **184**, 55 (1969).
16. See R. Zeblisky and J. McCormack, NEPCON 1971 Central Proceedings. This paper also contains a brief review of the history of colloidal noble metal sensitizers.
17. R. L. Cohen and K. W. West, *Chem. Phys. Letters*, **16**, 128 (1972).
18. D. Schroeer, R. F. Marzke, D. J. Erickson, S. W. Marshall, and R. M. Wilenzick, *Phys. Rev.*, **B2**, 4414 (1970).
19. L. D. Roberts, D. O. Patterson, J. D. Thomson, and R. P. Levey, *Phys. Rev.*, **179**, 656 (1969).
20. H. S. Moller, *Z. Physik*, **212**, 107 (1968).
21. F. W. C. Boswell, *Proc. Phys. Soc. (London)*, **64A**, 465 (1951).
22. J. A. Emerson, Engineering Research Center, Western Electric, Private communication.

An Improved Model for Capillary Diffusion with No External Stirring

Leonard Nanis,* Mitchell Litt, and Joseph Chen[1]

Department of Chemical Engineering, School of Engineering and Applied Science, University of Pennsylvania, Philadelphia, Pennsylvania 19104

ABSTRACT

Average capillary concentration as a function of time has been determined by computer simulation of the diffusion process from a capillary into an infinite stationary medium. These results may be used as the basis for experimental determination of diffusivity to eliminate the usual errors associated with stirring, and to correct results obtained without stirring but using the zero concentration boundary condition solution.

In engineering practice, the diffusion coefficient enters into important parameters for mass transport correlations such as the Schmidt and Sherwood numbers. The importance of diffusion coefficient to electrochemical engineering is associated directly with the limiting current density of all electrode reactions. The several methods available for the calculation and measurement of diffusivity have been amply reviewed (1-4). Of all the methods for diffusivity measurement, the capillary technique is the most universally adaptable, provided some analytic method exists for the determination of the chemical concentration in the capillary after a given time has elapsed. For this method, the problem of obtaining accurate diffusivity data is associated with the hydrodynamic conditions which prevail at the capillary mouth. Anderson and Saddington (5) are generally credited with introducing (1949) the capillary method. They performed studies of diffusion without stirring, but analyzed results according to a treatment which implies a stirred fluid at the capillary mouth. This procedure will lead to calculated diffusivities which are less than the true value. Where attempts have been made to utilize stirring to insure the proper concentration boundary condition at the mouth of the capillary, further difficulties have arisen because of hydrodynamic effects. When real liquids stream along an interface which suddenly gives way to a change in cross section such as at the lip of the capillary, a substantial pressure gradient occurs, forcing liquid into the capillary and removing a small amount of more concentrated solution from the mouth. The apparent diffusion coefficient thus measured is invariably too great. This phenomenon is generally known as the Δl effect and has been empirically studied by Borucka (6), Berne and Berggren (7), and Nanis, Richards, and Bockris (8). For very long diffusion times, it would be expected that these two cases would converge. Such a recourse, however, would be experimentally most inconvenient.

An apparent solution to this dilemma would be to use an experimental technique with no stirring, to eliminate the Δl effect, together with a model of the diffusion process which takes into account the true boundary conditions at the mouth of the capillary. This paper presents a method for precise prediction of the diffusion coefficients by using a capillary without stirring. A computer simulation of the diffusion process without stirring provides a procedure for the estimation of diffusion coefficients from the residual amount in the capillary at any time. The results may also be used to correct literature values of diffusivity where no stirring has been used experimentally but results fitted to the "stirred" equation.

* Electrochemical Society Active Member.

[1] Current address: Westinghouse Electric Corporation, Pittsburgh, Pennsylvania 15200.

Key words: diffusion, capillary method, diffusivity, Δl effect.

Mathematical Formulation

The diffusion of electrolyte from a capillary to an external bulk solution as shown in Fig. 1 is governed by Eq. [1], in which diffusivity is assumed to be constant and the following dimensionless parameters are introduced

$$\phi = \frac{c}{c_o},\ \eta = \frac{x}{L},\ \xi = \frac{y}{L},\ \beta = \frac{z}{L},\ \tau = \frac{Dt}{L^2}$$

where c = concentration of diffusant, c_o = initial concentration of diffusant inside the capillary, L = length of the capillary, D = diffusivity, and t = time.

In the region $0 \leq \eta < 1$, the diffusion is assumed to be one-dimensional, governed by

$$\left(\frac{\partial \phi}{\partial \tau}\right)_1 = \left(\frac{\partial^2 \phi}{\partial \eta^2}\right)_1 \qquad [1]$$

The subscript 1 indicates the region where one-dimensional diffusion prevails. The zero flux boundary condition at the closed end ($\eta = 0$) of the capillary is

$$\left(\frac{\partial \phi}{\partial \eta}\right)_1 = 0;\ \eta = 0,\ \tau \geq 0 \qquad [2]$$

The initial condition is

$$\phi_1 = 1;\ 0 \leq \eta \leq 1,\ \tau = 0 \qquad [3]$$

In the region $\eta > 1$, for the absence of convection, the diffusion is three dimensional. The three-dimensional version of the diffusion equation is

$$\left(\frac{\partial \phi}{\partial \tau}\right)_3 = \left(\frac{\partial^2 \phi}{\partial \eta^2}\right)_3 + \left(\frac{\partial^2 \phi}{\partial \xi^2}\right)_3 + \left(\frac{\partial^2 \phi}{\partial \beta^2}\right)_3 \qquad [4]$$

The subscript 3 refers to the three-dimensional region. The boundary condition is

$$\phi_3 = 0;\ \eta \to \infty,\ \xi \to \infty,\ \beta \to \infty,\ \tau \geq 0 \qquad [5]$$

The symmetry of diffusion perpendicular to the axis of the capillary gives

$$\left(\frac{\partial \phi}{\partial \xi}\right)_3 = 0, \left(\frac{\partial \phi}{\partial \beta}\right)_3 = 0;\ \xi = 0,\ \beta = 0,\ \eta > 1,\ \tau \geq 0 \qquad [6]$$

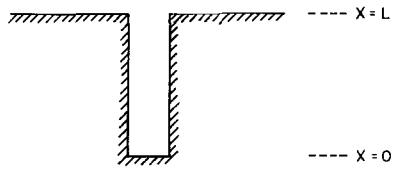

Fig. 1. Diffusion of electrolyte from a capillary to an external bulk solution.

The initial condition is

$$\phi_3 = 0;\ \eta > 1,\ 0 \leq \xi \leq \infty,\ 0 \leq \beta \leq \infty,\ \tau = 0 \quad [7]$$

At the mouth of the capillary ($\eta = 1$), where one- and three-dimensional regions join, equality of fluxes gives

$$\left(\frac{\partial \phi}{\partial \eta}\right)_1 = \left(\frac{\partial \phi}{\partial \eta}\right)_3 + \left(\frac{\partial \phi}{\partial \xi}\right)_3 + \left(\frac{\partial \phi}{\partial \beta}\right)_3 \quad [8]$$

at $\eta = 1$, $\xi = 0$, $\beta = 0$, and $\tau \geq 0$

The boundary conditions given here implicitly contain the assumption that the capillary mouth is a point source for the three-dimensional region, rather than an actual disk. The error arising from this assumption will be minimal unless the capillary diameter is a significant fraction (several per cent) of the length.

Finite Difference Formulation

An explicit form of the finite difference Eq. [9] was used to represent Eq. [1]-[8] for both one-dimensional and three-dimensional regions.

Let i = index for the step movement in x direction ($i = 1,2,3,...$), j = index for the step movement in y direction, k = index for the step movement in z direction, n = time, $\Delta\tau$ = step increment in dimensionless time, $\Delta\eta$ = step increment in η direction, $\Delta\beta$ = step increment in β direction, $\Delta\xi$ = step increment in ξ direction, $M = 1/\Delta\eta$: number of grid points in the capillary, $\lambda_1 = \Delta\tau/(\Delta\eta)^2$, $\lambda_2 = \Delta\tau/(\Delta\beta)^2$, and $\lambda_3 = \Delta\tau/(\Delta\xi)^2$.

For the one-dimensional diffusion region, $0 \leq \eta < 1$, Eq. [1] becomes

$$\phi_{i,1,1,n+1} = [1 - 2\lambda_1]\,\phi_{i,1,1,n} + \lambda_1\,[\phi_{i-1,1,1,n} + \phi_{i+1,1,1,n}] \quad [9]$$

where $1/\Delta\eta > i$

At the closed end of the capillary ($i = 1$), the zero flux boundary condition (Eq. [2]) leads to

$$\phi_{0,1,1,n} = \phi_{2,1,1,n} \quad [10]$$

The initial condition (Eq. [3]) becomes

$$\phi_{i,1,1,0} = 1 \quad [11]$$

For the three-dimensional diffusion region, $\eta > 1$, $0 \leq \xi \leq \infty$, $0 \leq \beta \leq \infty$, Eq. [4] becomes

$$\phi_{i,j,k,n+1} = (1 - 2\lambda_1 - 2\lambda_2 - 2\lambda_3)\,\phi_{i,j,k,n} + \lambda_1(\phi_{i-1,j,k,n} + \phi_{i+1,j,k,n}) + \lambda_2(\phi_{i,j-1,k,n} + \phi_{i,j+1,k,n}) + \lambda_3(\phi_{i,j,k-1,n} + \phi_{i,j,k+1,n}) \quad [12]$$

for $i > 1/\Delta\eta$.

Boundary conditions (Eq. [5], [6]) are

$$\phi_{i,j,k,n} = 0 \quad \text{as } i \to \infty,\ j \to \infty,\ k \to \infty \quad [13]$$

$$\phi_{i,0,k,n} = \phi_{i,2,k,n} \quad [14]$$

$$\phi_{i,j,0,n} = \phi_{i,j,2,n} \quad [15]$$

For simplicity, the capillary is considered as a drilled hole in a block. In order to account for the impermeable plane at the mouth level, $\eta = 1$, $\xi > 0$, $\beta > 0$, the following statement allows for zero flux perpendicular to the plane by the use of imaginary points below the plane, *e.g.*

$$\phi_{M+1,j,k,n} = \phi_{M-1,j,k,n} \quad [16]$$

The initial condition given by Eq. [7] becomes

$$\phi_{i,j,k,n} = 0 \quad \text{as } \tau = 0,\ i > \frac{1}{\Delta\eta},\ 0 \leq j \leq \infty,\ 0 \leq k \leq \infty \quad [17]$$

At the junction of the one- and three-dimensional regions just at the capillary mouth ($i = M$, $j = 1$, $k = 1$), Eq. [8] becomes

$$\phi_{M,1,1,n+1} = \frac{\phi_{M-1,1,1,n} + \phi_{M+1,1,1,n} + \phi_{M,2,1,n} + \phi_{M,1,2,n}}{4} \quad [18]$$

Equation [18] is based on implicit finite difference approximation, together with the assumption of equal spacing in the three-dimensional region ($\Delta\eta = \Delta\xi = \Delta\beta$).

Computation

Stability of the finite difference calculations required (9) that λ_1, λ_2, and λ_3 be smaller than 0.5. Ten grid points in the capillary ($\Delta\eta = 0.1$) and a dimensionless time increment of $\Delta\tau = 2 \times 10^{-4}$ were first used for the calculation except at early time ($\tau \leq 0.001$) where twenty grid points in the capillary were used to improve the computation of the average concentration by smoothing the concentration in the region $0 \leq \eta \leq 1$. The same step size ($\Delta\eta = \Delta\beta = \Delta\xi = 0.1$) was used in the three-dimensional diffusion region (Eq. [12]-[17]). Computation of the dimensionless concentration at all grid points was carried out as the dimensionless time, τ, increased to 1.5. The dimensionless concentrations in the three-dimensional diffusion region were calculated step by step from the mounth of the capillary to the infinite medium. However, computation was cut off and moved to the next time step when the dimensionless concentration, ϕ, at grid points became less than a preset value which, in this calculation, was chosen as 1.0×10^{-4}. Trial and error procedure showed that this value is the largest which can be neglected without affecting the final result for ϕ_{avg}. In this way, the actual computing time was reduced to about a quarter of that required to compute the concentration at every grid point out to $\eta = 2.5$. A computer time of about 10 min was required to carry out the calculation to $\tau = 1.5$ on the IBM 360/75.

Convergence was tested by reducing the time increment, λ, checking for changes in concentration profile and by checking the computed average concentration in the capillary as a function of dimensionless time with the analytical solution (Eq. [19]) for the case of diffusion with stirring and also one-dimensional diffusion along the axis of the capillary without stirring (Eq. [22]), the two limiting cases discussed below. The smallest time increment used ($\Delta\tau = 1.5 \times 10^{-4}$) provided for convergence of numerical results and also gave excellent agreement with analytic solutions for the fast and slow limiting cases. In Fig. 2, computer results are shown as points for comparison with the analytic limits given by Eq. [22] for the slowest possible bound and Eq. [19] for the fastest limit.

Analytic Solutions for Fast Limit

Anderson and Saddington (5) gave a solution to Eq. [1] with Eq [2] and [3] as boundary conditions which describes the average concentration remaining in the entire capillary at time t with the concentration at the mouth of the capillary maintained at zero. The solution, Eq. [19], permits the evaluation of a diffusion coefficient, D, for the limiting case of fastest extraction from the capillary.

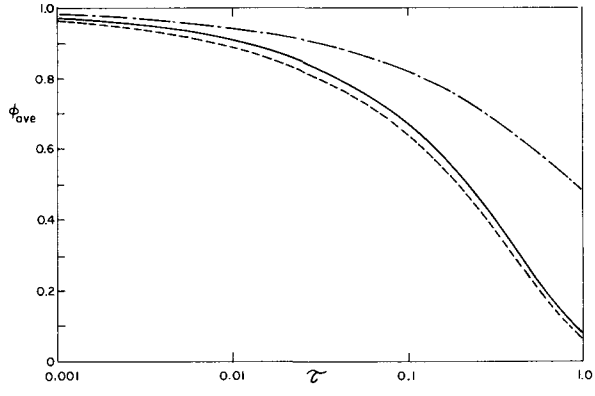

Fig. 2. Average capillary concentration vs. time (ϕ_{avg} vs τ). ——— No-stir, three dimensional, computed; —·—·—·— no-stir, one dimensional, analytic; - - - - - - stir, one dimensional, analytic.

$$\phi_{avg} = \frac{8}{\pi^2} \sum_{n=0}^{\infty} \frac{1}{(2n+1)^2} e^{\frac{-(2n+1)^2 \pi^2 \tau}{4}} \quad [19]$$

A result entirely equivalent to Eq. [19] may be obtained by the use of Laplace transform methods (9) and is much more useful for small time, although different in form.

$$\phi_{avg} = 1 - 2\tau^{1/2} \left\{ \frac{1}{\pi^{1/2}} + 2 \sum_{n=1} (-1)^n \left[\frac{e^{\frac{-n^2}{\tau}}}{\pi^{1/2}} - \frac{n}{\tau^{1/2}} \operatorname{erfc} \frac{n}{\tau^{1/2}} \right] \right\} \quad [20]$$

It may be readily determined that the entire summation in Eq. [20] may be ignored for times which are small, *i.e.*, where the criterion $\tau < 0.06$ is valid. The first term within the large brackets in Eq. [20] represents the limiting case equivalent to diffusion out of a semi-infinite region. Thus, for small time, Eq. [20] simplifies to

$$\phi_{avg} = 1 - \frac{2}{\pi^{1/2}} \tau^{1/2} \quad [21]$$

Analytic Solution for Slow Limit

By making no provision for sideways (radial) spreading of diffusant in the no-stirring case, an estimate is possible for a hypothetical slowest extraction of diffusant as though it moved outside the capillary in a virtual constrained tube within the exterior liquid. By the use of Laplace transform methods with the diffusion equation (Eq. [1]) together with only one boundary condition, given by Eq. [2] (no restriction on the capillary mouth concentration), the concentration as a function of distance and time may be readily obtained. The solution is

$$\phi_{avg} = 1 - \frac{\tau^{1/2}}{\pi^{1/2}} \left[1 - e^{-\frac{1}{\tau}} \right] - \operatorname{erfc} \frac{1}{\tau^{1/2}} \quad [22]$$

For small times, the decreasing exponential and complementary error function terms in Eq. [22] are very small and may be ignored in favor of the approximation

$$\phi_{avg} = 1 - \frac{\tau^{1/2}}{\pi^{1/2}} \quad [23]$$

If it were possible to arrange the bounded one-dimensional diffusion into the external liquid, Eq. [23] would describe the actual amount remaining in the capillary for small time. The diffusant actually spreads beyond the constraining envelope for the case of three-dimensional diffusion with no stirring, thus providing for a more rapid removal of material than the one-dimensional bound given in Eq. [22]. Thus, the "actual" amount remaining given by Eq. [23] appears to be associated with a smaller apparent diffusivity for the same ϕ_{avg} substituted in Eq. [21], valid for stirring.

Using the "actual" diffusivity for the no-stir, one-dimensional treatment as D_{act} in Eq. [23] and calling the apparent diffusivity computed from Eq. [21] D_{appt}, equating amounts in the capillary gives as a limit at short time

$$\frac{D_{appt}}{D_{act}} = 0.25$$

This bounding lowest possible value is indicated in Fig. 4 and provides a limit for the negative error in D measurement introduced by using Eq. [21] (incorrectly) without the necessary stirring conditions.

Table I. Numerical results for ϕ_{avg} vs. τ for three-dimensional diffusion without stirring

ϕ_{avg}	τ	D_{appt}/D_{act}*
0.9398	0.0048	0.5929
0.9228	0.0075	0.6241
0.8848	0.0153	0.6810
0.8219	0.0333	0.7480
0.7737	0.0513	0.7840
0.6972	0.0873	0.8249
0.5077	0.2160	0.8778
0.3339	0.3959	0.9078
0.2231	0.5699	0.9175
0.1470	0.7498	0.9228
0.09684	0.9298	0.9261
0.06034	1.134	0.9286
0.03949	1.316	0.9309
0.02605	1.496	0.9312

* D_{appt}/D_{act} obtained by substituting computed ϕ_{avg} in Eq. [20] or Eq. [21] to determine D_{appt}.

Results and Discussion

Table I gives the values from the numerical computation for three-dimensional diffusion from a capillary into a stationary bulk solution. The results of the slowest possible bound, Eq. [22], and the fast-stirred bound, Eq. [20], are shown together in Fig. 2. There is a surprisingly similar behavior of ϕ_{avg} *vs.* τ for the true extremes of stirring (Eq. [20]) and the nonstirred three-dimensional computed result. As shown in Fig. 3, curves of concentration *vs.* distance at selected values of τ bear a close resemblance to the shape expected for stirring conditions at the mouth. Even without stirring, the concentration gradients just at the mouth show a nearly similar flux behavior.

If stirring is not provided in an actual experiment, the apparent value of D computed using Eq. [20] (zero boundary condition) will clearly be less than the true value of the diffusion coefficient. These negative errors arising from misuse of Eq. [20] with ϕ_{avg} for no stirring are listed in Table I as D_{appt}/D_{act}. A plot of D_{appt}/D_{act} *vs.* ϕ_{avg} is given in Fig. 4. The lower limit (for $\phi_{avg} > 0.95$) of the ratio was not determined because of program time interval limitations. D_{appt}/D_{act} increases from 0.6 to 0.93 as the concentration of material remaining in the capillary decreases toward zero. Thus, if sufficient time elapses, diffusivity measurements may be made to within a close approximation of the correct value even if an incorrect equation for ϕ_{avg} *vs.* τ is used with no stirring, as expected. For a 3-cm long capillary and diffusion coefficient on the order of 5×10^{-6} cm²/sec, a misapplication of Eq. [20] for the

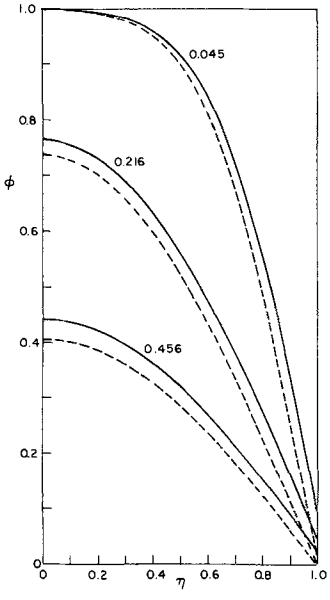

Fig. 3. Capillary concentration profiles for selected τ. ——— No-stir, $\phi \neq 0$, $\eta = 1$; - - - - - - - stir. $\phi = 0$, $\eta = 1$.

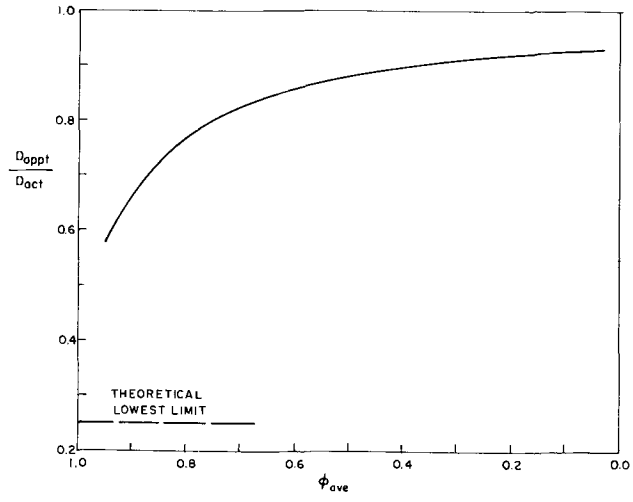

Fig. 4. Ratio of apparent to actual diffusivity obtained by using no-stir ϕ_{avg} in Eq. [20].

nonstirring case will result in less than 10% error only if the diffusion proceeds for longer than 375 hr. For a diffusion time of 32 hr, a 20% error will result from misapplication of Eq. [20]. Using the results shown in Fig. 2 and 4, however, it is possible to back-correct data in the literature where Eq. [20] has been used incorrectly with no stirring conditions. Furthermore, availability of these corrections implies that experimental use of the capillary technique with no stirring can be made to obtain accurate values of diffusivity and totally eliminate the ambiguity associated with stirring and the Δl effect. Errors may still arise from natural convection effects due to density differences between the diffusing and bulk solutions. For very dense solutions, such effects may be considerable and make stirring a preferable recourse. Preliminary results from an experimental test of the method indicate, however, that this problem can be overcome. Final results from that study will be the subject of a later communication.

Acknowledgment

This work was performed for the Jet Propulsion Laboratory, California Institute of Technology, sponsored by the National Aeronautics and Space Administration under Contract NAS7-100. Support of the University of Pennsylvania Computer Center is gratefully acknowledged. The assistance of George L. Schrenk, Associate Professor of Mechanical Engineering, University of Pennsylvania, in aspects of the computational effort is gratefully acknowledged.

Manuscript submitted March 27, 1972; revised manuscript received Oct. 21, 1972.

Any discussion of this paper will appear in a Discussion Section to be published in the December 1973 JOURNAL.

REFERENCES

1. R. Mills, *J. Electroanal. Chem.*, **9**, 57 (1965).
2. B. R. Sundheim, in "Fused Salts," B. R. Sundheim, Editor, McGraw Hill Publishing Co., New York (1964).
3. A. Klemm, in "Molten Salt Chemistry," p. 535, M. Blander, Editor, Interscience Publishers, New York (1964).
4. A. L. Geddes and R. B. Pontius, in "Technique of Organic Chemistry," Vol., 1, Part 2, Chap. XVI, p. 981, A. Weissberger, Editor, Interscience Publishers, New York (1959).
5. J. S. Anderson and K. Saddington, *J. Chem. Soc.*, S 381 (1949).
6. A. Z. Borucka, J. O'M. Bockris, and J. A. Kitchener, *Proc. Roy. Soc., London*, **A241**, 554 (1957).
7. E. Berne and J. Berggren, *Acta Chem. Scand.*, **14**, 428 (1960).
8. L. Nanis, S. R. Richard, and J. O'M. Bockris, *Rev. Sci. Instr.*, **36**, 673 (1965).
9. B. Carnahan, H. Luther, and J. Wilkes, "Applied Numerical Methods," John Wiley & Sons, Inc., New York (1964).
10. A. Thom and C. J. Apelt, Aeronautical Research Council, R & M, No. 3090, Her Majesty's Stationery Office, London (1958).

Technical Notes

Grain Boundary Attack of 316L SS in Ammonia-Rich Environments

J. M. A. Van der Horst*

Surface Research, Incorporated, Olean, New York 14760

Urea synthesis plants are often subject to very severe corrosion. The materials used most often are austenitic stainless steels of the types 316 and 317 (1). Titanium has been used but it is also subject to corrosion (2). Zirconium has found limited application and appears to be completely inert.

Two forms of corrosion should be distinguished in urea synthesis. First, corrosion in the reactor proper, which is mostly confined to the welds (3). This type of corrosion seems to be connected with the high level of carbamate in the reactor, or, as others claim, the presence of ammonium cyanate (4). At any rate, sigma phase in the weld metal is primarily attacked and it can be reduced to relatively low levels by employing a filler material which does not form sigma phase as rapidly as 316 or 317 (5).

The second form of corrosion is found in areas exposed to the gas phase in urea synthesis. It is characterized by general attack of austenitic stainless steels, sometimes by preferential leaching of some of the constituent elements of the alloy or by intergranular attack. This is the type of corrosion which will be discussed hereunder.

The Huey test (ASTM A262C) has been specified for stainless steels used in urea synthesis plants. This test is conducted at a high redox potential and a low pH, whereas urea synthesis takes place at a low redox

* Electrochemical Society Active Member.
Key words: intergranular corrosion, austenitic stainless steel, ammonia, ASTM tests, complexing.

potential and a high pH. It would therefore appear inappropriate to use the test for this purpose.

Some limited cases can be made for the Huey test in the case of the reactor, because this test also attacks sigma phase. For corrosion in areas exposed to the gas phase it is completely out of place (6), as will be demonstrated presently.

Case Histories and Experimental

Among internals from the high pressure section of a urea synthesis plant were present a series of collars consisting of two parts of 316L stainless steel welded together. A number of these assemblies were found to have one of the two parts severely corroded, the other not (Fig. 1). This indicated the presence of some condition in the particular part of 316L making it more subject to urea corrosion than the other part. The chemical analysis however did not show any significant differences:

	Ni	Cr	Mo
Corroded portion (steel A)	13.92	17.05	2.36
Noncorroded portion (steel B)	14.50	16.96	2.42

The assembly was therefore sliced into segments and the individual segments subjected to the oxalic acid test (ASTM A262A) (Fig. 2), the Streicher test (ASTM A262B) (Fig. 3), the Huey test (ASTM A272C) (Fig. 4), and the Strauss test (ASTM A262E) (Fig. 5). Fresh metal surfaces were exposed for the test. The grain-boundary etching visible in the cross section is due to metallographic preparation.

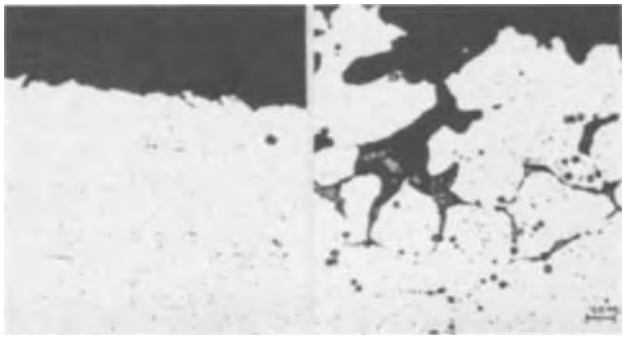

Fig. 1. 316L SS A (left) and B (right) after simultaneous exposure to the gas phase in urea synthesis.

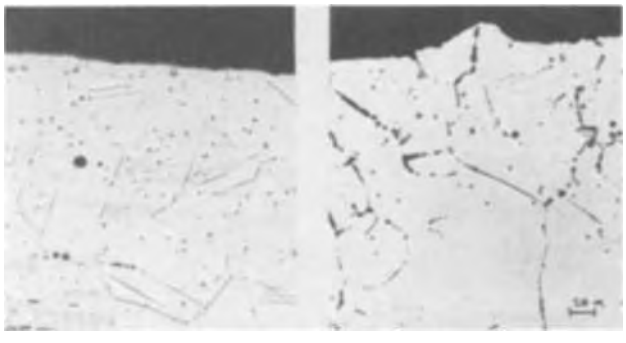

Fig. 2. 316L SS A (left) and B (right) after oxalic acid test (ASTM A262A).

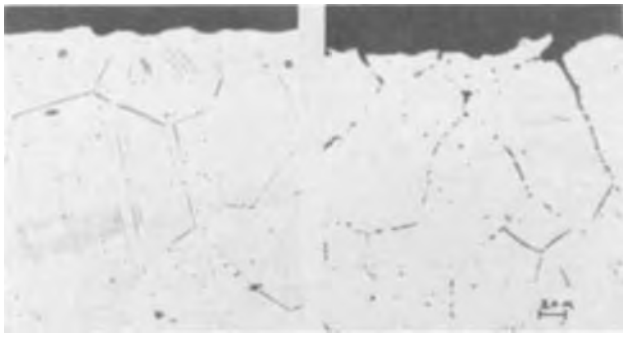

Fig. 3. 316L SS A (left) and B (right) after Streicher test (ASTM A262B).

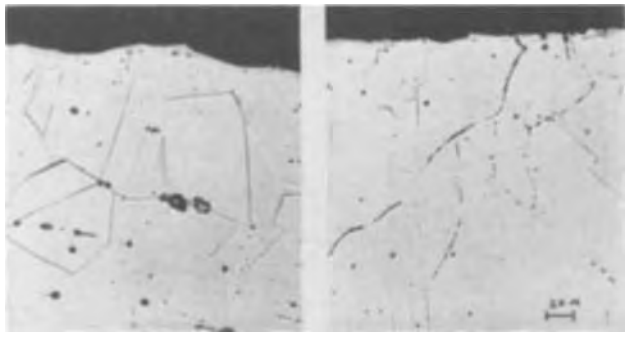

Fig. 4. 316L SS A (left) and B (right) after Huey test (ASTM A262C).

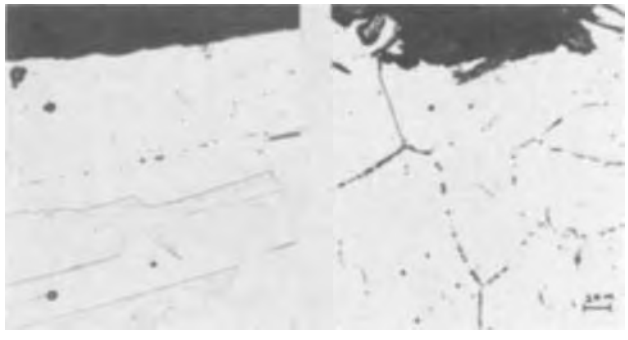

Fig. 5. 316L SS A (left) and B (right) after Strauss test (ASTM A262E).

Discussion

It is quite evident that while the urea synthesis environment can cause very severe intergranular corrosion in steel B, none of the ASTM intergranular corrosion tests does anything like it.

The photomicrographs (Fig. 1-5) clearly show a structural difference between steels A and B. They react quite differently to the metallographic etch, no

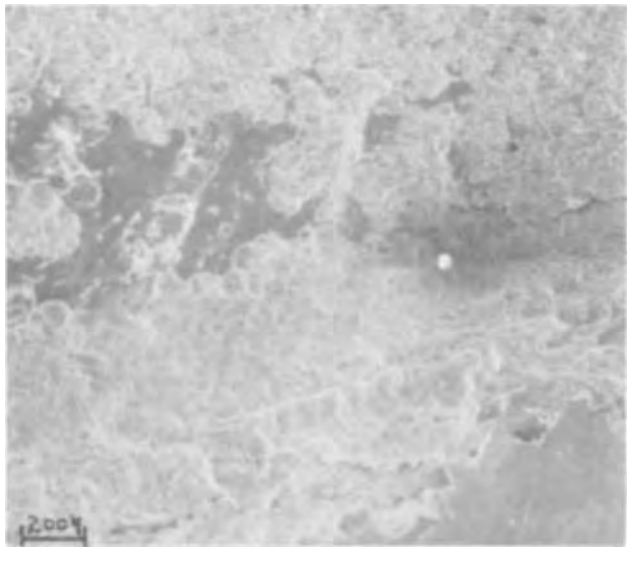

Fig. 6. SEM of partially leached out 316L SS; remaining metal lower left corner.

doubt due to a difference in heat-treatment. This difference however does not seem to have anything to do with Cr depletion at the grain boundaries, at which the tests of ASTM A262 are more or less aimed. Only the Strauss test (Fig. 5) caused considerable attack of steel B, but this attack appears to follow the internal grain structure rather than the grain boundaries.

The structure in Fig. 6-8 may clarify the matter somewhat. Apparently the corrosive environment we are dealing with in this case is an excellent solvent for Ni, a somewhat lesser solvent for Cr, and a poor solvent for Mo and Fe. This is also confirmed by the intergranular attack shown in Fig. 9-10, where the grain boundaries are Ni enriched. One might wish to make a case for corrosion caused by low C, but this would seem difficult.

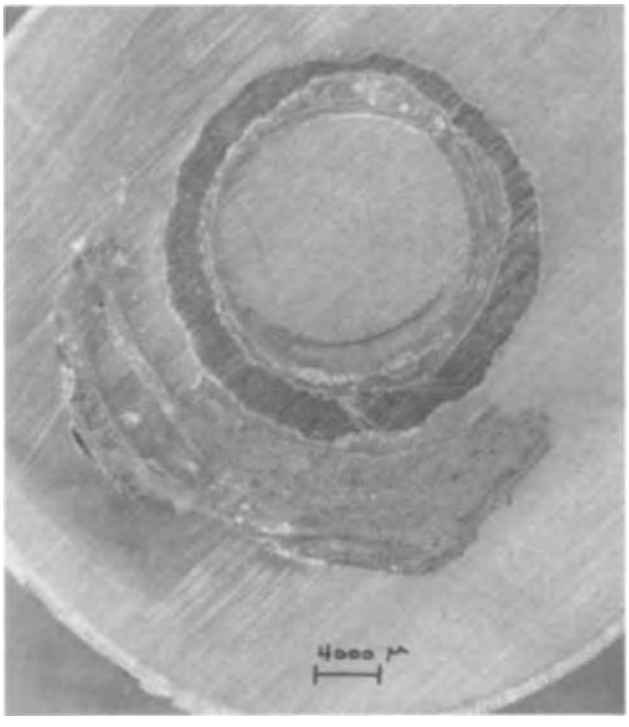

Fig. 7. Corroded assembly of 316L SS: inner circle rest of corroded tube, surrounded by partially corroded ring, and lower outside part of corroded plate.

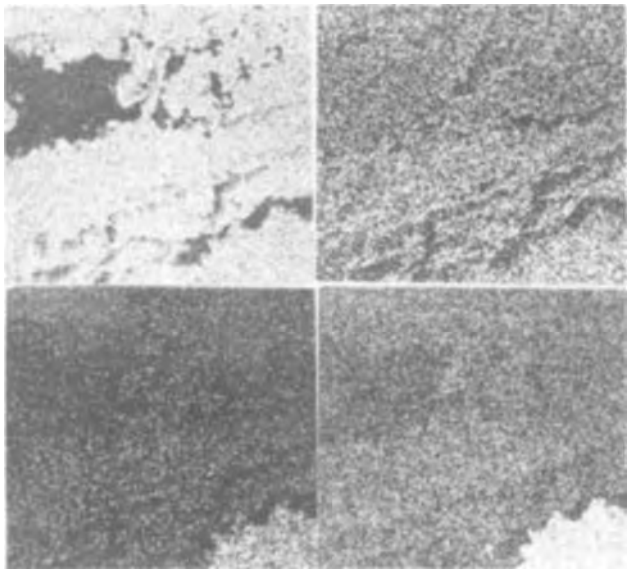

Fig. 8. Backscatter of Fig. 6 for Fe (upper left), Mo (upper right), Ni (lower left), and Cr (lower right).

The sequence of dissolution corresponds to the order of affinity for the formation of ammonia complexes, which has been widely investigated by Professor Janik Bjerrum (7), who confirmed to the author that increasing concentrations of ammonia are required to complex Ni, Cr, and Fe, in this order, while Mo is not complexed at all in this environment (8). These complexes are highly soluble in ammonia, and as a result the protective oxide layers of austenitic stainless steels become completely soluble.

Since all the metals concerned dissociate water when unprotected, and some water is always present in urea synthesis, the cycle, complexing, dissolution, dissociation, is continuous. At lower NH_3 concentrations it is capable only of complexing Ni, the result being preferential dissolution of areas with a high Ni concentration. At somewhat higher NH_3 concentrations both Ni and Cr are complexed and leached out of the matrix. At still higher NH_3 concentrations, Fe is also complexed and the stainless steel dissolves completely and cleanly.

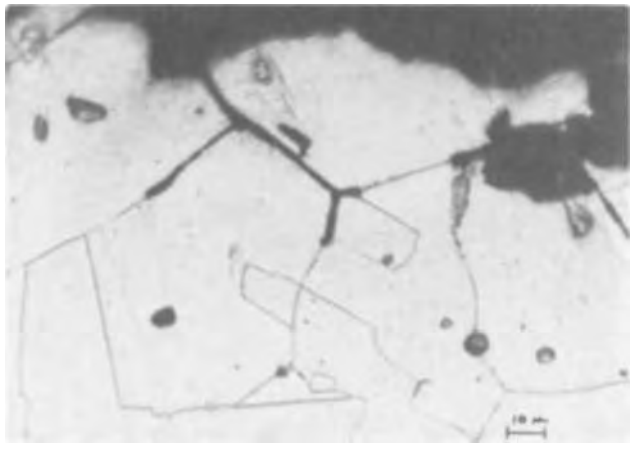

Fig. 9. 330 stainless corroded in a urea process stream

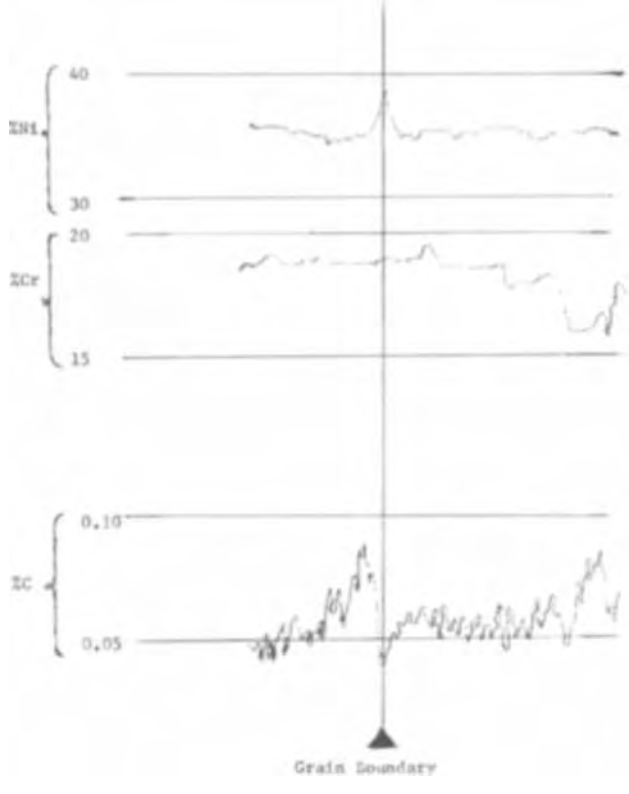

Fig. 10. Grain and grain-boundary composition of 330 SS for Ni, Cr, and C (electron microprobe).

Figure 6 shows a scanning electron micrograph of a piece of 316L SS (from the gas phase in urea synthesis) most of which is completely transformed into corrosion product. Only the lower left-hand corner is still metal. The corroded assembly is shown in Fig. 7. It was removed from a location close to that of the material shown in Fig. 1-5 and consists essentially of a tube, a ring, and a plate, only some of the ring still being in the form of metal.

In Fig. 8 one sees backscatter shots for the principal elements involved of the same area as Fig. 6. Quite obviously Fe and Mo have hardly been moved by the corrosion process, Cr has been considerably reduced, and Ni has virtually disappeared.

In another case, during testing in the gas phase of urea synthesis, a specimen of 330 SS showed severe intergranular attack (Fig. 9). Electron-microprobe traces (Fig. 10) for Ni, Cr, and C show no variation in Cr content, high Ni, and low C. Cr depletion, although obviously a cause, is apparently not the only cause for grain-boundary attack in austenitic SS. Ni enrichment, in the appropriate environment, can do the same thing.

Conclusions

The tests for intergranular corrosion in austenitic stainless steels specified in ASTM A262 are not applicable for this type of corrosion in highly ammoniacal environments.[1]

Intergranular corrosion of austenitic stainless steels in highly ammoniacal environments appear to be connected with increased Ni concentrations at the grain boundary.

The apparent corrosive mechanism is complexing of protective oxides by NH_3, dissolution of these oxides into ammonia, and dissociation of water by the unprotected metal.

[1] ASTM A262D not tested.

Manuscript submitted Nov. 1, 1972; revised manuscript received Dec. 14, 1972.

Any discussion of this paper will appear in a Discussion Section to be published in the December 1973 JOURNAL.

REFERENCES

1. N. H. Walton, *Safety Air Ammonia Plants*, **7**, 56 (1965); *ibid.*, **8**, 36 (1966).
2. Filippo Saraceno and Federico Turelli, *Quaderni Pignone*, **14**, 26 (1969).
3. V. V. Potapov, A. T. Strigin, and A. B. Gendel'man, *Khim. Prom.*, **47**, 125 (1971).
4. A. I. Krasil'shchikov, *Usp. Khim.*, **7**, 1041 (1938).
5. M. M. Kristal, A. L. Belinkii, N. A. Adugina, G. A. Zheltova, M. A. Dmitriev, and A. N. Krutikov, *Khim. i Neft. Mashinostr.*, **3**, 19 (1969).
6. M. Vassal, Conference Internationale des Arts Chimiques, Journées Techniques de Paris, Aciers speciaux, Paris (1965).
7. Jannik Bjerrum in "Theory of the Reversible Step Reactions," pp. 180-190, P. Haase and Son, Copenhagen (1957); "Stability Constants," Part II. Inorganic Ligands, pp. 46-51, The Chemical Society, London (1958); "On the Tendency of the Metal Ions Toward Complex Formation," p. 381, The Chemical Society, London (1955).
8. Jannik Bjerrum, Private communication.

Simultaneous Determination of Instantaneous Corrosion Rates and Tafel Slopes from Polarization Resistance Measurements

Florian Mansfeld*

North American Rockwell Science Center, Thousand Oaks, California 91360

Instantaneous corrosion rates are most commonly determined by the use of an electrochemical technique first described by Wagner and Traud (1) and Stern and co-workers (2, 3). This technique is now known as Stern-Geary technique, polarization resistance technique, or incorrectly (4) as linear polarization method.

It was shown by Wagner and Traud (1) and by Oldham and Mansfeld (4, 5) that for a polarization curve of the form

$$I = I_{corr}\left(e^{\frac{2.3(\phi-\phi_{corr})}{b_a}} - e^{-\frac{2.3(\phi-\phi_{corr})}{b_c}}\right) \quad [1]$$

the corrosion current I_{corr} is proportional to the slope of the polarization curve at the corrosion potential ϕ_{corr}

$$I_{corr} = \frac{1}{2.3}\frac{b_a b_c}{b_a + b_c}\left(\frac{dI}{d\phi}\right)_{\phi_{corr}} = \frac{1}{2.3}\frac{b_a b_c}{b_a + b_c}\frac{1}{R_p} = \frac{B}{R_p} \quad [2]$$

where R_p is the polarization resistance.

It is commonly believed that a serious limitation of the method discussed here is the fact that the actual current-potential measurement only leads to the value of R_p, while the values of the Tafel slopes b_a and b_c have to be guessed, taken from literature, or be determined in independent experiments. For this reason Hoar (6) expressed the opinion that the measurement of polarization resistance is superfluous in the electrical determination of corrosion rates. He overlooks, however, the important advantage of the polarization resistance method, namely that the system is disturbed only very little by the measurement which is especially important when the time behavior of corrosion rates is studied.

In the following it will be shown that the polarization resistance R_p and the Tafel slopes b_a and b_c can be determined simultaneously from the measured current-potential curve, thereby allowing calculation of instantaneous corrosion currents.

Combination of Eq. [1] and Eq. [2] leads to

$$I = \frac{1}{2.3}\frac{b_a b_c}{b_a + b_c}\frac{1}{R_p}\left(e^{\frac{2.3(\phi-\phi_{corr})}{b_a}} - e^{-\frac{2.3(\phi-\phi_{corr})}{b_c}}\right) \quad [3]$$

which can be written after rearrangement as

$$2.3\,R_p I = \frac{b_a b_c}{b_a + b_c}\left(e^{\frac{2.3\Delta\phi}{b_a}} - e^{-\frac{2.3\Delta\phi}{b_c}}\right) \quad [4]$$

where $\Delta\phi = \phi - \phi_{corr}$.

* Electrochemical Society Active Member.

Key words: time dependence of corrosion rates and Tafel slopes, corrosion of iron, curve fitting.

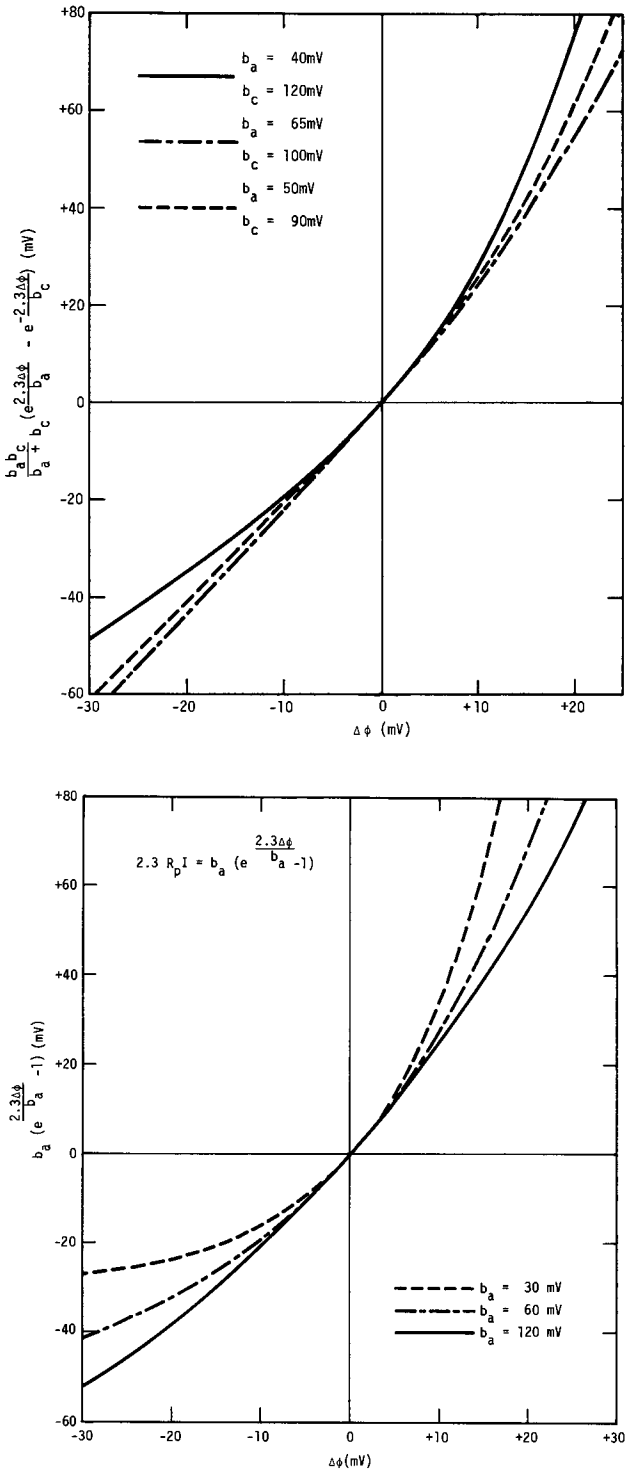

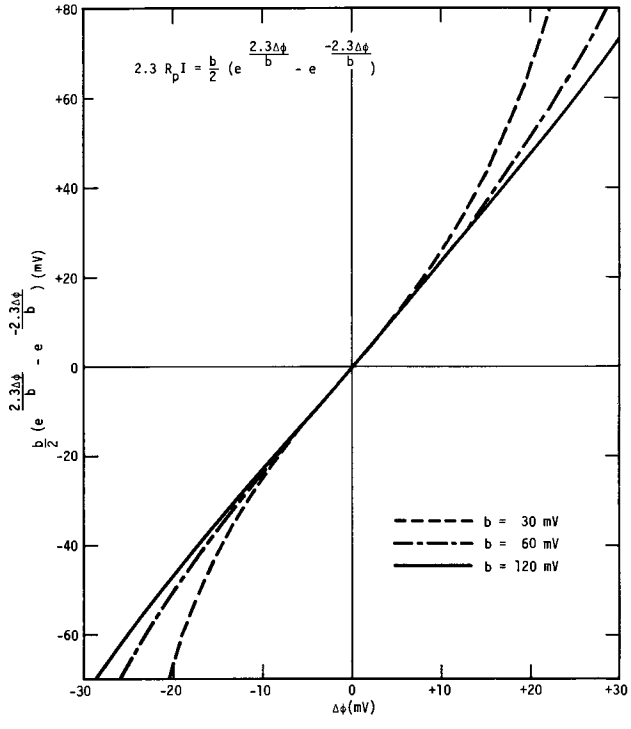

Fig. 1. Plots of right-hand side of Eq. [4] *vs.* $\Delta\phi = \phi$-ϕ_{corr}. (a, above left) Various combinations of Tafel slopes b_a and b_c, (b, left) $b_c = \infty$ (diffusion control), (c, above right) $b_a = b_c = b$.

It will be noted that the right hand side of Eq. [4] depends only on the Tafel slopes b_a and b_c. Figure 1 shows a plot of the right-hand side of Eq. [4] *vs.* $\Delta\phi$ for various combinations of Tafel slopes. It can be seen that the curvature of the plot depends on difference of the Tafel slopes b_a and b_c. Figure 1b shows a similar plot for the case where the cathodic reaction is under diffusion control ($b_c = \infty$), while in Fig. 1c it has been assumed that anodic and cathodic Tafel slopes are equal ($b_a = b_c = b$). Note the different curvature at cathodic potentials ($\Delta\phi < 0$) in Fig. 1b and Fig. 1c. These examples show that different kinetic behavior of a corroding metal, as expressed by different combinations of Tafel slopes, can be recognized based on plots according to Eq. [4].

The corrosion current I_{corr} can be calculated from the measured polarization curve in the following four steps which are based on Eq. [4] and Eq. [2]:

1. Determine the polarization resistance R_p from

$$\left(\frac{dI}{d\phi}\right)_{\phi_{corr}} = R_p^{-1}$$

by drawing a tangent at ϕ_{corr}.

2. Multiply the current I measured at a certain value $\Delta\phi$ by 2.3 R_p and plot

$$2.3\ R_p I \textit{ vs. } \Delta\phi$$

3. Determine from this plot the Tafel slopes b_a and b_c by curve fitting using theoretical curves calculated for various values of b_a and b_c.

4. Calculate I_{corr} from Eq. [2] using the R_p value determined in Step 1 and the Tafel slopes determined in Step 3.

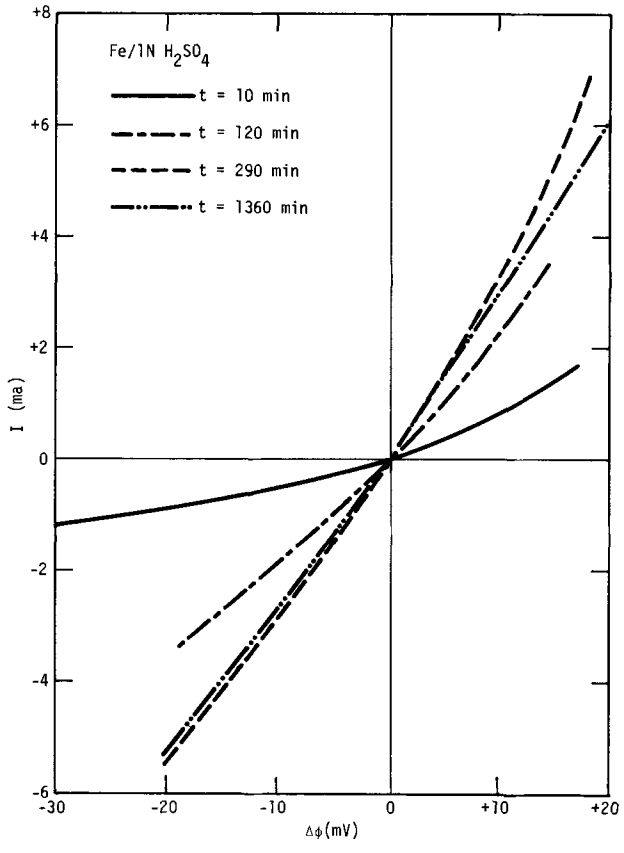

Fig. 2. Experimental polarization curves for iron in 1*N* H_2SO_4 as a function of time.

Experimental

This new type of analysis of polarization curves of corroding metals, described above, has been used for iron (99.9%, Johnson, Matthey & Company) corroding in 1*N* H_2SO_4. The polarization curves have been measured in the potentiodynamic mode using a sweep rate of 30 mV/min and $\Delta\phi = \pm 25$ mV. Duration of the experiment was 24 hr. Figure 2 shows some of the polarization curves obtained at various times of the experiment. From these curves the polarization resistance R_p has been determined graphically by drawing a tangent at $\Delta\phi = 0$. A plot of 2.3 R_pI *vs.* $\Delta\phi$ was then constructed according to Step 2. It was found using theoretical curves that the value of R_p could be determined within ±3%. An accurate determination of R_p is important for the success of the proposed method. If the graphically determined value of R_p is, for example, too high, then both b_a and b_c found by curve fitting will be somewhat too low. Experimental results are shown in Fig. 3a for the run recorded after 10 min and in Fig. 3b for the run recorded after 290 min. From Fig. 3a the values of b_a and b_c which fit the measured curve best are found to be $b_a = 30$ mV and $b_c = 95$ mV, while from Fig. 3b one finds $b_a = 55$ mV and $b_c = 105$ mV. The values of either the anodic or cathodic Tafel slope used to calculate the theoretical curves are varied in steps of 5 mV, since the procedure described here is not proposed for a quantitative determination of Tafel slopes but rather for a qualitative determination for situations where Tafel slopes are not known or where changes in Tafel slopes and corrosion rates are to be followed as a function of time, solution parameters, etc. While the calculations necessary for Steps 1-4 could be carried out best using a computer, the theoretical curves can be computed rather fast using desk top calculators. Once a set of theoretical curves corresponding to the right-hand side of Eq. [4] has been calculated, they can be used for analysis of any recorded polarization curve.

Results of the analysis of polarization curves for the system Fe/1*N* H_2SO_4 are summarized in Fig. 4. While there are some fluctuations of the cathodic Tafel slope b_c, there is a definite increase of the anodic Tafel

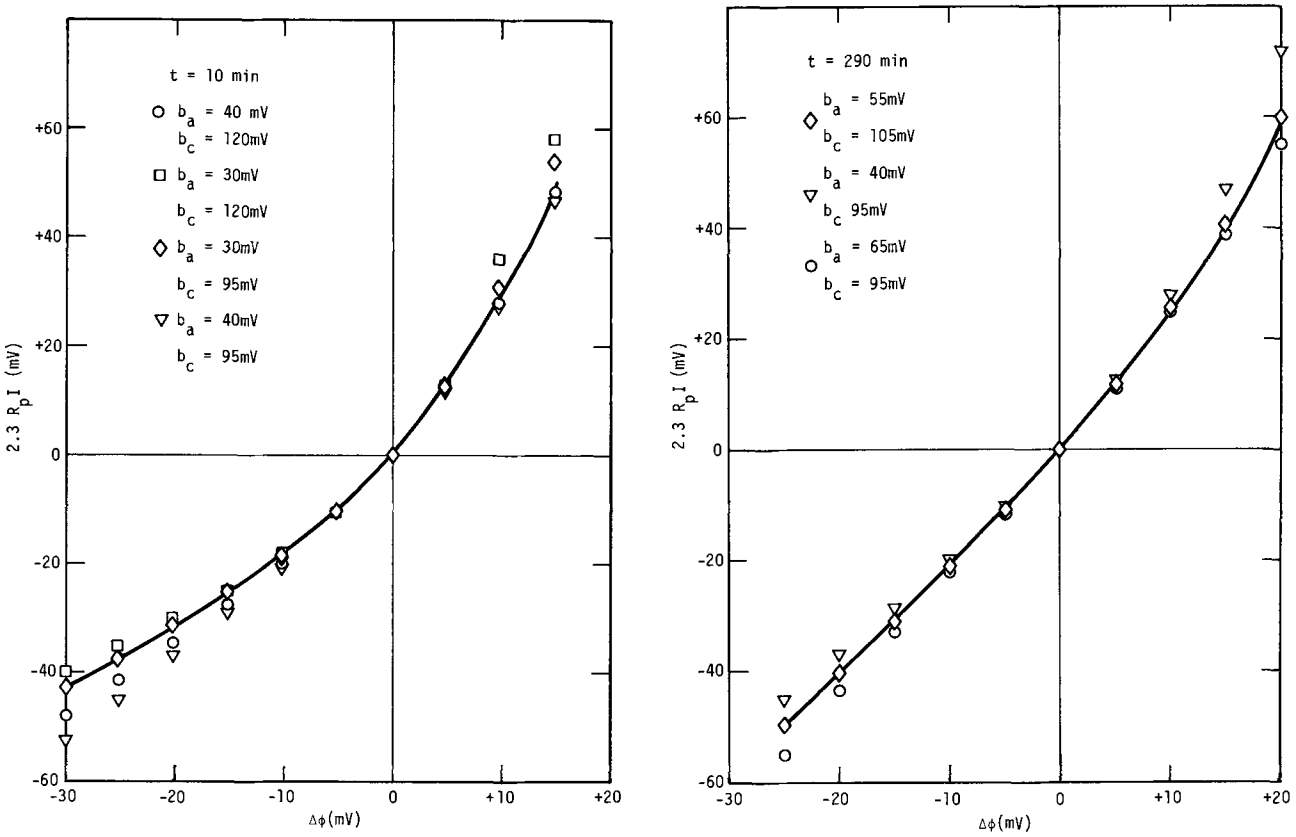

Fig. 3. Experimental curves (solid line) and theoretical curves, superimposed in order to obtain best values of b_a and b_c. (a, left) 10 min, (b, right) 290 min.

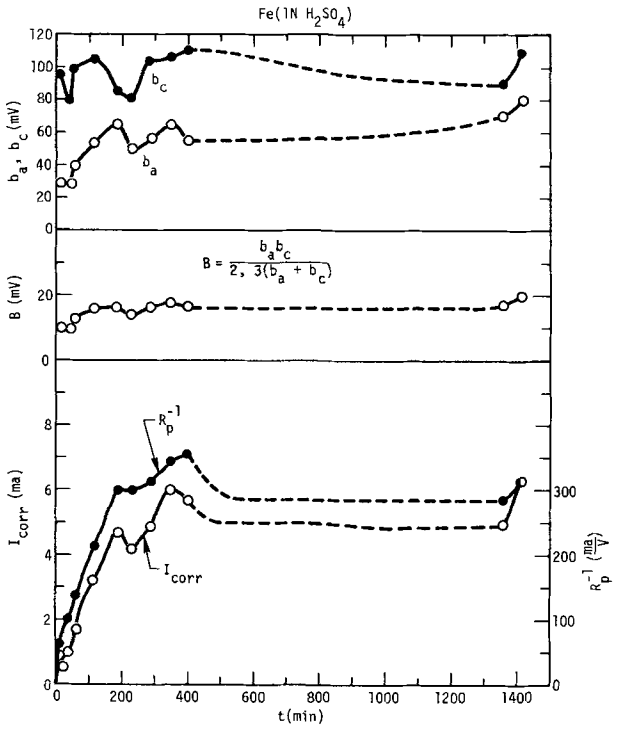

Fig. 4. Time behavior of corrosion parameters of iron in 1N H_2SO_4.

slope b_a with time. The factor $B = b_a b_c/2.3(b_a + b_c)$, which correlates polarization resistance R_p and corrosion current I_{corr} increases by about a factor of 2 from 9.9 to 20.2 mV during the 24 hr test.

Finally, the values of the inverse polarization resistance R_p^{-1} and the corrosion current $I_{corr} = BR_p^{-1}$ are shown in Fig. 4 for the 24 hr test. The corrosion current increases by about a factor of 10 in the first 6 hr of the experiment and then levels off. Similar results have been reported by Chin and Nobe (7) and Barnartt (8, 9). Since the factor B only increases slowly with time, the values of I_{corr} and R_p^{-1} show essentially similar behavior.

The experimental polarization curves, examples of which are shown in Fig. 2, have also been analyzed by a graphical method described recently by Oldham and Mansfeld (10). In this method the curvature of the polarization curve in the vicinity of ϕ_{corr} is used to obtain the corrosion current. A knowledge of the Tafel slopes b_a and b_c is not required for the determination of I_{corr}. In Fig. 5 corrosion current densities (C.D.) obtained with the two methods of analysis are plotted as a function of time. While there are some differences in the absolute values of i_{corr}, identical trends are observed. The fluctuations of i_{corr} between 200 and 400 min must be real because they appear in both analyses. It cannot be argued that they result from inaccurate determinations of the Tafel slopes b_a and b_c, because corrosion currents are determined directly from the measured polarization curve in the graphical method rather than being calculated from Tafel slopes and the polarization resistance.

After completion of the 24 hr test, the solution was analyzed for iron by atomic absorption spectroscopy. The amount of iron determined corresponds to a corrosion rate of 5700 mdd or a corrosion C.D. of 2.28

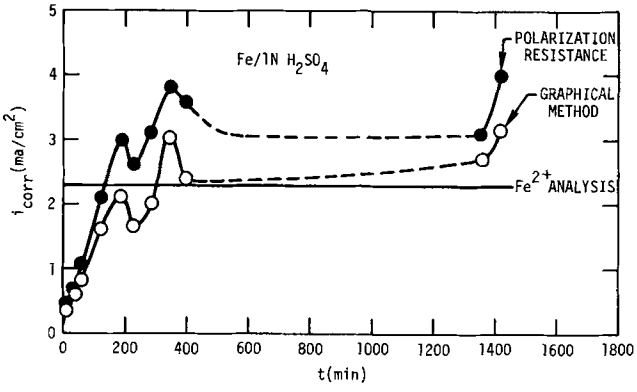

Fig. 5. Corrosion C.D. as a function of time obtained from two different analyses of experimental polarization curves and from chemical analysis of test solution.

mA/cm². This is in good agreement with the average corrosion C.D. from the electrochemical measurements especially when these are analyzed by the graphical method.

Barnartt using a galvanostatic procedure to obtain polarization curves which are then analyzed by a three-point method (11) has reported a similar time behavior of the corrosion parameters of iron in 1M $NaHSO_4$ (pH = 0.48) (8, 9).

Since the main purpose of this paper is to illustrate the new type of analysis of polarization curves of corroding metals, no attempts are being made to explain the observed variations of the Tafel slopes and corrosion rates with time. A complete analysis of the time behavior of all parameters of a corroding metal, would, however, certainly lead to a better understanding of mechanisms of corrosion.

Summary

It has been shown that polarization resistance values as well as Tafel slopes can be determined simultaneously from polarization curves in a potential region close to the corrosion potential so that instantaneous corrosion currents can be calculated. This new analysis of polarization curves is demonstrated in a study of the time dependence of the corrosion parameters of the system Fe/1N H_2SO_4.

Manuscript submitted Aug. 29, 1972; revised manuscript received Nov. 27, 1972.

Any discussion of this paper will appear in a Discussion Section to be published in the December 1973 JOURNAL.

REFERENCES

1. C. Wagner and W. Traud, *Z. Elektrochem.*, **44**, 391 (1938).
2. M. Stern and A. L. Geary, *This Journal*, **104**, 56 (1957).
3. M. Stern and E. D. Weisert, *Proc. Am. Soc. Test. Mater.*, **59**, 1280 (1959).
4. K. B. Oldham and F. Mansfeld, *Corrosion*, **27**, 434 (1971).
5. F. Mansfeld and K. B. Oldham, *Corrosion Sci.*, **11**, 787 (1971).
6. T. P. Hoar, *ibid.*, **7**, 455 (1967).
7. R. J. Chin and K. Nobe, *This Journal*, **118**, 545 (1971).
8. S. Barnartt, *Corrosion*, **27**, 467 (1971).
9. S. Barnartt, *This Journal*, **119**, 812 (1972).
10. K. B. Oldham and F. Mansfeld, *Corrosion Sci.*, In press.
11. S. Barnartt, *Electrochim. Acta*, **15**, 1313 (1970).

Brief Communication

A Copper Ion Conducting Solid Electrolyte by Substitution of Silver in $RbAg_4I_5$

Bruno Scrosati*

Laboratorio di Chimica Fisica ed Elettrochimica, Università di Roma, Rome, Italy

The advantages of $RbAg_4I_5$ as a solid electrolyte are well known. The practical use of this electrolyte, however, has been limited, mainly because of the cost of the anodic material. This in fact has to be silver since the conduction through the electrolyte is due to silver ion movements. It is therefore obvious that an electrolyte with comparable properties but conducting via copper ions would be of great interest because of the low cost and large availability of copper. I will report here very preliminary results obtained in our laboratory in a program for the development of a copper solid electrolyte.

One possible candidate is cuprous iodide. It is known in fact that CuI possesses predominant ionic conductivity at low temperature, provided that there is not excess of halogen (1, 2). This conductivity is very low and assumes high values only above 300°C (1). Therefore cuprous iodide cannot be used as such since the main requisite for a useful solid electrolyte is a reasonably good ionic conductivity at room temperature. To approach this condition, we have tried to substitute to a certain extent the silver ions with copper ions in $RbAg_4I_5$. To realize this we have assembled the cell

$$Ag/RbAg_5I_4/Cu \qquad [1]$$

by pressing into pellets a mixture of powdered copper and electrolyte, the electrolyte, and a mixture of powdered silver and electrolyte. The electrolyte was added to the electrode materials to reduce interfacial polarization effects (3). The surface of each pellet was 1.25 cm^2, and the thickness was about 0.15 cm.

Cell [1] was polarized with the copper electrode as positive and maintaining the voltage below the decomposition potential of $RbAg_4I_5$ [0.67V at 25°C (4)]. Under these conditions, since the electronic conductivity of $RbAg_4I_5$ is very low [about 10^{-11} ohm^{-1}-cm^{-1} at 25°C (3, 4)], if copper did not dissolve in the electrolyte in the form of ions, the resulting current, under steady-state conditions, would be almost negligible. This is not the case, as shown by the current-voltage curve of cell [1], which applies to the initial behavior of the cell, reported in Fig. 1. Therefore a cell similar to [1] was submitted to constant-current electrolysis and a typical result, at I = 0.05 mA, is shown in Fig. 2. The rise in voltage is probably due to increase in cell resistance because of dendritic deposition at the negative with consequent loss of electrode/electrolyte contact (5, 6). Generally after a few coulombs were passed through the cell (four in the case shown in Fig. 2), the electrolysis was interrupted and the silver electrode was replaced by an iodine-benzidine (I_2-B) charge-transfer complex pellet. The iodine charge-transfer complexes act as iodine electrodes with reduced iodine vapor pressure (6). The resulting cell

$$Cu/Cu_x\text{-}RbAg_{4-x}I_5/I_2\text{-}B \qquad [2]$$

had at room temperature an open-circuit voltage of about 0.6V. Cell [2] was then discharged at constant currents and showed good discharge capabilities, as indicated by the discharge curves reported in Fig. 3. These are further indications that Cu^+ ions are present and mobile in the "substituted" $RbAg_4I_5$. Therefore it is reasonable to admit that silver can be, at least partially, substituted with copper in $RbAg_4I_5$.

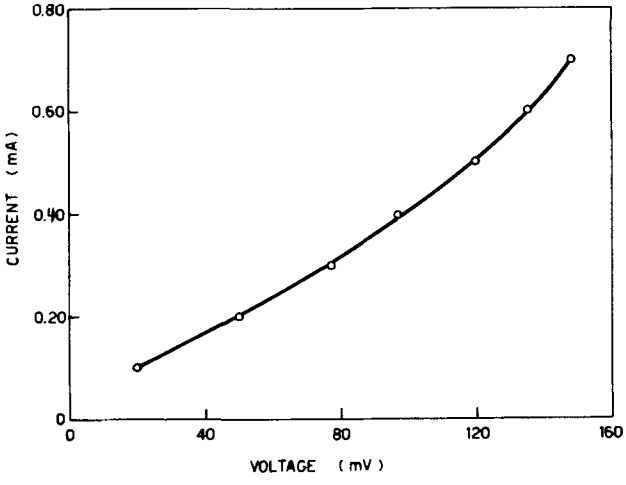

Fig. 1. Typical current-voltage curve of cell [1] at 25°C

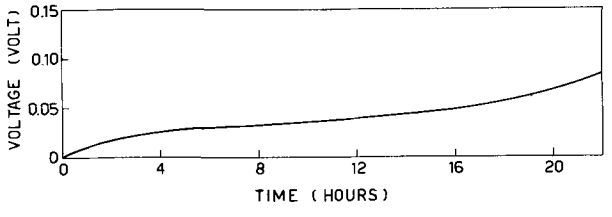

Fig. 2. Typical constant-current electrolysis (I = 0.05 mA) of cell [1] at 25°C.

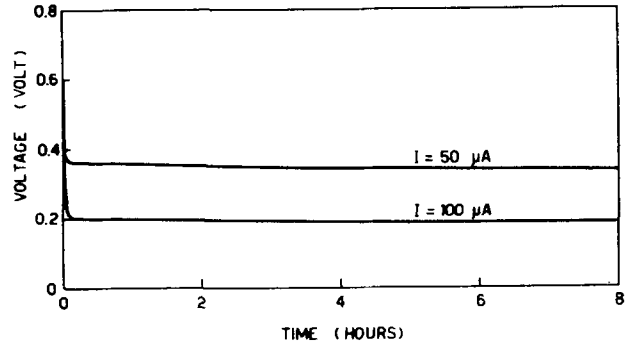

Fig. 3. Discharge curves of cell [2] at 25°C

* Electrochemical Society Active Member.
Key words: solid electrolyte, copper ions conductivity.

The study reported here is still in the very preliminary stage and further work is certainly needed to definitely characterize this electrolyte and determine the amount of silver which may be substituted with copper. Nevertheless, it seemed to be worthwhile to report these results since they tend to indicate that it could be possible to enhance the ionic conductivity of CuI by the formation of a double salt, as has been the case of AgI. Work in this direction is in progress in our laboratory and will be reported in a subsequent paper.

Acknowledgment

This work has been supported by the Consiglio Nazionale delle Ricerche.

Manuscript submitted Oct. 24, 1972; revised manuscript received Nov. 20, 1972.

Any discussion of this paper will appear in a Discussion Section to be published in the December 1973 JOURNAL.

REFERENCES

1. J. B. Wagner and C. Wagner, *J. Chem. Phys.*, **26**, 1597 (1957).
2. A. V. Joshi, "Fast Ion Transport in Solids-Solid State Batteries and Devices," Belgirate, Italy (1972).
3. G. R. Argue, I. J. Groce, and B. B. Owens in "Power Sources," D. H. Collins, Editor, p. 389, Pergamon Press, London (1970).
4. B. Scrosati, *J. Appl. Chem. Biotechnol.*, **21**, 223 (1971).
5. B. Scrosati and A. D. Butherus, *This Journal*, **119**, 128 (1972).
6. B. Scrosati, M. Torroni, and A. D. Butherus, Power Sources Symposium, Paper 18, Brighton, England (1972).

Errata

In the paper "Transient Mass Transfer at the Rotating Disk Electrode" by Leonard Nanis and Irving Klein which appeared on pp. 1683-1687 in the December 1972 JOURNAL, Vol. 119, No. 12, Eq. [14] should read as follows

$$J_{lim} = 1.58\, nFD \frac{C_b}{\delta_c}$$

The omission of the constant factor in no way affects the conclusions or any other equations.

The last sentence of the first paragraph in the Results section on page 1685 should read: "Data of Arvia (2) were used for the ratio of diffusion coefficients of the redox species."

In the paper "Electron Injection into Anodic Valve Metal Oxides. II. Further Experimental Results for Ta_2O_5, Nb_2O_5 and Al_2O_3" by N. I. Jaeger, G. P. Klein, and B. Myrvaagnes which appeared on pp. 1531-1538 in the November 1972 JOURNAL, Vol. 119, No. 11, the electric field should be MV/cm (M = mega) not mV/cm. Thus, the captions to Fig. 2, 3, 4, and 7 should read as follows:

Fig. 2. Current-time characteristic of the activation process for: 1, Nb/1960Å Nb_2O_5/200Å Fe_2O_3 electrode, activation field $F' = 3.5$ MV/cm; 2, Ta/1960Å Ta_2O_5/200Å Fe_2O_3 electrode, activation field $F' = 5.2$ MV/cm; 3, Al/1630Å Al_2O_3/200Å Fe_2O_3 electrode, activation field $F' = 6.2$ MV/cm; 4, reanodization curve of Nb/1960Å Nb_2O_5 anode following activation (curve 1) and subsequent dissolution of the Fe_2O_3 layer. $F' = 3.5$ MV/cm.

Fig. 3. Rate of activation as a function of the applied field $F' = V/d$ for Nb/1960Å Nb_2O_5/200Å Fe_2O_3 electrodes at 20°C; field range: 3.52-3.73 MV/cm.

Fig 4. Rate of activation as a function of the applied field $F' = V/d$ for Ta/1740Å Ta_2O_5/200Å Fe_2O_3 electrodes at 41.5°C; field range: 4.60-4.94 MV/cm.

Fig. 7. Slope of activation curves at constant applied field ($F = 4.81$ MV/cm) *vs.* $1/T$ for Ta/1740Å Ta_2O_5/200Å Fe_2O_3 electrode.

On page 1533, second column, second paragraph, the text should read: To obtain similar slopes the applied field had to be increased from 3.5 MV/cm for Nb_2O_5 to 5.2 MV/cm for Ta_2O_5 and 6.2 MV/cm for Al_2O_3, which corresponds to the decrease of the ionic conductivities of the anodic oxides given in the literature (5).

On page 1534, second column, first paragraph, the text should read: Log s *vs.* $1/T$ was plotted in Fig. 7 for constant field $F = 4.81$ MV/cm in Ta_2O_5 using the data from Fig. 6.

JOURNAL OF THE ELECTROCHEMICAL SOCIETY

SOLID-STATE SCIENCE AND TECHNOLOGY

APRIL 1973

Charge-Coupled Devices Fabricated Using Aluminum-Anodized Aluminum-Aluminum Double-Level Metalization

D. R. Collins,* S. R. Shortes,* W. R. McMahon, R. C. Bracken,* and T. C. Penn

Texas Instruments Incorporated, Dallas, Texas 75222

ABSTRACT

This paper describes a novel double-level metalization technique to fabricate charge-coupled devices (CCD's) where both metal levels are aluminum and the insulation between the two metalization levels is aluminum oxide formed by anodization. Anodization provides a simple, quick, method for forming the double-level system insulation. This technique relaxes the 3 μm (0.12 mil) electrode separation tolerance required for single-level metalization, since the thickness of the Al_2O_3 forms the interelectrode gap. The charge-transfer efficiency and stability of devices fabricated using this technique compare favorably with results obtained on devices fabricated using single-level metalization. A comparison of the Al-Al_2O_3-Al system with other double-level metalization systems indicates advantages in ease of fabrication and reliability, along with the capability of high speed operation of large arrays.

Charge-coupled devices (1-3), (CCD's) are semiconductor analog shift registers fabricated on a uniformly doped semiconductor substrate. The basic charge-coupling principle consists of storing minority carriers in potential wells at the semiconductor surface and transporting these carriers along the surface by translating the potential wells. The basic device structure is very simple and consists of a thermally oxidized semiconductor substrate with single-level metal electrodes on the oxidized surface. A cross section of the basic CCD structure is shown in Fig. 1 where silicon is the substrate material. The potential wells are produced by applying a voltage to the metal electrodes. The original, and the simplest, method of translating the potential wells along the silicon surface is to connect every third electrode to a separate clock line. Three electrodes then comprise an element: one electrode to hold and transmit the charge, the second electrode to receive the charge, and the third electrode to provide directionality to the charge flow. A three-phase pulse sequence may then be applied to the clock lines to transport a whole train of charge packets along the device surface. Diodes are generally used to inject charge into the potential wells at the input and to detect the presence of minority carriers at the output. The basis of the charge transport is the coupling of potential wells under adjoining electrodes so that the minority carriers may be transferred from under one electrode to the next. For reasonable substrate dopings and oxide thicknesses, this coupling requires electrode separations of approximately 3 μm or less. This metal separation is approximately four times narrower than present MOS production standards and presents one of the major problems in fabricating CCD's.

In addition to the tight metalization tolerances required, the single-level metal, three-phase system has two other drawbacks. The interconnection of three phases requires the use of a diffused tunnel to connect one of the sets of electrodes to the clock lines. Furthermore, the exposed oxide between the electrodes causes device operation to be sensitive to ambient effects. On a SiO_2 surface exposed to the ambient, ionic charges tend to accumulate and migrate under the influence of the electric fields. These migrating ions cause mirror charges in the silicon substrate which modify the potential barrier at the Si-SiO_2 interface, causing changes in the operating characteristics of the device. The problem of the close separation between metal electrodes can be alleviated by going to a double-level

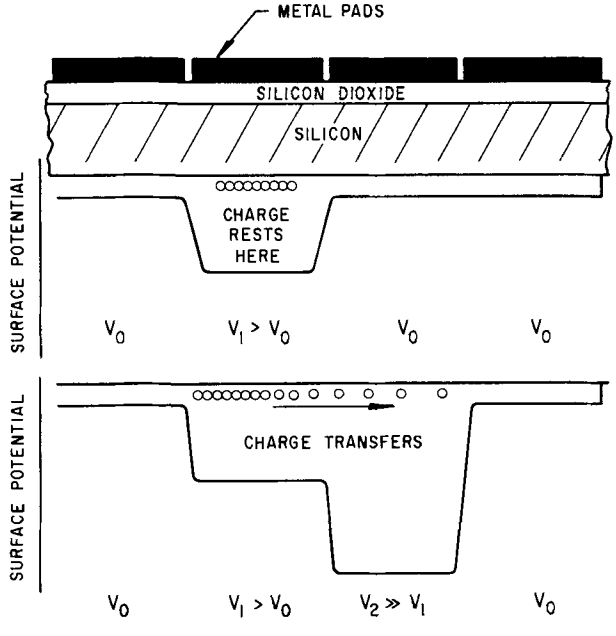

Fig. 1. Cross section of the basic CCD with surface potential diagrams

* Electrochemical Society Active Member.
Key words: high frequency operation, charge-transfer efficiency.

metal system (4, 5). In addition, a two-level system effectively seals the oxide surface from ambient effects. A double-level metal system has natural two- or four-phase symmetry. The two-phase system may be either a true two-phase, which uses a spatial asymmetry, or a pseudo two-phase system in which four electrodes actually are used for each element. True two-phase operation may be obtained by introducing an asymmetry in the fabrication process such as nonuniform oxide thickness (4-6) or an ion-implanted barrier (7). All of these two- or four-phase schemes have their own drawbacks, including additional processing steps. An excellent review article by Tompsett (8) provides a current evaluation of CCD development over the past two years.

This paper describes a novel double-level metalization technique in which both metal levels are aluminum and the insulation between the two metalization levels is aluminum oxide produced by anodization. The anodizing technique provides a simple, quick, method for forming the double-level system insulation. The insulation thickness of the Al_2O_3 forms the interelectrode gap, which allows normal metalization definition tolerances to be used. The double-level structure also seals the interelectrode gap from ambient effects and provides a coplanar, but overlapping, high conductivity metalization system.

Processing Concepts

The conversion of the surface of metallic interconnects to an insulating oxide by the process of anodization is used to form the interlevel insulator in this work. Aluminum has been chosen as the interconnect metal not only because of its capability of being anodized, but also because of its high conductivity. Any anodizable metal could, however, be used in the specific structure described above.

Aqueous and nonaqueous solutions of dibasic acids with finite solubility for the anodic oxide of aluminum have been used in this work. The resultant structures are assumed to be those modeled by Keller, Hunter, and Robinson (9). In this work, oxide thicknesses were determined by the product of current density and time, and the control parameter was that of time. Care must be exercised to eliminate extraneous current paths during the anodic process if adequate and simple controls are to be implemented. Specific details of the use of various electrolytes and the electrical characteristics of the anodization process are described by Young (10) and McMahon (11). Electrolytes which do not exhibit solubility for the anodic oxide may also be used to an advantage in that oxide thickness is then determined solely by the applied voltage and is found to be approximately 13.8 Å/V (12).

To ensure uniform rates of anodic conversion and uniform thickness of oxide coating, all surfaces subjected to the anodic processing must be at an equipotential during the anodization. In semiconductor processing this can be accomplished by connecting all clock electrodes to be anodized to a common potential and current-distribution bus during anodization. The distribution bus may be protected from the oxidation process by a photoresist coating during the anodic conversion. The lack of a protective oxide on the surfaces of such buses allows for their selective removal by etching during subsequent processing steps without additional masking operations.

Since the anodic oxide is grown atomistically from the metal itself, the adhesion between the metal and its oxide is excellent. It is also noteworthy that all surfaces exposed to the anodization condition, regardless of their topology or geometric orientation, are coated uniformly, since the propagation of the oxide-metal interface is perpendicular to the applied electric field. In addition, anodic processes are inherently self-healing, inasmuch as the maximum rate of conversion is found at the points of maximum field across the oxide film, *i.e.*, the thinnest oxide areas and pinholes in the oxide film are self-eliminating. The thin gate oxides exposed to the electrolyte and the applied field encountered in the anodic portion of the fabrication process are not affected if care is exercised in the selection of electrolyte and externally applied potentials.

Aluminum oxide is a recognized dielectric, and the electrical properties of the anodic form are well referenced in Young (10). Results of this work indicate that the anodic oxide of aluminum has a resistivity in excess of 10^{16} ohm-cm and a dielectric constant of approximately 8.6, with very little frequency dependence. Anodized films ranging from 700 to 6000Å are routinely grown in the fabrication of CCD's, and the breakdown strength of the films exceeds 6×10^6 V/cm (42V across 700Å). The pinhole density is less than 3/cm^2 with 5000Å of Al_2O_3.

Device Fabrication

The process steps used to fabricate a CCD using the aluminum-aluminum oxide-aluminum double-level metalization system are illustrated in Fig. 2; after the thick oxide is formed, the source-drain diffusion is made and the thin gate oxide is grown, (a), a layer of aluminum is evaporated over the entire wafer; (b), the aluminum is then patterned to form the first-level electrodes; (c), Patterning may be performed using standard photolithography techniques so that the minimum length of the electrodes and the separation between electrodes may be 10 μm (0.4 mil), as presently used in volume MOS production processes. Next, selected portions of the aluminum are covered with photoresist; these portions include, via holes from the first to second level, metal for bond pads and the anodizing connections. In a double-level metalization system there is no need for the clock electrodes to contact the semiconductor substrate; however, the electrochemical anodization process requires electrical contact to the CCD electrodes during anodization. The electrically isolated nature of the CCD electrodes in the finished device thus requires a temporary electrical connection to the anodizing contact. Typically, this anodizing contact (bus) is an extension of the first-level metal which is run to the scribe line. The first-level metal is then anodized; the portions covered with photoresist remain unanodized. In Fig. 2 (d), the anodizing converts an outer layer of the aluminum electrodes to Al_2O_3. The protecting photoresist is then stripped, and the second layer of aluminum is evaporated over the entire wafer. In Fig. 2 (e), this second level of aluminum is then patterned using standard photolithographic methods and acidic subtractive etching. In Fig. 2 (f), the patterning is performed so as to interleave the second-level CCD electrodes between the first-level CCD electrodes. The resulting structure consists of a set of coplanar, but overlapping, electrodes separated by a layer of anodized aluminum. During the patterning of the second-level electrodes, the anodizing contact (bus) to the first-level metal is also removed. The entire fabrication process can be accomplished with only one more additional photomask, the second-level metal photomask, than used to fabricate a single-level metal CCD. A reversal of the photomask normally used to open the protective oxide overcoat in the bond pad areas may be used to protect portions of the first-level metal from anodizing. The process of protecting the bond pads during anodization and of removing the bus bar along with second-level metal is illustrated in Fig. 3.

A photomicrograph of a finished device is shown in Fig. 4. The device was fabricated on 20 ohm-cm <111> n-type silicon using standard MOS techniques through the thin oxide growth step. The device shown is an eight-bit, four-phase, CCD shift register. The upper level metal (white in appearance) forms an interdigitated pattern consisting of the phase-one (ϕ_1) and phase-three (ϕ_3) electrodes. The lower level metal forms an interdigitated pattern consisting of phase-two (ϕ_2) and phase-four (ϕ_4) electrodes. Input and output

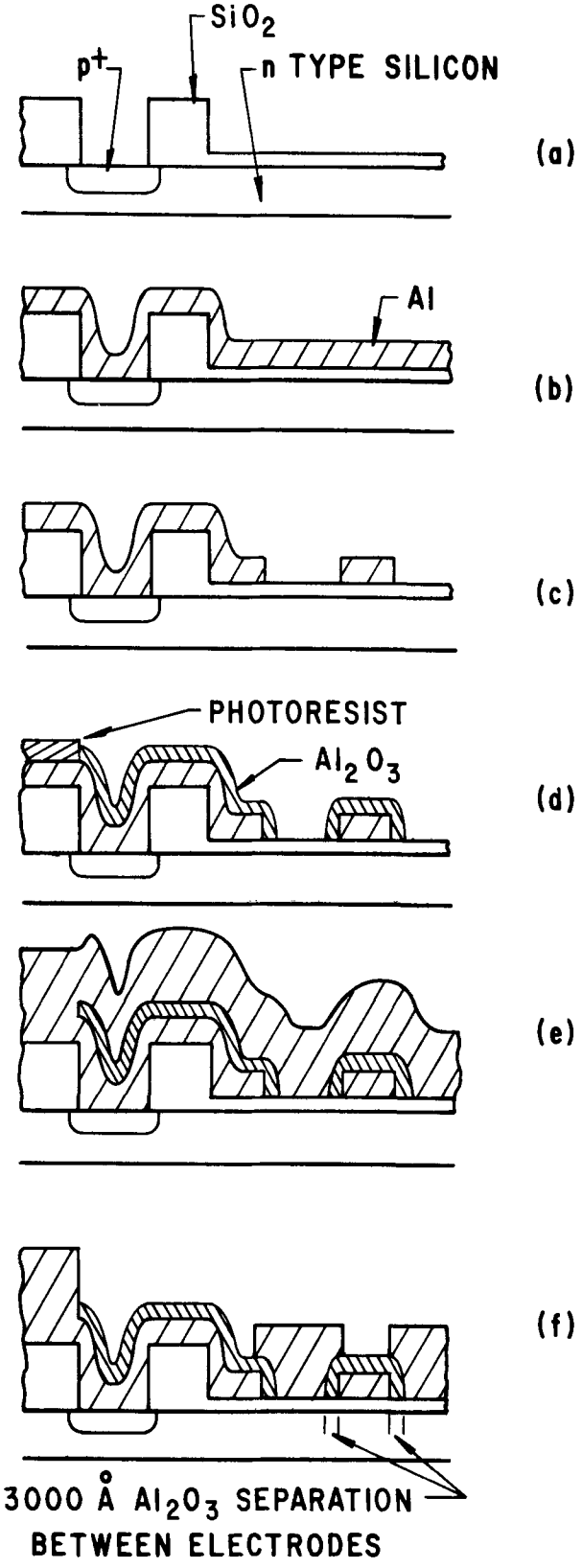

Fig. 2. Fabrication steps in the Al-Al_2O_3-Al double-level metalization system: (a), thick and thin oxides prior to metalization, ohmic contact region shown; (b), aluminum layer evaporated for first-level metal; (c), first-level metal patterned (including bus); (d), first-level metal anodized, photoresist protects via holes and bus; (e), aluminum evaporated for second-level metal; (f), second-level metal patterned.

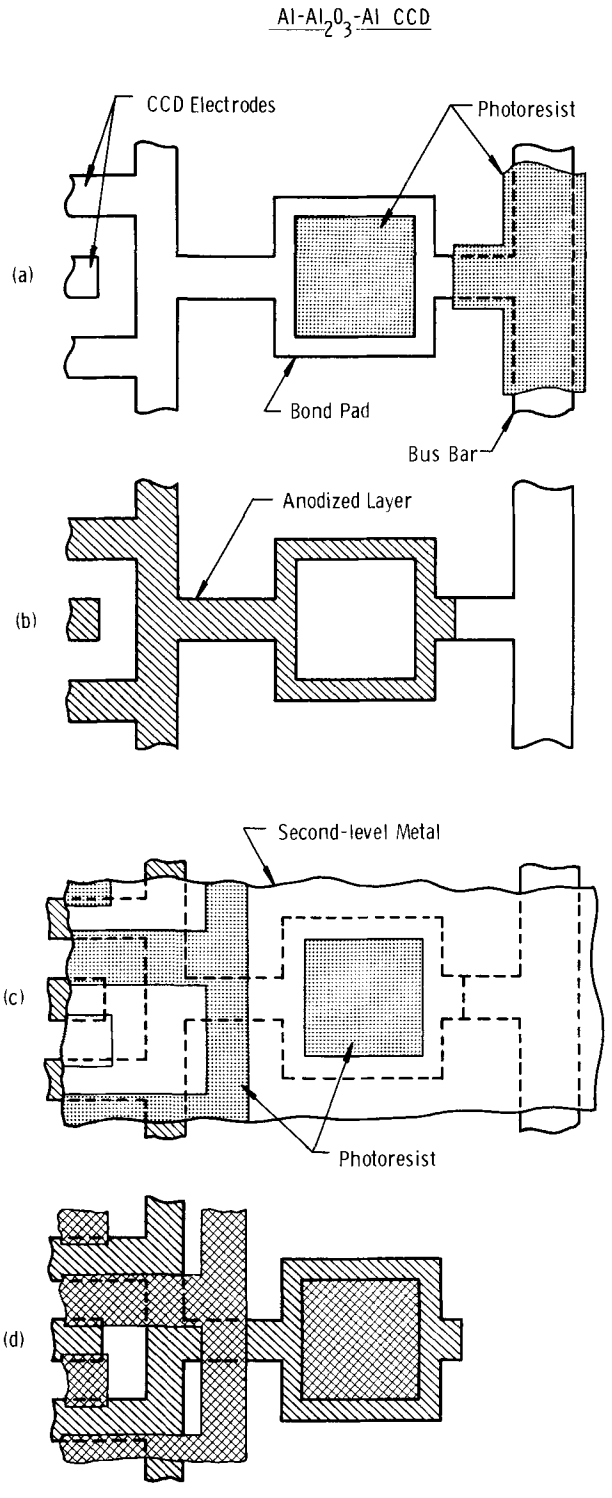

Fig. 3. Process of removing bus bar while protecting bonding pads: (a), bus bar and bond pads coated with photoresist prior to anodizing; (b), first-level metal after anodization and removal of photoresist; (c), second-level metal definition and bond-pad protection with photoresist prior to etching the second-level metal; (d), finished device.

diode connections, along with transfer electrodes, complete the structure. The electrode length (measured in the direction of current flow) is 25 μm (1.0 mil) and the width is 250 μm (10.0 mils). The device was designed to test-fabrication concepts and for comparison with existing single-level metalization devices; no attempt was made to minimize bit size.

Electrical Evaluation

The drive circuitry shown in Fig. 5 was used to operate the eight-bit CCD shift register at data rates

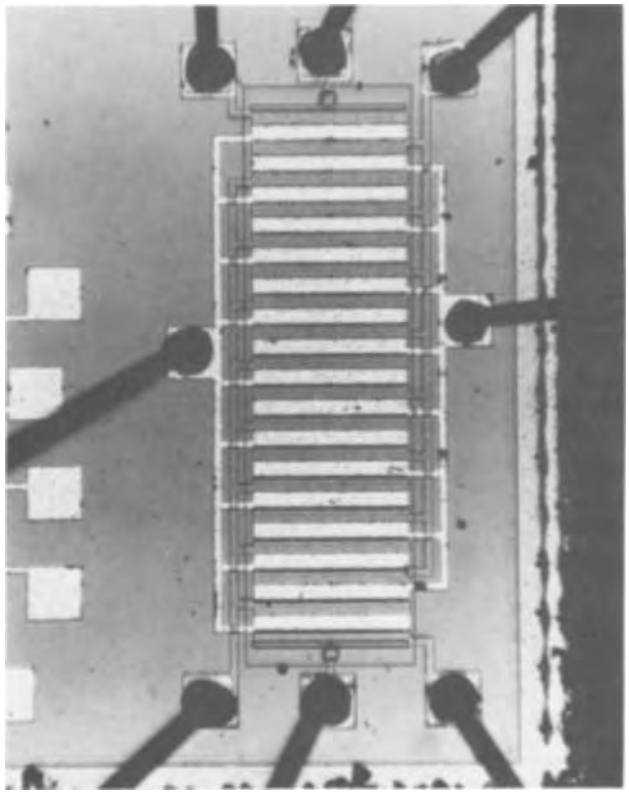

Fig. 4. Photomicrograph of eight-bit, four-phase Al-Al_2O_3-Al double-level metalization CCD shift register.

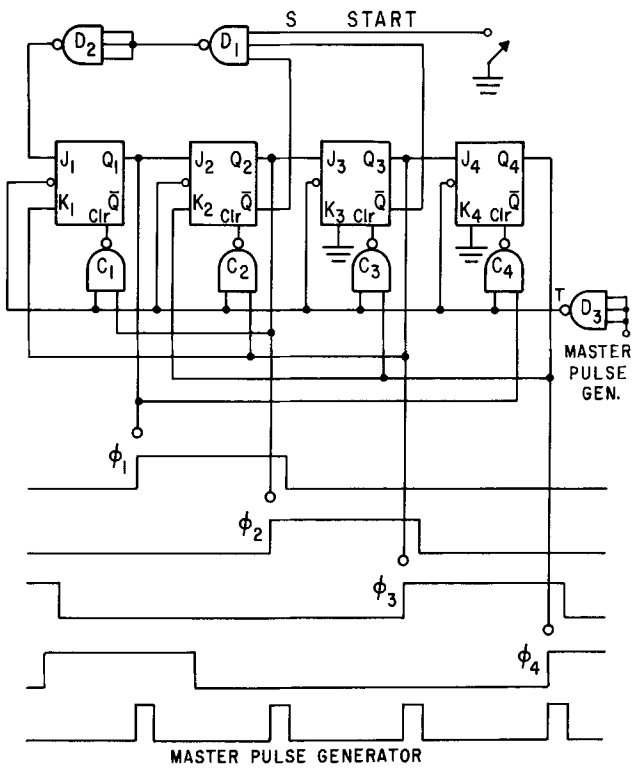

Fig. 5. Four-phase clock generator.

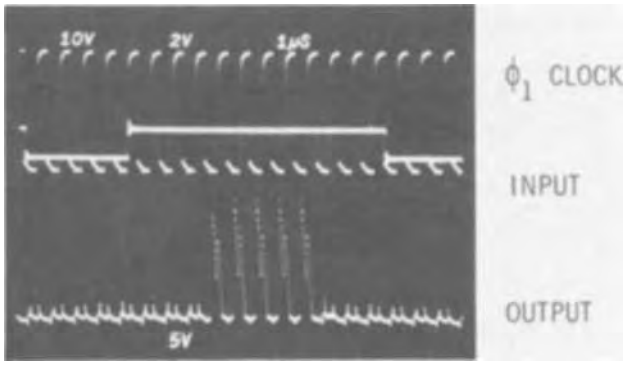

Fig. 6. Performance of anodized aluminum, double-level metalization, four-phase, eight-bit CCD shift register at 2 MHz, 25 μm (1.0 mil) electrode length, 15V clocks.

ranging from 100 kHz to 6 MHz.[1] Figure 6 shows the output of the shift-register, eight-clock periods after five "ones" are read into the register. The upper trace is the phase-one clock, the middle trace is the envelope of the input data, and the lower trace is the output. The output of five major pulses is followed by a small trailing pulse, illustrating the charge-transfer inefficiency associated with CCD (3). The charge-transfer inefficiency (percentage of charge not transferred from one electrode to the next) of this device is approximately 1.0×10^{-3} at 2 MHz. At 6 MHz the charge-transfer inefficiency increased to 7.0×10^{-3}. The departure from the ideal case of zero charge-transfer inefficiency is predicted by the time required for the thermal diffusion of minority carriers across an electrode of 25.4 μm (1.0 mil) length (13). The clock voltage used ranged from 9 to 15V, with the 15V necessary to obtain good charge-transfer efficiency at frequencies greater than 1 MHz. The stability of this device in an uncanned state was excellent. No change in operating parameters was observed over a testing period which extended over 1 month. The performance of a similar three-phase, single-level, metal shift register exhibited significantly poorer charge-transfer efficiency and stability. The three-phase device was fabricated in an identical manner to the double-level anodized device, except for the metalization, and had identical electrode geometry with 2.5 μm (0.1 mil) electrode separation.

Discussion

The primary advantage in using a double-level metalization system for the fabrication of CCD's is the elimination of the photolithographic requirement for close spacing between metal electrodes (<3 μm). However, if a significantly greater number of fabrication steps is required, or the technical problems involved in fabricating the double-level metalization system greatly exceed those encountered with single-level metalization, then little is gained by using a double-level system. The Al-Al_2O_3-Al system provides a simple fabrication method in which the separation between electrodes is determined by the Al_2O_3 thickness, not by photolithography, giving 3000Å rather than 3 μm electrode separation. Only one photomask, two photoresist definitions, one metal-etching step, and the anodizing are required in addition to the processing normally used for single-level metal devices. The anodization itself is quick, inexpensive, and simple. No high-temperature processing (>500°C) is necessary after the thin oxide growth. Both metalization levels are high-conductivity aluminum, and both levels have the same gate-insulator thickness, resulting in symmetric clock voltages. The insulation is quite reliable since the voltage used to form the Al_2O_3 is normally far higher than any voltages used in device operation.

The improved operating characteristics of the double-level metal anodized device shown in Fig. 6

[1] In the circuit shown in Fig. 5, each clock phase is overlapped by the preceding and following clock pulse in a controlled manner. At "start," a phase-one pulse appears first and at "stop," a phase-four pulse appears last. The circuit is self-correcting from any of the eight different error states which might occur due to noise transients or when power is first applied. Repetition rate and overlap are independently adjustable. Only four common TTL integrated circuits (two SN7473, one SN7410, and one SN7400) are used for input pulse rates ranging from 0.1 Hz to 24 MHz. The output phases are thus available up to 6 MHz with overlap equal to the width of the input pulse from the master pulse generator.

may be attributed to the close electrode separation on the n-type substrate. The narrow gap produced in the Al-Al_2O_3-Al system allows the fringing fields from the electrodes to suppress the potential barrier at the semiconductor surface. The removal of the barrier, in turn, allows a more complete transfer of charge to take place from one electrode to the next. The improved stability of the Al-Al_2O_3-Al system over the single-level Al system is explained by the sealed condition of the SiO_2 surface between electrodes. The SiO_2 surface between the electrodes in the Al-Al_2O_3-Al system is covered with a layer of Al_2O_3 which is covered with an equipotential layer of Al. Thus, surface migration of charged ions on the SiO_2 surface is prevented.

In addition to the Al-Al_2O_3-Al system, two other methods of fabricating CCD using double-level metalization have commonly been used. The first is the moly-SiO_2-aluminum (or the moly-SiO_2-moly) system (4). In this technology, one first deposits moly on the surface, patterns the moly, then insulates the first-level moly with a deposited oxide of some type. Finally, a second-level metal, either moly or aluminum, is deposited and patterned. In general, deposited oxides are less reliable than grown oxides and are subject to pinholes. Furthermore, the amount of insulation between two metal levels is critical, especially at the edges of the first-level moly, where the sharp corners, combined with high electric fields at these edges, have a tendency to cause breakdown in the weak deposited oxides. For reasonable fabrication yields, the deposited oxide must be at least as thick as the metal which it is covering. This would require approximately 2000Å of deposited oxide over the first-level metal and in the gap separating the first-level metal electrodes. This additional gate-oxide thickness under the second-level electrodes would necessitate asymmetric clock drives. Furthermore, since the higher oxides of moly are water soluble, any pinholes in the deposited oxide could cause reliability problems in a nonhermetic package. This system does have fairly high conductivity metal on both levels; and, as discussed below, with this system at reasonable frequencies we do not encounter the problem of two clock pulses getting out of phase as they travel down long electrodes. Because of the fabrication problems associated with this system, no large-scale MOS manufacturer is considering using it.

The second type of double-level system is the doped polysilicon-SiO_2-Al system (5) which is used extensively in MOS device manufacture. The attractive feature of this technology is that the insulator between the polysilicon and the aluminum is a uniformly grown insulator rather than a deposited insulator. This growth of the insulator makes it possible to have a reasonably thin insulating layer of SiO_2 of high integrity, as opposed to the deposited oxides, which never approach the integrity of a grown oxide. The problems with polysilicon revolve essentially around two aspects. First, due to the two oxide thicknesses, there is an asymmetry in the clock voltages necessary to run the device in a four-phase system. However, this system can be used very conveniently in a pseudo two-phase system where the polysilicon-work function difference, combined with the slight difference in oxide thickness under the two metalization layers, gives directionality.

The second problem with this system really lies in the difficulty of doping polysilicon to values near that of the conductivity of metal. The normal doping range of the polysilicon in MOS structures is in the 15-30 ohms per square range, which is approximately three orders of magnitude more resistive than aluminum. This high resistivity, along with an increased capacitance, causes clock pulses on different metalization levels to get out of phase. The propagation delay of a clock pulse in the distributed RC transmission line represented by the clock electrodes is approximately RC, where R and C are the lumped values of the line resistance and capacitance, respectively. Then

$$RC = \left(\frac{R_{\square} l}{w} \right) \left(\frac{\epsilon w l}{d} \right) = \frac{\epsilon R_{\square} l^2}{d} = \frac{8.8 \times 10^{-6}}{d(\text{Å})} R_{\square}$$

for $l = 200$ mils ($= 5080$ μm)

$$= \frac{5.5 \times 10^{-5}}{d(\text{Å})} R_{\square}$$

for $l = 500$ mils ($= 12{,}700$ μm)

where l is the length of the clock line, w is the width of the clock line, ϵ is the dielectric constant, and d is the thickness of the oxide under the clock line. In order to maintain proper phase relation between first- and second-level clock lines, the RC time constants for the two levels must differ by no more than a small fraction of the clock period. Assume a sheet resistance of 30 ohms/sq for for polysilicon, 3×10^{-2} ohms/sq for Al, and 5.7×10^{-2} ohms/sq for Mo. As shown in Table I, this requirement is best satisfied by the anodized aluminum electrode structure. The time constants associated with the polysilicon system will restrict operation to approximately 2 MHz for 200 mil long electrodes, and 300 kHz for 500 mil long electrodes. Since ultimate clock speeds of CCD's might exceed 5 MHz, this propagation delay is an important consideration in device layout. One could, of course,

Table I. Propagation delay along transfer electrodes, calculated as a distributed transmission line

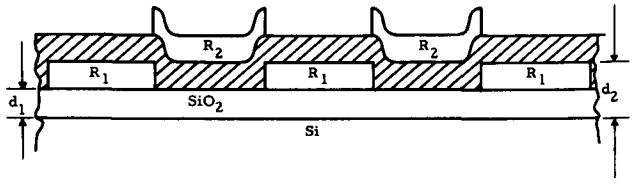

System	Time constant of first-level R_1C_1 (sec) $l = 200$ mils (5080 μm)	$l = 500$ mils (12,700 μm)	Time constant of second-level R_2C_2 (sec) $l = 200$ mils (5080 μm)	$l = 500$ mils (12,700 μm)
Al-Al_2O_3-Al	8.8×10^{-11}	5.5×10^{-10}	8.8×10^{-11}	5.5×10^{-10}
Poly-Si-SiO_2-Al	8.8×10^{-8}	5.5×10^{-7}	7.5×10^{-11}	4.7×10^{-10}
Moly-SiO_2-Al	1.6×10^{-10}	1.1×10^{-9}	5.3×10^{-11}	3.3×10^{-10}

Calculated assuming
Al = 3×10^{-2} ohm/sq, Mo = 5.7×10^{-2} ohm/sq, poly-Si = 30 ohm/sq
and
$d_{1_{\text{Al-Al}}} = d_{1_{\text{Mo-Al}}} = d_{1_{\text{Poly-Si-Al}}} = 3000$Å $\quad d_{2_{\text{Al-Al}}} = 3000$Å, $d_{2_{\text{Mo-Al}}} = 5000$Å, $d_{2_{\text{Poly-SiO-Al}}} = 3500$Å

contact the polysilicon system with periodic ohmic contacts to a parallel metal electrode running alongside the polysilicon, thereby decreasing the resistivity. However, the use of ohmic contacts is a very inefficient use of area, and a polysilicon system that relied on a metal electrode running parallel with it to provide high conductivity would have such a large bit size as to preclude use of this system in the fabrication of large arrays.

Acknowledgments

The authors wish to thank J. D. Awtrey and D. L. Splawn for performing the anodization and device testing and assisting in the device layout.

Manuscript submitted Sept. 8, 1972; revised manuscript received Nov. 29, 1972.

Any discussion of this paper will appear in a Discussion Section to be published in the December 1973 JOURNAL.

REFERENCES

1. W. S. Boyle and G. E. Smith, *Bell Syst. Tech. J.*, **49**, 587 (1970).
2. G. F. Amelio, M. F. Tompsett, and G. E. Smith, *ibid.*, **49**, 593 (1970).
3. M. F. Tompsett, G. F. Amelio, and G. E. Smith, *Appl. Phys. Letters*, **17**, 111 (1970).
4. W. E. Engler, J. J. Tiemann, and R. D. Baertsch, *ibid.*, **17**, 469 (1970).
5. W. F. Kosonocky and J. E. Carnes, *IEEE J. Solid-State Circuits*, **SC-6**, 314 (1971).
6. C. N. Berglund, R. J. Powell, E. H. Nicollian, and J. T. Clemens, *Appl. Phys. Letters*, **20**, 413 (1972).
7. R. H. Krambeck, R. H. Walden, and K. A. Pickar, *ibid.*, **19**, 520 (1971).
8. M. F. Tompsett, *J. Vacuum Sci. Technol.*, **9**, 1166 (1972).
9. F. Keller, M. S. Hunter, and D. L. Robinson, *This Journal*, **100**, 411 (1953).
10. L. Young, "Anodic Oxide Films," Academic Press, New York (1961).
11. W. R. McMahon, paper presented at International Electron Device Meeting, October 1970. Page 48 of Meeting Abstracts (IEEE Cat. No. 70 C45-ED); also see U.S. Pat. 3,634,203. "Thin Film Metallization Process for Microcircuits," assigned to W. R. McMahon and T. H. Ramsey.
12. G. Hass, *J. Opt. Soc. Am.*, **39**, 532 (1949).
13. J. E. Carnes, W. F. Kosonocky, and E. G. Ramberg, *IEEE Trans. Electron Devices*, **ED-19**, 798 (1972).

Anodic Oxidation of Silicon in Organic Baths Containing Fluorine

M. Croset* and D. Dieumegard

Laboratoire Central de Recherches, THOMSON-CSF/Corbeville, Orsay (91), France

ABSTRACT

The anodic oxidation of silicon in organic solvents containing fluorine traces has been investigated by using nuclear microanalysis and electrical measurements. The results obtained show that the fluorine incorporation into the oxide N_F increases with the oxide thickness N_o and with the fluorine content of the bath $|F|$ following the experimental law $N_F = k\sqrt{N_O \cdot |F|}$. Most of the fluorine incorporated is located in a region close to the Si-SiO_2 interface; its surface distribution, studied by ion microprobe mass spectrometry analysis, appears to be uniform. The fluorine incorporation probably obeys a two-step mechanism. The breakdown field of the anodic layer decreases as a function inversely proportional to the fluorine contamination of the layer. The C-V measurements of the contaminated layers after annealing in H_2 show that the density of charges at the Si-SiO_2 interface is about $10^{11}/cm^2$. By comparing composition and electrical measurements, one may predict that fluorine is linked to silicon atoms as is oxygen in silicon oxide.

Anodic oxidation of single crystalline silicon samples in an organic electrolyte was proposed for the first time in 1957 by Schmidt (1). Since then the influence of the nature of the oxidation bath on the mechanism and kinetics of oxidation has been the subject of a number of studies (2-6). These studies have revealed the fundamental part played by traces of water present in the organic electrolyte and have shown the possibility of incorporating in the oxide impurities such as phosphorus, by contaminating the oxidation bath with phosphate ions. No systematic study has been undertaken concerning the presence of fluorine compounds in the electrolyte. Schmidt (1) pointed out that oxidation in an organic bath containing fluorine ions increases the current yield of the oxidation. The considerable chemical affinity of the F^- ion for silicon oxide justified a detailed study of the effect of fluorine on the kinetics and mechanism of the anodic oxidation of silicon. In the work described in this paper, two aspects of contamination were envisaged depending on whether the oxidation was conducted in an organic bath intentionally or not contaminated with fluorine. The addition of salts which could limit the effect of this contamination was envisaged and will be described in detail in a forthcoming article. The localization of the fluorine incorporated in the oxide was also studied.

We shall briefly describe the experimental techniques of cleaning, oxidation, and characterization used. The results which will be presented relative to the quantitative determination of traces of fluorine incorporated in the oxide by the use of the technique of microanalysis by direct observation of nuclear reactions (7-9). This technique, developed by Amsel and co-workers permits quantitative determination of the oxygen and the fluorine contained in the silicon oxide. All the nuclear measurements were carried out on the Van de Graaf accelerator of the Groupe de Physique des Solides of the Ecole Normale Supérieure de Paris.

Experimental

Oxidation technique.—The electrolytes were prepared from the same organic solvent: diethylene glycol containing potassium nitrite or aluminum nitrate. The choice of potassium nitrite was justified by past studies;

* Electrochemical Society Active Member.

Key words: silicon dioxide, anodic oxidation, fluorine, oxygen, contamination, breakdown voltage, C-V measurements.

its concentration (4.7×10^{-2} mole/liter) assured a sufficient electrical conductivity. The aluminum nitrate had been selected for its possible effect on the fluorine ions contained in the bath, in view of the great affinity of aluminum and fluorine. The water content of the bath was adjusted to its optimum value (0.4% by weight) and verified by Karl Fischer determination. The fluorine-rich solutions were prepared by an addition of potassium fluoride. In order to eliminate the error due to a chance fluorine contamination of the starting glycol, the oxidation baths were prepared from the same batch solution of diethylene glycol and potassium nitrite.

Samples of N-type silicon supplied by Hoboken were used, with a resistivity close to 5 ohm · cm and orientation (1.0.0.), their surface being polished by a mechano-chemical process (11). Before oxidation, they were subjected to a cleaning cycle, the efficiency of which is discussed further on. The oxidation technique used was described in detail in Ref. (6). The Pyrex oxidation cell enables the sample to be placed as the anode opposite to a platinum cathode. The bath is homogenized throughout the oxidation by magnetic stirring. The electrical contact with the samples is effected by means of tantalum clamps previously oxidized at a voltage higher than that selected for the oxidation of the silicon. The contact surfaces of the clamps cleaned up with a file enable a satisfactory electrical contact to be obtained. The oxidation was performed at a constant current (most frequently 1 mA/cm^2) up to a predetermined voltage and was then followed by a stage at constant voltage. The final current was allowed to decrease to about 40 μA/cm^2 for all samples. After oxidation, the samples were rinsed in hot water and then in hot acetone.

Characterization of the layers obtained.—The composition of anodic SiO_2 films was characterized by nuclear measurement methods, their electrical properties were studied by C-V measurements and breakdown voltage determinations.

The growth law of the anodic film was studied by quantitative determination of the oxygen contained in the film as a function of the oxidation voltage; determination of the fluorine enabled the contamination of the silicon oxide in relation to a certain number of parameters (bath composition, oxidation voltage, etc.) to be followed. The O^{16} was determined by using the reaction O^{16} (d,p) O^{17*} initiated by a deuterons beam of 830 keV, the protons emitted being analyzed at a detection angle of 150°. The F^{19} was determined by using the reaction F^{19} (p,α) O^{16} initiated by a proton beam of 1270 keV, the α particles emitted being analyzed at a detection angle of 150°. The sensitivity calculated is 11×10^{14} atoms of F^{19}/cm^2 for a layer giving 100 counts for an irradiation of 200μ Cb and a solid detection angle of 0.12 steradians. The absolute oxygen standard was provided by a film of tantalum anodic oxide, the number of O^{16} atoms/cm^2 was known with an accuracy of about 3% (10). The absolute fluorine standard was a vacuum-deposited film of CaF_2 on a silicon substrate, known with an accuracy of about 7% (9).

C-V measurements were achieved on Si-SiO_2-Hg structures obtained by pressing an Hg drop at the oxide surface. This Hg probe technique permitted avoiding any change in the Si-SiO_2 interface state density and charge due to accidental thermal treatment during electrode deposition. Breakdown field determinations needed the use of well-defined capacitance geometry; Si-SiO_2-Al structures were obtained for the purpose by Al evaporation (1 μm thick, under a 10^{-6} Torr vacuum) and photolithographic localization of 650 μm diameter Al dots.

Results

Contamination of the surface of the silicon before oxidation treatment.—Influence of different cleanings.—The fluorine contamination of valve metal surfaces has already been studied by several authors (12-14). In the case of silicon, Kern (12) using F^{18} as a tracer showed that the surface immersed in HF solution adsorbs 10^{16}-10^{17} F atoms/cm^2; nevertheless, the major part of this contamination disappears by rinsing in cold water. Larrabee *et al.* (13) found contaminations of the order of 2×10^{14} atoms/cm^2 on silicon samples steeped in a buffer solution of fluorine (NH_4HF_2 + HF + H_2O) and rinsed in water. We have tried to reduce this contamination and to localize it. The results obtained after various types of cleaning are shown in Table I. It appears that the natural fluorine content on the surface of the silicon as delivered by the supplier is actually of the order of 10^{14} atoms/cm^2, whatever the origin of the silicon and the type of surface polishing used. This value thus seems typical of chemical post treatments of the surface rather than of its crystallographic state. The contamination does not disappear by simple dipping in solvents such as acetone and trichlorethylene. It increases after treatment in nitric acid but may drop below 10^{13} atoms/cm^2 after treatment in HF followed by rinsing in hot deionized water and acetone (duration of treatment in water was extended from 3 to 15 min without the fluorine content rising again above 10^{13} atoms/cm^2). Owing to these results, one may suppose that the fluorine is more probably incorporated in the layer of natural oxide at the surface of the silicon than located at the Si-SiO_2 interface or adsorbed on the natural oxide surface.

Fluorine contamination of the anodic oxide prepared in nonintentionally contaminated electrolytes.—The organic baths used for the oxidation were of the following composition: bath 1, diethylene glycol + ($4.7 \cdot 10^{-2}$ mole/liter) of KNO_2 and bath 2, diethylene glycol + ($6.7 \cdot 10^{-3}$ mole/liter) of $Al(NO_3)_3 \cdot 9H_2O$.

Bath 1 enables a formation voltage of 250-300V to be obtained without microbreakdown. At higher voltages, the oxide deteriorates, most frequently by the formation of pitting and local attack. Actually, the limit formation voltage V_{flim} is not absolute; it depends in particular on the silicon used (source, polishing, etc.). Thus certain samples of silicon free of dislocations enabled formation voltages of 350-400V to be reached in bath 1 without microbreakdown. In order to avoid these sources of irreproducibility, the measurements made were carried out on the same batch of silicon. Bath 2 enables distinctly higher voltages to be obtained which may exceed 600V without microbreakdown.

The fluorine content of the oxide layers, shown in Fig. 1, indicates that the incorporation increases with the formation voltage. The representative points of the linear part of the curves correspond to oxide layers which have no defects detectable by examination by optical dark field microscope. In that area, the amount of fluorine incorporated is proportional to the layer thickness, the F/O ratio being $2 \cdot 10^{-4}$. With high values of oxidation voltage ($V_f \geq 250$V), an excessive fluorine incorporation is found as compared with the linear law found previously. This excessive incorporation is associated with the occurrence of microbreakdowns which locally destroy the oxide layer.

Table I. Influence of different cleaning methods on fluorine contamination of silicon surface

	a	b	c	d
Specimen cleaning	1. Acetone	1. Acetone 2. HF 3. H_2O 4. Acetone	1. Acetone 2. HF 3. H_2O 4. Acetone 5. HNO_3 6. H_2O	1. C_2HCl_3 2. HNO_3 3. H_2O 4. Acetone
Atoms F^{19}/cm^2	$10 \cdot 10^{13}$	$<10^{13}$	$10 \cdot 10^{13}$	$20 \cdot 10^{13}$

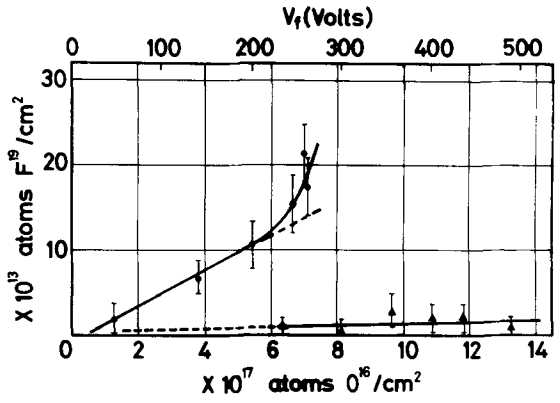

Fig. 1. Fluorine contamination of the silicon anodic oxide prepared in nonintentionally contaminated electrolytes as a function of the oxidation voltage and the oxygen content of the layers. (●) Bath 1: diethylene glycol + ($4.7 \cdot 10^{-2}$ mole/liter) of KNO_2. (▲) Bath 2: diethylene glycol + ($6.7 \cdot 10^{-3}$ mole/liter) of $Al(NO_3)_3, 9H_2O$.

The important effect of the aluminum ion on the limitation of contamination of the layers can be seen clearly in Fig. 1. It permits assuming that a stable aluminum-fluorine complex is formed in the oxidation bath. This effect, which occurs here in only slightly fluorine contaminated baths (natural contamination), shall be studied in detail for highly contaminated baths in a forthcoming publication.

Anodic oxidation of silicon in organic baths contaminated with fluorine.—The effect of electrolyte composition on the oxidation process and oxide composition has been studied in a more quantitative way by varying the fluorine ion concentration in the oxidation bath. Potassium fluoride has been selected to contaminate the bath, essentially because it yields a salt having the same cation as potassium nitrite and because its solubility limit in diethylene glycol permits high contamination levels.

The variation in fluorine content of layers prepared in baths with different KF concentrations is shown in Fig. 2 as a function of the oxygen content of the layers and their formation voltage, V_f. The same monotone variation of incorporation with oxide thickness as that in Fig. 1 is found qualitatively. Excessive incorporation at high thicknesses is associated in all cases with the occurrence of microbreakdowns during oxide growth. It appears that microbreakdowns occur for oxide thicknesses decreasing when bath contamination increases; however the highest quantity of fluorine which may be incorporated in the oxide without occurrence of microbreakdown is an increasing function of bath contamination. Thus, quantities up to 10^{15} atoms of fluorine per square centimeter can be incorporated in undisturbed oxide layers 100Å thick. In such layers, the average fluorine content defined by the ratio F/O reaches $F/O \simeq 2 \cdot 10^{-2}$. It should be pointed out that the proportionality between fluorine incorporation and oxide thickness for oxidation in a nonintentionally contaminated bath (Fig. 1) no longer applies to oxidation in contaminated baths. Here it seems (Fig. 2) that incorporation is proportional to the square root of oxide thickness, whatever the fluorine content of the electrolyte. Assuming that oxide thickness and bath contamination are independent variables, such incorporation may then be expressed by a law of the type

$$N_F = k \cdot \sqrt{N_O} \cdot g\,(|F|) \qquad [1]$$

where N_F and N_O are the quantities of fluorine and oxygen, respectively, contained in the oxide layer; $g\,(|F|)$ being a function of the independent parameter $|F|$ expressing the fluorine concentration in the bath.

The effect of the value of $|F|$ has been studied over a wide range of concentrations from $2 \cdot 10^{-3}$ to $2 \cdot 10^{-8}$ mole/liter of KF. The results obtained are shown in Fig. 3 which gives the variation in the ratio $N_F/\sqrt{N_O}$ for increasing formation voltages V_f *vs.* the bath composition. For potassium fluoride concentrations of the order of 10^{-5} mole/liter and over, the ratio $N_F/\sqrt{N_O}$ becomes saturated: the oxide layer formed is then fully disturbed. A typical aspect of a surface oxidized under these conditions is shown in Fig. 4; detachments of the oxide layer are noticeable and may result in corrosion of the silicon. In this region, the value of the ratio $N_F/\sqrt{N_O}$ is approximately 3% and can therefore correspond to the average limit composition of the nonadhering contaminated oxide layer. At KF concentrations in the bath below 10^{-5} mole/liter, the fluorine incorporation law is

$$\frac{N_F}{\sqrt{N_O}} = k\sqrt{|F|} \qquad [2]$$

This law is ascertained for various values of the oxidation voltage from 20 to 150V (Fig. 3). It confirms and defines Eq. [1] more accurately. The validity of the formula [2] for various oxide thicknesses permits assuming that the mechanism of fluorine incorporation in the oxide may be studied as a function of two parameters: the composition of electrolyte and the transport of the fluorine in the layer. These two parameters seem to be independent of each other. However, it should be noted that they seem to have

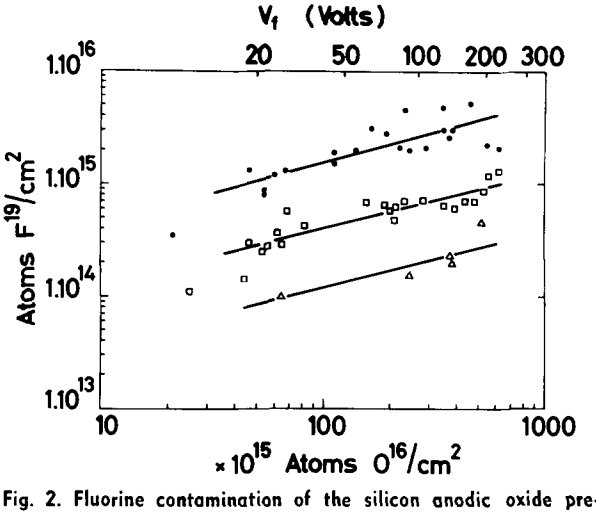

Fig. 2. Fluorine contamination of the silicon anodic oxide prepared in intentionally contaminated electrolytes as a function of the oxidation voltage and the oxygen content of the layers. (●) Bath: diethylene glycol + KNO_2 ($4.7 \cdot 10^{-2}$ mole/liter) + KF ($2 \cdot 10^{-6}$ mole/liter). (□) Bath: diethylene glycol + KNO_2 ($4.7 \cdot 10^{-2}$ mole/liter) + KF ($2 \cdot 10^{-7}$ mole/liter). (△) Bath; diethylene glycol + KNO_2 ($4.7 \cdot 10^{-2}$ mole/liter) + KF ($2 \cdot 10^{-8}$ mole/liter).

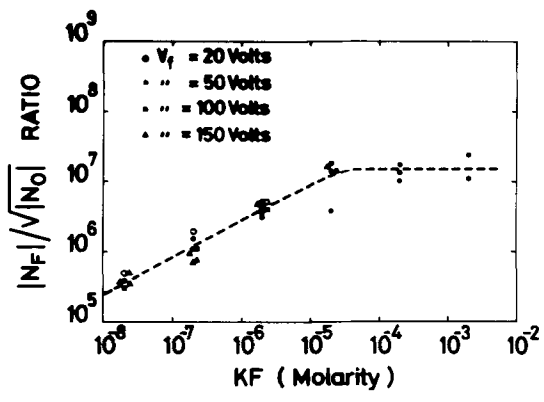

Fig. 3. Dependence of the $N_F/\sqrt{N_O}$ ratio on the KF concentration in the bath.

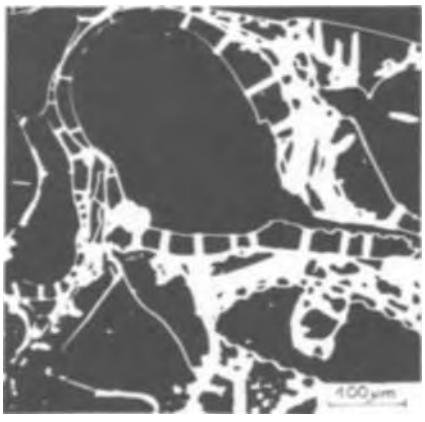

Fig. 4. Typical surface aspect of a silicon oxide layer obtained in highly fluorine contaminated electrolyte (V_f = 100V; |KF| = $2 \cdot 10^{-5}$ mole/liter).

a different action on the maximum fluorine incorporation into the oxide. This fact will be discussed further on.

The mean value of the oxidation yield has been obtained by comparing the electrical charge used throughout the phases at constant current and voltage, and the quantity of oxygen fixed. Results are shown in Fig. 5 *vs.* the fluorine content of the oxidation bath. For KF values below 10^{-5} mole/liter, oxidation yield increases slightly. For KF values above 10^{-5} mole/liter, efficiency increases rapidly but such increase is associated with disturbances in the oxide layer and an excessive incorporation of fluorine.

Locating the fluorine in the oxide layer.—Location of fluorine atoms in the layer has been obtained by determination of the total quantity of fluorine remaining in the contaminated layer during chemical dissolution steps. In such experiments, the layer of silicon oxide had to be sufficiently contaminated to permit determining the fluorine content with sufficient accuracy; it had to be sufficiently thick to permit dissolving by steps.

Several experiments using silicon of different origin, have enabled fairly thick layers to be obtained (V_f = 170V) with a sufficient contamination level (bath of 2×10^{-6} mole/liter of KF) and an adequate surface condition after oxidation. Oxidations were carried out on large silicon samples which were then cut out in several pieces, each of which was dipped for increasing dissolving times in a 1% HF solution. The fluorine contamination of the oxide surface by this dissolution bath has been estimated by partial chemical dissolution of thermal and anodic silicon oxide layers. No contamination could be evidenced on anodic films containing about 10^{13} F atoms/cm^2; with thermal layers containing less than 10^{13} F atoms/cm^2, one could detect a possible level of contamination in the 10^{13} F atoms/cm^2 range. The curve drawn on Fig. 6 shows the variation in the fluorine quantity remaining in the layer *vs.* the remaining oxide thickness. The figure also shows the total quantity of fluorine incorporated in oxides during their growth in the same contaminated bath *vs.* their thickness. Results given by these two types of experiments are very similar. They are on good accordance for films thicker than 200Å; for thin layers a slight deviation may exist which may be due to various experimental irreproducibilities, such as nonhomogeneous dissolution, cumulative contamination, or irreproducibility of bath composition. The analysis of the shape of the curve shows that the greatest part of the fluorine is located in a region close to the silicon-silicon oxide interface, with a thickness not exceeding 100Å (expressed in stoichiometric silicon oxide). Assuming that contamination of this layer is homogeneous, its fluorine content is of the order of F/O $\simeq$ 4%. This result is comparable with that found as a limit contamination of the disturbed layers (see above). Since the layers analyzed in Fig. 6 correspond to a maximum contamination prior to the occurrence of microbreakdowns, it can be assumed that microbreakdowns occur when fluorine contamination of the interface region reaches this limit value of F/O $\simeq$ 4%. It appears that except for interface region, the fluorine content of the oxide layer is low and seems homogeneously distributed in the layer. From the slope of the curve, one can evaluate this content to about F/O = 0.25%.

Owing to the similarity of the results obtained by partial dissolution and direct growth, it may be supposed that fluorine incorporated in the oxide layer moves in a similar manner to oxygen, either during the oxide growth phase or during the current decay phase. Then, the inhomogeneous distribution of fluorine in the layer would imply two successive incorporation mechanisms. These assumptions will be discussed further on.

Electrical characterization of the layers.—Determination of the breakdown field.—Circular aluminum dots, 650 μm in diameter, separated by 1 mm were distributed over the whole surface of the SiO_2 layer to be tested. A voltage ramp (duration 0.5 msec) was applied across the MOS capacitance in a direction

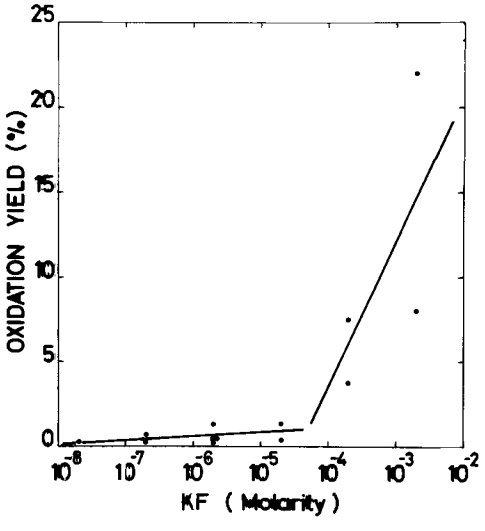

Fig. 5. Variation of the oxidation yield as a function of the KF concentration in the bath for SiO_2 films formed at V_f = 50V.

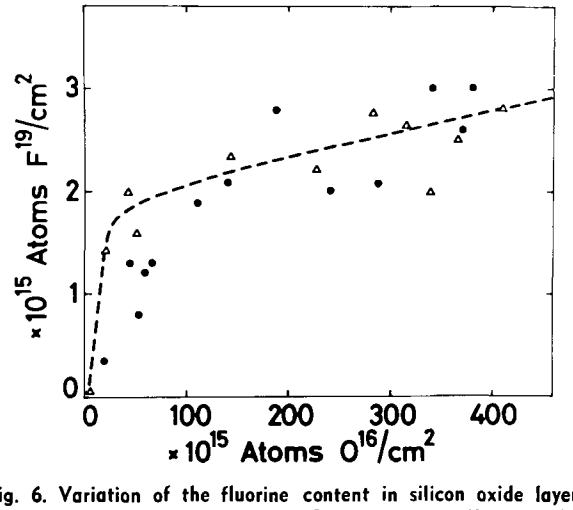

Fig. 6. Variation of the fluorine content in silicon oxide layers formed in glycol containing $2 \cdot 10^{-6}$ mole/liter of KF. The (Δ) distribution is obtained by determination of the fluorine quantity remaining in an oxide layer formed at V_F = 170V during its chemical dissolution by steps. The (●) distribution is obtained by counting the total quantity of fluorine incorporated as a function of oxide thickness.

such (positive bias on metal grid) that it created electron enrichment of the Si surface. The capacitance charging current $i(t)$ was stored and recorded immediately afterward on an XY recorder. The duration of this transcription (about 10 sec) enabled about a hundred MOS structures to be tested fairly quickly on each sample. Depending on the layers studied, various types of current *vs.* prebreakdown voltage curves are obtained, as shown in Fig. 7. For a given value of the breakdown voltage V_A of the oxide, the curve may exhibit (curve a) a first current peak corresponding to the first nondestructive microbreakdown. The increase of the electric field in the layer then causes breakdown V_D to occur. Note that the saturated value of the current is then defined by the electronic memory amplifier and has no experimental significance. Curve b corresponds to an exponential current increase up to breakdown V_D, with no appearance of pre-microbreakdown. Purposely contaminated layers (KF bath) lead to type a curves in all cases; layers prepared in nonintentionally KF-contaminated baths yield type a or type b curves.

Figure 8 is a breakdown field histogram taking electric field intervals of $1 \cdot 10^6$ V · cm^{-1} for layers slightly contaminated with fluorine and intervals of $0.1 \cdot 10^6$ V · cm^{-1} for contaminated layers. The thickness of the layers approximated 1000Å. The layers with a low level of contamination (about 1.4×10^{14} atoms/cm^2) has a maximum number of capacitors with a breakdown field within 6 and 7×10^6 V · cm^{-1}, this result is in agreement with those found by other

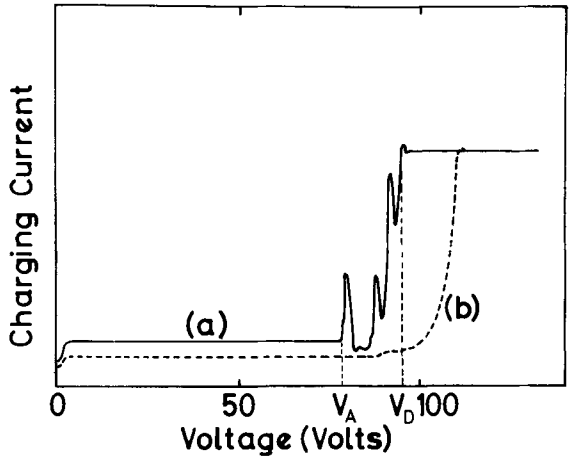

Fig. 7. Typical voltage current characteristics of Al-SiO_2-Si capacitance structures.

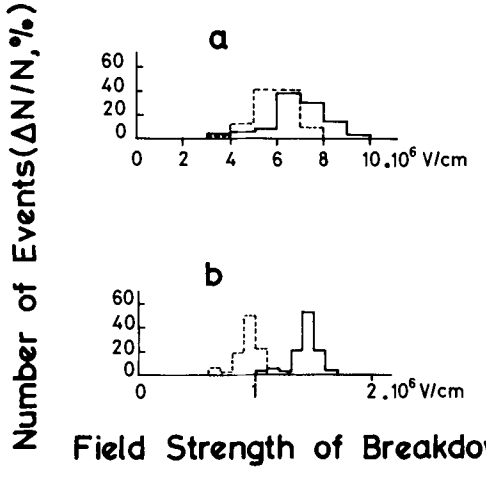

Fig. 8. Typical breakdown field distribution curves for Al-SiO_2-Si structures. The full and dotted lines correspond respectively to V_D and V_A defined on Fig. 7. a. SiO_2 layer 1000Å thick containing $14 \cdot 10^{13}$ atoms F^{19}/cm^2. b. SiO_2 layer 1000Å thick containing $66 \cdot 10^{13}$ atoms F^{19}/cm^2.

authors (15-17). The results achieved on highly contaminated layers show that the breakdown field decreases as a function inversely proportional to the fluorine content of the layer. This is illustrated in Fig. 9 giving the variation of E_a and E_d (at $\Delta N/N = 30\%$) with the fluorine content of the layer. The small scattering of the values of E_a and E_d for the contaminated layers implies that the fluorine distribution at the Si-SiO_2 interface is homogeneous, at least at the scale of a circular surface 650 μm in diameter.

C-V *measurements.*—As is known, plotting of the curve $C = f(V)$ of a MOS capacitance is an easy way of analyzing the properties of silicon oxide and of the Si-SiO_2 interface (18). This method has been widely described and used by many authors, and a few essential results will be recalled here. The translation ΔV between the theoretical and experimental capacitance *vs.* voltage curves is characteristic of the presence of electric charges Q moving within the dielectric and of the presence of a surface state Q_{ss} located at the interface. A distortion of the experimental curve implies the presence of acceptor or donor traps N_{ss} located in or near the interface.

Measurements were made at a frequency of 50 kHz. Contact with silicon was achieved through a silver lac, the metal grid on the silicon was most of the time produced by compression of a mercury drop. Just after oxidation, the capacitance-voltage curves obtained on contaminated layers are translated and distorted with respect to the theoretical curve; a hysteresis effect is sometimes observed. The relative position of the curves obtained is at random with the fluorine content of the layers.

The effect of annealing treatments between 400° and 500°C in hydrogen has been studied using SiO_2 films 900Å thick containing about 10^{15} fluorine atoms/cm^2. Nuclear measurements of layers before and after thermal treatment at 500°C did not evidence any fluorine content variation; no redistribution could be evidenced by using a CAMECA ion microprobe mass spectrometer which gave similar fluorine profiles in SiO_2 before and after annealing. The *C-V* curves obtained after different types of treatment (duration and temperature) are shown on Fig. 10; the experimental and theoretical curves appear to be parallel and translated by a low amount ($\Delta V \simeq 1$V for the lowest saturation value) which corresponds to a density of charges at the Si-SiO_2 interface of about 10^{11}/cm^2.

Discussion

The essential subject of this work was to study the effect on anodic silicon oxidation of the presence of fluorine traces in the oxidation bath. The results obtained relate to layers obtained by oxidation at con-

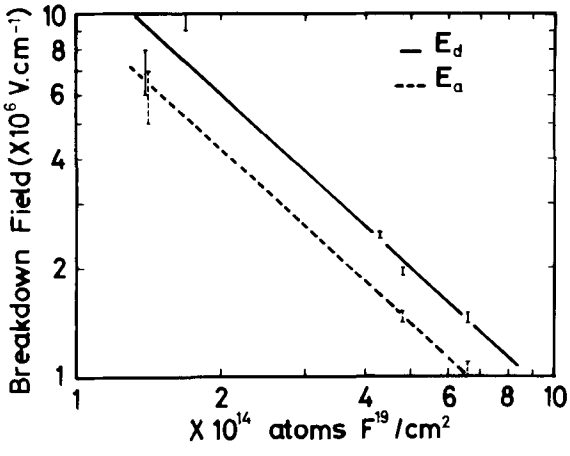

Fig. 9. Variation of breakdown field as a function of fluorine in SiO_2 film. The values E_d and E_a correspond, respectively, to V_D and V_A defined on Fig. 7.

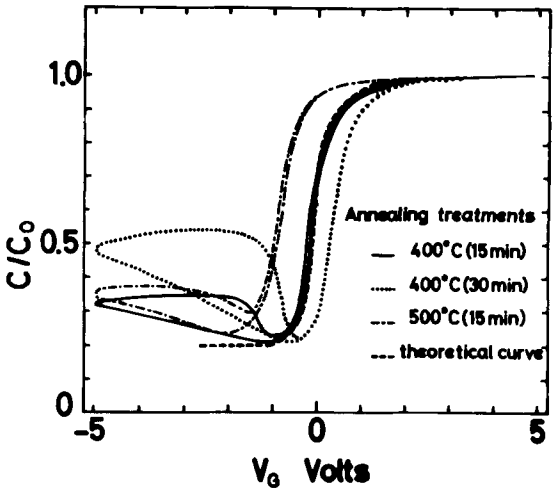

Fig. 10. Capacitance-voltage characteristic curves of MOS structures contaminated with fluorine. Influence of temperature and duration of annealing treatments in hydrogen ambient.

stant current followed by a phase at a voltage kept constant up to achievement of oxidation currents as low as 40 μA/cm^2. The influence of the value of the final oxidation current on the fluorine incorporation has not been studied in this work. A few preliminary oxidation experiments seem to show that incorporation is only slightly dependent on the value of the final current. Note that excessively long periods at constant voltage, seem to be associated with extra fluorine incorporation which might correspond to a recrystallization step of the oxide layer. More precise studies are being carried out on this subject.

In general, it was found that contamination of the electrolyte with fluorine results in a fluorine contamination of the silicon oxide obtained. This incorporation may be affected by the initial surface condition of the silicon sample, the oxidation parameters, and the electrolyte composition. Most of the oxidations have been carried out at a current density of 1 mA/cm^2; experiments at oxidation current densities varying between 0.5 and 10 mA/cm^2 have not evinced a significant variation in fluorine incorporation; it should be noted that in these cases the current decay phase may have masked possible differences associated with the initial value of the oxidation current.

The results obtained in the section on Contamination of the surface of the silicon show that natural contamination of the silicon surface of the order of 10^{14} atoms/cm^2 may be reduced to less than 10^{13} atoms/cm^2 by cleaning. It should be noted that exposure of such surface to the air results in the slow reconstitution of an oxide layer and in the restoration of the contamination level which depends on the environmental conditions. It seems that fluorine is incorporated in this natural oxide layer. Silicon surfaces, thus covered with their natural oxide, containing about 10^{14} fluorine atoms/cm^2, retain their contamination ratio, even after high-temperature heat-treatment in an oxidizing atmosphere. Thus, about 10^{14} atoms/cm^2 of fluorine are found again in a 1400Å oxide layer generated either at 1000°C in water vapor, or at 1100°C in dry oxygen. Oxidation under the same conditions of noncontaminated surface (less than 10^{13} atoms/cm^2) yields no noticeable incorporation of fluorine. Consequently, natural contamination of the silicon surface may be considered as stable and associated with the presence of a natural oxide layer. Anodic oxidations have all been carried out on surfaces free from such contamination.

The results obtained in the sections on Fluorine contamination and on Anodic oxidation of silicon show that the maximum oxidation voltage $V_{f\text{lim}}$ seems to depend on the origin and purity of the electrolyte. In particular, the addition of a fluorine salt involves a reduction of $V_{f\text{lim}}$ due to the early occurrence of microbreakdowns. The variation of $V_{f\text{lim}}$ *vs.* the level of contamination of the electrolyte (through addition of KF) permitted us to evaluate the order of magnitude of random contamination in the bath 1. The value found, about 10^{-9} equivalent mole/liter of KF, shows the predominant role of the handling of said baths on the oxidation results. In particular, their exposure to air in the laboratory, without precaution, may be the source of multiple irreproducibilities. In this work, all the oxidations were carried out in a sealed enclosure protected from the air; likewise, each series of experiments for the study of a given parameter has been carried out from the same batch solution of electrolyte.

Fluorine incorporation into the oxide increases with the oxide thickness and the fluorine content of the bath. Microbreakdowns of the oxide layer occur when the fluorine content of said layer reaches a limit value related to the bath contamination. Oxidation is then replaced by a corrosion of silicon due to successive periods of oxide formation and stripping of said oxide exposing local silicon areas which become oxidized in turn. The fluorine content of the disturbed oxide layer thus created (F/O = 3%), is unaffected by the fluorine content of the bath over the range studied. This limit content seems to be associated with the oxide stripping effect. It should be noted that there is a difference between contamination level of the oxide associated with the occurrence of microbreakdowns, which depends on the bath composition, and that associated with silicon corrosion, which does not seem to be related thereto over the concentration range considered. Fluorine incorporation into the oxide increases as the square root of the fluorine content in the electrolyte. This result may be due to a dissociation balance of the fluorine salt according to the law of mass action

$$KF \rightleftarrows F^- + K^+$$

where

$$|F^-| = K_C \frac{|KF|}{|K^+|}$$

and

$$|F^-| = |K^+|$$

Hence

$$|F^-| = \sqrt{K_C \cdot |KF|}$$

where only ionized fluorine fraction $|F^-|$ participates in the incorporation effect. The part played by the aluminum salt, limiting fluorine incorporation, may be attributed to the creation of an aluminum-fluorine complex which no longer participates either in full or part, in the incorporation. It should be noted that the variation of fluorine incorporation in the layers *vs.* intentional contamination of bath 1 with KF (Fig. 3) permitted the definition of the contamination level of bath 1; the result obtained (about 10^{-9} atom-gram/liter) is in agreement with the value estimated by analysis of the variation of $V_{f\text{lim}}$.

The results of the section on Locating the fluorine show that the fluorine distribution in the layer obtained by direct oxidation is very similar to that obtained by step dissolution. However, it should be emphasized that the oxide layers of the same thickness thus compared (by direct oxidation or after dissolution) have not been subjected to the same current decay phase at constant voltage. The model proposed below therefore presupposes that this final oxidation phase has a negligible effect on fluorine distribution. This point has to be verified. The result found means that the quantity of fluorine contained in a well-defined fraction of the oxide thickness (*e.g.*, within the first 100Å from the Si-SiO$_2$ interface) do not depend on the thickness of silicon oxide which covers this fraction; in other words, the quantity of fluorine in a silicon layer, x_0 thick, remains unchanged whether this layer is obtained by direct oxidation to x_0 or by oxidation to $x_0 + \Delta x$ and thinned by Δx, whatever the value

of Δx. Note that this interpretation is a schematic of the results which neglects the scattering of measurements clearly evinced in Fig. 6. It implies that at least the essential part of the fluorine incorporated during the growth is fixed at the very surface of the oxide in contact with the electrolyte and consequently that the fluorine does not migrate through the oxide layer by a long range migration mechanism.

Fluorine in the oxide exhibits a highly inhomogeneous distribution; the important part of the fluorine located at the $Si-SiO_2$ interface is fixed during the initial phase of the oxidation (corresponding to SiO_2 layer 100-150Å thick) and is not the result of an accumulation mechanism at the Si/SiO_2 interface during growth of thicker oxide film. It may be assumed that this high fluorine concentration in a region close to the $Si-SiO_2$ interface is associated with the existence in said region of silicon oxide layers more or less crystallized, such as that found for steam-grown oxide (19). This result seems to indicate the existence of two separate incorporation mechanisms, one affecting only an initial layer with a thickness approximating 100Å, the other affecting the remainder of the layer. In such a hypothesis, the square root dependence of fluorine incorporation on oxide thickness derived from Fig. 2 and 6 might only be the over-all result of these two successive steps. Then, both steps might independently obey a $\sqrt{|F|}$ law imposed by the electrolyte.

A separate study of the interface layer and of the bulk of the oxide would be required to define the fluorine incorporation mechanism more precisely.

The results obtained in the section on Electrical characterization show that after annealing of the MOS structures, the C-V curves have never exhibited an interface charge density higher than 10^{11} cm^{-2}. By comparing this value to the high concentration of fluorine atoms in this interface region (about 10^{15}/cm^2) and since annealing is associated with no detectable fluorine movement, one may suppose that fluorine is linked to silicon atoms, as is oxygen in silicon oxide.

It should be emphasized that the hysteresis of the C-V curves, from the viewpoint of an exchange of electrical charges between silicon and silicon oxide, confirms the existence of a disturbed interface whose composition and, probably, structure are different from those of the bulk silicon oxide.

The decrease in the dry breakdown field associated with fluorine incorporation into the layer was found to be very important. The uniform distribution of the breakdown field at the surface of the contaminated silicon oxide has shown, at least at the 650 μm scale, that surface fluorine distribution was homogeneous. Such a result has been complemented by ion microprobe mass spectrometry analysis of a thin silicon oxide layer highly contaminated with fluorine ($3 \cdot 10^{15}$ atoms/cm^2). The layer thickness, about 140Å, corresponded approximately to the thickness of the highly contaminated interface region. The image of the fluorine distribution was obtained with a CAMECA ion microprobe mass spectrometry apparatus which has a surface resolution of 1 μm; this image evidenced a uniform fluorine distribution on such a surface.

As a conclusion, this study has demonstrated that fluorine incorporation into silicon anodic oxide increases with the oxide thickness and with the fluorine content of the electrolyte. The essential fraction of fluorine incorporated is located at the Si/SiO_2 interface and has a uniform surface distribution. The fluorine incorporation obeys probably a two-step mechanism which is still under study. The fluorine contamination disturbs the growth kinetics of the oxide and its electrical properties.

Acknowledgment

The authors wish to acknowledge G. Amsel, C. Ortega, and S. Rigo for helpful discussions, and J. Diaz for assistance in the experimental work. The help of E. d'Artemare and E. Girard for the operation of the Van de Graaf accelerator has been much appreciated. This work was supported by the Centre National de la Recherche Scientifique (RCP No. 157), and the Délégation Générale à la Recherche Scientifique et Technique.

Manuscript submitted June 16, 1972; revised manuscript received Oct. 17, 1972. This was Paper 87 presented at the Cleveland Meeting of the Society, Oct. 3-7, 1971.

Any discussion of this paper will appear in a Discussion Section to be published in the December 1973 JOURNAL.

REFERENCES

1. P. F. Schmidt and W. Michel, *This Journal*, **104**, 230 (1957).
2. P. F. Schmidt and A. E. Owen, *ibid.*, **111**, 682 (1964).
3. P. F. Schmidt, T. W. O'Keeffe, J. Oroshnik, and A. E. Owen, *ibid.*, **112**, 800 (1965).
4. E. F. Duffek, C. Mylroie, and E. A. Benjamini, *ibid.*, **111**, 1042 (1964).
5. E. F. Duffek, E. A. Benjamini, and C. Mylroie, *Electrochem. Technol.*, **3**, 75 (1965).
6. M. Croset, E. Petreanu, D. Samuel, and J. P. Nadai, *This Journal*, **118**, 717 (1971).
7. G. Amsel, J. P. Nadai, E. d'Artemare, D. David, E. Girard, and J. Moulin, *Nucl. Instr. Methods*, **92**, 481 (1971).
8. D. Dieumegard, Thesis 3e Cycle, Orsay (1971).
9. G. Amsel, B. Maurel, and D. Dieumegard, "Microanalysis of F^{19}, Li^6, and Li^7 by Means of Nuclear Reactions," To be published.
10. G. Amsel, C. Cherki, G. Feuillade, and J. P. Nadai, *J. Phys. Chem. Solids*, **30**, 2117 (1969).
11. J. Regh and G. A. Silvey, *Electrochem. Technol.*, **6**, 155 (1968).
12. W. Kern, *Solid State Technol.*, **15**, 34 (1972).
13. G. B. Larrabee, H. G. Heinen, and S. A. Harrell, *This Journal*, **114**, 865 (1967).
14. B. Maurel, D. Dieumegard, and G. Amsel, *ibid.*, **119**, 1715 (1972).
15. C. R. Fritzsche, *Z. Angew. Phys.*, **24**, 48 (1967).
16. C. R. Fritzsche, *J. Phys. Chem. Solids*, **30**, 1885 (1969).
17. C. M. Osburn and D. W. Ormond, *This Journal*, **119**, 591 (1972).
18. B. E. Deal, M. Sklar, A. S. Grove, and E. H. Snow, *ibid.*, **114**, 266 (1967).
19. P. F. Schmidt and J. D. Ashner, *ibid.*, **118**, 325 (1971).

Electrically Active Stacking Faults in Silicon

K. V. Ravi, C. J. Varker,* and C. E. Volk*

Central Research Laboratories, Motorola Incorporated, Phoenix, Arizona 85008

ABSTRACT

The influence of oxidation induced stacking faults on the electrical characteristics of p-n junctions in silicon has been studied by employing scanning and transmission electron microscopy in conjunction with electrical measurements. Diodes were fabricated with a junction depth $X_j = 4$ μm and an integrated boron concentration of $\sim 3 \times 10^{16}$ cm^{-2} in 1-3 ohm-cm n-type epitaxial silicon.

The presence of decorated stacking faults in the field region of the diodes examined is found to introduce excess reverse leakage currents in the junction. However not all faults introduce the same degree of leakage and the electrical activity of the faults is found to vary. The concept of the "threshold voltage" of a stacking fault is introduced which is a measure of the specific electrical activity of the fault. Electrically active faults introduce excess reverse currents in the diodes which are characterized by a relationship between the reverse log I/V ratio measured at low voltages and the characteristic "threshold voltage" of the faults. The electrical activity is related to both the size and the structure of the faults. The smaller faults which are also more prone to impurity decoration are electrically more active than larger faults which are decorated to a lesser degree. Models are presented to account for the electrical activity of the faults. These models are based on the strain effects of the decorated faults and on the distortions produced in the p-n junctions by the presence of faults.

In the manufacture of semiconductor devices crystallographic defects such as dislocations, stacking faults, etc. are often introduced into the single crystal material as a result of the various thermal-diffusional steps associated with the processing sequence. The types of defects introduced at various stages in the process have been well characterized (1-5). The electrical effects associated with these defects however have not been unambiguously demonstrated. Apart from statistical correlation between the presence of certain defects and the attendant electrical aberrations (6-8) most of the discussion in the literature is speculative and ambiguous. The difficulty is usually of an experimental nature in that the interaction between a particular defect in the semiconductor and the depletion field of the p-n junction cannot be observed directly by any of the conventional techniques. Furthermore there has been a tendency to rely on low resolution techniques such as x-ray topography (6, 7) and surface decoration methods (8) to detect the presence of defects that might be influencing the junction characteristics. These techniques can at best provide a rough correlation between the presence or absence of a defect and the electrical characteristics of the p-n junction. More recently, the application of the scanning electron microscope has permitted the direct observation of electrical effects such as charge carrier generation and recombination in semiconductor devices containing a p-n junction. However, the detailed structure of the defects and the nature of the interaction with the depletion field of the p-n junction are not understood or correlated.

In attempting to better understand defect interactions with p-n junctions a number of questions need to be answered. A first requirement is to determine the structure of a particular defect on an atomic scale. For instance, if a dislocation is suspected of influencing the junction properties, it is necessary to know if the dislocation is "clean" or decorated by a second phase. It has been suggested that dislocations decorated by metallic precipitates, which cut across p-n junctions, are responsible for factors such as excessive reverse currents below the normal avalanche breakdown voltages of the junctions, emitter-collector pipes in bipolar transistors, etc.

Dislocations have also been suggested as providing paths for locally enhanced diffusion and hence cause leakage between the emitter and collector of shallow diffused transistors (8, 9). A contrary viewpoint (10) indicates that grown-in, or the so-called primary dislocations, are generally decorated with other impurities and are hence incapable of functioning as diffusion pipes during subsequent operations.

The problem becomes more complex if details of the decoration process around the dislocations are important in the electrical ramifications of this particular type of defect. If decoration is necessary then the question arises whether the decoration is due to metallic impurities or nonmetallic insulating precipitates such as the oxides of silicon. Dislocations can function as heterogeneous nucleating sites for both metals dissolved in the silicon as well as for silicon oxides (11).

In the present work we have attempted to determine the electrical activity associated with oxidation induced stacking faults. It has been demonstrated that elevated temperature oxidation of silicon in both dry and wet environments can generate stacking faults in the surface (4, 12). The nucleation and growth of these faults have been linked to the formation of second-phase particles in the bulk silicon, the second phase being an oxide of silicon (13). By employing a combination of scanning and transmission electron-microscopy in conjunction with measuring the I-V characteristics of diffused p-n junctions in the presence of stacking faults, the nature of the electrical activity of stacking faults has been investigated. Models are proposed to account for the experimental observations.

Experimental Procedure

The wafers used for diode fabrication consisted of 2 ohm-cm n-type epitaxial films (thickness ~ 20 μm) deposited on <111> oriented chemical-slurry polished silicon substrates of 0.005 ohm-cm resistivity. The wafers were oxidized in a steam ambient at 1100°C to obtain an SiO_2 film thickness of 0.5 μm. The boron diffused diodes ($\sim 0.1 \times 0.1$ cm) were fabricated with a junction depth $X_j \approx 4$ μm at a diffusion temperature of ~1250°C with an integrated boron concentration

* Electrochemical Society Active Member.
Key words: oxidation, diffusion, boron, diodes, precipitation.

$Q \approx 3 \times 10^{16}$ cm^{-2}. The dislocation density of the substrate and epitaxial layer was $<2 \times 10^3$ cm^{-2}.

Fully processed wafers containing diode arrays were electrically characterized by unit probe testing. Single data point measurements of individual diodes were obtained to determine the distribution and number of diodes exhibiting excess reverse leakage currents below the avalanche voltage. Typical diodes were selected for more complete electrical measurements and for subsequent structural analysis. The units were selected to cover the total range of *I-V* characteristics representing a given wafer. All diodes having anomalous reverse leakage currents due to process mask defects and surface damage were eliminated. Structural mapping and analysis was done nondestructively with the scanning electron microscope (SEM) utilizing the electron beam induced current mode (EBIC) (See Appendix I for a discussion of the EBIC technique).

The experimental procedure consists of mapping all selected devices at 0 bias to determine the total number of stacking faults. At relatively low magnifications, the complete diode structure is examined at 40 kV with a beam current of typically 5 nA. Under these conditions, the local recombination of beam generated electron-hole pairs produces sufficient contrast at 0V bias to reveal clearly the individual stacking faults. The total number of faults within the perimeter of each diode was recorded. Voltage-dependent current multiplication sites were observed at specific stacking faults in all diodes having a reverse leakage current above the nominal level for diodes selected at random. The current multiplication effects were observed to occur only at certain faults and these faults are termed "electrically active" faults. Electrically active faults were identified by applying a reverse bias less than or equal to the avalanche voltage.

Structural mapping of the electrically active faults at low magnifications was followed by a more detailed analysis of individual faults at higher magnifications. Instrument parameters for the SEM (*i.e.*, electron beam energy, probe current and magnification) were determined initially by optimizing display conditions and subsequently held constant throughout the investigation. This permitted a relative comparison of the current multiplication effects in terms of the "threshold voltage" of individual stacking faults. This "threshold voltage" is defined as the diode reverse voltage required to obtain local current enhancement at an active fault which corresponds to a video signal ~10% above the average background EBIC display level. This does not necessarily imply that a fault is inactive below the "threshold voltage" but that the current multiplication effects due to the fault are sufficiently small that the relative signal level is reduced by the noise generated in the device when biased. Further analysis with the SEM established the linear dimensions of individual faults and helped to detect the second phase particles associated with these defects.

The final detailed structural analysis at sub-micron resolution with the transmission electron microscope (TEM) required the preparation of thin silicon samples. The experimental technique consisted of chemical thinning selected regions of the diode with a jet polish assembly. Thin electron transparent regions permitted an extensive investigation of the defect structure and the second phase precipitates.

Experimental Results

Oxidation-induced stacking faults.—Transmission electron micrographs of a typical oxidation induced stacking fault are shown in Fig. 1. Figure 1(a) shows the fault fringes and the bounding partial dislocations in contrast while (b) shows the fringes out of contrast. Impurity precipitation is evident around the partials. These precipitates are very likely to be oxides of silicon which initiate and propagate the stacking faults (13). It is also observed that the precipitation around

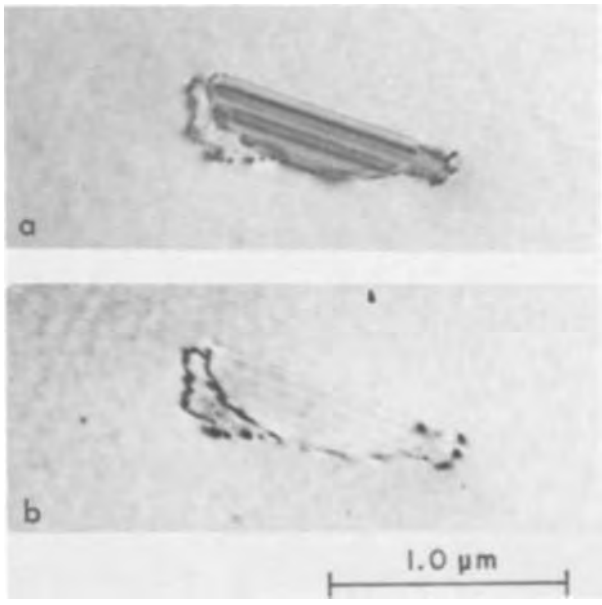

Fig. 1. Two beam bright field transmission electron micrographs of an oxidation induced stacking fault. The top micrograph shows the fault and the bounding dislocation in contrast. The bottom micrograph shows fault out of contrast.

the partial dislocation has resulted in the generation of other dislocations. It has been demonstrated elsewhere that oxidation-induced stacking faults can function as dislocation generating sources in silicon (22).

The stacking faults were typically ~1 μm in length and ~0.5 μm in depth following the oxidation process. However, the faults have been observed to grow during the subsequent diffusion operation, with the eventual size of the fault being related to the time and temperature of diffusion, *i.e.*, to the depth of the p-n junction. The following experimental results are obtained on boron diffused p-n diodes having a junction depth $X_j \approx 4$ μm.

Figure 2(a) is a typical fault as observed in the SEM operated in the EBIC mode. In the micrograph shown the scan direction is from left to right. As the beam encounters the fault, localized carrier recombination effects result in a decrease in signal and hence the fault has a dark leading edge. Since the d-c signal obtained has been capacitance blocked a bright trailing edge results as the beam moves away from the fault. Consequently recombination effects due to the presence of crystallographic defects result in the type of contrast shown in Fig. 2(a). A further point to be noted here is the presence of the two dark regions at the terminations of the stacking fault. This dark contrast results from the presence of second phase particles decorating the partial dislocation bounding the fault. This is more clearly evident in the transmission electron micrographs of a portion of the fault shown in Fig. 2(b) and (c). The micrographs show two beam images of the fault and the precipitate at the termination. In Fig. 2(a) both the fault and the precipitate are in contrast whereas Fig. 2(c) shows the fault out of contrast while the precipitate contrast remains.

Electrical activity of stacking faults.—Figure 3 illustrates EBIC displays of a diode having excess reverse leakage currents below the avalanche voltage. The individual stacking faults are evident in the 0V bias display as elliptically shaped recombination centers oriented along <110> directions. The reverse biased displays reveal the electrically active faults as local current enhancement sites while the inactive faults remain in a quiescent state with the bias applied. These displays show that the number of active faults in a given diode can be considerably less than the total number of stacking faults. Sirtl etch studies on sim-

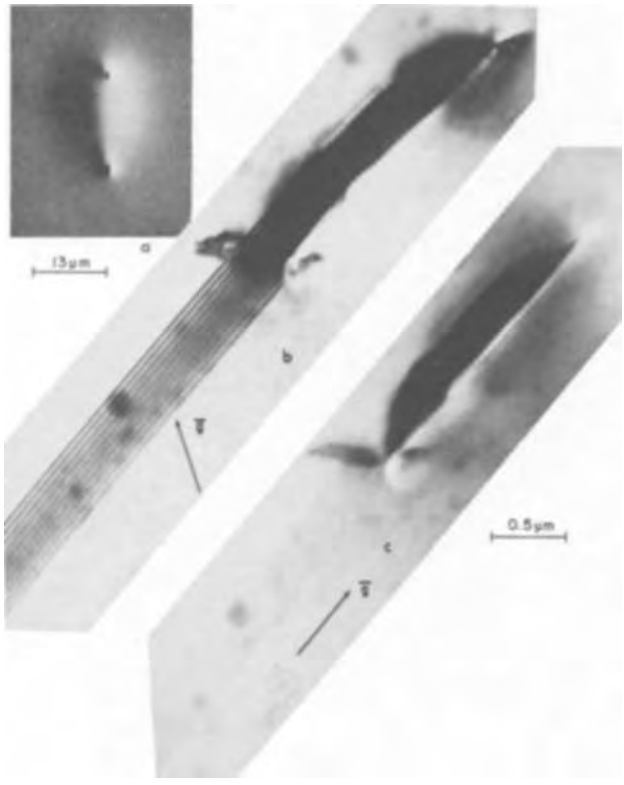

Fig. 2. Structure of a stacking fault following the formation of a p-n junction. (a) Fault as observed in the SEM operated in the EBIC mode; (b) and (c) show transmission electron micrographs of the fault and the precipitate decorating the partial dislocation at the fault terminations.

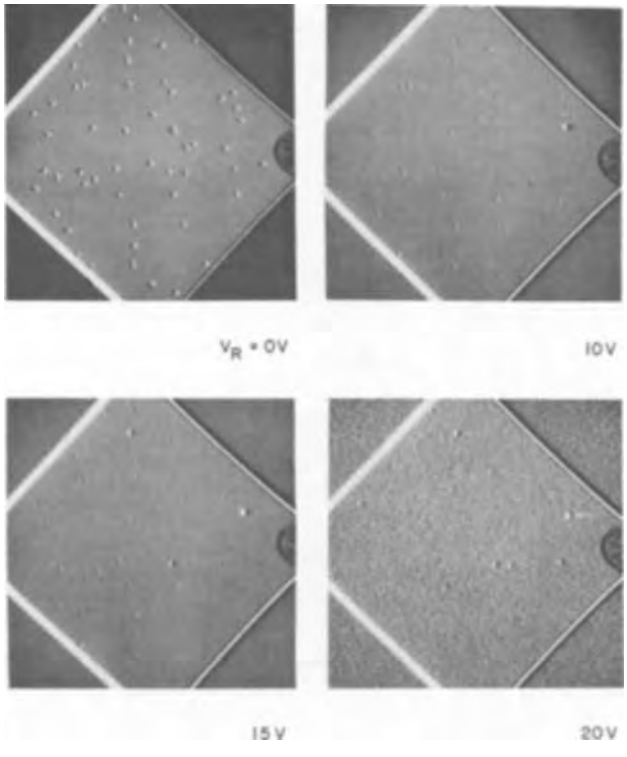

Fig. 3. EBIC displays of a diode with 0V bias and increasing reverse voltages to 20V illustrating the concepts of electrically active faults and the "threshold voltage" of a fault. The *I-V* plot corresponding to this diode is shown at the top of Fig. 4.

ilar structures indicate that a rather poor correlation exists between the total number of stacking faults in a given diode and the magnitude of the reverse leakage current at a given test voltage. Furthermore, it has been observed that a diode containing fewer stacking faults will often exhibit the greater leakage currents at a given voltage. These observations are more easily understood in view of the present results which suggest that the important parameter is more likely to be the number of electrically active faults. However, the "threshold voltage" for each fault within a given diode varies considerably. The diode shown in Fig. 3 contains ~55 faults of which eight are electrically active with "threshold voltage" levels distributed from ~4 to 20V. This series of micrographs suggests that in addition to the number of active faults, the "threshold voltage" for current multiplication effects also represents a significant parameter regarding excess leakage currents.

Test results are illustrated graphically in Fig. 4 which shows the reverse *I-V* characteristics of five diodes. The units were selected to sample the total range of *I-V* characteristics for a single wafer. The dark current limit represents the nominal characteristics of a diode containing no stacking faults, selected at random and represents the lower limit of leakage current for the ambient conditions existing during the measurements. The graph indicates the experimentally determined numerical values corresponding to the "threshold voltage," the number of active faults and the total number of stacking faults for each respective diode.

Note the poor correlation between the total number of stacking faults per diode, indicated at the end of each curve, and the current at a given voltage. For example the diode containing five faults has a reverse current of ≈50 μA at 60V, whereas, the diode containing three faults has a current of ≈200 μA at the same voltage. An even greater discrepancy exists between the two upper curves which are separated by less than an order of magnitude in current but differ by a factor of 18 in the number of faults.

A more convincing trend exists between the number of electrically active faults indicated at the center of

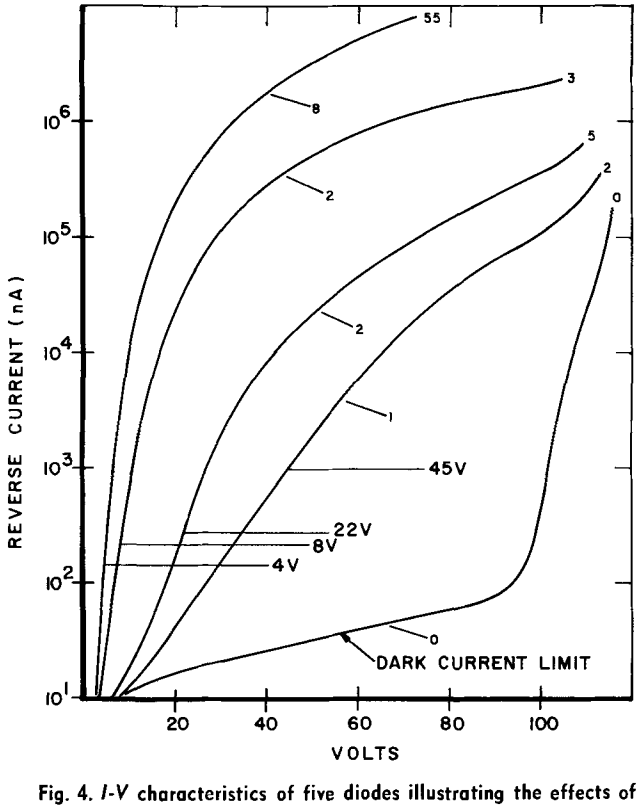

Fig. 4. *I-V* characteristics of five diodes illustrating the effects of electrically active stacking faults on excess reverse bias current. The total number of faults is shown at the ends of the curves and the total number of electrically active faults is indicated at the center. Arrows indicate the minumum threshold voltage for the group of active faults in a given diode.

each curve, but data obtained on a large number of diodes do not support a strong correlation. The values of "threshold voltage" indicated on this graph correspond to the stacking fault having the lowest "threshold voltage" for current multiplication in the electrically active group of each diode. A strong correlation between the "threshold voltage" and the reverse leakage current is indicated. The diodes containing faults of lowest "threshold voltage" display the greatest reverse leakage currents.

In Fig. 5 the reverse biased diode characteristics in decades of current per volt are plotted against the minimum "threshold voltage" V_{th} for a variety of diodes. A linear relationship is obtained with a negative slope which suggests a direct correlation between the "threshold voltage" of individual stacking faults and the excess leakage currents expressed in terms of reverse diode conductance. Moreover, the relationship indicates a current hogging effect which is dominated by the stacking fault having the lowest "threshold voltage," since many individual diodes contain more than one active fault.

Figure 6 shows a sequence of EBIC displays illustrating an electrically active fault as monitored under test conditions in the SEM. At 0V bias the fault exhibits primarily recombination contrast evident by the dark leading edge normal to the beam direction. At 15V a contrast reversal has occurred in a circular zone surrounding the fault which is characteristic of the current enhancement effect. With increased bias, annular contrast zones appear which are not presently understood in detail. A conservative calculation based on the geometry of the enhancement zone and on the current voltage characteristics of a low voltage fault indicates that a power density in excess of $\sim 10^4$ W/cm^2 can be realized locally. This high-power density may account for the particular type of contrast effects observed around the faults when biased.

Stacking fault structure and electrical activity.—In order to further understand the details of the electrical activity of stacking faults the detailed structure of the fault and the nature of the defect-depletion field interaction have to be examined. To illustrate this point, observe the fault displays in Fig. 7. Five distinct faults are shown with 0V bias on their respective diodes. The contrast observed in the EBIC display at 0V bias results from the recombination field of the stacking fault and the surface morphology of the fault particularly when second phase particles are present near the silicon surface. In Fig. 7 well-defined

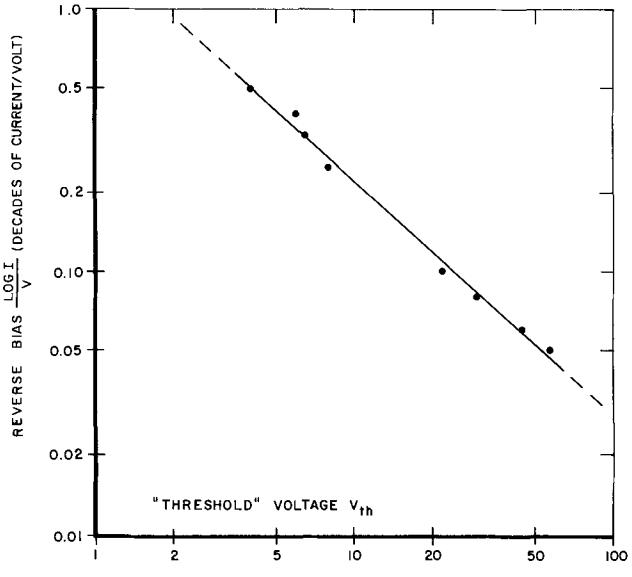

Fig. 5. Reverse biased diode characteristics in decades of current per volt plotted as a function of the minimum threshold voltage for electrically active faults.

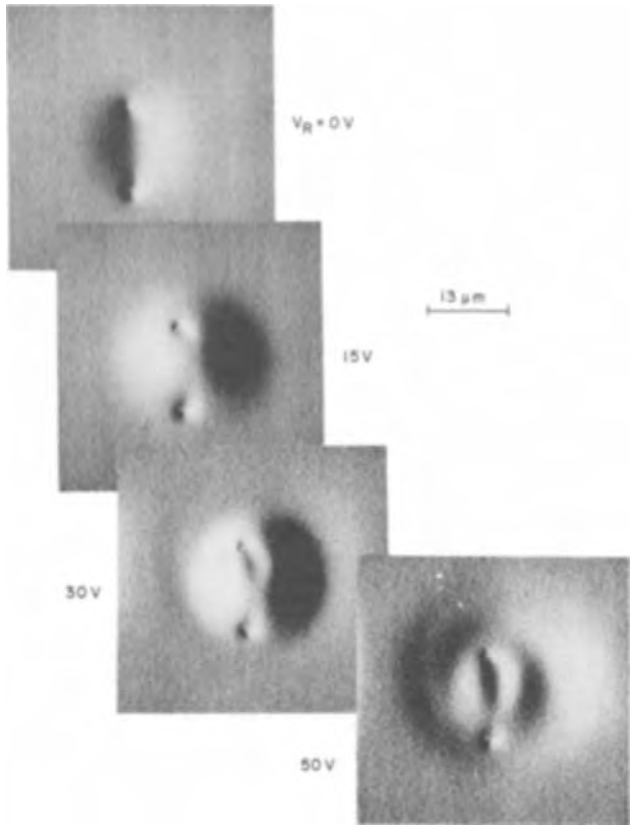

Fig. 6. Sequence of EBIC displays showing electrical activity associated with an active stacking fault.

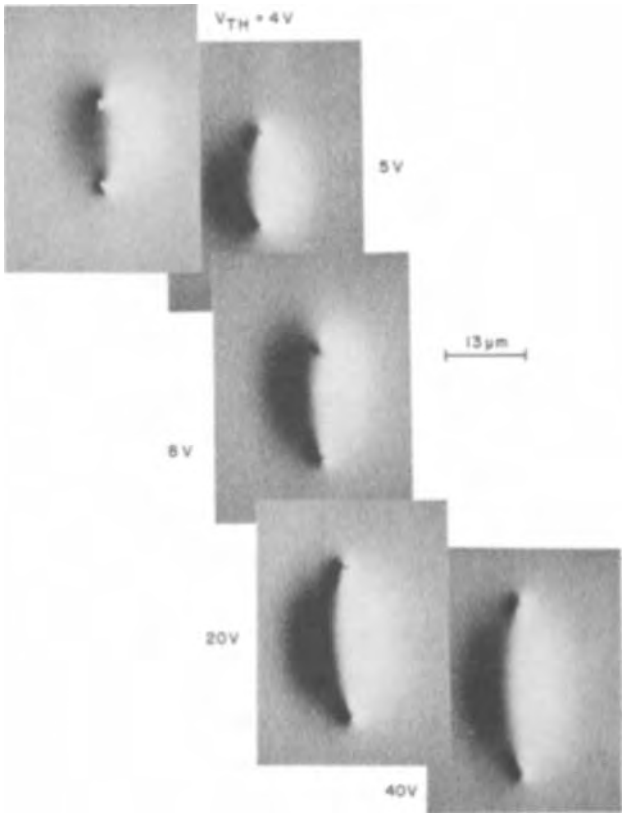

Fig. 7. EBIC displays showing the relation between stacking fault length and associated threshold voltages.

second-phase particles are evident at the ends of the stacking fault where the bounding partial dislocation intersects the silicon surface. The curved contrast ridge between the decorated ends of the partial dis-

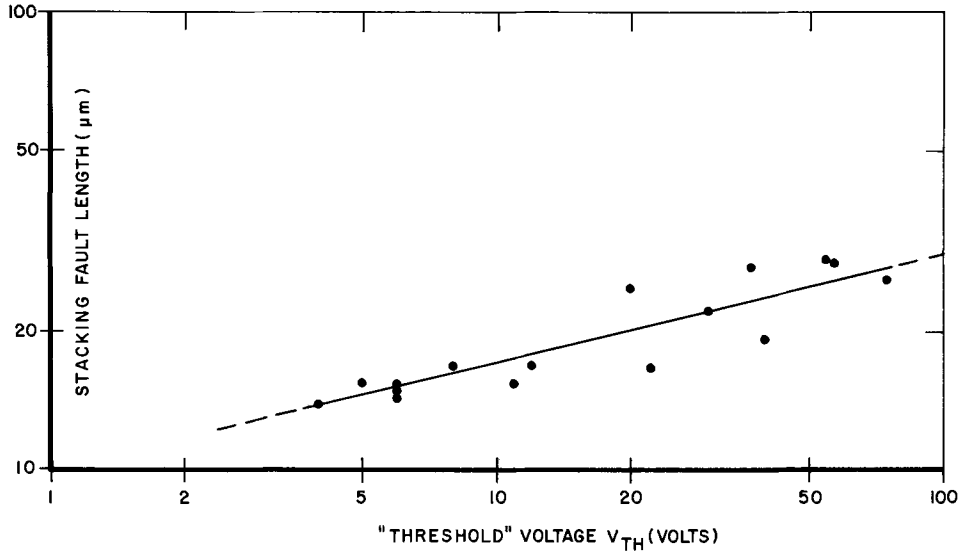

Fig. 8. Plot of threshold voltage as a function of fault length.

location results from the orientation of the stacking fault on a specific (111) type plane. The angle between the fault plane and the surface normal with respect to the beam direction will determine the geometry of the contrast ridge separating the leading and the trailing edge. Note the relationship between the measured value of "threshold voltage" which is indicated adjacent to each display and the linear dimensions of the faults. This observational trend which indicates that a correlation exists between fault length and "threshold voltage," is verified experimentally by the measurements plotted in Fig. 8.

The data cover the range of fault lengths (14 to 28 μm) for electrically active stacking faults in these structures. The "threshold voltage" measurements which correspond to these values range from 4 to 70V respectively. The upper limit of "threshold voltage" ($\sim$70V) represents $\sim$70% of the nominal avalanche voltage for these diodes (see Fig. 4). The extrapolated portion of the graph indicates that electrically inactive faults are represented by stacking faults having a length >30 μm (a "threshold voltage" approaching the avalanche limit of the diode). The lower value of "threshold voltage" ($\sim$4V) is apparently established by the detectability limit of the SEM utilizing the EBIC technique, particularly the signal to noise ratio inherent in the display. The greater data point scatter observed at the higher "threshold voltage" levels results from reduced sensitivity due to the increased noise level of the diode at voltages approaching the avalanche voltages.

Figures 5 and 8 reflect the strong correlation between the stacking fault length and the reverse diode conductance (decade of current per volt ratio). For example a factor of 2 decrease in the stacking fault length will increase the reverse diode conductance by one order of magnitude neglecting the current limiting effects which occur at higher current levels.

The significance of the defect structure on the degree of "electrical activity" for stacking faults in silicon requires a more detailed analysis of stacking fault structure. Figure 9 shows a series of TEM displays of four stacking faults with lengths ranging from $\sim$0.7 to 3.4 μm. The smallest faults (0.7 μm) consist of a partial dislocation loop bounding a faulted zone, both of which are heavily decorated with fine precipitates. The precipitates decorating the faults are thought to be predominantly silicon oxides and boron. Carbon can be eliminated as a likely candidate in view of the slower diffusion rates as compared to oxygen. Metallic impurities were ruled out by bulk phosphorus gettering (14) the diodes containing stacking faults and detecting no change in the excess reverse conductance before and after gettering. These micrographs were obtained following the diffusion of boron to establish the p-n junction. The decoration at the faults increases after the diffusion process. This is most obvious when the small fault in Fig. 9 is compared with the fault in Fig. 1. The fault shown in Fig. 1 shows the structure after oxidation and prior to boron diffusion. This effect of the diffusion on the fault and the resultant effect of the fault on the diffusion front is an important factor in determining the electrical activity of the faults as discussed subsequently. Note also the displacement-fringe contrast surrounding the fault which indicates the presence of local precipitate strain fields. The longer stacking faults are similarly decorated with precipitates; however, the decoration is in the form of well developed second-phase particles at the partial dislocation while the faulted region is generally free of precipitates. The bounding partial dislocation encloses a fault on an inclined (111) plane. The two

Fig. 9. Transmission electron micrographs of stacking faults of different lengths showing the effect of fault length on the degree of decoration of the fault.

longer faults are only partially visible because of the limited film thickness which is less than the fault depth after sample preparation, and consequently only the upper 0.4 μm of the fault is visible. Nevertheless, the common structural characteristic of these faults is the heavy precipitation, particularly at the partial dislocation and the attendant strain field. If one considers the fault structure in relationship to the metallurgical p-n junction of the diode we have the following observations; the upper limit for electrically active stacking faults in these diodes was 28 μm in length. Stacking faults greater than 28 μm in length were electrically inactive below the avalanche voltage. Because the junction depth $X_j \approx 4$ μm, the faults lie well within the depletion field of the p-n junction. Furthermore, the larger faults extend to a depth below the depletion edge at the avalanche voltage, the lower edge of the smaller faults will terminate within the depletion field. Since considerable experimental evidence has shown that the partial dislocation is decorated along its entire length, it seems highly probable that the second phase precipitates and their associated strain fields are interacting directly with the depletion field. However, since the growth and development of the fault is interrelated with the diffusion process itself, the complete physical model must include the mutual effects of both. Consequently hypothetical models are presented which attempt to visualize the mutual interaction which must include diffusion and precipitation processes occurring concurrent with the growth and development of these faults.

Discussion

The presence of decorated stacking faults in silicon has been shown to directly influence the reverse leakage characteristics of p-n junctions. The influence of the faults, however, is not straightforward in that not all faults in the active area of a diode interact with the depletion field of the junction and the degree of electrical activity is dependent on fault length. The concept of the "threshold voltage" of a stacking fault enables the specific electrical activity of a fault to be discussed in quantitative terms.

In order to develop a physical model for electrically active stacking faults it is necessary to consider the specific "threshold voltage" associated with individual faults. Furthermore the variation of "threshold voltage" with fault length also indicates that electrical activity is a function of the detailed structure of the fault. It was shown that the electrical activity of a fault varies with fault length, the smaller faults being more active than the larger faults.

The electrical effects associated with dislocations in the diamond cubic lattice have been dealt with theoretically (15) and experimentally (16) by the measurement of Hall mobilities in deformed crystals. The direct interaction between dislocations and charge carriers introduced in silicon by an electron beam has been reported previously (17). The existence of a one-dimensional energy band along edge and screw dislocations has been postulated to account for the electrical activity of dislocations (15). These models, however have been applied to fresh, undecorated dislocations. An oxidation-induced stacking fault is invariably formed in conjunction with a second phase. It has been observed that diffusion of boron into a surface decorated by these faults results in a further increase in the degree of decoration of the fault. Consequently the currently available theoretical treatments of dislocation-charge carrier interaction cannot be applied to the case of decorated stacking faults since the faulted region, the partial dislocation enclosing it, and the impurity decoration at the fault and at the dislocation introduce their own perturbations in the electronic structure of the otherwise perfect lattice.

The threshold voltage represents the onset of current multiplication at the stacking fault. Calculations on depletion layer width for 4 μm junctions suggest that the base of an active fault lies within ~1 μm of the upper edge of the depletion field at the threshold voltage of the fault (18). The base of the active fault is represented by the region where the Burger's vector of the bounding partial dislocation is approximately parallel to the electric field of the depletion region. This analysis assumes a planar diffusion front whose geometry is independent of the presence of stacking faults. However, since the growth of stacking fault is dependent on the diffusion process, the boron concentration profile in the vicinity of the fault is perhaps modified by the stacking fault structure and impurity decoration. Consequently, a simple analysis which assumes a planar diffusion front with a gaussian or erf distribution cannot be rigorously applied to determine the depletion-field width in the vicinity of the fault. Furthermore, severe contouring of the transition region may result from concentration profile anomalies which introduces geometry correction factors for the electric field in the depletion region. An added consideration is the degree of precipitation associated with stacking faults of different size, and the magnitude of the strain fields surrounding the partial dislocations. Based upon these hypotheses different models are discussed in an attempt to explain the experimental observations.

The schematic sketches in Fig. 10 show the two possible direct interactions of a stacking fault with the p-n junction. Since the junction is formed by the diffusion of boron into a surface covered with decorated stacking faults local contouring of the junction beneath the stacking fault can occur as shown in Fig. 10-1. The presence of precipitation at the fault (possibly SiO_2 precipitates) can retard the diffusion front by directly blocking the boron atoms, perhaps enhanced by the greater solubility of boron in the oxide precipitates. The accumulation of boron at the fault is also possible as a result of the differences in solubility of boron in the faulted and unfaulted regions of the crystal, *i.e.*, the Suzuki effect (19), although this is probably a secondary effect. The curvature introduced in the junctions can result in excessive reverse leakage currents (20).

In the event that the fault does not function as a block to the diffusion front, leakage can also be introduced in the junction due to the strain fields associated with faults as shown in Fig. 10-2. Elastic strains have

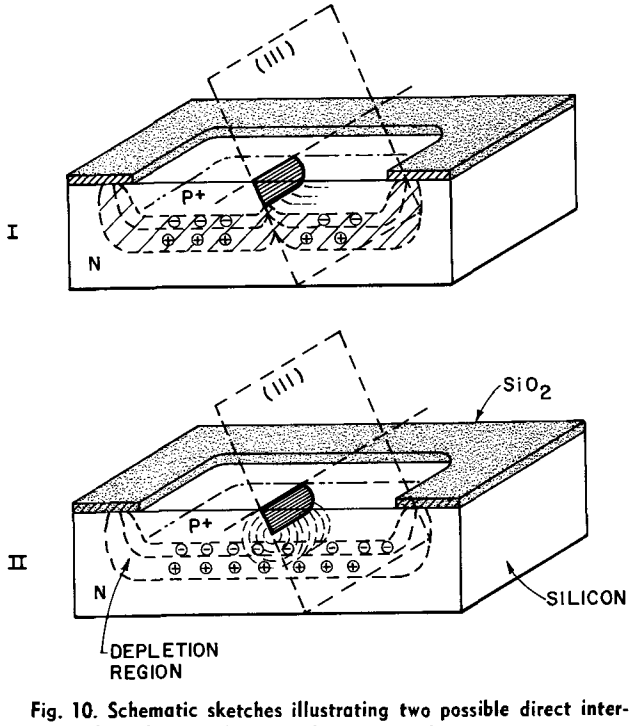

Fig. 10. Schematic sketches illustrating two possible direct interactions of stacking faults with the p-n junction.

been demonstrated to generate leakage currents in p-n junctions (21). The precipitation at the fault results in strong elastic strain fields in the lattice owing to the different specific volume of the precipitating phase (SiO_2) as compared to that of silicon. These strains can extend to considerable depths into the bulk of the material and interact with the depletion field of the junction.

A striking result of this study was the observation that the electrical activity of a fault was related to the fault length in an unexpected manner in that the smaller faults introduced greater leakage currents than the larger faults. The two models discussed above can be shown to account for this fact.

Figure 11 shows schematically the geometry of a diffused p-n junction beneath a stacking fault which is decorated both at the partial dislocation and within the fault. The physical p-n junction is curved all the way along the fault owing to the diffusion retarding effect of the decorated fault. The resulting structure of the fault is shown in the transmission electron micrograph in Fig. 11. The partial dislocation and the fault are observed to be decorated by a second phase. Such faults are typically small and extend to depths no greater than ~1 μm into the bulk. As discussed before they have also been observed to exhibit low "threshold voltages." Figure 12 shows schematically

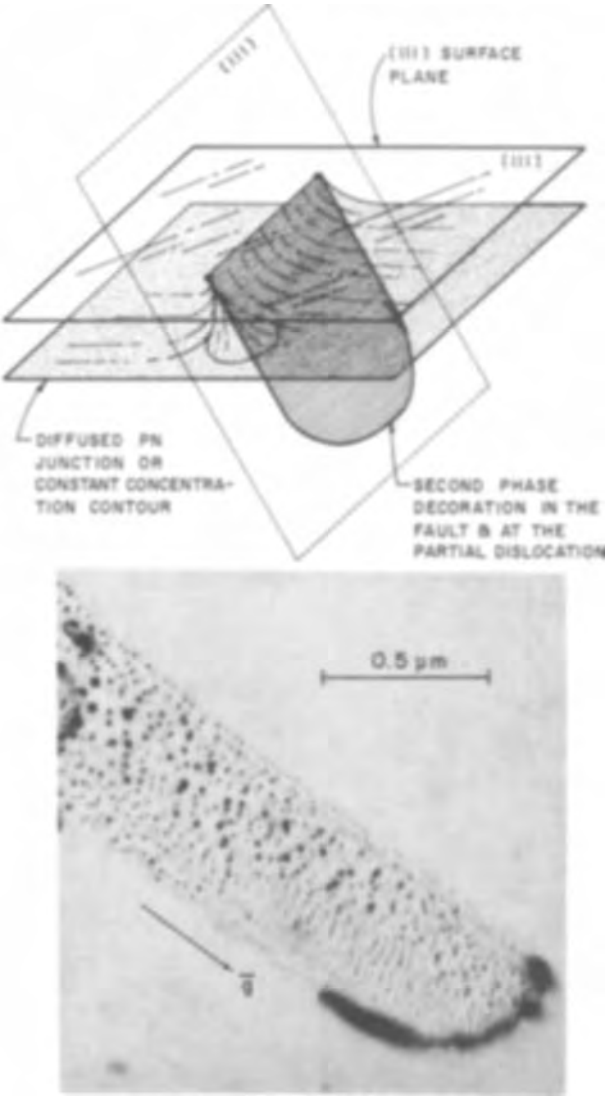

Fig. 11. Schematic of the contouring effect a decorated stacking fault has upon a p-n junction diffused into the faulted region. The TEM display shows a typical fault which is characterized by impurity decoration both at the bounding partial and within the fault.

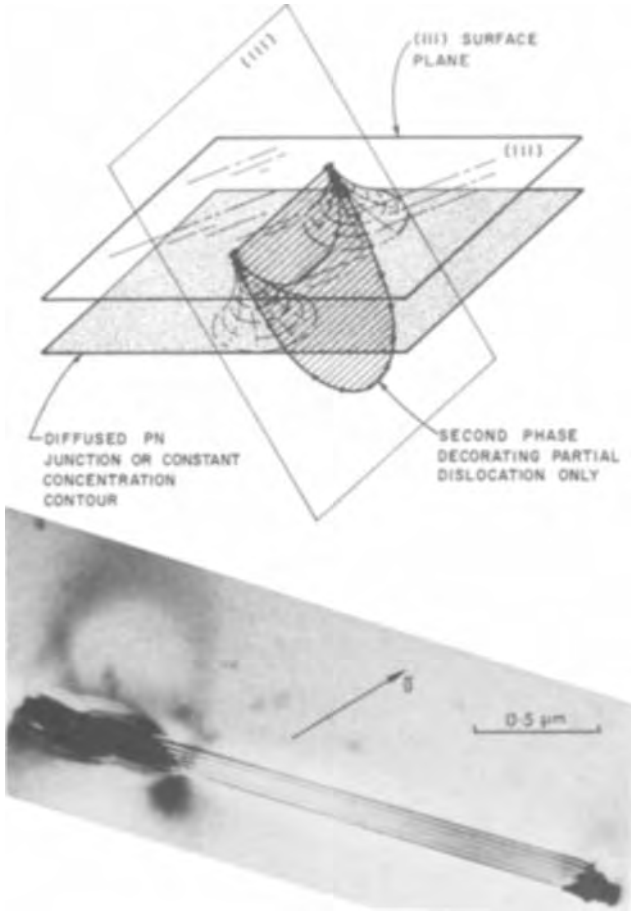

Fig. 12. Schematic of the contouring effect due to a fault which is decorated only at the bounding partial. The TEM display shows a typical fault of this kind.

the contouring effects of large faults where the second-phase decoration is primarily at the partial dislocations and not within the fault. The diffusion front is retarded only along the terminations of the fault and not within the faulted region. The transmission micrograph shows a large fault as observed after boron diffusion. The micrograph only shows a portion of the fault which can extend to considerable depths into the bulk. The terminations of the partial dislocation at the surface are profusely decorated whereas the fault is clean. The contouring introduced in the junction by such a fault is less severe than that due to small faults and hence the degree of leakage as a result of such faults is also less.

It must be emphasized that the process of diffusing impurities past a faulted region into the bulk results both in the modification of the diffused junction by the fault and a modification of the fault by the diffusing atoms. It has been shown elsewhere (22) that the diffusion process forces fault growth. Therefore the smaller stacking faults are more frequently found in diodes with shallow p-n junctions whereas deep junctions with their attendant long diffusion cycles force fault growth. Since the fault size and the distribution of segregated impurity in the fault are interrelated, the electrical activity is obviously related to both these factors. Furthermore, the position of the decorated fault in the depletion region of the p-n junction will also be related to the size and degree of decoration of the fault since the physical distortion introduced in the junctions will be a function of the fault size and associated impurity precipitation.

Fault growth can proceed by a combination of impurity precipitation and the diffusion of substitutionally diffusing atoms (boron) from within the fault into the surrounding silicon. Consequently large stack-

ing faults which have attained their final size as a result of the boron diffusing out of the faulted region are also prone to be less subject to decoration than the smaller faults which still have a large part of the accumulated boron decorating them. Consequently the electrical activity of smaller faults would be greater than large faults. The present study has been confined to the examination of the electrical activity of stacking faults on relatively deep p-n junctions (~4 μm). The effects of faults on shallow junctions (<1 μm) will be discussed in a subsequent publication.

Acknowledgments

The authors would like to acknowledge the invaluable technical assistance of E. Reed, D. Lopeman, and M. Jenkins. The excellent artwork was prepared by J. R. Preece. All of the above are associated with the Semiconductor Products Division of Motorola Incorporated.

Manuscript submitted Aug. 7, 1972; revised manuscript received Nov. 9, 1972. This was Paper 62 presented at the Houston, Texas, Meeting of the Society, May 7-11, 1972.

Any discussion of this paper will appear in a Discussion Section to be published in the December 1973 JOURNAL.

APPENDIX

The electron beam induced current (EBIC) mode (23-25) is illustrated schematically in Fig. A-1. A focused electron beam is scanned in a square raster pattern on the surface of diffused p-n diode. Directly under the focused electron spot (typically 0.01-0.10 μm in diameter) electron-hole pairs are generated within a volume defined by the practical range of the electrons in silicon at the particular beam energy. In the range of 5-50 keV which is typical for an SEM, the penetration range for electrons in silicon is approximately 0.4-17 μm. The number of charge carriers generated within this volume is proportional to the number of penetrating electrons and their energy dissipation. When the diffusion length of the induced carriers is greater than the distance from the point of generation to the underlying p-n junction a fraction of the total number of charge carriers will be swept across the space charge region of the p-n junction. The sampling resistor and voltage source shown in Fig. A-1 are connected in series with the p-n diode. The operational amplifier which is connected across the sampling resistor in a d-c mode provides the necessary gain to modulate the brightness of a display CRT scanned in synchronism with the electron beam. When the diode structure contains relatively perfect crystalline material the beam-generated charge carriers produce a steady-state d-c current which results in a scan raster of uniform intensity.

However, when the semiconductor crystal contains localized surface and bulk imperfections such as dislocations, precipitates, or stacking faults within or near the diffused p-n junction, localized charge-carrier

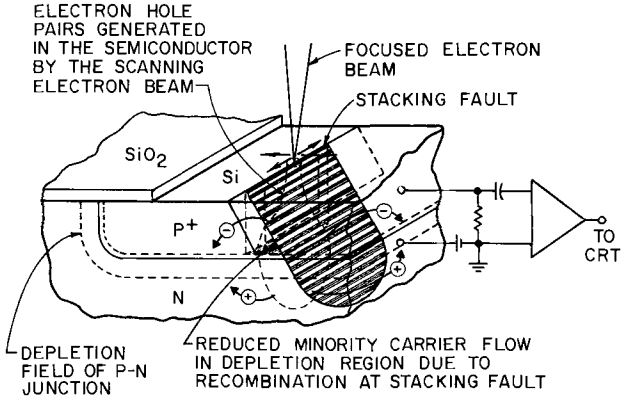

Fig. A-1. Schematic of the electron beam induced (EBIC) mode of operation.

recombination occurs. This reduces the number of charge carriers in the vicinity of the defect thereby reducing the net flow of charge carriers at the space-charge region. In this manner, the recombination processes associated with the defects modulate the charge-carrier flow, at the space-charge region revealing the structural imperfections of the diode in the video display.

With a reverse bias applied to the diode the electrical interaction between the defect and the depletion field can be investigated. The mechanism is attributed to charge carrier multiplication which increases the net flow of charge carriers in the depletion region. This effect produces a local current enhancement signal at the defect site which is dependent on the magnitude of the depletion field voltage and the degree of electrical activity of the particular defect. As a result of this interaction, electrically active defects are easily distinguished from electrically inactive sites, enabling a direct correlation between specific *I-V* characteristics and the associated defect centers.

The optimum electron beam energy depends on several considerations which involve the practical range of the electrons in the sample and the zone of maximum energy dissipation. These factors depend primarily on the density and thickness of the composite structure (*i.e.*, oxide layer and silicon). Additional considerations are the depth and distribution of the crystal defects with respect to the space charge region of the p-n junction and the minority carrier diffusion length near the point of generation of the beam-induced carriers.

When the depth of the defect is small compared to the metallurgical junction depth, low beam voltages are desirable for optimum resolution of the defects providing sufficient beam current is available to overcome the signal to noise limitations of the video amplifier including the sample. High-contrast displays often require a compromise of spacial resolution when increased beam current or voltage is required to improve the signal to noise ratio of the display. Practical considerations often involve the magnitude of leakage currents in diode structures containing defects. The leakage currents associated with the defects introduce current-voltage instabilities in a biased p-n diode resulting in scan rate dependent video noise. This requires a reduction of the video bandwidth by capacitive coupling or other means necessitating larger beam currents and voltages to increase the signal level at the sample.

In a typical EBIC display the reference voltage or ground for the video circuit is selected to obtain the desired signal polarity on the CRT when the beam crosses the vertical edge of the p-n junction. To avoid ambiguity in the interpretation of contrast the diode terminals are selected to provide an increased screen brightness when the p-n junction currents increase during the scan. Consequently, in the d-c coupled mode, the brighter areas of the display correspond to larger beam-induced currents at the p-n junction. In the capacitor-coupled EBIC display the bright and dark contrast levels correspond to the transient currents generated at regions where the junction currents change abruptly. The video circuit time constant is chosen to provide a display which approximates a time derivative of the d-c coupled display as illustrated in Fig. A-2.

The diodes used in this investigation have a p-n junction depth $X_j \approx 4.0$ μm. The stacking faults were typically 14-28 μm in length at the surface with a hemispherical boundary consisting of a partial dislocation enclosing the fault on the {111} planes. The depth of the fault measured normal to the surface is ~12 μm. For optimum interaction between the partial dislocation at the base of the faulted zone a beam energy of 40 keV was utilized. The electron penetration at this energy is ~12 μm. This energy was selected to insure that electron-hole pairs are generated near the base of the stacking fault. Since the depth of the stacking fault is greater than the metallurgical junction depth $X_j \simeq 4$ μm, a back diffusion of charge carriers is required to display the electrical interaction between the stacking fault and mobile charge carriers prior to their collection at the space charge region.

The capacitance coupled display was used exclusively to eliminate the d-c current instabilities of the reverse biased diode. A sampling resistor of 10^3 ohm

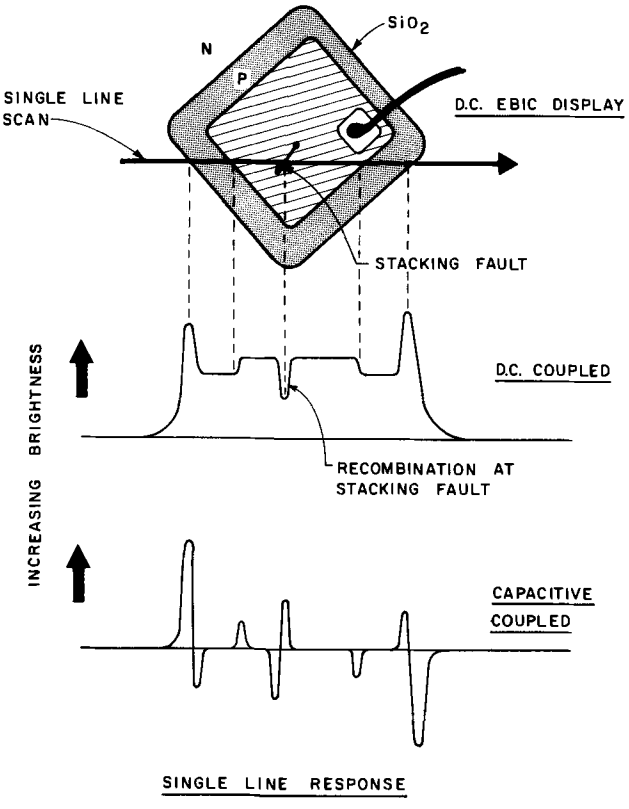

Fig. A-2. Schematic showing single line response of the EBIC display when used in the d-c and the capacitive coupled modes.

with a coupling capacitor of 0.02-0.05 μf provided adequate contrast at a nominal scan rate of 10 msec/line, with a beam current of $\simeq$ 1 nA at 40 keV.

REFERENCES

1. G. R. Booker and R. Stickler, *J. Appl. Phys.*, **33**, 3281 (1962).
2. M. L. Joshi, *This Journal*, **112**, 912 (1965).
3. E. Levine, J. Washburn, and G. Thomas, *J. Appl. Phys.*, **38**, 81 (1967).
4. A. W. Fisher and J. A. Amick, *This Journal*, **113**, 1054 (1966).
5. R. J. Jaccodine, *J. Appl. Phys.*, **39**, 3105 (1968).
6. G. H. Schwuttke, *Microelectronics & Relib.*, **9**, 397 (1970).
7. G. H. Schwuttke, K. Brack, and E. W. Hearn, *ibid.*, **10**, 467 (1971).
8. G. H. Plantinga, *IEEE Trans. Electron Devices*, **ED-16**, 394 (1969).
9. H. J. Queisser, *IRE Trans. Electron Devices*, **ED-8**, 429 (1961).
10. J. E. Lawrence, *This Journal*, **155**, 860 (1968).
11. D. Bialas and J. Hesse, *J. Mater. Sci.*, **4**, 779 (1969).
12. M. L. Joshi, *Acta Met.*, **14**, 1157 (1966).
13. G. R. Booker and W. J. Tunstall, *Phil. Mag.*, **13**, 71 (1966).
14. J. E. Lawrence, *Trans. AIME*, **242**, 484 (1968).
15. W. T. Read, *Phil. Mag.*, **45**, 775 (1954).
16. P. Haasen and W. Schroter, "Fundamental Aspects of Dislocation Theory," NBS Special Publication 317, Vol. 2, 1231 (1970).
17. J. J. Lander, T. M. Buck, H. Schreiber, Jr., and J. R. Mathews, *Appl. Phys. Letters*, **3**, 203 (1963).
18. C. J. Varker and K. V. Ravi, To be published.
19. H. Suzuki, *Sci. Rept. Res. Inst. Tohoku Univ.*, **A4**, 452 (1952).
20. S. M. Sze and G. Gibbons, *Solid-State Electron.*, **9**, 831 (1966).
21. W. Rinder, *J. Appl. Phys.*, **33**, 2479 (1962).
22. K. V. Ravi, *Met. Trans.*, In press.
23. J. J. Lander, H. Schreiber, and T. M. Buck, *Appl. Phys. Letters*, **3**, 206 (1963).
24. W. Czaja and J. R. Patel, *J. Appl. Phys.*, **36**, 1476 (1965).
25. C. J. Varker, T. E. Everhart, and A. J. Gonzales, Second International Conference on Ion Beam Science and Technology, April (1966) New York.

Submicron Epitaxial Films for GaAs Field Effect Transistors

R. D. Fairman*,[1] and R. Solomon*

Fairchild Research and Development Laboratory, Palo Alto, California 94306

ABSTRACT

Uniform submicron epitaxial films have been prepared by an optimized version of the $AsCl_3$, Ga, H_2 process. Film requirements and properties of films necessary for high performance GaAs FET's are discussed. Growth rate dependences of the Ga source and substrate temperature are shown. Growth rate dependence upon the $AsCl_3$ mole fraction and mass transport effects are shown in the range of interest. Effects of the thermal gradient imposed during deposition are related to the film thickness and doping uniformity obtained with a 5°C/cm and 0.5°/cm process. Vapor doping from H_2S and Sn-doped Ga sources is discussed and related to the character of the epitaxial doping profile. Epitaxial films grown by this technique have been produced in the range of 0.2-0.4μ with variations in film thickness and doping of $< \pm 10\%$.

In recent years, GaAs Schottky-barrier field-effect transistors have attracted much interest as an active device with usable gain at microwave frequencies.

Recently, our device research group has developed a device with a cutoff frequency >30 GHz and a unilateral gain of 10 dB at 10 GHz (1). These devices have a theoretical frequency-gain slope of 6 dB/octave and a very low noise figure.

The GaAs Schottky-barrier FET is a transit-time-limited device which operates in the depletion mode. The voltage required to pinch off conductance in the channel is given by the following expression

$$V_p = V_o + \frac{q}{2\epsilon}(N_D t^2) \qquad [1]$$

where V_o is the built-in voltage, N_D the donor concentration, and t the film thickness. Figure 1 shows the relationship between donor concentration and film

* Electrochemical Society Active Member.
[1] Present address: Varian Associates, Palo Alto, California 94303.

Key words: gallium arsenide epitaxy, thin-film growth.

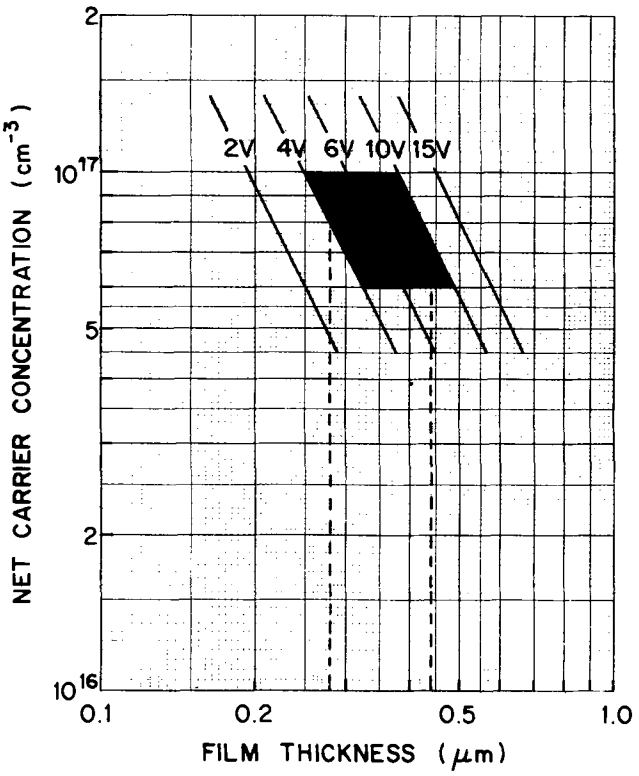

Fig. 1. Epitaxial film doping, film thickness relationship with pinch-off voltage, V_p, as a parameter.

thickness with the pinch-off voltage as a parameter. A desirable range of pinch-off voltages for an amplifier operating at 10 GHz lies between 4 and 10V. The useful range of donor concentrations in 6-10 $\times$ 10^{16} cm^{-3}. The upper end of this range is delimited by the gate breakdown voltage, whereas the lower end is constrained by backside gating from the semi-insulating substrate. Useful donor concentration and thickness combinations are shown in the cross-hatched trapezoidal region in Fig. 1. Film thicknesses lying between the dotted lines, *i.e.*, in the range from 0.28 to 0.44μ, have approximately an 85% probability of meeting the pinch-off voltage specification. In practice, we can extend the upper limit somewhat since thicker films can be etched into the useful range.

Experimental

The basic epitaxial process used to grow films for the GaAs FET is the $AsCl_3$, Ga, H_2 system (2). The $AsCl_3$ process has produced the highest purity vapor epitaxial GaAs to date (3). The principal reactions in the process are as follows

1. $4AsCl_3 + 6H_2 \rightarrow As_4 + 12HCl$ (400°-500°C)
2. $12HCl + 12GaAs \rightleftarrows 12GaCl + 3As_4 + 6H_2$ (800°C)
3. $6GaCl + As_4 \rightleftarrows 4GaAs + 2GaCl_3$

$AsCl_3$ is reduced to $As_{4(g)}$ and $HCl_{(g)}$ in the presence of H_2 at 400°-500°C. Both $As_{4(g)}$ and $HCl_{(g)}$ are transported over a Ga source held at 800°C until the source is saturated with As; following saturation a GaAs skin grows covering the As-saturated Ga source (4). Subsequent HCl passed over the saturated Ga source reacts with the GaAs skin as shown in Reaction 2 above. Thermodynamic calculations of the $AsCl_3$, Ga, H_2 system indicate that for source temperatures of 800°C and deposition temperatures of 750°C the deposition reaction is simply the reverse of Reaction 2. The contribution to deposition from the disproportionation Reaction 3 is negligible for the HCl concentrations involved in the present $AsCl_3$ process (5).

The experimental process parameters are as follows: gallium source temperature, 800°C; GaAs substrate temperature, 760°C; hydrogen flow rate, 200 cc/min; reactor tube diameter, 40 mm; $AsCl_3$ mole fraction, 1.0 $\times$ 10^{-2}.

The background doping of the process is controlled by the $AsCl_3$ mole fraction used (6). The residual background impurity is Si arising from a series of reactions between HCl, H_2, and Ga with the quartz reactor equipment (7). With an $AsCl_3$ mole fraction of 1 $\times$ 10^{-2} a net background doping of $\sim$1 $\times$ 10^{14} carriers cm^{-3} is experienced. The present work will deal with the optimization of the growth variables which affect growth rate and epitaxial film uniformity for films grown on (100) Cr-doped GaAs.

In order to achieve thickness control in the range from 0.25 to 0.5μ, it is desirable to operate at low growth rates so that reasonable deposition times can be used. The growth rate dependence on the Ga source temperature is shown in Fig. 2 for Ga source temperatures in the range from 770° to 810°C. The substrate temperature for these experiments was held constant at 760°C and the wafer was positioned in a thermal gradient of 5°C/cm. The $AsCl_3$ mole fraction was maintained at 10^{-2}. At this value the background donor concentration is several orders of magnitude lower than the final donor concentration. The growth rate is a rather steep exponential function of source temperature in the range measured. The dependence is similar to that obtained by Araki *et al.* (8) in the same range.

The growth rate dependence on the substrate deposition temperature is shown in Fig. 3 for substrate temperatures over the range of 760°-790°C. The Ga source temperature was held constant at 800°C, and the wafer was positioned in a thermal gradient of 5°C/cm.

The initial indication was that a substantial growth rate reduction could be made by a reduction of the Ga source temperature and by use of higher substrate temperatures. However, a vapor etch rate reduction occurs for substrate temperatures <800°C. Therefore a minimum source temperature of 800°C is maintained. Vapor etching of the substrate prior to thin film growth is required to eliminate interface states, traps, residual surface impurities, and to remove a thin surface film of

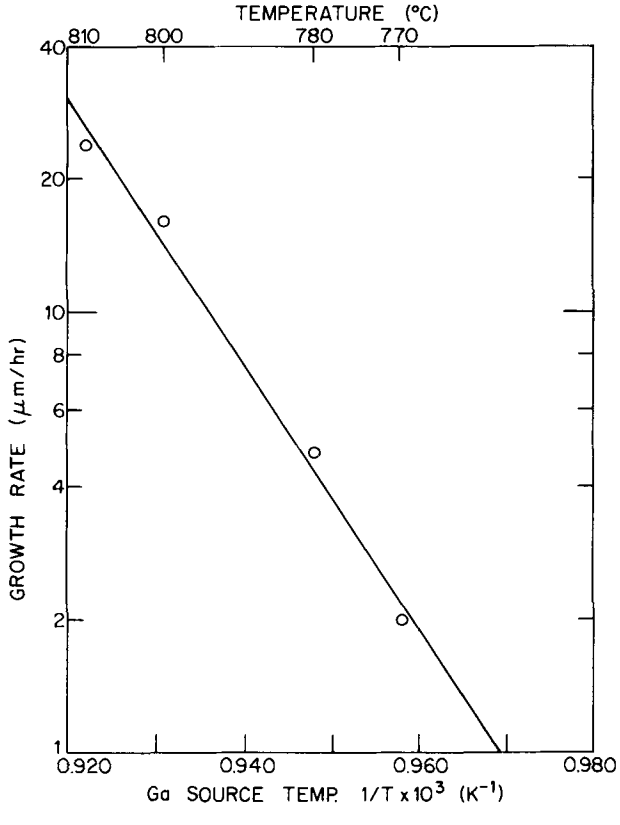

Fig. 2. Growth rate dependence of the Ga source temperature

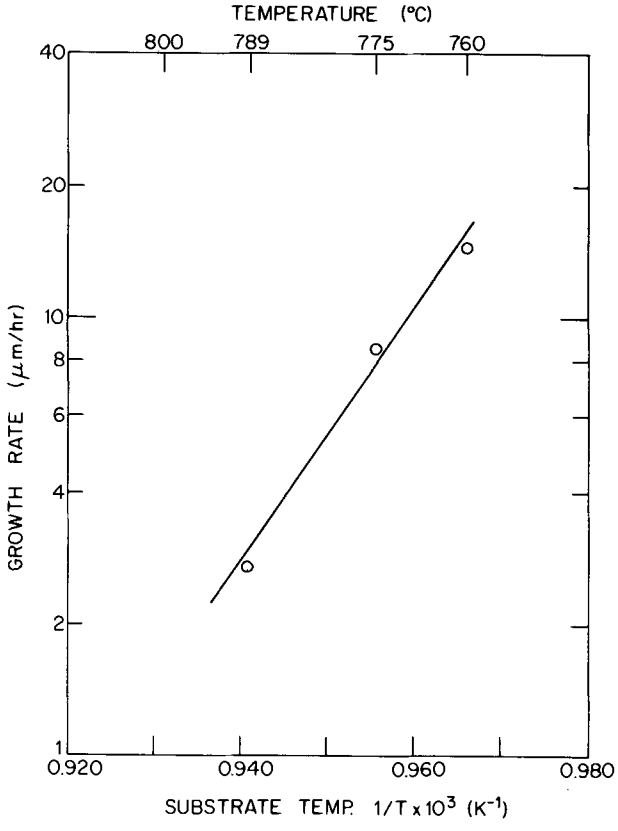

Fig. 3. Growth rate dependence of the GaAs substrate temperature

partially decomposed GaAs generated by As loss at 800°C. Thus, low growth rates are most easily achieved by increasing the substrate temperature. In the present work, a substrate temperature of 760°C was used, yielding an average growth rate of 0.1 μ/min.

For substrates held parallel to the gas flow direction an epitaxial film thickness gradient is observed in the direction of gas flow. This gradient is related to the ΔT imposed along the length of the substrate. Figure 4 shows the epitaxial film thickness gradient evaluated by Schottky-barrier profiling along the length of a wafer for a 5°C/cm and a 0.5°C/cm thermal gradient. The epitaxial thickness gradient produced by the 5°C/cm thermal gradient would reduce an FET device yield to ~15%, whereas the 0.5°C/cm gradient would allow a yield closer to 90%. The shallow thermal gradient also reduces the growth rate by a factor of 3 which greatly improves the growth rate reproducibility. The growth rate dependence on the $AsCl_3$ mole fraction is shown in Fig. 5. Changes made in the $AsCl_3$ mole fraction over the range of 6-9 $\times$ 10^{-3} mf makes a change in the growth rate of <10%. The growth rate dependence on the flow rate, with fixed $AsCl_3$ mf, is shown in Fig. 6. The independence of the growth rate on the

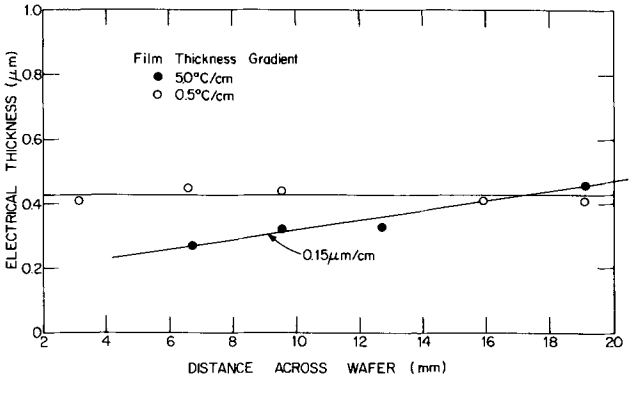

Fig. 4. Epitaxial film thickness gradient across the wafer as produced by two different deposition temperature gradients.

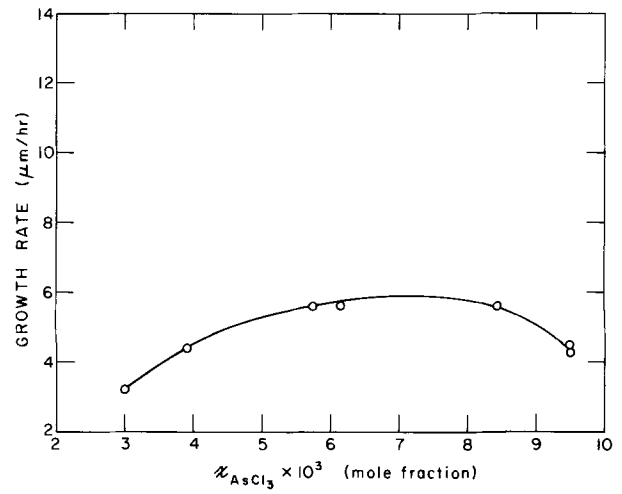

Fig. 5. Growth rate dependence upon the $AsCl_3$ mole fraction

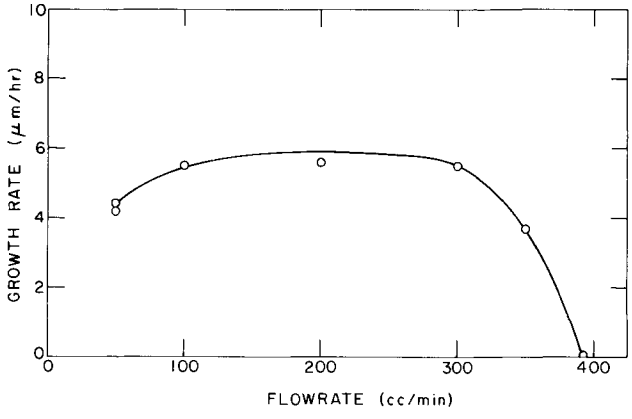

Fig. 6. Growth rate dependence upon mass transport with constant $AsCl_3$ mole fraction.

flow rate in the region of operation suggests that the process is not mass transport limited in this region. The decrease in growth rate with flow rates greater than 300 cc/min is related to the completion of the Ga source reaction.

Table I summarizes the results of a series of depositions performed with a 0.5°C/cm gradient, indicating the epitaxial film uniformity of both doping and thickness for two different dopants. The film thickness uniformity across a wafer and the corresponding pinch-off voltage uniformity are summarized in columns 3 and 4. The average doping variations are less than ±10% and the reproducibility is excellent. The yield on these films shows a combined 70% yield on both film doping and thickness.

The Sn vapor doping was accomplished by the use of a Sn-doped Ga source (9) and the S doping was achieved by metering H_2S into the reactor between the Ga source and the deposition region (7).

The epitaxial doping profile is another important factor in successful device processing. The film doping at the interface should drop an order of magnitude in approximately 0.1μ from the plateau of uniform doping as shown in Fig. 7. The doping profile for the Sn-doped case shows an extremely abrupt change in doping at the interface and a very uniform layer doping. In general, S-doped layers show a more graded profile as compared to the Sn-doped films. Both Czochralski-

Table I. Epitaxial film uniformity for H_2S and Sn dopants

Run series	Avg $N_D - N_A$ (cm^{-3})	$t_{elect.}$ (μm)	V_P (V)	Dopant
29-6 thru 15 (10)	$6.9 \times 10^{16} \pm 11.2\%$	$0.39 \pm 6.5\%$	5.2 ± 0.7	H_2S
31-4 thru 12 (8)	$8.2 \times 10^{16} \pm 7.3\%$	$0.36 \pm 8.7\%$	6.5 ± 0.8	Sn

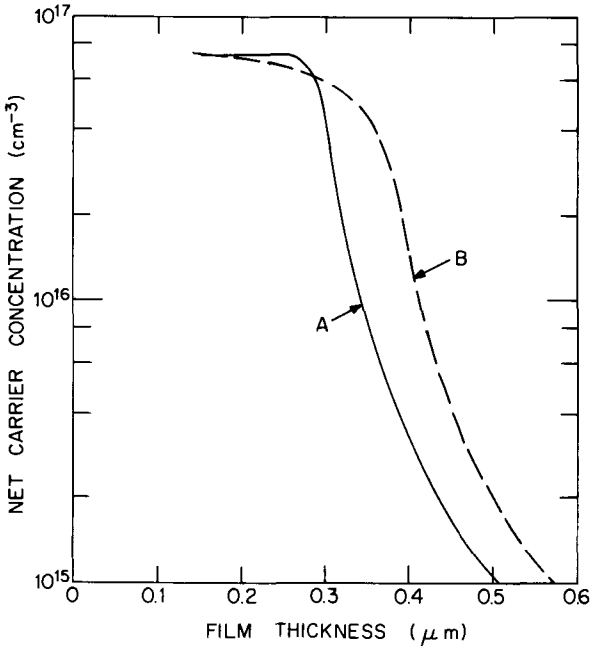

Fig. 7. Epitaxial doping profile for Sn-doped (A) and S-doped (B) (100) GaAs as deposited on Cr-doped semi-insulating substrates.

and boat-grown crystals have been used successfully. Figure 8 shows how the character of the substrate influences the shape of the doping profile. The sharp peaked profile (B) has been observed in selected lots of both Czochralski- and boat-grown substrates. Anomalous tails (A) are only observed for certain lots of Czochralski substrates. The epitaxial process variables have been monitored by alternating substrates from different lots and the doping profile anomalies have borne a 100% correlation with specific crystal lots rather than an uncontrolled process variable. We have not been able to determine which substrate defects are responsible for the graded profiles.

Figure 9 shows an example of the extremely thin film growth that is possible with this process, showing an electrical thickness of less than 0.1μ. The built-in surface barrier prevents us from profiling the flat portion of the profile. However, the mobility of this film is only about 10% lower than the average mobility

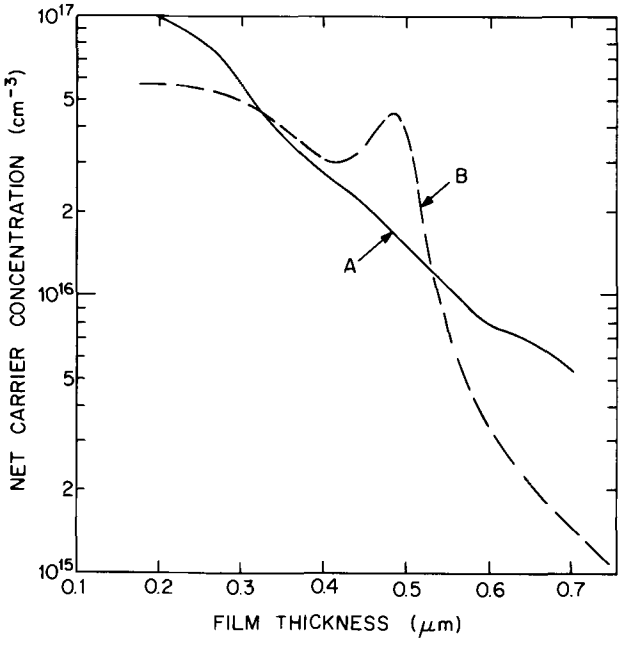

Fig. 8. Epitaxial doping profile characteristics of films grown on inferior substrates.

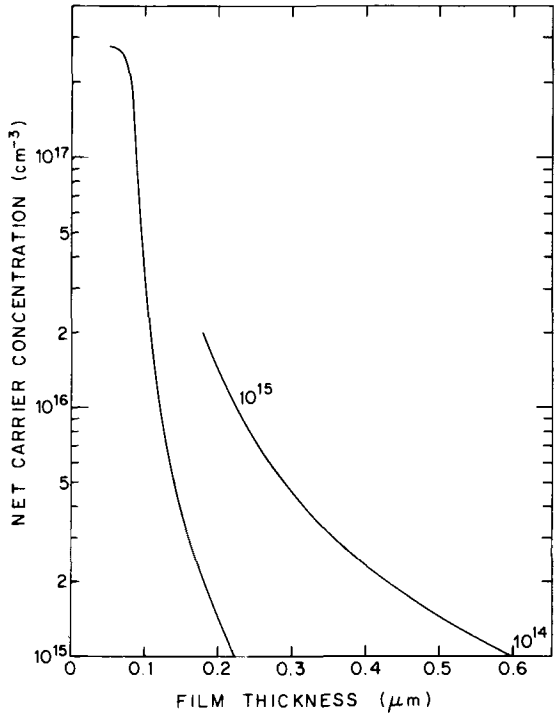

Fig. 9. Epitaxial doping profile of extremely thin film growth showing the capability of the vapor phase process.

for thick films which suggests that doping uniformity is still fairly good.

Hall mobilities of 4500 cm^2/V-sec have been measured on thin films at room temperature, and doping with either Sn or S to 1×10^{17} cm^{-3}. Thus reasonably high mobilities suitable for FET fabrication with high cut-off frequencies can be obtained with carrier densities as great as 10^{17} cm^{-3}.

In summary, it has been shown that careful control over substrate and source temperatures, temperature gradient, flow rate, and $AsCl_3$ mole fraction, can yield uniform films down to 1000Å. Devices fabricated from these films have exhibited cutoff frequencies of around 40 GHz with a noise figure of 2 dB at 3 GHz.

Acknowledgments

Appreciation is expressed to D. Tringali for his assistance in the experimental work.

This work was supported in part by the Air Force Avionics Laboratory, Wright-Patterson Air Force Base, Ohio, under contract F33615-60-C-1580.

Manuscript submitted March 21, 1972; revised manuscript received Oct. 27, 1972. This was Paper 193RNP presented at the Cleveland, Ohio, Meeting of the Society, Oct. 3-7, 1971.

Any discussion of this paper will appear in a Discussion Section to be published in the December 1973 JOURNAL.

REFERENCES

1. W. W. Hooper, R. D. Fairman, and N. G. Bechtel, "GaAs FET Technology and Performance," presented at the International Electron Device Meeting, Washington, D. C., October 11, 1971.
2. J. R. Knight, D. Effer, and P. R. Evans, *Solid-State Electron.*, **8**, 178 (1965).
3. C. M. Wolfe and G. E. Stillman in "Gallium Arsenide and Related Compounds," IPPS Conf. Series No. 9, London, p. 3 (1970).
4. D. W. Shaw, *J. Crystal Growth*, **8**, 117 (1971).
5. B. R. Cairns, Private communication.
6. B. R. Cairns and R. D. Fairman, *This Journal*, **115**, 327C (1968).
7. J. V. DiLorenzo, G. E. Moore, Jr., and A. E. Macbala, *ibid.*, **118**, 1823 (1971).
8. H. Araki, G. Iwane, and T. Aoki, *Rev. Electrical Commun. Lab.*, **18**, 608 (1970).
9. C. M. Wolfe, G. E. Stillman, and W. T. Linley, in "Symposium on Gallium Arsenide," IPPS Conf. Series No. 7, London, p. 43 (1968).

Iron Oxide See-Through Photomasks

Miles V. Sullivan

Bell Telephone Laboratories, Incorporated, Murray Hill, New Jersey 07974

ABSTRACT

The decomposition of $Fe(CO)_5$ in an oxidizing atmosphere was employed to obtain a film of Fe_2O_3 2600Å thick on a glass substrate. Using standard photoresist technology with dilute HCl as the etchant, see-through photomasks with 1 μm patterned elements were obtained.

Photoresist processing often involves the positioning of a photomask over a partially completed device in such a manner that the mask is aligned with certain features of the device. This alignment is greatly facilitated by a see-through mask: that is, a mask which is capable of transmitting visible light to aid in the alignment process and also of blocking the actinic radiation (predominantly uv) necessary for photoresist work.

The semiconductor industry is becoming more interested in a good see-through mask because:

1. The trend toward smaller geometries has made alignment more critical, and the see-through characteristic allows direct observation of the most critical elements of a device pattern rather than depending on remote registration marks.
2. The trend toward the use of positive resists has resulted in an increased number of masks which are mostly opaque and, therefore, more difficult to align with standard techniques. Recent developments in projection photolithography have accelerated this trend.
3. The masking is due to absorption of the unwanted light rather than reflection (as in Cr masks) of the unwanted light and consequently minimizes halation effects and enhances contrast to reflecting substrates.
4. The trend toward larger scale integration and smaller features puts a high premium on low defect density, and defects such as pinholes are reduced considerably by the use of the new see-through materials.

Early attempts to design such a mask made use of sputtering to form a thin inorganic oxide film on a glass substrate (1). In this phase of the work it was determined that a desirable combination of optical, mechanical, and chemical properties could be obtained from iron or vanadium oxides or mixtures of the two.

The next phase was concerned with finding the most practical fabrication techniques. Several existing techniques were evaluated and none appeared attractive. Therefore, a new chemical vapor deposition (CVD) technique based on $Fe(CO)_5$ was developed and proved to be very effective (2).

Continuing work on the sputtering technique brought to light some modifications which have made that method much more attractive than it originally was (3). Speed of sputtering has been increased by almost an order of magnitude, sputter cleaning of the substrates before deposition has reduced film defects, and control of the chemical and physical composition of the film has resulted in control of etchability (related to resolution).

There are other competitive techniques for making thin films of iron oxide for masks, *e.g.*, a spin-on process described by Reid and Cukor (4). However, these films do not seem to have as desirable a combination of durability, etchability, and freedom from pinholes as have CVD films.

The purpose of the present article is to describe the CVD method of making a see-through photomask. A thin uniform semitransparent film of Fe_2O_3 on a glass plate was obtained by reacting $Fe(CO)_5$ vapor with O_2 on or near the surface of the glass which was maintained at 100°C. This film was then etched with dilute HCl using photoresist techniques to obtain a useful photomask.

Key words: photoresist, transparent photomask, lithography, photolithography.

Deposition chamber.—In the original development of the CVD process (2), the deposition chamber consisted of a bell jar on a hot plate as shown in Fig. 1a. In an effort to minimize defects caused by particles, this system has been inverted as shown in Fig. 1b. Figure 2 is a densitometer trace across a 2-in. plate with Fe_2O_3 deposited in a chamber such as shown in Fig. 1b. Since the plate is supported by the edges, very little deposit forms there and the transmission at the edges is quite high.

For applications where it was desirable to have deposition all the way to the edges, the plate was supported as shown in Fig. 1c or 1d. Both of these systems gave uniform deposition. Figure 3 is a densitometer trace of a plate with iron oxide deposited in a chamber such as Fig. 1c.

In order to reduce the time required to obtain gaseous steady state, the chamber size has been succes-

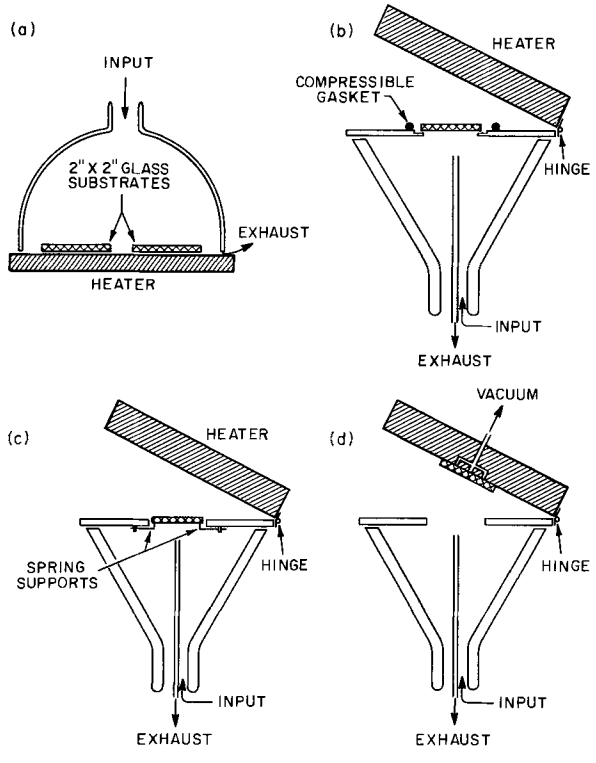

Fig. 1. (a) Bell jar on hot plate, 4 plates deposited simultaneously. (b) Inversion of system shown in Fig. 1 to minimize dust fall-out and reduction to one plate at a time. (c) Similar to Fig. 1b but plate supported by pins at the corners. This gives edge-to-edge coverage. (d) Similar to Fig. 1b but plate supported by a vacuum chuck in the heater block.

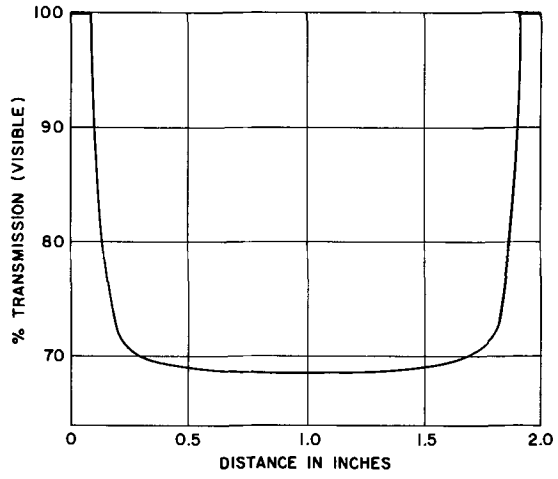

Fig. 2. Densitometer trace across a 2-in. plate deposited in a system such as in Fig. 1b. Note that transmission is high at the edges because of the method of plate support.

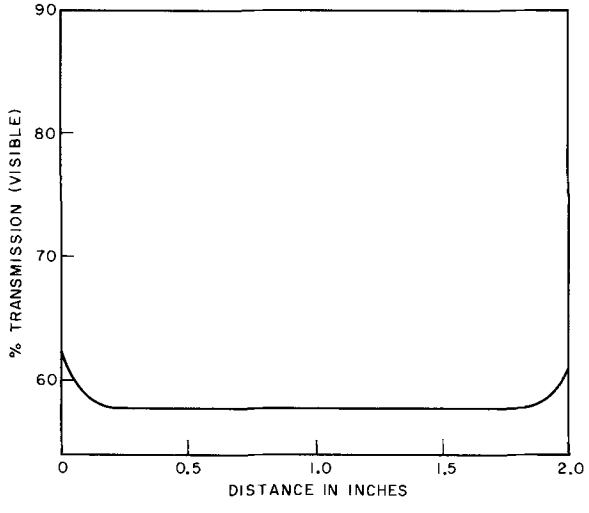

Fig. 3. Densitometer trace across a 2-in. plate deposited in a system such as in Fig. 1c.

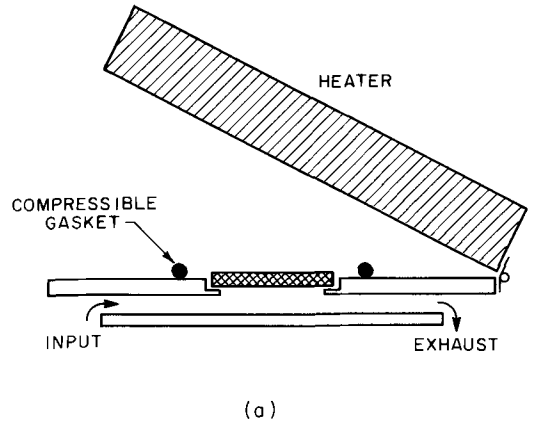

Fig. 4a. "Laminar" flow chamber with small volume (about 10 cc)

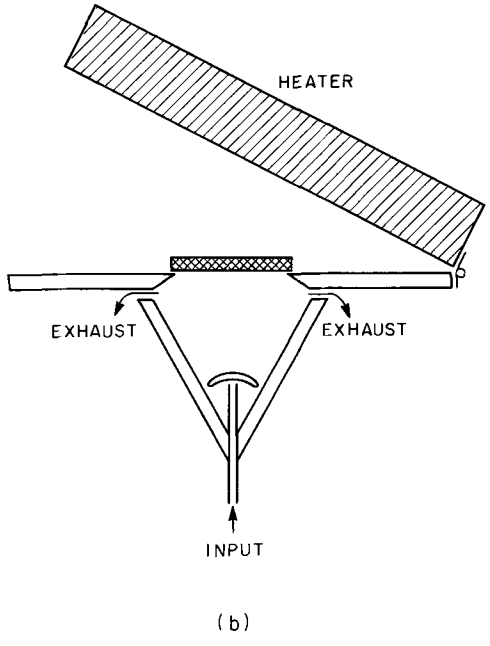

Fig. 4b. Most "successful" chamber design

sively reduced from over 1000 cc down to 10 cc. In this smallest chamber the gas was introduced along one edge and removed along the opposite edge as shown in Fig. 4a. With a high velocity of gas across the face of the plate, it was difficult to maintain uniform deposition. (The gas is not preheated but must be brought up to temperature by the glass plate on which deposition is taking place.)

The chamber that gave most consistently good results was funnel-shaped with the gas entering at the stem of the funnel and passing through a baffle as shown in Fig. 4b. The gas exited at the top edge in a symmetrical fashion. The chamber had a volume of 25 cc, and was made out of Plexiglas so that the deposition process could be monitored visually. To minimize deposition on the chamber walls they were water cooled or coated with a simple mineral oil. This not only makes visual observation easier but also increases the deposition rate on the desired area by maintaining a higher reactant concentration in the gas stream.

Heater.—The heater was a block of aluminum 1 × 6 × 6 in. in which was embedded a heating element, a controlling thermistor, and a thermometer. Since operating temperatures were within the range 80°-160°C, very little thermal insulation was necessary. A thin (0.03-0.07 cm) Teflon sheet placed between the aluminum block and the glass plate served two purposes: (*i*) it could be readily removed for cleaning, and (*ii*) it was a more uniform heat-transfer medium than the variable air gap that occurred between the imperfect glass plate and the polished metal surface of the heating block.

A proportional controller maintained the aluminum heating block within one degree of the desired temperature, and in a typical run the side of the glass on which deposition took place arrived within five degrees of this temperature in 27 sec (see Fig. 5).

Gas composition.—The two most essential gaseous ingredients for reasonable deposition rates are $Fe(CO)_5$ and O_2. The use of an inert gas carrier adds convenience, control, and increased safety. In the work reported earlier (2), Ar was always used as the inert carrier gas. It was suggested, however, that CO_2 be considered as a substitute for Ar on the basis of reducing the explosive range of CO-O_2 mixtures (CO is a product of the reaction). It was gratifying to discover that upon substituting CO_2 for the Ar, the deposition rate increased significantly. The deposition rate was so high that it was often desirable to have a diluent gas in the system to limit the deposition rate. Typical sets of operating conditions are shown in Table I. Under these conditions and with the glass plate held at 100°C, the deposition time is 2½ min for a film 2600Å thick.

The deposition rate can be increased or decreased by varying the O_2 flow rate as shown in Fig. 6. Optical transmission of these films are the same for equal film thickness. It is assumed, therefore, that they are similar chemically. Very low deposition rates (below 700

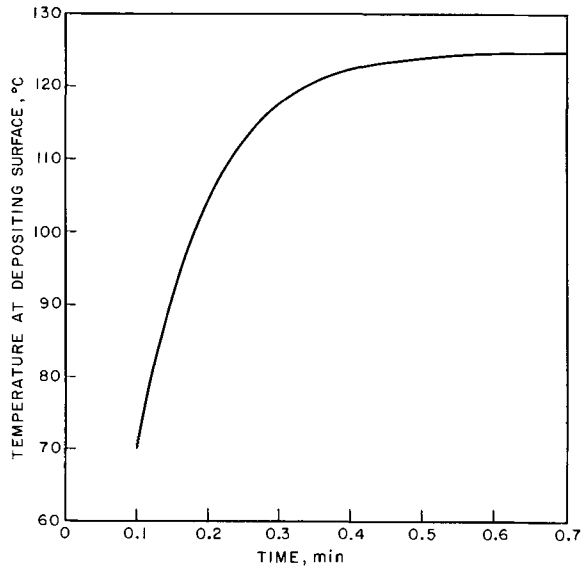

Fig. 5. Temperature of the outside surface (surface being coated) of 0.060-in. thick soda-lime glass plate in contact with a 125°C heating plate as measured with a 0.003-in. diameter thermocouple wire.

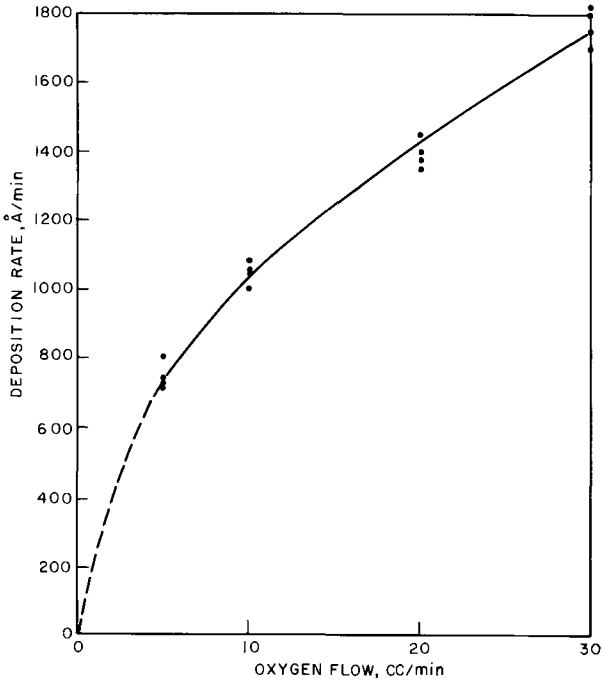

Fig. 6. Deposition rate as a function of oxygen flow at a constant CO_2 carrier gas flow rate of 200 cc/min.

Å/min) were of no particular interest and therefore, not investigated. At very high rates (over 1800 Å/min) it became increasingly difficult to maintain uniformity and reproducibility of the film. However, at higher deposition temperatures (140°-160°C) good films were obtained at rates as high as 9000 Å/min. This rate

Table I. Some typical flow compositions

Composition No.	Gas flow in cc/min CO_2*	O_2	N_2	Air
1	300	15	25	—
2	300	7	—	30
3	200	10	—	—

* Bubbled through liquid $Fe(CO)_5$ at room temperature.

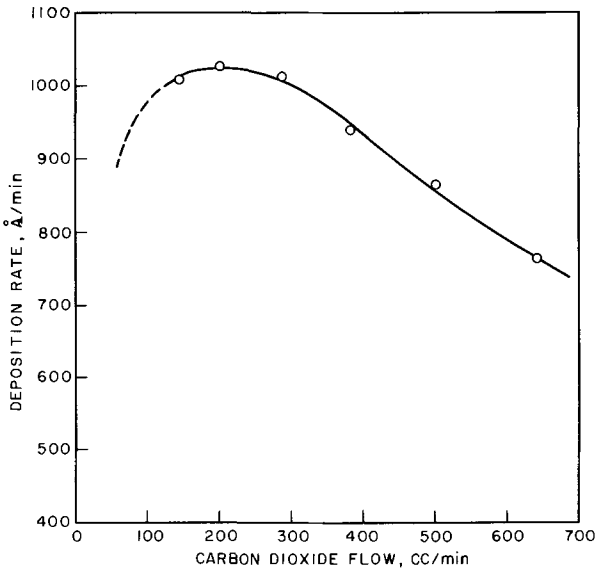

Fig. 7. Deposition rate as a function of CO_2 carrier gas flow at a constant oxygen flow rate of 10 cc/min.

means that a completed film can be deposited in about 20 sec.

The flow rate of the carrier gas also affects the deposition rate as shown in Fig. 7. The maximum in the curve seems to be real and may result from the cooling of the glass plate at high flow rates. It may also result from the decrease in $Fe(CO)_5$ concentration at high flow rates because of the evaporative cooling of the liquid in the bubbler and the resulting decrease in vapor pressure of the $Fe(CO)_5$. For higher deposition rates, the temperature of the bubbler and chamber may be raised. Only a modest increase can be tolerated because of the low temperature at which the desired reaction takes place (80°C).

Nitrogen is also an effective carrier gas for the carbonyl, and its substitution in place of the Ar used earlier increased the deposition rate still further. Indeed, when N_2 at 20 cc/min was bubbled through $Fe(CO)_5$ and mixed with oxygen at 5 cc/min the deposition rate was too fast to control easily. Therefore, such compositions are not recommended unless one is considering a continuous system for production.

The reason for the increased deposition rates with CO_2 or N_2 as compared with Ar is not clear. They both have higher thermal conductivity and higher specific heat than Ar, but to what degree this is responsible is not known.

Deposition temperature and etching.—Fe_2O_3 is not generally soluble in the dilute mineral acids that are most compatible with the photoresist processing. The oxide that is deposited from the CVD process is very difficult to dissolve in any concentration of HCl if the deposition temperature is over 180°C or if the film is given a postdeposition heat-treatment of over 400°C. Therefore, for ease of etching (and, thus, better pattern resolution) the temperature of deposition is kept below 160°C and all subsequent baking (before pattern delineation) below 200°C. Figure 8 is a graph showing the dependence of etching time (for a film 1700Å thick) on the deposition temperature. (See the section on Chemical analysis for a possible explanation of this relationship.) Resolution improves as the etch time becomes shorter, and the best resolution has been obtained at the lowest deposition temperature that has been used (80°C). The deposition rate, however, is relatively low at this temperature and also the absorption cutoff shifts too far toward the uv. Table II and Fig. 9 illustrate this shift in absorption cutoff. Optical transmission at 4000Å is plotted as a function of film thickness for films deposited at 100°, 120°, and 140°C. If transmission of 1% or less is desired in the spectral

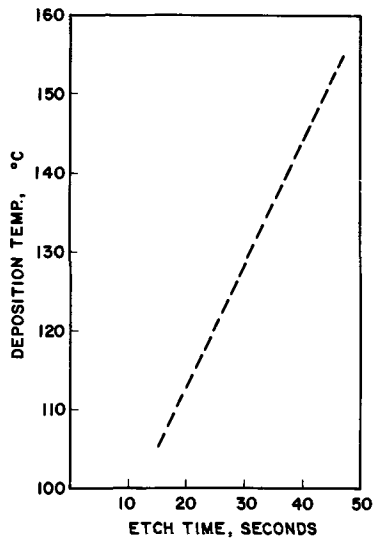

Fig. 8. Etch time as a function of the deposition temperature for films approximately 1700Å thick.

region below 4000Å, a film 1600Å thick will do if deposited at 140°C, but 2600Å will be required if deposited at 100°C. This shift in spectral transmission may be associated with the observed increase in what is assumed to be a carbonate content in the film (see section on Chemical analysis). Although some 4000Å light leaks through Fe_2O_3 films, absorption at 3600Å is very strong as indicated in Table II. Therefore, high contrast photomasking can be obtained with Fe_2O_3 by using visible cutoff filters (*e.g.*, Corning 5840) in the exposing source.

The transmission in the region 5500-7000Å is noticeably affected by interference and accounts for the occasional increase in transmission as the film gets thicker. This effect can be seen in Table II and also in Fig. 10.

Figure 10 is a graph of the transmission of a film about 2750Å thick which was deposited at 100°C. After photoresisting, a mask pattern was etched in this film in 1½ min using 6*N* HCl (1:1, concentrated HCl:water) at room temperature. A typical test pattern obtained under these conditions is shown by optical microscopy in Fig. 11 and by scanning electron microscopy in Fig. 12.

Because of the high vapor pressure of HCl it was also possible to use a vapor-etching process. It was satisfactory but did not seem to offer any real advantage over the simpler aqueous system. On the other hand, there are times when vapor etching can be very bothersome. For example, when experimenting with deposition chambers in which the glass plate would get a deposit on both sides, it was necessary to remove

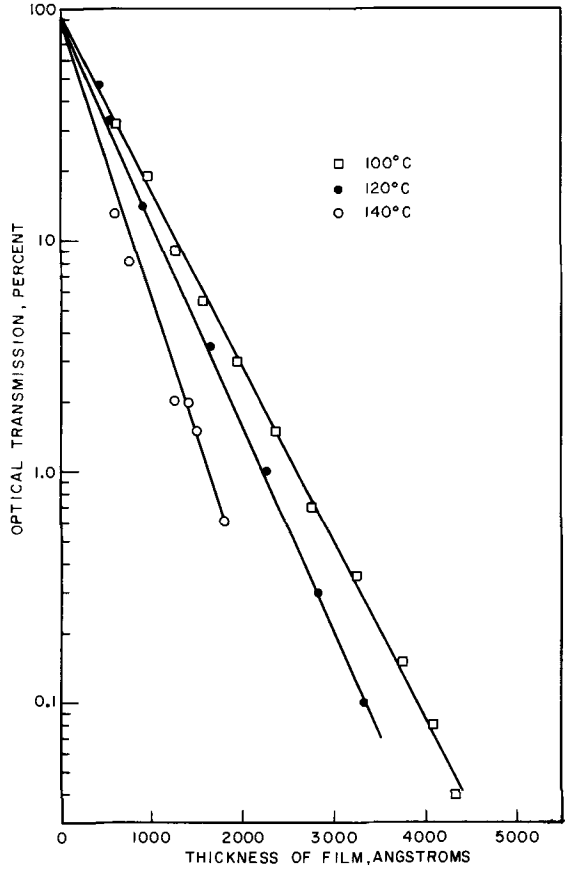

Fig. 9. Optical transmission at 4000Å as a function of film thickness for films depositel at 100°, 120°, and 140°C.

the deposit from one face with an etchant. If aqueous HCl was used as the etchant it was necessary to seal off the good Fe_2O_3 face to prevent its removal by HCl vapor along with the unwanted deposits. This was accomplished with an air curtain but a much more satisfactory solution to the problem is to use orthophosphoric acid which has a very low vapor pressure. The glass plate can readily be treated on one face only by saturating a filter paper with the acid and placing the plate on the filter paper. The etching rate is a little slower than for HCl.

Chemical analyses of Fe_2O_3 films.—In earlier work (2) it was indicated that the compositions of the CVD films "approximate that of Fe_2O_3 with possible minor concentrations of carbon and silicon." Specifically, it was noted that a film which was deposited at 155°C had 0.89% carbon, whereas a 200°C film had none.

Table II. Optical characteristics of iron oxide films of various thicknesses deposited at 100° and 120°C

Deposition temp, °C	Deposition time, min	Interference Order	Interference Color	Thickness, A	Per cent transmission at 3600A	4000A	6000A
100	0.5	—	—	308	42	51	84
100	0.8	—	—	500	21	32	65
100	1.1	1	Yellow	950	8	19	63
100	1.4	1	Red +	1275	2.5	9	76
100	1.7	1	Green	1562	1.2	5.5	67
100	2.0	2	Yellow +	1935	0.45	3	52
100	2.3	2	Red	2370	0.15	1.5	57
100	2.6	2	Green	2750	0.03	0.7	59
100	2.9	3	Yellow +	3250	<0.02	0.35	45
100	3.2	3	Red	3750	<0.02	0.15	48
100	3.5	3	Green	4100	<0.02	0.08	49
100	3.8	3	Green +	4312	<0.02	0.04	41
120	0.3	—	—	220	64	72	90
120	0.4	—	—	420	39	47	81
120	0.5	—	—	525	25	33	69
120	0.8	1	Yellow	900	5	14	63
120	1.1	1	Green	1640	0.7	3.5	58
120	1.4	2	Red	2280	0.1	1.0	51
120	1.7	2	Green	2810	<0.02	0.3	47
120	2.0	3	Red	3310	<0.02	0.1	42
120	2.3	3	Green	4030	<0.02	<0.02	38
120	2.6	4	Red	4640	<0.02	<0.02	35
120	2.9	5	Red	5400	<0.02	<0.02	29

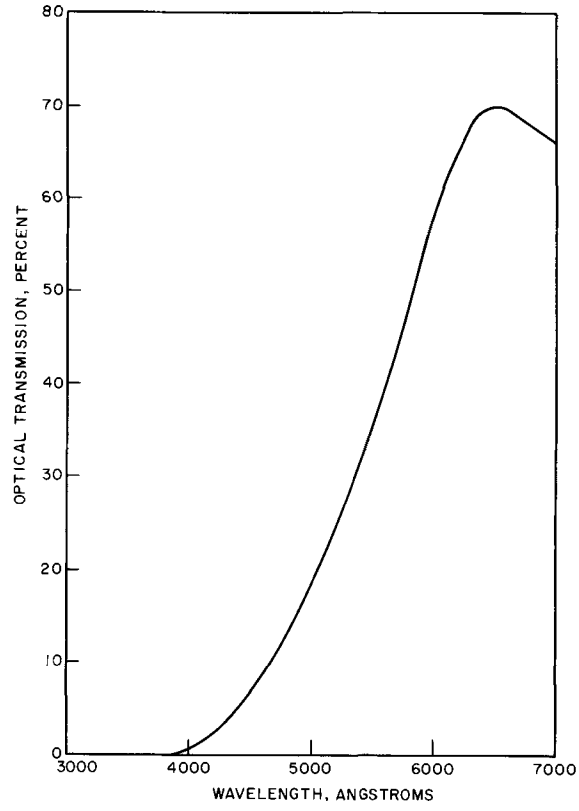

Fig. 10. Optical transmission of a 2750Å thick film of Fe_2O_3 deposited at 100°C.

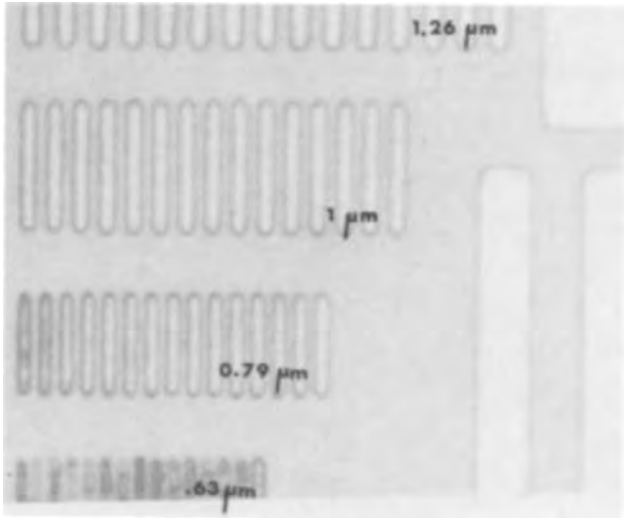

Fig. 11. Optical photograph of an Ealing test pattern contact printed in Fe_2O_3 using AZ 1350 photoresist.

However, the great solubility difference between those two films was not attributed to this difference in carbon content but was attributed to the more crystalline character of the higher temperature film.

More recently, Sinclair (5) has made some additional analyses that suggest a mechanism involving the carbon which may also account in part for this solubility difference. Infrared spectra were measured in the range 1-15μ. In the case of the CVD films this was done on very thick films which had spalled off of the glass substrate. With sputtered films (75% CO-25% CO_2 ambient), a calcium fluoride optical flat was used as the substrate. In both cases absorption was noted at about 6.7 and 7.4 μm which is consistent with the presence of carbonate or oxalate. Spot tests for oxalate were negative and chemical analyses for carbonate have been made by dissolving iron oxide films in 6M HCl

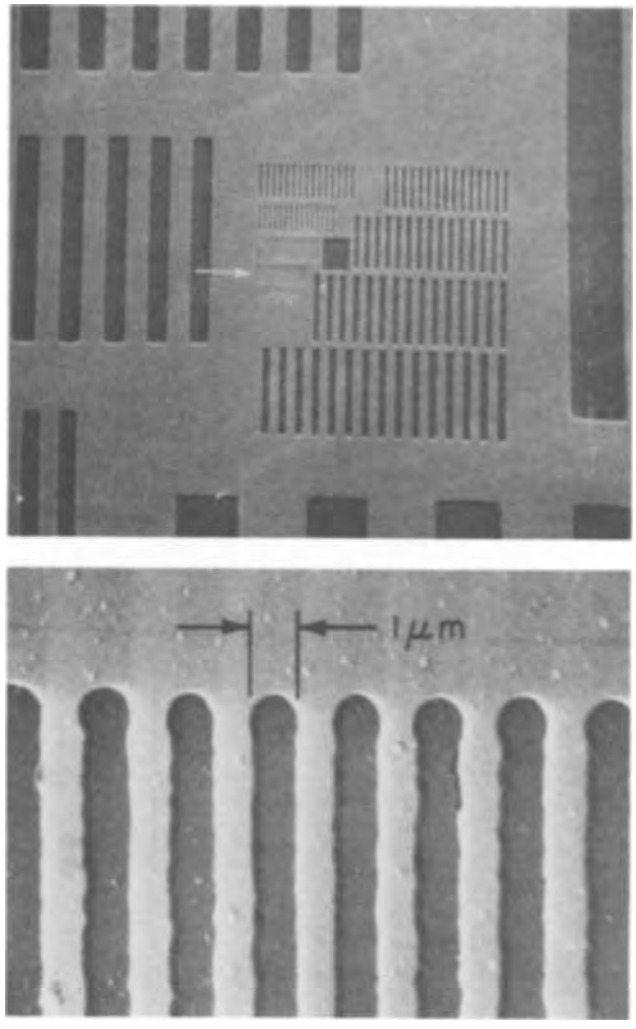

Fig. 12. Scanning electron microscope pattern of Ealing test pattern contact printed in Fe_2O_3 using AZ 1350 photoresist.

followed by gas chromatographic analysis of the liberated CO_2. The results are collected in Table III. These were unexpectedly large amounts of CO_2.

On the basis of these data it is suggested that the greater solubility of the CVD films and of the films sputtered in CO_2 as compared with films sputtered in Ar-O_2, may be due in part to the presence of a "carbonate" in the film. (The exact form of the compound from which the CO_2 was generated is not known. $Fe_2(CO_3)_3$ is not a recognized compound.) This mechanism would also account for the rapid conversion from the soluble to insoluble form by subsequent heat-treatment since the "carbonate" would decompose on heating. Such a treatment may be useful to decrease the solubility or increase the durability of the finished mask. It must be noted that the "carbonate" content is proposed as a possible influence on etching in addition to the crystal size influence described earlier (2). It is not obvious at this time which is the more important.

Defects.—Early in the development of the CVD process it was anticipated that the Fe_2O_3 film would have less tendency to form pinholes than the currently

Table III. Analyses for CO_2 evolved from Fe_2O_3 films

Sample description	mg CO_2 evolved/g of film
100° CVD film	99.8
Film sputtered in 100% CO_2	106
Film sputtered in 75% CO-25% CO_2	78.6
Film sputtered in 90% Ar-10% O_2	3.6

popular Cr films. This view was based in part on the higher degree of similarity between the Fe_2O_3 and the glass substrate and in part on the belief that the fluid precursor of the Fe_2O_3 may spread on the glass before the final reaction. Simple optical inspection as well as photoresist etching experiments designed to amplify pinholes indicate that the Fe_2O_3 films have fewer than 0.5 pinholes/cm^2. A more serious problem at present seems to be "antipinholes," that is, areas that etch with more difficulty than the majority of the film and thus tend to leave islands of unetched material behind. Elo (6) has compared Fe_2O_3 films with currently available Cr films and has suggested that "partial antipinholes" are due to residual photoresist arising from several sources. This is consistent with the observation that freshly deposited films dissolve uniformly in acids whereas after days of storage, antipinholes are noted. In other words, clean fresh films are reasonably free of defects, while films which have been exposed to possible contaminants (grease from airborne particles or bits of photoresist from poor processing) tend to show antipinholes. All Fe_2O_3 masks (~250) made over a three-month period were examined by a technique capable of detecting 2 μm defects. It was reported in that study that: "The R.M.S. concentration of defects 2 μm or larger in size is 0.5 defect/cm^2 in Fe_2O_3 films." Elo concluded that: "A significant reduction in the defect level (vis-a-vis evaporated Cr) appears possible with Fe_2O_3 semitransparent masks."

Summary and Conclusions

The decomposition of $Fe(CO)_5$ and oxidation of the decomposition product at 100°C in an O_2 or air ambient produces a films of Fe_2O_3 about 2600Å thick in 1-3 min. This film will block most of the actinic light employed with commercial photoresists. Using standard photoresist techniques and HCl as the etchant, photomasks have been made with 1 μm features.

The main advantage of such a photomask is the see-through characteristic which greatly simplifies alignment procedures in semiconductor processing. In addition, these masks have an impressive combination of other desirable qualities. For example, they are comparable to chromium masks in resistance to scratching, they have less halation effect than chromium, they are easier on the operator's eyes than chromium because of lower reflectivity, and finally the defect density is low.

Manuscript submitted Aug. 15, 1972; revised manuscript received Nov. 2, 1972. This was Paper 126 presented at the Los Angeles Meeting of the Society, May 10-15, 1970.

Any discussion of this paper will appear in a Discussion Section to be published in the December 1973 JOURNAL.

REFERENCES

1. W. R. Sinclair, M. V. Sullivan, and R. A. Fastnact, *This Journal*, **118**, 341 (1971).
2. J. B. MacChesney, P. B. O'Connor, and M. V. Sullivan, *ibid.*, **118**, 776 (1971).
3. F. G. Peters, W. R. Sinclair, and M. V. Sullivan, To be published in *This Journal*.
4. F. J. Reid and P. Cukor, Paper 127 presented at Electrochem. Soc. Meeting, Los Angeles, May 10-15, 1970.
5. W. R. Sinclair, Private communication.
6. R. B. Elo, Private communication.

The Epitaxial Growth and Properties of Silicon on Stoichiometric Spinel and Sapphire Substrates Using Silane-Helium Mixtures *vs.* Silane-Hydrogen Mixtures

Y. S. Chiang* and G. W. Looney

RCA Laboratories, Princeton, New Jersey 08540

ABSTRACT

Epitaxial growth of silicon on (111) and (100) stoichiometric spinel, $(1\bar{1}02)$, (0001), and $(11\bar{2}3)$ sapphire using silane in helium has been studied. (100) Si seems to be more compatible with sapphire than (111) Si, and exactly the opposite is true with stoichiometric spinel. Higher growth rate is preferred for epitaxial growth on sapphire and lower growth rate is favored for growth on stoichiometric spinel. Silicon films grown in hydrogen tend to have a smoother surface than that grown in helium, but larger contamination and interdiffusion effects. Lower optimum growth temperatures have also been observed for the silicon growth in helium than in hydrogen.

Effects of various growth parameters on the properties of the silicon layer using silane in helium were investigated. Hall mobilities comparable to bulk Si were realized in p-type films on (111) spinel. Hall mobility dependence, for both holes and electrons, on film thickness was found to be nearly constant for Si layers on spinel beyond 1 μm. The effect of stress on the mobility of (111) and (100) Si has been discussed.

The usual method of single crystalline Si deposition involves the silane-hydrogen system, where the deposition rate decreases to very low values below 1000°C. Silane-helium system, on the other hand, has been shown to give quite a high deposition rate (0.1 μm/min or higher) at 900°C both on Si (1) and on sapphire (2, 3). Furthermore, as discussed later, certain surface problems are always encountered in growth of Si on (111) stoichiometric spinel using hydrogen as the carrier gas which are not found with helium. Thus, the use of helium as a carrier gas instead of hydrogen

* Electrochemical Society Active Member.

Key words: silicon epitaxy, insulating substrate heteroepitaxy, spinel, sapphire, epitaxy by SiH_4-He system.

might be advantageous. However, the growth parameters and properties of the silicon change markedly when helium is substituted for hydrogen.

In this study, a variety of growth parameters such as surface treatment of substrate, growth temperature, and growth rate have been investigated using helium as the carrier gas. Comparison of the experimental results for silicon epitaxial growth on sapphire and stoichiometric spinel, as well as in hydrogen *vs.* helium, is made and discussed.

Experimental

The growth system used in this study has already been described in an earlier report (4). The silane source was 5% in He unless otherwise specified. The carrier gas was ultrahigh purity helium, passed through two molecular sieves at 77°K, and then filtered through a 0.8 μm filter. The dopant gases used were diborane and arsine of a concentration of 100 ppm in helium. Dilution of either of the dopants was effected by mixing the 100 ppm source gas with more ultrahigh purity helium in a glass mixing bulb. Fractions of the diluted mixtures were then bled into the reactant gas stream, while the rest was vented through an exhaust. In this manner, a few orders of magnitude of dilution of the dopant gas could be readily and reproducibly achieved in the resulting carrier gas stream.

The Czochralski stoichiometric spinel and sapphire were obtained from Linde Division of Union Carbide. All the sapphire wafers were cut and polished by Insaco (Quakertown, Pennsylvania), whereas the spinel wafers were polished either by our own in-house facilities or by Linde or Insaco. The finished wafers have been examined by electron diffraction for crystallinity and constitution. A cleaning procedure composed of trichloroethylene degreasing, alcohol rinsing, Caro's acid (5 parts H_2SO_4, 1 part 30% H_2O_2, and 1 part H_2O) cleaning, distilled water rinsing, and spin drying is used with all the substrates just prior to insertion into the growth chamber.

Layer thicknesses were determined exclusively by *IR* interference (transmission mode) technique (5) using a Cary 14 spectrophotometer. We have employed the Hall mobility of the majority carrier as the quality indicator of the electrical properties of the epitaxial Si films similar to many other investigators.

Results

Silicon on Czochralski Stoichiometric Spinel

Effect of substrate treatments prior to growth.—For both (111) and (100) oriented wafers, no apparent differences in Hall mobility can be distinguished from Si films grown on substrates mechanically polished by different sources. In addition, further chemical polishing of the substrates by phosphoric acid or borax fails to improve the Si films deposited on them.

Few *in situ* annealing schemes at elevated temperatures either in hydrogen or helium have been experimented. The effect of these treatments on Si films subsequently grown on (111) and (100) spinel is given in Tables I and II, respectively. For (111) Si on (111) spinel, the results indicate clearly that no predeposition annealing is necessary. Hydrogen annealing at 1000°C, however, has no adverse effect on Hall mobility for p-type films but slightly increases the acceptor concentration. More important, the hydrogen treatment produces a smoother surface of the Si deposit. Higher temperature hydrogen annealing is very undesirable even for p-type films. A 1040°C annealing would cause the Hall mobility to decrease by 50%, and from 1100°C upwards microcracking of the (111) spinel substrate would be observed.

In contrast with the (111) spinel, the (100) oriented substrate needs hydrogen or helium annealing for a smoother surface of the Si deposit, as well as higher Hall mobility. Hydrogen annealing is slightly more favorable than helium annealing for obtaining a smooth surface of the silicon layer.

Table I. Effect of surface treatment of melt-grown (111) stoichiometric spinel on epitaxial silicon films grown from silane-helium mixtures

A. P-type films

Surface treatment	Deposition temperature (°C)	Thickness of Si layer (μm)	Acceptor concentration (cm^{-3})	Hall mobility (cm^2/V-sec)
H_2, 1 hr at 1000°C	1040	1.8	3×10^{16}	310
H_2, 1 hr at 1040°C	1040	0.8	2×10^{15}	160
No annealing	1040	0.8	3×10^{15}	350
		1.0	1×10^{16}	370
He, 20 min at 1040°C	1040	0.8	3×10^{15}	320

B. N-type films

Surface treatment	Thickness of Si layer (μm)	Donor concentration (cm^{-3})	Hall mobility (cm^2/V-sec)
No annealing	1.0	3×10^{16}	535
H_2 annealing (1 hr at 1020°C)	1.0	2×10^{16}	400

Table II. Effect of surface treatment of melt-grown (100) stoichiometric spinel on epitaxial silicon films grown from silane-helium mixtures

A. P-type films

Surface treatment	Thickness of Si layer (μm)	Acceptor concentration (cm^{-3})	Hall mobility (cm^2/V-sec)
H_2 annealing (1 hr at 1000°C)	1.0	9×10^{16}	135
No annealing	1.0	4×10^{16}	120

B. N-type films

Surface treatment	Thickness of Si layer (μm)	Donor concentration (cm^{-3})	Hall mobility (cm^2/V-sec)
No annealing	1.3	2×10^{16}	70
Hydrogen annealing (1 hr at 1000°C)	1.4	5×10^{16}	320
Helium annealing (1 hr at 1000°C)	1.3	3×10^{16}	355

Influence of growth conditions.—The optimum epitaxial growth temperature on (111) spinel is found to lie around 1020°-1060°C. For p-type films, the Hall mobility at a growth temperature of 960°C is only one-half of that obtained in the optimum range, while at 1070°C three-quarters of the optimum value is obtained. In general, growth made at the higher end of the optimum temperature range tends to yield more uniform and smoother Si deposits.

The optimum growth temperature on (100) spinel is located similarly at 1020°-1050°C. But the surface smoothness of the Si deposit is much inferior to that obtained on (111) spinel; and at temperatures outside the optimum range, the appearance of the Si film is significantly degraded.

The Hall mobility of p-type Si films on (111) spinel grown at high silane concentration and helium flow rate is invariably much lower than that grown at low silane concentration and helium flow rate. The same is true for n-type Si films on (111) spinel as well as both n- and p-type Si films on (100) spinel except that inhomogeneity is also being introduced.

Resulting electrical properties of the Si films.—The Hall mobility of holes and electrons is measured and found to be essentially independent of carrier concentration in the range of 10^{15}-10^{17} cm^{-3} for Si films on both (111) and (100) spinel.

P-type Si layers on (111) spinel yield an almost linear dependence of Hall mobility on thicknesses from 0.2 to 0.8 μm (see Fig. 1). For 0.8 μm and thicker films, the Hall mobility of holes is approximately the value for bulk silicon (high 10^{15} to low 10^{17} acceptors/cm^3). Oxidation of the Si films at 1100°C for 1 hr

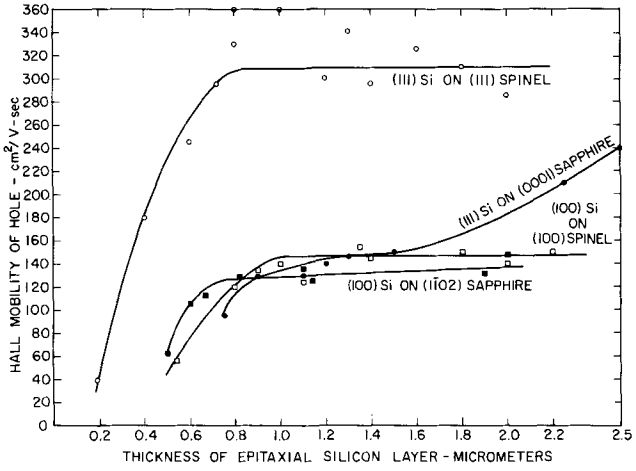

Fig. 1. Dependence of Hall mobility of holes in as-deposited (100) and (111) silicon on stoichiometric spinel and sapphire as a function of film thickness (carrier concentration: 3 to 8 × 10^{16} cm^{-3}) using silane-helium mixtures.

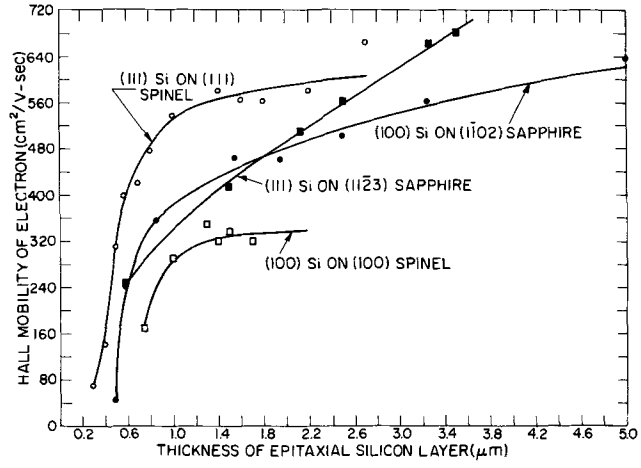

Fig. 2. Dependence of Hall mobility of electrons in as-deposited (100) and (111) silicon on stoichiometric spinel and sapphire as a function of film thickness (carrier concentration: 3 to 8 × 10^{16} cm^{-3}) using silane-helium mixtures.

usually would not degrade the Hall mobility value as exemplified by the few samples listed in Table III. On the other hand, a silicon layer grown in the same apparatus, but using hydrogen as the carrier gas, gives a Hall mobility of 60 at a 1 μm thickness (2 × 10^{17} acceptors/cm^3), about one-fifth of that obtained from films grown in helium.

The dependence of Hall mobility on film thickness of n-type films on (111) spinel is depicted in Fig. 2. At a thickness of 1 μm and more, the Hall mobility of electrons becomes independent of film thickness with a value of about 600 cm^2/V-sec.

The dependence of Hall mobility on film thickness of p- and n-type Si films on (100) spinel is very similar to that of Si on (111) spinel described above. Details of them are shown in Fig. 1 and 2, respectively. In contrast with the case of (111) spinel, excellent

Table III. The effect of thermal oxidation of p-type silicon epitaxial films on (111) melt-grown stoichiometric spinel

Thickness of Si layer (μm)	Acceptor concentration, N_A, cm^{-3}	Hall mobility, μ_p, cm^2/V-sec	After oxidation at 1100°C for 1 hr: Acceptor conc., N_A, cm^{-3}	After oxidation at 1100°C for 1 hr: Hall mobility, μ_p, cm^2/V-sec
0.6	4 × 10^{16}	245	2 × 10^{16}	195
1.3	5 × 10^{15}	330	2 × 10^{15}	345
1.4	1 × 10^{16}	295	6 × 10^{15}	275

epitaxial silicon films on (100) spinel can be grown in hydrogen at 1085°-1090°C (as compared with 1020°-1050°C in helium). The Hall mobilities of the films grown in hydrogen and helium are the same. For example, a 1.8 μm thick p-type film grown in hydrogen gives a Hall mobility of 140 cm^2/V-sec at an acceptor concentration of 3 × 10^{16} cm^{-3}. A n-type film grown in hydrogen has a Hall mobility of 300 cm^2/V-sec at a film thickness of 1 μm and a donor concentration of 1 × 10^{17} cm^{-3}.

Silicon on Sapphire

Effect of substrate treatments prior to growth.—The phosphoric acid chemically polished substrates were observed to offer no advantage over the normal mechanically polished wafers for growth of silicon films on sapphire. Among the various predeposition *in situ* treatments evaluated, hydrogen annealing at elevated temperatures (above 1200°C) is the most desirable process for both (1$\bar{1}$02) and (11$\bar{2}$3) oriented sapphire. And sulfur hexafluoride etching of the substrate in helium was found to be not as desirable as the hydrogen annealing.

Influence of growth conditions.—For (1$\bar{1}$02) and (11$\bar{2}$3) oriented sapphire, the optimum growth temperature was found to be 950°-1000°C; and for (0001) sapphire, 1030°-1050°C. As growth temperature departs more from the optimum range, the surface smoothness suffers.

Higher silane concentrations and higher flow rates of helium (higher deposition rate) are observed to be more favorable growth conditions in distinct contrast to the case of growth on spinel.

Resulting electrical properties of the Si films.—The dependence of Hall mobility on film thickness for p- and n-type (100) Si layers on (1$\bar{1}$02) sapphire is shown in Fig. 1 and 2, respectively. For p-type films, no appreciable increase in Hall mobility with film thickness can be seen for film thicknesses exceeding 1 μm. Also, the value of the measured Hall mobility of holes for helium-deposited films approximates closely the value of the Si film grown in hydrogen in the same epitaxial system with the same film thickness. In turn, the Hall mobilities measured on films grown in hydrogen agree well with the values reported (6). If the Si film grown in helium is oxidized at 1100°C for 1 hr, hardly any change in the value of the Hall mobility occurs. For example, a Hall mobility of 130 is measured from a 1.1 μm thick film at an acceptor concentration of 5 × 10^{16}; a Hall mobility of 120 is measured after the oxidation. The n-type (100) Si films on (1$\bar{1}$02), on the other hand, yield Hall mobilities ever increasing with film thickness up to 5 μm, the thickest film we have grown.

The dependence of Hall mobility on film thickness for p-type (111) Si on (0001) sapphire is also shown in Fig. 1. The Hall mobility continually increases with increasing thickness of the silicon layer. Epitaxial silicon films grown in the same system, but using hydrogen as the carrier gas, usually yield a comparable but slightly higher Hall mobility value than those grown in helium. For example, a 1.2 μm thick Si film grown in hydrogen at 1030°C gives a Hall mobility of 170 cm^2/V-sec (at an acceptor concentration of 9 × 10^{16} cm^{-3}) *vs.* 140 cm^2/V-sec for a helium grown film.

Similar to the case of (100) Si on (1$\bar{1}$02) sapphire, the Hall mobility of n-type (111) Si on (11$\bar{2}$3) sapphire rises with thickness of the layer as depicted in Fig. 2. The dependence of Hall mobility on thickness is almost linear throughout the range of practical interest, *i.e.*, 0.5-3.5 μm.

Discussion

The Hall mobility of holes for (111) Si on spinel is invariably greater than that of (100) Si on spinel. And at a film thickness exceeding 0.9 μm, the hole mobility

of (111) Si on sapphire is always larger than (100) Si on sapphire (see Fig. 1). These observations can be accounted for by a model of the effect of stress on the film properties (7, 8). Schlotterer (7) and Heywang (8) have postulated from theoretical considerations that stress enhances the hole mobility in (111) silicon but degrades the electron mobility in (100) silicon. The stress in the Si film is generated through the different thermal-expansion coefficient of silicon and the substrate. As the lattice mismatch between silicon and stoichiometric spinel is very small, *i.e.*, 0.3-0.9% (9), the stress effect is observed in the case of spinel from the very beginning. On the other hand, the larger lattice mismatch between silicon and sapphire, 4-12% (9), dominates at small thicknesses, and only at thicknesses greater than 0.9 μm does the stress effect become apparent in silicon on sapphire films.

Just as in the situation for p-type films, the n-type (111) Si on spinel invariably has a greater Hall mobility than that of (100) Si, and the n-type (111) Si on sapphire at first shows a lower mobility value than that of (100) Si, and subsequently surpasses the value of the latter at thickness greater than 2 μm (see Fig. 2). The effect of stress on the film properties as postulated by Schlotterer (7) and Heywang (8) is once again being observed.

Silicon films grown on the two sapphire orientations in either hydrogen or helium give very comparable if not identical results. But for Si on (111) spinel, the hole mobility for films grown in hydrogen is only about one-fifth of that grown in helium, suggesting a probable surface reaction of hydrogen with the substrate. Furthermore, comparable hole mobility is measured from the Si films on (100) spinel grown either in hydrogen or in helium. It seems that the (111) oriented spinel possesses a much higher surface reactivity with hydrogen than the (100) oriented material.

Surface treatments of the substrate, both sapphire and stoichiometric spinel, are of crucial importance in obtaining good quality silicon films. For sapphire, a prior *in situ* high-temperature annealing in hydrogen is necessary for growing a smooth silicon layer with acceptable Hall mobility. For (100) spinel, again an *in situ* high-temperature annealing in hydrogen or in helium is necessary to subsequently obtain a silicon film with reasonable appearance. As for (111) spinel, no *in situ* predeposition high-temperature annealing is necessary, and hydrogen annealing invariably degrades the electron Hall mobility.

In most aspects, epitaxial growth of Si on stoichiometric spinel and sapphire are very similar. For instance, the optimum growth temperatures (in helium) lie in the range of 950°-1050°C for both kinds of substrates. But the optimum silane concentration and helium flow rate for the two kinds of substrates are drastically different. Higher growth rate (higher silane concentration and helium flow rate) is more desirable for growth of Si on sapphire. And lower growth rate (lower silane concentration and helium flow rate) is more favorable for growth of Si on stoichiometric spinel. This is most likely related to the much reduced crystallographic mismatch of silicon to stoichiometric spinel than silicon to sapphire (9). Contamination by the constituents of the substrate is consistently less for stoichiometric spinel than for sapphire, as has been observed for alumina-rich spinel and sapphire (10).

The silicon films grown in helium, with the exception of Si on (111) stoichiometric spinel, are often not as smooth as that grown in hydrogen. On the other hand, the Si films grown in helium resist the degradation of Hall mobility by oxidation much better than those grown in hydrogen. The former is possibly caused by the larger amount of homogeneous nucleation in the gas phase of silicon in helium than in hydrogen, and the latter may be related to the inclusion of a reactive gas (hydrogen) in the Si film. The optimum growth temperature on sapphire as well as on stoichiometric spinel is usually 50°-100°C lower when helium is used instead of hydrogen as the carrier gas. In general the Si films grown in helium also have less contamination from constituents of the substrate. But they are much more sensitive to oxygen leaks in the epitaxial growth systems than their hydrogen counterparts.

Acknowledgments

The authors are grateful to C. W. Mueller, D. Richman, and G. W. Cullen for technical advice and stimulating discussions. The authors are also in debt to F. C. Dougherty for his assistance in making Hall mobility measurements.

Manuscript submitted March 22, 1972; revised manuscript received Dec. 11, 1972.

Any discussion of this paper will appear in a Discussion Section to be published in the December 1973 JOURNAL.

REFERENCES

1. D. Richman and R. H. Arlett, *This Journal*, **116**, 872 (1969); Y. S. Chiang and D. Richman, *Metal. Trans.*, **2**, 743 (1971).
2. D. Richman, Y. S. Chiang, and P. H. Robinson, *RCA Rev.*, **31**, 613 (1970); D. J. Dumin, P. H. Robinson, G. W. Cullen, and G. E. Gottlieb, *ibid.*, **31**, 620 (1970).
3. J. Mercier, *This Journal*, **118**, 962 (1971).
4. D. Richman and R. H. Arlett, in "Semiconductor Silicon," Rolt R. Haberecht and Edward L. Kern, Editors, p. 200, The Electrochemical Society Softbound Symposium Series, New York (1969).
5. O. S. Heavens, "Optical Properties of Thin Solid Films," Butterworths, London (1955).
6. J. D. Filby and S. Nielson, *Brit. J. Appl. Phys.*, **18**, 1357 (1967).
7. H. Schlotterer, *Solid-State Electron.*, **11**, 947 (1968).
8. W. Heywang, *Mater. Res. Bull.*, **3**, 315 (1968).
9. Crystal Products Bulletin, SIS-1 Epitaxial Wafer, Union Carbide Corp., San Diego, Calif. (1970).
10. P. H. Robinson and D. J. Dumin, *This Journal*, **115**, 75 (1968).

Heteroepitaxial Growth of Si_xGe_{1-x} Alloys by Thermal Decomposition of SiH_4 and GeH_4

G. M. Oleszek*,[1] and R. L. Anderson*

Microelectronics Laboratory, Department of Electrical and Computer Engineering, Syracuse University, Syracuse, New York 13210

ABSTRACT

Epitaxial layers of Si_xGe_{1-x} alloys have been grown on germanium substrates by the simultaneous thermal decomposition of SiH_4 and GeH_4 in hydrogen. Growth was in the 800°-850°C temperature range at growth rates on the order of 0.1 μm/min for alloy epitaxy. Using the back-reflection Laue method, the alloys were determined to be single crystal with the substrate orientation, while x-ray diffractometer measurements indicated alloy compositions with x in the range $0 < x \leq 0.25$. The defect density of lower Si concentration alloys ranged from 10^4 to 10^7 cm^{-2}. Hall measurements of alloy layers without intentional doping indicated p-type alloy material with Hall (hole) mobility in the 250-400 cm^2/V-sec range at carrier concentrations of 2-5 $\times$ 10^{17} cm^{-3} for 4-5 atomic per cent Si in the alloy. Current-voltage characteristics of p-n heterojunctions formed between alloy and substrate were found to be rectifying while p-p heterojunctions were weakly rectifying. A frequency dependence of the junction capacitance was observed which presumably is a result of defect states at the interface between the substrate and alloy.

Germanium and silicon have the same crystal structure (diamond-cubic) and their lattice constants differ by 4% at room temperature. It is well known that Si and Ge form solid solutions over the entire range of composition where, presumably, the atomic positions are random (1). In the late 1950's and early 1960's Si_xGe_{1-x} alloys were made covering the full range of composition (2-6). However, these crsytals were grown from the melt and single-crystal material was obtained only for the alloy represented by the extreme Si and Ge ends of the phase diagram. Sandulova *et al.* (7) in 1962 reported growth over the entire alloy range from the vapor phase using Se as a carrier in a closed tube system. The method proved impractical because of growth times requiring 2-5 days and the poor control associated with the closed tube process.

Also in 1962, Miller and Grieco (8) reported epitaxial growth of Si-rich alloys containing up to 30 a/o (atomic per cent) Ge by the simultaneous vapor-phase reduction of $SiCl_4$ and $GeCl_4$. Si wafers were used as substrates and hydrogen carrier gas was bubbled through a solution of $SiCl_4$-$GeCl_4$ which then carried the halides to the reaction chamber. Different compositions were obtained by varying the proportions of the halides. X-ray diffraction and electron diffraction measurements indicated that the films were epitaxial. The dislocation count was on the order of 10^7 cm^{-3} although the films were not extensively characterized. Results complementary to those of Miller and Grieco were obtained in 1963 by Newman and Wakefield (9). Attempting to deposit Si onto Ge substrates by the disproportionation of SiI_2, they actually produced Si_xGe_{1-x} alloys in which x varied appreciably. They reported appreciable cavity formation in the resultant material.

Recent work in the U.S.S.R. (10, 11) has reported growth of silicon-rich Si_xGe_{1-x} alloys over an appreciable composition range by hydrogen reduction of $GeCl_4$ and $SiCl_4$. Separate evaporators were used for the two chlorides which were then mixed before entering the reaction chamber. Little has been reported on the vapor-phase growth of Ge-rich alloys, however Feucht (12) recently reported growth of Ge-rich alloys with $x = 0.1$ by the simultaneous pyrolytic decomposition of GeH_4 and SiH_4.

The purpose of this paper is to define growth conditions for achieving germanium-rich Si_xGe_{1-x} epitaxial alloys in the range $0 < x \leq 0.25$ by thermal decomposition of SiH_4 and GeH_4 in H_2 and to discuss the growth and material characteristics of the alloy material. This particular method is potentially advantageous for alloy growth since (*i*) undesirable impurity transport does not occur because the thermal decomposition of silane and germane is not a reversible process, (*ii*) epitaxial growth processes using both silane and germane occur at relatively low temperatures which minimize substrate and impurity out-diffusion, and (*iii*) the alloy composition may be easily changed by varying the gas stream concentrations of the hydrides.

Experimental

Epitaxial reactor system.—The epitaxial growth system used was a vertical reactor unit[2] in which the process gases pass downward, perpendicular to the substrates. All gas lines in the reactor are of 316 stainless steel and valves and regulators are stainless steel with Teflon packing. The reaction dome is constructed of quartz and is air cooled. The essential features of the epitaxial reactor are shown schematically in Fig. 1. Purification of the hydrogen is accomplished by passing it through a palladium purifier. Specified concentration of GeH_4 in H_2, SiH_4 in H_2, and HCl were obtained commercially in cylinders. The graphite susceptor, 5 in. in diameter, is heated by a pancake coil located directly below the susceptor and energized by a 10 kHz, 15 kW motor-generator set.

Growth procedure.—The Si_xGe_{1-x} alloys were grown epitaxially by the simultaneous thermal decomposition of SiH_4 and GeH_4 in H_2. The substrates were chemically-mechanically polished single-crystal germanium wafers. Prior to epitaxy the substrates were boiled in a 50:50 mixture of ethyl alcohol and trichloroethylene, boiled in a saturated potassium hydroxide-deionized water solution, consecutively immersed in hydrofluoric acid, deionized water, and ethyl alcohol, and then blown dry with nitrogen. The growth process consisted of the following procedures: with the substrates in place, the reaction chamber was initially purged with nitrogen. Hydrogen was then introduced

* Electrochemical Society Active Member.
[1] Visiting Research Professor on leave from IBM Systems Development Laboratory, Endicott, New York. Present address: IBM Systems Development Laboratory, Kingston, New York 12401.
Key words: epitaxial growth, silicon-germanium alloys, heterojunction.

[2] Phoenix Materials Corporation, Kittanning, Pennsylvania.

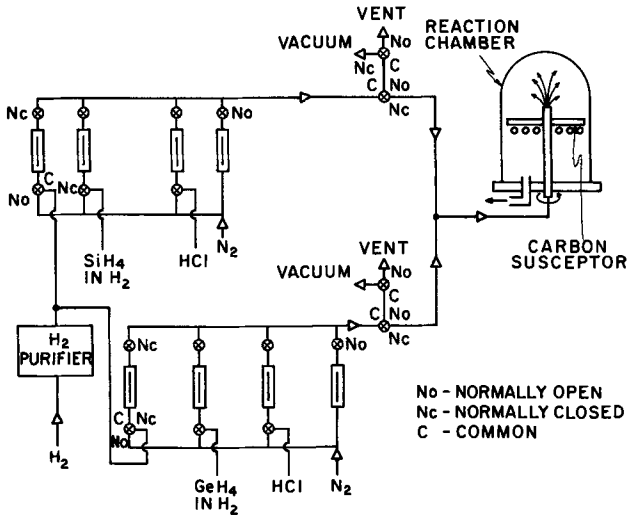

Fig. 1. Essential features of epitaxial reactor used in Si_xGe_{1-x} alloy growth.

into the chamber and the germanium substrates heated to 850°C for 15 min. HCl was then admitted for 10 min to etch the substrates. The reaction chamber was then purged with H_2; the temperature adjusted to the growth temperature; and SiH_4, GeH_4, and H_2 introduced into the reaction chamber for the Si_xGe_{1-x} alloy growth. After completion of the growth, the chamber was purged with H_2 until the substrates cooled to room temperature. The reaction chamber was then purged with N_2 and the substrates removed.

Measurement techniques.—The temperature was measured using an infrared optical pyrometer. The instrument was initially calibrated by heating a polished Ge wafer to its melting point in the reactor chamber with an emissivity setting corresponding to Allen's (13) emissivity data for Ge. In this work all temperatures correspond to the germanium substrate temperature prior to the alloy growth since some clouding of the dome prevented accurate monitoring of the temperature during growth.

The percentages of GeH_4 and of SiH_4 in the gas stream were computed using the specified concentrations of GeH_4 and SiH_4 in H_2, and the flow rates of the hydrides and main-stream hydrogen which were measured using calibrated glass tube-ball flowmeters.

Measurement of the alloy thickness was determined by the cylindrical grooving method (14). In most cases, the alloy sample did not have to be chemically stained to see the boundary line between the alloy and substrate.

The crystallinity of the epitaxial layer was established by back-reflection Laue and x-ray diffraction techniques. The back-reflection Laue method was primarily used to establish the single-crystal nature of the alloys; however, information concerning crystal distortion was obtained as well. A copper x-ray tube, operated at 30 kV and 22 mA, was used as the x-ray source which results in a depth of penetration of the x-ray beam of about 25 μm in pure germanium.

The alloy composition was determined using a General Electric XRD-6 x-ray diffractometer. A cobalt tube was used as the x-ray source and operated at 24 kV and 10 mA. The diffraction peaks of both the alloy and the Ge substrate were observed for the $K\alpha_1$, $K\alpha_2$, and $K\beta$ radiation. The $K\beta$ peaks were used to determine the lattice constant of the alloy. Because the lattice constant varies slowly with Si concentration (15), accurate alignment of the sample is normally required to determine the concentration. However, since the epitaxial growths were thin (2-7 μm), the responses from both the alloy and the substrate were observed. The difference in the 2θ angle between response peaks and the known 2θ angle of the Ge substrate was used to determine the interplanar spacing (16) of the alloy and thus its composition. Following Cullity (17) we calculate that for Ge using Co $K\beta$ radiation, 30% of the total diffracted intensity originates in the first 2.4 μm of material, 67% in the first 7.7 μm, and 99% in the first 20.6 μm. The diffracted intensity for the alloy would not be expected to differ markedly from these values and thus diffraction from the substrate would be expected to be observed.

Room temperature resistivity, conductivity type, concentration and mobility were determined from Hall effect measurements on alloys which were electrically isolated from the substrates (those grown on n-type substrates since all deposits were p-type). Both Standard and Van der Pauw d-c methods (18, 19) were used for Hall measurements with a magnetic field of 2.5 kgauss and a current of 1 mA. Current and voltage leads were attached using silver contact paint[3] and cured at 60°C for 15 min in air. Resistivity was also measured by the standard four-point probe method.

Dislocations were delineated by etching the samples in 30% H_2O_2 at room temperature for periods on the order of 1 hr.

Si_xGe_{1-x}/Ge heterojunctions were fabricated from epitaxial alloys grown on polished Ge wafers. Small pieces of the wafer, usually about 2.5 mm square, were obtained by scribing and breaking. The small pieces were then dip etched, cleaned, and the Ge side bonded to a transistor header. Contact to the alloy was made using a silver contact paint. The silver contact area, lead wires, and header leads were then waxed, etched, and rinsed in deionized water. The etching was allowed to proceed until all unmasked areas of the alloy were etched away.

A transistor curve tracer was used for qualitative observations of the *I-V* characteristics at room temperature with and without incandescent (microscope light) illumination. *C-V* measurements were made using a Boonton Model 71A capacitance/inductance meter, at 1 MHz, and a signal level of 15 mV peak to peak. Measurements at 500 and 100 kHz were obtained using a Boonton Model 75C capacitance bridge.

Results and Discussion

Si_xGe_{1-x} epitaxial growth characteristics.—Both n and p conductivity type Ge substrates of (100) and (110) orientations respectively were etched *in situ* at 850°C in mixtures of up to 7% HCl in H_2. The resultant surfaces were mirror-smooth and structureless. The etch rate was linearly proportional to both HCl concentration and time at a hydrogen flowrate of 10 liters/min.

The past history of the reaction chamber was found to be important to the appearance of the wafer after etching. When the reaction chamber had been thoroughly cleaned after a prior Si_xGe_{1-x} growth or had been used exclusively for Ge growth, the Ge substrate remained highly polished and structureless during etching. However, if the reaction chamber was not cleaned after an alloy run, a deposit was seen to form on the Ge substrate during the etching cycle. It was found that by allowing the etching to continue until the susceptor was etched clean of the previous Si_xGe_{1-x} growth, the deposit could then be completely etched off the substrate surface. It is thought that the deposit which grows on the Ge substrate during the HCl etch step is a Si_xGe_{1-x} alloy which occurs through the use of HCl as a transport agent.

It was found that single-crystal epitaxial layers could be grown without HCl etching prior to epitaxy provided that care was taken during substrate cleaning and subsequent handling. However, without the HCl etching step the alloy layer usually was not electrically isolated from the substrate, since four-point probe and Hall measurements were characteristic of the substrate layer while the heterojunction devices did not rectify.

Si_xGe_{1-x} alloys were epitaxially grown onto n-type and onto p-type Ge substrates with (100) and (110) crystallographic orientations, respectively. Experi-

[3] Materials for Electronics Inc., Jamaica, New York.

Table I. Growth and material characteristics of Si_xGe_{1-x} alloy for different process conditions

Process run	Substrate Type	Substrate Resistivity (ohm-cm)	Substrate Orientation	% GeH_4 in gas stream	% SiH_4 in gas stream	Temp (°C)	Total flow rate (liters/min)	Alloy Layer thickness (μm)	Alloy Growth rate (μm/min)	Alloy Resistivity (ohm-cm) (center)	Alloy Composition (x)
1	n	0.5	(100)	0.14	0.004	800	10	3.5	0.12	0.12	0.03
2	p	0.5	(110)	0.14	0.004	800	10	3.0	0.10	—	0.03
3	n	0.5	(100)	0.14	0.004	800	20	7.6	0.26	0.11	0.04
4	n	0.5	(100)	0.14	0.004	800	30	6.0	0.40	0.40	—
5	n	0.5	(100)	0.14	0.008	800	10	4.0	0.13	0.07	0.05
6	n	0.5	(100)	0.075	0.004	800	10	2.4	0.08	0.11	0.04
7	n	0.5	(100)	0.14	0.004	820	20	4.3	0.28	0.16	0.02
8	n	0.5	(100)	0.14	0.004	850	20	3.0	0.20	0.03	0.03
9	n	0.5	(100)	0.037	0.016	800	10	5.6	0.13	0.13	0.22
10	p	0.5	(110)	0.037	0.016	800	10	5.5	0.12	—	0.23
11	n	0.5	(100)	0.037	0.016	830	10	4.6	0.12	0.20	0.25
12	p	0.5	(110)	0.037	0.016	840	10	4.6	0.12	—	0.24

ments were conducted to determine the effects of process variables on the growth and material characteristics of the alloy layers. Table I lists the results of process runs for which analysis of the Si_xGe_{1-x} layers were made. The data shown in this table will be referred to in the following paragraphs.

An examination of Table I indicates that at constant flow rates and constituent concentration, the growth rate is reasonably independent of temperature (compare runs 3,7; 9,11; and 10,12), and that the growth rate is the same for (100) and (110) surfaces under similar conditions. In Fig. 2, it is seen that at fixed composition in the gas stream, the growth rate is linearly dependent on the total flow rate at constant temperature (runs 1-4). These data would indicate that the growth process of the Ge (since it is the major component of the alloy) is mass transfer controlled. Joyce and Bradley reported (20) that below 1100°C (to 950°C) the growth rate of Si by the pyrolytic decomposition of SiH_4 onto Si substrates is surface-reaction controlled. They suggest that surface reaction is limited by the rate of removal of hydrogen from the growth surface.

If the growth rate were limited by the rate of removal of hydrogen from the surface, it would be expected that for our case it would inhibit the growth of Ge and of Si. If, however, the Ge growth rate were mass-transfer controlled while the growth of Si were surface-reaction controlled, it would be expected that for an increase in flow rate at constant gas composition and temperature the alloy growth would become more Ge-rich, while for an increase in temperature with gas composition and flow rate fixed the Si content would increase. An examination of Table I shows that these do not happen, indicating that the growth rate of both Si and Ge are mass-transfer controlled. It must be emphasized, however, that this is merely a tentative conclusion since the range of temperature and flow rate used is small.

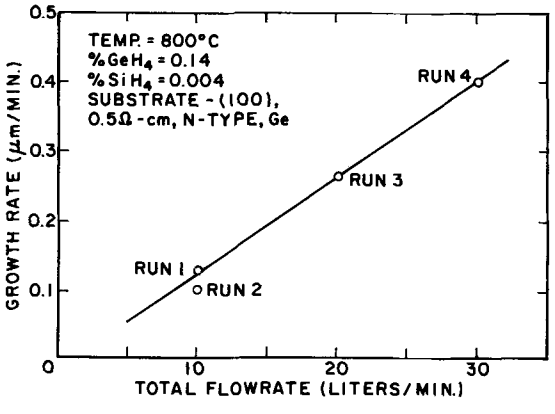

Fig. 2. Growth rate as a function of total flow rate at fixed composition and temperature.

Material characterization.—The surface characteristics of the Si_xGe_{1-x} alloy layers were observed by optical microscopy. The surfaces, in general, have a sandy appearance as shown in Fig. 3a. Surfaces of alloys grown on p-type (110) wafers appear to have a somewhat smoother and less textured surface than those grown on n-type (100) wafers. In general, as the growth rate was increased, the surfaces of low silicon concentration alloys ($x \simeq 0.05$) became more textured. As the alloy concentration or growth rate was increased the temperature of the growth process became the most important parameter with respect to surface appearance. For example, clusters or protrusions of the type shown in Fig. 3b were obtained for a 22 a/o Si alloy growth process at 800°C (run 9). Keeping all other process parameters constant but raising the temperature to 830°C (run 11) eliminated all the cluster defects and resulted in a surface comparable to that shown in Fig. 3a. Surface protrusions were also observed for runs 3 and 4 which were grown at 800°C at growth rates of 0.26 and 0.40 μm/min, respectively. However, run 7 which was grown under similar conditions to run 3, except that the temperature was raised 20°C (to 820°C), did not have surface protrusions. The elimination of these surface protrusions for higher growth temperatures is thought to be due to the fact that at the higher temperature the surface mobility of the silicon is larger. Thus the silicon atoms are able to diffuse more readily to the "growth steps" and complete growth planes rather than result in growth from localized nucleation sites associated with low surface mobility.

Etch-pit counts revealed dislocation densities from 10^4 to 10^7 cm^{-3} for alloys of low Si concentration. For higher Si content, the defect density was much higher than this; however the concentration could not be determined because of the tendency for the defects to be clustered.

From Laue back-reflection analysis it was determined that the Si_xGe_{1-x} growth was crystalline with the same crystal orientation as the substrate. In general, the spots were sharp. However, for those crystals which had surface protrusions as shown in Fig. 3b, partial Debye rings were observed indicating some lattice distortion.

Lattice parameters were determined from diffractometer measurements. All the alloys were found to be highly oriented with two distinct diffraction peaks corresponding to the alloy layer and the germanium substrate. Figure 4 shows a diffractogram, for cobalt radiation, of an alloy layer with $x = 0.25$ grown on (100) Ge substrate. The peak at $2\theta \simeq 71°$ results from diffraction in the alloy while that near 70° results from the Ge substrate.

Also in Fig. 4, it can be seen that the alloy diffraction peak is somewhat asymmetric. It was determined that the asymmetry was not due to misalignment of the diffractometer. It may be that the asymmetry is due to a transient variation in the SiH_4 and GeH_4 flow rates at the start of the epitaxy process. The hydrides

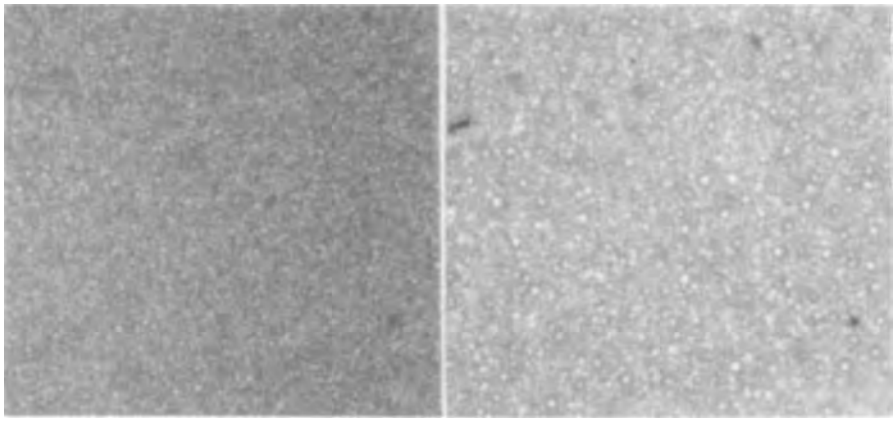

Fig. 3. Surface of Si_xGe_{1-x} epitaxial alloy layer with (a, left) orientation (110), $x = 0.25$ and (b, right) orientation (100), $x = 0.22$. (Magnification ×155.)

were not continually purged prior to their introduction into the reaction chamber and it is expected that a transient period is required before the flow rates attain their steady-state values. Thus, during the transient period the alloy growth layer would differ in composition from the remaining part with a resultant asymmetry in the alloy diffraction peak.

It is also seen in Fig. 4 that there is some broadening of the diffraction peak of the Si_xGe_{1-x} alloy in comparison to the Ge substrate peak. This type of broadening was observed for all of the alloy peaks and is thought to be due to the presence of some nonuniform strain in the alloy layer (17). We believe that this results from two effects: the mismatch in the lattice constant of the two materials and the different coefficients of thermal expansion. The latter would create a strain as the sample is cooled from the growth temperature even if crystal defects are introduced during growth to reduce the strain resulting from lattice mismatch.

For samples grown at growth rates 0.08-0.13 μm/min with low Si concentration (less than 5 a/o) the two peaks could be resolved using an input slit angle (1°), exit slit (0.05°), and high resolution Soller slits. However, for samples grown more rapidly than this, the alloy peak was broadened and the exit slit had to be reduced to resolve these peaks. An exit slit of 0.02° coupled with an entrance slit of 2° was adequate. We

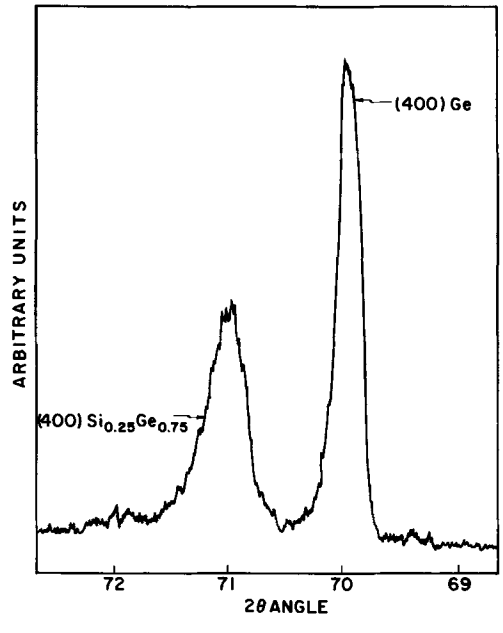

Fig. 4. X-ray diffractogram showing Kβ(400) $Si_{0.25}Ge_{0.75}$ and (400) Ge diffraction peak for cobalt radiation.

tentatively attribute this broadening to strain due to defects introduced during growth at these higher growth rates.

Although no impurity was intentionally introduced into the reaction chamber, Hall effect and thermal probing measurements indicated that the alloy was p-type. The alloy resistivity could be measured only for growths on n-type substrates since these cases provided the necessary junction isolation between the epitaxial growth and the substrate. The resistivity as measured with a four-point probe was generally on the order of 0.10 ohm-cm and reasonably independent of process parameters. The uniformity across a wafer surface was better than 10%. Some of the runs in which the HCl etch was not used gave considerable variation of resistivity with position. It is thought that this results from poor isolation at the interface and an influence of the substrate on the measurements.

From standard Hall measurements, the alloy resistivity was found to be comparable to that obtained from four-point probe measurements. The carrier concentration, obtained from the Hall data under the assumption that the ratio of drift to Hall mobility was unity, was determined to be $2\text{-}5 \times 10^{17}$ cm^{-3} with a Hall (hole) mobility in the 250-400 cm^2/V-sec range for 4-5 a/o Si in the alloy. In general, the resistivity and Hall mobility were somewhat larger as determined by the Van der Pauw method. This is thought to be a consequence of the fact that the contacts were not points nor were they located exactly on the boundary of the sample. This results in an additive error as shown by Van der Pauw (18, 19).

At a carrier concentration of 3×10^{17} cm^{-3}, the Hall mobilities of p-type Ge and Si are approximately 800 cm^2/V-sec and 200 cm^2/V-sec (21, 22), respectively. Since our measurements were made on alloys of 4-5 a/o Si we would expect the mobilities to be approximately equal to those of Ge instead of the measured values of 250 to 400 cm^2/V-sec. This reduced hole mobility could result from the increased carrier scattering expected from random positions of the Si atoms. However, it may be that the increased scattering is associated with the large defect concentration.

The origin of the p-type conductivity is not known. Acceptors may be introduced during growth from the reaction chamber (although depositions using $GeCl_4$ and $SiCl_4$ at higher temperatures result in high resistivity layers). Alternately they may be introduced from the gas streams or may result from the defects which occur in the growth, or from the strain introduced upon cooling. It is reported that regions of high deformation in germanium tend to be p-type (23).

Device characteristics.—Although without HCl etching just prior to growth, there appeared to be many regions of electrical shorting between the alloy and substrate, devices made from those runs in which the

HCl etch step was included yielded heterojunctions with electrical characteristics which seem to be qualitatively consistent with predictions based on heterojunction theory (24). Si_xGe_{1-x}/Ge p-n heterojunctions were found to be rectifying while p-p heterojunctions were found to be weakly rectifying and in some cases their *I-V* characteristics were not reproducible from unit to unit. The weakly rectifying characteristic observed for the p-p heterojunctions is expected because of the small discontinuity in the valence band edge and defect states at this interface (25). Some of the nonlinearity of the *I-V* characteristics can be attributed to the silver contacts used.

It should be pointed out, however, that if the acceptor is a typical shallow acceptor atom, considering the temperatures and times associated with the growth, it would be expected that the acceptor would diffuse into the Ge, creating a p-n junction in n-type substrates within the Ge and merely a p-p junction at the interface. If the p-type conductivity results from defects, on the other hand, negligible diffusion would be expected and the junction would be expected to be at the interface.

In Fig. 5 $1/C^2$ *vs.* voltage is plotted for a p-n Si_xGe_{1-x}/Ge heterojunction ($x = 0.22$) at three frequencies. The effective carrier concentration was calculated from the slope of the 1 MHz data and found to be 3×10^{15} cm^{-3}. This corresponds to the substrate doping level. This is as expected since the epitaxial layer is much more heavily doped than the substrate and so the depletion region would be expected to extend predominately into the lower doped substrate. The reverse breakdown (avalanche) voltage was also characteristic of the substrate doping level as expected.

A decrease in $1/C^2$ or an increase in capacitance under illumination with a microscope light was also observed at 1 MHz as shown. The carrier density as calculated from the slope, however, remained unchanged. Similar increases in capacitance with illumination were observed at the other frequencies. The frequency dependence of the capacitance is not expected from simple junction theory. However, Van Opdorp and Kanerva (26) have shown that interface states in heterojunctions can lead to such a dependence of capacitance on frequency. The influence of illumination on capacitance has been reported by Yawata and Anderson (27) and Oldham and Milnes (25) who attribute this effect to interface states. From this we conclude that enough interface states exist in our junction to affect the electrical properties. The origin of these states is not clear however. They may result from the lattice mismatch between alloy and germanium substrate, the strain introduced during cooling due to the different thermal coefficients of expansion or perhaps by defects present on the germanium substrate surface as growth started. These all have been reported to result in interface states.

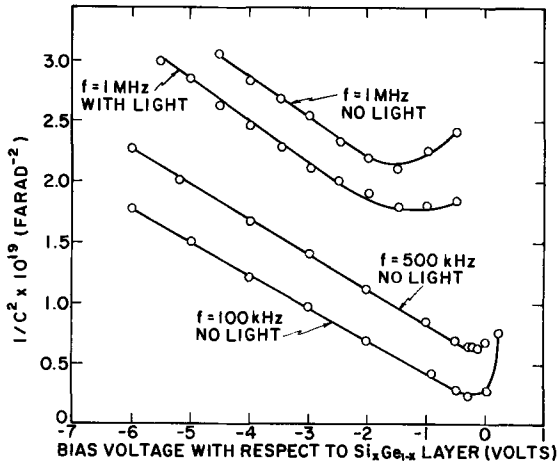

Fig. 5. $1/C^2$ *vs.* voltage for p-n Si_xGe_{1-x}/Ge heterojunction device with $x = 0.22$.

Summary

Si_x-Ge_{1-x} alloys with $0 < x \leq 0.25$ were grown epitaxially on Ge substrates by simultaneous thermal decomposition of SiH_4 and GeH_4 in hydrogen in the 800°-850°C temperature range. A vertical reactor was used in which the process gas passes downward and perpendicular to the substrate. The epitaxial growth process of both Si and Ge is thought to be mass-transfer controlled although the data is insufficient to conclude this. The surface morphology of low Si concentration ($x < 0.05$) layers was found to be dependent upon the growth rate at 800°C. For Si_xGe_{1-x} alloys with $0.22 \leq x \leq 0.25$, growth at 800°C resulted in the formation of defect clusters on the surface; increasing the temperature to 830°C yielded surfaces comparable to those of low Si concentration. Using the Laue back-reflection technique the alloys were found to be single crystal with the substrate orientation. Alloy compositions were determined using the x-ray diffractometer technique. Sharp spots in the Laue back-reflection patterns indicate that the strain in those films grown at less than 0.13 μm/min is not severe. However, partial Debye rings in the Laue patterns and broadening of diffractometer peaks indicate that strain is present in films with surface protrusions, *e.g.*, those grown at increased rates.

Although epitaxial growth occurs with or without *in situ* HCl etching, only those runs in which this etching step was included resulted in electrical isolation between substrate and growth. All deposits were p-type although no intentional doping was introduced. The origin of the p-type impurity is not known although it may be the high defect concentration as revealed by etch-pit counts (10^4-10^7 cm^{-2} on alloys of low Si content).

Si_xGe_{1-x}/Ge p-n heterojunctions were found to be rectifying and the general shape of the current-voltage characteristics are in qualitative agreement with heterojunction theory. The p-p heterojunctions were found to be weakly rectifying which was presumably due to the small potential barrier and defect states at the interface. The reverse breakdown voltage of the p-n structure and the slope of the $1/C^2$-*V* characteristics are characteristic of the substrate region as expected since the deposits were of higher net doping concentration.

The junction capacitance was found to be frequency and light dependent and presumably this effect is a result of lattice defect states at the interface.

Acknowledgments

The authors wish to acknowledge the assistance of Dr. Robert Thomas, RADC, in the design of the epitaxial reactor, Mr. Richard Gardner for the etch-pit studies, and Miss Martha Schwartzmann for many helpful suggestions and discussions during the course of this work. We are also indebted to Mr. Erwin Selleck for help with the diffractometer measurements and Drs. Bernard Waldman and John Schenck for critically reviewing the results. We also wish to thank the manuscript reviewers of this Journal for many helpful suggestions.

Manuscript submitted Feb. 15, 1972; revised manuscript received Nov. 27, 1972. This was Paper 272 presented at the Miami Beach Meeting of the Society, Oct. 8-13, 1972.

Any discussion of this paper will appear in a Discussion Section to be published in the December 1973 JOURNAL.

REFERENCES

1. See for example: C. Kittel, "Introduction to Solid State Physics," 3rd ed., p. 576, John Wiley & Sons, New York (1966).
2. R. Braunstein, A. R. Moore, and F. Herman, *Phys. Rev.*, **109**, 695 (1958).

3. G. Dresselhaus, A. F. Kip, H. Y. Ku, and G. Wagoner, *ibid.*, **100**, 1218 (1955).
4. A. Levitas, C. C. Wang, and B. H. Alexander, *ibid.*, **95**, 846 (1954).
5. R. Braunstein, *ibid.*, **130**, 869 (1962).
6. E. Schmidt, *Phys. Status Solidi*, **27**, 57 (1968).
7. A. V. Sandulova, P. S. Bogoyavlenskii, and M. I. Bronyuk, *Akad. Nauk SSR* (Proceedings, Chem. Sect.), **143**, 224 (1962).
8. K. J. Miller and M. J. Grieco, *This Journal*, **109**, 70 (1962).
9. R. C. Newman and J. Wakefield, *ibid.*, **110**, 1068 (1963).
10. I. P. Akimchenko and K. L. Lyutovich, *Soviet Phys.—Semiconductors*, **5**, 864 (1971).
11. K. L. Lyutovich, T. A. Ukhorskaya, and F. A. Gimel'farb, *Soviet Phys.—Crystallography*, **15**, 1109 (1971).
12. D. L. Feucht, "Proceedings of the International Conference on Heterojunctions," G. Szigeti, Editor, Vol. 1, p. 39, Akademiai Kiado, Budapest (1971).
13. F. G. Allen, *J. Appl. Phys.*, **28**, 1510 (1957).
14. W. W. Happ, and W. Shockley, *Bull. Am. Phys. Soc., Ser. II.*, **1**, 382 (1956).
15. F. D. Rosi, *Solid State Electron.*, **11**, 833 (1968).
16. H. Garret and R. Brock ehurst, "Tables of Interplanar Spacings Computed for the Characteristics Radiation of Copper, Molybdenum, Iron and Cobalt," WADC Technical Report 57-381, ASTIA Document No. AD 142344, Wright Air Development Center (1968).
17. B. D. Cullity, "Elements of X-Ray Diffraction," 3rd ed., Addison-Wesley, Inc. (1967).
18. L. J. Van der Pauw, *Philips Tech. Rev.*, **20**, 220 (1958/59).
19. L. J. Van der Pauw, *Philips Res. Rept.*, **13**, 1 (1958).
20. B. A. Joyce and R. R. Bradley, *This Journal*, **110**, 1235 (1963).
21. R. M. Warner, Jr. and J. N. Fordemwalt, "Integrated Circuits," McGraw-Hill Book Co., New York (1965).
22. F. A. Trombore and A. M. Tartaglia, *J. Appl. Phys.*, **29**, 1511 (1958): see also O. A. Golgova, B. Ya. Maizhes, and L. S. Stil'bans, *Soviet Phys. Solid State*, **3**, 2259 (1962).
23. W. C. Dunlap, Jr., "An Introduction to Semiconductors," p. 265, John Wiley & Sons, Inc., New York (1960).
24. R. L. Anderson, *Solid State Electron.*, **5**, 341 (1962).
25. W. G. Oldham and A. G. Milnes, *ibid.*, **7**, 153 (1964).
26. C. Van Opdorp and H. K. J. Kanerva, *ibid.*, **10**, 400 (1967).
27. S. Yawata and R. L. Anderson, *Phys. Status Solidi*, **12**, 297 (1965).

Kinetics of the Chemical Vapor Deposition of Tungsten

W. A. Bryant

Westinghouse Astronuclear Laboratory, Pittsburgh, Pennsylvania 15236

and G. H. Meier*

Department of Metallurgical and Materials Engineering, University of Pittsburgh, Pittsburgh, Pennsylvania 15213

ABSTRACT

The kinetics of the chemical vapor deposition of tungsten by the hydrogen reduction of WF_6 were studied over the system pressure range from 6 to 60 Torr and over the temperature range from 500° to 870°C to determine the operative rate controlling mechanisms. Within the pressure and temperature ranges studied HF desorption from the substrate was determined to be rate limiting for lower pressure-temperature combinations. An activation energy of 7300 cal/mole was associated with this mechanism. At higher pressure-temperature combinations WF_6 diffusion to the substrate was rate controlling. The activation energy for this process was found to be 1650 cal/mole.

The production of tungsten either in the form of coatings or free-standing shapes by chemical vapor deposition (CVD) has, in the last ten years, become an important manufacturing process. The over-all chemical reaction most usually associated with tungsten deposition and the one considered throughout this paper is given by

$$WF_{6(g)} + 3H_{2(g)} = W_{(s)} + 6HF_{(g)} \qquad [1]$$

A pertinent problem associated with this reaction is the nonuniformity of deposit thickness that is obtained when a substrate of considerable surface area (such as a removable mandrel or an item to be coated) is utilized. Deposit nonuniformity is the result of variations in reaction rate throughout the system. These variations are related to differences in temperature, pressure, and gas composition. To achieve deposit uniformity it is thus essential that the kinetics of the process be understood.

Holman and Huegel (1) have measured tungsten deposition rates under conditions of presumed negligible HF concentration and concluded that an unspecified surface process was rate controlling over a wide range of temperature and pressure. Data from the highest pressure-temperature combinations could not be explained by this analysis and were thought to represent the effect of inadequate supply of reactants. Haskell (2) developed a model in which the rate controlling mechanism for tungsten deposition was assumed to be HF desorption from the substrate. The model was checked by comparing its pressure dependence to that of a portion of Holman and Huegel's data for which the gas composition was considered to consist of essentially all hydrogen. Brecher (3), using the rate data of Berkeley *et al.* (4) obtained in a relatively high-pressure static system, has attempted to formulate a sorption-surface reaction model of the tungsten deposition process.

The work presented here is an investigation of the total range of pressure (6-60 Torr) and temperature (500°-870°C) normally associated with this CVD process. Rate-controlling mechanisms and involved species were tentatively identified by an analysis based on active-site theory. These findings were verified and a model was found to explain the experimentally determined behavior noted in both the high and low pressure-temperature subregions.

Experimental Procedure

The equipment used in this study is shown schematically in Fig. 1. An Inconel 718 deposition chamber

* Electrochemical Society Active Member.
Key words: tungsten fluoride (WF_6), tungsten preparation, desorption, diffusion, coating materials.

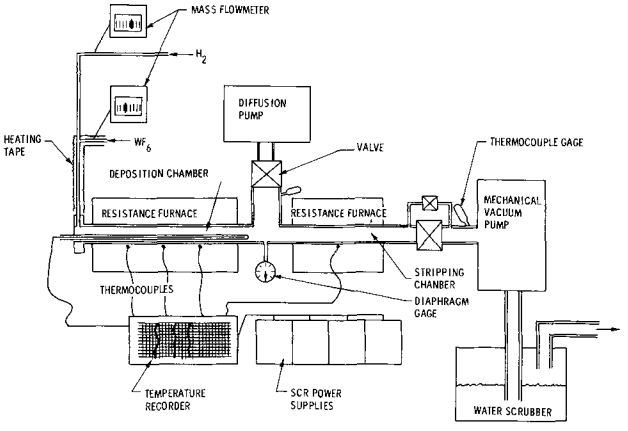

Fig. 1. Schematic drawing of CVD equipment

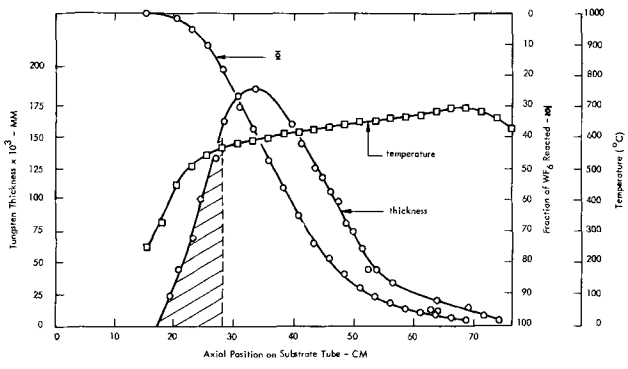

Fig. 2. Typical data used in calculation of gas composition

was heated by a surrounding clamshell resistance furnace whose three heating zones were each powered by a saturable core reactor and whose temperature was monitored with a Chromel-Alumel thermocouple. The downstream portion of the Inconel chamber was filled with stainless steel tubing and heated to approximately 700°C with a second clamshell furnace. This arrangement allowed this portion of the unit to serve as a stripping chamber wherein WF_6 not reacted in the deposition chamber could be spent to prevent its condensation further downstream in the system. Deposition pressure was controlled by the valves located forward of the mechanical vacuum pump and was measured with a diaphragm gauge. HF product gas was trapped in the water scrubber to prevent its discharge to the atmosphere. The unit was equipped with an integral high vacuum system to permit it being helium mass spectrometer leak checked prior to the start of a deposition trial.

Controlled flows of reactant gases entered the deposition chamber through an "O"-ring sealed, water cooled flange. Other features of the chamber included a removable, stainless steel liner tube and a thermocouple well equal in length to that of the tube.

The 4.88 cm ID liner tube, which served as the deposition substrate, was degreased and weighed prior to being inserted into the chamber. Further cleaning was provided during heat-up in flowing hydrogen to the deposition temperature. Hydrogen and WF_6 were admitted to the chamber at the respective rates of 2000 cc/min and 300 cc/min (STP). Temperatures between 500° and 870°C and pressures between 6 and 60 Torr were investigated. During deposition, temperature was measured as a function of axial position within the tube. A temperature profile was prepared from these data. Following deposition, the coated tube was removed from the chamber and its weight gain measured and compared with that calculated from the WF_6 flow rate and time of deposition. Tungsten was then removed from the tube along a line running 90° from vertical either by cutting a section from the coated tube and selectively dissolving the stainless steel or by repeated chipping of the nonadherent tungsten following cracking by application of a radial compressive force. Tungsten thickness was determined as a function of tube length to provide deposit thickness profiles as typified by the plot of Fig. 2.

The further use of a plot of this type to obtain the data necessary for kinetics analysis is best shown by the following sample calculation involving a tungsten thickness measurement at the position 28 cm from the inlet of the substrate indicated by the vertical dashed line in Fig. 2. Since the total amount of WF_6 injected during the 53-min run period was accounted for by the weight gain of the substrate tube, the fraction of WF_6 reacted at the 28-cm position was given by the area beneath the tungsten thickness profile from the point of its origin up to the 28-cm point (27.5 arbitrary area units) divided by the total area beneath the curve (152.5 arbitrary units). This calculation gave a value of 0.18 for Φ, the fraction of WF_6 reacted. (A plot of this parameter is included in Fig. 2)

Since the inlet gas flows (2000 cc/min hydrogen and 300 cc/min WF_6) are in the ratio 6.7 to 1, the over-all equation describing the deposition process can be written as follows

$$(6.7 - 3\Phi)H_{2(g)} + (1 - \Phi)WF_{6(g)} = (\Phi)W_{(s)} + (6\Phi)HF_{(g)} \quad [2]$$

The system pressure of 11 Torr was thus proportional to the sum of the coefficients for the terms involving gases $(7.7 + 2\Phi)$. Thus the partial pressure of hydrogen, for example, was given by

$$p_{H_2} = \left(\frac{6.7 - 3\Phi}{7.7 + 2\Phi}\right) 11 \text{ Torr} \quad [3]$$

which for the appropriate value for Φ of 0.18 gave 8.41 Torr. In a similar manner the partial pressures for WF_6 and HF were found to be 1.12 and 1.47 Torr, respectively.

The deposition rate, R, in cc/min $\times 10^3$ was found by division of the appropriate value for the tungsten thickness (150 mm $\times 10^3$) by the run time of 53 min to yield $R \times 10^3$ of 2.83.

The corresponding temperature was read from the measured temperature profile (superimposed on tungsten thickness profile in Fig. 2) and found to be 575°C.

Results

Numerous temperature, gas composition, and deposition rate combinations were found within a single deposition trial. This large amount of data made it possible to critically analyze the kinetics of tungsten deposition.

The deposition process was considered to consist of five steps as follows: (*i*) gas phase diffusion of reactants to the substrate, (*ii*) adsorption of reactants at the substrate, (*iii*) chemical reaction of reactants on the substrate, (*iv*) desorption of gaseous product at the substrate, and (*v*) gas phase diffusion of gaseous product from the substrate.

Steps (*ii*), (*iii*), and (*iv*) were examined with the aid of active site theory (5). With adsorption being the rate-controlling mechanism, an increased concentration of reactants due to a pressure increase would increase the deposition rate. Adsorption control is normally associated with low system pressure. At higher pressure the substrate surface would tend toward saturation with reactants. If the adsorbed molecules react faster than the product gas can be desorbed, desorption would become rate controlling. Desorption rate is dependent only on the fractional surface coverage of gaseous product and is independent of reactant concentrations. Thus, the deposition rate, if controlled by desorption, should be essentially independent of changes in system pressure (6). If chemical reaction of neighboring adsorbed species is the controlling mechanism at this same higher pressure, the deposition rate at a fixed ratio of reactant concentrations would

be pressure dependent while for a fixed value of pressure the deposition rate as a function of reactant concentrations should pass through a maximum.

To apply this means of analysis to the vapor deposition of tungsten by the hydrogen reduction of WF_6, experimentally determined deposition rates were plotted as a function of pressure for two combinations of reactant concentration ratios and temperature (Fig. 3). The observed strong dependence of reaction rate on pressure at very low pressures (less than 6 Torr) suggests adsorption control in this region. In the pressure range of interest in this work (6-60 Torr) reaction rate is essentially independent of pressure in the lower portion of the range. This suggests that desorption is the rate-controlling mechanism there. The low activation energy for HF desorption in comparison to that for F_2 desorption (2) suggests the former molecule to be important for this mechanism of rate control. The critical tests for chemical reaction control suggested above failed to identify this mechanism as rate controlling in this pressure-temperature region. It is reasonable to assume that for the higher pressures gas phase diffusion is the rate-limiting process (7, 8) and, since it is the least mobile molecule, WF_6 is the species of interest.

The validity of the two rate-controlling mechanisms (WF_6 diffusion and HF desorption) and their respective pressure-temperature region of dominance were ascertained by comparing experimentally determined deposition rates with rates predicted from models of each mechanism.

Following the analysis of Haskell (2), a model for HF desorption was formulated based on the equation

$$H_{(x)} + F_{(x)} = HF_{(g)} \qquad [4]$$

where the subscript x denotes atoms attached to sites on the substrate. Use was made of the postulate of absolute reaction rate theory that the reactants are in equilibrium with the activated complex $HF_{(x)}$ which decomposes to the product $HF_{(g)}$. The flux of HF from the substrate (which is proportional to the tungsten deposition rate) is the product of the concentration of surface sites occupied by the activated species and their frequency of vibration in a direction normal to the substrate surface. By combining all the constants and temperature-dependent terms into a single term, C_{des}, it was possible to express the deposition rate, R, in terms of the partial pressures of the reactants as follows

$$R_w = C_{des}\, p_{H_2}{}^{1/2}\, p_{WF_6}{}^{1/6} \qquad [5]$$

Partial pressure data from three temperatures (510°, 625°, and 705°C) were reduced to the appropriate values dictated by their fractional powers in Eq. [5]. Plots of actual deposition rates *vs.* $p_{H_2}{}^{1/2}\, p_{WF_6}{}^{1/6}$ are shown for each of the three temperatures in Fig. 4 through 6. Each data point, before being plotted, was

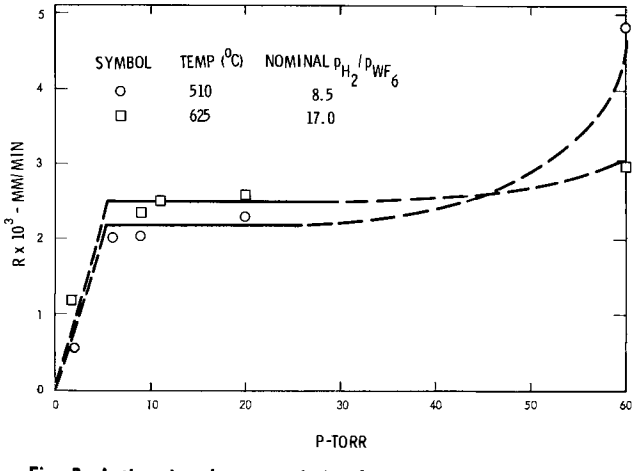

Fig. 3. Active-site theory analysis of tungsten deposition process

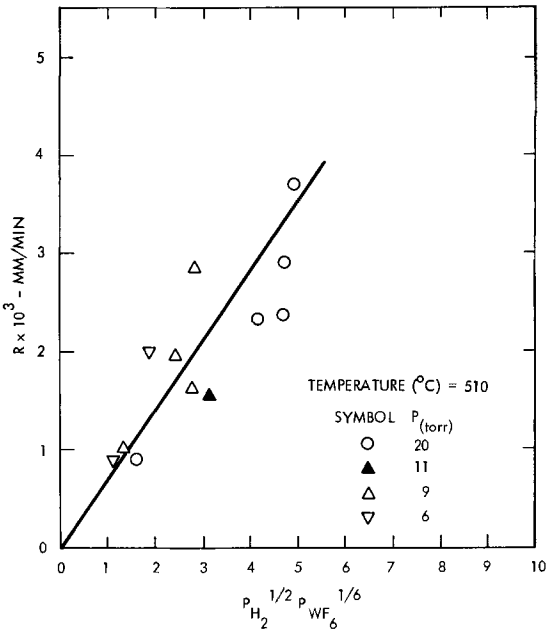

Fig. 4. Comparison at 510°C of experimentally observed deposition rates with rates predicted from the model for HF desorption.

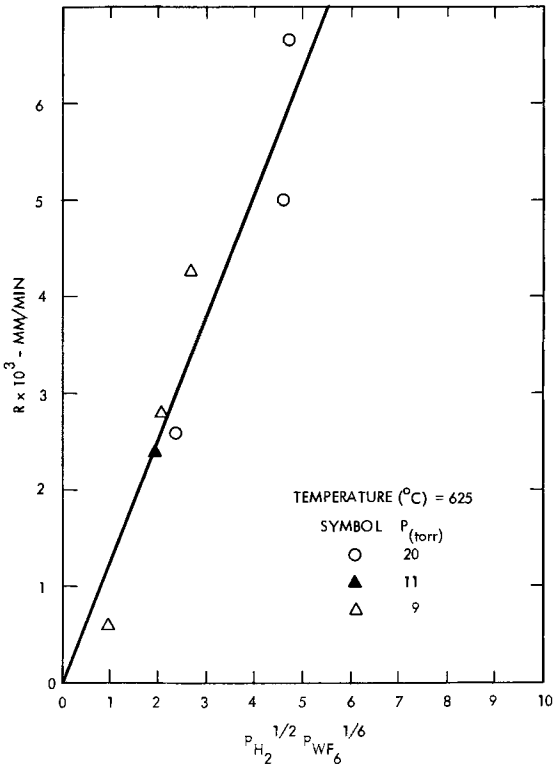

Fig. 5. Comparison at 625°C of experimentally observed deposition rates with rates predicted from the model for HF desorption.

first checked for agreement with the WF_6 transport model to be discussed subsequently. Only those points not fitting the latter model were used in this analysis. Good agreement between experimentally observed deposition behavior and that described by the model is indicated by each figure. To obtain a meaningful value for the activation energy of the HF desorption Arrhenius plots were made at constant values of concentration (constant $p_{H_2}{}^{1/2}\, p_{WF_6}{}^{1/6}$). From these plots (Fig. 7) an activation energy of 7300 cal/mole was obtained.

The data which did not fit the desorption model were generally from the higher pressure trials. It was reasonable to assume, therefore, that gas-phase diffusion was the rate-limiting step in the process for the

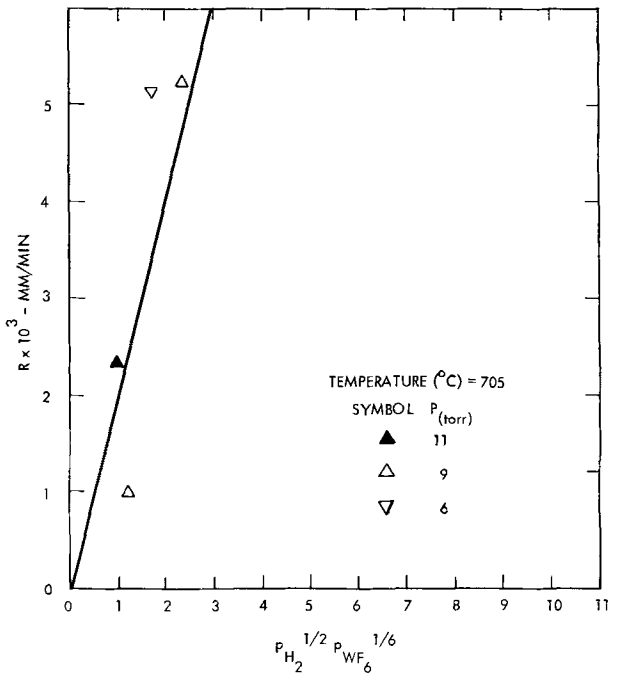

Fig. 6. Comparison at 705°C of experimentally observed deposition rates with rates predicted from the model for HF desorption.

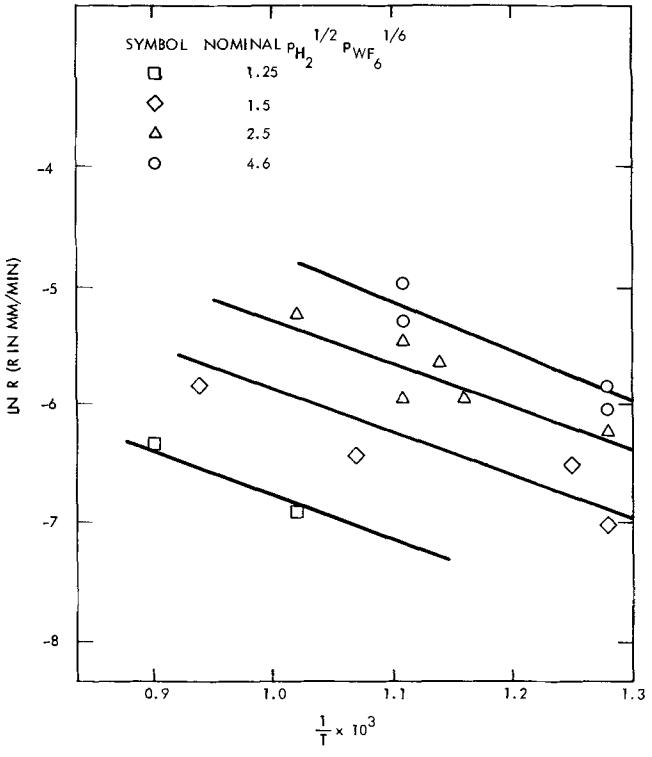

Fig. 7. Arrhenius plots for determination of activation energy for HF desorption.

experimental conditions associated with these data. WF_6 was assumed to be the diffusing species of interest because it is the heaviest and largest molecule in the system.

A model which considered nonequimolar counter-diffusion (8) was used. Thus, the diffusion-controlled deposition rate is given by the relation

$$R_w = k_1 k_g \Delta y \quad [6]$$

Here k_1 is a proportionality constant, k_g is a mass transfer coefficient, and Δy is the diffusion potential. Evaluation of these terms (described in the Appendix) led to the final relation

$$R = C_{diff}\, p_{WF_6}\, T^{1/2}/P \quad [7]$$

in which P is the total pressure and C_{diff} is the combined proportionality constant.

The experimentally determined deposition rates which were not described by the desorption model were plotted against corresponding values of $p_{WF_6} T^{1/2}/P$ (Fig. 8). The WF_6 diffusion model is seen to describe the rate data fairly well. Two minor deviations from model-predicted behavior are noted: the very low deposition rate data are not represented by the line of best fit nor does this line pass through the origin as it should.

Arrhenius plots at constant gas composition (represented by constant values of p_{WF_6}/P) yielded an activation energy of 1650 cal/mole for diffusion of WF_6 to the substrate surface (Fig. 9).

Discussion

The experimental results show that the kinetics of tungsten deposition by the reaction of WF_6 and hydrogen in the pressure and temperature ranges of 6-60 Torr and 500°-870°C, respectively, are well described by a model based on WF_6 transport to the substrate for high temperature-pressure combinations and by a model of HF desorption from the substrate at lower temperature-pressure combinations.

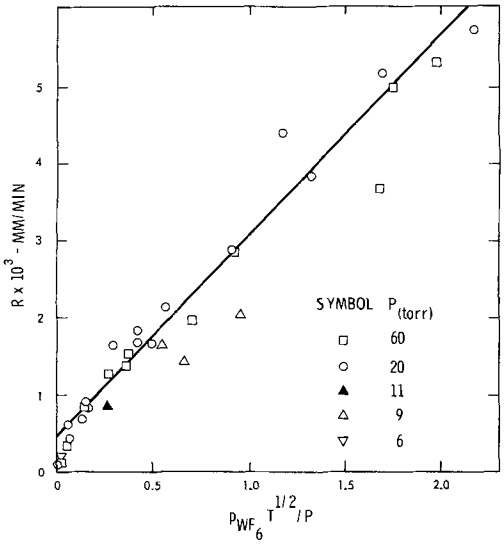

Fig. 8. Comparison of experimentally observed deposition rates with rates predicted from the model for WF_6 gas phase diffusion.

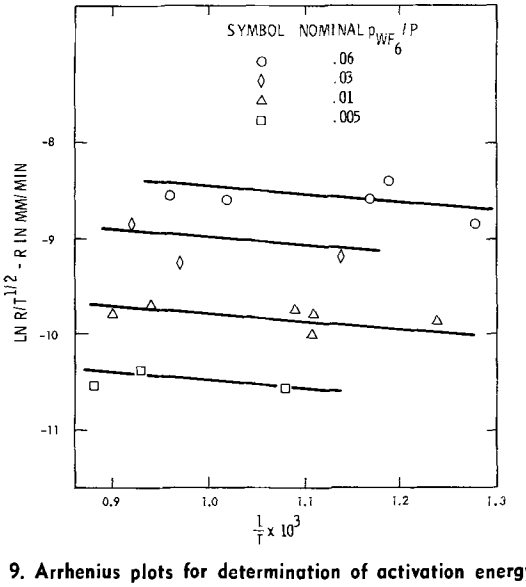

Fig. 9. Arrhenius plots for determination of activation energy for WF_6 gas phase diffusion.

The two regions of deposition control are separated by a boundary occurring at a pressure of approximately 20 Torr at 500°C and decreasing to approximately 6 Torr at 870°C.

HF desorption.—Tungsten deposition at the lower pressure-temperature combinations within the ranges studied is controlled by the rate of HF desorption from the substrate. This finding is in agreement with Haskell's analysis of the lower pressure-temperature data of Holman and Huegel for the same reaction. However, the latter investigators have calculated an activation energy of 16,000 cal/mole for the process as compared to the 7300 cal/mole found in the present study. At least part of this discrepancy is due to the manner in which Holman and Huegel plotted their rate data. They chose to plot the logarithm of the deposition rate as a function of the reciprocal of the absolute temperature in order to obtain the activation energy. This procedure is strictly correct only where the reactant concentration terms in the rate equation are constant. That this condition was obtained in their work is very doubtful. Their rate equation

$$R_m = C \exp(-16{,}000/RT) P^{1/2} \quad [8]$$

contains only one concentration related term, $P^{1/2}$. (The concentration of a single gas in a mixture of gases is given by the ideal gas law as $N/V = p/kT$ where N is the number of molecules and V is the volume.) Such an expression would be expected to be a reasonable approximation only where the gas phase is predominantly comprised of a single species. Thus, only for the conditions of high initial H_2/WF_6 ratio and low reaction temperature would this expression be reasonable and the activation energy value obtained therefrom be meaningful.

Several calculations were made to determine the magnitude of the adjustment to Holman and Huegel's gas compositions necessary to bring their value for activation energy in line with that found in the present work. The required fractional depletions of WF_6 necessary to effect this adjustment are greatly in excess of any value which would be considered reasonable in view of Holman and Huegel's experimental setup. Therefore, the difference in values for activation energy can only be partially explained by Holman and Huegel's not correcting their gas composition by allowing for WF_6 depletion.

Consideration was given to the possibility that the difference in activation energy was attributable to differences in experimental conditions, namely, deposition efficiency and temperature of the deposition gases. In the present work, the efficiency was very high, and the gas temperature was likely high owing to a relatively long period of contact with the hot substrate. In Holman and Huegel's setup both efficiency and gas temperature would necessarily be low.

To examine this effect further the deposition data of Shroff (10) were evaluated and compared (Fig. 10) to that of the investigations already discussed. Since Shroff employed a WF_6 flow of only 50 cc/min, the efficiency of his system would be expected to be high. However, judging from a description of his experimental setup (11), it would also be expected that the gases would be only moderately heated by the substrate. Thus, it could be considered that Shroff's experimental conditions were approximately intermediate to those of the other two investigations. Since the Shroff deposition rates were generally of intermediate value for fixed deposition parameters of temperature and $p_{H_2}^{1/2} p_{WF_6}^{1/6}$ product (Fig. 10) it would appear that experimental conditions do influence the rate of the deposition process. The activation energy of 10,000 cal/mole determined for the Shroff work further establishes this influence.

Based on the comparisons made here it seems reasonable to presume that the activation energy for the desorption-controlled deposition process is inversely related to the temperature of the deposition gas.

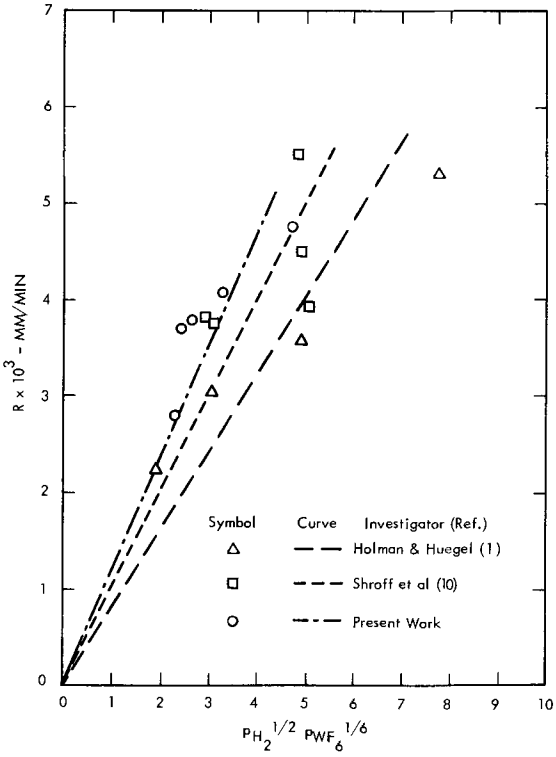

Fig. 10. Comparison of rate data at 600°C

Brecher's formulation of a model of sorption-surface reaction rate control produced the rate expression for tungsten deposition

$$R_w = k_r X_{WF_6} X_{H_2}^3 \quad [9]$$

where X is the mole fraction of the reactant at the substrate and k_r is the reaction rate constant given by

$$k_r = AP^2 \exp(-B/T) \quad [10]$$

The dependence of k_r on P^2 is not well established. This relation was obtained from rate data taken at 100-760 Torr and at temperatures between approximately 480° and 820°C. It was shown in the present work, however, that in this pressure-temperature regime sorption-surface reactions are not rate controlling. Instead, for these conditions, deposition is likely controlled (at low mole fractions of WF_6 at least) by WF_6 diffusion to the substrate or near the upper limit of pressure, even possibly by convection transport. The activation energy for Brecher's unspecified sorption-surface reaction (27,000 cal/mole) is therefore not easily interpreted.

WF_6 transport model.—From Fig. 8 it is noted that the data are not all represented by a straight line passing through the origin as required by the expression for deposition controlled by WF_6 transport (Eq. [7]). Two minor deviations from the behavior predicted by the model are responsible. In the formation of the model it was assumed that the diffusion coefficient was proportional to $T^{3/2}$ in agreement with kinetic theory for gases. It has been shown in actuality, however, that a $T^{7/4}$ dependence is more realistic (12). Use of this latter value yields a corrected rate equation given by

$$R_w = C_{diff} p_{WF_6} T^{0.55}/P \quad [11]$$

This correction offsets the data plot of Fig. 8 sufficiently to permit its passage through the origin.

The second deviation from predicted behavior is constituted by the failure of the measured rates corresponding to very low $p_{WF_6}T^{1/2}/P$ values to equal those predicted by the model. The one feature common to each of these deviant data points is the very low associated values of p_{WF_6} and p_{HF}. Thus at low R_W values the presence of hydrogen cannot be ignored as it was

in the formulation of the WF_6 transport model since in this region the rate of WF_6 diffusion through hydrogen rather than through HF is controlling.

The activation energy for WF_6 transport in this system has not been previously determined. The value of 1650 cal/mole obtained in the present work is reasonable since gas-phase diffusion is generally associated with very low activation energies.

It is interesting to note that WF_6 diffusion controlled the deposition kinetics for the higher pressure-temperature combinations. This result is in disagreement with that of Holman and Huegel (1) who, for the same pressure-temperature regime, attributed control of the deposition rate to the same surface reaction that they found controlling at lower pressure-temperature combinations. In their work an inadequate supply of reactants was offered as the cause of the difference in deposition rate dependence on temperature on going from the lower pressure-temperature regime to the higher.

Conclusions

It is concluded from the results of this work that two tungsten deposition rate-controlling mechanisms are operative in the pressure and temperature ranges usually associated with hydrogen reduction of WF_6. At the lower pressure-temperature conditions HF desorption is the controlling step in the process, while for higher pressure and temperature, WF_6 gas-phase diffusion is the rate-limiting mechanism.

APPENDIX

Formulation of Model for WF_6 Transport

If it is assumed in the system of gases WF_6-HF-H_2 that the hydrogen can be ignored (and such is the case as is shown subsequently in this development) the rate of tungsten deposition as a function of the nonequimolar counterdiffusion of WF_6 and HF to and from the substrate is given by the relation

$$R_w = k_1 k_g \Delta y \qquad [A\text{-}1]$$

where k_1 is a proportionality constant, k_g is a mass transfer coefficient, and Δy is the diffusion potential.

The diffusion potential (determined from the Stefan-Maxwell equations) for WF_6 transport in this system is given by (9)

$$\Delta y = \frac{1}{1-x} \ln \frac{1-(1-x)X_{s1}}{1-(1-x)X_{g1}} \qquad [A\text{-}2]$$

where x is the ratio of molar flow to the substrate to the molar flow away from the substrate (taken to equal 1/6 from the stoichiometry of the deposition reaction) and X_{g1} and X_{s1} are, respectively, the mole fractions of WF_6 in the gas stream and at the substrate surface. With the assumption of negligible WF_6 at the substrate (owing to the greater rate of the surface reaction as compared to the rate of WF_6 transport) and substitution of the value 1/6 for X, Δy can be expressed as

$$\Delta y = \frac{6}{5} \ln \frac{1}{1-5/6X_{g1}} \qquad [A\text{-}3]$$

For the small X_{g1} values investigated ($X_{g1} \leq 0.13$), Eq. [A-3] can be rewritten within an error of 1% as

$$\Delta y \approx -\frac{6}{5} \ln (1-5/6X_{g1}) \qquad [A\text{-}4]$$

Substitution of p_{WF_6}/P for X_{g1} and again utilizing the fact that only small molar fractions of WF_6 are being considered permits the diffusion potential to be written as

$$\Delta y = X_{g1} = p_{WF_6}/P \qquad [A\text{-}5]$$

The mass transport coefficient is given by

$$k_g = D_{12}P/ZRT \qquad [A\text{-}6]$$

where Z is a geometric constant and D_{12} is taken to be the concentration dependent diffusivity of the pair WF_6-HF in the WF_6-HF-H_2 mixture. Recalling the assumption that the hydrogen can be ignored in this particular case and assigning the subscript 3 to this gas permits D_{12} to be expressed as follows (13)

$$D_{12} = \mathcal{D}_{12}\left\{1 + \frac{X_3\left[\frac{M_3}{M_2}\mathcal{D}_{13} - \mathcal{D}_{12}\right]}{X_1\mathcal{D}_{23} + X_2\mathcal{D}_{13} + X_3\mathcal{D}_{12}}\right\} \qquad [A\text{-}7]$$

Here X_i and M_i are the mole fraction and molecular weight of species i, respectively, and $\mathcal{D}_{ij}$ is the binary diffusivity in the system i-j and is virtually independent of composition.

$\mathcal{D}_{ij}$ values were calculated from Bird's expression

$$\mathcal{D}_{ij} = 0.0018583 \frac{\sqrt{T_3\left(\frac{1}{M_i} + \frac{1}{M_j}\right)}}{P\sigma_{ij}^2 \Omega_{\mathcal{D}_{ij}}} \qquad [A\text{-}8]$$

Maximum and minimum values for the dimensionless parameter $\Omega_{\mathcal{D}_{ij}}$ were calculated for the range of temperatures covered in this investigation and found to be 1.01 and 0.92, respectively. Thus in the calculation of $\mathcal{D}_{ij}$ values it was reasonable to take $\Omega_{\mathcal{D}_{ij}}$ equal to unity. The other Lennard-Jones parameter appearing in Eq. [A-8], σ_{ij}, can be considered to be a collision diameter equal to $\frac{1}{2}(\sigma_i + \sigma_j)$. Calculations of these collision diameters and the subsequent evaluation of each $\mathcal{D}_{ij}$ value permitted the reduction of Eq. [A-7] to the form

$$D_{12} = \mathcal{D}_{12}\left\{1 - \frac{1.11X_3}{8.51X_1 + 7.28X_2 + 1.84X_3}\right\} \qquad [A\text{-}9]$$

Since the composition of the gas mixture is given by the chemical reaction (where Φ is the fractional amount of WF_6 reacted) as

$$(1-\Phi)p_{WF_6} + (6.7 - 3\Phi)p_{H_2} + (6\Phi)p_{HF} = (7.7 + 2\Phi)P \qquad [A\text{-}10]$$

and the condition

$$X_1 + X_2 + X_3 = 1 \qquad [A\text{-}11]$$

must be satisfied, D_{12} can be written solely as a function of $\mathcal{D}_{12}$ and Φ.

In the current study the value of Φ ranged from 0.42 to essentially 1.0 to give a corresponding range of D_{12} values of $0.818\mathcal{D}_{12}$ to $0.918\mathcal{D}_{12}$. Thus over the range of gas compositions studied D_{12} is essentially a fixed fraction of $\mathcal{D}_{12}$ (taken to be $0.868\mathcal{D}_{12}$) and thus the earlier assumption that the hydrogen can be ignored is supported. That such an assumption would be invalid over all possible gas compositions (represented by Φ varying in value from zero to 1.0) is shown by the corresponding calculated values of D_{12} of $0.643\mathcal{D}_{12}$ to $0.918\mathcal{D}_{12}$.

Using the relation

$$D_{12} = 0.868\mathcal{D}_{12} \qquad [A\text{-}12]$$

the diffusivity of WF_6 in the system (D_{WF_6}) can be written as

$$D_{WF_6} = D_{12} = 0.868(1.84 \times 10^{-5})T^{3/2}/P \qquad [A\text{-}13]$$

Further substitution into [A-6] yields for the mass transport coefficient

$$k_g = \frac{0.868(1.84 \times 10^{-5})T^{1/2}}{ZR} \qquad [A\text{-}14]$$

Substitution of [A-14] and [A-5] into [A-1] combined with a consolidation of constants into C_{diff} yields the final relation for the WF_6 diffusion limited deposition rate

$$R_w = C_{diff} p_{WF_6} T^{1/2}/P \qquad [A\text{-}15]$$

SYMBOLS

R_m	tungsten deposition rate (maximum), mm/min
R_w	tungsten deposition rate, mm/min
p	partial pressure, Torr
D	concentration dependent diffusion coefficient for gaseous pair, cm^2/sec
T	absolute temperature, °K

P	total pressure of system, Torr
N	number of molecules
V	volume, cc
k	Boltzmann's constant
k_r	reaction rate constant
X	mole fraction
n	number of particles per unit volume, liter^{-1}
S_d	average particle cross section, mm^2
M	molecular weight, g/mole
N_o	Avogadro's number
R	gas constant, cal/mole °K
k_g	mass transfer coefficient, g/sec cm^2
Δy	diffusion potential, (dimensionless)
Z	characteristic dimension of system, cm
Φ	fractional amount of WF_6 reacted, (dimensionless)
$\mathcal{D}$	binary diffusivity (concentration independent), cm^2/sec
σ	Lennard-Jones parameter (collision diameter), cm
$\Omega_{\mathcal{D}}$	Lennard-Jones parameter, (dimensionless)
x	ratio of molar flow to substrate to molar flow from substrate
X_{g1}	mole fraction of WF_6 in the gas stream
X_{s1}	mole fraction of WF_6 at substrate surface
A, B, C	constants
k_1, k_2, k_3	constants

Subscripts

g	gas phase
s	solid phase
x	substrate site attached species
des	desorption
diff	diffusion
1	WF_6
2	HF
3	H_2

Acknowledgment

This paper is based on a thesis submitted by W. A. Bryant in partial fulfillment of requirements for the M.S. degree to the University of Pittsburgh, June 1971.

Manuscript submitted Aug. 16, 1971; revised manuscript received Nov. 9, 1972.

Any discussion of this paper will appear in a Discussion Section to be published in the December 1973 JOURNAL.

REFERENCES

1. W. R. Holman and F. J. Huegel, "Proceedings of the Conference on Chemical Vapor Deposition of Refractory Metals, Alloys, and Compounds," A. C. Schaffhauser, Editor, p. 127, The American Nuclear Society, Hinsdale, Ill. (1967).
2. R. W. Haskell, "Chemical Vapor Deposition—Second International Conference," J. M. Blocher, Jr. and J. C. Withers, Editors, p. 63, The Electrochemical Society, New York (1970).
3. L. E. Brecher, *ibid.*, p. 37.
4. J. F. Berkeley, A. Brenner, and W. E. Reid, Jr., *This Journal*, **114**, 561 (1967).
5. O. Levenspiel, "Chemical Reaction Engineering," John Wiley & Sons, Inc., New York (1962).
6. S. M. Walas, "Reaction Kinetics for Chemical Engineers," McGraw-Hill Publishing Co., New York (1959).
7. H. Schafer, "Chemical Transport Reactions," Academic Press, New York (1964).
8. J. H. Oxley, Report DMIC 170 (June 1962).
9. C. F. Powell *et al.*, "Vapor Deposition," John Wiley & Sons, Inc., New York (1966).
10. A. M. Shroff *et al.*, "Proceedings of the 1970 Thermionic Conversion Specialists Conference," p. 58, Miami (1970).
11. A. M. Shroff, "High Temperature Materials—Papers Presented at the Sixth Plansee Seminar," F. Benesovsky, Editor, p. 854, Springer-Verlag, New York (1969).
12. E. H. Kennard, "Kinetic Theory of Gases," McGraw-Hill Publishing Co., New York (1938).
13. R. B. Bird *et al.*, "Transport Phenomena," John Wiley & Sons, Inc., New York (1960).

Dissolution Kinetics of Precipitates of Divalent Cadmium in Sodium Chloride Studied by means of Ionic Thermoconductivity

Rosanna Capelletti and Emico Okuno[1]

Istituto di Fisica dell'Università, Parma-Italia
Gruppo Nazionale di Struttura della Materia del C.N.R., Parma, Italy

ABSTRACT

In OH^- "free" NaCl:Cd system the isothermal time evolution of the solution process of I.V. (impurity-vacancy) dipoles to achieve the thermodynamical equilibrium was studied by means of the I.T.C. (ionic thermoconductivity) method in the annealing temperature range from 323° to 423°K. Two stages were found, both described by a monomolecular first order kinetics. The early fast stage and the subsequent slow one are characterized by activation energies of $\epsilon_1 \sim 1$ eV and $\epsilon_2 \sim 0.8$ eV, comparable with the activation energy for impurity diffusion, and pre-exponential frequency factors $\nu_{01} \sim 6 \times 10^{11}$ and $\nu_{02} \sim 3 \times 10^6$ sec^{-1}. The sources of I.V. dipoles in the two stages were tentatively identified with dipolar precipitates responsible for the additional peaks in I.T.C. spectrum. The energy required to decompose one kind of the above microprecipitates $\epsilon_B^S \sim 0.24$ eV is close to the solution energy of I.V. dipoles. The role of preannealing on thermodynamical equilibrium value n_s and on the solution kinetics was also analyzed.

Recent precipitation and solubility measurements (1-8) show that the knowledge of the aggregation state of divalent cation impurities in alkali halides is preliminary to both optical and electrical studies. Information about precipitation phenomena is still restricted and sometimes contradictory (1-6), chiefly with regard to the nature of the first precipitation products. The occurrence of an initial stage of dimerization (4) of I.V. (impurity-cation vacancy) dipoles

[1] On leave from Instituto de Fisica da Universidade de S.Paulo and Instituto de Energia Atômica, S.Paulo, Brazil.

Key words: alkali halides, solution of impurities, dielectric properties, dissolution kinetics.

was recently discussed by Crawford (9, 10) and Wintle (11): the latter has shown that a diffusion-controlled dimerization reaction can simulate the third order kinetics, experimentally detected by many authors by means of various techniques in different alkali halide systems (1-6, 10). Precipitation of divalent impurities out of the solid solution is accompanied by the growth, in addition to microprecipitates, of larger aggregates of metastable phases and stable segregated ones, which were detected by means of x-ray diffraction (12), electron microscopy (13), and Mössbauer spectroscopy (14).

On the other hand the solution of the impurities can supply a complementary view on the nature of the precipitates. The study of the thermodynamical equilibrium (8, 15) concentration of I.V. dipoles *vs.* temperature gave considerably lower solution activation energies for I.V. dipoles of the order of 0.1-0.2 eV in various systems. Moreover it was shown that the thermodynamical equilibrium value is reached quite slowly even at rather high annealing temperatures.

In our opinion a detailed analysis of the isothermal time evolution of I.V. dipole concentration in the solution process can throw light both on the dynamics of the solution reaction and on the nature of I.V. dipole sources. Moreover additional information can be gathered from the solution kinetics by affecting the nature and distribution of the early precipitates by submitting the sample to suitable preannealing.

To monitor the I.V. dipole concentration we employed the ionic thermoconductivity method (16) which, due to its high sensitivity, allows the detection of relaxation peaks associated with even low concentration of dipolar microprecipitates. Moreover I.T.C. runs are performed at temperatures below 273°K so that the point defects situation determined by annealing at higher temperatures can be frozen in. We chose NaCl:Cd system because precipitation measurements (4) suggested that defect mobility is high, so the thermodynamical equilibrium concentration can be achieved in a reasonably short time.

Experimental Procedures

The samples were grown in our laboratory by means of the Kyropoulos method in controlled atmosphere (dry nitrogen) in order to minimize contamination by OH^-, H_2O, and oxygen (17), which are present in air and affect solubility and precipitation phenomena (18). Cadmium dichloride salt was added to the molten NaCl in percentages ranging from 10^{-4} to 10^{-2} by weight.

In order to get samples with very low OH^- concentration ($<10^{14}/cm^3$), the starting powders were submitted to a suitable procedure. An alternative treatment with Cl_2 followed by HCl (at the pressure of ~250 mm Hg) is very efficient in eliminating OH^-, O^{--}, Br^-, and I^- if the gases react in the powdered salt at about 700°C, *i.e.*, about 100°C below the melting point of NaCl (19, 20).

The I.T.C. measurements were performed by the usual technique (16). The crystal slab (area: 2-3 cm^2, thickness: 0.5-1 mm) was polarized in a static electric field (ranging from 10^4 to 3×10^4 V/cm) for 3 min at the temperature T_p and then cooled down to the temperature T_f, generally 120°K; after which the field was switched off. During these steps the dipoles become polarized at saturation and remain orientated in the same configuration obtained at the polarization temperature, because at low temperature the relaxation time is practically infinite. The crystal was then warmed up at the nearly constant rate of 0.1°K/sec: the dipole relaxation time for orientation gets shorter and the dipoles lose their preferred orientation giving rise to a depolarization current. This was detected at linearly increasing temperature by a vibrating reed electrometer (Cary 31V) and recorded by Speedomax. The apparatus can measure currents as low as 10^{-16}A.

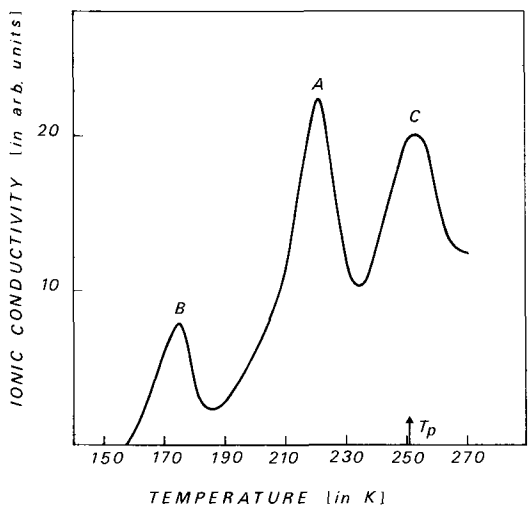

Fig. 1. Ionic thermocurrent of NaCl:Cd (OH^- free): the polarization temperature is indicated by an arrow.

The procedure followed in order to obtain solubility and precipitation curves is described in detail in a previous paper (8).

The aging of samples at temperatures below 530°K was performed directly in the measuring cryostat; in order to "quench" the sample the cryostat was filled with dry N_2 and cooled down to 273°K in a time shorter than 4 min.

Two cryostats with different performances were employed: the former, with vertical identical shaped aluminum electrodes assured the minimum temperature gradient through the sample; in the latter, with horizontal gold electrodes, the top one can be put in contact with liquid nitrogen in order to get a very fast quenching of the sample. The electrical contact between sample and electrodes was improved with colloidal graphite. The reproducibility of measurements was within 2%.

Results

The ionic thermoconductivity curve for a sample of NaCl:Cd "chlorinated" as described above, and polarized at $T_p = 252$°K shows three principal peaks at 174°, 220°, and 250°K. The activation energies for orientation of the dipole responsible for the three peaks are 0.4, 0.67 (16), and 0.62 eV. The peak at 220°K (peak A) is due to I.V. dipole relaxation, the peak at 174° (peak B) is related to microprecipitates, and that at 250°K (peak C) was usually detected in samples with very high Cd concentration (8). The curve in Fig. 1 corresponds to the I.T.C. of a sample "as received," *i.e.*, after aging for a long time at room temperature. The isothermal time evolution of I.V. dipole concentration to achieve the thermodynamical equilibrium value was studied by measuring the I.V. dipole concentration[2] as a function of the aging time at a given temperature, until a saturation is reached.

The isothermal time evolutions of I.V. dipoles were studied for annealing temperatures T_a: 323°, 331°, 340°, 346°, 353°, 364°, 374°, 390°, 405°, and 423°K. In Fig. 2 are shown the solubility curves at $T_a = 353$°K for peak A (curve 1) and for peak B (curve 2) in a sample aged only at temperatures lower than 346°K. Solubility curves always at $T_a = 353$°K for peak A (curve 3) and peak B (curve 4) are related to the same sample but annealed at room temperature after obtaining curves 1 and 2. Figure 2 exemplifies the behavior of solubility curves in the annealing temperature range between 323° and 374°K both for first and second run. It must be pointed out that the higher the annealing temperature T_a, the faster the saturation value was achieved. A change in the solubility curve behavior

[2] The concentration can be evaluated from the area under dipole peak or from the height if the warming rate during I.T.C. measurements is held constant (8).

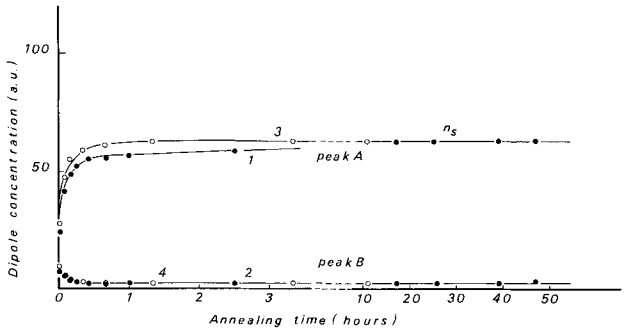

Fig. 2. Solubility curves at T_a = 353°K. Intensity of peak A (curve 1) and peak B (curve 2) vs. annealing time in a sample aged only at temperatures lower than 346°K (first run). Curve 3 and 4, the same as above, but related to same sample annealed at R.T. after getting curves 1 and 2 (second run).

occurred between 374° and 390°K, as can be observed in Fig. 3, where the I.V. dipole concentration normalized to the saturation value at each T_a *vs.* annealing time are compared for T_a = 364°, 374°, and 390°K, respectively curves a, b, and c. On going from 374° to 390°K the solubility process was slowed down and the saturation value was attained in a longer time. Starting from T_a = 390°K the rate of solution became again faster by increasing the annealing temperature.

The isothermal time evolution of the solution process was strongly affected by the "thermal history" of the sample. In Fig. 4 are shown the precipitation and solubility curves at T_a = 331°K. Curve a shows the precipitation of I.V. dipoles after quenching from T_q = 470°K; curve b, the solubility after quenching from T_q = 470°K followed by a precipitation at room temperature; curve c (open circles), the solubility of a sample annealed at room temperature after obtaining curve a; curve c (full circles), the solubility of a sample annealed previously at the same T_a and left at room temperature. Both curves a and c show a monotonic decrease and increase, respectively, to the saturation value n_s, while curve b shows an initial overshoot followed by a smooth decrease to n_s.

From Fig. 2 and 4 it turns out that the same saturation value n_s at a given T_a is obtained independently of the previous "thermal history" of the sample.

The results reported above were checked on different samples.

Discussion

Influence of preannealing on the solution reaction.— The experimental results show that the solution process at a given T_a is a complex one depending on the

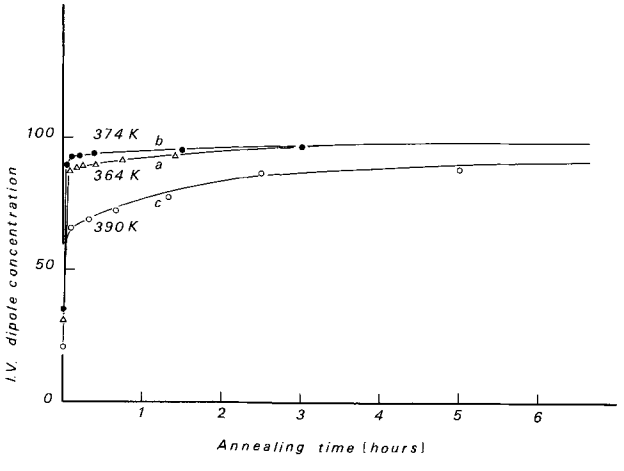

Fig. 3. Solubility curves (first run) at different annealing temperatures T_a for I.V. dipoles (peak A). The dipole concentration was normalized to the saturation value at each annealing temperature. Curve a: T_a = 364°K, curve b: T_a = 374°K, and curve c: T_a = 390°K.

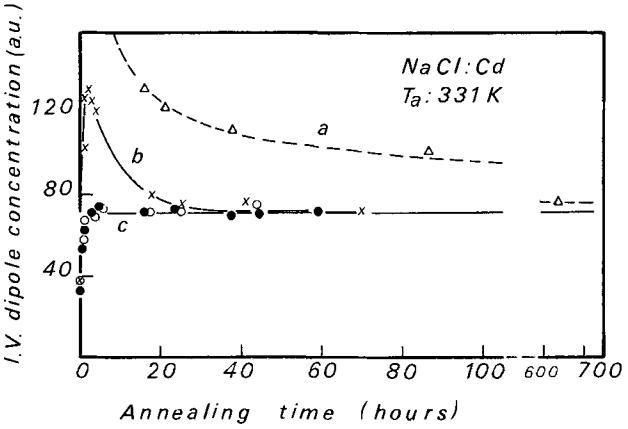

Fig. 4. Precipitation and solubility curves for I.V. dipoles at T_p = 331°K. Curve a: precipitation, after quenching from T_q = 470°K (only a part of curve is drawn for the sake of convenience; the ordinate at t = 0 is ~1200; curve b: solubility after quenching from T_q = 470°K followed by precipitation at R.T.; and curve c: (open circles) solubility of the sample annealed at R.T. after getting curve a; (full circles) solubility of the sample annealed at R.T. after getting curve c (open circles).

thermal history of the sample, even if the saturation value n_s is the same, as one would expect for thermodynamical equilibrium situation. As shown in Fig. 2 the I.V. dipole concentration grows monotonically with the annealing time while dipoles responsible for the small peak B decrease to a saturation value in both runs. This behavior supports that peak B must be related to precipitates, whose dissolution contributes to the I.V. dipole growth. The saturation value of I.V. dipole concentration is reached more quickly in the second annealing, for instance, at T_a = 353°K the saturation is obtained after ~15 hr and after 1½ hr in the first and second runs, respectively, further runs show practically the same features as the second one. The disparity between the first and second run in the early stage of the solution reaction can be explained by different kinds and distribution of the precipitates in the sample, due to different preannealing. In fact at the beginning of the second run (also at higher T_a) the concentration of B dipoles is always higher than that at the beginning of the first run.

The role of preannealing is still more evident in Fig. 4, where the overshoot which appears in curve b can be interpreted as follows: during the annealing at room temperature after quenching from T_q, the thermodynamical equilibrium among I.V. dipoles and microprecipitates is not yet achieved, due to the low mobility of defects. The latter ones are in excess with respect to the thermodynamical equilibrium, so the subsequent annealing at T_a > room temperature breaks readily the microprecipitates to give I.V. dipoles in concentration higher than n_s at T_a; n_s is then reached by precipitation of I.V. dipole excess. Moreover it is noteworthy that n_s is reached more quickly by solution process than by precipitation from supersaturated solution (curves a and c) even if the early stage of precipitation is extremely fast.

Analysis of solubility curves.—As reported in a previous work (18) dissolution of I.V. dipoles to reach thermodynamical equilibrium value n_s in KBr:Sr at relatively high temperature (334°K) takes long annealing times (~100 hr) and can be described by the simple law

$$n = n_o + (n_s - n_o)\,[1 - \exp(-t/\tau)] \qquad [1]$$

where n, n_o are the actual and initial I.V. dipole concentration, t is the time, and τ the time constant. A logarithmic plot *vs.* annealing time t of $n_s - n$ obtained from our solubility data at T_a ranging from 346° to 423°K does not show a behavior as simple as that predicted by [1]. Curve a of Fig. 5 exemplifies the

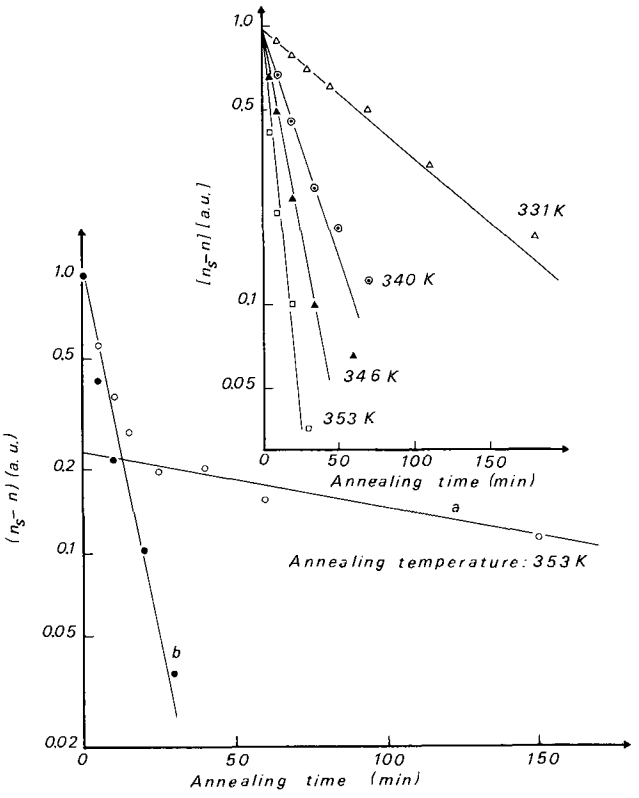

Fig. 5. Logarithmic plot vs. annealing time of $n_s - n$ at T_a = 353°K: open circles, first run; full circles, second run. The inset gives the logarithmic plot vs. annealing time at various T_a (second run).

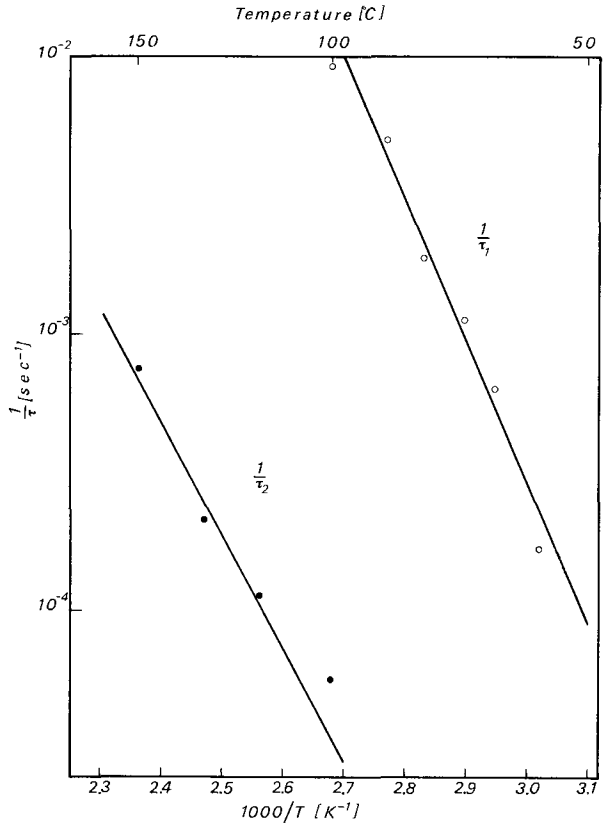

Fig. 6. Arrhenius plot of the reciprocal of time constants τ_1 and τ_2 vs. 1000/T.

solution reaction (first run) in our NaCl:Cd at T_a = 353°K. Two straight lines instead of one alone fit the experimental data well enough. The solution reaction appears more complex, with a "fast" early stage followed by a slower one. Hence the experimental results suggest that solubility reaction is better described by introducing two time constants τ_1 and τ_2 for the "fast" and "slow" stages, respectively. The second run data always at 353°K, reported for comparison in Fig. 5 (curve b) show surprisingly that the early "fast" stage predominates and now the reaction appears to follow closely the simple equation [1]. The inset in Fig. 5 shows the logarithmic plot at various T_a, for second run solubility data. The occurrence mainly of a "fast" stage in the second run can be explained by the presence of small microprecipitates. These, grown during the former annealing at T_a and subsequent precipitation at room temperature, are easily and rapidly broken during the latter annealing at T_a. The "slow" stage can be attributed to the slow dissolution of "hard" and larger microprecipitates. Hence the whole isothermal time evolution of I.V. dipoles is assumed to be governed by the following monomolecular kinetics combination

$$n_s - n = A_1(n_s - n_0)\exp(-t/\tau_1) + A_2(n_s - n_0)\exp(-t/\tau_2) \quad [2]$$

where $A_1 + A_2 = 1$, A_1 and A_2 are the statistical weights of the "fast" and "slow" stages, respectively. Moreover A_1 and A_2 can be related to the concentration of different kinds of microprecipitates: the easily and the hardly soluble ones. It is worthwhile noticing that the drastic change in the solubility curves between 374° and 390°K in Fig. 3, can be interpreted as follows: at 390°K the fast stage contributes at comparatively lower extent to the solution reaction, while the slow stage fractional contribution increases. This effect will be better understood in the light of different kinds of precipitates, discussed in the section on Microprecipitates and thermodynamical equilibrium.

τ_1 and τ_2 characteristics.—From Fig. 5 it turns out that the information about τ_1 and τ_2 can be more conveniently obtained utilizing data from second and first runs, respectively. The values of $1/\tau_1$ and $1/\tau_2$ are then reported in the Arrhenius plot shown in Fig. 6: activation energy $\epsilon_1 \sim 1$ eV and $\epsilon_2 \sim 0.8$ eV and pre-exponential factor $\nu_{01} \equiv (\tau_{01})^{-1} \sim 6 \times 10^{11}$ sec^{-1} and $\nu_{02} \equiv (\tau_{01})^{-1} \sim 3 \times 10^6$ sec^{-1} are evaluated for the first and second stage, respectively. The activation energy values are comparable with $\epsilon_d = 0.92$ eV, the activation energy for diffusion, *i.e.*, the exchange energy (21), chiefly if one takes into account that the data for the ϵ_2 calculation are not precise enough.[3] Therefore one can assume that the solution process is ruled by diffusion of impurity-vacancy dipole far from the precipitates in a similar way as that proposed by Wintle (11) for the precipitation reaction in a supersaturated solid solution. An appreciable insight on the nature of precipitates is pursued by comparing ν_{01} and ν_{02}. The rather high value of ν_{01} permits the assumption that only a few atomic jumps are required to release the I.V. dipole from the parent microprecipitate, and to give it the reorientability necessary to be monitored by I.T.C. technique. On the other hand ν_{02} is at least five orders of magnitude lower than ν_{01}, indicating that a convenient sequence of events able to liberate the I.V. dipole occurs with a very low probability and requires a very large number of atomic jumps. These results are consistent with the assumption that the solution stage characterized by τ_1 involves the break-up of simple I.V. clusters, so the free dipoles can escape easily enough. The extremely long sequence of atomic jumps which precedes the solution of a I.V. dipole in the stage described by τ_2 can be accounted for if large and "hard" precipitates are the only I.V. dipole sources still present. Geometrical and correlation factors can play a very important role in determining the most favorable jump sequence.

[3] It must be outlined that in the temperature range 346°-364°K the values obtained for τ_2 do not show a definite temperature dependence, possibly due to a mixing of different processes.

Microprecipitates and thermodynamical equilibrium. —The study of thermodynamical equilibrium concentration of dipoles responsible for peak A, B, and C *vs.* annealing temperature can throw light on the nature of microprecipitates involved in the solution process. In Fig. 7 the logarithmic plot of the saturation value of peak B is reported *vs.* $1000/T_a$ as obtained from the present work; for comparison the similar plot for peak A (I.V. dipoles) and peak C are drawn from Ref. (8). The behavior of peak A was also checked by using the present data. Moreover the temperature ranges where τ_1 and τ_2 were more conveniently measured, are indicated. In thermodynamical equilibrium, the dipoles responsible for peak B decrease with increasing temperature, further supporting the assumption that they are microprecipitates and I.V. dipole contributors. At annealing temperatures higher than 375°K the B dipole contribution becomes negligible. Peak C after a moderate growth till 365°K shows a sharp decrease in temperature range between 365° and 415°K. It is worthwhile noticing that in the temperature ranges where τ_1 and τ_2 were more conveniently studied, there occurs the decrease of peak B and C, respectively. This coincidence strongly supports that B and C dipoles are the principal sources of I.V. dipoles during the fast and slow stages, respectively. In the section on Results it was pointed out that on raising the annealing temperature from 374° to 390°K the solution process is slowed down: this can be understood by considering that decomposition of B dipoles contributes to I.V. dipole solution for a smaller fraction, and the thermodynamical equilibrium concentration n_s can be achieved only by the slow dissolution of the hard microprecipitates. From the straight line of Fig. 7 an activation energy of 0.24 eV is obtained for the B dipoles dissolution, which is quite close to the I.V. dipole solution energy $\epsilon_s^{I.V.} = 0.235$ eV (8).

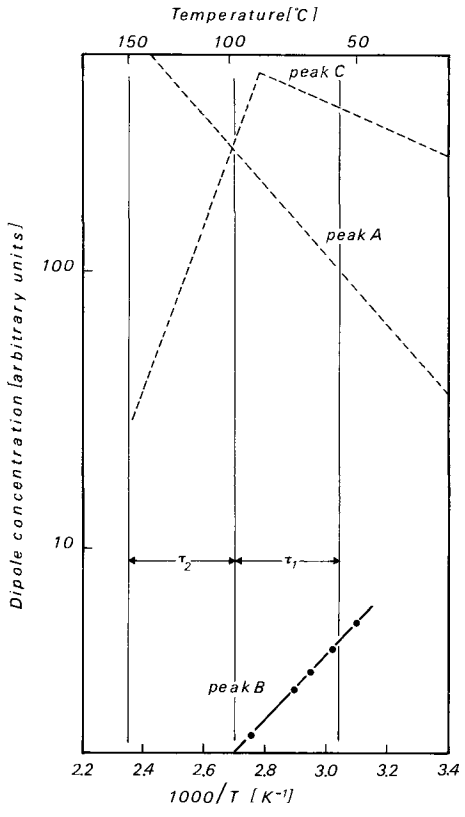

Fig. 7. Arrhenius plot of the thermodynamical equilibrium concentration of A(I.V.), B, and C dipoles *vs.* 1000/T. The dotted lines are taken from Ref. (8). The temperature ranges, where the time constants τ_1 and τ_2 were measured more conveniently, are indicated.

Conclusions

The accurate analysis of the time evolution of I.V. dipole concentration to achieve the thermodynamical equilibrium value has shown that:

1. The saturation value does not depend on the previous thermal history of the sample, as thermodynamical equilibrium requires.
2. The saturation value is reached more readily if the solution process is preceded by a proper preannealing which breaks the hard precipitates and allows the growth of the simpler ones.
3. At least two stages can be distinguished in the solution process: the early one is much faster than the subsequent one. Both can be separately described by a first order monomolecular kinetics, in which the time constants τ_1 and τ_2 are temperature dependent. The difference in activation energy for diffusion (21) is within 8 and 13% of the activation energies of our fast and slow stages, so the time evolution of the solution process is assumed to occur through a diffusion of I.V. dipoles from precipitates, in fact the energy to release an I.V. dipole from precipitates, *i.e.*, $\epsilon_s^{I.V.}$ turns out to be considerably less (0.235 eV) (8). Both the relatively high diffusion energy and the pre-exponential factors of τ_1 and chiefly of τ_2 explain why the solution reaction is so slow even at moderately high temperatures.

Moreover the study of thermodynamical equilibrium values *vs.* annealing temperature of dipoles responsible for peak B and C suggests that:

1. The growth of I.V. dipoles in the fast and in the slow stage can be related mainly to the decay of B and C dipolar precipitates.
2. The activation energy for the thermal decomposition of B dipoles is the same as the solution energy of I.V. dipoles (8) as expected if a single I.V. dipole is released from the dipolar microprecipitate B.

From the above results one has the general impression that the precipitation and dissolution of impurities in solids is a rather intricate phenomenon. In order to understand it, a careful and detailed study of its behavior is necessary avoiding schematic and oversimplified descriptions.

Acknowledgments

One of the authors (E.O.) wishes to thank the Fundação de Amparo á Pesquisa do Estado de S.Paulo (FAPESP) for financial support. The authors are deeply indebted to Professor Roberto Fieschi for constant encouragement and helpful discussions, and to Mr. Primo Allegri for the skillful help in performing I.T.C. measurements.

Manuscript submitted Sept. 11, 1972; revised manuscript received Nov. 15, 1972. This was Paper 93 presented at the Miami Beach, Florida, Meeting of the Society, Oct. 8-13, 1972.

Any discussion of this paper will appear in a Discussion Section to be published in the December 1973 JOURNAL.

REFERENCES

1. J. S. Cook and J. S. Dryden, *Proc. Phys. Soc., (London)*, **80**, 479 (1962).
2. G. Alzetta, P. R. Crippa, and S. Santucci, *Nuovo Cimento*, **42**, 100 (1966).
3. H. F. Symmons and R. C. Kemp, *Brit. J. Appl. Phys.*, **17**, 607 (1966).
4. R. Capelletti and E. De Benedetti, *Phys. Rev.*, **165**, 981 (1968).
5. R. Capelletti, R. Fieschi, G. Martegani, and L. Pirola, *J. Phys.*, **28**, Suppl. No. 8-9, C-4-130 (1967).
6. J. S. Dryden and G. G. Harvey, *J. Phys. C (Solid St. Phys.)*, **2**, 603 (1969).
7. R. Capelletti, *Nuovo Cimento*, **54B**, 233 (1968).
8. R. Capelletti and R. Fieschi, *Cryst. Latt. Defects*, **1**, 69 (1969).
9. J. H. Crawford, Jr., *J. Phys. Chem.*, **31**, 399 (1969).
10. W. C. Collins and J. H. Crawford, Jr., *Phys. Rev.*, **B4**, 3745 (1971).
11. H. J. Wintle, *ibid.*, **179**, 769 (1969).

12. K. Suzuki, *J. Phys. Soc. Japan*, **16**, 67 (1961).
13. E. Lilley and J. B. Newkirk, *J. Mater. Sci.*, **2**, 567 (1967).
14. R. Capelletti, R. Fieschi, and C. Lamborizio, "Radiation Effects," S. C. Jain and L. T. Chadderton, Editors, p. 85, Gordon and Breach, London (1970).
15. V. Trnovcova, *Fys. Cas.*, **18**, 211 (1968).
16. C. A. Bucci, R. Fieschi, and G. Guidi, *Phys. Rev.*, **148**, 816 (1966).
17. R. W. Dreyfus, *Appl. Phys. Letters*, **3**, 157 (1963).
18. R. Capelletti and R. Fieschi, Int. Conf. Col. Centres, Reading, 1971, H 163.
19. R. Capelletti, V. Fano, and M. Scalvini, *Ric. Sci.*, **38**, 886 (1968).
20. R. Capelletti, V. Fano, and M. Scalvini, *J. Cryst. Growth*, **5**, 73 (1969).
21. C. A. Allen, D. T. Irelands, and W. J. Fredericks, *J. Chem. Phys.*, **47**, 3068 (1967).

Galvanic Cell Studies Involving Calcium Carbide Solutions

D. R. Morris,*,[1] C. Aksaranan,*,[2] B. S. Waldron, and S. H. White[3]

Department of Chemical Engineering, University of New Brunswick, Fredericton, New Brunswick, Canada

ABSTRACT

The galvanic cell

$$\text{Fe[C]}_{(s)}\,|\,\text{CaC}_2,\ \text{CaCl}_{2(l)}\,|\,\text{C}_{(s)}$$

has been studied in detail in the temperature range 800°-1000°C using electrodes containing carbon at different activity levels. Calcium metal, the electroactive species, is present in the electrolyte by virtue of the heterogeneous equilibrium

$$\text{CaC}_{2(\text{soln})} \rightleftharpoons \text{Ca}_{(\text{soln})} + 2\text{C}_{(\text{electrode or crucible})}$$

The electromotive force of an electrode couple is given to a precision of about 1% by the Nernst equation for the theoretical emf in terms of the ratio of calcium activities, and hence indirectly of the ratio of carbon activities, at the electrodes.

An electronic conduction model has been developed to describe the observed irreversible behavior. A time-independent electromotive force is achieved when an external current, equal to that predicted by the model, is imposed upon the cell.

In earlier work with the cell (1)

$$\text{Fe[C]}_{(s)}\,|\,\text{CaC}_2,\ \text{CaCl}_{2(l)}\,|\,\text{C}_{(s)} \qquad [\text{I}]$$

where [C] represents carbon in solid solution, the cell reaction was postulated to be

$$\text{C}_{(s)} \rightarrow [\text{C}] \qquad [1]$$

and the cell electromotive force to be given by

$$E_\text{I} = -\frac{RT}{F}\ln a_\text{C} \qquad [2]$$

However, possible problems with the cell were indicated by (*i*) cell voltages corresponding to carbon activities lower by 0-10% than those from gas equilibration studies using CO/CO_2 and CH_4/H_2 gas mixtures (2), (*ii*) a need to introduce a nickel gauze partition between the electrodes to prevent carburization, and (*iii*) the possibility of less than equilibrium voltages because of electronic conduction in the melt as has been discussed for similar cells (3-5).

In this paper we present evidence that the galvanic cell is more complex than is implied by [I]; that it is more accurately represented by

$$\begin{array}{ll|ll} \text{anode} & \text{Fe[C]}_{(s)} & \text{Ca, CaC}_2\text{, CaCl}_{2(l)}, & \\ & a'_\text{C} & a'_\text{Ca} & \end{array}$$
$$\begin{array}{l|ll} \text{Ca} & \text{C}_{(s)} & \text{cathode} \\ a''_\text{Ca} & a''_\text{C} & \end{array} \qquad [\text{II}]$$

This evidence is founded upon a thermodynamic argument (6), and is supported by unpublished chronopotentiometric and voltammetric studies of the electrolyte used in the galvanic cell, and by experiments upon the multiple cell

$$\begin{array}{l|l} \multicolumn{2}{c}{\longleftarrow\!\!-\!\!-\!\!-\!\!-\,[\text{III}]\,-\!\!-\!\!-\!\!-\!\!\longrightarrow} \\ \underline{\text{Fe}}\ \ \text{Ca, CaC}_2\text{, CaCl}_{2(l)} & \text{CaC}_2\text{, CaCl}_{2(l)} \\ \quad\ \text{Ca}_{(\text{sat})}\quad \text{CaC}_{2(\text{sat})} & \text{CaC}_{2(\text{sat})} \\ \quad\ \text{calcium electrode} & \\ \qquad\quad a^\text{o}_\text{Ca} & \end{array}$$

$$\begin{array}{|c|c|c} \multicolumn{3}{c}{\longleftarrow\!\!-\!\!-\!\!-\!\!-\,[\text{IV}]\,-\!\!-\!\!-\!\!-\!\!\longrightarrow} \\ \text{Fe[C]}_{(s)} & \text{CaC}_2\text{, CaCl}_{2(l)} & \text{C}_{(s)} \\ & \text{CaC}_{2(\text{sat})} & \\ \text{austenite} & & \text{carbon} \\ \text{electrode} & & \text{electrode} \\ a'_\text{C}\ a'_\text{Ca} & & a''_\text{C}\ a''_\text{Ca} \end{array}$$

in which the calcium electrode and carbon electrode were introduced into the electrolyte alternately. In the above representation $\underline{\text{Fe}}$ represents the iron thimble containing the calcium metal-salt mixture constituting the calcium electrode and the dotted line, the porous metal diffusion barrier. Further, we show that the observed irreversible behavior is consistent with a model in which it is assumed that electronic conduction occurs in the electrolyte.

Experimental

Equipment

Two types of electrical furnace have been used in the experimental work. These were, (*i*) a "cold wall" vacuum furnace which employed a tantalum heating element drawing a current of the order 10^2-10^3A. The temperature was controlled using a tungsten-rhenium thermocouple situated in the hot zone coupled to a saturable reactor-control circuit, and (*ii*) a vertical, wire-wound, tube furnace fitted with an Inconel vacuum envelope; the heating current was of the order 10^0-10^1A, a.c. or d.c. The temperature was controlled using a Chromel-Alumel thermocouple positioned close

---

* Electrochemical Society Active Member.

[1] Present address: Department of Chemical Engineering, University College London, London, England (sabbatical leave 1972-1973).

[2] Present address: Chulalongkorn University, Bangkok, Thailand.

[3] Present address: University of West Indies, St. Augustine, Trinidad, West Indies.

Key words: galvanic cells, calcium carbide solution, iron-carbon system, electronic conduction model.

to the furnace windings, coupled to a Eurotherm controller. Because oxide and boron nitride crucibles react with CaC_2, steel, nickel, and graphite crucibles were used. The design of the steel crucible used in the "cold wall" furnace is shown in Fig. 1; this crucible permitted the simultaneous measurement of the emf of 7 anode/cathode couples including the steel crucible/cathode couple. Simple cylindrical crucibles of steel, nickel, or graphite were also used. Experiments were conducted with and without the partition described by Hawkes and Morris. When a graphite crucible was used, it also served as the cathode of the galvanic cell.

The cell emf was measured by the use of a potentiometer (Leeds and Northrup 8691), a digital voltmeter (Solartron LM 1420.2), or by a Keithley Electrometer Model 601 used in conjunction with a two-channel "YEW" (Yokogawa Company) recorder. The input impedance of the electrometer was of the order 10^{14} ohms. The cell temperature was measured by Pt/Pt 13% Rh thermocouples positioned in the wall of the crucible or placed inside a nickel thimble immersed in the electrolyte. The cell temperature fluctuation was ±2°C.

Electrodes

The carbon cathodes (3.2 mm diameter) were machined from a high-purity graphite (Grade AUC) supplied by Union Carbide or from spectra pure graphite supplied by Johnson Matthey and Company Incorporated. The austenite electrodes of known composition were supplied by the British Iron and Steel Research Association and by the Guest, Keen and Nettlefold Company, Limited, England. These were machined to a diameter of 3.2 mm, approximately 8 cm long.

The design of the calcium electrode for cell [III] was similar to that used by Bronstein (7) for various metal/metal halide electrodes. It was fabricated from a steel thimble 6.4 mm ID, 9.5 mm OD, by 7 cm long, in the side of which were incorporated two layers of steel felt (Feltmetal Grade FM 1501 rolled to about 65% density *ex* Huyck Metals Company). A steel cover plate with a 0.25 mm diameter hole was welded to the steel thimble over the steel felt. Steel was used for the construction of this electrode as calcium does not alloy with iron (8). Prior to use, the thimble was purified by placing it in a closed steel crucible containing a quantity of calcium metal. The crucible and contents were maintained at a temperature of 900°C for 75 hr under an argon atmosphere. The thimble was then washed with boiling distilled water and diluted hydrochloric acid, and the purification process repeated. Calculation indicated that this would be sufficient time to remove more than 90% of the carbon contained in the steel thimble. This procedure also removed many other impurity elements from the steel (*e.g.*, S, O, N). Finally, the thimble was again washed in boiling dilute hydrochloric acid, boiling water, then dried, and heated to 950°C under vacuum. The thimble was closed by a threaded plug, incorporating a bleed hole to ensure pressure equality. A steel rod was attached to the plug to serve as the electrode lead. The thimble was charged with 2.5g dried calcium chloride, 0.5g of calcium, and 0.5g calcium carbide. These quantities were sufficient to saturate the calcium chloride with calcium (9) and with calcium carbide (10).

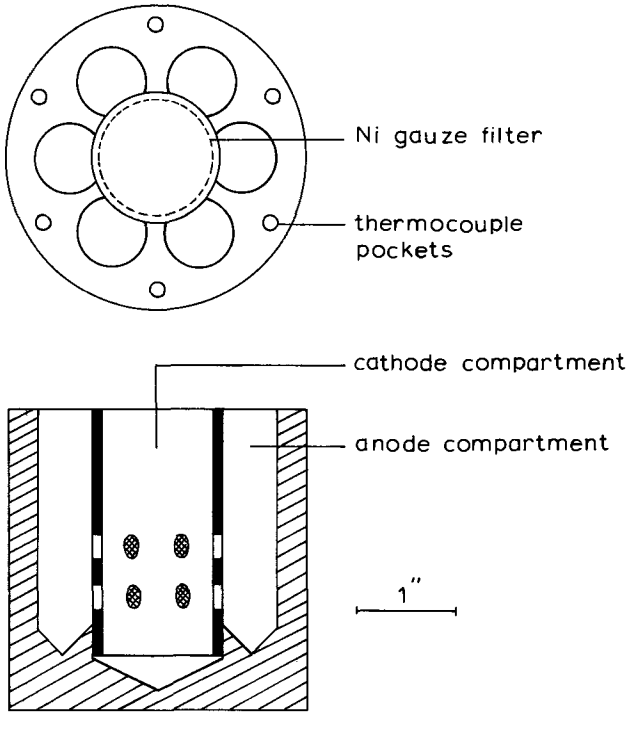

Fig. 1. Design of multicompartment steel crucible

Two types of electrode suspension have been used: (*i*) an assembly in which the electrodes were supported by "fired" pyrophyllite legs suspended from a water-cooled metal tube arrangement passing through a vacuum seal installed in the furnace closure flange (1). The electrical resistance between the electrodes, and between an electrode and ground, with the electrodes in the raised position at the cell operating temperature was of the order 10^7 ohms, and the leads to the electrodes were of platinum wire; and (*ii*) an assembly consisting of precision glass tubular sliding joints (Jencons Limited, England) situated on a water-cooled brass head (11), the electrodes being supported by steel rods which were also used as the electrode leads and where the order of magnitude of the electrical resistance between the electrodes in the raised position at the operating temperature was 4×10^8 ohms By the use of either assembly, the electrodes were immersed into the molten electrolyte approximately 2.5 cm, and raised at the completion of the experiment.

Electrolyte

Calcium chloride (reagent grade, J. T. Baker Chemical Company) was dried by heating stepwise in an oven to 200°C for approximately 6 days, after which it was transferred to a vacuum furnace in which the temperature was raised stepwise to the melting point.

Two modes of preparation of the electrolyte solution have been used, (*i*) by the addition, to the prefused $CaCl_2$, of CaC_2 synthesized from the elements, according to the procedure described by Aksaranan (12), and (*ii*) by the addition, to the prefused $CaCl_2$, of Ca metal and carbon in the stoichiometric proportions. Further Ca metal was added to the electrolyte in some experiments. In those crucibles in which a partition had been fitted, the CaC_2 or the Ca and C mixture was added to the carbon electrode compartment. A time period of the order of hours was allowed for reaction and, or solution prior to immersion of the electrodes.

Samples of the electrolyte were analyzed for calcium carbide, oxide, chloride, calcium metal, and carbon according to the procedure of Aksaranan *et al.* (6). The samples were taken either by drilling the solidified electrolyte as quickly as possible to minimize contact with air, or by use of a graphite sampling crucible which could be dipped into the melt and withdrawn.

Results

Galvanic Cell [II]

Experiments conducted in steel crucibles.—Experiments conducted in the "cold wall" furnace using multicompartment steel crucibles (Fig. 1) were characterized by a fairly rapid (of the order of 2-4 hr) attainment of approximately the same emf by all the Fe[C]-C couples, irrespective of the initial anode composition. Further, it was observed that this emf was some 10-20 mV above the emf of the steel crucible-C couple. This observation suggested that all the austenite electrodes had attained the same composition.

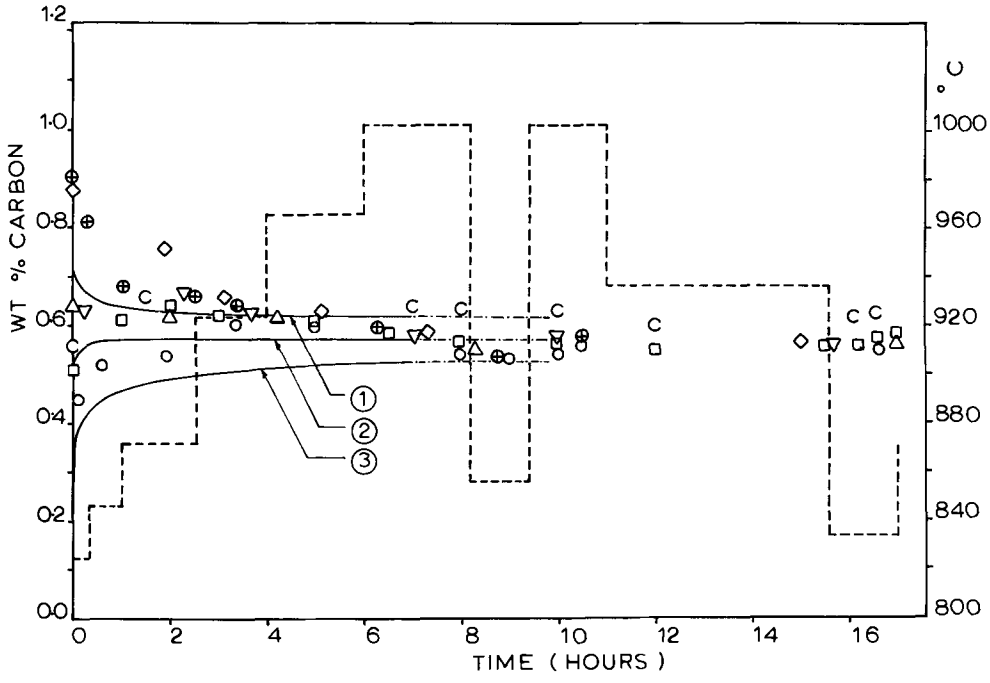

Fig. 2. Results of typical experiment (BSW 11) using multicompartment steel crucible. (For austenite electrode ref. No. see Table I.) □, BISRA V1827; ▽, BISRA S345; ⊕, BISRA V1664; ○, GKN66; △, GKN2; ◇, GKN37; C, crucible; - - - - - -, temperature history of experiment; ——·—·—·—, electronic conduction model: calculations based upon temperature of 860°C; mean value $\overline{\Delta G^\circ}$. line 1, initial C conc 0.72 weight per cent (w/o) C; line 2, initial C conc 0.51 w/o C; line 3, initial C conc 0.20 w/o C.

This was verified by chemical analysis. The results of a typical experiment are summarized in Table I. It is noteworthy that electrodes of relatively high carbon concentration had partially decarburized. This behavior was observed irrespective of the detail of the cell assembly or ancillary equipment. The results of the typical experiment are presented in more detail in Fig. 2 as a plot of the surface carbon concentration of the austenite electrodes as a function of time. The carbon concentration was calculated from the measured emf and temperature using Eq. [2] in conjunction with the correlation given by Ban-ya, Elliott, and Chipman (13) for a_C based upon gas equilibrium studies

$$\log a_C = \frac{3770}{T} + 2.72 \log T - 10.525 + \frac{3860}{T} y_C + \log Z_C \qquad [3]$$

This procedure has been adopted to demonstrate the response of the cell emf to the concentration (activity) of the carbon in the austenite electrode. It is seen that the surface carbon concentration is essentially independent of time and temperature, some 2-4 hr after insertion of the electrodes into the electrolyte. This calculated carbon concentration is in reasonable agreement with the results of chemical analysis of "bulk" samples of the electrodes taken from that part of the electrodes which had been immersed in the electrolyte (see Table I).

Table I. Typical experiment conducted in multicompartment steel crucible (BSW 11)

Austenite electrode ref. No.*	C, weight per cent as received	Emf of Fe[C]-C couple, mV: Time zero 825°C	Time 1 hr 850°C	Time 2 hr 860°C	Final analysis of electrode C, weight per cent: Above Electrolyte Surface†	Below Electrolyte Surface†
GKN 37	0.72	9	41	58	0.72	0.58
BISRA V1664	0.72	6	72	74	0.79	0.60
GKN 2	0.51	48	63	71	0.55	0.55
BISRA S345	0.50	48	63	70	0.53	0.53
GKN 66	0.20	87	87	86	0.19	0.44
BISRA V1827	0.21	76	72	74	0.21	0.47
Crucible	—	66	64	62	—	—

* GKN: Guest, Keen Nettleford.
BISRA: British Iron and Steel Research Association.
† Averages of duplicates which agreed within the limits of error of the analytical technique.
Analyses performed in the laboratories of the Department of Energy, Mines and Resources, Ottawa.

Experiments conducted in nickel or graphite crucibles.—The results of experiments conducted in nickel or graphite crucibles were qualitatively the same; characterized by the attainment of an emf of the Fe[C]-C couple near zero corresponding to essentially complete carburization of the austenite electrode as confirmed by chemical analysis. The results of typical experiments conducted in a graphite crucible are presented in Fig. 3 and in a nickel crucible in Fig. 4, again as a plot of the calculated surface carbon concentration of the austenite electrodes as a function of time. The asymptotic approach of the carbon concentration in the electrode to the saturation concentration at the operating temperature is seen. The final calculated carbon concentration agrees closely to that determined by chemical analysis.

During the course of the experimental work, considerable effort was directed toward the elimination of electrical interference upon the galvanic cell from

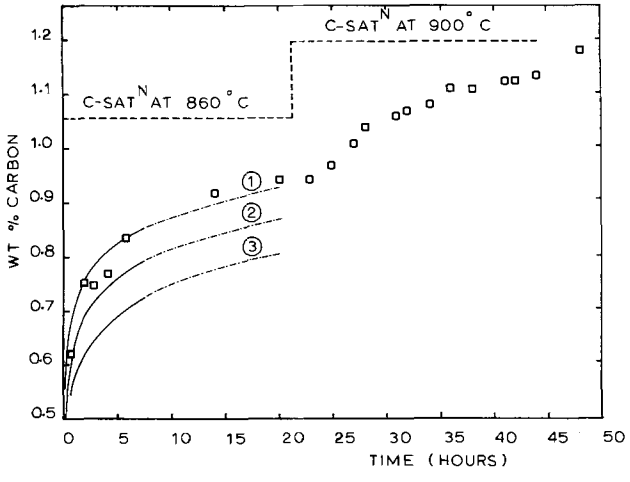

Fig. 3. Results of typical experiment (CCA 14) using graphite crucible. □, Experimental points. Austenite electrode initial conc 0.12 w/o C, final conc 1.19 w/o C; - - - - -, C saturation composition of austenite at operating temperature; ——·—·—·—, electronic conduction model, t = 860°C. Line 1, calculations based upon ($\overline{\Delta G^\circ}$ − 8400); line 2, calculations based upon $\overline{\Delta G^\circ}$; line 3, calculations based upon ($\overline{\Delta G^\circ}$ + 8400).

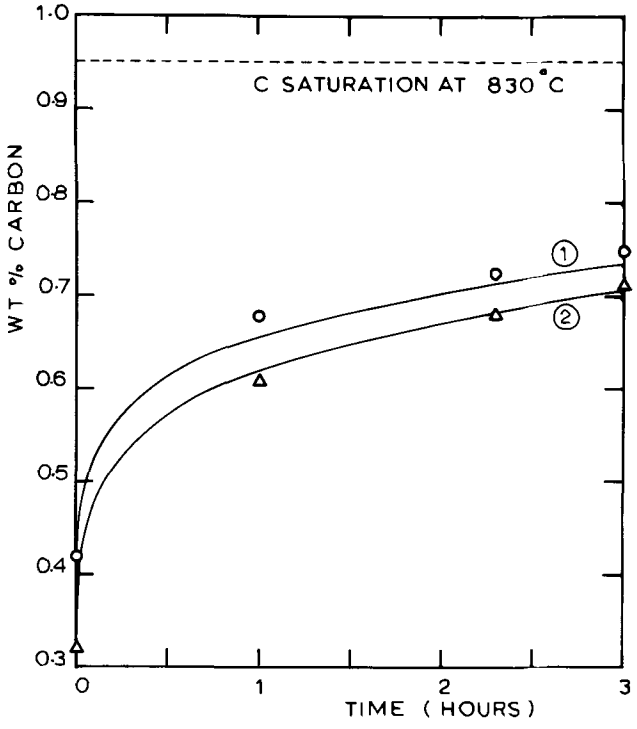

Fig. 4. Results of typical experiment (CCA 19) using nickel crucible at a temperature of 830°C. ○, experimental points austenite electrode initial conc 0.30 w/o C; △, experimental points austenite electrode initial conc 0.21 w/o C; - - - - -, C saturation conc of austenite at operating temperature; ———, electronic conduction model: calculations based upon $\overline{\Delta G}°$, line 1, 0.30 w/o C electrode; line 2, 0.21 w/o C electrode.

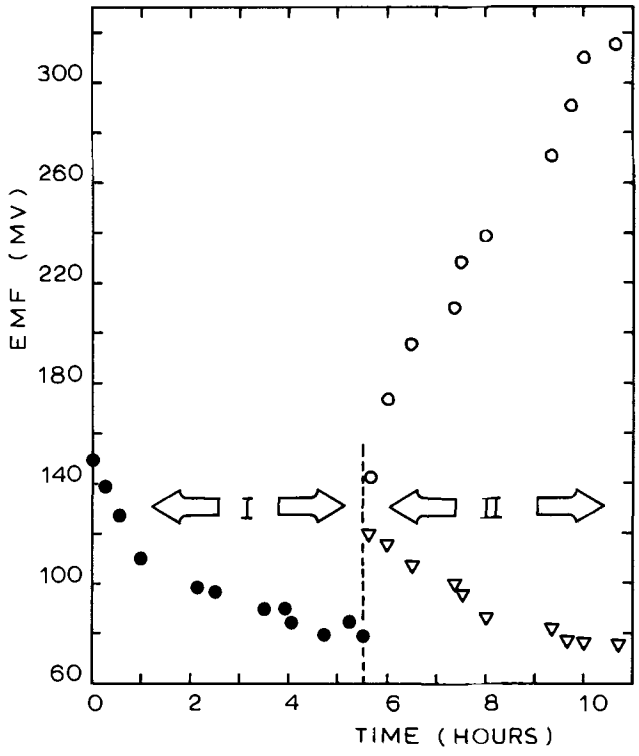

Fig. 5. Multiple galvanic cell experiment (CCA 40) conducted in nickel crucible at a temperature of 815°C. ●, Fe[C]-C couple, period I, $E_{[IV]}$; ○, Fe[C]-C couple, period II $E_{[IV]}$; ▽, Ca-Fe[C] couple, period II, $E_{[III]}$.

external sources, *e.g.*, the furnace heating circuits. Thus some experiments were conducted using a d-c power supply to the furnace and the whole assembly was independently earthed. The adoption of such procedures made no substantial difference to the behavior of the galvanic cell. The fitting of a gauze partition between the electrodes had little influence.

Multiple Galvanic Cell [III] and [IV]

The multiple cell experiment was conducted using a nickel crucible to contain the electrolyte which consisted of fused calcium chloride containing an excess of calcium carbide. The experimental procedure was to immerse the carbon and austenite electrodes in the electrolyte at time zero and record $E_{[IV]}$ as a function of time. After approximately 5 hr, the carbon electrode was raised clear of the electrolyte and the calcium electrode immersed. $E_{[III]}$ was recorded continuously as a function of time and $E_{[IV]}$ measured upon momentary immersion of the carbon electrode. The results are presented in Fig. 5. It is seen that in the first period $E_{[IV]}$ declined with time; in the second period $E_{[III]}$ declined with time, but $E_{[IV]}$, measured intermittently, increased. This cycle was reproducible.

Theoretical Analysis

It is well known that calcium metal is soluble in its halides, possibly in the form of a molecule-ion Ca_2^{2+} (14). The results of chemical analysis of calcium carbide-chloride solutions equilibrated in graphite crucibles have been interpreted using a thermodynamic argument based upon equilibrium [4] (6). Chronopotentiometric studies by White (11) and voltammetric studies by Dosaj (15) have been interpreted in terms of a dissociative equilibrium preceding the electrochemical step at low current densities.

A model is postulated for the galvanic cell in which calcium metal in solution is viewed as the electroactive species, and at the electrode-electrolyte phase boundary there exists the chemical equilibrium

$$CaC_{2(soln)} \rightleftharpoons Ca_{(soln)} + 2C_{(electrode)} \qquad [4]$$

and the electrochemical equilibrium

$$Ca_{(soln)} \rightleftharpoons Ca^{2+}{}_{(soln)} + 2e \qquad [5]$$

Cell [I] is therefore more accurately represented by cell [II] in which the calcium metal activities at the two electrodes are determined by equilibrium [4]. It is thus similar to the bimetallic cells with alkali metal anodes in which Hesson *et al.* (5) have found an irreversible (non-Faradaic) transfer of alkali metal from the anode to the bimetallic cathode to take place. They termed this transfer the self-discharge of the cell and presented a theoretical analysis of the cell based upon the equations of irreversible thermodynamics. They concluded that the self-discharge was largely due to the presence of dissolved alkali metal in equilibrium with alkali metal ions and electrons in the electrolyte resulting in partial electronic conduction in the electrolyte. They further stated that the predictions of the theory were in qualitative agreement with their experimental results. It is of interest to apply this theory to cell [II].

Carbon concentration at the electrode surface.—Following Hesson *et al.* (5) and Heyne (16) an equation may be derived assuming the electrolyte is of uniform composition in CaC_2, for the carbon flux, j_C at the austenite electrode surface, by noting the equivalence of the carbon flux to the electron current density. The equation is

$$j_C = \frac{RT\sigma_i}{F^2BA} \ln \left[\frac{K_e K^{1/2} a^{1/2}_{CaC_2} (a''_C)^{-1} + \sigma_i}{K_e K^{1/2} a^{1/2}_{CaC_2} (a'_C)^{-1} + \sigma_i} \right] \qquad [6]$$

The concentration of carbon at the electrode surface as a function of time is given by an appropriate solution to Fick's second law. Neglecting the change in the diffusion coefficient of carbon in iron with changing composition, the solution is (17)

$$\frac{4}{3} D_C t = \int_{c_i}^{c_s} \frac{2(c_s - c_i) f(c_s) - (c_s - c_i)^2 f'(c_s)}{f^3(c_s)} d(c_s) \qquad [7]$$

Equation [7] may be shown to be valid for $t \not> 15$, 4.5, and 1.0 hr at 800°, 900°, and 1000°C, respectively (18).

Emf of the galvanic cell.—The cell emf may be shown to be

$$E_{[II]} = -\frac{RT}{\mathbf{F}} \ln\left(\frac{a'_C}{a''_C}\right) - \frac{AB}{\sigma_i}(i_t - i_e) \quad [8]$$

For $i_t = 0$ (open-circuit condition) the second term in Eq. [8] is small (approximately 10^{-2} times) relative to the first term; it is zero when $i_t = i_e$. The current in the external circuit is then given by

$$I = i_t A = \frac{K_e}{B}\frac{RT}{\mathbf{F}} K^{1/2} a^{1/2}_{CaC2}\left(\frac{1}{a''_C} - \frac{1}{a'_C}\right) \quad [9]$$

Interpretation of Results

Galvanic Cell [II]

It is apparent from Eq. [6] that the magnitude and sign of the carbon flux is determined by the relative magnitudes of a'_C and a''_C. In the simplest case with $a''_C = 1$ (graphite crucible-cathode) the carbon flux is to the austenite anode. The results of a typical computation are shown in Fig. 3 including the uncertainty limits due to the uncertainty in K. It is seen that the surface composition calculated from the measured cell potential is within these limits.

The use of steel or nickel crucibles will lead to fluxes between the various cell components. The additional assumption was made that the dominant flux was that between the electrodes and the crucible. This is justified in view of the large mass (10^2-10^3 times) and large surface area (10^1-10^2 times) of the crucible relative to the electrodes, then $a''_C = \exp(-\mathbf{F}E_{cr}/RT)$. For nickel crucibles, E_{cr} was zero ± 20 mV. This is a consequence of the relatively high solubility of calcium in nickel (19) whence it may be shown that the nickel crucible is identical to a graphite crucible in the sense that $a''_C = 1$. The results of typical computations for an experiment using two austenite electrodes and a graphite cathode are shown in Fig. 4. The effects of the eccentricity of the geometrical arrangement were not taken into account. It is seen that the surface compositions of the austenite electrodes calculated from the measured cell potentials are in good agreement with those calculated by the above procedures. In the case of steel crucibles, E_{cr} was typically in the range 50-100 mV. The observed rate of change of this emf was small relative to the rate of change of the emf of the austenite test electrode. The results of a typical computation for an experiment using the multicompartment steel crucible (Fig. 1) are shown in Fig. 2. The model predicts carburization ($a'_C < a''_C$) or decarburization ($a'_C > a''_C$) of the austenite electrodes in accord with experimental observation. The computed steady-state compositions attained by the electrodes agree closely with the results of chemical analysis (see Table I).

Multiple Galvanic Cell [III] and [IV]

The multiple cell experiment represents an excellent qualitative demonstration of the influence of the calcium activities at the reference electrode (graphite or calcium) relative to the calcium activity at the austenite electrode, upon the cell emf (see Fig. 5). Thus in the first period of the experiment in which the austenite and carbon electrodes were immersed in the electrolyte, $a'_C < a''_C$ (and hence $a'_{Ca} > a''_{Ca}$) and carburization of the austenite electrode will ensue. In the second period in which the calcium and austenite electrodes were immersed, $a^o_{Ca} > a'_{Ca}$ leading to decarburization of the austenite electrode. These deductions from the model are in accord with experiment.

Further it should be noted that the emf of the calcium-carbon couple should correspond to $E^\circ_{CaC_2} = \Delta G^\circ/2\mathbf{F}$ and is given by

$$E^\circ_{CaC_2} = E_{[III]} + E_{[IV]} \quad [10]$$

neglecting terms accounting for the finite electronic conductivity of the electrolyte (cf. Eq. [8]). From Fig. 5, $E^\circ_{CaC_2}$ is found to be 350 ± 40 mV; from ΔG°, $E^\circ_{CaC_2}$ is calculated to be 360 ± 40 mV. The large standard deviation on the experimental value is a consequence of the short periodic time of immersion (approximately 30 sec) of the carbon electrode in the second period.

Influence of External Current

According to Eq. [8], $E_{[II]}$ equals the theoretical emf when $i_t = i_e$; Eq. [9] gives I, the current in the external circuit, in terms of the carbon activities of the electrodes and other relevant quantities.

In order to test these predictions, an experiment was performed using a graphite crucible-cathode and a single, centrally located, austenite electrode of known composition. External circuitry was assembled consisting of a Hewlett Packard Model 6206 B d-c power supply operating in the constant current mode, and a standard 10 ohm resistor connected in series with the electrode terminals. Upon immersion of the electrode, the current in the external circuit was adjusted such that the theoretical emf calculated according to Eq. [2] and [3] was attained. The cell emf was observed to remain constant. The current in the external circuit was calculated from the measured potential drop across the standard resistor. This procedure was repeated at several temperatures. The results of this experiment are summarized in Table II, in the fourth column of which are also shown the values of I calculated from Eq. [9]. The agreement between the measured and calculated values of I is seen to be excellent.

Conclusions

1. The electromotive force of a Fe[C]-C couple immersed in an electrolyte of calcium carbide dissolved in molten calcium chloride is a function of the temperature and the carbon activity in the alloy electrode, and the electronic conductivity of the electrolyte.
2. The particular form of the irreversible process in this galvanic cell is associated with the partial electronic conductivity of the electrolyte due to the finite concentration of calcium in the electrolyte.
3. A mechanism of the galvanic cell has been proposed based upon the chemical equilibrium $CaC_2 \rightleftharpoons Ca + 2C$ and the electrochemical equilibrium $Ca \rightleftharpoons Ca^{2+} + 2e$ in solution.
4. A mathematical model to calculate the carbon concentration at the surface of the austenite electrode as a function of time has been constructed. Results show a close agreement to those obtained from the measured emf of the galvanic cell.
5. The model predicts that by supplying current from an external source, a time independent emf can be achieved. This has been demonstrated. Further the magnitude of the current agrees closely with that calculated from the model.
6. The experimental results of Hawkes and Morris who used this cell to measure the carbon activity in Fe[C] alloy, have not been confirmed. The reasons for this are not known.

Table II. Influence of current in external circuit

Temp, °C	Theoretical emf of Fe[C]-C couple from Eq. [2] and [3], mV	External current I, mA: Experimental	External current I, mA: Calculated from Eq. [9]
810	137	−10.60	−10.41
843	158	−14.76	−16.35
874	176	−22.40	−23.70
887	183	−26.90	−27.32
902	190	−32.30	−31.63

Experiment No.: CCA 51.
Austenite electrode: BISRA 0.27 weight per cent C.
Crucible (cathode): graphite.
Electrolyte composition: 5.0 mole % CaC_2.

Acknowledgments

The authors wish to record their thanks to the National Research Council of Canada and the American Iron and Steel Institute for their financial support. Thanks are also due to the British Iron and Steel Research Association and the Guest, Keen Nettlefold Company, England, for the supply of steel specimens and to the Department of Energy, Mines and Resources, Ottawa for the carbon analysis of the steel specimens used. The fellowship awarded to C. Aksaranan by the Aluminium Company of Canada and the post-doctoral fellowship given to S. H. White by the University of New Brunswick are gratefully acknowledged.

We thank Dr. J. J. C. Picot of the Department of Chemical Engineering, University of New Brunswick, for his assistance leading to the solution of the diffusion equation.

Manuscript submitted Aug. 28, 1972; revised manuscript received Dec. 4, 1972. This was Paper 142 presented at the Houston, Texas, Meeting of the Society, May 7-11, 1972.

Any discussion of this paper will appear in a Discussion Section to be published in the December 1973 JOURNAL.

LIST OF SYMBOLS

a	activity a^o, a', a'', pertaining to indicated electrode
A	surface area of austenite electrode, m^2
B	geometrical factor, m^{-1}
c_i, c_s	initial and surface concentrations of carbon, mole m^{-3}
D_e, D_C	electron and carbon diffusion coefficients, m^2 sec^{-1}
D^o_e	constant (Eq. [A-2]), m^2 sec^{-1}
E, E_{cr}	cell and crucible emf, V
$E^\circ_{CaC_2}$	standard emf of formation of CaC_2, V
$f(c_s)$	$= -\delta c/\delta x$; $f'(c_s) = \delta/\delta c_s\,[f(c_s)]$
$\mathbf{F}$	Faraday constant, 9.648×10^4 C $mole^{-1}$
ΔG°	standard free energy change. (Eq. [4]) J $mole^{-1}$ $\Delta G^\circ = \overline{\Delta G^\circ} \pm 8400 = (28500 + 2.9T + 11.6T \log T) \pm 8400$ (6)
i_e, i_t	electron and total current density at austenite electrode, A/m^{-2}
I	current in external circuit, A
j_C	carbon flux at austenite electrode, mole-m^{-2} sec^{-1}
k	Boltzmann constant, 1.38×10^{-23} J K^{-1}
K	equilibrium constant, $\exp(-\Delta G^\circ/RT)$
K_e, K'	constants, see Eq. [A-4] and [A-1]
n_e	electron concentration, m^{-3}
q	electron charge, 1.602×10^{-19}C
R	gas constant, 8.314 J mol^{-1} K^{-1}
t	time, sec
T	temperature, K
T_b	normal boiling temperature of metal K
u_e	electron mobility, m^2 V^{-1} sec^{-1}
x	distance into austenite electrode from surface, m
y_C	n_C/n_{Fe} atom ratio of carbon to iron
Z_C	$n_C/(n_{Fe} - n_C)$ lattice ratio
σ_e, σ_i	electron and ion conductivity, ohm^{-1}-m^{-1}

APPENDIX

Estimation of Constant K_e

In order to calculate K_e it is assumed that conduction electrons are formed in the electrolyte by equilibrium [5] and hence

$$n_e = K' a_{Ca}{}^{1/2} \qquad [A\text{-}1]$$

According to Rice (20) electron movement in metal/metal salt solutions proceeds by a hopping mechanism akin to diffusion with activation energy of $4kT_b$. Hence the electron diffusion coefficient D_e may be written

$$D_e = D^o_e \exp(-4T_b/T) \qquad [A\text{-}2]$$

Use of this relation with the Einstein relation $u_e = q\,D_e/kT$, and the defining relation $\sigma_e = n_e\,q\,u_e$, gives

$$\sigma_e = \frac{K'\,q^2\,D^o_e \exp(-4T_b/T)}{kT}\,a^{1/2}_{Ca} \qquad [A\text{-}3]$$

Dworkin *et al.* (14) have measured the electrical conductivity of solutions of calcium in calcium chloride at 1128°K. The conductivity was found to increase with increasing concentration of metal. Assuming the excess conductivity is due to electrons, a relation of the form of Eq. [A-3] is readily verified. For $a_{Ca} = 1$ (saturated solution), $T = 1128$°K, $T_b = 1756$°K, $\sigma_e = 40$ ohm^{-1}-m^{-1}, Eq. [A-3] becomes $\sigma_e = K_e\,a^{1/2}_{Ca}$ with

$$K_e = \frac{2.28 \times 10^7}{T} \exp(-4T_b/T)\ ohm^{-1}\text{-}m^{-1} \qquad [A\text{-}4]$$

REFERENCES

1. G. L. Hawkes and D. R. Morris, *Trans. Met. Soc. AIME*, **242**, 1083 (1968).
2. J. Chipman, *ibid.*, **239**, 1332 (1967).
3. F. J. Salzano, L. Newman, and M. R. Hobdell, *Nucl. Technol.*, **10**, 335 (1971).
4. C. Aksaranan and D. R. Morris, *J. Appl. Electrochem.*, 2, 309 (1972).
5. J. C. Hesson, M. S. Foster, and H. Shimotake, *This Journal*, **115**, 787 (1968).
6. C. Aksaranan, V. Dosaj, D.R. Morris, and S. H. White, *Can. J. Chem.*, **49**, 2014 (1971).
7. H. R. Bronstein, *This Journal*, **112**, 1032 (1965).
8. J. F. Elliott, M. Gleiser, and V. Ramakrishna, "Thermochemistry for Steelmaking," Vol. II, p. 357, Addison-Wesley Publishing Co., Inc., Reading, Mass. (1963).
9. L. Staffanson, Ph.D. Thesis, Imperial College, London (1960); see B. R. Sundheim, "Fused Salts," McGraw-Hill Book Company, New York (1964).
10. W. A. Barber and C. L. Sloan, *J. Phys. Chem.*, **65**, 2026 (1961).
11. S. H. White, Internal Report, Dept. of Chem. Eng., Univ. of New Brunswick, Canada (1970).
12. C. Aksaranan, M.Sc. Thesis, Dept. of Chem. Eng., Univ. of New Brunswick, Canada (1969).
13. S. Ban-ya, J. F. Elliott, and J. Chipman, *Met. Trans.* **1**, 1313 (1970).
14. A. S. Dworkin, H. R. Bronstein, and M. A. Bredig, *Discussions Faraday Soc.*, **32**, 188 (1961).
15. V. Dosaj, M.Sc. Thesis, Dept. of Chem. Eng., Univ. of New Brunswick, Canada (1970).
16. L. Heyne, N.B.S. Special Publication No. 296,149 (1968).
17. M. N. Ozisik, "Boundary Value Problems in Heat Conduction," Chap. 7, Intext Educational Publishers, Scranton, Pa. (1968).
18. P. J. Schneider, "Conduction Heat Transfer," pp. 245-246, Addison-Wesley Publishing Co., Inc., Reading, Mass. (1955).
19. Y. Takeuchi, *Metallwissenschaft und Technik*, **1**, 2 (1966).
20. S. A. Rice, *Discussions Faraday Soc.*, **32**, 184 (1961).

Oxidation of GaP in an Aqueous H_2O_2 Solution

B. Schwartz* and W. J. Sundburg

Bell Laboratories, Murray Hill, New Jersey 07974

ABSTRACT

The oxidation of GaP in aqueous H_2O_2 has been accomplished by both galvanic action at ~100°C and by externally applied anodic reaction at room temperature. Films as thick as 1400 and 3500Å, respectively, have been prepared using these two approaches. A detailed examination of the kinetics of galvanic oxide growth indicates that: (*i*) the oxidation mechanism involves predominantly the transfer of holes, (*ii*) the rate-controlling step in the growth mechanism involves the diffusion of the oxidant, through the grown oxide, (*iii*) the index of refraction of the grown oxide is 1.58 ± 0.01, and (*iv*) a drying procedure to remove the water of hydration is necessary in order that the passivating amorphous oxide required for device use may be obtained. The growth of an oxide by externally applied anodic bias has resulted in the facts that: (*i*) the oxide thickness is linearly dependent on the applied bias up to about 100V, with the constant of proportionality being 12 Å/V, (*ii*) an upper forming voltage of about 200V has been found for obtaining uniformly colored (*i.e.*, thickness) films, and (*iii*) the index of refraction of the grown films depends on the forming voltage used, and (*iv*) a drying procedure to remove the water of hydration is necessary in order to obtain a stable amorphous oxide.

The achievement of controlled oxidation of silicon surfaces has been a major factor in the attainment of the very complex integrated circuits available today on the open market. With the advent of compound semiconductor devices as a commercial reality, it was obvious that the question of the availability of equivalent native surface oxides would be asked. It has not been obvious, however, that totally equivalent native oxides do exist (1, 2).

In a recent paper, Schwartz (3) described the results of a preliminary study on the oxidation of gallium arsenide and gallium phosphide. When GaP was placed in room-temperature water for seven days, approximately 60Å of amorphous oxide was grown on the surface; this is to be compared with a native oxide of only ~25Å on a freshly polished surface. When GaP was exposed to a concentrated[1] solution of H_2O_2 for seven days at room temperature, approximately 250Å of an amorphous oxide was grown.

In this paper some additional studies on the oxidation of GaP will be described.[2] Two techniques have been pursued: (*i*) boiling the GaP in concentrated H_2O_2 and (*ii*) anodic oxidation of GaP in concentrated H_2O_2 at room temperature. Thick oxides (>1000Å) have been obtained by the two techniques. The influence of conductivity type and the effect of a nonreactive ohmic contact will be shown. A linear dependence of the oxide thickness on forming voltage with a slope of about 12 Å/V, as well as an apparent upper forming voltage limit of about 200V, has been found in the anodic approach.

To be able to measure the oxide thickness it has been necessary to develop the reference curves for the ellipsometer, and reference will be made to these data.

Experimental Procedure

Oxidation in boiling hydrogen peroxide.—A 30% aqueous solution of H_2O_2 boils at about 106°C. Since the explosion hazard with this material is minimal [see Ref. (4)] it was decided to go directly to this temperature for the first phase of this study.

A simple all-quartz system was used, consisting of a 1000 ml tall-form beaker, a watch glass, a sample holder[3] (see Fig. 1B) and a commercial heating mantle. Because the beaker always extended well beyond the hot zone of the heating mantle, a simple reflux system was operative and the open pour spout acted as the pressure release. In this configuration, when the beaker was filled to the top of the heating mantle (approximately 500-600 ml) with concentrated H_2O_2 and boiling commenced, it took about 2 hr for the surface of the solution to fall about ¼-½ in. (about 50-100 ml of loss); at this point, fresh H_2O_2 solution was added to the beaker. A check of the temperature of the system during a continuous 6-hr boiling-and-refill operation showed that the temperature of the solution always

[3] A number of kinds of sample holders were constructed, but only holder B in Fig. 1 was used for the oxidation of GaP slices; the other two holders were constructed for use on packaged devices.

Fig. 1. Photograph of the simple beaker oxidation system used early in the studies. The quartz holders in the foreground are for use with (A) TO-18 packages, (B) slices, and (C) V-packages.

* Electrochemical Society Active Member.

Key words: compound semiconductor surfaces, native oxides, anodization.

[1] The concentrated H_2O_2 solution referred to in this paper was sold under the trade name Superoxol (CP) by Merck & Company, Rahway, New Jersey, and is nominally a stabilized 30% aqueous solution.

[2] All the oxidation data in this paper were obtained on Br_2-CH_3OH polished, P-faces of (111)-oriented GaP slices cut from liquid encapsulated Czochralski-grown ingots.

ranged between 105° and 106°C. This very narrow boiling range was taken to indicate that there was relatively little composition change of the H_2O_2 solution and that prolonged boiling of this kind was feasible.[4]

In order that oxidation-rate data might be obtained, samples were prepared from a slice of n-type, sulfur-doped GaP ($N_D \cong 10^{18}/cm^3$) which was polished and then broken into nine pieces. One piece was put aside as the reference and the other eight were placed in holder B, Fig. 1, and immersed in boiling H_2O_2. One piece was then removed every hour,[5] rinsed in 15 megohm deionized water, and blot dried. All of the samples, including the reference piece, were then put through the standard bake-drying procedure (see section on Sample drying procedure) and subsequently measured with an ellipsometer to determine the thickness of the grown film.

Thickness measurement.—The method of determining film properties by ellipsometry is to characterize a beam of monochromatic polarized light before and after the beam has been reflected from a test surface at some angle of incidence. The parameters that characterize the reflected light are ψ, the arctan of the ratio of the electric vectors of the beam in the perpendicular to the plane of incidence, and Δ, the phase difference between them. From the values of these two angles the thickness and index of refraction of the film can be determined.

Before one can do much in ellipsometry it is necessary to generate a series of reference curves for any new material which plots ψ and Δ as a function of film index of refraction. This was done for GaP using a computer program developed by Cox (5), the fundamentals of which will be found in the Appendix. Once these curves have been developed, the experimentally determined ψ and Δ for each sample is plotted on these reference curves. The particular curve on which the point falls corresponds to the index of refraction of the film, and the position along that curve, or the value of δ, indicates the thickness of the film.

Figures 2 and 3 are computer-generated curves for $\lambda = 5461$ and 6328Å, respectively, and for fixed thin film refractive index $n_1 = 1.58$.[6] The two curves are not identical because the index of refraction of the substrate changes with the wavelength of the impinging radiation; the values for n and k of the substrate were obtained from the literature (6, 7) and are indicated on each figure. Segments of curves for $n_1 = 1.57$ and 1.59 are also presented to indicate the sensitivity of the function to the input information. Total curves were not drawn because they converge for all values of n_1 as δ gets small and would only confuse the diagram.

The thickness and index of refraction of the films under study were measured with an L119 Gaertner (5461Å) and a 200E Rudolph (6328Å) ellipsometer. Both instruments were arranged in the manner described by Archer (8) with a constant angle of incidence of 70°. More than one wavelength was used because proximity of the bandgap of GaP to that of the available light sources (*i.e.*, 2.26 eV for GaP at room temperature, as compared with 2.28 eV for the 5461Å source and 1.97 eV for the 6328Å source) offered the possibility of errors associated with rapidly changing substrate optical properties near the band edge. We shall see that there is very good agreement between the two sets of measurements, and that this potential source of error is unimportant.

Sample drying procedure.—Because the oxidizing solution under study is an aqueous solution of hydrogen peroxide, it was thought very probable that the formed oxide would contain an appreciable quantity of water in the as-grown condition. An examination of the effect of baking freshly prepared oxidized samples at 200°-400°C for a short time (a few hours) always indicated that the films became about 20-25% thinner. In order that the baking process might be examined, a slice of n-type, Te-doped GaP with $N_D \cong 10^{18}/cm^3$ was pulverized in an agate mortar and pestle. The GaP powder was then divided into two equal parts. One part was not treated further, but the second portion was oxidized in boiling H_2O_2 for about 6½ hr, then filtered and air dried at room temperature on the filter paper. Samples of oxidized powder and unoxidized powder were then sent for both thermogravimetric and thermomass spectrographic analyses. Another set of equivalent powder samples was sent for infrared absorption analysis. The latter measurement was inconclusive because of (*i*) the lack of attenuation due to the limited mass of oxidized material on the surface of the powder and (*ii*) the hindrance by the obviously incorporated H_2O in the wavelength region of interest. However, thermogravimetric analysis showed (see Fig. 4A) that for the H_2O_2-oxidized powder there was a small weight loss up to about 250°C,[7] after which the weight of the sample stabilized and remained constant. Meanwhile, the unoxidized powder neither lost nor gained weight when exposed to the same temperature excursion (see Fig. 4B). During the time the oxidized sample was being heated so that the weight-change data could be obtained, the output gas was collected and passed into a mass spectrometer. The major component measured was water, indicating

[4] M. L. McNamara of Bell Laboratories, Reading, Pennsylvania, informs us that if a small quantity (about 25-50 ml) of concentrated H_2O_2 is boiled for about 1 to 2 hr, enough water is boiled off to cause an increase of the H_2O_2 concentration well into the explosive range; a simple reflux condenser system eliminates this hazard and is now the standard reactor for all high temperature oxidations.

[5] The last three samples were removed at 2-hr intervals.

[6] A complete set of curves has been calculated for each wavelength and for n_1 varying from 1.2 to 2.4, but the curves are not included because of their bulky nature. The curves can be generated from the information in the Appendix and in Ref. (5-8).

[7] The technique used is to raise the temperature 10°C/min while monitoring the mass of the sample; see Ref. (9) for details.

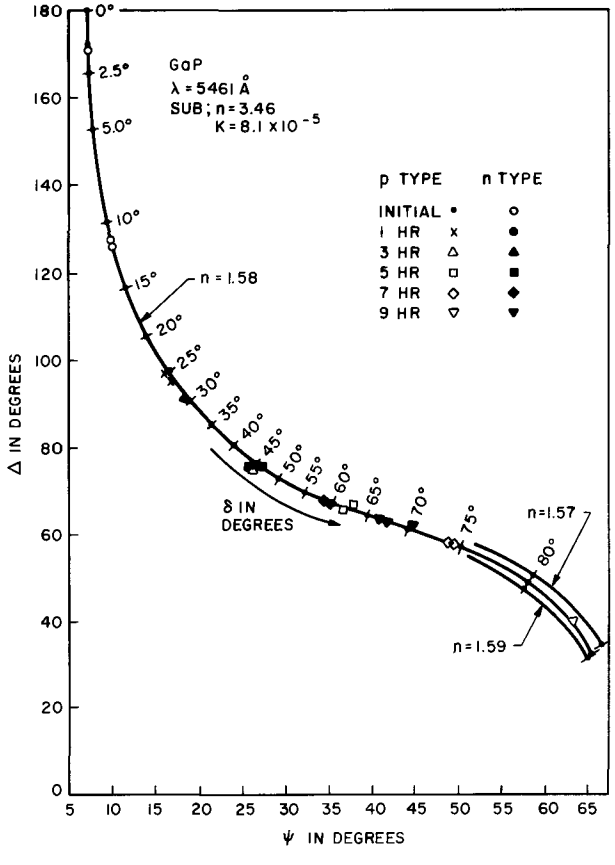

Fig. 2. Computer-generated curve of Δ *vs.* ψ for the wavelength 5461Å and a film refractive index of 1.58. Partial curves for index of refractions 1.57 and 1.59 are also included. In addition, the experimentally determined values of Δ and ψ are indicated to show the precision of the measurement.

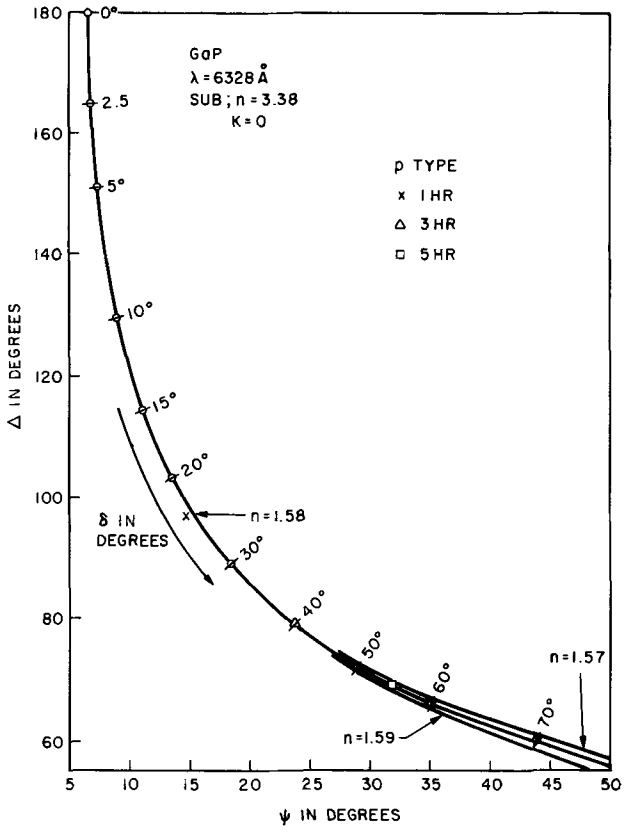

Fig. 3. Computer-generated curve of Δ vs. ψ for the wavelength 6328Å and a film refractive index of 1.58. Partial curves for index of refractions 1.57 and 1.59 are also included. In addition, the experimentally determined values of Δ and ψ are indicated to show the precision of the measurement.

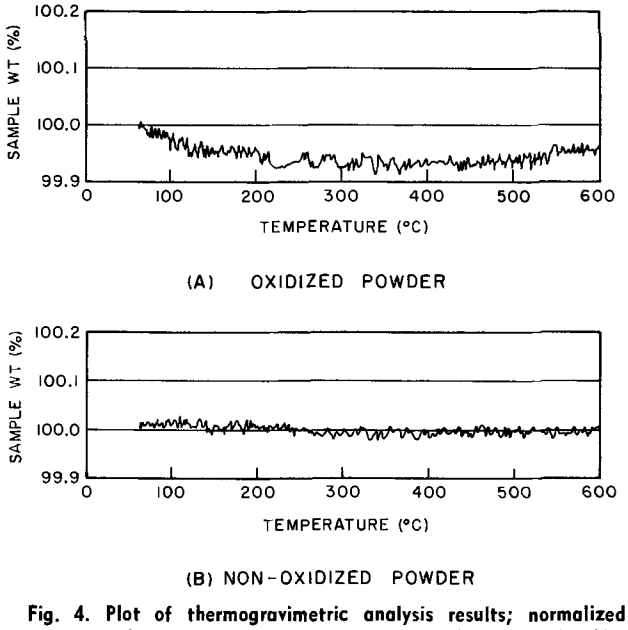

Fig. 4. Plot of thermogravimetric analysis results; normalized weight as a function of temperature for oxidized GaP powder (A), and for nonoxidized GaP powder (B).

that a drying of the oxide film was indeed taking place. As a consequence of all these findings, an arbitrary drying procedure was instituted, except where otherwise noted, for all subsequent oxidations which consisted of drying the samples in a nitrogen-purged oven at 95°C for 1 hr, at 150°C for 2 hr, and then at 250°C for 2 hr.

Anodic oxidation.—Since all oxidation-reduction reactions involve electron transport, one can also envision the reaction as an electrochemical cell, and it is a natural extrapolation to attempt to substitute external electrical driving forces for the thermal conditions described in the preceding section. A study of the anodic oxidation of GaP at room temperature was undertaken with concentrated H_2O_2 as the electrolyte. The choice was made to investigate a constant voltage system with a platinum cathode (see Fig. 5) and to monitor the current with time. The decay of current with time in Fig. 6 is a clear indication of the growth of a resistive oxide on the surface of the GaP anode. An examination of the anodized samples showed that very uniform oxides were grown over the entire exposed surface area.

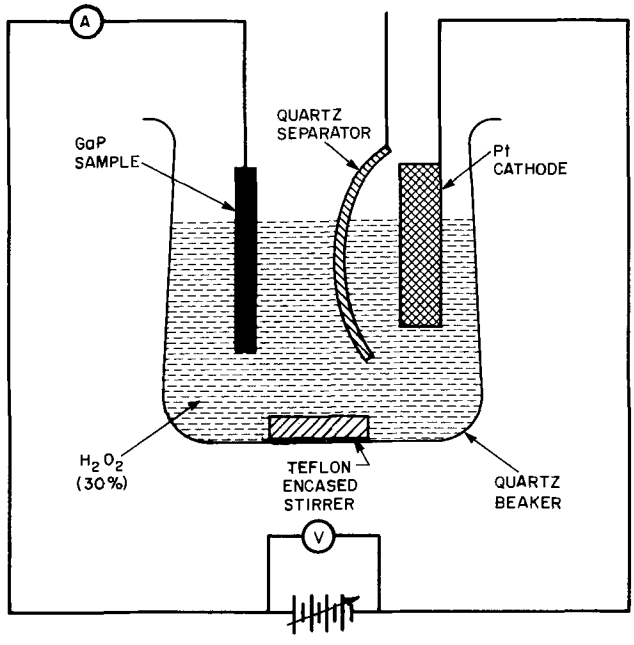

Fig. 5. Schematic of the anodization system

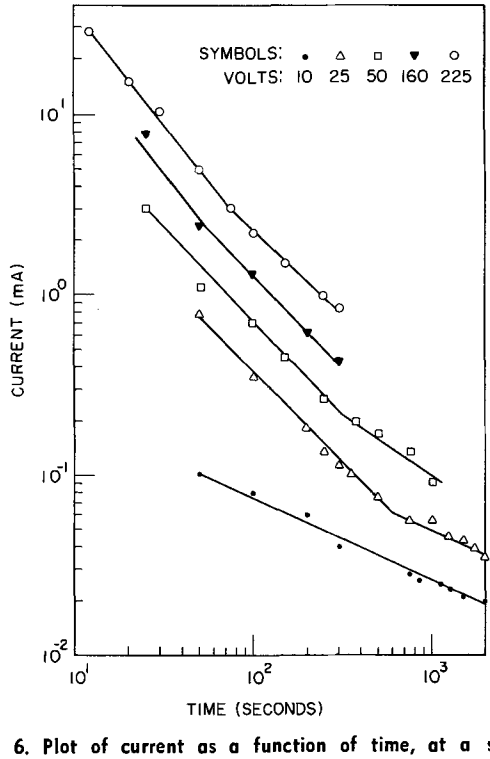

Fig. 6. Plot of current as a function of time, at a series of constant voltages, for the anodization of the $(\bar{1}\bar{1}\bar{1})$ face of n-type GaP.

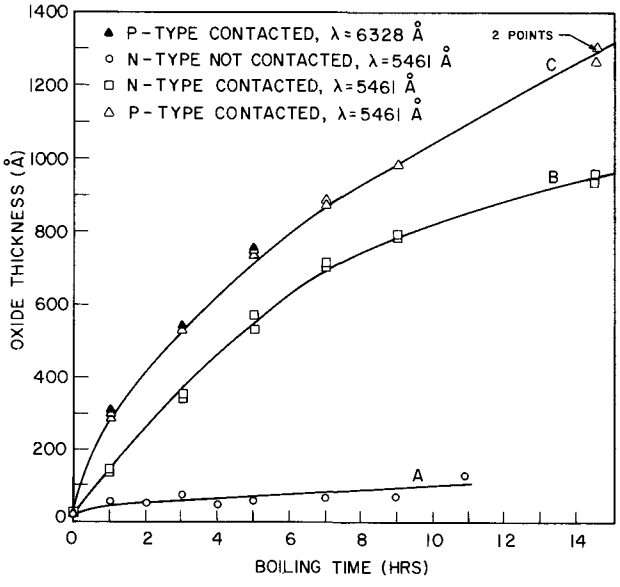

Fig. 7. Plot of oxide thickness as a function of time in boiling 30% H_2O_2 for chemical (noncontacted, curve A) and galvanic (contacted, curves B and C) oxides.

Results and Discussion

Boiling H_2O_2.—The results of the experiment to determine the oxidation rate of GaP in boiling H_2O_2 are shown as curve A in Fig. 7. Merely raising the temperature of the oxidizing system from 25° to 106°C did not produce an increased oxide film thickness. However, when another (111)-oriented, n-type slice (*i.e.*, Se-doped to an $N_D \cong 5 \times 10^{17}/cm^3$) containing a large area Au-Si ohmic contact on the Ga face was exposed to boiling H_2O_2 for periods up to 9 hr, the data shown as curve B of Fig. 7, 0-9 hr,[8] were obtained; the difference between the contacted and noncontacted situation is striking. Repeating this procedure on a p-type $3 \times 10^{17}/cm^3$, Zn-doped slice containing a large area Au-Be ohmic contact on the Ga face resulted in the data shown as curve C, Fig. 7, time 0-9 hr. As a verification that the data of curves B and C were meaningful, two other slices, one from each of the same ingots used to obtain curves B and C, were equivalently contacted and boiled in H_2O_2 for 8 hr, then removed, rinsed in D.I. water, blot dried, stored overnight at room temperature in a laminar flow hood before being boiled in fresh H_2O_2 for 6½ hr the next day, and then baked. These two data points are included in curves B and C of Fig. 7 as the 14½ hr values. Since the latter two points fall on the curves projected from the initial data points, the oxidation times appear to be additive.[9]

The explanation of the effect of the ohmic contact is very straightforward. Without the ohmic contact the entire surface is oxidized, and because the oxide is a "dielectric," the cathodic component of the oxidation-reduction reaction is quenched and oxidation ceases. With the nonreactive ohmic contact in place, the cathodic reaction proceeds on the noble metal surface and thus acts to drive the oxidation of the GaP forward. This is, in effect, a galvanic action, and we will therefore refer to the oxide grown in boiling H_2O_2 with the contact present as the galvanic oxide.

It should be noted here that the measurements of ψ and Δ used for obtaining curves B and C of Fig. 7 are shown in Fig. 2 and 3. The data indicate that the index of refraction of the galvanic oxide is 1.58 ± 0.01 independent of conductivity type of the GaP.

We can now look at curves B and C of Fig. 7 and obtain two more points of understanding. The first is that the p-type specimen clearly oxidizes faster than the n-type specimen. An oxidation reaction can be written as an electron loss, or a hole addition, or a combination of both. Therefore, it would not be surprising to see conductivity type and/or charge concentration effects in the oxidation of GaP. Since we have evaluated only one carrier concentration in this study, we cannot comment further on the effects of doping level except to note that such an effect has been reported for the oxidation of GaAs in H_2O (10). However, the primary influence of hole concentration previously reported in the anodization of germanium (11) is clearly evident in the data of Fig. 7. The second point concerns the fact that curves B and C look very much like a square root of time relationship which is normally found in diffusion-controlled reactions; from the p- and n-type data of Fig. 7, the exponents have been found to be 0.6 and 0.4, respectively. Combining this information with the fact that the GaP ratio is constant in depth into the oxide film, as determined from a Rutherford scattering analysis of thick galvanic films (12), we can conclude that diffusion of the ionic oxidant through the oxide is the rate-controlling step in this process.

Anodic oxidation.—Let us consider the data obtained on the anodically grown oxides. Table I presents the results of a study of the effect of voltage on oxide thickness. On examination of these data, three factors become obvious: (*i*) the oxide thickness is linearly dependent on voltage with a slope of about 12 Å/V up to about 100V, (*ii*) the index of refraction appears to decrease as the films get thicker, and (*iii*) there seems to be an upper anodization voltage above which uniformly colored films cannot be grown.

The linear dependence of the oxide thickness on voltage is a standard phenomenon well known for silicon and germanium anodization (13). The observation that the index of refraction changes with thickness (*i.e.*, forming voltage) is consistent with the observation from Rutherford scattering analysis (12) that the composition of the film is not uniform in depth. Whereas the galvanic oxide was uniform with a stoichiometric analysis of approximately $Ga_2O_3 \cdot P_2O_5$, the anodic oxide appears to be depleted of the Ga_2O_3 component at the oxide semiconductor interface and this region is believed to be almost exclusively vitreous P_2O_5. Studies are under way that should produce a better understanding of this phenomenon. It is believed that a study of the influence of field on the composition of the oxide grown anodically should explain the upper voltage limit on uniform oxide growth.

General results.—With reference to the composition of the oxides, it is worth noting that all attempts, [*i.e.*, x-ray diffraction, reflection electron diffraction, transmission electron diffraction (14), etc.] to determine

Table I. Effect of voltage on oxide thickness

Anodic bias* (volts)	Thickness** (Å)	Apparent refractive index	Interference color
10	125	1.70-1.75	None
25	300	1.70-1.75	None
50	525	1.68	Brownish
100	1125	1.61	Blue
100	1230	1.63	Blue
160	3500†	~1.2	Gold
≥225	—	—	Mottled surface over purplish range

* Constant oxidation time of 2000 sec at constant specified bias.
** Samples not bake-dried.
† Because of the large change in the refractive index, this value is to be used only as an approximation.

[8] Multiple data points for a given growth time indicate that the sample was measured at different positions on the surface or at different wavelengths. The very close agreement in the values implies the good uniformity achieved in oxide thickness over the surface as well as the high degree of precision measuring the thickness at both 5461 and 6328Å. It has been estimated that there is an error of only about 2% caused by errors in reading the ellipsometer or the computer-generated curves.

[9] Additional experiments indicate that the oxidation time is additive only if the drying bake is performed at the conclusion of the series of oxidations and is not interposed between two successive oxidations.

if there was any crystal structure to the galvanic or anodic oxides once they had been properly baked have shown that the film was amorphous (*i.e.*, of ordered dimension less than 20Å). It was found that baking caused the films to get thinner and water to be lost; in addition, the dielectric properties of the oxide were found to improve greatly (15). It has been determined that heating either of these films, galvanic (12) or anodic (16), to temperatures of 650°C and above for short times in nitrogen results in the appearance of polycrystalline $GaPO_4$ in the x-ray diffraction pattern. It is interesting to speculate that in the as-grown condition the oxide is a hydrated "gel" and that baking at 250°C results in the formation of a metastable "vitreous" composite; subsequent heating at the higher temperature (>650°C) merely causes a transformation to the crystalline modification.

It should also be noted that the native oxide, once grown, either by the galvanic or the anodic technique, and subsequently baked, appears to be attacked by many mineral acids and inorganic bases, but is insoluble in most organic solvents.

Conclusions

The results of this study may be summarized as follows:

1. Native oxide films of the order of 1000Å or more can be grown on GaP in aqueous H_2O_2.
2. Both a galvanic system, operating at ~106°C, and an anodic system, operating at 25°C, can be used to grow thick oxides on GaP.
3. The rate-limiting step in the growth of the galvanic oxide is the diffusion of the oxidant ion to the oxide-semiconductor interface.
4. The oxide as initially grown, by either the galvanic or the anodic technique, is rich in water, and adequate drying is required before a useful oxide is achieved.
5. The predominance of the hole transfer mechanism in the oxidation of GaP is shown by the higher oxidation rate of p-type GaP over n-type GaP.
6. There is a linear dependence of the anodic oxide thickness on forming voltage (*i.e.*, 12 Å/V) up to a limiting voltage of about 200V.
7. The index of refraction of the galvanic oxide is 1.58 ± 0.01.
8. The index of refraction of the anodically grown oxide varies from over 1.7 to about 1.2, depending on the forming voltage.
9. When these films are heated to 650°C and above for short periods of time, crystalline $GaPO_4$ appears.
10. These oxides are soluble in many mineral acids and common bases, but is not attacked by the standard Br_2-CH_3OH etchant.

It is obvious that much more work is required before the system reported on here can be fully understood.

Acknowledgment

The authors would like to thank numerous people for assistance and encouragement during the course of this work: J. P. Luongo for his infrared absorption measurements, P. K. Gallagher for the thermogravimetric analyses, Mrs. M. Read for the x-ray analyses, G. Kamlott for the reflection electron diffraction analyses, T. T. Sheng and R. C. Manz for the transmission electron diffraction analysis, S. M. Spitzer for the analysis of dielectric properties, R. L. Fields, Jr. for the information on heat-treatment effects, and R. A. Furnanage for applying the ohmic contacts. In addition, discussions with the following people have been both enlightening and stimulating: P. J. Boddy, J. M. Poate, J. Yahalom, T. M. Buck, R. L. Hartman, M. Kuhn, and F. A. Trumbore. The extremely able assistance of R. C. Manz and A. J. Sayko deserves a special note of thanks.

Manuscript submitted July 14, 1972; revised manuscript received Nov. 23, 1972.

Any discussion of this paper will appear in a Discussion Section to be published in the December 1973 JOURNAL.

APPENDIX

The following equations, taken from Archer (8), may prove useful in constructing a computer program to generate curves such as those shown in Fig. 2 and 3 for other values of n_1.

The fundamental equation of ellipsometry in terms of the Fresnel reflection coefficients is

$$\tan \psi e^{i\Delta} = \frac{r_{1p} + r_{2p}e^{-2i\delta}}{1 + r_{1p}r_{2p}e^{-2i\delta}} \cdot \frac{1 + r_{1s}r_{2s}e^{-2i\delta}}{r_{1s} + r_{2s}e^{-2i\delta}} \quad [A\text{-}1]$$

when

$$\delta = \left(\frac{360}{\lambda}\right) X_o \, (n_1^2 - \sin^2\phi)^{1/2} \quad [A\text{-}2]$$

In Eq. [A-2], λ = the wavelength of measuring light, X_o = the oxide thickness, ϕ = the angle of incidence, and n_1 = the index of refraction of the film.

In the equations above, the subscript numbers 1 and 2 refer to the film and substrate, respectively, and the subscript letters p and s refer to the electric vector of the light in and perpendicular to the plane of incidence.

The general Fresnel equation for reflection of light from a surface "b" into a medium "a" can be written as

$$r_p = \frac{n_a \cos \phi_b - n_b \cos \phi_a}{n_a \cos \phi_b + n_b \cos \phi_a} \quad [A\text{-}3]$$

$$r_s = \frac{n_a \cos \phi_a - n_b \cos \phi_b}{n_a \cos \phi_a + n_b \cos \phi_b} \quad [A\text{-}4]$$

where n_a and n_b are indices of refraction of the two media and in general are complex. ϕ_a and ϕ_b are the angles of incidence and reflection, respectively. Since these angles can be related by Snell's law, the Fresnel coefficients of Eq. [A-1] can be written in terms of the optical constants of the film and substrate. Equations for ψ and Δ may be obtained by substituting Eq. [A-2], [A-3], and [A-4] in Eq. [A-1] and separating the resulting expression into real and imaginary parts.

REFERENCES

1. H. T. Minden, *This Journal*, **109**, 733 (1962).
2. M. Rubinstein, *ibid.*, **113**, 540 (1966).
3. B. Schwartz, *ibid.*, **118**, 657 (1971).
4. Chemical Safety Data Sheet SD-53, Hydrogen Peroxide, Manufacturing Chemists Association, Inc., Washington, D.C. (1969).
5. R. E. Cox, *Appl. Optics*, **3**, 1188 (1964).
6. B. O. Seraphin and H. E. Bennett, "Semiconductors and Semimetals, Vol. 3—Optical Properties of III-V Compound," R. K. Willardson and A. C. Beer, Editors, pp. 499-543, Academic Press, New York (1967).
7. W. L. Bond, *J. Appl. Phys.*, **36**, 1674 (1965).
8. R. J. Archer, *J. Opt. Soc. Am.*, **52**, 970 (1962).
9. P. K. Gallagher and F. Schrey, *Thermochemica Acta*, **1**, 465 (1970).
10. B. Schwartz, S. E. Haszko, and D. R. Wonsidler, *This Journal*, **118**, 1229 (1971).
11. W. H. Brattain and C. G. B. Garrett, *Bell System Tech. J.*, **34**, 129 (1955).
12. T. M. Buck, J. M. Poate, and B. Schwartz, To be published in *Journal of Physics and Chemistry of Solids*.
13. L. Maisel and R. Glang, "Handbook of Thin Film Technology," pp. 5-17, McGraw-Hill Book Co., New York (1970).
14. T. T. Sheng and R. C. Manz, Private communication.
15. S. M. Spitzer, B. Schwartz, and M. Kuhn, *This Journal*, **119**, 242C (1972).
16. R. L. Fields, Jr., Private communication.

Technical Notes

Auger Spectra of HCl Vapor-Etched n^+ GaAs {100} Substrates

R. L. Moon* and L. W. James

Central Research Laboratories, Varian Associates, Palo Alto, California 94303

Often incorporated into the procedures used for vapor-phase epitaxy (VPE) of III-V materials is an etching phase to ensure a clean substrate prior to growth. The effect of this etching is usually judged by the final device characteristics or by carrier-concentration profiles. During the course of our investigations of possible contaminants present on the surface of vapor-grown GaAs, we examined the effects of HCl etching on the Auger spectra of n^+ GaAs {100} substrates.

Our procedure consisted of preparing the GaAs substrate for VPE, taking an Auger spectrum, etching with HCl and H_2 in the vapor reactor, and finally taking a second Auger spectrum. Auger analysis was performed with a Varian Cylindrical Mirror Analyzer system at a vacuum of 1×10^{-10} Torr. Substrates were Czochralski grown {100} GaAs doped to about 1×10^{18} cm^{-3} with Si, Sn, or Te. Final substrate preparation before beginning the test included, besides the appropriate intermediate rinses, a hot trichlorethylene and acetone degrease, a $5H_2SO_4:H_2O_2:H_2O$ etch, and a Br_2–methanol etch. The wafer was placed in methanol for transfer between the various stages.

At least for short periods, immersion of GaAs wafers in electronic-grade methanol does not appear to affect the surface-impurity distribution within the sensitivity of the Auger analysis. Besides Ga and As, only C and O peaks are seen; oxygen will always disappear with heating. Sulfur is the next most common contaminant seen, but only when the wafer is stored in methanol for several hours. Putting the methanol in a dry nitrogen atmosphere did not eliminate the sulfur contamination. The source of the sulfur is unknown.

Vapor etching was carried out in a vapor reactor designed for the $Ga|AsH_3|HCl$ process (1). The wafer was inserted through an H_2-purged antechamber into the hot zone of a reactor held at temperature. Approximately 3-5 min were required for the wafer to reach the steady-state temperature of 780°C. Then the wafer was etched for 10 min, followed by a 3 min wait before removing the sample. An etch rate of 0.3 μm/min was obtained with flow rates of 4 cm^3/min of a 10% HCl/H_2 mixture plus 1000 cm^3/min of H_2.

A typical Auger spectrum for GaAs {100} substrates just before etching is seen in Fig. 1. (This particular spectrum is from a Sn-doped wafer.) Substrates placed into the hot reactor with only H_2 flowing produce the same spectrum.

Some samples, after receiving the HCl etch, produce a different type of Auger spectrum. Figure 2, taken from a Te-doped sample after etching, shows an essentially unchanged spectrum. The same results are obtained from Si-doped substrates. Only C, O, N, Ga, and As peaks are seen. For Si-doped wafers, at energies above the final As peak, the spectrum is again featureless even when the sensitivity and sweep time are increased by a factor of 5; in particular, at secondary energies between 1500 and 1650 eV, where Si peaks are expected, nothing is seen. Tin-doped samples after etching produced the Auger spectrum seen in Fig. 3. In this case, an accumulation of Sn on the surface is noted.

Although this behavior may seem anomalous at first glance, it is understandable upon examination of the thermodynamic data of the dopants. Looking first at the vapor pressure of the dopants (Table I) at 800°C (2) it is apparent that Te would not be expected to accumulate on the surface because of its high vapor pressure. However, from vapor pressure considerations

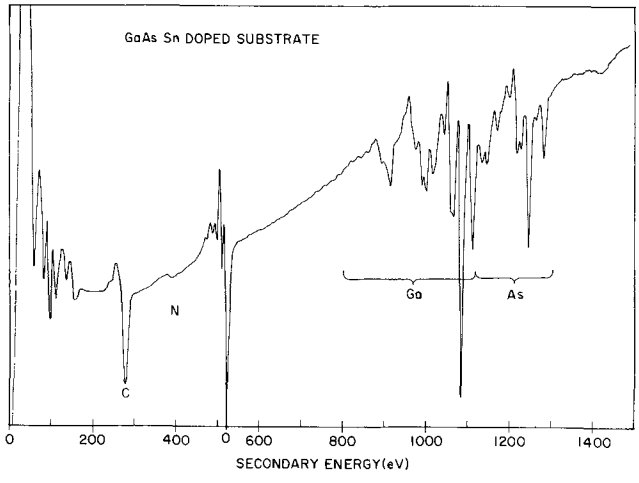

Fig. 1. Typical Auger spectrum of a n^+ GaAs {100} substrate before HCl etching in a VPE reactor. The substrate used in this case was Sn doped to 1×10^{18} cm^{-3}.

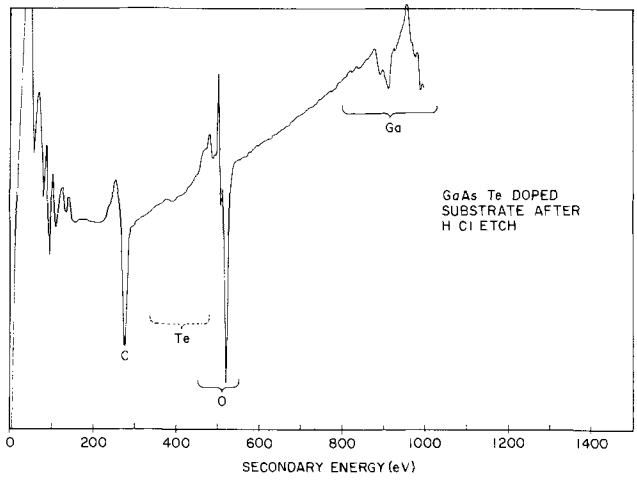

Fig. 2. Auger spectrum seen after etching Te and Si-doped GaAs substrates in HCl vapor. Shown here is a spectrum taken from a Te-doped substrate.

* Electrochemical Society Active Member.

Key words: Auger, vapor etching, gallium arsenide, substrate doping.

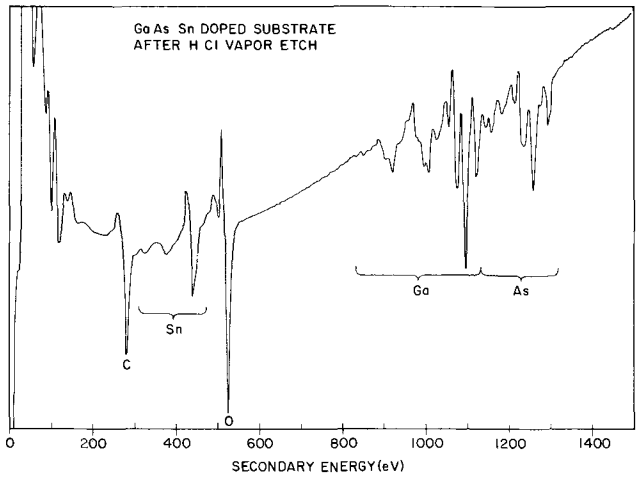

Fig. 3. Auger spectrum of a Sn-doped GaAs substrate after etching at 780°C in HCl vapor.

alone, Si, not Sn, would be expected to segregate on the surface.

The behavior of Si and Sn becomes clear when the stabilities of their chlorides are taken into consideration. Standard free energies at 800°C for the production of 1 mole of metal chloride were obtained by calculating the standard enthalpy and entropy (3), $\Delta H°_{298}$ and $\Delta S°_{298}$, respectively, for the reaction and then computing the free energy, $\Delta G°_T$, from $\Delta H°_{298} - T\Delta S°_{298}$. Since both $\Delta H°$ and $\Delta S°$ are functions only of the change in heat capacity and of the temperature, a change in one tends to cancel the change in the other, thus not greatly affecting $\Delta G°_T$ (4). Data for the thermochemical computations are from JANAF (5) and NBS (6) tables. From the equilibrium constants for the formation of the divalent and tetravalent chlorides, it is apparent that the equilibrium pressures are always greater for the Si chlorides than for the Sn chlorides (Table II). In the case of tetravalent chlorides for example, P_{SiCl_4}/P_{SnCl_4} is 10^7, assuming the Henry's Law constants for Sn and Si in the solid are the same. If HCl is considered to react with the metal oxides rather than the elemental metal, a stabilization against metal-chloride formation is seen. Since all standard energies of formation are positive, while the entropies of formation of MCl_4 and MCl_2 are negative and positive, respectively.

These observations should help in clarifying the relationship between substrate dopant and I-layer formation when undoped GaAs is grown by vapor epitaxial methods. Wolfe *et al.* (7) have shown that a high-resistance region appears at the undoped GaAs layer/Si-doped GaAs substrate interface when growth takes place in a low As_4-pressure atmosphere. At low arsenic pressures silicon outdiffusing from the substrate will be preferentially incorporated into arsenic sites, hence acting as an acceptor. Since the Ga in any $Ga/AsCl_3/H_2$ reactor requires a short period to resaturate as a result of dissolution and exposure of fresh Ga to the decomposed $AsCl_3$ vapor (8), the initial growth of high purity GaAs is always at low As_4 pressures unless special precautions are taken. These results have been substantiated by the work of Hirao and Nakashima (9) and also Saito and Hasegawa (10) who have shown that a critical pressure of arsenic vapor of about 3 Torr is necessary before I-layer formation is prevented. Of particular relevance are etching experiments (9) performed on Si, Sn, and Te-doped GaAs substrates with an impurity concentration of $\sim 1 \times 10^{18}$ cm^{-3} where high resistance regions were formed in all cases if growth commenced before arsenic saturation was complete. If the Ga was saturated and the substrates vapor etched, high resistance regions were not observed for layers grown on substrates doped with Sn or Te, but a slight dip in carrier concentration was seen for those doped with Si.

During growth, some HCl is always present as a result of incomplete reaction with the GaAs crust. Silicon chlorides can then form at the surface, thereby reducing the number of Si atoms available for the preferred Ga site when the As_4 pressure is high. A region having a lower donor concentration results. Further evidence supporting the idea of silicon chlorides being very stable in a GaAs VPE reactor is shown in another study by Hasegawa and Saito (11) where the final carrier concentrations of films grown from a Si-doped GaAs source or a Si-Ga mixture were always lower than those of the source; values of $N_d + N_A$ for films grown with a Ga-Si or just a Ga source were almost the same.

In the same work (11), Sn-doped layers with a 4-6 $\times 10^{16}$ cm^{-3} carrier concentration deposited on a 2×10^{16} cm^{-3} Sn-doped substrate showed a peak rather than a dip in carrier concentration near the interface. This is consistent with our observation of Sn accumulation on the surface after etching. The reason for the beneficial behavior of Te-doped substrates is not as clear, but is probably related to its totally donor nature and the stability of both GaTe and As_2Te_3.

Complete clarification of the relationship between I-layer formation, HCl etching, As_4 pressure, and substrate doping will require more detailed experiments. From our evidence here, coupled with carrier-concentration profiles (7, 9, 11), substrates doped with Sn appear to be superior to those doped with Si and possibly even to those doped with Te because of Sn accumulation at the surface during etching.

Table I. Vapor pressure of Te, Si, and Sn at 800°C

	Te	Si	Sn(l)
Vapor pressure (Torr) at 800°C	10^2	10^{-11}	7×10^{-7}

Table II. Standard heat and entropy of formation at 298°C, and equilibrium constants at 800°C, for the formation of divalent and tetravalent chlorides of Si and Sn from HCl by the following reactions:

$$M + n\text{HCl} \rightarrow MCl_n + \frac{n}{2}H_2 \text{ where } n = 2 \text{ or } 4$$

	$\Delta H°_{298}$, kcal/mol	$\Delta S°_{298}$, cal/deg per mole	$K_{800°C}$
$SiCl_4$	−69.0	−41.4	10^5
$SnCl_4$	−24.7	−40.9	8×10^{-8}
$SiCl_2$	+4.4	+5.5	2.0
$SnCl_2$	>4.4	~5.0	<2.0

Acknowledgments

The authors would like to acknowledge the experimental assistance of S. Hikido and H. Gilliland. We would also like to thank R. Fairman for useful comments.

Manuscript received Sept. 25, 1972.

Any discussion of this paper will appear in a Discussion Section to be published in the December 1973 JOURNAL.

REFERENCES

1. J. J. Tietjen and J. A. Amick, *This Journal*, **113**, 724 (1966).
2. R. E. Honig and D. A. Kramer, *RCA Rev.*, **30**, 285 (1969).
3. W. J. Moore, "Physical Chemistry," 3rd ed., Prentice Hall, New Jersey (1962).
4. A. W. Searcy, *Surv. Progr. Chem.*, **1**, 35 (1963).
5. D. R. Stull and H. Prophet et al., *JANAF Thermochemical Table*, 2nd ed., NSRDS-NBS-37, U.S. Government Printing Office (1971).
6. D. D. Wagman, W. H. Evans, U. B. Parker, I. Halow, S. M. Bailey, and R. H. Schumm, Selected Values of Thermodynamic Properties, NBS Tech.

Note 270-3, U.S. Government Printing Office (1968).
7. C. M. Wolfe, A. G. Foyt, and W. T. Lindley, *Electrochem. Technol.*, **6**, 208 (1968).
8. D. W. Shaw, *J. Crystal Growth*, **8**, 117 (1971).
9. M. Hirao and H. Nakashima, *J. Japan Soc. Appl. Phys., Suppl.*, **40**, 46 (1971).
10. T. Saito and F. Hasegawa, *Japan J. Appl. Phys.*, **10**, 197 (1971).
11. T. Saito and F. Hasegawa, *ibid.*, **7**, 1342 (1968).

Current-Controlled Growth and Dopant Modulation in Liquid Phase Epitaxy

M. Kumagawa,[1] A. F. Witt,* M. Lichtensteiger, and H. C. Gatos*

Department of Metallurgy and Materials Science and Center for Materials Science and Engineering, Massachusetts Institute of Technology, Cambridge, Massachusetts 02139

A crystal growth method is reported which uses Peltier cooling at the crystal-melt interface (associated with the flow of electric current from seed to solution) to initiate and sustain liquid phase epitaxial growth while the temperature of the over-all growth system is maintained constant.

"Rate striations" (1), which permit the determination of microscopic growth rates and the interface morphology during the growth process, were introduced (through current pulses of short duration) both in regular epitaxial growth obtained by decreasing the temperature of the system and in epitaxial growth induced by Peltier cooling. The width and intensity of these striations can be controlled by the amplitude and duration of the current pulses. Thus current pulses were also used to modulate the growth rate and consequently the dopant concentration.

The method was applied to the growth of InSb layers (doped with tellurium) on InSb substrates from indium and antimony solutions. The apparatus used is shown in Fig. 1. The growth cell is similar in design to those commonly employed (2), however, it permits controlled flow of electric current through the growth interface.

In a growth experiment, seed-solution contact is established after thermal equilibration by appropriately positioning the boron-nitride slide between the seed and the solution.

Representative results with rate striations introduced in epitaxial layers obtained with controlled furnace cooling at a rate of approximately 0.1°C/min and 0.04°C/min respectively, are shown in Fig. 2 and 3. The "rate striations" (revealed by etching) (3) were introduced by current pulses (56 A/cm^2) of 1 sec duration applied at intervals of 17.5 (Fig. 2) and 20 min (Fig. 3) with the first pulse transmitted 11 and 32 min after starting the respective cool-down cycles. These striations delineate unambiguously the morphology of the interface during the growth process and permit the determination of the microscopic growth rate from the known repetition rate of the current pulses and the spacing of the striations.

In the case of Fig. 2, it can be seen that at constant cooling rate, the microscopic growth rate changed

* Electrochemical Society Active Member.
[1] On leave from Research Institute of Electronics, Shizuoka University, Hamamatsu, Japan.
Key words: liquid phase epitaxy, dopant segregation, current controlled crystal growth, growth rates, solution growth.

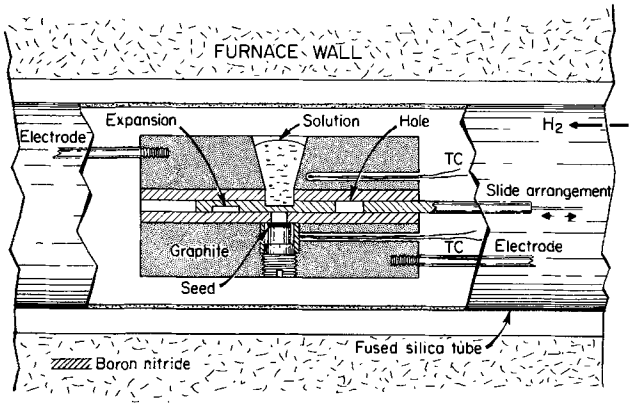

Fig. 1. Schematic diagram of epitaxial growth system

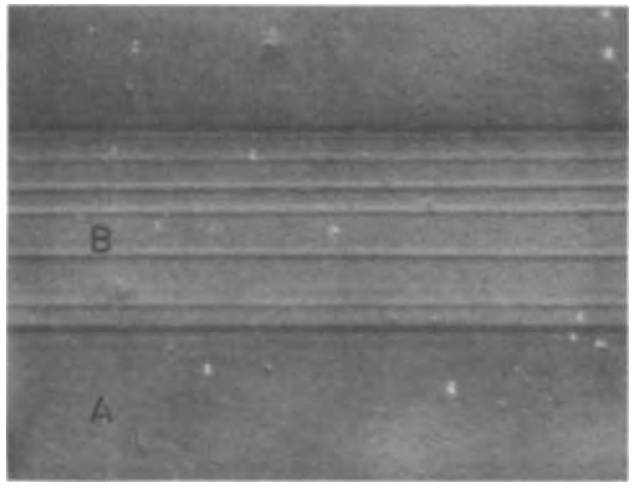

Fig. 2. Epitaxial layer of InSb (B) on InSb substrate (A) grown from a 75 atomic per cent (a/o) In and 25 a/o Sb solution at a cooling rate of 0.096°C/min. The rate striations were introduced by current pulses across the growth interface (see text). ×270.

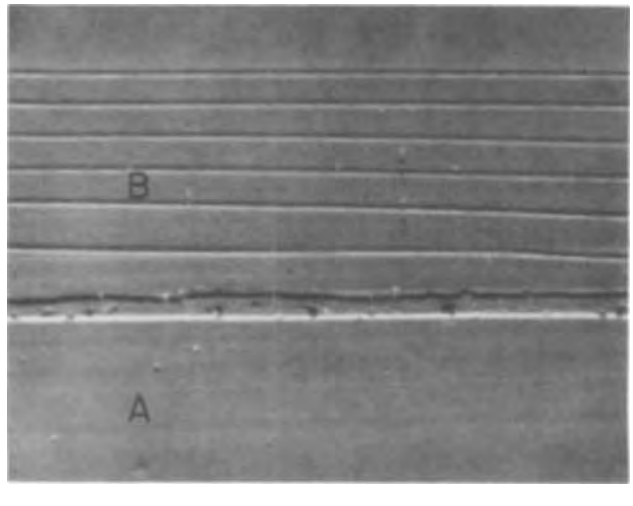

Fig. 3. Epitaxial layer of InSb (B) on InSb substrate (A) grown from a 75 a/o In and 25 a/o Sb solution at a cooling rate of 0.039°C/min (see text). ×330.

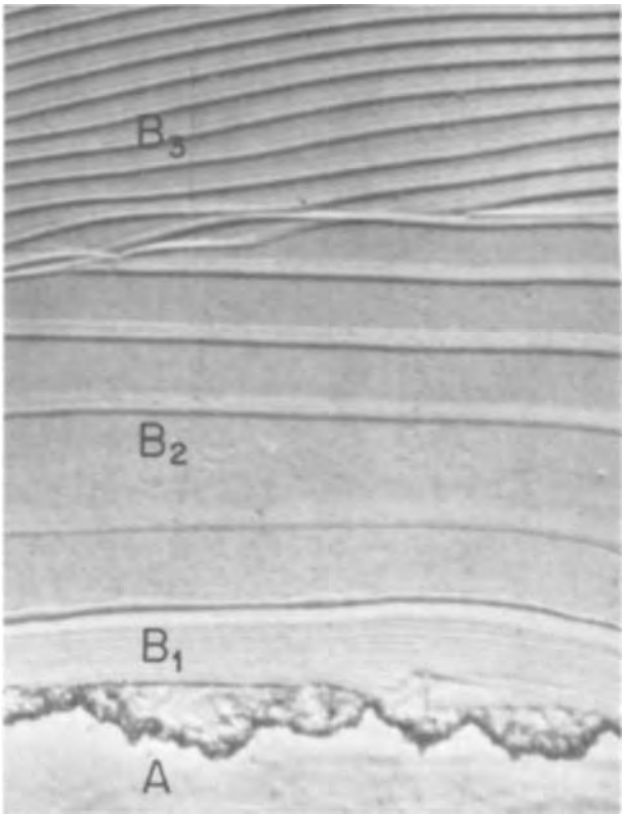

Fig. 4. Epitaxial layer of InSb grown by Peltier cooling (at constant furnace temperature) from a 60 a/o In and 40 a/o Sb solution (see text). ×470.

from 1.5 μm/min at the beginning to 0.45 μm/min toward the end of the growth. In the case of Fig. 3, seed-solution contact was established while the temperature of the system was slightly higher than its equilibrium value. Consequently a small fraction of the seed was dissolved and a flat seed solution interface was formed. Upon lowering the temperature (by about 1.2°C) to its equilibrium value (457.0°C), a new irregular interface was formed. It is seen from the morphology of the rate striations that this irregular interface becomes smooth upon initiation of growth and remains smooth throughout the growth process. The rate striations in Fig. 2 and 3 indicate clearly pronounced differences in the microscopic growth behavior with the growth rate going through a minimum in Fig. 2 and decreasing steadily in Fig. 3.

Epitaxial growth achieved by passing electric current across the seed-solution interface at constant furnace temperature is shown in Fig. 4. The unidentified precipitates at the original growth interface, which as can be seen do not interfere with epitaxial growth, are presumed to be the result of inadvertent oxidation during equilibration. The three growth regions B_1, B_2, and B_3 seen in the figure were obtained by passing continuous electric current of 0, 5.5, and 1 A/cm^2, respectively, through the growth interface. In all three regions rate striations were introduced by superimposing current pulses of 0.1 sec duration (100 A/cm^2) at a repetition rate of 0.01, 0.02, and 0.01 sec, respectively. The growth irregularities upon transition from regions B_2 to B_3 (changing interface morphology) are as yet unexplained and are subject to further investigations. It is seen that in the first growth region (B_1) where only intermittent pulses were applied but no "base current" was passed, the growth was very limited. Over a period of 5000 sec, an epitaxial layer of a total thickness of 25 μm was intermittently formed (due to cooling brought about by the pulses) at a net growth rate of 3×10^{-1} μm/min. A base current of 5.5 A/cm^2 for a period of 1200 sec (middle region) led to a layer (B_2) of a total thickness of 1.25 μm at an average growth rate of about 6 μm/min. It should be noted that in this region the growth rate during the superposition of each pulse was about 4000 μm/min (as determined from the width of the rate striations associated with the 0.1 sec pulse duration), *i.e.*, about 670 times greater than the average growth rate. The epitaxial region obtained at a base current density of 1 A/cm^2 (B_3 in Fig. 4) grew at an average rate of 3 μm/min; during the superposition of the pulses the rate was approximately 1500 μm/min.

In the region grown at a base current of 5.5 A/cm^2 the rate striations resulting from the pulses appear as bands rather than lines. This result reflects a high growth rate induced by the base current which is further increased by a factor of close to 700 for the duration of each high current density pulse. This sudden increase in growth rate should lead to a substantial increase in dopant concentration, which in turn is expected to be attenuated within the duration of the pulse, because of boundary layer depletion. Such a segregation behavior is indeed observed through the etching characteristics of the bands (4) which reveal pronounced concentration increases at their lower edge (beginning of pulse) and gradual transitions on their upper edge (termination of pulse). Thus, controlled modulation of chemical composition may be achieved by the appropriate choice of pulse shape and duration.

It is shown that Peltier cooling associated with current flow across the growth interface can be successfully used to achieve controlled crystal growth. Superimposed current pulses can serve for the introduction of rate striations as well as for localized modulation of dopant segregation.

Acknowledgment

This work was supported by the National Science Foundation under grant GK-28343X. One of us (A.F.W.) wishes to acknowledge the staff of the Materials Division of the I.B.M. research center, in particular Dr. T. S. Plaskett for assistance and stimulating discussions.

Manuscript submitted Aug. 28, 1972; revised manuscript received Nov. 16, 1972.

Any discussion of this paper will appear in a Discussion Section to be published in the December 1973 JOURNAL.

REFERENCES

1. M. Lichtensteiger, A. F. Witt, and H. C. Gatos, *This Journal*, **118**, 1013 (1971).
2. M. B. Panish, S. Sumski, and I. Hayashi, *Trans. AIME*, **2**, 795 (1971).
3. A. F. Witt, *This Journal*, **114**, 298 (1967).
4. D. C. Johnston, A. F. Witt, and H. C. Gatos, *ibid.*, **115**, 438 (1968).

Resistivity Characterization of Semiconductor Crystal Ingots

F. Padovani* and G. Valant

Texas Instruments Incorporated, Dallas, Texas 75222

The resistivity characterization of semiconductor crystal ingots is an important step in the manufacture of slabs or slices suitable for device manufacture. Such characterization is usually performed by a two-point probe or four-point probe measurement on the ingot surface. Such resistivity measurements are usually found not to be in agreement with each other and with subsequent measurements performed on slices obtained from the ingot. It is the purpose of the present work to demonstrate that four-point probe and two-point probe measurements performed at the same location on an ingot surface, can be used to estimate more accurately the resistivity profile of the ingot than either of the measurements independently. The presence of a radial resistivity gradient is first shown to affect the resistivity derived from a two-point probe resistivity measurement and hence to be a reason for discrepancy between two-point probe and four-point probe resistivity measurements. Correction factors to the two-point probe resistivity measurement are then calculated for two different radial resistivity profiles. Finally, it is shown that, assuming a given radial resistivity profile, combined two-point probe and four-point probe resistivity measurements can be used to evaluate the axial resistivity of the semiconductor ingot but cannot be used to deduce the local radial resistivity gradient.

Influence of a Radial Resistivity Gradient on Two-Point Probe Resistivity Measurement

Let us consider a two-point probe resistivity measurement arrangement as shown in Fig. 1. The crystal ingot will be assumed to have a uniform diameter $2R$, a uniform resistivity along the crystal axis, and a radial gradient with cylindrical symmetry. It will be further assumed that current is supplied to the crystal at two equipotential planes normal to the cylinder axis and located at distance from the probes much larger than the crystal diameter. Under these assumptions the equipotential surfaces in the crystal will be planes normal to the crystal axis and the crystal electrical properties can be described by an infinite number of concentric cylinders of resistivity, $\rho(r)$, thickness, dr, and cross-sectional area, $2\pi rdr$. If V is the potential existing between two probes separated by a distance, l, the current density, i, flowing in a cylinder of radius, r, will be

$$i = v/\rho(r)l \qquad [1]$$

where $\rho(r)$ is the resistivity of the cylinder considered. The total current, I, flowing in the crystal is

$$I = \int_0^R 2\pi irdr \qquad [2]$$

Hence, by combining Eq. [1] and [2] it is clear that

$$v/I = l/2\pi \left[\int_0^R \frac{rdr}{\rho(r)} \right]^{-1} \qquad [3]$$

Since the resistivity ρ_2 derived from a two-point probe measurement is equal to

$$\rho_2 = \pi R^2 v/Il \qquad [4]$$

we conclude that ρ_2 is equal to

$$\rho_2 = R^2 \left[2 \int_0^R \frac{rdr}{\rho(r)} \right]^{-1} \qquad [5]$$

It thus appears that the resistivity of an ingot as deduced from two-point probe resistivity measurements can be significantly affected by the radial resistivity profile of the ingot. This might explain the often encountered discrepancies occurring between resistivity measurements performed at the same location of an ingot surface by the four-point probe and the two-point probe techniques. Most four-point probe systems use a probe spacing of 40 mils and therefore the resistivity deduced from such a technique will reflect the ingot surface resistivity provided that the crystal diameter is very large compared to 40 mils. If one denotes by ρ_4 the resistivity deduced from such a four-point probe resistivity measurement, one can write that

$$\rho_4 = \rho(R) \qquad [6]$$

and thus in general

$$\rho_4 \neq \rho_2 \qquad [7]$$

We will now show that Eq. [6] and [5] can be used to estimate both the resistivity of an ingot along its axis and the radial resistivity gradient.

A Technique for Estimating Ingot Axial Resistivity and Radial Resistivity Gradient

As noted in the preceding section, four-point probe measurements and two-point probe measurements performed at the same location on an ingot surface will generally disagree as a result of the radial, nonuniformity of the ingot resistivity. The purpose of this section is to demonstrate that this difference in deduced resistivity can be used to more accurately characterize the ingot provided one has a knowledge of the functional dependence of the radial resistivity profile. This knowledge is required, as demonstrated by Eq. [5], if one desires to relate the resistivity deduced from a two-point probe resistivity measurement to the resistivity at a given point of the crystal radius.

Most semiconductor crystals produced today exhibit small (0-30%), uniform radial resistivity profiles. As a result, a semiconductor slice resistivity is usually characterized by the resistivity at the center of the slice and an average radial resistivity gradient (1). Let us assume thus that through experience one has gathered information on the functional dependence of the radial resistivity gradient and that although the magnitude of this gradient may vary from crystal to crystal its functional dependence is fairly constant. This is a good assumption since the radial resistivity gradient is a representation of the growth conditions which should be fairly reproducible for a given crystal growth apparatus.

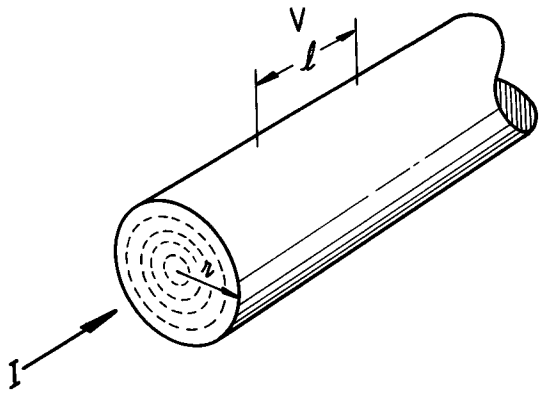

Fig. 1. Two-point probe resistivity measurement

* Electrochemical Society Active Member.

Key words: ingot radial resistivity gradient.

Through experience it has been found in our laboratory that two types of functional dependence of the radial resistivity profiles are usually encountered: the linear and the quadratic profiles. These two simple radial resistivity distributions will be used to illustrate the proposed technique.

Linear profile.—In this case, it is assumed that, if ρ_o is the axial resistivity, the resistivity of the ingot at a distance, r, from its axis is given by

$$\rho(r) = \rho_o + ar \qquad [8]$$

combining Eq. [8] and [5] yields

$$\rho_2 = \frac{a^2R^2}{2}\left[aR - \rho_o \ln\left(1 + \frac{aR}{\rho_o}\right)\right]^{-1} \qquad [9]$$

and, since $\rho_4 = \rho_o + aR$, we have

$$\frac{\rho_4}{\rho_2} = 2(1 + x)[x - \ln(1 + x)]/x^2 \qquad [10]$$

and

$$\rho_o = \rho_4/(1 + x) \qquad [11]$$

where $x = aR/\rho_o$ is the radial resistivity gradient. Equations [10] and [11] demonstrate that four-point probe and two-point probe resistivity measurements performed at the same location on a crystal ingot surface can be used to estimate the resistivity of the ingot axis as well as the radial resistivity gradient. Figure 2 shows a plot of the resistivity gradient x *vs.* the ratio ρ_4/ρ_2 as given by Eq. [10].

Quadratic profile.—In this case it is assumed that, if ρ_o is the axial resistivity, the ingot resistivity at a distance, r, from its axis is given by

$$\rho(r) = \rho_o + ar^2 \qquad [12]$$

Following the above treatment one deduces that

$$\rho_4/\rho_2 = \frac{(1 + x)}{x}\ln(1 + x) \qquad [13]$$

and that ρ_o is given again by Eq. [11]. Figure 2 also shows a plot of the resistivity gradient x *vs.* the ratio ρ_4/ρ_2 as given by Eq. [13]. Note that in this particular case the gradient n is equal to a R^2/ρ_o.

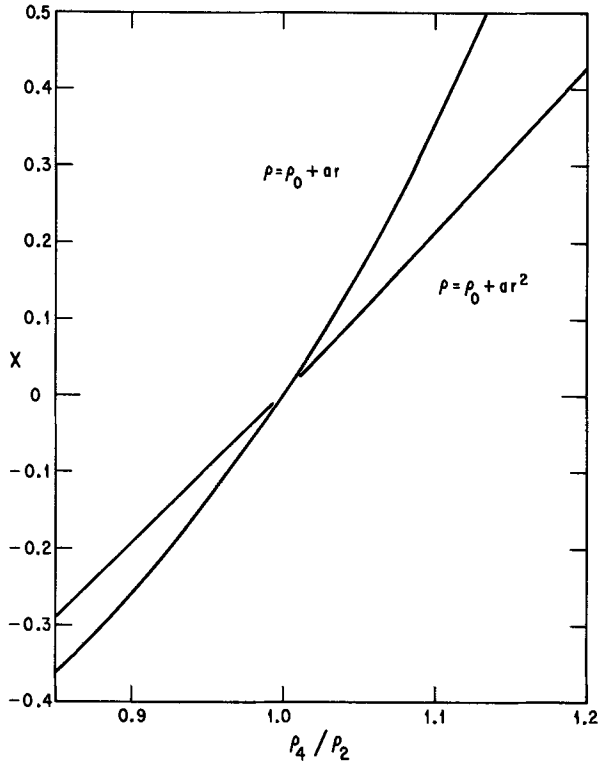

Fig. 2. Variation of the ratio ρ_4/ρ_2 *vs.* radial resistivity gradient x

Examination of Eq. [10], [11], and [13] reveals that, provided a radial resistivity profile is assumed, the radial resistivity gradient, x, and the axial resistivity profile, ρ_o, can be determined from simultaneous two-point probe and four-point probe resistivity measurements performed on the ingot surface. In practice, provided a set of measurements ρ_4 and ρ_2 one would first evaluate the radial gradient x by use of appropriate curve shown on Fig. 2. Having done so, one would subsequently use Eq. [11] to determine the axial resistivity.

An estimate of the errors encountered in the determination of the axial resistivity and of the radial resistivity profile can be obtained through an error calculation performed on Eq. [10], [11], and [13]. It can readily be shown that the relative error existing on the value of the axial resistivity is equal to the relative error existing on either the four-point probe or two-point probe resistivity measurements provided that these two relative errors are equal. As evidenced by Ref. (1) this is a good approximation.

Similar error calculations can be performed to obtain the relative error on the deduced radial resistivity gradient. Figure 3 shows the results of such calculations for both types of radial resistivity profiles previously considered, when the total relative error resulting from the two-point probe and four-point probe resistivity measurements is taken to be equal to 10% (1). Note that the proposed technique does not offer a great deal of accuracy toward the determination of the ingot radial resistivity gradient. Typical silicon crystals for example may exhibit a radial resistivity gradient of up to 30%. The proposed technique will only enable a one to 200% accuracy in the determination of the radial resistivity gradient of such crystals.

Experimental Verification of the Technique

In order to verify the applicability of this technique, silicon crystals were grown in the laboratory. These

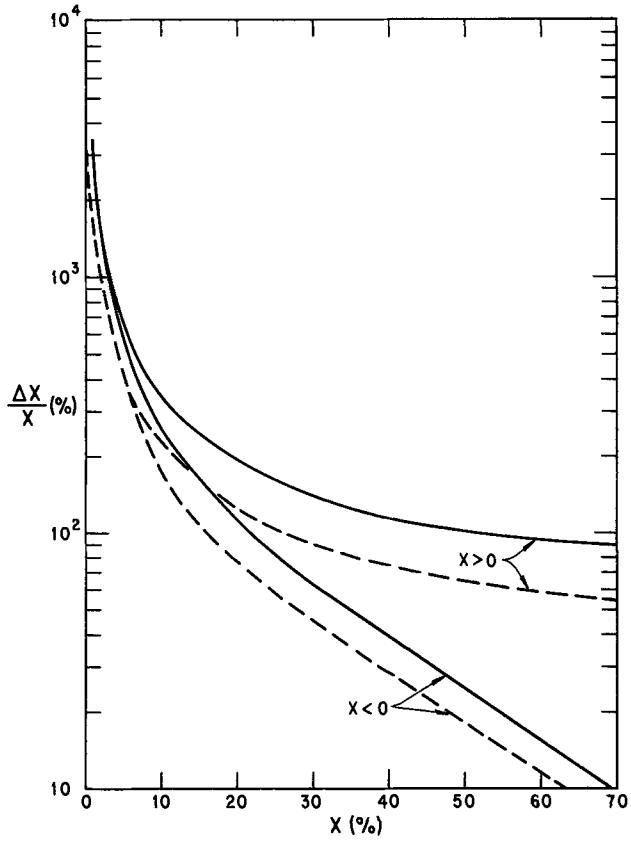

Fig. 3. Relative error on the deduced resistivity gradient *vs.* deduced resistivity gradient. Solid line is for a linear profile and dashed line for a quadratic profile.

crystals were grown using the Czochralski method from a 4 kg charge and had a nominal diameter of 2.25 in. Pull rate was maintained at one thousand of an inch per second during the whole growth. These crystals prior to resistivity characterization were centerless ground to 2 in. diameter to insure that diameter fluctuations would not give rise to erroneous readings. The crystals were subsequently heat-treated to dissolve oxygen donors and stabilize the resistivity. Two-point probe and four-point probe resistivity measurements were subsequently performed along the ingot axis at well-defined locations. Slices 20 mils in thickness were subsequently obtained at these locations and their resistivities characterized using a four-point probe technique. The various resistivities obtained from these measurements are shown on Fig. 4 for a typical crystal together with the values deduced from the four-point and two-point probe resistivity measurements by assuming a linear or quadratic functional dependence of the radial resistivity profile. Note that, assuming a linear resistivity profile, the resistivity along the crystal axis can be found to corrolate reasonably well with the resistivity subsequently measured at the center of the slices: namely both set of data points are within ±5% of each other.

The radial resistivity gradient deduced from these measurements is compared on Fig. 5 with the resistivity gradient subsequently measured on slices. Note there, as predicted, the agreement between any two sets of data points is poor. This technique should certainly not be used to estimate the magnitude of the radial resistivity gradient.

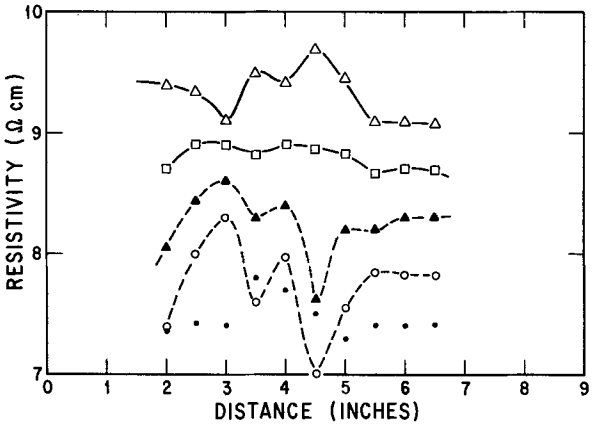

Fig. 4. Comparison of resistivity data obtained on an experimental crystal. Data designated by △ represent measurements performed along the ingot surface using a colinear four-point probe. Data designated by □ represent measurements performed along the ingot surface using a two-point probe. Axial resistivities deduced from the two above measurements by assuming a linear radial resistivity profile are represented by ○ while resistivity deduced under the assumption of a quadratic radial resistivity profile are denoted by ▲. Resistivities measured at the center of slices cut from the ingot are denoted by ●.

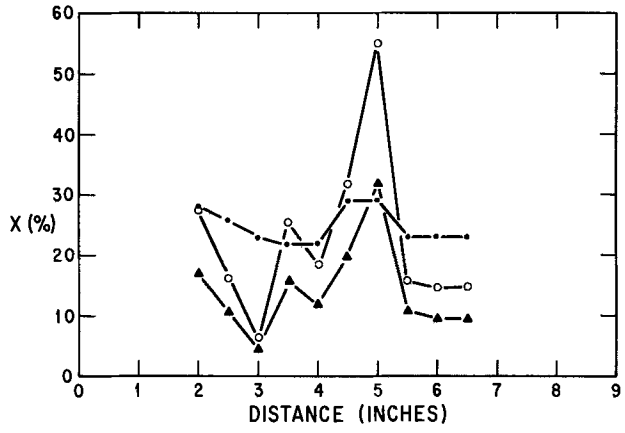

Fig. 5. Radial resistivity gradient vs. distance. The ● indicate values measured on slices; the ○ indicate values deduced assuming a linear profile, the ▲ indicate values deduced assuming a quadratic profile.

Conclusion

The influence of a radial resistivity gradient on two-point probe resistivity measurements along a semiconductor crystal ingot has been considered. The relationship existing between two-point probe resistivity measurements, four-point probe resistivity measurements, and radial resistivity variation was derived in the case of two typical resistivity profiles. Finally, an empirical technique was proposed to evaluate the resistivity gradient as well as the axial resistivity of an ingot. This technique was finally used to characterize an experimental crystal. It was found that for the particular crystal considered use of a linear resistivity profile gave results for the crystal axis resistivity within at most 8.5% of the value measured on subsequently cut slices. This type of agreement can be considered as quite acceptable in view of the fact that four-point probe and two-point probe resistivity measurement techniques have a basic accuracy of ±5% (1). Finally, it was shown that, although the proposed technique results in a good determination of the ingot axial resistivity, this technique should not be used to evaluate the radial resistivity gradient of an ingot because of its inherent inaccuracy.

Manuscript submitted Sept. 14, 1972; revised manuscript received Nov. 20, 1972.

Any discussion of this paper will appear in a Discussion Section to be published in the December 1973 JOURNAL.

REFERENCE

1. 1971 ASTM Annual Book of Standards, part 8. F81-70 "Standard Methods of Test for Bulk Semiconductor Radial Resistivity Variation."

Brief Communications

Growth of Low Strain GaP by Liquid-Encapsulation, Vertical-Gradient Freeze Technique

S. E. Blum* and R. J. Chicotka

IBM Thomas J. Watson Research Center, Yorktown Heights, New York 10598

Liquid-encapsulated Czochralski crystal pulling (LEC) was first described by Metz *et al.* (1) in 1962. In 1967 Bass *et al.* (2) showed how this technique can be used for the growth of single crystal gallium phosphide. Since then several manufacturers have been marketing high pressure Czochralski pullers able to withstand the pressures (>35 atmospheres) and temperatures (~1500°C) required for the single crystal growth of this compound, and growth in these pullers has become the "standard" means for preparing single crystal GaP. The experimental procedures of LEC growth have been described adequately by Bass and Oliver (2) and Nygren *et al.* (3).

With the increasing interest in devices made from GaP, most especially light-emitting diodes, there is a trend to produce larger diameter crystals for the obvious advantage these could offer the manufacturing process. However, the LEC growth of GaP invariably produces crystals that: (*i*) are highly strained, (*ii*) have high dislocation densities (10^4-10^6/cm^2), (*iii*) are somewhat difficult to grow with a uniform diameter, (*iv*) exhibit growth striae, and (*v*) require relatively close attention during the growth cycle. When large diameter (~35 mm) crystals are grown most of the above problems are even more severe. These difficulties were described recently by Nygren (4) who showed that a knowledge of the complex thermal properties of the high pressure ambient-GaP melt-B_2O_3 encapsulant system must be combined with a knowledge of the cooling processes that are normally found in the Czochralski growth system in order to successfully design a system for the growth of large crystals of controlled diameter. Crystals so grown will still exhibit strain and will have dislocation densities in the interior of the ingot of 10^4-10^5/cm^2.

We have developed and tested a technique that has produced GaP single crystals that: (*i*) can be grown with virtually no attention during the growth period, (*ii*) are uniform in diameter, (*iii*) are significantly less strained than the conventional LEC grown GaP, (*iv*) have dislocation densities that are ~10^3/cm^2, *i.e.*, one to three orders of magnitude less than LEC grown GaP, and (*v*) exhibit no growth striae. The technique we have used is a combination of the principles of liquid-encapsulation and vertical-gradient freezing. The entire apparatus can be enclosed in a relatively simple pressure vessel. The vessel should be sufficiently sturdy to contain an operating pressure of about 1000 psi of neutral gas and be fitted with the appropriate rf and thermocouple feedthroughs. A schematic representation of the apparatus we used is shown in Fig. 1. The gallium phosphide polycrystalline ingot we used was obtained by a synthesis method previously described by us (5). The ingot along with the boric oxide encapsulant and a single crystal GaP seed is placed within a boralloy (pyrolytic boron nitride) crucible as shown in Fig. 1. The crucible is positioned within the susceptor and the system is closed, evacuated to remove the air, and backfilled to 900 psi of nitrogen. The susceptor is heated by 500 kHz rf and the temperature within the susceptor is monitored by thermocouple (TC1) and controlled by a conventional L&N-CAT control system. The temperature at the ingot-seed interface is brought to a few degrees above the GaP melting point in order to effect wetting of the seed crystal. The temperature at the top of the melt, at the B_2O_3-melt interface (TC2), is approximately 50°-100°C above the melting temperature. Freezing of the melt is obtained by slowly lowering the control temperature (TC1) until the top of the melt (TC2) is below the GaP melting point. The system is then cooled slowly to room temperature. Typically the crystal is grown at about 1 in./hr and the solidified ingot cooled to room temperature in about 1 hr. This method has produced a crystal that is virtually strain free. A transmission micrograph of a polished-liquid encapsulation, vertical-gradient freeze (LE-VGF) wafer taken between crossed Nicol prisms is shown in Fig. 2 with two conventionally grown LEC wafers for comparison. In addition, a transmission micrograph of a wafer cut parallel to the growth direction shows the crystal to be striae free. LEC crystals always exhibit striae whose spacings obey the f/ω relationship.

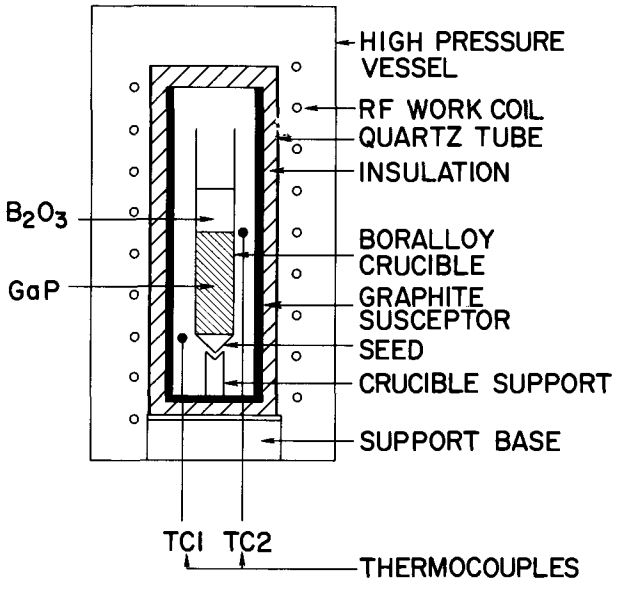

Fig. 1. A schematic representation of the apparatus used to grow single crystal gallium phosphide by the liquid-encapsulation, vertical gradient, freeze technique (LE-VGF).

* Electrochemical Society Active Member.

Key words: gallium phosphide, crystal growth, low strain crystals, light-emitting diodes, liquid encapsulation.

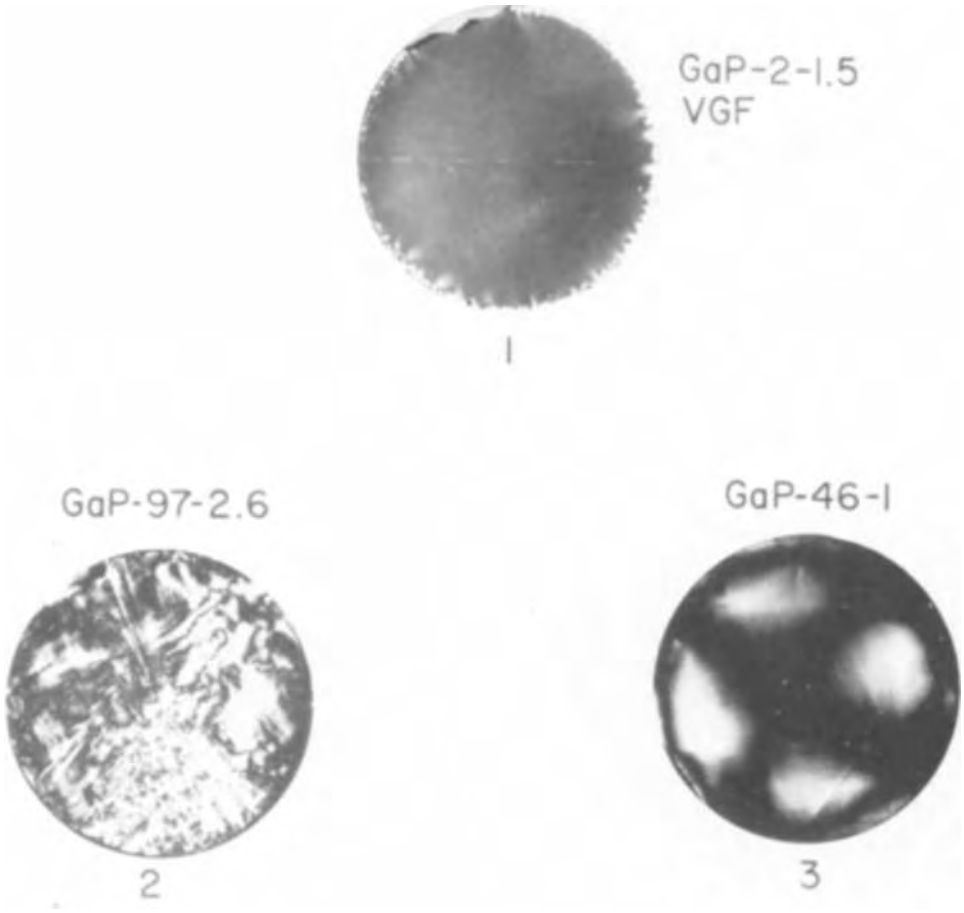

Fig. 2. Transmission micrographs taken between crossed Nicol prisms. The samples are transverse cuts of 1, 1.5 cm diameter crystal grown by LE-VGF, 2, and 3, 1.1 cm and 1.5 cm in diameter crystals, respectively, grown by conventional LEC.

The dislocation density of crystals grown by the LE-FGF technique and by conventional LEC were obtained by etching polished <111> wafers with the ferricyanide-KOH-H_2O etch (3). Dislocation densities of about $10^3/cm^2$ were obtained in the LE-VGF crystal and $>10^4/cm^2$ in LEC crystals.

Crystals grown by the LE-VGF technique are appreciably less strained, lower in dislocation density, excellent in diameter control, and easier to grow than the conventional LEC GaP.

Manuscript received Nov. 2, 1972.

Any discussion of this paper will appear in a Discussion Section to be published in the December 1973 JOURNAL.

REFERENCES

1. E. P. A. Metz, R. C. Miller, and R. Mazelsky, *J. Appl. Phys.*, **33**, 2016 (1962).
2. S. J. Bass and P. E. Oliver, *J. Crystal Growth*, **3**, 286 (1968).
3. S. F. Nygren, C. M. Ringel, and H. W. Verleur, *This Journal*, **118**, 306 (1971).
4. S. F. Nygren, To be published, Invited talk presented at the AACG Meeting, Princeton, New Jersey, August 1, 1972.
5. S. E. Blum, R. J. Chicotka, and B. K. Bischoff, *This Journal*, **115**, 324 (1968).

Use of Sirtl Etch for Silicon-Slice Evaluation

W. A. Porter, A. Gupta, and D. L. Swindle

Electrical Engineering Department and Activation Analysis Research Laboratory, Texas A & M University, College Station, Texas 77843

In recent years research on the influence of crystallographic defects on devices has been done to establish that yield problems are definitely related to material defects, and the importance of having defect-free starting material has been recognized by many researchers (1-3). The advent of LSI has given added importance to obtaining high quality starting material because of the inherent larger chip sizes and shallower base widths associated with LSI arrays. Gupta and Lathrop (4) have recently discussed this problem. As devices and their geometries become more complicated, the importance of having a nondestructive technique for evaluating silicon starting material, before device processing is begun, cannot be overemphasized. Some of the more common nondestructive techniques for evaluating silicon are x-ray diffraction, infrared spectrometry, and electron microscopy. In general, these techniques are unsuitable during mass production because of the time and expense associated with their use. This note describes the results of an investigation into the possibility of using Sirtl etch as a "nondestructive" evaluation step for categorizing silicon wafers before device fabrication is begun. It is known that chromium is deposited as a residue during the chemical reaction associated with etching silicon in Sirtl etch (5, 6). The detection of chromium as a cation contamination has been explained as due to either an irreversible electro-

Key words: crystal defects, surface damage, defect measurement.

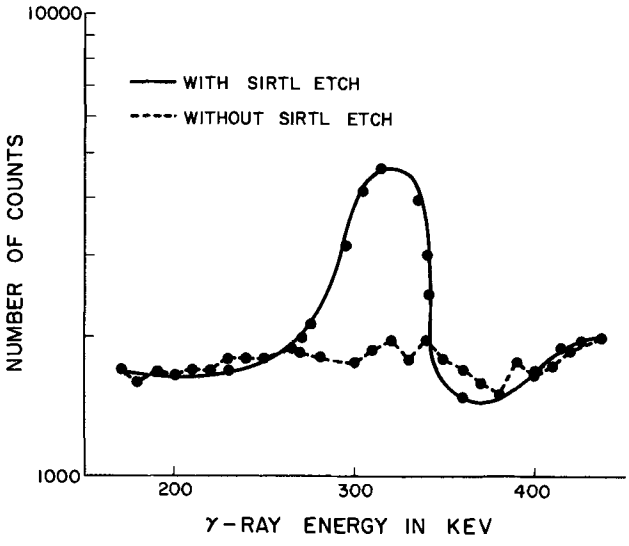

Fig. 1. Chromium content on silicon slice

chemical reaction at the silicon-liquid interface, or by reversible physical absorption (6). Contrary to the usual concern about the use of Sirtl etch resulting in chromium diffusing into the silicon slice during subsequent high-temperature processing steps, this note reveals that the residual chromium resides only on the surface of the slice and can easily be removed.

Experimental

Chemically polished silicon slices grown in the [111] direction were Sirtl etched for varying time periods. The amount of residual chromium on the slice after etching was determined by using neutron activation analysis. Gamma-ray spectrometry was used to detect the 320 keV γ-rays emitted by radioactive Cr^{51} produced by neutron bombardment.

Results

The 1 in. diameter silicon slices initially had less than 10^{12} atoms of chromium. After Sirtl etching, the total number of chromium atoms on the slice was 4×10^{16}. This indicated that chromium is deposited on the slice surface during Sirtl etching. Figure 1 shows a comparison γ-ray spectrum of two irradiated silicon slices; only one slice was Sirtl etched while the other was also subjected to irradiation and counting to establish any chromium background.

The slices were subsequently given various treatments to remove the chromium. Both the standard slice-cleaning procedure of hot (water-nitric-water cycle) and an aqueous solution of saturated KOH and 30% H_2O_2 in equal volumes, were sufficient to remove all the chromium deposited during Sirtl etching. Hence, the residual chromium is easily removed from the silicon surface. It was also found that it is sufficient to Sirtl etch for only 2 min to reveal all the defects on the slice. Surface defects are revealed with a much shorter etch time. In order to record the presence of both surface and bulk defects the wafer should be etched in 15 sec intervals and inspected at each interval (7).

It has been found during this investigation that wafers that are Sirtl etched from both sides result in low yields when MOS devices are subsequently fabricated. On the other hand, wafers that are Sirtl etched from the backside only have been successfully used to repeatably build standard yield MOS devices. Apparently, when the silicon wafer is etched from the front side the general flatness of the material is not maintained and the resulting fabrication problems associated with bowed wafers reduce the yields (8).

The use of Sirtl etch from the backside only has not yet been proven to be a definitive technique of identifying the starting quality of the wafer. However, the ability to fabricate devices with good yields on silicon material that has been Sirtl etched renders the possibility of using Sirtl etch as a "nondestructive" evaluation technique more feasible than it is generally accepted to be. Nondestructive here is used in the sense that operational semiconductor devices can still be fabricated on the material after etching. Thus, it has been shown that chromium impurities can be successfully removed, and operational MOS devices with standard yields fabricated, after the silicon material is exposed to the chromium atoms during a chemical-etch evaluation.

Acknowledgment

This research is supported by NASA Marshall Space Flight Center and the Air Force at Rome Air Development Center.

Manuscript submitted Aug. 14, 1972; revised manuscript received Dec. 4, 1972.

Any discussion of this paper will appear in a Discussion Section to be published in the December 1973 JOURNAL.

REFERENCES

1. G. H. Schwuttke, *Microelectronics and Reliability*, **9**, 397 (1970).
2. H. F. John, *Proc. IEEE*, **55**, 1249 (1967).
3. P. Rai-Choudhury, *This Journal*, **118**, 1183 (1971).
4. A. Gupta and J. W. Lathrop, *IEEE J. Solid-State Circuits*, **SC-7**, 389 (1972).
5. V. E. Sirtl and A. M. Adler, *Z. Metallk.*, **52H**, 529 (1961).
6. P. F. Kane and G. B. Larrabee, "Characterization of Semiconductor Materials," McGraw-Hill Book Company, New York (1970).
7. W. A. Porter, Interim Report on the Study of Process-Induced Imperfections in Silicon, NASA Contract NAS8-26379, September 1972.
8. H. R. Huff, R. C. Bracken, and S. N. Rea, *This Journal*, **118**, 143 (1971).

JOURNAL OF THE ELECTROCHEMICAL SOCIETY

REVIEWS AND NEWS — JANUARY 1973

Report of the Electrolytic Industries for the Year 1971[1]

L. C. Fuhrmeister*

Monsanto Enviro-Chem Systems, Incorporated, Chicago, Illinois 60600

and A. T. Emery

Hooker Industrial Chemicals Division,
Subsidiary of Occidental Petroleum Corporation, Niagara Falls, New York 14300

Chlorine—Caustic Soda

I. Production.—U.S. chlorine output declined in 1971 for the first time in 10 years. 1971 production was 9,308,500 tons, down 4.2% from 1970, the highest year on record. This total does not include production from a major new plant that went into production in Puerto Rico during 1971. Canadian production was 860,900 tons, up about 1% from 1970 (1).

At the year's end, production rates were increasing. U.S. operations dipped to 84.9% of capacity in May and increased over 92.2% in November and December. The average operating rate was about 87.9%. In Canada, operations rose from a low of 82.8% in May to a high of 91.4% in September. In the United States, new capacity offset shutdowns during the year and as of December 1, 1971, capacity was 29,005 tons/day, essentially unchanged from 1970. Canadian capacity increased 5% to 2,769 tons (1).

The high demand for caustic continued for the second year. As a result, caustic prices, which were being discounted in 1970 from $66/ton for 50% caustic, were firm at $71-$76/ton ($81/ton west of the Rockies). Chlorine which is "loose" is continuing at $75/ton with probable discounting (6, 9, 10, 11, 14).

PPG Industries provides the following breakdown of recent caustic sales, which is close to the industry total: chemical process industries, 45%; aluminum and petroleum, 19%; pulp and paper, 15%; soaps and detergents, 5%; textiles, 1%; and miscellaneous and export, 14% (5).

The drop in chlorine demand is due to the slump in its major market areas; chlorinated hydrocarbons such as vinyl chlorides, PVC and chlorinated solvents, chlorinated pesticides, and paper (5-7).

The drop in chlorine demand, together with plant shutdowns and a lagging economy were held responsible for the caustic shortage, rather than any radical growth in demand for any of caustics applications. Some producers disagree and feel users who switched from other sources of alkalinity will not switch back (18). The use of caustic soda to replace soda ash is occurring in the glass and alumina processing industries (19).

[1] This report is sponsored by the Industrial Electrolytic Division of The Electrochemical Society. While it is primarily a summary of production and developments in the chlor-alkali industry, reports of other electrolytic industries are included.
The material presented herein has been gathered from many sources, as noted in the references, and does not necessarily represent the opinions of the authors.
* Electrochemical Society Active Member.

II. Shutdowns and Expansions (2-5, 8, 12, 20)

Company and Location	Type of Cell	Capacity tons/day	Completion date
A. Shutdown			
BASF Wyandotte Wyandotte, Mich.	Mercury	150	March 1971
American Magnesium Corp. Snyder, Texas	Magnesium	175	July 1971 (temporary for alterations)
Sobin Chemicals, Inc. Niagara Falls, N. Y.	All Cl_2 production	40	February 1972
Olin Corp. Saltville, Va.	All Cl_2 production	300	March 1972
Dow Chemical of Canada Sarnia, Ontario	All Hg cell Cl_2 production	700	Early 1973
GAF Corp. Linden, N. J.	Mercury	235	October 1971
BASF Wyandotte Geismar, La.	Mercury	150	1973
B. Production Started			
Hooker Chemical Corp. Taft, La.	Hooker S4 Diaphragm	120	Partial 2nd Quarter 1971, Balance 2nd half 1971 conversion to DSA
Dow Chemical Co. Freeport, Texas	Dow Diaphragm	—	1971 Expansion
PPG Industries Guayaville, Puerto Rico	DeNora Mercury	500	2nd Quarter 1971
Dow Chemical Co. Midland, Mich.	Dow Diaphragm	—	1971-1972 Modernization
Standard Chemical Ltd. Beauharnois, Quebec	Uhde Mercury	220	February 1971
Hooker Chemical Co. Montague, Mich.	Hooker S3B Diaphragm	220	1971-1972 Conversion to DSA plus expansion
Hooker Chemical Co. Nanimo, B.C.	Hooker Diaphragm	100	1971-1972 Conversion S4 to H2 at higher load
Hooker Chemical Co. North Vancouver, B.C.	Hooker Diaphragm	500	1971-1972 Conversion to DSA plus expansion
C. Building or Planned			
NL Industries, Inc. Grantsville, Utah	BASF Magnesium	45,000 T/yr Magnesium 80,000 T/yr Cl_2	Early 1972
PPG Industries Lake Charles, La.	PPG-DeNora Bipolar	1,500	Not Announced
Hooker Chemical Corp. Niagara Falls, N. Y.	Hooker Diaphragm	1,000	1973-1976 Modernization

BASF Wyandotte Corp. Geismar, La.	Diamond Diaphragm	Two plants 350 each	Modernization
Dow Chemical of Canada. Ltd. Sarnia, Ontario	Convert Mercury to Diaphragm	700	Early 1973
Vulcan Materials Co. Wichita, Kan.	Hooker Diaphragm	275	Convert to DSA May 1972
Diamond-Shamrock Deer Park, Texas	Diaphragm	—	Convert to DSA
Dow Chemical Co. Dallesport, Wash.	Dow Magnesium	24,000 T/yr Magnesium 50,000 T/yr Cl_2	1st Quarter 1975

III. Developments.—A. Metals anodes.—Metal Anode Associates, a joint venture of Union Carbide Corporation and Engelhard Minerals and Chemical Corporation announced withdrawal from metal anode field in December 1971 (17).

A new titanium anode for chlorine cells has been jointly developed by Olin and ICI's Imperial Metal Industries, Limited (Birmingham, England). Olin will install the first commercial system at Augusta, Georgia. The anodes are made from titanium, utilizing advanced technology in titanium fabrication and surface-coating techniques, and will be used with the new Olin anode adjuster (18).

Electrode Corporation reports that 50% of the North American mercury-cell capacity has expanded capacity using the higher current densities available with Dimensionally Stable Anodes with (DSA^r). DeNora, Uhde, Solovay, and Olin mercury cells of various sizes are satisfactorily operating with DSA in 18 mercury cellrooms using sodium and potassium salts. Electrode Corporation's new DSA's account for 3 million tons chlorine capacity/yr, or 30% of U.S. chlorine capacity (13).

DSA installations in diaphragm cells are expanding rapidly through the association between Electrode Corporation and Hooker Chemical Corporation. Hooker has North American rights for conversion of Hooker Diaphragm cells. Using DSA's in diaphragm cells results in savings in power and labor because of less frequent maintenance, longer diaphragm life, and better cell efficiency.

Modern mercury cells generally operate at currents from 100,000-300,000A. Diaphragm cells with graphite anodes operate to 60,000A. The first diaphragm cells using DSA's operated at 70,000-80,000A (20).

DSA's are being supplied to a number of companies developing new design of chlorine cells. Commercial tests are being evaluated to use DSA's for chlorate, hypochlorite, copper, and nickel production (13).

B. New cell designs.—The environmental problem with mercury has resulted in the development and perfection of new types of diaphragm cells. Hooker Chemical Corporation has developed a new H-2 diaphragm cell using DSA's. The new cell operates at 90,000A and test cells have been operated at 150,000A (20).

The new bipolar cell announced in 1970 and developed jointly between PPG Industries and DeNora has been named the Glanor V cell. After successful testing, it is available in two sizes; 11/22 rated at 36 kA and 11/44 rated at 72 kA (15).

Other cells offered with metal anodes include the Diamond-Shamrock, Elcinore Cell and two from Japan manufactured by Showa Denko and Nippon Soda (21).

C. New hypochlorite cell.—Four companies have developed cells to produce sodium hypochlorite using sea water as cell feed instead of brine. New York City is planning to test 3 systems to disinfect effluents from the city's sewage treatment plants: (*i*) the Pepchlor unit made by Pacific Engineering and Production Company of Henderson, Nevada; (*ii*) the Sea-cell manufactured by A. Johnson and Co., Limited, of London, England, and marketed by Parkson Corporation, Fort Lauderdale, Florida; and (*iii*) the Sanilec cell made by Diamond-Shamrock Corporation, Cleveland, Ohio.

Estimates for production from the new units range from 3-5.5¢/lb for hypochlorite compared to 13¢/lb at present market price (16).

Sodium hypochlorite, generated on site, will be used as a bacterecide at the Department of the Interior's desalting plant at Wrightsville Beach, North Carolina. Engelhard Minerals and Chemicals will install one of is chloropoc plants at Wrightsville (22).

D. Mercury.—The widespread publicity given to mercury in the environment, and the health hazards of mercury in 1970 continued in 1971. Mercury cell chlor-alkali producers, in an incredibly short period of time, found ways and means to reduce the mercury content of plant wastes. These programs were continued and perfected in 1971. These programs cost money. The problem of removing past accumulation of mercury from the beds of downstream lakes and rivers of these plants is difficult, or in some cases impossible, to solve. The result is that many mercury cell plants have been, or are being, closed (21).

Proposed air-emission standards for mercury were published in the December 7, 1971 Federal Register by the Environmental Protection Agency. The standard requires mercury cell chlorine plants and primary mercury plants to limit emissions to a maximum of 5 lb of mercury over a 24 hr period (23).

The 1971 consumption of mercury was estimated at 54,000 flasks, a decline of 12% from 1970. The largest decreases from 1970 were in agriculture, catalysts, electrolytic chlorine production, and industrial instruments. The use of mercury for gold production ceased, and the use of mercurial slimicides in the pulp and paper industry was negligible. Gains were registered for paint and electrical apparatus.

U. S. production of mercury in 1971 was the lowest since 1964. Eighteen thousand flasks were produced from about 60 mines compared to 27,303 from 79 mines in 1970. By the end of the year only about 30 mines were active. About 16,000 flasks of mercury became available due to the closing of several mercury-cell chlorine plants and releases by the General Services Administration. California produced 73% of the mercury, Nevada 7%, with the remainder from Alaska, Arkansas, Idaho, Oregon, and Texas.

Imports were up to 27,000 flasks compared to 21,672 in 1970. Canada supplied 60%, Mexico 15%, Spain 13%, Turkey 5%, and Italy less than 1%.

The GSA exported 5,700 flasks of mercury to India under programs of the Agency for International Development.

The average New York price was estimated at $295/flask compared to $407.77 last year. Year end prices were in the $250-$260/flask range.

Other Alkalis and Electrolytic Processes

Caustic potash.—Caustic potash production in 1971 was 186,819 tons, up 7% over 1970 production (24).

PPG Industries, Incorporated announced in December that they had converted their 8,000 ton/yr liquid caustic-potash facilities at Natrium, West Virginia to produce liquid caustic soda. The company will continue to produce both liquid and flake caustic potash at Corpus Christi, Texas (25).

Under terms of a proposed agreement between Hooker Chemical Corporation and Sobin Chemical Company, the mercury-cell unit at Hooker's Niagara Falls plant will continue in operation producing chlorine and caustic potash (28). Sobin plans to shut down its Niagara Falls plant, with a caustic potash capacity of 23,000 tons/yr, in February 1972 (3). The Hooker facility has a 36,000 tons/yr capacity.

In May, Sobin Chemicals initiated a price increase for caustic potash from west coast terminals to $7/cwt. for 50% liquid, FOB terminal, while others posted $6.70 and $6.77 (26). On July 5, all producers were at $7.00 (27)

Soda ash.—Production of natural sodium carbonate in 1971 totaled 2.8 million short tons valued at $62.5

million, an increase of over 7% in quantity and nearly 11% in value over 1970, according to the Bureau of Mines. The trona mines of Wyoming supplied a major portion of the output, and the remainder came from dry lake beds in California (29). Synthetic soda ash production in 1971 was 4.3 million tons, down 3.2% from 1970. Production included 1,829,769 tons synthetic, light, and 2,337,037 tons, dense (30).

About half of the total sodium carbonate produced in the U. S. goes to the manufacture of glass, 40% to the manufacture of other chemicals, and 8% to the processing of wood pulp into paper. About 4-6% of production is exported (29). Some replacement of soda ash by caustic soda is occurring in the glass and alumina processing industries (31).

Year end soda ash prices were quoted at $2.35/100 lb for light, and $2.40-$2.45/100 lb for the dense. Bulk soda ash in carlots was quoted at $1.65/100 lb for light, and $1.65-$1.80/100 lb for dense (29). However, increases of $2.50/ton for light and dense soda ash have been proposed, but must be approved by federal officials under the terms of the price freeze ruling in the U. S. (32).

Hooker Chemical's $20 million plant at Searles Lake, California will use a new solar evaporation process to produce borax, soda ash, and potassium sulfate from mineral deposits in the area (33).

Allied's Green River, Wyoming soda ash plant is undergoing a 550,000 tons/yr expansion which will boost Green River's annual capacity to about 4.2 million tons by early 1973. This represents an increase of roughly 50% in total U. S. capacity for natural soda ash (34).

Olin Mathieson has closed down its Solvay process soda ash plant (300,000 tons/yr) at Saltville, Virginia as a result of state legislation reducing permissible effluent chloride levels The availability of cheap soda ash in the United States apparently made it uneconomical to modify the plant to reduce chloride levels (35). This was apparently the reason for PPG's decision to shut down its Barberton, Ohio, Solvay system soda ash facility (36).

Sodium chlorate.—U. S. production of sodium chlorate in 1971 was 196,469 tons, down 1% from 1970 production of 198,460 tons (30).

Production facilities in the U. S. are (37):

Company	Capacity (tons/yr)
Hooker Chemical Corp. Niagara Falls, N. Y. Columbus, Miss.	15,000 65,000
American Potash & Chemical Corp. Hamilton, Miss. Henderson, Nev.	60,500
Penn-Olin Corp. Calvert City, Ky.	31,000
Penwalt Corp. Portland, Ore.	15,000
PPG Industries, Inc. Lake Charles, La.	15,000
Huron Chemicals Co. Butler, Al. Riegelwood, N. C.	11,000
Georgia-Pacific Corp. Bellingham, Wash.	5,000
Brunswick Chemical Co. Brunswick, Ga.	7,000
Pacific Engineering & Production Co. Henderson, Nev.	6,000
	230,500

Hooker Chemical announced plans to build a new 45,000 tons/yr plant at Taft, Louisiana. The plant will use radically new cell design which was 4 yr in development. The site was chosen to be near the southern pulp and paper industry. This industry uses about 70% of the chlorate production to make chlorine dioxide bleach. Hooker anticipated increased demand as a result of the Hooker "SVP" (single vessel process) chlorine dioxide generating system which is said to produce lower cost product with no acid effluent (37).

Sodium chlorate prices for pulp and paper grade product was lowered from $140/ton to $134.50/ton which continued throughout the year (38).

Sodium.—Metallic sodium production in 1971 totaled 153,075 short tons, a decrease of about 10% from 171,190 tons in 1970 (39, 40).

The decrease is undoubtedly due to the decline of the manufacture of lead alkyls for gasoline additives in the U. S. Exportation of tetraethyl lead and tetramethyl lead have also declined as the European and Japanese manufacturing facilities have been expanded, thereby affecting the production rate of sodium in the U. S. (40, 41).

Prices for sodium were increased during the year and are quoted at $0.27½/lb for regular fused material in drums (Reactor grade $0.32). The 12 lb bricks are up $0.04-$0.30/lb. Smaller bricks are up $0.05-$0.35/lb for 5 lb bricks, $0.40/lb for 2.5 lb bricks, and $1.06/lb for 1 lb bricks (42, 43).

Fluorine.—Fluorine is derived from the mineral fluorite, commonly known as fluorspar. Three grades of fluorspar are generally recognized: Metallurgical—60, 70, and 72.5% effective calcium fluoride (CaF); Ceramic—85-96% CaF; and Acid—more than 97% CaF.

Cryolite (Na_3AlF_6) is a fluorine mineral required by the aluminum industry to dissolve alumina in the process of reducing alumina to aluminum by electrolysis. Greenland is the only known natural source of the natural mineral. However, large quantities are produced synthetically from caustic soda, alumina, and hydrofluoric acid.

In 1968, the U. S. produced 118,000 tons fluorine, or 18% of total U. S. demand. The remaining 82% is imported, chiefly from Mexico, or supplied from stockpiles. U. S. dependence on foreign supplies has existed since 1952 and is increasing (44).

Consumption patterns
(Based on 1968 figures)

A. Form used	Per cent
Fluorspar	44
Cryolite	18
Hydrofluoric acid	35
Fluosilicates	3
	100

B. Use	1,000 Tons fluorine	Per cent
Refrigerant, aerosols, solvents, and plastics	228	35.3
Steel fluxing	215	33.3
Auminum	114	17.6
Electrometallurgy flux	30	4.6
Gas opacifier and flux	16	2.5
Iron foundry flux	12	1.9
Ferroalloy and non-ferrous flux	11	1.7
Other*	20	3.1
	646	100

* Other uses include cement production, water fluorination, uranium isotope separation, catalyst for high octane gasoline production; polymerization, esterification, acidifying oil wells to increase oil production, extracting silica from carbon and graphite electrodes and many other processes.

The following data concerns fluorspar (45). In 1971, 14 companies shipped 269,000 tons of finished fluorspar from mines in 7 states. Two firms in Illinois provided over half the total shipments. Twelve other firms in Illinois, Colorado, Montana, Nevada, and Utah provided the rest.

Fluorspar statistics
(1,000 Tons)

		1968	1969	1970	1971*
Production		252	183	269	269
Imports:	Acid grade	638	695	676	697
	Metallurgical	412	455	416	341
Exports:	Ceramic and acid	13	4	15	15
Consumption:	Acid grade	678	736	767	650
	Metallurgical and ceramic	565	621	605	670
Price:	Average mine value per ton	$46.18	$46.07	$61.00	$62.00

* Estimated.

Imports were from Mexico, 76%, Spain 14%, Italy, 8%, other, 2%.

At 1971 production rates, the U. S. has a 25 yr supply before deposits are depleted.

Aluminum.—Output of primary aluminum metal was estimated at 3,935,000 tons, just slightly below the production level in 1970 of 3,976,148 tons. Domestic aluminum demand was slightly higher in 1970. Imports of aluminum in crude form increased 60% to a record 750,000 tons while exports dropped precipitously from 612,000 tons in 1970 to 300,000 tons in 1971, changing the balanced trade established in 1969 and 1970 (46).

Total inventories of aluminum metal in all forms increased to an estimated 2.5 million tons, up from 2.2 million at the end of 1970. The low demand level for primary metal resulted in the shutdown of reduction lines to reduce output. By year end, approximately 15% of available capacity was shut down (46).

Two new primary aluminum plants were started early in 1971. In February, Noranda Aluminum, Incorporated started production at New Madrid, Missouri, marking an entry of the tenth primary aluminum producer in the United States and the twenty-eighth plant. In March, Gulf Coast Aluminum Corporation, a subsidiary of Swiss Aluminum, Limited, started production at its new plant at Lake Charles, Lousiana (47, 48).

Aluminum Company of America is starting a new aluminum potline at its Warwick plant in Evansville, Indiana. The 50,000 tons/yr line, built earlier this year but so far unused, will raise the annual capacity of the facility to 190,000 tons/yr. Total capacity at Warwick is 275,000 tons/yr.

Two older potlines were closed because of a coal shortage. These two lines, with an annual capacity of 85,000 tons/yr, remain closed, but a third line with a capacity of 45,000 tons/yr reopened in late November (49).

Amax Pacific postponed the start-up of its proposed $120 million two-pot aluminum reduction plant at Warrenton, Oregon. Construction for this 150,000 tons/yr plant is scheduled to begin in the spring of 1972 with completion by the spring of 1974 (50).

The Battelle Development Corporation is touting aluminum alloy electroplating as an attractive alternative to cadmium plating in terms of corrosion resistance and the absence of pollution. Licensed from National Steel Corporation, Battelle further developed the process. Incorporating 10-18% manganese results in a smooth, dense, but dull coating. Increasing manganese to 20-30% results in a bright fine grain coating. Coating is done in a fused salt at 350°F. Compared with cadmium plating, the economies are a trade-off. Capital costs are higher for the alloy system, but raw materials are cheaper (51).

Magnesium.—The production of primary magnesium in 1971 is estimated at 115,000 short tons, up slightly from 1970. Shipments for the first three quarters were up 4% from 1970 and output was up 13% for the same period. Imports of magnesium from January through September were 2,362 tons and exports were 19,685 tons. Production of magnesium compounds decreased from 1970. Magnesite, brucite, and olivine production remained at about the 1970 level (52, 53).

Imports of caustic-calcined magnesia for January through October were 10,967 tons, while in the same period importation of dead-burned and grain magnesia, and periclase totaled 126,008 tons, up from 30,000 tons in 1970 (53).

The General Services Administration continued the disposal of magnesium metal in the national stockpile; at the end of the third quarter 99,790 tons remained in the stockpile.

New magnesium plants and expansions announced include Alcoa's proposal to build a plant in Addy, Washington and NL Industries 45,000 ton/yr plant in Utah. The magnesium will be cast into ingots following recovery from electrolytic cells (54). Norsk Hydro plans to invest $14 million in a 7,000 ton/yr plant at its magnesium operation at Heroya, Norway, bringing production up to 47,000 tons/yr. The expansion will incorporate a newly developed Norsk-Hydro process using magnesium chloride brine as the raw material and yields chlorine as a by-product (55).

Manganese.—There was no production of manganese ore concentrate, or nodules, containing 35% or more manganese in the U.S. in 1971. However, manganiferous ore continued to be produced in Minnesota and New Mexico. Domestic consumption of ore containing 35% or more manganese, expected to total 2 million short tons, was lower than in 1970. Consumption of ferromanganese and silicomanganese also dropped (56).

Major manganese ferroalloy producers reported progress in their installation of equipment to reduce air pollution. Foote Mineral Company announced that it was phasing out its Knoxville, Tennessee electrolytic manganese operations in favor of its newer New Johnsonville, Tennesee plant.

The GSA was authorized to dispose of 4,424,840 short tons of metallurgical grade manganese and 4,805 short tons of synthetic manganese dioxide from national stockpiles. GSA policy continued to limit deliveries of metallurgical manganese to 300,000 short tons per year, divided evenly between quarters (56).

The price of metallurgical ore containing 46-48% manganese was increased from 56-59¢/ton to 59-63¢/ton. Standard high carbon ferromanganese (74-76% manganese) continued to be priced at $184.50/long ton, FOB producer plant, and 78% minimum grade continued at $190. Imported standard ferromanganese was quoted by Metals Week at $180/long ton until March, then increased to $182-$184. Standard electrolytic manganese metal sold at 33.25¢/lb. FOB producer plant for shipment of 30,000 lb or more (56).

Imports of manganese ore (35%) from Brazil and Gabon were expected to approach 2 million short tons, over half of total U. S. imports. Ferromanganese imports were comparable to those of 1970 with the Republic of South Africa and France as principal suppliers, followed by India. Manganese metal imports were considerably increased from those of 1970, principally from the Republic of South Africa (56).

Two subsidiaries of Armcor, Metallorp, Limited and Ferrometals, Limited announced a $42 million expansion program in the Republic of South Africa which will make Amcor one of the world's largest ferroalloy producers (56).

Bureau of Mines RI 7473, "Processing Manganiferous Sea Nodules," reported Bureau research on manganese nodules from both the Atlantic and Pacific ocean floors. RI 7051, "Autoclave and Ambient Pressure Leaching of Lake Superior Manganiferous Ores," reported leaching studies on ores from three Cuyuna Range mines (56).

The commercial potential of ocean nodules has attracted some 18 commercial and governmental organizations in 5 countries. Deapsea Ventures, Incorporated appears to hold the lead, and has already spent $20 million on exploration and development, and anticipates an additional $200 million to achieve production. Plans call for progressive scale-up from present 1 ton/day pilot plant, to 75 and 750 ton pilot plants before building a full scale 3,000 ton/day plant. By processing 1,000,000 tons/yr of nodules they expect to produce 12,600 tons nickel, 10,000 tons copper, 2,400 tons cobalt, and 260,000 tons manganese.

The present process involves an HCl reaction, leaching, ion exchange, stripping, electrolysis, crystallization, and metal reduction (57, 58).

Beryllium.—The consumption of beryllium ores decreased slightly in 1971, from 6,000 tons in 1970. Of the total consumption, 53% is used in electrical equipment, 21% in electronic components, 18% in nuclear reactors, and 8% for miscellaneous uses (59). Domestic produc-

tion was from 3 states and consisted almost entirely of bertrandite.

Imports, largely from Brazil, declined in 1971 and are estimated at 4,200 tons and valued at $1.5 million. Midyear government stockpile inventories included 21,008 tons of beryl (11% BeO equivalent), 7,387 tons of beryllium-copper master alloy, or metal from 1970 inventories.

Kawecki Berylco Industries, Incorporated installed a 4 ft reversing mill producing the widest beryllium metal sheet available. Kawecki have also formed a joint venture with Trefimetaux GP to produce and market beryllium-copper products in Europe.

Brush Wellman, Incorporated planned to begin mining in new open pit reserves near their present pit in Utah (60).

The Environmental Protection Agency has proposed an emissions ceiling of 10g per day per plant to maintain an ambient ceiling of 0.01 $\mu g/m^3$ on a 30 day average. This will mainly affect facilities that extract beryllium from ore (61).

Chromium.—The U. S. continued to rely on imports and purchases from government stockpiles for its chromite requirements (62).

U.S. Salient Chromite Statistics (63)
(Short tons)

Year	Imports for consumption	Exports	Consumption
1970	1,405,527	40,877	1,400,538
1971	1,298,886	34,818	1,086,229
% Change	−7.6	−14.9	−22.6

U.S. Consumption and Stocks of Chromite by Industry (63)
(Short tons)

Consumption

Year	Metallurgical	Refractory	Chemical	Total
1970	911,697	277,646	213,195	1,402,538
1971	719,779	186,524	179,926	1,086,229

Stocks at end of year

Year	Metallurgical	Refractory	Chemical	Total
1970	387,572	309,616	110,792	807,980
1971	666,638	229,908	119,620	1,016,166
% Change	+72.0	−25.7	+8.0	+25.8

Various grades of chromite were offered for sale during the year by the General Services Administration. However, only refractory grade was sold, 21,048 tons for nonrefractory use and 8,300 tons for refractory use.

Union Carbide was authorized in October by the Department of the Treasury to import 150,000 tons of chromite from Southern Rhodesia which was paid for prior to United Nations economic sanctions. To date only 26,000 tons have been imported.

Published prices for chromite ore for 1971, per long ton delivered at Atlantic ports were as follows:

Country	% Cr_2O_3	Ratio	Price $/ton
Turkish	48	3-1	55-56
So. African Transvaal	44	no ratio	25-27
Russian Chromite (quoted per metric ton FOB loading point)			
	48	4-1	51.50-55.00
	55	—	59-63

Titanium.—Through October 1971, sponge-metal production had dropped 26% below the corresponding period for 1970, and 2 of the 3 domestic producers had closed down. Stocks of sponge and scrap increased 25 and 16%, respectively, during the ten month period as ingot production dropped 18% (64).

Type	Metal production (short tons) 1970	1971	% Change	Metal consumption (65) 1970	1971	% Change
Sponge			−34%	16,413	12,145	−26%
Ingot	24,331	18,450	−24%			
Scrap				7,242	6,149	−15%

There are 10 consumers of sponge, 15 of scrap, and 18 of ingot (64). Estimated industry capacities are 85 million lb/yr for ingot and 30 million lb/yr for sponge (66). Production of ilmenite was down 21%, while imports were down 32%, from 1970. No rutile was produced domestically and imports, mostly from Australia, declined by 24%. Importation of titanium sponge, mostly from Japan, totalled 3,905 short tons, a decrease of 40.5% from 1970 (65). Exports of sponge were expected to total about 1,500 tons for the year reflecting a decrease of about 48% from the 1970 level. Exports of wrought titanium and mill products were down 78% (64).

The General Services Administration stockpiles remained unchanged at 35,015 tons of sponge and 56,525 tons of rutile (64).

Domestic prices for titanium sponge (99.3% purity) remained unchanged from the previous year at $1.32/lb while the same grade Japanese and United Kingdom sponge was $1.20-$1.25. The price of rutile pigment at year end was 26-27¢/lb.

First quarter indications of an increased demand for titanium disappeared with the elimination of the Boeing SST and lower than anticipated production of both military and commercial aircraft.

Additionally, the titanium pigment industry capacity decreased by 36,000 tons with the closing of American Cyanamid's Piney River, Virginia plant and PPG's shutdown of its Natrium, West Virginia chloride process plant. NL announced abandonment of the chloride process of TiO_2 manufactured in the United States and Canada with closing of plants at Sayreville, New Jersey, St. Louis, Missouri, and Varennes, Quebec (64, 67).

At the same time, du Pont has announced development of a process to produce anatase TiO_2 pigments using the chloride route. The new development permits manufacture of both anatase and rutile crystal forms of TiO_2 pigment by one process (67).

Other interesting developments include the marketing of the Benilite Process by Cabot to reduce the manufacturing cost of upgraded titanium ores and expanded uses of diffusion bonding processes (68, 69).

The Soviet Union is building its largest sulfate process TiO_2 plant to date (about 20,000 tons/yr), which will double USSR sulfate process TiO_2 (65).

The American Smelting and Refining Company announced development of a new ilmenite mine in New Jersey expected to begin production in 1973 at a rate of 150,000 tons/yr of concentrate.

The Ceylon Mineral Sand Corporation is expanding the ilmenite extraction plant at Pulmoddai Beach and integrating it with a rutile and zircon recovery plant. The expansion will enable exports of 60,000 metric tons/yr of ilmenite and 11,000 metric tons of rutile by mid 1975 (70).

Lithium.—Domestic production of spodumene and lithium carbonate was the largest ever reported. Domestic and international consumption of lithium products was at an all time high.

Three domestic companies continued to process primary lithium products (production data not available): (*i*) Foote Mineral Company, Sunbright, Virginia, and Silver Peak, Nevada; (*ii*) American Potash and Chemical Corporation, Trona, California; and (*iii*) Lithium Corporation of American, Bessemer City, North California.

The Great Salt Lake Minerals and Chemical Corporation, formed by Lithium Corporation of America and Salzdetfurth, A.G., West Germany, harvested salts from the Great Salt Lake in Utah, but do not have facilities to recover lithium (71).

Honeywell, Incorporated announced the development of a small high-energy lithium battery for industrial applications requiring long term storage. Developing markets for lithium included large scale use of lithium carbonate by the aluminum industry and increased use of lithium hypochlorite for bleaches as a sanitizing agent for swimming pools. Other domestic industrial uses were in ceramics, glass, welding and brazing fluxes, air conditioning equipment, rubber, and pharmaceuticals.

United States Imports of Lithium, 1971 (72)

		Quantity	Value ($)
A.	Minerals: short tons		
	Brazil	5,292	225,899
	Republic of South Africa	1,115	82,613
		6,407	308,512
B.	Compounds: lb	18,200	51,257
C.	Lithium metal: lb	53	459
D.	Lithium salts: lb	33	1,166

Exports of lithium hydroxide (9 months) were 227 tons valued at $228,648. Figures for mineral and metal exports were not available. December 1971 prices for lithium products were (71):

Lithium metal, 1,000 lb lots	$8.18/lb
Lithium carbonate, carload lots	$0.50½/lb
Lithium chloride	$0.89/lb

Copper.—During 1971, the domestic copper industry experienced curtailed mine, smelter, and refinery outputs due to labor strikes at most plants during July, August, and September. In addition to production lost as a result of strikes, several mines curtailed operations during the latter part of the year due to utilization of smelter capacity for processing accumulated stocks of copper concentrates.

Mine production was 1.533 million tons, a decrease of 11% and the smallest output since 1968. Smelter output from domestic ores was 1.470 million tons, a decrease of 8.4% from the record high of 1970. Refinery production was 1.41 million tons from domestic ores and 0.181 million tons from foreign ores for a total of 1.591 million tons of primary metal, down 10% from 1970. Secondary metal production was 0.40 million tons (73).

Demand for refined copper was sluggish at the start of the year, increased to a relatively high level during the second quarter, and then slumped during the labor strikes in the third quarter. The total consumption of refined copper during 1971 was 2.00 million tons, down 1.5% from 1970 (73, 74).

U. S. imports of unmanufactured copper totaled 359,431 short tons for 1971, down 8% from 1970. U. S. exports of refined and scrap copper totaled 206,100 short tons, down 13% from 1970 (74).

Stocks of refined copper decreased from a level of 130,000 tons in January to 75,000 tons by the end of December. Fabricators' stocks of copper in all forms decreased from 515,000 tons at the start of 1971 to 487,000 tons by the end of October (73).

Price cutting by several copper companies in late November underscored the pessimism in the industry during the last quarter of 1971. Several of the larger producers indicated that they did not expect the problems of overcapacity and low prices to improve soon. Domestic producers changed prices three times during 1971 with a net decrease of 2.5¢ to a year end quote of 50.25-50.5¢/lb. Prices on the London Metal Exchange increased from an average of 45.2¢/lb equivalent for January to 56.3¢ for April, then declined erratically to 46.7¢ in December (73, 75). At one point the LME price was as low as 44.625¢/lb.

With copper demand off, prices down, new restrictions on air pollution, and previously announced facilities coming on stream, there was no significant expansion activity during 1971. Newmont Mining Corporation announced that their Magma Copper Company permanently closed its Superior, Arizona smelter in July. Magma will process all concentrates at their enlarged San Manuel, Arizona smelter (73, 76).

American Smelting and Refining announced a $300 million, 5 year program to boost production of copper, lead, zinc, and silver at its Mount Isa, Australia complex (76). Noranda announced a $19 million prototype continuous copper smelter as part of a $123 million expansion in Quebec. This unit will add 55,000 tons/yr smelting capacity for Noranda's Gaspe Copper Mines.

A continuous copper smelting process that is economical and does not pollute the air will be used in Japan's Onahama Smelting and Refining Company in a 1,500 metric ton/month plant. The process runs continuously using a converter which is higher than the furnace and slag flows downward while copper matte moves upward. SO_2 generated during smelting is completely recovered (83).

A new factor in copper production is ecology which has already deterred exploration operations in the western U.S. Stringent new regulations on sulfur emissions from copper smelters imposed by Arizona, Montana, and Nevada require that producers install equipment and have it operable by 1974. A number of processes have been proposed and are undergoing pilot-plant evaluation for removal of sulfur oxides from stack gases. Among the processes being considered are continuous resmelting, making it easier and more economical to couple to an acid plant requiring continuous gas feed, electrostatic precipitation, caustic or ammonia scrubbing, catalytic oxidation and reduction to elemental sulfur, chemical refining of ores, and absorption techniques for smoothing out of the flow and composition of the smelter off-gases (77-82).

Nickel.—Nickel consumption, excluding secondary nickel, was approximately 130,000 tons, down 18.7% from 1970. Nickel imports were about 145,000 tons, and domestic mines produced 17,000 tons of nickel laterite ore. The year was marked by a substantial excess of supply over demand and unusually high imports in the form of ferrous nickel (84).

On February 10, 1971, the Office of Emergency Preparedness announced that the nickel national stockpile objective was changed from 55,000 tons to 0. Thus, 40,096 tons became excess to stockpile needs. Congress did not enact the laws necessary to dispose of the excess nickel. Under the Strategic and Stockpiling Act, congressional approval of sales plans is necessary to protect producers, processors, and consumers against disruption of their usual markets. American Metal Climax, Incorporated (AMAX) purchased the Port Nickel Refinery at Braithwaite, Louisiana in February. Originally built in 1959 to process nickel concentrates from Cuba, the plant had been maintained in standby condition since 1960 due to the Cuban nationalization of U.S. owned mines (84).

International Nickel Company of Canada announced production cutbacks of 7% in August followed by another 15% in November, necessitated by the sharp decline in nickel sales in 1971 (85).

Zinc.—U.S. mine production of recoverable zinc declined 8% from 1970 to 491,419 tons, the lowest for any year since 1961. Only 19 states reported mine production of zinc in 1971; 4 states registered increases, 15 showed decreases, and no production was reported for Kansas or Oklahoma (86, 87).

Smelter production of zinc slab was 840,178 tons, down 12% from 1970. Imports of ores and concentrates dropped to 342,600 tons, down 35% from the previous year. However, imports for consumption jumped from a deficit of 22% for the year at the end of August to a

plus of 32% in September when 204,445 tons of zinc in concentrates was withdrawn from bonded warehouses pursuant to a notification by the Secretary of the Treasury exempting all warehouse entries prior to August 16, 1971, from the surtax if withdrawn from the warehouse before October 1, 1971 (86).

Imports of slab zinc increased to 319,072 tons in 1971, an increase of 18.5% over 1970. Exports of zinc slab increased from 289 tons in 1970 to 13,347 tons in 1971. Exports of scrap were projected to decrease to 2,000 tons for 1971, a decrease of 34% from 1970.

U. S. consumption of zinc in 1971 is indicated below:

Basis: recoverable zinc content	Tons 1970	Tons 1971	Per cent change
Zinc slab	1,186,591	1,259,043	+6.1
Ores	124,781	123,400	−1.0
Zinc-base scrap	93,451	87,600	−6.2
Copper-base scrap	160,027	135,200	−15.5
Al-Mg base scrap	6,386	6,000	−6.0
Total	1,571,596	1,611,243	+2.5

The mounting cost-price squeeze, prevalent throughout the zinc producing industry, was a major factor contributing to the loss of almost one-fourth of all U. S. slab-zinc smelter and refinery capacities in 1971, according to the Bureau of Mines, U. S. Department of the Interior. Five mines and 4 slab-zinc producing plants were shut down during 1971. However, what is reportedly the largest single zinc mining operation in the U. S. was opened in Balmat, New York by St. Joe Minerals Corporation. This should help ease an increasing dependency on the use of imported concentrates and metals (88). Strong demands for galvanized products in construction and die casting for the automobile and appliance markets were evident in the first half of the year.

Comparing the principal broad use categories for 1971 with 1970, galvanizing was up 8%, brass and bronze up 14%, and zinc base alloys up 7%. The minor uses declined, including rolled zinc by 22%, zinc oxide by 4%, and other uses by 8%.

General Services Administration (GSA) sales of zinc continued during the year amounting to 2,017 tons through December, leaving 20,580 tons in the existing disposal authorization. Sales to government agencies amounted to 90 tons; 22,097 tons remain of the original 50,000 tons authorized for government use in 1965.

The need for the zinc industry to reduce costs and control pollution has put more emphasis on electrolytic production of the metal. Electrolytic production now accounts for about 60% of the total. Significant improvements and modifications in electrolytic practices should further reduce costs and upgrade recoveries. Such modifications include fluid bed roasters, Jarosite leaching process for iron removal, automatic and continuous purification of leaching solution, and improved electrolysis and cathode stripping (89).

Prime western zinc was quoted at 17¢/lb at the end of 1971. During the year 2½¢ increases and a 1¢ increase were posted. The average monthly London Metal Exchange price varied between 12.33 and 13.05¢/lb (U. S. equivalent) January through June and between 14.05 and 14.62¢/lb July through December.

The foreign producers price increased from 13.93 to 16.46¢/lb in June which remained unchanged through the end of the year. Changes in the sterling exchange rate caused fractional changes in the average monthly U. S. equivalent price.

Electrical Energy

U. S. generation.—The following tables summarize the production and consumption of electrical energy for the 12 month period January through December 1971:

Production of electric energy (90, 91)
(Million-kWhr)

	1970	1971	% Change
Production by electric utilities			
Coal fired plants	706.1	714.8	+1.2
Gas fired plants	372.0	375.9	+1.0
Oil fired plants	182.5	218.2	+19.6
Nuclear plants	21.8	37.9	+73.9
Total fuel burning	1,282.3	1,347.6	+5.1
Hydroelectric	247.3	266.3	+7.7
Total	1,529.5	1,613.9	+5.5
Private industy, self-generated	108.4	103.5	−4.5
Total U. S. power consumption	1,638.0	1,717.5	+4.9

Installed generating capacity (90)
(Million-kW)

	1970	1971
Public owned capacity		
Steam	35.6	42.8
Hydro	36.3	36.8
Nuclear	6.5	0.9
Total	78.4	80.5
Investor owned capacity		
Steam	238.2	260.0
Hydro	18.8	19.1
Nuclear	5.7	7.8
Total	262.7	286.9
Total electrical utility industry capacity*	341.1	367.4

* Not including privately owned capacity.

Fuel consumption—electric utility (90)
(12 months ending Dec. 31, 1971)

	1970	1971	% Change
Coal—millions of tons	322.36	327.93	+1.73
Gas—billions of cu ft	3894.00	3992.98	+2.54
Oil—millions of barrels	332.10	396.24	+19.31
Coal and coal equivalent—millions of tons	583.14	618.16	+6.0

Sales to ultimate consumers (90, 91)
(12 months ending Dec. 31, 1971)
Total industry (million-kWhr)

	1970	1971	% Change
Residential	465.9	499.1	+7.1
Commercial	306.4	328.6	+7.2
Industrial	570.4	589.8	+3.4
Other	48.0	50.6	+5.4
Total	1,390.7	1,468.1	+5.6

On December 1, 1971, electric utility coal stocks on hand for production of electric energy totaled 76.1 million tons, or an 88 day supply, compared with 70.8 million tons, or an 80 day supply, as of December 1, 1970. Stocks of oil as of December 1, 1971 were 50 million barrels, or a 37 day supply, compared with 38 million, or a 40 day supply a year earlier (92).

Fuel problems resulting from the coal miners' strike affected a number of coal-burning power plants, and coal stocks at some locations are now low enough that serious shortages of electricity could occur in some areas if coal production and deliveries cannot be maintained at a sufficiently high rate to compensate for low stockpiles (93).

The Federal Power Commission's National Power Survey Task Force on Environment has urged the electric utility industry, as a whole, toward resolving environmental problems associated with energy supply. Environmental conflicts are only one source of major threats to the national power supply, according to the task force. Others include fossil fuel shortages, equipment failures, and underestimated forecasts of demand. The task force also pointed out the delays in

new power plants may result from changes in air and water quality standards.

While it might be assumed that the presently decreasing population growth would slow the rate at which demand for electric power is growing, this effect may be offset by increased family incomes and rising standards of living; reflected in increased per capita consumption of electric energy. Additionally, environmental requirements will place a heavy demand on available energy supplies (94).

Federal Power Commissioner, Pinkney Walker, has stated that a fundamental of the current energy problem is that it is becoming increasingly difficult and costly to obtain incremental increases in the domestic supply of primary fuels. This results from the basic economics of exploiting finite natural resources. The most accessible and promising fossil-fuel reserves were exploited first and now the industry faces developing those reserves which are not so accessible or promising (108).

Nuclear power.—Only 2.2% of our present electrical energy requirements are provided by nuclear power, up from 1.3% in 1970. This may increase to 15% or 300 Mwe. by 1985. This is equivalent to 8.5 million barrels/day of oil, or 55 billion cu ft/day of natural gas (95).

During 1971, 21 new nuclear units with a total design capacity of 20,810 Mw of electricity were ordered by U. S. utilities. The AEC licensed 2 nuclear power reactors for fuel-power operation and 4 units for fuel loading and/or low power testing and issued construction permits for 4 others (96).

At the end of 1971, the status of nuclear power plants in the U.S. was as follows (97, 98):

23 operable plants	10,040,800 Mwe.
54 being built	45,779,000 Mwe.
52 ordered	51,571,000 Mwe.
Total 129	107,390,800 Mwe.

Of the plants ordered, 39 have not yet received construction permits.

During 1971 the AEC undertook a major reshaping of its regulating process for nuclear facilities; the objectives being a proper regard for environmental quality, increased efficiency in licensing and regulation of nuclear power plants, and more effective participation of the public in the licensing process (99).

As a result of this new policy the licensing of plants from the AEC is becoming more and more difficult as the AEC switches from its "booster" to "neutral" role, deciding to abide rather than contest a circuit court's judgment in favor of environmentalists. Under this ruling, the AEC is required to conduct a thorough review of any such plants' environmental effects, including thermal effects, before granting a license for construction or operation (100). Environmentalists believe one result of this will be a requirement by the AEC that nuclear plant operators install cooling towers or cooling ponds (101).

Although 1971 will be the first year in which more than half of newly orderd electrical generating capacity will be based on nuclear energy, the near-term outlook is for a slowdown in the trend to nuclear power generation. What this slowdown means to the chemical process industries is: (i) a slowdown in demand for fuel, coolants, moderators, and other components of nuclear plants, (*ii*) higher costs of fossil fuels (coal, petroleum, and natural gas) and fossil fuel derivatives, and (iii) spot shortages of low cost interruptable power for aluminum smelters, chlor-alkali plants, and other large users of electrical energy (100).

The annual growth of nuclear power since 1957, when the first commercial plant (Shippingport, Pennsylvania) went into operation has been (102):

Year	Nuclear units ordered	Installed capacity (Mwe.)
1971	21	20,810
1970	14	14,252
1969	7	7,225
1968	15	13,955
1967	31	26,233
1966	20	16,384
Thru 1965	21*	8,532
Total	129	107,391

* Excludes 6 small prototype plants no longer in operation or which are now used only for experimental work.

Demand for nuclear fuel.—According to the AEC, the U. S. nuclear power capacity will rocket from 10,000 Mwe. now, to possibly 150,000 Mwe. by 1980, and demand for uranium will rise from 2,658 tons in 1968 to 63,400 tons in the year 2000, according to the U. S. Bureau of Mines (103). The demand for uranium will present additional demands on reprocessing plants. Assuming 1 ton/day fuel reprocessing capacity for every 10,000 Mw of generating capacity, this will create a demand for at least 15 tons/day of reprocessing capability. Two new reprocessing plants now under construction will more than double today's commercial capacity of about 5 tons/day. Without any recovery process, uranium stocks would dwindle rapidly, because fissionable U-235 makes up only 3-4% of nuclear fuel. The remainder is nonfissionable U-238 (104).

The AEC has ended its 1967 ban on private research on uranium enrichment; however, uranium enrichment technology will remain classified under terms of an AEC contract. No federal funds will be available to assist the private work (105).

New developments.—In the next decade, U. S. electric utilities will not only have to double their generating capacities, but also their existing transmission capacity. Consolidated Edison and Cleveland Electric Illuminating Company are installing short transmission lines of very high voltage that are insulated with sulfur hexafluoride (SF_6). Because of the gas insulation, these 345 kV lines can be placed so close together that they will occupy as little as 1/20 of the normal space.

The technology also applies to utility substations. Generally, an SF_6 station is expected to cost anywhere from 20-100% more than conventional ones, not counting savings on land costs, which are expected to be a significant factor in the years ahead (106).

Fuel cell systems have been developed to generate electricity from natural gas at the point of use. The unit feeds on natural gas and reforms it to produce hydrogen which goes to a hydrogen-air fuel cell. The d-c electricity output can be converted to a-c in an inverter (107).

Manuscript received October 16, 1972. This report was presented at the Industrial Electrolytic Division Luncheon at the Houston, Texas, Meeting of the Society, May 7-11, 1972.

Any discussion of this report will appear in a Discussion Section to be published in the December 1973 JOURNAL.

REFERENCES

1. Helmuth W. Schultze, President, Chlorine Institute (Feb. 2, 1972).
2. Chlorine Institute, Pamphlet No. 10 (July 1971).
3. *Ibid.* (Jan. 1972).
4. *Chemical Week*, p. 13, Oct. 6, 1971.
5. *Barron's*, p. 11, March 6, 1972.
6. *Chemical Week*, p. 22, July 28, 1971.
7. *Chem. Eng. News*, p. 10, Nov. 8, 1971.
8. *Wall Street Journal*, p. 3, Jan. 15, 1971.
9. *Chemical Week*, p. 29, June 9, 1971.
10. *Wall Street Journal*, p. 6, June 9, 1971.
11. *Oil, Paint and Drug Reporter*, Dec. 13, 1971.
12. Mr. M. P. Grotheer, Hooker Industrial Chemicals.
13. Mr. H. Stuart Holden, Electrode Corporation.
14. *Chem. Eng. News*, p. 16, Dec. 6, 1971.

15. DeNora, Press Release No. 724.
16. *Chemical Week*, p. 52, Jan. 12, 1972.
17. *Ibid.*, p. 39, Dec. 15, 1971.
18. *Oil, Paint and Drug Reporter*, Jan. 17, 1972.
19. *Ibid.*, June 7, 1971.
20. *Chemical Week*, p. 35, April 5, 1972.
21. *Chem. Eng. News*, p. 63, Feb. 28, 1972.
22. *Chemical Week*, p. 39, March 15, 1972.
23. Mineral Industry Surveys, U.S. Dept. of the Interior Annual Preliminary, "Mercury in 1971."
24. Current Industrial Reports, Inorganic Chemicals, U.S. Dept. of Commerce, Bureau of Census.
25. *Oil, Paint and Drug Reporter*, Dec. 13, 1971.
26. *Ibid.*, May 24, 1971.
27. *Ibid.*, July 5, 1971.
28. *Ibid.*, Nov. 15, 1971.
29. Mineral Industry Surveys, U.S. Dept. of the Interior, Bureau of Mines, Annual Preliminary, "Sodium Compounds 1971."
30. Current Industrial Reports, Inorganic Chemicals, U.S. Dept. of Commerce, Bureau of Census.
31. *Oil, Paint and Drug Reporter*, June 7, 1971.
32. *European Chemical News*, p. 8, Dec. 10. 1970.
33. *Chemical Week*, p. 52, May 5, 1971.
34. *Ibid.*, p. 22, Oct. 20, 1971.
35. *European Chemical News*, p. 8, Oct. 23, 1970.
36. *Chemical Week*, p. 25, June 2, 1971.
37. *Oil, Paint and Drug Reporter*, Feb. 22, 1971.
38. *Ibid.*, Jan. 18, 1971.
39. *Ibid.*, Aug. 23, 1971.
40. *Ibid.*, Oct. 18, 1971.
41. Mr. W. L. Amos, Dept. of Commerce, Chemical Division.
42. *Oil, Paint and Drug Reporter*, Feb. 28, 1972.
43. *Ibid.*, June 14, 1971.
44. Mineral Facts and Problems, Bulletin 650, U.S. Dept. of the Interior, p. 989-1000, "Fluorine 1970."
45. Commodity Data Summary, U.S. Dept. of the Interior, "Fluorspur, January 1972."
46. Mineral Industry Surveys, U.S. Dept. of the Interior, Annual Preliminary, "Aluminum and Bauxite in 1971."
47. Mineral Industry Surveys, U.S. Dept. of the Interior, "Aluminum Industry in February 1971."
48. Mineral Industry Surveys, U.S. Dept. of the Interior, "Aluminum in March 1971."
49. *Oil, Paint and Drug Reporter*, Dec. 13, 1971
50. *Chemical Week*, p. 13, March 17, 1971.
51. *Chem. Eng. News*, p. 10 Feb. 8, 1971.
52. *Chemical Week*, p. 29, Dec. 1, 1971.
53. Mineral Industry Surveys, U.S. Dept. of the Interior, Annual Preliminary, "Magnesium and Magnesium Compounds in 1971."
54. *Oil, Paint and Drug Reporter*, April 26, 1971.
55. *Chem. Eng.* p. 23, Feb. 8, 1971.
56. Mineral Industry Surveys, U.S. Dept. of the Interior, Annual Preliminary, "Manganese in 1971."
57. *Chem. Eng. News*, p. 56-57, May 10, 1971.
58. Mr. J. J. Victory, Deapsea Ventures, Inc.
59. Mineral Industry Surveys, U.S. Dept. of the Interior, Annual Preliminary, "Beryllium in 1971."
60. *American Metal Market*, Oct. 14, 1971.
61. *Chem. Eng.*, p. 76, Oct. 18, 1971.
62. Mineral Industry Surveys, U.S. Dept. of the Interior, Annual Preliminary, "Chromium in 1971."
63. Mineral Industry Surveys, U.S. Dept. of the Interior, "Chromium in December 1971."
64. Mineral Industry Surveys, U.S. Dept. of the Interior, Annual Preliminary, "Titanium in 1971."
65. Mineral Industry Surveys, U.S. Dept. of the Interior, "Titanium in the Fourth Quarter 1971."
66. *Metalworking News*, p. 1, March 29, 1971.
67. *Chem. Eng. News*, p. 15, Jan. 3, 1972.
68. *Journal of Commerce*, p. 8, Feb. 24, 1971.
69. *American Metals Market*, May 7, 1971.
70. *Chem. Eng. News*, p. 6, Jan. 17, 1972.
71. Mineral Industry Surveys, U.S. Dept. of the Interior, Annual Preliminary, "Lithium in 1971."
72. Mr. D. C. Wininger, U.S. Dept. of the Interior.
73. Mineral Industry Surveys, U.S. Dept. of the Interior, Annual Preliminary, "Copper in 1971."
74. Mineral Industry Surveys, U.S. Dept. of the Interior, "Copper Industry in December 1971."
75. *Chemical Week*, p. 18, Dec. 1, 1971.
76. *Ibid.*, p. 15, Dec. 8, 1971.
77. *Ibid.*, p. 23, Feb. 24, 1971.
78. *Ibid.*, p. 35, March 17, 1971.
79. *Ibid.*, p. 33, Nov. 24, 1971.
80. *Business Week*, p. 52, Feb. 19, 1972.
81. *Chemical Week*, p. 65, April 14, 1971.
82. *Ibid.*, p. 13, March 14, 1971.
83. *Chem. Eng.*, p. 18, Nov. 29, 1971.
84. Mineral Industry Surveys, U.S. Dept. of the Interior, Annual Preliminary, "Nickel in 1971."
85. *Oil, Paint and Drug Reporter*, Nov. 8, 1971.
86. Mineral Industry Surveys, U.S. Dept. of the Interior, Annual Preliminary, "Zinc in 1971."
87. Mineral Industry Surveys, U.S. Dept. of the Interior, "Zinc Industry in December 1971."
88. *Oil, Paint and Drug Reporter*, Oct. 4, 1971.
89. *Engineering and Mining Journal*, p. 69, Feb. 1972.
90. Mr. P. Rederer, Edison Electrical Institute.
91. Federal Power Commission, News Release No. 18154, March 24, 1972.
92. Federal Power Commission, News Release No. 18087, Feb. 25, 1972.
93. Federal Power Commission, News Release No. 17894, Nov. 26, 1971.
94. Federal Power Commission, News Release No. 18032, Feb. 4, 1972.
95. *Chem. Eng.*, (Dec. 27, 1971).
96. Annual Report to Congress of the Atomic Energy Commission for 1971.
97. *Chem. Eng. News*, p. 16, Jan. 24, 1972.
98. Annual Report to Congress of the Atomic Energy Commission for 1971.
99. Annual Report to Congress of the Atomic Energy Commission for 1971.
100. *Chemical Week*, p. 15, Nov. 3, 1971.
101. *Ibid.*, p. 32, Aug. 4, 1971.
102. Annual Report to Congress of the Atomic Energy Commission for 1971.
103. *Chemical Week*, p. 16, Nov. 3, 1971.
104. *Chem. Eng.*, p. 34, Aug. 23, 1971.
105. *Chemical Week*, p. 16, June 30, 1971.
106. *Business Week*, p. 58, March 20, 1971.
107. *Chem. Eng.*, May 31, 1971.
108. Federal Power Commission, News Release No. 18023, Jan. 28, 1972.

JOURNAL OF THE ELECTROCHEMICAL SOCIETY

REVIEWS AND NEWS

APRIL 1973

Design and Materials of Construction for Electrolytic Cells

R. B. MacMullin*

R. B. MacMullin Associates, Niagara Falls, New York 14303

The scope of this paper is broader than it sounds. Clearly, it is the essence of electrochemical engineering. Like all engineering disciplines, it combines two ingredients, theory and practice, or, if you will, science and art. Historically, the art has preceded the science by decades. We have been making chlorine and caustic soda by electrolysis long before we understood electrode kinetics. We have been making aluminum long before we understood the chemistry of fused-salt baths. We have been electroplating gold and silver long before we had knowledge of complex ions and ligands.

Theory is at last catching up with practice and it is now possible to think in terms of applying theory to practical electrochemistry in ways previously ignored. So, it behooves the present generation of electrochemical engineers to have a working knowledge of theory. My remarks, however, will be focused on the application. I think it worthwhile to first consider the fundamental difference between a purely chemical reactor and an electrochemical reactor, that is, a cell.

In a chemical reactor (Fig. 1), the various reaction steps are limited to those which are thermodynamically possible. The selectivity and the space-time yield are foreordained by temperature, pressure, the composition of the reactants, and the catalysts that may be present.

In an electrochemical reactor (Fig. 2), reactions that are *a priori* thermodynamically impossible are forced by supplying the missing free energy at the electrodes. The reactions take place on a heterogenous surface which is capable of accepting or donating electrons to the reacting species in accordance with Faraday's law.

* Electrochemical Society Active Member.

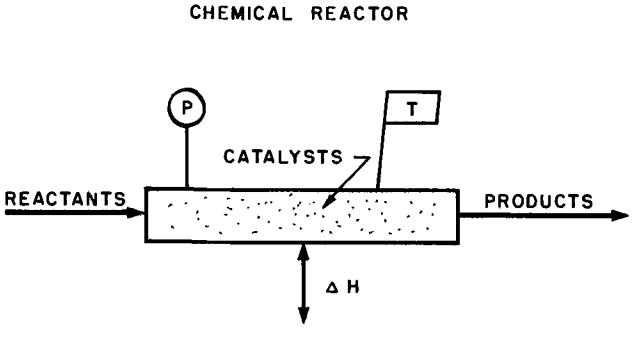

	Δ H°	Δ G°
	k cal	k cal
$N_2 + 3\,H_2 \longrightarrow 2\,NH_3$	- 22.08	- 7.95

Fig. 1. Chemical reactor. To obtain products, the free energy change must be negative.

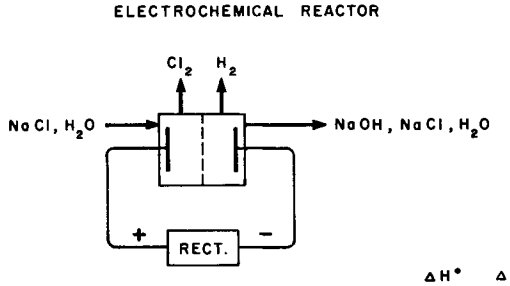

	ΔH°	ΔG°	E°
	k cal	k cal	volt
$2\,NaCl + 2\,H_2O \xrightarrow{2\,F} 2\,NaOH + Cl_2 + H_2$	+ 106.8	+ 100.9	- 2.18
2 FARADAYS x CELL VOLTAGE = ENERGY INPUT	- 166.0	- 166.0	+ 3.60
EXCESS ENERGY USED	- 59.2	- 55.1	+ 1.42

Fig. 2. Electrochemical reactor. To obtain products, the free energy change is made negative by applying energy at the electrodes.

The selectivity depends on the usual laws of mass transport, but the action takes place in the incredibly attenuated layer adjacent to the electrode. The electrical energy consumed is invariably greater than the Gibbsian free-energy requirement, the excess depending on the efficiency of the transport processes required to bring reacting species up to the electrode and to take away the reaction products.

To reduce this to a quickly grasped metaphor, chemical reaction, like politics, is the art of the possible; electrochemical reaction, like military tactics, is the art of overriding the impossible by applying electrical force.

The Scope of Industrial Electrolysis

Before we get too involved in our subject, I must caution you that it covers a very broad field, as shown in Table I. You can classify electrolytic systems in many arbitrary ways, as illustrated in Table II. Every practical industrial cell represents a particular combination of these eight categories. There are over 200,-

Table I. Some industrial applications of electrolysis

Category	Examples
1. Inorganic chemicals, preparative	Chlor-alkali; chlorate
2. Inorganic chemicals, purification	NaOH
3. Metals, electrowinning	Al, Mg, Na, Mn, Ni
4. Metals, electrorefining	Cu, Pb, Zn
5. Metals, electroplating	Ag, Cu, Ni, Cr
6. Metals, electroforming	Steel, alloys
7. Metals, electromachining	Steel, alloys
8. Metals, electropolishing	Steel, alloys
9. Metals, anodizing	Al, Ti
10. Organic chemicals, preparative	Adiponitrile; p-aminophenol; fluorocarbons, TEL
11. Electrodialysis	Desalting/conc'n. saline water
12. Batteries	Primary, secondary
13. Fuel cells	H_2/O_2, Na/S
14. Films, electrophoretic deposition	Rubber latex

Table II. Cells classified by various functions

By mode	Example
Charge	Electrowinning cells, power consumed
Discharge	Prim. batteries, fuel cells, power generated
Reversible	Sec. batteries, power stored

By polarity	Example
Monopolar assemblies	Hooker Cl cell
Bipolar assemblies	Erco chlorate cell
Combination assemblies	Dow Cl cell

By type of anode	Cell type	Anode
Consumable	Al pot	Carbon
Soluble, solid	Ni cell	Nickel matte
Soluble, liquid	Al ref.	Molten Al
Insoluble, solid	Cl/Alk. cells	Graphite, DSA
Insoluble, porous	Phillips ECF	Carbon
Insoluble, packed particles	Nalco TEL	Pb
Insoluble, fluidized particles	Newcastle, CN removal	Metal, graphite

By type of cathode	Cell type	Cathode
Rigid metal	Metal win., refin.	Start. metal/plated metal
Rigid metal	Cl/Alk. (dia.)	Steel mesh
Rigid porous solid	Fuel, H_2/O_2	C, graph., metal
Packed particles	Cl/Alk., Hg	Graphite in decomposer
Fluidized particles	Newcastle	Metal, graphite
Liquid metal	Cl/Alk. (Hg)	Amalgam
Liquid metal	Chlor metal (Na)	Molten Pb/Na
Liquid metal	Ford Na/S bat.	Liquid Na

By type of electrolyte	Example
Aqueous solutions	Brine
Nonaqueous organics	THF, DMSO, Et_2O plus support. electrolyte
Nonaqueous inorganic	KH_2F_3
Homogenous combinations	Monsanto EHD, H_2O, QAS, AN/ADN
Heterogenous emulsions	Phillips EHD, H_2O, buffer salt, DS, AN/ADN
Fused salts	NaCl, $CaCl_2$, $MgCl_2$, LiCl/KCl
Solid electrolytes, (liq./liq.)	Ford Na/S, beta Al_2O_3
Solid electrolytes, (gas/gas)	G.E. H_2/O_2, stab. ZrO_2

By type of divider	Type of cell	Divider
Undivided cells	Chlorate cells	None
Partly divided		
Curtain walls	MEL Mg	Ceramic
Baffles, screens	Downs Na	St. steel mesh
Isolated by fluid metal	Cl/Alk., Chlormetals Na	Mercury, Molten Pb
Permeable diaphragms		
Rigid, porous	Wet batteries, fuel cells	Ceramic, metal
Flexible, porous	Cl/Alk.; Mn	Asbestos; textiles
Ion selective membranes		
Organic	Electrodialysis, desalting	Anionic, cationic
	Electro hydrodimerization	Cationic
Solid electrolyte	Ford Na/S battery	Beta alumina, Na^+
Solid electrolyte	G.E. H_2 generator	Stabilized ZrO_2, $O^=$

By hierarchy	Cell type	Products
Cell products = electrode products	Chlor-alkali	Cl_2, NaOH, H_2
Cell products formed by secondary chem. react. away from electrodes	Hypo cells	Na OCl
	LeDuc	Ethylene oxide
Combinations of above	Erco, Krebs	$NaClO_3$

By change of state at electrode	Examples	
	At anode	At cathode
No change, prods. sol. in bath	Oxidation	Reduction
Gas is evolved	O_2, Cl_2	H_2
New liquid phase forms		
Heavier than bath		Al, Mg
Lighter than bath	S (Ford bat.)	Na, Mg
Solid phase forms		
Adherent deposit	PbO_2	Mn
Nonadherent deposit	MnO_2	$Mg(OH)_2$

000 combinations of these categories, but the industrially important types probably number less than 50. This suggests that there is plenty of room left for innovative designs, and alternate, but not necessarily economic, cell designs for making even the commonly produced electrolytic products.

It is certainly worthwhile to evaluate the advances made in one branch of electrochemistry in terms of application to another branch. For example:

(*i*) The polarograph is an analytical tool which makes separations on a scale measured in microamperes (Fig. 3). Some of these separations have been duplicated in commercial amalgam cells in the multikiloampere range (Fig. 4).

(*ii*) New close-coupled cell geometries, found useful in oxyhydrogen fuel cells (Fig. 5), are now being applied in reverse, to oxyhydrogen generators (1).

(*iii*) Porous, carbon anodes, long useful in the air-depolarized zinc batteries of commerce, find application in cells for Phillips Petroleum Company's new ECF process for the electrochemical fluorination of hydrocarbon vapors (2). We will take a closer look at these later.

(*iv*) The Ford sodium/sulfur rechargeable battery (Fig. 6), employing a β-alumina solid electrolyte, which is selective to sodium ions, is attracting attention as a possible new way of making metallic sodium (Fig. 7) (3).

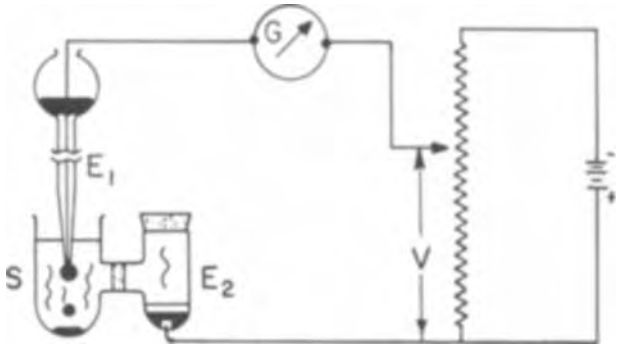

Fig. 3. Basic electrical circuit for polarography. This is a mercury cell in its simplest form. Current is usually in the microampere range.

Fig. 4. A mercury cathode chlor-alkali cell. This cell, of the DeNora type, can handle currents up to 450 kA.

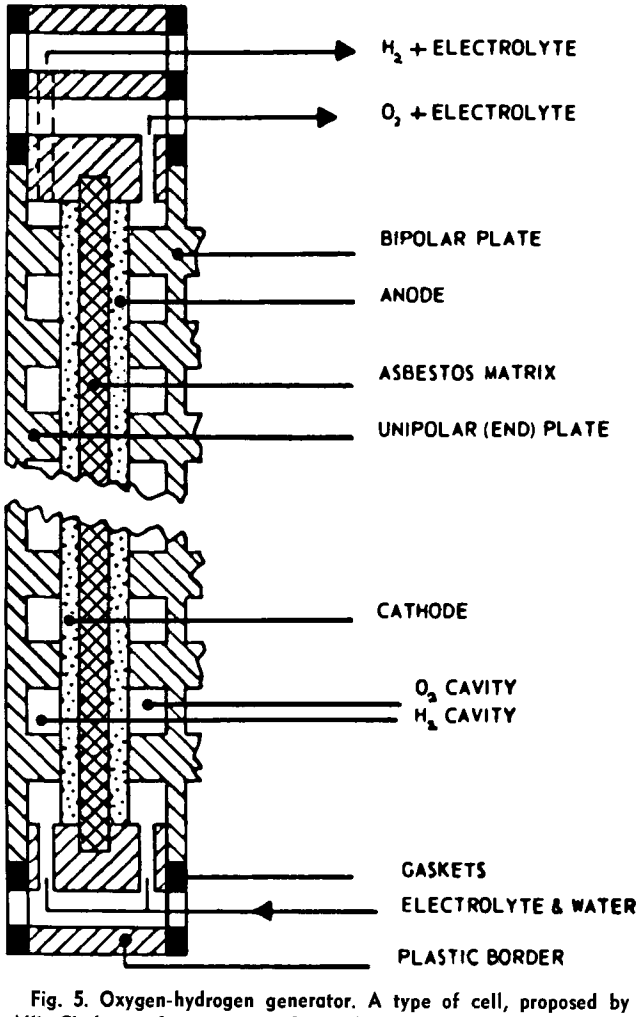

Fig. 5. Oxygen-hydrogen generator. A type of cell, proposed by Allis-Chalmers, for running a fuel cell in the charge mode.

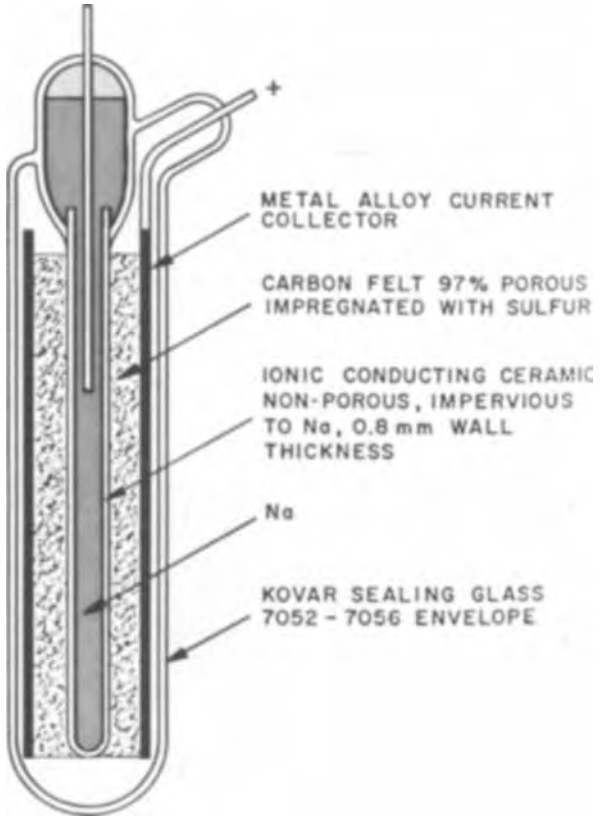

Fig. 6. A small Na-S secondary battery. The solid electrolyte is polycrystalline beta alumina. (Courtesy Ford Motor Company.)

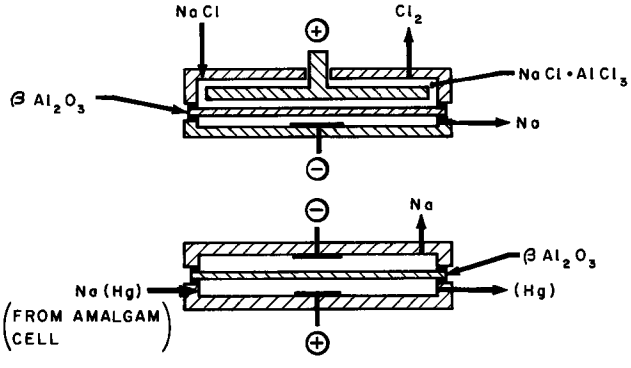

Fig. 7. Two schemes for recovering sodium from NaCl. Upper, from NaCl rich melt of NaCl · $AlCl_3$; lower, from Na(Hg) made in amalgam cell.

(*v*) The discovery that organic free radicals can be generated in certain kinds of nonaqueous electrolytes led to a new commercial process for making tetraalkyl lead (4).

(*vi*) The development of ion exchange membranes for the desalination of water is now being put to use to produce salt, and chlor-alkali from seawater (5) (Fig. 8), and also tonnage electro-organics, like adiponitrile (6).

Since it is obviously impractical to cover the whole field of applied electrochemistry, I will devote the rest of my paper to specific examples of (*i*) advances in design concepts, and (*ii*) advances in materials available to carry out those concepts.

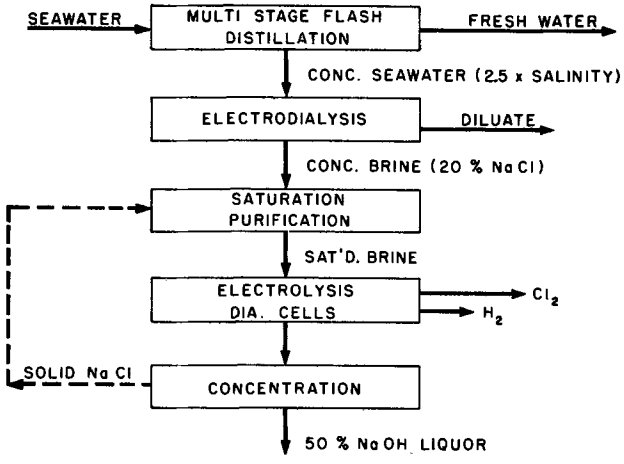

Fig. 8. A Japanese scheme for making chlor-alkali from seawater. This scheme combines seawater desalination with the diaphragm cell process for chlor-alkali.

Techniques of Design and Scale-Up

In 1962 I presented a pioneering paper in *Electro-Chemical Technology* on the problems of scale-up of electrolytic processes (7). The processes considered were the preparative ones, in which power is used to make chemicals or to win metals. Within this field, the recommended procedures were fairly comprehensive, and are just as applicable today as then. This primer was extended, in 1964, to include electro-organic processes (7).

In a magnificent paper Eisenberg covers the principles of design and scale-up of fuel cells (8). The techniques are equally applicable to running cells in the charge mode to make chemicals.

I will now mention a number of new techniques which have come to light since 1962. I will first deal with those only indirectly related to materials of construction.

Porous electrodes.—These have been with us for a long time, but modeling what takes place inside is extremely complex. Much work has been done, and some progress made, in developing models for mass transport, current distribution, and heat transport (9, 10). Flow regimes may be dead-ended, as in most fuel cells, or flow-through (the electrolysis zone), as in making chlorohydrin from ethylene, or flow-by, as in the cells for the Phillips ECF process already referred to.

The flow-by concept is new and seems to involve action at a distance like a gravitational field (Fig. 9). A specie of elemental fluorine, identified as a C...F complex, is generated at the surface of the anode, yet is quite effective in fluorinating hydrocarbon gas flowing by, even as far away as 1 or 2 cm. The electrolyte, KH_2F_3, is repelled by surface-tension effects and very little penetrates into the pores. The gas is free to rise through the porous anode like flue gas up a chimney. The system has been modeled and simulated on a computer. Naturally, experimentally determined design factors have to be fed into the program, in order to use the program for design purposes.

Extended surface electrodes.—The idea of carrying out electrolysis in fluidized beds of solid particles was conceived by our British friends at the University of Newcastle upon Tyne (11). They have come up with a number of interesting applications, and have also learned something about its limitations. Being good electrochemical engineers, they have modeled the technique and are presenting papers on this subject later in this symposium. One extraordinary result has been to increase the voltage gradient to the point where each (conducting) particle acts as a bipolar electrode.

Forced circulation of electrolyte.—There is really nothing conceptually new in boosting limiting current

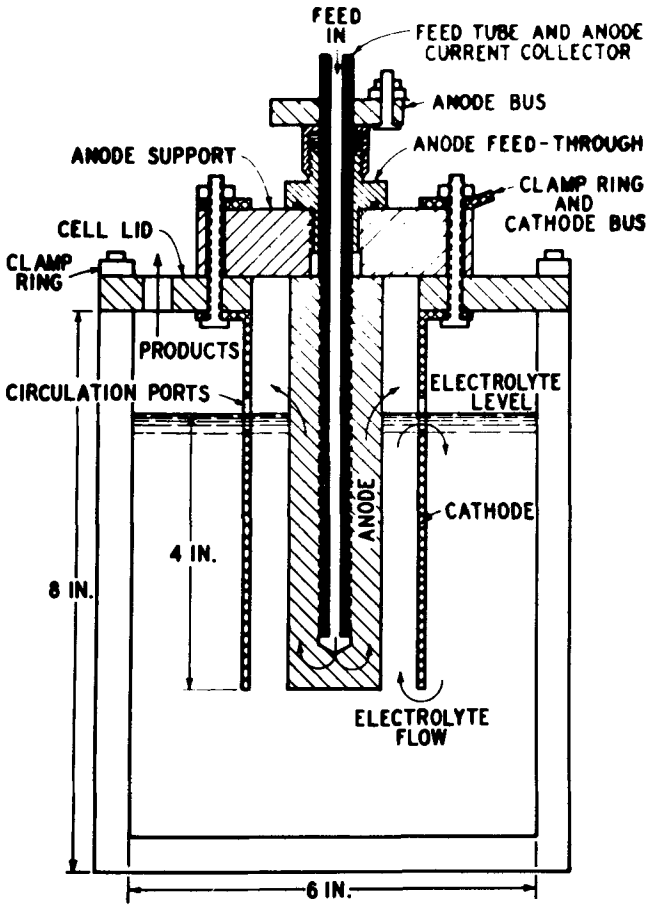

Fig. 9. Experimental fluorination cell. This illustrates the flow-by technique for electrochemical fluorination of hydrocarbon gases in a porous carbon anode. (Courtesy Phillips Petroleum Company.) See *This Journal*, 118, 1248 (1971).

density by increasing turbulence in the electrolyte flowing past an electrode. You can spin the electrode, or promote circulation by the gas-lift effect created by gas evolved on the electrode. Or you can force the electrolyte to flow by at high velocity. The diffusion film thickness depends on the velocity. The only remarkable thing is that cell designers have made so little use of forced circulation.

Certain electro-organic syntheses would have little commercial interest without forced circulation at velocities in the range 0.5-1.5 m/sec. This is particularly true in EHD cells for making adiponitrile. These cells are expensive, and since forced circulation permits higher current density, it also cuts capital cost. Lastly, a great light has dawned on electro-organikers: the selectivity of the electrode toward the desired product often depends on shear velocity. I speak from experience.

Anode effects.—These annoying interruptions in an otherwise smooth electrolysis are more frequently encountered at graphite or carbon anodes, in fused-salt baths, particularly in fluoride baths. The cause and cure of anode effects, when they occur, has been pretty well mastered in an aluminum-cell pot line. It is generally the signal to stir more alumina into the cryolyte bath.

In oxide-free systems, the anode effect is generally more serious. In an ECF cell, the voltage may suddenly rise from 7 to 70V, the porous anode may be "electro-machined" in places where free fluorine is generated, and the free fluorine, in contrast to the C...F complex, may cause the coking of the hydrocarbon gases being fluorinated. The cure is quite simple: when the anode effect occurs, force full current through the polarized electrode for about 1 min, then drop the current to

zero. Within seconds, normal electrolysis may be resumed. The technique has been extended to multiple anode cells and for series circuits of such cells, without unduly complicating the rectifier. Incipient anode effect can be detected and cured by inducing the anode effect by momentarily increasing the current supply to the sick anode (12, 13).

Current reversal and pulsing.—The effect of superimposing alternating current on direct current has been a favorite pastime for inquisitive electrochemists for years, usually with disappointing results. The a.c. contributes no Faradays, only I^2R heat. If you try to depassivate platinum-coated titanium anodes by this scheme, you quickly lose the platinum.

On the other hand, periodic reversal of the d.c. in bipolar cells is sometimes quite useful. If both electrodes are alike in size and materials, as in a bipolar chlorate cell with graphite electrodes, occasional periodic reversal evens wear and prolongs life. In bipolar cells with similar electrodes which corrode while anodic (*e.g.*, lead), frequent and automatic current reversal can be used to prevent the accumulation of adherent oxide films which lead to total polarization, or shorts, or blockage to flow of electrolyte (12).

Currently, there is great interest in the use of either d-c reversal or pulsed d.c. in the electroplating of metals (14). It has been demonstrated that the technique gives smooth, level deposits at high current density, and it relaxes the usual built-in stresses of electroplated metal. In fact, two papers on this technique are being presented at this symposium (15). For industrial application, the circuitry and power supply are not without their problems, but the answers do not seem unduly complicated.

Halide polyanions.—The equilibrium between free halogen and halogen ion to form polyanions is pretty well known. Among these, Br_3^- and I_3^- are quite stable. This property can be put to good use in new kinds of batteries, for example the H/Br cell. On charge, the liberated Br_2 is stored as $LiBr_3$.

On the other hand, if you set out to electrolyze NaBr in an ordinary diaphragm cell, most of the bromine stays in the brine as $NaBr_3$, and after passing through the diaphragm is reduced back to NaBr at the cathode. Result: impossibly low current efficiency. Additionally, graphite anodes are intercalated by bromine and fall apart. If you are still interested in making tonnage bromine in a diaphragm cell, do not give up. You only have to shift the polyanion equilibrium. If you run the cell at the boiling point, very high current efficiencies are obtained. If you substitute amorphous carbon for graphite, you achieve reasonable anode life (12).

Enhancement of heat transfer on gas-evolving electrodes.—The enhancement of mass transfer by gas evolution has been much studied. It seems natural to expect a similar enhancement of heat transfer. The degree of enhancement has now been measured, and it is of the order of threefold. Occasionally an electrochemical engineer has need of cell cooling for temperature control, particularly when chemical reactions, following electrode reactions, liberate excessive heat. Now cooling of electrodes is an old technique. Making use of the enhancement factor is new (Fig. 10) and has led to some innovative and economically optimum cell designs (16).

Conformal plotting as an aid in predicting current distribution.—Conformal plotting is an old technique, much used by civil engineers to predict distribution of fluid flow through porous soils, and by mechanical engineers for predicting distribution of heat flow. Electroplaters have tried to use it for predicting current distribution and deposit thickness. There are complications: when the overvoltages are an appreciable percentage of the over-all potential differences, you have to allow for the fact that overvoltage is usually not a

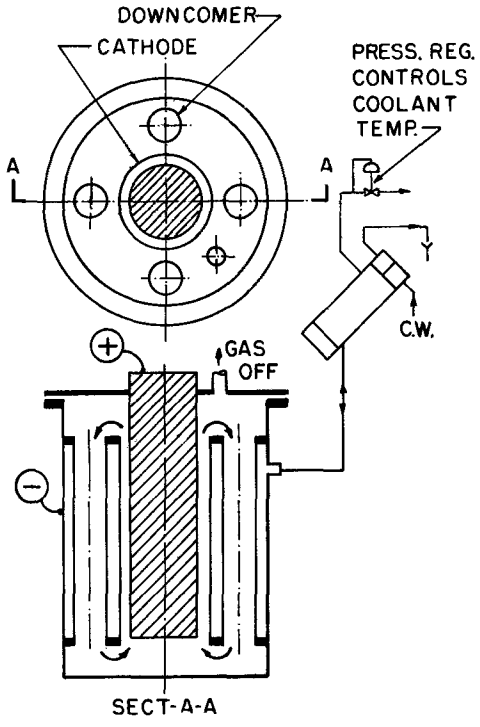

Fig. 10. Cell used to demonstrate enhancement of heat transfer on a gas evolving electrode. The evolution of H_2 gas on the heat transfer surface enhances the coefficient of heat transfer by a factor of about 3. See *This Journal*, 118, 1582 (1971).

linear function of current density (17). For some electrode configurations, a mathematical solution is beyond the ken of the average engineer. For the average person, conformal plotting is easy, and gives surprisingly realistic results. Figures 11-14 show how this was done in a Hall-type cell for producing molten uranium metal from uranium oxide. Where overvoltage is a complication, the trick is to change the shape of the areas between the intersecting flux and potential lines from squares to appropriately proportioned rectangles. Three-dimensional estimates are no problem (12).

Shock removal of metal from cathodes.—There are plenty of problems in the electrowinning of manganese metal, that is, putting a good deposit onto a starting cathode. Getting the deposit off, and reconditioning the starting sheet, is another. Foote Mineral has developed a neat way of doing this, by sonic shock in a water bath. The shock is produced by a sudden electrical arc discharge from an electrical condenser (18). This technique has greatly simplified cell house practice. The lesson is, not all electrochemical problems are confined to the cells proper.

Computer simulation in cell design.—Computer simulation of almost anything has become "old hat." The program shown in Fig. 15 was a pioneer effort in 1970, to do this for an old style Hooker diaphragm cell (19). The computer print out did not tell us much in the way of results that we did not know before. To set up the program, however, forced us to investigate in detail, and for the first time, the many separate relations between the variables. The computer merely solved the problem of how all these separate relations interacted.

I highly recommend the discipline of computer simulation, because it so often brings to the surface many embarrassing problems of which we have been blissfully ignorant. The solution of these problems always leads to improved design.

Directive salts.—In the electro-hydrodimerization of acrylonitrile to produce adiponitrile, various alkyl quaternary ammonium salts are added to the catholyte

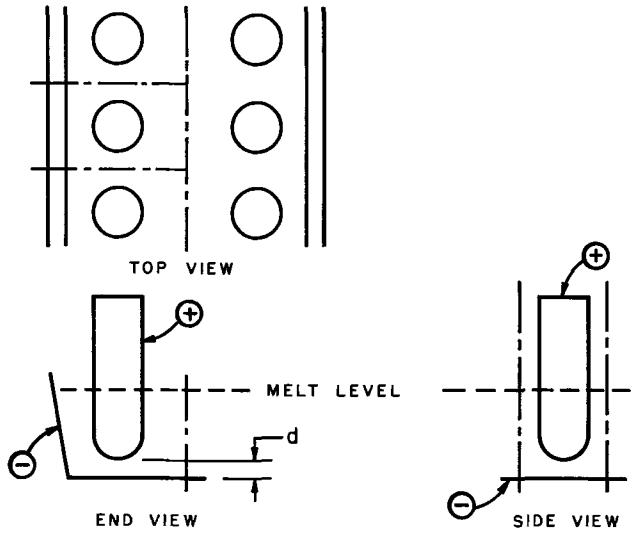

Fig. 11

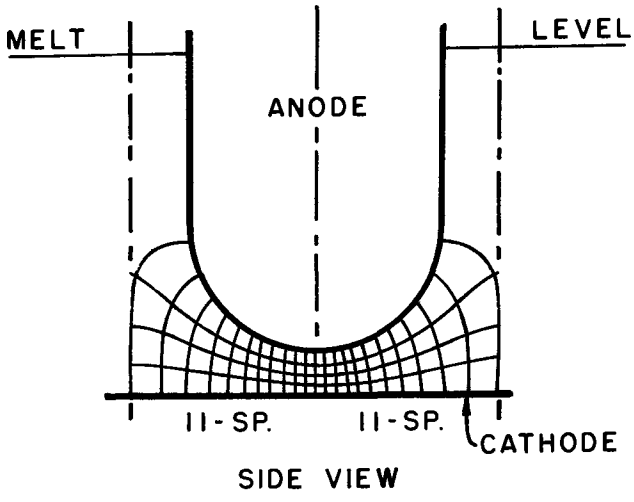

BOUNDARIES of MODULE

Fig. 12

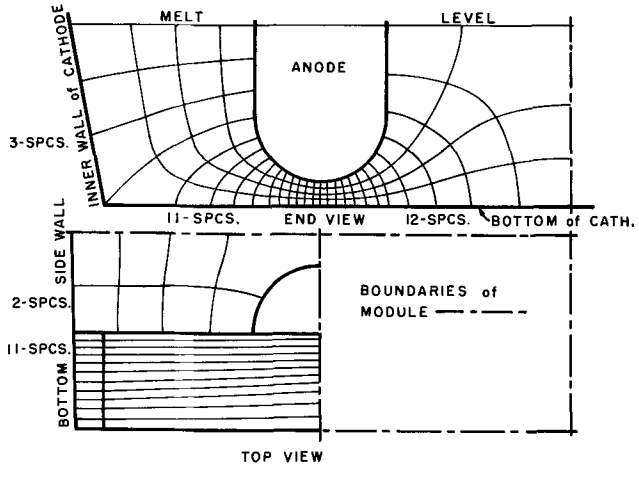

Fig. 13

RESULTS, CONFORMAL PLOT.

As shown, IR drop is quartered.

Keeping $\Delta E \times \Delta I$ paths square

No. SPACES	END VIEW		SIDE VIEW	TOTAL
Bottom	23	x	22	506
Side Wall	3	x	4	12
Total no. equal current paths				518

L, gap at tip	=	d
A, path at tip	=	$(d/4)^2$
R, any path	=	$16\ \rho/d$
I_n per path	=	$I/518$
V = IR	=	$I \cdot \rho/32.4\ d$

Fig. 14

Fig. 11-14. Conformal plotting as a means of estimating current distribution. A proposed high temperature fused salt cell for reduction of UO_2 to liquid uranium metal, uses multiple graphite anodes, common cathode. Fig. 11. A typical module is first selected. Fig. 12. Flux and equipotential lines are sketched in for side view. Fig. 13. Flux and equipotential lines are sketched in for end view and plan. Fig. 14. The results for 3 dimensions are tabulated.

to control selectivity (current yield) of the desired product. The nature of the cathode is also important. Neither factor taken separately is self-sufficient. A proper combination can lead to very high current yields indeed. Clearly, we are dealing with surface chemistry and catalysis. Some theories of reaction mechanisms have been advanced, but are not too helpful (20). The point is, here is a new tool for improving electro-organic reactions, that could spell the difference between success and failure for industrial exploitation.

Exotic fields for metal deposition.—We ordinarily think of metal as being plated out on a cathode in an electric field. That is, there is a voltage gradient between bulk solution and cathode, and with it, an associated concentration gradient. Until recently, little thought has been given to the possible effect of other kinds of energy fields. The following effects have now been studied, some of them with beneficial results in electroplating:

(*i*) Thermal field—Should the cathode be hotter or colder than the bulk solution (21)?

(*ii*) Magnetic field—Should this be parallel or perpendicular to the plane of deposition (22)?

(*iii*) Acoustic field—What wave length is most effective (23)?

Materials for Cell Construction

The engineer's term for this is "hardware." Traditionally, cells have been built of the best materials available at the time. You recall the couplet about the bridal gown, which consists of

"Something old, something new,
Something borrowed, and something blue."

Cells are like that. The something blue is often pure whimsy, like a blue garter.

The way a cell is fashioned invariably reflects the properties, and especially the limitations and cost of the available materials. The way a cell performs is thus a compromise, generally somewhere between a "solid gold Cadillac" and a "tin Lizzie."

A more sophisticated approach, if you have the time, is to first design an ideal cell, write the specifications, and then hunt for the materials. If you cannot buy them you invent them, which of course means research and development. Some of the recent spectacular advances in chlor-alkali cell design were made possible by the ultimate success of a deliberate ten year campaign to find another kind of anode, better than graphite.

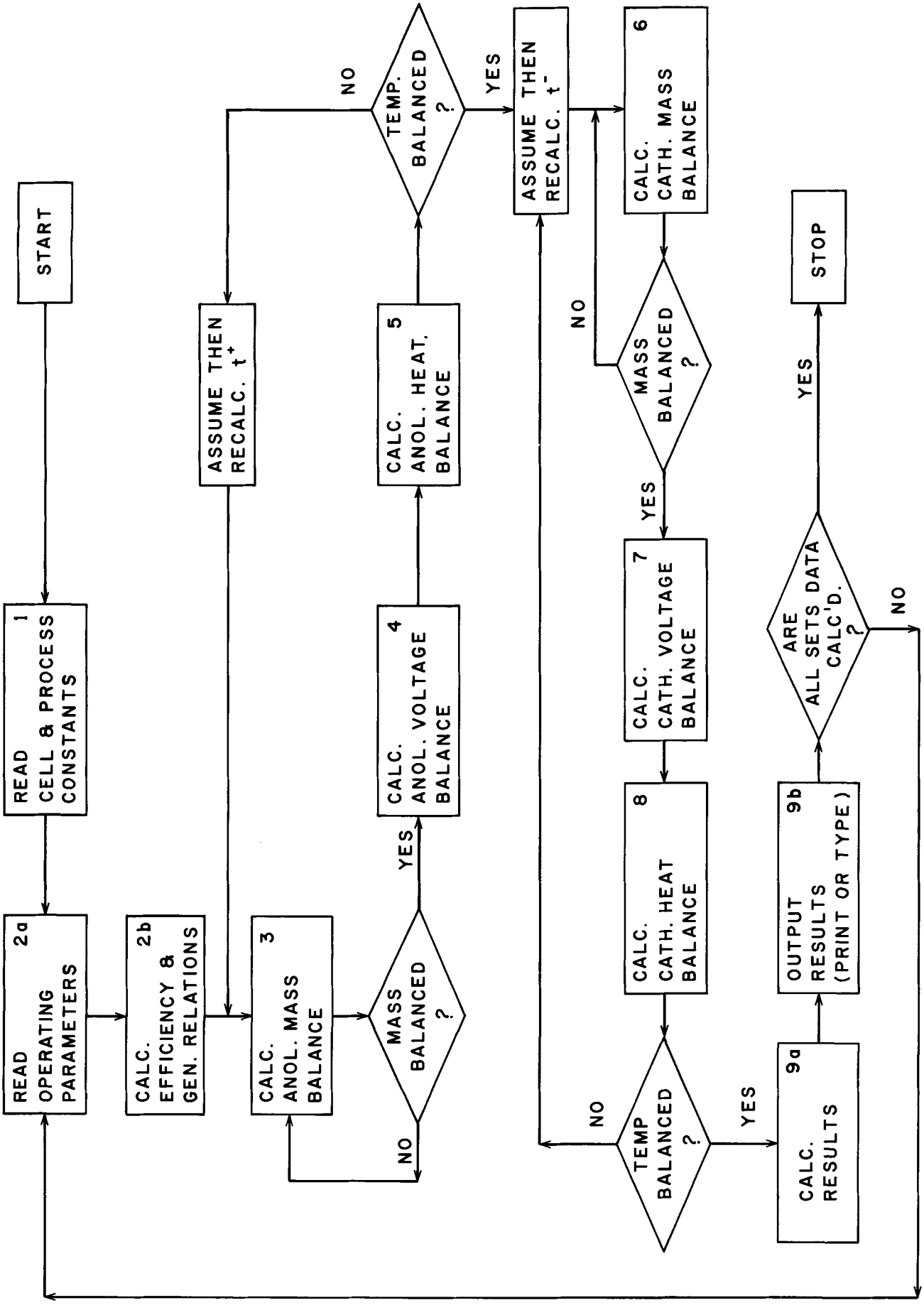

Fig. 15. Program for computer simulation of a diaphragm-type chlor-alkali cell, with graphite anodes. The computer predicts the day-to-day conditions in a single typical cell throughout its life cycle. The average results conform to performance of a cell line comprising a large number of such cells.

Some new, or at least different, materials for cell components are:

Anodes.—Graphite still plays an important role in industrial cells, particularly in fused salt systems. For aqueous systems, the quality of anode graphite is better than ever. The old stand-by, linseed oil impregnated graphite, was never good enough for mercury cells, but Nippon Carbon Company has come up with a vinyl polymer impregnant that gives about 70% longer life in actual cells running at 10 kA/m^2 (24).

Some other forms of carbon, quite expensive and not necessarily better for anodes, are: pyrolytic carbon, glassy carbon, and filaments, felt, and woven cloth of both carbon and graphite. You can get superdense graphite, and porous graphite composites which include built-in catalysts and surface-tension control agents. You can even "ruthenize" graphite and arrive at a compromise between ordinary graphite and DSA's in performance. And lead dioxide, electroplated onto a graphite or metal substrate, is used extensively in chlorate, perchlorate, and hypochlorite cells.

The most exciting new kind of anode is of course, the dimensionally stable anode, or DSA®, which consists of a metal substrate, usually titanium, on which an adherent catalytic coating is deposited (25). The titanium is quite stable in oxidizing aqueous solutions, but it is a valve metal, and of no use as an anode by itself. Platinum, and other metals of the same group will activate the titanium. However, these are not good enough, and the loss of the noble metal is prohibitive in most applications, like chlor-alkali. There are a number of metal oxides which are good electronic conductors, and some of these exhibit remarkable resistance to corrosion. Ruthenium dioxide is one of the best (26). Various other oxides are used in combination with RuO_2, to reduce cost. The patent and technical literature on metal anodes is by now extensive and known to most of you. DeNora will tell you, later on, about the new Glanor diaphragm cell, which employs DSA's (27). A few pertinent points to keep in mind are: (*i*) Completely new and more advantageous cell geometries are possible. (*ii*) Higher current densities, and/or lower cell voltages are possible. (*iii*) The field of application is much wider than chlor-alkali, but there are some limitations. (*iv*) Watch out for nitrogen compounds in the electrolyte—they could strip the coating. (*v*) DSA's cannot be used in anhydrous fused salt baths that contain halides. Under these conditions, the titanium anodically dissolves.

Cathodes.—In electro-organic synthesis, the choice of metal is important (28). Hydrogen overvoltage can be used as a rough guide in selecting the proper metal. Having made a choice, from tests *in vitro*, the cell designer must be careful to exclude other, less noble metals from the cell parts, feed materials, and the system in general, that might plate out on top of the selected cathode and reduce or destroy its selectivity.

In diaphragm type chlorine cells, the cathode is most commonly a woven steel wire screen. The hydrogen overvoltage on steel is an appreciable component of the total cell voltage. A number of other metals are available that exhibit lower H_2 overvoltage. When these are used as cathodes they do not remain active, because it is almost impossible to eliminate iron as a trace impurity in the system. One possible way of reducing the voltage is to depolarize the cathode with air. This is not new, of course, and lots of technology can be borrowed from the fuel cell experts.

Ion exchange membranes.—A great variety of these are now available, and much progress has been made along these lines: (*i*) Mechanical strength, built-in glass fiber reinforcement. (*ii*) Greater stability in aggressive environments, higher range of temperature. A recent example is duPont's new cation exchange membrane, a modified fluorocarbon polymer (29). (*iii*) Improved selectivity at higher electrolyte concentrations, where selectivity has heretofore been too low to be interesting. (*iv*) Specific selectivity to particular ions.

Past attempts to use cation exchange membranes in place of permeable diaphragms in chlorine cells have been frustrating, using the membranes then available. A recent news item, perhaps only a rumor, seems to indicate that Asahi Chemical Industry Company is more optimistic about such an application (30).

Permeable diaphragms.—I have little new to report here, except that it is a sadly neglected subject and worthy of attention (31). Asbestos diaphragms have wide usage, but nobody seems to know why they work as well as they do, or how to make them work better.

Synthetic fibers have largely replaced cotton duck for separators and anode bags in many metal winning and refining cells. Woven PVC cloth can be heat-shrunk to give the desired low permeability in commercial periodate cells.

Solid electrolytes.—This is an exciting new development in solid-state science, which opens up new vistas of application in electrochemical technology. Solid electrolytes are usually polycrystalline ceramic materials which, in certain ranges of temperature, are good conductors for certain ions, while being substantially nonconductive to electrons. They are also, ideally, impermeable to liquids and gases.

As a first example, there is β-alumina, essentially $Na_2O \cdot 11Al_2O_3$, and β''-alumina, $Na_2O \cdot 5Al_2O_3$, usually doped with minor amounts of MgO or other oxides. These are excellent conductors for sodium ions, at 300°C and over. In the Ford sodium/sulfur battery, the ceramic membrane separates liquid sodium on one side from liquid sodium polysulfide on the other. The open-circuit voltage is about 2V, and on discharge Na reacts with sulfur to form Na_2S_x. On charge, metallic sodium and S are regenerated, all at 100% current efficiency. The use of β-alumina for the electrowinning of sodium is a distinct possibility. The membrane can be modified to conduct other alkali metal ions (32).

As a second example there is zirconium oxide usually doped with yttria, which is an excellent conductor for oxygen ions $O^=$ at temperatures above 900°C (33). This material is used in a new type of fuel cell, and also in new types of instruments that measure the oxygen content of liquid metals (34). It has also been proposed as a way to make cheap hydrogen, by the electrolysis of superheated steam. The water vapor dissociates, the oxygen is ionized at a cathode and passes through the solid electrolyte, then gives up its electrons at an anode to form oxygen gas. The hydrogen is left behind, and is easily separated from the steam (35).

As a third example, there is the double salt $RbAg_4I_5$, which easily conducts silver ion even at room temperature. This forms the basis for a new type of battery (36, 37).

These are but the first indications of the possible development of a wide class of solid-state materials, engineered for use in industrially important electrolytic cells.

Baths.—Although not properly part of the hardware, the nature of the electrolyte used is a determining factor in cell design. The bath can be engineered as well as the hardware. Supporting electrolytes are added to increase conductivity; hydrotropes, to increase solubility of aromatic organics; directive salts to control selectivity; and buffers, inhibitors, levelers, and so on. Cations can be complexed into anions, and *vice versa.*

Tanks.—Concrete, a poor material at best, can be greatly improved in strength and corrosion resistance by including resins in the mix. Het-crete (38) is such a material, which contains a chlorinated polyester resin. Epoxy-sand mixtures, are useful. Solid PVC plastic tanks are in use in periodate cells. Glass fiber reinforced plastics can be used standing, or as liners

for steel tanks. Titanium or titanium-clad steel is sometimes used. Flexible plastic bag liners have also been used in concrete tanks, or even wood tanks, in place of lead.

For low temperature fused salt baths, cells of carbon steel or alloy steel are often quite satisfactory, if maintained cathodic in respect to the bath. For higher temperatures, brick, carbon or graphite linings are standard. There are cases where "skulls" of frozen bath have been used to protect exposed metal.

Cover and seals.—Tank covers need not be rigid. DeNora amalgam cells have two-ply flexible covers, the inner ply to resist chlorine, the outer to resist air oxidation. It is also commonplace to bring anode conductors right into the anode chamber. If these are of copper, they can be protected with sleeves of ceramic, vinyl polymers, or they may be titanium clad. Flexible seals can be made of neoprene, PVC, or poly vinylidene fluoride.

Insulators.—There are many new ceramic materials that have proved their worth in such difficult spots as thermocouple wells, reference cell probes, or simply as insulators in aggressive environments where glass, alumina, or plastics have proved unsuitable. Boron nitride is one such ceramic (39).

Bus and conductors.—Aluminum is now widely used in place of copper. Joints should be welded if possible, and good bolted joints must be carefully engineered. Sodium in a steel pipe makes an excellent bus. Sodium-filled polyethylene pipe is quite acceptable and inexpensive for underground cable.

Conclusion

Electrochemical engineering has indeed established a foothold as a scientific discipline. There seem to be endless opportunities for more advanced design of cells and materials of construction for producing chemicals from energy or energy from chemicals on the industrial scale, and in the service of mankind. This paper marks the end of my own lifetime effort in this field, and I hope that some of my own optimism about the future has rubbed off onto the competent people taking part in this wonderful symposium arranged by my good friend Dr. Wranglén.

Acknowledgment

This paper was presented at the 23rd Meeting, International Society of Electrochemistry, Stockholm, Sweden, 1972.

Manuscript received Oct. 4, 1972.

REFERENCES

1. R. L. Costa and P. G. Grimes, *Chem. Eng. Prog.*, **63**, 56 (1967).
2. H. M. Fox, F. N. Ruehlen, and W. V. Childs, *This Journal*, **118**, 1246 (1971).
3. Imperial Chemical Industries, Ltd., Brit. Pat. 1,155,927 (1969) and 1,200,103 (1970).
4. Private communication; see also *Chem. Eng.*, **75**, 102 (1965) and U.S. Pat. 3,007,857, 3,287,249.
5. *Chem. Econ. Eng. Rev. (Jap.)*, **3**, 13 (1971).
6. C&EN, July 26, 1965.
7. R. B. MacMullin, *Electrochem. Technol.*, **1**, 5 (1963) and **2**, 106 (1964).
8. M. Eisenberg, *Advan. Electrochem. Electrochem. Eng.*, **2**, 235 (1962).
9. A. Winsel, *Chemie Ingr.-Tech.*, **43**, 191 (1971).
10. R. E. Sioda, *Electrochim. Acta*, **16**, 1569 (1971).
11. Chem. Engr., Jan. 1, 1968.
12. Private source.
13. W. V. Childs, U.S. Pat. 3,616,315 (1971).
14. Bulgarian ref.: *CA* **76** (1972), 30007, 30009. Russian ref.: *CA* **76** (1972), 30019, 30023, 30039, 30087.
15. A. Despic, ISE Ext. Abstra. (1972) 20. J. Vereeken, *ibid.*, 63.
16. R. B. MacMullin, K. L. Mills, and F. N. Ruehlen, *This Journal*, **118**, 1582 (1971).
17. "Technology of Electrodeposition," Vagramyan & Solov'eva and Trans. by Behr, Robert Draper Ltd. (1961).
18. Charles Sheer, U.S. Pat. 3,420,758 (1969).
19. R. B. MacMullin, *Denki Kagaku (Japan)*, **38**, 570 (1970).
20. I. E. Gillet, *Chemie Ingr.-Tech.*, **40**, 573 (1968).
21. Russian ref.: CA **76** (1972), 30020.
22. J. Dash and W. W. King, *This Journal*, **119**, 51 (1972).
23. Russian ref.: CA **76** (1972), 30045, 30046.
24. T. Ishikawa and K. Tokutomi, ECS, Houston Mtg., May 1972.
25. Dimensionally stable electrodes are licensed by Electronor Corp., Panama, under the trademarks "DSA" and "DSE."
26. S. M. Marcus, Physics Letters, 28A, 191 (Nov. 1968).
27. V. DeNora, ISE Ext. Abstr. (1972), 51.
28. A favorite theme of Sherlock Swann, dean of American electroorganic chemists.
29. W. G. F. Grot, G. E. Munn, and P. N. Walmsley, Paper 154 presented at Electrochem. Soc. Meeting, Houston, Texas, May 7-11, 1972.
30. *Chem. Week*, June 14, 1972, p. 39.
31. There have been some publications. See F. Hine and Y. Masaki, *This Journal*, **118**, 166 (1971).
32. J. T. Kummer, Paper 162 presented at Electrochem. Soc. Meeting, Houston, Texas, May 7-11, 1972.
33. H. S. Spacil and C. S Tedmar, Jr., *This Journal*, **116**, 1627 (1969).
34. T. H. Etsell and S. N. Flengas, *ibid.*, **119**, 1 (1972).
35. *Chem. & Eng. News*, Nov. 4, 1968, p. 48.
36. T. Takahashi and J. Yamamoto, *This Journal*, **118**, 1051 (1971).
37. A. D. Butherus, Paper 177 presented at Electrochem. Soc. Meeting, Houston, Texas, May 7-11, 1972.
38. Made by Hooker Chemical Co.
39. Made by Carborundum Co.

JOURNAL OF THE ELECTROCHEMICAL SOCIETY

ELECTROCHEMICAL SCIENCE AND TECHNOLOGY

MAY 1973

Phase Diagram of the Pseudoternary System Li_2Se-Se-(LiBr-RbBr Eutectic)

P. T. Cunningham, E. J. Cairns,* E. J. Hathaway, S. A. Johnson, and V. A. Maroni

Argonne National Laboratory, Chemical Engineering Division, Argonne, Illinois 60439

ABSTRACT

The phase diagram of the Li_2Se-Se-(LiBr-RbBr eutectic) system at 360°C has been determined using data obtained from a variety of physicochemical measurements and emf studies. Of particular interest is a large region of three-liquid equilibrium.

Phase-equilibria studies on systems comprised of alkali metals, chalcogens, chalcogenides, and alkali halide salts have been investigated extensively in this laboratory (1-5). Interest in these systems stems primarily from their application in the development of high-specific-energy, high-specific-power secondary cells based on alkali metal-chalcogen couples utilizing molten alkali halide electrolytes (6-10). In this paper we describe results of physicochemical studies on the pseudoternary system Li_2Se-Se-(LiBr-RbBr eutectic) and related systems using solubility, thermal analysis, centrifugation, and quenching techniques. The following article (11) in This Journal presents results of electromotive force (emf) measurements for the Li_2Se-Se-(LiBr-RbBr eutectic) pseudoternary system and related systems. The physicochemical and emf data are herein interpreted in terms of a ternary phase diagram in which the eutectic salt mixture is considered as a single component.

Experimental

Materials.—The selenium (99.999+ % purity, obtained from American Smelting and Refining Company, South Plainfield, New Jersey) and lithium (99.98+ % purity, obtained from Foote Mineral Company, Philadelphia) were used as received. The Li_2Se was prepared from the elements by a method that has been described elsewhere (1). The compositions of the alkali metal halide eutectic mixtures used in these studies are listed in Table I together with their melting points. They were prepared from the anhydrous salts in a purified-helium-atmosphere glove box (13) in which the maximum concentrations of H_2O, O_2, and N_2 are less than 1, 5, and 10 ppm, respectively. The preparative procedure consisted of contacting molten mixtures of the eutectic compositions with lithium for several hours to remove any water and to reduce heavy metal ions, followed by filtration of the eutectic through a double quartz frit filter. The LiCl, LiI, LiBr, and RbBr were obtained from Anderson Physics Laboratories, Champaign, Illinois, and were reportedly 99.99% pure. The LiF was single-crystal optical grade obtained from Harshaw Chemical Company, Cleveland.

Solubility studies.—The solubility studies were carried out in a furnace well attached to the floor of a helium-atmosphere glove box (13). Samples were equilibrated in quartz tubes 460 mm long and 13 mm in diameter. These tubes were inserted into a 16-mm-diameter hole drilled to a depth of 150 mm in a copper block which was positioned in the hot zone of the furnace well. In all cases an excess of the solute material was provided so that the solvent phase would be saturated. Enough solute plus solvent mixture was added to fill the sample tube to a depth of about 100 mm. After equilibration for 4-6 hr with periodic stirring, a 3-mm-diameter quartz extraction tube with a fine quartz frit fused in the lower end was immersed into the phase to be sampled using a vernier depth gauge. The entire assembly was then allowed to come to thermal equilibrium and a sample was drawn into the extraction tube. The extraction tube was then withdrawn from the hot zone and the sample above the frit was submitted for chemical analysis.

Centrifugation studies.—A high-temperature centrifuge similar in design to one described by Friedman (14), was constructed for the centrifugation studies. A drawing of the centrifuge has appeared elsewhere (15). Samples of the desired composition were loaded into quartz tubes, sealed under vacuum, and equilibrated at temperatures of about 400°C in a rocker furnace for times in excess of 24 hr. The equilibrated samples were then removed from the quartz tubes, ground to fine powder, and loaded into special quartz ampules, which were placed in the metal holding

Table I. Compositions and melting points for LiF-LiCl-LiI and LiBr-RbBr eutectics

Eutectic composition, m/o	Melting point, °C
LiF — 11.7 LiCl — 29.1 LiI — 59.2	340.9
LiBr — 59 RbBr — 41	277[a]

[a] This value is 18° higher than the value reported by Gromakov and Gromakova (12).

* Electrochemical Society Active Member.

Key words: selenium, lithium selenide, alkali halide, phase diagram, cathode.

buckets of the centrifuge. The samples were heated to 360°C and centrifuged for periods of 8-10 hr at speeds in excess of 1200 rpm and with a minimum centrifugal force on the sample of 100*g*. The temperature in the sample compartment of the centrifuge was found to vary by less than 2°C during operation. After centrifugation, the holding buckets (containing the ampules) were removed from the centrifuge and immersed in liquid nitrogen. In most cases all of the samples could be removed from the centrifuge and quenched in less than 2 min from the time at which the furnace was opened. The ampules were then transferred to the helium-atmosphere glove box for examination prior to analysis.

Analytical procedures.—Solid samples obtained in solubility, centrifugation, and quenching experiments were subjected to chemical analyses using the following general procedure. The samples were first digested in glacial acetic acid for several hours. Selenium present in the elemental form appeared as a precipitate whereas selenium present as selenide evolved as gaseous hydrogen selenide, which was recovered in a nitric acid trap. The precipitated selenium was recovered from the acetic acid solution and combined with the selenide in the HNO_3 trap by dissolution. The resulting solution (now containing all of the selenium) was spot-checked for halogen (none was ever found) and analyzed for selenium using the standard potassium iodide method (16). The acetic acid solution from the digestion step (now free of selenium) was analyzed for bromide amperometrically using a silver electrode and for lithium and rubidium using flame photometry. For samples containing the LiF-LiCl-LiI eutectic, no attempt was made to analyze for the halogens.

Other procedures.—The methods used in mounting and polishing the samples for microscopic examination as well as procedures used for differential thermal analysis (DTA) have been described elsewhere (1). The experimental procedures used in the emf studies are described in detail in the following paper (11).

Results

Solubility studies.—Prior to examination of ternary samples containing lithium selenide (Li_2Se), selenium (Se), and salt eutectic (LiX), a series of solubility studies was conducted to determine important phase relationships for the Li_2Se-LiX and Se-LiX binary systems. The phase boundaries for the Li_2Se-Se system were known from the work of Cunningham *et al.* (1).

A study of the solubility of Li_2Se in three lithium halide-containing eutectics indicated that the amount of Li_2Se dissolved in these molten salts does not exceed 1 m/o (mol per cent) for temperatures below 450°C. These data are given in Fig. 1. The points for the all-lithium halide eutectics appear to lie on a straight line with a slope corresponding to a heat of solution of 13.3 kcal/mol. Data for the LiBr-RbBr eutectic lie on a line of nearly the same slope but displaced to significantly lower solubility values.

Results of a series of measurements of the solubility of selenium in two lithium halide-containing eutectics are given in Table II. Although there is considerable scatter in the data for the LiF-LiCl-LiI eutectic, it is clear that the solubility of elemental selenium in these eutectics is less than 0.1 m/o at temperatures below 500°C. A linear least squares analysis of the data for the LiF-LiCl-LiI eutectic yielded the equation

$$\log_{10} n_{Se} = 2.628 - 2776/T$$

where n_{Se} is the mole fraction of selenium and T is temperature in degrees Kelvin. The single determination for the LiBr-RbBr eutectic indicates that the selenium solubility is not appreciably affected by changing the constituents of the eutectic.

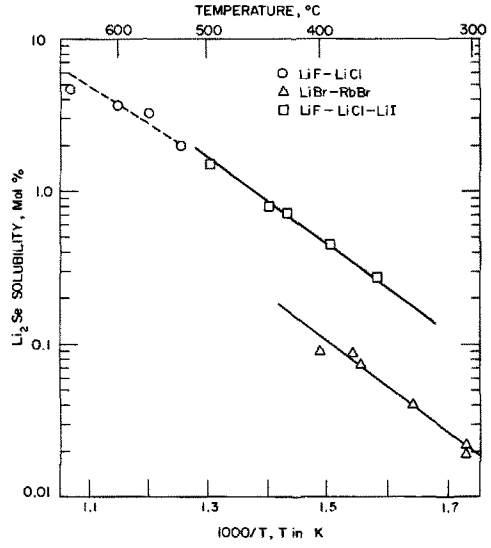

Fig. 1. Solubility of Li_2Se in eutectics containing lithium halides

A single measurement was made of the solubility of a molten salt eutectic in selenium. In this experiment the quantity of LiBr-RbBr eutectic dissolved in selenium at 394° ± 10°C was found to be less than 0.01 m/o. From this result and the data given in Table II for selenium solubilities in lithium halide-containing eutectics, it appears that at 360°C an extensive miscibility gap exists in the pseudobinary systems Se-(LiBr-RbBr eutectic) and Se-(LiF-LiCl-LiI eutectic) extending from <0.1 m/o selenium to >99.9 m/o selenium.

Preliminary studies of the solubility of Li_2Se-Se mixtures in LiX indicated that the quantities of selenium dissolved in the salt were enhanced considerably by the presence of Li_2Se. For example, the respective solubilities of Li_2Se and Se separately in LiBr-RbBr eutectic are only 0.030 and 0.026 m/o at 363°C, but a LiBr-RbBr sample equilibrated at 364°C with a Li_2Se-Se mixture (moles Se/mole Li_2Se = 4.0) was found to contain 1.45 m/o selenium. This observation of increased selenium solubility in the salt-rich phase for samples containing both Li_2Se and Se provided the basis for a clearer understanding of the emf and phase-equilibrium results which follow.

Emf studies.—Typical emf results, such as those presented in Fig. 3 through 7 of the following paper (11), were in qualitative agreement with results expected from the phase equilibria for the Li_2Se-Se binary system (1) in that composition ranges for which emf was decreasing or constant at a given temperature had a one-to-one correspondence with those regions of the phase diagram where such variation was expected on the basis of the phase rule. However, the compositions at boundary crossings where the slope of emf-*vs.*-composition plots changes abruptly did not agree with the compositions of corresponding boundaries as determined by other methods.

Table II. Solubility of selenium in LiBr-RbBr and LiF-LiCl-LiI eutectics

Eutectic	Temp, °C	Total dissolved selenium, m/o Se[a]
LiF-LiCl-LiI	378	0.009
	379	0.034
	429	0.078
	432	0.093
	483	0.071
	484	0.080
	516	0.119
	516	0.115
LiBr-RbBr	364	0.030

[a] m/o Se = (moles of selenium × 100)/(moles of halide + moles of selenium).

Table III. Summary of emf data from Li/LiBr-RbBr(eutectic)/Li in Se cells at 360°C

Cell No.	Composition range, $n_{Li}/(n_{Li}+n_{Se})$	$n_{Se}/(n_{Se}+n_E)$	Location of breaks in emf vs. log x_{Li}, atom fraction Li	m/o Li_2Se at phase boundary locations: $(L_1+L_3)-L_3$	$(Li_2Se(s)+L_3)-L_3$	$(L_1+L_3)-(L_1+L_2+L_3)$	$(L_1+L_2+L_3)-(L_2+L_3)$	$(Li_2Se(s)+L_2+L_3)-(L_2+L_3)$	$(L_1+L_2+L_3)-(L_1+L_2)$
129	0-0.28	0.0838	0.105	0.493	—	—	—	—	—
147	0-0.21	0.160	~0.21	~2.13	—	—	—	—	—
189	0-0.46	0.188	0.24, 0.335	2.96	4.72	—	—	—	—
18	0-0.47	0.384	0.19, 0.27, 0.32	—	—	4.50	7.10	9.03	—
72	0-0.12	0.714	0.04	—	—	1.64	—	—	—
32, 41	0-0.375	0.835	0.023, 0.252, 0.298	—	—	0.98	13.82	17.43	—
5	0-0.21	0.903	0.008, 0.152	—	—	0.326	—	—	8.28

In view of the solubility-study results and of the discrepancy noted above between the early emf data and the phase equilibria found for the Li_2Se-Se binary system, it was concluded that the behavior of Li/LiBr-RbBr (eutectic)/Li in Se emf cells should be interpreted in terms of a pseudoternary system. A summary of the data on the locations of phase boundaries based on emf measurements for Li/LiBr-RbBr (eutectic)/Li in Se cells at 360°C is given in Table III and the locations are shown in Fig. 2.

The emf cells were operated so that the atom fraction of lithium with respect to selenium in the cathode was varied while the atom fraction of selenium with respect to the electrolyte was constant. The values for these atom fractions are listed in columns 2 and 3 of Table III. The atom fractions of lithium at the break points, which are listed in column 4, were converted to mole per cent Li_2Se for plotting on Fig. 2. The constant selenium to eutectic ratio in the emf cell means that the data from any one cell lie on a line parallel to the Se-Li_2Se boundary of the phase diagram.

DTA, quenching, and centrifugation studies.—To further characterize the pseudoternary systems, a series of DTA curves were obtained for samples of various compositions containing the LiBr-RbBr eutectic. The results are presented in Table IV. These data show three thermal effects at about 280°, 249°, and 220°C which are apparently associated with the disappearance of L_3, L_2, and L_1, respectively. The thermal data provide qualitative limits to the range of compositions covered by L_2 and L_3. For example, for compositions lying near the lithium selenide-selenium binary, the thermal effect associated with the disappearance of L_3 is not observed. This would indicate that L_2 extends far enough into the phase diagram to prevent formation of L_3 from these compositions.

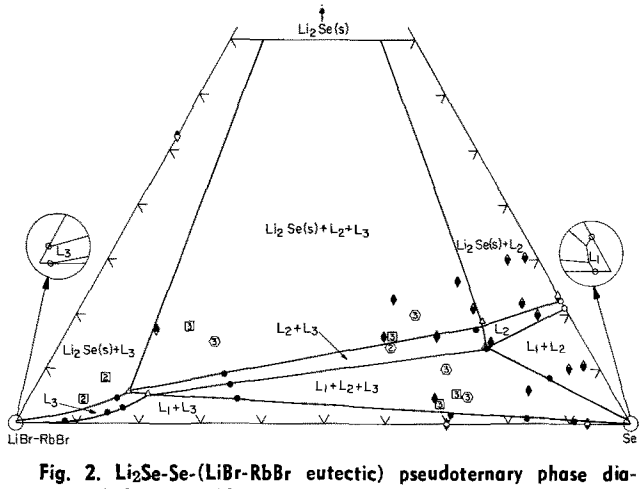

Fig. 2. Li_2Se-Se-(LiBr-RbBr eutectic) pseudoternary phase diagram at 360°C. ●, Phase boundary locations determined by emf measurements. ○, Phase boundary locations for the binary systems determined by solubility studies and from Ref. (1). △, Phase boundary locations determined by chemical analysis. ⬡ and □, regions found to contain the number of phases indicated by quenching and emf methods, respectively. ◇, Compositions examined by DTA. See text for explanation of shading.

These data are also plotted on Fig. 2 using diamond-shaped symbols which are shaded at the bottom, middle, or top indicating thermal effects at 220°, 249°, and 280°C, respectively. A fully shaded diamond would indicate that all three effects were observed.

An effort was made to determine the degree to which L_2 and L_3 extend into the phase diagram by equilibration and quenching of samples having compositions lying within the three-liquid region. Microscopic examination of the quenched samples showed that, in addition to L_1, there were indeed two other liquid phases present, but their densities were apparently quite similar and separation was not adequate to permit chemical analysis. Other quenched samples having compositions in the two-liquid region between L_2 and L_3 were examined and were found to contain two liquid phases, as expected.

In view of the difficulties encountered in separating the three liquid phases, L_1, L_2, and L_3 during quenching studies, an attempt was made to accomplish this separation using a high-temperature centrifugation technique. Centrifuged samples consistently showed nearly quantitative separation of all of the constituent phases. The selenium-rich liquid, L_1, was always found to be the most dense phase with the selenide phase, L_2, intermediate, and the salt-rich phase, L_3, the lowest-density phase. In cases where solid Li_2Se was present, it appeared in the upper portion of the salt-rich liquid phase. Normally, four samples were centrifuged simultaneously for each composition. The phases of two of these samples were separated at the interfaces between the phases and were submitted for chemical analysis. The other two samples were mounted, polished, and examined microscopically. By examining compositions near the upper boundary of the $L_1 + L_2$

Table IV. Summary of DTA data on Se, Li_2Se, LiBr-RbBr eutectic and their binary and ternary mixtures

Composition (m/o) Li_2Se	Se	Eutectic	Peak temperatures of endothermic effects noted (°C)[a]		
100					1302[b]
	100		221		
		100			280
23.4	76.6		223		352[c]
16.2	60.3	23.5	221	247	275
22.1	71.4	6.5	221	245	(267)
	70.0	30.0	221		283
	93.0	7.0	221		284
10.0	85.0	5.0	222	247	(270)
20.0	75.0	5.0	222	246	(270)
30.0	65.0	5.0	221	244	(260)
6.0	80.5	13.5	222	247	277
14.9	69.8	15.3	221	247	280
21.2	63.8	15.0	225	246	(263)
26.2	58.7	15.1	221	247	282
4.7	65.8	29.5	222	247	277
16.0	51.8	32.2	222	247	276
22.8	50.1	27.1	228	247	272
52.4		47.6			278
10.7	86.8	2.4	222	248	(274)
30.4	67.5	2.1	223	246	
17.4	14.2	68.4		245	274

[a] The exact temperature of a reaction is difficult to determine using DTA. Here we consistently report peak temperature. Uncertainties of ±2°C due to changing peak size might be expected. Values in ( ) are shoulders (not peaks) and may be associated with a liquidus crossing.

[b] The only effect seen is the mp of Li_2Se at 1302°C. This value is confirmed by other methods (1).

[c] The Li-Se binary has a monotectic reaction at 350°C (1).

+ L_3 field and near the lower boundary of the $Li_2Se(s)$ + L_2 + L_3 field (see Fig. 2) we were able to determine the boundaries of the L_2 + L_3 field from chemical analyses.

Discussion

The experimental data in Fig. 1 and Tables I through IV, as well as results of other solubility studies discussed above, are consistent with the pseudoternary phase diagram for the Li_2Se-Se-(LiBr-RbBr eutectic) shown in Fig. 2. The determination of this diagram started with a consideration of the binary systems from which it is constituted. The Li_2Se-Se system has been well-studied by Cunningham *et al.* (1). The terminal phases melt at 1302°C (Li_2Se) and 220°C (Se). There are no intermediate phases and the system has a simple monotectic structure. Starting from the Li_2Se phase, the upper liquidus drops sharply with the liquid which becomes L_2 in the pseudoternary system undergoing monotectic reaction at 350°C to form the selenium-rich liquid, L_1, and $Li_2Se(s)$. The monotectic composition is about 22 m/o Li_2Se. The L_1 phase freezes at 220°C with considerable tendency to undercool. Both the tendency to under-cool and the freezing point (indistinguishable from that of pure Se) confirm the very slight solubility of Li_2Se in Se. The miscibility gap between L_1 and L_2 extends from about 22 m/o Li_2Se to less than 0.5 m/o Li_2Se and has very steep boundaries. The phase boundaries in the Li_2Se-Se system at 360°C obtained from the work of Cunningham *et al.* (1) are indicated in Fig. 2. Phase relationships in the LiX-Se and Li_2Se-LiX binary systems as determined from the solubility studies[1] are also indicated in Fig. 2.

Results of the solubility studies, the centrifugation experiments, and the Li_2Se-Se phase-diagram work locate the corners of the L_1 + L_2 + L_3, L_2 + L_3, L_2, and L_3 regions as shown in Fig. 2. The emf data in Table III establish the boundaries of L_3 and locate the boundaries between two- and three-phase regions implied by the other studies. The compositions corresponding to boundary crossings as given in Table III are shown in Fig. 2. When microscopic or chemical analyses were performed, the nature of the phases present was always consistent with Fig. 2. In particular, both microscopic and chemical analyses of equilibrium samples from the L_1 + L_2 + L_3 field obtained in centrifugation experiments clearly showed the presence of all three liquid phases.

The phase diagram of this pseudoternary system is particularly interesting because of the region of three-liquid equilibrium and the presence of a salt phase, L_3, which can contain appreciable quantities of dissolved selenium-bearing species. The single-phase regions, L_1, L_2, and L_3, probably expand monotonically across the diagram with increasing temperature. Coincidentally, the L_2 + L_3 region would be expected to expand steadily in the direction of the three-phase fields, L_1 + L_2 + L_3 and L_2 + L_3 + $Li_2Se_{(s)}$, while giving way laterally to L_2 and L_3 and eventually disappearing. With decreasing temperature (from 360°C), the salt-rich phase, L_3, must retreat rapidly since that phase was shown (by DTA) to freeze within a few degrees of the freezing point of pure LiBr-RbBr eutectic (277°C).

[1] The existence of Rb_xSe_y compounds may not show up in the solubility studies. Emf studies (11) show effects possibly attributable to these compounds but their limited presence does not seem to invalidate the assumption of pseudoternary behavior.

The pseudoternary phase diagram of the Li_2Se-Se-(LiBr-RbBr eutectic) system is important to the understanding of the operation of the Li/LiBr-RbBr(eutectic)/Se cell (6-9), which has been investigated as a rechargeable electrochemical power source. The extent of the L_3 phase is related to the degree of (undesirable) transfer of selenium to the lithium electrode (9). Steps have been taken to reduce the extent of L_3 by decreasing the activity of selenium through the use of thallium (17).

Acknowledgment

The authors wish to thank Dr. R. C. Vogel and Dr. A. D. Tevebaugh for their interest in this work. Chemical analyses were performed by the Chemical Engineering Division Analytical Support Group. This work was performed under the auspices of the United States Atomic Energy Commission.

Manuscript received Oct. 4, 1972.

Any discussion of this paper will appear in a Discussion Section to be published in the December 1973 JOURNAL.

REFERENCES

1. P. T. Cunningham, S. A. Johnson, and E. J. Cairns, *This Journal*, **118**, 1942 (1971).
2. P. T. Cunningham, S. A. Johnson, and E. J. Cairns, *ibid.*, **119**, 1448 (1972); *ibid.*, **120**, 328 (1973).
3. C. E. Johnson and E. J. Hathaway, *ibid.*, **118**, 631 (1971).
4. R. Shridhar, C. E. Johnson, and E. J. Cairns, *J. Chem. and Eng. Data*, **15**, 244 (1970).
5. C. E. Johnson and M. S. Foster, *This Journal*, **116**, 1612 (1969).
6. E. J. Cairns and H. Shimotake, *Science*, **164**, 1347 (1969).
7. E. J. Cairns, R. K. Steunenberg, and H. Shimotake, "Kirk-Othmer Encyclopedia of Chemical Technology," Supplement Volume, 2nd edition, p. 120, John Wiley & Sons, Inc., New York (1971).
8. H. Shimotake, A. A. Chilenskas, R. K. Steunenberg, and E. J. Cairns, Proc. Fifth Intersociety Energy Conversion Engineering Conference, American Nuclear Society, Hinsdale, Ill. (1970).
9. E. C. Gay, L. E. Trevorrow, M. L. Kyle, V. M. Kolba, and E. J. Cairns, Paper 61 presented at Atlantic City Meeting of the Society, Oct. 4-8, 1970; Abstract No. 61, p. 150, Electrochem. Soc. Extended Abstracts, Fall Meeting, Atlantic City, Oct. 4-8, 1970.
10. M. L. Kyle, H. Shimotake, R. K. Steunenberg, F. J. Martino, R. Rubischko, and E. J. Cairns, 1971 Intersociety Energy Conversion Conference Proceedings, p. 80, Society of Automotive Engineers, Inc., New York (1971).
11. E. J. Cairns, G. H. Kucera, and P. T. Cunningham, *This Journal*, **120**, 595 (1973).
12. S. D. Gromakov and L. M. Gromakova, *Zh. Fiz. Khim.*, **27**, 1545 (1953).
13. C. E. Johnson, M. S. Foster, and M. L. Kyle, *Nucl. Applications*, **3**, 563 (1967).
14. H. A. Friedman, *J. Sci. Instr.*, **44**, 454 (1967).
15. V. A. Maroni and E. J. Hathaway, in Physical Chemistry of Liquid Metals and Molten Salts—Semiannual Report, January-June 1971, USAEC Report ANL 7823, p. 42 (1971).
16. W. W. Scott, "Standard Methods of Chemical Analysis," 5th ed., D. Van Nostrand Co., Inc., Princeton, N. J. (1939).
17. W. J. Walsh, A. A. Chilenskas, L. E. Trevorrow, E. C. Gay, and E. J. Cairns, Paper 146 presented at the Houston Meeting of the Society, May 7-12, 1972; Abstract No. 146, p. 375, Electrochem. Soc. Extended Abstracts, Spring Meeting, Houston, Texas, May 7-12, 1972.

Thermodynamic Studies of the Lithium-Selenium System by an EMF Method

E. J. Cairns,* G. H. Kucera, and P. T. Cunningham

Argonne National Laboratory, Chemical Engineering Division, Argonne, Illinois 60439

ABSTRACT

Emf measurements on cells of the type Li/lithium halide eutectic mixture/Li in Se have been used to determine thermodynamic quantities for the Li-Se system. For low lithium concentrations in the cathode, the over-all cell reaction can be written as $2Li + xSe \rightarrow Li_2Se_x$. From the cell data, the activity coefficient of lithium was calculated to be 6×10^{-32} in the dilute Li region; the standard free energy of formation of Li_2Se at 360°C was calculated to be −94.0 kcal/mol.

The thermodynamics of lithium-selenium mixtures are of interest in connection with the chemistry of alkali metal-containing binary systems having components of widely differing electronegativities because of the applicability of these systems to electrochemical energy conversion (1, 2). A study of secondary cells involving lithium-chalcogen couples has been underway at this laboratory for several years. The potential of these cells in various applications requiring high-specific-energy, high-specific-power batteries has been discussed (1-5). The phase diagram of the lithium-selenium system has been previously reported (6) and phase equilibria in pseudoternary systems of selenium, lithium selenide, and alkali metal-halide mixtures are presented in the preceding paper (7). In this paper we report the results of a series of emf measurements on cells of the type Li/LiF-LiCl-LiI (eutectic)/Li in Se, and Li/LiBr-RbBr (eutectic)/Li in Se, and the thermodynamic quantities calculated therefrom.

Experimental

The sources and purities of lithium, selenium, and the electrolyte salts have been described in the preceding paper (7). The emf data were obtained from cells of two different designs.

The type I cell, shown in Fig. 1, consisted of a lithium reference electrode and a lithium-selenium-alloy electrode, which were positioned in separate compartments and immersed in the molten-salt electrolyte. The lithium electrode was a porous stainless steel cylinder (~10 mm in diameter and 10 mm high) saturated with lithium, which was retained within the voids of the porous metal structure by surface-tension forces. The lithium-selenium-alloy electrode was prepared by mixing selenium pellets with the desired amount of powdered Li_2Se. The Li_2Se was prepared by the reaction of selenium vapor with lithium metal (6). The selenium-Li_2Se mixture was placed in a niobium cup (700 mm^3) which had a tight-fitting niobium lid containing a porous Al_2O_3 wick to insure contact between the mixture and the electrolyte. Two different eutectic salt mixtures were used as electrolytes: 59 m/o (mole per cent) LiBr-41 m/o RbBr (mp 277°C) and 11.7 m/o LiF-29.1 m/o LiCl-59.2 m/o LiI (mp 340.9°C). The type I cell was operated in a furnace well attached to the floor of a high-purity-helium-atmosphere glove box (<2 ppm O_2 and N_2, <1 ppm H_2O) (8) in which the cell was assembled. This type of cell has been used primarily to study the effect of temperature variation on cell emf for various fixed-cathode-alloy compositions.

The type II cell, which is shown in Fig. 2, utilized a three-compartment quartz housing. The lithium electrode was again a porous stainless steel cylinder impregnated with lithium. The selenium alloy electrode was contained in the lower end of one leg of the housing and was contacted with a niobium wire coil which served as a current collector. The compartments were loaded with weighed amounts of lithium, selenium, and electrolyte in the helium-atmosphere glove box and sealed. The cell was operated outside the glove box in a molten $NaNO_3$-KNO_3 bath to insure temperature uniformity. The helium atmosphere inside the cell was maintained at a slight positive pressure to limit dif-

* Electrochemical Society Active Member.

Key words: lithium, selenium, emf measurement, lithium selenide.

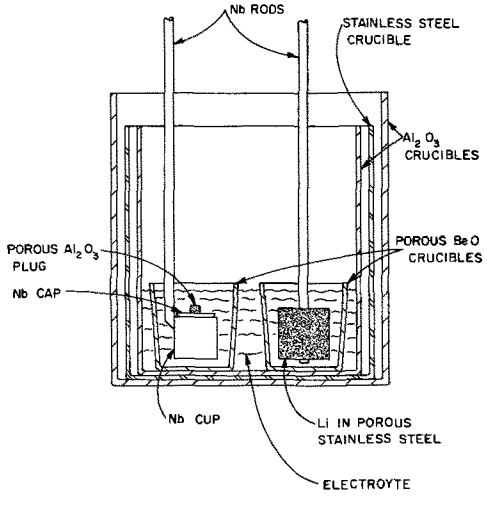

Fig. 1. EMF cell of type I

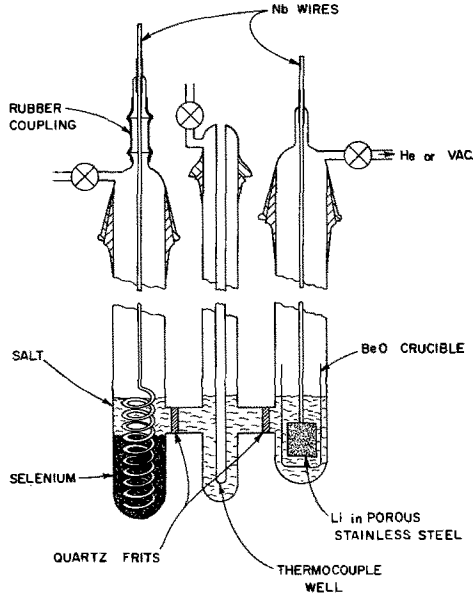

Fig. 2. EMF cell of type II

fusion of impurities into the cell. The type II cell was used primarily to study the effect of changing composition on cell emf at constant temperature, although some temperature-variation studies were performed with this type of cell. The cell was usually started with pure selenium, and the composition of the alloy electrode was changed by electrochemical transfer of lithium into the alloy, keeping count of the number of coulombs involved. The ratio of selenium to electrolyte was also varied over a wide range from one cell to another so that the effects of the solubility of selenium-bearing species in the electrolyte (7) could be evaluated. For cells with a large selenium-to-electrolyte ratio, the details of the H-cell construction were modified slightly from those shown in Fig. 2 so that the volume of the selenium compartment could also be varied. Thus the increased volume of the lithium-selenium alloy with increasing lithium content could be accommodated without altering the electrolyte level within the selenium electrode compartment. Corrosion of cell parts by reactants, products, or electrolyte was not detected.

The emf measurements were made with a Hewlett-Packard Model 3420B differential d-c voltmeter having an input impedance of 10^{10} ohms (some early measurements were made with a Keithley Model 630 having 10^{13} ohms input impedance). Individual measurements had a precision of 1.0 mV or better and the accuracy of the measurements is estimated to be ±10 mV or better. The current for changing the composition of the lithium-selenium alloy was supplied by a Wenking Model 61RS potentiostat connected as a galvanostat and was measured with a standard resistor and a L&N Type K-3 potentiometer. Cell temperature was measured using Chromel-Alumel thermocouples and the K-3 potentiometer. All data were monitored on strip-chart recorders as appropriate.

Results and Discussion

Typical results for emf as a function of temperature for various mole ratios of lithium to lithium plus selenium $[n_{Li}/(n_{Li} + n_{Se})]$ for the selenium alloy electrode are shown in Fig. 3. The data points for the composition $n_{Li}/(n_{Li} + n_{Se}) = 0.10$ through 0.276 have been eliminated for clarity because they are too numerous and closely spaced to be shown. The data used in this figure were taken from a cell using the LiBr-RbBr eutectic as electrolyte and having a mole ratio of selenium to selenium plus electrolyte in the alloy compartment $[n_{Se}/(n_{Se} + n_E)]$ equal to 0.384. In Fig. 4 results are shown for emf as a function of lithium content of the alloy electrode at 360°C and for $n_{Se}/(n_{Se} + n_E)$ again equal to 0.384.

Four general types of behavior can be noted based on the data shown in Fig. 3 and 4: (*i*) for lithium mole ratios less than about 0.19 [*i.e.*, $n_{Li}/(n_{Li} + n_{Se}) < 0.19$], $(\partial E/\partial T)$ is positive and $(\partial E/\partial \ln x_{Li})$ is equal to $RT/2F$; (*ii*) in the range of lithium mole ratio from about 0.19 to about 0.28, $(\partial E/\partial T)$ and $(\partial E/\partial \ln x_{Li})$ are both zero; (*iii*) in the range of lithium mole ratio from about 0.28 to about 0.32, $(\partial E/\partial T)$ is probably negative and $(\partial E/\partial \ln x_{Li})$ certainly negative; and (*iv*) for lithium mole ratios greater than 0.32 and up to at least 0.46, $(\partial E/\partial T)$ is negative and $(\partial E/\partial \ln x_{Li})$ is zero.

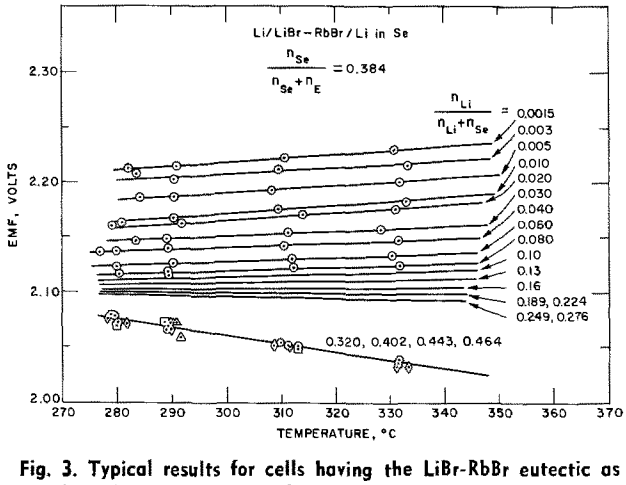

Fig. 3. Typical results for cells having the LiBr-RbBr eutectic as electrolyte showing emf as a function of temperature for various lithium contents of the alloy electrode.

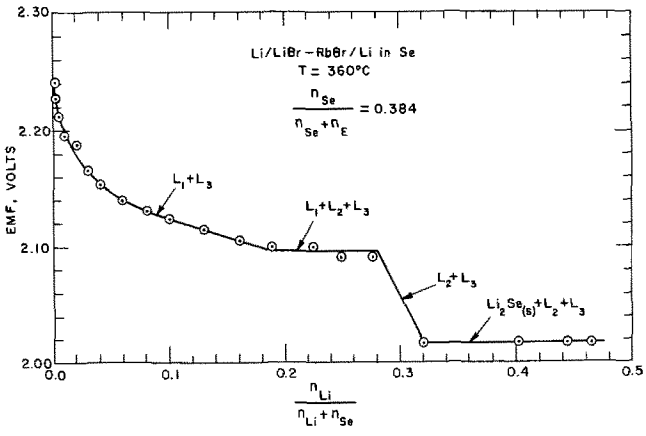

Fig. 4. Typical results for cells having the LiBr-RbBr eutectic electrolyte showing emf as a function of the lithium content of the alloy electrode at 360°C.

The significance of these four regions is clear when considered in connection with the pseudoternary phase diagram presented in the preceding paper (7). The results shown in Fig. 4 represent the emf of the cell as the composition progressed across the phase diagram along a line parallel to the Li_2Se-Se side and intersected the (LiBr-RbBr)-Se side of the diagram at a point corresponding to 0.384 mole fraction selenium. The discontinuous change of slope at 0.188 mole fraction lithium in Fig. 4 corresponds to the point in the pseudoternary phase diagram located at 4.4 m/o Li_2Se, 33.9 m/o Se, and 61.7 m/o LiBr-RbBr which lies on the boundary between the $L_1 + L_3$ and $L_1 + L_2 + L_3$ regions (see Fig. 2 of the preceding paper). The additional slope discontinuities correspond to the crossing of other phase boundaries.

As the extent of the solubility of the lithium-selenium alloy electrode in the lithium halide-containing electrolyte became clear (7), the modified H-cells described above were used to obtain data where the mole fraction of selenium with respect to electrolyte $[n_{Se}/(n_{Se} + n_E)]$ was made as large as the cell design would permit. Results from three such cells are shown in Fig. 5 and are quite similar to those shown in Fig. 4. In Fig. 5 the composition is plotted on a log scale in the low lithium range to emphasize the observed relation $\partial E/\partial \ln x_{Li} = RT/2F$ and on a linear scale in the high lithium range to prevent crowding so that the four distinct regions are apparent. In the two regions corresponding to three-phase equilibrium, however, there is a definite negative slope to the emf-*vs.*-com-

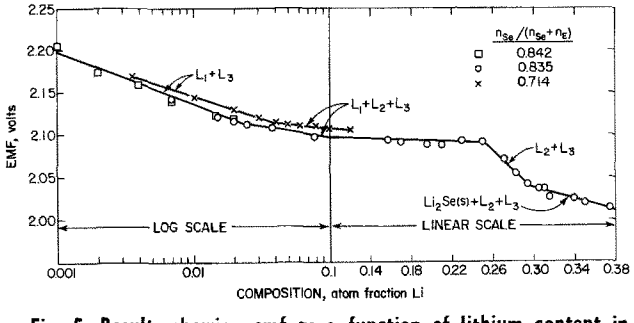

Fig. 5. Results showing emf as a function of lithium content in the alloy electrode for cells using LiBr-RbBr eutectic as electrolyte and for which $n_{Se}/(n_{Se} + n_E)$ has been maximized.

position plot instead of a zero slope line as expected for a three-phase region in a three-component system. This variation is attributed to exchange of rubidium and lithium at the electrolyte-cathode interface in the cathode chamber. The formation of some Rb_2Se_x would be expected to lower the cell potential slightly as the lithium concentration increases in the cathode alloy. This interpretation is also supported by the observation that, for cells using only lithium cations in the electrolyte, negative slopes were not obtained in the three-phase regions for $n_{Se}/(n_{Se} + n_E)$ up to 0.53.

Typical emf-*vs.*-temperature and emf-*vs.*-composition curves for cells in which the LiF-LiCl-LiI eutectic was used as electrolyte are shown in Fig. 6 and 7. The resemblances to the corresponding figures for the LiBr-RbBr eutectic are clear. Data were obtained using this eutectic in a number of cells having different selenium to selenium plus eutectic mole ratios. The information obtained relating to phase equilibria and the location of phase boundaries at 390°C is presented in Fig. 8. In this figure the data have been tentatively interpreted in terms of a pseudoternary system similar to that presented in the preceding paper (7) for the LiBr-RbBr eutectic containing system.

As stated above, the data for low-lithium regions (such as the data presented in Fig. 4, 5, and 7) correspond to $\partial E/\partial \ln x_{Li} = RT/2\mathbf{F}$, indicating that two electrons and two lithium atoms are involved in the over-all cell reaction, which may be written

$$2Li + xSe \rightarrow Li_2Se_x$$

The corresponding Nernst equation (with pure lithium as the reference electrode) is then

$$E = -\frac{RT}{2\mathbf{F}} \ln \gamma_{Li_2} x_{Li_2}$$

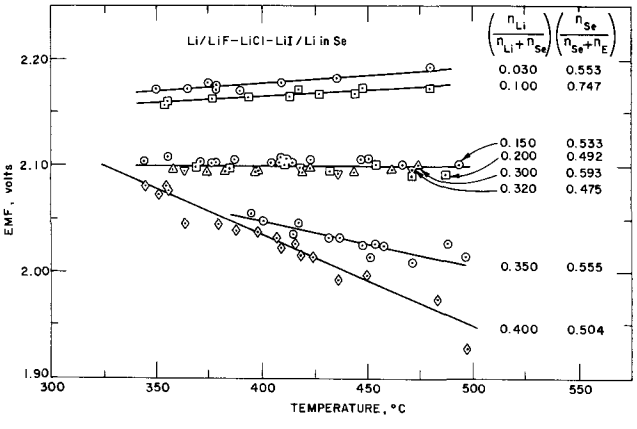

Fig. 6. Typical results for cells having the LiF-LiCl-LiI eutectic electrolyte showing emf as a function of temperature for various lithium contents of the alloy electrode.

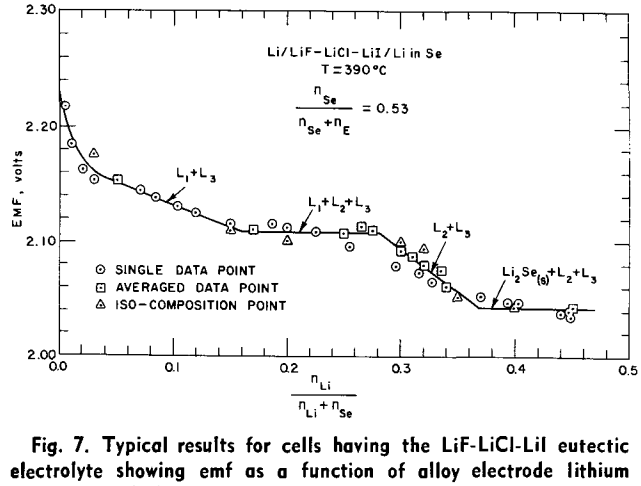

Fig. 7. Typical results for cells having the LiF-LiCl-LiI eutectic electrolyte showing emf as a function of alloy electrode lithium content at 390°C.

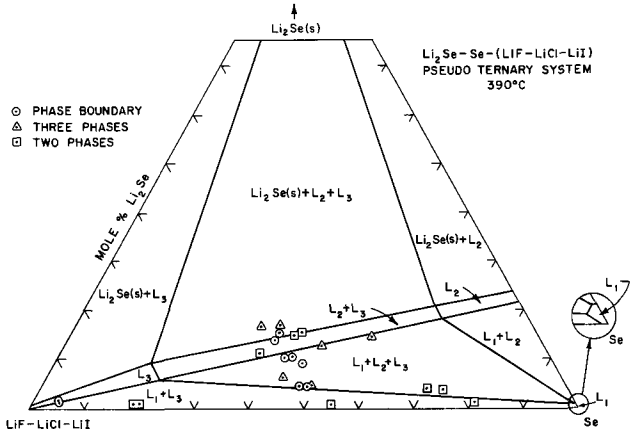

Fig. 8. Phase equilibrium data and phase boundary locations determined by emf measurements on cells using the LiF-LiCl-LiI eutectic electrolyte. Data are tentatively interpreted in terms of a pseudoternary system.

The activity coefficient (γ_{Li_2}) of lithium in liquid L_1 at 360°C has been calculated using data from Li/LiBr-RbBr(eutectic)/Li in Se cells. The activity coefficient was found to be 6×10^{-32} and is quite insensitive to variation in composition in the region where L_1 and L_2 are in equilibrium.

From the emf in the $Li_2Se(s) + L_2 + L_3$ region, and the knowledge that the lithium activity in L_1 saturated with L_2 (and L_3) is equal to the lithium activity in L_2 saturated with L_1 (and L_3), it was possible to apply the Gibbs-Duhem equation (assuming that the activity coefficient of the salt in L_2 and L_3 was constant) in correcting the free energy of formation of Li_2Se to unit activities of lithium and selenium. At 360°C, $\Delta G°_f$ (Li_2Se) = −94.0 kcal/mol.

Acknowledgment

The authors wish to thank Dr. R. C. Vogel and Dr. A. D. Tevebaugh for their encouragement and support, and Mr. P. D. Hunt for help with some of the experiments. This work was performed under the auspices of the United States Atomic Energy Commission.

Manuscript submitted Oct. 4, 1972, revised manuscript received Dec. 28, 1972.

Any discussion of this paper will appear in a Discussion Section to be published in the December 1973 JOURNAL.

REFERENCES

1. E. J. Cairns and H. Shimotake, *Science*, **164**, 1347 (1969).
2. E. J. Cairns, R. K. Steunenberg, and H. Shimotake, "Kirk-Othmer Encyclopedia of Chemical Technology," Supplement Volume, 2nd edition, p. 120, John Wiley & Sons, Inc., New York (1971).
3. H. Shimotake, A. A. Chilenskas, R. K. Steunenberg, and E. J. Cairns, Proc. Fifth Intersociety Energy Conversion Engineering Conference, American Nuclear Society, Hinsdale, Ill. (1970).
4. E. C. Gay, L. E. Trevorrow, M. L. Kyle, V. M. Kolba, and E. J. Cairns, Paper 61 presented at Atlantic City Meeting of the Society, Oct. 4-8, 1970; Abstract No. 61, p. 150, Electrochem. Soc. Extended Abstracts, Fall Meeting, Atlantic City, Oct. 4-8, 1970.
5. M. L. Kyle, H. Shimotake, R. K. Steunenberg, F. J. Martino, R. Rubishko, and E. J. Cairns, 1971 Intersociety Energy Conversion Engineering Conference Proceedings, p. 38, Society of Automotive Engineers, Inc., New York (1971).
6. P. T. Cunningham, S. A. Johnson, and E. J. Cairns, *This Journal*, **118**, 1941 (1971).
7. P. T. Cunningham, E. J. Cairns, E. J. Hathaway, S. A. Johnson, and V. A. Maroni, *ibid.*, **120**, 591 (1973).
8. C. E. Johnson, M. S. Foster, and M. L. Kyle, *Nucl. Applications*, **3**, 563 (1967).

Mathematical Characterization of Corrosion Currents in Local Electrolytic Cells

L. Gal-Or, Y. Raz,[1] and J. Yahalom

Israel Institute of Metals and the Department of Materials Engineering, Technion-Israel Institute of Technology, Haifa, Israel

ABSTRACT

A previous mathematical analysis of Simmons *et al.* related to the corrosion currents in local rectangular electrolytic cells is extended here to the more realistic case of circular cells which develop in pitting processes. The present work is based on a typical local electrolytic cell, in which the anode and cathode are represented by coplanar concentric circles. The cell current is calculated as a function of the anode and cathode radius, thickness, and conductivity of electrolyte, potential difference between anode and cathode at zero current flow, and a linear polarization parameter. The present results are then compared with the theoretical results of Simmons *et al.* and with experimental data obtained in this study for a system of two coplanar circular electrodes made of Fe and Ni in an 0.01*N* NaBr aqueous solution.

Many corrosion reactions proceed through an electrochemical mechanism based on the action of local electrolytic cells (1, 2). The local cells are developed due to the electrochemical heterogeneity of the metal surface or of the electrolyte. The causes of electrochemical heterogeneity of the metal include: heterogeneous metal structure, grain boundaries, pores in protective films, nonuniform deformations, etc.

The mechanism of such corrosion processes, mainly the pitting reaction, has been extensively studied (3-5). Nevertheless, so far, only two theoretical attempts have been made to characterize quantitatively the corrosion current of local electrolytic cells (6, 7).

Waber *et al.* (6, 8) used a one-dimensional model, in which the anodes and cathodes of the local cells were described as an array of alternately infinitely long electrodes. They calculated the current of the cell as a function of the width of the electrodes, thickness of the electrolyte layer, the conductivity of the electrolyte, and the polarization parameters.

In 1967 Simmons *et al.* (7) generalized the one-dimensional geometry employed by Waber *et al.*, and calculated the current for a cell in which the cathode and anode are described as coplanar concentric rectangulars.

However, in many actual cases of local corrosion the geometry of the anode is much closer to a circular cross section than to a rectangular one. Therefore, the aim of the present analysis is to quantitatively characterize the corrosion current of a local cell with a circular geometry.

Cell Geometry

The geometry of the local electrolytic cell used in this analysis is illustrated in Fig. 1. The anode and cathode are coplanar, and are represented by two concentric circles, with radii a and b, respectively. The electrolyte thickness is designated by c, and it represents the height of the cylinder formed. Therefore, the mathematical treatment is done with cylindrical coordinates, whose origin is located at the center of the upper plane, where $Z = 0$, so that the anode and cathode lie in the plane $Z = -c$. This model represents a typical (statistically averaged) circular electrolytic cell analogous to cell models employed in, for instance, statistical thermodynamics (9), or hydrodynamics (10).

The expected corrosion current of the cell, I_{total}, is to be derived as a function of the following parameters

$$I_{total} = f(a, b, c, E, \sigma, k)$$

where: a = radius of anode; b = radius of cathode; c = electrolyte thickness; E = potential difference between anode and cathode at zero current flow; σ = conductivity of electrolyte; and k = linear polarization parameter, $k = \sigma(dV/di)$, where dV/di represents the slope of the polarization curve at the operating current densities (for further elucidation of k see the following assumptions).

The following simplifying assumptions employed in this work are similar to those employed by Waber *et al.* (6) and Simmons (7).

1. Variations in the composition of the electrolyte, of cell geometry, and of surface conditions of the electrodes, during the corrosion process, are neglected.

2. The polarization parameter k is the same for both electrodes, and is independent of the current density. This independence is a result of the assumption of a linear relation between potential and current density, so that dV/di = const. For many practical cases these assumptions may be considered as reasonable approximations.

3. The envelope $r = b$, as well as the upper plane of the cylinder $Z = 0$, are perfect insulators (*i.e.*, no current flows between the numerous electrolytic cells on the metal surface).

Governing Equations and Boundary Conditions

1. The total cell current can now be derived by integration of the equation describing the local current distribution, over the area of the anode or cathode. This integration is based on the aforementioned assumptions.

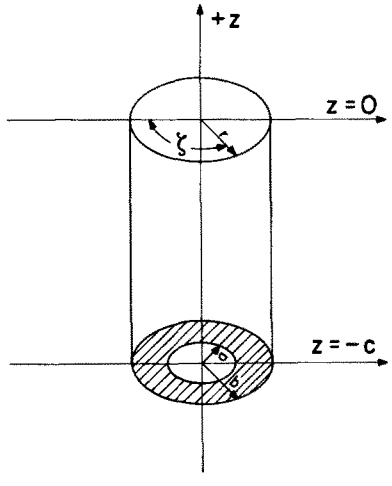

Fig. 1. Geometry of the mathematical model for an electrolytic cell.

[1] Department of Computer Science.

Key words: pitting, mathematical model, localized corrosion.

2. The local current flow to or from the electrodes, is characterized by the potential distribution through Ohm's law, *i.e.*

$$I_{(r,\zeta,-c)} = -\delta \frac{\partial \phi}{\partial z} \Bigg|_{(r,\zeta,-c)} \quad [1]$$

where r,ζ,z are the cylindrical coordinates and $\partial\phi/\partial z$ the local gradient of the potential normal to the metal surface.

3. The potential distribution in the cell is governed by the Laplace equation

$$\nabla^2\phi = 0 \quad [2]$$

The solution of this equation with suitable boundary conditions, should give the distribution of the potential in the cell.

Equation [1] stems from the Poisson law, which states that the relation between potential and charge density is given by

$$\text{divgrad}\,\phi = \nabla^2\phi = -\frac{4\pi\rho'}{\epsilon} \quad [3]$$

where ρ' is the charge density and ϵ the dielectric constant.

Since the net charge in an electrolytic cell is zero, $\rho' = 0$ and $\nabla^2\phi = 0$.

In cylindrical coordinates the Laplace equation becomes

$$\nabla^2\phi = \frac{\partial^2\phi}{\partial r^2} \perp \frac{1}{r}\frac{\partial\phi}{\partial r} \perp \frac{1}{r^2}\frac{\partial^2\phi}{\partial\zeta^2} \perp \frac{\partial^2\phi}{\partial z^2} = 0 \quad [4]$$

The total expected cell current will be derived by solution of Eq. [4], differentiation of the solution with respect to z to obtain $\partial\phi/\partial z$, substitution of $\partial\phi/\partial z$ in Eq. [1] to obtain $I_{(r,\zeta,-c)}$, and integration of the resulting equation of $I_{(r,\zeta,-c)}$ over the anode surface area as follows

$$I_{\text{total}} = \int\int_{s(\text{anode})} I_{(r,\zeta,-c)}\, ds = \int_0^a I(r,-c)\, 2\pi r dr$$

4. The boundary conditions used for the solution of Eq. [1] are

$$\frac{\partial\phi}{\partial r/r = b} = 0 \quad [5]$$

and

$$\frac{\partial\phi}{\partial z/z = 0} = 0 \quad [6]$$

Equations [5] and [6] stem from the assumption that the envelope of the cylinder describing the typical cell (except the metal planes of the electrodes) are insulators.

The third boundary condition is derived as follows:

On the cathode area (*i.e.*, $a < r < b$)

$$\phi_{(r,\zeta,-c)} = E_c \perp k\frac{\partial\phi}{\partial z/z = -c} \quad [7]$$

where E_c is the open-circuit single potential of the cathode.

5. Choosing the potential scale so that $E_c = 0$ we obtain

$$\phi_{(r,\zeta,-c)} = k\frac{\partial\phi}{\partial z/z = -c} \quad [8]$$

for $a < r < b$.

On the anode (*i.e.* at $r < a$)

$$\phi_{(r,\zeta,-c)} = E \perp k\frac{\partial\phi}{\partial z/z = -c} \quad [9]$$

where E is the difference between E_a (open-circuit single potential of the anode) and E_c.

Equations [8] and [9] can thus be combined to give

$$\phi_{(r,\zeta,-c)} = ES(r) \perp k\frac{\partial\phi}{\partial z/z = -c} \quad [10]$$

where $S(r)$ is a step function with the properties

$$S(r) = 0 \quad a < r < b$$

$$S(r) = 1 \quad r < a$$

Mathematical Solution

Equation [4] is solved by the separation of variables technique, *i.e.*, by assuming that the solution is given as a product of three separate functions, each being dependent on a single variable

$$\phi_{(r,\zeta,z)} = R(r)\theta(\zeta)Z(z) \quad [11]$$

Introducing now the dimensionless parameters

$$a^* = \frac{a}{b},\quad c^* = \frac{c}{b},\quad r^* = \frac{r}{b},\quad z^* = \frac{z}{b},\quad k^* = \frac{k}{b}$$

the Laplace equation and its boundary conditions take the form

$$\frac{\partial^2\phi}{\partial r^{*2}} \perp \frac{1}{r^*}\frac{\partial\phi}{\partial r^*} \perp \frac{1}{r^{*2}}\frac{\partial^2\phi}{\partial\zeta^2} \perp \frac{\partial^2\phi}{\partial z^{*2}} = 0 \quad [12]$$

and

$$\frac{\partial\phi}{\partial r^*/r^* = 1} = 0 \quad [13]$$

$$\frac{\partial\phi}{\partial z^*/z^* = 0} = 0 \quad [14]$$

$$\phi_{(r,\zeta,-c^*)} = ES(r^*) \perp k^*\frac{\partial\phi}{\partial z^*/z^* = -c^*} \quad [15]$$

where

$$S(r^*) = \begin{cases} 1 & r^* < \dfrac{a}{b} \\ 0 & \dfrac{a}{b} < r^* < 1 \end{cases} \quad [16]$$

Equation [11] is thus represented as

$$\phi_{(r^*,\zeta,z^*)} = R(r^*) \times \theta(\zeta) \times Z(z^*) \quad [17]$$

By substituting Eq. [17], and its derivatives, in Eq. [12], and dividing by $R\theta Z$, we obtain

$$\frac{1}{R}\left[\frac{d^2R}{dr^{*2}} \perp \frac{1}{r^*}\frac{dR}{dr^*}\right] \perp \frac{1}{r^{*2}\theta}\frac{d^2\theta}{d\zeta^2} \perp \frac{d^2Z}{Zdz^{*2}} = 0 \quad [18]$$

which can be rewritten as

$$\frac{R''}{R} \perp \frac{1}{r^*}\frac{R'}{R} \perp \frac{\theta''}{\theta} \times \frac{1}{r^{*2}} \perp \frac{Z''}{Z} = 0 \quad [19]$$

Since

$$\frac{Z''}{Z} = k^2\,\text{const} \quad [20]$$

$$Z = c_1e^{-kz^*} \perp c_2e^{-kz^*} \quad [21]$$

where c_1 and c_2 are constants.

Now

$$\frac{\theta''}{\theta} = -\nu^2 \quad [22]$$

and

$$\theta = c_3e^{i\nu\zeta} \perp c_4e^{-i\nu\zeta} \quad [23]$$

where c_3 and c_4 are constants.

Equation [19] can be written now (after multiplying by r^{*2}/R) as

$$r^{*2}R'' \perp r^*R' \perp (k^2r^{*2} - \nu^2)R = 0 \quad [24]$$

substituting $x = kr^*$ in Eq. [24] we obtain

$$x^2\frac{d^2R}{dx^2} \perp x\frac{dR}{dx} \perp (x^2 - \nu^2)R = 0 \quad [25]$$

Equation [25] is a Bessel equation whose regular solu-

tions at $x = 0$ are $J_\nu(x)$, the Bessel functions. Therefore $R(r^*) \sim J_\nu(kr^*)$.

Since the problem is axi-symmetric (no dependence on ξ), $\nu = 0$ and, therefore

$$\theta(\xi) = 1 \quad [26]$$

$$R(r^*) \sim J_0(kr^*) \quad [27]$$

and

$$\phi_{(r^*,z^*)} = R(r^*)Z(z^*) = J_0(kr^*)[c_1e^{kz^*} \perp c_2e^{-kz^*}] \quad [28]$$

Boundary condition [13] gives

$$\left.\frac{dR(r^*)}{dr^*}\right|_{r^*=1} = \frac{d}{dr^*}[J_0(kr^*)]_{r^*=1} = 0 \quad [29]$$

using the identity

$$J'_0(x) = -J_1(x) \quad [30]$$

Eq. [30] becomes

$$\left.\frac{d}{dr^*}J_0(kr^*)\right|_{r^*=1} = -kJ_1(k) = 0 \quad [31]$$

The solutions k_n of [31] are the zeroes of $J_1(x)$.

Boundary condition [14] demands that for any n

$$\left.\frac{d\phi}{dz^*}\right|_{z^*=0} = \frac{dZ(z^*)}{dz^*} = c_1k_n - c_2k_n = 0 \quad [32]$$

so that $c_1 = c_2$.

The potential field (Eq. [28]) will be given by

$$\phi(r^*,z^*) = \sum_{n=1}^{\infty} C_nJ_0(k_nr^*)\cosh(k_nz^*) \perp C_0 \quad [33]$$

The above series are the Dini series and by differentiation of Eq. [33] with respect to z^*, at $-c^*$, and by substituting in boundary condition [15], we obtain

$$ES(r^*) = \sum_{n=1}^{\infty} C_nJ_0(k_nr^*)\cosh(k_nc^*) \perp k^*k_n\sinh(k_nc^*) \perp C_0 \quad [34]$$

C_n will be calculated by differentiation of Eq. [34] with respect to r^* with the use of identity [31], and the relation

$$2\int_0^1 J_1(k_nr^*)J_1(k_mr^*)r^*dr^* = \delta_{mn}[J'_1(k_m)]^2 \quad [35]$$

where

$J'_1(k_n) = J_0(k_m)$ and δ_{mn} is the Kronecker delta

$$\delta_{mn} = \begin{cases} 1 & m = n \\ 0 & m \neq n \end{cases}$$

This gives

$$C_n = \frac{2a^*EJ_1(k_na^*)}{[J_0(k_n)]^2k_n[\cosh(k_nc^*) \perp k^*k_n\sinh(k_nc^*)]} \quad [36]$$

Since the expansion [34] is a Dini series, $C_0 = Ea^{*2}$.

Substituting C_n and C_0 into Eq. [33] we obtain

$$\phi(r^*,z^*) = 2a^*E \times \sum_{n=1}^{\infty} \frac{J_0(k_nr^*)\cosh[k_nz^*]J_1(k_na^*)}{[J_0(k_n)]^2k_n[\cosh(k_nc^*) \perp k^*k_n\sinh(k_nc^*)]} \perp Ea^{*2} \quad [37]$$

The current density on the electrode surface is thus given by

$$I_{(r^*,-c^*)} = \frac{-\sigma}{b}\left.\frac{\partial\phi}{\partial z^*}\right|_{z^*=-c^*} = \frac{2}{b}a^*E\sigma \times \sum_{n=1}^{\infty} \frac{J_0(k_nr^*)J_1(k_na^*)\sinh(k_nc^*)}{[J_0(k_n)]^2[\cosh(k_nc^*) \perp k^*k_n\sinh(k_nc^*)]} \times \frac{1}{[\coth(k_nc^*) \perp (k^*k_n)]} \quad [38]$$

and the total corrosion current by

$$I_{\text{total}} = 2\pi\int_0^{a^*b} I(r^*,-c^*)r^*dr^* = 4\pi a^{*2}bE\sigma\sum_{n=1}^{\infty}\frac{[J_1(k_na^*)]^2}{[J_0(k_n)]^2} \times \frac{1}{[\coth(k_nc^*) + k^*k_n]k_n} \quad [39]$$

For the integration step we used

$$\int x^nJ_{n-1}(x)dx = x^nJ_n(x)$$

I_{total} had been computed from Eq. [39] by employing a digital computer, as described in Appendix A. The analysis of the error involved in computing I_{total} is also given in Appendix B.

To express I_{total} for a wide spectrum of systems, independently of specific values of E, a, and σ, one can transform I_{total} to the dimensionless expression

$$I^*_{\text{total}} = \frac{k\,I_{\text{total}}}{4Ea^2\sigma} = \frac{k\,I_{\text{total}}}{4\pi E\sigma(\text{anode area})} \quad [40]$$

Results and Discussion

The dependence of I^*_{total} on a^*, c^*, and k^*, is given in Fig. 2. This figure shows that I^*_{total} increases with c^* for various values of k^* and a^* up to a saturation level.

Figure 3 shows the dependence of the cell current, I_{total}, on the anode radius, a, the polarization parameter, k, and the electrolyte thickness, c. I_{total} increases with c up to a saturation level.

Comparison of the results of the present model with the results of Simmons et al. (7).—To compare the results obtained by the present model with the results of Simmons *et al.* (7), I^*_{total} was computed from Eq. [40], for different values of a^*, k^*, and c^* (see Table I). The error, R, involved in the above computations of I^*_{total} is related to N, the number of terms employed in the calculation of the series which appears in Eq. [39]. In the present study N was taken as 1000. The error involved can be calculated as follows:

According to Eq. [A-B-9] of Appendix B one obtains that for $a^* >> 10^{-3}$, $R \leq 1/a^* \times 10^{-4}$.

Therefore, for $a^* = 0.5$, $R \leq 0.0002$; and for $a^* = 0.1$, $R \leq 0.001$.

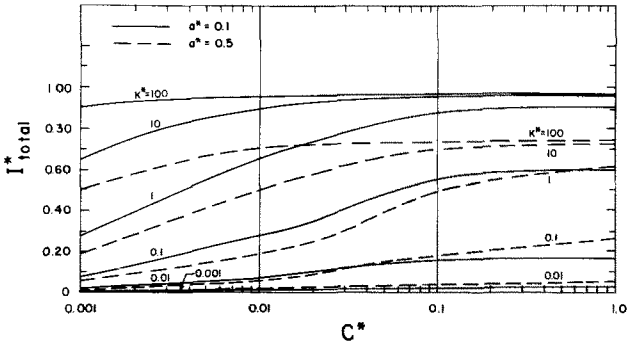

Fig. 2. Dependence of dimensionless cell current I^*_{total} on k^*, a^*, and c^*.

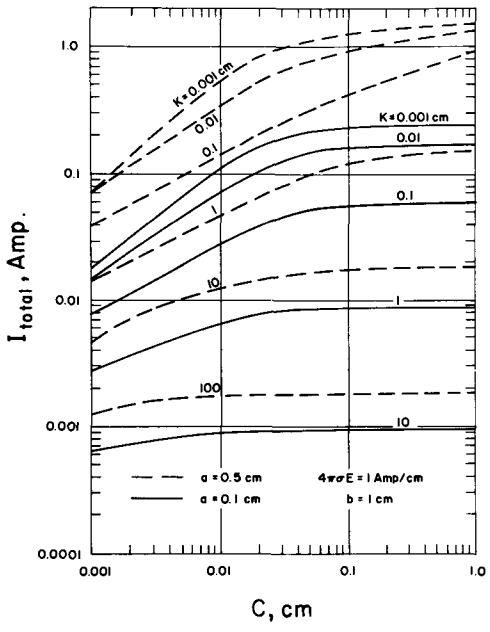

Fig. 3. Dependence of cell current I_{total} on polarization parameter k, anode radius a, and electrolyte thickness c.

The terms in the series were computed with an accuracy of 10^{-7}, therefore, the accumulative truncation error, which can have a positive or negative value, would not exceed a value of 10^{-4}. Therefore, the total error $\overline{R}$ must be for $a^* = 0.5$, $0 < \overline{R} < 0.0003$; and for $a^* = 0.1$, $0 < \overline{R} < 0.0011$.

Since $\overline{R} > 0$ the exact value of I^*_{total} is to be within the interval $[I^*_{total}, I^*_{total} + \overline{R}]$.

In general, as the value of a^* decreases, the number of terms employed in the calculation of the series in Eq. [39] should increase, in order to obtain a given accuracy (*q.v.* Eq. [A-B-9]-[A-B-11] in Appendix B).

Table I gives the values thus computed, compared to the values of I^*_{total} computed by Simmons *et al.* The comparison shows that there is a good agreement between the predicted results of the two analyses at relatively high values of a^*, k^*, and c^*. The discrepancy between the two models grows with a decrease of c^* and k^*. This implies that there is a greater effect of the cell geometry on the computed cell current for low polarization and thin electrolytes, than for high polarization and thick electrolytes.

Table I. Values for I^*_{total} based on the present model and as obtained by Simmons *et al.* (7)

	$a^* = 0.5$		$a^* = 0.1$	
	I^*_{total}	I^*_{total}, Simmons	I^*_{total}	I^*_{total}, Simmons
$c^* = 1.000$				
$k^* = 100.0$	0.744	0.75	0.969	0.99
$k^* = 10.0$	0.730	0.73	0.962	0.98
$k^* = 1.0$	0.616	0.61	0.904	0.92
$k^* = 0.1$	0.367	0.26	0.599	0.60
$k^* = 0.01$	0.052	0.054	0.171	0.18
$k^* = 0.001$	0.006	0.0084	0.024	0.033
$c^* = 0.10$				
$k^* = 100.0$	0.741	0.74	0.969	0.99
$k^* = 10.0$	0.706	0.70	0.958	0.98
$k^* = 1.0$	0.495	0.47	0.880	0.89
$k^* = 0.1$	0.172	0.17	0.562	0.56
$k^* = 0.01$	0.037	0.04	0.161	0.17
$k^* = 0.001$	0.0050	0.0068	0.023	0.031
$c^* = 0.01$				
$k^* = 100.0$	0.708	0.70	0.961	0.99
$k^* = 10.0$	0.505	0.48	0.901	0.91
$k^* = 1.0$	0.192	0.19	0.658	0.65
$k^* = 0.1$	0.058	0.061	0.278	0.28
$k^* = 0.01$	0.014	0.018	0.0172	0.0188
$k^* = 0.001$	0.0022	0.0041	0.0114	0.020
$c^* = 0.001$				
$k^* = 100.0$	0.505	0.48	0.901	0.91
$k^* = 10.0$	0.192	0.19	0.660	0.65
$k^* = 1.0$	0.059	0.062	0.283	0.28
$k^* = 0.1$	0.016	0.020	0.080	0.097
$k^* = 0.01$	0.003	0.0062	0.015	0.031
$k^* = 0.001$	0.0003	0.0018	0.009	0.0092

Experimental Comparison

An experimental system was built for the purpose of comparing the theoretical predictions with an actual system. The system was designed to enable measurement of the current of an electrochemical cell with a defined geometry as a function of the parameters employed in the theoretical analysis. The experimental results are then compared with the predicted values of the analytical model at the same operating conditions.

The experimental set up is described in Fig. 4. It includes a galvanic cell made of two circular coplanar concentric electrodes. The anode is made of Swedish Pure Steel 0.4 cm in diameter and the cathode is made of 99.85% nickel 0.8 cm in diameter. The two electrodes are isolated by a thin Teflon tape of 0.01 cm thickness. The plane of the electrode surfaces is maintained above and parallel to the bottom of the solution container. A micrometric screw enables varying the distance between the electrode plane and the plane of the glass vessel bottom. In this way the electrolyte thickness c can be varied.

I_{total}, the cell current, is measured as the potential drop on a known resistance using a Hewlett Packard V.T.V.M. Model 412A and an amplifier with a 10^{12} ohm impedance, Knick Model 72Z. I_{total} was measured as a function of c.

The following parameters of the cell needed for the computation of I_{total} were measured:

E the open-circuit potential was measured using the Hewlett Packard V.T.V.M. and the Knick amplifier.

σ the conductivity of the solution was measured by using a standard conductivity measuring system previously calibrated with a KCl solution of similar conductivity.

k the polarization parameter has been deduced from the anodic polarization curve of the Swedish Pure Steel. The polarization measurements were carried out in a standard polarization cell. The approximated slope, M, of the V *vs.* i curve was used in the estimation of k ($k = \sigma M$). It is assumed that because of the smaller anodic area the reaction is anodically controlled (also concentration polarization effects in the cathodic reaction are not expected since I_{total} was recorded shortly after the circuit was closed).

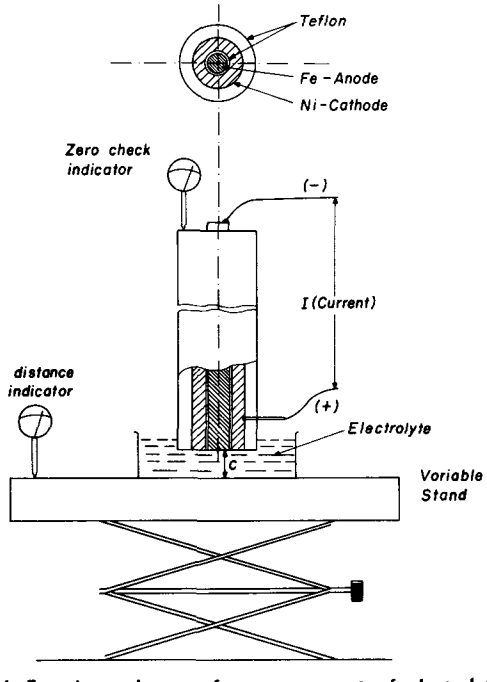

Fig. 4. Experimental setup for measurement of electrolytic current as function of electrolyte thickness.

Table II. Experimental data for calculation of I_{total}

k, cm	M, ohm-cm²	σ, ohm⁻¹-cm⁻¹	E, V	b, cm	a, cm
0.80	55.5	0.0145	0.175	0.4	0.2

The measurements were carried out in an aqueous solution of 0.01N NaBr buffered to pH = 2.2 with a 0.05M sulfate buffer. (The bromide solution was chosen because of its relevance to a study on the mechanism of corrosion by bromine which was studied at the same time.) Table II summarizes the measured parameters.

I_{total} was computed by Eq. [39] using an Elliott 503 computer. In each computation 1000 terms of the series in Eq. [39] were summarized. The comparison of experimental and theoretical results of I_{total} as a function of c is given in Fig. 5.

Figure 5 shows that the theoretical and experimental curves are qualitatively similar. Quantitatively the theoretical and experimental results differ by a factor up to 2. This discrepancy probably stems partly from the simplifying assumptions employed in the deduction of the analytical model, as well as from the experimental errors involved in the measurements of the parameters. As to the simplifying assumptions, the one involving a linear relation between the potential and the current density is probably the weakest one, since it is theoretically justified only for small values of current density. In our experiments, the current densities were of the order of 1 mA/cm² and were still in the approximate linear region. Variations of k due to nonlinearity of the extension of the curve are of the order of ±30%. The reproducibility of k, for the same current density and different polarization curves, was in the range of ±20%. (A typical polarization curve for the system studied is given in Fig. 6.) While the aforementioned variations of k introduce inaccuracies in the computed cell currents, they do not account for the entire discrepancy between the essentially exact theoretical results and the experimental ones, as can be judged from Fig. 3. Other factors, such as the assumption that the whole electrode area acts as an anode, or cathode, contribute to the discrepancy. A large number of experimental data, under various operating conditions, is required in order to distinguish between the influence of the various individual factors.

APPENDIX A

Computation of total cell current I_{total}

I_{total} is computed from Eq. [39]. The number of terms in the series is dictated by the chosen degree of accuracy (see Appendix B).

k_n which are the zeroes of J_1 have been computed by a combination of the regula falsi and bisection methods using the asymptotic expression

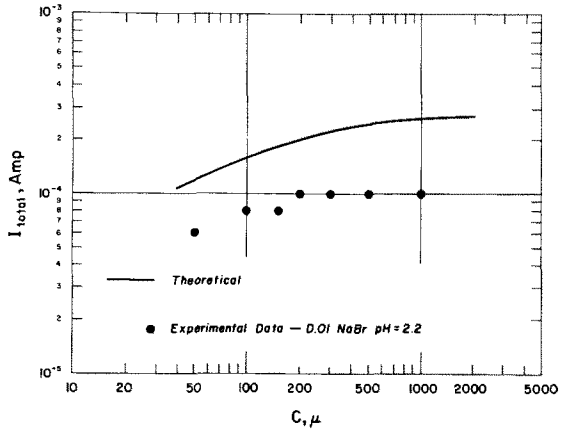

Fig. 5. Comparison of experimental and theoretical results for effect of electrolyte thickness on cell current.

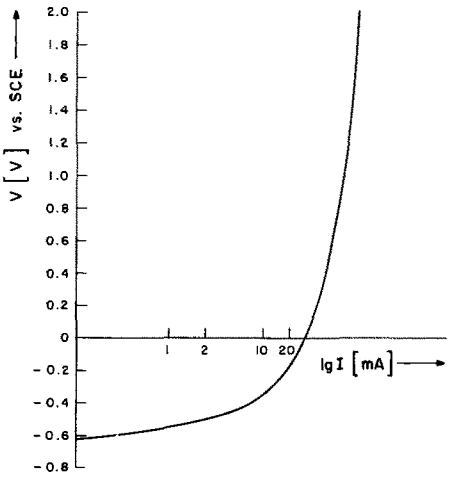

Fig. 6. Anodic polarization curve for Swedish Pure Steel in 0.01N NaBr, pH 2.2

$$k_n = \left(n \perp \frac{1}{4}\right)\pi \perp O\left(\frac{1}{n}\right) \text{ and the inequality}$$

$$n\pi < k_n < \left(n \perp \frac{1}{2}\right)\pi \text{ for } n = 1, 2, \ldots$$

An appropriate number of k_n were computed with an accuracy of 7 decimals and stored on the computer tape. The stored values were used for any computation of I_{total}.

$J_0(x)$ and $J_1(x)$ were computed up to 8 decimals.

The computation was carried out by an Elliott 503 computer.

APPENDIX B

Evaluation of the error in computing I_{total}

I_{total} is computed from Eq. [39] which contains a series that can be expressed as

$$A = \sum_{n=1}^{\infty} a_n \qquad \text{[A-B-1]}$$

where

$$a_n = 4\bar{k}\left[\frac{J_1(k_n a^*)}{J_0(k_n)}\right]^2 \cdot \frac{1}{[\coth(k_n c^*) \perp k^* \cdot k_n]k_n} \qquad \text{[A-B-2]}$$

The truncation error in the computation of a_n is of the order of 10^{-7}, while the round off error is much smaller. Therefore in order to achieve a chosen accuracy the necessary number of terms in the series A has to be determined.

In the following the "tail" of the series

$$R_n = \sum_{n=N\perp 1}^{\infty} a_n \qquad \text{[A-B-3]}$$

is estimated.

The following asymptotic expression is valid for the Bessel function

$$J_\nu Z = \sqrt{\frac{2}{\pi Z}}\cos\left[Z - \left(\nu \perp \frac{1}{2}\right)\frac{\pi}{2}\right] \perp O\left(\frac{1}{Z^{3/2}}\right) \qquad \text{[A-B-4]}$$

therefore

$$\frac{J_1(a^*k_n)}{J_0(k_n)} = \frac{1}{\sqrt{a^*}} \frac{\cos\left[a^*k_n - \frac{3}{4}\pi\right] \perp O\left[\frac{1}{(na^*)}\right]^{3/2}}{\cos\left[k_n - \frac{\pi}{4}\right] \perp O\left[\frac{1}{n}\right]^{3/2}} \qquad \text{[A-B-5]}$$

Using

$$k_n = \left(n \perp \frac{1}{4}\right)\pi \perp O\left(\frac{1}{n}\right) \qquad \text{[A-B-6]}$$

We obtain

$$\frac{J_1(a^*k_n)}{J_0(k_n)} = \frac{1}{\sqrt{a^*}} \frac{\cos\left[a^*k_n - \frac{3}{4}\pi\right] \perp O(na^*)^{-3/2}}{\cos\left[\left(n \perp \frac{1}{4}\right)\pi - \frac{1}{4}\pi\right] \perp O\left(\frac{1}{n}\right)}$$

$$= \frac{1}{\sqrt{a^*}} \frac{\cos\left[a^*k_n - \frac{3}{4}\pi\right] \perp O[(na^*)^{-3/2}]}{(-1)^n \perp O\left(\frac{1}{n}\right)}$$

or

$$\left[\frac{J_1(a^*k_n)}{J_0(k_n)}\right]^2 \leq \frac{1}{a^*} \frac{1 \perp O[(na^*)^{-3/2}]}{1 \perp O\left(\frac{1}{n}\right)} \quad \text{[A-B-7]}$$

Therefore

$$|a_n| = a_n \leq \frac{4k^*}{a^*} \frac{1 \perp O(na^*)^{-3/2}}{1 \perp O\left(\frac{1}{n}\right)} \cdot \frac{1}{\left\{\coth(k_n\pi c^*) \perp k^*\left[\left(n \perp \frac{1}{4}\right)\pi \perp O\left(\frac{1}{n}\right)\right]\right\}\left[\left(n \perp \frac{1}{4}\right)\pi \perp O\left(\frac{1}{n}\right)\right]}$$

$$\leq \frac{4k^*}{a^*} \frac{1 \perp O[(na^*)^{-3/2}]}{k^*\pi^2\left(n \perp \frac{1}{4}\right)^2} = \frac{4(1 \perp O[(na^*)^{-3/2}]}{a^*\pi^2\left(n \perp \frac{1}{4}\right)^2} \quad \text{[A-B-8]}$$

Therefore

$$|R_N| = R_N \leq \frac{4(1 \perp O[(Na^*)^{-3/2}])}{a^*\pi^2} \int_N^\infty \frac{dx}{x^2} = \frac{4(1 \perp O[(Na^*)^{-3/2}])}{Na^*\pi^2} \quad \text{[A-B-9]}$$

To obtain a chosen accuracy of R the number of terms N has to fulfill

$$N >> \frac{1}{a^*} \quad \text{[A-B-10]}$$

$$N \geq \frac{4}{\pi^2 R a^*} \quad \text{[A-B-11]}$$

Since $I^*_{\text{total}} < 1$, R will always be $R < 0.1$ and therefore condition [A-B-11] is sufficient.

Manuscript submitted April 3, 1972; revised manuscript received Dec. 14, 1972.

Any discussion of this paper will appear in a Discussion Section to be published in the December 1973 JOURNAL.

REFERENCES

1. N. D. Tomashov, "Theory of Corrosion and Protection of Metals," p. 154, McMillan Co., New York (1966).
2. H. H. Uhlig, Proceedings 2nd Inter. Congress on Metallic Corrosion, NACE, 1966, p. 1.
3. I. L. Rosenfeld and I. S. Danilov, *Corrosion Sci.*, **7**, 129 (1967).
4. T. P. Hoar, *ibid.*, **5**, 279 (1965).
5. M. A. Streicher, *This Journal*, **103**, 375 (1956).
6. J. T. Waber, *ibid.*, **101**, 271 (1954).
7. J. A. Simmons, S. R. Coriell, and F. Ogburn, *ibid.*, **114**, 782 (1967).
8. E. Kennard and J. T. Waber, *ibid.*, **117**, 880 (1970).
9. J. O. Hirschfelder, C. F. Curtiss, and R. B. Bird, "Molecular Theory of Gases and Liquids," John Wiley & Sons, Inc., New York (1954).
10. J. Happel and H. Brenner, "Low Reynolds Number Hydrodynamics," Prentice Hall, Inc., Englewood Cliffs, N. J. (1965).

Effects of Molybdenum on the Pitting Potentials of Ferritic Stainless Steels at Various Temperatures

A. P. Bond*

Research Laboratory, Climax Molybdenum Company of Michigan, Ann Arbor, Michigan 48106

ABSTRACT

Pitting potential measurements were performed by potentiodynamic scanning at 200 mV/hr in 1M NaCl and in 1M NaBr, each saturated with nitrogen. Over the entire temperature range studied, 1°-70°C, molybdenum additions up to the limit of solid solubility caused a continuous increase in the pitting potentials of 18% Cr ferritic stainless steels. Exposure tests were also performed in various chloride-containing environments, and it was found that pitting rate decreased as the molybdenum content increased.

It has been suggested that at low temperatures molybdenum additions may not be beneficial to the pitting resistance of austenitic stainless steels exposed to chloride solutions (1). Data have also been presented indicating that above room temperature, the beneficial effects of molybdenum on resistance to pitting may decrease (2). Furthermore, it has been reported that molybdenum additions are ineffective in sodium bromide solutions (2, 3).

In view of the present interest in molybdenum-containing ferritic stainless steels, it was thought important to investigate these questions and establish more clearly the range of conditions under which molybdenum content has a favorable effect on pitting resistance of ferritic stainless steels. To do this, pitting potential measurements were undertaken on a series of

* Electrochemical Society Active Member.
Key words: corrosion, polarization.

18% chromium steels containing 0-5% Mo. These measurements were made in 1M NaCl and 1M NaBr over a temperature range from 1° to 70°C. Concurrently, some exposure tests were performed in various media containing chlorides or bromides.

Experimental

The experimental alloys were produced by induction-melting in an argon atmosphere using the split-heat technique. By this technique, the base composition was melted and part of the melt was poured off to produce an ingot. To the balance of the melt, the required molybdenum addition was made and the next ingot was cast. This process was repeated until the desired compositions were cast. By this procedure, the impurity levels were held nearly constant within each series. The compositions of the steels produced are given in Table I.

The resulting ingots were hot-forged and hot-rolled to 0.76 cm thick strips and then cold-rolled to 0.38 cm thickness. All strips were given a 1-hr anneal at 815°C and water-quenched before the test specimens were prepared.

The electrodes for the potentiodynamic studies were mounted in epoxy plastic with a single exposed surface parallel to the rolling plane. Electrical contact was made by soft-soldering a nickel wire to the back of the electrode. Contact between the solder or lead wire and the electrolyte was excluded by the plastic and glass tube. The 0.5 by 0.6 cm exposed surface was polished by using standard metallographic techniques, finishing with a distilled water slurry of 0.3μ alumina. The edges of the electrode were masked with clear Glyptal varnish to prevent crevice corrosion.

The coupons for the exposure tests, 2.5 by 2.5 by 0.3 cm, were surface ground and then polished through No. 600 wet silicon carbide paper. They were solvent degreased and rinsed in methanol before exposure.

The potentiodynamic scanning experiments were performed using standard equipment and techniques. The platinum auxiliary electrode was isolated from the test solution by means of a glass frit. The solution used was nitrogen-saturated 1.0M NaCl or 1.0M NaBr. All potential measurements were made using a saturated calomel reference electrode. The scans were started at −0.7V and continued in the noble direction at 200 mV/hr. The temperature was controlled within ±0.5°C of the reported temperature. Below room temperature an ice bath was used, while the elevated temperatures were maintained by a heating mantle and temperature controller.

Results and Discussion

A typical pitting potential determination is shown in Fig. 1. It can be seen that the current rise corresponding to pitting is extremely sharp. This was true at all temperatures investigated. It can also be seen that very short pulses of current were sometimes observed as the pitting potential was approached. As discussed previously (4), these pulses correspond to formation of very tiny pits that do not propagate if the potential scan is stopped below the pitting potential for time periods up to 24 hr.

The effect of variation in the rate of potential scan was checked for the 18% Cr-2% Mo alloy (Table II).

Table I. Compositions of steels tested

Designation	Composition (%)						
	Cr	Mo	Ni	Si	Mn	C	N
4354A	17.61	0.035	0.091	0.22	0.55	0.028	0.032
4354B	NA[a]	0.96	NA	NA	NA	NA	NA
4354C	NA	2.06	NA	NA	NA	NA	NA
4354D	NA	3.51	NA	NA	NA	NA	NA
4354E	17.31	4.67	NA	NA	NA	0.031	0.033
4073A	18.45	1.97	0.11	0.13	—	0.034	0.045

[a] NA = not analyzed, but assumed to be in the range of the series.

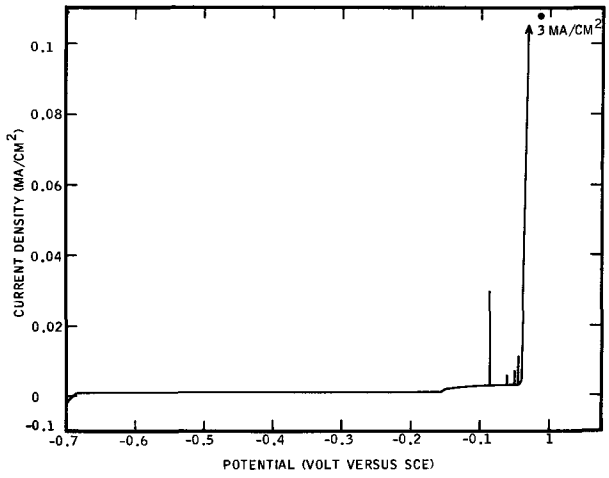

Fig. 1. Polarization curve obtained on scanning a masked electrode of alloy 4354D (3.5% Mo at 200 mV/hr in nitrogen-saturated 1.0M NaCl at 70°C).

No significant difference in pitting potential was obtained when the scan rate was increased from 200 to 2000 mV/hr. This is in contrast to results obtained in a previous study of an 18% Cr-14% Ni-3% Mo austenitic steel (4). This austenitic steel showed a significant decrease in pitting potential as scan rate increased. In general, it has been observed that pitting potentials of ferritic steels are less affected by variations in experimental conditions than are pitting potentials of austenitic steels of similar chromium and molybdenum content.

After each run, the electrode was examined under the microscope. Only if well-developed pits, away from the masked edges, were present was a run accepted as valid. In many cases, there was simultaneous attack at the edges where crevices may have existed, but this was disregarded if distinct pits were visible. The crevice attack was more likely to occur as the test temperature decreased. At 70°C, most electrodes were free of any crevice attack, while at 1°C, most electrodes suffered crevice attack as well as pitting. This effect may be partially a result of the physical properties of the Glyptal mask, which tended to be brittle at low temperatures.

When pitting occurred, a large number of pits were usually found. If the scan was stopped at this point, but without the potentiostat switched off, the pits would continue to grow until the electrode was destroyed.

Results of the tests in 1M NaCl are shown in Fig. 2. While temperature had a very large effect on pitting potentials of these alloys, it is striking that the effect of molybdenum was nearly the same at each of the test temperatures. Thus, over the temperature range studied, molybdenum exerts a definite beneficial effect on pitting potentials. Note that an increase in the pitting potential in the noble direction corresponds to an increase in resistance to pitting corrosion. However, the pitting potentials of the 4.7% Mo alloy did tend to be lower than those observed for the 3.5% Mo steel. Since this difference was observed at each temperature, it appears to be a true effect and not the result of experimental variation.

A similar tendency for a maximum in pitting potential to occur at intermediate molybdenum content was also observed for an austenitic stainless steel series (4). This behavior in the austenitic series was attri-

Table II. Effect of scanning rate on pitting potential of the 18% Cr-2% Mo alloy (4354C) in N_2 saturated 1M NaCl at 45°C

200 mV/hr	2000 mV/hr
0.08V (SCE)	0.02V (SCE)
0.06V (SCE)	0.085V (SCE)

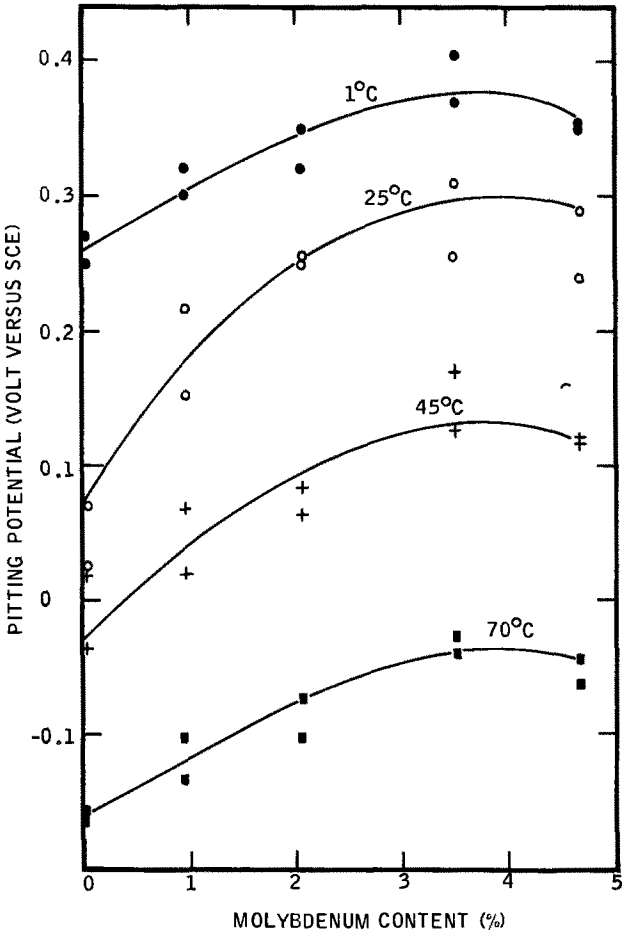

Fig. 2. Pitting potentials obtained from potentiodynamic polarization scans at 200 mV/hr in nitrogen-saturated 1.0M NaCl.

buted to the occurrence of a second phase at high molybdenum contents. In the present series of ferritic steels, a second phase also occurs in the high molybdenum steels. According to the work of McMullin *et al.* (5), at 815°C, this phase is chi, a compound containing about 25% Mo, 18% Cr, and the balance iron. According to the phase diagram, at 815°C the maximum solubility of molybdenum is about 3.5% in 18% Cr-Fe (5). Thus, the 4.7% Mo alloy does not have any more molybdenum dissolved in the matrix than does the 3.5% Mo alloy. Examination of the microstructures of the steels annealed at 815°C indicated that a very small amount of chi was present in the 3.5% Mo steel and a large amount in the 4.7% Mo steel (Fig. 3). Therefore, it is concluded that the failure of the 4.7% Mo alloy to exhibit a higher pitting potential than the 3.5% Mo steel is a consequence of the phase constitution of the alloys. The slight decrease in pitting potential that was apparently observed could either indicate that chi itself is not as resistant as the matrix to pitting or that the chi-ferrite interface forms preferential pitting sites. In any event, the decrease in pitting potential of the 4.7% Mo steel as compared to the 3.5% Mo steel was too small to be of practical significance.

In an effort to avoid the chi phase, the three alloys with the highest molybdenum content were annealed at 980°C and water-quenched. Microscopic examination confirmed that all of these steels did not contain appreciable chi after treatment. However, the pitting potentials found in 1.0M NaCl at 25°C were considerably reduced by the 980°C treatment (Table III).

It is known that this heat-treatment also sensitizes these steels to intergranular corrosion (6). It is thought that the intergranular corrosion is the result of precipitation of carbides and nitrides rich in chromium and molybdenum, causing depletion of the adjacent matrix (7). Thus, it is to be expected that steels heat-treated so as to be sensitive to intergranular corrosion would

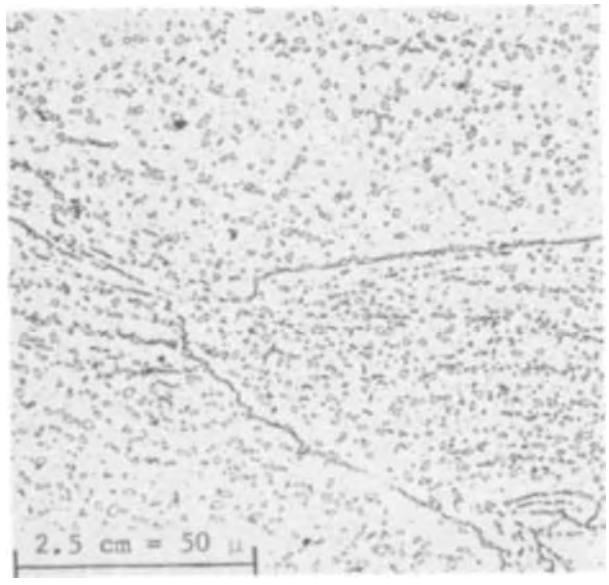

Fig. 3. Structure (islands of chi in a ferrite matrix) of the 18% Cr-5% Mo alloy (4354E) annealed 1 hr at 815°C and water-quenched; 500×.

be more susceptible to pitting corrosion than would properly annealed steels, as was recently reported for 26% Cr ferritic alloys (8). A similar effect has been observed for austenitic stainless steels exposed in ferric chloride (9).

The foregoing results lead to the conclusion that the maximum useful molybdenum content of 18% Cr steels containing the usual amounts of interstitial elements and not fully stabilized is about 3.5%. Steels fully stabilized by titanium or columbium additions that tie up all carbon and nitrogen, or steels of such low interstitial content that carbides or nitrides do not precipitate, could be annealed at high enough temperatures to dissolve chi without suffering chromium depletion because of carbide or nitride precipitation. In this case, larger molybdenum additions can contribute to corrosion resistance, as was demonstrated in work on high-purity 25% Cr steels containing up to 5% Mo (10).

In order to demonstrate that titanium stabilization can prevent loss of pitting resistance as well as sensitization to intergranular corrosion as a result of exposure to high temperatures, the pitting potential of an 18% Cr–2% Mo–0.5% Ti alloy was determined as a function of heat-treatment. It was found (Table IV)

Table III. Effect of heat-treatment on pitting potentials in N_2-saturated 1M NaCl at 25°C

Heat	% Mo	Pitting potential, V (SCE) 815°C, WQ	980°C, WQ
4354C	2	0.25 0.26	−0.01
4354D	3.5	0.31 0.26	0.04
4354E	4.7	0.29 0.24	−0.01

Table IV. Effect of heat-treatment on the pitting potential of Ti-stabilized 18% Cr-2% Mo ferritic stainless steels in nitrogen-saturated 1M NaCl at a scanning rate of 2000 mV/hr at 45°C

Heat	Ti content (weight) per cent)	Pitting potential, V (SCE), after water quenching from the indicated temperatures 815°C	925°C	1035°C
4073A	0.47	0.27 0.35 0.29	0.30	0.53 0.59 0.50

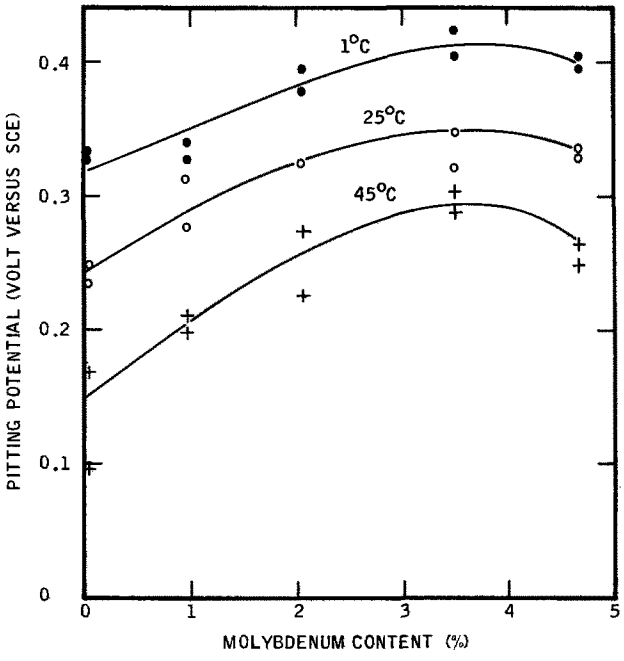

Fig. 4. Pitting potentials obtained from potentiodynamic polarization scans at 200 mV/hr in nitrogen-saturated 1.0M NaBr.

that, as expected, heat-treatment at temperatures up to 1035°C had no deleterious effect on pitting potential. In fact, after treatment at 1035°C, the pitting potential was more noble than it was after the normal anneal at 815°C. It was also noted that the titanium-containing alloy had a more noble pitting potential than the titanium-free alloy under the same conditions. Earlier work with this alloy at 25°C also indicated that titanium was beneficial to pitting resistance (11).

Pitting potentials measured in 1M NaBr varied with composition in the same way as in 1M NaCl (Fig. 4). Pitting potentials were more noble in NaBr, especially at higher temperatures. The beneficial effect of molybdenum additions on pitting potentials of this series of steels in NaBr is just as clearly defined as it is in NaCl. The pitting potentials measured in 1M NaCl and in 1M NaBr at 25°C indicate that all the steels studied should be subject to pitting in 0.33M $FeCl_3$, 0.5M $CuCl_2$, and 0.33M $FeBr_3$ solutions. Exposure tests did indeed show pitting of all the test steels in these solutions at 25°C (Table V). In all cases, the rate of attack decreased with increasing molybdenum content up to 3.5%. The behavior of the 4.7% Mo steel was erratic in these solutions.

Exposure tests were also performed in less aggressive media at 90°C (Table VI). In both solutions, the molybdenum-free steel was severely pitted, while the steels containing molybdenum were attacked only very slightly or not at all. These exposure test results were in good qualitative agreement with the pitting potential results.

Table V. Results of exposure tests in acidified halide salts at 25°C

Medium	Corrosion rate (mdd) of indicated alloys				
	4354A 0% Mo	4354B 1% Mo	4354C 2% Mo	4354D 3.5% Mo	4354E 5% Mo
0.33M $FeCl_3$ + 0.1*N* HCl	7200	7700	5300	670	220
0.33M $FeBr_3$ + 0.1*N* HBr	920	230	120	75	140
0.5M $CuCl_2$ + 0.1*N* HCl	740	610	650	330	560

Table VI. Results of 30 day complete immersion tests in oxygen-saturated aqueous solutions at 90°C

Solution	Corrosion rate (mdd) of the indicated alloys				
	4354A 0% Mo	4354B 1% Mo	4354C 2% Mo	4354D 3.5% Mo	4354E 5% Mo
3% NaCl	63	nil	0.4	nil	0.3
125 ppm Cl^-, 60 ppm Cu^{++}	95	0.4	0.4	nil	0.3

As a result of the polarization measurements, it is clear that molybdenum has a beneficial effect on pitting potentials in 1M NaCl over a range at least from 1° to 70°C. This result is in partial conflict with the results of others on some austenitic steels. The conflict is more definite at 1°C, since Horvath and Uhlig (1) found that molybdenum had a detrimental effect on pitting potentials of an austenitic stainless steel series in 0.1M NaCl at 0°C. The small differences in experimental conditions and technique do not appear sufficient to explain a reversal in direction of pitting potential change with molybdenum content. Thus, the effect of molybdenum may be different in austenite than it is in ferrite even though there is no obvious rationalization for the difference. These same considerations also apply to the difference in molybdenum effect on austenite and ferrite tested in NaBr.

There is less obvious conflict in the behavior of molybdenum-containing steels at higher temperatures in NaCl. The previously reported results (2) were obtained by counting pits formed at constant current density. This involved driving the potential beyond that required to produce pitting without determining any pitting or breakthrough potential. It is quite possible that the number of pits found in this manner does not correlate at all with pitting potentials as measured in the present work.

Conclusions

In fully annealed (815°C) 18% Cr ferritic stainless steels, molybdenum additions up to the limit of solid solubility increase pitting potentials. This is true over the entire temperature range studied *i.e.*, 1°-70°C in 1M NaCl and 1°-45°C in 1M NaBr. Heat-treatments that sensitize the steels to intergranular corrosion also drastically lower the pitting potential.

Manuscript submitted Nov. 9, 1972; revised manuscript received Jan. 5, 1973. This was Paper 53 presented at the Cleveland, Ohio, Meeting of the Society, Oct. 3-7, 1971.

Any discussion of this paper will appear in a Discussion Section to be published in the December 1973 JOURNAL.

REFERENCES

1. J. Horvath and H. H. Uhlig, *This Journal*, **115**, 791 (1968).
2. M. A. Streicher, *ibid.*, **103**, 375 (1956).
3. H. H. Uhlig and J. Wulff, *Trans. AIME*, **135**, 494 (1939).
4. A. P. Bond and E. A. Lizlovs, *This Journal*, **115**, 1130 (1968).
5. J. G. McMullin, S. F. Reiter, and D. G. Ebeling, *Trans. ASM*, **46**, 799 (1954).
6. A. P. Bond and E. A. Lizlovs, *This Journal*, **116**, 1305 (1969).
7. A. P. Bond, *Trans. AIME*, **245**, 2127 (1969).
8. C. R. Rarey and A. H. Aronson, *Corrosion*, **28**, 255 (1972).
9. N. D. Tomashov, G. P. Chernova, and O. N. Marcova, *ibid.*, **20**, 166t (1964).
10. E. A. Lizlovs and A. P. Bond, *This Journal*, **118**, 22 (1971).
11. E. A. Lizlovs and A. P. Bond, *ibid.*, **116**, 574 (1969).

On the Role of Iron Dissolution in Crack Propagation During Hydrogen Charging of an Fe-Pt Alloy

H. W. Pickering*,[1] and P. J. Byrne[2]

Edgar C. Bain Laboratory for Fundamental Research, United States Steel Corporation Research Center, Monroeville, Pennsylvania 15146

ABSTRACT

Iron dissolution during cathodic charging of iron and its alloys is generally negligible, in agreement with thermodynamic conditions at the surface. This is not true, however, of iron alloys for which hydrogen discharge is easy, and also may not in general be true within cracks or cavities. For Fe-10 atom per cent (a/o) Pt in 1*N* H_2SO_4 at 293°K appreciable iron dissolution (~0.05 A/cm^{-2}) occurs for hydrogen-charging currents as high as 1.6 A/cm^{-2}. Crack propagation occurs for specimens loaded in tension which (*i*) is independent of the level of hydrogen charging and (*ii*) has anodic dissolution of iron associated with it. Internal (hydrogen-produced) cracking does not occur. The role of ohmic drops in promoting anodic dissolution at the base of the cracks during hydrogen charging is discussed.

A possible role of hydrogen in crack propagation of anodically polarized specimens has generally been recognized in recent years (1-4). The occurrence of hydrogen discharge within a cavity or crack when the outer surface of the specimen is held at potentials positive or noble of the standard hydrogen electrode (SHE) is understandable in terms of the ohmic drop through the electrolyte within the cavity. The sign of the ohmic drop for anodic polarization is such that the electrode potential becomes less noble or less positive with increasing distance into the cavity or with increasing anodic current density in the cavity (4). The occurrence of hydrogen discharge requires that the electrode potential be in the vicinity of, or less noble than (depending on the *p*H), 0.0V (SHE). Potentials in this region have been directly measured within cavities in Fe while the outer surface was held at potentials as positive as 1.4V (SHE) (4, 5). Potential variations within crevices in stainless steels and Ti alloys have also been measured (6-8).

The purpose of the present paper is to consider the analogous situation which exists for cathodic polarization. This is of interest since the occurrence of an anodic process within cracks and cavities during cathodic polarization is generally disregarded, and in view of the practical consequences of anodic dissolution in cavities in connection with hydrogen cracking of metals.

Theoretical

When a net cathodic current flows in a cavity, it can readily be shown that the electrode potential at the bottom of the cavity increases in the positive (noble) direction with increasing depth of the cavity, *i.e.*, for all other conditions the same, the oxidizing power of the system is greatest at the base of the cavity. Thus, during hydrogen charging of a metal, anodic reactions may in principle occur at the base of cavities, even though they may not be thermodynamically possible at the outer surface of the metal.

The magnitude of the potential drop in the electrolyte within the cavity as a function of depth may be calculated for certain simple situations. Such calculations, however, give only the smallest potential changes, whereas under actual conditions much larger (>0.5V) ohmic drops may occur within the cavity as a result of the presence of gas (4). If the latter occurs, the measured potential at the outer surface is of little value for the determination of the electrode potential or, hence, of the possibility of anodic reactions, at the base of the cavity. For example, at high hydrogen discharge rates on iron in 1*N* H_2SO_4 the potential at the outer surface may be several tenths of a volt negative of the standard potential for the formation of ferrous ion, in which case no iron is dissolved. If, however, the surface contains a cavity or crack which in turn contains a hydrogen bubble, the electrode potential within the cavity may be in the region of iron dissolution.

This situation is analogous to that found for conditions of anodic polarization within a pit, as mentioned above, but differs in the sign of the ohmic drop. In the absence of constrictions (gas bubbles), on the other hand, the shifts in potential are relatively small; calculations for anodic polarizations (4, 9, 10) show that the ohmic drop per unit depth into a cavity is on the order of 0.1 V/mm^{-1} in the less noble direction, at a current density of 0.1 A/cm^{-2}.

Experimental

A study of the amount of iron dissolution and of its role, if any, on crack propagation during hydrogen charging of Fe-10 atomic per cent (a/o) Pt (Fe10Pt) alloy follows. The use of Fe-Pt alloy specimens provides the special features: (*i*) the occurrence of iron dissolution is easily recognized by the formation of a porous reaction layer; (*ii*) hydrogen discharge occurs at low overpotentials and, consequently, at high rates in the potential region of iron dissolution; and (*iii*) platinum does not dissolve at the potentials of interest.

Materials and procedure.—Results were obtained for a Fe-10 a/o Pt (Fe10Pt) alloy in 1*N* H_2SO_4. The Fe10Pt alloy was induction vacuum-melted from pure Fe (99.95) and Pt (99.95). The ingot was homogenized at 1373°K (2012°F) in the stable austenite (γ) region for 168 hr in an evacuated capsule. On cooling to room temperature a martensitic γ to α transformation is expected (11) and indicated in the etched microstructures (Fig. 1c and 4c). The absence of macrosegregation in the ingot was shown by chemical analysis. The ingot was then swaged and wire drawn with one intermittent anneal to 0.22 cm diameter. Specimens cut to 1.42 cm were held in evacuated capsules at 1373°K for 20 hr and water quenched. Some of the specimens were then annealed at 973°K (1292°F) for 12 hr in the stable, two-phase, austenite/ferrite region. After a light emery treatment (4/0 paper) and attachment to a Teflon-covered, stainless steel rod they were rinsed in

* Electrochemical Society Active Member.
[1] Present address: Metallurgy Section, Department of Material Sciences, The Pennsylvania State University, University Park, Pennsylvania 16802.
[2] Present address: Pennsylvania State Environmental Resources, Pittsburgh, Pennsylvania 15200.
Key words: iron, hydrogen cracking, embrittlement, alloy corrosion, stress corrosion.

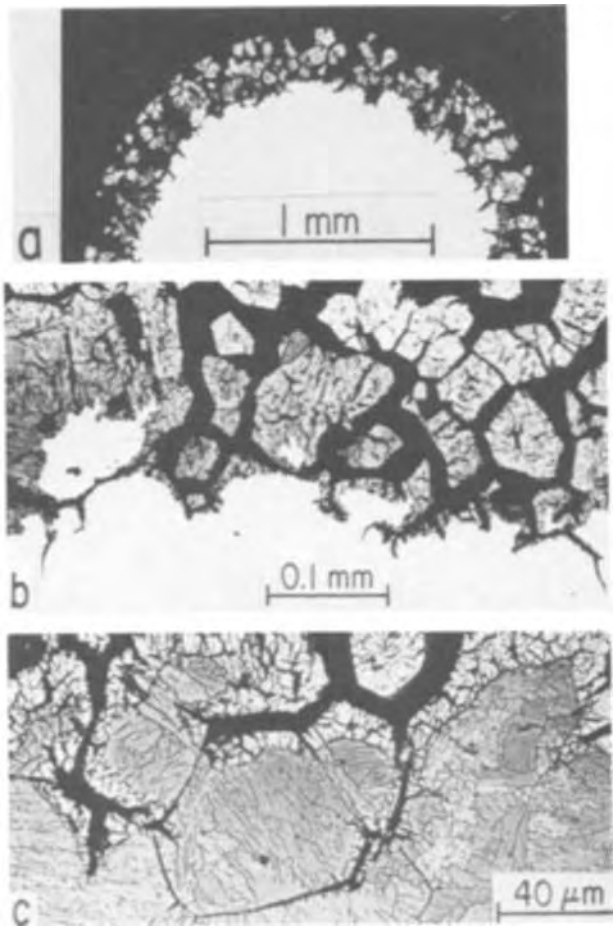

Fig. 1. Cross-section micrographs showing anodically produced reaction layer for austenized specimens. The reaction front has proceeded into the alloy from the top to about the midline of each micrograph. (a) $E_a = -1.00$V (SHE), 2 hr, $i_{Fe} = 60$ mA/cm^{-2}; (b) same as (a); (c) etched, $E_a = -0.40$V.

methanol and distilled water and placed in a cell of all Pyrex construction for the polarization runs.

The potential at the outer surface of the specimen was held constant throughout the test with a Wenking potentiostat. The 130 cm^3 cell also contained the Pt counterelectrode and Luggin capillary. Purified He was passed continuously through the cell to reduce oxygen and also to provide mixing of the electrolyte. Neither He nor mixing appeared, however, to influence the dissolution reaction. The (net) current in the external circuit was recorded and the partial current due to iron dissolution was determined by periodic chemical analysis of the electrolyte by the 1, 10 orthophenanthroline color procedure (12) using a Beckman DU spectrophotometer. The rate of hydrogen discharge is the difference in these currents

The procedure for determination of the amount of dissolved iron was as follows. Prior to draining the cell, any iron which may have deposited on the Pt counterelectrode during the (anodic) polarization runs was redissolved by an impressed current from an auxiliary circuit; the counterelectrode of this circuit was in an adjoining cell (1N H_2SO_4 bridge) connected through a closed stopcock. The electrolyte was then drained from the cell for chemical analysis, and fresh 1N H_2SO_4 was added. Further dissolution at the same potential occurred upon reinsertion of the specimen in the cell.

Tensile specimens, 1.5 cm in length and 0.10 × 0.32 cm reduced cross section, were prepared from the homogenized ingot, and subsequently annealed at 1373°K and quenched. For a run a specimen was connected to the potentiostat, placed in a cell similar to the above-described one but specially designed for the Instron Tensile Testing Machine, and strained a given amount at a constant rate of extension of 0.034 min^{-1}. The electrode potential was preset at a value in the same range as for the nonstressed cylindrical specimens, and the polarization treatment begun by filling the cell with the test electrolyte. The cell was continuously flushed with He. The load on the specimen at constant extension (crosshead stopped) and the current were monitored. Grips and other parts of the apparatus which were in contact with the electrolyte were made of titanium alloy and coated with Halocarbon wax.

All experiments were performed at room temperature, 293°K. Potentials are given in terms of the standard hydrogen electrode (SHE).

The scanning-electron micrographs were taken in stereo with a Cambridge Stereoscan microscope. Examination of the micrographs in stereo gives a much more complete and correct impression of the corrosion structure than does a monocular examination. The stereo figures in this paper may be seen in stereo with the aid of a stereo viewer.

Results for cylindrical (nonstressed) specimens.— The Fe10Pt cylindrical specimens were held at applied potentials, E_a, in the range, −1.00 to +0.15V (SHE) in 1N H_2SO_4. At each potential, the net current and the iron-partial current were obtained from the ammeter in the potentiostat circuit and from periodic chemical analysis of the electrolyte, respectively. The meter current is cathodic over most of this potential range ($E_a < 0$V) in accord with an expected and observed profuse hydrogen evolution, Table I. Since the net (meter) current at the more negative potentials is of the order of 1 A/cm^{-2} cathodic, the actual potential across the surface is considerably more noble than the applied value, E_a. Corrected potentials, E, are given in Table I; the correction equals the ohmic drop between the tip of the Luggin capillary and the specimen surface (2 mm); each E is an approximate calculated value using the conductivity of the bulk electrolyte. At $E > 0$V, for which only iron dissolution occurs, the meter current is anodic, *i.e.*, $i_{meter} = i_{Fe} \cong 0.065$ A/cm^{-2}. This is in excellent agreement with i_{Fe} determined by periodic chemical analysis of the electrolyte: $i_{Fe} = 0.066$ and 0.064 A/cm^{-2} at $E = 0.12$ and 0.02V, respectively. The precision of the chemical analysis method was determined to be ±3% in the amount of dissolved iron.

After an initial period of less than 1 hr the rate of iron dissolution at all potentials was found by chemical analysis to approach a quasi-stationary value in the range 0.040-0.065 A/cm^{-2}, Table I.[3] The occurrence of iron dissolution was confirmed at all potentials by the gradual development of a pale yellow-green color of the electrolyte and by the results (to be described) of electron-microprobe and x-ray diffraction analyses of these specimens. The occurrence of iron dissolution during cathodic charging follows most directly from a superposition of cathodic and anodic current-poten-

[3] The listed current densities are apparent values based on the original area. The true surface area increases with time. The electrochemically active surface area for iron dissolution, however, is expected essentially to level off, since iron dissolution will occur mainly at the advancing front of the developing surface perturbations.

Table I. Net (meter) and partial currents, i_{Fe} and i_H, for applied potentials, E_a, and corrected potentials, E

E_a, V (SHE)	E, V (SHE)	i_{meter}, A/cm^{-2}	i_{Fe}, A/cm^{-2}	i_H, A/cm^{-2}
0.15	0.12		0.066	~0
0.05	0.02	0.065	0.064	~0
−0.10	−0.07	−0.058	0.064	−0.12
−0.40	−0.1	−0.70	0.043	−0.74
−0.80	−0.3	−1.2	0.051	−1.3
−0.80	−0.3	−1.2	0.047	−1.3
−1.00	−0.4	−1.2	0.051	−1.3
−1.00	−0.4	−1.5	0.060	−1.6

tial curves as demonstrated by Wagner and others (13-15).

The hydrogen partial current is the algebraic difference between the meter current and the partial iron current. The hydrogen partial current predominates at the more negative potentials with values of $i_H \gtrsim 1$ A/cm^{-2}. When the specimens were removed from the test cell and rinsed, the evolution of a gas, presumably H_2, was observed within the adherent water film. A large amount of heat is also given off during the rinse (H_2O followed by methanol). The heat is so high that on occasion the paper towel used for drying the specimen was singed.

A porous metal layer forms on specimens polarized at all potentials. The morphology and general appearance of the reaction layer are the same over the entire potential range in Table I, *i.e.*, at the negative potentials of simultaneous hydrogen evolution and iron dissolution and at the positive potentials of sole-iron dissolution. Typical morphologies are shown in cross section in Fig. 1. The large amount of porosity appears in the form of a continuous network of crack-like cavities varying in size from 10 μm down to less than 0.1 μm. The cavities of all sizes have faceted surfaces, as shown by scanning-electron microscopy (SEM) in Fig. 2 and 3. These are typical structures of the reaction layer at all depths and at all potentials. Figures 2 and 3 are stereo pairs and provide a much easier to interpret view of the corrosion structure than does a monocular view. The alloy microstructure (1373°K, quenched) is shown in the bottom portion of Fig. 1C.

Examination of etched specimens reveals that the alloy microstructure influences the course of the corrosion process. The attack (cavities) penetrates faster along prior austenite-grain boundaries than elsewhere, and this often results in encirclement of original alloy, Fig. 1b. Much finer cavities than those that form along grain boundaries grow along the interfaces of the martensite plates, Fig. 1c. These are by far the most numerous cavities in accord with the high density of martensite plates.

This influence of the microstructure is illustrated further by comparison with specimens annealed in the ferrite/austenite region after quenching from the

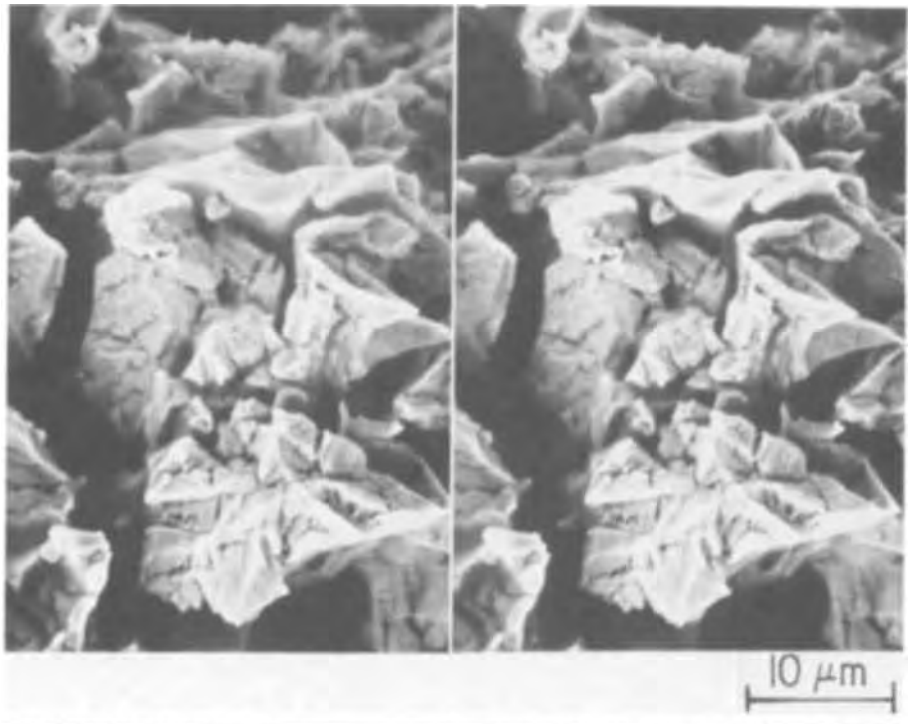

Fig. 2. SEM stereo pair of reaction layer. $E_a = 0.05$V.

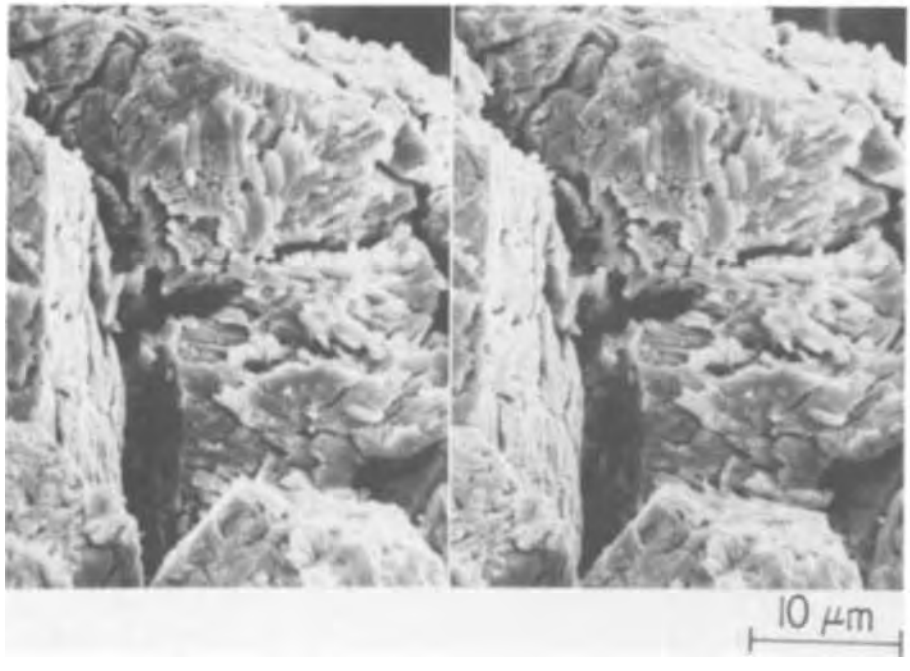

Fig. 3. SEM stereo pair of reaction layer. $E_a = -1.00$V.

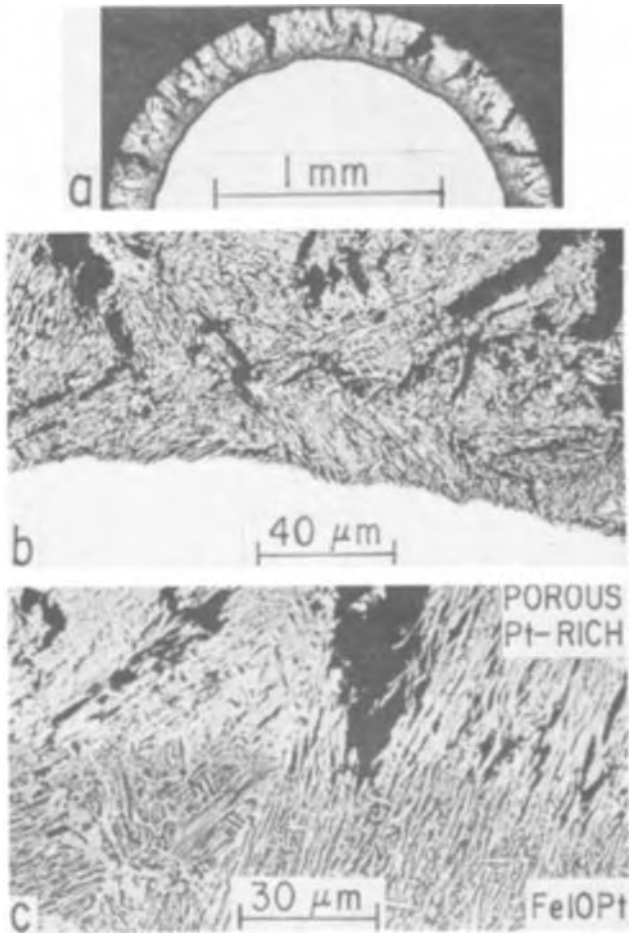

Fig. 4. Cross-section micrographs showing anodically produced reaction layer for austenized and annealed specimens. (a) E_a = 0.13V, 3 hr; (b) Same as (a); (c) Same as (b) but etched.

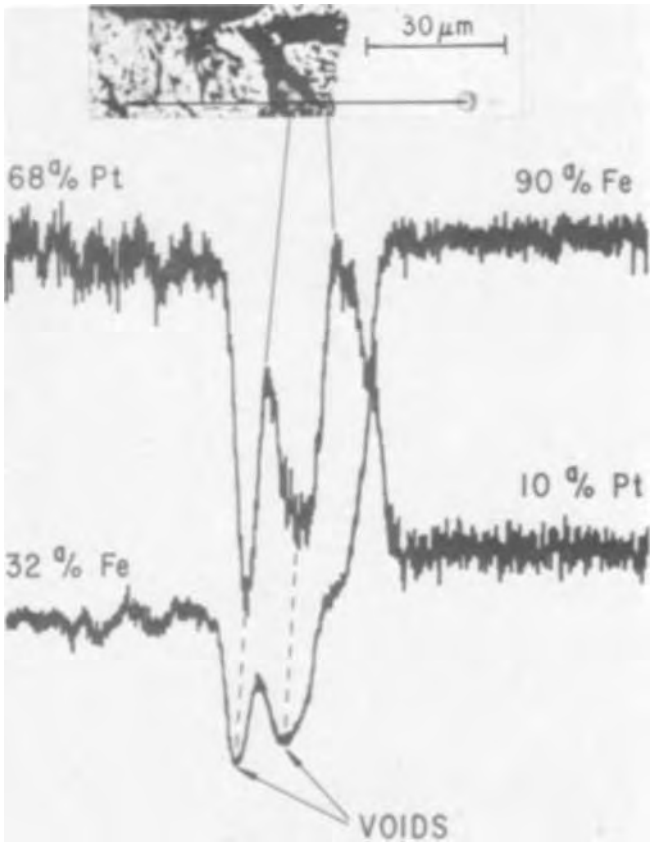

Fig. 5. Electron-microprobe traces of Fe and Pt. Arrow in micrograph shows path of electron beam starting in original alloy at right and proceeding into reaction layer. E_a = — 1.00V, 3 hr.

austenite region, Fig. 4. Much less grain-boundary attack occurs in the annealed specimens. The attack is localized, though, to the interface (presumably Fe-rich ferrite) regions of the plate-like structure, Fig. 4c. The alloy microstructure (1373°K, quenched, followed by 12 hr at 973°K) is shown in the bottom portion of Fig. 4c.

Results of the electron-microprobe and x-ray diffraction analysis of the porous layer were the same at all of the potentials. The microprobe results are shown in Fig. 5. A sharp change in the Fe and Pt contents occurs at the boundary between the porous metal and the unattacked portion of the alloy; the porous metal is rich in Pt. An x-ray diffraction analysis (Fig. 6) shows in addition that the porous metal at all potentials is a single-phase solid solution of Fe in Pt (~60-100% Pt) in agreement with diffraction analyses of other alloys undergoing preferential dissolution (16, 17).

Results for tensile specimens.—The Fe10Pt tensile specimens were held at applied potentials in the range —1.00 to + 0.50V in 1*N* H_2SO_4. At all potentials the load was observed to fall for the polarized tensile specimens at a rate faster than that for room-temperature creep of (nonpolarized) specimens in air; in a matter of minutes the rate of falloff began to increase with time for the polarized specimens, followed by fracture of the specimen within about 1 hr. A typical result is shown in Fig. 7 in which the load has been converted to stress. The cross-sectional area for the fracture (solid) curve at the start of load relaxation (time = 0) is assumed to be $A^o(l^o/l)$; A^o and l^o are the original cross-sectional area and length, respectively, and l is the length after elongation. This relation presupposes uniform elongation. The "creep-in-air" and "corrected" fracture curves for the specimen are also included; this correction takes into account a continuous reduction in cross section as a result of corrosion generally over the surface during the test.

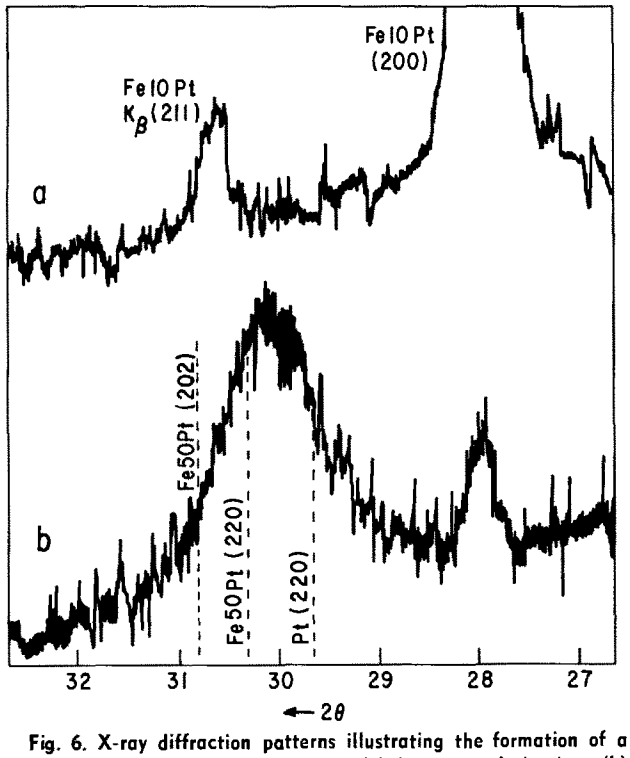

Fig. 6. X-ray diffraction patterns illustrating the formation of a Pt-rich alloy of variable composition. (a) Prior to polarization; (b) E_a = — 0.05V, 8 min.

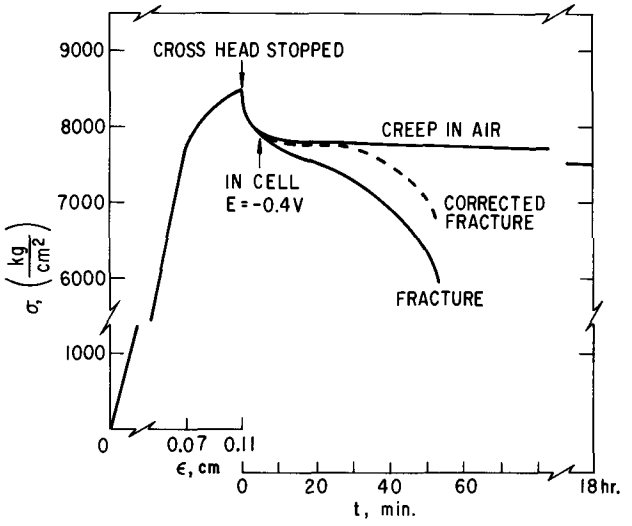

Fig. 7. Stress-relaxation curve showing accelerated falloff in stress to failure of a sample polarized at $E_a = -1.00$V.

Prior to the onset of cracking the "corrected fracture" and "creep-in-air" curves nearly superimpose.

Visual observation of the specimens during load relaxation revealed the evolution of large gas bubbles from several stationary sites which presumably were cavities or cracks. These bubbles were readily distinguished from the much smaller hydrogen bubbles which evolve generally over the surface at all negative potentials.

Cross-section examination of the failed specimens showed that there usually were a few cracks in addition to the main fracture crack, Fig. 8. The cracks propagate in a mixed mode, *i.e.*, along, as well as across, prior austenite-grain boundaries.

Anodically produced porous structure can be resolved along the fracture surface by scanning-electron microscopy. The amount of anodic dissolution associated with crack propagation varied. On the basis of only a few runs it appears to increase with decreasing propagation rate, the latter being at least in part a function of the elongation prior to load relaxation. Figure 9 shows the anodically produced porous structure at the very tip of a crack. In this case the electrolyte was removed after some crack propagation had occurred and the specimen immediately elongated to ultimate failure so that fracture of the remaining cross section was by the ductile mode. The porous structure extends to (into) the dimpled (ductile) structure (Fig. 9a) which shows that anodic dissolution was occurring right at the crack tip. This same result was obtained at different potentials, E_a ranging from -1.00 to $+0.50$V (SHE) and, hence, for widely different hydrogen-charging rates. Figure 9b is a stereo pair and shows the marked three-dimensional nature of the fracture surfaces. Anodically produced crack growth has also been observed for anodically polarized Cu-Au alloys in instances of slow crack growth. Anodic dissolution was found to occur at the crack tip; here again the anodic dissolution process was identified by the formation of a porous reaction layer along and ahead of the crack (18). The same result has been found for a Ni-Au alloy by Swann and Duff (19).

Discussion

It is shown by chemical analysis of the electrolyte and by electron-microprobe, x-ray diffraction, and cross-section metallographic analyses of the porous metal layer that iron dissolves rapidly from Fe10Pt alloy over a broad range of negative potentials including those for which the rate of hydrogen discharge is greater than 1 A/cm^{-2}. The thickness of the anodically produced porous metal layer may be calculated from the moles of dissolved iron. The number of moles of

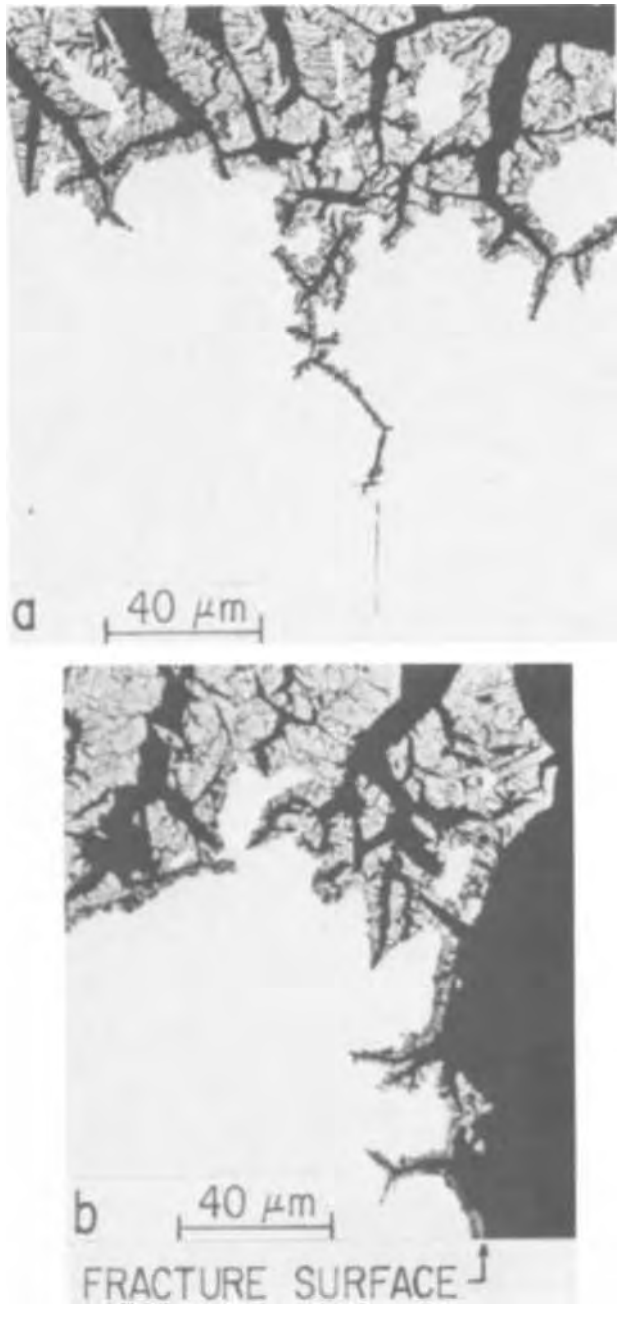

Fig. 8. Cross-section micrographs showing (a) secondary crack and (b) one half of main crack which propagated through a tensile specimen. $E_a = -1.00$V.

dissolved iron is $i_{Fe}t/n\mathbf{F}$, in which i_{Fe} is the partial iron current density, t is the time of iron dissolution, and n and $\mathbf{F}$ have their usual meaning. For $i_{Fe} \cong 0.06$ A/cm^{-2}, $t = 2$ hr, and $n = 2$ for the formation of ferrous ions, 0.0021 mole-cm^{-2} of iron dissolve. Multiplying by the molar volume of the alloy, $V_M \cong 8$ cm^3 mole^{-1} and dividing by 0.7, the fraction of iron removed according to the microprobe analyses, gives 0.026 cm for the depth of the reaction layer. This is in good agreement with the average measured values, *e.g.*, 0.025 cm in Fig. 1c, and 0.022 cm in Fig. 4c.

The identification of the reaction layer by x-ray diffraction as a Pt-rich solid solution of variable composition agrees with data found for other alloys, and indicates that interdiffusion of the components within a (shallow), vacancy supersaturated surface layer, rather than some other transport mechanism, is mainly responsible for the preferential dissolution of iron from Fe-Pt alloy (16, 17). Cuddy (20) has shown that there is a point defect in iron with an activation energy

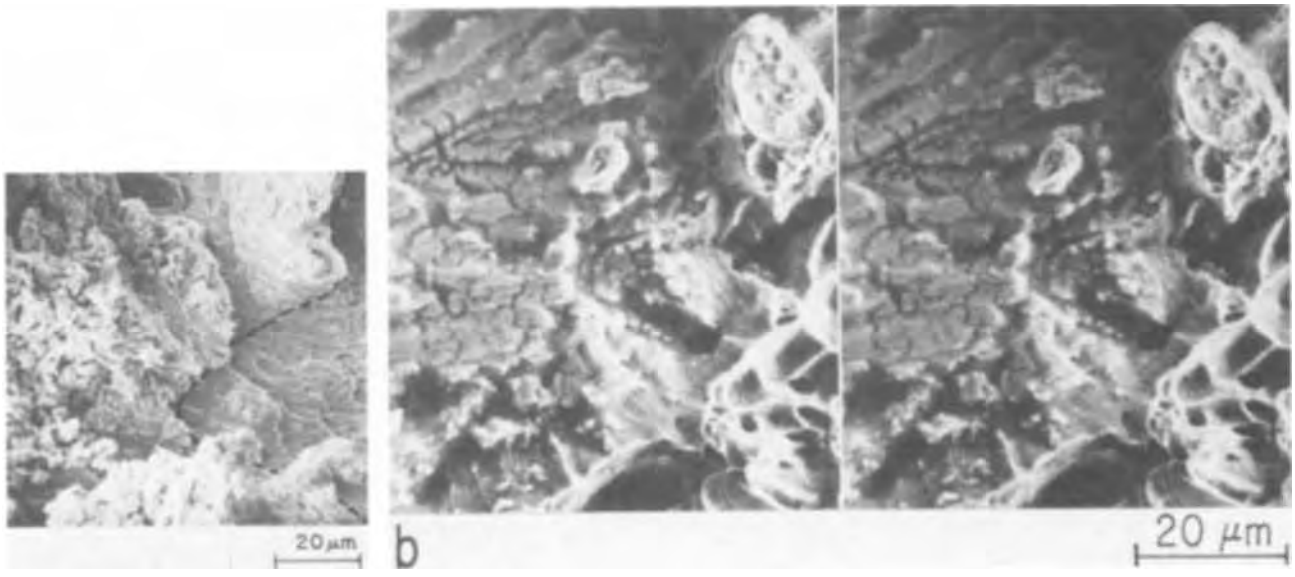

Fig. 9. SEM micrographs showing anodically produced porous material at the crack tip. (a) $E_a = -1.00V$. Anodically produced fracture has proceeded from left to dashed line; mechanically produced (ductile) fracture is to the right of the dashed line. (b) $E_a = -0.40V$. Stereo pair. Anodic fracture progressed from left to right of center.

of 0.55 eV. If, as Cuddy concludes, these are single vacancies, the mean-square displacement, $\overline{\Delta x^2}$, of a single vacancy in iron is $2D_{\square}t$ or $2t\nu a_o^2 \exp(-E_m/kT)$ in which ν is the jump frequency, a_o is the lattice parameter, E_m is the migration energy of a single vacancy, T is the temperature, t is the time, k is the Boltzmann constant, and $D_{\square}$ is the diffusivity of a single vacancy.

For $\nu = 5 \times 10^{13}$ sec^{-1} and $a_o = 2.86 \times 10^{-8}$ cm, one obtains at 25°C after 10^3 sec the rather large value of $\overline{\Delta x^2} = 4 \times 10^{-8}$ cm^2, or an average migration distance of 2 μm for a single vacancy. This value is larger than that for mono- or divacancies at 25°C in Cu (21, 22). Consequently, somewhat lower concentrations of excess vacancies, or conversely larger pore sizes, will yield dissolution rates which are comparable to those in the Cu-Au or Cu-Zn alloy systems discussed elsewhere (16, 17).

In view of the occurrence of hydrogen evolution, absorption of some hydrogen by the metal must occur. The heat evolved during rinsing of specimens polarized at the negative potentials could be the oxidation of hydrogen which had been absorbed in the metal or which had been present as bubbles trapped within the electrolyte of the porous structure. Certain usual features of hydrogen absorption however, were not present, *e.g.*, internal cracks were not observed in either the cylindrical or tensile specimens. Furthermore, the over-all rate of crack propagation observed in the tensile specimens is approximately the same at all the applied potentials, and, hence, the same for all rates of hydrogen discharge insofar as it occurs generally over the surface, *i.e.*, for zero as well as for 1 A/cm^{-2} hydrogen discharge; this observation, coupled with the observed high rates of iron dissolution, indicate that crack propagation is by anodic dissolution. The cracking observed in this system, thus, is similar to the anodically produced cracking which has been observed in anodically polarized Cu-Au alloys (18), an alloy system in which hydrogen discharge can be ruled out on thermodynamic grounds, both at the outer surface and within cavities, since the standard potentials of Cu and of Au are both noble to that of hydrogen by $>> RT/n\mathbf{F}$. The absence of a major role of hydrogen in the formation of the porous structure or in crack propagation does not mean, of course, that hydrogen-induced cracking may not occur in this alloy for other conditions of cathodic charging.

Formation of hydrogen gas within the cavity or crack may, in general, be important, as already discussed in the theoretical section of this paper for obtaining large ohmic drops within the cavity. Hence, hydrogen gas which forms a constriction at the crack tip may cause ohmic drops of whatever values are necessary to shift the electrode potential (in the positive sense) into a potential region of rapid iron dissolution.

In the present research a large shift in potential was not required for the occurrence of iron dissolution in the crack since the actual potentials, E, at the outer surface were in the region of iron dissolution. Therefore, gas bubbles, though probably present in the cavities, were not necessary for the occurrence of iron dissolution at the bottom of the cavities. A large shift in potential would be needed, however, at more negative applied potentials, and for most conditions of hydrogen charging of iron and steels of high, rather than low, hydrogen overvoltage.

Conclusions

The partial iron i_{Fe} and hydrogen i_H currents at several potentials E ranging from 0.12 to about −0.40V (SHE) are given for Fe10Pt in 1N H_2SO_4 at 293°K. The partial iron current varies little over this potential range, approaching a quasi-stationary value of between 0.040 and 0.065 A/cm^{-2} in less than 1 hr. The partial hydrogen current varies from zero at $E \cong 0$ to 1.6 A/cm^{-2} at $E = 0.40V$. Since platinum does not dissolve at these potentials the surface is enriched in Pt, and the surface area increases sharply. X-ray diffraction shows the resulting porous structure to be a solid solution of Fe in Pt, in agreement with results for other alloys undergoing preferential anodic dissolution of the less noble component, and indicative of the occurrence of volume diffusion during the dissolution process.

Crack propagation is observed for specimens loaded in tension which is independent of the level of hydrogen charging. These cracks are deduced to be anodically produced. The presence of porous (anodically produced) metal at the crack tip supports this conclusion. Internal (hydrogen produced) cracking is not observed.

The role of ohmic drops in promoting anodic dissolution at the base of cracks during hydrogen charging is discussed.

Acknowledgments

We gratefully acknowledge the assistance of C. E. Brickner and W. Gundaker who performed the scanning-electron microscopy and electron-microprobe analyses, respectively, and discussions with P. Wray and R. P. Frankenthal, all of this laboratory.

Manuscript submitted July 6, 1972; revised manuscript received Dec. 8, 1972.

Any discussion of this paper will appear in a Discussion Section to be published in the December 1973 JOURNAL.

REFERENCES

1. J. H. Shively, R. F. Hehemann, and A. R. Troiano, *Corrosion*, **23**, 215 (1967); *ibid.*, **22**, 253 (1966).
2. C. F. Barth, E. A. Steigerwald, and A. R. Troiano, *ibid.*, **25**, 353 (1969).
3. B. E. Wilde, *ibid.*, **27**, 326 (1971); B. E. Wilde and C. D. Kim, *ibid.*, **28**, 350 (1972).
4. H. W. Pickering and R. P. Frankenthal, *This Journal*, **119**, 1297 (1972); *ibid.*, **119**, 1304 (1972); Proc. 1971 International Conference on Localized Corrosion, R. W. Staehle, Editor, Williamsburg, Va., N.A.C.E. (1973).
5. G. Herbsleb and H. J. Engell, *Z. Elektrochem.*, **65**, 881 (1961).
6. N. D. Greene, W. D. France, Jr., and B. E. Wilde, *Corrosion*, **21**, 275 (1965).
7. W. D. France, Jr. and N. D. Greene, Jr., *ibid.*, **24**, 247 (1968).
8. C. M. Chen, F. H. Beck, and M. G. Fontana, *ibid.*, **27**, 234 (1971).
9. T. R. Beck and E. A. Grens, II, *This Journal*, **116**, 177 (1969).
10. D. A. Vermilyea and C. S. Tedmon, Jr., *ibid.*, **117**, 437 (1970).
11. E. J. Efsic and C. M. Wayman, *Trans. AIME*, **239**, 873 (1967).
12. ASTM Standards on Chemical Analysis of Metals, p. 173, Philadelphia, Pa. (1970).
13. C. Wagner and W. Traud, *Z. Elektrochem.*, **44**, 391 (1938).
14. J. Elze and H. Fischer, *This Journal*, **99**, 259 (1952).
15. H. Kaesche, "Die Korrosion der Metalle," p. 123, Springer-Verlag, New York (1966).
16. H. W. Pickering and C. Wagner, *This Journal*, **114**, 698 (1967).
17. H. W. Pickering, *ibid.*, **115**, 143 (1968); *ibid.*, **117**, 8 (1970).
18. H. W. Pickering, *Corrosion*, **25**, 289 (1969).
19. P. R. Swann and W. R. Duff, *Met. Trans.*, **1**, 69 (1970).
20. L. J. Cuddy, *Acta Met.*, **16**, 23 (1968).
21. R. Ramstetter, G. Lampert, A. Seeger, and W. Schule, *Phys. Status Solidi*, **8**, 863 (1965).
22. R. O. Simmons and R. W. Balluffi, *Phys. Rev.*, **129** 1533 (1963).

Electroless Deposition of Nickel-Boron Alloys

Mechanism of Process, Structure, and Some Properties of Deposits

K. M. Gorbunova, M. V. Ivanov, and V. P. Moiseev

Institute of Physical Chemistry, Academy of Sciences of USSR, Moscow, USSR

ABSTRACT

The conditions for electroless nickel-boron plating, the process mechanism, and the structure of the alloys as-plated and after annealing at 150°-700°C were investigated. A correlation of the mechanical and magnetic properties with the changes of phase structure was established.

Following the success of electroless plating of the transition metals by the use of the hypophosphite ion, investigations were begun to find other reducing agents to obtain coatings with new properties meeting the requirements of modern industry.

In this respect alkali metal borohydrides and alkyl amine boranes (borazanes) appeared to be of the greatest interest (1-4).

The present paper presents data on both the conditions of nickel reduction by borohydride and the mechanism of reactions involved, as well as data on the deposit structure which revealed the correlation of some of their properties, such as magnetic, hardness, wear resistance, etc., with phase transformations proceeding during annealing of nickel-boron plates.

Electroless Nickel Bath

The plating bath as described contains nickel salt, sodium borohydride as the reducing agent, sodium hydroxide, complexing agent (ligand), and stabilizer.

Ligands.—In order to find the most effective ligands the following substances were investigated: ethylenediamine, mono-, di-, tri-ethanolamine, iminodiacetic, nitrilotriacetic, ethylenediaminetetraacetic, 2-oxyethyliminodiacetic, oxyethylidendiphosphonic, and ethylenediaminebisisopropylphosphonic acids. These substances were selected on the basis of their ability to interact with nickel ions to form rather stable complexes.

Key words: electroless plating, nickel-boron alloys, borohydrides.

The results of the study of the behavior of these ligands indicated that ethylenediamine was the most appropriate one. The comparison of the characteristics of the ethylenediamine complex and other complexes allows one to state some considerations concerning the choice of ligands. It was revealed, in particular, that the data on the stability constants are not sufficient to evaluate the ligand efficiency in this process. The important part seems to be played by both the formed complex structure and its charge. On the basis of the plating rate and the solution stability one may conclude that conditions favorable for the process are those which lead to the formation of coordinationally saturated complexes with zero or positive charge. Under these conditions the probability of the destruction of complexes in the bulk of the solution appears to be the smallest owing to the hindrances to the penetration of both water molecules and borohydride ions to a nickel ion. Also, the absence of a charge or a positive charge favors the adsorption of a complex on the negatively charged surface of the metal catalyst.

Stabilizers.—It should be noted that in spite of the presence of the most effective ligands the solution shows insufficient stability as manifested by the formation of metal powder in the bulk of the solution. For preventing or lessening this undesirable phenomenon some substances, stabilizers, are introduced into solution. As a result of studying the stabilization effect of different sulfur-containing substances of organic nature, some inorganic salts and oxides (5),

Table I. Compositions of plating solutions and conditions of process

Composition of solution	Concentration, g/liter A	B	C
Nickel chloride	30	30	30
Sodium borohydride	1.2	1.2	1.2
Sodium hydroxide	40	40	40
Ethylenediamine (70%), ml/liter	86	86	86
Thallium nitrate	0.1	—	—
Lead chloride	—	—	$4 \cdot 10^{-2}$
2-mercaptobenzothiasole	—	—	$5 \cdot 10^{-3}$
Temperature, °C	95	95	95
pH	14	14	14
Rate of deposition, μ/hr	25	10	13
Stability of the solution, %	95	57	88
Content of the boron in deposit, wt %	4.3	5.7	6.4

including substances proposed in the patent literature (6, 7), thallium nitrate and lead chloride together with 2-mercaptobenzothiazole were chosen for investigation, the results of which are given below. Table I represents the compositions of the plating solutions. The solution stability was estimated as the ratio of the weight of plate to the total weight of reduced alloy including the metal deposited as a powder in the bulk of solution. The boron content in the alloys was determined by a photocolorimetric method using acetylchinalizarin (8). Figures 1, 2, and 3 show the influence, respectively, of the concentration of the sodium borohydride, ethylenediamine, and temperature on the deposition rate of nickel-boron plates and the solution stability. The data of Fig. 1 draw attention to the important role of the nature of the stabilizing additives; Fig. 3 reveals the specific influence on the deposition rate of $TlNO_3$, which allows the process to be carried out at a relatively low temperature with a rather high rate.

Mechanism of Electroless Nickel-Boron Plating

The available literature concerning the mechanism of nickel-boron plating is rather limited and proposed ideas are not confirmed by experimental data. According to the notions of different authors (2, 9, 10)

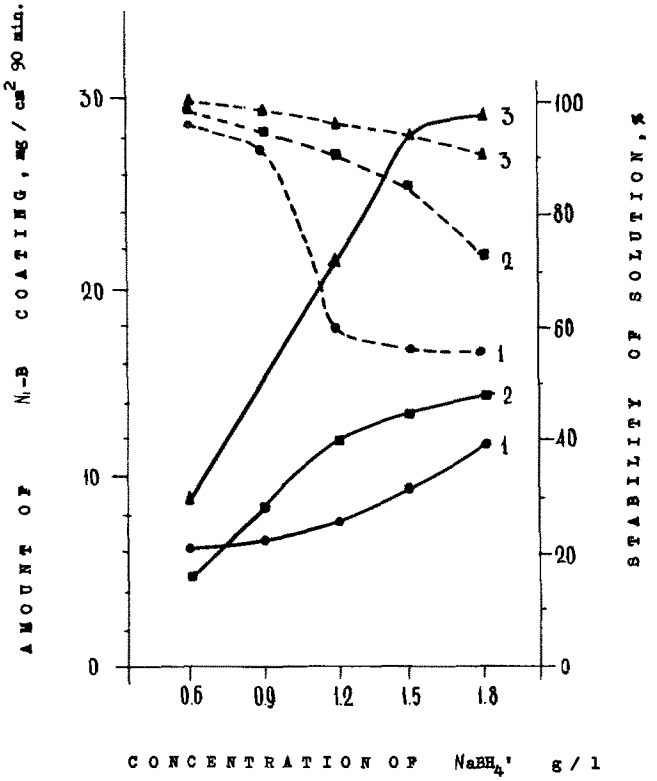

Fig. 1. Influence of the concentration of $NaBH_4$ on the plating rate (solid lines) and solution stability (dashed lines): 1, solution without a stabilizer; 2, solution with $PbCl_2$ and 2-mercaptobenzothiazole; 3, solution with $TlNO_3$.

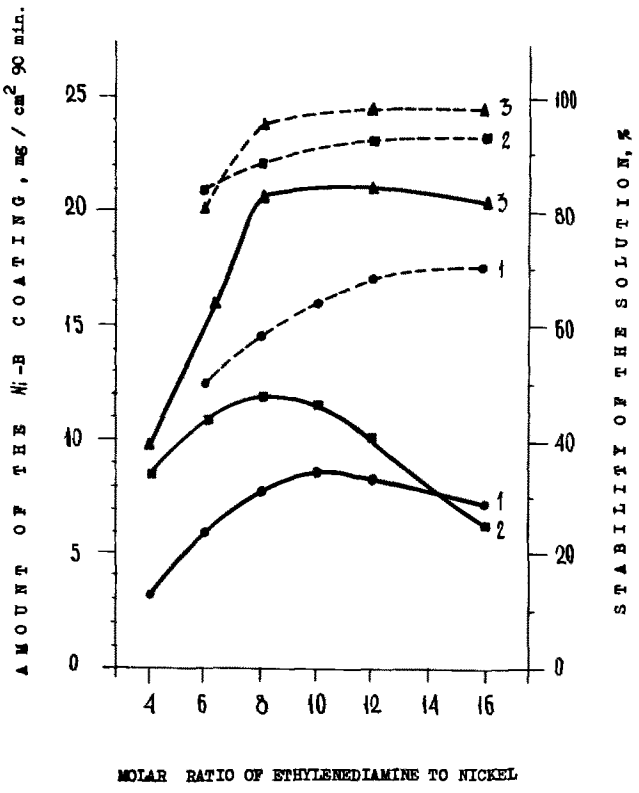

Fig. 2. Influence of the molar ratio of ethylenediamine to nickel on the plating rate (solid lines) and solution stability (dashed lines). Numbers correspond to those in Fig. 1.

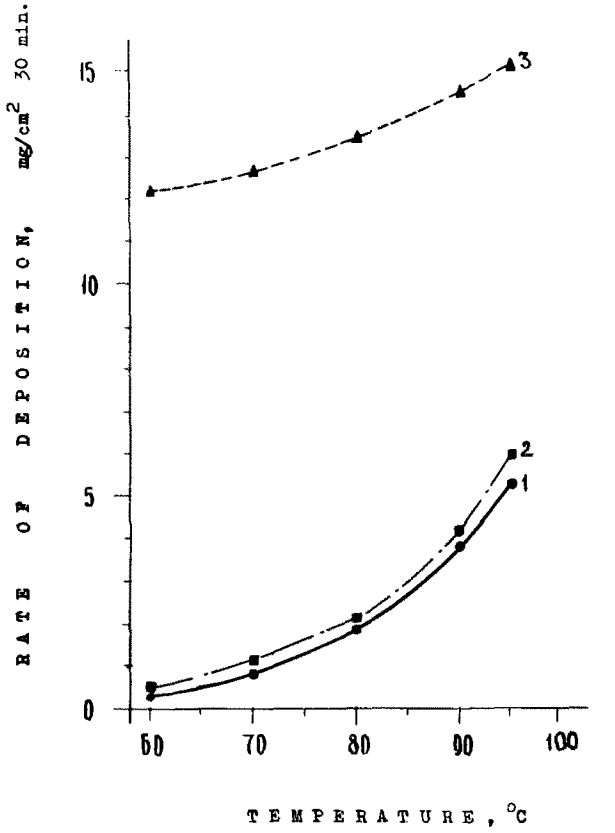

Fig. 3. Influence of the temperature on the plating rate. Numbers correspond to those in Fig. 1.

each borohydride ion reduces four nickel ions (Table II), *i.e.*, all four hydride ions of borohydride are oxidized to the proton state.

The reduction of boron is discussed by these authors from various points of view. Thus, in Ref. (2) it is

Table II. Reaction equations of the process of formation of Ni-B coating proposed in the literature

Reduction of nickel

$NaBH_4 + 4NiCl_2 + 8NaOH = 4Ni + NaBO_2 + 8NaCl + 6H_2O$ (2, 9, 10)

Reduction of boron

1. $2NaBH_4 + 4NiCl_2 + 6NaOH = 2Ni_2B + 8NaCl + 6H_2O + H_2$ (2)
2. $2NaBH_4 + 5NiCl_2 + 8NaOH = 2B + 5Ni + 10NaCl + 8H_2O$ (9)
3. $2NaBH_4 + 2H_2O = 2B + 5H_2 + 2NaOH$ (10)

assumed that only three hydride ions are oxidized to protons. The fourth hydride ion is oxidized to the atomic state, leading to the formation of a molecule which is evolved as a gas (Table II, Eq. [1]). However, in Ref. (9) it is supposed that all hydride ions are oxidized to protons (Table II, Eq. [2]). The reaction of boron reduction is considered by authors (10) as a catalytic process of decomposition of the borohydride ion, which takes place independently of the reduction of the metal (Table II, Eq. [3]).

However, the hypothesis that hydrogen atoms, formed during oxidation of hydride ions of borohydride, are an intermediate product which can take part in the reduction of nickel or boron is subject to serious objections based on earlier data relating to the reduction process by hypophosphite (11-13). Based on the results of these investigations and on the data about the stepwise hydrolysis of borohydride in alkali solution (14), the scheme of the reactions proceeding at the formation of Ni-B plates shown in Table III was proposed (5, 16). According to this scheme the hydrogen atoms arising from hydrolysis of borohydride combine to form hydrogen molecules and do not take part in nickel reduction. The increase of the acidity observed in this process is due to the proton from the water molecules only. The reduction of boron proceeds according to the idea proposed in Ref. (15) as a catalytic decomposition reaction of the reductant.

The proposed mechanism was confirmed by the results of mass-spectrometric measurements of the isotope composition of the gaseous hydrogen evolved in the process carried out using heavy water (16). The investigations were carried out by use of a solution prepared with D_2O (99.7%) containing (grams/liter): $NiCO_3$, 13; NaOD, 41; ethylenediamine (70%), 86 ml/liter; $NaBH_4$, 0.8 at 95°C, and pH 14. The hydrogen evolved during the reaction was passed through a liquid nitrogen trap and collected in evacuated ampoules. The isotopic composition of the hydrogen was established by using the mass spectrometer MI-1311; the absolute error in the measurements was below 1.5-2.0%. Results of these measurements are presented in Table IV. The data of the measurements are in accordance (within 6-8%) with those of the gas composition calculated following the reduction scheme given in Table III. The calculations made on the basis of the ideas of the feasibility of hydride ion oxidation to a proton results in a considerable (~200%) deviation from the experimental data.

Structure of Nickel-Boron Plates

The as-plated nickel-boron alloys containing 4.3% B consist of two phases: a solid solution of boron and

Table III. Proposed scheme for the mechanism of electroless nickel-boron plating

Reduction of nickel

$BH_4^- + 4HOH \longrightarrow B(OH)_4^- + 4H + 4H^+ + 4e$

$2Ni^{2+} + 4e \longrightarrow 2Ni$

$BH_4^- + 4HOH + 2Ni^{2+} \longrightarrow 2Ni + B(OH)_4^- + 2H_2 + 4H^+$

Reduction of boron

$BH_4^- + H^+ \longrightarrow BH_3 + H_2 \longrightarrow B + 2.5H_2$

Hydrolysis of reductant

$BH_4^- + 4HOH \longrightarrow B(OH)_4^- + 4H + 4H^+ + 4e \longrightarrow B(OH)_4^- + 4H_2$

Table IV. Results of mass-spectrometric measurements and data calculated according to the different reaction mechanisms

No. of experiment	Experimental data: Consumed $NaBH_4$, mg	Reduced: Nickel, mg	Reduced: Boron, mg	Mechanism Ref. No.	Content of deuterium in hydrogen, %: Calculated data	Content of deuterium in hydrogen, %: Mass-spectrometric data
1	16.2	26.37	1.53	(2)	38.2	15.5
				(9)	41.0	
				(10)	33.9	
				Proposed	16.4	
2	16.1	25.42	1.48	(2)	38.3	16.1
				(9)	41.0	
				(10)	34.1	
				Proposed	17.4	
3	16.6	25.61	1.49	(2)	38.5	19.0
				(9)	41.0	
				(10)	34.5	
				Proposed	18.4	

hydrogen in face-centered cubic β-nickel and an amorphous phase. The samples with 5.7 and 6.4% B are single-phase alloys of amorphous structure. The cross section of Ni-B deposits shown in Fig. 4 revealed a column-lamellar structure which is similar to that of electroless Co-P alloys (17). This type of deposit seems to reflect the periodic change of the ratio of the reduction rates of nickel and boron; this change is due to pH alternations in the layer adjacent to the surface.

Peculiarities of the phase transformations proceeding during annealing of Ni-B alloys were revealed by using the combination of the thermographic, x-ray methods (18) and electronmicroscopic examinations. Figure 5 shows the thermograms of the alloys of different composition which were heated in a helium atmosphere at the rate of 10°/min. In the thermograms one can see the three exothermic effects at 305°, 405°, and 425°C.

The thermographic investigations of the alloys containing 6.4-6.9% boron allowed one to distinguish more clearly exothermic effects in the range 400°-430°C (Fig. 6).

The results of x-ray analysis have shown that the effect at 305°C relates to the formation of the Ni_3B phase, the effect at 425°C to the formation of the Ni_2B. According to the thermographic data of Fig. 5 the higher the boron content in the alloy, the higher is the relative quantity of the Ni_2B phase. It is of interest that in this case the absolute quantity of the Ni_3B phase decreases.

There is reason to suppose that the exothermic effect at 405°C is due to the appearance of the very unstable phase of the Ni_7B_3 compound, revealed first in Ref. (19).

In Table V are given the data on the phase compositions of the deposits isothermally annealed over the temperature range of 150°-700°C. The annealing was

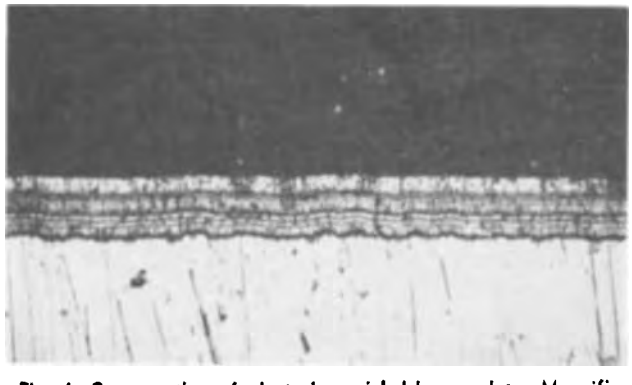

Fig. 4. Cross section of electroless nickel-boron plate. Magnification ×225.

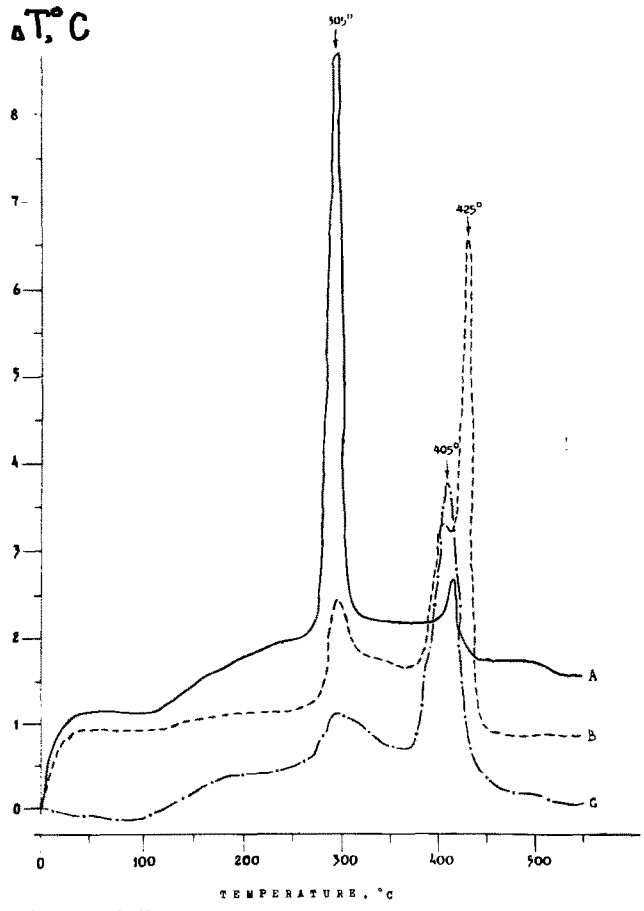

Fig. 5. Differential thermograms of electroless nickel-boron alloys containing 4.3(A), 5.7(B), and 6.4(C) % boron.

carried out in vacuum ($5 \cdot 10^{-4}$ Torr) for 1 hr. After cooling and investigating the structure and properties at room temperature, the specimens were subjected to further annealing at a temperature 50° higher than the preceding one.

The data of this table show that the higher the content of the boron in the alloys the higher the temperature of the formation of Ni_3B. It is consistent with the results of thermographic analysis.

The estimation of the quantity of hydrogen which was included in the Ni-B plate and investigation of the process of its evaluation during heating these plates at the rate of 10°/min were carried out by use of the method of vacuum extraction. It should be noted that the hydrogen content in the alloys is almost independent of the boron content, and equal to about 200 cm^3/100g, but the intensity of its evolution reflects the phase transformation in the coatings proceeding during annealing. Figure 7 shows that the formation of the Ni_3B and Ni_2B (Ni_7B_3) is associated with the additional hydrogen evolution.

Some Properties of Nickel-Boron Plates

The observed dependence of the phase composition on the annealing temperature allows one to under-

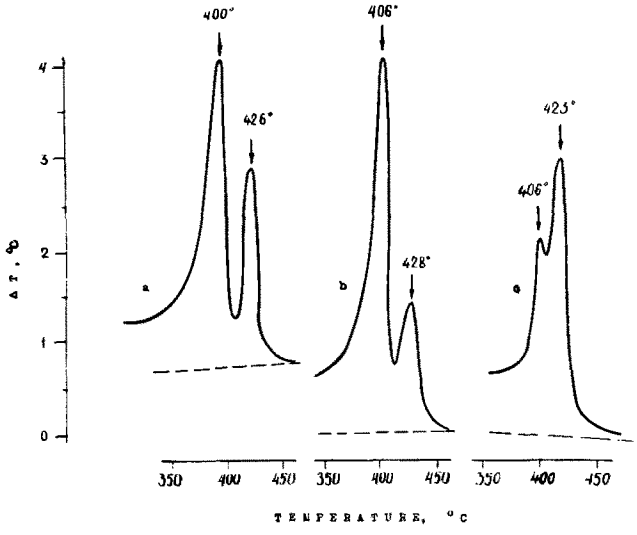

Fig. 6. Differential thermograms of electroless nickel-boron alloys containing 6.9(a), 6.6(b), and 6.5(c) % boron.

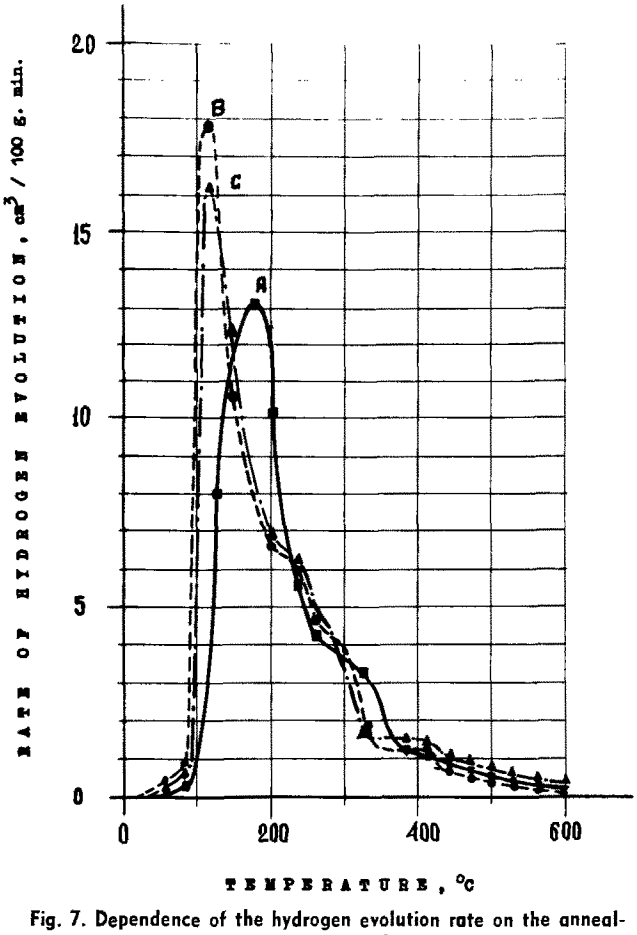

Fig. 7. Dependence of the hydrogen evolution rate on the annealing temperature. Letters correspond to those in Fig. 5.

Table V. Structure of the as-plated and annealed nickel-boron plates

Stabilizer of solution	Specimen	Content of boron in coating, % Wt.	At.	Temperature of heat-treatment, °C: Solid solution of boron in nickel, Amorph.	Crystal.	Ni + Ni_3B	Ni + Ni_3B + Ni_2B	Ni_3B + Ni_2B
$TlNO_3$	A	4.3	19.6	95*	95*	150-700	—	—
—	B	5.7	24.7	95*-150	—	200-250	300-550	600-700
2-mercaptobenzo-thiazole + $PbCl_2$	C	6.4	27.1	95*-200	—	250-300	350-400	450-700

* Without heat-treatment.

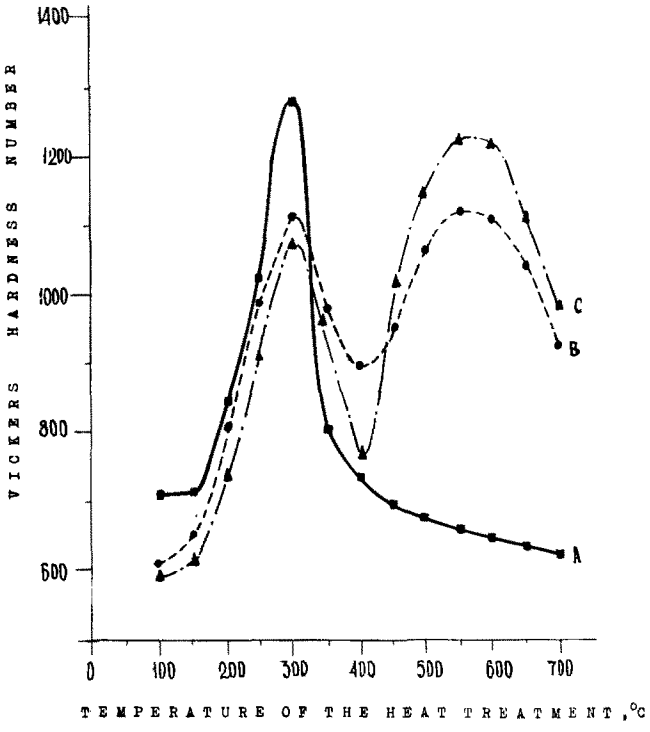

Fig. 8. Dependence of the plate hardness on the annealing temperature. Letters correspond to those in Fig. 5.

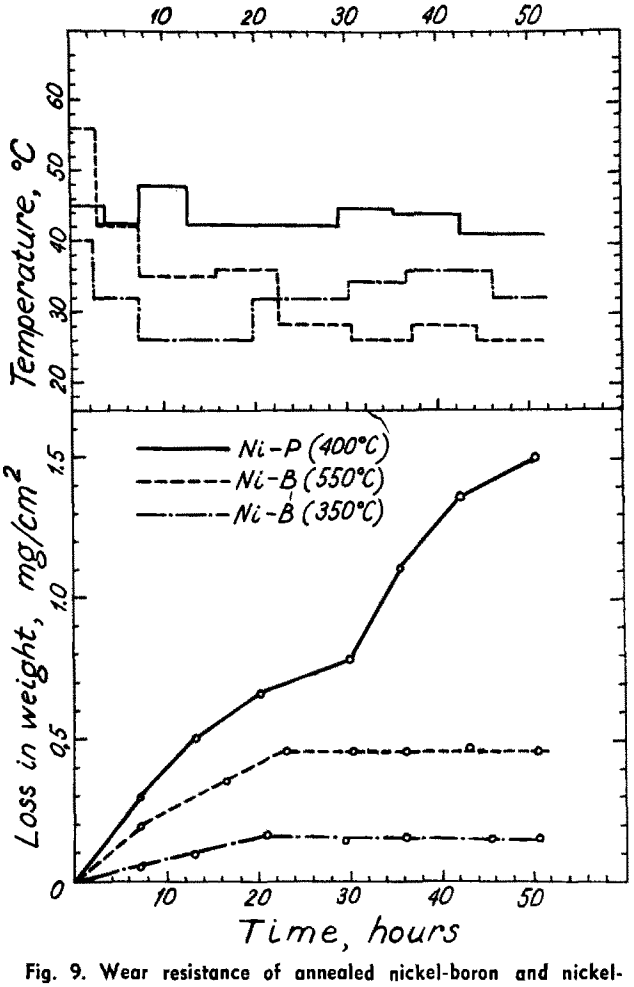

Fig. 9. Wear resistance of annealed nickel-boron and nickel-phosphorus plates.

stand the nature of the changes of the coating properties, observed after heat-treatment.

Hardness.—The hardness of Ni-B deposits plated on a copper substrate was examined on the hardness meter (by Vickers) with diamond pyramid and a load of 50g; the thickness of deposits was in the range of 35-45μ. The increase of plating hardness after isothermal annealing in the ranges 150°-300°C and 400°-550°C shown in Fig. 8 appears to be due to both the dispersion hardening as a result of the Ni_3B and Ni_2B phase formation and their high hardness; the decrease of plating hardness after reaching its maximum value can be considered to be a result of relaxation of the internal stresses and coagulation of boride particles. A very high hardness (~1500 kg/mm²) exceeding the hardness of chromium coatings can be reached if the annealing is carried out in nonisothermal conditions with a rate of heating of 400°/min.

Wear resistance.—The wear resistance of the Ni-B and Ni-P coatings deposited on the hardened steel CT-45 was studied by use of the butt-end friction apparatus; the friction was applied to the nickel-plated specimens by contact with the same steel. The tests were carried out at the specimen rotation rate of 300 rpm under a load of 5 kg/cm² with alcohol-glycerine lubrication. The temperature of the specimens during tests was measured by a thermocouple introduced into the hole of the immovable part of the friction pair.

Figure 9 shows comparative data on the wear resistance of annealed nickel-boron (6.4% B) and

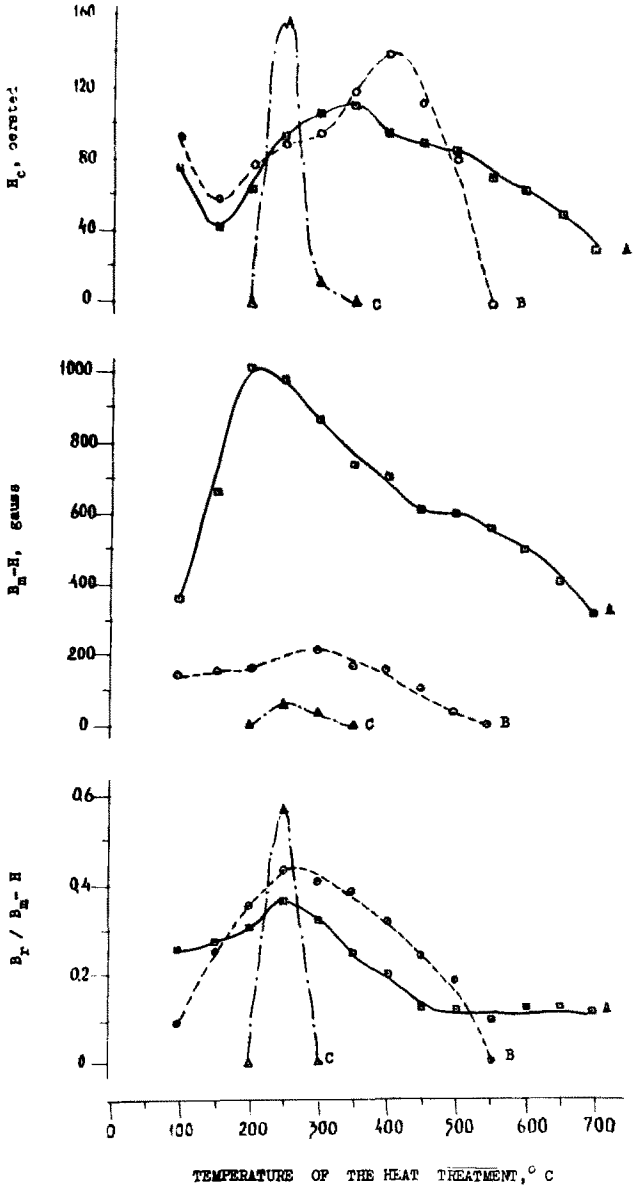

Fig 10. Dependence of the magnetic properties of the electroless nickel-boron plates on the annealing temperature. Letters correspond to those in Fig. 5.

nickel-phosphorus (9.7% P) plates. It is evident from this figure that the wear resistance of the nickel-boron deposits is much higher than that of the nickel-phosphorus alloys. The almost complete absence of the dependence of wear resistance on time is restricted to the nickel-boron deposits. The temperature measurements in the course of testing show the friction coefficient to be lower for the nickel-boron alloys than for the nickel-phosphorus alloys.

Magnetic properties.—It was of special interest to determine to what extent boron incorporation affects the magnetic characteristics of nickel. The measurments of magnetic properties of nickel-boron alloys 35μ thick were carried out by using a combination of ballistic and oscillographic methods in the magnetizing field of 1200 oersteds. The coatings were deposited on copper rods; the length of the specimen was 50 mm and their diameter was 3 mm.

Figure 10 gives the data on the effect of isothermal annealing temperature on the value of maximum induction, the loop rectangularity, and the coercive strength of nickel-boron alloys of different compositions. The effect of boron incorporation on the magnetic properties of nickel is not as strong as that of phosphorus, although in the as-plated state the ferromagnetic properties in nickel-boron alloys cannot be detected beginning with 6.4% B. However, the heating of these coatings to 250°C also resulted in a sharp rise of their magnetic characteristics. It is due to the appearance of the weakly ferromagnetic Ni_3B phase. The changes of magnetic characteristics with further increase of annealing temperature resulting in the formation of the Ni_2B phase, suggest the latter boride to be completely nonferromagnetic.

Acknowledgments

The authors would like to thank Mrs. A. A. Nikiforova for helpful discussions; Mrs. L. S. Barybina for technical assistance; and Dr. V. P. Shcheredin for the mass-spectrometric measurements.

Manuscript submitted June 15, 1972; revised manuscript received Dec. 13, 1972.

Any discussion of this paper will appear in a Discussion Section to be published in the December 1973 JOURNAL.

REFERENCES

1. E. B. Saubestre, *Metal Finishing*, **60** (9), 59 (1962).
2. K. Lang, *Galvanotechnik*, **56** (6), 347 (1965).
3. H. Narcus, *Plating*, **54** (4), 380 (1967).
4. K. M. Gorbunova, M. V. Ivanov, M. M. Melnikova, and A. A. Nikiforova, "Itogi Nauki. Elektrokhimiya 1968," p. 112, VINITI, Moscow (1970).
5. K. M. Gorbunova, M. V. Ivanov, and A. A. Nikiforova, *Zashchita Metal.*, **6** (5), 522 (1970).
6. E. Zirngiebl and H-G. Klein, U.S. Pat. 3,234,031 (1966).
7. E. Zirngiebl and H-G. Klein, U.S. Pat. 3,295,999 (1967).
8. M. V. Ivanov, A. A. Nemodruk, and A. A. Nikiforova, Deponirovano VINITI, No. 1322-70 (1970).
9. L. E. Tsupak, Kandidatskaya dissertatsiya, Moscow, 1969.
10. A. Yu. Prokopchik, Ya. I. Valsyunene, Yu. P. Butkyavichyus, and D. P. Kimtene, *Zashchita Metal.*, **6** (5), 517 (1970).
11. R. M. Lukes, *Plating*, **51**, 969 (1964).
12. T. V. Ivanovskaya and K. M. Gorbunova, *Zashchita Metal.*, No. 2, 477 (1966).
13. A. A. Nikiforova and G. A. Sadakov, *Elektrokhimiya*, **3** (10), 1207 (1967).
14. V. I. Mikheeva and V. Yu. Surs, *Dokl. Akad. Nauk USSR*, **93**, 1, 67 (1953).
15. K. N. Mochalov, N. V. Tremasov, and Kh. V. Shifrin, *Tr. Kazansk. Khim.-Tekhnol. Inst.*, **33**, 95 (1965).
16. M. V. Ivanov, K. M. Gorbunova, A. A. Nikiforova, and V. P. Shcheredin, *Dokl. Akad. Nauk USSR*, **199** (6), 1317 (1971).
17. V. P. Moiseev, G. A. Sadakov, and K. M. Gorbunova, *Zh. Fiz. Khim.*, **42**, 2751 (1968).
18. M. V. Ivanov, V. P. Moiseev, and K. M. Gorbunova, *Dokl. Akad. Nauk USSR*, **194** (3), 610 (1970).
19. Yu. N. Petrov, V. V. Kovalev, and M. M. Markus, *ibid.*, **198** (1), 118 (1971).

The Effect of Third Metal on the Magnetic and Storage Properties of Electrodeposited Permalloy Films

H. V. Venkatasetty*,[1]

Honeywell Corporate Research Center, Bloomington, Minnesota 55420

ABSTRACT

Controlled quantities of reducible metal ions like molybdenum and indium are introduced in the appropriate form into a nickel-iron bath and the magnetic properties of the ternary alloy films of Ni-Fe-Mo and Ni-Fe-In are measured over a wide range of concentration of molybdenum and indium in the bath. These films show much improved magnetic properties as well as some improvement in creep resistant characteristics when compared with permalloy films. The improved properties of these films are discussed in terms of the improved magnetic parameters and thickness.

In recent years electrodeposited ferromagnetic thin films of nickel-iron and nickel-iron containing small quantities of elements like cobalt, copper, molybdenum, arsenic, phosphorus, and sulfur have received considerable attention as possible memory elements in digital computers (1-8). These films have moderately low coercive force (H_c) and uniaxial anisotropy field (H_k), have rectangular hysteresis loops, and much faster switching mode for flux reversal compared to ferrite core material. The magnetic properties such as the wall motion coercive force (H_c), the anisotropy field (H_k), the dispersion of the easy axis (α_{90}), and creep threshold of thin films are important parameters for use as memory elements and these properties are influenced by the substrate characteristics, the composition, and thickness of the films. The most useful memory properties of nickel-iron films are obtained at zero magnetostrictive composition of 80% Ni and 20% Fe. The composition of the electrodeposited films is dependent on the composition of the bath and on the

* Electrochemical Society Active Member.
[1] Present address: Honeywell, Inc., Power Sources Center, Montgomeryville, Pennsylvania 18936.
Key words: magnetic thin film, electrodeposition, ternary alloy, memory element, switching.

plating parameters. In the case of the deposition of nickel-iron films from their simple salt solution (Watts type of bath) the rate of iron deposition is higher (>30%) in the initial stages (~500Å) of the deposit even though the nickel to iron ratio in the bath is about 50:1, and their standard electrode potentials indicate that nickel ($E°$, Ni = −0.25V) should plate out faster than ferrous iron ($E°$, Fe = −0.44) (9). This anomalous codeposition has been attributed to local hydrolysis of iron ions at the cathode and the adsorbed hydroxide causes preferential iron deposition (10). The nonzero magnetostrictive deposit not only results in increased dispersion of the easy axis (α_{90}) and the anisotropy field (H_k) but the memory properties of the film become very sensitive to strain (11). In thin films, a good control on gradients in composition during electrodeposition is necessary to improve the magnetic properties and the storage characteristics. This paper describes the results of experiments carried out in an effort to achieve this.

Experimental Procedure

A citrate complexed nickel-iron bath with nickel to iron ratio ~22:1 was prepared as described elsewhere (12). The Ni-Fe-Mo bath preparation was essentially similar to that described by Freitag and Mathias (3). It was made by dissolving reagent grade chemicals in distilled water, 100g $NiSO_4 \cdot 7H_2O$, 6.9g $FeSO_4 \cdot 7H_2O$, 0.37-1.88g $Na_2MoO_4 \cdot 2H_2O$, 32g citric acid, 15g sodium citrate, 2.5g K_2SO_4, ~0.2g sodium lauryl sulfate, and 1g saccharin, and diluting the solution to one liter. The pH was adjusted to 5.2 by NaOH and/or citric acid, the bath operated at temperatures from 26° to 40°C at a current density of 15.3 mA/cm² to get zero magnetostrictive films. The Ni-Fe-In system was also a citrate-complexed bath but to prepare zero magnetostrictive films, the bath had to contain more iron, 7.5 g/liter $FeSO_4 \cdot 7H_2O$ indium as indium sulfate varied from 0.25 to 2.5 g/liter, the bath *p*H was adjusted to 5.2 and the bath operated from 25° to 35°C at 15:3 mA/cm² current density. As substrates, 10 mil and 40 mil glass slides with chromium and gold evaporated on them were used. The procedure for preparing these films and making magnetic measurements has already been described (12). The reported magnetic parameters represent an average value of at least five samples and the difference between the samples was less than 5%.

The standard spectrophotometric method using a Cary 14 spectrophotometer was used to carry out quantitative estimation of various elements present in the electrodeposits. Iron was separated from the other metals and complexed with 2, 2′-dipyridyl and estimated at 522 mμ (13). Molybdenum was complexed with mercapto acetic acid and estimated at 365 mμ (14). Indium was determined by complexing with 5, 7-dibromo 8-quinolinol and extracting the complex with chloroform and measuring absorbance at 415 mμ (15). These determinations are accurate to ±2%.

In creep measurements large area films (24 × 15 mm), varying in thickness from about 1000 to 5000Å, that were deposited on 10 mil microsheet glass and made conducting with evaporated chromium (~300Å) and gold (~1000Å) were used to minimize demagnetizing field effects. Measurements were made by applying a combination of an a-c field in the hard direction and a d-c field in the easy direction. The observations of the extent of film switching were made by detecting the associated flux changes with a suitable pickup loop and observing the induced signal with the help of an oscilloscope. The various creep and switching curves refer to about 50% of film switching.

Background

In the case of codeposition of two or more metals from a bath prepared by complexing the metal ions with suitable ligands, the resultant deposition potentials of the metals, the relative rates of dissociation of metal complexes, and the diffusion of metal and complex ions control both the deposition process and the structure of the deposit. Although the theory of alloy formation by codeposition which has been treated elsewhere (16, 17) is not well understood (18), it is apparent that the bath composition, the substrate crystal structure, and surface topography (19) as well as the structure of the double layer at the electrode-solution interface influence the deposition process and the properties of the deposit.

It has been shown that in flat thin ferromagnetic films, when a d-c magnetic field is applied in both easy and hard direction, magnetization reversal takes place at a smaller critical field. A plot of this critical field as a function of hard direction d-c field is known as the critical curve for wall motion. However, when an a-c field whose amplitude is equal to the magnitude of the d-c field is substituted in the hard direction, magnetization will creep into a demagnetized state even though the applied field combination is below the uniaxial switching threshold curve (20). The creep threshold has been shown to be dependent on the type of domain walls existing in the film and the types of fields applied (21). It has been shown that the wall creeping is caused by Block-Néel-Bloch wall transitions in thick film (>850Å) and Block line motions in thin film (<850Å) which occur under the influence of the hard direction a-c field (21, 22). Attempts have been made to analyze the nature of domain wall creeping and several mechanisms and models proposed, but the creep mechanism is not well understood (21, 23).

Results and Discussion

When nickel and iron ions were complexed with organic ligands like citrate to control the concentration of free metal ions and to prevent hydrolysis of iron ions and nickel-iron deposited using pulsing current, the composition gradient was minimized, but not eliminated (12). Recently it has been shown that the composition gradient in the initial stages of the deposition process of nickel-iron films can be controlled by adding small quantities of cathodically easily reducible ions like antimony, selenium, or tellurium to the electrolyte so that these nonmagnetic elements are incorporated preferentially in the initially deposited film zones and thus produce more homogeneous films with good magnetic properties (24). It has been shown that zero magnetostrictive films of Ni-Fe-Cu with excellent control over alloy composition and magnetic properties from 400 to 2000Å can be prepared (4). It was thought desirable to investigate Ni-Fe-Mo and Ni-Fe-In systems over a wide range of molybdenum and indium concentration in an appropriate bath because these metals are not only nonmagnetic but may be more easily reduced electrochemically than iron. To prepare such films with zero magnetostriction, the deposition has to be done within a narrow concentration range. Zero magnetostrictive films of Ni-Fe-Mo and Ni-Fe-In covering the thickness range of ~1000-5000Å from a bath with wide range of molybdenum and indium concentrations at known concentration of nickel-iron were prepared and their magnetic properties like H_c, H_k, and α_{90} measured and their composition determined. It should be pointed out that Ni-Fe-Mo films prepared by Freitag and Mathias (3) were 600-800Å thick and were highly magnetostrictive and hence not suited for examining their storage characteristics.

The composition of the deposits as a function of molybdate and indium concentration of the baths are shown in Fig. 1 and 2. It is interesting to note that the iron content remains about 20% (weight) over the entire range of composition in both the systems. The magnetic properties of Ni-Fe-Mo films (~5000Å) as a function of molybdenum content are shown in Fig. 3, while those of Ni-Fe-In films (~5000Å) are shown in Fig. 4. Magnetic parameters and composition measured on zero magnetostrictive thin films (~1200Å) of Ni-Fe-Mo and Ni-Fe-In show similar behavior to those of

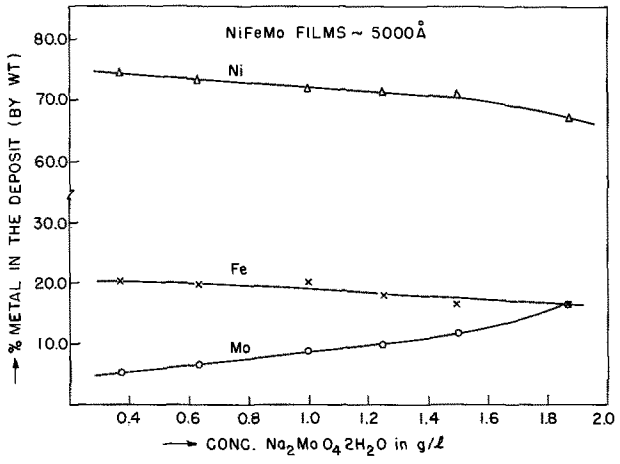

Fig. 1. Variation in the composition of Mo, Fe, and Ni with change in the concentration of molybdenum in the bath.

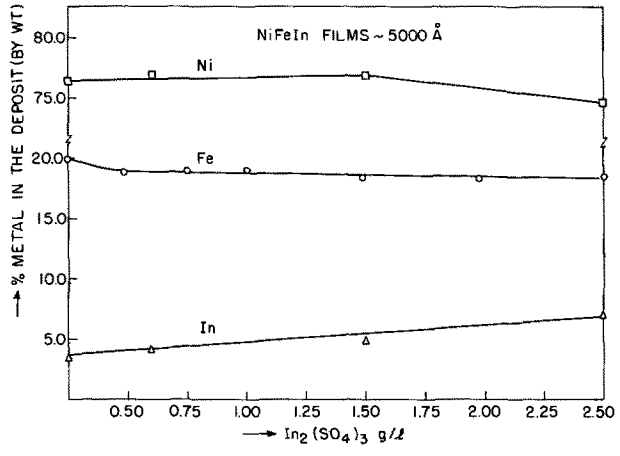

Fig. 2. Variation in the composition of In, Fe, and Ni with change in the concentration of indium in the bath.

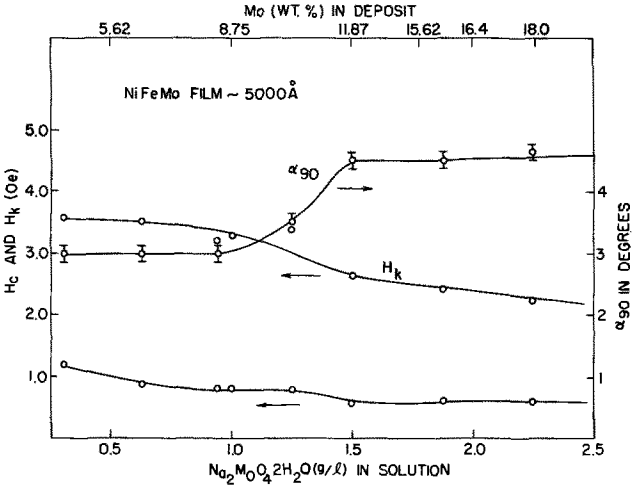

Fig. 3. Variation of H_c, H_k, and α_{90} of Ni-Fe-Mo films with amount of molybdenum in the bath and the amount of molybdenum in the deposit.

5000Å films. The magnetic parameters and iron content in zero magnetostrictive Ni-Fe-In films were determined as a function of thickness from 1000 to 5000Å and are shown in Fig. 5. The iron content of the film remains very close to 20% (weight) above 2000Å but appears to be slightly higher in the initial stages of the deposit. The decrease in H_k with thickness can be attributed to the reduced influence of the initial deposit in the thicker films.

Since very thin films (~1000Å) have low output signals and their magnetic properties are very sensi-

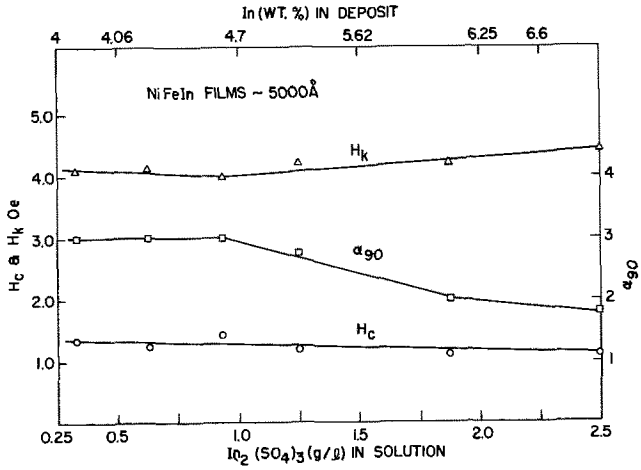

Fig. 4. Variation of H_c, H_k, and α_{90} of Ni-Fe-In films with amount of indium in the bath and the amount of indium in the deposit.

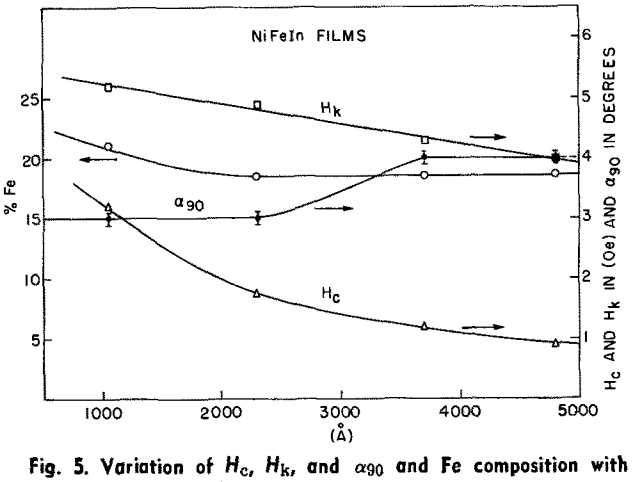

Fig. 5. Variation of H_c, H_k, and α_{90} and Fe composition with thickness of Ni-Fe-In films.

tive to substrate characteristics, it was decided to deposit films of about 5000Å with zero magnetostriction. The wall motion coercive force (H_c) for zero magnetostrictive permalloy films has a logarithmic relationship with thickness of the form $H_c = At^{-B}$ where t is thickness, the constant A relates to substrate roughness, and B to plating conditions (25, 26). In order to increase H_c of these films (~5000Å) with a view to increase their creep threshold, experiments were conducted to relate the magnetic properties of zero magnetostrictive films of Ni-Fe-Mo, Ni-Fe-In, and Ni-Fe with substrate surface roughness by preplating copper at varying current densities and measuring roughness by a radioactive tracer technique (19). As a result of such a study, optimum plating conditions were developed to obtain zero magnetostrictive films of Ni-Fe-Mo, Ni-Fe-In, and Ni-Fe with good magnetic properties.

Some of the parameters that influence the creep threshold in flat magnetic films are the film thickness, film composition, coercive force, anisotropy field, dispersion of the easy axis, and film geometry. The creep threshold measurements are important because the information stored in these memory elements can be destroyed by domain wall creeping under the influence of disturbances occurring in actual memory environment, thus limiting the bit density in memory design. It is therefore necessary to know the maximum field combination for which domain wall creeping still does not occur. Various attempts have been made to increase the disturb threshold for flat films. Although very thin films (~300Å) which have Néel walls have better disturb threshold, they have small signals and

are very sensitive to substrate characteristics. Another approach is to use multilayer films wherein the wall motion coercive force of the composite film is influenced through magnetostatic and exchange coupling effects (27). It has also been shown that the storage properties of Ni-Fe films can be improved either by directly diffusing (28) or electroplating nonmagnetic metal and diffusing (29) into permalloy.

Although a great deal of data on creep measurements is available on vacuum-deposited binary and ternary flat films, very little data are available on electrodeposited films (20, 23, 30, 31). Therefore, zero magnetostrictive films (~1000 and ~5000Å) of Ni-Fe-Mo, with the composition 72.4% Ni, 20% Fe, and 7.6% Mo, and Ni-Fe-In films (~1000 and ~5000Å), with the composition 74% Ni, 20% Fe, and 6% In, with suitable magnetic properties were selected and their creep threshold and switching properties measured and compared with those of 80:20 Ni-Fe films (~1200 and ~5000Å). By noting the separation between the switching and creep curves for each of the films, it is apparent from Fig. 6 that the curves for the Ni-Fe-Mo films (~1000Å) are closer and therefore they exhibit better creep threshold characteristics than those of Ni-Fe-In and Ni-Fe films. In the case of ~5000Å films (Fig. 7) the Ni-Fe-In films have slightly better creep threshold characteristics than Ni-Fe-Mo and Ni-Fe films although the differences are smaller than those in the 1000Å films.

The improved creep thresholds observed in the case of thinner films (~1000Å) compared to those of 5000Å films (Fig. 6 and 7) can be attributed partly to their increased coercive force and partly to reduced demagnetizing field effects. Since the domain wall structure changes with film thickness (12), the dependence of the creep process on film thickness is expected (32, 33). It has been observed recently that in addition to film thickness, film composition also influences creep threshold (34).

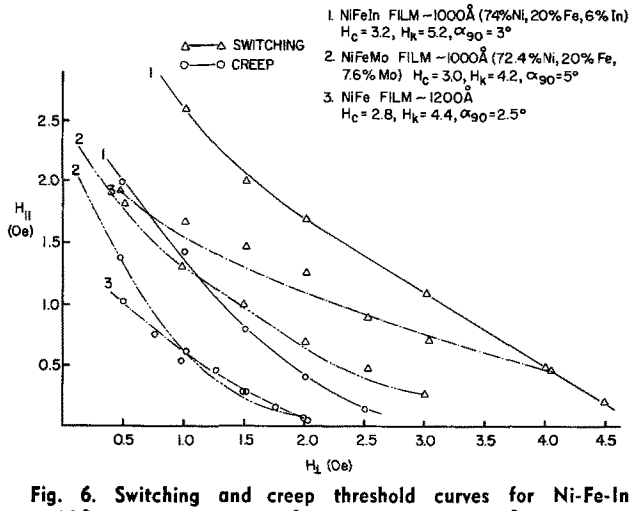

Fig. 6. Switching and creep threshold curves for Ni-Fe-In (~1000Å), Ni-Fe-Mo (~1000Å), and Ni-Fe (~1200Å) films.

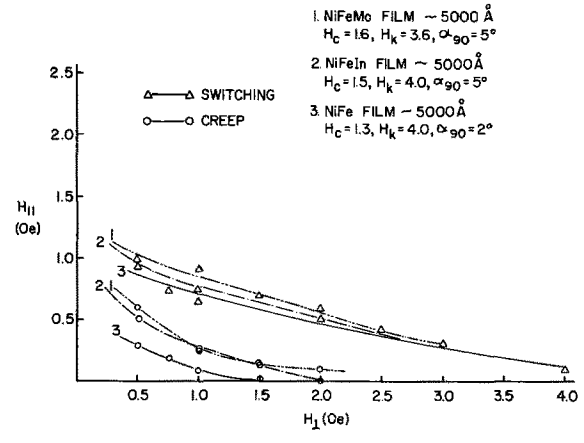

Fig. 7. Switching and creep threshold curves for ~5000Å Ni-Fe-In, Ni-Fe-Mo, and Ni-Fe films.

Conclusion

Zero magnetostrictive Ni-Fe-Mo and Ni-Fe-In films of varying thickness have been prepared. The magnetic properties such as H_c, H_k, and α_{90} of these films containing a wide range of molybdenum and indium have been measured and their composition determined. The films of different thickness with optimum composition were evaluated for their creep threshold and switching properties and compared to those of Ni-Fe films. The improved disturb thresholds of Ni-Fe-Mo and Ni-Fe-In films are attributed to improved magnetic properties and film thickness.

Acknowledgment

The author thanks L. L. Egan, D. Bergum, and C. A. Griep for their technical assistance.

Manuscript submitted May 25, 1972; revised manuscript received Dec. 14, 1972. This was Paper 149 presented at the Cleveland Meeting of the Society, Oct. 3-8, 1971.

Any discussion of this paper will appear in a Discussion Section to be published in the December 1973 JOURNAL.

REFERENCES

1. T. R. Long, *J. Appl. Phys.*, **31**, 1235 (1960).
2. M. W. Segal, *This Journal*, **112**, 174 (1965).
3. W. O. Freitag and J. S. Mathias, *ibid.*, **112**, 64 (1965).
4. J. M. Brownlow, *J. Appl. Phys.*, **38**, 1440 (1967).
5. W. O. Freitag, G. Diguilio, and J. S. Mathias, *This Journal*, **113**, 441 (1966).
6. W. O. Freitag, J. S. Mathias, and G. Diguilio, *This Journal*, **111**, 35 (1964).
7. F. E. Luborsky, *J. Appl. Phys.*, **38**, 1445 (1967).
8. J. S. Mathias and G. A. Fedde, *IEEE Trans. Magnetics*, **MAG-5**, 728 (1969).
9. G. H. Cockett and E. S. Spencer-Timms, *This Journal*, **108**, 906 (1961).
10. H. Dahms and I. M. Croll, *ibid.*, **112**, 771 (1965).
11. E. M. Bradley, *J. Appl. Phys.*, **33**, 1051 (1962).
12. H. V. Venkatasetty, *This Journal*, **117**, 403 (1970).
13. M. L. Moss and M. Y. Mellon, *Ind. Eng. Chem., Anal. Ed.*, **14**, 862 (1942).
14. F. Will, III and J. H. Yoe, *Anal. Chem.*, **25**, 1363 (1953).
15. J. E. Johnson, M. C. Lavine, and A. J. Rosenberg, *Anal. Chem.*, **30**, 2055 (1958).
16. A. Brenner, "Electrodeposition of Alloys," Vol. I and II, Academic Press, New York (1963).
17. Z. Kovac, *This Journal*, **118**, 51 (1971).
18. K. M. Gorbunova and Yu M. Polukarov, "Advances in Electrochemistry and Electrochemical Engineering," Vol. 5, p. 290, C. W. Tobias, Editor, Interscience Publisher, New York (1967).
19. H. V. Venkatasetty, *Plating Journal*, 571 (1972).
20. A. L. Olson and E. J. Torok, *J. Appl. Phys.*, **36**, 1058 (1965).
21. S. Middelhoek, *Z. Angew, Phys.*, **14**, 191 (1962), **18**, 524 (1965).
22. S. Middelhoek, *IBM J. Res. and Dev.*, **6**, 140 (1962).
23. W. Kayser, *IEEE Trans. Magnetics*, **MAG-3**, 141 (1967).
24. J. L. Jostan and A. F. Bogenschutz, *ibid.*, **MAG-5**, 112 (1969).
25. J. C. Lloyd and R. S. Smith, *J. Appl. Phys.*, **30**, 274S (1959).
26. I. W. Wolf, *This Journal*, **108**, 959 (1961).
27. E. Feldtkeller, *Z. Angew, Phys.*, **18**, 532 (1965).
28. A. R. Von Neida and F. B. Hagedorn, *J. Appl. Phys.*, **38**, 1436 (1967).
29. B. Littwin, *IEEE Trans. Magnetics*, **MAG-5**, 511 (1969).
30. S. Middelhoek and D. Wild, *IBM J. Res. and Dev.*, **11**, 93 (1967).
31. W. R. Beam and F. L. Thiel, *IEEE Trans. Magnetics*, **MAG-2**, 31 (1966).
32. E. E. Huber, D. O. Smith, and J. B. Goodenough, *J. Appl. Phys.*, **29**, 294 (1958).
33. S. Methfessel, S. Middelhoek, and H. Thomas, *IBM J. Res. and Dev.*, **4**, 96 (1960).
34. T. H. Beeforth, *Int. J. Contr.*, **1**, 375 (1965).

Molybdenum Carbide by Electrolysis of Sodium Molybdate

A. K. Suri, T. K. Mukherjee, and C. K. Gupta

Metallurgy Division, Bhabha Atomic Research Centre, Trombay, Bombay-85, India

ABSTRACT

Preparation of di-molybdenum carbide from sodium molybdate dissolved in fused bath of sodium carbonate, sodium tetraborate, sodium fluoride, and potassium fluoride was investigated. Under the optimum conditions established, a maximum electrodeposition rate corresponding to 0.5 g/A-hr of the carbide was obtained. In the follow-up investigation the carbide was admixed with monitored amounts of molybdenum dioxide for vacuum thermal sintering treatment to yield molybdenum metal of purity comparable to conventional molybdenum extraction process.

Production methods of molybdenum carbide have been extensively researched. A review on this subject has been forwarded by Schwarzkopf and Kieffer (1), and more recently by Kosolapova (2). Processes based on molybdenum or molybdic oxide carburized with graphite, carbon black, carbonaceous gases, or calcium carbide for the manufacture of di-molybdenum carbide have been patented. There has also been parallel interest in electrometallurgical routes in carbide production. Electrolyses of alkali fluoride-carbonate-borate-molybdic oxide baths have been conducted, and conditions of di- and mono-molybdenum carbide deposition have been established by Andrieux and Weiss (3). In a recent work Heinen *et al.* (4) from the U.S. Bureau of Mines have reported electrolysis of potassium fluoride-potassium chloride-sodium metasilicate and sodium fluoride-potassium fluoride-sodium carbonate-sodium tetraborate baths containing molybdenite for the production of di-molybdenum carbide, the maximum yield being 0.42 g/A-hr. No reference is found on any previous work producing molybdenum carbides from molybdates such as calcium and sodium molybdate. Molybdenum electrowinning processes on laboratory scale from calcium molybdate have been recently investigated (5). With sodium molybdate on the other hand Campbell (6) reported that not much success on metal deposition was achieved in aqueous or organic electrolytes. This alkali molybdate, because of its low fusion temperature (627°C) without any decomposition, has been considered as a preferred salt in molten electrolyte systems also. Senderoff and Brenner (7) examined the possibility of inert atmosphere fused salt electrolysis of molybdenum in various baths. In the instance of sodium molybdate dissolved in molten sodium chloride-potassium chloride the cathodic deposit consisted of molybdenum metal, di-molybdenum carbide, and lower oxides.

Studies incorporated in the present paper pertain to production of di-molybdenum carbide by molten salt electrolysis of sodium molybdate. A similar tungsten compound, sodium tungstate which has been successfully electrolyzed for tungsten carbide production may be pointed out here as a reference (8) of interest. The paper also embodies an extension of work involving metal preparation from the carbide electrowon from sodium molybdate.

Electrolysis

Chemicals used in the electrolytic investigation included sodium fluoride, potassium fluoride, sodium tetraborate, sodium carbonate, and sodium molybdate. With the exception of sodium molybdate these were commercial or technical grade available from the open market. Sodium molybdate was prepared in the laboratory through chemical dissolution of commercial molybdenum trioxide in soda-ash solution.

Key words: fused salt electrolysis, sodium molybdate, molybdenum carbide, molybdenum.

Electrolyses were conducted in 8 in. high by 2 in. ID open cells made of high density graphite serving as both anode and electrolyte container. A ½ in. diameter graphite rod suspended centrally into the molten bath functioned as the cathode. The cell was heated externally by a resistance furnace and the direct current for electrolysis was furnished by a 0-250A, 0-12V stepless selenium rectifier. In batch electrolysis, 350g of total salt mixture was formed according to the composition desired, charged into the graphite crucible, furnaced, and the temperature was raised gradually to the intended level. At any desired test temperature the graphite cathode rod was lowered and held above the molten bath for drying before immersion. Positioned at 1 in. from the crucible bottom (total bath depth 3.5 in.) the cathode rod was allowed to attain the electrolyte temperature before starting the electrolysis. Amperage appropriate to a desired initial cathode current density was regulated with voltage varying between 0.5 and 1V. At the end of 10 A-hr the cathode was lifted and the deposit immediately scraped, leached first in water and then in 10% HCl solution before final washing and drying. The effects of different experimental parameters, viz., the cathode current density, sodium molybdate, sodium carbonate concentrations, and temperature on the quality and yield of electrodeposits as shown in Table I were investigated. These are discussed below.

Cathode current density.—An electrolyte bath at 10 weight per cent (w/o) sodium molybdate composition, maintained at 1000°C, was tested at different cathode current densities varying from 300 to 1350 A/ft^2. In each case adherent shining silvery crystals, identified as Mo_2C by x-ray diffraction determination, were obtained. There was, however, no observable effect on the yield. In the cathode current density range investigated, the rate of di-molybdenum carbide deposition varied from 0.225 to 0.3 g/A-hr.

Sodium molybdate.—From electrolyses carried out at 1000°C and a cathode current density of 800 A/ft^2, the following corresponding values of sodium molybdate content (w/o) and di-molybdenum carbide deposition rate (g/A-hr) were obtained: 10, 0.3; 16, 0.42; 18, 0.315; 20, 0. It can be seen that at 16 w/o sodium molybdate concentration a maximum deposition rate of 0.42 g/A-hr occurred. Further addition of sodium molybdate in the bath resulted in a declining deposition rate. Almost no carbide deposition at 20 w/o composition suggested the bath to be in a condition where carbide redissolution appeared competitive to its cathodic deposition.

Sodium carbonate.—Holding the bath composition at 16 w/o sodium molybdate, with other operational parameters, cathode current density (800 A/ft^2) and temperature (1000°C) fixed, experiments were performed to examine the cathodic deposition with sodium carbonate additions varying from 0 to 30 w/o.

Table I. Influence of cathodic current density, bath composition, and temperature in the molten-salt electrolysis of sodium molybdate

Run No.	Electrolyte composition (weight per cent) Na_2MoO_4	Na_2CO_3	$Na_2B_4O_7$	NaF	KF	Temp. (°C)	Cathode current density (A/ft²)	Deposition rate (g/A-hr)	Product X-ray diffraction determination Major	Minor	Trace	Remarks
1	10	14	4	37	35	1000	300	0.26	Mo_2C	—	—	Adherent silvery crystals of Mo_2C
2	10	14	4	37	35	1000	800	0.30	Mo_2C	—	—	Adherent silvery crystals of Mo_2C
3	10	14	4	37	35	1000	1000	0.28	Mo_2C	—	—	Adherent silvery crystals of Mo_2C
4	10	14	4	37	35	1000	1350	0.225	Mo_2C	—	—	Adherent silvery crystals of Mo_2C
5	16	14	4	34	32	1000	800	0.42	Mo_2C	—	—	Adherent silvery crystals of Mo_2C
6	18	14	4	33	31	1000	800	0.315	Mo_2C	—	—	Adherent silvery crystals of Mo_2C
7	20	14	4	32	30	1000	800	—	—	—	—	Practically no deposition
8	16	0	4	43	37	1000	800	0.365	Mo_2C	Mo	[a]	Grayish appearance of deposit
9	16	10	4	36	34	1000	800	0.34	Mo_2C	—	—	Adherent silvery crystals of Mo_2C
10	16	20	4	31	29	1000	800	0.273	Mo_2C	—	—	Adherent silvery crystals of Mo_2C
11	16	30	4	26	24	1000	800	0.22	Mo_2C	—	—	Adherent silvery crystals of Mo_2C
12	16	14	4	34	32	960	800	0.50	Mo_2C	—	—	Adherent silvery crystals of Mo_2C
13	16	14	4	34	32	900	800	0.345	Mo_2C	—	—	Adherent silvery crystals of Mo_2C

[a] Unidentified.

The electrolysis with no sodium carbonate produced lusterless electrodeposits at 0.365 g/A-hr. The material on x-ray examination was found to be a mixture of di-molybdenum carbide, molybdenum metal, and trace amount of unidentified phase. Di-molybdenum carbide free from other associations started appearing at and above 10 w/o sodium carbonate concentrations. A maximum rate of 0.42 g/A-hr was obtained at 14 w/o of sodium carbonate. Any further increase of concentration was ineffective in improving the carbide yield as shown in run No. 10 and 11 in Table I.

Temperature.—The electrolysis at a cathode current density of 800 A/ft², with a bath composition (in w/o) of: 16 Na_2MoO_4, 14 Na_2CO_3, 4 $Na_2B_4O_7$, 34 NaF, and 32 KF, produced a maximum rate of deposition of 0.5 g/A-hr at a test temperature of 960°C. Electrolyses carried out at lower (900°C) and higher (1000°C) temperatures yielded reduced deposition rates as shown in run No. 13 and 5, Table I.

Adopting the optimum operational parameters with which maximum yield (0.5 g/A-hr) was obtained, a larger scale electrolysis was conducted in a 4 in. ID by 8 in. high graphite cell. In a 200 A-hr electrolysis test about 100g of carbide was recovered. The electrodeposit after initial x-ray examination as di-molybdenum carbide was further evaluated. Combustion of the carbide in air gave a weight gain of 40.6% compared to the theoretical value of 41.2%. The carbon and oxygen content of the electrowon carbide were 6 (theoretical 5.9%) and 0.03%, respectively.

Metal Preparation

Utilization of di-molybdenum carbide electroextracted from sodium molybdate was studied in an additional area of interest. In a reference quoted earlier, preparation of di-molybdenum carbide by electrosynthesis of molybdenite was pointed out. In addition, the work also was concerned with metal preparation by inert atmosphere sintering of the electrosynthesized carbide and molybdenum trioxide mixture. Sintered product was finally arc-melted into buttons for which a lowest hardness value of 172 VPN was reported. Except for this single reference there seemed to have been no other work involving carbide conversion to metal. The present work dealt with the metal preparative route through vacuum thermal treatment of di-molybdenum carbide and molybdenum dioxide.

Molybdenum dioxide was prepared by hydrogen reduction of molybdenum trioxide at 450°C. The reduced product was then calcined under a flowing HCl gas stream at red heat to effect removal of residual MoO_3 as $MoO_3 \cdot 2HCl$. A series of charges composed of 5g of di-molybdenum carbide dry mixed intimately with variable amounts of molybdenum dioxide were prepared. These charges were pelletized at 25 tons/in.² and subsequently each was examined for its response to vacuum thermal treatment carried out in a 12 kW tantalum resistance furnace. The thermal treatment commenced at the vacuum level of 5×10^{-5} Torr. The first break in vacuum indicating the onset of carbide-oxide reaction, was observed around 600°C. Under controlled heating and vacuum conditions the temperature was gradually raised to 1400°C and soaked for 30 min. During the final stage the furnace vacuum levelled at better than 2×10^{-5} Torr. The sintered products were argon arc-melted and evaluated rapidly for the purity by hardness testing. The percentage of molybdenum dioxide in the carbide-oxide mixture was varied from 0 to 15% excess over stoichiometric. The product resulting from using 10% molybdenum dioxide in excess of stoichiometric on melting recorded the lowest hardness value of 170 VPN. This hardness value, it may be mentioned here, is close to the value reported for the arc-cast molybdenum produced by hydrogen reduction of molybdenum trioxide.

Conclusion

The preparation of Mo_2C type molybdenum carbide was demonstrated by molten salt electrolysis of sodium molybdate. Carbide yield corresponding to 0.5 g/A-hr was achieved under the following conditions: bath composition (w/o) 16 Na_2MoO_4, 14 Na_2CO_3, 4 $Na_2B_4O_7$, 34 NaF, 32 KF; bath temperature 960°C; and the cathode current density of 800 A/ft².

Electrowon Mo_2C in further work was thermally reacted under vacuum with monitored amounts of MoO_2 to yield a product whose melt hardness was 170 VPN, similar to arc-cast molybdenum values.

Acknowledgments

The authors gratefully acknowledge Shri C. V. Sundaram, Head, Extractive Metallurgy Section, for his interest in the present work and Dr. V. K. Moorthy, Head, Metallurgy Division, for his kind approval in the publication of this research report.

Manuscript received July 26, 1972.

Any discussion of this paper will appear in a Discussion Section to be published in the December 1973 JOURNAL.

REFERENCES

1. P. Schwarzkopf and R. Kieffer, "Refractory Hard Metals," pp. 128-137, The MacMillan Co., New York (1953).
2. T. Ya. Kosolapova, "Carbides," pp. 59, 159, Plenum Press, New York and London (1971).
3. J. L. Andrieux and G. Weiss, *Bull. Soc. Chim. France*, **15**, 598 (1948).
4. H. J. Heinen, C. L. Barber, and D. H. Baker, Jr., *U.S. Bur. Mines, Rept. Invest. 6590* (1965).
5. B. I. Khlebnikov and A. P. Nadolskii, *Tr. Ivkutsk. Politekh Inst. No. 47*, 20 (1969).
6. T. T. Campbell, *This Journal*, **106**, 119 (1959).
7. S. Senderoff and A. Brenner, *ibid.*, **101**, 25 (1954).
8. J. M. Gomes and M. M. Wong, *U.S. Bur. Mines, Rept. Invest. 7247* (1969).

Behavior of the Silver, Silver Chloride Electrode in Concentrated Aqueous Sodium Chloride

H. Frank Gibbard, Jr.

Department of Chemistry and Biochemistry, Southern Illinois University, Carbondale, Illinois 62901

ABSTRACT

The reported solute and solvent activities of concentrated aqueous sodium chloride are not thermodynamically consistent within the apparent experimental errors. This result is attributed to a deviation of the silver, silver chloride electrode owing to the formation of a solid solution of silver chloride and sodium chloride. Electrochemical cell measurements and x-ray diffraction results are reported in support of these conclusions. The mole fractions and activities of silver chloride in the solid solutions are calculated from solubility equilibria and are correlated with literature values of the activity coefficients of sodium chloride.

The thermodynamic properties of aqueous sodium chloride have been studied more extensively than those of any other electrolyte. The activity of the solvent has been measured in dilute solutions (1) and in concentrated solutions (2, 3) by freezing point measurements and in concentrated solutions near room temperature (4-6) by direct vapor pressure measurements. The solute activity has been determined from electrochemical cell measurements in both dilute (7) and concentrated (8-10) solutions.

The thermodynamic consistency of the solvent and solute activity data is quite important owing to the use of sodium chloride as the standard reference substance in most isopiestic vapor pressure studies. In dilute solution the osmotic coefficients calculated from solute activity data by integration of the Gibbs-Duhem equation are in satisfactory agreement with the values obtained directly from solvent activity data. At concentrations higher than 2*M* the osmotic coefficients calculated from solute and solvent activities differ, and this difference reaches nearly 2% for saturated sodium chloride at 25°C (6, 9). This discrepancy seems quite large in view of the apparent precision of 0.1-0.2% in the osmotic coefficients determined by vapor pressure measurements (4-6, 11).

The electrochemical cell measurements of Harned and Nims (8), Lanier (9), and Caramazza (10) all rely on the silver, silver chloride electrode, and they are in agreement within a few tenths of a millivolt from 0 to 4*M*. Because of the variety of ways in which reference electrodes may fail in concentrated electrolyte solutions, we suspected a failure of the silver, silver chloride electrode to be responsible for the inconsistency in the solvent and solute activities. In this paper electrochemical experiments which confirm the imperfection of the silver, silver chloride electrode in concentrated aqueous sodium chloride are reported. Further experiments and calculations are used to explain this behavior in terms of the formation of a solid solution of silver chloride and sodium chloride.

Key words: activity, electrolyte, solution, electrochemical.

Experimental

Electrochemical Measurements

An H-type cell with a stopcock in the horizontal arm was constructed to measure the emf of the cell

$$Ag(s) \mid AgCl(s) \mid NaCl(aq) \mid Hg_2Cl_2(s) \mid Hg(l) \quad [1]$$

as a function of sodium chloride concentration. Silver, silver chloride electrodes of the thermal-electrolytic type were made according to the method of Bates (12) and calomel electrodes by the method of Hills and Ives (13). The extensive precautions suggested by these authors regarding purification of materials and preparation of the electrodes were followed carefully. Precipitated rather than electrolytic calomel (13) was used in these studies. The outside of the cell was painted black to avoid possible deterioration of the light-sensitive halides.

Sodium chloride was purified by the following procedure: chlorine gas was bubbled through a nearly saturated salt solution to remove bromide; then hydrogen chloride gas was passed through the solution to precipitate sodium chloride. The precipitate was fused in platinum crucibles under dry nitrogen, cooled, and ground to a fine powder, and stored in a desiccator.

The H cell was placed in a water bath at 25.00 ± 0.01°C. EMF measurements were made with a calibrated Leeds and Northrup Type K-5 potentiometer. All recommendations of the manufacturer regarding grounding and shielding of the electrochemical cell, the potentiometer and its power supply, null detector, and standard cell were followed. Nitrogen passed first over red-hot copper turnings in a quartz tube and then through presaturators was bubbled through the cell compartments to exclude oxygen. The presaturators were immersed in the water bath and contained solution of the same concentration as that in the cell. Their use permitted operation of the cell for several days without appreciable changes in the concentration of the cell solution.

Six silver, silver chloride electrodes were prepared; the largest difference in potential between any two of these electrodes in 0.01*M* hydrochloric acid was 20 μV. After their preparation these electrodes were stored immersed in conductivity water in the dark.

Measurements were made at sodium chloride concentrations of 0.100, 3.658, and 4.597*M*. Separate portions of the two more concentrated solutions were shaken for 48 hr with amounts of silver chloride and calomel just sufficient to saturate the solutions at room temperature. These saturated or nearly saturated solutions were used in the cell compartments to prevent excessive dissolving of the electrode materials. At 0.100 and 3.658*M* the cell required 2 days to reach a stable equilibrium; the most concentrated solution required 3 days. The criterion of equilibrium was taken as stability of the cell potential within 10 μV for 2-3 hr. The extreme sluggishness of the cell was caused by the calomel electrode. A fresh silver, silver chloride electrode, rinsed several times with solution of the same concentration as the cell solution, would reach equilibrium within 4-5 hr after its insertion into the cell.

Two silver, silver chloride electrodes were used at each concentration, and the cell potential was taken as the average of the readings of these two *vs.* the calomel electrode. The largest deviation between a pair of silver, silver chloride electrodes at equilibrium was 19 μV.

X-Ray Powder Studies

Materials.—Matheson, Coleman and Bell analytical reagent grade sodium chloride and silver nitrate were dried overnight at 115°C and used without further purification. Silver chloride was prepared by dropwise addition of 0.1M silver nitrate to 0.1M sodium chloride. The precipitate was filtered and washed thoroughly with 0.01M nitric acid and dried overnight at 115°C.

Procedure.—A 5g sample of silver chloride was ground with a mortar and pestle to a fine powder. The powdered sample was placed in an Erlenmeyer flask, 250 ml of 4, 5, or 6*M* sodium chloride was added, and the flask was capped. The solution was stirred for 72 hr at 25° ± 1°C. The solid was recovered by filtration in a porcelain crucible, dried for 30 min by suction, and dried several hours at 115°C.

The suspected solid solutions and samples of pure sodium chloride and silver chloride were ground to fine powders and sieved. Initially powder x-ray diffraction patterns were recorded on the General Electric XRD-5 Diffractometer; more precise a_o values were obtained by the use of a precision back-reflection symmetrical focusing powder camera (14, 15). Positions of the Cu K_α lines were estimated to 0.01 mm by the use of a Nikon optical comparator. Best values for the a_o parameters were obtained by plotting apparent a_o values against $\cos^2\theta$ and extrapolating to $\cos^2\theta = 0$.

Results and Discussion

Because of the known tendency of silver chloride to form complex anions in concentrated chloride solutions (16), a junction potential in our cell due to the increased solubility of silver chloride might be suspected. However, Gerke (17) and Randall (18), in careful measurements on the cell

$$Ag(s) \mid AgCl(s) \mid HCl(aq) \mid Hg_2Cl_2(s) \mid Hg(l) \qquad [2]$$

found the potential to be independent of chloride concentration up to nearly 15*M*. This result suggests that the suspected anomalous potential of the silver, silver chloride electrode must be related to the presence of sodium ion, not chloride ion.

The present electrochemical cell measurements strongly support a change in the silver, silver chloride electrode induced by sodium ion at high concentrations. For the cells [1] and [2] the change in state for the passage of one Faraday of electricity is

$$Ag(s) + \tfrac{1}{2}\,Hg_2Cl_2(s) = AgCl(s) + Hg(l) \qquad [3]$$

The emf of this cell should be independent of electrolyte concentration unless the activity of one of the solids or of liquid mercury should vary from unity. The experimental potentials presented in Table I clearly show a variation with sodium ion concentration. The values at 0.100*M* may be compared with the values obtained from the standard reduction potentials at 25° of the calomel electrode on the first day after its preparation (19), 0.26797V; the calomel electrode at equilibrium (20) 0.26812V; and the silver, silver chloride electrode (21), 0.22234V. The corresponding values for the "first day" and stable calomel electrode for cell [1] are 0.04562 and 0.04578V, respectively. The agreement with the values of Table I shows the remarkable reproducibility of both electrodes in dilute solutions.

The deviations of the potential ξ of cell (1) from the standard potential ξ° are consistent with a silver chloride activity of less than unity. This follows if it is assumed that calomel, silver, and mercury are at unit activity, in which case for cell [1] at 25°

$$\xi - \xi^\circ = -0.05915 \log_{10} a_{AgCl} \qquad [4]$$

That the activity of silver chloride might be less than unity is suspected because of the known complete miscibility of silver chloride and sodium chloride in the solid phase at high temperatures (22-28). Below about 170°C a miscibility gap appears in the phase diagram for the solid solutions; at room temperature the gap extends from about 5 to 87 mole per cent (m/o) sodium chloride (28, 29). A reasonable assumption is that silver chloride in equilibrium with a concentrated sodium chloride solution forms a solid solution dilute in sodium chloride.

Formation of a solid solution should affect the mechanical, electrochemical, and other properties of solid silver chloride. However, the most direct evidence for solid solution formation comes from the x-ray diffraction results which are discussed below.

The extrapolations used to find the lattice parameters a_o for pure silver chloride and the solid solutions are shown in Fig. 1. Only the lines corresponding to diffraction angles greater than 65° were used in making the extrapolation. The variation of a_o with the concentration of sodium chloride in which the precipitates were immersed is reproducible and independent of sample equilibration time from 48 to 108 hr. We have found no suitable explanation for this variation except solid solution formation. No sodium chloride diffraction lines were present in the solid solution diffraction films. The lattice parameters determined from Fig. 1 and a similar extrapolation for sodium chloride are given in Table II. In the first column the solids are identified; the second column gives the a_o parameters determined from our measurements. The third column shows the mole percentage of sodium chloride in the

Table I. Electromotive force of cell [1] at 25°C

m_{NaCl} (mol kg^{-1})	ξ_{avg} (V)
0.100	0.045812
	0.045622*
3.658	0.046242
4.597	0.046414

* "First day" calomel electrode.

Table II. Results of x-ray diffraction measurements

Solid	a_o (Å)	Mole per cent NaCl
NaCl	5.6406	100.0
AgCl	5.5504	0.0
AgCl (4*M* NaCl)	5.5515	1.2
AgCl (5*M* NaCl)	5.5530	2.9
AgCl (6*M* NaCl)	5.5546	4.7

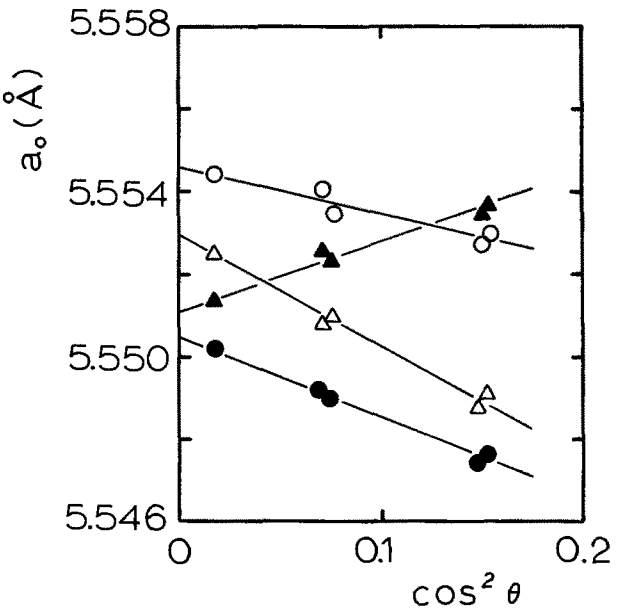

Fig. 1. Determination of lattice parameters for silver chloride and solid solutions. Filled circles, pure AgCl; filled triangles, solid treated with 4M NaCl; open triangles, solid treated with 5M NaCl; open circles, solid treated with 6M NaCl.

solids calculated by Vegard's law, which has been shown to be valid for NaCl-AgCl solid solutions (26).

An independent method of calculating the compositions of the solid solutions in equilibrium with aqueous sodium chloride of any concentration may be derived from the criterion for equilibrium in this heterogeneous system. At equilibrium at constant temperature and pressure the chemical potential of sodium chloride has the same value in the solid and aqueous phases; thus the activity of sodium chloride in the solid phase is proportional to its activity in the aqueous phase. This relation may be written

$$f_2 x_2 = m_{Na^+} m_{Cl^-} \gamma_\pm^2 / K \qquad [5]$$

where f_2 and x_2 are the activity coefficient and mole fraction of sodium chloride in the solid phase, m_i is the molality of ion species i, $\gamma_\pm$ is the mean molal ionic activity coefficient of sodium and chloride ions in the aqueous phase, and K is the solubility product constant of sodium chloride. The constant K is evaluated from the equilibrium solubility of sodium chloride at 25°C, 6.144M, and the activity coefficient, 1.0004 (6). Setting $x_2 = f_2 = 1$, we find $K = 37.78$.

In order for Eq. [5] to be used for an accurate calculation of x_2, the dependence of f_2 on x_2 must be known. This may be found from an expression for the Gibbs function of mixing and the limits of miscibility of the solid solution at 25°C. The Gibbs function of mixing the pure components to form the solid solution is defined by

$$G^M \equiv n_1(\mu_1 - \mu_1^\circ) + n_2(\mu_2 - \mu_2^\circ) \qquad [6]$$

where μ_i is the chemical potential of component i in the solution, and μ_i° is the molar Gibbs function of pure component i. We assume that the Gibbs function of mixing per mole of solid solution, $\bar{G}^M$, may be expressed by

$$\bar{G}^M/RT = x_1 \ln x_1 + x_2 \ln x_2 + Bx_1x_2 + Cx_1x_2(1 - x_2/2) \qquad [7]$$

where R is the gas constant, T is the absolute temperature, and B and C are functions of temperature and pressure but not of composition. Expressions for the logarithms of the activity coefficients of the components may be derived from Eq. [7]; these are given by

$$\ln f_1 = (B + 3C/2)x_2^2 - Cx_2^3 \qquad [8a]$$

$$\ln f_2 = Bx_1^2 + Cx_1^3 \qquad [8b]$$

The condition for a miscibility gap in the solid solution is that a single straight line be tangent at the two solubility limits to the curve of $\bar{G}^M/RT$ *vs.* x_2. After some algebra this condition with the solubility gap extending from $x_2 = 0.05$ to $x_2 = 0.87$ gives $B = 1.5445$; $C = 1.7408$. Insertion of these values into Eq. [5] and [8b] gives

$$x_2 = (m^2\gamma_\pm^2/37.78)\, e^{-(1.5445x_1^2 + 1.7408x_1^3)} \qquad [9]$$

where it is assumed that the effect on m_{Cl^-} and $\gamma_\pm$ of dissolved silver chloride is negligible, so that $m_{Cl^-} = m_{Na^+} = m$.

With the use of sodium chloride activity data (6) Eq. [9] may be solved iteratively for the mole fraction of sodium chloride in the solid solution at various sodium chloride concentrations. The results of these calculations are presented in the first three columns of Table III. Comparison of the values of x_2 at 4.0, 5.0, and 6.0M sodium chloride with the experimental values of Table II shows fairly good agreement.

The calculation of the effect of solid solution formation on electrochemical cell measurements is straightforward. Harned and Nims (8) and Caramazza (10) used sodium amalgam cells which may be written

$$\text{Ag(s)} \mid \text{AgCl(s)} \mid \text{NaCl(aq,m')} \mid \text{Na(in Na}_x\text{Hg)} \mid \text{NaCl(aq,m")} \mid \text{AgCl(s)} \mid \text{Ag(s)} \qquad [10]$$

The reference solution with molality m' is so dilute that solid solution formation is entirely negligible in the left side of the cell. For thermodynamic comparisons we are interested in the value of the logarithm of the apparent mean activity coefficient, $(\gamma_\pm")_{app}$, calculated with the neglect of solid solution formation, less the true value of the logarithm of the activity coefficient. This difference is given by

$$\log(\gamma_\pm")_{app} - \log\gamma_\pm" = -(\tfrac{1}{2})\log a"_{AgCl} \qquad [11]$$

Values of the right side of Eq. [11] calculated by Eq. [8a] and [9] are given in the fourth column of Table III.

For a comparison with experimental results we identify the "true" values of $\gamma_\pm"$ with those calculated from solvent activities (6, 11) and the "apparent" values with those determined by electrochemical cell measurements. Values of the left side of Eq. [11] are plotted in Fig. 2 for the measurements of Harned and Nims (8) and Caramazza (10), and for the results of Lanier (9), who used a sodium-sensitive glass electrode in combination with a silver, silver chloride electrode. The broken curve shows the prediction of Eq. [8a], [9], and [11]. The agreement of the calculated curve with Caramazza's values is good up to 4M. At higher concentrations his values of the activity coefficients give large positive deviations from our curve and from Lanier's results. The points labeled "this work" are calculated from Eq. [4] and [11] and the experimental results of Table I. The calculation from solubility considerations of both the compositions of the solid solutions and the deviations of the

Table III. Mole fractions and activities of silver chloride in solid solutions at 25°C

m_{NaCl} (mol kg^{-1})	a_{NaCl}	x_{AgCl}	$-0.5 \log_{10} a_{AgCl}$
1.0	0.4365	0.9996	0.00005
1.5	0.9807	0.9990	0.0002
2.0	1.8031	0.9982	0.0004
2.5	2.9817	0.9970	0.0006
3.0	4.6204	0.9952	0.0010
3.5	6.8594	0.9928	0.0015
4.0	9.8646	0.9893	0.0022
4.5	13.870	0.9844	0.0032
5.0	19.149	0.9771	0.0046
5.5	26.056	0.9660	0.0065
6.0	34.985	0.9473	0.0093

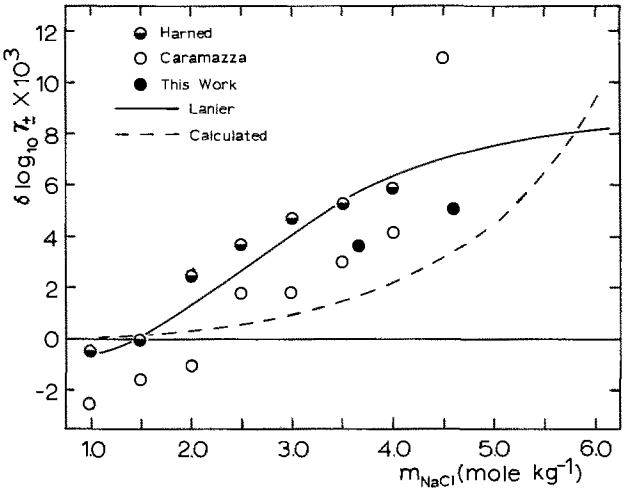

Fig. 2. Deviations of activity coefficients derived by electrochemical cell measurements from those determined by solvent activities.

emf results yields strong support to the present interpretation of those deviations.

Further evidence in support of solid solution formation comes from the mechanical properties of silver chloride immersed in concentrated aqueous sodium chloride. Levine *et al.* (30) and Westwood *et al.* (31) found that treatment of both polycrystalline and single-crystal forms of silver chloride with concentrated sodium chloride solution greatly embrittles the solid. The effect becomes evident at concentrations of 2-3*M* sodium chloride but is not found with potassium chloride or cesium chloride. These observations are consistent with solid solution formation at the surface of silver chloride crystals. It is just at concentrations of 2-3*M* that solid solution formation begins to cause significant deviations in the emf measurements. Neither potassium ion nor cesium ion is compatible with the silver chloride lattice, so no solid solution formation would be expected with these ions.

Acknowledgments

The author thanks Research Corporation and the Southern Illinois University Office of Research and Projects for financial aid, and Mr. Joseph Tucker and Mr. Larry Yen for their help in the x-ray studies.

Manuscript received June 14, 1972.

Any discussion of this paper will appear in a Discussin Section to be published in the December 1973 JOURNAL.

LIST OF SYMBOLS

a_{AgCl}	activity of solid silver chloride
B, C	Margules coefficients
f_i	rational activity coefficient of ith component in the solid state
G^M	Gibbs function of mixing, cal
$\overline{G}^M$	molar Gibbs function of mixing, cal/mole
K	solubility product constant
m_i	molality of ith species, mole/kg
n_i	number of moles of ith component, mole
R	gas constant, cal mole^{-1} K^{-1}
T	absolute temperature, °K
$\gamma_\pm$	mean molal ionic activity coefficient
μ_i, μ_i°	chemical potential and standard chemical potential of ith component, cal/mole
ξ_i, ξ_i°	cell potential and standard cell potential, V

REFERENCES

1. G. Scatchard and S. S. Prentiss, *J. Am. Chem. Soc.*, **55**, 4355 (1933).
2. W. H. Rodebush, *ibid.*, **40**, 1204 (1918).
3. H. F. Gibbard, Jr. and A. F. Gossmann, "Freezing Points of Aqueous Electrolyte Mixtures. The System NaCl-$MgCl_2$-H_2O," Symposium on Electrolyte Solutions, Fifth Middle Atlantic Regional Meeting, American Chemical Society, Newark, Del., April 1970.
4. S. S. Negus, Thesis, Johns Hopkins University (1922); J. C. W. Frazer, "The Direct Measurement of Osmotic Pressure. Contemporary Developments in Chemistry," Columbia University Press, New York (1927).
5. P. Olynyk and A. R. Gordon, *J. Am. Chem. Soc.*, **65**, 224 (1943).
6. G. Scatchard, H. F. Gibbard, Jr., and R. A. Rousseau, *J. Chem. Thermodyn.*, In press (1972).
7. A. S. Brown and D. A. MacInnes, *J. Am. Chem. Soc.*, **57**, 1356 (1935).
8. H. S. Harned and L. F. Nims, *ibid.*, **54**, 423 (1932); H. S. Harned and M. A. Cook, *ibid.*, **61**, 495 (1939).
9. R. D. Lanier, *J. Phys. Chem.*, **69**, 2697 (1965).
10. R. Caramazza, *Gazz. Chim. Ital.*, **90**, 1839 (1960).
11. R. A. Robinson, *Trans. Roy. Soc. New Zealand*, **75** (2), 203 (1945).
12. R. M. Bates, "Determination of pH: Theory and Practice," pp. 281-284, John Wiley and Sons, New York (1964).
13. G. J. Hills and D. J. G. Ives, *J. Chem. Soc.*, 311 (1951).
14. R. A. Vandermeer, *Norelco Reporter*, **6**, 87 (1959).
15. The author is grateful to Dr. J. Amoros and Dr. J. H. Fang for making this equipment available.
16. E. Berne and I. Leden, *Svensk. Kem. Tidskr.*, **65**, 88 (1953).
17. R. H. Gerke, *J. Am. Chem. Soc.*, **44**, 1684 (1922).
18. M. Randall and L. E. Young, *ibid.*, **50**, 989 (1927).
19. G. J. Hills and D. J. G. Ives, *J. Chem. Soc.*, 319 (1951).
20. A. K. Grzybowski, *J. Phys. Chem.*, **62**, 550 (1958).
21. R. G. Bates and V. E. Bower, *J. Res. Nat. Bur. Std.*, **53**, 282 (1954).
22. G. Tammann, *Z. Anorg. Chem.*, **107**, 1 (1919).
23. B. H. Broome, *ibid.*, **143**, 60 (1925).
24. S. F. Zernezrezny, *ibid.*, **153**, 47 (1926).
25. G. F. Hüttig and E. Menzel, *Z. Anal. Chem.*, **68**, 343 (1926).
26. M. LeBlanc and J. Quenstadt, *Z. Physik. Chem.*, **150**, 321 (1930).
27. A. Wachter, *J. Am. Chem. Soc.*, **54**, 919 (1932).
28. R. J. Stokes and C. H. Li, *Acta Met.*, **10**, 535 (1962).
29. A. A. Nazarov, *Russ. J. Phys. Chem.*, **39**, 768 (1965).
30. E. Levine, H. Solomon, and I. Cadoff, *Acta Met.*, **12**, 1119 (1964).
31. A. R. C. Westwood, D. L. Guldheim, and E. N. Pugh, *ibid.*, **13**, 695 (1965).

Concentration Recovery in the Downstream of a Rotating Disk Electrode

Der-Tau Chin*

Electrochemistry Department, Research Laboratories, General Motors Corporation, Warren, Michigan 48090

ABSTRACT

A simple and systematic method based on the principle of maximal balance is used to discuss mass transfer mechanisms in various diffusion regions on a finite rotating disk electrode. A wake solution is presented to describe the concentration distribution in the far downstream of the electrode. It is shown that the wake length behind the disk electrode is ten times smaller than that behind a flat-plate electrode in plane flow.

The rotating disk electrode (RDE) is one of the most versatile tools used in the study of electrode kinetics. In theory (1), the electrode is assumed to be infinitely large, and the diffusion field to be one-dimensional, independent of the radius. This leads to a "uniformly accessible surface" for the electrode and has the advantage that the reaction rate at the electrode is everywhere the same. In practice, the electrode is finite and is usually made of a circular disk electrode mounted flush in the center of an electrically inert rotating disk. At the limiting current potentials, the concentration of the diffusing ion becomes zero at the electrode surface, whereas on the insulating surface there is no reaction taking place. This difference in the surface conditions in effect produces a radial diffusion flux near the edge of the disk electrode as well as on the insulating disk; consequently, the concept of the uniformly accessible surface fails to hold in these regions.

To attack the diffusion problem for such a finite rotating disk electrode, we divide the concentration boundary layer into three regions as shown in Fig. 1. The first region is the MAIN region over the disk electrode, where the diffusion field can be approximated as one-dimensional. The second region is the EDGE region, which is a narrow zone spanning a portion of the electrode surface near the edge of the disk electrode and a portion of the insulating plane in the immediate neighborhood of the disk electrode. The third region is the WAKE region in the far downsteam of the disk electrode. In the main region the Levich theory (1) gives a fair description of the rate of diffusion at high Schmidt numbers (Sc). The diffusion problem in the edge region has been discussed recently by Smyrl and Newman (2). Presently, we are interested in the concentration recovery of the diffusing ion in the wake region. Such information would not only serve as a complement to the transfer theory of the RDE, but would also be most useful in connection with the rotating ring-disk electrode.

Since different regions involve different transport mechanisms, the problem of deducing differential equations for each of the regions is a tricky one. In the classical procedure, the deduction is often made by setting forth a number of prior assumptions, such as $\partial C/\partial r = 0$, etc. The modern method of order-of-magnitude estimate based on a principle of "maximal balance" appears not to have been widely used in the electrochemical literature. According to this principle, the deduction should be performed in such a way that the maximum amount of physical knowledge can be retained in the resulting differential equation. Quite often there appears to be a number of ways to simplify the transfer equation for a given region. However, the most desirable way is the one achieved by use of a set of order-of-magnitude information which gives the least simplification, and which maintains the maximum number of comparable terms in the simplified equation. Thus, the principle of maximal balance is also called the principle of "maximal complication," or the principle of "least degeneracy." Good illustrations of this principle can be found in the works by Van Dyke (3), Kruskal (4), and Chin (5).

The purpose of this paper is: (*i*) to use the RDE as an example to demonstrate that the principle of maximal balance is a simple and systematic method for deduction of transport equations for various concentration regions, and (*ii*) to present a wake solution describing the concentration distribution in the far downstream of the disk electrode.

* Electrochemical Society Active Member.
Key words: principle of maximal balance, mass transfer, concentration boundary layer, ring-disk electrode.

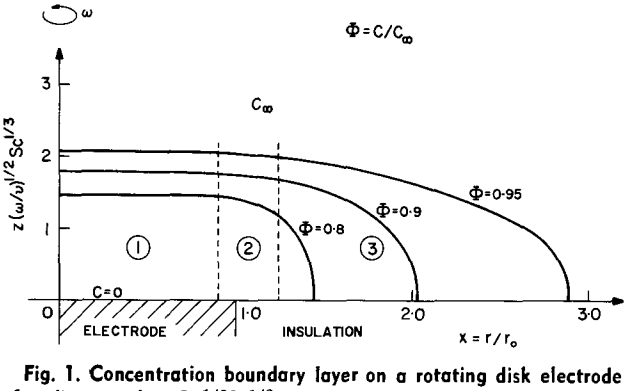

Fig. 1. Concentration boundary layer on a rotating disk electrode of radius r_0 when $Re^{1/2}Sc^{1/3} \to \infty$. (1) The MAIN region; (2) the EDGE region; (3) the WAKE region. The concentration profiles in the main region are calculated from the Levich equation, and those in the wake region are the results of the present analysis.

Theoretical

Maximal balance and diffusion layer equations.—In this analysis we assume that a disk electrode of radius, r_0, is embedded concentrically in an insulating rotating disk of infinite size as shown in Fig. 1. The disk is rotating with an angular velocity, ω, in a solution of constant properties. The solution contains an excess of supporting electrolyte, and the Schmidt number of the diffusing ion is assumed to have a large value. Under these conditions, the equation of convective diffusion in the neighborhood of the disk electrode may be given as

$$\left(a\eta - \frac{1}{2}\eta^2 + \ldots\right)x\frac{\partial\Phi}{\partial x} + \left(-a\eta^2 + \frac{1}{3}\eta^3 + \ldots\right)\frac{\partial\Phi}{\partial\eta} = \frac{1}{Sc}\frac{\partial^2\Phi}{\partial\eta^2} + \frac{1}{ReSc}\frac{\partial^2\Phi}{\partial x^2} + \frac{1}{ReSc\,x}\frac{\partial\Phi}{\partial x} \quad [1]$$

with the boundary conditions

$$\begin{aligned} &(i) && \Phi = 0 && \text{at } \eta = 0 \text{ for } x < 1 \\ &(ii) && \frac{\partial \Phi}{\partial \eta} = 0 && \text{at } \eta = 0 \text{ for } x > 1 \\ &(iii) && \Phi = 1 && \text{at } x \text{ and } \eta \to \infty \\ &(iv) && \frac{\partial \Phi}{\partial x} = 0 && \text{at } x = 0 \end{aligned} \qquad [2]$$

Our task here is to apply the principle of maximal balance to obtain a simplified equation for each of the concentration regions shown in Fig. 1. This requires an estimate of the order of magnitude of every single term in Eq. [1]; the terms with smaller orders will be dropped, retaining only those having the same order of magnitude. Since Sc is assumed to have a large value, we will make our order-of-magnitude estimation in terms of this parameter. To do this, we introduce a set of stretched coordinates defined as

$$\left.\begin{aligned} Z &= \mathrm{Sc}^{\alpha}\eta \\ X &= \mathrm{Sc}^{\beta}(x-1) \end{aligned}\right\} \alpha > 0,\ \beta \geqq 0 \qquad [3]$$

Substituting the new variables into Eq. [1], we have

$$\begin{aligned} &\left(a\mathrm{Sc}^{\beta-\alpha}Z - \frac{1}{2}\mathrm{Sc}^{\beta-2\alpha}Z^2 + \dots\right)\frac{\partial \Phi}{\partial X} \\ &\quad + \left(a\mathrm{Sc}^{-\alpha}Z - \frac{1}{2}\mathrm{Sc}^{-2\alpha}Z^2 + \dots\right)X\frac{\partial \Phi}{\partial X} \\ &\quad + \left(-a\mathrm{Sc}^{-\alpha}Z^2 + \frac{1}{3}\mathrm{Sc}^{-2\alpha}Z^3 + \dots\right)\frac{\partial \Phi}{\partial Z} \\ &\quad = \mathrm{Sc}^{2\alpha-1}\frac{\partial^2 \Phi}{\partial Z^2} + \mathrm{Sc}^{2\beta-1}\frac{1}{\mathrm{Re}}\frac{\partial^2 \Phi}{\partial X^2} \\ &\quad + (\mathrm{Sc}^{\beta-1} - \mathrm{Sc}^{-1}X + \dots)\frac{1}{\mathrm{Re}}\frac{\partial \Phi}{\partial X} \end{aligned} \qquad [4]$$

The exponents of Sc in the leading terms in Eq. [4] are

$$\beta - \alpha : -\alpha : -\alpha : 2\alpha - 1 : 2\beta - 1 : \beta - 1 \qquad [5]$$

The objective of the principle of maximal balance is to determine values of α and β for each of the concentration regions such that the maximum number of comparable terms can be preserved in the governing equation. To achieve this, a trial and error method is used. Numerical values are assigned to α and β, and a comparison is carried out among the terms in Eq. [5]. The terms with smaller order in Sc are dropped, retaining only the terms of the highest order in Sc. This procedure is repeated until one finds a set of values for α and β which keeps the maximum number of terms. It should be noted that the main region and the wake region do not include the point, $x = 1$. Thus, in these two regions, the stretch of the x-coordinate in the vicinity of $x = 1$ is not necessary, and β is zero. On the other hand, the edge region is located in the immediate neighborhood of $x = 1$, and β is nonzero.

Using the above procedures we find that in the main and the wake regions, $\alpha = 1/3$, and $\beta = 0$. Substituting these values into Eq. [4] and rearranging, we have

$$\begin{aligned} &aZx\frac{\partial \Phi}{\partial x} - aZ^2\frac{\partial \Phi}{\partial Z} - \frac{\partial^2 \Phi}{\partial Z^2} \\ &\quad = \mathrm{Sc}^{-1/3}\left(\frac{1}{2}Z^2x\frac{\partial \Phi}{\partial x} - \frac{1}{3}Z^3\frac{\partial \Phi}{\partial Z}\right) + 0\,(\mathrm{Sc}^{-2/3}) \end{aligned} \qquad [6]$$

where $Z = \mathrm{Sc}^{1/3}\eta$.

To the zeroth-order approximation of Sc, we may neglect the right-hand side of Eq. [6], and the equation is simplified to

$$aZx\frac{\partial \Phi}{\partial x} - aZ^2\frac{\partial \Phi}{\partial Z} - \frac{\partial^2 \Phi}{\partial Z^2} = 0$$

(for the main and the wake regions) [7]

Using the method of separation of variables and making use of the boundary conditions, (*i*) (*iii*), and (*iv*), it can be shown that the main-region solution takes the form of the Levich solution (1), being independent of the dimensionless radial coordinate, x

$$\Phi_M = 0.62\int_0^Z \exp\left(-\frac{a}{3}Z^3\right)dZ \qquad [8]$$

For the edge region, we find $\alpha = \beta = \frac{1}{2}$. Furthermore, by stretching the independent variables again with respect to large Re, Eq. [4] can be reduced to

$$\frac{\partial^2 \Phi}{\partial Z^{*2}} + \frac{\partial^2 \Phi}{\partial X^{*2}} - aZ^*\frac{\partial \Phi}{\partial X^*} = 0 \qquad [9]$$

with $X^* = \mathrm{Re}^{3/4}\mathrm{Sc}^{1/2}(x-1)$ and $Z^* = \mathrm{Re}^{1/4}\mathrm{Sc}^{1/2}\eta$.

This equation implies that (*i*) the radial diffusion and convection terms have the same order of magnitude as the axial diffusion term in the edge region; (*ii*) for $N = \mathrm{Re}^{1/2}\mathrm{Sc}^{1/3} \to \infty$, the size of the edge region diminishes to a single point at $x = 1$ and $\eta = 0$, and its existence can be ignored for practical calculations. The second point is especially important in electrochemical applications, for now the wake region equation can be solved by directly matching with the main region solution at $x = 1$. This has been the basic assumption in deriving the prevalent ring-disk theory (6, 7), although none of the previous investigators explicitly mentioned it.

Equation [9] has been solved numerically by Smyrl and Newman (2). Their results concerning the contribution of the edge region to the average mass flux on the surface of the disk electrode can be summarized as

$$J_E/J_M = 1.92/\mathrm{Re}^{3/4}\,\mathrm{Sc}^{1/2} \qquad [10]$$

Here J_E and J_M are the contributions to the mass flux from the edge- and the main-region solutions, respectively. The total average rate of transfer to the electrode surface is the sum of these two quantities.

Wake-region solution.—For $N = \infty$, Smyrl and Newman (7) have used a Stieltjes integral method to obtain a surface concentration distribution in the downstream of the disk electrode by matching the boundary conditions with Eq. [8]. For finite values of N, we have found the following equation

$$\Phi_W = 1 + \frac{A}{x^2}\exp\left(-\frac{a}{3}Z^3\right) \qquad [11]$$

satisfying both Eq. [7] and the boundary conditions (*ii*) and (*iii*) of Eq. [2]. To determine the constant, A, one needs to match Eq. [11] with the solution on the insulator side of the edge region. Since there is no general solution available for the edge region when N is finite, the matching operation is not possible. An alternative way is to apply the principle of mass balance. Accordingly, the flux of the diffusing ion carried by the electrolyte flow to the rotating disk should be equal to the sum of the flux consumed at the surface of the central disk electrode and the flux returning to the bulk of the electrolyte in the downstream of the disk electrode. Mathematically, this criterion may be obtained by integrating Eq. [1] over the concentration boundary layer

$$\int_0^{2\pi}\int_0^{\infty} \text{Eq. [1]} \cdot d\eta \cdot r_0 x d\theta$$

At high Schmidt numbers, this integration can be simplified to

$$\frac{d}{dx}\int_0^{\infty} ax^2Z\,(\Phi - 1)\,dZ = -x\left(\frac{\partial \Phi}{\partial Z}\right)_{Z=0}$$

In the wake region, we have $x > 1$, and the above equation can be integrated to give

$$\int_0^\infty ax^2Z\,(\Phi - 1)_{x>1}\,dZ = -\int_0^1 x\left(\frac{\partial\Phi}{\partial Z}\right)_{Z=0} dx \quad [12]$$

Substituting Eq. [8] and [10] in the right-hand side of Eq. [12], and Eq. [11] in the left-hand side of Eq. [12], we find

$$A = -0.413\left(1 + \frac{1.92}{Re^{3/4}Sc^{1/2}}\right)$$

Thus, the concentration distribution in the far downstream of a rotating disk electrode is described by

$$\Phi_W = 1 - \frac{0.413}{x^2}\left(1 + \frac{1.92}{Re^{3/4}Sc^{1/2}}\right)\exp\left(-\frac{a}{3}Z^3\right) \quad [13]$$

Discussion of Results

The concentration recovery of the diffusing ion on the insulating surface is shown in Fig. 2 for three different values of $Re^{1/2}Sc^{1/3}$. The thick solid curves are calculated from Eq. [13] by setting $Z = 0$. The thin solid curves are Smyrl and Newman's numerical solutions (2) for the edge region. It is seen that the present results correctly predict that the surface concentration would asymptotically approach $\Phi = 1$ at large radial distances in the downstream of the disk electrode; however, it fails to give a zero concentration at the edge of the electrode ($x = 1$). On the other hand, Smyrl and Newman's edge-region solution correctly predicts the concentration recovery in the immediate vicinity of $x = 1$; it gives a false value of Φ larger than the bulk concentration ($\Phi = 1$) at some distance from the disk electrode. In a later report, Smyrl and Newman published a more complete solution (7) for the surface concentration on the insulating surface when $N \to \infty$. This solution is plotted in Fig. 2 as the dashed curve, which appears to be a smooth connection between the edge-region and the wake solutions. It is seen that the edge-region solution is valid only for $x < 1.1$. On the other hand, the present wake solution represents only an asymptotic behavior of the diffusing ion at large x. It begins to be valid at $x \geq 1.5$; within this region the accuracy is expected to be better than 98%.

Equation [13] shows that the concentration deficiency, $1 - \Phi_W$, in the far downstream of the disk electrode is inversely proportional to the square of the radial distance. For large values of $Re^{1/2}Sc^{1/3}$, it takes a distance about twice the radius of the disk electrode to attain a 95% recovery (Fig. 1). This rate of recovery is faster than that found in the downstream of a flat-plate electrode in channel flow. For flows over a flat-plate electrode embedded in an insulating plane, the recovery of the surface concentration in the wake region is shown to be proportional to the 2/3 power of the distance from the leading edge of the electrode (8), and it would take twenty-four times the length of the electrode to reach a 95% recovery. Thus, the length of the wake region on the rotating disk is ten times smaller than that in plane flow. From the electroanalytical point of view, this leads to a disadvantage for the ring-disk electrode because the ring-disk distance is more critical than if one places the indicator electrode in the downstream of a flat-plate electrode in plane flow. The results of this analysis also indicate that the existing ring-disk theory is valid only for $N \to \infty$; correction to the theory for finite N requires further investigation.

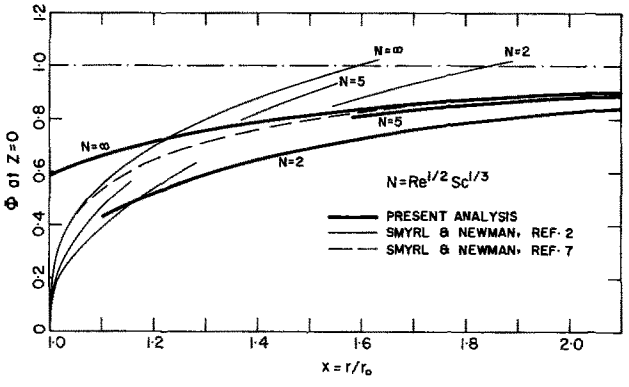

Fig. 2. Concentration recovery on the insulating surface in the downstream of the disk electrode. The present wake solutions are given as the thick solid curves. The thin solid curves are Smyrl and Newman's edge-region solutions. The dashed lines represent graphically interpolated values which would smoothly connect the two solutions.

Summary

In summary, we have used the principle of maximal balance to discuss transfer mechanisms in various diffusion regions on a finite rotating disk electrode. An analytical solution is presented to describe the concentration distribution in the wake region. It is shown that the wake length behind the disk electrode is ten times smaller than that in the downstream of a flat-plate electrode.

Manuscript submitted Jan. 18, 1972; revised manuscript received Oct. 26, 1972.

Any discussion of this paper will appear in a Discussion Section to be published in the December 1973 JUORNAL.

SYMBOLS

- a dimensionless constant, 0.510
- A integration constant in the wake solution, dimensionless
- C concentration of the diffusing ion, g-mole/cm³
- C_∞ bulk concentration of the diffusing ion, g-mole/cm³
- D diffusivity, cm²/sec
- J average rate of mass transfer on the surface of the disk electrode, g-mole/cm² sec
- J_E contribution to the rate of mass transfer on the electrode surface from the edge-region solution, g-mole/cm² sec
- J_M contribution to the rate of mass transfer on the electrode surface from the main-region solution, g-mole/cm² sec
- N dimensionless parameter defined as $Re^{1/2}Sc^{1/3}$
- r radial coordinate, cm
- r_0 radius of the disk electrode, cm
- Re Reynolds number defined as $r_0^2\omega/\nu$, dimensionless
- Sc Schmidt number defined as ν/D, dimensionless
- x dimensionless radial distance defined as r/r_0
- X^* dimensionless radial distance (for the edge-region) defined as $Re^{3/4}Sc^{1/2}(x - 1)$ or $N^{3/2}(x - 1)$
- z axial coordinate, cm
- Z dimensionless axial distance defined as $Sc^{1/3}\eta$, or $Sc^{1/3}(\omega/\nu)^{1/2}z$
- Z^* dimensionless axial distance (for the edge-region) defined as $Re^{1/4}Sc^{1/2}$ or $N^{1/2}Z$

Greek Symbols

- α a nonzero positive number for the stretch of the axial distance, see Eq. [3]
- β a positive number for the stretch of the radial distance, see Eq. [3]
- η dimensionless axial distance defined as $(\omega/\nu)^{1/2}z$
- θ circumferential coordinate, rad
- ν kinematic viscosity of the electrolyte, cm²/sec
- Φ dimensionless concentration defined as C/C_∞
- Φ_M concentration profile in the main region, dimensionless
- Φ_W concentration profile in the wake region, dimensionless
- ω angular velocity of the rotating disk, rad/sec

REFERENCES

1. V. G. Levich, "Physicochemical Hydrodynamics," Prentice-Hall, Englewood Cliffs, N. J. (1962).
2. W. H. Smyrl and J. Newman, *This Journal*, **118**, 1079 (1971).
3. M. Van Dyke, "Perturbation Methods in Fluid Mechanics," Academic Press, New York (1964).

4. M. D. Kruskal, "Asymptotology," in "Mathematical Models in Physical Sciences," S. Drobot, Editor, pp. 17-48, Prentice-Hall, Englewood Cliffs, N. J. (1963).
5. D. T. Chin, "Mass Transfer and Flow Instability: a Study Using Electrolytic Probes on the Surface of a Rotating Disk," Ph.D. Dissertation, University of Pennsylvania, Philadelphia (1969).
6. W. J. Albery and S. Bruckenstein, *Trans. Faraday Soc.*, **62**, 1920 (1966).
7. W. H. Smyrl and J. Newman, *This Journal*, **119**, 212 (1972).
8. S. C. Ling, *J. Heat Transfer, Trans. ASME*, **85C**, 230 (1963).

A Rotating Ring-Hemispherical Electrode for Electroanalytical Applications

Der-Tau Chin*

Electrochemistry Department, Research Laboratories, General Motors Corporation, Warren, Michigan 48090

ABSTRACT

A study has been made of the combination of a rotating hemispherical electrode with a ring electrode of a larger radius for use in investigations of reaction intermediates. Cyclic voltammetry in an acid copper solution was used to test the feasibility of the combination, and a ferricyanide/ferrocyanide redox reaction was used to measure the collection efficiency at the ring electrode. The collection efficiency was found to be independent of the rotational speed in laminar flow, and its value was comparable to that obtained from the rotating ring-disk electrode theory. The results indicate that the ring-disk theory can be used as a rough approximation for the ring-hemisphere electrode if the inner radius of the ring electrode is a minimum of 1.08 times the radius of the hemispherical electrode. Easy replacement of the central hemispherical electrode is a big advantage of this new geometry. This offers electrochemists an alternative choice where the use of a ring-disk electrode would fail to give a meaningful result and where frequent replacement of the disk electrode is needed.

In electrochemistry a powerful technique that permits the quantitative study of reaction intermediates is the rotating ring-disk electrode (RRDE) (1). The RRDE consists of a circular disk electrode and a ring electrode of a larger diameter mounted flush and concentrically in the surface of an insulated rotating disk. An intermediate that is produced by an electrochemical reaction occurring at the central disk electrode is transported by a radial flux to the ring, and the ring electrode then serves as an indicator to analyze the electrochemical properties of such an intermediate. From these properties, the nature of the intermediate and the kinetics of the intermediate reaction can be identified. Experimentally, the RRDE requires a perfectly flat surface. This requirement has impeded the application of the RRDE to high-rate dissolution reactions such as electrochemical machining, electrochemical polishing, high-rate corrosion, etc., because the disk electrode made of the metal being dissolved would recede into the support surface and upset the fluid flow characteristics. This would result in a greater loss of the intermediate being transferred to the ring electrode.

Recently, the electrochemical application of a rotating hemispherical electrode was discussed in a number of papers (2-5). A theory of convective diffusion was formulated for the rate of ionic transfer at the spherical surface, and an experimental setup for the use of such an electrode was described. There are several advantages in the use of this geometry:

1. The basic theory of the rotating sphere differs from that of the rotating disk by only a numerical factor in the proportional constant; thus, the method of application for electrochemical studies will be the same as that for the rotating disk electrode.

2. The hemispherical electrode protrudes from the surface of the inert support. The electrode can be replaced easily; only one support rod is needed. On the other hand, the fabrication of a replaceable rotating disk electrode is difficult because the disk electrode has to be flush with the support surface.

3. The hemispherical electrode merely reduces in size during the dissolution reaction. This change will not alter the fluid flow characteristics within a reasonable duration of experimental runs.[1]

4. The primary current distribution is uniform across the surface of the hemispherical electrode.

Considering these advantages, it was thought that by replacing the central disk electrode on the RRDE with a hemispherical electrode (HSE) as shown in Fig. 1, one might offer electrochemists an alternative method for the study of reaction intermediates, especially for dissolution reactions. We call the electrode combination of this kind the rotating ring-hemispherical electrode (RRHSE). The fluid flow around the HSE, observed in a previous study (4), involves an inflow of the electrolyte toward the spherical surface along the axis of rotation, and a swirling motion of the electrolyte along the electrode surface toward the equator. In the vicinity of the equator, the flow bends smoothly 90° toward the radial direction, and then moves along the support surface to the bulk of the electrolyte. No vortex was observed at the equator when the flow was laminar (for Reynolds number less than 10^4). Thus, any intermediate generated at the hemispherical electrode is carried by the electrolyte flow to the ring electrode, where the nature of the intermediate can be analyzed.

The purpose of this study was to investigate the feasibility of the RRHSE for electroanalytical applications. Cyclic voltammetry in acid copper solutions was used to demonstrate the ability of the RRHSE to detect the reaction intermediate, and a ferricyanide/ferrocyanide redox system was used to measure the collection efficiency at the ring electrode. This paper describes the results of these investigations.

* Electrochemical Society Active Member.
Key words: ring-disk electrode, cuprous/cupric reactions.

[1] It has been found that slight deviation from sphericity does not effect the flow pattern appreciably, however, a severely etched surface may produce localized disturbances and cause an early transition to turbulent flow. Prolonged experimental runs should be avoided for dissolution reactions.

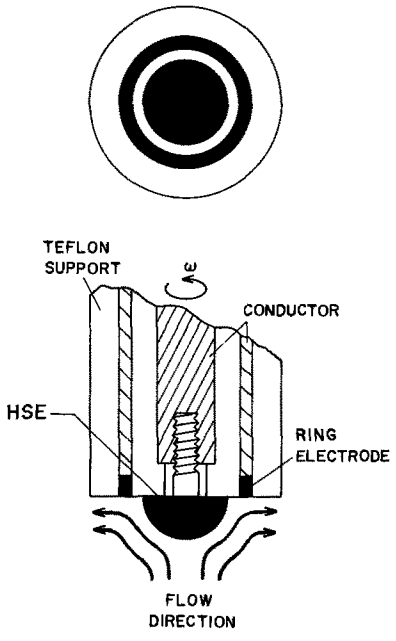

Fig. 1. Rotating ring-hemispherical electrode

Experimental

Rotating ring-hemispherical electrode.—The RRHSE used was modified from a Pine Instrument DT ring electrode. It consisted of a Teflon support rod, a platinum ring electrode, and a replaceable gold-plated hemispherical head electrode. Figure 1 illustrates the construction details.

The Teflon support was a 1.9 cm diameter rod. A platinum ring electrode, 0.798 cm ID × 1.003 cm OD, was embedded in the end of the support. At the center of this support end, there was a 0.396-cm hole which reached to a stainless steel shaft inside. The steel shaft had a 6-32 female thread to accommodate the hemispherical electrode. The other end of the Teflon support rod was attached to a stainless steel collet which was machined to fit into a high speed rotator.

A 6-32 brass screw having a hemispherically shaped head was used as the replaceable hemispherical electrode. The surface of the hemispherical head was electroplated with a smooth layer of gold. To assemble the RRHSE, a thin film of silicone grease was applied to the backside of the hemispherical head; the hemispherical electrode was then screwed into the steel shaft until the under surface of the screw head mated tightly with the Teflon support surface. Six such hemispherical electrodes were constructed, with the diameter of the hemispherical head varying from 0.634 to 0.788 cm.

Cell arrangement and electrical measurements.—An acrylic plastic vessel, 16.5 cm ID × 15 cm high, was used as the cell container. It was equipped with several baffles on the sidewall and two platinum counterelectrodes on the cell bottom. Each of the counterelectrodes had an approximate surface area of 2.5 cm^2 exposed to the electrolyte. The container also had two reference electrode compartments which had capillary tubes extending to the downstream side of the RRHSE. Two saturated calomel electrodes (SCE) placed in the compartments were used as the reference electrodes: one for the HSE, and the other for the ring electrode.

The potential of the hemispherical electrode was controlled by a Magna 4700M potentiostat. A Magna 4510 linear scan unit was used in conjunction with the potentiostat in order to sweep the HSE potentials. The ring potential was controlled by a battery-powered potentiostat designed and constructed at the General Motors Research Laboratories. This potentiostat was floating with respect to ground; thus together with the second reference and counterelectrodes, it offered an electric circuit independent of the HSE. The electric currents collected from the hemispherical and the ring electrodes were measured by passing the currents through two standard resistors; the voltage drops across the resistors were fed to the vertical channels of a Honeywell 540 XYY' recorder. The horizontal channel of the recorder was used to indicate the HSE potentials.

Rotation of the RRHSE was provided by a Pine Instrument PIR high-speed rotator, which had a speed range of 400 to 10,000 rpm. Electrical connections to the hemispherical and the ring electrodes were made by two silver/carbon slip-ring contacts mounted on the rotator. For each run, the surface of the ring electrode was lightly polished on a 600 grit Carbimet wet grinding paper; the hemispherical electrode was then fastened to the Teflon support. The assembled RRHSE was cleaned with ethanol and was cathodically treated at −2V in a 2M NaOH solution for 2 min followed by a rinse in running distilled water. The clean RRHSE was transferred immediately to the cell filled with the test electrolyte and was installed on the rotator. To provide approximately infinite surroundings for the RRHSE, the spacing between the RRHSE and the counterelectrodes was kept at 4 cm throughout the experiments. All the runs were performed at a temperature of 24°±1°C.

Feasibility test.—To test the ability of the RRHSE to detect reaction intermediates, a triangular voltammetric sweep was carried out for the Cu^{2+}/Cu^{0} reactions. The electrolytes used for the tests were: (*i*) 0.01M $CuCl_2$ plus 0.5M HCl; and (*ii*) 0.01M $CuSO_4$ plus 0.5M H_2SO_4. These solutions were saturated with nitrogen before and during the experimental runs. The potential of the Au-HSE was scanned between 0.4 to −0.4V *vs.* SCE in the chloride solution, and between 0.2 to −0.2V *vs.* SCE in the sulfate solution. To detect the formation of Cu^{+} ion during the scan, the potential of the Pt-ring electrode was maintained at 0.4V *vs.* SCE for the chloride system, and at 0.58V *vs.* SCE for the sulfate system. At these potentials cuprous ion is oxidized to cupric ion.

Measurement of collection efficiency.—Limiting current measurements for the reduction of $Fe(CN)_6^{3-}$ to $Fe(CN)_6^{4-}$ at the HSE and the oxidation of $Fe(CN)_6^{4-}$ to $Fe(CN)_6^{3-}$ at the ring electrode were used to determine the collection efficiency. A nitrogen-saturated solution containing 0.01-0.05M $K_3Fe(CN)_6$ and 0.5M NaOH was used for the measurements. The potentials of the HSE and the ring electrode were maintained at −0.1 and 0.4V *vs.* SCE, respectively, and the collection efficiency was calculated as the ratio of the ring current (minus any residual current when the HSE was at open circuit) to the HSE current.

Results and Discussion

Effect of the hemispherical head on the rate of mass transfer to the ring electrode.—Before the RRHSE experiments, a run was made to investigate the behavior of the ring electrode in the presence of an HSE on the upstream side of the electrolyte flow. The reduction of ferricyanide ion in a solution containing 0.01M $K_3Fe(CN)_6$, 0.01M $K_4Fe(CN)_6$, and 0.5M NaOH was used for the study. Limiting currents were measured on the ring while the HSE was at open circuit. The results are given in Fig. 2, where the ratio of the ring current in the presence of the HSE to the ring current in the absence of the HSE (same size ring electrode) is plotted against rotational speeds for various sizes of the hemispherical electrodes. The experimental data are represented by the symbols, ○, □, △, etc., and the average of these values is shown as the solid line. The dashed lines are the reproducibility of the measurements. It is seen that within the experimental error of ±5%, the limiting current on the ring electrode is not affected by the presence of the central hemispherical head; the average of the ratio data shown in the figure is 1.005. This is an interesting discovery, for despite a convex geometry presented by the HSE in the upstream, the ring behaves as though it were mounted on the surface of a flat rotating disk. The

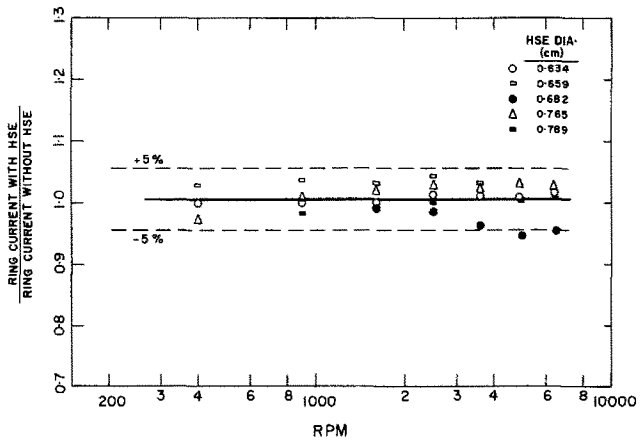

Fig. 2. Effect of HSE on the limiting current on the ring electrode. The ring electrode used was 0.798 cm ID x 1.003 cm OD in size, and the currents were measured while the central hemispherical electrodes were at open circuit.

significance of this point will be discussed in a later section.

Results of feasibility tests.—The ability of the RRHSE to detect reaction intermediates is shown in Fig. 3, where a series of cathodic sweep curves are given for a 0.765 cm diameter Au-HSE in acidic cupric chloride solution. Two waves are obtained for the HSE current during the scans (Fig. 3A). The first wave corresponds to the reduction of Cu^{2+} to Cu^{+}. The second wave, which begins at a potential of −0.2V *vs.* SCE, corresponds to the reduction of Cu^{2+} to metallic copper at the HSE. Figure 3b is a plot of ring current against the HSE potential; the ring potential was maintained at 0.4V *vs.* SCE to oxidize any Cu^{+} generated at the HSE and carried by the electrolyte flow to the ring surface. It is seen that the ring current increases with the HSE potential as the first wave reaction occurs and then levels off when the reaction reaches the limiting current potentials. The level of the ring current increases correspondingly with the level of the HSE current as the speed of rotation increases. When the HSE reaches the potential where the second wave reaction starts to occur, the ring current drops immediately, and becomes zero at a potential corresponding to the limiting current for the reduction of cupric ion to copper at the HSE. The collection efficiency of cuprous ion, calculated by dividing the magnitude of the ring current plateau by the magnitude of the first HSE current plateau, is found to be 33%, independent of the speed of rotation.

Figure 4 shows the results of a triangular sweep in the cupric chloride solution for the same RRHSE used above. The rate of scan was 0.8 V/min, and the rotational speed of the electrode was 1600 rpm. The result for the cathodic scan is seen to be the same as in Fig. 3 and will not be discussed further. For the anodic sweep, a current peak is obtained for both the ring and the hemispherical electrodes. These peaks are caused by the dissolution of deposited copper on the HSE and by the pickup of a dissolution product in the form of Cu^{+} at the ring electrode. The ratio of the height of the ring peak to that of the HSE peak is 32%, in close agreement with the result of the cathodic sweeps shown in Fig. 3. This indicates that within the potential range scanned, cuprous ion is the primary product formed during the dissolution of copper in HCl.

That the ring-hemispherical electrode is capable of differentiating the Cu^{2+}/Cu^{0} reaction in H_2SO_4 from that in HCl is shown in Fig. 5, where the triangular sweep curves from the same RRHSE are plotted for the acid cupric sulfate solution. Figure 5 shows that only one reaction wave occurs at the HSE during the cathodic scan and no detection of Cu^{+} is made at the ring electrode. For the anodic scan, a current peak is observed for the ring electrode as well as for the HSE. However, the ring current is very small compared to the HSE current (note the μA scale of the ring current in Fig. 5B). This implies that Cu^{+} ion is not the major dissolution product, but rather is a soluble species resulting from a secondary reaction at the HSE. By setting the ring electrode at −0.2V *vs.* SCE, the potential at which Cu^{2+} ion is reduced to Cu^{0}, it was found that the major product resulting from the dissolution of copper in H_2SO_4 is Cu^{2+}. Thus, the generation of Cu^{+} may be the result of a secondary chemical reaction between the copper deposit on the HSE and

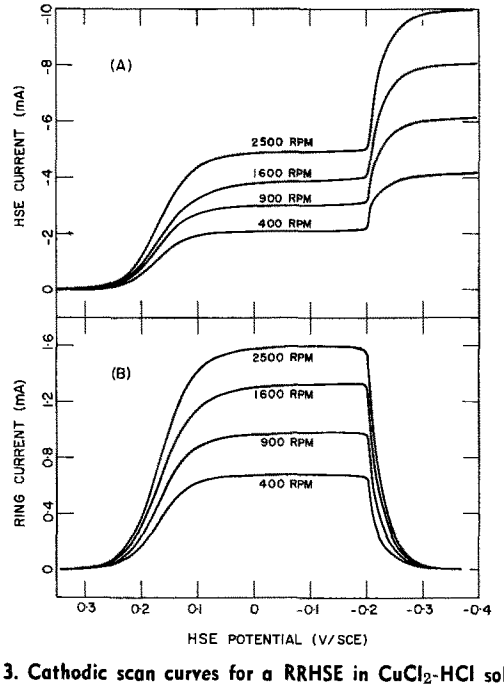

Fig. 3. Cathodic scan curves for a RRHSE in $CuCl_2$-HCl solution. The ring potential was maintained at 0.4V *vs.* SCE while the HSE potential was scanned at a rate of 0.27 V/min.

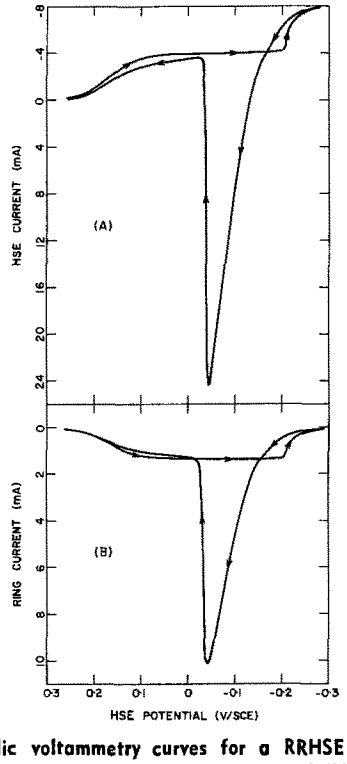

Fig. 4. Cyclic voltammetry curves for a RRHSE in $CuCl_2$-HCl solution. The ring potential was maintained at 0.4V *vs.* SCE, while the HSE potential was scanned between 0.4 and −0.4V *vs.* SCE at a scan rate of 0.8 V/min. Rotational speed was 1600 rpm.

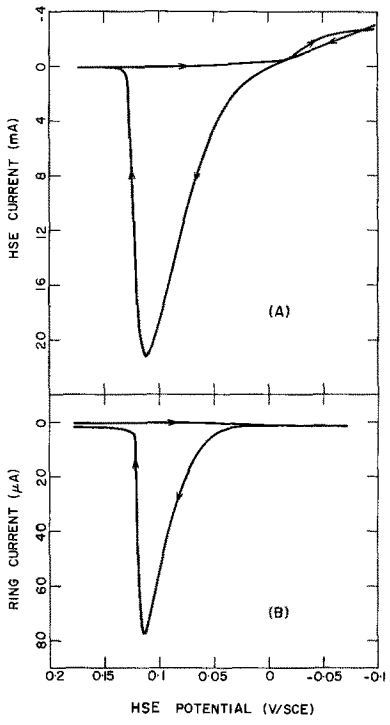

Fig. 5. Cyclic voltammetry curves of a RRHSE in $CuSO_4$-H_2SO_4 solution. The size of the RRHSE used was the same as that used for data in Fig. 3 and 4. The ring potential was maintained at 0.58V vs. SCE, while the HSE potential was scanned between 0.2 and —0.2V vs. SCE at a scan rate of 0.4 V/min. Rotational speed was 1600 rpm.

cupric ions in the electrolyte. These results agree with a ring-disk experiment reported earlier (6).

Collection efficiency.—The results of the collection efficiency measurements are presented in Fig. 6 as a function of the spacing between the equator of the HSE and the inner edge of the ring electrode. The spacing between electrodes was varied by using different sizes of hemispherical electrodes, and the measurements were made for two different ferricyanide concentrations. It was found that the collection efficiency was independent of the speed of rotation. Each data point represents an average of the measurements over a speed range of 400-4900 rpm, and the scattering of the data is given as the I-bars. This speed range covered a span of Reynolds numbers from 1000 to 13,000 for the ring electrode, and 400 to 8000 for the HSE, which was well within the laminar flow region. The thick line in the figure represents a smooth curve

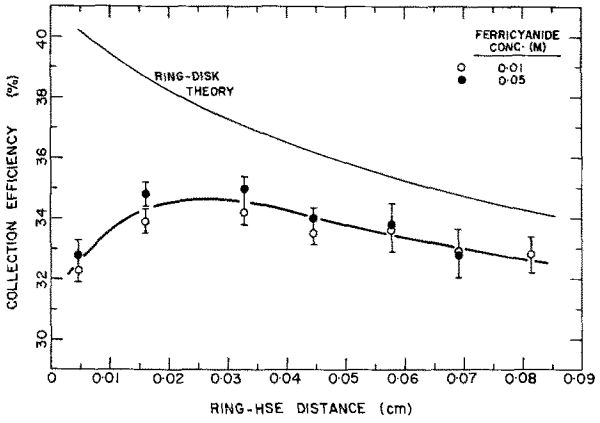

Fig. 6. Results of collection efficiency measurements. A ring electrode of 0.798 cm ID x 1.003 cm OD was used, and the ring-HSE spacing was varied by using different sizes of hemispherical electrodes. The measurements were made in a ferricyanide/ferrocyanide redox system over a speed range of 400-4900 rpm.

drawn between the data points. For comparison, the collection efficiency calculated from the ring-disk theory (7), using the projected area of the HSE, is plotted as the thin curve.

It is seen that the change in the ferricyanide concentration had no significant effect on the measurement. The measured collection efficiency increases slowly with decreasing spacing between the HSE and the ring electrode. After reaching a maximum, it then decreases with a further decrease in spacing. In the region to the right of the maximum, *i.e.*, at a ring-HSE spacing greater than 0.03 cm, the ring-disk theory gives a collection efficiency only 2-3% higher than that of the RRHSE. However, for ring-HSE spacings less than 0.03 cm, the theory predicts a continuous increase in the collection efficiency with decreasing electrode separation. This difference in behavior between the ring-disk electrode and the RRHSE can probably be attributed to an uneven distribution of the local reaction rate near the equator of the HSE rather than to the ring electrode, for the limiting current at the ring is not affected by the presence of an HSE at open circuit (Fig. 2).

According to the diffusion theory of the rotating sphere (5), the local limiting current density is highest at the pole and decreases meridionally toward the equator. Thus, the rate of the diffusion-controlled reaction would be expected to reach a minimum at the equator, where the least amount of the reaction intermediates (or products) would be generated. Since the steamlines of the electrolyte flow bend smoothly in the neighborhood of the equator toward the support surface (Fig. 1), there would be a "corner space," within a short distance from the equator, where the concentration of the reaction intermediate would be smaller than that in the main stream. If the ring electrode, or a portion of the ring electrode, is located within this corner space, it is expected that a lower collection efficiency would be obtained as is shown to the left side of the maximum point in Fig. 6. The transport details in this corner space are not clear because no mathematical theory pertaining to such hydrodynamic flow is available at the present time. However, if one regards the region to the left of the maximum in Fig. 6 as the corner space, it can be calculated that the corner space is located within 1.08 radii of the hemispherical electrode. Thus, to achieve the best electrode combination for the RRHSE, it is recommended that the inner radius of the ring electrode be at least 1.08 times greater than the radius of the HSE. Under these conditions, the ring-disk theory gives a good approximation of the collection efficiency at the RRHSE.

Conclusions

The results of the feasibility tests have clearly demonstrated that the rotating ring-hemispherical electrode can be used for electrochemical studies. Easy replacement of the central hemispherical electrode is a big advantage of the RRHSE. In laminar flow, the collection efficiency is found to be independent of the rotational speed, and its value is comparable to that obtained from the ring-disk electrode theory. The RRHSE offers an alternative choice where the use of the ring-disk electrode would fail to give a meaningful result and where frequent replacements of the disk electrode would be needed. However, in view of the lack of a mathematical theory, it is recommended that each RRHSE should be calibrated beforehand with a known electrochemical reaction. The ring-disk theory can be used as an approximation for the estimate of the collection efficiency if the inner radius of the ring electrode is at least 1.08 times greater than the radius of the hemispherical electrode.

Manuscript submitted Aug. 28, 1972; revised manuscript received Dec. 11, 1972.

Any discussion of this paper will appear in a Discussion Section to be published in the December 1973 JOURNAL.

REFERENCES

1. W. J. Albery and M. L. Hitchman, "Ring-Disc Electrodes," Oxford University Press, London (1971).
2. D. T. Chin, *This Journal*, **118**, 1434 (1971).
3. D. T. Chin, *ibid.*, **119**, 1049 (1972).
4. D. T. Chin, *ibid.*, **118**, 1764 (1971).
5. J. Newman, *ibid.*, **119**, 69 (1972).
6. G. W. Tindall and S. Bruckenstein, *Anal. Chem.*, **40**, 1402 (1968).
7. W. J. Albery and S. Bruckenstein, *Trans. Faraday Soc.*, **62**, 1920 (1966).

Evaluation of Porous Electrodes Through Cell Power Maximum Measurements

S. Szpak[1] and G. E. McWilliams[1]

Chemistry Laboratory, Mare Island Naval Shipyard, Vallejo, California 94592

ABSTRACT

A method for the analysis of porous electrodes, based on cell power maximum *vs.* time measurements, has been developed. The electrode effectiveness factor was determined without resorting to tedious chemical procedures. Good agreement with published analyses was obtained for the HgO(C)/30% KOH system.

Discharge of a primary battery is an energy-producing process accompanied by structural changes of the electrodes. The fundamental difference in the analytical approach to primary batteries and to some other types of energy conversion devices, *e.g.*, fuel cells, is in the manner in which reactants are supplied. In the latter case, reactants are continuously admitted from an external source; in the former case, they are incorporated into the electrode structure, usually in the form of sparingly soluble substances. Because of this difference, a fuel cell can operate indefinitely and a true steady state can be achieved. In contrast to this, in the course of battery operation the supply of reactant diminishes and, when all active material is used up, the battery ceases to function. Thus, a true steady state cannot be realized.

In what follows, we are concerned with monitoring changes that occur on discharge via measurements of the power maximum. It will be shown that, in certain cases, measurements of the power maximum provide information on the electrode performance and, in those cases, they can be used to determine the rate of penetration of the reaction zone into the electrode structure.

Relevant Concepts and Equations

For convenience, we begin the analysis by considering an idealized system: a galvanic cell consisting of two smooth electrodes, spaced d cm apart. Electrode reactions are well defined but otherwise quite arbitrary. The open-circuit potential is assumed to be equivalent to the thermodynamic potential. The conductivity of the solution and the cell geometry remain invariant during cell operation. Furthermore, we adapt the following definitions and properties: (*i*) cathode is positive and anode is negative, (*ii*) reaction is spontaneous on discharge, (*iii*) potential drop at the electrode is modified by the passage of cell-generated current, and (*iv*) the sign of the cell-generated current is such that the quantity $i \cdot \eta$ is always positive. The thermodynamic potential, $V_r = V_{r,c} - V_{r,a}$, plays a dominant role. It determines the reaction's driving force, $V_r - V_i(i)$, which in turn, is modified by the flow of cell-generated current, i. For this reason, the electrochemical cell discussed here—a primary battery—cannot be regarded in terms of a single electrode concept, unless we clearly define properties of the other electrode.

When a variable external load, R_e, is engaged, current i begins to flow and a potential difference at the battery terminals, $V_e(i)$, is established. In particular

$$V_e(i) = V_r - V_i(i) - iR_i \qquad [1]$$

where $V_i(i) = \eta_c(i) + \eta_a(i)$ is the sum of overpotentials developed at the cathode and anode, respectively. R_i is the cell internal resistance, so that iR_i is the ohmic drop in the electrolyte. Subscripts i and e denote the internal and external part of the complete circuit.

One of the properties of a galvanic cell that we wish to examine is the cell power, P. Evidently, it is zero at $i = 0$, *i.e.*, at the open-circuit potential and when $V_e(i) = 0$. Since at $0 < i < i_{lim}$, alternatively at $V_r > V_i(i) > 0$, P is positive, it follows that there exists at least one value of current and/or potential where P is maximum.

Starting with Eq. [1], multiplying it by i differentiating it with respect to i, we obtain the following

$$P = i\,[V_r - V_i(i)] - i^2R_i \qquad [2]$$

and

$$\frac{dP}{di} = V_r - V_i(i) - i\frac{dV_i(i)}{di} - 2iR_i \qquad [3]$$

The quantity, $dV_i(i)/di$, appearing in Eq. [3], may be identified as the differential resistance of the electrochemical cell, being in many cases approximately constant over roughly 60% of the cell currents. The deviation from constancy is evident at the extreme ends of cell operation. At low currents it is due to activation control while at the other extreme it exhibits the effects of limiting current.

The condition of power maximum, P_m, together with the corresponding i_m, may be calculated by taking $dP/di = 0$. Thus

$$P_m = \frac{[V_r - V_i(i_m)]^2}{2R_i + \dfrac{dV_i(i_m)}{di}}\left[1 - \frac{R_i}{2R_i + \dfrac{dV_i(i_m)}{di}}\right] \qquad [4]$$

and

$$i_m = \frac{V_r - V_i(i_m)}{2R_i + \dfrac{dV_i(i_m)}{di}} \qquad [5]$$

For the operating region exhibiting constant differential resistance, $dV_i(i)/di = kR_i$ (with $k \geq 0$), Eq. [4] is somewhat simplified and takes the form

$$P_m = \frac{(k+1)\,[V_r - V_i(i_m)]^2}{(k+2)^2\,R_i} \qquad [6]$$

[1] Present address: Electronic Materials Sciences Division, Code 2600, Naval Electronics Laboratory Center, San Diego, California 92152.

Key words: primary battery, porous electrode, electrode effectiveness factor, mercuric oxide electrode, cell power maximum.

The shape of the P-i curves and thus, the position of P_m, depends on electrode kinetics and the cell geometry. The P-i curves for various kinetic and geometric parameters were examined by Bockris and Srinivasan (1). They found that the maximum power is close to the limiting current, except in cases where the internal resistance is high or the kinetics even for one electrode is slow. To illustrate this, computer generated $dV(i)/di$ *vs.* i and P *vs.* i curves for a selected set of parameters are shown in Fig. 1 and 2, respectively. Evidently, the $dV(i)/di$ *vs.* i curves are constant over the range of currents and/or potentials of interest, thus Eq. [6] implies parabolic representation in the vicinity of power maximum.

The displacement of power maximum as a function of internal cell resistance is clearly displayed in Fig. 2. Similarly, a shift is indicated in the potential or current at which P_m occurs. These two displacements are characteristic of battery performance and depend on internal cell resistance. If the battery construction involves smooth electrodes, then according to Eq. [6], the P_m^{-1} *vs.* R_i plot is a straight line with a slope $(k + 2)^2/(V_r - V_i)(i_m)^2(k + 1)$. In the case of a battery employing even one porous electrode, a more complex dependence is expected.

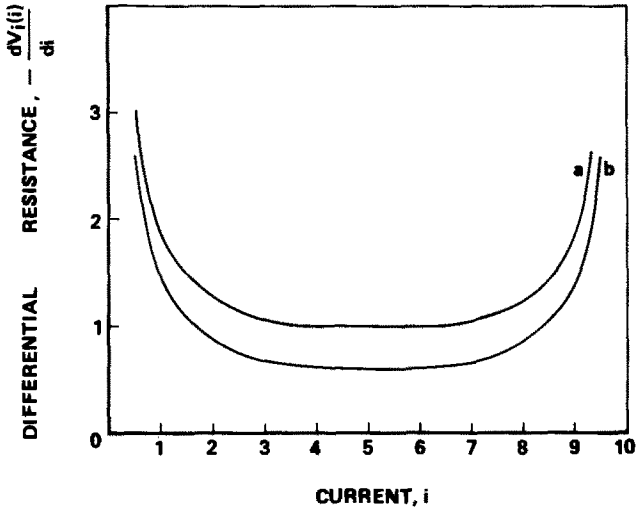

Fig. 1. Differential cell resistance as function of R_i. Data: $i_{o,c} = 10^{-3}$ Acm^{-2}; $\alpha_c = \frac{1}{2}$, $i_{o,a} \geq 1$ Acm^{-2}, $\alpha_a = \infty$. Curve a, $R_i = 0.5$ ohm and curve b, $R_i = 0.1$ ohm.

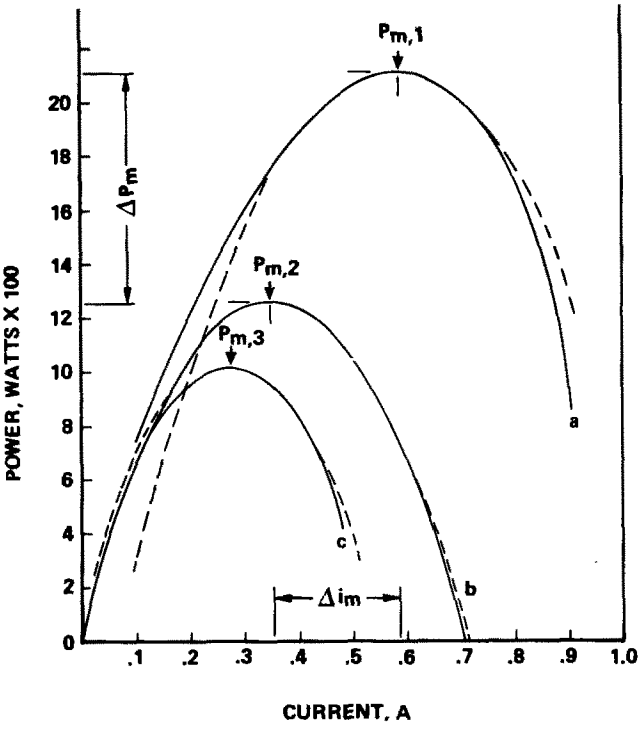

Fig. 2. Power-current curves as a function of cell resistance. Data: $V_r = 1.29$V; other as in Fig. 1. Curves: a, b, and c, $R = 0.1$, 0.5, and 0.75 ohm respectively. (Broken lines refer to computer generated parabolas.)

P-i Curves for Cell with Porous Electrode

Basic cell components of a battery with a porous electrode are shown in Fig. 3. Cathode (A) represents a porous electrode consisting of a conductive matrix with a uniformly distributed active material. For simplicity, anode (B) is assumed to be nonpolarizable.

It is known from the theory of porous electrodes that there exists a reaction zone, *i.e.*, the electrochemical process takes place within a relatively narrow part of the electrode volume. In the case of devices operating with a continuous supply of reactants, *e.g.*, fuel cells, this zone is immobilized. In the case of batteries, the reaction zone travels across the electrode volume. At the beginning of the discharge, it is usually localized at the electrode/solution interface. At the end of the discharge, it is in the vicinity of the "back-up" plate. Such behavior is expected in most batteries, with the exception of cases where the current density distribution is anomalous (2).

Upon initiation of battery discharge, *e.g.*, at constant current density, a reaction profile (current-density profile) is established throughout the electrode volume, having highest density at the electrode/solution interface, *i.e.*, at $x_o(t) = 0$. In the course of battery discharge, active material is used up, forcing the $x_o(t)$ plane to proceed inwards and, in effect, increasing the ohmic part of the cell internal resistance by a factor proportional to $x_o(t)$. Because of the porous structure, the increases may be substantial and therefore experimentally detectable.

In deriving the P-i curves for a cell employing porous electrodes and, for example, operating under galvanostatic conditions, it is necessary to compute the $V_i(i)$ measured with respect to the reference point located at the electrode/solution interface when the reaction zone has penetrated to a new position, $x_o(t)$. This reference point is convenient, since $V(i)$ can be decomposed into its ohmic part and a component due

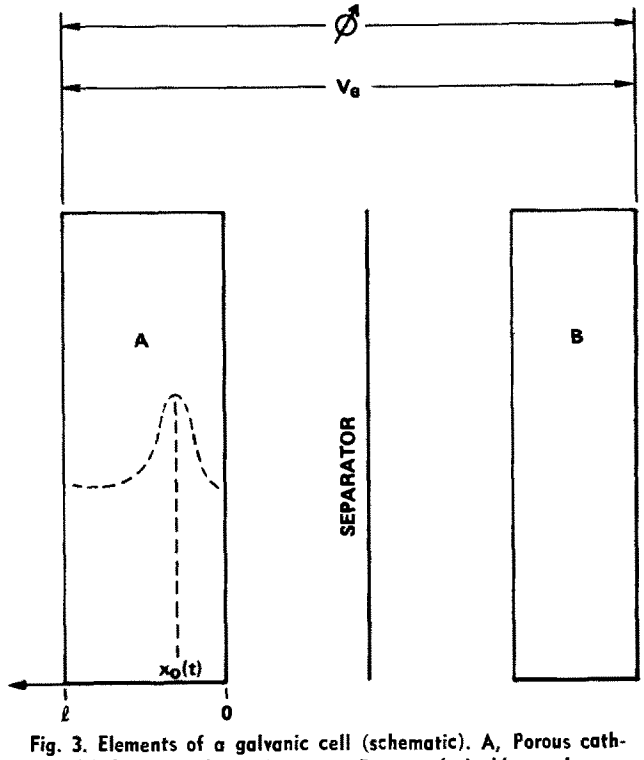

Fig. 3. Elements of a galvanic cell (schematic). A, Porous cathode; $x_o(t)$, location of reaction zone; B, nonpolarizable anode.

to the porous electrode behavior of a length $[l - x_o(t)]$ discharging under specified current.

Following Winsel (3), we write for the galvanostatic case

$$V_i(i) = \frac{\rho I}{a^2\pi} x_o(t) + \frac{\rho I\lambda}{a^2\pi} \coth [(l - x_o(t))/\lambda] \quad [7]$$

where ρ and a are solution resistivity and pore diameter, respectively. I is the discharge current (per pore), and λ is a constant depending upon the electrochemical system and electrode construction. Evidently, both the ohmic part, $[\rho I/a^2\pi]\ x_o(t)$, and the potential $[\rho I\lambda/a^2\pi]$ coth $[(l - x_o(t))/\lambda]$, which operates at the electrode/solution interface, when the latter has shifted to a new position, are time dependent. This clearly indicates and also defines the transient behavior of a battery when it operates under constant current output. Substitution of Eq. [7] into Eq. [2] yields

$$P = i\,[V_r - \rho i\lambda \coth\,(l - x_o(t))/\lambda] - i^2[R_i + \rho x_o(t)] \quad [8]$$

(The factor $a^2\pi$ has been removed, because the pore current I has been replaced by current density i).

Equation [8] is of little value in this form, since $x_o(t)$ is experimentally not accessible without destructive examination of the electrode. More effective use of Eq. [8] can be made, if the position of the reaction zone is related to the active material available, alternatively, to the time needed for complete cell discharge, $t_m = Q_o/i$ (Q_o is the total charge available). Again following Winsel (3), this relationship is

$$\frac{x_o(t)}{l} + \frac{\lambda}{l} \tan\left[\left(1 - \frac{x_o(t)}{l}\right)\frac{l}{\lambda}\right] = t/t_m \quad [9]$$

Equation [9] was derived subject to following restrictions: (*i*) linear potential/current dependence within the reaction zone, *i.e.*, for $x_o(t) \leq x \leq l$, and (*ii*) absence of faradaic current outside the reaction zone, *i.e.*, for $0 \leq x \leq x_o(t)$. The rate of penetration of the reaction zone was determined by differentiation of an expression formed by equating the time-integrated local faradaic current with the amount of active material stored on the pore wall. The position of the $x_o(t)$-plane was obtained upon integration of this expression and upon setting the integration constant equal to the time necessary for the complete discharge of the active material located at $x = 0$. Graphical solution of Eq. [9] in the form of a plot of $x_o(t)/l$ *vs.* t/t_m [cf. Ref. (3), Fig. 7], was used in subsequent analysis and computations.

Experimental

The experimental arrangement employed in this investigation is shown in the form of a block diagram in Fig. 4. The power *vs.* cell voltage was continuously plotted on the XY recorder (Hewlett-Packard, Model 7001 A) with the cell voltage connected to the X-axis input. The battery under test was driven by a linear current sweep (0.7 $Asec^{-1}$) supplied by a power source (Kepco, Model BOP-36-5M) controlled by a function generator (Exact, Model G1103 with A 1202 amplifier). Cell power was computed using Philbrick multiplier (Model 4430) with the output fed into the Y-axis input.

Examples of experimental *P-i* curves for the HgO(C)-Zn battery at various stages of discharge are shown in Fig. 5. Even a cursory examination reveals similarities to the calculated curves of Fig. 2, as evidenced by the decline in power maximum with time and a shift in potential in the direction predicted by the elementary treatment (cf., Eq. [4] and [5]). In particular, curve a represents initial behavior, curves b and c after 5 and 10 hr of discharge at 60 mA, respectively.

A plot of P_m^{-1} *vs.* t/t_m for a series of type BA-1516 U batteries is shown in Fig. 6. This plot consists of two regions. The first region, AB, terminated at $t/t_m = 0.3$,

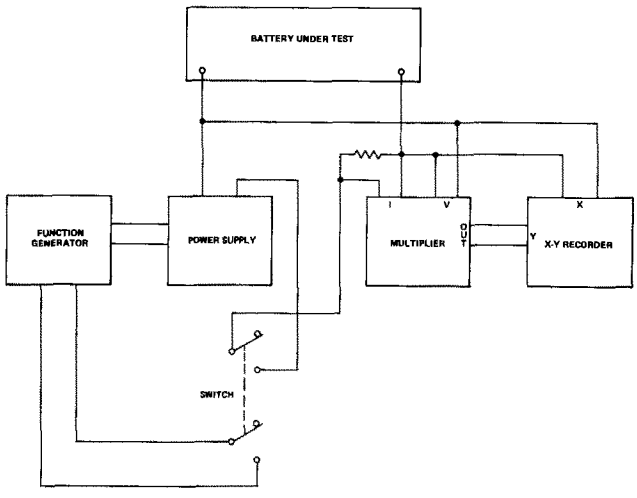

Fig. 4. Block diagram for measurements of battery power maximum.

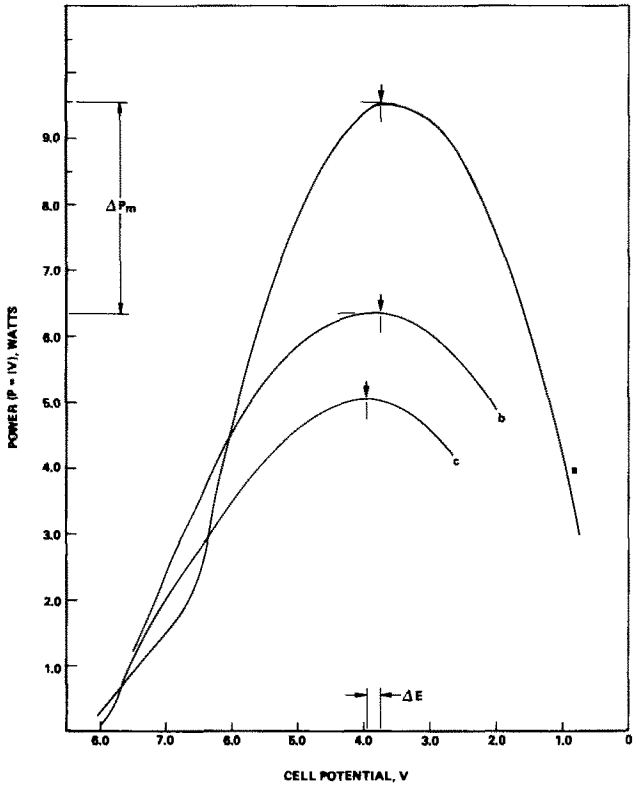

Fig. 5. Power maximum *vs.* cell potential curves. Data: HgO(C)-30% KOH-Zn, battery type AB 1516 U. Discharge current, — 60 mA. Curves: a, new battery; b, after 5 hr of discharge; c, after 10 hr of discharge.

roughly 10 hr after commencement of discharge at 60 mA. The second, less steep segment, BC, persisted until total discharge occurred. When the reciprocal of the power maximum was plotted against the discharge time, each time, 16 hr after interruption of battery discharge, the lower plot (curve b) was obtained. This new plot probably reflects the well-known fact of "recovery" characteristic of mercuric oxide batteries.

Before attempting any interpretation of presented results, we will consider the construction of the type BA-1516 U battery in some detail. This battery consists of 6 HgO(C)-30% KOH-Zn(Hg) cells. Electrodes are flat disks, 3.5 cm in diameter. The cathode is a mixture of HgO (14g) and graphite in the form of a pellet, 0.25 cm thick; the anode is constructed from amalgamated zinc ribbon, weighing 3.5g and wound to

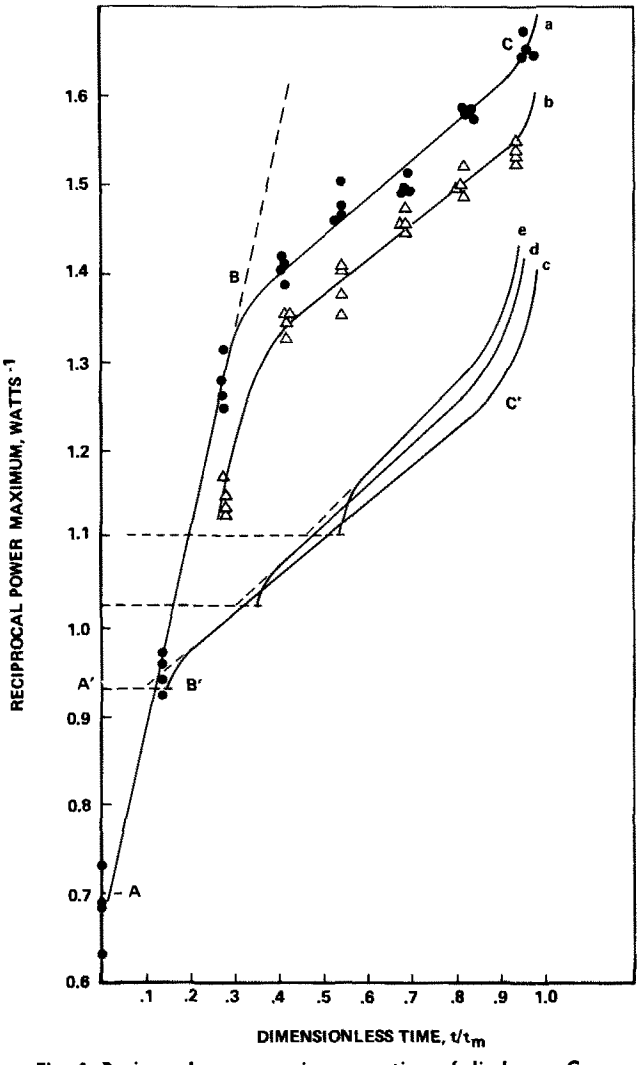

Fig. 6. Reciprocal power maximum vs. time of discharge. Curves: a, HgO(C)-Zn battery, immediately after interruption of discharge; b, same as a, after 16 hr on open circuit; c, calculated for $l/\lambda = 10$; d, calculated for $l/\lambda = 3$; e, calculated for $l/\lambda = 2$.

form a 0.62 cm thick electrode. A separator, 0.04 cm thick, is used. All dimensions and weights are approximate.

Discussion

For comparison, calculated P_m^{-1} *vs.* t/t_m curves are shown also in Fig. 6. They were drawn for the effectiveness factor, $l/\lambda = 10$, 3 and 2; curves c, d, and e, respectively, employing Winsel's (3) model. Qualitatively good agreement between calculated and experimental curves is displayed for $t/t_m > 0.3$. A less satisfactory situation prevails for $t/t_m < 0.3$.

In order to resolve this difficulty, consider Eq. [8] which, as $x_o(t) \to 0$ and for $l/\lambda > 3$, yields

$$\lim_{x_o(t) \to 0} P_m = i_m [V_r - \rho i_m \lambda - i_m R_i] \qquad [10]$$

Equation [10] applies during the initial period of cell discharge, specifically before total depletion of reactant at $x_o(t) = 0$ has occurred. Because of the time required for a complete depletion of reactant at the electrode/solution interface, the initial slope of the P_m^{-1} *vs.* t/t_m curve should be zero (segment A'B', Fig. 6). This is just the opposite of what has been observed. Evidently, the initial behavior must be attributed to changes in λ.

Physical significance of λ.—The parameter λ arises in the solution of the second order differential equation with respect to potential, *e.g.*, Ref. (3). For a tubular geometry and negligible matrix resistance, $\lambda = \sqrt{ar/2\rho}$, where r specifies the local current/potential relationship, $i = r^{-1}V$. This quantity has the dimension of length, and it is usually referred to as the reduced pore length or depth of penetration. It is within this distance that most of the reaction occurs. By multiplying and dividing the terms under the square root by $a^2\pi$, we obtain after rearrangement

$$\lambda = \sqrt{\frac{r/\delta S}{\rho/\delta V}}$$

where δS is the surface element associated with the volume element δV, or simply $\lambda = \sqrt{R_{chem}/R_{ohmic}}$. Consequently, λ, may be viewed as a relative measure of the ratio of surface resistance to resistance in the electrolyte. Thus, in principle, it is applicable to any porous electrode provided certain dimensional criteria are met (4, 5). It is noteworthy that λ can be related to certain characteristic group of general interest to electrochemical engineering (5).

Time evolution of λ *for* $t/t_m < 0.3$.—The effect of parameter λ on the power maximum enters through the expression for potential. Thus, the time evolution of λ can be determined from experimentally obtained data points of P_m and $V_{e,m}$ as a function of t/t_m. Such data for the HgO(C) electrode are presented in Fig. 7. For convenience, i_m-data were used.

It is seen that $V_{e,m}$ remains constant up to $t/t_m = 0.18$, approximately. By Eq. [10], the constancy of $V_{e,m}$ requires that $\lambda = \frac{1}{\rho}\left[\frac{V_r - V_{l,m}}{i_m} + R_l\right]$, that is to say, λ must increase, since i_m decreases with time. Evidently, the characteristic number for the HgO(C) electrode increases with the depletion of HgO. At later times, when $t/t_m > 0.3$, it becomes stabilized and the electrode effectiveness, is $3 < l/\lambda < 5$, as inferred from Fig. 6.

Formation of reaction zone.—Upon initiation of electrode discharge and shortly thereafter, the highest local current density is at the electrode/solution interface, estimated to be not less than sixfold its average value (6). Qualitatively, as the active material is used up, the reaction rate (local current density) is less and the reaction zone extends somewhat into the electrode structure. When all active material is exhausted or is reduced to a level which only slowly varies with time, the reaction zone is said to be fully developed. Quantitatively, for λ = const, the reaction zone is fully developed when the time-integrated faradaic current exceeds certain known value, q_o Asec/cm^2. At this time, t_o, all the available active material at the electrode/solution interface is consumed. Other methods of calculations require the assumption of a reaction path (7).

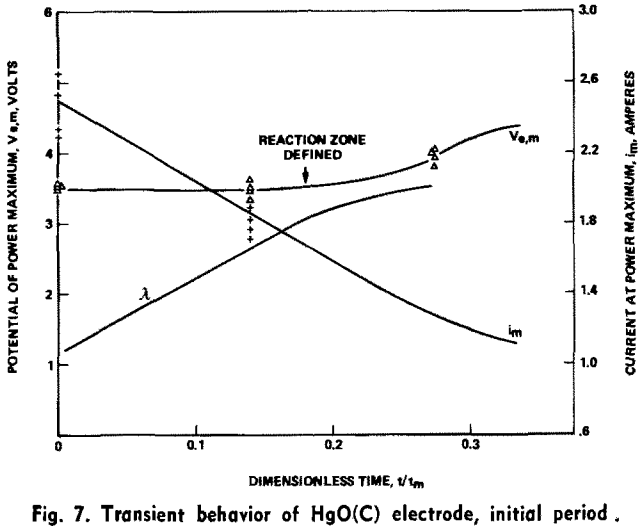

Fig. 7. Transient behavior of HgO(C) electrode, initial period.

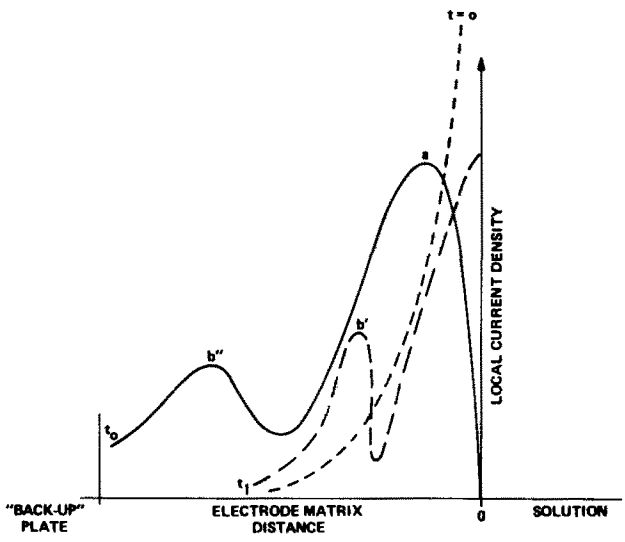

Fig. 8. Formation of reaction zone (schematic).

The evolution of the reaction zone in a practical electrode, such as HgO(C), is more complex. Discharging this kind of electrode at constant current, Euler (6) found a secondary peak in local current-density distribution. The existence of the secondary maximum is consistent with our observation concerning the time evolution of the parameter λ.

The formation of a secondary maximum is shown schematically in Fig. 8. Upon initiation of discharge (at $t = 0$), a reaction profile is established. At some later time, t_1, owing to the increase in relative measure of surface to ohmic resistance, the local current densities at corresponding locations are less than they were at $t = 0$. Condition of constant-charge current forces the reaction to occur in adjacent areas with lower λ. Consequently, secondary maximum is formed.

On the basis of the experimental data reported in Fig. 6 and 7, it can be concluded that the formation of the fully developed reaction zone took place when approximately 18% of the total active material was used up, *i.e.*, when there is a noticeable shift in $V_{e,m}$. More or less regular current density distribution occurred at $t/t_m > 0.3$. The regularity in current distribution, or the constancy of λ, may be attributed to the disappearance of the secondary current maximum. This interpretation is in good agreement with Euler's (6) findings.

Conclusions

Electrode behavior upon discharge can be examined by following the decline in cell power with time of discharge. In principle, any point of the cell power *vs.* voltage curve can be utilized; in practice, however, the position of the power maximum is sought and expressed in terms of the time needed to complete the electrode discharge.

The decline of the cell power is associated with the penetration of the reaction zone into the electrode structure. The rate of penetration depends on the mode of cell discharge. The presented analysis is based on galvanostatic discharge. Analytical expressions for the potentiostatic mode are also known (3).

The electrode effectiveness factor, l/λ, was determined for the HgO(C) electrode in the BA-1516 U battery. The decrease in the effectiveness factor is associated with the initial battery discharge, followed by its stabilization to a value $3 < l/\lambda < 5$ after 30% of all the active material has reacted. The formation of a fully developed reaction zone required approximately 18% of the total time needed for completion of cell discharge.

Acknowledgments

This work was supported by Naval Air Systems Command, under Air Task No. A310310C/410A/1 R010-01-020. The authors wish to thank Dr. H. Rosenwasser, AIR 310, for continuous interest, Professor L. Nanis (University of Pennsylvania, Philadelphia, Pennsylvania) and Dr. T. Katan (Lockheed Research Laboratories, Palo Alto, California) for comments in the course of manuscript preparation.

Manuscript submitted April 25, 1972; revised manuscript received Nov. 6, 1972.

Any discussion of this paper will appear in a Discussion Section to be published in the December 1973 JOURNAL.

REFERENCES

1. J. O'M. Bockris and S. Srinivasan, Proc. S.E.R.I. Vol. 2, p. 68, Brussels (1965).
2. K. J. Euler, *Naturwissenschaften*, **56**, 326 (1969); *Z. Angew. Phys.*, **27**, 271 (1959); *Z. Phys.*, **220**, 199 (1969).
3. A. Winsel, *Z. Elektrochem.*, **66**, 287 (1962).
4. E. A. Grens, *Electrochim. Acta*, **15**, 1047 (1970).
5. L. Nanis, *Plating*, **58**, 805 (1971).
6. K. J. Euler, *Electrochim. Acta*, **13**, 1533 (1968); *Z. Angew. Phys.*, **31**, 81 (1971).
7. J. S. Dunning, D. N. Bennion, and J. Newman, *This Journal*, **118**, 1251 (1971).

Technical Notes

Asymmetric Induction by Alkaloids in Electrolytic Reductions

E. Kariv, H. A. Terni, and E. Gileadi*

Institute of Chemistry, Tel-Aviv University, Ramat-Aviv, Israel

Chemical and electrochemical reactions, in which an asymmetric center is generated, normally lead to an optically inactive racemic mixture. It was shown recently that optical activity can be induced in the electrolytic reduction of certain compounds if a chiral electrolyte is present in the solution. Appreciable optical yields have been reported by Grimshaw *et al.* (1) in the reduction of coumarin derivatives in the presence of certain alkaloids. These authors related the activity of alkaloids in inducing asymmetry to their activity in catalytic hydrogen evolution, and postulated a similar mechanism. Horner *et al.* (2-5)

* Electrochemical Society Active Member.
Key words: asymmetric, electroreduction, acetophenone.

studied the reduction of various unsaturated functions in the presence of different alkaloids and asymmetric ammonium salts. These authors found no correlation between the ability of a compound to induce optical activity and its function as a catalyst for electrolytic hydrogen evolution. Their interpretation of this phenomenon was that the asymmetric electrolytes create an asymmetric environment in the near vicinity of the electrode, thus inducing optical activity of the product.

In the present note, the effect of several alkaloids on the electroreduction of acetophenone [1] on a mercury pool cathode is reported, with particular reference to the optical activity of 1-phenylethanol [2] formed and the ratio between the yields of the alcohol [2] and the pinacol [3] produced during electrolysis.

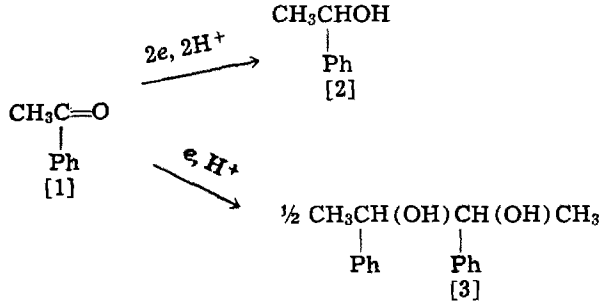

A mercury pool (25 cm^2) served as the cathode, with a platinum foil (4 cm^2) anode and a mercury-mercuric sulfate (MSE) reference electrode. The reference electrode compartment was separated from the bulk of the solution and electrolytic contact was made through a Luggin capillary which was brought to within 1 mm of the surface of the cathode. The cathode compartment contained alkaloid in 70 ml aqueous acetate buffer ($pH = 4.8$) and 15 ml methanol. The anode compartment contained 20 ml of the aqueous acetate buffer only. The two compartments were separated by "thirsty glass" (Corning Type 7930 glass). Nitrogen was bubbled through the catholyte during electrolysis. A solution of 2 ml of acetophenone [1] in 25 ml methanol was added to the cathode compartment drop by drop during electrolysis at a rate of *ca.* 4 drops per min. The concentration of the alkaloid in the catholyte at the beginning of electrolysis was $3.2 \times 10^{-2}M$ and reduced gradually with the addition of the acetophenone solution to a final value of $2.3 \times 10^{-2}M$. The amount of acetophenone [1] added corresponds to a final concentration of $0.15M$ if no reaction has taken place. The actual concentration of [1] in solution at any time during the electrolysis was lower than the above value.

Electrolysis was conducted at a potential of −1.90V (MSE). After all the acetophenone was added, electrolysis was continued until the current (which was initially *ca.* 250 mA) dropped to its background value (*ca.* 50 mA) measured in the absence of acetophenone [1]. The average duration of a run was 16 hr. Methanol was removed from the product under reduced pressure at room temperature. The organic fraction was extracted with ether and washed free of alkaloids with a 10% HCl solution. The mixture obtained after evaporation of the solvent was distilled at 52°-56°C (1 mm Hg). The pot residue, a white solid, was found (by comparison with an authentic sample) to be a mixture of the three isomers of pinacol [3]. It caused no optical rotation, indicating that the amounts of the (R),(R)- and (S),(S)-isomers in it were equal. The ratio between the meso-isomer and the racemic mixture of [3] was determined by analysis of the nmr spectrum. The ratio of the yields of the isomers of [3] formed during the reaction was not affected by addition of alkaloids to the catholyte. The distillate consisted of a mixture of (R)- and (S)-1-phenylethanol [2]. The $[\alpha]_D$ of this fraction was measured and the optical yield was calculated.[1] Results are shown in Table I.

Some of the alkaloids tested were electrochemically active and could be reduced at less negative potentials than those required to reduce acetophenone. When this was the case, the solution was pre-electrolyzed at −2.00V (MSE) before addition of acetophenone for about 5 hr, until the current dropped to the background value.

Detailed consideration of Table I reveals several phenomena. It may be seen that the addition of any of the alkaloids tested increased the relative amount of alcohol [2] produced during electrolysis. This is probably due to the fact that the alkaloid is adsorbed on the electrode (6) and in this way inhibits surface recombination of the intermediate radicals leading to pinacol [3], either by reducing the concentration of the radical intermediate or by hindering its lateral motion on the surface. All the alkaloids tested induced preferential formation of one of the enantiomers of the alcohol [2] but the absolute configuration and the yield of the one formed in excess seems to depend on the detailed structure of the alkaloid used. Thus, for example, the effect observed for cinchonine and cinchonidine is substantially smaller than for quinidine and quinine, although these compounds differ only by one methoxy group on the quinoline ring. This observation can also be best explained by the effect of the methoxy group on the adsorbability of the alkaloid. It is also noteworthy that quinidine and quinine (and likewise cinchonine and cinchonidine), which are diastereomers (opposite configurations at C-8 and C-9), induce symmetry in opposite directions. This finding, although not surprising, is reassuring and indicative of the specific interaction which must exist between the (adsorbed) alkaloid molecule and the reactant or

[1] The value of $[\alpha]_D$ for (S)-1-phenylethanol in methanol (4) is −45.5° and for the (R)-isomer its value is +45.5°. The optical yield is defined as

$$\frac{[\alpha]_D \text{ of product}}{[\alpha]_D \text{ of pure enantiomer}} \times 100$$

Table I. Product distribution and optical yield in the reduction of acetophenone[a]

Asymmetric electrolyte	Chemical yield of alcohol [2] (%)	Chemical yield of pinacol [3] (%)	Ratio of alcohol [2] fraction to pinacol [3] fraction	$[\alpha]_D$ of the alcohol [2] fraction	Optical yield (%)
—	14	73	0.19	0.0°	0.0
Quinidine[b]	22	63	0.35	−6.80°	14.9
Quinine[b]	34	39	0.88	+3.11°	6.9
Cinchonine[b]	20	77	0.26	−4.39°	9.7
Cinchonidine[b]	27	48	0.56	+0.97°	2.2
Yohimbine	17	55	0.31	+1.80°	4.0
Reserpine	20	74	0.27	+0.86°	1.9
Sparteine	26	52	0.50	−0.63°	1.4
Eserine[b]	16	76	0.21	−0.62°	1.4

[a] Each of the results in Table I represents the average of four experiments, at least. The spread of results was ±0.15° on $[\alpha]_D$, ±0.5% on optical yield, and ±0.1 on the ratio of yields of alcohol and pinacol.
[b] Pre-electrolysis required.

intermediate(s) formed in the electrochemical reaction sequence.

Reduction of acetophenone was conducted at a potential of −1.90V (MSE), less cathodic than the potential at which catalytic activity on hydrogen evolution of any of the alkaloids tested could be observed in the same solution. Thus, a mechanism in which the critical step is the homogeneous charge transfer, as proposed by Grimshaw *et al.* (1), cannot be operative in the systems studied here. A detailed study of the reduction of acetophenone in the presence of quinidine, which was found to be the most effective in inducing optical activity, under a wide range of experimental conditions, will be published elsewhere (7).

Acknowledgment

Partial support of this work by the Bat-Sheva de Rothschild Fund is gratefully acknowledged.

Manuscript submitted Oct. 24, 1972; revised manuscript received Dec. 8, 1972.

Any discussion of this paper will appear in a Discussion Section to be published in the December 1973 JOURNAL.

REFERENCES

1. R. N. Gourley, J. Grimshaw, and P. G. Millar, *Chem. Commun.*, 1278 (1967); *J. Chem. Soc.*, (C), **17**, 2318 (1970).
2. L. Horner, D. Degner, and D. Skaletz, *Chem.-Ing.-Tech.*, **44**, 209 (1972).
3. L. Horner and D. Skaletz, *Tetrahedron Letters*, 1103 (1970); *ibid.*, 3679 (1970).
4. L. Horner and D. Degner, *ibid.*, 5889 (1968); *ibid.*, 1241 (1971); *ibid.*, 1245 (1971).
5. L. Horner and H. D. Ruprecht, *ibid.*, 2803 (1970).
6. B. E. Conway, J. O'M. Bockris, and B. Lovreček, *Proc. 6th Intern. Comm. Electrochem. Thermodynam.*, 207 (1955).
7. E. Kariv, H. A. Terni, and E. Gileadi, *Electrochim. Acta*, In press (1973).

Calculation of Liquid Junction Potentials

E. C. Moreno and R. T. Zahradnik

Physical Chemistry Section, Forsyth Dental Center, Boston, Massachusetts 02115

In chemical and biological systems it is often desirable to assess the junction (or diffusion) potentials originating when two solutions of the same electrolyte are brought into contact. Thus, in studying the permselectivity of membranes, the liquid junction potential constitutes the minimum "membrane potential" when the system does not display any permselectivity. Solutions to the problem are available if ideal behavior is ascribed to the electrolyte (1-3) or if the ionic transference numbers are considered invariant with concentration (4). In most real systems, however, these assumptions are not warranted even if the solutions are in the dilute range; this is particularly true in the case of nonsymmetrical electrolytes. For uni-univalent electrolytes an expression was derived (5) on the assumption that the ion activities of the positive and negative ions are both equal to the mean ion activity. Recently, the calculation of liquid junction potentials has been reported using simulation techniques (6, 7). These techniques may become useful in ascertaining time rises and estimates of individual ionic activity coefficients; they, however, do not provide analytical solutions to the problem nor yield unique values for liquid junction potentials (7). In the present research, we were interested in establishing an analytical expression in closed form for the calculation of the LJP that takes into account the concentration dependence of both the ionic activity coefficient and the transport numbers.

In this communication we derive a generalized expression in closed form for the liquid junction potential ψ_j applicable to nonsymmetrical binary electrolytes. Ionic activity coefficients are defined by an extension of the Debye-Hückel limiting law and use is made of empirical functions of transference numbers on concentrations. It is shown that the calculated junction potentials for various electrolytes are consistent with the over-all emf values of concentration cells reported in the literature up to ionic strengths of about 0.3M.

The flux J_i of the ith ionic species at an absolute temperature T is defined by

$$J_i = -\frac{c_i|u_i|}{|z_i|e}\left(\frac{\partial\bar{\mu}_i}{\partial x}\right)_T \qquad [1]$$

in which c, u, z, and $\bar{\mu}$ are the concentration, the electrical mobility, the charge number, and the electrochemical potential of the subscripted ionic species i; the gradient is taken in the direction x.

Considering the components of $\bar{\mu}_i$, we can write

$$\frac{\partial\bar{\mu}_i}{\partial x} = \frac{\partial\mu_i}{\partial x} + z_i\mathbf{F}\frac{\partial\psi}{\partial x} \qquad [2]$$

in which μ, $\mathbf{F}$, and ψ are the chemical potential, the Faraday, and the electrical potential, respectively. In terms of the chemical activity a_i, μ_i can be defined as $\mu_i = \mu_i^\circ + RT \ln a_i$ (R being the gas constant). Introducing the ionic activity coefficient γ_i, $a_i = c_i\gamma_i$. Therefore, we may write

$$\frac{\partial\mu_i}{\partial x} = RT\left(\frac{1}{\gamma_i}\frac{\partial\gamma_i}{\partial x} + \frac{1}{c_i}\frac{\partial c_i}{\partial x}\right) \qquad [3]$$

The activity coefficient is defined here logarithmically as

$$\ln\gamma_i = -\frac{z_i^2A\sqrt{I}}{1 + B\,\alpha_i\sqrt{I}} \qquad [4]$$

in which I is the ionic strength ($I = (\frac{1}{2})\Sigma_j c_j z_j^2$), A and B are temperature and solvent dependent constants and α_i (often referred to as the distance of closest approach) is a length parameter the value of which depends on the ionic species considered. The coefficient $\partial\gamma_i/\partial x$ is given by

$$\frac{\partial\gamma_i}{\partial x} = \frac{d\gamma_i}{dI}\frac{\partial I}{\partial x} \qquad [5]$$

since γ_i is a function of I only. It is convenient to define a function $\Phi_i(I)$ by

$$\Phi_i(I) = -\frac{A\sqrt{I}}{1 + B\,\alpha_i\sqrt{I}}$$

therefore

$$\frac{d\gamma_i}{dI} = \frac{\gamma_i z_i^2\Phi_i(I)}{2I(1 + B\,\alpha_i\sqrt{I})} \qquad [6]$$

Also, from the definition of I, it follows that

$$\frac{\partial I}{\partial x} = \sum_j \frac{\partial I}{\partial c_j}\frac{\partial c_j}{\partial x}\ (j = 1,2,\ldots\ldots i) \qquad [7]$$

Substitution of Eq. [6], [7], and [5] into Eq. [3] yields

Key words: transference, activity, cell, mobility, electrolyte.

$$\frac{\partial \mu_i}{\partial x} = RT\left[\frac{z_i^2\Phi_i(I)}{2I(1+B\,a_i\sqrt{I})}\sum_j \frac{\partial I}{\partial c_j}\frac{\partial c_j}{\partial x} + \frac{1}{c_i}\frac{\partial c_i}{\partial x}\right] \quad [8]$$

and substitution of Eq. [8] into Eq. [2] followed by substitution of the resulting expression into [1] gives a generalized form for the flux equation

$$J_i = -\frac{c_i|u_i|}{|z_i|e}\left(RT\left[\frac{z_i^2\Phi_i(I)}{2I(1+B\,a_i\sqrt{I})}\sum_j \frac{\partial I}{\partial c_j}\frac{\partial c_j}{\partial x} + \frac{1}{c_i}\frac{\partial c_i}{\partial x}\right] + z_i F\frac{\partial \psi}{\partial x}\right) \quad [9]$$

In the subsequent equations the quantities related to the properties of the cation and the anion of the binary electrolyte will be subscripted with the numerals 1 and 2, respectively. The condition of zero current is

$$\sum_{i=1}^{2} z_i J_i = 0 \quad [10]$$

Substitution of Eq. [9] into [10] and subsequent use of the condition for electrical neutrality, $\Sigma_j z_j c_j = 0$, and the definition of the transport number, $t_i = c_i|u_i|/\Sigma_j c_j|u_j|$, yield the general differential equation

$$\frac{\partial \psi}{\partial x} = \frac{RT}{4F}\left[\frac{(z_1^2z_2 - z_1^3)t_1\Phi_1(I)}{I(1+B\,a_1\sqrt{I})} + \frac{(z_2^2z_1 - z_1^2z_2)t_2\Phi_2(I)}{I(1+B\,a_2\sqrt{I})}\right]\frac{\partial c_1}{\partial x} - RT\left(\frac{t_1}{z_1}+\frac{t_2}{z_2}\right)\frac{1}{c_1}\frac{\partial c_1}{\partial x} \quad [11]$$

The transport numbers t_i appearing in Eq. [11] are not independent of concentration. It has been found empirically (8-10) that for many binary electrolytes, the dependence of t_1 on concentration is described very adequately by

$$t_1 = \frac{K_1}{I + K_2\sqrt{c_1}} - 1 \quad [12]$$

in which the values of the constants K_1 and K_2 depend on the electrolyte considered. Equation [2] is now substituted into Eq. [11] recalling that $t_2 = 1 - t_1$ and that $I = [z_1^2 - z_1z_2]c_1/2$. The integration of the resulting differential equation is done across the boundary, from solution "to solution," considering that this region is made up of an indefinite number of layers with concentrations intermediate between the two solutions in question. Thus one obtains

$$\psi'' - \psi' = \psi_j = \left(1 + \frac{K_1B\alpha_1}{K_3 - B\alpha_1}\right)\Gamma_1(I) - \left(2 + \frac{K_1B\alpha_2}{K_3 - B\alpha_2}\right)\Gamma_2(I) + L_1(I) - L_2(I) + \frac{RTK_1}{F}\left[\left(\frac{1-K_1}{z_1K_1} - \frac{2-K_1}{z_2K_1}\right)\ln\frac{I''}{I'} - \left(\frac{2}{z_2} - \frac{2}{z_1}\right)\ln\frac{1+K_3\sqrt{I''}}{1+K_3\sqrt{I'}}\right] \quad [13]$$

The new terms in Eq. [13] are defined as

$$\Gamma_i(I) = \frac{RTAz_i(\sqrt{I'} - \sqrt{I''})}{F(1+B\alpha_i\sqrt{I'})(1+B\alpha_i\sqrt{I''})};$$

$$K_3 = \sqrt{2}\,K_2/(z_1^2 - z_1z_2)^{1/2}$$

$$L_i(I) = \frac{RTA}{F}\frac{K_1K_3z_i}{(K_3 - B\alpha_i)^2}\ln\frac{(1+K_3\sqrt{I''})(1+B\alpha_i\sqrt{I'})}{(1+K_3\sqrt{I'})(1+B\alpha_i\sqrt{I''})}$$

Equation [13] is rather cumbersome but it constitutes an analytical solution to the stated problem; its validity, of course, depends on the validity of the extra-thermodynamic functions used in its derivation, namely, the use of the Debye-Hückel theory to calculate ionic activity coefficients and the empirical dependence of transport numbers on concentrations. We have tested the adequacy of Eq. [13] using emf values reported in the literature for concentration cells with NaCl, LiCl, KCl, $BaCl_2$, $CaCl_2$, and $LaCl_3$ at 25°C. For this purpose we defined the calculated potentials, E_c, of these cells as

$$E_c = -\frac{RT}{F}\ln\frac{c_2''\gamma_2''}{c_2'\gamma_2'} + \psi_j \quad [14]$$

The activity coefficients γ_i and the junction potential ψ_j were calculated from Eq. [4] and [13], respectively. Thus, assessment of the adequacy of Eq. [13] can be obtained by comparison of the E_c with the observed emf values E_{ob} for the various electrolytes. Typical results for four of the electrolytes studied are given in Table I. For the case of $BaCl_2$ the values used for the constants K_1 and K_2 in Eq. [12] as well as the values for E_{ob}, were those reported by Jones and Dole (8). For $LaCl_3$, the values used for K_1 and K_2 were those reported by Jones and Prendergast (10) and the E_{ob} values were those reported by Shedlovsky and MacInnes (11). Values used for K_1 and K_2 for LiCl were those reported by Jones and Bradshaw (9) and the E_{ob} values were those reported by MacInnes and Beattie (12). For NaCl the best values for K_1 and K_2 were obtained by a least squares procedure (index of determination, 0.994) from the data on transference numbers reported by Longsworth (13). Values for E_{ob} for NaCl were those reported by MacInnes (14). The values used (15) for $a_i \times 10^8$ were: 4.5, for Na^+; 5 for Ba^{2+}; 9, for La^{3+}; and 3, for Cl^-. Values for the constants $A/2.303$ and B in Eq. [4] were 0.512 and 0.329×10^8, respectively (16), for water at 25°C.

The data in the last two columns of the table show good agreement (within 3%) between E_c and E_{ob} for systems with ionic strengths up to 0.3M. It is evident that a more satisfactory agreement was obtained for NaCl and $BaCl_2$ than for $LaCl_3$. This is not surprising since the use of the Debye-Hückel theory for single ionic activity coefficients is less satisfactory the higher the ionic charge number. Lack of agreement between the E_c values calculated by Eq. [4] and the E_{ob} values reported in the previously mentioned references became larger at higher ionic strengths; for systems (not included in the table) with ionic strengths from 0.5 to 3M the two values differed from about 5 to 10%. It is conceivable that the use of higher order terms in Eq. [4] might result in an expression that could give satisfactory results at higher concentrations; its concomitant increased complexity, however, would probably prevent its use in most practical situations.

Table I. Calculated liquid junction potentials at 25°C for concentration cells with transference together with observed and calculated cell emf's

Electrolyte	m', M	m'', M	ψ_j (Eq. [13]), mV	E_{ob}, mV	E_c (Eq. [14]), mV
NaCl	0.005	0.1	15.45	−56.46[a]	−56.19
	0.01	0.05	8.31	−30.35	−30.23
	0.02	0.1	8.17	−29.80	−29.62
	0.08	0.1	1.11	−4.05	−4.02
LiCl	0.03	0.3	18.49	−35.21[b]	−34.35
	0.1	0.3	8.78	−16.41	−15.97
$BaCl_2$	0.001	0.05	35.52	−58.50[c]	−58.03
	0.005	0.05	21.22	−33.26	−32.74
	0.01	0.05	14.92	−22.75	−22.40
	0.025	0.05	6.48	−9.42	−9.37
$LaCl_3$	0.00061	0.03333	40.84	−52.69[d]	−54.23
	0.00322	0.03333	24.28	−29.05	−30.04
	0.01094	0.03333	11.69	−13.24	−13.72
	0.02526	0.03333	2.93	−3.21	−3.31

[a] Ref. (8).
[b] Ref. (6).
[c] Ref. (2).
[d] Ref. (5).

Equation [14] is substantially simplified if t_i values, intermediate between the two electrolyte concentrations, are considered to be independent of concentration. However, calculations made on this basis for the examples listed in the table yielded disagreements between E_{ob} and E_c in the order of about 3-6% for the cases of NaCl and $BaCl_2$ and it amounted to 6-12% for the case of $LaCl_3$.

Acknowledgment

This work was partially supported by U. S. Public Health Grant DE-03187.

Manuscript submitted Aug. 3, 1972; revised manuscript received Jan. 25, 1973.

Any discussion of this paper will appear in a Discussion Section to be published in the December 1973 JOURNAL.

LIST OF SYMBOLS

ψ_j	liquid junction potential, V
J	flux, mole-ions/(cm² sec)
c	concentration, mole-ions/dm³
u	electrical mobility, cm²/(V sec) (negative for anions)
z	charge number (negative for anions)
e	electronic charge, A sec or coulomb
$\bar{\mu}$	electrochemical potential, erg or joule
μ	chemical potential, erg or joule
ψ	electrical potential, V
x	direction of potential gradient, cm
F	Faraday coulomb/eq
R	gas constant, (erg or joule)/(mole K)
T	temperature, °K
a	chemical activity, mole-ions/dm³
γ	ionic activity coefficient
I	ionic strength, (mol-ion/dm³)²
A	Debye-Hückel parameter, mole$^{-1/2}$ dm$^{1/2}$
B	Debye-Hückel parameter, cm^{-1} mole$^{-1/2}$ dm$^{1/2}$
α	distance of closest approach, cm
t	transport number
K_1, K_2	parameters for empirical transport equation (Eq. [13])
E_{ob}	observed concentration cell potential, V
E_c	calculated cell potential (Eq. [14]),V

REFERENCES

1. M. Planck, *Ann. Phys. Chem.*, **39**, 161 (1890); **40**, 561 (1890).
2. P. Henderson, *Z. Physik. Chem.*, **59**, 118 (1907); **63**, 325 (1908).
3. L. Bass, *Trans. Faraday Soc.*, **60**, 1914 (1964).
4. G. Bianchi, G. Faita, R. Galli, and T. Mussini, *Electrochimia Acta*, **12**, 439 (1967).
5. D. A. MacInnes, "The Principles of Electrochemistry," pp. 222-225, Reinhold Publishing Corp., New York (1939).
6. D. R. Hafemann, *J. Phys. Chem.*, **69**, 4226 (1965).
7. R. N. Goldberg and H. S. Frank, *J. Phys. Chem.*, **76**, 1758 (1972).
8. G. Jones, and M. Dole, *J. Am. Chem. Soc.*, **51**, 1073 (1929).
9. G. Jones and B. C. Bradshaw, *ibid.*, **54**, 138 (1932).
10. G. Jones and L. T. Prendergast, *ibid.*, **58**, 1476 (1936).
11. T. Shedlovsky and D. A. MacInnes, *ibid.*, **61**, 200 (1939).
12. D. A. MacInnes and J. A. Beattie, *ibid.*, **42**, 1117 (1920).
13. L. G. Longsworth, *ibid.*, **57**, 1185 (1935).
14. D. A. MacInnes, *ibid.*, **57**, 1359 (1935).
15. J. Kielland, *ibid.*, **59**, 1675 (1937).
16. R. A. Robinson and R. H. Stokes, "Electrolyte Solutions," 2nd ed., p. 468, Butterworths, London (1968).

ECM of Nickel in $NaClO_3$ Solution

Mitchell A. LaBoda,* Armand J. Chartrand, James P. Hoare,* Charles R. Wiese, and Kao-Wen Mao*

Electrochemistry Department, Research Laboratories, General Motors Corporation, Warren, Michigan 48090

A certain amount of success has been achieved by correlating the electrochemical machining (ECM) behavior of steel in a given electrolyte with the passivation characteristics of steel in the electrolyte determined from polarization, film stripping, and mass balance studies (1-7). There is some evidence (8-10) that the results valid for iron and steel may not be valid for some other metals. Consequently, the machining of Ni by ECM may be an entirely different proposition.

Since the ECM behavior of a given metal in a given electrolyte has been shown to depend on the nature of the anodic film formed on the metal surface (1-6) and on the interaction of the anodic film with the anions present in the electrolyte (7), it would seem highly probable that the machining of iron or steel in $NaClO_3$ solutions would be much different from that of nickel in $NaClO_3$ solutions. It is the purpose of this note to present the results of an investigation showing that the polarization, film stripping, and mass balance data for steel and nickel anodes in 3M $NaClO_3$ solution are very different, and that the machining characteristics of steel and nickel samples in a laboratory ECM plunge-cut machine are equally so.

All experimental techniques have been described in earlier reports (6, 7). The samples were mild steel (Type 1020) and nickel (99.5% pure). The electrolyte studied was a solution of 350g of $NaClO_3$ per liter. The steel and nickel tubes machined in the ECM machine had the same geometric dimensions.

The steady-state polarization curves along with the film stripping data are plotted in Fig. 1. The difference between the two curves for steel and nickel is striking. At low potentials (below 0.5V), steel is active and surface films are undetectable; whereas nickel is passive in the same potential region and the surface is well covered with an anodic film. Instead of a negative resistance region (active-passive transition) exhibited by steel anodes, a limiting current region appears on the polarization curve obtained on Ni anodes. In the transpassive region, the anodic film on steel anodes becomes thinner with increasing potential, but that on nickel anodes not only becomes thicker but also a new phase appears (filled circles in Fig. 1b) at potentials where O_2 evolution begins (11).

Nearly all the current is consumed in O_2 evolution on Ni anodes at current densities below about 2 A/in.². After a polarization run, the Ni wires remained bright and the electrolyte was clear and colorless. Under similar experimental conditions, the diameter of a steel wire was greatly reduced and $Fe(OH)_3$ sludge collected in the electrolyte. Such behavior indicates that the anodic film on Ni anodes in $NaClO_3$ solution possesses a higher degree of electronic conductivity. Oxygen is evolved by the chemical decomposition of a higher oxide and current is consumed in the electrochemical formation of the higher oxide from the lower form (11).

Although the current efficiency for metal removal at Ni anodes in $NaClO_3$ solution increases with increasing current density as noted by Landolt (10), it does not increase as fast with current density as that at steel anodes in $NaClO_3$ solution, nor does it reach as high values at high current densities ($\sim$ 300 A/in.²). These facts are contained in the data of Table I. For this

* Electrochemical Society Active Member.

Key words: electrochemical machining, nickel anodes, $NaClO_3$ electrolytes, passive films, anodic films.

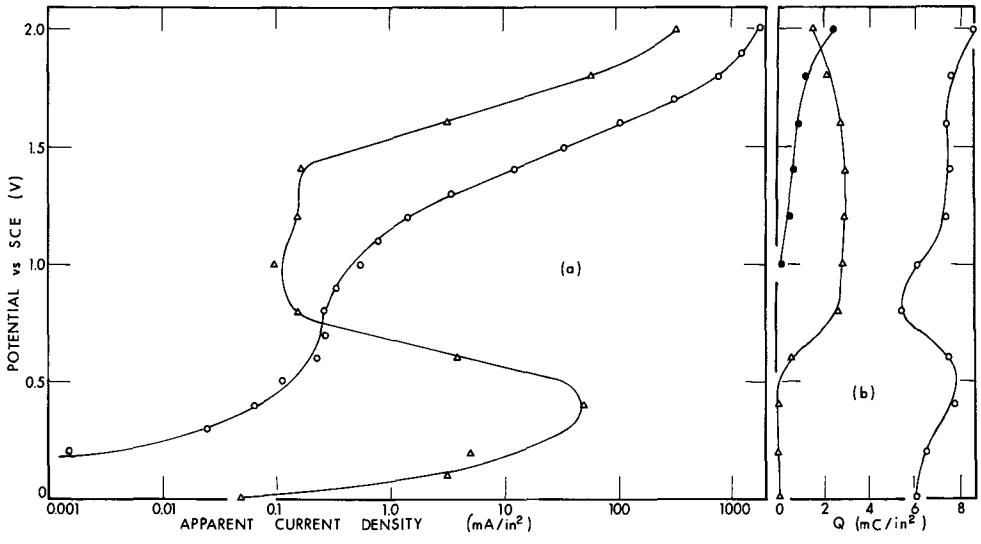

Fig. 1. (a) Steady-state polarization curves for nickel (open circles) and steel (open triangles) anodes in O_2-saturated $NaClO_3$ solution (350 g/liter). (b) A plot of the charge (Q) associated with anodic film formed on the surface of nickel (open circles) and steel (open triangles) anodes as a function of potential in $NaClO_3$ solution (350 g/liter); the filled circles represent the charge associated with a higher oxide formed on Ni anodes in the potential range where O_2 is evolved.

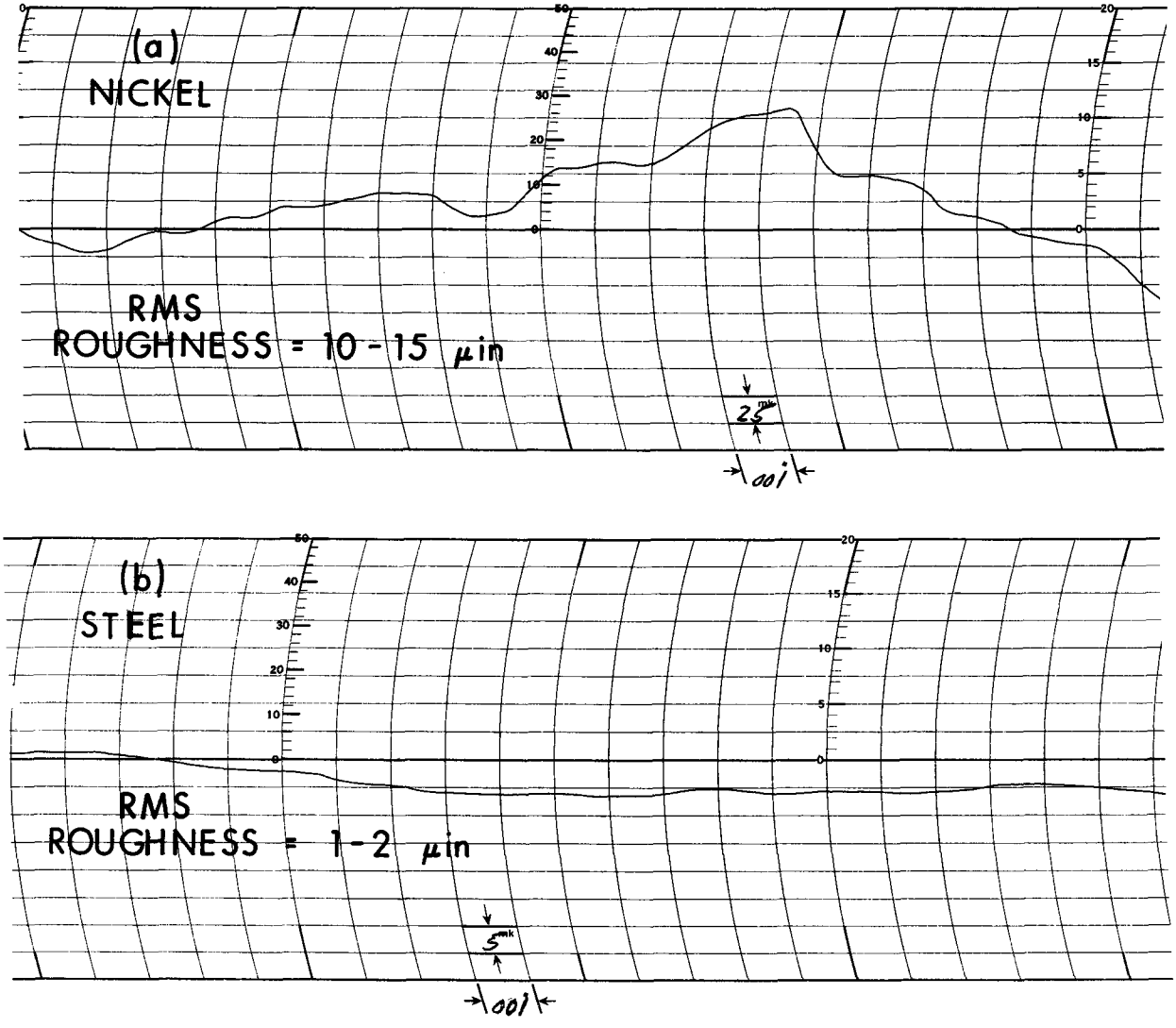

Fig. 2. Proficorder traces of the sides of holes plunge-cut by an ECM machine in nickel (a) and steel (b) samples using $NaClO_3$ solution (350 g/liter). The x-axis for both (a) and (b) is 0.001 in./div; the y-axis for (a) is 25 μin./div and for (b) 5 μin./div. RMS surface roughness is determined as 1/3 of the peak-to-valley distance.

reason, one would expect the machining rate of Ni to be slower than that of steel in the $NaClO_3$ electrolyte. In Table II is listed the highest machining rate obtained during the plunge-cutting of a sample in the laboratory ECM machine without the automatic cutoff being activated. As noted, steel can be machined almost twice as fast as Ni under the same experimental conditions in $NaClO_3$ electrolytes.

With increasing potentials, the anodic film on steel becomes uniformly thinner and highly porous producing an electropolishing of the metal surface (7). On the contrary, the anodic film on Ni anodes thickens

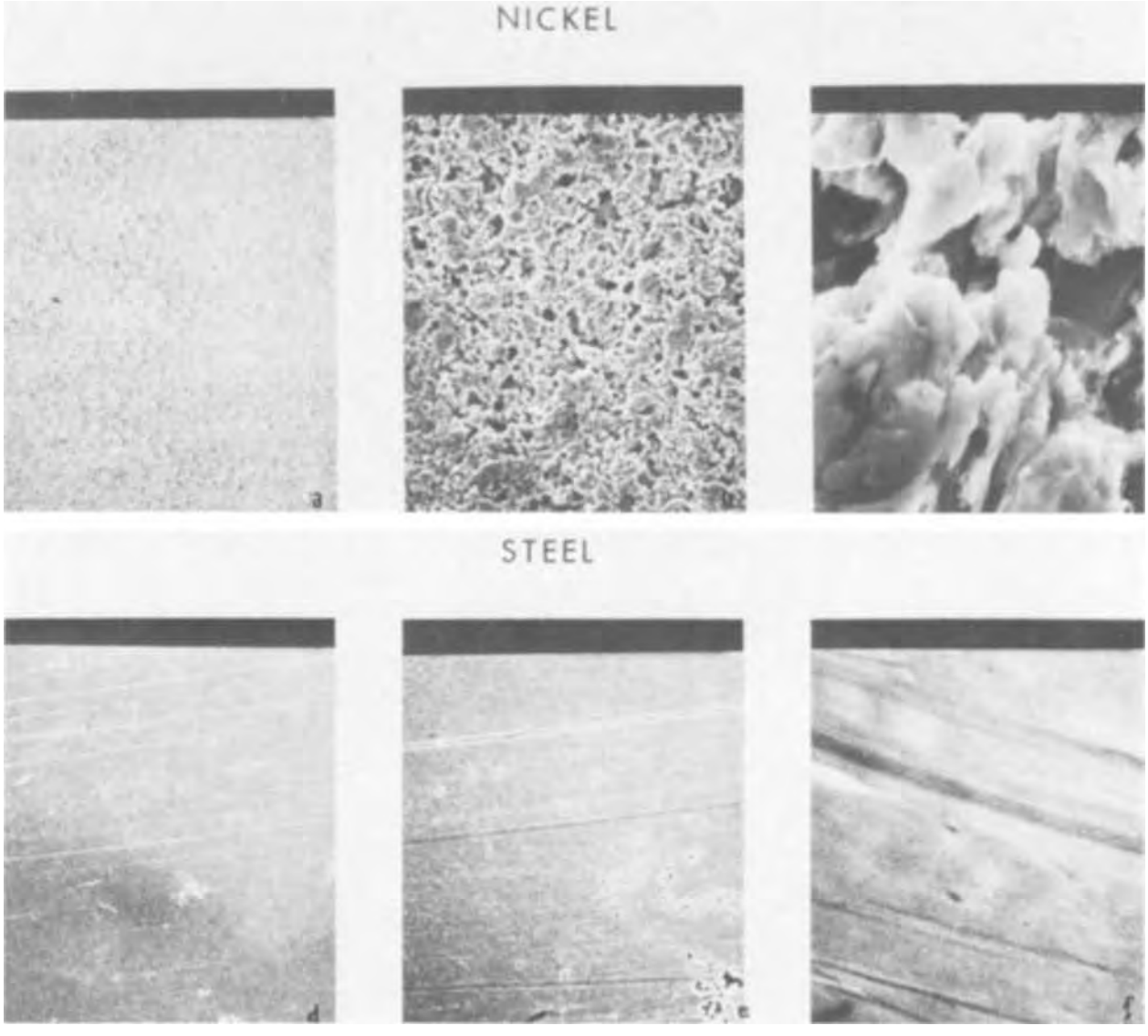

Fig. 3. Scanning-electron micrographs of the machined surface of the side of a hole plunge-cut by an ECM machine in nickel (a, b, and c) and steel (d, e, and f) samples using $NaClO_3$ solution (350 g/liter). Magnification of (a) and (d) is 100×; of (b) and (e) 1000×; of (c) and (f) 10,000×. Angle of incidence was 12°.

with increasing potential, and a less smooth surface is obtained on Ni anodes. The Proficorder traces along the sides of a hole plunge-cut in the sample by the ECM laboratory machine are reproduced in Fig. 2. It is seen that there is nearly an order of magnitude difference in the degree of surface roughness recorded on the machined surfaces of Ni and steel samples. Confirmation of this observation is obtained in Fig. 3 which shows scanning electron micrographs of the machined surfaces of plunge-cut Ni and steel samples at three magnifications.

These data confirm the contention that the ECM behavior of a given metal in a given electrolyte is highly dependent on the type and nature of the anodic films formed on the metal surface and on the interaction of the film with the anions in solutions as a function of potential. A good understanding of these two conditions can be obtained from polarization, film stripping, and mass balance studies of the given system. To obtain acceptable results from ECM, the choice of electrolyte and experimental parameters must be determined for each kind of metal under consideration.

Table I. Current efficiency for nickel and steel tubes machined in $NaClO_3$ (350 g/liter) electrolyte

Metal	Current density (A/in.²)	Current efficiency for metal removal (%)	Current efficiency for O_2 evolution (%)
Nickel	40	7.7	—
	80	14.8	78.5
	150	58.2	—
	300	66.5	39.6
Steel	40	0.3	—
	80	22.4	77.8
	150	61.5	39.5
	300	85.5	17.8

Table II. Machining rate of plunge-cut samples in $NaClO_3$ solution (350 g/liter)

Metal	Applied voltage (V)	Pump pressure PSIG	Machining rate (in./min)	RMS surface roughness (μin.)
Nickel	20	72	0.175	10-15
Steel	20	68	0.310	1-2

Manuscript submitted Oct. 26, 1972; revised manuscript received Jan. 16, 1973.

Any discussion of this paper will appear in a Discussion Section to be published in the December 1973 JOURNAL.

REFERENCES

1. M. A. LaBoda and M. L. McMillan, *Electrochem. Technol.*, 5, 340 (1967).

2. J. P. Hoare, M. A. LaBoda, M. L. McMillan, and A. J. Wallace, *This Journal*, **116**, 199 (1969).
3. J. P. Hoare, *ibid.*, **117**, 142 (1970); *Nature*, **219**, 1034 (1968).
4. M. A. LaBoda, J. P. Hoare, and S. E. Beacom, *Collection Czech. Chem. Commun.*, **36**, 380 (1970).
5. J. P. Hoare, K-W. Mao, and A. J. Wallace, *Corrosion*, **27**, 211 (1971); *Corrosion Sci.*, **12**, 571 (1972).
6. K-W. Mao, *This Journal*, **118**, 1870 (1971); *ibid.*, **118**, 1876 (1971).
7. K-W. Mao, M. A. LaBoda, and J. P. Hoare, *ibid.*, **119**, 419 (1972).
8. P. J. Boden, and J. M. Evans, *Nature*, **222**, 337 (1969); *This Journal*, **116**, 1715 (1969).
9. J. P. Hoare, M. A. LaBoda, and A. J. Wallace, *ibid.*, **116**, 1715 (1969).
10. D. Landolt, *ibid.*, **119**, 708 (1972).
11. J. P. Hoare, *Nature*, **241**, 44 (1973).

JOURNAL OF THE ELECTROCHEMICAL SOCIETY

SOLID-STATE SCIENCE AND TECHNOLOGY

MAY 1973

Solid-State Ionics: A New High Ionic Conductivity Solid Electrolyte $Ag_6I_4WO_4$ and Use of This Compound in a Solid-Electrolyte Cell

Takehiko Takahashi,* Shoichiro Ikeda, and Osamu Yamamoto

Department of Applied Chemistry, Faculty of Engineering, Nagoya University, Nagoya, Japan

ABSTRACT

A new high ionic conductivity solid $Ag_6I_4WO_4$ has been found in the system AgI-Ag_2WO_4 at ambient temperature. This compound has a silver ion conductivity of 0.047 $(ohm \cdot cm)^{-1}$ at 25°C and an activation energy for conduction of 3.6 kcal/mole between 20° and 293°C. The transport number measurement using Tubandt's method shows that the transport number of silver ions in this compound is 1.00 within the experimental error. A $Ag/Ag_6I_4WO_4/I_2$ solid-electrolyte cell shows an open-circuit voltage of 687 mV which agrees well with the value of 686.7 mV calculated from $\Delta G°$ of the cell reaction at 21°C. Characteristics of the solid-state cells using $Ag_6I_4WO_4$ as the electrolyte have been investigated. The phase diagram of the system AgI-Ag_2WO_4 has been determined also.

In a previous paper (1) the phase diagrams of the systems AgI-Ag_3PO_4 and AgI-$Ag_4P_2O_7$ were reported, and the solid ionic conductors $Ag_7I_4PO_4$ and $Ag_{19}I_{15}P_2O_7$ were described. The compounds $Ag_7I_4PO_4$ and $Ag_{19}I_{15}P_2O_7$ are more stable than the MAg_4I_5 group ($M = K$, Rb, or NH_4) (2, 3) in iodine atmosphere and in moisture. In this paper, a new high ionic conductivity solid in the silver-iodide and silver-tungstate system is described which has better stability in iodine atmosphere than the other high ionic conductors previously known.

The system AgI-Ag_2WO_4 has been examined by the same procedure as previously mentioned (1) to determine its phase diagram, and the performance of the solid-state silver-iodine cell has been investigated using this system as the electrolyte.

Experimental

Preparation of samples.—G.R. grade $AgNO_3$, KI, and $Na_2WO_4 \cdot 2H_2O$ were used as starting materials. Silver tungstate was prepared by precipitation from aqueous solutions of silver nitrate and sodium tungstate. The precipitate was washed seven or eight times with distilled water and dried under nitrogen flow at 120°C for several hours. The preparation method of AgI was described in the previous paper (1).

Weighing of silver iodide and silver tungstate was followed by mixing and grinding, and the mixture was sealed in a Pyrex tube under vacuum and heated for about 18 hr at 400°C and then the resulting material was allowed to cool to room temperature.

Conductivity measurement.—In order to reduce the contact resistance in the measurements of the conductivity change with temperature, a mixture of 0.9g of the sample and 0.3g of 200 mesh silver powder was used as the electrode material. The sample of 1.2g was stacked between the electrodes and pressed into a pellet of 13 mm in diameter by a hand press under 4000 kg/cm². The electrical conductivity was measured with an 1 kHz impedance bridge (YEW, Model BV-Z-13A).

The transport number of silver ions in this new high conductivity solid was measured by Tubandt's method (4), where a cell of the type of

$$\underset{(+)}{Ag,Hg/X_1/X_2/X_3/X_4/}\underset{(-)}{Ag} \qquad [I]$$

was used, where $X = Ag_6I_4WO_4$. In order to reduce the anodic polarization, an amalgamated silver plate was used for the anode material, and the change of the mass of X_2, X_3, X_4, and cathode was measured. A solution of 10 w/o (weight per cent) silver nitrate was used as the electrolyte of the silver coulometer. A stabilized direct current was passed through the cell for about 4 hr at the current density of 1.5 mA/cm².

Galvanic cell.—A solid-state galvanic cell of the type of

$$Ag,Ag_6I_4WO_4/Ag_6I_4WO_4/I_2,\ Ag_6I_4WO_4,C \qquad [II]$$

was constructed, the schematic of which is shown in Fig. 1. In order to reduce the contact polarization effects at the anode-electrolyte interface, a mixture of 0.4g of $Ag_6I_4WO_4$ and 0.15g of 200 mesh silver powder, and 1.0g of $Ag_6I_4WO_4$ were stacked in laminar arrangement and pressed at 4000 kg/cm² into a single pellet of 13-mm diameter to form the anode and the electrolyte, respectively.

The cathode material was a mixture of iodine, $Ag_6I_4WO_4$, and graphite (0.40g:0.40g:0.07g), and pressed into a pellet of the same shape. In order to measure the anodic and cathodic polarizations of this cell, the anode layer was divided into two pieces of an

* Electrochemical Society Active Member.

Key words: silver iodide-silver tungstate, ionic conductivity, solid-state battery.

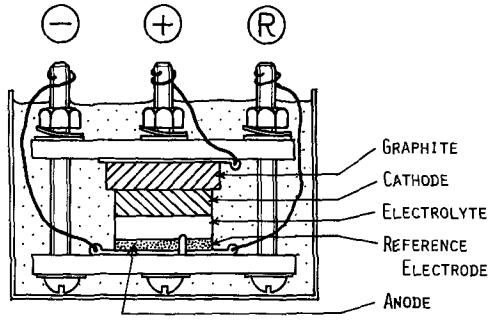

Fig. 1. Schematic diagram of the solid-electrolyte cell for polarization measurement.

original anode and a reference electrode, where the area ratio was 10:3. Silver plates 0.05-mm thick were used as the current collectors contacted directly with the anode and the reference electrode, and indirectly with the cathode via a graphite plate. The cell was sealed with polyester resin to prevent the sublimation of iodine.

X-ray diffraction.—Geigerflex D-3F (Rigaku Denki Company, Ltd.) was used for the x-ray diffraction analysis. A copper anode tube was operated at 15 mA and 35 kV. The shape of each sample was a pellet of 13 mm in diameter and about 1.5-mm thick pressed by a hand press under 4000 kg/cm^2.

Differential thermal analysis (DTA).—A sample of 0.8g was sealed in a Vycor tube under vacuum, and an α-alumina powder sealed in a Vycor tube of the same size was used for the standard material. The heating rate was 3.5°C/min, controlled by a PID controller (YEW, Model EGC 5-10) and a programmer (YEW, Model PGE-12).

Results and Discussion

Electrical conductivity of the system AgI-Ag_2WO_4.—A plot of the electrical conductivity of the system AgI-Ag_2WO_4 at room temperature against the Ag_2WO_4 content is shown in Fig. 2. The conductivity curve suggests that an intermediate compound with high electrical conductivity may be present in this system, because the curve shows a maximum at about 20 m/o (mol per cent) Ag_2WO_4 when the conductivity is of the order of 10^{-2} (ohm · cm)$^{-1}$. The conductivity of Ag_2WO_4 shown in the figure was obtained from an extrapolation of the Arrhenius plots of Ag_2WO_4 shown in Fig. 3 to 25°C.

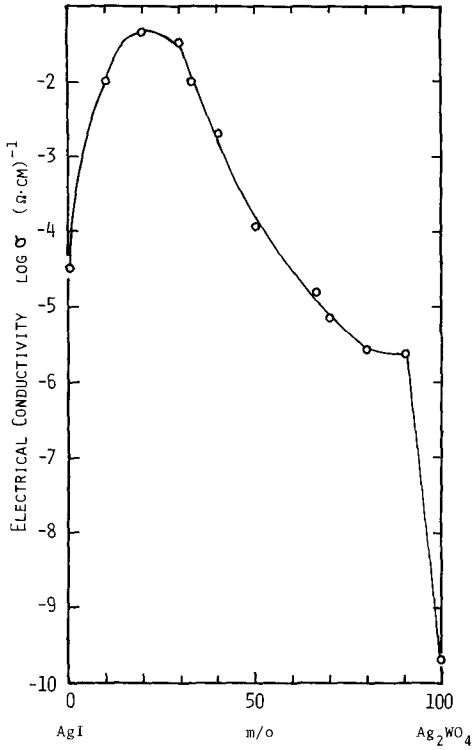

Fig. 2. Electrical conductivities in the system AgI-Ag_2WO_4 vs. the composition of Ag_2WO_4 at 25°C.

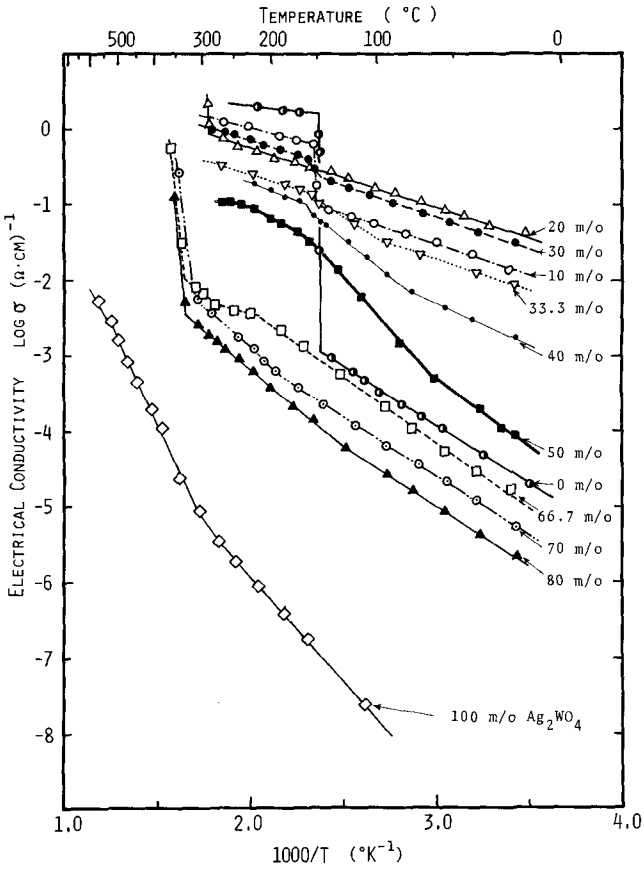

Fig. 3. Electrical conductivities of the system AgI-Ag_2WO_4 vs. the reciprocal of the absolute temperature.

The electrical conductivities of the system AgI-Ag_2WO_4 plotted as a function of the reciprocal of the absolute temperature are shown in Fig. 3. The conductivity curves of the samples containing 0 and 10 m/o of Ag_2WO_4 show abrupt change at 147°C, corresponding to the transition of silver iodide from β to α phase. The curves of the samples of 30 and 33.3 m/o of Ag_2WO_4 show the small bends near 150°C.

The conductivity curve of 20 m/o of Ag_2WO_4, however, shows no abrupt change and bend near these temperatures, and increases linearly up to 293°C, which corresponds to the incongruent melting point described in a later section. This result indicates that a new high conductivity compound, which may be written as $Ag_6I_4WO_4$, would be present at the composition of 20 m/o Ag_2WO_4-80 m/o AgI.

In order to determine the charge carrier of this compound, Tubandt's method was used. It was found that the total charge passed through cell [I] corresponded to the quantity of silver deposited at the cathode as shown in Table I, and the transport number of the silver ion is unity within the experimental error. Therefore, the electrical conductivity of

Table I. Transport number in $Ag_6I_4WO_4$

	Change in mass (mg)
Ag-Hg anode	—
X_1	—
X_2	+0.01
X_3	±0.00
X_4	+28.12
Ag cathode	±0.00
Ag deposited in coulometer	+28.30
Transport number of Ag^+	0.994

$Ag_6I_4WO_4$ shown in Fig. 3 is a silver ion conductivity and is 0.047 ± 0.001 $(ohm \cdot cm)^{-1}$ at 25°C. The activation energy for conduction obtained from the Arrhenius plot is 3.6 kcal/mole, which is comparable to the values of the other high ionic conductivity solids (1). The high ionic conductivity and low activation energy suggest that the silver ions in this new compound may be statistically distributed in the lattice taking an averaged structure.

X-ray diffraction.—The results of the x-ray diffraction of the samples carried out at room temperature using nickel filtered Cu-Kα radiation are listed in Table II. In the composition range of 0-18 m/o Ag_2WO_4, the diffraction peaks due to γ-phase silver iodide appeared. The lines due to Ag_2WO_4 were observed in the samples containing 67 m/o or more Ag_2WO_4. The lines due to β-AgI and Ag_2WO_4 were not observed in the samples containing 20-67 m/o Ag_2WO_4. The patterns of the samples containing 20, 33, and 67 m/o Ag_2WO_4 showed that the new phases were formed in these compositions. These patterns, however, are too complex to determine the crystal structure only by the powder x-ray diffraction analysis.

Phase diagram of the system AgI-Ag_2WO_4.—The results of the DTA of the system AgI-Ag_2WO_4 in the temperature range of 20°-200°C are shown in Fig. 4. Although the DTA of this system showed an endothermic peak at 147°C in the heating process in the composition range of 0-17.5 m/o of Ag_2WO_4 which is due to the transformation of silver iodide from β to α phase, the peak did not appear at this temperature in the samples of 20 and 22.5 m/o Ag_2WO_4. Another endothermic peak at 150°C appeared in the composition range of 25-60 m/o Ag_2WO_4. These results correspond to those of the electrical conductivity measurements shown in Fig. 3. In the samples containing more than 67 m/o of Ag_2WO_4, however, no peaks were observed near these temperatures. The endothermic peaks at 293°, 290°, and 348°C were also observed in the composition ranges of 0-20, 20-67, and 50-90 m/o of Ag_2WO_4 in the heating process.

Figure 5 shows the phase diagram of the system AgI-Ag_2WO_4 determined by the x-ray diffraction measurements and the differential thermal analysis. In this system, there are three intermediate compounds at the compositions of 20, 33, and 67 m/o of Ag_2WO_4, which may be written as $Ag_6I_4WO_4$, $Ag_4I_2WO_4$, and $Ag_5IW_2O_8$, respectively, at room temperature. $Ag_6I_4WO_4$ and $Ag_5IW_2O_8$ incongruently melt at 293° and 348°C, respectively. $Ag_4I_2WO_4$ decomposes to $Ag_6I_4WO_4$ and $Ag_5IW_2O_8$ above 150°C. The melting

Table II. Powder x-ray patterns for the system AgI-Ag_2WO_4

Ag_2WO_4 d (Å)	I	$Ag_5IW_2O_8$ d (Å)	I	$Ag_4I_2WO_4$ d (Å)	I	$Ag_6I_4WO_4$ d (Å)	I	γ-AgI d (Å)	I
4.08	W	4.17	VW	4.31	W	4.44	W	3.75	VS
3.80	W	3.97	W	3.79	S	4.25	VW	2.31	S
3.49	VW	3.77	VW	3.48	W	4.13	VW	1.97	M
3.28	W	3.62	VW	3.02	M	3.79	MWB*		
3.14	W	3.22	MW	2.94	M	3.68	MB		
2.96	M	3.06	M	2.87	MW	3.48	MSB*		
2.85	VS	2.99	S	2.71	M	3.18	MB		
2.72	M	2.86	M	2.31	M	2.96	MB		
2.65	W	2.80	MB*	2.25	VW	2.92	M		
2.44	VW	2.72	MW	1.97	MW	2.87	M		
2.37	VW	2.66	M	1.92	W	2.71	SB*		
2.20	VW	2.50	W			2.56	WB		
2.16	VW	2.37	W			2.46	W		
2.01	S	2.30	W			2.38	WB		
1.96	W	2.21	W			2.31	MB		
		2.16	W			2.18	MB		
		2.13	VW			1.93	WB		
		2.04	W						
		2.01	W						
		1.87	VW						
100 m/o Ag_2WO_4		66.7 m/o		33.3 m/o		20 m/o		0 m/o	
90, 80, 70 m/o		60, 50, 40 m/o		30, 25 m/o		17.5, 10, 5 m/o			
Mixed pattern		Mixed pattern		Mixed pattern		Mixed pattern			

* MB, MWB, MSB, and SB: B means that the peak is rather broad.

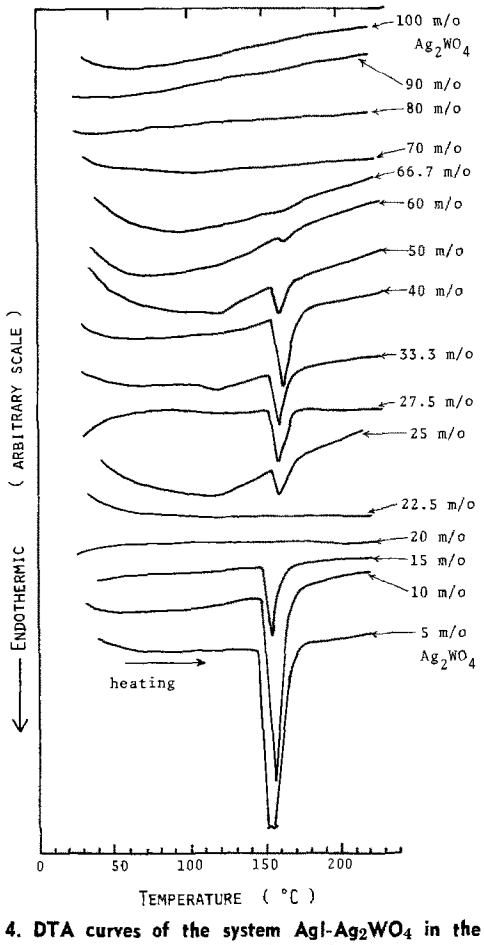

Fig. 4. DTA curves of the system AgI-Ag_2WO_4 in the heating process in the temperature range of 20°-200°C.

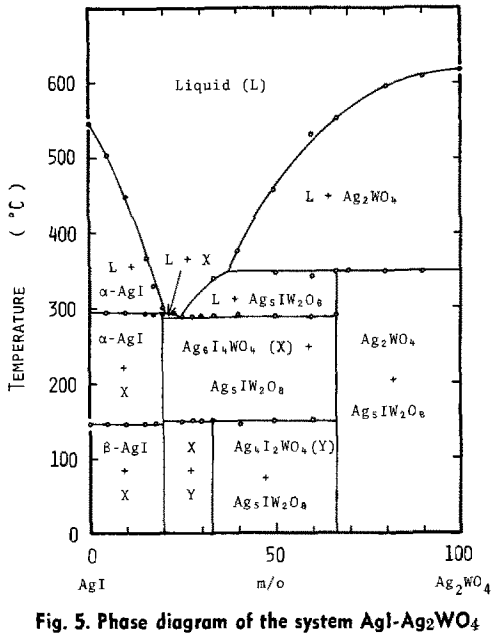

Fig. 5. Phase diagram of the system AgI-Ag_2WO_4

point of Ag_2WO_4 is 620° ± 5°C, and the eutectic composition is estimated to be 25 m/o Ag_2WO_4, at 290°C.

Galvanic cell.—The high ionic conductivity solid electrolytes have been mainly used in solid-electrolyte galvanic cells (5-10). In these applications, the solid electrolyte should have a high ionic conductivity, high stability for the cathode material, and low electrode polarization. Figure 6 shows the result of the change of the internal resistance of the cell, Graphite/$Ag_6I_4WO_4$ + I_2/Graphite, with time. A mixture of 1.3g of the electrolyte and 0.3g of iodine was used. The

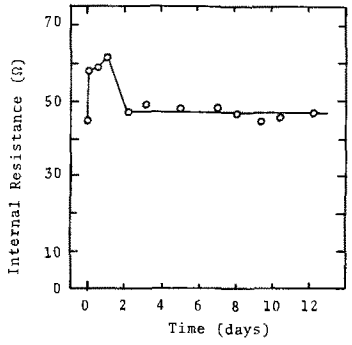

Fig. 6. Change of internal resistance of the cell; Graphite/$Ag_6I_4WO_4$ + I_2/Graphite.

resistance of the cell has been maintained at a constant value of about 50 ohm for two years.

$Ag_6I_4WO_4$ has the best stability in an iodine atmosphere among the high ionic conductivity compounds of silver previously known, such as Ag_3SI (11, 12, 13), $Ag_7I_4PO_4$, $Ag_{19}I_{15}P_2O_7$ (1), $RbAg_4I_5$ (1, 2, 3, 14), and $Ag_6I_4WO_4$, and is a promising material for solid-state silver-iodine batteries.

As $Ag_6I_4WO_4$ has been found to be a high ionic conductivity compound and stable in an iodine atmosphere, the silver-iodine solid-state cell of type [II] was constructed with $Ag_6I_4WO_4$ for the electrolyte material. This cell shows an open-circuit voltage of 687 mV at 21°C, which agrees well with the value of 686.7 mV calculated from the change of free energy of the formation of silver iodide according to the equation

$$Ag(s) + \tfrac{1}{2}I_2(g) = AgI(s) \qquad [1]$$

indicating that the ionic transport number of this compound is unity. This is confirmed with the result of the transport number measured by Tubandt's method.

Figure 7 shows the result of the measurement of the anodic and cathodic polarizations of the cell in the temperature range of −20° to 68°C. The polarization was recorded 1 min after passing the current. At 30°C, the anodic and cathodic overvoltages were 31 and 44 mV, respectively, at the current density of 1 mA/cm^2; and they were 50 and 60 mV, at 100 μA/cm^2 at −20°C, respectively. These values were relatively lower than those of the solid ionic compounds except for $RbAg_4I_5$ at ambient temperature.

Figure 8 shows the discharge curves of the cells at constant load measured at room temperature. The cell loaded 7.5 kohm showed a terminal voltage of 550 mV at 50% anode efficiency.

In Fig. 8 and 9, abbreviations E_o and E_c mean the open-circuit voltage and the cell voltage immediately after the beginning of discharge, respectively.

In order to measure the performance at low temperature, the discharge curve of the cell was measured

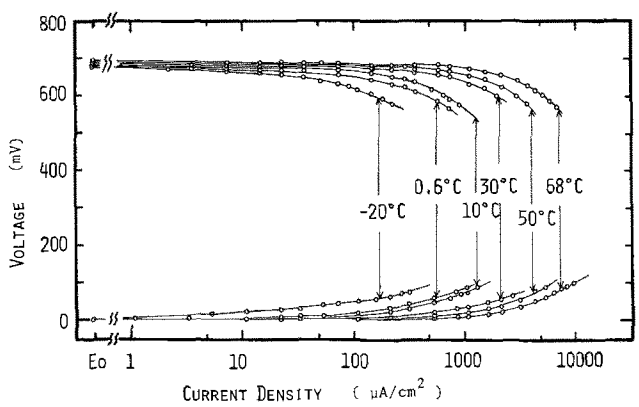

Fig. 7. Anodic and cathodic polarizations of the cell Ag, $Ag_6I_4WO_4/Ag_6I_4WO_4/I_2$, $Ag_6I_4WO_4$, C at various temperatures.

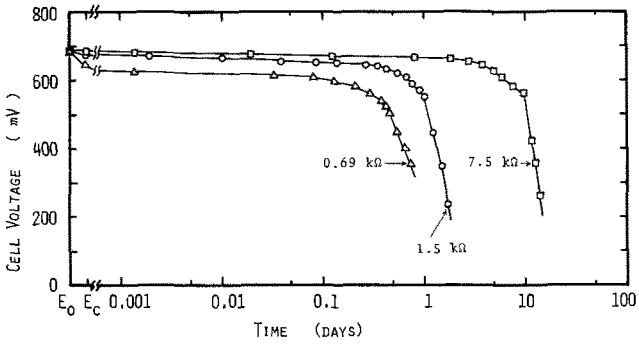

Fig. 8. Time dependence of the voltage of the cell Ag, $Ag_6I_4WO_4/Ag_6I_4WO_4/I_2$, $Ag_6I_4WO_4$, C at various constant load discharges at room temperature.

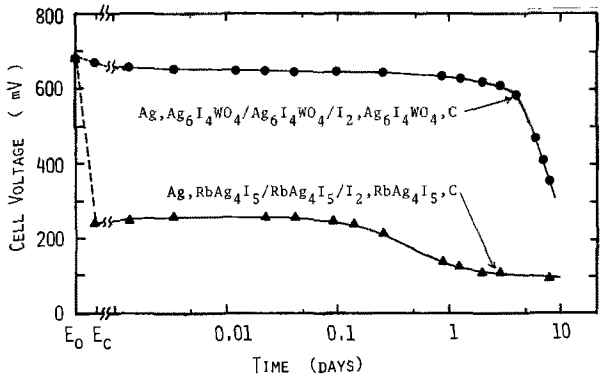

Fig. 9. Time dependence of the voltage of the cell Ag, $Ag_6I_4WO_4/Ag_6I_4WO_4/I_2$, $Ag_6I_4WO_4$, C at constant load discharge of 7.5 kohm at 0°C.

at constant load of 7.5 kohm at 0°C, and the result is shown in Fig. 9. The cell showed the open-circuit voltage of 681 mV and the terminal voltage of 668 mV at the initial stage of discharge. It showed a terminal voltage of 575 mV at 21% anode efficiency at 0°C.

Conclusion

In an investigation to find a new high ionic conductivity solid electrolyte, which was carried out on the system $AgI-Ag_2WO_4$, it has been found that $Ag_6I_4WO_4$ has a pure silver ion conductivity as high as 0.047 $(ohm \cdot cm)^{-1}$ at 25°C and an activation energy for conduction of 3.6 kcal/mole. $Ag_6I_4WO_4$ is a stable yellow-colored solid in the temperature range of 20°-293°C, and extremely stable in an iodine atmosphere. The transport number of silver ions in $Ag_6I_4WO_4$ is 1.00 within the experimental error. The silver-iodine solid-state battery using $Ag_6I_4WO_4$ as the electrolyte material showed the open-circuit voltage of 687 mV at 21°C, which is in good agreement with the value, 686.7 mV calculated from $\Delta G°$, the free energy of formation of silver iodide(s) from silver(s) and iodine(g) at 21°C. The anodic and cathodic overvoltages of this cell are 31 and 44 mV at the current density of 1 mA/cm^2 at 30°C, and 50 and 60 mV at 100 μA/cm^2 at −20°C, respectively. This cell showed the terminal voltage of 550 mV after the discharge of 50% anode efficiency at room temperature, and 575 mV after discharging 21% at 0°C.

The phase diagram of the system $AgI-Ag_2WO_4$ has been determined. There are three intermediate compounds of $Ag_6I_4WO_4$, Ag_4IWO_4, and $Ag_5I_2WO_8$ at room temperature.

Manuscript submitted Aug. 16, 1972; revised manuscript received Jan. 3, 1973.

Any discussion of this paper will appear in a Discussion Section to be published in the December 1973 JOURNAL.

REFERENCES

1. T. Takahashi, S. Ikeda, and O. Yamamoto, *This Journal*, **119**, 477 (1972).

2. J. N. Bradley and P. D. Greene, *Trans. Faraday Soc.*, **62**, 2069 (1966); **63**, 424 (1967).
3. B. B. Owens and G. R. Argue, *Science*, **157**, 308 (1967).
4. C. Tubandt, Handbuch Exp. Phys., **12**, 383 (1932).
5. T. Takahashi and O. Yamamoto, *This Journal*, **117**, 1 (1970).
6. M. de Rossi, G. Pistoia, and B. Scrosati, *ibid.*, **116**, 1642 (1969).
7. G. R. Argue, I. J. Groce, and B. B. Owens, *Power Sources*, **2**, 389 (1968).
8. J. E. Oxley and B. B. Owens, *ibid.*, **3**, 535 (1970).
9. M. N. Hull, *Energy Conversion*, **10**, 215 (1970).
10. L. D. Yushina, S. V. Karapachev, and Yu. M. Ovchinikov, *Elekrokhimiya*, **6**, 1425 (1970).
11. B. Reuter and K. Hardel, *Z. Anorg. Allgem. Chem.*, **340**, 158 (1965).
12. T. Takahashi and O. Yamamoto, *Electrochim. Acta*, **11**, 779 (1966).
13. B. B. Owens, G. R. Argue, I. J. Groce, and L. D. Hermo, *This Journal*, **116**, 312 (1969).
14. L. E. Topol and B. B. Owens, *J. Phys. Chem.*, **72**, 2106 (1968).

The Interaction of Some Atmospheric Gases with a Tin-Lead Alloy

Harland G. Tompkins

Bell Telephone Laboratories, Columbus, Ohio 43213

ABSTRACT

A study is made of the interaction of O_2, SO_2, NO_2, H_2S, Cl_2, CO, and NH_3 with a tin-lead alloy (50-50% by weight). Studies were made at both high (10-100%) and low (0.1-100 ppm) concentrations. At the high concentrations, some interaction is observed for all except CO and NH_3. At concentrations below 100 ppm, only NO_2 and Cl_2 interact with the tin-lead to any extent. Products formed are $Pb(NO_3)_2$ for NO_2 and $SnCl_2$ and $PbCl_2$ for Cl_2. Kinetic data are presented for the interaction of these two gases with SnPb along with the effect of relative humidity. Relative humidity is shown to have a strong effect on the interaction, with high relative humidity enhancing the interaction for Cl_2 but inhibiting the interaction for NO_2.

Most of the investigations of tin-lead alloys have been concerned with degradation of appearance, solderability, and wettability (1), etc. Very little has been done in the area of kinetic studies of the interaction of gases with tin-lead, particularly at room temperature. Two of the few works available are oxidation studies made on tin (2) and lead (3) individually. A previous paper (4) deals with the interaction of NO_2 with tin-lead. This work is a continuation of that previous paper and deals with the interaction of several additional gases sometimes found in the atmosphere. Gases studied were O_2, SO_2, H_2S, Cl_2, NH_3, and CO. The results of the work on NO_2 are summarized for completeness.

From a corrosion point of view, studies should be carried out at a low concentration in order to more closely approximate the actual atmosphere conditions. Accordingly most of the present studies were done at concentrations of 0.1-100 ppm. Prior to this study, however, an exploratory investigation was made at high concentrations to determine which gases affected tin-lead appreciably. This study was to indicate the area of most fruitful effort in research. The exploratory investigations at high concentration were much less exact than the low-concentration studies. In the high-concentration studies, the concentration is estimated, and some of the film thickness values are lower limits rather than actual values. The purpose of including the high-concentration studies in this paper is not to provide kinetic data, but to indicate roughly which gases interact appreciably with tin-lead, and which do not.

Although it is an accepted rule of thumb that high relative humidity accelerates corrosion, the mechanism of this acceleration is not understood in many cases. Accordingly, the effect of relative humidity is included in the low-concentration study. Both the high-concentration exploratory study and the low-concentration study were conducted at room temperature.

Key words: corrosion, lead-tin alloys.

Experimental Setup

Low concentration.—The experimental setup for the weight gain measurements at low concentrations has been described previously (4). Briefly, weight gain was measured under various gaseous environments. The microbalance setup is shown schematically in Fig. 1. The output from a Cahn microbalance, which is used to measure weight gain continuously as the corrosive gas was passed over the sample, is presented on a chart recorder. The samples were solid tin-lead coupons having an area of about 9 cm^2. The tin-lead, nominal composition 50-50 by weight, was purchased in 0.1 cm sheets, rolled to 0.018 cm, and then annealed at 125°C in mild vacuum for 30 min.

The coupons were ultrasonically degreased in trichloroethylene and rinsed in acetone prior to annealing. This surface preparation appears adequate to obtain reproducible data.

The corrosive atmosphere was obtained by flowing a carrier gas, dry air, over a permeation tube (5) which releases the corrosive gas (*e.g.*, Cl_2) at a constant rate. The permeation tubes were purchased from

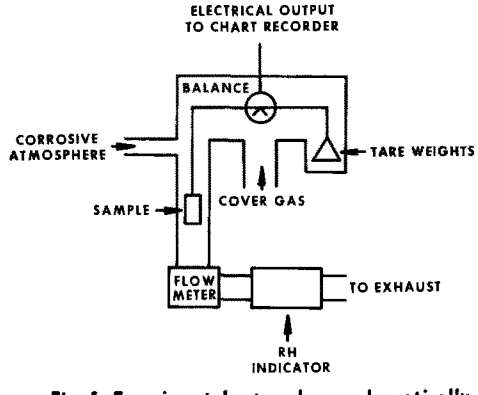

Fig. 1. Experimental setup shown schematically

Analytical Instrument Development, Inc., and consisted of liquid Cl_2 (or NO_2, H_2S, SO_2) in FEP Teflon tubes. The Cl_2 permeates out through the walls of the tube at a rate which is dependent only on the size of the tube, and temperature. Moist air was added after the carrier gas had passed over the permeation tube in order to give the desired relative humidity. Relative humidity was measured with an hygrometer indicator manufactured by Hygrodynamics, Inc., which has a quoted accuracy of ±3% RH. The permeation rates were determined by weight loss of the tube. The flow rate of the gas over the sample was 100 ml/min (0.4 cm/sec) and a typical permeation rate was 3 μg/min of Cl_2 (3 μg of Cl_2 in 100 ml corresponds to approximately 10 ppm). Concentration was varied by varying the temperature of the permeation tube. This in turn changed the permeation rate which changed the amount of corrosive gas being put into the carrier gas.

High-concentration exploratory study.—For the high-concentration work, the samples were exposed by flushing the appropriate atmosphere through a closed glass container which held the sample. The stopcocks were then closed and the sample was allowed to sit in the chosen atmosphere for the allotted time. The samples were again solid tin-lead coupons.

The dry atmospheres were obtained by flowing the appropriate gas from a lecture bottle directly into the sample chamber. The relative humidity was not measured but is estimated to be between 0 and 20%. The wet atmospheres were obtained by bubbling the gas through water and then flowing it through the sample chamber. Flow was continued for several minutes to insure saturation of the water. Relative humidity was estimated to be between 80 and 100%.

The presence or absence of film growth was noted by using cathodic reduction (6). This is an old technique whereby the film is reduced electrically and the amount of charge required is a measure of the film thickness. This method does not give accurate results for films which are soluble in water, so for these films, the value obtained from cathodic reduction is lower than the actual thickness.

Results

High-concentration exploratory study.—No film growth was observed for concentrations of approximately 100% CO or 100% NH (wet), for times of several days.

The oxygen in air causes a limiting film of tin oxide and/or lead oxide to form. Under normal room conditions, this film is of the order of 30-60Å. If excessive relative humidity (100%) or temperature (168°C) are used, films up to 300Å are obtained. These data agree with the results of Anderson and Tare (3) and Britton and Bright (2) who indicate that the oxide formed is limiting.

Sulfur-containing gases used were SO_2 with concentrations from 10 to 100%, both wet and dry, and wet H_2S (concentration 80-100%). Results were very erratic but in no case did a film thicker than 1600Å form (thickness calculated by assuming SnS with density 5.08 g/cm³). Exposure varied from 16 to 76 hr and longer times did not generally give thicker films. The conclusion is that these films are limiting.

Chlorine and oxides of nitrogen caused films to grow in excess of 10,000Å calculated by assuming $SnCl_2$, density (3.39 g/cm³) and these films appear to be nonlimiting. Concentrations from 20 to 100% were used, both wet and dry. In Cl_2, a liquid film formed on the sample. When removed from the sample chamber, the sample dried leaving a white deposit of lead chloride and hydrated tin chloride as determined by x-ray diffraction. The low-concentration section deals with the liquid film more extensively.

When the samples were viewed with an optical microscope, the surface roughness of the films grown in SO_2 and H_2S did not appear significantly different from the unexposed sample. The films grown in NO_2 and Cl_2, on the other hand, appeared very rough and grossly rearranged. These films were undoubtedly very porous.

Low concentrations.—Based on the results of the study at high concentrations, SO_2, H_2S, NO_2, and Cl_2 were used for the low-concentration study.

NO_2.—The results for NO_2 have been reported previously (4). They are summarized here for completeness. The reaction product was determined to be $Pb(NO_3)_2$ by x-ray diffraction. Presumably no interaction occurs with the Sn. The weight gain *vs.* time curves are linear indicating that a nonprotective film is being formed. The film is undoubtedly porous, but no loss of adhesion was noted, even on very thick films.

Curves were obtained with various concentrations at 32% relative humidity. In all cases, the curves were linear. The slope of these curves is the rate of the weight change. The rate of weight gain *vs.* concentration is shown in Fig. 2.

The linearity of this curve (above 10 ppm) indicates that when the concentration is doubled, the film growth rate is doubled. This is to say that when more gas arrives at the surface, more gas reacts with the surface, and the relationship is linear. The limiting process would then be the gas phase diffusion of the NO_2 to the gas-solid interface.

Curves were obtained using various relative humidities and a constant concentration (42 ppm). The slopes of these curves are plotted in Fig. 3. Here we see that high rates of film growth are obtained for intermediate relative humidities and low rates of film growth for low and for high relative humidities. The implication of the decrease in rate for higher RH values is discussed in the previous work and the conclusion was that the mechanism probably involved a simultaneous chemisorption of NO_2 and H_2O with each species competing for adsorption sites.

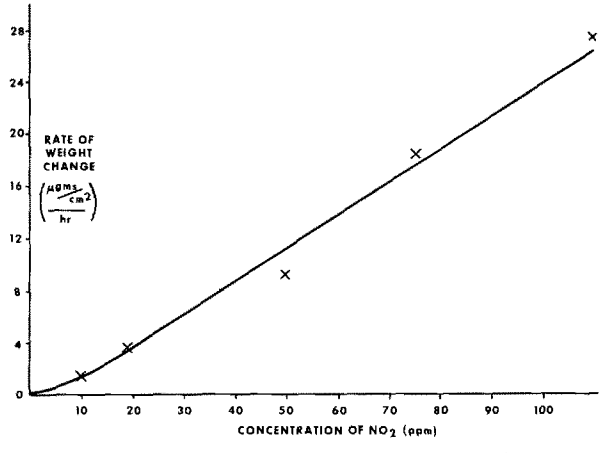

Fig. 2. Rate of weight change *vs.* concentration of NO_2 (RH is 32%).

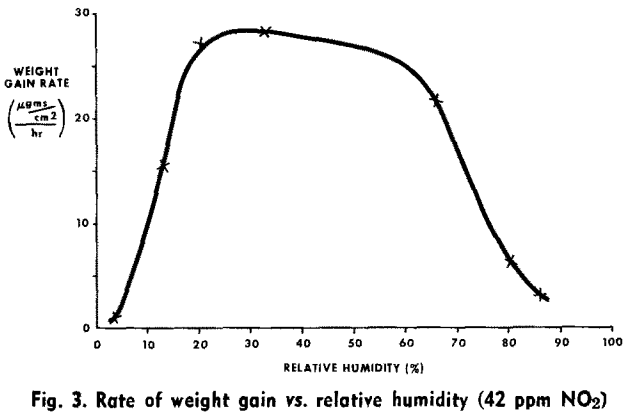

Fig. 3. Rate of weight gain *vs.* relative humidity (42 ppm NO_2)

H_2S and SO_2.—For SO_2, a concentration of 37 ppm and relative humidities of 40, 72, and 90% were used. No film growth was observed in three days for 40 and 90%. For 72% RH a slight film growth (0.15 $\mu g/cm^2$-hr) was observed. This was not repeatable and subsequent exposures of different SnPb coupons to the same conditions gave no film growth. For H_2S, concentrations of 40 ppm and relative humidities of 59 and 88% gave no film growth.

Summarizing the sulfur-containing gases, we see that we get some film growth for extremely high concentrations (10% and up) but with concentrations of less than 100 ppm we get very little, if any, film growth.

Cl_2.—Coupons of SnPb were exposed to various concentrations of Cl_2 from 0.2 to 10 ppm and relative humidities of 25 to 90%. The weight gain *vs.* time curves were linear in all cases. The reaction products observed with x-ray diffraction were $SnCl_2$ and $PbCl_2$. Visibly, the film growth was not particularly uniform, but seemed to grow from nucleation sites. For the larger weight gains, a visible liquid film formed on the sample.

A peculiar phenomenon was observed for the samples which had developed the liquid film. We would expect that, if we removed the Cl_2 and H_2O from the gas stream, a weight loss might occur. It is not at first obvious what would happen if we removed only one of these gases. It was found that if the H_2O is removed, but the Cl_2 remains, a weight loss of about 10% of the total weight gain occurred. This is not particularly surprising and is basically in agreement with the results of growth rate *vs.* relative humidity (see below). At low relative humidity the film growth stops and some of the water evaporates. The surprising phenomenon is that when the relative humidity was left unchanged and the Cl_2 was taken out of the gas stream, weight losses from 14 to 45% of the total weight gained were observed.

In the previous section we have shown that the reaction of NO_2 with SnPb appears to be simply a gas-solid interaction. We see here that the reaction of Cl_2 with SnPb is much more complex and involves at least a liquid-solid interaction and a gas-liquid interaction.

The gas-liquid interaction is simply the establishment of equilibrium of the H_2O and Cl_2 going into and coming out of the liquid from the gas phase. Since $SnCl_2$ and $PbCl_2$ are soluble in water, the liquid probably contains Sn^{+2}, Pb^{+2}, Cl^-, H_2O, H^+, and OH^-.

The weight loss might be due to a reaction which first causes tin and chlorine to form a tin chloride which then reacts with the water to form an oxide or hydroxide. HCl could then come off as a gas. The oxide or hydroxide does not show up in x-ray diffraction patterns, but this might be due to its being amorphous. This reaction, if it occurs, does not go to completion since some $SnCl_2$ is observed in x-ray diffraction patterns.

It would seem that the loss of whatever gas is going off probably occurs even while the film is growing. Because of the rather complex interaction the quantity which we call weight gain is the difference between what is going onto the sample and what is coming off the sample. We cannot directly relate the weight gain to "film growth" as in the case of NO_2, unless we were able to determine the reaction mechanism and the stoichiometry. On the other hand, weight gain does give an indication as to the conditions which cause "something to happen." Accordingly, then, weight gain *vs.* time curves were obtained for various concentrations at a constant relative humidity. The slopes of these curves are plotted in Fig. 4, taken with 80% relative humidity. It should be noted that the concentrations of Cl_2 are much lower than the concentrations of NO_2 studied.

The effects of relative humidity are shown in Fig. 5. Rate of weight gain *vs.* relative humidity is plotted for two concentration levels. It is not clear why the

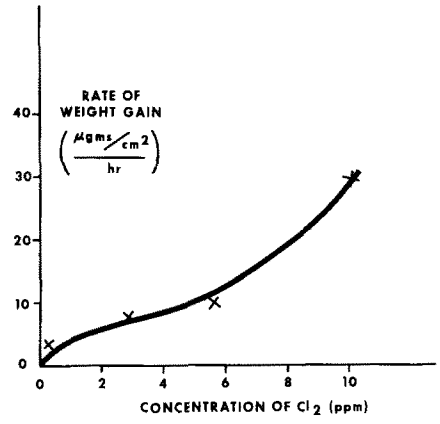

Fig. 4. Rate of weight gain *vs.* concentration of Cl_2 (RH is 80%)

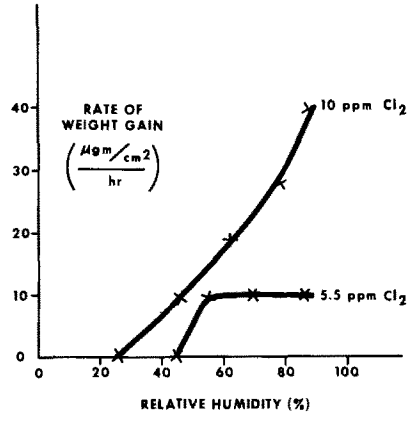

Fig. 5. Rate of weight gain *vs.* relative humidity

curve for 5.5 ppm levels off while the curve for 10 ppm continues to increase. It is, however, obvious that films will not grow in low relative humidities, and that intermediate and high relative humidity enhances film growth.

These curves, along with the weight gain-weight loss phenomenon (and the liquid film) show that relative humidity has a very complicated effect on the reaction of Cl_2 with SnPb.

Summary

The room temperature interaction of NO_2, Cl_2, H_2S, SO_2, O_2, CO, and NH_3 with a tin-lead alloy was investigated at high concentrations. No interaction was observed using CO and NH_3. The interaction of O_2 was a normal oxidation as described in the literature. A significant interaction was observed using SO_2, H_2S, NO_2, and Cl_2. This high-concentration study stimulated the low-concentration study where the interactions of NO_2, Cl_2, H_2S, and SO_2 with a tin-lead alloy at levels of 0.2-100 ppm were studied. The interaction of H_2S and SO_2 is negligibly small (below the limits of detectability of the microbalance), and the interaction of NO_2 and Cl_2 is significant with $Pb(NO_3)_2$, $SnCl_2$ and $PbCl_2$ being the reaction products.

At constant relative humidity, the interaction increases for higher concentrations for both NO_2 and Cl_2 with no sign of leveling off. At constant concentrations, the effect of relative humidity on the interaction is different for NO_2 than for Cl_2. Very high relative humidity enhances the interaction of Cl_2 but inhibits the interaction for NO_2.

Acknowledgments

The author wishes to thank E. T. Eisenmann for fruitful discussions and G. V. McIlhargie for sample preparation.

Manuscript submitted Aug. 8, 1972; revised manuscript received Nov. 5, 1972.

Any discussion of this paper will appear in a Discussion Section to be published in the December 1973 JOURNAL.

REFERENCES

1. H. Leidheiser, Jr., "The Corrosion of Copper, Tin, and Their Alloys," John Wiley & Sons, Inc., New York (1971).
2. W. E. Boggs, R. H. Kachik, and G. E. Pellissier, *This Journal*, **108**, 6 (1961); W. E. Boggs, P. S. Trozzo, and G. E. Pellissier, *ibid.*, **108**, 13 (1961); W. E. Boggs, *ibid.*, **108**, 124 (1961); S. C. Britton and K. Bright, *Metallurgia*, **56**, 163 (1957).
3. J. R. Anderson and V. B. Tare, *J. Phys. Chem.*, **68**, 1482 (1964).
4. H. G. Tompkins, *Surface Sci.*, **32**, 269 (1972).
5. A. E. O'Keefe and G. C. Ortman, *Anal. Chem.*, **38**, 760 (1966).
6. W. E. Campbell and U. B. Thomas, *Trans. Electrochem. Soc.*, **76**, 303 (1939).

A Study of Eu^{3+} Fluorescence in Some Silicate Oxyapatites

T. J. Isaacs

Westinghouse Research Laboratories, Pittsburgh, Pennsylvania 15235

ABSTRACT

Five silicate oxyapatites were activated with Eu^{3+} and their emission and excitation spectra were determined, as well as their peak emission intensities relative to $Y_2O_3:Eu^{3+}$.

The mineral apatite ($Ca_{10}(PO_4)_6(F,Cl)_2$), when doped with Mn^{2+} and Sb^{3+} is a well-known phosphor, and it is used extensively in present-day fluorescent lamps. Silicates having the apatite structure have been reported (1, 2), and the fluorescence of several oxyapatites when activated with Eu^{3+} was studied (1). An intense red luminescence was seen when $Ca_2Gd_8(SiO_4)_6O_2:Eu^{3+}$, $Sr_2Y_8(SiO_4)_6O_2:Eu^{3+}$ and $NaYb_8(SiO_4)_6O_2:Eu^{3+}$ were excited with 3130Å radiation. The strongest line was at approximately 6190Å, with moderate lines at approximately 7050, 6500, 6260, 5980, and 5850Å for each of these compounds.

Silicate apatites are hard, stable materials and lend themselves to a variety of compositional substitutions. In this work, we studied emission and excitation of five silicate oxyapatites [including $Ca_2Gd_8(SiO_4)_6O_2$] when activated with Eu^{3+}. The other compounds were $Ca_2Y_8(SiO_4)_6O_2$, $Ca_2La_8(SiO_4)_6O_2$, $Mg_2Y_8(SiO_4)_6O_2$, and $Mg_2La_8(SiO_4)_6O_2$.

Experimental Details

Spectrographic grade [99.99+ weight per cent (w/o)] starting materials which consisted of the oxides of yttrium, lanthanum, magnesium, silicon, and europium, and the carbonate of calcium were used. They were weighed out in stoichiometric proportions and were mixed for 15 min in a SPEX mixer mill. These mixes were then fired in air at approximately 1300°C, and the runs were of 4 hr duration.

The products of the experiments were examined under the polarizing microscope and by x-ray diffraction using the Debye-Scherrer technique to ascertain that the desired compound had been made and that the material was single phase. The radiation used was CuKα, and the exposure times were in the order of 9 hr.

Emission and excitation spectra were determined at room temperature on a double beam monochrometer system of the type described by Riedel (3). The relative intensities of the main emission peaks were also determined on this instrument.

Results and Conclusions

The optimum concentration of Eu^{3+} was found to be between 5 and 7 mole per cent (m/o) of the trivalent ion. The samples discussed below all had a 7% concentration of Eu^{3+}.

1. $Ca_2Gd_8(SiO_4)_6O_2:Eu^{3+}$ had a complex emission spectrum with the main peak at 6147Å, moderate peaks at 6120, 6240, 6270, and 7075Å, and numerous lesser peaks (Fig. 1a). Its excitation spectrum showed two main bands between 2100 and 2850Å and several lesser bands to 4200Å (Fig. 1b).

2. $Ca_2La_8(SiO_4)_6O_2:Eu^{3+}$ had its main emission peak at 6261Å, with moderate peaks at 5870, 5960, 6140, 6862, and 7079Å (Fig. 2a). Its excitation spectrum showed two bands, one from approximately 2100 to 2400Å and the other from approximately 2600 to 3100Å (Fig. 2b).

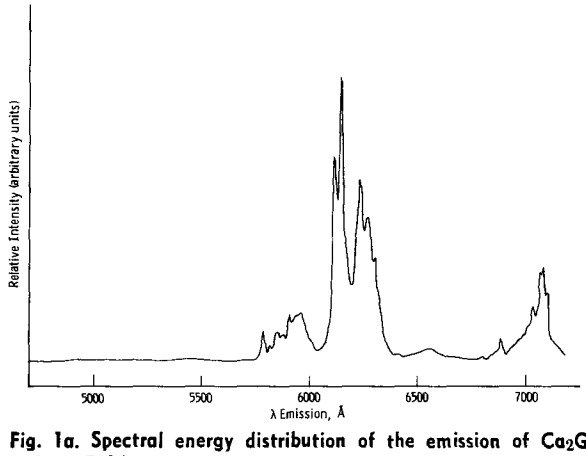

Fig. 1a. Spectral energy distribution of the emission of $Ca_2Gd_8(SiO_4)_6O_2:Eu^{3+}$

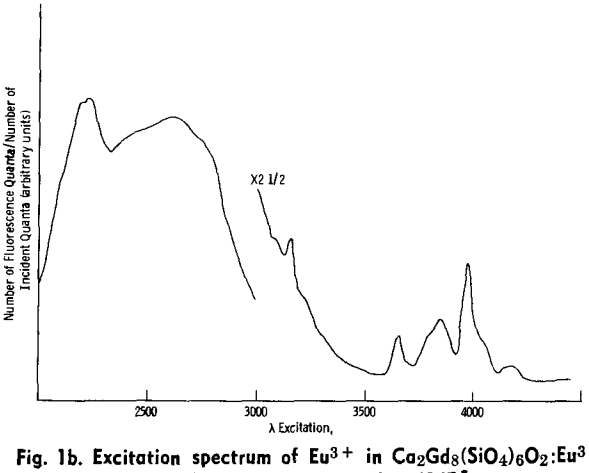

Fig. 1b. Excitation spectrum of Eu^{3+} in $Ca_2Gd_8(SiO_4)_6O_2:Eu^{3+}$. The fluorescence wavelength was monitored at 6147Å.

Key words: oxyapatites, europium, emission, excitation.

Any discussion of this paper will appear in a Discussion Section to be published in the December 1973 JOURNAL.

REFERENCES

1. H. Leidheiser, Jr., "The Corrosion of Copper, Tin, and Their Alloys," John Wiley & Sons, Inc., New York (1971).
2. W. E. Boggs, R. H. Kachik, and G. E. Pellissier, *This Journal*, **108**, 6 (1961); W. E. Boggs, P. S. Trozzo, and G. E. Pellissier, *ibid.*, **108**, 13 (1961); W. E. Boggs, *ibid.*, **108**, 124 (1961); S. C. Britton and K. Bright, *Metallurgia*, **56**, 163 (1957).
3. J. R. Anderson and V. B. Tare, *J. Phys. Chem.*, **68**, 1482 (1964).
4. H. G. Tompkins, *Surface Sci.*, **32**, 269 (1972).
5. A. E. O'Keefe and G. C. Ortman, *Anal. Chem.*, **38**, 760 (1966).
6. W. E. Campbell and U. B. Thomas, *Trans. Electrochem. Soc.*, **76**, 303 (1939).

A Study of Eu^{3+} Fluorescence in Some Silicate Oxyapatites

T. J. Isaacs

Westinghouse Research Laboratories, Pittsburgh, Pennsylvania 15235

ABSTRACT

Five silicate oxyapatites were activated with Eu^{3+} and their emission and excitation spectra were determined, as well as their peak emission intensities relative to $Y_2O_3:Eu^{3+}$.

The mineral apatite ($Ca_{10}(PO_4)_6(F,Cl)_2$), when doped with Mn^{2+} and Sb^{3+} is a well-known phosphor, and it is used extensively in present-day fluorescent lamps. Silicates having the apatite structure have been reported (1, 2), and the fluorescence of several oxyapatites when activated with Eu^{3+} was studied (1). An intense red luminescence was seen when $Ca_2Gd_8(SiO_4)_6O_2:Eu^{3+}$, $Sr_2Y_8(SiO_4)_6O_2:Eu^{3+}$ and $NaYb_8(SiO_4)_6O_2:Eu^{3+}$ were excited with 3130Å radiation. The strongest line was at approximately 6190Å, with moderate lines at approximately 7050, 6500, 6260, 5980, and 5850Å for each of these compounds.

Silicate apatites are hard, stable materials and lend themselves to a variety of compositional substitutions. In this work, we studied emission and excitation of five silicate oxyapatites [including $Ca_2Gd_8(SiO_4)_6O_2$] when activated with Eu^{3+}. The other compounds were $Ca_2Y_8(SiO_4)_6O_2$, $Ca_2La_8(SiO_4)_6O_2$, $Mg_2Y_8(SiO_4)_6O_2$, and $Mg_2La_8(SiO_4)_6O_2$.

Experimental Details

Spectrographic grade [99.99+ weight per cent (w/o)] starting materials which consisted of the oxides of yttrium, lanthanum, magnesium, silicon, and europium, and the carbonate of calcium were used. They were weighed out in stoichiometric proportions and were mixed for 15 min in a SPEX mixer mill. These mixes were then fired in air at approximately 1300°C, and the runs were of 4 hr duration.

The products of the experiments were examined under the polarizing microscope and by x-ray diffraction using the Debye-Scherrer technique to ascertain that the desired compound had been made and that the material was single phase. The radiation used was CuKα, and the exposure times were in the order of 9 hr.

Emission and excitation spectra were determined at room temperature on a double beam monochrometer system of the type described by Riedel (3). The relative intensities of the main emission peaks were also determined on this instrument.

Results and Conclusions

The optimum concentration of Eu^{3+} was found to be between 5 and 7 mole per cent (m/o) of the trivalent ion. The samples discussed below all had a 7% concentration of Eu^{3+}.

1. $Ca_2Gd_8(SiO_4)_6O_2:Eu^{3+}$ had a complex emission spectrum with the main peak at 6147Å, moderate peaks at 6120, 6240, 6270, and 7075Å, and numerous lesser peaks (Fig. 1a). Its excitation spectrum showed two main bands between 2100 and 2850Å and several lesser bands to 4200Å (Fig. 1b).

2. $Ca_2La_8(SiO_4)_6O_2:Eu^{3+}$ had its main emission peak at 6261Å, with moderate peaks at 5870, 5960, 6140, 6862, and 7079Å (Fig. 2a). Its excitation spectrum showed two bands, one from approximately 2100 to 2400Å and the other from approximately 2600 to 3100Å (Fig. 2b).

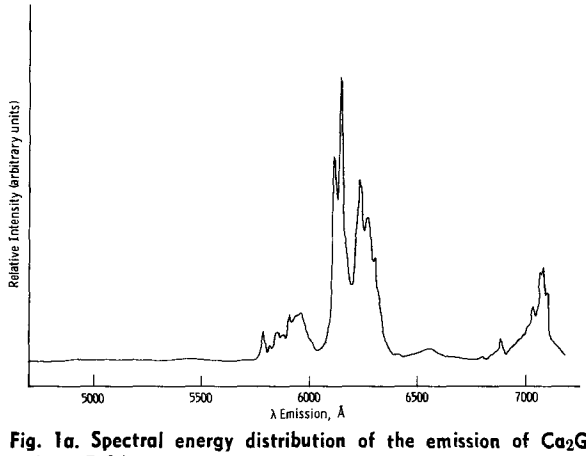

Fig. 1a. Spectral energy distribution of the emission of $Ca_2Gd_8(SiO_4)_6O_2:Eu^{3+}$

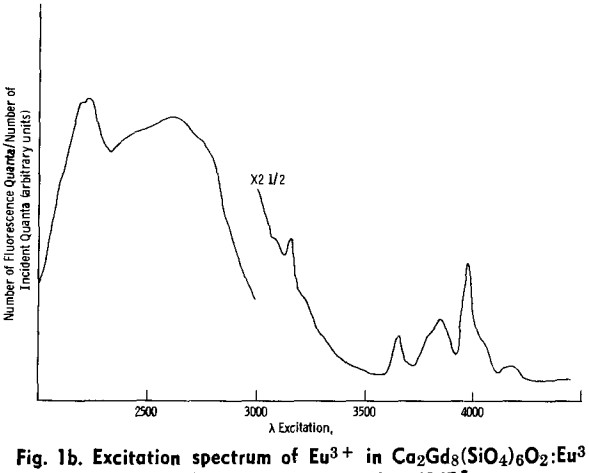

Fig. 1b. Excitation spectrum of Eu^{3+} in $Ca_2Gd_8(SiO_4)_6O_2:Eu^{3+}$. The fluorescence wavelength was monitored at 6147Å.

Key words: oxyapatites, europium, emission, excitation.

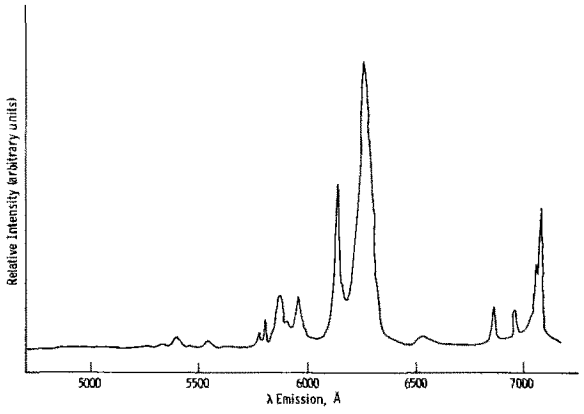

Fig. 2a. Spectral energy distribution of the emission of $Ca_2La_8(SiO_4)_6O_2:Eu^{3+}$

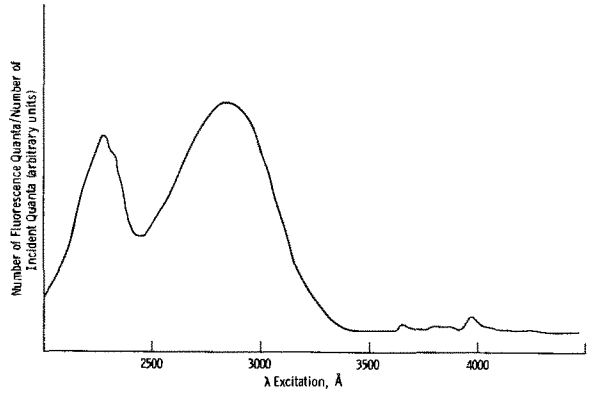

Fig. 2b. Excitation spectrum of Eu^{3+} in $Ca_2La_8(SiO_4)_6O_2:Eu^{3+}$. The fluorescence wavelength was monitored at 6261Å.

3. $Ca_2Y_8(SiO_4)_6O_2:Eu^{3+}$ had its main emission peak at 6114Å, a moderate peak at approximately 6150Å, and a number of lesser peaks from 5800 to 7100Å (Fig. 3a). Its excitation spectrum showed one broad band from below 2000 to approximately 2500Å (Fig. 3b).

4. $Mg_2La_8(SiO_4)_6O_2:Eu^{3+}$ had a complex emission spectrum with the main peak at 6260Å and numerous moderate to small peaks throughout the spectrum (Fig. 4a). Its excitation spectrum showed two main bands between 2100 and 3100Å, with several small bands to 4200Å (Fig. 4b).

5. $Mg_2Y_8(SiO_4)_6O_2:Eu^{3+}$ had its main emission peak at 6112Å, a moderate peak at 6145Å, and a number of small peaks from 5800 to 7100Å (Fig. 5a). The excitation spectrum showed a large two-humped broad band extending from approximately 2000 to 2600Å, and some small bands to 4200Å (Fig. 5b).

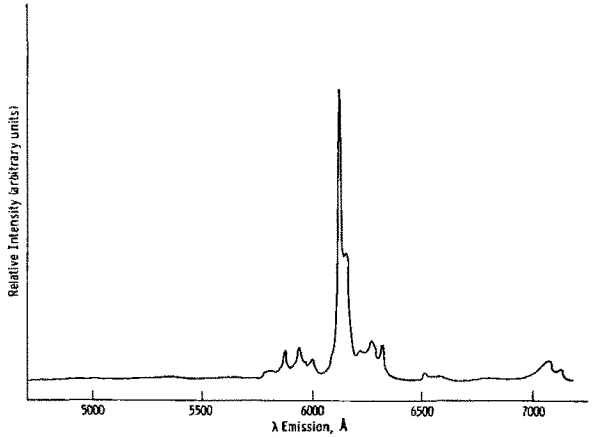

Fig 3a. Spectral energy distribution of the emission of $Ca_2Y_8(SiO_4)_6O_2:Eu^{3+}$.

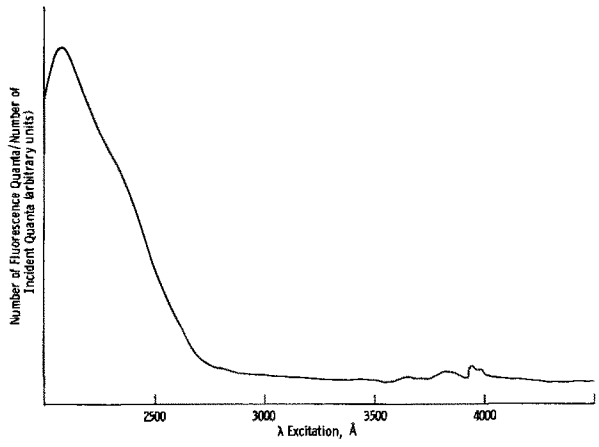

Fig. 3b. Excitation spectrum of Eu^{3+} in $Ca_2Y_8(SiO_4)_6O_2:Eu^{3+}$. The fluorescence wavelength was monitored at 6113Å.

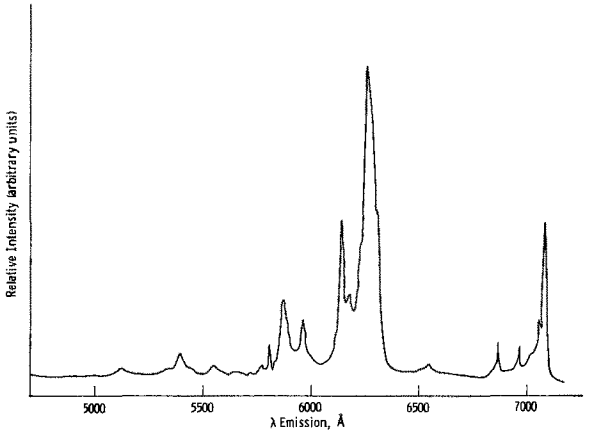

Fig. 4a. Spectral energy distribution of the emission of $Mg_2La_8(SiO_4)_6O_2:Eu^{3+}$.

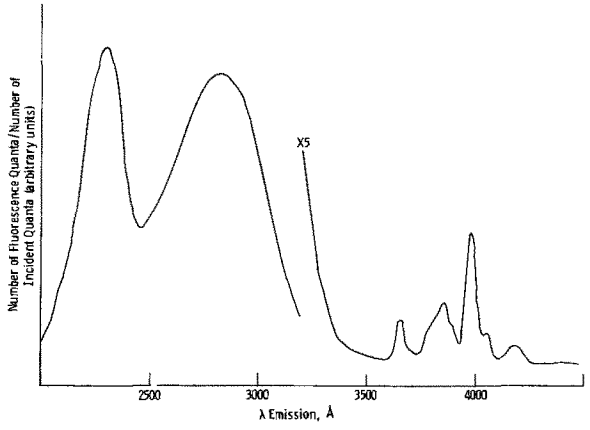

Fig. 4b. Excitation spectrum of Eu^{3+} in $Mg_2La_8(SiO_4)_6O_2:Eu^{3+}$. The fluorescence wavelength was monitored at 6260Å.

In order to compare emission intensity among these samples, we measured the luminescence intensity of the main peak in each of the compounds against a standard $Y_2O_3:Eu^{3+}$ which contained 7% Eu_2O_3. The results are given in Table I. We can see that the two

Table I. Relative intensities of emission of the main peaks compared with $Y_2O_3:Eu^{3+}$ at 2537Å excitation

(The Eu^{3+} content was 7% for all the compounds)

Compound	% intensity *vs.* $Y_2O_3:Eu^{+3}$
$Ca_2Gd_8Si_6O_{26}:Eu^{3+}$	10
$Ca_2La_8Si_6O_{26}:Eu^{3+}$	4
$Ca_6Y_8Si_2O_{26}:Eu^{3+}Si_6$	20
$Mg_2La_8Si_6O_{26}:Eu^{3+}$	4
$Mg_2Y_8Si_6O_{26}:Eu^{3+}$	20

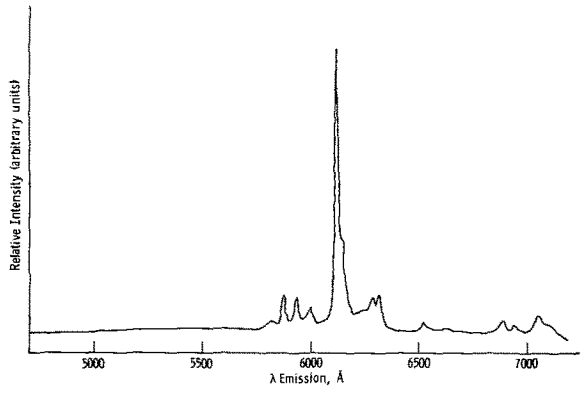

Fig. 5a. Spectral energy distribution of the emission of $Mg_2Y_8(SiO_4)_6O_2:Eu^{3+}$.

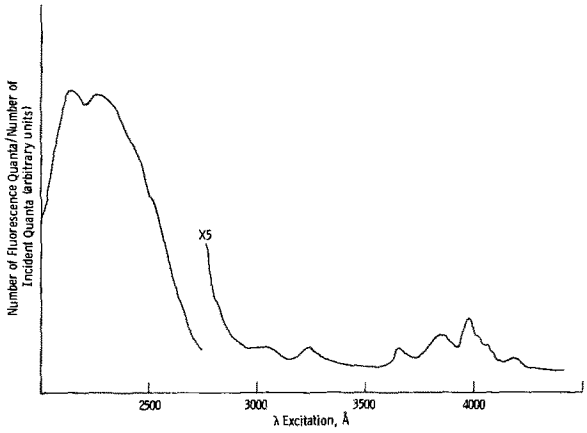

Fig. 5b. Excitation spectrum of $Eu^{3+}Mg_2Y_8(SiO_4)_6O_2:Eu^{3+}$. The fluorescence wavelength was monitored at 6112Å.

materials which had yttrium as the trivalent cation had the best relative intensities, and their emission spectra showed them to have a large part of their emission concentrated at approximately 6110Å. Their excitation spectra showed them to be poorly excited at 2537Å, with the intensity being approximately 20% that of the highest part of the curve for $Ca_2Y_8(SiO_4)_6O_2:Eu^{3+}$, and approximately 35% for $Mg_2Y_8(SiO_4)_6O_2:Eu^{3+}$.

The spectra of these compounds depends upon the trivalent cation and were independent of the divalent cation. The yttrium members had better spectral energy distributions as more of their emission was concentrated in one peak, but the lanthanum members were sensitive to excitation at longer wavelengths.

It is known that there are two sites available for cation substitution in Y_2O_3, and that there also are two sites for divalent cation substitution in the normal apatite. The materials reported on in this work are all modifications of the apatite structure and they would have at least two such sites. Spin resonance studies of fluorapatites used as laser materials show that there are more than two sites, and may be as many as eight (R. Warren, private communication). We did not attempt to interpret our spectra in terms of the symmetry of sites because of the complications involved.

Acknowledgments

I wish to thank Andrea Price for helping to make the compounds and taking the x-ray photographs, and Roy Williams for taking the emission and excitation curves and determining the relative intensities.

Manuscript submitted Nov. 9, 1972; revised manuscript received Jan. 8, 1973.

Any discussion of this paper will appear in a Discussion Section to be published in the December 1973 JOURNAL.

REFERENCES

1. J. Ito, *Am. Mineralogist*, **53**, 890 (1968).
2. R. H. Hopkins, G. W. Roland, K. B. Steinbruegge, and W. D. Partlow, *This Journal*, **118**, 637 (1971).
3. E. P. Riedel, *J. Luminescence*, **1**, 176 (1969).

Epitaxial Growth and Characterization of Pyrolytic-Grown $GaAs_{1-x}P_x$ for Electroluminescent Diodes

Tadashi Saitoh and Shigekazu Minagawa

Central Research Laboratory, Hitachi Ltd., Kokubunji, Tokyo, Japan

ABSTRACT

Epitaxial layers of $GaAs_{1-x}P_x$ on GaAs substrates were prepared using trimethylgallium, arsine, and phosphine. The growth was primarily mass transport limited and the phosphorus content in the layers increased linearly with the phosphine content in the vapor and the substrate temperature. Growth pyramids appeared at high phosphine content in the vapor and were brighter than flat regions in the cathodoluminescent image. A diode, fabricated by diffusing zinc into $GaAs_{0.6}P_{0.4}$ layers, showed brightness of 43 ft-L at 8 A/cm^2 with an external quantum efficiency of about 0.01%. The external efficiency has been found to depend strongly on the generation-recombination current and the deep level impurity concentration in the depletion layer.

The method most commonly used to prepare $GaAs_{1-x}P_x$ for electroluminescent devices is a vapor transport system using a halide (1). Manasevit and Simpson (2) have reported on the use of organometallics in the preparation of III-V compounds. This method has two advantages over the conventional process. The one is that compound semiconductors can be grown in a rf-heated furnace, which requires only a short time for heating up or cooling down, and the other is that it can avoid autodoping from a substrate, because it does not include any halogen atoms which react with a substrate.

Key words: $GaAs_{1-x}P_x$ pyrolytic growth, light-emitting diodes, growth pyramids, cathodoluminescence.

Although various compound semiconductors have been prepared using organometallics (2-9), no efficient visible electroluminescence has been reported for the diodes fabricated from these crystals. The present

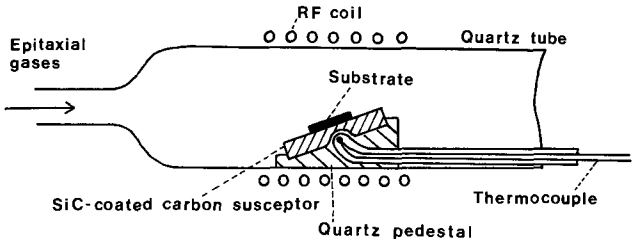

Fig. 1. Schematic representation of an epitaxial reactor

paper describes the epitaxial growth of $GaAs_{1-x}P_x$ on GaAs substrate by the pyrolytic method, and also describes morphological and cathodoluminescent characterization of these layers. Finally, several features of electrical and optical properties of pyrolytic-grown $GaAs_{0.6}P_{0.4}$ diodes are discussed.

Experimental

Apparatus.—A schematic representation of a horizontal epitaxial reactor is shown in Fig. 1. A substrate was placed on a SiC-coated carbon susceptor inclined by 20°. The substrate temperature was measured by an optical pyrometer and was controlled by an electronic control system whose thermocouple was inserted into the susceptor.

Trimethylgallium, contained in a stainless steel bubbler cooled by a thermoelectric element, was transported by passing hydrogen through it.

Procedure.—The substrates were n-type (100) GaAs with an electron concentration of 1.3×10^{18} cm^{-3}. They were mechanically polished and chemically etched (etchant; $4H_2SO_4$: $1H_2O_2$: $1H_2O$) prior to growth.

After the growth of an initial layer of GaAs, the phosphorus content of the layer was gradually increased by increasing the PH_3/AsH_3 ratios in the vapor to obtain a final composition of $x = 0.4$. The total thickness of the epitaxial layers were normally about 70μ.

Typical growth parameters are given in Table I. A higher flow rate of H_2 was adopted to prevent $GaAs_{1-x}P_x$ crystals from depositing before the substrate unlike the hitherto reported experiment (2). H_2Se was added to obtain n-type epitaxial layers with the carrier concentration of 10^{17} cm^{-3} to 10^{18} cm^{-3}.

Evaluation of epitaxial layers.—Surface morphology of the epitaxial layers was examined by a conventional optical microscope. Thickness of epilayers was measured by examining stained sections of the layers. The phosphorus content of the layers was determined by the electron microprobe analysis. Cathodoluminescence of the layers excited by 30 kV electrons was analyzed with a Hitachi Model S-12B monochrometer and a S-10 photomultiplier.

Diode fabrication and characterization.—The p-n junctions were made by diffusing Zn into the Se-doped $GaAs_{0.6}P_{0.4}$ epilayers with the electron concentration of 3×10^{17} cm^{-3} at the temperature ranges of 700°-850°C for 30 min. An array of small Au contacts was evaporated and alloyed to the Zn-diffused p-type $GaAs_{0.6}P_{0.4}$ surface, and a continuous Sn contact was evaporated and alloyed to the n-type GaAs substrate. The wafer was cleaved into chips, which were mounted on TO-18 transistor headers to measure junction characteristics and luminescent properties. The concentration of deep level impurities in the depletion layer was calculated from the difference of the junction capacitance (10) at 300° and 77°K.

Table I. Growth parameters

Substrate temperature	650°-800°C
Total flow rate	5 liters/min
Gas concentration	
$(CH_3)_3Ga$	0.056% (calc.)
AsH_3	0-0.24%
PH_3	0-0.11%
SeH_2	2 ppm
Growth rate	0.7 μ/min
Substrate	Te doped, (100) $n \simeq 3 \times 10^{18}$ cm^{-3}

Results and Discussion

Deposition reaction.—The principal parameters which affect the deposition reaction of $GaAs_{1-x}P_x$ by pyrolysis were the flow rate of H_2, the growth temperature, the PH_3/AsH_3 ratio, and the concentration of reaction gas. The growth rate as a function of temperature indicated in Fig. 2, shows that the rate is almost independent of the substrate temperature. It was also found that the growth rate is proportional to the $(CH_3)_3Ga$ concentration in the vapor. These results suggest that the growth is most probably mass transport limited.

Compositions.—Another quantity of interest is the composition of the epitaxial layer, *i.e.*, an effective vapor-solid distribution coefficient for the group V element. PH_3 mole fraction in the gas, x_g, is defined as

$$x_g = \frac{p_{PH_3}}{p_{AsH_3} + p_{PH_3}} \quad [1]$$

where p is the partial pressure of the subscript molecule in the gas. GaP mole fraction in the solid, x_s, is defined as

$$x_s = \frac{n_P}{n_{As} + n_P} \quad [2]$$

where n is the number of moles of the subscript element in the solid.

Then, the distribution coefficient for phosphorus is given by

$$k_p = \frac{x_s}{x_g} \quad [3]$$

Figure 3 shows the relation between the GaP mole fraction in the epitaxial layer and the PH_3 content in the gas. The composition increases in proportion to

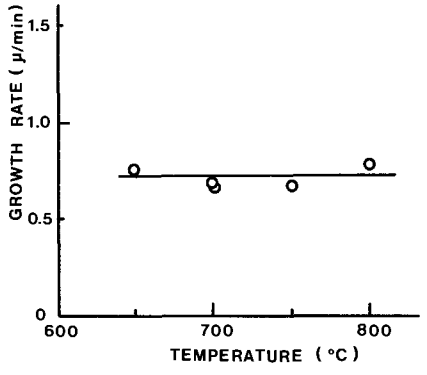

Fig. 2. Growth rate of $GaAs_{1-x}P_x$ as a function of substrate temperature.

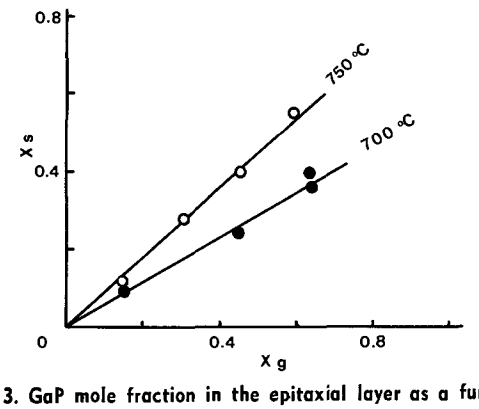

Fig. 3. GaP mole fraction in the epitaxial layer as a function of PH_3 content in the gas.

the PH_3 content in the range of $x_g = 0$ to $x_g = 0.6$, and the slope, k_p, depends on the growth temperature. The temperature dependence of the slope at $x_g = 0.54$ in the temperature range of 650°-850°C is given by

$$k_p = 3.7 \times 10^{-3} T - 2.9 \quad [4]$$

where T is the growth temperature in the absolute unit.

The equation indicates that GaAs is more easily deposited at low temperatures, and the GaP mole fraction increases with the growth temperature. The pyrolytic growth is a dynamic system in which a thermodynamical equilibrium state is not expected. A recent mass spectrometric study of $GaAs_{1-x}P_x$ system (11) showed that the vapor resulting from the thermal decomposition of AsH_3 and PH_3 mixtures has a very complex composition and the temperature variation of reactivities of P- and As-containing species reflects itself in the composition of $GaAs_{1-x}P_x$ layers. In the pyrolytic growth, dependence of the composition on the growth temperature may be explained also by the temperature variation of the reactivities of P- and As-containing species.

Structural characteristics.—The appearance of the epitaxial layers was primarily dependent on growth temperature and AsH_3/PH_3 ratios in the gas. Structural imperfections were found to be growth pyramids shown in Fig. 4. The ranges of growth pyramids generally run in the [110] direction parallel to the surface. Examination of cross sections of the layers indicated that the pyramids generally originate in the graded layer and develop with the increase of the thickness of the epitaxial layer. A few cracks, probably consisting of the [110] {111} slip system (12), were observed at the epitaxial layer-growth pyramid interface.

To evaluate crystallinity of the epitaxial layers, cathodoluminescence was studied on the surface of the epilayers and on the cross sections. Figure 5 shows the variation of the cathodoluminescent intensity and the composition with the thickness of the layer. The intensity which is almost constant in the GaAs epitaxial layer, decreases rapidly in the graded layer, but increases with the thickness. The decrease of the intensity in the graded layer is probably caused by the misfit dislocations. It seems to us that the grading rate at the initial layer should be low enough to minimize

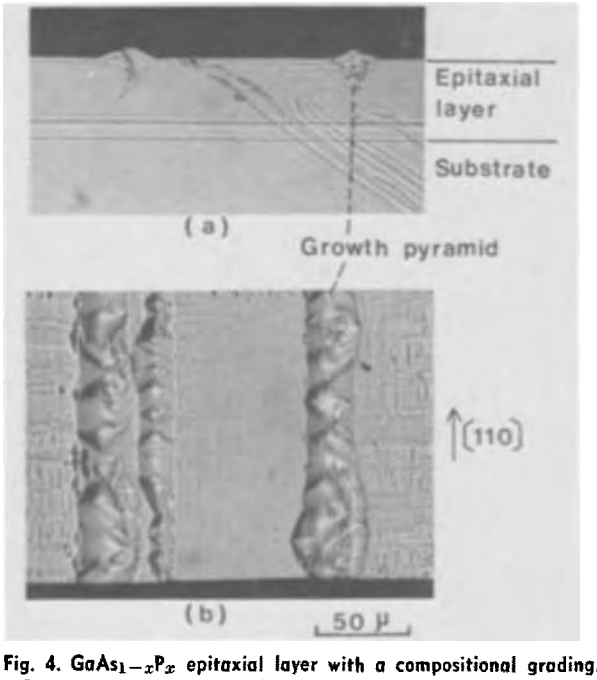

Fig. 4. $GaAs_{1-x}P_x$ epitaxial layer with a compositional grading. (a) Cross section (stained), (b) as-grown surface. Growth temperature 700°C.

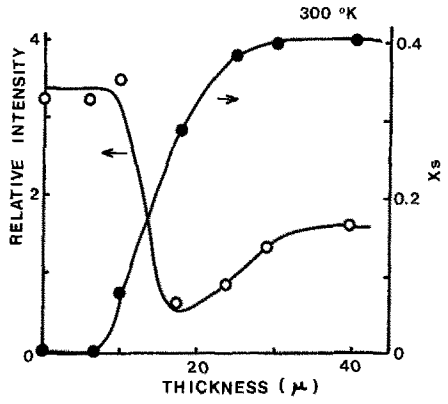

Fig. 5. Cathodoluminescent intensity or composition vs. epitaxial layer thickness.

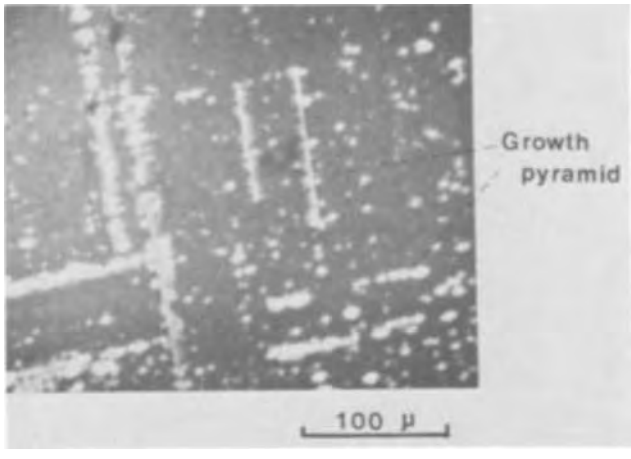

Fig. 6. Cathodoluminescent image of a $GaAs_{0.6}P_{0.4}$ surface

the misfit dislocations. A cathodoluminescent image of the epitaxial surface shown in Fig. 6 consisted of bright areas and dark areas. The bright areas where radiative recombination occurs more efficiently than the dark areas, correspond to the growth pyramids such as those shown in Fig. 4. The good crystal quality of the pyramids may be interpreted as a result of the reduction of misfit dislocations, which is caused by the stress-relaxation through the introduction of cracks at the bottom of the pyramids.

Diode characteristics.—Junction properties such as I-V and C-V characteristics were examined. The log I-V plot is linear for forward bias up to 1.3V with current varying as exp $(qV/2.3\ kT)$. The value 2.3 which is larger than 1.5 of commercial $GaAs_{0.6}P_{0.4}$ diodes, shows that almost all the carriers are consumed in the depletion layer and is not effective to produce electroluminescence. The C^{-2}-V plot is linear for reverse bias of 0-3V, indicating that the junction is abrupt. The built-in voltage and the depletion layer width calculated from the plot are 1.6 ~ 1.9V and 0.08 ~ 0.11μ, respectively.

A luminance of 43 ft-L at 8 A/cm^2 with an external quantum efficiency of 9×10^{-5} was obtained for a diode whose emission peaked at 6600Å. The efficiency was about an order of magnitude lower than the commercial $GaAs_{0.6}P_{0.4}$ diodes.

In order to examine the factors leading to reduced quantum efficiencies of the diodes prepared by pyrolysis, the forward current at 1.0V in the linear regions of log I-V plot, and the deep level impurity concentration (N_{TT}) in the depletion layer were measured. Figure 7 shows the relation between the forward current in the depletion layer and the quantum efficiency. The decrease of efficiency with the forward current means that the efficiency is reduced by the waste current, *i.e.*, the generation-recombination current in the depletion layer. The results for the deep

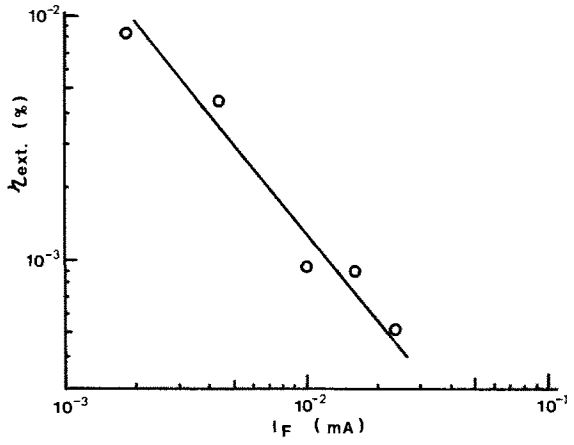

Fig. 7. External quantum efficiency vs. forward current at 1.0V. Diode area 0.25 mm².

level impurity concentration are shown in Fig. 8. The efficiency decreases rapidly with deep level impurity concentration. Deep levels may consist of lattice defects or impurities segregated at the lattice defects, related to the surface inhomogeneities shown in the cathodoluminescent image of the $GaAs_{0.6}P_{0.4}$ surface.

Conclusions

The $GaAs_{1-x}P_x$ epilayers to fabricate light emitting diodes were successfully prepared by the pyrolytic method. The main conclusions are as follows:

1. The epitaxial growth is primarily mass transport limited because the growth rate is independent of temperature and proportional to the $(CH_3)_3Ga$ concentration.
2. The phosphorus content in the epitaxial layer increases linearly with the increase of the phosphine content in the gas and the substrate temperature.
3. Apparent structural imperfections are found to be growth pyramids which generally originate in the graded layer and develop with the increase of the layer thickness.
4. The bright areas in the cathodoluminescent image of the layers correspond to the growth pyramids. The efficient cathodoluminescence may be ascribed to the reduction of lattice defects in the pyramids.
5. The external efficiency of the diodes is about an order of magnitude lower than the commercial diodes. The relatively low efficiency can be understood in view of the relatively large generation-recombination current and the substantial amount of the deep level impurity in the depletion layer.

Acknowledgments

The authors wish to thank Dr. Y. Otomo for his encouragement, Mr. S. Hosoki for measuring the cathodoluminescent spectra, and Dr. J. Umeda for his helpful suggestions and discussions.

Manuscript submitted Nov. 8, 1972; revised manuscript received Dec. 29, 1972.

Any discussion of this paper will appear in a Discussion Section to be published in the December 1973 JOURNAL.

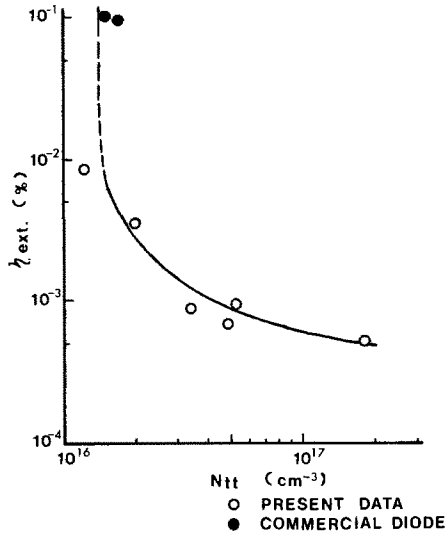

Fig. 8. External quantum efficiency vs. deep level impurity concentration.

REFERENCES

1. T. J. Tietjen and J. A. Amick, *This Journal*, **113**, 724 (1966).
2. H. M. Manasevit and W. I. Simpson, *ibid.*, **116**, 1725 (1969).
3. P. Rai-Choudhury, *ibid.*, **116**, 1745 (1969).
4. K. Lindeke, W. Sack, and J. J. Nickl, *ibid.*, **117**, 1316 (1970).
5. R. W. Thomas, *ibid.*, **116**, 1449 (1969).
6. H. M. Manasevit, F. M. Erdmann, and W. I. Simpson, *ibid.*, **118**, 1864 (1971).
7. C. H. Lee, H. B. Pogge, and B. M. Kemlage, Abstract No. 180, p. 466, Electrochem. Soc., Extended Abstracts, Fall Meeting, Cleveland, Ohio, Oct. 3-7, 1971.
8. C. C. Wang and S. H. McFarlane, *J. Crystal Growth*, **13-14**, 262 (1972).
9. I. Ladany and C. C. Wang, *J. Appl. Phys.*, **43**, 236 (1972).
10. C. T. Sah, L. L. Rosier, and L. Forbes, *Appl. Phys. Letters*, **15**, 161 (1969).
11. V. S. Ban, *J. Appl. Phys.*, **43**, 2471 (1972).
12. G. B. Stringfellow and P. E. Greene, *ibid.*, **40**, 502 (1969).

Fluorescence Properties of Alkaline Earth Tellurates

S. Natansohn*

The Waltham Research Center of GTE Laboratories, Inc., Waltham, Massachusetts 02154

ABSTRACT

The emission characteristics of phosphors based on alkaline earth tellurates as host lattice are described. The fluorescence of hexavalent uranium in compounds of the formula M_nTeO_{3+n} with $n = 2$ or 3, was studied. The spectral energy distribution of the fluorescence is affected by the cationic species and crystal structure of the compound. Two of the more interesting phosphors are $Ca_3TeO_6:U^{6+}$ and $Ba_2TeO_5:U^{6+}$ which emit in the blue-green and orange region of the spectrum, respectively. The effect of structural variations on the nature of the emission center in uranium-activated phosphors is discussed.

The voluminous literature describing the fluorescence properties of a great number of inorganic compounds is conspicuous in its lack of reports on compounds based on oxyanions of hexavalent tellurium; yet these compounds are particularly suitable for the study of the fluorescence of hexavalent uranium in solids. The uranium activator is readily incorporated in the tellurate host lattice. Furthermore, in the course of this and previous work (1) it was found that the fluorescence intensity of U^{6+}-activated tellurates is significantly greater than that of the analogous tungstates or molybdates. The fluorescence characteristics of activated rare earth tellurates, R_2TeO_6, were reported previously (1). The current discussion is concerned with U^{6+}-activated alkaline earth tellurates of the formula M_3TeO_6 (M = Mg, Ca, Sr) and with Ba_2TeO_5. The synthesis of these materials was reported by Merz (2).

Experimental

These compounds were readily prepared by reacting the stoichiometric amounts of the appropriate reagent-grade alkaline earth carbonates with reagent-grade orthotelluric acid, $Te(OH)_6$, at elevated temperatures. The U^{6+} activator was added as the uranyl acetate. The reagents were reacted in silica crucibles in an oxidizing atmosphere at temperatures in the range of 1100°-1300°C for the Mg, Ca, and Sr compounds, and 800°-900°C for the Ba phosphors. Single-phase products were obtained after two or more heating steps with intervening mortaring.

The presence of the desired phases was confirmed by x-ray diffraction using Ni-filtered Cu-Kα radiation at a scanning speed of 1° (2θ)/min. Selected diffractograms used to establish the crystal class of the compounds were obtained at a scanning speed of ¼° (2θ) and ⅛° (2θ)/min and a silicon standard was used to calibrate the instrument. The chemical composition of certain compounds was established by analysis. The metal ion content was determined by gravimetric and/or x-ray fluorescence techniques while the oxygen content was determined by neutron activation analysis.

The method described by Amster and Wiggins (3) was used to obtain corrected emission and excitation spectra which are given in terms of relative energy *vs.* wavelength. The diffuse reflectance spectra were obtained on the Cary 14 spectrophotometer using $MgCO_3$ as a standard.

Results and Discussion

Compound identification.—The host compounds thus synthesized are well-crystallized, optically inert, and stable under ordinary conditions. The x-ray powder diffraction pattern of Ba_2TeO_5 (Table I) can be satisfactorily indexed on the basis of an orthorhombic unit cell or, by doubling one of the cell parameters, on the basis of a tetragonal unit cell of twice the volume (Table II). In the former case, the observed reflections are consistent with the space groups $Pna2_1$ or Pnma, while in the latter case the space group $P4_12_12$ is possible. Single crystals of Ba_2TeO_5 were not available to permit the unambiguous determination of the space group of the compound.

The crystal structure of Mg_3TeO_6 was recently the subject of study by several investigators (4) and it has been established as rhombohedral with the space group $R\bar{3}$. An earlier publication (5) reported that the crystal class of Ca_3TeO_6 is monoclinic with a space group $P2_1$ and that Ca_3TeO_6 is isostructural with Ca_3UO_6. The structure of Sr_3TeO_6 is related to that of Ca_3TeO_6. In the orthotellurates,[1] as in the Ca_3UO_6, the hexavalent ion is at the center of an octahedron formed by six oxygen ions.

The results of chemical analyses were consistent with the desired formulations. The amounts of constit-

[1] The nomenclature of Scholder (6) is used here which defines an oxyanionic "ortho" compound as one containing as many oxygen ions as the valence of the central ion in the anion complex.

Table I. Tetragonal indexing of the powder diffractogram of Ba_2TeO_5

hkl	d_{obs}	d_{calc}	I*	hkl	d_{obs}	d_{calc}	I*
101	6.24	6.232	5	600	1.922	1.920	8
200	5.76	5.760	6	004 }	1.852	1.852	11
221	3.56	3.569	7	522 }			
102	3.53	3.527	20	442	1.784	1.784	7
301	3.41	3.409	4	204	1.764	1.764	19
320	3.197	3.195	100	541	1.747	1.748	10
202	3.116	3.116	68	214 }	1.742	1.743	12
212	3.010	3.008	44	532 }			
400	2.881	2.880	49	630	1.716	1.717	17
222	2.741	2.741	27	602	1.704	1.705	7
302	2.667	2.666	18	503	1.684	1.685	12
421	2.435	2.433	8	304	1.668	1.668	10
402	2.276	2.274	12	622	1.634	1.634	13
412	2.232	2.231	17	542	1.618	1.618	7
501	2.201	2.200	16	640	1.598	1.597	11
422 }	2.114	2.115	35	404 }	1.558	1.558	5
223 }		2.112		632 }			
303	2.078	2.077	5	613	1.503	1.503	8
502	1.957	1.956	25	623	1.466	1.466	6
				504	1.443	1.444	16
				524 }	1.400	1.400	6
				732 }			
				703	1.369	1.369	9

* The intensity of the reflections is estimated from the peak heights.

Table II. Crystallographic data on Ba_2TeO_5

Crystal class	Tetragonal	Orthorhombic
Unit cell parameters (Å)		
a_o	11.52_0	7.41_0
b_o		5.75_7
c_o	7.41_0	11.52_6
d_{theor} (g/cm³)	6.52	6.52
d_{meas} (g/cm³)	6.39	6.39
Z	8	4
Possible space group	$P4_12_12$	$Pna2_1$ or Pnma

* Electrochemical Society Active Member.

Key words: luminescence, phosphors, uranium, calcium orthotellurate, barium pentaoxotellurate.

uents found in Ca_3TeO_6 were (weight per cent): 35.1% Ca, 37.0% Te, and 27.8% of O which is in excellent agreement with the calculated values of 34.97, 37.12, and 27.91% for the respective elements. The analysis of Ba_2TeO_5 showed this material to contain 56.6% Ba and 26.9% Te as compared to the calculated amounts of 56.96% for Ba and 26.46% for Te.

Luminescence properties of U^{6+}-activated M_3TeO_6.— Most intense fluorescence in these compounds is observed in uranium-activated calcium orthotellurate and barium pentaoxotellurate. The calcium orthotellurate, $Ca_3TeO_6:U^{6+}$, phosphor fluoresces brightly under a variety of excitation modes. Its emission spectrum at room temperature (Fig. 1) consists of a single band peaking at 501 nm with a halfwidth of 30 nm. The excitation spectrum (Fig. 2) shows a broad band peaking at 340 nm and another peaking at 280 nm so that the phosphor is responsive to both long and short wavelength uv radiation. The photoluminescent response of $Ca_3TeO_6:U^{6+}$ is among the most intense observed in uranium-activated phosphors and compares favorably with other uv-excited phosphors having similar emission spectra. The cathodoluminescent response of $Ca_3TeO_6:U^{6+}$ is about 40% that of Zn_2SiO_4:Mn. This is substantially better than that of other U^{6+}-activated phosphors, which are generally inefficient under cathode-ray excitation. The threshold voltage for cathodoluminescence is low, about 50V, and the luminescence decay time to 1/10 of I_0 is of the order of 1 msec.

The concentration dependence of the fluorescence intensity (Fig. 3) shows the critical concentration for quenching to be 2 a/o (atom per cent) for the phosphor in which the activator was formulated to substitute for the tellurium in the lattice ($Ca_3Te_{1-x}U_xO_6$)

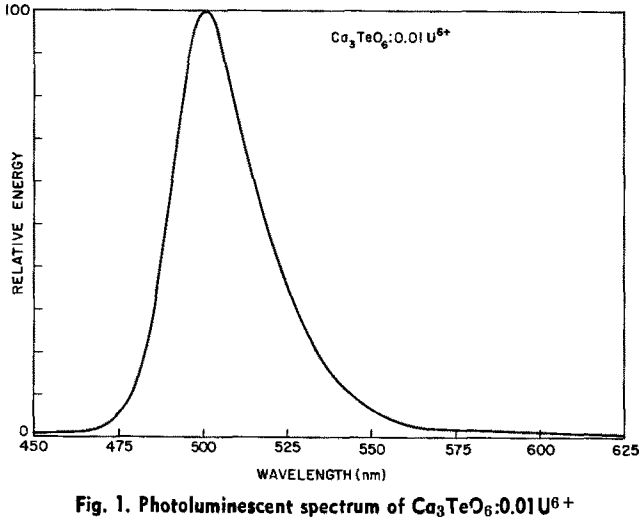

Fig. 1. Photoluminescent spectrum of Ca_3TeO_6:0.01 U^{6+}

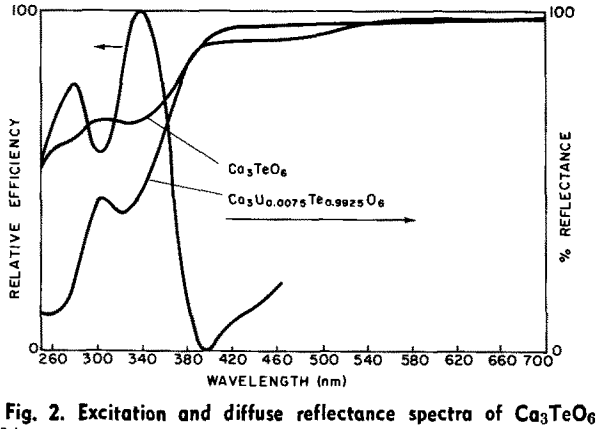

Fig. 2. Excitation and diffuse reflectance spectra of Ca_3TeO_6: U^{6+}.

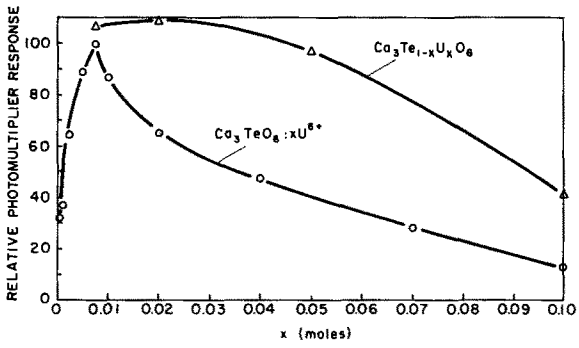

Fig. 3. Concentration dependence of the fluorescence intensity in U^{6+}-activated Ca_3TeO_6 phosphors.

and 0.75 a/o for the phosphor where no stoichiometric compensation was provided ($Ca_3TeO_6:xU^{6+}$). The former phosphor maintains the high efficiency of the photoluminescence response over much wider concentration range than $Ca_3TeO_6:xU^{6+}$, the luminescence of which is strongly dependent on activator concentration. The observed trends are consistent with the prevalent considerations of concentration quenching. Dexter and Schulman (7) and later Blasse (8) relate this phenomenon to the presence of quenching centers in the lattice, such as imperfections or impurities, at which the absorbed excitation energy is dissipated radiationlessly. The $Ca_3Te_{1-x}U_xO_6$ phosphor is likely to provide fewer lattice imperfections to serve as traps for the excitation energy and therefore its maximum fluorescence intensity is less concentration dependent than the noncompensated $Ca_3TeO_6:xU^{6+}$.

The green fluorescence of uranium-activated phosphors has been ascribed to the molecular uranyl ion UO_2^{2+} whose identity in a crystalline matrix may be preserved by having the uranium coordinated by two oxygen ions at a distance distinctly closer than that of the other oxygen ligands (1). Runciman (9) and then Blasse (10) state that the green emission can also be ascribed to an octahedrally coordinated uranium in a UO_6 emission center. In an attempt to elucidate the nature of the luminescence center in the compounds under investigation, the emission and excitation spectra were obtained at room and liquid nitrogen temperatures for Mg, Ca, and Sr orthotellurate and for calcium orthouranate, Ca_3UO_6, which is isomorphous with Ca_3TeO_6. As mentioned earlier, in each of these compounds the uranium activator is surrounded by six oxygen ligands in an octahedral configuration.

The fluorescence spectra of these compounds at room and liquid N_2 temperatures are shown in Fig. 4. At room temperature they all emit in the green spectral region; Mg, Ca, and Sr orthotellurates have reasonably symmetric emission bands peaking at 545, 501, and 530 nm, respectively, with the respective halfwidths of the emission band being 55, 30, and 35 nm. The fluorescence intensity of Mg and Sr orthotellurates, however, is only a fraction of that of the $Ca_3TeO_6:U^{6+}$. Calcium orthouranate, on the other hand, has a broad emission band skewed toward the red which peaks at 515 nm with a halfwidth of 50 nm. At liquid N_2 temperature the fluorescence spectra of the alkaline earth orthotellurate phosphors show sharp structure superimposed on the broad emission band. These sharp bands are most distinct in the $Mg_3TeO_6:U^{6+}$ phosphor and are similar to those observed by Blasse (10) in the $Y_6WO_{12}:U^{6+}$ compound. In fact, Newnham *et al.* (4c) established that the crystal structure of Mg_3TeO_6 is closely related to that of Y_6UO_{12} which in turn is isomorphous with Y_6WO_{12}. The space group of these compounds is $R\bar{3}$, with the hexavalent ion (U, Te, or W) being coordinated by six equispaced oxygens. This structural similarity is the probable reason for the close analogy between the de-

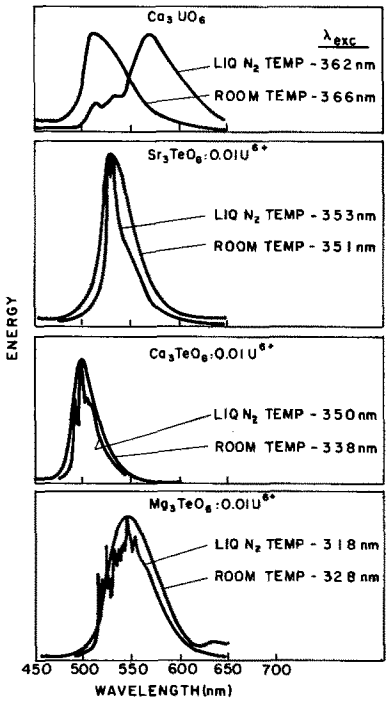

Fig. 4. Emission spectra of Ca_3UO_6 and of U^{6+}-activated M_3TeO_6 phosphors at room and liquid N_2 temperatures.

tail structure of the spectral energy distribution of U^{6+}-activated Mg_3TeO_6 and Y_6WO_{12} at liquid N_2 temperatures except that the emission of the latter is shifted toward lower energies.

The fluorescence spectra of the U^{6+}-activated alkaline earth tellurates at liquid N_2 temperature are resolved into a number of sharp bands, whose spacing is in most cases in the range of 40-210 cm^{-1} (Table III). Thus, $Mg_3TeO_6:U^{6+}$, has 12 clearly distinguishable spectral bands in the region of 515-558 nm. Blasse (10) identifies the emission center of $Y_6WO_{12}:U^{6+}$ as the UO_6 octahedron and in view of the aforementioned similarity of the spectra of $Y_6WO_{12}:U^{6+}$ and $Mg_3TeO_6:U^{6+}$, it is plausible to make the same assumption for the latter compound, the related alkaline earth orthotellurates and the calcium orthouranate. However, if one assumes a UO_6 luminescent center, then it is difficult to explain the drastic difference in the spectrum of the Ca_3UO_6 at liquid N_2 temperature when compared to those of the alkaline earth orthotellurates, particularly to that of the isostructural $Ca_3TeO_6:U^{6+}$. While there is no shift in the emission bands of the alkaline earth tellurates at liquid N_2 temperatures, the principal emission band of Ca_3UO_6 shifts from 515 nm at room temperature to 570 nm at liquid N_2 and the observed splittings are broader and more widely spaced. It has been established (11) that the uranium is in an octahedral coordination in Ca_3UO_6 although the six U-O coordinate bonds are not of equal length. If the green emission center of the aforementioned compound is the UO_6 group, then the spectral characteristics of the $Ca_3TeO_6:U^{6+}$ (or of the spectrally undistinguishable $Ca_3Te_{1-x}U_xO_6$) should be very similar to those of Ca_3UO_6, because Ca_3TeO_6 is isostructural with Ca_3UO_6 with the Te site being equivalent to the U site. But there is considerably more similarity among the spectral characteristics of the alkaline earth tellurates, although they are not all isostructural, than between Ca_3UO_6 and $Ca_3TeO_6:U^{6+}$.

Table III. Fluorescence peaks of U^{6+}-activated compounds at liquid N_2 temperature

Mg_3TeO_6		Ca_3TeO_6		Ca_3UO_6		Sr_3TeO_6	
λ (nm)	ν (cm^{-1})	λ (nm)	ν (cm^{-1})	λ (nm)	ν (cm^{-1})	λ (nm)	ν (cm^{-1})
515	19420	492	20320	504	19840	525	19050
517	19340	494	20240	513	19490	527	18980
520	19230	497	20120	528	18940	529	18900
526	19010	498	20080	530	18870	532	18800
528	18940	500	20000	534	18730	536	18660
531	18830	502	19920	570	17540	546	18320
536	18660	507	19720				
539	18550	511	19570				
543	18420						
549	18220						
551	18150						
557.5	17940						

It is possible to reconcile this difference by assuming a UO_2^{2+} emission center in the M_3TeO_6 compounds and a UO_6 emission center in Ca_3UO_6. An indication of the presence of a uranyl linkage may be obtained from an examination of the fluorescence spectrum of $Mg_3TeO_6:U^{6+}$ at liquid N_2 which resembles somewhat the series of strongest fluorescence bands of $CsUO_2(NO_3)_3$ obtained at 20°K (12). There are 14 of these bands between 479 and 571 nm and they have been interpreted as combinations of the resonance frequency ν_F and the frequencies ν_s, ν_a, and ν_b which represent, respectively, the symmetric, antisymmetric, and bending vibrations of the uranyl ion (13). A simple analysis of the observed splittings in the spectra of $Mg_3TeO_6:U^{6+}$ and $Ca_3TeO_6:U^{6+}$, such as done by Rabinowitch and Belford (12), can lead to $\nu_s \simeq 760$ cm^{-1}, $\nu_a \simeq 850$ cm^{-1}, and $\nu_b \simeq 200$ cm^{-1} for the two compounds. This is not unreasonable when compared to typical values of $\nu_s \simeq 810$-890 cm^{-1} and $\nu_a \simeq 860$-960 cm^{-1} measured on solid uranyl salts at 20°K (14). The ratio of ν_a/ν_s arrived at for Mg_3TeO_6 and Ca_3TeO_6 is 1.1 as compared to the theoretical value of 1.065 (15).

Luminescence properties of U^{6+}-activated Ba_2TeO_5.— The U^{6+}-activated Ba_2TeO_5 phosphor has an intense photoluminescent response in the orange-red spectral region. Its emission spectrum (Fig. 5) consists of a broad-band skewed toward the longer wavelength in which two maxima are discernible, at 590 nm and at 605 nm, with a composite halfwidth of 55 nm. Under cathode-ray excitation it is possible to distinguish a weak emission band in the green peaking at 520 nm in addition to the characteristic luminescence in the orange-red.

The red emission of uranium-activated compounds has been ascribed by Gobrecht and Weiss (16) and more recently by Blasse (10) to uranium tetrahedrally coordinated by oxygen, for example in a UO_4 complex. Although detailed structural data are not as yet available, it is possible that in the Ba_2TeO_5 compound the uranium, which is assumed to occupy a tellurium site in the lattice, is in the center of a UO_4 coordination tetrahedron.

The dominant excitation band of Ba_2TeO_5 is in the near ultraviolet, peaking at 375 nm, and therefore the phosphor is excited primarily by long wavelength ra-

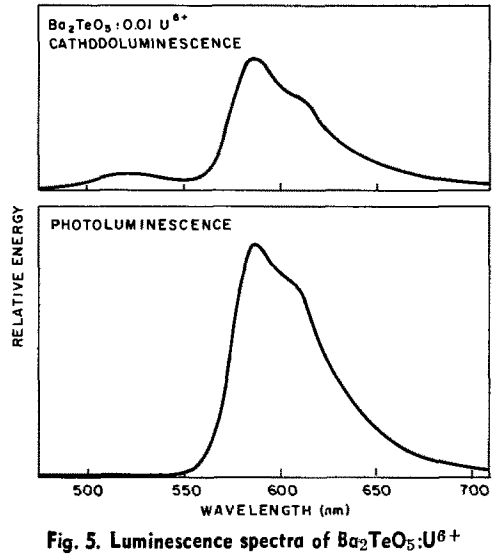

Fig. 5. Luminescence spectra of $Ba_2TeO_5:U^{6+}$

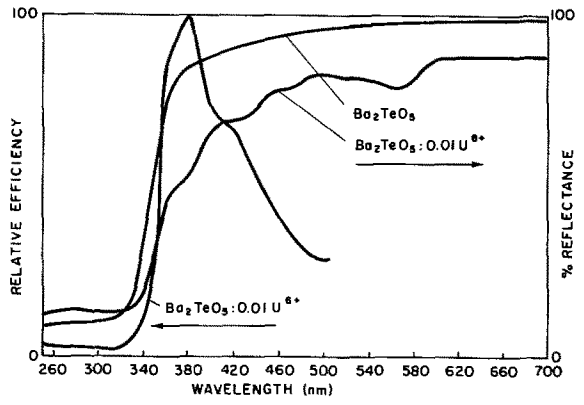

Fig. 6. Excitation and diffuse reflectance spectra of Ba_2TeO_5: U^{6+}.

diation. The comparison of the diffuse reflectance spectra of the unactivated and activated Ba_2TeO_5 (Fig. 6) shows that the presence of uranium results in several absorption bands in the visible and near ultraviolet region, the most intense of which is at 375 nm, the main excitation band of the phosphor. Thus it appears that the fluorescence results from direct excitation of the activator center rather than through energy absorption by the lattice and subsequent transfer to the activator site. The host compound absorbs strongly throughout the uv region where no excitation bands for the phosphor are found.

There are two experimental facts which indicate the strong effect of the crystalline environment on the spectroscopic properties of the U^{6+} emission. There is the substantial difference in the intensity of fluorescence between compounds in which the U^{6+} is formulated to substitute for the Te^{6+} ($Ba_2Te_{1-x}U_xO_5$) and those in which no stoichiometric compensation is provided (Ba_2TeO_5:xU^{6+}). The latter formulation is substantially brighter throughout the concentration range evaluated (Fig. 7) even though the excitation and emission spectra at room temperature are identical for the two formulations. The dependence of the fluorescence intensity on activator concentration shows concentration quenching at rather high U^{6+} content (2-5 a/o) in the Ba_2TeO_5:xU^{6+} phosphor, a concentration which is one to two orders of magnitude greater than that found in other red-emitting uranium activated phosphors.

It is noteworthy that the dependence of the fluorescence intensity on activator concentration in the barium pentaoxotellurate phosphor is contrary to that observed in the calcium tellurate and thus not consistent with the argument advanced earlier. As a first approximation one could assume fewer lattice imperfections in $Ba_2Te_{1-x}U_xO_5$ phosphor than in Ba_2TeO_5:xU^{6+} and thus one would expect higher efficiency and a higher value of critical concentration in the former material. However, the data show the Ba_2TeO_5:xU^{6+} phosphor to be substantially more efficient. The large difference in fluorescence intensity between

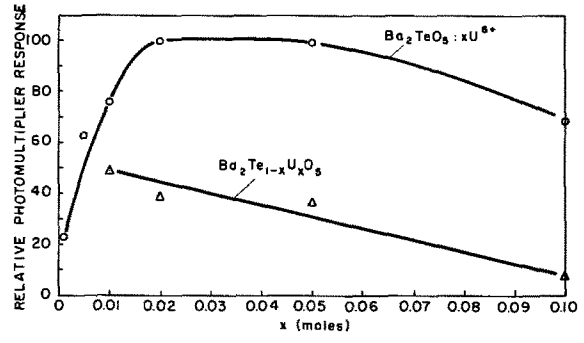

Fig. 7. Concentration dependence of the fluorescence intensity in U^{6+}-activated Ba_2TeO_5 phosphors.

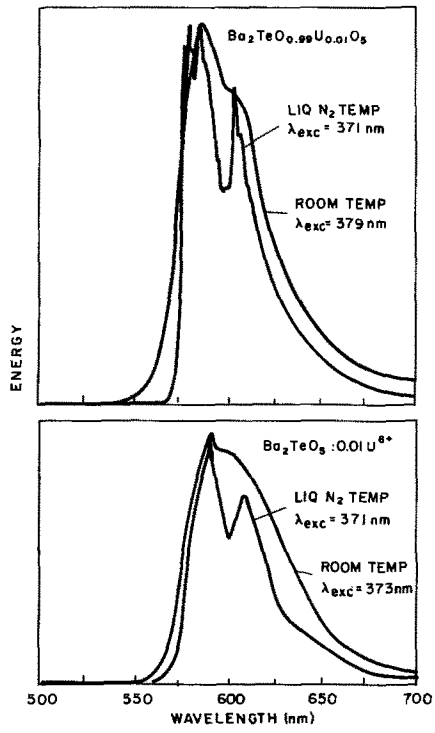

Fig. 8. Emission spectra of U^{6+}-activated Ba_2TeO_5 phosphors at room and liquid N_2 temperatures.

$Ba_2Te_{1-x}U_xO_5$ and Ba_2TeO_5:xU^{6+} phosphors implies a small variation in the nature of the activator center in the two compounds. This is also evident in the fluorescence spectra taken at liquid nitrogen temperature. While the spectroscopic data at room temperature are identical for the two materials, the emission spectra at liquid N_2 are slightly different (Fig. 8). The asymmetric RT emission curve of Ba_2TeO_5:$0.01U^{6+}$ is split at liquid N_2 into two bands whose peaks are separated by ~500 cm^{-1}. The fluorescence band of $Ba_2Te_{1.99}U_{0.01}O_5$ at liquid N_2 temperature also consists of two major bands separated by ~500 cm^{-1}; however, each of these has a distinct vibrational structure. Thus, there seems to be a tangible difference in the properties of these two virtually identical phosphors which probably is related to small changes in the ligand arrangement around the uranium activator. It is possible that some of the U^{6+} ions in Ba_2TeO_5:xU^{6+} are located in sites coordinated in a slightly different manner than the Te in Ba_2TeO_5 or may even be in interstitial positions. Such an arrangement would explain the absence of structure in the liquid N_2 spectrum of Ba_2TeO_5:xU^{6+}, because the contributions from various sites would tend to be superimposed; but it still would not account for the difference in the observed fluorescence intensities.

The conclusion reached here is that the knowledge of the spectroscopic behavior of uranium-activated phosphors is too scant to permit the unambiguous identification of the nature of the emission center. Such identification would necessarily have to reconcile all available experimental evidence which may superficially appear to be in conflict. It is hoped that the present work has contributed to stimulating this effort by posing some of the apparent questions.

Acknowledgment

The author gratefully appreciates the assistance of R. Francis in much of the experimental work, the spectroscopic measurements of S. Mosca, the analytical measurements of C. Persiani, W. Shelby, and R. Weberling, the diffuse reflectance spectra of E. Lanning, the helpful discussions with J. Baglio and the critical comments of F. Avella, T. Peters, F. Palilla, and O. Sovers.

Manuscript submitted Sept. 19, 1972; revised manuscript received Nov. 20, 1972. This was Paper 61 presented at the Los Angeles Meeting of the Society, May 10-15, 1970.

Any discussion of this paper will appear in a Discussion Section to be published in the December 1973 JOURNAL.

REFERENCES

1. S. Natansohn, *This Journal*, **116**, 1250 (1969).
2. G. Merz, Thesis, Technische Hochschule Karlsruhe, 1956.
3. R. Amster and C. Wiggins, *This Journal*, **116**, 68 (1969).
4a. G. Bayer, *Z. Krist.*, **124**, 131 (1967).
b. H. Kasper, *Z. Anorg. Allgem. Chem.*, **356**, 329 (1968).
c. R. E. Newnham, J. F. Dorrian, and E. P. Meagher, *Mater. Res. Bull.*, **5**, 199 (1970).
5. J. A. Baglio and S. Natansohn, *J. Appl. Cryst.*, **2**, 252 (1969).
6. R. Scholder, *Angew. Chem.*, **70**, 583 (1958).
7. D. L. Dexter and J. H. Schulman, *J. Chem. Phys.*, **22**, 1063 (1954).
8. G. Blasse, *This Journal*, **115**, 1067 (1968).
9. W. A. Runciman, *Brit. J. Appl. Phys., Suppl. No. 4*, S78 (1955).
10. G. Blasse, *This Journal*, **115**, 738 (1968).
11. H. M. Rietveld, *Acta Cryst.*, **20**, 508 (1966).
12. E. Rabinowitch and R. L. Belford, "Spectroscopy and Photochemistry of Uranyl Compounds," pp. 62-63, Macmillan Co., New York (1964).
13. *Ibid.*, pp. 6-10.
14. *Ibid.*, p. 48.
15. *Ibid.*, p. 7, 46.
16. H. Gobrecht and W. Weiss, *Z. Physik*, **140**, 139 (1955).

Selective Silicon Epitaxy and Orientation Dependence of Growth

P. Rai-Choudhury* and D. K. Schroder

Westinghouse Research Laboratories, Pittsburgh, Pennsylvania 15253

ABSTRACT

Silicon was grown epitaxially on oxidized silicon substrates in which the oxide was removed over selected areas. Both planar substrates and etched pedestals standing above the substrates were used. (110) oriented substrates had the highest growth rates, followed by (100), (115), and (111). (110) also had the grown surfaces with best planarity. Pattern displacement was very noticeable on (115) substrates. Alignment of the patterns with major crystal axes had a significant influence on the growth perfection. Some of the experimental observations can be explained by surface energy considerations.

Epitaxial layers of silicon are either grown over the entire wafer surface (nonselective growth) as in the case of the collector and/or base of a transistor, or grown selectively through an oxide mask as in the case of the silicon photodiode array (1, 2). In the past, device designers have paid little attention to the orientation of the starting substrate. For example, when compared with the (111) substrates, the deposition temperature could be lowered considerably by using (100) substrates without producing any increase in the defect density (3). We have succeeded in growing device quality epitaxial silicon on (100) substrates at temperatures as low as 900°C. One of the implications of this is to produce a very abrupt junction on degenerate substrates. In most transistor or integrated circuit applications the layer thickness is very much less than the substrate diameter and any faceting due to edge effects can be neglected. However, even for thin layers, selective buried layer resolution often becomes a problem due to pattern translation from faceting.

When the layer thickness becomes comparable to the size of the growth pattern, as in the case of silicon photodiode arrays, then faceting becomes very important. For example, the orientation of the substrate and hence the faceting determine the width-to-height ratio of the epitaxially grown material. In the application of this technique to diode arrays it is advantageous to have these "mushrooms" grow high with relatively little lateral growth, for good electron beam acceptance. Other applications may demand a high width/height ratio. The planarity of the surface and the geometric shape may be important for some device applications, and we show that the orientation has a major influence on these.

* Electrochemical Society Active Member.

Key words: faceting, surface energy, alignment, silicon dioxide, masking.

Energetics and Nucleation Considerations

When epitaxial silicon is deposited from hydrogen reduction of $SiCl_4$ at about 1150°C in a conventional horizontal reactor, the orientation dependence of growth is not pronounced. For example, at a $SiCl_4$ partial pressure of 7×10^{-3} atm the growth rates on unmasked wafers varied as (111) : (110) : (115) : (100) :: 1.0 : 2.3 : 1.9 : 2.2. The relative growth rates on different orientation substrates do not change noticeably when HCl gas is injected for selective epitaxial growth, although a considerable decrease in the deposition rate is observed. The presence of excess HCl tends to favor the reverse reactions and probably causes the system to approach thermodynamic equilibrium. Thus, the selective epitaxial growth may be considered to be under isothermal and quasi-equilibrium conditions. It is well known that the crystals formed under these conditions are bounded, as much as possible, by the slowest growing surfaces (4). Therefore, in silicon, layers on different orientation substrates will eventually develop {111} facets under unconstrained growth.

Before presentation of the experimental results, a brief summary of the growth habits of different crystal faces and their relative stabilities is helpful. The main driving force in the development of different facets is the tendency for the crystal surface to approach minimum free energy configuration. The enthalpy, ΔH^{SV}, of the (111) face of silicon has been measured at liquid nitrogen temperature by Jaccodine (5) to be 1230 ergs/cm^2. From the measured enthalpy (which is equal to the energy, ΔE^{SV}, in this case), the Si-Si bond strength, and hence the surface energies of other orientations can be calculated. The surface energy values

for the orientations of interest here are given below:

Orientation	Surface energy, ergs/cm^2
(111)	1230
(110)	1510
(115)	1650
(100)	2130

Thus, at low temperatures, growth in the <111> direction will be minimized whereas in the <100> direction growth will be maximized. However, at the temperatures of interest here (T = 1400°-1500°K) the entropy term (ΔS^{SV}) becomes very significant and the observed order of stability of these planes is most likely to change. In fact, with a reasonable guess at the entropy values and considering the number of broken bonds per atom, it can be shown that at the growth temperature of 1500°K, (110) would be the plane of highest surface-free energy. The plane with high surface-free energy will tend to grow faster along its axis rather than generate new surfaces.

Recently, Sangster (6) has treated the crystal growth phenomena in III-V compounds in a qualitative manner much of which applies to the present case. If the growth is not constrained (by mass transfer rates and other operator variables), surfaces like the diagonal faces would grow very rapidly. When the face diagonal is perpendicular to the growth front, the growing interface would possess a great multitude of growth steps so that nucleation and growth could occur anywhere on the surface.

{110} surfaces.—Atoms in {110} surfaces are arranged in planar zigzag chains, each atom being bonded to two nearest neighbors in the chain with the remaining two bonds extending diagonally out on each side. Thus, each surface atom has one unsatisfied bond. The first deposited atom to start the formation of a new layer makes only one bond to the existing surface creating three dangling bonds. The net increase of two unsatisfied bonds forms a potential energy barrier for nucleation of growth of a new layer. Once the first atom is in place, other atoms can deposit adjacent to it without change in the number of unsatisfied bonds. Some inherent tendency towards maintenance of surface planarity exists, since deposition of part of a second new layer requires the presence of adjacent portions of two chains in the first layer. (110) plane might be relatively difficult to extinguish by the slow growing {111} faces since four of the six {111} planes are at right angles to the (110), while the other two {111} are at 35.26° from the (110). Thus, there are only two planes to extinguish the fast growing face.

{100} surfaces.—In a (100) surface, each atom is bonded to two atoms in the bulk and has two unsatisfied dangling bonds. A depositing atom can approach the surface and bond to two surface atoms leaving unsatisfied the other two bonds. Thus, atoms can be added to the surface without an increase in the surface energy. The four bounding {111} faces are at 54·74° from (100) and under optimum growth conditions (as will be shown later) will extinguish the (100) face in a rather well-defined manner.

{111} surfaces.—The {111} surfaces consist of two closely spaced planes of atoms. Each atom in one plane is bonded to three nearest neighbor atoms in the other plane. The fourth bond extends normal to the plane of this "double layer" and connects with an atom in the next such layer. Three-fourths of the crystal binding energy or cohesive energy is involved in the internal bonding of these double layer units. This is why the {111} face has the lowest surface energy. The depositing atoms can form only one bond each to a specific {111} surface. Addition of one atom causes the net creation of two unsatisfied bonds. Since no atom can bond both to this first one and to the existing layer, deposition of one atom does not allow subsequent barrier-free growth. For such to be possible, a second atom must attach itself to the existing layer as a second nearest neighbor of the first, again with a net increase of two unsatisfied bonds. Then a third atom can bond to the two nucleus atoms, and one of the first type from this one back to the underlying surface, without any increase in the number of dangling bonds, to generate a triangular structure. This two-dimensional nucleus is the smallest portion of the {111} double layer that can be stable. Thus, the difficulty of nucleation and the low surface energy of {111} faces are responsible for its slow growth rate and high stability.

{115} surfaces.—The (115) face makes an angle of 15 · 8° to (001). With $l \geqq 5$, (l is one of the Miller indices), the axes rapidly become indistinguishable from [001]. Thus, (115) face has two unsatisfied bonds per surface atom and can be treated very similar to the {100}.

Experimental Procedure

Epitaxial layers were deposited by hydrogen reduction of $SiCl_4$ in an rf heated horizontal reactor. In order to prevent growth over the oxide masked regions, a controlled amount of HCl was injected into the main gas stream (2). The substrates used were of (111), (110), (115), and (100) orientations, polished chem-mechanically to a damage-free surface. The substrates for the selective growth were prepared to provide two basically different geometries. One geometry consisted of small raised pedestals with oxide-passivated sides and these substrates were prepared by a process described by Appels *et al.* (7). Si_3N_4 was deposited on the silicon wafer and etched into square patterns. With the nitride as the etch mask, the silicon was etched to a depth of 4 μm. The etched regions were then oxidized and the nitride subsequently removed. This resulted in pedestals of dimensions 8 μm × 8 μm, which were oxide-passivated except for the top surface. In addition to these pedestals, there were some of the size 40

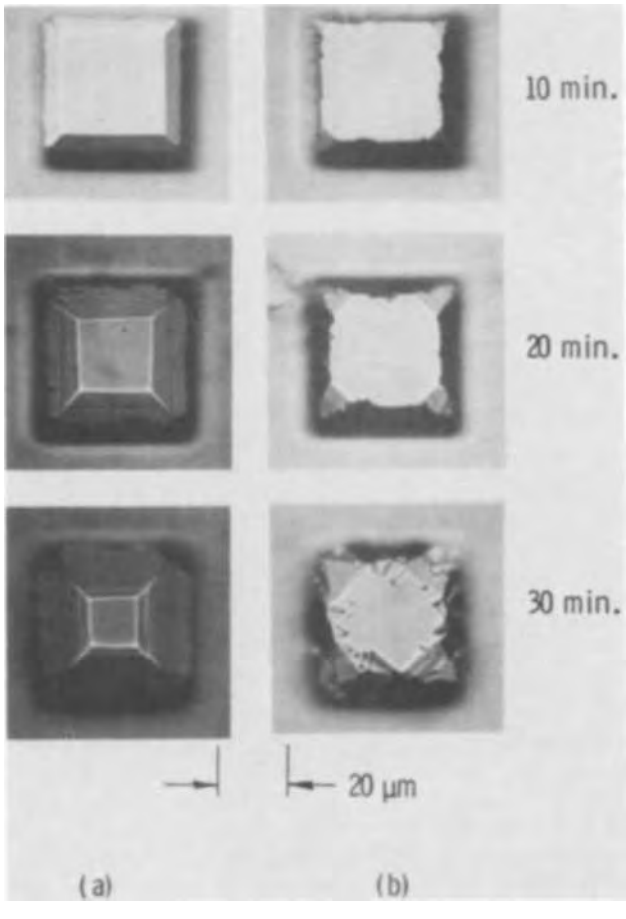

Fig. 1. Growth of silicon on 40 μm × 40 μm pedestals on a (100) substrate as a function of time. (a), sides of the square patterns aligned with {110} faces; (b), sides 45° off the {110} faces.

μm × 40 μm (see Fig. 1 and 2). Some of these pedestals were deliberately aligned with other crystal planes, *e.g.*, the sides of the square patterns on (100) wafers aligned with the {110} faces.

Substrates with the second type of geometry were prepared by simply oxidizing the silicon slices to a thickness of 1 μm and photolithographically opening windows in the oxide. No attempt was made here to align the patterns with any particular crystal faces.

Results

In conventional epitaxial growth, the layer thickness (typically 10-20 μm) is very much smaller than the substrate diameter (typically 3 × 10^4 μm) so that the boundary conditions of a semi-infinite body apply. That is, any growth facets that normally develop near the wafer edges can be neglected for all practical purposes. However, in selective epitaxy, the layer thickness is often comparable to the diameter of the growth plane, and therefore, the facets that normally initiate from the edges of the pattern cannot be overlooked. The relative stability of the different faces depend on their surface-free energies as mentioned earlier. In the following discussion, some results are presented showing how the initial growth planes are modified and the development of the low energy faces.

Figure 1 shows some photomicrographs of layers grown on etched square pedestals raised above the oxide-masked (100) surface, as shown in the insert of Fig. 3. When the sides of the square pedestals are aligned with {110} planes, four well-defined {111} facets develop from the four sides of the pedestal, as shown in Fig. 1(a). These {111} planes make an angle of 54·74° with the initial (100) plane. It can be seen from the photomicrograph of the layers grown for 30 min that a new set of faces is developing from the edges where the previous adjacent {111} faces failed to join. This type of faceting is also seen in Fig. 2(b),

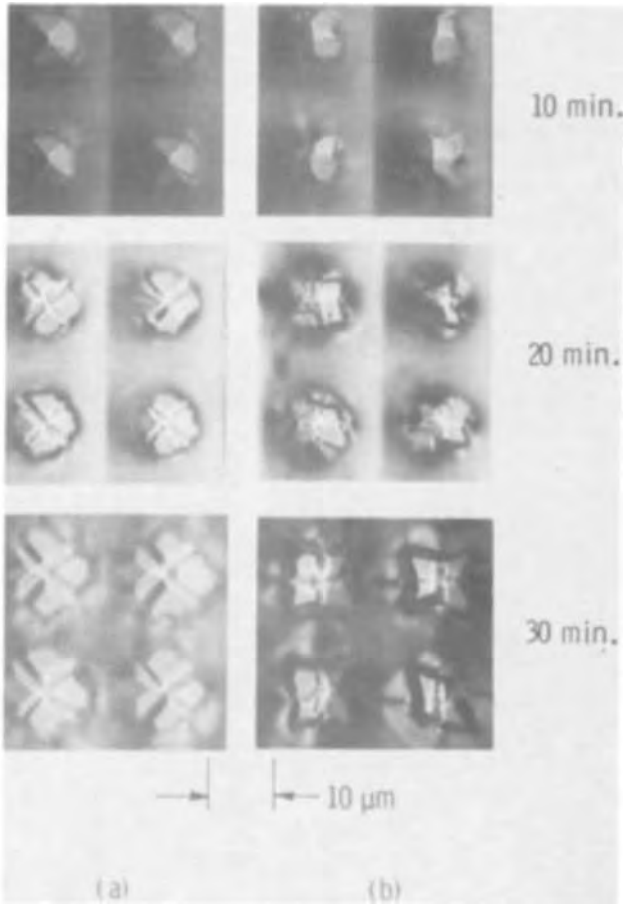

Fig. 2. Patterns on the same wafer as in Fig. 1, except that the dimensions are 8 μm × 8 μm. Alignment, same as in Fig. 1.

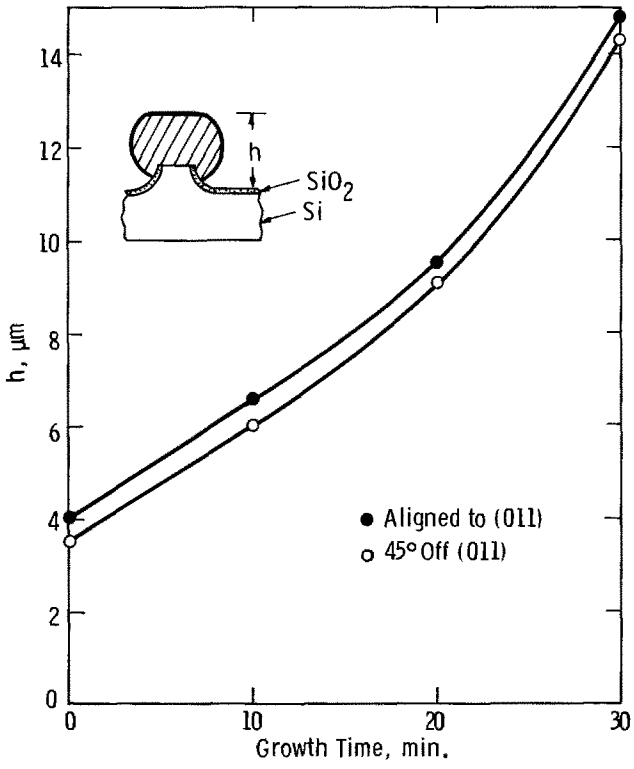

Fig. 3. Height of etched pedestal plus grown "bump" for the wafers of Fig. 1 and 2 as a function of growth time.

where here, the sides of the square are aligned 45° off the {110} planes.

The effect of multiple well-defined {111} facet development becomes more significant as the ratio of layer

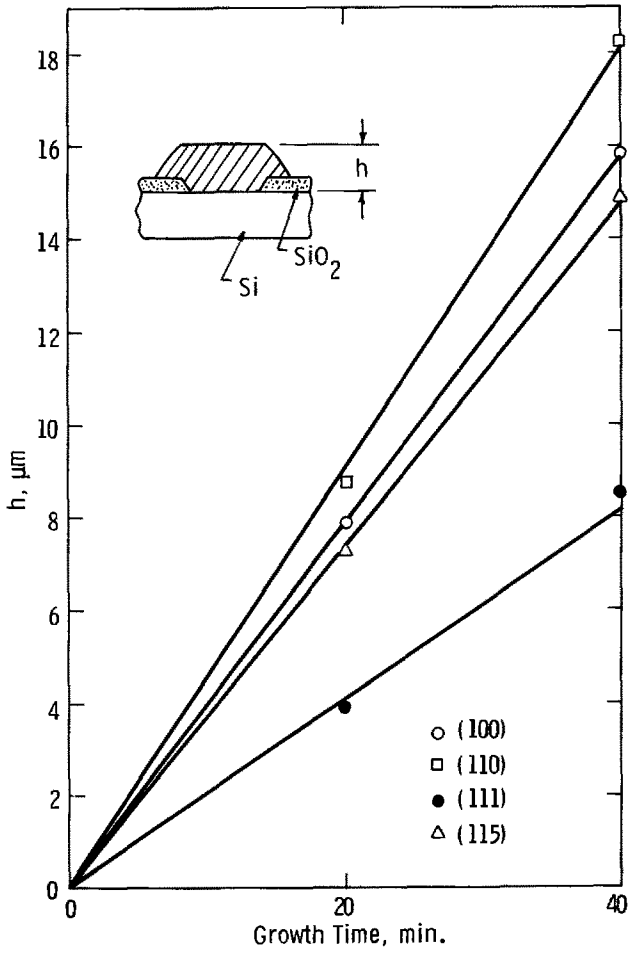

Fig. 4. Height of grown "bumps" on planar wafers as a function of time for 4 different substrate wafer orientations.

thickness to pedestal or pattern size increases. This is observed in Fig. 2, where the size of the pedestals is 8 μm $\times$ 8 μm, instead of 40 μm $\times$ 40 μm as in Fig. 1. Even for only 10 min growth time, we see the new sets of faces developing in the corners. These faces become much more obvious in the 30 min photograph in Fig. 2(a).

The random development of numerous facets is seen on the wafer where the sides of the squares are not aligned to the {110} planes [see Fig. 1(b) and 2(b)].

The growth rate of the patterned structures is not affected by the pattern alignment on a given substrate orientation. This is shown in Fig. 3 where the total pedestal height is plotted as a function of growth time. The heights of the small area structures (Fig. 2) were approximately the same as those of the larger area ones shown in Fig. 1. Note that at zero time the height corresponds to that of the etched, oxide-passivated pedestal alone. It appears that the growth rate increases as the pedestals grow higher. One possible explanation for this is that the high density of the small pedestals (1.5×10^5 cm^{-2}) in this pattern might be effective in increasing the turbulence near the wafer surface, in thinning the boundary layer for mass transfer, and/or making available higher concentration of $SiCl_4$ for growth by virtue of their raised position. These pedestals grow larger in diameter as well as reach further into the gas stream as the growth progresses. The growth rates on the pedestals were generally found to be somewhat less than that on similar density patterns on planar structures in which the patterns are etched windows in thermally grown oxide. This is expected since the pedestals form potential barriers for surface migration of any depositing species landing on the valleys. Thus, the results of growth on (100) wafers indicate that the surface planarity and the orientation of the initial pattern are lost at a very early stage of growth, which is consistent with the large difference in the surface energies between {100} and {111}. This has implications for some device applications where the growth height plus the initial etched pedestal height allow the top of the grown structure to be significantly above the oxide in the valleys.

With the objective of determining an orientation which grows further above the substrate surface without losing its identity and without touching its neighbors (to preserve the discrete nature of the structures), experiments were carried out on four different substrate orientations, namely, (100), (115), (111), and (110). Figure 4 shows a comparison of growth behavior on these four different orientations where the patterns for selective growth were formed by etching windows of the various shapes into the oxide of plane, thermally oxidized Si wafers, as opposed to raised pedestals. Also the sizes of the unmasked regions were much larger than those of the pedestal pattern. The ratio of the unmasked to oxide masked areas is 0.1 compared to 0.25 for the earlier "etched pedestal" wafers. As can be seen, no enhancement of growth with time is observed. (111) is the slowest growing plane which is consistent with its lowest surface energy and the associated nucleation difficulty. Because of the ease of nucleation

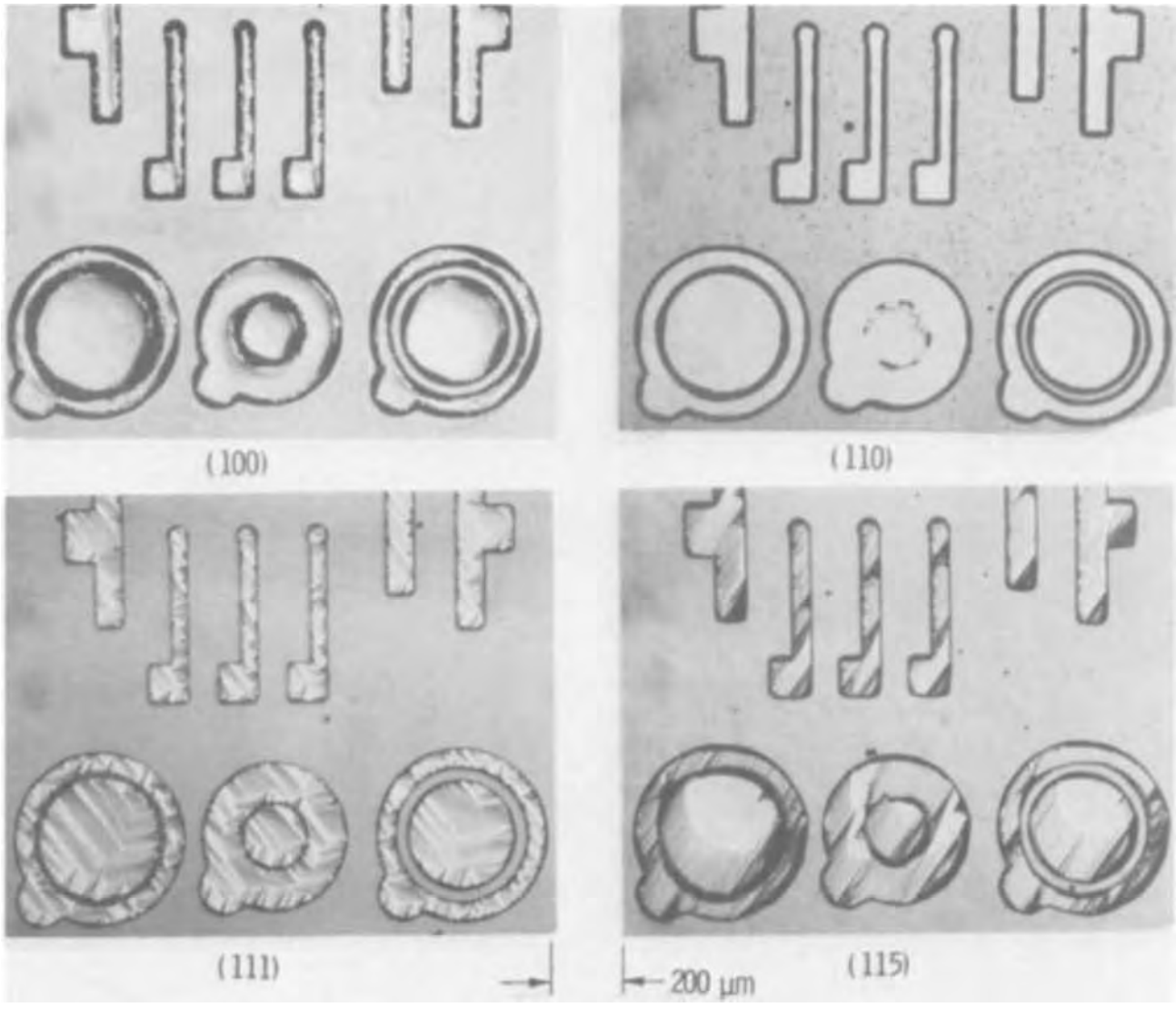

Fig. 5. Growth patterns on planar wafer of different orientations for a growth time of 40 min

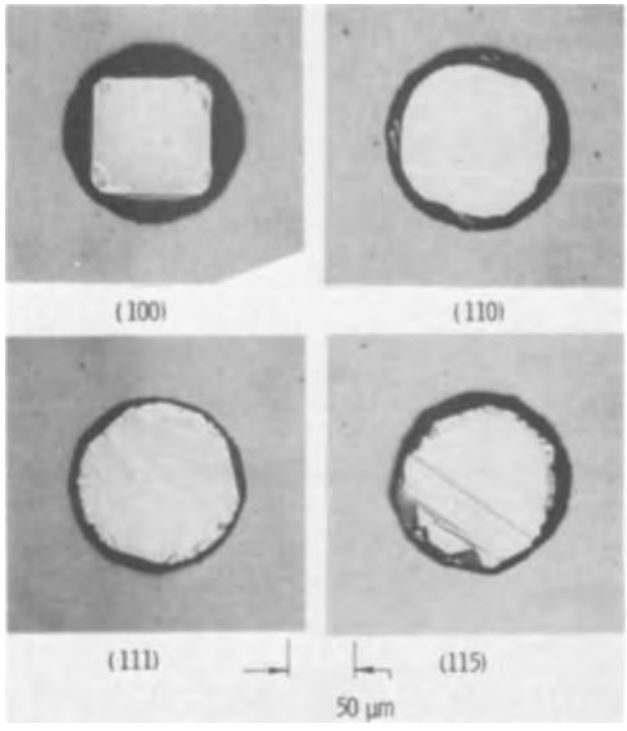

Fig. 6. Growth patterns on the same wafers as in Fig. 5 in circular oxide openings for a growth time of 40 min.

and high surface energy of the (100) plane, the growth rate on this plane is higher than that on (111). The (115) plane, being close to (100), encounters no nucleation difficulties and the growth proceeds at a rate slightly under that for (100). It is not obvious why (110) has the highest growth rate. The (110) plane has considerably lower surface energy than (100), and the nucleation is energetically not as favorable as in (100). One conjecture is that the {111} facets develop very early during the growth on (100), thus decreasing its effective growth rate. Whereas in (110) the {111} facets take considerably longer time before a significant portion of the growing (110) surface is transformed.

Figure 5 shows photomicrographs of the growth facets on the four orientations. It is noteworthy that the most planar growth occurred on the pattern on the (110) plane. This may be expected from the nucleation constraints and the availability of only two {111} faces that could extinguish the growing (110) as discussed earlier. The growth on (111) loses its planarity completely and new sets of {111} facets initially originating from the oxide-silicon interface are formed. The growth on (115) plane develops numerous {111} facets and a very distinct lateral translation of the patterns is noticeable. Therefore, in terms of pattern stability, their heights above the initial surface, and minimum interference from facet growth, (110) substrates are preferred.

The facet formation is especially evident in the photographs of Fig. 6. Here, the pattern was a 5 mil diameter circular window in the oxide. Note the square shape of the (100) orientation and the beginnings of the typical triangular configuration for the (111) substrate. The (110) again has the most planar top surface with the (100) next. As in Fig. 5, both (111) and (115) have very irregular top surfaces.

Summary

Silicon was epitaxially deposited selectively on silicon substrates, by using thermally grown SiO_2 as the mask. Both raised silicon pedestals with oxidized sides and planar surfaces were used. The effect of various substrate orientations and crystal face alignment on growth were studied with the following results:

1. The growth rate on planar structures is highest on (110) wafers and decreases in the order (100), (115), and (111).
2. The size of the area in which Si is grown has no noticeable influence on the growth rate.
3. The planarity of the growth surface is best for (110) and deteriorates in the order (100), (115), (111).
4. Alignment of the pattern with major crystal axes has an effect on the perfection of the grown patterns.
5. Pattern displacement is very noticeable for (115) oriented devices.

Acknowledgment

The authors would like to thank G. A. Gruber for the preparation of the silicon nitride films, W. Cifone and R. A. Wickstrom for assistance with the experiments.

Manuscript submitted Sept. 25, 1972; revised manuscript received Dec. 15, 1972.

Any discussion of this paper will appear in a Discussion Section to be published in the December 1973 JOURNAL.

REFERENCES

1. W. E. Engeler, M. Blumenfeld, and E. A. Taft, *Appl. Phys. Letters*, **16**, 202 (1970).
2. P. Rai-Choudhury and D. K. Schroder, *This Journal*, **118**, 107 (1971).
3. P. Rai-Choudhury, *ibid.*, **118**, 1183 (1971).
4. H. E. Buckley, "Crystal Growth," Chap. 4, John Wiley & Sons, Inc., New York (1951).
5. R. J. Jaccodine, *This Journal*, **110**, 524 (1963).
6. R. C. Sangster, "Compound Semiconductors," Vol. 1, p. 241, Reinhold Publishing Corp., New York (1962).
7. J. A. Appels, E. Kooi, M. M. Paffen, J. J. H. Schaturje, and W. H. C. G. Verkuylen, *Philips Res. Rept.*, **25**, 118 (1970).

Electrical Properties of a Native Oxide on Gallium Phosphide

S. M. Spitzer,* B. Schwartz,* and M. Kuhn*

Bell Laboratories, Murray Hill, New Jersey 07974

ABSTRACT

A vitreous native oxide can be grown on GaP by oxidation in a concentrated solution of hydrogen peroxide, and this oxide effectively passivates GaP light-emitting devices. This paper reports the first electrical characterization of this native oxide. Electrical measurements were performed on MOS structures prepared by growing a native oxide film 500-1000Å thick on the $(\bar{1}\bar{1}\bar{1})$ face of an n- or p-type GaP wafer and evaporating an Au field plate on the oxide. The refractive index of the oxide film was 1.58. Current-voltage and capacitance-voltage characteristics show that the native oxide is an electrical insulator, with a low frequency dielectric constant $\epsilon \approx 5.5$, and a dielectric breakdown strength of 6-8 $\times$ 10^6 V/cm after annealing in nitrogen at 250°C. Current-voltage behavior shows a linear dependence of ln J on $E^{1/2}$, typical of field-enhanced thermionic emission. The I-V characteristics are nonsymmetric with respect to field plate polarity, suggesting the conduction mechanism to be surface-barrier-controlled emission, with a barrier height $\phi_b \approx 1.2$ eV, as determined from the temperature dependence of the I-V characteristics. The dielectric constant determined from the slope of the I-V characteristics by using a field-enhanced thermionic emission model agrees with the value obtained from capacitance measurements. Capacitance-voltage characteristics show accumulation and deep depletion behavior. Analysis of deep depletion curves yields a surface charge density $Q_s \approx 4 \times 10^{12}/cm^2$ for both p- and n-type GaP samples. Values of $|N_D - N_A|$ for the GaP substrates obtained from deep depletion data are in good agreement with the values obtained from Hall measurements on the substrate material.

Development of a technology for the fabrication of gallium phosphide light-emitting diodes requires a reliable method for the formation of insulating layers on the processed surface. Such insulating layers serve to electrically isolate and passivate active junctions, as well as to insulate metalization required for device interconnections. These layers should be pinhole-free, have good adherence to the GaP substrates, and be able to act as a processing mask, while being inert to subsequent processing steps. In addition such layers should have low optical absorption in order to be used in light-emitting diode structures.

The importance of electrically insulating layers has been amply demonstrated in the silicon planar device technology. For compound semiconductors, insulating layers of such materials as SiO_2 or Si_3N_4 may be deposited but these layers typically have had poor uniformity, high pinhole density, and poor adherence.

A native oxide has been grown on GaP (1) which exhibits good adherence, acts as a mask for the etching of GaP (2) and for metalization, and is transparent in the visible region. This oxide can be grown on p- and n-type material (3) by a relatively simple process occurring at ~100°C.

The electrical properties of the native oxide are reported in this paper. It is shown that this oxide is a good insulator, satisfying the electrical requirements for GaP processing. The sample preparation and oxidation procedure are described, as well as the electrical measurements and resulting experimental data. The electrical data are analyzed and the results discussed.

Sample Preparation and Oxidation

Gallium phosphide wafers were cut with a diamond saw from n-type Te-doped and p-type Zn-doped liquid-encapsulated-Czochralski-grown crystals of {111} orientation. Carrier concentrations were 1-4 $\times$ 10^{17} cm^{-3} for the n-type and 4-5 $\times$ 10^{17} cm^{-3} for the p-type samples. The wafer surfaces were prepared by lapping with 0.3 μm alumina and then etching 75 μm off the P $(\bar{1}\bar{1}\bar{1})$ face with a bromine-methanol solution for a final wafer thickness of 0.3 mm. A full-surface back contact was made to the Ga (111) face by evaporating 5000Å layers of Si-Au and Be-Au on n- and p-type wafers, respectively; a 10,000Å overlay of Au was subsequently deposited. These contacts were then alloyed at 600°C for 10 min to form ohmic contacts to the substrate.

A galvanic oxide was then grown on the $(\bar{1}\bar{1}\bar{1})$ faces of the GaP samples by boiling them in a concentrated solution of hydrogen peroxide for several hours and subsequently baking them in dry nitrogen at 250°C for 2 hr (3). This glassy oxide was found to be an amorphous mixture of Ga_2O_3 and P_2O_5. The thickness and refractive index of the oxide were determined by ellipsometry. The films used in this study ranged in thickness from 500 to 1000Å and after baking had an index of refraction $n \approx 1.58$ independent of thickness.

Electrical Characteristics

The electrical properties of the oxide films were investigated by means of measurements on metal-oxide-semiconductor structures prepared by evaporating 15-mil diameter Au field plates on the oxide. Contact was made by a W probe to the Au field plate and by a Pt base to the full-surface alloyed Si-Au or Be-Au back contact.

The dielectric breakdown strength of the oxide film at room temperature was measured by increasing the voltage across the MOS structure until the current underwent a sharp increase-limited only by external series resistance. For as-grown, unbaked films, breakdown occurred at electric fields of 0.5-2 $\times$ 10^6 V/cm. Since the oxide was grown in aqueous solution, water of hydration incorporated in the films was expected to reduce the dielectric strength. In order to verify this effect, the oxides were annealed in dry nitrogen at 250°C for 2 hr. During annealing the film thickness decreased by approximately 20% (3), the dielectric breakdown strength increased to 6-8 $\times$ 10^6 V/cm, and the index of refraction decreased slightly. Additional annealing at 250°C caused no further changes. The

* Electrochemical Society Active Member.

Key words: compound semiconductors, MOS, conduction mechanisms.

Table I. Properties of native oxide films on GaP

	RD269-2 n-type				RD313-2 p-type			
	Sample A		Sample E		Sample A		Sample E	
	Unbaked	Baked	Unbaked	Baked	Unbaked	Baked	Unbaked	Baked
Oxide thickness, Å	550	425	600	500	725	525	1125	975
Index of refraction	1.60	1.58	1.60	1.58	1.60	1.58	1.61	1.58
Relative dielectric constant as determined from *I-V*	—	5.52	—	5.53	—	5.54	—	5.54
C-V	—	5.4	—	5.4	—	5.4	—	5.45
Dielectric breakdown strength, V/cm	1.1×10^6	6.4×10^6	0.5×10^6	6×10^6	2.0×10^6	8×10^6	0.9×10^6	7×10^6
Barrier height, eV	—	1.18	—	1.20	—	1.18	—	1.23
Flatband voltage, V	—	7.5	—	12	—	−8	—	−14
Surface charge density, cm^{-2}	—	5×10^{12}	—	7×10^{12}	—	4×10^{12}	—	4×10^{12}

physical properties of the oxide films before and after annealing are summarized in Table I.

Current-voltage measurements were taken on the MOS structures with the samples shielded from the light in a specimen holder flushed with dry nitrogen, in order to avoid photo-excited and surface-leakage current components. The *I-V* data were collected using a Keithley 602C electrometer and Lambda LS-515 digital voltage source in series with the MOS structure. Point-by-point, rather than continuous, measurements were taken to minimize any error due to lengthy response time of the electrometer and to conveniently cover the large range of current.

At room temperature the current through the oxide for applied voltages below breakdown is too small for detection ($<10^{-13}$ A/cm^2). However, the conductivity was found to be strongly temperature dependent, and *I-V* characteristics could be measured at temperatures in the range of 75°-150°C. The data were checked for reproducibility on the same sample and on different samples. All results in this temperature range were found to be consistent, indicating that sample hysteresis or drift was not a serious problem. A typical family of *I-V* curves obtained for an MOS structure incorporating an annealed oxide film is shown in Fig. 1. The current is asymmetric with respect to bias polarity and depends strongly on voltage and temperature. Analysis of these data to determine the mechanism for current transport through the oxide are given in the Section on Discussion. *I-V* measurements were not made at temperatures above 150°C owing to an experimental limitation. This limitation has now been overcome, and the results of higher temperature measurements will be reported later.

The properties of the oxide films, as well as those of the GaP oxide interface, were also investigated by capacitance-voltage measurements on the MOS structures. The *C-V* characteristics at 1 mHz for MOS structures on both n- and p-type GaP substrates show accumulation and deep depletion behavior. A typical *C-V* curve at room temperature for an n-type substrate is shown in Fig. 2. The low-frequency dielectric constant calculated from the accumulation capacitance and film thickness is $\epsilon = 5.4$. Surface inversion due to minority carrier generation could not be observed at room temperature using voltage sweep rates (4, 5) as low as 10 mV/sec, unless the sample was illuminated with a tungsten lamp. Pulsed capacitance measurements were made at room temperature in an attempt to determine bulk and surface minority carrier generation rates by using the Zerbst (6) analysis technique. Generation rates on the order of tens of hours were measured. While such slow minority carrier generation is to be expected with wide bandgap semiconductors, additional analysis of the temperature dependence of pulsed capacitance will be required to relate these generation rates to bulk minority carrier lifetimes and surface recombination velocities at the semiconductor-oxide interface.

Ramp measurements (7) were made at 250°C to determine whether the oxide exhibits ionic instabilities similar to those caused by Na or K in SiO_2 (8), which give rise to well-defined ionic current peaks about zero bias in SiO_2-on-Si MOS structures (7). Such peaks were not observed in the present experiments, suggesting that this kind of fast ionic drift does not occur in the oxide on GaP at temperatures below 250°C. In addition, *C-V* curves were measured before and after bias-temperature stress experiments performed at 200°C and ±15V for 30 min. No significant changes in flatband voltage were observed, again suggesting that the oxide is relatively free of mobile ion contamination.

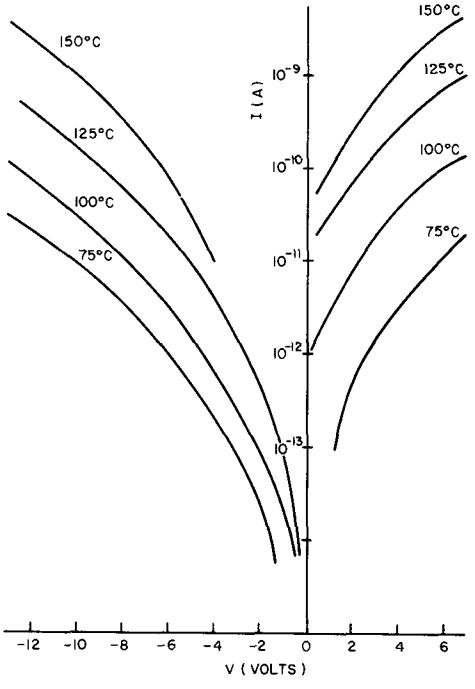

Fig. 1. Current-voltage characteristics of Au-native oxide-GaP structure. Substrate is Te-doped $\approx 3 \times 10^{17}$/cm^3 with a 500Å thick native oxide. (Sample RD269-2E, Table I).

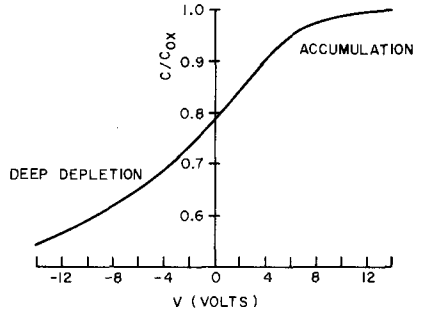

Fig. 2. Capacitance-voltage characteristics of Au-native oxide-GaP structure at room temperature. Oxide capacitance is 112 pF for 15 mil diameter Au field plates. (Sample RD269-2E).

Discussion

Current-voltage characteristics.—Current flow through an insulating oxide can take place by several different conduction mechanisms (9). These mechanisms include ionic conduction, ohmic conduction, tunneling, field emission, and field-enhanced thermionic emission either over an interfacial barrier (Schottky-Richardson mechanism) or from localized coulombic traps in the oxide (Frenkel-Poole mechanism).

In the Section on Electrical Characteristics, the discussion on ionic drift suggests that ionic conduction is not significant here. Furthermore, an ionic current would be expected to decay in time with constant applied bias, but no such decay is observed. Ionic conduction can therefore be eliminated as a significant transport mechanism for these samples.

The nonlinear, asymmetric *I-V* characteristics (Fig. 1) preclude ohmic conduction, and their strong temperature dependence precludes tunneling. The relationship between current and voltage calculated for the Schottky-Richardson (SR) and Frenkel-Pool (FP) (10) mechanisms are given by Eq. [1] and [2], which are quite similar in form, but the barriers are different, *i.e.*, an interfacial barrier and a coulombic potential well, respectively.

$$J_{SR} = A^*T^2 \exp\left[-q(\phi_b - \sqrt{qE/4\pi\epsilon_{ox}})/kT\right] \quad [1]$$

$$J_{FP} = CE \exp\left[-q(\phi_b - \sqrt{qE/\pi\epsilon_{ox}})/kT\right] \quad [2]$$

where A^* = effective Richardson constant, ϕ_b = barrier height, ϵ_{ox} = dielectric constant of oxide, and C = constant, independent of field and temperature. The experimental *I-V* data are consistent with the form of either equation, as shown by the linear plots of *I/V* and *I vs.* $E^{1/2}$ shown in Fig. 3 for one of the MOS structures.

FP emission is a bulk process and would be expected to exhibit symmetric *I-V* characteristics, while the SR mechanism is dependent on the barrier height at the metal-oxide or semiconductor-oxide interface, and the current would then be quite polarity dependent. The observed, asymmetric *I-V* characteristics suggest that conduction occurs via the SR mechanism.

Equations [1] and [2] can be used to obtain alternative values of the high frequency dielectric constant, ϵ_{ox}, from the slopes of the two lines in Fig. 3. Using the SR model (*I vs.* $E^{1/2}$), $\epsilon_{ox} = 5.53$ is calculated, a value one-fourth that determined from the FP model (*I/E vs.* $E^{1/2}$), $\epsilon_{ox} = 22.12$. It is expected that the high frequency value of ϵ_{ox} should approximate $(n)^2$, *i.e.*, 2.5, according to the Maxwell relation. The fact that the calculated ϵ_{ox} for the SR mechanism is closer to the high frequency value than ϵ_{ox} for FP emission, along with the observation that the SR value of ϵ_{ox} is close to the 1 mHz (low frequency) value of ϵ_{ox} as determined from *C-V* data, provides another indication that conduction through the oxide occurs via the SR mechanism.

The effective barrier height (assuming SR) controlling current flow, *i.e.*, the interfacial barrier ϕ_b reduced by the applied electric field due to Schottky lowering, was determined from an Arrhenius plot of ln I/T^2 *vs.* $1/T$ as shown in Fig. 4, at applied electric fields of 2 and 10 $\times$ 10^5 V/cm, by using Eq. [1]. By adding the estimated Schottky lowering, $(qE/4\pi\epsilon_{ox})^{1/2}$, the interfacial barrier was found to be $\phi_b \approx 1.2$ eV (for the sample of Fig. 4) for both positive and negative field polarity. This apparent discrepancy between symmetric barrier height and nonsymmetric *I-V* characteristics is explained in terms of the experimental uncertainty in determining ϕ_b ($\pm$40 meV) and the relatively small difference in barrier heights (5-20 meV) required to produce such *I-V* data. For a barrier height of ~1.2 eV, the incremental room temperature resistivity would be expected to be on the order of 10^{19} ohm-cm. Thus any current measured at room temperature would result from surface leakage or from the measurement instrument.

Capacitance-voltage characteristics.—As discussed in the Section on Electrical Characteristics, the capacitance-voltage characteristics show both accumulation and deep depletion behavior. Deep depletion results from the very long minority carrier generation times, while the more familiar inversion behavior is observed in semiconductors with fast generation rates (Ge, Si, GaAs). The relation between capacitance and voltage for deep depletion (11) is given by

$$(C_{ox}/C)^2 - 1 = (C_{ox}/A)^2 \frac{2}{qN\epsilon_s}(V - V_{fb}) \quad [3]$$

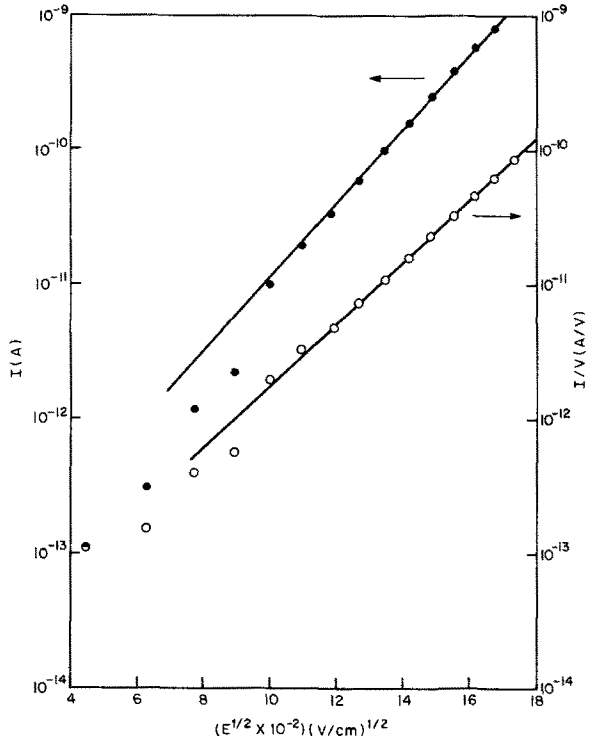

Fig. 3. Plot of *I* and *I/V* vs. $E^{1/2}$ obtained from *I-V* data of Fig. 1 with negative voltage applied to field plate at 125°C.

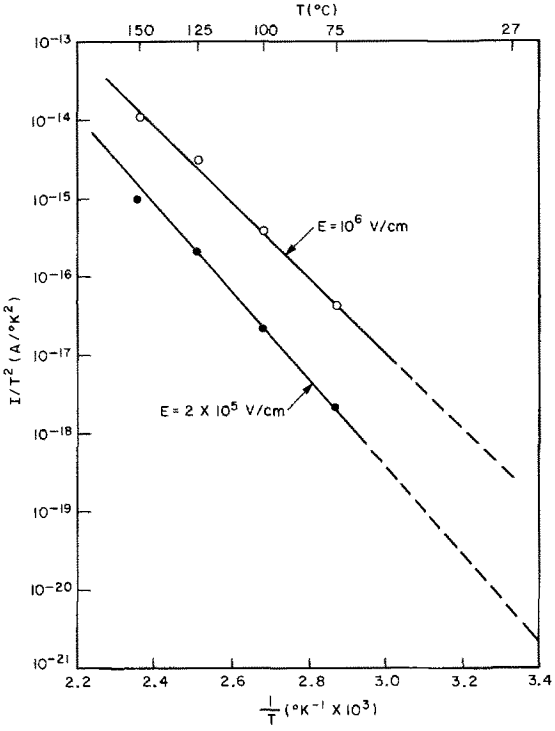

Fig. 4. Plot of I/T^2 vs. $1/T$ obtained from *I-V* data of Fig. 1 with —5V and —1V applied to field plate.

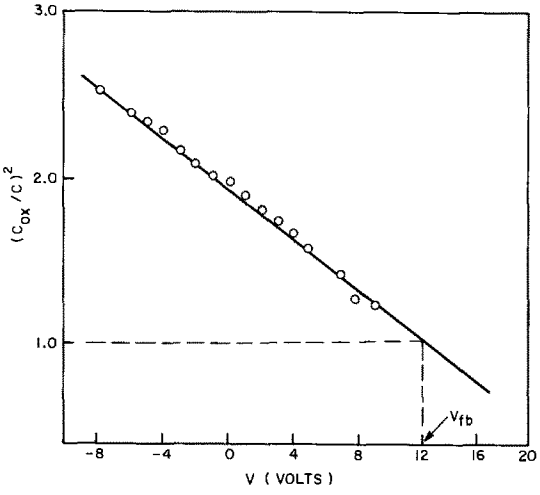

Fig. 5. Plot of $(C_{ox}/C)^2$ vs. V obtained from C-V data of Fig. 2

where C_{ox} = oxide capacitance as determined from MOS capacitance-voltage measurement in the accumulation region, A = field plate area, N = net carrier concentration $|N_D - N_A|$ in the semiconductor, ϵ_s = low-frequency dielectric constant of the semiconductor, and V_{fb} = flatband voltage.

If a plot of $(C_{ox}/C)^2$ *vs.* V is constructed from experimental C-V data, Eq. [3] can be used to obtain values of $|N_D - N_A|$ and V_{fb}. This determination of $|N_D - N_A|$ is independent of Hall data, and thus provides a consistency check. The surface charge density, Q_s, may be calculated from

$$Q_s = CV_{fb}/Aq \qquad [4]$$

A typical plot of $(C_{ox}/C)^2$ *vs.* V for a MOS structure on an n-type GaP substrate (sample RD269-2E, Table I) is shown in Fig. 5. The value of $|N_D - N_A|$ obtained from this plot, $3.17 \times 10^{17}/cm^3$, agrees within 20% with the value determined by Hall measurements on the GaP substrate material. From this plot V_{fb} is found to be 12V, corresponding to a surface charge density, Q_s, of $7 \times 10^{12}/cm^2$. Similar values were found for structures on p-type substrates (see Table I). With such large V_{fb} values, only MOS structures incorporating oxide films with relatively high dielectric breakdown strength can be biased into accumulation. If the breakdown strength is too low, as in films that have not yet been annealed, the devices go into breakdown before accumulation is obtained, making surface-state analysis quite difficult. The similarity in V_{fb} values (with a polarity change) for p- and n-type samples and the constancy of V_{fb} under temperature and bias stress suggest that the rather large surface charge density may be due to interface states rather than to mobile ions or fixed charge. It should be noted that the presence of interface states could influence the polarity dependence of the I-V characteristics. Such effects will be reported in future efforts.

Conclusions

This paper describes the electrical properties of a galvanic native oxide grown on n- and p-type GaP. This oxide is an electrical insulator, having a relative dielectric constant $\epsilon \approx 5.5$, which exhibits a dielectric breakdown strength of $6\text{-}8 \times 10^6$ V/cm after annealing in nitrogen at 250°C. Conduction in MOS structures incorporating the oxide appears to proceed via field-enhanced thermionic emission over a barrier $\phi_b \approx 1.2$V, which is believed to be an interfacial barrier at the oxide-semiconductor interface. A large surface charge density, $Q_s \approx 4\text{-}8 \times 10^{12}/cm^2$, has been found; it is attributed to interface states rather than mobile ion contamination or fixed charge. These initial findings suggest that the native oxide should serve a valuable function in GaP device technology.

Acknowledgments

We are grateful to R. C. Manz, R. A. Furnanage, and A. J. Sayko for sample preparation and oxidation. We wish to thank G. D. Weigle for his help in performing some of the electrical measurements and W. J. Sundburg for measurements of film thickness and index of refraction.

Manuscript submitted July 25, 1972; revised manuscript received Dec. 27, 1972. This was Paper 292 presented at the Miami Beach Meeting of the Society, Oct. 8-13, 1972.

Any discussion of this paper will appear in a Discussion Section to be published in the December 1973 JOURNAL.

REFERENCES

1. B. Schwartz, *This Journal*, **118**, 657 (1971).
2. B. Schwartz and R. C. Manz, Submitted to *This Journal*.
3. B. Schwartz and W. J. Sundburg, *ibid.*, **119**, 241C (1972).
4. R. Castagne, *C. R. Acad. Sci. Paris*, **267**, 886 (1968).
5. M. Kuhn, *Solid-State Electron.*, **13**, 873 (1970).
6. M. Zerbst, *Z. Angew. Phys.*, **22:1**, 30 (1966).
7. M. Kuhn and D. J. Silversmith, *This Journal*, **118**, 966 (1971).
8. E. H. Snow, A. S. Grove, B. E. Deal, and C. T. Sah, *J. Appl. Phys.*, **30**, 1164 (1965).
9. D. R. Lamb, "Electrical Conduction Mechanisms in Thin Insulating Films," Methuen and Co., London (1967).
10. S. M. Sze, "Physics of Semiconductor Devices," pp. 492-501, Wiley-Interscience, New York (1969).
11. A. Goetzberger and E. H. Nicollian, *Appl. Phys. Letters*, **9**, 444 (1966).

Etch Pit Studies of GaP Liquid Phase Epitaxial Layers

G. A. Rozgonyi* and T. Iizuka[1]

Bell Laboratories, Murray Hill, New Jersey 07974

ABSTRACT

In investigations of the influence of defects on the luminescence properties of compound semiconductors, the relative importance of purely structural defects, *e.g.*, dislocations, *vs.* imperfections of a chemical or stoichiometric nature, such as impurities, vacancies, etc., is invariably discussed. Recent photoluminescence studies on GaAs and GaP have shown that dislocations are an important factor only if they are decorated with impurities. For GaP the decorated dislocations only occur when there is also present another type of etch feature called a saucer or S-pit. In the present report further comparisons of dislocations and S-pits are made in GaP material typical of that used in electroluminescent devices made by liquid phase epitaxy (LPE). The etch pit studies on LPE material have been examined in terms of using S-pits as an observable in evaluating the device potential of different LPE layers.

A continuing area of study in semiconductor device materials has been in evaluating the relative importance of purely structural defects, *e.g.*, dislocations, *vs.* imperfections of a chemical or stoichiometric nature, such as impurities, vacancies, etc., or complexes of different types of these defects. This question has arisen often recently by workers describing possible nonradiative recombination centers which affect the electroluminescence (EL) and photoluminescence (PL) efficiencies (η) of GaP liquid phase epitaxial (LPE) layers (1-3) and liquid encapsulated Czochralski (LEC) (4-6) and solution grown (SG) substrates. With the advent of the chemical etch pit-optical microscopy studies first described by Iizuka (7), and subsequently used by Rozgonyi and co-workers (5, 6), it has been possible to differentiate between dislocation, or D-pits, and another type of etch feature which is referred to as a saucer or S-pit. Although the nature of the defect or defect-impurity complex responsible for the formation of the S-pits has not been identified, it has been demonstrated that a reduction in S-pit density can be correlated with improved PL η, while the D-pits play a secondary role in the evaluation of GaP LEC substrates (5, 6). The object of the present report is to make a similar comparison of S- and D-pits in GaP LPE layers and LEC and SG substrates to see if the correlation with EL η is the same. Thus, by using the S-pits as an observable in characterizing the luminescence behavior of GaP, further information about the possible behavior of nonradiative centers will be described.

Experimental Procedures and Etch Pit Characteristics

The samples used in this study consisted of LPE layers grown by Saul (8) on the $(\bar{1}\bar{1}\bar{1})$ P-face of LEC substrates pulled by Nygren *et al.* (9), or on SG platelets provided by L. Derick. Both n (Te-doped) and p (Zn, O doped) type layers and substrates were examined. Initially, all the optical studies were performed on $(\bar{1}\bar{1}\bar{1})$ P-surfaces which had been chemically polished. However, angle lapping at 2° to the $(\bar{1}\bar{1}\bar{1})$ P-face was later found to be more advantageous since the layer and substrate could be studied simultaneously on the same sample. Damage due to lapping was removed by etching the sample for 30 sec in chlorine-saturated methanol prior to the actual pit delineation etch. The etching solutions used were the same as those previously described by Saul (10) and by Iizuka (7). Table I describes the solutions, etching times, and temperatures, and range of applicability of each etch. The AB and RC designations are used since these solutions are modifications of etches originated by Richards and Crocker (11) and Abrahams and Buiocchi (12). Examination of the etch pits was carried out in a Zeiss interference contrast microscope, and occasionally in a scanning electron microscope (SEM).

Table I. Etching solutions used for delineating S- and D-pits in GaP

Etch, Ref.	Solution	Temp and Time	Comments
RC, Ref. (11)	8 ml H_2O, 4 ml HF, 6 ml HNO_3, 10 mg $AgNO_3$	4 min at 65°C	Can be used on $(\bar{1}\bar{1}\bar{1})$ P face of either p- or n-type GaP
Ref. (10), (12)	10 ml H_2O, 8 ml HF, 5g CrO_3, 40 mg $AgNO_3$	50 min at 65°C	Best for $(\bar{1}\bar{1}\bar{1})$ P face of p-type material, or for delineating dislocation grooves on $(1\bar{1}0)$ cleavage faces of both p- or n-type GaP

The difference between S- and D-pits is illustrated in Fig. 1. The identification of the pits is quite straightforward, D-pits have an apex or point and tend toward a triangular shape typical of {111} surfaces, while S-pits are shallow, round, and flat-bottomed, see arrows D and S in the optical photomicrograph shown in Fig. 1a. The D-pits are generally ~10μ in diameter while the S-pits vary in size from ~1μ to slightly less than the size of the D-pits. Figure 1b is an SEM

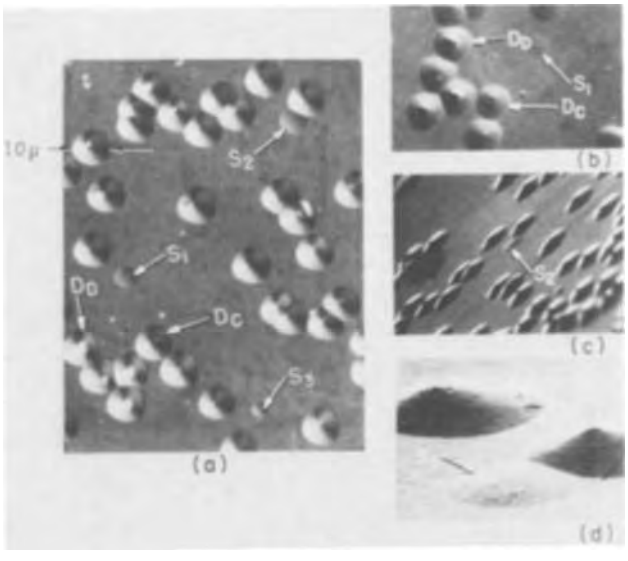

Fig. 1. Identification of saucer and dislocation pits in a GaP LPE layer. (a) Optical photomicrograph illustrating S-pits, see arrows S, and clean and decorated D-pits, D_c and D_d, respectively. (b) SEM photo with field of Fig. 1a rotated ~60° clockwise. Incident beam ~80° to surface. (c) SEM photo of S_2 with incident beam ~10° to surface. (d) Higher magnification SEM view of S_2.

* Electrochemical Society Active Member.
[1] Present address: Electrotechnical Laboratory, Tokyo, Japan.
Key words: defects, III-V compounds, electroluminescence.

photomicrograph of the same area taken at an incident beam angle of ~80° to the surface. Note that because the S-pits are shallow and the local secondary electron yield does not differ from the host crystal the contrast at the S-pits is very poor. However, using an incident beam angle of ~10° shadows the pits quite nicely as shown in Fig. 1c and d. Actually, the SEM photographs do not give any more information about the S-pits than can be obtained with interference contrast microscopy. However, the SEM does enable us to look inside the D-pits. It has, therefore, been possible to distinguish between what we have designated as a clean D-pit, *i.e.*, one that has smooth sides and undergoes no geometric discontinuities from the edge of the pit down its walls to the apex, see arrows D_C; and a decorated D-pit, see arrows D_D for the somewhat knobby and irregular appearance of decorated D-pits. It has been shown (6) that decorated D-pits are generally found in material containing a high density of S-pits, while clean D-pits occur when the S-pits are reduced or eliminated. These simple etch features will now be compared in GaP material typical of that used to fabricate red-emitting EL diodes.

Experimental Results

N-type LEC substrates and LPE layers.—The results of the etch pit analysis of an LEC substrate, tellurium doped to 3×10^{17} cm^{-3}, are presented in Fig. 2a. Three classes of surface features are to be found in this photomicrograph; they are: (*i*) a moderately high ($\sim 1 \times 10^5$ cm^{-2}) density of deep, tripyramidal-shaped, decorated dislocation etch pits, see arrows D, (*ii*) a high density (greater than 1×10^7 cm^{-2}) of shallow, flat-bottomed, saucer-shaped etch pits, see arrow S, and, (*iii*) regions surrounding D-pits which are denuded of S-pits, presumably due to depletion of impurities by incorporation into nearby dislocations (5, 7).

Figure 2b is the etched surface of an LPE layer grown on a substrate from an adjacent wafer of the same LEC ingot shown in Fig. 2a. The LPE layer was n-type, tellurium doped to $\sim 1 \times 10^{18}$ cm^{-3} at its outer surface. Note that the density of S-pits has been reduced by three orders of magnitude compared to that in the substrate. In addition, a comparison of the D-pits in Fig. 2a and b shows that the pits in the LPE layer are definitely of the clean variety. Of the more than 20 n-type LPE layers examined the great majority had an S-pit density of $\sim 1 \times 10^3$ cm^{-2}, however, several had a zero or vanishingly small number of S-pits. Note that the S-pit density in the LPE layer has been reduced even though the tellurium concentration was increased by a factor of three or four over that in the LEC substrate. This is to be contrasted to the results of Iizuka (7) who studied n-type LEC substrate material and found that the S-pit density was reduced only in undoped LEC samples.

P-type LEC substrates and LPE layers.—The etch pits typical of zinc-oxygen doped p-type LEC material with a carrier concentration of $\sim 1 \times 10^{18}$ cm^{-3} is shown in Fig. 3a. Whereas the S-pit density in n-type LEC substrates was always greater than 1×10^7 cm^{-2} the p-type material varied from 1×10^5 to $\sim 2 \times 10^7$

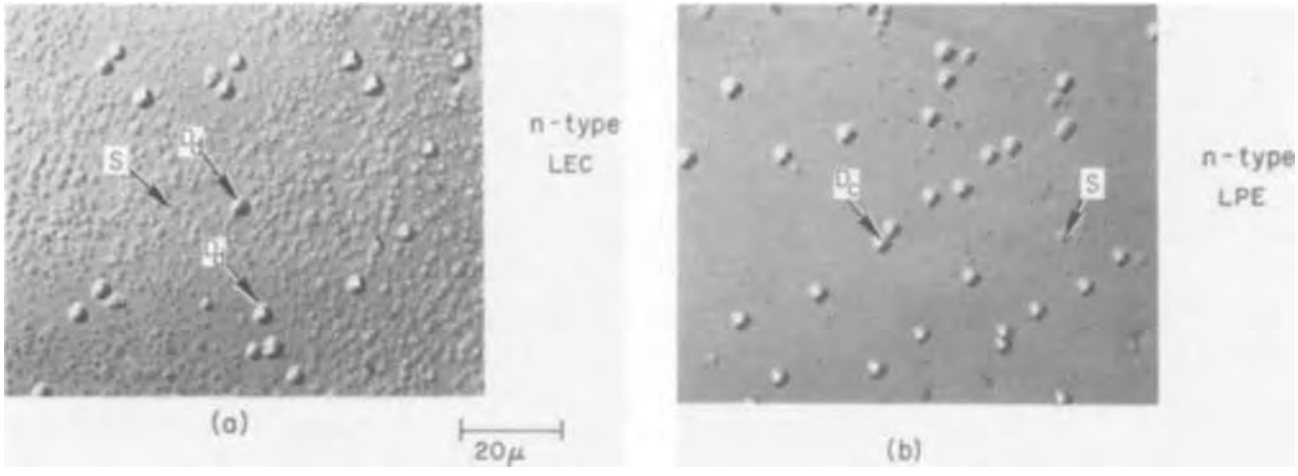

Fig. 2. Optical photomicrographs of S- and D-pits in n-type (a) LEC substrate with $|N_D\text{-}N_A| \simeq 2\times10^{17}$ cm^{-3}, and (b) LPE layer with $|N_D\text{-}N_A| \simeq 1\times10^{18}$ cm^{-3}.

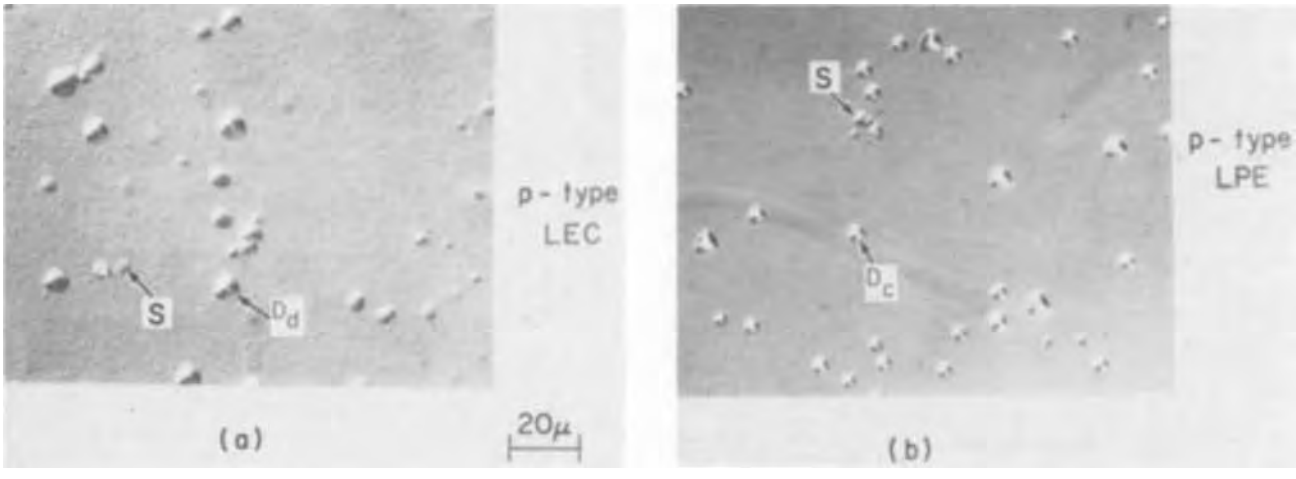

Fig. 3. Optical photomicrographs of S- and D-pits in p-type (a) LEC substrate with $|N_D\text{-}N_A| \simeq 2\times10^{17}$ cm^{-3}, and (b) LPE layer with $|N_D\text{-}N_A| \simeq 2\times10^{17}$ cm^{-3}.

cm^{-2}. Again, the D-pits are of the decorated variety and occur at a density of $\sim 1 \times 10^5$ cm^{-2}.

For p-type LPE layers very smooth and clean looking D-pits are found, see arrow D in Fig. 3b, while the S-pit density is reduced to zero. A zero S-pit density was always observed in p-type LPE layers unless there were inclusions or some other growth anomaly. The layer in Fig. 3b was (Zn,O) doped to $\sim 2 \times 10^{17}$ cm^{-3} and grown on the n-type LEC substrate shown in Fig. 2a.

Another aspect of the etched p-type material, both substrates and layers, was a generally rough or coarse texture of the surface between the different etch pits. This background feature is uniformly distributed and does not appear to be depleted in the vicinity of dislocation etch pits. Whether these features are related to a unique type of crystal defect has not been established. It should be noted, however, that in certain LEC crystals pulled from nonstoichiometric melts (6) which have high PL η, a very smooth background surface is obtained. In the present report we limit our discussion of p-type material to the previously identified S- and D-pits.

P-type LPE layers on n-type SG substrates.—The materials system which has consistently yielded electroluminescent diodes with the highest efficiencies is one consisting of a p-type LPE layer grown on an n-type SG substrate (1, 8). If the S-pits were playing an active role in the electroluminescence process we would expect their density to be a minimum for this material. This was, in fact, found to be the case as can be seen in the two optical photomicrographs shown in Fig. 4. These should be compared to the p-type LPE layer/n-type LEC substrate combination shown in Fig. 2a and 3b. It was not possible to locate any etch feature which could be identified as an S-pit in the LPE layer, Fig. 4b or in the SG substrate, Fig. 4a.

Note that the dislocation etch pit density of the LPE layer was as high as 3×10^5 cm^{-2}, which is more than three orders of magnitude higher than that in the SG substrate on which the LPE layer was grown. This large increase in structural, *i.e.*, purely geometric, defect density actually puts the LPE layers grown on LEC or SG substrates, see Fig. 2b and 3b, at the same level. However, they differ considerably in terms of chemical, *i.e.*, impurity, vacancy, etc., defect density as determined by the saucer etch pit counts. The approximate range of D- and S-pits in these two samples is given in Table II along with data on the relative device performance, which is discussed in the next section.

Relative electroluminescence efficiencies.—Electroluminescence data on red-emitting p-n junctions fabricated from adjacent pieces of the samples discussed in Fig. 2b and 3b are presented in Table II along with etch pit data. Three LPE layer-substrate combinations have been evaluated. They are the p/n (LEC), p/n (SG), and n/n (LEC), *i.e.*, the buffer layer

Table II. Etch pit and device efficiency data for GaP LPE layers and LEC substrates

Surface	Property $\lvert N_D - N_A \rvert$* (cm^{-3})	D-pit density (cm^{-2})	S-pit density (cm^{-2})	Diode efficiency** (%)
P-type LPE layer (Fig. 2b)	2×10^{17}	5×10^3-5×10^5	0-100	0.35
N-type LEC substrate (Fig. 1a)	3×10^7	1×10^4-1×10^6	1×10^7	0.35
P-type LPE layer (Fig. 3b)	2×10^{17}	5×10^3-3×10^5	0	1.4
N-type SG substrate (Fig. 3a)	8×10^{17}	0-100		1.4
N-type LPE layer (Fig. 1b) on	1×10^{18}	5×10^3-5×10^5	0-1×10^4	Not applicable
N-type LEC substrate (Fig. 1a)	3×10^{17}	1×10^4-1×10^6	1×10^7	Not applicable

* Schottky barrier measurement at outer surface.
** Average peak external quantum efficiency of point contacted, unencapsulated red-emitting mesa diodes.

situation. First, we note that the range of D-pit densities is approximately the same in all the layers and is a factor of two to five below that in the LEC substrate material. This reduction in D-pit density is typical of that previously reported for III-V LPE systems (13, 14), but is in marked contrast to the many orders of magnitude difference in the S-pit density for both n- and p-LPE/LEC substrates. Recall also that the D-pits were of the clean variety once the S-pit density was reduced, indicating that it is the crystal defect responsible for the formation of S-pits that is of main concern and not the dislocations. This is confirmed by comparing the peak external quantum efficiencies of point contacted unencapsulated diodes shown in Table II for the p-type LPE layers on LEC and SG substrates. The factor of four difference in efficiency is typical of that previously reported (1) for single LPE layers grown on LEC or SG substrates, while the absolute values are within a factor of two of data typical of "single tipped" material.

It should be noted that if a p-type LPE layer is grown on an n-type buffer layer, thereby moving the p/n junction away from the high S-pit density LEC substrate, then the EL η jumps a factor of three or four and is comparable to devices fabricated on SG substrates. This "double tipping" approach is what is almost universally used in GaP light emitting diode technology. For these p/n/n structures the LEC substrate functions as a large area "breadboard" for the active p/n device which consists of two LPE layers.

Analysis of angle lapped LPE junctions.—In discussing the D- and S-pit densities in EL device material it was shown that "double tipping," or moving the active p/n junction away from a region of high S-pit density, *i.e.*, the LEC substrate, results in improved EL η. In this section an example will be given of how the S-pits can be used as an observable in the evalua-

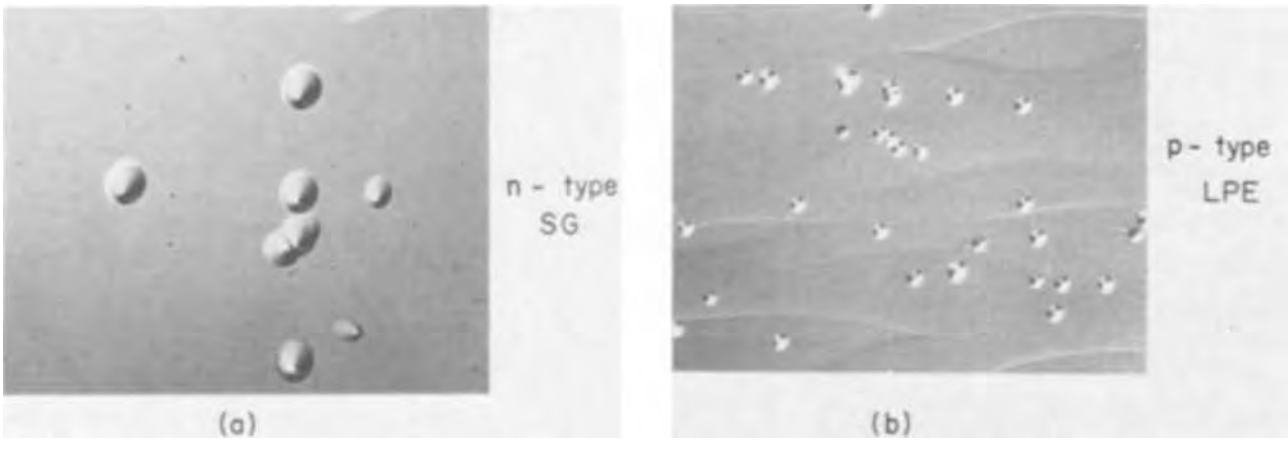

Fig. 4. Optical photomicrographs of D-pits in (a) n-type SG substrate, and (b) p-type LPE layer grown on SG substrate

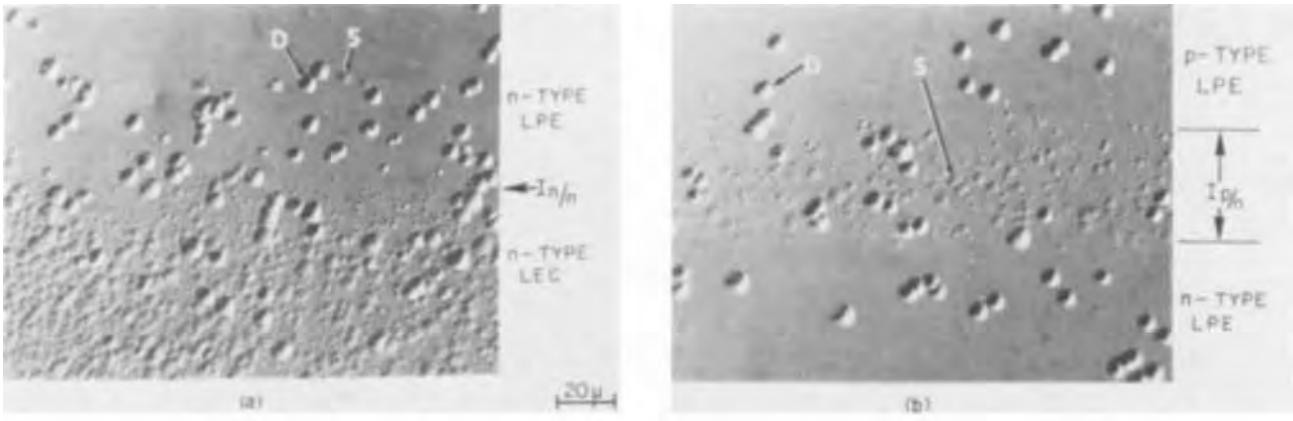

Fig. 5. Optical photomicrographs of angle-lapped sample showing (a) abrupt reduction in S-pit density at LEC substrate-LPE layer interface, $I_{n/n}$, and (b) band of S-pits localized at LPE p/n junction interface, $I_{p/n}$.

tion of p/n junctions where the junction lies between two LPE layers. For junction or interface studies it has been found that angle lapping the sample at ~2° to the $(\bar{1}\bar{1}\bar{1})$ P growth face, which enhances the depth resolution by a factor of ~30, provides an extremely useful approach to this problem. The delineation of the two interfaces on a double tipped p/n/n sample is shown in Fig. 5. The previously described reduction in S-pit density on going from an LEC substrate to an LPE layer is shown in Fig. 5a.[2] The transition is extremely abrupt and occurs within a thickness of ~1μ. A simultaneous change in the character (but not necessarily the density) of the D-pits occurs and they assume a smooth, clean appearance. The n-type LPE layer is then quite uniform until the interface with the p-type LPE layer is reached, see $I_{p/n}$ in Fig. 5b. At this point a localized band of S-pits is observed at a density of $\sim 1 \times 10^6$ cm^{-2}. The p-type layer then immediately reverts to a zero S-pit density situation. Localized bands of S-pits at p/n junction interfaces have only been observed in material which yields very poor EL device efficiencies. Similar results have been recently described by Asao and Akasaki (20) who found that the η of vapor grown LED's depends primarily on the S-pit density at the p/n junction.

The occurrence of interfacial layers containing high concentrations of residual impurities at GaAs epi-substrate junctions has recently been described by DiLorenzo *et al.* (15). Using an ion-probe mass analyzer with imaging capabilities, in conjunction with a depth profile of the active device carrier concentration, they demonstrated that a correlation exists between the occurrence of a high resistivity, or *i*-layer, and the presence of impurity contamination, most notably silicon, which was highly localized at the epi-substrate interface. Subsequent work by DiLorenzo (16), also on GaAs, gave procedures for reducing or eliminating the localized impurities by a combination of careful substrate cleaning, *in situ* vapor etching, and the growth of a "buffer" layer of epi-GaAs.

Cleavage face analysis of D- and S-pits.—In the etch pit data presented above we have assumed that the S-pits were not associated with the emergence of a dislocation line at the sample surface, but could be used to characterize the presence of an impurity or defect-impurity complex. Because of the importance of this assumption in our subsequent discussion, additional work on the nature of the D- and S-pits was carried out. Specifically, a p-type LEC crystal with isolated D- and S-pits was cleaved and examined at the intersection of the cleavage edge and the isolated pits. In this way, it was possible to examine the defect in-depth, first by identifying either a D- or S-pit on the $(\bar{1}\bar{1}\bar{1})$ P face, and then looking around the corner of the sample down the cleavage face. Although chemical etchants do not reveal individual dislocation pits on the {110} cleavage faces of GaP, Iizuka has shown (6) that etch grooves corresponding to dislocation line segments are revealed by the AB etching solution described in Table I.

The results of this type of analysis are shown in Fig. 6 which gives two composite photomicrographs of adjacent regions on a $(\bar{1}\bar{1}\bar{1})$ P surface and $(01\bar{1})$ cleavage face. Note that the S-pits, designated by the arrows S in Fig. 6a, are only revealed by a very slight depression on the matching $(01\bar{1})$ cleavage face, as shown by the arrows S' in Fig. 6a. However, the dislocation etch pit in Fig. 6b has a deep, sharply faceted profile with a dislocation etch groove, see arrow DG, extending from the apex of the pit on down the cleavage face. It was found that each D-pit which was intercepted by the cleavage has a corresponding $(01\bar{1})$ dislocation groove associated with it. Therefore, we can conclude that the crystal imperfection responsible for S-pit formation is not linear in extent, but is associated with a defect that perturbs the crystal in a limited volume with a spherical or possibly disk-shaped symmetry.

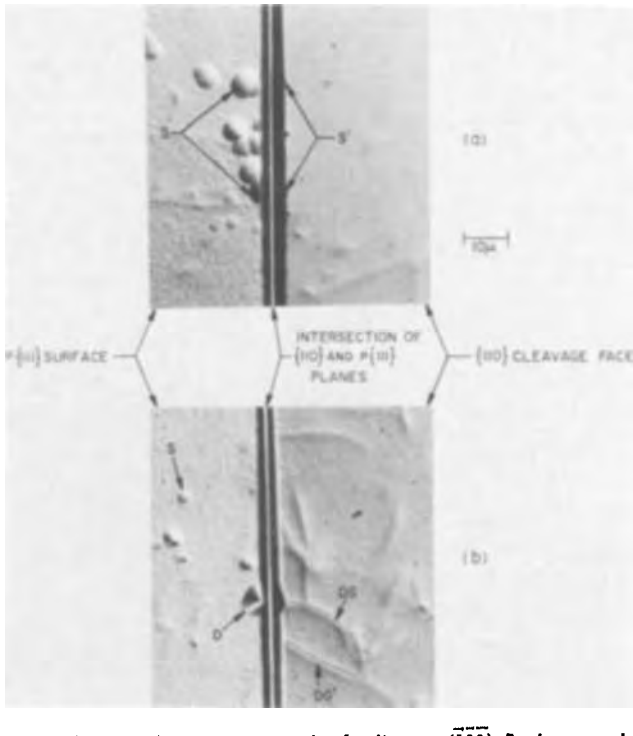

Fig. 6. Optical photomicrograph of adjacent $(\bar{1}\bar{1}\bar{1})$ P planes and {110} cleavage face showing (a) S-pits, and (b) D-pits and dislocation grooves.

[2] The lower half of this figure is labeled (a) in order to retain the actual sequence of substrate-layer growth.

Note that in Fig. 6b there were several dislocation grooves, see arrow DG', which appeared to terminate at the surface without the appearance of a D-pit. The failure of a D-pit to be revealed at the point of emergence of a dislocation line on the $(\bar{1}\bar{1}\bar{1})$ P surface could be related to whether the dislocation is of the α-(Ga) or β-(P) variety as described by Haasen (17). Abrahams and Buiocchi (12) have previously shown that for {111} surfaces of GaAs their etch will only reveal β-(As) type dislocations, unless the dislocations are decorated with an impurity. Similar behavior for GaP would help explain the observations shown in Fig. 6b. However, since it has previously been established that the D-pits in doped GaP LEC crystals are mainly of the decorated variety, see Fig. 2a and 3a, there appears to be an additional factor involved in the GaP case.

Discussion of Results

In discussing the etch pit observations on LPE layers presented above, along with the complementary information previously obtained by photoluminescence mapping (5) of LEC substrates pulled from stoichiometric melts and by etch pit comparisons on LEC material pulled from nonstoichiometric melts (6) several definite conclusions can be made about the nature of the S-pits and their ability to classify that material which is best for EL devices. For example, in dealing with the possible effects of dislocations on EL and PL (5) device performance, it has been shown that dislocations, by themselves, are of secondary importance in correlating luminescence efficiency. However, decorated dislocations, which only occur when there is a corresponding high density of S-pits, can be a significant factor. Similar conclusions have been arrived at by Stringfellow and Green (18) for defects in Ga(As, P). In addition to the association of S-pits with decorated dislocations, it has been found that very localized, high density layers of S-pits occur at p/n junction interfaces of material with poor device performance. These observations are consistent with ion probe mass analysis results on GaAs (15, 16) which have revealed the presence of high resistivity impurity layers at epi-substrate interfaces. Preliminary ion-probe studies on GaP (19) indicate that the interfacial impurity problem is very similar to that in GaAs and in fact the "buffer" layer approach used by DiLorenzo is somewhat equivalent to "double tipping" in LPE growth. However, in the vapor phase epitaxial system used by DiLorenzo the final active device layer was immediately grown on the "buffer" layer, whereas in LPE systems the p-and n-layer growth are usually separate procedures. Therefore, the elimination of *i*-layers, interfacial impurities, and ultimately S-pits at GaP p/n junctions is expected to be a more difficult procedure than it was in GaAs vapor growth.

Although we have de-emphasized the importance of dislocations and implied that an impurity is at least partly responsible for the formation of S-pits it should be noted that the dopant itself, *e.g.*, tellurium or zinc, does not appear to be a dominant factor. This is supported by the fact that the density of S-pits in tellurium-doped LPE layers is greatly reduced even though the doping level is usually a factor of four higher than that in the substrate. Iizuka (7) had previously attributed a decrease in S-pit density in certain undoped substrates to the lower doping level. However, it now appears that if Te is involved it is most likely either associated with another element, *e.g.*, Si, O, C, or B, or possibly with a native defect such as a Ga vacancy (4), or a small structural defect like a dislocation loop. Since the LPE growth temperature (as well as that for SG platelets and certain LEC crystals pulled from nonstoichiometric melts), is several hundred degrees below that of the LEC substrates it is very likely that all three possibilities, *i.e.*, impurity incorporation, defect chemistry, and dislocation mechanics, will have to be considered in finding the origin of the S-pits in LEC substrates. Although the problem of a positive identification of the imperfection responsible for formation of S-pits in GaP is not an insurmountable one, it appears that analytic tools more powerful and versatile than the optical microscope will most certainly have to be used. Foremost among these would be the transmission electron microscope for structural and precipitation information, and the direct imaging ion-probe mass analyzer for chemical identification.

In terms of using the S-pits as an observable in evaluating GaP EL material two important points are to be stressed. The first is that moving the active p/n junction away from a substrate containing a high density of S-pits, *i.e.*, double tipping; or tipping directly on substrates with low or zero S-pit density, *i.e.*, SG or LEC pulled from a nonstoichiometric melt (6), produces superior device material. Second, maintaining proper processing conditions such that interfacial layers of S-pits are not present also leads to improved device results.

Summary

The results of the above discussion can be summarized as follows:

(*i*) The dislocation density is of secondary importance when comparing the luminescence η of LPE layers with other layers or with SG and LEC crystals,

(*ii*) The association of S-pits with the presence of decorated dislocations, and with *i*-layers at p-n junction interfaces indicates that the S-pit formation mechanism is associated with some form of impurity precipitation, or defect-impurity complex,

(*iii*) The η of EL devices is considerably improved if the active p/n junction is removed from a substrate containing a high density of S-pits,

(*iv*) Conversely, the presence of a band of S-pits at the interface of an otherwise S-pit free p/n LPE layer device results in reduced EL η,

Acknowledgments

The authors would like to thank R. H. Saul for providing the LPE layers and EL device η data, G. W. Kammlott for the SEM photos, T. J. Ciesielka and F. A. Thiel for assistance with the angle lapping and optical microscopy, and R. B. Marcus for comments on the manuscript. S. E. Haszko also participated in some of the early optical microscopy work.

Manuscript submitted Oct. 26, 1972; revised manuscript received Dec. 21, 1972. This was Paper 86 at the Washington, D. C., Meeting of the Society, May 9-13, 1971.

Any discussion of this paper will appear in a Discussion Section to be published in the December 1973 JOURNAL.

REFERENCES

1. W. H. Hackett, Jr., R. H. Saul, H. W. Verleur, and S. J. Bass, *Appl. Phys. Letters*, **16**, 477 (1970).
2. I. Ladany, S. H. McFarlane, and S. J. Bass, *J. Appl. Phys.*, **40**, 4984 (1969).
3. A. Calverly and D. R. Wight, *Solid State Electron.*, **13**, 382 (1970).
4. A. S. Jordan, R. Caruso, A. R. Von Neida, and M. DiDomenico, *Appl. Phys. Letters*, **19**, 394 (1971).
5. G. A. Rozgonyi and Martin Afromowitz, *ibid.*, **19**, 153 (1971).
6. G. A. Rozgonyi, A. R. Von Neida, T. Iizuka, and S. E. Haszko, *J. Appl. Phys.*, **43**, 3141 (1972).
7. T. Iizuka, *This Journal*, **118**, 1190 (1971).
8. R. H. Saul, J. Armstrong, and W. H. Hackett, Jr., *Appl. Phys. Letters*, **15**, 229 (1969).
9. S. F. Nygren, C. M. Ringel, and H. W. Verleur, *This Journal*, **118**, 306 (1970).
10. R. H. Saul, *ibid.*, **115**, 1184 (1968).
11. J. L. Richards and A. J. Crocker, *J. Appl. Phys.*, **31**, 611 (1960).
12. M. A. Abrahams and C. J. Buiocchi, *ibid.*, **36**, 2855 (1965).
13. G. A. Rozgonyi and S. E. Haszko, *This Journal*, **117**, 1162 (1970).
14. R. H. Saul, *ibid.*, **118**, 793 (1971); M. Weinstein *et al.*, *J. Appl. Phys.*, **38**, 2913 (1967).
15. J. V. DiLorenzo, R. B. Marcus, and R. Lewis, *J.*

Appl. Phys., **42**, 729 (1971).
16. J. V. DiLorenzo, *This Journal*, **118**, 1645 (1971).
17. P. Haasen, *Acta Met.*, **5**, 598 (1957).
18. G. Stringfellow and P. Green, *J. Appl. Phys.*, **40**, 502 (1969).
19. R. L. Hartman, Unpublished data.
20. I. Asao and I. Akasaki, *This Journal*, **119**, 235C (1972).

Defects in Garnet Substrates and Epitaxial Magnetic Garnet Films Revealed by Phosphoric Acid Etching

D. C. Miller

Bell Laboratories, Murray Hill, New Jersey 07974

ABSTRACT

Phosphoric acid between 140° and 170°C has been used to reveal strain and chemical heterogeneities in nonmagnetic garnet substrates and magnetic garnet epitaxial films, principally $Gd_3Ga_5O_{12}$ and $Y_1Gd_1Tm_1Ga_{0.8}Fe_{4.2}O_{12}$, respectively. Dislocations, growth striations, and residual polishing damage have all been observed. Dislocations perpendicular to the film-substrate interface in (111) films were shown to be generated by inclusions whether at the interface or in the interior of the film. Dislocations in the substrate will also propagate into the layer. Interface or misfit dislocations were not observed either by etching or x-ray transmission and reflection topography.

Magnetic garnet films grown by liquid phase epitaxy (1-3) on nonmagnetic garnet substrates (4,5) must be essentially free of crystalline defects to be suitable for use in magnetic bubble domain devices (6, 7). To aid in the defect analysis of both the rare earth gallium garnet substrates and rare earth iron garnet films, an etchant was sought in which the dissolution rate of the garnets would be altered by the presence of strain and chemical heterogeneities such as dislocations and growth striations, respectively. Since phosphoric acid has been used successfully to chemically polish a number of other oxide single crystals at high temperatures (8-11) it seemed likely that it could also be used to etch the rare earth gallium and iron garnets selectively at lower temperatures, and this proved to be true. Many other etchants were investigated including phosphoric-sulfuric acid mixtures, and phosphoric acid containing chrome trioxide, potassium permanganate, and other additions. Some of these mixtures had higher etch rates, but none had any advantage over pure orthophosphoric acid (H_3PO_4) between 140° and 170°C, which was used throughout this investigation. Polarized light microscopy and x-ray reflection and transmission topography were used to verify the results of the etching experiments.

Experimental

Commercial 85% orthophosphoric acid with an initial density of 1.68 g/cm^3 was used for all of the etching experiments reported here. The acid was contained in platinum beakers. However, below about 200°C Teflon and Pyrex (which dissolves at the rate of approximately 0.05 μm/min at 150°C) may also be used. Specimens were held with Teflon forceps.

Samples to be etched for defects were dipped directly into the acid at 165°C for 1-15 min depending on the size of features desired and the composition of the material. The acid bath temperature was monitored with a platinum-encased Chromel-Alumel thermocouple immersed in the bath. Control of the bath temperature to within ±3° is adequate for defect delineation. Very large specimens such as whole boules were preheated to avoid the possibility of cracking due to thermally induced stresses. Following etching, the samples were quenched in heavy oil at 70°C to reduce thermal shock, then dipped in consecutive hot Alconox solutions, the first containing about 15 w/o (weight per cent) KOH to aid in neutralizing any acid remaining on the specimens. The specimens were then rinsed in distilled water and blown dry.

Key words: growth striations, topography, polishing damage.

Etch Pits

The etch rate of the garnet in phosphoric acid in the 140°-170°C temperature range is extremely sensitive to the presence of strain and chemical heterogeneities in the crystals and is edge preserving. Variations in the acid composition which occur on heating affect the etch rate (12) but do not change the etching characteristics of the acid, which remains selective up to about 270°-280°C. Therefore, the shape of pits that are formed due to the presence of inclusions or dislocations will enlarge as etching continues while maintaining their over-all initial shape even though the cause of the pit, such as an inclusion, has been etched away. This has been found to be the case with all orientations and a number of the rare earth gallium and iron garnets including solid solutions, although the pit shapes and rates of formation differ. Most of the garnet films now being produced are grown on $Gd_3Ga_5O_{12}$ {111} surfaces and thus most of the data reported here is for this material and orientation, but the techniques apply equally well to other compositions and orientations.

On {111} surfaces, pits formed in the presence of strain fields, which were detected using birefringence prior to etching, have six sides with over-all three-fold symmetry, while those formed without observable strain fields are purely triangular. This is illustrated in Fig. 1. None of these pits are dislocation etch pits. All have been generated due to the intersection of an inclusion (or possibly a void) with the surface. Dirt on the substrate may also cause this type of pit if it reacts with or becomes firmly bonded to the surface. The pit with six sides was caused by an inclusion with a strain field and has the same shape as a dislocation etch pit. However, the strained inclusion pit has a flat bottom. Upon further etching this pit will enlarge while maintaining the same cross-sectional shape near its intersection with the surface even though the strain field had been etched away. The bottom will remain flat or assume a triangular morphology as in the case of a pit formed in the absence of a strain field.

Dislocation etch pits, however, will continue to deepen on further etching, maintaining a sharp pointed tip, and thus if there is doubt about whether pits are caused by dislocations or inclusions with strain fields, continued etching will enable the two to be distin-

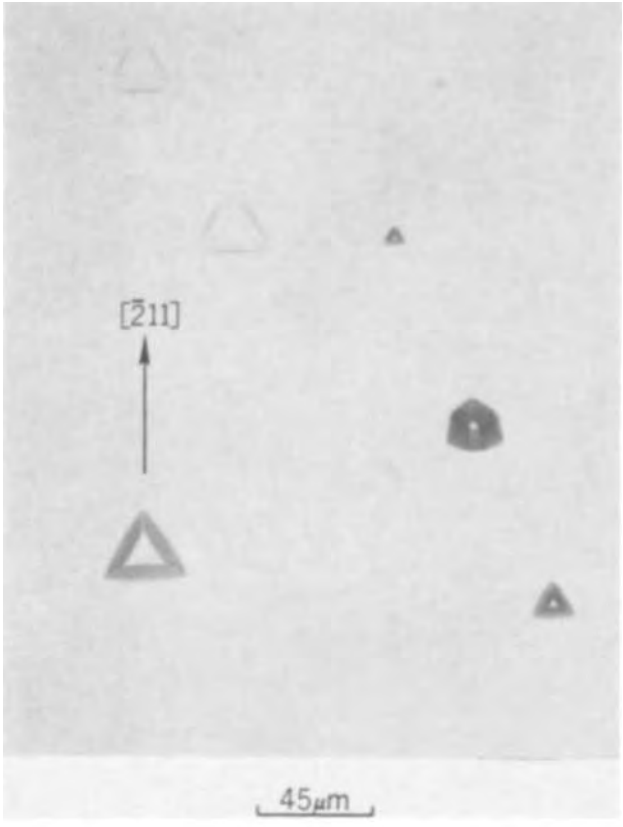

Fig. 1. Etch pits produced by phosphoric acid at 165°C in 10 min on the (111) surface of $Gd_3Ga_5O_{12}$.

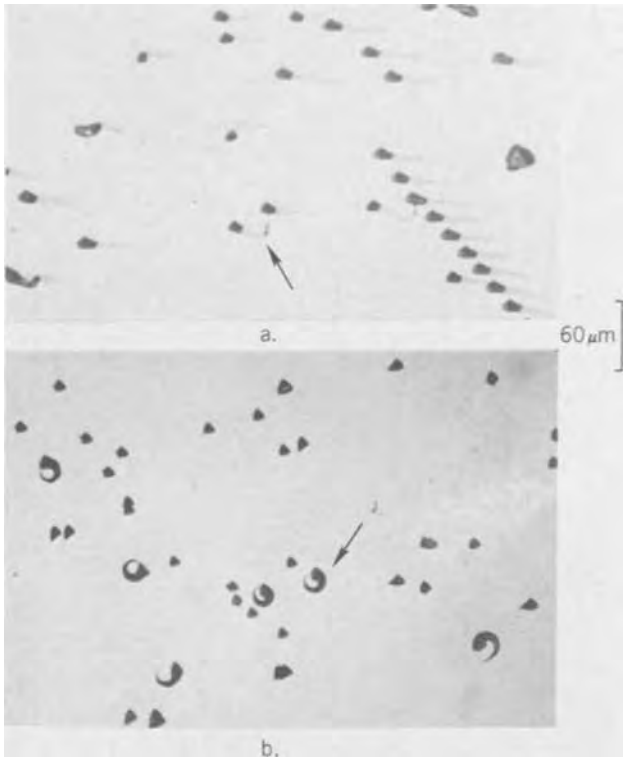

Fig. 2. Dislocation etch pits on the (111) surface of $Gd_3Ga_5O_{12}$ produced by phosphoric acid at 165°C in 10 min.

guished. Roughly 15 min in H_3PO_4, at 165°C, is sufficient time to develop pits easily visible under 200X magnification. Dislocation pits formed in the (111) surface of a $Gd_3Ga_5O_{12}$ substrate are shown in Fig. 2. The extraordinary length of the pits can be used to determine the orientation of the dislocations. Their paths as well as Burgers vectors can also be determined using birefringence in the case of edge dislocations, but pure screw dislocations cannot be seen in this way (13-15). In the $Gd_3Ga_5O_{12}$ boule of which a slice is shown in Fig. 2, roughly 15% of the dislocations present are of the spiral type denoted by the arrows, and these dislocations are not visible when viewed between crossed polarizers. The Burgers vectors of the edge dislocations in $Gd_3Ga_5O_{12}$ determined using birefringence appeared to be similar to those observed in $Y_3Al_5O_{12}$ (15) (i.e., a/2<111>, a<100>, and a<110>) and all appeared to etch in the same way. No preferred orientation of the dislocations has been observed.

Having determined the shape of pits formed by various defects, the etching technique can now be used to analyze more complicated types of defects, a great variety of which occur in the garnet crystals. For example, two different variations of a type observed in some garnet boules whose analysis is aided by the use of phosphoric acid are shown between crossed polarizers in Fig. 3a and b. Both appear to consist of an inclusion, perhaps a post-growth precipitate, surrounded by dislocation loops. Normally, inclusions which generate enough stresses to cause plastic deformation punch out small loops of the order of the particle size (16). However, in this case the dislocation loops appear to surround the central inclusion, with the planes of the loops inclined to the (111) surface.

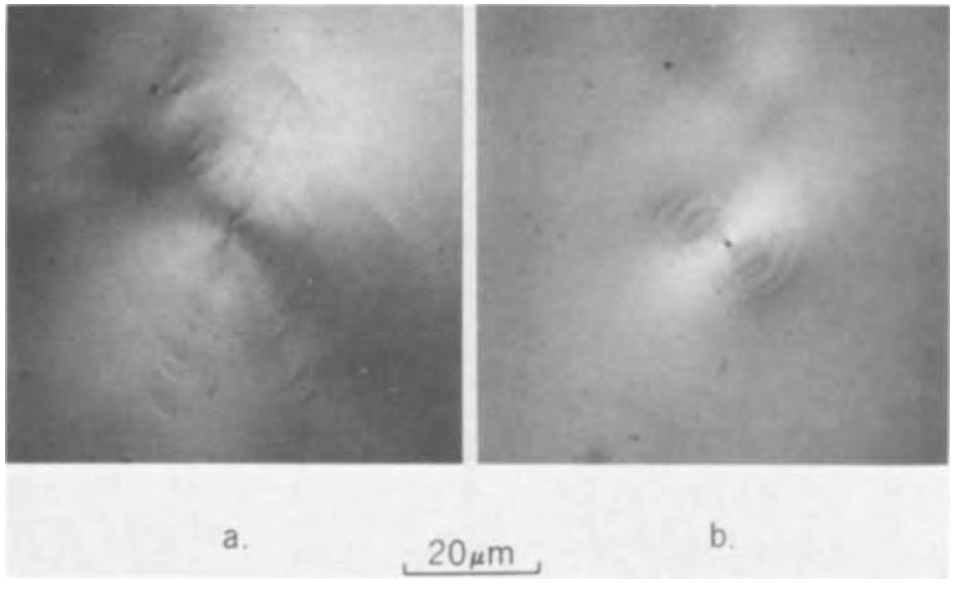

Fig. 3. A defect within $Gd_3Ga_5O_{12}$ between crossed polarizers: (a) with central inclusion only, (b) with central inclusion and an array of small inclusions or voids.

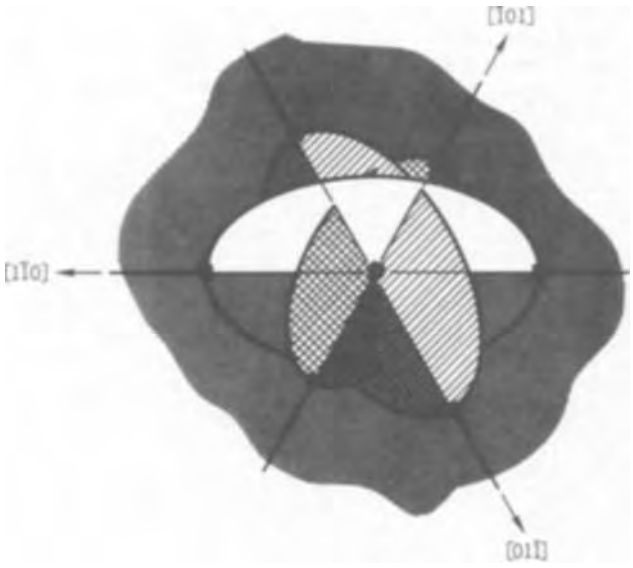

Fig. 4. Schematic illustration of a possible configuration of the defect shown in Fig. 9a.

The cluster in Fig. 3a appears to consist entirely of dislocations while the cluster in 3b appears to have associated with it an array of small (<0.2 μm) inclusions or voids lying in the planes of the loops, not along the line of the loops themselves. A possible configuration for the loops is shown schematically in Fig. 4. If sectioned through the central precipitate and etched, pits should develop at the intersection of the loops with the plane of section, here parallel to the (111) surface and through the center of symmetry of the defect. This was done on defects similar to those of Fig. 3a and b and the results are shown in Fig. 5a and b, respectively. The strong correlation in both cases of an equal number of pits on either side of the center strongly supports the view that large loops are present. The array of nondislocation pits in Fig. 5b are identical to those generated by inclusions without strain fields and are consistent with the array of small particles or voids present in Fig. 3b.

It would be very difficult for a defect of this configuration to be entirely grown into the crystal. Thus, it must form after solidification while the temperature and stress are great enough for plastic deformation to occur. A defect with a structure similar to that suggested above could result from small dislocation loops which form by vacancy coalescence and collapse or by inclusion generated stresses, and then grow due to the effect of thermal induced stress near the interface. The particle in the center of the structure, which appears to be a gadolinium gallium suboxide crystallite (5), may either have formed in the melt and been included into the crystal or have precipitated after growth from the solid which had become supersaturated with suboxide. This supersaturation would be brought about by an oxygen deficiency and a decreasing temperature associated with continued growth of the crystal. The temperature profile in the crystal and supersaturation of the precipitating species, which govern the formation and growth rate of precipitates, are in turn controlled by the thermal geometry of the apparatus, growth rate, crystal rotation rate, stoichiometry of the melt, and many other variables. Since some inclusions have strain fields and some do not and others are associated with the prismatic loop clusters, it is clear that a variety of defect generation mechanisms operate during growth. In no instance, however, have straight dislocations been observed to have been generated by isolated inclusions with or without strain fields.

In any case, all bulk defects which intersect the surface of the substrate will cause defects in an epitaxial layer subsequently grown on the substrate, and this will be discussed below. First, however, surface defects in the substrates arising from processing must be considered.

Residual Polishing and Handling Damage

Residual surface damage, such as polishing induced damage and handling scratches cause defects in films grown over them. Often, the topological result of a

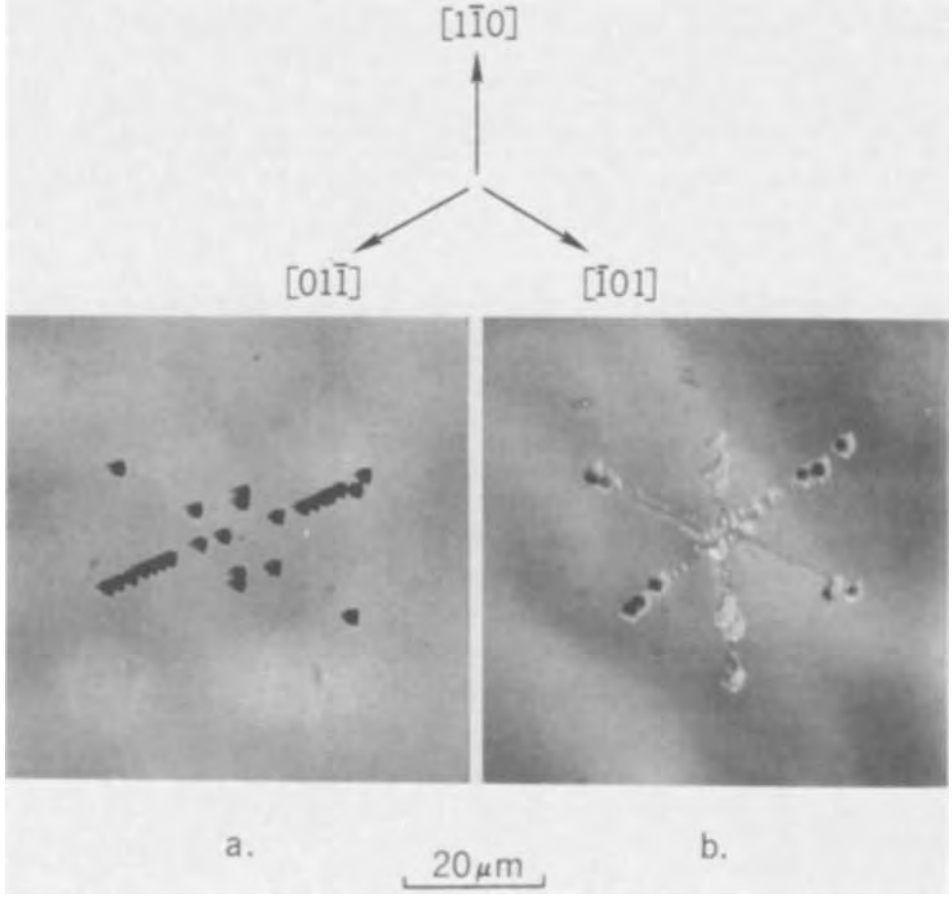

Fig. 5. Defects similar to those of Fig. 9a-b, respectively after sectioning and etching.

Fig. 6. (111) surface of a $Nd_3Ga_5O_{12}$ crystal etched in phosphoric acid at 165°C for 30 sec to reveal residual polishing damage.

scratch resulting from contamination of the polishing compound with larger grit or dirt will be polished off leaving only the subsurface residual damage which will be invisible, even under careful microscopic examination. Yet, this too will cause magnetic defects (17, 18) in the subsequently grown magnetic layer. Such residual damage will be preferentially etched during a 30-45 sec exposure to phosphoric acid at 165°C, and a groove will form at the location of the surface damage. Any other scratches present will be enlarged. The brief etch is also a cleaning step, since polishing compound, dirt, grease, etc., adhering to the specimen are removed by the acid. The grooves produced as a result of etching can be easily seen with an interference contrast microscope and even with the naked eye under sufficiently intense illumination. An example of a $Nd_3Ga_5O_{12}$ crystal that has had an inadequate amount of Syton[1] polishing to remove all of the residual damage from previous diamond polishing steps is shown in Fig. 6. The intermittent nature of some of the damage tracks suggests that the particle which caused the damage was rolling over and of irregular shape. The black spots are dislocation etch pits. $Nd_3Ga_5O_{12}$ etches much faster than any of the other gallium garnets and such pits of microscopic size will not form during the 30-40 sec etch times used to reveal polishing damage on $Gd_3Ga_5O_{12}$. The brief etch also does not affect the substrate in any deleterious way as no differences in the magnetic properties could be observed on films grown on etched and unetched substrates.

Film Defects

Crystalline defects which locally retard magnetic domain wall motion in the magnetic garnet films are caused by inclusions and dislocations in the substrate which intersect the surface, residual surface damage such as scratches, dirt which remains on the substrate surface after immersion in the flux, and inclusions, dislocations, and scratches in the films themselves.

Dislocations in the substrates will propagate into the epitaxial layers, and this is illustrated in Fig. 7. The large pits (Fig. 7a) are on the $Gd_3Ga_5O_{12}$ side of a substrate which has an LPE layer on only one side. The small pits (Fig. 7c) are on the film side. The dislocations in the substrate which have caused the pits and have propagated into the film can be seen by birefringence within the substrate in Fig. 7b. The small size of the pits on the film side relative to those on the $Gd_3Ga_5O_{12}$ side is due to the much lower etch rate of the $Y_1Gd_1Tm_1Ga_{0.8}Fe_{4.2}O_{12}$ film.

Having thus established that dislocation etch pits also form in the films, phosphoric acid etching can be used to further analyze the defect structure of the epitaxial layers. For example, shown in Fig. 8b is an etched $Y_1Ga_1Tm_1Ga_{0.8}Fe_{4.2}O_{12}$ film containing many dislocations. However, by observing the substrate side (Fig.

[1] Product of Monsanto Chemical Company.

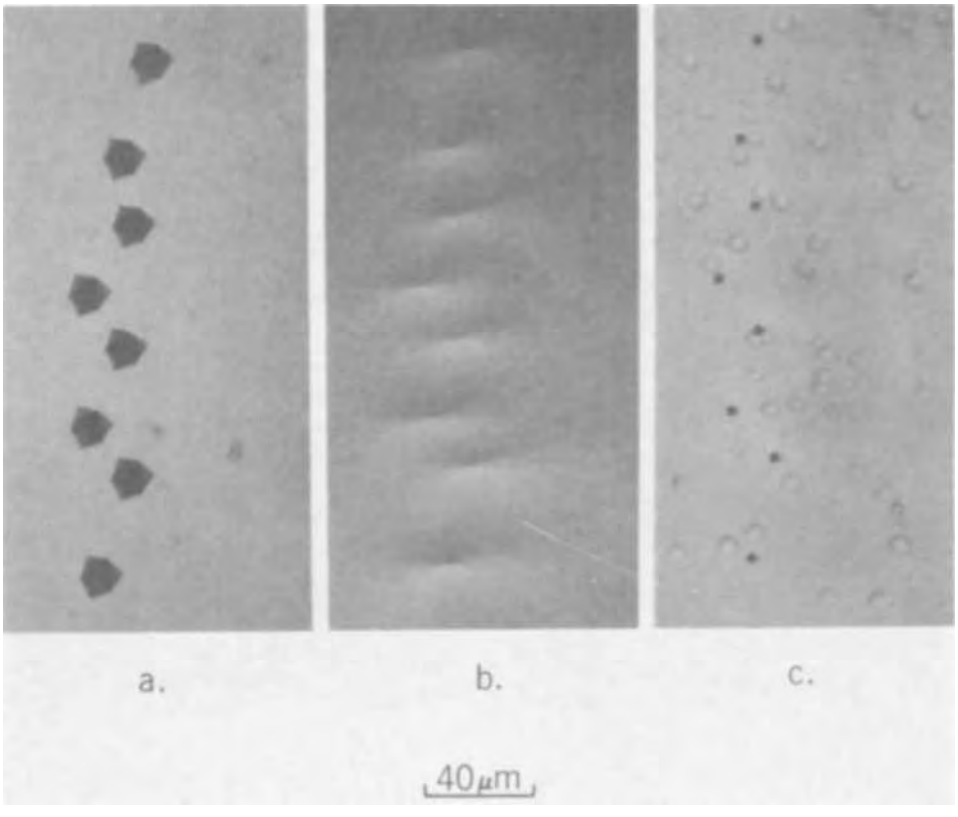

Fig. 7. (a) Dislocation etch pits on the surface of a $Gd_3Ga_5O_{12}$ crystal with a magnetic film on one side only. (b) The dislocations causing the pits as seen between crossed polarizers in the interior of the substrate. (c) The corresponding dislocation etch pits in the $Y_1Gd_1Tm_1Ga_{0.8}Fe_{4.2}O_{12}$ magnetic film.

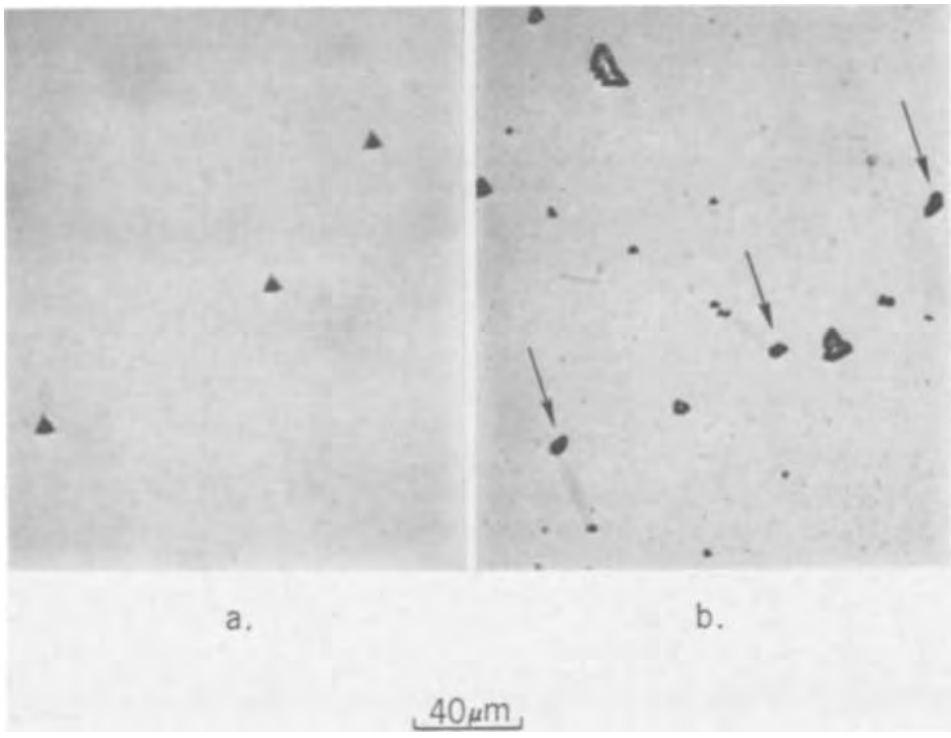

Fig. 8. (a) Dislocation etch pits on the $Gd_3Ga_5O_{12}$ side and (b) on the magnetic film side of a substrate with a $Y_1Gd_1Tm_1Ga_{0.8}Fe_{4.2}O_{12}$ layer on one surface only.

8a), it can be seen from the etch pits present that only three of the dislocations, marked with arrows in Fig. 8b, arose from bulk dislocations in the substrate. The remainder originated at the film-substrate interface. The large pits are formed by the coalescence of the etch pits of clusters of dislocations generated by large inclusions at the interface. Such large inclusions can be easily observed, but the cause of every dislocation originating at the interface cannot always be so conclusively established. However, it has been established that dirt, microinclusions, and surface damage can cause dislocations in the films when they are present at the interface. For example, it was found that previously, easily moved dirt and grease drops reacted with and became bonded to the surface of the substrate during a 1-hr anneal at 1000°C in O_2, a treatment somewhat analogous to the conditions a substrate encounters when being lowered into the furnace prior to dipping into the flux. Approximately one third resulted in dislocations in the subsequently grown magnetic layer.

Inclusions within the films themselves may or may not cause dislocations, but in either case domain wall motion will be impeded. The presence of an inclusion and whether or not it has generated dislocations can be ascertained by observing the surface of the epitaxial layer using interference contrast microscopy. For example, shown in Fig. 9a is the as-grown surface of a $Y_1Gd_1Tm_1Ga_{0.8}Fe_{4.2}O_{12}$ film which contains a group of depressions or pits. The outlined region in Fig. 9a is shown in transmission in Fig. 9b with the microscope focused about 5 μm down into this 9 μm thick film. Precipitates can be seen corresponding to the pits observable in Fig. 9a. Next, this film was etched for 3 min in phosphoric acid at 170°C in order to reveal dislocations. The outlined region in Fig. 9b is shown in Fig. 9c, after etching. In this case, only one of the inclusions generated dislocations (two). This corresponds to the type "A" growth pits so labeled in Fig. 9a. Thus, the deep conical pits are formed over inclusions which have generated dislocations, and the shallow "saucer" shaped pits form over inclusions which have not gen-

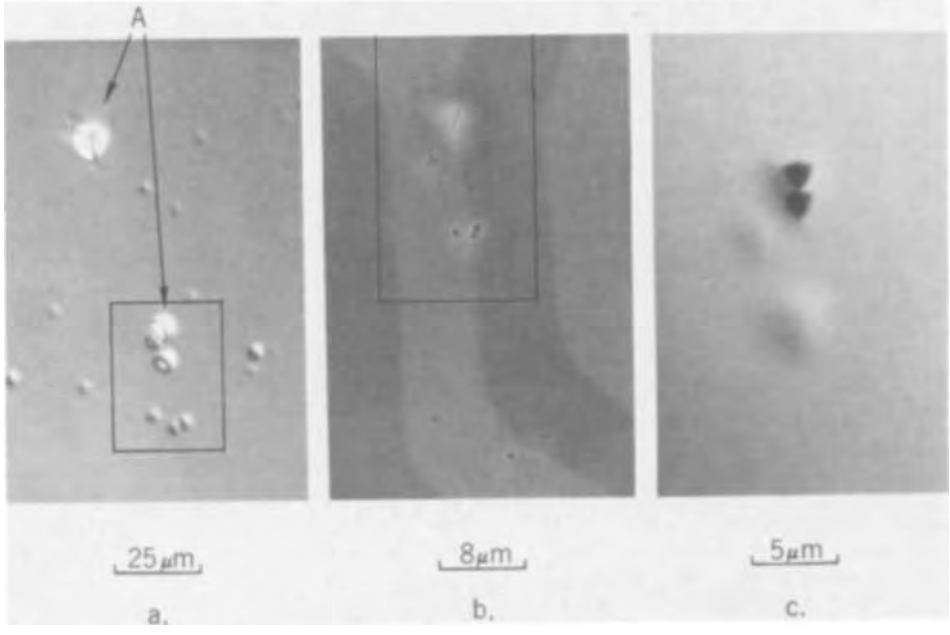

Fig. 9. The as-grown surface of a $Y_1Gd_1Tm_1Ga_{0.8}Fe_{4.2}O_{12}$ film, (b) the interior of the region of the film outlined in (a), and (c) the surface of the region of the film outlined in (b) after etching.

erated dislocations. Often, as in the case of dislocations originating at the interface, these types of surface features may be observed where no inclusions can be detected in the films. Presumably, the inclusions causing the defects in these instances are too small to be observed using optical microscopy. Even when visible, however, it is difficult to identify the inclusion unless its shape, color, and other features can be ascertained. For example, red, "cubic" inclusions which display extinction every 90° between crossed polarizers can be identified as being most probably orthoferrite crystallites which had been floating in the flux. Inclusions such as these have not been observed to generate dislocations other than perpendicular, or nearly so, to the interface.

The much greater depth of the growth pits which form over inclusions with dislocations may indicate that the presence of dislocations reduces the growth rate. This result may be explained by a plausible argument based on the observed growth behavior of the garnets. Because <111> growth facets do not form on Czochralski grown $Gd_3Ga_5O_{12}$ and other rare earth gallium garnets it can be concluded that little undercooling is required for the nucleation of new layers on {111} planes, and thus the growth of garnet in the [111] direction should also require little undercooling. Therefore, the growth rate of $Gd_3Ga_5O_{12}$ should vary directly with undercooling (19) in the [111] direction. Epitaxial films grown on {111} surfaces should behave in the same way, except for the possible influence of diffusion boundary layer effects, and this has been observed (3). However, the strain field which surrounds a dislocation is a higher energy nucleation site than a perfect (111) surface. In general, then, for any given growth temperature, the growth rate should be inversely proportional to the amount of strain associated with the site of attachment of an adatom. An inclusion which does not generate dislocations will be surrounded by a relatively weak strain field, and thus according to the above reasoning, a reduced growth rate will result until the inclusion is well covered by many atomic layers and the strain diminishes. Therefore, the size of the growth pit associated with an inclusion without dislocations should be directly proportional to the size and magnitude of its strain field. However, if dislocations are generated by the inclusion, then a larger growth pit should form than would otherwise be the case. This occurs because even though the dislocations may reduce the over-all stress in the vicinity of the inclusion, dislocations grow through the layer and thus the reduced growth rate will persist for the duration of film growth.

The situation will be different in the case of a growth plane on which the nucleation of new layers requires substantial undercooling, such as the {211} planes in garnet. Depending on the relative magnitude of the strain energy associated with a dislocation and lattice parameter mismatch, the presence of a dislocation with a Burgers vector other than parallel to the interface may increase the growth rate of the film for a given amount of undercooling. This occurs because the step produced when the dislocation intersects the interface becomes a growth step, obviating the need for the high undercooling necessary for the nucleation of new layers (20, 21).

Whether or not the above arguments can be applied to other than localized strain, *i.e.*, to the possible effect of lattice mismatch strain on the growth rates of epitaxial layers, will be investigated.

Growth Striations

The etch rate of the various garnets studied is very sensitive to small variations in composition. This can be used effectively qualitatively to study compositional fluctuations caused by growth rate variations as in the case of semiconductor crystals (22, 23). The growth rate fluctuations essentially span the entire growth front and thus can be used to study the interface shape as influenced by changes in growth parameters.

Fig. 10. $(\bar{2}11)$ surface of a sectional $Gd_3Ga_5O_{12}$ boule etched in phosphoric acid for 10 min at 165°C. The growth direction is vertically downward.

Shown in Fig. 10 is the $(\bar{2}11)$ surface of a $Gd_3Ga_5O_{12}$ boule sectioned lengthwise perpendicular to the growth direction, polished, and etched for 10 min in phosphoric acid at 165°C. The (112) faceted growth region is to the right and the nonfaceted region to the left while the pulling direction was vertically upward.

The closely spaced striations appear to have resulted from rotation of the crystal in the presence of thermal asymmetry in the apparatus. Since the rotation rate is constant, the spacing of these striations can be used to detect and analyze growth rate fluctuations arising from other sources. For example, in the off-facet region many fewer striations with greater spacing can be counted than in the core region, indicating that the crystal grew much faster in this region and that part of the crystal was remelted with each cycle. Thus, it can be calculated that the growth rate in the off-facet region is about four times greater than the pull rate of 0.18 in./hr or about 0.7 in./hr. The widely spaced "remelt" striations in the off-facet region, which have a period of about 40 sec, may result from regular low frequency fluid flow fluctuations in the melt (24, 25). It should be noted that the effective average growth rate will always be greater than the pull rate in the presence of growth rate fluctuation (26).

In this crystal the interface in the center of the boule (to the left in the figure) is almost flat, and therefore the striations will intersect the surfaces of substrates cut from this boule at a shallow angle. Thus, the lattice parameter changes associated with the striations are diffused enough so that no strain gradients large enough to interfere noticeably with bubble motion in an LPE layer grown over them will be generated. This flattened interface can be produced by using high crystal rotation rates (27), which will pump more hot liquid up the center of the crucible, thus raising the temperature there and counteracting the loss of heat by radiation up the center of the crystal. Under conditions of slow rotation the [211] facets become grouped at the center of the boule due to the highly convex interface shape. The intersection of the [211] facets with the (111) surface of a substrate cut from a boule grown with a highly convex interface is shown in Fig. 11. This also illustrates that the acid is equally selective on the {111} surfaces.

Striations may also be observed between crossed polarizers due to the strain birefringence generated by the compositional variations. This technique lacks the resolution of etching methods but, along with topography, is a useful tool.

The sensitivity of the acid to impurity or compositional heterogeneities can also be used to study growth fluctuations in the magnetic garnet films, as is shown in

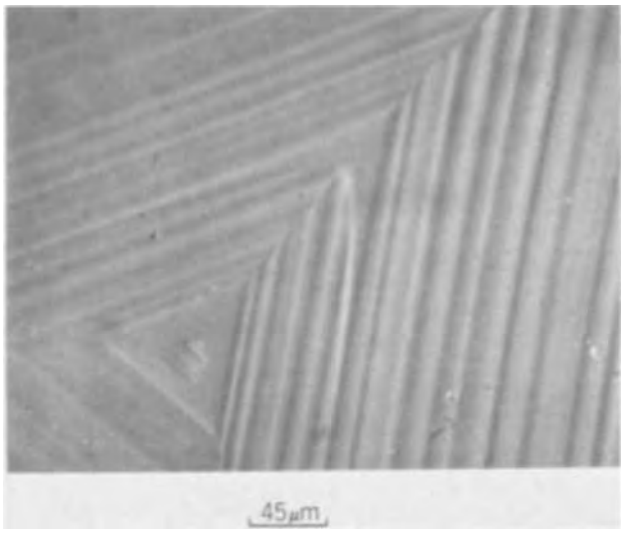

Fig. 11. (111) surface of a $Gd_3Ga_5O_{12}$ substrate after etching

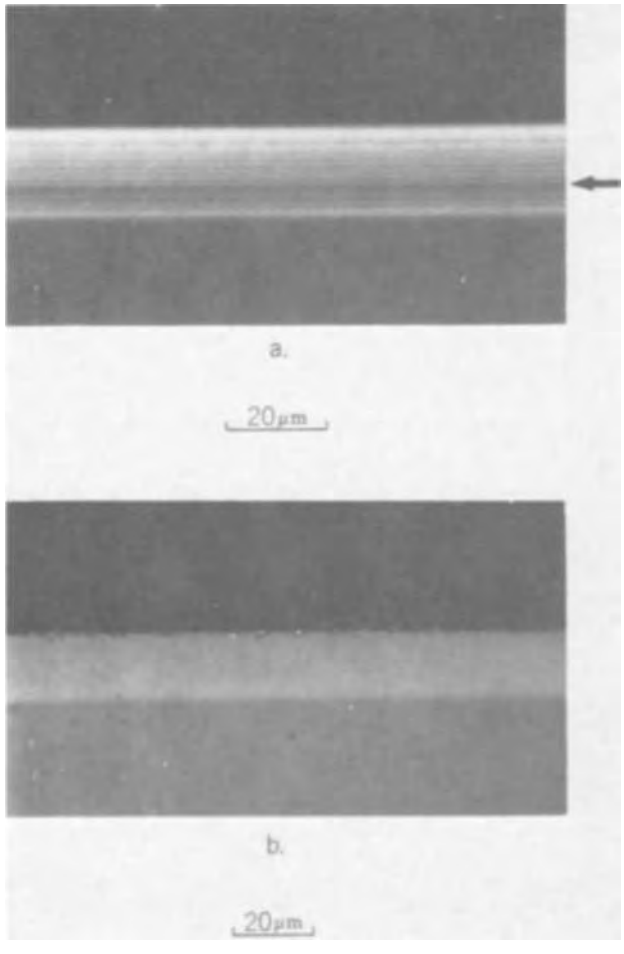

Fig. 12. Cross section of a $Er_2Eu_1Ga_{0.7}Fe_{4.3}O_{12}$ film after (a) and before (b) etching.

Fig. 12a. Figure 12b is the sectioned (by scribing and fracturing) view before etching. The origin of the striations in this film are related to boundary layer thickness changes caused by intermittent rotation of the substrate during film growth. The periods of rotation are regular, thus the variations in their spacing, as well as other topological variations produced by the etchant, can be used to measure growth rate changes during film growth and relative changes in film composition, respectively. In the film shown, after 3.5 μm of growth marked by the arrow, the over-all growth rate dropped by 15%. From the change in shading, which indicates a difference in height in interference contrast, it can be concluded that this lower part also etched faster than the upper part. This is caused by a difference in composition which is probably related to changes in the effective distribution coefficients of the constituents due to the higher growth rate. The cause of the abrupt change in rate is not known.

It is important to note here as well that there is no preferential etching at the interface as would be the case if a network of dislocations were present there. In fact, misfit or interfacial dislocations or dislocations parallel to the interface within the films have not been observed on any LPE film thus far examined which was not faceted. Dislocations have been observed parallel to the interface around the entire periphery of an LPE layer, indicating that pits form equally well on all orientations. However, these dislocations do not penetrate into the LPE layer itself, but rather are entirely contained in the material which grew epitaxially on to the outer edge of the substrate. Films in tension will crack before enough stress is generated for dislocation generation, at a mismatch of about 0.015Å. The defect structure of films grown under large compressive stress are currently being investigated.

Topography

In order to confirm the absence of interface dislocations and learn more about the strain state of the films, x-ray reflection (Berg-Barrett) (28, 29) topographs were taken. For example, an $Er_2Eu_1Ga_{0.7}Fe_{4.3}O_{12}$ film grown in tension with about 0.012Å mismatch in which cracks have formed around the periphery of the crystal was taper etched and a topograph taken. A schematic diagram of the diffraction conditions is shown in Fig. 13 and the resulting topograph in Fig. 14. Copper $K\alpha_1$, radiation and {10, 4, 0} reflecting planes were used and the image recorded on an Ilford L-4 nuclear plate. The light areas correspond to reduced intensity because a double negative was made during reproduction. The light area near the top is the substrate surface, while the lower ¼ of the crystal is unetched. The reduced intensity reflected from the substrate results because the crystal was aligned using the film and the different d spacing in the substrate renders it slightly out of alignment. There are many contrast features observable in the topograph which arise from topological variations, such as mesas resulting from flux retention, ridges due to contact with the platinum wire holders, etch pits, as well as defects in the emulsion. However, no dislocations can be resolved parallel to the interface throughout the thickness of the film or at the interface. Furthermore, no contrast (darkening) is present near the interface either (save for one weak pendellosung fringe), as would be the case if there were a network of dislocations present there too close together to be individually resolved. The cracks present can also be seen on the topograph due to the strain caused by stress relief near the crack edges.

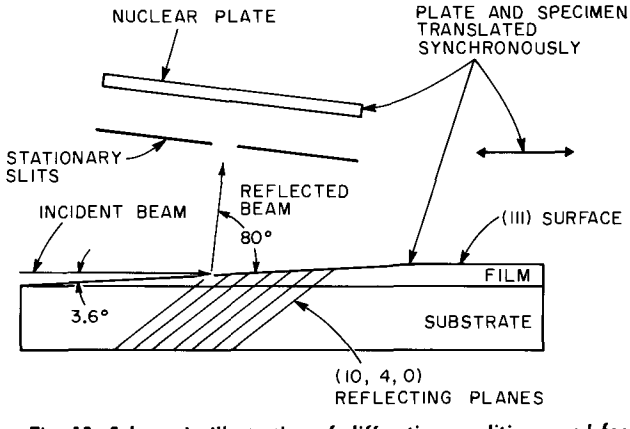

Fig. 13. Schematic illustration of diffraction conditions used for reflection topography.

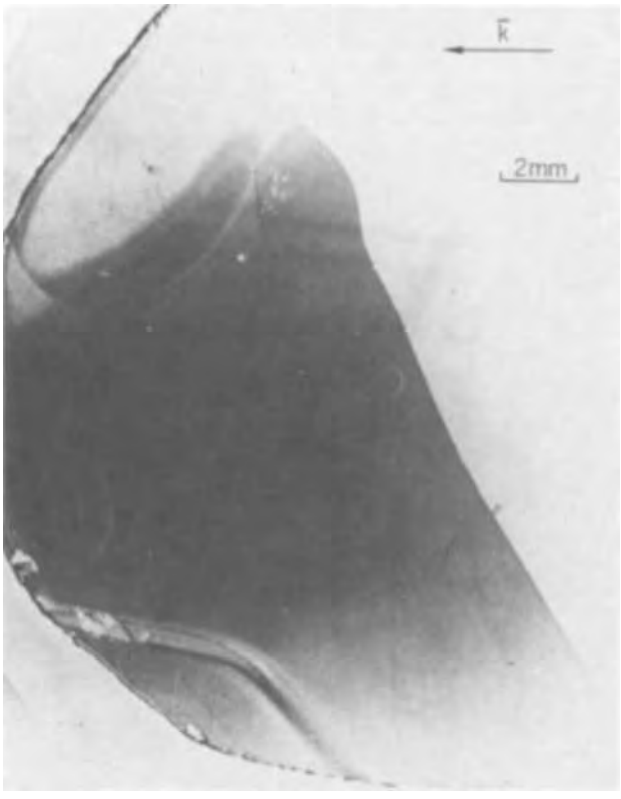

Fig. 14. Berg-Barrett reflection topograph of a taper-etched $Er_2Eu_1Ga_{0.7}Fe_{4.3}O_{12}$ film.

Such cracks when etched as grooves into the substrate due to the masking effect of the film do not have contrast since there is no strain or bending of planes.

Summary

Phosphoric acid etching combined with optical microscopy and x-ray topography can be used to study many properties of the garnet substrates and films, both qualitatively and quantitatively. An overview has been presented here of the use of these techniques to study defects found in both the substrates and epitaxial layers. Through the use of these techniques the occurrence of the defects can be related to preparation and growth conditions and then successfully eliminated, as has now been accomplished with the defects known to limit the utilization of epitaxial magnetic garnet films in large bubble domain devices. Other aspects of these materials such as growth striations in the films and substrates, the effects of strain on the growth rate, and the structure of mixed defects have also been revealed using phosphoric acid and will be studied in more detail. Even though operation of magnetic bubble circuits does not now appear to be limited by some of these phenomena, a knowledge of them may become important as work progresses and more subtle relationships between the magnetic and structural properties of these materials are revealed.

Acknowledgments

The author wishes to thank C. D. Brandle for growing the substrate crystals, and S. L. Blank and B. S. Hewitt for growing the LPE layers. Helpful comments and suggestions made by J. W. Nielsen and L. J. Varnerin are also gratefully acknowledged.

Manuscript submitted Oct. 17, 1972; revised manuscript received Dec. 15, 1972. This was Paper 5 presented at the Houston Meeting of the Society, May 7-11, 1972.

Any discussion of this paper will appear in a Discussion Section to be published in the December 1973 JOURNAL.

Note added in proof: A detailed analysis by J. W. Matthews of the type of defect shown in Fig. 3 appears in the March 1973 issue of *Acta Metallurgica.*

REFERENCES

1. R. C. Linares, *J. Cryst. Growth,* **3, 4,** 443 (1968).
2. H. J. Levinstein, S. Licht, R. W. Landorf, and S. L. Blank, *Appl. Phys. Letters,* **19,** 486 (1971).
3. S. L. Blank and J. W. Nielsen, *J. Cryst. Growth,* **17,** 302 (1972).
4. C. D. Brandle and A. J. Valentino, *J. Cryst. Growth,* **12,** 3 (1972).
5. C. D. Brandle, D. C. Miller, and J. W. Nielsen, *ibid.,* **12,** 195 (1972).
6. A. H. Bobeck, *Bell System Tech. J.,* **46,** 1901 (1967).
7. A. H. Bobeck, *IEEE Trans. Magnetics,* **MAG-6,** 445 (1970).
8. B. Cockayne and D. S. Robertson, *Brit. J. Appl. Phys.,* **15,** 643 (1964).
9. J. Basterfield, *ibid.,* (*J. Phys. D.*), **2,** 1169 (1969).
10. L. K. Shick, *This Journal,* **118** 179 (1971).
11. D. C. Miller, *J. Elect. Materials,* **1,** 499 (1972).
12. D. C. Miller, Submitted to *This Journal.*
13. W. L. Bond and J. Andrus, *Phys. Rev.,* **101,** 1211 (1956).
14. R. Bullough, *ibid.,* **110,** 620 (1958).
15. M. J. Prescott and J. Basterfield, *J. Mater. Sci.,* **2,** 583 (1967).
16. J. Friedel, "Dislocations," p. 232, Pergamon, London (1964).
17. R. J. Pierce, Private communication.
18. P. W. Shumate, *IEEE Trans. Magnetics,* **MAG-8,** 586 (1971).
19. H. A. Wilson, *Phil. Mag.,* **50,** 238 (1900).
20. F. C. Frank, *Discussions Faraday Soc.,* **5,** 48 (1949).
21. W. B. Hillig and D. J. Turnbull, *J. Chem. Phys.,* **24,** 473 (1956).
22. J. A. M. Dikhoff, *Solid State Electron.,* **1,** 202 (1960).
23. A. F. Witt and H. C. Gatos, *This Journal,* **118,** 70 (1968).
24. J. R. Carruthers and K. Nassau, *J. Appl. Phys.,* **39,** 5205 (1968).
25. K. K. Kim, A. F. Witt, and H. C. Gatos, *This Journal,* **119,** 1218 (1972).
26. D. T. Hurle, E. Jakeman, and E. R. Pike, *J. Cryst. Growth,* **3, 4,** 633 (1968).
27. B. Cockayne, M. Chesswas, and D. B. Gasson, *J. Mater. Sci.,* **3,** 224 (1968).
28. W. F. Berg, *Naturwiss.,* **19,** 391 (1931).
29. C. S. Barrett, *Trans. AIME,* **161,** 15 (1945).

Chemical Vapor Deposition of Thin-Film Platinum

Myron J. Rand*

Bell Telephone Laboratories, Incorporated, Allentown, Pennsylvania 18103

ABSTRACT

Chemical vapor deposition of platinum for microelectronic applications has been studied with the aim of avoiding the radiation damage to dielectrics caused by sputter or e-gun deposition. Two known CVD methods—the pyrolysis of Pt acetylacetonate and the reduction of $Pt(CO)_2Cl_2$—were tried and judged unsatisfactory for either purity or adherence. A novel method of Pt deposition using the trifluorophosphine complex is reported. The process is simple and reliable, and produces adherent bright films of ~100Å Pt crystals on a variety of substrates at 200°-300°C in 1 atm hydrogen. The Pt contains small amounts of residual phosphorus, mostly concentrated at the surface. Resistivity of 750Å films is 1.8 times that of bulk Pt. MOS capacitors with CVD Pt field plates on both Al_2O_3/SiO_2 and SiO_2 alone have shown good stability under bias-temperature aging. CVD Pt and Si interdiffuse readily to form ohmic or Schottky diode PtSi contacts.

Thin films of platinum are used extensively in semiconductor device processing in making platinum silicide ohmic and Schottky diode contacts to silicon. Platinum is also the best diffusion barrier metal in the Ti-Pt-Au metalization scheme for beam leads. For these uses Pt thicknesses range from as little as 100Å (for some contacts) to about 2000Å. Unfortunately Pt is difficult to filament-evaporate; its vapor pressure is low, and it alloys rapidly with tungsten. Pt is usually deposited by electron-beam evaporation or by sputtering.

In addition to the relatively complex—and sometimes temperamental—equipment required by these vacuum operations, there is the more serious disadvantage of radiation damage to thin insulating films by x-rays, energetic electrons, and far uv radiation. The charge injected into the dielectric results in shifts of the MOS characteristic, especially during bias-temperature aging. Since stability of threshold voltage is the *sine qua non* of IGFET's, platinum is seldom used in their metalizations.

The obvious way to avoid radiation damage is to use chemical vapor deposition (CVD), which employs only thermal energy, and which is usually done in relatively simple apparatus. The prospects for platinum CVD have been reviewed by Powell *et al.* (1). They suggest two classes of volatile platinum compounds: organometallics such as the acetylacetonate (acac), and the carbonyl chlorides, especially the dicarbonyl dichloride, $Pt(CO)_2Cl_2$. It is probably significant that no articles on the acac as source could be located in the primary literature, and that the last papers on the carbonyl chloride appeared in 1934 (2-4). There is no literature specifically on thin film CVD Pt, to say nothing of films of a quality useful for microelectronics.

This paper first reports experience using both the sources given above for the CVD of Pt thin films. Next a novel deposition method will be described, the pyrolysis of the trifluorophosphine complex of platinum. This reaction employs a liquid source and has decided advantages in simplicity and temperature requirements. It has been studied in detail not only for its own sake but also because volatile PF_3 complexes of most of the transition metals have now been synthesized but as yet have been little investigated for suitability as CVD sources.

Platinum from the Acetylacetonate

The acetylaceton of zero-valent platinum is prepared from potassium chlorplatinite and acetylacetone in aqueous solution made strongly alkaline in order to displace the β-diketone equilibrium toward the enol form. The chelate may be formulated

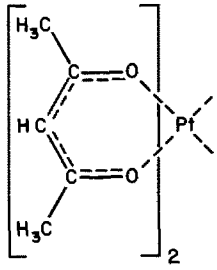

on the assumption that Pt is bonded to oxygen. While metal-oxygen bonding is usually the case in these complexes, Lewis *et al.* (5) have shown that in some Pt(II) acac derivatives there is Pt-C bonding. The distinction is important to the pattern of pyrolysis of the compound.

$Pt(acac)_2$ is an air-stable yellow powder, available commercially (6). For CVD its vapor pressure becomes significant at about 150°C. Powell *et al.* (1) recommend vaporization at 180° *in vacuo* and a substrate temperature of 350°-450°C. Hydrogen ambient may often be used instead of vacuum to accomplish a clean pyrolytic decomposition of organometallics, but we find $Pt(acac)_2$ heated in hydrogen turns black without vaporizing. The black powder persists at red heat, in air; evidently hydrogen reduces the compound to platinum.

For vacuum CVD experiments the apparatus of Fig. 1 was used. Heating the pedestal by hot gases from a torch flame is unconventional but should not be scorned. The method permits rapid attainment of any temperature up to 700°C, constancy to ±5°, and flexible temperature adjustment by control of the size and gas mixture of the flame.

With the $Pt(acac)_2$ pressure 20-200μ Torr, deposition of Pt at 10-100 Å/min occurred at substrate temperatures of 500°-600°C. On Si substrates one would therefore expect PtSi, but reflection electron diffraction gave only the pattern of randomly oriented fcc Pt. The metallic deposit had a distinct tan or bronze cast, and it was resistant to aqua regia etching. Electron beam microprobe analysis revealed heavy carbon contamination, in fact about one carbon atom per Pt atom. The codeposition of carbonaceous residue was not suppressed by adding CO_2 to the ambient to act as oxidizer. The carbon was completely removed by oxygen-baking the deposit at 550° for a few minutes, but ohmic contact to the 0.01 ohm-cm n-Si substrate was still not achieved. No case of low-resistance ohmic contact to Si has been observed with Pt deposited from the acac, with or without a deliberate siliciding step.

Carbon has little solubility in solid Pt. Considering the electron diffraction result, the probe analysis, the

* Electrochemical Society Active Member.
Key words: platinum, chemical vapor deposition, thin films.

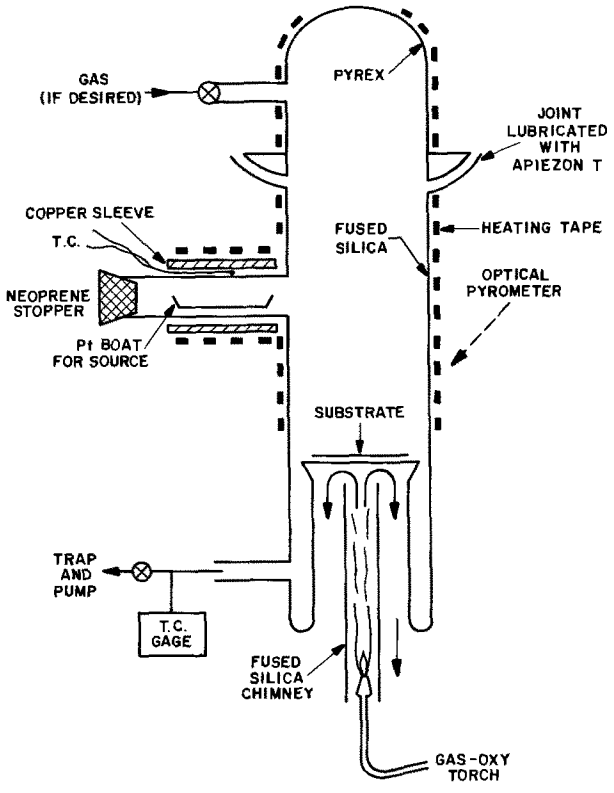

Fig. 1. Apparatus for vacuum pyrolysis of Pt acetylacetonate

result of oxygen-baking, and the failure of Pt-Si interdiffusion, the picture that emerges is one of small crystallites of Pt surrounded by heavy concentrations of carbon, very probably at grain boundaries. We conclude that Pt from the pyrolysis of the acetylacetonate contains too much codeposited carbon to be of interest for most device purposes.

Platinum from the Carbonyl Chloride

For volatile inorganic platinum sources for CVD, Powell *et al.* (1) recommend the carbonyl chlorides, especially the dicarbonyl dichloride, $Pt(CO)_2Cl_2$, as having the greatest difference between the sublimation and decomposition temperatures. They state that deposition may be carried out at 600°C at low pressures (10-20μ), or at 1 atm in hydrogen at much lower temperatures, using carbon monoxide as $Pt(CO)_2Cl_2$ carrier gas to suppress premature decomposition. Saturator temperatures were 100°-150°C. The discussion mentions problems with nonadherent or acicular deposits.

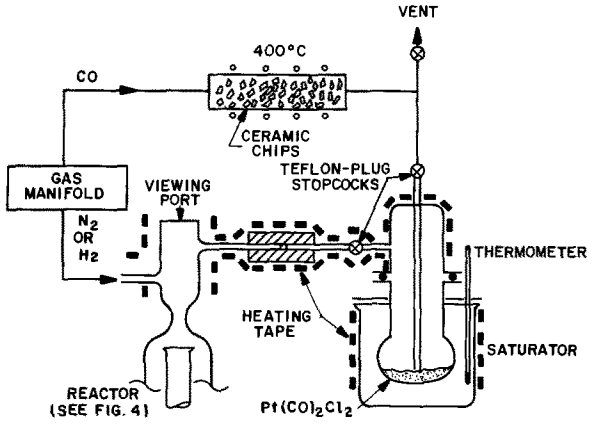

Fig. 2. Schematic diagram of apparatus for the deposition of Pt from the carbonyl chloride.

$Pt(CO)_2Cl_2$ occurs as colorless needles when pure, but is usually dark because of Pt liberated by reaction with atmospheric moisture. Our material was prepared by the method of Lutton and Parry (7) by the Pressure Chemical Company, Pittsburgh, Pennsylvania, and stored under carbon monoxide. Pt depositions were carried out both in the vacuum apparatus of Fig. 1 and the apparatus shown schematically in Fig. 2 and 4. A summary of typical conditions and results appears in Table I; available analytical data are collected in Table II.

Bright films of Pt on Si were obtained without difficulty at low pressures, but adherence was invariably poor. Characteristically, the film suddenly turned from bright to frosty in appearance during deposition, usually not long after it had become opaque, *i.e.*, 300-400Å thick. Often the rough zone continued to spread after the sample was cold. Under the microscope a dense network of folds, puckers, or wrinkles was visible, and there is little doubt that Pt had separated from the substrate. Scoring a smooth area caused instant peeling. The failure of the film to adhere is surprising; at these deposition temperatures considerable Pt-Si interdiffusion should occur. The electron beam microprobe was unable to detect either C or Cl in the Pt, and the electron diffraction pattern was normal.

Table I. Depositions from platinum carbonyl chloride

(For analytical data see Table II)

Run	Substrate	Dep'n temp (°C)	Ambient	Source temp (°C)	Dep'n rate (Å/min)	Appearance, etc.	Ohmic contact? (*)	Comment
11	0.01 n-Si	450	50μ $Pt(CO)_2Cl_2$		100	Bright to frosty		Wrinkling during dep'n.
12	0.01 n-Si	600	40μ			Tan, hazy	No	Poor adherence
16	0.01 n-Si	350	20μ		50	Bright to frosty		Wrinkling during dep'n.
3	0.01 n-Si	550	1 atm N_2 or H_2	120	nil			
4	0.01 n-Si	245	1 atm H_2	125	nil	Tan, hazy		
5	0.01 n-Si	350	1 atm H_2	140	10-40	Lt. tan, hazy		
				Gas flow pattern modified				
6	0.01 n-Si	250	1 atm H_2	143	20-100	Bright to frosty	Yes	Portion wrinkled during dep'n.
7	0.01 n-Si	187	1 atm H_2	140	15	Bright	No	Pt did not alloy at 650°C
		Heated 30 min, 750°C, Ar				Dull	Yes	
				Carbon monoxide purifier added				
8	0.01 n-Si	300	1 atm H_2	145	15-50	Frosty	Yes	Wrinkling during dep'n., some peeling
9	dep. SiO_2	250	1 atm H_2	145-150	35	Bright, islands		Islands 1000-5000Å diam.
	dep. Al_2O_3				75	Bright		Peeled on scoring. (1500Å thick)
10	dep. SiO_2 dep. Al_2O_3 th. SiO_2 5 n-Si	485	1 atm H_2	155	10	Bright, semiopaque on all		

* After standard 650°C, 10 min in Ar.

Table II. Depositions from platinum carbonyl chloride
(Analytical data for Table I)

Run	Substrate	Dep'n temp (°C)	Microprobe analysis (atomic per cent) Pt	Si	O	Others	Electron diffraction and other data
12	Si	600	98.2	1.8		Cl, C, n.d.*	
16	Si	350					fcc Pt
6	Si	250	85.5	2.1	2.2	Ni, 9.3; Fe, 0.9; C, n.d.	
7	Si	187	70.0	19.9	4.1	Ni, 7.2: Fe, 0.4; C, n.d.	
	Carbon monoxide purifier installed						
8	Si	300	95.5	4.5		Fe, Ni, Cr, n.d.	(Thin deposit)
			99.6	0.4			(Thick deposit)
9	Si	250					fcc Pt, xtal size ~225Å
	dep. SiO_2						fcc Pt, xtal size ~150Å. Islands.
	dep. Al_2O_3						fcc Pt, xtal size ~2000Å
10	Si	485					Anomalous pattern, xtal size ~100Å
	th. SiO_2						Anomalous pattern
	dep. Al_2O_3						fcc Pt
	dep. SiO_2						Anomalous pattern

* n.d. = not detected.

In depositions in 1 atm hydrogen the necessity for a carbonyl scavenger for the carbon monoxide carrier soon became evident. The CO was research grade (Matheson Company, 99.9% min.), but at 1500 psi there is probably reaction with the tank materials, so that iron and nickel carbonyl contaminants are pyrolyzed on the substrate and Fe and Ni end up in the Pt. A 400°C tube packed with porcelain chips took care of this problem.

Hydrogen-ambient depositions also produced bright Pt films, and for the first time some of these could be alloyed into Si to produce good ohmic contacts. Adherence was still marginal. Proper dispersion of the gas flow over the substrate surface was troublesome, as it is with many CVD reactions, and keeping the $Pt(CO)_2Cl_2$ from condensing out in cool places requires careful attention to the heated saturator lines, since they cannot be permitted to be hot enough to decompose the compound.

The substrate definitely influenced the Pt film morphology in these depositions. In run 9 (Table II) relatively large islands composed of randomly oriented 150Å Pt crystals formed on a deposited silica surface giving a sheet resistance of >20-Kohm/□, while an adjacent deposited alumina surface accumulated a continuous film of ~2000Å crystals of 1.8 ohm/□. In run 10, done at 485°C, four different substrates were deposited simultaneously, but only Pt on the Al_2O_3 substrate gave the expected electron diffraction pattern. The others gave a much more complex, and somewhat variable, pattern with many d-spacings larger than any in fcc Pt. Among these were two strong reflections at about double the spacing of the two most intense fcc lines, the (111) and the (200). We have seen these anomalous patterns also on several e-gun evaporated films and two 3 kV-sputtered Pt's, but not on low voltage triode-sputtered samples. The glancing angle electron beam penetrates only ~50Å in Pt; x-ray diffraction has shown normal fcc structures for Pt with anomalous surface patterns. The existence of superlattice surface structures on Pt has been reported (8); it is not known whether they are impurity-stabilized. At 485°C, the disproportionation of CO to give some carbon is a distinct possibility, especially on Pt.

The source temperatures in Table I are to be noted. Over the course of only seven runs it was necessary to raise the $Pt(CO)_2Cl_2$ temperature from 125° to 155°C (which is above the melting point) to maintain reasonable deposition rates. This suggests that in spite of the CO atmosphere the compound was decomposing to one less volatile. After the last run of Table I the cake of source material was analyzed, with the following results:

$Pt(CO)_2Cl_2$	78.6%
$PtCl_2$	19.0%
Pt	0.63%
Fe, Ni, Cr oxides	0.1-0.2%

It seems clear that the material in the saturator was slowly decomposing to nonvolatile $PtCl_2$, which coated the solid particles and made the volatile carbonyl chloride inaccessible. The elemental Pt may have been present originally or have resulted from further decomposition.

While the carbonyl chloride process in hydrogen can produce pure Pt films, the limited source life, corrosive vapor, necessity for heated lines, and poor adherence combine to make the method unattractive. Furthermore, it is probably more than ordinarily sensitive to the various deposition parameters, owing to the complicated equilibria existing among the various carbonyl chlorides, $PtCl_2$, CO, Cl_2, and Pt (7).

Platinum from the Trifluorophosphine Complex

Phosphorus trifluoride resembles carbon monoxide, at least formally, in forming a wide variety of stable complexes with transition metals. Although $Ni(PF_3)_4$ has been known for twenty years (9), it has been only since 1965 that Thomas Kruck and his co-workers have achieved the preparation of the complexes of all the metals of Groups VI-VIII of the periodic chart. Nixon (10) has tabulated the known PF_3 complexes, and Schmutzler (11) gives a useful review of the properties of PF_3 itself.

In spite of the good volatility of the metal-PF_3 compounds, there is only one mention of their use for CVD, a patent (12) teaching the use of $W(PF_3)_6$ to deposit W on Si at 450°C in making Schottky barrier contacts.

The PF_3 complex of platinum is of particular interest because no stable carbonyl of platinum is known. Tetrakistrifluorophosphine platinum, $Pt(PF_3)_4$, was first prepared by Kruck and Baur (13). Our samples were made using their procedure by PCR, Incorporated, Gainesville, Florida, and Pressure Chemical Company, Pittsburgh, Pennsylvania. The compound is a colorless, mobile liquid boiling at 87°C, apparently stable to dry air but hydrolyzed by moisture to Pt, H_3PO_3, and HF. The compound appears to be a good solvent for simple halogenated organics and for various mixed halides of phosphorus, and it is advisable to check its purity by infrared spectra. Arsenic trifluoride (bp 65°C) is another common impurity, originating in the manufacture of the PF_3, and can contaminate Pt deposits with as much as 1% As.

In considering $Pt(PF_3)_4$ for the CVD of Pt, the hope is of course that simple pyrolysis will occur, with selective rupture of the Pt-P bond and liberation of the thermally-stable PF_3. In considering the results reported below, however, one should keep some additional chemistry in mind: that PF_3 is reported to attack SiO_2 at elevated temperatures, forming P_2O_3 and SiF_4 (both gases at the deposition temperatures); and that freshly formed Pt will certainly be a strong chemisorber and highly catalytic. In other words, the reactivity of the products may complicate the pyrolysis, degrade the Pt purity, or result in attack on the substrate.

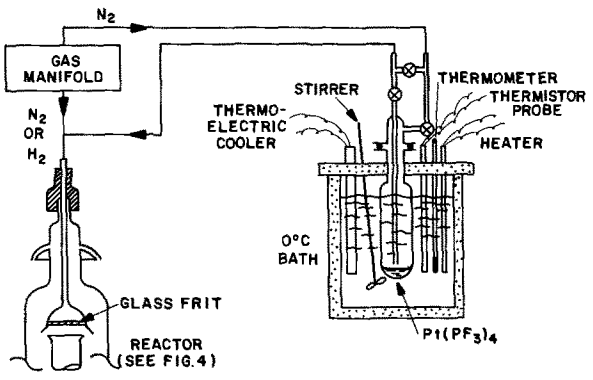

Fig. 3. Schematic diagram of source system and apparatus for the deposition of Pt from $Pt(PF_3)_4$.

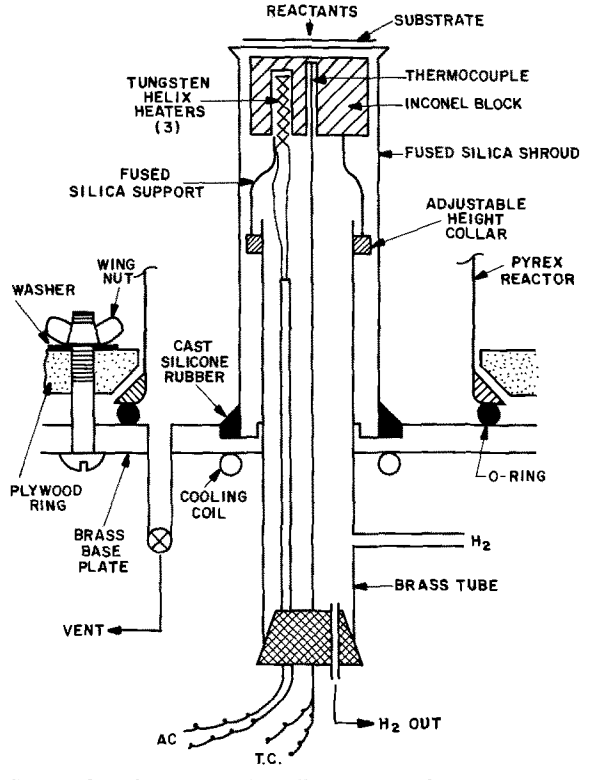

Fig. 4. Detail of the cold-wall reactor with resistance-heated silica pedestal for the substrate.

The apparatus used for Pt deposition from the PF_3 complex is shown schematically in Fig. 3 and 4. The complex is stored under dry nitrogen in a saturator at 0°C, at which temperature its vapor pressure is estimated to be ~15 Torr. After dilution by the main gas stream (usually hydrogen) its concentration is 0.01-0.1%. The total gas flow displaces the reactor volume 1-5 times a minute. A coarse glass frit distributes the reactants over the substrate wafer; deposit thickness uniformity of ±10% is easily obtained. The resistance-heated pedestal (Fig. 4) is preferred to tube furnace or rf-heated equipment because the reactor wall remains fairly cool. A hot wall would soon become opaque. The temperatures quoted in this report are not readings of the heater block thermocouple but estimated substrate temperatures derived from measurements of the temperature difference between the heater thermocouple and the horizontal surface of the fused silica shroud.

Results—Deposition of thin-film Pt.—With optimum deposition conditions the pyrolysis of $Pt(PF_3)_4$ produces a uniform, smooth, continuous, adherent layer of mirror-bright Pt indistinguishable in appearance from sputtered or e-gun-evaporated Pt. The following substrates have been coated: Si, thermal and deposited SiO_2, deposited Al_2O_3 and Si_3N_4, fused silica, soft glass, sapphire, Ta_2N, evaporated Ti, CVD tungsten, GaP, and GaAs. The preferred ambient is hydrogen, and the preferred temperature range 200°-300°C. At 175°C and below nonspecular rough deposits indicate incomplete pyrolysis; at 350°C and above a brown fume in the gas phase suggests decomposition before the vapor reaches the hot substrate. A deposition rate of 50-100Å Pt/min is most convenient.

Glancing angle or transmission electron diffraction has invariably shown only the pattern of fcc Pt. The as-deposited grain size, as seen by transmission electron microscopy, is 90-120Å, whether on Si or SiO_2. Only on single-crystal sapphire has strong preferred orientation been observed. When CVD Pt on SiO_2 is heated to 500°C or so, as would happen when PtSi contacts were being formed, rapid growth to grains several microns across occurs.

CVD Pt resistivity has been measured on 750 ± 25Å films using a four-point probe. The films were deposited on thermal silica at 225°C. The result was 18 μohm-cm. The accepted value for bulk Pt is 10 μohm-cm. Sputtered or e-gun Pt films also are in the range 1.5—2 times bulk resistivity. CVD Pt films heated to 525°C for 30 min had resistivities of 11 μohm-cm.

Adherence.—This property is always of particular interest for microelectronic applications, especially with a noble metal where adhesion is not expected to be aided by chemical bonding with the substrate. For a quick comparative adherence measurement we have used a Kentron microhardness tester with a 5 mil radius diamond stylus which could be loaded with from 1 to 1000g. The sample was moved by a micrometer stage while in contact with the stylus, and the resulting scratch was examined under the microscope. Any exposure of the substrate anywhere along the track, or any detached metal debris, was called an adherence failure. In Table III typical results for a number of films are given, so that CVD Pt may be located on a scale with other common film-substrate combinations.

Considering the mild deposition conditions, the adherence of CVD Pt is remarkably good. Adherence to insulators is comparable to that of active metals such as Al or Ti. Pt on deposited Al_2O_3 (where double-dielectric IGFET's now use Ti as a "glue" for metalization) is especially tenacious; we have not seen a sample which failed at less than 500g. At such loads the silicon is as likely to fail as the Pt-insulator bond. In fact, such a failure occurred in attempting a gold "nailhead" pull test (1 mm diam 90° thermal compression bond) on the structure Au/CVD Pt/Al_2O_3/SiO_2/Si. At 10 lb the Si ruptured. The Pt samples of Table III were remeasured 3 months later with no substantial changes.

All adherence testing is empirical and often ambiguous and subjective. Scratch testing does not predict beam lead adherence. Certainly the most meaningful adherence test is one which most closely mimics the conditions the actual structure is subject to. But CVD Pt does appear to stick very well, as well as sputtered Pt does; indeed, no case of spontaneous peeling from

Table III. Scratch tests for adherence

(5 mil radius diamond stylus)

System	Approx. failure load (g)
Metal film marginal for Scotch tape pull test	5-10
Evap. Au on SiO_2, dep'd. Si_3N_4, dep'd. Al_2O_3	3-5
Evap. Al on SiO_2	100
Evap. Al on dep'd. Al_2O_3	500
E-gun evap. Pt on Si or SiO_2	80-500 (quite variable)
Low-voltage triode-sputtered Pt on Si or SiO_2	350-500
CVD Pt: on Si, SiO_2, Sapphire	50-300
on dep'd. Al_2O_3, Si_3N_4	≧500
on evap. Ti/dep'd. Al_2O_3	>100 (Ti/Al_2O_3 failed first)
on CVD W/dep'd. Al_2O_3	>500

any substrate has ever been observed. Possibly conditioning of the substrate by PF_3 plays a role in this adherence.

Analysis of the Pt.—The deposited Pt films have been analyzed by two techniques: electron beam microprobe analysis and Auger electron spectroscopy combined with argon or xenon ion sputtering (14). Microprobe results must be based on the assumption that the film is homogeneous, whereas the Auger analysis can establish a profile.

The only foreign element detected in significant amount by the microprobe is phosphorus, with the reported content varying with deposition parameters. The actual figure is meaningless, since the Auger spectra have repeatedly shown that the phosphorus is concentrated in the outer 50Å of the Pt film. At the surface it is a major component; in most of the film it is undetectable, *i.e.*, <0.5 atomic per cent (a/o). The phosphorus content is four or five times higher if the deposition is carried out in nitrogen instead of hydrogen—not a recommended procedure, although there is little change in the appearance of the film.

Trace amounts of fluorine, oxygen, or carbon have been detected irregularly by the electron microprobe.

Whether there is phosphorus enrichment at the Pt-substrate interface is still moot at this writing. It is certainly much less than at the Pt surface. The question is not trivial because of the possibility of n-doping of Si during PtSi formation. The Auger spectra also show that the Pt-Si interface is not sharp after 225°C deposition: there is a zone roughly 300Å thick with major amounts of both elements (14). This result agrees with the conclusions of Hiraki *et al.* (15) that Si diffuses rapidly through some metal films at temperatures far below the eutectic.

Auger spectra have confirmed the presence of small amounts of carbon scattered through some of the CVD Pt film samples. The source is probably a volatile organic impurity in the $Pt(PF_3)_4$. There is evidence from the infrared absorption spectrum for an impurity absorbing at 1026 cm^{-1}, but it cannot be identified.

Film stress.—Stresses in deposited Pt films are of interest because they must be balanced by stresses induced into the substrate, and because they influence the interdiffusion of Pt and other metals or Si. Average film stress on (111) Si was measured by interferometric determination of beam bending (16), with results as given in Table IV. Two PtSi samples are included. All the films were under considerable tension, with the CVD Pt, at 4.7×10^9 dynes/cm^2, only about a quarter of the stress of a low-voltage sputtered Pt. It can be calculated that the thermal expansion mismatch between Pt and Si in cooling from 225°C to room temperature can account for about 2.8×10^9 dynes/cm^2; the remainder must be "intrinsic" stress.

The tensive stresses in Table IV are far above those that pure bulk Pt could sustain without plastic flow. The shear modulus μ of Pt is 6×10^{11} dynes/cm^2, and for single-crystal metals the flow stress is of the order of $10^{-4}\mu$. It is well known that much higher stresses may be observed in films of very small randomly oriented crystals. Chaudhari *et al.* (18) have presented a mechanism accounting for stresses of $1\text{-}2 \times 10^{-2}\ \mu$ for crystallite sizes of 100-200Å. For Pt this would allow flow stresses of $\sim 10^{10}$ dynes/cm^2, in close accord with our measurements. The data of Table IV thus very likely represent the elastic limits of the films, and differences can be accounted for by small amounts of Pt-Si alloying. In fact, the Auger spectra showed considerably more Si in as-deposited sputtered Pt than in CVD Pt—and, of course, very similar amounts in the silicides made from them.

Table IV. Average film stress on (111) Si at room temperature

Film	Thickness (Å)	Substrate temp (°C)	Stress (10^{10} dynes/cm²)
E-gun evaporated Pt[a]	1000	225	+1.2
Low-voltage sputtered Pt	500	?	+1.8
CVD Pt	600	225	+0.47
PtSi, l.v. sputtered	1000[b]	625[c]	+1.9
PtSi, CVD	2000[b]	525[c]	+1.0

[a] Calc. from Ref. (17).
[b] PtSi assumed twice Pt thickness.
[c] Sintering temp.

The high stress in deposited Pt films may be implicated in what we observe when Pt is deposited over films of active metals. When CVD Pt was deposited on evaporated Ti or CVD tungsten a dendritic crystal pattern developed on the surface within a few days, appearing to the eye as haze. Reflection electron diffraction gave complicated patterns whose only certain interpretation was that the crystals were not merely Pt. Some of the spacings agreed with those for Ti (or W) oxides, or with intermetallics like Ti_3Pt. In any case, there is a strong hint that at the 225°C deposition temperature the underlying metal diffused into or through the Pt. There is other evidence that at such temperatures Ti may diffuse through Pt and form rutile at the surface (19).

The crystallization may be stress-nucleated. Figure 5 shows crystals growing from the edges of a stylus trace in CVD Pt on ~1000Å CVD W (from $WF_6 + H_2$) on deposited Al_2O_3. In areas where the W was masked against Pt deposition there were no crystals along the stylus mark.

CVD Pt for field plates.—Pt electrodes of various sizes for MOS testing have been delineated on both SiO_2 and Al_2O_3 using Shipley AZ 1350H resist. The etch was 4 H_2O: 3 HCl: 1 HNO_3, 1-2 min at ~85°C. Resist adherence appeared good; there was no difficulty with edge lifting.

The first question to be answered is whether the CVD Pt process is in any way detrimental to the IGFET Al_2O_3/SiO_2 double insulator. Typical IGFET material was Pt-deposited, heated to 600°C (as would be done to form the PtSi contacts), cooled, and the Pt stripped off with aqua regia. The C-V characteristic was taken with a mercury probe before and after this procedure. A portion of each slice received the temperature cycling but not the Pt deposition, and therefore served as control.

Results of these tests are summarized in Table V. The 600° heating has caused some shift in the flatband voltage. In all cases, however, the shift is virtually identical for the Pt-deposited samples and the controls. The changes in Si doping level are also insignificant. We conclude that the CVD Pt process could be used for IGFET's without harm to the gate insulation.

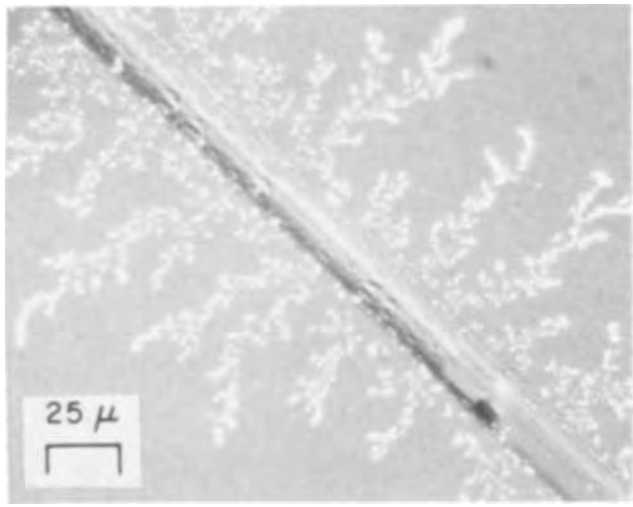

Fig. 5. Development of crystal dendrities along a stylus trace in CVD Pt over CVD W. Interference contrast, 410X.

Table V. Effect of CVD platinum deposition and sintering on Al_2O_3/SiO_2 dielectric

(Measurements with mercury probe)

Heat treatment (°C)	Conditions	V_{FB}	ΔV_{FB}	$\Delta N_D \times 10^{-11}$
600°, 30 min, H_2	Before Pt dep'n.	1.07 ± 0.05		
	After Pt, heat, Pt strip	1.82, 1.80	+0.74	+0.65
	Control, no Pt	1.72, 1.68	+0.63	+0.76
600°, 30 min, N_2	Before Pt dep'n.	1.06 ± 0.05		
	After Pt, heat, Pt strip	1.75, 1.81	+0.72	+0.63
	Control, no Pt	1.75, 1.73	+0.68	+0.42
600°, 30 min, H_2	Before Pt dep'n. (A)	1.86 ± 0.03		
	(B)	1.80 ± 0.05		
	After Pt, heat, Pt strip (A)	1.59 ± 0.03	−0.27	+0.5
	Control, no Pt (B),	1.50 ± 0.04	−0.30	+2.3

Limited stress-aging experiments using CVD Pt field plates have been carried out on both the Al_2O_3 (500Å)/SiO_2 (1000Å) double dielectric and on 1150Å dry-oxygen-grown SiO_2 annealed at 1100°C. For the former the conditions were: 300°C, 24 hr, ±10V; for the latter, 200°C, 30 min, ±10V. For most of the work, controls were available in the form of evaporated Al dots on another portion of the same slice used for the Pt tests. (In any case, there is a considerable history on bias-temperature aging of these insulators with Al electrodes.) C-V curves were taken with ±20V sweeps. Electrodes were contacted with gravity probes with Pt tips; these have been superior to any others in maintaining reliable contact, especially on Al, without serious damage to the metal film.

A summary of conditions and results appears as Table VI. In general, the Pt diodes aged very well, and clearly outperformed their Al controls. In only one case, with positive bias on the Pt with the double dielectric, was ΔV_{FB} >0.2V. Results were very reproducible—note the tight statistical distribution of V_{FB}'s. On occasion shifts of 0.1-0.4V were observed on heating the diodes without bias, or shorted, but this behavior is also characteristic of Al or Au metalization. There was no instance of peeling of Pt dots as a result of B-T aging.

Interface state density determinations are available on the second sample of Table VI. Diodes which had been heated without bias showed N_{fs} in the high 10^{10} cm^{-2} eV^{-1} range near midgap, while B-T aged diodes showed $N_{fs} = 4\text{-}7 \times 10^{10}$. These are slightly high; for Al, $N_{fs} < 5 \times 10^{10}$ is expected, but no Al controls for this run were available. Judging solely by the shapes of the C-V curves, Pt metalization and B-T aging never degraded interface state density, and in some cases (notably with the SiO_2 capacitors) definitely improved it. A CVD Pt deposition represents a 225° hydrogen bake.

With (100) n-Si, Pt field plates on the double dielectric give $V_{FB} \sim +1.6$V, V_T (calc.) $\sim +0.8$V. Pt on SiO_2 shows $V_{FB} \sim +0.2$V, with V_T (calc.) ~ -0.8V.

While the data of Tables V and VI are inadequate to establish firmly the aging behavior of CVD Pt-metalized diodes, there is certainly no evidence that phosphorus or fluorine impurities in the Pt are diffusing into the dielectric or drifting under bias. So far CVD Pt has been a stable, reproducible, adherent noble metal electrode, and one which should have a useful place in stress aging. Pt should not react with the dielectric, it will not react with atmospheric moisture and produce hydrogen, and the instability of Pt oxide at elevated temperatures keeps its surface clean and easy to maintain contact to.

Ohmic contact.—Generally the first Pt deposited on a device is interdiffused with Si in selected areas, forming PtSi (probably with some Pt_2Si) contacts to the underlying Si. These may be ohmic or Schottky diode contacts, depending mostly on the doping level of the Si. In any case, Pt deposited by any process must interdiffuse readily and reproducibly with Si at 400°-600°C, and Pt deposited on insulator areas must then be removed without damaging the silicide.

There has been extensive investigation of the formation of PtSi between Si and Pt from the $Pt(PF_3)_4$ process. It is planned to present information on the electrical characteristics of the resulting contacts in a separate report. For present purposes it is sufficient to say that CVD Pt has invariably alloyed readily with Si under identical time-temperature conditions used for sputtered Pt. A smooth silicide of normal appearance results. Under all conditions where a PtSi-Si contact is expected to give an ohmic characteristic, the contact using CVD Pt infallibly has done so. This includes n-Si of $N_D > 10^{18}$, and practically all levels of p-Si, since here the PtSi-Si barrier height is only 0.25 eV (20).

PtSi made from CVD Pt shows a somewhat greater susceptibility to attack by aqua regia than does conventional silicide. We believe this is due to the relatively high phosphorus content at the surface, which degrades the integrity and chemical resistance of the thin film of SiO_2 which ordinarily protects PtSi (21).[1] However, the silicide may be made immune to attack by deliberate superficial oxidation, for example by heating in air to ~500° for a few minutes. The oxide may be removed afterwards by a brief HF treatment.

The behavior of a CVD Pt film on an insulator when it is heated ≥600°C is believed to be another conse-

[1] Platinum silicide made in even the purest available inert ambient is covered with about 100Å of silica. If this protection is removed, the PtSi is rapidly and completely dissolved by the aqua regia used to strip unreacted Pt from the insulator areas of a circuit pattern.

Table VI. Bias-temperature aging with CVD platinum field plates

Sample	Dielectric	Field plate	Conditions[a]	V_{FB}	ΔV_{FB}	No. of diodes
6 ohm-cm (As) bulk (100) Si	500Å Al_2O_3/1000Å SiO_2	Pt	As deposited	1.77 ± 0.08[b]		9
			300°, 25 hr, no bias	1.75	−0.02	1
			300°, 1 hr, −10V	1.95 ± 0.03	+0.18	9
			300°, 25 hr, −10V	1.88 ± 0.06	+0.11	9
		Al	As deposited	0.19 ± 0.02		9
			300°, 25 hr, −10V	0.66 ± 0.06	+0.47	9
8 ohm-cm (As) epi/(100) n-Si	500Å Al_2O_3/1000Å SiO_2	Pt	As deposited	1.47 ± 0.03		9
			300°, 1 hr, short	1.81 ± 0.08	+0.34	9
			(A) shelf, 2 weeks	1.59 ± 0.03	+0.12	9
			300°, 24 hr, no bias	1.79 ± 0.03	+0.20	3
			300°, 24 hr, −10V	1.63 ± 0.03	+0.04	9
			(B) shelf, 2 weeks	1.54 ± 0.02	+0.07	9
			300°, 24 hr, no bias	1.68 ± 0.03	+0.14	3
			300°, 24 hr, +10V	1.21 ± 0.03	−0.33	9
5 ohm-cm bulk (100) n-Si	1150Å SiO_2 (dry O_2 oxide, annealed 1100°C)	Pt	As deposited	0.19 ± 0.02		12
			(A) 200°, 30 min, −10V	−0.01 ± 0.02	−0.20	6
			(B) 200°, 30 min, +10V	0.26 ± 0.03	+0.07	6
		Al	As deposited	−0.24 ± 0.03		12
			(A) 200°, 30 min, −10V	−0.84 ± 0.07	−0.60	6
			(B) 200°, 30 min, +10V	−0.89 ± 0.05	−0.65	5

[a] Tests were made in the order given.
[b] Variances are standard deviations.

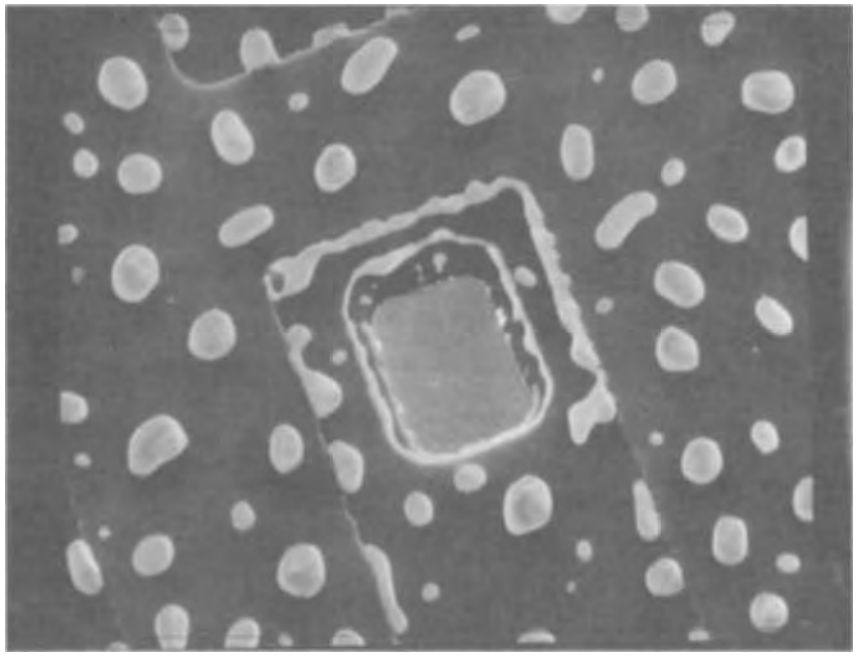

Fig. 6. Scanning electron microscope photograph of 0.3 x 0.4 mil PtSi contact formed from CVD Pt at 625°C, showing separation of Pt film on insulator into islands. The picture was taken at 45° tilt, 5000X.

quence of phosphorus segregation at the interfaces. The Pt-P system has a eutectic at 588°C. As this temperature is approached the film breaks abruptly into islands of metal with bare insulator in between. We suspect localized melting occurs where the Pt contacts the insulator, allowing strong surface tension forces to contract the film. The phenomenon is shown in Fig. 6, a 5000× scanning electron micrograph of a 0.3 × 0.4 mil contact hole in the Al_2O_3/SiO_2 double insulator. The smooth PtSi contact is seen near the center of the picture; note also the adherence of the Pt to the exposed edge of the Al_2O_3 layer. If the Pt-Si interdiffusion is carried out at temperatures below the Pt-P eutectic the film on the insulator remains smooth and unbroken.

The islanding phenomenon may impose limitations on the use of CVD Pt in some multilevel structures, since the better insulators are usually deposited at >600°C. It may be possible to find deposition conditions which will reduce the phosphorus content, or alternatively to remove most of the P from the surface chemically. Neither of these approaches has been tried as yet; doubtless it would be simpler to avoid temperatures over 550°C after the application of CVD Pt if the Pt, as such, is to remain a permanent part of the structure.

Conclusions

In solid-state device and integrated circuit technology, platinum has important applications in contacts and in metalization systems. However, present deposition methods cause radiation damage to insulating layers which may be unacceptably severe for some unipolar devices. Chemical vapor deposition of thin film Pt has consequently been studied. The two known methods were both found unsatisfactory. Pyrolysis of platinum acetylacetonate yields a film heavily contaminated with carbon. Reduction of platinum dicarbonyl dichloride yields a pure film, but adherence is poor, the source life is short, and the reaction is difficult to control.

A new method of Pt deposition, pyrolysis of $Pt(PF_3)_4$, has been studied in detail. The process is simple and reliable, and produces adherent bright films of very small crystals on a variety of substrates at 200°-300°C in hydrogen. Adherence to deposited Al_2O_3 and Si_3N_4 is particularly tenacious. The Pt contains small amounts of residual phosphorus, most of which apparently accumulates at the outside surface during deposition, or else is deposited last. Resistivity is normal for Pt thin films. The film is under tensile stress, but less so than those from e-gun evaporated or sputtered Pt.

MOS structures with CVD Pt field plates have shown good stability under bias-temperature aging, in fact better than their Al-metalized controls. CVD Pt on the usual IGFET $Al_2O_3/SiO_2/(100)$ Si gives $V_{FB} \sim +1.6$V, and on $SiO_2 \sim +0.2$V. The corresponding calculated threshold voltages are +0.8 and −0.8V, respectively. The stress-aging stability is considered evidence that residual phosphorus in CVD Pt does not permeate the dielectric, at least not in any electrically active form.

CVD Pt films behave like sputtered Pt in alloying readily with Si at 400°-600°C to form a smooth layer of PtSi. A low-resistance ohmic contact to Si is produced in all cases where theory predicts such a contact.

Finally, there is an important area of potential usefulness of the $Pt(PF_3)_4$ process which this report has not considered but which will be obvious to chemists. This is the platinum coating of particulate solids, porous materials, screens, irregularly shaped objects, plastics, etc., for corrosion resistance or catalytic activity.

Acknowledgments

The author acknowledges with gratitude the aid of the following: J. F. Roberts, for much experimental work; D. R. Wonsidler, for electron microprobe analyses; J. Drobek, for electron microscopy; and J. M. Morabito, for Auger electron spectroscopy.

Manuscript submitted Aug. 14, 1972; revised manuscript received Dec. 26, 1972. This was Paper 253 presented at the Miami Beach Meeting of the Society, Oct. 8-13, 1972.

Any discussion of this paper will appear in a Discussion Section to be published in the December 1973 JOURNAL.

REFERENCES

1. C. F. Powell, J. H. Oxley, and J. M. Blocher, Jr., "Vapor Deposition," pp. 310-314, and references therein, John Wiley & Sons, Inc., New York (1966).
2. E. H. Reerink, *Z. Anorg. Allgem. Chem.*, **173,** 45 (1928).
3. J. A. M. Van Liempt, *Metallwirtschaft,* **11,** 357 (1932).
4. A. E. Van Arkel, *ibid.*, **13,** 405 (1934).
5. J. Lewis *et al., J. Chem. Soc.*, **1965,** 6740.
6. Ventron Corporation, Chemicals Division, Beverly, Mass.
7. J. M. Lutton and R. W. Parry, *J. Am. Chem. Soc.*, **76,** 4271 (1954).

8. H. B. Lyon and G. A. Somorjai, *J. Chem. Phys.*, **46**, 2539 (1967).
9. G. Wilkinson, *J. Am. Chem. Soc.*, **73**, 5501 (1951).
10. J. F. Nixon, *Advan. Inorg. Chem. Radiochem.*, **13**, 364-469 (1970).
11. R. Schmutzler, *Advan. Fluorine Chem.*, **5**, 31 (1965).
12. E. Sirtl, Ger. Offenleg. 1,900,119 (Aug. 13, 1970); U.S. Pat. 3,619,288.
13. Th. Kruck and K. Baur, *Angew. Chem. Internat. Ed.*, **4**, 521 (1965); *Z. Anorg. Allgem. Chem.*, **364**, 192 (1969).
14. J. M. Morabito and M. J. Rand, To be published.
15. A. Hiraki *et al.*, *Appl. Phys. Letters*, **18**, 178 (1971); *Phys. Status Solidi (a)*, **7**, 401 (1971).
16. C. M. Drum, *Rev. Sci. Instr.*, **40**, 853 (1969).
17. R. E. Rottmayer and R. W. Hoffman, *J. Vacuum Sci. Tech.*, **8**, 151 (1971).
18. P. Chaudhari *et al.*, *ibid.*, **6**, 618 (1969).
19. T. C. Tisone and J. Drobek, Private communication.
20. M. P. Lepselter and J. M. Andrews, in "Ohmic Contacts to Semiconductors," Bertram Schwartz, Editor, pp. 159-186, The Electrochemical Society Softbound Symposium Series, New York (1969).
21. M. J. Rand and J. F. Roberts, To be published.

Technical Notes

An Optical Study of the Chemistry of Mn^{2+} During the Formation of Calcium Fluorophosphate Phosphors

A. Wachtel*

Westinghouse Lamp Division, Bloomfield, New Jersey 07003

and F. M. Ryan*

Westinghouse Research Laboratories, Pittsburgh, Pennsylvania 15235

In 1967, Parodi (1) reported a study which was concerned with the distribution of Mn between different phases which can form in the course of solid-state synthesis of Ca-fluorophosphate. One of the important findings was that one of the phases, namely CaO, has a very high affinity for Mn, so that a large fraction of the total Mn is found in CaO during early stages of the reaction. Parodi used electron-spin resonance to identify the Mn activated phases, and therefore the total Mn concentration had to be kept very low, typically about 1/100 of that normally employed in commercial halophosphate phosphors.

In order to avoid this difficulty, we used the excitation spectra to identify the phases. This enabled us to dope the halophosphates with the higher manganese concentration of 0.085 Mn/3P such as is used in typical cool-white formulations. The excitation spectra of the d^5 configuration of Mn^{2+} consists of a combination of sharp lines which involve transitions between energy levels whose separations are independent of crystal field strength, and broad lines which involve transitions between energy levels whose separations are strongly dependent on crystal field strength. In addition, the spectra are influenced by the site symmetry in which the Mn is located. These variations are sufficient to yield excitation spectra which are unique for each of the compounds.

In addition to higher Mn concentrations, we also included Sb or Cl or both in some of our preparations, since these compounds are normal constituents of Ca halophosphate phosphors. Raw mixes consisted of $Ca_2P_2O_7$, $CaCO_3$, and CaF_2 with the Mn incorporated in solid solution in one of these three compounds for each sample. Cl containing phosphors were prepared with NH_4Cl as usual, and Sb, where used, was added as Sb_2O_3. In order to follow the formation of intermediate phases, firings which lead to equilibrium conditions (*e.g.*, 1150°C for several hours) were avoided in most cases. Thus, most of the firing times were shorter and firing temperatures lower than are commonly used in preparing halophosphate phosphors. Under these conditions it was important to avoid oxidation of Sb which reaches a maximum in air at 900°C (2), as this would prevent its incorporation into the apatite phase. All firings were therefore conducted in a purified nitrogen atmosphere. In view of the limited firing conditions it was also important to avoid any possibility of incomplete mixing which could allow some local excesses in the ratio of total metal ions to phosphorous over the stoichiometric ratio of 5/3. Although Rabatin, Gillooly, and Hunter (3) have shown that the luminescent phase in halophosphate phosphors is stoichiometric apatite, it is well known that deviations from stoichiometry in which the metal to phosphorous ratio exceeds 5/3 are disastrous to luminescence efficiency, while ratios below 5/3 have a much smaller effect (4). We, therefore, deliberately employed formulations calculated to yield the slightly nonstoichiometric metal to phosphorous ratio of 4.95/3. The second phase of $Ca_2P_2O_7$ which could form due to this nonstoichiometry was considered to be a small effect compared to the large amounts of second phases present due to the limited firing conditions.

Results

Table I summarizes the twelve major variables investigated, and also presents relative line heights of the major reflections for apatite, $\beta Ca_2P_2O_7$, and $\beta Ca_3(PO_4)_2$ (in the order shown) as obtained by x-ray powder diffraction analyses. It can be seen that in most cases, preparations in which the Mn is added in solid solution to $Ca_2P_2O_7$ showed somewhat stronger apatite lines; however these differences are not very great. The only appreciable influence due to the form of Mn addition was noted in the 254 nm excited luminescence of fluoroapatite containing Sb but no Cl. In no case were we able to detect free CaO by x-ray powder diffraction analyses where present in appreci-

* Electrochemical Society Active Member.
Key words: halophosphate, manganese, phases, spectra, phosphors.

Table I. Properties of phosphors fired at 900°C for 30 min. as a function of composition

Cl	Sb	Measurements	Source of Mn $(Ca,Mn)_2P_2O_7$	$(Ca,Mn)CO_3$	$(Ca,Mn)F_2$
		X-ray diffraction*	75, 8, 5	77, 9, 0	72, 7, 4
–	–	Ex. spectra—apatite	Moderate	Very weak	Moderate
		Ex. spectra—CaO	Moderate	Strong	Moderate
		X-ray diffraction*	93, 3, 0	83, 0, 0	83, 4, 0
+	–	Ex. spectra—apatite	Strong	Strong	Strong
		Ex. spectra—CaO	Absent	Absent	Absent
		X-ray diffraction*	90, 0, 0	71, 8, 0	73, 6, 0
–	+	Ex. spectra—apatite	Strong	Strong	Strong
		Ex. spectra—CaO	Absent	Absent	Absent
		254× luminescence**	56.8	6.94	7.70
		X-ray diffraction*	87, 0, 0	88, 0, 0	83, 0, 0
+	+	Ex. spectra—apatite	Strong	Strong	Strong
		Ex. spectra—CaO	Absent	Absent	Absent
		254× luminescence**	42.0	37.0	39.2

* Numbers refer to line heights of strongest reflections for apatite, $\beta Ca_2P_2O_7$, and $\beta Ca_3(PO_4)_2$, respectively.
** Numbers refer to per cent brightness compared to a typical standard cool-white halophosphate, excited at 254 nm.

able quantity (top row). It was, however, easy to demonstrate its presence by the high pH of an aqueous slurry of the phosphor.

Figure 1 shows the excitation spectra of Mn activated phases which one might encounter during solid-state reactions leading to fluoroapatite. It was easy to identify those of $Ca_2P_2O_7$, $CaCO_3$, and CaF_2 in our raw mixes, but we found no more evidence of these in the mixtures after firing at 900°C. At least in the case of $\beta Ca_2P_2O_7$ that may be due to the similarity of its excitation spectrum with that of apatite. To detect it, one relies on the sharp line at 4025Å. We estimate that 5% of $\beta Ca_2P_2O_7$ would be undetectable in apatite, provided that the distribution coefficients of Mn are the same in both compounds and that equilibrium conditions exist. Among the remainder, only the excitation spectra of Mn in apatite and in CaO could be clearly identified in phosphors fired at 900°C or higher. This is shown in Fig. 2 where we see the effect of the source of Mn and of firing temperature. The top spectrum is that of a phosphor obtained at 900°C from a raw mix which contained the Mn in solid solution

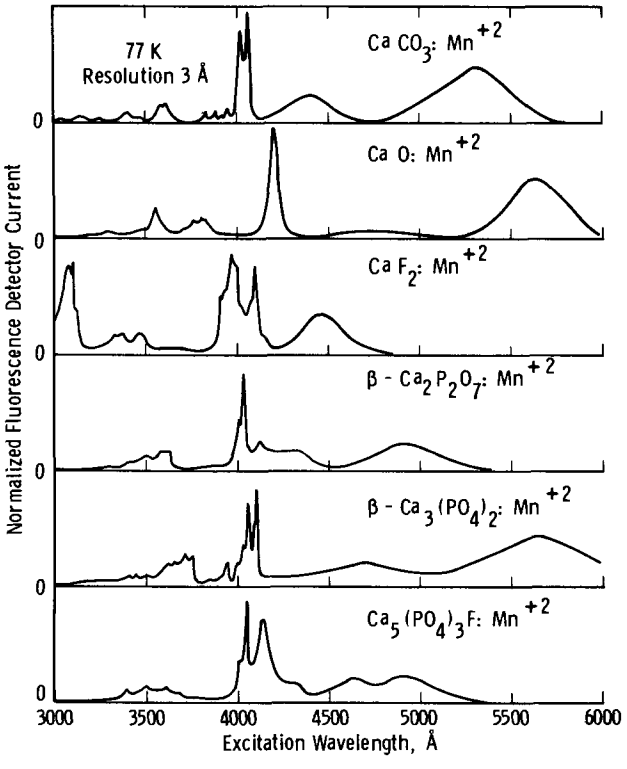

Fig. 1. Excitation spectra of Mn in raw materials and intermediates formed during solid-state reaction leading to fluoroapatite.

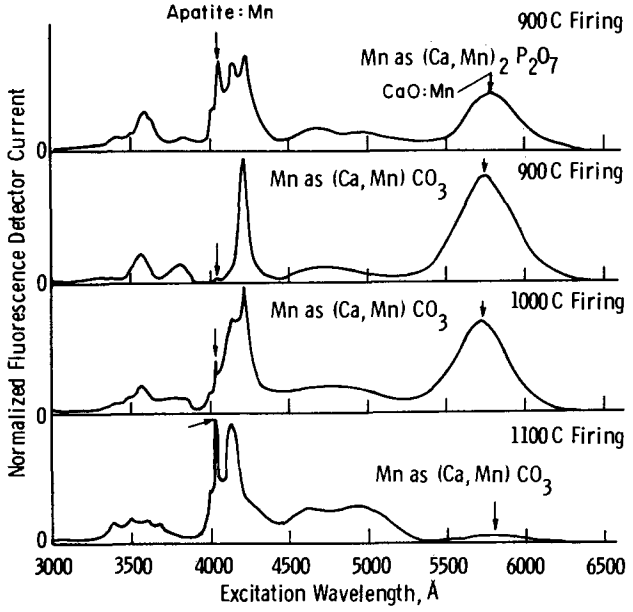

Fig. 2. Excitation spectra of Mn in fluoroapatite phosphor compositions. Detector currents of the individual spectra have been normalized to make them appear of equal height. No correction has been applied for the wavelength-dependent response of the system as a function of source of Mn and firing temperature. The arrows indicate the presence of Mn in the apatite phase as evidenced by the dominant sharp line in its excitation spectrum at 4037Å.

in $Ca_2P_2O_7$ (top left in Table I). It consists of fairly strong lines due to apatite, as well as evidence of strong fluorescence due to CaO:Mn. On the other hand, the fluorescence, if any, of the $\beta Ca_2P_2O_7$ and $\beta Ca_3(PO_4)_2$, shown to be present by x-ray powder diffraction analysis, could not be identified over the background. Phosphors derived from a mix containing the Mn in solid solution in CaF_2 show essentially the same spectra. The remainder of the figure shows the excitation spectra of phosphors derived from a mix containing the Mn in solid solution in $CaCO_3$. Here we note that at 900°C, the spectrum consists almost entirely of that of CaO:Mn. Only with increasing firing temperature does the excitability of Mn in apatite gain in strength, so that after firing at 1100°C, almost all of the CaO has disappeared.

Figure 3 shows the excitation spectra of phosphors containing Cl and Sb after firing at low temperatures. The spectra are restricted to a region near 3500Å because the fine structure there is suitable for showing

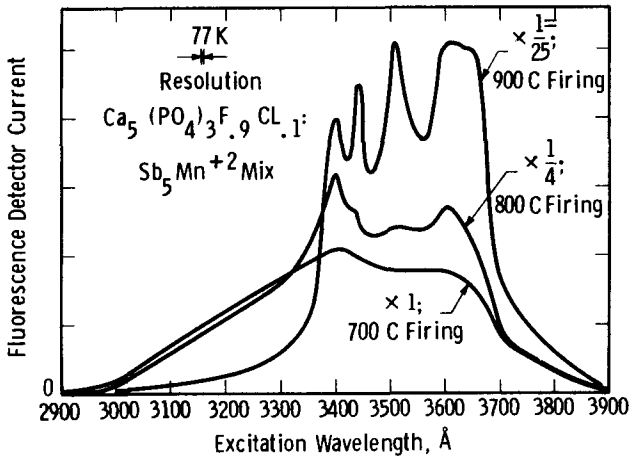

Fig. 3. Excitation spectra of Mn in fluoro-chloroapatite composition containing Sb, as a function of firing temperature.

the formation of a well-defined matrix. As one goes from 700° to 900°C, we note a very rapid rise in signal strength which is entirely due to Mn activated apatite. Although these phosphors were also derived from a mix containing the Mn in solid solution in $CaCO_3$, there was no evidence of CaO:Mn after firing at any temperature, or in any other region of the excitation spectrum.

Inasmuch as the presence of either Sb_2O_3 or NH_4Cl in the raw mix seemed to inhibit the formation of a separate CaO phase at low temperatures, we investigated these phenomena further by means of additional preparations. The effect of Sb was studied on a fluoroapatite containing 5.1 metal/3P, *i.e.*, designed to form with a separate phase of CaO even after firing to equilibrium conditions. This was accomplished by firing at 1200°C for 3 hr. Excitation spectra of a phosphor prepared without Sb did, indeed, show luminescence of Mn in apatite and in CaO of approximately equal intensity. However, the same phosphor, also doped with Sb, showed only a strong excitability of Mn activated apatite with no trace of CaO:Mn luminescence evident. This was so in spite of the fact that at this high metal/P ratio, there was none of the characteristic energy transfer from Sb to Mn, and indeed no Sb fluorescence could be observed.

The mechanism whereby NH_4Cl inhibited the formation of CaO may be twofold and was tested by (*i*) preparing chloro-fluoroapatite with $CaCl_2$ instead of NH_4Cl, and (*ii*) preparing fluoroapatite with 10% of the F addition as NH_4F instead of CaF_2, both followed by firing at 900°C for 30 min. The previous observations were now reversed, *i.e.*, the Cl containing phosphor showed free CaO, while the Cl-free phosphor contained no second phase of CaO. However, the amount of CaO in the chloro-fluoroapatite was appreciably lower than that observed in fluoroapatites prepared with CaF_2 as the sole source of F (*e.g.*, Table I and Fig. 2).

Discussion

The appearance of strong CaO:Mn luminescence in materials consisting mainly of apatite and containing less CaO than can be detected by x-ray powder diffraction analyses suggests that the apatite contained very little Mn, otherwise its signal would have swamped that of the CaO:Mn luminescence. Therefore, the affinity of CaO for Mn is very high, and concentration quenching is not pronounced. In particular, the high affinity of CaO for Mn is demonstrated by the fact that much of the Mn diffused from its original location in solid solution in $Ca_2P_2O_7$ or CaF_2 into freshly formed CaO, while in the case where it was originally located in $CaCO_3$, essentially all of it remained associated with the CaO which was formed by decomposition of the $CaCO_3$. Release of Mn for incorporation into apatite occurs only with the disappearance of the CaO, either by completing the apatite-forming reactions at higher temperatures, or by other means, *e.g.*, by reaction with excess ammonium halide to form the corresponding calcium halide.

The fact that phosphors prepared with 0.9 CaF_2 + 0.1 $CaCl_2$ contained less CaO than phosphors prepared with 1.0 CaF_2 is probably due to fluxing by the relatively low-melting $CaCl_2$ or $CaCl_2$-CaF_2 eutectics; the effect of excess ammonium halide (Cl or F) was considerably more pronounced.

The mechanism by which Sb_2O_3 inhibits the formation of free CaO is almost certainly due to formation of Ca-antimonites or antimonates (5) not only because the effect is obtained also at equilibrium conditions (prolonged high-temperature firing), but also because, at high metal/P ratio, there is no Sb luminescence, *i.e.*, the Sb does not seem to enter the apatite lattice. The fact that at 5.1 metal/3P one obtains the normal excitability of Mn in apatite also suggests that the generally observed dependence of halophosphate phosphor luminescence on the metal/P ratio is primarily governed by the efficiency of Sb luminescence.

Manuscript submitted Oct. 10, 1972; revised manuscript received Dec. 20, 1972.

Any discussion of this paper will appear in a Discussion Section to be published in the December 1973 JOURNAL.

REFERENCES

1. J. A. Parodi, *This Journal*, **114**, 370 (1967).
2. W. L. Wanmaker, A. H. Hoekstra, and M. P. A. Tak, *Philips Res. Rept.*, **10**, 11 (1955).
3. J. G. Rabatin, G. R. Gillooly, and J. W. Hunter, *This Journal*, **114**, 956 (1967).
4. A. Wachtel, *ibid.*, **113**, 128 (1966).
5. K. H. Butler, M. Y. Bergin, and V. M. Hannaford, *ibid.*, **97**, 117 (1950).

Emission Color of Y_2O_2S:Eu Phosphor

Harvey Forest

Zenith Radio Corporation, Melrose Park, Illinois 60160

Since the introduction of narrow-lined, red-emitting phosphors such as YVO_4:Eu, Y_2O_3:Eu, and Y_2O_2S:Eu into the color-television industry there has been a constant need for fast and accurate color measurements. Simple colorimetric techniques employing a combination of three or four filters cannot be used for narrow-lined emitting phosphors because the filters only approximate the gross features of the C.I.E. tristimulus curves and may be in considerable error at particular wavelengths. The need has become even greater with the increasing use of Y_2O_2S:Eu, since the emission color and brightness of this phosphor depends upon Eu concentration and synthesis procedure to a greater degree than Y_2O_3:Eu or YVO_4:Eu. Accordingly, samples of Y_2O_2S:Eu from various phosphor manufacturers show significant variations in color which are important when evaluating the brightness of a phosphor lot.

The color coordinates of Y_2O_2S:Eu at different Eu concentrations under cathode-ray excitation are shown in Fig. 1, indicating the well-known shift of the emission color from yellow to red with increasing Eu concentration. The color shift has been attributed to the sequential quenching of the $^5D_2$, $^5D_1$, and $^5D_0$ emitting states (1). The emission spectrum consists of many narrow lines from all three emitting states resulting in a composite color. The dominant emissions from $^5D_2$ fall in the blue-green region, $^5D_1$ in the green-yellow region, and $^5D_0$ in the yellow-red region so that as the $^5D_2$ and $^5D_1$ emissions are quenched with increasing Eu concentration, the emission color becomes more red. At commercial Eu concentrations [~3.6 mole per cent (m/o)] the $^5D_2$ emissions are not important and the emission color of the phosphor is determined by the relative amounts of $^5D_1$ and $^5D_0$ emissions.

In this paper, it is shown that the color of Y_2O_2S:Eu phosphors can be routinely determined by measuring the $^5D_0/^5D_1$ line intensity ratio (LIR) from the emission spectrum. Since $^5D_1$ and $^5D_0$ emissions belonging to the $^5D_1 \rightarrow {}^7F_3$ and $^5D_0 \rightarrow {}^7F_0$ transitions occur be-

Key words: phosphor, color, spectrum.

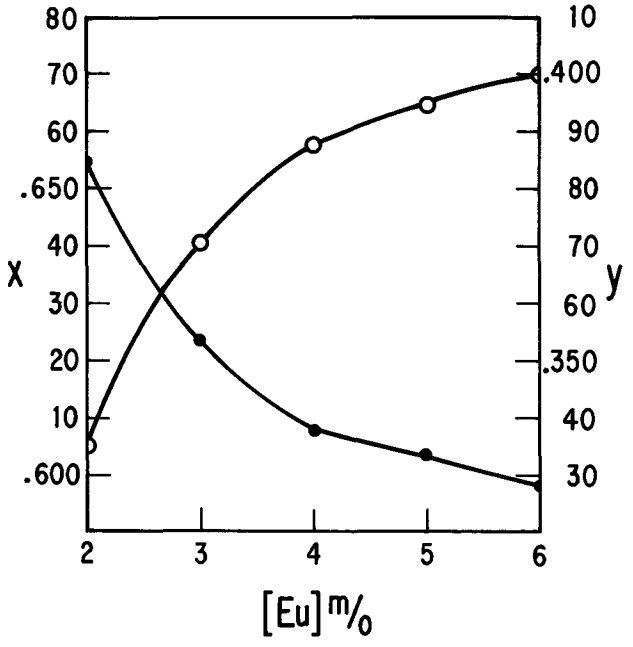

Fig. 1. Color coordinates (x,y) of Y_2O_2S:Eu under cathode-ray excitation for different Eu concentrations expressed in mole per cent. The open circles refer to the left ordinate (x) and the closed circles refer to the right ordinate (y).

tween 5800 and 5900Å, it is necessary to scan only this narrow wavelength range to determine the emission color of the phosphor. The emission spectrum can be obtained using shortwave ultraviolet excitation which eliminates the need for special sample preparation and vacuum techniques necessary for cathode-ray excitation. The entire measurement can be done in less than 5 min.

Since the $^5D_0 \rightarrow {}^7F_0$ transition is unsplit by the crystal field, the emission occurs as a narrow singlet, but the $^5D_1 \rightarrow {}^7F_3$ transition can be resolved into several emission lines. For all our measurements, a 0.25M Jarrell-Ash Monochromator with a 6Å bandpass was used which is sufficient to resolve the $^5D_1 \rightarrow {}^7F_3$ transition into two emission lines, although more lines can be resolved by decreasing the bandpass. The wavelengths of the $^5D_0 \rightarrow {}^7F_0$ and $^5D_1 \rightarrow {}^7F_3$ emissions are shown in Table I. The line intensities are measured directly from the emission spectrum after a baseline is drawn. No corrections are made for spectral sensitivity of the monochromator or phototube. Ratios are then determined from the line intensity of the $^5D_0 \rightarrow {}^7F_0$ emission line to either of the $^5D_1 \rightarrow {}^7F_3$ lines. So expressed the $^5D_0/{}^5D_1$ ratio would numerically increase as the emission color of the phosphor becomes more red.

A series of Y_2O_2S:Eu phosphors were prepared with varying Eu concentration from 2.5-6.0 (m/o) by the usual Na_2CO_3 + S flux synthesis procedure which directly converts Y_2O_3:Eu into Y_2O_2S:Eu with greater than 99% yield (3). The $^5D_0/{}^5D_1$ LIR were measured as described above and are plotted (open circles) in Fig. 2 *vs.* Eu concentration in mole per cent. A smooth curve can be drawn through the points and reproducibility of the ratio for different samples at the same Eu concentration is ±3%. The curve in Fig. 2 formed a working calibration curve for all our synthesis and color monitoring procedures.

Table I

Transition	Wavelength[a] (A)
$^5D_0 \rightarrow {}^7F_0$	5830
$^5D_1 \rightarrow {}^7F_3$	5865 5885

[a] Measured at 6A bandpass.

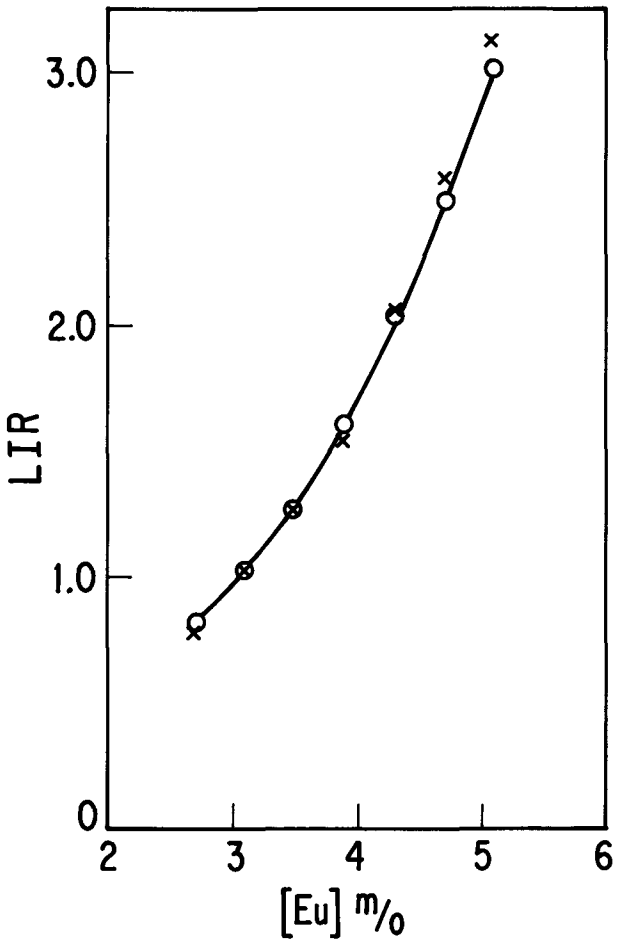

Fig. 2. $^5D_0 \rightarrow {}^7F_0/{}^5D_1 \rightarrow {}^7F_3$ line intensity ratio (LIR) *vs.* Eu concentration expressed in mole per cent. The open circles refer to Y_2O_2S:Eu phosphors made and measured at Zenith and the crosses refer to phosphors made and measured at Sylvania.

It now becomes a simple matter to determine quantitatively how close a particular sample of yttrium oxysulfide phosphor agrees with a standard color. The standard yttrium oxysulfide phosphor used by Rauland Tube Division has an LIR equal to 1.37 (3.63 m/o) while the phosphors manufactured domestically tend to fall in the range of 1.0-1.5. The more useful relationship between LIR and color coordinates (not shown) can be obtained by combining Fig. 1 and 2.

The curve in Fig. 2 has also been used by us as an analytical method for determining Eu in Y_2O_3 by converting an unknown Y_2O_3:Eu into Y_2O_2S:Eu and obtaining the mole per cent from the LIR. The reproducibility of the synthesis is within 3% so that the accuracy of the Eu determination using Fig. 1 is about 1.5% in the range of 2-6 m/o. It is possible to extend the range to either higher or lower concentrations. At the lower concentrations the $^5D_1$ emission lines can be used in some ratio combination with $^5D_1$ or $^5D_0$. A complete investigation comparing this procedure with other analytical methods for Eu is beyond this paper but we have used it in preference to atomic absorption (4).

A similar series of yttrium oxysulfide phosphors was synthesized at Sylvania Electric Products. The LIR were measured using their spectrometer and the normalized data (crosses) are plotted in Fig. 2. The agreement of their data with our data is very good. The average discrepancy between the two sets of data points is about 2% which seems to be greatest at the higher concentrations. Both sets of data points are listed in Table II. It is a little surprising that the proportionality between the data is linear even though the synthesis procedure and spectrometer used by each laboratory are not identical. This means that the

Table II. $^5D_0/^5D_1$ line intensity ratios

m/o Eu	Zenith's data	Sylvania's data	Sylvania's normalized
2.70	0.82	1.00	0.79
3.10	1.03	1.30	1.03
3.49	1.26	1.60	1.27
3.90	1.60	1.95	1.54
4.30	2.04	2.60	2.06
4.70	2.49	3.25	2.58
5.08	3.02	3.95	3.13

Normalization factor = 1.26 ± 0.26.
$^5D_1 \rightarrow {}^7F_3$ emission at 5865Å.

LIR method for determining the color of Y_2O_2S:Eu phosphors can be used to define a point of reference between two phosphor laboratories or more importantly between a phosphor manufacturer and a phosphor user.

Acknowledgment

I am indebted to Jim Mathers of Sylvania Electric Products for his cooperation and interest in supplying the data for his phosphor samples. Also I would like to acknowledge the assistance of Lyuji Ozawa of Zenith Research Laboratory in preparing this paper.

Manuscript received Dec. 1, 1972.

Any discussion of this paper will appear in a Discussion Section to be published in the December 1973 JOURNAL.

REFERENCES

1. L. Ozawa and P. M. Jaffe, *This Journal*, **118**, 1678 (1971).
2. O. J. Sovars and T. Yoshioka, *J. Chem. Phys.*, **49**, 4945 (1968).
3. M. R. Royce, U.S. Pat. 3,418,246 (1968).
4. L. Ozawa and H. Forest, *Anal. Chem.*, To be published.

Photoluminescence of Gel-Grown Pb(OH)I Single Crystals

A. Schwartz and J. C. O'Connell

U. S. Army Electronics Technology and Devices Laboratory (ECOM), Fort Monmouth, New Jersey 07703

Crystalline growth in gels containing a lead cation source and an iodine anion source will produce predominantly lead hydroxy-iodide with some lead iodide for gel *p*H greater than 7.0. Dennis *et al.* (1) have reported the growth of lead hydroxy-iodide in alkaline sodium metasilicate gels along with a few basic properties of the material. The purpose of this paper is to report some recent photoluminescent measurements on this double salt.

The method of growth which is essentially the same as in previous work has been modified somewhat resulting in increased crystal size. Acidified sodium metasilicate gels were prepared at room temperature in glass U-tubes in the *p*H range 6.0-7.3. The cation source was a 0.2-0.4M lead nitrate or lead acetate solution. The anion source was a 0.1-0.3M potassium iodide. The reaction was allowed to proceed at room temperature with crystal growth beginning in approximately 2 weeks.

The resulting crystals were rods up to 30 mm in length and 2 mm^2 cross section. Hexagonal lead iodide and its spherulitic polymorph were also present (Fig. 1). The clarity of the lead hydroxy-iodide crystals varied considerably with most having some occluded regions. A representative spectrographic analysis averaged over a number of crystals shows that Si is incorporated in the crystal from the gel (Fig. 2). Iron and other impurities are present in lower concentration.

Lead hydroxy-iodide has been reported to be a p-type semiconductor with an optical absorption edge at room temperature of 430 nm as determined from absorption and photoconductivity measurements (1). It was felt that investigation of the photoluminescence at liquid nitrogen temperature would provide additional information on crystalline growth and structure.

Lead hydroxy-iodide single crystals were mounted in an optical dewar and coated to liquid nitrogen temperature. Monochromators were used to provide u.v. excitation and to analyze the luminescent emission. The resulting emission curves were corrected for source, monochromator, and photomultiplier response.

The lead hydroxy-iodide emission spectrum is a broad band whose peak wavelength occurs at 560 nm (Fig. 3). Measurements were made for the *E* vector perpendicular and parallel to the *c*-axis of the crystal with the curves differing by a factor of three. Excitation for these curves was 350 nm.

Excitation spectra are shown for three crystals in Fig. 4. A sharp absorption edge occurs at 355 nm in all crystals. Variations in response at shorter wavelengths are large most probably due to surface influences.

Key words: lead hydroxy-iodide, photoluminescence, gel-growth, single crystals.

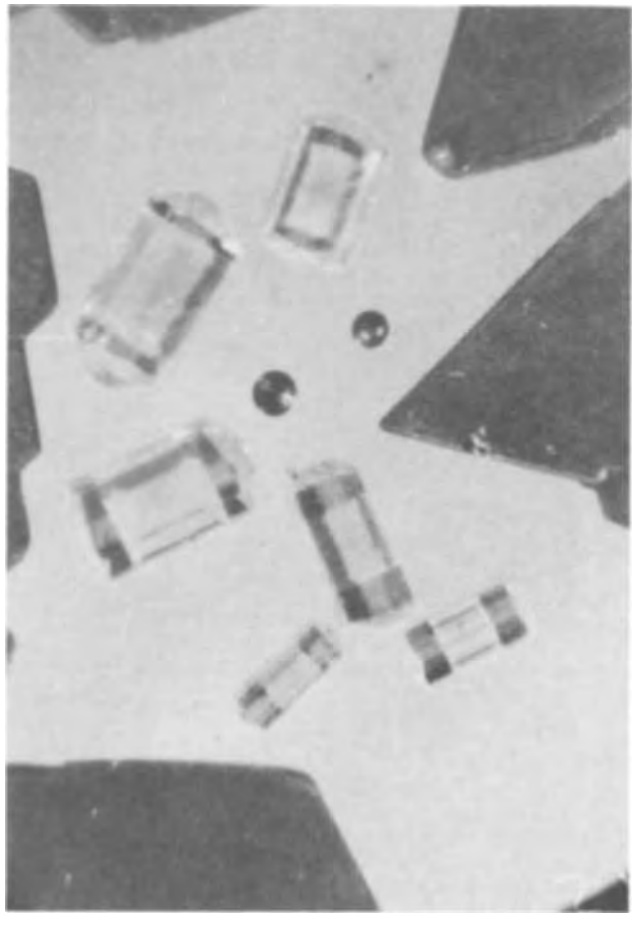

Fig. 1. Lead hydroxy-iodide crystals in which lead iodide and its spherulitic polymorph were also present.

Element	Wt. %
Pb	Major
Si	0.07
Fe	0.02
B	0.01
Mg	0.002
Ag	0.001
Ca	0.001
Cu	0.0002
Al	0.0002
Sn	0.0001

Fig. 2. Averaged spectrographic analysis of lead hydroxy-iodide showing that Si is incorporated in the crystal from the gel.

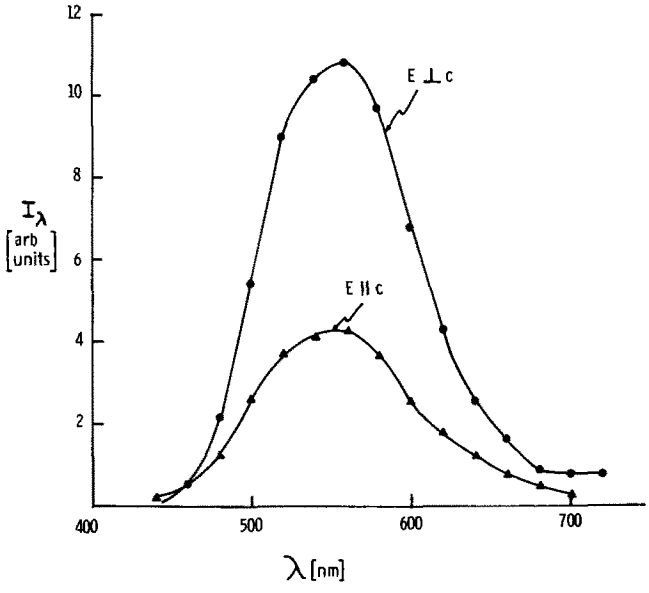

Fig. 3. Photoluminescent spectra of Pb(OH)I single crystals at 77°K.

While monitoring the peak emission of the lead hydroxy-iodide crystals the temperature was increased to room temperature (Fig. 5). Above 200°K the luminescence was thermally quenched with an activation energy of 0.3 eV.

Microscopic examination of the crystals showed that emission is inhomogeneous and occurred near and at occluded areas.

In summary, during the growth of lead hydroxy-iodide single crystals in gels, Si as well as other impurities are incorporated in the crystal. The Si may be in the form of silicon dioxide as in the case in certain gel-grown calcite. Since emission occurs primarily at or near occluded areas rather than transparent ones, impurity activation is highly probable although no identification can be made at this time. A series of rare-earth doped lead hydroxy-iodide has been grown and photoluminescent measurements along with microprobe data on impurity distribution will be pursued.

Acknowledgments

We would like to express our appreciation to D. W. Eckart for x-ray diffraction work and to J. W. Mellichamp for the spectrographic analysis.

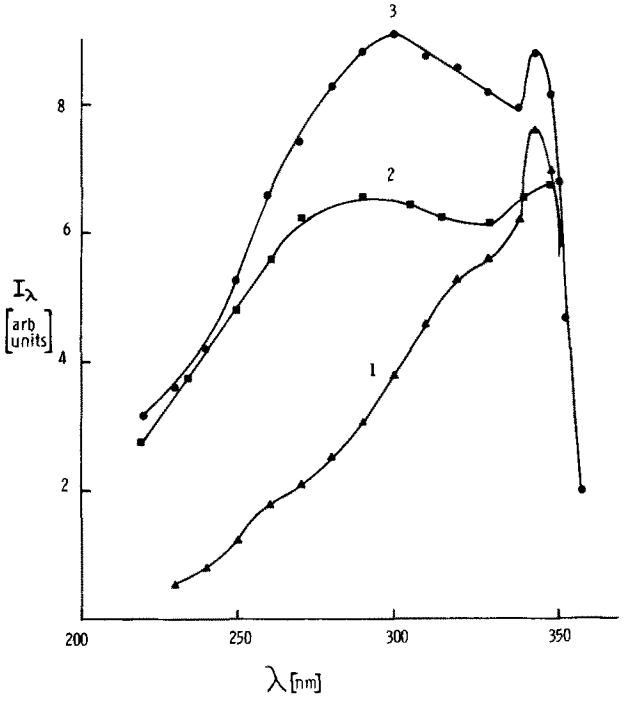

Fig. 4. Excitation spectra of Pb(OH)I single crystals at 77°K

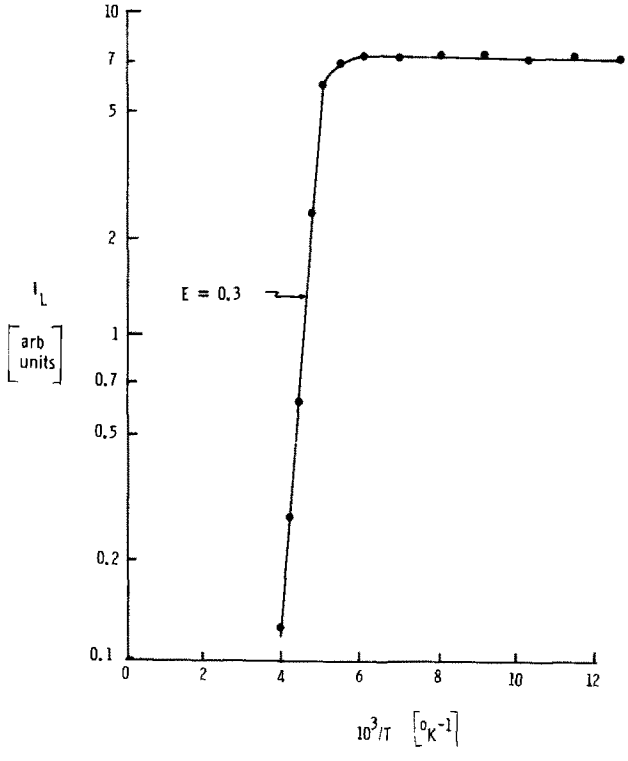

Fig. 5. Temperature dependence of photoluminescence of Pb(OH)I single crystals.

Manuscript submitted Nov. 13, 1972; revised manuscript received Dec. 18, 1972.

Any discussion of this paper will appear in a Discussion Section to be published in the December 1973 JOURNAL.

REFERENCE

1. J. Dennis, H. J. Henisch, and P. J. Cherin, *This Journal*, **112**, 120 (1965).

Method for Determining the Metallurgical Layer Thickness of Epitaxially Deposited Silicon from SiH_4 down to 0.5 μm

F. C. Eversteyn and G. J. P. M. van den Heuvel

Philips Research Laboratories, Eindhoven, The Netherlands

The thickness of epitaxially deposited silicon films can be determined with different techniques. Widely used methods are bevel and stain and infrared interference on highly doped substrates. A survey of these techniques has been given by Schumann (1). Each technique results in a thickness peculiar to the method used. For epitaxial silicon layers thinner than about 5 μm especially there is a need for a simple technique with which the metallurgical layer thickness, defined as the deposited layer thickness, can be determined because: (*i*) accepted methods for thick layers (*e.g.*, more than 5 μm) become less accurate or cannot be used: (*ii*) investigation of the actual impurity profile, as affected by various processing steps, finds a well-defined reference point in the metallurgical interface; and (*iii*) quantitative knowledge resulting from (*ii*) gives a sound basis for the design of integrated circuits and discrete devices.

In this paper a method is described for determining the metallurgical layer thickness of silicon epitaxially deposited from SiH_4. To use such a method as a standard technique, specially for thin epitaxial layers (*e.g.*, less than 5 μm), it is necessary that the technique be (*i*) simple and rapid, (*ii*) accurate to the second decimal place, and (*iii*) applicable also for ultrathin epitaxial layers, *e.g.*, 0.5 μm.

It will be shown that the proposed method fulfills the above-mentioned conditions. Essentially the metallurgical layer thickness of epitaxially deposited silicon is derived from the thickness of the polycrystalline silicon layer deposited on an Si_3N_4-coated check slice simultaneously processed.

The relation between the metallurgical layer thickness of epitaxially deposited silicon and the thickness of polycrystalline silicon simultaneously deposited on Si_3N_4 has been F determined by using silicon substrates partially covered with about 1500Å Si_3N_4. The depositions have been carried out from an H_2-SiH_4 mixture in a horizontal, water-cooled, epitaxial reactor, basically without an HCl-etching treatment prior to epitaxial growth, at a temperature of 1020°-1050°C (pyrometer reading). The thickness of the polycrystalline silicon layer deposited on Si_3N_4 as well as the thickness of the epitaxially deposited silicon have been determined with a Taylor-Hobson Talystep with a conical tip of radius 12.5 μm. The polycrystalline silicon is partly removed with an etch containing 1 part HF (49%) and 1 part CrO_3 solution (500 gram CrO_3 in 1000 ml water), whereafter the thickness of the polycrystalline silicon layer can be measured. Subsequent removal of the Si_3N_4 with HF marks the original substrate surface as a reference for the measurement of the metallurgical film thickness of epitaxially deposited silicon. For the range of layer thicknesses between 0.1 and 10 μm the results of these measurements are given in Fig. 1. It turns out that the relation between the metallurgical layer thickness of epitaxially deposited silicon ($d_{\text{met.Si}}$) and the thickness of polycrystalline silicon simultaneously deposited on Si_3N_4 can be given by the relation

$$d_{\text{met.Si}} = d_{\text{poly-Si(T)}} - 0.10\ \mu\text{m}, \qquad [1]$$

in which $d_{\text{met.Si}}$ = metallurgical layer thickness of epitaxially deposited silicon and $d_{\text{poly-Si(T)}}$ = thickness of polycrystalline silicon simultaneously deposited on Si_3N_4 and measured with a Talystep.

Key words: thickness determination, epitaxy, polycrystalline silicon, SiH_4, Si_3N_4.

Equation [1] can be used to determine the metallurgical layer thickness of epitaxially deposited silicon. However, for routine operation it is too cumbersome. That is why we have looked for an alternative which would permit a rapid determination of the thickness of polycrystalline silicon on Si_3N_4. For this purpose the thickness of the polycrystalline silicon on Si_3N_4 has also been determined by infrared multiple interference. We have used a Hitachi EPI-G3 spectrophotometer (k = 400-4000 cm^{-1}). The infrared interference spectra have been interpreted according to the method proposed by Severin (2) and shown in Fig. 2. The layer thickness [$d_{\text{poly-Si(i.r.)}}$] can be derived from the wave-number difference between two extrema as indicated in Fig. 2(a). To minimize the experimental error in determining the positions of the maxima and minima a more accurate method is given in Fig. 2(b). Since the wave-number difference between maxima and minima is constant, a straight line can be drawn through the extrema when the order of the interference extrema is plotted *vs.* the wave number. The slope of this line represents $2nd_{\text{poly-Si(i.r.)}}$ with n the refractive index of silicon (=3.42). In Fig. 3 the i.r. thickness of polycrystalline silicon on Si_3N_4 [$d_{\text{poly-Si(i.r.)}}$] is plotted *vs.* the corresponding Talystep thickness [$d_{\text{poly-Si(T)}}$]. It appears from this figure that up to 10 μm the thickness of polycrystalline silicon as measured with a Talystep is equal to the thickness as derived from multiple interference.

$$d_{\text{poly-Si(i.r.)}} = d_{\text{poly-Si(T)}} \qquad [2]$$

Combining Eq. [1] and [2] we obtain

$$d_{\text{met.Si}} = d_{\text{poly-Si(i.r.)}} - 0.10\ \mu\text{m}$$

The corrective term of 0.10 μm, which has to be substracted from the thickness of the polycrystalline silicon film on Si_3N_4 is due to the roughness of the poly-

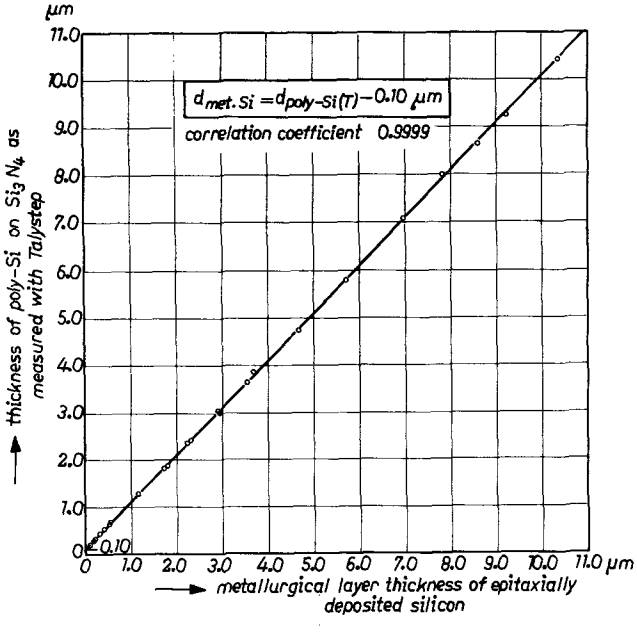

Fig. 1. Metallurgical layer thickness of epitaxially deposited silicon *vs.* thickness of polycrystalline silicon simultaneously deposited on Si_3N_4 as measured with a Taylor-Hobson Talystep.

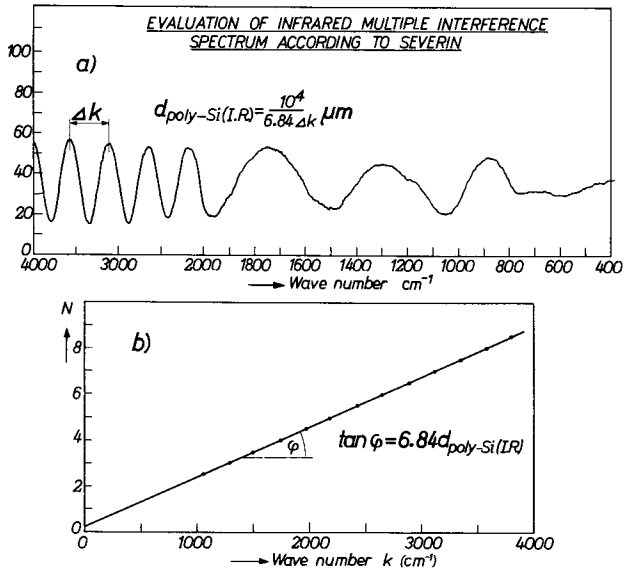

Fig. 2. (a), Infrared reflection spectrum of a 3.19 μm polycrystalline silicon layer; in this figure the way of determining the i.r. thickness is also indicated. (b), Wave number (*k*) vs. order of interference extrema (*N*) of the spectrum given in Fig. 2(a).

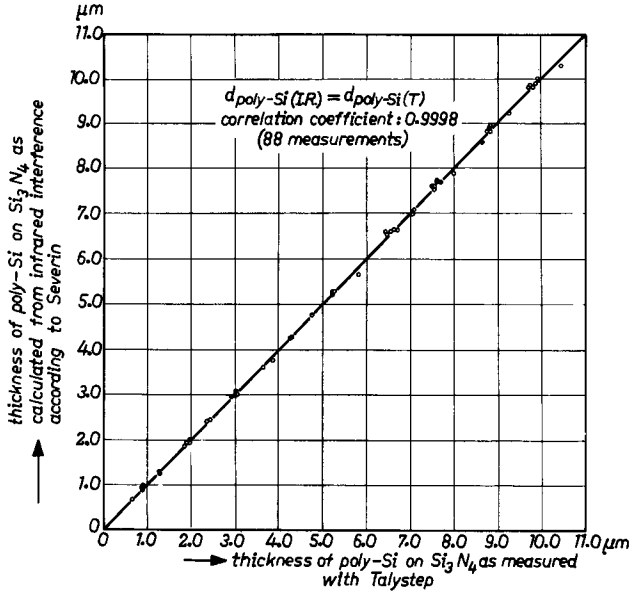

Fig. 3. Thickness of polycrystalline silicon on Si_3N_4 as measured with a Taylor-Hobson Talystep vs. thickness of polycrystalline silicon on Si_3N_4 as calculated from infrared multiple interference according to the method described by Severin.

crystalline silicon surface. Electron micrographs revealed the crystallites to have dimensions between 0.5 and 1.0 μm for the present process conditions. Because the thickness determination of the polycrystalline silicon on Si_3N_4 has been verified with a Talystep with a conical radius of the tip of 12.5 μm, the Talystep probe moves over the top of the grains of the polycrystalline silicon. In Fig. 4 a rough approximation is made of the correction necessary to derive the metallurgical layer thickness from the thickness of the polycrystalline silicon layer on Si_3N_4 in the case where the deposition rate is determined by mass transport from the gas phase. Assuming the crystallites to protrude through the surface by hemispheres, and assuming further that the bulk densities of polycrystalline and monocrystalline silicon are equal, we came to a correction value of 0.1 and 0.2 μm for crystallite sizes between 0.5 and 1.0 μm, respectively. The experimental value of 0.10 μm corresponds reasonably well to the calculated value taking the oversimplification into account.

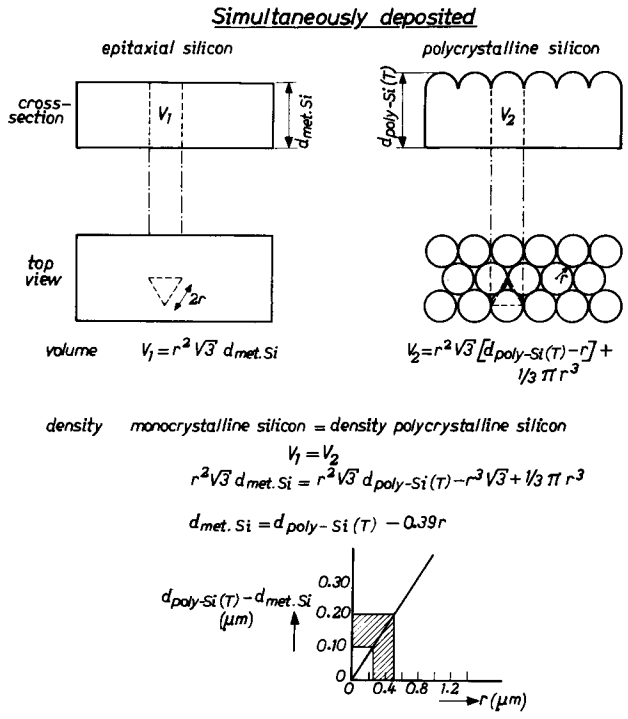

Fig. 4. Simplified model of the influence of surface roughness on correction necessary to derive the metallurgical layer thickness from the thickness of simultaneously deposited polycrystalline silicon.

It has been verified that *in situ* gas etching with hydrogen chloride does not affect the subsequent film growth and consequently this method can be used regardless of whether or not it has been applied. Also no difference has been found for (111)2-5° off and (100)1-3° off oriented substrates.

An SiO_2 coated check slice might be an obvious alternative for Si_3N_4, but the latter is preferable for the following reasons: (*i*) SiO_2 is less resistant to an HCl-vapor etch prior to epitaxial growth than Si_3N_4; and (*ii*) with SiO_2 near its edges a nonuniform deposition occurs, resulting in separately positioned crystallites, while with Si_3N_4 uniform deposition is observed all over the slice.

The influence of the thickness of Si_3N_4 on the value of the i.r. thickness of polycrystalline silicon on Si_3N_4 has been investigated. In Table I measurements are presented of polycrystalline silicon deposited on Si_3N_4 of various thicknesses. It turns out that up to 3000Å Si_3N_4, the i.r. thickness is equal to the Talystep thickness.

The proposed method for determining the metallurgical layer thickness can be used down to thicknesses of 0.5 μm. Below 0.5 μm no infrared interference fringes are obtained in the wave-number region of 400-4000 cm^{-1}.

The experimental error in the i.r. thickness is determined by the accuracy with which the positions of the extrema in the infrared-interference spectrum can be determined. This results in a final accuracy to within ±0.02 μm for silicon layers thinner than about 4 μm and ±0.5% for silicon layers thicker than 4 μm.

Table I. I. R. thickness and Talystep thickness of polycrystalline silicon deposited on Si_3N_4 of various thicknesses

Thickness of Si_3N_4 (Å)	I.R. thickness (μm)	Talystep thickness (μm)
500	3.18	3.19
500	3.22	3.23
1,500	3.18	3.17
1,500	3.27	3.25
3,000	3.22	3.17
3,000	3.26	3.25
6,000	3.35	3.20
6,000	3.36	3.28

Manuscript submitted June 20, 1972; revised manuscript received Nov. 30, 1972. This was Paper 214RNP presented at the Houston, Texas, Meeting of the Society, May 7-11, 1972.

Any discussion of this paper will appear in a Discussion Section to be published in the December 1973 JOURNAL.

REFERENCES

1. P. A. Schumann, Jr., in "Semiconductor Silicon," Rolf R. Haberecht and Edward L. Kern, Editors, p. 662, The Electrochemical Society Softbound Symposium Series, New York (1969).
2. P. J. Severin, *Appl. Opt.*, 9, 2381 (1970); *ibid.*, 11, 691 (1972).

Chemical Composition and Electrical Properties of Tin Oxide Films Prepared by Vapor Deposition

J. A. Aboaf* and V. C. Marcotte

IBM System Products Division, East Fishkill Facility, Hopewell Junction, New York 12533

and N. J. Chou*

IBM Thomas Watson Research Center, Yorktown Heights, New York 10598

Tin oxide films have been widely used as conductive electrodes on glass substrates because of their transparency in the visible region of the spectrum. They can be prepared either by reactive sputtering (1, 2) or by hydrolysis of $SnCl_4$ in various ambients (3-5). To attain high electrical conductivity the SnO_2 films are usually doped with antimony or bismuth (1-3, 6, 7). However, highly conductive films have also been obtained by hydrolysis without intentional doping (4, 6). In the latter case, the increased conductivity was attributed to the oxygen deficiency (or excess tin) in the SnO_2 films (4). In this brief note we report the experimental evidence relating the changes in electrical conductivity and current-carrier concentration to the chemical composition of the polycrystalline SnO_2 films prepared by vapor deposition from the reaction of $SnCl_4$ with water vapor. Our x-ray and electron microprobe analyses suggest that the observed variation in these films can be attributed to a combination of the departure from stoichiometry and the incorporation of chlorine in the films. A more accurate investigative technique is, however, necessary in order to relate them quantitatively.

The SnO_2 films were vapor-deposited on oxidized Si substrates in a resistance-heated tube furnace (59 mm inside diameter) from the reaction of $SnCl_4$ with water vapor at various temperatures and ambients. About 200 cm^3/min of N_2 gas was used to transport the $SnCl_4$ vapor (high-purity grade) into the furnace tube in which either a N_2, H_2, or O_2 ambient maintained a flow of 5000 cm^3/min. Water-vapor saturated nitrogen was fed into the furnace at a rate of 400 cm^3/min through a nozzle situated at a distance of about 2 in. from the uniform hot zone. Such arrangement was essential in minimizing the reaction of $SnCl_4$ with H_2O prior to reaching the hot zone. The films obtained were clear and virtually insoluble in acids and bases.

The SnO_2 films deposited between 380° and 600°C were polycrystalline. Low-angle x-ray diffraction and reflection electron diffraction studies of the films indicated the presence of a second phase, most likely SnO, in the surface layer of the films. The thickness of this layer containing what was thought to be SnO appeared to decrease with increased temperature of deposition. The grain size of the films also increased with the deposition temperature. For 380°C, the grain size was less than 1000Å (see Table I).

The electron microprobe analysis has detected chlorine in the film deposits. Quantitative information regarding the composition of the films was obtained by using pure tin and fused quartz specimens as the standards for the analysis. The composition of the film samples was calculated from the raw intensities using Colby's MAGIC Program (8). A comparison was also made with a pure single crystal of SnO_2.[1] The results are presented in Table II. All samples including the single crystal appeared to be oxygen deficient. The oxygen content in the films was found to decrease with an increase in deposition temperature, regardless of the deposition ambient. However, the chlorine concentration was much lower for the films deposited in a hydrogen atmosphere. The reduction in Cl concentration is probably due to the effect of hydrogen in preventing the formation of intermediates containing chlorine, which cause subsequent doping of the films.

The resistivity and Hall effect measurements were made at 24° and −196°C, respectively, on films (≃2000Å thick) deposited in various ambients. The results for those deposited in a nitrgoen ambient are

[1] Courtesy of Professor D. A. Wright, University of Durham, Department of Applied Physics and Electronics, South Road, Durham City, England.

Table I. Crystalline structure of SnO_2 films deposited in N_2 at various temperatures

Deposition temperature (°C)	Low angle x-ray diffraction (bulk)	Reflection electron diffraction (surface)
380	SnO_2 + 1 extra line*	SnO_2 + 3 extra lines*
450	SnO_2	SnO_2 + 3 extra lines
525	SnO_2	SnO_2 + 3 extra lines
600	SnO_2	SnO_2 + 3 extra lines

* Extra lines match best with SnO.

Table II. Electron microprobe analysis of SnO_2 films deposited at various temperatures in N_2, O_2, and H_2 ambients

	Deposition ambient Composition*								
	N_2			O_2			H_2		
Deposition temperature (°C)	% Sn	% O_2	% Cl_2	% Sn	% O_2	% Cl_2	% Sn	% O_2	% Cl_2
380	77.4	19.1	1.2						
450	77.4	18.6	1.1	76.7	18.1	1.2	76.9	18.5	0.3
525	77.1	18.0	0.8	76.5	16.9	0.8			
600	76.6	16.5	**						
		% Sn			% O			% Cl	
Single crystal		79			19.4			—	
SnO_2 theoretical		78.8			21.2			—	
Precision limit		±0.4			±0.9			±0.4	

* In weight per cent.
** Below detectability limit.

* Electrochemical Society Active Member.
Key words: SnO_2, vapor-deposited films, resistivity and Hall effect measurements.

Table III. Electrical properties of tin oxide films deposited in a nitrogen ambient at various temperatures

Deposition temperature, °C	Measurement temperature, °K	Resistivity, ohm-cm	Coefficient Hall	Mobility, cm^2 V^{-1} sec^{-1}	Carriers, cm^{-3}
380	RT	1.1×10^{-2}	-6.2×10^{-2}	6.1	1×10^{20}
	77	1.2×10^{-2}	-6.6×10^{-2}	5.4	
450	RT	7.0×10^{-3}	-6.8×10^{-2}	9.6	9.1×10^{19}
	77	7.7×10^{-3}	-6.8×10^{-2}	8.8	
525	RT	2.3×10^{-3}	-2.21×10^{-2}	9.5	2.8×10^{20}
	77	2.4×10^{-3}	-2.2×10^{-2}	9.3	
600	RT	1.9×10^{-2}	-4.01×10^{-2}	2.78	1.55
	77	2.7×10^{-2}	-5.3×10^{-2}	1.95	1.2×10^{20}

shown in Table III. All films were found to be of n-type, the carrier concentration being $\sim 10^{20}$ electrons/cm^3. The electrical conductivity and carrier concentration measured at room temperature were essentially the same as measured at the liquid nitrogen temperature, implying an almost complete ionization of impurity centers at −196°C. This is in agreement with Kuznetsov's results (4), which showed that the impurity level was ≤ 0.02 eV below the conduction band edge of SnO_2. The conductivity of the films deposited in nitrogen is weakly dependent on the deposition temperature; the films deposited at 525°C are more conductive. A reduction in conductivity and carrier concentration was observed for the film deposited under comparable conditions in a reducing or oxidizing ambient.

A nitrogen-deposited SnO_2 film annealed in oxygen at 960°C for 1½ hr showed not only a decrease in oxygen content (18-16.9%), but also a reduction of chlorine concentration from 1.1 to 0.5%. The conductivity and carrier concentration of the film decreased in the process by an order of magnitude. It thus appears that the change in conductivity and carrier concentration cannot be attributed to the departure from stoichiometry alone. Our x-ray data have shown that chlorine was incorporated in the SnO_2 lattice either interstitially or substitutionally, since no chlorine-containing phases were detected. Substitutional or interstitial incorporation of chlorine should give rise to donor levels, thus increasing the conductivity and carrier concentration in n-type SnO_2 films. This is consistent with our observation that the conductivity and carrier concentration of a nitrogen-deposited film which contains 1.1 weight per cent (w/o) Cl is an order of magnitude higher than the film which was deposited at the same temperature in hydrogen but contains only 0.3 (w/o) Cl.

SnO_2 has a rutile structure; its unit cell contains four oxygen and two tin atoms, and has a volume of 71.6A^3 (9). One atomic per cent (a/o) of substitional chlorine (or singly ionized interstitial) would give rise to a carrier concentration of $\sim 8 \times 10^{20}$ electrons/cm^3. Our Hall effect data thus suggest that part of the chlorine incorporated is electrically inactive. For example, although the film deposited in nitrogen at 380°C contains 1.7 a/o Cl, it has a carrier concentration of only 1×10^{20} electrons/cm^3 (Table III). It is probable that the oxygen vacancies interact with chlorine to render the latter inactive. For the nitrogen-deposited films, the chlorine concentration decreases whereas the oxygen deficiency increases with the deposition temperature. The virtually constant carrier concentration over the same range of deposition temperatures lends further support to the contention that both the oxygen deficiency and the chlorine incorporation contribute to the carrier concentration in these films. Since the film deposits are polycrystalline, the grain boundary effect, coupled with the presence of SnO in the surface layer, makes it difficult to predict the behavior of electrical conductivity, even in qualitative terms. It is evident that a quantitative interpretation of the relationship between the chemical composition and the transport properties of the SnO_2 films would require analytical techniques of much greater accuracy than those we have used in this investigation.

Acknowledgment

The authors wish to thank J. E. Woods, R. Martin, and J. Keller for making x-ray, Hall effect, and conductivity measurements.

Manuscript submitted Sept. 26, 1972; revised manuscript received Dec. 27, 1972.

Any discussion of this paper will appear in a Discussion Section to be published in the December 1973 JOURNAL.

REFERENCES

1. W. R. Sinclair, F. L. Peters, D. W. Stillinger, and S. E. Koonce, *This Journal*, **112**, 1096 (1965).
2. J. L. Vossen, Symposium on Sputtering, Vacuum Society Meeting, Rochester, September 1969.
3. Hajime Sasaki, Yasuro Nishimura, and Tatsuji Yamamote, Proceedings Elec. Comp. IEEE, p. 79, May 1966.
4. A. Y. Kuznetsov, Translated from *Fisika Tverdogo Tela*, **2**, 35 (1960).
5. B. P. Kryzhanovski and A. V. Kruglova, *Russian Journal of Chemistry*, **45**, 2 (1971).
6. O. V. Vorob'eva and T. F. Polurotova, *Izvestiya Akad. Nauk SSSR*, **7**, 206 (1971).
7. C. A. Vincent and D. G. C. Weston, *This Journal*, **119**, 515 (1972).
8. J. Colby, *Adv. X-Ray Anal.*, **11**, 287 (1968).
9. D. A. Wright, *Proc. Brit. Ceram. Soc.*, **10**, 103 (1968).

JOURNAL OF THE ELECTROCHEMICAL SOCIETY

ELECTROCHEMICAL SCIENCE
— AND TECHNOLOGY —

JUNE
1973

The Thermal Power of the Solid Electrolytes Ag_4MI_5 and of Molten Mixtures of the Same Composition

K. E. Johnson,* S. J. Sime,[1] and J. Dudley[2]

Department of Chemistry, University of Saskatchewan, Regina, Saskatchewan, Canada

ABSTRACT

Measurements are reported of the thermal power with reversible silver electrodes of polycrystalline samples of Ag_4MI_5 (M = K and Rb) and of molten mixtures of the same composition (M also = Cs). The Wagner-Pitzer approximation for the entropy of a single ion is extended to molten mixtures and to nonbinary solid compounds and is used to calculate the heterogeneous contribution to the thermal power of Ag_4RbI_5. Then the heat of transport of Ag^+ in Ag_4RbI_5 solid may be calculated and is found to be 2.1 kcal mole^{-1}. The term $\sum_i \frac{t_i Q_i}{z_i}$ for molten Ag_4RbI_5 is found to be 3.2 kcal mole^{-1}. This same term is estimated from the variation of the homogeneous thermal power with temperature to be 2.5 ± 0.4 for the rubidium mixture, 2.7 ± 0.4 for the potassium mixture, and 3.7 ± 0.6 for the cesium mixture. The self-consistency of the results and the agreement between the heat of transport in solid Ag_4RbI_5 and the activation energy for diffusion (of Ag^+) support the use of the extended form of the Pitzer equation.

The high-conductivity solid electrolytes Ag_4MI_5 (M = K, Rb, and NH_4) were discovered independently by Bradley and Greene (1, 2) and by Owens and Argue (3). The crystal structure of the rubidium salt (4) shows that the silver lattice is highly disordered, there being 56 sites per unit cell for 16 silver ions. Measurements have been reported of the electrical conductivity (3, 5, 6) and silver ion diffusion (7) in Ag_4RbI_5 and activation energies for these processes have been determined. Johnston, Wiedersich, and Lindberg (8) have investigated the specific heat of this compound from 5° to 350°K, and reported values of the standard entropy, entropy of silver disorder at 300°K, and the disorder contribution to the specific heat. We have recently determined the enthalpy contents of the systems Ag_4MI_5 [M = K, Rb, Cs, NH_4, and $(CH_3)_4N$] as a function of temperature (9) and reported the heats of incongruent melting of the compounds (M = K, Rb, and NH_4).

Except for the recent publication of Chandra *et al.* (10) there have been no previous investigations of the thermal power of these systems. The major problem in the analysis of thermal power is in assigning a value to the partial molar entropy of the ion to which the electrode is reversible. Single-ion entropies are not independent thermodynamic properties and thus cannot be determined by experiment. The only expression available for the calculation of a single-ion entropy is the approximation of Wagner (11), extended by Pitzer (12), and this applies only to simple binary compounds. We have extended it to nonbinary solid compounds and molten mixtures, and further modified it to allow for the disorder of the silver sublattice. Using the available thermodynamic data one is then able to calculate the heterogeneous contribution to the thermal power of Ag_4RbI_5. The measurement of the thermal power thus allows one to calculate the heat of transport of Ag^+ in the solid and this may be compared with the activation energies for diffusion and conductance.

We have measured the thermal power of Ag_4RbI_5 and Ag_4KI_5 in the solid and liquid states and also that of the molten mixture Ag_4CsI_5.

Theory

The thermal power, θ (dE/dT of the thermocell) of a system with electrodes reversible to an ion j^+ is given by (13)

$$\theta = \theta_{hom} + \theta_{het} \quad [1]$$

where θ_{het}, the heterogeneous contribution, is given, for a reversible metal electrode with reaction $J \rightleftarrows J^+ + e$, by

$$F\theta_{het} = S_j - \overline{S}_{j+} - \overline{S}_{e(j)} \quad [2]$$

and θ_{hom}, the homogeneous term, is

$$F\theta_{hom} = \sum_i \frac{t_i Q^*_i}{z_i T} \quad [3]$$

In these expressions S_j, $\overline{S}_{j+}$, and $\overline{S}_{e(j)}$ are the partial molar entropies of pure j, the ion j^+, and the electron in the metal j, respectively; t_i, z_i, and Q^*_i are the transport number, the charge, and the heat of transport, respectively, of species i, and F is the Faraday. In the expression for θ_{hom}, the values of t_i and Q^*_i are dependent on the frame of reference chosen for the ion fluxes (14, 15). In the present work the crystal lattice is chosen as the reference for the solid compounds, and the iodine ions as the reference frame in the melt [the Hittorf frame (16)].

* Electrochemical Society Active Member.
[1] Present address: Department of Chemistry, University of Ife, Ife-Ife, Nigeria.
[2] Present address: University of Saskatchewan, Saskatoon, Saskatchewan, Canada.
Key words: entropy of transport, heat of transport, solid electrolyte, thermal power.

It has been shown that $\overline{S}_{e-(j)}$ is essentially zero (17) and Q^*_e may be neglected too; thus, as pointed out above, the major problem in the interpretation of thermal power data is the determination of $\overline{S}_{j+}$. The Wagner (11)-Pitzer (12) approximation assumes that short range interactions do not contribute significantly to the molar entropy of the system, or, if they do, that they are identical for each species present. In this case the configuration contribution to the molar entropy is equally divisible among the species. Thus, if classical statistical mechanics is applicable, Pitzer showed the entropy of an ion in a simple binary salt to be

$$\overline{S}_{M+} = \tfrac{1}{2}\left[S_{MX} + 3/2R \ln\left(\frac{M_{M+}}{M_{X-}} \right) \right] \quad [4]$$

where S_{MX} is the molar entropy of the salt and M_{M+} and M_{X-} are the molecular weights of the positive and negative species, respectively.

We may easily extend Pitzer's expression to the case of a molten mixture. Consider a system of $2N$ homovalent ions, N_i of species i. If x_i, the ion fraction of i, is defined as N_i/N, then the canonical ensemble partition function is given by

$$Q[2N] = \prod_i \frac{(q_i)^{N_i}}{N_i!} Z(R) \quad [5]$$

where $q_i = (2\pi m_i kT/h^3)^{3/2}$ and $Z(R)$ is the configuration integral.

The partial molar entropy of a species j is given by

$$\overline{S}_j = Nk \frac{\partial}{\partial N_j} \frac{\partial}{\partial T} T \ln (Q[2N]) \quad [6]$$

Thus the nonconfigurational contribution may be found directly to be

$$S_j^{nc} = R\left[\ln\left(\frac{q_j}{Nx_j} \right) + 3/2 \right] \quad [7]$$

We can thus determine the configurational contribution from the measured entropy for the systems S_{mes}. The expression is

$$S(Z) = \frac{S_{mes}}{2} - \sum_i \frac{x_i}{2} R\left[\ln\left(\frac{q_i}{Nx_i} \right) + 3/2 \right] \quad [8]$$

Dividing this equally among the species one obtains, noting that $\sum_i \frac{x_i}{2} = 1$

$$\overline{S}_j = 1/2\, S_{mes} - 3/2\, R \ln\left(\prod_i \frac{m_i^{x_i/2}}{m_j} \right) + R \ln\left(\prod_i \frac{x_i^{x_i/2}}{x_j} \right) \quad [9]$$

The last term in this equation arises from the entropies of mixing of the species. In the perfect crystal this term is zero (correspondingly the term $N!$ is not present in the partition function of a solid) and one obtains

$$\overline{S}_j = \frac{S_s}{n} - 3/2\ R \ln\left(\prod_i \frac{m_i^{n_i/n}}{m_j} \right) \quad [10]$$

where S_s is the molar entropy of the compound, and n is the number of ions per formula unit, n_i of species i.

In the case of solids in which one sublattice is highly disordered this expression does not apply directly. Before one can evaluate $S(z)$ from the measured molar entropy, one must subtract the part of the total entropy due to disorder of the sublattice and assign it separately to the disordered species. If this is done the final expression is, if j^+ is the disordered species

$$\overline{S}_{j+} = \frac{S_s - S_{dis}}{n} + \frac{S_{dis}}{n_j} - 3/2\, R \ln\left(\prod_i \frac{m_i^{n_i/n}}{m_j} \right) \quad [11]$$

Experimental

All the chemicals used were supplied by British Drug Houses (reagent grade). Mixtures of the correct stoichiometry were made and filtered through a sintered glass frit to remove any silver metal formed by photo decomposition of the silver iodide. The resultant solid was powdered, and stored in the dark before use.

The apparatus used for the measurements is shown in Fig. 1. It consisted of a Pyrex "H" tube (about 13 cm high, 10 cm wide), with fritted disks A, at the entrance to each arm to prevent thermal diffusion in the melts, and a central tube B. The electrodes, C, consisted of silver wire sealed inside an alumina tube so that only a small bead of silver, at the end of the tube, had contact with the melt. The Pt/Pt, 13% Rh thermocouples were mounted in Pyrex wells D so that the junction was level with the point of the electrode. The cell was wrapped in aluminum foil, the sensing elements of the temperature controllers put against each arm, and the whole wrapped in more foil. This served the dual purpose of reducing temperature gradients within each arm, and, when the foil was grounded, of isolating the electrodes from the heating elements. These were lengths of heating tape wound separately around each arm of the cell. The current through each was controlled by a separate temperature controller (Cole-Palmer Proportional 1300 series). The whole was mounted in a mass of vermiculite for insulation.

The cell was filled by heating both arms above the melting point of the mixture, filling them with the powdered solid, and then sucking the melt through the frits by applying a vacuum to the tube B.

The thermal power at a temperature t_m was determined by measuring the thermal emf at five different temperature gradients (between 0 and 17°C) with the mean temperature within ±0.4°C of t_m. These points fell in a good straight line, and the gradient was determined by linear least squares.

For convenience, within each set of five points, the temperature gradient was in the same direction across the cell. It was general practice, however, to reverse the direction before commencing the next set. Intercepts on the ΔT axis were generally less than a millivolt, and explicable in terms of thermal diffusion within the electrode compartment.

Potentials were measured with a Guildline potentiometer (Model 9174) using a preamplifier (9460 A) and a galvanometer (9461 D) as a null detector.

In any run measurements were made first on the melts, t_m being cycled between 10°C above the melting

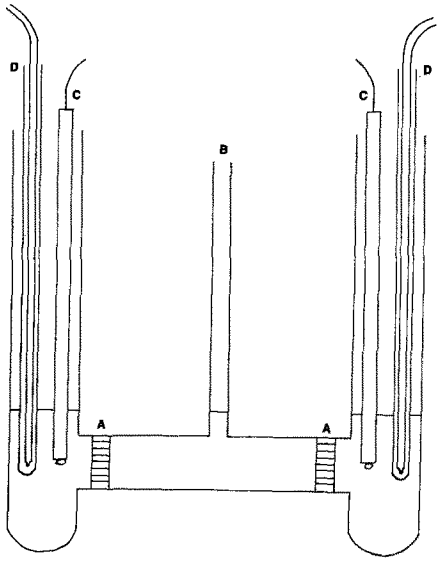

Fig. 1. Cell for measuring thermal power of melts. A, fine porosity sintered glass frits; B, central tube to aid filling; C, silver electrodes fused into alumina tubes; D, Pt/Pt, 13% Rh for thermocouples in glass wells.

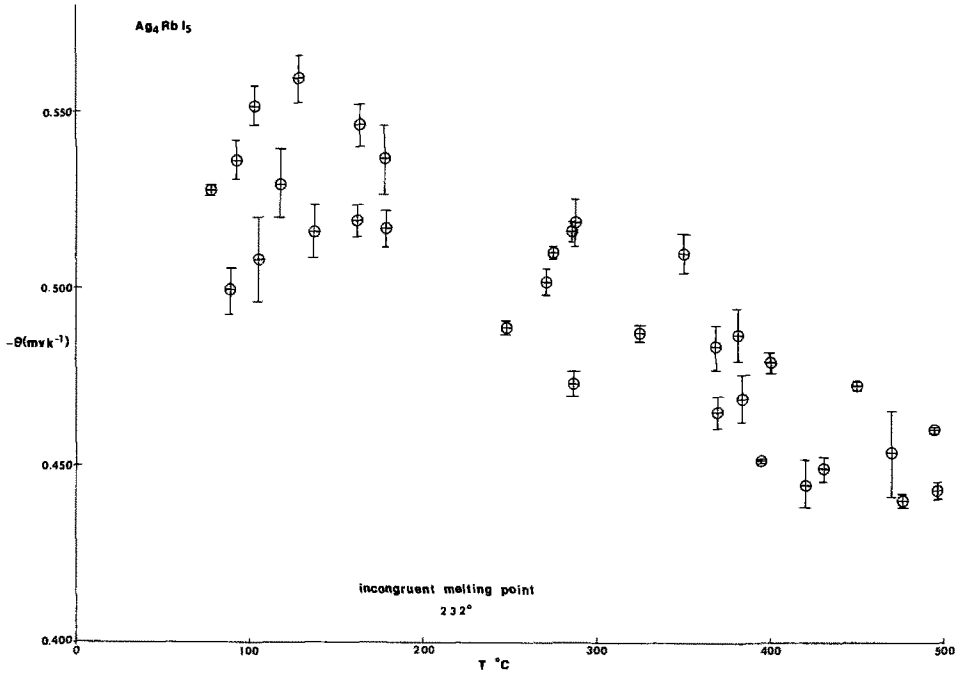

Fig. 2. Thermal power vs. temperature for Ag_4RbI_5.

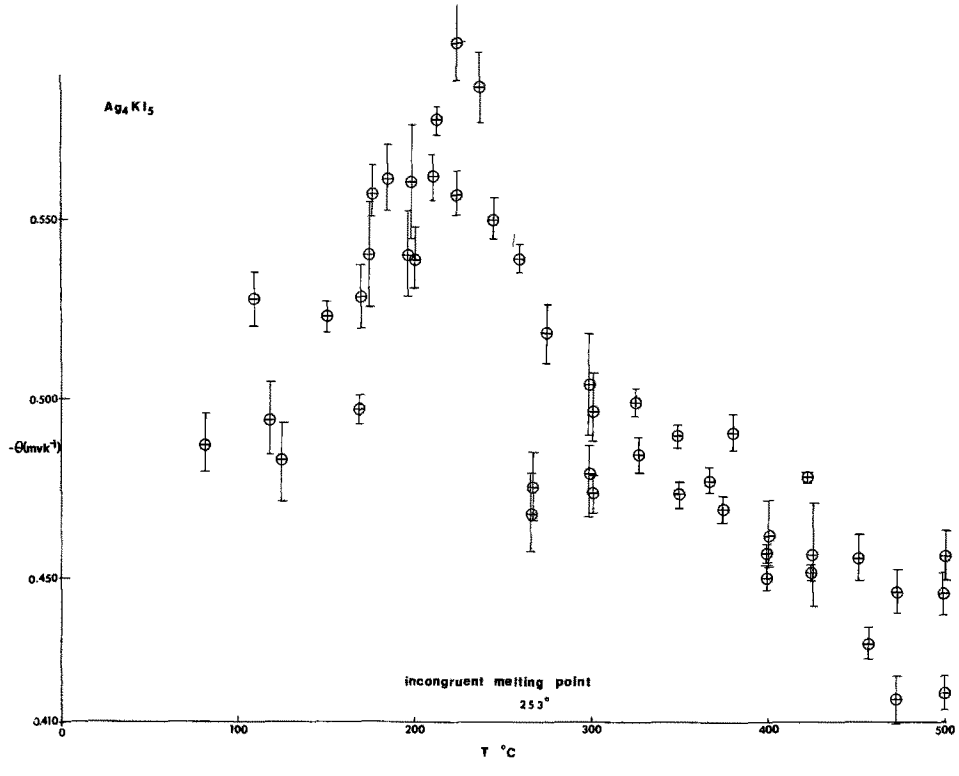

Fig. 3. Thermal power vs. temperature for Ag_4KI_5.

point and 500°C. Then, for the potassium and rubidium salts the apparatus was cooled below the eutectic temperature for the system and annealed overnight. Measurements of the thermal power of these polycrystalline samples were made in the same way as the melts. For each substance studied three runs were performed, each with different batches of mixtures. Attempts were made to obtain the thermal power of single crystals and compressed pellets of Ag_4RbI_5. However, no satisfactory silver electrode could be found. Using massive silver the contact resistance was too high and the results irreproducible. Using silver paint, the silver quickly diffused into the sample and the results were highly erratic. Attempts were also made to measure the thermal power of the ammonium salt but it was found impossible to fill the cell without decomposition.

Results and Discussion

The experimental results obtained are shown in Fig. 2 through 4. Plotted there are the values of the thermal power against temperature in degrees centigrade. The error bars are the probable errors in the slopes of the experimental points at each t_m as calculated by least squares analysis. The scatter in the data for the melt is probably explained by gradual thermal diffusion within each arm of the cell, and, possibly, through the frits. The scatter in the solids is almost certainly due to strain potentials existing in the polycrystalline mass.

The results for the rubidium salt were analyzed using the equations developed above in conjunction with the data of Johnston, Wiedersich, and Lindberg (8), and of the authors (9). A list of the data used is given in Table I. θ_{het} was calculated at each t_m and subtracted from the measured thermal power. The re-

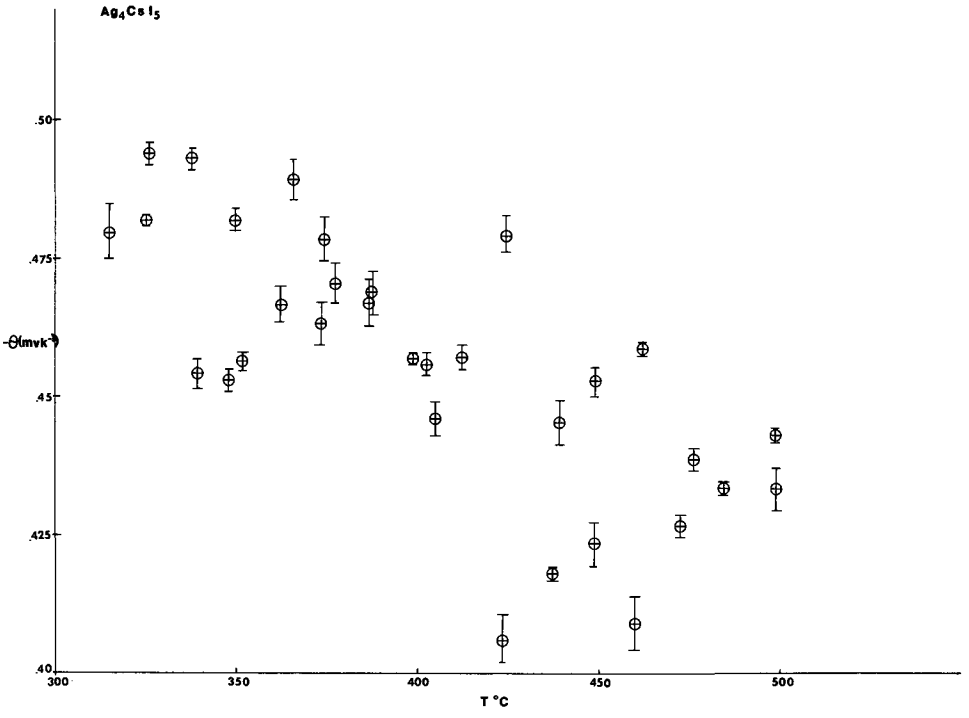

Fig. 4. Thermal power vs. temperature for Ag_4CsI_5.

sultant θ_{hom} was fitted against $10^3/T$ by least squares. For solid Ag_4KI_5 detailed analysis was not possible as the disorder contribution to the heat capacity is not known; however, if it is assumed to be in the same order as that of Ag_4RbI_5 then, as in the case of the rubidium salt, the major part of the temperature dependence of θ may be attributed to the heterogeneous term. In fact the slopes of the plots shown in Fig. 2 and 3 are in the order of 0.5×10^{-4} mV K^{-2}. The slope calculated for θ_{het} is 0.53×10^{-4} m K^{-2}.

For the potassium and cesium melts the standard entropy is not known; however, it is possible to calculate a modified heterogeneous thermal power $\theta^*_{het}(T)$ defined as

$$\theta^*_{het}(T) = \theta_{het}(T) - \theta_{het}(T^o) \qquad [12]$$

directly from the specific heats, where T^o is any reference temperature (conveniently the melting point of the mixture). If θ^*_{het} is subtracted from the measured value and the result fitted against $10^3/T$, then the slopes of such plots will be $t_{Ag} + Q^*_{Ag+} + t_{M+}Q^*_{M+}$, providing the transport numbers are not significantly temperature dependent.

The results of the least squares plots are shown in Table II. In Table III are listed the values of the heats of transport obtained from the slopes, and, for Ag_4RbI_5, by direct calculation from the magnitude of θ_{hom}. It is seen that for Ag_4RbI_5 the values calculated directly from the values of θ_{hom} are in the same order as those values predicted from the slope. This is particularly gratifying in the case of the solid in which the bulk of the temperature dependence of the measured thermal power arises from the heterogeneous term. The agreement between direct calculation and the values from the slopes in the melt indicates that the transport numbers are not significantly temperature dependent in the region studied, and allows one to place some confidence in the values predicted for the potassium and cesium mixtures.

The fact that the intercepts of the least squares plots for the rubidium system are close to zero (particularly in the case of the melt) serves to indicate that the calculated values of θ_{het} are reasonably accurate.

The calculated value for Q_{Ag+} in Ag_4RbI_5 (2.1 kcal $mole^{-1}$) is in excellent agreement with the activation energy for silver ion diffusion measured by Bentle (1.994). This agreement is predicted by the earlier theory of the heat of transport (18, 20). More elaborate theories (21) indicate that the major term in the heat of transport is the activation energy for diffusion, but that this is modified by complicated terms involving the nonisothermal friction constants. The agreement with Bentle's value would suggest that these corrections are small for Ag^+ in Ag_4RbI_5. The values for the molten systems are in the same order as Q^*_{Ag+} calculated from Kvist's (22) data for molten AgI (3.0 kcal $mole^{-1}$). The differences between the values might be understood if it is assumed that the heat of transport increases with increasing ionic radius (*i.e.*, the "activation energy" for diffusion increases) whereas the transport number, and hence its contribution to $t_{M+}Q^*_{M+} + t_{Ag+}Q^*_{Ag+}$ decreases.

Table I. Data used in the calculations of thermal powers

Quantity	Value (Cal K^{-1} $mole^{-1}$)	Reference
Standard entropy of Ag_4RbI_5	147.07	8
Entropy due to lattice disorder in Ag_4RbI_5	10.81	8
Disorder contribution to the heat capacity of Ag_4RbI_5	22	8
Heat capacities of:		
Ag_4RbI_5 solid	73.4	9
liquid	77.0	9
Ag_4KI_5 solid	71.4	9
liquid	79.1	9
Ag_4CsI_5 liquid	80.9	9
Standard entropy of silver metal	10.2	19
Specific heat of silver metal at 298°K	0.056	19

Table II. Least squares fits of θ_{hom} (θ^*_{hom}) against $10^3/T$

		$-\theta_{hom}(mV) = a + b\ 10^3/T$			
Substance	Phase	a	Error	b	Error
Ag_4RbI_5	Solid	0.095	±0.07	0.052	±0.026
	Melt	0.045	±0.030	0.110	±0.018
$Ag_4KI_5(\theta^*_{hom})$	Melt	0.808	±0.028	0.118	±0.018
$Ag_4CsI_5(\theta^*_{hom})$	Melt	0.874	±0.037	0.162	±0.025

Table III. Values of the heat of transport terms

Substance	Phase	Term	Method	Value
Ag_4RbI_5	Solid	$Q^*_{Ag^+}$	Direct	2.07
	Solid	$Q^*_{Ag^+}$	Slope	1.2 ± 0.8
	Melt	$t_{Ag^+}Q^*_{Ag^+} + t_{Rb^+}Q^*_{Rb^+}$	Direct	3.2
	Melt	$t_{Ag^+}Q^*_{Ag^+} + t_{Rb^+}Q_{Rb^+}$	Slope	2.5 ± 0.4
Ag_4KI_5	Melt	$t_{K^+}Q^*_{K^+} + t_{Ag^+}Q^*_{Ag^+}$	Slope	2.7 ± 0.4
Ag_4CsI_5	Melt	$t_{Cs^+}Q^*_{Cs^+} + t_{Ag^+}Q^*_{Ag^+}$	Slops	3.7 ± 0.6

Chandra *et al.* (10) reported that they have measured the thermal power of compressed pellets of Ag_4KI_5 using massive silver and brass electrodes. They observed unusually large values of θ (-1.5 mV K^{-1}), and state that the potential was not a linear function of the temperature gradient. It seems likely that in their work the silver electrodes were not reversible to Ag^+. This is supported by the fact that there is little difference between the values of θ obtained with brass electrodes, which cannot be reversible, and those obtained with silver electrodes.

Manuscript submitted May 4, 1972; revised manuscript received Jan. 25, 1973.

Any discussion of this paper will appear in a Discussion Section to be published in the December 1973 JOURNAL.

REFERENCES

1. J. N. Bradley and P. D. Greene, *Trans. Faraday Soc.*, **62**, 2069 (1966).
2. J. N. Bradley and P. D. Greene, *ibid.*, **63**, 424 (1967).
3. B. B. Owens and G. R. Argue, *Science*, **157**, 308 (1967).
4. S. Geller, *ibid.*, **157**, 310 (1967).
5. J. N. Bradley and P. D. Greene, *Trans. Faraday Soc.*, **63**, 2516 (1967).
6. D. O. Raleigh, *J. Appl. Phys.*, **41**, 1876 (1970).
7. G. G. Bentle, *ibid.*, **39**, 4036 (1968).
8. W. V. Johnston, H. Wiedersich, and G. W. Lindberg, *J. Chem. Phys.*, **51**, 3739 (1969).
9. K. E. Johnson, S. J. Sime, and J. Dudley, *J. C. S. Faraday II*, **68**, 2015 (1972).
10. S. Chandra, H. B. Lal, and K. Shahi, *J. Phys. D.*, **5**, 443 (1972).
11. C. Wagner, *Ann. Physik*, **3**, 629 (1929); **6**, 370 (1930).
12. K. S. Pitzer, *J. Phys. Chem.*, **65**, 147 (1961).
13. See, *e.g.*, P. Mazur, *ibid.*, **58**, 700 (1954).
14. De Groot and Mazur, "Non Equilibrium Thermodynamics," p. 239, North Holland Publishing Co., Amsterdam.
15. B. R. Sandheim, "Fused Salts," p. 181, McGraw Hill Book Co., New York (1964).
16. See, *e.g.*, C. Sinistri and E. Pezzati, *Z. Naturforsch.*, **25**, 893 (1970).
17. M. I. Temkin and A. V. Khoroshin, *Zh. Fiz. Khim.*, **26**, 500 (1952).
18. K. Wirtz and J. W. Hiby, *Physik. Z.*, **44**, 369 (1943).
19. K. K. Kelley, *U.S. Bur. Mines Bull.*, 477 (1950).
20. A. R. Allnatt and S. A. Rice, *J. Chem. Phys.*, **33**, 573 (1960).
21. A. R. Allnatt, *Z. Naturforsch.*, **26(a)**, 10 (1971).
22. A. Kvist, A. Rondsalu, and I. Svanson, *ibid.*, **21(a)**, 184 (1966).

Hydrogen Overpotential on Zinc Containing Small Amounts of Impurities in Concentrated Alkaline Solution

T. S. Lee*

Union Carbide Corporation, Consumer Products Division, Research Laboratory, Cleveland, Ohio 44101

ABSTRACT

Hydrogen overpotentials on zinc uniformly alloyed with 500 ppm Cd, Fe, Ca, and Mn, as well as 200 ppm Hg, were measured in 9*N* KOH at room temperature. Exchange current densities and transfer coefficients for each alloy for the hydrogen evolution process were obtained. Except for Cd, all the other impurities including Hg will cause zinc to be more readily corroded in alkaline medium.

Hydrogen overpotentials on zinc in alkaline solution have been measured in an open vessel (1) and in closed systems under experimentally carefully controlled conditions (2, 3). The overpotential on zinc containing electrodeposited impurities (Fe and Tl) in alkaline solution has also been measured (4). In this case, the impurities are deposited on the electrode surface and their distribution and uniformity are not well defined. The purpose of this paper is to report measurements of hydrogen overpotential on zinc containing small amounts of impurities uniformly alloyed with the zinc in highly purified 9*N* KOH solution.

Experimental

The cell used for the measurements is a closed system under a hydrogen atmosphere. It is made from epoxy-lined Pyrex so that the inner walls are highly alkaline resistant. The details of the cell, the lining technique, and tests for resistance to concentrated alkaline solution were reported previously (3).

The samples are prepared by alloying the pure elements obtainable on the market with high-purity zinc. The zinc is obtained from American Smelting and Refining Company and has a purity of 99.999+%. Analysis shows 1 ppm Cu and less than 1 ppm of Mg and Si. Other elements such as Sb, Ti, Mn, Sn, Cr, Fe, Ni, Bi, Al, Ca, In, Cd, and Ag are not detected. The purity of the alloying elements and their vendors are as follows: iron, from Battelle Memorial Institute, has a purity of 99.99+%; calcium, from J. T. Baker, has a purity of 99.0+%; mercury, from National Lead, has a purity of 99.996+%; manganese, from Foote Mineral, has a purity of 99.99+%; and cadmium, from American Smelting and Refining Company, has a purity of 99.999+%. The process of alloying is carried out by melting about 100g charges in high-purity graphite crucibles in a small resistance muffle furnace under argon. The melt is homogenized with a high-purity graphite stirrer. A graphite-coated molybdenum skimmer is used to remove the dross. Melt temperature is measured with a calibrated thermocouple adjacent to the crucible. After stirring and skimming, the melt is poured into a graphite-coated copper chill mold. Before starting, the crucible and stirrer are scraped and then cleaned with dilute HNO_3 each time. After rinsing and drying, the final cleaning is done by using a wash heat of the zinc base metal.

All alloys used in this study are made from master zinc alloy and pure zinc. The master alloys are made from pure metals which contain a higher percentage of the different alloying metals.

For the alloys of iron and mercury, the casting is followed by rolling the cast slabs from 3/8 in. to about

* Electrochemical Society Active Member.

Key words: hydrogen overpotential, hydrogen overvoltage, hydrogen evolution process in alkaline solution, electrode kinetics hydrogen evolution process, zinc corrosion.

40 mil thickness on a 35 in. diameter, 2 high flat mill with unheated rolls lubricated with 50-50 tallow-paraffin mixture. On each pass a reduction of about 10% is obtained.

To determine whether the impurities introduced into the zinc are well mixed and that no zinc oxide is introduced in the alloying process, a metallographic examination and electron-microprobe analysis of each of the specimens are done. All tests show that the small amount of impurities introduced into the zinc is evenly distributed and that no evidence of zinc oxide is present in the sample.

All the impurities introduced for this study are at a level of 500 ppm except mercury which is only 200 ppm.

The electrodes prepared for this study are made from a piece of the alloy cut from the center of the casts or rolls.

The counterelectrode is made from pure nickel and its area is about 8-10 times that of the working electrode. The reference electrode is a Hg/HgO electrode in contact with the same KOH solution. The working electrode, which has an exposed area of about 1 cm^2, is electrically insulated with the epoxy that was used to line the cell. The electrode surface is prepared and treated by following the same procedure as described before (3).

The constant current is supplied by a Harrison Laboratories' Model 855C power supply through a variable power resistor in series. The potentials are measured by a Keithley Model 630 potentiometric electrometer which has a minimum input resistance of 10^{13} ohm. All the measurements are carried out at room temperature which is controlled at 25° ± 1°C. Measurements are carried out from the high current density to the low current density region and back again; this process is then repeated.

At each current density, the steady potential is obtained in a few minutes. Once the steady potential is reached, the electrode will stay at the same potential as long as ½ hr without any change. The data presented here are the average values of at least four runs. The deviation of each run from the average value is only a few millivolts. There is no hysteresis in any of the runs. After the measurement, the electrodes are washed, dried, and examined under a microscope. The surface does not appear to have changed from its original appearance.

Results and Discussion

Hydrogen evolution on metal surfaces in alkaline solution is known to have the over-all reaction $2H_2O + 2e = H_2 + 2\,OH^-$. In the case where the rate-determining step is electron transfer and the transfer coefficient $\alpha = ½$, the hydrogen overpotential (η) for the reaction as shown before (3), is

$$\eta = \text{const.} + \frac{RT}{\mathbf{F}} \ln \alpha_{H_2O}\alpha_{OH^-} - \frac{2RT}{\mathbf{F}} \ln I$$

where α denotes activity, I is the current density, and the other symbols have their usual meaning. At constant temperature and definite KOH concentration, the above equation reduces to the Tafel equation $\eta = A + B \log I$ where A and B are constants.

In the experiments, the hydrogen overpotential is obtained by substracting the reversible hydrogen potential from the measured potential. The reversible hydrogen potential in 9*N* KOH at 25°C, as measured as well as calculated before, is −0.938V against a Hg/HgO electrode (3).

The plots of hydrogen overpotential against logarithmic current density for zinc containing 500 ppm Cd, Ca, and Fe are shown in Fig. 1, and those for zinc containing 200 ppm Hg and 500 ppm Mn are shown in Fig. 2. In each figure the overpotential for pure zinc is also plotted for comparison. (Please note that curves 3 and 4 in Fig. 1 are referred to the right-hand scale only.)

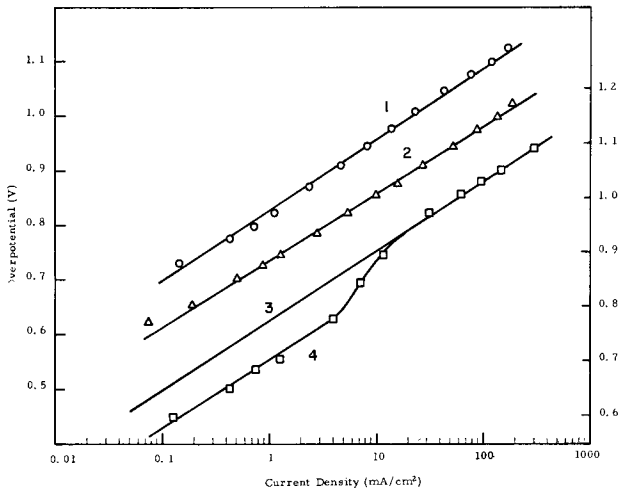

Fig. 1. Hydrogen overpotential in 9*N* KOH at 25°C: curve 1, Zn as well as Zn-0.05% Cd; curve 2, Zn-0.05% Ca; curve 3 (right-hand scale) Zn; curve 4 (right-hand scale) Zn-0.05% Fe.

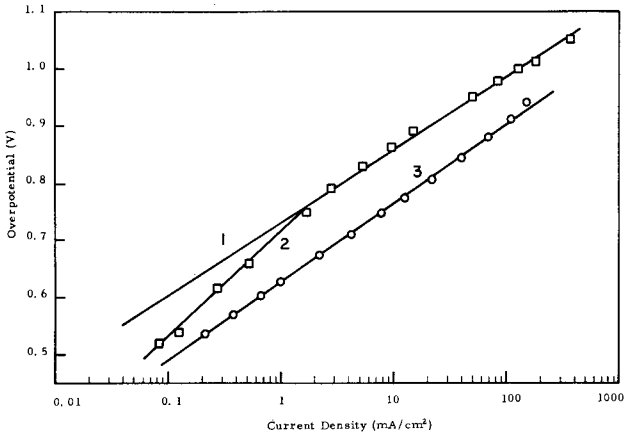

Fig. 2. Hydrogen overpotential in 9*N* KOH at 25°C: curve 1, Zn; curve 2, Zn-0.02% Hg; curve 3, Zn-0.05% Mn.

In Fig. 1, curve 1 is the hydrogen overpotential plot for Zn-0.05% Cd, which is identical to that for pure zinc. Curve 2 is the overpotential plot for Zn-0.05% Ca which is about 0.1V lower than that for zinc. Curve 3 is the plot for zinc, and curve 4 is that for Zn-0.05% Fe. Comparing curves 3 and 4, one can see that the effect of 500 ppm of Fe appears only in the low current density region, which is about 72 mV lower than that for pure zinc. In the high current density region, the small amount of iron does not have any effect. In Fig. 2, curve 3 is the plot for Zn-0.05% Mn, and the value of the overpotential is about 0.1V lower than that of pure zinc.

In Fig. 2, curve 1 is the hydrogen overpotential plot for zinc, and curve 2 is that for Zn-0.02% Hg. One can see that the small amount of mercury in zinc does not affect one way or the other the overpotential on zinc in the high current density region. However, in the low current density region, the small amount of mercury decreases the overpotential on zinc. In order to clarify the fact that the lowering of the overpotential in the low current density region is not due to impurities other than small amounts of mercury, the sample has been subjected to emission spectroscopic analysis. No impurities other than mercury have been found. Also, the measurements have been made on different samples in different purified solutions and the results are all the same. It is generally believed that amalgamated zinc is more corrosion resistant to alkaline solution than is zinc alone because mercury has a high hydrogen overpotential (5). This finding suggests that when small amounts of mercury are alloyed with zinc this belief may no longer be valid, since the hydrogen over-

potential of the alloy is lower than that of pure zinc (6). Consequently, the alloy will corrode more readily in the alkaline medium.

With the result obtained here, in conjunction with the explanation given in the preceding paragraph for the zinc-mercury alloy, one can visualize that almost all the impurities, including mercury in the zinc, will make zinc more readily corroded in the alkaline medium. Cadmium is the only exception which will not affect the zinc corrosion.

The electrochemical parameters, transfer coefficients (α), and exchange (I_0), which are derived from the Tafel slopes, are shown in Table I. For Fe and Hg-alloyed zinc, the parameters based upon the low current density region are given. Their values in the high current density region are the same as that of pure zinc. It appears that in most cases the small amounts of impurities in zinc only lower the hydrogen overpotential and do not change the mechanism of the hydrogen evolution process in alkaline solution. The Tafel slopes are in the vicinity of 120 mV per decade. The rate determining step is an electron-transfer process of the Volmer type (3), $H_2O + e = H_{ad} + OH^-$. For zinc with small amounts of mercury in the low current density region, the mechanism of hydrogen evolution in alkaline solution might be different as indicated by the high Tafel slope.

Table I. Electrochemical parameter for hydrogen evolution reaction on various Zn surfaces in 9N KOH

Electrode	Slope	α	I_0 (mA/cm^2)
Zn	124	0.48	8.5×10^{-7}
Zn-0.05% Ca	124	0.48	8.5×10^{-6}
Zn-0.05% Cd	128	0.47	3.5×10^{-6}
Zn-0.05% Fe*	124	0.48	7.0×10^{-6}
Zn-0.02% Hg*	180	0.33	1×10^{-4}
Zn-0.05% Mn	138	0.43	5.1×10^{-5}

* Based upon the lower current density region.

Acknowledgment

The process of alloying the sample was carried out at Battelle Memorial Institute by B. C. Allen. Thanks to Mrs. H. M. Joseph for editing the manuscript.

Manuscript submitted Aug. 10, 1972; revised manuscript received Feb. 2, 1973.

Any discussion of this paper will appear in a Discussion Section to be published in the December 1973 JOURNAL.

REFERENCES

1. M. D. Zholuder and V. V. Stender, *Zh. Prikl. Khim.*, **31**, 711 (1958).
2. Z. A. Iofa, L. V. Komlev, and V. S. Bagotskii, *Zh. Fiz. Khim.*, **35**, 1571 (1961).
3. T. S. Lee, *This Journal*, **118**, 1278 (1971).
4. T. I. Popova, V. S. Bagotskii, and B. V. Kabanov, *Zh. Prikl. Khim.*, **36**, 1743 (1963).
5. For example, see Falk and Salkind, "Alkaline Storage Batteries," p. 546, John Wiley and Sons, Inc., New York (1969).
6. For detailed analysis see, for example, Hampel, "Encyclopedia of Electrochemistry," p. 830, Reinhold Publishing Corp., New York (1964).

Properties of LiCl and $(CH_3)_4NCl$ Solutions in Water-Methanol Mixtures

M. H. Miles* and V. Jiamsakul[1]

Department of Chemistry, Middle Tennessee State University, Murfreesboro, Tennessee 37130

ABSTRACT

Solutions of both 1.0M LiCl and 1.0M $(CH_3)_4NCl$ in methanol-water mixtures were investigated to determine the effect of solvent composition on viscosity, electrolytic conductance, and surface tension. The viscosity-composition curves suggest that interactions between solvent molecules attain a maximum effect at a composition of about 0.3 mole fraction methanol, and that these interactions increase as the temperature is lowered. In the methanol-rich mixtures, the conductivity of the $(CH_3)_4NCl$ solution becomes considerably larger than that of the LiCl solution. Cyclic voltammetric measurements on platinum, gold, and molybdenum electrodes indicate that oxidation of methanol is insignificant in these solutions despite favorable thermodynamics. Wide, useful potential ranges are available at all solvent compositions.

There is very little reported research on the use of mixed solvents in batteries or fuel cells. Desired properties of electrolyte solutions in mixed solvents for such applications include high electrolytic conductivity, a wide liquid temperature range, and inertness of the solution to electrochemical oxidation and reduction over a wide potential range. These properties were investigated as a function of the solvent composition for both 1.0M LiCl and 1.0M $(CH_3)_4NCl$ solutions in methanol-water mixtures. Methanol was selected due to its attractive properties of low viscosity (0.0054 poise at 25°C) and low freezing point (−98°C). The LiCl and $(CH_3)_4NCl$ salts were selected to represent the extremes of a small, highly solvated cation given by Li^+, and of a large, relatively unsolvated cation given by $(CH_3)_4N^+$. Despite numerous reported studies in water-alcohol mixtures during the past century (1-12), no literature data could be located for our selected three-component systems. However, data on the conductivity and viscosity of 0.05M LiCl solutions in methanol-water mixtures is already available (3).

Experimental

All solution preparations were made using Baker spectrophotometric reagent grade methanol and deionized distilled water. The lithium chloride used was Baker reagent grade, and tetramethylammonium chloride was obtained from Eastman. All chemicals were used without further purification.

Measurements of electrolytic conductivity were made with a Sargent conductivity bridge which had a

* Electrochemical Society Active Member.
[1] Present address: Faculty of Science, Prince of Songkla University, Haadyai, Songkla, Thailand.
Key words: activation energy, conductivity, electrostability, surface tension, viscosity.

potential of the alloy is lower than that of pure zinc (6). Consequently, the alloy will corrode more readily in the alkaline medium.

With the result obtained here, in conjunction with the explanation given in the preceding paragraph for the zinc-mercury alloy, one can visualize that almost all the impurities, including mercury in the zinc, will make zinc more readily corroded in the alkaline medium. Cadmium is the only exception which will not affect the zinc corrosion.

The electrochemical parameters, transfer coefficients (α), and exchange (I_0), which are derived from the Tafel slopes, are shown in Table I. For Fe and Hg-alloyed zinc, the parameters based upon the low current density region are given. Their values in the high current density region are the same as that of pure zinc. It appears that in most cases the small amounts of impurities in zinc only lower the hydrogen overpotential and do not change the mechanism of the hydrogen evolution process in alkaline solution. The Tafel slopes are in the vicinity of 120 mV per decade. The rate determining step is an electron-transfer process of the Volmer type (3), $H_2O + e = H_{ad} + OH^-$. For zinc with small amounts of mercury in the low current density region, the mechanism of hydrogen evolution in alkaline solution might be different as indicated by the high Tafel slope.

Table I. Electrochemical parameter for hydrogen evolution reaction on various Zn surfaces in 9N KOH

Electrode	Slope	α	I_0 (mA/cm^2)
Zn	124	0.48	8.5×10^{-7}
Zn-0.05% Ca	124	0.48	8.5×10^{-6}
Zn-0.05% Cd	128	0.47	3.5×10^{-6}
Zn-0.05% Fe*	124	0.48	7.0×10^{-6}
Zn-0.02% Hg*	180	0.33	1×10^{-4}
Zn-0.05% Mn	138	0.43	5.1×10^{-5}

* Based upon the lower current density region.

Acknowledgment

The process of alloying the sample was carried out at Battelle Memorial Institute by B. C. Allen. Thanks to Mrs. H. M. Joseph for editing the manuscript.

Manuscript submitted Aug. 10, 1972; revised manuscript received Feb. 2, 1973.

Any discussion of this paper will appear in a Discussion Section to be published in the December 1973 JOURNAL.

REFERENCES

1. M. D. Zholuder and V. V. Stender, *Zh. Prikl. Khim.*, **31**, 711 (1958).
2. Z. A. Iofa, L. V. Komlev, and V. S. Bagotskii, *Zh. Fiz. Khim.*, **35**, 1571 (1961).
3. T. S. Lee, *This Journal*, **118**, 1278 (1971).
4. T. I. Popova, V. S. Bagotskii, and B. V. Kabanov, *Zh. Prikl. Khim.*, **36**, 1743 (1963).
5. For example, see Falk and Salkind, "Alkaline Storage Batteries," p. 546, John Wiley and Sons, Inc., New York (1969).
6. For detailed analysis see, for example, Hampel, "Encyclopedia of Electrochemistry," p. 830, Reinhold Publishing Corp., New York (1964).

Properties of LiCl and $(CH_3)_4NCl$ Solutions in Water-Methanol Mixtures

M. H. Miles* and V. Jiamsakul[1]

Department of Chemistry, Middle Tennessee State University, Murfreesboro, Tennessee 37130

ABSTRACT

Solutions of both 1.0M LiCl and 1.0M $(CH_3)_4NCl$ in methanol-water mixtures were investigated to determine the effect of solvent composition on viscosity, electrolytic conductance, and surface tension. The viscosity-composition curves suggest that interactions between solvent molecules attain a maximum effect at a composition of about 0.3 mole fraction methanol, and that these interactions increase as the temperature is lowered. In the methanol-rich mixtures, the conductivity of the $(CH_3)_4NCl$ solution becomes considerably larger than that of the LiCl solution. Cyclic voltammetric measurements on platinum, gold, and molybdenum electrodes indicate that oxidation of methanol is insignificant in these solutions despite favorable thermodynamics. Wide, useful potential ranges are available at all solvent compositions.

There is very little reported research on the use of mixed solvents in batteries or fuel cells. Desired properties of electrolyte solutions in mixed solvents for such applications include high electrolytic conductivity, a wide liquid temperature range, and inertness of the solution to electrochemical oxidation and reduction over a wide potential range. These properties were investigated as a function of the solvent composition for both 1.0M LiCl and 1.0M $(CH_3)_4NCl$ solutions in methanol-water mixtures. Methanol was selected due to its attractive properties of low viscosity (0.0054 poise at 25°C) and low freezing point (−98°C). The LiCl and $(CH_3)_4NCl$ salts were selected to represent the extremes of a small, highly solvated cation given by Li^+, and of a large, relatively unsolvated cation given by $(CH_3)_4N^+$. Despite numerous reported studies in water-alcohol mixtures during the past century (1-12), no literature data could be located for our selected three-component systems. However, data on the conductivity and viscosity of 0.05M LiCl solutions in methanol-water mixtures is already available (3).

Experimental

All solution preparations were made using Baker spectrophotometric reagent grade methanol and deionized distilled water. The lithium chloride used was Baker reagent grade, and tetramethylammonium chloride was obtained from Eastman. All chemicals were used without further purification.

Measurements of electrolytic conductivity were made with a Sargent conductivity bridge which had a

* Electrochemical Society Active Member.
[1] Present address: Faculty of Science, Prince of Songkla University, Haadyai, Songkla, Thailand.
Key words: activation energy, conductivity, electrostability, surface tension, viscosity.

specified accuracy of ±1% over the experimental range of resistances. The cell constant was determined using 0.1000M KCl. An Ostwald viscosimeter was used to determine solution viscosities. Kinetic-energy corrections were negligible in each case. The capillary rise method was used to determine the surface tension of the solutions. Experimental details of these various measurements are given by Shoemaker and Garland (13).

Measurements at 25° and 35°C were performed in a Sargent thermostatic water bath controlled by a thermistor sensor to ±0.01°C of the stated temperature. A distilled water-ice bath was used for measurements at 0°C.

Cyclic voltammetric measurements were made with a Beckman Electroscan 30 using a potential sweep rate of 100 mV/sec. These experiments were conducted in a 50 ml beaker containing the working electrode (platinum, molybdenum, or gold), counterelectrode, and solution. The potential was measured with respect to an aqueous saturated calomel electrode (SCE) contained in a separate compartment by using an aqueous 1.0M KCl salt bridge to establish electrolytic contact. Solution contamination was minimized by restricting the contact between the salt bridge and solution to a narrow strip of filter paper. From the Henderson equation, the liquid junction potentials were estimated to be less than 10 mV for all solution compositions.

Results

The viscosities of 1.0M LiCl solutions in water-methanol mixtures are shown in Fig. 1 for temperatures of 0°, 25°, and 35°C. Results for 1.0M $(CH_3)_4NCl$ solutions (TMAC) are also shown for the temperature of 25°C. Maxima on the viscosity-composition curves occur in each case at about 0.3 mole fraction methanol. These maxima in viscosity become more intense as the temperature decreases.

The conductivity measurements, shown in Fig. 2, reflect the influence of the viscosity. There is an initial marked decrease in conductivity on adding methanol due largely to the increase in viscosity. As the methanol content of the solution increases beyond 0.3 mole fraction, the change in conductivity becomes much more gradual. For the TMAC solution, the conductivity passes through a flat minimum at about 0.5 mole fraction of methanol. At high methanol concentrations, the TMAC solutions have much greater conductivities (and lower viscosities) than the LiCl solutions.

Figure 3 illustrates that addition of methanol causes an initial marked decrease in surface tension. Changes in this property become more gradual as the methanol content increases.

Cyclic voltammetry was used to obtain the current *vs.* potential traces shown in Fig. 4. These results were produced using a platinum electrode in 1.0M LiCl solutions at 24°C. The dashed line shows the trace for an aqueous solution, the dotted line for a methanol solution, and the solid line for the mixed solvent containing 0.5 mole fraction methanol.

The horizontal line segments shown in Fig. 4 represent an arbitrary limit where the current density exceeds 10 mA/cm² (geometrical area) using a potential sweep rate of 100 mV/sec. Within the potential region established by these anodic and cathodic limits, electrochemical oxidation or reduction of the solvent,

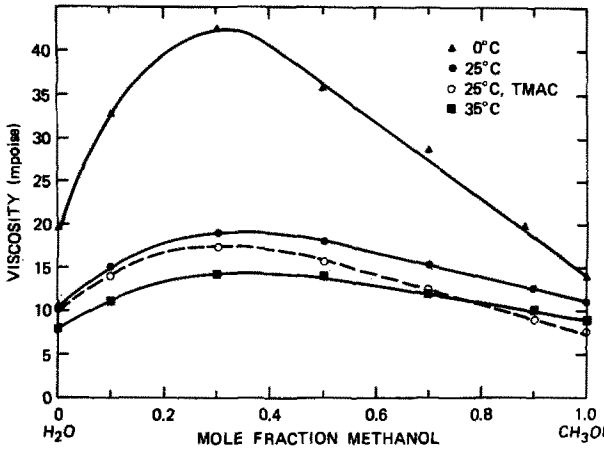

Fig. 1. Variation of the viscosity with mole fraction methanol for 1.0M LiCl solutions at 0°, 25°, and 35°C and for 1.0M $(CH_3)_4$ NCl solutions at 25°C.

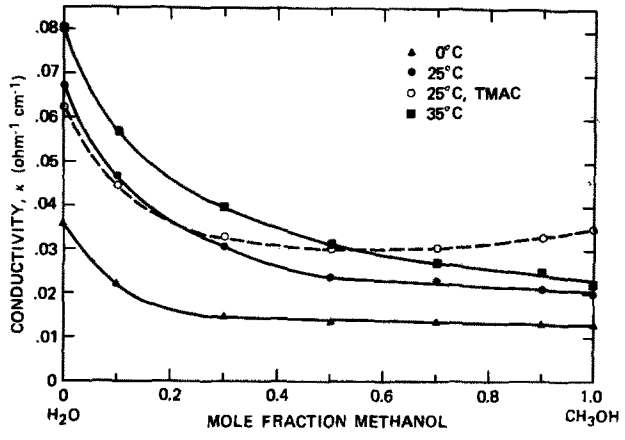

Fig. 2. Variation of the specific conductivity with mole fraction methanol for 1.0M LiCl solutions at 0°, 25°, and 35°C and for 1.0M $(CH_3)_4$ NCl solutions at 25°C.

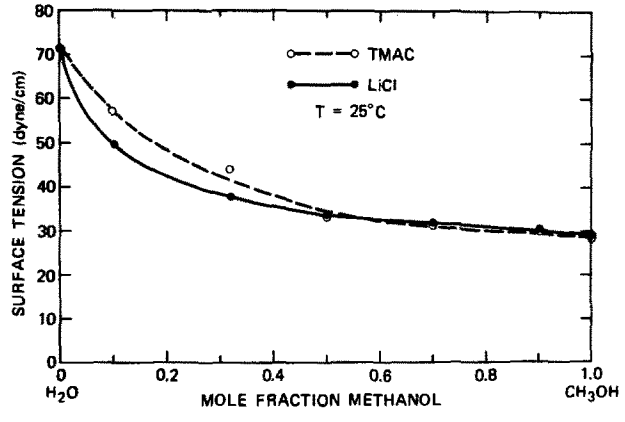

Fig. 3. Variation of the surface tension with mole fraction methanol for 1M salt solutions at 25°C.

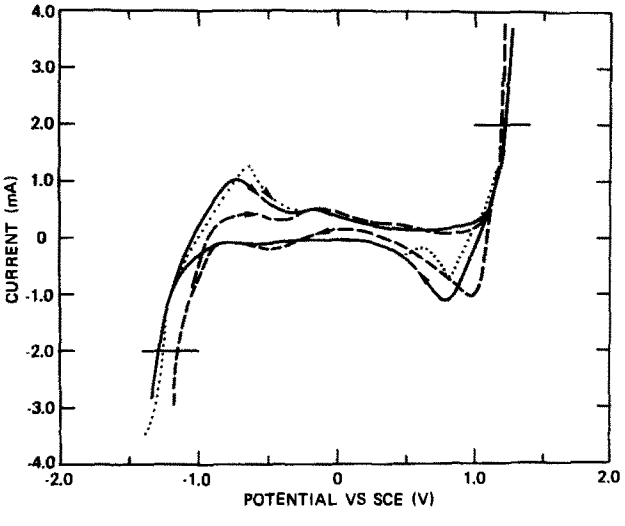

Fig. 4. Cyclic voltammograms for 1.0M LiCl solutions at 24°C on a platinum wire electrode with geometrical area equal to 0.2 cm². Sweep rate = 100 mV/sec. - - - - Aqueous solution, ——— 0.5 mole fraction methanol, and · · · · methanol solution.

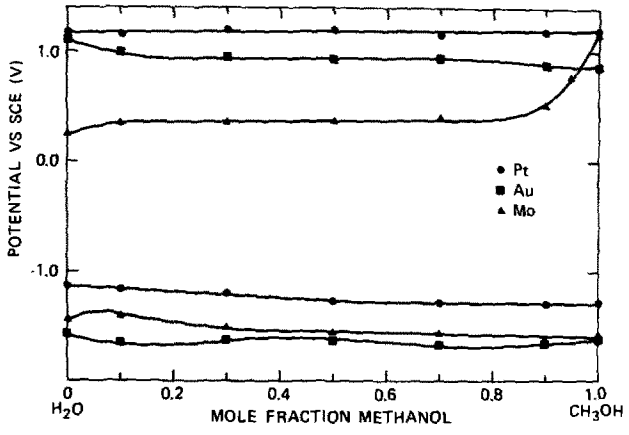

Fig. 5. Variation of the anodic and cathodic electrostability limits with mole fraction methanol for platinum, gold, and molybdenum electrodes in 1.0M LiCl solutions at 24°C.

electrolyte, or electrode is relatively insignificant. This defines the electrostability region for the selected solvent-electrolyte-electrode system (14).

The electrostability limits for 1.0M LiCl solutions in methanol-water mixtures at room temperature (24°C) are shown in Fig. 5 for platinum, gold, and molybdenum electrodes. Thermodynamically, methanol can be electrochemically oxidized to formaldehyde or to carbon dioxide at potentials considerably lower than the potential at which water is oxidized (15). Experimentally, however, the potential at which appreciable electrochemical oxidation is observed is virtually unaffected at room temperature by the addition of methanol. Similarly, the potential at which significant reduction of the solutions is observed shows only slight change as the mole fraction of methanol is increased. At all solvent compositions there are wide useful potential ranges available for fundamental electrochemical investigations.

For 1.0M TMAC solutions, somewhat erratic changes in the electrostability regions are observed as the mole fraction of methanol increases (Fig. 6). Nevertheless, wide useful potential ranges are also available in these solutions.

Discussion

Properties of water-methanol mixtures are characteristic for systems with strong interactions (6). The maxima on the viscosity-composition curves in Fig. 1 can be explained by hydrogen bonding between methanol and water molecules. Theoretical studies of seven open-chain trimers in water-methanol mixtures show that the methanol-water-water trimer is the most stable (16). The viscosity maximum at about 0.3 mole fraction methanol suggests that the strongest interactions occur when two or three water molecules are available for each methanol molecule. Other studies on pure water-methanol mixtures (5) and on $LiClO_4$, $NaClO_4$, and NaCl solutions in water-methanol mixtures (12) also show viscosity maxima at about this composition. The large increase in the viscosity maximum as the temperature decreases suggests increasing interactions between methanol and water molecules with decreasing temperatures.

From Stokes' viscosity law, the product of specific conductivity, k, and viscosity, η, is given approximately by

$$k \cdot \eta = C^+ \left(\frac{1}{r^+} + \frac{1}{r^-} \right) \times \text{constant} \qquad [1]$$

where C^+ is the ionic concentration of the cation, r^+ is the radius of the cation in solution, and r^- is the radius of the anion in solution. If the extent of ionization of the 1.0M salt solutions and the radii of the solvated ions are independent of the solvent composition, and if the viscosity experienced by the moving ion is the same as the measured bulk viscosity, then the product, $k\eta$, should remain constant for all solvent compositions. Figure 7 shows this $k\eta$ product as a function of solvent composition for LiCl solutions at 0°, 25°, and 35°C, and for $(CH_3)_4NCl$ solutions at 25°C. Slight maxima in the $k\eta$ product are often observed in the predominantly aqueous regions (9, 11, 17). This is usually attributed to the viscosity experienced by the moving ion being less than the measured bulk viscosity (9, 17).

The large decrease in the $k\eta$ product at higher alcohol concentrations is usually attributed to either decreasing ionization of the electrolyte (11, 17) or to the increasing size of the ionic radii with increasing mole fraction of alcohol (3, 4, 9). Since both $(CH_3)_4N^+$ and Cl^- ions are believed to be only slightly solvated in water (18), it is difficult to rationalize that this decrease in the $k\eta$ product is due entirely to enlargement of the solvated radii as methanol is added. However, the decrease in $k\eta$ is noticeably less for $(CH_3)_4NCl$ than for LiCl. Probably both decreasing ionization and increasing solvated radii as methanol is added contribute to the decreasing $k\eta$ product. The decrease in the $k\eta$ product with increasing temperature in the predominantly aqueous solutions suggests that the ions become more highly solvated as the solvent structure is destroyed by the increased temperature (18).

The activation energies for conductivity (E_k) and for viscosity (E_η) can be calculated from the well-known equations

$$k = Ae^{-E_k/RT} \text{ and } \eta = Be^{E_\eta/RT} \qquad [2]$$

by assuming that A and B are constants which are in-

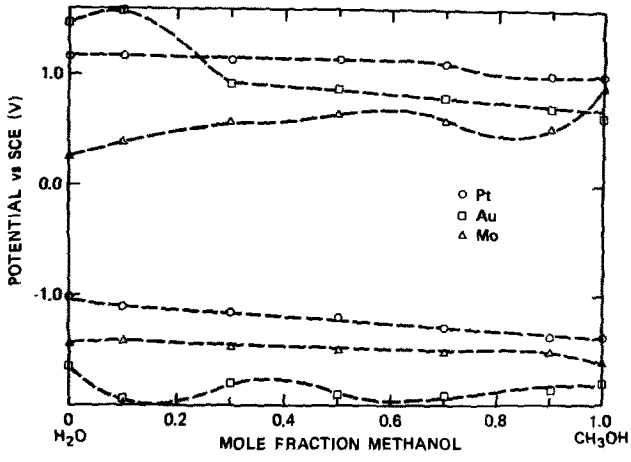

Fig. 6. Variation of the anodic and cathodic electrostability limits with mole fraction methanol for platinum, gold, and molybdenum electrodes in 1.0M $(CH_3)_4NCl$ solutions at 24°C.

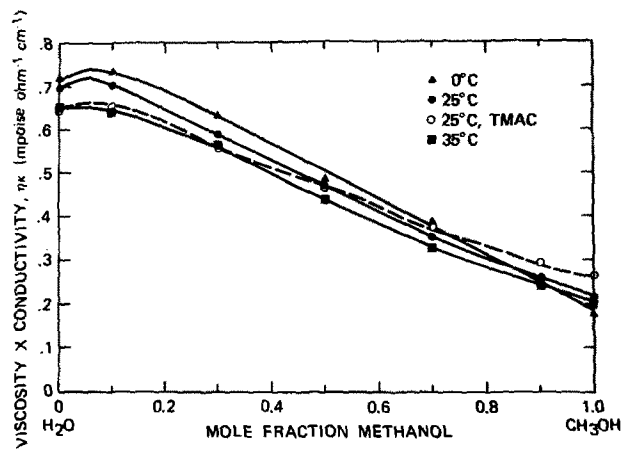

Fig. 7. Variation of the product of viscosity times conductivity with mole fraction methanol for 1.0M LiCl solutions at 0°, 25°, and 35°C and for 1.0M $(CH_3)_4NCl$ solutions at 25°C.

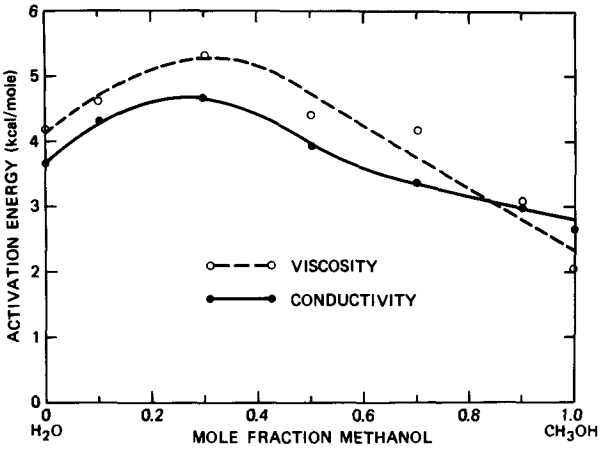

Fig. 8. Activation energies for viscosity and conductivity as a function of the solvent composition for 1.0M LiCl solutions.

dependent of the temperature. The results for such calculations are shown in Fig. 8 for the 1.0M LiCl solutions.

Two interesting features of Fig. 8 are the maxima in activation energies and differences in activation energies for the two processes. Since the energy barriers for both ionic motion and viscous flow are determined largely by solvent molecules exchanging positions (19), it is reasonable that the maxima in activation energies for these two processes are observed at about the composition of maximum interactions between water and methanol molecules. The generally lower activation energies for conductivity indicate that the intense electric field of the ions tends to loosen the solvent structure in the vicinity of the ions, which reduces the required activation energy for movement of solvent molecules (9). At high methanol concentrations, the activation energy for conductivity exceeds that for viscosity. Increasing ionization of LiCl with increasing temperature at high methanol concentrations would result in the calculated activation energy being larger than the true value determined solely from ionic mobility. Another possible factor is that the structure of the methanol-rich solutions is less influenced by the electric field of the larger, methanol-solvated ions (9).

Gibbs isotherm

$$\Gamma_2 = -\frac{1}{RT}\frac{\partial\gamma}{\partial \ln a_2} \qquad [3]$$

relates the surface concentration, Γ_2, and activity, a_2, of component 2 to the surface tension, γ, of the solution (20). This equation indicates that a component such as methanol which decreases the surface tension of the solution (Fig. 3), will tend to accumulate strongly at the surface. Rapid changes in surface potentials of LiCl solutions in water-methanol solutions observed at small methanol concentrations (21) verify this tendency of methanol to accumulate at surfaces in these solutions. Therefore, in electrochemical studies in this mixed solvent, the concentration of methanol molecules at the electrode surface will be considerably greater than the bulk concentration. Despite favorable surface concentrations and favorable thermodynamics, significant oxidation of methanol does not occur in these solutions.

Recent studies of LiCl solutions in methanol have established that the limiting anodic potential on platinum is controlled by oxidation of the chloride ion to chlorine gas (22). Due to the high overvoltage for oxygen evolution, the evolution of chlorine is likely the predominant anodic reaction on platinum in the aqueous solutions as well (23). For molybdenum, and possibly also for gold, the limiting anodic potential is likely controlled by surface oxidation of the electrode metal.

The limiting cathodic potentials on Pt, Au, and Mo for all solution compositions unquestionably represent reduction of the solvent to hydrogen gas (21). The addition of methanol generally tends to shift the cathodic limit toward slightly more negative potentials.

Summary

Favorable electrostability regions are available for the use of water-methanol mixtures in batteries or fuel cells. However, strong interactions between water and methanol molecules will limit the usefulness of such solutions at low temperatures. These interactions between solvent molecules attain a maximum effect at a composition of about 0.3 mole fraction methanol. The main differences observed between the LiCl and $(CH_3)_4NCl$ solutions are a slightly lower viscosity and a markedly higher conductivity for the $(CH_3)_4NCl$ solutions in methanol-rich mixtures.

Manuscript submitted Oct. 25, 1972; revised manuscript received Jan. 18, 1973. This was Paper 16 presented at the Miami Beach Meeting of the Society, Oct. 8-13, 1972.

Any discussion of this paper will appear in a Discussion Section to be published in the December 1973 JOURNAL.

REFERENCES

1. H. C. Jones and C. F. Lindsay, *Am. Chem. J.*, **28**, 329 (1902).
2. H. C. Jones and L. McMaster, *ibid.*, **36**, 325 (1906).
3. L. G. Longsworth and D. A. MacInnes, *J. Phys. Chem.*, **43**, 239 (1939).
4. A. N. Campbell and G. H. Debus, *Can. J. Chem.*, **34**, 1232 (1956).
5. S. Z. Mikhail and W. R. Kimel, *J. Chem. Eng. Data*, **6**, 533 (1961).
6. H. A. Neidig, R. T. Yingling, K. L. Lockwood, and T. G. Teates, *J. Chem. Ed.*, **42**, 309 (1965).
7. H. A. Neidig, R. T. Yingling, K. L. Lockwood, and T. G. Teates, *ibid.*, **42**, 368 (1965).
8. D. Feakins, D. J. Freemantle, and K. G. Lawrence, *Chem. Commun.*, 970 (1968).
9. T. Erdey-Grúz, E. Kugler, and L. Majthényl, *Electrochim. Acta*, **13**, 947 (1968).
10. H. H. Emons, F. Winkler, D. Dümke, M. Förtsch, K. Schneider, and R. Tröger, *Z. Chem.*, **11**, 293 (1971).
11. M. H. Miles and H. Gerischer, *This Journal*, **118**, 837 (1971).
12. L. Werblan, A. Rotowska, and S. Minc, *Electrochim. Acta*, **16**, 41 (1971).
13. D. P. Shoemaker and C. W. Garland, "Experiments in Physical Chemistry," 2nd. Ed., McGraw-Hill Book Co., New York (1967).
14. M. H. Miles and P. M. Kellett, *This Journal*, **115**, 1225 (1968).
15. K. R. Williams, Editor, "An Introduction to Fuel Cells," pp. 116-123, Elsevier Publishing Co., New York (1966).
16. J. E. Del Bene, *J. Chem. Phys.*, **55**, 4633 (1971).
17. V. S. Griffiths, *J. Chem. Soc.*, 686 (1954).
18. E. R. Nightingale, *J. Phys. Chem.*, **63**, 1381 (1959).
19. S. Glasstone, K. J. Laidler, and H. Eyring, "The Theory of Rate Processes," pp. 557-559, McGraw-Hill Book Co., New York (1941).
20. F. Daniels and R. A. Alberty, "Physical Chemistry," 3rd. ed., pp. 283-284, John Wiley & Sons, Inc., New York (1966).
21. S. Minc and I. Zagórska, *Electrochim. Acta*, **16**, 1213 (1971).
22. C. Iwakura, T. Hayashi, S. Kikkawa, and H. Tamura, *ibid.*, **17**, 1085 (1972).
23. E. C. Potter, "Electrochemistry," pp. 340-341, Cleaver-Hume Press, London (1961).

Electrodeposition of Coherent Boron

Jordan D. Kellner

United Aircraft Research Laboratories, East Hartford, Connecticut 06108

ABSTRACT

Pure coherent boron has been electrodeposited from a fused fluoride mixture. A eutectic mixture of LiF and KF is used as the electrolyte, with BF_3 gas dissolved to form the tetrafluoborate ion which reacts at the cathode to produce boron. The boron as plated is of 95% or better purity, and is homogeneous and uncracked, up to 25 mils thickness. The substrates plated include steel, copper, graphite, tungsten, and molybdenum. Temperatures of plating range from 600° to 700°C, with plating rates up to 6 mils/hr.

Pure boron has been produced electrolytically in fused salts by Cooper (1) and others (2). However, these methods for producing boron electrolytically have produced spongy, dendritic, or compacted powder deposits. These deposits were crushed and treated with hot water and acid to leach out salts and other impurities. In contrast, the method presented in this paper produced 95+% pure boron as a single homogeneous material, dense, and structurally coherent. Boron is of interest as a coating due to its high hardness, low rate of corrosion, and high specific strength and modulus. Due to the hardness and brittleness of the material, it is difficult to machine, and electroforming offers an attractive technique to prepare useful parts made of boron. Substrates that have been plated include copper, graphite, steel, tungsten, and molybdenum.

Experimental

The electrolyte consists of a 50-50 mole per cent (m/o) mixture of reagent grade LiF and KF melting at about 495°C. These salts are partially dried by exposure for two weeks in an argon-filled dry box and then weighed and mixed mechanically. The BF_3 gas is 99.9% pure obtained in a 1400 psi cylinder. The melt is contained in a graphite crucible machined from UCAR Grade CS graphite rod obtained from Graphite Products Corporation. Figure 1 shows the crucible in its stainless steel can. The stainless steel cover is welded and provides threaded openings for fittings through which various electrodes are placed in the melt. Boron nitride inserts are used in the fittings to electrically insulate the electrodes from the can.

Key words: boron, electrodeposition, fused salts.

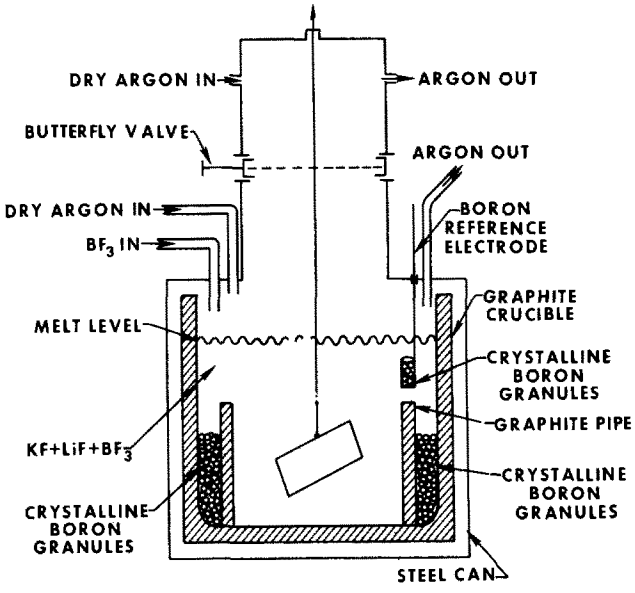

Fig. 1. Diagram of cell

The 6 in. opening at the top is fitted with a 6 in. nickel butterfly valve to provide an argon antechamber. This prevents air and moisture from reaching the melt surface, when the cathode is put in place and removed.

The dried mixed powder is held for 4-5 days in the crucible at 450°C under a stream of argon to remove residual moisture, then brought to 650°C for BF_3 addition.

A nickel tube held at ½ in. above the melt surface is used to add pure BF_3 gas for solution into the melt until the concentration reaches approximately 25 g/100 cm^3. Flow rates for gas addition are about 100 cm^3/min. Concentrations up to 100g BF_3/100 cm^3 of melt can then be obtained by immersing this tube and again flowing 20-50 cm^3/min. We have found that if the tube is below the liquid surface at low BF_3 concentrations it will become clogged easily, due to a partial vacuum being formed and forcing the liquid up the tube. The BF_3 concentration in the melt falls by about 0.5g BF_3/100 cm^3/day due to the appreciable vapor pressure of the gas above the melt, and necessitates the further addition of BF_3 periodically. The BF_3 concentration in the melt is monitored weekly by dissolving a small melt sample in water and determining fluoborate ion with an Orion specific ion tetrafluoroborate electrode.

The carbon electrodes used were all spectroscopic grade graphite rod obtained from Ultracarbon Corporation.

A power supply is used to establish a constant current between cathode and cell while the cathode-reference potential is monitored. An integrator using a Keithley 301 differential operational amplifier is used to determine the charge passed during an experiment. A Duffers Model 600 potentiostat was used to obtain constant voltage potentiograms recorded on a Mosely X-Y recorder.

Results

Plating conditions and coating appearance.—Coating appearance and purity are affected by three parameters: concentration of BF_3, current density, and temperature. Concentration of BF_3 has been varied from 3 to 25 g/100 cm^3, current density from 15 to 500 mA/cm^2 and temperatures from 550-750°C. At the lower temperatures, high BF_3 concentration and low current density are necessary for good deposits, while at high temperature, high current densities must be used. Some typical plating parameters are shown in Table I. Figure 2 shows typical coating surfaces with hemispherical nodules formed on the surface.

In general, the nodules were flatter at the high current densities, resulting in a shiny surface, while at

Table I. Plating conditions

Temperature (°C)	600		650		700	
Current (mA/cm^2)	15	50	25	100	50	200
Concentration (g BF_3/100 cm^3)	5	20	5	20	3	20

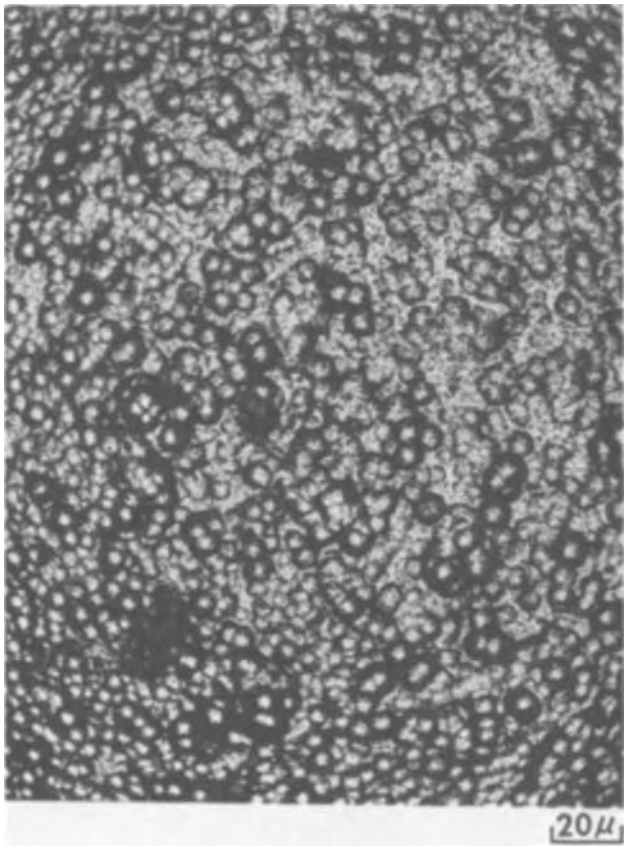

Fig. 2. Photograph (500×) showing hemispherical surface nodules.

low currents, the relatively large nodules produced a dull "matte" finish.

Coulometry and chemical analysis.—The number of electrons transferred in the deposition reaction, n, can be calculated according to

$$n = \frac{MC}{WF}$$

where M is the molecular weight of boron, 10.81, C is coulombs passed, W is weight of coating, and $\mathbf{F}$ is Faraday's constant. Table II shows the n numbers obtained from weighed cathodes at various current densities and temperatures. Each of these n numbers is the average of at least 10 determinations with a variation of ±2%. These data indicate an n number of 3 at lower current densities and higher temperatures, with numbers lower than 3 at high current densities and low temperatures.

Table III presents data on the boron content of some of the coatings used to obtain Table II.

Chemical analyses were performed by a modified Cooper technique where the coating and the copper foil substrate was dissolved in a mixture of HNO_3, HCl, and H_2SO_4 with refluxing. After removal of copper by precipitation of $Cu(OH)_2$ with NaOH, and adjusting pH, the solution was titrated with mannitol and NaOH. Table III shows that when the n number is close to 3, the boron content of the coating is close to 100%,

Table II. n Numbers

T (°C)	i (mA/cm²) 30	40	50	60	70	80
570-585	2.78	2.66	2.54	2.42	2.31	2.19
600-605	2.86	2.72	2.57	2.43	2.29	2.15
630-640	2.93	2.85	2.77	2.69	2.61	2.53
660-675	3.03	3.01	2.99	2.98	2.96	2.94

Table III. Coulometry of boron deposits

n	% boron by analysis
3.02	99
3.01	98
3.02	98.5
2.97	100
2.83	88
2.71	87
2.02	65

while lower n number coatings produced at high rates of deposition or low temperatures showed a corresponding low boron content.

This value is consistent with the cathode reaction

$$BF_4^- + 3e^- \rightarrow B + 4F^-$$

Since KF, from free energy calculations, (Janaf Thermochemical Data) would have a decomposition potential differing by about a volt from that of BF_3 (4.7 for KF, 3.7 for BF_3) one would suspect a small amount of potassium to codeposit with boron, especially at high overpotentials. If potassium were codepositing, only 1 mole of electrons would be necessary to reduce a mole of potassium weighing 39.1g whereas 3 moles of electrons are required to reduce a mole of boron weighing 10.81g. Thus a little current used for a potassium reaction goes a long way toward reducing the purity of the boron coating. The total weight of the deposit is

$$W = \frac{M_B C_B}{3F} + \frac{M_K C_K}{F}$$

For a total of 1000 coulombs

$$W = \frac{10.81\ (1000 - C_K)}{3\ (96{,}487)} + \frac{39.1\ (C_K)}{96{,}487}$$

The number of coulombs used to deposit potassium is

$$C_K = 2718W - 101.5$$

In the limit when $W = 37.3$ mg, C_K is zero, and the deposit is all boron. The value of C_K can be used to determine the weight of potassium in the deposit

$$W_K = \frac{M_K C_K}{F}$$

and the boron purity is

$$\%\ \text{boron} = \frac{W - W_K}{W} \times 100$$

Table IV shows results for seven samples that were analyzed for boron. The boron content of these samples as calculated by the above method is shown in the last column. These calculated values show good agreement with the actual values shown in the third column. It is interesting to note that in the fourth sample only 10.21 coulombs out of 1000 coulombs can be attributed to potassium deposition, and yet this is enough to limit the boron content of this sample to 87%. A spectral analysis qualitative test on a few of these samples showed potassium was present as a major impurity.

Table IV

W(g)	n	% boron by anaysis	C_K	Mg_K	Calc % B
0.0372	3.02	99	−0.4[a]	0	99.6
0.0372	3.05	98.5	−0.4[a]	0	99.6
0.0396	2.83	88	6.13	2.48	93.7
0.0411	2.73	87	10.21	4.14	89.9
0.0464	2.42	77	24.62	9.98	78.5
0.0524	2.14	69	40.92	16.58	68.4
0.0555	2.02	65	49.35	20.00	63.1

[a] These negative values of C_K are the result of an experimental error of 0.1 Mg in weighing the deposit.

Apparently, although the appearance of specimens plated was good, pure boron was obtained only at temperatures of about 700°, current densities below 50 mA/cm², and BF_3 concentrations above 20 g/100 cm³. Since there was good correlation between n numbers and boron purity, this can be used as a check on the quality of deposit.

Physical properties.—Samples of electroplated boron were exposed to Cu radiation for 12 hr in a Debye Camera 114.6 mm, and no crystalline peaks were observed. The pattern was typical of what has been called "amorphous" boron showing 2 diffuse rings similar to the pattern formed by high-strength vapor-deposited filament boron.

Strength and modulus of elasticity in bending was measured for copper and steel foil plated strips on a "Rigidometer" made by Galileo, Incorporated. The modulus is calculated from

$$E = \frac{M_O L}{3I \tan \theta}$$

where M_O is moment in lb-in., L is length of strip in inches, I is moment of inertia (for a flat rectangular beam $I = 1/12\ bh^3$, where b is the width and h is the thickness of the beam), and θ is the angle of deflection. The moment and the angle of deflection are read directly from the instrument. The stress at which the stress-strain curve becomes nonlinear was taken as the breaking stress of the coating, given by

$$S = \frac{6M_O}{bh^2}$$

These measurements yielded moduli for the boron coating of 57-70 $\times$ 10^6 psi and strengths of 30,000-95,000 psi.

Plating stress.—Qualitative measurements of plating stress were obtained from boron plating a bimetallic strip. A stainless steel 5 mil foil strip was copper plated on one side only, since the boron does not adhere to the steel but does adhere to the copper. Observations of the strip after coating with boron, and before cooling have shown a large compressive stress at low current densities, and a large tensile stress at high current densities. By measuring the curvature of the strip prior to cooling, effects due to differential thermal expansion were eliminated. An intermediate current density could be found where the plating stress was zero; however, this produced a coating of only 90% purity. In other words, plating for maximum purity of boron at low current densities always produced coatings with a high compressive stress. It is interesting to note that the boron produced by vapor deposition in BCl_3-H_2 gas mixture also exhibits expansion and resulting compressive stress. In vapor deposition on tungsten wires, the boriding and subseqeunt expansion of this wire tends to relieve this stress.

Hardness.—Figure 3 shows an eleven mil boron coating on graphite. Hardness measurements, using a Reichert microhardness tester at 100g load yielded a value for five impressions of 2505 ± 150 D.P.H. The same operator on the same apparatus obtained a value of 3027 ± 150 for vapor deposited boron fiber. It is apparent that the hardness of the electrodeposited boron is very dependent on the purity obtained, since lower hardness values were obtained for less pure boron deposits.

Chronopotentiometry.—Electrodes of small surface area were used to generate chronopotentiometric curves. A boron reference electrode was used, and proved to be extremely stable over long periods of time. This reference is properly called a "quasi" reference electrode (3) because its potential is not precisely defined. At BF_3 concentrations of 5 g/100 cm³ and 700°C, current densities of about 1 A/cm² produced a plateau at −0.52 and then a shallow decrease to −1.3,

Fig. 3. Boron coating on graphite rod (200×) showing five impressions of a diamond pyramid.

with a transition time of about 1 sec. This transition is too slow to be caused by diffusion control limiting the reaction, and it is probably caused by a series of reactions in which alkali borides and borates are deposited along with boron.

Voltammetry.—Current voltage curves using a copper working electrode, boron reference electrode, and a boron indicator were run with the results shown in Fig. 4. The sweep rate was 1 V/min, and little change was noted at slower sweep rates. The figure indicates the boron deposition potential is −0.55V relative to the boron reference, with a limiting current extending

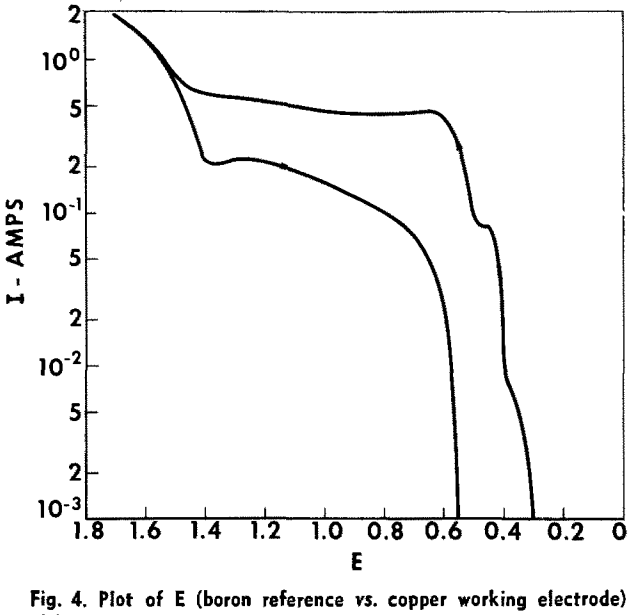

Fig. 4. Plot of E (boron reference vs. copper working electrode) vs. I (total current).

to −1.5V where alkali metal begins to deposit. Chronopotentiometric curves discussed previously indicate this is not a diffusion-limited current but a reaction-limited current. Thus, it is likely that a small amount of alkali metal deposits along with the boron at all potentials, while increasing amounts are deposited at more negative potentials.

Discussion

The essential feature of the present method for depositing boron is the low level of oxygen contamination that is necessary. After the KF-LiF mixture is melted, and before BF_3 is added, the oxygen-moisture contamination is checked by voltammetry. Two carbon rods are used, with a third carbon rod acting as a "quasi-reference." An anodic sweep at 20 mV/min produced a consistent current maximum at about +1.5V the height of which could be related to the oxide contamination level. Assignment of the current to oxygen discharge was possible from the observed evolution of carbon dioxide and carbon monoxide from the working carbon electrode as measured in the argon purge gas. Good boron deposits could be obtained only if the peak current due to the oxyanions was less than 10 mA/cm^2 and the best deposits were obtained when this current was less than 1 mA/cm^2. Boron deposited in a clean melt was of high purity (95%+) without any further purification treatment, and had a smooth surface. The thickness of the coating was varied from 0.5 to 25 mils with the thicker coatings being somewhat less pure and prone to cracks. There was no difference in the quality of the coating deposited on steel, graphite, copper, molybdenum, niobium, tungsten, titanium, or nickel. Of these substrates titanium required a thin protective coat of electroplated copper because of its corrosion by the melt. Both steel and nickel substrates required the presence of a boride layer before the boron would adhere to the surface. The boride layer would form if low current densities were chosen so that the cathode potential *vs.* a boron reference electrode was about −0.1V, *i.e.*, much less than the −0.55V necessary for boron to accumulate on the surface. Cook (4) in his boriding patent states that one should avoid the accumulation of boron on the surface which occurs at high deposition rates because the boron so obtained is crystalline, dendritic, or powdery. Numerous authors (1, 2) in the patent literature have described methods for producing this salt-boron composite mixture. The author can only conclude that the prime requisite in the present method is nearly complete absence of oxyanion contamination. Mellors and Senderoff (5) have discussed the undesirable high vapor pressure of BF_3 in fluoride melts, and the difficulties encountered by rapidly changing melt composition. The author has found that BF_3 composition changes are very small at temperatures of 600°-700°C in the KF-LiF eutectic mixture. Also, the melt can dissolve up to 50% by weight of BF_3 and still remain a single liquid phase. In melts that do not contain KF, it was found that BF_3 is nearly insoluble in this temperature range. On the other hand, attempts to use other sources of boron such as boric oxide do not produce smooth coherent pure boron deposits.

Manuscript submitted May 25, 1972; revised manuscript received Jan. 22, 1973.

Any discussion of this paper will appear in a Discussion Section to be published in the December 1973 JOURNAL.

LIST OF SYMBOLS

b	Width of beam (in.)
C	Charge passed (total) (coulombs)
C_K	Charge passed for potassium deposition (coulombs)
E	Modulus of elasticity (psi)
$\mathbf{F}$	Faraday's constant
h	Thickness of beam (in.)
i	Current density (mA/cm^2)
I	Moment of inertia (in.$^{+4}$)
L	Length of beam (in.)
M	Molecular weight
M_B	Molecular weight of boron
M_K	Molecular weight of potassium
M_O	Moment (lb-in.)
n	Electron number
S	Yield strength (psi)
W	Weight of deposit
W_K	Weight of potassium in deposit
θ	Angle of deflection (degrees)

REFERENCES

1. H. S. Cooper, U.S. Pat. 2,984,605 (1961); 2,572,249 (1950); 2,918,417 (1959); 2,572,248 (1951).
2. D. R. Stern, U.S. Pat. 3,030,284 (1962); N. F. Murphy and R. S. Tinsley, U.S. Pat. 2,848,396 (1958); R. B. Ellis, U.S. Pat. 2,810,683 (1957).
3. D. L. Manning, *J. Electroanal. Chem.*, **6**, 227 (1963).
4. N. C. Cook, U.S. Pat. 3,024,176 (1962).
5. G. W. Mellors and S. Senderoff, *This Journal*, **118**, 220 (1971).

Photoconductivity in Anodic Oxide Films on Bismuth

S. Ikonopisov,* L. Andreeva, and Ts. Nikolov

Department of Physical Chemistry, Higher Institute of Chemical Technology, Sofia 56 (Darvenitsa), Bulgaria

ABSTRACT

Photoconduction of bismuth anodic films in different contacting and forming electrolytes is studied as a function of formation voltage, U_f, (film thickness, l_f); electrode potential, U_a; light intensity, L_o; and wavelength, λ. Oscillations of the photocurrent, I_{ph}, were observed when the film is obtained by galvanostatic anodization, these oscillations being eliminated by prolonged constant voltage anodization. Photoconduction is observed only under anodic polarization of the oxide-covered electrode. I_{ph} was found to be proportional to U_a and L_o, and to increase with U_f (or l_f). The spectral distribution I_{ph} (λ) is independent of the contacting electrolyte and for films anodized in a glycol-borate electrolyte or in dilute aqueous solutions shows an optical activation energy $W_{opt} \sim 2.8$ eV. For films anodized in a phosphate electrolyte [$(C_2H_5)_3PO_4 + H_3PO_4 + H_2O$] W_{opt} decreases to *ca.* 2.5 eV. This is attributed to the incorporation of ions from the electrolyte into the film. An attempt to explain the properties of the photoconduction is made on the assumption that a high density of trapping levels exists in the forbidden band of the structurally disordered anodic film.

De Smet and Hopper (1) have observed that visible light produces a sharp decrease in the potential of the bismuth anode during galvanostatic oxidation at low current density. This indicates that the anodic film exhibits photoconductivity in the visible region. The purpose of this paper is to clarify the origin and to study the properties of this phenomenon.

Experimental

The samples used in this study were cylinders (0.92 cm diameter) cut from a block of high purity (99.9995%) bismuth. A wire lead was soldered to the back-face of each cylinder. The specimen was then immersed in Araldite and, after curing, the front-face was uncovered by abrading with emery paper. The working surface was subsequently electropolished, brightened, and washed by the method described by Masing and Young (2). Conventional galvanostatic and potentiostatic techniques (3) were used for growing the anodic oxide films.

The precise measurements of the spectral distribution of photosensitivity requires operation at very low light intensities. In this case the photocurrent is only a small fraction of the dark current and the latter ought to be fully compensated. The compensating circuit designed to detect the photocurrents alone is given in Fig. 1. The electrode was polarized by an electronic constant voltage supply through a bleeder, the resistance (γ_b) of which was made proportional to the ratio of the applied voltage (U_a) to the formation voltage (U_f), viz., $\gamma_b = 500(U_a/U_f)$ kohms. The potential drop through the bleeder after stabilization of the dark current, was compensated by a second potentiostat. The anode potential was then measured by a vacuum tube voltmeter and overpotentials were calculated by subtracting the value of the open-circuit potential. Despite the high input impedance of the voltmeter the latter was disconnected during photocurrent measurements.

The electrode was subsequently irradiated with monochromatic light from a 100W incandescent lamp and photocurrent values were taken down only after a stabilization period of *ca.* 5 min. A monochromator with 11 nm half-width (Specol-C.Z.Jena, ± 1 nm wavelength accuracy) carefully calibrated against a Hg arc lamp, was used.

In the following the term formation voltage (U_f) is used to designate the potential up to which the electrode has been anodized under galvanostatic conditions or the overpotential at which the anodization has been carried out at a constant voltage and the term applied potential (U_a) refers to the overpotential at which the photoconductivity is measured.

All experiments were carried out at room temperature.

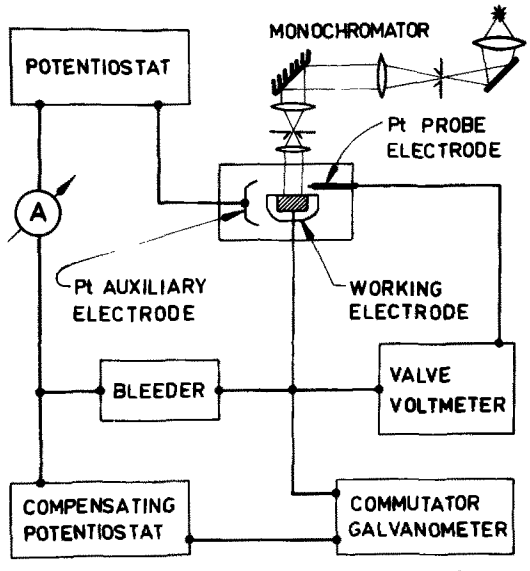

Fig. 1. Compensating circuit used for photoconduction measurements.

Results

Selection of the formation electrolyte.—Various alkaline (1, 2, 4-8) and acid (9-11) aqueous solutions are known to favor the formation of insulating anodic films on bismuth. The kinetics of anodization are strongly affected by the electrolyte composition and concentration. In many cases the dissolution of the anodic film is appreciable. Therefore investigations were carried out for the selection of an electrolyte which has no dissolution action on the film. Such appeared to be the mixture [$(H_2CO)_4B$]H + [$(H_2CO)_4B$]Na (1:1), produced by reacting appropriate amounts of H_3BO_3, NaOH, and $(CH_2OH)_2$ and removing the water obtained in the esterification by heating to 120°C. Prolonged (10 hr and more) polarization at potentials well below U_f or keeping the electrode for 100 hr in this electrolyte did not change the dielectric characteristics of the anodic film. Unless otherwise stated, the anodization and photoconductivity measurements were performed in this electrolyte, which will be designated as glycol-borate electrolyte.

* Electrochemical Society Active Member.

Key words: bismuth, anodic films, photoeffect, electronic conduction.

Influence of the film-formation method on the photoconductivity.—Preliminary experiments indicated that photosensitivity of the anodic film is strongly affected by the mode of anodization. After galvanostatic oxidation irregular oscillations of the photocurrent were observed. The amplitude of oscillation increased with the bias potential and near the formation voltage the measurements become almost impossible. A hysteresis in the photocurrent/wavelength curve was also observed.

When the galvanostatic film formation is followed by a constant voltage anodization, the current oscillations diminish the longer the anodization time. After sufficiently long (*e.g.*, 16 hr) anodization the oscillations vanish and the photoconduction can be easily measured at potentials as high as the formation voltage.

As shown in Fig. 2, all photosensitivity spectra have similar shapes and the increased duration of the constant voltage anodization results only in a reduction of the photocurrent. This is quite explicable, taking into account the increase in the film thickness (*i.e.*, the lowering of the field strength across the film) during the process.

All these results suggest the presence of imperfections in the anodic film grown under galvanostatic conditions, these imperfections being removed after a prolonged constant voltage anodization. The latter mode of oxidation was used throughout the following investigations.

Occurrence and reproducibility of photoconduction.—Photoconductivity is observed only during anodic polarization of the oxide-covered electrode. At cathodic potentials close to U_f the dark current density is very high and increases until film breakdown commences. At lower cathodic potentials the dark current decreases with time to a steady-state value, which is still many times higher than that at anodic polarization. The irradiation with visible light after current stabilization at cathodic potentials either does not cause photoconduction, or the feeble photocurrent eludes detection on the background of the very large dark current, although it is compensated.

The photosensitivity spectra have a good reproducibility and are independent of the history of the film, whether the electrode has been previously polarized at higher or lower anodic potentials or even at low cathodic potentials.

Effect of the contacting electrolyte and the film thickness on photosensitivity.—Photoconductivity was found to be independent of the nature of the contacting electrolyte. As shown in Fig. 3, the change of the glycol-borate electrolyte (after the anodic film formation) with an aqueous acid or alkaline solution has no influence over the spectral sensitivity curve.

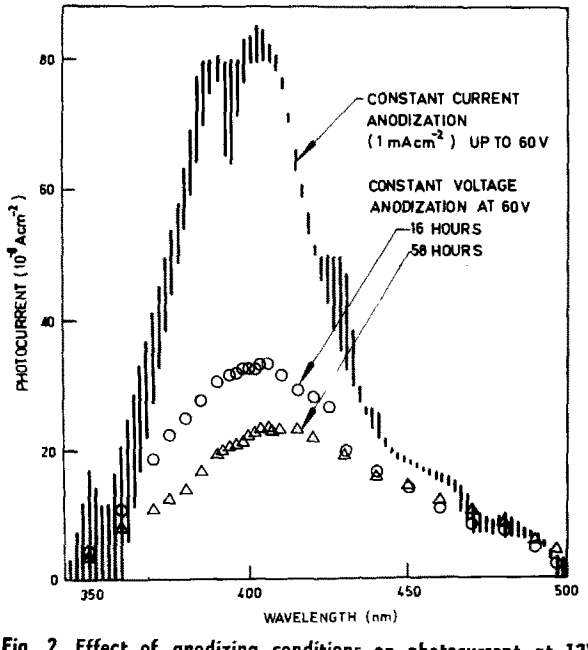

Fig. 2. Effect of anodizing conditions on photocurrent at 12V bias of anodic films formed to or at equal potentials.

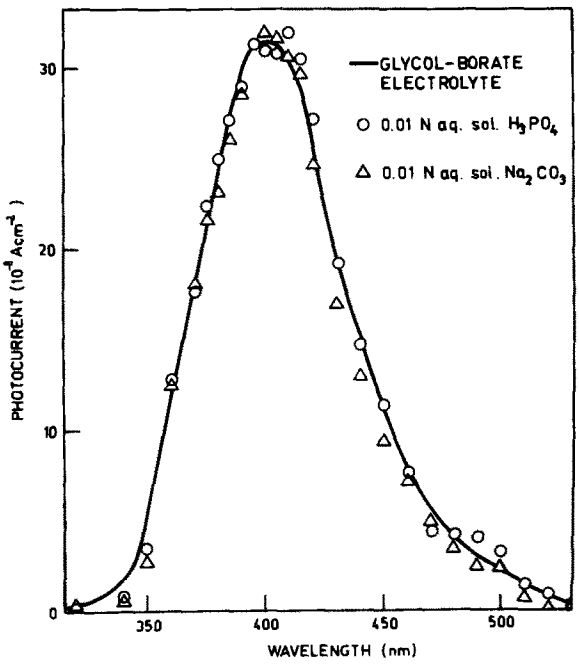

Fig. 3. Spectral distribution of photoconduction at 12V bias in various electrolyte solutions. (Film formed 16 hr at 48V in the glycol-borate electrolyte.)

The photocurrent increases with the film thickness. Figure 4 shows a plot of the peaks of the photosensitivity spectra against U_f, which is approximately proportional to the film thickness, and at $(U_a/U_f) = \text{const}$, providing for an almost constant field strength in the anodic film.

Potential and light intensity dependence of photocurrent.—The photocurrent (I_{ph}) increases with the bias potential (U_a). The shapes of the spectral response curves (Fig. 5) are, however, identical for various U_a, having a peak at $\lambda_p \sim 400$ nm. The peak photocurrent for a given film thickness was found to be proportional to U_a, and consequently to the field strength across the film. This is illustrated in Fig. 6.

As shown in Fig. 5, the wavelengths at half-maximum sensitivity ($\lambda_{1/2}$), determined as the wavelengths where I_{ph} has fallen to half its maximum value, were found to lie very close ($436 < \lambda_{1/2} < 442$ nm) for vari-

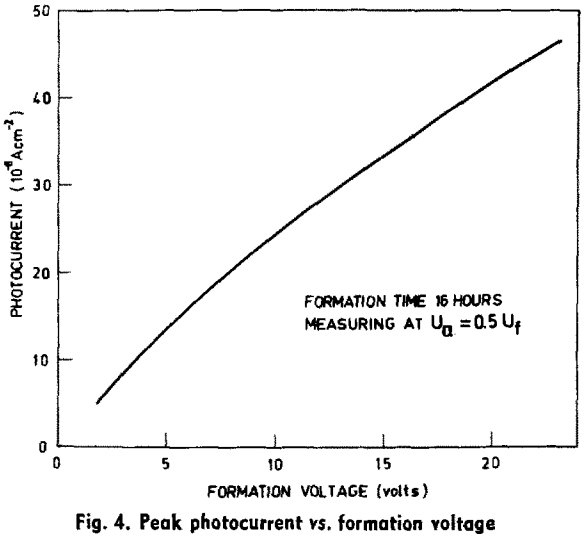

Fig. 4. Peak photocurrent vs. formation voltage

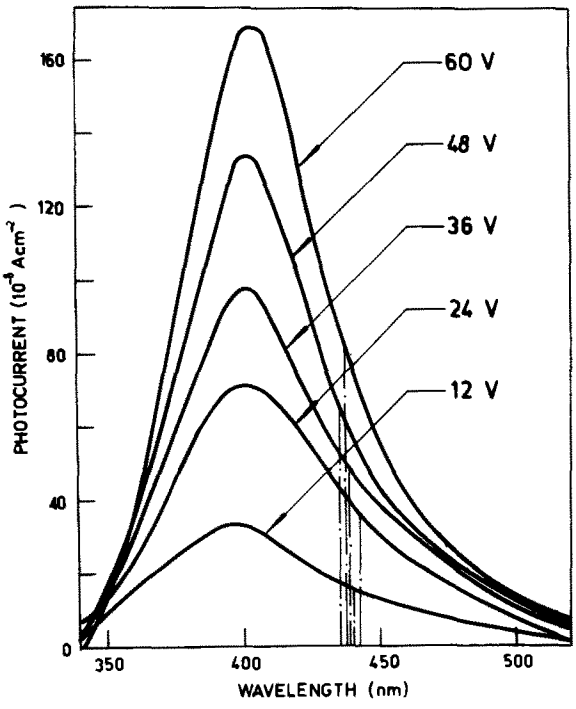

Fig. 5. Spectral distribution of photoconduction at various electrode potentials. Film formed 16 hr at 60V in glycol-borate electrolyte. Mean values. Dotted lines mark values of $\lambda_{1/2}$.

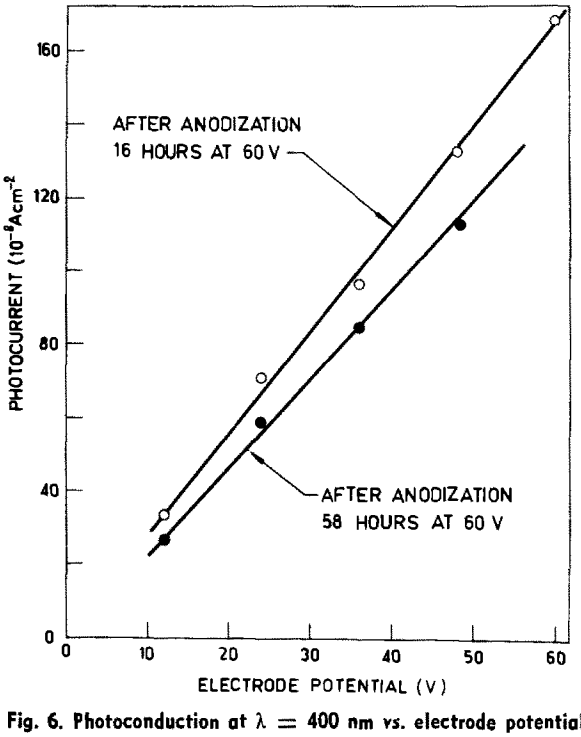

Fig. 6. Photoconduction at $\lambda = 400$ nm vs. electrode potential

ous U_a. By the way, for all runs in glycol-borate electrolyte the mean value of $\lambda_{1/2} = 445 \pm 10$ nm.

Intensity dependence of photoconduction was measured with monochromatic light of λ_p (400 nm). The light intensity (L_o) was changed by placing various numbers (N_f) of equal neutral filters between the monochromator and the electrolytic cell. The diminution of L_o was determined by the relation $L_o \propto \exp(-\text{const } N_f)$. In this way the photocurrent was found to be proportional to the intensity of illumination within the range of intensities employed (Fig. 7).

Effect of the forming electrolyte on the spectral distribution of photocurrent.—The galvanostatic anodization in sufficiently diluted aqueous acid or alkaline

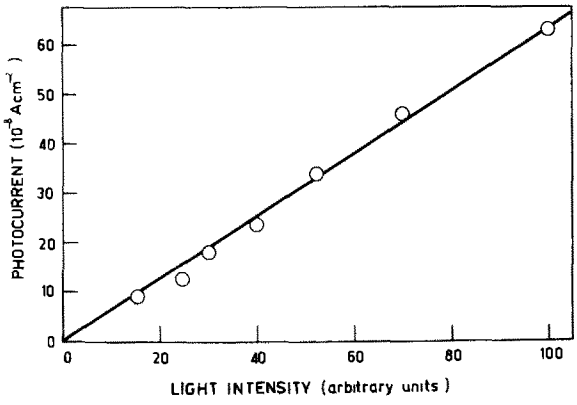

Fig. 7. Intensity dependence of photoconduction. Film formed 58 hr at 60V and tested at 24V. $\lambda = 400$ nm.

solution is known to proceed according to quite identical kinetics (8, 11). Some preliminary investigations revealed that the anodization kinetics in the glycol-borate is similar. The spectral sensitivity curves of anodic films obtained in various dilute aqueous solutions have similar shapes as for anodization in glycol-borate electrolyte and almost the same characteristic wavelengths (λ_p and $\lambda_{1/2}$). As an example the spectral distribution of photocurrent for an anodic film obtained in dilute citric acid solution is shown in Fig. 8. In spite of the great difference in the electrolyte composition and the forming conditions, the values $\lambda_p = 412$ nm and $\lambda_{1/2} = 437$ nm lie very close to the mean values for the glycol-borate electrolyte (*ca.* 400 and *ca.* 440 nm, respectively).

The case where the anodic film is formed in a phosphoric acid + triethyl-phosphate mixture with a low water content is different. For this electrolyte abnormally high rates of galvanostatic anodization are reported (11), which can be twice the rates for the dilute aqueous solutions or the glycol-borate electrolyte. This high apparent current efficiency (up to 200%) has been attributed to the incorporation of ions from the electrolyte into the film (11). Corresponding differences in the film properties, including photosen-

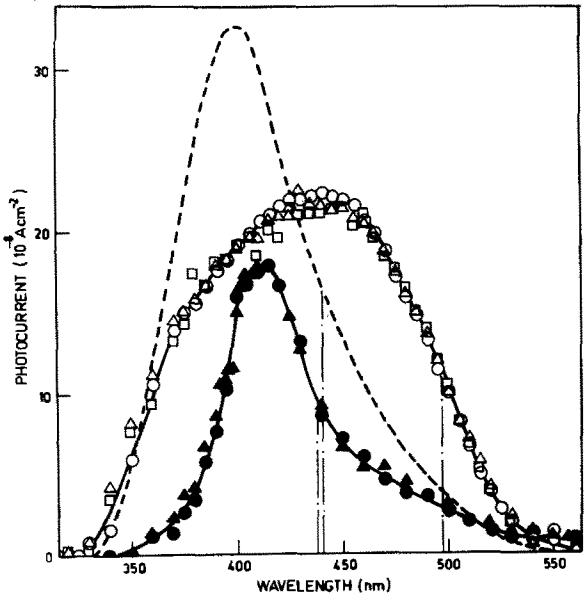

Fig. 8. Photoconduction data for anodic film formed in various electrolyte solutions and tested in glycol-borate electrolyte. Open symbols: formation in phosphate electrolyte 16 hr at 48V, testing at 12V; closed symbols: formation in 0.01*N* aqueous solution citric acid at 0.5 mA/cm^2 up to 200V, testing at 60V. For comparison the spectral sensitivity curve of anodic film formed in glycol-borate electrolyte at the same conditions as in the phosphate electrolyte is shown with dashed line. Dotted lines represent the value of $\lambda_{1/2}$.

sitivity, are to be expected. Such differences in the spectral sensitivity curves were actually observed. Thus, as shown in Fig. 8, in the case of anodization in an electrolyte of 62 w/o (weight per cent) $(C_2H_5)_3PO_4$ + 20 w/o H_3PO_4 + 18 w/o H_2O both λ_p and $\lambda_{1/2}$ are shifted by more than 50 nm to longer wavelengths as compared to the mean values of λ_p and $\lambda_{1/2}$ for oxides formed in the glycol-borate electrolyte.

Discussion

Origin of photoconductivity.—The film-thickness dependence of photoconduction indicates that the investigated phenomenon should be regarded as a bulk-limited (internal) photoeffect. This is also strongly supported by the lack of dependence of photocurrents on the nature of the contacting electrolyte. Hence the electrolyte/oxide interface does not take part in the photoexcitation process, and yet the electrolyte contact appears to be indispensable for the establishing of photoconduction, because the latter is observed only during anodic polarization of the oxide-covered electrode, *i.e.*, in the case of electron transfer from the electrolyte to the metal.

The lack of photoconduction under cathodic polarization of the metal, as well as the rectification effect of the system in question could be explained admitting a difference in the work functions of the electrolyte and the metal. The electron energy of anions in electrolytes is known to lie several electron volts below the Fermi level of metals and thus electrolytes realize one of the most blocking contact with semiconductors (12).

Thanks to the blocking electrolyte contact under anodic polarization of the metal, it is possible to apply electric fields sufficiently high to pull the photoelectrons before trapping. Conversely, the comparatively low potential barrier for electron emission from the metal gives rise to a high dark-current density at such a low cathodic potential (low field strength across the film), which are insufficient for detection of any photoconductivity. The different height of the potential barriers at the metal/oxide and the electrolyte/oxide interface presents, of course, an explanation also of the rectifying effect of the system Bi/anodic film/electrolyte, but this point is beyond the scope of the present paper.

The rectification and photoeffects for some valve metals have been related to p-n or p-i-n junctions within the oxide film (13-18). The existence of space charge in the anodic film of these metals is strongly supported by the observed corresponding variation of the film capacity with applied bias potential (17-19). But the capacity of anodic films formed on bismuth is known to be independent of potential (19), thus indicating the lack of space charge. This fact and the described independence of photosensitivity from the film history leads us to conclude that the model of p-n or p-i-n junction, which is applicable in some instances, is unacceptable in the case of anodic films on bismuth.

Photoconductive spectra and optical activation energy for films obtained in glycol-borate electrolyte.—The spectral sensitivity curves exhibit a peak, characteristic of materials with high surface recombination velocities (20, 21). At higher wavelengths the photocurrent rapidly decreases. An exponential fall of I_{ph} at longer wavelengths with photon energy, $I_{ph} \propto \exp(-\text{const } h\nu)$, was found to give a good fit to all experimental results, in accordance with theory (20).

It is known that the "absolute" threshold wavelength, that is, the wavelength at which the sensitivity vanishes completely, is condition-dependent and gives only a rough idea of the optical activation energy (W_{opt}), but nevertheless, it has been frequently used for the purpose. For the anodic film on Bi we estimated the absolute threshold wavelength to vary between 520 and 575 nm, the corresponding energies being *ca.* 2.4 and 2.15 eV.

An exact method of determining W_{opt} is proposed by Moss (20). By this method W_{opt} is determined from the spectral sensitivity curve as a point (wavelength $\lambda_{1/2}$) where the sensitivity has fallen to half its maximum value. Actually, this method is derived and regarded as valid only in the case where thermal (W_{th}) and optical (W_{opt}) activation energies are equal, *i.e.*, for nonpolar monatomic crystals (20). Nevertheless, it appeared that for sufficiently thin films (*e.g.*, $\lesssim 10$ μm) this method gives correct values of both W_{th} and W_{opt} for highly polar (even structureless) inorganic (21) and organic (22) materials.

In our case the threshold wavelength was found to be $\lambda_{1/2} = 445 \pm 10$ nm, corresponding to $W_{opt} = 2.78 \pm 0.06$ eV. The shape of the spectral response curves and the lack of sensitivity in the near uv region suggest an intrinsic photoconduction and that the energy of 2.78 eV corresponds to the energy gap (E_g) of the oxide.

Two values for E_g of Bi_2O_3 are known to the present authors. One of them, $E_g = 3.2$ eV (23), is considerably higher and probably pertains to a crystalline structure of Bi_2O_3. Nevertheless, this discrepancy could not be attributed to the glassy structure of the anodic film. It is known (24) that a band model is applicable and remains valid for amorphous structures also, the energy gap being similar in respect to the crystalline condition, or broader because of the larger interparticle distances. The outer value, $E_g = 2.7$ eV [see (25)], is quite close to the one found here.

Photoconductive properties.—Generally under an applied voltage U_a the photocurrent density I_{ph} is

$$I_{ph} = N_e(l_f, L_o)\, e\mu U_a / l_f \qquad [1]$$

where N_e is the number of photoelectrons per square centimeter in steady state, l_f is the film thickness, L_o is the intensity of the incident light, e is the electronic charge, and μ is the electron mobility.

At constant l_f, if the irradiation excites N photoelectrons per square centimeter per second, the increase of photoelectron density (n) in the conduction band with time (t) is given by

$$(dn/dt) = N - \beta n(n + M) \qquad [2]$$

where β is the recombination coefficient and M is the number of the trapped electrons (or of the trapping levels for sufficiently deep traps). Assuming a great number of trapping levels ($M >> n$) because of the amorphous structure of the film, when equilibrium is attained [*i.e.*, $(dn/dt) = 0$ and $n = N_e$], we may write

$$N_e = N/\beta M \qquad [3]$$

For monochromatic light with appropriate wavelength, taking into account the exponential decay of the light intensity with the depth into the film, we have

$$N = AL_o \int_0^{l_f} \exp(-\alpha l_f)\, dl_f \qquad [4]$$

where A is the number of photoelectrons per unit absorbed radiation and α is the absorption coefficient.

Combining Eq. [1], [3], and [4] relationship $I_{ph}(L_o U_a l_f)$ is obtained

$$I_{ph} = \frac{Ae\mu L_o U_a}{\beta M l_f} \int_0^{l_f} \exp(-\alpha l_f)\, dl_f \qquad [5]$$

Hence at constant L_o and l_f

$$(I_{ph})_{L_o, l_f} \propto U_a \qquad [6]$$

and at constant U_a and l_f

$$(I_{ph})_{U_a, l_f} \propto L_o \qquad [7]$$

Equations [6] and [7] are in accordance with the relationships found experimentally (Fig. 6 and 7).[1]

[1] Relation [7] is of course valid only at very low L_o where condition $M >> n$ is satisfied. At higher L_o Eq. [2], [4], and [5] lead to $(I_{ph})_{U_a, l_f} \propto L_o^f$ where $1 > f > 1/2$.

We have no data about the dependence $[I_{ph}(l_f)]_{U_a,L_0}$, but, if l_f is approximately proportional to the formation voltage (U_f), the observed nonlinearity of $[I_{ph}(U_f)]_{U_a,L_0}$ (see Fig. 4) becomes comprehensible from Eq. [5].

Production of donor impurity levels by incorporation of ions from the anodizing electrolyte.—The anodic film obtained by anodization in sufficiently diluted aqueous solutions or in glycol-borate electrolyte give similar photoconduction spectra, implying that the films have similar structure and composition.

This is not the case when a phosphate electrolyte is used for anodization. The threshold wavelength is shifted from *ca.* 445 nm to *ca.* 495 nm, the activation energy becoming $W_{opt} = 2.5$ eV. This indicates the appearance of new donor impurity levels reducing the optical activation energy by about 0.3 eV. This is in accordance with the assumption concerning the incorporation of ions in bismuth anodic films formed in phosphate electrolyte. The assumption was proposed to explain the higher (up to two times) rate of potential rise during galvanostatic anodization in a phosphate electrolyte (11). Incorporation of ions from the electrolyte into the oxide during anodization of other valve metals in phosphoric acid or phosphate solutions has been experimentally observed in several cases (26-30). Our results indicate that the incorporated ions from the phosphate electrolyte give impurity levels in the forbidden band of the bismuth anodic films.

Summary

It has been found that the photoconduction of the anodic films on bismuth is thickness dependent and hence is a bulk-effect. It is observed only at anodic polarization of the oxide-covered electrode and increases linearly with the applied voltage and light intensity. The spectral distribution of photoconduction is independent of the contacting electrolyte and for films obtained by anodization in glycol-borate electrolyte or dilute aqueous solutions shows an optical activation energy of *ca.* 2.8 eV. When the anodization is carried out in phosphate electrolyte, this activation energy decreases to *ca.* 2.5 eV, due in all probability to the incorporation of ions from the electrolyte into the film. An attempt to explain all these properties of photoconductivity is made on the assumption that a great number of trapping levels exists in the forbidden band because of the disordered structure of the film.

Manuscript submitted Sept. 29, 1972; revised manuscript received Jan. 10, 1973.

Any discussion of this paper will appear in a Discussion Section to be published in the December 1973 JOURNAL.

REFERENCES

1. D. J. De Smet and M. A. Hopper, *This Journal*, **116**, 1184 (1969).
2. L. Masing and L. Young, *Can. J. Chem.*, **40**, 903 (1962).
3. S. Ikonopisov and L. Andreeva, *Electrokhimiya*, **5**, 1358 (1969); **6**, 1412 (1970); L. Andreeva, S. Ikonopisov, and D. Tokarev, *ibid.*, **7**, 1698 (1971).
4. A. Güntherschulze and H. Betz, *Z. Phys.*, **71**, 106 (1931); V. Cupr and E. Dvorakova, *Chem. Listy*, **50**, 1492 (1956); *Collection Czech. Chem. Commun.*, **22**, 305 (1957).
5. W. McNeill and L. Gruss, *This Journal*, **110**, 853 (1963).
6. F. F. Faysullin and B. S. Mironov, *Electrokhimiya*, **8**, 215 (1972).
7. I. A. Ammar and M. W. Khalil, *Electrochim. Acta*, **16**, 1601 (1971).
8. Ts. Nikolov and S. Ikonopisov, *Compt. Rend. Acad. Bulgare Sci.*, **25**, No. 11 (1972).
9. I. A. Ammar and M. W. Khalil, *Electrochim. Acta*, **16**, 1379 (1971).
10. S. Ikonopisov and Ts. Nikolov, *This Journal*, **119**, 1544 (1972).
11. S. Ikonopisov and Ts. Nikolov, *Compt. Rend. Acad. Bulgare Sci.*, **25**, No. 12 (1972).
12. A. Rose, "Osnovy teorii fotoprovodimosti," Publ. Mir, Moscow (1966), translation of "Concepts in Photoconductivity and Allied Problems," John Wiley & Sons, Inc., New York (1963).
13. W. Ch. van Geel, *Physica*, **17**, 761 (1951); W. Ch. van Geel and J. W. A. Scholte, *Philips Res. Rept.*, **6**, 54 (1951); J. W. A. Scholte and W. Ch. van Geel, *ibid.*, **8**, 47 (1953).
14. B. M. Tareev and M. M. Lerner, *Fiz. Tverd. Tela*, **2**, 2487 (1960).
15. Y. Sasaki, *J. Phys. Chem. Solids*, **13**, 177 (1960).
16. A. P. Belova, L. G. Gorskaya, and L. N. Zakgeim, *Fiz. Tverd. Tela*, **3**, 1851 (1961); T. I. Komolova and D. N. Nasledov, *ibid.*, **3**, 3400 (1961).
17. F. Huber, *Solid State Electron.*, **5**, 410 (1962); *This Journal*, **110**, 846 (1963); **115**, 203 (1968).
18. K. Hirata, H. Yoneyama, and H. Tamura, *Electrochim. Acta*, **17**, 793, 805 (1972).
19. D. A. Vermilyea, *J. Phys. Chem. Solids*, **26**, 133 (1965).
20. T. S. Moss, "Photoconductivity in the Elements," Butterworths Scientific Publications, London (1952).
21. T. S. Moss, "Optical Properties of Semi-conductors," Butterworths Scientific Publications, London (1959).
22. A. T. Vartanyan and I. A. Karpovich, *Dokl. Akad. Nauk SSSR*, **111**, 561 (1956); *Zh. Fiz. Khim.*, **32**, 274, 543 (1958); A. T. Vartanyan, *ibid.*, **30**, 1028 (1956); A. T. Vartanyan and L. D. Rosenshteyn, *Dokl. Akad. Nauk SSSR*, **124**, 295 (1959).
23. R. H. Bube, "Fotoprovodimost tverdyh tel," Publ. Izd. Inostr. Lit., Moscow (1962), translation of "Photoconductivity of Solids," John Wiley & Sons, Inc., New York (1960).
24. N. F. Mott, "Electrony w neuporyadotshennyh strukturah," Publ. Mir, Moscow (1969); W. A. Harrison, "Teoriya tverdogo tela," Publ. Mir, Moscow (1972), translation of "Solid State Theory," McGraw-Hill Book Co., New York (1970).
25. A. K. Vijh, *Electrochim. Acta*, **17**, 91 (1972).
26. P. F. Schmidt and A. E. Owen, *This Journal*, **111**, 682 (1964).
27. J. J. Randall, W. J. Bernard, and R. R. Wilkinson, *Electrochim. Acta*, **10**, 183 (1965).
28. J. C. Banter, *This Journal*, **114**, 508 (1967).
29. L. N. Bokiy, M. N. D'yakonov, and L. L. Odynets, *Elektrokhimiya*, **8**, 298 (1972).
30. C. J. Dell'Oca and L. Young, *This Journal*, **117**, 1548 (1970).

Space-Charge and Concentration-Gradient Effects on Anodic Oxide Film Formation

A. T. Fromhold, Jr.[1] and J. Kruger*

National Bureau of Standards, Washington, D. C. 20234

ABSTRACT

Numerical computations illustrate the effects of space charge and a concentration gradient on the steady-state mobile-defect concentration profile and the kinetics of anodic film formation. The position-dependence of the concentration of mobile defects producing growth is shown to vary with current density and film thickness. Of especial interest is a series of curves illustrating the total electrostatic potential developed across the oxide as a function of thickness for growth under constant current conditions. Space charge is shown to have the capability of being a critical factor in retarding the growth rate of the anodic film.

Background

Introduction to the problem.—The approach of considering forward and reverse currents over discrete energy barriers within a diffusion medium was first proposed by Verwey (1) in 1935. Since that time Mott (2) and Cabrera and Mott (3) have extended the concept by emphasizing the possibility of a rate-limiting barrier located at the interface of a growing, anodically formed (or thermally formed) metal oxide. Dewald (4) extended the model of Verwey by an approximate analytical development which included the space-charge electric field, with the major emphasis placed on the Tafel slope (5) in the high-field limit. The primary purpose of the present work (6) is to evaluate numerically the effect of space charge on the kinetics in the intermediate-field regime; simultaneously the specific role of the concentration gradient is examined (7, 8).

Physical origin of the concentration gradient.—The first question is whether or not there is a concentration difference in the diffusing species across the anodic film, and if so, whether or not it provides a driving force for mass transport through the film. In the case of equilibrium of a given species in an anodic film, the electrochemical potential for the species must be uniform in the film and there will be no particle current of that species through the film. If there is no electric field in the film, then the uniformity of the electrochemical potential may require that the concentration be uniform also, in which case there will be no concentration gradient in the film. On the other hand, if the electric field in the film is nonzero, the electrostatic potential within the film will be position-dependent. Since the electrochemical potential is made up of contributions due to electrostatic potential and defect concentration, the uniformity of the electrochemical potential then requires in general that the concentration be position-dependent. That is, a concentration gradient is to be expected even in equilibrium when the electric field is nonzero. In addition to illustrating that the equilibrium case can involve concentration gradients, the conclusion is reached that concentration gradients and electric fields do not necessarily produce any net current.

Suppose that we perform a *gedanken* experiment in which we attempt to go from the equilibrium condition of zero current with some given electric field to a nonequilibrium condition of nonzero current by changing the value of the field. There can likewise be equilibrium with some different value of the electric field, provided that the concentration profile of the defect species is allowed to rearrange itself to maintain uniformity of the electrochemical potential. Does the change in electric field then drive a net current through the film, or does the concentration profile readjust itself with the change in field in order to maintain a uniform electrochemical potential for that species in the film? The answer is intuitive: the concentration of the diffusing species is constantly depleted at the reaction interface, so that the concentration profile cannot adjust itself arbitrarily to maintain a uniform electrochemical potential. The interfacial reactions play an important role in determining the boundary concentrations, so these concentrations are more or less fixed independently of the electric field. Thus by changing the electric field, an accompanying change in the species current can be produced. This qualitative argument should not be misconstrued as a statement that the boundary concentrations are entirely independent of the electric field. Instead, it merely represents an argument that the concentration profiles are determined in accordance with conditions imposed by the interfacial reactions as well as by the electric field, and hence the profiles are not entirely free to adjust arbitrarily with the electric field. Thus we arrive at an idealized picture of the metal-oxide-solution system as an asymmetrical system with boundary concentrations of the defect species determined to a large extent by the interfacial reactions. In the absence of a particular model for the interfacial reactions, or merely for reasons of simplicity, we can choose the boundary concentrations of the diffusing defect species to have arbitrary fixed values at the interfaces. This will serve to give an indication of the general effect of the concentration gradient in anodic film growth.

The asymmetry of the metal-oxide-oxygen system as described above means that there will be a built-in electrochemical potential gradient for the ionic species which tends to give rise to film growth even before an external electrostatic potential is superimposed onto the system from some external source. To the extent that the built-in electrochemical potential is undisturbed by an applied electric field, it can be considered to be added algebraically to the externally applied electrostatic potential in order to obtain the total driving potential for mass transport. This essentially is a thermodynamic argument, which does not aid us directly in obtaining the rate constant for film growth.[2] A self-consistent solution of the relevant microscopic equations does lead to the rate constant. Numerical evaluation of the appropriate microscopic equations is the essence of the presently described work.

* Electrochemical Society Active Member.
[1] Permanent address: Physics Department, Auburn University, Auburn, Alabama 36830.
Key words: anodization, corrosion, oxidation.

[2] Such electrochemical potential gradients can produce large stresses in the growing anodic films, as shown theoretically (9). This may account for the amorphous nature of many anodic oxides.

Discrete hopping model including space charge.—Figure 1 in Ref. (7) illustrates the model utilized to ascertain both concentration-gradient and space-charge effects. Let us consider a particular barrier in the oxide located at position x_k. The net current J_k is the difference between the forward current $J_k^{(f)}$ and the reverse current $J_k^{(r)}$. The concentrations at the endpoints O and N are considered in the present work to have fixed values which are determined entirely by the interfacial reactions. If these two boundary concentrations are different, then there will be a net transport current even in zero electric field [cf. upper curve in Fig. 1 of Ref. (7)]. With an applied electric field, the electrostatic potential is position-dependent. In the usual manner of illustrating applied potentials, we superimpose this potential energy variation on the periodic (or aperiodic) potential of the crystalline (or amorphous) diffusion medium, so the barriers slope downward under forward bias [cf. lower curve in Fig. 1 of Ref. (7)]. The energy difference between forward and reverse motion is noted to be (at least to lowest order) equal to $2\Delta W = 2Z|e|E_k a$, where $Z|e|$ is the charge on the diffusing defect and E_k is the field at the kth barrier. We generally denote the electronic charge magnitude $|e|$ by e. The hopping distance is $2a$. The thickness $L = 2Na$ is the product of the number of barriers and the distance $2a$ between barriers.

Let us now summarize the pertinent equations which have been described in greater detail in Ref. (7) and (8). Denote by n_{k-1} the number of charged particles of a given species per unit area in a planar slice of thickness $2a$ which is perpendicular to the hopping direction and in front of the barrier labeled k; denote by n_k the corresponding number located just beyond the same barrier. Then the number J_k surmounting the barrier in unit time is

$$J_k = J_k^{(f)} - J_k^{(r)}$$
$$= \nu \exp(-W/k_BT)\,[n_{k-1}\exp(ZeE_k a/k_BT) - n_k \exp(-ZeE_k a/k_BT)] \quad [1]$$

where ν is the attempt frequency for the particle and W is the corresponding zero-field activation energy for diffusion. This quantity J_k is the net particle current at the position of the kth potential barrier. The major assumption inherent in this equation is that of the applicability of Boltzmann statistics; this assumption should be very good for the presently considered situation of ionic diffusion, although it might not always be such a good assumption for smaller mass particles such as electrons or electron holes.

The second important equation which we utilize is

$$J_{k+1} = J_k \quad (k = 1, 2, \ldots, N-1) \quad [2]$$

This constitutes the steady-state approximation, which is premised on the assumption that there is little or no build-up (or depletion) of the diffusing species in comparison to the number diffusing through at any point within the anodic film. It is not difficult to show that this assumption is generally quite good.[3] Transients (10) are neglected in the present computations.

The third equation which we utilize is based on Poisson's equation relating the electric field in the medium to the charge density

$$E_{k+1} = E_k + \frac{4\pi Zen_k}{\epsilon} \quad (k = 0, 1, 2, \ldots, N-1) \quad [3]$$

This expression determines the electric field everywhere within the medium in terms of the surface-charge field E_0 and the diffusing defect densities n_k. The surface-charge field E_0 is determined by the net charge density per unit area on the parent metal crystal at the metal-oxide interface. It can be negative, corresponding to an electron excess, or it can be positive, corresponding to an electron deficit. This is distinct from the quantity n_0 which is the ionic charged defect density within the oxide adjacent to the metal interface.

Finally, the electrostatic potential is given in terms of the electric field

$$V_k = V_{k-1} - 2aE_k \quad (k = 1, 2, \ldots, N) \quad [4]$$

The potential V_0 is arbitrary, and thus it is conveniently chosen to be zero. The total potential V_N across the film is thus determined in terms of E_0 and the space charge densities. For a constant applied potential, V_N is given and the current J_k is determined from numerical evaluation of the above equations; for a constant applied current, J_k is given and the total potential V_N is determined from numerical evaluation of the above equations. In both cases straightforward iterative schemes are utilized to achieve self-consistency with the chosen values for the boundary concentrations.

Coordinate system conventions.—If cation interstitials or anion vacancies (positively charged ionic species) are the primary mobile species, then the boundary concentrations can be expected to be larger at the metal-oxide interface than at the oxygen-solution interface. It is then convenient to choose the origin ($x = 0$) of the coordinate system at the metal-oxide interface. The corresponding positive x-direction is from metal to oxide to solution, which is the direction of flow of the primary mobile species.[4]

For growth by the transport of negatively charged ionic species, we choose to utilize the alternate coordinate system in which the origin ($x = 0$) is located at the oxide-solution interface. Then the positive direction is from solution to oxide to metal, which is the direction of flow of the primary mobile species. The surface-charge field [viz., $E(x)$ at $x = 0$] is in this case determined by the interfacial charge density at the oxide-solution interface instead of by the interfacial charge density at the metal-oxide interface.

The convention chosen for the coordinate system will of course have no bearing on the actual species and charge distributions in the system. Thus a simple mathematical transformation can be devised to convert from one coordinate system to another. This coordinate-system transformation is not developed herein since it is not essential to our primary purpose.

The results deduced for a physical model in which the mobile species is negatively charged can be readily transformed to corresponding results for a physical model in which the mobile species is positively charged. This second type of transformation (namely, a species transformation) is especially easy in the case of the presently utilized convention of choosing the origin of the coordinate system at the particular interface having the larger boundary concentration. Then the species transformation is effected simply by reversing the sign of the charge of the species, together with making the corresponding reversals in sign for the electric field and potential.

At this point it may be evident that we do not attempt to answer by means of our numerical computations the important physical question of which ionic species is responsible for growth in any given metal-oxide-solution system. Instead, we deduce results illustrative of concentration-gradient and space-charge effects which are (apart from incidental details such as directions and signs) generally applicable to any mobile ionic species.

For our model numerical calculations we choose a negatively charged mobile ionic species, with the origin

[3] The total build-up of defect species within the film when the film increases in thickness by one monolayer is much less than the amount of defect species which must be transported to build the monolayer. Thus a minor departure from Eq. [2] allows the profiles and electric fields to adjust continuously to new steady-state values as the film increases in thickness.

[4] For the alternant situation for which the primary mobile species are either cation vacancies or anion interstitials (negatively charged ionic species) the coordinate system could be chosen to be the same if desired, in which case the boundary concentration at the origin would be lower than at $x = L$. Flow of ionic species would then be in the negative direction. We do not choose to utilize this convention in the present work.

Table I. Values utilized for parameters in numerical computations

Symbol	Units	Definition	Value
n_0	No./cm²	Defect density at position $x = 0$	10^{11}
n_N	No./cm²	Defect density at position $x = L$	10^{10}
W	eV	Activation energy for diffusion	0.3
T	°K	Temperature	300
ν	sec⁻¹	Attempt frequency	10^{13}
$2a$	A	Lattice parameter	4
Z	—	Valence of diffusing species	−1
ϵ	—	Relative dielectric constant	10

of the coordinate system located at the oxide-solution interface and the positive direction from solution to oxide to metal. The results as they stand will be immediately applicable to either cation vacancy motion or anion interstitial motion. The results can be easily converted by the above species transformation to cation interstitial or anion vacancy motion.

Scaling of the numerical results.—It can be seen from the basic Eq. [1] that

$$J \propto \nu \exp(-W/k_BT) \quad [5]$$

If a quantity Υ is defined

$$\Upsilon \equiv J/[\nu \exp(-W/k_BT)] \quad [6]$$

then the basic Eq. [1] can be looked upon as a difference equation dependent on Υ but not otherwise dependent on the specific values of the parameters J, ν, and W. For a given value of Υ, the numerical solution deduced will be generally applicable to all possible combinations of J, ν, and W consistent with the given value of Υ. In particular, the results of the present numerical calculations with W chosen to have the value 0.3 eV (cf. Table I) will be equally valid for a different value of W (*e.g.*, $W = 0.8$ eV), provided only that the currents are changed accordingly (*e.g.*, for $W = 0.8$ eV the currents will reduce by a factor of $e^{-0.8/k_BT}/e^{-0.3/k_BT} = e^{-0.5/k_BT}$, which at room temperature is approximately $e^{-20} \simeq 2 \times 10^{-9}$). The currents scale linearly with the value of ν, with no change in the profiles. The time scale dilates reciprocally as the currents, so our numerical results in actuality cover the range from large currents (corresponding to rapid growth on a laboratory time scale) to extremely small currents (corresponding to a growth rate which may be negligible on a laboratory time scale). Of course, we exclude situations in which the currents are so large that appreciable heating of the sample might occur.

Numerical Results

Diffusing defect concentration profiles.—The distribution of defects in an anodic oxide film which is growing under various applied currents is shown as a function of thickness N (in monolayers) in Fig. 1-3. The curves were produced by drawing straight lines between the numerically computed values at discrete points separated by one monolayer in the lattice. (The discrete model yields only one point per monolayer.) The values chosen for the microscopic parameters are listed in Table I. In all figures the numbers 1 through

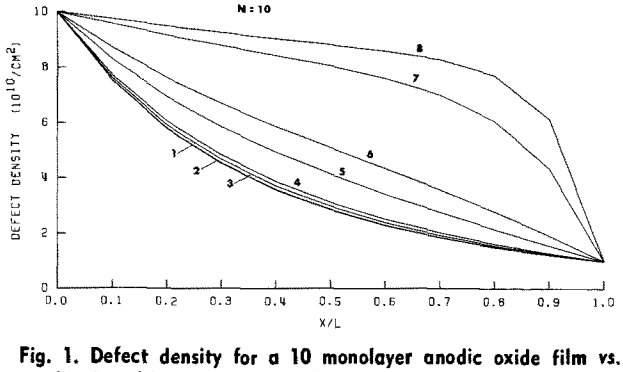

Fig. 1. Defect density for a 10 monolayer anodic oxide film vs. normalized position for several values of the current.

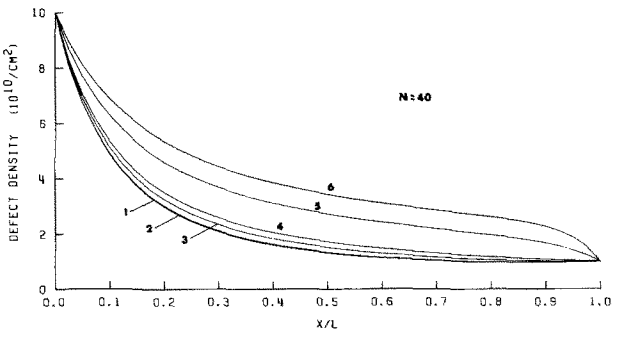

Fig. 2. Defect density for a 40 monolayer anodic oxide film vs. normalized position for several values of the current.

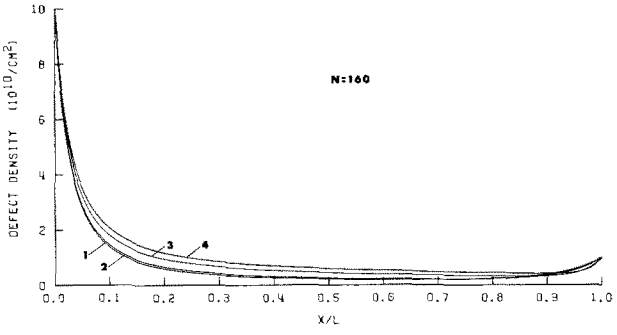

Fig. 3. Defect density for a 160 monolayer anodic oxide film vs. normalized position for several values of the current.

10 correspond respectively to currents of 5×10^{15}, 1×10^{16}, 5×10^{16}, 1×10^{17}, 5×10^{17}, 1×10^{18}, 5×10^{18}, 1×10^{19}, 5×10^{19}, and 1×10^{20} particles/cm²-sec, respectively, as listed for reference purposes in Table II.[5] Fixed boundary concentrations are chosen for simplicity in performing the numerical computations, since the purpose of the present work is to examine the general effects of concentration gradients and space charge.

A factor of 10 is chosen for the difference in the two boundary concentrations, as is evident from Fig. 1-3. This difference will in practice vary with the system in question, being larger in general for anodic films having a larger free energy of formation. The effects of the concentration difference across the film are quite apparent in these figures; this factor can be expected to influence markedly the concentration profiles found experimentally in such anodic films.

It is interesting to note (cf. Fig. 1-3) that a relatively high density of defects prevails throughout most of the film of a given thickness whenever the current is relatively large. Note especially in Fig. 1 that curve 8 has a defect density at the midpoint of the film which is at least a factor of 3 larger than curve 1. (The ratio of the currents for these two curves is $1 \times 10^{19}/5 \times 10^{15}$

[5] It can be noted from Fig. 1-3 that the higher current density curves for the thicker films are missing. These cannot be computed accurately by means of the present computer program. The curves which are shown meet a very stringent criterion for accuracy. The presently considered field and voltage range is of interest from the standpoint that it illustrates the interplay of electrostatic-field effects and concentration-gradient effects.

Table II. Currents associated with a given curve number in the figures

Curve number	Current J (No./cm²-sec)
1	5×10^{15}
2	1×10^{16}
3	5×10^{16}
4	1×10^{17}
5	5×10^{17}
6	1×10^{18}
7	5×10^{18}
8	1×10^{19}
9	5×10^{19}
10	1×10^{20}

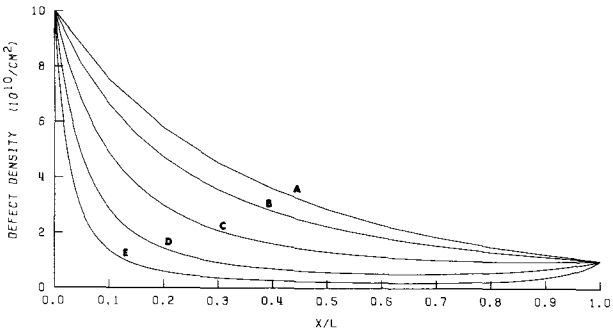

Fig. 4. Defect density for a given current vs. normalized position in growing anodic oxide films for various film thicknesses in monolayers. ($J = 5 \times 10^{15}$ particles/cm^2-sec.)

= 2000.) An important general conclusion can thus be drawn from this set of three figures: (*a*) Larger current densities for a given thickness are accompanied by greater numbers of diffusing defects in the growing film.

It is quite interesting to compare Fig. 1 through 3. It can be seen that the defect densities for a given current density become relatively lower throughout the film as the thickness increases. This effect is associated specifically with the space charge. It can be understood qualitatively somewhat as follows. Increasing the thickness tends to yield a greater total space charge and correspondingly larger space-charge fields, which requires in turn a modification in the concentration profiles to decrease the space charge in order that the concentration difference across the film may be maintained. The general conclusion to be drawn is: (*b*) Larger film thicknesses are accompanied by decreasing concentrations of diffusing defects at a given normalized position within the film for a given current density. This can also be looked upon from the standpoint that the regions of large space-charge density become relatively more confined to the interfaces as the film thickness increases.

Figure 4 illustrates quite clearly the lowering of the diffusing defect concentration with increasing thickness at a given current density. Curves A through E in all figures represent thicknesses of 10, 20, 40, 80, and 160 monolayers, respectively, as listed for reference purposes in Table III. The usefulness of plotting as a function of normalized position x/L, where x is the position in the film and L is the film thickness, is evident in this figure.

Space-charge density and electrical conductivity profiles.—The charge density is given by the product of the defect density with the charge per defect. In addition, the ionic conductivity is given by the product of the charge density with the mobility. Thus Fig. 1-4 are also representative of the charge density profile and ionic conductivity profile in growing anodic films.

Total space charge.—The total charge located in the region of the film between the origin $x = 0$ and a given normalized position x/L in the film is given by an integral of the charge density from zero to x. Figure 5 illustrates this quantity (in units of the electronic charge magnitude) as a function of normalized position for five different film thicknesses, and Fig. 6 illustrates this quantity for four different current densities. From

Table III. Thicknesses associated with a given curve symbol in the figures

Symbol on curve	Thickness (in monolayers)
A	10
B	20
C	40
D	80
E	160

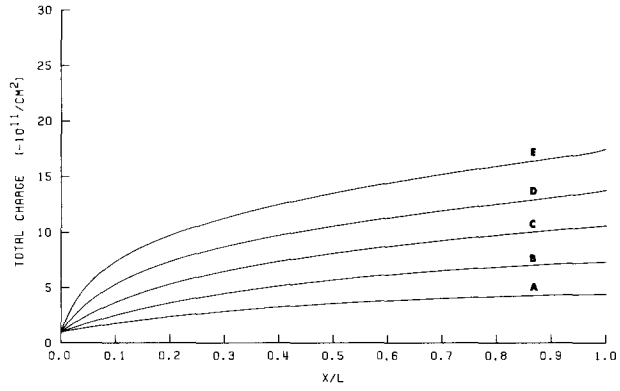

Fig. 5. Total charge up to position x within a growing anodic oxide film vs. normalized position for various film thicknesses with $J = 1 \times 10^{17}$ particles/cm^2-sec.

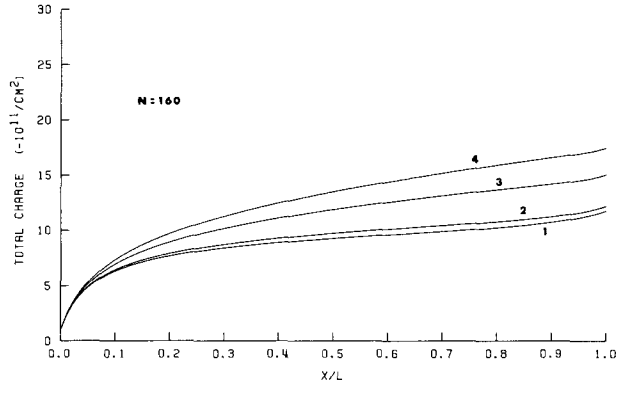

Fig. 6. Total charge up to position x within a growing anodic oxide film 160 monolayers in thickness vs. normalized position for various applied currents.

Fig. 5 we can draw the following conclusion: (c) Larger thicknesses contain greater total amounts of space charge for a given current density. From Fig. 6 we can conclude that higher current densities yield more space charge for a given thickness, which is in accord with our previously stated conclusion (*a*). A comparison of our previously stated conclusion (*b*) with conclusion (c) shows us that even though the defect concentration at a given normalized position decreases with increasing thickness at a fixed current density, the total number of defects still increases somewhat with increasing film thickness.

Figure 7 is an extensive plot for the total space charge within the growing film which serves to delineate sharply conclusions (*a*) and (c) drawn from the intensive plots discussed above. (An intensive plot contains curves for some given quantity *vs.* normalized position x/L in the film, whereas an extensive plot contains curves for some given quantity *vs.* film thick-

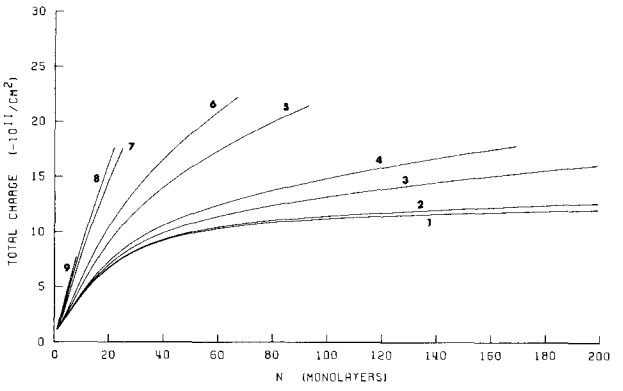

Fig. 7. Total charge within a growing anodic oxide film vs. thickness in monolayers with different applied currents.

ness.) Each curve (corresponding to a given current density) shows, for example, the increase in total space charge in the film with increasing thickness. This is basically stated in conclusion (c). A comparison of the curves in Fig. 7 shows that the total space charge at a given thickness increases with current density, which is essentially conclusion (*a*). In addition, a new conclusion can be drawn from this figure: (*d*) For growth under constant current conditions, the total space charge in the film has a tendency to level off with increasing thickness to a constant value characteristic of the current density. For lower current densities this is found to occur at smaller thicknesses. This effect can be attributed entirely to space charge, since corresponding homogeneous-field computations predict a total number of defects which increases almost linearly with thickness without any tendency to level off with increasing thickness.

Electric fields.—The electric field is nonhomogeneous in the film due to the large space-charge concentrations. Figure 8 illustrates the electric field *vs.* position in a 10 monolayer film and in a 160 monolayer film for various current densities. The increased curvature evident at 160 monolayers is indicative of the increased amount of space charge for thicker films. This effect is emphasized in Fig. 9 where the electric field *vs.* normalized position is shown for the five thicknesses at a given current density. The decreasing field with increasing x shows that the space charge happens to be of opposite sign to the surface-charge field for this particular current density.

Also it is of interest to note in Fig. 8 the algebraically decreasing electric fields associated with increasing current densities. This is simply a matter of the requirement of a larger electric driving force to produce larger current densities. The fact that the electric field has the opposite polarity for different values of the current (*e.g.*, compare curves 1 and 7 for $N = 10$ in Fig. 8) is also of interest. This is readily explained as follows. The concentration gradient in the absence of an electric field will produce a certain particle current, the exact value of which depends on the film thickness. Whenever the particle current due to the concentration gradient alone is larger than the net particle current in question, then the field has the polarity needed to retard charged particle transport. On the other hand, the field must have the polarity required to aid charged particle transport when the current produced by the concentration gradient alone is insufficient to yield the net particle current under consideration.

Figures 10 and 11 are very illuminating extensive plots illustrating the electric field at the two oxide interfaces as a function of thickness. A comparison between the two figures leads us to the following conclusion: (*e*) With increasing thickness the surface-charge field at the higher defect-density interface levels off to some constant value characteristic of the current

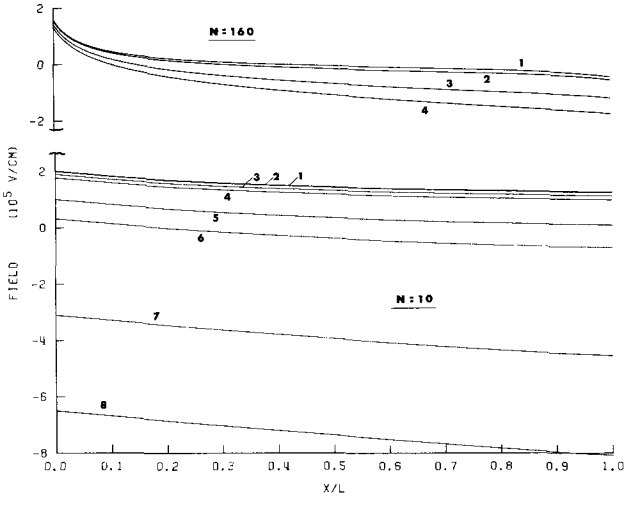

Fig. 8. Electric field *vs.* normalized position in growing 10 monolayer (lower set) and 160 monolayer (upper set) anodic oxide films for several currents.

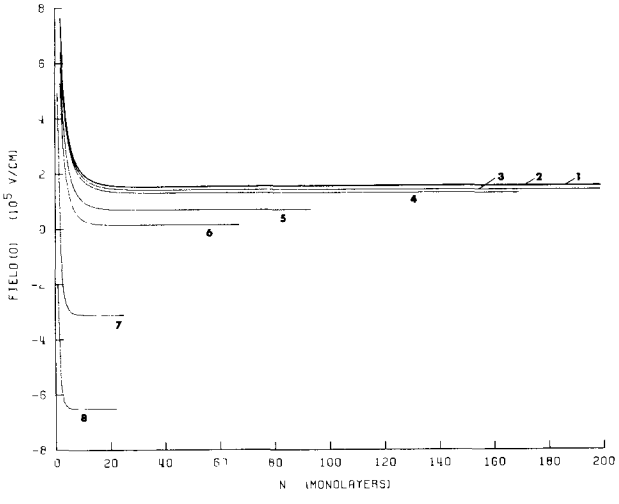

Fig. 10. Electric field at the larger defect-density interface *vs.* thickness in monolayers for a growing anodic oxide film with different applied currents.

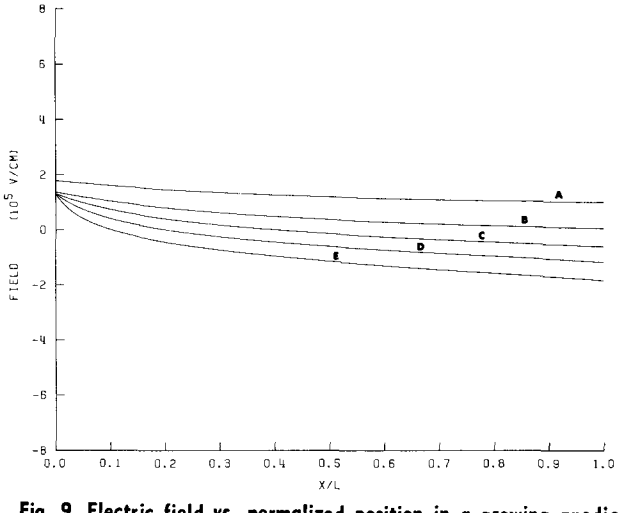

Fig. 9. Electric field *vs.* normalized position in a growing anodic oxide film with $J = 1 \times 10^{17}$ particles/cm^2-sec for several thicknesses.

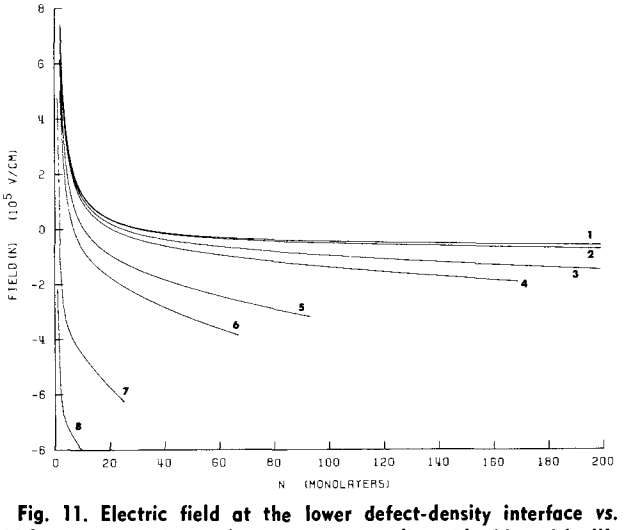

Fig. 11. Electric field at the lower defect-density interface *vs.* thickness in monolayers for a growing anodic oxide film with different applied currents.

density quite rapidly as compared to the electric field at the opposite interface. The difference between the electric fields at the inner and outer interfaces can be attributed of course to the total space charge within the film. (Without space charge, the electric fields at the two interfaces would be the same.) Note the similarity between the curves in the two figures for very small values of thickness. This reflects the fact that the total space charge within the film approaches zero as the thickness of the film approaches zero, so the electric fields at the inner and outer interfaces approach one another in this limit. The change in polarity of the field with increasing thickness is also very apparent in these curves. For thin enough films, the currents produced by the concentration gradient can be very large, so an opposing electric field is required to balance the current density to a given net value. With increasing thickness, the concentration gradient becomes a lesser driving force, so the electric field must gradually change from an opposing to an aiding polarity to maintain the fixed current density.

Electrostatic potentials.—The electrostatic potential $V(x)$ is generally obtained from an integral of the macroscopic electric field

$$V(x) = -\int_0^x E(x)\,dx \qquad [7]$$

or in the present model of a discrete lattice, from Eq. [4]. In the absence of space charge, $E(x)$ would have a constant value E_0 throughout the film and $V(x)$ would be a linear function of position x. With space charge, however, $E(x)$ varies with position as was noted in Fig. 8-9. Therefore space charge causes $V(x)$ to be a nonlinear function of position x. The potential is shown as a function of normalized position in Fig. 12 and 13. A comparison of the curves for a 20 monolayer thickness with corresponding curves for a 160 monolayer thickness in Fig. 12 shows an increased curvature appropriate for the thicker films. It therefore can be stated: (*f*) The electrostatic potential as a function of normalized position within the film is more nonlinear for thicker films. Another interesting feature illustrated in Fig. 12 is the larger potentials associated with the higher current densities. Also in Fig. 12 it is especially evident at $N = 160$ that: (*g*) The curvature in the potential *vs.* normalized position curves is greater at higher current densities, which reflects the greater amount of space charge in the film at higher current densities.

Figure 13 illustrates a set of different thickness curves (A through E) at two given current densities differing by a factor of five. Note that the potential (for a given current density) in the thicker films has

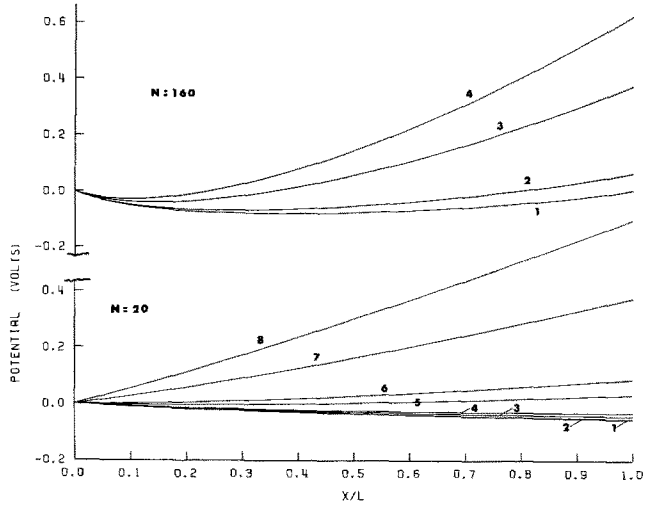

Fig. 12. Electrostatic potential *vs.* normalized position in growing anodic oxide films 20 monolayers (lower set) and 160 monolayers (upper set) in thickness for several currents.

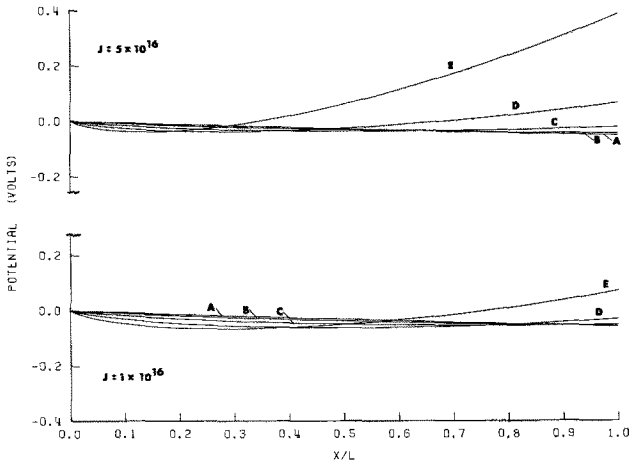

Fig. 13. Electrostatic potential *vs.* normalized position in a growing anodic oxide film with $J = 1 \times 10^{16}$ (lower set) and $J = 5 \times 10^{16}$ (upper set) particles/cm^2-sec for several thicknesses.

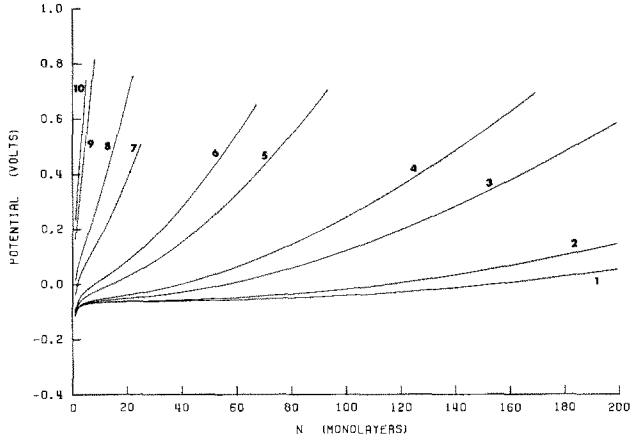

Fig. 14. Electrostatic potential *vs.* thickness in monolayers for a growing anodic oxide film with different currents.

an increased curvature which is directly associated with the greater total amount of space charge in the thicker films. Note also the increased curvature for the potential in a film of given thickness when the current density is increased.

Figure 14 represents some of the most important results of the numerical computations. The total electrostatic potential[6] $V(L)$ developed across the anodic film is shown as a function of thickness for ten different current densities. It can be noted that: (*h*) There are two separate regions of interest in the potential *vs.* thickness curves, the very thin-film region (convex curvature) where concentration gradient effects predominate, and the thicker film region (concave curvature) where space-charge effects predominate. The potential increases with thickness, as illustrated, since a greater total driving potential is needed at thicker films to maintain a fixed value for the current. It is also clear from the figure that higher current densities require considerably higher potentials at any given thickness.

Figure 15 gives the total electrostatic potential as computed as a function of thickness in the homogeneous-field limit (*viz.*, when space charge is ignored). Note that the curves are essentially linear in the thick-film region. A comparison with the corresponding curves of Fig. 14 shows that a given current at a given thickness is obtained at a significantly lower potential when space-charge effects can be ignored. Thus it can

[6] This quantity represents the electrostatic potential difference (or voltage drop) across the anodic film exclusive of any electrostatic potential differences developed within the solution phase and excluding the driving force contribution given by the concentration gradient.

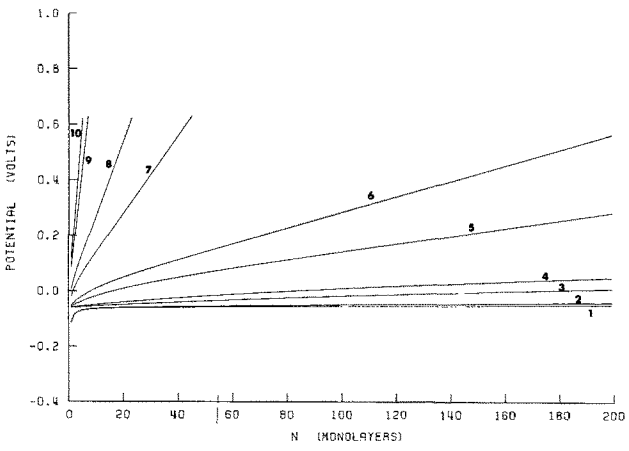

Fig. 15. Homogeneous-field results for the electrostatic potential vs. thickness in monolayers for a growing anodic oxide film with different currents.

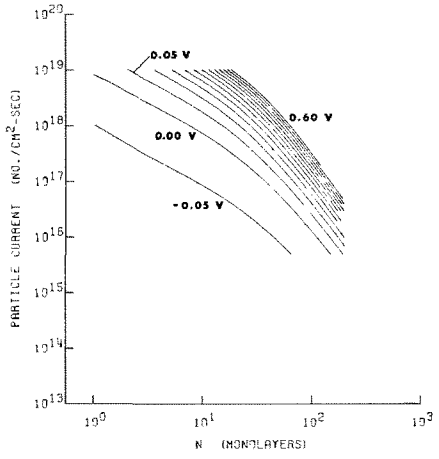

Fig. 16. Logarithm of the particle current vs. logarithm of the thickness for growth under constant electrostatic potentials ranging from −0.05 to 0.60V in increments of 0.05V.

be concluded that: (*i*) Space charge retards the rate of anodic film growth, and (*j*) Space charge gives rise to curvature in the potential *vs.* thickness characteristics.

The curvature in Fig. 14 therefore represents a measure of the effects of space charge. This plot should be quite useful in a correlation with appropriate experimental results. Unfortunately there appear to be no available experimental data in the thin-film low-voltage range to provide more than a qualitative comparison (11) with the predictions of this work. Experiments designed to yield such data are to be greatly encouraged, since the results would be most useful in delineating the possible role of space charge in anodic film formation.

Kinetics of film growth.—An examination of the range of electric fields (*cf.* Fig. 10-11) shows them to be of the order of or below 10^6V/cm. The quantity $\delta \equiv ZeEa/k_BT$ consequently has values which lie between 0.0 and 0.8 in magnitude. The fields thus reach large enough values so that the exponentials $e^{\pm\delta}$ cannot be accurately approximated by $1\pm\delta$ (for example, $e^{\delta} \simeq 2.23$ and $e^{-\delta} \simeq 0.45$ for $\delta = 0.80$). On the other hand, the fields are not so large that $e^{-\delta}$ can be neglected with respect to e^{δ}, which is the usual high-field limit. Therefore, neither of the commonly used constant potential plots of log(current) *vs.* log(thickness) and log(current) *vs.* reciprocal thickness could be expected to yield straight lines even in the absence of space-charge and concentration-gradient effects.

In order to interpret to some extent the kinetics at constant voltage, the following commonly used semi-empirical plots were made: (*a*) ln J *vs.* $1/N$, (*b*) ln J *vs.* ln N, and (c) ln J *vs.* N. In the absence of space charge and concentration gradients, the first of these would yield a straight line in the high-field limit, whereas the second would yield a straight line if growth occurred according to some empirical power law (*i.e.*, $J \propto 1/L^n$, where L denotes thickness). The third of the possibilities would yield a straight line if growth were logarithmic.

Perhaps not surprisingly, none of the three types of plot yielded good straight lines. Plots of the type (*a*) turned out to provide the poorest representation of a straight line, while plots of type (c) were somewhat better but still quite poor. Plots of type (*b*), while by no means perfectly linear as can be noted from Fig. 16, were at least quasilinear over certain thickness regions for the case of the higher potentials. At the lower potentials, the curves can be noted to be affected markedly by the presence of the concentration gradient.

The choice of the type (*b*) plot as providing the best empirical representation of the kinetics is at best somewhat arbitrary due to the fact that a log-log plot has an innate tendency to minimize variations. It does have the distinct virtue, however, that the slopes give some indication of whether or not the growth curves are severely rate-limiting in character. The slopes of the higher potential curves in Fig. 16 range between −1 and −3, so that an empirical power law for growth would be of the form

$$L \propto t^{1/n} \quad (2 \lesssim n \lesssim 4) \qquad [8]$$

This tells us that growth is more sharply rate-limiting than would be expected on the basis of a parabolic law.

Corresponding computations (cf. Fig. 17) have been carried out in the homogeneous-field limit to ascertain specifically the effects of space charge. The curves can be noted to be more linear than those in Fig. 16. In addition, the slopes are generally found to be much less than the slopes of the corresponding curves in Fig. 16 (not greatly exceeding the value $n = 2$), so that growth is more nearly parabolic. Thus it can be concluded that: (*k*) Space charge gives rise to growth kinetics curves which have a greater limiting-thickness character than the corresponding homogeneous-field growth kinetics curves. In addition, the currents in the thick-film homogeneous-field limit are as much as an order-of-magnitude larger than the corresponding currents in Fig. 16. To summarize the results of our present numerical computations, then, we can state that: (*l*) Under constant potential conditions space charge severely retards the growth rate and gives rise to growth curves which have a marked limiting-thickness character.

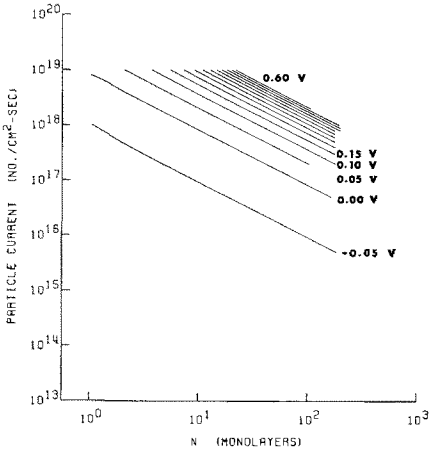

Fig. 17. Homogeneous-field results for the logarithm of the particle current vs. logarithm of the thickness for growth under constant electrostatic potentials ranging from −0.05 to 0.60V in increments of 0.05V.

Summary and Conclusions

A space-charge-gradient model computation for anodic oxidation has been carried out to delineate the effects of the concentration gradient and space charge of an arbitrary diffusing ionic species on the kinetics of film formation. The fundamental transport equation (8) is based on the concept of a thermally activated hopping (1) of charged point defects obeying Boltzmann statistics; a net mass transport takes place because of the built-in concentration gradient and the net electric field in the film due to space charge and the externally applied potential. An iterative technique has been employed to obtain extensive numerical solutions as a function of thickness and current density for reasonable values of the microscopic physical parameters involved in the model. Our major observations are summarized as follows:

1. With respect to corresponding curves computed in the homogeneous-field limit, the kinetic growth curves under constant voltage conditions are without question severely rate-limited by relatively moderate space-charge concentrations. Plots of the logarithm of the current *vs.* thickness, reciprocal thickness, and logarithm of the thickness have been made in an effort to deduce an empirical growth law, but none of the curves were found to be entirely linear. Space charge causes the growth kinetics to have an increased limiting-thickness character.

2. For growth under constant current conditions, the potential *vs.* thickness curves possess a concave curvature region which is most pronounced at low voltages. This constitutes a promising region to explore from the standpoint of verifying experimentally the existence of space-charge effects.

3. The potential *vs.* thickness curves under constant current conditions exhibit in addition a region of convex curvature which is most pronounced for thin films and very low voltages where the concentration gradient produced by the chemical reaction of film formation at the interface competes with the externally applied potential.

4. Under constant current conditions, the total amount of space charge within a film increases with thickness with a tendency to level off toward some constant value with increasing thickness. This takes place at smaller film thickness for the lower current densities.

5. Under constant current conditions, the surface-charge field at the higher defect-density interface approaches a characteristic asymptotic value very rapidly with increasing thickness. The electric field at the opposite interface levels off at a rate more in accordance with the behavior of the total space charge in the film.

6. At a given current density, the regions of large space charge become relatively more confined to the interfaces as the film thickness increases. The ionic carrier density in the central region of the film can thus become quite low for thick films.

7. For a given thickness, the order of the current density profiles shows that the total amount of space charge contained in the anodic film increases with increased current levels. The corresponding point defect density at a given position thus tends to be lower for films grown to the same thickness under low current conditions.

8. The computed electrostatic potential *vs.* position within the film is more nonlinear for thicker films due to the greater amount of space charge. In addition, at a given film thickness the electrostatic potential is more nonlinear at higher current densities due to the greater amount of space charge.

Acknowledgments

The authors wish to thank the personnel of the Computing Centers of the National Bureau of Standards and Auburn University for their aid and cooperation.

Manuscript submitted Nov. 6, 1972; revised manuscript received Jan. 26, 1973.

Any discussion of this paper will appear in a Discussion Section to be published in the December 1973 JOURNAL.

REFERENCES

1. E. J. W. Verwey, *Physica*, **2**, 1059 (1935).
2. N. F. Mott, *Trans. Faraday Soc.*, **43**, 429 (1947).
3. N. Cabrera and N. F. Mott, *Rept. Prog. Phys.*, **12**, 163 (1949).
4. J. F. Dewald, *This Journal*, **102**, 1 (1955).
5. L. Young, "Anodic Oxide Films," p. 12, Academic Press, New York (1961).
6. An oral report of this work has been given: A. T. Fromhold, Jr. and J. Kruger, "Space Charge Effects on Anodic Oxide Film Formation," presented at the Anodic Film Symposium, Electrochemical Society Meeting, Cleveland, Oct. 3-7, 1971.
7. A. T. Fromhold, Jr., and E. L. Cook, *J. Appl. Phys.*, **38**, 1546 (1967).
8. A. T. Fromhold, Jr., *Phys. Letters*, **28A**, 176 (1968).
9. A. T. Fromhold, Jr., *Surface Sci.*, **22**, 396 (1972).
10. W. H. Butler, E. T. Kinzer, Jr., and A. T. Fromhold, Jr., *Phys. Letters*, **40A**, 57 (1972).
11. Jerome Kruger and Joan P. Calvert, *This Journal*, **114**, 43 (1967).

Effect of Metaphosphate and Temperature on Silver Deposition

Richard J. Roethlein*[1]

Research and Development Laboratories, Sprague Electric Company, North Adams, Massachusetts 01247

ABSTRACT

Effects of metaphosphate and temperature on the electrodeposition of silver from a phosphoric acid electrolyte were investigated by both steady-state and transient electrochemical techniques. Electron-microscope and x-ray diffraction techniques were used to study the morphology and structure of the electrodeposited silver. The addition of metaphosphate and the lowering of electrolyte temperature were found to change the morphology and crystal orientation of the electrodeposited silver. Possible explanations as to the cause of these changes are discussed.

Recently interest was generated in the use of silver coulometers in electronic circuits for a variety of timing applications. The device makes use of the voltage rise associated with the removal of a predetermined quantity of silver from an inert electrode (anode) which is then used to activate a relay. Due to the wide temperature span needed in many applications, a concentrated solution of phosphoric acid is used for the electrolyte system. Electroplating silver from a silver phosphate/phosphoric acid electrolyte produces rough granular deposits with poor adherence. It was found that when small quantities of metaphosphoric acid were added to the electrolyte, smoother silver deposits were obtained having better adhesion to the underlying substrate. Electrodeposition of silver at low temperature in the absence of metaphosphate was also found to have a pronounced effect on deposit texture.

Metaphosphoric acid was first used as a leveling agent for the electrodeposition of silver by Mathers (1) in an acidified silver nitrate electrolyte. Early studies indicated that the presence of this additive in silver nitrate solutions caused the formation of complex cations with silver which the authors (2) deduced were responsible for the reduction in crystal grain size. Later studies (3) have shown that although complexing may take place between the additive and cation, there is no direct correlation between complex ion formation and reduction in crystal size. Presently, the view is held that most addition agents are adsorbed on the electrode surface and thus cause modifications in the steps of the electrocrystallization process (4). Fischer (5) maintains that some form of inhibition is present in every electrode process.

Previous studies by a number of authors (6-12) on the mechanism of silver deposition in other electrolytes have revealed the presence of several alternate paths that can be rate controlling. Bockis and co-workers (7, 8) have presented evidence that at low overvoltage the rate-controlling process is surface diffusion of silver adions to lattice-building sites, which gradually changes to a charge-transfer controlled reaction at higher overvoltages. Studies (13-15) of the effects of electrode pretreatment have shown that the rate-controlling step is extremely dependent on the number of dislocations and the active growth sites present on the electrode surface. Fleishmann and Thirsk (16, 17) have maintained that the path in metal deposition would be better represented by a mechanism which would involve direct transfer to a growth site preceded by diffusion through solution. Rangarajan (18) has also shown that if the rate-controlling step was slow lattice incorporation, it would exhibit similar characteristics, such as long rise time, as predicted for a slow surface-diffusion model. Studies made by Budevskii *et al.* (10) on dislocation-free monocrystals of silver have supported the view that crystal growth involves the formation of two-dimensional nuclei and propagation by monoatomic layers. This view has also been supported with metal deposition studies employing a vitreous carbon electrode substrate (19).

In the present study, an attempt was made to investigate the steady-state and transient kinetics associated with the deposition of silver from phosphoric acid at low temperatures and in the presence of various concentrations of metaphosphoric acid. Morphology studies of the electrodeposit under various conditions have also been examined.

Experimental

A standard Pyrex glass test cell was used in making all electrochemical measurements. The cell had a separate reference compartment which could be isolated by means of a stopcock and a Luggin capillary tip extending to the edge of the study electrode. The cell also contained appropriate gas inlet and outlet ports and was cleaned before each run with a sulfuric-chromic acid mixture and then rinsed several times in doubly distilled water. The silver phosphate/phosphoric acid electrolyte was prepared by dissolving silver metal (99.97%) into a two-to-one mixture of concentrated phosphoric acid and 30% hydrogen peroxide, both reagent grade. After dissolution of the metal, the solution was heated for several hours at 125°C to remove all traces of hydrogen peroxide, which has the added benefit of oxidizing any organic impurities in the electrolyte. The electrolyte was then diluted to its appropriate concentration and stored in a taped flask, all operations being carried out in a dimly lit room to prevent formation of colloidal silver. Metaphosphate was obtained from colorless crystals of analytical reagent-grade quality containing 40% HPO_3 and 60% $NaPO_3$. Molar concentrations were calculated by averaging the molecular weight of each compound.

The reference and counterelectrodes used in these experiments were 99.99% silver. The study electrode consisted of a section of 20 mil diameter silver wire (99.99%) which was sealed to Pyrex tubing by a special Teflon tubing, Flotite. All electrodes were thoroughly cleaned before immersion into the electrolyte by rinsing in acetone, distilled water, nitric acid, and finally distilled water.

All measurements were taken immediately after the addition of metaphosphate since in phosphoric acid it slowly converts to the ortho form. A 10^{-4}M concentration will be entirely converted to the ortho form after several hours. The electrolyte was thoroughly purged by bubbling nitrogen through the system before and during each experimental run. Prepurified

* Electrochemical Society Active Member.
[1] Present address: Pratt and Whitney Aircraft Corporation, Hartford, Connecticut 06074.
Key words: deposition, silver, crystal morphology, mechanism.

nitrogen was further scrubbed before entering into the cell by passing it through a gas train containing columns of ascarite, copper filings at 300°C, and finally a liquid nitrogen cold trap. Low temperature experiments were carried out in either a cold box containing ethylene glycol as the coolant or by immersing the test cell in a Dewar flask which contained freezing mixtures of dry ice and either carbon tetrachloride or chlorobenzene. Electrical measurements were carried out after the test cell had come to a constant temperature which did not vary by more than ±0.5°C during the course of the experiment.

Steady-state polarization measurements were made using a Wenking potentiostat or an electronic measurement constant-current power supply, and potentials were recorded with a Hewlett-Packard digital voltmeter having an input impedance of 10^{10} ohms. Galvanostatic transients were obtained using an electronic circuit containing a mercury-wetted relay system that has been described previously in the literature (20). Overpotential-time measurements were recorded on a Tektronix Oscilloscope, Model 535, and photographed with an attached Polaroid camera. An electron-probe analysis for phosphorous on electrodeposited silver samples was carried out at 21 keV, and x-ray diffraction analysis for crystal orientation was done with a Phillips diffractometer using a Cu tube at 1°/min scan rate. Morphology studies of the electrodeposit were made with an American Optical 2400-P Metallograph and an electron microscope employing the carbon replica method.

Results

Effect of temperature.—The steady-state deposition and dissolution of silver was studied at various temperatures and silver ion normalities in a concentrated phosphoric acid electrolyte. At room temperature, a semilog plot of the current-potential characteristics of this reaction are almost symmetrical and do not exhibit a hysteresis effect, Fig. 1. Current-voltage data for the deposition reaction at several silver ion concentrations when plotted on rectangular coordinates exhibit linear slopes which are proportional to the silver ion concentration, Fig. 2. Curves taken in the presence of stirring show a marked reduction in overvoltage while the electrolyte is being agitated.

With decreasing temperature electrode polarization increases and a large hysteresis is observed to occur between the ascending and descending current-potential values. At a temperature of approximately −10°C or less, an inflection in the current-potential curve appears which seems to indicate a shift in the electrode process is occurring. Figure 1 reveals that under potentiostatic conditions, the initial ascending cathodic portion (curve 2) of the current-potential curve has a pronounced inhibition inflection at approximately 25 mV polarization. Further increases in polarization

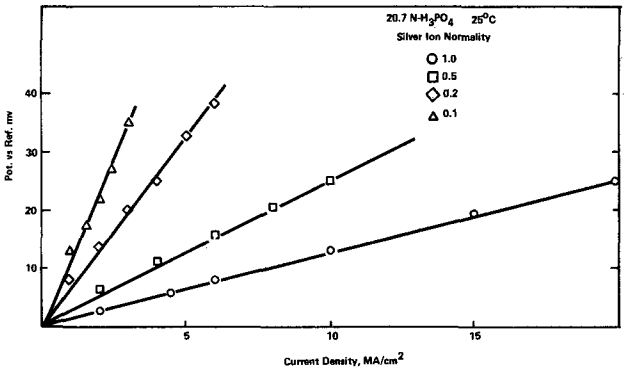

Fig. 2. Steady-state deposition of Ag

indicate that a subsequent electrode process takes place at higher overvoltages. After the transition region has been passed, descending cathodic potentials (curve 3) follow the second curve and at low current densities exhibit a higher overvoltage than the ascending cathodic portion of the curve (curve 2). Further decreases in potential produce an anodic current and the dissolution (curve 4) of the electrodeposited layer exhibits a large hysteresis when compared to the original dissolution curve (curve 1) until enough charge has been passed to remove the quantity of silver deposited during the cathodic portion of the curve. After removal of the electrodeposited layer, current-potenital parameters follow the original dissolution curve (curve 1).

A coulometric study of the potential variation between the dissolution of the silver substrate and the electrodeposited silver layer at −22°C has shown that the potential difference exists only until the electrodeposited silver has been removed from the silver-electrode substrate, Fig. 3. A stable dissolution potential was first established for a given current density; the current was then reversed and silver deposited for a given period of time. The rest potential after electrodeposition is approximately 25 mV more cathodic than the silver-reference potential and has been observed to be stable over 24 hr. Upon reversal of the same current in the anodic direction, a potential plateau is observed which is approximately 35 mV more cathodic than the initial dissolution potential. The potential remains at this value only until the amount of time corresponding to the deposition of silver has elapsed; the potential then drops to its original anodic value. At 25°C, no potential variation between the dissolution of the silver substrate and an electrodeposited layer was observed.

Morphology studies of the electrodeposited silver obtained at different temperatures and overvoltages, Table I, are shown in Fig. 4. At room temperature,

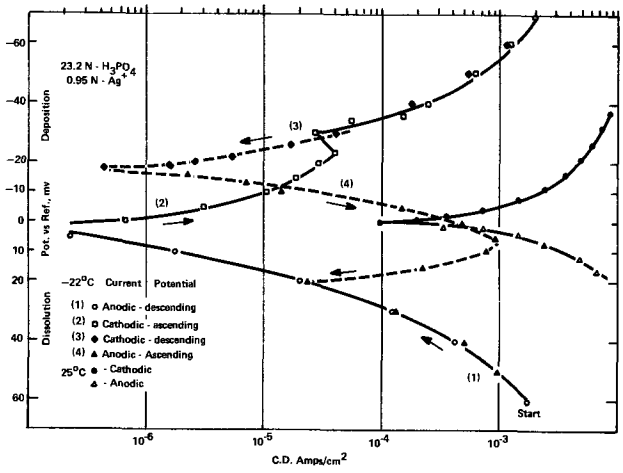

Fig. 1. Steady-state dissolution deposition of Ag

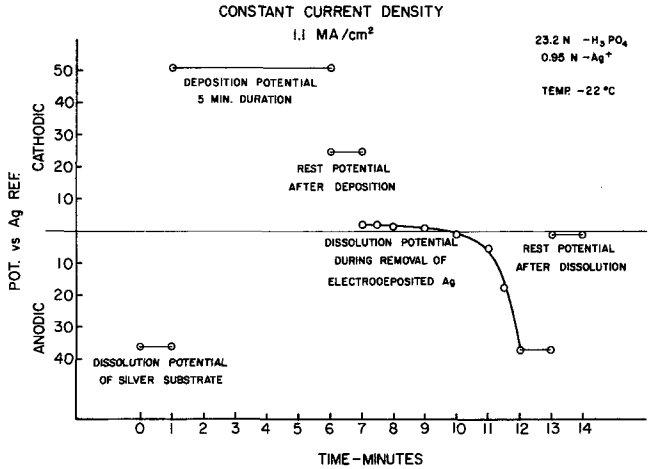

Fig. 3. Silver-dissolution potentials at low temperature

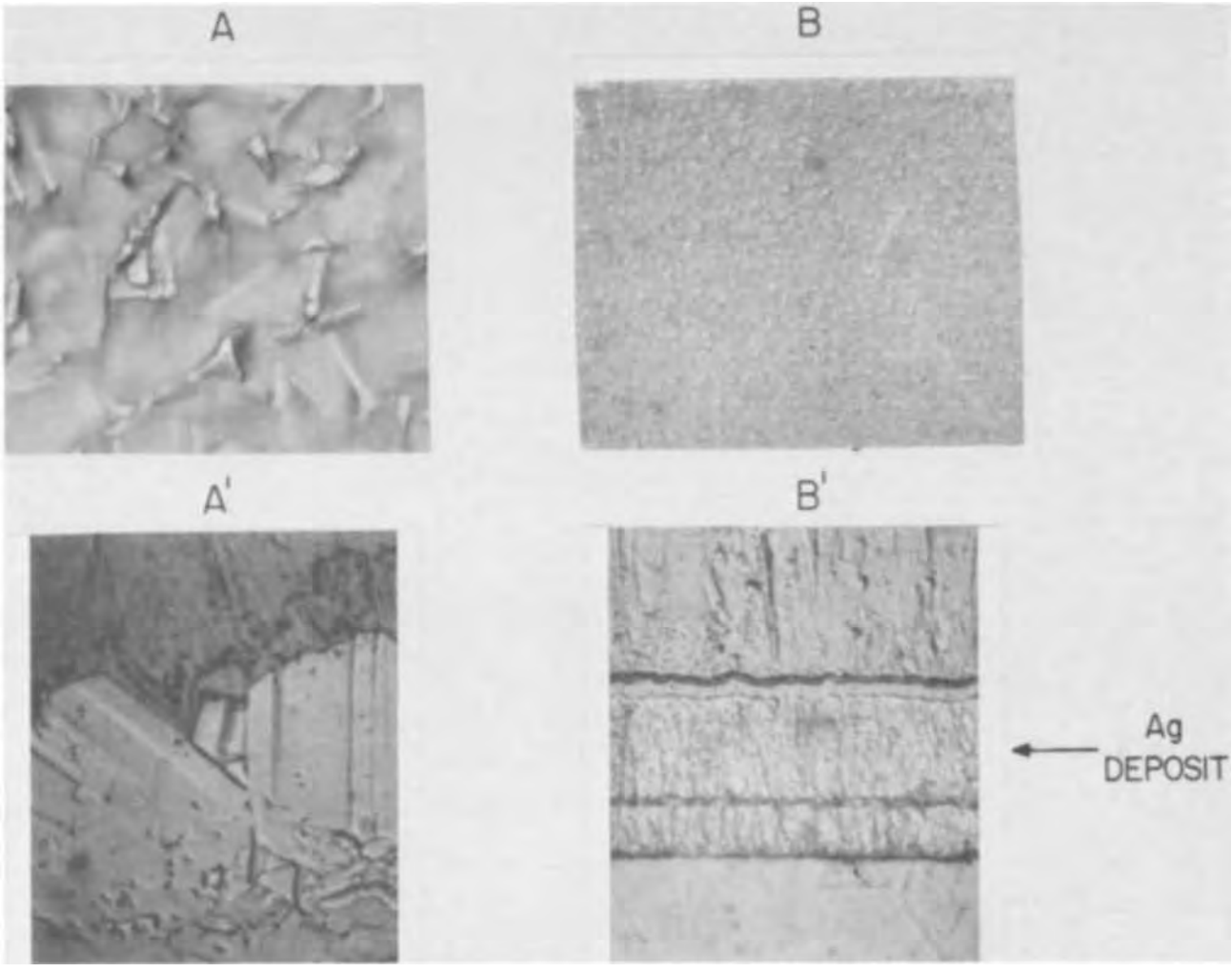

Fig. 4. Silver crystal growth as a function of temperature. A', cross section of A; B', cross section of B. Magnification 1200×

silver tends to grow large polyhedral crystals; a cross section of these crystals also indicates that a large amount of twinning occurs. These large crystals have been observed to grow over a large current-density range. Electrodeposition carried out for prolonged periods of time, up to 1 month, at low current density, 10 μA/cm^2, have produced large platelike crystal structures. Deposits obtained at lower temperatures (−20°C) are composed of much smaller crystals having a white matlike appearance. Cross section indicates the deposit is finer grained and is composed of a large amount of columnar-type structure.

The preferred orientation of electrodeposited silver also changed with decreasing temperature. X-ray diffraction studies were made of the crystal orientation of the electrodeposit at room temperature and low overvoltage. The orientation is predominantly with the <111> plane parallel to the surface with only small contributions from other planes. With decreasing temperature and higher overvoltages, a larger proportion of the crystal orientation is in the <110> plane. Examination of crystal orientation as a function of overvoltage at −20°C showed that the <110> plane was a major orientation for electrodeposited silver over the range of potentials investigated, 20-70 mV.

Table I. Morphology studies of the electrodeposited silver obtained at different temperatures and overvoltages

	23.8N $-H_3PO_4$, 1.08N $-Ag^+$ (see Fig. 4)		
C.D.	Deposition time (min)	η (mV)	Temp
A, 1 mA/cm^2	150	6.8	25°C
B, 1 mA/cm^2	150	70	−20°C

Nonsteady-state transient studies of the electrode process were made employing the galvanostatic-pulse method. Activation polarization was found to increase with decreasing temperature and an analysis of the initial portion of the charging curve supplied a value of the silver adion concentration. At 25°C, the silver adion concentration has an average value of 3.4 × 10^{-10} mole/cm^2 for a 1.0N silver ion concentration, which is in agreement with previously obtained values of this parameter (6-9). For an equivalent bulk-silver ion concentration, values of the silver adion concentration declined slightly with decreasing electrolyte temperature; at −20°C values of silver adion concentration were 50% lower. Values of the rise time to reach activation overvoltage were also obtained from the charging curve and were compared to calculated values of the rise time assuming charge-transfer control. Experimental rise times were found to be slower, up to an order of magnitude, than the calculated value of 10 μsec.

Figure 5 is a semilog plot of activation overvoltage *vs.* current density for the deposition of silver at two different temperatures. At 25°C, very little activation polarization is associated with the process up to current densities the order of 1 A/cm^2 and a linear slope is observed over the range of current densities investigated having a value the order of 10 mV/decade. At −20°C, two consecutive slopes are observed with an inflection occurring at approximately 25 mV polarization. The slope occurring in the low current-density region has a value of 10 mV/decade which increases to 30 mV/decade in the higher current-density range.

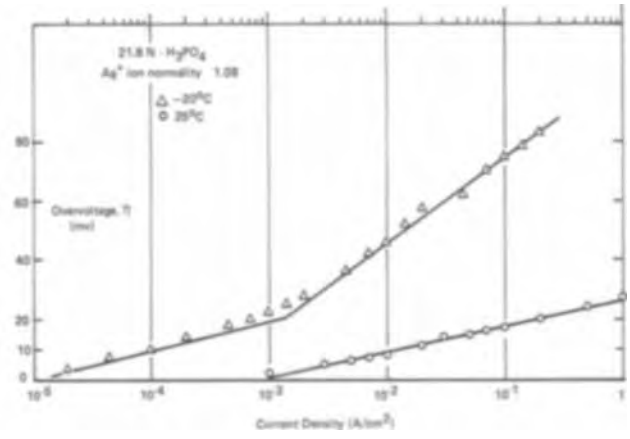

Fig. 5. Activation overvoltage for Ag deposition

Effect of metaphosphate.—Steady-state polarization curves for silver deposition show a successive increase in overvoltage with increasing metaphosphate concentration and exhibit linear current-potential behavior, Fig. 6. In the presence of metaphosphate, there is no appreciable change in slope until the metaphosphate concentration is greater than the silver ion concentration. Since metaphosphate does form weak complexes (21) with silver ions, the amount of silver ion complexing can be estimated from a reduction in the amount of silver ions present in solution. In the absence of metaphosphate, the potential difference between a silver study and reference electrode immersed in a $0.1N$-$Ag^+/20N$-H_3PO_4 electrolyte is essentially zero. With the addition of 0.1M metaphosphate to the study electrode compartment, there is a potential change of 1.5 mV indicating a very small degree of complexing is occurring. A large amount of complexing is not indicated until the metaphosphate concentration is at least an order of magnitude greater than the silver ion concentration.

Steady-state polarization curves taken on silver electrodes show that in the presence of metaphosphate, a shift in anodic (dissolution) overvoltage occurs, similar to that obtained at low temperatures in the absence of metaphosphate. Similarly, it was found that the hysteresis observed during the dissolution of silver corresponded exactly to the amount of silver deposited on the electrode during the cathodic section of the curve. A coulometric study revealed that the dissolution of an electrodeposited layer is approximately 20 mV more cathodic than the initial dissolution potential of the substrate. The potential remained at this value only until the amount of time corresponding to the deposition of silver had elapsed. The potential then dropped to its original anodic value.

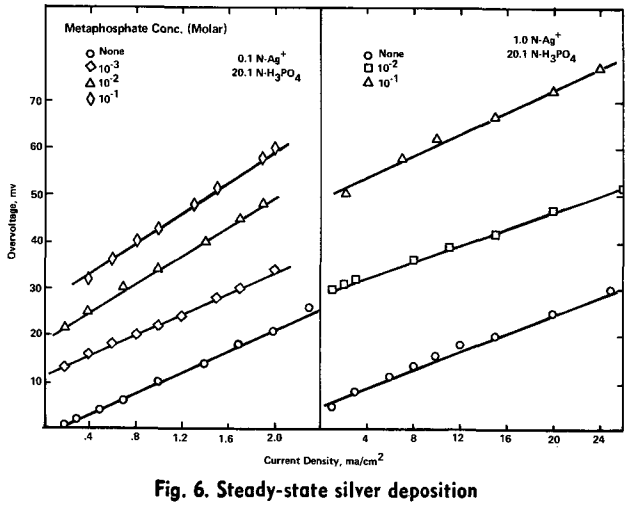

Fig. 6. Steady-state silver deposition

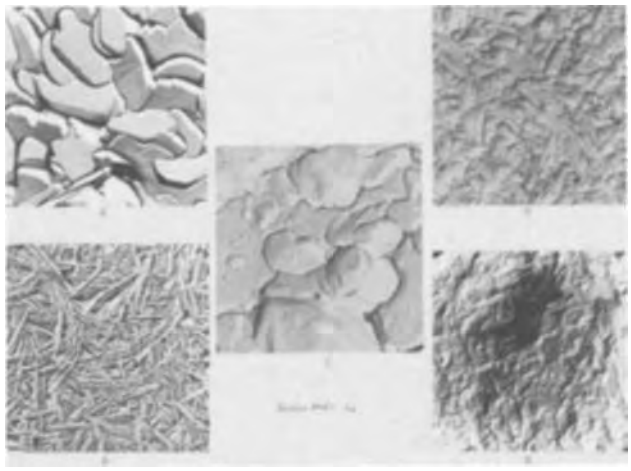

Fig. 7. Silver-crystal growth in the presence of metaphosphate

Electron-microscopy photographs were taken, Fig. 7, of electrodeposited silver surfaces under varying conditions, Table II. At the higher magnification, the samples plated in the absence of metaphosphate showed a granular structure with well-defined growth of crystal faces; the lower silver ion concentration still retained the large-grain structure but with less individual crystal definition. Growth in the presence of metaphosphate produced a smooth structure, consisting of fine needles in the presence of a $1.0N$ silver ion concentration. At the lower silver ion concentration, the grains, which ranged in size from 1.5 to 4.0μ, had little texture. For purposes of comparison, a silver deposit obtained in a cyanide bath shows the smooth, layered, crystal growth that occurs under these conditions. A comparison of deposit texture with electrode overvoltage indicates an increasingly smoother deposit is obtained with higher cathodic polarizations. The texture or crystal orientation of electrodeposited silver in the presence of metaphosphate revealed that for overvoltages greater than 20 mV the preferential orientation is mainly in the <110> plane.

In order to obtain more direct evidence for the adsorption of metaphosphate an electron-probe analysis for phosphorous was carried out on silver deposits that had been electrodeposited on gold in the presence of the additive. Table III shows that in the presence of metaphosphate, there is a large increase in the amount of phosphorous found in the deposit, which increases with a higher additive concentration. The values obtained, less than 1%, are in the range generally found for the inclusion of additives in an electrodeposit.

Table II. Studies of electron-microscopy photographs of electrodeposited silver-surfaces under varying conditions

	$20.1N-H_3PO_4$ (see Fig. 7)				
Electrode	Ag^+ conc.	HPO_3 conc.	C.D. (mA/cm^2)	Time (sec)	η (mV)
A	$1.0N$	—	1.0	2000	4
B	$1.0N$	0.1M	2.0	1000	50
C	$0.1N$	—	1.0	5400	12
D	$0.1N$	0.1M	1.0	5400	44
E	Silver cyanide	—	5.0	1000	197

Table III. Phosphorous content of a silver deposit

$20.7N-H_3PO_4$, $1.0N-Ag^+$	
Metaphosphate conc.	Weight per cent
—	0.02
10^{-2}M	0.40
10^{-1}M	0.75

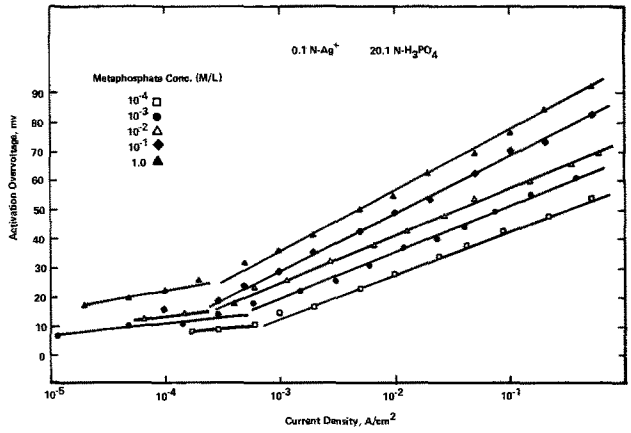

Fig. 8. Activation overvoltage vs. log C.D.

Transient potential-time traces indicate a successive increase in activation overvoltage with higher metaphosphate concentrations. A semilog plot, Fig. 8, of these values for the deposition of silver shows that at each metaphosphate concentration, a linear region exists over a considerable portion of the current-density range investigated. Values of the slope for this linear region range from 16 to 20 mV/decade. Examination of the voltage-time characteristics of the traces revealed that the rise time to an activation-controlled potential decreased with increasing metaphosphate concentration. Values of the amount of charge, Q_A, required to reach the activation potential showed little variation with current density but did decrease with increasing metaphosphate concentration; representative values are shown in Table IV. The overpotential-time transients were analyzed by the same procedure mentioned previously for silver adion concentration; the values did not show much variation with current density but do decrease with the addition of metaphosphate, remaining fairly constant for additive concentrations greater than 10^{-3}M, Table IV.

Discussion

Previous studies of the silver-deposition reaction have shown that the reaction mechanism is composed of several steps; mass transport of silver ions to the interface, discharge to the electrode surface, and the surface diffusion of silver adions to lattice-building sites. The above steps are also accompanied by losses of several waters of hydration associated with the various stages of silver ion crystallization. There has been some disagreement over the role surface diffusion plays in the over-all electrochemical process, but we have found in this study that this is an important step under certain conditions.

For the steady-state deposition and dissolution of silver in phosphoric acid the over-all rate-controlling step is the mass transport of silver ions from the bulk electrolyte solution. This is indicated by the decrease in overvoltage accompanying electrolyte agitation, the linearity observed between the current-potential curves at low overvoltages, and the slopes of these curves being proportional to the bulk-silver ion concentration. For reactions with high exchange currents linear steady-state, current-potential behavior has previously been shown to be due to concentration polarization (12). Although the over-all electrochemical reaction rate is mass-transport controlled, the rates of individual steps in the reaction mechanism can vary.

Table IV. Values of charge, Q_A to an activation overvoltage and silver adion concentration

$20.7N - H_3PO_4$, $1.0N - Ag^+$

Metaphosphate conc. molar	—	10^{-4}	10^{-3}	10^{-2}	10^{-1}	1
Q_A, μcoul/cm²	87	36	25	19	15	14
$C_o \times 10^{10}$, mole/cm²	3.4	1.27	0.27	0.24	0.27	0.23

Studies (6-9) of the silver-deposition mechanism in aqueous electrolytes have shown that at low overvoltages, the surface diffusion of silver adions is an intermediate step in the over-all reaction mechanism. In the present study, the results obtained from galvanostatic pulsing also indicate that at ambient temperatures and low overvoltages, surface diffusion is a slower intermediate step than charge transfer. Values of the silver adion concentration are similar to those observed by Bockris, activation polarization is extremely low, and the rise time is greater than that calculated for a charge-transfer controlled step. Slow adion diffusion would also be consistent with the type of deposit obtained at ambient temperatures, where deposit morphology indicates crystal growth occurs on a relatively limited number of nucleation sites with the eventual formation of large crystal structures. Under these conditions, partially hydrated silver adions migrate over the surface in a random walk manner until they collide with an active site such as a kink position where the growth via a step or screw dislocation can be maintained.

At lower temperatures, $<-10°C$, deposit morphology, along with crystal orientation, changes accompanied by a large increase in the number of nucleation sites on the electrode surface. Steady-state, current-potential curves indicate a change in the electrode process occurs at overvoltages greater than 25 mV and a large hysteresis is observed between the removal of the electrodeposited species and the polycrystalline-electrode substrate. This variation in current-potential behavior can be related to the change in crystal orientation obtained at higher overvoltages. Since changes in crystal orientation will give rise to different bond strengths between adions and surface metal atoms, a shift in the amount of energy needed to remove them will be required. Piontelli (22) has also shown that the current-potential relationships for metal deposition and dissolution vary considerably on different crystal faces.

A shift in electrode process at low temperatures is also suggested from the nonsteady-state plot of current *vs.* activation overvoltage. The two linear slopes with an inflection at 25 mV indicates that another consecutive reaction is rate controlling at higher overvoltages. Since electrochemical rate constants, for various steps in a reaction, depend on potential it would be reasonable to assume that some other reaction such as the direct transfer of silver ions becomes more rate controlling at higher potentials. At higher overvoltages, sufficient energy would be realized to nucleate more energetic deposition sites; concurrently the rate of silver adion diffusion would increase to where it is no longer the slowest intermediate step in the reaction. Due to the high dislocation density of the etched silver-electrode surface used in these experiments, the possibility of deposition occurring via two-dimensional nucleation would be unlikely.

In the presence of metaphosphate, a change in silver-deposit morphology is also accompanied by a large increase in overvoltage. Linear steady-state, current-potential behavior in the presence of metaphosphate indicates the over-all reaction rate is mass-transport controlled. Evidence of metaphosphate adsorption on the electrode surface is indicated by the decrease in silver adion concentration and the amount of charge required to reach activation overvoltage. Electron-probe analysis also indicates metaphosphate coverage increases with larger additive concentrations. Similar values of the slope obtained from the nonsteady-state plot of current *vs.* potential indicate a consistent rate-controlling step over the range of metaphosphate concentrations investigated. These facts tentatively suggest that with the adsorption of metaphosphate, low energy sites become blocked and deposition is forced to occur on higher energy sites with a subsequent increase in overvoltage. This would gradually make direct transfer of silver ions from solution to nuclea-

tion sites a more favorable intermediate reaction step in the over-all electrochemical process. With increasing overvoltages, more nucleation sites for silver deposition become available, resulting in an over-all more fine-grained electrodeposited surface.

Manuscript submitted Oct. 8, 1971; revised manuscript received Dec. 13, 1972.

Any discussion of this paper will appear in a Discussion Section to be published in the December 1973 JOURNAL.

REFERENCES

1. F. Mathers and I. Kuebler, *Trans. Electrochem. Soc.*, **29**, 417 (1916).
2. G. Fuseya and K. Murata, *ibid*, **50**, 235 (1926).
3. E. Neal and L. Shreir, *Trans. Faraday Soc.*, **49**, 703 (1955).
4. O. Volk and H. Fischer, *Electrochim. Acta*, **5**, 112 (1961).
5. H. Fischer, *ibid.*, **2**, 50 (1960).
6. H. Gerischer, *Z. Elecktrochem.*, **62**, 256 (1958); *ibid.*, **61**, 1159 (1957).
7. W. Mehl and J. Bockris, *J. Chem. Phys.*, **27**, 818 (1957); *Can. J. Chem.*, **37**, 1959.
8. A. Despic and J. Bockris, *J. Chem. Phys.*, **32**, 389 (1960).
9. Z. Lorenz, *Physik. Chem. Frankfurt*, **17**, 136 (1958).
10. E. Budevskii, V. Bostanov, T. Vitanov, Z. Stoinov, A. Kotseva, and R. Kaisher, *Elekrokhimiya*, **3**, 856 (1967).
11. N. Pangarov, *Electrochim. Acta*, **11**, 1753 (1966); *ibid.*, **7**, 139 (1962).
12. T. Reddy, *This Journal*, **113**, 117 (1966).
13. J. Bockris and H. Kita, *ibid.*, **109**, 920 (1962).
14. A. Damjanovic and J. Bockris, *ibid.*, **110**, 1035 (1963).
15. H. Kita, M. Enyo, and J. Bockris, *Can. J. Chem.*, **39**, 1670 (1961).
16. M. Fleischmann and H. Thirsk, *Electrochim. Acta*, **2**, 22 (1960).
17. M. Fleischmann, S. K. Rangarajan, and H. Thirsk, *Trans. Faraday Soc.*, **63**, 1240 (1967).
18. S. K. Rangarajan, *J. Electroanal. Chem.*, **16**, 485 (1968).
19. D. Astley, J. Harrison, and H. Thirsk, *Trans. Faraday Soc.*, **64**, 192 (1968).
20. E. Mattsson and J. Bockris, *ibid.*, **55**, 1586 (1959).
21. J. Wager and J. Campanella, *J. Am. Chem. Soc.*, **72**, 666 (1950).
22. R. Piontelli, Trans. of the Symposium on Electrode Processes, John Wiley and Sons, Inc. New York (1961).

A Study of Surface Chromium on Tinplate

S. E. Rauch, Jr. and R. N. Steinbicker

Homer Research Laboratories, Bethlehem Steel Corporation, Bethlehem, Pennsylvania 18016

ABSTRACT

The reactions occurring during the anodic polarization of tinplate passivated cathodically in a dichromate solution (CDC tinplate) were ascertained by applying Faraday's law to analyses of the oxidation products generated. It was found that a large portion of the CDC passivation film consists of chromium in the metallic state.

Most of the tinplate used for making cans and other containers, particularly containers for foods and beverages, is produced commercially by the electroplating of steel strip with a thin coating of metallic tin. After the strip has been plated, the tin coating is flow-brightened to convert the tin from a condition in which it presents a matte surface to a condition in which it presents a bright surface. The flow brightening is accomplished by melting and subsequently solidifying the tin coating. If the tin surface were permitted to remain in the flow-brightened condition, it would be susceptible to the formation of an oxide film during storage that is very detrimental to lacquer or enamel adhesion if the tinplate is subsequently coated. In addition, untreated tin surfaces are susceptible to discoloration or yellowing when heated during the enamel-drying process and to sulfide staining when sulfur-containing foods are packed in such tinplate. Such discolorations are objectionable from an esthetic standpoint.

For these reasons and also to improve the corrosion resistance of the tin surface, it is customary to electrochemically treat the flow-brightened tin surface in a dilute solution of sodium dichromate. The tinplate is made cathodic in this solution maintained at a temperature of approximately 80°-85°C, about 4 coulombs/dm^2 being passed at a current density of 5-10 A/dm^2.

This treatment applies a layer of chromium amounting in weight to 60-100 $\mu g/dm^2$ to the surface of the tinplate. The nature and composition of such a passivation film has been a subject of controversy for many years, but it has generally been felt that the film consists of various hydrated and/or unhydrated oxides of chromium. Although the solution to the problem is complicated by the extreme thinness of the film ($\simeq$10 Å), recent evidence has indicated the possibility that some portion of the film might consist of chromium in the metallic form (1). Along these lines the anodic polarization at constant current (galvanostatic) of cathodic dichromate (CDC)-treated tinplate and the relationships of the resulting potential-time (charge) curves to various surface properties have been independently explored and reported by several investigators, notably Rocquet and Auburn (1), Britton (2), and Becker (3).

Britton's investigations provided the basic work in this field, and his general procedure was used by most of the other investigators. Using Britton's electrolyte (0.75% Na_2HPO_4, adjusted to pH 7.4 with H_3PO_4), engineers in Bethlehem Steel's Research Department examined the procedure and attempted to correlate the results with plain plate and underfilm sulfide stain ratings. However, the correlations were poor and the lack of a clearcut relationship between the test and total surface chromium prevented Britton's procedure from being used as a routine analytical method.

During preliminary work that led to the study reported on in the present paper we found that the substitution of 3% aqueous ammonia for the 0.75% Na_2HPO_4 electrolyte and the use of a higher current density than that used by Britton permitted a larger percentage of the total surface chromium to be electrochemically oxidized and hence brought about better correlation between coulometric results and the total surface chromium present as measured by standard colorimetric procedure.

Key words: chromium passivation films, tinplate passivation, chromium analysis, tinplate surface analysis.

Experimental

During the course of our preliminary investigation it became apparent that precise experiments could be performed which would explain the coulometry involved and prove or disprove the existence of metallic chromium in the CDC passivation film.

Accordingly, our experimental program employed accurate and precise measurements of the charge passed and the oxidation products generated (except O_2) during the galvanostatic polarization, followed by potentiokinetic polarizations to discern the contribution of O_2 evolution to the coulometry. Faraday's law was then applied to these data to establish the original valence state of the chromium.

Description of specimens.—For this study a quantity of sheets were sheared from a coil of normal production CDC-treated tinplate produced on an alkaline tinning line at Bethlehem's Sparrows Point Plant. The experimental specimens (surface area = 0.324 dm^2) were die-punched sequentially from the center position of these sheets and hence can be considered to be identical. Wet chemical analysis established that the experimental face of these specimens had a chromium level of 94 $\mu g/dm^2$.

Apparatus for coulometric experiments.—The galvanostatic experiments were performed in a glove box under an argon atmosphere. All solutions used were deaerated with argon to minimize analytical errors due to chemical oxidation of the tin surface. Currents were measured with a milliammeter (0.25% accuracy), and potentials were measured with a potentiometric recorder (0.1% accuracy). The power supplies used were low-ripple constant voltage supplies modified to supply constant current.

The potentiokinetic experiments were performed outside of the glove box, since no chemical analyses of oxidation products were to be performed. The potentiostat used was controlled by a motor potentiometer. The current *vs.* applied potential measurements were made by passing the cell current through a precision 1.0 ohm series resistor and recording the resultant *IR* drop *vs.* specimen potential on an X-Y recorder.

The electrochemical cell (Fig. 1) was a 600 ml beaker modified with a glass tee connecting tube centered on the bottom. The glass tee accommodated an electrical connection to the specimen and permitted the application of vacuum to hold the specimen tight against a Tygon gasket mounted in the bottom of the beaker. Reference and counterelectrodes were mounted in a No. 15 gum rubber stopper, which fitted snugly into the top of the beaker. The cathode was isolated from direct contact with the electrolyte by means of a fritted glass junction.

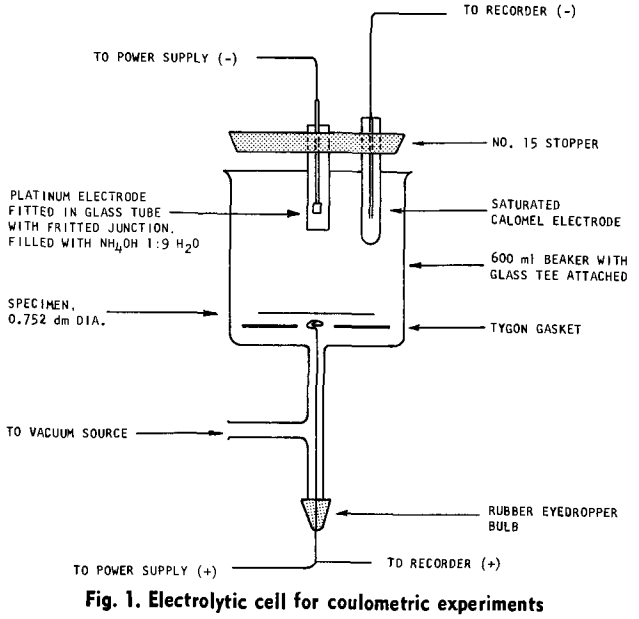

Fig. 1. Electrolytic cell for coulometric experiments

Galvanostatic Experiments

To determine the rates of the reactions occurring during galvanostatic polarization the specimens were polarized for various increments of time. The surface tin oxides were then determined by electrochemical analysis, and the tin and chromium in the electrolyte by chemical analysis.

Polarization procedure and surface tin oxide determination.—Seven specimens (labeled A through G) of the experimental material were transferred into the glove box. First, the original tin oxide level on the surface of specimen A was established coulometrically using a method generally referred to in the industry as the MCE test (4). Essentially, this test consists of the coulometric reduction, at constant current, of stannous and stannic oxides in very dilute HBr (1:5000).

Specimens B through G were then exposed to an electrolyte of 3% aqueous ammonia (NH_4OH 1:9 H_2O) for precisely 3 min, during which time they were anodically polarized at 8.00 mA (18.0 mA/dm^2) for intervals of 0, 15, 30, 45, 75, and 105 sec. After each polarization the electrolyte was set aside for chemical analysis of tin and chromium and the specimens were analyzed for surface tin oxides with the MCE test. The potential *vs.* time curve in Fig. 2 shows the levels to which the experimental materials were polarized.

Analysis for tin and chromium in the electrolyte.—The electrolytes were removed from the glove box, acidified with H_2SO_4, and diluted to volume in 200 ml volumetric flasks. Dissolved tin was determined polarographically after 100 ml aliquots were concentrated in 25 ml solutions of NH_4Cl by coprecipitation with Al and redissolution with HCl. The other half of the solutions were analyzed colorimetrically for Cr^{+6} with the sensitive diphenylcarbazide procedure, after a preliminary oxidation with silver catalyzed $(NH_4)_2S_2O_8$. The oxidation step was precautionary, because it was found that a small amount of tin dissolved chemically (no current) into the NH_4OH electrolyte which (if present as Sn^{+2}) could conceivably reduce a portion of the Cr^{+6}, and thus cause low results.

Quantitative results of the analyses are shown together with polarization times in Table I, with all quantities expressed as quantity/square decimeter. It can be seen from Table I that a tin oxide value of 11 MCE/dm^2 was originally present on the surface (sample A). A 3-min exposure to the electrolyte under static (no current) conditions (sample B) caused no increase in this quantity, but did result in the chemical dissolution of 16 $\mu g/dm^2$ of Sn.

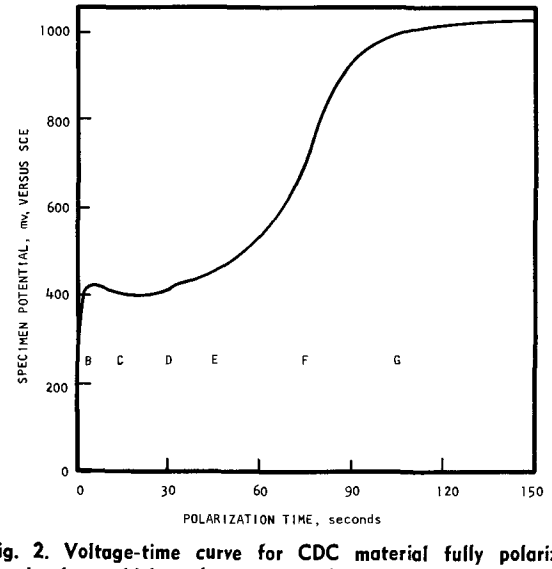

Fig. 2. Voltage-time curve for CDC material fully polarized. Shows levels to which each experimental specimen was polarized.

Table I. Results of tin and chromium analyses

Specimen	A Polarization time, sec	B Surface tin oxides, MCE/dm²	C Dissolved tin, μg/dm²	D Dissolved chromium, μg/dm²
A	—	11	—	—
B	0.0	11	16	0.0
C	15.0	54	41	18.0
D	30.0	111	59	34.5
E	45.0	165	83	48.2
F	75.0	288	133	65.8
G	105.0	392	171	69.9

Potentiokinetic Experiments

In order to discern the contribution of oxygen evolution ($2\,OH^- \rightarrow O_2 + 2H^+ + 4e$) to the coulometry of the galvanostatic experiments, potentiokinetic polarizations of the same material were made for the determination of the minimum potential at which that reaction can occur.

Procedure and results.—Using a potentiostat controlled by a motor-driven potentiometer, the potential of the specimen (*vs.* SCE) was increased linearly from 0 to 1100 mV at a rate of 50 mV/min. Figure 3 shows the resultant cell current *vs.* potential up to 1000 mV, as recorded on an X-Y recorder.

From 0 to 300 mV (*vs.* SCE) the cell current slowly increased from 0.0 to 0.4 mA. From this point it rapidly increased to a maximum (6.5 mA) at 420 mV, which is approximately the same voltage as the potential arrest (400 mV) noted during galvanostatic experiments (Fig. 2). The current then declined to a minimum of 1.5 mA at 750 mV. As the potential increased above 800 mV the current again increased rapidly to a maximum of 14 mA at 1100 mV (off scale) and the evolution of gas bubbles was observed on the specimen's surface.

This same specimen was polarized a second time, and no significant current flowed until the potential reached 750 mV. After 800 mV the current again increased to a maximum (Fig. 4).

When this experiment was repeated with a specimen of chromium-free tinplate the resultant curve was very similar to Fig. 4, except that a current of 0.2 mA began to flow at 250 mV. Again, when this specimen was polarized for a second time no current flowed until a potential of 750 mV was attained.

Discussion

Having obtained both the experimental data from the potentiokinetic experiments (which will show the potential at which O_2 evolution became significant) and the analytical data from the galvanostatic experiments, we can now determine the original oxidation state of the chromium.

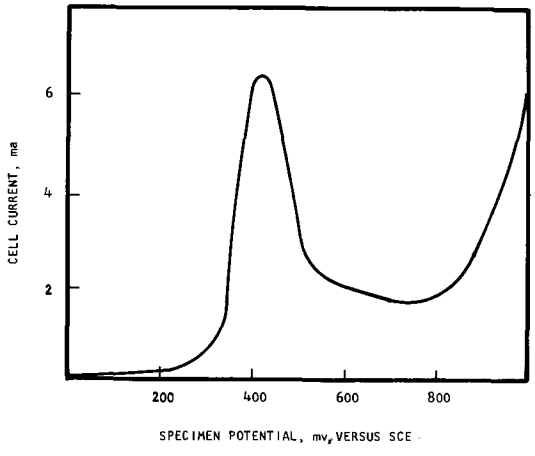

Fig. 3. Current-voltage relationship for first potentiokinetic polarization of CDC material. Potential increased 50 mV/min.

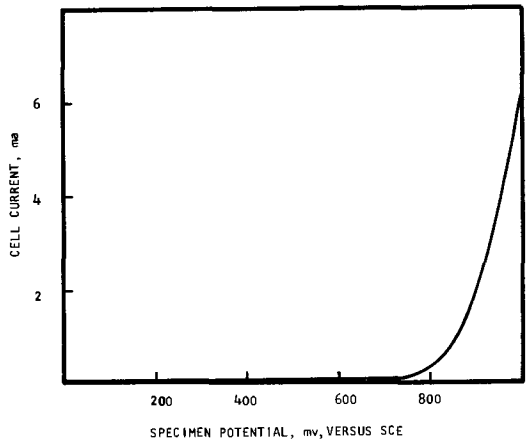

Fig. 4. Current-voltage relationship for CDC material polarized potentiokinetically a second time. Potential increased 50 mV/min.

Potentiokinetic experiments.—The recorded current peak at 420 mV for the CDC-treated specimens (Fig. 3) and the lack of such a peak for untreated tinplate indicate that the CDC passivation film was oxidized at that potential. However, the small current which began early for both CDC-treated and untreated samples must be due to the oxidation of the tin surface. In the case of the unpassivated specimen this current was smaller than for CDC-treated tinplate, because air oxidation of the unpassivated surface had proceeded to a higher degree.

The absence of measurable current until 750 mV was reached on the specimens polarized for a second time (Fig. 4) indicates that O_2 evolution ($2\,OH^- \rightarrow O_2 + 2H^+ + 4e$) was not an appreciable factor prior to that potential. This, in turn, means that O_2 played no significant role in the coulometry of the galvanostatic experiments before 750 mV was reached.

Galvanostatic experiments.—As previously stated, a tin oxide value of 11 MCE/dm² was originally present on the specimens, and the 3-min exposure to the electrolyte caused the chemical dissolution of 16 μg Sn/dm². In Table II these values are subtracted from the data, so that only electrochemical oxidation products are shown. Dissolved tin is now expressed as MCE/dm², since tin dissolving electrochemically at these potentials (≧400 mV *vs.* SCE) would be expected to be oxidized to the +4 state. Our experiments showed this to be the case, allowing the electrochemical equivalent of 3.25 coulombs/mg to be assigned. Figure 5 shows the electrochemical rates of tin dissolution and oxide formation.

Table II also presents another quantity, referred to as the "delta charge," which is that quantity of electricity (millicoulombs/square decimeter) not explained by the total oxidation of tin. The delta charge must therefore be the charge used in the oxidation of chromium and/or the evolution of oxygen on a specimen surface above 750 mV.

Figure 6 shows the dissolution of chromium *vs.* the delta charge. Chromium dissolves at a constant rate of 0.117 μg/Δmcoulomb for slightly more than 320

Table II. Relationship of coulometric charge to electrochemical oxidation products

Specimen	a Anodic charge, mcoulombs/dm²	b Surface tin oxides, MCE/dm²	c Dissolved tin, MCE/dm²	a − (b + c) Delta charge, Δmcoulombs/dm²	d Dissolved chromium, μg/dm²
B	0	0	0	0	0.0
C	270	43	81	146	18.0
D	540	100	135	305	34.5
E	810	154	220	436	48.2
F	1350	278	380	692	65.8
G	1890	381	505	1004	69.9

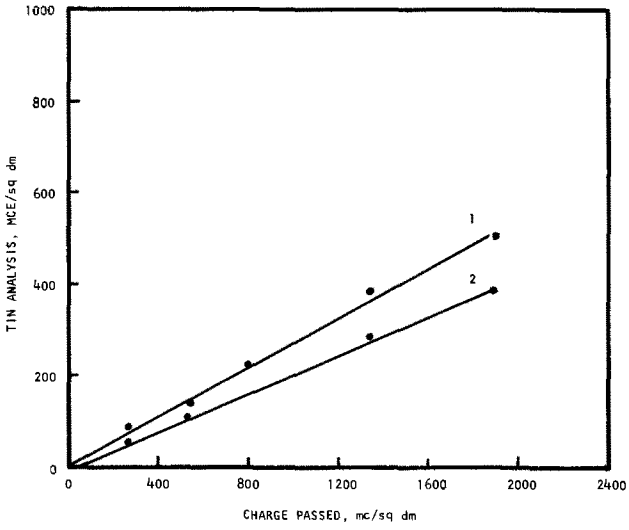

Fig. 5. Oxidation of tin vs. charge passed during galvanostatic polarization of experimental specimens. Shows: curve 1, the tin found in the electrolyte, and curve 2, the oxides formed on the surface.

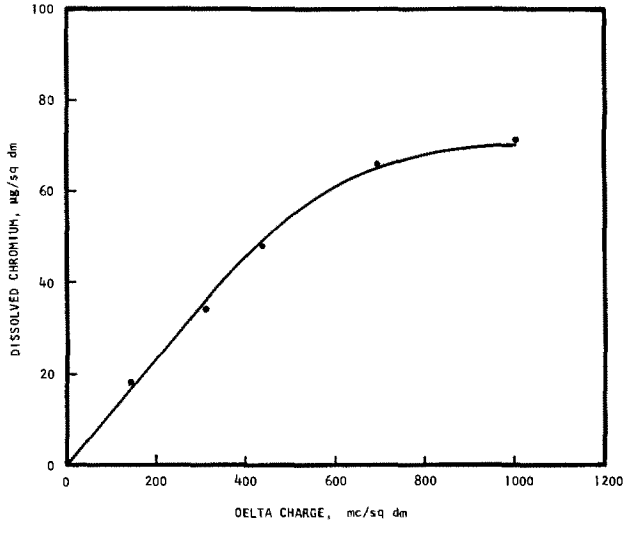

Fig. 6. Chromium dissolved in electrolyte during galvanostatic polarizations vs. delta charge.

Δmcoulombs/dm², a value which corresponds closely to the duration of the galvanostatic potential arrest at 400 mV (*vs.* SCE). From this point the rate decreases until chromium dissolution ceases and the decomposition potential of the electrolyte (O_2 overvoltage) is reached ($\simeq$1000 mV *vs.* SCE). At this potential the evolution of oxygen is easily observed.

The initial chromium dissolution rate of 0.117 µg/Δmcoulomb supposedly could be interpreted as the oxidation of Cr^{+3} at a current efficiency of 65%. However, since this initial rate occurs at a potential far below that at which oxygen evolution can occur (as shown in the potentiokinetic experiments) and since all other oxidation products have been accounted for, it follows that Cr° and Cr^{+3} are being oxidized simultaneously. When applied to data from Fig. 6, a simple equation (µg Cr° = [Δmcoulombs/5.565] − µg ΣCr), derived algebraically from the electrochemical equivalents of Cr° and Cr^{+3}, can be used to calculate the weight of Cr° oxidized and, by simple difference, that of the Cr^{+3}.

This equation shows that Cr° and Cr^{+3} are initially oxidized at a constant rate of (0.063 µg Cr° + 0.054 µg Cr^{+3})/Δmcoulomb. After 320 Δmcoulombs, the oxidation of Cr^{+3} rapidly decreases, ceasing entirely after 460 Δmcoulombs at a total weight of 19 µg/dm². The oxidation of Cr° consumes the excess charge until the potential reaches approximately 750 mV (*vs.* SCE), at which point oxygen evolution begins. By the time 970 Δmcoulombs has passed, chromium oxidation has ceased and the decomposition potential of the electrolyte has been reached. The amount of Cr° oxidized is about 51 µg/dm², or the difference between total dissolved chromium and the Cr^{+3}. This quantity corresponds to roughly 54% of the total surface chromium (94 µg/dm²).

Investigators have disagreed as to the identification of the residual chromium left on the specimen after polarization to the decomposition potential (24 µg/dm²). For example, Britton, who reported a much greater quantity of residual chromium than we found in our work, theorized that the residual material might be Cr^{+6} united with SnO_2. However, if his hypothesis were correct, the chromium would have been oxidized to the +6 state during galvanostatic polarization, a result which was not borne out by data we obtained in the following experiment.

The experiment consisted of exposing a fully polarized specimen to a solution of 0.1M oxalic acid for 5 min under an argon atmosphere to avoid air oxidation of the tin surface. (The work done during the development of the MCE test for the quantitative determination of tin oxide films had shown that the oxalic acid solution dissolves these films (4). This solution also dissolves Cr^{+6}.) After an oxidation step the solution was analyzed colorimetrically for chromium. None was found, indicating that the residual is not Cr^{+6} combined with the tin oxide film.

It is more reasonable to assume that the residual chromium is in its trivalent form and is either an inherently poor conductor or one with which good electrical continuity was lost due to the large growth of tin oxides. In any event, given the fact that the residual chromium was not oxidized during the galvanostatic tests, this chromium is not a factor in the coulometry of the polarization.

Conclusion

To sum up, the results of galvanostatic and potentiokinetic experiments interpreted analytically using Faraday's law proved that a substantial portion of the CDC passivation film on tinplate is chromium in the metallic state, the following reactions having occurred during the anodic polarization of the tinplate in 3% aqueous ammonia:

$$Cr^\circ \rightarrow Cr^{+6} + 6e$$

$$Cr^{+3} \rightarrow Cr^{+6} + 3e$$

$$Sn^\circ \rightarrow Sn^{+4} + 4e$$

$$Sn^\circ \rightarrow SnO_2 + 4e$$

$$2\,OH^- \rightarrow O_2 + 2H^+ + 4e$$

(only occurs above 750 mV *vs.* SCE)

For the specimens studied in detail the passivation film was found to contain approximately 54% metallic chromium.

Manuscript submitted Oct. 10, 1972; revised manuscript received Dec. 15, 1972.

Any discussion of this paper will appear in a Discussion Section to be published in the December 1973 JOURNAL.

REFERENCES

1. P. Rocquet and Ph. Auburn, *Corrosion* (Fr.), **5**, 229 (1968).
2. S. C. Britton, *Brit. J. Corrosion*, **1**, 91 (1965).
3. J. J. Becker, *This Journal*, **117**, 1211 (1970).
4. A. R. Willey and D. F. Kelsey, *Anal. Chem.*, **11**, 1804 (1958).

An Electrochemical Study of Electroless Gold-Deposition Reaction

Yutaka Okinaka*

Bell Laboratories, Murray Hill, New Jersey 07974

ABSTRACT

The electroless (autocatalytic) gold-deposition reaction, using potassium borohydride as the reducing agent, was studied by electrochemical methods. The results support the assumptions made previously that (*i*) the species that reduces aurocyanide ions is BH_3OH^-, an intermediate formed during the hydrolysis of BH_4^-, and (*ii*) the deposition reaction is preceded by competitive adsorption of reacting species.

The hydrolysis kinetics of borohydride ions, under conditions of the electroless process, was also studied using a polarographic method. The results allowed the calculation of rate constants and the variation of concentrations of BH_4^- and BH_3OH^- as a function of time during operation of the electroless plating bath.

The electroless gold-plating bath developed recently in this laboratory (1) contains $KAu(CN)_2$, KCN, KOH, and KBH_4, and is operated at 70°-80°C. The process is autocatalytic and deposits pure gold on gold substrates without incorporation of boron. In the initial study of this system of the dependence of deposition rate on various experimental variables, two rather unexpected results were noted (1). One was the decrease in deposition rate with increasing KOH concentration, a dependence which is opposite from what might be expected from the over-all deposition reaction which is believed to involve hydroxyl ions as a reactant. In view of the reasonably well-established reaction of borohydride ions (2-4), this result was accounted for by assuming that the species that actually reduces $Au(CN)_2^-$ to gold metal is not BH_4^- but BH_3OH^-, an intermediate formed during the course of hydrolysis of BH_4^-. Since the hydrolysis reaction is catalyzed by acids, the concentration of BH_3OH^- is expected to be lower at higher alkalinities. The other unexpected result was that with increasing $KAu(CN)_2$ concentration, the deposition rate increased to a maximum followed by a gradual decrease. This unusual dependence was one of the important factors considered in formulating optimum bath compositions to obtain not only an acceptable deposition rate, but also deposits of satisfactory physical properties (5, 6). In order to explain the observed effect of $KAu(CN)_2$ concentration on the deposition rate, it was postulated (1) that the deposition reaction is preceded by competitive adsorption of BH_3OH^- and $Au(CN)_2^-$ on the substrate surface. The purpose of this communication is to present and discuss results of an electrochemical study that supports the above assumptions.

Experimental

Chemicals.—Potassium hydroxide and potassium cyanide were of C.P. grade. Potassium aurocyanide (68+% Au) was a product of Technic, Incorporated, and potassium borohydride (98%) was obtained from City Chemical Corporation.

Equipment.—Current-potential curves were obtained with a set of equipment consisting of a Wenking potentiostat, motor potentiometer, and X-Y recorder. The electrolytic cell was a jacketed 200 ml Pyrex glass beaker, and the temperature was maintained at 75°C by circulating constant temperature water from a Lauda circulator.

Electrodes.—A rotating platinum disk electrode (diameter 0.77 cm), precoated with about 25 μm thick electrolytic gold, was used for the experiment of Fig. 11. For all other experiments involving the use of gold as the working electrode, a piece of rectangular gold sheet with an area of 1 cm^2 was employed. No insulating or masking material was used. A fine gold wire was welded onto a corner of the gold sheet, and the electrode was hung through a small hole drilled through the Teflon cover of the cell. The solution was gently stirred at a constant speed with a magnetic stirrer. Current fluctuation of ±5-10% was unavoidable under these experimental conditions, but the precision and reproducibility were considered to be acceptable for the purpose of this investigation. The current values reported for gold-sheet electrode experiments are the average of such fluctuating currents. The counterelectrode was a platinum coil placed in a compartment separated from the main cell by a fritted glass disk. A Hg/HgO reference electrode in 1M KOH at room temperature was connected to the cell through a salt bridge with a capillary tip filled with 1M KOH.

The dropping mercury electrode used had the following characteristics: $m = 2.07$ mg·sec^{-1} and $t = 4.02$ sec at −0.40V in 0.2M KOH at 75°C. Current measurements were made at the end of the life of mercury drops. Dissolved air was removed by bubbling purified nitrogen through solutions in all experiments.

Results and Discussion

BH_3OH^- as the reducing species.—It is fairly well established that the hydrolysis of BH_4^- proceeds in two steps (2-4)[1]

$$BH_4^- + H_2O \xrightarrow{k_1} BH_3OH^- + H_2 \qquad [1]$$

$$BH_3OH^- + H_2O \xrightarrow{k_2} BO_2^- + 3H_2 \qquad [2]$$

The polarographic investigation carried out by Gardiner and Collat (4) shows that at the mercury electrode, the BH_3OH^- ion formed as the intermediate is much more readily oxidized than BH_4^-. The anodic wave for the oxidation of BH_3OH^- according to

$$BH_3OH^- + 3\,OH^- \rightarrow BO_2^- + 3/2H_2 + 2H_2O + 3e^- \qquad [3]$$

appears at a potential about 0.5V more negative than that of BH_4^-

$$BH_4^- + 8\,OH^- \rightarrow BO_2^- + 6H_2O + 8e^- \qquad [4]$$

At platinum the anodic oxidation of these two ions does not occur at such discrete potentials (9, 10). The be-

* Electrochemical Society Life Member.

Key words: electroless plating, autocatalytic plating, gold plating, borohydride, electrocatalysis, adsorption.

[1] Species such as $(BH_3)_{aq}$ (7), $BH(OH)_2$ (7), or $BH(OH)_3^-$ (8) have also been suggested for the hydrolysis intermediate, but the formula BH_3OH^- appears to have the most convincing experimental support.

havior of these ions at a gold electrode has not been reported in the literature to the author's knowledge. Thus, the question arises as to whether the species directly responsible for the electroless deposition of gold is BH_3OH^-, or BH_4^-, or both. An answer to this question was obtained by comparing potentials measured during the deposition of gold with current-potential curves for the anodic oxidation of borohydride solutions at a gold electrode.

Figure 1 shows the variation of open-circuit potential with the concentration of $KAu(CN)_2$ in the absence (line 1) and presence (line 2) of 0.1M KBH_4 in a mixture of 0.2M KOH and 0.2M KCN. The measurement was made at 75°C, a typical operating temperature of the electroless bath. In the absence of KBH_4 the potential changed linearly with $\log[Au(CN)_2^-]$, and the slope of the line, 64 mV, agreed well with the theoretical Nernst value of 69 mV for the reaction

$$Au(CN)_2^- + e^- \rightleftarrows Au + 2CN^- \qquad [5]$$

With KBH_4 in the solution, the measured potential was always more negative than the corresponding equilibrium potential and ranged from −0.7 to −1.0V in the concentration range studied (line 2, Fig. 1). The potential shift was greater at higher KBH_4 concentrations (line 3) as expected for a typical mixed potential reaction.

Anodic current-potential curves obtained in various solutions at 75°C are shown in Fig. 2. Currents varied with time, as will be shown later, because the concentrations of both BH_4^- and BH_3OH^- changed with time due to hydrolysis. Recording of the curves shown in Fig. 2 was begun approximately 10 min after the solution temperature reached 75°C. Curve 1 was obtained with 0.1M KBH_4 in a mixture of 0.2M KOH and 0.2M KCN. Curve 1′ was obtained without KBH_4 in the solution and represents the anodic dissolution of the gold electrode. The difference in current between curves 1 and 1′ is due to the anodic oxidation of a borohydride species, but because of the interference caused by the large dissolution current of the electrode, these two curves do not provide information as to which borohydride species is responsible for the anodic current. Curve 2 was obtained in a solution containing 0.1M KBH_4 and 0.2M KOH in the absence of KCN. Comparison of curves 1 and 2 shows that cyanide ions greatly inhibit the anodic oxidation of the species in question. It is likely that this inhibiting effect results from the adsorption of CN^- on the electrode surface. (The adsorption of CN^- also accounts for the fact that the cathodic hydrogen evolution in the presence of KCN occurs at a potential about 0.1V more negative than that in the absence of KCN. Compare cathodic ends of curves 1 and 2.) Because of the high concentration of KBH_4 used for curve 2, it was not possible to record the current over the entire potential range. A much smaller concentration of KBH_4 (2×10^{-4}M) was used to obtain curve 3. In the potential range of curve 2, no current is visible in curve 3 because of the low KBH_4 concentration, but it is clear that the reaction which causes the sharp increase in anodic current in curve 2 starting at about −0.7V is responsible for the large anodic wave in curve 3. From these two curves and their similarity to the known polarographic behavior of borohydride solutions (4) (see also the next section), it may be assumed that the first wave (curve 2) is due to the oxidation of the hydrolysis intermediate, BH_3OH^-, whereas the second wave (curve 3) results from the oxidation of BH_4^-.[2] From the proximity of curves 1 and 2 the reaction corresponding to curve 1 is most likely to be the oxidation of BH_3OH^- partially inhibited by the adsorption of CN^-. These assumptions were further substantiated by examining the dependence of current on time as described below.

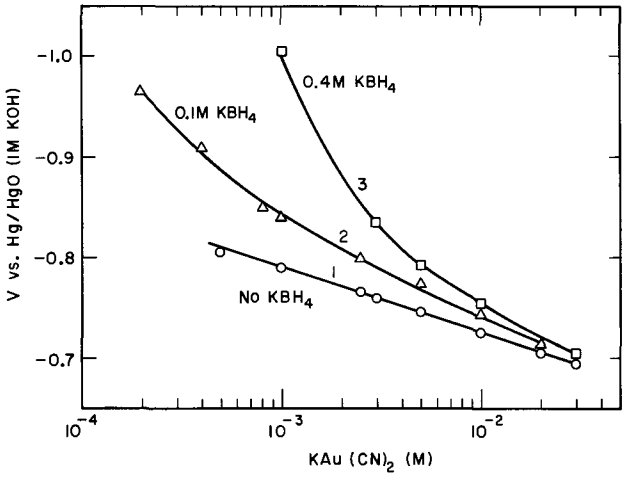

Fig. 1. Zero-current potential as function of $KAu(CN)_2$ concentration at various KBH_4 concentrations at 75°C. 0.2M KOH, 0.2M KCN.

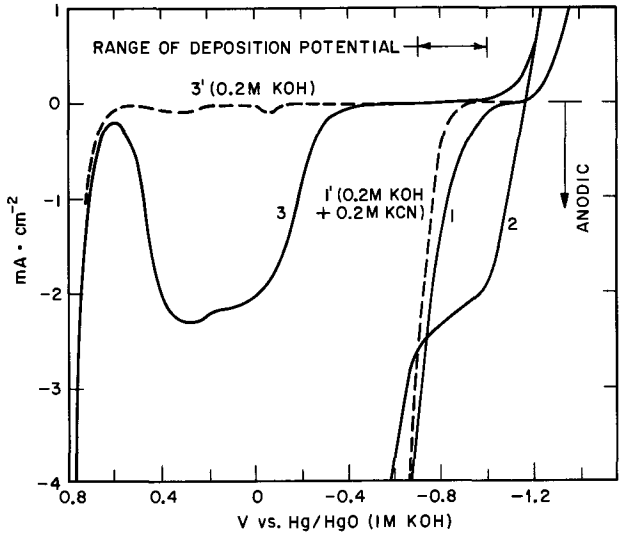

Fig. 2. Current-potential curves for oxidation of borohydride at gold electrode in various solutions at 75°C. Curve 1, 0.1M KBH_4 in 0.2M KOH plus 0.2M KCN; curve 1′, same as curve 1 without KBH_4; curve 2, 0.1M KBH_4 in 0.2M KOH; curve 3, 2×10^{-4}M KBH_4 in 0.2M KOH; curve 3′, same as curve 3 without KBH_4. Potential scanned from negative to positive at 5.56 mV/sec^{-1}.

According to the hydrolysis reaction scheme, Eq. [1] and [2], the concentrations of BH_4^- and BH_3OH^- at time t after the commencement of hydrolysis are given by the following equations (2)

$$(BH_4^-) = (BH_4^-)_o \, e^{-k_1 t} \qquad [6]$$

$$(BH_3OH^-) = \frac{(BH_4^-)_o}{(k_2/k_1) - 1} (e^{-k_1 t} - e^{-k_2 t}) \qquad [7]$$

where $(BH_4^-)_o$ is the initial concentration of BH_4^-, and k_1 and k_2 are the pseudo first-order rate constants of reactions [1] and [2] expressed in sec^{-1}. Thus, the mass-transfer controlled limiting current for the oxidation of BH_4^- should decrease exponentially with time, whereas that for the oxidation of BH_3OH^- is expected to increase first from zero at $t = 0$ to a maximum followed by a decrease with increasing t. The experimental results are shown in Fig. 3. The current measured at +0.100V in 0.2M KOH containing 2×10^{-4}M KBH_4 decreased continuously with time (curve 1), which is expected for the variation of (BH_4^-). On the other hand, the currents measured at −0.850V in mixtures of 0.1M KBH_4 and 0.2M KOH showed maxima in

[2] In 0.2M KOH without KBH_4 (curve 3′, Fig. 2) two small dips are noted: a well-defined narrow one with a peak at −0.06V and a broad, shallow one with a peak at about +0.3V. Comparison of this curve with curve 3 shows that the substance formed at the first dip (perhaps Au_2O) does not interfere with the oxide of BH_4^-, whereas this oxidation is greatly inhibited by the substance that forms at the second dip (Au_2O_3). The final current rise is undoubtedly due to the oxygen-evolution reaction.

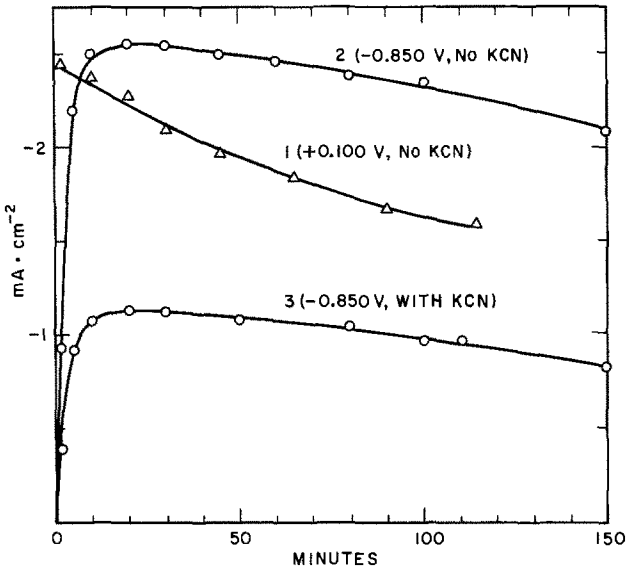

Fig. 3. Variation of oxidation current of borohydride with time at gold electrode at 75°C. Curve 1, 2 × 10^{-4}M KBH_4 in 0.2M KOH at +0.100V; curve 2, 0.1M KBH_4 in 0.2M KOH at −0.850V; curve 3, 0.1M KBH_4 in 0.2M KOH plus 0.2M KCN at −0.850V.

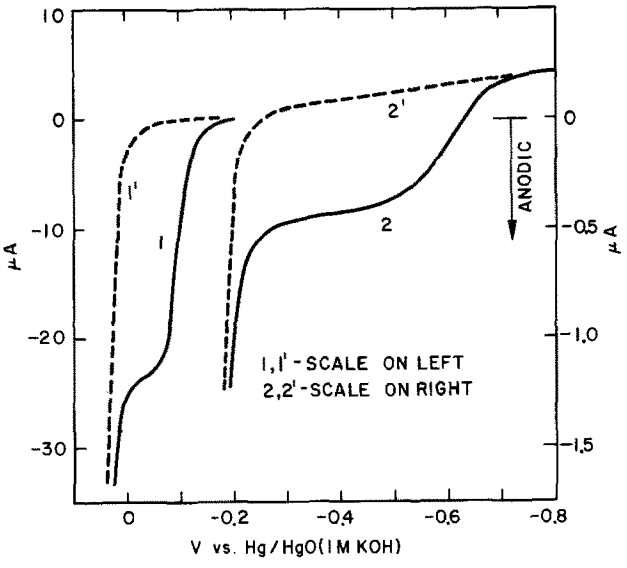

Fig. 4. Polarograms for anodic oxidation of BH_4^- (curve 1) and BH_3OH^- (curve 2) in 0.2M KOH at 75°C. Curve 1 taken with 5 × 10^{-4}M KBH_4 immediately after its addition, curve 2 with 2.5 × 10^{-3}M KBH_4 10 min after its addition. Broken lines, curves 1' and 2', residual current.

both the presence (curve 2) and absence (curve 3) of 0.2M KCN. This behavior is expected for the change in (BH_3OH^-) with time. In principle it should be possible to analyze quantitatively the current-time curves of Fig. 3 to calculate the rate constants. However, since the polarographic method using a dropping mercury electrode allowed much more precise measurements of current as described in the subsequent section, the data shown in Fig. 3 were not analyzed for quantitative purposes. Nevertheless, observed difference in the mode of variation of current with time at the two different potentials is sufficient to draw the conclusion that the current at −0.850V is due to the oxidation of BH_3OH^-, while that at +0.100V results from the oxidation of BH_4^-. As already noted in Fig. 1 and 2, the electroless deposition of gold takes place in the potential range of −0.7 to −1.0V, which precisely corresponds to the range where the oxidation of BH_3OH^- occurs. Thus, it is concluded that it is this intermediate species, and not BH_4^-, that acts as the reducing agent for the deposition of gold from $Au(CN)_2^-$.

Polarographic investigation of hydrolysis kinetics.— Knowledge of the rate constants, k_1 and k_2, for reactions [1] and [2] is of interest because it allows calculation of the concentrations of BH_4^- and BH_3OH^- at any time during the hydrolysis. This information is also useful because it can be used to calculate the amount of potassium borohydride to be added for the purpose of replenishment during the operation of the bath (11).

Gardiner and Collat (2) reported polarographically determined rate constants in various buffer solutions of pH values between 8.9 and 10.2 at temperatures below 35°C. Since estimation of the rate constants under operating conditions of the electroless bath from the data of Gardiner and Collat involves a large degree of extrapolation and uncertainty, it was decided to make actual polarographic measurements of rate constants. Polarographic waves for the anodic oxidation of BH_4^- (curve 1) and BH_3OH^- (curve 2) in 0.2M KOH at 75°C are shown in Fig. 4. The electrode reactions are given by Eq. [3] and [4]. The presence of KCN interfered because the anodic oxidation of the mercury electrode to form $Hg(CN)_2$ (12) occurred at a potential about 0.3V more negative than that for the oxidation of BH_4^-, and therefore all polarographic measurements were made in the absence of KCN. It was found that the effect of KCN on the rate of hydrolysis is relatively small, as may be expected from the fact that the hydrolysis reaction is catalyzed by acids (2) and the only acidic species present in the electroless system at a significant concentration is H_2O, regardless of the concentration of KCN. The following experimental result shows the small KCN effect. Ten milliliters of solution containing 0.2M KOH and 0.4M KBH_4 were heated to 75°C and the rate of hydrogen-gas evolution was measured. A closed vessel connected to a gas burette was used in this experiment. The gas volume increased approximately linearly with time over a period of 1 hr. The volume measured at the end of the 1-hr period was 56.0 ml at 1 atm and room temperature (average of three determinations). This corresponds to the hydrolysis rate of 15.6% per hour as calculated on the basis of the over-all hydrolysis reaction $BH_4^- + 2H_2O \rightarrow BO_2^- + 4H_2$, ignoring the effect of partial hydrolysis to BH_3OH^-, which is small as will be shown later. The measurement was repeated with the addition of 0.2M KCN to the above solution. The volume of hydrogen gas measured was 50.4 ml, corresponding to a hydrolysis rate of 14.0%. Thus, the effect of KCN was to decrease the hydrolysis rate by about 10% with respect to the rate in the absence of KCN. This is perhaps an effect of the increased ionic strength (2).

The experiment for the calculation of rate constants consisted of measuring the diffusion currents at −0.05 and −0.40V (see Fig. 4) as a function of time to follow the change in BH_4^- and BH_3OH^- concentrations, respectively. The very small ratio of $i_{BH_3OH^-}/i_{BH_4^-}$ found in a single solution necessitated separate measurements of the two currents in solutions containing different concentrations of KBH_4. The equations used were those derived by Gardiner and Collat (2); namely

$$i_{BH_4^-} = R_{BH_4^-}\,(BH_4^-)_0\, e^{-k_1 t} \qquad [8]$$

$$k_1 t_{max} = \frac{1}{(k_2/k_1) - 1} \ln (k_2/k_1) \qquad [9]$$

where $R_{BH_4^-}$ is the proportionality constant determined by the characteristics of the polarographic capillary used, and t_{max} is the time at which $i_{BH_3OH^-}$ is maximum. Equation [8] predicts that plotting log $i_{BH_4^-}$ against t yields a straight line, and k_1 can be calculated from the slope of this line. Equation [9] permits the calculation of k_2 from the value of k_1 thus determined, and t_{max} found in the $i_{BH_3OH^-}$ *vs.* t curve. The experimental results obtained are shown in Fig. 5 and 6. The rate constants calculated were as follows:

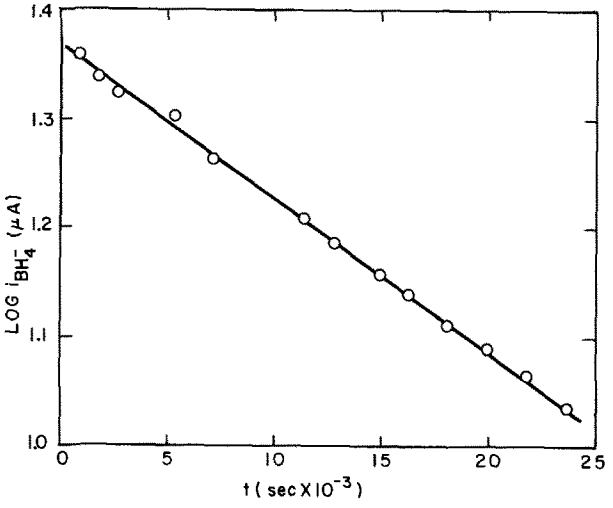

Fig. 5. Plot of log $i_{BH_4^-}$ vs. time. Current measured at −0.05V in 0.2M KOH at 75°C. Initial KBH_4 concentration, 5 × 10^{-4}M.

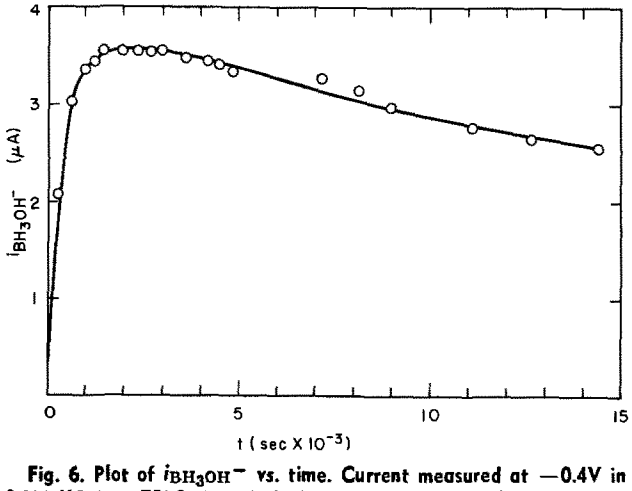

Fig. 6. Plot of $i_{BH_3OH^-}$ vs. time. Current measured at −0.4V in 0.2M KOH at 75°C; initial KBH_4 concentration. 0.01M.

$k_1 = 3.29 \times 10^{-5}$ sec^{-1}, $k_2 = 1.43 \times 10^{-3}$ sec^{-1} in 0.2M KOH at 75°C.

These values now being known, the instantaneous concentrations of BH_4^- and BH_3OH^- can be calculated for any initial concentration of BH_4^- with the aid of Eq. [6] and [7]. The ratios $[BH_4^-]/[BH_4^-]_o$ and $[BH_3OH^-]/[BH_4^-]_o$ calculated in this manner over a period of 8 hr are shown in Fig. 7. The curves represent the calculated values, and the points are the experimental values found polarographically. It is significant to note that the concentration of BH_3OH^- never exceeds about 2.2% of the initial KBH_4 concentration. Since BH_3OH^- is the species that acts as the reducing agent, it can be stated that the efficiency of utilization of KBH_4 in the electroless gold-deposition process is very low, and most of KBH_4 is lost by hydrolysis.

Competitive adsorption of reacting species.—The dependence of the deposition rate on $KAu(CN)_2$ concentration is quite unusual in that it exhibits a maximum at about 0.003M (1). The appearance of the maximum was previously assumed to be due to a competitive adsorption of $Au(CN)_2^-$ and BH_3OH^- on the substrate surface prior to the heterogeneous redox reaction. If $Au(CN)_2^-$ is more strongly adsorbed than BH_3OH^-, an increase in $Au(CN)_2^-$ concentration will tend to interfere with the adsorption of BH_3OH^-, thus decreasing the deposition rate beyond a certain $Au(CN)_2^-$ concentration. Experimental results and discussions presented below support this assumption.

Adsorption of BH_3OH^-.—In Fig. 2 it is seen that the anodic oxidation current of BH_3OH^- at the gold

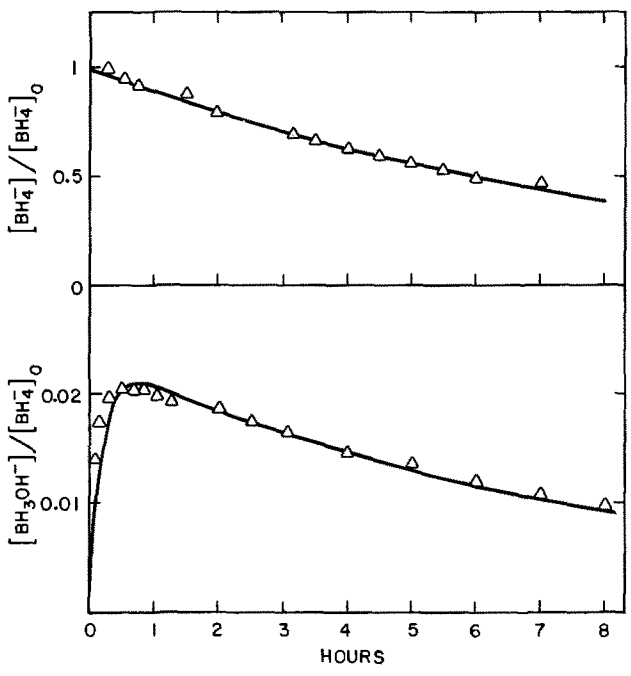

Fig. 7. Variation of concentrations of BH_4^- and BH_3OH^- with time with respect to the initial BH_4^- concentration in 0.2M KOH at 75°C. Lines calculated from rate constants; points experimental.

electrode in 0.2M KOH (curve 2) merges at the cathodic end (−1.2V) with the hydrogen-evolution current observed in the absence of borohydride (curve 3). This means that the BH_3OH^- oxidation occurs at a potential at least as negative as, or possibly more negative than, the hydrogen-evolution potential. At mercury, on the other hand, the oxidation of BH_3OH^- takes place at about −0.6V (see Fig. 4, curve 2), which is at least 0.5V less negative than the corresponding potential at gold. This potential difference corresponds to a difference in rate constant by several orders of magnitude, the exact difference being dependent on other kinetic parameters of the reaction. Such a large effect of electrode material (13) can be understood only by postulating a considerably greater electrocatalytic activity of gold due to the chemisorption of BH_3OH^-.

The dependence of the rate of electroless gold deposition on the crystalline orientation of the substrate is also of interest in this context. Sard and Wonsiewicz (14), using single-crystal copper substrates, found that the gold deposition rate decreases in the order (111) > polycrystal > (100) > (110). The rate on (111) surfaces was found to be about four times greater than that on (110). It is significant to note that this sequence is identical to that reported recently by Bagotzky, Vassiliev, and Pyshnograeva (15) for the electrocatalytic activity of various crystalline faces of platinum toward the hydrogen and oxygen evolution reactions as well as the anodic oxidation of methanol. Discussion of the cause of the orientation effect is beyond the scope of this paper, but there is little doubt that the chemisorption of reacting species is involved in these electrocatalytic reactions (13, 15) as well as in the electroless gold-deposition process.

Adsorption of $Au(CN)_2^-$.—On the basis of the dependence of current on concentrations at a constant overpotential, Maja (16) proposed a mechanism for the reduction of $Au(CN)_2^-$ in which this ion is postulated to be adsorbed on the gold electrode prior to the reduction. However, there is no direct experimental evidence available to prove the adsorption. On the other hand, it was found that $Au(CN)_2^-$ adsorbs strongly on the surface of mercury. This is evidenced by the large effect of $Au(CN)_2^-$ on the electrocapillary curves at potentials less negative than the potential where $Au(CN)_2^-$ begins to be reduced (Fig. 8). It is

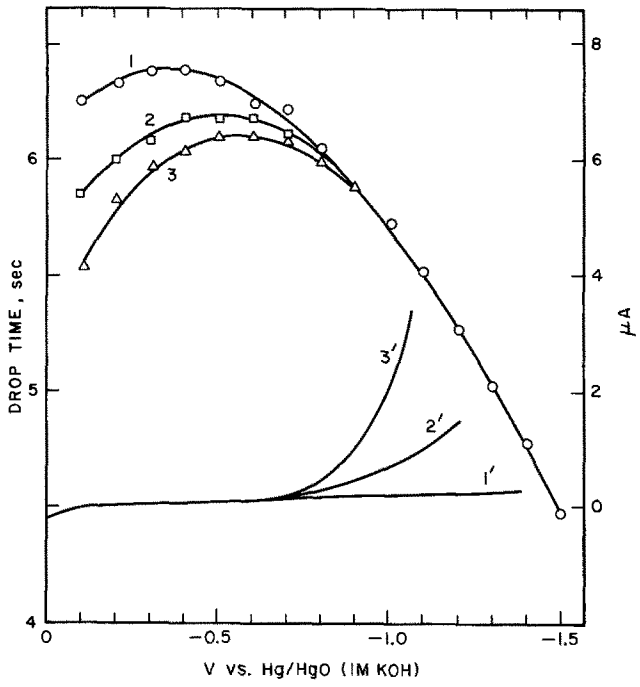

Fig. 8. Electrocapillary curves (1,2,3) and polarograms (1', 2', 3') at various concentrations of $KAu(CN)_2$ in 0.2M KOH at room temperature. Curves 1 and 1', no $KAu(CN)_2$; curves 2 and 2', 0.001M; curves 3 and 3', 0.005M.

also seen in Fig. 8 that the electrocapillary maximum is shifted toward more negative potentials and that the decrease in drop time is greater at less negative potentials. These results show that the adsorbed species is negatively charged.

Effect of $Au(CN)_2^-$ on anodic oxidation of BH_3OH^-.— The over-all deposition reaction can be considered to consist of the two partial electrochemical reactions, Eq. [3] and [5], occurring at an equal rate at the mixed potential. Thus, if there is no secondary kinetic interaction between the two partial reactions (*e.g.*, a reactant or product of one partial reaction affects the kinetics of the other), the cathodic-reduction current of $Au(CN)_2^-$ measured at the mixed potential in the absence of BH_3OH^- should be equal to the anodic-oxidation current of BH_3OH^- measured in the absence of $Au(CN)_2^-$. This relationship was found to hold when the $KAu(CN)_2$ concentration was very low as illustrated in Fig. 9 for the case of 2×10^{-4}M $KAu(CN)_2$.

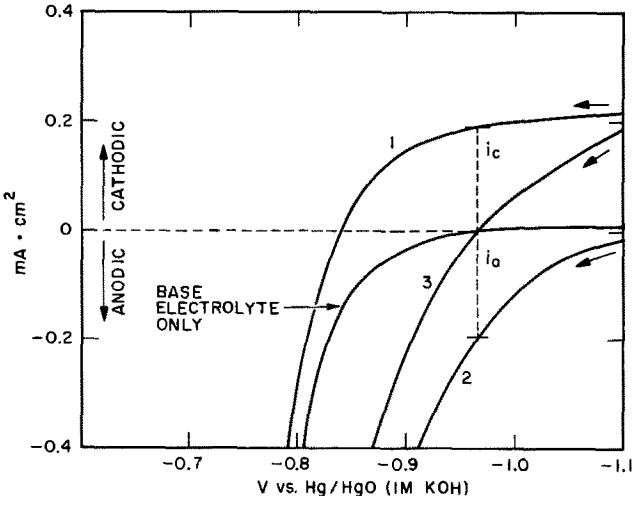

Fig. 9. Current-potential curves at gold electrode at 75°C. Base electrolyte, 0.2M KOH plus 0.2M KCN; curve 1, 2×10^{-4}M $KAu(CN)_2$ without KBH_4; curve 2, 0.1M KBH_4 without $KAu(CN)_2$; curve 3, 2×10^{-4}M $KAu(CN)_2$ and 0.1M KBH_4. Potential scanned from negative to positive at 5.56 mV/sec^{-1}.

The curves for solutions containing KBH_4 were recorded between 10 and 30 min after the addition of KBH_4, during which period the concentration of BH_3OH^- was practically constant (see Fig. 3). With increasing $KAu(CN)_2$ concentration, the deposition potential shifts in the positive direction (Fig. 1), and the contribution of the anodic-oxidation current of gold to the total anodic current becomes significant. Figure 10 illustrates the situation for the case where the $KAu(CN)_2$ concentration was 10^{-3}M. It is seen that the oxidation current of BH_3OH^-, designated as $i_{BH_3OH^-}$, must be calculated by subtracting the oxidation current of gold measured in the base electrolyte alone (0.2M KOH + 0.2M KCN) from the total anodic current i_a. Note that $i_{BH_3OH^-}$ is significantly greater than i_c in this case. This inequality was observed at all higher $KAu(CN)_2$ concentrations studied (up to 0.02M). In separate experiments it was found that gravimetrically determined deposition rates are equivalent to i_c rather than $i_{BH_3OH^-}$. These results show that the presence of $Au(CN)_2^-$ at concentrations greater than about 10^{-3}M does interfere with the anodic oxidation of BH_3OH^-. It is considered reasonable to ascribe this phenomenon to the adsorption of $Au(CN)_2^-$ on some of the sites where BH_3OH^- would adsorb if the solution did not contain $Au(CN)_2^-$.

Effect of $Ni(CN)_4^{--}$ on anodic oxidation of BH_3OH^-.— It was found that the $Ni(CN)_4^{--}$ ion exerts a similar effect on the oxidation of BH_3OH^-. This phenomenon is described here because the effect of $Ni(CN)_4^{--}$ is much more clearly visible than that of $Au(CN)_2^-$ owing to the fact that $Ni(CN)_4^{--}$ is not reduced in the potential range where BH_3OH^- is oxidized. Effects of 1×10^{-4} and 3×10^{-4}M $NiSO_4$[3] on the current-potential curve for the oxidation of BH_3OH^- are illustrated in Fig. 11 (curves 1-3). The reduction current of $Au(CN)_2^-$ is unaffected by nickel ions (curve 4). Striking similarities in the form of the two ions, $Ni(CN)_4^{--}$ and $Au(CN)_2^-$, and in their effect on the electrocatalytic activity of gold are noteworthy.

The poisoning effect of $Ni(CN)_4^{--}$ also accounts for the observation that the deposition rate of electroless gold decreases drastically when small amounts of nickel ions are added in the bath (18). A decrease in deposition rate with use of the bath was also noted when nickel metal was employed as substrate. This is due to the fact that the gold deposition on nickel metal takes place initially by the displacement reaction, in which nickel metal dissolves into the bath to

[3] In the 0.2M KOH-0.1M KCN mixture used, nickel is most likely to be present in the form of $Ni(CN)_4^{--}$ (17).

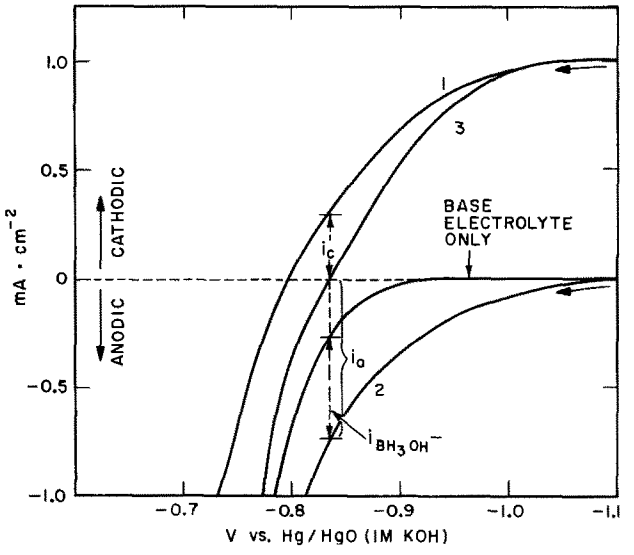

Fig. 10. Current-potential curves at gold electrode at 75°C. Conditions were the same as for Fig. 9 except that the $KAu(CN)_2$ concentration was 10^{-3}M.

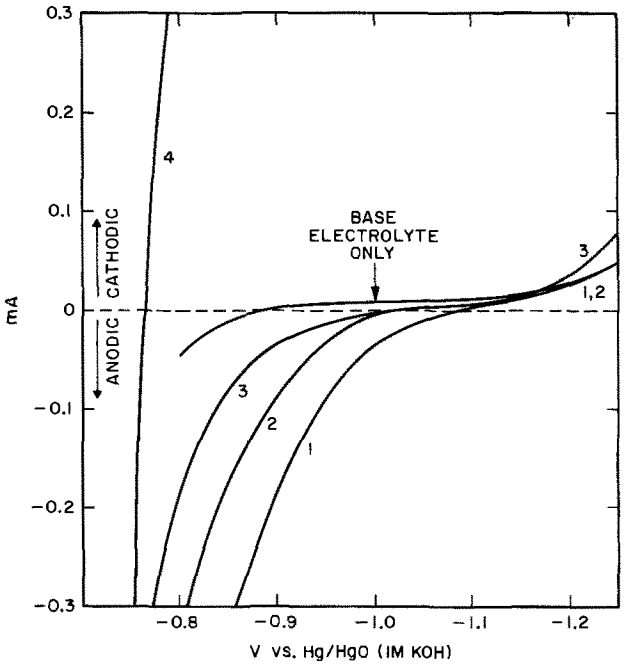

Fig. 11. Effect of nickel ions on anodic oxidation of BH_3OH^- at gold-plated rotating-platinum disk electrode (1600 rpm) at 75°C. Base electrolyte, 0.2M KOH + 0.1M KCN; curve 1, 0.1M KBH_4, no $NiSO_4$; curve 2, 0.1M KBH_4, 1×10^{-4} $NiSO_4$; curve 3, 0.1M KBH_4, 3×10^{-4}M $NiSO_4$; curve 4, 1×10^{-3}M $KAu(CN)_2$, no KBH_4, with or without 1×10^{-3}M $NiSO_4$.

form $Ni(CN)_4^{--}$ until it is completely covered with gold deposits.

Experimental evidences presented above are considered sufficient to support the originally proposed concept of competitive adsorption of $Au(CN)_2^-$ and BH_3OH^-. Further details of the reaction mechanism cannot be derived from the results of this study alone. However, based on the recent study of Holbrook and Twist (19) on the mechanism of surface-catalyzed hydrolysis of BH_4^-, it may be speculated that the chemisorption of BH_3OH^- is dissociative involving the splitting of B-H bonds to form adsorbed hydrogen atoms and boron-containing radicals. It is likely that the electrons necessary for reducing adsorbed $Au(CN)_2^-$ are supplied by the adsorbed boron-containing radicals, and two adsorbed hydrogen atoms simply combine with each other to form molecular hydrogen.

Summary and Conclusion

(*i*) The species that reduces $Au(CN)_2^-$ is BH_3OH^- and not BH_4^-. The former is an intermediate of the hydrolysis reaction of BH_4^-, and its concentration during the electroless deposition is only 2% or less of the initial BH_4^- concentration.

(*ii*) The pseudo first-order rate constants, k_1 and k_2, for the two stages of hydrolysis of borohydride ions were determined by the polarographic method in 0.2M KOH at 75°C. The values found were $k_1 = 3.29 \times 10^{-5}$ sec^{-1} and $k_2 = 1.43 \times 10^{-3}$ sec^{-1}. The addition of KCN decelerates the hydrolysis to a small extent.

(*iii*) Results of this study and the dependence of deposition rate on $KAu(CN)_2$ concentration reported previously (1) are both consistent with the assumption that the deposition process is preceded by competitive adsorption of $Au(CN)_2^-$ and BH_3OH^-.

Acknowledgment

The assistance of Mrs. C. Wolowodiuk in the polarographic experiment is gratefully acknowledged.

Manuscript submitted Dec. 15, 1972; revised manuscript received Jan. 30, 1973.

Any discussion of this paper will appear in a Discussion Section to be published in the December 1973 JOURNAL.

REFERENCES

1. Y. Okinaka, *Plating*, **57**, 914 (1970).
2. J. A. Gardiner and J. W. Collat, *J. Am. Chem. Soc.*, **86**, 3165 (1964).
3. J. A. Gardiner and J. W. Collat, *ibid.*, **87**, 1692 (1965).
4. J. A. Gardiner and J. W. Collat, *Inorg. Chem.*, **4**, 1208 (1965).
5. R. Sard, Paper 134 presented at Electrochem. Soc. Meeting, Cleveland, Ohio, October 3-7, 1971.
6. R. Sard, Y. Okinaka, and J. R. Rushton, *Plating*, **58**, 893 (1971).
7. R. E. Davis, E. Bromels, and C. L. Kibby, *J. Am. Chem. Soc.*, **84**, 885 (1962).
8. W. L. Jolly and T. Schmitt, *ibid.*, **88**, 4284 (1966).
9. J. P. Elder and A. Hickling, *Trans. Faraday Soc.*, **58**, 1852 (1962).
10. J. P. Elder, *Electrochim. Acta*, **7**, 417 (1962).
11. Y. Okinaka and C. Wolowodiuk, *Plating*, **58**, 1080 (1971).
12. I. M. Kolthoff and J. J. Lingane, "Polarography," Vol. 2, p. 541, Interscience Publishers, New York (1952).
13. J. O'M. Bockris and A. K. N. Reddy, "Modern Electrochemistry," Vol. 2, Chap. 10, Plenum Publishing Corp., New York (1970).
14. R. Sard and B. C. Wonsiewicz, Unpublished results.
15. V. S. Bagotzky, Yu. B. Vassiliev, and I. I. Pyshnograeva, *Electrochim. Acta*, **16**, 2141 (1971).
16. M. Maja, *Atti Accad. Sci. Torino: Classe Sci. Fis. Mat. Nat.*, **99**, 1111 (1965).
17. "Stability Constants," Special Publication No. 17, The Chemical Society, London, England (1964).
18. Y. Okinaka, R. Sard, W. H. Craft, and C. Wolowodiuk, Paper 206 presented at Electrochem. Soc. Meeting, October 8-13, 1972.
19. K. A. Holbrook and P. J. Twist, *J. Chem. Soc. (A)*, 890 (1971).

Electrolytic Oxidation of Nitroalkane Anions

S. Wawzonek* and Tsung-Yuan Su

Department of Chemistry, University of Iowa, Iowa City, Iowa 52240

ABSTRACT

Voltammetric studies have been carried out with nitroalkanes in basic buffers in aqueous medium. Similar studies in dimethylformamide and in methanol were limited to 2-nitropropane. Large scale electrolyses of 2-nitropropane were carried out in dimethylformamide and methanol and gave 2,3-dimethyl-2,3-dinitrobutane. In methanol, 1-nitropropane gave a low yield of 1,1-dinitropropane, and 2,5-dinitrohexane in the same solvent gave 2,5-hexanedione.

Studies of the electrochemical oxidation of nitroalkane anions in the past have dealt mainly with large scale electrolyses and report the formation of a variety of products. Phenylnitromethane and 9-nitrofluorene (1) form in alkaline solution 1,2-dinitro-1,2-diphenylethane and 9,9'-dinitro-9,9'-difluorenyl, respectively.

In aqueous alkali, 2-nitropropane gave 2,3-dimethyl-2,3-dinitrobutane and 2,2-dinitropropane; 2-nitrobutane behaved similarly. If the oxidation is carried out in the presence of sodium nitrite, the amount of the 2,2-dinitropropane is increased (2).

The cross-coupling of sodium nitrite with nitroethane (3) and 1,1-dinitroalkanes (4) gave 1,1-dinitroethane and 1,1,1-trinitroalkanes, respectively.

Primary nitroalkanes are oxidized to vicinal dinitroalkanes and olefins (5). On the other hand, 1,6-dinitrohexane gave no cyclohexane derivative (6).

The use of triethylamine as a base in nitromethane, nitroethane, and 2-nitropropane gave nitroethanol, 3-nitro-2-butanol, and acetone, respectively (7).

The free radical nature of the reaction was demonstrated by the electrolysis of anions from 2-nitropropane and nitrocyclohexane in the presence of styrene and ethyl vinyl ether. Products were obtained containing both monomers (8).

Voltammetric studies of the oxidation of nitroalkane anions has been limited to a report of the oxidation potential of nitroethane and 2-nitropropane in methanol-benzene (1:1) (8).[1] Information of this type was considered to be desirable in understanding the mechanism of the oxidation and in devising electrolysis conditions which would maximize the yields of the dinitro derivatives.

Experimental

Voltammetric studies were carried out using a microplatinum electrode which was rotated at a constant speed of 571 rpm.

General procedure.—The stock solution (1 ml) which contained 0.01*M* nitroalkane in 30% methanol, was added to 9 ml of the buffer and the resulting solution was degassed at 25°C with nitrogen for 20 min. Polarograms were recorded with a Sargent Model 21 polarograph. The proximity of the oxidation curves to the residual current required a correction for the latter in order to obtain the half-wave potentials and limiting currents. The values for the latter using the saturated calomel electrode as a reference electrode were usually higher and more irregular than those obtained with a mercury pool cathode.

Polarographic reductions were carried out at the DME in the same solution prior to the oxidation. Values for capillary characteristics are given in Table I.

The buffer solutions were prepared according to the procedure described by Robinson and Stokes (9). The *p*H values were checked with a Beckman *p*H meter.

Lithium 2-propanenitronate (10), potassium 2-propanenitronate (11), 3,5-dinitroheptane (12), and 2,5-dinitrohexane (6) were prepared according to the directions in the literature.

Nitromethane, nitroethane, 1-nitropropane, and 2-nitropropane were purified by distillation. Reagent grade methanol and reagent grade inorganic chemicals were used without further purification. Benzyltrimethylammonium methoxide (40% solution in methanol) was obtained from Aldrich Chemical Company and 2,5-hexanedione was obtained from Eastman Kodak Company.

General procedure.—Large scale electrolyses were carried out in a beaker with a rotating (571 rpm) platinum cylinder anode. The cathode was a copper wire coil and was placed in a porous porcelain cup. The procedure for a typical electrolysis is illustrated by the following. A solution of 2-nitropropane (44.5g) in 40% benzyltrimethylammonium methoxide in methanol (227g) was placed in a 600 ml beaker. The cathode

Table I. Voltammetric and polarographic behavior of nitroalkanes[a] (vs. SCE) in aqueous buffers

*p*H	$E_{1/2}$(anodic), RPE	$I^{b,c}_{lim}$	$E_{1/2}$(cathodic), DME	I_d
		CH_3NO_2[d]		
8	No wave	—	−0.91	12.83
11.2	0.91	9.6	−0.90	1.47
11.9	0.82	15.4	−0.90	0.11
		$CH_3CH_2NO_2$[d]		
8	No wave	—	−0.92	8.42
11.2	0.91	11.1	No wave	—
11.9	0.82	22.4	No wave	—
		$CH_3CH_2CH_2NO_2$[d]		
8	No wave	—	−0.90	7.49
11.2	0.90	11.4	No wave	—
11.9	0.82	14.0	No wave	—
		$CH_3CHNO_2CH_3$[d]		
8	No wave	—	−0.94	7.82
11.2	0.95	14.5	−0.97	2.34
11.9	0.85	17.0	No wave	—
		2,5-Dinitrohexane[e]		
8	No wave	—	−0.82	13.31
11.2	0.94	27.0	−0.94	1.74
11.9	0.84	47.4	No wave	—
		3,5-Dinitroheptane[f]		
8	No wave	—	−0.84	8.10
		—	−1.41	1.12
11.2	1.01	20.4	−0.93	1.43
11.9	0.82	46.6	−0.98	0.71
		Sodium nitrite[e]		
8	No wave	—	No wave	—
11.2	1.05	6.8	No wave	—
11.9	0.87	13.4	No wave	—

[a] Concentration 0.001*M*.
[b] I_{lim} = microamperes/millimole.
[c] All curves were normal S-shaped except for nitromethane at *p*H 11.9; the curve showed a drop at positive potentials.
[d] Capillary characteristics $m^{2/3}t^{1/6} = 1.486$ mg$^{2/3}$ sec$^{-1/2}$.
[e] Capillary characteristics $m^{2/3}t^{1/6} = 1.607$ mg$^{2/3}$ sec$^{-1/2}$.
[f] Capillary characteristics $m^{2/3}t^{1/6} = 1.969$ mg$^{2/3}$ sec$^{-1/2}$.

* Electrochemical Society Active Member.

Key words: 2-nitropropane, 2,3-dimethyl-2,3-dinitrobutane, voltammetry, large scale electrolyses.

[1] This work appeared after the completion of the present study.

Table II. Voltammetric behavior of alkali salts of nitroalkanes in dimethylformamide and in methanol

Compound[a]	Electrolyte	Cathode	$E_{1/2}$(anodic)	I_{11m}[b]
	Dimethylformamide			
$Li^+[(CH_3)_2CNO_2]^-$	0.1*M* $LiNO_3$	Hg pool	0.91	2.3
Hydroquinone	0.1*M* $LiNO_3$	Hg pool	1.30	5.0
	Methanol			
$K^+[CH_3CH_2CHNO_2]^-$	0.1*M* $LiNO_3$	Hg pool	0.79	4.6
		SCE	0.76	4.4
	0.1*M* $KOCH_3$	Hg pool	0.72	7.6
		SCE	0.68	7.7
$K^+[(CH_3)_2CNO_2]^-$	0.1*M* $LiNO_3$	Hg pool	0.72	4.4
		SCE	0.70	4.4
	0.1*M* $KOCH_3$	Hg pool	0.84	7.9
		SCE	0.65	7.3

[a] Concentration 0.001*M*.
[b] I_{11m} = microamperes/millimole.

compartment consisted of a 5.3 by 10 cm porous cup and was filled with 40% benzyltrimethylammonium methoxide in methanol. A voltage of 12V gave a current of 2A which was maintained at this value for 7 hr by adding more electrolyte to the cathode compartment and methanol to the anode compartment during the electrolysis. The anolyte was cooled and the solid was filtered and washed with water. The yield of essentially pure 2,3-dimethyl-2,3-dinitrobutane was 23g, mp 209°-210° [literature (2) 208°-209°]. A mixture with an authentic sample melted at the same point. The *IR* spectra were identical. The methanol filtrate when treated with water gave an additional 3g of the dinitro compound.

Data obtained from other electrolyses using the cell described are given in Table III. The 1,1-dinitropropane (13) and the 2,5-hexanedione were identified by comparison of their *IR* spectra with those of authentic samples.

Chemical dimerization.—A solution of 2-nitropropane (90g) in methanol (300 ml) containing potassium hydroxide (56g) was treated dropwise at room temperature with a solution of iodine (127g) in methanol (900 ml). The solution turned dark after 80% of the iodine solution was added and was refluxed for 2 hr. Partial removal of the methanol followed by cooling gave a solid which was washed with water. The yield of 2,3-dimethyl-2,3-dinitrobutane was 49g; mp 209°-210°.

Results and Discussion

Voltammetric oxidation of nitroalkane anions was carried out in aqueous buffers, in methanol, and in dimethylformamide. The formation of the anion in the buffers was monitored by observing the polarographic reduction waves at a dropping mercury electrode. The results obtained in aqueous alkaline buffers are given in Table I.

Similar studies in acetonitrile, dimethylformamide, and dimethylsulfoxide were prevented by low solubilities of the alkali salts of the nitroalkanes. Lithium 2-propanenitronate is an exception and is moderately soluble in dimethylformamide. The same salts are very soluble in methanol and were prepared before hand or generated in this solvent. The data obtained are listed in Table II.

The yields obtained in large scale electrolyses are listed in Table III.

Examination of the polarographic results in Table I indicate that the nitroparaffin reduction waves diminished in alkaline solutions to zero with two exceptions; this decrease is caused by the tautomeric change of the nitroparaffins into the aci-form, which was not reducible within the range of potentials (down to 2.0V) used (14).

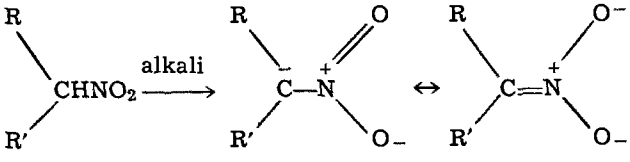

The two exceptions, nitromethane and 3,5-dinitroheptane, gave small waves in the pH 11.9 buffer. The wave for nitromethane is caused by the presence of a small amount of nitromethane. This compound has a pK_a of 10.24 (15) and therefore would not be converted completely to the anion.

The behavior of 3,5-dinitroheptane can be explained by a cleavage of this compound by alkali (reverse Michael reaction) to the anion of 1-nitropropane and 2-nitro-1-butene. The latter is converted by base to 2-nitro-1-butanol which undergoes a reverse aldol at

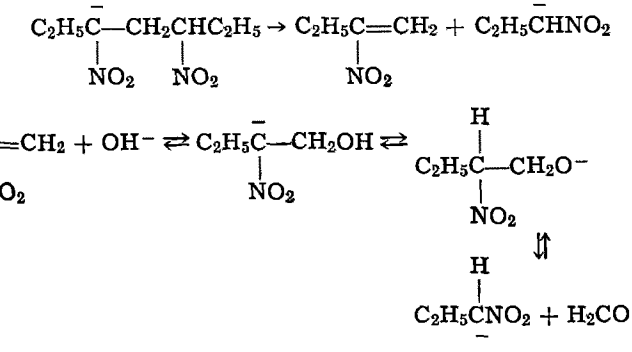

Table III. Large scale electrolyses of nitroalkanes

Compound	Electrolyte	Solvent	Conditions	Product yield
2-Nitropropane (44.5g)	40% Benzyltrimethylammonium methoxide (227g)	CH_3OH	12V, 2A, 7 hr	DMDNB[a] 58%
2-Nitropropane (89g)	40% Benzyltrimethylammonium methoxide (anolyte) (454g), 8.5% KOH-CH_3OH (catholyte)	CH_3OH	12V, 3A, 10 hr	DMDNB[a] 44%
Potassium 1-propanenitronate (40g)	0.3*M* $KOCH_3$	CH_3OH (100 ml)	13V, 0.4A, 17 hr, 0°, N_2	1,1-Dinitropropane 4.8%, KNO_2 (12.0g)
Potassium 2-propanenitronate	0.5*M* $KOCH_3$	CH_3OH (100 ml)	13V, 0.5A, 26 hr, 0°, N_2	DMDNB[a] 56%
2-Nitropropane (22.3g)	40% Benzyltrimethylammonium methoxide	CH_3OH (125 ml)	14V, 0.5-0.05A, 22 hr, 0°, N_2	DMDNB[a] 64%
Lithium-2-propanenitronate (9.5g)	1*N* $LiNO_3$	DMF (120 ml)	20V, 0.1-0.01A, 24 hr, 0°, N_2	DMDNB[a] 13%
2,5-Dinitrohexane (8g)	0.1*N* $KOCH_3$	CH_3OH	20V, 1.2-0.05A, 3 hr, 0°, N_2	2,5-Hexanedione 13.6%

[a] DMDNB = 2,3-dimethyl-2,3-dinitrobutane.

pH 8 since a reduction wave was observed for formaldehyde. The half-wave potential of −1.41 (SCE) is in good agreement with that reported in the literature (16). At higher pH values the reverse aldol reaction apparently does not occur since the formaldehyde wave is absent. The more positive reduction waves observed are probably due to the 2-nitro-1-butanol since the half-wave potentials approximate values reported by others (17).

The results in Table II indicate that a one-electron oxidation occurs for the 2-nitropropane anion; in dimethylformamide its limiting current is approximately one-half of that observed for hydroquinone.

The limiting current in methanol varies with the electrolyte employed. The low value observed in a lithium nitrate solution can be ascribed to the lower concentration of the anion which would result from the following reaction

$$K^+[(CH_3)_2CNO_2]^- + CH_3OH \rightleftarrows KOCH_3 + (CH_3)_2CHNO_2$$

The close proximity of the anodic wave for the nitroalkanes to the residual current in aqueous media offers an explanation for the 2,2-dinitropropane formed in the electrolytic oxidation of 2-nitropropane in basic medium. At this potential either hydroxyl radicals or oxygen is produced and cross-coupling or oxidation of the radical can occur (12) and forms acetone and nitrite ion. The latter oxidizes at 0.87 at a pH 11.9 and would cross-couple with the 2-nitropropyl radical and form 2,2-dinitropropane.

In order to avoid these complications large scale electrolyses were carried out in methanol and in dimethylformamide as solvents and the results are given in Table III. Methanol proved to be the superior solvent and gave the best yield of 2,3-dimethyl-2,3-dinitrobutane from 2-nitropropane, and in contrast to aqueous solutions (2) gave no 2,2-dinitropropane. The maximum yield obtained was 64% using a nitrogen atmosphere and a temperature of 0°. Electrolysis in the presence of air with no temperature control gave only a slightly lower yield of 58%. This lower yield is no doubt caused by oxygen diffusing into the reaction mixture and oxidizing the intermediate radical to acetone and nitrite (18). Both yields are much higher than that (15%) obtained in aqueous media (2).

A similar yield of dimer was obtained chemically by treating 2-nitropropane in methanol containing potassium hydroxide with iodine. The yield (55%) is smaller than that (86%) obtained by treating the sodium salt of 2-nitropropane with 2-bromo-2-nitropropane (19) but the reaction is simpler and can be carried out in one step.

One possible side reaction which can occur and would prevent better yields in the electrolytic method is the decomposition of the intermediate radical into acetone and nitric oxide. Such a decomposition has been observed in the electrolysis of nitroalkanes containing triethylamine as a base (7). The nitric oxide thus formed in methanol would result in methyl

$$(CH_3)_2\dot{C} - NO_2 \rightarrow CH_3C(=O) - CH_3 + NO$$

nitrite which is volatile. In aqueous basic medium sodium nitrite would be formed. This type of decomposition is substantiated by the results obtained with the electrolysis of 2,5-dinitrohexane in methanol with potassium methoxide as the electrolyte at 0° under nitrogen; a 13.0% yield of 2,5-hexanedione was isolated. The other products formed in this oxidation were a resin and a solid (3% based on 2,5-dinitrohexane) which was not investigated further because of the small amount available.

A primary nitroalkane such as 1-nitropropane gave in methanol similar products to those found in water. The coupled product in the anion form

$$CH_3CH_2CHNO_2 \rightarrow NO_2^- + CH_3CH_2CH(=CH_2)$$
$$CH_3CH_2\dot{C}(NO_2)^- \qquad\qquad CH_3CH_2\dot{C}(NO_2)$$

eliminates nitrite ion and the resulting potassium nitrite partially precipitates from the methanol and can be isolated. The yield of the cross-coupled product 1,1-dinitropropane, because of the small amount of dissolved sodium nitrite, was therefore low. Only a very small amount of a liquid with a boiling point corresponding to the unsaturated nitro compound was isolated. The majority of the product was a tar.

Acknowledgment

The authors wish to acknowledge the support of the United States Army Research Office under Contract DA 31-124-ARO-D-406, and Grant No. DA-ARO(D)-31-124-G 351. This paper is abstracted in part from the Ph.D. Thesis of Tsung-yuan Su, February 1967.

Manuscript submitted April 21, 1972; revised manuscript received Jan. 5, 1973.

Any discussion of this paper will appear in a Discussion Section to be published in the December 1973 JOURNAL.

REFERENCES

1. C. D. Nenitzescu and D. A. Isacescu, *Ber.*, **63**, 2491 (1930).
2. C. T. Bahner, *Ind. Eng. Chem.*, **44**, 317 (1952).
3. C. M. Wright and D. R. Levering, *Tetrahedron*, **19**, Suppl. 1, 3 (1963).
4. A. P. Hardt, F. G. Bogardt, W. L. Reed, and P. Noble, Jr., *Electrochem. Technol.*, **1**, 375 (1963).
5. C. T. Bahner, U.S. Pat. 2,485,803 (1949).
6. J. K. Stille and E. D. Vessel, *J. Org. Chem.*, **25**, 478 (1960).
7. R. Pearson and W. V. Evans, *Trans. Electrochem. Soc.*, **84**, 173 (1943).
8. H. Schäfer, *Chem.-Ing.-Tech.*, **41**, 179 (1969).
9. A. Robinson and R. H. Stokes, "Electrolyte Solutions," 2nd Edition, Butterworths, London, Academic Press, Inc., New York (1959).
10. N. Kornblum and P. Pink, *Tetrahedron*, **19**, Suppl. 1, 17 (1963).
11. H. Feuer and R. F. Vincent, Jr., *Anal. Chem.*, **35**, 598 (1963).
12. G. B. Bachman and M. T. Atwood, *J. Am. Chem. Soc.*, **78**, 484 (1956).
13. H. E. Ungnade and L. W. Kissinger, *J. Org. Chem.*, **22**, 1088 (1957).
14. E. W. Miller, A. P. Arnold, and M. J. Astle, *J. Am. Chem. Soc.*, **70**, 3971 (1948).
15. G. W. Wheland and J. Farr, *ibid.*, **65**, 1433 (1943).
16. R. Bieber and G. Trümpler, *Helv. Chim. Acta*, **30**, 1109 (1947).
17. W. J. Seagers and P. J. Elving, *J. Am. Chem. Soc.*, **72**, 3211 (1950).
18. G. A Russell and W. C. Danen, *ibid.*, **88**, 5663 (1966).
19. G. A. Russell and W. C. Danen, *ibid.*, **90**, 347 (1968).

Electrohydrodimerization Reactions

III. Rotating Ring-Disk Electrode, Voltammetric and Coulometric Studies of Mixed Reductive Coupling of Dimethyl Fumarate in the Presence of Cinnamonitrile and Acrylonitrile in Dimethylformamide Solution

Vincent J. Puglisi and Allen J. Bard

Department of Chemistry, University of Texas at Austin, Austin, Texas 78712

ABSTRACT

The electrohydrodimerization reaction of dimethyl fumarate in the presence of cinnamonitrile and acrylonitrile was studied in dimethylformamide solution by rotating ring-disk electrode, voltammetric and coulometric techniques. At potentials where only dimethyl fumarate is electroactive, the rate and mechanism of decay of the dimethyl fumarate anion radical are only slightly perturbed from the results obtained in the absence of cinnamonitrile and acrylonitrile. This is an indication that little or no cross-coupling was occurring. At potentials where both dimethyl fumarate and cinnamonitrile are electroactive evidence for the occurrence of a solution oxidation-reduction reaction consuming cinnamonitrile anion radical and dimethyl fumarate parent was obtained. In addition, the role of *cis-trans* isomerization of radical anions in electrohydrodimerization reactions is discussed. Differences in the cyclic voltammograms of diethyl maleate in the presence of acrylonitrile when compared with those obtained in the absence of acrylonitrile and for dimethyl fumarate in the presence of acrylonitrile are observed.

We have previously reported (1) the use of rotating ring-disk electrode (RRDE) voltammetry, cyclic voltammetry, and coulometry in the elucidation of the mechanism of the electrohydrodimerization (electrolytic reductive coupling) of the three di-substituted olefins dimethyl fumarate (DF), cinnamonitrile (CN), and fumaronitrile (FN) in anhydrous dimethylformamide (DMF) solution. Potential-step chronoamperometry has also been employed to determine the electrohydrodimerization mechanism of diethyl fumarate (2). These studies showed that these hydrodimerizations proceed predominantly via a one-electron reduction

$$R + e \rightleftarrows R^{\cdot -} \qquad [1]$$

followed by a radical ion dimerization (EC reaction scheme) for each olefin

$$2R^{\cdot -} \xrightarrow{k_2} R_2^{2-} \qquad [2]$$

It is also of interest to examine the hydrodimerization reaction of a disubstituted olefin in the presence of a second activated olefin (R') by RRDE voltammetry (3) and coulometric techniques. The aim was to explore the conditions under which formation of cross-coupled products can occur, thus obtaining more insight into the mechanism of electrolytic reductive coupling.

This approach was first undertaken by Baizer *et al.* (4-7). These investigators discovered cross-coupled products of the form $R'RH_2$ after electrolysis of aqueous-DMF solutions at mercury electrodes containing high concentrations (up to 5*M*) acrylonitrile (AN) at potentials where R, but not R', was electroactive. They attributed these results, on the basis of this as well as cyclic voltammetric evidence (8), to the occurrence of an ECE mechanism; *i.e.*, a one-electron reduction (Eq. [1]) followed by nucleophilic attack by the radical anion on the parent molecule

$$R^{\cdot -} + R \xrightarrow{k_2'} R_2^{\cdot -} \qquad [3]$$

to form the electroactive species $R_2^{\cdot -}$ which can undergo further reduction to yield the

$$R_2^{\cdot -} + e^- \rightarrow R_2^{2-} \qquad [4]$$

nonelectroactive species R_2^{2-}. They surmised that in the presence of a second olefin R', because of its greater concentration at the electrode surface when compared with R, nucleophilic attack by $R^{\cdot -}$ on R' to form the electroactive species

$$R^{\cdot -} + R' \xrightarrow{k_2''} (RR')^{\cdot -} \qquad [5]$$

$(RR')^{\cdot -}$ occurs. This species can undergo further reduction to yield a cross-coupled product (9)

$$(RR')^{\cdot -} + e^- \rightarrow (RR')^{2-} \qquad [6]$$

The ratio of cross-coupled product to simple dimer (R_2H_2) would be dependent on the concentration ratio of R and R', on the rate of formation of the cross-coupled product relative to the rates of formation of the simple dimers (R_2H_2 and R'_2H_2), and on the rates of formation of the simple dimers relative to each other. They also found that the yield of cross-coupled product was substantially increased when electrolysis was conducted at potentials where both R and R' were reduced; this is an indication that cross-coupling via a radical ion-radical ion-coupling mechanism was occurring at a faster rate than the ECE

$$R^{\cdot -} + R'^{\cdot -} \rightarrow (RR')^{2-} \qquad [7]$$

mechanism postulated in Eq. [5] and [6].

Dimethyl fumarate was chosen to serve as the species R. Its radical decay rate constant (*i.e.*, dimerization rate constant) is at the lower limit of rate constants measurable with the particular RRDE used and thus any increase in the velocity of that reaction, as explained above, would still result in reasonable current levels at the ring. Also, the $E_{1/2}$ of its first reduction occurs well before that of cinnamonitrile and acrylonitrile (AN), the two species which would function as the R' species. CN was chosen because its hydrodimerization has been studied (1), because its second-order rate constant is only eight times that of dimethyl fumarate, and because it is more difficult to reduce than dimethyl fumarate. Acrylonitrile was chosen because of its use in previous studies (4-7). The mechanism and rate of dimerization of AN, however, have not been determined because the electrogenerated product reacts very quickly (9).

The diagnostic criteria which were used to determine the reaction path consisted of a qualitative examina-

* Electrochemical Society Active Member.

Key words: reductive coupling, electrochemical dimerizations, cross-coupled products, *cis-trans* isomerization.

tion of the dependence of the ring current (i_r) on disk potenital (E_d) at constant ring potential (E_r), a quantitative examination of the dependence of the kinetic collection efficiency, N_K, on the rotation rate and concentration ($XKTC$) (10-12), where

$$XKTC = (0.51)^{-2/3}\nu^{-1/3}D^{1/3}C^{\circ}\omega^{-1}k_2 \quad [8]$$

and ν is the kinematic viscosity, D is the diffusion coefficient, C° is the initial concentration, ω is the rotation rate, and k_2 is the second-order homogeneous rate constant, on the behavior of N_K with various disk currents ($CONI$) (3)

$$CONI = i_d/i_{d,l} \quad [9]$$

where i_d is the disk current and $i_{d,l}$ is the disk current at the limiting current plateau, and finally, controlled potential coulometric analysis.

Experimental

Reagents.—N,N-dimethylformamide (DMF), obtained from Baker Chemical Company, was purified by vacuum distillation and stored under He. Solvent purity was ascertained by cyclic voltammetric analysis of DMF solutions of tetrabutylammonium iodide (TBAI) obtained from Southwestern Analytical Chemicals, Inc. TBAI and tetrabutylammonium perchlorate (TBAP), also obtained from Southwestern Analytical Chemicals, Inc., were vacuum dried and stored over Drierite. Dimethyl fumarate (DF), sublimed prior to use, and cinnamonitrile, used as received, were obtained from K. and K. Laboratories. Acrylonitrile, Matheson, Coleman and Bell Chemicals, was used as received.

Apparatus.—A Tascussel Electronique Bipotentiostat, Model Bipad 2, was used for all RRDE experiments. A Digitec digital voltmeter, Model 204, and a Fairchild digital multimeter, Model 7050, were used to measure the steady-state ring and disk currents simultaneously. A Wavetek function generator provided a d-c potential ramp for voltammetric experiments recorded on a Mosley Model 2D-2 X-Y recorder. The platinum-Teflon rotating ring-disk electrode, having a disk radius (r_1) of 0.187 cm and inner (r_2) and outer (r_3) ring radii of 0.200 and 0.332 cm, respectively, was constructed by Pine Instrument Company, Grove City, Pennsylvania. The maximum collection efficiency, N, for the RRDE used in these experiments was 0.555 (1). The electrochemical cell, dispensing vessel, and motor and controller used to rotate the RRDE have been described previously (1). The reference electrode was a silver wire spiral (Ag-RE) whose potential was dependent on the identity and concentration of the supporting electrolyte. TBAI was used as supporting electrolyte in all RRDE experiments. A Model 170 Electrochemistry System (Princeton Applied Research, Princeton, New Jersey) was employed for all controlled potential coulometric experiments. A conventional coulometry cell was used. In these experiments, a platinum gauze served as the working electrode and a platinum spiral as the auxiliary. A saturated calomel electrode (SCE) was used as the reference electrode. The reference and auxiliary compartments were separated from the cathode compartment by medium porosity glass frits.

Procedure.—DMF, dispensed from the storage vessel into the dispensing vessel by positive He pressure, together with supporting electrolyte and, in most cases, the depolarizer, was subjected to a minimum of three freeze-pump-thaw cycles. In experiments where CN was present, it was first necessary to conduct a pre-electrolysis to remove an electroactive impurity present in the CN prior to addition of the DF. This was carried out at a Hg pool electrode in the RRDE electrochemical cell. In these experiments the DF concentration was determined from a working curve of the disk limiting current ($i_{d,l}$) *vs.* concentration. This curve was compiled from measurements on solutions of dimethyl fumarate in the absence of cinnamonitrile and validated with known mixtures of DF and CN.

Results

Dimethyl Fumarate-Cinnamonitrile

Electrochemical generation of the DF radical ion.—RDE voltammograms of DF and CN are illustrated in Fig. 1 and 2. DF (Fig. 1a) exhibits a one-electron reduction with half-wave potential, $E(i = i_{d,l}/2)$ of -0.8V *vs.* silver reference electrode (Ag-RE) followed by a current dip commencing at approximately -1.55V. This dip has been shown to occur at potentials corresponding to formation of the dianion and has been interpreted as resulting from polymerization initiated by that ion (8). Curve b is a ring current (i_r) *vs.* disk potential (E_d) trace with the ring potential (E_r) maintained at a constant value of 0.0V *vs.* Ag-RE. The ring current increase results from oxidation of the DF radical anion being formed at the disk electrode. At sufficiently negative disk potentials ($E_d > -1.55$V) reduction of DF to the dianion begins and the ring current decreases because of instability of the dianion in solution.

Figure 2 curves a and b, which describe the CN system, are analogous in interpretation to curves a and b in Fig. 1, respectively. The CN dianion participates to a lesser extent in polymerization reactions than does the DF dianion, thus an increase in cathodic current and a reduction wave 1.5 times the height of the first wave results. The half-wave potentials of the one- and two-electron reductions for CN are -1.21 and -1.83V, respectively.

Figure 3, curve a, shows a disk current-potential trace of the mixed DF-CN system in 0.15*M* TBAI-DMF. For convenience this voltammogram will be considered as consisting of four regions, as shown. Comparison with Fig. 1 and 2 reveals that reductions occurring in regions 1 and 3 can be ascribed to DF reductions, whereas those in regions 2 and 4 are CN reductions. The DF one-electron reduction limiting current is, within experimental error, unchanged upon addition

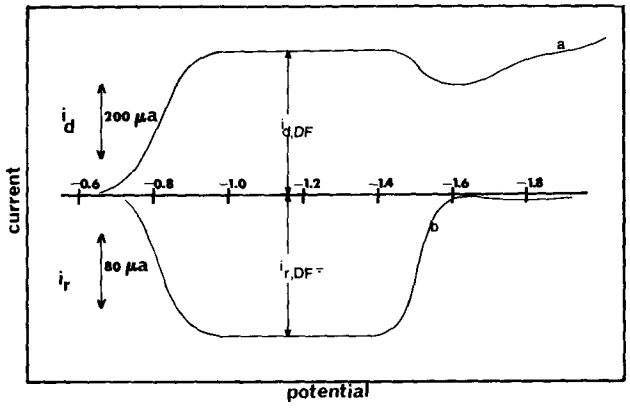

Fig. 1. Dimethyl fumarate (8.2 mM) RRDE voltammograms in 0.15M TBAI-DMF solution. $\omega = 47.6$ sec^{-1}; (a) i_d *vs.* E_d and (b) i_r *vs.* E_d, $E_r = 0.0$V.

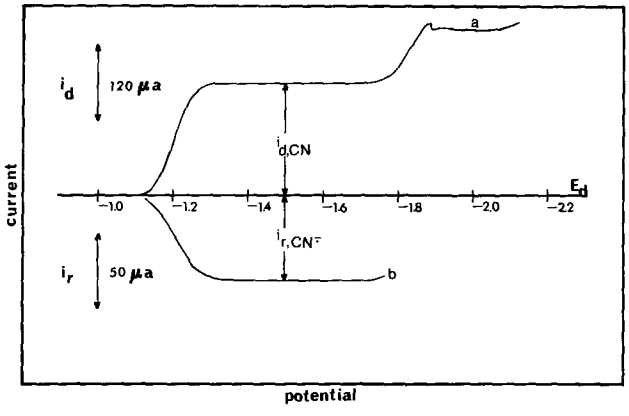

Fig. 2. Cinnamonitrile (3.8 mM) RRDE voltammograms determined at $\omega = 47.6$ sec^{-1}; (a) i_d *vs.* E_d and (b) i_r vs. E_d, $E_r = 0.0$V.

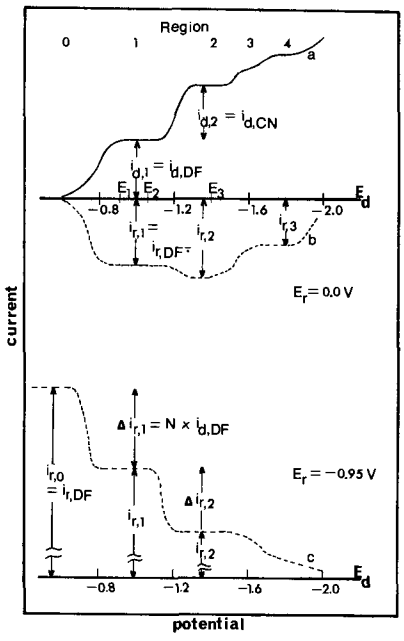

Fig. 3. Typical DF-CN RRDE voltammograms: (a) i_d vs. E_d; (b) i_r vs. E_d, $E_r = 0.0$V; and (c) i_r vs. E_d, $E_r = -0.95$V.

of CN. Further, the disk limiting current plateau (curve a, region 1), as well as the ring current plateau (curve b, region 1), exhibits essentially zero slope; evidence that processes occurring at the potential denoted E_1 do not differ from those at E_2. These results differ from those obtained from product analysis after exhaustive electrolysis of diethyl maleate (DEM) (6), where it was found that the products varied as a function of the working electrode potential and it was concluded that the processes occurring on the DEM limiting current plateau are a function of the applied potential in the mixed system.

Determination of N_K as a function of *CONI* for $i_d < (i_{d,l})_a$, where $(i_{d,l})_a$ is the DF limiting disk current in region 1, resulted in the experimental data shown in Fig. 4 and tabulated in Table I. This trend, N_K increasing with increasing 1-*CONI*, is the one reported to be characteristic of the EC dimerization mechanism

Table I. Collection efficiency (N_K) for dimethyl fumarate reduction as a function of the disk current

Compound (conc-m*M*)						
Olefin R	Olefin R′	ω (sec^{-1})	i_r (μA)	i_d (μA)	N_K	*CONI*
Dimethyl fumarate (1.85)	Cinnamonitrile (3.85)	47.6	4.4	8.0	0.550	0.080
			8.8	16.4	0.536	0.164
			14.4	26.0	0.554	0.260
			20.8	37.6	0.553	0.376
			24.8	45.6	0.544	0.456
			30.8	59.0	0.522	0.590
			35.6	68.0	0.524	0.680
			40.8	79.0	0.517	0.790
			45.2	89.0	0.508	0.890
			46.8	93.0	0.503	0.930
Dimethyl fumarate (8.19)	Acrylonitrile (200)	98.6	17	42	0.405	0.080
			40	88	0.454	0.169
			70	140	0.500	0.268
			91	186	0.489	0.356
			105	222	0.473	0.425
			137	288	0.476	0.552
			152	336	0.452	0.644
			166	378	0.439	0.724
			179	418	0.428	0.800
			188	452	0.416	0.866
			218	518	0.421	0.992

(Eq. [2]), but not of ECE mechanisms II and III (3). N_K *vs.* 1-*CONI* theoretical curves for the EC mechanism with *XKTC* equal to 0.06 and 0.25 are also given in Fig. 4. Calculation of the second-order rate constant for dimerization of DF anion radicals yields a value of $1.1 \pm 0.1 \times 10^2$ liter/mole-sec; the same value is obtained in the absence of CN (1).

A theoretical curve depicting the dependence of N_K on *XKTC* for the EC (I) mechanism, together with experimental values of N_K measured at potentials on the DF limiting current plateau and determined as functions of the rotation rate, are presented in Fig. 5. It can be seen that the experimental points closely fit the curve generated for the radical ion dimerization mechanism; this provides additional evidence that mechanism I is the path of choice, even in the presence of a second olefin.

These similarities, both qualitative and quantitative, which appear in the RRDE experimental dimethyl fumarate currents measured in the presence and in the absence of cinnamonitrile, are also evident from cyclic voltammetric studies. Figure 6 shows cyclic voltammograms of DF (curve a), CN (curve b), and the mixed DF-CN system (curves c and d). As with the RRDE data, curves c and d can be compared with curves a and b for purposes of assignment. The first reduction of DF exhibits a sizable anodic current on

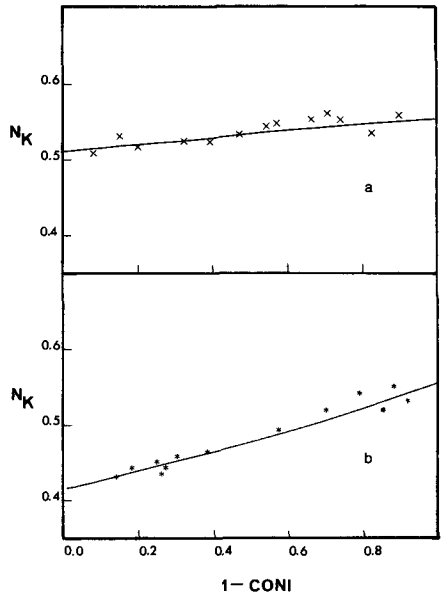

Fig. 4. Dimethyl fumarate collection efficiency (N_K) vs. 1-*CONI* at $\omega = 47.6$ sec^{-1} in the presence of cinnamonitrile: (a) DF = 1.85 mM and CN = 3.85 mM; (b) DF = 7.3 mM and CN = 3.8 mM. Solid lines are theoretical curves corresponding to mechanism I and (a) *XKTC* = 0.06 and (b) *XKTC* = 0.25.

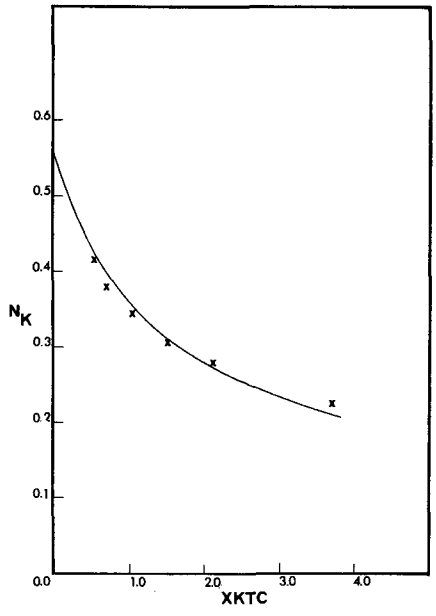

Fig. 5. Dimethyl fumarate (1.8 mM) collection efficiency (N_K) vs. *XKTC* plot in the presence of cinnamonitrile (3.8 mM). Solid line corresponds to the theoretical curve depicting the behavior of N_K for mechanism I.

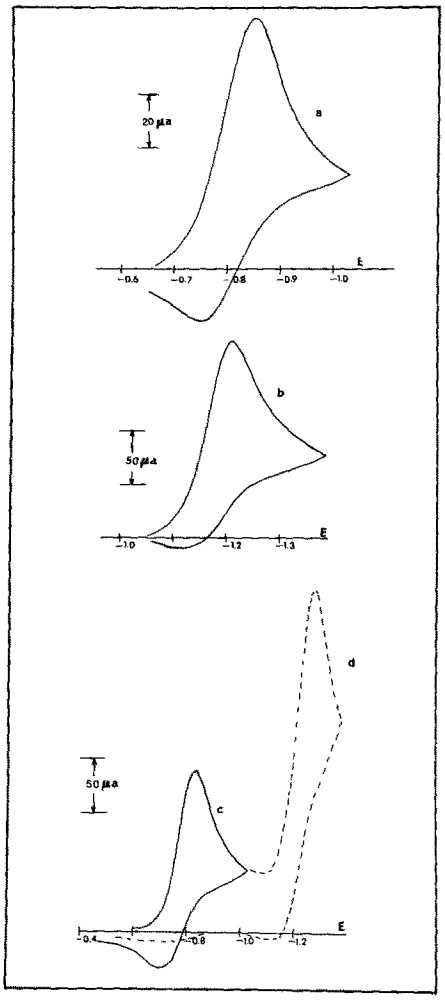

Fig. 6. Cyclic voltammograms recorded at 0.1 V/sec; (a) dimethyl fumarate (3.5 mM); (b) cinnamonitrile (2.6 mM); (c) dimethyl fumarate (1.8 mM), cinnamonitrile (3.8 mM); and (d) same as (c).

reversal (curve a) even in the presence of cinnamonitrile (curve c). The ratio of peak currents ($i_{p_l DF^-}/i_{plDF}$) and the peak current function ($i_{plDF}/C^o_{DF}V^{1/2}$) were found to be 0.38 and 96 μA/mM V sec^{-1}, respectively, in the absence, and 0.42 and 99 μA/mM V sec^{-1} in the presence of CN.

In addition, coulometric analysis at -1.425V *vs.* SCE, a potential on the DF first reduction current plateau but positive of potentials necessary for reduction of CN, resulted in an n_{app}-value of 0.63 for an equimolar DF-CN solution. The n-value predicted by each of the postulated hydrodimerization mechanisms is one (3). An n_{app}-value less than one results because of the occurrence of polymerization side reactions during the time scale of the coulometric experiment. Coulometry at -1.625V *vs.* SCE in the absence of cinnamonitrile yielded an n_{app}-value of 0.62. If the ECE mechanism involving reactions [5] and [6] occurred, the n_{app} in the presence of CN should have been greater than 0.62, and possibly even greater than one.

Simultaneous electrochemical generation of the dimethyl fumarate ($DF^{-\cdot}$) and cinnamonitrile ($CN^{-\cdot}$) radical anions.—To determine the extent of cross-coupling arising from a radical ion-radical ion mechanism (Eq. [7]), an examination of the DF-CN mixed system at potentials where both DF and CN undergo reduction to form their respective radical anions was undertaken.

Ring current *vs.* disk potential voltammograms where $E_r = 0.0$V (curve b) and $E_r = -0.95$ (curve c) are shown in Fig. 3. Curve b shows the oxidation of electroactive species being formed at the disk during processes shown in Fig. 3a or of any electroactive species being formed from reactions of disk products. From the study of the DF radical anion alone, we know that the ring current in region 1 under the electrode conditions imposed to obtain curve b [denoted $(i_{r,1})_b$] results solely from oxidation of the DF radical anion. If there were no interaction in the bulk between DF parent or radical anion and CN parent or radical anion, the measured ring current, $(i_{r,2})_b$, would simply equal the sum, $i_{r,s}$, of the DF and CN ring currents measured independently (*i.e.*, the ring currents i_{r,DF^-} and i_{r,CN^-} illustrated in Fig. 1 and 2, respectively). This is not the case and $i_{r,s}$ is greater than $(i_{r,2})_b$. Typical experimental values are given in Table II. These experimental values were collected at various concentrations and rotation rates. To determine the magnitude of the current contribution to $(i_{r,2})_b$ from oxidations other than that of the DF radical anion, the experiment recorded as Fig. 3c was conducted. The ring current $(i_{r,0})_c$, results from reduction of DF at the ring electrode. At disk potentials sufficiently negative (*e.g.*, $E = E_1$, shown in Fig. 3a), DF reduces at the disk and a decrease, $\Delta(i_{r,1})_c$, in the cathodic current measured at the ring electrode results because of a decrease in the amount of DF reaching the ring. This is termed shielding and $\Delta(i_{r,1})_c$ equals N times $(i_{d,1})_a$, the DF disk limiting current shown in Fig. 3a, region 1. The DF radical anion is not oxidized at the potential applied at the ring electrode and is, therefore, not detected. At more negative disk potentials (*i.e.*, Fig. 3a, $E = E_3$) both DF and CN are reduced at the disk electrode to the respective radical anions

$$DF + e^- \rightarrow DF^{-\cdot} \quad \text{(at the disk electrode [Fig. 3a, region 2])} \quad [10]$$

$$CN + e^- \rightarrow CN^{-\cdot} \quad [11]$$

and a second decrease in the ring current, $(\Delta i_{r,2})_c$ is observed. The measured current, $(i_{r,2})_c$, is the sum of two currents; a cathodic current component resulting from the one-electron reduction of DF and an anodic current component resulting from the oxidation of the CN radical anion

$$DF + e^- \rightarrow DF^{-\cdot} \quad \text{(at the ring electrode [Fig. 3c, region 2])} \quad [12]$$

$$CN^{-\cdot} - e^- \rightarrow CN \quad [13]$$

Table II. Disk and ring currents at different values of E_d and E_r*

Concentration (mM)										
DF	CN	ω	$(i_{d,1})_a$	$(i_{d,2})_a$	$(i_{r,1})_b$	i_{r,CN^-}	$(i_{r,2})_b$	$(i_{r,3})_b$	$\Delta(i_{r,1})_c$	$\Delta(i_{r,2})_c$
1.62	2.46	47.6	112	123	55	30	74	47	—	68
1.62	2.46	67.2	133	137	66	42	88	54	79	78
2.20	4.42	47.6	152	226	69	52	87	65	96	92
2.20	4.42	98.6	208	311	98	91	148	108	104	158
2.85	3.10	47.6	143	144	68	—	94	52	78	63
3.78	3.58	47.6	178	174	84	44	104	60	104	82

* DMF solution containing 0.15*M* TBAI. See Fig. 3 for definition of terms. All currents in microamperes.

At the applied ring potential, neither the CN parent nor the DF radical are electroactive. The current decrease, $|\Delta(i_{r,2})_c|$, cannot result simply from oxidation of the cinnamonitrile radical anion, since $|\Delta(i_{r,2})_c| > |(i_{r,CN^{\cdot-}})|$, where $i_{r,CN^{\cdot-}}$ is the ring current resulting from oxidation of CN radical anion in the absence of DF (Fig. 2b and Table II). For example, item 6 in Table II shows that the $CN^{\cdot-}$ ring current (*i.e.*, $|i_{r,CN^{\cdot-}}|$) for C = 3.58 m*M* and $\omega = 47.6$ sec^{-1} in the absence of DF is 44 μA. The decrease in the ring current, $\Delta(i_{r,2})_c$, is 82 μA. One would have anticipated a decrease less than or equal to 44 μA, but not greater than this if oxidation of $CN^{\cdot-}$ were the only additional process occurring in this region. Radical ion-radical ion cross-coupling could occur but this would decrease the stability of the CN and DF radical anions, leading to a smaller value of $\Delta(i_{r,2})_c$. One must also take into account, however, the occurrence of the electron transfer reaction

$$CN^{\cdot-} + DF \rightarrow CN + DF^{\cdot-} \qquad [14]$$

In the absence of any other kinetics (*e.g.*, dimerization) contributing to the instability of the species $CN^{\cdot-}$ and DF, the occurrence of reaction [14], in terms of measured ring current at $E_r = -0.95$, would have no observable effect and $\Delta(i_{r,2})_c$ would equal *N* times $i_{d,CN}$, where $i_{d,CN}$ is the CN disk limiting current. However, in this case both $DF^{\cdot-}$ and $CN^{\cdot-}$ undergo further dimerization reactions ([15] and [16]). Moreover, the rate constant of the CN dimerization reaction

$$2CN^{\cdot-} \rightarrow (CN)_2^{2-} \qquad [15]$$

is about eight times larger than that of the DF dimerization reaction (1)

$$2DF^{\cdot-} \rightarrow (DF)_2^{2-} \qquad [16]$$

Hence, the effect of reaction [14], if its rate is much larger than that of reaction [15], is to remove a less stable intermediate ($CN^{\cdot-}$) and form a more stable one ($DF^{\cdot-}$) in transit from disk to ring. This leads to a smaller amount of DF available for reduction at the ring and hence a larger-than-expected value of $\Delta(i_{r,2})_c$. This hypothesis, *i.e.*, the effect of the oxidation-reduction represented in Eq. [14], is supported by digital simulation of the RRDE experimental conditions.

This program assumed that the disk electrode was maintained at a potential where reduction of DF (Eq. [10]) and CN (Eq. [11]) to their respective radical anions proceeded at mass transfer controlled rates. The ring electrode was maintained at a potential where mass transfer controlled oxidation of the CN radical anion (Eq. [13]) and reduction of DF parent (Eq. [12]) occurs. Three homogeneous reactions were assumed to occur in the gap region: the radical ion-radical ion dimerizations of DF (Eq. [16]) and CN (Eq. [15], and the oxidation-reduction reaction represented in Eq. [14]). The rate constants for the DF (1.1×10^2 liters/mole-sec) and CN (8.8×10^2 liters/mole-sec) dimerizations, together with the specific experimental conditions (*e.g.*, concentrations, diffusion constant, etc.), were used to calculate the appropriate *XKTC* values. The oxidation-reduction reaction was assumed to occur at a diffusion-controlled rate. The simulation output parameters of interest were a dimensionless current parameter proportional to the disk current, and dimensionless current parameters proportional to the currents resulting from reduction of the DF and from oxidation of the CN radical anion at the ring electrode.

The current decrease, $\Delta(i_{r,2})_c$, was found to occur totally from a decline in the cathodic current due to loss of DF parent species in transit to the ring electrode, and with essentially no contribution to the current decrease from anodic current resulting from oxidation of the $CN^{\cdot-}$ species. That is, the velocity of the reaction represented in Eq. [14] is of such a high order of magnitude that the CN dimerization does not successfully compete with that reaction and all the $CN^{\cdot-}$ is consumed in reaction [14]. Under these conditions, the simulation accounted for approximately 90% of the experimentally measured current, $\Delta(i_{r,2})_c$.

Cyclic voltammograms of the DF-CN system show no oxidizable species other than the DF and CN radical anions that were observed. In addition a coulometric experiment, in which a solution of DF and CN, in approximately equimolar concentrations, electrolyzed at −1.90V *vs.* SCE was carried out. This potential is sufficient to produce both the DF and CN radical anions but not negative enough to produce the DF dianion. An over-all n_{app}-value of 0.81 was obtained. The average n_{app}-value obtained for the CN reduction in the absence of DF was 0.96. Assuming $n = 1.0$ for the CN reduction, the n_{app}-value for DF in the presence of CN is 0.64, essentially the same value obtained in the absence of CN. This value is less than that anticipated if the cross-coupling reaction [Eq. 7] was occurring to an appreciable extent, since this should reduce the extent of polymerization and result in $0.62 < n_{app} < 1.0$. The unchanged n_{app}-value for DF suggests that the DF radical anion is effectively insensitive to the presence of CN parent and the CN radical anion being electrochemically generated. The equivalents *vs.* time (*t*) and the current (*i*) *vs.* time curves for this experiment are shown in Fig. 7. The presence of two slopes in the equivalent *vs.* *t* curve and the break in the *i vs.* *t* curve indicate the possible existence of two consecutive reductions as opposed to two simultaneous reductions, although simultaneous reduction of DF and CN is occurring at the potential of the working electrode. The coulometric data can be explained by the occurrence of the oxidation-reduction reaction (Eq. [14]) in the bulk solution. The $CN^{\cdot-}$ produced at the electrode reacts with DF parent to yield CN parent and $DF^{\cdot-}$. Until a sizable amount of the DF parent has been consumed, the electrolysis is completely characteristic of a DF electrolysis, but at a faster rate than the controlled potential electrolysis of DF alone because of the additional coulometric titration of DF by $CN^{\cdot-}$. Thus, the coulometric, as well as the RRDE, results point to the importance of the oxidation-reduction reaction represented in Eq. [14], in the over-all reaction scheme.

Simultaneous electrochemical generation of the dimethyl fumarate dianion (DF^{2-}) and the cinnamonitrile radical anion.—In the DF-CN mixed system, the current dip anticipated at potentials where formation of the DF dianion commences, Eq. [17] does not occur, but instead additional cathodic current (Fig. 3a, re-

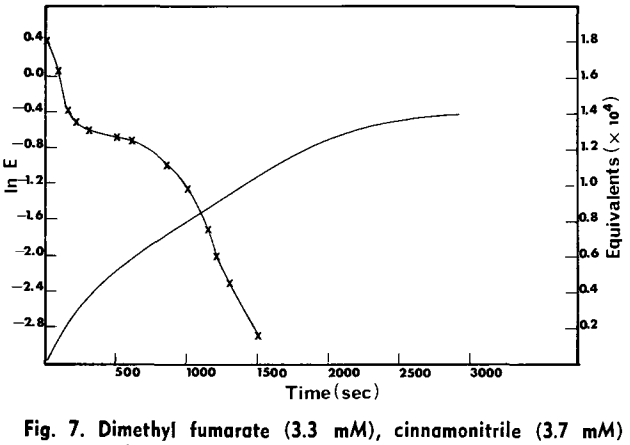

Fig. 7. Dimethyl fumarate (3.3 mM), cinnamonitrile (3.7 mM) equivalents electrolyzed *vs.* time (*t*) and current (*i*) *vs.* time experimental curves.

gion 3) results.

$$DF + 2e^- \rightarrow DF^{2-} \quad [17]$$

A possible explanation for the increase in cathodic current here is either the formation of an electroactive cross-coupled dimer

$$DF^{2-} + CN \rightarrow [(DF)(CN)]^{2-} \quad [18]$$

or the occurrence of the redox reaction

$$DF^{2-} + CN \rightarrow DF^{\cdot -} + CN^{\cdot -} \quad [19]$$

Either [18] or [19] would be expected to compete with polymerization of DF

$$DF^{2-} + p\,DF \rightarrow (DF)_{p+1}{}^{2-} \quad [20]$$

resulting in increased currents.

Dimethyl Fumarate-Acrylonitrile

Dimethyl fumarate in the presence of acrylonitrile (AN).—Figure 8 illustrates typical disk current-potential (curves a, b, and c) as well as ring current-disk potential (curves d and e) scans obtained at constant ring potential (E_r = 0.0V *vs.* Ag-RE) for DF in the absence (curves a, b, and d) or presence (curves c and e) of AN. The significance of curve a has been explained. Curve b is a voltammogram of a quiescent solution ($\omega = 0$). Curve c is a repeat of curve a following the addition of 0.2*M* AN. Curves d and e represent the ring current recorded as a function of disk potential while the disk electrode is simultaneously undergoing the processes shown in curves a and c, respectively. Values of N_K measured in the absence and in the presence of AN are given in Table III. In approximately equimolar concentrations there is no apparent perturbation. When AN is present in large excess, the rate of decay of the dimethyl fumarate radical is seen to increase as a function of DF concentration, but not to the extent anticipated were the ECE mechanism a major path. The N_K *vs.* 1-*CONI* plots for $i_d < i_{d,DF}$ are consistent with the trend predicted by digital simulation techniques for the EC dimerization (mechanism I) being the primary reaction path (Fig. 9).

Cyclic voltammetric studies reveal that the $DF^{\cdot -}$ has a measurable lifetime even in the presence of 0.2*M* AN

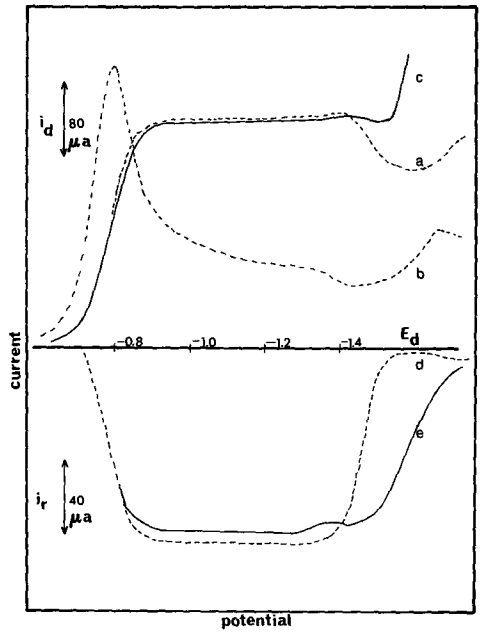

Fig. 8. Dimethyl fumarate (4.8 mM) RRDE voltammograms; (a) i_d *vs.* E_d, ω = 47.6 sec^{-1}; (b) i_d *vs.* E_d, ω = 0; (c) i_d *vs.* E_d, ω = 47.6 sec^{-1}, AN (0.2M) present; (d) i_r *vs.* E_d, E_r = 0.0V, ω = 47.6 sec^{-1}; and (e) i_r *vs.* E_d, E_r = 0.0V, ω = 47.6 sec^{-1}; 0.2M AN present.

Table III. RRDE collection efficiency data for the dimethyl fumarate radical anion

Concentration (mM)			
DF	AN	ω (sec^{-1})	N_K
4.0	0	47.6	0.480
		67.2	0.501
4.0	~4	47.6	0.475
		67.2	0.500
4.8	0	47.6	0.436
4.8	200	47.6	0.422
8.2	0	47.6	0.394
8.2	200	47.6	0.356

(Fig. 10). The $(E_p)_c$ remained unchanged but $(i_p)_c$ exhibited a 5% decrease.

Controlled potential coulometric experiments employing potentials sufficient to reduce DF to the radical anion but insufficient to reduce AN were undertaken. The results are presented in Table IV. The n_{app}-values given for a single solution were obtained by the addi-

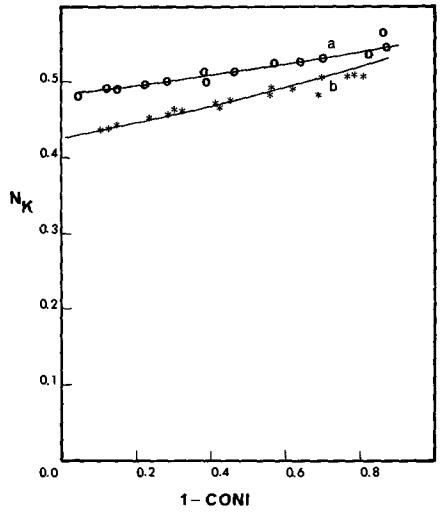

Fig. 9. Collection efficiency (N_K) vs. 1-*CONI* at ω = 47.6 sec^{-1} for 4.0 mM (o) and 4.8 mM (*) dimethyl fumarate solution in the presence of 0.2M acrylonitrile. Solid lines are theoretical curves corresponding to mechanism I and *XKTC* = (a) 0.12 and (b) 0.25.

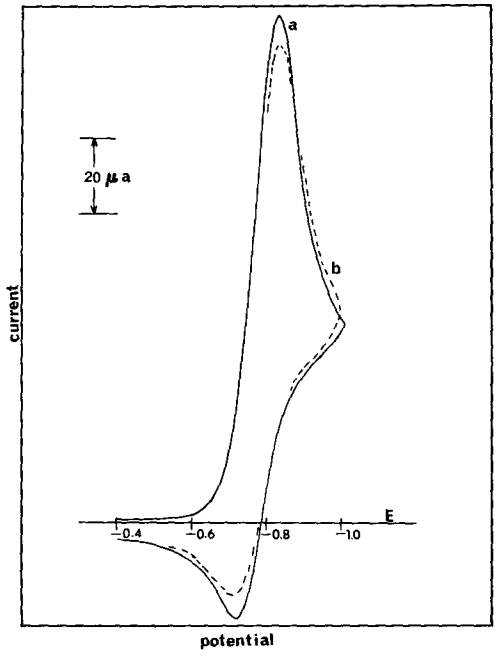

Fig. 10. Dimethyl fumarate (4.8 mM) cyclic voltammograms recorded at 0.1 V/sec; (a) acrylonitrile absent, (b) acrylonitrile (0.2M) present.

Table IV. Coulometric results for mixtures of dimethyl fumarate and acrylonitrile[a]

Solution	E (vs. SCE)	Moles present DF (×10⁴)	Moles present AN	n_{app}-value
1	−1.625	0.66	0	0.62
2	−1.450	1.10	Equimolar	0.62
	−1.600	0.98	Equimolar	0.76
	−1.525	1.07	Equimolar	0.78
	−1.450	1.02	Equimolar	0.79
3	−1.750	1.09	Large excess	0.77
	−1.550	1.00	Large excess	0.80

[a] The solution was 0.15*M* TBAI in DMF and the working electrode was Pt.

tion of a DF sample following exhaustive electrolysis of the previous sample. The average n_{app} was 0.78. Thus, the presence of AN does perturb, on the coulometric time scale, the following reaction of the DF radical. Whether this perturbation in the n_{app} results from some cross-coupling or from interference by the AN in some other manner with the reactions which result in the n_{app}-value less than one in the absence of AN (*e.g.*, polymerization), it is difficult to determine with the experimental evidence at hand. Were n_{app} greater than one, cross-coupling by an ECE path would have been probable.

Electrochemical generation of the DF dianion.—The DF-AN system differs from the DF-CN system in that formation of the DF dianion occurs prior to the first reduction step of the R′ species (AN), as can be seen by comparing curve a to c (Fig. 8). Further, the DF radical anion is detected by the ring electrode over a greater potential range in the presence of AN (Fig. 8e) when compared with the potential range for detection of the radical anion in the absence of AN (Fig. 8d). In other words, in the presence of AN, $DF^{\cdot -}$ is being generated in a potential region normally associated with formation of the DF dianion. The anodic current measured at the ring electrode (curve e) is now seen to decrease at disk potentials corresponding to reduction of AN (curve c) at potentials more negative than those necessary to form the DF dianion (curve a). A possible explanation is the occurrence of a rapid oxidation-reduction reaction consuming dimethyl fumarate dianion and acrylonitrile parent and yielding the radical anions of DF and AN

$$DF^{2-} + AN \rightarrow DF^{\cdot -} + AN^{\cdot -} \qquad [21]$$

Thus, the amount of DF radical anion reaching the ring electrode remains relatively unchanged up to disk potentials corresponding to reduction of AN. Other possible explanations of this occurrence include the stabilization of the DF dianion by AN toward fragmentation or polymerization. However, no oxidations other than the oxidation of $DF^{\cdot -}$ were observed on varying the ring potential in RRDE voltammetry or on reversal in cyclic voltammetric experiments. In addition, the fact that the ring current does not change significantly at the more negative potentials is another indication that the identity of the species in transit to the ring is not a function of potential. Another possible explanation for this occurrence is the stabilization of the DF parent toward acceptance of the second electron. This, too, however, does not seem likely, since one would likewise expect stabilization of the DF parent species to acceptance of the first electron, and this is not observed.

Discussion

The mixed system results indicate that the mechanism which serves as the primary route for the disappearance of the dimethyl fumarate radical anion is not altered appreciably by the presence of a second olefin which is itself not electroactive at potentials sufficient to produce the DF radical anion under the conditions of our experiment. Further, the velocity of the radical decay remains, within experimental error, unchanged from the velocity measured in the absence of the second olefin when the second olefin is present in amounts about equal to that of DF; when AN is present in large excess, $DF^{\cdot -}$ decay increases to some extent. Considering the arguments presented, these RRDE results confirm the conclusion (1) that the major pathway in the electrodimerization of dimethyl fumarate in anhydrous DMF is the EC dimerization path (Eq. [16]).

The interpretation of the processes following the first DF reduction wave is more difficult. In the case of the DF-CN system, the CN one-electron reduction occurs prior to the DF two-electron reduction and appears unperturbed up to potentials necessary for formation of the dimethyl fumarate dianion. Analysis of the ring currents at various ring electrode potentials reveals that the stability of the $CN^{\cdot -}$ is decreased from its value in the absence of DF. This additional instability is attributed mainly to the electron transfer reaction between DF parent and CN radical anion, forming DF radical anion and CN parent. This hypothesis is supported by results of controlled potential coulometry conducted at electrode potentials where the radical anions of both DF and CN are formed which qualitatively indicate the occurrence of two independent reactions and quantitatively indicate little or no change in the coulometric n_{app}-value for the reduction of DF.

In the DF-AN system, the reduction of DF to the dianion occurs prior to reduction of AN. Thus, simultaneous generation of the DF and AN radical anions is not possible. The DF current-potential curve does not exhibit a dip at the second reduction potentials when AN is present. Further, the ring current resulting from oxidation of the DF radical anion extends into the region of disk potential normally associated with formation of the DF dianion and falls off only when the AN reduction commences. Here again the possibility of a redox reaction, this time involving the DF dianion, seems likely. That the ring current plateau does not change significantly at these potentials from its value in the disk potential region where formation of the DF radical anion occurs would lead one to conclude that the DF radical anion is the electroactive species being produced.

It is necessary to compare the results found here with previous studies of cross-coupling (4-7, 13). Our findings demonstrate that the DF-CN and DF-AN systems do not follow the path where cross-coupling occurs when the radical ion of only one species is produced in the presence of an equimolar concentration of the second olefin. For DF-AN concentration ratios of approximately 1 to 40 and 1 to 25, a slightly accelerated decay of the DF radical ion is observed, perhaps due to cross-coupling. Certainly, the cross-coupling reaction will be favored by very high concentrations of the second olefin. When radical ions of both reactants are produced, then the electron transfer reaction must be considered in addition to, or as a path to, the cross-coupling reaction. Baizer and co-workers (6) studied the cross-coupling reaction of the *cis*-isomer diethyl maleate (DEM) and AN and showed appreciable cross-coupled product formation at potentials where only the DEM radical ion is produced. Baizer also found coupling of DEF with AN under conditions of a very high ratio of AN to DEF (DEF added dropwise to AN containing tetraethylammonium p-toulene-sulfonate and a small amount of water) (4). Baizer and Chruma (14) have recently repeated this experiment and found substantial quantities of cross-coupled product (about one-fifth of the amount of the hydrodimer of DEF, tetraethylbutane tetracarboxylate) and no AN reduction products. The amount of cross-coupled product when DEM and AN are used

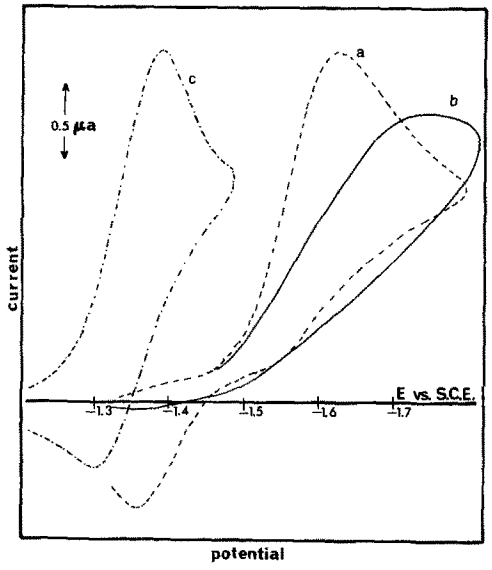

Fig. 11. Cyclic voltammograms at 200 mV/sec on a Pt working electrode: (a) diethyl maleate (3.9 mM), TBAP (0.15M), DMF; (b) diethyl maleate (3.9 mM) after the addition of AN (0.2M): (c) dimethyl fumarate (3.7 mM) in the presence of diethyl maleate and AN.

appears higher (6). On preliminary consideration, one would predict that the DEF-AN and the DEM-AN reactions would follow identical pathways, since DEF and DEM ultimately produce the same radical anion on reduction (15). However, recent results in our laboratory have shown that the behavior of DEM is very different from that of DEF. DEM is more difficult to reduce than its *trans*-isomer form, DEF; in addition, the diethyl maleate radical anion undergoes fast isomerization to form the diethyl fumarate radical and it appears that the direction of the isomerization lies exclusively toward the *trans* form (16, 17). Figure 11 is a cyclic voltammogram of a DEM-TBAP-DMF solution illustrating this isomerization. Following addition of excess AN, the wave shape becomes altered and no anodic current is observed on reversal (Fig. 11b). However, a cyclic voltammogram of the solution taken after the addition of dimethyl fumarate shows that the DF wave shape is qualitatively unaltered from that reported (1) and that anodic current is observed on reversal. One must conclude on the basis of this series of voltammograms that the *cis*-radical anion reacts with AN prior to isomerization, whereas the *trans*-radical anion is more stable with respect to reaction with AN. Cross-coupling of diethyl maleate and AN at potentials where only the diethyl maleate is electroactive and indeed, the occurrence of increasingly greater amounts of cross-coupled product with increasingly negative electrode potential when electrolyzing a mixture of DEM and DEF in the presence of AN can be explained in the light of the above observations. Further experiments are currently under way to uncover the nature of the difference between the reactivity of the *trans*- and *cis*-isomers. In conclusion these experiments demonstrate that cross-coupling will compete with dimerization only when the ratio of the second olefin (*e.g.*, AN) to the reduced olefin (DEF) is very large, and that cross-coupling can probably be carried out more efficiently by reducing both reactants (7).

Acknowledgment

The support of the Robert A. Welch Foundation and the National Science Foundation (GP 31414X) are gratefully acknowledged.

Manuscript submitted Nov. 16, 1972; revised manuscript received Jan. 31, 1973.

Any discussion of this paper will appear in a Discussion Section to be published in the December 1973 JOURNAL.

REFERENCES

1. V. J. Puglisi and A. J. Bard, *This Journal*, **119**, 829 (1972).
2. W. V. Childs, J. T. Maloy, C. P. Keszthelyi, and A. J. Bard, *ibid.*, **118**, 874 (1971).
3. V. J. Puglisi and A. J. Bard, *ibid.*, **119**, 833 (1972).
4. M. M. Baizer, *J. Org. Chem.*, **29**, 1670 (1964).
5. M. M. Baizer and J. P. Petrovich, *This Journal*, **114**, 1023 (1967).
6. M. M. Baizer, J. P. Petrovich, and D. A. Tyssee, *ibid.*, **117**, 173 (1970).
7. M. M. Baizer and J. L. Chruma, *ibid.*, **118**, 450 (1971).
8. J. P. Petrovich, M. M. Baizer, and M. R. Ort, *ibid.*, **116**, 743 (1969).
9. J. P. Petrovich, M. M. Baizer, and M. R. Ort, *ibid.*, **116**, 749 (1969).
10. K. B. Prater and A. J. Bard, *ibid.*, **117**, 207 (1970).
11. K. B. Prater and A. J. Bard, *ibid.*, **117**, 335 (1970).
12. K. B. Prater and A. J. Bard, *ibid.*, **117**, 1517 (1970).
13. Yu. D. Smirnov, S. K. Smirnov, and A. P. Tomilov, *Zh. Organ. Khim.*, **4**, 216 (1968).
14. M. M. Baizer and J. L. Chruma, Private communication, December 1972.
15. S. F. Nelson, *Tetrahedron Letters*, **39**, 3795 (1967).
16. J. Kenkel, Unpublished results, University of Texas (1972).
17. A. V. Il'zasov, Yu. M. Kargin, and V. Z. Kondranina, *Izv. Akad. Nauk SSSR, Ser. Khim.*, **5**, 927 (1971).

Origin of Activation Effects of Acetonitrile and Mercury in Electrocatalytic Oxidation of Formic Acid

H. Angerstein-Kozlowska, B. MacDougall, and B. E. Conway

Chemistry Department, University of Ottawa, Ottawa, Ontario, Canada

ABSTRACT

In the presence of catalyst poisons such as acetonitrile or mercury, it is shown that the currents for formic acid oxidation, measured in the potential range +0.4 to +0.8V E_H at Pt can be substantially increased. The effect is shown to originate from blocking of the surface at less positive potentials mainly in the H adsorption/desorption region (+0.05 to +0.35V E_H) where an inhibitor for the main formic acid oxidation reaction is normally formed in the absence of additive.

Under the latter conditions, steady-state oxidation currents are normally small and decrease with time due to build-up of an inhibiting species from the *HCOOH* or intermediates involved in its oxidation. Increases in the formic acid oxidation peak in the "double-layer" potential region at Pt can also be brought about in potentiodynamic experiments in the absence of additive, by cycling over a restricted potential range which excludes the H adsorption region. The inhibitor for formic acid oxidation is formed at potentials negative to 0.6V E_H by dimerization of COOH groups to give adsorbed formic anhydride. Its formation requires both time and available free surface. The competitive effects of Hg and CH_3CN are different insofar as a given extent of surface blocking causes different effects on the formic acid oxidation current. Comparative experiments on the effect of CH_3CN on methanol oxidation are described.

A general problem in the electro-oxidation of small organic molecules is the progressive decrease of rate (current density) of the reaction at a given potential and temperature, which occurs with time (1). This is usually not due to physical changes of the electrocatalyst structure except at elevated temperatures (2). Build-up of adsorbed species which inhibit (3) the main reaction sequence causes these effects. Periodic activation of the electrode, particularly by pulsing (4) to surface oxide formation potentials (5, 6), or by auto-oscillation (3, 7) regenerates electrode activity.

Activating effects in electrode reactions by what would normally be regarded as catalyst poisons were first observed by Monblanova and Kobosev (8); Binder *et al.* (9) found that partial coverage of the electrode by sulfur from sulfide enhanced the electrocatalytic activity of the surface for formic acid oxidation. Bockris and Conway (10) observed activating effects of traces of As and KCN in the H_2 evolution reaction. Satisfactory explanations for these effects have not yet been provided.

In the present paper, we report some interesting activating effects which arise in the electro-oxidation of formic acid at platinum electrodes when small concentrations of acetonitrile are present. The behavior is compared with that exhibited with methanol.

The present work indicates that the activating effect may be a general one in the case of formic acid oxidation and an account of the behavior may be given in terms of competitive adsorption effects (3) in an electrocatalytic process (11).

The electrochemistry of CH_3CN in aqueous medium has been described in previous papers (12, 13) from this laboratory and we have shown that acetonitrile itself is electroactive at Pt and the adsorbed species causes anodic H displacement (12, 14). Below 0.7V E_H, the adsorbed CH_3CN becomes progressively reduced. The molecule is attached to the Pt surface through the N atom at low concentrations while at high [CH_3CN] associative adsorption involving more Pt sites is involved.

Experimental

Methods of approach.—The kinetics of formic acid and formate oxidation have been studied previously and the results reported in various papers (15-18). Both "steady-state" galvanostatic (16, 19) and potentiodynamic (17) experiments have been described. Repetitive linear potential sweep experiments have been useful (17) in defining the potential ranges at Pt electrodes where appreciable anodic currents pass or where inhibition effects (3) arise. Although the steady-state approach is always necessary for defining the kinetic characteristics of the over-all reaction (since in the nonsteady-state, the surface concentrations of inhibiting or coreacting intermediates are not the steady-state or representative values, so that the reaction mechanism may be different from that in the steady state) the potentiodynamic method affords a convenient and sensitive way of controlling the prehistory of the electrode over various ranges of potential. Also, if the potential sweep is sufficiently slow (20), the main kinetic characteristics of the reaction are similar to those in the steady state. In the present work, both the steady-state and potentiodynamic current (i)-potential (V) characteristics of the reactions were examined.

Electrodes.—Pt electrodes were prepared by sealing Johnson-Matthey spec-pure Pt wire into glass bulbs in H_2 as described in previous work (21). The bulbs were broken beneath the solution in an all-glass cell (22) when required.

Solutions.—Solutions of 1N aq H_2SO_4, used as the supporting electrolyte, were prepared from B.D.H. micro-analytical grade H_2SO_4 using triply distilled water, the second stage of distillation being from alkaline $KMnO_4$. Electrochemical purity of the initial solutions was judged by the exhaustive criteria reported elsewhere (14), namely (in brief) resolution of the three surface oxidation regions of Pt between 0.85 and 1.1V together with the broad oxidation region from 1.2 to 1.5V; resolution of the H deposition and oxidation regions between 0.0 and +0.35V; and maintenance of the resolved H region without significant decrease of H coverage in potentiodynamic cycling between +0.05 and +0.75V (*i.e.*, in the absence of surface oxide formation) for 30 min. In all experiments, the reference i-V profile for the normal surface processes at Pt occurring between +0.05 and +1.4V E_H was first established before addition of formic acid

Key words: electrocatalysis, activation effects, formic acid oxidation, acetonitrile, mercury.

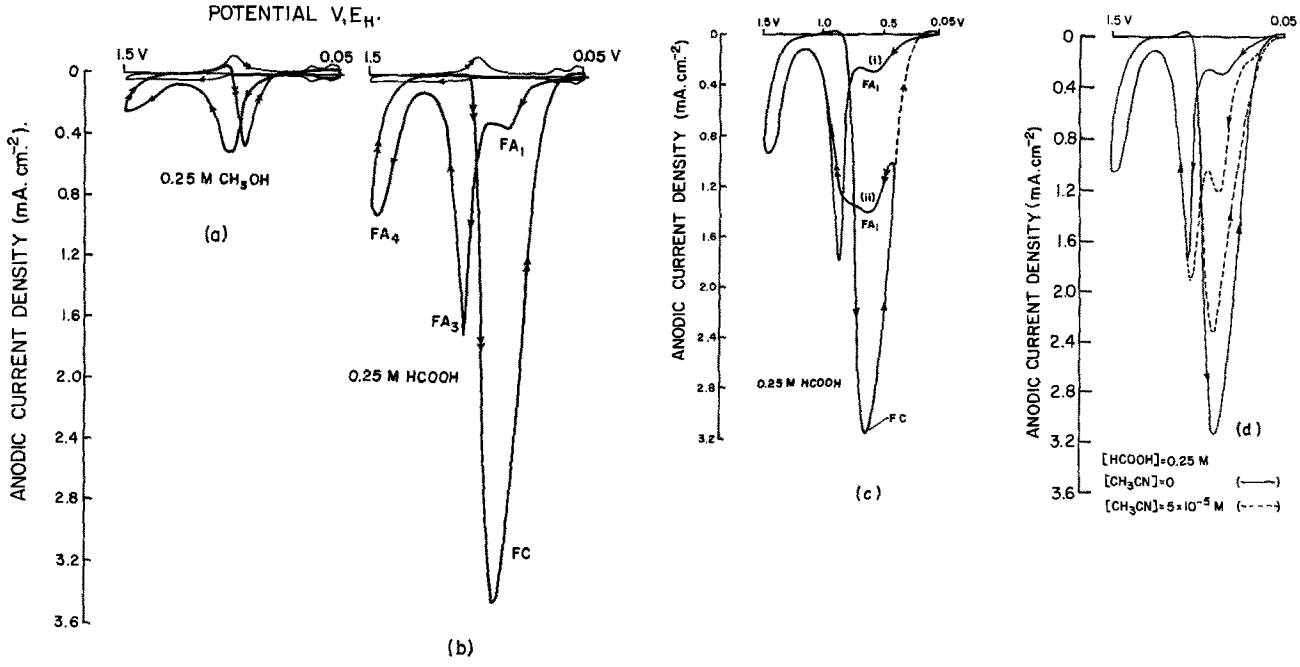

Fig. 1. Potentiodynamic *i-V* profiles at 50 mV·sec^{-1} for (a) 0.25M methanol and (b) 0.25M formic acid oxidation at Pt in 1*N* aq H_2SO_4 at 25°C over the potential range +1.5 to +0.05V E_H. (Current peaks "FA_1" and "FC", discussed in the text, are indicated.) Curve ii in (c) shows the *i-V* profile for formic acid oxidation over a restricted potential range, excluding the H region, in comparison with curve i in (c) over the full range to +0.05V. The curve in (d) shows the effect of 5 x 10^{-5} M CH_3CN.

and the other additives. All experiments were conducted at 25°C.

Formic acid and acetonitrile.—Formic acid was purified as described previously (16). Acetonitrile was purified according to the procedure of Mann *et al.* (23) using the Union Carbide reagent as starting material [as discussed previously (13)].

Instrumentation.—A Wenking fast-rise potentiostat was employed in the steady-state and potentiodynamic experiments. Linear potential sweeps were established using a Servomex LF 141 function generator. Current-potential relations were recorded on a Hewlett Packard XY recorder through a cathode follower.

Results and Discussion

Effects of Acetonitrile on the Oxidation of Formic Acid and Methanol in Aqueous Media

General: oxidation behavior of HCOOH and CH_3OH at Pt.—In an anodic-going potential sweep, formic acid exhibits distinct oxidation current peaks over three potential ranges (17) (Fig. 1b): (*i*) the H adsorption and double-layer (d.l.) regions, 0.25-0.6V E_H (FA_1);[1] (*ii*) the region where surface oxidation begins, *i.e.*, +0.85 to +0.95V E_H (FA_3), and (*iii*) a region of higher anodic potentials, *i.e.*, +1.225 to 1.525V E_H (FA_4). In the cathodic-going potential sweep, a large anodic current peak arises in the potential region where surface oxide reduction is nearing completion. Similar electrooxidation behavior at platinum is observed with methanol (24) (Fig. 1a) although, in this case, there is no current peak in the anodic-going potential sweep in the d.l. region. The potentiodynamic *i-V* profiles are shown for reference in Fig. 1a and b, while 1c shows the higher FA_1 peak when the scan is reversed at 0.35V E_H.

The oxidation of formic acid and methanol was first studied at platinum under anhydrous conditions with CH_3CN as solvent (25). Complete lack of reactivity of methanol and relatively small reactivity of formic acid was observed under these conditions; this led to an examination of the effects of large and small quantities of CH_3CN on the oxidation of the organic molecules at platinum in aqueous media. In this way, information could be obtained regarding the extent to which the concentration of CH_3CN determines surface blocking for the reaction of formic acid or methanol at platinum anodes. Effects of Hg on the formic acid oxidation reactions were also investigated.

Elsewhere (13), we have shown that CH_3CN is chemisorbed at Pt and undergoes reduction and oxidation entirely in an adsorbed state in cyclic voltammetry between +0.05 and +0.8V E_H, with a reversible reduction-oxidation peak in the d.l. (+0.35 to +0.8V E_H) region (13). Further reduction occurs in the H region (0.0 to +0.35V E_H) but even when the surface coverage by CH_3CN has reached its saturation value, H can be co-adsorbed to an extent of $\theta_H = 0.35$.

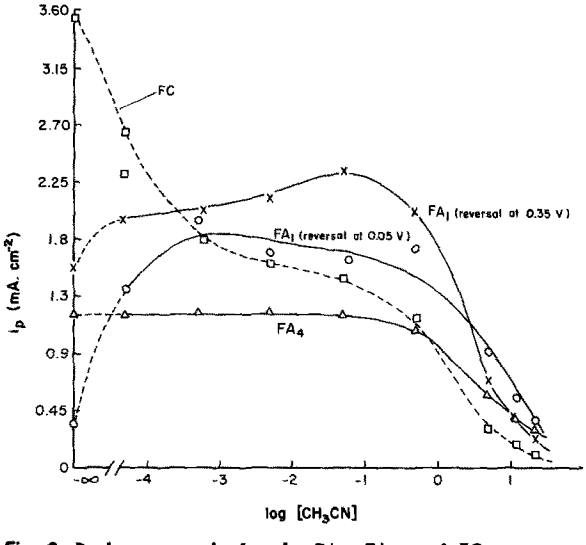

Fig. 2. Peak currents i_p for the FA_1, FA_4, and FC processes in formic acid oxidation at Pt at 25°C in 1*N* aq H_2SO_4 as a function of CH_3CN concentration: for FA_1 process with sweep reversal at +0.05V, for FA_1 process with sweep reversal at +0.35V outside H region, FA_4 process in oxide region, and FC process in cathodic sweep. When [CH_3CN] = 0, the difference between the initial points ○ and X represents the change of $(i_p)_{FA_1}$ when sweeps are taken to 0.05V compared with 0.35V.

[1] The symbol, FA_1, refers to the formic acid anodic oxidation reaction in the double-layer region at platinum; in an anodic-going sweep, it is the "first" process to be distinguished. In the remaining parts of this paper, the peak current for this "FA_1" process will be referred to, for brevity, as $(i_p)_{FA_1}$. Other processes, over the indicated potential ranges, are referred to as FA_3, FA_4. A second peak, "FA_2", arises under some conditions (13) but is not involved in the present work.

Effect of CH_3CN on formic acid oxidation in the double-layer potential range.—The most significant observation in the present work is that CH_3CN has an appreciable effect on the formic acid oxidation peak FA_1 over the d.l. potential region in an anodic-going potential sweep at platinum; the effect is one of activation rather than inhibition as shown in Fig. 1d. Figure 2 shows how the peak current $(i_p)_{FA1}$ for the process FA_1 increases with CH_3CN concentration in potentiodynamic sweep experiments. Results are shown for two ranges of potential, including and excluding the H adsorption region, for reasons to be discussed below. In a potentiodynamic cycling experiment conducted bewteen +1.5 and +0.05V E_H, the increase is about 600% for CH_3CN concentrations up to 5×10^{-2}M. At higher concentrations of the additive, the current begins to decrease; however, even at 2M, $(i_p)_{FA1}$ is still greater than its value measured in the absence of CH_3CN.

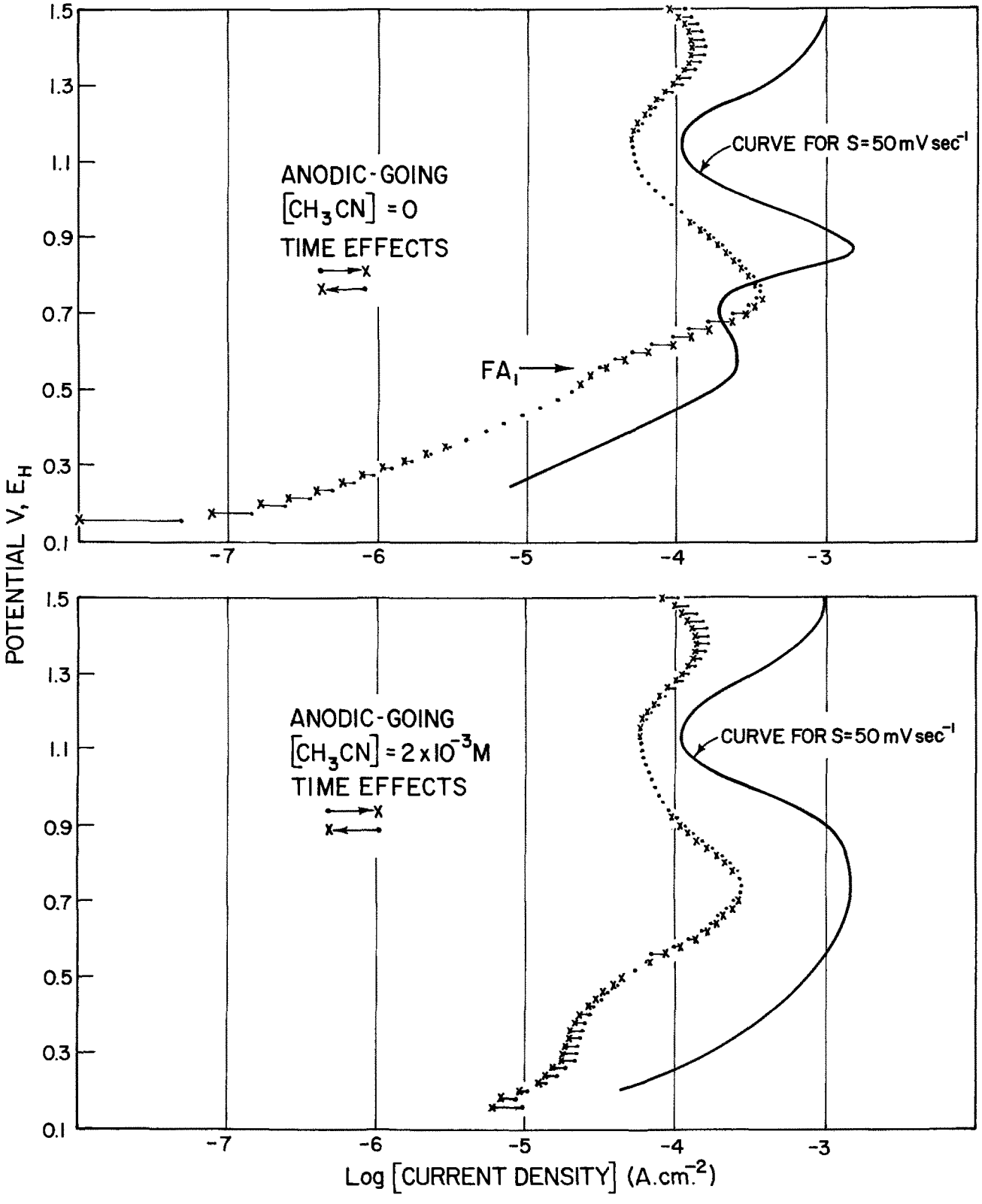

Fig. 3. Relation between steady-state point-by-point *i-V* curves for 0.25M formic acid oxidation in the presence and absence of CH_3CN (2×10^{-3}M in 1N aq H_2SO_4, 25°C) and the potentiodynamic *i-V* profiles taken at 50 mV·sec^{-1} over the same potential range in cathodic and anodic-going directions. Time effects in "steady-state" points are indicated by ●→—X over 90 sec.

That the effect of CH_3CN is not due to some trivial nonsteady-state effect under potentiodynamic conditions, is shown by the results in Fig. 3, where the steady-state, point-by-point i-V profiles are compared with the 50 mV sec^{-1} profiles. Slow time effects in the point-by-point curve are indicated by the direction of change from the X to the O points during 90 sec observation times. It is clear that the activating effects of CH_3CN on FA_1 peak currents are even larger on the steady-state curve than for the dynamical one and all the features of the results of Fig. 1b and 1d are retained in the steady-state behavior. Above 0.7V, both the steady-state and the potentiodynamic i-V curves are independent of the presence of CH_3CN. (Fig. 3).

Relation to the mechanism of formic acid oxidation in the double-layer region.—The effects of CH_3CN must be examined in the context of the mechanism of oxidation of formic acid itself, particularly with regard to the FA_1 process of HCOOH oxidation at the "bare" platinum surface and at a surface on which coadsorbed H is present.

Two main pathways for HCOOH oxidation have been proposed (16), one involving oxidative electrosorption at the carboxylic acid group, (particularly for the case of formate ion oxidation)

$$HCOOH \rightleftharpoons HCOOH_{ads.d.l.} \quad [1]$$

$$Pt + HCOOH_{ads.d.l.} \rightarrow HCOO\cdot/Pt + H^+ + e \quad [2]$$

$$HCOO\cdot/Pt \rightarrow CO_2 + H^+ + e \quad [3]$$

and the other (15, 17, 19) involving dissociative chemisorption with coupled electrochemical steps

$$HCOOH \rightleftharpoons HCOOH_{ads.d.l.} \quad [1]$$

$$2Pt + HCOOH_{ads.d.l.} \rightarrow PtH + PtCOOH \quad [4]$$

$$PtH \rightarrow Pt + H^+ + e \quad [5]$$

$$PtCOOH \rightarrow Pt + CO_2 + H^+ + e \quad [6]$$

The reaction mechanism [1], [4], [5], [6] is the principal one in acid media.

One of the main features of interest in the kinetics of formic acid oxidation is that the rate of the reaction at various potentials does not increase in relation to the coverage of chemisorbed species on the electrode as deduced from oxidative and reductive (by H accommodation measurement) transients. In fact, under some conditions (15, 18), the oxidation current falls as the coverage by adsorbed species increases, a conclusion which can only be interpreted (26) in terms of formation of a blocking species "P" produced in a step in parallel with the main reaction sequences shown above. P cannot, therefore, be $HCOO\cdot$ or $\cdot COOH$. P is also responsible for long-time deactivation effects (27) in HCOOH oxidation; its nature will be discussed in a later section.

Two proposals may be offered for the reaction which forms the inhibitor and leads to the effect of CH_3CN:

(*i*) The inhibitor is produced (15, 26) in a reaction between adsorbed H and an adsorbed species derived from formic acid, *e.g.*, $\cdot COOH$ (15) (from reaction [4]) which is involved in the main reaction sequence.

(*ii*) The poison is formed in a potential-dependent reaction between —COOH species, without the participation of atomic hydrogen. In this case, an additive such as CH_3CN could act as a "third body" interfering in an inhibitor-forming reaction (see below) between —COOH species.

Summary of Results and Conclusions from Experiments on CH_3CN and HCOOH Addition to aq H_2SO_4 in a Potentiodynamic Sweep Especially in or near the H Region

Experiments were carried out at a sweep rate of 50 mV sec^{-1} in 1*N* aq H_2SO_4. In some experiments, HCOOH was already present at 0.25M concentration and CH_3CN was added at selected potentials within a given potentiodynamic cycle; in other experiments, HCOOH was added during the potentiodynamic cycle in 1*N* aq H_2SO_4 in the absence of CH_3CN at selected potentials in either the cathodic-, or anodic-going sweep, *i.e.*, before or after H had been electrosorbed on the surface.

The purpose of these experiments was to establish if the CH_3CN acted independently as a catalytic material for the formic acid oxidation reaction or if it acted by diminishing the coverage by another inhibiting substance formed near or within the range of potentials over which H coverage is significant (0 to +0.35V E_H). The results and conclusions of these experiments are most conveniently recorded by means of Table I, in which reference is made to appropriate figures which provide the basis for the conclusions enumerated.

With increasing $[CH_3CN]$, $(i_p)_{FA_1}$ increases by *ca.* 7 times until about 66% of the H sites [full coverage by CH_3CN (13)] are blocked relative to those available at 0.05V; at higher concentrations, $(i_p)_{FA_1}$ falls somewhat. Although it would initially appear from this result and from the results in Table I that acetonitrile increases $(i_p)_{FA_1}$ by decreasing sites available for hydrogen adsorption, it will be shown that the role of acetonitrile in the formic acid reaction originates for different and indirect reasons, connected with blocking of sites for —COOH adsorption so that formation of P from such species is diminished.

Blocking of Surface Sites for H and/or COOH Species by Hg Electrosorption

In the experiments with CH_3CN and HCOOH, it was possible that CH_3CN could be displaced to some extent by formic acid depending on their relative concentrations (points 5 and 6 in Table I). It was desirable, therefore, to provide an alternative way of blocking the surface, for H and —COOH species, by an adsorbate which cannot be displaced by HCOOH. Electrodeposited mercury was found to meet this requirement very well.

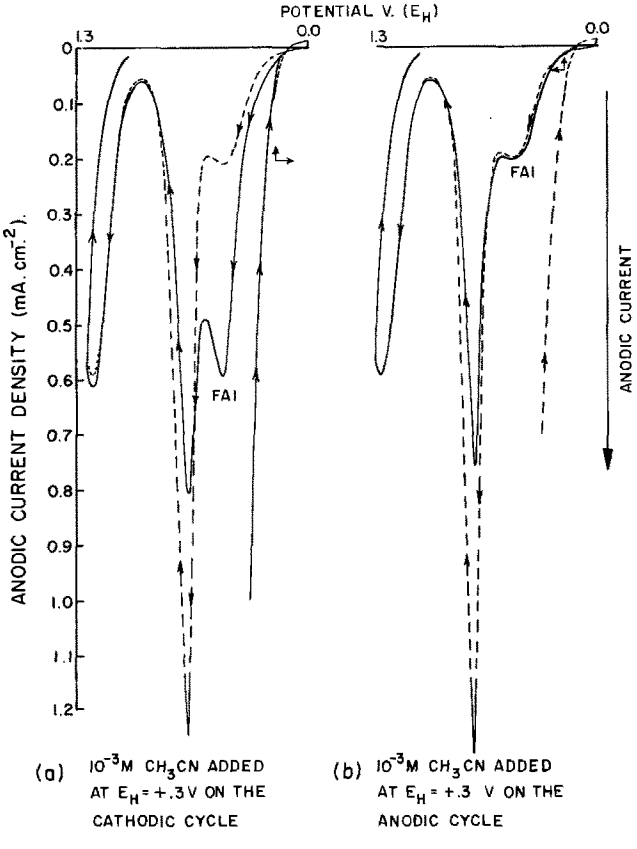

Fig. 4. Potentiodynamic *i*-*V* profiles for 0.25M formic acid oxidation at 50 mV·sec^{-1} at Pt showing effects of CH_3CN addition at 0.3V E_H (a) before and (b) after traversal of the H adsorption region in the sweep.

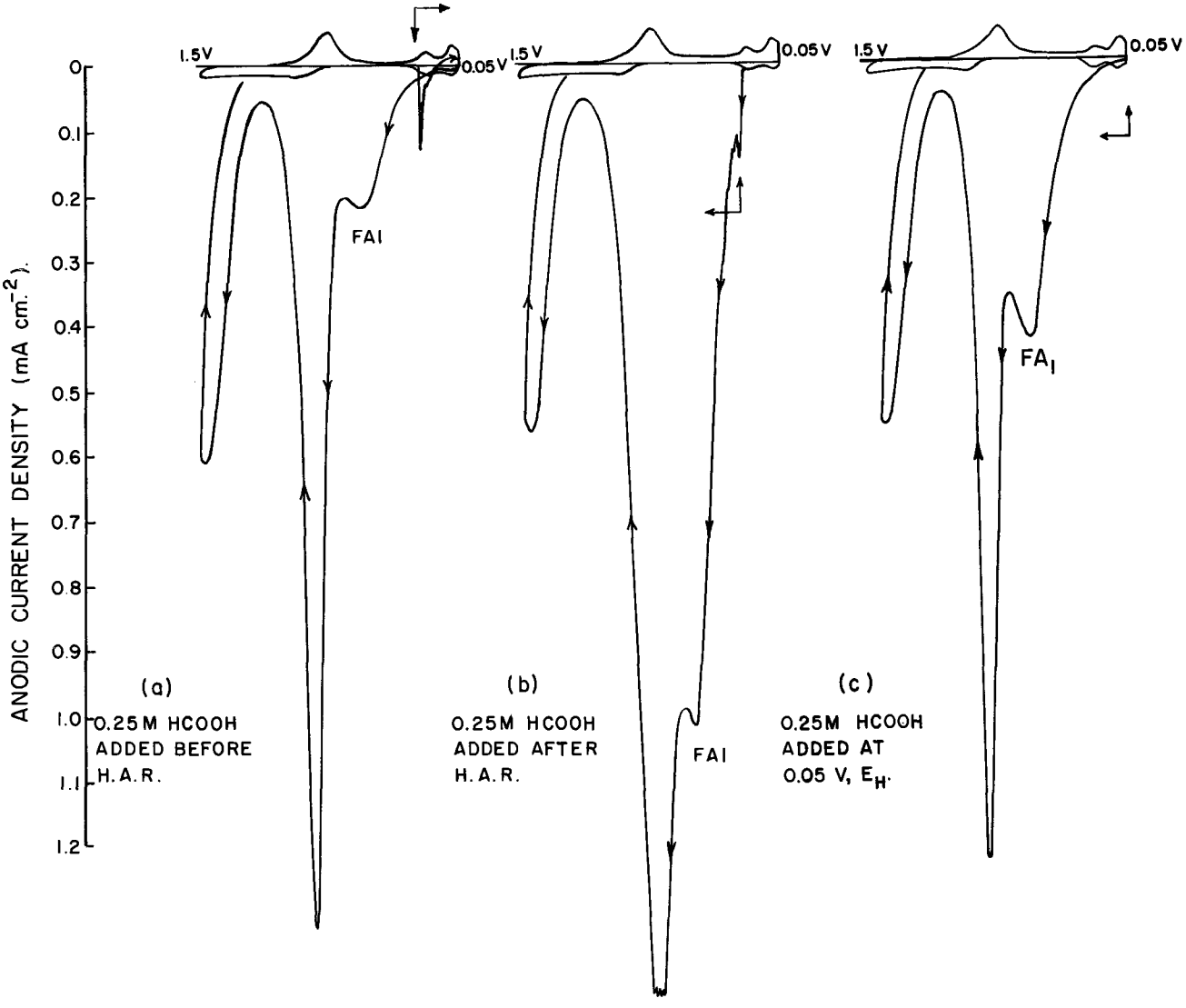

Fig. 5. Potentiodynamic *i-V* profiles for formic acid oxidation at Pt at 50 mV·sec^{-1} at Pt in the absence of CH_3CN: (a) for HCOOH addition at 0.3V on the cathodic-going sweep, (b) for HCOOH addition at 0.3V on the anodic-going sweep, and (c) for HCOOH addition at 0.05V as the sweep is reversed, where Θ_H is a maximum.

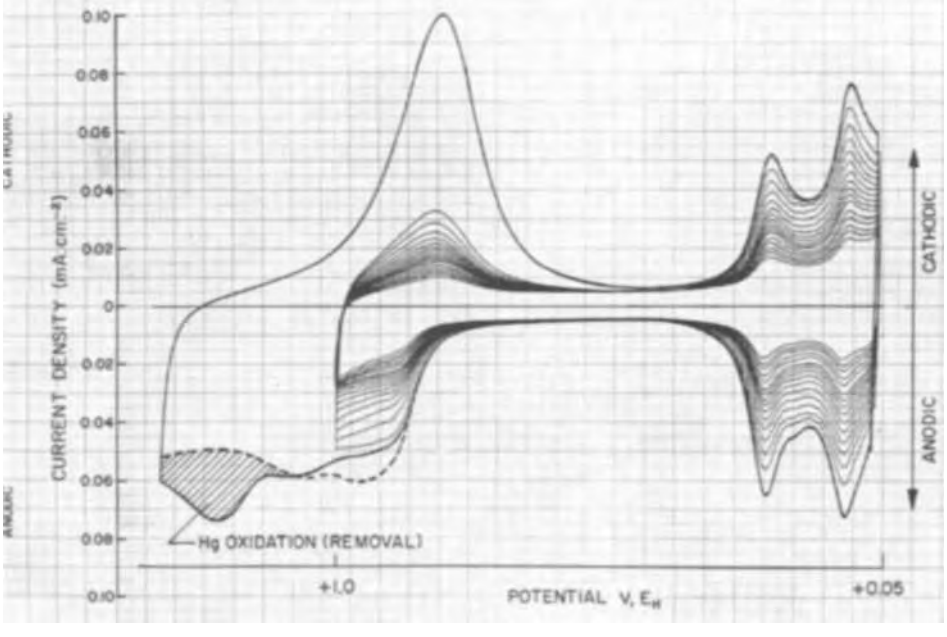

Fig. 6. Progressive blocking of H adsorption peaks (but with maintenance of their resolution) upon electrodeposition of Hg from 3 x 10^{-6}M aq $HgSO_4$ in successive cathodic sweeps. Quantitative oxidation of deposited Hg is measured in sweeps taken to 1.4V.

Mercury can be conveniently and controllably electrodeposited in submonolayer quantities at the platinum surface in aqueous H_2SO_4 using $HgSO_4$ under repetitive sweep conditions with the anodic reversal potential <1.0V E_H; cathodically deposited mercury is not then oxidized off the surface so that the mercury

Table I. Summary of results and conclusions from selected experiments on inhibitor formation and additive effects

Result number	Solution	Added substance	Potential of addition	Potential range of linear sweep (V)	Change in FA_1 peak current %	Comment	Figure reference	Conclusions
1.	1N aq H_2SO_4 + 0.25M HCOOH	—	—	0.05-1.5	—	i_{FA_1} taken as a reference current	1b	—
2.	1N aq H_2SO_4 + 0.25M HCOOH	5×10^{-5}M CH_3CN	In solution	0.05-1.5	+600	—	1d	Stimulation of HCOOH oxidation.
3.	1N aq H_2SO_4 + 0.25M HCOOH	—	—	0.35-1.5	+450		1c	CH_3CN is not itself a catalyst for HCOOH oxidation but a poison P is formed in the H adsorption/desorption region.
4.	1N aq H_2SO_4 + 0.25M HCOOH	5×10^{-4}M CH_3CN	In solution	0.35-1.5	+630		5b	CH_3CN prevents the formation of P.
5.	1N aq H_2SO_4 + 0.25M HCOOH	5×10^{-4}M CH_3CN	0.3V on cathodic cycle	0.05-1.5	+600 as in result number 2			
6.	1N aq H_2SO_4 + 0.25M HCOOH	5×10^{-4}M CH_3CN	0.3V on anodic cycle	0.05-1.5	0	No influence	4a	CH_3CN prevents the formation of P.
7.	1N aq H_2SO_4 + 0.25M HCOOH	5×10^{-4}M CH_3CN	0.05V at potential of cycle reversal	0.05-1.5	10		4b	CH_3CN does not affect P, once it is formed. P is 90% formed before full coverage by H is reached.
8.	1N aq H_2SO_4	HCOOH 0.25M	0.3V on cathodic cycle	0.05-1.5	0	As in result number 1	5a	P formed in H region is removed at higher potentials, *viz.*, 0.3V or higher.
9.	1N aq H_2SO_4	HCOOH 0.25M	0.3V on anodic cycle	0.05-1.5	500		5b	From result numbers 5 and 2 it is to be deduced that CH_3CN can displace species derived from HCOOH on the surface.
10.	1N aq H_2SO_4	HCOOH 0.25M	0.05	0.05-1.5	200		5c	With increasing potential, i_{FA_1} increases due to less P being formed.
11.	1N aq H_2SO_4 + 0.25M HCOOH	—	—	0.035-0.50	300-600		—	Effect continues beyond region of significant H coverage.

coverage on successive sweeps progressively increases as indicated by corresponding decreases of hydrogen coverage (Fig. 6). The electrodeposited mercury can, however, be quantitatively oxidized from the surface in a sweep to 1.4V E_H, giving rise to the new peak seen in Fig. 6 at 1.2V E_H.

θ_H could be controlled over a wide range of values with only one concentration of mercury in solution. For progressively increasing Hg deposition, the two main H peaks still remain completely resolved down to $\theta_H = 0.1$. This indicates that mercury blocks H adsorption on an individual site-by-site basis[2] rather than changing the "state" of adsorbed H. This situation is of particular value for the studies with HCOOH where a large range of H coverages and corresponding values of free surface area were of interest.

Figure 7 shows the variation of the FA_1 peak current with θ_H controlled by Hg deposition in the presence of formic acid. It is supposed (see below) that θ_H observed in the absence of formic acid when the surface is progressively blocked by electrodeposited Hg (Fig. 6) changes in proportion to θ_H when formic acid is present.

The initial increase in $(i_p)_{FA_1}$ as mercury begins to decrease θ_H and/or the available free space for HCOOH adsorption, continues until approximately 25% of the platinum sites at which H can be electrochemisorbed has been blocked by mercury. Since the percentage of sites blocked at the inflection point is important when considering the reaction of formation of P, the 25% figure was checked by a procedure which did not involve the above assumption. In this case, known coverages of mercury were first electrodeposited on the surface and the formic acid was added afterwards; the FA_1 peak currents were then registered. This procedure was repeated in separate experiments for a series of θ_H values and the 25% figure was confirmed.

Relation between the Effects of Mercury and Acetonitrile

When $(i_p)_{FA_1}$ in Fig. 2 is plotted with respect to θ_H, corresponding to various acetonitrile concentrations, the reversal of direction of the increase in $(i_p)_{FA_1}$ was found to occur at *ca.* 70% surface coverage by nitrile; the same results were obtained when θ_H was controlled with a particular [CH_3CN] initially in the absence of formic acid, followed by formic acid addition to the system.

The difference between the results with mercury and acetonitrile must be attributed to the ability of formic acid to displace, to some extent, acetonitrile from the surface as mentioned above. Then the free space available for formic acid adsorption, measured by θ_H determined in the presence of acetonitrile, can be substantially different from the space actually occupied by formic acid molecules when the latter are coadsorbed with acetonitrile. Coverage by species derived from HCOOH can hence be higher, with resultant [cf. (14) and below] formation of P. Electrodeposited Hg is not easily displaced in the above manner and requires anodic oxidation for its removal (Fig. 6).

Effects of Time spent in the H Region during Potentiodynamic Sweeps on Inhibitor Formation

The time τ_H spent in a sweep over the potential range ΔV_H in the H region $\left(\tau_H = 2\Delta V_H \frac{dV}{dt} \right)$, is an important factor in the reaction which produces the inhibiting species P. The percentage change in $(i_p)_{FA_1}$, after sharply decreasing initially, soon approaches a limiting value with increasing τ_H, *e.g.*, to *ca.* 30 sec on going to lower dV/dt. Evidently, under the latter conditions, τ_H is sufficient to allow the production of P to be more or less complete.

[2] The possibility that the electrodeposited Hg simply forms two-dimensional islands of Hg with otherwise free Pt sites is ruled out because the FA_1 peak current is increased by Hg (Fig. 7). If Hg had the effect of simply cutting the available surface area, all currents would be uniformly decreased.

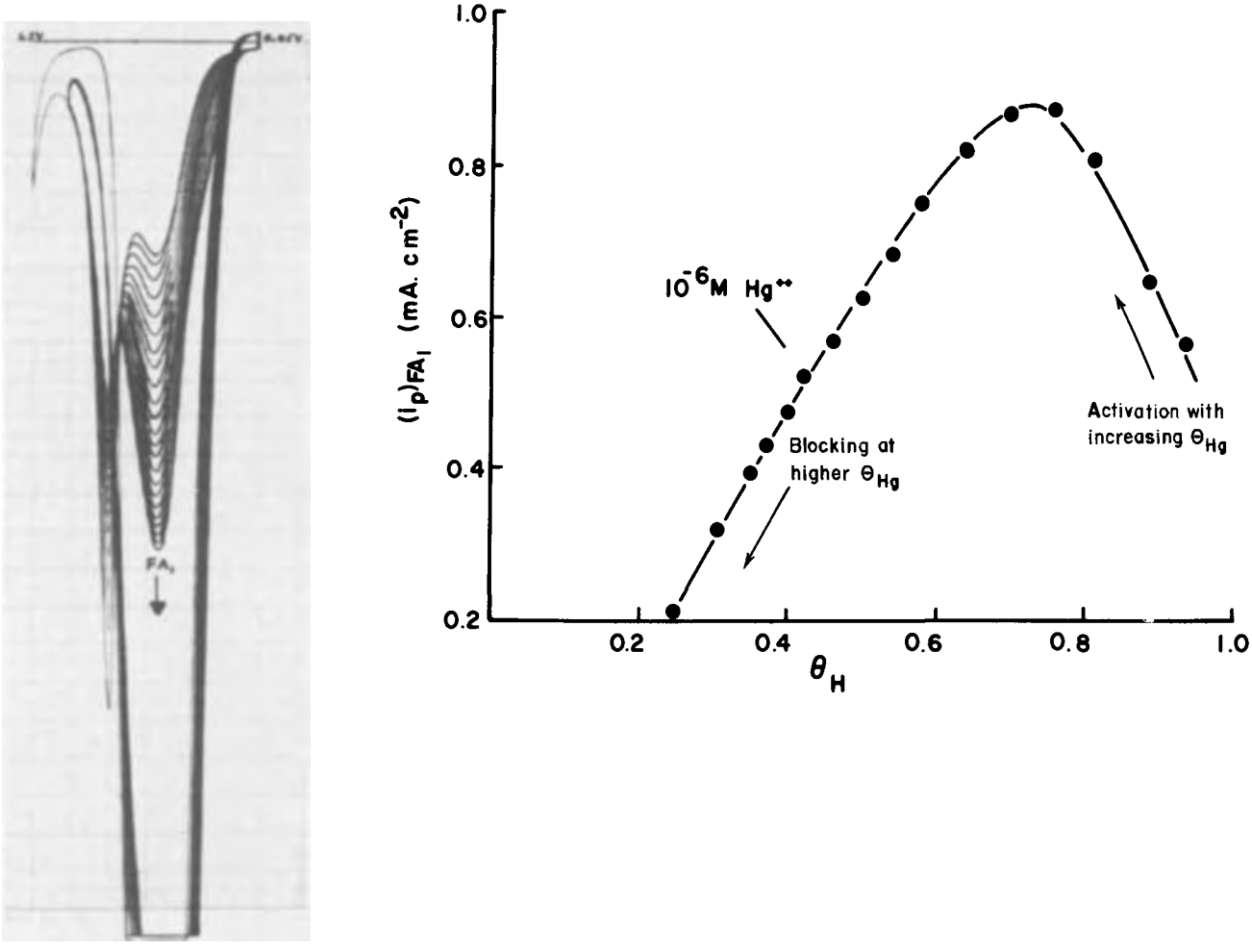

Fig. 7. Variation of $(i_p)_{FA_1}$ with H coverage at Pt controlled by Hg electrodeposition (Fig. 8) (HCOOH concentration 0.25M, 1*N* aq H_2SO_4, 25°C). (Lefthand set of curves shows the progression of *i-V* profiles with decreasing Θ_H down to 0.75).

Although the increase of $(i_p)_{FA_1}$ as the cathodic termination potential of the sweep is made more positive can be explained in terms of the production of less P, due to the tendency for Θ_H to diminish with increasing potential, the same, or an even higher degree of poisoning of the FA_1 reaction can be achieved by holding the potential for various times t_h at more positive values in the H region, where Θ_H is, of course, smaller. Figure 8 shows how $(i_p)_{FA_1}$ values depend on various holding times t_h at different reversal potentials in the cathodic-going sweep. It is to be noted that the maximum decrease of FA_1 peak current occurs at a reversal potential of *ca.* 0.22V E_H; in fact, 5 sec of cathodic holding at this potential gives a value of $(i_p)_{FA_1}$ as low as that observed after 40 sec of cathodic holding at +0.1V E_H.

There are evidently three factors which may determine the production of P: (*i*) the time spent at a given potential, (*ii*) the potential itself in the H region and/or Θ_H (Fig. 8), (*iii*) the free space available for dissociative adsorption of HCOOH to —COOH species which can then form the inhibitor P.

Support for the role of factor (*iii*) follows from the observation that the maximum poisoning effect with cathodic holding for times t_h occurs at about +0.20V E_H, where Θ_H can only be $\leq$0.25, *i.e.*, some free space is available. However, free space is not the only important factor since cycling to a potential of +0.20V E_H in the cathodic sweep results in an increase of $(i_p)_{FA_1}$ in comparison with that for cycling to +0.1V E_H (curve for t_h = 0 in Fig. 8). This complication can be rationalized in terms of the observation that formation of P is a slow reaction so that the extra time τ_H provided by cycling to a more cathodic reversal potential in the H region compensates for the increased Θ_H.

The time and potential effects in the H region on the FA_1 peak current are evidently complex but the two main factors determining P formation will be: competition of dissociative HCOOH adsorption with increasing tendency for H chemisorption at the least positive potentials; and decrease of —COOH coverage as the potential is made more positive, a situation that results from the mechanism [1], [4], [5], [6]. The minimum in $(i_p)_{FA_1}$ at finite t_h corresponds approximately with maximum adsorption of "HCOOH" species (18) and hence with maximum P coverage.

That the above effects are not due primarily to actual surface reactions with H was demonstrated by another holding experiment at 0.5V where $(i_p)_{FA_1}$ still fell to 27% of its value on the repetitive sweep during 60 sec holding at 0.5V, *i.e.*, outside the region where H is significantly adsorbed and at a potential where any H arising from HCOOH dissociation would be immediately ionized.

Nature of Inhibiting Species and Its Formation in Relation to Effects of CH_3CN and Hg

The results considered above indicated that formation of P is slow, the maximum rate occurring at *ca.* 0.2V E_H where coverage with formic acid species is a maximum. Also, the formation of P while influenced by H or potential in the H region does not require H. This leaves proposal (*ii*) on page 759 as a basis for formation of P and the effects of acetonitrile in the reaction.

Various possible inhibiting species, such as CO, "reduced CO_2,"≡C·OH, Cl^-, $HCOO^-$ anions, and CHO·COOH formed by dehydration of 2 HCOOH or by reductive coupling of CO, have been discussed (15). The first three have been discounted as the inhibitor (15, 19)

and adsorbed HCOOH itself (17) cannot be responsible for the observed behavior. CHO·COOH requires 3e for its oxidation to $CO_2 + H^+$, and it is difficult to see that it can occupy less than 3 or 4 sites; that is, its electron oxidation number per site will be <1. Brummer's experiment (15, 19) indicates oxidation charges in anodic galvanostatic experiments of *ca.* 370 μcoulomb per real cm². However, the galvanostatic method operated at large currents cannot be used reliably for desorption of a slowly oxidized intermediate while at smaller currents, reaction charge passes due to the diffusion-controlled reaction of reagent in solution in addition to the charge for oxidation of the adsorbed species. The end of the oxidation transient is also more difficult to define in comparison with that in potentiostatic-step or potential sweep-transients.

The results suggest that a formation of P must arise by a "dimerization" type of reaction on the electrode surface between adsorbed formic acid species leading to the lowering of coverage by the main electrochemically reactive species, —COOH. It cannot be a poison arising independently of the adsorbed formic acid species, *e.g.*, chloride ion (15), since there is no reason why displacement of one such a poison by another, acetonitrile, should increase $(i_p)_{FA1}$. The most plausible reaction between two adsorbed formic acid (—COOH) residues adjacent to each other on the electrode surface is dehydration leading to adsorbed formic anhydride[3]

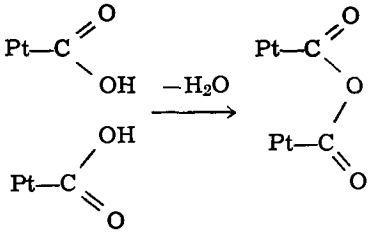

[7]

This reaction diminishes the surface available for reactive —COOH species, transforming them instead into the anhydride species which is unreactive except at higher anodic potentials (> *ca.* 0.9V E_H). Adsorbed acetonitrile acts as a "third body," decreasing the coverage with neighboring adsorbed —COOH groups so that there is less chance for two reactive species to become adjacent to one another and undergo dehydration leading to dimerization.

The mechanism of reaction [7] may be written following known mechanisms of, and substituent effects in, anhydride formation (29). Although formic anhydride is unknown as a stable substance in solution, it is proposed that the above reaction is possible since the intermediate [I] is in a two-point adsorbed state on the platinum surface so that the resulting anhydride [II] can be stabilized.

The identity of the P species as formic anhydride is supported by the observed potential-dependence of the rate of formation of P. Significant P formation only occurs in the less positive potential regions, *i.e.*, when the electrode acts relatively as a source of electrons. This is consistent with the above reaction mechanism since increase of electron donating tendency by the platinum will tend (*i*) to increase the protonation of adsorbed COOH groups, leading to stabilization of the

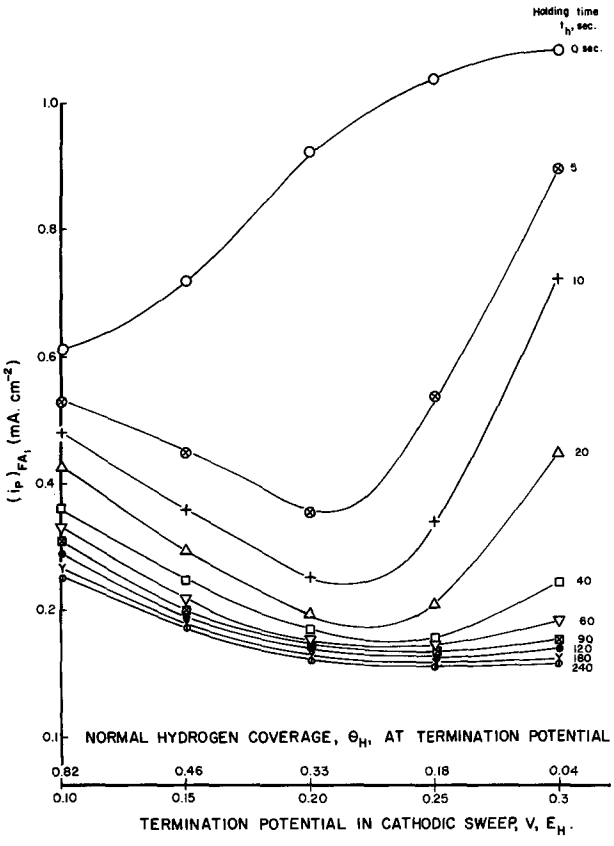

Fig. 8. Dependence of $(i_p)_{FA_1}$ on termination potential in the cathodic sweep for various holding times t_h at that potential. Also shown on nonlinear scale are corresponding H coverages (HCOOH concentration = 0.25M, dV/dt = 100 mV·sec^{-1} to minimize τ_H effect, in comparison with t_h in the H region.)

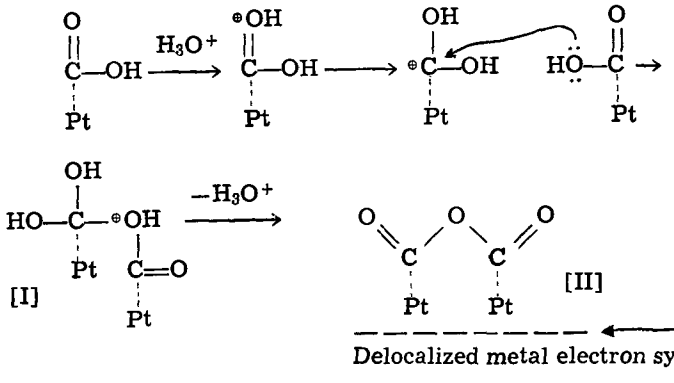

[8]

[3] A requirement for the above reaction will exist that would limit the reaction of anhydride formation to those adjacent COOH species on the surface which have the proper geometry. Formation of Brummer's intermediate, glyoxalic acid, requires dehydration between the OH and CH groups of two free formic acid molecules. This seems unlikely for organic mechanistic reasons and also because the inhibitor appears to be formed rather from already adsorbed intermediates, *e.g.*, -COOH, than from the normal free molecule HCOOH.

resulting protonated species and (*ii*) to increase the nucleophilicity of those adsorbed species which are not protonated, *i.e.*, the attacking species (29). At more positive potentials, the rate of reaction [7] should decrease since the platinum then acts as an electron withdrawing agent and the surface coverage by —COOH is also diminished as potential becomes more positive. Eventually, reaction [7] will become reversed, which is consistent with the change of direction of time effects with potential shown in Fig. 3.

The mechanism [7], [8], and the suggestion that the activating effect of CH_3CN arises from a "third body" effect which diminishes the probability of the dimerization reaction [7], receives further support from the results described earlier with controlled electrodeposition of Hg below monolayer coverage.

It is concluded that mercury acts in the same way as acetonitrile with regard to the FA_1 reaction by providing a "third body" which decreases the formation of poison P (reaction [7]). The situation giving rise to the maximum $(i_p)_{FA1}$ should correspond to the highest coverage by formic acid which can be attained without the presence of adsorbed "formic acid" (—COOH) species close enough to one another to give rise to reaction [7]. The maximum $(i_p)_{FA1}$ arises when the platinum surface is *ca.* 25% covered with mercury and the subsequent decrease of $(i_p)_{FA1}$ at higher mercury coverages (Fig. 7) is probably simply caused by mercury deposition on platinum sites where the main FA_1 reaction itself would normally occur. It is seen, however, that even when mercury has blocked 75% of the surface, $(i_p)_{FA1}$, after passing through its maximum value, has about the same value it had in the initial formic acid solution in the absence of mercury. This is consistent with the experimental findings of Brummer *et al.* (15) who concluded that the normal formic acid oxidation reaction occurs on only *ca.* 10% of the available platinum surface.

An approximate value of the mercury coverage which should give rise to a maximum $(i_p)_{FA1}$ by blocking dimerization between nearest neighbor —COOH groups can be obtained by reference to the geometry of adsorbed formic acid on a Pt (III) face (Fig. 9a). While one molecule of formic acid (as —COOH) can form a chemisorption bond to one Pt site, the whole unit effectively shields three platinum sites.[4] Maximum coverage by such adsorbed COOH groups arises when the surface is occupied as shown in Fig. 9b, as may be seen from space-filling models (Fig. 9a). For dimerization to be inhibited, nearest neighbor COOH positions must be blocked, *e.g.*, by Hg atoms. The highest coverage of COOH groups consistent with blocking adjacent positions (Fig. 9b) for COOH adsorption corresponds to that shown in Fig. 9c, where one in every four Pt sites has been blocked by electrodeposited Hg. This is consistent with the extent of blcoking of H adsorption (25%) at which the maximum in $(i_p)_{FA1}$ arises in Fig. 7. The blocking effects of Hg hence quantitatively support the view that the inhibitor P arises from COOH groups by a dimerization surface reaction. The corresponding situation for acetonitrile adsorption is shown in Fig. 9d where CH_3CN groups occupy 3 Pt sites each (13). In this case, CH_3CN must occupy all successive trigonal sites on two lines of Pt atoms and alternate groups of trigonal sites on the next two pairs of lines of Pt atoms. The pattern is then repeated.

[4] The adsorbed formic acid molecules are drawn as triangles in Fig. 9b (shielding three platinum atoms) for convenience of representation. The formic anhydride molecule can be seen from space-filling models to shield 5 platinum atoms. H coverage is assumed to correspond to approximately 1 atom per Pt of the lattice as found experimentally for the (111), (110), and (100) crystal faces. On the (111) face, this means that there are two trigonal holes for every H atom adsorbed.

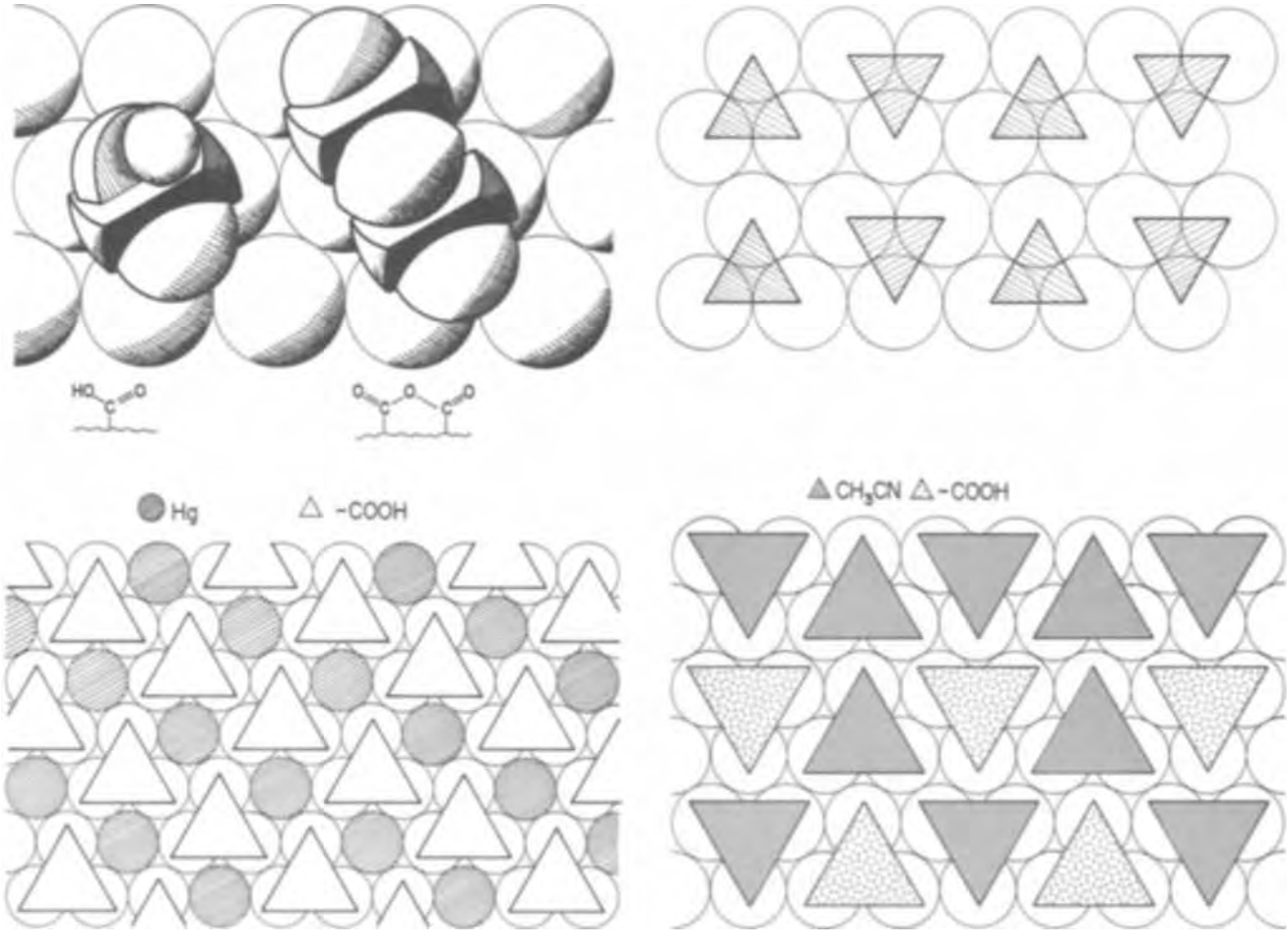

Fig. 9. Schematic diagram of (a, above left) adsorption of —COOH and the inhibitor in relation to (b, above right) H blocking, (c, below left) blocking by Hg, and (d, below right) blocking by CH_3CN.

This situation corresponds to 66% of the normal (13) maximum CH_3CN coverage attainable at Pt and is hence consistent with the observation that the maximum in $(i_p)_{FA_1}$ in the presence of CH_3CN occurs at *ca.* 70% relative blocking referred to H coverage at 0.05V. This does not represent saturation geometrical coverage by CH_3CN as it would (13) if CH_3CN were the only organic chemisorbed species. In the presence of HCOOH, co-adsorption of COOH must occur as shown in Fig. 9d. The results with Hg and CH_3CN cannot be easily accounted for if P were CO arising in a first order surface dehydration of HCOOHg nor are they consistent with the intermediate ≡C—OH involved in methanol oxidation (18).

Of course, the ordered arrangements of Fig. 9b-d are an idealization and the real surface undoubtedly has more random arrangements. The ordered patterns give, however, quite a good account of how the activating effects arise from partial blocking of sites for COOH adsorption. This blocking by the additive, Hg or CH_3CN, will also block H adsorption in the absence of HCOOH but it can be seen from the above diagrams how this can be a secondary effect so that H need not directly be involved in the production of P.

We stress the desirability, in interpretation of electrocatalytic processes, of considering the geometry of the metal lattice[5] in relation to the geometries of the probable chemisorbed species.

In impure solutions, but without an additive such as CH_3CN or Hg, potentiodynamic cycling over a potential range, which excludes (<0.85V) the Pt surface oxidation region, allows accumulation of adsorbed or electrodeposited impurities which are not then removed in the usual oxidative desorption provided by reaction with the oxidized Pt surface. After cycling for various periods of time, formic acid was added and $(i_p)_{FA_1}$ recorded. The peak current progressively increased as the surface became occupied with adsorbed impurities, evidently acting as a "third body," similar to Hg or CH_3CN, blocking the formation of P. Extension of the anodic limit of the potential sweep to +1.1V immediately lowered $(i_p)_{FA_1}$ on the next cycle due to removal, between 0.85 and 1.1V, of the impurities that had blocked formation of P. In pyrodistilled water (32), the above impurity effects are eliminated completely.

Effects of Acetonitrile on Other Formic Acid Oxidation Reactions and Comparison with the Behavior of Methanol

In addition to the FA_1 process, formic acid oxidation occurs by other mechanisms (15-19) near 0.9V E_H (FA_3), as surface oxide formation on Pt commences (31) and also at 1.3V (FA_4) on the more highly oxidized "PtO" surface. In the cathodic sweep, facile oxidation occurs ("FC" reaction, Fig. 2) again, just before completion of surface oxide reduction. The peak current FA_4 at +1.30V E_H is independent of the previous history of exposure of the electrode to formic acid in the H region and hence does not vary like that for peak FA_1. This is to be expected since the species P formed in the H region is oxidatively desorbed before a potential of 1.3V is reached.

The dependence on $[CH_3CN]$ of the peak currents $(i_p)_{FC}$ (see Fig. 1) and $(i_p)_{MC}$ for formic acid and methanol oxidations observed on the cathodic-going sweep is shown in Fig. 10. In these cases, there is a current decrease which follows, in a general way, the dependence of CH_3CN coverage at platinum on its concentration, reported elsewhere (13).

The rate of decrease of the current peak for the FC process on the cathodic sweep with $[CH_3CN]$ can be compared with that for methanol under similar conditions where the current has decreased to zero already at $[CH_3CN] = 2.5 \times 10^{-3}$ M (Fig. 10). The less

[5] Elsewhere (30), we have shown that the initial stages of oxidation of Pt which are resolvable below monolayer coverage by OH species ("PtOH") can be attributed to various stages of occupation of the Pt surface lattice by OH species in different geometrical arrays (cf. the conclusions from LEED work on surfaces not contaminated by carbonaceous residues).

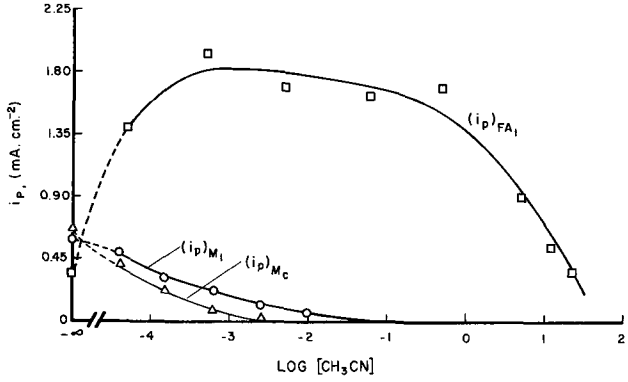

Fig. 10. Peak currents for the processes M_1 in the anodic-going, and M_c in the cathodic-going sweep for methanol oxidation in 1*N* aq H_2SO_4, 25°C, as a function of log [acetonitrile concentration] in comparison with $(i_p)_{FA_1}$ values for formic acid oxidation.

sensitive dependence of the currents for formic acid oxidation on $[CH_3CN]$ can be correlated with the requirement that only two free platinum sites are required for the dissociative chemisorption, HCOOH + Pt → PtH + PtCOOH, in comparison with that for methanol, represented (25) by: Pt + CH_3OH → Pt≡COH + 3PtH which requires a total of 6 sites.

While the formic acid oxidation peak FA_4 at +1.3V E_H is almost independent of $[CH_3CN]$ up to 5×10^{-2} M, the peak current for methanol oxidation on the anodic sweep at +1.3V E_H is found to continuously decrease with increasing $[CH_3CN]$ but it was not possible to separate this peak from that for oxidation of adsorbed (12) acetonitrile itself (13). The decrease in methanol oxidation current at *ca.* +1.3V E_H can be correlated with observations made previously (12, 13), that acetonitrile remains adsorbed on the electrode surface even at potentials in the oxygen evolution region at platinum.

Trace quantities of CH_3CN already decrease the two main current peaks for the methanol oxidation reaction at platinum. Figure 10 shows the dependence on CH_3CN concentration of the peak current M_1 (Fig. 1) for methanol oxidation in the potential region where surface oxidation of Pt commences. Methanol electrosorption requires (25, 28), as indicated above, three adjacent platinum sites so that coverage of the surface by CH_3CN species (12) and the corresponding blocking of sites for H chemisorption when $[CH_3CN] \geq 2 \times 10^{-4}$M makes it difficult for this site requirement to be fulfilled so that the reaction is very sensitive to poisoning of Pt sites.

Summary

The current for formic acid oxidation in the d.l. range of potentials at Pt is substantially increased in the presence of CH_3CN, adsorbed impurities, or Hg atoms. This arises from an indirect effect associated with prevention of formation of an inhibitor for formic acid oxidation which is otherwise spontaneously formed, particularly in the potential range 0.05 to 0.6V E_H. The additives which chemisorb and block inhibitor formation do so by a "third body" effect in which the rate of inhibitor production by a supposed dimerization reaction involving —COOH groups is diminished by blocking sites for nearest neighbor —COOH adsorption. It is shown that the inhibitor is probably adsorbed formic anhydride. The role of H coverage in inhibitor formation and in the activating effects is considered but it is shown that it is not a primary factor in the behavior reported. Similar activating effects do not arise in methanol oxidation because the electrochemical reaction does not involve the production of an inhibitor in a side reaction in that case.

Acknowledgment

Grateful acknowledgment is made to the Defence Research Board, Department of National Defence,

Canada, for support of this work on D.R.B. Grant No. 5412-01.

Manuscript submitted Sept. 8, 1972; revised manuscript received Dec. 11, 1972.

Any discussion of this paper will appear in a Discussion Section to be published in the December 1973 JOURNAL.

REFERENCES

1. J. Giner, *Electrochim. Acta*, **9**, 63 (1964).
2. G. McKee, *J. Phys. Chem.*, **67**, 841 (1963).
3. D. Gilroy and B. E. Conway, *ibid.*, **69**, 1259 (1965).
4. P. Gentile, M. Leitz, H. Porter, and G. Sarma, U.S. Govt. Report, A.D.-272-352 (1960); see K. Williams, Editor, "Introduction to Fuel Cells," p. 127, Elsevier Publishing Company, Amsterdam (1966).
5. D. Gilroy and B. E. Conway, *Can. J. Chem.*, **46**, 875 (1967).
6. S. Gilman, *J. Phys. Chem.*, **66**, 2657 (1962); *ibid.*, **67**, 1898 (1963).
7. J. Wojtowicz, N. Marincic, and B. E. Conway, *J. Chem. Phys.*, **48**, 4333 (1968).
8. N. Kobosev and W. Monblanowa, *Acta Physicochim. U.R.S.S.*, **1**, 611 (1934).
9. H. Binder, G. Sanstede, and A. Köhling, *Nature*, **214**, 268 (1964); see also *J. Electroanal. Chem.*, **17**, 111 (1968).
10. J. O'M. Bockris and B. E. Conway, *Trans. Faraday Soc.*, **45**, 989 (1949).
11. P. Stonehart, *Electrochim. Acta*, **12**, 1185 (1967).
12. B. MacDougall, B. E. Conway, and H. A. Kozlowska, *J. Electroanal. Chem.*, **32**, App. 15-20 (1971).
13. H. Angerstein-Kozlowska, B. MacDougall, and B. E. Conway, *ibid.*, **39**, 287 (1972).
14. B. E. Conway, B. MacDougall, and H. Angerstein-Kozlowska, *J. Chem. Soc., Faraday Trans. I*, **68**, 1566 (1972).
15. See S. Brummer and A. C. Makrides, *J. Phys. Chem.*, **68**, 1448 (1964); S. B. Brummer, *ibid.*, **69**, 1363 (1965); *Elektrokhimiya*, **4**, 243 (1968).
16. B. E. Conway and M. Dzieciuch, *Can. J. Chem.*, **41**, 21; *ibid.*, **41**, 55 (1963).
17. M. Breiter, *Electrochim. Acta*, **8**, 447 (1963); *ibid.*, **10**, 503 (1965).
18. V. S. Bagotskii and Y. B. Vasil'ev, *ibid.*, **9**, 869 (1964); see also *Elektrokhimiya*, **6**, 157 (1970) (Suppl).
19. S. Brummer, *J. Phys. Chem.*, **69**, 562 (1965).
20. S. Srinivasan and E. Gileadi, *Electrochim. Acta*, **11**, 321 (1966).
21. J. O'M. Bockris and B. E. Conway, *J. Sci. Instr.*, **25**, 423 (1949).
22. J. J. MacDonald and B. E. Conway, *Proc. Roy. Soc. (London), Ser. A*, **269**, 419 (1962).
23. J. F. O'Donnell, J. T. Ayres, and C. M. Mann, *Anal. Chem.*, **37**, 1161 (1968); J. F. Coetzee and G. P. Cunningham, *ibid.*, **34**, 1138 (1962).
24. M. Breiter, *Electrochim. Acta*, **8**, 457 (1963).
25. B. E. Conway, B. MacDougall, H. Angerstein-Kozlowska, and V. B. Tilak," Proc. 2nd International Conference on Fuel Cells, Brussels, 1968," S.E.R.A.I., Brussels, Belgium (1969).
26. C. W. Fleischman, G. K. Johnson, and A. T. Kuhn, *This Journal*, **112**, 602 (1964); see also S. B. Brummer, *Elektrokhimiya*, **4**, 243 (1968).
27. H. Angerstein-Kozlowska and B. E. Conway, In course of publication.
28. V. S. Bagotskii and Y. B. Vasil'ev, *Electrochim. Acta*, **12**, 1323 (1967).
29. E. Berliner and L. H. Altschul, *J. Am. Chem. Soc.*, **74**, 4110 (1952).
30. H. Angerstein-Kozlowska, B. E. Conway, and W. Sharp, *J. Electroanal. Chem.*, To be published April 1973; H. Angerstein-Kozlowska, B. V. Tilak, and B. E. Conway, Abstract No. 109, p. 292, Electrochemical Society Extended Abstracts, Spring Meeting, Houston, Texas, May 7-11, 1972.
31. B. E. Conway, N. Marincic, D. Gilroy, and E. J. Rudd, *This Journal*, **113**, 1143 (1966).
32. B. E. Conway, H. Angerstein-Kozlowska, and W. B. A. Sharp, *Anal. Chem.*, In press (1973).

The Anodic Oxidation of Hydrogen on Platinized Tungsten Oxides

II. Mechanism of H_2 Oxidation on Platinized WO_3 Electrodes

B. S. Hobbs[1] and A. C. C. Tseung

Department of Chemistry, The City University, St. John Street, London EC1V 4PB, United Kingdom

ABSTRACT

Electrochemical measurements on the anodic oxidation of hydrogen on platinized boron carbide and WO_3 supports reveal that the latter is an "active" support, participating directly in the over-all electrode reaction. In contrast, boron carbide is an "inert" support and takes no part in the electrode reaction. This work and previous investigations on the composition of the WO_3, confirm that the electrode reaction proceeds by the formation and oxidation of hydrogen tungsten bronzes (H_xWO_3)

$$WO_3 + x\text{Pt} - \text{H} \rightarrow H_xWO_3 + \text{Pt}$$

$$H_xWO_3 \rightarrow WO_3 + xe^- + xH^+$$

In this way the effective reaction zone area is extended onto the support, increasing the net electrode current.

Previous studies based on polarization curves of electrodes fabricated from various platinized substrates (*e.g.*, tantalum carbide, graphite, tungsten trioxide) indicated a synergic mechanism on WO_3 (1). Later, it was shown that hydrogen tungsten bronzes (H_xWO_3) are the sole products when platinized WO_3 electrocatalysts are exposed to hydrogen in $5NH_2SO_4$ between 20° and 80°C (2). A mechanism was proposed whereby these bronzes participated in the anodic oxidation of hydrogen, thereby enhancing the output of electrodes using Pt/WO_3 catalysts, viz

$$2\text{Pt} + H_2 \rightarrow 2\text{Pt}H_{ads}$$

$$\text{Pt}H_{ads} \rightarrow \text{Pt} + H^+ + e \quad \text{normal route}$$

$$x\text{Pt}H_{ads} + WO_3 \rightarrow \text{Pt} + H_xWO_3$$
$$H_xWO_3 \rightarrow xH^+ + WO_3 + xe \quad \Big) \text{ bronze route}$$

[1] Present address: Electrical Research Association, Cleeve Road, Leatherhead, Surrey, United Kingdom.

Key words: electrocatalysis, H_2 oxidation, WO_3 support.

The original polarization studies, however, do not confirm the above mechanism since the observed activity differences on the various substrates could also have arisen from differences in Pt morphology or physical electrode parameters such as wetting, permeability, etc. The extent of support participation in the electrode reaction can be determined in the presence of these complicating structural effects by examining the relationship between electrode activity and Pt loading, the support loading being held constant. Thus, assuming all the electrode current at a given overvoltage originates from the Pt, we can define a specific Pt activity ($j_{(p)}$), expressed in milliamperes/milligram of platinum

$$j_{(p)} = \frac{i(\eta)}{W_{(p)}}$$

where $i(\eta)$ is the electrode current density at a fixed overvoltage, η, in mA cm^{-2}, and $W_{(p)}$ is the Pt loading in mg cm^{-2}.

Alternatively, the Pt activity can be expressed in terms of milliamperes/unit surface area of Pt

$$j_{(ps)} = \frac{i(\eta)}{S_{(p)}} \quad \text{(mA per cm}^2\text{ Pt)}$$

where $S_{(p)}$ is the Pt area/cm^2 electrode.

Now $j_{(p)}$ (or $j_{(ps)}$) should remain independent of variations in the Pt loading, provided the Pt specific surface area and morphology remain constant. In this case $j_{(p)}$ represents the true Pt activity.

If however, the support also contributes to the electrode current, $j_{(p)}$ will apparently increase as the Pt loading decreases. Furthermore, if the support contributes the major fraction of the current, the relationship between $j_{(p)}$ and W_p will approximate to an inverse proportion, *e.g.*, halving the Pt loading will produce little effect on $i(\eta)$ if the support accounts for most of the current, but $j_{(p)}$ will apparently double.

Experimental

Catalyst preparation.—To ensure Pt morphology and specific surface area remained constant, loadings were varied by first impregnating a batch of WO_3 with Pt, then mixing samples of this with varying proportions of unplatinized oxide when preparing electrodes. In order to produce a high, uniform dispersion of Pt on the oxide, impregnation was carried out by means of a freeze-drying technique (2). The Pt content was analyzed by gravimetric extraction with NaOH solution as previously described (2).

Electrode preparation.—Electrodes of the polytetrafluorethylene (PTFE) bonded type, having very similar physical structures, while varying significantly in their Pt loadings, were prepared according to an optimized procedure described by Giner *et al.* (3): "weighed quantities of impregnated and plain WO_3 powders were slurried with aqueous P.T.F.E. dispersion and pasted onto 80 mesh, 18 Standard Wire Gauge (S.W.G.) gold-plated Pt gauze screens. After drying at 70°C, the electrodes were 'cured' at 300°C for one hour."

Complete transfer of the mix to the screen was impossible and the Pt loadings were therefore estimated from the screen weight changes before and after fabrication, assuming the components of the catalyst/PTFE paste to be transferred in the same ratio as the original pot mix.

Pt loadings were kept low to avoid masking any substrate activity by the intrinsic Pt activity. Oxide loadings of about 10 mg/geometric cm^2 of screen were used, with Pt contents ranging between 0.1 and 1% of the oxide weight (0.1-0.01 mg/cm^2 electrode). PTFE loadings were in the range 3-4 mg/cm^2 electrode.

Electrode testing.—Electrochemical measurements were made with a floating electrode cell described by Giner *et al.* (3) employing a gold counterelectrode, 5*N* sulfuric acid thermostated at 25°C, and a dynamic hydrogen reference electrode (DHE) (4), whose potential was −25 mV with respect to a normal hydrogen electrode in the same electrolyte. Hydrogen from a palladium diffuser was fed to the test electrode and steady-state anodic polarization curves were obtained using a Chemical Electronics TR40-3 Amp potentiostat. The resultant polarization curves were corrected for ohmic effects by the interrupter technique (5).

The limits of experimental deviation were determined from the maximum spread of measurements obtained from several electrode samples made from each batch of catalyst powder.

Boron carbide electrodes.—Boron carbide (B_4C) is an acid resistant (6, 7), conducting [$\rho = 0.455$ ohm-cm (8)] material which has been extensively employed in fuel cells as a catalyst or support (9-15). It possesses no activity toward H_2 oxidation, being inert to H_2 chemisorption, either directly or via predissociation on Pt (13). Hence B_4C is an ideal substrate to test the "Pt loading effect" for an inert support, and is preferred to either graphite, which can deactivate Pt (16), or TaC which can form resistive oxide films. It is emphasized however, that we cannot directly compare the polarization curves for B_4C and WO_3 substrates, owing to structural and morphological variations between the two types of electrode. We can only confirm the independence of $j_{(p)}$ on platinum loading for inert supports, such as B_4C.

Platinizing was carried out in an analogous manner to WO_3, but owing to the difficulty of dissolving B_4C to separate it from the Pt, no check on the Pt content was possible. Instead, Pt contents were calculated from the chloroplatinic acid used in the impregnation and since good agreement was obtained with WO_3 between this method and the gravimetric analysis, it can be assumed to be so for B_4C.

Electrode curing and drying were performed in a nitrogen stream to avoid oxidation of the B_4C.

Materials purification.—As previously described, H_2 was purified with a palladium diffuser. Analar sulfuric acid and distilled/deionized water were used to prepare the electrolyte, which was electrolyzed for several hours between gold electrodes before use.

The WO_3 and B_4C were repeatedly refluxed with 5*N* H_2SO_4 and analyzed by mass spectrography before use. Iron was the only significant impurity which was reduced to 20 and 150 ppm in the WO_3 and B_4C, respectively.

Results and Discussion

WO_3 electrodes.—None of the polarization curves exhibited a Tafel region and were essentially linear throughout the overpotential ranges studied (Fig. 1). The unusually wide overpotential range of linearity can be attributed to mass transfer effects (17). Platinum activities $j_{(p)}$ were determined from the

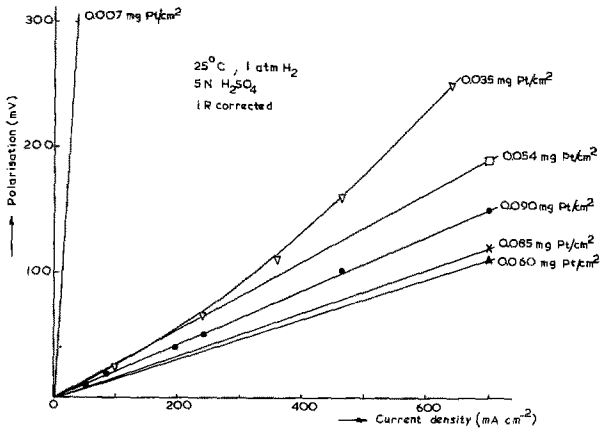

Fig. 1. Polarization curves for platinized WO_3 electrodes

electrode current at an arbitrarily chosen overpotential of 50 mV.

Figures 2 and 3 show the variations of specific Pt activity as a function of platinum loading and reciprocal Pt loading, respectively. In the range of Pt loading between 0.2 and 1% of the support weight (0.02 to 0.1 mg/cm^2) the experimental points lie very closely to the theoretical curves for an active support supplying the majority of electrode current.

When the Pt content was reduced below 0.2% of the oxide weight however, the electrode performance sharply declined. This critical Pt loading was observed during hydrogen uptake and bronze compositional studies (2) and corresponds to the condition at which the ratio of Pt to WO_3 particles was unity, calculated from the average particle sizes [from BET measurements on the WO_3 powder and extracted Pt black (2, 18)], assuming the particles to be perfect spheres. This effect is expected under steady-state polarization, if the oxide interparticle H-transfer rate is slower than the anodic oxidation of H_xWO_3. Ohmic polarization will then limit the electrode performance as WO_3 accumulates in the electrode. The fact that electrode activity is very high when there is at least one Pt particle per oxide particle, indicates that the Pt/oxide interparticle and WO_3 intraparticle H-migration rates are extremely fast.

Boron carbide electrodes.—Polarization curves were again essentially linear over the overpotential ranges investigated (Fig. 4) and Pt activities were similarly measured from currents at an arbitrary 50 mV.

Figures 5 and 6 show that the specific Pt activity was independent of Pt loading, as expected of an inert support.

A plain B_4C electrode showed some residual activity under H_2. This probably arose from trace impurities, especially iron, which is not easily removed completely from B_4C (7). Other current sources were exposed Pt at the electrode edges when cutting to size and possible pin holes or other defects in the gold plate.

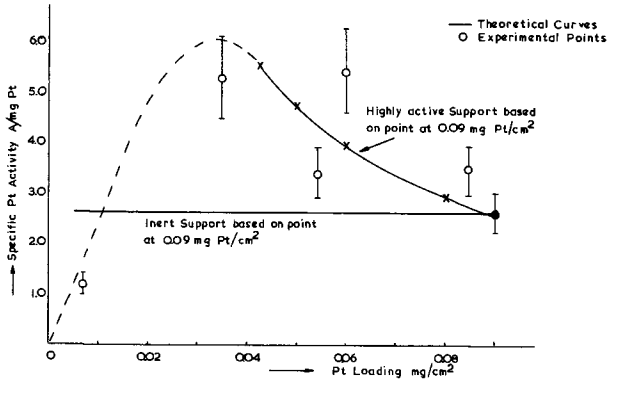

Fig. 2. Variation of specific Pt activity with Pt loading using WO_3 support.

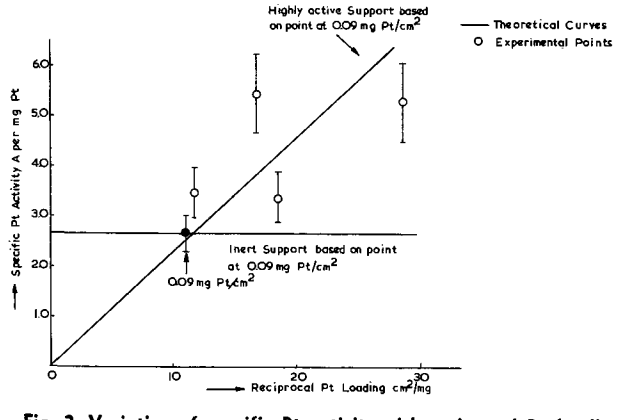

Fig. 3. Variation of specific Pt activity with reciprocal Pt loading using WO_3 support.

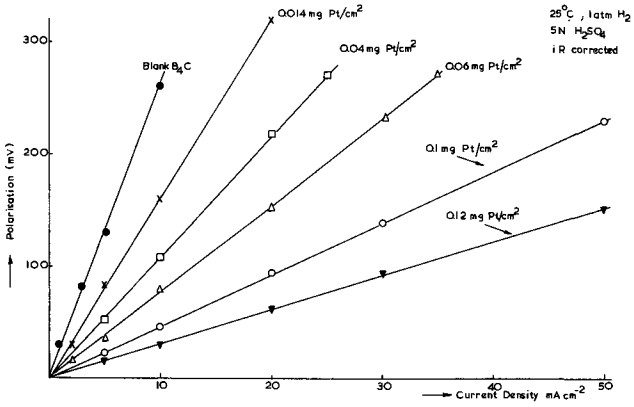

Fig. 4. Polarization curves for platinized B_4C electrodes

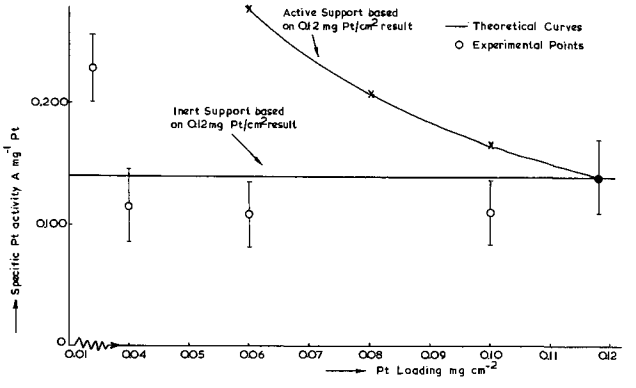

Fig. 5. Variation of specific Pt activity with Pt loading using B_4C support.

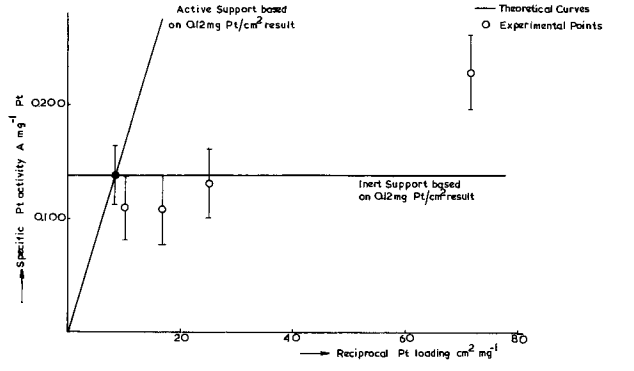

Fig. 6. Variation of specific Pt activity with reciprocal Pt loading using B_4C support.

Conclusions

Hydrogen bronzes, formed in platinized WO_3 hydrogen electrodes, contribute to the net anodic current, being formed chemically by H-atom migration from the Pt to the oxide, and oxidizing electrochemically. Thus the reaction zone is extended onto the support and the over-all electrode activity is increased. With Pt loadings in the range of 0.02-0.1 mg/cm^2 (or 0.2-1% of the WO_3 loading) high electrode performance was obtained which originated principally from the bronze reaction

$$H_xWO_3 \rightarrow xH^+ + WO_3 + xe$$

The rate of hydrogen atom migration to form bronzes is rapid provided there is direct contact between Pt and WO_3 particles. Hydrogen atom migration between oxide particles is relatively slow and, under conditions where this is necessary for current generation, a severe decline in activity is observed.

Although the oxide composition and H_2 oxidation mechanism has been conclusively established for platinized WO_3, complementary work is required on related substrates, *e.g.*, the lower tungsten oxides and

sodium bronzes, which show similar evidence of synergic effects (1, 20).

Acknowledgments

This work was supported by Ministry of Defence.

Manuscript submitted Dec. 14, 1971; revised manuscript received Dec. 22, 1973.

Any discussion of this paper will appear in a Discussion Section to be published in the December 1973 JOURNAL.

REFERENCES

1. B. S. Hobbs and A. C. C. Tseung, *Nature*, **222**, 556 (1969).
2. B. S. Hobbs and A. C. C. Tseung, *This Journal*, **119**, 580 (1972).
3. J. Giner, J. M. Parry, S. Smith, and M. Turchan, *ibid.*, **116**, 1692 (1969).
4. J. Giner, *ibid.*, **111**, 376 (1964).
5. K. R. Williams, "An Introduction to Fuel Cells," Elsevier Publishing Co., New York (1966).
6. T. R. Mueller, Ph.D. Thesis, Univ. Kansas, Dissertation Abst. 24, 4952 (1964).
7. T. N. Nazarchuk, *Zh. Neorgan. Khim.*, **4**, 2665 (1959).
8. G. V. Samsonov, "High Temperature Materials Property Index," Reinhold, Plenum Press, New York (1964).
9. D. W. McKee and A. J. Scarpellino, *Electrochem. Technol.*, **6**, 101 (1968).
10. D. T. Sawyer and E. T. Seo, *J. Electroanal. Chem.*, **3**, 410 (1962).
11. S. G. Meibuhr, *Nature*, **210**, 409 (1966).
12. General Electric Co. Ltd., Brit. Pat. 1,157,124 (1965).
13. W. T. Grubb and D. W. McKee, *Nature*, **210**, 192 (1966).
14. O. J. Adlhart and A. J. Hartner, *Proc. Ann. Power Sources Conf.*, Atlantic City, No. 11 (1966).
15. M. A. Liebhafsky and E. J. Cairns, "Fuel Cells and Fuel Batteries," p. 392, John Wiley & Sons, Inc., New York (1968).
16. L. J. Hillenbrand and J. W. Lacksonen, *This Journal*, **112**, 245 (1965).
17. A. Charkey and G. A. Daliu, *Proc. Ann. Power Sources Conf.*, **20**, 79 (1966).
18. B. S. Hobbs, Ph.D. Thesis, The City University, London, 127 (1970).
19. L. W. Niedrach and I. B. Weinstock, *Electrochem. Technol.*, **3**, 270 (1965).
20. L. W. Niedrach and H. I. Zeliger, *This Journal*, **116**, 152 (1969).

Technical Notes

Detection of CO_2 in Cavities in NiO Scales

M. J. Graham and D. Caplan

Division of Chemistry, National Research Council of Canada, Ottawa, Ontario, Canada

In an investigation of the oxidation of Ni at high temperatures (1), cavities (voids) were observed to form in the NiO layer. Cavities are expected at the oxide-metal interface as the result of the condensation of cation vacancies, but voids throughout the oxide layer are less readily explained. One possible explanation is that gas pockets are formed in the oxide by oxidation of the carbon impurity in the metal to CO or CO_2. If so, higher carbon contents should produce more cavity, and CO or CO_2 should occupy the voids. To test this thesis a procedure was devised to analyze the gas content of cavities.

Three specimens, 1 × 5 × 0.03 cm, of pure Ni with carbon contents of 100, 9, and 2 ppm atomic were oxidized at 1270°C for 20 hr in 760 Torr O_2, producing oxide layers ~75 μm thick. To analyze for gases the oxidized sheet was placed on a flange in a metal, ultrahigh vacuum apparatus (Fig. 1) below a steel chisel which could be raised magnetically and dropped onto the specimen to break into the oxide. Any gas liberated was monitored by an A.E.I. Minimass spectrometer. Before a breaking experiment, weakly held gases were desorbed from the chisel, specimen, and apparatus walls by baking at 180°C. Metallographic cross sections were prepared from separate pieces of specimen. Figure 2 shows that many voids formed throughout the oxide on the Ni with 100 ppm atomic carbon, and few on the low-carbon Ni except near the oxide-metal interface.

Each blow of the chisel evolved a strong pulse of CO_2 from the oxidized Ni that had contained 100 ppm atomic carbon,[1] occasional pulses from Ni with 9 ppm atomic carbon, and no CO_2 from Ni with the lowest carbon. The relative amounts of CO_2 evolved are

[1] From the quantity of CO_2 evolved per pulse (~10^{-9} Torr liters), the pressure within the cavities can be estimated to be between 50-5000 Torr.

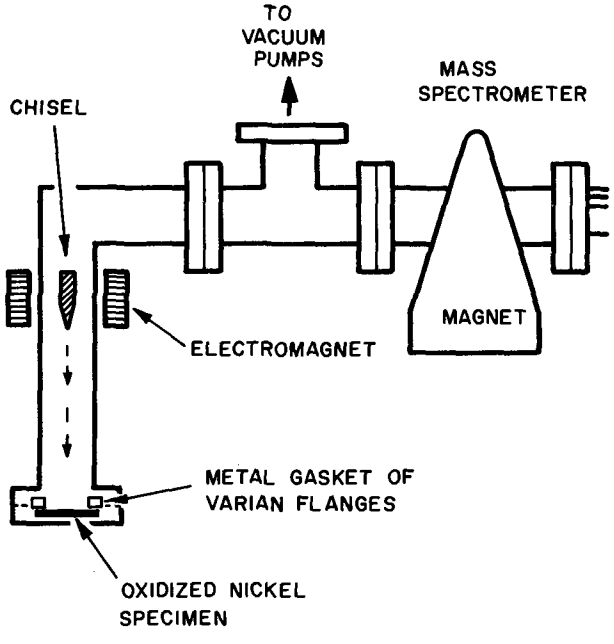

Fig. 1. Schematic diagram of oxide-cracking apparatus

Key words: nickel oxidation, cavities in oxide, CO_2 detection.

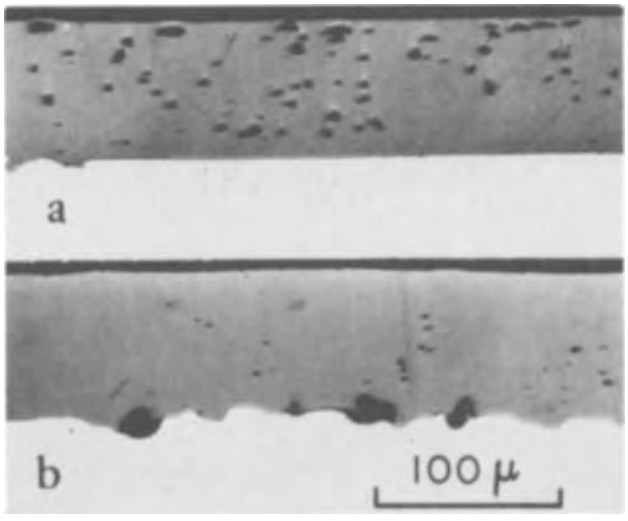

Fig. 2. Metallographic cross sections through oxide formed on Ni in 20 hr at 1270°C in 760 Torr O_2. (a), initial carbon 100 ppm atomic, cavities scattered through oxide; (b) initial carbon 2 ppm atomic, cavities near Ni-NiO interface, but few within the oxide. (×250)

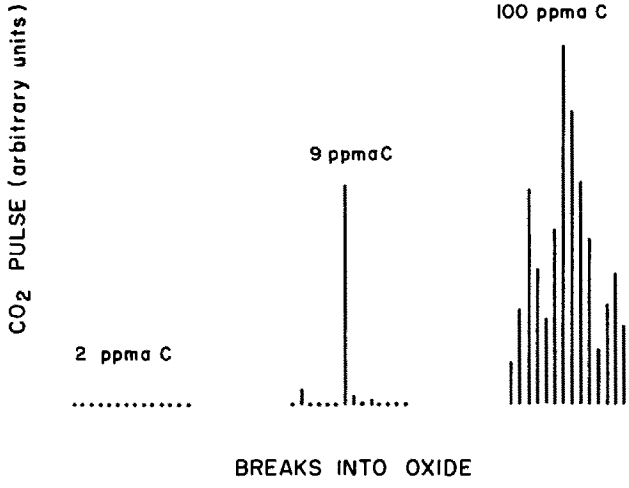

Fig. 3. CO_2 pressure pulses released by cracking of oxide. Bars represent 14 consecutive blows on nickel of 3 different initial carbon contents.

illustrated in Fig. 3, where the pulse height is recorded for an equal number of blows of the chisel into the oxide. The average CO_2 peak heights for the three grades of oxidized Ni are in the ratio 100:8:0. Analysis by spark-source mass spectrometry showed that oxidation reduced the carbon levels from 100:9:2 to 17:2:2, indicating that during oxidation the maximum possible CO_2 production would be in the ratio 83:7:0 (normalized to 100:8:0), which is in agreement with the observed CO_2 peak heights. (The close correspondence is fortuitous since the carbon analysis is uncertain by a factor of two.) Pulse heights of CO were monitored also but no similar correlation was observed; none was expected since the thermodynamics predict a high ratio of CO_2 to CO (2).

These experiments demonstrate that cavities in the NiO scales contain CO_2 at appreciable pressures and that the amount of cavity is related to the carbon content of the nickel. Carbon impurities apparently can have a significant effect on the formation of cavities in oxide layers. The general subject of cavities in Ni oxidation will be reported in a subsequent paper.

Acknowledgment

The authors thank Mssrs. P. E. Beaubien, G. I. Sproule, and Dr. R. J. Hussey for their assistance.

Manuscript received Jan. 24, 1973.

Any discussion of this paper will appear in a Discussion Section to be published in the December 1973 JOURNAL.

REFERENCES

1. D. Caplan, M. J. Graham, and M. Cohen, *This Journal*, **119**, 1205 (1972).
2. F. D. Richardson and J. H. E. Jeffes, *J. Iron Steel Inst.*, **160**, 261 (1948).

The Activity of In in Liquid In-Sb Alloys

D. Chatterji* and J. V. Smith

Aerospace Research Laboratories, Metallurgy and Ceramics Research Laboratory, Wright-Patterson Air Force Base, Ohio 45433

The physical and electrical properties of In-Sb alloys, especially the intermetallic compound InSb, have been studied in considerable detail (1). The thermodynamic properties of this alloy system have received only limited attention.

Schottky and Bever (2) measured the heat of formation of the compound InSb at 273°K by solution calorimetry and the heat of fusion by quantitative thermal analysis. From their measurements and the published In-Sb phase diagram (3), they calculated the free energy of the liquid phase, and concluded that the In-Sb melts showed negative deviations from ideality. Unfortunately, Schottky and Bever did not extend their experimental work to the entire In-Sb system.

Terpilowski (4) conducted a systematic study of the thermodynamic properties of liquid In-Sb alloys using galvanic cells based on fused-salt electrolytes. From open-circuit emf measurements on cells of the type

$$\text{In(l)}\,|\,\text{In Br in NaBr-KBr}\,|\,\text{In-Sb(l)} \qquad \text{[I]}$$

he determined the activity of In in a series of liquid In-Sb melts. He observed a negative deviation from ideality in the liquid phase in agreement with the conclusion reached by Schottky and Bever (2). However, free-energy calculations (5) based on Terpilowski's data for the alloy of equimolar composition did not agree with the values reported by Schottky and Bever for InSb.

Recently, Hoshino *et al.* (5) conducted a thorough investigation of the thermodynamic properties of liquid-In-Sb alloys using cells of the type

$$\text{In(l)}\,|\,\text{InI in NaI-KI}\,|\,\text{In-Sb(l)} \qquad \text{[II]}$$

The activity and free energy data obtained by Hoshino *et al.* at 900°K are in fair agreement with those determined by Terpilowski (4) at the same temperature.

* Electrochemical Society Active Member.

Key words: emf measurements, electrochemical cells, solid electrolytes, thermodynamic properties.

However, the excess enthalpies and entropies reported in the two investigations are quite different.

Terpilowski (4) as well as Hoshino and co-workers (5) assumed that the In ions in their electrolytes were monovalent, and used the relationship

$$\ln a_{In} = -FE/RT \quad [1]$$

to obtain the In-activity (with pure liquid In as the reference state) from the measured-cell emf. There is, however, no direct evidence to support the above-mentioned assumption. We therefore decided to reinvestigate the In-Sb system using cells where the In ions would exhibit an unambiguous oxidation state. With this objective in mind, the following types of cells were constructed

$$W, In\text{-}Sb(l), In_2O_3(s)|Zr_{0.85}Ca_{0.15}O_{1.85}|Air, Pt \quad [III]$$

$$W, In(l), In_2O_3(s)|Zr_{0.85}Ca_{0.15}O_{1.85}|Air, Pt. \quad [IV]$$

The electrolyte in these cells, $Zr_{0.85}Ca_{0.15}O_{1.85}$, is a well-known oxygen ion-conducting solid. In such oxygen-concentration cells, the In ions are clearly trivalent and the O ions divalent, and the over-all cell reaction involves the transfer of 3g equivalents of O ions. The In activity in the In-Sb alloy is then given by

$$\ln a_{In} = -3F(E_{IV} - E_{III})/RT \quad [2]$$

This procedure of taking the difference of the emf outputs of cells IV and III to calculate the In activity is obviously equivalent to, but less accurate than, direct emf measurement on the cell

$$W, In(l), In_2O_3(s)|Zr_{0.85}Ca_{0.15}O_{1.85}|In\text{-}Sb(l), In_2O_3(s), W \quad [V]$$

Nevertheless, cells [III] and [IV] were used instead of cell [V] for the following reason. Preliminary experiments indicated that W could be used as the lead material only if it contacted the liquid electrodes for a short time; long-time contact resulted in W dissolution. Consequently, arrangements had to be made in the cell assembly to lower and raise the W lead wires into and out of the molten electrodes. Such arrangements were easy to install (6) in cells [III] and [IV], but relatively difficult in cell [V].

Experimental

The cell assemblies used in the present work were similar to the ones described in an earlier paper (6). The details of the experimental procedure are also outlined in that publication.

Cell IV.—In a typical experiment, weighed amounts of In shot (99.99% pure) and In_2O_3 powder (99.99% pure) were placed in the electrolyte tube, and melted under a He atmosphere. The emf measurements were started when the cell temperature reached about 550°C. The equilibrium emf data obtained at different temperatures during repeated heating and cooling are presented in Fig. 1 (line 1). These emf values were found to remain constant to within ±0.5 mV for hours and were reproducible to within ±0.5 mV.

Cell III.—At the end of emf measurements on cell [IV], the cell was cooled down to room temperature, and a weighed amount of Sb metal (99.9% pure) was added to the In-In_2O_3 mixture. The system was evacuated and backfilled with He and heated to above 800°C to insure homogeneity in the molten alloy. Equilibrium emf measurements were then carried out at selected temperatures. Additional amounts of Sb were added at the end of successive runs and the procedure repeated. The upper limit of Sb concentration allowable in our cells was found to be only 50 atomic per cent (a/o) because small amounts of Sb_2O_3 formed over alloys containing more than 50% Sb. Although such a situation is thermodynamically unfavorable, it frequently occurs for kinetic reasons. Presence of Sb_2O_3 in addition to In_2O_3 caused undefined oxygen potentials to develop in the alloys, and resulted in erroneous emf readings. The present study was thus confined to four alloys: In-16.0 a/o Sb; In-27.5 a/o Sb; In-43.1 a/o Sb; and In-50.0 a/o Sb. Emf data from the cells containing these alloys are presented in Fig. 1.

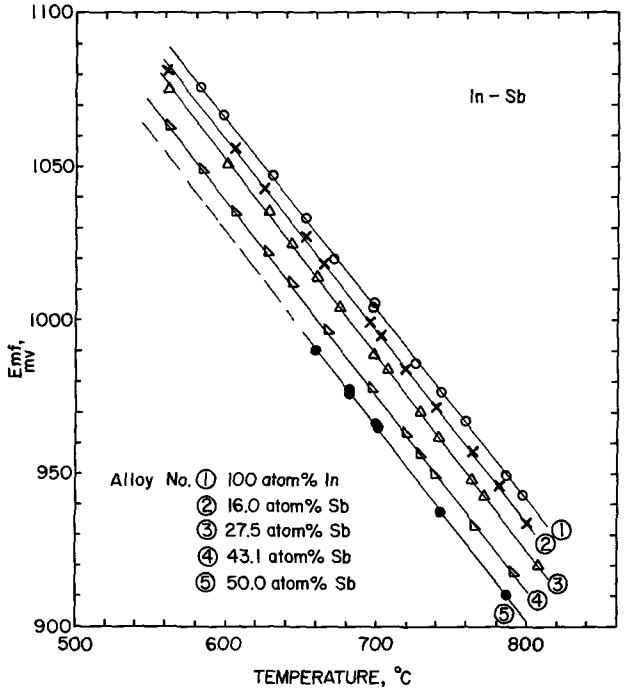

Fig. 1. Emf-temperature data from cell [IV] (alloy) and cell [III] (alloys 2-5) from 550° to 800°C.

Results and Discussion

Free energy of formation of In_2O_3.—As explained earlier, the emf data from cells [IV] and [III] were combined to calculate the In activities in the alloys through Eq. [II]. In addition, the standard molar free energy of formation of In_2O_3 could be directly calculated from the emf of cell [IV] after necessary thermal emf corrections (6) for the W-Pt couple

$$\begin{aligned} E_{IV}^{corr.} &= E_{IV}^{meas.} + E_{W\text{-}Pt}^{therm.} \\ &= (1606.9 - 0.620T) + (-21.4 + 0.037T) \\ &= 1585.5 - 0.583T \pm 0.5 \text{ mV} \\ \Delta G^\circ_{In_2O_3} &= -6FE_{IV}^{corr.} + 1.5\,RT \ln (0.21) \\ &= -219{,}400 + 76.03T \pm 200 \text{ cal/mole} \end{aligned}$$

The free-energy values calculated from this expression are in excellent agreement with the calculations based on similar expressions published in the literature (7, 8). This was considered to be convincing evidence of the correctness of our experimental techniques.

In activity in the alloys.—Table I presents the $(E_{IV} - E_{III})$ values for the four alloys at 900°, 973°, and 1073°K, and the corresponding In activities calculated from Eq. [3]. The activity values are plotted in Fig. 2 as a function of molar composition, and compared with the results obtained by Hoshino *et al.* (5). It is obvious that our results are in excellent agreement with the findings of Hoshino and co-workers for the same temperature (900°K). Our results also agree

Table I. Activity of In* in liquid In-Sb alloys at 900°, 973°, and 1073°K

Alloy No.	X_{In}	X_{Sb}	900°K $E_{IV}-E_{III}$	900°K a_{In}	973°K $E_{IV}-E_{III}$	973°K a_{In}	1073°K $E_{IV}-E_{III}$	1073°K a_{In}
2	0.840	0.160	6.5	0.778	7.0	0.778	7.5	0.784
3	0.725	0.275	13.5	0.590	15.0	0.584	16.5	0.585
4	0.569	0.431	27.0	0.352	28.0	0.367	29.5	0.384
5	0.500	0.500	37.0	0.239	38.0	0.256	40.0	0.273

* Reference state: pure liquid In.

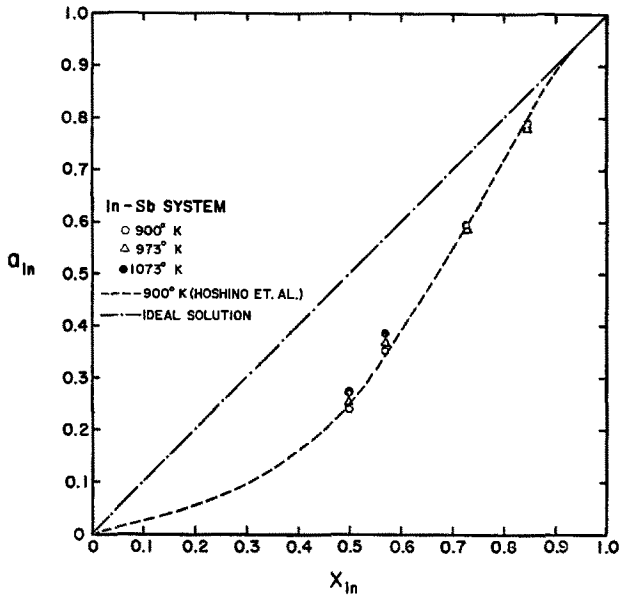

Fig. 2. Activity of In in liquid In-Sb alloys at 900°, 973°, and 1073°K.

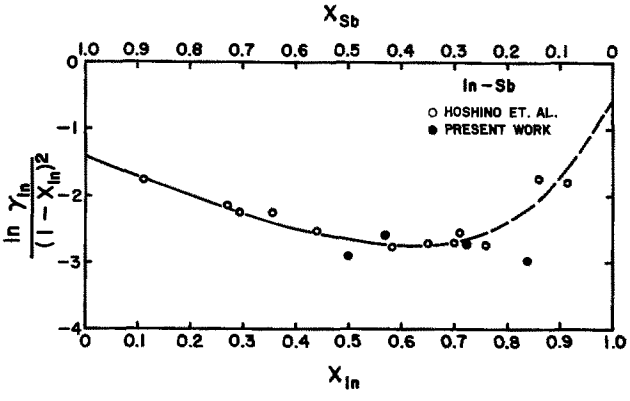

Fig. 3. α_{In} in liquid In-Sb alloys at 900°K

reasonably well with the activity values obtained by extrapolation of Terpilowski's data (4). These extrapolated activity values are not included in Fig. 2 for the sake of clarity; they are included in the paper by Hoshino *et al.*

As a further test of the agreement between our and Hoshino's work at 900°K, the two sets of activity data were converted to corresponding alpha functions (9)

$$\alpha_{In} = \ln \gamma_{In}/(1 - x_{In})^2$$

The calculated α_{In} values are shown in Fig. 3. The agreement is again satisfactory except for the In-16.0 a/o Sb alloy, where small errors in emf measurements may cause large errors in activity calculations.

The agreement between the results from our solid oxide-based investigation and the results from earlier studies involving In-halide based fused-salt electrolyte cells indicates that the assumption of monovalent In ions in halide melts is indeed valid. In light of this indication, it appears that the Sb activities (from In activities through Gibbs-Duhem integration using alpha functions) and excess thermodynamic properties calculated by Hoshino *et al.* (5) may be considered reliable. No such calculations were attempted in the present study because of the limited number of alloys investigated and the consequent uncertainties in Gibbs-Duhem integration.

Conclusions

Oxygen-concentration cells based on the electrolyte, $Zr_{0.85}Ca_{0.15}O_{1.85}$, have been successfully used to determine the In activity in liquid In-Sb alloys over 560°-800°C. Only In-rich alloys could be studied.

Our results are in agreement with the data obtained by earlier workers who used halide-based concentration cells, and assumed presence of monovalent In ions in their electrolytes. The present investigation therefore serves not only as an independent source of In-activity data but also as an indirect evidence of correctness of the assumption regarding the oxidation state of In ions in In-halide melts.

Acknowledgments

One of the authors (D. C.) wishes to thank National Research Council and Air Force Systems Command for providing a Resident Research Associateship. Useful discussions with Dr. J. Wimmer are gratefully acknowledged.

Manuscript received Jan. 24, 1973.

Any discussion of this paper will appear in a Discussion Section to be published in the December 1973 JOURNAL.

REFERENCES

1. H. Welker and H. Weiss, in "Solid State Physics," Vol. 3, Academic Press, New York (1956).
2. W. F. Schottky and M. B. Bever, *Acta Met.*, **6**, 320 (1968).
3. T. S. Liu and E. A. Peretti, *Trans. Am. Soc. Metals*, **44**, 539 (1952).
4. J. Terpilowski, *Arch. Hutnictwa*, **3**, 227 (1958).
5. H. Hoshino, Y. Nakamura, M. Schimoji, and K. Niwa, *Ber. Bunsengesellsch. Physik. Chem.*, **69**, 114 (1965).
6. D. Chatterji and J. V. Smith, Paper 17 presented at Electrochem. Soc. Meeting, Miami Beach, Florida, October 8-13, 1972.
7. D. Chatterji and R. W. Vest, *J. Am. Ceram. Soc.*, **55**, 575 (1972).
8. G. R. Newns and J. M. Pelmore, *J. Chem. Soc (A)*, **2**, 360 (1968).
9. L. S. Darken and R. W. Gurry, "Physical Chemistry of Metals," McGraw Hill Book Co., Inc., New York (1953).

Brief Communication

A Preparative Graphite-Paste Electrode

J. M. Bobbitt,* J. F. Colaruotolo, and Samuel J. Huang

Department of Chemistry, University of Connecticut, Storrs, Connecticut 06268

Pastes of graphite in various organic liquids have been developed and used extensively as analytical electrodes by Adams and his co-workers (1). Such electrodes have a good working range and are remarkably free of problems. We have been intrigued by the role that the liquid component of such a paste might play in determining the products of the reaction, and, to this end, have devised and tested a preparative form of the electrode.

Several possible configurations of such an electrode have been investigated including one in which the paste is pressed out of a tube into the cell rather like Adam's original idea (1). However, the best configuration is a simple one. The paste, prepared according to Adams (1), and about 5 mm thick, is packed into the bottom of a beaker against a platinum foil contact about the same size as the bottom of the beaker. Contact is made with the foil by an insulated Pt wire attached to the inside wall of the beaker. The reference electrode is placed just over the paste, and the electrolyte is layered over it. The auxiliary electrode (Pt foil) is placed over the center of the paste in a second compartment separated from the anode by a glass frit. Currents of 2-3 mA/cm^2 were obtained on a Nujol-graphite paste electrode, and the effective range is about the same as that of the analytical electrode (-0.9 to $+1.3$V *vs.* SCE in 0.1*M* $HClO_4$).

The cell was tested with two compounds, potassium hexacyanoferrate and the isoquinoline alkaloid corypalline (2-4). Aqueous solutions (200 ml) of 0.1*M* $HClO_4$ containing 0.6 mM of potassium hexacyanoferrate was oxidized at 0.6V (5) on a Nujol-graphite electrode about 35 cm^2 in area. The initial current was 30 mA which dropped off to the residual current of about 0 mA in about 10 hr. In one experiment, a coulometric measurement showed that 0.913 electrons per molecule were released. The oxidation of 1.0g of corypalline was carried out on the sodium salt in aqueous 0.1*M* KCl. The initial current at 0.35V was 85 mA which fell to 15 mA in 6 hr. The products were isolated as previously described (4) giving an over-all yield of dimeric products of 42% (38% carbon-carbon and 4% carbon-oxygen). In addition, 16% of a trimer (6) was obtained. On graphite felt (4) in acetonitrile, the products obtained were about 90% dimers (86% carbon-carbon and about 4% carbon-oxygen) and no trimer. However, the graphite felt reactions were carried out at lower potentials (0.0V *vs.* SCE). When higher potentials were applied to the felt system, appreciable amounts of trimer were formed. On a platinum working electrode in aqueous $Na_2B_4O_7$, the yields of dimeric products ranged from 44-60% (2) at potentials of about 0.35V. Thus, it would appear, in agreement with Adams (7), that the paste electrode is comparable to platinum.

The nature of the charge-transfer reactions within and on the surface of graphite pastes appears to be largely unknown (7) although it has been ascertained that the graphite particles are covered with a liquid film. Thus far, we have explored pastes made with Nujol and bromoform (1), benzonitrile (inferior because of paste fragmentation), optically active liquids such as α (+)-pinene and (+)-2-octanol, and the quaternary liquid-anion exchanger Aliquat 336.[1] The ion exchanger has been used in its chloride form and its hydroxide form. Although all of the pastes gave results comparable with those described above for phenol coupling reactions, the liquid-ion exchangers offer the greatest potential. It is possible, using them as a matrix, to prepare electrodes which, in themselves, have any desired *p*H or contain a large variety of ions. We have initiated work to further explore these possibilities with both liquid-anion exchangers and liquid-cation exchangers.

Acknowledgments

We would like to thank Professor J. T. Stock of this Department for his many helpful suggestions, and the National Science Foundation (Grant No. GP-30574X) and the National Institutes of Health (CA-10494) for financial support.

Manuscript received Jan. 2, 1973.

Any discussion of this paper will appear in a Discussion Section to be published in the December 1973 JOURNAL.

[1] General Mills Chemicals, Incorporated, Mineral Industries Division, Tucson, Arizona.

* Electrochemical Society Active Member.

Key words: graphite, electrode, paste, phenol, electro-oxidation.

REFERENCES

1. R. N. Adams, "Electrochemistry at Solid Electrodes," pp. 26, 281, Marcel Dekker, Inc., New York (1969).
2. G. F. Kirkbright, J. T. Stock, R. D. Pugliese, and J. M. Bobbitt, *This Journal*, **116**, 219 (1969).
3. J. M. Bobbitt, K. H. Weisgraber, A. S. Steinfeld, and S. G. Weiss, *J. Org. Chem.*, **35**, 2884 (1970).
4. J. M. Bobbitt, H. Yagi, S. Shibuya, and J. T. Stock, *ibid.*, **36**, 3006 (1971).
5. W. M. MacNevin and B. B. Baker, *Anal. Chem.*, **24**, 986 (1952).
6. B. Umezawa, O. Hoshino, H. Hara, and J. Sakakibara, *Chem. Pharm. Bull. (Tokyo)*, **16**, 381 (1968).
7. R. N. Adams, *Rev. Polarog. (Kyoto)*, **11**, 71 (1963).

DISCUSSION SECTION

This Discussion Section includes discussion of papers appearing in the *Journal of The Electrochemical Society*, Vol. 119, No. 5, 8, and 10; May, August, and October, 1972.

Anodic Oxidation of Ethylenediaminetetraacetic Acid on Pt in Acid Sulfate Solutions

J. W. Johnson, H. W. Jiang, S. B. Hanna, and W. J. James

(pp. 574-580. Vol. 119, No. 5)

P. Sidheswaran, V. K. Venkatesan, and H. V. K. Udupa:[1] During the steady-state oxidation of EDTA at platinum electrodes in acid sulfate solutions, Johnson *et. al.*, in the paper under discussion, identified various reaction products. A definite clue to the presence of CH_2O was obtained from the melting point of the DNP derivative. However, it is very easy to establish the presence of CH_2O with chromotropic acid by the method described elsewhere.[2] After 3 hr of electrolysis, we also noticed[3] a concentration of $>10^{-2}$M CH_2O formed from 0.5M EDTA. Our evidence strongly supports their observation that CH_2O is thrown out into the solution.

The formation of CH_2O has been indicated to be due to a reverse Schiff-type reaction and the authors of the above-mentioned paper proposed the following two steps

$$R{-}\overset{\displaystyle Ac}{\overset{|}{N}}{-}CH_2\cdot + H_2O \rightarrow R{-}\overset{\displaystyle Ac}{\overset{|}{N}}{-}CH_2OH + H\cdot \qquad [19]$$

$$R{-}\overset{\displaystyle Ac}{\overset{|}{N}}{-}CH_2OH \rightarrow R{-}\overset{\displaystyle Ac}{\overset{|}{N}}{-}H + CH_2O \qquad [20]$$

However, the second step should be either less probable or a simultaneous reaction occurs on the platinum electrode. This opinion stems from the following evidence: Podlovchenko *et al.*[4] have demonstrated that the presence of a hydroxyl function weakens the C-C bond; it has also been noticed by us[3] that primary alcohols preferentially get disintegrated into two fragments of which CH_2OH is one. The mechanism of formation of CH_2O from CH_2OH has already been proposed.[2] Hence, the following mechanism appears to be operative

$$2Pt + R{-}\overset{\displaystyle Ac}{\overset{|}{N}}{-}CH_2OH \rightarrow R{-}\overset{\displaystyle Ac}{\overset{|}{N}}{-}\underset{\displaystyle Pt}{\overset{|}{Pt}} + CH_2OH \qquad [1]$$

$$H{-}\overset{\displaystyle H}{\overset{|}{C}}{-}O{-}H \rightarrow H{-}\overset{\displaystyle H}{\overset{|}{C}}{=}O + Pt + Pt \qquad [2]$$

The observed Tafel slope of ~120 mV is in sharp agreement with $\beta \approx 0.5$ and $\Delta Ea/\Delta\psi r \approx 14$ kcal/mole/V. However, it is very difficult to establish exactly which step decides the rate of the entire reaction in as much as so many reaction intermediates are getting formed and oxidized.

J. W. Johnson, H. W. Jiang, S. B. Hanna, and W. J. James: We were very interested to learn of the similar work with EDTA that has been done by Sidheswaran, Venkatesan, and Udupa, and of the close agreement of the experimental results of the two studies. Our difference in interpreting the results appears to center around the disposition of the species, $R{-}\overset{\displaystyle Ac}{\overset{|}{N}}{-}CH_2OH$, which was proposed as an intermediate. In particular we have proposed a homogeneous, nonelectrochemical step (reverse Schiff-type) by which formaldehyde is ejected from the intermediate. Venkatesan *et al.* propose a heterogeneous step that results in two adsorbed fragments, one of which (CH_2OH) is the precursor of formaldehyde.

A sequence such as proposed by Venkatesan *et al.* was among the many that we considered. The one presented in our paper was favored because of the following reasons.

If bonding should occur between Pt and the nitrogen atom as shown in Step I (SVU sequence), several desorption and readsorption steps would be necessary to account for all the observed reaction products, *e.g.*, ED3A, U-EDDA, S-EDDA, and EDMA. This does not seem likely. A further consideration is the geometrical crowding around the nitrogen atom by other attached groups that makes its accessibility unfavorable for bonding with the electrode. Finally, protonation of the unshared electron pair on the nitrogen atom is also quite likely which would further hinder its adsorption.

If formaldehyde were produced as shown in Step II of the SVU sequence, the further ionization of the adsorbed H would be almost certain, and be associated with a 1 CO_2/2F coulombic relationship. This relationship was not observed experimentally, though the observed value could be accounted for by a combination of the SVN and JJHJ sequences.

Our studies indicate that EDTA is oxidized on Pt at potentials up to *ca.* 1.6V. It is doubtful that oxide-free sites would be available for bonding at these potentials[5] as required by the SVN sequence. Since no change in the reaction sequence with potential is indicated by the experimental results, we feel that direct bonding (adsorption) between Pt atoms and the EDTA species or any fragments therefrom should be excluded.

In summary, the sequence proposed by Venkatesan *et al.* is a logical one and cannot be completely eliminated as a possibility. Indeed it may be that both sequences (or others) are occurring. However, the above mentioned items caused us to favor the sequence we proposed.

Kinetics of Iron Corrosion in Concentrated Acidic Chloride Solutions

E. McCafferty and Norman Hackerman (pp. 999-1009, Vol. 119, No. 8)

G. Bech-Nielsen:[6] This paper, and also a virtually simultaneous publication by Darwish, Hilbert, Lorenz, and Rosswag,[7] report some important and rather unusual kinetic data for iron electrodes in strongly acid, strongly concentrated, chloride solutions. In the two papers reaction schemes of a similar type are proposed for explaining the observed kinetic parameters.

We would like to point out that such unusual kinetic parameters have been reported previously, to-

[1] Fundamental Electrochemistry Section, Central Electrochemical Research Institute, Karaikudi 3, Tamil Nadu, India.
[2] P. Sidheswaran, *J. Electroanal. Chem.*, 38, 101 (1972).
[3] P. Sidheswaran, Unpublished work.
[4] B. I. Podlovchenko and V. F. Stenin, *Elektrokhimiya*, 3, 649 (1967).
[5] S. Gilman and M. W. Breiter, *This Journal*, 109, 1099 (1962).
[6] Chemistry Department A, The Technical University of Denmark, Lyngby, Denmark.
[7] N. A. Darwish, F. Hilbert, W. J. Lorenz, and H. Rosswag, 23rd Meeting of ISE, Extended Abstracts p. 213, Stockholm, 1972.

gether with the more usual ones, for iron electrodes in a wide variety of solutions.[8-11] It may well be that all of the unusual parameters will be found simultaneously only when using extremely concentrated solutions, whereas it has been shown that dilute, less concentrated, solutions present conditions for observing first (at lower anodic potentials) the usual behavior called the I_1-reaction[8-11] and then, following a characteristic transition region, the less usual or less often examined behavior of the I_2-reaction.

The most constant feature of this latter reaction is the higher Tafel slope (from *ca.* 80 to more than 120 mV), while the reaction orders with respect to different anions may be negative[10] or positive,[9] and the reaction order with respect to *p*H has been reported to be positive[10] or zero.[11] (A further indication of transition from negative to positive values has been found, but not yet published, in data from the experiments with an NH_4ClO_4-$NaClO_4$ solution, *p*H 5.5-3.0 described elsewhere.[9])

It is not surprising that neither the discussed paper nor that of Darwish *et al.* include descriptions of simultaneous observation of the two distinct reactions, since it can be seen,[11] and may be shown by general considerations,[12] that the regions, where a distinct behavior in accord with either of the reactions will be found, are likely to be separated by some 1-3 decades of current density (C.D.). When the I_2-reaction is recorded in the range of moderate anodic C.D.'s, it may be inferred that the I_1-reaction is only found in the C.D. range below the corrosion C.D., which is in accord with the usual inhibitive influence on this reaction of low *p*H and high chloride concentration together with the promotion of the hydrogen evolution reaction caused by lower *p*H.

Since we have observed that the I_1 and the I_2 reaction usually occur together as coupled, parallel reactions, we have suggested an outline of a kinetic model, which accounts for the potential-dependent transition between the two processes.[9] An explanation of this feature is evidently of primary importance, and further examination of the influences of *p*H and anions in the individual steps of the two reactions are now in progress.

In the last part of this comment we should like to consider the so-called reaction orders with respect to *p*H ($-\partial \log i/\partial \log [H^+]$). The analysis of coupled, parallel reactions developed by us indicates that the I_2 reaction proceeds via an intermediate complex of the composition $Fe^{II}(OH^-)_3(X)$, where X is a ligand, usually an anion.[8,9] In most cases known to us (of which one has been reported),[10] the reaction order with respect to *p*H for the I_2 reaction is between 0.2 and 0.3, *i.e.*, much lower than the number of OH^- ions taken up during formation of the intermediate complex. We therefore suggest that the observation of a negative reaction order with respect to *p*H for the I_2 reaction does not necessarily require the assumption of uptake of H^+ ions (especially not when the observation is possible at intermediate *p*H values, as we have seen). The steps in the mechanism following the formation of the above-mentioned complex should merely involve removal of one or more of the OH^- ions (in exchange for halide ions, for example) by H^+ ions, in order to result in an over-all negative reaction order with respect to *p*H (and at the same time a positive one for the halide ion).

E. McCafferty and Norman Hackerman: We thank G. Bech-Nielsen for his interesting comments and for calling our attention to the work of Darwish, Hilbert, Lorenz, and Rosswag.[7] These workers have confirmed our observation that both H^+ and Cl^- ions promote iron corrosion in concentrated acidic chloride solutions (*i.e.*, the reaction orders z_{H+} and z_{Cl-} are positive), in contrast to the usual cases more frequently examined (more dilute solutions) for which both z_{H+} and z_{Cl-} are negative.

Table I. Polarization resistance for iron in 6*N* chloride solutions.

N [H+]	Polarization resistance (ohm-cm²) Polarization curve	Calc'd from Stern-Geary Eq.
1.2	38.6	40.1
2.4	20.4	24.1
3.6	21.4	18.8
4.8	10.3	15.7
6.0	6.3	9.5

Both our results in the paper under discussion and the Darwish data[7] have shown that a high concentration of hydrogen ions in combination with a high concentration of chloride ions is necessary to give the new set of parameters $z_{H+} = +1$[7] as compared to $+1.8$ in our paper; $z_{Cl-} = +0.5$ in both our results; and $b_a = 60$-80 mV in our paper as compared to 120 mV in the work of Darwish *et al.*

These parameters are unusual in the sense that the signs of z_{H+} and z_{Cl-} in certain concentrated solutions are opposite to those in differing, dilute solutions. In contrast, in the work of Bech-Nielsen, the unusual parameters emerged only after considerable anodic polarization (usually about 200 mV) in the same solution. The possibility that the original surface could have been modified seems to have been recognized by the authors, who usually attributed the second Tafel region to the appearance of passivation precursors.

Whether or not the two sets of observations are linked through a general scheme of coupled, parallel, reactions having widespread validity remains to be seen. We did not examine the region below the corrosion current density in any great detail, but our own data do tend to show simple pre-Tafel behavior rather than the existence of a different, *i.e.*, I_1, reaction. Table I compares polarization resistances obtained from the linear polarization curve near the corrosion potential (Fig. 1) with those calculated from the Stern-Geary equation.[13] Agreement between the two sets of values is generally good, although a more thorough examination of the region close to the corrosion potential should be made, as suggested by Bech-Nielsen.

We next consider the suggestion that replacement of adsorbed OH^- ions by Cl^- (to give positive z_{H+} and z_{Cl-}) is equivalent to uptake of H^+ ions by adsorbed Cl^-. Consider the two reaction mechanisms in Table II. Mechanism I involves adsorption of Cl^- ions by replacement of chemisorbed water molecules,[14] followed by attraction of H^+ ions onto chemisorbed $FeCl^-_{ads}$, as

[8] H. Nord and G. Bech-Nielsen, *Electrochim. Acta*, 16, 849 (1971).
[9] G. Bech-Nielsen and J. C. Reeve, 6th Scandinavian Corrosion Congress, chap. 8, Gothenburg, 1971.
[10] G. Bech-Nielsen, 23rd Meeting of ISE, Extended Abstracts, p. 213, Stockholm, 1972.
[11] I. Epelboin and M. Keddam, *Electrochim. Acta*, 17, 177 (1972).
[12] G. Bech-Nielsen, Submitted to *Electrochim. Acta*.
[13] M. Stern and A. L. Geary, *This Journal*, 104, 56 (1957).
[14] T. N. Andersen and J. O'M. Bockris, *Electrochim. Acta*, 9, 347 (1964).

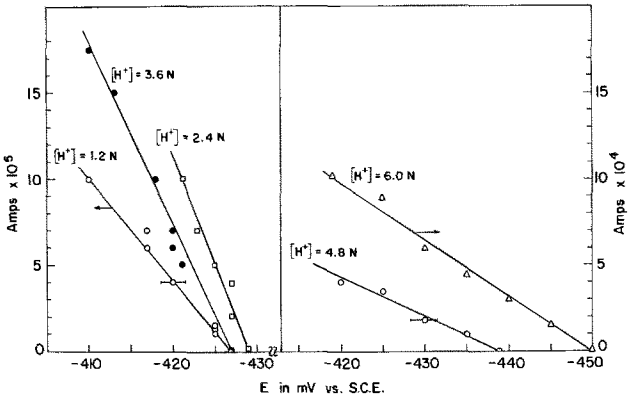

Fig. 1. Polarization curves near the corrosion potential for 6*N* chloride solutions of various acidities.

Table II. Comparison of different reaction mechanisms to test equivalence of H^+ attraction to OH^- expulsion

Mechanism I (Electrostatic attraction of H^+ ions to adsorbed chloride irons)	Mechanism II (Displacement of adsorbed hydroxyl ions by chloride ions)
$Fe + H_2O \underset{-1}{\overset{1}{\rightleftharpoons}} Fe \cdot H_2O_{ads}$	
$Fe \cdot H_2O_{ads} + Cl^- \underset{-2}{\overset{2}{\rightleftharpoons}} FeCl^-_{ads} + H_2O$	$Fe \cdot H_2O_{ads} \underset{-2}{\overset{2}{\rightleftharpoons}} FeOH^-_{ads} + H^+$
$FeCl^-_{ads} + H^+ \underset{-3}{\overset{3}{\rightleftharpoons}} FeCl^- \cdot H^+$	$FeOH^- + Cl^- \underset{-3}{\overset{3}{\rightleftharpoons}} FeCl^-_{ads} + OH^-$
$FeCl^- \cdot H^+ \xrightarrow{4} FeCl^+ + H^+ + 2e^-$	$FeCl^-_{ads} \xrightarrow{4} FeCl^+ + 2e^-$
$FeCl^+ \underset{-5}{\overset{5}{\rightleftharpoons}} Fe^{++}(aq) + Cl^-$	

Table III. Results for Mechanism II

Case	Assumption	z_{H^+}	z_{Cl^-}
A	$\theta_{Cl^-} >> \theta_{OH^-}$	0	$(1-\theta_{Cl^-})$; $1 \rightarrow 0$ as θ_{Cl^-} goes from $0 \rightarrow 1$
B	$\theta_{OH^-} >> \theta_{Cl^-}$	θ_{OH^-}; $0 \rightarrow 1$	$+1$
C	$\theta_{OH^-} \approx \theta_{Cl^-}$	$(1-2\theta_{OH^-})$; $1 \rightarrow 0$ as θ_{OH^-} goes from $0 \rightarrow 0.5$	0
D	$\theta_w >> \theta_{OH^-} + \theta_{Cl^-}$	0	$+1$
E	$\theta_{OH^-} >> \theta_w + \theta_{Cl^-}$	θ_{OH^-}; $0 \rightarrow 1$	$+1$
F	$\theta_{Cl^-} >> \theta_w + \theta_{OH^-}$	0	$(1-\theta_{Cl^-})$; $1 \rightarrow 0$ as θ_{Cl^-} goes from $0 \rightarrow 1$
G	$\theta_w + \theta_{Cl^-} >> \theta_{OH^-}$	Same as case A	Same as case A
H	$\theta_w + \theta_{OH^-} >> \theta_{Cl^-}$	Same as case B	Same as case B
J	$\theta_{Cl^-} + \theta_{OH^-} >> \theta_w$	θ_{OH^-}; $0 \rightarrow 1$	$(1-\theta_{Cl^-})$; $1 \rightarrow 0$ as θ_{Cl^-} goes from $0 \rightarrow 1$

proposed earlier in the paper under discussion. In mechanism II, the chloride ion adsorbs by replacing chemisorbed hydroxyl ions rather than water molecules. In the steady state, mechanism I gives $b_a = 60$ mV, $z_{H+} = +1$, and $z_{Cl-} = 1 - \theta_{Cl-}$, so that z_{Cl-} is always positive and goes from 1 to 0 as θ_{Cl-} goes from 0 to 1. Necessary assumptions are $v_{-3} >> v_4$ and $\theta_{Cl-} >> \theta_{complex}$, where complex refers to $FeCl^- \cdot H^+$. Note that mechanism I is not exactly the same as proposed in our original paper under discussion, but differs in that only one rather than two H^+ ions are involved (to make a clear distinction between the different roles of H^+ in mechanisms I and II).

Results for mechanism II are given in Table III for various cases which compare: (*i*) the coverage of $FeCl^-_{ads}$ to $FeOH^-_{ads}$ (cases A-C); (*ii*) the coverage of one of the adsorbed species to the other two (cases D-F, θ_w refers to $Fe \cdot H_2O_{ads}$); and finally, (*iii*) the coverages of two of the adsorbed species to the other one. None of the cases yield both z_{H+} to be exactly $+1$ and $z_{Cl-} = 1 - \theta_{Cl-}$, as in mechanism I, but cases B, E, and J do give both z_{H+} and z_{Cl-} to be positive. However, in each instance, in order that $z_{H+} \cong +1$, θ_{OH-} must be near full coverage. This, in turn, makes it more likely that the reaction would proceed through the species $FeOH^+$, as for systems lower in $[Cl^-]$ or $[H^+]$, instead of through $FeCl^+$. Thus, replacement of adsorbed hydroxyl ions by chloride is not kinetically equivalent to H^+ attraction onto adsorbed chloride.

Calculation of the adsorption energy for $FeCl^-_{ads}$ and $FeOH^-_{ads}$ also suggests that Cl^- will not displace OH^- from an iron surface. These calculations follow Andersen and Bockris.[14] The attractive contributions to the adsorption energy are due to image and dispersion forces

$$U_{image} = -\frac{e^2}{4r} + \frac{e^4}{64W_a \cdot r^2} \qquad [1]$$

where e is the ionic charge, r the distance from the center of the ion to the outer surface of the metal atoms, and W_a the sum of the electronic work function and Fermi energy of the metal (1.83×10^{-11} ergs for iron). Also,

$$U_{disp} = -\frac{\pi N m c^2 \alpha_{Fe} \alpha_{ion}}{r^3 \left(\frac{\alpha_{Fe}}{\chi_{Fe}} + \frac{\alpha_{ion}}{\chi_{ion}} \right)} \qquad [2]$$

where N is the number of iron atoms per unit volume (8.50×10^{22} cm^3), and α and χ are the polarizabilities and diamagnetic susceptibilities of the interacting species (2.42×10^{-24} cm^3/atom and 1.68×10^{-29} cm^3/atom, respectively, for iron).[15] The repulsion term is

$$U_{repul} = \frac{2\pi NA}{(n-3)(n-2)r^{(n-3)}} \qquad [3]$$

where A and n are repulsion parameters. The total energy of adsorption for the unsolvated anion is then

$$U_{ads} = U_{image} + U_{disp} + U_{repul} \qquad [4]$$

Values of various parameters used in calculating U_{ads} are listed in Table IV. Calculation of U_{repul} is the least certain because the parameters A and n are not known for the interaction between an iron atom and a chloride (or hydroxyl) ion. However, these parameters can be estimated by comparison with data for alkali halide crystals,[20] because A and n are determined by the sizes of the ionic cores. Andersen and Bockris[15] used values of A and n for RbCl to calculate the repulsion between Hg and Cl^- because the radii of Hg (1.51Å) and Rb^+ (1.48Å) are nearly the same. In the case of Fe (1.24Å), there is no alkali metal ion of similar radius. G. A. Wright, with whom one of us has previously corresponded[21] on the problem of calculating adsorption energies for the series FeX^-_{ads} (X = Cl, Br, I) has suggested that n for Fe^0Cl^- be obtained from inter-

[15] J. O'M. Bockris and D. A. J. Swinkels, *This Journal*, 111, 736 (1964).
[16] L. Pauling, "The Nature of the Chemical Bond," p. 518, Cornell University Press, Ithaca, New York (1960).
[17] H. Triche, *Compt. Rend.*, 217, 687 (1943).
[18] J. A. A. Ketelaar, "Chemical Constitution," p. 102, Elsevier Publishing Co., Amsterdam (1958).
[19] P. W. Selwood, "Magnetochemistry," p. 78, Interscience Publishers, New York (1956).
[20] E. A. Moelwyn-Hughes, "Physical Chemistry," p. 557, Pergamon Press, New York (1961).
[21] G. A. Wright, University of Auckland, New Zealand, to E. McCafferty, Personal communication, Nov., 1968.

Table IV. Summary of calculations of the adsorption energy for $FeCl^-_{ads}$ and $FeOH^-_{ads}$

Term	$FeCl^-_{ads}$	$FeOH^-_{ads}$	Source
Ionic radius (A)	1.81	1.33	Footnote 16, 17
Polarizability, σ_{ion} (cm^3/ion)	2.98×10^{-24}	1.89×10^{-24}	Footnote 18
Diamagnetic susceptibility, χ_{ion} (cm^3/ion)	4.32×10^{-29}	1.99×10^{-29}	Footnote 19
n	8.81	8.03	Interpolation
log A	−79.504	−73.603	Eq. [5]
Equilibrium distance, r_e (A)	1.82	1.34	Eq. [5]
U_{image} (kcal/mole)	−43.7	−58.4	Eq. [1]
U_{disp} (kcal/mole)	−17.7	−25.0	Eq. [2]
U_{repul} (kcal/mole)	+16.0	+25.3	Eq. [3]
U_{ads} (kcal/mole)	−45.4	−58.1	Eq. [4]

polation of graphs of n *vs.* cation radius for LiCl, NaCl, KCl, and RbCl. The radius of the OH^- anion (1.33Å) is nearly the same as for F^- (1.34Å),[16] so n for Fe^0OH^- was interpolated by drawing a smooth plot through values for LiF, NaF, KF, and RbF. Values of n used in calculation of U_{ads} are given in Table IV.

The values of A corresponding to n can be obtained from solving the equation which results from the requirement that

$$\frac{\partial U_{ads}}{\partial r} = 0, \text{ when } r = r_{equil} \qquad [5]$$

with the equilibrium distance taken to be the ionic radius listed in Table IV. Results of the calculations are given in Table IV.[22] It is seen that the adsorption energy for $FeOH^-_{ads}$ is significantly higher than for $FeCl^-_{ads}$, so that replacement of adsorbed hydroxyls by chloride ions is not favored on an enthalpy basis. These calculated adsorption energies are for small initial coverages, but both values are expected to fall off in some complicated manner with increasing coverages.

Thus adsorption of Cl^- by competition with OH^- seems more likely than replacement of the latter by the former. For high bulk concentrations of Cl^- and H^+, adsorption of OH^- will not be favored, as shown in Eq. [44] of our paper under discussion, so that dissolution does not proceed through $FeOH^+$ but via the species $FeCl^+$.

Finally, evidence has been accumulating to indicate that there is attraction of H^+ ions in solution to the adsorbed chloride ions $FeCl^-_{ads}$. For example, various organic amines were more effective in inhibiting the corrosion of iron in HCl than in $HClO_4$.[23] This observation suggests that the inhibitor adsorbs not only at the metal surface, but also attaches via electrostatic attraction of the protonated amine to the adsorbed chloride ion. Similarly, additions of quinoline or dimethyl aniline reduced the double layer capacitance of iron more in HCl than in $HClO_4$,[24] again suggesting cooperative adsorption between the protonated inhibitor and the adsorbed anion. The kinetic data, of Darwish *et al.*[7] and in our paper under discussion, which show that a high Cl^- concentration alone will not give the unusual kinetic parameters but that a concomitant high concentration of H^+ ions is necessary also, point to cooperative adsorption between the two species. The positive value of z_{H^+} also persists if organic inhibitors are present in the concentrated acidic chloride solutions.[25]

Corrosion Fatigue of Copper and Alpha-Brass

Stuart S. Birley and Desmond Tromans

(pp. 1278-1285, Vol. 119, No. 10)

Ugo Bertocci:[26] In the paper under discussion the authors refer to a paper of mine[27] and describe the model in it as an electrochemical reaction under cathodic control. I would like to point out that this is incorrect. My model consists of a system in which anodic and cathodic electrode reactions occur without hindrance, so that both processes are diffusion controlled. Specifically, I commented that stirring would increase the corrosion rate but would not change the concentrations of the reactants at the metal surface. This, of course, is equivalent to predicting no change in electrode potential, which, in the absence of charge-transfer overvoltage, is the equilibrium potential for both reactions (not indicating ammonia ligands)[28]

$$Cu \rightarrow Cu^+ + e^- \qquad [1]$$

$$Cu^+ \rightarrow Cu^{++} + e^- \qquad [2]$$

Such a behavior with stirring can hardly be ascribed to a system under cathodic control.

It is not difficult to extend the consequences of my model to conditions under which the solubility product for Cu_2O is reached and a film is formed. Then the Cu^+ concentration at the metal surface is kept constant, and therefore for a given thickness of the diffusion layer, the amount of Cu^+ diffusing away depends only on the oxygen concentration in solution, but no longer on Cu^{++}. If equilibrium at the surface is maintained (that is, Cu^{++} at the metal surface is constant) more Cu^{++} will diffuse in and be reduced than Cu^+ will diffuse out. The material balance (as well as the electroneutrality of the corroding metal) is achieved by a continuous Cu_2O film growth. Stirring would only affect the rate of film formation, but no shift from the equilibrium value of the potential would be observed, contrary to the experimental results, but also inconsistent with a system under cathodic control.

In order to explain the results, a larger degree of irreversibility for the anodic reaction than for the cathodic one has to be postulated. After all, the assumption of complete reversibility for the electrode reaction made in my paper, although perhaps adequate for the purpose of estimating corrosion rates, cannot be taken literally, so as to exclude potential shifts of 10 to 20 mV when corrosion rates are fairly high. The authors of the paper under discussion favor a mechanism related to the protective properties of the Cu_2O film. This might be right, although the fact that the film is formed by precipitation does not seem to suggest a large degree of protection. I would like to propose that the charge-transfer overvoltage for reaction [1] could be larger than that for reaction [2], an explanation which is in qualitative agreement with recent faradaic impedance measurements.[29] If this explanation were correct, stirring should affect the potential in the same direction whether a film is present or not. I wonder if the authors of the paper under discussion have experimental data bearing on this point.

Stuart S. Birley and Desmond Tromans: We wish to thank the author of the above discussion for correcting our description of his model. In retrospect, we should have stated more explicitly that Bertocci's model was based upon diffusion control and that experimental testing of the model by Pugh and Green [30] (Ref. (36) in our paper which is being discussed) indicated that dissolution was cathodically controlled by the transport of cupric complex ions to the metal surface.

Bertocci's proposal regarding the effect of charge-transfer overvoltage is interesting. Unfortunately, all our studies concerning stirring effects were conducted in environments which produced corrosion films.

[22] G. A. Wright assessed A in a different manner (by graphical interpolation from values for the alkali chlorides), and calculated U_{ads} of $FeCl^-_{ads}$ to be −43.2 kcal/mole.

[23] N. Hackerman, E. S. Snavely, Jr., and J. S. Payne, Jr., *This Journal*, 113, 677 (1966).

[24] T. Murakawa and N. Hackerman, *Corrosion Sci.*, 4, 387 (1964).

[25] N. Hackerman and E. McCafferty, Extend Abstracts, 5th International Congress on Metallic Corrosion, Tokyo, 1972.

[26] Corrosion Section, National Bureau of Standards, Washington, D. C. 20234.

[27] U. Bertocci, *Electrochim. Metal.*, 3, 275 (1968).

[28] A formal contradiction arises here with the statement in my paper[27] that the Cu^{++} activity at the metal solution interface is zero, a value inconsistent with the equilibrium of reaction [2]; the contradiction is solved if one observes that the equilibrium concentration of Cu^{++} is very small (probably less than 10^{-5}M) and although significant for defining the potential, is negligible for the evaluation of the concentration gradient.

[29] A. W. M. Verkroost, M. Sluyters-Rehbach, and J. H. Sluyters, *J. Electroanal. Chem.*, 39, 147 (1972).

[30] E. N. Pugh and J. A. S. Green, *Met. Trans.*, 2, 3129 (1971).

JOURNAL OF THE ELECTROCHEMICAL SOCIETY

SOLID-STATE SCIENCE AND TECHNOLOGY

JUNE 1973

The Kinetics of Thin Oxide Film Formation on Iron Using Proton-Impact-Excited X-Ray Analysis

P. B. Needham, Jr., H. W. Leavenworth, Jr., and T. J. Driscoll

College Park Metallurgy Research Center, Bureau of Mines, United States Department of the Interior, College Park, Maryland 20740

ABSTRACT

Studies of the oxidation of high-purity iron samples at 224°, 285°, and 350°C have been conducted in an oxygen partial pressure of 4×10^{-6} Torr for exposure times ranging from 25 to 2000 sec. The oxide films were measured and quantitatively analyzed for trace carbon impurities using proton-impact-excited characteristic x-rays. Analytical surface sensitivities to the equivalent of 10^{-3} monatomic layers have allowed direct studies of ultrathin (<50Å) oxide film kinetics. A two-stage logarithmic oxidation rate law was observed at all temperatures with the transition from the first to second stage occurring at oxide thicknesses of 25, 36, and 52Å at 224°, 285°, and 350°C, respectively. This observation is discussed in terms of Uhlig's theory for logarithmic oxidation. Quantitative measurements of carbon impurities on the iron surfaces show that an increase in the preoxidation surface coverage from 0.1 to 1.0 monolayer results in a significant suppression of the oxidation process. Detailed studies were made of the removal of residual carbon and oxygen impurities and 12-14Å air-formed oxide films from the iron surface by vacuum annealing at 715°C. Without H_2 reduction techniques, preoxidation iron surface coverages of 0.4 monolayer oxygen and one monolayer carbon were routinely obtained. Also, the residual surface carbon, present prior to oxidation, does not oxidize off of the surface during the oxidation process at these temperatures.

Previous studies (1-3) on the ultrathin film oxidation kinetics of iron at temperatures ranging from 100° to 500°C have been limited by the sensitivity of the techniques utilized for film measurement, and the data are most reliable only for oxide films thicker than 100Å. There have been no techniques used in iron oxidation studies which could quantitatively characterize trace impurities on the iron surface before, during, and after the oxidation process. Oxidation studies have generally been initiated with samples for whose preoxidation surfaces the assumption of uniformity with respect to the initial surface impurity coverage (including the air-formed oxide film) is based on standardization of the preoxidation sample preparation techniques; *i.e.*, electropolishing, chemical etching, vacuum annealing, and reduction of the iron surface using H_2 partial pressures at elevated sample temperatures (2-6).

Uhlig (7, 8) has proposed an oxidation theory in which an electron transfer mechanism is rate controlling, resulting in logarithmic rate law kinetics. According to Uhlig's model, a two-stage logarithmic oxidation process could occur where the electron transfer process from metal to oxide is initially controlled by formation of a constant density space charge region and, at some critical film thickness, is subsequently controlled by the succeeding formation of a diffuse space charge region. A two-stage logarithmic oxidation process has been experimentally observed by several workers (9-13), including one reported observation by Lustman (13) for thick iron oxide films. However, no results have been reported for ultrathin iron oxide films in which this two-stage logarithmic mechanism has been observed. Logarithmic oxidation kinetics on polycrystalline Ferrovac E[1] samples have been reported by Graham *et al.* (4) for oxidation temperatures ranging from 25° to 200°C, with a parabolic rate law observed at 200°C for O_2 exposures longer than 1.56×10^3 Torr-sec, and by Yolken and Kruger (14) for oxidation at 24°C. For temperatures above 200°C, thicker oxide films, and higher ($>10^{-5}$ Torr) O_2 partial pressures, the oxidation kinetics of iron have usually been found to obey a parabolic rate law (1, 2, 4, 6). Graham and Cohen (2) have also reported the effect of oxidation partial pressures (10^{-6}-60 Torr O_2) on the limiting oxide thickness and morphology for iron oxidation at 350° and 400°C. An induction period at the lowest ($<10^{-5}$ Torr) oxygen partial pressures was observed and attributed to the possible removal of oxidizable impurities (carbon) or to slow nucleation. Ferrovac E iron was used as their principal sample material, but they also reported data at 350°C for high-purity, floating-zone refined Battelle iron on which they found a much thicker final oxide film than was obtained for Ferrovac E samples under the same experimental conditions. It was suggested that this was due to grain size and orientation differences, the Battelle iron samples having larger, more highly oriented grains exposed.

Key words: double-logarithmic oxidation, proton-impact-excited x-rays, iron, carbon surface impurities.

[1] Reference to specific equipment is made to facilitate understanding and does not imply endorsement by the Bureau of Mines.

In the present paper, we are reporting on the ultrathin film oxidation kinetics of polycrystalline iron at 224°, 285°, and 350°C in an oxygen partial pressure of 4×10^{-6} Torr for exposures ranging from 100 to 8000 Torr-sec. These exposures are of considerably shorter duration than those generally reported by other authors (1, 3-6). A new and extremely sensitive technique, proton excitation of characteristic x-rays, was used for *in situ* measurements of the oxide film thickness and quantitative measurements of the surface impurity carbon atom content at every stage of the oxidation process. Measurements were made of initial carbon and oxygen impurity concentrations on the iron surface as a result of preoxidation cleaning procedures. The effects of varying amounts of initial carbon surface impurities on the oxidation kinetics at 285°C were also studied.

Experimental

Film measurement technique.—Direct oxygen and carbon impurity measurements obtained by the use of proton-impact-excited characteristic x-rays have been reported elsewhere in detail (15-17), and only a brief review is given here. Except for the system used by Sewell *et al.* (18-20), the standard x-ray techniques do not offer either the required degree of sensitivity or the required degree of quantitativeness for the measurement or elemental analysis of thin (<100Å) oxide films. The use of proton-excited x-rays (PEX) has several distinct advantages: essentially only characteristic x-rays are excited by proton impact, eliminating the need to separate the x-ray signal from a large continuum x-ray background; very high x-ray yields for low Z elements are obtained; and x-ray production cross sections are available which allow direct quantitative analysis without reliance on data calibration based on the use of a standard sample.

In these experiments, a proton beam from an ion accelerator was directed onto the iron samples, which were mounted and oxidized in an ultrahigh-vacuum target chamber (Fig. 1). Protons with kinetic energies of 120 keV were used for the carbon, oxygen, and sulfur impurity determinations. Proton beam currents were in the 50-2000 nanoampere region, and we have found that sputtering effects during any of the measurements reported here were no more than the equivalent of 10^{-2} monatomic layer.

In order to discriminate between carbon or oxygen x-rays that originate from the iron sample bulk impurities and those that originate from surface impurities, the processes of exciting the bulk impurity x-rays and extracting them from the sample have been considered in detail elsewhere (21). The depth into the sample from which bulk impurity x-ray information is extracted is determined by both the rate of energy loss for the proton as it penetrates the sample (resulting in a reduction in the x-ray yield in x-rays/proton) and the absorption of the carbon K (44.5Å) or oxygen K (23.7Å) x-rays by the sample itself as they return to the surface. For these x-ray wavelengths the bulk impurity x-ray information depth is determined primarily by the target self-absorption of the x-rays. In an iron sample, less than $1/e$ of the oxygen K x-rays detected at the surface originate deeper than 1485Å into the sample, and, similarly, less than $1/e$ of the carbon impurity x-rays originate deeper than 390Å (21). This bulk oxygen and carbon impurity contribution was considered as the background x-ray field which established the theoretical limit of analytical sensitivity in terms of signal-to-noise ratio (a conservative signal-to-noise ratio equal to one was chosen to define the sensitivity limit), where the noise is defined as x-rays due to bulk impurities, and the signal is defined as the x-rays due to oxygen or carbon impurities on the iron surface. To avoid model problems in considering the distribution of the oxygen and carbon bulk impurities throughout their information depths (1485 and 390Å, respectively), the assumption was made that all the bulk impurities in these sample depths reside on the sample surface. This, from the technique's sensitivity standpoint, is a worst-case-assumption.

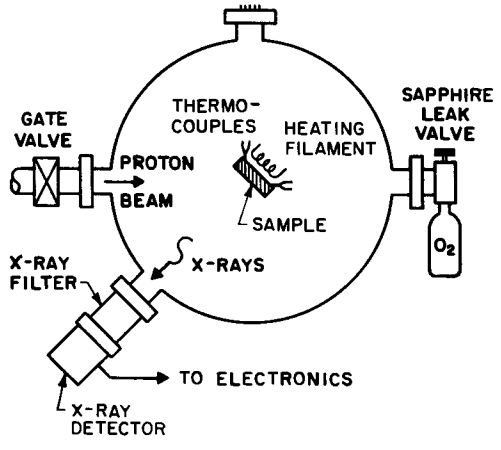

Fig. 1. Ultrahigh vacuum chamber in which the iron samples were mounted and vacuum annealed at 715°C, oxidized at 4×10^{-6} Torr O_2, and then analyzed by proton-impact-excited x-rays. Thermocouples were welded to the top and bottom edges of the samples, and the distance from the back of the sample to the tungsten heating filament was approximately ¼ in.

For the Battelle iron samples used in these experiments, the bulk impurity concentration of oxygen was 2.3 ppm and of carbon was 0.9-5 ppm,[2] contributing a background x-ray field equivalent to 10^{12} atoms of surface carbon per square centimeter and to 3×10^{12} atoms of surface oxygen per square centimeter. For an iron surface, this is equivalent to approximately 6×10^{-4} monatomic layer of carbon and 1.9×10^{-3} monatomic layer of oxygen, where a monolayer of impurity is defined as a one-to-one correspondence with 1.6×10^{15} iron surface atoms/cm² (22). In the studies reported here, therefore, the bulk impurity x-ray contribution to the measurement of one atomic layer of a surface impurity was six parts per ten thousand for carbon and two parts per thousand for oxygen.

The experimentally obtained x-ray yield, I_μ, is used to obtain oxide thickness or impurity coverage in micrograms/square centimeter from the equation $I_\mu = N\Delta r\sigma_x$ where N is the number of atoms/gram, Δr is surface coverage in grams/square centimeter, and σ_x is thick target x-ray production cross section in square centimeters/atom. This linear relationship between x-ray yield and coverage is valid for use where the x-ray yield is obtained from a thin layer in which the incident proton has lost less than 10% of its initial energy, and the accuracy has been shown to decrease with increasing film thickness from 0.01% at monolayer coverages to 15% at 10^3Å of Al_2O_3 (15). The calculation of Δr results in an uncertainty due principally to the uncertainty in σ_x; approximately ±5% for CK_α and ±12% for OK_α. For the case where I_μ represents the oxygen K_α x-ray yield, N is the number of oxygen atoms/gram in the oxide formed and Δr is the oxide thickness in grams/square centimeter. For these experiments, the oxide films were assumed to be magnetite, based on recent work (2,

[2] The analysis of the Battelle iron was kindly supplied to us with the iron ingot by Battelle Memorial Institute. All concentrations are in ppm. *Nonmetallics* [4]: oxygen (2.3), nitrogen (<0.1), hydrogen (<0.1), carbon (5 by combustion-conductometric, 0.9 by internal friction), sulfur (1.0). *Metallics* [19]: arsenic (0.2), boron (0.002), calcium (0.07), chromium (1.0), cobalt (3.0), copper (7.0), magnesium (0.2), manganese (4.0), molybdenum (0.2), nickel (0.1), phosphorus (0.1), potassium (0.2), sodium (0.3), tantalum (0.6), tin (0.3), titanium (0.6), vanadium (0.03), zinc (<0.6), zirconium (0.1). Although the bulk sulfur concentration was reported to be 1 ppm, during vacuum annealing processes we consistently observed the segregation of approximately ½-¾ monolayer of the bulk impurity sulfur onto the iron surface. Although the iron samples were repeatedly re-electropolished and vacuum annealed at 715°C, no reduction in the amount of sulfur segregating onto the surface from the bulk was observed, indicating that the bulk sulfur impurity concentration was at least 10-15 ppm rather than 1 ppm.

4, 23) in which Fe_3O_4 was the only oxide phase found to grow at oxygen partial pressures $<10^{-5}$ Torr.

Specimen preparation.—All oxidation measurements were made on square tabs, 25 × 25 × 1 mm, cut from electron beam-zone refined polycrystalline iron obtained from Battelle Memorial Institute. Preparation of the samples consisted of fine grinding with 180-600 grit paper, electropolishing in a 20/1 solution of acetic acid/perchloric acid, rinsing in distilled water, drying in a dry nitrogen blast, and vacuum annealing at a temperature of 715°C. The samples were mounted in the vacuum chamber (Fig. 1) within 1 min after the last of the external cleaning steps above. The chamber was pumped using a 450-liter/sec Orb-Ion pump and a 2000-liter/sec titanium sublimation pump. Prior to the chamber bakeout, a preliminary oxygen and carbon analysis of the sample surface was performed at 2×10^{-8} Torr. In this manner, a rigid control was maintained of the initial sample surface condition as a result of the external cleaning procedures. By establishing upper limits to the oxygen and carbon contamination at this stage, it was easier to attain specific ranges of impurity coverage during subsequent vacuum annealing procedures. After the preliminary surface analysis, the vacuum chamber was baked out and the operating pressure of 6×10^{-10} Torr was attained. The sample was then subjected to various cycles of heating by electron beam heating and, in some cases, an additional surface cleaning by argon ion bombardment. We have found that, by proper selection of the sample heating temperatures and heating times, a particular surface impurity coverage can be reproduced within 15% from one sample to another. In this present work, each iron sample was vacuum annealed at 715°C for two 300-sec cycles with a carbon and oxygen impurity determination performed after each cycle. The analysis time was approximately 30 sec for the carbon impurities and 120 sec for the oxygen. When a surface impurity level of 0.4 monolayer for oxygen and 1 monolayer for carbon (assuming carbon is present in the form of graphite on the surface) was attained, the oxidation cycles were begun. Argon ion bombardment was used to obtain further reductions in the surface impurity coverages in only one series of experiments which was performed to study the effect of carbon impurities on the oxidation process.

Oxidation technique.—For the oxidation cycles, the samples were heated radiatively by the thoriated tungsten filament used for the electron beam heating-annealing processes. The sample was heated to temperature (±2°C) within 180 sec and stabilized for an additional 120 sec. The temperature was measured by thermocouples welded to the top and bottom edges of the iron sample. The sample was at ground potential during oxidation runs with the heating filament at a temperature of approximately 1410°C. With the residual vacuum chamber background pressure at 1×10^{-9} Torr, oxygen was then leaked into the vacuum chamber through a sapphire seal leak-valve. The oxygen was an analyzed research grade obtained from Mathieson Company and contained 10 ppm total impurities. The oxygen pressure was raised in <2 sec to 4×10^{-6} Torr for oxidation times ranging from 25 to 2000 sec. At the end of the oxidation run, the oxygen was shut off and the chamber pumped to 2×10^{-8} Torr within 3 sec, reaching 5×10^{-9} Torr within 240 sec, at which time the gate valve to the accelerator beam line was opened, the proton beam directed onto the sample, and the oxygen and carbon measurements made. The beam-line gate valve was closed after completion of the analyses (180 sec), and the O_2 was reintroduced for another oxidation exposure. For a given total exposure of oxygen, it was found that the same oxide thickness was obtained at a given sample temperature no matter how many exposure increments were used to obtain that total exposure.

The same three tabs of Battelle iron were used for all oxidation runs and were mounted on the sample holder in such a manner that the proton beam analyzed the same 1/4-in.-diameter spot every time the sample was re-electropolished, rinsed, dried, and remounted in the vacuum chamber. Metallographic and scanning electron microscopic studies showed that the number and grain size distribution of each sample beam spot was reasonably equal. No attempt was made to determine the orientation of the major grains. The beam spot positions were chosen in order to minimize orientation and grain size effects so that the carbon impurity effects could be studied. Each sample was re-electropolished and reoxidized five to ten times.

Results and Discussion

Preoxidation cleaning.—The preliminary analyses of the Battelle iron samples performed at 5×10^{-8} Torr showed mean residual surface coverages of 12-14Å of oxide and 0.335 $\mu g/cm^2$ of carbon. After the two 300-sec, 715°C annealing cycles, the surface coverages were reduced to mean values of 0.125 ± 0.015 $\mu g/cm^2$ of carbon and 0.017 ± 0.003 $\mu g/cm^2$ of oxygen ($\simeq$0.4 monolayer). When utilized, an argon ion bombardment reduced the surface coverage of both oxygen and carbon another order of magnitude. Another result of the vacuum annealing process which we have observed was the diffusion of bulk impurity sulfur atoms to the iron surface, with the segregation of an equivalent of approximately 1/2-3/4 monolayer onto the surface. The accuracy for the sulfur impurity coverage determinations is less than those for the carbon and oxygen measurements since only a few sulfur measurements were performed.

For these present kinetic studies, no attempt was made to obtain a so-called "atomically clean" surface, and the preoxidation surface carbon and oxygen impurity levels (0.125 ± 0.015 $\mu g/cm^2$ and 0.017 ± 0.003 $\mu g/cm^2$, respectively) were obtained without the use of either argon ion bombardment or hydrogen reduction techniques.

Kinetics.—Figure 2 shows the results of oxidation at 224°, 285°, and 350°C in an oxygen pressure of 4×10^{-6} Torr. The curves are plotted directly as the measured oxide film thickness *vs.* the exposure time. Each point on a curve represents the mean value (listed in Table I) for three samples, each of which was re-electropolished and reoxidized three times. The total experimental uncertainty in the measurements was ±4%. The oxide thickness scale factor is uncertain to ±12% due to the uncertainty in the value of the

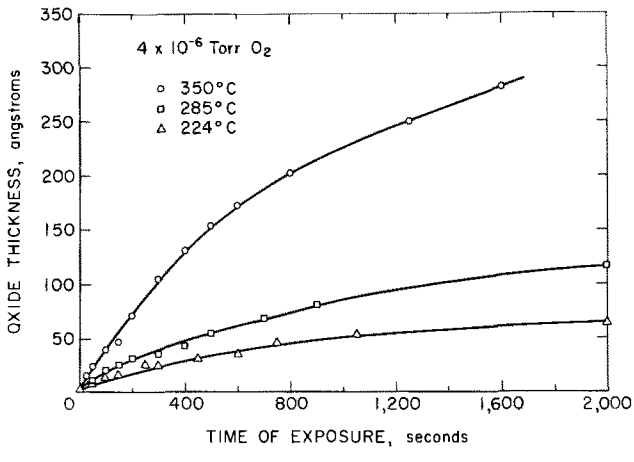

Fig. 2. Measured oxide film thickness *vs.* the exposure times in seconds are shown for Battelle iron samples at 224°, 285°, and 350°C. The oxygen partial pressure was 4×10^{-6} Torr O_2, and each point is the mean of nine oxidation runs. The estimated uncertainty is approximately twice the size of the data point symbols.

Table I. Measured oxide thicknesses as a function of temperature and exposure. Each thickness is the mean for three different Battelle iron samples, each of which was run three times at each temperature

Langmuirs (10^{-6} Torr-sec)	Seconds at 4×10^{-6} Torr O_2	Battelle iron oxide thickness (A) 224°C	285°C	350°C
0	0	0.017*	0.017*	0.017*
100	25	—	—	15.3
200	50	7.8	11.8	23.0
400	100	13.4	20.2	39.2
600	150	16.8	25.8	47.0
800	200	—	30.8	71.1
1,000	250	24.6	—	—
1,200	300	24.6	35.8	104.2
1,600	400	—	42.0	131.6
1,800	450	30.8	—	—
2,000	500	—	53.2	153.4
2,400	600	35.8	—	172.5
2,800	700	—	68.9	—
3,000	750	46.5	—	—
3,200	800	—	—	202.7
3,600	900	—	80.6	—
4,200	1,050	52.1	—	—
5,000	1,250	—	—	250.3
6,400	1,600	—	—	282.8
8,000	2,000	65.0	115.0	—
10,000	2,500	—	—	322.0
32,000	8,000	—	179.2	—
64,000	16,000	—	210.6	—

* These zero exposure values are the mean values of the preoxidation impurity coverage in micrograms/square centimeter of oxygen.

oxygen K_α x-ray production cross section. The maximum total durations of the oxygen exposures were 10^{-2} Torr-sec, or approximately 2.5×10^3 sec, except for the 285°C oxidation runs during which the effect of the initial carbon coverage was being studied. For the latter runs, the total exposure time was extended to 16×10^3 sec. In these experiments the oxygen exposures were not sufficient in length to allow the oxide films on the samples to reach their maximum thickness, since the initial stages of the oxidation process were of principal interest.

The kinetic data in Fig. 2 were plotted in Fig. 3 as two-stage logarithmic oxidation curves using a least squares fit. Logarithmic oxidation of the form $X = A \ln t + B$ (X = film thickness, t = exposure time) on iron at 24°, 100°, and 200°C has been reported by Graham, Ali, and Cohen (4), and both logarithmic and inverse logarithmic kinetics at 25°C were reported by Yolken and Kruger (14).

In most oxidation theories, logarithmic oxidation kinetics are associated with the transport of electrons from the metal to the oxide-oxygen interface being the rate-limiting (slowest) step. The electronic transport can occur either by thermionic emission of electrons

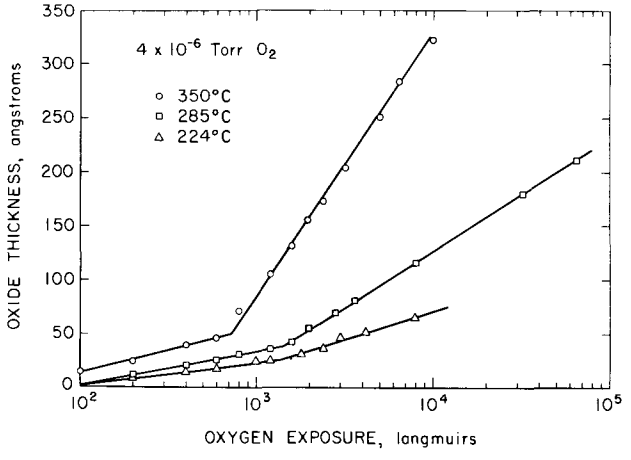

Fig. 3. Data from Fig. 2 are fitted to two-stage logarithmic oxidation kinetics by a least squares fit. The oxygen exposure is given in Langmuirs (≡ 10^{-6} Torr-sec). The transition points from 1st to 2nd stage are determined from the curves to occur at 25, 36, and 52Å for 224°, 285°, and 350°C, respectively.

from the metal or by quantum mechanical tunneling through the oxide layer. Several authors have suggested that for the early stages of oxidation (up to a few tens of angstroms) electrons can reach the oxide-oxygen interface very rapidly by quantum mechanical tunneling, in which case the rate-limiting step in the oxidation process would be ionic diffusion (iron or oxygen ions). Assuming substantial quantum mechanical tunneling, Mott (24) obtained a parabolic equation for the growth kinetics in low-temperature regions where there is no thermionic emission, and Cabrera and Mott (25) obtained inverse logarithmic kinetics for higher temperatures where thermionic emission also contributed to the electronic transport. For low-temperature oxidation, Fromhold and Cook (26) derived a kinetic rate law similar to that of Cabrera and Mott for oxide films up to 20-30Å, but beyond which electron tunneling became rate limiting and logarithmic kinetics would be obtained.

The logarithmic oxidation kinetics which we have observed for the studies reported here indicate that electronic rather than ionic transport was the rate-limiting step. However, the abrupt change in the rate constant of the logarithmic oxidation at each temperature is less easily explained. The separate oxidation stages may be associated with a change in the phase of the growing oxide film, or with a change in occupancy conditions associated with the trapping centers of the growing oxide as described by Uhlig (7) for thicker oxide films.

Uhlig (7) has proposed a theory of double logarithmic oxidation which assumes that thermionic emission of electrons through the oxide layer is the rate-limiting step. At some particular oxide thickness, where the energy difference between the Fermi level of the oxide film and the trapped charge in the oxide film approaches the thermal energy kT, all of the trapping levels will not be filled, and a diffuse space charge region can form in the oxide, overlaying the initially formed uniform oxide space charge region. An increase in the rate constant for logarithmic oxidation should occur at this transition thickness, L, where (27)

$$L = k_0 [\Delta E/kT - 1] \qquad [1]$$

and k_0 and ΔE are the rate constant and activation energy, respectively, for the first stage of oxidation. To test this theory with our data, we used for our first stage kinetics

$$X = k_0 \ln (t/\tau) \qquad [2]$$

where X is the oxide thickness, t is the exposure time, and τ is a constant. The values for k_0 and τ (Table II) were obtained from the curves in Fig. 3 and were used in the Arrhenius plot of Fig. 4 to obtain the apparent activation energy for the first stage, 3.58 kcal/mole. The values of k_0 and the activation energy were then used with Eq. [1] to calculate the transition point thicknesses, L (calc), and these were compared to our experimentally determined values, L (exp), in Table II. The ratio L (calc)/L (exp) ranges from 0.94 at 224°C to 0.67 at 350°C. The agreement between these experimentally measured and theoretically calculated values of L is reasonably good. However, we feel that this agreement may be fortuitous, since questions concerning the effects of the initial surface impurities (discussed below), of the precise stoichiometry of the oxide films, and of the crystallographic

Table II. Comparison of experimental values to theoretical transition point values calculated by Uhlig's theory

Temperature (°C)	k_0 (A)	τ, Langmuirs	L (calc), Å	L (exp), Å	Ratio L (calc)/L (exp)
224	8.91	73	23.4	25	0.94
285	13.29	80	29.6	36	0.83
350	18.38	43	34.8	52	0.67

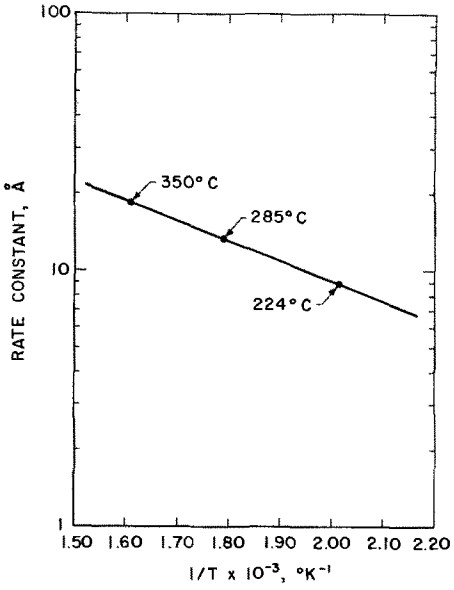

Fig. 4. Arrhenius plot of the oxidation rate constants determined from the curves of Fig. 3 yields an apparent activation energy of 3.58 kcal/mole for the 1st stage kinetics.

orientation of the large substrate grains remain to be answered.

Effect of initial carbon and sulfur coverage.—Kinetic data are given in Fig. 5 for oxidation studies of iron samples having different preoxidation carbon impurity coverages. The samples were oxidized in 4×10^{-6} Torr O_2 at 285°C. The lower curve (Δ) is for the iron samples with the mean preoxidation surface impurity coverage of 0.125 ± 0.015 μg/cm² of carbon and 0.017 ± 0.003 μg/cm² of oxygen obtained by vacuum annealing at 715°C for 10 min. The data for the upper curve (0) are for the same samples, with the preoxidation carbon and oxygen coverages reduced an additional order of magnitude by using an argon ion bombardment as the final preoxidation surface cleaning step. For these data runs the mean initial coverages were 0.012 ± 0.005 μg/cm² for carbon and less than 0.002 ± 0.002 μg/cm² for oxygen. Again, each data point is the mean for the results of three different Battelle iron samples, each of which was oxidized three times.

The data for the samples with the cleaner preoxidation surface clearly indicate a much higher oxidation rate and resulting oxide thickness. At an exposure of 7×10^{-2} Torr O_2-sec, the data for surfaces with 0.125 μg/cm² of carbon (approximately one monolayer if we assume it is present in a graphite form) reaches

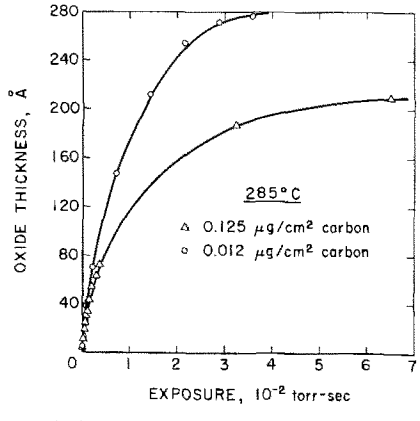

Fig. 5. Battelle iron samples with different initial carbon impurity coverages were oxidized at 285°C at 4×10^{-6} Torr O_2. Each iron sample was run at both initial carbon impurity levels in order to smooth out microstructure differences from sample to sample. The maximum oxide thickness in the upper (o) curve is estimated to be 300Å, whereas for the lower curve (representing the dirtier sample) the maximum oxide thickness is estimated to be 215Å.

an oxide thickness of approximately 215Å. The samples with the cleaner surfaces (0.012 μg/cm² carbon) reach an oxide film thickness estimated to be 300Å from extrapolation of the data curve. The creation of highly active oxidation sites by the argon ion bombardment as a possible explanation for thicker film on the cleaner surface was eliminated, we feel, by the use of a post-argon-ion-bombardment anneal at 550°C for 900 sec.

The role of the residual carbon impurities in slowing the oxidation process may be (*i*) through an oxidizing process whereby the oxygen gas phase molecules are utilized initially in the formation of CO, possibly resulting in the removal of carbon from the surface, or (*ii*) the utilization by the impurity carbon atoms of iron bonds which would otherwise be available for the iron oxidation process itself. The possibility of carbon oxidizing from the iron surface during the initial stages of oxidation was studied for all sample runs reported here. In the temperature range investigated here, the reduction in the initial carbon impurity level that could be attributed to removal of carbon from the surface during the oxidation process averaged less than 10%. The removal of carbon through oxidation would be expected to be very slight for lower oxidation temperatures. Evidence has been reported elsewhere (28) as indicating that these residual carbon impurities tend to continuously redistribute themselves throughout the growing iron oxide film, with a slight concentration at the iron oxide-gas phase interface.

Finally, a brief discussion should be made concerning the role of the other major surface impurity, sulfur, which was present during our oxidation experiments. The effect on the initial oxidation process of these sulfur surface impurities, which are a result of segregation onto the iron surfaces of the bulk sulfur impurities, has not been reported. During vacuum annealing at 600°-900°C, Harris (29) observed, using Auger electron spectroscopy, the segregation of sulfur onto the surfaces of nickel, iron, and other metals. He demonstrated, for nickel, that the source of the sulfur was bulk sulfur impurities in the metal. Sickafus (30) observed sulfur segregation on nickel (110) surfaces using low-energy electron diffraction and Auger electron spectroscopy, and concluded from his studies that sulfur is nonhomogeneously distributed over the surface in domains less than 40Å wide.

The iron samples of Fig. 5 with the 0.125 μg/cm² initial carbon coverage also had a 1/2-3/4 monolayer equivalent of sulfur on the surface. For the argon-ion bombarded samples, this initial sulfur coverage was reduced by about 80%, although the sulfur impurity measurements for the experiments reported here were not nearly as reproducible as the carbon impurity masurements. However, during the post-argon-ion-bombardment annealing cycle at 550°C for 900 sec, an equivalent of about 30% of the original (pre-ion-bombardment) coverage segregated back onto the iron surface, resulting in a net reduction of about 50% in the preoxidation surface coverage due to the ion bombardment process. From Fig. 5, the active impurity appears to have a large effect on the oxidation rate even at later (exposures longer than 1.2×10^{-3} Torr O_2 · sec) stages of the oxidation process. During iron oxidation at 200°C in 4×10^{-6} Torr O_2, preoxidation sulfur impurity coverages have been found (28) to remain at the metal-oxide interface during the growth of oxide films up to 20Å thick. We feel, therefore, that any direct, active role which the sulfur impurities play probably occurs only during the initial (chemisorption) stages of the oxidation process. Extensive work is continuing in this laboratory on the role of this sulfur or sulfur layer in the early stages of iron oxidation.

Graham and Cohen (2) have reported results comparing the oxidation of Ferrovac E iron and Battelle iron at 350°C in 10^{-3} Torr O_2. They detected little difference in the oxidation rates for both types of iron

during the first 600 sec of exposure. Subsequently, the Battelle iron oxidized at a higher rate with a larger final oxide film thickness. This was attributed to the difference in grain sizes of the two types of polycrystalline iron, the Battelle iron having larger and more highly oriented crystallites exposed than the Ferrovac E. They attributed the higher net oxidation rate of Battelle iron to its either having more exposed grains with higher oxidation rates or to its larger grain size preventing the spread of α-Fe_2O_3 from grains with high α-Fe_2O_3 formation rates onto grains less susceptible to α-Fe_2O_3 formation. Our results (Fig. 5) suggest that the variance in the final oxide film thickness may also be attributable to subtle variations in the surface carbon impurities at approximately monolayer equivalent levels.

A recent paper by Swanson and Uhlig (9) on thin film oxidation of copper concentrated on the effect on oxidation kinetics of the submicroscopic faceting of sample surfaces caused by pretreatment vacuum annealing in H_2 and N_2 atmospheres. They suggested that their results indicate that surface impurities are of no importance for the formation of thin oxide films on other metals as well as copper. While gaseous pretreatments of the iron surfaces were not used here, we suggest that for the initially formed thin film (0-200Å) on any metal surface, the role of the initial impurities cannot be dismissed.

Conclusions

The use of proton-excited characteristic x-rays has allowed us to quantitatively define iron surfaces with respect to impurities at every stage of cleaning, reduction, and oxidation at 224°, 285°, and 350°C in 4 $\times$ 10^{-6} Torr O_2. We have found that:

1. A two-stage logarithmic oxidation process occurs on Battelle iron at 224°, 285°, and 350°C for oxygen pressures of 4 $\times$ 10^{-6} Torr. The kinetics of this process were discussed in terms of Uhlig's oxidation theory, and good agreement at all temperatures was found between our experimentally measured oxide thicknesses at which the transition from the first stage to the second stage occurs, and empirical calculations suggested by Nwoko and Uhlig (27). It is felt that this agreement may be fortuitous in light of uncertainties relating to the roles played in the early stages of the oxidation process by initial carbon and sulfur surface impurities, stoichiometry of the growing oxide film, and orientation of the exposed grains on the iron substrate.

2. Vacuum annealing at 715°C resulted in removal of the natural air-formed oxide films and partial removal of the carbon impurities. All of the oxidation results reported here were initiated on preoxidation iron surfaces with oxygen impurity levels of about 0.4 monolayer equivalent and carbon impurity levels slightly greater than one monolayer equivalent.

3. Reduction of the preoxidation carbon impurity coverage on the iron surfaces from 0.125 to 0.012 $\mu g/cm^2$ resulted in a sharp increase in the oxidation rate and the oxide film thickness for extended oxidation times. This result is in the range of oxide film thicknesses where other authors (2, 9) have attributed similar effects entirely to submicroscopic structure of the metal surface.

Brief mention has also been made of the segregation of sulfur from the bulk onto the iron surface during preoxidation vacuum annealing. For Battelle iron the equivalent of 1/2-3/4 of a monolayer of sulfur diffused rapidly to the sample surface at an annealing temperature of 715°C.

Manuscript submitted June 14, 1972; revised manuscript received Jan. 15, 1973.

Any discussion of this paper will appear in a Discussion Section to be published in the December 1973 JOURNAL.

SYMBOLS

I_μ	x-ray yield, photons/microcoulomb
N	number of atoms/gram
$\Delta\tau$	surface coverage, g/cm^2
σ_x	thick target x-ray production cross-section, cm^2/atom
X	film thickness, Å
t	exposure time, sec, or exposure, Langmuirs
A, B	constants of logarithmic oxidation equation, Å
L	oxide thickness representing the transition between first and second stage of oxidation, Å
k_0	oxidation rate constant for the first stage of oxidation, Å
ΔE	activation energy for the first stage of oxidation, kcal/mole
k	Boltzmann constant, kcal/°K
T	absolute temperature, °K
τ	empirical constant of logarithmic oxidation equation, sec or Langmuirs

REFERENCES

1. N. Ramasubramanian, P. B. Sewell, and M. Cohen, *This Journal*, **115**, 12 (1968).
2. M. J. Graham and M. Cohen, *ibid.*, **116**, 1430 (1969).
3. W. E. Boggs, R. H. Kachik, and G. E. Pellissier, *ibid.*, **114**, 32 (1967).
4. M. J. Graham, S. I. Ali, and M. Cohen, *ibid.*, **117**, 513 (1970).
5. W. E. Boggs, R. H. Kachik, and G. E. Pellissier, *ibid.*, **112**, 539 (1965).
6. E. J. Caule, K. H. Buob, and M. Cohen, *ibid.*, **108**, 829 (1961).
7. H. H. Uhlig, *Acta Met.*, **4**, 541 (1956).
8. H. H. Uhlig, *Corrosion Sci.*, **7**, 325 (1967).
9. A. W. Swanson and H. H. Uhlig, *This Journal*, **118**, 1325 (1971).
10. W. Bradley and H. H. Uhlig, *ibid.*, **114**, 669 (1967).
11. R. Tylecoat, *J. Inst. Metals*, **78**, 327 (1950).
12. H. H. Uhlig, J. Pickett, and J. MacNairn, *Acta Met.*, **7**, 111 (1959).
13. B. Lustman, *Trans. Electrochem. Soc.*, **81**, 359 (1942).
14. H. T. Yolken and J. Kruger, *This Journal*, **114**, 796 (1967).
15. L. J. Christensen, J. M. Khan, and W. F. Brunner, *Rev. Sci. Instr.*, **38**, 20 (1967).
16. P. B. Needham, Jr., Proc. of Second Oak Ridge Conf. on the Use of Small Accelerators for Teaching and Research, CONF-700322, USAEC, 155 (1970).
17. P. B. Needham, Jr., and B. D. Sartwell, *Advan. X-Ray Analy.*, **14**, 184 (1971).
18. P. B. Sewell and M. Cohen, *Appl. Phys. Letters*, **11**, 9, 298 (1967).
19. P. B. Sewell and D. F. Mitchell, *J. Appl. Phys.*, **42**, 14, 5879 (1971).
20. P. B. Sewell, D. F. Mitchell, and M. Cohen, *Surface Sci.*, **29**, 173 (1972).
21. P. B. Needham, Jr., and T. J. Driscoll, To be published.
22. G. K. Hall and C. H. B. Mee, *Surface Sci.*, **28**, 598 (1971).
23. R. J. Hussey and M. Cohen, *Corrosion Sci.*, **11**, 699 (1971).
24. N. Mott, *Trans. Faraday Soc.*, **43**, 431 (1947).
25. N. Cabrera and N. F. Mott, *Rept. Progr. Phys.* **XII**, 163 (1949).
26. A. T. Fromhold and E. L. Cook, *Phys. Rev.*, **158**, 600 (1967).
27. O. Nwoko and H. H. Uhlig, *This Journal*, **112**, 1181 (1965).
28. P. B. Needham, Jr., T. J. Driscoll, and D. Schlain, Paper 91 presented at Electrochem. Soc. Meeting, Miami Beach, Florida, Oct. 8-13, 1972.
29. L. A. Harris, *J. Appl. Phys.*, **39**, 1428 (1968).
30. E. N. Sickafus, *Surface Sci.*, **19**, 181 (1970).

Study by Nuclear Microanalysis and O^{18} Tracer Techniques of the Oxygen Transport Processes and the Growth Laws for Porous Anodic Oxide Layers on Aluminum

C. Cherki and J. Siejka*

Groupe de Physique des Solides de l'Ecole Normale Supérieure, Tour 23, 11 Quai Saint-Bernard, Paris 5ème, France

ABSTRACT

The method of nuclear microanalysis of stable oxygen isotopes by the reactions O^{16} (d, p) O^{17*} and O^{18} (p, α) N^{15} was used to investigate the mechanisms of growth, dissolution, and transport associated with oxygen during the formation of relatively thin ($\leq$7000Å) porous anodic layers on aluminum. The average charge associated with an oxygen ion fixed in the film was calculated on the basis of the direct measurement of sulfur incorporation in the films. The current efficiency of the oxidation was determined (and found to be low, ~55%) by comparing the amount of oxygen fixed on the metal surface deduced from nuclear microanalysis to that deduced from the amount of charge fed into the circuit. The rate of chemical dissolution of the oxide was measured in open circuit and under polarization and was found to be two orders of magnitude lower than that which would explain the low current efficiency. Hence the existence of an electrochemical process of cation transfer must be assumed. It was found, by using oxygen 18 tracer techniques, that the growing oxide layer is formed at the metal/oxide interface by oxygen transport through the base layer. The results show that about 60% of the ionic current is transported by oxygen ions and about 40% by cations during the growth of porous oxide layers on aluminum.

Porous oxide layers produced by anodic oxidation of aluminum in acid solutions have been investigated for many years; however, no consistent model has as yet been elaborated to explain the formation of these films. The present paper reports new data on the growth and dissolution of porous anodic oxide films on aluminum in H_2SO_4 [15 w/o (weight per cent)]. The method of nuclear microanalysis of the O^{16} and O^{18} isotopes used in this paper has been applied previously to the investigation of anodic oxidation of metals (1-3) and semiconductors (4).

The nondestructive method of nuclear microanalysis allows one to determine the number of oxygen atoms/square centimeter fixed by oxidation on the surface of the metal specimen under investigation. Moreover, by using a solution in which the water was enriched[1] in O^{18} and by measuring and locating this isotope in films formed in solutions having various O^{18} isotopic concentrations, it is possible to tackle the problem of oxygen transport during growth and dissolution of porous films in a more direct way than would be possible by using other techniques, such as tracing with radioactive sulfur (5).

An analysis of previous work (6-8) leads to considering two main types of growth mechanism of porous layers: (*a*) migration of cations across the film, together with the oxygen bearing anions (OH^-, O^{2-}, SO_4^{2-}); these cations form directly a porous oxide at the film-electrolyte interface. Mechanisms of this type have been suggested to explain the uniform distribution of polyatomic anions incorporated in the films; and (*b*) cations and anions which migrate across the barrier layer continue to form a compact layer at the oxide-electrolyte and metal-oxide interfaces, respectively; then, by some process, this layer is transformed into a porous layer at a rate equal to that of barrier layer formation, thereby keeping the thickness of the latter at a constant value.

The latter type of growth mechanism seems to have been generally accepted in the literature; however, there is still much controversy, in particular as regards the conversion mechanism of the barrier layer into a porous layer. Keller *et al.* (9) have suggested a purely chemical process of transformation: the convergent flow of current was supposed to raise the temperature and concentration of the solution at the base of the pores, thereby accelerating the chemical dissolution of the oxide formed. Such a mechanism consisting in Joule heating of the solution has been accepted by numerous authors (7, 10). However, recent calculations by Nagayama and Tamura (11) have shown that the rise of temperature at the pore base is practically always negligible.

Hoar and Mott (6) have explained the dissolution at the pore base as being a field-assisted process. They assume that the oxide film formation occurs at the oxide-metal interface by OH^- migration. Under the effect of the electric field, the protons produced by this reaction would migrate toward the oxide-solution interface at the pore base. This process favors the dissolution of Al ions from the oxide into the solution. However, the origin of the OH^- ions and the mechanism of electrochemical dissolution have not been specified. Moreover, as pointed out by Young (12), no experimental evidence has been obtained for these mechanisms. Finally, this model has been in part rejected by Hoar himself and Yahalom (7).

Moreover, Nagayama and Tamura (11) have shown that the quantity of Al^{3+} in the solution after oxidation exceeds that of Al^{3+} originating from the formation of the pores. From this they inferred the existence of electrochemical dissolution of Al at the pore bases. This conclusion has been criticized several times by Diggle et al. (13). By S^{35} tracing, they have shown that the above difference is probably caused by an extensive chemical dissolution of the oxide all over the oxide-solution interface.

To gain some insight into these problems, in a first series of experiments we investigated the current efficiency of the formation of porous layers. The quantity of oxygen atoms/square centimeter of N_O fixed on the specimen surface, measured by nuclear microanalysis, was compared to the quantity N_{qox} of oxygen which is equivalent to the ionic charge Q_{ox} applied during anodic oxidation. To determine N_{qox} on the

* Electrochemical Society Active Member.

Key words: nuclear microanalysis, O^{18} tracing, aluminum, porous oxide, sulfuric acid, dissolution current, current efficiency, oxygen movement.

[1] Normalized O^{18} enriched water produced at the Weizmann Institute, Rehovot, Israel. The natural abundance of O^{18} is 0.204%.

basis of coulometric measurements, it is necessary to know the value of electronic losses and the charge associated with an oxygen atom. Information about this was found in the literature. Spooner (14) has shown that the electronic losses can be disregarded. This result was confirmed in Ref. (8).

Moreover, it is well known (2) that anodic films formed in concentrated acids contain a large number of anionic impurities of the $A_xO_y^{n-}$ type. According to Ref. (15), for aluminum oxidized in H_2SO_4 (15%) the incorporation of sulfate anions can be estimated to represent 14% of the total weight of oxide in the case of thick layers.

Using the method of back-scattering with $^4He^+$ ions at 1800 keV [see Ref. (1)] we measured the rate of sulfur incorporation during the formation of thin oxide layers and we evaluated the average charge of the oxygen atoms under our experimental conditions.

In a second stage, we investigated the dissolution of the oxide in open circuit and during growth. In a certain way, this investigation complemented the one described above, since the dissolution of the outer part of the oxide, which has been proposed to explain the poor current efficiency observed by the other authors, has not yet received quantitative evidence. In the present experiments, we produced a thin porous layer, enriched in O^{18}, superimposed on a porous layer depleted in O^{18}. Determining the O^{16} and O^{18} losses of this duplex layer after dissolution, it is possible to obtain quantitative information about the rate of dissolution in the pores and on the oxide surface, as well as to specify the origin of Al^{3+} in the oxidation bath.

The last part of these experiments was devoted to a study of the nature of charge carriers during the oxide formation by means of O^{18} tracer techniques. This method was introduced by Amsel and Samuel (16) for investigating the transport mechanism during the formation of compact films. In the present experiments, films of different thickness were obtained in solutions of the same chemical type (H_2SO_4, 15%) with various O^{18} isotopic concentration and the O^{18} was then located in these duplex films.

Experimental

Measurement of O^{16} and O^{18}.—The method of nuclear microanalysis used in this paper is based on the determination of the number of particles coming from the following nuclear reactions: O^{16} (d, p) O^{17*} and O^{18} (p, α)N^{15}. The basic principles of this method have been described in a series of papers by members of our laboratory [see Ref. (1) and (17].

Measurement of sulfur.—The energy of back-scattered particles is a function of the incident energy and of the masses of the incident particle and the target nuclei. This method, described elsewhere (1), allows one to measure the quantity of heavy impurities contained in a light matrix. A 1800 keV $^4He^+$ beam was used in the present experiments to determine the sulfur contained in aluminum oxide formed on an extra pure metal (99.999%) (see paragraph on Preparation of solution and specimens, below).

Location of O^{18}.—Isotopic analysis of oxygen at various depths in anodic layers was used for the first time by Amsel and Samuel (16) to investigate the migration mechanism of ionic charge carriers during the growth of compact aluminum anodic oxide films. This method consists in an analysis of the excitation curve as a function of bombarding energy in the vicinity of a narrow resonance of the O^{18} (p, α)N^{15} reaction, measured for the sample under investigation.

In this paper, we used the 2.5 keV wide resonance at 629 keV, according to a technique described by Amsel *et al.* (1, 18). By fitting the theoretical excitation curve, calculated for a given concentration profile, with the experimental curve we deduced the O^{18} concentration profile $C(x)$ in the oxide obtained by successive oxidation in two solutions of different isotopic concentrations.

Preparation of solutions and specimens.—We used annealed, rolled aluminum pure to 99.9 or 99.999%. Specimens of the latter type were supplied by Materials Research Corporation. The natural oxide layer on this metal is of the order of 50Å. The specimens were rectangular having an area of 2 cm^2. Before oxidation the surfaces were thoroughly cleaned with acetone and then washed with bidistilled water. The method of electrochemical polishing was not used here for the same reasons as explained in (3).

Two types of solutions were used: "$s_O{}^{18}$" enriched to about 10% and O^{18} and "$s_O{}^{16}$" depleted 20-30 times in O^{18}. A special oxidation cell (5 cm^3) was used because of the high cost of labeled electrolytes. The specimen holder has been described in (2) and (3). The temperature of the cells was controlled with an accuracy of 0.5°C and was equal to 15°C.

Experiments were carried out at constant voltage $V_{ox} = 10V$ for a fixed time by applying the voltage between the specimen and a helical platinum cathode. It was shown that there was practically no isotopic exchange between the oxygen of the oxide and that of the water (see below). For this reason the specimens were washed with running distilled water to remove any residual acid and then dried.

In agreement with the literature (19) we found that the isotopic exchange of oxygen between SO_4^{2-} and H_2O is negligible under the present experimental conditions. Therefore, the O^{18} labeling of the SO_4 groups is equal to 0.204% (natural abundance) both in $s_O{}^{18}$ and $s_O{}^{16}$ solutions.

Results and Interpretation

Analysis of back-scattering spectra.—For 1800 keV incident $^4He^+$ ions, Fig. 1 shows typical back-scattering amplitude spectra obtained: (*a*) from the pure metal and (*b*) from the metal covered with a 210Å oxide layer. The presence of the neatly resolved peak at 1126 keV corresponds to the presence of sulfur. Calculations, based on the Rutherford formula for elastic scattering cross sections, led us to the value of 7×10^{15} sulfur atoms/cm^2 with an accuracy of 10%,

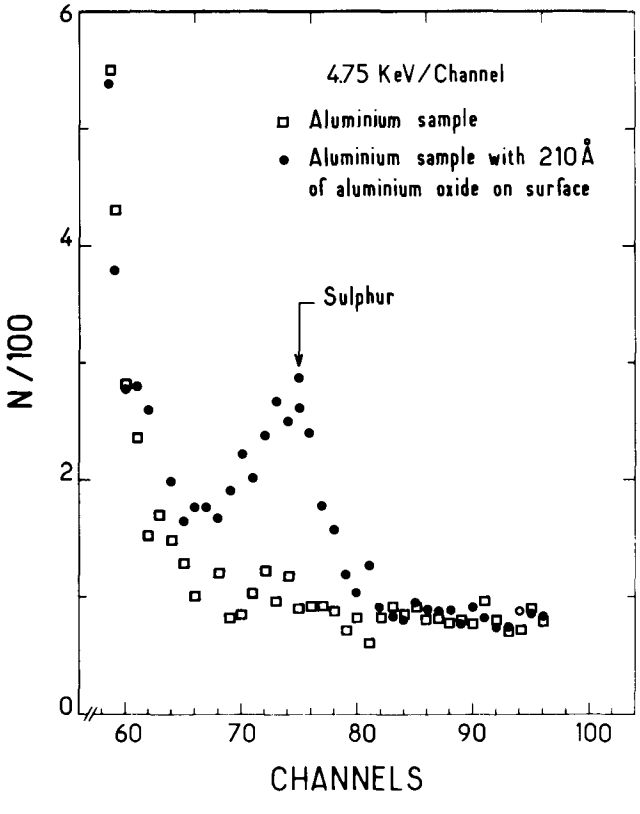

Fig. 1. Back-scattering amplitude spectra for $^4He^+$ ions at 1800 keV obtained on pure and oxidized aluminum.

this film containing on the other hand 122 × 10^{15} oxygen atoms/cm². Assuming that all the sulfur is in the form SO_4^{2-}, the percentage of oxygen incorporated in the form of sulfates is equal to 23 ± 6%. The literature gives (15) the sulfur content of those films as the weight percentage of the SO_3 group in thick films: the value reported is 12-14%. Recalculating the similar quantity on the basis of our results we find 14 ± 3% in reasonable agreement.

We shall now calculate the average charge required to fix an oxygen atom in the oxide. Let us assume first (assumption *a*) that the oxide is of the form

$$Al_2^{3+}\ [(O^{2-})_x,\ (SO_4^{2-})_y] \qquad [a]$$

We find readily that $x = 2.79$ and $y = 0.21$. The average charge is then: $(0.77 \pm 0.06) \cdot (-2) + (0.23 \pm 0.06) \cdot (-0.5) = -1.65 \pm 0.1$ where -2 is the average oxygen charge for pure oxide and -0.5 for pure sulfate.

It is reported in the literature (8) that SO_4^{2-} anions may be fixed by adsorption and can be accompanied by protons. The extreme assumption [*b*] will therefore be made that the oxide is of the form

$$(Al_2^{3+}\ O_3^{2-}),\ (H_2SO_4)_y \qquad [b]$$

with the oxygen charge in the sulfate being zero. Then $y = 0.22$, and the average charge is $(-2) \cdot (0.77 \pm 0.06) = -1.54 \pm 0.1$.

Current efficiency.—Experiments were performed at constant voltage ($V_{ox} = 10$V) and in steady-state conditions. The time when the porous film begins to grow under constant current, *i.e.*, when the steady-state conditions are reached, was used as an arbitrary reference. In our experiment, this time was equal to 30 sec. Coulometric measurements were made taking this instant as the origin of the time, *t*. Figure 2 shows the time dependences of: curve 1, the number of oxygen atoms/cm² N_O (t) measured by nuclear analysis (the initial quantities of oxygen fixed up to 30 sec being substracted); and curve 2, the quantities of oxygen N_{qox} calculated from coulometric measurements by giving to each oxygen atom the limits of the average charge deduced from model [*a*], *i.e.*, 1.55 and 1.75 electron charges (curve 2a and 2b), respectively. The variation of $N_O(t)$ and $N_{qox}(t)$ are linear and the ratio of the mean slopes gives the efficiency of the reaction which is constant over the range of oxidation times investigated ($t_{ox} \leq 10$ min). The efficiency obtained is 53 ± 3%. If the average charge deduced from model [*b*] is used the current efficiency obtained is 48 ± 3%.

Mason and Slundler (20), Mason and Fowle (21), and Spooner (14) measured the current efficiency, expressed in terms of coating ratio, of aluminum anodically oxidized in H_2SO_4 solutions under different concentrations, temperature, and current density conditions. The coating ratio is given by the expression

$$\frac{\text{weight of oxide formed}}{\text{weight of aluminum consumed}}$$

If the current efficiency for the conversion of aluminum to alumina were 100%, the coating ratio would be 1.89 (2.20 if SO_3 incorporated in the oxide represents 14% of the oxide weight).

Experimental observations suggest that the coating ratios measured are always less than these values and decrease as the electrolyte temperature and concentration increase and current densities decrease. Oxidation time is a complicated function of current density and temperature. For small current densities, the coating ratio decreases with time. If it is measured for very short oxidation times and at constant current densities ($t_{ox} \leq 2$ min, for $I \simeq 5$ mA/cm²), the coating ratios are obviously influenced by the coating ratio of barrier film formation which could be much higher than during porous film formation (7). This effect can be neglected for $t_{ox} = 10$ min. For these reasons, we have compared our results to those of Ref. (14), (20), and (21) obtained at $t_{ox} = 10$ min. For the oxide formation at conditions similar to ours ($t_{ox} = 10$ min, 15% H_2SO_4, $I \simeq 5$ mA/cm² at steady-state conditions) we found that according to Mason and Fowle (21) the coating ratios were equal to 1.47 at 10°C and 1.33 at 21.1°C (theoretical value: 2.20). These values correspond to current efficiencies of 66% and 60%, respectively. Similar results can be deduced from the measurements by Mason and Slundler (20) and Spooner (14). The current efficiency calculated from Ref. (11) is equal to 66% ($t_{ox} = 10$ min). This value was obtained from chemical analysis of the aluminum dissolved in the solution and compared to the coulometric curve. It can be noted that the value of the current efficiency calculated in Ref. (11) is independent of the model chosen for the oxide formed, *i.e.*, independent of the average charge of the oxygen fixed in the oxide. This value of current efficiency, although obtained at different conditions ($t = 27$°C, $I = 9.5$ mA/cm², 10% H_2SO_4), is practically the same as that measured by gravimetric methods (14, 20, 21) at our experimental conditions. Our value 53 ± 3% is about 20% smaller than those mentioned in the above literature data. It can be noted that the experimental errors due to the methods used in Ref. (11), (14), (20), and (21) were not discussed in these papers.

It is interesting to note that if one gives the average oxygen charge -2 to all oxygen fixed in the oxide, the current efficiency measured in our experiments comes to 64%. This value is practically the same as these deduced from Ref. (11), (14), (20), and (21). However, it is difficult to consider a mechanism which could explain the presence of sulfur in the oxide not in the form of sulfate but in some reduced form due, for example, to the chemical action of water. Therefore, on the basis of some data in the literature (8) we cannot exclude the hypothesis that incorporation of sulfates is lower in steady-state conditions than measured at the beginning of the oxidation (210Å). Thus the current efficiency would be in reality somewhat greater than 53 ± 3% and equal to a value within the limits 53-64%. Hereafter, we will base the discussion of these results on the assumption that the current efficiency is equal to 53 ± 3%. Anyway, the general conclusion of this work does not change if the current efficiency is taken to be equal to 64% instead of 53 ± 3%.

A simple calculation of the size and number of pores, based upon numerical estimations by Keller *et al.* (9) shows that the poor current efficiency is not simply due to the loss of aluminum from the volume of the pores. For oxidation in a 15% H_2SO_4 solution at 10°C, Keller *et al.* found that the radius of the pore r_o, at

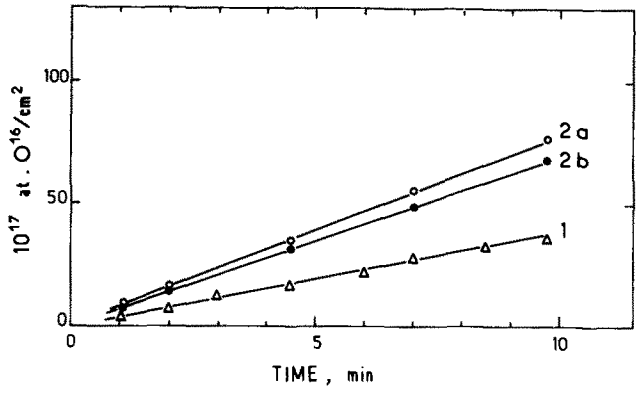

Fig. 2. Quantity of oxygen fixed on aluminum oxidized in steady-state conditions as a function of oxidation time in 15% H_2SO_4 at 10V and 15°C. Curve 1 is deduced from nuclear microanalysis and curves 2a and 2b from coulometric measurements assuming the average charge of oxygen to be 1.55 and 1.75, respectively.

the outer surface of the film, is equal to 60Å. The volume of the pores expressed in per cent of the total volume of the oxide, V_o, can be calculated from the empirical formula: $V_o = 78.5 \cdot r_o^2/R^2$, R being the radius of the cell; $R = AV + r_o$, where the wall thickness A is equal to 8 Å/V and V is the film formation voltage. One finds $R = 140$Å and the volume of the pores is calculated to be 14% of the total volume of the oxide.

It follows that the total surface, S, of the pores per square centimeter on the outer surface of the oxide is equal to 0.14 cm^2 assuming that the pores are cylindrical, *i.e.*, that lateral dissolution along their walls is negligible during film formation (this hypothesis will be confirmed in the following section). The number of pores per square centimeter, N, can be evaluated by dividing the total surface of the pores, S, by πr_o^2, *i.e.*, the surface of one individual pore. $N = 1.27 \times 10^{11}$ pores/cm^2 is the result obtained.

Recently, Wood *et al.* showed (22) by sectioning a film perpendicularly to the aluminum surface that the barrier layer and the pores were clearly visible. However, the dimensions of the cells displayed in this way were somewhat different from those indicated by Keller *et al.* (9). In particular Wood *et al.* found the diameter of the pores for films formed in 15% H_2SO_4, to be about 100Å, instead of 120Å as measured by Keller. It should be noted that in spite of certain quantitative disparities, Wood gives a perfect confirmation of the structural model proposed by Keller. Obviously, the volume of the pores (14%) cannot explain the poor current efficiency even if it is 64 ± 3% and not 53 ± 3%.

Open-circuit dissolution.—The ratio of the quantity of oxygen lost to the initial quantity of oxygen in the film is shown in Fig. 3 (curve 1) as a function of dissolution time in open circuit. Films formed at 10V, 15°C, for 6 min, 3 min, and 1 min 50 sec were dissolved in a 15% H_2SO_4 solution. An analysis of the results leads us to the following conclusions: (*a*) the apparent dissolution rate expressed as the percentage of oxygen lost depends only slightly on time throughout the range investigated (up to 200 min); and (*b*) the percentage of oxygen lost from the specimens investigated are independent of the initial thickness of the film.

In order to compare the dissolution rates of the frontal and lateral oxides (v_2, v_1) (see Fig. 4), we formed a duplex layer in a solution enriched to 10% in O^{18} (~150Å) and then in a solution depleted in O^{18} (~1800Å). When the total oxygen losses ($O^{16} + O^{18}$) are considered as a function of time the relation is the same as that given by curve 1, Fig. 3. Curve 2, Fig. 3, shows the time dependence of the percentage of O^{18} lost relative to the initial O^{18} content of the film; this percentage indicates the relative oxygen loss of the surface layer.

In order to be able to fully interpret these experiments, it appeared necessary to investigate the isotopic exchange of the oxygen contained within the film with oxygen contained in the solution, as, in principle O^{18} losses may be due not only to the dissolution of the film, but also to isotopic exchange. In order to increase the accuracy of our measurements, we investigated the oxygen exchange between films formed in solutions depleted in O^{18} and then immersed in a solution enriched in O^{18}. There appears to be no increase in the quantity of O^{18} inside the film after a 2-hr contact with the solution. On the other hand, there is a decrease of the total quantity of oxygen due to the dissolution. Although, due to this dissolution, such an experiment does not allow us to draw precise conclusions as to the value of the electrochemical oxygen exchange current, it appears clearly that the rate of isotopic exchange (the uptake of oxygen atoms per unit time) seems to be negligible compared with the rate of chemical attack.

We shall attempt to discuss the results obtained above under the assumption (suggested by several authors) that the constant rate of dissolution v_1 (cm/min) along the walls of the pore differs from the rate

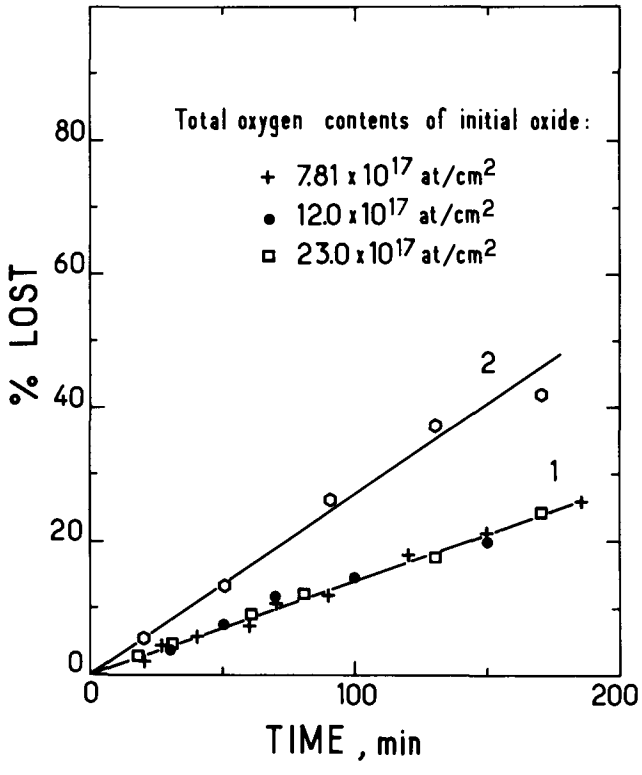

Fig. 3. Percentage of oxygen lost with respect to the initial quantity of oxygen in the film as a function of the open-circuit dissolution time in 15% H_2SO_4 at 15°C. Curve 1: films formed in $s_0 16$ solution; O^{16} losses with respect to the total initial quantity of oxygen. Curve 2: duplex film; O^{18} losses with respect to the initial amount of O^{18} in the film (see Fig. 4).

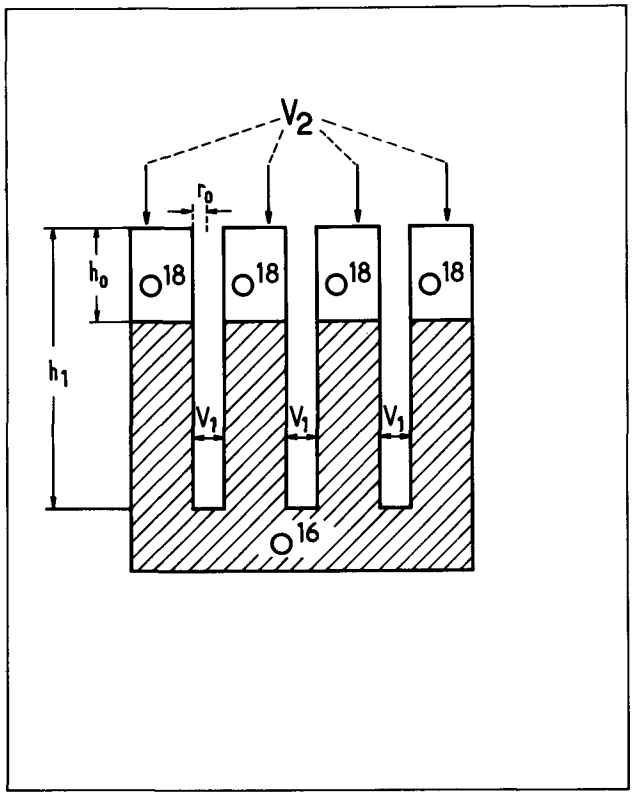

Fig. 4. Schematic structure of a porous layer: v_2 and v_1 are the frontal and lateral rates of dissolution of the oxide, respectively; r_o is the pore radius; h_o is the thickness of the enriched layer; h_1 is the total thickness of the porous layer.

of dissolution v_2 at the outer surface of the film (see Fig. 4). We shall apply Keller's geometrical model and quantitative evaluations in order to determine v_1 and v_2 which may be calculated by a method similar to that used in Ref. (11).

The ratio g_1 of the pore wall surface to the apparent surface of the specimen, at a given time θ is

$$g_1 = 2\pi rhN$$

where r is the average radius of a pore at time θ, and h is the thickness of the film (the thickness of the compact base layer is assumed to be negligible compared with the total thickness of the film). At a given time θ, the ratio g_2 of the outer film surface to the apparent surface of the specimen is

$$g_2 = 1 - \pi r^2 N$$

Because the rate of dissolution remains constant, r increases and h decreases linearly with time

$$r = r_1 + v_1\theta \text{ and } h = h_1 - v_2\theta$$

where h_1 and r_1 are the thickness of the film and the average pore diameter at $\theta = 0$, respectively.

The quantity of oxygen dissolved at a time t is given by

$$N_O(t) = \alpha v_1 \delta \int_o^t g_1 d\theta + \alpha v_2 \delta \int_o^t g_2 d\theta$$

where α is the fraction by weight of oxygen in the film and δ is the density of the film. After calculations this expression becomes

$$N_O(t) = \alpha\delta v_1 2\pi N \left[h_1 r_1 t + (v_1 h_1 - v_2 r_1)\frac{t^2}{2} - v_1 v_2 \frac{t^3}{3} \right] + \alpha\delta v_2 \left[(1 - \pi N r_1^2)t - 2\pi N r_1 v_1 \frac{t^2}{2} - N\pi \frac{v_1^2 t^3}{3} \right]$$

The total quantity of oxygen in the film prior to dissolution is

$$N_O = \alpha h_1 \delta - \alpha\pi r_1^2 h_1 N\delta = \alpha h_1 \delta (1 - \pi r_1^2 N)$$

In this expression, $\alpha\delta h_1$ is the quantity of oxygen which would be present in the film of thickness h if the film were free of pores and $\alpha\pi r_1^2 h_1 N\delta$ is the quantity of oxygen which would be contained within the pores.

The ratio of oxygen lost after a dissolution time t to the initial quantity of oxygen is

$$p = \frac{N_O(t)}{N_O} = \left[\frac{2\pi N r_1 v_1}{1 - \pi N r_1^2} + \frac{v_2}{h_1} \right] t + \frac{\pi N [v_1^2 h_1 - 2 v_1 v_2 r_1]}{h_1 (1 - \pi N r_1^2)} t^2 - \frac{\pi N v_1^2 v_2 t^3}{h_1 (1 - \pi N r_1^2)} \quad [1a]$$

Equation [1a] shows that the general expression for p as a function of dissolution time contains t^2 and t^3 terms, as well as a linear term. Experimental results show (Fig. 3) that under our conditions (dissolution time $t \leq 200$ min), p is essentially a linear function of the dissolution time. Thus, we shall only keep

$$p = \left[\frac{2\pi N r_1 v_1}{1 - \pi N r_1^2} + \frac{v_2}{h_1} \right] t. \quad [1b]$$

or

$$p = [A \cdot v_1 + v_2 \cdot h_1^{-1}]t \quad [1c]$$

where $A = 5.55 \times 10^{-3}$ Å^{-1}.

From Fig. 3, we can deduce two values of p; one for a total film thickness of 1800Å (curve 1) and a second value deduced using the thickness of the oxygen 18 enriched surface layer presented in Fig. 4 as h_o, *i.e.*, 150Å (curve 2). For an arbitrary dissolution time equal for example to 100 min, we can calculate from Eq. [1c] the values of v_1 and v_2. We find that these values are practically the same and equal to 2×10^{-9} cm/min: Consequently, the term v_2/h_1 (curve 1) is ten times smaller than the term $2\pi N r_1 v_1/1 - \pi N r_1^2$. In addition the nonlinear terms are indeed negligible in Eq. [1a] for these values of the parameters.

For $h_1 \geq 1800$Å the v_2 term can be neglected and

$$p \approx \frac{2\pi N r_1 v_1}{1 - \pi N r_1^2} t$$

This means that the oxygen loss is independent of the initial thickness of the film as was shown experimentally (curve 1, Fig. 3)

In fact, the value v_1 determined in this way depends on quantitative hypotheses based on the data of Keller *et al.* which certain authors consider to be underestimated. Furthermore, the determination of the value v_2 depends on the accuracy of the value h_o used for the surface film thickness (Fig. 4). Although these remarks cast a certain doubt on the reliability of the values of v_1 and v_2, it should be clear that the dissolution rates along the pore walls and on the outer surface are of the same order of magnitude. On the other hand, it seems significant that the values of v_1 and v_2 established by investigating the oxygen losses (15% H_2SO_4 at 15°C) are of the same order of magnitude as those obtained by Nagayama and Tamura at 27°C in 10% H_2SO_4 (7.5×10^{-9} cm/min) by analyzing the aluminum dissolved.

Dissolution during oxide growth.—In the previous paragraph we showed that in the case of open-circuit dissolution there is no appreciable difference between the dissolution rate at the outer oxide-solution interface and the dissolution rate along the pore walls. We are now faced with the problem of knowing whether there is a high dissolution rate at the outer oxide-solution interface during film formation and, if so, whether this can account for the poor current efficiency observed. To settle this question, we attempted to estimate the variations of the quantity of O^{18} in the films initially formed in an enriched solution and subsequently reoxidized in a depleted solution. Such a film was formed for 15 sec in s_o18 at 10V and then reoxidized for 10 min in s_o16. Measurements showed that there was an increase in O^{18} of $2.6 \pm 0.1 \times 10^{15}$ atoms/cm^2 in the final duplex film compared to the original film which contained 15×10^{15} atoms O^{18}/cm^2.

Further measurements showed that a film formed for 10 min in s_o16 at 15°C, 10V, contains $3 \pm 0.15 \times 10^{15}$ atoms O^{18}/cm^2, which comes partly from the O^{18} of the depleted solution and, above all, from the incorporation of SO_4 ions of natural isotopic concentration. It can be concluded from the difference between the values measured that there is a loss of $0.4 \pm 0.25 \times 10^{15}$ atoms O^{18}/cm^2 at the film-solution interface during reoxidation. Curve 2 of Fig. 3 shows that open-circuit dissolution for 10 min results in a loss of 0.4×10^{15} atoms O^{18}/cm^2 for a film which contains, like the original duplex film specimen, 15×10^{15} atoms O^{18}/cm^2. Thus, the oxygen losses during reoxidation and the losses under open-circuit dissolution seem to be of the same order of magnitude.

Growth mechanism.—In order to understand the physical meaning of the above results, it was thought necessary to examine the possible configurations of the isotope distribution throughout the duplex film, according to various transfer mechanisms.

During reoxidation, a new layer having a different isotopic composition from that of the first layer can form at the three interfaces: (*i*) porous layer-solution (Fig. 5a), (*ii*) compact layer-porous layer (Fig. 5b), and (*iii*) metal-compact layer (Fig. 5c).

(*i*) In the case of the first configuration (Fig. 5a), the oxide forms at the porous layer-solution interface

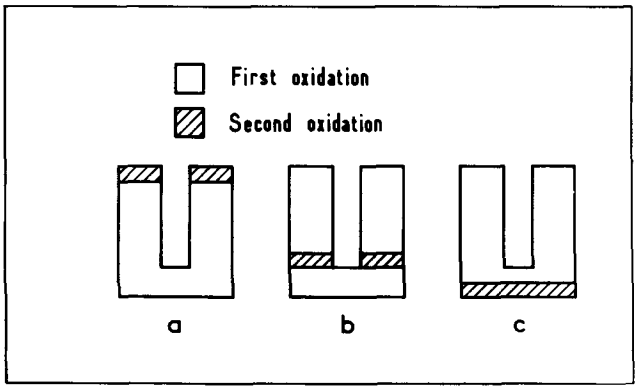

Fig. 5. Oxygen transport during porous formation. New layer formed (a) on the top of the porous film, (b) at the porous/compact layer interface, and (c) at the compact layer/metal interface.

by cation migration across the compact and porous layers.

(*ii*) According to Fig. 5b, the oxide forms at the compact layer-porous layer interface either by long range cation migration or by an order conserving oxygen propagation transmitted from neighbor to neighbor across the compact layer. The new layer immediately transforms into a porous layer maintaining constant the thickness of the compact layer.

(*iii*) In the third configuration (Fig. 5c), oxide formation occurs at the compact layer-metal interface by long-range migration of oxygen coming directly from the solution. In this case, too, the thickness of the compact layer does not change because of immediate transformation into a porous layer.

Figure 6 shows the excitation curves for three types of specimen obtained near the resonance at 629 keV. Curve 1 refers to a porous oxide film formed for 15 sec in 15% H_2SO_4 enriched in O^{18} (solution $s_0 18$) at 10V. Curve 2 has been obtained for a duplex film, first formed for 3 min at 10V in 15% H_2SO_4 depleted in O^{18} ($s_0 16$) and then reoxidized at the same potential for 15 sec in $s_0 18$. The quantity of O^{18} added is equal within 10% to the quantity of O^{18} in the specimen of curve 1. Curve 3 refers to a duplex layer formed under conditions similar to those described above, with an initial oxidation time in $s_0 16$ equal to 6 min. Analysis of the curves shows that the resonance maximum is shifted toward higher energies. This seems to indicate that all the O^{18} atoms added during reoxidation are embedded in the bulk of the oxide and that their depth relative to the film-solution interface depends on the original porous layer formed in $s_0 16$. However due to energy straggling of the protons the spread of the O^{18} distribution around its mean value cannot be determined with sufficient accuracy from the observed broadening of the excitation curves. In particular, no assertion can be made as to whether the oxygen atoms coming from reoxidation accumulate near the metal-compact layer interface (Fig. 5c) or whether they are distributed throughout the duplex film. Anyway, this consideration makes configuration 5a impossible.

To gain a deeper knowledge of this fundamental aspect of the transport mechanism, tests were carried out exchanging the two oxidations. After formation of an original layer with O^{18} followed by reoxidation with O^{16}, the original O^{18} layer would remain at the surface if the oxygen atoms coming from reoxidation were located at the metal-compact film interface. In this case, one would observe a narrow resonance peak corresponding to that obtained from the layer prior to reoxidation, whatever the additional thickness of the oxide layer. If the oxygen atoms were found at the compact film-porous film interface, there would be two peaks originating from deep-seated and surface O^{18}, respectively. Figure 7 shows the theoretical excitation curve corresponding to such a case (curve 3).

Figure 7, curve 1, shows the excitation curve for a film formed in $s_0 18$ (10V, 15 sec). Curve 2 shows the excitation curves for duplex films formed in $s_0 18$ (10V, 15 sec) and then reoxidized at the same potential in $s_0 16$ for various fixed times (1 min, 30 sec; 3 min; 6 min).

It can be seen that there is only one peak coinciding with the resonance peak, whatever the additional thickness. Thus, the actual picture of the isotopic distribution is shown by Fig. 5c. It is impossible to ascer-

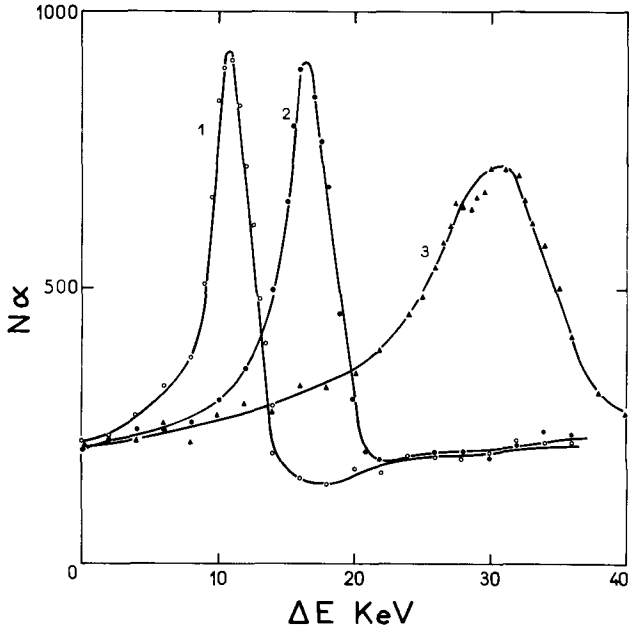

Fig. 6. Excitation curves of O^{18} (p, α) N^{15} reaction near the 629 keV resonance. Curve 1: thin porous film formed in O^{18} enriched solution (15 sec); curves 2 and 3: duplex films, first formed in a solution depleted in O^{18} for 3 and 6 min, respectively, and then reoxidized at the same potential for 15 sec in an O^{18} enriched solution (v = 10V; t = 15°C; 15% H_2SO_4).

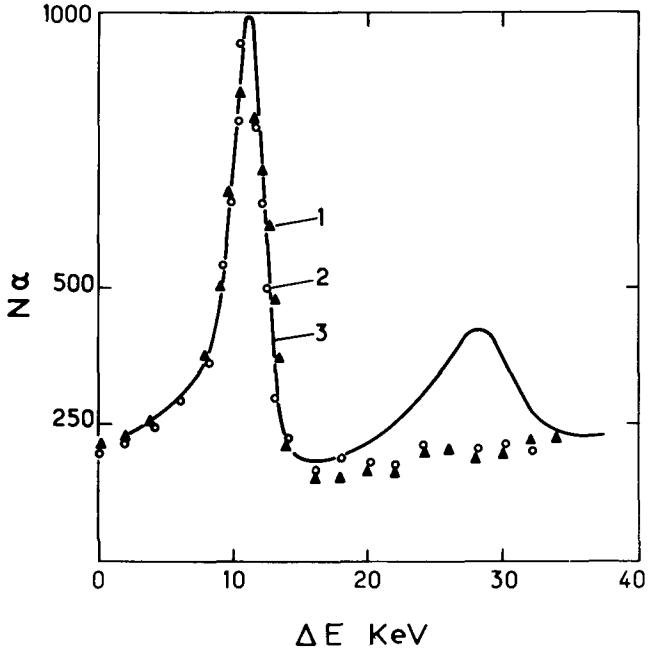

Fig. 7. Excitation curves of O^{18} (p, α)N^{15} reaction near the 629 keV resonance. Curve 1: thin porous film formed for 15 sec at 10V and 15°C in O^{18} enriched solution: curve 2; duplex film, first formed in an O^{18} enriched solution (see above) and then reoxidized at the same potential in an O^{18} depleted solution for fixed times of 1 min 30 sec, 3 min, 6 min; curve 3: theoretical curve of the duplex film (6 min reoxidation) calculated when one-half of the initial O^{18} layer remains at the metal-oxide interface.

tain whether there is a mixing of O^{18} and O^{16} beyond a depth of ~200Å below the surface layer, because of the limited investigating possibilities of our experiment.

Nevertheless, it should be noted that the validity of the conclusions as regards the choice of the transport mechanism does not depend on the absence or presence of this relatively small mixing.

Discussion

The above experimental results lead to the determination of the various terms of the current forming the porous layers disregarding electronic losses (8, 14). For steady-state conditions [see Ref. (3)]

$$I_{tot} = I_{ox} + I_{dis} \quad [2]$$

Obviously, I_{ox} is proportional to the current efficiency of film formation, which is found to be constant in our experimental conditions ($t_{ox} \leq 10$ min). It represents 53 ± 3% of I_{tot} (I_{tot} = const). Thus, I_{dis} is 47 ± 3% of I_{tot}. According to Diggle *et al.* (5, 8), I_{dis} is the sum of two terms; I_{dec} and I_{chim}:

I_{dec} is the charge per unit area, per unit time, required to form a volume of oxide equal to the volume of the pores.

I_{chim} is the charge per unit area, per unit time needed to form the oxide dissolved chemically. Therefore

$$I_{dis} = I_{dec} + I_{chim} \quad [3a]$$

I_{chim} depends on the pore geometry which is itself dependent on the anodizing time used in film formation

$$I_{chim} = i_{chim} \cdot S$$

where i_{chim} is the oxide dissolution rate of the oxide per real square centimeter; in our experimental conditions, we obtained $v_1 = v_2 = 2 \times 10^{-9}$ cm/min, *i.e.*, equivalent to a current density per real unit surface of 0.3 μA/cm^2; S is the ratio of the total real surface of the pores to the apparent surface of the specimen. S can be calculated from the expressions

$$S = 2\pi r_1 \cdot h_1 \cdot N$$

For $r_1 = 60 \times 10^{-8}$ cm, $N = 1.27 \times 10^{11}$ pores/cm^2, and $h_1 = 7 \times 10^{-5}$ cm, (which is the maximum thickness of films studied in this work), we found: $S = 33.7$. Thus, the maximum value of I_{chim} is equal to 10.1 μA/cm^2. In our experiment, $I_{tot} \approx 5$ mA/cm^2 and I_{dis} (47% of I_{tot}) $\approx$ 2.4 mA/cm^2. This means that for $t_{ox} \leq 10$ min the maximum value of I_{chim} is much smaller than 1% of I_{dis} and can be disregarded.

The value of I_{dec}[2] can be deduced from the volume of the pores and can be determined from the data of Keller *et al.* (9) to be about 9% of I_{tot}. It should be noted that the value of I_{dec} is independent of the oxide dissolution mechanism for producing pores. According to literature data [see for example Diggle *et al.* (23)], it is a field-assisted process, the mechanism of which, however, has not been specified.

Thus, our results cannot be explained by Eq. [3a]. It is logical to suppose that I_{dis} has a third component (I_{Al}) and can be written as Eq. [3b]

$$I_{dis} = I_{dec} + I_{Al} + I_{chim} \quad [3b]$$

which, in our experimental conditions ($t_{ox} \leq 10$ min) is reduced to [3c]

$$I_{dis} \simeq I_{dec} + I_{Al} \quad [3c]$$

According to our results ($I_{dis} \approx 47\%$ of I_{tot}), I_{Al} is equal to 38% of I_{tot}. Using the data from Ref. (11), ($I_{dis} \approx 33\%$ of I_{tot}), I_{Al} was found to be about 22% of I_{tot}. It should be noted that Nagayama and Tamura (11) arrived at the same conclusions but the physical meaning of this effect was not discussed in their paper.

We found above that the dissolution current I_{dis} is not accompanied by significant losses of oxygen. Thus it is logical to suppose that all the dissolution current (I_{dis}) is purely a cationic effect, *i.e.*, that is represented in the solution only by aluminum cations.

[2] $I_{dec} = I_{ox} \cdot 0.14/0.86$.

It must be emphasized that I_{Al} and I_{dec} are completely different from the physical point of view. I_{Al} can be represented by the movement of the aluminum sublattice (hole movement) or by the interstitial movement of cations from the metal to the solution. Thus I_{Al} can be defined as the current of direct discharge of cations in the solution; whereas I_{dec} arises in the bottom of the pores at the oxide-solution interface as a result of field assisted "dissolution" of the oxide to form the pores. It is probably represented by the movement of aluminum species toward the solution and oxygen species toward the oxide-metal interface, where the new oxide is formed. It should be noted that I_{ox} (53% of I_{tot}) is caused by the movement of oxygen coming from the solution which ensures the growth of the oxide at the metal/oxide interface. The results concerning the ionic movements during the field-assisted dissolution of the oxide and the discussion of the asserting models will be reported in a separate paper.

It should be recalled that the numerical values of the different terms of the current were calculated on the basis of the current efficiency equal to 53 ± 3%; replacing this value by 64%, one obtains: I_{ox} = 64% of I_{tot}; I_{dis} = 36% of I_{tot}; I_{dec} = 10% of I_{tot}; and I_{Al} = 26% of I_{tot}. The numerical values of these terms are different for both cases; anyway, they provide evidence for the existence of a direct discharge of cations in the solution current (I_{Al}). This current exceeds by at least one hundred times the chemical oxide dissolution current for oxide thicknesses less than 10^{-4} cm. Similar conclusions have been drawn from experiments on the formation of compact alumina layers in ammonium citrate (3), in agreement with the data of Davies *et al.* (24).

The value of the dissolution rate of the oxide determines a limiting value of thickness beyond which there occurs no further growth of the oxide layer, defined by the increase of oxygen content in the films. At 15°C and V_{ox} = 10V this limiting thickness h corresponds to the formation of pore surfaces ensuring a chemical dissolution current equal to the maximum value of I_{ox} (56% of $I_{tot} \sim 2.7$ mA/cm^2). The precise value of h is difficult to calculate. However, assuming the pores to be cylindrical by neglecting the pore widening process, the maximum value is readily found to be $\sim 2 \times 10^{-2}$ cm.

On the basis of the results obtained, we shall attempt to shed some light on certain aspects of the growth mechanism of porous layers. It should be emphasized that the oxygen atoms coming from the solution migrate across the base layer, thereby ensuring oxide growth at the oxide-metal interface. Experiments performed previously in our laboratory on the mechanism of oxygen transport (16, 25) have shown that the oxygen atoms are fixed according to their order of arrival during the formation of amorphous compact layers on aluminum or tantalum. In other words, the oxygen atoms belonging to a new layer are located at the oxide-solution interface. If the base layer formed during porous growth also had an amorphous structure, a reversing of the order of oxygen atoms would involve an interstitial type of oxygen migration. Such a type of oxygen transport in the form OH^- has been taken into consideration by Hoar and Mott (6); as mentioned in the beginning of this paper, it has been frequently criticized in the literature. This type of oxygen transport, which is very different from the transport mechanism during the formation of compact layers, seems quite untenable if the base layer is also amorphous. However, there is some experimental evidence [see, *e.g.*, Dorsey (26)] that the base layer has a substructure and that it is composed of anhydrous microcrystallites (highly polymerized Al_2O_3) and of a hydrated microphase equivalent to aluminum trihydroxide. Similar conclusions were obtained by La Vecchia *et al.* (27) on the basis of results obtained by electron micrographs. According to these authors,

the base layer contains microchannels which should not be considered as ordinary channels but rather as easy paths through which charge carriers flow preferentially. The existence of such a substructure of the base layer would account for the inversion of the order of oxygen during the growth process, if the isotopic oxygen exchange between oxygen traveling through the easy paths and oxygen contained within the crystallites can be disregarded.

A partial inversion of the order of oxygen has been observed during the formation of compact layers on zirconium (28). Since the mobility of oxygen in the microchannels (containing hydrated alumina) exceeds that of oxygen in the anhydrous microcrystallites, it could be concluded that oxygen migration increases in the presence of OH^- groups. Recent investigations on the isotopic effect of hydrogen on the rate of porous growth (29) seem to confirm this hypothesis. Results of these investigations will be reported in a separate paper.

Acknowledgments

The authors wish to thank Dr. G. Amsel for his numerous comments and suggestions during this work. They are grateful to Mr. C. Ortega and Dr. J. P. Nadai for enlightening discussions. The technical assistance of Mr. A. Laurent was much appreciated. The comments of Dr. R. S. Alwitt, which contributed to a better presentation of this paper, were greatly appreciated too. This work was supported by the Centre National de la Recherche Scientifique (RCP No. 157), the DRME, and the DGRST.

Manuscript submitted June 5, 1972; revised manuscript received Jan. 25, 1973. This was Paper 90 presented at the Cleveland, Ohio, Meeting of the Society, Oct. 3-7, 1971.

Any discussion of this paper will appear in a Discussion Section to be published in the December 1973 JOURNAL.

REFERENCES

1. G. Amsel, J. P. Nadai, E. D'Artemare, D. David, E. Girard, and J. Moulin, *Nucl. Instr. Methods*, **92**, 481 (1971).
2. G. Amsel, C. Cherki, G. Feuillade, and J. P. Nadai, *J. Phys. Chem. Solids*, **30**, 2117 (1969).
3. J. Siejka, J. P. Nadai, and G. Amsel, *This Journal*, **118**, 727 (1971).
4. M. Croset, E. Petreanu, D. Samuel, G. Amsel, and J. P. Nadai, *ibid.*, **118**, 717 (1971).
5. J. W. Diggle, T. C. Downie, and C. W. Goulding, *ibid.*, **116**, 1347 (1969).
6. T. P. Hoar and N. F. Mott, *J. Phys. Chem. Solids*, **9**, 97 (1959).
7. T. P. Hoar and J. Yahalom, *This Journal*, **110**, 614 (1963).
8. J. W. Diggle, T. C. Downie, and C. W. Goulding, *Chem. Rev.*, **69**, 365 (1969).
9. F. Keller, M. S. Hunter, and D. L. Robinson, *This Journal*, **100**, 411 (1953).
10. M. S. Hunter and P. E. Fowle, *ibid.*, **101**, 514 (1954)
11. M. Nagayama and K. Tamura, *Electrochim. Acta*, **12**, 1097 (1967); M. Nagayama, K. Tamura, and H. Takahashi, *Corrosion Sci.*, **12**, 133 (1972).
12. L. Young, "Anodic Oxide Films," Academic Press, New York (1961).
13. J. W. Diggle, T. C. Downie, and C. W. Goulding, *J. Electroanal. Chem.*, **18**, 192 (1968).
14. R. C. Spooner, *This Journal*, **102**, 156 (1955).
15. R. B. Mason, *ibid.*, **102**, 671 (1955).
16. G. Amsel and D. Samuel, *J. Phys. Chem. Solids*, **23**, 1707 (1962).
17. G. Amsel and D. Samuel, *Anal. Chem.*, **39**, 1689 (1967).
18. G. Amsel, J. P. Nadai, and B. Maurel, To be published.
19. T. C. Hoering and J. W. Kennedy, *J. Am. Chem. Soc.*, **79**, 56 (1957).
20. R. B. Mason and C. J. Slunder, *Ind. Eng. Chem.*, **39**, 1602 (1947).
21. R. B. Mason and E. Fowle, *This Journal*, **101**, 53 (1954).
22. G. C. Wood and J. P. O'Sullivan, *Electrochim. Acta*, **15**, 1865 (1970); J. P. O'Sullivan and G. C. Wood, *Proc. Roy. Soc. London*, **A317**, 511 (1970).
23. J. W. Diggle, T. C. Downie, and C. W. Goulding, *This Journal*, **116**, 737 (1969).
24. J. A. Davies, B. Domeij, J. P. S. Pringle, and F. Brown, *ibid.*, **112**, 675 (1965).
25. C. Cherki, Thesis, Paris (1969).
26. G. A. Dorsey, Jr., *This Journal*, **113**, 169 (1966); **113**, 172 (1966); **113**, 284 (1966).
27. La Vecchia, G. Piazzesi, and F. Siniscalco, *Electrochim. Metal.*, **2**, 71 (1967).
28. C. Ortega and J. Siejka, Paper 86 presented at the Cleveland Meeting of the Society, Oct. 3-7, 1971; Extended Abstracts, p. 221.
29. J. Siejka and C. Cherki, Paper 90 presented at the Cleveland Meeting of the Society, Oct. 3-7, 1971; Extended Abstracts, p. 231.

The Incorporation of Tellurium in Liquid Phase Epitaxial (LPE) GaP: Implications for Oxygen Incorporation

A. S. Jordan, F. A. Trumbore,* K. B. Wolfstirn, M. Kowalchik, and D. D. Roccasecca

Bell Laboratories, Murray Hill, New Jersey 07974

ABSTRACT

The dependence of the Te concentration in GaP LPE layers was studied as a function of doping level and temperature in the range from ~935° to ~1135°C. The results are interpreted in terms of surface-controlled, as well as bulk-equilibrium, incorporation of the Te, and indicate that, at the lower doping levels, the Te solubility is appreciably lower than the bulk equilibrium value. A similar behavior is postulated to explain conflicting data on the solubility of O in GaP.

Group VI donor impurities play a major role in GaP red and green light-emitting diodes (LED's). In particular, oxygen, in the form of Zn-O nearest neighbor pairs, is the center responsible for the red electroluminescence in GaP (1), while tellurium is a commonly used donor for the preparation of n-type regions in both red and green LED's (2). Thus, it is of practical importance to understand the incorporation of these impurities in GaP. In addition, there is considerable fundamental interest in the incorporation mechanism of Group VI donors, since their solid-solu-

* Electrochemical Society Active Member.

Key words: light-emitting diodes, crystal growth, compound semiconductors, impurity incorporation, defect chemistry.

bility behavior disagrees with the conventional thermodynamic analysis of impurity incorporation for bulk phases in equilibrium. In essence, this analysis predicts that the functional variation of the ionized donor or acceptor concentration on the dopant concentration in the external phase (*i.e.*, liquid solution) changes from linear to square-root dependence at $\sim n_i$, the intrinsic electron concentration (3-5). Zn-doped GaP (3, 5) and GaAs (4) are the prototype systems where the above behavior is clearly manifested and best understood. However, the available experimental data for Te, Se, and S-doped GaP (3) and GaAs (6, 7) cannot be reconciled with the consequences of the thermodynamic analysis invoking bulk equilibrium. On the one hand, the 1000°C solid-solubility isotherm of Te (7), as well as the 1238°C (melting point) solubilities of Te and Se in GaAs (6), is linear at all observed donor concentrations, much exceeding the estimated values of n_i (8). On the other hand, a break to a square-root solubility behavior has been observed to occur above n_i for the incorporation of Te, Se, and S in GaP at 1040°C (3), and S in GaAs at 1238°C (6).

In this paper, we present the results of radiotracer (^{129m}Te) and surface-barrier capacitance measurements on Te-doped GaP layers grown by liquid-phase epitaxy (LPE) over limited temperature ranges using a sealed-tube slider technique (9). The major objectives of this work were the following: (*i*) To more accurately determine the solid solubility isotherm of Te at ~1040°C, especially at lower doping levels than previously studied [*i.e.*, $\lesssim 10^{-2}$ atomic per cent (a/o) Te additions to the LPE solution corresponding to doping levels employed to grow LED material]; (*ii*) To obtain solid solubility isotherms below and above 1040°C in order to establish whether the presence and anomalous position of the break was temperature dependent; (*iii*) To relate these results to the surface band-bending model of Zschauer and Vogel (10) and Casey *et al.* (7); (*iv*) To compare the results on Te-doped GaP prepared by different techniques (sliding, tipping, vapor-transport, liquid-encapsulated Czochralski, and thermal gradient).

As a final objective, an attempt was made to examine the consequences of the findings with respect to Te incorporation in the apparently disparate results concerning the incorporation of O donors in GaP.

Experimental

Crystal growth.—The Te-doped GaP layers were grown on liquid-encapsulated Czochralski (LEC) substrates,[1] by LPE from GaP-saturated Ga solutions containing Te or ^{129m}Te. To eliminate vapor transport of the dopant and to ensure the termination of growth at any chosen temperature, a sealed-tube slider assembly (9) located in an isothermal furnace (with less than 1°C variation over the capsule) was used to grow the epitaxial films. Although most experiments were performed in an Al_2O_3 (G. E. Lucalox) slider, occasionally a fused-quartz slider was also employed.

In a typical run, the substrate and the solution containing Te, ^{129m}Te, or a mixture of the two were placed into the appropriate compartments of the slider assembly which was sealed in a quartz capsule after evacuation to 10^{-6} Torr. Next the ampoule was heated to about 15°C above the initial growth temperature and held for 30 min to achieve saturation. Subsequently, epitaxial growth was initiated by moving the Ga-rich solution contained in an opening cut through the slider, onto the GaP substrate. After cooling the solution at a rate of ~0.8°C/min over a limited temperature range, growth was terminated by retracting the slider to its original position following which the ampoule was removed from the furnace. The GaP LPE layers were grown in the following limited temperature ranges: 1145°-1125°C, 1050°-1030°C, and 950°-920°C. The typical epitaxial film thicknesses were ~50, 25, and 15 μm, respectively, corresponding to the average growth temperatures 1135°, 1040°, and 935°C.

Tellurium analysis.—Radiochemical analysis and surface-barrier capacitance measurements were the two methods used to determine the solid solubility of Te in the GaP LPE layers. The radiochemical analysis procedure was similar to that previously applied to the solubility of Te in GaAs (7) and was based on the detection of the 0.48 MeV gamma-emission peak resulting from the decay of ^{129m}Te (half-life = 33.5 days). From counting statistics an accuracy of ±3% is estimated for this analytical method and the detection sensitivity was 3×10^{-9}g of Te.

In order to ascertain that Te was not lost during a run via vapor transport or a refractory reaction, and to eliminate weighing errors, a radiochemical analysis of the LPE solution following growth was performed. In essence, the solution was dissolved in HNO_3 and its ^{129m}Te content determined by comparing the count-rate of an aliquot of this acid solution with that of a ^{129m}Te standard.

Essentially, two complementary methods were used in the LPE layer analysis. In the first method, following lapping the edge and back growth, the LPE layer was sectioned by incrementally removing ~3 μm thick layers using a chlorine-methanol solution. During sectioning the uniformity of the dopant distribution across the layer was frequently checked by means of autoradiographs. The Te concentration in a given section was determined by a comparison of the count-rate in the etching solution with appropriate ^{129m}Te standards and from the weight loss and area of the sample. In the second method, subsequent to the removal of between 2 to 6 sections, the average Te concentration in the remaining layer was evaluated from its total count-rate, area and thickness, the latter being obtained by microscopic measurement of cleaved or angle-lapped surfaces. Since sectioning is a laborious procedure, it was hoped that after a few sectioning steps, the Te concentration in the last increment would approach that in the remaining layer. Unfortunately, this condition could not be met for the LPE layers grown at the highest temperature (~1135°C). At that temperature mechanical difficulties were often encountered with the slider, preventing the desired abrupt termination of growth and resulting in a thick layer with a heavy Te accumulation in the last portion to crystallize.

The net impurity profile (N_D-N_A) was determined for several Te-doped layers by means of surface-barrier capacitance measurements on angle-lapped samples as described previously for the analysis of Zn (11) and Te (12) in GaP LPE layers. The background value of $N_D - N_A$ was $\sim 9 \times 10^{15}$ cm^{-3} for a LPE layer grown from an undoped solution.

Results and Discussion

Surface controlled and equilibrium incorporation.—The Te concentrations in the LPE alloys (x^l_{Te}) and the corresponding solid solubilities of Te (C^s_{Te}) in the GaP LPE layers expressed in units of atom fraction and atoms/cm^3, respectively, are summarized in Table I. In general, good agreement was achieved between the values of x^l_{Te} derived from radiotracer analysis of the solutions and those determined by weighing. A comparison of the two methods by statistical means[2] yields a standard deviation of ~6%. However, for minute ^{129m}Te additions to the solution, tracer analysis was considered more reliable than weighing; hence, below 10^{-3} a/o additions, tracer concentrations are listed in Table I.

[1] The source materials used for these experiments were phosphine-grown polycrystalline GaP (Monsanto) and Te (United Minerals), both with 99.9999% nominal purity. A batch of 99% enriched ^{128}Te was irradiated for 6 weeks in a neutron flux of 9×10^{13} cm^2/sec to yield ^{129m}Te (Union Carbide, Tuxedo, New York). The undoped LEC substrates, mechanically polished on the phosphorus (B) face, were obtained from Bell Laboratories, Reading.

[2] In the absence of errors, the ratio of the i'th concentration determined by the tracer and weighing techniques, C^i_t/C^i_w should be unity. Hence, the standard deviation $\sqrt{(\Sigma_i (C^i_t/C^i_w - 1)^2)/n}$ where n is the number of measurements, is a reasonable representation of the pertinent error.

Table I. Solid-solubility data for Te in GaP

Average growth temperature (°C)	x^{l}_{Te} (atom fraction)	C^{s}_{Te} (atoms/cm³)
935	5.22×10^{-6}*	$5.7_2 \times 10^{16}$
	1.06×10^{-5}*q	$1.5_0 \times 10^{17}$
	8.70×10^{-5}	$4.5_0 \times 10^{17}$
	6.16×10^{-4}q	$6.8_1 \times 10^{18}$
	7.10×10^{-4}	$7.0_2 \times 10^{18}$
1040	2.54×10^{-6}*	$2.9_5 \times 10^{16}$
	2.70×10^{-6}	2.1×10^{16}†
	4.73×10^{-6}*	$5.0_6 \times 10^{16}$
	1.00×10^{-5}q	7.5×10^{16}†
	2.50×10^{-5}	2.5×10^{17}†
	3.52×10^{-5}q	4.0×10^{17}†
	6.80×10^{-5}	5.1×10^{17}†
	6.80×10^{-5}	6.2×10^{17}†
	3.00×10^{-4}	1.2×10^{18}†
	1.13×10^{-3}	$3.3_0 \times 10^{18}$
1135	5.41×10^{-6}*	$3.4_9 \times 10^{16}$
	5.41×10^{-6}*	4.0×10^{16}†
	6.88×10^{-6}*	$4.6_0 \times 10^{16}$
	9.39×10^{-6}*	$9.0_3 \times 10^{16}$
	2.20×10^{-5}	$7.3_6 \times 10^{16}$
	4.49×10^{-5}	$1.1_4 \times 10^{17}$
	1.09×10^{-4}	$4.0_4 \times 10^{17}$
	1.09×10^{-4}	3.1×10^{17}
	9.39×10^{-4}	$3.5_5 \times 10^{18}$
	9.20×10^{-3}	$2.1_7 \times 10^{19}$

The value of x^{l}_{Te} and C^{s}_{Te} were obtained by weighing and radiochemical analysis, respectively, and the LPE layers were grown in an Al_2O_3 slider except when otherwise denoted.
* Radiochemical.
† $N_D - N_A$.
q Fused quartz slider.

The tabulated ^{129m}Te solubility data for ~935° and ~1040°C were obtained, in general, by averaging the concentrations determined by the two above mentioned methods. However, on account of the previously discussed heavy Te accumulation in the first few sections, the listed ~1135°C solubility data are based on the analysis of the remaining layer. Extrapolation of the N_D-N_A profiles to the electrical junction yielded the additional data presented in Table I where it is assumed that $C^{s}_{Te} = N_D$-N_A.

The tabulated values of C^{s}_{Te} as a function of x^{l}_{Te} are plotted in Fig. 1 for the LPE layers grown at ~1040°C, and in Fig. 2 for those grown at ~935° and ~1135°C. Solid-solubility data from the investigations of Trumbore *et al.* (3) and Saul and Hackett (12) are also shown. The data of Trumbore *et al.* (3) were based on the spectrophotometric analyses of the total Te concentration in crystals grown by a thermal gradient transport (TGT) technique over a period of 5

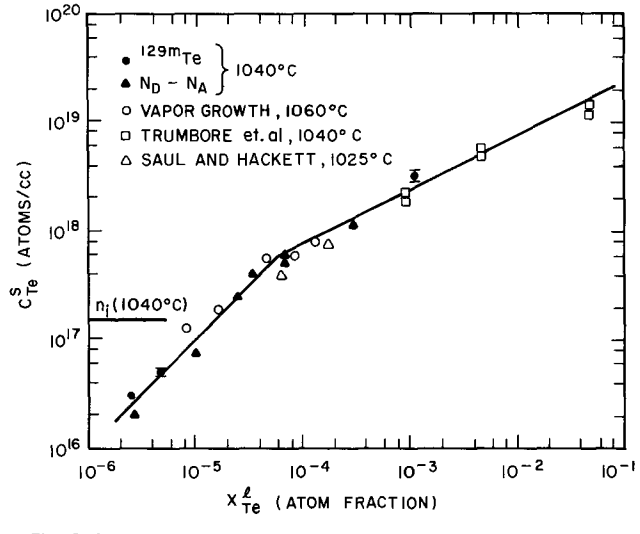

Fig. 1. Te concentration in GaP as a function of the Te content of the LPE solution at ~1040°C. The error bars indicate the concentration limits obtained by sectioning and the total count-rate of the remaining layer. In the linear incorporation regime, the solid line was based on Eq. [8]. The abscissas for vapor-grown crystals are actually calculated Te activities which correspond to Te atom fractions for an ideal solution.

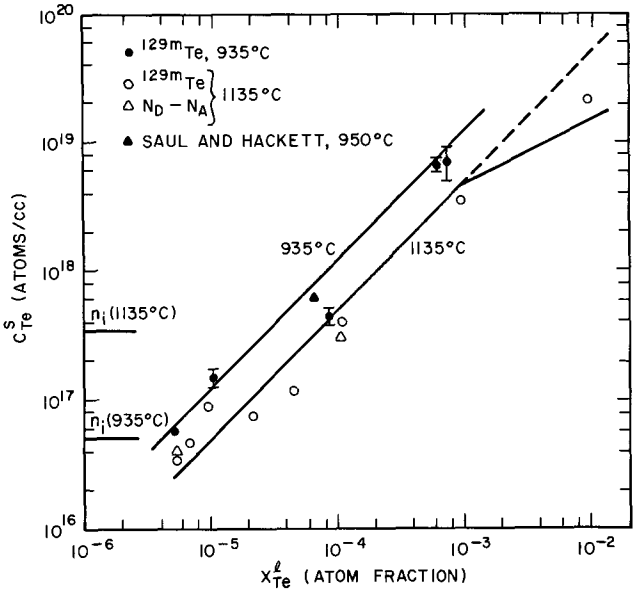

Fig. 2. Te concentration in GaP as a function of the Te content of the LPE solution at ~935° and ~1135°C. The error bars indicate the concentration limits obtained by sectioning and the total count-rate of the remaining layer. In the linear incorporation regimes, the full lines were based on Eq. [8]. The dashed line at ~1135°C shows the extrapolation of surface-controlled incorporation behavior to high doping levels.

weeks at ~1040°C.[3] Combining the N_D-N_A and calculated temperature profiles of epitaxial layers, Saul and Hackett (12) determined at a constant x^{l}_{Te} the temperature dependence of the Te solubility in GaP grown by sealed-tube tipping over a wide temperature range. Here only values of N_D-N_A at the junction corresponding to their two measured initial tipping temperatures are shown. The agreement among the three sets of data, where they overlap, is reasonably good and is probably within the experimental errors of the various investigations.

In addition to the above data obtained for crystals grown from saturated solutions, Fig. 1 also includes the Te solubility in epitaxial layers prepared at ~1060°C by the water-vapor transport process (13). The Te-doping of these samples was accomplished via the gas phase by the H_2 transport of Te from a reservoir held at a constant temperature to the deposition zone. The plotted values of C^{s}_{Te} were obtained from x-ray fluorescence analysis (14), while the following thermodynamic reasoning led to the assignment of x^{l}_{Te}. Knowing the reservoir temperature, the weight-loss of Te, the flow-rate, and the duration of a run the partial pressure of Te was calculated as a function of reservoir temperature from the ideal gas law. The recently tabulated vapor pressure (15) of $Te_2(g)$ is in reasonable agreement with the values derived from the experimental data (13). However, in the absence of kinetic factors, $Te_2(g)$ almost completely dissociates to Te(g) of partial pressure p_{Te} at the deposition temperature. Hence, the activity $a_{Te} = p_{Te}/p^{o}_{Te}$ can be computed for vapor growth where p^{o}_{Te} is the vapor pressure of pure superheated Te(l) (15) at the deposition temperature. In Fig. 1 values of a_{Te} are plotted on the abscissa which equal x^{l}_{Te} assuming ideal liquid-solution behavior. In view of these approximations and the differences in growth temperatures, the similarity in the solubility behavior between vapor growth and solution growth is quite striking.

An analysis of the solubility data requires a knowledge of the incorporation chemistry of Te in GaP. By analogy with the incorporation of Te in GaAs (7), the simplest defect reaction describing the incorporation

[3] The N_D-N_A data of Trumbore *et al.* (3) are not included in Fig. 1; they generally disagree with the present results at low concentrations and also show heat-treatment effects, the cause of which was not determined.

of a singly ionized donor from an external phase (liquid) is given by

$$Te(l) + V_P = Te_P^+ + e^- \quad [1]$$

Assuming that species in the crystalline solid form an ideal dilute solution and Te is completely ionized, then the equilibrium constant K for Eq. [1] can be written as

$$K = \frac{C^s_{Te}\, n}{\gamma_{Te} x^l_{Te} C_{VP}} \quad [2]$$

where n and C_{VP} are the electron and phosphorus vacancy concentrations in GaP, respectively, and γ_{Te} is the activity coefficient of Te in the ternary (Ga-P-Te) solution. At a constant temperature and for dilute solutions, γ_{Te} and C_{VP} can be assumed to be constant so that Eq. [2] becomes

$$\kappa \simeq \frac{C^s_{Te}\, n}{x^l_{Te}} \quad [3]$$

where $\kappa = K\gamma_{Te}C_{VP}$ is the new equilibrium constant.

Combining Eq. [3] with the electroneutrality condition ($C^s_{Te} + p = n$) and the mass action relationship for electrons and holes ($pn = n^2_i$) (an operation permissible if the external phase is in equilibrium with the bulk of the growng crystal) an explicit expression between C^s_{Te} and x^l_{Te} is obtained. From this relationship the following two limiting results are derived

$$C^s_{Te} \simeq K' x^l_{Te} \text{ if } C^s_{Te} < n_i \text{ (intrinsic case)} \quad [4]$$

$$C^s_{Te} \simeq K'' (x^l_{Te})^{1/2} \text{ if } C^s_{Te} > n_i \text{ (extrinsic case)} \quad [5]$$

with a break from linear to square-root behavior centered at $C^s_{Te} \simeq n_i$.

Taken as a whole, the data in Fig. 1 confirm the change from a linear to square-root dependence of C^s_{Te} on x^l_{Te} with increasing doping, as suggested by Trumbore *et al.* (3). However, the break occurs at $\sim 6 \times 10^{17}$ cm^{-3},[4] well above the presently accepted value of $n_i \simeq 1.5 \times 10^{17}$ cm^{-3} at 1040°C (8) and is lower by 1-2 orders of magnitude than the break points for S and Se in GaP at the same temperature (3).

No such shift from linear to square-root behavior was found by Casey *et al.* for Te in GaAs (7). These authors reported a linear dependence of C^s_{Te} on x^l_{Te} in LPE layers grown at 1000°C even at doping levels nearly two orders of magnitude higher than n_i. To explain the lack of a square-root behavior, Casey *et al.* (7) invoked the surface-band bending (SBB) model of Zschauer and Vogel (10). According to this model, for a slowly diffusing impurity, such as Te, at rapid growth rates equilibrium is established between the external phase and the semiconductor surface, but not between this surface and the bulk of the crystal. Considering the growth interface as a liquid-metal semiconductor Schottky barrier, the electron concentration at the surface, n_s, remains constant, independent of doping, due to the pinning of the Fermi level at the surface. Thus a constant n_s (function of temperature only) would be substituted for n in Eq. [3] and hence a linear dependence of C^s_{Te} on x^l_{Te} represented by

$$C^s_{Te} = K'_{SBB} x^l_{Te} \quad [6]$$

is to be expected at all doping concentrations (7).

There is no doubt that surface-controlled incorporation (SCI) of slowly diffusing impurities is a common occurrence in semiconductor crystal growth as evidenced by the well-known "facet" (orientation) effect. Whether or not the SBB model can explain all of the observed results to date is not yet clear and other mechanisms have been proposed to explain SCI in elemental as well as III-V semiconductors. For example, Banus and Gatos (16) interpreted the orientation dependence of S-doping in pulled InSb crystals in terms of adsorption isotherms which vary with orientation but approach each other at high impurity concentrations. Lavrent'eva *et al.* (17) have recently explained the orientation dependence of doping in heteroepitaxial Ge films by means of Chernov's theory of step-layer growth, which assumes that the diffusion length of the adsorbed impurity atom is much greater than that of Ge. That "faceting" also occurs in GaP is shown by the recent observation of "coring" in n-type LEC ingots (18). Recognizing the possibility of alternate SCI mechanisms, we shall attribute the linear portion of the curve in Fig. 1 to Te incorporation controlled by SBB.

The fact that within experimental error the chemically determined Te concentration is equal to N_D-N_A is taken as evidence that the simple incorporation reaction given in Eq. [1] is indeed the appropriate reaction to consider in the concentration range involved. If we accept Eq. [1], we conclude that the square-root regime corresponds to bulk-equilibrium behavior presented in Eq. [5]. Naturally, the question arises as to the reasons for the switch from surface-controlled to bulk-equilibrium behavior. A possible explanation may be provided by the work of Zschauer and Vogel (10) showing that bulk equilibrium is approached if the diffusion coefficient of the impurity (*e.g.*, Te) is sufficiently large compared to the growth rate of the crystal.[5] Hence, if the diffusion coefficient sharply increases with increasing impurity concentration, a shift to the square-root regime occurs. Unfortunately, at present there is only limited data on the concentration dependence of the diffusion coefficients of Group VI impurities in GaP to decide whether this factor governs the apparent equilibrium behavior of relatively highly Te-doped GaP (as well as S, and Se-doped GaP, and S-doped GaAs).[6] However, the temperature dependence of the solid solubility to be discussed below, may shed some light on this question.

Regardless of the mechanism involved, the observed equilibrium behavior at higher doping levels leads to the following interesting conclusion: at the lower doping levels, less than the bulk equilibrium solubility of Te in GaP is being achieved.[7] This is a consequence of the fact that Eq. [4] and [5] require a break from linear to square-root behavior to occur around n_i. Hence, we may extrapolate the bulk equilibrium portion of the curve to lower doping levels to a first approximation as shown in Fig. 3. As discussed later, this observation could have important implications in connection with the incorporation of oxygen in GaP and the efficiency of red LED's.

Temperature dependence of the solubility behavior: evaluation of the distribution coefficient.—The Te solid-solubility data obtained at ~935°C (Fig. 2) shows a linear dependence of C^s_{Te} on x^l_{Te} up to nearly $\sim 10^{19}$ cm^{-3} doping levels, more than two orders of magnitude above n_i at that temperature.[8] There is no break to a square-root behavior as at ~1040°C (Fig. 1) and the observed linearity is similar to the behavior reported by Casey *et al.* (7) for Te in GaAs at 1000°C. It seems reasonable to attribute this difference in the ~1040° and ~935°C behavior to lower diffusion coefficients for Te at the lower growth temperature, thus permitting SCI, in general, or SBB, in particular, to prevail at all doping concentrations.

However, this rather plausible explanation of the temperature effect is tempered by the ~1135°C data (Fig. 2). Here, one presumably would expect higher diffusion coefficients than at ~935° or ~1040°C, resulting in a closer approach to bulk equilibrium. Apparently, this is not the case at ~1135°C, since the

[4] This break is about a factor of three lower than the one reported by Trumbore *et al.* (3) which was inferred from questionable N_D-N_A data (see footnote 3).

[5] The fact that Zn in GaP follows bulk-equilibrium behavior was attributed to its large diffusion coefficient by Trumbore *et al.* (3).

[6] It is interesting to note that Young and Pearson (19) observed a cusp in the 1235°C diffusion coefficient of S in GaP at the same concentration where the break appears ($\sim 2 \times 10^{19}$ cm^{-3}) in S-doped crystals grown by TGT at ~1040°C.

[7] Earlier Trumbore and Nash (20) arrived at this same conclusion in a comparison of the solubility behavior of Bi with S, Se, and Te in GaP.

[8] Similarly, in vapor-grown GaP, Taylor (35) has observed a linear dependence at a temperature as low as 800°C.

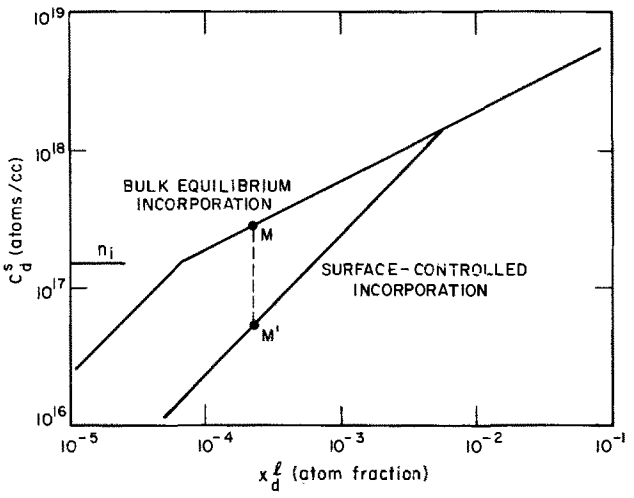

Fig. 3. A schematic comparison of bulk-equilibrium and surface-controlled incorporation at ~1040°C. This diagram is essentially a generalization of the behavior found in Fig. 1. It shows the donor concentration (C^s_d) in GaP as a function of the donor content (x^l_d) of the tipping solution. The points M' and M roughly correspond to the substitutional oxygen solubility approached by surface-controlled and bulk-equilibrium incorporation at oxygen saturation in the ternary Ga-P-Ga_2O_3 solution.

break to square-root behavior, if present at all, occurs in the mid 10^{18} cm^{-3} doping level range, well above the break point found at ~1040°C. (The increase in n_i in going to ~1135° from ~1040°C is a little over a factor of two). The appreciable scatter in the experimental data at ~1135°C, together with the fact that the diffusion coefficient of Te is an unknown function of both doping level and temperature, precludes a self-consistent explanation in terms of diffusion at this time.

Nonetheless, the linear segment at low Te concentrations, extending well above n_i, is a common feature of the solid-solubility isotherms at all three temperatures. Hence, a concentration-independent, distribution-coefficient, k_{Te}, can be derived as a function of the average growth temperature. Since data have been obtained over a wide concentration range and there is appreciable scatter, it was thought appropriate to apply the method of logarithmic least squares to the analysis (5). Briefly, at a given temperature for the i'th solubility determination the following relationship holds

$$\log x^{s,i}_{Te} = \log k_{Te} + \log x^{l,i}_{Te} \qquad [7]$$

where $i = 1, 2 \ldots n$ and $x^{s,i}_{Te}$ is the atom fraction of Te in GaP. The n equations represented by Eq. [7] can be solved for the "best" value of log k_{Te} (intercept) by the method of single parameter least squares (21) to yield

$$\log k_{Te} = \frac{\Sigma \log x^{s,i}_{Te} - \Sigma \log x^{l,i}_{Te}}{n} \qquad [8]$$

The solid lines drawn in Fig. 1 and 2 in the linear regime were based on the "best" values of k_{Te} calculated according to Eq. [8].

In Fig. 4 we present values of k_{Te} as a function of reciprocal-growth temperature, together with the standard deviations of k_{Te}.[9] These results are complemented with values of k_{Te} at ~1025° and ~950°C, obtained from the previously discussed work of Saul and Hackett (12), and at the melting point of GaP (1465°C), determined by Nygren *et al.* (18) on Te-doped LEC ingots, all derived from surface-barrier capacitance measurements. A monotonic decrease of k_{Te} with increasing temperature is apparent from the data in Fig. 4. Indeed, such temperature dependence of

[9] Transforming the well-known expression for the standard deviation in the intercept of linear least squares (21) we obtain the formula $[\Sigma(\log k^{i}_{Te}/k_{Te})^2]^{1/2}/n$ for use in this analysis where $k^{i}_{Te} = x^{s,i}_{Te}/x^{l,i}_{Te}$.

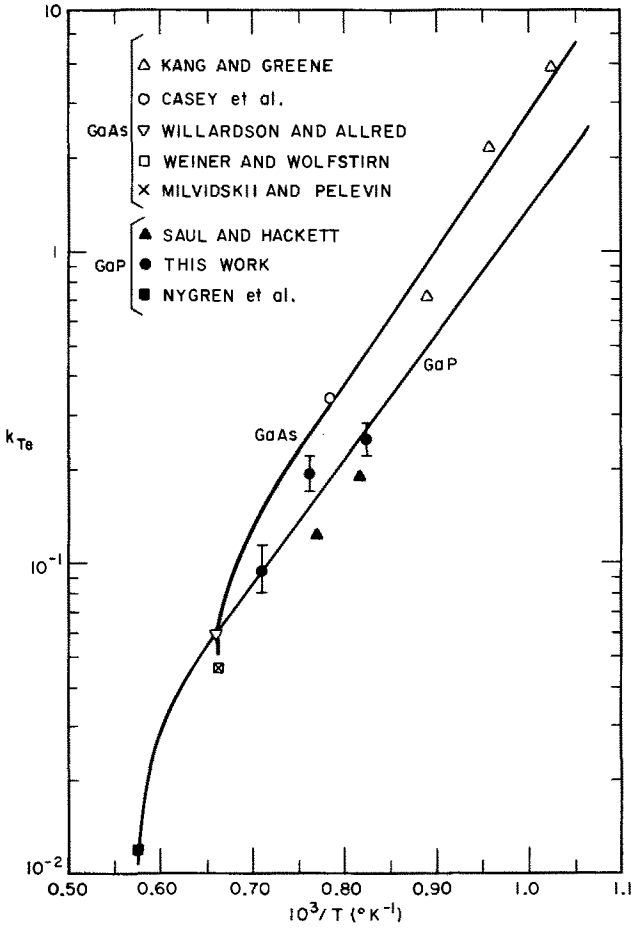

Fig. 4. A comparison of the calculated (Eq. [11]) and experimental distribution coefficients for Te in GaP and GaAs (along the respective Ga-rich liquidus curves) as a function of reciprocal temperature.

k_{Te} has been observed by Saul and Hackett (12) in their temperature range.

In addition to values of k_{Te} for Te-doped GaP, Fig. 4 also includes similar data for Te-doped GaAs. The 1000°C data of Casey *et al.* (7) on LPE layers were determined by radiochemical analysis. The melting point (1238°C) data of Willardson and Allred (22) on Czochralski pulled ingots, and of Milvidskii and Pelevin (6) on crystals grown by horizontal directional crystallization, were obtained by Hall coefficient measurements (confirmed by mass spectroscopy) and chemical analysis, respectively. The k_{Te} values derived from all three investigations were based on linear-solubility behavior which was shown to extend over a wide concentration range. However, a single doping concentration at a given temperature characterizes the surface-barrier capacitance results of Kang and Greene (23) on epitaxial films grown by a modified TGT technique and the radiochemical determination of Weiner and Wolfstirn (24) on a LEC ingot pulled at 1238°C, all of which we assume to belong to the linear incorporation regime.

It is immediately obvious from Fig. 4 that, although at a given temperature the k_{Te} values for GaAs are somewhat higher than for GaP, similar trends prevail in the temperature dependence of k_{Te} for both compounds, the slopes being nearly equal. Hence, we conclude that if surface-band bending is responsible for the linearity of Te incorporation in GaAs at 1000°C, as advocated by Casey *et al.* (7), then it seems likely that the linear region for both compounds at all temperatures is associated with the same mechanism.

Having established the common features of k_{Te} for GaAs and GaP, it is desirable to devise an extrapolation and interpolation technique to describe the ex-

perimental data. Although in principle the analysis could proceed directly from Eq. 2, we begin with a modification of Eq. [1] due to computational convenience as C_{VP} is not known. Let us add the defect reaction

$$P_P = V_P + P(l)$$

to Eq. [1]. Then, eliminating C_{VP} we obtain

$$Te(l) + P_P = P(l) + Te_P^+ + e^- \quad [9]$$

Since the concentration of phosphorus atoms on their own sites is nearly constant and we provisionally accept the SBB model, the equilibrium constant for Eq. [9], K_{Te}, can be written in the form

$$K_{Te} = \frac{a_P C^s_{Te} n_s}{\gamma_{Te} x^l_{Te}} = \frac{a_P k_{Te} n_s \times 4.94 \times 10^{22}}{\gamma_{Te}} \quad [10]$$

where a_P is the phosphorus activity in the Ga-P-Te ternary liquid solution which for small Te additions nearly equals a_P in the Ga-P binary.

In general, log K_{Te} varies linearly with $1/T$ over the entire temperature range, while the log k_{Te} *vs.* $1/T$ plot is linear only at low temperatures. Thus, to extrapolate log k_{Te} up to the melting point of the compound, some assumptions must be made concerning the temperature dependence of the unknown quantities in Eq. [10]. Specifically, we assume that log γ_{Te} and log n_s, compared to the variation with temperature of the other relevant quantities, are linear functions of $1/T$ within a good approximation over the entire temperature range. Hence, a new equilibrium constant, K'_{Te}, is defined and Eq. [10] becomes

$$\frac{K_{Te}\gamma_{Te}}{n_s \times 4.94 \times 10^{22}} \approx K'_{Te}(T) = a_P k_{Te} \quad [11]$$

Obviously, if the subscript As is introduced in place of P, equations similar to Eq. [10] and [11] also hold for Te-doped GaAs.

Values of $K'_{Te}(T)$ were evaluated for GaP and GaAs by combining the k_{Te} data plotted in Fig. 4, excluding results at the melting points, with the activities a_P and a_{As} obtained from the work of Thurmond (25). The linear dependence of log $K'(T)$ on $1/T$, which follows from Eq. [11] and the assumptions involved in its derivation permitted the application of the method of least squares to the $K'(T)$ data to calculate the line of best fit. Then, the solid curves, illustrated in Fig. 4, for k_{Te} in GaP and GaAs were evaluated over the entire temperature range by combining the respective line of best fit with values of a_P and a_{As} according to Eq. [11].

As seen in Fig. 4, a generally good agreement is achieved between the calculated k_{Te} curves and the experimental points.[10] Of particular importance here is the predicted downturn in k_{Te} for both compounds in the vicinity of their melting points. This indicates that the calculation is self-consistent since the melting point data which were excluded from the analysis are also described by the curves. Although not shown in Fig. 4, log k_{Te} is actually a double-valued function of $1/T$, thus for crystals grown from a P or As-rich solution, k_{Te} should turn over, *i.e.*, probably rise again with decreasing temperature. Finally, as is the case for the equilibrium constants for the incorporation of Zn in GaP and GaAs (5), the k_{Te} curves are nearly parallel for Te-doped GaP and GaAs.

Implications for the surface-controlled and bulk-equilibrium incorporation of O in GaP.—A high concentration of substitutional oxygen in GaP is considered to be desirable for the attainment of high efficiency LED's since it leads to an increased number of nearest neighbor pairs. However, in spite of its importance, the incorporation chemistry of oxygen is the least well understood of the significant dopants in GaP. Recently, several investigators have reported on the oxygen solubility in GaP. Although many of these results disagree, they generally lie within a concentration range which is less than an order of magnitude.

The solubility of oxygen in GaP, taken from Saul (26) and Lightowlers *et al.* (27) is shown as a function of reciprocal temperature in Fig. 5. By a combination of surface-barrier capacitance measurements on Zn and Zn-O-doped LPE layers, Saul (26) deduced the concentration of ionized oxygen donors on phosphorus sites $C^s_{O_P}{}^+$. Surprisingly his $C^s_{O_P}{}^+$ data exhibit a maximum ($\sim 2.7 \times 10^{17}$ cm^{-3}) in the vicinity of the normal LPE growth temperatures ($\sim$1000°-1050°C).[11] The results of Lightowlers *et al.* (27), based on prompt α-particle nuclear microanalysis of the total oxygen concentration in Zn-O-doped LPE layers grown by a sealed-tube slider technique (9) in a restricted temperature range, are about a factor of five lower ($\sim 5 \times 10^{16}$ cm^{-3}) for layers grown at a temperature near Saul's maximum, although the analytical value very likely includes interstitial oxygen. Both studies took note of the work of Kowalchik *et al.* (9) concerning the coprecipitation of Ga_2O_3 with GaP from tipping solutions which contain Ga_2O_3 additions in excess of values permitted by the Ga-P-Ga_2O_3 ternary eutectic valley (9). Since they were grown from solutions with a large excess of Ga_2O_3 added, Saul's (26) LPE layers contained precipitates, assuring oxygen saturation. In contrast, the LPE solutions used by Lightowlers *et al.* (27) were barely saturated with Ga_2O_3, since the

[11] It should be noted that Saul's results (26) at the higher temperatures may be affected by a significant background contribution.

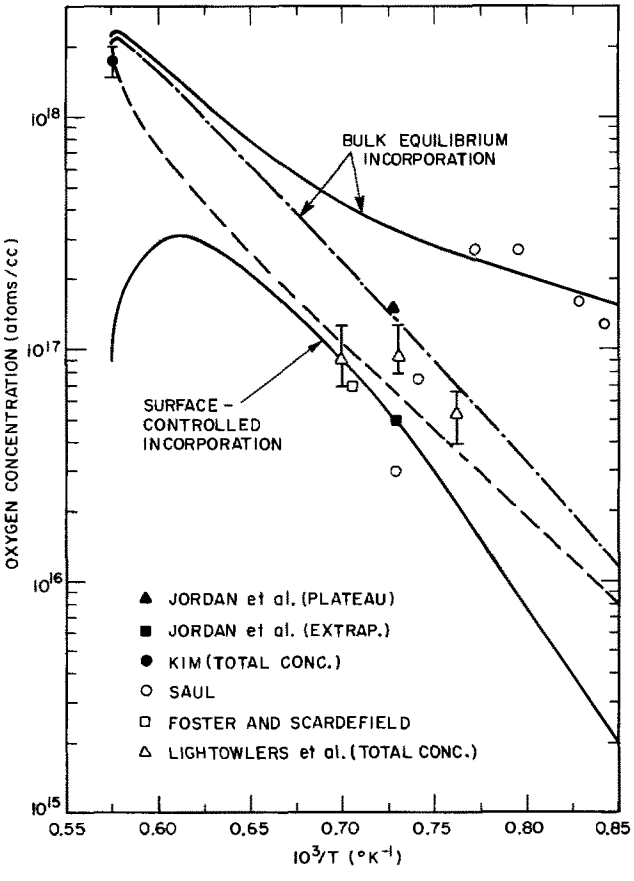

Fig. 5. Oxygen solid solubility in GaP as a function of reciprocal temperature. The lower solid line shows the estimated oxygen solubility by surface-controlled (Eq. [13]) incorporation. The upper solid line and the line -·-·-·- represents bulk equilibrium incorporation (Eq. [16], [17]) for $\bar{C}^s_{ZnGa^-} = 5 \times 10^{17}$ and $\bar{C}^s_{ZnGa^-} = 0$, respectively. The line – – – – represents interstitial solubility and is based on the data of Berman (30) which was obtained between ~900° and 1325°C.

[10] Note that the intermediate k_{Te} data of Saul and Hackett (12), based not on a measured, but calculated, growth-temperature history of an LPE layer, are in accord with the k_{Te} line for GaP. Likewise, for Zn-doped GaP their simple method (11) led to good agreement with independently obtained solid-solubility calculations (5).

presence of precipitates precludes any meaningful determination of the oxygen in solid solution.

Accepting the validity of both sets of data, we attempt to resolve their disagreement in terms of the absence or presence of precipitates which governs, in our view, the predominant mode of oxygen incorporation, namely surface controlled or bulk equilibrium. We have previously concluded, in conjunction with Fig. 3, that for a slowly diffusing impurity, such as Te, at lower doping levels the solubility corresponding to SCI is less than that by bulk-equilibrium incorporation. Let us assume a similar situation prevails for oxygen. In the absence of precipitates (Lightowlers *et al.*'s case), SCI predominates and the solubility of substitutional oxygen increases with increasing Ga_2O_3 addition to the maximum value M' (Fig. 3). However, if the Ga_2O_3 contained in the LPE solution exceeds the abscissa of M' (Saul's case), coprecipitation of Ga_2O_3 takes place simultaneously with the initial SCI of M' oxygen atoms. Once a segment of the epitaxial film is grown, the presence of Ga_2O_3 precipitates permits equilibration with the GaP matrix, in a manner that eventual O solubility is no longer surface controlled. For a sufficiently large density of precipitates, diffusional limitations, even for a slowly diffusing impurity, are minimized; hence the bulk-equilibrium value of substitutional oxygen solubility can be reached while the crystal is still at a relatively high temperature in the LPE furnace. Thus the actual value of $C^s_{O_P+}$ moves from M' to M (Fig. 3) as measured by Saul (26).

The substitutional oxygen concentration estimated from photoluminescence measurements on $Zn(PO_3)_2$ doped, solution-grown platelets (28) seems to support the above interpretation. A linear extrapolation of the oxygen concentration for platelets grown from a solution containing $\sim 3.1 \times 10^{-2}$ a/o O to the ternary liquid-solubility limit ($\sim 4.8 \times 10^{-2}$ a/o O) yields $5 \pm 2.5 \times 10^{16}$ cm^{-3} at the average growth temperature of 1100°C. The oxygen concentrations in three other crystals grown from solutions with higher and varying amounts of $Zn(PO_3)_2$ added to the melt lie on a plateau closely centered around 1.5×10^{17} cm^{-3}. With respect to these values which are plotted in Fig. 5, we suggest that the low one corresponds to SCI, while the plateau point reflects bulk-equilibrium incorporation.[12]

A more concrete description of these two modes of incorporation can be given by estimating the temperature dependence of oxygen incorporation in GaP by means of simplified defect chemical analysis. First, we attempt to calculate the variation of $C^s_{O_P+}$ with temperature if SCI predominates. Let us rewrite Eq. [9] to represent O instead of Te incorporation. Then, we have

$$O(l) + P_P = P(l) + O_P^+ + e^- \qquad [12]$$

Accepting the assumptions leading to Eq. [11] including specifically the SBB model, we find

$$K'_O(T) = a_P k_O \qquad [13]$$

A combination of the $\sim$1100°C value of $C^s_{O_P+} = 5 \times 10^{16}$ cm^{-3}, derived from the work of Jordan *et al.* (28) with the O solubility in the Ga-P-Ga_2O_3 (9) ternary solution, yields $k_O = 2.25 \times 10^{-3}$. We may assume, as before, that for the SBB model log $a_P k_O$ is a linear function of $1/T$, but lacking any information concerning the slope of log k_O as a function of $1/T$, additional assumptions are required.

Let us assume that at low doping levels the incorporation of the Group VI dopants O, S, Se, and Te obeys the SBB model and that equivalents of Eq. [9] hold for S and Se. This permits a correlation of the slopes of these Group VI distribution coefficients. In particular, the slope of log k_{Te} *vs.* $1/T$, related to the enthalpy of incorporation, was directly obtained from the low temperature portion of Fig. 4. The corresponding slopes for S and Se were obtained from curves similar to Fig. 4. These curves were constructed on the basis of equations of the type given in Eq. [9] from the data of Trumbore *et al.* (3) at 1040°C and Nygren *et al.* (21) at the melting point of GaP in combination with values of a_P taken from the work of Thurmond (25). Then, by a linear extrapolation of the slopes $d \log k_d / d\ 1/T$ as a function of the normalized Pauling tetrahedral (29) radius differences $(r_d - r_P)/r_P$, where d denotes the donors S, Se, or Te, d log k_O/d 1/T corresponding to the abscissa $(r_O - r_P)/r_P$ was determined. A knowledge of the low temperature slopes d log k_O/d $1/T$ and d log a_P/d $1/T$ together with the 1100°C values of k_O and a_P yields the function $K'_O(T)$. Finally, a combination of the ternary eutectic valley (9) describing the liquid composition, the $K'_O(T)$ function and a_P provides the maximum solid-solubility $C^s_{O_P+}$ allowed by surface-controlled incorporation in the absence of Ga_2O_3 precipitates. This is plotted as the lowest curve in Fig. 5.

Next, we estimate the variation of $C^s_{O_P+}$ with temperature for bulk-equilibrium incorporation. If precipitates are present in the matrix (or if excess Ga_2O_3 is contained in the growth system), the incorporation of O can be described by the equilibrium

$$Ga_2O_3(s) = 2Ga_{Ga} + V_{Ga} + 3O_P^+ + 3e^- \qquad [14]$$

To find a more convenient relationship for subsequent analysis, let us add the reaction

$$V_{Ga} + P_P = P(l)$$

to Eq. [14]. Then, we have, eliminating V_{Ga}

$$Ga_2O_3(s) + P_P = 2Ga_{Ga} + 3O_P^+ + 3e^- + P(l) \qquad [15]$$

The equilibrium constant, K_B, for Eq. [15] is given by

$$K_B = (C^s_{O_P+})^3 n^3 a_P \qquad [16]$$

Assuming that the oxygen donors are completely ionized in p-type (Zn-doped) material, a detailed consideration of the simultaneous Zn and O incorporation yields n in Eq. [16] in the form

$$n = 2n^2 \frac{C^s_{O_P+} + \sqrt{(C^s_{O_P+})^2 + \zeta^2}}{\zeta^2} \qquad [17a]$$

where

$$\zeta \equiv \sqrt{(\bar{C}^s_{Zn_{G\bar{a}}})^2 + 4n_i^2} + \bar{C}^s_{Zn_{G\bar{a}}} \qquad [17b]$$

and the bar in $\bar{C}^s_{Zn_{G\bar{a}}}$ signifies that it is the zinc acceptor concentration in GaP grown from a solution containing only Zn at the same zinc and phosphorus activities and temperature which are employed in the growth of the Zn-O-doped crystal.[13] Accepting that bulk-equilibrium incorporation of oxygen alone is responsible for the solubilities reported by Saul (26) up to perhaps 1025°C, we evaluated log K_B as a function of $1/T$ from Eq. [16] and [17] in combination with the experimental data. Extrapolation of the log K_B data to the melting point of GaP allows the calculation of $C^s_{O_P+}$ from Eq. [16] and [17] at all temperatures and zinc acceptor levels of interest.

[12] Likewise, recently Saul and Hackett (36) have shown for GaP layers grown at $\sim$1025°C that increasing the oxygen addition to the solution from 1.5×10^{-2} a/o (which is below the solubility limit of 2×10^{-2} a/o) to the range between 6×10^{-2} and 1.05 a/o leads to a drastic rise in the oxygen donor concentration from 3×10^{16} to a constant plateau value of 2.7×10^{17} cm^{-3}.

[13] The basis for this calculation has been presented by Saul and Hackett (11). Briefly, six equations are available for the eight unknown variables $\bar{C}^s_{Zn_{G\bar{a}}}$, $C^s_{Zn_{G\bar{a}}}$, $C^s_{O_P+}$, $\bar{p}$, p, $\bar{n}$, n, and K_{Zn}. Hence, one can express at any T, n as a function of $C^s_{O_P+}$ and $\bar{C}^s_{Zn_{G\bar{a}}}$. The equations for Zn and Zn-O-doped crystals are the hole-electron equilibrium relationships ($\bar{p}\bar{n} = n_i^2$, $pn = n_i^2$), the electroneutrality conditions ($\bar{p} = \bar{n} + \bar{C}^s_{Zn_{G\bar{a}}}$, $p + C^s_{O_P+} = n + C^s_{Zn_{G\bar{a}}}$) and the defect equilibria

$$P(l) + Zn(l) = Zn_{G\bar{a}} + e^+ + P_P$$

for which $K_{Zn} = \bar{C}^s_{Zn_{G\bar{a}}} \bar{p}/a_{Zn} a_P = C^s_{Zn_{G\bar{a}}} p/a_{Zn} a_P$

In Fig. 5 we show two zinc isoconcentration curves for the bulk-equilibrium incorporation of substitutional oxygen. One curve (dash-dot) at $\overline{C}^{s}_{Zn_{Ga}} = 0$ is for a hypothetical n-type oxygen-doped crystal; the other one (solid line) corresponds to $\overline{C}_{Zn_{Ga}} = 5 \times 10^{17}$ cm^{-3}. The two curves nearly overlap at the melting point and the position of the curves for intermediate values of $\overline{C}^{s}_{Zn_{Ga}}$ can be easily imagined.

In addition to these curves representing the two modes of substitutional oxygen incorporation in GaP, we also give in Fig. 5 (dashed line) an extrapolation to the GaP melting point of the interstitial oxygen data of Berman (30) based on an analysis of the infrared absorption spectra of annealed LEC crystals (31). To perform the extrapolation let us add the following reactions, assuming the presence of neutral interstitials, to Eq. [14]

$$3O_P^+ + 3V_i + 3e^- = 3O_i + 3V_P$$
$$2P(l) = 2V_{Ga} + 2P_P$$
$$3V_{Ga} + 3V_P = 0$$

Then, we find

$$2P(l) + 3V_i + Ga_2O_3(s) = 2Ga_{Ga} + 2P_P + 3O_i \quad [18]$$

where the subscript i refers to interstitial species. Since the concentration of V_i is large and insensitive to temperature, the equilibrium constant K_i for Eq. [18] can be written as

$$K_i = \frac{(C^{s}_{O_i})^3}{a_P^2} \quad [19]$$

where $C^{s}_{O_i}$ is the concentration of interstitial oxygen atoms. Applying Eq. [19] to Berman's data (30), log K_i was evaluated as a function of $1/T$ and extrapolated to the melting point of GaP. Subsequently $C^{s}_{O_i}$ was calculated from Eq. [19] over the entire temperature range of interest.

Finally, Fig. 5 includes the oxygen solubilities reported by Foster and Scardefield (32), deduced from the degree of compensation in Zn, O-doped crystals grown from solutions at 1144°C,[14] and Kim (33), obtained by ^{3}He activation analysis (34) of O-doped LEC crystals.

The following interesting, although tentative conclusions can be drawn from Fig. 5:

(*i*) It appears that the total oxygen concentration reported by Lightowlers *et al.* (27) is the sum of the interstitial and surface-controlled substitutional solubilities.

(*ii*) The value of Jordan *et al.* (28) along the plateau is likely due to bulk-equilibrium incorporation since it is comparable to the low temperature results of Saul (26), if the temperature range for solution growth and the error associated with the optical estimate (~50%) is taken into account.

(*iii*) Although the average growth temperature of Foster and Scardefield (32) is to some extent uncertain, their incorporation mechanism is probably surface controlled which is also consistent with the small Ga_2O_3 additions employed (0.048 a/o O).

(*iv*) The maximum and downturn in the data of Saul (26) (above ~985°C) is caused by a transition from bulk-equilibrium to surface-controlled incorporation as the density of precipitates for a constant Ga_2O_3 addition to the solution decreases with increasing temperature.

(*v*) Kim's result (33), a total oxygen measurement, seems to be predominantly due to interstitial oxygen.

If the above explanation is indeed correct, some precipitation is desirable to obtain higher oxygen concentrations and consequently higher efficiency red LED's. However, excessive precipitation leads to contacting difficulties and degraded device performance (9). In addition, the postulated importance of Ga_2O_3 precipitates could account for much of the difficulties in reproducing the same efficiency from run to run or even obtaining uniform efficiencies. Obviously, further experimental work is required to confirm these ideas concerning the two modes of oxygen incorporation in GaP.

[14] Actually Foster and Scardefield (32) terminated their solution-growth experiments at 850°C; hence, the average growth temperature may be lower than the reported liquidus temperature.

Acknowledgments

The authors are grateful to C. D. Thurmond, H. C. Casey, M. Weiner, and R. H. Saul for fruitful discussions. We are also grateful to M. Weiner, R. Berman, C. Kim, and R. H. Saul for the use of their unpublished data.

Manuscript received October 21, 1972. This was Paper 51 presented at the Chicago Meeting of the Society, May 13-18, 1973.

Any discussion of this paper will appear in a Discussion Section to be published in the December 1973 JOURNAL.

REFERENCES

1. T. N. Morgan, B. Welber, and R. N. Bhargava, *Phys. Rev.*, **166**, 751 (1968); C. H. Henry, P. J. Dean, and J. D. Cuthbert, *ibid.*, **166**, 754 (1968).
2. See, for example, R. H. Saul, J. Armstrong, and W. H. Hackett, Jr., *Appl. Phys. Letters*, **15**, 229 (1969); R. A. Logan, H. G. White, and W. Wiegmann, *Solid-State Electron.*, **14**, 55 (1971).
3. F. A. Trumbore, H. G. White, M. Kowalchik, R. A. Logan, and C. L. Luke, *This Journal*, **112**, 782 (1965).
4. M. B. Panish and H. C. Casey, Jr., *J. Phys. Chem. Solids*, **28**, 1673 (1967).
5. A. S. Jordan, *This Journal*, **118**, 781 (1971).
6. M. G. Milvidskii and O. V. Pelevin, *Inorg. Mater.*, **3**, 1024 (1967), (Translated from *Izv. Akad. Nauk SSSR, Neorgan. Materialy*, **3**, 1159 (1967).
7. H. C. Casey, Jr., M. B. Panish, and K. B. Wolfstirn, *J. Phys. Chem. Solids*, **32**, 571 (1971).
8. H. C. Casey, Jr. in "Atomic Diffusion in Semiconductors," D. Shaw, Editor, Plenum Press, New York (1972).
9. M. Kowalchik, A. S. Jordan, and Mildred H. Read, *This Journal*, **119**, 756 (1972).
10. K. H. Zschauer and A. Vogel, "Proceedings of the Third International Symposium on GaAs," Aachen (1970); The Institute of Physics, London and Bristol (1971).
11. R. H. Saul and W. H. Hackett, Jr., *This Journal*, **117**, 921 (1970).
12. R. H. Saul and W. H. Hackett, Jr., *J. Appl. Phys.*, **41**, 3354 (1970).
13. C. J. Frosch, *This Journal*, **111**, 180 (1964).
14. C. L. Luke, *Anal. Chim. Acta*, **41**, 237 (1968).
15. R. Hultgren, October 1964 Supplement issued to R. Hultgren, R. L. Orr, P. D. Anderson, and K. K. Kelley, "Selected Values of Thermodynamic Properties of Metal and Alloys," John Wiley & Sons, Inc., New York (1963).
16. M. D. Banus and H. C. Gatos, *This Journal*, **109**, 829 (1962).
17. L. G. Lavrent'eva, I. S. Zakharov, and Yu. M. Rumyantsev, *Soviet Phys.-Cryst.*, **16**, 348 (1971).
18. S. F. Nygren, C. M. Ringel, and H. W. Verleur, *This Journal*, **118**, 306 (1971).
19. A. B. Y. Young and G. L. Pearson, *J. Phys. Chem. Solids*, **31**, 517 (1970).
20. F. A. Trumbore and D. L. Nash, Unpublished results.
21. L. G. Parratt, "Probability and Experimental Errors in Science," John Wiley & Sons, Inc., New York (1961).
22. R. K. Willardson and W. P. Allred, "Proceedings of the (First) International Symposium on GaAs," Reading, England (1966); The Institute of Physics, London (1967).
23. C. S. Kang and P. E. Greene, "Proceedings of the Second International Symposium on GaAs," Dallas (1968); The Institute of Physics, London (1969).
24. M. E. Weiner and K. B. Wolfstirn, Unpublished data.
25. C. D. Thurmond, *J. Phys. Chem. Solids*, **26**, 785 (1965).

26. R. H. Saul, *J. Electron. Materials*, **1**, 16 (1972).
27. E. C. Lightowlers, J. C. North, A. S. Jordan, L. Derick, and J. L. Merz, *J. Appl. Phys.*, To be published.
28. A. S. Jordan, L. Derick, R. Caruso, and M. Kowalchik, *This Journal*, **119**, 1585 (1972).
29. L. Pauling, "The Nature of the Chemical Bond," 3rd ed., Cornell University Press, Ithaca (1960).
30. R. Berman, Unpublished data.
31. A. S. Barker, Jr., R. Berman, and H. W. Verleur, *J. Phys. Chem. Solids*, **34**, 123 (1973).
32. L. M. Foster and J. Scardefield, *This Journal*, **116**, 494 (1969).
33. C. K. Kim, Unpublished data.
34. C. K. Kim, *Radiochem. Radioanal. Letters*, **2**, 53 (1969).
35. R. C. Taylor, *This Journal*, **118**, 364 (1971).
36. R. H. Saul and W. H. Hackett, Jr., *ibid.*, **119**, 542 (1972).

Characteristics of [115] Dislocation-Free Float-Zoned Silicon Crystals

T. F. Ciszek[1]

Dow Corning Corporation, Hemlock, Michigan 48626

ABSTRACT

Dislocation-free silicon crystals with [115] crystallographic orientation were grown by the float-zone method. The relatively high (115) surface free energy allows more uniform growth, particularly for dopant incorporation, than that which is characteristic of low surface free energy planes such as (111). The macroradial variation of resistivity in phosphorus-doped [115] crystals is typically less than 5%. Also, low surface-state charge densities can be achieved using low oxygen content [115] float-zoned crystals. (100) wafers, circular within 4%, may be cut from these crystals.

The majority of float-zoned silicon crystals for semiconductor use have historically been grown in <111> orientations. This was favorable for early alloy junction devices since the {111} planes tended to define a sharp junction boundary. In the early 1960's, crystal suppliers attempted <100> crystal zoning and were successful up to diameters of about 18 mm. As diameters were increased above 20 mm, large angle grain boundaries were found to occur, preventing the growth of good quality crystals; thus essentially all zoning efforts again reverted to the <111> orientations. Recently, the advances in dislocation-free and large diameter <111> float-zoning technology have made float-zoned crystals attractive for MOS devices. For this application, <100> crystals are desirable because of the low {100} Si/SiO_2 surface-state charge density (1) and favorable device die separation. Thus there is a revival of interest in <100> growth by the float-zone method.

The <115> crystallographic directions have been found to be viable orientations for dislocation-free silicon float-zoning; and <115> crystals have several properties of interest for MOS applications as well as other applications where uniform doping is of importance.

[115] Orientation

Figure 1 illustrates the geometric relationship between the [115] direction and other common directions in the silicon lattice. There is an angle of 15.8° between [001] and [115] directions and a 39° angle between [115] and [111] directions. The <115> directions are significant in that growth twins, which occasionally occur during the growth of <111> axis silicon crystals, change the growth axis to either <115> or another <111> orientation since the twin plane is of the {111} family (2). Normally, the occurrence of such growth twins during dislocation-free <111> zoning leads to degradation of the crystal perfection (dislocations, subsequent twins, or large angle grain boundaries usually occur shortly after twinning).

[1] Present address: IBM East Fishkill Laboratory, Hopewell Junction, New York 12533.

Key words: silicon crystal growth, float-zoned silicon crystals, [115] oriented silicon crystals, [115] silicon crystal properties, radial resistivity, dislocation-free [115] silicon crystals.

Back-reflection and transmission Laue x-ray diffraction photographs taken of a (115) silicon surface with a 5 cm sample to film distance are shown in Fig. 2 along with a simplified stereographic projection. Little symmetry is present in the arrangement of the diffraction spots; there is only mirror symmetry across the (110) plane which is vertical and perpendicular to the page. The prominent spots present in the back-reflection pattern are (001), (113), and (112). Standard Laue or diffractometer x-ray techniques can be used for specimen orientation; the (115) interplanar separation is 1.04510Å based on the lattice constant value $a = 5.43050$Å (3).

Comparison of [115] and [111] Crystal Growth Mechanisms

A difference in growth mechanism of (115) *vs.* (111) solidification fronts is believed to account for the more uniform electrical properties seen in [115] crystals. Dislocation-free, float-zone silicon crystal growth is apparently dominated by the lateral or sheet-like propagation of (111) planes (4). When dislocation-free

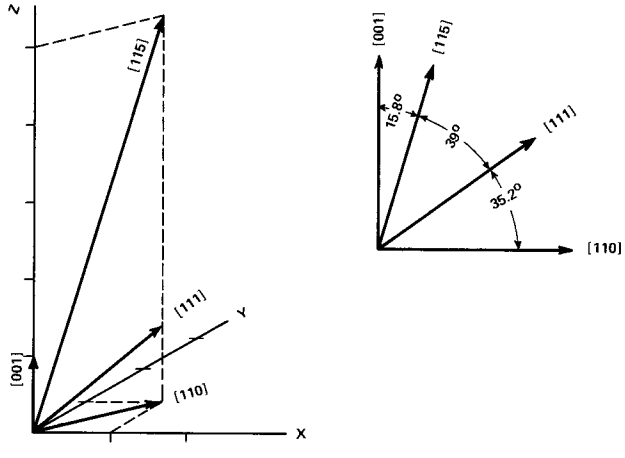

Fig. 1. Geometry of the [115] direction in the cubic lattice and its relationship to common silicon crystal growth orientations.

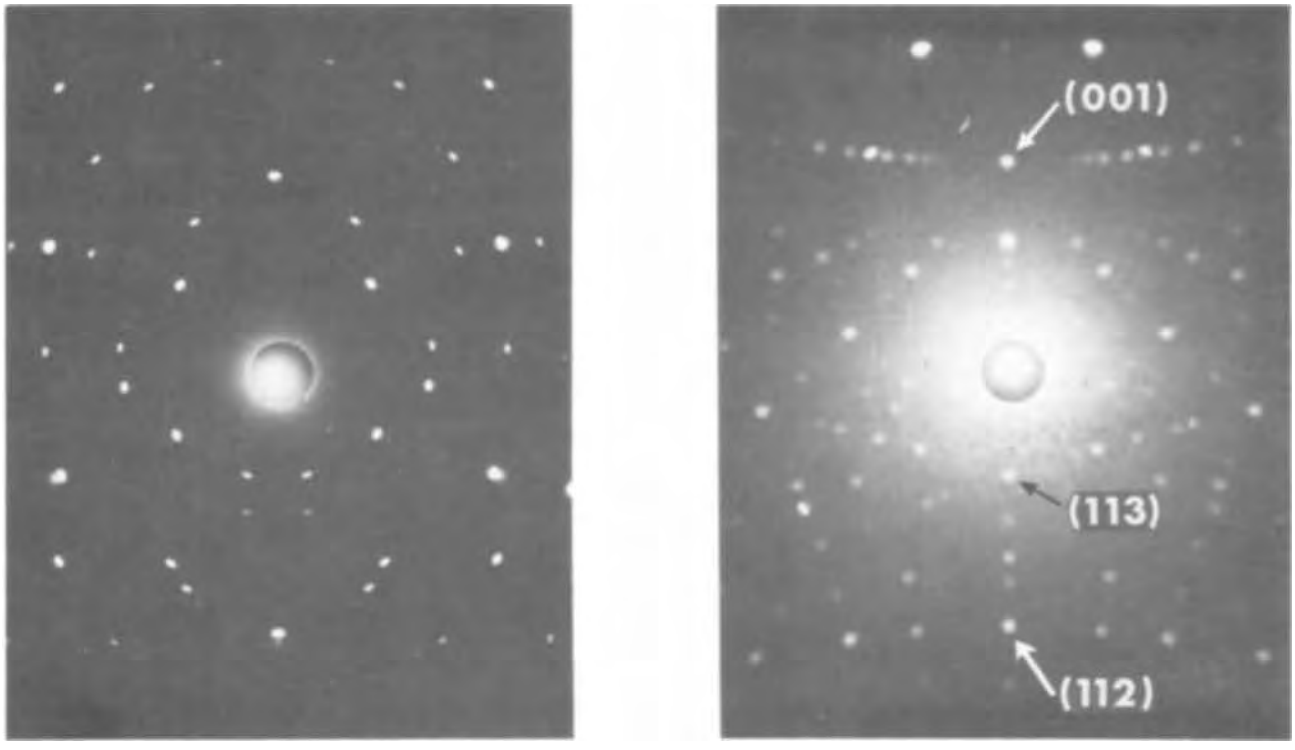

Fig. 2a (left). (115) transmission Laue x-ray diffraction at 5 cm sample to film distance. b (right). Laue back-reflection at 5 cm sample to film distance.

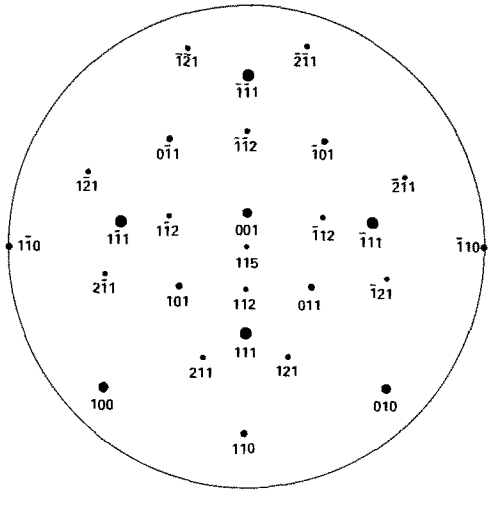

Fig. 2c. (115) stereographic projection.

crystals are zoned close to the [111] orientation, substantial (111) singular or faceted planar regions develop on those supercooled portions of the interface where new (111) layers nucleate (4, 5). For example, if the sold-liquid interface is convex toward the melt, the singular region will be in the central core of the crystal (Fig. 3), while normal or rough growth will take place on the remainder of the interface.

The tendency for facet-like growth to dominate the coolest or "leading" regions of the interface is predominantly an inverse function of the angle between (111) and the leading interface surface. This occurs because the (111) surface has the lowest surface free energy, is the atomically smoothest, and is the only surface to show strong faceting tendencies during melt growth. However, it is possible that other low indice surfaces corresponding to less prominent minima in the polar surface free energy plot may also have some tendency (albeit less pronounced) to form faceted or singular interfaces. Ideally, the most uniform electrical properties for crystals grown with a curved interface should result when the average interface plane corresponds to a maximum in the polar surface free energy plot, is the atomically roughest, and is angularly distant from (111) planes and other low indice planes. While there is no experimental evidence that the (115) surface totally fulfills these criteria, it should be more likely to do so than low indice surfaces.

In [115] zoning, {111} planes are inclined to the interface at angles of 38.9°, 56.3°, and 70.5°; thus, only minute regions develop facets on the crystal periphery, and crystal growth is essentially uniformly normal or rough in nature over the entire interface area.

The [115] and [111] dislocation-free crystals were zoned under attempted identical experimental conditions, in that the same apparatus (ECCO zone refiner), operator, growth speed (3 mm/min), rotation rate (20 rpm) and geometry (two-turn stationary rf coil) were used. Seeds were oriented to the appropriate direction and dislocation-free growth was initiated by the "necking" technique (6, 7). Both crystals were vertically zoned with the crystal beneath the melt and the feed rod above, in argon, from silicon doped with phosphorus to a resistivity of approximately 50 ohm-cm. A half dozen attempts were made to zone [100] dislocation-free crystals under these same conditions and none were successful; dislocations and loss of singularity occurred early in growth in every case.

Comparison of [115] and [111] Crystal Properties

Solid-liquid interface shapes of the two crystals were determined by etching longitudinal sections (4), and

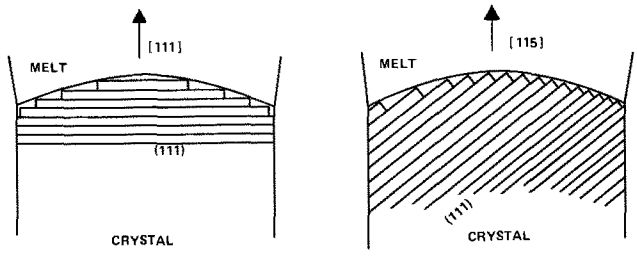

Fig. 3. Schematic representation of (111) layer growth in [111] and [115] float-zoned, dislocation-free crystals.

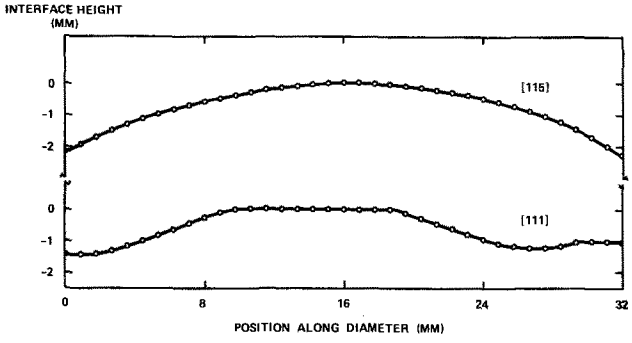

Fig. 4. Solid-liquid interface profiles for [115] and [111] dislocation-free crystals zoned under similar conditions.

are in accord with the growth mechanisms discussed above. The interface of the [115] crystal was continuously curved and convex toward the melt, while the interface of the [111] crystal was partially curved and partially flat. The flat or faceted areas occurred at the center and at the periphery of the solidification front (Fig. 4). It has been previously shown (5) that the peripheral (111) facets give rise to ridges or bulges which extend along the length of the crystal and cause a deviation from roundness in the cross section of the crystal; the lack of these facets in [115] crystals allows a nearly circular cross section. Figure 5 shows x-ray topographs of cross-sectional slices from the two crystals and illustrates the difference in cross-sectional shape as well as the absence of dislocations.

It has also been shown previously (4) that the central (111) facet on [111] crystal interfaces is associated with a greater adsorption of impurities or dopants with segregation coefficients, k_o, less than 1.0. For example, the incorporation of phosphorus ($k_o = 0.4$) is approximately 20% greater in the faceted or "core" region. Resistivity measurements were made by the one-probe technique at 0.5 mm increments on thin filaments (1 × 1 mm cross section) cut along the diameter of the [115] and [111] 50 ohm-cm, n-type crystals. The resultant radial resistivity profiles are shown in Fig. 6. Decreased resistivity values (increased dopant concentrations) are seen in the faceted region of the [111] crystal, whereas the [115] crystal, free of interface facets, exhibits a more uniform (±5%) resistivity. Although the [115] crystal resistivity is relatively uniform on a long range (axis to periphery) basis, it does exhibit resistivity striations on a smaller microscale which are similar to those seen in [111] crystals. The extreme to which these can be observed is a function of the spatial resolution of the measuring technique.

In addition to the preceding growth-related consequences of the [115] geometry, there are some purely orientation-dependent properties of interest. Since there is an angle of 15.8° between the (115) and (001) planes, {100} wafers which deviate from roundness by only $[(1/\cos 15.8°) - 1] \times 100\% = 4\%$ can be cut from [115] crystals. Thus, nearly round {100} wafers of float-zone purity[2] can be attained (direct [100] zoning is difficult). Also, the (115) surface is comparatively rough on an atomic scale, which may have implications for epitaxy or alloying treatments. Surface-state charge density at Si/SiO_2 interfaces is another orientation-dependent property, and has been found to be lowest for (100) surfaces, highest for (111) surfaces, and midway between for (110) surfaces [see for example, Gray and Brown (8)]. Since the [115] direction is relatively close to the [100] direction, a relatively low surface-state charge density is expected for the (115) surface. Preliminary measurements indicate that the value for the (115) surface is between that for (100) and that for (110) (9).

Summary

The float-zone growth of [115] dislocation-free silicon crystals is a means of obtaining high purity, low defect wafers for applications where low radial resistivity gradients, low surface-state charge densities, or atomically rough, high surface free energy wafer surfaces are desirable. In addition, nearly round (within 4%) (100) wafers can be cut from [115] crystals.

Most of the differences between [111] and [115] float-zoned crystals are expected to also hold true in Czochralski growth; an exception is that [111] and [115] Czochralski crystals are comparable in roundness.

[2] The oxygen content of float-zoned crystals is typically 10^{16} atoms/cm^3.

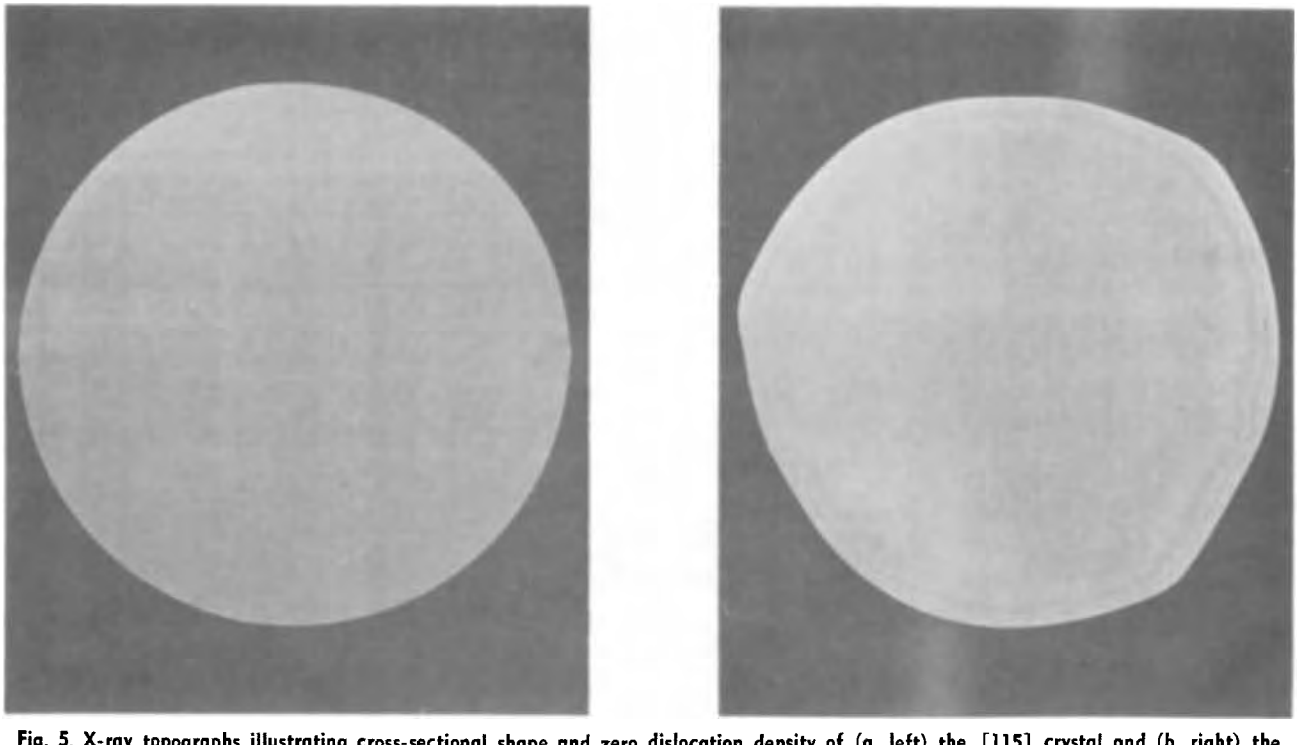

Fig. 5. X-ray topographs illustrating cross-sectional shape and zero dislocation density of (a, left) the [115] crystal and (b, right) the [111] crystal of Fig. 4.

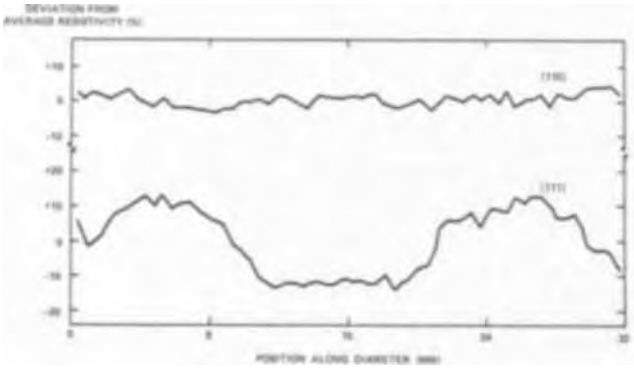

Fig. 6. Radial resistivity profiles for the [115] and [111] crystals of Fig. 4.

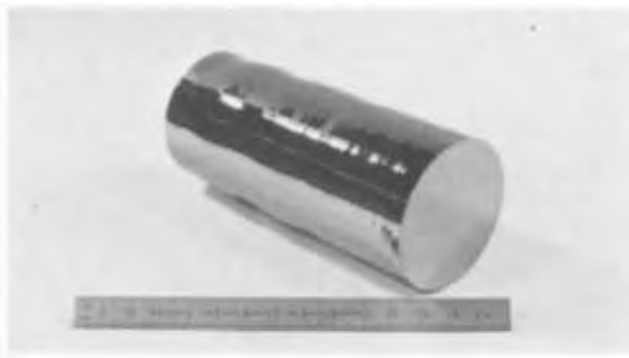

Fig. 7. A 55 mm diameter float-zoned, dislocation-free [115] crystal.

The largest dislocation-free [115] crystals zoned to date are in excess of 55 mm in diameter (Fig. 7).

Manuscript submitted Feb. 9, 1972; revised manuscript received Dec. 11, 1972. This was Paper 200RNP presented at the Cleveland, Ohio, Meeting of the Society, Oct. 3-7, 1971.

Any discussion of this paper will appear in a Discussion Section to be published in the December 1973 JOURNAL.

REFERENCES

1. Y. Miura, *Jap. J. Appl. Phys.*, **4**, 958 (1965).
2. E. I. Salkouitz and F. W. Von Batchelder, *J. Metals*, **4**, 165 (1952).
3. W. Parrish, *Acta Cryst.*, **13**, 838 (1960).
4. T. F. Ciszek, in "Semiconductor Silicon," R. R. Haberecht and E. L. Kern, Editors, pp. 156-168, The Electrochemical Society Softbound Symposium Series, New York (1969).
5. T. F. Ciszek, *J. Cryst. Growth*, **10**, 263 (1971).
6. W. C. Dash, *J. Appl. Phys.*, **30**, 459 (1959).
7. W. Keller and G. Ziegler, U.S. Pat. 3,175,891 (1965).
8. P. V. Gray and D. M. Brown, *Appl. Phys. Letters*, **8**, 31 (1966).
9. P. Rai-Choudhury, Private communication.

The Crystal Growth of Boron Monophosphide from Metal Phosphide Solutions

T. L. Chu,* J. M. Jackson, and R. K. Smeltzer*

Electronic Sciences Center, Southern Methodist University, Dallas, Texas 75222

ABSTRACT

The crystal growth of boron phosphide, BP, has been investigated using two approaches: (*i*) the addition of phosphorus to a boron-nickel or boron-copper melt, and (*ii*) the recrystallization of boron phosphide from a nickel phosphide or copper phosphide solution in a temperature gradient. To determine the optimum conditions for the growth processes, the solubility of boron phosphide in nickel phosphide ($Ni_{12}P_5$) and copper subphosphide (Cu_3P) was determined over a wide temperature range. The solubility of boron phosphide in nickel phosphide was found to be higher than that in copper phosphide. Boron phosphide crystals of about 3-mm size were obtained by the addition of phosphorus to a boron-nickel or boron-copper melt at 1300°C or above, followed by slow cooling. The temperature gradient recrystallization of boron phosphide from nickel phosphide at 1200°C has produced larger crystals. The solution-grown crystals were in the form of hoppers and platelets with platelets dominating. The platelets had main faces of {111} orientation and were formed by the twin-plane re-entrant-edge mechanism. The solution-grown crystals are usually n-type with a room temperature resistivity of about 0.5 ohm-cm and a dopant concentration of about 10^{18} cm^{-3}. They have been used successfully as substrates for the epitaxial growth of boron phosphide.

Boron monophosphide (BP, referred to as boron phosphide hereafter) crystallizes in the zincblende structure and has an indirect energy gap of about 2 eV (1). Because of its relatively large energy gap, this material has potential applications for high-temperature devices and for visible light-emitting devices. However, these devices have not been developed because of the difficulties involved in the growth of single crystals of boron phosphide of controlled chemical and structural perfection. Conventional melt-growth techniques are not feasible for the crystal growth of boron phosphide because of its high melting point (3000°C) and its dissociation into boron subphosphide (B_6P) at temperatures considerably below the melting point (2). Boron phosphide crystals have been grown from metal phosphide solutions and by the chemical transport technique under conditions where its thermal dissociation is negligible.

The growth of boron phosphide crystals from metal phosphide solutions has been briefly reported in several investigations (1, 3-5); however, no information concerning the effects of various process parameters is available. In the present work, the process parameters in the solution growth of boron phosphide have been extensively studied with the objective of producing

* Electrochemical Society Active Member.

Key words: boron phosphide, crystal growth, nickel phosphide, semiconductors, twin planes.

larger crystals suitable as substrates for the epitaxial growth of boron phosphide (6); the epitaxial growth technique is believed to be the most promising approach for the preparation of boron phosphide device structures, since the concentration and distribution of dopants in the epitaxial layer can be reproducibly controlled. Copper and nickel phosphides were used as solvents, and the growth process was carried out by the addition of phosphorus to a boron-metal melt and by the recrystallization of boron phosphide from a metal phosphide solution in the presence of a temperature gradient. The experimental procedures and results are summarized below.

Solubility of Boron Phosphide in Metal Phosphides

The most important parameter in the solution-growth process is the choice of a suitable solvent. The solvent must either be essentially insoluble in boron phosphide, or it must be electrically inactive if it has significant solubility.

Several metals, such as copper, iron, nickel, and platinum, are possible solvent-formers for the solution growth of boron phosphide, and copper and nickel phosphides appear to be the most useful ones on the basis of the available information. An examination of binary phase diagrams (7-9) reveals the following relations: (*i*) boron is soluble in copper and nickel over a wide temperature range: nickel forms four borides (Ni_2B, Ni_3B_2, NiB, and Ni_2B_3) and copper forms no borides, (*ii*) nickel forms at least eight phosphides: Ni_3P, Ni_5P_2, $Ni_{12}P_5$, Ni_2P, Ni_5P_4, NiP, NiP_2, and NiP_3, and the first four phosphides have melting points below 1200°C, and (*iii*) copper forms two phosphides: Cu_3P and CuP_2 (10). Thus, the B-Cu-P system is relatively simple, and the use of nickel phosphide for the solution growth of boron phosphide may involve rather complicated mixtures.

To determine the conditions for the growth of boron phosphide crystals from solutions, the solubilities of boron phosphide in nickel and copper phosphides were determined over a wide temperature range. Polycrystalline boron phosphide, nickel phosphide, and copper phosphide were first prepared as follows.

Boron phosphide was prepared by the thermal reduction of a boron tribromide-phosphorus trichloride mixture with hydrogen in a gas flow system. A mixture of hydrogen, boron tribromide, and phosphorus trichloride, at flow rates of 8×10^{-2}, 1.5×10^{-3}, and 3×10^{-3} moles/min, respectively, was introduced into a fused silica tube heated at about 1100°C in a resistance-heated furnace. The reaction took place on the wall of the silica tube, depositing boron phosphide. The excess of phosphorus trichloride in the reactant prevented any phosphorus deficiency in the deposit. The deposit was confirmed to be boron phosphide by the x-ray Debye-Scherrer technique. Approximately 30g of boron phosphide was formed during an 8-hr period.

Nickel phosphide was synthesized by the reaction of phosphorus vapor with nickel under conditions similar to those used for the solution growth of boron phosphide, and a schematic diagram of the apparatus is shown in Fig. 1. An alumina boat containing a nickel ingot was fitted into a cylindrical graphite sleeve of 1 in. ID and 1¼ in. OD, which was used as a susceptor for rf heating. The susceptor was positioned in a fused silica spacer so that the graphite contacted the spacer only at four points. This assembly and an excess of red phosphorus were placed in a fused silica tube of 50 mm ID and 55 mm OD which was evacuated to less than 10^{-5} Torr and sealed. The reaction tube was about 45 cm long after sealing. The end of the tube containing the susceptor and phosphorus was heated to sublime all phosphorus to the other end of the tube. The susceptor was heated at the desired temperature, 1200°-1400°C, with an rf generator, and a resistance heater surrounding a major portion of the reaction tube was used to maintain the phosphorus pressure in

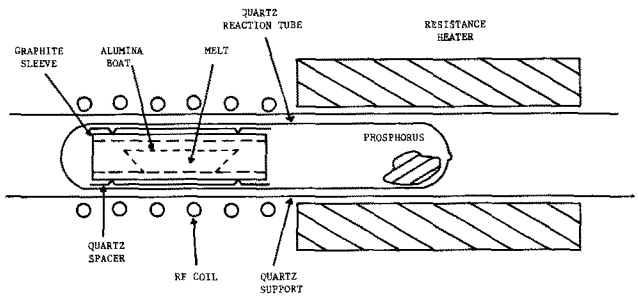

Fig. 1. Schematic diagram of the apparatus used for the synthesis of nickel phosphide and the solution growth of boron phosphide.

the tube at about 2 atm. The nickel appeared to be saturated with phosphorus after several hours; however, the reaction time was usually 24 hr or longer to assure saturation. The x-ray Debye-Scherrer pattern of the resulting product was identical with that of $Ni_{12}P_5$ (11). Nickel phosphides with higher phosphorus content were not obtained.

Copper phosphide was synthesized by the reaction of phosphorus vapor with copper in a closed tube. Weighed amounts of copper and red phosphorus were placed in a fused silica tube, evacuated to less than 10^{-5} Torr, and sealed. The reaction tube was then placed in a two-temperature zone furnace. Copper located at one end of the tube was heated at 1150°C, and the temperature of the other zone was maintained to yield a phosphorus pressure of about 1 atm. Depending on the Cu/P molar ratio in the reactants, Cu_3P or CuP_2, identified by their x-ray Debye-Scherrer patterns (10, 12), were obtained.

To determine the solubility of boron phosphide, a pulverized mixture of 1.0g boron phosphide, 0.04g red phosphorus, and 10.0g nickel phosphide ($Ni_{12}P_5$) was sealed in an evacuated fused silica tube of 10 mm ID and 16 mm OD; phosphorus was used to suppress the decomposition of boron phosphide at high temperatures. The boron phosphide was sieved through a 74μ screen so that the amount of recrystallized material, which would have considerably larger particle size, could be easily determined. The silica tube was fitted into a cylindrical graphite susceptor. The susceptor was sealed into a second silica tube containing about 0.2 atm of argon (the argon pressure was used to suppress the expansion of the inner tube at high temperatures), and the susceptor was at least 1 cm from the tube wall so that the susceptor could be heated to high temperatures. The graphite susceptor was then heated with an rf generator at the desired temperature, 1200°-1400°C for 5-24 hr. The content of the reaction tube was treated with a nitric acid-hydrofluoric acid mixture to dissolve all species except boron phosphide. Whenever recrystallization had occurred, the residual boron phosphide was found to contain small orange-red crystals in addition to the original powder material, and the crystals were separated by sieving the mixture through a 74μ screen. The recovered powder material was undissolved boron phosphide, and the collected crystalline material was recrystallized boron phosphide. In all cases, boron phosphide was not completely recovered due presumably to the complexity of the Ni-B-P system. At 1300°C, for example, 0.75g of boron phosphide dissolved in 10g of nickel phosphide, whereas only 0.23g recrystallized from the solution. The weights per cent of boron phosphide dissolved in, and recrystallized from, nickel phosphide at various temperatures is shown in Fig. 2. It is seen that it has a significant solubility in nickel phosphide at 1200°C, even though this temperature is just above the melting point of nickel phosphide.

The melting point of copper subphosphide, Cu_3P, is 1022°C. The solubility of boron phosphide in copper subphosphide was determined at 1150° and 1220° in a manner similar to that described above. Boron phosphide was found to be essentially insoluble in copper

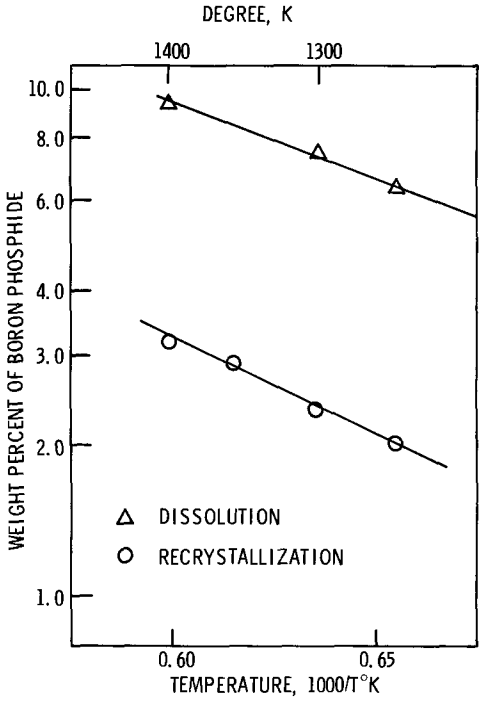

Fig. 2. Dissolution and recrystallization of boron phosphide as a function of temperature using nickel phosphide as a solvent.

subphosphide at 1150°C. When the experiment was carried out at 1220°C for 48 hr, about 85% of the boron phosphide was recovered, and 0.64% (weight) of the initial boron phosphide recrystallized. Thus, boron phosphide is less soluble in copper subphosphide than in nickel phosphide. Also, boron phosphide was found to be insoluble in copper diphosphide, CuP_2, at temperatures up to 1200°C.

Growth of Boron Phosphide Crystals by the Addition of Phosphorus to a Boron-Metal Melt

The slow cooling of a phosphorus-saturated solution of boron in nickel was used for the growth of boron phosphide crystals. The apparatus is the same as that used for the preparation of nickel phosphide shown in Fig. 1. A boron-nickel ingot was prepared by melting weighed quantities of boron and nickel in an alumina boat in a hydrogen atmosphere. Typically, 40g of nickel was used, and the melt was maintained at 1400°C for at least 1 hr to form a homogeneous mixture. The resulting ingot was then sealed in the reaction tube in a manner as shown in Fig. 1. After maintaining a phosphorus pressure over the melt at a predetermined temperature, boron and nickel were converted into the corresponding phosphides. The solution was slowly cooled, and the resulting material was treated with nitric acid to isolate the boron phosphide crystals.

The important process parameters including the phosphorus pressure over the solution, the initial concentration of boron in solution, the temperature of the solution, the reaction time, and the cooling rate, were studied in a number of experiments. A phosphorus pressure of 2-3 atm was found to be optimum; lower pressure resulted in the formation of boron subphosphide B_6P, and higher pressures created such strong convection currents in the reaction tube that the phosphorus pressure could not be controlled. The concentration of boron in nickel was first selected on the basis of the data shown in Fig. 2. The boron-nickel alloy used for crystal growth at 1325°C should contain 2.3% (weight) boron so that, after saturating with phosphorus, the resulting solution of boron phosphide in nickel phosphide would be slightly undersaturated. The solution was maintained at 1325°C for 4 hr and then cooled at a rate of 10°C/hr to about 1150°C. The boron phosphide crystals obtained in this manner were up to 3 mm in size, and the yield was about 50% on the basis of the amount of boron used. Several changes in the process parameters were then made. Higher temperatures did not noticeably change the size distribution or yield of the crystals; however, crystals were smaller on the average at temperatures below 1300°C. The use of higher concentrations of boron in nickel, up to 10%, also did not change significantly the size of boron phosphide crystals. By maintaining the solution at high temperatures under the phosphorus pressure over extended periods, the yield of boron phosphide crystals was slightly increased, but the results were no better in other aspects. Also, no improvements in crystal size were obtained with cooling rates of less than 10°C/hr. Experiments were also carried out by slowly pulling the reaction tube out of the rf coil, and the results were inferior to the slow cooling of the entire solution. To eliminate the possibility that particulate matter from the graphite susceptor had induced excessive nucleation in solution, one experiment was carried out using a molybdenum susceptor and produced very similar results.

A series of experiments was carried out using the addition of phosphorus to a boron-copper melt. Although the solubility of boron in copper is less than that in nickel, the effects of the alloy composition, temperature, reaction time, and cooling rate on the size distribution of crystals were essentially the same as the use of a boron-nickel melt.

Growth of Boron Phosphide Crystals by Recrystallization from Metal Phosphide Solutions

The addition of phosphorus to a boron-nickel or boron-copper melt requires a reaction temperature of at least 1300°C for obtaining boron phosphide crystals of reasonable size. Lower temperature techniques are preferable, and the temperature dependence of the solubility of boron phosphide in metal phosphides was utilized for the crystal growth of boron phosphide by the temperature gradient recrystallization technique. In this technique, a small temperature gradient is maintained across a saturated solution of boron phosphide in a metal phosphide with a polycrystalline boron phosphide source in the higher temperature region. A concentration gradient is thus set up across the solution, and this gradient results in the transport of boron phosphide from the polycrystalline source to the lower temperature region in the solution. The nucleation process in this region can be controlled to yield relatively large crystals.

The recrystallization experiments were carried out in vertical fused silica tubes using a resistance-heated furnace for recrystallization temperatures up to 1200°C and rf heating for higher temperatures. Since the density of boron phosphide is considerably lower than that of metal phosphide solutions, the top of the reaction tube was in the highest temperature region in the majority of the experiments. In a typical high-temperature experiment, 1.5g of polycrystalline boron phosphide and 35g of copper subphosphide were placed in a graphite cylinder of 1 in. ID and 3 in. in height. The crucible was supported by a fused-silica holder and sealed in a fused-silica tube with sufficient phosphorus to yield 2 or 3 atm pressure during recrystallization. The graphite crucible was heated with an rf generator. The top of the solution was maintained at about 1300°C and the bottom was a few degrees cooler. The crucible was slowly cooled after one day, and the resulting boron phosphide was completely recrystallized with crystals up to 2 mm in size. These results were not significantly improved by using nickel phosphide as the solvent or by using a silica liner in the graphite crucible. The relatively small size of boron phosphide crystals obtained in these experiments are presumably due to the high recrystallization rate resulting from the difficulty of controlling a small temperature gradient with rf heating.

The recrystallization experiments at lower temperatures have produced crystals superior to the high-temperature experiments. The best results were obtained with nickel phosphide solutions. In a typical experiment, 0.5g of boron phosphide, 15g of nickel phosphide, and 0.08g of phosphorus were placed in a fused silica tube of 10 mm ID × 16 mm OD, which was evacuated and sealed. The tube was held in a vertical furnace so that the top of the solution was at the highest temperature, 1200°C, and a 5°C gradient existed across the solution. After three weeks, boron phosphide crystals, mostly in the form of platelets up to 4 mm in size, were obtained. At 1150°C or below, no measurable recrystallization was observed after two weeks. Thus, among the techniques investigated in this work, the temperature gradient recrystallization of boron phosphide from nickel phosphide at 1200°C appears to be best suited for the growth of boron phosphide crystals.

Properties of Solution-Grown Boron Phosphide Crystals

Boron phosphide crystals obtained in this work were in the form of hoppers and platelets, with platelets dominating among crystals grown by the recrystallization technique. They are chemically inert, insoluble in aqueous acids and alkalis. Molten potassium hydroxide or a molten mixture of 3:1 sodium hydroxide-sodium peroxide was used as a preferential etchant to reveal structural defects in boron phosphide crystals.

The platelets are usually in the six-sided form, intermediate between a regular hexagon and an equilateral triangle. Figure 3 shows several boron phosphide platelets obtained by the recrystallization technique. The platelets usually have one smooth main face, and the x-ray Laue back-reflection technique indicated that the main face is of {111} orientation. The platelets are also characterized by a twinned structure with twinning taking place about {111} planes. Figure 4 shows the angle-lapped and chemically etched surface of a boron phosphide platelet; the parallel lines are grooves and are the intersections of the twin planes with the angle-lapped surface. In this case, the twin planes are 2-4μ apart. Twinning has been shown to be essential for the growth of the platelets (13). Since the {111} faces are the slowest growing, a stable octahedral structure bounded by these planes would be formed without twinning, and additional growth onto this structure would be difficult because of the high energy of nucleation on the {111} faces. In the twinned structure, however, intersection of the twins forms re-entrant grooves on alternating edges in three of the six equivalent <211> directions that lie in the plane of the twins. The twins intersect at ridges on the other three edges. The grooves provide locations for multiple attachment of new atoms so the energy of nucleation is lowered and growth can ensue preferentially in those directions.

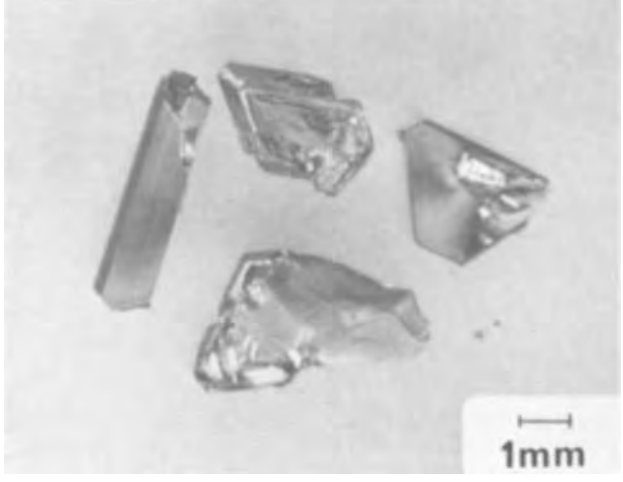

Fig. 3. Typical boron phosphide platelets grown by recrystallization from a nickel phosphide solution at 1200°C.

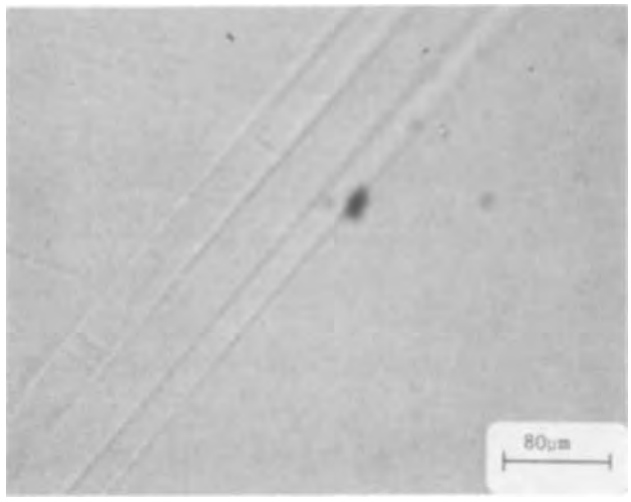

Fig. 4. Angle-lapped and chemically etched surface of a boron phosphide platelet showing the presence of twins.

The hopper-faced boron phosphide crystals were frequently obtained from solutions with a high boron concentration. The crystals consist of separate but often interleaved {111} platelets grown out at different levels from intersecting faces. Edges are favored growth sites in this structure. Although the presence of hopper crystals indicates that many of the solutions were too concentrated, the size and shape of the well-formed twinned crystals did not vary with the presence or absence of the hopper type.

The solution-grown boron phosphide crystals exhibit both n- and p-type conductivity with the n-type predominant. Their electrical conductivities have been measured in the temperature range 77°-500°K. Ohmic contacts were obtained by evaporating indium onto the surface of the crystal followed by annealing at 500°C. A typical conductance-temperature relation of an n-type crystal is shown in Fig. 5. An activation energy of about 0.13 eV dominates in the temperature range 200°-500°K; however, the conductivity is controlled by shallow levels which could not be determined from the data here. Typical resistivities are 0.5 ohm-cm at room temperature and 50 ohm-cm at 77°K.

The room-temperature carrier concentration in solution-grown boron phosphide crystals was estimated from Schottky barrier measurements. Gold dots of 0.01-in. diameter evaporated onto the surface of the crystal were used as the barrier. Capacitance-voltage data from a number of samples has yielded net donor concentrations on the order of 10^{18} cm^{-3}.

The solution-grown boron phosphide crystals are not directly useful for device purposes because the dopant concentration and distribution in these crystals cannot be readily controlled. However, they are ideal as substrates for the epitaxial growth of boron phosphide. Both n- and p-type epitaxial layers with controlled dopant concentration have been deposited on the solution grown crystals by the thermal reduction of a boron tribromide-phosphorus trichloride mixture with hydrogen. The properties of these epitaxial layers will be discussed in another publication.

Summary and Conclusions

Single crystals of boron phosphide have been prepared from metal phosphide solutions by two techniques: (*i*) the addition of phosphorus to a boron-nickel or boron-copper melt at 1300°C followed by slow cooling of the resulting solution, and (*ii*) the recrystallization of boron phosphide from a nickel phosphide or copper phosphide solution at 1200°C in a temperature gradient. The solution-grown crystals are in the form of hoppers and platelets with platelets domi-

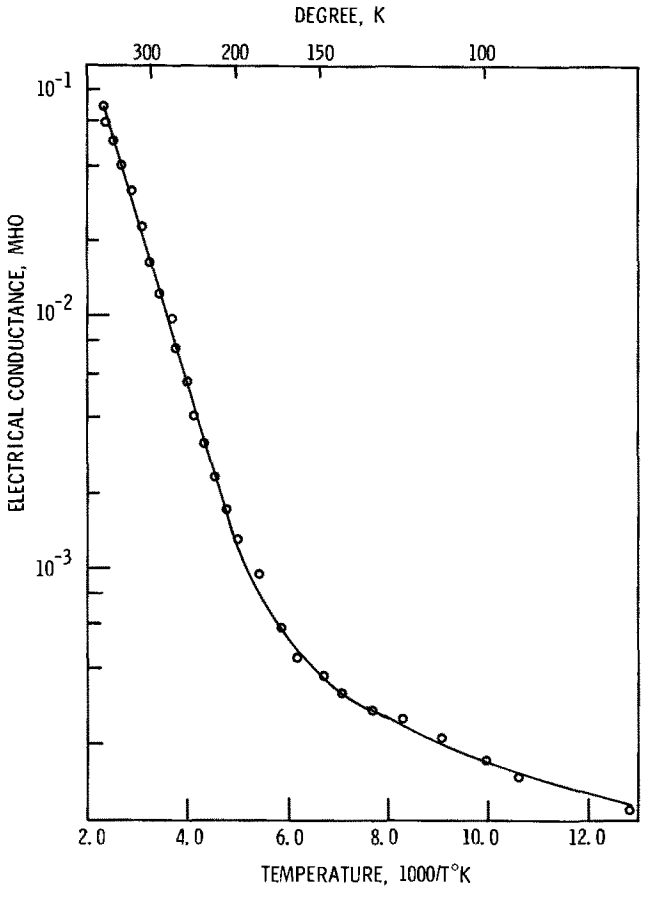

Fig. 5. Electrical conductance of a solution-grown boron phosphide crystal as a function of temperature.

nating. The twin-plane re-entrant-edge mechanism is responsible for the formation of platelets The solution-grown crystals have a dopant concentration on the order of 10^{18} cm^{-3} and are not useful directly for device purposes. They have been used successfully as substrates for the epitaxial growth of boron phosphide.

Acknowledgment

This research was supported by the Langley Research Center of the National Aeronautics and Space Administration under Grant NGL 44-007-042.

Manuscript submitted July 5, 1972; revised manuscript received Dec. 19, 1972. This was Paper 53 presented at the Houston, Texas, Meeting of the Society, May 7-11, 1972.

Any discussion of this paper will appear in a Discussion Section to be published in the December 1973 JOURNAL.

REFERENCES

1. C. C. Wang, M. Cardona, and A. G. Fischer, *RCA Rev.*, **25**, 159 (1964).
2. F. V. Williams and R. A. Ruehrwein, *J. Am. Chem. Soc.*, **82**, 1330 (1960).
3. B. Stone and D. Hill, *Phys. Rev. Letters*, **4**, 282 (1960).
4. B. V. Baranov, V. D. Proclukhan, and N. A. Goryunova, *Izv. Akad. Nauk SSSR, Neorgan. Materialy*, **3**, 1691 (1967) [English translation, p. 1477].
5. M. Iwami, N. Fujita, and K. Kawabe, *Jap. J. Appl. Phys.*, **10**, 1746 (1971).
6. T. L. Chu, J. M. Jackson, A. E. Hyslop, and S. C. Chu, *J. Appl. Phys.*, **42**, 420 (1971).
7. M. Hansen, "Constitution of Binary Alloys," McGraw-Hill Book Co., New York (1958).
8. F. A. Shunk, "Constitution of Binary Alloys, Second Supplement," McGraw-Hill Book Co., New York (1969).
9. E. Larsson, *Arkiv Kemi*, **23**, 335 (1965).
10. O. Olofsson, *Acta Chem. Scand.*, **19**, 229 (1965).
11. S. Rundqvist and E. Larson, *ibid.*, **13**, 551 (1959).
12. H. Haraldsen, *Z. Anorg. Chem.*, **240**, 337 (1939).
13. J. W. Faust, Jr. and H. F. John, *J. Phys. Chem. Solids*, **25**, 1407 (1964).

The Equilibrium Behavior of the Silicon-Hydrogen-Bromine and Silicon-Hydrogen-Iodine Systems

L. P. Hunt* and E. Sirtl*

Dow Corning Corporation, Solid State Research and Development, Hemlock, Michigan 48626

ABSTRACT

A thorough evaluation of the Si-H-Br and Si-H-I systems was made by considering many compounds to coexist at equilibrium. Compound partial pressures are presented as a function of temperature (300°-1700°K) for a halogen to hydrogen ratio of 0.01. Diagrams relating the X/H ratio (0.01-10) to the Si/X ratio indicate the equilibrium state of the system with respect to the corresponding increase or decrease of silicon in the gaseous phase. Experimental data are presented proving the existence of a high-temperature ($\gtrsim$ 1300°K) cold-to-hot transport reaction in the Si-H-I system in contrast to what is predicted in the Si-H-Br and known in the Si-H-Cl systems. The cold-to-hot transport reaction is the result of the high-equilibrium partial pressure of monatomic iodine at temperatures approaching the melting point of silicon.

The common methods used in the semiconductor industry for the chemical vapor deposition of silicon involve either the pyrolysis of silane or the hydrogen reduction of the chlorosilanes $SiCl_4$, $SiHCl_3$, and more recently SiH_2Cl_2 (1). In comparison to the chlorosilanes, the body of information available concerning the decomposition of the other halosilanes is very slight. The fluorosilanes have attracted little attention because of their comparatively high thermal stability, while the bromo- and iodosilanes have been largely ignored for both economic and technical handling reasons.

* Electrochemical Society Active Member.
Key words: silicon, thermochemical equilibrium, transport, vapor deposition.

Within the Si-H-Br system, silicon tetrabromide has been studied (2, 3) on a very limited basis as a source material for silicon deposition. In the other extreme, the etching of silicon by H_2-HBr mixtures has been shown (4) to have advantages over the more commonly used H_2-HCl mixtures. Interest in the Si-H-I system, or more specifically the Si-I system in the absence of hydrogen, has been higher than in the corresponding bromine system since the chemistry is somewhat altered by the low stability of SiI_4 at medium temperatures and the greater stability of monatomic iodine at higher temperatures. Although work in the etching area has been somewhat limited (5), studies in polycrystalline silicon deposition (6-8) initiated additional investigation into epitaxial deposition (9-14) from SiI_4 by pyrolysis, hydrogen reduction, and chemical transport reactions.

The purpose of this paper is to generally describe the equilibrium behavior of the Si-H-Br and Si-H-I systems in order to provide a frame of reference to which experimental data can be compared. Calculations are based on a detailed thermodynamic analysis of each system in a manner very similar to that used for the Si-H-Cl system (15). Earlier thermodynamic analyses of the Si-H-I system (10-13) have been quite specific in terms of interpreting experimental data of a limited nature.

Thermodynamic Data

The computational method, based on that reported by Cruise (16), and described more thoroughly elsewhere (15), requires a knowledge of the standard enthalpy of formation, $\Delta Hf°_{298}$, the standard entropy, $S°_{298}$, and the temperature function of the heat capacity equation, $C_p°(T)$, for each species in an equilibrium system. Since many of these basic quantities have not been determined for the halosilanes and subhalides in the Si-H-Br and Si-H-I systems, a thorough analysis of the equilibrium situation requires a careful evaluation and estimation of the missing data.

Standard enthalpy of formation.—As is the case with chlorosilanes, the absence of enthalpy of formation data for the tri-, di-, and monohalosilanes (X = Br, I) necessitates their estimation by interpolating between the well-established values for the tetrahalosilanes (17) and for monosilane (18). This method has been shown (15) to be accurate to within about 1 kcal/mol for trichlorosilane. The interpolated values appear in Table I.

Table I. Thermochemical data

Species	$\Delta Hf°_{298}$ (kcal/mol)	Ref.	$S°_{298}$ (eu)	Ref.	$C_p° = A + BT + CT^{-2}$ (eu) A	B ×10³	C ×10⁻⁵	Ref.
Si(s)	0	[a]	4.50	(22)	5.70	0.70	−1.04	(27)
Si(g)	107.7	(22)	40.12	(22)	4.82	0.18	0.42	(28)
H_2(g)	0	[a]	31.21	(28)	6.52	0.78	0.12	(28)
HBr(g)	−8.71	(22)	47.47	(22)	6.41	1.24	0.15	(27)
Br(g)	26.74	(20)	41.81	(20)	4.90	0.22	0	(27)
Br_2(g)	7.39	(20)	58.64	(20)	8.92	0.12	−0.30	(27)
SiH_4(g)	7.3	(18)	48.87	(29)	15.38	4.88	−6.35	(22)[c]
SiH_3Br(g)	−19.4	[b]	62.65	(29)	17.96	3.67	−6.08	(30)
SiH_2Br_2(g)	−46.0	[b]	74.18	(29)	20.54	2.48	−5.14	(29)
$SiHBr_3$(g)	−72.7	[b]	83.24	(29)	23.05	1.33	−3.81	(29)
$SiBr_4$(g)	−99.3	(17)	90.24	(29)	25.60	0.15	−2.18	(29)
$SiBr_3$(g)	−38	[b]	83.2	[b]	19.80	0.04	−1.20	[b]
$SiBr_2$(g)	−12.2	(17)	72	(17)	14.36	0.08	−0.80	[b]
SiBr(g)	61	[b]	58.7	(31)	8.92	0.13	−0.40	[b]
Si_2Br_6(g)	−149	[b]	112	[b]	43.52	0.11	−2.98	[b]
HI(g)	6.30	(22)	49.35	(22)	6.39	1.42	0.14	(27)
I(g)	25.54	(20)	43.18	(20)	4.80	0.16	0.11	(27)
I_2(g)	14.92	(20)	62.28	(20)	8.94	0.14	−0.17	(27)
SiH_3I(g)	−2.0	[b]	64.72	(30)	18.08	3.61	−5.82	(30)
SiH_2I_2(g)	−11.3	[b]	78.0	[b]	20.63	2.42	−5.0	[b]
$SiHI_3$(g)	−20.6	[b]	89.1	[b]	23.18	1.23	−3.5	[b]
SiI_4(g)	−29.9	(17)	98.65	(29)	25.74	0.05	−1.56	(29)
SiI_3(g)	15	[b]	89.5	[b]	20.04	0.14	−0.91	[b]
SiI_2(g)	17.9	(17)	76	(17)	14.56	0.22	−0.35	[b]
SiI(g)	78	[b]	60.1	[b]	9.54	0.12	0.09	[b]
Si_2I_6(g)	−45	[b]	120	[b]	43.60	0.06	−2.44	[b]

[a] Zero by definition.
[b] Estimated in this paper.
[c] A regression analysis was performed on the cited data.

Reliable data for the standard enthalpy of formation of both $SiBr_2$(g) and SiI_2(g) have been published by Schäfer *et al.* (17). No known experimental determinations of the enthalpies of the silicon mono- and trihalides have been made however. Therefore, their values are estimated using the data for the silicon subchlorides (15) as a guide line. Since the deviation from the straight line between Si(g) and $SiCl_4$(g) of the enthalpy values of SiCl and $SiCl_3$ are about 5 and 10 kcal/mol, respectively, we have algebraically added these off-set values to the "straight line" values in the bromine and iodine series to accordingly obtain the enthalpies of SiBr, $SiBr_3$, SiI, and SiI_3. Even though this type of estimation leads to values of limited accuracy, later calculations will show equilibrium partial pressures of the mono- and trihalides to be quite negligible under the conditions studies.

Since experimental enthalpy of formation data have not been published for either Si_2Br_6(g) or Si_2I_6(g), the values were estimated in the same manner as has been explained earlier for Si_2Cl_6 (15). This method essentially involves adding twice the enthalpy of the hypothetical "ideal" SiX_3(g) molecule, obtained by linear interpolation, to one-half of the atomic sublimation energy of silicon.

Standard entropy.—The standard entropy of $SiHI_3$(g) and SiH_2I_2(g) can be accurately estimated by plotting the known data for the halosilanes in the coordinating diagram (19) shown in Fig. 1. Here use is made of the near linear relationship between the logarithms of the entropy and molecular weight for similar series of compounds. This same approach was also used to calculate the entropy of $SiBr_3$(g), SiI(g), and SiI_3(g) as shown in Fig. 2.

The entropies of Si_2Br_6(g) and Si_2I_6(g) were calculated from the entropy of Si_2Cl_6(g) based on the near constant incremental standard entropies of 11 eu between the chlorine and bromine compounds and 8 eu between the bromine and iodine compounds for gaseous CX_4, SiX_4, and C_2X_6 (20).

Heat capacity.—Where heat capacity data were not available in the equation form $C_p° = A + BT + C/T^2$, a regression analysis was performed on the originally tabulated data. Although reliable data exist for all the bromosilanes, there are no available values for either di- or triiodosilane. The coefficients of the heat capacity equation for these compounds can be very accurately estimated in a diagram, such as Fig. 3, where the value of each coefficient is plotted as a function of the compounds in the series $SiH_4 \rightarrow SiI_4$. The smoothness of such curves can be seen in the case of the chloro- and bromosilanes where all data are available. This method has also proved very successful in estimating missing

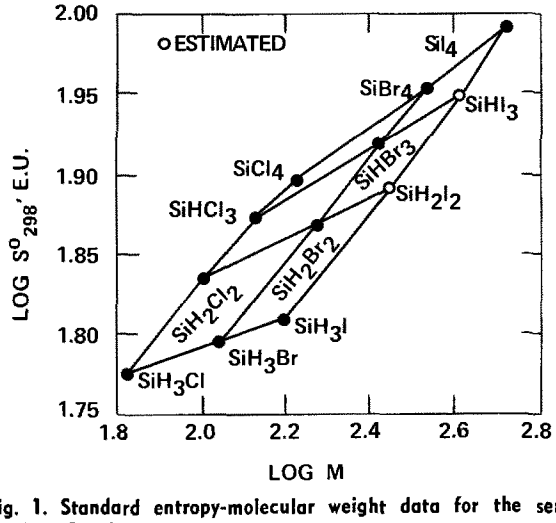

Fig. 1. Standard entropy-molecular weight data for the series $SiH_3X(g) \rightarrow SiX_4(g)$.

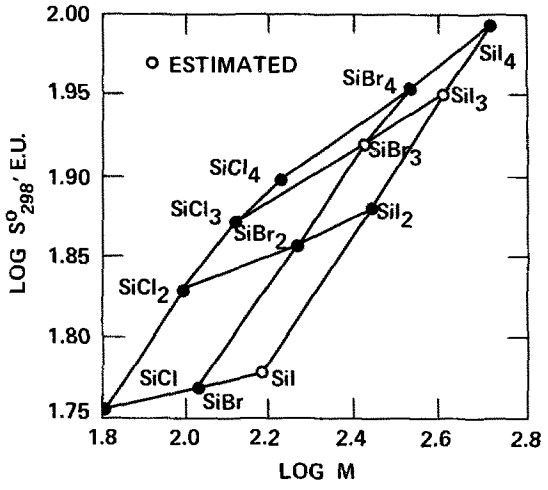

Fig. 2. Standard entropy-molecular weight data for the series $SiX(g) \rightarrow SiX_4(g)$.

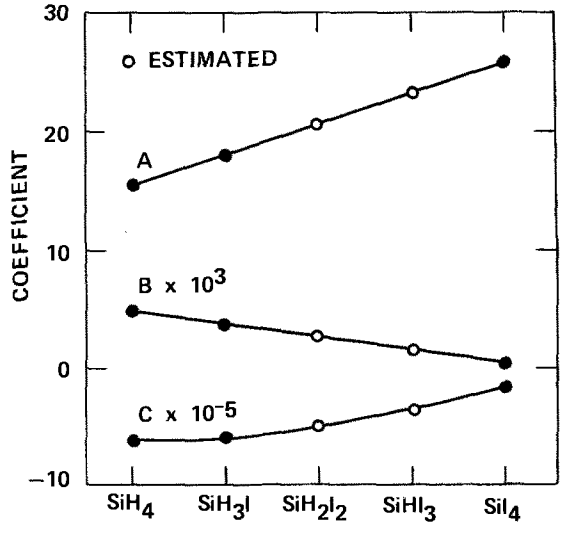

Fig. 3. Heat capacity coefficients from the equation $C_p^\circ = A+BT+C/T^2$ for the series $SiH_4(g) \rightarrow SiI_4(g)$.

heat capacity data for the methysilanes and methychlorosilanes (21).

Heat capacity data for the silicon subbromides were assumed equal to that of the JANAF (22) data for the corresponding aluminum bromides due to close agreement in the data for the silicon and aluminum subchlorides. The unavailability of data for $AlBr_2(g)$ required that it be interpolated, as in Fig. 3, from the series $Al(g) \rightarrow AlBr_3(g)$.

Since reliable data do not exist for either the silicon or aluminum subiodides, the heat capacities of SiI, SiI_2, and SiI_3 were estimated, as in Fig. 3, from the series $Si(g) \rightarrow SiI_4(g)$ by comparison to the similar series for the subchlorides and subbromides.

The heat capacity of $Si_2Cl_6(g)$ was assumed earlier (15) to be equal to that of $C_2Cl_6(g)$. The lack of published data for $C_2Br_6(g)$ and $C_2I_6(g)$, however, makes it necessary to estimate the heat capacities of $Si_2Br_6(g)$ and $Si_2I_6(g)$ from their corresponding aluminum analogs (22). Even though comparison of the heat capacity-temperature curves for C_2Cl_6 and Al_2Cl_6 shows them to be somewhat different (their molecular structures are different), the approximation is justified here due to the very low partial pressure of Si_2Cl_6 found to exist at equilibrium (23). Since initial calculations using the heat capacity of Al_2Br_6 and Al_2I_6 for Si_2Br_6 and Si_2I_6, respectively, showed the latter compounds also to have very low partial pressures at equilibrium, the estimates were assumed to be accurate enough for this work.

Results and Discussion

Si-H-Br and Si-H-I systems.—Calculations for the Si-H-Br system assumed various initial bromosilane-hydrogen mixtures to be in contact with a solid phase of silicon at specified temperatures. The resulting equilibrium partial pressures of the various species are presented in Fig. 4 for an initial Br/H ratio of 0.01 (0.5% SiI_4) over a temperature range of 300°-1700°K. The absence from the diagrams of some of the species listed in Table I is due to their very low equilibrium partial pressures. It is possible to ignore the following gaseous species while maintaining greater than 98% accuracy: Si, Br, Br_2, SiBr, $SiBr_3$, SiH_4, SiH_3Br, and Si_2Br_6.

Comparison of the equilibrium gas phase data in Fig. 4 for the Si-H-Br system to analogous data for the Si-H-Cl system (23) shows nearly exact agreement except for two species, one of which, of course, is Br(g). The partial pressure of $SiHBr_3$ is lower relative to that of $SiHCl_3$ since the enthalpy of the latter compound was determined (15) to be 1.2 kcal/mol more negative than the interpolated value between SiH_4 and $SiCl_4$.

The Si-H-I system was treated similarly to the Si-H-Br system. The iodine system can be calculated to greater than 97% accuracy by leaving out all the species corresponding to those already mentioned in the bromine system with the exception of I(g). The equilibrium partial pressures of the compounds in Fig. 5 are found to be very nearly equal to the partial pressures of the corresponding compounds in the Si-H-Cl and Si-H-Br systems up to about 1200°K. Above this temperature, however, the stability of monatomic iodine results in the Si-H-I system being quite different from the chlorine and bromine systems. The stability of I(g) increases with temperature to such an extent that it actually causes a maximum to occur in the partial pressures of HI and SiI_2. This is in contrast to the chlorine and bromine systems where HX and SiX_2 are monotonic functions of temperature.

Further insights into the Si-H-Br and Si-H-I systems are available through Fig. 6 and 7 which show the silicon content (Si/X ratio) of the gas phase as a function of the initial gas phase composition (X/H ratio) for temperatures between 300°-1700°K. A thorough description of the general trends found in curves

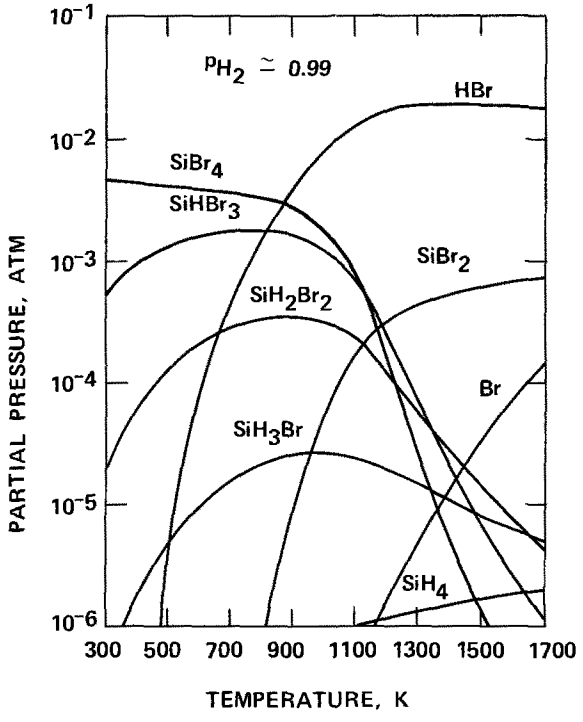

Fig. 4. Equilibrium partial pressures of species in the Si-H-Br system as a function of temperature for Br/H=0.01.

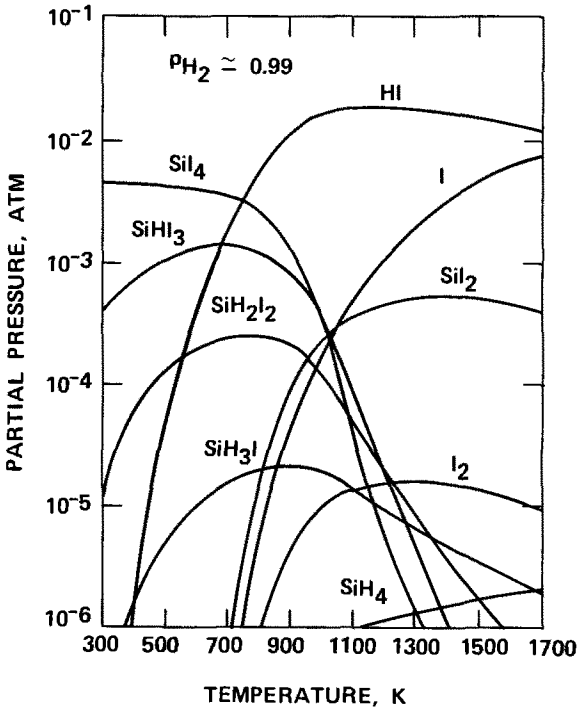

Fig. 5. Equilibrium partial pressures of species in the Si-H-I system as a function of temperature for I/H=0.01.

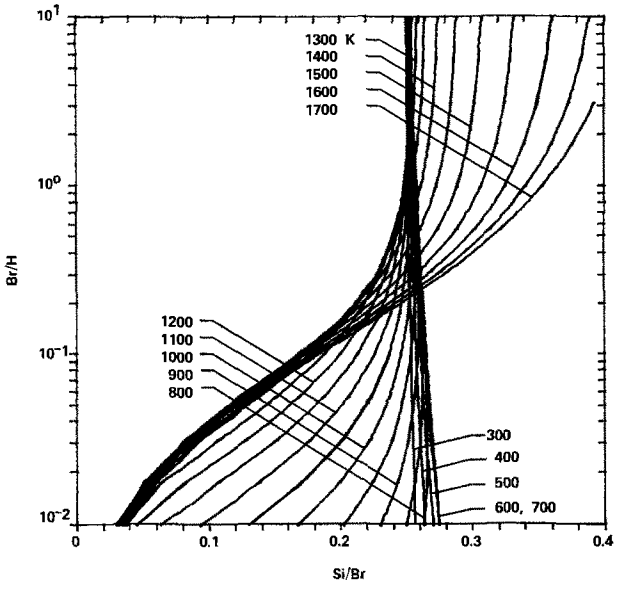

Fig. 6. Silicon content of the Si-H-Br system gas phase as a function of the Br/H ratio at 1 atm total pressure for 50° temperature increments.

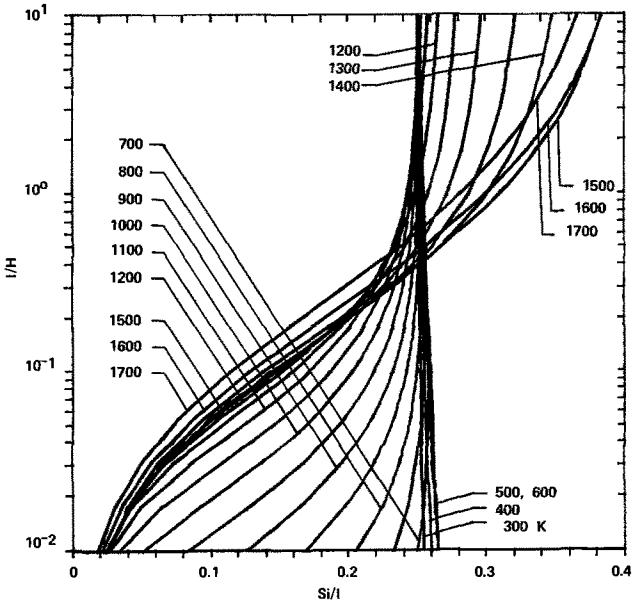

Fig. 7. Silicon content of the Si-H-I system gas phase as a function of the I/H ratio at 1 atm total pressure for 50° temperature increments.

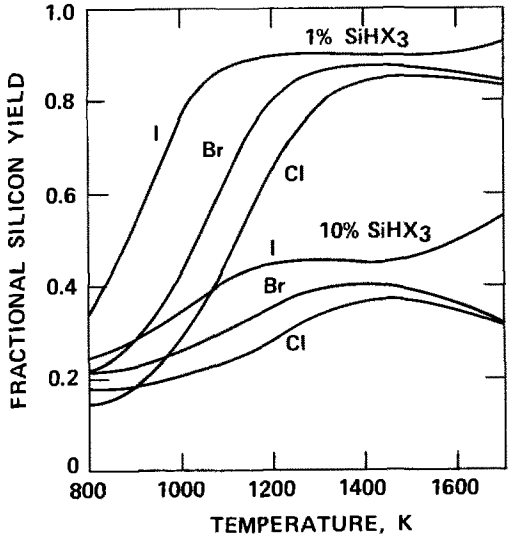

Fig. 8. Temperature variation of the fractional silicon yield from various $SiHX_3$-H_2 mixtures.

of this type has been given elsewhere (15). At low X/H ratios and temperatures $\lesssim$ 1200°K, the isothermal curves in the bromine and iodine systems show a shift toward lower Si/X values when compared to the chlorine system due to the higher partial pressure of SiX_4 (Si/X = 0.25) relative to $SiHX_3$ (Si/X = 0.33). This is attributed to the standard enthalpy of $SiHCl_3$ not being an interpolated value as is the case of $SiHBr_3$ and $SiHI_3$.

Figure 8 shows the temperature function of the silicon yield for 1 and 10% initial mixtures of $SiHCl_3$, $SiHBr_3$, and $SiHI_3$ in H_2. The thermal stability of the compounds are found to be $SiHCl_3 > SiHBr_3 > SiHI_3$ for temperatures up to the melting point of silicon. Although the data in Fig. 8 show nearly the same silicon yields from both the Si-H-Cl and Si-H-Br systems at high temperatures, equivalent experiments in this laboratory have indicated that 5% $SiHBr_3$ in H_2 yields a 40% greater polycrystalline silicon deposition rate than the corresponding $SiHCl_3$ mixture at 1400°K (24). It is obvious, however, that silicon deposition in flow systems is kinetically controlled and that equilibrium conditions are not attained in either case.

The high partial pressure of monatomic iodine at $\geqslant$ 1200°K is the reason for the increased complexity of Fig. 7 for the Si-H-I system over Fig. 6 for the Si-H-Br system. At approximately 1400°K, the partial pressure of I(g) becomes so high that the major silicon-containing compound in the gas phase, SiI_2, passes through a maximum and consequently causes the silicon yield, as seen in Fig. 8, to pass through a minimum. Since a similar behavior has been theoretically predicted and experimentally verified in the germanium-iodine system (25), the transport experiments described in the Appendix were performed to prove our thermodynamically predicted yield curve.

In the Si-H-Br system the only experimental yield or deposition rate data available in the literature for comparing our thermodynamically determined data to is the hydrogen reduction of silicon tetrabromide by Miller and Grieco (3). Their deposition rate-mole fraction curve was found to be considerably below the

calculated curve as has been shown to also be the case for $SiCl_4$ and $SiHCl_3$ as source materials in the Si-H-Cl system (23). The same case is found to exist for the data by Seki and Araki (13) in the Si-H-I system.

Si-I system.—The two common processes carried out in this more limited system (hydrogen concentration equals zero) are silicon transport using an initial gas phase of SiI_4 or I_2 and silicon deposition by the pyrolysis of SiI_4. The partial pressure-temperature data in Fig. 9a and b show that SiI_4, SiI_2, and I are the only species that must be considered to be in equilibrium with solid-phase silicon over a total pressure range of 0.01-1.0 atm. In addition to these data, Fig. 10 indicates that SiI_4 can be expected to be stable up to a temperature of about 800°K. The Si-I system is

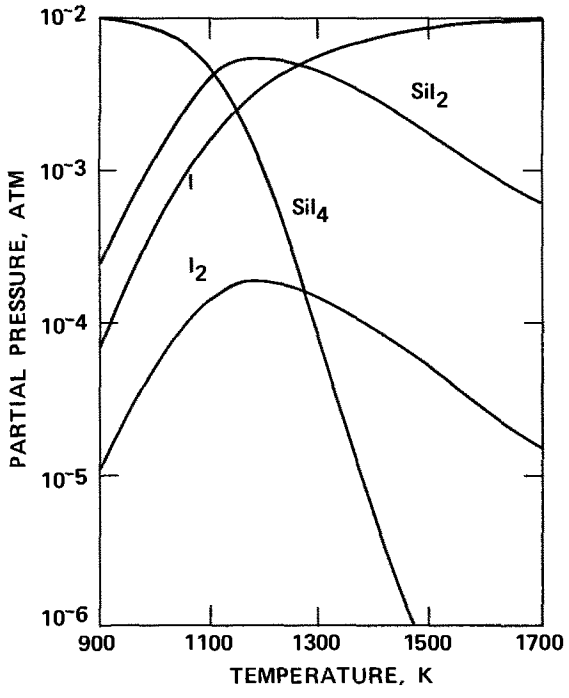

Fig. 9a. Equilibrium partial pressures of species in the Si-I system as a function of temperature at 0.01 atm total pressure.

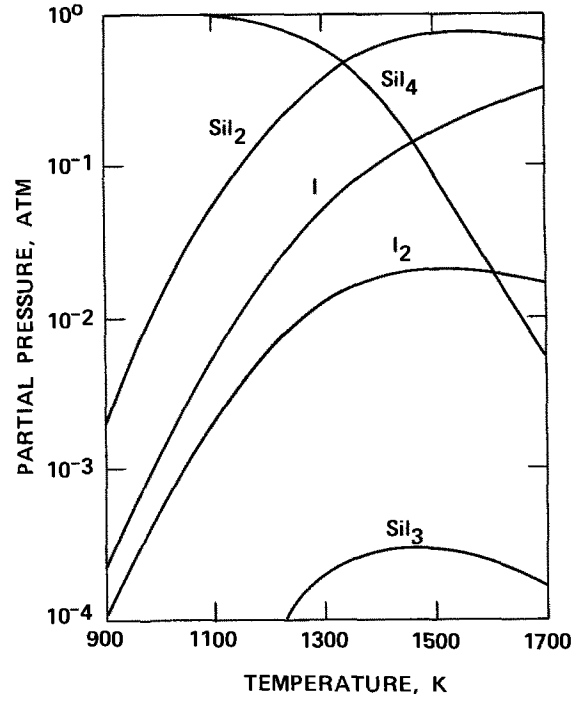

Fig. 9b. Equilibrium partial pressures of species in the Si-I system as a function of temperature at 1.0 atm total pressure.

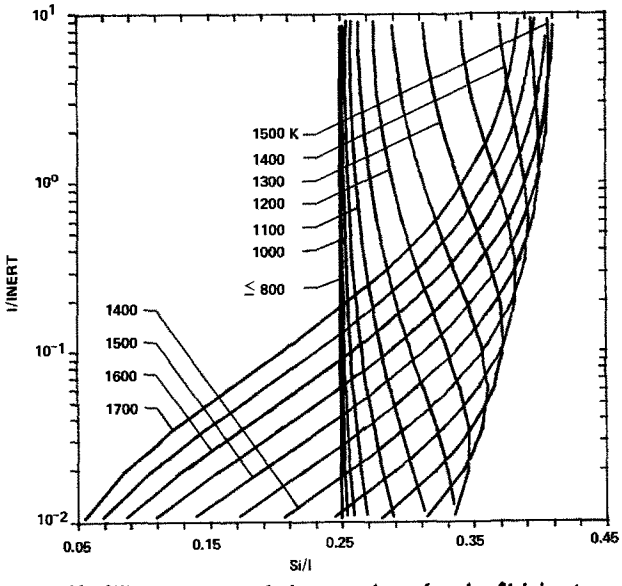

Fig. 10. Silicon content of the gas phase for the Si-I inert gas system as a function of the I/H ratio at 1.0 atm total pressure for 50° temperature increments.

unique with respect to the Si-H-X systems in that it is theoretically possible to obtain the same silicon yield (Si/I ratio) from different initial compositions of the gas phase at a high constant temperature, *e.g.*, 1300°K.

A check on the accuracy of our calculated data has been made by comparing it to the equilibrium data reported by Schäfer and Morcher (26) in their studies of the pressure dependence of the transport direction of silicon by silicon diiodide. Their data showed no transport to exist between temperature zones of 1223° and 1423°K at a total pressure of 79 mm. This is seen to be the case in Fig. 10 when one assumes the value of 79 mm (0.104 atm) is nearly equal to an I/inert ratio of 0.1. Fair agreement is also found between our computed silicon yield data and the ones calculated by Wajda and Glang (10) based upon reported (26) equilibrium constant data.

In a final attempt to set all the previously described systems in proper perspective to themselves and to the Si-H-Cl system, we have presented four threshold curves in Fig. 11. These curves indicate the threshold

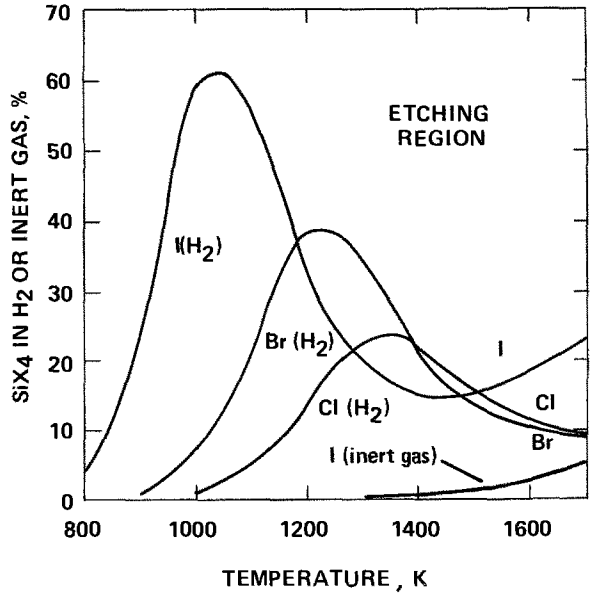

Fig 11. Threshold curves as a function of temperature for various SiX_4-H_2 mixtures.

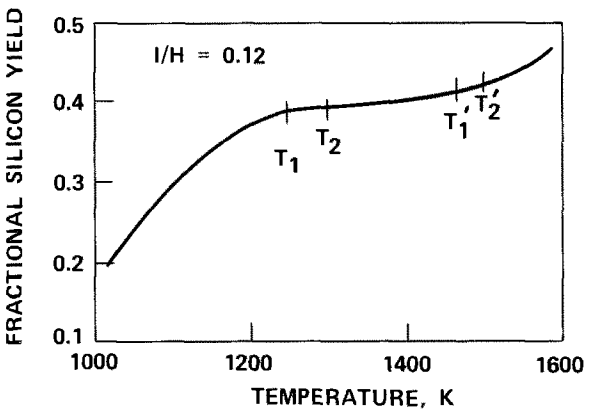

Fig. 12. Calculated and experimental data for transport reactions in the Si-H-I system.

Temperature, °K		Deposition rate, μ/min	Transport direction
T_1	1246		
T_2	1299	0 ± 0.5	Not detected
T_1'	1463		
T_2'	1499	16.9 ± 0.7	Cold-to-hot

between silicon etching and deposition for various temperatures and initial silicon tetrahalide concentrations.

Conclusions

A thorough thermodynamic analysis of the Si-H-Br and Si-H-I systems allowed many potential compounds to be rejected as being significant due to their low equilibrium partial pressures. Good reliability was therefore associated with the computed equilibrium data since thermodynamic data was either available or could be estimated with sufficient accuracy for the remaining predominate compounds. Consistency was found between our calculated data and the limited amount of experimental data found in the literature for the Si-H-Br, Si-H-I, and Si-I systems. A high-temperature minimum in the silicon yield curve theoretically postulated for the Si-H-I system was experimentally verified by the study of transport reactions. The high-temperature Si-H-I system differs from the Si-H-Cl and Si-H-Br systems because the concentration of the main silicon-bearing species SiI_2 passes through a maximum due to the increasing stability of monatomic iodine with temperature.

Acknowledgment

We wish to thank D. H. Sawyer for performing all of the experimental work associated with the transport reactions.

Manuscript submitted July 26, 1972; revised manuscript received Jan. 2, 1973. This was Paper 270 presented at the Miami Beach, Florida, Meeting of the Society, Oct. 8-13, 1972.

Any discussion of this paper will appear in a Discussion Section to be published in the December 1973 JOURNAL.

APPENDIX

The general trend of the silicon yield-temperature curve shown in Fig. 12 was determined by measuring the rate of silicon transport in a temperature gradient between two silicon slices using the "sandwich technique" (32). A horizontal, induction-heated, quartz tube reactor was fed with a 250 ml/min hydrogen stream that passed through an iodine sublimator so as to maintain an 11% I_2 mixture. The source and substrate were 0.6 mm by 13 mm diameter, polished, float-zoned silicon wafers of <111> orientation that had been previously cleaned in solvents. The wafers were separated by 0.2 mm spacers.

Transport reactions were carried out at the corrected pyrometric temperatures (±5°K) for time periods up to 60 min. Deposition rates were determined microscopically by measuring the deposited layer thickness on a cross section of the substrate.

REFERENCES

1. W. C. Benzing and A. E. Ozias, Abstract 75, p. 184, Electrochem. Soc. Extended Abstracts, Spring Meeting, Washington, D.C., May 9-13, 1971.
2. R. C. Sangster, E. F. Maverick, and M. L. Croutch, *This Journal*, **104**, 317 (1957).
3. K. J. Miller and M. J. Grieco, *ibid.*, **110**, 1252 (1963).
4. L. V. Gregor, P. Balk, and F. J. Campagna, *IBM J.*, **9**, 327 (1965).
5. A. Reisman and M. Berkenblit, *This Journal*, **112**, 812 (1965).
6. F. B. Litton and H. C. Andersen, *ibid.*, **101**, 287 (1954).
7. G. Szekely, *ibid.*, **104**, 663 (1957).
8. S. C. Herrick and J. C. Krieble, *ibid.*, **107**, 111 (1960).
9. E. S. Wajda, B. W. Kippenhan, and W. H. White, *IBM J.*, **4**, 288 (1960).
10. E. S. Wajda and R. Glang, in "Metallurgy of Elemental and Compound Semiconductors," p. 229, R. O. Grubel, Editor, Interscience Publishers, New York (1961).
11. R. A. A. Lieth and A. G. M. Eggels, *J. Appl. Phys.*, **35**, 3015 (1964).
12. J. E. May, *This Journal*, **112**, 710 (1965).
13. H. Seki and H. Araki, *Jap. J. Appl. Phys.*, **4**, 645 (1965).
14. E. A. Taft, *This Journal*, **118**, 1535 (1971).
15. L. P. Hunt and E. Sirtl, *ibid.*, **119**, 1741 (1972).
16. D. R. Cruise, *J. Phys. Chem.*, **68**, 3797 (1964).
17. H. Schäfer, H. Bruderreck, and B. Morcher, *Z. Anorg. Allgem. Chem.*, **352**, 122 (1967).
18. S. R. Gunn and L. G. Green, *J. Phys. Chem.*, **65**, 799 (1961).
19. E. Sirtl, *Z. Naturforsch.*, **21a**, 2001 (1966).
20. D. D. Wagman, W. H. Evans, V. B. Parker, I. Halow, S. M. Bailey, and R. H. Schumm, *NBS Tech. Note 270-3* (1968).
21. L. P. Hunt, Unpublished work.
22. D. R. Stull, Editor, JANAF Thermochemical Tables, Dow Chemical Co., Midland, Mich. (1965-1968).
23. E. Sirtl, L. P. Hunt, and D. H. Sawyer, Submitted to *This Journal*.
24. G. H. Barnes, Dow Corning Corp., Private communication.
25. F. Jona, R. F. Lever, and H. R. Wendt, *This Journal*, **111**, 413 (1964).
26. H. Schäfer and B. Morcher, *Z. Anorg. Allgem. Chem.*, **290**, 279 (1957).
27. K. K. Kelley, *U.S. Bur. Mines Bull. 584* (1960).
28. O. Kubaschewski, E. L. Evans, and C. B. Alcock, "Metallurgical Thermochemistry," Pergamon, Press, New York (1967).
29. S. Mikawa, *Nippon Kagaku Zasshi*, **81**, 1512 (1960).
30. A. Müller, R. Kebabcioglu, B. Krebs, and O. Glemser, *Z. Phys. Chem.*, **240**, 92 (1969).
31. K. K. Kelley and E. G. King, *U.S. Bur. Mines Bull. 592* (1961).
32. E. Sirtl, *J. Phys. Chem. Solids*, **24**, 1285 (1963).

Circular and Hexagonal Stacking Faults in Bulk Silicon Crystals

Lawrence D. Dyer* and Fred W. Voltmer

Texas Instruments Incorporated, Dallas, Texas 75222

ABSTRACT

Circular and hexagonal defects were formed in bulk silicon crystals by annealing and slow cooling. Some of these circular defects were unusual in possessing spoke-like radial lines in <110> directions. By use of the rule that the Burgers vector is invariant against displacement of the Burgers circuit through good crystal regions, the radial lines are shown to have zero net Burgers vector and thus are probably dislocation dipoles. A mechanism is presented that accounts for the observed defects in terms of the formation of Frank sessile loops and half-loops. The principal significance of this interpretation is that when the circular defects containing radial lines appear, precipitates are present in the material.

In the course of a development program to improve yields of polished slices for epitaxial substrates, some rather peculiar defects were noted in slices from ordinary silicon boules that had been annealed. These defects were identified by their etching characteristics as circular and hexagonal stacking faults. Similar faults have previously been observed in annealed bulk silicon crystals doped with gold (1-4) or oxygen (5). Also, truncated circular stacking faults occur when silicon is annealed in steam or wet oxygen, particularly if polishing damage remains (6-13). These defects can seriously affect device performance and yields, either by themselves or by causing further defects in epitaxial layers grown after their generation.

The source of the circular stacking faults in bulk silicon has previously been attributed to line defects (3, 4) and to precipitates (3-5). Dislocation networks have been reported within the circular stacking faults, but details are lacking (5). The present article shows that circular faults can form in annealed bulk crystal without intentional gold or oxygen treatment. In addition, in the present work radial dislocation lines (spokes) occur within the faults. In this case, precipitates are almost certainly present, although they have not been positively identified in this study. The Burgers vectors of the various dislocation lines in the ring-spoke combinations are worked out and a mechanism for their formation is presented. A later paper will show infrared evidence for precipitates and will deal with the nature of the precipitation and the distribution of the faults.

Experimental Procedure

The silicon crystals used in this study were grown in the <111> orientation by the Teal-Little modification of the Czochralski technique (14). The crystals were sawed into 3-4 in. lengths and were annealed in this form, either at 1100°C for 20 hr or at 1225°C for 4 hr. Cooling times to 700°C varied from 5 min to 2 hr, and the furnace atmosphere was 99% N_2, 1% O_2.

A number of 2-in.-diameter samples were sliced from the silicon crystals 1½°-2½° off the {111} face and were chemically-mechanically polished on one side to a thickness of approximately 0.012 in. The slices were Sirtl etched (15) for 4 min and inspected with a Reichert Zetopan microscope equipped with Nomarski interference contrast equipment.

Observations

Figure 1 shows a group of defects on one of the slices. They appear as circles and grooves lying in three <110> directions. (In all the photographs, a <110> direction is parallel to the bottom of the picture). The circles are generally as large as the grooves in the same vicinity.

The etched circular defects may exhibit any or all of six radial lines which lie in $<1\bar{1}0>$ directions. These will hereafter be called spokes. Figure 2 shows all the types of rings with 1, 2, 5, and 6 spokes. Figure 3 shows all the types of rings with 3 and 4 spokes. Figure 4 shows other types that can occur: a, hexagonal; b, c, and d, concentric rings of various types; e, rings with a central dot; f, cases of non-$<1\bar{1}0>$ spokes within the ring. In the latter case note the etch pits that occur in the $<1\bar{1}0>$ grooves. Figure 5 shows an example of a ring with a diametral line that terminates in two etch pits.

Some rings appear with one side open (Fig. 6). When this happens all such partial rings on the slice are open

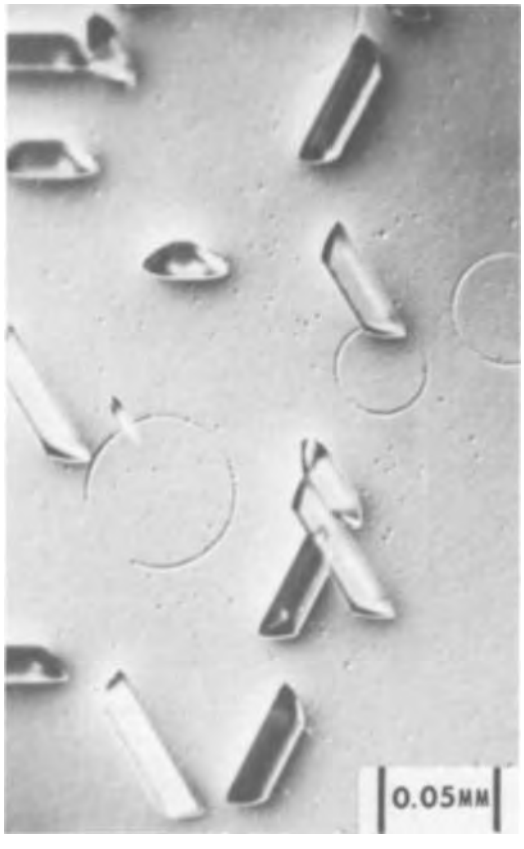

Fig. 1. Circular defects in <111> bulk silicon crystal. Interference contrast.

* Electrochemical Society Active Member.

Key words: precipitates in silicon, dipoles, fault nucleation.

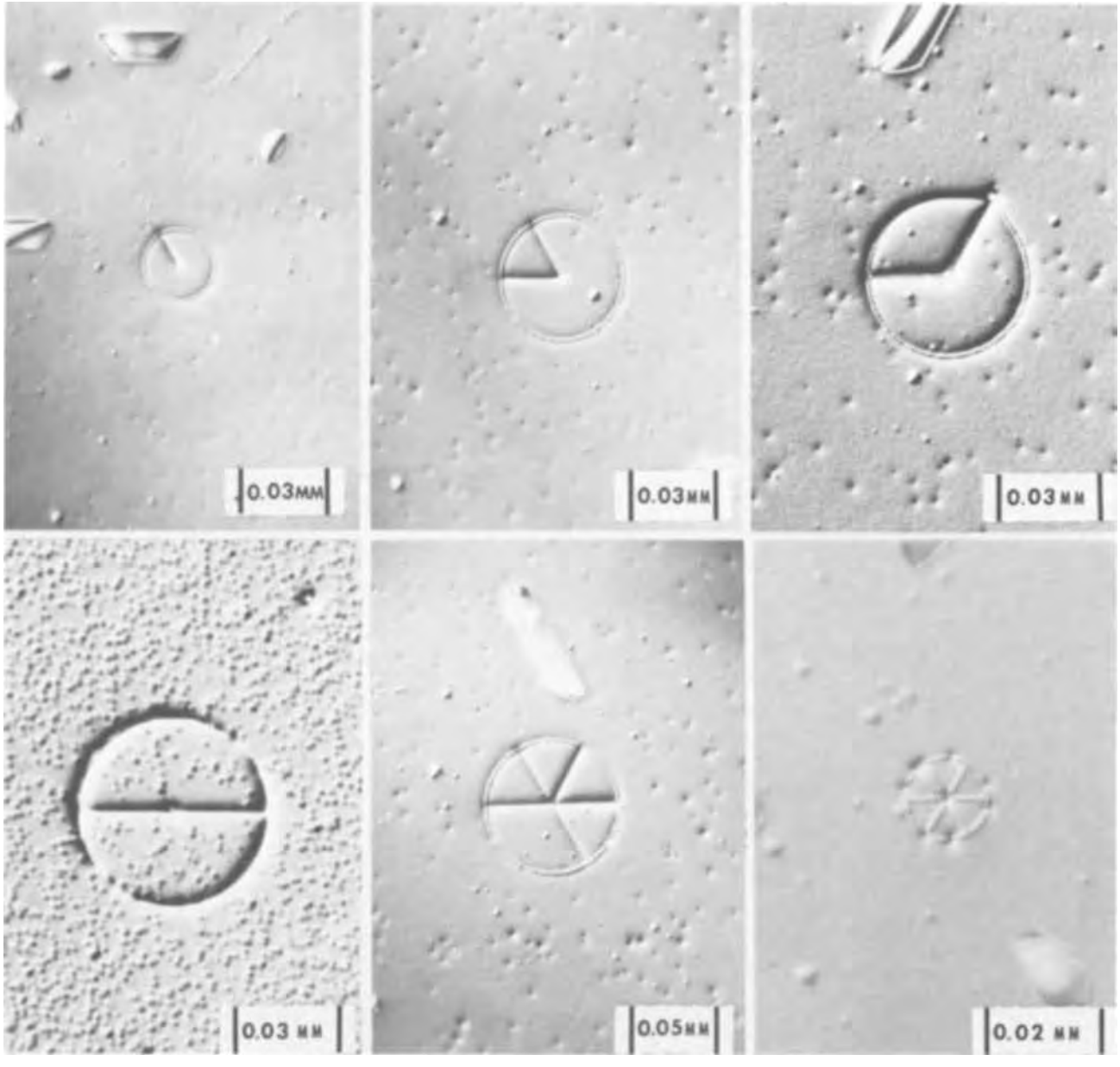

Fig. 2. Circular defects with 1, 2, 5, and 6 radial lines (spokes). Interference contrast

on the same side. No etch pits appear where the partial rings terminate.

The rings and the spokes etch differently. Figure 7 shows a polarization interferogram of a fault having a diametral line. The line is a ridge 0.3 μm high, while the ring is a shallow groove with raised edges.

No dislocation etch pits from plastic deformation were observed in the slices.

The faults were observed in both n- and p-type slices having resistivities of 10-200 ohm-cm. There was a general tendency for the defects to be larger in the case of slower cooling rates and in the lower portion of the boule. Also, there was a radial variation of defect size within the slices. These aspects will be discussed in a later paper.

Discussion and Interpretation of Results

The Sirtl etch technique is known to reveal circular stacking faults in the same manner as seen here, *i.e.*, a stacking fault leaves a deeply etched groove when it intersects the (111) plane of the slice surface, and the surrounding partial dislocation etches as a shallow groove when the stacking fault is parallel to the (111) surface of the slice (3, 4). Patrick (5) has shown that when the circles and the grooves appear in the same region of the slice, the grooves are (111) intersections of loops, identical with the circular ones. Thus it is supposed that we are dealing with four sets of circular stacking faults, three on inclined {111} planes and the fourth in the (111) plane that is 1½°-2½° off the slice surface. The latter set would give rings open on one side should the slicing operation happen to cut through any circular faults. It appears that the spokes are some type of dislocation, since they are revealed as etch pits in cases where they intersect the (111) surface at a large angle. (See Fig. 4, lower right). The possibility that the spokes are precipitates emanating from a nucleation center is eliminated by the existence of forms such as Fig. 4c.

First it will be shown that the spokes lying inside the circular faults are dislocation dipoles by virtue of having a zero net Burgers vector. Various possible sources of formation of the fault are eliminated by this finding. Next, a probable mechanism of ring and spoke formation will be presented. Finally, it will be shown that all of the partial dislocations in the rings and spokes have the 1/3 <111> Burgers vector normal to the plane of the ring, so that each sector of a ring-spoke combination consists of a Frank sessile loop (16).

Net Burgers vector of spokes.—The spokes will be shown to have a net Burgers vector of zero by refer-

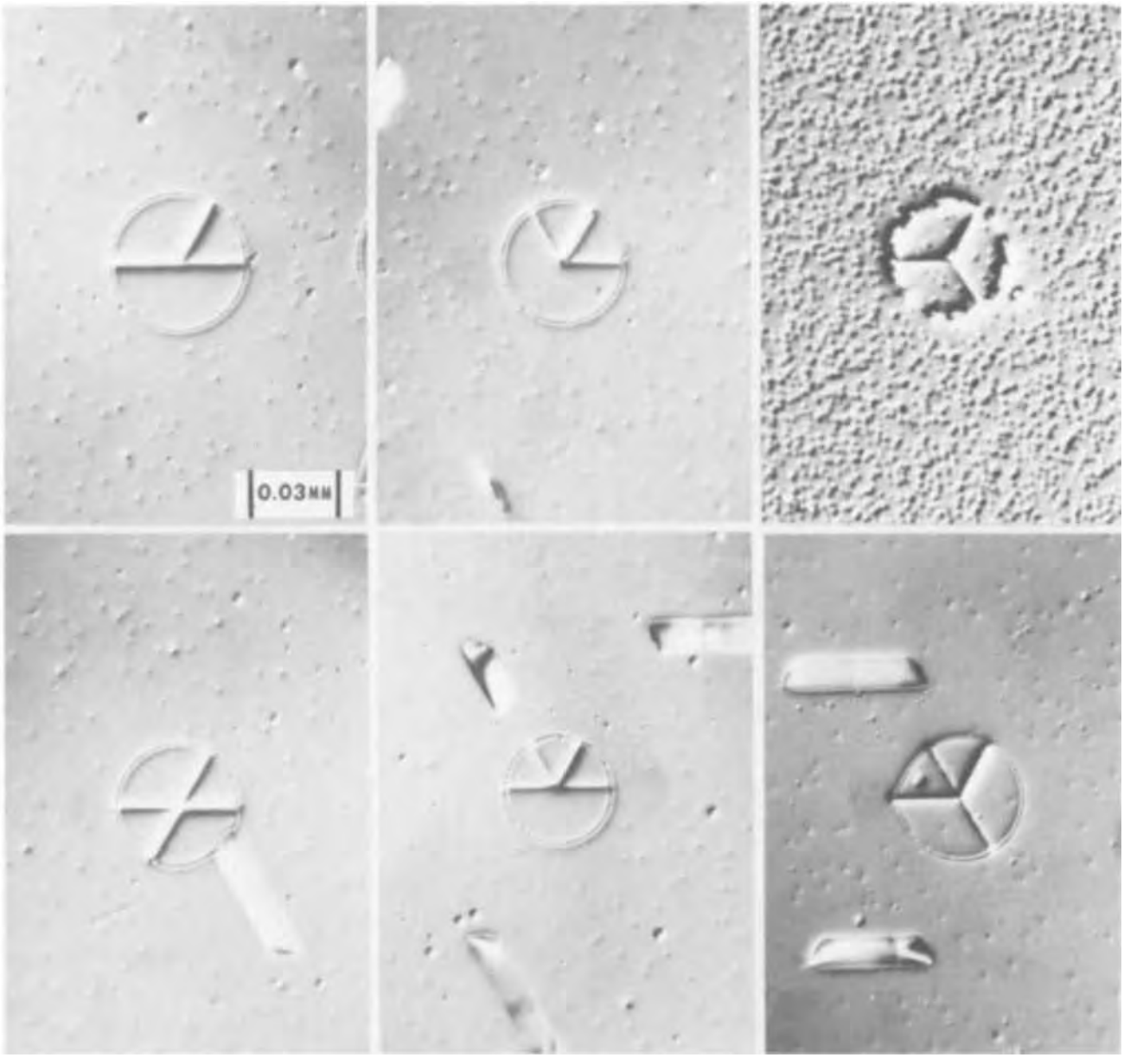

Fig. 3. Circular defects with 3 and 4 spokes. Interference contrast

ence to Fig. 8. The rule that the Burgers vector is invariant against displacements of the circuit through good crystal regions (17) will be used. The Burgers circuits are indicated on the figure by •−−−−−+ (• in, + out). By this is meant a polygonal circuit around the dislocations, such as given by Hornstra (18), which circuit is to be compared with an associated path in the ideal reference crystal for determining the resultant Burgers vector of all the dislocations within the circuit. On the figure, the dislocations are labeled by numbers where necessary: 11′, 22′, etc.; writing the two numbers on either side of the dislocation secures the proper reversal of sign as the dislocation is looked at from one end or the other. With this notation, the addition and subtraction of Burgers vectors may be handled in the same way as with the Thompson notation (19). In the following analysis note that no specific Burgers vector needs to be determined by the fundamental lattice comparison procedure, and that, since the circuits are always taken in good crystalline regions, the construction of Burgers circuits is not complicated by the presence of the stacking fault.

The two circuits taken in Fig. 8a show that any dislocation ring has a zero net Burgers vector, in other words, the two opposite sides of the ring have equal and opposite Burgers vectors when viewed from the same end (19).

In Fig. 8b, the circuits taken show that the net Burgers vector of the single spoke is also zero. In Fig. 8c, we cannot thus far assume that arc 4 has the same Burgers vector as arc 1, so they are separately labeled. First, taking the two Burgers circuits lying horizontal in the figure

$$11' + 22' + 33' + 1'1 = 0 \quad [1]$$

Then taking the other two circuits

$$11' + 22' + 44' = 0 \quad [2]$$

and

$$11' + 3'3 + 44' = 0 \quad [3]$$

Therefore

$$22' + 3'3 = 0 \quad [4]$$

Combining [1] and [4]

$$22' = 0 \quad [5]$$

Substituting in [4]

$$3'3 = 0 \quad [6]$$

Replacing [5] and [6] in [2] and [3]

$$11' = 4'4$$

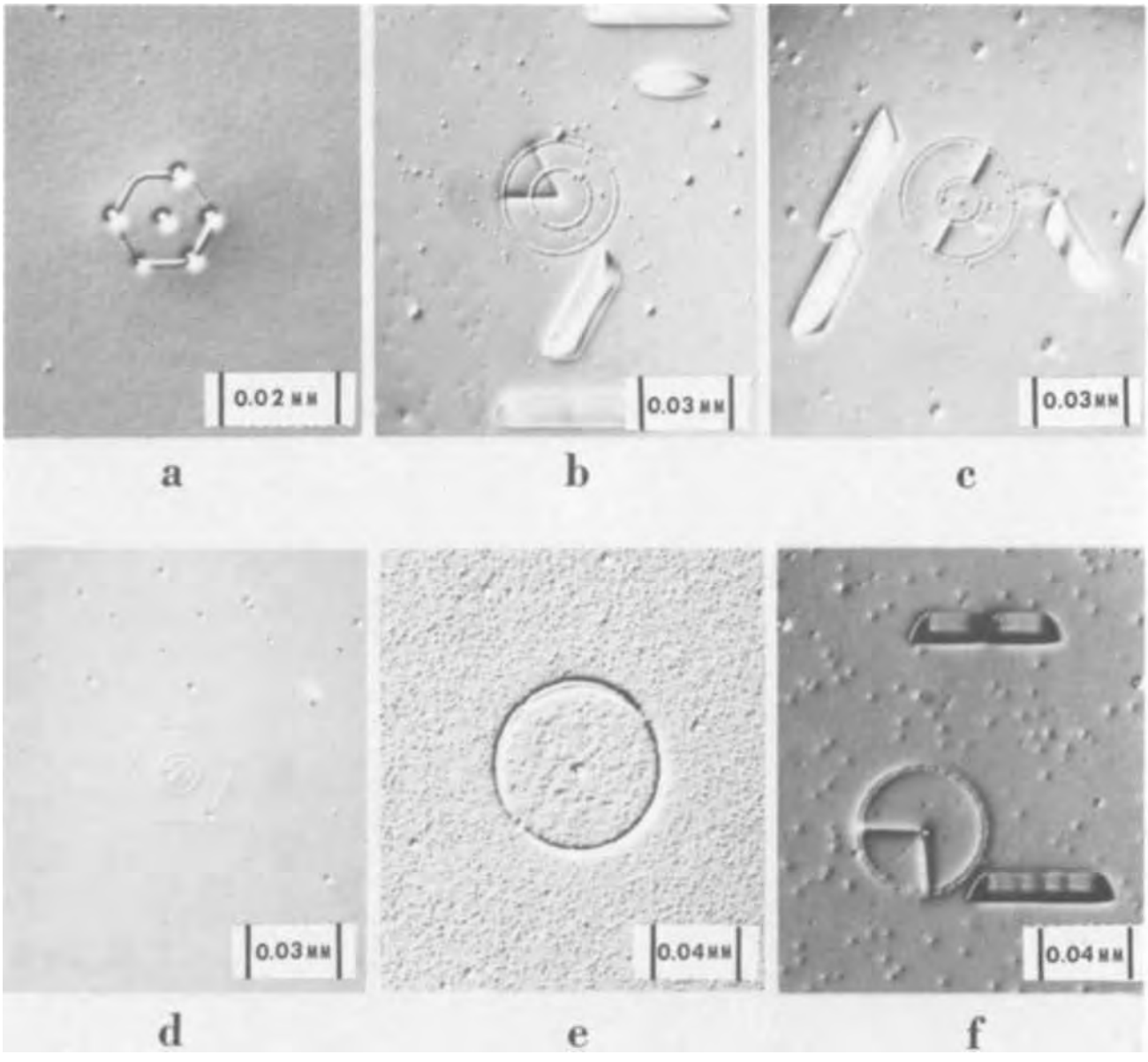

Fig. 4. Ring defects of various types: a, hexagonal; b, concentric rings with spokes in both rings; c, concentric rings with spokes between rings; d, concentric rings with spokes in inner ring; e, ring with a central dot, f, ring with non-<110> spoke. Interference contrast.

i.e., the entire ring has the same Burgers vector. By the same process as for Fig. 8a, the spokes have zero net Burgers vector and are therefore dislocation dipoles.

Although it cannot be shown, it is reasonable to expect that the forms with more spokes are similarly constituted of dislocation dipoles as spokes and a ring having one Burgers vector.

The termination of a diametral line within the circular stacking fault (Fig. 5) can now be understood as the pinching off of a dislocation dipole at both ends and the attendant formation of short lengths of dislocation at either end of the dipole. These short lengths are sufficiently vertical to the plane of the slice to leave standard dislocation etch pits.

The circular stacking fault that contains only one spoke (Fig. 2) deserves some attention. The one spoke should exhibit a dislocation etch pit at the center of the fault unless the dipole terminates at a precipitate at this point. Justification will be presented in the following section for such a precipitate.

Sources of ring and spoke formation.—In the previous section it was shown that the spokes within the rings were dislocation dipoles and that all arcs of each ring had the same Burgers vector. The various possible sources of the ring-spoke combinations. *i.e.*, line sources dislocation loops, and precipitates, will now be discussed.

Two types of line sources will be considered: single lines and multiple lines. Bardeen-Herring line sources have been suggested as the cause of the circular stacking faults (3, 4). Also, the line source in the Silcock and Tunstall mechanism (8, 9, 20) is attractive for explaining the formation of the faults, since a stacking fault is produced in back of a partial dislocation and this partial has what will later be shown to be the correct Burgers vector. For one of these sources to generate the ring-and-spoke combinations of Fig. 1-6, it would have to encounter multiple obstacles that were located close to the source and were arranged around the source, then encounter no other such obstacles during the growth of the fault to full size. The obstacles would have to be capable of diverting the various sectors of fault to separate levels in the crystal. In addition, some evidence for the pinning of the source by dislocations or precipitates should be seen, such as etch pits at both ends of the source. These considerations show that it is very improbable that the circular faults originate at single line sources.

Multiple line sources could conceivably generate the observed combinations. However, since the overwhelming majority of dipoles radiate from a center,

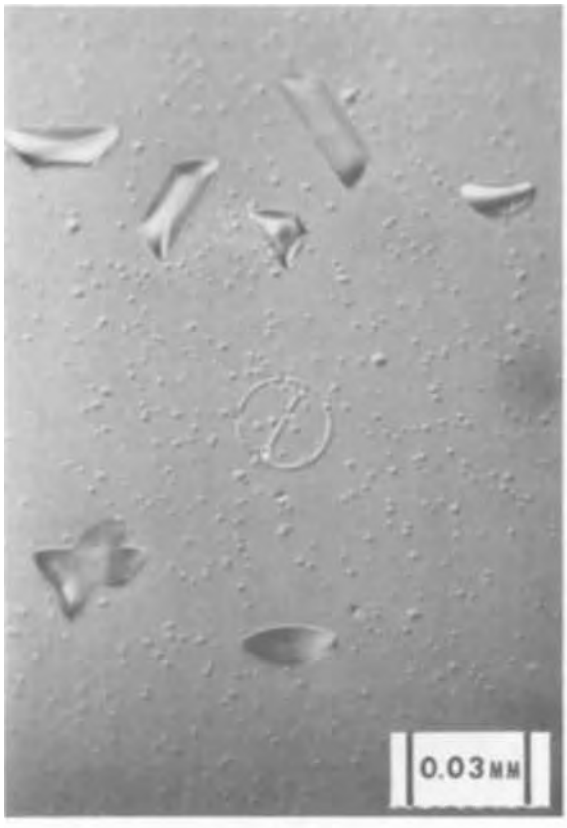

Fig. 5. Ring with diametral line terminating in etch pits. Interference contrast.

Fig. 7. Ring with diametral line. Polarization interference

Fig. 6. Rings with one side open. Interference contrast

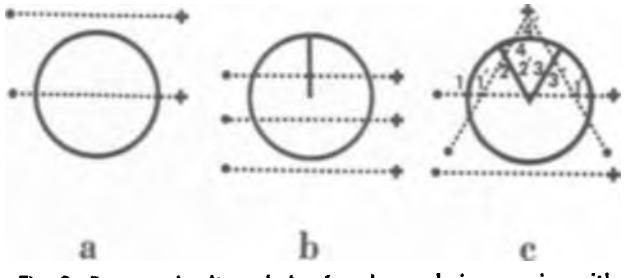

Fig. 8. Burgers circuit analysis of spokes and ring: a, ring with no spokes; b, one spoke; c, two spokes.

these sources would again have to be close to that center and be arranged about it. They would also have to have the same Burgers vector. Such a situation is not likely since we are assuming the line sources to be independent.

Single dislocation loops would also have to form the spokes by passing through an unlikely arrangement of obstacles. Such loops are not considered the probable sources, therefore, whether they are faulted or unfaulted. With the elimination of line sources and single dislocation loops as possible sources, precipitates seem to be the only plausible remaining cause.

Iizuka and Kikuchi (3, 4) suggested that the faulted loops are Frank sessile loops that are nucleated from oxygen precipitates and that they grow by a mechanism similar to that controlling the climb of straight dislocations. In the following section a mechanism is presented by which each circular fault containing dipoles is formed from several Frank sessile loops that are nucleated on a precipitate.

Mechanism of ring and spoke formation.—The fact that the spokes are dipoles implies that they were formed by dislocations arriving on parallel but separate planes. The fact that the fault consists of sectors bounded by circular arcs of partial dislocations suggests that each sector originated from a faulted dislocation loop or half-loop on a center of nucleation such as a precipitate. Spherical precipitates could form circular faults on four intersecting {111} planes. Since most of the present faults occur singly, the precipitate

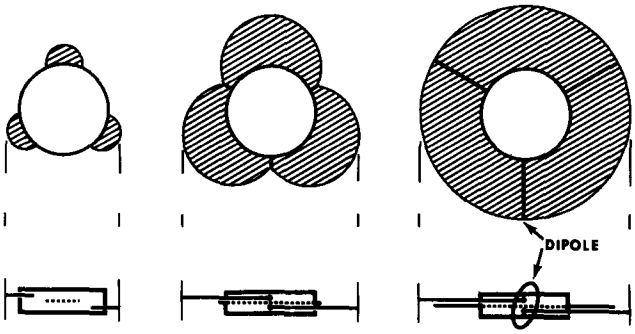

Fig. 9. Mechanism of ring and spoke formation in the case of ring with three spokes: a, faulted loops arise on three separate levels around a precipitate of tabular habit; b, loops expand by climb and form dipoles where they meet; c, continued growth of faulted loops results in ring with spokes (dipoles).

is probably of tabular habit. Figure 9 shows the mechanism by which the faulted loops can arise around a precipitate of tabular habit and result in one of the observed ring-spoke combinations. As the half-loops expand they are attracted to one another at their edges, but only annihilate readily if they were created on the same plane. Thus, in many cases dipoles are formed and take the $<1\bar{1}0>$ directions for minimum energy. The fact that non-$<1\bar{1}0>$ spokes sometimes appear may mean that other energy minima occur besides $<1\bar{1}0>$ around the [111] zone.

The observation that the rings and spokes etch differently can now be understood, because the rings consist of single partial dislocations whereas the spokes consist of a pair of oppositely oriented partial dislocations.

Burgers vector of ring.—Let us consider the possible Burgers vectors of all the loops making up ring-spoke combinations having two or more regions (such as those in Fig. 3 and 4). We will assume that each region separated from others by spokes is formed from an independent faulted dislocation loop. If nonvertical Burgers vectors are possible, then the rotational symmetry of the crystal face requires that at least three such vectors are possible for each loop. But some spokes could then exist in which the net Burgers vector was finite, which was shown to be false. The only vector that would not violate the rotational symmetry condition is vertical to the ring, *i.e.*, $<111>$. The actual Burgers vector is very probably 1/3 $<111>$; in other words, each loop is a Frank sessile loop.

The formation of the Frank sessile dislocations around the precipitate can now be visualized as the insertion of either an extra layer of silicon atoms or of the collapse of a layer of vacancies at each place of nucleation around the precipitate, and the subsequent expansion of each Frank partial dislocation by climb. One might ask why the dipoles do not readily annihilate by climb which would involve much smaller distances than the climb taking place in expansion of the fault. Such annihilation would require bending of the fault which has a very strong kinematic restraint (17). This probably occurs only when the two faults are created on planes that are very close to one another, possibly one or two atom diameters apart.

The foregoing explanation may also account for the formation of stacking faults in steam-oxidized silicon, especially when there is no surface damage to generate Frank sessile loops (10). In this case the faults have been found to be extrinsic, which implies that the growth of the fault occurs by evolution, rather than accumulation, of vacancies.

If the precipitate is large enough, more than six Frank sessile dislocations could presumably form simultaneously on separate planes. These would grow and yield more than six spokes. The most that have been observed thus far have been six. This result may be due to the decreased probability of forming more Frank loops, or it may mean that there is some other constraint on the formation of the loops, such as having a preferred azimuth (such as $<110>$) at which loop generation can take place.

Conclusions

Circular and hexagonal stacking faults formed during the annealing treatment of melt-grown silicon crystals were found to contain radial line defects. The circular faults are formed by the nucleation of one or more Frank sessile dislocations around a precipitate of tabular habit, followed by the growth of the sessile half-loops by climb and the formation of radial lines (dislocation dipoles) where the loops meet on parallel but separate planes.

The mechanism may also be applicable to stacking faults formed in damage-free steam-oxidized silicon.

Manuscript submitted July 21, 1972; revised manuscript received Feb. 12, 1973.

Any discussion of this paper will appear in a Discussion Section to be published in the December 1973 JOURNAL.

REFERENCES

1. W. C. Dash, *J. Appl. Phys.*, **31**, 2275 (1960).
2. V. A. Phillips and W. C. Dash, *ibid.*, **33**, 568 (1962).
3. T. Iizuka and M. Kikuchi, "Lattice Defects in Semiconductors," International Symposium, Sept. 5-6, 1966, Tokyo, R. R. Hasiguti, Editor, University of Tokyo Press, Tokyo, and Pennsylvania State University Press, University Park, and London (1968).
4. T. Iizuka, *Jap. J. Appl. Phys.*, **5**, No. 11, 1018 (1966).
5. W. J. Patrick, "Silicon Device Processing," Symposium, June 2-3, 1970, Charles Marsden, Editor, NBS Special Publication 337, Lib. Cong. No. 74-608543.
6. D. J. D. Thomas, *Phys. Status Solidi*, **3**, 2261 (1963).
7. H. J. Queisser and P. G. G. van Loon, *J. Appl. Phys.*, **35**, 3066 (1964).
8. G. R. Booker and R. Stickler, *Phil. Mag.*, **11**, 1303 (1965).
9. G. R. Booker and W. J. Tunstall, *ibid.*, **13**, 71 (1966).
10. M. L. Joshi, *Acta Met.*, **14**, 1157 (1966).
11. A. W. Fisher and J. A. Amick, *This Journal*, **113**, 1054 (1966).
12. A. Mayer, *RCA Rev.*, p. 414, (June 1970).
13. S. Dash and M. L. Joshi, *IBM J. Res. Dev.*, p. 453, (July 1970).
14. G. K. Teal, and G. B. Little, *Phys. Rev.*, **78**, 647 (A) (1950).
15. E. Sirtl and A. Adler, *Z. Metallk.*, **52**, 529 (1961).
16. F. C. Frank, *Proc. Phys. Soc., A*, **62**, 202 (1949).
17. F. C. Frank, *Phil. Mag., Ser. 7*, **42**, 809 (1951).
18. J. Hornstra, *J. Phys. Chem. Solids*, **5**, 129 (1958).
19. N. Thompson, *Proc. Phys. Soc., B*, **66**, 481 (1953).
20. J. M. Silcock and W. J. Tunstall, *Phil. Mag.*, **10**, 361 (1964).

Stability and Stirring in Crystal Growth from High-Temperature Solutions

Hans J. Scheel

IBM Zurich Research Laboratory, 8803 Rüschlikon, Switzerland

and D. Elwell

Physics Department, Portsmouth Polytechnic, Portsmouth, United Kingdom

ABSTRACT

Crystals normally grow in solution in a destabilizing supersaturation gradient. The observation of inclusion-free growth to large crystal sizes may be described in terms of a metastable region of the supersaturation gradient which is associated with the mechanism of growth on the habit faces. Stirring has a beneficial effect on growth stability especially by reducing or removing the supersaturation inhomogeneity across the face of a polyhedral crystal. The effect of convection and of various stirring techniques is briefly described.

The widespread use of high-temperature solution techniques for the growth of bulk crystals (as distinct from crystalline films) has been retarded by a tendency towards the formation of small crystals by multinucleation and by the frequent occurrence within the crystals of solvent inclusions. The former problem may in general be overcome by the use of seeding, by cyclic temperature variations, or by careful control of the temperature distribution within the crucible, and many examples are now known of crystals weighing 50g or more.

On the other hand, the conditions under which stable growth may occur up to large crystal sizes in solution have not been clearly established, and quantitative criteria of growth stability which may be readily used by experimentalists are still lacking. "Stable growth" in the context of growth from solution may be taken to imply inclusion-free growth, since solvent inclusions will result from various forms of growth irregularities.

Formal theoretical treatments of growth stability normally treat the problem of morphological stability, or whether a specified shape is stable against infinitesimal perturbations. This problem differs from the related question of whether a given shape or habit is preserved as the crystal grows.

Morphological stability treatments are restricted to simple crystal shapes. Mullins and Sekerka (1) examined the stability of a spherical crystal with isotropic surface kinetics growing in a supersaturated medium. They concluded that the sphere is stable only if its radius is below a critical value, in the region of 0.1 μm. This value may be increased to about 10 μm by the inclusion of surface diffusion (2), but even the latter value is much below the size of inclusion-free crystals which can be grown from solution.

In the case of a plane surface of unlimited extent growing in a doped melt, there is general agreement between the perturbation treatment (3) and the constitutional supercooling criterion (4, 5) which was introduced independently by Ivantsov (6) as "diffusional undercooling." According to this criterion, instability results if the growth rate exceeds some critical value which depends on the temperature gradient at the crystal-liquid interface.

In this paper the concepts of a critical size and critical growth rate will be examined in detail with reference to the theory of solution growth and, where possible, to experiments on high-temperature and aqueous solutions. The importance must be recognized in any treatment of crystal growth from solution of the strong tendency of the crystals to form facets. A realistic theory must therefore treat the growth of finite polyhedra, and the stabilizing effect of the interface kinetic processes on the habit faces must be taken into account.

The importance of stirring for the enhancement of growth stability will be demonstrated, and the effectiveness of stirring by natural and forced convection will be discussed.

Key words: crystal growth, hydrodynamics, growth mechanism, growth stability, crystal/solution interface.

Stages in Growth from Solution

The factors which are of crucial importance in determining whether or not growth will be stable under chosen experimental conditions is likely to depend on which stage in the growth process is rate-determining. The process of crystal growth from solution may be treated as a sequence of stages as discussed, for example, in the review of Parker (7) or by Laudise (8), and as illustrated in simple form in Fig. 1. The removal of solute from the solution by the growing crystal creates a flow of solute towards the crystal surface. This flow is mainly by diffusion which can be imagined to take place through an "unstirred" boundary layer

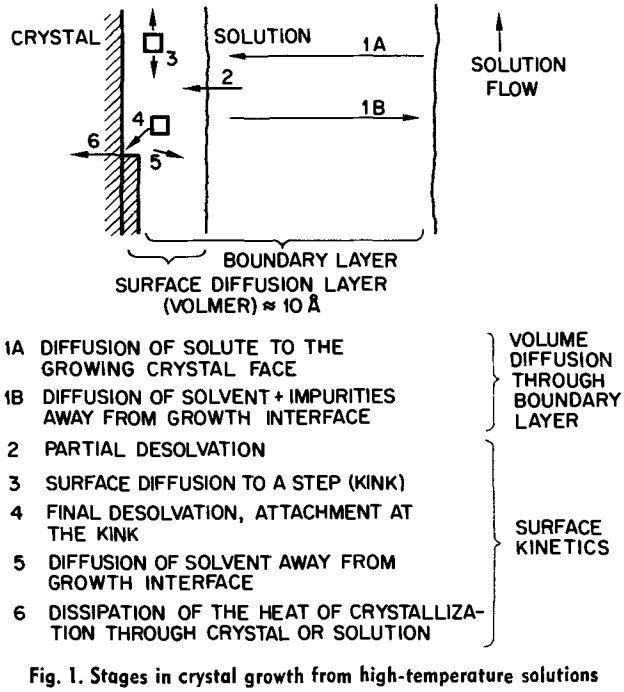

Fig. 1. Stages in crystal growth from high-temperature solutions

(9) of thickness δ (stage 1A)[1] and there will be a corresponding counterdiffusion of solvent and of impurities away from the crystal-liquid interface (stage 1B). At the surface, partial desolvation (stage 2) and surface diffusion of solute (step 3) will occur in the adsorption or Volmer layer which will be a few molecular diameters in thickness. The integration of solute into the crystal (stage 4) will occur at a kink site, with further desolvation. On a habit face, growth takes place by the spreading of steps over the crystal surface and kinks will be present at the edges of these steps. The heat of crystallization is dissipated (stage 6) through the solution or through the crystal if the latter is cooled. Stages 2-6 may be regarded as the surface kinetic mechanism which has been treated in the classical paper of Burton, Cabrera, and Frank (10); by Bennema (11); Gilmer, Ghez, and Cabrera (12); in the Parker review (7) and; with special reference to high-temperature solutions, by Elwell and Neate (13).

Apart from a choice of solvent and temperature, the experimenter normally attempts to influence the growth conditions by varying the supersaturation (either directly or indirectly by changing the cooling rate or rate of solvent evaporation) or by varying the boundary layer thickness δ by changing the rate of relative motion between crystal and solution. If the solution flows at a rate u past a stationary crystal face of length l, the value of δ has been estimated by Carlson (14) and by Bennema (11) as

$$\delta = \left[0.463 \left(\frac{\eta}{\rho_s D} \right)^{1/3} \left(\frac{\rho_s u}{\eta l} \right)^{1/2} \right]^{-1} \qquad [1]$$

where η is the viscosity and ρ_s the density of the solution and D the diffusion coefficient of the solute. Carlson prefers a model with nonuniform solute concentration along the crystal surface, whereas Bennema assumes a uniform concentration, in which case the factor 0.463 should be replaced by 2/3.

If diffusion through the boundary layer is rate-limiting, stirring will tend to increase the growth rate as originally postulated by Nernst (15). The linear growth rate is given by

$$v = \frac{n_e K \sigma}{\rho_c} \qquad [2]$$

where ρ_c is the density of the crystal, n_e the equilibrium concentration of solute, and σ the relative supersaturation $(n_s - n_e)/n_e$, with n_s the concentration in the bulk solution. K is an activity coefficient which, for volume-diffusion limited growth, is D/δ. Therefore the growth rate in this case is

$$v = \frac{n_e D \sigma}{\rho_c \delta} \qquad [3]$$

At low supersaturation (and for strong agitation) K is determined by surface kinetics and is a function of the supersaturation.

When both volume diffusion and surface kinetics influence the growth rate, the value of v may be approximated by the relation

$$\frac{v \delta \rho_c}{D n_e} + \left(\frac{v}{A} \right)^{1/m} = \sigma \qquad [4]$$

which is similar to that derived by Brice (16). Equation [4] reduces to Eq. [3] in the limit where $A \to \infty$, while $v = A\sigma^m$ is the kinetic-controlled limit as $\delta/D \to 0$. The variation of the linear growth rate with δ for various values of supersaturation is illustrated in Fig. 2. In a normal crystal-growth experiment, the rate at which solute is deposited from the solution will be determined only by the volume of solution, by the solubility curve, and by the rate at which the solution is cooled. For a given surface area of crystal on which growth is occurring the supersaturation will adjust itself (for a given value of δ) until the linear growth rate has the value indicated by Fig. 2. As shown on the diagram, too high a value of the supersaturation will lead to nucleation of more crystals. Stirring thus has the beneficial effect of permitting growth at lower supersaturation through a reduction in the value of δ, according to Eq. [1]. The limitation of the growth rate by surface kinetics at high stirring rates (small δ) is indicated approximately on the diagram for $\sigma = 0.005$ and $\sigma = 0.01$.

At high supersaturation and high stirring rate a maximum stable growth rate is reached which is independent of σ, n, or δ. This ultimate rate of stable growth will be determined by the surface kinetics (possibly by desolvation or the density of kink sites) or by the heat flow, especially at high values of the solute concentration. In the limiting case of growth from a pure melt, the maximum growth rate is given (17) by

$$v_{max} = \frac{K_s}{\Delta H_v} \frac{dT_s}{dx} \qquad [5]$$

where ΔH_v is the latent heat per unit volume, K_s the thermal conductivity of the solid, and dT_s/dx the temperature gradient in the solid. In the more typical case of the growth of oxides from molten salts at solute concentrations of 10-30%, the maximum stable growth rate appears from experiment to be in the region of 200-500Å sec^{-1} (18). The origin of an ultimate stable growth rate is not clearly established and techniques which would permit stable growth from solution at faster rates than those indicated above would be highly beneficial. In the subsequent discussion we shall as-

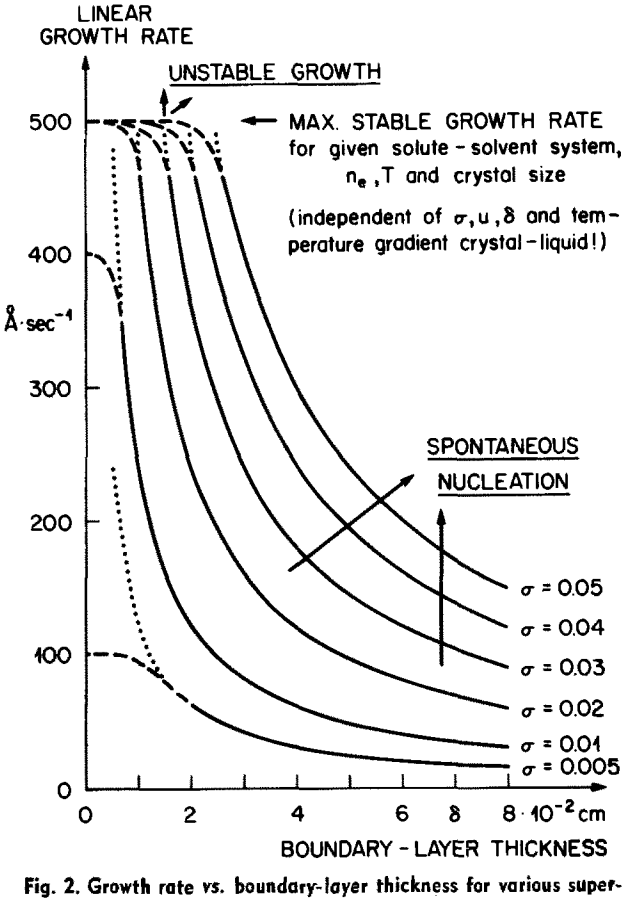

Fig. 2. Growth rate vs. boundary-layer thickness for various supersaturations.

[1] In this paper δ refers to the solute diffusion boundary layer which in solution growth is normally of the same order of magnitude as the hydrodynamic boundary layer.

sume that growth occurs at some value below this limit and that the rate of removal of the heat of crystallization has a negligible effect on the growth rate. The latter assumption appears to be justified under normal conditions of solution growth (13).

Supersaturation Gradient Criterion

In growth from the pure melt, the stability criterion which has been of greatest value is that of constitutional supercooling. A similar condition may be expected to apply to solution growth, since the rejection of solvent by the growing crystal is closely analogous to the rejection of impurities in melt growth. However the term "constitutional supercooling" is not wholly appropriate for growth from solution, and it is desirable to re-examine the stability condition specifically for the case of solution growth.

The occurrence of volume diffusion in some boundary layer is inevitably associated with a gradient of solute at the crystal-solution interface. If a protuberance develops by random fluctuation on an otherwise flat interface, this protuberance will encounter a higher solute concentration than that of the flat region and will therefore tend to grow with respect to this region. This tendency towards instability of the interface may be eliminated by the application of a sufficiently large temperature gradient, the important factor being whether or not there exists a gradient in the supersaturation normal to the crystal surface. For stable growth of an interface at $x = 0$, we therefore require that

$$\left(\frac{d\sigma}{dx}\right)_{x=0} < 0 \qquad [6]$$

or, as is equivalent for small supersaturations

$$\left(\frac{dn}{dx}\right)_{x=0} < \left(\frac{dn_e}{dx}\right)_{x=0} \qquad [7]$$

where dn/dx is the solute gradient normal to the interface and n_e the equilibrium concentration of solute as before.

If the capture of solute by the moving crystal surface is neglected as a first approximation, the solute gradient is related to the linear growth rate by

$$v = \frac{D}{\rho_c}\left(\frac{dn}{dx}\right)_{x=0} \qquad [8]$$

For an ideal solution $n_e = n_\infty \exp(-\Delta H/RT)$, with n_∞ a constant, so that

$$\frac{dn_e}{dx} = \frac{\Delta H\, n_e}{RT^2}\frac{dT}{dx} \qquad [9]$$

and substitution from Eq. [8] and [9] into [7] gives the condition for stability as

$$v < \frac{Dn_e\,\Delta H}{\rho_c RT^2}\left(\frac{dT}{dx}\right)_{x=0} \qquad [10]$$

This condition is in substantial agreement with that obtained by Tiller (19) by a modification of the constitutional supercooling criterion.

Using typical experimental values of $D = 10^{-5}$ cm^2 sec^{-1}, $n_e = 1$g cm^{-3}, $\Delta H = 50$ kJ mole^{-1}, $\rho_c = 5$g cm^{-3}, and $T = 1500$°K, the maximum stable growth rate according to Eq. [10] will be about 0.5Å sec^{-1} for $(dT/dx)_{x=0} = 1$ deg cm^{-1} and a gradient of 1000 deg cm^{-1} will be required for the stable growth of crystals at 500Å sec^{-1}, which has been mentioned above as typical of the highest growth rates to be achieved experimentally. Equation [10] is therefore in clear conflict with experiment, since growth at 100-200Å sec^{-1} has been widely reported to occur in crucibles located in an enclosure at uniform temperature or even in a negative temperature gradient, with the heat of crystallization ΔH being removed by conduction through the melt.

In order to account for this discrepancy it must be assumed that the supersaturation gradient is insufficient for the growth of a protuberance relative to the rest of the surface. Therefore the crystals grow in a metastable region of the supersaturation gradient in which the protuberance grows at a negligibly slow rate with respect to the crystal surface. This region may be considered analogous to the well-known metastable (Ostwald-Miers) region in which a melt or solution is cooled below its equilibrium liquidus temperature without onset of nucleation.

The metastable region of the supersaturation gradient is illustrated in Fig. 3, in which the temperature distribution is particularly considered since this may be conveniently varied. Figure 3(a) shows the variation in the solute concentration ahead of the crystal surface together with the equilibrium value at the crystal-solution interface. The solute concentration at the interface is close to the equilibrium value, a condition which will be fulfilled if volume diffusion is the rate-limiting stage. The validity of the latter assumption for the examples of $NiFe_2O_4$ and $NaNbO_3$ in unstirred borate solutions is supported by experiment (20, 21).

Figure 3(b) shows the liquidus temperature T_L corresponding to the actual solute concentration n_s and the actual temperature distribution T_{eff} in the solution. Stable growth according to Eq. [10] requires that the temperature gradient at the interface should exceed that of the line denoted T_0 which is tangential to the curve of T_L at $x = 0$. T_{crit} represents the assumed

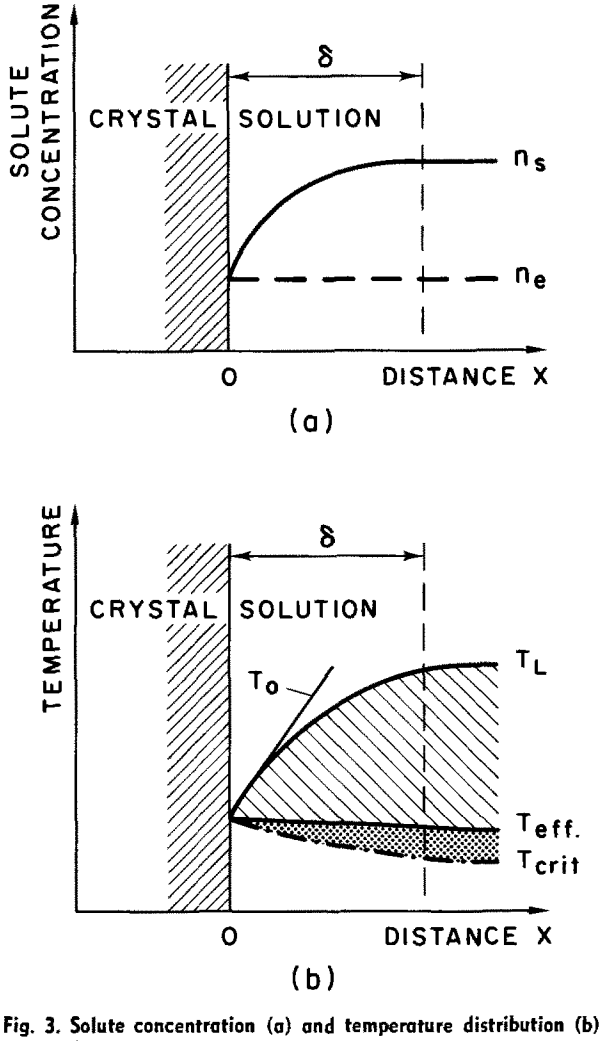

Fig. 3. Solute concentration (a) and temperature distribution (b) in front of a crystal growing from unstirred solution.

metastable limit so that the shaded area denotes the metastable region. Growth will occur without solvent inclusions so long as the gradient of T_{eff} at the interface is higher than that of T_{crit}, as is assumed in the example shown. The value of this critical gradient of temperature (or supersaturation) may be expected to depend on the crystal growth rate, the solute concentration, the interface temperature, the type of solvent and on impurities. Of particular importance is complex formation in front of the growing crystals which may have either a positive or negative effect on the critical supersaturation gradient. Also by analogy with the Ostwald-Miers region, the probability that an instability will develop should be increased if the growing crystal is subjected to any thermal or mechanical shock or vibration. Experience has shown that the size of inclusion-free crystals which can be grown increases if vibrations are minimized and the furnaces are located in separate enclosures in order to reduce any disturbances.

The increased stabilization which permits the stable growth of crystals in solution in a supersaturation gradient must result from the growth mechanism on the faceted habit planes. That interface kinetics can stabilize growth has been demonstrated by Coriell and Parker (22) and by Tarshis and Tiller (23). The particular case of growth on large facets has been considered qualitatively by O'Hara *et al.* (24), who postulate two main sources of stabilization. The first is the lower driving force for lateral growth of surface layers compared with normal growth and this will oppose the effect of any perturbation which tends to create more layers. The second is the capillarity term which is a consequence of the low energy associated with the habit planes, the orientation of which normally corresponds to a cusp in a Wulff (surface energy *vs.* orientation) plot. These effects could in principle be included by the introduction of appropriate anisotropic terms in the morphological stability treatment, but quantitative calculations would be very difficult and have not yet been reported.

Effect of Stirring on the Supersaturation Gradient

According to the simple model of the solution growth process outlined above, the effect of stirring is to reduce the width of the boundary layer and thus to cause a transition from diffusion-controlled to kinetic-controlled growth. The first effect tends to increase the supersaturation gradient, while the second decreases it so the net effect depends on the interface kinetics.

The flow of solute towards the crystal surface is given (25) in the steady state by

$$\frac{Dd^2n}{dx^2} + v\frac{\rho_c}{\rho_s}\frac{dn}{dx} = 0 \qquad [11]$$

the solution of which equation gives for the solute distribution

$$n - n_i = (n_s - n_i)\frac{[1 - \exp(-xv\rho_c/\rho_s D)]}{[1 - \exp(-\delta v\rho_c/\rho_s D)]} \qquad [12]$$

Here n_i is the solute concentration at the interface and the thickness δ of the boundary layer has been defined by the boundary condition that $n = n_s$ when $x = \delta$. The second term in Eq. [11] represents the capture of solute by the moving crystal surface, which has been neglected in our earlier approximations.

Equation [12] gives the solute concentration gradient at $x = 0$ as

$$\left(\frac{dn}{dx}\right)_{x=0} = \frac{(n_s - n_i)v\rho_c}{[1 - \exp(-\delta v\rho_c/\rho_s D)]\rho_s D} \simeq \frac{n_s - n_i}{\delta} \qquad [13]$$

The approximation is expected to be generally good since $v/D \sim 10^{-1}$ cm^{-1} and $\delta \sim 10^{-1} - 10^{-3}$ cm depending upon the solution flow rate.

The value of the solute gradient for a given n_s and solution flow rate u (and hence δ) will thus be determined by the value of n_i, and hence on the kinetic coefficient A of Eq. [4]. The solute distribution ahead of the crystal in a stirred solution is shown in Fig. 4(a), and the corresponding temperature distribution is indicated in Fig. 4(b). It has been assumed in this diagram that the solvent gradient is reduced by the stirring so that stability is enhanced. Figure 4 differs from a similar diagram of Tiller (19) whose interpretation of a sharp increase of the supersaturation gradient with increasing flow rate may hold only for a sudden increase of agitation. If a stabilizing temperature gradient is applied, this will tend to steepen due to mixing within the solution on stirring and some additional stabilization may be expected on this account (21).

Morphological stability treatments by Hurle (26) and Delves (27) confirm that stirring can provide some degree of stabilization of a plane interface. Experimental confirmation of the stabilizing effect of stirring is provided by observations of the surface of crystals grown from a melt in which the stirring is suddenly interrupted. Stability theory predicts (3, 27) a self-excited oscillatory motion of the interface near the breakdown of stability. In Fig. 5 a set of fine inclusions may be seen at the surface of a large $GdAlO_3$ crystal grown from a high-temperature solution in which stirring was stopped prior to removal of the excess solu-

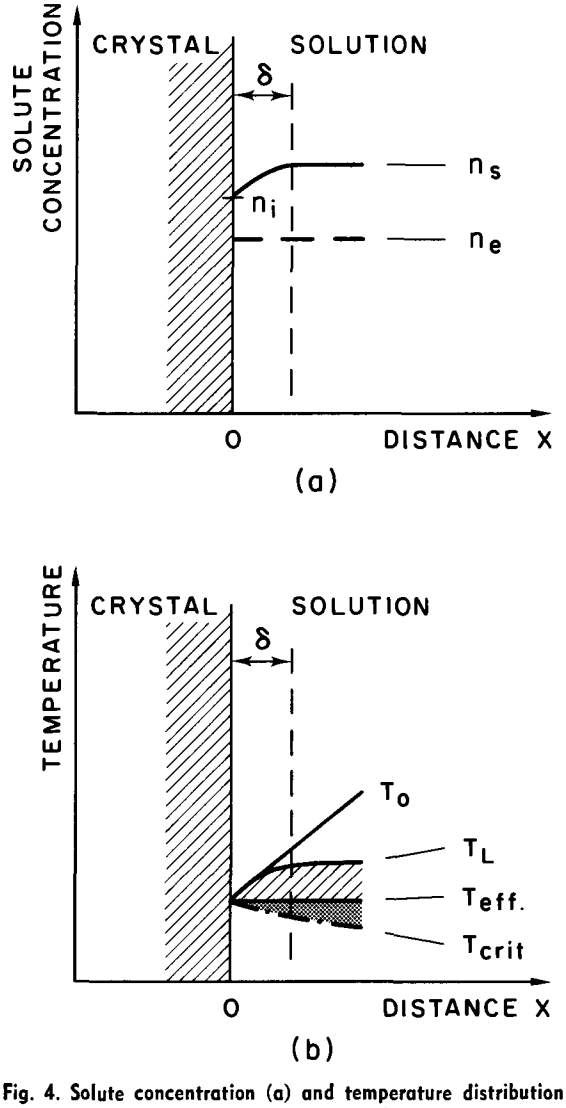

Fig. 4. Solute concentration (a) and temperature distribution (b) in front of a crystal growing from a stirred solution.

Fig. 5. Solvent inclusions near the surface of a 210g $GdAlO_3$ crystal due to interruption of stirring at the end of the growth experiment.

tion. The periodicity of the inclusions is about 30 μm which is in good agreement to the order of magnitude with theoretical predictions. A coarse inclusion structure intersecting the fine bands at an angle of 35°-36° may be due to a complex transient flow pattern on sudden cessation of forced stirring.

Stability of Polyhedral Crystals

The discussion of the previous sections was concerned with crystal surfaces of unlimited extent, whereas crystals in reality are finite polyhedra. The new problem introduced by taking into account the finite size of crystals is that of the supersaturation inhomogeneity across the surface. Because of the enhanced diffusional flow to the corners and edges of a crystal, the supersaturation in these regions is much higher than that at the face centers. This inhomogeneity has been measured in many examples of crystals growing from aqueous solution and amounts to about 25% in the case of sodium chlorate (28).

The stability of polyhedral crystals growing in solution has been considered by Cahn (29) and Chernov (30). Cahn took as his stability condition the requirement that the supersaturation should not vanish in the center of a face and provided theoretical justification for the well-established observation (31-33) that the stable linear growth rate must decrease as the crystal size increases. Chernov (30) proposed that the supersaturation inhomogeneity is compensated by the development of vicinal faces. The slope to the crystallographic habit plane at the face center may differ from that at the edges by about 2° if the increased kinetic coefficient at the center is to balance the lower supersaturation, but instability will result if the curvature at the center exceeds some critical value.

In both Cahn's and Chernov's treatments, substitution of typical data leads to a predication that the maximum size of crystals for stable growth should be of the order of 10^{-1} mm, which is clearly in conflict with experiment. The discrepancy arises from the assumption that solute is distributed over the crystal surface only by volume diffusion. In practice some allowance must be made for convective mixing within the solution, since it is clear that a crystal growing in a well-mixed solution will generally preserve its shape during growth. Carlson (14) demonstrated the necessity of stirring for the growth of large inclusion-free crystals of ammonium dihydrogen phosphate and derived an expression for the maximum size l of inclusion-free crystal

$$l = \frac{0.214\, Du(n_s - n_e)^2}{(\eta/\rho_s D)^{1/3}\rho_c^2 v^2} \qquad [14]$$

Equation [14] has been found to give values for the maximum linear growth rate for crystals of macroscopic size which are in general agreement with experiment, and temperature programs for crystal growth by slow cooling have been proposed by the authors (34).

For a given value of l, the maximum value of v which can be used without the onset of instability will increase according to Eq. [14] with the solution flow rate u. If the value of u is too low to achieve the necessary homogeneity, the higher supersaturation at the edges of the crystal will lead to enhanced growth in these regions and the mechanism of growth will be by layers nucleated at the crystal edges. Layers spreading towards the center of the face are frequently overgrown by those nucleated subsequently, with the formation of large inclusions at the face centers. Further increase in the supersaturation beyond the stability limit results in terraced or "hopper" growth and eventually in dendritic growth with branched projections spreading in the fast growth directions.

Role of Natural Convection in Flux Growth

In the foregoing discussion the necessity of high-solution flow rates at the growing crystal face was demonstrated. In unstirred solutions as in the normal flux practice with stationary crucibles the only means of producing some solution flow is thermal and solutional convection. This has been discussed by Parker (7), Wilcox (35), Cobb and Wallis (36), and by Schulz-DuBois (37).

For idealized systems a critical dimensionless number characterizes the onset of thermal convection according to the Rayleigh criterion as reviewed by Chandrasekhar (38). In crystal-growth experiments, convection currents almost always occur because of temperature gradients and solute flow due to crystallization. However, no quantitative data are available on the magnitude of convection flow rates. For a simple model as shown in Fig. 6 the average flow rate of thermal convection can be estimated (36) by

$$u = \frac{K}{\rho_s L c_p}\left[0.208\,(L^3\alpha\theta)^{1/4} - 1\right] \qquad [15]$$

where α is the convection parameter $\rho_s^2 c_p g\beta/\eta K$ with c_p specific heat of the liquid, β the volume expansion coefficient, and K the thermal conductivity. It can be seen from Eq. [15] that the convection flow rate depends on the solution and on the liquid height L and the temperature difference θ which may be varied by the experimenter. Figure 7 shows flow rate *vs.* liquid height L for various convection parameters and a temperature difference of 10°C. After the first steep increase due to the critical Rayleigh number, the flow rate is not much influenced by L. Even for extremely large values of α (a typical value of α in high-temperature solutions is 1500) the flow rate does not exceed 0.05 cm sec^{-1}.

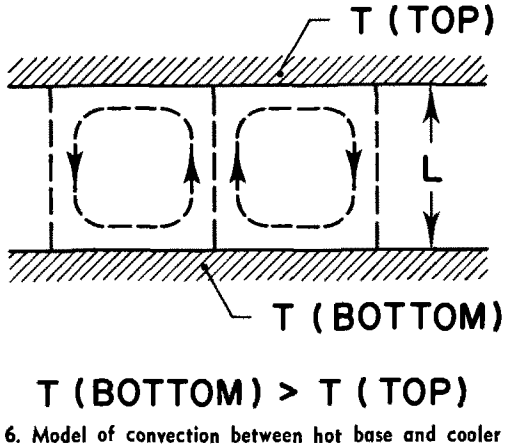

Fig. 6. Model of convection between hot base and cooler top

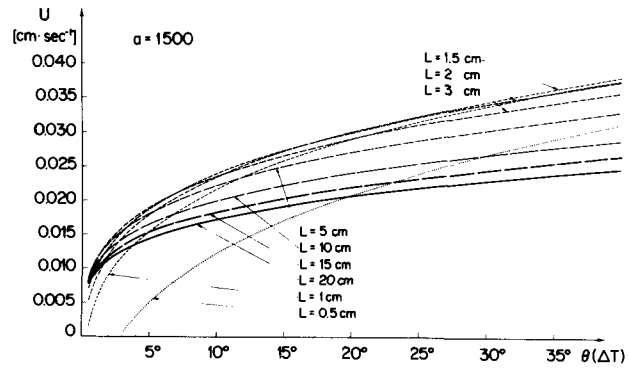

Fig. 7. Convection flow rates vs. liquid height L for various convection parameters α and temperature difference of 10°C.

The effect of the temperature gradient on the flow rate for the convective modulus 1500 and for various liquid heights L is demonstrated in Fig. 8. For small θ the critical value of L is 1 cm, below which convection decreases rapidly. For $L > 1$ cm a temperature difference of 5° is sufficient to achieve flow rates of approximately 0.02 cm sec^{-1} which do not increase much with larger θ.

It follows that natural convection produces too small solution flow rates for the achievement of high stable growth rates. Solutional convection as discussed by Wagner (39) and Jakeman and Hurle (40) will improve the situation. However, the convection flow rates will not increase by more than an order of magnitude under typical growth conditions. Therefore forced convection by stirring is applied in crystal growth from solutions wherever possible.

Stirring Techniques in Flux Growth

In flux growth, immersed rotating seed crystals have been used by Laudise, Linares, and Dearborn (41) with nonvolatile solvents. Pulling of rotating seed crystals was summarized by Scheel (18). Growth of rotating seed crystals slightly below the liquid surface, thereby decreasing excessively steep temperature gradients in the growing crystals, was first reported by Miller (42) and recently by Belruss *et al.* (43) as "top-seeded solution growth." The stirring action of a rotating seed is the same as that in Czochralski growth which has been described by Carruthers and Nassau (44) and by Robertson (45) and is possible only with nonvolatile fluxes. The Ekman flow pattern has been analyzed by Hide and Titman (46) and by Ellison and Cornet (47), and the boundary-layer thickness along a rotating disk was estimated by Burton, Prim, and Slichter (48).

Experimentally, it is extremely difficult to apply conventional stirring with the excellent but volatile

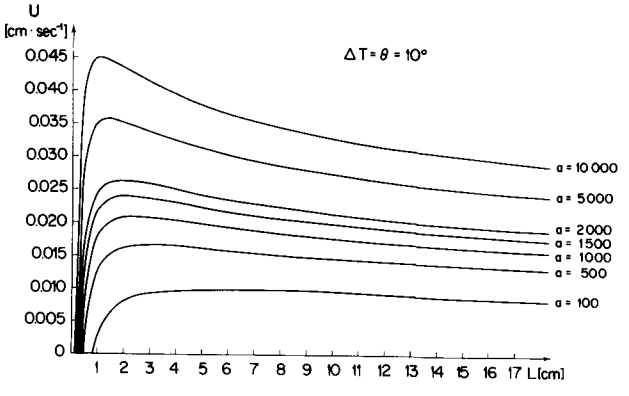

Fig. 8. Convection flow rates vs. temperature difference for various liquid heights and the convection parameter 1500.

lead oxide, lead fluoride, and other volatile solvents. Here the beneficial effect of the accelerated crucible rotation technique (ACRT) was discovered (18, 37, 49), which allows, by its homogenization of the solution and by combination with localized cooling, the growth of large inclusion-free crystals. By periodic acceleration and deceleration of the crucible rotation, a smooth and more or less laminar solution flow can be produced.

Conclusions

The necessity of stirring in crystal growth from high-temperature solutions has been demonstrated. The concepts of the boundary layer and of the metastable region of supersaturation gradient are necessary for an optimum choice of all experimental parameters in order to achieve good results in high-temperature solution growth. The high quality of solution-grown crystals proven by their low dislocation densities (50) as well as the general applicability of this method will lead to its technical use for the growth of special crystals with applications in electronics, optics, magnetics, or acoustics.

A more detailed discussion of many of the points raised in this paper will be given in a forthcoming book on high-temperature solution growth (51).

Acknowledgment

Stimulating discussions with Dr. P. Sahm are gratefully acknowledged.

Manuscript submitted Jan. 18, 1972; revised manuscript received Jan. 12, 1973. This was Paper 112 presented at the Washington, D.C., Meeting of the Society, May 9-13, 1971.

Any discussion of this paper will appear in a Discussion Section to be published in the December 1973 JOURNAL.

REFERENCES

1. W. W. Mullins and R. F. Sekerka, *J. Appl. Phys.*, **34**, 323 (1963).
2. F. A. Nichols and W. W. Mullins, *Trans. AIME*, **233**, 1840 (1965).
3. W. W. Mullins and R. F. Sekerka, *J. Appl. Phys.*, **35**, 444 (1964).
4. J. W. Rutter and B. Chalmers, *Can. J. Phys.*, **31**, 15 (1953).
5. W. A. Tiller, K. A. Jackson, J. W. Rutter, and B. Chalmers, *Acta Met.*, **1**, 428 (1953).
6. G. P. Ivantsov, *Dokl. Akad. Nauk. SSSR*, **81**, 179 (1951); *ibid.*, **83**, 573 (1952).
7. R. L. Parker, *Solid State Phys.*, **25**, 151 (1970).
8. R. A. Laudise, "The Growth of Single Crystals", pp. 86 and 92, Prentice Hall, Englewood Cliffs, N. J. (1970).
9. W. R. Wilcox, *Mater. Res. Bull.*, **4**, 265 (1969).
10. W. K. Burton, N. Cabrera, and F. C. Frank, *Phil. Trans. Roy. Soc.*, **A243**, 299 (1951).
11. P. Bennema in "Crystal Growth," H. S. Peiser, Editor, p. 413, Pergamon Press, Oxford (1967).
12. G. H. Gilmer, R. Ghez, and N. Cabrera, *J. Cryst. Growth*, **8**, 79 (1971).
13. D. Elwell and B. W. Neate, *J. Mater. Sci.*, **6**, 1499 (1971).
14. A. E. Carlson, Ph.D. Thesis, Univ. of Utah (1958); in "Growth and Perfection of Crystals," R. H. Doremus, B. W. Roberts, and D. Turnbull, Editors, p. 421, John Wiley & Sons, Inc., New York (1958).
15. W. Nernst, *Z. Phys. Chem.*, **47**, 52 (1904).
16. J. C. Brice, *J. Cryst. Growth*, **1**, 161 (1967).

17. J. C. Brice, "The Growth of Crystals from the Melt," p. 124, North-Holland Publishing Co., Amsterdam (1965).
18. H. J. Scheel, *J. Cryst. Growth*, **13/14**, 560 (1972).
19. W. A. Tiller, *ibid.*, **2**, 69 (1968).
20. D. Elwell and R. D. Dawson, *ibid.*, **13/14**, 555 (1972).
21. R. D. Dawson, D. Elwell, and J. C. Brice, To be published.
22. S. R. Coriell and R. L. Parker, in "Crystal Growth," H. S. Peiser, Editor, p. 703, Pergamon Press, Oxford (1967).
23. L. A. Tarshis and W. A. Tiller, in "Crystal Growth," H.S. Peiser, Editor, p. 709, Pergamon Press, Oxford (1967).
24. S. O'Hara, L. A. Tarshis, W. A. Tiller, and J. P. Hunt, *J. Cryst. Growth*, **3/4**, 555 (1968).
25. W. R. Wilcox, *ibid.*, **12**, 93 (1972).
26. D. T. J. Hurle, *ibid.*, **5**, 162 (1969).
27. R. T. Delves, *ibid.*, **8**, 13 (1971).
28. C. W. Bunn, *Discussions, Faraday Soc.*, **5**, 132 (1949).
29. J. W. Cahn, in "Crystal Growth," H.S. Peiser, Editor, p. 681, Pergamon Press, Oxford (1967).
30. A. A. Chernov, *Soviet Phys. Cryst.*, **16**, 734 (1972).
31. T. Yamamoto, *Sci. Papers Inst. Phys. Chem. Res.*, **35**, 228 (1939).
32. P. H. Egli and S. Zerfoss, *Discussions, Faraday Soc.*, **5**, 61 (1949).
33. H. V. Alexandru, Paper presented at Chisa Congress, Czechoslovakia (1972).
34. H. J. Scheel and D. Elwell, *J. Cryst. Growth*, **12**, 153 (1972).
35. W. R. Wilcox, in "Aspects of Crystal Growth," R. A. Lefever, Editor, p. 37, Marcel Dekker, New York (1971).
36. C. M. Cobb and E. B. Wallis, Report AD 655 388 (1967).
37. E. O. Schulz-DuBois, *J. Cryst. Growth*, **12**, 81 (1972).
38. S. Chandrasekhar, "Hydrodynamic and Hydromagnetic Stability," Oxford University Press (1961).
39. C. Wagner, *J. Phys. and Coll. Chem.* **53**, 1030 (1950).
40. E. Jakeman and D. T. J. Hurle, *Rev. Phys. Technology*, To be published (1972).
41. R. A. Laudise, R. C. Linares, and E. F. Dearborn, *J. Appl. Phys.*, **33**, Suppl., 1362 (1962).
42. C. E. Miller, *ibid.*, **29**, 233 (1958).
43. V. Belruss, J. Kalnajs, A. Linz, and R. C. Folweiler, *Mater. Res. Bull.*, **6**, 899 (1971).
44. J. R. Carruthers and K. Nassau, *J. Appl. Phys.*, **39**, 5205 (1968).
45. D. S. Robertson, *Brit. J. Appl. Phys.*, **17**, 1047 (1966).
46. R. Hide and C. W. Titman, *J. Fluid Mech.*, **29**, 39 (1967).
47. B. T. Ellison and I. Cornet, *This Journal*, **118**, 68 (1971).
48. J. A. Burton, R. C. Prim, and W. P. Slichter, *J. Chem. Phys.*, **21**, 1987 (1953).
49. H. J. Scheel and E. O. Schulz-DuBois, *J. Cryst. Growth*, **8**, 304 (1971).
50. C. S. Sahagian and M. Schieber, in "Growth of Crystals," N. N. Sheftal, Editor, Vol. 7, pp. 183-194 (1969).
51. D. Elwell and H. J. Scheel, "Crystal Growth from High-Temperature Solutions," Academic Press, London, To be published.

Mechanism and Kinetics of Nickel Chromite Formation

J. S. Armijo

General Electric Company, Breeder Reactor Development Operation, San Jose, California 95114

D. L. Douglass*

University of California at Los Angeles, Department of Materials Science, Los Angeles, California 90000

and R. A. Huggins*

Stanford University, Department of Materials Science, Stanford, California 94305

ABSTRACT

Nickel chromite formation was studied using dense polycrystals and single crystals of NiO and Cr_2O_3. The influence of time, temperature, and oxide purity on spinel structures and formation rates was determined. Experiments were performed by reacting pure Cr_2O_3 pellets with pure and manganese-doped pellets of NiO. All reactions were done in air for times ranging from 24 to 640 hr, and at temperatures from 1200° to 1500°C.

The rates of nickel chromite formation in dense, crack-free specimens are two orders of magnitude smaller than the rates of formation in porous specimens, or at surfaces of dense specimens. These solid-state reaction rates are affected, and possibly controlled, by the rate of chromium dissolution in the nickel oxide, while the reaction rates at free surfaces are controlled by diffusion of Ni^{2+} and Cr^{3+} through the spinel.

There have been several experimental attempts to determine the mechanism of formation of nickel chromite from its component oxides (1-6). In a prior review (7) it was shown that none of these experiments provided conclusive determination of the rate-controlling mechanism. Prior experiments were inconclusive for two major reasons. First, the starting oxides used were too porous to eliminate complications arising from vapor-phase transport. Second, marker experiments failed. Inert metal markers disappeared during the reactions at elevated temperatures (2, 5), while natural markers (interface between polycrystal and single crystal starting oxides) produced results which did not support the mechanism concluded by the author (6).

The purpose of this paper is to describe studies of nickel chromite formation in which dense high-purity oxides were used and for which metal markers provided definitive information of the reaction mechanism.

Experimental

Oxide preparation.—Techniques for the preparation of high-purity oxides commonly consist of purification of salts followed by thermal decomposition. Of these various methods, the oxalate decomposition method of Brown (8, 9) was reported to yield oxides of high purity (99.999%) which would also sinter to high density after simple cold pressing and sintering. Similar procedures were used to prepare the high-purity and manganese-doped nickel oxides used in this study.

Pellets of high-purity and manganese-doped nickel oxides (2.5 cm diameter, 2-5 mm thick) were prepared by cold pressing, drying, and firing in air at 1500°C for 250-350 hr. After initial firing, groups of pellets of each type were equilibrated with air at 1200°, 1300°, and 1400°C in order to provide starting oxides for experiments to be made at such temperatures.

Pellets (5 cm diameter, 3-5 mm thick) of reagent-grade chromium oxide were prepared by hot pressing for 1 hr at 1450°C. After pressing, the pellets were fired in air for 250-350 hr at 1500°C. Groups of chromium oxide pellets were then equilibrated with air by firing for 100 hr at 1200°, 1300°, and 1400°C. In addition to the studies using the polycrystalline oxides, a limited number of experiments were made with single crystals of nickel oxide and chromium oxide. These crystals were obtained from sources listed in Table I.

* Electrochemical Society Active Member.
Key words: nickel chromite, mechanism, kinetics.

Table I. Purities and densities of starting oxides

Material	Source	Metallic impurity concentrations* (ppm by wt) Co	Ni	Si	Mn	Cu	Fe	Co + Zn + Mg + Cd	Dopant (m/o)	Purity level (w/o)	Average density g/cm³	theoret.**
NiO, reagent grade	J. T. Baker Chemical Co. "Analyzed Reagent"	450	M	ND	ND	30	50	470	None	99.90	6.38	94
NiO, high purity	Prepared by oxalate precipitation	100	M	ND	ND	30	ND	50	None	99.98	6.45	95
NiO-1MnO	Prepared by oxalate precipitation	100	M	ND	7200	10	ND	50	0.97 MnO	98.26	6.40	94
NiO, single crystal	Argonne National Lab. Argonne, Ill.	190	M	10	30	30	60	60	None	99.96	6.67	98
Cr_2O_3, reagent grade	Fisher Scientific Co. "Certified Reagent"	ND	ND	250	ND	20	250	200	None	99.93	5.15	99
Cr_2O_3, single crystal	Adolph Meller Co. P. O. Box 6001 Providence, R. I.	ND	ND	150	ND	50	300	300	None	99.9	5.20	100

* ND, not detected; M, major constituent. Determined by spectrographic analysis.
** Based on the following theoretical densities: NiO, 6.808 g/cm³; Cr_2O_3, 5.202 g/cm³.

Spinel formation reactions.—The following procedures were closely followed for most spinel formation experiments. Pellets for reaction at a given temperature were selected from groups that had previously been equilibrated at or near the desired temperature. Pellets were selected on the basis of density and freedom from obvious flaws such as cracks.

Three types of markers were used in these studies: (*i*) thick platinum foils (6μ by 1 mm by 1 cm); (*ii*) thin platinum foils (1.5μ by 1 mm by 1 cm); and (*iii*) iridium powder approximately 0.1-1μ diameter.

The assembled specimens with markers were placed in silicon carbide heated muffle furnaces capable of temperatures to 1550°C. Alumina blocks were then placed on top of each specimen to produce a compressive stress of approximately 1 kg/cm^2. The furnaces were then rapidly heated to the desired reaction temperature. All experiments were done in air, and temperatures were measured with two Pt + Pt-10%Rh thermocouples. Temperatures measured with both thermocouples were always within ±5°C of each other, and the temperatures remained within ±10°C of the reported value during each experiment.

Results

Compositions, densities, and structures of starting oxides.—The compositions and densities of the oxides used are shown in Table I. The nickel oxides prepared by oxalate precipitation and decomposition were of somewhat higher purity than commercial reagent-grade oxide. The major impurity was cobalt oxide. As shown in Table I, the manganese oxide concentration in the nickel oxide was very close to the desired 1 mole per cent (m/o) value.

The immersion densities of all the nickel oxides prepared by cold pressing and firing ranged from 92 to 97% of the theoretical value. These percentages were based on a theoretical density of 6.808 for nickel oxide. The densities obtained with hot-pressed chromium oxide were always within 98% of theoretical density. In addition, the densities of the surfaces of these pellets were higher than the over-all density. In general, all spinel reactions were made with chromium oxides approaching 100% of theoretical density.

Nickel chromite formation from pure oxides.—The observations to be discussed in this section apply to the spinel formation from the reaction of reagent-grade chromium oxide with both reagent-grade and high-purity nickel oxide. For ease of presentation, the surface effects and the internal effects will be described separately.

Surface features.—During early experiments, the chromium oxide pellets appeared to shrink during the spinel reaction anneals. Details of this shrinkage were determined by cutting prebonded pellets into small rectangular prisms and firing at temperatures from 1200° to 1500°C. All such specimens took the shape shown in Fig. 1 after firing, the most pronounced shape changes occurring at the highest temperatures and longest times. The initial shape of the specimen is shown by the dashed lines. The nickel oxide half of the specimen expanded, the maximum expansion occurring near the reaction interface.

Examination of the reaction interface in greater detail revealed small crystallites on the surface of the spinel. These crystallites were not strongly bonded to the spinel and could easily be brushed off. The crystallites were small octahedrons and were identified as nickel chromite by x-ray diffraction. In addition to these features, small crystallites resembling etch pits formed on the surfaces on the nickel oxide during the spinel reaction. These crystallites appeared to form preferentially on cube faces of the nickel oxide crystals. The amount of crystallite formation on the nickel oxide decreased as the distance from the reaction interface increased. No such crystallite formation was ever observed on the surfaces of nickel oxides that had been fired in the absence of chromium oxide. These observations suggest that the crystallites on the surface of the nickel oxide may be the first stages of nickel chromite spinel formation by a solid NiO-"vapor" Cr_2O_3 mechanism. The spinel crystallites on the surface of the spinel probably form by a vapor-phase reaction of both nickel and chromium oxides.

Internal features.—Characteristics of the internal features of nickel chromite spinel formation are summarized schematically in Fig. 2 and examples of some of these features are shown in Fig. 3-8. The thickness of the spinel formed during a given diffusion anneal varied considerably depending on the location within the specimen. At the surface of the reaction interface (location A in Fig. 2), the spinel was very thick. However, inside the dense, crack-free, regions of the specimen (location B), the spinel layer was thin. Thick spinel layers also formed at internal cracks exposed to air (location D). These internal layers could either be thicker or thinner than the surface layers, depending on the geometry of the crack. Although cracking of the reactants was common, the diffusion couples were generally well bonded. This behavior contrasted sharply with the easy separation of reactants which had been observed in prior studies (1, 5, 6). In this

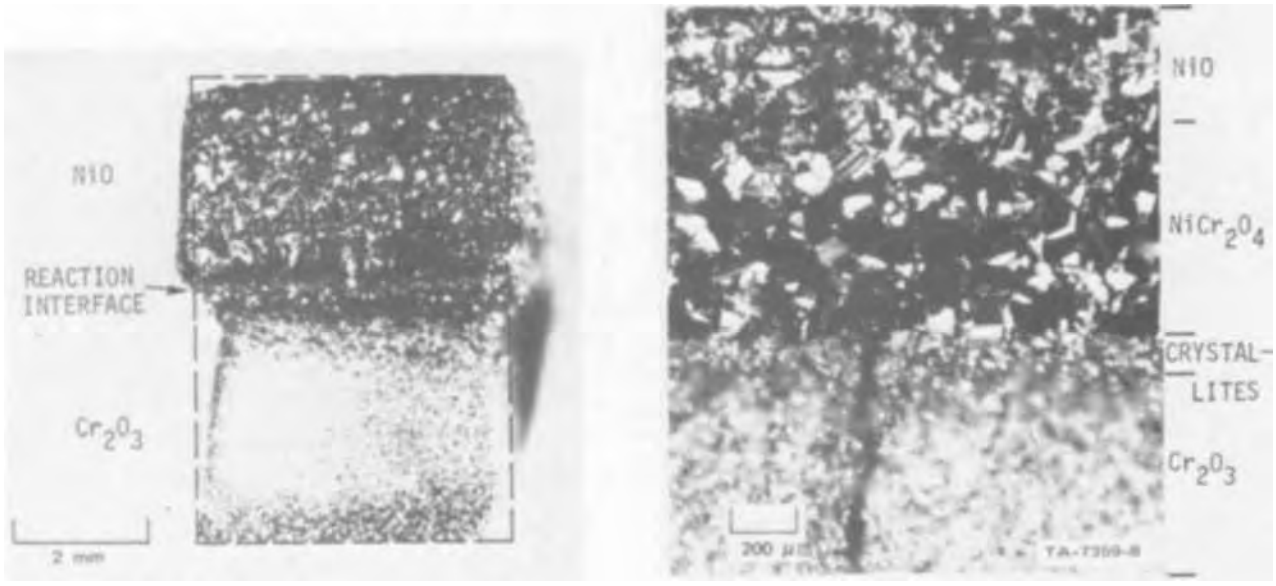

Fig. 1. Nickel oxide/chromium oxide diffusion couple: (a, above left) microstructure showing nonuniform shrinkage of chromium oxide; (b, above right) details of surface at reaction interface.

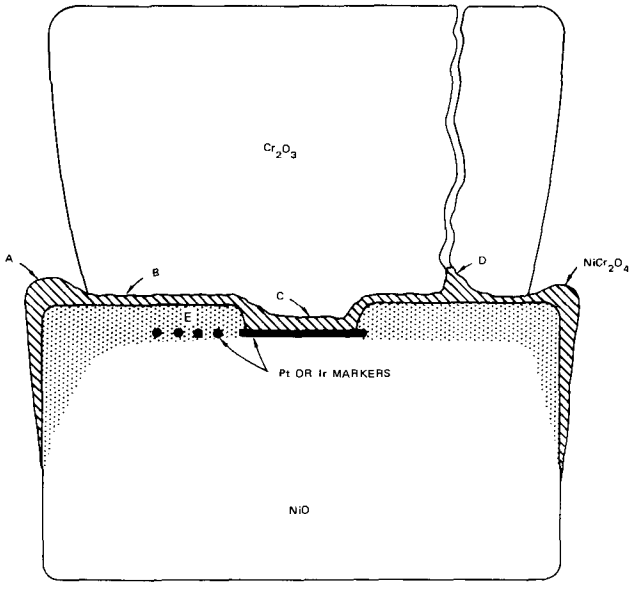

Fig. 2. Schematic representation of internal features observed in nickel chromite formation from pure oxides: (a) surface spinel (spinel formed at corners of pellet exposed to air); (b) internal spinel (spinel formed in dense, crack-free, regions of pellets); (c) spinel formed at thick marker; (d) spinel formed internally but exposed to air by a crack; (e) spinel precipitate in nickel oxide.

study, easy separation of the reactants was observed in only one special experiment. The details of this experiment and its implications in the mechanism of spinel formation will be given in a later section. Thick spinel layers also formed at thick (approximately 6μ) platinum markers (location C). An example of thick spinel formation at such a marker and thin spinel formation from a region of the specimen that has no marker is shown in Fig. 3. The large difference in the thickness of the spinel at these two locations is evident.

The last predominant internal features (location E) were found at the thin (1-2μ) or discontinuous platinum or iridium markers. These thin markers were always buried within the nickel oxide. The depth to which the markers were buried increased with the time and temperature of exposure. The time dependence was parabolic, and the temperature dependence was Arrhenius in form. No differences were observed in the depths of the platinum and iridium markers after identical reactions. Examples of buried markers are shown in Fig. 4 for a specimen reacted for 64 hr at 1300°C. Also visible in the nickel oxide, both in specimens that contained markers and in specimens that did not contain markers, were very fine Widmanstatten precipitates. These precipitates extended well into the nickel oxide, and could be resolved on both sides of the markers. In addition to these features it was observed that nonplanar diffusion interfaces formed between the spinel layer and the chromium oxide (Fig. 4). However, the interface between the spinel and the nickel oxide was always planar (when complications arising from the presence of thick markers did not interfere).

Phase analysis and precipitate identification.—The precipitates were identified by combining x-ray diffraction and metallographic techniques. A specimen that had been reacted and slowly cooled to room temperature (to accentuate the precipitation) was carefully ground parallel to the reaction interface. The ground face was examined by x-ray diffraction using Cr Kα radiation. The NiO (111), Cr_2O_3 (104), and $NiCr_2O_4$ (220) reflections were measured after grinding. The results of these measurements (Fig. 5) showed that the precipitates were nickel chromite spinel. The spinel precipitates could readily be detected at a distance of 80μ from the dense spinel layer.

Marker behavior.—The identification of the nickel chromite precipitate particles in the nickel oxide provides an explanation for the formation of thick spinel layers at (defect-free) thick markers and thin spinel layers away from the markers. The nickel chromite precipitation in the nickel oxide is the result of dissolution of the spinel ($NiCr_2O_4 + 3Ni^{2+} \rightarrow 4NiO + 2Cr^{3+}$) at the nickel oxide/spinel reaction interface. Consequently, if the rate of dissolution of the spinel by nickel oxide is of the same order of magnitude as the rate of formation of the spinel, one can expect the resultant layer to be thin where there are no dissolution barriers and thick where barriers are present. A confirmation of this model was provided in part by morphology of the reaction interface at an imperfect platinum marker and by the chromium and nickel concentration profiles at defected and defect-free regions of the marker.

The structure and composition of the reaction interface at a defected platinum marker are shown in Fig. 6. The electron backscatter image and the Ni Kα x-ray image show the spinel layer to be very irregular at the spinel chromium oxide interface. More impor-

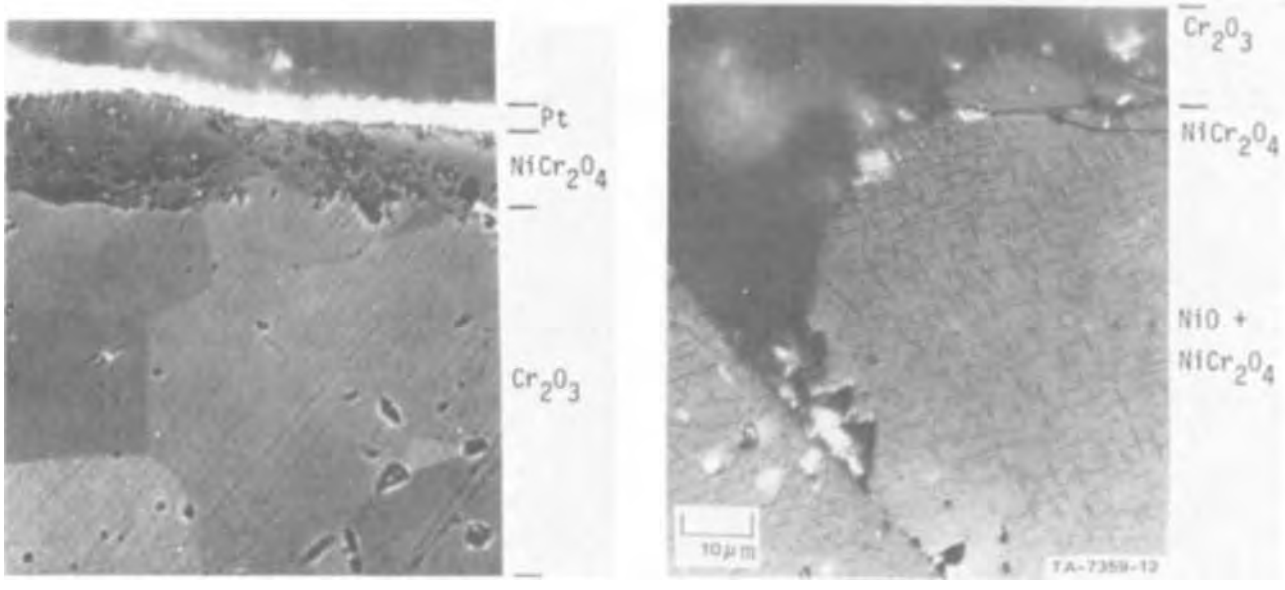

Fig. 3. Comparison of nickel chromite layers formed (a) at thick markers and (b) at marker-free locations. Note spinel precipitates in NiO. Specimen reacted at 1200°C for 1.3 x 10^6 sec.

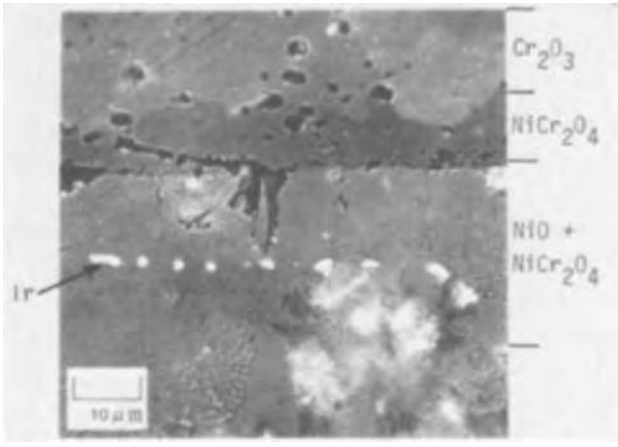

Fig. 4. Marker locations in nickel oxide. Specimen reacted at 1300°C for 2.3×10^5 sec

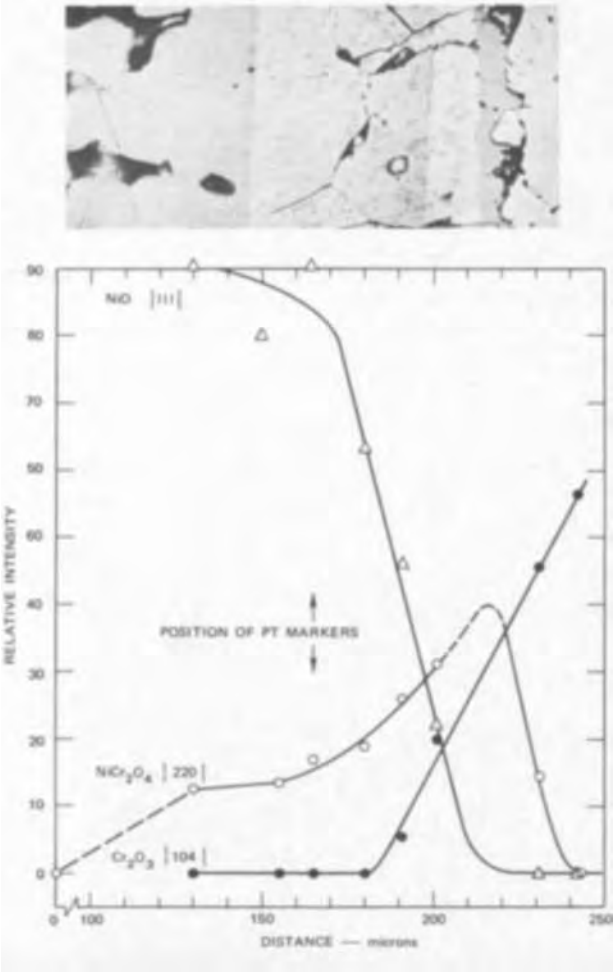

Fig. 5. Structure and phase analysis of reaction zone formed during solid-state spinel formation. Specimen reacted at 1200°C for 1.3×10^6 sec, then reheated to 1480°C for 4.3×10^5 sec and slowly cooled to room temperature.

tantly, both images show that a small defect in the marker resulted in the formation of a hemispherical intrusion of nickel oxide into the chromium oxide. Electron-microprobe scans across the specimen along paths A and B of Fig. 6 revealed the composition profiles shown in Fig. 7. As shown, the chromium concentration in the nickel oxide intrusion is significantly higher than in the nickel oxide at the planar reaction interface. Consequently, it can be concluded that the thick platinum markers cause the formation of thicker

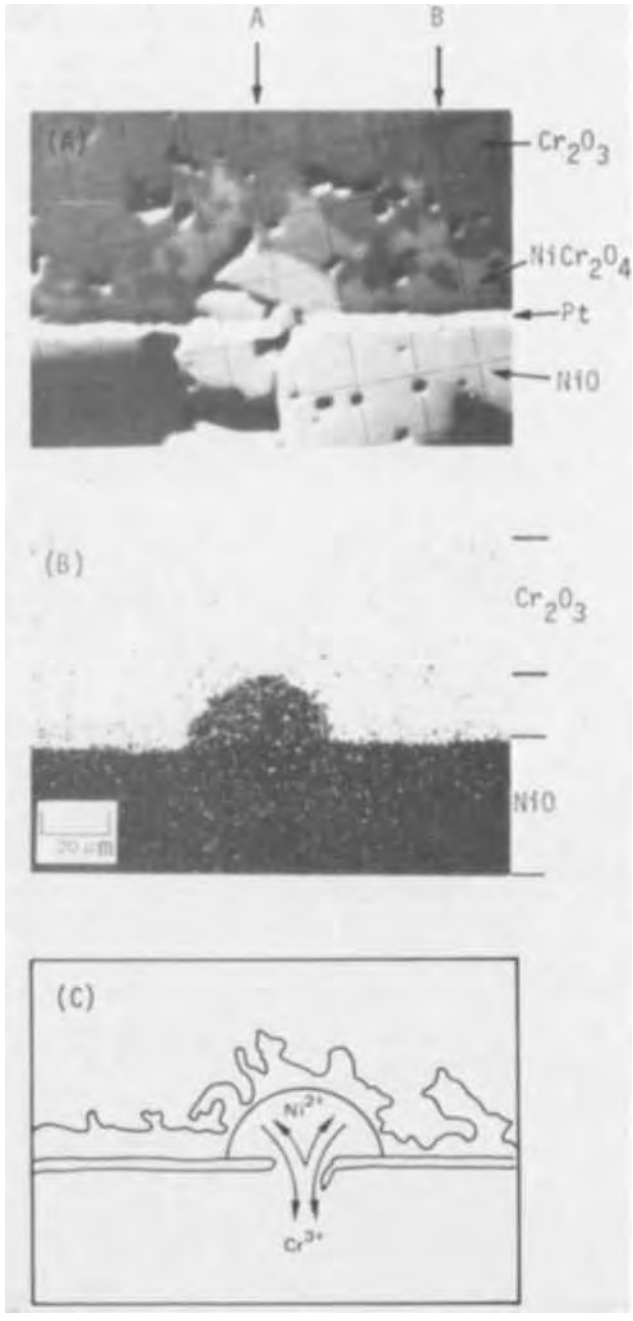

Fig. 6. Details of structure at defect in platinum marker. Chromium and nickel composition profile scans shown in Fig. 7 were made at locations A and B. Specimen reacted at 1235°C for 7.8×10^5 sec.

spinel layers because they are barriers to chromium dissolution in the nickel oxide.

The structures shown in Fig. 6 and 7 also help explain the location of the thin and/or discontinuous markers in the nickel oxide (location E, Fig. 2). If the markers are discrete particles, they do not interfere with the simultaneous formation of spinel at the NiO/Cr_2O_3 interface and spinel dissolution in the nickel oxide. Thus the simple countercurrent diffusion reaction is replaced by a moving-boundary diffusion reaction, in which there is a flux of material into the spinel and a concurrent flux (of the same order of magnitude) into the nickel oxide (2, 10). Consequently, the markers remain at the original interface, and the spinel layer moves toward the chromium oxide half of the diffusion couple. When thick platinum markers are used, spinel dissolution is prevented, and the spinel will remain at the original interface.

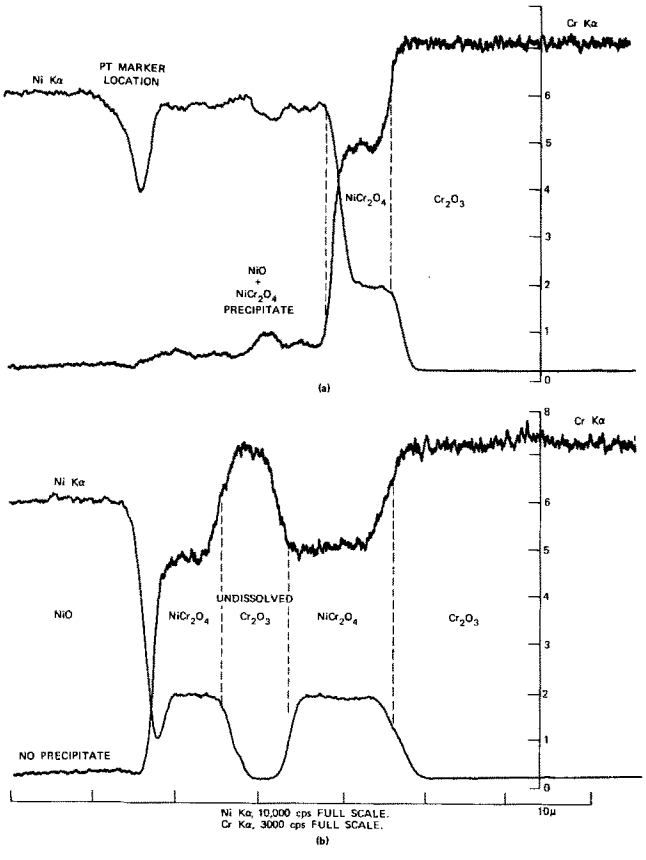

Fig. 7. Influence of thick platinum marker on the concentration of dissolved chromium in nickel oxide. (a) at marker defect and (b) at continuous marker.

An example of this effect with thick markers is shown schematically in Fig. 2 and explicitly in Fig. 8 where the final interface has advanced away from the initial interface defined by the thick platinum marker.

Single crystal experiments.—Experiments with single crystals were performed for comparison with the various observations of spinel formation from dense polycrystalline specimens. In general, results obtained with single crystal reactants were similar to results obtained with polycrystals. Reaction of single crystals of NiO and Cr_2O_3 produced structures identical to those produced by reaction of polycrystals. Thin spinel layers were formed (Fig. 9) between the starting oxides, and precipitation of nickel chromite spinel was clearly visible in the nickel oxide. In addition, the reaction interfaces between the spinel and both starting oxides were not planar.

The single crystal experiments proved that the penetration of the chromium into the nickel oxide occurred by a solid-state diffusion mechanism, and not by a vapor-transport mechanism through pores (as was possible with the polycrystalline nickel oxide specimens). In addition, it was evident that this penetration occurred without the formation of porosity in either the nickel or chromium oxide single crystals. Further, the calculated parabolic reaction rate constants (described in a later section) were consistent with the rate constants derived from dense polycrystalline specimens. These observations therefore supported the conclusion that the results obtained with the polycrystalline specimens used in this study reflect the solid-state spinel reaction mechanism. The lack of visible porosity in the single crystals allowed for the determination of a mass balance across the reaction interface.

Electron-microprobe measurements of the chromium Kα radiation from the same area shown in Fig. 9 were made by point counting at 3-6μ intervals using a beam

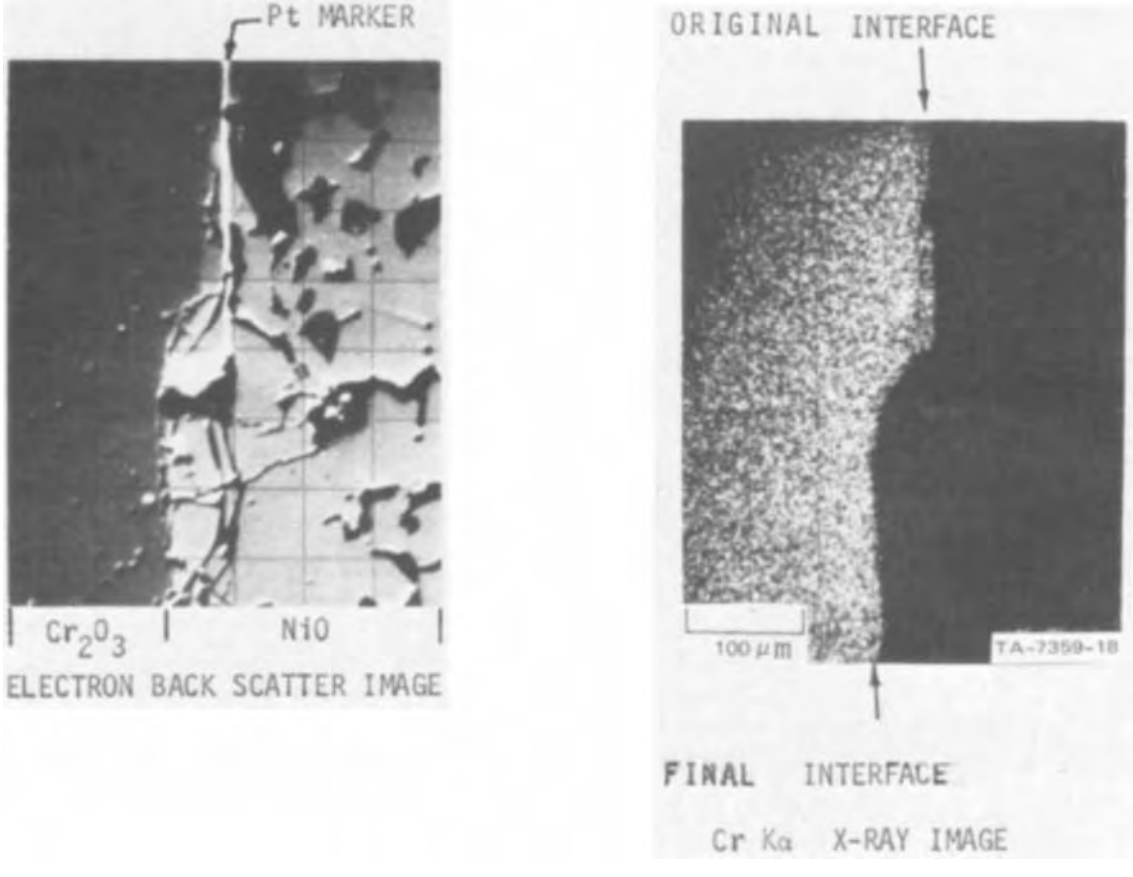

Fig. 8. Example of moving interface during nickel chromite formation. The thick (~6μ) platinum marker does not move during the reaction. Specimen reacted at 1235°C for 1 x 10^6 sec.

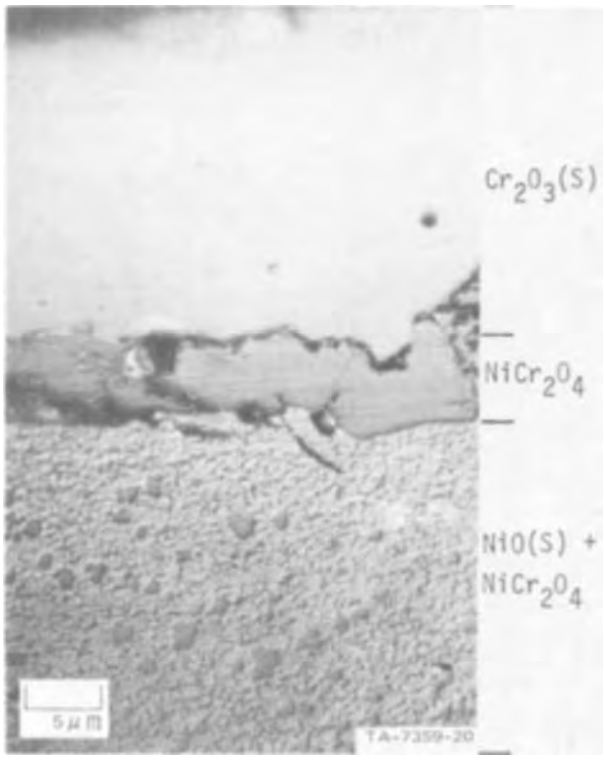

Fig. 9. Structure of nickel chromite reaction layer between nickel oxide and chromium oxide single crystals. Specimen heated at 1410°C for 7.6 x 10^5 sec.

diameter of ~6μ. The chromium Kα x-ray intensity profile across the reaction interface (Fig. 10) showed the depth to which the chromium had penetrated into the nickel oxide. Measurable amounts of chromium could be detected at a distance of 625μ from the spinel/nickel oxide interface. Figure 10 shows that the intensity-distance profile in the nickel oxide was very irregular, as would be expected from the presence of spinel precipitates in the single crystal nickel oxide. The spinel layer itself was too thin to be resolved by the point counting technique, however, the chromium spinel intensity was calculated from comparison with the intensity data from thicker layers and the 6μ spinel layer was drawn accordingly. The position of the platinum marker in another area of the specimen is also shown, and will be used in the discussion of the reaction mechanism.

Vapor-transport experiment.—Vapor-phase transport of one or more of the reacting species has been widely reported in the literature (1, 5, 6, 11-13) and has been used as a general explanation for the commonly observed phenomenon of easy separation of reactants

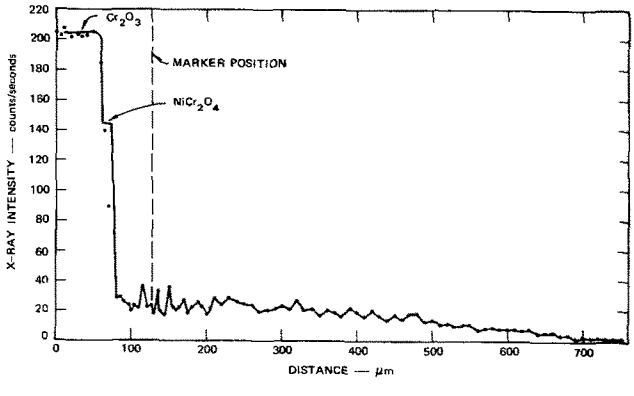

Fig. 10. Cr Kα composition profile. Point count data show sufficient dissolved chromium in nickel oxide to account for marker position.

after the spinel reaction. Schmalzried (11) has stated that this phenomenon results from the vapor transport of the more volatile species to the other reactant when nonideal contact conditions exist between the two pellets. According to this mechanism, the more volatile species travels, via the gas phase, to the less volatile pellet, and reacts to form the spinel. Since there is never any solid contact, the pellets separate easily, and the spinel layer is bonded to the less volatile material. For example, in the formation of zinc aluminate, one would expect the spinel to bond to the aluminum oxide, while in the formation of magnesium chromite, one would expect the spinel to bond to the magnesium oxide. Extrapolating this generalization to the nickel chromite system, one would expect the spinel to bond to the nickel oxide after an experiment in which nonideal contact exists, because the vaporization rate of chromium oxide is greater than that of nickel oxide (5).

An experiment utilizing nonideal contact was performed to test this model and to provide a comparison with experiments in which ideal contact was assumed. The specimen assembly consisted of a flat, polished, nickel oxide pellet separated from a flat, polished, chromium oxide pellet by 2μ thick foil markers. No load other than the nickel oxide pellet was placed on the diffusion couple, and the resultant compressive stress level was of the order of 2 g/cm². The experiment was performed at 1450°C in order to produce a high vapor pressure of the chromium oxide, and thus assure nonideal contact. After the diffusion anneal was completed, the specimen was slowly cooled to room temperature.

The reactants were easily separated by lifting the nickel oxide pellet off the chromium oxide pellet. The reaction surfaces of the two pellets were similar in appearance, and both showed traces of the former marker locations. The surface of the nickel oxide pellet had depressions at the marker locations while the surface of the chromium oxide pellet was elevated at the marker location. The markers themselves could not be seen, and were either buried in the spinel, in the nickel oxide, or at the spinel/chromium oxide interface.

Micrographic examination of the cross-sectioned pellets revealed spinel formation on the chromium oxide, platinum markers buried in the nickel oxide, and spinel precipitation in the nickel oxide.

The spinel layer thickness on the chromium oxide was used to calculate a reaction rate constant, and this rate constant was consistent with the rate constants obtained at the same temperature using ideal contact. Consequently, the specimens behaved as though they were under ideal contact during the spinel reaction, although they were very lightly loaded and they separated readily. If nonideal contact had existed, the spinel should have formed on the nickel oxide (as it forms on the corners of nickel oxide specimens exposed to chromium oxide vapors and air). Since this structure did not occur, one can conclude that the easy separation of pellets does not necessarily provide any indication of the reaction mechanism.

A schematic drawing of the proposed sequence of events which occurred in this experiment is shown in Fig. 11. At the first stage of reaction, ideal contact occurred between the two pellets by a combination of deformation of the markers and the oxides. Reaction to form nickel chromite then proceeded with simultaneous chromium dissolution by the nickel oxide. The dissolution of the spinel at the marker, however, was inhibited by the presence of the markers. In the third stage, the spinel/nickel oxide interface continued to move away from the original interface, and intrusions of nickel oxide began to form as defects formed in the marker by surface tension forces. In stage four, the marker had agglomerated enough that the spinel/nickel oxide interface moved away from the marker. The discontinuity in the reaction interface at the prior

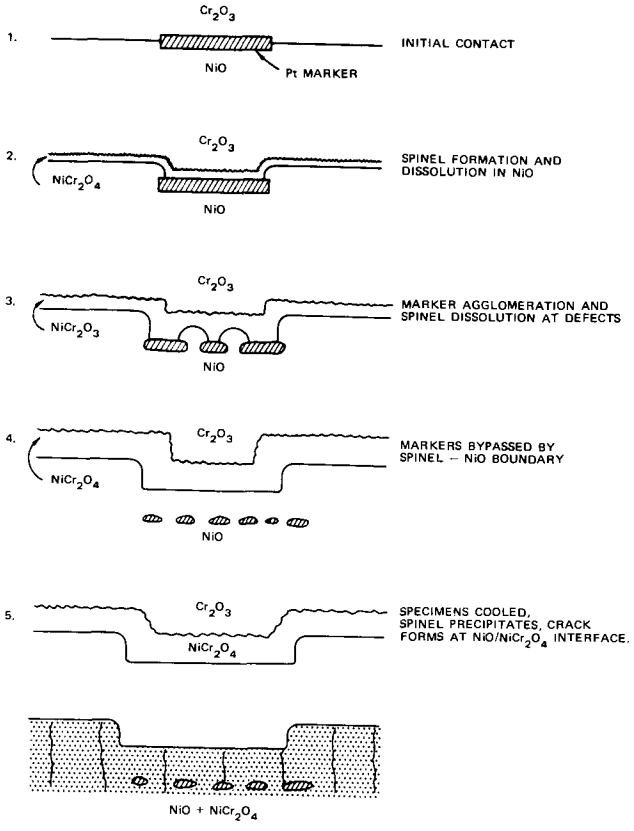

Fig. 11. Schematic representation of reaction mechanism in vapor-transport experiment.

marker location remained, however, because the starting time for the dissolution reaction was delayed by the presence of the marker. At stage five, the specimen was cooled and separated at the spinel/nickel oxide interface by the formation of interfacial cracks. This mechanism leaves the spinel bonded to the chromium oxide, elevations on the chromium oxide at the former marker location, and depressions in the nickel oxide at the former marker location as observed experimentally.

Additional information on the mechanism of nickel chromite formation from the solid state can be determined from the electron-microprobe data of Fig. 10. As is shown, the spinel layer thickness formed between single crystal nickel oxide and single crystal chromium oxide was approximately 6μ thick. In addition, the marker was buried in the nickel oxide single crystal at a distance of 56μ from the nickel oxide/nickel chromite interface. By measuring the area under the Cr Kα penetration curve in the nickel oxide, and dividing by the Cr Kα intensity for pure nickel chromite, a dissolved spinel layer thickness of 75μ was determined. From these measurements, the ratio of the spinel thickness on the nickel oxide side of the markers to the spinel thickness on the chromium oxide side was determined to be 1:3[1] in qualitative agreement with the Wagner mechanism of countercurrent diffusion of Cr^{3+} and Ni^{2+}.

Nickel chromite formation from Mn-doped nickel oxide.—Various experiments were performed with diffusion couples in which the nickel oxide was doped with 1 m/o manganese oxide. In general the spinel formation reaction with the manganese-doped nickel oxide was the same structurally and kinetically as the spinel formation reaction with the pure oxide. The only significant difference between the spinel formed from the pure and the manganese-doped nickel oxide was the manganese enrichment of the spinel phase when formed from the latter oxide. A quantitative estimate of the degree of manganese enrichment in the spinel was obtained by electron-microprobe scans across the reaction interface. These scans showed that the manganese concentration in the spinel is approximately 4 times greater than in the doped nickel oxide.

Kinetics of nickel chromite spinel formation.—To confirm the previously reported observations that spinel formation was diffusion controlled (1, 2, 5), the thickness of the spinel surface layer was determined as a function of $t^{1/2}$ for two reaction temperatures. These measurements (Fig. 13) showed that the spinel thickness was indeed a linear function of $t^{1/2}$, and therefore controlled by diffusion processes. The reaction constant (K_p) for each experiment was calculated from the measured thickness (Δx) and the reaction time (t) using Eq. [1]

$$K_p = \Delta x^2/2t \qquad [1]$$

The spinel thicknesses at the specimen surface (Fig. 2, location A) and the dense interior of the specimen (Fig. 2, location B) were measured and used to calculate rate constants. In addition, the distance from the spinel/nickel oxide interface to the markers buried in the nickel oxide was measured and used to calculate a rate constant. It is proposed that each of these rate constants represent different reactions. The influence of temperature on the reaction rate constants for surface spinel and internal spinel formation is shown in Fig. 13.

There was a difference of two orders of magnitude between the reaction rate constant for spinel formed at the surface of the specimens (Fig. 2, location A) and for spinel formed inside the dense, crack-free, parts of

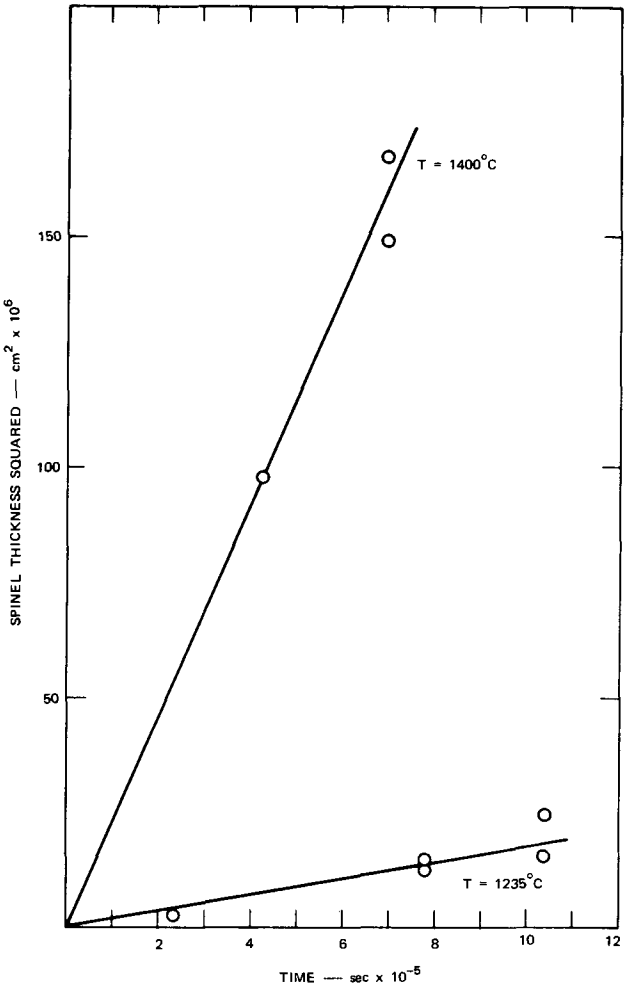

Fig. 12. Time dependence of nickel chromite thickness

[1] To maintain electrical neutrality, 3 Ni^{2+} ions must pass through the reference interface to balance the charge of 2 Cr^{3+} ions diffusing in the opposite direction. The nickel ions form three molecules of $NiCr_2O_4$ on the chromium oxide side of the marker while the chromium ions form one molecule of $NiCr_2O_4$ on the nickel oxide side.

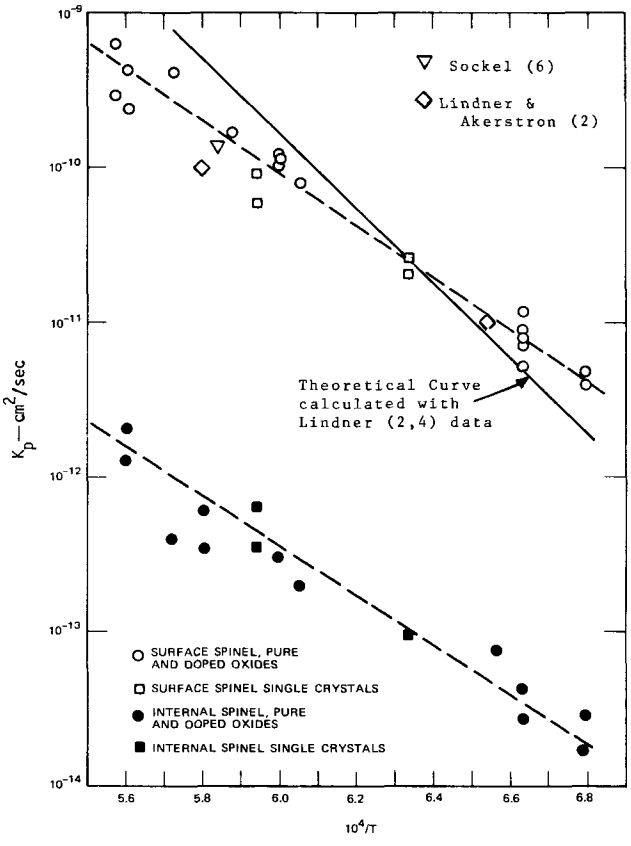

Fig. 13. Reaction rate constants for nickel chromite formation

the specimen (Fig. 2, location B). Even though there is considerable scatter in these data, the extreme difference in these rates clearly shows that two different mechanisms are operating.

Also apparent from Fig. 13 is the absence of any impurity effects in either the surface or internal reaction rate constants. The rates are essentially the same (within experimental scatter) for nickel chromite formed from pure chromium oxide, high purity, or manganese-doped nickel oxide. In addition, the rates of surface and internal spinel formation are the same for single crystal specimens as for dense polycrystalline specimens.

The reaction rate constants reported in prior studies (2, 6) are also shown in Fig. 13. These constants agree well with the surface spinel rate constants of the present work. This agreement is further proof of the porosity of the specimens used in prior studies, and the influence of vapor-phase transport on the rate constants. A least squares fit through the data reveals that the temperature dependences are

$$K_p \text{ (surface)} = 1.04 \exp(-76.4 \times 10^3/RT)$$

$$K_p \text{ (internal)} = 3.26 \times 10^{-4} \exp(-68.3 \times 10^3/RT)$$

The temperature dependence of the rate constants for interface motion with respect to the markers is given by

$$k_{\text{marker}} = 2.20 \times 10^{-2} \exp(-67.5 \times 10^3/RT)$$

The activation energy for the nickel oxide/nickel chromite interface motion is identical to that for internal spinel formation, and does not appear to be significantly affected by oxide composition or by the crystalline structure of the starting material.

Discussion

These experiments form the basis for the following model of nickel chromite spinel formation. The model is simple and is supported by the experimental data. Internal, or solid-state nickel chromite formation (*e.g.*, Fig. 2, location B) occurs by the countercurrent diffusion of Ni^{2+} and Cr^{3+} through the spinel, and simultaneously, through the nickel oxide. The rate of spinel growth is strongly affected by the rate of chromium dissolution and diffusion in the nickel oxide. Because the rates of transport through the spinel and the nickel oxide are of the same order of magnitude, there is a coupling of these two processes and it is not possible to specify one or the other as rate controlling. This model explains: (*i*) spinel precipitation in NiO; (*ii*) marker effects, including intrusion formation at marker defects, and thick spinel formation at thick markers; (*iii*) internal spinel thickness; and (*iv*) the motion of the spinel layer with respect to the markers.

Surface (*e.g.*, Fig. 2, location A) spinel formation occurs by a modified Wagner mechanism in which spinel dissolution is compensated for by geometrical effects. The cooperative diffusion of Cr^{3+} from vertical and horizontal surfaces of the specimen rapidly saturates the nickel oxide (17), and allows the spinel to grow by countercurrent diffusion of Ni^{3+} and Cr^{3+} through the spinel layer.

Comparisons were made of the measured spinel formation rates with the Wagner-Schmalzried theory.

Data for the free energies of formation were taken from Tretjakow and Schmalzried (18), and diffusion coefficients were chosen on the basis that the diffusion rate of Ni^{2+} controls spinel formation. This is basically correct, because the diffusivity of Ni^{2+} is less than that of Cr^{3+} over the temperature range of interest (2, 4, 19).

Two sets of diffusivity data for Ni^{2+} in $NiCr_2O_4$ are available. Although both sets were measured by the same authors, the diffusion coefficients calculated from one set (2, 4) are approximately one order of magnitude larger than those calculated from the other set (3). As would be expected, the values of the diffusion coefficients totally control the theoretical values of K_p. For example, at (T = 1400°C) the reaction rate constant equals $1.2D_{Ni}$. At lower temperatures (1200°C), K_p equals $0.45D_{Ni}$. The theoretical values of the reaction rate constants were calculated by using both sets of Lindner diffusivity data. The rate constants calculated on the basis of one set of data (2, 4) are shown in Fig. 13 and are in good agreement with measured rate constants. The rate constants calculated on the basis of the other set of data (3) were a factor of 7 lower than the measured rate constants.

In an earlier analysis of these data (20) it was concluded that agreement between the experimental and theoretical rate constants for nickel chromite formation was fortuitous. This conclusion was supported by the following facts. The theory was developed to apply to the formation of dense, defect-free, reaction product layers, while the experimental measurements were made with porous specimens or dense specimens whose surfaces were exposed to air (as in this study). In addition, the experimental rates for surface spinel formation are affected by chromium dissolution in the nickel oxide. Therefore, the theory, which does not account for vapor transport through pores, and dissolution of one component of the spinel by the other reactant, should not agree with the measured rates in which these effects prevail. However, it is possible that the structure of porous specimens (or surfaces of dense specimens) compensates for spinel dissolution by rapidly saturating the nickel oxide with chromium via vapor-phase transport. If the spinel layer is densified in the process, the experimental conditions will approach those required by theory.

Only qualitative statements will be made concerning the influence of impurities on the mechanism of spinel formation. There are two reasons for this. First, this is the first experimental study in which these effects have been considered. Second, these systems are more complex than normal spinels with respect to phase structure, defect structure, and thermodynamic definition (21). As described in the text, the addition of 1 m/o manganese oxide to nickel oxide did not sig-

nificantly affect the structure rate of formation of nickel chromite. However, manganese enrichment in the spinel (by a factor of 4) was observed.

A qualitative explanation for the enrichment of manganese in the spinel can be based on the polyvalent characteristics of the ions. Manganese can exist either as $MnO(Mn^{2+})$ or $Mn_2O_3(Mn^{3+})$ and can form its own spinel (Mn_3O_4) in which it exists in two valence states (22, 23). Consequently, the manganese ions can fit in both octahedral and tetrahedral sites in the spinel lattice. Therefore, the reaction of 1 mole of nickel oxide to form 1 mole of nickel chromite produces 3 times the initial number of sites in which the manganese ion can fit.

Conclusions

There are a number of conclusions from this work which have general application to spinel studies. These conclusions are associated with the two major experimental observations of this study: density effects and spinel dissolution effects. First, and perhaps most important, it has been shown that experimental results obtained from the reactions of high-density oxides can be significantly different from those obtained from the reactions of porous oxides. Spinel formation rates from dense oxides can be orders of magnitude slower than rates in porous oxides. Mechanisms of spinel formation from porous oxides can be affected, or controlled, by vapor-phase transport phenomena, while reaction mechanisms in dense oxides cannot. Simple marker experiments can be interpreted when dense oxides are used, whereas these markers are often destroyed or lost when porous oxides are used.

Dissolution effects, of the spinel in the reactants or the reactants in the spinel, must be accounted for in future studies. As has been shown in this work, such effects can control both the mechanism and kinetics of spinel formation. It is recognized that dissolution effects would be accounted for if observed. However, the experimental observations of these effects requires the use of dense reactants and careful specimen preparation and examination.

Another general conclusion from this work is that reaction mechanisms must be determined by direct experimental techniques. Determination of reaction mechanisms by comparison of experimental and theoretical reaction rate constants are totally dependent on measured rates of diffusion of cations through their respective spinels. There is sufficient variability in the diffusion data for these systems that nearly any experimental measurement will fit within an order of magnitude of a theoretical value. Any true test of the validity of a theoretically determined rate constant must be based on precise diffusion data through fully dense polycrystalline or single crystalline spinels, and theoretical data must be compared with experimental kinetic data determined from similar or (preferably) identical oxides.

Specific conclusions obtained from this study are:

1. The mechanism of nickel chromite formation from its component oxides is countercurrent diffusion of Ni^{2+} and Cr^{3+} through the spinel layer.
2. The rates of nickel chromite formation at surfaces of dense specimens or at interfaces of porous specimens are equal.
3. The rate of nickel chromite formation in dense oxides is two orders of magnitude less than the rate of formation at surfaces, and is strongly affected by the rate of chromium dissolution in nickel oxide.
4. Dissolution of Cr^{3+} in nickel oxide occurs at high (>1200°C) temperatures. The solubility of chromium oxide in nickel oxide is of the order of 10 weight per cent. On cooling to room temperature, the Cr^{3+} precipitates as nickel chromite in the nickel oxide.
5. The location and morphology of thin inert markers after spinel reactions can be explained as a result of chromium dissolution.
6. Additions of manganese (at the level of 1 m/o) to nickel oxide will not affect the rate of nickel chromite growth. However, manganese enrichment of the chromite layer will occur.

Acknowledgment

This work performed under NASA Contract NAS 3-11165.

Manuscript submitted June 5, 1972; revised manuscript received Jan. 22, 1973.

Any discussion of this paper will appear in a Discussion Section to be published in the December 1973 JOURNAL.

REFERENCES

1. K. Hauffe and K. Pschera, *Z. Anorg. Allgem. Chem.*, **262**, 147 (1950).
2. R. Lindner and A. Akerstrom, *Z. Physik. Chem. (N.F.,)* **6**, 162 (1956).
3. R. Lindner and A. Akerstrom, *ibid.*, **18**, 303 (1958).
4. R. Lindner, *Naturforsch.*, **10a**, 1027 (1955).
5. H. Schmalzried, *Z. Physik. Chem. (N.F.)*, **33**, 111 (1962).
6. H. G. Sockel, Thesis, University of Goettingen, West Germany (1965).
7. J. S. Armijo, *Oxidation of Metals*, **1**, 171 (1969).
8. R. A. Brown, *Am. Ceram. Soc. Bull.*, **44**, 483 (1965).
9. R. A. Brown, *ibid.*, **44**, 693 (1965).
10. C. Greskovich, *J. Am. Ceram. Soc.*, **53**, 498 (1970).
11. H. Schmalzried, *Ber. Deut. Keram. Ges.*, **42**, 11 (1965).
12. B. Bengston and R. Jagitsch, *Arkiv Kemi*, **24A**, 1 (1947).
13. F. S. Pettit, E. H. Randklev, and E. J. Felton, *J. Am. Ceram. Soc.*, **49**, 199 (1966).
14. C. Wagner, *Z. Physik. Chem.*, **34**, 309 (1936).
15. J. Moreau, *Compt. Rend.*, **236**, 85 (1953).
16. G. H. Meier and R. A. Rapp, To be published, *Metallurgical Trans.*
17. C. Wagner, Private communication.
18. J. D. Tretjakow and H. Schmalzried, *Ber. Bunsenges. Phys. Chem.*, **69**, 396 (1965).
19. A. Morkel and H. Schmalzried, *Z. Physik. Chem. (N.F.)*, **32**, 76 (1962).
20. J. S. Armijo, Ph.D. Dissertation, Stanford University, California (1969).
21. H. Schmalzried, *Progr. Solid State Chem.*, **2**, 265 (1965).
22. R. S. Gurnick and W. M. Baldwin, Jr., *Trans. Am. Soc. Metals*, **42**, 308 (1950).
23. E. B. Evans, C. A. Phalnikar, and W. M. Baldwin, Jr., *This Journal*, **103**, 367 (1956).

Technical Notes

Nondestructive Location of Oxide Breakdowns on MOSFET Structures

P. L. Garbarino and R. D. Sandison

IBM System Products Division, East Fishkill Facility, Hopewell Junction, New York 12533

An experimental investigation of the mechanism of silicon dioxide degradation leading to MOS oxide breakdown has highlighted the need for a reliable nondestructive method of pinpointing the breakdown location. A situation commonly presents itself where electrical test has pointed to a short (breakdown) in a "chain" of as many as several hundred thin oxide regions, all tied in electrical common by a metalization pattern. The use of an oxide chain arises naturally and necessarily from the limited number of terminals on a test chip, and the requirement that extremely large numbers of individual regions be tested to generate just a few breakdown failures at high bias-temperature stress. The problem is then to narrow the short location to an area that is manageable for meaningful study by visual, x-ray, or electron-optical means. That is, the breakdown must be located nondistructively to a single thin oxide area; or better, to a fraction of one area.

The purpose of this note is to report that cholesteric liquid crystal together with a thin amorphous carbon coating is ideally suited to breakdown location in the small areas typical of thin oxides on MOS devices. The procedure should have wide applicability in the failure analysis of bipolar LSI devices as well.

Liquid crystals (1, 2) are substances which selectively scatter incident white light, the wavelength of the scattered light scaling inversely with the temperature. The thermal characteristics of the liquid crystal are operationally specified by two parameters: (*i*) the lowest temperature at which color first appears, which we call the transition temperature; and (*ii*) the temperature range over which the entire spectrum is displayed, which is referred to as the thermal bandwidth (3). The crystal can be simply considered to be a thermometer which translates the thermal gradient around the powered short into a color pattern. As Fig. 1 indicates, the location of the short is revealed as a color profile on a colorless background.

Procedure

The mounted chip (either header or otherwise) is placed in good thermal contact with a thermally massive temperature controlled substage. The liquid crystal, mixed with its volatile suspension medium, is applied to the chip either with an eyedropper or an air brush to a thickness of 3-5μ. The temperature of the as yet unpowered chip may be cycled through the thermal bandwidth of the crystal several times (the color transition of the crystal is reversible) and the color quality observed. It is important to have a continuous film of as uniform a thickness as possible. If the color quality is poor, an additional liquid crystal application may be used to enhance it. However, a crystal thickness of more than 10μ is detrimental as it broadens the thermal profile around the short, compromising the obtainable spatial resolution.

Key words: SiO_2 degradation, oxide breakdown, shorting, failure analysis, nondestructive.

The temperature of the substage is adjusted to be about 2°C below the transition temperature of the crystal, and the device powered until the temperature at the short is well into the thermal bandwidth of the crystal. A schematic of the substage assembly is shown in Fig. 2.

In practice, it is found that the reflected white light from the metalization pattern is of much greater intensity than that of the selectively scattered radiation,

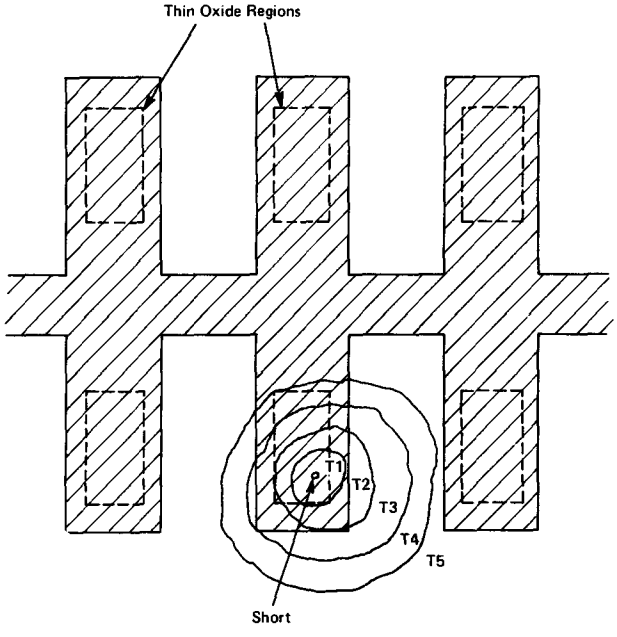

Fig. 1. Schematic of a defective gate chain. The cross-hatched areas indicate the metalization pattern forming the chain. Gate areas are outlined by dashed lines. The rough circles around the short represent isotherms of the temperature profile around the powered short. Temperatures $T_1 > T_2 > \cdots > T_5$ are the average temperatures in their respective regions. Under action of the liquid crystal region 1 will appear blue; region 2, green; region 3, yellow; region 4, red; and region 5, colorless.

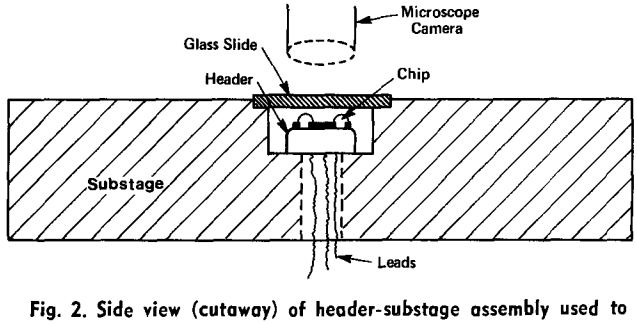

Fig. 2. Side view (cutaway) of header-substage assembly used to provide temperature control.

rendering the color pattern difficult or impossible to see. A layer of carbon black deposited on the chip surface prior to crystal application will counter this difficulty. The carbon layer must be thick enough to shield most of the reflected light but thin enough so that the metalization pattern may still be seen; carbon thicknesses of from 0.2 to 0.4μ will strike this balance. Commercial mixtures of dye and liquid crystal, and flat black paints are not adequate because of nonhomogeneity of coverage or complete opaqueness.

Carbon layers of the above thickness were found to be of high enough electrical impedance so as not to alter the electrical characteristics of the test chip. The carbon may be deposited in an evaporator, or most simply by rapidly passing the chip through the sooty flame of a paraffin candle several times. The carbon layer as well as the liquid crystal can be removed by ultrasonic agitation in a chloroform bath.

Spatial Resolution

Based on a study of extremely thin chromium resistors deposited on glass substrates, Lukianoff (3) has concluded that the limit of spatial resolution of liquid crystal is 1μ. In the case of fault location on MOSFET structures, one must contend with a heat source that is not directly on the surface but is buried under the metal of the gate electrode and the applied carbon coating. For our devices, the resolution limit, due to the broadening of the thermal pattern by the material over the heat source, is about 0.3 mils (7.3μ). That is, in a one-mil square gate area one can, by careful observation of the thermal profile, expect to narrow the short location to about 1/10 of the gate area. These numbers are estimates and may vary with the construction characteristics of the particular MOSFET device in question.

This technique eliminates the tedium involved in cutting and probing the metalization pattern to narrow the short location electrically, and has proven to be highly reliable in locating the breakdown. In several instances, visual inspection of a failed thin oxide region after metalization removal, showed more than one abnormally. Comparison with the liquid crystal photograph was indispensible in determining which fault was actually responsible for the electrical short. An SEM photograph of an oxide breakdown located with liquid crystal is shown in Fig. 3.

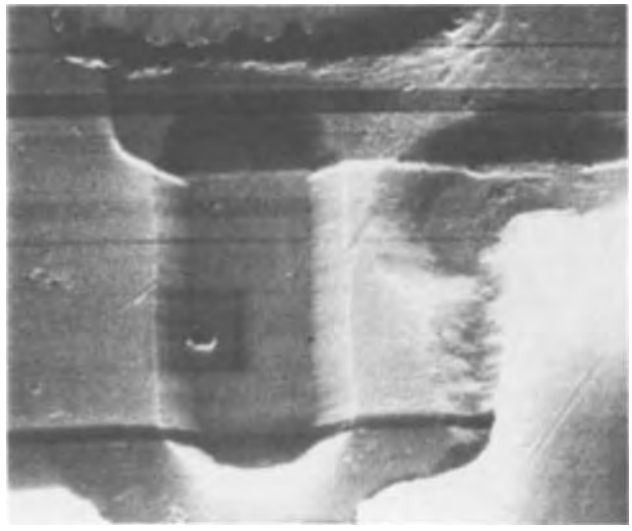

Fig. 3. SEM photograph of breakdown in thin oxide

Acknowledgment

The authors wish to thank D. E. Stabell and D. Fox for their interest and support.

Manuscript submitted Jan. 4, 1973; revised manuscript received Feb. 10, 1973.

Any discussion of this paper will appear in a Discussion Section to be published in the December 1973 JOURNAL.

REFERENCES

1. J. L. Fergason, *Appl. Opt.*, **7**, 1729 (1968).
2. W. E. Woodmanesse, *ibid.*, **7**, 1721 (1968).
3. G. V. Lukianoff, *Molec. Cryst. Liq. Cryst.*, **8**, 389 (1969).

Some Factors Influencing the Luminous Decay Characteristics of $Y_3Al_5O_{12}: Ce^{3+}$

E. F. Gibbons, T. Y. Tien,* R. G. DeLosh, P. J. Zacmanidis, and H. L. Stadler*

Ford Motor Company, Scientific Research Staff, Dearborn, Michigan 48121

Fast decay phosphors based on Ce^{3+} activation have been used for many years. Under electron beam excitation these phosphors typically have a decay time (I_{max}/e) of less than 100 nsec and have a broad-band emission spectrum peaking in the near ultra violet or blue. Several recently developed phosphor materials have moved the cerium emission peak to much longer wavelengths, green emission being reported for $CaS:Ce^{3+}$ (1) and green to yellow-orange for various garnet hosts (2-4).

Visible emitting fast decay phosphors have a number of useful applications. One such application, which was the primary motivation for this investigation, is in flying-spot scanner tubes such as those used by the Post Office in their automatic letter sorting system. The phosphors mentioned above, however, have one disadvantage which limits their usefulness, *i.e.*, the luminescent decay curve is very nonexponential. Bril *et al.* (3) report that for $Y_3Al_5O_{12}:Ce^{3+}$ the emission intensity is still 6% of its maximum value 80 μsec after cessation of excitation, while Lehmann and Ryan (1) observed that $CaS:Ce^{3+}$ had an afterglow lasting for several milliseconds. This nonexponential decay behavior is very undesirable for flying spot scanner applications since it creates a large background illumination which appears as noise to the signal processing system. This, of course, lowers the signal to noise ratio of the system and, in the case of the Post Office mail sorter, reduces the percentage of the mail that can be sorted.

This note reports the effect of several parameters on the decay characteristics of $Y_3Al_5O_{12}:Ce^{3+}$, with some sets of conditions resulting in almost purely exponential decay curves.

Experimental

Phosphor samples used were 2 mole per cent (m/o) Ce^{3+} activated $Y_3Al_5O_{12}$. The preparation of this phosphor has been reported previously (5).

The phosphors were settled on 1 in. $\times$ 3 in. microscope slides using the conventional potassium silicate-barium acetate settling technique. The slides, after

* Electrochemical Society Active Member.

Key words: luminescence, phosphors, cerium, $Y_3Al_5O_{12}$.

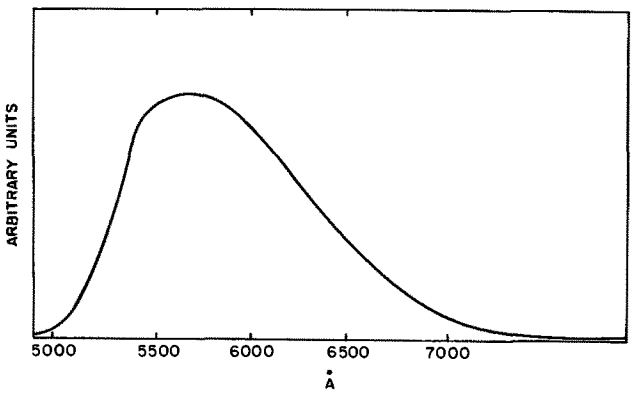

Fig. 1. Cathodoluminescent emission spectrum of $Y_3Al_5O_{12}:Ce^{3+}$

aluminizing, were measured in a demountable electron beam gun system. All measurements were made at 15 kV beam voltage and current densities of approximately 10 mA/cm². The electron beam gun, normally biased into cutoff, was pulsed on by means of an external pulse generator capacitively coupled to the grid. Pulse widths used in these experiments were 0.2, 3, and 20 μsec.[1]

The light pulse was detected by a 9558Q photomultiplier tube with the resulting signal being analyzed by a PAR Model 160 Boxcar Integrator. It was found that the photomultiplier tube required an electrically shielded, noninductive 50 ohm load to insure the elimination of spurious electrical effects. Also, with such a small load resistor, care had to be taken not to overload the photomultiplier. If the incident light intensity on the photomultiplier cathode was too high, the resulting high electron density at the anode would produce an electrical signal lasting tens of microseconds after the termination of the light pulse. This is probably caused by a momentary heating effect at the anode. Suitable neutral density filters eliminated this "tail" effect.

The output from the boxcar integrator was plotted on an x-y recorder. Since the minimum gate open time for the boxcar integrator was 10 nsec, this represented the ultimate resolution obtainable from the system.

Intensity data were taken by applying a 1 in. by 1 in. raster to the phosphor-coated slide and measuring the luminous intensity by means of a Spectra Pritchard photometer, Photo Research Corporation Model 1970 PR.

The emission spectra were measured in a second demountable system attached to a ¾ meter Czerny-Turner spectrometer.

Results

The emission spectrum for $Y_3Al_5O_{12}:Ce^{3+}$ is shown in Fig. 1. This spectrum did not change with different firing atmospheres as long as the cerium concentration remained constant. The emission peak does shift, however, with cerium concentration. Firing in an oxidizing atmosphere limited the amount of cerium that the garnet would accept to 2%, with a second phase appearing if the starting concentration of cerium was higher than that, while a reducing atmosphere permitted up to 6% cerium to be incorporated into the host. These solubility limit and emission peak shift results are presented in detail elsewhere (5). All systems studied in this experiment had a cerium concentration of 2%.

Figure 2 shows the luminescent decay curves for a 3 μsec excitation pulse resulting from three different firing conditions. It can be seen that the afterglow becomes progressively more pronounced as the firing atmosphere goes from oxidizing to inert to reducing. Also, for the material formed in an inert or reducing environment, there is a gradual build-up of the emission intensity during the period of excitation. These two results would be consistent with the idea of energy storage traps in the phosphor. These traps would slowly fill during the excitation period, taking up less and less of the excitation energy as more traps become filled. This would produce the sort of cerium emission increase seen during the excitation period. These traps could then slowly feed their energy to the cerium ions after the electron beam pulse was turned off, thus producing the observed afterglow. A likely candidate for such energy traps would be lattice defects, possibly oxygen vacancies, since the build-up and afterglow effects are greatly diminished when the phosphors are prepared in an oxygen atmosphere. If this is true, then one would expect to be able to anneal out at least some of these traps by refiring in air material that had been prepared in a reducing atmosphere. Figure 3 shows the results of such an experiment where a 20 μsec duration excitation pulse has been used. It is obvious that the refiring has greatly diminished the build-up and afterglow observed in the original material.

Also, since the number of traps that are filled depends on the duration of the excitation, one would expect that the afterglow effect would be more pronounced for long excitation pulses. This trend is shown

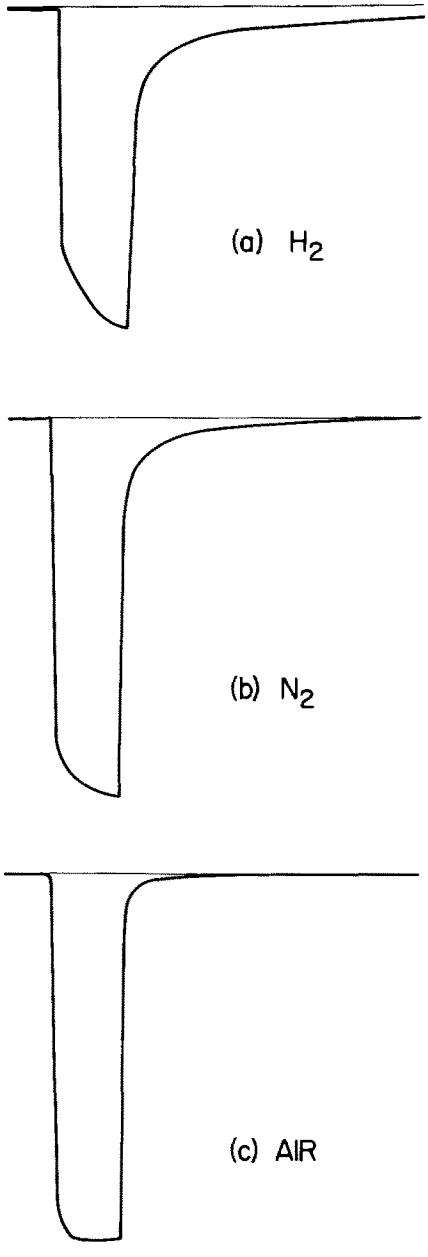

Fig. 2. Light intensity profiles for 3 μsec excitation pulses for materials fired in (a) H_2, (b) N_2, and (c) air.

[1] The 0.2 and 3 μsec values correspond to the beam dwell time on a phosphor particle in a Post Office Optical Character Reader when the system is in either its "search" or "read" mode (6).

Table I. Effect of firing atmosphere and excitation pulse width on the luminous decay of Ce^{3+} and effect of firing atmosphere on relative intensity

Material	Firing atmosphere	0.2 μsec pulse		3 μsec pulse		20 μsec pulse		
		$I_{max/10}$ (μsec)	$I_{max/20}$ (μsec)	$I_{max/10}$ (μsec)	$I_{max/20}$ (μsec)	$I_{max/10}$ (μsec)	$I_{max/20}$ (μsec)	Relative intensity
$Y_3Al_5O_{12}$: 2% Ce	Air	0.23	0.30	0.26	0.42	0.28	0.75	85
	H_2	0.32	0.62	3.2	8.5	12.0	35.0	100
	H_2-Air*	0.21	0.30	0.72	1.4	0.75	2.7	70
	N_2	0.29	0.48	1.1	2.0	4.4	13.5	70
$Y_{2.7}Gd_{0.3}Al_5O_{12}$: 2% Ce	Air	0.29	0.49	1.0	2.3	2.9	8.6	85

* Sample was fired for 2 hr in H_2, then refired 5 min in air.

in Table I which lists the time after excitation for the light intensity to fall to its 10% point and 5% point. These data are given for different pulse widths and for different firing conditions. All samples show a tendency toward longer decay times under longer pulse conditions. However, the effect for the air-fired sample is only very slight, while the H_2-fired sample shows a much greater afterglow for the longer excitation pulses. The material refired in air has a much more improved decay characteristic than did the original H_2-fired material, being equivalent to the air-fired sample at the shortest pulse width, and only slightly worse for the longer pulses. The N_2-fired sample is intermediate to the above cases.

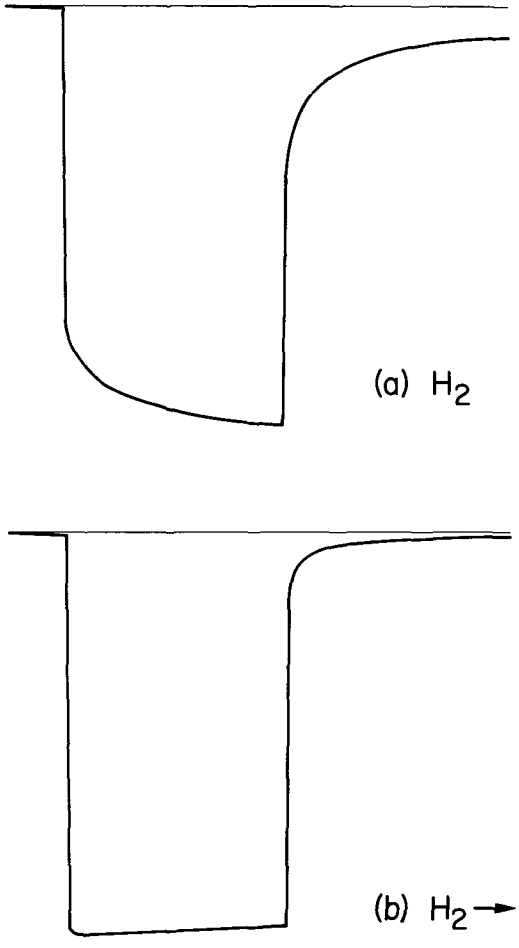

Fig. 3. Light intensity profiles for 20 μsec excitation pulses for material fired in (a) H_2, and (b) same material refired in air.

The table also gives data for $Y_{2.7}Gd_{0.3}Al_5O_{12}:Ce^{3+}$, a material in which 10% of the yttrium has been replaced by gadolinium. Although this material was fired in air, the longer excitation conditions show an afterglow effect considerably more pronounced than the pure $Y_3Al_5O_{12}:Ce^{3+}$ fired in air. It could be that the addition of Gd to the system caused sufficient distortion of the garnet crystal to introduce other types of energy traps.

Table I also shows the relative intensity data for the samples fired in different atmospheres. Hydrogen-fired samples have a somewhat greater intensity, as measured by a spot photometer, than do the air-fired samples.

The results then indicate that under certain firing conditions and excitation conditions, $Y_3Al_5O_{12}:Ce^{3+}$ shows very little afterglow effect. Even in cases of long pulse width excitation, nonexponential decay characteristics can be minimized by using the appropriate forming conditions.

Manuscript submitted Aug. 23, 1972; revised manuscript received Jan. 22, 1973.

Any discussion of this paper will appear in a Discussion Section to be published in the December 1973 JOURNAL.

REFERENCES

1. W. Lehmann and F. M. Ryan, *This Journal* **119**, 275 (1972).
2. G. Blasse and A. Bril, *Appl. Phys. Letters*, **11**, 53 (1967).
3. A. Bril, G. Blasse, and J. A. dePoorter, *This Journal*, **117**, 346 (1970).
4. W. W. Holloway, Jr. and M. Kestigian, *J. Opt. Soc. Am.*, **59**, 60 (1969).
5. T. Y. Tien, E. F. Gibbons, R. G. DeLosh, P. J. Zacmanidis, D. E. Smith, and H. L. Stadler, *This Journal*, **120**, 228 (1973).
6. F. P. Keiper, U.S. Pat. 3,196,208 (1965).

Anomalies Observed in Some Discrete Device and Integrated Circuit Substrates

Ivars Irbe

Rome Air Development Center, RBRM, Griffiss Air Force Base, New York 13441

Several phenomena, not yet reported in the literature to the author's knowledge, have been observed during physical analysis of in house fabricated avalanche diodes and some commercially available integrated circuits and ion-implanted MOS field effect devices.

The first of the phenomena, denoted "bulk stain effect," was observed on freshly angle-lapped surfaces of samples which had previously been angle lapped and stained (concentrated HF under intensive light), or the top surfaces of which had been treated with concentrated HF. In each case, without application of the staining agent to the freshly angle-lapped surfaces, stainlike discolorations were evident in the p-diffused areas, generally not exceeding laterally the respective diffusion window boundaries and extending down to a varying fraction of the diffusion depth. Since bulk silicon material is removed during an angle-lapping operation, the appearance of such discoloration implies that staining had occurred inside the silicon material during the preceding staining cycles, hence the term "bulk stain effect." Comparison of horizontal and vertical dimensions of the volumes removed by the angle-lapping cycles indicates that the bulk staining occurs predominantly from the top of the silicon chips, *i.e.*, from the top surfaces of the respective diffusion windows. The total time of HF treatment applied to the chip surfaces before the appearance of bulk stain effect ranged from 20-30 sec (circuit chip shown in Fig. 2) to well over 30 min (time accumulation from 15 angle lapping and staining cycles applied to a circuit chip during failure analysis; not shown here). Application of the staining agent to angle-lapped surfaces which already display the bulk stain effect produces the normal staining patterns, except that the bulk stained areas remain distinguishable due to different shades of discoloration and/or depressions in these areas. The effect was observed within devices or circuit configurations fabricated in epitaxial silicon substrates, and within some ion-implanted devices. In the latter case, it was not known if the substrates were epitaxial wafers. On circuit chips with silicon nitride surface protection, the bulk stain was observed only in areas which were not covered by silicon nitride during the preceding staining cycles.

An etching of silicon surfaces was in some instances observed to occur during chemical treatments (concentrated HF or KOH) of devices and circuits by chemicals which normally [KOH at room temperature on (111) surface] would not attack silicon, or would do so at a very slow rate. The etching was most pronounced within devices and structures formed by high impurity concentration diffusions, especially n^+ (phosphorus) diffusion. The etching was also observed on some silicon surfaces following only a thermal oxidation in steam. All of the areas in which etching was observed had received at least a 20 min aqua regia treatment after the silicon dioxide had been removed (etched away). In the case of the MOS device, the etching occurred in areas which had been diffused and subsequently ion implanted. This device was not subjected to aqua regia or other nitric acid based chemical treatment.

Figure 1 displays the bulk stain effect and a normal subsequent staining pattern on the same angle-lapped surface observed within an avalanche diode structure fabricated by p^+ diffusion (7.5×10^{19} boron atoms/cc final impurity concentration at the surface) into an $n^- \text{-} n^+$ epitaxial silicon substrate (10.0 ohm-cm, 8.0μ thick epitaxial layer on 0.01 ohm-cm substrate. These parameters apply also to devices shown in Fig. 3 and 4). Note in Fig. 1b the darker shade of color and the depression of the bulk stained area within the normal staining pattern. The bulk stain effect within a silicon nitride passivated circuit chip is shown in Fig. 2b. A 30 sec staining cycle, sufficiently long to remove all the exposed silicon dioxide, was applied to the surface shown in Fig. 2a. A subsequent lapping cycle revealed the bulk stain effect, except for the areas which had been protected by the silicon nitride layer and that part of the silicon dioxide layer removed last by the preceding staining cycle. This behavior was observed also during consecutive staining and lapping cycles. Note the appearance of the bulk stain in the contact areas which were not protected by silicon nitride. In addition to the bulk stain effect shown in Fig. 3a, both Fig. 3a and 3b display silicon surface etching effects inside the device diffusion window and on the chip surface outside the laterally diffused areas. The differences in height are indicated by the interference fringes. The silicon areas outside the diffusion window did not receive any processing other than initial oxidation (2½ hr at 950°C in steam) and boron drive in (20 min at 1150°C in steam) cycles. Surface etching is also evident in Fig. 4. The structure indicated by the arrow constitutes a scribe line from which the oxide was removed prior to aluminum metalization. The area was alloyed (450°C for 15 min) during the contact formation process. A preferential surface etching outside the laterally diffused areas is evidenced by a ridgelike structure on the right side of this photograph. Based on junction depth measurements, it appeared that the scribe lines and the laterally diffused areas were etched very little or not at all. The devices in Fig. 3 and 4 were treated with aqua regia for an additional 20 min after the removal of the metalization lines and silicon dioxide layer. Bulk stain and surface etching effects within the structure of a diffused and

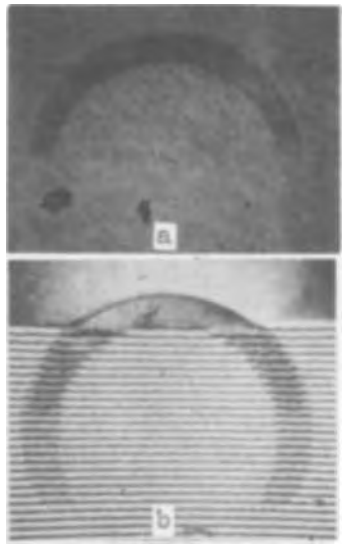

Fig. 1. (a) A freshly angle-lapped surface of a device chip displaying bulk stain effect; (b) the same surface after staining. Magnification 130×.

Key words: silicon, failure analysis, process induced defects.

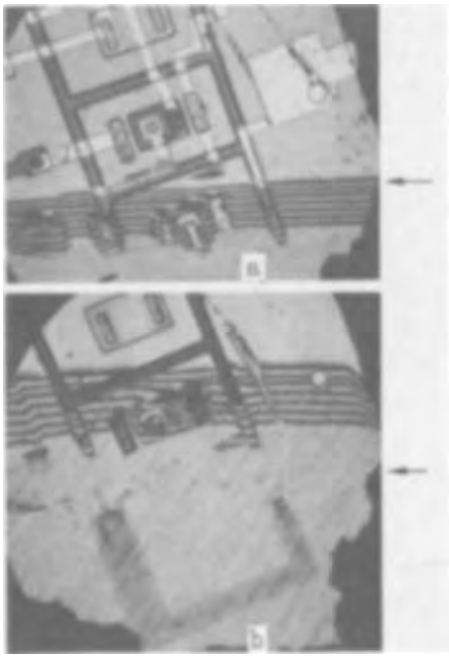

Fig. 2. (a) A freshly angle-lapped surface of a circuit chip with silicon nitride passivation; (b) same chip after a staining and an additional lapping cycle. Arrow indicates the level of the silicon nitride layer during staining cycle. Magnification 130×.

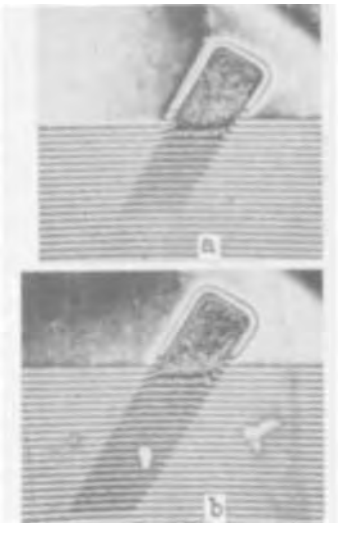

Fig. 3. (a) A freshly angle-lapped surface displaying bulk stain effect; (b) same surface after staining. A ridgelike structure covering the laterally diffused area is evident in both photographs. Magnification 130×.

ion-implanted MOS field effect device are shown in Fig. 5. Previous angle-lapping and staining cycles indicated 1.9μ diffusion and 0.4μ ion-implantation depth. Subsequent angle-lapping cycles revealed a bulk stain effect up to 1.5μ depth (Fig. 5a). A consecutive 2 min treatment with concentrated KOH completely removed all silicon (Fig. 5b) in areas outlined by the bulk stain discoloration leaving the channel areas intact as a ridge-like structure. Note the interference fringes on the angle-lapped parts of the channel structure. All angle lapping shown in the photographs was done with a 2° lapping block. A Zeiss interferometer (thallium light, $\lambda/2 = 0.27\mu$) was used for the measurements.

Based on these observations and on additional work done on devices fabricated by high concentration diffusion into single resistivity (nonepitaxial) silicon substrates, which showed no bulk staining, it is postulated that both effects are primarily caused by imperfections in, and/or gross damage to, the crystalline structure of the substrate material. The bulk stain effect takes place whenever the silicon material can be penetrated by the staining agent (HF) causing, upon reaction with available p-type impurities, discolorations in the bulk material. In the cases of the surface etching effects, the penetrants would be provided by the nitric acid components of the applied chemicals. Absence of etching in alloyed and laterally diffused areas indicates that it might be possible to improve the crystalline structure of the material by judiciously applied processes. The possibility of penetration of silicon substrate material by chemical agents points to a potential problem area with respect to device and integrated circuit reliability.

Fig. 4. Display of surface etching effect. Arrow indicates the scribe line area. Ridgelike structure similar to the one shown in Fig. 3 can be seen on the right side of the photograph. Magnification 130×.

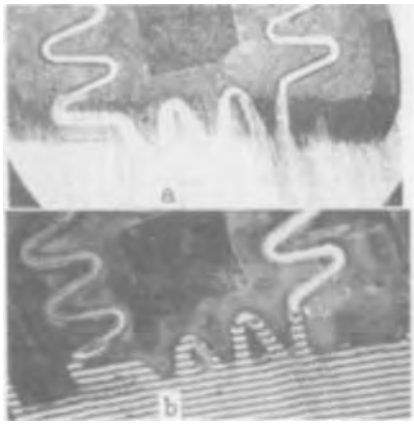

Fig. 5. (a) Display of bulk stain effect on a freshly angle-lapped surface; (b) same area after KOH treatment, displaying etching effect as evidenced by the remaining ridgelike channel structure.

Acknowledgments

Some of the work undertaken in the Solid State Applications Section of Rome Air Development Center for the purpose of investigating the nature and causes of these effects is described in RADC-RC-TM-71-7 "Development and Analysis of Diffusion Techniques."

Appreciation is expressed to the personnel of the Advanced Studies Group for the help provided in the preparation of this article.

Manuscript submitted May 25, 1972; revised manuscript received Oct. 23, 1972.

Any discussion of this paper will appear in a Discussion Section to be published in the December 1973 JOURNAL.

Porous Carbides as Evaporation Sources for Vacuum Deposition of Metal and Semiconductor Layers

J. J. A. Ploos van Amstel and E. Kooi*

Philips Research Laboratories, Eindhoven, Netherlands

In vapor deposition techniques the material in question is usually evaporated from a crucible or a filament. In this paper we will describe the preparation of evaporators of a porous nature, usually rod or tube shaped, and consisting of the carbide of either aluminum, silicon, titanium, or zirconium. The porosity of these evaporators, which is due to their particular manufacturing process, makes it possible for them to contain a fairly large amount of material to be evaporated. Capillary action causes a rapid distribution of molten material in the porous structure. This enables such an evaporator to be connected to a separate source of material, so that a continuous supply of fresh material may occur during a vapor deposition process.

Possibilities for continuous supply of material have been described earlier by one of us (1) and an example is shown schematically in Fig. 1. A long rod-shaped evaporator, as indicated, is heated by passing through an electric current. One end of the evaporator is connected to a crucible, placed at the top end in Fig. 1. The crucible contains the material to be evaporated and has a small hole in its bottom, through which the evaporator is connected to the material in the crucible. This material can be melted by heating with aid of a small furnace, as indicated in the figure. The molten material flows along the evaporator only when the latter is hot. If the temperature of the evaporator is sufficiently high, evaporation will occur from it in all directions. Substrates on which deposition is to take place can be arranged around the evaporator. In this manner homogeneous deposition can be obtained over large areas. The choice of the material for the evaporator will depend on the material to be evaporated. It is obvious that the evaporator must be able to withstand sufficiently high temperatures to permit evaporation. Further, it is desired that there be a certain amount of wetting of the evaporator by the molten material in the crucible. Otherwise a flow of droplets may occur to the lower end of the evaporator without resulting in effective evaporation. We have found that in many instances twisted wires of refractory metals can be very useful. Twisted tungsten wire evaporators, for example, have been applied successfully for evaporation of metals like Cu, Au, and Ag.

In search of useful materials for this evaporation method, we have developed methods of preparing the carbide evaporators to be described. They may indeed be applied as indicated in Fig. 1, but their use is certainly not limited to that procedure. The preparation of Al_4C_3, SiC, TiC, and ZrC was performed via reactions between the elements, using commercially available graphite cords as the starting material for the carbon constituent. These cords are flexible and can easily be handled; they can even be knotted, if desired. As the cords are "hollow," one may be pulled over another; this is useful for the preparation of thicker evaporators. The cords have a woven structure; consequently, a carbide formed from it looks similar (see Fig. 2) and has a high degree of porosity. Due to capillary action, flow of molten material in such a carbide evaporator is not restricted to the direction of gravity. In a set-up like that shown in Fig. 1, a vertically placed carbide evaporator may be connected to a molten source of material even at its lower end. An upward flow of molten material then occurs to replace material which is evaporated, thus guaranteeing a constant evaporation rate.

In Table I we have listed the melting points of the four carbides as well as those of the elements Al, Si, Ti, Zr, and Cr, and the temperatures at which the vapor pressure of the pure elements is 10^{-2} Torr. The latter values indicate the temperatures needed to get a reasonable rate of evaporation of the given element. Usually Al is evaporated from Al_4C_3, Si from SiC, and so on. The element Cr has been added to the list because we consider this a useful example of another element which can be evaporated via one of the above carbide evaporators (ZrC). The special method to perform this will be described later in this paper.

Preparation of Aluminum Carbide and Silicon Carbide Evaporators

In Fig. 3 the method of preparing Al_4C_3 and SiC evaporators is shown. The crucible contains either Al or Si and can be heated. It is placed either at the top end or at the lower end of a vertically stretched graphite cord. In the case of SiC, preparation reaction between Si and C can be started simply by heating the whole assembly. The reaction then proceeds along the cord, thus converting it completely to a SiC rod. Due to the contact with the liquid in the crucible, the rod contains an excess of silicon. Figure 2 shows a photograph of a carbon cord and a resulting SiC rod-shaped evaporator.

For the preparation of an aluminum carbide rod it is necessary to heat the cord to a higher temperature. This can easily be done by passing an electric current through the cord. After the reaction has started, a reaction zone is seen to pass along the cord. The aluminum carbide formed contains an excess of aluminum because of the contact with the aluminum in the crucible.

Preparation of Titanium Carbide and Zirconium Carbide Evaporators

Because of the high melting points of TiC and ZrC as well as of elementary Ti and Zr, the method of preparation as used for Al_4C_3 and SiC is hardly possible as crucible materials for contamination-free melting are not available. In these cases contact between Ti or Zr and the graphite cord is established either by pulling the cord into a spiral of Ti or Zr wire, or by threading a wire of one of these elements through the

Table I. Melting points of a few elements and carbides

Element	Melting point (°C)	Temp for 10^{-2} Torr (°C)	Carbide	Melting point (°C)
Al	670	1200	Al_4C_3	2100
Si	1420	1550	SiC	2800[d]
Ti	1700	1700	TiC	3100
Zr	1850	2400	ZrC	3500
Cr	1900	1400		

The third column indicates the temperatures at which the vapor pressure of the elements is 10^{-2} Torr and may thus be considered as an indication of the temperature needed for evaporation at a reasonable rate.

* Electrochemical Society Active Member.

Key words: vapor deposition, aluminum carbide, silicon carbide, titanium carbide, zirconium carbide.

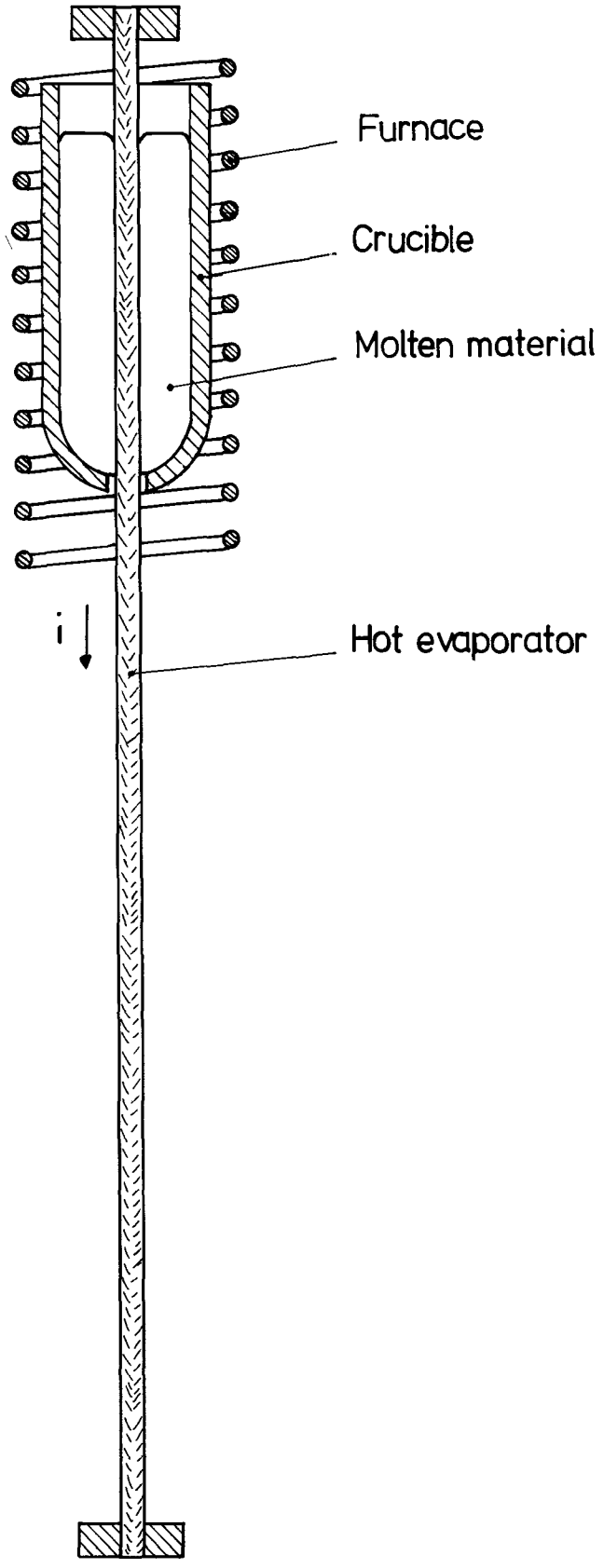

Fig. 1. Basic setup for vacuum deposition from a long evaporator supplied continuously from a crucible with molten material at the top.

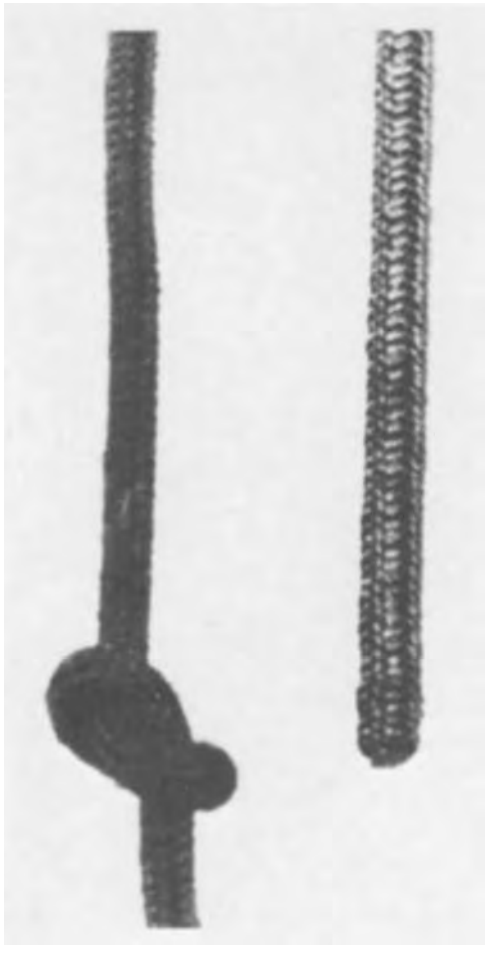

Fig. 2. Photographs of a graphite cord and of an SiC evaporator made from such a cord. The diameter may be a few mm, the length several dm.

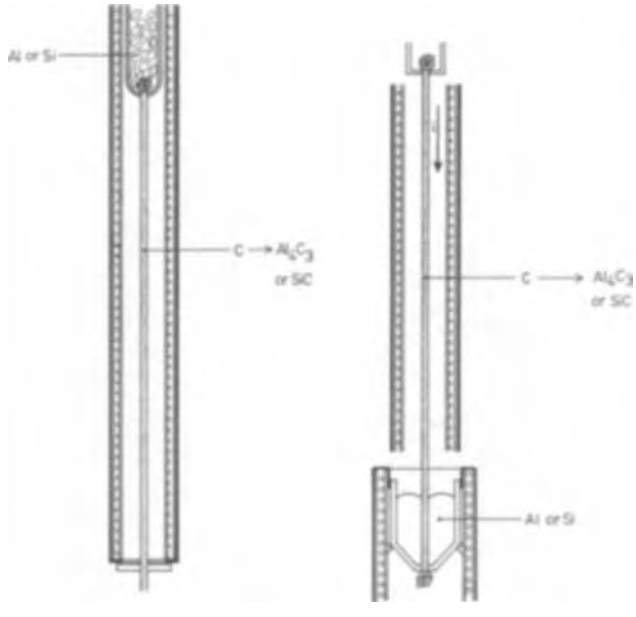

Fig. 3. Methods of preparation of Al_4C_3 and SiC evaporators. A graphite cord is connected to a crucible with molten aluminum or silicon, placed either at the upper or the lower end of the cord. Note that the cord is stretched by knots at the ends. Reaction occurs along the cord if sufficient heat is supplied.

cord (Fig. 4). The reaction can be made to occur by the heating produced by passing of an electric current. It starts near one of the contacts and a very hot zone can be seen to move quickly along the cord. These carbide evaporators may also contain a large excess of the metallic element. It should be remarked that, if an evaporator is formed by inserting a metal wire inside the cord, the resulting carbide will show a hollow structure (see Fig. 5).

The Use of Carbide Evaporators

Preparation by one of the methods described above yields carbide evaporators containing an excess of

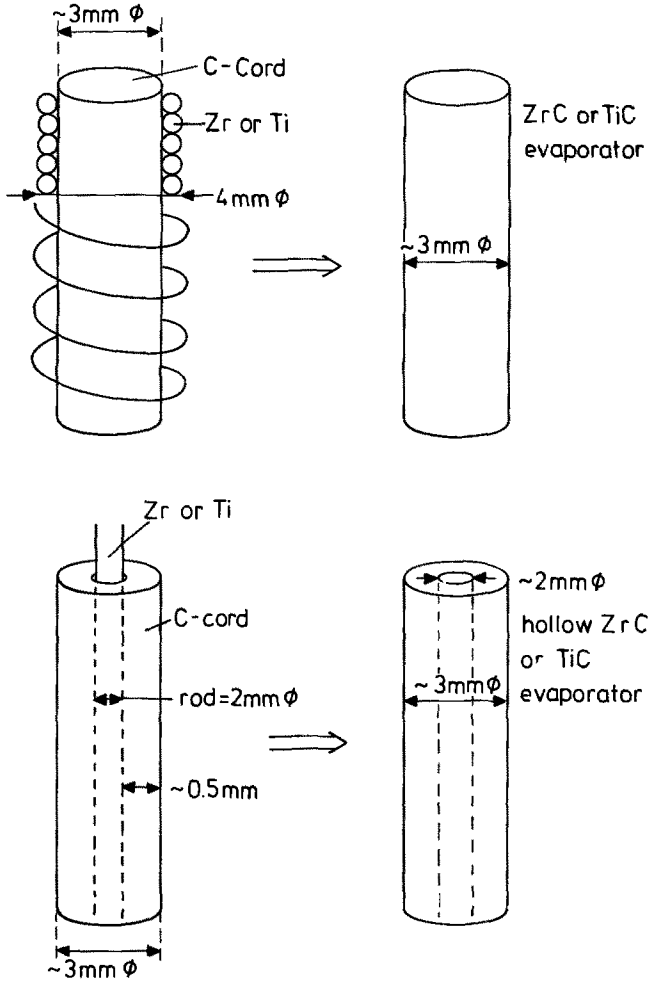

Fig. 4. Preparation of TiC and ZrC evaporators. A metal wire is either wound spirally around a graphite cord or inserted in it. In the latter case a hollow evaporator results (see Fig. 5).

Fig. 5. Photograph of a tubular ZrC evaporator. Inner diameter about 1.5 mm, outer diameter 3 mm. The length may be several dm.

either Al, Si, Ti, or Zr. They may thus be used for vacuum deposition of these elements by heating them (for example by passing an electric current) to a sufficiently high temperature. By using setups like that of Fig. 1 it is possible to supply material to the evaporator continuously, so that thick layers can be deposited. As an example of a deposition rate used to obtain thick layers, we have observed silicon deposition at a rate of 20 μm/min on substrates placed at a distance of 3 cm from the evaporator by passing 200A through the evaporator (about 0.5V per cm length needed). In Fig. 6 a cross section of a dielectrically isolated transistor structure of an integrated circuit is shown. The transistors are in this case made in monocrystalline silicon islands in a polycrystalline substrate, produced by the described deposition technique. A silicon oxide layer separates the islands from the substrate.

Another useful application in the semiconductor industry is the deposition of metal films or silicon devices and integrated circuits. In particular for MOS (metal oxide semiconductor) devices, the use of "clean" aluminum films is desirable. It is often found that aluminum deposited from tungsten filaments is not "clean." Instability effects in MOS structures attributed to the presence of sodium are then observed. These sodium ions probably originate from the tungsten filament, and electron-beam evaporation of aluminum from a cooled crucible is often utilized to produce stable MOS structures. We have found that evaporation from a carbide evaporator results in MOS structures of a quality similar to that of MOS structures obtained by means of electron-beam evaporation.

The deposited films may contain some carbon, especially when high deposition rates are used, *i.e.*, when the evaporator is heated to a high temperature. For the case of the system Si-SiC, for example, it is known that the partial pressure of Si_2C can be a few per cent, if the temperature is high enough (3). In fact, we have been able to detect the presence of a few per cent of carbon in silicon films which had been deposited at a high rate (chemical analysis). In aluminum films we have not been able to detect carbon.

It should be realized that during evaporation the solid carbide phase of the evaporator is in equilibrium with a melt which may contain rather a large amount of carbon. As an example, Fig. 7 shows part of the phase-diagram of the system Zr-C. Assuming a temperature of about 2400°C to be necessary for a reasonable rate of evaporation (see Table I), the melt apparently contains a few per cent of carbon. The percentage becomes greater as the temperature is increased. Given the presence of an excess of metal, complete melting can occur below the melting point of ZrC. Such an effect is occasionally observed to occur at one spot of the evaporator, where, due to some inhomogeneity, the electrical resistance is highest, and therefore also the temperature. When this occurs the evaporators fall into two parts.

Except for Al_4C_3 the above types of carbide evaporators can be stored in atmospheric air. Aluminum carbide reacts slowly with water; if such an evaporator is not kept dry, it may crumble to powder in a few weeks.

The use of the carbide evaporators is not restricted to the evaporation of the four elements mentioned. As one very useful example we would mention the vacuum deposition of chromium layers from ZrC evaporators. In this case a tubular evaporator is filled with small chromium particles and then heated; again simply by the passing of an electric current. Table I

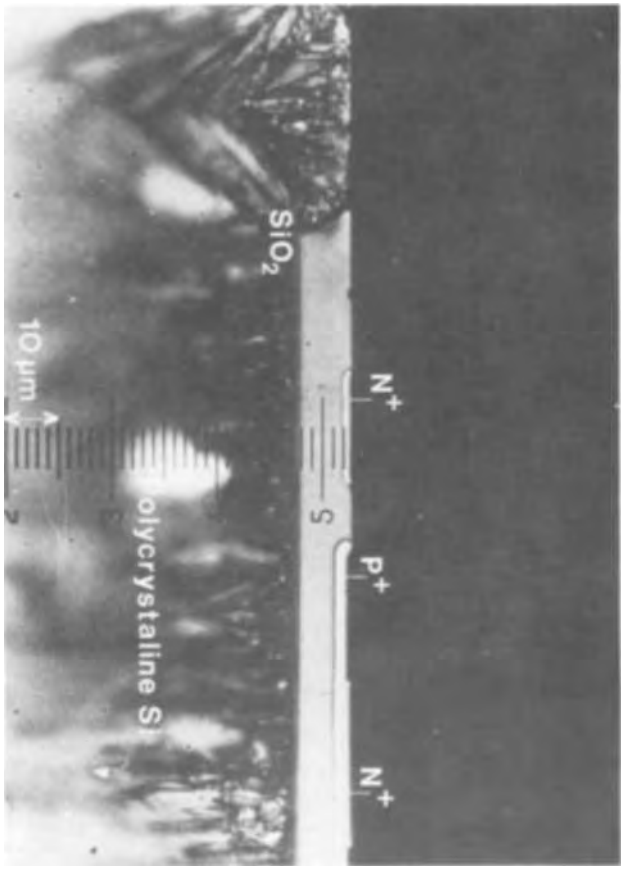

Fig. 6. Dielectrically isolated transistor structure. The polycrystalline substrate consists of silicon deposited from an SiC evaporator.

indicates that it is not necessary to melt chromium in order to obtain evaporation. Sublimation occurs at a reasonable rate even at about 1400°C. At this temperature the partial pressure of zirconium is still negligible and this element could not in fact be detected in the deposited chromium layers. With reference to Fig. 7 it may be remarked that the sublimation temperature is still too low to lead to melting in the Zr-C system. It is not known exactly how the Cr penetrates through the wall of the ZrC(+Zr) tube in this vacuum deposition process, the rate of which was about 0.1 μm/min (distance between evaporator and substrate 10 cm). The deposition was found to be homogeneous over a total substrate area as large as 2000 cm². The length of the evaporator was in this case 25 cm; with an applied voltage of 20V the current through the evaporator was 65A.

Vacuum deposition from carbide evaporators can also be used to getter gases from the vacuum system. For this purpose we are applying the titanium evaporation from a TiC evaporator which we have set up in experimental laboratory equipment and which has worked satisfactorily already for a few years. One might fear that the carbon content of the evaporator might cause the formation of CH_4, but this appears not to be the case. This is probably due to the fact that during the evaporation the TiC phase is surrounded completely by molten titanium.

Conclusion

Long porous evaporators consisting of the carbides of either Al, Si, Ti, or Zr can be prepared by reaction of these elements with commercially available graphite cords. The resulting evaporators are rod or tube

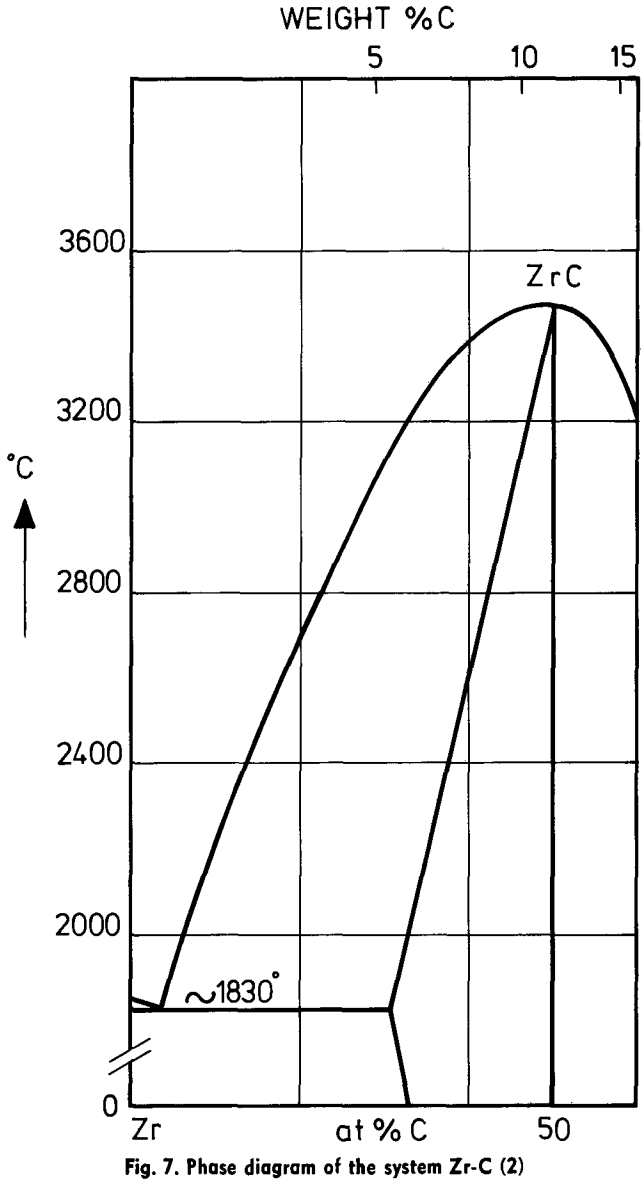

Fig. 7. Phase diagram of the system Zr-C (2)

shaped and may contain a fairly large amount of material to be evaporated. Connection to a continuous supply system is possible as capillary action causes a rapid distribution of molten material along the evaporator.

Acknowledgments

G. C. Cornelissen and H. J. H. Wilting have been very helpful in the preparation of the evaporators and the setup for vacuum deposition.

Manuscript submitted June 2, 1972; revised manuscript received Dec. 21, 1972. This was Paper 210RNP presented at the Cleveland, Ohio, Meeting of the Society, Oct. 3-7, 1971.

Any discussion of this paper will appear in a Discussion Section to be published in the December 1973 JOURNAL.

REFERENCES

1. J. J. A. Ploos van Amstel, *Philips Tech. Rev.*, **28**, 57 (1967).
2. R. P. Elliott, "Constitution of Binary Alloys," First Supplement, McGraw Hill Book Co., New York (1965).
3. J. Drowart and G. De Maria, in "Silicon Carbide," Proceedings of a 1959 conference in Boston, pp. 16-23, Pergamon Press, Inc., New York (1960).

Brief Communications

Anodic Oxide Films on GaP

J. M. Poate, P. J. Silverman, and J. Yahalom[1]
Bell Laboratories, Murray Hill, New Jersey 07974

The growth of oxides on compound semiconductors is of considerable importance in such problems as surface passivation and the formation of insulating or masking films. In the pioneering work of Dewald (1), anodic films were grown on InSb; more recently, several groups have examined anodic oxides on GaAs (2-4). In the previous work on GaP (5), oxides were

[1] Permanent address: Department of Materials Engineering, Technion Israel Institute of Technology, Technion City, Haifa, Israel.

Key words: gallium phosphide (GaP), anodic oxide films, Rutherford scattering.

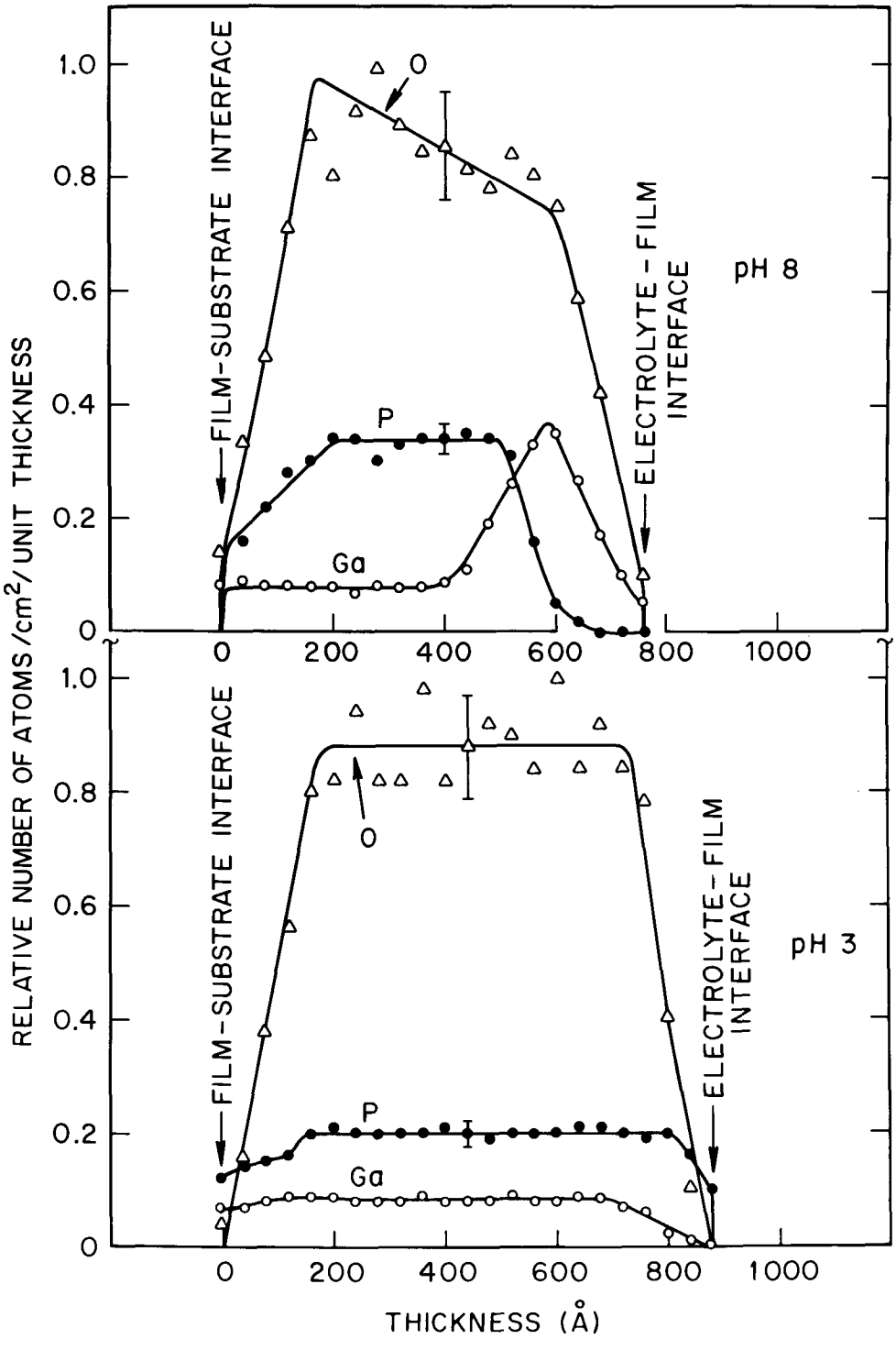

Fig. 1. Depth profiles of Ga, P, and O extracted directly from the backscattered energy spectra of (a) a nonuniform film grown in a pH 8 electrolyte and (b) a uniform film grown in a pH 3 electrolyte. The lines are drawn simply to guide the eye, not necessarily as a best fit for the data points. Typical error bars are shown on the O and P profiles; the error bar on the Ga is ~ the dot size.

grown anodically and galvanically in H_2O_2. Because the anodic oxides could be grown with more facility than the galvanic oxides, and the growth mechanisms of the anodic oxides should include the particular case of the galvanic oxides, it was decided to undertake a systematic study of GaP anodization.

(111)-oriented GaP slices were cut from n-type, Se-doped, Czochralski-grown crystals. The P-face of each slice was etched and polished in bromine-methanol. Anodization was carried out in a Teflon cell with a platinum counterelectrode; anodic connection was made to the unpolished side of the slice with a gold electrode. Because studies (6) have indicated a strong pH dependence of the dissolution of gallium oxides, aqueous buffered solutions ranging from pH 3 to 10 were used as electrolytes. A range of constant current densities between 1 and 100 mA/cm^2 was used so that the resistive voltage drop across the GaP substrate was essentially constant throughout an anodization and could be subtracted to obtain the actual voltage drop across the anodic film. A slice area of 1 cm^2 was exposed to the electrolyte, and anodization was terminated after passage of 0.2 coulomb. The wafer was then quickly removed from the electrolyte, rinsed with water and methanol, blown dry, and stored under vacuum.

The composition and depth profiles of the anodic films were analyzed by Rutherford backscattering of 1.7-2.0 MeV He ions in combination with ion channeling. The technique has proved eminently suitable (7) for the analysis of such films on single crystal substrates in that no calibration procedures are required and depth information is obtained in a straightforward fashion. This method revealed two distinct types of films: those with uniform composition throughout the thickness of the film, and those in which there is a Ga-rich and P-deficient layer near the film-electrolyte interface. Figure 1 shows the Ga, P, and O depth profiles extracted directly from the backscattered energy spectra of typical uniform and nonuniform films grown in pH 3 and 8 solutions, respectively (see Table I). Depth resolution for these films was ~100Å. The extreme peaking of the Ga in the outer half of the nonuniform film and the almost complete lack of P within ~200Å of the surface are clearly seen in Fig. 1a. Ga apparently migrates through the films during anodizing much more rapidly than P and forms an outer layer, probably of the form Ga_2O_3, in the nonuniform case. Between this layer and the substrate, the anodic film contains P in excess of Ga by a factor of ~3. Figure 1b illustrates the uniformity of the pH 3 grown film over most of its thickness. The composition of the uniform film is somewhat similar to the deep layer in the nonuniform film, indicating that in the uniform case a large fraction of the migrating Ga is continually being dissolved as it arrives at the oxide-electrolyte interface. The growth mechanism of this uniform core may depend on the in-diffusion of the oxidizing species to form a matrix which grows as the majority of the Ga diffuses through it.

Table I. Integrated stoichiometries and thicknesses of films produced in typical aqueous buffered electrolytes

pH	Electrolyte composition	Current (mA/cm^2)	Integrated Ga:P:O	Thickness Å
3	Potassium hydrogen phthalate, sulfuric acid	10	1:2.4:6.5	550
		100	1:2.4:8.5	800
8	Potassium dihydrogen phosphate, sodium hydroxide	10	1:1.2:3.7	600
		100	1:1.6:4.9	900

Film thickness was calculated using the densities of P_2O_5 and Ga_2O_3, weighted according to the P:Ga ratio in the oxide. Errors in the stoichiometries and thicknesses are expected to be ~10-15%.

In all cases it was found that for the same anodization charge higher current densities produced thicker films, as judged by surface densities and interference colors. This is to be expected if dissolution during anodization is an important factor, since a lower current density requires the slice to be immersed in the electrolyte for a longer time. In certain electrolytes, particularly at high pH values, the voltage rose linearly to typical values during anodization, but little or no film was found on the slices after they were removed from solution. The voltage rise indicated that film was growing during anodization; apparently strong dissolution occurred mainly after the current was stopped. This dissolution may have been prevented during anodization by either a field repulsion of film-dissolving cations or by a local decrease in pH, caused by H^+ production near the anode, which disappeared when the current was stopped. Since the electrolyte was buffered and stirred, the latter explanation seems unlikely. Several slices were also anodized in buffered solutions of identical pH but different composition. The differences between these oxides indicate that the properties of the anodic films may depend on the constituents of the electrolyte as well as on the pH.

Films of sufficient thickness exhibit interference colors similar to those seen in anodic Ta_2O_5, ranging from pale yellow for the thinnest to purple or blue for the thickest. Of all the electrolyte used, phosphate solutions (pH 6-8) produced films that were the most stable and uniform in appearance. Oxides produced in other solutions were often mottled or became so shortly after exposure to air, apparently by absorption of water.

This Rutherford backscattering examination of GaP anodic films has revealed the complex film structures that can arise in compound or alloy systems because of such competing factors as varying cationic mobilities and dissolution rates. A particularly interesting manifestation of these processes is the surfeit of Ga that can occur at the oxide-electrolyte interface. A complete account of the results and interpretation of this experiment will be given elsewhere (8).

Acknowledgments

We are indebted to Bert Schwartz for introducing us to the problem and for his helpful discussions.

Manuscript received Dec. 28, 1972.

Any discussion of this paper will appear in a Discussion Section to be published in the December 1973 JOURNAL.

REFERENCES

1. J. F. Dewald, *This Journal*, **104**, 244 (1957).
2. A. K. Revesz and K. H. Zaininger, *J. Am. Ceram. Soc.*, **46**, 606 (1963).
3. C. J. Dell'Oca, G. Yan, and L. Young, *This Journal*, **118**, 89 (1971).
4. W. W. Harvey and J. Kruger, *Electrochim. Acta*, **16**, 2017 (1971).
5. B. Schwartz and W. J. Sundburg, *This Journal*, **119**, 241C (1972).
6. M. Pourbaix, Atlas D'Equilibres Electrochimiques, Gauthier-Villars, Paris (1963).
7. J. M. Poate, T. M. Buck, and B. Schwartz, To be published, *J. Phys. Chem. Solids*.
8. J. M. Poate, P. J. Silverman, and J. Yahalom, To be published.

Bonding of Gallium Arsenide Crystals

T. L. Chu* and R. K. Smeltzer*,[1]

Electronic Sciences Center, Southern Methodist University, Dallas, Texas 75222

Gallium arsenide crystals are grown commercially by the Czochralski or the gradient freeze technique, and available crystals are usually no larger than 1½ in. in diameter. These crystals are much too small for some applications, such as optical windows. One approach of obtaining large area gallium arsenide crystals is to bond a number of commercially available crystals by the alloying technique. In this investigation, germanium was selected as an alloying agent on the basis of three reasons: (*i*) germanium does not react chemically with gallium arsenide and their mutual solubility is very small; (*ii*) the lattice parameter and thermal expansion coefficient of germanium (5.66A and 5.8 $\times$ 10^{-6} $°C^{-1}$, respectively) are essentially the same as those of gallium arsenide (5.65A and 5.9 $\times$ 10^{-6} $°C^{-1}$, respectively); and (*iii*) the germanium-gallium arsenide pseudobinary system has a simple eutectic containing 15 mole per cent (m/o) gallium arsenide and melts at a conveniently low temperature, 865°C (1). The experimental procedures and results are summarized below.

To utilize the alloying technique for the bonding of gallium arsenide crystals, germanium is deposited on the faces of the crystals to be bonded, and the two faces are placed in contact with each other so that they are crystallographically parallel. This assembly is then heated in an arsenic atmosphere at a temperature above the eutectic temperature of the germanium-gallium arsenide system. The extent of dissolution of gallium arsenide and the amount of liquid solution are determined by the thickness of the germanium layer and the alloying temperature in accordance with the phase diagram. After equilibrium is established, the germanium-gallium arsenide assembly is slowly cooled to yield epitaxial, single crystalline, gallium arsenide and germanium which are bonded to the original gallium arsenide crystals. The bond is expected to be strong mechanically because of the nearly identical lattice parameters and thermal expansion coefficients of germanium and gallium arsenide. The important parameters in this process are therefore the thickness of the germanium layer, the alloying temperature, and the cooling rate.

Gallium arsenide crystals used in the bonding experiments had main faces of {100} orientation and were polished on a Pellon pad using sodium hypochlorite as an etchant. In a typical experiment, 1-2μ of germanium were deposited onto the polished faces by vacuum evaporation. The faces to be bonded were placed in contact and heated at 900°C in a sealed silica tube containing a few Torrs of arsenic pressure. According to the phase diagram of the germanium-gallium arsenide system (1), the thickness of gallium arsenide dissolved at 900°C under equilibrium conditions is approximately one-half of that of the germanium layer. The cooling was carried out at a rate of 10°C/hr, and a strong bond was formed between the two crystals. A series of experiments were carried out using different thicknesses of germanium at alloying temperatures up to 1000°C, and a strong bond was formed in all cases. Angle-polishing and chemical-etching techniques were used to examine the interface region of several samples, and this region was found to be 4-14μ in thickness, in qualitative agreement with what one would expect from phase diagram considerations. The flatness and cleanliness of the gallium arsenide surfaces were found to be important factors affecting the perfection of the interface region, particularly when very thin layers of germanium were used. Figure 1 shows the angle-polished surface of a bonded specimen where the voids in the interface region are due presumably to nonuniform wetting of the gallium arsenide surface.

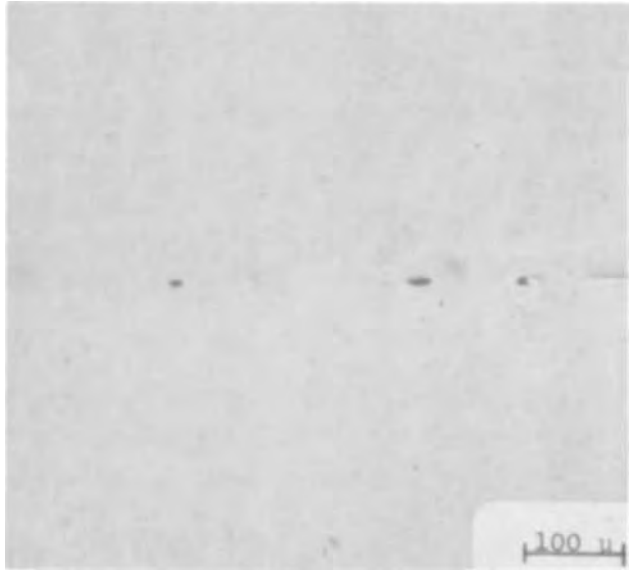

Fig. 1. Angle-polished surface of a bonded gallium arsenide crystal showing defects in the interface region.

In summary, germanium has been shown to be a suitable alloying agent for the bonding of gallium arsenide crystals at relatively low temperatures. The extent of dissolution of gallium arsenide is determined by the thickness of the germanium layer and the alloying temperature, and the perfection of the interface region is determined predominately by the surface preparation of gallium arsenide.

Acknowledgment

This research was supported by the Robert A Welch Foundation, Houston, Texas, under Grant N-298.

Manuscript received Dec. 27, 1972.

Any discussion of this paper will appear in a Discussion Section to be published in the December 1973 JOURNAL.

REFERENCE

1. Y. Takeda, T. Hirai, and M. Hirao, *This Journal*, **112**, 363 (1965).

* Electrochemical Society Active Member.
[1] Present address: Texas Instruments, Incorporated, Dallas, Texas 75222.

Key words: gallium arsenide, germanium, semiconductors, alloying.

DISCUSSION SECTION

This Discussion Section includes discussion of papers appearing in the *Journal of The Electrochemical Society*, Vol. 119, No. 3 and 11; March and November, 1972.

Control of the Deposition of Silicon Nitride Layers by 2537Å Radiation

C. H. J. v. d. Brekel and P. J. Severin
(pp. 372-376, Vol. 119, No. 3)

K. Navrátil and I. Ohlídal:[1] Brekel and Severin in the paper under discussion described a method of control and determination of the thickness of the deposition of Si_3N_4 on silicon from the extremes of the curve expressing the dependence of the reflectance of the system Si_3N_4–Si on the phase angle at a constant wavelength of light 2537Å.

In our discussion we would like to raise some critical objections concerning the theoretical part and hence the following conclusions of the paper cited. The authors characterize the system mentioned as a nonabsorbing layer on a nonabsorbing substrate. On the basis of measurements by Reizmann and van Gelder[2] the authors of the paper under discussion assume the index of refraction of Si_3N_4 for the given wavelength to be $n_1 = 2.18$; and the index of refraction of silicon according to Philipp and Taft[3] is $n_2 = 1.65$, where they have neglected the index of absorption of silicon as indicated in Appendix A by the authors. Here the authors of the paper being discussed, as shown in the following discussion have committed a comparatively relevant error. Philipp and Taft[3] give for the index of absorption the value $k_2 = 3.5$. It is evident that, in the region of the wavelengths, silicon cannot be considered to be nonabsorbing, but on the contrary, a relatively considerable absorbing matter.

Next we shall give a short outline of a correct procedure of deriving the reflectance of the system Si_3N_4–Si in the case where the absorption of silicon, *i.e.*, the system of nonabsorbing layer/absorbing substrate, is considered.

According to Vašíček[4] the resulting Fresnel coefficient for reflectance on a thin layer has the form

$$\hat{r} = \frac{r_1 + \hat{r}_2 e^{-ix}}{1 + r_1 \hat{r}_2 e^{-ix}} \qquad [1]$$

where $\hat{r} = re^{i\delta}$, and

$$r_1 \equiv \frac{n_0 - n_1}{n_0 + n_1} = r_1 e^{i\beta}, \quad \hat{r}_2 \equiv \frac{n_1 - \hat{n}_2}{n_1 + \hat{n}_2} = r_2 e^{i\alpha} \qquad [2]$$

$$\hat{n}_2 = n_2 - ik_2, \quad x = \frac{2\pi}{\lambda} 2n_1 d_1$$

In relation [2] $n_0 = 1$, n_1 is the index of refraction of the layer, $\hat{n}_2$ is the complex index of refraction of silicon, $n_2 = 1.65$ is the real part of the index of refraction of silicon, and $k_2 = 3.5$ is the index of absorption of silicon, r_1 and $\hat{r}_2$ are the Fresnel coefficients of the upper and lower boundary, x is the phase angle, d_1 is the thickness of the layer, α is the phase change at the boundary Si_3N_4–Si, and the angle β obtains the values

$$\beta = \begin{cases} 0 \text{ for } n_0 > n_1 \\ \pi \text{ for } n_0 < n_1 \end{cases}$$

From this point of view the assumption by the authors of the paper under discussion that change of the phase occurs about π at the boundary of Si_3N_4–Si is not correct. In their paper they consider silicon as a nonabsorbing matter; it is $n_2 < n_1$ and the phase change cannot occur.

Relation [1] may be rewritten into the form

$$re^{i\delta} = \frac{r_1 e^{i\beta} + r_2 e^{i\alpha} e^{-ix}}{1 + r_1 e^{i\beta} r_2 e^{i\alpha} e^{-ix}} \qquad [3]$$

here r_1 and r_2 are the absolute values of the Fresnel coefficients. From Eq. [3] it may be easy to obtain the formula for reflection

$$R = \frac{r_1^2 + r_2^2 + 2r_1 r_2 \cos(x - \alpha - \beta)}{1 + r_1^2 r_2^2 + 2r_1 r_2 \cos(x - \alpha - \beta)} \qquad [4]$$

The phase change at the boundary layer with silicon follows then by simple calculation from Eq. [2]

$$\tan \alpha = \frac{2k_2 n_1}{n_1^2 - n_2^2 - k_2^2} \qquad [5]$$

Optical constants of our system will then evidently hold $\tan \alpha < 0$. According to Vašíček[4] it is valid that

$$\tan \alpha_0 = \frac{2k_2 n_1}{n_2^2 + k_2^2 - n_1^2}$$

and thus $\tan \alpha_0 > 0$ in this case. The differences in expressions correspond with the introduction of single parameters. It may, however, be written $\alpha = \pi - \alpha_0$. By substitution in Eq. [4] we obtain a relation agreeing with Vašíček[4]

$$R = \frac{r_1^2 + r_2^2 + 2r_1 r_2 \cos(x + \alpha_0)}{1 + r_1^2 r_2^2 + 2r_1 r_2 \cos(x + \alpha_0)} \qquad [4a]$$

as in our case is $\beta = \pi$.

In Fig. 1 the dependence of R on the phase angle $(x + \alpha_0)$ is plotted. A qualitative difference of the course of dependencies in comparison with Fig. 4 of the paper being discussed is apparent. The reflectance with increasing thickness decreases from the value for a clean surface of silicon without the layer to a minimum, and then increases to a maximum value $R_{max} > R_0$, where R_0 is the reflectance of clean silicon. This course is in accordance with that of the reflectance of the system of nonabsorbing layer metal as mentioned[4] for approximately the same optical constants of the substrate and layer.

In Table I conditions are indicated for which the extreme values of reflectance occur according to a correct relation [4a] and those when assuming silicon to be nonabsorbing. We would like to direct the authors' attention to the misinterpretation of the phase angle in the form

$$x = \frac{2\pi}{\lambda} n_1 (d_1)_0$$

The difference of the thickness of the layer determined under the assumption of silicon to be nonabsorbing and according to the correct relation (see Table I) may be stated. This difference is constant

[1] Department of Solid-State Physics, Faculty of Science, Purkyně University, Brno, Czechoslovakia.
[2] T. Reizmann and W. van Gelder, *Solid-State Electron.*, **10**, 625 (1967).
[3] H. R. Philipp and E. A. Taft, *Phys. Rev.*, **120**, 37 (1960).
[4] A. Vašíček, "Optics of Thin Films, North-Holland Publishing Co., Amsterdam (1960).

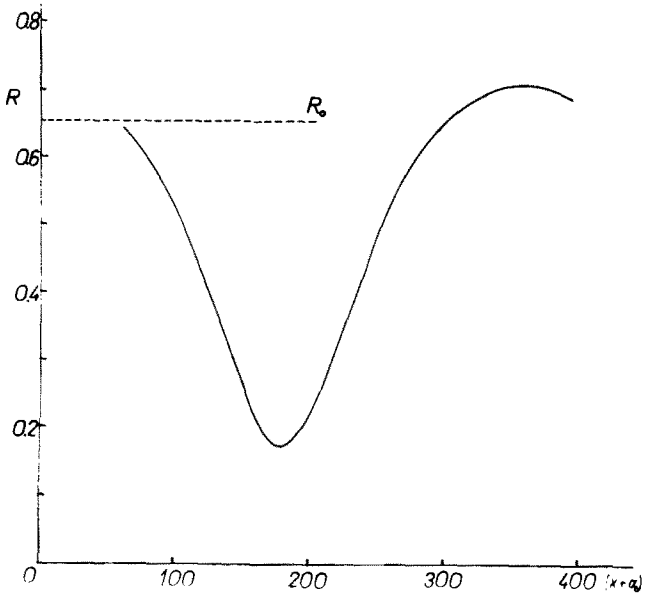

Fig. 1. Dependence of reflectance of the system Si_3N_4–Si on the value of the phase angle $(x + \alpha_0)$. The dependence is calculated using relation [4a].

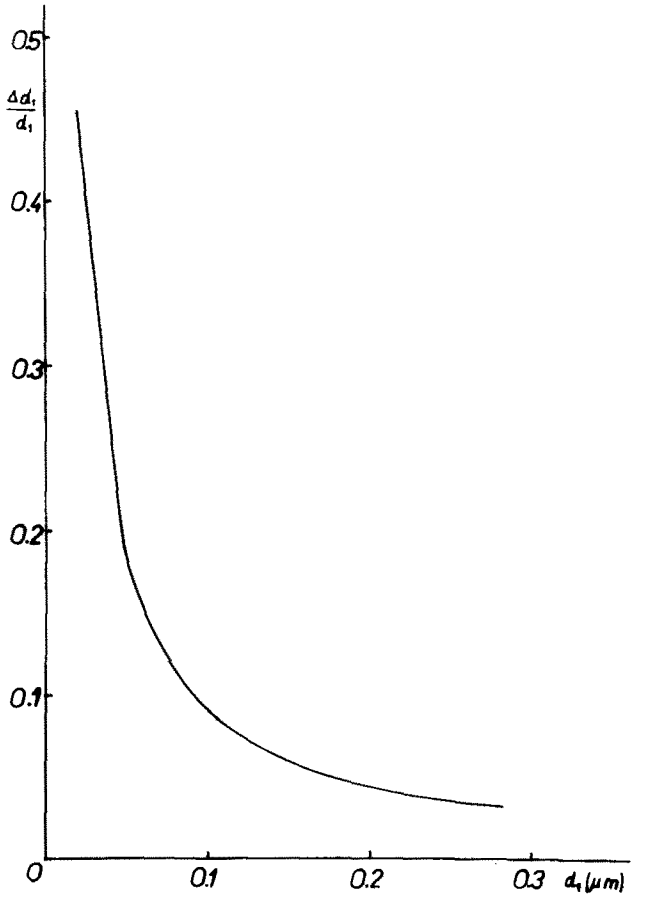

Fig. 2. Dependence of the relative error when determining the thickness dependent on the magnitude of the thickness of the layer.

$\Delta d_1 \equiv (d_1)_0 - d_1 = \alpha\lambda/4\pi n_1$ and is equal to 91Å. The relative error in determining the thickness of dependence on that of the layer d_1 is given in Fig. 2. It is evident that this error is considerable, namely, in the region of small values of d_1.

This discussion was intended to show how neglect of the absorption of the substrate can affect the statement, especially for small thicknesses. In case the relative experimental error is greater than $\Delta d_1/d_1$, the correction stated does not take place. Nevertheless, Chopra[5] mentions the sensitivity in determining thickness by this method $\lambda/300$. Hence it is apparent that neglecting the absorption of silicon takes place substantially when controlling the thickness by the method mentioned at $\lambda = 2537$Å.

Table I

	Correct conditions for occurrence of the extreme	Conditions for occurrence of extremes under the assumption of silicon to be nonabsorbing
Minimum	$x + \alpha_0 = (2k - 1)\pi$	$x = 2k\pi$
	$\frac{4\pi}{\lambda} n_1 d_1 + \alpha_0 = (2k - 1)\pi$	$\frac{4\pi}{\lambda} n_1 (d_1)_0 = 2k\pi$
Maximum	$x + \alpha_0 = 2k\pi$	$x = (2k - 1)\pi$
	$\frac{4\pi}{\lambda} n_1 d_1 + \alpha_0 = 2k\pi$	$\frac{4\pi}{\lambda} n_1 (d_1)_0 = (2k - 1)\pi$

k are the integers.

C. H. J. v.d. Brekel and P. J. Severin: In their comment on our paper Navrátil and Ohlídal quite rightly state that the vacuum-Si_3N_4–Si system should not be characterized by simply assuming that the absorption is negligible. In fact we indicated in appendices A and B of our paper under discussion along which lines a calculation could possibly be undertaken assuming real refractive indices. Knowing that this assumption does not hold we only used the model to show the agreement with the periodic dependence actually measured. Knowing that the relevant parameters were not available we did not compare the experiments to a more sophisticated theory.

Navrátil and Ohlídal are right in their conclusion that the introduction of the phase shift δ_{12} at the Si_3N_4–Si interface modifies the thickness of the layers by a fixed amount. However, the actual magnitude is subject to the following considerations. The refractive index of silicon has been deduced by Philipp and Taft[3] from the spectral dependence of the reflectance, 65% at 4.8 eV. They found $n = 1.65$ and $k = 3.5$, but it should be doubted whether the frequency range used to evaluate the Kramers-Kronig integral relation was large enough,[6,7] particularly in the range of strong absorption near 5 eV. Verleur[8] also measured the reflectance, 80% at 4.8 eV, and fitted it to an expansion in terms of a set of classical oscillators. Matching the whole spectrum between 0.5 and 10.0 eV he finds $n = 0.9$ and $k = 3.1$. This set of data is also quoted by Moses.[9] The above data refer to room-temperature measurements whereas the parameters needed at the growth temperature of 200°C are not available. Using the results of Philipp and Taft, Navrátil and Ohlídal calculated the difference in thickness due to δ_{12}, neglected in our simplified model, to be 91Å. However, this claim to accuracy and precision exceeds the experimental possibilities to a large extent.

Chemical Vapor Deposited Polycrystalline Silicon

M. E. Cowher and T. O. Sedgwick (pp. 1565-1570, Vol. 119, No. 11)

C. M. Wolfe, G. E. Stillman, and J. A. Rossi:[10,11] In their interesting paper under discussion on polycrystal-

[5] K. L. Chopra, "Thin Film Phenomena," p. 107, McGraw-Hill Book Co., New York (1969).
[6] H. R. Philipp and E. A. Taft, *Phys. Rev.*, 113, 1002 (1959).
[7] P. N. Schatz, S. Maeda, and K. Kozima, *J. Chem. Phys.*, 38, 2658 (1963).
[8] H. W. Verleur, *J. Opt. Soc. Am.*, 58, 1356 (1968).
[9] A. J. Moses, "Handbook of Electronic Materials," Vol. 1, p. 70, I.F.I.I., Plenum Publishing Corp., New York (1971).
[10] Lincoln Laboratory, Massachusetts Institute of Technology, Lexington, Massachusetts 02173.
[11] This work was sponsored by the Department of the Air Force.

line silicon, Cowher and Sedgwick discuss Hall mobilities for both n- and p-type samples which are as high as 1/2-1/3 of bulk mobility values in the 10^{14}-10^{17} cm^{-3} concentration range. In this doping range mobilities have typically been much lower than this, presumably because of potential barriers at the grain boundaries which have a greater scattering effect at lower carrier concentrations than at higher concentrations. Also, they find that the total dopant concentration (phosphorous), as determined from neutron-activation analysis, is much larger than the electrically active dopant concentration as determined from Hall measurements. To explain their unusually high mobility values and the discrepancy between total and electrically active dopant concentrations, Cowher and Sedgwick propose a model in which the electrically inactive dopant atoms are preferentially deposited at the grain boundaries where they compensate local structural defects and reduce carrier scattering. They also postulate an alternative model in which the hydrogen ambient at their low growth temperatures eliminates or compensates the structural defects at the grain boundaries. Either of these models seems reasonable and could explain their mobility values being 1/2-1/3 of bulk values.

However, Cowher and Sedgwick in the paper under discussion state that our previously developed conducting inhomogeneity model[12,13] cannot explain their high mobility values because the total amount of dopant required greatly exceeds that which is present in their samples. (It is not clear whether they are referring to total or electrically active dopant concentration.) This statement, of course, is misleading, since our conducting inhomogeneity model is independent of doping level. It is not obvious how this misinterpretation could have occurred. We have previously discussed in our work why high apparent mobilities might be observed in polycrystalline samples.[13] In as-grown single crystalline GaAs samples we have observed mobility values which are twice bulk values[14] in the same concentration range where in polycrystalline silicon Cowher and Sedgwick in their work see 1/2-1/3 of bulk values. These results are easily explained with the conducting inhomogeneity model. Theoretically, we have also shown that conducting inhomogeneities in a Hall sample can result in apparent (not real) mobilities which are too high by as much as several orders of magnitude.[12,13] This is because in a Hall sample with conducting inhomogeneities the resistivity measurement gives an average resistivity for the sample including the conducting inhomogeneities, whereas the Hall constant measurement preferentially gives the Hall constant of the medium surrounding the conducting inhomogeneities, Thus, the mobility calculated from the Hall constant divided by the resistivity is too high. Physically, this is because there is less current flow in the inhomogeneities in a magnetic field (Hall constant measurement) than in zero magnetic field (resistivity measurement).[15]

This can be shown to hold true for any arbitrarily shaped, three-dimensional conducting inhomogeneity in the following manner: the component of current density normal to the surface of the inhomogeneity, J_{ni}, at any point is related to the normal and tangential components of the electrical field, E_{ni} and E_{ti}, respectively, at the same point by

$$J_{ni} = \left(\frac{\sigma_i}{1 + \beta_i^2} \right) (E_{ni} + \beta_i E_{ti}), \quad i = 1, 2$$

where σ_i is the conductivity, β_i is the product of the real mobility; μ_i, and the orthogonal magnetic field, B, and $i = 1, 2$ denote the surrounding medium and the inhomogeneity, respectively. Since there are no current sources at the boundary between the inhomogeneity and the surrounding medium, $J_{n1} = J_{n2}$, and because of conservation of energy, $E_{t1} = E_{t2}$. With these relations it is easy to show that

$$J_{ni} = \frac{\left(E_{n1} - \frac{\beta_1}{\beta_2} E_{n2} \right)}{\left(\frac{1 + \beta_1^2}{\sigma_1} \right) - \frac{\beta_1}{\beta_2} \left(\frac{1 + \beta_2^2}{\sigma_2} \right)}$$

From this expression it can be seen that the current into any inhomogeneity decreases with increasing magnetic field, and, in fact, approaches zero as the magnetic field approaches infinity.

For the case in point then, it is clear that the conducting inhomogeneity model is generally valid, is independent of doping level, and cannot be arbitrarily discounted for any sample with unusually high measured values of mobility without more extensive measurements, as has been previously discussed.[12,13]

M. E. Cowher and T. O. Sedgwick: The authors of the above discussion correctly point out that the applicability of their model[13] for the anomalously high mobility of inhomogeneous semiconductors is independent of doping and cannot be ruled out as a possible partial explanation of the high mobilities observed in our lightly doped polycrystalline Si samples in the paper being discussed. However, this inhomogeneity model probably cannot account for more than a factor of two, at most, in our results. First, our samples were measured at a $\beta \leq 4 \times 10^{-2}$ (assuming a maximum $\mu = 10^3$ cm^2/V sec) which according to their Fig. 4[16] gives at most $\mu_{App}/\mu = 2$ which occurs at $\alpha = 0.7$. We have no way of estimating α for our samples, but μ_{App}/μ is less than 2 for all other values of α. Secondly, it is difficult to know how precisely their model, for a sample with a single inhomogeneity, may be applied to our samples which are very fine grained, and where the inhomogeneities, if they exist, are small, but possibly large in number.

[12] C. M. Wolfe and G. E. Stillman, *Appl. Phys. Letters*, **18**, 205 (1971).
[13] C. M. Wolfe, G. E. Stillman, and J. A. Rossi, *This Journal*, **119**, 250 (1972).
[14] C. M. Wolfe, G. E. Stillman, D. L. Spears, D. E. Hill, and F. V. Williams, *J. Appl. Phys.*, **44**, 732 (1973).
[15] C. Herring, *J. Appl. Phys.*, **31**, 1939 (1960).
[16] C. M. Wolfe, Private communication.

Errata

In the paper "Control of the Deposition of Silicon Nitride Layers by 2537Å Radiation" by C. H. J. v. d. Brekel and P. J. Severin which appeared on pp. 372-376 in the March 1972 JOURNAL, Vol. 119, No. 3, the authors have found that the parameter ϕ as used in the paper should be $\phi = 4\pi hn/\lambda$, twice as large as defined in Eq. [1a]. Then Eq. [A-4a] and [A-4b] should read $h = 635$Å and $h = 317$Å, respectively.

The authors further state that the experiments appear to be in agreement with the erroneous definition of ϕ. This could be traced to be caused as follows. The thickness measurements made every minute were noted with the detailed color chart (1) for SiO_2 as if the layer grown were SiO_2. The thickness of the Si_3N_4 layer actually grown should be obtained by multiplying by the refractive index ratio 1.48/1.97 = 0.7, but the observer divided by 0.7 so that the thickness plotted is too large by a factor of two. This did not arouse suspicion because of the mistake made in the definition of Eq. [1a], which, subconsciously perhaps, generated the error. Hence after correction of Eq. [1a] and dividing the ordinate scale in Fig. 5 by a factor of two, the model adequately describes the experiments.

Equations [A-2] and [B-3] should read

$$R = 1 - \frac{(1 - r_{01}^2)\ (1 - r_{12}^2)}{(1 - r_{01}r_{12})^2 + 4r_{01}r_{12}\sin^2(-\phi/2)} \qquad [A\text{-}1]$$

$$\frac{1}{G} = \frac{1}{2}\frac{ED}{E^2\sin^2\phi/2 + \cos^2\phi/2} \qquad [B\text{-}3]$$

In the section on Theory, first paragraph, lines 13-15 should read "Absorption in the Si_3N_4 layer is neglected and light reflects at the Si_3N_4 surface with a phase change π.

REFERENCE

1. W. A. Pliskin and E. E. Conrad, *IBM J. Res. Dev.*, **8**, 43 (1964).

In the paper "Electrochemical Behavior of Germanium in Fused LiCl-KCl Eutectic" by Joseph M. Shafir and James A. Plambeck which appeared on pp. 18-22 in the January 1973 JOURNAL, Vol. 120, No. 1, page 19, second column, first paragraph, should read: "The average is −0.665V, standard deviation 0.002V."

In the paper "Solvent Equilibria of $AlCl_3$-NaCl Melts" by L. G. Boxall, H. L. Jones, and R. A. Osteryoung which appeared on pp. 223-231 in the February 1973 JOURNAL, Vol. 120, No. 2, the values of d for $NaAlCl_4$ and $NaAl_2Cl_7$ in Table III should read:

		d
$NaAlCl_4$	$\Delta H_f°$	−6.96
	$S°$	15.12
$NaAl_2Cl_7$	$\Delta H_f°$	−5.31
	$S°$	26.02

This would change the value of the calculated ΔHm, referred to on page 227, to 6.6 kcal mole^{-1} and make $\Delta H°$ values for solid $NaAlCl_4$ appear about 12 kcal mole^{-1} too positive.

In the paper "Measurement of Zincate Permeation in a Polyethylene Battery Separator with Controlled External Hydrodynamic Conditions" which appeared on pp. 324-328 in the March 1973 JOURNAL, Vol. 120, No. 3, the data quoted from Adams and Harlowe on page 328, first column, second paragraph, should read: 2.39 × 10^{-6} mole in.$^{-2}$ min^{-1}. The calculations from these numbers are correct but incorrect units were quoted.

JOURNAL OF THE ELECTROCHEMICAL SOCIETY

ELECTROCHEMICAL SCIENCE AND TECHNOLOGY

JULY 1973

A Battery Analog

Clarence M. Shepherd*

Electrochemistry Branch, Naval Research Laboratory, Washington, D. C. 20390

ABSTRACT

The current density distribution inside a battery can be very well approximated by assuming the current flow is perpendicular to the electrodes. The ratio of electrode spacing to electrode height is found to have a negligible effect on this approximation. A battery analogue was constructed that consisted of resistances alone and eliminated any polarization effects. Measurements made on it were in excellent agreement with those predicted mathematically.

A number of mathematical equations have been and are being developed that describe the current density distribution and other cell characteristics inside a battery during charge and discharge. Many of these derivations are based on the proposition that the current flow in the electrolyte is perpendicular to the electrodes, an assumption that is an excellent approximation when the ratio of the electrode spacing D to the electrode height H is sufficiently small. The effect on cell characteristics as D/H becomes large is considered here.

A thorough discussion of the mathematical model and symbols have been given previously and is applicable here (1, 2). It is assumed that the electrodes are thin, flat, parallel, rectangular, of uniform width and spacing, and are in a close fitting cell case.

H = total electrode height, cm
h = height above bottom of electrode, cm
m = H $-$h, cm
D = distance between electrodes, cm
d = distance measured perpendicularly from the anode, cm
L = resistance of a parallelogram 1 cm^2 in cross section extending from anode to cathode, ohm-cm^2
$R_e = LD^{-1}$ = resistivity of electrolyte, ohm-cm
R_o, R_d = resistance of a 1 cm wide section of the anode and the cathode, respectively, per unit length in the h direction, ohm
$R = R_o + R_d$, ohm
e is the sum of the potential drop in the anode and cathode measured from the top of the electrode to a point at height h, V
$x = -R^{-1}\, de/dh$ is the current per unit width flowing vertically past a point on the electrode at height h, A-cm^{-1}
$i = dx/dh$ is the current flowing between electrodes, per unit area at height h, A-cm^{-2}
i_H = current density, i, at top of electrode ($h = H$)
i_M = current density at the midpoint of electrode
i_o = current density at the bottom of the electrode
E_d = the potential drop due to the discharge current I and is the sum of all the potential drops in the cell due to resistances and polarization, V

$\lambda_o = R_o DHL^{-1}$, dimensionless
$\lambda_D = R_d DHL^{-1}$, dimensionless
$\lambda = \lambda_o + \lambda_d$
b_o, b_d = absolute values of the slopes of the single electrode potential *vs.* current density curves for anode and cathode, respectively, ohm-cm^2
$K = b_o + b_d$
$\mu_o = Db_o L^{-1}H^{-1}$, dimensionless
$\mu_d = Db_d L^{-1}H^{-1}$, dimensionless

$$\Psi = \left(\frac{\lambda_o + \lambda_d}{DH^{-1} + \mu_o + \mu_d}\right)^{1/2} \text{ dimensionless}$$

$$= \left(\frac{R}{L + K}\right)^{1/2} H \text{ dimensionless} \qquad [1]$$

$J(m, d)$ = value of the stream function at (m, d) in the cell (2), A-cm^{-1}

Tobias and Wijsman (2) have shown that

$$\frac{J(m,d)}{I} = \frac{m}{h} + \sum_{n=1}^{\infty} \frac{2}{n\pi}\left(\sin n\pi \frac{m}{H}\right)\frac{A}{B} \qquad [2]$$

where

$$A = [\lambda_d(\lambda_o + n^2\pi^2\mu_o)\mathrm{Sh}(n\pi dH^{-1}) + \lambda_o(\lambda_d + n^2\pi^2\mu_d)\mathrm{Sh}(n\pi\{D-d\}H^{-1}) + n\pi\lambda_d \mathrm{Ch}(n\pi dH^{-1}) + n\pi\lambda_o \mathrm{Ch}(n\pi\{D-d\}H^{-1})] \qquad [3]$$

and

$$B = [\lambda_o\lambda_d + n^2\pi^2(1 + \lambda_o\mu_d + \lambda_d\mu_o) + n^4\pi^4\mu_o\mu_d]\mathrm{Sh}n\pi DH^{-1} + [n\pi(\lambda_o + \lambda_d) + n^3\pi^3(\mu_o + \mu_d)]\mathrm{Ch}n\pi DH^{-1} \qquad [4]$$

If it is assumed that the current flow in the electrolyte is perpendicular to the electrodes then it can be easily shown that the cell characteristics at the beginning of a discharge are described by the following equations (1, 2)

$$\frac{x}{I} = \frac{\sinh[h/H)]}{\sinh \Psi} \qquad [5]$$

$$\frac{iH}{I} = \frac{\Psi \cosh[\Psi(h/H)]}{\sinh \Psi} \qquad [6]$$

* Electrochemical Society Active Member.

Key words: current density distribution, battery design, cell, electrode resistance, electrolyte resistance, polarization, cell characteristics.

$$\frac{e}{HIR} = \frac{\coth \Psi}{\Psi} - \frac{\cosh [\Psi(h/H)]}{\Psi \sinh \Psi} \quad [7]$$

$$\frac{E_d}{HIR} = \frac{\coth \Psi}{\Psi} \quad [8]$$

where (x/I), Ψ, (iH/I), (e/HIR), and (h/H) are dimensionless.

Results and Discussion

It can be shown here that Eq. [2] approaches Eq. [6] as a limiting value when D/H approaches zero in value by putting $D/H = 0$ and $d = 0$ in Eq. [2] and taking the derivative with respect to m/H. As a result

$$\frac{iH}{I} = 1 + \sum_{n=1}^{\infty} 2 \left(\cos n\pi \frac{m}{H}\right) \left(\frac{n\pi\lambda_d + n\pi\lambda_o}{n\pi\lambda_d + n\pi\lambda_o + n^3\pi^3\{\mu_o + \mu_d\}}\right) \quad [9]$$

Substituting Eq. [1] gives

$$\frac{iH}{I} = 1 + \frac{\Psi^2}{\pi^2} \sum_{n=1}^{\infty} 2 \left(\cos n\pi \frac{m}{H}\right)\left(\frac{1}{n^2 + \Psi^2/\pi^2}\right) \quad [10]$$

$$= 1 + \frac{\Psi^2}{\pi^2} \cdot \frac{\pi}{\Psi} \cdot 2 \frac{\Psi}{\pi} \sum_{n=1}^{\infty} \frac{\cos n\pi\, m/H}{n^2 + \Psi^2/\pi^2} \quad [11]$$

From Ref. (3) or (4)

$$\frac{iH}{I} = 1 + \frac{\Psi}{\pi}\left[\frac{\pi \cosh \Psi/\pi\,(\pi - \pi\, m/H)}{\sinh \Psi} - \frac{\pi}{\Psi}\right] \quad [12]$$

$$= \frac{\Psi \cosh [\Psi(h/H)]}{\sinh \Psi} \quad [13]$$

which is identical to Eq. [6] and can be used to derive Eq. [5], [7], and [8] by integration. Thus Eq. [5] to [8] can be derived from Eq. [2] as a limit that is approached when D/H approaches zero in value or they can be derived by assuming that the current flow is perpendicular to the electrodes. It will be shown here how the error in Eq. [5] to [8] increases as D/H increases above zero in value.

The derivation of Eq. [5] to [8] as well as that of Eq. [2] is based on an assumption that the total drop in potential due to polarization is a linear function of the current density (1, 2). The coefficient of polarization K has the same dimensions as the electrolyte resistance L and since the two are added in defining Ψ, it makes no difference in Eq. [5] to [8] whether the polarization is large or small; the results are defined only by the sum of $L + K$.

The techniques used in deriving Eq. [2] are not readily adaptable to nonlinear polarization. The assumption of perpendicular current flow, which will be studied here, makes possible a simple numerical analysis for any nonlinear polarization and in a number of cases makes possible a mathematical solution. By applying a correction factor to Ψ, Eq. [5] and [6] can give a good description of many of the nonlinear solutions (1). The relationships described in Eq. [5] to [8] have been plotted in Ref. (1) and to a limited extent in Fig. 4 and 5. It can be seen from Eq. [6] that i_H/i_o, the ratio of the current density at the top of the electrode to that at the bottom, is equal to cos Ψ. This relationship has been plotted in Fig. 1 as a function of Ψ and shows the current density distribution over the face of the electrode to be fairly even for values of $\Psi < 1$. As Ψ approaches zero, i_H/i_o approaches one in value and the current density distribution becomes uniform. As Ψ increases above one in value, the variation in current density distribution increases rapidly and eventually other factors such as nonlinearity of the polarization will become significant and affect the accuracy of the mathematical descriptions. Large variations in current density can cause or be associated with appreciable lowering of the discharge potential, the capacity, the efficiency, and the maximum discharge rate and may also cause serious overheating at the top of the battery. A major purpose of this paper is to eliminate such undesirable conditions by establishing here some of the underlying principles that can be used to properly design batteries so that the value of Ψ will be small. It is desired to determine here what limitations are placed on using Eq. [5] to [8], particularly at low values of Ψ, by comparing the results obtained from Eq. [6] to those obtained from Eq. [2].

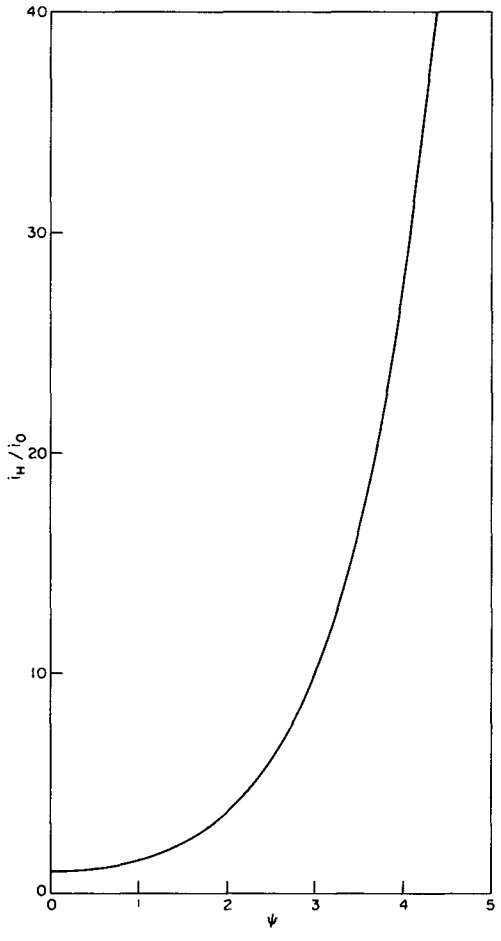

Fig. 1. i_H/i_o, the ratio of the current at the top to the current flowing at the bottom of a battery.

By putting $d = 0$ and $d = D$ in Eq. [2] the current distribution at the electrodes can be obtained and is found to be different on the two electrodes when one has a high resistance and one has a low resistance. Tobias and Wijsman have studied the case where polarization and terminal effect are restricted to one electrode by putting $\lambda_d \cong 0$ and $\mu_d \cong 0$. They also studied this case in the absence of polarization effects by making $\lambda_d \cong 0$, $\mu_d \cong 0$, and $\mu_o \cong 0$ and found that as D/H decreased in value the current density distribution approached in value the approximation described in Eq. [6]. This is illustrated in Fig. 2 where iH/I, the ratio of the current density at a given height to the average current density, is plotted as a function of h/H, the ratio of that height to the total height. At $\Psi = 0$, $iH/I = 1$ and the discharge current is distributed evenly over the face of the electrode as seen in curve C. Curve A, Fig. 2 is the approximate solution for $\Psi = 1$ using Eq. [6]. Curve B is the exact result obtained from Eq. [2] for $\Psi = 1$ where $D/H = 0.5$, $\lambda_d = 0.5$, $\lambda_o = 0$, $\mu_d = 0$, and $\mu_o = 0$. When D/H is reduced to 0.1 and Ψ is kept equal to 1 by decreasing λ_d to 0.1, the results, which are shown as circles in Fig. 2, move much closer to the approximate solution and

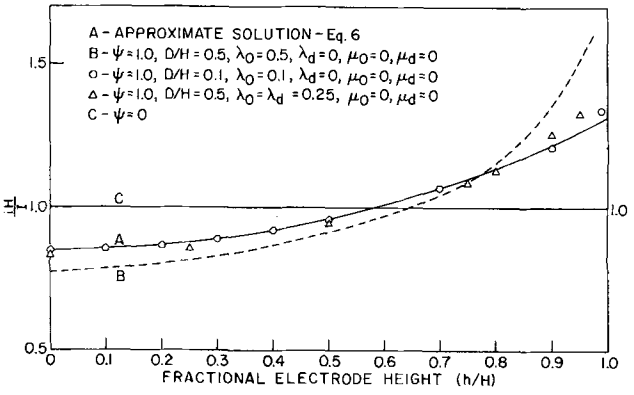

Fig. 2. Effect of *D/H* on the accuracy of the approximate solution

nearly coincide with it. At the extreme top of the electrode the current density predicted by Eq. [2] would be quite large and in a cell would be greatly reduced by the polarization that would be incurred.

A case such as this where the resistance of one electrode was quite large and the other quite small, would not be found in most battery constructions. In general, the grid resistances are kept as small as feasible and are generally fairly equal in value. This case can be studied in the absence of polarization by putting $\mu_o = 0$, $\mu_d = 0$, and $\frac{1}{2}\lambda = \lambda_o = \lambda_d$. Under these conditions Eq. [2] is symmetrical and the current distribution at each electrode for $d = 0$ and $d = D$ is the same. Consequently (2)

$$\frac{J(m,0)}{I} = \frac{J(m,D)}{I} = (1 - x/I)$$

and Eq. [2] becomes

$$(1 - x/I) = \frac{m}{H} + \sum_{n=1}^{\infty} \frac{2}{n\pi} \left(\sin n\pi \frac{m}{H} \right) C \qquad [14]$$

where

$$C = \frac{(n\pi)^{-1}(\frac{1}{2}\Psi^2 D/H)\,\mathrm{Sh}(n\pi D/H) + 1 + \mathrm{Ch}(n\pi D/H)}{(n\pi)^{-1}(\frac{1}{2}\Psi^2 D/H)\,\mathrm{Sh}(n\pi D/H) + n\pi(\frac{1}{2}\Psi^2 D/H)^{-1}\mathrm{Sh}(n\pi D/H) + 2\mathrm{Ch}(n\pi D/H)} \qquad [15]$$

Differentiating Eq. [14] with respect to m/H, gives the current density, i, flowing between electrodes at a height equal to h.

$$\frac{iH}{I} = 1 + \sum_{n=1}^{\infty} 2 \left(\cos n\pi \frac{m}{H} \right) C \qquad [16]$$

Equation [6] can be obtained from Eq. [16] by putting $D/H = 0$.

The triangles in Fig. 2 show values, calculated from Eq. [16] for $\Psi = 1$, $D/H = 0.5$, and equal electrode resistances. They are in much better agreement with curve A than curve B which has the same value of Ψ and very unequal electrode resistances.

The per cent error introduced in the current density by assuming current flow is perpendicular to the electrodes and using Eq. [6] instead of Eq. [16] has been plotted in Fig. 3 for various values of D/H and Ψ at a point at the bottom of the electrode which is fairly typical. As h/H increases from 0, this per cent of error decreases, and near the top of the electrode becomes larger again as can be seen in Fig. 2. A study of Fig. 3 shows that the error increases as D/H increases. A well designed battery will have a fairly even current density which means the value of Ψ must be small, probably less than 1.0. At $\Psi = 1.0$, the use of Eq. [6], gives an error of about 1% for $D/H = 0.5$ which is acceptable for design purposes.

In virtually all battery constructions a high value of D/H is not compatible with a high value of Ψ, since the former requires a relatively low value of H and the latter a relatively high value of H. Rewriting Eq. [1], neglecting polarization and substituting the defined values of λ_o, λ_d, and R_e gives

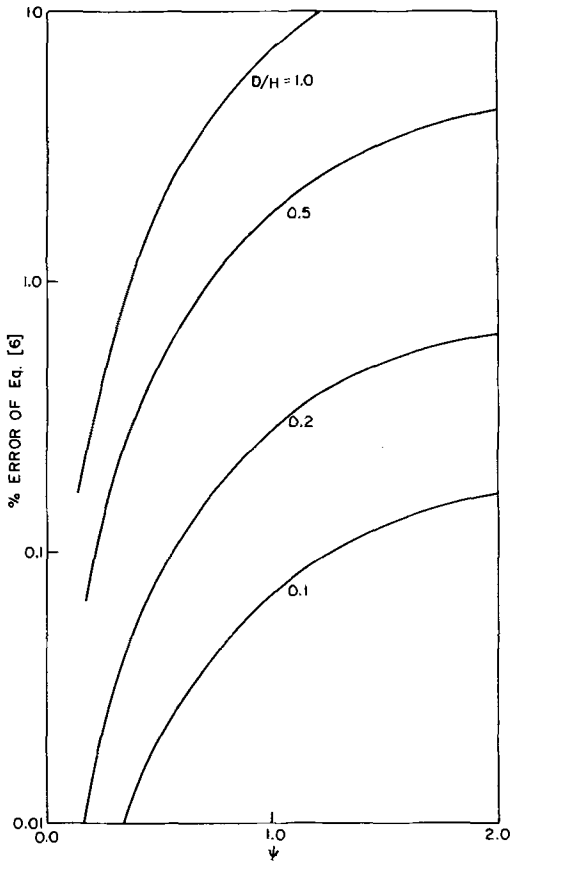

Fig. 3. Effect of *D/H* and Ψ on the accuracy of the approximate solution.

$$\frac{D}{H} = \frac{RH}{\Psi^2 R_e} \qquad [17]$$

The smallest value of R_e that is found among most electrolytes is approximately 2 ohm-cm. At a value of $\Psi = 1$ this would give $DH^{-1} = \frac{1}{2}\,RH$ from Eq. [17]. It would take an unusual combination of very high resistance grid material in one electrode plus very tall, very widely spaced electrodes to give a value of RH that would make D/H much greater than 0.01, a value that Fig. 3 indicates would be in a region of very low error. Conversely, if we assume a value of DH^{-1} equal to 0.5, then Ψ^2 would be approximately equal to RH and Ψ would be very much less than 1.0 in value and would be in the region of low error. Consequently, the assumption is tenable that the current flow in batteries is approximately perpendicular to the electrodes and it can be used as a basis for deriving the characteristics of batteries where the polarization is nonlinear as well as where it is linear as in Eq. [5] to [8].

It was desired to construct battery analogs with resistances connected together analogous to the way they are in a battery, which would not be subject to polarization effects and which could be used experimentally to check Eq. [5] to [8] and which could also be used to determine either Ψ or R, the electrode or grid resistance for an unknown battery. In many cases R is difficult to measure since it is very small in value and it is difficult to calculate because of the nature of most grid construction.

In the first attempt, two plates of good conducting material such as copper or silver which corresponded to the electrodes were clamped on each side of a poorer

conducting material which corresponded to the electrolyte. This failed due to the low resistances involved and the poor electrical contacts. Next various relatively high resistance alloys were melted and allowed to solidify between copper plates. While occasional successes were obtained, most cases failed, once again due to poor contacts. Experiments using thick metal sheets of copper or silver to correspond to the electrodes and mercury in place of the electrolyte were highly successful. A typical construction used two silver plates 3/8 in. thick, 3 in. wide, and 9 3/4 in. high, spaced 3/8 in. apart in a Lucite cell case. An electrical lead was connected to the back of one silver plate and brought out through the Lucite case which was then sealed. A similar connection was made on the other plate at the same height and the entire operation was repeated at a number of different heights. Connections were made at the top of the two silver plates, mercury was added to the desired height, and a constant high amperage d-c current (200-400A) was passed through the system. Measurements were made rapidly to avoid amalgamation effects. Potential drops were measured between the plates at the various heights and also down the plates at the various heights. Various characteristics, such as the variation of current density distribution with height, can be calculated from this data. The system is analogous to a battery in which there is no polarization.

In Fig. 4 current density distributions measured at different electrode heights for various values of Ψ are compared to curves plotted from Eq. [6]. In Fig. 5 values of e/HIR, which is proportional to the potential drop down the electrode, are compared to curves plotted from Eq. [7]. Equally good fits have been obtained from Eq. [5] and [8].

These results show that the assumption that current flow is perpendicular to the electrodes is quite

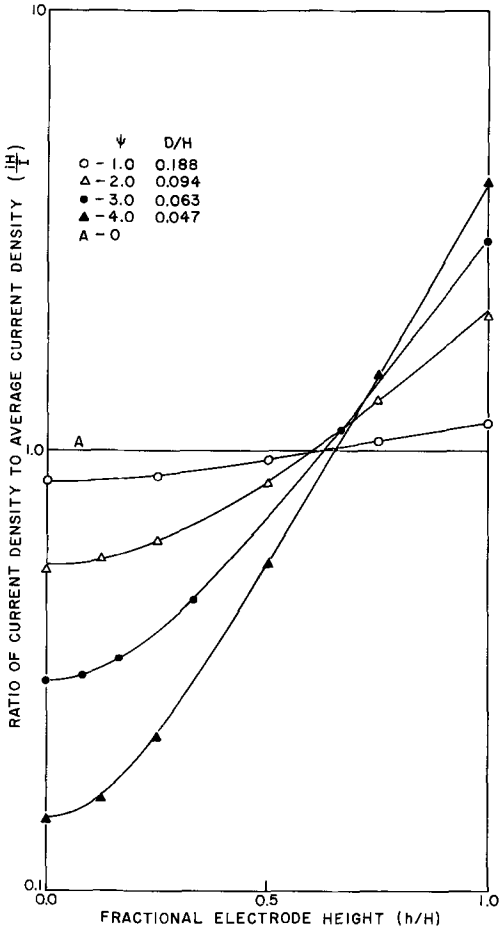

Fig. 4. Measured values of current density distributions over the face of the electrode compared to curves calculated from Eq. [6].

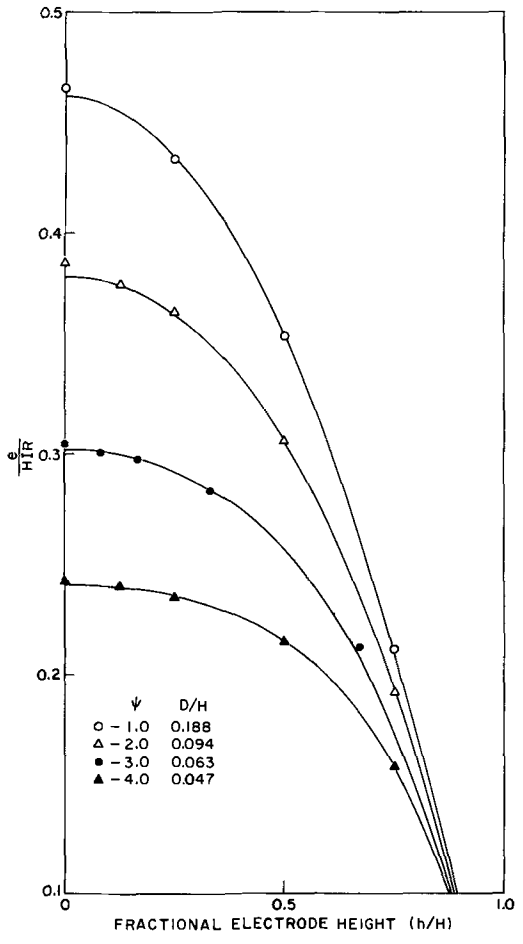

Fig. 5. Measured values of potential drop down the electrodes compared to curves calculated from Eq. [7].

accurate if D/H is not too large in value. Consequently, Eq. [5] to [8] can be used to describe the cell characteristics of almost any battery whenever the polarization is negligible or is a linear function of the current density, i. The above assumption also makes it relatively easy to analyze these cases where the polarization is nonlinear (1).

The value of Ψ is readily calculated from the electrode height, H, the spacing, D, the electrolyte resistivity, R_e, and the electrode resistance, R, using Eq. [1]. Since most grids have various kinds of holes or pockets in them, R may be difficult to calculate mathematically and it may be difficult to measure directly due to its low resistance. However, R can be measured readily by use of the battery analog. Two of the grids or plates or a suitable fraction thereof are spaced a fairly large distance apart, in a moderately close fitting container which is then filled with mercury. Insulated leads are sealed to the bottoms of the two electrodes. Potential drops between the two electrodes are measured at the top and the bottom of the electrodes. The ratio of these two potential drops, i_H/i_o, equals cosh Ψ which is plotted in Fig. 1. From Eq. [1] it can be seen that $R = L\Psi^2H^{-2}$. If i_o is very small, it may be more practical to measure the potential drop between the mid-points of the two electrodes. The potential ratio B is equal to i_H/i_M and

$$\cosh \Psi = 0.25B^2 + (0.5B^2 + 0.0625B^4)^{1/2} \quad [18]$$

In each of these cases there is no polarization present. The difference between the open-circuit potential of a cell and the potential when a given current, I, is flowing should theoretically be, and often is, equal to E_o. This value of E_o can be used in Eq. [8] to determine a value of Ψ. If the polarization is linear, Ψ can be compared to the value of Ψ as calculated or measured by the analog, which we will call Ψ_o. Since

$$\Psi_0 = \left(\frac{R}{L}\right)^{1/2} H \quad [19]$$

and Ψ is defined by Eq. [1], the two equations can be combined to show that

$$K = \frac{L(\Psi_0^2 - \Psi^2)}{\Psi^2} \quad [20]$$

thus determining the coefficient of linear polarization.

Calculations such as these are easily made and are of importance in cell design whenever Ψ becomes sufficiently large in value as it may whenever H is large and/or very thin, closely spaced electrodes are being used.

The analyses discussed here are applicable only at the beginning of a discharge. In the early stages of a constant current discharge, the active material is being consumed faster in a high current density region, the true surface area is decreasing faster, and the polarization is increasing faster than in a low current density region. As a result, the current densities in the high current density region will decrease and those in the low current density region will increase as the discharge progresses.

Manuscript submitted Aug. 23, 1972; revised manuscript received Feb. 5, 1973.

Any discussion of this paper will appear in a Discussion Section to be published in the June 1974 JOURNAL.

REFERENCES

1. C. M. Shepherd, *This Journal*, **112**, 252 (1965).
2. C. W. Tobias and R. Wijsman, *ibid.*, **100**, 459 (1953).
3. L. B. W. Jolley, "Summation of Series," p. 104, Eq. 559, Dover Publications, New York (1961).
4. T. J. I'a Bromwich, "Introduction to the Theory of Infinite Series," 2nd ed., revised, p. 393, McMillan and Co., New York (1942).

Investigations of an Alkaline Electrolyte for Zn-PbO_2 Cells

M. L. B. Rao*

Laboratory for Physical Science, P. R. Mallory and Company, Incorporated
Northwest Industrial Park, Burlington, Massachusetts 01803

ABSTRACT

Investigations of electrolytes for the operation of Zn-PbO_2 primary cells indicated that an ammoniacal zinc salt solution was satisfactory for the purpose. The stability of PbO_2, the solubility of PbO, and the corrosion rate of zinc in the electrolyte were acceptable. Cell evaluation was carried out in wound-electrode and bobbin-type C-size cells. The cell characteristics and performance are compared with zinc-carbon cells. The limitations of the new system are discussed.

Various metal oxide cathodes have been reported (1, 2) for application in primary cells. Of these, manganese dioxide and mercuric oxide are used extensively in commercial cells. The economic advantage of the former and the high volumetric energy density of the latter are key factors in the widespread employment of these active materials with zinc anodes. New battery systems that may be competitive with zinc-carbon or Zn-HgO cells would have to possess either or both the virtues of MnO_2 and HgO cathodes. One such candidate that is of interest in the context is lead dioxide. This is illustrated in Table I.

The application of PbO_2 as active material in storage cells is well known (3). Reserve cells containing acid electrolytes and PbO_2 cathodes have also been described (4-8). A nonreserve primary cell using a sulfamic acid electrolyte has been proposed by Ruben (9). McCallum (10) has patented a Pb-PbO_2 cell in phosphoric acid. Zn-PbO_2 primary cells based on ammonium phosphate electrolyte is disclosed by Johnson (11).

The instability of zinc and PbO_2 in acid (12, 13) and the high solubility of PbO, the discharge product of PbO_2 in sodium or potassium hydroxide (14), renders both very low and very high pH electrolytes unsuitable for Zn-PbO_2 cells. A lower limit of pH 4 was considered for the electrolyte as zinc is expected to be stable and PbO_2 would cease spontaneous evolution of oxygen in the medium (15). In a search for electrolytes meeting these requirements, attention was given to investigations on PbO_2 cathodes in ammonium hydroxide solutions. The choice of the electrolyte was based on the fact that PbO solubility was measured to be 10^{-4} moles/liter. This paper reports some aspects of this investigation.

Experiments and Results

Stability of PbO_2.— The stability of PbO_2 in 8M NH_4OH solution was determined by iodimetry in acetic acid media in the presence of ethylenediaminetetraacetic acid (EDTA). Experiments carried out by treating 2g of PbO_2 in 50 ml 8M NH_4OH at 80°C for 100 hr indicated no change in the oxidation number of the test sample. Hence PbO_2 was concluded to be reasonably stable in the ammoniacal medium.

Electrolyte conductivity.—The conductivity of ammonium hydroxide was three orders lower than potassium hydroxide of comparable molarity. To improve the conductivity of the solution 1M $ZnCl_2$ was added. The conductance data are given in Table II.

PbO solubility.—The solubility of PbO was measured by polarography by taking known volumes of

Table I. Comparison of cathode-active materials

No.	Feature of comparison	MnO_2*	HgO**	PbO_2**
1	g/A-hr	3.24	4.04	4.46
2	cm^3/A-hr	0.65	0.36	0.48
3	~$/1000 A-hr	2.20	70.20	4.70
4	Cell with zinc anode			
	(a) open-circuit voltage	1.5V	1.35V	1.5V***
	(b) theoretical-energy density			
	(i) Whr/lb	152.4	117.6	123.8
	(ii) Whr/$in.^3$	30.1	41.8	39.2

* One-electron transfer reaction.
** Two-electron transfer reaction.
*** Alkaline system.

* Electrochemical Society Active Member.
Key words: lead dioxide, zinc, zinc-lead dioxide cell, alkaline primary cell, ammoniacal zinc chloride electrolyte.

Table II. Properties of electrolyte at 25°C

Electrolyte	Sp. conductivity (ohm^{-1}-cm^{-1})	Solubility of PbO (moles/liter)	Zinc corrosion rate (g/cm^2/day)
8M NH_4OH	9.75×10^{-4}	2.6×10^{-4}	2.6
8M NH_4OH, 1M $ZnCl_2$	1.29×10^{-1}	1.1×10^{-4}	1.3
8M KOH + 6% ZnO	3.41×10^{-1}	10^{-2}	1.3

PbO equilibrated ammoniacal solution in acetate buffer.

Zinc corrosion.—Weight loss method was used to determine the zinc corrosion rate in the ammoniacal solution. The data are given in Table II and are compared with similar experimental data in zinc hydroxide containing potassium hydroxide solution.

Wound electrode cells.—To test the material efficiency of discharge of PbO_2 in the ammoniacal zinc chloride solution, cathode limiting C-size cells were assembled using pasted plate electrodes in wound structures. The cathodes were 1 × 15 in. in dimension and contained 75% PbO_2, 10% graphite, 10% carbon, 5% proprietory binder, and a stainless steel expanded metal grid. Anodes were also of pasted plate configuration with 95% zinc (10% Hg) powder, 5% binder. The cells were of 2.8 A-hr PbO_2, 3.9 A-hr zinc, and contained filter paper as the separator material. The cells were discharged at 0.2, 0.6, and 1.0A after filling with 1M $ZnCl_2$ in 8M NH_4OH electrolyte. The open-circuit voltage of the cell was 1.52V, and the discharge curves (Fig. 1) indicated 60.7%, 44%, and 25% utilization of PbO_2 (2*e* basis) at 0.2, 0.6, and 1.0A currents, respectively.

Leclanché type cells.—The applicability of ammoniacal-electrolyte to bobbin-type Zn-PbO_2 cells was tested. Thick nonporous cathodes formulated for C-cells gave poor performance. Upon modification of the cathode structure by incorporating a soluble salt such as NH_4HCO_3 to generate porosity, the cell performance improved. The cathodes used in the test cells were fabricated according to the following procedure.

Twenty-eight to thirty-two grams of PbO_2 was mixed with 4g of graphite powder, 4-8g of ammonium bicarbonate, and 2-3g of binder. The mixture was pressed to a cylindrical bobbin of 0.75-0.81 in. diameter and 1.2-1.375 in. height with a carbon rod of 0.25 in. diameter driven through the axis of the pellet. The Leclanché type cells were assembled using the cathodes, two layers of filter paper separator, 1M $ZnCl_2$, 8M NH_4OH electrolyte, and a calculated excess of amalgamated zinc anode. The C-cells so assembled were of 6 A-hr based on PbO_2 capacity. In the presence of ammonium bicarbonate in the cathode, the

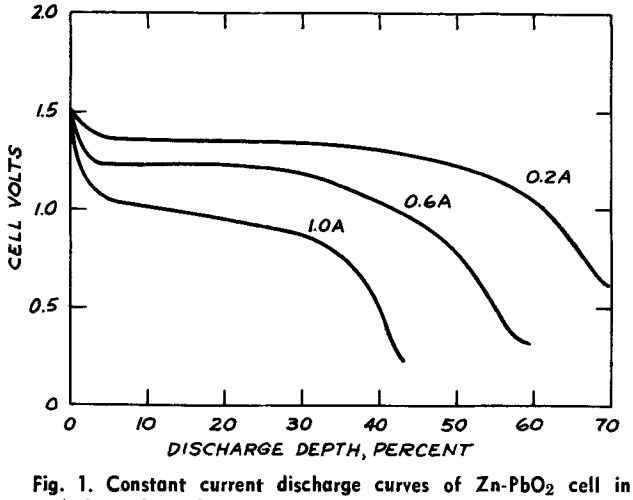

Fig. 1. Constant current discharge curves of Zn-PbO_2 cell in wound electrode configuration.

Table III. Discharge data of Zn-PbO_2 bobbin-type C-Cells

No.	Type of anode	Cathode	Hours of service at 4 ohm load (0.75V cutoff)
1	Zinc can	PbO_2 bobbin	0.5 ± 0.2
2	Carboxyl-methyl cellulose-coated zinc powder along with zinc can	PbO_2 bobbin	2.6 ± 0.3
3	Zinc expanded metal along with zinc can	PbO_2 bobbin	3.9 ± 0.3

open-circuit voltage of the cell was 1.8V. The freshly assembled cells were subjected to continuous discharge across a 4-ohm load. The number of hours of service for cells assembled with different types of zinc anodes is provided in Table III. Figure 2, curve 2, illustrates the discharge data of a typical cell.

Discussion

One of the major problems in adopting potassium or sodium hydroxide electrolyte for Zn-PbO_2 cells is the solubility of PbO formed during discharge. This is because the dissolved lead species reacts with zinc anode and causes self-discharge of the cells. It is seen from the data in Table II that by the use of 1M $ZnCl_2$, 8M NH_4OH electrolyte the solubility of PbO has been reduced to 10^{-4} moles/liter. This magnitude of solubility may be considered acceptable. Although the specific conductivity of the ammoniacal electrolyte is lower than that of KOH solutions, the decreased solubility of PbO is of considerable merit. It has been shown that PbO_2 is reasonably stable, and the zinc corrosion rate is similar to that in alkali in the ammoniacal electrolyte. These characteristics and the discharge data in Fig. 1 and Table III, render this electrolyte interesting for application in Zn-PbO_2 cells.

The open-circuit voltage of the Zn-PbO_2 cells tested is 1.52V. This value is close to that expected from the following

$$Zn + 2\,OH^- = ZnO + H_2O + 2e \quad E^\circ_b = 1.24V \quad [1]$$

$$PbO_2 + H_2O + 2e = PbO + 2\,OH^- \quad E^\circ_b = 0.25V \quad [2]$$

Cell reaction

$$Zn + PbO_2 = ZnO + PbO \quad E^\circ_b = 1.49V \quad [3]$$

Half-cell measurements carried out employing cathode-limiting cells indicated the discharge efficiency of PbO_2 electrode correspond to a 2 electron transfer reaction as proposed in Eq. [2]. X-ray diffraction studies, on partially discharged PbO_2 cathodes indicated the presence of PbO_2, PbO, $Pb(OH)_2$, $PbCl_2$, and lead oxychloride. The presence of PbO and $Pb(OH)_2$ in the

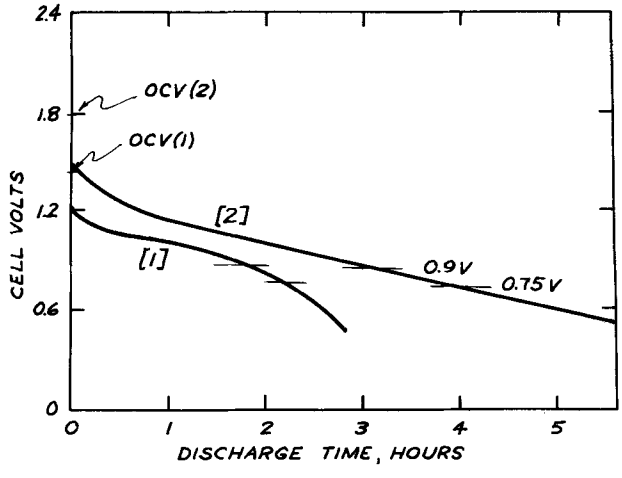

Fig. 2. Constant load discharge curves of Zn-MnO_2 and Zn-PbO_2 cells in Leclanché cell configuration. (4 ohm load). Curve 1, Zn-MnO_2 cell; Curve 2, Zn-PbO_2 cell.

Table IV. Comparison of $Zn-MnO_2$ and $Zn-PbO_2$ C-Size Leclanché type cells

Factor of comparison	$Zn-MnO_2$ C-Cell	$Zn-PbO_2$ C-Cell
Nominal capacity (cathode limiting)	4 A-hr	6 A-hr
cell weight	1.4 oz	2.5 oz
cell volume	1.25 $in.^3$	1.25 $in.^3$
Open-circuit emf	1.5V	1.8V
Energy density (assembled cell values)		
Whr/lb	69.0	69.0
Whr/$in.^3$	4.8	8.6

discharge product is according to Eq. [2]. The presence of $PbCl_2$ and lead oxychloride is hypothesized as due to the kinetic factors dependent upon the effect of rate of discharge on the reaction mechanism.

A change in open-circuit voltage from 1.52V to 1.8V is observed to occur in the presence of ammonium bicarbonate in the cathode matrix. This may be due to reactions leading to the formation of $PbCO_3$ and the changes in pH in the interior of the cathode. The differences observed in the service hours delivered by various cells in Table III indicated that a large surface area zinc anode is necessary for the operation.

A comparison of the characteristics and performance capability of $Zn-PbO_2$ and zinc-carbon cells is provided in Table IV and Fig. 2.

It is seen from the data in Table IV that the gravimetric energy density of $Zn-PbO_2$ cells are of similar magnitude as that of zinc-carbon cells, and the volumetric energy density of the former is approximately double that of the latter. Based on this data and the performance characteristics represented in Fig. 2, it is concluded that the development of $Zn-PbO_2$ cells is feasible in the ammoniacal zinc chloride electrolyte. It is of interest to point out the following limitations of the new system.

(*i*) The low conductivity of the electrolyte renders the rate capability of the $Zn-PbO_2$ system inferior to that of alkaline $Zn-MnO_2$ cells.

(*ii*) The freezing point of the electrolyte is $-10°C$. Thus a limited low temperature performance is expected for the $Zn-PbO_2$ cells.

(*iii*) The electrolyte is highly corrosive, hence commonly used container materials such as nickel coated steel should be avoided in the cell formulation.

(*iv*) The electrolyte has higher vapor pressure than acidic zinc chloride solution used in Leclanché cells. Hence, cells based on the electrolyte under investigation are not suitable for vented cell structures.

(*v*) It is an open question whether PbO_2 reacts with the ammonia in the electrolyte during long term storage.

Acknowledgment

The author wishes to thank Dr. P. Bro, Dr. R. G. Selim, and Dr. A. N. Dey for useful discussions and Mr. S. Fantasia for discussion of x-ray diffraction studies.

Manuscript submitted Nov. 8, 1972; revised manuscript received March 19, 1973.

Any discussion of this paper will appear in a Discussion Section to be published in the June 1974 JOURNAL.

REFERENCES

1. G. W. Vinal, "Primary Batteries," John Wiley & Sons, Inc., New York (1950).
2. G. W. Heise and N. C. Cahoon, "The Primary Battery," John Wiley & Sons, Inc., New York (1971).
3. G. W. Vinal, "Storage Batteries," John Wiley & Sons, Inc., New York (1962).
4. G. W. Heise and N. C. Cahoon, "The Primary Battery," pp. 27-28, John Wiley & Sons, Inc., New York (1971).
5. L. W. Pucher, *This Journal*, **99**, 204C (1952).
6. W. J. Shlotter, *ibid.*, **99**, 205C (1952).
7. P. A. Brook and A. E. Davis, *J. Appl. Chem. (London)*, **6**, 174 (1956).
8. Chloride Batteries Ltd., Brit. Pat. 842,931 (1960).
9. S. Ruben, U.S. Pat. 2,954,418 (1960).
10. J. McCallum, U.S. Pat. 2,954,418 (1960).
11. T. B. Johnson, U.S. Pat. 2,952,572 (1960).
12. W. H. Beck and W. F. K. Wyne-Jones, *Trans. Faraday Soc.*, **50**, 972 (1954).
13. P. Ruetschi and B. D. Cahan, *This Journal*, **105**, 369 (1958).
14. W. F. Linke, "Solubilities Inorganic and Metal Organic Compounds," Vol. 2, p. 1314, American Chemical Society, Washington, D.C. (1965).
15. M. Pourbaix, N. Zoubov, and J. Van Muylder, "Altas d'Equilibres ElectroChemiques," Cebelcor, Paris (1963).

Laboratory Cell and Hydrodynamic Model Studies of Magnesium Chloride Reduction in Low-Density Electrolytes

R. D. Holliday and P. McIntosh

University of Newcastle, New South Wales 2308, Australia

ABSTRACT

A large laboratory cell of a new type, which uses low-density electrolytes and electrodes inclined at a small angle to the vertical, has been used to study production of magnesium from anhydrous $MgCl_2$. Current efficiency and power efficiency have been measured to within 1% at current densities up to 2.0 A/cm^2 in both LiCl-KCl and pure KCl solvents at temperatures between 700°-850°C. The gas-lift pumping of the electrolyte between the electrodes by chlorine evolved at the anode has been simulated in a hydrodynamic model. The model has shown that the back mixing of electrode products which causes loss of current efficiency is strongly influenced by cell geometry, and the important parameters are the electrode slope, interelectrode spacing, depth of melt above the electrodes, and the surface area available for gas liberation from the melt. The observations provide an explanation for the effects of changes in cell-operating conditions on current efficiency and have provided a basis for design improvements. The design finally evolved has a much higher productive capacity and lower specific energy requirement than conventional cells.

Magnesium is produced commercially by electrolysis of $MgCl_2$ dissolved in molten chloride solvents, and conventional cells use electrolytes of higher density than the metal produced, so that the product accumulates at the melt surface (1). In recent years a number of chloride solvents for $MgCl_2$ have been developed which are of lower density than the metal, and so permit collection of the metal on the base of cells, similar in concept to the Hall cells used in aluminum manufacture (2).

In magnesium electrolysis, the use of low-density electrolytes opens the way to development of new cell designs in which full advantage is taken of the fact that both the anode and the cathode reactions take place on solid nonconsumable electrodes. One such design, proposed and developed in the present work, embodies pairs of parallel planar electrodes, inclined at a small angle to the vertical and arranged so that metal deposited on the upward-facing cathodes flows to the bottom of the cell, while chlorine is held by buoyancy forces within an envelope near the down-facing anode surfaces.

The resulting countercurrent flow of electrode products contrasts with the cocurrent flow pattern of the conventional cells. It was postulated that cells of the new type should be much less subject to metal losses caused by back reaction between magnesium and chlorine than conventional cells in which efficient separation of electrode products is difficult (1). The main prospective advantages of the proposed design are that operation at a higher current density and with reduced interelectrode spacing would be possible without serious impairment of current efficiency, while cell structure would be greatly simplified by avoidance of the need to separate products above the electrolyte. These improvements should bring about reductions in both operating and capital costs of the process.

To evaluate the design, experiments were conducted in which a large laboratory cell was operated over a range of conditions likely to be considered for commercial use. The design of the cell, and the interpretation of results obtained from it, were facilitated by the use of a room-temperature hydrodynamic model. In this model, the flow patterns of gas and liquid could be readily followed and recorded photographically. The necessary conditions for modeling of the fused-salt system by aqueous solutions are well established (3, 4), and in fact models of similar type have been used in studies of flow patterns in conventional magnesium cells.

Key words: electrolysis, current efficiency, molten chlorides, magnesium.

Experimental

Objectives.—The primary aim of the experimental program was to measure the main operating characteristics, current efficiency, and power efficiency, in cells of the new type sized large enough to permit predictions of the performance of production-scale cells. It was desired to measure the performance characteristics with a precision and reproducibility of better than 1% under conditions of current flow and melt circulation identical to those in the full-size cells. This could be achieved by using a laboratory cell with planar, parallel electrodes, geometrically similar to the scaled-up version in section perpendicular to the electrodes. The essential difference between laboratory and full-size cells was the reduction of the electrode width, so that the model constituted a slice of an electrode pair of the full-scale unit. Moreover, the model contained only one set of electrodes rather than the multiple pairs necessary to attain high amperages in the scaled-up version.

In the addition to the measurement of current efficiency and power efficiency in the laboratory cell, the melt-flow patterns induced by the gas-lift pumping action of chlorine at the anode were studied in a separate program using a hydrodynamic model of the laboratory cell. This program was designed to elucidate the influence of geometrical parameters, melt properties, and current density on the recirculation and retention of anode gas before the final cell design was prepared.

It was recognized that data obtained under rigorously monitored laboratory conditions would likely represent the upper limit of efficiency figures attainable under commercial conditions, which would, of necessity, be less stringently controlled. The aim of the program, accordingly, was to obtain basic data on the effects of geometry and electrolyte properties in cells of the new type. It was of course not intended, even if it were possible, to duplicate the types of disturbances which might occur in an industrial plant; in this sense, the work represents a feasibility study rather than a final economic evaluation.

The cell was operated with reagent-grade electrolyte materials and with anhydrous $MgCl_2$ feed of the highest purity attainable. This was considered neces-

sary in order to simplify as far as possible the interpretation of data on response of the cell to changes in electrolyte composition and operating conditions. The data so obtained should then provide a base line against which the effects of such factors as operating disturbances and electrolyte contamination can be assessed.

Design and construction of the experimental cell.— The large planar-electrode cell used in the main part of the experimental program is shown in Fig. 1. This cell embodies many features that were evolved during preliminary work with small cells of 100-500A capacity and of cylindrical geometry, one form of which is shown in Fig. 2.

The main feature of the design is the use of parallel, planar electrodes with working surfaces inclined at a small angle to the vertical. The central electrode is the anode, constructed from graphite plates 24 in. in over-all length, and tapered over the lower 12 in. to an included angle of 20°. Cathode plates of mild steel conform to the anode slope, and are welded to the steel shell at their upper ends to maintain a uniform separation [anode-cathode distance (A.C.D.)] of 1.5 in. between anode and cathode surfaces. The current flow path is perpendicular to the electrodes and leakage of current to the sides of the cell is prevented by 1 in. thick insulator sheets cut from fused-cast alumina brick.

The shell to which the cathode plates are welded is constructed in two parts. The upper section of ½ in. mild steel plate houses the gas-collection chamber and

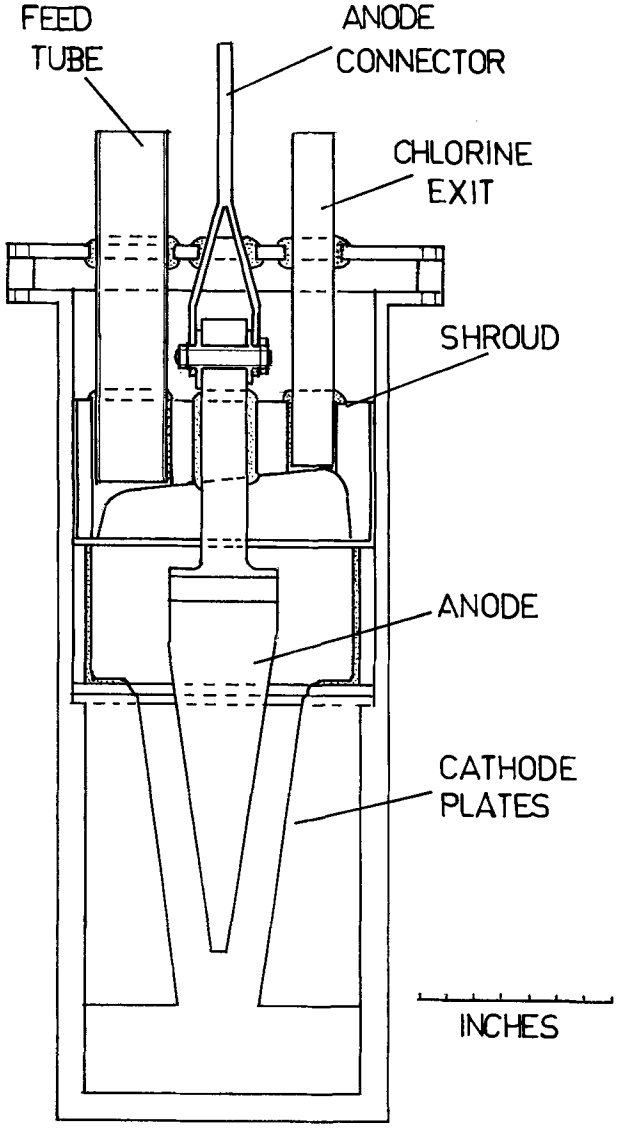

Fig. 1. Planar-electrode cell, cathode area 1100 cm²

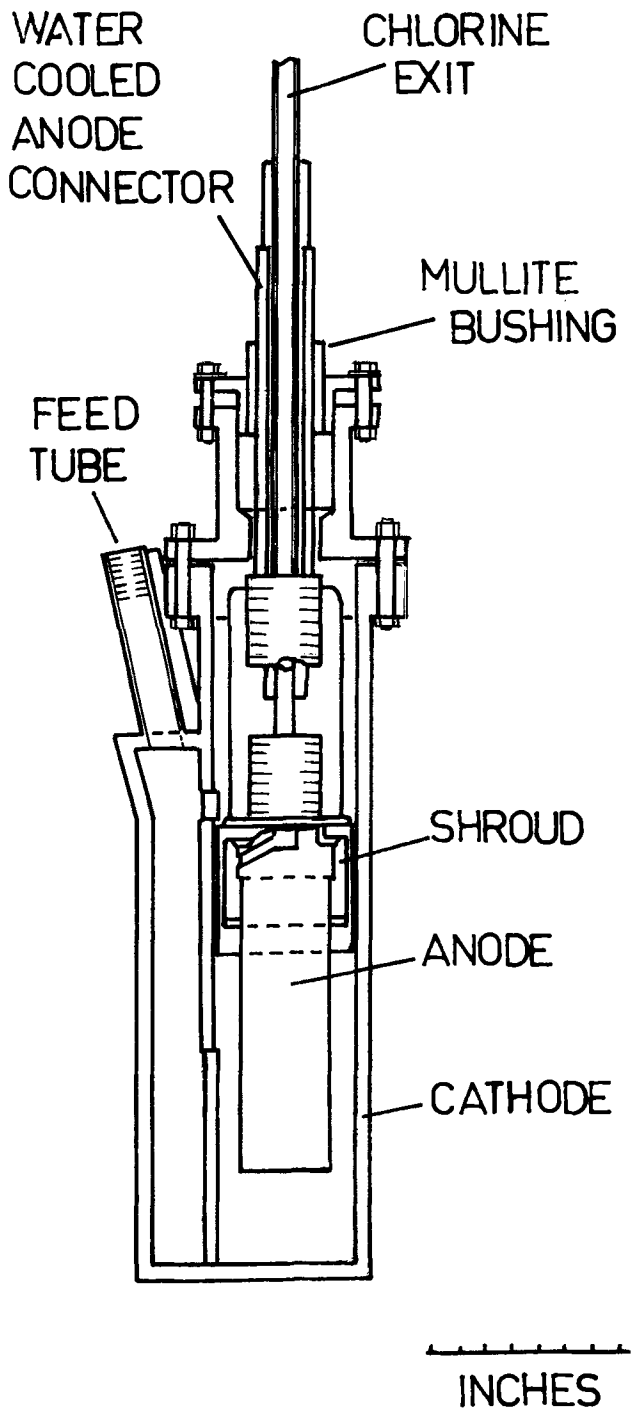

Fig. 2. Cylindrical cell, cathode area 500 cm²

permits a cold seal to be made at the upper flange, which is located some 12 in. above the heater zone of the auxiliary furnace. The flange temperature is always below 200°C, and an asbestos gasket with a silicone-based filler may be used. Although the flange seal is vacuum tight, the gas space is maintained at 2 in. water gauge below atmospheric pressure and back purged with Ar to ensure that no loss of chlorine can occur.

Direct contact between chlorine and metal is avoided throughout the structure. A rectangular-box shroud made from impermeable high-alumina castable refractory serves as a gas-tight cover over the entire melt surface. The shroud is supported on a ledge in the steel shell where the gas collection chamber joins the lower 1 in. thick M.S. chamber housing the electrodes. The height of the shroud above the electrodes is increased as required by mounting it on a sillimanite liner, and sealing it with alumina cement. During cell opera-

tion the electrolyte level is maintained well above the base of the liner so that chlorine above the melt contacts only the refractory. Mullite tubes sealed into the shroud afford access for feeding, chlorine exit, temperature measurement, and melt-level control.

The lower part of the cell houses the electrodes and communicates via a 1 in. slot at the base with a compartmented side chamber. The side chamber is designed so that as metal accumulates in the base of the cell, a barometric leg of metal in the side chamber overflows a weir. In this way, a constant metal-pad depth is automatically maintained and metal may be tapped from the cell without disturbance of the electrode compartment.

The cathodes are connected to the power supply by copper flexes joining the shell to the negative terminal, and measurable voltage losses occur only at the contacts. The connection to the anode is made above the shroud by a water-cooled copper pressure pad. A size limit is imposed on the upper section of the anode by the dimensions of the shroud and the gas collection chamber which houses it. As a result, resistive-voltage losses in this section of the circuit account for 80% of the total loss external to the electrolyte. In a full-scale cell, this loss would be halved because of the freedom to increase conductor dimensions.

Cell operation.—The electrolyte is premelted in gas-tight steel crucibles under Ar purge in a gas-fired muffle furnace. By pressurizing the crucible with Ar, the melt may be syphoned into the electrode compartment via a stainless-steel feed tube. The melt may be withdrawn from the cell by reversing the procedure and syphoning into the crucibles under reduced pressure. Metal is removed in the same way, from the overflow weir in the side chamber.

The as-received feed material was a good quality Kroll process recycle $MgCl_2$, supplied in the form of massive blocks cast in drums by Commonwealth Scientific and Industrial Research Laboratories, Melbourne, Australia. Before use, this material was further purified by remelting and stirring in contact with pure molten Mg under carefully controlled conditions, so that essentially all the MgO, dissolved H_2O, and metallic impurities were removed. Feed to the cell assayed above 99.85% $MgCl_2$, the major impurities being a maximum of 0.1% MgO and 0.05% metallics, principally Fe and Ti.

The $MgCl_2$ was syphoned from the purification chamber and solidified as cylindrical slugs which were fed into the cell via the mullite feed tube under a protective Ar purge.

Power is supplied to the cell by a Westinghouse Type RXAF 5.5/5000 silicon diode rectifier with a maximum output of 5000A at 5.5V. Changes in cell current are detected by recording the voltage drop across a calibrated shunt on the 1 mV scale of a Bausch and Lomb recorder fitted with a zero suppressor. Manual adjustment of a saturable-reactor controller is made to ensure that current does not deviate on the average by more than 0.1% from the set point during a run. Total cell voltage is measured at the output terminals of the rectifier, and voltage drops across sections of the circuit are measured by probe contacts at intervals during a run.

Chlorine is withdrawn from the cell under slightly reduced pressure, and passed through a filter and a bubbler to remove entrained particulate before it is absorbed by NaOH solution flowing countercurrent through a packed tower. The NaOH solution is recycled and samples are withdrawn at intervals from the accumulator for analysis by a modified Mohr titration. The absolute error in the analysis results in an uncertainty of 0.5% in the measured yield of chlorine during 30 min at the 700A level, and 0.2% at 2000A.

Basis for design of the hydrodynamic model.—Bukhbinder, in modeling gas evolution in the conventional magnesium cell, has established which physical factors control the flow pattern within the electrolyte (3). The average electrolyte velocity, w, under conditions of pumping by gas evolved at the anode, is determined by the kinematic viscosity (ν), the total anode immersion depth (h), the A.C.D. (1), and the specific rate of gas evolution (v). The average size of bubbles evolved also exerts an important effect, and it is suggested (5) that the critical detaching diameter, α, of the bubbles is given by the semi-empirical equation

$$\alpha = 0.0208\theta(\sigma/\gamma)^{1/2}$$

involving contact angle θ, surface tension σ, and density γ of the electrolyte.

Dimensional analysis (4) leads finally to the relationship

$$(wh/\nu) = B \cdot (vh/\nu)^m \cdot (gh^3/\nu^2)^n \cdot (\sigma/\gamma v^2 h)^q \cdot (h/l)^p$$

which contains the term $(\sigma/\gamma v^2 h)^q$ to take into account the melt properties that affect bubble size. In this relationship, B is a constant of proportionality; the exponents m, n, q, and p are numerical constants for a particular flow regime, and g is the gravitational constant. From this relationship the conditions for similarity between the fused-salt system of the experimental cell and an aqueous model are obtained. These conditions are

(*i*) v cell = v model

(*ii*) ν cell = ν model

(*iii*) σ/γ cell = σ/γ model

together with equality of linear dimensions. Conditions (*ii*) and (*iii*) are satisfied if 10% $NaNO_3$ solution is used as model fluid (Table I).

An additional factor of importance is the contact angle, θ, which determines the average bubble size. Ukshe (4) found in studies of chlorine evolved by electrolysis on graphite in $MgCl_2$-KCl-NaCl electrolyte, that bubble size ranged from 0.35 to 0.70 mm. A similar size distribution was found for bubbles obtained by forcing N_2 gas through porous graphite in 10% $NaNO_3$ solution.

Marrucci and Nicodemo (6) found that the bubble size depended upon the ionic concentration but decreased asymptotically to a limiting value as concentration increased, independently of the nature of the electrolyte. The size of the bubbles decreases as the concentration increases because mutual repulsion between bubbles is promoted by increased surface concentration of ions.

It is apparent that the required similarity between the chloride melts and the modeling solution is satisfied by using strong ionic solutions which have comparable densities, viscosities, and surface tensions to chloride melts. Such solutions should show comparable size distributions for bubbles liberated at a submerged surface, regardless of their mode of origin.

Construction and operation of hydrodynamic model.—The physical model is hence based on the use of concentrated ionic solutions, and geometrical similarity is achieved by constructing the model to the same dimensions as the cell itself. The width of the model may be made much less than that of the cell, since only the A.C.D. and vertical dimensions can affect the flow pattern.

Exploratory observations showed that only the anode gas evolution had a major effect on the flow of electro-

Table I. Comparison of physical properties for molten-salt electrolytes and aqueous $NaNO_3$ solution

Property	Ternary electrolyte (10% $MgCl_2$, 67% KCl, 23% NaCl, at 700°C)	Quaternary electrolyte (10% $MgCl_2$, 40% $CaCl_2$, 12% KCl, 38% NaCl, at 700°C)	10% $NaNO_3$ at 20°C
ν (m^2/sec)	0.82×10^{-6}	1.32×10^{-6}	1.00×10^{-6}
σ/γ (m^2)	0.0616	0.0632	0.0695

lyte, and the effect of liquid-metal flow in a layer approximately 0.1 in. thick at the cathode would be negligible.

A two dimensional model was constructed in which it was possible to vary the geometrical factors such as A.C.D., surface area for gas evolution, electrode-immersion depth and slope, as well as current density. The general construction of the model is shown in the cinephotographs, Fig. 7-9, and the important geometrical parameters are indicated in Fig. 3. It consists of a tank of transparent plastic in which a 2 in. layer of salt solution, *i.e.*, the model electrolyte, is contained between ¼ in. walls. Both electrodes fit tightly within the walls, but can be manipulated by means of attached rods after supporting clamps are loosened. The cathode and the melt reservoir above it are constructed from metal sheet and serve essentially to define the electrolyte flow path.

The simulated anode consists of a closed box with an active wall of porous material, through which gas is forced to simulate evolution of chlorine. The active face is constructed from sillimanite and is tapered in thickness to allow for the effect of liquid head on gas-evolution rate. Nitrogen gas is supplied to the anode at flow rates equal to the volumetric production rate of chlorine at cell temperatures and current densities from 0.5 to 2.5 A/cm^2. With the profile adopted, gas evolution is uniform over the immersed surface, and the range of bubble diameters, 0.3-0.7 mm, is close to that expected in chloride melts.

Two different techniques were used to photograph the bubble patterns. The first was a stop-motion still technique which employed illumination from behind the tank, using a diffuser screen and a Mayer Type 035 strobe light. The camera, a Linhof 4 in. by 5 in. with a Symmar F 5.6/100 mm lens, was located on the opposite side of the tank and synchronized with the strobe to achieve very low exposure times.

In the second approach, high speed cinephotography was used to obtain a large number of frames under a particular combination of cell parameters to ensure that the photographic data were representative of average flow conditions. A 16 mm Vinten camera with a speed range of 100-250 fps was used, and it was found that at 100 fps bubble movement could be stopped on an individual frame, and the movement of individual bubbles could be followed in adjoining frames.

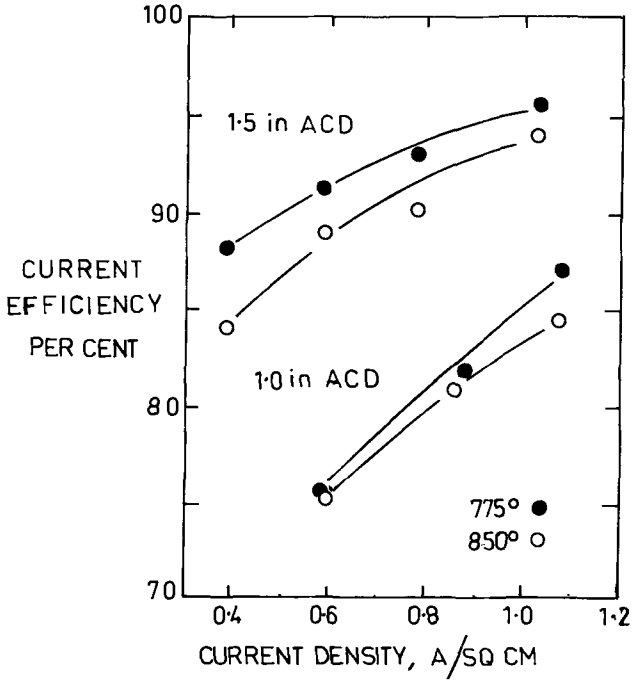

Fig. 3. Dependence of C.E. on interelectrode distance in 500A cell

Experimental Results

Hydrodynamic model studies of cell geometry.—An initial survey was undertaken to determine which geometrical factors controlled the evolution of gas from the melt and the back mixing of electrode products. The first experiments used the cell geometry, as initially proposed, and revealed that the design did not secure efficient separation of products (Fig. 4).

The early experiments showed that the ascending gas forms an envelope of discrete bubbles along the surface of the anode, and the electrolyte near the anode is drawn into the envelope to acquire an upward velocity equal to that of the gas. At the surface the two-phase mixture forms a well-defined foam layer, the thickness of which depends upon the gas rate, the area of the liquid surface, and the physical properties of the liquid.

The liquid which has been pumped to the surface flows horizontally from the face of the anode and along the surface until it meets the cell wall and is directed downwards to form a vortex. Gas that has not escaped at this stage is carried down into the liquid, where it may flow in one of two directions: around the vortex and back to the surface, or into the interelectrode space with the returning melt. As the liquid flows back between the electrodes, it is again influenced by the ascending gas stream and its velocity decreases as it moves toward the bottom of the cathode.

The preliminary experiments showed that it was necessary to clarify the roles played by each of the geometrical parameters shown in Fig. 5 in determining the flow pattern.

Anode slope proved to be of major importance because the thickness of the gas envelope is strongly affected by the buoyancy forces which compress the bubbles against the anode surface. However, if the slope is large, compactness of the cell is sacrificed.

The A.C.D. must be large enough to permit melt to flow back between the electrodes without interfering with the ascending gas envelope.

The importance of the other parameters, the surface area and the depth of liquid above the electrodes, was only fully appreciated after observations had been made on the model. The surface area of the melt in fact controls the rate of gas evolution while the upper liquid layer serves to accommodate the foam and exerts an important effect on the circulation rate of the liquid.

The effects of anode slope at two levels of current density are shown in Fig. 6. The marked decrease in the amount of gas carried back between the electrodes at the higher angle results from a lessening of the

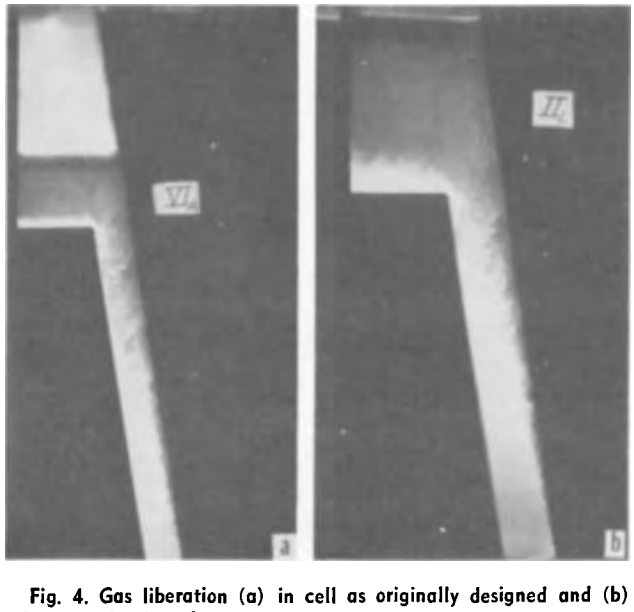

Fig. 4. Gas liberation (a) in cell as originally designed and (b) after optimization of geometry

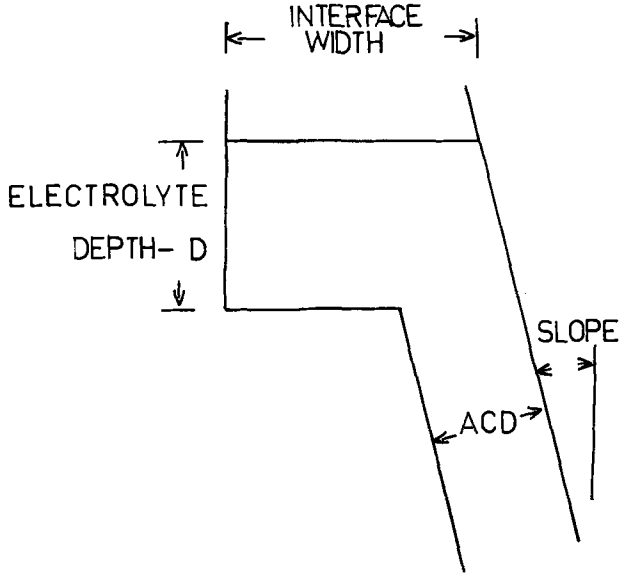

Fig. 5. Cell dimensions controlling flow pattern due to anode gas pumping

interaction between returning electrolyte and the gas envelope.

A.C.D. functions similarly to the electrode slope in controlling the interaction between the envelope and the returning electrolyte. Figure 7a shows that at 1 A/cm^2 and 1 in. A.C.D. a substantial quantity of gas is torn from the envelope by returning melt; at 1.5 in. the quantity is markedly reduced, and at 2.0 in. the effect is eliminated, as shown in Fig. 7b. At 2.0 A/cm^2, even a 2 in. A.C.D. does not suppress the interaction completely, and quite strong interaction is observed at 1.5 in.

The strong influences of surface area and melt depth are illustrated in Fig. 8, where it is apparent that a decrease in melt depth from 4.0 to 1.5 in. above the cathode forces the two-phase layer well into the region between the electrodes at 1.0 A/cm^2. Reduction of the surface area of the melt by a factor of 2.5 has a similar and even more pronounced effect even if melt depth is adequate. The most compact cell geometry is attained only by joint variation of these parameters to secure optimum gas liberation from electrodes of given size.

As a result of a systematic investigation of the geometrical parameters the dimensions selected for the experimental cell were: A.C.D., 1.5 in.; anode slope, 10°; melt depth, 4 in.; surface width, 3.5 in. A comparison of gas liberation in a model with these dimensions and in one conforming to the original cell design shows a clear improvement (Fig. 4).

Table II. Effect of melt depth on current efficiency

Large Planar Electrode Cell

Temp. (°C)	Melt level (in. above cathode)	Current density (A/cm^2)	Current efficiency (%)
850	1.5	0.36	75
850	4.0	0.36	82
850	5.0	0.36	81
800	1.5	0.36	82
800	4.0	0.36	87
800	5.0	0.36	79
850	1.5	0.64	82
850	4.0	0.64	90
850	5.0	0.64	72
800	1.5	0.64	86
800	4.0	0.64	88
800	5.0	0.64	78

Verification of the hydrodynamic model.—Initial electrolysis runs in the large cell were designed to check the validity of the hydrodynamic model. Once optimum values for the geometrical parameters had been established in the model, it was necessary to select as experimental variable a parameter that could be easily varied without structural modification of the cell. One of the easiest to vary, and one which showed an unexpectedly strong effect on gas recirculation in the model tests, was the depth of the liquid layer above the cathode, dimension D in Fig. 5.

Runs were conducted at two temperature levels and at two levels of current density, using melt depths ranging from 1.5 to 5.0 in. above the cathode. Results shown in Table II support the conclusion drawn from the aqueous model tests. The effect of increasing the depth to 5 in. in the cell as constructed was to raise the foam level in the gas space so that the gas-exit tube was partially blocked and gas-space recirculation markedly increased. The result is a severe fall in current efficiency.

Further evidence for the validity of the model was obtained from current efficiencies measured in the 500A cells, which were operated at two levels of interelectrode spacing, 1.0 and 1.5 in. The predicted falloff in current efficiency occurs as A.C.D. is decreased, as indicated in Fig. 3. The geometry of the 500A cell is such that current densities at anode and cathode are unequal, so that quantitatively the data do not describe behavior of the large planar electrode cell, but the trend predicted by the model is supported.

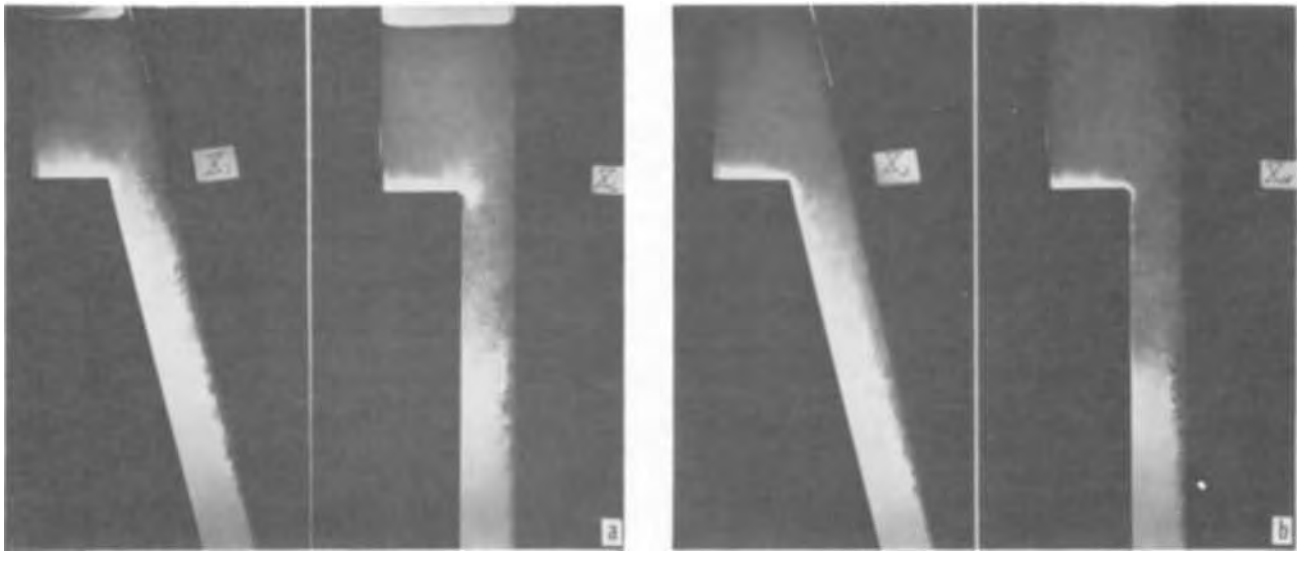

Fig. 6. Effect of electrode slope on gas liberation (a) at 1 A/cm^2 and (b) at 2 A/cm^2

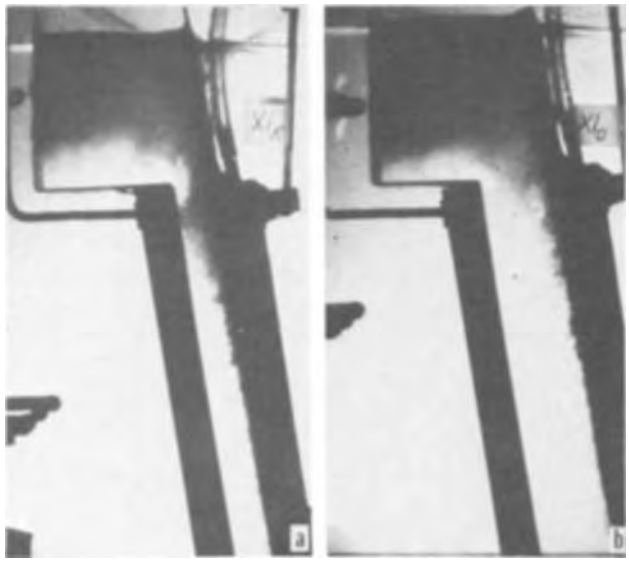

Fig. 7. Effect of A.C.D. on gas liberation at 1 A/cm² (a) at 1 in. A.C.D. and (b) at 2 in. A.C.D.

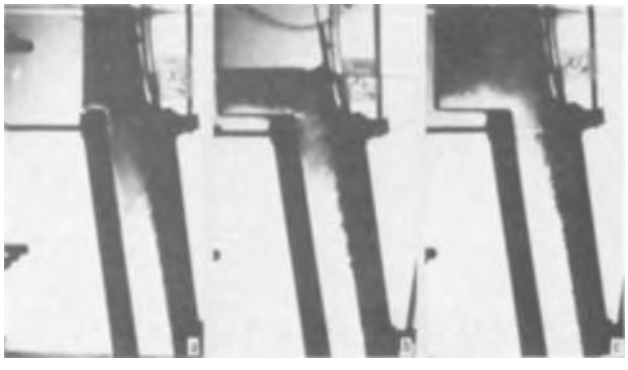

Fig. 8. Effect of interface width and liquid depth on gas liberation at 1 A/cm² and 1.5 in. A.C.D.: (a) width 1.5 in., depth 4 in.; (b) width 4 in., depth 1.5 in., and (c) width 4 in., depth 4 in.

Reliability of current-efficiency measurements.—An essential preliminary part of the program was the assessment of the accuracy and reproducibility of measurements of current efficiency, the main index of cell performance. This was accomplished by conducting a series of replicate runs at relatively low current, where the effects of errors of measurement would be most pronounced. A typical set of replicate data is shown in Table III. At 700A results are reproducible within 0.45%, while at 400A the spread is 1.4%, again only slightly greater than the error in the measurement of the yield of chlorine.

As more data accumulated, it became possible to obtain a further check on the efficiency measurements by establishing a mass balance between the directly measured yield of chlorine in the absorber and the chlorine equivalent of the $MgCl_2$ fed to the cell. A typical balance obtained in this way is summarized in Table IV. In general the $MgCl_2$ content of the melt by

Table III. Replication of current-efficiency measurements

Large Planar Electrode Cell

Duration of run (min)	Cell current (A)	Current efficiency (%)	Estimated error (%)
100	700	84.7	0.33
70	700	85.1	0.45
110	400	82.2	0.46
75	400	83.6	0.71

Table IV. Representative mass balance for $MgCl_2$ over a 12 run campaign

Large Planar Electrode Cell
(mass in grams)

Run No.	Adjustments	$MgCl_2$ additions	$MgCl_2$ consumed	Melt % $MgCl_2$ calculated	Melt analysis, % $MgCl_2$
	Fill cell	5461	—	17.2	17.2
1001-1005	Change melt depth, add 8035 KCl	7259	6713	16.6	16.4
1006-1009	Syphon and adjust melt level removing 152 KCl	5428	3295	19.5	19.5
1010-1012		3639	3465	19.6	19.1
	$MgCl_2$ in cell		8374		
	Balance	21787	21847		

direct analysis of syphoned samples was in agreement with calculations based on the mass balance to within 0.5%.

Further check runs interspersed in the later campaigns confirmed that the absolute error in the current-efficiency (C. E.) measurements was of the order 0.2% at 2000 A, that is, near the upper end of the range of current investigated.

Influence of cell-operating conditions and electrolyte properties on current efficiency.—The main benefit of the cold-model studies was that they permitted an optimum geometrical design to be established, within the limits of the size of the equipment, with a minimum number of high-temperature experiments in the cell itself. Once the parameters were selected, the cell was constructed and used to determine the effects of nongeometrical variables on current efficiency and power efficiency.

The factors expected to influence current efficiency (C.E.) were the physical properties which affect melt circulation and gas liberation from the surface of the melt. The most important of these physical properties are density and viscosity, both strongly dependent on composition and temperature. The other primary variable affecting melt circulation was the rate of gas production, which is proportional to current density.

In all the systems investigated, C. E. was found to increase as current density was raised through the range 0.36-1.5 A/cm². Above 1.5 A/cm², the C.E. fell off; the hydrodynamic model shows that re-entry of chlorine into the electrode gap is becoming significant above this current density (Fig. 9). Typical C.E. data

Fig. 9. Retention of chlorine at high current density in cell with optimum dimensions, 2 A/cm² at 1.5 in. A.C.D.

Table V. Dependence of current efficiency on current density at 850°C

Large Planar Electrode Cell

Electrolyte composition (w/o)	Total current (A)	Current density (A/cm²)	Current efficiency (%)
19 $MgCl_2$-81 KCl	400	0.36	83
19 $MgCl_2$-81 KCl	700	0.64	89
21 $MgCl_2$-75 KCl-4 LiCl	400	0.36	83
21 $MgCl_2$-75 KCl-4 LiCl	700	0.64	87
20 $MgCl_2$-45 KCl-35 LiCl	700	0.64	84
20 $MgCl_2$-45 KCl-35 LiCl	1650	1.50	91
22 $MgCl_2$-28 KCl-50 LiCl	700	0.64	86
22 $MgCl_2$-28 KCl-50 LiCl	1650	1.50	90
22 $MgCl_2$-28 KCl-50 LiCl	2200	2.00	86

for a range of electrolyte compositions are shown in Table V.

Sampling of melts was carried out by syphoning from the interelectrode space during runs and also immediately after current was switched off. In all samples, globules of Mg, 1-3 mm in diameter, were found. It was not possible to decide whether the proportion of dispersed metal changed with operating conditions, but the indications were that such variations were small.

It is proposed that the main mechanism by which current-inefficiency losses occur is back reaction between chlorine in the anode-gas envelope and globules of metal dispersed within the melt. At the highest current densities, direct contact between the gas envelope and the coherent film of metal on the cathode probably occurs also.

At low current densities the loss due to back reaction is a significant fraction of the total metal produced, and for all the electrolytes investigated, C.E. is below 85% at 0.36 A/cm². C.E. in fact is lowest in melts of high LiCl content at low current densities, and at 0.64 A/cm² C.E. in the 35% LiCl melt is only 84%, compared to 89% in the straight KCl-$MgCl_2$ binary at this current density.

As current density is increased, C.E. improves because even if the total amount of metal dispersed per unit of volume of the electrolyte is unaffected, the proportion of the deposit that is brought into contact with the anode gas envelope will diminish. The improvement is particularly significant in the case of melts containing medium to high proportions of LiCl. In the 35% LiCl electrolyte, C.E. increases to 91%, and at 50% LiCl to 90%, when current density is raised to 1.5 A/cm².

The model studies suggest that a second factor contributing to improved separation of electrode products as current density is raised in the low to medium range is the downward motion of the melt returning to the region between the electrodes. This downward flow is strongest in the vicinity of the upper cathode, and will tend to direct entrained metal particles away from the anode-gas envelope.

However, at the highest levels of current density, 2.0 A/cm² and above, a new feature of the flow patterns begins to control contact between electrode products. As the thickness of the ascending gas envelope and the velocity of the stream of electrolyte returning to within the electrode gap both increase, a point is reached at which interference between the two streams occurs, and gas starts to become torn away from the anode envelope to form incipient vortexes within the interelectrode space itself. At still higher current densities, gas is incompletely removed within the vortex above the electrodes, and an increasing proportion is redirected to the interelectrode region with returning electrolyte. It is this behavior that causes the efficiency to decrease from 90% to 86% as current density is raised from 1.5 to 2.0 A/cm² (Table V).

Physical properties of the electrolyte appear to exert a relatively small but still significant effect on the flow pattern, and hence on the C.E. The most pronounced effects attributable to differing physical properties are found in the lower ranges of current density and at relatively low temperatures (Table VI and VII). For all compositions investigated, it was found that in the range of 0.36-0.64 A/cm² C.E. rose as temperature decreased, but the increase was far less marked in the high LiCl melts. At high current densities, C.E. was practically independent of temperature. At low current densities, viscosity exerts a dominant effect on the rate of melt circulation and on the rate of separation of globules from the cathode deposit. Thus higher viscosity will tend to reduce the degree of back reaction at a particular current density. The viscosity of the KCl-$MgCl_2$ binary increases quite strongly as the temperature is lowered from 850° to 800°C, since the lower temperature is close to the liquidus, and in this system the strongest effects of temperature on C.E. are to be expected. In the systems containing LiCl, the viscosity of the melts is lower and the effect of temperature on viscosity is smaller because the cell operating temperature range is well above the liquidus. The result is that in the 35 and 50% LiCl melts the C.E. changes very little between 700° and 850°C.

At high current densities, gas pumping rather than viscosity will control the melt circulation rate; consequently C.E. should show a relatively weak dependence on temperature. In fact, above 1.5 A/cm² essentially no change of C.E. with temperature occurs at the 50% LiCl level, and only a 1% decrease is observed in the 35% melts as temperature is changed by 150°.

Voltage and power efficiency.—Gross cell voltage is the primary factor determining specific energy consumption during electrolysis. Accordingly, an important part of the study was the determination of the total voltage required to maintain electrolysis, and the distribution of this voltage between components of the circuit as operating conditions were varied. Total operating voltages were measured between anode and cathode bus outlets of the power supply, and thus included components due to contact resistances at bus and electrode connections as well as the conductor resistances of the anode, cathode shell, flexes, and electrolyte itself. Also included within the over-all measured values were overvoltages for both anode and cathode reactions.

Table VI. Dependence of current efficiency on temperature at low-current densities

Large Planar Electrode Cell

Electrolyte composition (w/o)	Temperature (°C)	Current density (A/cm²)	Current efficiency (%)
19 $MgCl_2$-81 KCl	850	0.36	83
19 $MgCl_2$-81 KCl	800	0.36	90
19 $MgCl_2$-81 KCl	850	0.64	89
19 $MgCl_2$-81 KCl	800	0.64	91
21 $MgCl_2$-75 KCl-4 LiCl	850	0.36	83
21 $MgCl_2$-75 KCl-4 LiCl	800	0.36	87
21 $MgCl_2$-75 KCl-4 LiCl	850	0.64	87
21 $MgCl_2$-75 KCl-4 LiCl	800	0.64	88
20 $MgCl_2$-45 KCl-35 LiCl	850	0.64	84
20 $MgCl_2$-45 KCl-35 LiCl	700	0.64	85
22 $MgCl_2$-28 KCl-50 LiCl	850	0.64	86
22 $MgCl_2$-28 KCl-50 LiCl	700	0.64	87

Table VII. Dependence of current efficiency on temperature at high-current densities

Large Planar Electrode Cell

Electrolyte composition (w/o)	Temperature (°C)	Current density (A/cm²)	Current efficiency (%)
20 $MgCl_2$-45 KCl-35 LiCl	850	1.50	91
20 $MgCl_2$-45 KCl-35 LiCl	700	1.50	90
22 $MgCl_2$-28 KCl-50 LiCl	850	1.50	90
22 $MgCl_2$-28 KCl-50 LiCl	700	1.50	90
22 $MgCl_2$-28 KCl-50 LiCl	850	2.00	86
22 $MgCl_2$-28 KCl-50 LiCl	700	2.00	86

The least reproducible components were those arising at contact resistance. Voltage drops at each accessible contact point were checked during runs, but the contact voltages at internal connections and the resistive voltage drop through the anode could not be measured directly when the cell was operating. Experience coupled with resistivity measurements made on cell components before assembly, indicated that the uncertainty introduced by variation in these components did not exceed 0.02V, but no attempt was made to routinely determine voltages with greater accuracy than this.

Measurements were made of resistances of all components of the cell circuit at room temperature, and all accessible components were checked again at operating temperature. The resistance of the path through the electrolyte itself could be calculated with good accuracy for the $MgCl_2$-KCl binary, and with somewhat less confidence for the LiCl-KCl-$MgCl_2$ ternary. The total cell resistance may be compared with the resistance estimated from the gradient of the plot of total cell voltage *vs.* total cell current and agrees to within 2%. Over the current range of 500-2000A, cell-voltage requirements changed by 2.5V in the case of the best conducting electrolyte, containing 50% LiCl.

The voltage loss in connectors, electrodes, and contacts ranged from 0.42 to 1.31V as current density ranged from 0.64 to 2.0 A/cm^2. The greater part of this ohmic loss occurs within the upper thin section of the anode, and at the anode-connector contact. In a normal production scale cell, both resistances would be halved. The relatively high experimental-cell resistance causes the power requirement to be exaggerated, and the power efficiency to be understated. In Table VIII, the directly measured power requirements for representative electrolytes are compared with figures typical of conventional production scale cells.

An important check on cell operations was afforded by measurement of the open-circuit emf developed when current was interrupted after steady-state electrolysis had been established. Reproducible values of back emf were attainable after only 1 or 2 min of electrolysis, and these values remained constant until electrode products had been dispersed, which took several minutes.

No attempt was made to determine transient components of the emf with decay times of less than 0.01 sec, and transients with decay times greater than this were detected only at the highest levels of current density.

The open-circuit emf values measured in this way agreed with values calculated from the free energy of formation of $MgCl_2$ and the excess free energy of solution in a particular solvent (7, 8). Typical data are shown in Table IX, from which it is apparent that the voltage increase attributable to nonideality or complex-ion formation is markedly less in pure LiCl than in solvents containing KCl. At 800°C, in 20% $MgCl_2$ solutions, the difference is a significant contributor to the lower energy requirement for production of Mg from the high LiCl electrolytes.

Table VIII. Specific energy requirements for metal production in conventional cells and in large planar electrode cell

System	Current density (A/cm^2)	Cell voltage measured (full-scale)		Current efficiency (%)	Specific energy (kw-hr/lb Mg measured)
Conventional Dow	0.5		7.0	85	8.2
Conventional I.G.-M.E.L.	0.6		6.5	85	7.6
Sloped electrode, 20 $MgCl_2$-80 KCl	0.64	4.65	—	89	5.2
Sloped electrode, 20 $MgCl_2$-80 KCl	1.09	5.75	—	88	6.5
Sloped electrode, 20 $MgCl_2$-45 KCl-35 LiCl	1.50	5.40	—	91	5.9
Sloped electrode, 22 $MgCl_2$-28 KCl-50 LiCl	1.50	5.10	—	90	5.7

Table IX. Comparison of cell open-circuit emf and calculated decomposition potential for $MgCl_2$

Electrolyte composition (w/o)	Temperature (°C)	Reverse emf (V)	Decomposition potential (V)
20 $MgCl_2$-80 KCl	800	2.75	2.71
20 $MgCl_2$-80 KCl	850	2.70	2.68
20 $MgCl_2$-80 LiCl	775	2.55	2.50
20 $MgCl_2$-80 LiCl	850	2.45	2.45

Conclusions

The vertical-electrode cell designed for the study of reduction of $MgCl_2$ has proved capable of yielding data on current efficiency consistently to within 0.5% in relatively short experimental runs. The cell is adaptable to study of similar electrolytic processes in which metal of higher density than the electrolyte is deposited as a liquid at an inert cathode and chlorine is evolved at the anode.

One of the most pleasing features observed in operating the cell with the magnesium system was the ease with which it was possible to form and collect a very clean pad of metal on the base of the cell; indeed, this factor made it possible to use an underflow weir to collect metal without disturbance of the electrolysis compartment. The ability to operate without opening the cell was undoubtedly a major factor responsible for the absence of sludging. Over the course of several months, no noticeable oxide buildup occurred in either the electrolysis chamber or the tapping weir. Melt samples at all stages were water clear, further confirming the absence of oxide within the cell.

The Mg system studied is one in which the liquid metal is deposited at a cathode of mild steel inclined at a small angle to the vertical, and accumulates to form a coherent layer at the base of the cell. Chlorine evolved at the anode causes vigorous circulation of the electrolyte by gas-lift pumping. The anode gas flowing upwards is released through the surface of the electrolyte, or may recirculate in a complex flow pattern involving vortex production at the surface and formation of a well-defined foam layer.

The gas-liquid system has proved amenable to study in a room-temperature hydrodynamic model, and by this means the important parameters which promote the liberation of gas from an electrode system of given A.C.D. have been identified. The main geometrical factors are the surface area of melt available to the electrodes, the depth of liquid in the zone above the electrodes, and the angle of inclination of the electrodes to the vertical.

The cell data and the model studies support the conclusion that the main factor which determines the degree of back reaction between electrode products is the contact between the anode-gas envelope and the metal on the surface of the cathode or dispersed within the electrolyte near the cathode. The main support for this view is provided by the way in which current efficiency measurements conform to changes of flow pattern produced by changes of electrolyte depth, A.C.D., and current density.

The hypothesis that the reaction at the interface between chlorine gas and metal is the prime mechanism for reduction of faradaic yield is also in agreement with recent measurements of the relative rates of reaction between magnesium metal, either dissolved or dispersed within the melt, and chlorine gas, again either dissolved or dispersed in the electrolyte (9). The inference from these reaction-rate studies is that only the reaction between liquid magnesium and chlorine gas can yield over-all rates sufficiently high to account for observed rates of loss of metal.

Additional support is obtained from the way in which physical properties of the electrolyte affect the current

efficiency. Basically two types of flow regime are possible in the electrolyte-anode gas system: one predominates at low current density, and is controlled by viscosity, while a second, controlled by gas-evolution rate, becomes established at high current density. Consequently, the variation of current efficiency with temperature is larger at lower current densities and in melts of high viscosity.

Cell experiments have demonstrated that the system using parallel electrodes inclined at a small angle to the vertical with mainly downward flow of metal is actually more efficient than the conventional system for Mg production in which both metal and gas flow toward the top of the cell. The improvement is such that current efficiencies above 90% are attainable at current densities of 1.5 A/cm^2, some three times the operating level of the conventional cells.

The improved operating characteristics of cells with the counterflow separation of electrode products lead to higher power efficiencies and much lower specific energy requirements. Performance figures for the cells are compared with those for conventional types in Table VIII.

It is recognized that to demonstrate the ability of new systems of the present type to sustain current efficiencies over very long periods of operation, and to assess the effects of operating disturbances that might occur under industrial-plant conditions, a suitably long-term pilot plant evaluation will be necessary. In this program, evaluation of the durability of cell materials, the stability of the geometry, and the effects of progressive buildup of even minute concentrations of contaminants, will all be of the highest importance. It is again emphasized that the data obtained in the present program refer to a relatively small element of a commercial cell, and to one operating under rigorous conditions of control with high-purity materials.

Subject to these qualifications, it appears that the most important benefit conferred by the new system is the increase in output attainable from a cell structure of given shell dimensions. This results directly from the ability to operate at high current density with relatively high current efficiency and at low interelectrode spacing. If no additional engineering problems are revealed during scale-up, so that the experimental-cell data can be translated directly into performance of full-scale units, then the initial capital cost of the electrolysis plant can clearly be substantially reduced.

Besides contributing to lowering the cost of magnesium metal, a less expensive cell improves the case for using magnesium metal as a reducing agent in the CRASO process (10) for manufacture of aluminum from $AlCl_3$. In the CRASO process a combined electrolytic cell and chemical reactor is used, and the cell is the main item of capital expense.

Acknowledgments

The authors wish to express their thanks to Conzinc Riotinto Corporation of Australia for the financial support that made this work possible.

Manuscript submitted July 28, 1972; revised manuscript received Jan. 12, 1973. This was Paper 343 presented at the Miami Beach, Florida, Meeting of the Society, October 8-13, 1972.

Any discussion of this paper will appear in a Discussion Section to be published in the June 1974 JOURNAL.

REFERENCES

1. N. Hoy-Petersen, *J. Metals*, **21**, 43 (1969).
2. Dow Chemical Company, Brit. Pat. No. 923,709 (1963).
3. A. I. Bukhbinder, *Tr. Leningr. Politekhn. Inst.*, **188**, 115 (1957).
4. E. A. Ukshe, G. V. Polyakova, and G. A. Medvetskaya, *J. Appl. Chem. USSR*, **33**, 2246 (1960).
5. W. Fritz and W. Ende, *Z. Physik.*, **37**, 391 (1936).
6. G. Marucci and L. Nicodemo, *Chem. Eng. Sci.*, **22**, 1257 (1967).
7. D. E. Neil, H. M. Clark, and R. H. Wishall, *J. Chem. Eng. Data*, **10**, 21 (1965).
8. B. F. Markov, Yu. K. Delimarskii, and I. D. Panchenko, *Zh. Fiz. Khim.*, **29**, 51 (1955).
9. O. A. Lebedev, A. N. Antonov, K. D. Muzhzhavlev, and O. N. Dronyaeva, *Tsvetn. Metal.*, **43**, 52 (1970).
10. Conzinc Riotinto of Australia and Commonwealth Scientific and Industrial Research Organisation, Fr. Pat. No. 1,499,326 (1967).

The Influence of Unsaturated Organic Molecules in the Electrocrystallization of Nickel

Th. Ap. Costavaras, M. Froment, and A. Hugot-Le Goff

Groupe de Recherche No. 4 du C.N.R.S. "Physique des Liquides et Electrochimie," associé à l'Université de Paris, Paris VI, France

and C. Georgoulis

Equipe de Recherche du C.N.R.S. "Cinétique et Mécanisme des Réactions Organiques," associé à l'Université de Paris, Paris VI, France

ABSTRACT

The fiber textures of nickel electrodeposits grown in the presence of unsaturated organic compounds are studied by x-ray diffraction and shown to be related to the nature of the unsaturation present in the molecule. The structural environment of this unsaturation influences the magnitude of the additive activity. A number of compounds with an ethylenic unsaturation were extensively studied. The [110] axis fiber texture is then preferentially formed. In the presence of other compounds, *e.g.*, acetylenic or aryl-sulfonic compounds, the fiber texture is [100] or [211]. These modifications of crystal growth are interpreted by the adsorption-hydrogenation-desorption process. The nature of bonds between the metallic surface and the adsorbed molecule can differ according to the unsaturation, and so the quantity of adsorbed hydrogen atoms involved in the hydrogenation step.

It is known that the addition of extremely small quantities (10^{-5}-10^{-3} molar) of a wide variety of organic compounds in electrolytic solutions for nickel deposition, considerably modifies the mechanism of crystal growth of the deposit. The activity of an organic molecule depends on the presence of certain types of unsaturations between atoms of carbon, nitrogen, and oxygen (or certain sulfur-containing radicals). Numerous unsaturated compounds, of various and often complex structure have been classified by Brown (1, 2) and Saubestre (3, 4). These additives are considered as "brighteners" or "leveling agents." The leveling effect, which is a macroscopic phenomenon related to transport of the molecules toward the cathode by convective diffusion, is not considered here. We are interested only in modifications of the structural properties of the deposit and particularly the fiber texture and the grain size. The latter is of interest because the brightening effect is related to the ability of the metal to be deposited as small crystallites.

Only fragmentary experimental data and theory are available concerning the fiber texture formation in the presence of organic compounds. In this mode of crystal growth, all the crystallites constituting the deposit present the same (hkl) axis perpendicular to the cathode plane. No theory exactly accounts for the experimental observations, even if organic molecules are not present in the electrolytic solution. Among the factors proposed in these theories to cause a fiber texture, are the cathodic overvoltage in the two-dimensional nucleation (5), or the hydrogen coverage modifying the growth rates of the different crystal faces (6) The eventual structural defects of metallic lattice may also play a major role. When the organic molecules are present in the electrolyte, sparse results appear in the literature: DuRose (7) points out that acetylenic alcohol favors a [211] texture; Weil notes the presence of a [100] texture due to coumarin (8); Leidheiser and co-workers (9, 10) relate the grain size and the orientation of deposit to the chemical structure of the compounds, which were, however, studied in only one concentration.

Now it appears that a systematic study on how the fiber textures are modified, or initiated, by the presence of organic compounds and how this phenomenon is affected by their chemical structure, is a good method to reach a better knowledge of their role. This role seems essentially to modify the sites of incorporation in the crystal lattice of the nickel ions, certain sites being blocked by adsorbed molecules. The relation between activity and unsaturation suggests indeed the formation of interactions between π-orbitals and metallic atoms of the cathode, as in a hydrogenation reaction over a nickel catalyst. As experimental proof of the electrolytic hydrogenation of unsaturated bonds on nickel, Rogers and Taylor (11), introducing 2-butyne 1,4 diol or cinnamic alcohol into a Watts-type solution, after electrolysis, recovered the saturated derivative in yields exceeding 90%.

Key words: adsorption, ethylenic alcohols, fiber texture axis.

Experimental Procedure

Choice of organic compounds.—Among the numerous unsaturated compounds classified by Brown and by Saubestre, a simple and interesting choice is that of doubly or triply bound carbon atoms; the ethylenic bond permits greater possibilities in the choice of the environment, in that the number of variable adjacent substituents is four instead of two, and the reduction in a single step to the saturated state can simplify the understanding of the involved phenomena. We have therefore chosen to study the ethylenic alcohols. These have a good solubility in Watts solution and there are no problems of pH change which may result from organic acids. It is, however, necessary to verify that there is no specific effect of the alcoholic hydroxy group. Thus, we selected fourteen compounds, starting with the simplest ethylenic alcohols with an aliphatic chain of four carbon atoms; this permits comparison with an acetylenic additive, 2-butyne 1,4 diol, which is, in practice, one of the most important brighteners. In order to determine the possible action of the alcoholic hydroxy group, we have also studied four saturated compounds. Table I gives the formula, preparation, and control of purity for each organic compound used.

Study of the deposits.—Taking in account our objective, we attempted to relate the action of organic compounds to the structural properties of the electrolytic deposit, particularly the fiber texture. To determine the latter, we used x-ray diffraction at an oblique angle. An apparatus with a cylindrical chamber al-

Table I. Formula, preparation, and purity control for organic compounds

Organic compound	Formula	Origin	Control of purity
Butane-1,4 diol	$CH_2—OH—CH_2—CH_2—CH_2—OH$	Commercial product, Prolabo, France	bp 280°C
Cyclohexane-1,2 diol, *cis*		(a)	mp 103°-104°C, VPC, IR
Cyclohexane-1,2 diol, *trans*	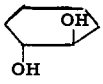	(b)	mp 97°C, VPC, IR
Cyclohexane-1,4 diol, *cis*		Commercial product, Prolabo, France	mp 98°-99°C
2-Butene-1,4 diol, *cis*	$HOCH_2—C=C—CH_2OH$ (H, H)	(c)	bp 139°-140°C under 19 mm Hg, n_D^{20} = 1.478, VPC
2-Butene-1,4 diol, *trans*	H; $HOCH_2—C=C—CH_2OH$; H	(d)	bp 112°C under 4 mm Hg, VPC
2-Butene-1 ol, *cis*	$CH_3—C=C—CH_2OH$ (H, H)	(e)	bp 123°, 6°C under 767 mm Hg, VPC, IR
2-Butene-1 ol, *trans*	H; $CH_3—C=C—CH_2OH$; H	(f)	bp 120°, 6°C under 767 mm Hg, VPC, IR
γ-Phenyl propyl alcohol	$C_6H_5—CH_2—CH_2—CH_2CH$	(g)	bp 92°C under 0.5 mm Hg, VPC
Cinnamic alcohol, *cis*	$C_6H_5—C=C—CH_2OH$ (H, H)	(h)	VPC, IR
Cinnamic alcohol, *trans*	H; $C_6H_5—C=C—CH_2OH$; H	Commercial product, Givaudan, France	VPC, IR
Dimethyl maleate	CH_3OCO $OCOCH_3$; C=C; H H	(i)	VPC, IR
Dimethyl fumarate	CH_3OCO H; C=C; H $OCOCH_3$	(j)	VPC, IR
Coumarin	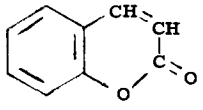	Commercial product, Touzart et Matignon, France	mp 66°-67°C

The noncommercial products were synthetized in this laboratory as indicated.

(a) Hydroxylation of cyclohexene by Woodward's procedure (iodine and silver acetate in wet acetic acid), and subsequent saponification by a hydroalcoholic potassium hydroxide solution. VPC analysis showed only one product excluding the presence of the *trans* isomer.

(b) Hydroxylation of cyclohexene by Prevost's procedure (iodine and silver benzoate in dry benzene) and subsequent saponification by a hydroalcoholic potassium hydroxide solution. VPC analysis showed only one product excluding the presence of the *cis* isomer.

(c) Selective hydrogenation of pure 2-butyne-1,4 diol over Lindlar's catalyst and subsequent fractionation under reduced pressure. VPC analysis showed only one product, excluding the presence of the acetylenic starting material, the ethylenic *trans* isomer, and the saturated corresponding compound.

(d) Hydrolysis of pure *trans* 1,4-dibromo-2 butene by an aqueous solution of sodium carbonate and purified by crystallization and subsequent distillation under reduced pressure. VPC analysis showed only one product. The starting material was prepared by addition of bromine to butadiene in chloroform solution and purification by fractional crystallization.

(e) Selective hydrogenation of the corresponding pure acetylenic alcohol over Lindlar's catalyst and subsequent fractional distillation. VPC analysis showed only one product excluding the presence of the acetylenic starting material, the *trans* isomer, and the saturated corresponding compound.

(f) Reduction of crotonaldehyde by lithium aluminum hydride, followed by fractional distillation. VPC analysis showed only one product.

(g) Reduction of commercial cinnamic alcohol by lithium aluminum hydride.

(h) Selective hydrogenation of the corresponding acetylenic compound over Lindlar's catalyst and subsequent distillation under reduced pressure (0.5 mm Hg). VPC and IR analysis excluded the presence of the acetylenic starting material, the ethylenic *trans* isomer, and the saturated corresponding compound.

(i) Reaction of dimethyl sulfate with maleic acid disodium salt. VPC and IR analysis showed only one product, excluding the presence of the *trans* isomer.

(j) Reaction of dimethyl sulfate with fumaric acid disodium salt. VPC and IR analysis showed only one product excluding the presence of the *cis* isomer.

lowed us to obtain diffraction patterns in the form of concentric circles. The presence of an oriented crystal structure is manifested by an enhancement of the intensity at certain points on the circles. The orientation is deduced directly from the position of the spots, with the aid of charts established by Bozorth (12). Uniform circumferential intensity of the rings corresponds to a sample devoid of preferred orientation.

We have also studied the deposits in the electron microscope. The crystal habits are examined by the medium of surface carbon replicas. In certain cases, thin foils of deposit are also examined by transmission. This examination allows us to measure the width of the crystallites.

It is convenient to measure also the average height of the crystallites. In fact, we determined the root-mean-square roughness, σ, of the surface by a spectrophotometric method (13). This method is an application of the theory of reflection of electromagnetic waves for the cases where the dimensions of the irregularities of

the surface are much less than one wavelength. The diffuse (Rd) and global (Rt) reflection factors of the surface are recorded as a function of the wavelength λ from 0.25 to 2.5 μm. The roughness σ is related to the ratio Rd/Rt by $Rd/Rt = 4\pi\sigma/\lambda^2$ and it is characteristic of an average roughness of the deposit over an extended area (of the order of 0.3 cm^2). One can thus associate a simple quantitative factor with the "brightness" of the surface, an essentially subjective concept which is an interpretation of the relative fraction of the specularly reflected luminous energy. The simultaneous determination of σ and of the lateral grain dimensions, estimated by electron microscopy, permits complete characterization of the brightening action of an additive.

Preparation of the deposits.—The electrolytic nickel deposits were all obtained from a Watts solution of the following composition: 300 g/liter $NiSO_4 \cdot 7H_2O$, 35 g/liter $NiCl_2 \cdot 6H_2O$, 40 g/liter H_3BO_3. The temperature was 50°C and the *p*H was 4.5. The electrolytic cell has a volume of 200 cm^3, and the solution was stirred by a revolving paddle. Both position of the stirrer, with respect to the cathode, and its speed of rotation were kept constant from one experiment to another. As certain additives are transported to the cathode by convective diffusion, their concentration near the cathode surface depends on the speed of stirring. The soluble anode of nickel was large compared to the cathode. It was important that the anode be ultrasonically cleaned after each use, because pits in the anode can retain decomposition products of the additives. Our analytical technique required a deposit of several square centimeters. or spectrophotometric and electron microscope studies, the cathodic substrate was the plane face of a brass cylinder, 23 mm in diameter, prepared with abrasive papers, and then polished with different diamond pastes to 1 μm size. For the x-ray study, a sheet of brass was used which was later dissolved in a mixture of sulfuric and chromic acids, leaving the deposits stripped of their substrates. We adopted a constant 15 μm thickness for all the deposits studied here by maintaining the electrolysis for a time inversely proportional to the employed current density. The results are presented, as most authors have done, as a function of "current density" since deposits were produced under galvanostatic control and not by a control of the cathodic overpotential. The results have a slightly different presentation when expressed in the one or the other parameter, because the additives can change the overpotential.

Experimental Results

The experimental results are presented in the form of graphs where the abscissa is the current density at which the deposit was prepared, and the ordinate is the concentration of additives. The abscissa therefore corresponds to the distribution of textures for a Watts bath devoid of additives. In Fig. 1, we have reproduced the *p*H-potential diagram of textures (14) for this Watts bath. At a *p*H equal to 4.5, the succession of orientations with increasing current density is [110], [211], [100], [110]. We must note that, at low *p*H, the [211] orientation does not exist; instead, a [210] texture appears, corresponding to deposits with a strong hydrogen inclusion.

However, the current density at which one texture is replaced by another one is a somewhat fluctuating value; this value is very sensitive to a number of factors, such as the geometry of the cell; for example, according to this geometry, the current density corresponding to the transition from [110] to [211] can possibly change from 0.5 to 1 A/dm^2. Even for a well-defined cell geometry, the current density corresponding to this transition must be considered as a medium value, because we generally observe the coexistence of the two types of crystallites with [110] and [211] fiber axis texture between 0.5 and 1 A/dm^2. An analogous phenomenon exists for the transition from [211] to [100]: the transition between two fiber textures is never sharp, but generally gradual.

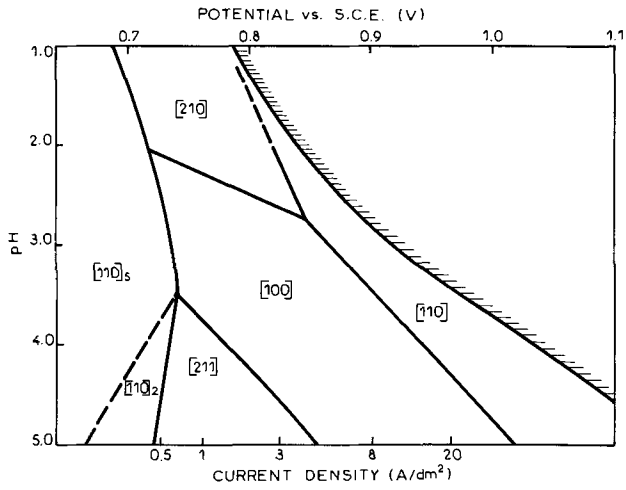

Fig. 1. Diagram of *p*H-potential (or current density) for deposits obtained in a Watts-type solution. Temperature 50°C.

In the following experimental results, we limited ourselves to a range of current densities from 0.5 to 20 A/dm^2, because in the presence of organic additives, the deposits are generally poorly formed at high current densities. This range excludes the [110] texture which appears in the deposits placed under a high current density in a Watts bath. In Fig. 2, 3, 5, and 6, the displacements of the current densities corresponding to the change from [110] to [211], and from [211] to [100] texture are shown as the concentration of organic additives increased. A medium value of the transition current density is retained to draw the lines separating the regions of existence of each orientation.

These graphs show two characteristics of the additives. The first is the texture axis favored by the presence of the additive, which characterizes its action on the mode of crystal growth. Second, for a specific growth mode, it is useful to be able to associate a quantity to the activity of each compound. The concentration, Cm, of the additive, at which the texture characteristic of a Watts bath without additives is replaced by the texture characteristic of the additive for a current density of 3 A/dm^2, was selected. The choice of 3 A/dm^2 is somewhat arbitrary; it is a current density used in practice and at which the deposits in the Watts bath present the [211] texture; now, the [211] orientation can be considered as typical of the Watts bath free of active organic additives, as it generally disappears as soon as such compounds are present in the electrolyte.

For a particular texture, several habits can exist. In certain cases, the regions of existence of the texture are separated in "sub-regions" corresponding to the different habits, see Fig. 2, 3, 5, and 6.

In Table II, the main characteristics of the deposits obtained in the presence of the studied additives are summarized. The table shows the texture axis favored by the additive, the value of Cm, and the minimum value of rms roughness, σm, of the deposits obtained in the presence of the additive. In certain cases, the type of the more common habit is given.

The unsaturated compounds are generally employed up to the maximum concentration, above which the deposits have poor mechanical resistance, as a result of excessive internal stresses. This explains the different ranges of the additive concentrations, on Fig. 2, 3, 5, and 6. But we should be able to further increase the concentration of the saturated additives, without damaging the deposits.

Figure 2 points out the specificity of the role of each unsaturated bond. Butane-1,4 diol, even at high concentrations, does not modify the texture and the roughness of the deposits. The slight effect observed for

Table II. Characteristics of deposits

Compound	Figure No.	Favored texture	Habit	Cm, mM	σm, A
2 Butyne-1,4 diol	2c	Weak [211]	—	—	50
Butane-1,4 diol	2a	No effect	—	—	580
Cyclohexane-1,4 diol	—	No effect	—	—	570
Cis cyclohexane-1,2 diol	—	No effect	—	—	520
Trans cyclohexane-1,2 diol	—	No effect	—	—	600
Trans 2 butene-1,4 diol	2b	[110]	2-fold sym.	2.5	450
Cis 2 butene-1,4 diol	3a	[110]	5-fold sym.	1.5	150
Trans 2 butene-1 ol	3c	[110]	2-fold sym.	1.5	600
Cis 2 butene-1 ol	3b	[110]	2-fold sym.	0.7	400
Phenylpropyl alcohol	5a	[110]	"Cauliflower"	0.8	800
Trans cinnamic alcohol	5c	[110]	5-fold sym.	0.4	300
Cis cinnamic alcohol	5b	[110]	5-fold sym.	0.4	400
Dimethyl fumarate	6b	[100], then weak [110]	—	0.5	300
Dimethyl maleate	6a	[100], then weak [110]	—	0.4	150
Coumarine	6c	Weak [110]	"Cauliflower"	0.1	200
Sodium benzenesulfonate		[100]	—	3	100

concentrations higher than 25 mM can be explained because the cathodic surface is crowded by numerous organic molecules, which hinder the discharge of nickel ions. The small size of the crystallites which develop when 2-butyne-1,4 diol is present in the solution makes study of this compound difficult. Recent results seem to indicate that 2 butyne-1,4 diol favors the growth of the [211] fiber texture, or more exactly that it involves the disappearance of all orientations, except the [211] axis texture. These results obtained by a goniometric method of x-ray diffraction (15) are at the present time difficult to construe for the 2-butyne-1,4 diol concentrations higher than 5 mM. In this case, the brightening is effected by a reduction in all crystal dimensions, with conservation of the habits, at least down to crystallites too small to be observed on the replicas by the electron microscope.

In the presence of 2 butene-1,4 diol, the region of existence of the [110] texture is extended, initially at the expense of the [211] texture. The [110] texture exits at all current densities when the concentration of the additive attains 7.5 mM. The [110] oriented crystals are always large (16) and this fact can explain why the activity of ethylenic compounds in the electroplating bath went unnoticed by authors who only observed their brightening effects. The region of existence of the [110] orientation is separated in three sub-regions, and analogous separation is effected on the graphs of Fig. 3. These graphs are relative to three ethylenic al-

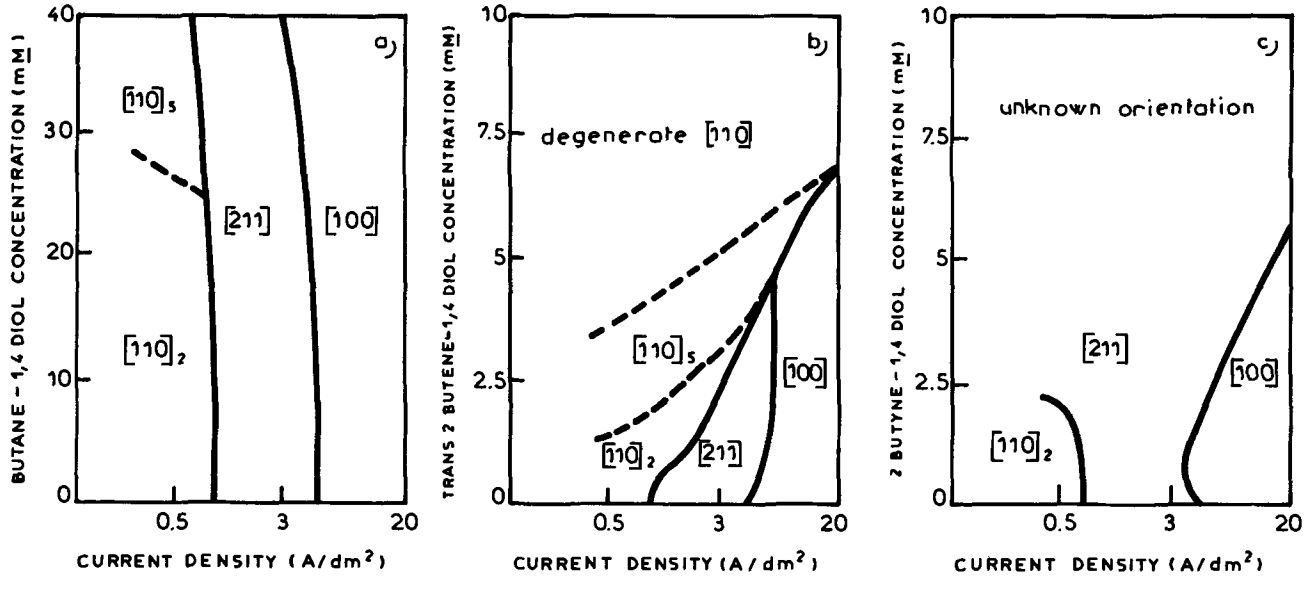

Fig. 2. Comparison between the texture axis of deposits obtained in presence of saturated compound (a), ethylenic homologue compound (b), and acetylenic homologue compound (c).

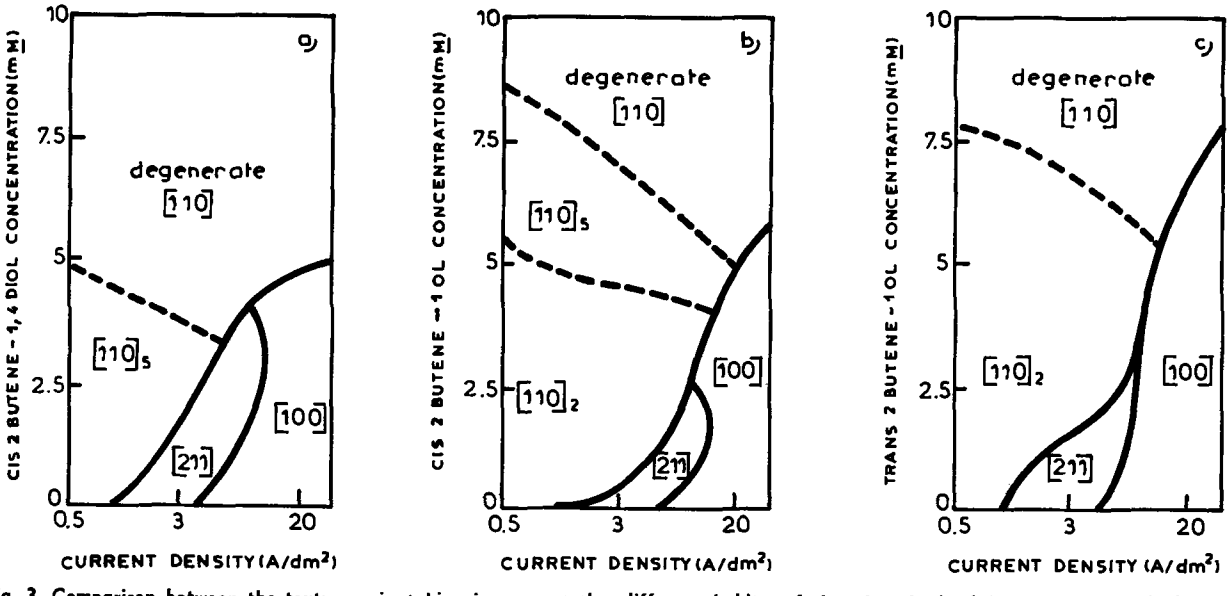

Fig. 3. Comparison between the texture axis, taking in account the different habits, of deposits obtained in presence of *cis* (b) and *trans* (c) monoalcohols, and with the corresponding *cis* diol (a)

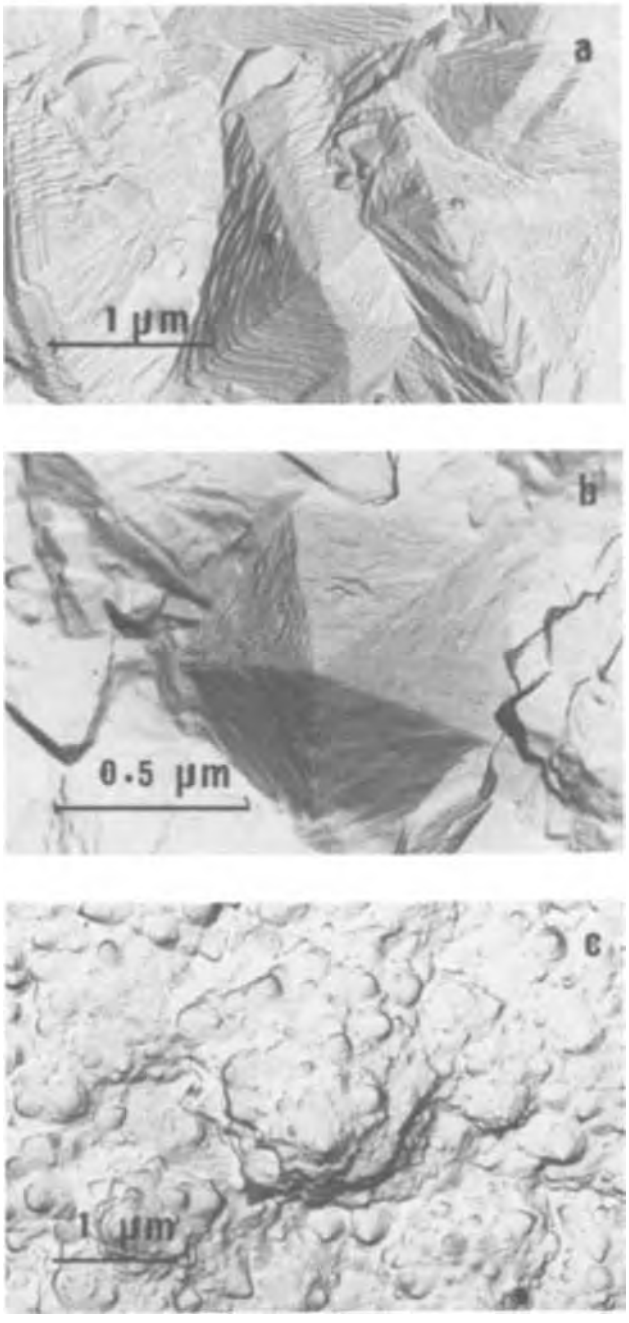

Fig. 4. Three typical habits of deposits with [110] axis fiber texture: two-fold symmetry (a), five-fold symmetry, (b) and cauliflower-like habit (c).

cohols, which evidently show the same effect in electroplating as does *trans* 2 butene-1,4 diol. However, the difference in the number and position of the functional groups around the double bond involves the difference of activity.

In the region marked $[110]_2$, the habit is constituted by large pyramids of two-fold symmetry formed around a twinning plane at the center of the grain (Fig. 4a). The angles between the faces [two (111) planes and two (100) planes] and the base of the deposit are 35° or 45°, respectively. The growth mode of these pyramids is similar to that of pyramids having a [211] axis, where the faces are placed symmetrically around twinning planes. Therefore, replacement of a [211] orientation by a $[110]_2$ does not constitute a significant structural change by the additive.

In the region marked $[110]_5$, the crystallites are arranged in a star around five twinning planes (Fig. 4b), the angles between the faces [(111) planes] with the basal plane are 35°. In a Watts solution without additives, at a pH equal to 4.5, this habit is only found at low overpotential. It characterizes a crystal mode produced by defects; the five-fold symmetry requires a minimal nucleation energy, as was shown in the case of vapor growth (17). In the last region marked "degenerate [110]," where the x-ray diffraction indicates only a weak [110] orientation, very small pyramids derived of five-fold symmetry pyramids are lumped to form irregular hummocks with a "cauliflower-like" appearance (Fig. 4c). The habit is no longer limited by crystallographic planes with simple indexes. This habit characterizes a very perturbed crystal growth.

The comparison between the activity of the four ethylenic alcohols shows a somewhat higher activity of the monoalcohols toward the dialcohols, and a higher activity of the *cis* compounds, toward the *trans* homologous compound: the Cm values and the σ values are lower for the *cis* compound than those for the *trans* homologue, at all current densities (16). The differences in σ are related to the formation of the several types of habits. In the presence of the *cis* isomer, the habit with five-fold symmetry and the disordered one occur at lower additive concentrations than for the *trans* one.

Figure 5 shows that a benzene ring presents the same type of activity toward the plating process as does ethylenic unsaturation. The similarity of the activity seems perhaps surprising; but, the enhancement of this activity in respect to that of ethylenic alcohol is in agreement with the results of Bockris and coworkers (18) that have shown in a similar situation (adsorption on mercury) that the order of increasing activity is butyl < phenyl < naphtyl.

The activity is further enhanced by conjugation with a double bond. The strong reactivity of the phenyl group masks the differences anticipated between the *cis* and *trans* isomers about the double bond.

Figure 6 shows that the three compounds present a different kind of activity from those already described, which must be due to the influence of the C=O unsaturation on the molecule-metal interactions. We shall not dwell on the case of the esters, whose presence leads to a rapid disappearance of the [211] texture zone of existence, with simultaneous preponderance of [100] and [110], followed by disorientation and varied habits. Examination of the habits and determination of σ values have shown, however, the formation of smaller crystallites in the presence of the *cis* compound, whose more accessible double bond favors the activity. In the presence of coumarine, on the other hand, the [110] texture is unequivocally favored, although weak. The habit is cauliflower-like, but it becomes flat enough for lesser concentrations than those of other ethylenic compounds.

Discussion

Using the growth of fiber textures in polycrystalline nickel deposits as an analytical criterion, we have clearly established the specificity of different unsaturations known to influence the course of electrodeposition. Whereas the acetylenic bond favors the [211] axis fiber texture, the ethylenic bond favors a [110] orientation, and the aryl-sulfone group favors a [100] orientation. In this work, we have particularly studied the role of some ethylenic compounds as addition agents in electrodeposition. Their action can be interpreted by an adsorption-desorption process, accompanied by hydrogenation of the adsorbed species before desorption. Our experimental results show that the neighboring of the unsaturated bonded groups can modify markedly the adsorption or desorption of the organic additives, and they are a matter for a number of reflections.

Comparison between cis and trans isomers.—The observed differences between the activity of *cis* and *trans* homologue alcohols or esters are easy to explain. The roughness of deposits, obtained in the presence of *cis* compounds are always lower than those obtained in the presence of *trans* homologues: the adsorption of

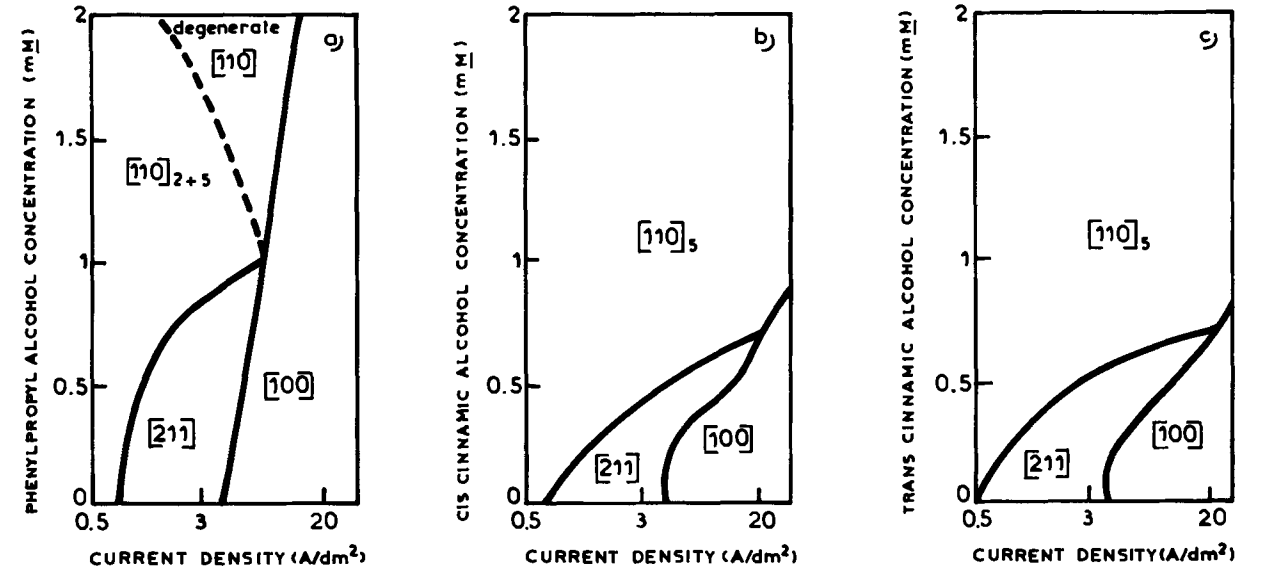

Fig. 5. Comparison between the role of a phenyl ring when it is found in a molecule having elsewhere a saturated side chain (a), an ethylenic side chain *cis* (b) or *trans* (c).

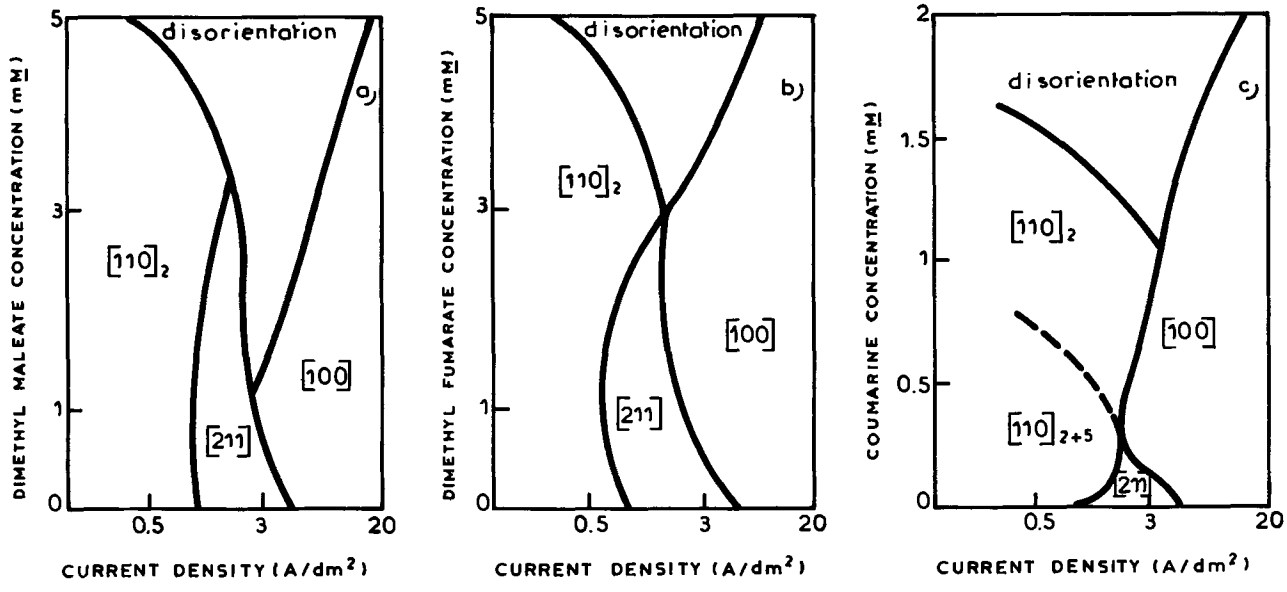

Fig. 6. Comparison between the role of a carbonyl group when it is associated to an ethylenic bond *cis* (a) or *trans* (b), and to a phenyl ring (c).

the *cis* isomer is facilitated by a relatively lower steric hindrance. The number of molecules lying on the surface is greater, thus more sites are occupied, and one observes formation of more crystallites of smaller size, limited in their lateral extension.

Role of hydroxy group.—Our present results seem to indicate that the hydroxy groups cannot, when they are alone, establish adsorption interactions with the cathode during the nickel electrocrystallization, which can lead to an alteration of texture. However, it is believed that butane-1,4 diol possesses some properties of a weak inhibitor in the corrosion of iron (19), and also that an addition agent behaves very much alike in both corrosion inhibition and electrocrystallization. Newman and colleagues (20) studied the role of butane-1,4 diol, 2 butene-1,4 diol, and 2 butyne-1,4 diol in the inhibition of cadmium and silver corrosion. They stated that the organic additives are oriented in one case parallel to the surface, and in the other case perpendicular to the surface. When the addition agent is adsorbed parallel to the surface, although the main interaction takes place between the unsaturated site and the cathode, the hydroxy group may establish some rather weak interactions. By this way, we cannot explain the higher activity of the monoalcohols toward the homologue dialcohols. We rather consider that the hydroxy group can interact with the constituents of the electrolyte, perturb the charge transfer reaction by substituting a complex metallic ion for the MOH^+ species normally discharged by the Heusler mechanism (21), and therefore modify the adsorption rate. These associations also could perturb the desorption rate. Examination of the habits tends to confirm the possibility of the discharge of complexed ions. The deposits obtained in the presence of monoalcohols have more frequently the $[110]_2$ habit. On the other hand, examination of the replicas obtained in the presence of aliphatic and cyclic saturated compounds shows a slight diminution of the crystallite size and a clearer appearance of the $[110]_5$ habit as one passes from butene-1,4 diol to *cis* 1,4 cyclohexanediol, then to *trans* 1,4 cyclohexanediol, and finally to *cis* 1,2 cyclohexanediol. This series of compounds is in a reasonable order for increasing the probability of complexing with the solution. It would seem that, in this case, a number of anions arrive complexed at the interface, where superficial crowding causes a slight diminution in the lateral extension of the crystallites.

Role of phenyl ring.—The observed modifications of the fiber texture suggest that the phenyl ring, when it is alone, is adsorbed by the same type of interactions as the ethylenic double bond. However, when a double bond is present in the molecule along with the phenyl group, the double bond has a higher probability of interaction with the metal than has the phenyl group. One supposes that the phenyl group activates the double bond by enhancing the π-electron density, but does not itself interact directly with the surface. Examination of the crystal habits permits further progress in the discussion of the phenomena. The deposits obtained in the presence of the cinnamic alcohols generally present a regular $[110]_5$ appearance, and then these alcohols perturb the crystal growth no more than the 2 butene diols/or ols. In contrast, the deposits obtained in the presence of phenyl propyl alcohol, even at low concentrations, have the cauliflower habit, characterizing an extensive crystallographic perturbation (even in the region marked $[110]_{2+5}$ on Fig. 5a, the habit is irregular enough). In this case the phenyl group only can interact with the surface. These major perturbations of the crystal form suggest that the phenyl group is flat on the surface. The size of this group is of the order of a unit cell on nickel, and it thus has a profound effect on the crystal formation. For the case of chemisorption of benzene in heterogeneous catalysis, different models have been proposed: benzene chemisorbed flat on the surface with six bonds (22), or perpendicular to the surface of catalyst with two bonds and rupture of the ring (23). But, for the case of electrocrystallization, the only experimental evidence is that the benzene ring is always found intact after electrolysis. Dubsky and Kozak (24) have studied the products of reduction and decomposition for a series of sulfone compounds. The authors found that the sulfur part is included in the deposit, while the undestroyed aromatic ring returns in the solution. The more probable model for the electrocrystallization then is the benzene molecule flat on the surface, adsorbed on nickel in the same way as an ethylenic double bond, but the following steps, hydrogenation and desorption, are not clearly explained at the present time.

Competition between unsaturations.—The interest in the study of the coumarin is that this study permits comparison between the interactions established by C=C and C=O with the cathode. The reduction product distribution studied by Rogers and Taylor (11) indicates that the interaction is preferentially located at the C=C unsaturation of the lactone ring, rather than at the C=O unsaturation. The melilotic acid (*i.e.*, 2 hydroxyphenylpropanoic acid), hydrogenation product of the C=C double bond in the lactone ring is always present in much greater quantity than o-hydroxyphenylpropanol, the reduction product of the carbonyl group (it is the principal product at low *p*H). One may therefore suggest that the influence of C=O and C=C unsaturations on electrodeposition follows the same mechanism of adsorption on nickel atoms, and then they are both hydrogenated, but that the carbonyl reduction at *p*H = 4.5 is more difficult, because this reaction requires the presence of more available H-adions than for ethylenic linkage.

Once again, in this case, the stability of the phenyl group is evident: inclusion of carbon-containing fragments has been extensively studied by tracer methods: Edwards and Levett (25) have been able to show that the rupture of a molecule of coumarin occurs in the lactone ring, the carbon atom of which is included in the deposit, while the aromatic ring is not destroyed and returns intact to the solution. It is likely that the melilotic acid and the other reduction products intervene in a second stage in a similar manner to that of phenyl propyl alcohol and reinforce formation of the [110] axis fiber texture. The presence in the molecule of coumarin of different groups able to adsorb on varied sites of the surface may be a reason for its very great activity on the electrodeposition process. Once again, it is shown that a phenyl group, when it is not alone in an otherwise saturated compound, cannot interact by itself with the metal surface but enhances the activity of the double bonds conjugated with it.

Role of hydrogen.—A last point of the discussion is the comparison of diagrams Fig. 2b, 3a, 3b, and 3c, with the *p*H overpotential diagram of Fig. 1. It reveals a remarkable similarity between the effect of increasing the concentration of organic compounds, or decreasing the *p*H, and especially in the disappearance of the [211] texture. The difference between the area covered by the organic molecules, and that covered by H-adions shows that it is not a simple effect of coverage but, rather, that of a modification of the charge transfer reaction. In fact, the reduction of the C=C unsaturation, by consuming substantial quantities of H-adions, displaces the equilibrium $H^+ + e \rightleftarrows$ H-adions and the reaction is driven to the right. The rate of this reaction may become as fast at *p*H = 4.5, as at lower *p*H in the absence of additives. This confirms that the hydrogen charge transfer reaction plays an important role in the formation of textures.

We must note that, in certain cases (coumarin and esters), we observe a slight increase in the *p*H of the electrolyte during the course of electrolysis: their reduction involves a consumption of a substantial quantity of H-adions, and evidently the boric acid is not able to furnish enough H^+ to adequately buffer the solution.

Specificity of adsorption.—In the previous discussion, we referred to adsorption without definition of the adsorption sites. However, the similarity with the catalysis phenomenon suggests that there is a possibly selective adsorption on the different crystallographic planes. DuRose (7) has tried to determine the adsorption sites, using spherical cathodes of monocrystalline nickel. Unfortunately, this method is questionable in that the adsorption is inferred from modifications in the aspect of the sphere surface in regions corresponding to simple crystalline orientations. Now, the greatest difficulty is that the initial plane (and the initial orientation) of the substrate for the deposit intervenes only in the first moments of nucleation, before the habit is constituted. After that, the interactions occur at the level of the growth-limiting faces, since the organic molecules are adsorbed on the crystal faces limiting the habit. Making deposits on a monocrystalline substrate is of interest only while growth figures limited by other planes have not appeared on the surface. On the other hand, the modification of aspect is not a good criterion and may correspond to very different phenomena: for example, the brightening can occur as a result of a process corresponding to distinct mechanisms of the modification of crystal growth. There may be a similar reduction in all dimensions of the crystallites, or there may be a reduction of the surface relief without a decrease of the grain size. There is sometimes also a degeneracy of the habits. Therefore, a direct method does not exist to determine the adsorption sites.

The determination of adsorption sites would allow the use of bond energy calculations, such as Bond's (26) relative to alcynes, olefins, and conjugated diolefins, to predict the most probable interactions between the unsaturated bond and a crystallographic face; the comparison between experimental data and energy calculations would permit a better understanding of the electrocrystallization mechanism. However, even in the simplest case of the catalysis, the results obtained by LEED (27) on the adsorption of ethylene and acetylene on nickel monocrystals do not agree with the theory. The LEED results show a greater catalytic activity for the (111) face than Bond's theory predicts. In electrocrystallization, the complexity of the interface is very much greater than in catalysis. The cathode-electrolyte interface can never be considered as a perfect and static plane, but it is in continuous evolution. Even

before the formation of the growth habit, and in the simplest case of an epitaxial growth on a monocrystalline face, the edges of the growth steps present the most favorable sites for adsorption, furthermore the appearance of dislocations and twinning create additional low-energy sites. The possibility of adsorption on a crystalline face depends on its perfection on an atomic scale, in a large measure.

The Ni^{++} adions, more or less hydrated or complexed, and H^+ migrate in company with molecular fragments toward their sites of discharge, or incorporation into the lattice. One does not know *a priori*, if the organic groups are strongly bound to a particular site, or if they remain mobile; this depends on the particular strength of the adsorption forces. In any case, the presence of these molecules or fragments (with a volume relatively large compared to that of an adion) should necessarily perturb the electrocrystallization process, and in certain cases of high concentrations, simply by a superficial crowding effect.

To conclude, we shall show that it is possible to describe the mode of action of an unsaturated compound without taking a position about the adsorption selectivity, but advancing the hydrogenation-desorption process, and the role of imperfections and low-energy sites.

Ethylenic compounds.—Adsorption is secured by the π-electrons of the carbon-carbon unsaturated linkage and by the establishment of localized bonds with nickel atoms, preferentially, to minimum energy sites such as twinning planes and dislocations. The cathode is thus covered partly with chemically bound organic molecules, and partly with relatively mobile adsorbed hydrogen, which can replace the metal in the organic molecule-metal linkage, and so permits the desorption of the former. The points liberated by this desorption are then very active sites for nucleation. The organic molecule acts as an intermediate, reinforcing the natural tendency to the crystalline growth from the surface defects at low overpotential, by improving these defects. It favors therefore the formation of a [110] axis. Adsorption is facilitated on the dense planes, *i.e.*, (111) against (100). The growth rate of the (111) faces is limited; the (100) faces must disappear, and the $[110]_2$ habit which involves (100) faces must also disappear in favor of the $[110]_5$ habit which involves only (111) faces. This process seems, finally, general enough, and other double bonds, C=O for example, and others not studied here, must act in this manner.

Acetylenic compounds.—The particularity of this class of compounds is to require a large quantity of adsorbed hydrogen in the reduction step. We suppose therefore that the rate of desorption is limited by the rate of hydrogen supply; the molecule stays a long time on the surface before desorption, involving a substantial blocking of the surface, *i.e.*, a great increase in the frequency of nucleation, as shown by the very small size of the crystallites observed with the electron microscope, and also a great increase of the surface coverage, as shown by the displacement of the cathodic overpotential. The nucleation intervenes, not at the place of the desorbed molecule as in the case of ethylenic compounds, but around the molecule adsorbed with formation of very numerous crystallites limited in their lateral extension.

Aryl-sulfonic compounds.—The mechanism is in this case different, as suggested by analysis of the decomposition products: a molecular rupture takes place, with phenyl returning into solution (it plays its activator role without directly interacting with the surface), and the sulfur-containing fragment incorporated in the deposit. This incorporation takes place along the denser direction. Organic fragments have been found along the >110< directions in the course of electrodeposition of the [100] textured nickel in the presence of sodium benzene sulfonate (28). Indeed, very strong interactions can be formed between the orbitals of sulfur and nickel, and rupture of the molecule occurs at the level of the phenyl sulfur bond. An essential difference with the preceding mechanisms is that, in the latter case, only adsorbed hydrogen atom is involved. This is in line with the kinetic measurements of Wiart (29) who has shown that 2 butyne-1,4 diol modifies the rate constant of the last step of the transfer reaction $NiOH\text{-adions} + NiOH^+ + 3e = 2Ni + 2\,OH^-$, which is influenced by the local pH. In contrast, it was shown experimentally that the presence of sodium benzene sulfonate does not modify the rate constant of the transfer reaction, and it brings only a slight change in the local pH.

We have shown that the organic molecule involved in a process of electrodeposition can, along its chemical structure, favor either a growth mode, perpendicular to the substrate, initiated from surface structural defects, or a lateral mode generally explained by a two dimensional nucleation theory. Then, the different theories of crystal growth being available for a particular growth mode, we understand why their fitting with the experiment is not often good. Very numerous parameters of the interface must be taken into account; we have shown that, at the present time, there is no experiment which allows a conclusion on the absorption selectivity of the organic molecules during an electrocrystallization process. We have pointed out the role played by the adsorbed hydrogen, and the modifications of the adsorption and desorption rates of the different species present on the interface.

Manuscript submitted Oct. 16, 1972; revised manuscript received March 13, 1973.

Any discussion of this paper will appear in a Discussion Section to be published in the June 1974 JOURNAL.

REFERENCES

1. H. Brown, U.S. Pat. 366,385 (1940).
2. H. Brown, *Plating*, **55**, 1047 (1968).
3. E. Saubestre, "Guidebook of Electroplating," p. 348 (1957).
4. E. Saubestre, *Plating*, **45**, 925 (1958).
5. N. Pangarov, *J. Electroanal. Chem.*, **9**, 70 (1965).
6. A. Reddy and S. Rajagopalan, *ibid.*, **6**, 141 (1963).
7. A. DuRose, 7th International Metal Finishing Conference, Hanover (1968).
8. R. Weil and R. Paquin, *This Journal*, **107**, 87 (1960).
9. F. Denise and H. Leidheiser, *ibid.*, **100**, 490 (1953).
10. L. Roth and H. Leidheiser, *ibid.*, **100**, 553 (1953).
11. G. Rogers and K. Tailor, *Electrochim. Acta*, **11**, 1685 (1966).
12. R. Bozorth, *Phys. Rev.*, **26**, 390 (1925).
13. A. Hugot-Le Goff, *Galvanotech. Oberflächenschutz*, **8**, 97, 121, 143 (1967).
14. I. Epelboin, M. Froment, and G. Maurin, *Plating*, **56**, 1357 (1969).
15. J. Amblard, M. Froment, and G. Maurin, *Compt. Rend., Série C*, **272**, 995 (1971).
16. M. Froment, C. Georgoulis, and A. Hugot-Le Goff, *ibid.*, **267**, 1099 (1968).
17. E. Gillet and M. Gillet, *J. Cryst. Growth*, **13/14**, 212 (1972).
18. N. Blomgren, J. O'M. Bockris, and H. Jesch, *J. Phys. Chem.*, 65, 2000 (1961).
19. M. Froment and A. Desestret, 2th Symp. Européen sur les Inhibiteurs de Corrosion Ferrare, Annali dell'Universitá di Ferrara, 223 (1965).
20. D. S. Newman, J. McCarthy, and M. Heckaman, *This Journal*, **118**, 541 (1971).
21. K. E. Heusler and L. Gaiser, *Electrochim. Acta*, **13**, 59 (1968).
22. A. Balandin, *Z. Phys. Chem.*, **B2**, 289 (1929).
23. G. A. Martin and B. Imelik, *J. Chim. Phys.*, **68**, 1550 (1971).
24. I. Dubsky and P. Kozak, *Metalloberflaeche*, **24**, 423 (1970).
25. J. Edwards and M. Levett, *Trans. Inst. Met. Finishing*, **41**, 157 (1964); **45**, 12 (1967).
26. G. Bond, *Discussions Faraday Soc.*, **41**, 200 (1966).
27. G. Dalmai-Imelik and J. C. Bertolini, *Compt. Rend., Série C*, **270**, 1079 (1970).
28. M. Froment, G. Maurin, and J. Thevenin, *J. Microscopie*, **8**, 521 (1969).
29. I. Epelboin and R. Wiart, *This Journal*, **118**, 1577 (1971).

Electron Microscope Studies of an Improved Sensitizer Solution

N. Feldstein*

RCA Corporation, David Sarnoff Research Center, Princeton, New Jersey 08540

and S. L. Chow and M. Schlesinger*

Department of Physics, University of Windsor, Windsor, Ontario, Canada

ABSTRACT

A comparative study of the transmission electron micrographs in the different stages of the autocatalytic plating process has been made. The comparison was made between conventional $SnCl_2/HCl$ sensitizer solution and a newly developed system based upon the incorporation of aged stannic component. Results have demonstrated an increase in catalytic site density of approximately one order of magnitude. This improved method has further resulted in the formation of finer and denser metal crystallites during the early stages of nucleation and growth.

In the art of plating on dielectric substrates, chemical treatment of the surface is an essential step required for the initiation of the autocatalytic (electroless) plating processes. During the chemical treatment procedure, sites are formed which provide a chemical path for the initiation of the plating process. At present, there are two basic procedures used in the formation of the catalytic sites: (*i*) sensitization (via acidic stannous chloride) followed by activation (via acidic palladium chloride), or (*ii*) a colloidal system (via palladium chloride in excess acidic stannous chloride). Although both of the above procedures are widely utilized, this investigation is concerned with modifications related to the first approach only.

In recent publications (1-4) it has been demonstrated that the effectiveness of conventional tin sensitizer solutions ($SnCl_2/HCl$) may be altered through proper solution modification. Specifically, the incorporation of aged stannic chloride solutions were found to provide the improvements in performance. During the

* Electrochemical Society Active Member.
Key words: electroless, sensitizers, microscopy.

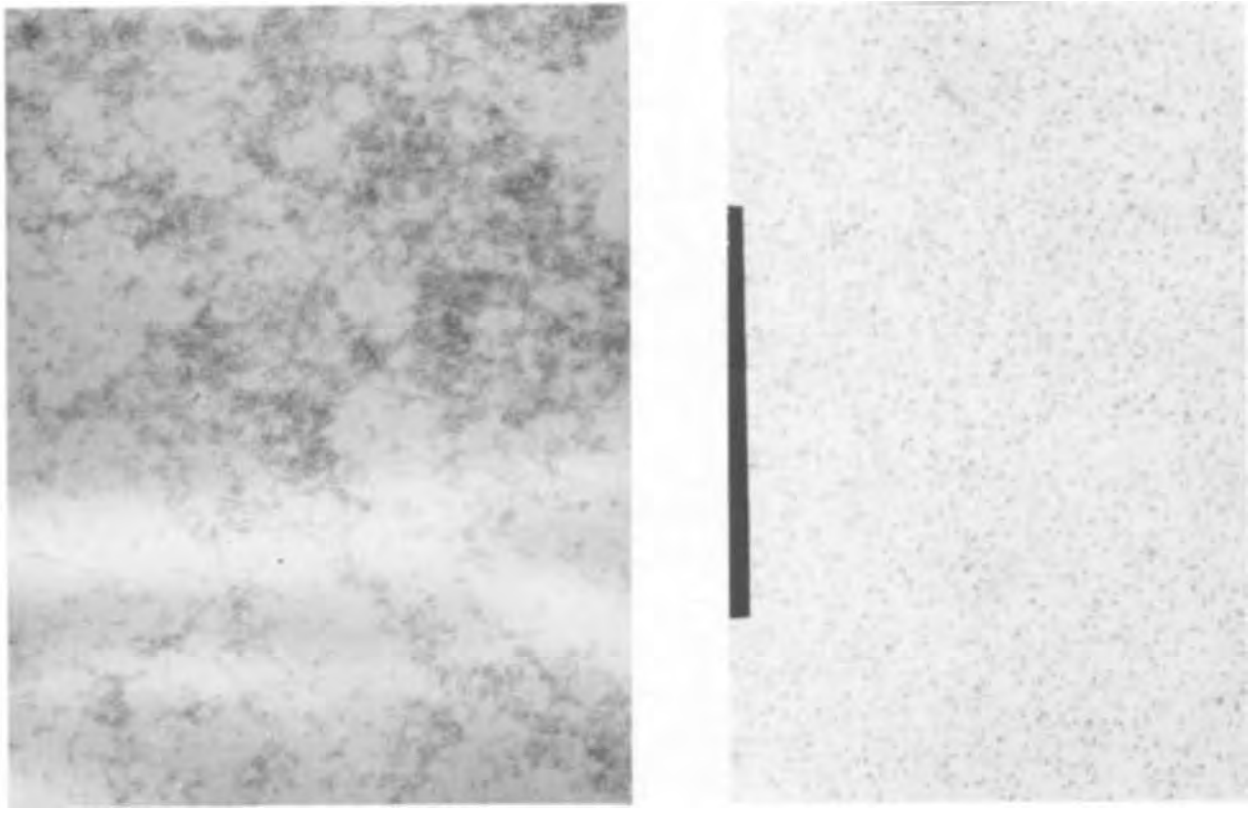

Fig. 1. Electron micrographs of sensitized Formvar surface, at magnification 116,000× (1 cm = 860Å). A (left), conventional sensitizer; B (right), improved sensitizer.

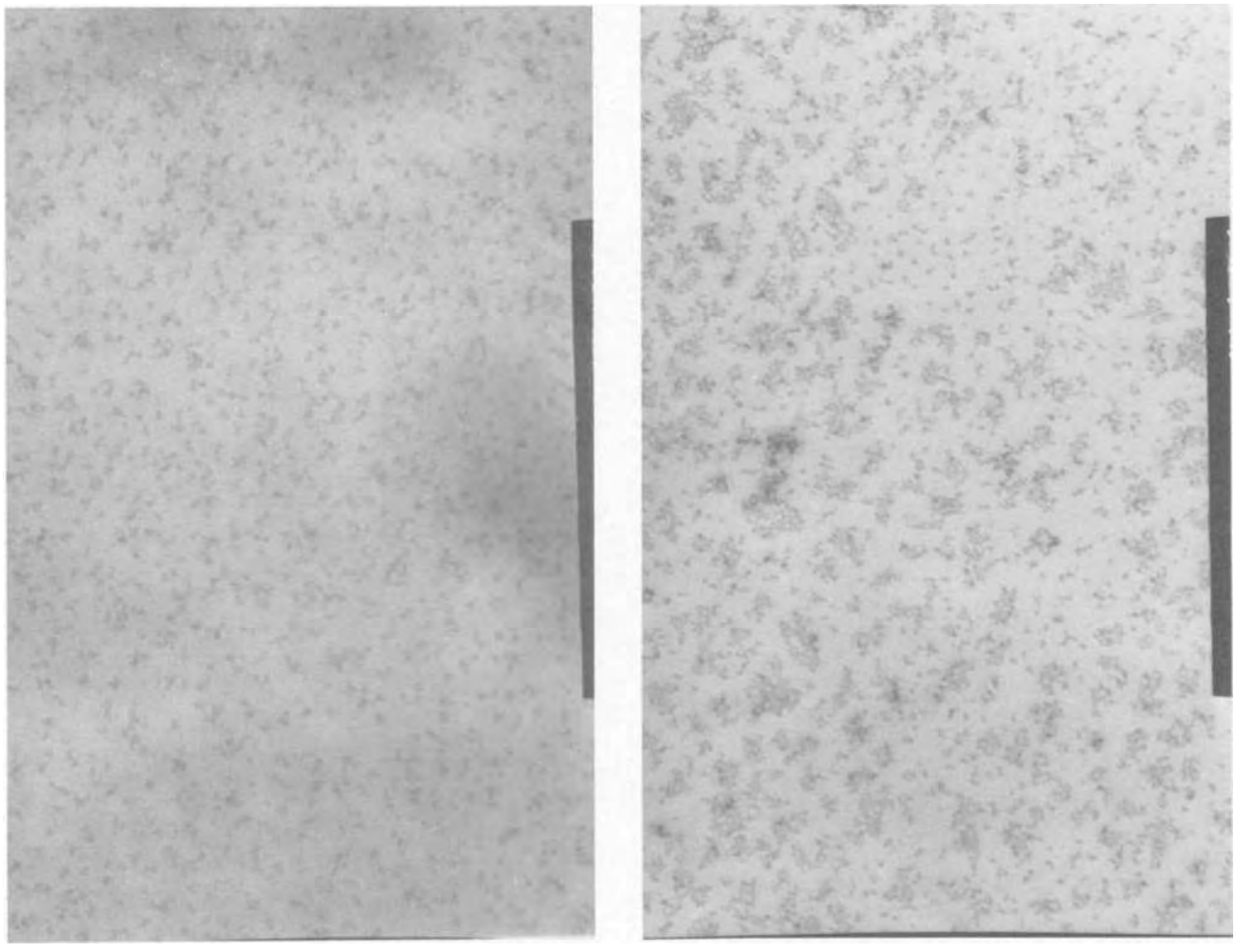

Fig. 2. Electron micrographs after the activation step on Formvar surface, at magnification 200,000× (1 cm = 500Å). A (left) conventional sensitizer; B (right), improved sensitizer.

aging process, a colloidal compound of tin (IV) was formed (1). It was also found (2, 3) that the aged stannic chloride solution may either be added to conventional tin sensitizers or used in a separate step prior to the immersion in conventional tin sensitizers. In either case, the same results were obtained by examining the uniformity of metallic coverage, by measuring the resulting surface through contact angle measurements (1-3), and by monitoring the concentrations of active components by radiochemical adsorption measurements (5). This development was of special significance in the metalization of hydrophobic substrates (Teflon, photoresists, etc.). Moreover, visual examination of thin films deposited onto hydrophilic surfaces showed also a greater degree of uniformity in comparison to films deposited by the use of conventional sensitizers.

Improvement in sensitizer performance was also obtained (7) through the aging of dilute acidic stannous chloride solutions. This procedure, which utilized an aging period of 1-2 weeks, is limited to solutions having a low acidity or chloride content. More recently (8), improvements in conventional sensitizers were also reported through the incorporation of colloidal tin or iron salts.

In examining the nucleation and growth of thin Ni-P deposits, Schlesinger *et al.* (9) have shown that the nucleation process is initiated at activation centers. The process of nucleation continues until the coalescence into a continuous layer takes place. The initial product derived from conventional sensitization ($SnCl_2$/HCl) appears to consist of particles approximately 20Å in diameter. These particles are agglomerated into clumps of an order of magnitude larger. The clumps themselves are randomly distributed on the surface. The activated surface shows particles of about 50Å in size. This is presumably a deposit of metallic palladium, although recent studies (5, 10, 11) have suggested that ionic palladium may be still present at the conclusion of the activation step.

Sard (12) has carried out similar studies with electroless copper films. His observations agree essentially with the previous findings by Marton and Schlesinger (9). The nucleation of Co-P deposits has been studied earlier to some extent by Frieze *et al.* (13). Their findings were corroborated by the above (9). With the development of the new sensitizing system (1-4), the question as to the actual microscopic processes responsible for both the conventional and improved sensitization became even more interesting. In the present work, Formvar surfaces were examined after being subjected to various treating solutions. The results of this work will show that the visual observation of more homogeneous metallic distribution is attributed to a more homogeneous distribution of sensitizer component on a microscopic scale.

Experimental Procedure

The main aim in the current investigation was to study the microstructure of the premetalizing stages in the electroless deposition procedure. The complete process of copper deposition was also included. The presensitizing solution was an "aged" (1 week at 25°C)

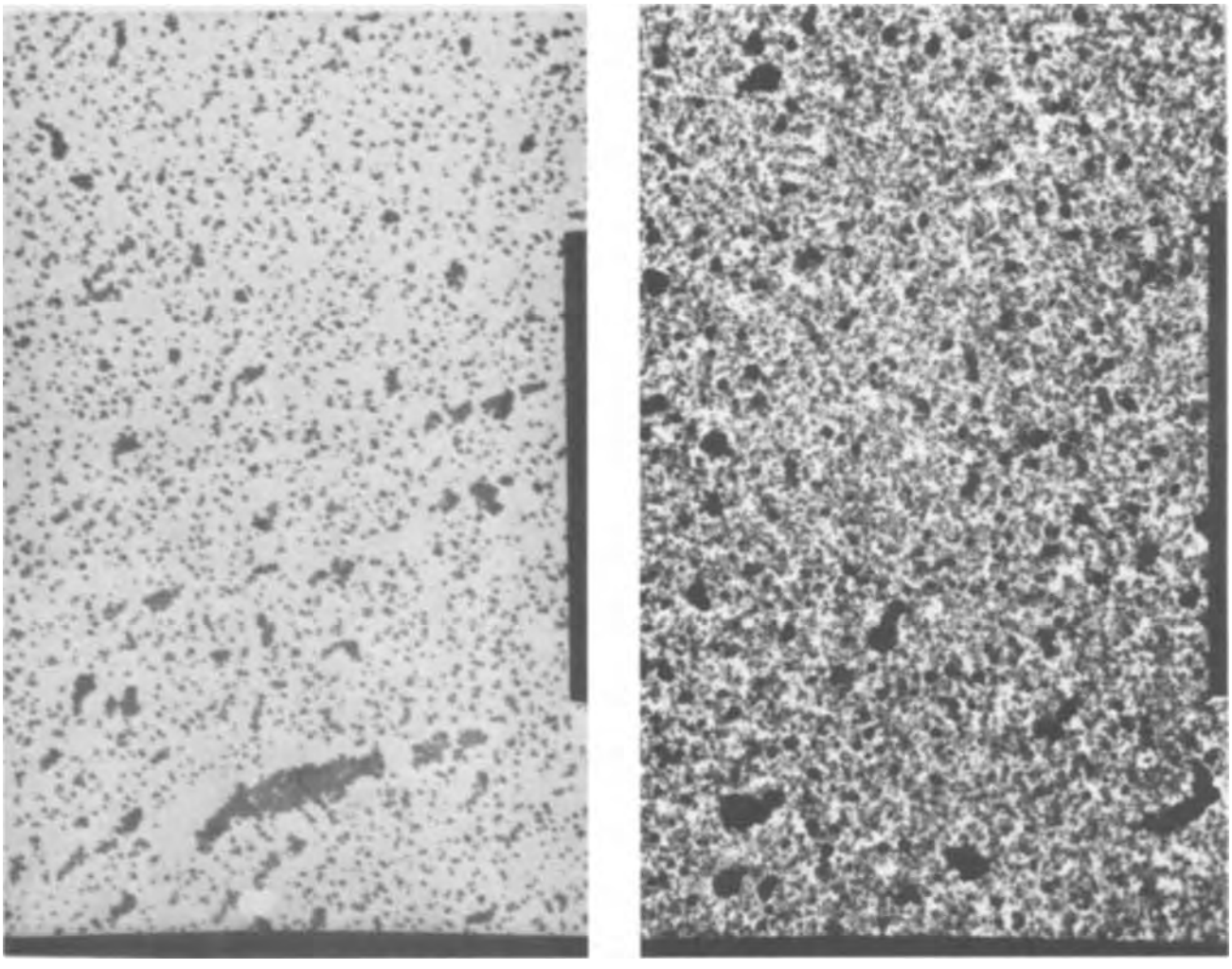

Fig. 3. Electron micrographs of a Formvar surface after 1 min immersion in electroless copper bath, at magnification 14,200× (1 cm = 7050Å). A (left), conventional sensitizer; B (right), improved sensitizer.

0.5M stannic chloride. Working solutions were made by 1:100 dilution using deionized water. The conventional sensitizer medium ($SnCl_2$/HCl) and activating solution ($PdCl_2$/HCl) were identical with those described previously (9). An identical procedure (9) of a 1 min deionized water rinse after each of the sensitizing and activating steps, was followed. In all cases, the sensitizer solutions were freshly prepared and used. The electroless copper metalizing bath was "bath B" described by Sard (12). All chemical treatments were carried out at room temperature.

All chemicals were reagent grade supplied by Fisher or Canlab, and were used without further purification.

Microscope slides glasses coated with Formvar (4g polyvinylformal in 1 liter of ethylene dichloride) were used as substrates. The coated Formvar was floated off the glass in distilled water. The samples were examined with a Hitachi HU-12 electron microscope operated at 100 kV.

Results and Discussion

In Fig. 1, the electron micrographs of tin-sensitized surfaces are presented. Figure 1A represents the micrographs of Formvar immersed for 1 min in freshly prepared conventional sensitizer. Figure 1B is the micrograph representing the Formvar surface after 1 min immersion in aged stannic chloride solution (presensitizer solution) followed by 1 min immersion in the same sensitizer solution used in Fig. 1A. Comparison of the results reveals a denser and a more uniform distribution of particles and clusters. The density of particles resulting from the improved procedure is about 10^{12} particles/cm^2. In comparison, the density resulting from conventional sensitizer is about 10^{11} particles/cm^2.

Identical electron micrograph results were obtained using the improved procedure whether the aged stannic chloride component was used prior to the conventional $SnCl_2$/HCl) sensitizer or mixed along with the sensitizer. This result, *i.e.*, that one may use the aged $SnCl_4$ prior to, or together with, the $SnCl_2$ sensitizer, is consistent with previous observations (1, 2, 5). It is consistent also with the model proposed (see below) to account for sensitization. It has also been observed that when diluted conventional sensitizer solutions are aged at room temperature for 1 week or more, they serve as effective presensitizing baths, rendering results similar to Fig. 1B.

Although the basic particles of Fig. 1 are about 20-30Å, it should be apparent that the improved sensitizer medium results in a decreased tendency for cluster formation. In fact, the clusters formed through the conventional approach are a few times larger in comparison with those obtained using the improved procedure. The results of Fig. 1B were independent of the tin (II) concentrations used.

Figure 2 represents the electron micrographs of Formvar surfaces at the conclusion of the activation step. Figure 2A represents the surface after 1 min immersion in sensitizer solution followed by 1 min immersion in activating solution. Figure 2B is the same except for the immersion for 1 min in the aged solution prior to the sensitizer solution. Here, too, the product of the improved procedure is denser in comparison with the conventional approach. Some tendency for clustering is evident in both cases.

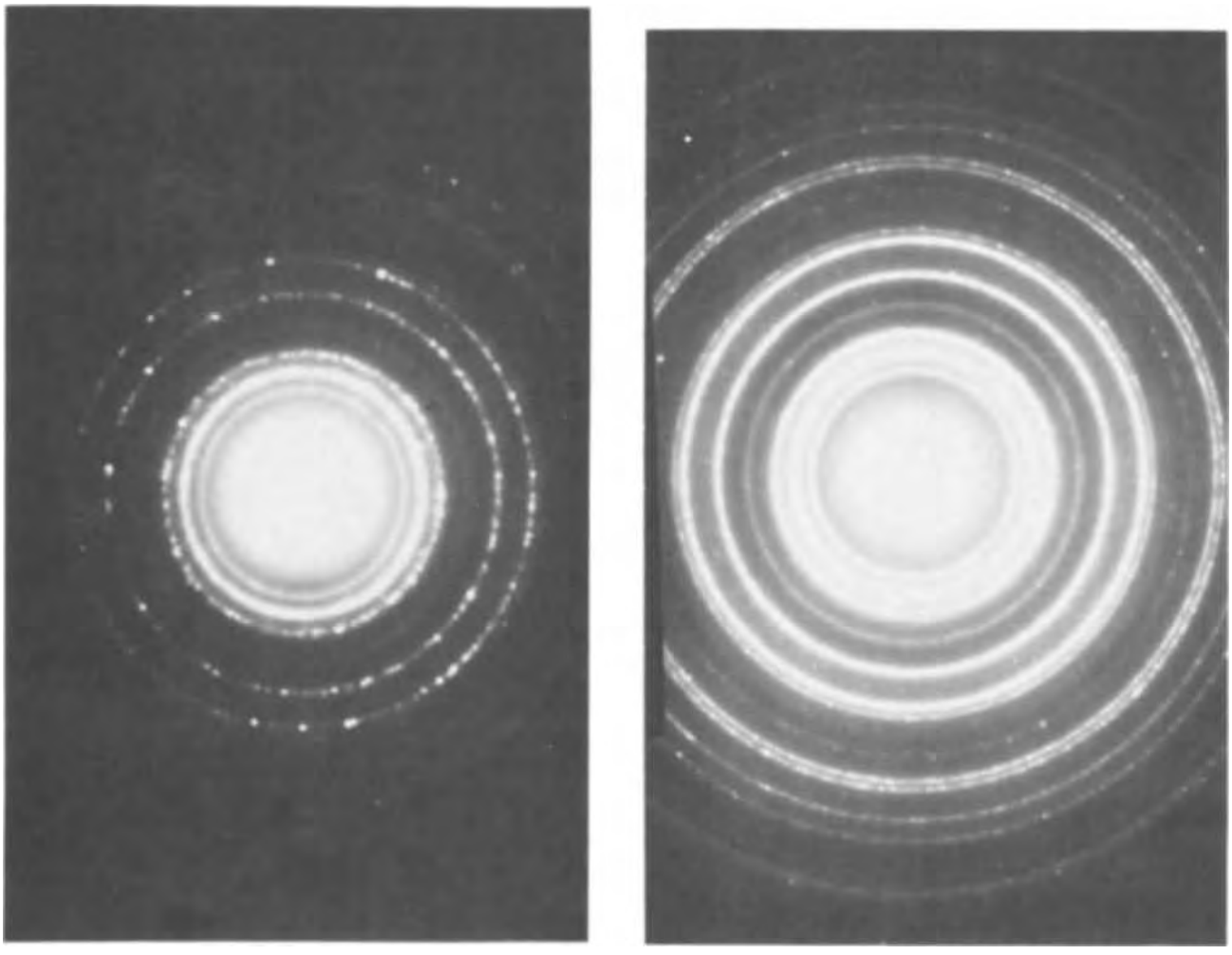

Fig. 4. Electron diffraction patterns corresponding to Fig. 3

Figure 3A represents the electron micrographs of electroless deposited copper using a conventional sequence, with 1 min immersions in each of the sensitizing, activating, and metalizing solutions. Figure 3B corresponds to a surface with the same treatment except for an immersion of 1 min in the aged solution, preceding the above treatment. Once again the finer and denser particle distribution is seen to result from the improved procedure. The finer size particles in Fig. 3B manifests itself in the corresponding diffraction patterns given in Fig. 4.

Preliminary analyses of the electron diffraction patterns corresponding to the micrographs presented in Fig. 1 and 2 indicate that the product of conventional sensitization is most probably hydrated stannic oxide. This is consistent with the previous findings (9, 14) and the model proposed by Cohen *et al.* (15) for the surface characteristics resulting from conventional sensitizer treatment. The surface product obtained by the improved method exhibits a diffraction pattern markedly different from that obtained using conventional sensitizers. It may well be argued that the chemical species responsible for this pattern is a polymeric substance of the type (1, 16)

$$(HO)_3 - Sn - [OSn - (OH)_2]_n - OH$$

or

$$(HO)_2 - Sn - [O_2Sn]_n - (OH)_2$$

where n is an integer, *i.e.*, 1, 2, 3, etc. This polymeric material was formed during the aging process.

It should be noted that three major experimental difficulties are inherent in the quantitative interpretation of the diffraction patterns: (*i*) the amount of material present on the surface is very small, and consequently, the intensity of patterns is rather low; (*ii*) the size of the "crystallites" present is such as to give diffuse patterns; and (*iii*) there is also the possibility of dehydration of the "hydrous Sn polymer" by the vacuum and/or irradiation of the electron beam.

Table I presents the derived d-spacing for the surface formed as a result of treatment with conventional and the improved sensitizers.

Conclusions

Although the improved sensitizer solution was initially aimed at achieving good plating uniformity of hydrophobic surfaces, the current results show significant improvements in hydrophilic substrates as well. The adsorbed sensitizer clusters and particles are more uniformly distributed on the surface in comparison to those obtained using conventional sensitizers. The density of adsorbed center is about 10^{12} centers/cm^2, which is approximately an order of magnitude greater in comparison with the results derived from conventional sensitizers on Formvar. No significant

Table I. d-spacing (Å) for sensitized surfaces

Conventional	Improved
3.155 (s)	3.255 (s)
1.969 (s)	3.095 (w)
1.652 (s)	2.142 (w)
1.356 (w)	2.065 (w)
1.095 (d)	1.678 (s)
	1.424 (w)
	1.142 (d)

s, w, and d refer to strong, weak, and diffuse, respectively.

differences were observed with respect to the basic particle size.

It was also confirmed that the results of the improved sensitization are independent of the specific procedure used in that specifically identical results were obtained whether the aged tin (IV) is used prior to conventional sensitizers or is incorporated into the same medium.

Following the activation step, it has been observed that the size of the clusters is increased; this trend is consistent with the behavior encountered with conventional sensitizers as well.

Examination of the electroless copper films in which deposition was interrupted during the early stage of nucleation and growth shows major differences. Similar differences would be expected for other electroless systems. The new sensitizer medium shows a greater degree of metallic coverage for the same immersion time in the electroless copper bath. This observation is not surprising in view of the fact that the improved sensitizer medium yields a greater number of active centers which are distributed more uniformly on the surface. From this observation, it is reasonable to speculate that thin films deposited by chemical plating will exhibit variations in physical properties such as conductivity, complex index of refraction, adhesion, etc., depending on the sensitizer solution used.

Acknowledgment

Experimental work was carried out in the Department of Physics, University of Windsor, Windsor, Ontario, Canada.

Manuscript submitted Dec. 19, 1972; revised manuscript received March 14, 1973.

Any discussion of this paper will appear in a Discussion Section to be published in the June 1974 JOURNAL.

REFERENCES

1. N. Feldstein, J. A. Weiner, and G. L. Schnable, *This Journal*, **119**, 1486 (1972).
2. N. Feldstein and J. A. Weiner, *Plating*, **59**, 140 (1972).
3. N. Feldstein and J. A. Weiner, *This Journal*, **119**, 668 (1972).
4. N. Feldstein and T. S. Lancsek, U.S. Pat. 3,666,527 (1972).
5. N. Feldstein and J. A. Weiner, *This Journal*, **120**, 475 (1973).
6. N. Feldstein, "Proc. of the AES Fourth Plating in the Electronics Industry Symposium," Indianapolis, Ind. (1973).
7. G. Bernhardt, U.S. Pat. 3,616,296 (1971).
8. W. P. Townsend, J. A. Emerson, and J. T. Kenney, Abstract No. 216, p. 530, The Electrochem. Soc. Extended Abstracts, Fall Meeting, Miami Beach, Florida, Oct. 8-13, 1972.
9. J. P. Marton and M. Schlesinger, *This Journal*, **115**, 16 (1968).
10. N. Feldstein and A. W. Levine, Unpublished results.
11. P. F. J. v. d. Boom and C. H. DeMinjer, Private communications (1972).
12. R. Sard, *This Journal*, **117**, 864 (1970).
13. A. S. Frieze, R. Sard, and R. Weil, *ibid.*, **115**, 587 (1968); A. S. Frieze and R. Weil, Sixth International Conference for Electron Microscopy, p. 533, Kyoto, Japan (1966).
14. S. L. Chow, N. E. Hedgecock, M. Schlesinger, and J. Rezek, *This Journal*, **119**, 1013 (1972).
15. R. L. Cohen, J. F. D'Amico, and K. W. West, *ibid.*, **118**, 2042 (1971).
16. J. Gueron, *Ann. Chim.*, **11**, 225 (1935).

Measurement of the Potential of Zero Charge of Solid Electrodes by the Time-of-Contact Method

S. Efrima and E. Gileadi*

Institute of Chemistry, Tel-Aviv University, Ramat-Aviv, Israel

ABSTRACT

A new technique has been developed for the measurement of the potential of zero charge (PZC) of solid electrodes. The technique utilizes the repulsion between identically charged double layers (DL) and electrodes. This potential (or charge) dependent repulsion is shown to affect the time of contact (TOC) between two electrodes when one is struck by the other. It is shown that the TOC is a minimum at the PZC. Measurements on gold electrodes in perchloric acid solutions showed minima in the TOC near the potential +0.01V SCE. In sodium iodide solutions the minimum of TOC was shifted cathodically corresponding to the expected shift of the PZC resulting from specific adsorption of iodide. This technique, after several improvements, is suggested for measuring the PZC of solid electrodes.

The potential of zero charge (PZC) is a fundamental physical quantity in electrochemistry. It is very important in the research of the electric double layer, in studies of adsorption of charged and uncharged species on the electrode, and when treating kinetics of electrochemical reactions (1-4). Thus, it has an essential role in pure fundamental research as well as in applications of technology. Nevertheless, there is still no method to determine the PZC of solid electrodes unambiguously and with sufficient precision. For liquid electrodes there are several methods which are "thermodynamic" in the sense that they do not depend on any specific model of the system, and exact (5-8), and lately also some which are relatively easy to practice (9). They are based, in one way or the other, on the measurement of the surface tension. On solid electrodes such measurements are, of course, not as straightforward. One must then apply approximate thermodynamic methods [organic adsorption (10, 11), measurement of electrode elongations (12), electrode vibrations (13), and others], or go over to nonthermodynamic methods (capacity measurements, friction measurements, etc.).

The large spread of PZC values of solid electrodes which are reported in the literature (1, 2, 14-17) and which cannot be attributed entirely to differences in electrode pretreatments, indicates the unsatisfactory state of affairs in the PZC research. It is evident that further efforts in this field are needed. Below is a report of such an effort to develop a new method. It

* Electrochemical Society Active Member.

Key words: potential of zero charge (PZC), gold electrodes, time-of-contact method.

is based on the measurement of the time of contact (TOC) between two electrodes constructed of the same metal and polarized to virtually the same potential, when one is struck by the other. Application of this method for the determination of the PZC on gold electrodes is described.

The principle of the method.—A schematic diagram of the apparatus is shown in Fig. 1. A rodlike electrode is suspended from a metal strip which acts as a spring. This electrode is pulled back by means of a small electromagnet. When released, the electrode at the end of the spring moves through the solution and hits the face of the planar electrode which is held at virtually the same potential. The time of contact (TOC) between the two electrodes is the quantity being measured in these experiments. This depends on the charge density q_M (and hence on the potential) of the two electrodes. As q_M increases more work must be expended to overcome the coulombic repulsion and bring the two electrodes together. This work will be done at the expense of the initial energy given to the moving electrode by the spring, so that the velocity of the moving electrode "just before making contact," will decrease as the absolute value of the charge increases. Hence at the PZC this velocity will be the greatest. The TOC is expected to decrease with increasing velocity, since the depth of penetration of the moving electrode into the planar electrode will be essentially independent of it. It may be concluded from the above qualitative reasoning that the TOC will be a minimum at the PZC and will increase with increasing rational potential on both sides.

Experimental

The mechanical system.—The mechanical system (Fig. 2) was built in and onto a large box constructed of Perspex (30 × 30 × 35 cm) which served the double purpose of establishing a base for the electrodes and ensuring an inert gas atmosphere. One of the side panels was easily removable. A round hole was bored into the top panel, through which a PVC rod (point 1), with a bore throughout its length (point 2), was pressure fitted. On the lower end of the PVC rod a cylindrical Teflon bar (point 3) could be attached with the aid of a sleeve (point 4). A gold pin (point 5) was pushed into the lower end of the Teflon bar. This gold pin screwed into a gold block (point 6) (8 × 10 × 5 mm), which was the stationary planar electrode. A brass rod passing through the bore (point 2) provided the electrical contact and contributed to the mechanical stability of this electrode.

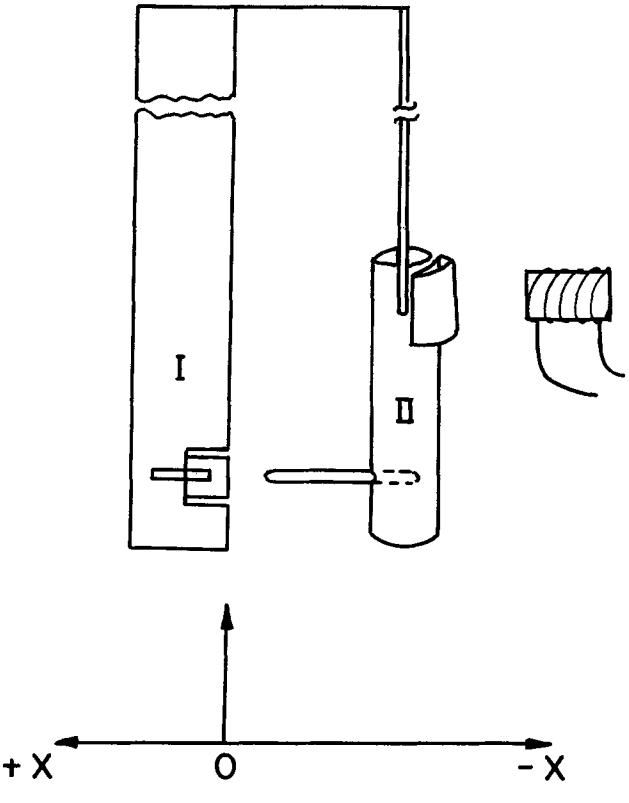

Fig. 1. A schematic diagram of the apparatus. I, Stationary electrode; II, moving electrode.

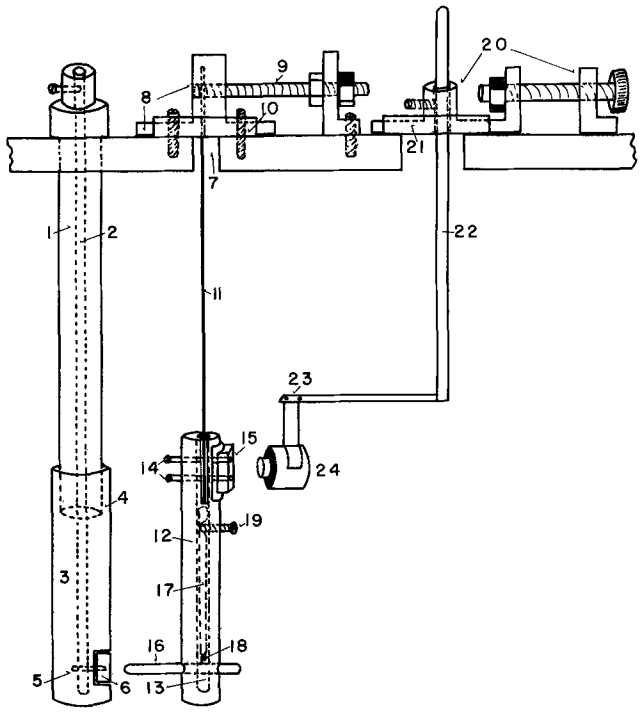

Fig. 2. Full scale diagram of apparatus

Not far from the first hole in the upper panel, another one was bored (point 7). This was a rectangular opening permanently covered by a metal device (point 8), which could move horizontally in tracks (point 10) by turning the nut (point 9). A steel band (point 11) serving as a spring was attached to the lower part of this device. The moving electrode was built of a Teflon rod (point 12) with a bore in the middle (point 13) almost all the way to the lower end. At that end a 3 cm long and 3 mm diameter gold rod (point 16) was inserted with pressure. Its point which faced the planar electrode was shaped as a truncated cone (the diameter of the small circle was ca. 0.5 mm). The upper end of the Teflon rod (point 12) was split in two, and the spring was inserted there and fastened by two screws (point 14), which screwed into an iron block (point 15). The electrical contacts of this electrode were conducted through the central bore. A brass rod (point 17) pressed a small spring (point 18) against the gold rod. The upper end of the brass was held tight by a small screw (point 19), to which the electric lead was soldered.

On the top panel of the Perspex box another movable device (point 20) with tracks (point 21) was built. It connected inside the box to a handle (point 22) carrying an electromagnet (point 24). When current passed through it the electromagnet could attract the moving electrode by the iron block (point 15). Stopping the current released the spring and the electrode moved forward to strike the planar electrode.

The two movable devices (points 8 and 20) were needed in order to control the velocity of the moving electrode. The Perspex box was kept on a special shock absorber to eliminate mechanical disturbances.

It was essential to ensure, as much as possible, the rigidity of the fixed electrode, the electromagnet setting, and the box. It was also important to ensure that the moving electrode should have freedom of motion

only in the forward and backward directions and should not be able to move sideways.

The electronic circuits.—There were two separate circuits. One provided current to the electromagnet; this current could be stopped by applying a voltage step for a controlled span of time. The time between current intermissions could also be controlled. Generally there were 3 sec for current intermission and 18 sec in between for the solution to calm down. In each cycle the direction of the current in the electromagnet was inverted to avoid residual magnetism in the magnetic core.

The second circuit controlled the potential of the electrodes and allowed the measurement of the TOC (Fig. 3). A potentiostat (Elron CHP-1) was used. The working electrode terminal was connected directly to the moving electrode and, through the resistance R_m, to the planar electrode. R_m was a 400 k-ohm helipot. The voltage on R_m was read on the y axis of an oscilloscope (Tetronix 564 with 3A3 and 3B3 plug-in units for the y and x axes, respectively).

Measurement of the TOC depends on the existence of a small residual current (*ca.* 0.5-1.0 μA/cm^2). The resistance R_m was set to give a potential drop of 8 mV between the moving and the stationary working electrodes. (This requires a different setting of R_m for each applied potential since the residual current depends on potential.) During contact there is no current through R_m and the potential across it drops to zero. This fast drop in potential is used to trigger the oscilloscope. When the electrodes detach, current again passes through R_m and the voltage assumes its previous value (Fig. 4). (The rise in the voltage is generally much slower than the fall.)

Cell, electrodes, and materials.—The cell was covered with a glass plate with a hole for the auxiliary electrode and openings for the working electrodes. The opening for the moving electrode was elongated, allowing enough free space for movement. The reference electrode was installed in a special compartment separated from the main cell by two fine sinters. An inert gas atmosphere was kept by flowing nitrogen into the Perspex box. Before beginning the measurements, nitrogen was passed through the solution for a period of about 1 hr. The nitrogen was cleaned first by passing it through an oven with copper files, through distilled water, through concentrated sulfuric acid, and again through water. The working electrodes were 99.99% pure gold. They were treated by abrading with alumina powder (0.05μ) until bright, then were rinsed with water, acetone, and again water in an ultrasonic cleaner. A platinum foil (*ca.* 2 cm^2) served as the counterelectrode and a saturated calomel electrode (Radiometer K-401) served as the reference electrode. All potentials are reported with respect to this electrode. Triple-distilled water was used to prepare solutions.

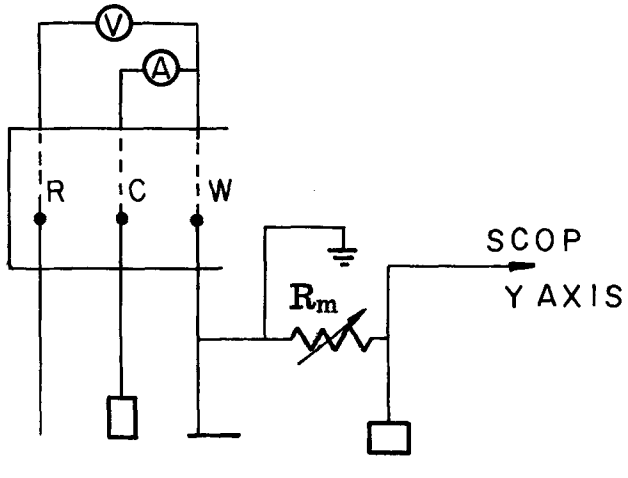

Fig. 3. Circuit for potential adjustment and TOC measurement

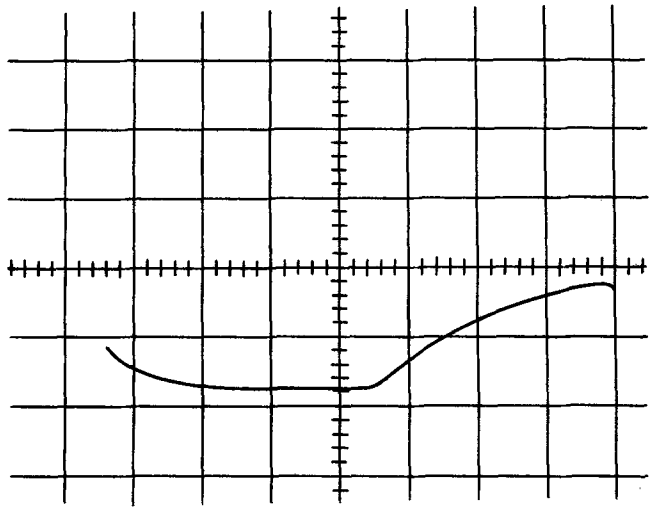

Fig. 4. An oscilloscope trace of the voltage on R_m during contact. The sudden rise marks the end of contact.

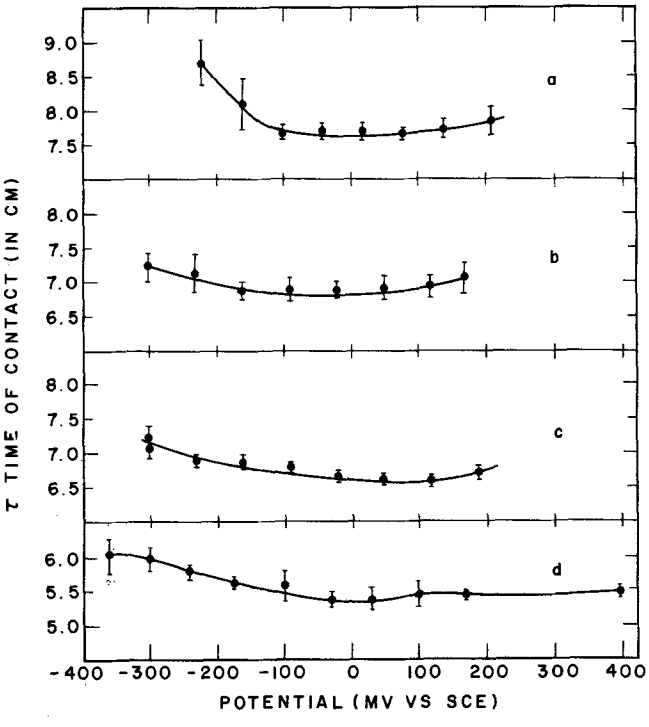

Fig. 5. TOC *vs.* potential curves measured in perchloric acid solutions. Time scale: a, 20 μsec/cm; b, 100 μsec/cm; c, 120 μsec/cm; d, 200 μsec/cm.

All chemicals were AR grade, used without further purification. Iodine solutions were prepared in water which was deaerated by bubbling nitrogen through it for 1 hr.

Results and Discussion

The variation of the TOC with potential was measured for gold electrodes in 1×10^{-3}M $HClO_4$ and in 5×10^{-3}M KI solutions with and without 5×10^{-4}M $HClO_4$.

The plots of the TOC *vs.* potential in 1×10^{-3}M $HClO_4$ showed rather wide minima (Fig. 5, a-d) in the range of -0.05 to $+0.10$V as seen in Table I.

The average value of the PZC in this solution is 0.01V. The limits of uncertainty are of the order of 0.05-0.1V. This result falls in the same region where most of the reported values of the PZC of gold (14, 16, 17).

In sodium iodide solutions we obtained minima which were generally sharper and clearer than in perchlorate solutions (Fig. 6, a-d). This corresponds

Table I. Minimum of TOC in perchloric acid solutions

No. of curve (see Fig. 5)	Potential of minimum (V)
a	0.00
b	−0.05
c	0.10
d	0.01

Table II. Minimum of TOC in sodium iodide solutions

No. of curve, see Fig. 6	Potential of minimum (V)
a	−0.28
b	−0.32
c	−0.23
d	−0.25

to the fact that in the case of specific adsorption, q_M changes more rapidly with potential. The average value of the PZC in this solution was −0.27V as seen in Table II, and shifted about 0.28V in the cathodic direction relative to the average observed in perchloric acid, in qualitative agreement with the shift expected for the PZC due to specific adsorption of anions.

It is important to note that the reproducibility in these experiments was not very high. There are many difficulties stemming from sudden, unpredictable jumps in the measured TOC which are probably caused by a change of the exact point of contact, or by a change of the surface structure of the electrodes at the point of contact under the influence of the blows. Notwithstanding this, almost all the results revealed the same general behavior; namely, a decrease in TOC when approaching the potential region where better runs yielded minima. These mechanical difficulties express themselves in the standard deviations which are rather large. The main factors which now limit the accuracy and reproducibility are mechanical, and improvements in this direction are feasible.

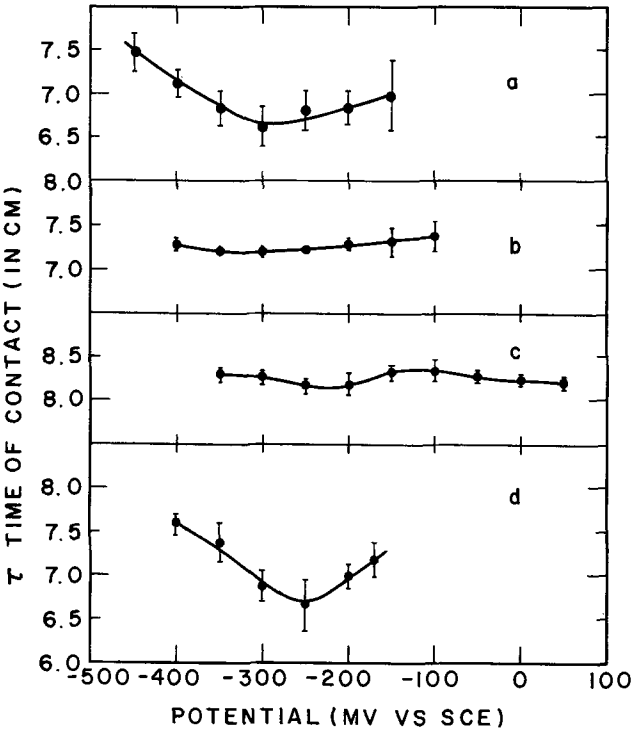

Fig. 6. TOC vs. potential curves measured in iodide solutions. Time scale: a, 380 μsec/cm; b, 150 μsec/cm; c, 100 μsec/cm; d, 400 μsec/cm.

Conclusions

It may be concluded that the time of contact between a moving and a stationary electrode can serve as a method for determining the potential of zero charge on solid electrodes. Measurements with the instrument described here are rather tedious, and limited in accuracy, but the measurement can be automated, and by further introducing small improvements in the mechanical construction, this may serve as a useful method for measurements of the PZC on solids.

Acknowledgments

The authors wish to thank Mr. Y. Drielinger for construction of the mechanical parts of the instrument and Mr. N. Tshernikovski for his assistance in the design of the electronic circuitry.

Financial support for this work by the Ford Foundation, under Grant No. 6/C/IV, is gratefully acknowledged.

Manuscript submitted Oct. 16, 1972; revised manuscript received Feb. 12, 1973.

Any discussion of this paper will appear in a Discussion Section to be published in the June 1974 JOURNAL.

REFERENCES

1. S. D. Argade and E. Gileadi, in "Electrosorption," E. Gileadi, Editor, p. 87, Plenum Press, New York (1967).
2. A. N. Frumkin, *Svensk Kem. Tidskr.*, **77**, 6 (1965).
3. P. Delahay, "Double Layer and Electrode Kinetics," Interscience Publishers, New York (1965).
4. L. I. Antropov, "Kinetics of Electrode Processes and the Null Points of Metals," Council of Scientific and Industrial Research, New Delhi, India (1960).
5. D. C. Grahame, *Chem. Rev.*, **41**, 441 (1947).
6. D. C. Grahame, R. P. Larsen, and M. A. Poth, *J. Am. Chem. Soc.*, **71**, 2978 (1949).
7. G. Kucera, *Ann. Phys.*, **11**, 529, 698 (1903).
8. G. Lipmann, *Ann. Chim. Phys.*, **5**, 494 (1875); *ibid.*, **12**, 265 (1877); *Ann. Phys.*, **149**, 547 (1873); *J. Phys. Radium*, **2**, 116 (1883).
9. J. Lawrence and D. M. Mohilner, *This Journal*, **118**, 1596 (1971).
10. M. Green and H. Dahms, *ibid.*, **110**, 446 (1963).
11. J. O'M. Bockris, S. D. Argade, and E. Gileadi, *Electrochim. Acta*, **14**, 1259 (1969).
12. T. R. Beck, *J. Phys. Chem.*, **73**, 466 (1969).
13. A. Ya. Gokhstein, *Elektrokhimiya*, **2**, 1315 (1966); *Electrochim. Acta*, **15**, 219 (1970).
14. R. S. Perkins and T. N. Andersen, in "Modern Aspects of Electrochemistry," Vol. 5, J. O'M. Bockris and B. E. Conway, Editors, Plenum Press, New York (1969).
15. L. Campanella, *J. Electroanal. Chem.*, **28**, 228 (1970).
16. J. P. Carr and N. A. Hampson, *This Journal*, **119**, 325 (1972).
17. S. Efrima, Thesis, Tel-Aviv University, Israel (1972).

Silver/Silver Chloride Electrode: Reaction Paths on Discharge

T. Katan*

Materials and Structures, Lockheed Palo Alto Research Laboratory, Palo Alto, California 94304

S. Szpak[1]

Chemistry Laboratory, Mare Island Naval Shipyard, Vallejo, California 94590

and Douglas N. Bennion*

Energy and Kinetics Department, University of California at Los Angeles, Los Angeles, California 90023

ABSTRACT

Elementary processes for the reduction of thin films of silver chloride on silver have been investigated using rotating disk techniques. Experiments were carried out in 1, 2, and 4*N* solutions of KCl. The effective diffusion coefficients of the prevalent species of silver ion in 2 and 4*N* KCl are about 1.42 and 0.31 $\times$ 10^{-5} cm^2/sec, respectively. Reduction of thin AgCl films on Ag can be carried out at high rates, 100-200 mA/cm^2 at 300 mV overpotential, two orders of magnitude higher than that for the reduction of dissolved AgCl from bulk solution at 2000 rpm. A linear $i = \eta$ relationship and its independence of the state of charge suggest that liquid phase transport occurs, possibly followed by a rate controlling process of surface diffusion.

The silver/silver chloride electrode is an example of the class of battery electrodes which consists of a dispersed, sparingly soluble reactant within a continuous, conductive matrix. Electrodes of this class have a structure which is repeatedly encountered in practical batteries. Recent theoretical studies (1, 2) have indicated that a great variety of current density distributions may exist in such systems, *e.g.*, exhibiting maxima and/or minima in the discharge profile, depending on local conditions governing mass and charge transfer. Identification and evaluation of local conditions during electrode charge or discharge are consequently necessary not only for more accurate assessment of electrode behavior in terms of the developing theory, founded on firm experimental bases and corresponding closely to reality, but also to help ascertain conditions of the recently predicted current distributions. The present work on the reaction paths of reduction at silver/silver chloride electrodes was accordingly undertaken to provide information that may be of use in interpreting behavior of electrodes in this important class.

Summary of Reaction Paths

Sparingly soluble reactants.—In general, the processes governing the local mass and charge transfer can be represented by a diagram as shown schematically in Fig. 1. An element of the electrode structure is visualized as consisting of a metal which is partially covered with its salt and which is immersed in an electrolyte. The process of electrode discharge (metal ion reduction) can proceed along the paths indicated. The charge transfer process may occur at the metal/salt interface (path a), or at preferred sites of the metal/solution interface (path b). The first or film mode of transfer involves ion transport in the solid salt and is relatively simple to describe if the cation is the only species with a nonzero mobility in the solid salt phase (2). It is the second mode, the reduction of metal ions at the metal/solution interface, which may lead to unexpected distributions because of the several possible kinetic steps involved, including the dissolution rate, the diffusion flux, and various interfacial phenomena, such as adsorption, surface diffusion, and nucleation (crystallization). It is evident why a clear distinction between the numerous local complex paths is needed in order to avoid ambiguity and to allow a simple and clear development of theory.

A reasonably complete description of the isothermal operation of such electrodes, the so-called "solution-diffusion" model (1), requires the solution of five second-order partial differential equations. A considerable simplification can be made without seriously impairing the results through the use of a characteristic number, similar in many respects to the Thiele parameter (3-5). Dunning (2) showed that this characteristic number, λ^2/L^2 [N^2 in Nanis's (4) notation] contains the rate constants of a set of consecutive elementary steps, such as those shown in Fig. 1, and is of the form

$$\lambda^2/L^2 = A\kappa \sum_i k_i^{-1} \qquad [1]$$

where k_i is the rate or transport constant of the ith step, κ is the electrolyte conductivity, and A, a constant related to the electrochemical system. It is necessary to arrive experimentally at the numerical values of the coefficients in Eq. [1], or, at least to determine the relative magnitude of the steps involved in

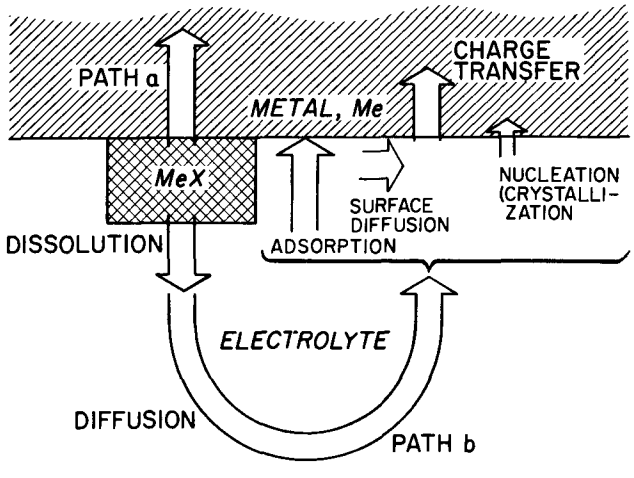

Fig. 1. Possible reaction paths for sparingly soluble reactant-conductive matrix electrode system. Path a: charge transfer at the Me/MeX interface. Path b: dissolution, diffusion, interfacial steps, and charge transfer.

* Electrochemical Society Active Member.

[1] Present address: Electronic Materials Sciences Division, Naval Electronics Laboratory Center, San Diego, California 92152.

Key words: porous electrodes, silver/silver chloride, batteries.

order to establish the governing or controlling steps for the "solution-diffusion" model (1, 2).

Ag/AgCl electrode.—The Ag/AgCl electrode has found practical applications in both primary and secondary batteries for operating conditions described as electrode discharge, electrode charge, or electrode cycling. Since an excess of Cl^- ions is formed on discharge while a deficiency results on charge in the vicinity of the reaction zone, variations in Cl^- ion concentration must be considered in the course of electrode analysis.

The set of elementary steps comprising the over-all discharge process, shown in Fig. 1, may also apply to the Ag/AgCl electrode. This set of events can be divided into two groups, those connected with the reduction via a solid-state path (path a) and those occurring via liquid phase (path b). Past work has been concerned primarily with the reduction of thick silver chloride films where reduction takes place at the Ag/AgCl interface, path a (6, 7). The detailed mechanism has not been definitely established although valuable microscopic observations were made by Jaenicke *et al.* (6) and Briggs and Thirsk (7), indicating that the reaction begins at the AgCl grain boundaries and the Ag/AgCl interface. Shortly after impressing external cathodic current, pores are formed in the thick layers of AgCl which are considered to be initially present in an essentially pore-free condition. Aleskovskii *et al.* (8) have recently presented evidence for the reduction of solid AgCl occurring via reduction of solvated silver ions. A quite different view, expressed by Dorosh and Galushko (9), implies that adsorbed hydrogen is required for the reduction of silver chloride on silver electrodes.

Conceivably, more than one reduction mechanism can operate, depending on experimental conditions such as thickness of the AgCl layer and its porosity, electrolyte concentration, and electrode potential. We shall only consider the reduction of films having physical dimensions on the order of 1 μm or less, *i.e.*, having physical dimensions compatible with the construction of a model AgCl electrode which has practical analogies in other battery systems and which is amenable to theoretical treatment.

Since thin silver chloride films are porous, it appears likely that the mechanism proposed by Aleskovskii *et al.* (8) should dominate the discharge process. The experimental work reported here is concerned with ascertaining the validity of this mechanism and with determining conditions under which it may operate in practical electrodes.

Experimental

In the experimental arrangement, a rotating disk silver electrode, 0.83 cm in diameter, centered in an epoxy cylinder, 2.43 cm in diameter, was employed. A Wenking, fast rise potentiostat and an Electronics Model C 612 galvanostat were used to impose the desired experimental conditions. The electrode response to a predetermined set of conditions was recorded on a Sargent MR recorder, a Tektronix Model 551 oscilloscope, or a Greibach Model 500 milliammeter, as applicable.

The electrolyte was an aqueous 1, 2, or 4*N* KCl solution prepared from triply distilled water and ACS reagent grade KCl, used as purchased. No additional purification was performed. The electrolyte in the electrolytic cell, approximately 500 cm^3 in volume, was continuously purged with nitrogen. All experiments were carried out at 22.5° ± 0.5°C in the deaerated solutions.

The sequence of experimental procedures to elucidate the reaction path and to assign relative importance of each step is suggested from an inspection of Fig. 1. The diffusion part of reaction path b was isolated and studied by observing silver ion transport from a bulk solution to the surface of the rotating disk. The bulk solutions were the various concentrations of KCl saturated with AgCl. Results were compared to experiments in which solid AgCl was previously formed on the electrode surface. The comparison provided insight into the effects of surface coverage by AgCl and dissolution kinetics limitations.

Results

Reduction of AgCl from KCl solutions.—Typical i-η curves for the reduction of silver ions from potassium chloride solutions saturated in AgCl are shown in Fig. 2. In particular, curves a and c together with curves b and d show the effect of Cl^- ion concentration and, therefore, total silver ion concentration, while curves a and b together with curves c and d indicate the influence of the speed of electrode rotation.

It is seen that in 2*N* KCl electrolyte, a diffusion-limiting current density, $i_l(2N, 100)$, is realized. As the speed of rotation is increased further, a limiting current density, $i_l(2N, 500)$, is again obtained. At still higher rotational speeds, when the current densities become appreciably higher, a deviation occurs from the usual form of the potential/current curve, namely, a relatively sharp break toward higher currents is recorded, segment AB, curve b, Fig. 2. With further increase in electrode rotation, this break is shifted to lower overpotentials, suggesting that a critical current density must be exceeded before the break occurs, about 0.5 mA/cm^2 in 2*N* KCl. The sharp increase in current density, together with the requirement of some minimum critical current density or time of electrolysis, is readily associated with the onset of an increase in electrode surface area by silver nucleation (10).

The situation remains qualitatively the same as chloride ion concentration is increased. However, the marked increase in current (electrode area) then coincided approximately with the occurrence of the mass transport limiting current density and partly obscured the plateau, Fig. 2, i_l (4*N*, 100) segments A'B' and A"B". A dense, whisker-like growth was noted on the electrode surface upon completion of the experimental run. This confirms the view that substantial increase in the electrode surface is responsible for current densities which exceed the diffusion-limiting values.

Formation of AgCl film.—Silver chloride films can be easily formed on a silver substrate in chloride solutions when an anodic (positive) overpotential is applied. The galvanostatic potential-time curve, shown in Fig. 3, exhibits typical characteristics for the formation of

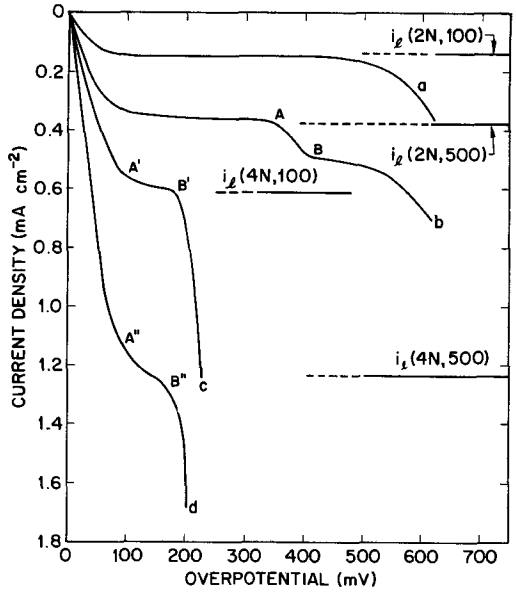

Fig. 2. Typical cathodic potential-current curves for selected chloride concentrations and electrode rotation. Curve a, 2*N* KCl + sat. AgCl, 100 rpm; curve b, 2*N* KCl + sat. AgCl, 500 rpm; curve c. 4*N* KCl + sat. AgCl, 100 rpm; and curve d, 4*N* KCl + sat. AgCl, 500 rpm.

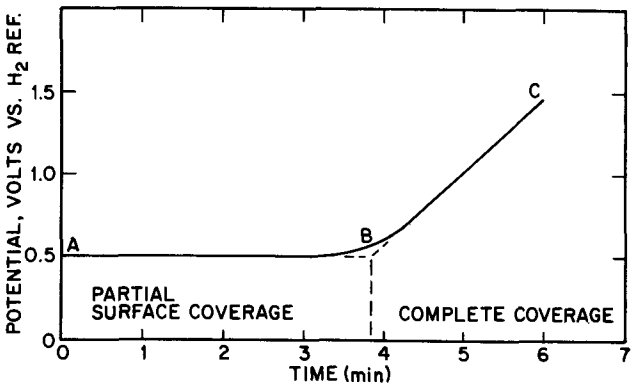

Fig. 3. Potential-time curve for galvanostatic (anodic) charging. Electrolyte, 1*N* KCl + sat. AgCl; charging current, 5.0 mA/cm².

an ion-conducting layer. The initial, flat portion, AB, corresponds to the formation of a porous film; the rising portion, BC, indicates a complete surface coverage with ohmic resistance proportional to film thickness (11), after 1.14 coulomb-cm^{-2} are passed.

The anodic films used in this investigation were formed at the rate of 0.5 μm/min, *i.e.*, at $i = 5$ mA/cm², and, assuming no porosity and 100% coulombic efficiency, their thickness did not exceed 2 μm. As a rule, thinner films were studied and, unless otherwise noted, the films were porous, being formed under conditions corresponding to the formation of fractional surface coverage, part AB, Fig. 3.

It was found that silver chloride films can also be obtained by simply immersing silver in a 1 or 2*N* potassium chloride solution saturated with silver chloride; no films were detected from 4*N* potassium chloride solutions saturated with silver chloride. Here, the mechanism of film formation is probably different than when anodic current is applied or, in the absence of applied current, when an oxidant, *e.g.*, Br_2, I_2, is added to the electrolyte (12). These solutions were purged with nitrogen to insure the absence of oxygen from the electrolytic solutions.

To differentiate between the various modes of film formation, the electroless films will be referred to as "charge accumulation" to distinguish them from the anodically formed films. The evidence presented in Fig. 4 and 5 suggests that transport of dissolved silver from bulk solution to the electrode surface governs the rate of electroless film formation. In particular,

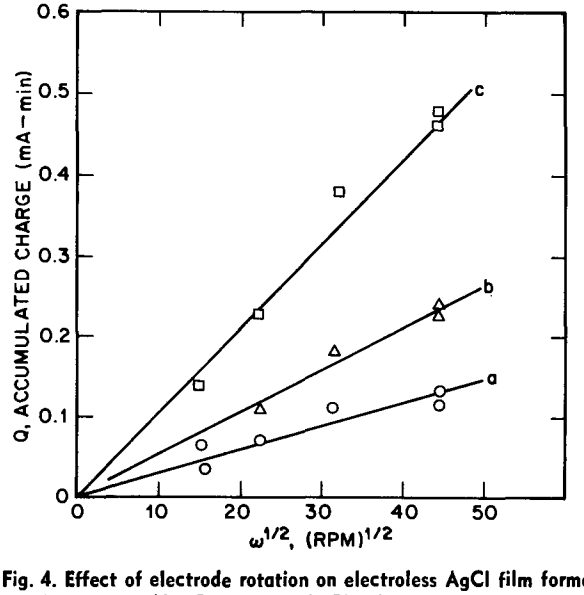

Fig. 4. Effect of electrode rotation on electroless AgCl film formation. Electrolyte, 1*N* KCl + sat. AgCl; charging time: 2, 4, and 8 min, curves a, b, and c, respectively.

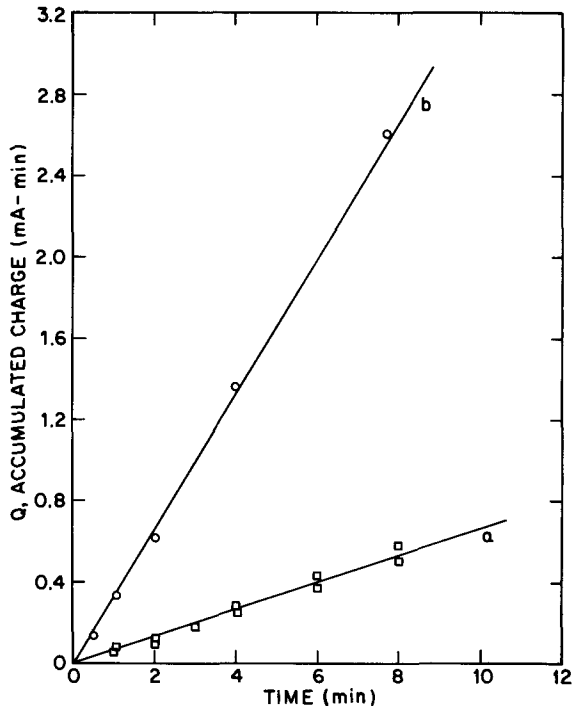

Fig. 5. Effect of chloride concentration on electroless film formation. Electrode rotation, 2000 rpm; curve a, 1*N* KCl + sat. AgCl; curve b, 2*N* KCl + sat. AgCl.

results of Fig. 4 clearly indicate the importance of diffusion in the charge accumulation, since the latter is shown to be proportional to the square root of rotational velocity. Results presented in Fig. 5 indicate that complex silver ions, $AgCl_{n+1}^{-n}$ with $n = 1, 2, 3$, are the diffusing species. This latter conclusion is reached by inspection of Table I, where it can be seen that the ratio of total silver in the form of various complexes, 5.9, agrees well with the ratio calculated on a basis of diffusional transport, 6.1, for 1 and 2*N* KCl, Fig. 5.

Reduction of thin AgCl films.—The determination of the reaction profile within a porous electrode structure requires the specification of the local current-potential relation, $i = f(\eta, c)$, where c is a relevant parameter, *e.g.*, concentration. The form of this expression can be derived if the reaction mechanism is known, alternatively, its form can be established experimentally.

Usually, steady-state values are employed to construct the current density-potential relationship. Here however, because in the course of measurements the stored active material is used up, it is advantageous to select some distinctive feature of the potentiostatically obtained *i-t* curves for the *i*-η plots.

The i-t curves.—The potentiostatically recorded *i-t* curves for the reduction of silver chloride films are shown in Fig. 6. The general shape of these curves

Table I. Concentration of $AgCl_{n+1}^{-n}$ in KCL + AgCl (sat.) solutions, 25°C

Species	Concentrations in normality, KCl		
	1*N*	2*N*	4*N*
Ag^{+}[a]	2.3×10^{-10}	1.2×10^{-10}	0.59×10^{-10}
$AgCl_2^{-1}$[a]	3.0×10^{-5}	5.9×10^{-5}	11.8×10^{-5}
$AgCl_3^{-2}$[a]	4.1×10^{-5}	15.6×10^{-5}	64.0×10^{-5}
$AgCl_4^{-3}$[a]	2.15×10^{-5}	8.0×10^{-5}	328.0×10^{-5}
AgCl[a]	5.4×10^{-7}	5.4×10^{-7}	5.4×10^{-7}
$AgCl_{n+1}^{-n}$[b] (total dissolved silver)	10.1×10^{-5}	61.6×10^{-5}	637.0×10^{-5}

[a] Calculated values using instability constants (13).
[b] Experimental values (14).

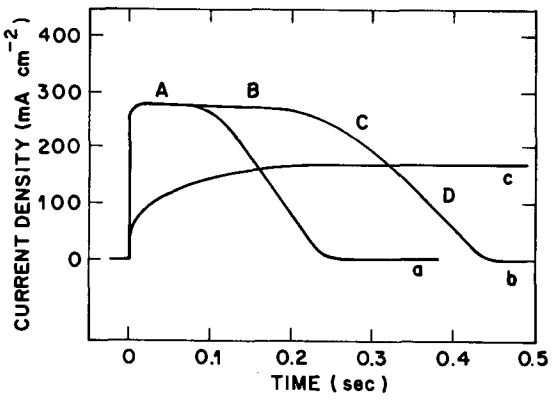

Fig. 6. Typical current-time curves for potentiostatic reduction of AgCl films. Curves a and b, thin films (thickness less than 2μm); curve c, thick films (thickness more than 2μm); electrolyte, 2*N* KCl + sat. AgCl; electrode rotation, 2000 rpm.

remained unchanged, as long as the AgCl film was porous, that is to say, as long as the charge on the electrode surface corresponded to the horizontal portion of the charging curve shown in Fig. 3.

It is seen that the *i-t* curves are characterized by a rapid attainment of a plateau, whose extent in time and height depend on the initial electrode charge and applied discharge potential, respectively. These curves, however, are not affected by externally imposed transport conditions, *i.e.*, electrode rotation. Also, their shape was essentially independent of the manner in which the film was formed, *i.e.*, whether the film was formed anodically, or the charge was accumulated by the electroless process from AgCl-saturated KCl solutions. However, if sufficiently large charge was placed on the electrode surface so that the film was no longer porous, then the *i-t* curve exhibited a gradual increase in the discharge current, cf. Fig. 6, curve c, until a more or less flat region was attained, followed by the decrease in the discharge current. Such behavior was also reported by Briggs and Thirsk (7).

The i-η curves.—The current potential plots, shown in Fig. 7 clearly display linear dependence for the plateaus of the *i-t* curves, examples of which are shown in Fig. 6. In particular, for overpotentials greater than *ca.* 50 mV they follow the relationship

$$i = a\eta + b \qquad [2]$$

with $a = 0.323$ ohm^{-1}/cm^2, $b = -7$ mA/cm^2; for 1*N* KCl, $a = 0.773$ ohm^{-1}/cm^2, $b = -45$ and -20 mA/cm^2 for 2 and 4*N* KCl, respectively.

For overpotentials less than 50 mV, higher order polynomials would have to be used to fit the experimental data. The linear dependence is maintained even when the electrode surface contains only a small fraction of the initial amount of AgCl. This situation is illustrated in Fig. 8, where the *i-η* curves for nearly discharged electrodes are shown. It is also seen that slopes of the *i-η* curves decrease with increasing electrode discharge. Thus, the form of above equation is retained, but now *a* becomes a function of the charge, *Q*, remaining on the electrode surface.

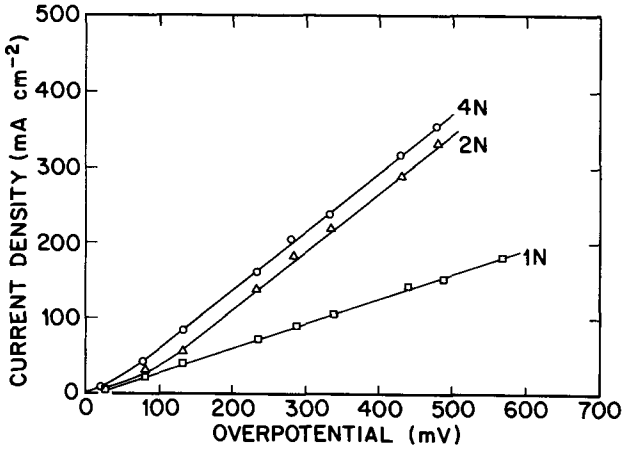

Fig. 7. Effect of chloride on AgCl-electrode discharge. Discharge current read from the flat portion of the *i/t* curves (cf. Fig. 6).

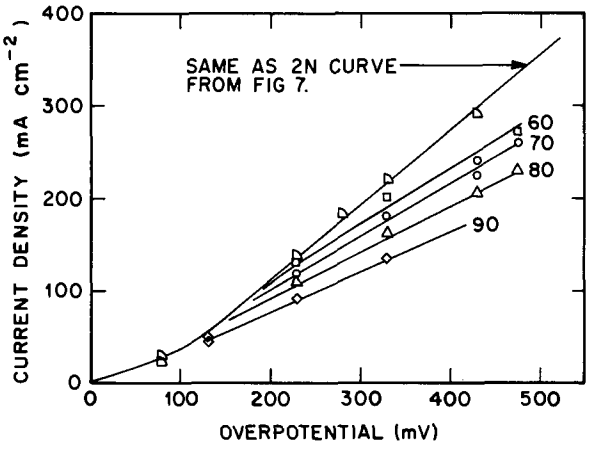

Fig. 8. Discharge characteristics for residual charge. Discharge percentage level indicated by numbers, 2*N* KCl.

Discussion

Recently, the rotating disk electrode has been employed in the investigation of the passivation of metals (22) and also in the study of events occurring at the electrode surface during metal deposition (23). In this study, the rotating disk technique was used in an attempt to separate the elementary processes from the complex over-all reaction path. Thus, further insight into the mechanism for silver deposition and confirmation of an assumed reaction path was obtained through the analysis of the $i(\eta)$ *vs.* $\omega^{1/2}$ relationship.

Deviation from linearity occurred toward higher currents, Fig. 9, in the sense that the limiting current was exceeded many times over. This effect can be attributed to the formation of nuclei and dendritic-type growth into the boundary layer, and consequent increases in surface area of the rotating disk electrode.

Based on the limiting current plateaus in Fig. 2 and the limiting current slope shown in Fig. 9. (these are, in fact, independent data) the effective diffusion coefficient for the silver ions can be calculated by direct application of the Levich equation (17)

$$i_l = \frac{D^{2/3}\, n\mathbf{F}\, \omega^{1/2}\, c}{1.61\, \nu^{1/6}} \qquad [3]$$

The limiting currents are difficult to determine accurately because of the interference or disruption of the boundary layer due to formation, after a short time, of surface roughness or whisker-like growth. To within ±10%, the values are 1.4×10^{-5} and 0.31×10^{-5} cm^2/sec at 2 and 4*N* KCl, respectively, saturated with AgCl at 22.4°C. The large decrease in the effective diffusion coefficient is apparently due to the much larger proportion of $AgCl_4^{-3}$ present at the higher KCl concentration (see Table I).

Experimental evidence presented thus far (Fig. 2 and 9) indicates that silver diffusion from the bulk solution is the rate controlling process in depositing silver under some conditions. It also appears that nucleation phenomena must be included. The fact that the estimated mass transport limiting currents are exceeded under certain conditions must be considered in interpreting observed behavior.

The discharge current densities reported in Fig. 7 and 8, are about two orders of magnitude higher than those from AgCl-saturated KCl solutions, cf., Fig. 2. This observation suggests that the diffusion resistance for transport from the AgCl crystal to reaction sites is

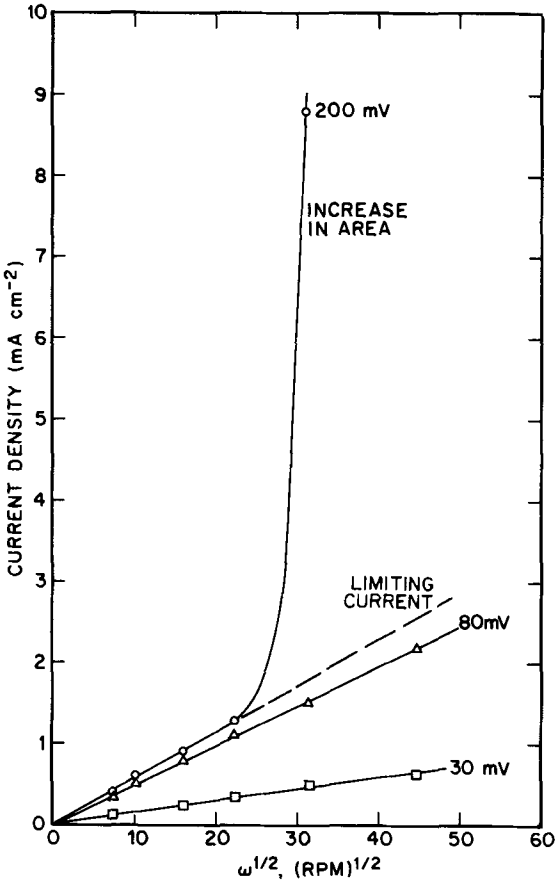

Fig. 9. Effect of overpotential and electrode rotation on cathodic current density. Electrolyte, 4*N* KCl + sat. AgCl; slope for dotted line showing diffusion transport for $D = 0.31 \times 10^{-5}$ cm^2/sec.

much less than diffusion resistance across the rotating disk boundary layer. The linear i-η relationship, Fig. 7 and 8, might be ascribed to the ohmic drop across a continuous nonporous film covering the electrode surface. This case seems unlikely because, if the ohmic-type resistance is ascribed to film thickness, resistance should decrease as the reaction progresses. Similarly, if the ohmic resistance is due to solid-state ion conductance followed by charge transfer at the metal/salt interface, the flat portion of the i-t curve (Fig. 6) could not exist, since the current density should increase as the film thickness decreases. This argument indicates that path a, Fig. 1, is unlikely under the observed conditions. Returning to path b, we consider metal deposition. In outline, the process of metal deposition consists of ions crossing the crystal-solution interface, liquid phase diffusion, surface diffusion to the growth center, and inclusion into the lattice. The linear dependence of the peak currents on overpotential (see Fig. 7) and the independence of the current peak heights (see Fig. 6) on the state of charge Q over a wide range can be explained by assuming that surface diffusion is the slow step. In surface diffusion, ions located within the Helmholtz layer will migrate to points just opposite the "growth sites" and traverse the Helmholtz layer at these points. That is to say, an inhomogeneous electric field is set up in a Helmholtz layer to guide the metal ions to their destination, resulting in a linear i-η relationship (18). The active metal area which is adjacent to the silver chloride crystals is assumed to be constant over a wide range of Q. Since the surface concentration of growth sites at the metal-liquid interface remains constant at fixed potential (19, 20), the independence of current peak heights on Q can then be accounted for.

The flat portion of the potentiostatic i-t curve, its magnitude and duration (see Fig. 6) provides additional clues for identification of the controlling steps in the reaction path. In accordance with Giles' concept (21) of the porous silver chloride film and the perimeter-advancement mechanism of reduction of thick AgCl films (6, 7), we may anticipate a movement of an Ag/AgCl perimeter during reduction and a surface diffusion to nucleation centers of fixed surface concentration. Eventually the patches of AgCl become small enough so that the electrode discharge rate drops as the resistance due to combined dissolution increases, and the resistance due to liquid phase diffusion increases. Qualitatively, these steps can explain both the linearity of the i-η curves, the shapes of the i-t curves, and the independence of the plateau current density of the i-t curves on Q.

The phenomenon of the "charge accumulation," that is, the film formation in the absence of impressed anodic potential or dissolved oxidants is of interest, both theoretical and practical.

The ratio of the rates of charge accumulation in 2 and 1*N* solutions (see Fig. 5) was found to be 5.9, which agrees rather well with the predicted ratio of 6.1 (see Table I) based on total silver content. It is to be noted that the proportions of the various species of silver complexes remain fairly constant between 1 and 2*N* KCl. However, on going to 4*N* KCl the proportion of $AgCl_4^{-3}$ increases dramatically. The self-charging characteristic was absent in 4*N* KCl saturated with AgCl. No self-charging was observed when no AgCl was present for any KCl concentration.

The explanation of the self-charging phenomenon, which may be of practical interest, is sought through an analysis of conditions and processes occurring within the metal/solution interphase (22). Consider Fig. 10 showing schematically the dynamic situation within the metal/solution interphase. The letters in parentheses in the figure indicate location of species and are as follows: (b) adsorbed, (c) the metal side of the diffusion layer, (d) the solution side of the diffusion layer, and (s) at the surface, not necessarily in the "adsorbed state."

In the absence of silver complexes in the bulk, only the equilibrium involving chloride ions exists for negatively charged species, set 1; the adsorption of water molecules is neglected and considered to be irrelevant for the present purpose. In the presence of silver complexes, however, additional competitive adsorption processes may enter, sets 2 and 3.

If the solubility of AgCl in the adsorbed state is less than in the bulk solutions, adherent "patches" of AgCl will form and at the same time produce an excess of adsorbed Cl^- ions, nCl^-. On the strength of evidence

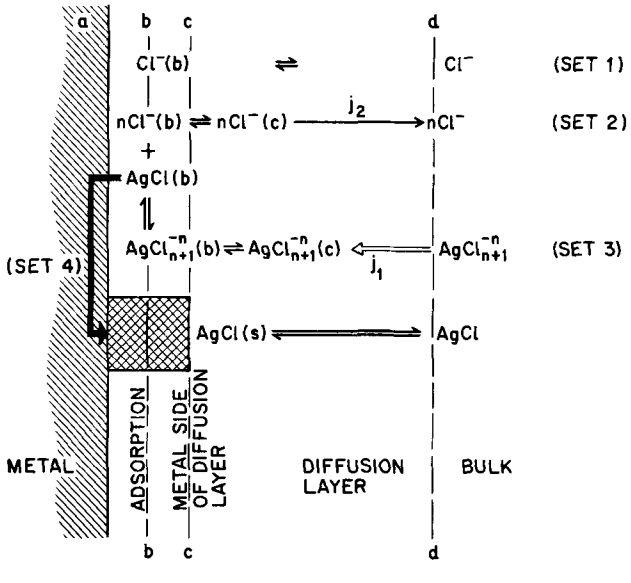

Fig. 10. Schematic representation of surface reactions and transport for saturated AgCl in KCl solutions, after Van Ryssel-berghe (22).

presented in Fig. 5, the rate of accumulation of silver chloride is governed by the transport of complex silver ions to the electrode surface, i_1, as indicated by the events of set 3, Fig. 10. The transport of charged species across any distance is equivalent to flow of current. Thus, in the absence of external current, electroneutrality condition requires a counterflow of species of the same charge or a co-current transport of species of opposite sign. The origin of these mass fluxes resides in the precipitation of silver chloride on the electrode surface. The precipitation of silver chloride from complex ions releases an excess of chloride ions, and a concentration gradient is established giving rise to the transport of Cl^- ions away from the electrode surface, j_2.

The adsorbed AgCl may form multiple layers on the solid surface, set 4, indicated as AgCl(s) which eventually attains equilibrium with bulk solution saturated with solid silver chloride. The nature of this transformation cannot be deduced on the basis of available information. Some inference, however, can be drawn from the detailed mapping of the potential within the metal/solution interphase (17).

In 4*N* KCl, saturated AgCl, the spontaneous formation of AgCl films did not occur, although the observations with 1 and 2*N* KCl, saturated AgCl, indicated that the rate of charge accumulation would increase with increase in silver complex ion concentration. The existence of an upper limit of chloride concentration for spontaneous film formation might be explained by the formation of different dominant complex species in the bulk solution and different species in the adsorbed state (see Table I and Fig. 10). The rates of electroless charge accumulation in 1 and 2*N* KCl solutions are almost constant for a period of ca. 30 min, after which they slowly diminish with time. These processes are of interest in battery technology because they may contribute to charge redistribution on cycling.

Conclusions

The identification and more precise description of some of the elementary processes occurring in silver/silver chloride porous electrodes have been investigated. The principal conclusions of this work are as follows:

1. The effective diffusion coefficient of silver ion in potassium chloride solution depends on the chloride ion concentration and is estimated to be 1.42 and 0.31 $\times$ 10^{-5} cm^2/sec at 22.4°C in 2 and 4*N* KCl, respectively.

2. The controlling step in the reduction of anodically formed AgCl films on Ag/AgCl electrodes in 2 and 4*N* KCl can be explained by surface diffusion to growth sites on the silver surface except when the state of surface charge is very small when the area of the silver chloride crystallites is small so that dissolution of AgCl becomes controlling.

3. Over a wide range of the state of charge, the local transfer current density is independent of the state of charge and is linearly dependent on local overpotential for the Ag/AgCl electrode.

4. At 1 and 2*N* KCl, AgCl from a saturated AgCl solution spontaneously precipitates on a silver surface. This did not occur in 4*N* KCl. This phenomenon may be of importance in redistribution of AgCl in AgCl/Ag porous electrodes on cycling.

5. The current densities possible with silver chloride crystallites on a silver electrode surface are much higher than when the limiting process is liquid phase transport from bulk solution to a rotating disk up to 2000 rpm, and suggest that high current densities are inherently possible in porous electrode structures because of the short diffusion paths.

6. Complete surface coverage by silver chloride during anodic oxidation in an aqueous solution of potassium chloride saturated with silver chloride occurred after the passage of 19 $\times$ 10^{-3} coulombs/cm. The onset of rapidly increasing polarization linearly with time, *i.e.*, with charge passed, is associated with this event.

Acknowledgment

This work was supported by Naval Air Systems Command under Contract No. N00019-71-C-0342 and N00019-71-C-0369. The authors wish to acknowledge the continued interest of Dr. H. Rosenwasser.

Manuscript submitted Aug. 14, 1972; revised manuscript received March 6, 1973.

Any discussion of this paper will appear in a Discussion Section to be published in the June 1974 JOURNAL.

SYMBOLS

- A constant characteristic of the porous electrode system, ohm-sec. See Ref. (2), Appendix 5.
- a empirical constant defined in Eq. [2], mho/cm^2
- b empirical constant defined in Eq. [2], A/cm^2
- c electrolyte concentration, mol/cm^3
- D diffusion coefficient, cm^2/sec
- $\mathbf{F}$ Faraday constant, 96,487 coulomb/equiv.
- i current density, A/cm^2
- i_l limiting current density, A/cm^2
- k_i transport constant for the *i*th elementary process, cm/sec
- L electrode thickness, cm
- n number of electrons transferred in electrode reaction
- η local overpotential, V
- κ specific conductance of electrolytic solution, mho/cm
- λ characteristic length for a porous electrode, may be potential dependent, cm. See Ref. (2), Appendix 5.
- ν kinematic viscosity, cm^2/sec
- ω rotation rate, radians/sec

REFERENCES

1. J. S. Dunning, D. N. Bennion, and J. Newman, *This Journal*, **118**, 1251 (1971).
2. J. S. Dunning, Ph.D. Thesis, University of California, Los Angeles (1971).
3. P. Bro and H. Y. Kang, *This Journal*, **118**, 519 (1971).
4. L. Nanis, *Plating*, **58**, 805 (1971).
5. E. W. Thiele, *Ind. Eng. Chem.*, **31**, 916 (1939).
6. W. Jaenicke, R. P. Tischer, and H. Gerischer, *Z. Elektrochem.*, **59**, 448 (1955).
7. G. W. D. Briggs and H. R. Thirsk, *Trans. Faraday Soc.*, **48**, 1171 (1952).
8. V. B. Aleskovskii, E. V. Bairashnyi, E. G. Ivanov, and V. A. Nikoskii, *Sb. Rab. Khim. Istochnikam*, **4**, 241 (1969).
9. T. P. Gorosh and V. P. Galushko, *Ukrain. Khim. Zh.*, **28**, 66 (1962).
10. K. J. Vetter, "Electrochemical Kinetics," p. 678, Academic Press, New York (1967).
11. G. Kortum, "Treatise on Electrochemistry," p. 517, Elsevier Publishing Co., New York (1965).
12. W. Jaenicke, *Z. Elektrochem.*, **55**, 186 (1951); **56**, 728 (1952).
13. L. G. Sillen and A. E. Martell, "Stability Constants," Spec. Pub. No. 17, The Chemical Society, London (1964).
14. W. F. Kinke, "Solubilities (Seidell)," Vol. I, p. 67, 4th Ed., D. Van Nostrand Co., Inc., New York (1958).
15. J. A. Harrison, *J. Electroanal. Chem.*, **36**, 71 (1972).
16. R. D. Armstrong and J. A. Harrison, *J. Electroanal. Chem.*, **36**, 79 (1972).
17. V. G. Levich, "Physicochemical Hydrodynamics," p. 69, Prentice Hall, Englewood Cliffs, N. J. (1962).
18. J. O'M. Bockris and A. K. N. Reddy, "Modern Electrochemistry," Vol. 2, Chap. 10, Plenum Press, New York (1970).
19. A. R. Despic and J. O'M. Bockris, *J. Chem. Phys.*, **32**, 389 (1960).
20. V. Bostanov, R. Roussinova, and E. Budevski, Abstract No. 140, p. 355, Electrochem. Soc. Extended Abstracts, Fall Meeting, Cleveland, Ohio, Oct. 3-7, 1971.
21. R. D. Giles, *J. Electroanal. Chem.*, **27**, 11 (1970).
22. P. Van Rysselberghe, in "Modern Aspects of Electrochemistry," Vol. 4, Plenum Press, New York (1966).
23. K. J. Vetter, *loc. cit.*, p. 742.

Free Energy of Formation of Bi_2O_3, Sb_2O_3, and TeO_2 from EMF Measurements

D. Chatterji*,[1] and J. V. Smith

Metallurgy and Ceramics Laboratory, Aerospace Research Laboratories, Wright-Patterson AFB, Ohio 45433

ABSTRACT

The solid electrolyte cell technique was employed for the direct determination of the free energy of formation of Bi_2O_3, Sb_2O_3, and TeO_2 at temperatures above 520°C. The high-temperature free energy data obtained in the present investigation were used to calculate the thermodynamic properties for the three oxides at 298°K. The calculations depended in part on the accuracy of the published thermochemical data.

In recent years, considerable effort has been directed toward developing materials for thermoelectric devices. Alloys prepared from the tellurides of bismuth and antimony have been found to be promising for such applications. Therefore a research program has been initiated to determine the thermodynamic properties of Bi-Te and Sb-Te alloys using the solid oxide galvanic cell technique of Kiukkola and Wagner (1). The technique demands accurate free energy of formation data for Bi_2O_3, Sb_2O_3, and TeO_2. A literature search revealed that reliable values for thermodynamic properties, especially free energy of formation, are not available for these oxides. Therefore, we have used the cell technique for direct determination of the free energy change, $\Delta G°$, for the following formation reactions over the temperature ranges indicated:

$$520°\text{-}820°: \quad 2Bi\ (c) + 3/2\ O_2\ (g) = Bi_2O_3\ (c) \qquad [a]$$

$$520°\text{-}740°: \quad 2Sb\ (c) + 3/2\ O_2\ (g) = Sb_2O_3\ (c) \qquad [b]$$

$$520°\text{-}720°: \quad Te\ (c) + O_2\ (g) = TeO_2\ (c) \qquad [c]$$

* Electrochemical Society Active Member.
[1] Present address: General Electric Research and Development Center, Schenectady, New York 12309.
Key words: thermodynamic properties, solid electrolytes, galvanic cells, enthalpy and entropy of formation.

Literature Review

Rossini *et al.* (2) critically reviewed all papers published before 1952 on thermodynamic properties of Bi_2O_3, Sb_2O_3, and TeO_2, and included the best available data in their compilation. The present discussion will be, therefore, restricted mainly to the papers published in the last two decades. However, some of the earlier work reviewd by Rossini *et al.* will be mentioned whenever required for the sake of comparison. Table I presents the data selected by Rossini and coworkers in a tabular form. It also includes the results of all later investigations to be discussed below.

Bi_2O_3.—The experimental data on the Bi-O system have been compiled by Hansen (3), Elliot (4), and Shunk (5). Two stable polymorphs of Bi_2O_3 are reported to exist; the low-temperature form, α-Bi_2O_3 transforms to the high-temperature form, δ-Bi_2O_3 at about 720°C. The melting point of δ-Bi_2O_3 is 825°C.

Mah (6) has determined the heat of formation of Bi_2O_3 by combustion calorimetry. He has also calculated the entropy and free energy of formation.

Sb_2O_3.—Elliot (4) and Shunk (5) have reviewed the available thermodynamic information on the Sb-O

Table I. Published thermodynamic data for Bi_2O_3, Sb_2O_3, and TeO_2

Bi_2O_3

Property	Rossini *et al.* (2)	Kubaschewski, Evans, and Alcock (15)	Wicks and Block (16)	Mah (6)
$\Delta H°_{298}$, kcal/mole	−137.9	−137.2 ± 1.0	−137.9	−137.16 ± 0.30
$\Delta S°_{298}$, eu	—	—	—	−64.3
$S°_{298}$, eu	36.2	36.7 ± 0.7	36.2	—
$\Delta G°_{298}$, kcal/mole	−118.7	—	−118.7	−118.0

Sb_2O_3*

Property	Rossini *et al.* (2)	Kubaschewski, Evans, and Alcock (15)	Wicks and Block (16)	Gorgoraki and Tarasov (8)	Mah (7)
$\Delta H°_{298}$, kcal/mole	−166.5	−169.4 ± 1.0	−168.5	—	−169.4 ± 0.17
$\Delta S°_{298}$, eu	—	—	—	—	—
$S°_{298}$, eu	—	29.4 ± 0.6	29.4	31.65, 33.71	—
$\Delta G°_{298}$, kcal/mole	—	—	−149.1	—	−156.2 ± 0.8

TeO_2

Property	Rossini *et al.* (2)	Kubaschewski, Evans, and Alcock (15)	Schuhmann (12)	Gadzhiev and Sharifov (11)	Schneider and Zintl (10)
$\Delta H°_{298}$, kcal/mole	−77.69	−77.0 ± 1.5	−77.7	−90.6 ± 0.3	−76.9 ± 1.2
$\Delta S°_{298}$, eu	—	—	—	—	—
$S°_{298}$, eu**	16.99	19.0 ± 1.0	—	—	—
$\Delta G°_{298}$, kcal/mole	−64.60	—	−64.32	—	—

* The data quoted are for orthorhombic Sb_2O_3.
** The $S°_{298}$ data of Mezaki and Margrave (9) for TeO_2 (= 14 ± 2 eu) was not included in the table for lack of space.

system. Solid Sb_2O_3 occurs in two modifications, and the transformation temperature is reported to be 570°C. Sb_2O_3 melts at 655°C.

Using combustion calorimetry, Mah (7) has determined the heat of formation of Sb_2O_3, and calculated the entropy and free energy of formation. Gorgoraki and Tarasov (8) used adiabatic calorimetry to obtain heat capacity and enthalpy of Sb_2O_3. They calculated $S°_{298}$ values for the two modifications by graphical integration and extrapolation of their data to 0°K.

TeO_2.—The Te-O system has been reviewed by Elliot (4) and Shunk (5). TeO_2 prepared by precipitation from aqueous solution or oxidation of tellurium metal is reported to be tetragonal. The melting point of TeO_2 is 733°C.

Mezaki and Margrave (9) measured the heat contents of TeO_2 in a drop-type calorimeter over 446°-1146°K (173°-873°C). From an approximate fitting of the high-temperature heat content data with a Debye equation, they estimated $S°_{298}$ for TeO_2.

Schneider and Zintl (10) determined the heat of formation of TeO_2 by combustion of elemental tellurium in a bomb calorimeter. Gadzhiev and Sharifov (11) used the same technique but obtained a different $\Delta H°_{298}$ value (see Table I).

One of the earliest investigations of thermodynamic properties of TeO_2 deserves special attention. Schuhmann (12) in 1925 measured the emf of the cell

$$Te\text{-}TeO_2|HClO_4, H_2O|H_2, Pt$$

at 25° and 45°C, and directly measured the free energy of formation. He also estimated the heat of formation from the temperature dependence of free energy. This is the only direct free energy measurement to date for any of the three oxides under discussion.

Experimental Details

In the present investigation, the open-circuit emf of the following oxygen concentration cells were measured as a function of temperature

$$W, Bi\text{-}Bi_2O_3|0.85\ ZrO_2 + 0.15\ CaO|Air, Pt \quad [I]$$

$$W, Sb\text{-}Sb_2O_3|0.85\ ZrO_2 + 0.15\ CaO|Air, Pt \quad [IIa]$$

$$C, Sb\text{-}Sb_2O_3|0.85\ ZrO_2 + 0.15\ CaO|Air, Pt \quad [IIb]$$

$$W, Te\text{-}TeO_2|0.85\ ZrO_2 + 0.15\ CaO|Air, Pt \quad [III]$$

For cells of these types, the open-circuit emf (after necessary thermal emf corrections) is related to the equilibrium oxygen partial pressures at the two electrodes by the expression

$$E = \frac{RT}{4F} \ln [P'_{O_2}/P''_{O_2}];\ P'_{O_2} > P''_{O_2}$$

where P'_{O_2} = oxygen pressure at the reference electrode (air) = 0.21 atm; P''_{O_2} = oxygen pressure at the metal-metal oxide electrode for the experimental temperature, T; and all of the other symbols have their usual meaning.

Since the oxygen partial pressure for a metal-metal oxide equilibrium is related to the free energy of formation of the oxide, we obtain the following emf-free energy relations for the cells under consideration

$$\Delta G°_{Bi_2O_3} = -6FE_I + 1.5\ RT \ln (0.21) \quad [1]$$

$$\Delta G°_{Sb_2O_3} = -6FE_{II} + 1.5\ RT \ln (0.21) \quad [2]$$

$$\Delta G°_{TeO_2} = -4FE_{III} + RT \ln (0.21) \quad [3]$$

where the subscripts in $\Delta G°$ refer to the reactions [*a*], [*b*], and [*c*], respectively, and the subscripts in E refer to the cells [I], [IIa-IIb], and [III], respectively.

The cell assemblies used in the four experiments were similar. Figure 1 shows the main features of a typical set-up. The entire assembly was placed inside a quartz protection tube. The open end of the calcia-stabilized zirconia electrolyte tube was sealed to a vacuum manifold with epoxy. One end of a short platinum lead wire was brought out through the epoxy seal, and the other end was spot-welded to a tungsten lead wire (cells [I], [IIa], and [III]) or force-fitted to a graphite rod (cell [IIb]). For cell [I], the tungsten lead wire could be allowed to remain in contact with the $Bi\text{-}Bi_2O_3$ electrode for the entire duration of the experiment since no reaction between tungsten and bismuth was observed. This conclusion could be deduced from the fact that identical emf values were observed during repeated heating and cooling cycles.

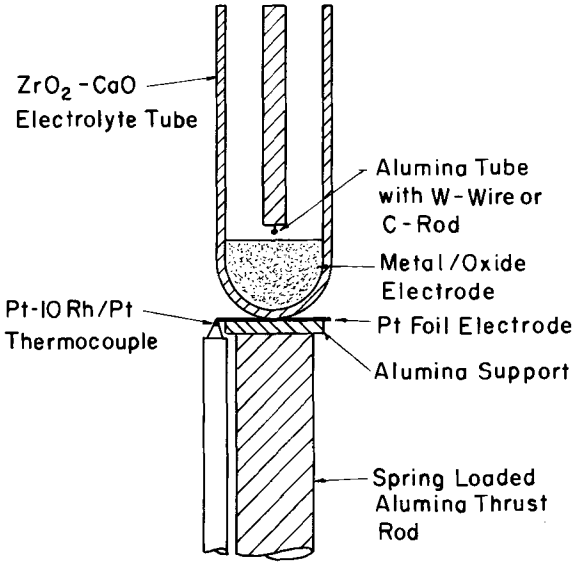

Fig. 1. Cell assembly (schematic)

Liquid antimony metal was found to slowly react with tungsten. It was therefore necessary to avoid prolonged contact between these two metals, or to seek a new lead element that would not react with liquid antimony. A minor modification in the cell design allowed us to raise or lower the tungsten lead wire into the $Sb\text{-}Sb_2O_3$ electrode only during emf measurements. This was accomplished by attaching a piece of soft iron to the tungsten wire, and moving the iron piece with an externally located magnet. This procedure prevented any appreciable tungsten dissolution from taking place. The cell where this technique was adopted is designated cell [IIa]. An alternative cell, denoted as cell [IIb], made use of a graphite rod as the lead element. The graphite rod was allowed to remain in contact with the molten electrode. As will be discussed later, the results obtained with cells [IIa] and [IIb] were consistent.

The reaction between tungsten and liquid tellurium was found to be rapid in agreement with earlier observations (13). Attempts to use graphite lead element were not successful since it quickly reduced TeO_2 to the liquid metal. It was, therefore, necessary to lower the tungsten lead wire into the electrode melt only when an emf measurement was desired, as in cell [IIa]. This procedure kept the electrode contamination to a minimum; the tungsten-content of the $Te\text{-}TeO_2$ electrode at the end of the experiment was found to be less than 30 ppm. The error in the free energy measurements due to electrode contamination is estimated to be less than 10 cal/mole.

In a typical experiment, the cell was placed in a wire-wound furnace at room temperature and assembled under a fume hood because of the toxic nature of the fumes involved in some of these systems. The metal-metal oxide electrodes were prepared by mixing the metal granules with the oxide powder in about 5:1 volume ratio. The mixture was then placed in the electrolyte tube and the tube closed off. The system was slowly heated to above 500°C, and the emf measurement was started. A DORIC integrating-type digital voltmeter (Model DS-100) was used to measure the

Table II. Details of electrode materials

Material	Source	Grade/purity
Bi	Fisher Scientific Company	Certified (>99.9%)
Bi_2O_3	Fisher Scientific Company	Certified (>99.9%)
Sb	Fisher Scientific Company	Certified (>99.9%)
Sb_2O_3	Matheson, Coleman, and Bell	Reagent (>99%)
Te	Alfa Inorganics	99.99%
TeO_2	Prepared by oxidation of Te metal in our laboratory	≈99.9%

open-circuit cell emf to a precision of 0.1 mV. The high input impedance of this voltmeter prevented loading of the cell and allowed reversible measurements. On reaching the desired temperature, the cell emf assumed a stable value within about half an hour. The emf remained constant to within ±1 mV for 24 hr or longer if allowed. The reversibility of the measured emf was checked frequently by shorting the cell for about 10 sec, and then allowing the emf to return to a stable value. The cell emf always returned to the original value within a minute. Once a constant cell emf was obtained for a controlled temperature, the set point of the controller (Tem-Pres Research Inc., Model CP-1V-M) was changed to a new value and the sequence of measurements was repeated. In the present investigation, the cell temperatures could be controlled to within ±2°C.

A typical experiment consisted of many heating and cooling schedules, and lasted from one to two weeks. The electrolyte tubes did not crack on thermal cyclings of this type.

The 15 m/o (mole per cent) CaO-stabilized ZrO_2 tubes were purchased from Zirconium Corporation of America. The tubes were 12 in. long with an outer diameter of 1/2 in. and wall thickness of 1/16 in. and were certified to be helium leak tested to 5×10^{-7} or less standard cubic centimeter per second at room temperature by the manufacturer. Tubes of this type from the same manufacturer have been shown to be acceptable as electrolyte materials for oxygen concentration cells (14).

Table II lists the electrode materials used in this study, their sources, and purity levels claimed by the suppliers.

Since the cells used in the present work employed dissimilar lead elements, the observed emf data had to be corrected for the thermal emf generated between tungsten and platinum (cells [I], [IIa], and [III]) or carbon and platinum (cell [IIb]). Couples of these types were, therefore, prepared and their thermal emf measured over wide temperature ranges. The system used to measure the thermal emf for the W-Pt couple is schematically shown in Fig. 2. Only minor modifications were necessary for the C-Pt couple. Thermal emf experiments were conducted in helium atmospheres to prevent the non-noble element from oxidation.

Results and Discussion

Figures 3, 4, and 5 present the emf-temperature data from cells [I], [IIa-IIb], and [III], respectively. Within the limits of experimental uncertainties, the emf-temperature plots are linear. It should be pointed out that for cells [I] and [III], the sample electrodes consisted of a liquid metal (Bi or Te) and a solid oxide (Bi_2O_3 or TeO_2). No phase transformations involving large heat effects (such as fusion) occurred in these cells over the temperature ranges selected. Linear emf-temperature plots are therefore expected for these cells. On the other hand, for cells [IIa] and [IIb], the sample electrode consisted of Sb(s) and Sb_2O_3(s) below 631°C, Sb(l) and Sb_2O_3(s) below 655°C but above 631°C, and Sb(l) and Sb_2O_3(l) above 655°C. The emf-temperature plots for these cells are thus expected to consist of three linear segments. However, the heat effects due to the melting of the metal and of the oxide tend to cancel each other. Moreover, the melting points of Sb and Sb_2O_3 are quite close (within 25°C). The emf-temperature plots for cells [IIa] and [IIb] thus appear as single straight lines over the entire temperature range.

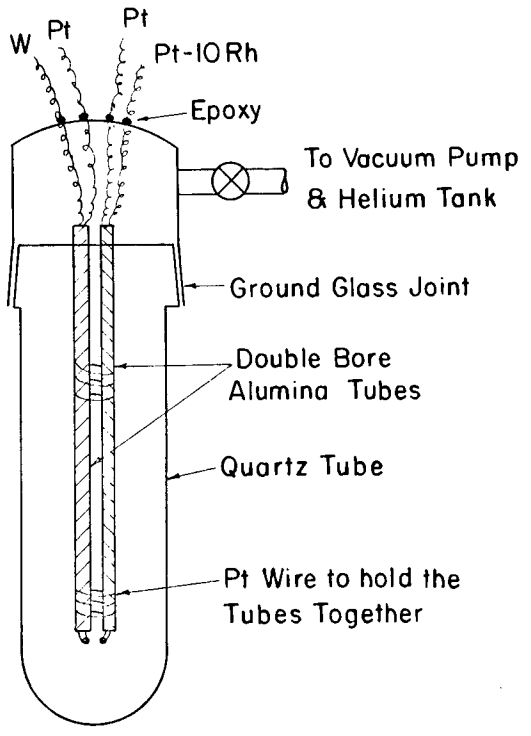

Fig. 2. Experimental arrangement for thermal emf measurements

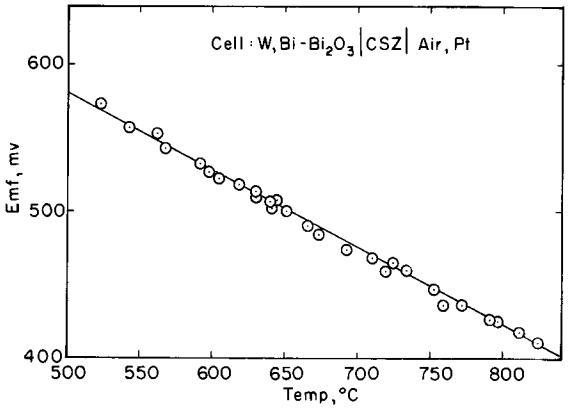

Fig. 3. Emf-temperature data from cell [I]

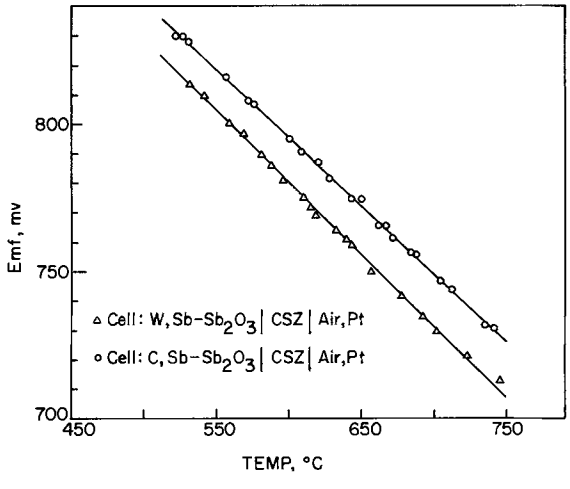

Fig. 4. Emf-temperature data from cell [11a] and cell [11b]. The difference in emf of the two cells is due to different lead wire combinations (W-Pt and C-Pt).

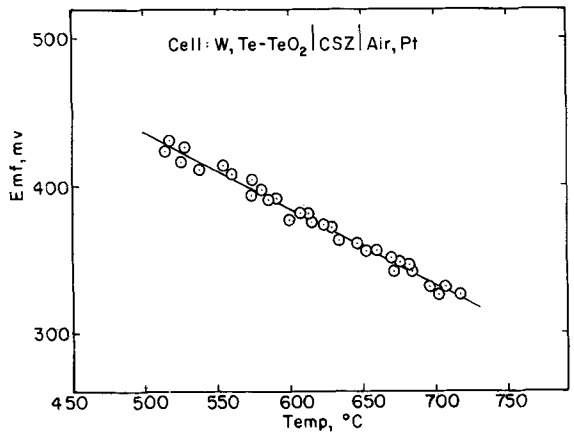

Fig. 5. Emf-temperature data from cell[III]

As mentioned earlier, the data presented in Fig. 3, 4, and 5 had to be corrected for thermal emf's due to dissimilar lead elements. The results of our thermal emf measurements on W-Pt and C-Pt couples are shown in Fig. 6 and 7, respectively. Table III presents the emf-temperature relationships for the cells under consideration before and after thermal emf corrections. It is obvious from Table III that the accuracy of the present emf measurements was high. The consistency between the cell [IIa] and cell [IIb] data is also good; at 900°K, the two sets of measurements agree within ±3 mV after necessary thermal emf corrections.

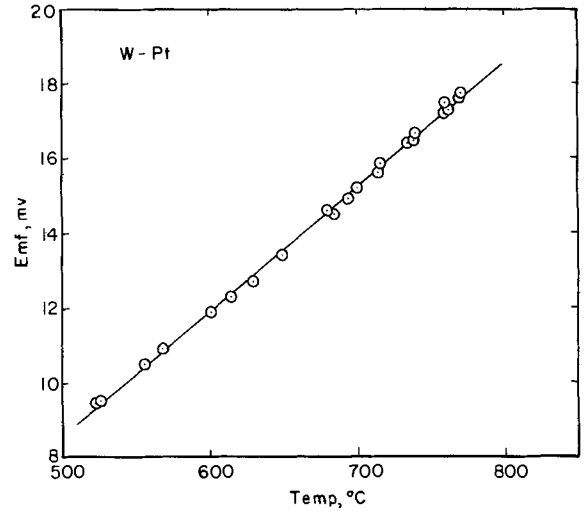

Fig. 6. Thermal emf of W-Pt couple as a function of temperature

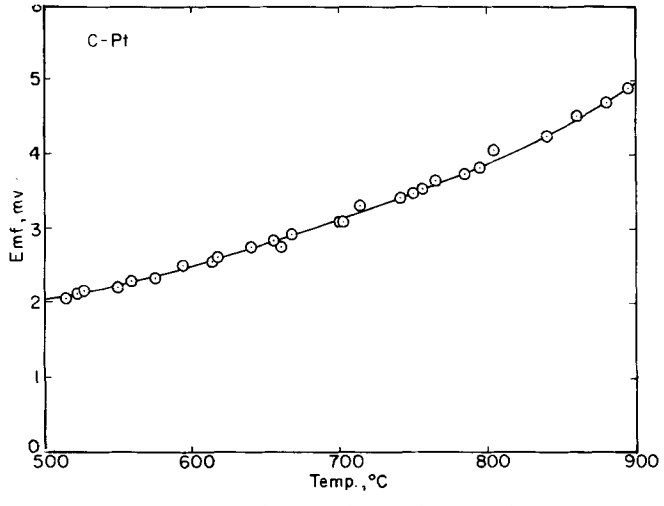

Fig. 7. Thermal emf of C-Pt couple as a function of temperature

Table III. EMF-temperature relationships for the cells under investigation

Cell No.	E (mV) = A-BT (K°) Emf data before thermal emf correction	Standard deviation	Emf data after thermal emf correction	Standard deviation
[I]	E = 989.0 − 0.529T	±0.6	E = 967.6 − 0.492T	±1.0
[IIa]	E = 1201.2 − 0.482T	±0.4	E = 1179.8 − 0.445T*	±0.5
[IIb]	E = 1197.9 − 0.461T	±0.3	E = 1195.6 − 0.455T*	±0.5
[III]	E = 835.7 − 0.517T	±0.7	E = 814.3 − 0.480T	±1.0

* E_{II} = 1/2 [$E_{[IIa]}$ + $E_{[IIb]}$] = 1187.7 − 0.450T ± 3.0 mV.

The corrected emf-temperature relationships given in Table III were used to obtain the following free energy-temperature expressions for the formation reactions [a], [b], and [c]

$$\Delta G^\circ_{Bi_2O_3} = -133{,}890 + 63.43T \pm 140 \text{ cal/mole}$$

$$\Delta G^\circ_{Sb_2O_3} = -164{,}340 + 57.62T \pm 400 \text{ cal/mole}$$

$$\Delta G^\circ_{TeO_2} = -75{,}120 + 41.18T \pm 100 \text{ cal/mole}$$

When a linear relation is found to exist between the free energy of reaction and the temperature, the slope of the line represents the entropy and the intercept the enthalpy of the reaction. The above equations, therefore, not only give reliable free energy values, but also offer working values for the enthalpy and entropy of formation for the three reactions at high temperatures.

It is possible to calculate standard thermodynamic properties for the three oxides under discussion from our high-temperature data. Such calculations are useful in providing a common basis for comparing results from different investigations. For such calculations to be of any real value, it is imperative that accurate heat capacity and heat of fusion data be available for the metals and oxides being studied. Unfortunately, only estimated heat capacity and heat of fusion values are available for some of our materials (15). Nevertheless, calculations were carried out for the three oxides taking all heat effects into account. Table IV presents the results of our extrapolation from the mean experimental temperatures. A comparison of our results with the available literature data (Table I) reveals large differences. The differences are too large to be totally attributed to the inaccuracy of published thermochemical data. Our calculated results are probably less accurate than the direct calorimetric measurements of Mah (6, 7), since our method is an indirect one. The high-temperature free energy values, however, are the first reported values obtained from direct experimental data.

Summary

The solid electrolyte cell technique has been successfully employed for the direct determination of the free energy of formation of Bi_2O_3, Sb_2O_3, and TeO_2 at temperatures above 520°C. Since the cells consisted of liquid metal-oxide electrodes, platinum lead wire was found unsuitable. The problem of electrode-lead wire interaction and methods used to minimize it have been discussed.

Table IV. Thermodynamic properties of Bi_2O_3, Sb_2O_3, and TeO_2 from the present investigation*

Property	Bi_2O_3 (s)	Sb_2O_3 (s)	TeO_2 (s)
ΔH°_{298}, kcal/mole	−131.6 ± 0.5	−158.1 ± 1.0	−72.0 ± 0.5
ΔS°_{298}, eu	−59.2 ± 2.0	−52.8 ± 3.0	−37.5 ± 3.0
S°_{298}, eu	41.4 ± 2.0	42.5 ± 3.0	23.4 ± 2.0
ΔG°_{298}, kcal/mole	−144.0 ± 1.0	−142.4 ± 2.0	−60.8 ± 1.0

* Heat capacity, heat of fusion, and standard entropy values needed in the calculations were obtained from the tables given by Kubaschewski *et al.* (15).

The high-temperature free energy data obtained in the present investigation were used to calculate the thermodynamic properties for the three oxides at 298°K. The calculations depended in part on the accuracy of the published thermochemicl data.

Acknowledgment

Financial assistance from the Air Force Systems Command in the form of National Research Council Associateship is gratefully acknowledged by one of the authors (D. C.).

Manuscript submitted Aug. 14, 1972; revised manuscript received Jan. 23, 1973. This was Paper 17 presented at the Miami Beach, Florida, Meeting of the Society, Oct. 3-8, 1972.

Any discussion of this paper will appear in a Discussion Section to be published in the June 1974 JOURNAL.

REFERENCES

1. K. Kiukkola and C. Wagner, *This Journal*, **106**, 379 (1957).
2. F. D. Rossini, D. D. Wagman, W. H. Evans, S. Levine, and I. Jaffe, "Selected Values of Chemical Thermodynamic Properties," NBS Circular 500, February (1952).
3. M. Hansen, "Constitution of Binary Alloys," McGraw-Hill Book Co., Inc., New York (1958).
4. R. P. Elliot, "Constitution of Binary Alloys, First Supplement," McGraw-Hill Book Co., New York (1965).
5. F. A. Shunk, "Constitution of Binary Alloys, Second Supplement," McGraw-Hill Book Co., New York (1969).
6. A. D. Mah, *U.S. Bur. Mines Rept. 5676* (1961).
7. A. D. Mah, *U.S. Bur. Mines Rept. 5972* (1962).
8. E. A. Gorgoraki and V. V. Tarasov, *Tr. Mosk. Khim.-Tekhnol. Inst.*, **49**, 11 (1965); *C. A.*, **65**, 3094b (1966).
9. R. Mezaki and J. L. Margrave, *J. Phys. Chem.*, **66**, 1713 (1962).
10. A. Schneider and G. Zintl, *Z. Anorg. Allgem. Chem.*, **308**, 290 (1961).
11. S. N. Gadzhiev and K. A. Sharifov, *Izv. Akad. Nauk. Azerb. SSR, Ser. Fiz. Mat. i. Tekhn. Nauk*, No. 1, 47 (1962); *C. A.*, **57**, 4114i (1962).
12. R. Schuhmann, *J. Am. Chem. Soc.*, **47**, 356 (1925).
13. L. H. Brixner, *J. Inorg. Nucl. Chem.*, **24**, 257 (1962).
14. G. G. Charette and S. N. Flengas, *This Journal*, **115**, 796 (1968).
15. O. Kubaschewski, E. Ll. Evans, and C. B. Alcock, "Metallurgical Thermochemistry," 4th ed., Pergamon Press, Oxford (1967).
16. C. E. Wicks and F. E. Block, *U.S. Bur. Mines Bull. 605* (1963).

Formation and Surface Characteristics of Hydrous Metal Oxide Sols

Egon Matijević, Alexander Bell, Roger Brace, and Peter McFadyen

Institute of Colloid and Surface Science and Department of Chemistry, Clarkson College of Technology, Potsdam, New York 13676

ABSTRACT

Methods for preparation of chromium(III), aluminum, and zirconium(IV) hydrous oxide sols consisting of spherical particles, and of copper(I) oxide sols of cubic particles, have been described. Under certain experimental conditions the particle size distribution is very narrow. Various properties of these sols are described and the mechanism of their formation and particle growth discussed.

Precipitation of metal hydroxides or, more appropriately, of metal hydrous oxides, is of continuing interest in various applications such as corrosion, water pollution, and catalysis. Although numerous studies have been initiated throughout the years attempting to elucidate the chemistry and physics of the formation of these systems, the results have been largely qualitative owing to the complex kinetics and equilibria involved. Numerous difficulties are encountered in the investigations of hydrous metal oxide precipitations. For example, the solids formed are generally amorphous; additional chemical reactions (hydrolysis, condensation, complexation, etc.) occur which may affect nucleation and particle growth; the extent of precipitation is highly dependent upon concentration, pH, temperature, and time (1). Furthermore, the particles produced are mostly of irregular shape and of broad size distribution. This makes it very difficult to characterize, on a quantitative basis, the particle formation, growth, surface properties, and sol stability (when the hydrous metal oxides appear in the colloidal state).

Ideally, the particles should be of simple shape (*e.g.*, spherical, cubic), of narrow size distribution ("monodispersed"), and stable enough so that their composition and properties, such as surface charge, might readily be determined. In addition, the electrolyte environment from which the particles are formed or in which they are suspended often contains complex solute species. These must be sufficiently inert (kinetically) to make their separation and identification possible, often via a variety of suitable analytical techniques (2).

Despite innumerable studies dealing with precipitation of various hydrous metal oxides, the methods for generation of hydrosols of these materials, uniform in size and shape, have only recently been described. "Monodispersed" chromium hydroxide sols consisting of spherical particles (3-5) and copper(I) oxide sols consisting of cubic particles (6) can now be reproducibly prepared over a range of modal size parameters. In addition to this work the preparation of "monodispersed" aluminum hydrous oxide sols having spherical particles will be described for the first time. Finally, preliminary work shows that zirconium hydrous oxide sols of spherical particles can also be produced. All these systems were obtained by aging of salt solutions of the corresponding metal ions at elevated temperatures in the presence of certain complexing anions. Many of the sols are of sufficient uniformity to show higher order Tyndall spectra (HOTS), which in the case of the chromium and aluminum hydrous oxides, permits a particle size distribution anal-

Key words: chronomal, electrophoresis, monodispersed sols, particle growth, penetrating anions, precipitation.

ysis and an estimation of the number concentration *in situ* from light-scattering measurements.

As well as describing the methods for the preparation of these "monodispersed" metal hydrous oxide sols and some of their characteristics, we will report here in greater detail recent studies on the kinetics of the formation and growth of the solids from chromium salt solutions. These shed some light on the mechanism of the hydrous metal oxide particle formation which has been hitherto very poorly understood.

Preparation of Metal Hydrous Oxide Sols of Narrow Size Distribution

Materials.—All chemicals were reagent grade and used without further purification. Generally, the stock solutions were filtered through Millipore filters (for Cr salt solutions, 1.2 μm; and for copper and aluminum salt solutions 0.2 μm), although for experiments involving Cr(III) solutes, filtration does not appear to be necessary to ensure reproducibility. An assay of all stock solutions was made by means of standard analytical methods. Water was distilled twice, the second time in an all glass apparatus. Pyrex culture tubes with Teflon-lined, screw-type caps were employed as reaction vessels.

Techniques.—Light-scattering data were obtained in a Brice-Phoenix photometer Model 2000. When possible, the particle size distribution was determined *in situ* from the polarization ratios of the scattered light using a method described earlier (7).

The histograms of all sols having particles of uniform shape and narrow size distribution were obtained from electron microscopy. Samples were prepared by placing a drop of the suspension on a collodion-covered copper grid and removing the liquid with a micropipette after several minutes. It could be shown that the size distributions determined by electron microscopy and by light scattering (in cases in which the latter technique was applicable) were in excellent agreement (8).

The change in light-scattering intensities was also employed to determine the precipitation boundaries. In the latter case, in a series of systems the concentration of the metal salt was kept constant whereas the *p*H was changed systematically in small increments. A plot of scattering intensity *vs.* *p*H showed a sharp increase at the *p*H at which solid phase first formed. The critical *p*H of precipitation for a given metal ion concentration was determined by extrapolation of the line of steepest slope to that of the homogeneous solutions.

Electrophoretic mobilities were measured in a microelectrophoresis apparatus with a van Gils cell.

The concentration of chromium in the dispersion medium after the removal of sol particles by filtration was determined by atomic absorption spectroscopy in a blue flame (9). Samples heated for 1 hr (and filtered) were used as standards.

All *p*H adjustments were made by means of glass-calomel combination electrodes. Where necessary the *p*H was measured at higher temperatures (75°C) and the combination electrode (Beckman 39500) was appropriately standardized with a KH-phthalate buffer.

Procedures.—The chemical composition, the morphological characteristics, and the surface properties of precipitated metal hydrous oxides depend on a number of experimental parameters, the most important among these being the concentration of the metal salt, the presence of complexing species (particularly of certain anions), *p*H, temperature, time of aging, method of mixing, and in some instances, the history of the solution preparation.

To illustrate some of these effects, with special reference to particle size and shape of the precipitated metal hydrous oxides, Fig. 1 gives a copper(II) sulfate concentration-*p*H precipitation domain (10). The systems on the left and right were aged for 18 hr at 25°C and 75°C, respectively. In region I (Fig. 1) solutions remain homogeneous; in region II (Fig. 1) a pale blue precipitate is formed consisting of the basic copper sulfate, $Cu_4(OH)_6SO_4$, whereas in region III (Fig. 1) the red-brown particles are tenorite, CuO. Dashed lines in Fig. 1 show calculated boundaries between regions I/II and II/III using corresponding equilibrium constants given by Barton and Bethke (11). The experimental and calculated boundaries for systems aged at 75°C (and then cooled to 25°C) are in reasonably good agreement whereas no such correlation was found for the systems aged at 25°C. Obviously, in the latter case the aging period was too short for the equilibrium to be established.

Also included in the various regions of the precipitation domain are the electron micrographs of the corresponding sols. The particle sizes and shapes change considerably with the concentration of the precipitating components and the temperature of aging. Quite uniform, oval-shaped particles were obtained by aging at 75°C solutions containing $CuSO_4$ and NaOH in the molar ratio of 1:2, these particles are shown in the electron micrograph at the extreme right of Fig. 1. They were not observed when a similar procedure was followed with $Cu(NO_3)_2$ in place of the copper(II) sulfate. However, using copper(II) nitrate solution to which sodium sulfate had been added, such that the sulfate concentration was equal to that of Cu^{2+}, very similar particles were again formed, strongly pointing to the role SO_4^{2-} ions play in their production.

Needless to say the precipitation domains obtained with solutions of salts of other metals show different boundaries because in each case the composition of the solid separated, and the composition of the solute complexes in the dispersion medium may vary considerably. Also the rates of formation and thermodynamic properties will differ.

The involved nature of metal hydrous oxide precipitation processes is most likely the reason that "monodispersed" sols containing particles of simple shapes (*i.e.*, spheres or cubes) have been reported only recently (3-6). It is therefore, even more remarkable that we have succeeded in the preparation of such sols of several metals. Significantly, certain conditions resulting in systems of narrow size distribution are similar in all cases. The metal salt solutions from which the sols form must be hydrolyzed, usually at elevated temperatures, for extended periods of time. More importantly these sols are produced only in the presence of certain coordinating or "penetrating" ions. In this regard, sulfate ions seem to play a special role, although preparations of monodispersed chromium hydroxide sols were successful also in the presence of phosphate ions (4). This would indicate that a similar mechanism underlies the formation of hydrous oxides of different metals, which, if resolved, would help in understanding many phenomena involving these materials.

Essential procedures for the preparation of metal hydrous oxide sols of narrow size distribution are given below.

Chromium(III) hydrous oxide sols were obtained if solutions of chrom alum or solutions containing chromium(III) nitrate and alkali sulfate were kept at 75.0° ±0.3°C for an extended period of time (from several hours to several days), after which the sample tubes were immersed in ice water and cooled to room temperature (3-5). An electron micrograph of such a sol is given in Fig. 2a. Uniform spherical particles could also be formed directly in the electron microscope if solutions of chrom alum were exposed to the electron beam in a "wet cell" (8, 12).

Similarly, aluminum hydrous oxide sols consisting of spherical particles uniform in size form upon aging at elevated temperatures of aluminum salt solutions. The latter contain either aluminum sulfate or aluminum nitrate to which sodium sulfate was added in concentrations approximating the aluminum sulfate

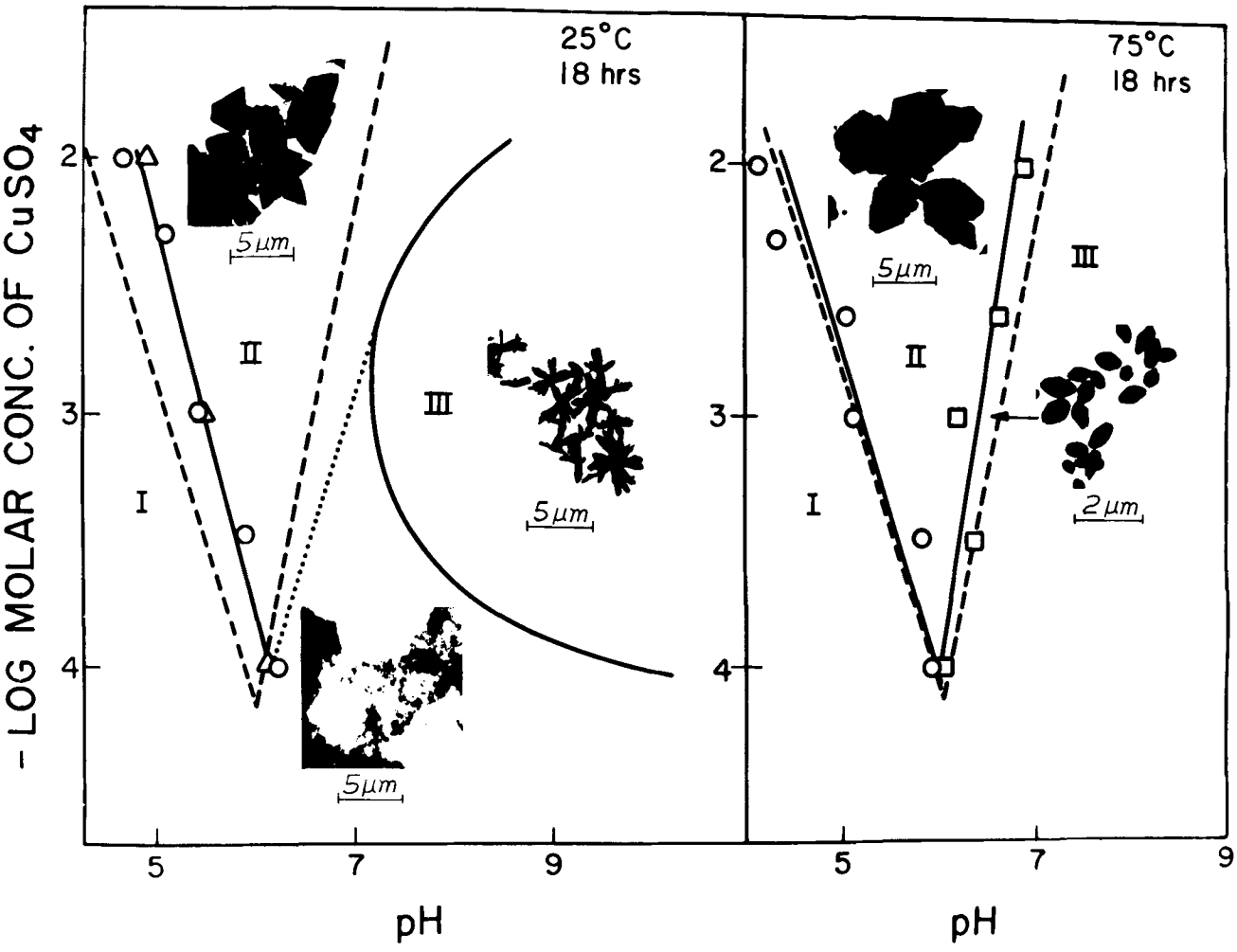

Fig. 1. Precipitation domains of copper sulfate as a function of pH for systems aged for 18 hr at 25°C (left) and at 75°C (right). Region I, homogeneous solution; region II, blue precipitate; region III, red-brown precipitate. Solid lines indicate boundaries between the various regions, the individual experimental data points being represented by the circle and the box symbols. (The triangles indicate data obtained with the ion-specific electrode.) The theoretical boundaries are indicated by the dashed lines; the dotted line indicates the boundary between the regions of large and small particles within region II at 25°C. The electron micrographs show particles typical of those formed thoughout the corresponding region except for the one at the extreme right, for which the preparation conditions are indicated by the arrow.

stoichiometry. The major difference as compared to the chromium hydrous oxides is in regard to the temperature of aging, which for aluminum salt solutions had to be in excess of ~90°C. Also in the latter case the rate of heating the solutions to the equilibrium temperature seemed to be important for the production of monodispersed sols. In the present work the rate of temperature rise was ~0.5°C/min during the first 2-3 hr of aging. In contrast, chromium salt solution, if chosen in proper concentrations, gave monodispersed sols regardless of how quickly they reached thermal equilibrium. An example of the aluminum hydrous oxide sols prepared as described above is shown in Fig. 2b.

The latest experiments indicate that similar sols can be obtained by hydrolysis of aluminum alkoxides at elevated temperatures if the pH and the sulfate concentrations are carefully adjusted.

Zirconium(IV) sulfate solutions on aging at 75°C also give sols containing spherical particles although in this case only sols of rather broad distribution have been obtained so far (Fig. 2c).

In all preceding cases the sols consisted of spherical particles. All attempts to produce similar copper hydrous oxide sols failed. However, it was possible to prepare copper(I) oxide hydrosols having cubic particles of narrow size distribution. Again the presence of complexing solutes seemed to be essential as such sols were obtained by reduction of an alkaline solution of copper tartrate complex (diluted Fehling's solution) with glucose (10). This reaction does not proceed stoichiometrically due to the changes in the sugar molecule caused by the alkaline medium (13) and the glucose concentration used actually was in excess in all cases. The solutions were mixed and heated rapidly until precipitation occurred (at about 92°C) and then cooled in an ice-water mixture. Typical particles are shown in Fig. 2d.

The conditions which will result in systems of narrow size distribution and uniform particle shape are rather restricted. As a rule such sols form over a narrow pH range just above the solubility boundary. By far the greatest effect on their appearance has been the concentration of the complexing solute, particularly of the sulfate ion. To illustrate this, Fig. 3 gives the reactant concentrations of a number of solutions containing aluminum and sulfate ions which were heated at 99°C for 40 hr in order to establish in which of these monodispersed sols are formed. At the end of the aging period systems designated by triangles showed no separation of the solid phase, whereas aluminum hydrous oxide separated in all other systems. Black circles (Fig. 3) designate sols exhibiting higher order Tyndall spectra (HOTS), which are most sensitive indicators for the presence of particles of rather narrow size distribution, particularly of spheres in the micron diameter range. It can be seen that "monodispersed" sols are obtained at aluminum ion concentrations from 2×10^{-4} to 6×10^{-3}F but only when sulfate ions were present to give an aluminum

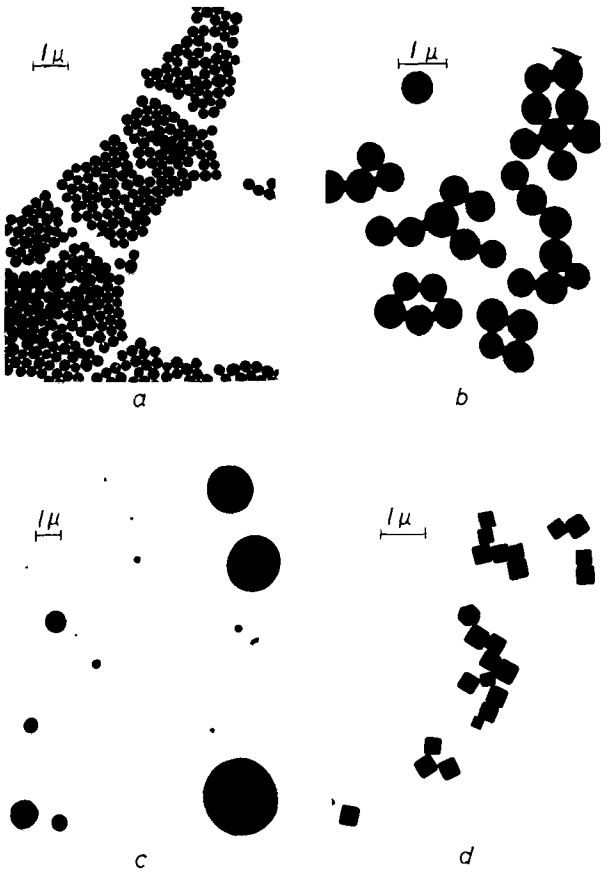

Fig. 2. Electron micrographs of various metal hydrous oxide sol particles obtained by aging of (a) chrom alum, 4 × 10^{-4}F, at 75°C; (b) aluminum sulfate, 1 × 10^{-3}F, at 99°C; (c) zirconium (IV) sulfate, 5 × 10^{-3}F, at 75°C; and (d) Cu_2O sol formed by reduction of Fehling's solution by glucose.

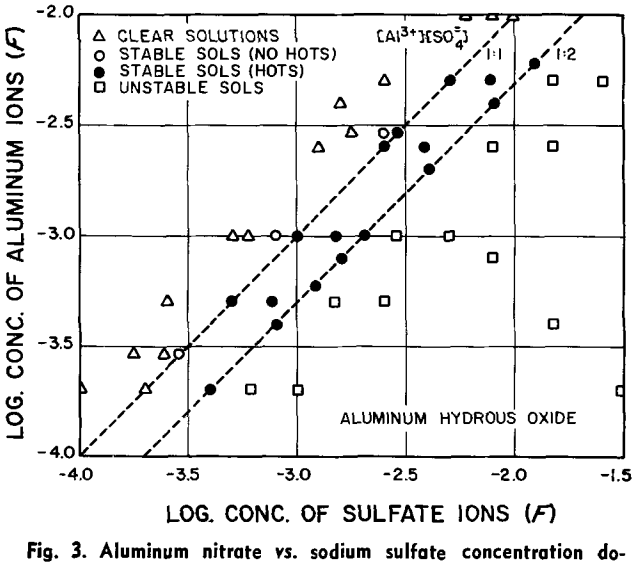

Fig. 3. Aluminum nitrate vs. sodium sulfate concentration domain of solutions aged for longer than 24 hr at 99°C resulting in △ no sol formation; ○ stable sols, small particles; ● sols showing HOTS; □ coagulated and settled sols.

to sulfate ratio between 1:1 and 1:2 (delineated by dashed lines). In larger excess of sulfate ions the particles grow considerably larger and in many cases flocculate and settle (indicated by squares). The pH in all systems showing HOTS was self-adjusted and upon aging and cooling of the sols to room temperature ranged from 3.1-3.5, the lower values being for systems of higher aluminum ion content. The great effect of pH on the formation of monodispersed metal hydrous oxides was demonstrated earlier with chromium hydroxide sols (4).

The size of the sol particles depends on the reactant concentrations. Again, in this regard, the complexing anion exhibits a considerable effect. Figure 4 (left) shows that the modal diameters of the spherical aluminum hydrous oxide particles increase with increasing sulfate concentration in the solution from which the sols are formed. Interestingly, at a given sulfate concentration the modal diameter does not seem to change if the aluminum ion concentration is varied over the narrow range which produces sols exhibiting HOTS. Similar observations have been made with the chromium hydroxide sols to be described in greater detail below.

The effect of the Cu^{2+} ion concentration on the edge length of cubes prepared by reduction of the Fehling's solutions is shown in Fig. 4 (right). In this case, the modal particle size is strongly affected by the metal ion concentration if the concentration of glucose is kept constant.

Properties of Monodispersed Metal Hydrous Oxide Sols

Because of their reproducibility and well-characterized morphology the metal hydrous oxides of narrow size distribution lend themselves uniquely to the study of their sol stability and of particle surface properties.

Whereas sol particles generated from solutions of chromium salts remain unchanged once formed, the aluminum hydrous oxide particles produced at higher temperatures (>90°C), slowly redissolve upon cooling to 25°C. The latter sols can, however, be permanently stabilized against dissolution if, after their formation, the pH is changed to ~10. No secondary precipitation of aluminum hydrous oxide takes place as the pH is made sufficiently high to complex excess aluminum ions in the form of solute aluminate species.

The pH of all sols prepared by aging as described earlier has been lower than the corresponding zero point of charge (ZPC); thus, the particles carry a positive charge. The surface charge can be readily altered by changing the pH of the medium. Consequently pH exercises a significant effect on sol stability. In general the sols coagulate when the pH is adjusted to be around the ZPC of a given system. However, they peptize completely if pH is sufficiently high or low to give strongly charged particles. Figure 5 shows the electrophoretic mobilities as a function of pH of three different sols. The ZPC of hydrous chromium and aluminum oxides are in agreement with the "best" values cited by Parks (14); the corresponding value

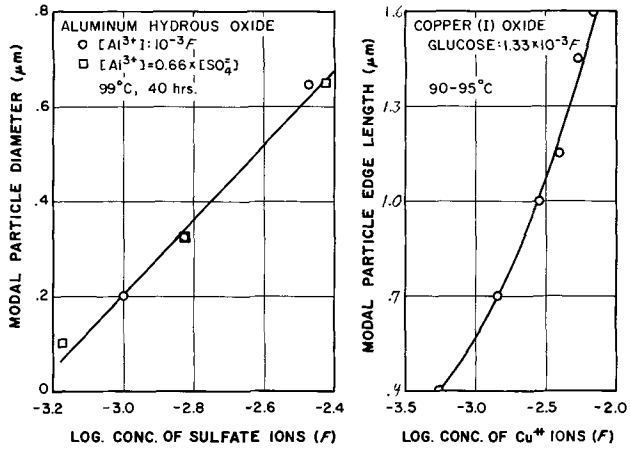

Fig. 4. Left, modal particle side of aluminum hydrous oxide sols formed by aging solutions containing 1 × 10^{-3}F Al (III) at 99°C in the presence of varying sulfate concentrations (○) and from a range of aluminum concentrations at a constant aluminum/sulfate ratio (□). Right, modal particle size of copper (I) oxide sols as a function of initial Cu(II) concentrations in the presence of constant initial concentration of glucose.

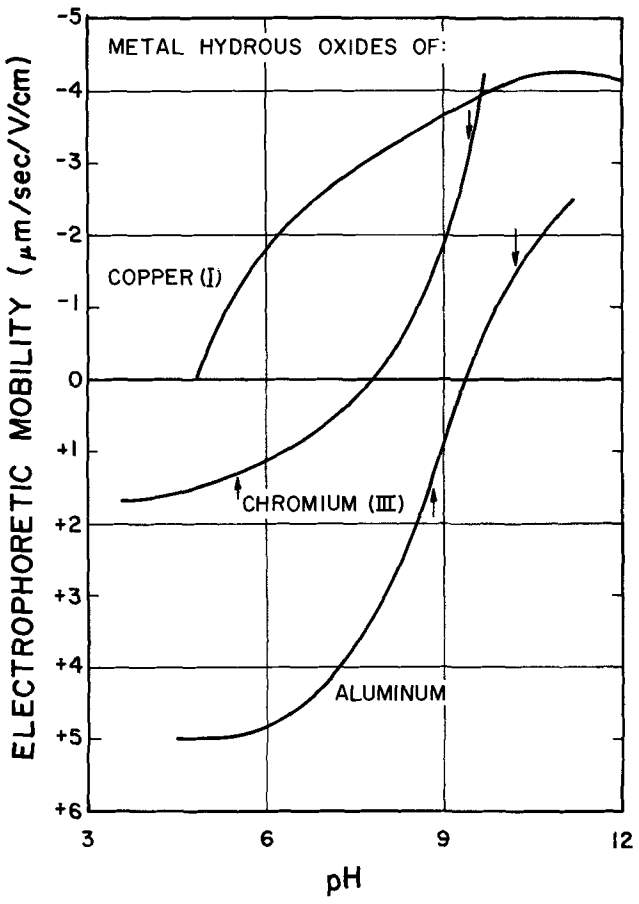

Fig. 5. Electrophoretic mobilities of monodispersed copper (I) oxide, chromium (III), and aluminum oxide particles as functions of pH at 25°C; between arrows, sols flocculate.

for copper(II) hydrous oxide is much lower than that reported elsewhere. Within the pH range indicated by arrows the chromium and aluminum hydrous oxide sols coagulate whereas outside of this range the sols remain stable.

Data for the aluminum hydrous oxide were obtained on a sol which was washed to remove the excess of reactant ions and then resuspended in solutions of different pH values. The original sol in the presence of sulfate ions showed much lower positive or higher negative mobilities as compared to the "washed" sol at the same pH values. The effect of sulfate ions is similar to that reported earlier on corundum in the presence of various anions (15). More recently, Alwitt showed a considerable influence of certain anions on the mobilities of pseudoboehmite (16).

The "monodispersed" sols could also be used to establish whether the particle size remains the same when pH, and consequently the charge, is changed. For this purpose the chromium(III) hydrous oxide sols are best suited since the light scattering could be used to establish the particle size distribution *in situ* with great precision (3, 8). A sol consisting of uniform, spherical, positively charged particles was prepared by aging chrom alum solutions at low pH and then the pH was increased sufficiently to give a stable sol of negatively charged particles. The size distribution was determined by light scattering before and after recharging. Both the modal particle diameter and the size distribution of chromium hydroxide sols remained essentially unchanged (Table I).

Kinetics of Formation and Growth of Chromium Hydrous Oxide Sols

The results described above showed that metal hydrous oxide sols of uniform size and shape may now be reproducibly prepared, although the conditions

Table I. Size distribution parameters and mobilities of a chromium hydroxide sol [4×10^{-4}M solution of $CrK(SO_4)_2$ aged for 21 hr at 75°C] at different pH

pH (25°C)	3.80	9.60
Particle diameter (μm)	0.314	0.318
Width of the size distribution, σ	0.12	0.10
Mobility (μm/sec/V/cm)	+1.48	−4.18

are somewhat restricted. These sols are suitable for the study of kinetics of particle formation and growth, since most theories apply to monodispersed systems of spherical particles. For this purpose chromium hydrous oxide seems to be most convenient since it is the least sensitive system to the changes in the experimental conditions (such as the rate of heating or the presence of impurities, etc.) leading to the formation of monodispersed sols. Also the complexes formed in chromium salt solutions are sufficiently kinetically inert (2, 5) to allow their identification.

Effect of sulfate ion concentration.—A previous study (5) described the change of particle diameter and of the content of soluble chromium species in a 4.0×10^{-4}F solution of chrom alum as a function of time of aging at 75°C. Here the effects of changing the sulfate concentration (added as sodium sulfate) at the constant concentration of chromium(III) nitrate on the formation of the hydrous oxide sols will be shown. In Fig. 6 the concentration of solute chromium is given as a function of time of aging the solutions at 75°C in the presence of three different sulfate concentrations and in the absence of this anion. It is apparent that with increasing content of sulfate ions the solution is more rapidly depleted of soluble chromium species.

Figure 7 shows that the pH at 75°C of the dispersion media for sols which have reached equilibrium (at 96 hr of aging) remains essentially constant at sulfate concentrations $<2 \times 10^{-3}$F but increases at higher sulfate additions. The latter indicates that sulfate ions are replacing hydroxyl groups in the basic chromium species formed during the aging process, which should influence the properties of the sols produced at elevated temperatures. Finally, Fig. 8 is a plot of the modal particle diameter of sols formed by aging 4.0×10^{-4}F chromium(III) nitrate solution at 75°C for 96 hr as a function of the initial sulfate concentrations. The nature of the particles formed is also indicated in this figure. At the lowest sulfate concentrations the particles are spherical but of broad size distribution. Because of polydispersity and small particle diameters, light scattering could not be applied for determination

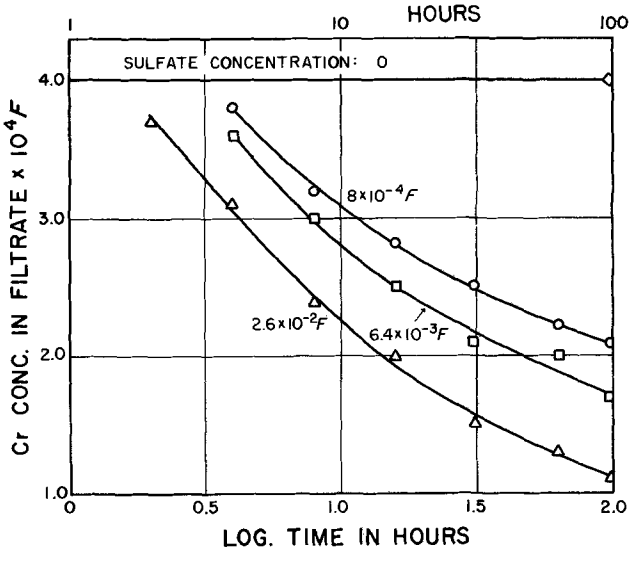

Fig. 6. Concentration of Cr (III) species remaining in solution after removal of sol particles from solutions containing three different sulfate concentrations each initially 4.0×10^{-4}F in Cr (III).

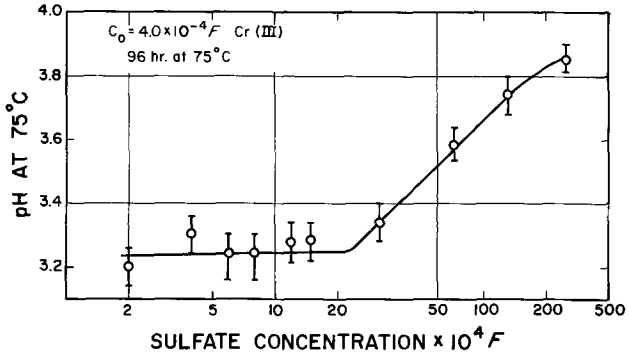

Fig. 7. The pH of the dispersion medium after 96 hr at 75°C as a function of sulfate concentration for solutions initially 4.0 × 10^{-4}F in Cr (III).

of the size distribution. Instead the electron microscopic results are given. At the intermediate sulfate concentrations the particle size distribution is sufficiently narrow for sols to show intense higher order Tyndall spectra (HOTS) and the particle size data are from the light-scattering analysis. At the highest sulfate concentrations studied the solids formed are aggregates of spherical particles. It is interesting to note that the onset of increase in pH (Fig. 7) and the formation of aggregates occur at approximately the same sulfate concentration. The aggregation apparently is caused by the lowering of the surface-charge density in the presence of higher concentrations of sulfate ions (as demonstrated by mobility measurements) and by the bridging of the particles by different coordinated chromium basic sulfate complexes which seem to form under these conditions (as indicated by the pH effects, Fig. 7).

These observations show the essential role which sulfate ions play both in the nucleation and in the growth process during the formation of chromium hydrous oxide sols. A more explicit mechanism of the particle generation will be possible once the chromium basic sulfate complexes are more precisely identified.

Growth mechanism.—When precipitation results in particles of uniform shape and size, and the number concentration remains nearly constant, the "chronomal" analysis (17) may be used to establish the growth mechanism. In principle this analysis permits dis-

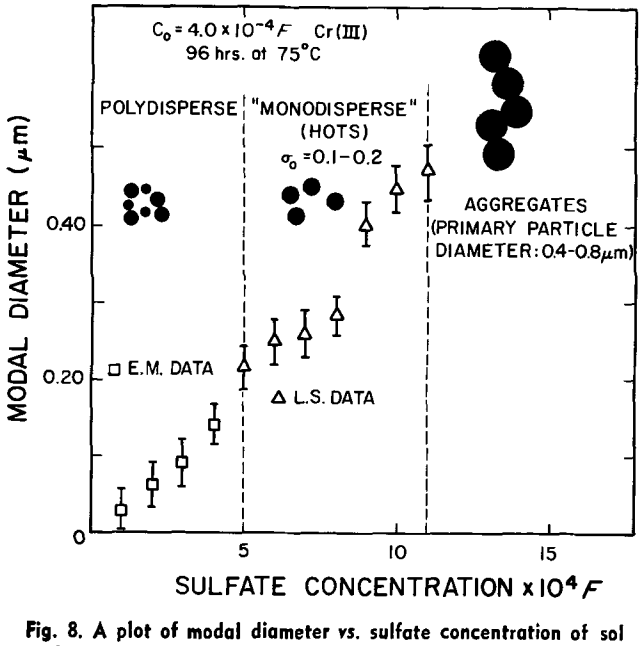

Fig. 8. A plot of modal diameter vs. sulfate concentration of sol particles formed in solutions aged at 75°C for 96 hr initially 4.0 × 10^{-4}F in Cr (III). E.M., electron microscopy; L.S., light scattering.

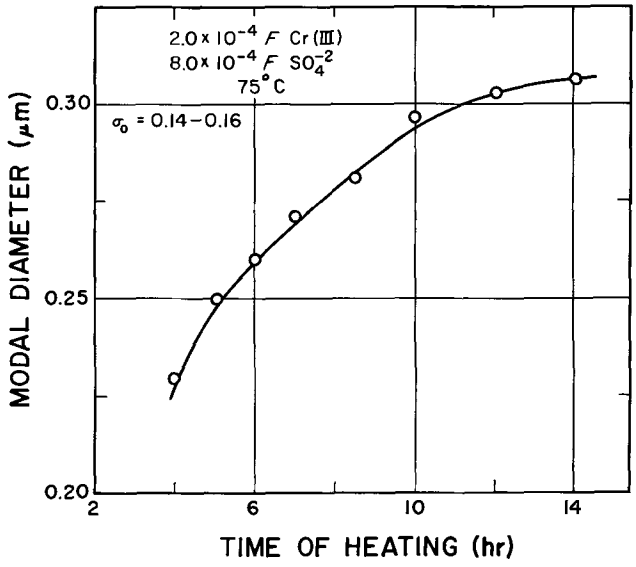

Fig. 9. Modal diameter of particles vs. time of aging at 75°C formed in solutions initially 2.0 × 10^{-4}F in Cr (III) and 8.0 × 10^{-4}F in SO_4.

tinguishing between diffusion controlled, polynuclear layer, and mononuclear layer growth.

The chromium hydrous oxide sols under certain experimental conditions meet the requirements necessary to apply the chronomals. For example, Fig. 9 shows the change of the modal particle diameter with time of sol generated by aging at 75°C a solution 2.0 × 10^{-4}F in chrom alum and 4.0 × 10^{-4}F in K_2SO_4. Assuming a constant particle composition (36% Cr) (5), throughout the entire period of particle growth shown in Fig. 9, a constant particle concentration of (2.0 ±0.5) × 10^8 cm^{-3} was calculated by means of the expression (18)

$$N = \frac{6\pi^2 w}{\rho\lambda^3} \cdot \left[\int_{\alpha_M \exp(-3\sigma_0)}^{\alpha_M \exp(3\sigma_0)} \alpha^3 p(\alpha)\, d\alpha \right]^{-1}$$

where w is the mass of particles per cm^3, ρ is the particle density (2.4 g/cm^3), $\lambda = 3.25 \times 10^{-5}$ cm, σ_0 is the distribution width parameter, and $p(\alpha)$ is the zeroth order logarithmic distribution function (19), α being the size parameter, $\alpha = 2\pi r/\lambda$, for which r is the radius of the spherical particle.

Nielsen (17) defines several chronomals, two of which are of interest in this work. The diffusion chronomal, I_D, is given as

$$I_D = \tfrac{1}{2} \ln [(1 - x)/(1 - x^{1/3})^3] - 3^{1/2} \tan^{-1} [3^{1/2}/(1 + 2x^{-1/3})]$$

where x is the degree of reaction (the ratio between the amount of substance that has reacted, and the total amount able to react, *i.e.*, solubility).

At time, t_D

$$t_D = K_D I_D$$

and

$$K_D = [48\pi^2 v N^2 (C_0 - S)]^{-1/3} D^{-1}$$

where v is the molar volume, D the diffusion coefficient, and $(C_0 - S)$ is the total amount reacted.

For the polynuclear controlled growth chronomal

$$I_P = \int_0^{X_P} X^{-2/3} (1 - X)^{-(m+2)/3} dx$$

where X is now defined as the fraction of the total initial species which has reacted to form the precipitate at time t_p. As above, $t_p = K_p I_p$ where

$$K_p \sim 0.6 r_1 [k_m v^{7/3} D^2 C_0^{(m+2)}]^{-1/3}$$

and r_1 is the equilibrium particle radius, k_m is a rate

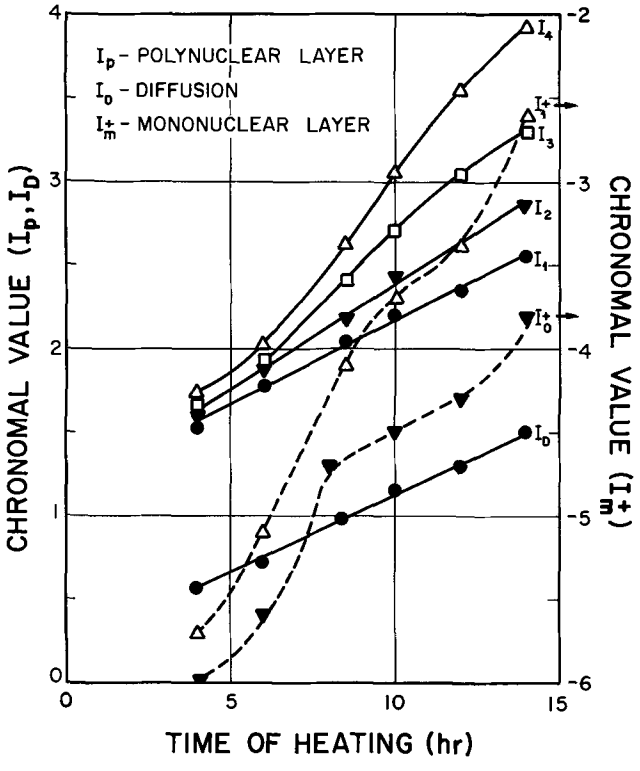

Fig. 10. Chronomal values assuming three different growth mechanisms designated by Nielsen as functions of time of aging at 75°C for solutions initially 2.0 × 10^{-4}F in Cr (III) and 8.0 × 10^{-4}F in SO_4^{-2} (see text).

constant, C_o is the initial concentration of the reacting species, and m is a constant.

For the chromium hydrous oxide sol described in this section, I_D and I_p, chronomals gave linear plots as a function of time (Fig. 10). Mononuclear controlled growth chronomals (I^+_m) did not give a linear relationship, and therefore, were not defined here.

To test whether a linear plot of a given chronomal properly indicates the growth mechanism, the diffusion coefficient, D, calculated from the corresponding K quantities, should have a reasonable value. In our case K_D did not yield a meaningful value for D over a wide range of values for the molar volume (the precipitate is amorphous). For example, assuming $v = \sim 50$ cm³/mole, $D = \sim 10^{-9}$ cm²/sec; a similar result is obtained using the expression $r(t) = [2Dv(C_o - S)t]^{1/2}$ which is valid for $v(C_o - S) << 1$ (1, 17). On the other hand, more reasonable values for D could be calculated from K_p values. It would appear that a polynuclear mechanism may be involved in the particular growth period studied although this is by no means certain; conceivably a compound growth mechanism might also be operative.

Acknowledgment

This work was carried out with support of the National Science Foundation grant GP 12220, and by grants from the Unilever Research Laboratory and the International Copper Research Association. The hydrous zirconia sols were prepared by Mr. D. L. Catone.

Manuscript submitted Sept. 27, 1972; revised manuscript received Jan. 22, 1973. This was Paper 181 presented at the Miami Beach, Florida, Meeting of the Society, Oct. 8-13, 1972.

Any discussion of this paper will appear in a Discussion Section to be published in the June 1974 JOURNAL.

LIST OF SYMBOLS

C	concentration at time t, mole/cm³
C_o	initial concentration, mole/cm³
D	diffusion coefficient of reacting species, cm²/sec
D_M	modal particle diameter, μm
K	factor converting a chronomal to time, sec
k_m	rate constant for nucleation controlled growth (units dependent upon m)
I	chronomal, dimensionless parameter proportional to time
I_D	diffusion chronomal
I^+_m	mononuclear layer chronomal
I_P	polynuclear layer chronomal
m	kinetic order of precipitation
N	particle number average concentration, cm^{-3}
p	kinetic order of polynuclear layer growth
$p(\alpha)$	zeroth order logarithmic distribution function
r	particle radius, cm or μm
r_1	equilibrium particle radius, cm
S	solubility of particles, mole/cm³
t	time, sec or hr
t_D	time of diffusional growth, sec
t_p	time of polynuclear layer growth, sec
v	molar volume of precipitating species, cm³/mole
w	mass per unit volume, g/cm³
x	degree of reaction
x_P	degree of reaction, polynuclear layer growth
α	particle size parameter
α_M	modal particle size parameter
σ_o	particle size distribution width parameter
λ	wavelength of scattered light in medium, cm
ρ	density of particles, g/cm³

REFERENCES

1. K. H. Lieser, *Angew. Chem. Intern. Ed. Engl.*, **8**, 188 (1969).
2. F. J. C. Rossotti and H. Rossotti, "The Determination of Stability Constants," Chap. 6, McGraw Hill Book Co., New York (1961).
3. R. Demchak and E. Matijević, *J. Colloid Interface Sci.*, **31**, 257 (1969).
4. E. Matijević, A. D. Lindsay, S. Kratohvil, M. E. Jones, R. I. Larson, and N. W. Cayey, *ibid.*, **36**, 273 (1971).
5. E. Matijević and A. Bell, in Proc. Soc. Chem. Ind. on "Particle Growth in Suspensions," London, 1972, In press.
6. P. McFadyen and E. Matijević, *J. Colloid Interface Sci.*, In press.
7. M. Kerker, E. Matijević, W. F. Espenscheid, W. A. Farone, and S. Kitani, *J. Colloid Sci.*, **19**, 213 (1964).
8. R. I. Larson, E. F. Fullam, A. D. Lindsay, and E. Matijević, *A.I.Ch.E. J.*, In press.
9. "Analytical Methods for Atomic Absorption Spectrophotometry," Perkin Elmer Corp., Norwalk, Conn. (1968).
10. P. McFadyen and E. Matijević, *J. Inorg. Nucl. Chem.*, In press.
11. P. B. Barton, Jr. and P. M. Bethke, *Am. J. Sci.*, **258A**, 21 (1960).
12. E. F. Fullam, *Rev. Sci. Instr.*, **43**, 245 (1972).
13. J. Staněk, M. Černý, J. Kocourek, and J. Pacák, "The Monosaccharides," pp. 180-181, Academic Press, New York (1963).
14. G. A. Parks, *Chem. Rev.*, **65**, 177 (1965).
15. H. J. Modi and D. W. Fuerstenau, *J. Phys. Chem.*, **61**, 640 (1957).
16. R. S. Alwitt, *J. Colloid Interface Sci.*, **40**, 195 (1972).
17. Arne E. Nielsen, "Kinetics of Precipitation," Pergamon Press, Oxford, England (1964).
18. G. Nicolaon, M. Kerker, D. D. Cooke, and E. Matijević, *J. Colloid Interface Sci.*, **38**, 460 (1972).
19. W. F. Espenscheid, M. Kerker, and E. Matijević, *J. Phys. Chem.*, **68**, 3093 (1964).

A Theoretical Study of Bipolar Porous Electrodes

Richard Alkire*

Department of Chemical Engineering, University of Illinois, Urbana, Illinois 61801

ABSTRACT

When electrical current passes through a porous metal diaphragm, the potential gradient in the electrolyte can serve to drive an electrochemical reaction provided that reactive species are present. One portion of the metal will act as an anode while the remainder will act as a cathode. A one-dimensional model is presented for determining how the reaction rate distribution is affected by system parameters including charge-transfer, resistance of the diaphragm, diffusion of solute species, and forced convection through the diaphragm. The results are presented in a series of dimensionless figures.

Nearly all current distribution studies have heretofore been conducted on electrodes of single polarity, either anodes or cathodes. A variety of important electrochemical systems, however, involve "bipolar" electrodes which are characterized by localized anodic and cathodic areas which coexist on adjacent regions of a single conductive surface. The following current distribution study has therefore been conducted in order to arrive at several features which are characteristic of one simple type of bipolar electrode.

The particular system under investigation involves a porous metal diaphragm of uniform porosity and thickness which is placed between two electrodes in a cell as shown schematically in Fig. 1. When current passes through the cell, a potential difference arises across the porous metal diaphragm so that electrochemical reactions may occur provided that reactive species are present. One portion of the diaphragm acts as an anode while the remainder acts as a cathode. Current, therefore, passes through the diaphragm both by ionic conduction in the electrolytic solution and by electronic conduction between anodic and cathodic regions.

Previous fundamental studies on bipolar systems have mostly focused attention on determining the current and potential distribution in a system of fixed anode/cathode geometry. In a series of publications, Waber *et al.* (1) calculated the primary and secondary current distribution in local cells having coplanar adjacent cathodes and anodes of known geometry ratio. Wagner (2) investigated the behavior of local cell action when the cathodic reaction was diffusion limited. Along different lines, Levich (3) employed concepts of convective diffusion to determine the rate of dissolution of inclusions of known size in both horizontal and vertical metal surfaces. In contradistinction to these studies, however, situations can arise where one has no *a priori* knowledge of which areas of a metal tend to be anodic or cathodic, or how the system properties influence the size of the anodic area. Analyses of bipolar systems which do not specify the size of the anodic or cathodic region are less common. For example, bipolar resistive wire electrodes have been analyzed by a linear network model (4), and bipolar electrochemical reactors have been treated as differential chemical reactors (5). Although no studies are known to exist which examine the behavior of bipolar porous electrodes, the following work is based on related analyses of porous battery electrode behavior (6). The simple model discussed below contains the salient features of many systems which exhibit bipolar behavior and, in addition, provides a basis for investigating more complex phenomena.

Derivation of the Model

The porous electrode under consideration is of uniform thickness, l, and is of uniform specific surface area throughout. Current enters the porous electrode in the solution phase at $y = 0$ and exits from the porous region at $y = l$. The concentration of reacting species is the same on both sides of the porous diaphragm.

Since rigorous calculations are cumbersome, several assumptions have been introduced: (*i*) The metal and void volumes of the porous diaphragm have a sufficiently fine structure that variations in potential and concentration occur along a single spatial dimension; the current distribution along each external surface is assumed to be uniform. (*ii*) Operation proceeds in the steady-state without structural changes, depletion, or insulation effects. (*iii*) Only one reversible electrochemical reaction occurs. (*iv*) The electrolyte is flooded with a nonreactive supporting electrolyte so that electrical migration of reactive species is not important. (*v*) Mass transfer limitations do not exist external to the porous diaphragm. (*vi*) Convection through the porous electrode takes place by forced plug flow along the same spatial direction as the flow of electrical current so that a one-dimensional analysis remains appropriate. Although these restrictions limit the applicability of the following model, they do not obviate the essential features which are of interest. As discussed in a later section, most of the assumptions may be altered to suit special circumstances without appreciable complication of the general procedures.

The transport equations which describe the model will be developed for an electrode reaction having the stoichiometric form

$$\sum_i \nu_i M_i^{z_i} = ne^- \qquad [1]$$

The reversible electrode reaction rate expression used in this investigation has concentration dependent forward and reverse rates

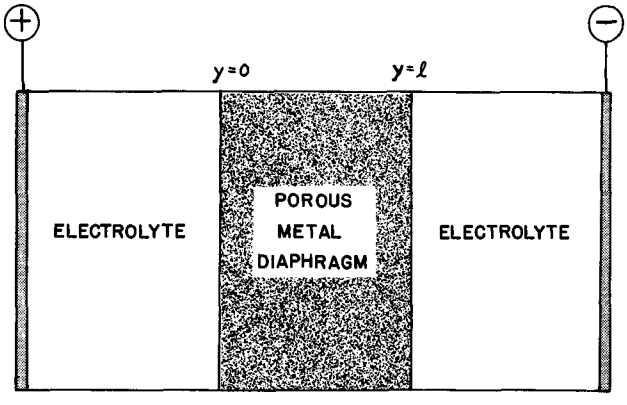

Fig. 1. Schematic diagram of bipolar porous metal diaphram

* Electrochemical Society Active Member.

Key words: current distribution, mathematical model, bipolar, porous electrode.

$$j(y) = i_0 \left[\frac{c_1(y)}{c_1^0} \exp\left(\frac{\alpha_a n\mathbf{F}}{RT} [\phi_s(y) - \phi_m(y)] \right) - \frac{c_2(y)}{c_2^0} \exp\left(-\frac{\alpha_c n\mathbf{F}}{RT} [\phi_s(y) - \phi_m(y)] \right) \right] \quad [2]$$

The notation is provided in the section on Symbols at the end of the paper. The four variables which appear on the right side of Eq. [2] (concentrations of both reactant and product species, potentials in both the electrode and solutions phases) are, in general, dependent on spatial position within the porous electrode; the four variables are to be determined by solving a set of equations as outlined in the following paragraphs.

In the solution phase, Ohm's law is

$$i_s(y) = -\kappa \frac{d\phi_s(y)}{dy} \quad [3]$$

The current in the solution, $i_s(y)$, varies with position since the electrochemical reaction acts as a sink

$$\frac{di_s(y)}{dy} = -aj(y) \quad [4]$$

The quantity "a" is the specific surface area in units of square centimeter surface area per cubic centimeter void volume. Combination of Eq. [2], [3], and [4] gives

$$\frac{d^2\phi_s}{dy^2} = \frac{i_0 a}{\kappa} \left[\frac{c_1}{c_1^0} \exp\left(\frac{\alpha_a n\mathbf{F}}{RT} [\phi_s - \phi_m] \right) - \frac{c_2}{c_2^0} \exp\left(-\frac{\alpha_c n\mathbf{F}}{RT} [\phi_s - \phi_m] \right) \right] \quad [5]$$

In a similar manner, Ohm's law may be applied to the passage of electronic current in the electrode phase

$$i_m = -\sigma \frac{d\phi_m(y)}{dy} \quad [6]$$

with the result

$$\frac{d^2\phi_m}{dy^2} = -\frac{i_0 aP}{\sigma(1-P)} \left[\frac{c_1}{c_1^0} \exp\left(\frac{\alpha_a n\mathbf{F}}{RT} [\phi_s - \phi_m] \right) - \frac{c_2}{c_2^0} \exp\left(-\frac{\alpha_c n\mathbf{F}}{RT} [\phi_s - \phi_m] \right) \right] \quad [7]$$

The group $[(aP/(1-P)]$ corresponds to the specific surface area in units of square centimeter surface area per cubic centimeter electrode volume.

The movement of reacting species within the electrode occurs by diffusion and by convection

$$N_i = -D_i \frac{dc_i}{dy} + vc_i \quad [8]$$

The anodic reactant concentration, $c_1(y)$, varies with position owing to the electrochemical reaction which acts as a sink so that

$$D_1 \frac{d^2c_1}{dy^2} - v\frac{dc_1}{dy} = \frac{\nu_1 i_0 a}{n\mathbf{F}} \left[\frac{c_1}{c_1^0} \exp\left(\frac{\alpha_a n\mathbf{F}}{RT} [\phi_m - \phi_s] \right) - \frac{c_2}{c_2^0} \exp\left(-\frac{\alpha_c n\mathbf{F}}{RT} [\phi_m - \phi_s] \right) \right] \quad [9]$$

Similarly, the anodic reaction product, $c_2(y)$, obeys the transport equation

$$D_2 \frac{d^2c_2}{dy^2} - v\frac{dc_2}{dy} = \frac{\nu_2 i_0 a}{n\mathbf{F}} \left[\frac{c_1}{c_1^0} \exp\left(\frac{\alpha_a n\mathbf{F}}{RT} [\phi_m - \phi_s] \right) - \frac{c_2}{c_2^0} \exp\left(-\frac{\alpha_c n\mathbf{F}}{RT} [\phi_m - \phi_s] \right) \right] \quad [10]$$

Equations [5], [7], [9], and [10] are sufficient for determining the four unknown variables which appear in Eq. [2]. Each of the differential equations contains all four unknown variables so that, in general, simultaneous integration is required. The model is completed by specification of the boundary conditions. At $y = 0$

$$\phi_s = \phi_{cell},\ c_1 = c_1^0$$

$$\frac{d\phi_m}{dy} = 0,\ c_2 = c_2^0 \quad [11]$$

while at $y = l$

$$\phi_s = 0,\ c_1 = c_1^0$$

$$\frac{d\phi_m}{dy} = 0,\ c_2 = c_2^0 \quad [12]$$

In order to render the calculations more compact, the following dimensionless quantities are defined

$$\mathrm{Y} = \frac{y}{l} \qquad \pi_i = \frac{D_i}{D_r}$$

$$\mathrm{C}_i(\mathrm{Y}) = \frac{c_i(y)}{c_r} \qquad \gamma_i = \frac{c_i^0}{c_r}$$

$$\Phi_m(\mathrm{Y}) = \frac{n\mathbf{F}}{RT}\phi_m(y) \qquad \beta = \frac{i_s^* l n\mathbf{F}}{\kappa RT}$$

$$\Phi_s(\mathrm{Y}) = \frac{n\mathbf{F}}{RT}\phi_s(y) \qquad J = \frac{alj}{i_s^*} \quad [13]$$

When these groupings are substituted into the equations which define the model, the following parameters arise

$$\xi = \frac{ai_0 l^2 n\mathbf{F}}{\kappa RT}$$

$$\chi = \frac{aPi_0 l^2 n\mathbf{F}}{(1-P)\sigma RT}$$

$$\Xi = \frac{i_0 a l^2}{n\mathbf{F} c_r D_r}$$

$$\zeta = \frac{vl}{D_r} \quad [14]$$

In dimensionless notation, the four equations which define the model can be arranged to the somewhat compact form

$$\Phi_s'' = \xi \left[\frac{C_1}{\gamma_1} \exp\left[\alpha_a(\Phi_s - \Phi_m)\right] - \frac{C_2}{\gamma_2} \exp\left[-\alpha_c(\Phi_s - \Phi_m)\right] \right] \quad [15]$$

$$\Phi_m'' = -\frac{\chi}{\xi}\Phi_s'' \quad [16]$$

$$C_1'' - \frac{\zeta}{\pi_1} C_1' = \frac{\nu_1 \Xi}{\pi_1 \xi}\Phi_s'' \quad [17]$$

$$C_2'' - \frac{\zeta}{\pi_2} C_2' = \frac{\nu_2 \Xi}{\pi_2 \xi}\Phi_s'' \quad [18]$$

Each "prime" superscript denotes differentiation with respect to the spatial variable Y. The boundary conditions given by Eq. [11] and [12] take on the form

$$\begin{aligned} &\text{at } \mathrm{Y} = 0: && \Phi_s = \Phi_a, && C_1 = \gamma_1 \\ & && \Phi_m' = 0, && C_2 = \gamma_2 \\ &\text{at } \mathrm{Y} = 1: && \Phi_s = 0, && C_1 = \gamma_1 \\ & && \Phi_m' = 0, && C_2 = \gamma_2 \end{aligned} \quad [19]$$

Once the four unknown variables are obtained, the current distribution along the porous electrode may be found from the dimensionless form of Eq. [2]

$$\beta J = \xi \left[\frac{C_1}{\gamma_1} \exp\left[\alpha_a(\Phi_s - \Phi_m)\right] - \frac{C_2}{\gamma_2} \exp\left[-\alpha_c(\Phi_s - \Phi_m)\right] \right] \quad [20]$$

Method of Solution

The solution of the Eq. [15]-[19], which describe the mathematical model, was carried out on a digital computer by a finite difference numerical procedure. Several computer programs were employed in order to examine the various cases presented below. In every case, the equations which describe the model were first linearized about a trial solution and then set into finite difference form. The set of tridiagonal matrices was then inverted (7) on an IBM 360 computer. Solutions to the nonlinear equations were subsequently obtained by iteration on the approximate linear solution; convergence was usually achieved within five iterations.

It may be noted that Eq. [15] becomes homogeneous when $\chi = 0$, that is, when the electrode conductivity is very large. The derivative boundary conditions on Φ_m will then no longer permit determination of the potential in the metal phase. In such cases, the boundary condition at $Y = 0$ was modified to

$$\Phi_m = \Phi_m^* \quad [21]$$

where Φ_m^* was chosen to be that value for which

$$\int_0^1 J\, dY = 0 \quad [22]$$

That is, the potential in the metal was chosen by inspection so that anodic and cathodic currents balance exactly.

Results and Discussion

Since the foregoing model contains a large number of system properties, it would be cumbersome to report detailed parameter studies for every possible case. Only a few features, which seem to be of special interest, have been chosen for discussion.

Effect of charge-transfer.—First consider the pristine situation when mass transport restrictions are altogether absent ($\Xi = 0$) and the electrode phase is of high conductivity ($\chi = 0$). Under these restrictions, the concentration of reacting species is uniform, and the potential in the metal is uniform. The system is described by Eq. [15] with the two appropriate boundary conditions, Eq. [19]. The potential in the electrode phase was chosen such that Eq. [22] was obeyed. The parameters under consideration are thus ξ, Φ_a, α_a, and α_c. Figure 2 illustrates how the electrochemical reaction rate varies along the porous diaphragm for various values of the parameter ξ. For small values of ξ, the reaction proceeds with difficulty (low i_0) so that current does not enter into the electrode phase; for large values, electrochemical reaction proceeds with ease so that a considerable amount of current flows in the electrode phase between anodic and cathodic areas. Fig. 3 provides a compilation of the current distributions for various values of the parameter ξ, as well as for two applied potentials across the diaphragm. The electrode reaction rate distribution depends on the value of applied potential, Φ_a, because the charge-transfer resistance is not constant but varies with Φ_a. For a given value of ξ, the current distributions shown in Fig. 3 have similar shapes which, in the interior regions of the diaphragm, are independent of the applied potential. For reactions having symmetric transfer coefficients ($\alpha_a = \alpha_c$) the reaction rate at the edges of the diaphragm is

$$J_{(Y=0 \text{ or } 1)} = 2\xi \sinh \frac{\alpha \Phi_a}{2} \quad [23]$$

Therefore, the current distributions for systems with different ξ or Φ_a than those provided in Fig. 3 may be

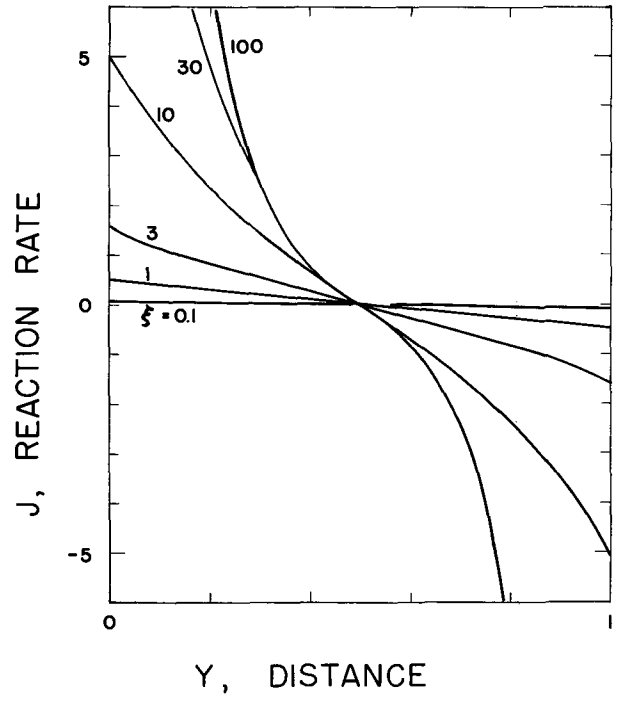

Fig. 2. Steady-state current density distributions within a bipolar porous electrode ($\alpha_a = \alpha_c = 0.5$, $\Phi_a = 1$, $\chi = \Xi = 0$).

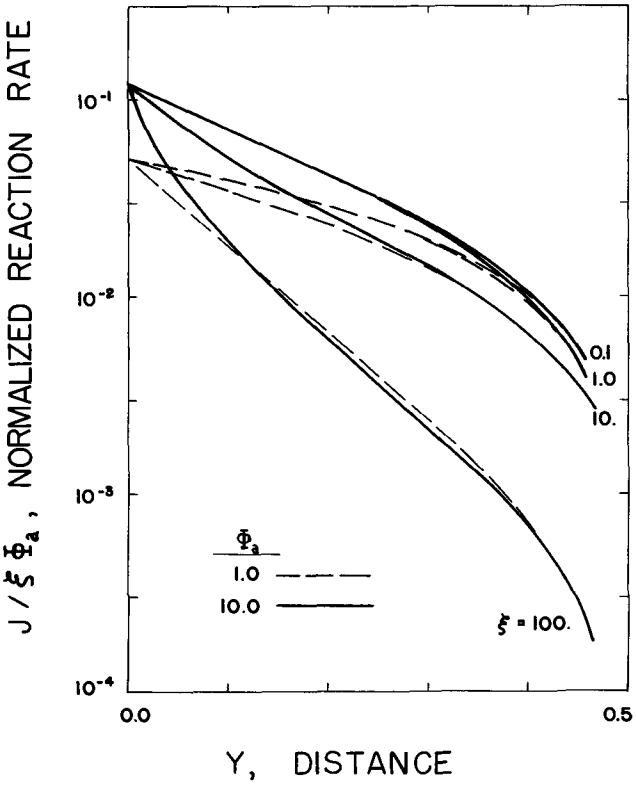

Fig. 3. Compilation of reaction rate distributions in bipolar porous electrodes ($\alpha_a = \alpha_c = 0.5$, $\chi = \Xi = 0$).

estimated by first computing $J_{(Y=0 \text{ or } 1)}$ from Eq. [23], and the interpolating between the appropriate lines in Fig. 3.

When the potential Φ_a is impressed across the diaphragm the magnitude of the current which flows will depend on the extent of electrochemical reaction taking place in the diaphragm as illustrated in Fig. 4. The quantity β_{avg}/Φ_a represents the over-all dimensionless conductivity of the diaphragm. The family of solid lines in Fig. 4 indicate that the over-all diaphragm conductivity increases as ξ increases; that is, electrochemical reaction permits passage of current through the

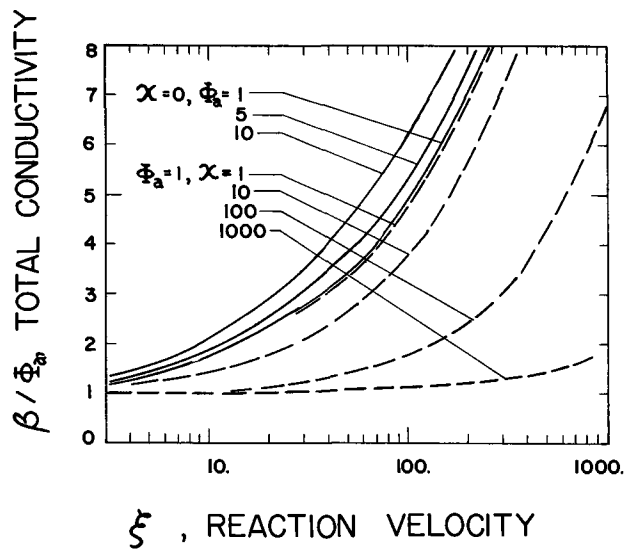

Fig. 4. Dependence of over-all electrode conductivity on system parameters ($\alpha_a = \alpha_c = 0.5$. $\Xi = 0$).

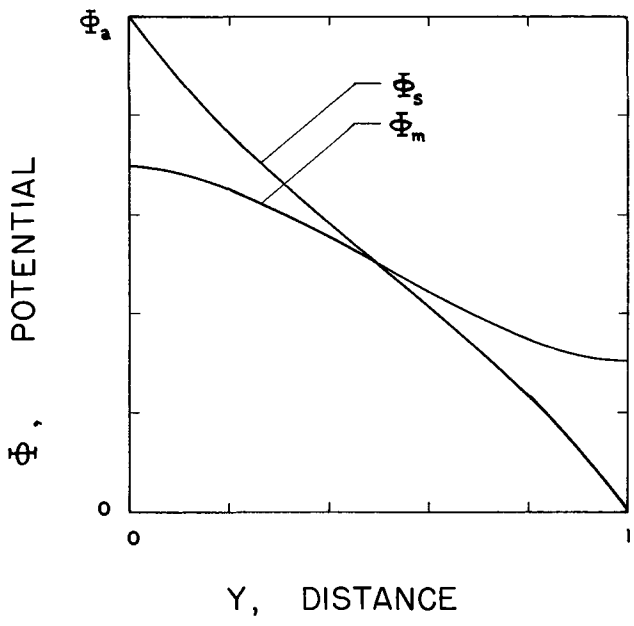

Fig. 5. Variation of potential in solution (Φ_s) and in metal (Φ_m) phases during electrolysis in a bipolar porous electrode ($\alpha_a = \alpha_c = 0.5$, $\Phi_a = 1$, $\xi = 10$, $\chi = 10$, $\Xi = 0$).

diaphragm in the electronic phase. At a given value of ξ, the over-all conductivity is somewhat potential dependent owing to the nonlinear reaction rate equation used in the present model. For the case $\Phi_a = 1$ and $\xi = 0.1$, it has been found that 98.7% of the current passes through the diaphragm in the electrolyte phase; on the other hand, with $\Phi_a = 1$ and $\xi = 100$, electrochemical reaction occurs to such a large extent that only 1.4% of the current flows in the electrolyte phase in the center of the diaphragm.

Effect of electrode resistance.—Now let us superimpose onto the foregoing pristine system the effect of finite electrode conductivity by increasing χ to nonzero levels; the potential in the electrode phase will no longer be constant. For the moment, however, Ξ will remain zero so that solute concentrations remain constant. The situation is modeled by Eq. [15] and [16] with the appropriate boundary conditions chosen from Eq. [19]. It was found that the most expedient method of integration was not to employ the two derivative boundary conditions on Φ_m but rather to chose the value of Φ_m on one side of the diaphragm such that Eq. [22] was obeyed.

Figure 5 illustrates how the potentials in the electrolyte and electrode phases vary with position within the diaphragm under the conditions $\xi = 10$, $\chi = 10$, $\Xi = 0$, and $\Phi_a = 1.0$. It is seen that potential gradients appear in both phases. The potential distributions in each phase exhibit inflection points since, by Eq. [15], their second derivatives change sign as one passes between electrode regions of opposite polarity. Figure 6 illustrates the effect of electrode resistance on the current distribution under the conditions of $\xi = 100$ and $\Phi_a = 1.0$. The electrode resistance tends to suppress electrochemical reaction by consuming a portion of the applied potential. The results shown by the dashed lines in Fig. 4 are helpful in estimating the effect of diaphragm resistance on over-all electrode conductivity. Even though the exchange current density may be very large (large ξ), it is clear that electrochemical reaction will tend not to occur if the metal has a sufficiently large resistance (large χ).

Effect of diffusion.—The importance of mass transfer limitations on electrode behavior is determined by the parameters Ξ and ζ. The first denotes the ratio of diffusion resistance to charge-transfer resistance insofar as it contains the ratio i_0/D_r; the quantity ζ provides the ratio of convective velocity to diffusive velocity. For the moment, consider pure diffusion control, that is, $\zeta = 0$. Further, let $\chi = 0$ so that the diaphragm is at a uniform potential. The system behavior is then deter-

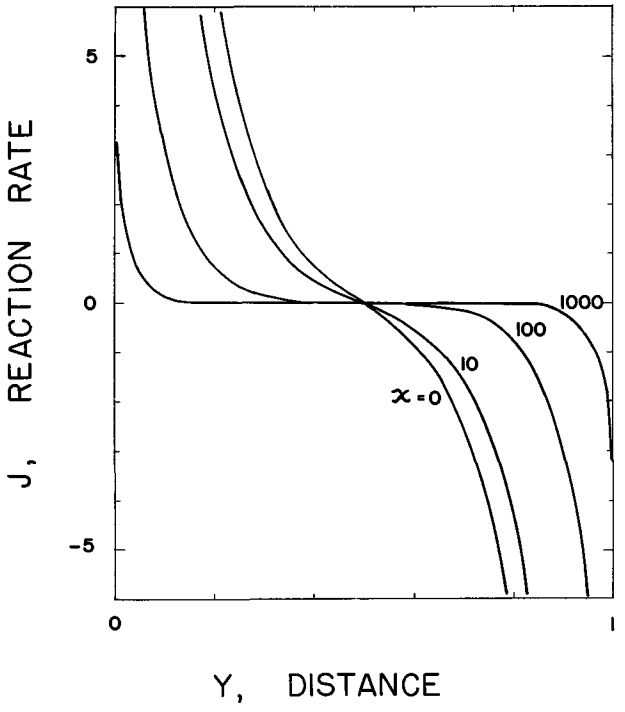

Fig. 6. Influence of electrode resistance on current density distribution in bipolar porous electrodes ($\alpha_a = \alpha_c = 0.5$, $\Phi_a = 1$, $\xi = 100$, $\Xi = 0$).

mined by Eq. [15], [17], and [18] along with the appropriate boundary conditions from Eq. [19]. As before, the potential in the metal is chosen such that Eq. [22] is obeyed.

When Ξ takes on nonzero values, concentration gradients may arise in the electrolyte if reaction rates are appreciable. The solid lines in the upper portion of Fig. 7 illustrate steady-state concentration profiles of the two reacting species for one particular set of conditions ($\xi = 10$, $\Xi = 1000$, $\Phi_a = 1$, $\chi = 0$). The concentration profiles are somewhat S-shaped since reactants consumed along the anodic region are generated by the reverse reaction along the cathodic region. An inflection point in the concentration profiles had been expected since the second derivatives in Eq. [17]

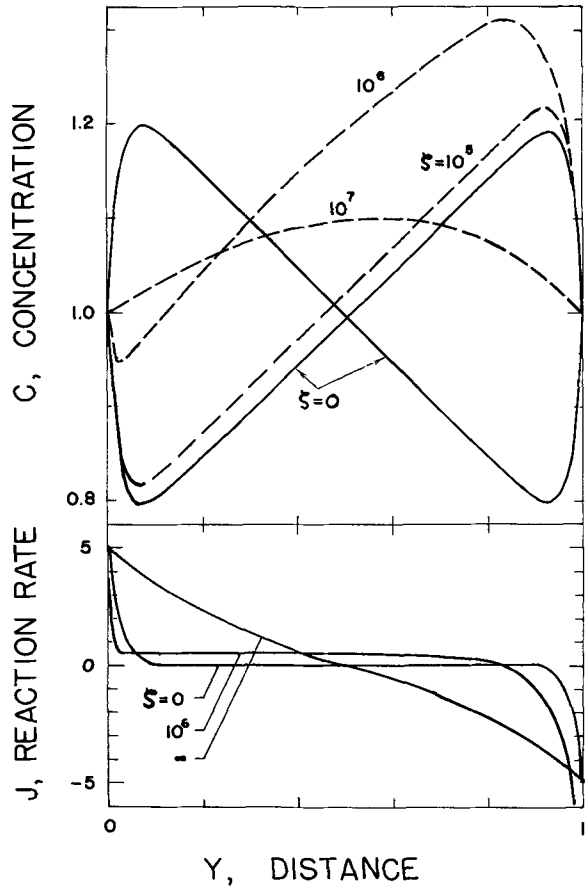

Fig. 7. Concentration and current distributions in a bipolar porous electrode under transport restrictions ($\alpha_a = \alpha_c = 0.5$, $\Phi_a = 1$, $\xi = 10$, $\chi = 0$, $\Xi = 1000$).

and [18] change signs as one passes between electrode regions of opposite polarity.

Naturally large concentration differences arise only if the electrochemical reaction proceeds at reasonably high velocities, that is for large ξ; otherwise, current merely passes through the diaphragm wtihout entering the metal phase and thus serving as a species sink. The existence of concentration differences, however, decreases the extent of electrochemical reaction by consuming a portion of the applied potential. Figure 8 illustrates how concentration overpotential acts to reduce the over-all conductivity of the porous diaphragm for the conditions $\Phi_a = 1$, $\chi = 0$, and $\zeta = 0$. The results shown in Fig. 8 are only weakly dependent on the applied potential in the range up to $\Phi_a = 10$. When Ξ takes on large values, the extent of electrochemical reaction is reduced and the reaction distribution becomes more uniform.

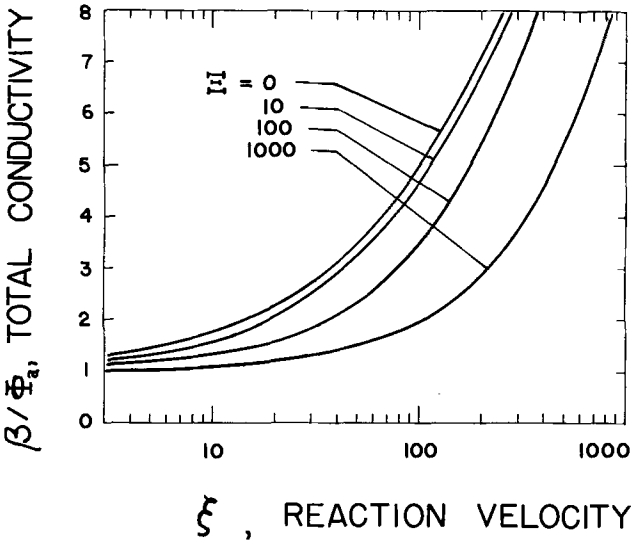

Fig. 8. Dependence of over-all electrode conductivity on system parameters ($\alpha_a = \alpha_c = 0.5$, $\Phi_a = 1$, $\chi = 0$).

Effect of electrolyte flow.—When mass transport limitations predominate electrode behavior, convection of electrolyte may naturally have a significant effect on performance. The parameter which determines the extent is ζ. The dashed lines in the upper portion of Fig. 7 illustrate the effect of forced flow on the concentration distribution of species C_1 which is consumed in the anodic regions. When ζ has the value zero, pure diffusion obtains and the concentration distribution is shown by the solid curve as mentioned previously. An increase in the value of ζ, corresponding to convection from right to left in the figure, distorts the concentration distribution as shown. At sufficiently high values of ζ the concentration distribution becomes uniform, that is, mass transport limitations are entirely removed. The lower portion of Fig. 7 illustrates the effect of convection on the electrochemical reaction rate distribution. Under pure diffusion control ($\zeta = 0$), the current distribution is symmetric and highly nonuniform. In the complete absence of mass transport effects ($\zeta = \infty$) the current distribution varies almost linearly with distance within the electrode. At intermediate levels (such as $\zeta = 10^6$), the current distribution is far from symmetric. For the example in Fig. 7, large local reaction rates are encountered in the (upstream) cathodic portion which, however, occupies less than 20% of the electrode volume. The cathodic reaction products are washed downstream onto the anodic surface where reaction occurs with remarkable uniformity over 60% of the electrode surface.

By relieving concentration overpotential, convection will increase the apparent diaphragm conductivity above the values for diffusion-controlled diaphragms as shown previously in Fig. 6. For the range of parameters reported in this investigation, it was found that pure diffusion behavior persisted for ζ values between 0 and 10^4. For values of ζ in excess of 10^7, on the other hand, the over-all diaphragm conductivity was within 1% of the value which corresponds to the absence of concentration overpotential. In all cases, convection affected electrode performance primarily in a narrow range of ζ between 10^5 and 10^6.

Conclusions

In the absence of concentration and electrode resistance effects, the electrochemical reaction distribution within the porous metal diaphragm depends solely on the parameter ξ. If ξ has a value greater than unity, electronic co-conduction via electrode reactions becomes appreciable. The effect of electrode resistance on electrode behavior is determined by the value of χ; if χ has a large value, the potential in the electrode phase varies with position. Similarly, the magnitude of the parameter Ξ determines the extent of concentration overpotential. The parameters χ and Ξ affect diaphragm behavior only insofar as they affect the electrochemical reaction; if ξ is small, electrochemical reaction does not occur, and the role of electrode resistance and concentration effects is of no concern.

The model presented above is based on a set of assumptions which naturally affect the applicability of the calculated results. For example, a potential difference across the porous diaphragm was chosen in this study for the driving force for occurrence of bipolar behavior. Other driving forces are possible. In order to investigate other systems having bipolar behavior, a significant number of the assumptions may be removed or substantially altered without appreciable complication of the over-all procedure. Several examples may be cited: assumption (*i*), concentration gradients often arise during high rate discharge of porous battery or fuel cell electrodes. After release of

the external load, the device proceeds to recover the terminal voltage by a process which depends in part on bipolar short-circuiting of the concentration gradients within the porous electrodes. Rate of recovery behavior may, thus, be investigated by removing assumption (*ii*) in favor of transient species conservation equations (8). Assumption (*ii*), many corrosion processes are driven by localized concentration, stress, or potential gradients which cause the metallic surface to become bipolar and thus corrode. Since at least two different electrochemical reactions are usually involved, assumption (*iii*) may be relieved in favor of, for example, oxygen reduction combined with iron dissolution/passivation kinetics. Assumption (*iii*), acid leaching of mineral ore pellets often takes place by corrosion-type reactions since many of the common sulfide and oxide ores are electronic conductors. Determination of leaching rates would, therefore, involve multiple bipolar reactions coupled, perhaps, with pore size variation considerations. Assumption (*iv*), electroless deposition processes consist of simultaneous corrosion-type reactions which have the net effect of depositing metal on an appropriately sensitized substrate. Bipolar concepts are involved in determining the local cathodic reaction rate, that is, the metal thickness distribution. Such studies are naturally of interest in improving quality control of electroless plating systems.

The bipolar porous electrode model described above, thus, provides a firm basis for further investigations on important electrochemical systems.

Acknowledgment

Acknowledgment is made to the donors of The Petroleum Research Fund, administered by the American Chemical Society, for partial support of this research. Funds for computation charges were contributed by the University of Illinois Research Board.

Manuscript submitted Oct. 4, 1972; revised manuscript received Feb. 7, 1973.

Any discussion of this paper will appear in a Discussion Section to be published in the June 1974 JOURNAL.

SYMBOLS

English characters

- a specific surface area, cm^{-1}
- c_i concentration of species i, g-mol/cm^3
- c_i^0 concentration of spcies i in bulk solution, g-mol/cm^3
- C_i c_i/c_i^0, concentration of species i, dimensionless
- c_r arbitrary reference concentration, g-mol/cm^3
- D_i diffusion coefficient of species i, cm^2/sec
- D_r arbitrary reference diffusion coefficient, cm^2/sec
- $\mathbf{F}$ Faraday's constant, 96,500 coulombs/g-equiv
- i_m current density in the electrode, A/cm^2
- i_0 exchange current density of the electrode reaction
- i_s current density in the electrolyte, A/cm^2
- i_s^* current density in the electrolyte at $Y = 0$ or 1, A/cm^2
- j local reaction rate, A/cm^2
- J ajl/i_s^*, local reaction rate, dimensionless
- l electrode thickness, cm
- M_i symbol for species taking part in electrode reaction, Eq. [1]
- n number of electrons taking part in electrode reaction
- N_i flux of species i, g-mol/cm^2-sec
- P electrode porosity
- R gas constant, 8.31 joules/g-mol °K
- T temperature, °K
- v electrolyte velocity, cm/sec
- y spatial distance, cm
- Y y/l, spatial distance, dimensionless
- z_i electric charge of species i

Greek characters

- α_a anodic transfer coefficient in reaction rate expression
- α_c cathodic transfer coefficient in reaction rate coefficient
- β $i_s^* l n\mathbf{F}/\kappa RT$, current density in solution at $y = 0$ or 1, dimensionless
- γ_i c_i^0/c_r, bulk concentration of species i, dimensionless
- ζ vl/D_r, convective velocity, dimensionless
- κ conductivity of electrolytic solution, ohm^{-1} cm^{-1}
- ν_i stoichiometric coefficient of species i, Eq. [1]
- ξ $ai_0 l^2 n\mathbf{F}/\kappa RT$, reaction velocity parameter, dimensionless
- Ξ $ai_0 l^2/n\mathbf{F}c_r D_r$, diffusion parameter, dimensionless
- π_i D_i/D_r, diffusion coefficient of species i, dimensionless
- σ conductivity of electrode material, ohm^{-1} cm^{-1}
- ϕ_{cell} potential difference, $[\phi_s(y = 0) - \phi_s(y = l)]$, V
- ϕ_m potential in electrode phase, V
- ϕ_s potential in electrolyte phase, V
- Φ_a $n\mathbf{F}[\phi_s(y = 0) - \phi_s(y = l)]/RT$, applied potential difference, dimensionless
- Φ_m $n\mathbf{F}\phi_m/RT$, potential in electrode phase, dimensionless
- Φ_s $n\mathbf{F}\phi_s/RT$, potential in electrolyte phase, dimensionless
- χ $aPi_0 l^2 n\mathbf{F}/(1 - P)\sigma RT$, electrode resistance parameter, dimensionless

REFERENCES

1. J. T. Waber, *This Journal*, **101**, 271 (1954); J. T. Waber and M. Rosenbluth, *ibid.*, **102**, 344 (1955); J. T. Waber and B. Fagan, *ibid.*, **103**, 64 (1956); J. T. Waber, J. Morrissey, and J. Ruth, *ibid.*, **103**, 138 (1956); J. T. Waber, *ibid.*, **103**, 567 (1956).
2. C. Wagner, *ibid.*, **107**, 445 (1960).
3. B. Levich, "Physicochemical Hydrodynamics," p. 343 ff, Prentice-Hall, Inc., Englewood Cliffs, N. J. (1962).
4. K. Nagata, T. Akimoto, and N. Fujise, *Denki Kagaku*, **38**, 763 (1970).
5. M. Fleischmann, J. Oldfield, and C. Tennakoon, Symposium on Electrochemical Engineering, Newcastle, 1971.
6. R. de Levie, in "Advances in Electrochemistry and Electrochemical Engineering," Vol. 6, P. Delahay and C. Tobias, Editors, Interscience, New York (1967).
7. J. Newman, *Ind. Eng. Chem., Fundamentals*, **7**, 514 (1968).
8. E. Grens and C. Tobias, *Ber. Bunseg. Physik. Chem.*, **68**, 236 (1964).

Analysis of Porous Electrodes with Sparingly Soluble Reactants

II. Variable Solution Properties, Convection, and Complexing

John S. Dunning* and Douglas N. Bennion*

Energy and Kinetics Department, School of Engineering and Applied Science, University of California, Los Angeles, California 90024

and John Newman*

Inorganic Materials Research Division, Lawrence Berkeley Laboratory, and Department of Chemical Engineering, University of California, Berkeley, California 94720

ABSTRACT

The galvanostatic operation of flooded porous electrodes employing metal/metal salt couples is analyzed. A model is developed for a single, circular pore configuration which accounts for the effects of differing equivalent volumes of the solid reactants. The model also includes effects of variation in solution properties and effects of complexing of the sparingly soluble salt with the bulk electrolyte anion. The $Cd/Cd(OH)_2$ couple in concentrated aqueous potassium hydroxide and the Ag/AgCl couple in concentrated potassium chloride solutions are considered. Overpotential is computed as a function of time for solid-film and solution-diffusion versions of the model. The solid film model shows a linear overpotential-time relationship and nearly uniform current distribution. The solution-diffusion model shows a variety of overpotential-time curves, based on different physical parameters. In general, anodic failure is caused by blockage of pores or by complete coverage of the metal surface by product crystallites. Cathodic failure is caused by low mass transport which leads to limiting currents in the electrode. The solution-diffusion model may generate extremely nonuniform current distributions, often with maxima inside the pore. These persistent nonuniform current distributions are important in terms of the analysis of cycling behavior.

Porous electrodes using sparingly soluble active species are common to most modern electrical storage cells. The negative plates in lead-acid batteries are porous structures containing lead and lead sulfate mixtures formed electrochemically from pastes pressed into lead alloy current collectors. The lead sulfate is sparingly soluble. Nickel-cadmium cells use sparingly soluble cadmium hydroxide and various nickel oxides and hydroxides on cadmium or nickel substrates. Sea water activated cells use the silver/silver chloride couple for the positive electrode reaction.

This study addresses itself to the formulation of a physical and mathematical model which describes the operation of flooded porous electrodes using a metal/sparingly soluble salt couple. Emphasis is on presenting an accurate description of the elementary processes believed to be the most important in establishing over-all electrode behavior. Comparison of critical aspects of the model to actual experimental observations is made insofar as such information is available.

Two specific examples of metal/salt couples have been considered. The first is cadmium/cadmium hydroxide in aqueous potassium hydroxide electrolytic solutions. Croft (1) and Farr and Hampson (2) have presented evidence supporting anodic film growth by ionic film transport as a controlling process. Dissolution and precipitation of a CdO intermediate has been proposed by Lake and Casey (3). Devanathan and Lakshmanan (4) suggest that a $CdOH^+$ ion is formed which may decompose into CdO and $Cd(OH)_2$. Armstrong *et al.* (5) found no CdO formed and that the primary product of oxidation was $Cd(OH)_2$. Croft (1) and Falk (6) also proposed that $Cd(OH)_2$ was formed directly on oxidation of Cd. Breiter and Weininger (7) suggested that a very thin layer of amorphous CdO could be formed. Yoshizawa and Takehara (8) proposed $HCdO_2^-$ as an intermediate in a sequence of elementary steps. Visco and Sonner (9) found that $Cd(OH)_3^-$ is formed on the dissolution of $Cd(OH)_2$ in KOH solutions from 2 to 15 molar. The results of Visco and Sonner make the Yoshizawa and Takehara sequence unlikely. Their observed third-order dependence of the equilibrium potential on OH^- activity can be explained by the mechanism proposed by Milner and Thomas (10) and by Okinaka (11).

$$Cd + 3\,OH^- \rightleftarrows Cd(OH)_3^- + 2e^-$$

$$Cd(OH)_3^- \rightleftarrows Cd(OH)_2 + OH^-$$

Okinaka concluded that in the active potential range the dissolution-precipitation mechanism is predominant. He also concluded that a thin film of CdO was responsible for the passivation of cadmium, rather than surface blockage by $Cd(OH)_2$ crystallites. In the passive region, continued growth was accomplished by ionic migration through the $Cd(OH)_2$ film which formed on top of the CdO film. Measurements of the conductivity of $Cd(OH)_2$ gave values of about 10^{-10} mho/cm. These results might be compared to $PbSO_4$ film results of 3.5×10^{-10} mho/cm found by Fleischmann and Thirsk (12). Okinaka (11) also estimated that the rate constant for the precipitation of $Cd(OH)_2$ was the order of 10^{-3} to 3×10^{-3} cm/sec.

The reduction of $Cd(OH)_2$ has been studied less than the oxidation of Cd even though this process is important in the charging of Ni-Cd cells. This is especially true with regard to possible hydrogen evolution in sealed cells. Croft (1) postulated that a direct solid-state mechanism was responsible for this process while Okinaka (11) found evidence for both solid- and solution-phase transport, with the contribution of the solution-diffusion mechanism increasing as the reduction progresses.

Will and Hess (13, 14) simulated a single pore by using a cadmium electrode covered with a thin (10-400μ) layer of electrolytic solution and arranged so that the counterelectrode was positioned side-by-side with the test electrode. Microscopic investigations of the resulting $Cd(OH)_2$ were interpreted as supporting the mechanism of solid-state ionic transport through passivating layers of $Cd(OH)_2$. It was noted that large

* Electrochemical Society Active Member.

Key words: porous electrodes, current distribution, cadmium, cadmium hydroxide, silver, silver chloride, batteries, failure mechanisms.

particles of $Cd(OH)_2$ were formed on repeated cycling. This effect was concluded to be responsible for the decrease in capacity during the first ten cycles. A study by Bro and Kang (15) gives experimental data on the discharge profiles in an actual cadmium anode. These investigators sliced the electrode after discharge and were thus able to determine current distributions by differentiating the depth of discharge with respect to time. They also showed the effect of pore blockage by $Cd(OH)_2$ crystallites through an empirical correlation. It was found that the per cent coulombic efficiency dropped as the integral current density of a galvanostatic discharge was increased. Some polarization data were also presented. No theoretical treatment of the data was attempted.

Vermilyea (16) has classified films of silver halides on silver and oxide and hydroxide films on cadmium as "noncontinuous films." Some of the metal substrate is exposed and ions diffuse to and from the metal through openings in the overlaying salt or oxide. A review of metal electrodes with surface films is given by Vetter (17).

The mechanism of the growth of silver chloride on silver electrodes is apparently a function of applied current density. Lal *et al.* (18) found a purplish, probably polycrystalline deposit which formed at 1-2 mA/cm^2. Jaenicke *et al.* (19) obtained white films, with apparently lower specific resistance, formed at current densities greater than 20 mA/cm^2. They showed that these films were nonporous if thicker than 2-4μ. Thus liquid-phase silver ion transport was not important in anodic growth past this thickness. On the other hand, Giles (20) found that a series of intermediate, soluble complexes was formed on oxidation of silver single crystals in chloride-containing media. Lal *et al.* (21) observed periodic phenomena associated with the breakdown of the anodic film. Jaenicke *et al.* suggested that the cathodic process is cation migration along grain boundaries at large film thicknesses. After some time the film breaks down and a diffusion process in the electrolyte solution becomes predominant.

Lal *et al.* (18) found that the conductivity of AgCl depended on the current density during formation, rising with current density. The conductivity was reported to vary between 10^{-6} and 10^{-4} mho/cm. Apparently the solid-state transference number of the silver ion is nearly unity. Indira and Doss (22) have explained the high cation mobility on the basis of a stoichiometric excess of silver in the AgCl film formed electrolytically.

The rate of the electrochemical reaction in the Ag/AgCl couple seems large. Giles (20) proposed that the complexation dissolution reaction

$$Ag + nCl^- \rightleftarrows AgCl_n^{1-n} + e^-$$

takes place at a rate too fast to measure by faradaic impedance methods. The subsequent production of AgCl by chloride elimination would then be rate limiting. These results apply only to salt-free surfaces. As the surface becomes covered with AgCl crystals (phase formation takes place at about +25 mV overpotential), the overpotential of the electrode rises at constant current. Giles also observed large changes in the real surface area after formation and reduction of AgCl nuclei.

A review by de Levie (23) describes the features of many porous electrode models. Most porous electrode models employ a one-dimensional approach as discussed by Grens (24). Winsel (25) analyzed a single pore of constant conductivity with a highly conducting wall. He calculated some transient effects by integrating the local transfer current density over time and considering a finite amount of reactant to be available at each point in the electrode. Thus Winsel was able to show overpotentials which increased markedly as the amount of charge consumed approached the amount available.

Newman and Tobias (26) presented a steady-state analysis of a one-dimensional homogeneous mixture model of a porous electrode. They considered effects of a finite matrix resistance and variations in concentration. Austin and Gagnon (27) applied a similar analysis to their experimental data on Ag/Ag_2O electrodes and found good agreement. Grens (24) and Grens and Tobias (28) reported on analysis of transient effects in a porous electrode due to concentration changes in the pore solution. The transient mode was analyzed by a time-stepping method in which the results of computations for a previous step are used as the initial conditions of each time step.

The work by Alkire and co-workers (29, 30) was the first effort to account quantitatively for structural changes in a dissolving porous anode. They used dilute-solution theory with constant transport and solution properties. It was assumed that the solubility limit of the copper salt formed on anodic dissolution was not exceeded. Thus the effects of a sparingly soluble metal salt couple were not considered.

Dunning and Bennion (31) considered the effect of crystallites of active material on the charge and discharge process. The concept of a mass transfer coefficient describing transport between active metal sites and reactant salt crystallites was employed. Later Dunning *et al.* (32) extended that work to cover transient operation and cycling behavior. Even though constant solution properties and other idealizations were used, results of the model showed a redistribution of active-material conversion on repeated anodic and cathodic polarization.

The common assumptions underlying many theoretical porous electrode treatments have been analyzed by Grens (33). He stated that the assumption of concentration independent electrolytic solution properties is highly questionable. Changes in volume of metal and metal salt with time were not included.

In this work a model for the operation of a porous electrode with sparingly soluble reactants is developed. The effects of varying solution properties are included as well as convection arising from differing densities of reactant and product species. The effects of local mass transfer between salt crystallites and metal surface with considerable attention to the detailed physical and mathematical description of this process is investigated. In addition, the effect of complexing between active species and the bulk electrolyte, and the associated bulk electrolyte concentration dependence, has been considered. The behavior of the porous electrode is determined by a numerical solution of the combined continuity, transport, and kinetic equations which describe the system. The electrode polarization can be determined as a function of applied current density and time. The distribution of transfer current density and state of charge can be determined as a function of position and time. The results can suggest certain idealized modes of failure and performance limitations.

Development of a Single Pore Model

A one-dimensional approach is used in which variations in properties occur only along the y direction. At the origin is a current collecting backing plate or center of symmetry. The total electrode thickness is L. At values of y greater than L it is assumed that the solution has the properties of the bulk. The geometric cross section of a model pore is shown in Fig. 1. The solid, sparingly soluble salt is imagined as being a series of crystallites on the surface of the active metal. The radius r_3 limits the region in space allocated to an "average pore" and defines the pore as a system. The radius r_3 is a constant. The space between r_2 and r_3 defines the quantity of active metal within the space allocated to the pore. The radius r_2 is a variable and changes as the quantity of active metal within the pore varies. The space between r_1 and r_2 is the effective volume of solid, sparingly soluble salt within the pore. The inner radius r_1 defines the area available for transport in the solution phase in the y direction. The radius

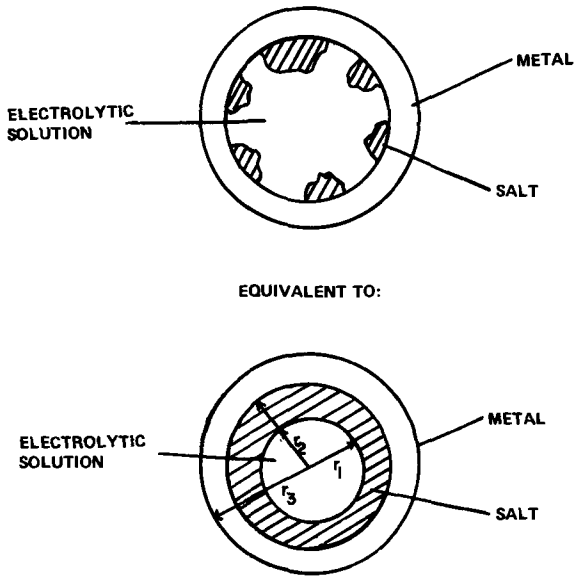

Fig. 1. Circular pore geometry

r_1 is a variable. This description is not to imply that the metal and salt are annular in shape. The radii, r_1, r_2, and r_3 are defined as bookkeeping artifacts to allow quantitative, mathematical treatment of the amounts of active metal and active salt as functions of time and position within the porous electrode.

The over-all, stoichiometric reaction representing the chemical process within the porous electrode is written

$$\sum_i s_i A_i^{z_i} = ne^- \qquad [1]$$

Examples are

$$Cd + 2\,OH^- - Cd(OH)_2 = 2e^-$$
$$Pb + SO_4^= - PbSO_4 = 2e^-$$
$$Ag + Cl^- - AgCl = e^-$$

The s_i are stoichiometric coefficients and can be positive or negative. The z_i are the charges on the species A_i and can be positive, negative, or zero. The n is the number of electrons transferred for the reaction as written and is a positive number.

The radius r_2 varies with time as the quantity of active metal varies. The local cathodic transfer current density, j, is a measure of the rate of appearance or disappearance of active metal. The two variables are related by the expression

$$\frac{dr_2}{dt} = \frac{-s_1 M_1}{n\mathbf{F}\rho_1} j \qquad [2]$$

The subscripts 1 imply the active metal. M_i is the molecular weight of species i, and ρ_i is the density of species i.

The variation of the radius r_1 depends on the relative rates of appearance and disappearance of the metal and salt. The relation between dr_1/dt and the transfer current density j depends on how both solid species vary with j. The relation is

$$\frac{dr_1}{dt} = -\sum_{\substack{\text{solid}\\ \text{species}}} \frac{s_i M_i}{n\mathbf{F}\rho_i} \frac{r_2}{r_1} j = A\frac{r_2}{r_1} j \qquad [3]$$

Equation [3] defines the constant A. The ratio r_2/r_1 appears because the quantities of salt and metal present are accounted for in terms of cylindrical geometry.

As the volume of solid species within the control element changes, the porosity or space available for liquid changes. In addition, the mass of liquid varies as liquid phase species also participate in the chemical reaction whose rate is characterized by j. As the relative volumes of liquid and solid change, the porous electrode "breathes," *i.e.*, a convective flow of the liquid into or out of the porous electrode is created. This bulk electrolyte solution convective motion can be described by an over-all continuity equation or molar balance on a control element

$$\frac{\partial}{\partial t}\left[\begin{pmatrix}\text{moles in electrolyte}\\ \text{solution phase}\end{pmatrix} + \begin{pmatrix}\text{moles in}\\ \text{solid phase}\end{pmatrix}\right] = \begin{bmatrix}\text{net increase in moles}\\ \text{due to convection}\end{bmatrix} + \begin{bmatrix}\text{net increase in moles}\\ \text{due to electrode reaction}\end{bmatrix}$$

In more mathematical terms, this relationship can be written as

$$\frac{\partial c_T}{\partial t} + \frac{2r_2}{r_1^2}\left(Ac_T - \frac{1}{\mathbf{F}}\right) j + \frac{1}{r_1^2}\frac{\partial}{\partial y}(r_1^2 c_T v^*) = 0 \qquad [4]$$

where c_T is the actual, total molar concentration in the liquid phase and v^* is the actual, molar average velocity in the liquid phase.

Two equations are needed to describe the concentration variations of water and electrolyte in the liquid phase. The first is the so-called species continuity equation

$$\frac{\partial}{\partial t}(c_+ \pi r_1^2) = -\frac{\partial}{\partial y}(\pi r_1^2 c_+ v_+) \qquad [5]$$

Here c_+ is the concentration of the positive ion and v_+ is the velocity of the positive ion. The positive ion is chosen for this balance since, for the electrodes being considered, the positive ion does not participate in the chemical reaction and no source term is needed in Eq. [5]. The species flux, c_+v_+, must be described as a function of the appropriate driving forces to complete the description of bulk electrolyte transport inside the porous electrode (34)

$$c_+ v_+ = -Dc_T\frac{dx_e}{dy} + \frac{i_2 t^*_+}{z_+\mathbf{F}} + c_+ v^* \qquad [6]$$

One can identify the diffusion, migration, and convection contributions to the electrolyte diffusion on the right-hand side of Eq. [6]. D is the diffusion coefficient for the electrolyte in water; x_e is the particle fraction of the electrolyte in the solution averaged across the pore diameter r_1; i_2 is the current density in the solution phase; and t^*_+ is the transference number relative to the molar average velocity, v^*.

The variation in potential in the solution, ϕ_2, and the variation of potential in the matrix phase, ϕ_1, must be described and related to the current density in the solution, i_2, and the current density in the matrix phase i_1. The simple form of Ohm's law does not hold in the solution phase; there must be a correction for variations in electrolyte activity, a_e, where, for example, a_e is the mean molal activity coefficient $\gamma_\pm$ times the molality

$$i_2 = -\kappa\frac{d\phi_2}{dy} - \frac{\kappa t^0_+}{\mathbf{F}}\nu RT\frac{d\ln a_e}{dy} \qquad [7]$$

Here κ is the conductivity of the electrolyte solution and ν is the number of ions per electrolyte molecule. It is assumed that there are no concentration variations within the matrix and that Ohm's law holds

$$i_1 = -\sigma\frac{(r_3^2 - r_2^2)}{r_3^2}\frac{d\phi_1}{dy} \qquad [8]$$

Here σ is the specific conductance of the matrix. The geometric terms are there to correct i_1 from an area basis of the whole volume element to that for the metal phase alone between r_2 and r_3. The current density i_2 is applied to the solution alone, by definition. This un-

usual variation in definitions is for mathematical convenience.

The two current densities, i_1 and i_2, are related to the over-all or total current density I through the conservation of charge

$$I = i_1 + \frac{r_1^2}{r_3^2} i_2 \qquad [9]$$

The physical and mathematical model developed up to here is similar to one presented earlier (32). In the earlier model, the detailed description of the transport of the active, sparingly soluble salt was handled using a single, constant transport coefficient and redox overpotential expression. In this study a more detailed description of the transport of the active salt and the effect of crystallization resistance and complexing are added. Two possible situations for transport of the active salt species to and from the salt lattice are described. The first is simply to assume that the salt completely covers the metal and ions arrive at the metal-salt or salt-electrolytic solution interfaces by solid-state transport through the salt film. If the transference number of the solid salt cation is unity, the film model simply means adding a series resistance to the surface overpotential. The redox expression relating the transfer current density to the surface overpotential between the matrix and solution, $\phi_1 - \phi_2$, is

$$j = -i_o \left\{ \exp\left[\frac{-\alpha_a \mathbf{F}}{RT} \left(\phi_1 - \phi_2 + \frac{j}{\kappa'} r_2 \ln \frac{r_2}{r_1} \right) \right] - \exp\left[\frac{-\alpha_c \mathbf{F}}{RT} \left(\phi_1 - \phi_2 + \frac{j}{\kappa'} r_2 \ln \frac{r_2}{r_1} \right) \right] \right\} \qquad [10]$$

Here i_o is the exchange current density, and α_a and α_c are transfer coefficients. The κ' is the specific conductance of the solid electrolyte film. The geometric term $r_2 \ln r_2/r_1$ accounts for the film thickness and the cylindrical geometry.

The solution-diffusion model assumes that the sparingly soluble salt must dissolve into the electrolytic solution and then diffuse in the liquid phase to the metal surface, or *vice versa*. It is possible that a rate-limiting step occurs at the salt interface due to limitations on how rapidly the salt ions can get out of or into the crystal, so-called crystallographic overpotential. There can also be a rate-limiting step in transport through the solution. The fraction of the metal surface exposed to the liquid electrolytic solution is defined as θ. The over-all mass transfer coefficient is k_m^* defined so that

$$j = n\mathbf{F}k_m^* c_{eq}(1 - c_0/c_{eq}) \qquad [11]$$

where c_0 is the active salt concentration at the metal surface and c_{eq} is the equilibrium concentration of the active salt in the electrolytic solution. The c_{eq} is assumed to depend on local electrolytic solution concentration through a complexing reaction of the form

$$MX_n + X^- = MX^-_{n+1} \qquad [12]$$

where MX_n is the active salt and X^- is the anion of the electrolyte in the liquid electrolyte solution. The species MX^-_{n+1} is the form in which the active metal ion moves through the solution. The equilibrium concentration of the complex MX^-_{n+1} c_{eq}, depends on the concentration of species X^- and the equilibrium constant, K, associated with the reaction [12]. This dependence of c_{eq} on the electrolyte concentration, c_e, and the equilibrium constant have been included in the mathematical calculations.

The over-all mass transfer coefficient, k_m^*, is related to the mass transfer and crystallographic resistances as follows

$$\frac{1}{k_m^*} = \frac{1}{k_m^o \dfrac{1 - 2\theta}{\ln\left(\dfrac{1-\theta}{\theta}\right)}} + \frac{1}{(1-\theta)k_{xtal}} \qquad [13]$$

Here k_m^o is twice the mass transfer coefficient when θ equals 1/2. The expression $(1 - 2\theta)/\ln((1 - \theta)/\theta)$ adjusts the mass transfer coefficient as it is expected to vary depending on the surface area of metal, θ, or surface area of active salt, $1 - \theta$, exposed. The term $(1 - \theta)k_{xtal}$ is the coefficient for the kinetics of dissolution (or deposition) of the salt.

The surface overpotential could be treated as a potential-dependent resistance for mass transfer in series in Eq. [13]. In this study it has been treated separately. The surface overpotential $(\phi_1 - \phi_2)$ and transfer current density are assumed to be related through a concentration-dependent expression of the form

$$j = -\theta i_o \left\{ \exp\left[\frac{\alpha_a \mathbf{F}}{RT} (\phi_1 - \phi_2) \right] - \frac{c_o}{c_{eq}} \exp\left[-\frac{\alpha_c \mathbf{F}}{RT} (\phi_1 - \phi_2) \right] \right\} \qquad [14]$$

Here i_o is the exchange current density when MX_{n-1}^- is at the concentration c_{eq}. The terms α_a and α_c are transfer coefficients.

It is convenient to define a new variable

$$C_1 \equiv c_0/c_{eq}$$

and substitute Eq. [14] into Eq. [11], rearrange terms and get

$$C_1 = \exp\left[\frac{(\alpha_a + \alpha_c)\mathbf{F}}{RT} (\phi_1 - \phi_2) \right] + \frac{(1 - C_1) n\mathbf{F} k_m^* c_{eq}}{\theta i_o} \exp\left[\frac{\alpha_c \mathbf{F}}{RT} (\phi_1 - \phi_2) \right] \qquad [15]$$

If just the first term on the right side is considered, Eq. [15] is seen to reduce to the Nernst equation. The second term on the right side accounts for the nonzero electrochemical kinetic contribution to the overpotential. If k_m^* is small and i_o is large, this contribution will be small under most conditions. However, even for k_m^* small and i_o large, the electrochemical kinetic overpotential becomes dominant as θ goes to zero.

A final but important aspect of the model is the relation between θ, the fraction of the active metal surface exposed, and the state of charge. Before this relation can be expressed, the maximum charge storage per unit volume must be established. There are two factors which may be limiting. First, the amount of active metal may limit the maximum charge, Q_{cm}. For example, when all the cadmium in a $Cd/Cd(OH)_2$ electrode is consumed, that will end the discharge. When the active metal is limiting, Q_{cm} can be expressed as

$$Q_{cm} = n\mathbf{F} \frac{\rho_M}{M_M} \left(1 - \frac{r_{2o}^2}{r_{3o}^2} \right) \qquad [16]$$

Here ρ_M and M_M are density and molecular weight respectively, of the active metal. The r_{2o} and r_{3o} are the initial or fully charged radii r_2 and r_3 (when active salt is converted entirely to metallic form).

A second limitation on the maximum charge per unit volume, Q_{cm}, might be the complete choking or filling of the pore by the active salt MX_n. The salt loading capacity limitation on Q_{cm} is then given by the expression

$$Q_{cm} = Q_{cmo} + n\mathbf{F} \frac{r_{1o}^2}{r_{3o}^2} \frac{1}{\left(\dfrac{M_{MX_n}}{\rho_{MX_n}} - \dfrac{M_M}{\rho_M} \right)} \qquad [17]$$

Here Q_{cmo} is the initial amount of active material, MX_n. The second term on the right side represents the additional MX_n that can be formed from the metal before the pore becomes completely plugged or "choked solid."

The value of Q_{cm} is calculated using both Eq. [16] and [17]. The smaller value of Q_{cm} is selected for use.

It may be that the charge storage is further limited by passivation, *i.e.*, θ going to zero before the maximum charge Q_{cm} is realized. A new charge parameter Q^* is defined

$$Q^* = \lambda Q_{cm} \qquad [18]$$

The coefficient λ represents the fraction of the theoretical maximum of charge per unit volume which can be realized prior to the metal surface becoming completely covered by salt and passivated. (Thus far, the film and solution diffusion models have not been combined. In this solution-diffusion model, the electrode cannot operate once θ goes to zero.)

The relation between θ and the state of charge, Q_c/Q^*, is assumed to be described by the expression

$$\theta = 1 - \left(\frac{Q_c}{Q^*}\right)^p \qquad [19]$$

Here p is essentially a fitting parameter. However, using simple geometric arguments it can be shown that for $p = 0$, film-type passivating active salt deposits are implied. For $p = 2/3$ cubic salt crystals are implied. As p gets very large, long needle-like crystals of the active salt are implied.

This completes the physical and mathematical description of the porous-electrode models. Of necessity, some aspects of the model are still rather highly idealized, and all possible processes are not included. For example, temperature effects are not included. Such effects could have a large effect on the parameter p as well as migration of various species within the pores. However, it is hoped that the more detailed description of transport of active species inside the porous structure will bring the mathematical modeling closer to actual electrode behavior and help in visualizing and describing quantitatively the effects of various processes.

Results of Calculations and Discussion

Details of the computational problem and a copy of the computer program are presented elsewhere (35). The equations have been solved for a few selected operating conditions and parameters. The use of an effective, efficient matrix inversion technique is most important to realizing solutions for a minimum cost. The method described by Newman (33, 34) has been used. Additionally, proper linearization of the nonlinear terms in the equations has been found to reduce greatly run time and therefore cost. Time-dependent results were achieved using the pseudo-steady-state approximation. This approximation means assuming time-independent behavior and solving the steady-state, ordinary differential equations. The steady-state solution is then used to predict the electrode conditions for one time increment later, *i.e.*, new values of r_1, r_2, and Q_c. A new steady-state solution is then found, and so on. The dr_i/dt terms are related to the transfer current, j, and are thus retained, in effect, while still eliminating the explicit time dependence. The actual concentration dependence of the physical properties of the binary solution was used, except t_+° was assumed constant. The exchange current density, i_o, was assumed to be directly proportional to the electrolyte concentration c_e. The correlations of solution properties are based on the work of Chapman, Newman, and Nisancioglu (38-40).

Several results are presented to illustrate a few of the features of this physical and mathematical description of porous electrodes of the second kind. Using input parameter characteristics of the cadmium electrode, overpotential as a function of time has been predicted for mass transfer, crystallization, and electrochemical kinetic rate-controlling steps as shown in Fig. 2. The initial decline in overpotential for crystallization rate control results because of initial lack of nuclei on which the product $Cd(OH)_2$ can precipitate. This leads to large supersaturation initially and higher overpotential. As more sites for $Cd(OH)_2$ precipitation are produced, the level of supersaturation decreases, and the overpotential decreases. Somewhat similar arguments apply to the solution-phase mass transfer; however, the effect is much less pronounced. In each case, the consuming of reactant, cadmium in this case, and blocking of the cadmium surface slowly forces the reaction zone back into the electrode. The resulting increase in resistance in the electrolytic solution causes the observed rise in electrode overpotential. In all cases, a limiting current condition finally terminates the discharge.

In all cases studied for the $Cd/Cd(OH)_2$ electrode, the transfer current is initially high near the front, *i.e.*, the interface with the bulk electrolyte, and "eats" its way back into the electrode as cadmium is consumed. The electrochemical kinetic resistance will always become controlling as the cadmium surface becomes blocked (recall the discussion of Eq. [15]). In Fig. 3, the dimensionless reaction distribution as a function of position is shown at various states of discharge for the electrochemical resistance controlling. The quantity AJ is the dimensionless current density corrected to the outer radius of the pore and defined as $AJ = -j2\pi r_2 L/I\pi r_3^2$. The shapes of the curves in Fig. 3 match quite well with similar experimental data on actual $Cd/Cd(OH)_2$ electrodes presented by Bro and Kang (15).

Although it has been possible to match Bro and Kang's (15) result with the mathematical model at 2 mA/cm² over-all current (35), the overpotential predicted by the solution-diffusion model at 50 mA/cm² is much lower than observed by Bro and Kang. Using the film model, a reasonably good fit of predicted and experimental overpotential time behavior is achieved for a salt-film specific conductance of 3.5×10^{-8} mho/cm, as shown in Fig. 4. However, although the solution-diffusion model predicts a cutoff, *i.e.*, sudden increase in overpotential indicating the electrode is discharged, no such sharp cutoff is predicted by the film model. This result suggests that a combination of the solution-diffusion and film-transport mechanisms in parallel

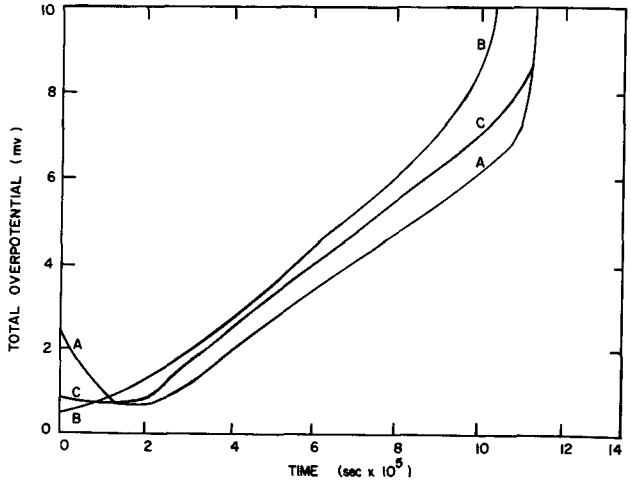

Fig. 2. Overpotential-time curves for a cadmium anode, solution diffusion model, current density 2 mA/cm². Input parameters: $r_1 = r_2 = 6.9 \times 10^{-4}$ cm, $r_3 = 8.93 \times 10^{-4}$ cm, $L = 0.508$ cm, $x_e^\circ = 0.11$, $K = 2 \times 10^{-5}$, $\lambda = 0.7$, $p = 2/3$, $\alpha_a = \alpha_c = 1$. Curve A, crystallization rate control, $k_m^\circ = 1.437$ cm/sec, $k_{xtal} = 1.47 \times 10^{-2}$ cm/sec, $nFc_{eq}/i_o = 0.696$ sec/cm. Curve B, electrochemical kinetic control, $k_m^\circ = k_{xtal} = 1.437$, $nFc_{eq}/i_o = 68.29$. Curve C, mass transfer control, $k_m^\circ = 1.47 \times 10^{-2}$, $k_{xtal} = 1.437$, $nFc_{eq}/i_o = 0.696$.

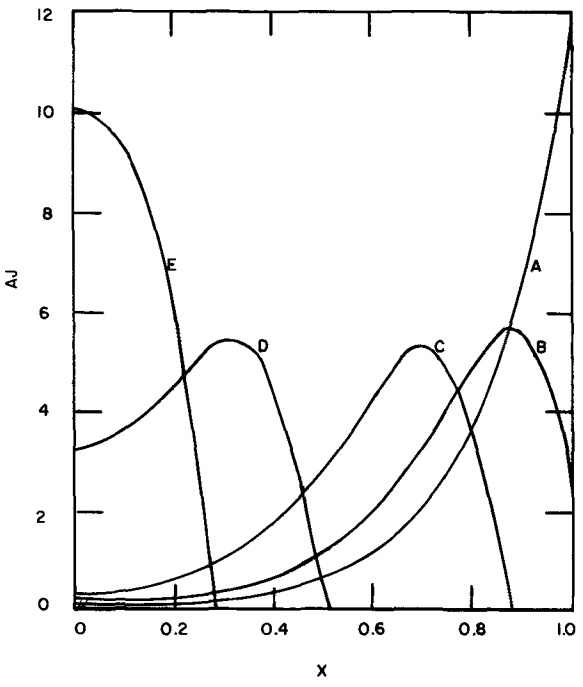

Fig. 3. Current distribution in cadmium anode at various times. Input parameters as in Fig. 2, curve B. Curve A, initial; curve B, 2×10^5 sec; curve C, 4×10^5 sec; curve D, 8×10^5 sec; curve E, 10^6 sec.

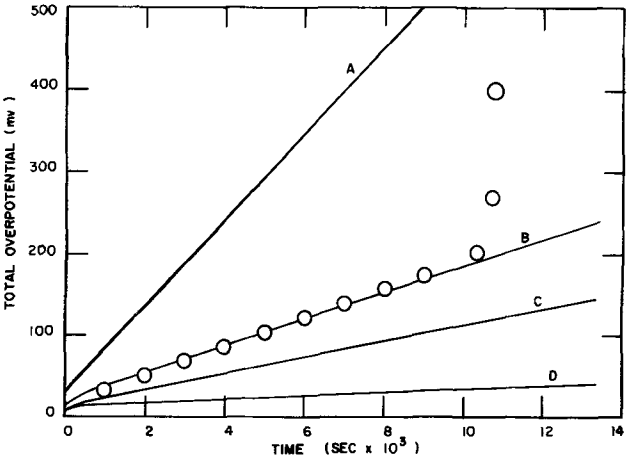

Fig. 4. Overpotential-time curves for cadmium anode at 50 mA/cm^2. Film model for various film conductances; curve A, 10^{-8} mho/cm; curve B, 3.5×10^{-8}; curve C, 10^{-7}; curve D, 10^{-6}. Circles are experimental data of Bro and Kang (16). Physical input parameters are the same as in Fig. 2. Exchange current density is 100 mA/cm^2.

or even series may be required to describe actual electrodes more accurately. Our conclusion here is similar to the explanation proposed by Nagy and Bockris (41) for the zinc-zinc oxide electrode behavior. Additionally the role of CdO may need to be more clearly understood and included as an explicit part of the model.

The model can be used to predict many combinations of current, overpotential, concentration, reaction rates, maximum power, etc., as functions of position, time, and cycling. However, only one more effect will be shown here to illustrate the type of information the mathematical model can produce.

It is generally to be expected that for a uniform state of charge or discharge, *i.e.*, Q_c uniform at different values of y, and a highly conducting matrix, the reaction distribution will be shifted toward the front of the electrode due to resistance losses in the electrolytic solution. This nonuniform reaction distribution is generally expected to become more nonuniform at higher

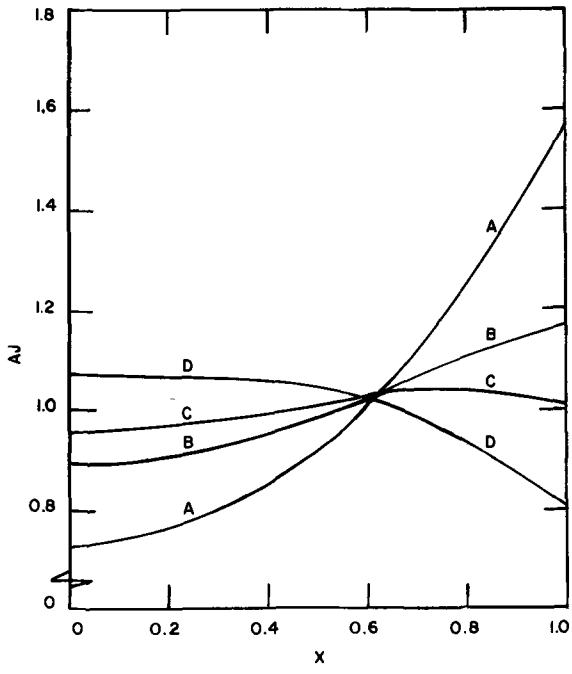

Fig. 5. Initial current distribution in Ag/AgCl cathode at various current densities. Curve A, 1 mA/cm^2; curve B, 7 mA/cm^2, curve C, 10 mA/cm^2; curve D, 15 mA/cm^2. Input parameters: $r_1 = 5.0 \times 10^{-4}$ cm, $r_2 = 7.2 \times 10^{-4}$ cm, $r_3 = 10^{-3}$ cm, $L = 0.1$ cm, $x_e^o = 0.02$, $K = 1.735 \times 10^{-5}$, $\lambda = 0.90$, $p = 2/3$, $\alpha_a = \alpha_c = 1/2$, $k_m^o = 0.1$ cm/sec, $k_{xtal} = 10^3$, $i_o = 1$ mA/cm^2.

currents. This effect is one explanation for lower charge utilization at higher currents or power levels. Using parameters characteristic of the Ag/AgCl electrode, the possible behavior was observed, as shown in Fig. 5. As the current was increased, the reaction distribution became more uniform, and at the highest current density explored, 15 mA/cm^2 in this sequence of runs, the reaction rate was higher toward the back. This behavior can lead to uniform utilization of active material and implies a continual high energy density at high power. The effect is caused by the complexing phenomena incorporated into the mathematical model in Eq. [11] through [15]. At higher cathodic currents, the electrolyte concentration, KCl in this case, increases toward the back of the electrode. The increased Cl^- concentration increases the concentration of the active complex, MX^-_{n+1}. This increased concentration, c_{eq}, increases the mass transfer, crystallization, and electrochemical rates. Thus, the back of the electrode may become a favored reaction zone in spite of the solution resistance losses. The proper use and control of this complexing phenomenon could lead to improved battery design and performance.

The current distribution as a function of position for various states of discharge at 40 mA/cm^2 is shown in Fig. 6 to illustrate further the effect of the complex formation on Ag/AgCl electrode behavior.

A final example of the predictive capability of the mathematical model for the Ag/AgCl electrode is the variation of the discharge efficiency or energy storage capability with applied current as shown in Fig. 7. A higher mass transfer coefficient, k_m^o, is seen to increase utilization efficiency at high currents. The discharge was at constant current in each case. The electrode was assumed to be discharged when the overpotential began to rise very rapidly and the numerical computations would no longer converge. Error bars are used at intermediate points because coarse time grids were used. Accurate convergence and fine time steps became expensive and time consuming under these conditions. However, the end points at 0% discharge efficiency are accurately determined, since they correspond to the limiting currents at the initial charge conditions.

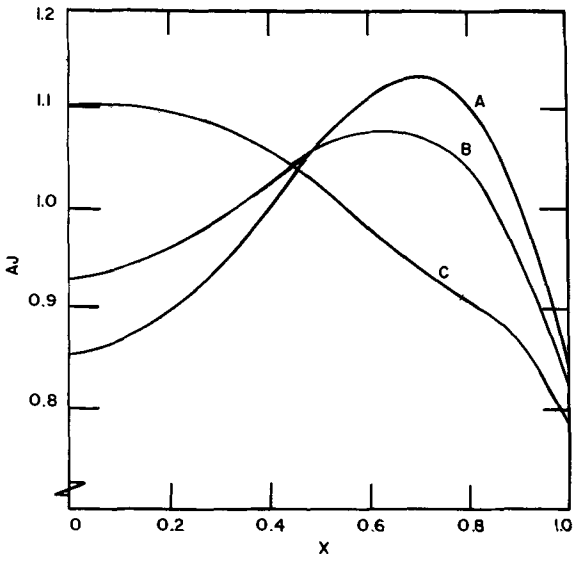

Fig. 6. Current distribution in Ag/AgCl cathode, 40 mA/cm², at various times. Input parameters same as Fig. 5 except k_m^o = 0.3 cm/sec. Curve A, initial; curve B, 1000 sec; curve C, 2000 sec.

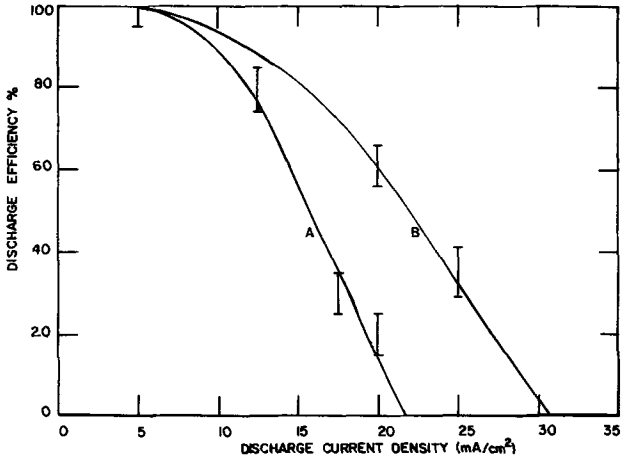

Fig. 7. Discharge efficiency as a function of discharge current density for Ag/AgCl cathode. Input parameters same as Fig. 5 except i_o = 100 mA/cm². Curve A, k_m^o = 0.10 cm/sec; curve B, k_m^o = 0.12 cm/sec.

Conclusions

A key to the validity and applicability of the models is the extent to which the local overpotential expressions approximate conditions inside the operating porous electrode. Apparently, the general behavior of a cadmium anode is best approximated by the solution-diffusion model at low current densities and the film model at higher current densities. The formation of a CdO layer may explain this result. A combination of the film and solution-diffusion models would be a logical extension of this work.

Solution-diffusion model results are very sensitive to the magnitude of k_m^o. Possibly further interpretation and investigation of this parameter can explain the failure of some systems to give higher energy and power densities. The results of this study show that cathodic failure is caused by low mass transport which leads to limiting currents in the electrode. Anodic failure is, in general, caused by blockage of pores or by complete coverage of the metal surface by product crystallites. All these effects are closely related to the magnitude and functional dependence for the mass transfer coefficient k_m^*.

Dunning *et al.* (31) calculated current distributions without considering the effects of concentration variations or of complexing reactions. By considering these effects, the present solution-diffusion model predicts that a peak in current distribution may occur at initial polarization and that the middle of a porous cathode may be exhausted before the front face. This effect has not been previously observed and suggests that experiments could be performed to look for it.

The film model presented here is simpler than the solution-diffusion model. It does not predict such subtle but important phenomena as variations of useful energy density with discharge current. Unless the films are very thin or highly conductive, the film model represents the mode of operation of passivated electrodes which, hopefully, is a condition not often encountered in battery operation. For highly conducting films, a more nearly correct model may involve competing or series solution-diffusion steps or more complex solid-state diffusion processes than those discussed here. The nickel oxide or lead dioxide electrodes may be in the latter classification.

Only a few computer results have been presented compared to the many possible performance predictions possible. The nonuniform current distributions predicted by all models lead to nonuniform reactant conversion. On cycling [see also Ref. (32)], these effects propagate and can ultimately lead to some sort of failure. The programs can keep accurate account of the state of charge. Battery performance (current-voltage curves for example) can be determined as a function of state of charge and possibly improved methods can be developed to determine more easily the state of charge for real batteries.

The usefulness of models and predictions of the type presented here is predicated on the faithful description of actual, physical processes. An important next step is experimental validation and improved descriptions of the elementary processes in real batteries.

Acknowledgments

Financial support for this work was provided in part by Naval Air Systems Command on Contract No. N00019-71-C-0342.

Manuscript submitted Oct. 2, 1972; revised manuscript received Feb. 21, 1973.

Any discussion of this paper will appear in a Discussion Section to be published in the June 1974 JOURNAL.

SYMBOLS

A_i	chemical symbol for species i
A	a structural parameter for the metal salt system, cm³/coulomb
a_e	activity of the electrolyte solution
AJ	a dimensionless reaction rate in the electrode, $-2jr_2L/Ir_3^2$
C_1	ratio of surface concentration to bulk saturation concentration of active species
c_T	total concentration $\Sigma_i c_i$, mole/cm³
c_i	concentration of species i, mole/cm³
c_{eq}	equilibrium concentration of complex species, mole/cm³
c_o	concentration of active species at the metal surface, mole/cm³
D	diffusion coefficient of the electrolyte, cm²/sec
e^-	symbol for the electron
$\mathbf{F}$	Faraday's constant, 96,500 coulombs/equivalent
I	superficial applied current density, A/cm²
i_1	superficial current density in metal phase, A/cm²
i_2	actual current density in solution phase, A/cm²
i_o	exchange current density, A/cm²
j	local (internal) cathodic current density, A/cm²
K	dissolution constant for complexation reaction
k_m^*	combined mass transfer and crystallization rate constant, cm/sec
k_m^o	mass transfer coefficient, cm/sec
k_{xtal}	a crystallization rate constant, cm/sec
L	total electrode thickness, cm
M_i	molecular weight of species i
MX_n	chemical symbol for a metal salt
n	number of electrons transferred in the electrode reaction as written
n	number of anions in a salt MX_n
N_i	flux of species i, mole/cm² sec
p	an adjustable parameter characterizing internal

crystal morphology
Q_c amount of charge stored at a point within the electrode, coulombs/cm³ of electrode
Q_{cm} the maximum amount of active material salt possible to store in the pore, coulombs/cm³
Q^* effective amount of active material available, coulombs/cm³
r_1 inner radius available for solution phase conduction, cm
r_2 inner radius of metal, cm
r_3 outer radius which defines over-all electrode area, cm
RT gas constant multiplied by the absolute temperature, joules/mole
s_i stoichiometric number for species i
t time, sec
t_+^* transference number of cation referred to molar average velocity
t_+° transference number of cation referred to solvent velocity
v^* molar average velocity, $\sum_i c_i v_i / \sum_i c_i$, cm/sec
v_i velocity of species i in solution, cm/sec
x_e particle fraction of the electrolyte, $c_e/(c_o + 2c_e)$
x dimensionless distance from backing plate, y/L
y dimensionless coordinate, cm
z_i charge number of species i

Greek symbols

α_c a kinetic parameter
α_a a kinetic parameter
θ microporosity of crystallite-surface system
κ specific conductance of electrolytic solution $ohm^{-1}\ cm^{-1}$
κ' conductivity of the solid film $ohm^{-1}\ cm^{-1}$
λ an adjustable parameter corresponding to the fraction of Q_{cm} reached before blocking of the surface occurs
ν number of ions per molecule of dissolved electrolyte (equals 2 for a 1-1 electrolyte)
ρ_i density of solid species i, g/cm³
σ conductivity of metal, mho/cm
ϕ_1 potential in metal phase, V
ϕ_2 potential in solution phase, V

REFERENCES

1. G. T. Croft, *This Journal*, **106**, 278 (1959).
2. J. P. G. Farr and N. A. Hampson, *Electrochem. Technol.*, **6**, 10 (1968).
3. P. E. Lake and E. J. Casey, *This Journal*, **105**, 52 (1958).
4. M. A. V. Devanathan and S. Lakshmanan, *Electrochim. Acta*, **13**, 667 (1968).
5. R. D. Armstrong, E. H. Boult, D. F. Porter, and H. R. Thirsk, *ibid.*, **12**, 1245 (1967).
6. S. U. Falk, *This Journal*, **107**, 661 (1960).
7. M. W. Breiter and J. L. Weininger, *ibid.*, **113**, 652 (1966).
8. S. Yoshizawa and Z. Takehara, *Electrochim. Acta*, **5**, 240 (1961).
9. R. E. Visco and R. H. Sonner, Abstract No. 7, p. 18, Electrochem. Soc. Extended Abstracts, Fall Meeting, Detroit, Michigan, Oct. 5-9, 1969.
10. P. C. Milner and U. B. Thomas, *Advanc. Electrochem. Electrochem. Eng.*, **5**, 1 (1967).
11. Y. Okinaka, *This Journal*, **117**, 289 (1970).
12. M. Fleischmann and H. R. Thirsk, *Trans. Faraday Soc.*, **51**, 71 (1955).
13. F. G. Will and H. J. Hess, Abstract No. 68, p. 168, Electrochem. Soc. Extended Abstracts, Fall Meeting, Atlantic City, N. J., Oct. 4-8, 1970.
14. F. G. Will and H. J. Hess, *Proc., Advances in Battery Technology Symposium*, Southern California-Nevada Section of Electrochem. Soc., **6**, 47 (December 1970).
15. P. Bro and H. Y. Kang, *This Journal*, **118**, 519 (1971).
16. D. A. Vermilyea, *Advan. Electrochem. Electrochem. Eng.*, **3**, 211 (1963).
17. K. J. Vetter, "Electrochemical Kinetics," Academic Press, New York (1967).
18. H. Lal, H. R. Thirsk, and W. F. K. Wynne-Jones, *Trans. Faraday Soc.*, **47**, 70 (1951).
19. W. Jaenicke, R. P. Tischer, and H. Gerischer, *Z. Elektrochem.*, **59**, 448 (1955).
20. R. D. Giles, *J. Electroanaly. Chem. Interfacial Electrochem.*, **27**, 11 (1970).
21. H. Lal, H. R. Thirsk, and W. F. K. Wynne-Jones, *Trans. Faraday Soc.*, **47**, 999 (1951).
22. K. S. Indira and K. S. G. Doss, *J. Electroanal. Chem. Interfacial Electrochem.*, **17**, 145 (1968).
23. R. de Levie, *Advan. Electrochem. Electrochem. Eng.*, **6**, 329 (1967).
24. Edward A. Grens, II, Ph.D. thesis in Chem. Eng., Univ. Calif., Berkeley, September 1963.
25. A. Winsel, *Z. Elektrochem.*, **66**, 287 (1962).
26. J. S. Newman and C. W. Tobias, *This Journal*, **109**, 1183 (1962).
27. L. G. Austin and E. G. Gagnon, *Am. Inst. Chem. Eng. J.*, **17**, 1057 (1971).
28. E. A. Grens and C. W. Tobias, *Ber. Bunsenges. Physik. Chem.*, **68**, 236 (1964).
29. R. C. Alkire, Ph.D. thesis in Chem. Eng., Univ. Calif., Berkeley, September 1968.
30. R. C. Alkire. E. A. Grens, and C. W. Tobias, *This Journal*, **116**, 1328 (1969).
31. J. S. Dunning and D. N. Bennion, *Proc., Advances in Battery Technology Symposium*, Southern California-Nevada Section of Electrochem. Soc., **5**, 135 (December 1969).
32. J. S. Dunning, D. N. Bennion, and J. Newman, *This Journal*, **118**,1251 (1971).
33. E. A. Grens, *Electrochim. Acta*, **15**, 1047 (1970).
34. John Newman, Douglas Bennion, and C. W. Tobias, *Ber. Bunsenges. Physik. Chem.*, **69**, 608 (1965).
35. John S. Dunning, Ph.D. dissertation. School of Engineering, Univ. California, Los Angeles, December 1971.
36. J. Newman, *Ind. Eng. Chem. Fundamentals*, **7**, 514 (1968).
37. J. Newman, Univ. California Lawrence Radiation Lab. Report UCRL-17739, August 1967.
38. Thomas W. Chapman, Ph.D. thesis in Chem. Eng., Univ. California, Berkeley, 1967.
39. T. W. Chapman, and John Newman, Univ. California Lawrence Radiation Lab. Report UCRL-17767, May 1968.
40. J. Newman and K. Nisancioglu, Unpublished results.
41. Z. Nagy and J. O'M. Bockris, *This Journal*, **119**, 1129 (1972).

On the Displacement Reaction in the Concentration Cells Involving Liquid Zinc and Cadmium Alloys

Z. Moser and K. Fitzner

Institute for Metal Research, Polish Academy of Sciences, Kraków, Poland

ABSTRACT

The equilibrium constant of displacement reaction $Zn + CdCl_2 \rightarrow Cd + ZnCl_2$ occurring in the concentration cell $Zn(l)\,|ZnCl_2$ in $(LiCl\text{-}KCl)_{eut}(l)\,|Zn\text{-}Cd(l)$ has been determined on the basis of the following parameters: (*i*) $\Delta F^{o}{}_{T}$ of the displacement reaction assuming ideal solutions for the salt and metal phases; (*ii*) data of dilute solutions of zinc in cadmium; (*iii*) thermodynamic properties of dilute solutions of $ZnCl_2$ and $CdCl_2$ in LiCl-KCl eutectic obtained in this paper from formation cells.

In this case of dilute solutions of zinc in cadmium the influence of displacement reaction is visible in the values of zinc activity coefficients at $X_{Zn} = 0.01$ molar fraction resulting in deviations from the linear dependence of $\ln \gamma_{Zn}$ *vs.* X_{Zn}. Investigations enabled the calculation of the correction for the measured emf values, which when taken into account prove the linear character of $\ln \gamma_{Zn}$ *vs.* X_{Zn} over the range $X_{Zn} = 0.01\text{-}0.1$ molar fraction in Zn-Cd system.

Investigations on dilute solutions of zinc carried out to determine the self-interaction parameter $\epsilon_{Zn}{}^{Zn}$, defined by Wagner (1), show that the dependence of $\ln \gamma_{Zn}$ *vs.* X_{Zn}, which is linear for dilute solutions, deviates from a linear relationship for some systems as $X_{Zn} \rightarrow 0$. The typical linear dependence of $\ln \gamma_{Zn}$ *vs.* X_{Zn} is illustrated in Fig. 1 by the Zn-Pb system (2), and deviations from a linear behavior as $X_{Zn} \rightarrow 0$ by the Zn-Cd (3) and Zn-In (4) systems. These deviations from linearity may be explained by a displacement reaction of the type

$$Me + ZnCl_2 = Zn + MeCl_2 \qquad [1]$$

(where Me = Cd, In, or Ga) occurring between $ZnCl_2$ in the metal salts and the metal of an alloy electrode of a concentration cell.

The closer Zn and the metal of the alloy electrode are to each other in the electromotive series, the further the equilibrium of reaction [1] lies to the right. Wagner (5) has assumed that the occurrence of reaction [1] is connected with the difference in standard-free energy of the formation of the metal chlorides. If the absolute value of the difference $\Delta F^{o}{}_{ZnCl_2} - \Delta F^{o}{}_{MeCl_2}$ is less than 7000 cal, the influence of the displacement reaction should be taken into account, and the range of the concentration of the components experimentally determined. Pursuing their considerations, Wagner and Werner (6) calculated the error resulting from reaction [1] in an experimentally determined activity.

Key words: concentration cell, displacement reaction, equilibrium constant, dilute $ZnCl_2$ and $CdCl_2$ solutions, formation cell, curve of equilibrium compositions.

However, the method of calculating the error given in (6) is unsatisfactory if the cation of the metal salt acting as a charge carrier changes in valency in the temperature range of the cell operation, as is the case with the gallium salts (7).

The present paper is an attempt to determine the composition of the alloy and the temperature range over which reaction [1] may occur by taking into consideration the metal-salt equilibrium.

The results of the investigations obtained for the Zn-Cd system are discussed, and the equilibrium of the reaction

$$Zn + CdCl_2 \rightarrow Cd + ZnCl_2 \qquad [2]$$

is determined.

From Fig. 1 in a paper by us (3) it appears that the displacement reaction occurs within the temperature range 773°-873°K, consequently our calculations have been made for three different temperatures: 773°, 823°, and 873°K. Utilizing the dependence

$$\Delta F^{o}{}_{T} = -2F\,(E^{oT}{}_{ZnCl_2} - E^{oT}{}_{CdCl_2}) \qquad [3]$$

and the data obtained by Hildebrand and Wachter (8),

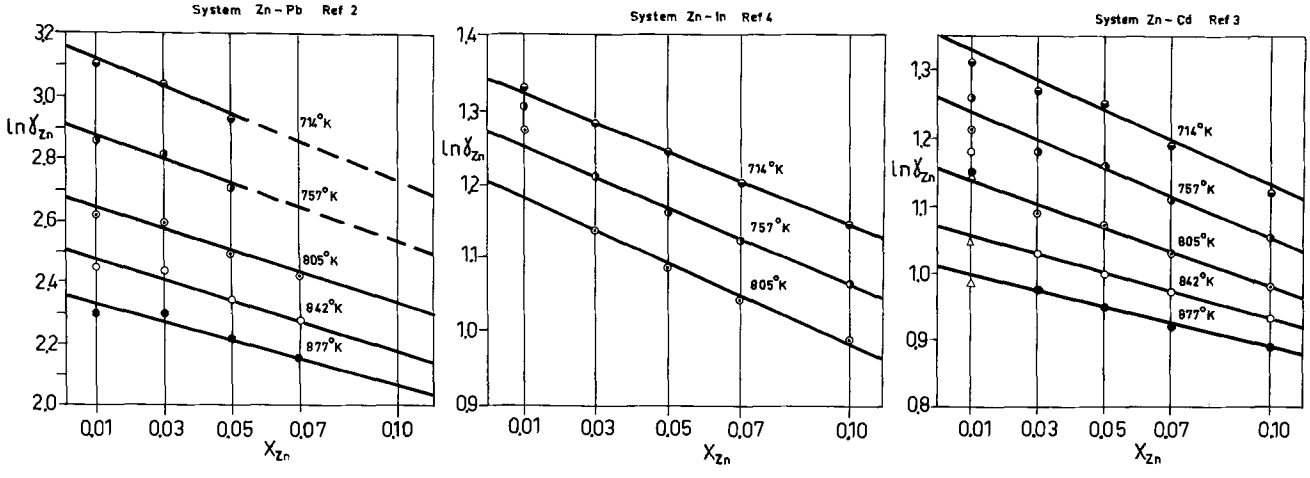

Fig. 1. Dependence $\ln \gamma_{Zn}$ *vs.* X_{Zn} for the Zn-Pb, Zn-Cd, and Zn-In systems. For the Zn-Cd system the graph includes points Δ calculated from corrected emf values.

Table I. The values of equilibrium constant of displacement reaction [2]

T°K	ln K	K
773	5.11502	166.5
823	4.66912	106.6
873	4.27116	71.6

Lorenz and Velde (9), and Lantratow and Alabyszew (10), which allows the following relationships to be determined

$$E^{\circ}_{ZnCl_2} = 1.9178 - 0.000696t \pm 0.0022V \quad [4]$$

$$E^{\circ}_{CdCl_2} = 1.6990 - 0.000599t \pm 0.0037V \quad [5]$$

(where t is the temperature in °C) the equilibrium constant K of reaction [2] was calculated and is summarized in Table I, and the dependence of ln K on temperature was determined to be

$$\ln K = \frac{5659}{T} - 2.208 \quad [6]$$

Use was made of the fact that reaction [2] occurs in the concentration cell in the solution LiCl-KCl which appears in excess relative to $ZnCl_2$ and $CdCl_2$. These solutions may be regarded as a solvent thus allowing the determination of the thermodynamic properties of $ZnCl_2$ and $CdCl_2$ in the eutectic LiCl-KCl for each metal chloride separately (1), since theoretical considerations show only slight differences in the activity coefficient on transition from a ternary to a quaternary system for dilute solutions. The concentration range of Zn in Cd, X_{Zn} — 0.01 — 0.09, permits the metal phase to be regarded in a similar way. Thus when $X_{Zn} \to 0$ in the system Zn-Cd we assume limiting values γ°_{Zn} instead of γ_{Zn}. Similarly when $X_{ZnCl_2} = X_{CdCl_2} \to 0$ in the salt phase the values $\gamma^{\circ}_{ZnCl_2}$ and $\gamma^{\circ}_{CdCl_2}$ may be assumed instead of γ_{ZnCl_2} and γ_{CdCl_2}.

Considering the negligible mutual solubility of the metals in salts, then $X_{Zn} + X_{Cd} \cong 1$ and $X_{CdCl_2} + X_{ZnCl_2} \cong 1$, thus the equilibrium constant of reaction [2] may be expressed in the form

$$\left(\frac{X_{[Cd]}}{1 - X_{[Cd]}}\right)\left(\frac{1 - X_{(CdCl_2)}}{X_{(CdCl_2)}}\right) = K\left(\frac{\gamma^{\circ}_{CdCl_2}}{\gamma^{\circ}_{ZnCl_2}}\right)\gamma^{\circ}_{Zn} = K'(T) \quad [7]$$

or in the form

$$\left(\frac{X_{[Cd]}}{1 - X_{[Cd]}}\right)\left(\frac{1 - X_{(CdCl_2)}}{X_{(CdCl_2)}}\right) = K \quad [8]$$

if it is assumed that the metal and the salt phases are both ideal solutions. It follows from Eq. [7] and [8] that to calculate the equilibrium composition of the phases the following are necessary:

(*i*) The calculation of the equilibrium constant of reaction [2] from the free-energy change, ΔF°_T, of that reaction according to formula [3].

(*ii*) Experimental determination of limiting activity coefficients of zinc in dilute solutions of zinc in cadmium. These values are available elsewhere (3) where the following formula was given

$$\ln \gamma^{\circ}_{Zn} = \frac{1131}{T} - 0.31 \quad [9]$$

which takes into account only those points having a linear dependence (Fig. 1). (The deviation from this linear dependence at $X_{Zn} = 0.01$ molar fraction is caused by the displacement reaction [2].)

(*iii*) Experimental evaluation of $\gamma^{\circ}_{ZnCl_2}$ and $\gamma^{\circ}_{CdCl_2}$ in dilute $ZnCl_2$-LiCl-KCl and $CdCl_2$-LiCl-KCl solutions obtained in this paper.

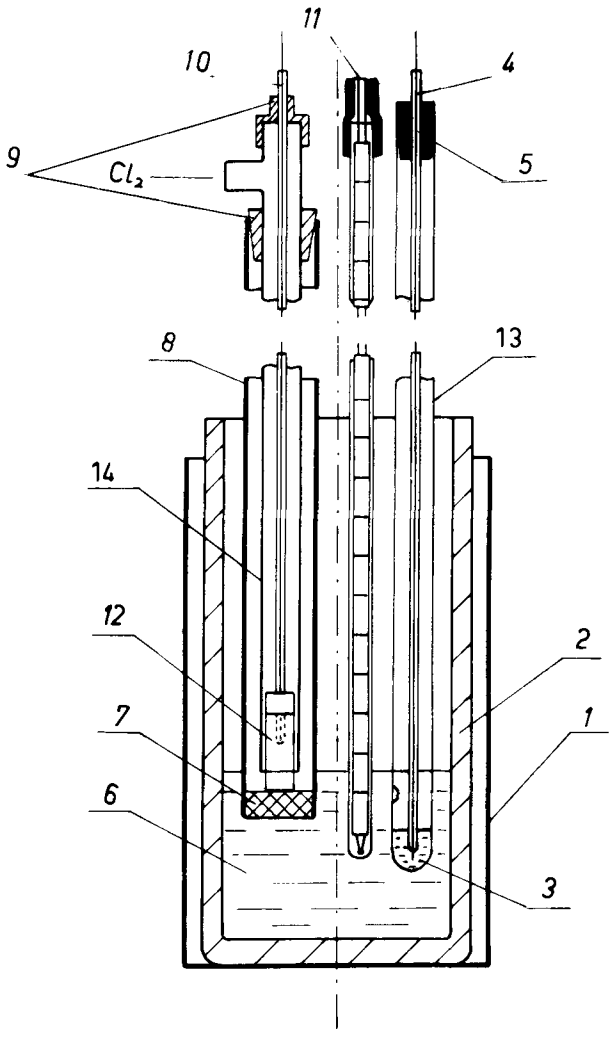

Fig. 2. Scheme of the experimental cell

Experimental

The investigation of the thermodynamic properties of $ZnCl_2$ and $CdCl_2$ were carried out using the reversible formation cells

$$Zn(l) \mid ZnCl_2 \text{ in } (LiCl\text{-}KCl)_{eut.}(l) \mid Cl_2(g)$$

$$Cd(l) \mid CdCl_2 \text{ in } (LiCl\text{-}KCl)_{eut.}(l) \mid Cl_2(g)$$

over the concentration range 0.01-0.09 X_{ZnCl_2} and X_{CdCl_2} molar fractions. The scheme of the cell is shown in Fig. 2. A crucible (point 2) made of silica and containing liquid salts (point 6) was placed in an alumina tube (point 1). The following were immersed in the liquid salts:

(*i*) A high-melting glass tube (point 13) closed at one end in the bottom of which was placed the liquid metal (point 3), Zn or Cd. An electrode made of tungsten wire (point 4) passing through the rubber stopper (point 5) of the tube (point 13) was introduced into the metal;

(*ii*) A Pt-PtRh thermocouple (point 11) was placed in a quartz tube enabling temperature measurements to ±2°C.

(*iii*) A diaphragm (point 8), with a sintered alundum cement plug (point 7) at the bottom, contains the chlorine electrode made of a high-melting glass tube (point 14), a graphite rod (point 12), and a Pt wire (point 10). Seals (point 9) were made of Teflon.

The preparation of the electrode and the diaphragm have been described elsewhere (11-12). The cell was placed in an ordinary resistant furnace with a longitudinal temperature gradient of ±2°C.

Temperature and emf were recorded on a Pye potentiometer having an accuracy of 0.01 mV.

Procedure

The eutectic LiCl-KCl mixture obtained by evaporating a water solution, was dried under vacuum for about 70 hr while the temperature was increased. The dried mixture was next placed in a crucible (point 2, Fig. 2) located in an operating furnace. The required amount of $ZnCl_2$ or $CdCl_2$ was added and the salts melted under an HCl atmosphere. After melting, HCl was passed through the melt for about 1 1/2 hr followed by argon for about 1 hr. The crucible was placed in the measurement furnace in an alumina sheath (point 1) and the cell arranged as shown in Fig. 2. Measurements were made for temperatures increasing or decreasing at a constant rate. The results of measurements were corrected for the thermoelectric emf between the tungsten and the platinum which were used as the leads from the electrodes. The composition of salts for the particular runs were determined analytically after a series of measurements had been completed.

The results of the measurements are given in Fig. 3 and 4 and show a linear dependence of emf on temperature. Applying the least squares method, the experimental data in the case of the $ZnCl_2$-LiCl-KCl system may be presented by the following equations for the $ZnCl_2$-LiCl-KCl system

$$X_{ZnCl_2} = 0.010 \quad E = 2.1299 - 0.000441t \pm 0.0041V \quad [10]$$
$$X_{ZnCl_2} = 0.023 \quad E = 2.1202 - 0.000490t \pm 0.0039V \quad [11]$$
$$X_{ZnCl_2} = 0.036 \quad E = 2.1088 - 0.000501t \pm 0.0037V \quad [12]$$
$$X_{ZnCl_2} = 0.050 \quad E = 2.0934 - 0.000512t \pm 0.0038V \quad [13]$$
$$X_{ZnCl_2} = 0.077 \quad E = 2.0907 - 0.000544t \pm 0.0041V \quad [14]$$

and for the $CdCl_2$-LiCl-KCl system

$$X_{CdCl_2} = 0.010 \quad E = 1.8646 - 0.000422t \pm 0.0047V \quad [15]$$
$$X_{CdCl_2} = 0.024 \quad E = 1.8354 - 0.000429t \pm 0.0039V \quad [16]$$
$$X_{CdCl_2} = 0.038 \quad E = 1.8264 - 0.000466t \pm 0.0038V \quad [17]$$
$$X_{CdCl_2} = 0.050 \quad E = 1.8256 - 0.000471t \pm 0.0038V \quad [18]$$
$$X_{CdCl_2} = 0.073 \quad E = 1.8062 - 0.000466t \pm 0.0037V \quad [19]$$

where t is the temperature in °C. The deviations given for E at each concentration in Eq. [10]-[19] are the sum of the standard deviation of the emf and the correction for the oscillation of chlorine pressure about 1 atm.

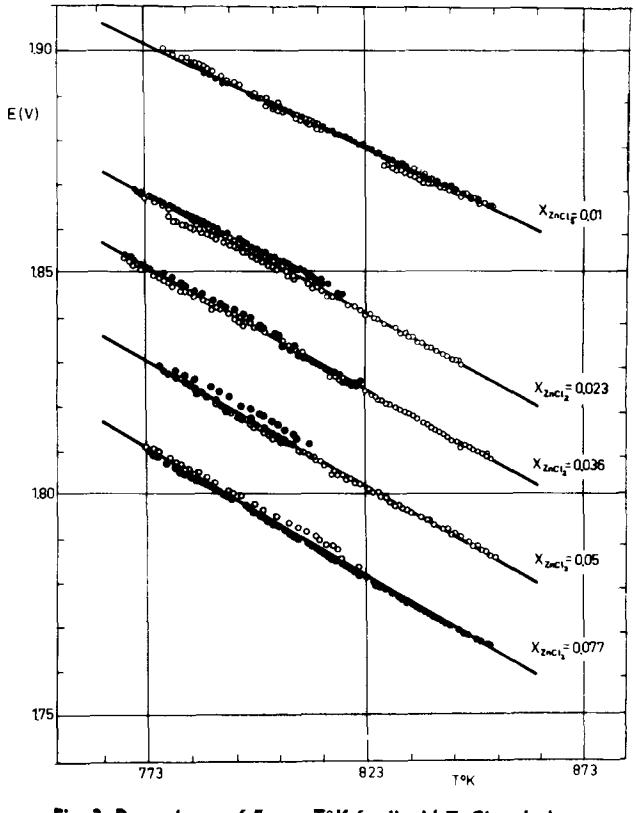

Fig. 3. Dependence of E_V vs. T°K for liquid $ZnCl_2$ solutions

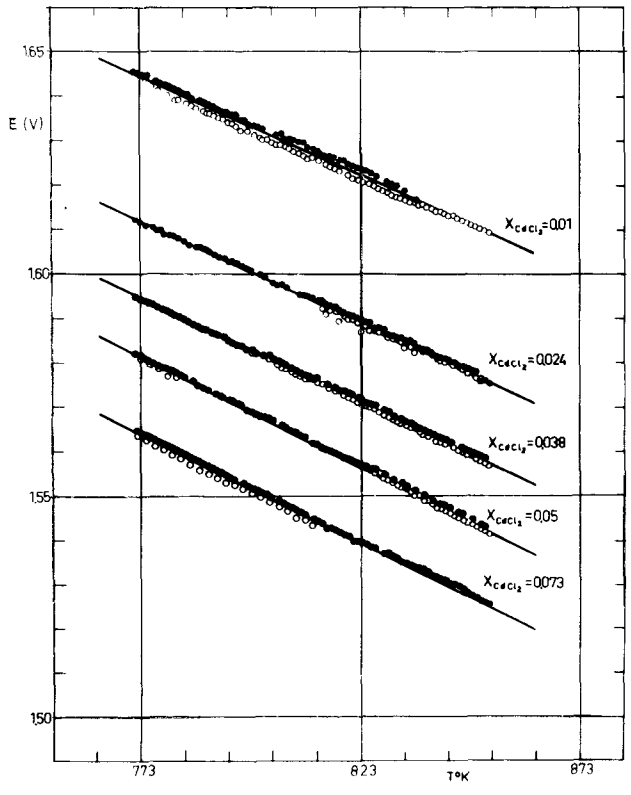

Fig. 4. Dependence E_V vs. T°K for liquid $CdCl_2$ solutions

Employing the relation

$$E_i - E^\circ_i = -\frac{RT}{nF} \ln a_i \quad [20]$$

where E°_i is the standard cell potential obtained with pure $ZnCl_2$ or $CdCl_2$, E_i is the emf value of the formation cell for the $ZnCl_2$-LiCl-KCl or $CdCl_2$-LiCl-KCl system, T is in °K, R is the ideal gas constant = 1.986 cal/deg, n is the electrochemical valency, $\mathbf{F}$ is Faraday's constant = 23,066 cal/V, and a_i is the activity of $ZnCl_2$ or $CdCl_2$. The ln γ_i was calculated for the particular salt compositions taking into account Eq. [10]-[19] and assuming $P_{Cl_2} = 1$ atm, and $n = 2$.

The results of the calculations are presented in Fig. 5 and 6. It was found that within the concentration range 0.01-0.1 molar fraction they may be described by a linear dependence as in the case of the metal systems. The calculated values $\gamma^\circ_{ZnCl_2}$ and $\gamma^\circ_{CdCl_2}$ for $X_{ZnCl_2} = X_{CdCl_2} = 0$ are given in Table II.

To verify the obtained results at a temperature of 773°K the activities calculated from [20] were compared with those determined experimentally by Yang and Hudson (13). Figure 7 shows the good agreement obtained between both sets of data.

Discussion

Equations [6] and [7] were transformed so that assuming the composition of the metal phase, it was possible to calculate the respective concentrations of the salt phase. The obtained results are given in Fig. 8 for the temperatures 773° and 873°K along with the data of Lorenz and Schulz (14) and Jellinek and Siewers (15).

To determine the composition of the metal phase, starting from which the reaction [2] may occur in the

Table II. The values of limiting activity coefficients of $CdCl_2$ and $ZnCl_2$

T°K	$\gamma^\circ_{ZnCl_2} \times 10^2$	$\gamma^\circ_{CdCl_2} \times 10^2$
773	0.346	4.538
823	0.451	5.586
873	0.572	6.730

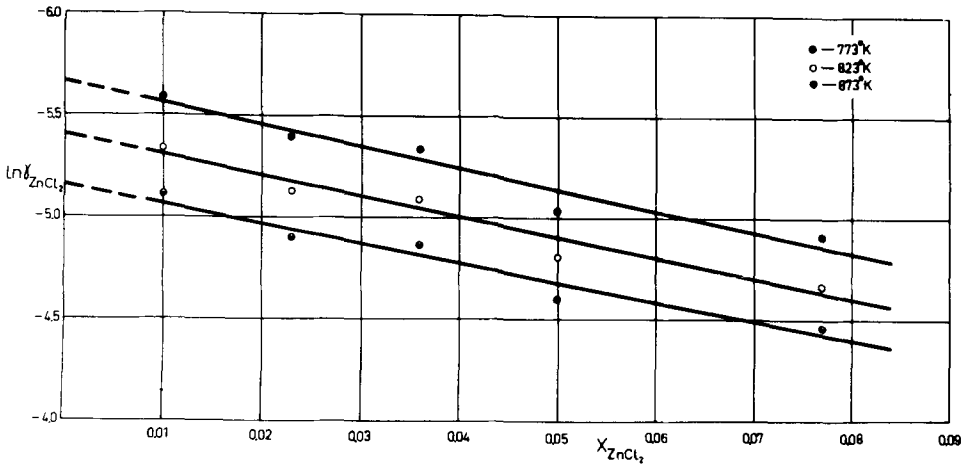

Fig. 5. Dependence ln γ_{ZnCl_2} *vs.* X_{ZnCl_2} for liquid $ZnCl_2$ solutions.

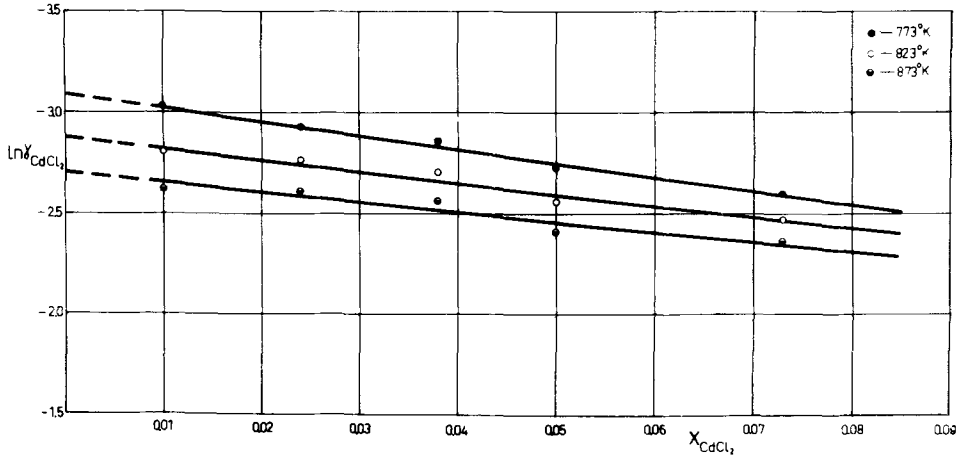

Fig. 6. Dependence ln γ_{CdCl_2} *vs.* X_{CdCl_2} for liquid $CdCl_2$ solutions.

cell, we assume that it corresponds to the extreme point of the curve of equilibrium composition in the coordinates $X_{CdCl_2} - X_{Cd}$ turned clockwise 45°. At this point the change in the metal-phase composition given by dX_{Cd}, corresponds to the change in the salt-phase composition dX_{CdCl_2}, which is defined by the condition

$$\frac{dX_{CdCl_2}}{dX_{Cd}} = 1 \qquad [21]$$

When the condition of reaction [21] is exceeded, the change in the metal-phase composition, given by dX_{Cd}, results in a great change in X_{CdCl_2} which corresponds to the formation of $CdCl_2$ in the salt phase as a result of reaction [2]. From Eq. [21] and [7] we obtained

$$X_{[Cd]} = \frac{\sqrt{K'}}{1 + \sqrt{K'}} \qquad [22]$$

which allowed the determination of the metal-phase composition (alloy electrode) for a given temperature.

The results are shown in Fig. 9 and this dependence may be presented by the equation

$$X_{[Cd]} = -9 \times 10^{-5}T + 1.058 \qquad [23]$$

Assuming that the lowest zinc concentration of the alloy electrode used in the investigations is $X_{Zn} = 0.01$, it is possible by means of Eq. [23] to determine the temperature, starting from which, as a result of reaction [2], the composition of the alloy electrode will be changed, the change eventually influencing the emf measurements. The temperature, 756°K, is in very good accordance with the plot ln γ_{Zn} *vs.* X_{Zn} for the Zn-Cd system in Fig. 1.

As can be seen from Fig. 8, the obtained results differ both from the experimental data obtained by Lorenz and Schulz (14) and from those of Jellinek and Siewers (15). It does not seem likely that the errors these

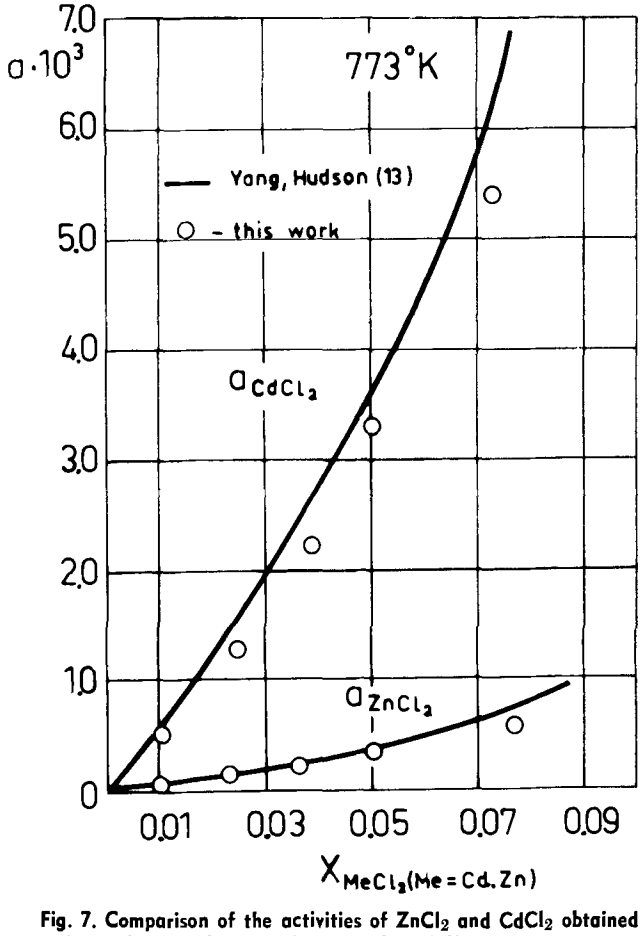

Fig. 7. Comparison of the activities of $ZnCl_2$ and $CdCl_2$ obtained experimentally with the data given elsewhere (13).

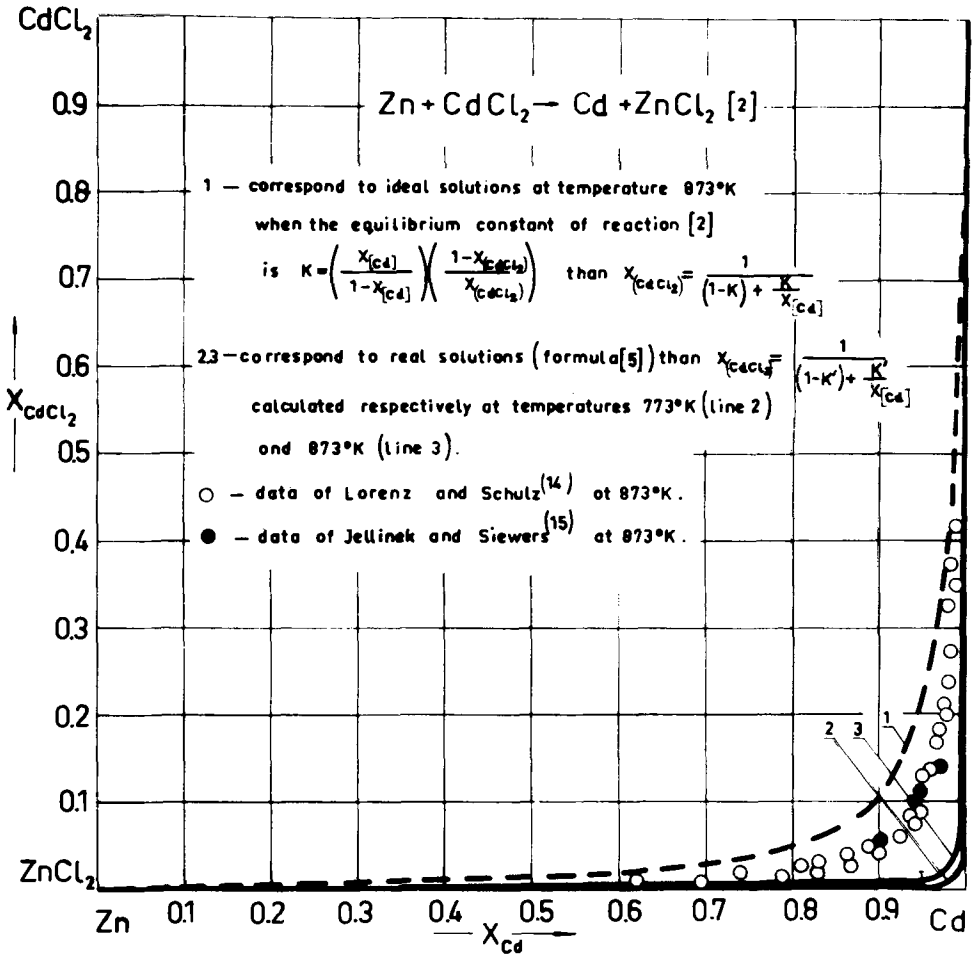

Fig. 8. Curve of the equilibrium composition of a displacement reaction compared with the ideal solutions and the data from literature.

authors (14, 15) may have made, resulting mainly from chemical analysis or poor dehydrating of salts, can account for these differences.

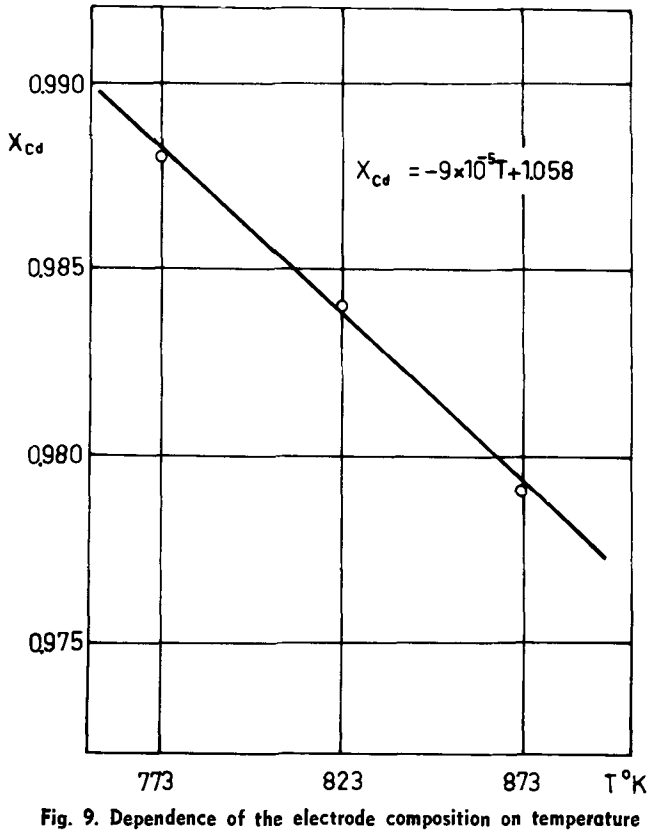

Fig. 9. Dependence of the electrode composition on temperature in the case of liquid Zn-Cd solutions.

In these papers (14, 15) the salt phase consisted of the solutions $ZnCl_2$-$CdCl_2$, while in our cell we were concerned with the $ZnCl_2$-$CdCl_2$-LiCl-KCl system, where $ZnCl_2$ and $CdCl_2$ are present only in small quantities, hence we consider that the main reason for the translocation of the curve is the eutectic LiCl-KCl. Assuming the salt phase is an ideal solution, from Eq. [7] $K' = K$, and $\gamma^{\circ}_{Zn} = 192.6$ at 873°K and we obtain almost the same values as in the papers (14, 15) in Fig. 8. This proves both the influence of the eutectic on the translocation of the curve of equilibrium composition and the fact that the solution $ZnCl_2$-$CdCl_2$ is ideal.

Conclusions

The investigations carried out prove the influence of the displacement reaction [2] on the emf of the concentration cell Zn(l) | $ZnCl_2$ in $(LiCl\text{-}KCl)_{eut}$(l) | Zn-Cd(l) and cause the value of the zinc activity coefficient at $X_{Zn} = 0.01$ for the higher temperatures to have considerable error. The displacement reaction [2] limits the applicability of the concentration cell method to $X_{Zn} = 0.01$ and a temperature of 756°K in the case of dilute zinc solutions in cadmium; in determining the linear dependence of ln γ_{Zn} *vs.* X_{Zn} the results at $X_{Zn} = 0.01$ molar fraction were not, therefore, taken into consideration.

Investigations on the equilibrium constant of reaction [2] and Eq. [28] for the dependence of the metal-phase composition *vs.* temperature enabled the calculation of the correction for the concentration $X_{Zn} = 0.01$ yielding agreement with the results for the higher zinc content. For this purpose a correction δ was introduced in the measured emf values at the temperatures 805°, 842°, and 877°K (Fig. 1). This correction was $\delta = \left(\frac{dE}{dX}\right)_T (X'_{Zn} - 0.01)$ where $X'_{Zn} = (1 - X_{[Cd]})$ and $X_{[Cd]}$ is calculated from Eq. [23]. After recalculation of the emf values at $X_{Zn} = 0.01$ corrected in this manner, the linear dependence of ln

γ_{Zn} *vs.* X_{Zn} was obtained over the whole range X_{Zn} = 0.01-0.1 molar fraction.

When undertaking experiments using the emf method of concentration cells it would appear necessary to determine experimentally the range of concentration of components and temperatures thus enabling the exclusion of the influence of various factors such as the displacement reactions between the components of electrodes and those of the electrolytes.

Acknowledgment

The authors are indebted to W. Ptak for assistance in the interpretation of the experimental results. This paper was presented at the 23rd I.S.E. Meeting in Stockholm, Sweden, 1972.

Manuscript submitted Aug. 16, 1972; revised manuscript received Feb. 16, 1973.

Any discussion of this paper will appear in a Discussion Section to be published in the June 1974 JOURNAL.

REFERENCES

1. C. Wagner, "Thermodynamics of Alloys," Addison-Wesley Publishing Co., Inc., Cambridge, Mass. (1952).
2. Z. Moser, *Arch. Hutnictwa*, **4**, 385 (1969).
3. Z. Moser, *Bull. Acad. Polon. Sci., Ser. Sci. Tech.*, **17**, 27 (1969).
4. Z. Moser, *ibid.*, **18**, 51 (1970).
5. C. Wagner, *Phys. Chem. Metallic Sol. Intermetallic Compds. Symp.*, **11B**, 16, (1959).
6. C. Wagner and A. Werner, *This Journal*, **110**, 326 (1963).
7. S. P. Jacenko, W. N. Danilin, and L. N. Wolkowa, *Zh. Fiz. Khim.*, **42**, 874 (1968).
8. J. Hildebrand and W. Wachter, *J. Am. Chem. Soc.*, **54**, 4655 (1930).
9. R. Lorenz and H. Velde, *Zeit. Anorg. Allgem. Chem.*, **183**, 81 (1929).
10. M. F. Lantratow and A. F. Alabyszew, *Zh. Prikl. Khim.*, **4**, 353 (1953); **7**, 722 (1954).
11. C. Krohn and Z. Moser, *Norsk Videnskabers Selskabs Skr.*, **1**, 9 (1967).
12. C. Krohn and Z. Moser, *ibid.*, **1**, 8 (1967).
13. L. Yang and R. G. Hudson, *Trans. AIME*, **215**, 589 (1959).
14. R. Lorenz and G. Schulz, *Zeit. Anorg. Allgem. Chem.*, **170**, 324 (1928).
15. K. Jellinek and H. Siewers, *Z. Elektrochem.*, **40**, 871 (1934).

Technical Notes

Electrical Conductivity and Structure of Molten Binary $LiF-AlF_3$ and $NaF-AlF_3$ Mixtures

K. Matiašovský and V. Daněk

Institute of Inorganic Chemistry, Slovak Academy of Sciences, Bratislava, Czechoslovakia

The study of the electrical conductivity of molten salts is one of the indirect methods which is used for determination of the structure of molten salts and of the interaction of the constituents in molten mixtures. The changes in the composition of a molten mixture are frequently accompanied by structural changes which affect the character of the dependence of the electrical conductivity on composition. Consequently, an analysis of this dependence should provide some information regarding the ionic species and their arrangement in the melt. Supplementary information, *i.e.*, that concerning the formation and decomposition of complex ions, the character of the bond cation-anion, and the character of the conductivity, cationic, anionic, electronic, etc., can be obtained from an analysis of the dependence of the activation energy, calculated from the temperature dependence of the electrical conductivity on the composition.

The shape of the isotherms of the electrical conductivity of binary mixtures is principally determined by two factors: (*i*) by the formation of new chemical compounds and consequently by the formation of new complex ions; and (*ii*) by the values of the electrical conductivity of the components and the newly formed compounds.

A theoretical interpretation of the concentration dependence of equivalent conductivity for simple binary mixtures was presented by Markov and Shumina (1). It should be pointed out that this theory, even when considering the structural aspect, represents rather a method of interpretation of the experimental data than a genuine picture of the structure of the melt. In molten salts generally only ions and not molecules are present, hence the conception of Markov and Shumina is to be considered also from this aspect. Their theory is based on the assumption that the electrical conductivity of a mixture of molten salts varies with temperature similarly to the case of pure components. In this respect, some general character of the dependence of the electrical conductivity on the composition, indicating the interaction of components in an ideal solution, could be expected. Considering this assumption, Markov and Shumina derived a relation for the dependence of the equivalent conductivity of a mixture of molten salts on the conductivity

$$\lambda_{mix} = x_1^2 \cdot \lambda_1 + x_2^2 \cdot \lambda_2 + 2x_1x_2 \cdot \lambda_2 \qquad [1]$$

where λ_i is the equivalent conductivity, ohm^{-1}-cm^2, and x_i is the mole fraction, with the presumption that $\lambda_1 > \lambda_2$. Thus for the calculation of the equivalent conductivity of a molten binary mixture according to Eq. [1], only the equivalent conductivities of the components at the same temperature must be known.

This problem was treated more generally by Kvist (2), who proposed for the equivalent conductivity of mixtures with one common ion and n interacting ions the equation

$$\lambda_{mix} = \lambda_1 \cdot x_1^n + \lambda_2(1 - x_1^n) \qquad [2]$$

For $n = 2$, Eq. [2] is transformed to Eq. [1].

In this work, the equivalent conductivity of the molten binary $LiF-AlF_3$ and $NaF-AlF_3$ mixtures was

Key words: conductivity, activation energies, molten salts.

calculated on the basis of experimental data and the values determined were compared with the theoretical ones calculated using Eq. [1]. On the basis of the experimentally determined values, the activation energies of the equivalent conductivity of the above mixtures at 1000°C were calculated. An analysis of the dependence of the equivalent conductivity and of the activation energy on the composition makes it possible to draw some qualitative conclusions on the structure and the character of the current transport as well as on the interaction of constituents in the above binary mixtures.

Calculation

The equivalent conductivity of both the molten components and of the molten binary mixture was calculated on the basis of the previously published experimental data on the specific conductivity and density (3-5) according to the equation

$$\lambda = \frac{\kappa \cdot M_e}{\rho} \qquad [3]$$

where λ is the equivalent conductivity, ohm^{-1}-cm^2, κ is the specific conductivity, ohm^{-1}-cm^{-1}, M_e is the mean equivalent weight of a mixture defined by the relation

$$M_e = \sum_i \frac{M_i \cdot x_i}{n_i} \qquad [4]$$

where M_i is the molecular weight, x_i the mole fractions of the components, and n_i is the number of the positive and negative charges of the cation and anion, respectively, and ρ the density, $g\text{-}cm^{-3}$.

Regarding the formation, in the system investigated, of a congruently melting compound of the type M_3AlF_6, which partially dissociates according to the equation

$$M_3AlF_6 = MAlF_4 + 2MF \qquad [5]$$

the presence of the products of dissociation in the melt has to be considered. In the calculation of the equivalent weight of the molten mixture the equilibrium concentration values of the constituents presented by Matiašovský *et al.* (6) were used. Assuming the primary dissociation of Na_3AlF_6 with the formation of $3Na^+$ cations and AlF_6^{3-} anion, for cryolite the value $n = 3$ was considered.

The values of the equivalent conductivity of molten LiF-AlF_3 mixtures at 900° and 1000°C, calculated with regard to the presence of LiF, Li_3AlF_6, and $LiAlF_4$ in the melt, are presented in Fig. 1. In Fig. 2, the calculated values of the equivalent conductivity of the molten NaF-AlF_3 mixtures at 1000° and 1100°C are presented.

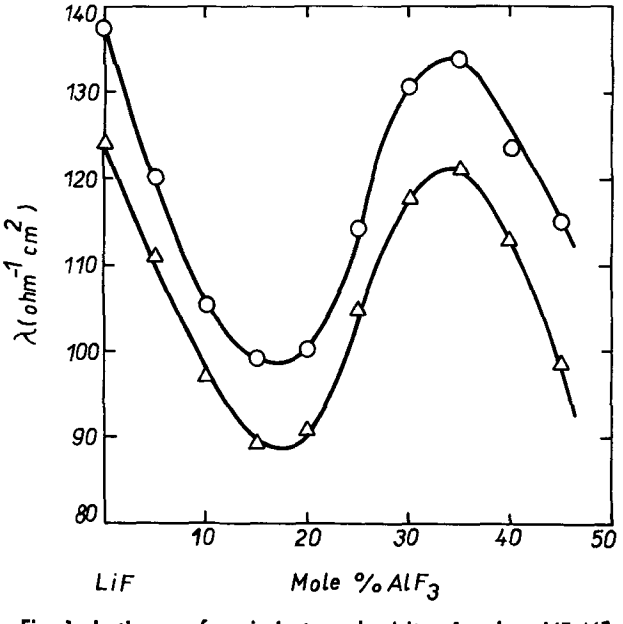

Fig. 1. Isotherms of equivalent conductivity of molten LiF-AlF_3 mixtures. ○, 1000°C; △, 900°C.

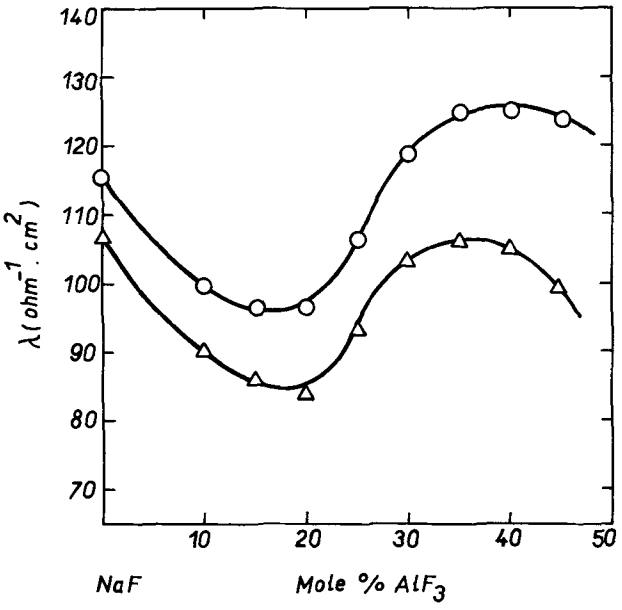

Fig. 2. Isotherms of equivalent conductivity of molten NaF-AlF_3 mixtures. ○, 1100°C; △, 1000°C.

The activation energies of the equivalent conductivity were calculated according to the equation

$$E_\lambda = R \ln (\lambda_2/\lambda_1)/(1/T_1 - 1/T_2) \qquad [6]$$

The values of the activation energies of the equivalent conductivity of the LiF-AlF_3 and NaF-AlF_3 mixtures at 1000°C are plotted in Table I. The dependence of the activation energy of the equivalent conductivity on the concentration in the above systems is presented in Fig. 3 and 4. The activation energy of the equivalent conductivity was found to be practically independent of the temperature in the temperature region investigated.

Discussion of Results

In the system LiF-AlF_3, the components react to form congruently melting lithium cryolite, Li_3AlF_6 (mp = 782°C) (7). According to the phase diagram, no other compound is formed in this system (7). However, in a series of papers the formation of $LiAlF_4$ was suggested (8-11). The existence of the complex AlF_4^- anion in the liquid phase was confirmed also by Malinovský and Matiašovský (12) on the basis of cryoscopic measurements in the system Li_3AlF_6-KCl. Hence, with regard to the investigated concentration range in the study of the specific conductivity and density of LiF-AlF_3 mixtures, this system can be divided in two partial systems: LiF-Li_3AlF_6 and Li_3AlF_6-$LiAlF_4$.

Similarly, in the system NaF-AlF_3, the analogous partial systems, NaF-Na_3AlF_6 and Na_3AlF_6-$NaAlF_4$, were considered. In the concentration range investigated, congruently melting sodium cryolite, Na_3AlF_6, (mp = 1006°C) is formed (13). The compound $NaAlF_4$

Table I. Activation energy of the equivalent conductivity, kcal-mole^{-1}, of molten LiF-AlF_3 and NaF-AlF_3 mixtures

LiF-AlF_3 Mole per cent AlF_3	E_λ	NaF-AlF_3 Mole per cent AlF_3	E_λ
0	2.05	0	2.75
5	2.33	10	3.34
10	2.47	15	4.12
15	3.16	20	4.36
20	2.95	25	4.50
25	2.68	30	4.91
30	3.04	35	5.64
35	3.02	40	6.12
40	3.59	45	7.72
45	4.57		

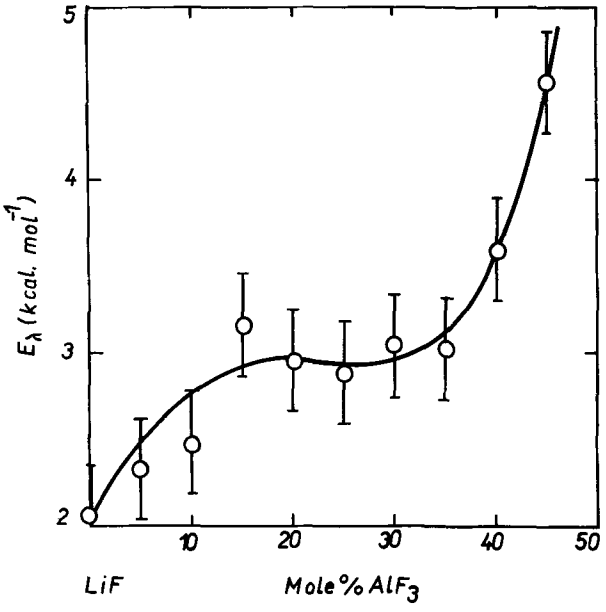

Fig. 3. Activation energy of equivalent conductivity of molten LiF-AlF$_3$ mixtures.

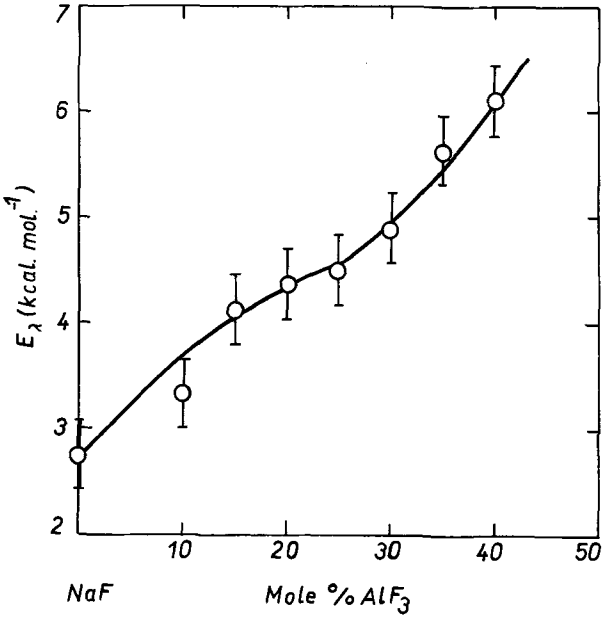

Fig. 4. Activation energy of equivalent conductivity of molten NaF-AlF$_3$ mixtures.

was first identified by Howard (14) by means of chemical analysis and x-ray powder diffraction of quenched vapors over the melt corresponding to the equimolar composition NaF · AlF$_3$. The existence of the complex AlF_4^- anion in molten cryolite was later confirmed by cryoscopic (15) and spectroscopic (16) measurements, and by investigations of the structure and the density (17) as well as on the electrical conductivity of cryolite close to the melting point (18, 19).

Besides Na_3AlF_6 and $NaAlF_4$, in the system NaF-AlF$_3$ the incongruently melting compound $Na_5Al_3F_{14}$, chiolite, is formed. However, this compound is not stable and decomposes by a peritectic reaction at 739°C (20). It was confirmed spectroscopically that at 1030°C there are no complex $Al_3F_{14}^{5-}$ anions in the melt (16). Therefore, this compound was not considered in the calculation of the equivalent conductivity of molten NaF-AlF$_3$ mixtures.

The course of the isotherms of the equivalent conductivity of molten MF-AlF$_3$ mixtures (Fig. 1 and 2) indicates significantly the character of interaction of the components. The inflection point on the isotherms corresponds to the formation of the complex compound M_3AlF_6. The decrease of the conductivity with increasing MF concentration in the partial system MF-M_3AlF_6 is due most probably to the suppression of the dissociation of the complex AlF_6^{3-} anion according to the scheme

$$AlF_6^{3-} = AlF_4^- + 2F^- \qquad [7]$$

effected by the introduction of F^- anions in the form of MF into the melt. The Li^+ and Na^+ ions, respectively, occupy the interstitial positions between the large AlF_6^{3-} and AlF_4^- complex anions and for this reason their positive influence on the increase of the electrical conductivitly is thus limited. It can be assumed that the minimum in the isotherms of the equivalent conductivity of the MF-M_3AlF_6 mixtures may be ascribed to the combined influence of both factors. The prevalent participation of cations in the current transport is evident only in the range of high MF concentrations. The course of the dependence of the activation energy of the equivalent conductivity on the composition in the investigated system agrees with the above assumption. From a comparison of the course of the isotherm at 1000°C with the isotherm calculated according to Eq. [1], it follows that the character of the interaction of components is in contradiction with the simplifying assumptions made by Markov and Shumina (1).

An entirely different isotherm shape of the equivalent conductivity was determined in the partial system M_3AlF_6-$MAlF_4$. This isotherm shape is very rare in the literature. Qualitatively, it can be explained by the simultaneous influence of several factors. First, it is the decrease of the relaxation influence of the F^- anions resulting in an increased conductivity caused by the prevalent cationic transfer. In the range of high $MAlF_4$ concentrations, the concentration of the particles taking part in the current transport is decreased which causes decreased electrical conductivity. Both these factors manifest themselves by a maximum on the isotherm of the equivalent conductivity in the M_3AlF_6-$MAlF_4$ partial systems.

From the course of the dependence of the activation energy of the equivalent conductivity of the MF-AlF$_3$ mixtures it follows that the activation energy generally increases in the entire concentration range, the inflection point corresponding to the formation of the compound M_3AlF_6. The course of the dependence confirms the conclusions on the character of the conductivity and on the interaction of the components.

Finally it should be said that in the case of such complicated systems as those of the type MF-AlF$_3$, only qualitative conclusions can be made. This scarcity of experimental data is due mainly to deficiencies in the theoretical aspects in the field of the chemistry and electrochemistry of fused salts.

Manuscript submitted July 20, 1972; revised manuscript received Jan. 20, 1973.

Any discussion of this paper will appear in a Discussion Section to be published in the June 1974 JOURNAL.

REFERENCES

1. B. F. Markov and L. A. Shumina, *Dokl. Akad. Nauk SSSR*, **110**, 411 (1956).
2. A. Kvist, *Z. Naturforsch.*, **22a**, 208 (1967).
3. V. Daněk and K. Matiašovský, *Electrochim. Acta*, In press.
4. K. Matiašovsky, M. Malinovský, and V. Daněk, *ibid.*, **15**, 25 (1970).
5. M. Paučírová, K. Matiašovský, and M. Malinovský, *Rev. Roumaine Chim.*, **15**, 33 (1970).
6. K. Matiašovský, M. Paučírová, and M. Malinovský, *Collection Czech. Chem. Commun.*, **37**, 1963 (1972).
7. M. Malinovský, I. Čakajdová, and K. Matiašovský, *Chem. Zvesti*, **21**, 794 (1967).
8. R. F. Porter and E. A. Zeller, *J. Chem. Phys.*, **33**, 858 (1960).
9. D. L. Hildebrand and L. P. Theard, *U.S. Dept. Comm. Office Tech. Serv., PBR*, **AD 258**, 410 (1961).

10. L. D. McCory, R. C. Paulo, and J. L. Margrave, *J. Phys. Chem.*, **67**, 1086 (1963).
11. G. Garton and B. M. Vanklyn, *J. Inorg. Nucl. Chem.*, **27**, 2461 (1965).
12. M. Malinovský and K. Matiašovský, *Chem. Zvesti*, **26**, 31 (1972).
13. J. Brynestad, K. Grjotheim, and S. Urnes, *Metallurgia Ital.*, **52**, 495 (1960).
14. E. H. Howard, *J. Am. Chem. Soc.*, **76**, 2041 (1954).
15. K. Grjotheim, T. Halvorsen, and S. Urnes, *Can. J. Chem.*, **37**, 1170 (1957).
16. C. Solomons, J. H. R. Clarke, and J. O'M. Bockris, *J. Chem. Phys.*, **49**, 445 (1968).
17. W. B. Frank and L. M. Foster, *J. Phys. Chem.*, **64**, 95 (1960).
18. G. J. Landon and A. E. Ubbelohde, *Proc. Roy. Soc. (London)*, **240**, 160 (1957).
19. G. J. Landon, *Congr. Intern. Chim. Pure Appl., 16, Paris, 1957.*
20. K. Grjotheim, J. L. Holm, C. Krohn, and J. Thonstad, "Selected Topics in High Temperature Chemistry," p. 151, Universitetsforlaget, Oslo (1960).

Electrochemistry of Nematic Liquid Crystals

M. Voïnov* and J. S. Dunnett

Battelle Geneva Research Centre, 1227-Carouge, Genève, Switzerland

Dynamic scattering in nematic liquid crystals has mostly been investigated with a view to making passive display devices. The devices work on a-c or d-c excitation. However low voltage d-c operation is desirable to make the display compatible with battery power sources. Several theories have been proposed to explain dynamic scattering (1, 2). It seems to be generally accepted that the current carriers in liquid crystals are ions (3, 4), and it would thus be surprising if there were no electrolysis at the potentials necessary to cause scattering.

Although it is generally felt among specialists in the field that degradation of liquid crystals under d-c excitation is due to parasitic electrochemical reactions, we are not aware of any investigation of these materials from the point of view of electrochemistry. Furthermore we propose that electrochemical reactions are not only parasitic but that they are essential to the operation of the liquid crystal device.

We have measured current-voltage curves for 10 μm thick layers of Merck's nematic phase *NV* sandwiched between two pyrolytic tin oxide electrodes (R = 1 k-ohm/□) deposited on flat glass plates. Merck's nematic phase *NV* is a mixture in undisclosed proportions of four compounds

$$R_1\,C_6H_4\,N(O)N\,C_6H_4\,R_2$$

where

$$R_1 = CH_3O, \quad R_2 = C_4H_9 \qquad [I]$$

$$R_1 = C_4H_9, \quad R_2 = CH_3O \qquad [II]$$

$$R_1 = CH_3O, \quad R_2 = C_2H_5 \qquad [III]$$

$$R_1 = C_2H_5, \quad R_2 = CH_3O \qquad [IV]$$

The characteristics of nematic phase *NV* are described in Merck's brochure (5).

We have also made measurements on a 12 μm thick cell containing a 1:1 mixture of p-methoxybenzilidene-p'-butylaniline with p-ethoxybenzilidene-p'-butylaniline (MBBA-EBBA). The cathode of this cell was vapor deposited aluminum and the anode tin oxide ($R \simeq$ 200 ohm/□), both supported on glass plates.

The current-voltage curve for nematic phase *NV* is shown in Fig. 1A. After correction for the high resistance of the cell estimated from the resistivity quoted by the manufacturer, the curve is seen to be characteristic of electrolysis (Fig. 1B). Two waves are apparent, the first at about 1V and the second at 2V. The current due to the first wave reaches a limiting value of 2 μA/cm^2 at about 1.7V, well before the start of the second wave.

Figure 1C shows the optical transmittance of the cell against applied voltage. The onset of scattering also occurs at a corrected voltage of about 1.7V (Fig. 1D), the tension at which the current reaches the plateau. Scattering reaches saturation before the second wave begins, that is over a span of only 1.3V once correction for the ohmic drop has been made.

The current-voltage curve (Fig. 2A) for the MBBA-EBBA mixture is less easy to interpret. After correction for the ohmic drop, several inflections become apparent in the ascending branch (Fig. 2B). The well-defined first wave, I, is presumably due to some impurity whilst the inflection at 1.5V, II, is possibly caused by the electrolysis of water which is more likely to be present in this hygroscopic mixture than in nematic *NV*. The main "scattering" wave, III, appears to commence at 3.8V although, as with nematic *NV*, visible scattering does not occur much below the inflection point at 4.5V, IV. We assume that this corresponds to the current plateau observed with nematic *NV*, possibly obscured in the case of the MBBA-EBBA mixture by some further electrochemical reaction. As with nematic *NV*, scattering increases rapidly above 4.5V, to reach saturation by 6V.

The descending branch recorded for the MBBA-EBBA mixture is also interesting. The current at corresponding voltages is lower than that for the forward curve and there are no well-defined inflections. This indicates that the products of electrolysis are only weakly or not at all electroactive, so that the stock of depolarizer in the cell is seriously depleted on continued electrolysis.

Discussion

An electrochemical mechanism can explain many well-known features of the behavior of nematic liquid crystals. First, it has been reported that the current increases with cell thickness at constant field. Now in the steady state, for an electrochemical reaction (8)

$$V = E_o + \eta(i) + l\rho i \qquad [1]$$

where the symbols are defined at the end of the paper.

Neglecting $\eta(i)$, which is reasonable for electron exchange reactions in high resistivity, nonaqueuos solvents, we have

$$i = V/l\rho - E_o/l\rho \qquad [2]$$

Thus at constant field, V/l, Eq. [2] correctly predicts the increase of current with the thickness of the sample. Of course, such a mechanism requires that there be sufficient ions in the solution to neutralize the space charge on the electrodes. This is consistent with the observation that for satisfactory operation, liquid crystals must possess a finite electrical conductivity. The current carrying ions are not necessarily the same as the electroactive species which may themselves be uncharged. Using the results of Heilmeier *et al.* (3) on anisylidene-p-aminophenylacetate (APAPA) and Eq.

* Electrochemical Society Active Member.

Key words: display devices, liquid crystals, dynamic scattering, electrochemistry.

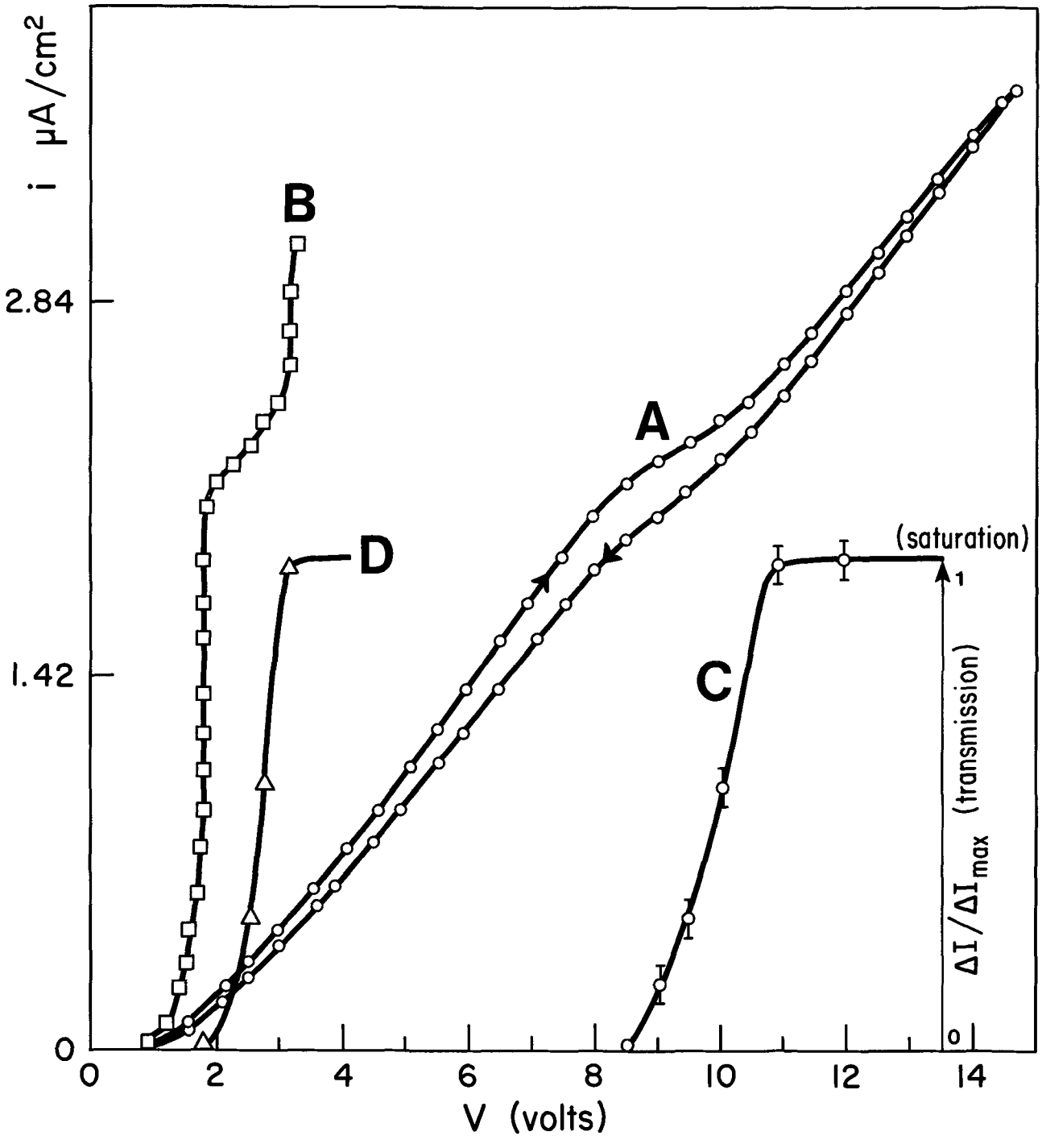

Fig. 1. Nematic phase *NV*. A, Current-voltage curve as measured, B, current-voltage curve after correcting for ohmic drop; C, dynamic scattering measured in transmission and normalized to saturation, *vs.* applied voltage; D, the same as C, voltage corrected for ohmic drop. Voltage scan rate, 8 mV/sec; cell thickness, 10 μm.

[2] we calculate reasonable values $E_0 \simeq 3.4$V and $\rho \simeq 4 \times 10^{10}$ ohm-cm.

Other features which can be interpreted electrochemically are the so-called rise and decay times. The time constant for relaxation of a steady-state concentration gradient (8) gives the observed dependence of the decay time on the square of the sample thickness. Furthermore the rise time has been reported to be inversely proportional to the current (3) and to the square of the applied tension (9, 10). For electrochemical reactions limited by diffusion and driven by a constant current, the interface concentrations of the reacting species vary in a well-known fashion (11). It can be shown that the time which elapses before this interface concentration becomes smaller or higher than a given value is inversely proportional to the square of the current. This is the basic equation in voltametry at controlled current (11)

$$i\tau^{1/2} = \text{constant} \qquad [3]$$

Because of the high resistance of liquid crystal devices the total tension, at voltages higher than the threshold tension, can be approximated by Ohm's law so that

$$\tau_{rise} \simeq R/V^2 \qquad [4]$$

in agreement with the experimental results (9, 10).

An intriguing aspect of nematic liquid crystals is that they can sustain direct current excitation for over 1000 hr before failure. For example, Sussman has shown (12) that, in a cell containing 0.5×10^{-5} M/cm² p-methoxybenzilidene-p'-aminophenylacetate

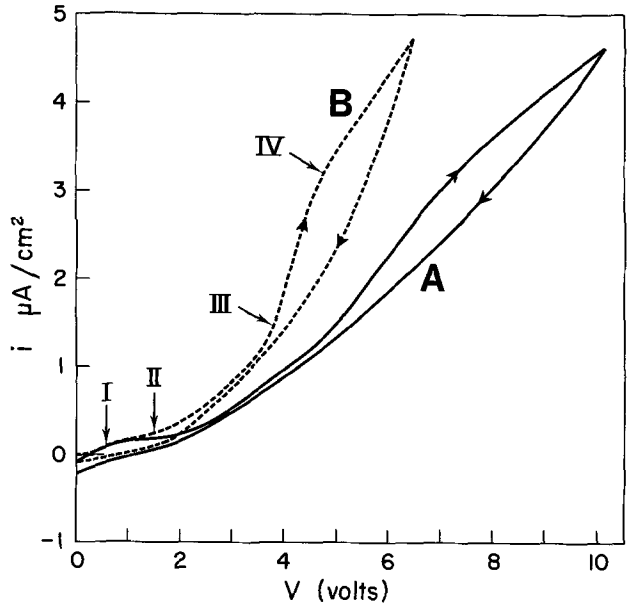

Fig. 2. MBBA-EBBA mixture. A, As measured; B, corrected for ohmic drop. Voltage scan rate, 10 mV/sec; cell thickness, 12 μm; resistivity of liquid crystal, 6 x 10^9 ohm-cm.

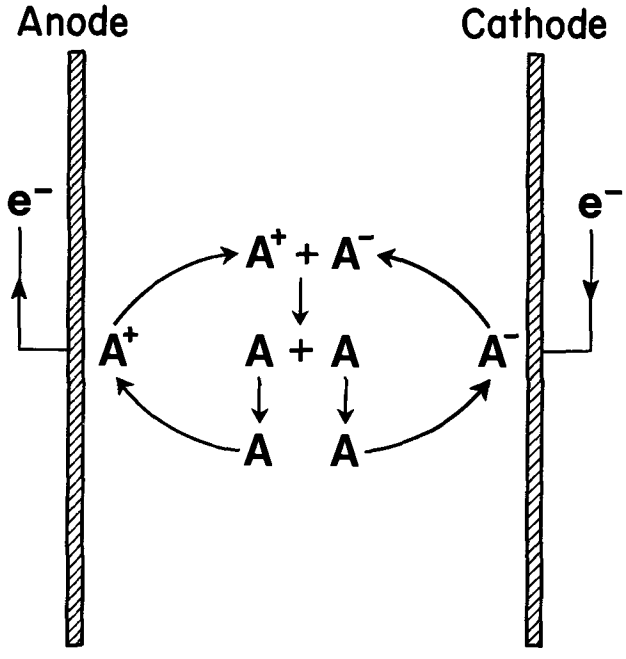

Fig. 3. Proposed scheme of cell reactions showing formation of ions, A^+, A^-, and regeneration of molecules, A.

(APAPA), it is possible to pass about 12.5 coulomb/cm² before 50% failure of the device. To electrolyze completely the APAPA contained in the cell 0.5 coulomb/cm² would be sufficient, assuming a one-electron process though the number of coulombs to electrolyze the impurities in the cell would be much smaller. Thus there must be at least partial regeneration of the APAPA or of other electroactive species if the long life under d-c excitation is to be explained. To this end, we propose that the ions created from the electrolysis of neutral molecules on the electrodes diffuse or migrate to the center of the cell where they react giving back the original molecules which, in turn, diffuse back to the electrodes to be electrolyzed again. This cyclic process is shown schematically in Fig. 3. One would expect these two opposing flows of ions and molecules to eventually cause turbulence. Failure of the device would be brought about if some of the recombination reactions at the center of the cell did not give back the original molecules, possibly because of alternative reactions with impurities or with the liquid crystal material itself.

There has been some speculation in the literature as to whether the work functions of the electrode material have any influence. According to our electrochemical mechanism these have no role to play in the scattering phenomenon.

The mechanism is essentially the same under a-c excitation. In this case two separate and independent recombination regions exist, as each electrode acts, alternately, as anode and cathode.

Acknowledgment

We wish to thank Dr. B. Zega for the liquid crystal cells and helpful discussions.

Authors' note.—After we submitted this note, a paper on electrochemistry of liquid crystals by A. Lomax, R. Hirasawa, and A. J. Bard was published [*This Journal*, **119**, 1679 (1972)]. The results in that paper are not inconsistent with our own conclusions.

Manuscript submitted Nov. 15, 1972; revised manuscript received Feb. 12, 1973.

Any discussion of this paper will appear in a Discussion Section to be published in the June 1974 JOURNAL.

LIST OF SYMBOLS

V	applied tension
E_o	minimum tension for electrolysis
i	current density
ρ	resistivity of the liquid crystal
l	distance between electrodes
$\eta(i)$	overvoltage
R	resistance of cell
τ	time constant for relaxation
τ_{rise}	rise time for dynamic scattering

REFERENCES

1. W. Helfrich, *J. Chem. Phys.*, **51**, 4092 (1969).
2. N. Felici, *Rev. Gen. Elec.*, **78**, 717 (1969).
3. G. H. Heilmeier, L. A. Zanoni, and L. A. Barton, *Proc. IEEE*, **56**, 1162 (1968).
4. G. Briere, F. Gaspard, and R. Herino, *Chem. Phys. Letters*, **9**, 285 (1971).
5. E. Merck, "Licristal," Darmstadt, Germany Company (Available in English).
6. G. H. Heilmeier, L. A. Zanoni, and L. A. Barton, *IEEE Trans. Electron Devices*, **ED-17**, 22 (1970).
7. G. Assouline, M. Hareng, and E. Leiba, *ibid.*, **ED-18**, 959 (1971).
8. K. J. Vetter, "Elektrochemische Kinetik," Springer Verlag, Berlin (1961).
9. Linda T. Creagh, A. K. Kmetz, and R. A. Reynolds, *IEEE Trans. Electron Devices*, **ED-18**, 672 (1971).
10. H. Koelmans and A. M. van Boxtel, *Phys. Letters*, **32A**, 32 (1970).
11. P. Delahay, "New Instrumental Methods in Electrochemistry," Interscience Publishers, New York (1954).
12. A. Sussman, *Appl. Phys. Letters*, **21**, 126 (1972).

Brief Communication

Antimony in the Lead-Acid Battery

Don E. Swets

Research Laboratories, General Motors Corporation, Warren, Michigan 48090

It is well known that antimony, which is alloyed in the grids of the lead-acid battery to improve their castability, corrosion resistance, and strength, affects the properties of the battery in various ways. Of particular interest is its apparent beneficial effect on the cycle life of the positive plate. This beneficial action has been the subject of much research (1) and various mechanisms have been proposed to explain it. For example, it has been suggested that antimony is responsible for maintaining a minimum concentration of αPbO_2 during cycling, which in turn stabilizes the plate structure. If this is so, the function of antimony may be to nucleate new αPbO_2 crystals during charge or to passivate already existing αPbO_2 during discharge.

In an effort to shed further light on this proposed mechanism we have studied the crystal structures of α and β PbO_2 and certain AB_2O_6 compounds to which they are related. [This approach was also suggested by Burbank (2) in a recent publication.] More specifically, we were interested in determining if the compound $PbSb_2O_6$ could reasonably be expected to grow epitaxially onto αPbO_2 (or vice versa) and passivate (or nucleate) it.

Key words: battery, nonantimonial, αPbO_2, βPbO_2, antimony.

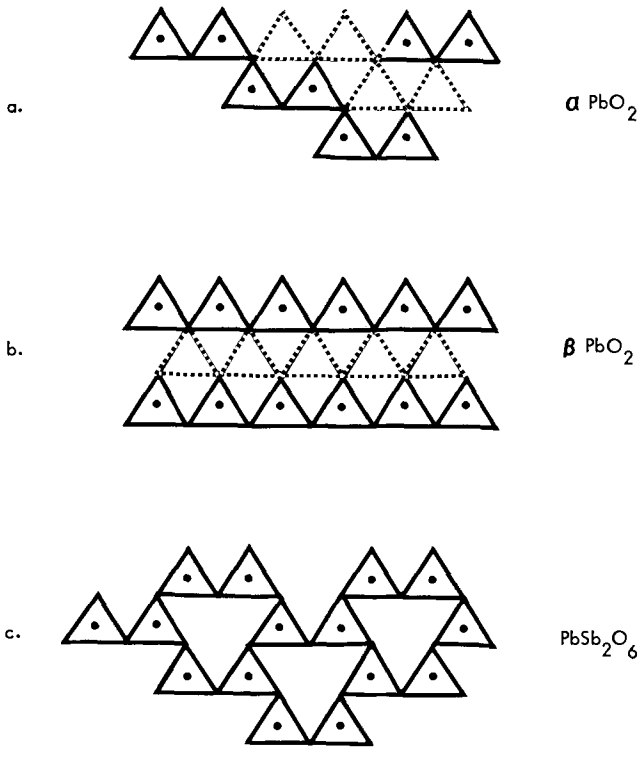

Fig. 1. In this figure the octahedra containing a metal ion are represented by triangles as viewed perpendicular to layers of close-packed oxygen. The metal ions filling octahedral holes in a given plane halfway between oxygen layers are represented by dots. The dashed triangles represent filled octahedra at higher or lower levels. a) αPbO_2; b) βPbO_2; c) $PbSb_2O_6$.

Alpha-PbO_2 is isostructural with columbite, (Fe, Mn)Nb_2O_6 whereas βPbO_2 has the structure of cassiterite, SnO_2. In both of these structures the cations are octahedrically coordinated to six oxygen ions but the pattern of cation-filled octahedra is different for the two types. Simply stated, the filled octahedra form zig-zag chains in αPbO_2 and linear chains in βPbO_2. This concept is illustrated schematically in Fig. 1.

In making the list of columbite type compounds for Table I we have taken three unit cells of αPbO_2 stacked along the a_o axis and written $PbPb_2O_6$ instead of $3PbO_2$ for comparison with the other columbite compounds. Similarly we have written $3\alpha PbO_2$ as $PbPb_2O_6$ for comparison with a series of compounds isostructural with the mineral tapiolite $FeTa_2O_6$. Wyckoff (3) describes this structure as a superlattice on cassiterite with three cassiteritelike units stacked end on end. In this group several of the compounds contain SbO_6 octahedra in linear chains.

Another family of structures is typified by lead metantimonate, $PbSb_2O_6$. In this structure the Sb^{5+} ion is again octahedrally coordinated to oxygen with the filled octahedra lying in sheets perpendicular to the C_o axis in a hexagonal pattern (see Fig. 1). The layers of octahedra are separated by the large Pb^{2+} ions. Magneli (4) lists several compounds with this structure (which we have included in Table I) and points out that the $(Sb_2O_6)^{2-}$ sheets are only slightly influenced by the bivalent cations between them. He also notes that, for this structure to form, the bivalent cations must be rather large; with smaller ions metantimonates will have the structure types columbite or mossite (similar to tapiolite).

Thus, in summary, there is a series of AB_2O_6 compounds whose structures are related in that they all contain BO_6 octahedra but fall into three separate types. In the columbite structure only one compound is listed in which Sb^{5+} is the *B* ion and in this case the *A* ion radius is 0.80Å, quite close to Pb^{4+} at 0.84Å.

Table I. AB_2O_6 crystals with the columbite, tapiolite, or lead metantimonate structure

Crystal	*A* ion radius (Å)	
$PbPb_2O_6$ (αPbO_2)	0.84	Columbite
$FeNb_2O_6$	0.76	
$MnNb_2O_6$	0.80	
$CdNb_2O_6$	0.97	
$CoNb_2O_6$	0.78	
$MgNb_2O_6$	0.65	
$NiNb_2O_6$	0.78	
$ZnNb_2O_6$	0.74	
$MnSb_2O_6$	0.80	
$PbPb_2O_6$ (βPbO_2)	0.84	Tapiolite
$FeTaO_6$	0.76	
$CeSb_2O_6$	0.78	
$FeSb_2O_6$	0.76	
$MgSb_2O_6$	0.65	
$NiSb_2O_6$	0.78	
$ZnSb_2O_6$	0.74	
$BaSb_2O_6$	1.35	Lead metantimonate
$CaSb_2O_6$	0.99	
$CdSb_2O_6$	0.97	
$HgSb_2O_6$	1.10	
$PbSb_2O_6$	1.20	
$SrSb_2O_6$	1.13	

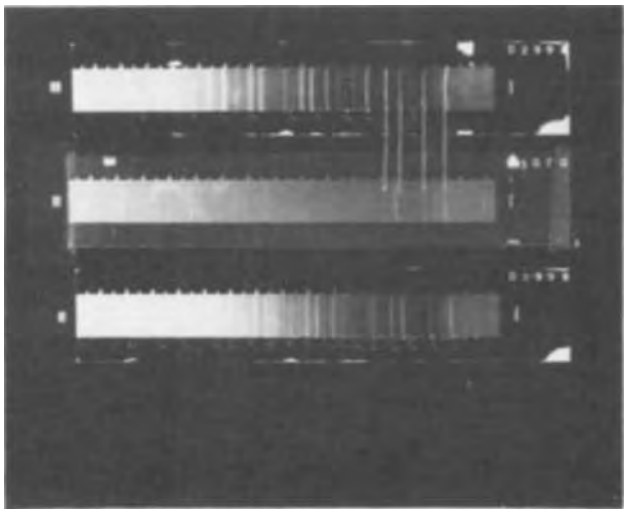

Fig. 2. X-ray patterns for 1) $PbSb_2O_6$; 2) old battery-active material residue after PbO_2 removal; and 3) residue from a cycled minicell to which $PbSb_2O_6$ had been added.

In the tapiolite group there are several compounds with Sb^{5+} all with *A* ion less than 0.80Å, and in the $PbSb_2O_6$ group all the *A* ions are greater than 0.97Å. So with SbO_6 octahedra the preferred structure is apparently determined by the *A* ion size. Burbank and Ritchie (1) suggested that Sb^{5+} ions may occupy vacant Pb^{4+} octahedral sites in the PbO_2 lattice. If this is true then from the relation between ion size and preferred structure one might speculate that, as Pb^{4+} (with ionic radius 0.84) is reduced to Pb^{2+} (with ionic radius 1.20Å) during discharge, some $PbSb_2O_6$ forms (along with the $PbSO_4$) and either nucleates new αPbO_2 crystals on subsequent charging, or passivates the surface of already existing αPbO_2 and prevents it from reacting in the next discharge.

Efforts to prove by experiment that antimony improves positive life via the compound $PbSb_2O_6$ have not been conclusive. Over 200 miniature three-plate batteries with various amounts of $PbSb_2O_6$ (or other materials, such as Nb_2O_5) added to the positive plate were cycle-life tested in a period of 2 yr. No significant difference in cycle life was found; however, the $PbSb_2O_6$ (which we synthesized according to the method of Magneli) had relatively large particle size, perhaps too large for nucleating αPbO_2. In another approach, some old batteries, which had failed in automotive use, were cut open; the positives were removed, and lead dioxide was removed from the plates. Care was taken to avoid breaking off pieces of the grid which was quite fragile. The PbO_2 was digested in HNO_3 and H_2O_2 to obtain a small residue which was analyzed by x-ray diffraction. In one out of five attempts a pattern was obtained which contained the major lines of our synthesized $PbSb_2O_6$ as shown in Fig. 2. Other materials were also present in the residue.

Whereas this result and the argument from comparing crystal structure give some credence to the concept that antimony acts in the positive plate via the compound lead metantimonate, it is not the intent of the author to imply that absolute proof or a final answer has been given, but rather to suggest another approach to a rather difficult and complex problem.

Manuscript received Feb. 2, 1973.

Any discussion of this paper will appear in a Discussion Section to be published in the June 1974 JOURNAL.

REFERENCES

1. E. J. Ritchie and J. Burbank. *This Journal*, **117**, 299 (1970).
2. J. Burbank, Naval Research Laboratory Report 7256 (1971).
3. R. W. G. Wyckoff, "Crystal Structures," Vol. 3, p. 361, John Wiley & Sons, Inc., New York (1965).
4. A. Magneli, *Arkiv Kemi Min. Geol.*, **1513**, 3 (1941); see also H. M. Kasper, *Mat. Res. Bull.*, **4**, 33 (1969).

Erratum

In the paper "A Soft X-Ray Study of the Near Surface Composition of Cu30Zn Alloy during Simultaneous Dissolution of Its Components" by J. E. Holliday and H. W. Pickering which appeared on pp. 470-475 in the April 1973 JOURNAL, Vol. 120, No. 4, the horizontal axis of Fig. 4 should be labeled x.

JOURNAL OF THE ELECTROCHEMICAL SOCIETY

SOLID-STATE SCIENCE AND TECHNOLOGY

JULY 1973

Selected Properties of Pyrolytic Ta_2O_5 Films

W. H. Knausenberger

Bell Telephone Laboratories, Incorporated, Whippany, New Jersey 07981

and R. N. Tauber

Bell Telephone Laboratories, Incorporated, Allentown, Pennsylvania 18103

ABSTRACT

Pyrolytic Ta_2O_5 films, in thicknesses up to 30,000Å, were produced by the $TaCl_5$-CO_2-H_2 reaction at 900°C. These films were characterized by use of transmission electron microscopy, electron microprobe analysis, measurement of dielectric, and optical properties. It was found that the films were orthorhombic Ta_2O_5 (β-Ta_2O_5) with a fine grained structure. The films did not etch appreciably in hydrofluoric acid. Ellipsometric measurements indicated that the films had an index of refraction of 2.20 ± 0.03 at 5461Å. In addition, certain areas of the films exhibited slight optical absorption. The optical energy gap was found to be 4.20 eV. The dielectric constant and the loss tangent of the pyrolytic Ta_2O_5 films were measured over the temperature range 78°-488°K and the frequency interval 1-100 kHz and exhibited a surprisingly strong temperature dependence. These results and the electron microprobe results indicate the films are not stoichiometric.

Tantalum pentoxide (Ta_2O_5) has played a very active role in electronic applications for over a decade. Ta_2O_5 has been used in thin film form long before the much studied thin film materials such as SiO_2, Si_3N_4, and Al_2O_3 came into positions of importance for applications such as integrated circuit (IC) passivation and insulated gate, field effect transistor gate dielectrics. It has been found for the latter materials that high-temperature (600°-1000°C) chemical vapor deposition (CVD) produced films with properties generally considered more desirable than those of films produced by other methods. In electronic applications Ta_2O_5 is usually produced anodically, or sometimes thermally, but pyrolytic Ta_2O_5 has not been used, nor its properties investigated. This paper reports selected details on the preparation and properties of Ta_2O_5 films produced by CVD.

Film Deposition

The general subject of oxide film preparation by CVD has been well-treated by Powell *et al.* (1). Pyrolytic Ta_2O_5 has been produced by Peacock (2) through the reaction of $TaCl_5$ vapor, H_2 gas, and CO_2 gas at 900°C, and by Wang *et al.* (3), through the reaction of tantalum alcoholate vapor, helium, and oxygen at 450°C. The properties of the films produced by the former reaction were not investigated, and those of the latter reaction were described as amorphous and annealable to polycrystalline β-Ta_2O_5 fter 30 min at 800°C.

The reaction between $TaCl_5$ vapor, H_2, and CO_2 at 900°C was used to prepare the films for this study. The presumed over-all reaction is

$$2TaCl_5 + 5H_2 + 5CO_2 \xrightarrow{900°C} Ta_2O_5 + 6CO + 10HCl$$

Key words: tantalum oxide, chemical vapor deposition, insulators, dielectric properties, optical properties.

The deposition apparatus, shown schematically in Fig. 1, is a modified version of the one reported by Tauber, Dumbri, and Caffrey (4) for the pyrolytic deposition of zirconium dioxide. The substrate rests on a molydenum susceptor, which is heated inductively at 480 kHz, The susceptor is rotated by a specially designed harmonic drive. The gases are carefully metered through Brooks rotometers and are carried through stainless steel lines to the deposition chamber. The $TaCl_5$ vapor is transferred to the chamber by passing hydrogen through a heated saturator. A schematic of the stainless steel saturator is shown in the enlarged section of Fig. 1. The carrier gas is forced to take a tortuous path over six layers of $TaCl_5$. It is assumed that the carrier is saturated with the vapor. All lines past the saturator are heated approximately 60°C above the saturator temperature, in order to prevent recondensation of the $TaCl_5$ prior to its arriving at the heated substrate.

All depositions were made at a substrate temperature of 900°C. The substrate usually used was 3-10 ohm-cm n-type (100) silicon, with the occasional use of fused silica disks, thermally grown SiO_2 on Si, and 0.001 ohm-cm silicon for special purposes. The typical concentrations by volume used were 0.02% $TaCl_5$ and 0.15% CO_2 with the remainder hydrogen. The total H_2 flow rate was 3270 cm³/min. These conditions yielded a deposition rate of approximately 300 Å/min.

Film Properties

General

The films deposited by the above procedure were clear, hard films of good quality which formed a tenacious coating on the substrate. Films as thick as 30,000Å deposited on polished silicon or fused silica showed no evidence of cracking, even when quenched to −195°C.

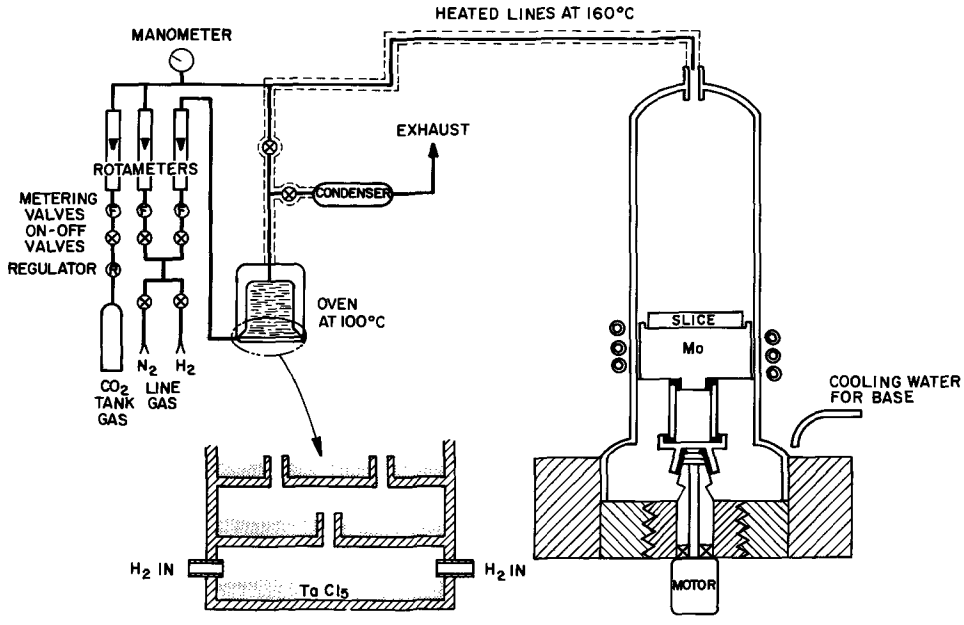

Fig. 1. Schematic representation of deposition equipment.

The characteristic ring interference color pattern revealed nonuniformity in the thickness of the films on the order of ±10%. Ellipsometric (5) and ultraviolet-visible reflection spectra (6) measurements indicated the center of the deposit to be the thickest area; no attempt was made to improve the thickness uniformity of the film.

Structure Identification

Transmission electron microscopy and electron diffraction analysis.—Pyrolytic Ta_2O_5 does not appear to etch appreciably, even in concentrated HF. Thus, in order to produce a thin sample for transmission electron microscopy, a 1000Å Ta_2O_5 film was pyrolytically deposited on a 1000Å thick layer of thermally grown SiO_2 on a silicon substrate. A long-term etch (15 hr) in 49% HF sufficed to undercut the Ta_2O_5 and lift it from the substrate. The etchant was then diluted and the film specimens were removed on a fine copper grid.

The specimens were examined in a Philips 300 Electron Microscope at an accelerating potential of 100 kV. Figure 2 is a transmission micrograph made at a magnification of 74,500 times. A well-defined and relatively uniform grain structure is observed with a 600Å average grain size.

Figure 3 shows an electron diffraction pattern of the same area. The film is crystalline and the pattern indexes to orthorhombic Ta_2O_5 (β-Ta_2O_5) (7). However, the line positions are such that one cannot rule out the presence of a small amount of Ta. The indexing is summarized in Table I.

Electron microprobe analysis.—The stoichiometry of a 5000Å pyrolytic Ta_2O_5 film deposited on silicon was studied by electron microprobe by the technique described by Colby (8). A Materials Analysis Corporation electron microprobe was used. The accelerating voltage was 5 kV, the beam current 0.4 μA, and the x-ray emergence angle 38.5°. The depth of analysis was approximately 1000Å, calculated from an assumed density of 8.70 g/cm^3. The elements analyzed were Ta, O, and Si, the latter being included to insure that the electron beam was not penetrating the film. Eight spots in regular increments of width from the center of the outer edge of the slice were analyzed. The result of analysis in depth on five of the spots is presented in Table II. Note the fact that the average oxygen to tantalum ratio is 2.37 ± 0.05, which is somewhat smaller than the 2.50:1 expected for stoichiometric Ta_2O_5. One can expect a slight overestimation of the amount of Ta present since the standard sample, of necessity, has on it a thin oxide layer on the order of 20-50Å thick. However, it is doubtful that this can be responsible for so large a difference. The comparison of a pyrolytic film on a relative basis with a film of known stoichiometry should allow the resolution of this question. Therefore, a Ta_2O_5 sample was prepared

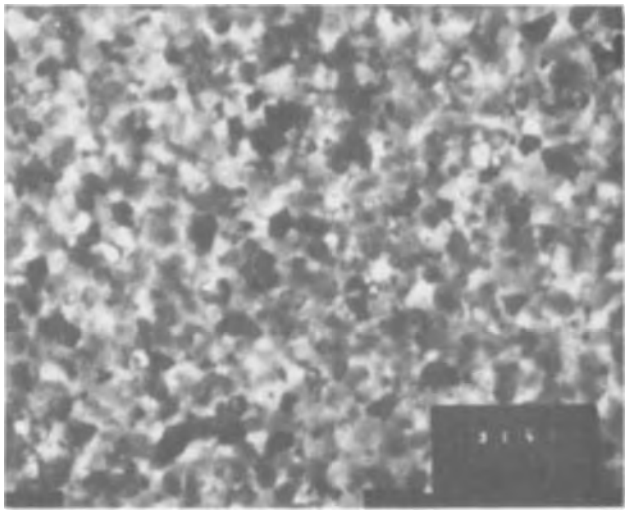

Fig. 2. Transmission electron micrograph of Ta_2O_5. Magnification 74,500×.

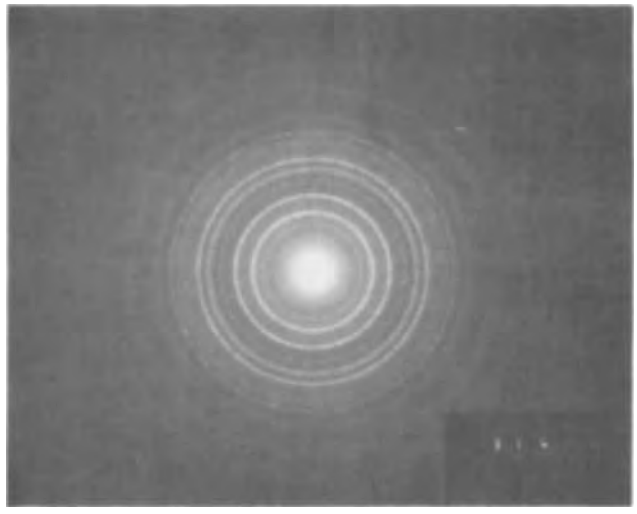

Fig. 3. Electron diffraction pattern of Ta_2O_5

Table I. Indexing of orthorhombic Ta_2O_5 electron diffraction pattern

Plane (hkl)	d(hkl) theoretical	d(hkl) observed	Theoretical intensity	Observed intensity
(001)	3.87	3.87	90	S
(110)	315	3.14	100	VS
(200)	3.09	3.08	50	VW
(111)	2.46	2.47	100	
		(band)		VS band
(201)	2.43	2.38	60	
(211)	2.02	2.04	30	W
(002)	1.95	1.94	50	W
(020)	1.83	1.86	40	
		(band)		S band
(310)	1.80	1.78	40	
(021)	1.66	1.67	100	S
(121)	1.63	1.64	30	W
(220)	1.58	1.59	30	W
(400)	1.55	1.56	30	W
(221)	1.46	1.46	40	W
(022)	1.34	1.35	70	
		(band)		S band
(312)	1.32	1.30	60	
(113)	1.20	1.20_5	80	S

VS: very strong.
S: strong.
W: weak.
VW: very weak.

by anodizing a sputtered β-Ta film at 120V in 0.01% citric acid with a 1 mA/cm^2 current density. The Ta_2O_5 film formed in this manner is reported to be stoichiometric (9). This film was analyzed by electron microprobe at the same time the pyrolytic Ta_2O_5 film was reanalyzed. The oxygen to tantalum ratio in the anodic film was 2.55 ± 0.05 and the average ratio in the pyrolytic film remained 2.37 ± 0.05. The over-all conclusion of this analysis is that the pyrolytic film, as examined across the width of the slice, is slightly oxygen deficient and not stoichiometric Ta_2O_5.

Infrared absorption and reflection study.—The specimens analyzed were 5000Å thick pyrolytic Ta_2O_5 films deposited on 50 ohm-cm silicon slices approximately 0.63 mm thick. Both the absorption and reflection spectra were obtained on a Beckman IR-12 double beam infrared spectrophotometer with appropriate attachments. The instrument scans in the wave-number range of 4000-200 cm^{-1}, but no peaks were observed above 1200 cm^{-1}.

The absorption spectrum obtained in this study is shown in Fig. 4. Two prominent and eight minor peaks were observed. McDevitt and Baun (10) have reported the absorption spectrum of β-Ta_2O_5 pressed powder in a Nujol mull over the wave-number range of 700-240 cm^{-1}. The peaks of the present study in that wave-number range roughly coincide with their three reported peaks, with a finite shift in positions having taken place. Sidorov (11), in an investigation of the absorption of β-Ta_2O_5 in the wave-number range of 1041-576 cm^{-1}, observed two peaks which coincide with peaks of the present study. Table III presents a comparison of results. Kihara-Morishita *et al.* (12) showed that the position of the prominent peaks is very sensitive to the voltage of anodization in making anodic films, and thus presumably to small differences in structure. Hence, from the *IR* absorption spectrum we can conclude that the deposited film is similar to β-Ta_2O_5 reported in the literature.

The infrared reflection spectrum (IRRS) obtained from the same specimens is seen in Fig. 5. Kihara-Morishita *et al* (12), recently reported the IRRS of

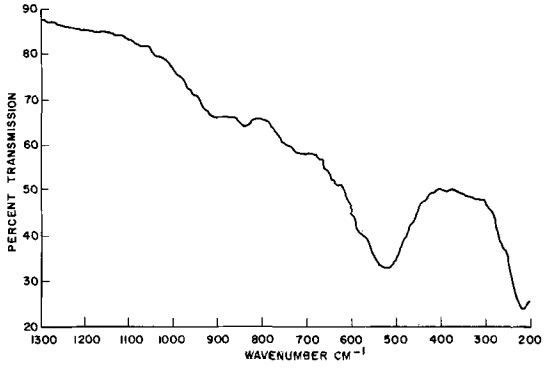

Fig. 4. Infrared transmission spectrum of Ta_2O_5

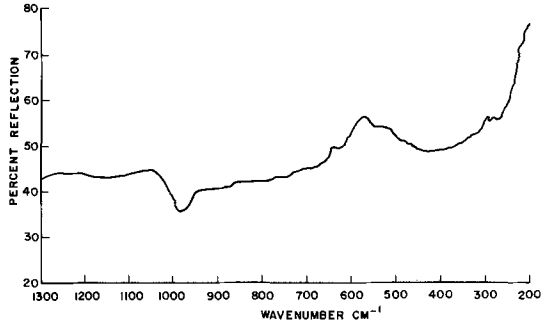

Fig. 5. Infrared reflection spectrum of Ta_2O_5

anodic tantalum oxide films in the wave-number range of 4000-7000 cm^{-1}. Two of their three reported peaks were observed in the present study, as seen in the comparison of results in Table IV. From the reflection spectrum it can be seen that the deposited films of the present study are related to but not identical to anodic tantalum oxide.

Optical Properties

Optical constants.—The index of refraction, n, of the pyrolytic Ta_2O_5 deposited on 1¼ in. diameter polished silicon slices was measured as a function of radial distance from the center of the slice by ellipsometry at 5461Å. The Ta_2O_5 film was assumed to be nonabsorbing. During this examination some concentric areas were observed, in which n was consistently 2.20 ± 0.03, as well as other concentric areas where the index of refraction had anomalously large values and changed strongly as a function of position. The value of n = 2.12-2.20 and 2.32-2.37 are found in the literature (13) for the two axes of β-Ta_2O_5 at 6710Å. Correction to 5461Å with the dispersion relationship reported for Ta_2O_5 (14) yields n = 2.23-2.31 and 2.43-2.48, in fair agreement for one of the axes with the present result of 2.20 ± 0.03. The anomalous values of n and their sensitivity to position indicate the film is absorbing in those areas.

Ellipsometry can be used for explicit measurements of an absorbing film (*i.e.*, a film with nonvanishing extinction coefficient) at the expense of adding an additional unknown parameter. If it is assumed that $k = 0$ in an absorbing film, ellipsometry will overestimate the value of n. However, once n in the nonabsorbing portions of the film is known the thickness and extinction

Table II. Summary of electron microprobe analysis of pyrolytic Ta_2O_5

Spot number; position on slice	Weight Ta	Per cent O	Atomic Ta	Per cent O	Ratio O:Ta
1 (center)	83.68 ± 0.78	17.42 ± 0.38	29.82 ± 0.39	70.18 ± 0.39	2.35:1
2	84.04 ± 0.81	17.40 ± 0.51	29.95 ± 0.49	70.05 ± 0.49	2.34:1
3	84.33 ± 0.67	17.91 ± 0.49	29.42 ± 0.49	70.58 ± 0.50	2.40:1
4	84.25 ± 0.77	17.75 ± 0.54	29.58 ± 0.58	70.42 ± 0.51	2.38:1
5 (outside edge)	84.10 ± 0.85	17.89 ± 0.45	29.38 ± 0.46	70.62 ± 0.47	2.40:1
				Average	2.37:1

Table III. Comparison of infrared absorption results

Observed absorption peaks (cm^{-1})	Previously reported absorption peaks (cm^{-1}) McDevitt and Baun (10) 700-240 cm^{-1}	Sidorov (11) 1041-576 cm^{-1}
220		
325 shoulder	315	
380 weak		This range not
425 shoulder	455 shoulder	covered
525 strong	575 strong	
630 shoulder		
710 shoulder	This range not	733
840	covered	860
900 shoulder		
1040 shoulder		

Table IV. Comparison of infrared reflection results

Observed reflection peaks (cm^{-1})		Previously reported reflection peaks Kihara-Morishita *et al.* (12) 4000-700 cm^{-1}	
270	medium		
425	broad	This range not	
550	shoulder	previously covered	
630	medium		
Not observed		810	weak to strong*
980	strong	950	weak to strong*
1140	weak	1100	weak

* The intensity of the peak is very dependent on the voltage of anodization.

coefficient of the film at all other points on the film can be obtained from the measured ellipsometric parameters Δ and Ψ by a method described elsewhere (15). Table V presents the optical constants calculated from Δ and Ψ, which were measured in approximately 2 mm increments across the slices.

The optical constant of the silicon substrate is taken to be $4.05-0.28i$ (5). Note the small amount of absorption in the Ta_2O_5 film that suffices to cause such a drastically different apparent n if it is assumed $k = 0$. For example, at spot 1 there is an apparent shift of 0.56 in n from neglecting the extinction coefficient of 0.044. The Drude ellipsometry equation (16), on which the program used for the present calculations is based, assumes an ideally homogeneous and optically isotropic substrate and film. Thus one cannot determine from ellipsometry whether the absorption in the film is isotropic through its depth, or whether it occurs in a specific region of the film, *e.g.*, at the substrate-film or film-ambient interfaces. The extinction coefficient k (where the absorption coefficient α is related to k by $\alpha = 4\pi/k\lambda$) which is listed in Table V is an average number applying to the whole depth of the film.

Optical energy gap.—The energy gap measurement samples were prepared by depositing Ta_2O_5 on fused silica disks. Absorbance *vs.* wavelength measurements in the wavelength region of 2000-7500Å were made on a Perkin-Elmer 202 UV-VIS double beam spectrophotometer. There was only one absorption peak observed, and this was assumed to be due to the fundamental energy gap absorption. The absorption coefficient α was calculated as a function of photon energy from this in the neighborhood of the absorption edge.

Table V. Optical study across width of slice pyrolytic Ta_2O_5 on silicon

Spot number; position on slice	Measured ellipsometric parameters Δ	Ψ	n of film assuming $k = 0$	Optical constants of film when allowing finite k	Thickness of film (Å)
1 (center)	297.7	13.3	2.76	$2.20-0.044\,i$	5150
2	307.3	15.5	2.68	$2.20-0.042\,i$	5090
3	319.3	19.8	2.52	$2.20-0.030\,i$	5000
4	337.6	25.0	2.42	$2.20-0.036\,i$	4910
5	42.7	29.6	2.19	$2.20-0.002\,i$	4680
6	64.2	24.8	2.18	$2.20-0.004\,i$	4265
7	94.0	18.0	2.20	$2.20-0.000\,i$	4115
8 (outside edge)	118.9	13.7	2.45	$2.20-0.013\,i$	4060

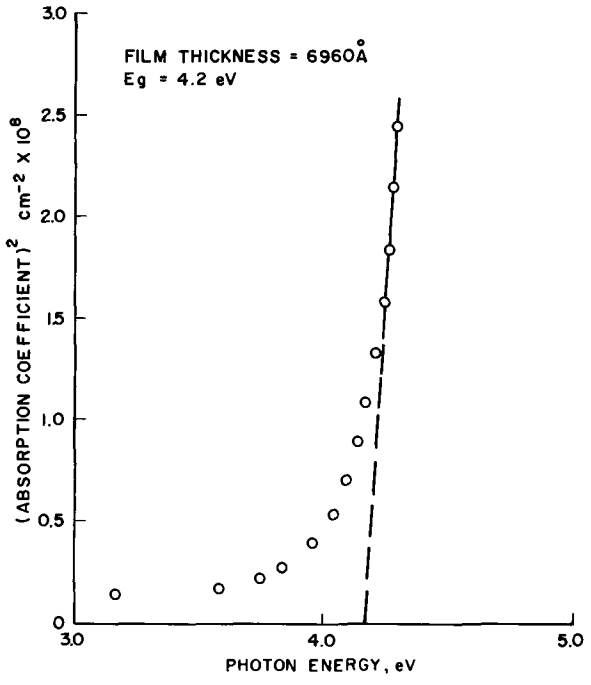

Fig. 6. (Absorption coefficient)^2 as a function of photon energy, $h\nu$, for Ta_2O_5.

This yielded values of α on the order of 10^4 cm^{-1}, which are indicative of direct optical transitions. Fan (17) has shown that for direct allowed transitions α is related to the photon energy by

$$\alpha = A(h\nu - E_g)^{1/2}$$

where A is a constant and E_g, the bandgap energy. Figure 6 shows α^2 as a function of energy. Extrapolation to $\alpha = 0$ yields an energy gap of 4.20 eV. This is well within the range of 3.58 eV reported for both α and β-Ta_2O_5 from conductivity measurements (18), and values of 4.5 and 4.6 eV from reflectivity and absorption measurements (19, 20).

Electrical Properties

Ta_2O_5 films approximately 1000Å thick were pyrolytically deposited on 0.001 ohm-cm silicon and aluminum dots 2.0×10^{-3} cm^2 in area were vacuum evaporated at a pressure less than 10^{-6} Torr. A 2000Å sheet of Al was evaporated as a back contact. The specimens were mounted in a temperature chamber and electrical connection was made using spring loaded contacts. The capacitance and loss tangent were measured in a temperature interval of 78°-488°K and a frequency interval of 1×10^3 to 1×10^5 Hz. Measurements of loss tangents at frequencies down to 1×10^2 Hz were made, but could not be continued through the whole temperature range because of excessively large loss tangent values. The measurements were performed on a General Radio Type 1615-A capacitance bridge using a three-terminal probe.

Dielectric constant.—The dielectric constant was calculated from the capacitance measured as outlined above and from the Ta_2O_5 film thickness measured by ellipsometry and the reflectivity minima in the ultraviolet and visible spectrum. Figure 7 shows the results as a function of temperature for the frequencies 1×10^3, 2×10^3, 1×10^4, and 1×10^5 Hz. At room temperature and 100 kHz the apparent dielectric constant is 44.0. To the authors' knowledge there are no published data on the dielectric constant of crystalline β-Ta_2O_5 available in the literature to make comparison with the present results. However, Pavlovic (21) reported the dielectric constant of β-Ta_2O_5 ceramic to be 24.1 at room temperature and 100 kHz. Gerstenberg found an average value of dielectric constant for anodic films of 21.7 (22). There is clearly a strong tempera-

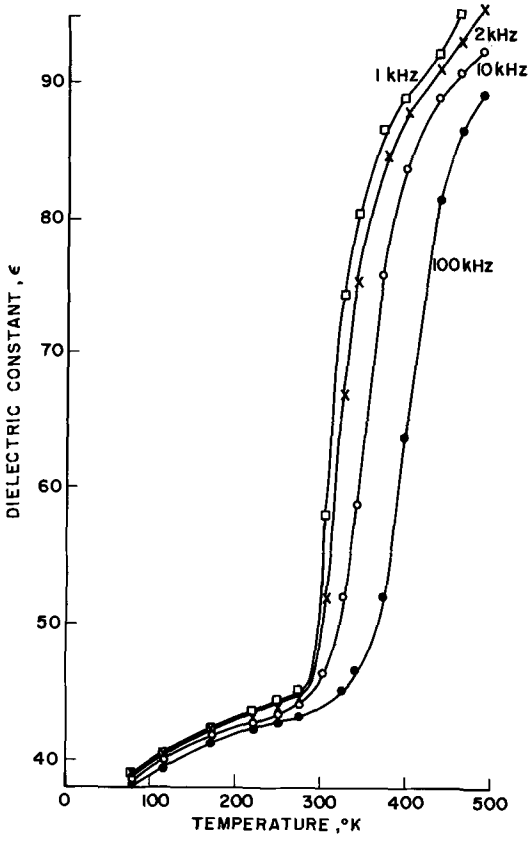

Fig. 7. Dielectric constant, ε, as a function of temperature with frequency as a parameter.

ture dependence which manifests itself above 290°K and suggests the existence of ionization sites in the Ta_2O_5 film. Smyth *et al.* (23), in their investigation of the effects of heat-treatment and reanodization on anodic Ta_2O_5 films, found strong temperature dependence under conditions in which there were oxygen vacancies in the film. An oxygen vacancy would contain two electrons, whose ionization would be temperature dependent. Thus the data presented in Fig. 7 indicates that the film investigated is probably not stoichiometric.

Loss tangent.—The loss tangent was calculated directly from the General Radio Type 1615-A capacitance bridge readings. Figure 8 presents these data as a function of temperature for the frequencies 1×10^3, 2×10^3, 1×10^4, and 1×10^5 Hz. At room temperature and 100 kHz, the loss tangent is 0.025, in contrast to Pavlovic's (22) value of 0.0001 for β-Ta_2O_5 ceramic. In this case also a strong temperature dependence, as in the case of the dielectric constant, could be attributed to the ionization of oxygen vacancies.

Acknowledgments

The authors would like to thank R. E. Caffrey for his encouragement throughout the course of this work. Thanks are also due to D. R. Wonsidler for his assistance with the microprobe analysis, L. P. Adda for assistance in measuring the dielectric properties, J. Drobek for assistance with electron microscopy, and D. Gerstenberg for helpful discussions.

Manuscript submitted Sept. 25, 1972; revised manuscript received Feb. 7, 1973. This was Paper 170 presented at the Miami Beach, Florida, Meeting of the Society, Oct. 8-13, 1972.

Any discussion of this paper will appear in a Discussion Section to be published in the June 1974 JOURNAL.

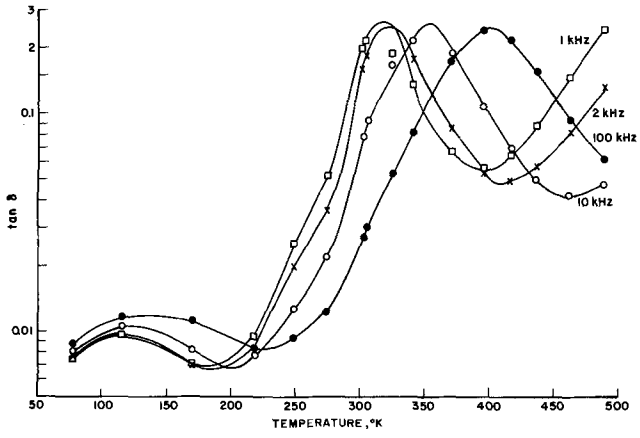

Fig. 8. Loss tangent, tan δ, as a function of temperature with frequency as a parameter.

REFERENCES

1. C. F. Powell, J. H. Oxley, and J. M. Bloecher, Jr., Editors, "Vapor Deposition," pp. 384-403, John Wiley and Sons, Inc., New York (1969).
2. D. J. Peacock, *Electrochem. Technol.*, **4**, 443 (1966).
3. C. C. Wang, K. H. Zaininger, and M. T. Duffy, *RCA Rev.*, **31**, 728 (1970).
4. R. N. Tauber, A. C. Dumbri, and R. E. Caffrey, *This Journal*, **118**, 747 (1971).
5. K. Vedam, W. H. Knausenberger, and F. Lukes, *J. Opt. Soc. Am.*, **59**, 64 (1969).
6. F. Reizman, *J. Appl. Phys.*, **36**, 3804 (1964).
7. X-Ray Power Data File, ASTM (1961).
8. J. W. Colby, in "Thin Film Dielectrics," F. Vratny, Editor, pp. 491-520, The Electrochemical Society Softbound Symposium Series, New York (1969).
9. D. G. Muth, *J. Vacuum Sci. Technol.*, **6**, 751 (1969).
10. N. T. McDevitt and W. L. Baun, *J. Am. Ceramic*, **47**, 622 (1964).
11. T. A. Sidorov, *Tr. Fiz. Inst. Akad., Nauk USSR*, **12**, 236 (1960).
12. H. Kihara-Morishita, T. Takamura, and R. Takeda, *Thin Solid Films*, **6**, R29 (1970).
13. J. T. Waber, G. E. Sturdy, E. M. Wise, and C. R. Tipton, *This Journal*, **99**, 121 (1952).
14. B. W. King, J. Schultz, E. A. Durbin, and W. H. Duckworth, *BMI*—1106, 8 (1957).
15. W. H. Knausenberger, To be published.
16. P. Drude, *Ann Physik Chemi.*, **39**, 481 (1890).
17. H. Y. Fan, *Rept. Progr. Phys.*, **19**, 107 (1956).
18. P. Kasstad, *This Journal*, **109**, 776 (1962).
19. P. Hortl and W. Schwarz, *Z. Naturforsch.*, **24a**, 296 (1969).
20. L. Apker and E. A. Taft, *Phys. Rev.*, **88**, 58 (1952).
21. A. S. Povlovic, *J. Chem. Phys.*, **40**, 951 (1964).
22. D. Gerstenberg, *This Journal*, **113**, 1542 (1966).
23. D. M. Smyth, G. A. Shirn, and T. B. Tripp, *ibid.*, **111**, 1331 (1964).

Measurement of Film Thickness from Lattice Absorption Bands

C. J. Mogab

Bell Laboratories, Murray Hill, New Jersey 07974

ABSTRACT

Many compound semiconductors and insulators exhibit characteristic infrared lattice absorption bands which can be quantitatively described by classical dispersion theory. When the dispersion parameters are known, the thickness of an absorbing film on a nonabsorbing substrate can be determined from a measurement of the lattice absorption. For thin films the dispersion parameters can differ from the values appropriate to bulk single crystals; however, it is shown that the parameter most susceptible to variation can be obtained directly from the measured absorption band without knowledge of the film thickness. It is also shown that the integrated optical density (the area under the band plotted as optical density *vs.* wave number) is a linear function of thickness when the refractive index of the substrate is unity, but departs from linearity as the substrate refractive index increases. The appropriate equations and a method for determining film thickness from a measured absorption band are given. The discussion is illustrated by data for thin SiC films on Si substrates.

Of the many techniques available for the measurement of film thickness (1), the use of infrared lattice absorption bands has received comparatively little attention despite the fact that it is a potentially useful technique for a variety of compound semiconductors and insulators of practical importance. Nakayama and Collins (2) used the optical density at the peak of the 9.3 μm infrared band of SiO_2 to determine the thicknesses of thin SiO_2 films on silicon substrates. This was accomplished by calibration against the Vamfo method (1) for several films in excess of 2400Å with a linear interpolation of the peak optical density between 2400Å and zero thickness assumed valid. In another study of SiO_2 films on Si, Pliskin and Esch (3) pointed out that the peak optical density is not a linear function of thickness and suggested the integrated band intensity (the area under a plot of optical density *vs.* wave number) as a more suitable function for linear interpolation. They measured the integrated optical density and film thickness, the latter quantity by use of the Vamfo technique, and observed a linear relation between these quantities over the range of their thickness measurements. Choudhury and Formigoni (4) attempted to determine the thickness of β-SiC films on Si substrates by comparing the transmission at the peak of the 12.6 μm band to the values expected for unsupported films on the basis of the dispersion parameters for β-SiC determined by Spitzer *et al.* (5).

In the course of a study of the growth of very thin epitaxial films of SiC on Si crystals (6), we have found it necessary to resort to infrared lattice absorption measurements in order to determine film thickness. More conventional methods such as ellipsometry at 5461Å failed to provide accurate thickness values due, we believe, to the peculiar topology of these films which allowed some scattering of visible light. In a survey of the literature we were unable to find any basis for the interpretation of infrared measurements insofar as the determination of film thickness is concerned. Moreover, in most instances where infrared measurements had been used for this purpose, we felt that an improper interpretation of these measurements was made leading to erroneous thickness values.

This paper considers the use of infrared lattice absorption measurements as a means for thickness determination for films for which the lattice absorption can be described in terms of classical dispersion theory (7) and which are supported on a substrate that is transparent within the region of the absorption band.

Key words: films, thickness, infrared, absorption.

(A partial listing of the many compounds exhibiting lattice absorption bands which can be quantitatively described by classical dispersion theory is given in Table I). In particular, the use of linear interpolation or extrapolation from calibration measurements, for materials whose dispersion constants are unknown, and the appropriate methods for dealing with film materials, for which dispersion parameters are available from measurements on bulk crystals, are discussed. Calculations and experimental data for β-SiC films on silicon substrates are used to illustrate the discussion.

As with most thickness measuring techniques, this method has certain advantages and limitations which will dictate its applicability for specific situations. It is contactless and nondestructive and does not require that the film be transparent in the visible, or that there be a step in the film; requirements which must be met in order to use several of the most widely employed techniques (1). Further, it does not depend on interference within the film and thus in certain instances can be used to measure thicknesses well below the minimum value at which interference techniques are applicable. Since infrared is used the method can be useful for films having rough (nonspecular) surfaces, on the scale of visible light, but negligible roughness in comparison to infrared wavelengths. Its main limitations are that it requires a substrate which is transparent in the region of the absorption band and, as will be discussed, the high and low frequency dielectric constants of the film material must be known or an auxiliary method of thickness measurement must be available for calibration. In addition the method involves a comparatively complicated analysis, although no more so than for ellipsometry. Consideration of the foregoing remarks suggests that this method may be most useful for opaque semiconductor films and possibly also for insulator films having sufficiently rough surfaces to preclude the use of simple techniques employing visible light.

Table I. Measured dispersion parameters for several materials

Material	w_o (cm^{-1})	ρ	γ	ϵ_∞	γ/ρ	Ref.
InSb	185	0.175	0.007	15.68	0.040	(8)
InAs	219	0.231	0.007	12.25	0.030	(8)
GaSb	230	0.099	0.007	14.44	0.071	(8)
GaAs	273	0.159	0.007	10.9	0.044	(9)
InP	307 ± 8	0.239	0.04	9.61	0.17	(8)
AlSb	318 ± 8	0.143	0.02	10.24	0.14	(8)
GaP	366	0.137	0.003	8.46	0.022	(10)
ZnO	413	0.332	0.025	4.0	0.075	(11)
SiC	793	0.263	0.0107	6.7	0.040	(5)

Theory

The classical dispersion theory (7) for a single resonance considers the interaction of monochromatic radiation of wave number w with a collection of charged oscillators undergoing damped harmonic motion with a resonant wave number w_0. The frequency dependence of the complex dielectric constant as deduced from this theory is

$$\epsilon_1 = \epsilon_\infty + 4\pi\rho \frac{1-\nu^2}{(1-\nu^2)^2+\gamma^2\nu^2} \quad [1]$$

$$\epsilon_2 = 4\pi\rho \frac{\gamma\nu}{(1-\nu^2)^2+\gamma^2\nu^2} \quad [2]$$

where ϵ_1 and ϵ_2 are the real and imaginary parts of the dielectric constant, ϵ_∞ is the high frequency dielectric constant, $\nu = w/w_0$, γ is a dimensionless damping constant, and ρ is a dimensionless parameter reflecting the strength of absorption. ρ is related to the static (low frequency) dielectric constant, ϵ_0, by

$$\rho = (\epsilon_0 - \epsilon_\infty)/4\pi \quad [3]$$

The parameters ϵ_∞, ρ, γ, and w_0 are referred to as the dispersion parameters and completely determine the optical properties, n, k, in the region of the absorption band (n and k are the real and imaginary parts of the refractive index) since

$$\left.\begin{aligned}\epsilon_1 &= n^2 - k^2\\ \epsilon_2 &= 2nk\end{aligned}\right\} \quad [4]$$

If the dispersion parameters are known for a specific film, the thickness of that film on a transparent substrate can be determined from a transmission measurement as described in the Appendix. A desirable alternative to computation of the thickness would be direct calibration of the integrated optical density against an independent thickness measuring technique, and subsequent use of linear interpolation or extrapolation over the thickness range of interest, as suggested by the work of Pliskin and Esch (3). The validity of this approach is discussed below.

The equations describing the transmission of a thin absorbing film on a transparent substrate (see Appendix) are sufficiently cumbersome that no direct relation between optical density and film thickness can be obtained from them. In order to arrive at simplified relations, an unsupported film, exhibiting a single lattice resonance,[1] is considered here. The applicability of these simplified relations to films on substrates is then tested by direct numerical computation using the exact equations as given in the Appendix and values of the dispersion parameters for β-SiC as determined by Spitzer *et al.* (5), which are representative of materials having a single lattice resonance.

A first-order approximation to the transmission, T,[2] of an unsupported film of thickness, d, valid when $2\pi wd\sqrt{n^2+k^2} << 1$, gives

$$\frac{1}{T} = 1 + \beta\epsilon_2 + \frac{1}{4}(\beta\epsilon_2)^2 + \frac{1}{4}[\beta(\epsilon_1 - 1)]^2 \quad [5]$$

where $\beta = 2\pi wd$. Substitution of Eq. [1] and [2] in [5] yields

$$\frac{1}{T} = 1 + \mathbf{F}(\nu) \quad [6]$$

with

$$\mathbf{F}(\nu) = \frac{4\pi\rho}{D}\left[\beta\gamma\nu + \frac{\beta^2}{2}(\epsilon_\infty - 1)(1-\nu^2) + \pi\rho\beta^2\right] + \frac{\beta^2}{4}(\epsilon_\infty - 1)^2 \quad [7]$$

where $D = (1-\nu^2)^2 + \gamma^2\nu^2$. Equations [6] and [7] describe the transmission in the vicinity of the absorption band. For typical dispersion parameters (see Table I) the last term in Eq. [7] is negligible over the entire band, and since ν is near unity throughout the band, Eq. [7] can be rewritten

$$\mathbf{F}(\nu) \simeq \frac{C}{(1-\nu)^2 + (\gamma/2)^2} \quad [8]$$

where

$$C = \pi^2\rho[2\gamma w_0 d + 4\pi^2\rho(w_0 d)^2] \quad [9]$$

The optical density is defined by

$$OD = \log(1/T) \quad [10]$$

Figure 1 illustrates computed absorption bands, plotted as optical density *vs.* reduced wave number (w/w_0), for a 600Å film of β-SiC on substrates of various refractive indexes. Note that the effect of increasing the substrate refractive index is to enhance the transmission; this results mainly from a reduced reflectivity at the film-substrate interface.

Substitution of Eq. [6] and [8] in [10] gives

$$OD \simeq \log\left[1 + \frac{C}{(1-\nu)^2 + (\gamma/2)^2}\right] \quad [11]$$

According to Eq. [11] and [9] the optical density has a maximum at $\nu = 1$ given by

$$OD_{max} = \log\left(\frac{\gamma^2 + 4C}{\gamma^2}\right) = 2\log\left(1 + \frac{4\pi^2\rho w_0 d}{\gamma}\right) \quad [12]$$

Expansion of Eq. [12] in powers of $w_0 d$ indicates that the peak optical density is linear in $w_0 d$, for typical values of ρ/γ, only up to values of $w_0 d$ corresponding to negligible absorption. From the exact equations it can be shown that the peak optical density becomes linear in thickness when $4\pi k w_0 d > 2$ where k is the value of the imaginary part of the film refractive index at the resonant frequency. For typical materials, the latter criterion implies that the peak optical density is linear in thickness only for thicknesses corresponding

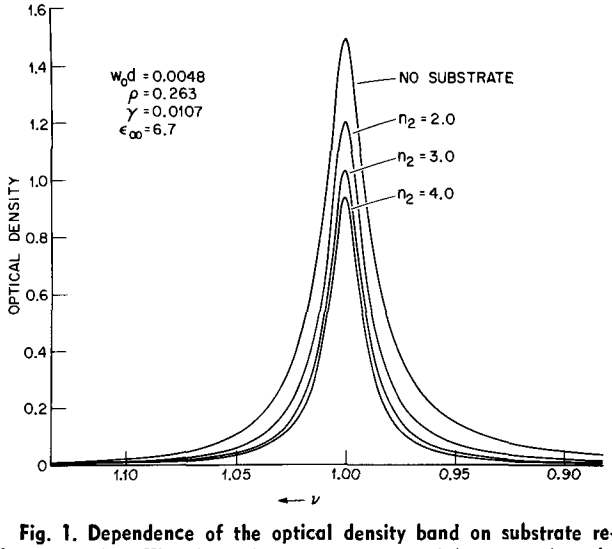

Fig. 1. Dependence of the optical density band on substrate refractive index. The dispersion parameters used in computing the band are those for β-SiC as reported in Ref. (5).

[1] Multiresonance absorption processes are described by equations analogous to [1] and [2]

$$\epsilon_1 = \epsilon_\infty + \sum_j 4\pi\rho_j \frac{(1-\nu_j^2)}{(1-\nu_j^2)^2 + \gamma_j^2\nu_j^2}$$

$$\epsilon_2 = \sum_j \frac{4\pi\rho_j\gamma_j\nu_j}{(1-\nu_j^2)^2 + \gamma_j^2\nu_j^2}$$

where ν_j and ρ_j are the dispersion parameters associated with the jth resonance. An extension of the discussion presented here to materials exhibiting multiresonance lattice bands will be evident.

[2] Throughout this paper it is assumed that the transmission, T, in the region of an absorption band is normalized relative to any observable background.

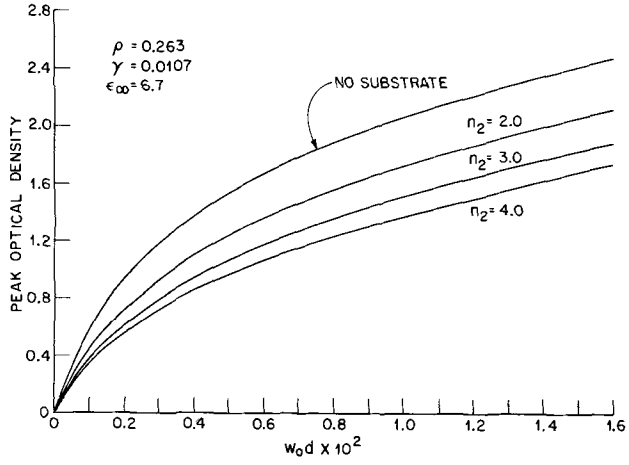

Fig. 2. Dependence of the peak optical density on film thickness and substrate refractive index for β-SiC films having the dispersion parameters given in Ref. (5).

to substantial absorption. Thus over the range of thicknesses where transmission measurements can be employed with high accuracy, the peak optical density is not a linear function of thickness. This is demonstrated in Fig. 2 for the case of β-SiC films having dispersion parameters as determined by Spitzer *et al.* (5). Accordingly, linear interpolation of peak optical density *vs.* thickness, as used by Nakayama and Collins (2), is certain to lead to considerable error.

The integrated optical density, A, can be obtained from Eq. [11] as

$$A = \int (OD)\, d\nu \cong \frac{1}{2.303} \int_{-\infty}^{\infty} \ln\left[1 + \frac{C}{(1-\nu)^2 + (\gamma/2)^2}\right] d\nu \quad [13]$$

and carrying out the integration with use of Eq. [9]

$$A = 4\pi^3 \rho w_0 d/2.303 \quad [14]$$

Thus, within the first-order approximation, which is expected to be valid even for the thickest films that can be measured, the integrated optical density is linear in thickness and independent of the damping constant γ when the film is unsupported. The validity of this conclusion. when a substrate is present, has been tested by use of the exact equations. Figure 3

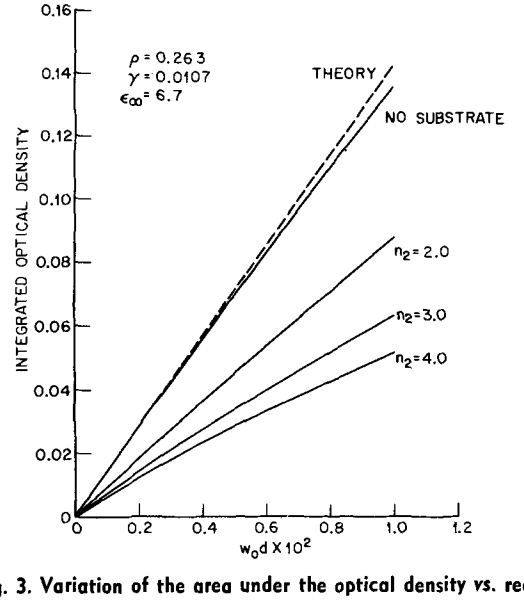

Fig. 3. Variation of the area under the optical density *vs.* reduced wave number (w/w_0) band with thickness and substrate refractive index. The dashed line represents Eq. [14].

shows the dependence of the integrated optical density on film thickness for a series of substrate indexes. The dashed line represents Eq. [14] while the solid lines correspond to numerical integrations of the exact equation for optical density. In carrying out the numerical integrations, infinite limits cannot be used thus leading to an error due to neglect of the band "wings" (see Fig. 1). If fixed limits are used (as was done here) this error increases with film thickness. For the "no substrate" case the error can be calculated exactly and can be shown to account for the divergence between the theoretical line and the "no substrate" curve in Fig. 3. As is evident from Fig. 1, for a given film thickness the wing correction is smaller the larger the substrate index. Accordingly, while the curves for $n_2 > 1$ in Fig. 3 are slightly in error for $w_0 d \gtrsim 0.004$, due to neglect of the wing correction, making this correction will not impart linearity to the curves since the maximum possible correction is given by the departure of the "no substrate" curve from the dashed line. We conclude, therefore, that the integrated optical density is strictly linear in thickness only when $n_2 \to 1.0$. However, it can be seen from Fig. 3 that, except for rather high substrate indexes, comparatively little error is involved in use of linear interpolation or extrapolation of the integrated optical density. The linearity observed by Pliskin and Esch (3) for SiO_2 films on silicon substrates ($n_2 \simeq 3.4$) probably results from the fact that the ρ value for the 9.3 μm band of SiO_2 is likely to be considerably smaller than the values indicated in Table I,[3] (this causes the initial linearity evident in Fig. 3 to be retained to higher $w_0 d$ values) and may also result in part from their inclusion of the small 8 μm shoulder on the 9.3 μm band in the integration. The effect of the damping constant on the computed areas was also tested. For the "no substrate" case the area was independent of γ as predicted by Eq. [14]. however for $n_2 \gtrsim 2.0$ there was a very slight dependence of the integrated optical density on γ, which if neglected would lead to a maximum error in derived thickness estimated to be about 5%.

One other noteworthy feature of the optical density band obtainable from Eq. [9] and [11] is that the band half-width (the width of the band at half the peak intensity) is not independent of film thickness as might customarily be assumed. In fact for the unsupported film

$$\Delta\nu = [\gamma(4\pi^2 w_0 \rho d + \gamma)]^{1/2} \quad [15]$$

where $\Delta\nu$ is the half-width. Figure 4 illustrates the effect of the substrate refractive index on the half-width of the optical density band, again for the case of β-SiC films.

In contrast to the behavior of the optical density function, it can be seen from Eq. [6] and [8] that the function $(1/T - 1)$ has a Lorentzian shape with a half-width equal to γ independent of the film thickness. It also has a maximum at the resonant frequency, however, both the peak height and the area under the peak are quadratic in thickness as can be deduced by the use of Eq. [6], [8], and [9]. Direct numerical computation of the half-width of the $[(1/T) - 1]$ function for several test cases, including the full range of dispersion parameters and substrate refractive indexes which might normally be encountered in practice indicates that the half-width is in fact equal to γ, well within probable experimental error, up to the maximum measurable thicknesses. Consequently an experimental plot of $[(1/T) - 1]$ *vs.* wave number can be used to obtain γ (and w_0) directly. This is significant because the damping "constant" is expected to be structure-sensitive.

[3] The films measured by Pliskin and Esch (3) were presumably amorphous. The author knows of no determination of the dispersion parameters for vitreous SiO_2, however for quartz, which exhibits multiresonance bands, Spitzer and Kleinman (11) report $\rho = 0.053$ for the 9.3 μm band.

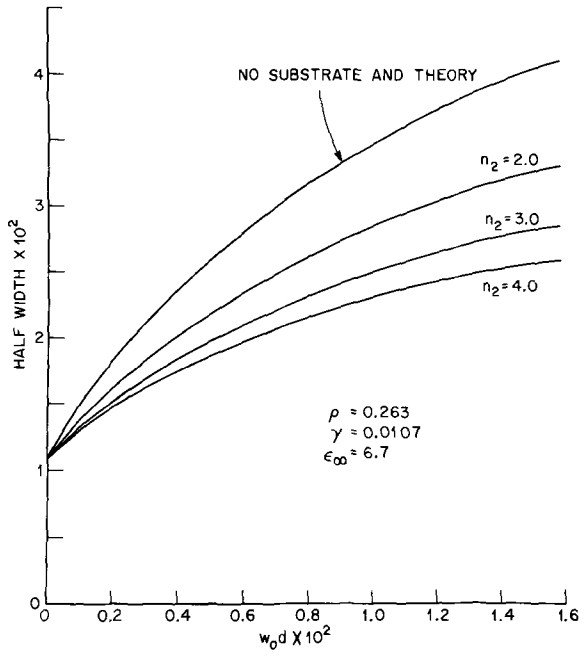

Fig. 4. Dependence of the half-width of the optical density band on film thickness and substrate refractive index.

Discussion and Comparison to Experiment

When the dispersion parameters for a particular material are available from the literature, it is imperative that their applicability be checked, when measurements are to be made on films, because of the anticipated structure-sensitivity. Once the appropriateness of a set of constants is confirmed, a simple measurement of peak optical density suffices for the determination of thickness. As an example of the error involved in applying published constants without regard to their validity, Fig. 5a compares experimental data for a thin epitaxial β-SiC film grown on Si with an absorption band computed from the dispersion parameters of Spitzer *et al.* (5) using a film thickness chosen to match the experimental peak height. (The carbide film was grown by reaction of C_2H_2 with a (111) silicon crystal. The absorption band was recorded on a Perkin-Elmer Model 621 grating spectrophotometer). It is evident from this comparison that the published dispersion parameters are not applicable to this film; varying the film thickness for the computed curve will vary its breadth as per Eq. [15] but will also change the peak height. When the experimental data of Fig. 5a were plotted as $(1/T) - 1$ *vs.* wave number it was found that the resonant frequency was identical to the value determined by Spitzer *et al.* but the damping constant γ was considerably larger ($\gamma = 0.0211$). Using this new damping constant and retaining the literature values for the other dispersion constants, a film thickness was found which resulted in a match between the computed and measured peak height and half-width. A new band was then computed which gave a good match to the experimental data as shown in Fig. 5b. The thickness determined in this way was 930Å which is to be compared to the 470Å film which matches only the peak height using the published damping constant.

To further emphasize the structure-sensitivity of the damping constant Table II lists the experimentally determined values of γ and w_0 for several β-SiC films grown on silicon under different conditions of time, temperature, and C_2H_2 pressure. Note that, even for films grown at the same temperature and C_2H_2 pressure, the damping constant varies with growth time and, therefore, with thickness. The large values of γ (compared to those of Spitzer *et al.*) shown here are not peculiar to the author's SiC films; similar values can be deduced from the data of Choudhury and Formigoni (4) for SiC films formed by reaction of

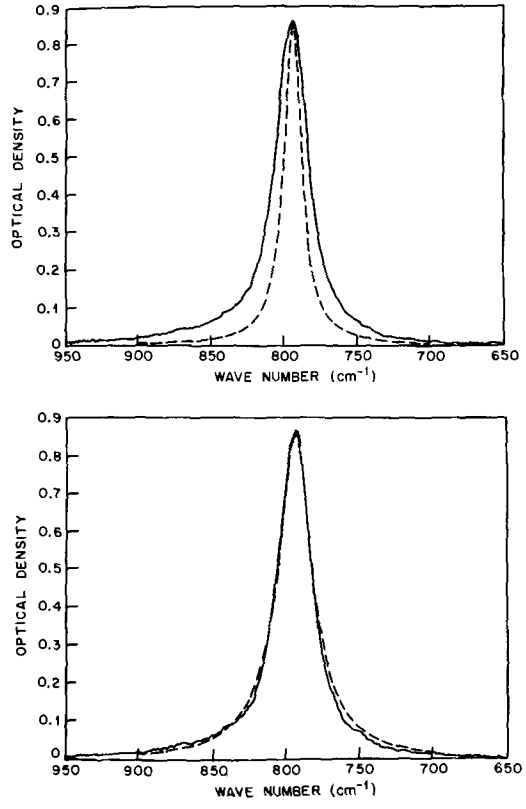

Fig. 5. (a, top) Comparison of an experimental absorption band (solid line) for a thin β-SiC film on silicon to a band (dashed line) computed from published dispersion parameters (Ref. 5) which matches the experimental peak intensity. (b, bottom) Comparison of measured and computed bands when the correct damping constant is used.

CH_4 with silicon. The reason for the variability of the γ parameter is open to conjecture, but whatever the case, the error involved in not accounting for it can be substantial.

One must also consider the possibility of variation of the parameters ρ and ϵ_∞. Unfortunately, if the film thickness is unknown there is no way to determine these parameters uniquely from a transmission measurement, or, for that matter, from a combination of transmission and reflection measurements. From Eq. [15] and [12] it can be seen that the width and intensity of the absorption band are independent of ϵ_∞, but depend directly on the product ρd. Indeed, using the exact equations as given in the Appendix it is found that large changes in ϵ_∞ have very little effect on the computed absorption bands. For example, changes in the bulk value of ϵ_∞ for SiC by factors of two and one-half lead to nearly imperceptible differences in the computed bands, over the wave number region where a fit to a measured band would be made. More importantly, variation of ϵ_∞ mainly affects the wings of the band and thus the thickness derived by matching

Table II. Observed values of damping constant and resonant frequency for thin β-SiC films on silicon

Sample	Growth temperature (°C)	C_2H_2 pressure (Torr)	Growth time (hr)	γ	w_0 (cm^{-1})
10-1	955	$5\cdot10^{-7}$	2	0.0283	794
10-2	955	$5\cdot10^{-7}$	4	0.0238	794
10-3	955	$5\cdot10^{-7}$	6	0.0220	794
10-4	955	$5\cdot10^{-7}$	8	0.0193	794
11-1	1000	$5\cdot10^{-7}$	2	0.0286	793
11-2	1000	$5\cdot10^{-7}$	4	0.0242	793
11-3	1000	$5\cdot10^{-7}$	6	0.0184	793
11-4	1000	$5\cdot10^{-7}$	8	0.0156	793
2-1SH	950	$1\cdot10^{-6}$	1	0.0261	793
2-2SH	950	$1\cdot10^{-6}$	2	0.0245	793
2-3SH	950	$1\cdot10^{-6}$	0.5	0.0305	794
2-4SH	950	$1\cdot10^{-6}$	5	0.0193	793

the peak region is not influenced by the choice of ϵ_∞. Thus values of ϵ_∞ obtained from the literature can be used with impunity. On the other hand, Eq. [15] and [12] imply that, given the correct values of w_0 and γ, one can fit an experimental band (as in Fig. 5b) by choosing any combination of values for ρ and d which give the correct product. Using the exact equations it is found that the wings of the band vary for different choices of ρ and d such that ρd is maintained constant. However, within the realm of typical experimental error one could fit a measured band using a rather wide range of thicknesses depending on the value of ρ selected.

In the simple Lorentz theory the parameter ρ is given by

$$\rho = \frac{Ne^2}{4\pi^2 m_r \nu_0^2} \qquad [16]$$

where N is the oscillator concentration, m_r is the reduced mass, ν_0 is the resonant frequency, and e is the effective charge. Thus, for a given material, ρ is essentially a measure of the oscillator density and can reasonably be expected to be considerably less structure-sensitive than the damping constant which reflects local interactions between an oscillator and its surroundings. For single-phase films whose densities and/or lattice parameters are not appreciably different from their bulk values, ρ can be expected to be approximately the same as the bulk value. Where some independent method exists, for example, determination of film thickness by some other technique, one can, of course, use the lattice absorption data to obtain the value of ρ.

Since the band intensity depends only on the product ρd, it follows that, if ρ is constant from film to film, but not necessarily equal to the bulk value, one can still obtain an accurate relative measure of thickness by using the bulk ρ value. Figure 6 is a plot of film thickness *vs.* growth time for several films of β-SiC grown under various conditions which were expected to yield a linear growth rate. The thickness values were determined by fitting the 12.6 μm absorption band

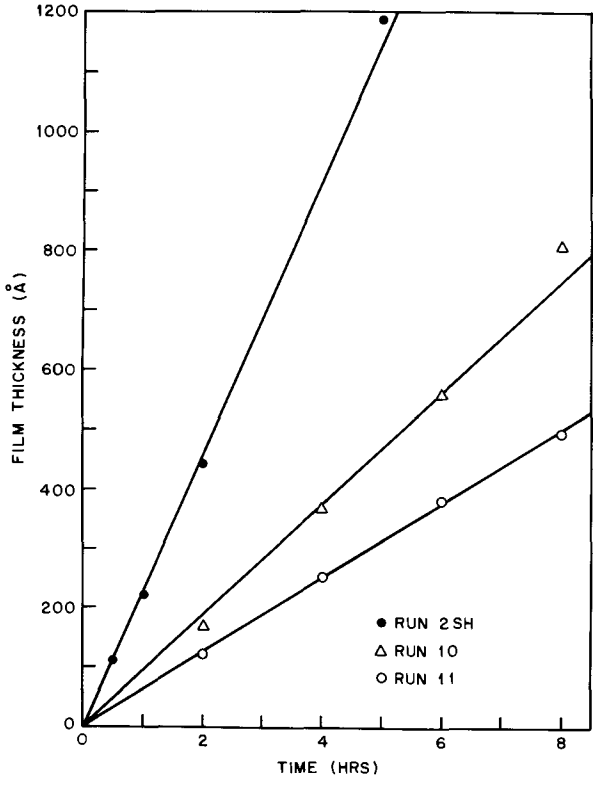

Fig. 6. Dependence of film thickness, determined from the experimental absorption bands, on film growth time for several films having variable damping constants (see Table I).

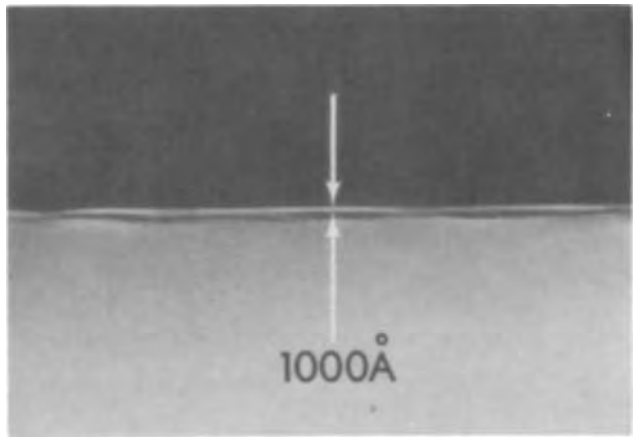

Fig. 7. Scanning electron micrograph of cleaved silicon substrate with a thin SiC film on the surface viewed edge-on. The film is delineated by the vertical arrows.

using experimentally determined values of γ and w_0 and the ρ (and ϵ_∞) value of Spitzer *et al.* (5). The values of γ vary widely for these films (see Table I) but the ρ value is apparently essentially constant, as evidenced by the reasonable fit to a straight line.

As noted at the beginning of this paper, we initially attempted determination of the thicknesses of our SiC films by the ellipsometric technique. These measurements generally gave results which were obviously affected by light scattering; the surfaces of the films were often not specular at visible wavelengths. Consequently, ellipsometry could not be used to check the infrared values. In lieu of a more sensitive technique, we endeavored to obtain a check on the thicknesses derived from the infrared bands by cleaving several samples and viewing the film-substrate composite edge-on in a scanning electron microscope. Within the resolution of this instrument. a good correspondence between the infrared and scanning microscope measurements was found. As an example, Fig. 7 illustrates a typical observation of a film on its substrate as seen edge-on. The thickness of this film, as determined from an infrared measurement, was 930Å. The interesting topological details evident in Fig. 7 (note particularly the film-substrate interface) will be discussed elsewhere (6).

Summary and Conclusions

Fundamental lattice absorption bands can be used to determine film thickness when the dispersion parameters are known. The damping constant and resonant frequency can be obtained directly from transmission measurements. If the high and low frequency dielectric constants are known no additional information is needed. However, the structure sensitivity of the dispersion constants, particularly the damping constant, requires that caution be exercised in deriving film thicknesses from measured absorption bands by the use of published dispersion constants. When the dispersion parameters are not available, the integrated optical density appears to be the most suitable function for linearization when direct calibration against an independent thickness measuring technique is to be used to generate a standard curve for subsequent thickness measurements.

Acknowledgment

The author is indepted to H. J. Leamy and S. D. Ferris for the scanning electron microscope measurements.

APPENDIX

The relations needed to derive film thickness from measured transmission bands are given here together with a brief discussion of a useful computational scheme. The thickness range over which measurements can be made is also estimated.

When a film-covered, transparent substrate is compared to an uncoated, but otherwise identical substrate in a double beam spectrophotometer (at normal incidence) the observed transmission, T_{obs}, is given by

$$T_{obs} = \frac{T_f(1 + R_f')}{1 - R_f'R_s'} \qquad [A\text{-}1]$$

provided the substrate is thick enough to suppress interference effects.[4] If n_2 is the substrate refractive index

$$R_s' = \left(\frac{n_2 - 1}{n_2 + 1}\right)^2 \qquad [A\text{-}2]$$

T_f and R_f' are given by (13)

$$T_f = \frac{n_2\{(1 + g_1)^2 + h_1^2\}\{(1 + g_2)^2 + h_2^2\}}{e^{2\alpha_1} + (g_1^2 + h_1^2)(g_2^2 + h_2^2)e^{-2\alpha_1} + C\cos 2\gamma_1 + D\sin 2\gamma_1} \qquad [A\text{-}3]$$

$$R_f' = \frac{(g_2^2 + h_2^2)e^{2\alpha_1} + (g_1^2 + h_1^2)e^{-2\alpha_1} + A\cos 2\gamma_1 - B\sin 2\gamma_1}{e^{2\alpha_1} + (g_2^2 + h_2^2)(g_1^2 + h_1^2)e^{-2\alpha_1} + C\cos 2\gamma_1 + D\sin 2\gamma_1} \qquad [A\text{-}4]$$

where

$$g_1 = \frac{1 - n_1^2 - k_1^2}{(1 + n_1)^2 + k_1^2}$$

$$h_1 = \frac{2k_1}{(1 + n_1)^2 + k_1^2}$$

$$g_2 = \frac{n_1^2 - n_2^2 + k_1^2}{(n_1 + n_2)^2 + k_1^2}$$

$$h_2 = \frac{-2n_2k_1}{(n_1 + n_2)^2 + k_1^2}$$

$$\alpha_1 = \frac{2\pi k_1 d}{\lambda};\ \gamma_1 = \frac{2\pi n_1 d}{\lambda}$$

$$A = 2(g_1g_2 + h_1h_2);\ B = 2(g_1h_2 - g_2h_1)$$

$$C = 2(g_1g_2 - h_1h_2);\ D = 2(g_1h_2 + g_2h_1)$$

here n_1 and k_1 are the real and imaginary parts of the film refractive index, d is the film thickness, and λ is the vacuum wavelength. n_1 and k_1 are computed from Eq. [1], [2], and [4]. The complexity of these expressions necessitates the use of a computer for obtaining the thickness. Two cases can be distinguished: (*i*) the dispersion parameters are known and are independent of film thickness and preparation conditions, (*ii*) the values of γ and/or w_o vary from film to film. In the former case, Eq. [1], [2], [4], and [A-1]-[A-4], are used to obtain a standard plot of peak height (*e.g.*, peak optical density) *vs.* thickness. In the latter case, the values of γ and w_o can be obtained from the experimental data by plotting $(1/T_{obs}) - 1$ *vs.* wave number as discussed in the text. Using known values of ρ and ϵ_∞ the thickness is then determined, by trial and error, so that the height of the $(1/T_{obs}) - 1$ peak is matched to any desired degree of accuracy. The height of this peak for an unsupported film is given by $4C/\gamma$ which allows for an initial estimate of d. For $n_2 > 1$ this initial estimate will be less than the actual thickness. As an alternative to plotting $(1/T_{obs}) - 1$, trial and error adjustments of both γ and d can be made until the peak height and half-width of an experimental optical density *vs.* wave number curve are matched. It can easily be shown that for fixed ρ, ϵ_∞, and w_o there is a unique pair (γ,d) which provides a match.

Applicable thickness range.—Assuming the availability of a spectrophotometer capable of measuring optical density from 0.1 to 2.0, Eq. [12] can be used to estimate the minimum and maximum film thicknesses which can be measured

$$d_{min} \approx 3 \times 10^{-3}\left(\frac{\gamma}{\rho w_o}\right) \qquad [A\text{-}5]$$

$$d_{max} \approx 2 \times 10^{-1}\left(\frac{\gamma}{\rho w_o}\right) \qquad [A\text{-}6]$$

These estimates are too small for substrate refractive indexes exceeding unity. As an example for β-SiC films, using the dispersion parameters in Table I and Eq. [A-5] and [A-6], the minimum and maximum detectable thicknesses are 15 and 1025Å, respectively, whereas, using the same dispersion parameters, for β-SiC films on Si substrates ($n_2 = 3.42$) films of 40 and 2400Å thickness correspond to the assumed limits on measurable optical density. Note that for typical γ/ρ values (see Table I) the measurable thickness range is determined primarily by the resonant frequency; lower resonant frequencies requiring proportionately larger film thicknesses to produce a given optical density.

Manuscript submitted Dec. 21, 1972; revised manuscript received March 8, 1973.

Any discussion of this paper will appear in a Discussion Section to be published in the June 1974 JOURNAL.

[4] The minimum thickness necessary to suppress interference depends on the substrate refractive index, n_2, and the resolution of the spectrometer used, $\Delta w(cm^{-1})$. Then $d_{subs} > (2\ n_2\Delta w)^{-1}$ cm will eliminate interference.

REFERENCES

1. W. Pliskin and S. J. Zanin, in "Handbook of Thin Film Technology," L. I. Maissel and R. Glang, Editors, McGraw-Hill Book Co., New York (1970).
2. T. Nakayama and F. C. Collins, *This Journal*, **113**, 706 (1966).
3. W. A. Pliskin and R. P. Esch, *Appl. Phys. Letters*, **11**, 257 (1967).
4. P. Rai-Choudhury and N. P. Formigoni, *This Journal*, **116**, 1440 (1969).
5. W. G. Spitzer, D. A. Kleinman, and C. J. Frosch, *Phys. Rev.*, **113**, 133 (1959).
6. C. J. Mogab and H. J. Leamy, To be published.
7. F. Seitz, "Modern Theory of Solids," McGraw-Hill Book Co., New York (1940).
8. M. Hass and B. W. Henvis, *J. Phys. Chem. Solids*, **23**, 1099 (1962).
9. S. Iwasa, I. Balslev, and E. Burstein, Proc. 7th Int'l. Conference on Semiconductors, 1964, p. 1061.
10. D. A. Kleinman and W. G. Spitzer, *Phys. Rev.*, **118**, 110 (1960).
11. R. J. Collins and D. A. Kleinman, *J. Phys. Chem. Solids*, **11**, 190 (1959).
12. W. G. Spitzer and D. A. Kleinman, *Phys. Rev.*, **121**, 1324 (1961).
13. O. S. Heavens, "Optical Properties of Thin Solid Films," pp. 76-77, Dover Publications, Inc., New York (1965).

Resistivity and Photoluminescence of Zn(S,Se):I Annealed in Liquid Zinc

Lyuji Ozawa and H. N. Hersh

Zenith Radio Corporation, Chicago, Illinois 60639

ABSTRACT

The resistivity and photoluminescence of Zn(S,Se):I single crystals annealed in liquid Zn at several temperatures have been studied. The change in resistivity with annealing temperature had a characteristic activation energy of 16 kcal/mole and was independent of the S:Se ratio suggesting that Zn is diffusing into the crystal. The photoluminescent spectra was not changed by annealing; however, the room temperature photoluminescence efficiency increased as Zn diffused in and decreased when Zn diffused out. It was concluded that diffused Zn only contributes to the resistivity and the thermal quenching centers. In addition it was found that excess iodine gave an additional yellow luminescent band centered at 2.23 eV (560 nm).

The photoluminescence of zinc sulfoselenide crystals, Zn(S,Se):halogen, as a function of ZnSe concentration is of basic interest in understanding II-VI compound semiconductors because ZnSe is isoelectronic with GaAs and Ge. From a practical point of view, the phosphor ZnSe:Cu:Br has been proposed as a possible red color TV phosphor (1) and is an electroluminescent material (2, 3); yellow-emitting Zn(S,Se):Cu:Br has been shown to be a brighter electroluminescent phosphor than ZnS:Mn:Cu and has been used in an EL TV display panel (4).

The majority carriers of ZnSe at room temperature are electrons. The resistivity of n-ZnSe as-grown single crystals is high but is lowered by annealing in Zn (5). Cu_2Se-ZnSe and Cu_2S-ZnS emit a brilliant d-c electroluminescence (6, 7). Stringfellow and Bube have measured the photoluminescence and excitation spectra at 85°K and the thermally stimulated luminescence of n-ZnSe(SA) annealed in Zn (8). They concluded that the fact that the center lies 0.5-0.6 eV above the valence band is an intrinsic defect.

In this work the resistivity and photoluminescence of Zn(S,Se):I single crystals before and after annealing in Zn were studied. This report will describe first the effect of annealing on Zn(S,Se):I crystals as determined by the change in resistivity, thus confirming that Zn diffuses into the crystals. Then the photoluminescence of Zn(S,Se):I crystals as-grown and annealed will be described.

Experimental

The Zn(S,Se):I single crystals were grown by an iodine transport technique (9, 10) from the amorphous powder mixture; the ZnSe powder was a vacuum deposition grade from the Apache Chemical Company and the ZnS powder was a luminescent grade from RCA. The crystals did not grow under conditions of excess Zn but only grew in an excess Se and S. X-ray diffraction analysis indicated that all Zn(S,Se) crystals formed solid solutions over the whole range of composition within 2% error from the expected composition.

The crystals, about 5g, were cut into slices along the <111> plane and were polished by carborundum (1μ grit size) to 0.5 mm thickness. These sliced pieces were used in the study of the photoluminescence and resistivity.

The crystals (about 100 mg) were placed in a quartz capsule (1 cm^3) which was evacuated to 5×10^{-6} Torr by means of an ion pump and were heated in liquid Zn (1g) with iodine (20 mg) at desired annealing conditions. Iodine was introduced into the evacuated capsule with vapor transport techniques. Then the crystals were taken out of the liquid Zn and cooled to room temperature. The samples were washed with alcohol in order to remove the excess ZnI_2 and I_2 from the crystal surface. Ohmic contact was made using indium which was rubbed onto the fresh cleaved surface; the crystals were then heated at 350°C for 2 min in nitrogen atmosphere. All of the resistivity measurements were made at room temperature.

The photoluminescent spectra at room temperature and liquid-nitrogen temperature were measured using a Bausch and Lomb grating monochromator (1300 lines/mm). A high pressure Hg-lamp plus Corning filter (7-60) was used as the excitation source. Correction of the spectral response to the combination of the monochromator and photomultiplier was made with a standard tungsten lamp.

Results and Discussion

Resistivity.—The change in the resistivity of ZnSe:I crystal as a function of temperature and time of annealing was essentially similar to the change in the resistivity of Zn(S,Se):I crystals. For this reason, the resistivity of ZnSe:I crystal is primarily discussed and then the difference of the Zn(S,Se):I crystals is described.

The resistivity of the as-grown ZnSe:I crystal was 7 ± 1 kohm-cm. This resistivity decreased upon annealing in an atmosphere of Zn. The resistivity of the ZnSe:I crystals annealed in Zn alone (either in Zn vapor or in liquid Zn) was about twice as high as the resistivity of the samples in Zn and iodine. Annealing in Zn vapor alone yielded transparent ZnSe plates but annealing in liquid Zn resulted in opaque plates due to the rough surface formed when a part of the crystal dissolved in liquid Zn.

The solubility of ZnSe in liquid Zn is shown in Fig. 1. These experimental determinations were done by a weight-loss method with a controlled weight of ZnSe and Zn in a controlled volume. The ZnSe samples were heated for 7 days at the given temperatures. The experiments at temperatures below 600°C were difficult because a small amount of Zn adhered to the surface of the ZnSe crystal when the ZnSe crystal was taken out from liquid Zn. The solubility markedly increased above 1000°C. Etch pit patterns were observed under a microscope on the surface of the annealed crystals.

The resistivities of ZnSe crystals as a function of the temperature and time of annealing in liquid Zn and iodine are shown in Fig. 2. Three to five samples were made for each annealing condition to check the variance (which is given by the vertical lines in the figure). The resistivity of the annealing samples at a given temperature decreased with annealing time and finally reached the constant value which is shown in Fig. 2. The annealing time required to reach a constant re-

* Electrochemical Society Active Member.
Key words: II-VI compound, luminescence, resistivity, annealing.

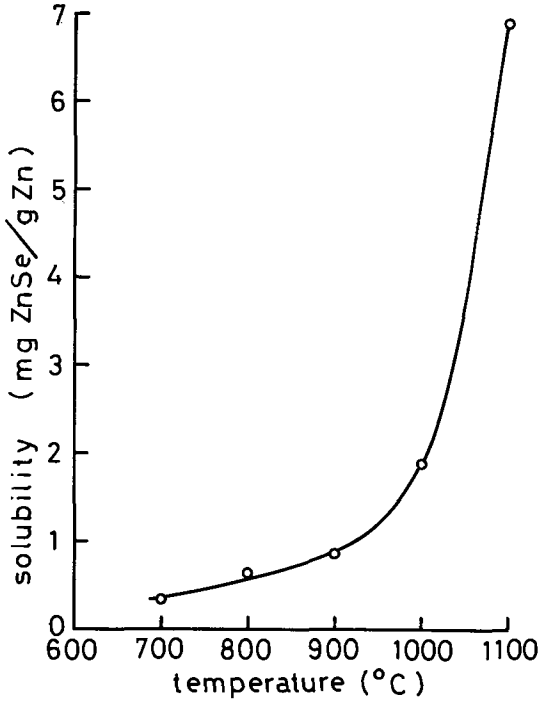

Fig. 1. Solubility of ZnSe in liquid Zn

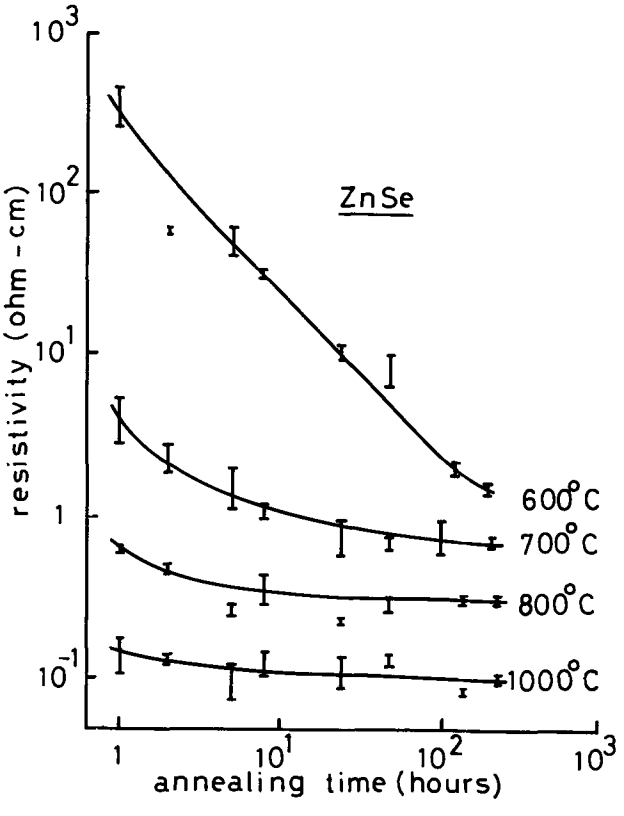

Fig. 2. Resistivities of ZnSe:I annealed at various temperatures and lengths of time.

sistivity decreased with an increase in the annealing temperature: 100 hr at 700°C, 20 hr at 800°C, and 10 hr at 1000°C.

It is assumed that the ZnSe crystals which were annealed for 160 hr reach the characteristic resistivity at a given annealing temperature. The logarithm of this resistivity is plotted against reciprocal temperature ($1/T$°K) in Fig. 3. It may be seen that there is an exponential relationship between the resistivity and reciprocal temperature, indicating that the resistivity follows a diffusion equation. Therefore, it is believed that the resistivity of the annealed ZnSe

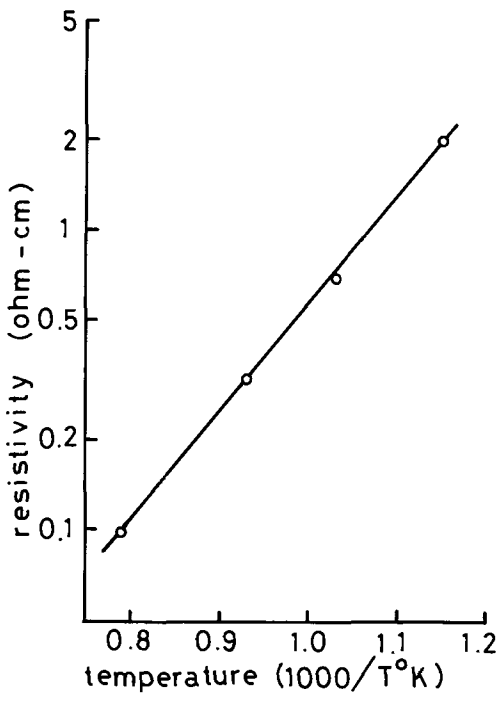

Fig. 3. Exponential relationship between resistivity of ZnSe:I and reciprocal annealing temperature. Activation energy was calculated at 16 kcal/mole.

crystal decreases in proportion to the amount of Zn diffused into ZnSe crystal, and activation energy is required to diffuse Zn into ZnSe:I crystal. This energy is determined from the slope to be 16 kcal/mole.

When the annealed crystals were heated in vaccum (5×10^{-6} Torr), the resistivity of the crystals became greater with an increase in the heating temperature and length of time. The change in the ZnSe resistivity by the heating at 1000° and 800°C in the absence of Zn and iodine is shown in Fig. 4. Since the resistivity of the annealed ZnSe crystal is proportional to the amount of Zn diffused into ZnSe, the increase in the resistivity must be due to an out-diffusion, of which the amount depends on vapor pressure and capsule volume. Since the capsule was kept at constant volume (1 cm^3), the amount of out-diffusion at equilibrium that was required for 20 min at 1000°C and for 100

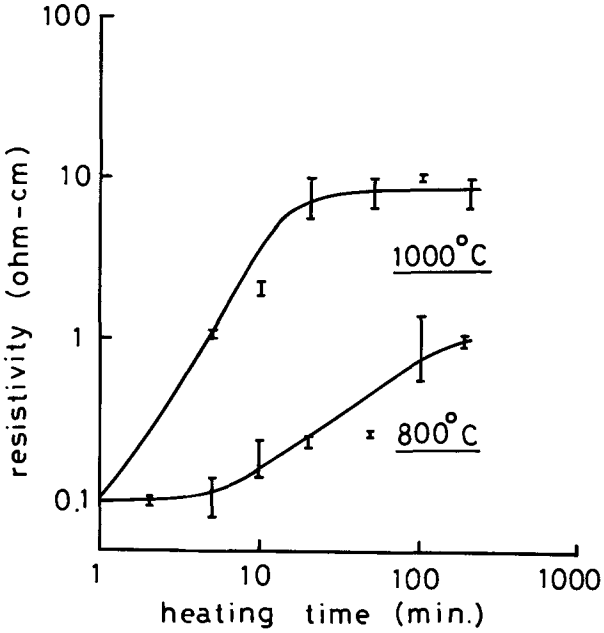

Fig. 4. Change in resistivity of annealed ZnSe:I by heating in vacuum, 5×10^{-6} Torr.

min at 800°C depended on the heating temperature. As a result of this out-diffusion, the room temperature photoluminescence of the annealed ZnSe:I crystal was diminished.

The activation energy required to diffuse Zn into the Zn(S,Se):I crystals was the same as into the ZnSe:I. The resistivity at a given temperature, however, differed. The resistivities of Zn(S, Se):I crystals annealed at 800° and 1000°C as a function of the amount of ZnSe in the Zn(S,Se) solid solution are shown in Fig. 5. It was found that an exponential relationship between the resistivity and mole per cent (m/o) of ZnSe was maintained at the annealing temperature from 600° to 1000°C. The reason why the resistivity exponentially increases with ZnS content is not understood as yet.

Photoluminescence.—To make sure that Zn diffused into the Zn(S,Se):I crystals, the annealed crystals were made by heating at 1000°C for 160 hr in liquid Zn and iodine. These samples were used to study the photoluminescence.

The photoluminescent spectra of as-grown Zn(S,Se):I crystals are shown in Fig. 6. The same spectra were also obtained with polycrystalline Zn(S,Se):I phosphor which were prepared by the firing at 950°C for 3 days with iodine. The photoluminescent intensity of ZnSe:I at room temperature was too weak to measure.

It may be seen that the room temperature spectra of Zn(S,Se):I (not ZnS:I) monotonically shifted to longer wavelengths with an increase in ZnSe content. At liquid-nitrogen temperature, the spectral behavior differs somewhat from that at room temperature: the short wavelength side of the spectra of Zn(S,Se):I containing above 60 m/o ZnSe did not move to longer wavelengths. The luminescent spectra of ZnSe:I seem to give the key to this spectral behavior. When the ZnSe:I crystal was annealed in Zn and iodine, a yellow photoluminescence was obtained; in Zn alone an orange photoluminescence was obtained.

The photoluminescent spectra at 77°K are shown in Fig. 7. Upon annealing in liquid Zn alone, spectrum (1) with center wavelength at 2.02 eV (614 nm) was always obtained. Spectrum 1 was also obtained with ZnSe:Br powder, prepared by using a small amount of NH_4Br (0.5 weight per cent (w/o). Spectrum 2, considerably broader than spectrum 1, was obtained with ZnSe:I crystals as-grown and/or annealed in liquid Zn and iodine. Spectrum 3, shown with dashed lines, was detected by subtracting spectrum 1 from spectrum 2. The center wavelength of spectrum 3 was 2.23 eV (560 nm). Spectrum 1 and spectrum 3 were completely Gaussian, as shown in Fig. 8 in which the photoluminescent spectra were plotted on a normal distribution graph. The position and distribution of the yellow luminescent band of ZnSe:I is very closely

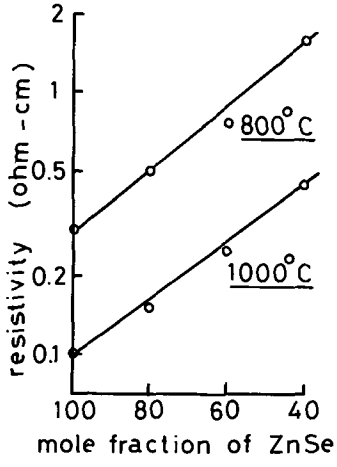

Fig. 5. Exponential relationship between resistivity of Zn(S,Se): I crystals annealed and ZnSe amount in Zn(S,Se) solid solution crystals.

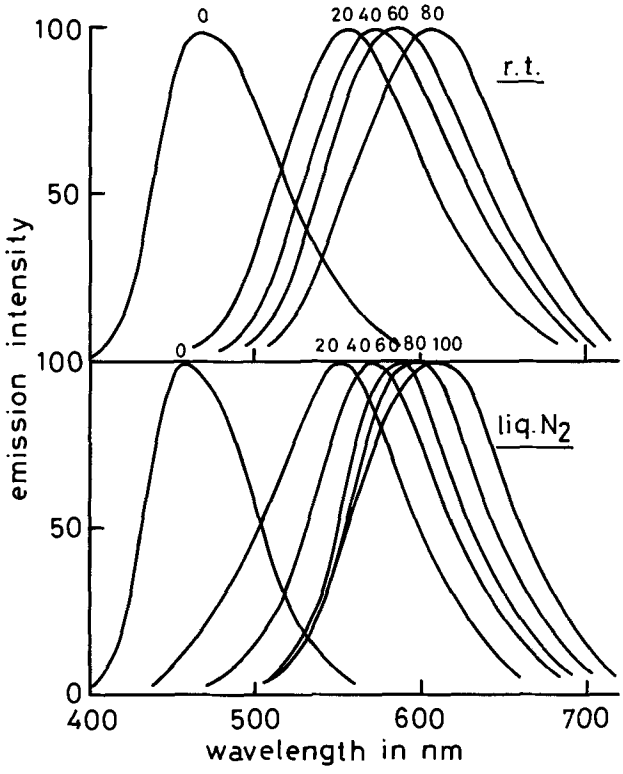

Fig. 6. Photoluminescent spectra of Zn(S,Se):I at room and liquid-nitrogen temperatures. The number above each spectrum indicates ZnSe m/o in Zn(S,Se) crystal.

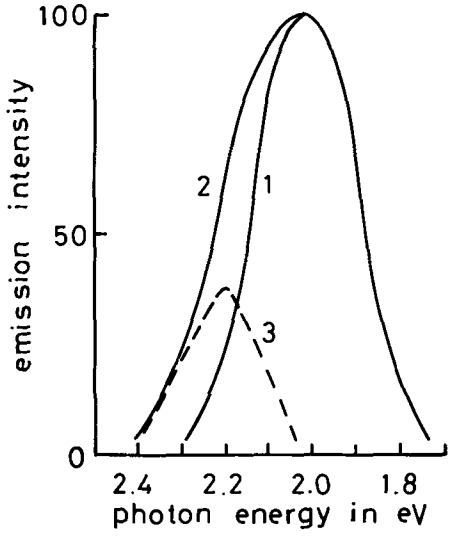

Fig. 7. Photoluminescent spectra of ZnSe:I at 77°K. Details in text.

matched to that of ZnSe:Ag:I. But the yellow luminescent band is not the Ag luminescent band. The intensity of the ZnSe:Ag:I band changes with Ag concentration and is quenched at room temperature and furthermore this Ag band completely disappears upon annealing in liquid Zn, whereas the yellow band of ZnSe:I emits at liquid-nitrogen temperature and does not diminish upon annealing in liquid Zn and iodine. The yellow band is also observed at room temperature in the samples annealed in liquid Zn and iodine. In addition, chemical determination of Ag in the samples indicated that Ag concentration was less than 10 ppm, suggesting that the intensity of the Ag band was weak.

Figure 9 shows the 2 photoluminescent spectra of ZnSe:I, annealed lightly in liquid Zn (for 3 hr at 1000°C) and annealed in ZnI_2 vapor for a long time (7 days). The yellow luminescent band was markedly enhanced by the annealing in ZnI_2 vapor and this luminescence is not quenched at room temperature.

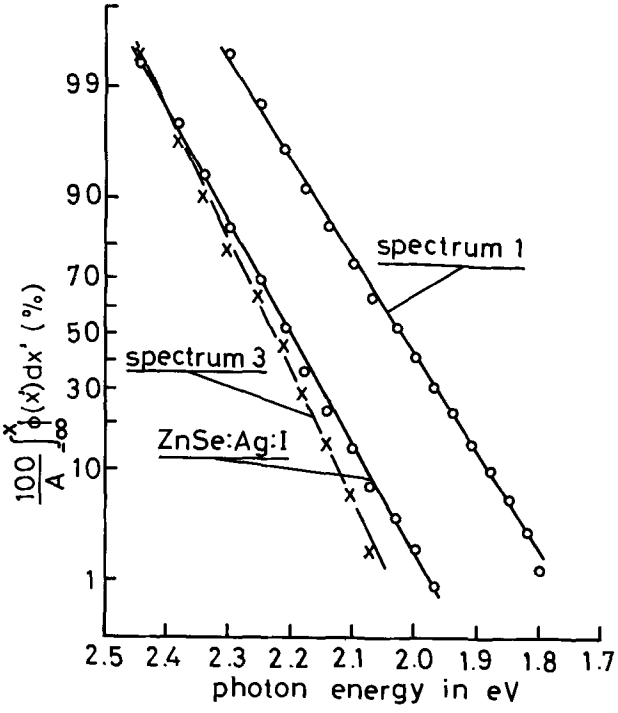

Fig. 8. Photoluminescent spectra of ZnSe:I and ZnSe:Ag:I plotted on normal distribution graph. A in ordinate is $\int_{-\infty}^{\infty} \phi(x')dx'$ and is 1.0 for normal distribution.

It is inferred from all these results that excess iodine is somehow responsible for the yellow luminescent band centered at 560 nm.

The room temperature luminescent spectra of Zn(S,Se):I crystals annealed in liquid Zn and iodine coincided with the spectra of as-grown Zn(S,Se):I crystals at liquid nitrogen temperature as indicated in Fig. 6. Considering that the position of the yellow luminescent band of ZnSe:I is at 560 nm, this yellow luminescent band seems to be contributing to the spectra of Zn(S,Se):I crystals containing more than 60 m/o ZnSe. It is inferred therefore that the yellow luminescent band of ZnSe:I appears in the spectrum of Zn(S,Se):I crystals containing more than 60 m/o ZnSe, and that spectral position is independent of the composition of host crystal. It is possible that the center of the yellow luminescent band involves molecular iodine.

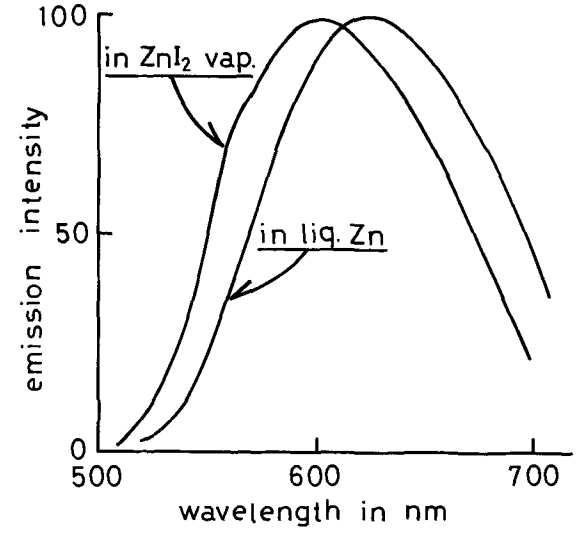

Fig. 9. Photoluminescent spectra of ZnSe:I crystals annealed lightly in liquid Zn for 3 hr at 1000°C and in ZnI_2 vapor for 7 days at 1000°C.

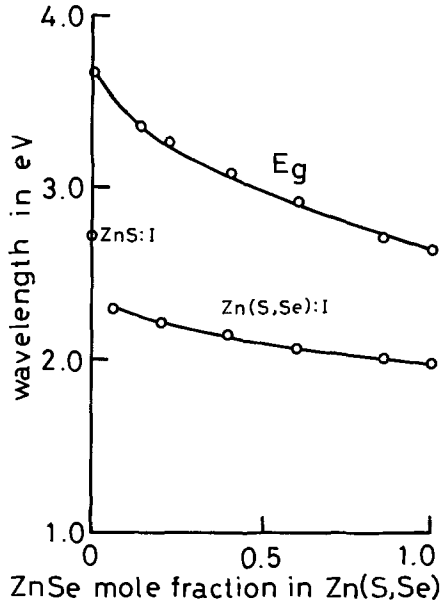

Fig. 10. Bandgap and peak wavelengths of Zn(S,Se):I annealed in liquid Zn alone at 900°C for 7 days.

The bandgap, E_g, and the peak position of the photoluminescent spectra of self-activated Zn(S,Se):I crystals annealed in liquid Zn alone are shown in Fig. 10. The bandgap was determined from the optical absorption spectra of Zn(S,Se):I single crystals. When a small amount of ZnSe was introduced into ZnS crystal to make a Zn(S,Se) solid solution, the blue luminescent band of ZnS "jumped" to the green spectral region and then monotonically shifted to longer wavelengths with an increase in ZnSe amount (11). The jumping of the blue luminescent band of ZnS to green does not happen in (Zn,Cd)S solid solution [in which the luminescent band monotonically shifts over the whole composition range (12)]. The results on Zn(S,Se):I, indicate therefore, that the self-activated center in Zn(S,Se):I crystal differs from that of ZnS:Cl, which is known to be a pair consisting of a vacancy and a halogen ion occupying the nearest neighbor site (13). The luminescent center of Zn(S,Se) crystals should be identical to that of ZnSe but not to that of ZnS

At 77°K, the identical photoluminescent spectrum and intensity were detected with the ZnSe:I crystals before and after annealing at 1000°C. Under this annealing condition, Zn surely diffused into ZnSe crystal, resulting in the change in the resistivity of the crystal. This diffused Zn did not affect the luminescent center. It is inferred, therefore, that the luminescent center of ZnSe:I may be an intrinsic defect, as suggested by Stringfellow and Bube (8).

Brilliant room temperature photoluminescence of ZnSe:I was always observed with the annealed samples. This room temperature photoluminescence diminished after heating in vacuum (Zn diffused out from the crystal). It is inferred from the results on annealing in liquid Zn that the diffused Zn occupies sites that form thermal quenching centers (resulting in the improvement of room temperature photoluminescence).

Other annealing effects were also observed; the impurities, such as Ag and Cu which were ubiquitous impurities in ZnSe, were removed from the crystals (14). The determination of Cu and Ag concentration in the annealed samples were made by atomic absorption spectrometry. The excess iodine in ZnSe:I crystal as-grown was also removed from the crystal by the annealing. The absorption spectra of ZnSe:I crystals before and after annealing at 1000°C for 7 days are shown in Fig. 11. The absorption spectrum of the annealed sample coincided with the absorption spectrum of the ZnSe crystal obtained from Eagle Picher.

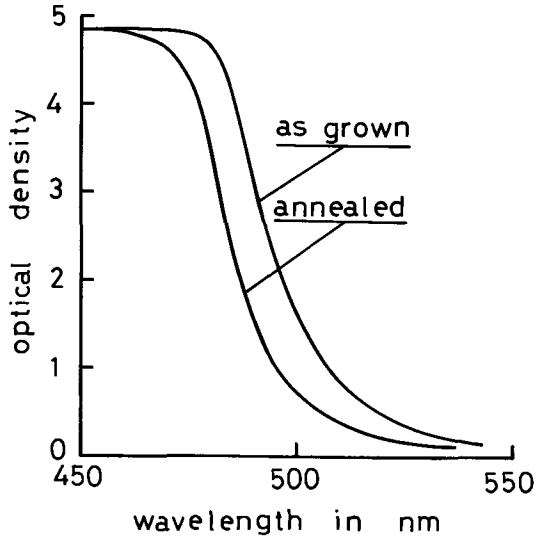

Fig. 11. Transparent spectra of ZnSe:I crystals before and after annealing at 1000°C for 7 days.

It is possible to say that Zn(S,Se):I crystals are purified by the annealing in liquid Zn; the Zn reduces the concentration of impurities and the crystal defects which form the temperature quenching centers; it also decreases the resistivity. On the other hand, the luminescent centers are not affected by annealing in Zn.

Summary

By the annealing in liquid Zn, Zn diffuses into ZnSe crystal with an activation energy 16 kcal/mole as determined by the change in resistivity at the annealing temperature. The activation energy required to diffuse Zn into Zn(S,Se) crystals is the same as the activation energy required to diffuse Zn into ZnSe. The actual resistivity at the given temperature, however, depends on the S:Se ratio in solid solution crystals. An exponential relationship between the resistivity and m/o of ZnSe was found. The photoluminescent spectra did not change upon annealing in liquid Zn and iodine but the luminescence at room temperature, which was diminished by heating the crystal in vacuum, was improved. A yellow luminescent band centered at 2.23 eV was found in samples having excess iodine.

Manuscript submitted Sept. 28, 1972: revised manuscript received Jan. 16, 1973.

Any discussion of this paper will appear in a Discussion Section to be published in the June 1974 JOURNAL.

REFERENCES

1. L. Ozawa and R. Toyonaga, *J. Inst. Elect. Eng. Japan*, in Japanese, **85**, 109 (1965).
2. I. J. Hegyi, S. Larach, and R. E. Shrader, *This Journal*, **104**, 717 (1957).
3. G. A. Saum, R. H. Glaenger, and J. E. Dueker, *J. Phys. Chem. Solids*, **30**, 2447 (1969).
4. H. Arai, T. Yoshizawa, K. Awazu, K. Kurahashi, and S. Ibuki, *IEEE Conf. Record, 1970 IEEE Conf. Display Device*, p. 52 (1970).
5. M. Aven, *J. Appl. Phys.*, **42**, 1204 (1971).
6. A. G. Fischer, *This Journal*, **118**, 139C (1971).
7. M. Aven and D. A. Cusano, *J. Appl. Phys.*, **35**, 606 (1964).
8. G. B. Stringfellow and R. H. Bube, *Phys. Rev.*, **171**, 903 (1968).
9. E. Kaldis, *J. Phys. Chem. Solids*, **26**, 1701 (1965).
10. S. G. Parker and J. E. Pinnell, *Trans Metal. Soc. AIME*, **245**, 451 (1969).
11. L. Ozawa and Y. Nagashima, *J. Electrochem Soc., Japan*, **32**, 26 (1964).
12. H. W. Leverentz, "An Introduction to Luminescence of Solid," John Wiley & Sons, New York (1950).
13. P. H. Kasai and Y. Otomo, *J. Chem. Phys.*, **37**, 1236 (1962).
14. M. Aven and H. H. Hoodburg, *Appl. Phys. Letters*, **1**, 53 (1962).

Efficient Mn(IV) Emission in Fluorine Coordination

A. G. Paulusz

Osram (GEC) Research Laboratories, The General Electric Company Limited, Hirst Research Centre, Wembley, England

ABSTRACT

The efficiency of Mn(IV) luminescence in fluorine coordination is discussed in the context of the chemical bonding in the MnF_6^{2-} center. It is possible that the lower degree of σ-antibonding in the e_g orbitals, and the greater degree of π-antibonding in the t_{2g} orbitals, compared with the effect observed in oxides, contributes to a high efficiency and quenching temperature of the emission. The excitation and emission spectra of Mn(IV) in K_2SiF_6, K_2GeF_6, and K_2TiF_6 are presented and compared.

The luminescent center in transition-metal ion-activated phosphors consists of the transition-metal ion itself together with its directly coordinated anions. This is often an octahedral or a tetrahedral group and is the same center treated by the ligand field theory. When this group is represented in the well-known configurational coordinate model of the center, (*e.g.*, Fig. 1) it is convenient to identify the configurational coordinate with the actual transition metal/anion separation so that changes in bond length can be represented by displacements of the potential curves along the configurational coordinate axis (1). It seems to be generally recognized that the bond lengths in such centers can change in the excited state, depending on the electron transition involved. For example, Orgel has explained the Stokes shift of Mn(II) activated phosphors by noting that the electron transition which occurs on excitation, $t_{2g}^3e_g^2 \rightarrow t_{2g}^4e_g^1$, involves a transition from an antibonding e_g orbital to a nonbonding t_{2g} orbital (2) The center is thus more tightly bound in the excited state than in the ground state with a corresponding decrease in the manganese-oxygen bond length. The excited state potential curve is shifted, relative to the ground-state curve, to a smaller internuclear separation on the configurational coordinate diagram and this can account for the observed Stokes shift.

As well as introducing a Stokes shift between emission and absorption, the relative displacement of the ground and excited state potential curves can also en-

Key words: luminescence, phosphors, fluorides, emission spectra, excitation spectra.

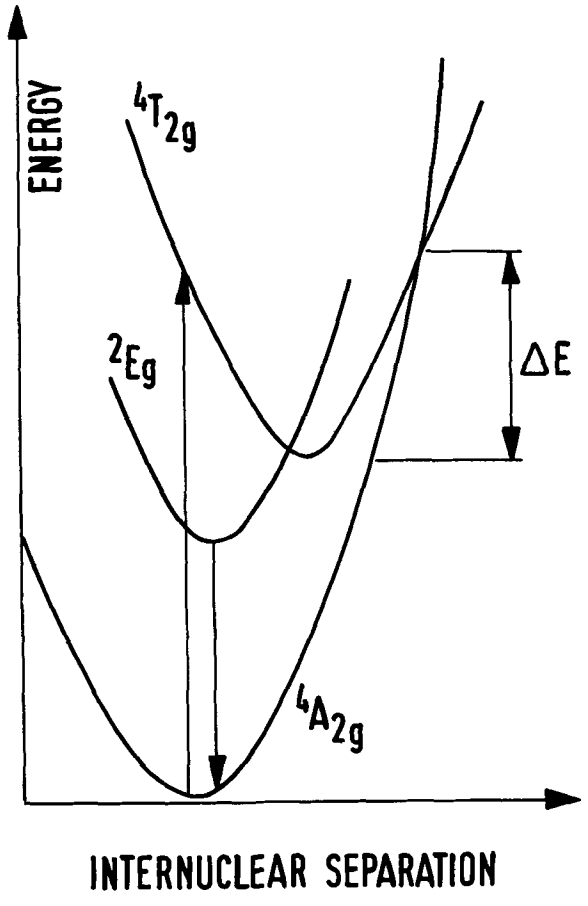

Fig. 1. Schematic configurational coordinate diagram of a d^3 center. Only one of the excited states ($^4T_{2g}$) derived from the electron configuration $t^2_{2g}e_g$ is shown.

hance nonradiative processes by lowering the energy of the crossover point of the curves. Furlani, for example, has suggested this as the reason why only a few cases of emission from d^6 ions, such as Co(III), have been reported (3). The excitation transition ($t_{2g}^6 \rightarrow t_{2g}^5 e_g^1$) involves the promotion of an electron to an antibonding e_g orbital with a corresponding increase in the cobalt-ligand bond length. The shift of the excited-state potential curve in this case is apparently sufficient to prevent efficient radiative processes except in a few cases.

In the case of d^3 ions in octahedral coordination the emitting level (^2E_g) derives from the same t_{2g}^3 electron configuration as the ground state. The transition to the ground state, $^2E_g \rightarrow {}^4A_{2g}$, only involves the net spin change $S = \frac{1}{2}$ to $S = 3/2$, so that the potential curves are not displaced relative to each other. This is illustrated in Fig. 1 which gives a schematic representation of a typical d^3 center. Several workers have noted that this fact may account for the emission of this center being comparatively well known, as in V(II), Cr(III), and Mn(IV) for example (3, 4). Emissions from other isoelectronic ions such as Re(IV) (5) and Mo(III) (6) have also been reported recently.

On the other hand, the emission of d^3 ions is most effectively excited by irradiation into the broad spin allowed bands $^4A_{2g} \rightarrow {}^4T_{2g}$ and $^4A_{2g} \rightarrow {}^4T_{1g}$ and not by direct excitation of the ^2E_g level. The excited states $^4T_{2g}$ and $^4T_{1g}$ derive from the electron configuration $t_{2g}^2 e_g^1$, *i.e.*, with an electron occupying an antibonding e_g orbital, and the excited-state curves are therefore displaced to greater internuclear separations on the configurational coordinate axis as shown in Fig. 1. In fact single crystal studies of Re(IV) in Cs_2ZrCl_6 have indicated that the rhenium-chlorine bond length increases about 7% in the excited state (7) and a similar increase probably occurs in other d^3 centers.

Because nonradiative processes can occur from the excited $^4T_{2g}$ state, either before energy is transferred to the emitting ^2E_g state, or subsequently after thermal repopulation of the $^4T_{2g}$ state, it is clear that the relative shift of the ground and excited state curves will be important for d^3 centers as well, although perhaps not so critical as in the cases mentioned earlier in which the displaced curve represents the emitting state itself.

It is well known that the activation energy, ΔE, is related to the quenching temperature, of the luminescence (8) and it is clear from Fig. 1 that the greater the displacement of the $^4T_{2g}$ curve relative to the ground-state curve $^4A_{2g}$, the lower will be ΔE and hence the quenching temperature. The activation energy is associated with the excited-state curve, and not the emitting level in this case, because as we have noted, nonradiative processes can occur from the $^4T_{2g}$ state. If the displacement could be restricted, a higher value of the quenching temperature might be obtained. Since the displacement is due to the difference in antibonding character between the e_g and t_{2g} orbitals it is possible that this could be minimized in materials in which the e_g orbitals become less strongly antibonding or alternatively in which the t_{2g} orbitals become more strongly antibonding. In the molecular orbital theory the t_{2g} orbitals are nonbonding and the e_g orbitals strongly antibonding if only σ-interactions are considered. On the other hand if π-interactions are also included the t_{2g} orbitals become π-antibonding (9).

Orgel has suggested that ligands occupying an early position in the spectrochemical series (9) have weaker σ-antibonding effects than later members (10). Thus, more favorable conditions for the luminescence of d^3 ions might very well be obtained in materials other than oxides in which the ligands occupy an early position in the spectrochemical series. The position of oxygen in the spectrochemical series is variable and in oxides will depend upon the crystal structure and the nature of other ions in the lattice, but in general we might expect the halides, for example, to be somewhat less σ-antibonding than oxygen ions. In oxide lattices particularly, the t_{2g} π-antibonding interaction is also dependent on crystal structure and the polarizing effect of more distant ions in the lattice. The CN^- ligand will however provide quite strong π-antibonding effects (9) and it is interesting to note that a higher quenching temperature is observed in $K_3Cr(CN)_6$ than in other Cr(III) complexes (11) and also that the only reported emissions from Co(III) have been in cyanide complexes (12). In the case of these complexes, however, a relatively high value of the crystal field parameter, 10 Dq, is also observed and this must also contribute to the efficiency of the radiative process.

Blasse has suggested a more physical way to limit the displacement of the excited-state curve: if the activator is substituted at a lattice site somewhat too small to accommodate it easily, the surrounding anions will be forced apart by the intruding ion even in the ground state so that further expansion of the center in the excited state will be strongly resisted by the lattice (13).

Mn(IV) Centers.—The application of these suggestions to Mn(IV) is particularly interesting because comparatively few cases of efficient emission above room temperature have been reported.

We shall consider first the question of the size of the manganese site. The radius of the ion is not known exactly (Pauling gives a radius of 0.52Å and Goldschmidt 0.54Å) but it is certainly very small. The smallest ions which regularly form octahedral groups in oxides are arsenic ($r = 0.47$Å), aluminum ($r = 0.50$Å), and germanium ($r = 0.53$Å), but unfortunately these ions are not significantly smaller than Mn(IV) itself. Nevertheless, it is interesting that the most efficient Mn(IV) emissions above room temperature have indeed been observed in arsenates, aluminates, and germanates. Examples are: $Mg_6As_2O_{11}$ (14), $6Al_2O_3 \cdot 6Li_2O \cdot As_2O_5$ (15), Al_2O_3 (8), alkaline earth aluminates (8, 16), AlN (17), $LiMgAlO_3$ (18),

'Mg_4GeO_6' (19), $LiMgGeO_4$ (18), $3Li_2O$, $8GeO_2$ (18). Smaller ions such as silicon (r = 0.41Å) and phosphorus (r = 0.34Å) are not found in octahedral coordination in oxides. In fluorides, however, octahedral coordination seems to be preferred, such groups as SiF_6^{2-} and PF_6^- being well known. The reason for this is probably partly a steric effect (the F^- ion is slightly smaller than O^{2-}) and also the greater electronegativity difference between the central ion and the ligands as Pauling has suggested. In any case the conditions for compressing the Mn(IV) into a small lattice site are easily available in fluorophosphates and fluorosilicates.

Turning next to the question of chemical bonding in the Mn(IV) center, the small size and instability of the manganese ion place severe restrictions on the type of material which might be considered. Strong π-antibonding effects might be expected in cyanides, as in the case of Cr(III), however these materials are likely to be unstable. A cyanide complex of Mn(IV), apparently $K_2Mn(CN)_6 \cdot 2KCN$, has in fact been reported (20), but we have not succeeded in preparing this compound by the method described. On the other hand weaker σ-antibonding interactions than generally observed in oxides may be observed at the other end of the spectrochemical series in halides. Again the small size and instability of Mn(IV) restrict the possibilities, but the F^- ion seems to be an exception. The MnF_6^{2-} group is quite stable out of contact with water and might be further stabilized in suitable fluoride or oxyfluoride lattices.

Finally we should remark that we have only considered the case of octahedrally coordinated Mn(IV) as the emission from the tetrahedrally coordinated ion has not been definitely observed.

Thus consideration of both the chemical bonding in the Mn(IV) center and the size of the ion lead to the conclusion that efficient emission above room temperature may be observed in fluorides. These considerations led us to examine Mn(IV) activated fluorosilicates. In order to check the importance of the manganese site size we also prepared Mn(IV) activated fluorogermanates and fluorotitanates, and we report here on the luminescence spectra of K_2SiF_6, K_2GeF_6, and K_2TiF_6 containing Mn(IV).

Experimental

The materials were prepared by recrystallizing mixtures of K_2MnF_6 and the host lattice material (K_2SiF_6, K_2GeF_6, or K_2TiF_6) from 40% aqueous hydrofluoric acid. The K_2MnF_6 was prepared by the method of Bode *et al.* (21): 100 volume hydrogen peroxide was added dropwise with constant stirring to an ice-cold 40% aqueous hydrofluoric acid solution of KHF_2 saturated with $KMnO_4$. As soon as the yellow precipitate of K_2MnF_6 began to form it was rapidly filtered off on polythene ware, washed with acetone, and then purified by recrystallizing from 40% HF.

The chemical purity of the materials was examined by x-ray fluorescence analysis and the purity of phase checked by x-ray diffraction. K_2SiF_6 crystallizes with a cubic K_2PtCl_6 structure while the other materials have a hexagonal β-$(NH_4)_2SiF_6$ lattice.

The excitation and emission spectra were measured at 90° and 300°K using a double prism Hilger D300 monochromator fitted with a trialkali photomultiplier (EMI 9558 QA). A 150W xenon lamp was used for excitation in the ultraviolet and a tungsten halogen lamp at longer wavelengths. The brightness of the phosphors as a function of temperature was measured with a Gamma Scientific Telephotometer (Model 2000) focused onto a plaque of the material which could be heated in a small enclosure in order to get a measure of the quenching temperature.

Results and Discussion

The brightness of the phosphors increases slightly with temperature up to about 200°C and then quenches very rapidly. Following Kröger (8) we have obtained the temperature at which the emission intensity has fallen to half its maximum value and called this $T_{1/2}$. The values are given in Table I. The quenching temperatures increase as the radius of the site at which Mn(IV) substitutes decreases, as expected from the model proposed by Blasse (13). On the other hand the quenching temperature also increases with the value of the crystal field parameter, 10 Dq. We have found that there is a fairly general relationship between the value of 10 Dq and $T_{1/2}$ in Mn(IV) luminescence, such that high values of 10 Dq are associated with high quenching temperatures (22), so that this fact could also explain the observed relationship. The two effects need not however be entirely independent because the small Mn(IV) site in K_2SiF_6 will in any case tend to increase the value of 10 Dq because of a compression effect. Reinen has demonstrated that this is the case for Cr(III) in oxides (23). A comparison of $T_{1/2}$ values in the series is complicated by the fact that the compounds are not isomorphous. Although the manganese is surrounded by an octahedron of fluoride ions in each case, K_2SiF_6 is cubic with a structure related to CaF_2 while the other two materials are hexagonal with a layer type structure resembling CdI_2 (24). In K_2TiF_6 where the manganese occupies a site almost 0.2Å larger than itself a relatively high quenching temperature of 450°K is observed. This is about 100°K higher than typical values of $T_{1/2}$ in oxides with about the same value of the crystal field parameter (20-21 kK) (22) and this suggests that other factors beside the radius of the Mn(IV) site are also important in this case.

Table I. Quenching temperature, site radius, and crystal field parameter of Mn(IV) in fluoride hosts

Host material	Radius of Mn (IV) site (Å)	10 Dq (kK)	$T_{1/2}$ (°K)
K_2SiF_6	0.41	22.12	490
K_2GeF_6	0.53	21.28	470
K_2TiF_6	0.68	21.19	450

The quantum efficiency of the phosphors has not been accurately measured but is estimated to be about 80%. The brightness of K_2SiF_6:Mn(IV) is up to two and a half times that of the well-known phosphor magnesium fluorogermanate [$Mg_4GeO_5F_2$:Mn(IV)]. It seems reasonable to suggest that the high efficiency and quenching temperature are connected with the fluorine coordination of the manganese, and that this could be associated with a smaller displacement of the excited-state ($^4T_{2g}$) curve than usually observed, due to the weaker σ-antibonding character of fluorine compared with oxygen.

The excitation spectra of the materials are interesting and show a well-resolved vibrational structure, as do a number of other transition-metal ions in fluorine coordination. The excitation spectra of the three phosphors are shown in Fig. 2.

The intense band peaking between 450 and 470 nm in the first spin allowed transition $^2A_{2g} \rightarrow {}^4T_{2g}$. In all three materials this consists of a number of components, with a spacing of 500-600 cm^{-1}, which are most clearly resolved in K_2SiF_6. Recent studies by Pfeil of the complex Cs_2MnF_6 have shown that the symmetric stretching (a_{1g}) mode of the MnF_6^{2-} group occurs at 608 cm^{-1} in the ground state (25). The structure of this band can therefore be understood as a vibronic progression of this fundamental frequency combined with an unsymmetrical vibration of the MnF_6^{2-} group (probably the e_g mode), superimposed on the electronic transition. The fact that the energy separation of the components is less than 608 cm^{-1} can be attributed to the weakening of the manganese-fluorine bond in the excited state due to the presence of an electron in the antibonding e_g orbitals. The true value of the crystal field parameter, 10 Dq, is given by the energy of the zero phonon transition in the spectrum (10). Unfortunately we have not succeeded in identifying this component and so we have taken the peak at the center of

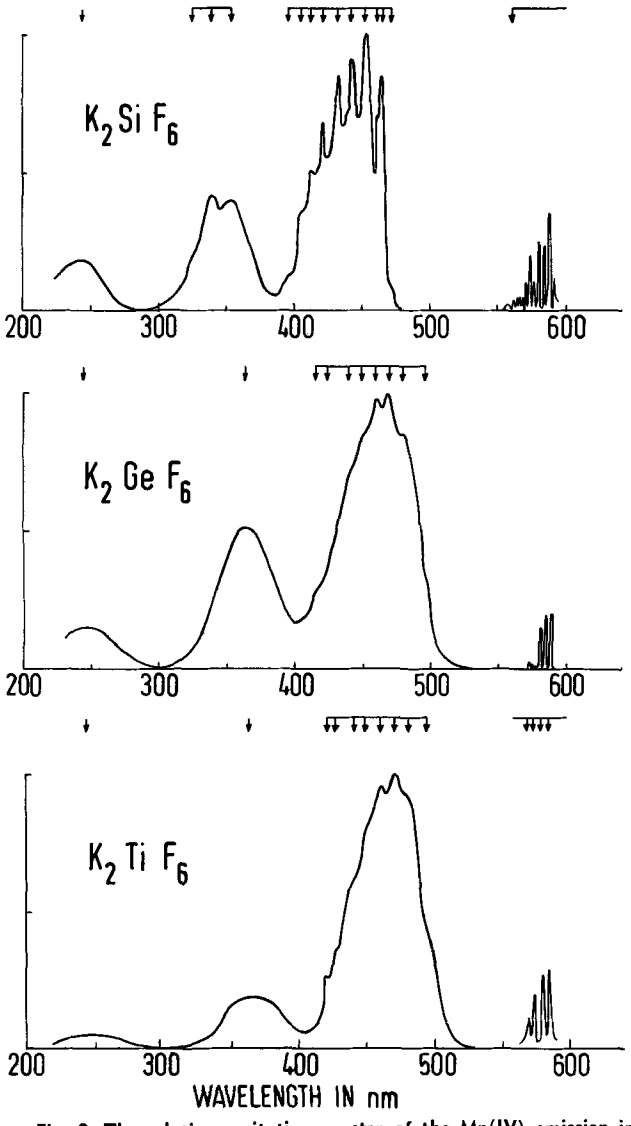

Fig. 2. The relative excitation spectra of the Mn(IV) emission in fluoride lattices containing 1 mole per cent Mn(IV) at 90°K. The ordinate represents relative radiant power per unit input power and is marked in arbitrary units.

the band to give a rough measure of 10 Dq. Although this is not correct it does allow a comparison to be made with other Mn(IV) phosphors where the absence of structure forces us to use the peak of the band as a measure of 10 Dq in any case.

The second broad excitation band between 340 and 360 nm is the $^4A_{2g} \rightarrow {}^4T_{1g}$ transition. In the case of K_2SiF_6 there is some structure in this band too. The component at 339 nm (29.5 kK) becomes much more prominent at 300°K. Apart from a slight broadening this is not detectable in the spectra of the other materials. Reisfeld *et al.* have recently discussed the absorption spectrum of Cs_2MnF_6 (26), and commenting on possible sources of splitting in the spin-allowed absorption bands have concluded that this could be due either to a vibronic progression, as observed in the first band, or a Jahn-Teller splitting assisted by a spin-orbiting coupling effect. The resolution of this band in these materials does not seem adequate to warrant further discussion of these possibilities at this stage.

There are two possible assignments of the third band near 240 nm. This could be either a fluorine-manganese charge-transfer band, or the third spin-allowed transition, $^4A_{2g} \rightarrow {}^4T_{1g}(^4P)$, of the manganese ion. The transition to $^4T_{1g}(^4P)$ is a two-electron transition, the state arising from the electron configuration $t_{2g}{}^1e_g{}^2$ (9), so that in the absorption spectrum of Cr(III), for example, it tends to be weaker than the first two spin-allowed bands. Because two electrons occupy the antibonding e_g orbitals the excited $^4T_{1g}(^4P)$ state is expected to be even further displaced along the configurational coordinate axis than the $^4T_{2g}$ and $^4T_{1g}$ states, and energy absorbed by the level is likely to be dissipated by a completely nonradiative process. This explains why this band is never observed in Mn(IV) excitation spectra (18). The absorption spectrum of Cs_2MnF_6 (26) and the diffuse reflectance spectrum of K_2MnF_6 (27) show an intense absorption at about 255 nm which has been assigned to a transition from a π-type antibonding orbital on a fluorine ion to the nonbonding t_{2g} orbitals on the Mn(IV) ion. We assign the band in these excitation spectra to the same transition although it is shifted to progressively higher energies in the titanate, germanate, and silicate, respectively.

It is interesting to note that the energy of the corresponding charge-transfer band in oxides should be at lower energies because the oxygen ion is, in general, less stable than the fluorine ion. In oxides however excitation into this band does not always lead to emission. In the case of K_2TiF_6 too, only very weak excitation is observed. A possible explanation of this is as follows. Blasse has argued that in the course of excitation into a charge-transfer band an electron is transferred from an orbital on an anion to an orbital predominantly localized on the central ion. There is thus a build up of charge on the central ion in the excited state which has a screening effect, lowering the effective positive charge of the central ion. As a result the anions relax slightly to a greater internuclear separation (13). The result of this relaxation is to shift the potential surface of the charge-transfer state relative to the ground-state curve so as to reduce the activation energy ΔE. This effect is minimized when the manganese occupies a small lattice site, so the intensity of the charge-transfer excitation band decreased in the order $K_2SiF_6 > K_2GeF_6 > K_2TiF_6$ as the radius of the Mn(IV) site increases. In oxides the charge-transfer absorption is expected at longer wavelengths, and the displacement of the potential curve to lower energies decreases ΔE so that effective excitation of the center in this band cannot be achieved even when the manganese enters comparatively small lattice sites. In a number of other centers too it is known that if the charge-transfer band lies at low energies luminescence may not be observed (28).

A number of narrow excitation bands can be observed in the region of 580 nm. These are most clearly resolved in K_2SiF_6 and have not previously been reported in a Mn(IV) excitation spectrum. An enlarged version of this part of the spectrum is shown in Fig. 3. We assign these bands to vibronic levels of the ^2E_g and $^2T_{1g}$ states. These transitions are not usually observed

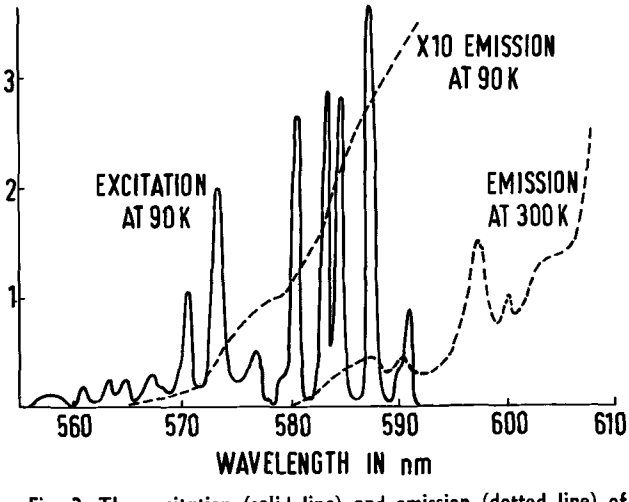

Fig. 3. The excitation (solid line) and emission (dotted line) of K_2SiF_6:0.01 Mn(IV) at 90°K in the region 18-18 kK. The excitation is plotted against the same ordinate as in Fig. 2 and the emission is plotted on an arbitrary scale.

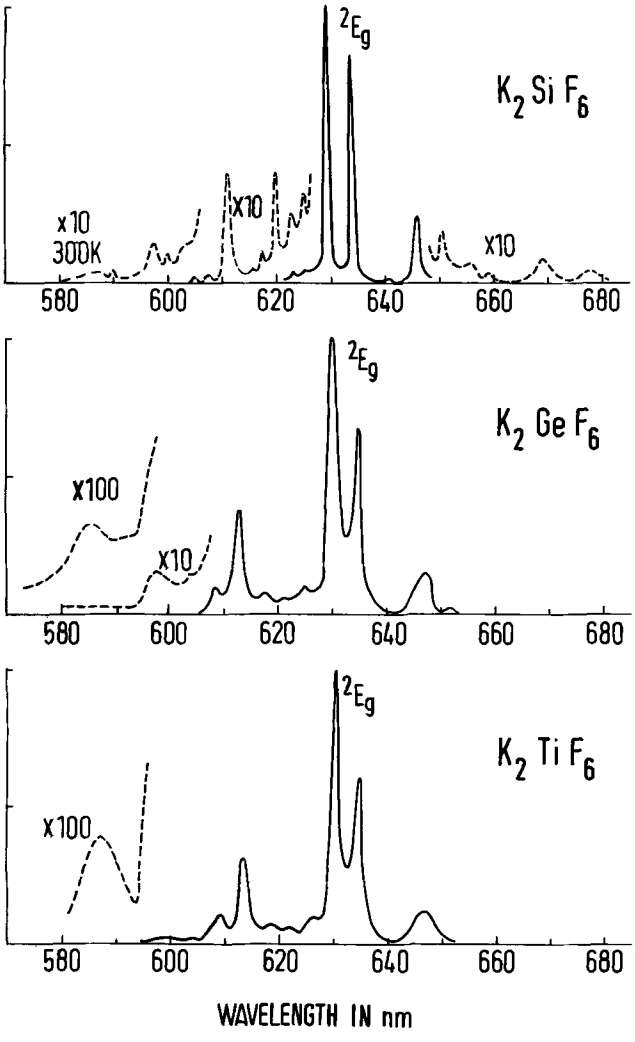

Fig. 4. The emission spectra of Mn(IV) in fluoride lattices containing 1 mole per cent Mn(IV) at 90°K. The ordinate represents relative radiant power per constant bandwidth and is marked in arbitrary units. The weak emission at shorter wavelengths is shown on an enlarged scale (dotted line).

in Mn(IV) absorption and excitation spectra because the tail of the $^4T_{2g}$ band extends into this region making them difficult to detect. A partial analysis of this structure indicates that not all these lines can be attributed to vibronic levels associated with the $^4A_{2g} \rightarrow {}^2E_g$ transition and that some must belong to the $^2T_{1g}$ state (18). The $^2T_{1g}$ state itself appears to be ~800 cm above ^2E_g; however more complete data are required before all these transitions can be satisfactorily explained.

The emission spectra of the materials are shown in Fig. 4. This must be assigned to transitions between the vibronic levels of the ^2E_g and $^4A_{2g}$ states. For electric dipole radiation the $^2E_g \rightarrow {}^4A_{2g}$ transition is forbidden in the octahedral MnF_6^{2-} ion, but may gain intensity by the activation of odd vibrational modes in the center. As in Cs_2MnF_6 (25) the most intense line at ~629 nm (15.891 kK) can be assigned to the transition to the $\nu_6(t_{2a})$ vibrational level of the ground state. The next most intense lines at ~634 nm (15.775 kK) and 646 nm (15.473 kK) are due to transitions to the $\nu_4(t_{1u})$ and $\nu_3(t_{1u})$ levels, respectively. The zero phonon line is rather weak at room temperature but can be identified as the transition at ~623 nm (16.124 kK) in the 90°K spectrum. The strong transitions to ν_6, ν_4, and ν_3 are separated from the zero phonon line by 233, 349, and 651 cm^{-1}, respectively, and these figures are in reasonable agreement with vibrational frequencies already observed in Cs_2MnF_6 (229, 334, and 616 cm^{-1}, respectively) (25). A higher quality spectrum is required before any attempt can be made to comment in more detail on the other lines in the spectrum.

Mn(IV) phosphors and complexes can also show a broad diffuse transition, mostly in the infrared peaking at about 750 nm, due to a Stokes-shifted emission from the $^4T_{2g}$ state (22) but this was not observed in these fluorides. The reason is that the relatively high value of the crystal field probably places the emitting ^2E_g level at a significantly lower energy than the $^4T_{2g}$ state. A similar effect is noticed in the emission of Cr(III) materials (29).

The first absorption band of Mn(IV) in oxides is typically observed at 20°-21°kK but it is not always certain that this is due to the $^4A_{2g} \rightarrow {}^4T_{2g}$ transition of Mn(IV) because there is often an equilibrium between Mn(IV) and Mn(III) ions (16). In these excitation spectra however there is no doubt that the excitation spectra must be attributed to Mn(IV) alone, and the value of the crystal field parameter, 10 *Dq*, is therefore interesting as it is derived from one of the few spectra where the assignment is least in question. It is well known that attempts to calculate the value of 10 *Dq* from considerations of electrostatic interactions, as in the crystal field model, lead to a negative value of 10 Dq. This only becomes positive with a value in reasonable agreement with experiment when σ-bonding interactions are included in molecular orbital calculations. The value of the parameter is thus largely a reflection of σ-bonding interaction in the center. The magnitude of 10 *Dq* is however also affected by π-bonding interactions. Low lying π-orbitals on the ligands tend to reduce the magnitude of 10 *Dq* to a lower figure than would be observed with σ-bonding alone. On the other hand high lying π-orbitals have the opposite effect, tending to increase 10 *Dq* [*e.g.*, see Ref. (32)]. These considerations allow some of the features of the chemical bonding in the Mn(IV) center to be connected with the luminescence. In fact π-bonding interactions may be quite important in these materials. ESR studies of MnF_6^{2-} in K_2GeF_6 have indicated that this is possible (33) and so the relatively small displacement of the excited-state potential curves of Mn(IV) centers in fluorides may be due to a combination of a generally low σ-antibonding effect in the e_g orbitals together with a greater π-antibonding effect in the t_{2g} orbitals.

Conclusions

These complex fluoride phosphors provide much more information than has been available previously on Mn(IV) luminescence spectra.

The relatively high value of the quenching temperature in K_2SiF_6 may very well be due to the small silicon site which compresses the Mn(IV) ion. This restricts the expansion of the center in the excited state, and at the same time causes a relatively high value of 10 *Dq* to be observed, and both these effects favor a high quenching temperature. On the other hand the high efficiency and quenching temperature, only 40°K lower in K_2TiF_6, suggest that the manganese-fluorine bonding is also important in determining the properties of these phosphors. The earlier position of F^- in the spectrochemical series than O^{2-} probably results in a weaker σ-antibonding effect in the e_g orbitals, and it also seems likely that π-antibonding in the t_{2g} orbitals is important. The difference in antibonding character between the t_{2g} and e_g orbitals is thus less in the MnF_6^{2-} center than in the $Mn(O^{2-})_6$ center so that the relaxation of the group in the excited state is minimized.

If the compression of the Mn(IV) ion is of importance the effect is likely to be enhanced in rigid ionic lattices which contain small highly charged ions (13). The comparatively large number of small doubly charged magnesium ions in the commercial phosphors $Mg_6As_2O_{11}$ (14) and Mg_4GeO_6 (19) [more accurately $Mg_{28}Ge_{10}O_{48}$ (34)] is noteworthy in this connection. Clearly this condition has not been very well satisfied in the potassium compounds reported here. However,

efficient Mn(IV) emission is also observed in other complex fluorides, and we hope to report details of the preparation and properties of these materials later.

Acknowledgments

Thanks are due to Messrs. A. H. McKeag and H. L. Burrus for encouragement and helpful discussions during the course of this work, and to members of the Chemistry and Technical Services Division for carrying out x-ray diffraction and spectroscopic measurements.

Manuscript submitted Nov. 27, 1972; revised manuscript received Feb. 16, 1973. This was paper 225RNP presented at the Houston, Texas, Meeting of the Society, May 7-11, 1972.

Any discussion of this paper will appear in a Discussion Section to be published in the June 1974 JOURNAL.

REFERENCES

1. D. L. Dexter, *Solid State Phys.*, **6**, 353 (1958).
2. L. E. Orgel, *J. Chem. Phys.*, **23**, 1958 (1955).
3. C. Furlani, *Coord. Chem. Rev.*, **1**, 51 (1966).
4. G. B. Porter and H. L. Schläfer, *Ber. Bunsenges*, **68**, 316 (1964).
5. A. R. Reinberg and S. G. Parker, *Phys. Rev.*, **B1**, 2085 (1970).
6. A. R. Reinberg, *ibid.*, **B3**, 41 (1971).
7. P. B. Dorain and R. G. Wheeler, *J. Chem. Phys.*, **45**, 1172 (1966).
8. F. A. Kröger, "Some Aspects of the Luminescence of Solids," American Elsevier Publishing Co., Inc., New York (1948).
9. H. L. Schläfer and G. Gliemann, "Basic Principles of Ligand Field Theory," Interscience Publishers, Inc., London and New York (1969).
10. D. S. McClure, in "Advances in the Chemistry of Coordination Compounds, S. Kirschner, Editor, p. 498, The MacMillan Company, New York (1961).
11. J. L. Laver and P. W. Smith, *Chem. Commun.*, **1970**, 497.
12. M. Mingardi and G. B. Porter, *J. Chem. Phys.*, **44**, 4354 (1966).
13. G. Blasse, *ibid.*, **51**, 3529 (1969).
14. M. Trivnicek, F. A. Kröger, P. J. Botden, and P. Zalm, *Physica*, **18**, 33 (1952).
15. K. T. Wilke, *Z. Physik. Chem.*, **210**, 260 (1959).
16. A. Bergstein and W. B. White, *This Journal*, **118**, 1166 (1971).
17. F. Karel, J. Pastrňák, J. Hejduk, and V. Losík, *Phys. Status Solidi*, **15**, 693 (1966).
18. A. G. Paulusz, Unpublished results.
19. F. A. Kröger and J. van den Boomgaard, *This Journal*, **97**, 377 (1950).
20. Al. Yakimach, *Compt. Rend.*, **190**, 681 (1930).
21. H. Bode, H. Jensen, and F. Bandte, *Angew. Chem.*, **1953**, 304.
22. A. G. Paulusz, To be published.
23. D. Reinen, *Structure and Bonding*, **6**, 30 (1969).
24. R. W. G. Wyckoff, "Crystal Structures," Vol. 3, Interscience Publishers, Inc., New York (1965).
25. A. Pfeil, *Theoret. Chim. Acta (Berlin)*, **20**, 159 (1971).
26. M. J. Reisfeld, N. A. Matwiyof, and L. B. Asprey, *J. Mol. Spectr.*, **39**, 8 (1971).
27. G. C. Allen, G. A. M. El-Sharkarwy, and K. D. Warren, *Inorg. Nucl. Chem. Letters*, **5**, 725 (1969).
28. G. Blasse, *J. Chem. Phys.*, **48**, 3108 (1968).
29. H. L. Schläfter, H. Gausmann, and H. Witzke, *ibid.*, **46**, 1423 (1967).
30. C. K. Jørgensen, *Advan. Chem. Phys.*, **46**, 1423 (1967).
31. C. K. Jørgensen, *Solid State Phys.*, **13**, 375 (1962).
32. D. Reinen, *Angew. Chem. (International Edition)*, **10**, 901 (1971).
33. L. Helmholz, A. V. Guzzo, and R. N. Sanders, *J. Chem. Phys.*, **35**, 1349 (1961).
34. R. B. Von Dreele, P. W. Bless, E. Kostiner, and R. E. Hughes, *J. Solid State Chem.*, **2**, 612 (1970).

Vapor Growth of $In_{1-x}Ga_xP$ for P-N Junction Electroluminescence

I. Material Preparation

A. G. Sigai,*[1] C. J. Nuese, R. E. Enstrom,* and T. Zamerowski

RCA Laboratories, Princeton, New Jersey 08540

ABSTRACT

Epitaxial layers of single-crystal $In_{1-x}Ga_xP$ have been deposited on GaP substrates by an open-tube vapor-growth technique. The dependence of alloy composition on the deposition temperature and the relative amounts of In and Ga transported have been established. The effects of substrate preparation, reaction temperatures, deviations from equilibrium, and gas-phase mixing on achieving material with controlled composition, purity, doping, and homogeneity have been investigated. *In situ* vapor-grown p-n junction structures employing Se and Zn as the respective n- and p-type dopants have been prepared with sufficient perfection to permit fabrication of efficient visible-light-emitting diodes and injection lasers.

Because of its direct band structure to energies as high as about 2.2 eV (1, 2), $In_{1-x}Ga_xP$ has recently received considerable attention as a luminescence source for efficient coherent and spontaneous emission throughout the red, orange, and yellow portions of the visible spectrum. Despite considerable efforts in the synthesis of the alloy, the quality of the material prepared to date has limited the performance of light-emitting diodes to well below expectations. For example, until recently, external quantum efficiencies for visible electroluminescence have been limited to typical values of 1 to 5 $\times$ 10^{-4} at room temperature (3-5), undesired low-energy emission peaks frequently have been large (6), and p-n junctions of sufficiently high quality to support laser emission have been difficult to fabricate (7). Many of the problems in the synthesis of homogeneous material may be directly related to the relatively large lattice mismatch between the compounds which constitute this alloy. The large separation of the solidus and liquidus curves in the temperature-composition phase diagram (8) of $In_{1-x}Ga_xP$ results in a large segregation of GaP for melt-growth, making the preparation of bulk alloys of uniform composition difficult. The large segregation

* Electrochemical Society Active Member.
[1] Present address: Xerox Research Laboratories, Webster, New York 14580.
Key words: $In_{1-x}Ga_xP$, vapor-phase growth, homogeneity, equilibrium, epitaxial deposition.

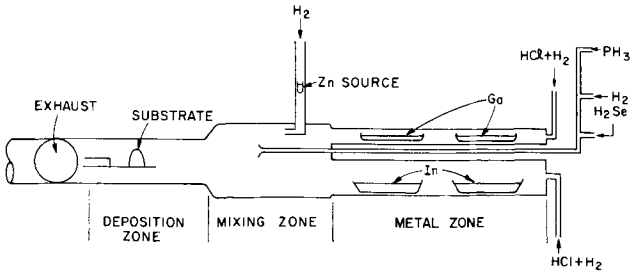

Fig. 1. Schematic diagram of the vapor-phase growth system used for the epitaxial deposition of $In_{1-x}Ga_xP$.

coefficient (4) also complicates liquid-phase epitaxial growth of $In_{1-x}Ga_xP$. Very little work has been done on the vapor-phase growth of this material.

Earlier work by Nuese, Richman, and Clough (6) demonstrated that epitaxial layers of $In_{1-x}Ga_xP$ could be prepared across the entire alloy system by an open-tube vapor-growth technique. However, diodes fabricated from this material yielded very low electroluminescence efficiencies ($\sim 10^{-6}$), perhaps due to crystal strain and compositional inhomogeneity. In this work, we report the development of vapor-growth techniques for preparing $In_{1-x}Ga_xP$ with controlled composition, doping, homogeneity, purity, and crystalline perfection. From such material, electroluminescent diodes and lasers have been obtained (9) with luminescence properties that are significantly improved relative to those of previous vapor-grown material, and which are comparable to the best reported (3) for this alloy system.

Vapor-Growth Technique

The apparatus used to prepare $In_{1-x}Ga_xP$ alloys is shown schematically in Fig. 1 and is similar to that used earlier (6). The use of separate quartz tubes to contain the In and Ga sources allows independent control of the HCl concentrations over each of the metal sources. Mass spectrometric analysis (10) of the gases in the growth tube has shown that HCl reacts with Ga and In metals to form monochlorides of these metals according to the reaction

$$y\,M(l) + HCl(g) = y\,MCl(g) + (1-y)HCl(g) + \frac{y}{2}H_2(g) \quad [1]$$

Here M is In or Ga and y is the mole fraction of HCl consumed in the reaction. The metal monochlorides are carried in hydrogen into the mixing zone where they mix, but do not react, with gaseous phosphine, the source of phosphorus. The reduced temperature in the deposition zone, where the substrate is positioned, allows the reaction between gases to give $In_{1-x}Ga_xP$ as an epitaxial film and HCl as the gaseous by-product (10) according to the reaction

$$MCl(g) + P^*(g) + H_2(g) = MP(s) + HCl(g) \quad [2]$$

Here, P* represents PH_3 and the products of the decomposition of PH_3, namely P_2 and P_4. The provisions for *in situ* n- and p-type doping using H_2Se and Zn vapor, respectively, are also shown in Fig. 1. For p-n junction formation, the dopants are sequentially introduced during growth, thereby eliminating the need for an extra high-temperature processing step.

An important feature of this system is the ability to uniformly and controllably grade the alloy composition between the substrate and the terminal alloy in order to minimize strain and reduce dislocations due to lattice-constant mismatch. This is particularly important in $In_{1-x}Ga_xP$ because the lattice parameters of the end components differ by almost 8%. Compositional grading previously has been shown to lead to enhanced electroluminescence in vapor-grown $GaAs_{1-x}P_x$ p-n junctions (11).

Choice of Growth Temperature

Since unknown background contaminants might introduce trapping states, nonradiative recombination centers, or compensating impurities, it is desirable to first achieve background concentrations as low as possible before introducing controlled amounts of dopants. Therefore, several temperatures and temperature profiles were examined in order to determine the optimum conditions for high-purity $In_{1-x}Ga_xP$ epitaxial growth. Three representative crystals grown under various growth conditions together with their mass spectrometric analyses and electrical properties are listed in Table I. Here, we see that the lower temperatures used for the three zones in Fig. 1 have led to significantly reduced background doping concentrations. In addition, note the correlation in each case between the free electron concentration (determined by Hall measurements) and the concentration of Si (determined by mass spectrometric analysis), suggesting that Si is the predominant electrically active impurity. This is consistent with the observation that Si is the predominant donor impurity in other III-V compounds such as AlAs (12, 13) and GaAs (14) prepared by similar vapor-growth techniques.

Substrate Preparation and Characterization

The $In_{1-x}Ga_xP$ epitaxial layers in this work were typically deposited on liquid-encapsulated Czochralski-grown (referred to as LEC) GaP substrates oriented 3° off the <100> direction toward the <010> direction. These layers were graded in alloy composition from GaP at the substrate to the final desired composition, which usually was between 50 and 65 m/o (mole per cent) GaP.

The GaP wafers were first chemi-mechanically polished using a bromine:methanol:phosphoric acid solution (15) (later referred to as BMP etch) to remove work damage. A bromine-methanol solution has been found to be particularly effective in revealing work-damaged areas which can remain after insufficient etching. The photomicrographs in Fig. 2 show a wafer prior to the test for work damage (Fig. 2a) and after etching for 2 min in bromine-methanol (Fig. 2b). Note how this etchant reveals minute surface damage. The white areas (in contrast to the light scratches) are artifacts of the bromine-methanol etching procedure and occur only when the solution contains trace amounts of moisture.

As a standard procedure in our substrate preparation, we performed a second chemical etching treatment

Table I. Comparison of mass spectrometric analysis and electrical properties of $In_{1-x}Ga_xP$ layers grown under different temperature conditions

Run No.	n(cm^{-3})	Mass spectrometric analysis (PPMA)*						Furnace temperatures (°C)			
		Cu	Ni	Fe	Cl	Si	F	Deposition	Center	Indium	Gallium
0115	2×10^{19}	0.08	N.D.	0.5	0.3	80	0.03	775	1000	980	850
1103	2×10^{17}	0.9	0.2	0.2	2	4	0.1	775	1000	850	760
1720	2×10^{15}	N.D.	N.D.	N.D.	1	1	N.D.	725	850	825	760

* 1 PPMA = 5×10^{16} cm^{-3}.
N.D.: not detected.

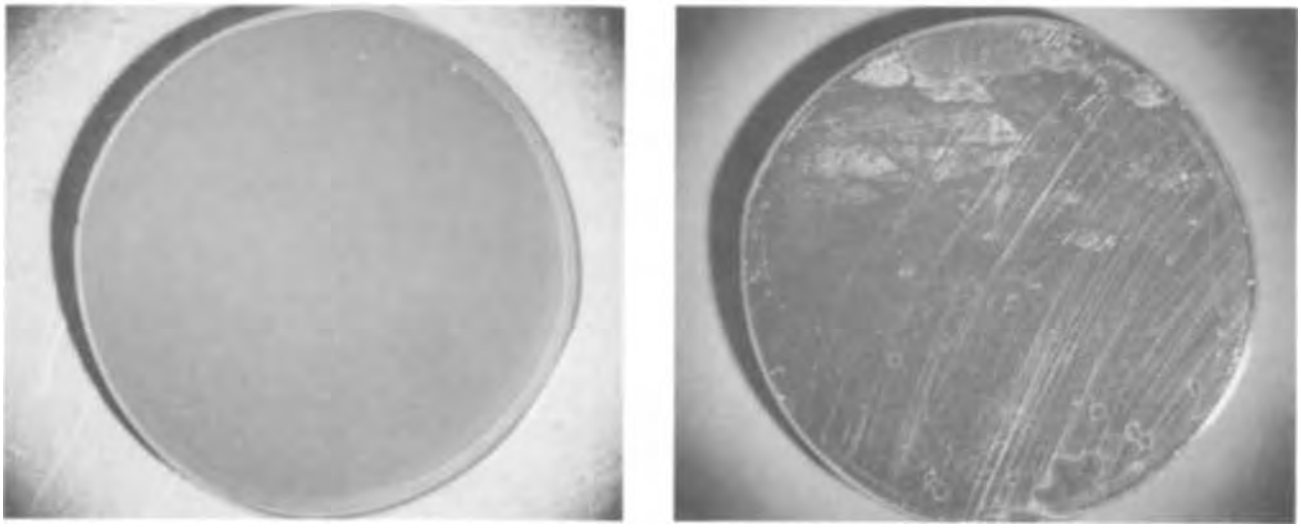

Fig. 2. Photomicrograph (a) of a liquid-encapsulated Czochralski-grown GaP substrate which is to be tested for work damage, and the corresponding photomicrograph (b) of the wafer after 2 min etching in a bromine-methanol solution. The white areas are artifacts of the etching procedure.

shortly before insertion into the vapor-growth system. A hot (80°C) Caro's acid ($5H_2SO_4:H_2O_2:H_2O$) etch was used for 5 min, followed by a hot (50°C) BMP etch. It should be noted that the etching rate for both the Caro's etch and the BMP etch are highly dependent on the temperature of the etchant, as indicated in Fig. 3. We have found that etching rates of greater than 5 μm/min (obtained at elevated temperatures) cause both etchants to become preferential, resulting in etch pits and nonplanar surfaces. Best results have generally been attained for etching rates of 0.6 μm/min for the Caro's etch and 1.5 μm/min for the BMP etch, which occur at 80° and 50°C, respectively.

We also have found that the BMP etch should be used immediately after the Caro's acid etching of the substrate. For example, a 24-hr delay between the use of the two etchants resulted in the appearance of pits after a 5 min BMP etch (50°C). These pits most likely originate from an oxide or other surface contaminant from the ambient in the interval between the etching steps. If the wafers are used immediately after chemi-

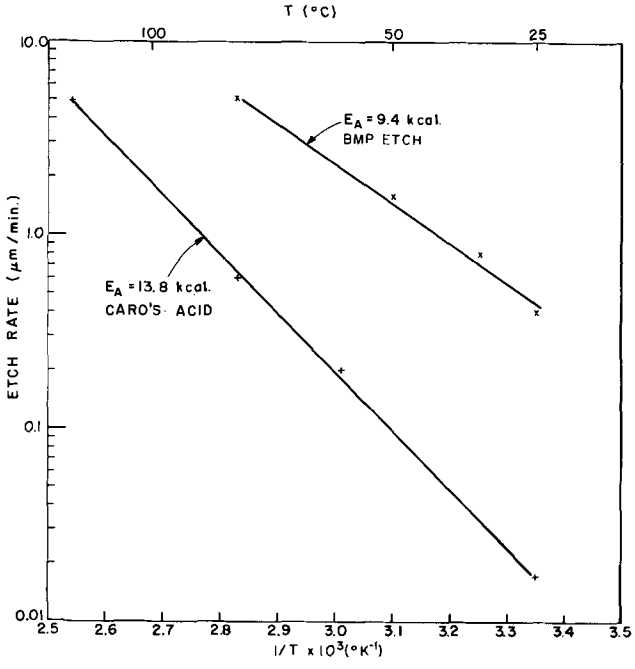

Fig. 3. Etch rate of Caro's acid and the BMP etch on <100>-oriented liquid-encapsulated GaP substrates as a function of etchant temperature.

mechanical polishing, single-crystal epitaxial layers are obtained; however, if a 24-hr delay occurs prior to growth, the layers are inevitably polycrystalline. These results suggest that removal of surface contamination is important for achieving high-quality single-crystal epitaxial layers.

Control of Composition

Since earlier work (6) on the vapor growth of $In_{1-x}Ga_xP$ has shown that the composition of the alloy depends strongly on the ratio of the HCl flow rates to the In and Ga sources (HCl_{In}/HCl_{Ga}), precision electronically activated gas-flow controllers were employed for each of the metal sources. However, to achieve reproducible control of alloy composition, it is necessary not only to have constant flow rates to the metal sources, but also to be certain that the conversion of HCl to the respective metal chlorides remains fixed with time. Both the Ga and In conversion have been examined in detail, the results of which are presented below.

Gallium source.—From mass spectrometric investigations (16) of the amount of HCl reacted during the transport of Ga for various hydrogen carrier flow rates, it is possible to calculate the per cent HCl reacted for various linear velocities (since the reaction temperature and the effective cross-sectional area of the metal zone tube are known).[2] If the length of the Ga boat is also known, the linear velocities can be expressed in terms of a "residence time," *i.e.*, the amount of time the HCl is in contact with the metal source boat. Using the mass spectrometric data (16) the dependence of the unreacted amount of HCl on residence time is plotted in Fig. 4 for a reaction temperature of 800°C. Here, the equilibrium (10) fraction of HCl not converted to GaCl is also shown. In the present work, an effective Ga zone tube cross-sectional area of 2.1 cm^2 and a flow rate of 600 cc/min are employed, resulting in a linear velocity of 16.7 cm/sec. Since two 15-cm boats are used in series in the gallium source zone in our experiments, the residence time is 1.7 sec. If the conditions employed in our work are similar to those reported for the mass-spectrometric studies (16), we would expect equilibrium to be approached rapidly with increasing residence time, as indicated in Fig. 4.

It should be noted that the smaller diameter tube used in the present case [1.7 cm *vs.* 2.5 cm used in the earlier study (16)] further increases the equilibration

[2] The effects of the displacement of the metal boats and the expansion of the carrier gas at reaction temperature on the linear velocities and residence times of the gases within the metal zone have been taken into account in the calculations reported here.

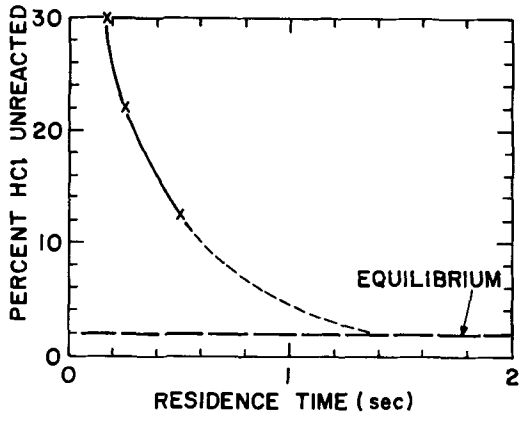

Fig. 4. Percentage HCl unreacted as a function of residence time, the amount of time the HCl is in contact with the Ga metal source boat.

rate in the Ga zone, since the ratio of the surface area of the Ga to the volume of gas above the boat must be somewhat higher than previously.

To experimentally determine the precise amount of HCl converted with the geometries employed here, the number of moles of Ga consumed (as determined by the weight difference of the boats before and after a series of six 3-hr runs) was compared to the number of moles of HCl passed over the source (measured by precision gas flowmeters). These findings, presented in Table II, assume that only reaction [1] leads to the transport of Ga. The calculated per cent conversion of 97.8% is in excellent agreement with values expected for equilibrium conversion of HCl to GaCl and, therefore, verifies that equilibrium is attained in the Ga zone under the experimental conditions employed. Note also that the second boat converts less than 3% of the total HCl entering the Ga zone, in approximate agreement with the curve in Fig. 4 for residence times between 0.85 and 1.7 sec. The data in Table II and the curve in Fig. 4 also indicate that small changes in the residence time should not cause large changes in the amount of GaCl formed.

Indium source.—Despite the fact that x-ray diffraction and electron microprobe findings indicated reasonable uniformity of composition, a gradual shift in alloy composition for runs employing essentially the same growth conditions was observed over a 15-hr period required to grow four to five samples, as illustrated in Fig. 5. Differences by as much as 15 m/o InP were observed. The fact that the percentage of InP decreased monotonically with time in Fig. 5 suggested a depletion of In as the source of the change; incomplete reaction

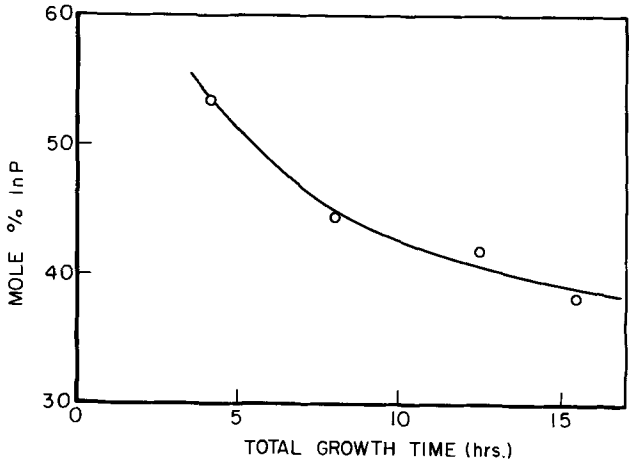

Fig. 5. Variation of composition for a series of $In_{1-x}Ga_xP$ epitaxial layers employing the same growth conditions. The HCl flow to the In source was 50 cc/min.

Table II. Number of moles of gallium consumed determined by the weight difference of the boats before and after a series of six 3-hr runs

Boat	Moles gallium consumed ($\times 10^8$)	Moles HCl introduced into Ga zone ($\times 10^8$)	Per cent conversion to GaCl
1	145.8		
2	4.22		
Combined	150.02	153.8	97.8

between In and HCl as the In source depleted would then cause a decrease in InCl concentration in the deposition zone. In addition, since HCl is a by-product of the deposition reaction [2], the composition would be further changed by the extent to which the unreacted HCl suppresses deposition of InP. Upon increasing the In source contact with the HCl either by increasing the volume of In or by using deflection baffles, reproducible compositions and compositional profiles have been achieved.

Experiments similar to those described for Ga concerning the per cent conversion of HCl to InCl also were carried out. The data in Table III are based on 50 cc/min of HCl to the In source, 600 cc/min of H_2 carrier, and an effective cross-sectional area of 7.8 cm^2, yielding a linear velocity of 7.5 cm/sec. Note that the final boat contributes only about 2% of the total HCl converted. The per cent conversion of 96% is in good agreement with that expected (10) for complete equilibrium in the In zone according to reaction [2]. The discrepancy between the 96% reported here and a value of only 80% measured in earlier work (10) can be attributed to the differences in the experimental conditions employed, in particular, the use of baffles and a larger In source in the present investigation.

One feature common to many of our earlier layers (which were graded from a GaP substrate) was a "lag" in alloy composition observed in the initial stages of the compositional grading (the first 10 μm of growth for the crystal in Fig. 6a), which would be expected to generate large concentrations of lattice-misfit dislocations. Analysis of the In source after the series of vapor depositions indicated a solubility of about 2 to 3% of InCl in the In metal. Consequently, the strong nonlinear variation in alloy composition at the onset of the grading was thought to be due to slow saturation of the In source with InCl. By allowing the metal source to become saturated prior to initiation of the grading schedule, it has been possible to eliminate such deviations, as illustrated in the microprobe profile of Fig. 6b.

Dependence of Alloy Composition on HCl Ratio and Deposition Temperature

The incorporation of InP in vapor-grown $In_{1-x}Ga_xP$ is strongly dependent on both the deposition temperature and the relative ratio of the HCl flows in the respective metal zones, as shown in Fig. 7. This results, in part, from the large difference in the free energy of formation, $\Delta G°_f$, of InP(s) and GaP(s). Under the range of experimental temperatures employed, the free energy of reaction is large and negative for the deposition of GaP. Therefore, the conversion of GaCl to GaP is nearly complete. But for InP the free energy of reaction is only slightly negative and then becomes

Table III. Number of moles of indium consumed determined by the weight difference of the boats before and after a series of runs

Boat	Moles In consumed ($\times 10^2$)	Moles HCl consumed ($\times 10^2$)	Per cent conversion to InCl
1	27.78		
2	19.79		
3	4.73		
4	1.07		
Combined	53.37	55.49	96.2

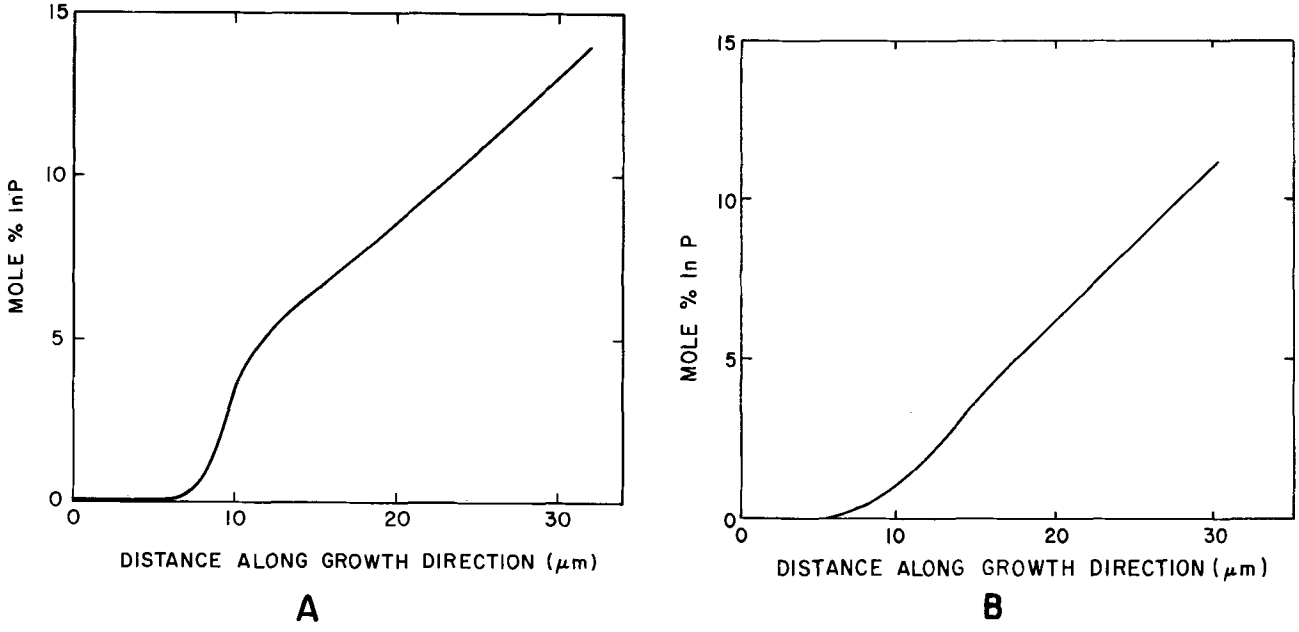

Fig. 6. Microprobe profile of the mole fraction of InP in the initial $In_{1-x}Ga_xP$ deposition for (A) incomplete saturation of the In sources with InCl, (B) complete saturation of the In sources with InCl.

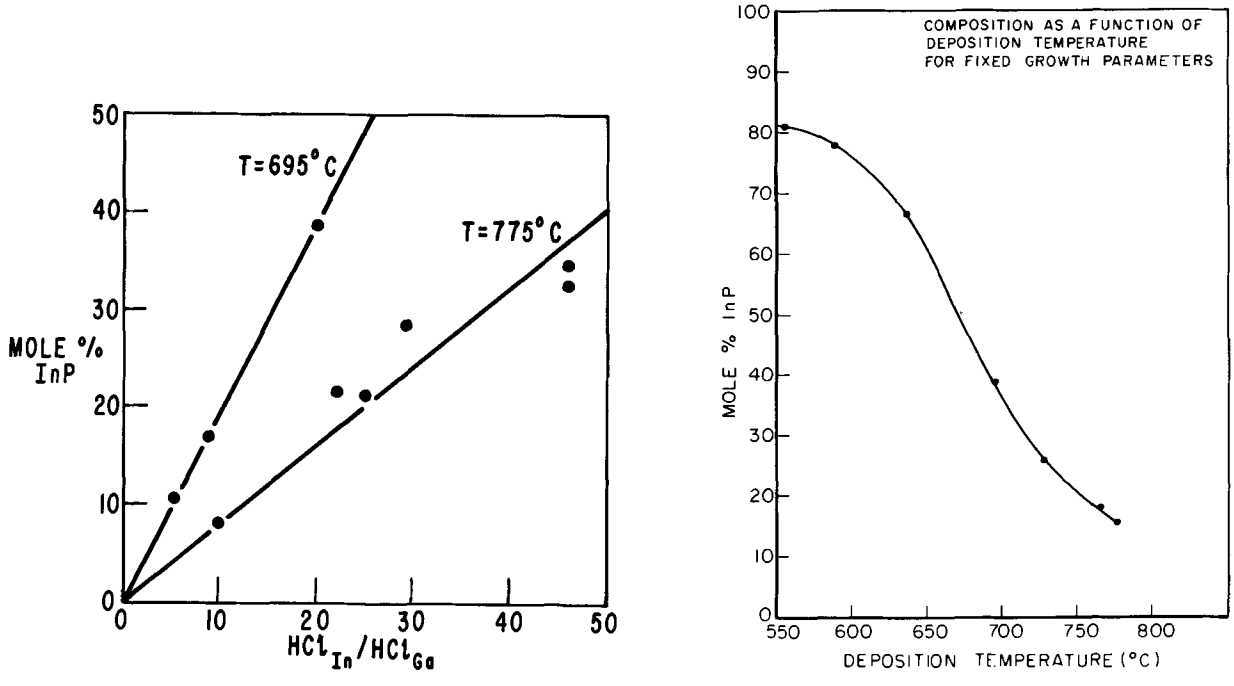

Fig. 7. Dependence of the mole fraction of InP in the $In_{1-x}Ga_xP$ alloy on (A, left) the ratio of the HCl flow rate over the In and Ga sources, and (B, right) deposition temperature.

positive with increasing temperature. As a result, only a small fraction of InCl is converted to InP under the experimental conditions employed, and the conversion becomes less efficient with increasing temperature.

Ban and Ettenberg (10) have carried out an elegant analysis of the deposition of $In_{1-x}Ga_xP$ alloys in our vapor-growth system, which takes into account the activity of the InP and GaP in the deposition reaction [2]. The close agreement between their equilibrium calculations and our experimentally determined data reported in that work indicates that equilibrium is closely approached, not only in the reaction between the Group III metals and HCl, as we have shown earlier, but also in the deposition under the experimental conditions used in this work.

Origin of Hillock Formation in Vapor-Grown $In_{1-x}Ga_xP$

Although hillock formation has been a minor problem in the vapor growth of several III-V compounds, such formation has been particularly severe in the $In_{1-x}Ga_xP$ epitaxial layers. For this reason, an investigation was carried out to determine the source of the surface imperfections. We have found that hillocks can originate from loose deposits which form on the walls of the quartz tube during growth, fall onto the substrate, and thereby create sites for heterogeneous nucleation. Therefore, by orienting the wafers vertically and parallel to the gas flow, the hillock density was substantially reduced.

In addition to the effect of substrate orientation, several observations during the course of our investigation suggested that ambient gas leaks are the origin

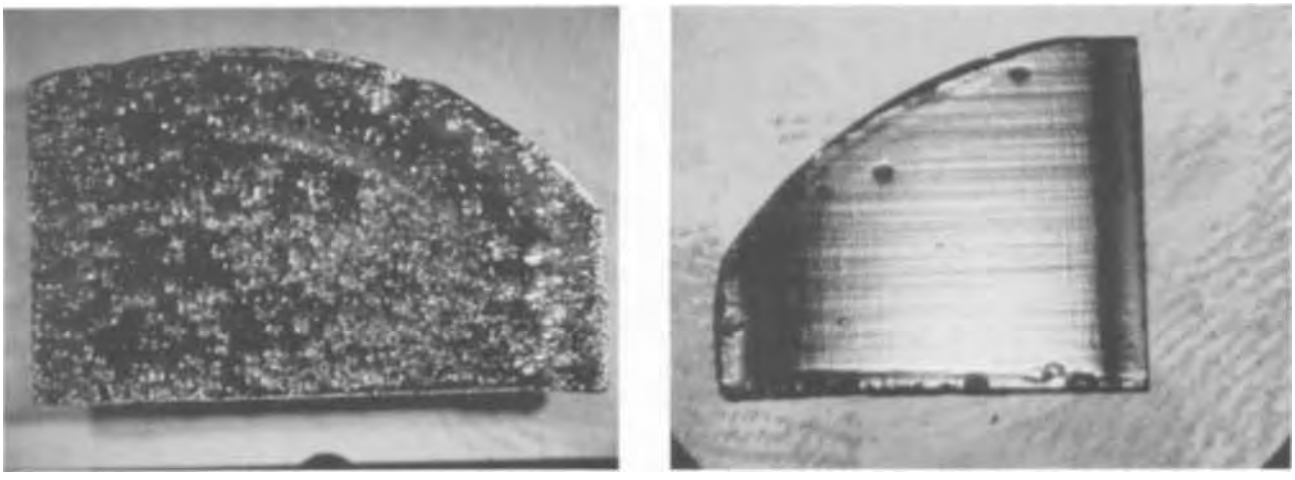

Fig. 8. Photomicrographs of the surface morphology of an $In_{1-x}Ga_xP$ epitaxial layer (A, left) grown in the presence of an ambient gas leak and (B, right) grown in the absence of an ambient gas leak.

of many of the hillocks. Most notably, upon ensuring that our growth system was leak tight, the hillock density was observed to decrease appreciably. To confirm this observation, a very small quantity of ambient gas to approximate a pinhole leak was intentionally introduced into the vapor growth system during the deposition of $In_{1-x}Ga_xP$ epitaxial layers. Figure 8 shows the surface morphology of wafers grown with and without the intentional leak. It is apparent that small ambient leaks can have a catastrophic effect on the crystal surface appearance. We also should mention that no correlation has been seen between hillock density and crystallographic orientation for GaP substrates oriented 0°, 2°, 3°, 4°, and 5° off {100} toward {010}, in contrast to Blakeslee's findings (17) on vapor-grown GaAs.

Under suitable growth conditions using a substrate free of work damage, a vertical substrate orientation, and a growth system free of leaks, large area macroscopically defect-free epitaxial layers can be routinely obtained. The surfaces of $In_{1-x}Ga_xP$ layers deposited on GaP substrates are comparable in appearance to high-quality epitaxial layers of GaP deposited on GaP substrates, as shown in Fig. 9. One notable difference between the $In_{1-x}Ga_xP$ and GaP surface structure is the presence of a grid network in the case of the $In_{1-x}Ga_xP$. This is related to the orthogonal array of dislocations (18) introduced during the compositional grading between the GaP substrate and the $In_{1-x}Ga_xP$ alloy.

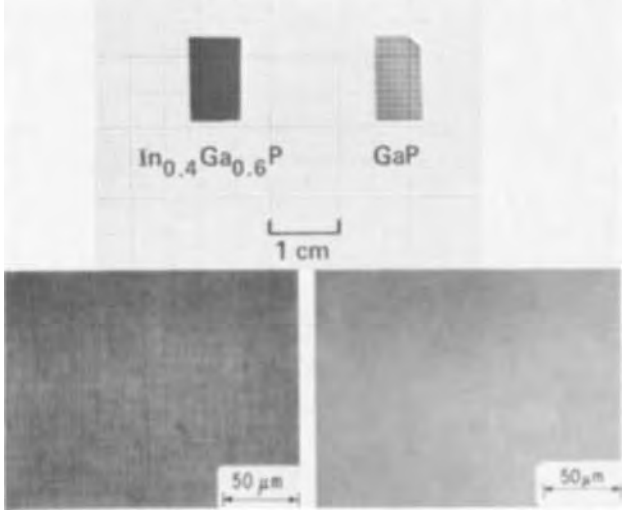

Fig. 9. Photograph of $In_{0.4}Ga_{0.6}P$ and GaP epitaxial layers deposited on GaP substrates with the vapor-growth refinements discussed in the text.

P- and N-Type Doping of $In_{1-x}Ga_xP$

Semi-insulating substrates are frequently used for the deposition of epitaxial layers because their high resistance allows Hall measurements to be made without removal of the substrate. Since semi-insulating GaP substrates were not available, a series of $In_{0.49}Ga_{0.51}P$ layers which were Zn- and Se-doped over a wide range of carrier concentrations were epitaxially deposited on <100>-oriented Cr-doped GaAs substrates. To minimize problems associated with lattice mismatch between the $In_{1-x}Ga_xP$ and GaAs, an alloy composition of 51 ± 1 m/o GaP [3] was chosen. In Fig. 10 the electron and hole concentrations determined by standard Hall measurements on the $In_{0.49}Ga_{0.51}P$ are plotted as a function of the zinc and H_2Se partial pres-

[3] Room-temperature lattice matching between GaAs and $In_{1-x}Ga_xP$ occurs at $x = 0.515$.

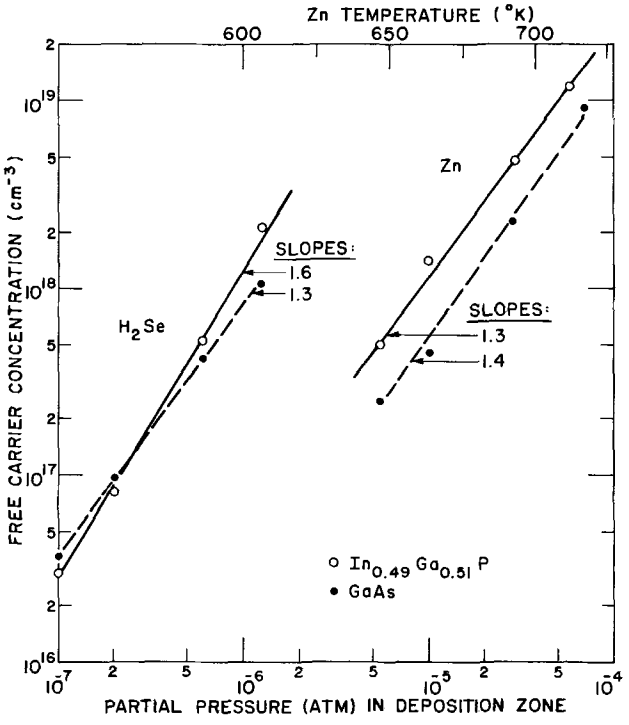

Fig. 10. Hole and electron concentrations in Zn- and Se-doped vapor-grown layers of $In_{0.49}Ga_{0.51}P$ and GaAs grown under similar growth conditions as a function of the zinc and H_2Se partial pressure in the deposition zone. Also shown above the Zn data are the temperatures of the Zn source.

sures in the deposition zone. Also included in Fig. 10 are the carrier concentrations for Zn- and Se-doped GaAs layers deposited under similar growth conditions.

The amount of Zn incorporated into the epitaxial layers was determined by the temperature of an elemental Zn source placed in an auxiliary sidearm to the main deposition chamber (see Fig. 1). In Fig. 10, the Zn partial pressures were calculated under the assumption that the elemental Zn and the hydrogen carrier gas have equilibrated in the Zn sidearm. This has been independently confirmed by measurements of the amount of Zn vaporized with time and the amount of hydrogen flowing over the source.

In general, the carrier concentration is a factor of two to three higher in Zn-doped $In_{0.49}Ga_{0.51}P$ than in GaAs. Since the ionization energy of Zn in these two compounds is not sufficiently large [$E_A \sim 59$ meV in $In_{0.5}Ga_{0.5}P$ (19, 20) and ~ 26 meV in GaAs (21)] to limit the carrier concentration at room temperature, the differences must represent the extent to which Zn is introduced into the respective materials, presumably due to differences in thermodynamic properties or the kinetics by which the impurity is incorporated during the growth processes.

In order to determine if equilibrium is achieved during the incorporation of Zn into our vapor-grown layers, the expected dependence of hole concentration on Zn partial pressure under equilibrium conditions can be independently established and compared with the experimental data of Fig. 10. At thermal equilibrium, the incorporation of Zn into both GaAs and $In_{0.49}Ga_{0.51}P$ can be described by the equation

$$Zn(g) = Zn^- \text{ (crystal)} + h^+ \qquad [3]$$

Since $[Zn^-] = [h^+]$, $[h^+]$ can be expressed in terms of the equilibrium constant, K_{eq}, for reaction [3] and the zinc partial pressure, P_{Zn}, in the deposition zone by the equation

$$[h^+] = (K_{eq} P_{Zn})^{1/2} \qquad [4]$$

Since the slopes of log $[h^+]$ *vs.* log P_{Zn} shown in Fig. 13 are 1.2 and 1.4 for the incorporation of Zn into $In_{0.49}Ga_{0.51}P$ and GaAs, respectively, we must conclude that thermal equilibrium is not established during the deposition process.

For the case of Se-doping, no empirical data exist on the decomposition of H_2Se in our growth system. The partial pressures in Fig. 10 were therefore calculated by assuming the absence of all polyatomic species of Se. Because of the strong dependence of carrier concentration on H_2Se partial pressure, an electronic gas flowmeter was used in conjunction with a micrometer needle valve to achieve reproducible doping of the layers. The incorporation of Se appears to be almost the same for GaAs and for $In_{0.49}Ga_{0.51}P$ over the donor concentrations measured. The slopes of 1.6 and 1.3 for n-type $In_{0.49}Ga_{0.51}P$ and GaAs, respectively, in Fig. 10 indicate that, like Zn incorporation, equilibrium is not achieved during the incorporation of Se. Comparison of the data for Se- and Zn-doping in Fig. 10 show that the incorporation of Se is over an order of magnitude higher than that of Zn at the same dopant partial pressure.

The smooth monotonic curves of Fig. 10 show that Zn- and Se-doping can be well controlled over a relatively wide range of carrier concentrations. Such control has been found to be essential for attaining optimum electroluminescence performance from vapor-grown $In_{1-x}Ga_xP$ p-n junctions (19). Finally, it should be noted that the background doping concentration for both $In_{0.49}Ga_{0.51}P$ and GaAs samples which were not intentionally doped was found to be about 2×10^{15} cm^{-3}.

Alloy Homogeneity

Independent evaluations by a variety of experimental techniques indicate that alloy homogeneity may be an important parameter governing the perfection and luminescence properties of vapor-grown $In_{1-x}Ga_xP$. We have explored this possibility by examining the near-bandgap photoluminescence half-width, x-ray line broadening, optical transmission, and bulk electrical properties of our layers, the results of which are presented below.

Near-bandgap photoluminescence half-width.—In a ternary III-V alloy, the width of the near-bandgap luminescence peak can be increased due to alloy inhomogeneity occurring within the volume of the crystal responsible for the luminescence. Such effects were reported for early $GaAs_{1-x}P_x$ crystals (22), where broadened spontaneous electroluminescence spectra were correlated with an inability to attain laser operation. Similar effects have been observed in our vapor-grown $In_{1-x}Ga_xP$ layers, where a general relationship has been noted for a large number of samples between narrow spontaneous emission spectra and efficient photoluminescence. To confirm this relationship quantitatively, and to separate the effect of doping on the half-width, a series of Zn-doped $In_{0.47}Ga_{0.53}P$ layers with acceptor concentrations of only 4×10^{17} cm^{-3} were prepared over a period of a few weeks. For these samples, room-temperature photoluminescence measurements, shown in Fig. 11, indicated a range of spectral half-widths between 55 and 110 meV. Since the spectral half-width at such low acceptor concentrations is only weakly dependent on doping (23, 24), small unintentional doping variations could not account for the range of half-widths shown in Fig. 11. We, therefore, conclude that the increased half-widths shown here are due to compositional inhomogeneities, and that such inhomogeneities can lead to reductions in the photoluminescence efficiency by as much as three orders of magnitude. The fact that compositional inhomogeneity does exist in our vapor-grown layers, and that it can significantly affect the optical and electrical properties of our material is further corroborated by independent measurements described below.

X-ray line broadening.—Despite the fact that x-ray diffraction patterns of our vapor-grown $In_{1-x}Ga_xP$ layers are typically well resolved in the back reflection into $K\alpha_1$ and $K\alpha_2$ doublets, notable differences are seen be-

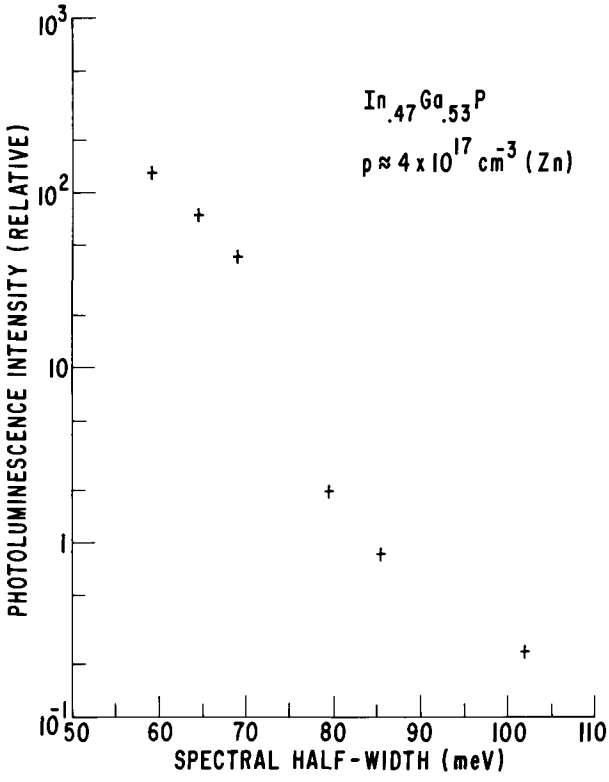

Fig. 11. Variation of the near-bandgap photoluminescence intensity as a function of the spectral half-width for a variety of p-type $In_{0.47}Ga_{0.53}P$ layers grown epitaxially on GaP substrates.

Table IV. Comparison of the x-ray line broadening of vapor-grown $In_{1-x}Ga_xP$ deposited on GaP, $GaAs_{1-x}P_x$ deposited on GaAs, and vapor-grown InP

Sample	Material	Composition*	Mean lattice constant (Å)	Range in lattice constant (Å)**
10001	InP		5.868	0.003
10231	Ga(As,P)	14.8% GaP	5.623	0.004
10232	Ga(As,P)	25.9% GaP	5.601	0.004
10624	(In,Ga)P	61.8% GaP	5.611	0.005
20202	(In,Ga)P	68.0% GaP	5.585	0.006
20014	(In,Ga)P	53.5% GaP	5.646	0.009
20005	(In,Ga)P	58.0% GaP	5.627	0.028

* Graded in alloy composition from the substrate, except for InP.
** Measured for $K\alpha_1$ on the highest angle reflection [(711) for all samples except InP for which (642) was used]; the estimated limit of resolution is ±0.0005Å.

tween the $In_{1-x}Ga_xP$ layers and InP or $GaAs_{1-x}P_x$ deposited by this vapor-growth technique. These differences are summarized in Table IV. The lattice constants were calculated using the highest angle reflection, the (711), except for InP for which the (642) reflection was chosen. The range in lattice constant was estimated from the maximum and minimum diffraction angle of the x-ray diffraction line, and, therefore, is a measure of line broadening. Note that the $In_{1-x}Ga_xP$ samples as a class have the least sharply resolved x-ray lines. In addition, in a few samples, efforts were made to homogenize the InCl and GaCl vapor by the use of baffles in the center zone. Samples 10624 and 20202 have somewhat less broadened lines than samples 20014 and 20005, which is attributed to more thorough mixing of the metal chlorides in the former samples. A clear correlation also was observed between the $In_{1-x}Ga_xP$ line broadening and the near-bandgap photoluminescence intensity, with the better-mixed chlorides consistently resulting in the higher photoluminescence intensities.

Optical transmission.—The optical transmission of several wafers was evaluated. Three representative layers, together with the optical density of the substrate on which they were grown, are plotted as a function of wavelength in Fig. 12. The optical density data have not been corrected for reflection losses. Since the refractive index of GaP ($n = 2.97$) is close to that of InP ($n = 3.3$), we can assume that for GaP-rich alloys the optical density should be close to that for the GaP substrate. Note that there are significant differences in the absorption depending on the degree of mixing of the InCl and GaCl. When the chlorides are mixed, the transmission properties are not far from those of the GaP substrate. The differences in the transmission properties at 9000Å between samples with mixed and unmixed chlorides are almost 40%. This loss would represent a significant attenuation of near-bandgap emission for an electroluminescent structure. Although the mechanism responsible for the increased absorption in the less homogeneous alloys is unknown, two possible causes are refractive index fluctuations and scattering at misfit dislocations.

Electrical properties.—Since the electron mobility is expected to be relatively large for direct energy-gap alloy compositions away from the direct-indirect transition, it should be a sensitive test for the crystalline quality of our layers. A series of Se-doped n-type $In_{0.49}Ga_{0.51}P$ layers were epitaxially deposited on Cr-doped GaAs substrates, as described earlier. Shown in Fig. 13 is the electron mobility of these samples as a function of free-electron carrier concentration both for the case of mixed and unmixed metal chlorides. Although the scatter in the data precludes interpolation of a precise curve, it is apparent that the electron mobilities are consistently higher where the metal chlorides are mixed. This is to be expected since chloride mixing has been shown earlier in this work to lead to more homogeneous alloys. Although the mobility of 1750 cm^2/V-sec at 2×10^{15} cm^{-3} is the highest we have measured in our vapor-grown layers, and is comparable to our results reported elsewhere (20), it is significantly smaller than a value of 2950 cm^2/V-sec at 1.8×10^{17} cm^{-3} reported by Clark (25) for vapor-grown InP deposited on InP substrates, or a value of 2560 cm^2/V-sec at 1.2×10^{17} cm^{-3} determined for Se-doped InP vapor deposited on InP in this work.

The alloy composition, $x = 0.51$, for these samples differs sufficiently from that at the direct-indirect transition ($x \sim 0.7$) (6) to minimize a mobility reduction due to subsidiary indirect conduction-band minima. In addition, since previous mobilty measurements in $GaAs_{1-x}P_x$ (26) indicate that alloy scattering is not prevalent over the direct-bandgap compositional range, the fact that our $In_{0.49}Ga_{0.51}P$ values are significantly lower than that of InP suggests that other scattering processes, perhaps those related to strain or residual inhomogeneity, still exist in the vapor-grown $In_{1-x}Ga_xP$.

Luminescence Properties

As a result of increasing the crystalline perfection of the vapor-grown layers, the resultant radiative properties have been considerably improved, particularly by a large-scale enhancement of the near-bandgap photoluminescence and a concomitant reduction in low-energy infrared emission. $In_{1-x}Ga_xP$ p-n junctions have

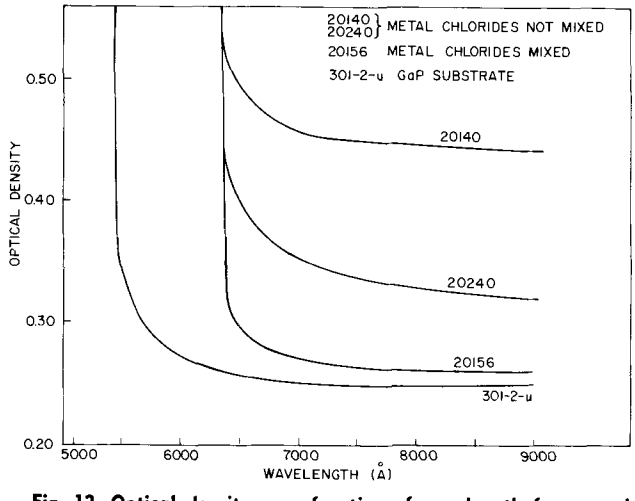

Fig. 12. Optical density as a function of wavelength for several $In_{1-x}Ga_xP$ epitaxial layers which employ mixed and unmixed metal chlorides compared to the GaP substrate on which they were grown.

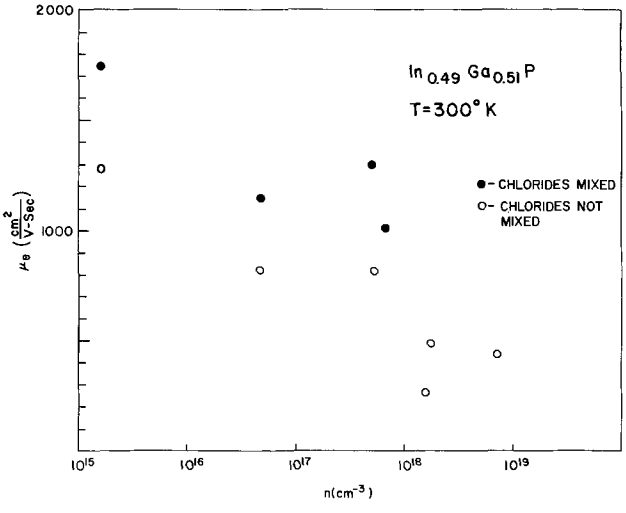

Fig. 13. Room-temperature electron mobilities of Se-doped $In_{0.49}Ga_{0.51}P$ deposited on GaAs as a function of free-electron carrier concentrations for the case of mixed and unmixed metal chlorides.

been prepared *in situ* on GaP substrates by using H_2Se and Zn vapor, as described previously. The electroluminescence emission spectra of diodes prepared from these structures also is primarily bandgap with very weak impurity peaks. This is in sharp contrast to diodes made from earlier vapor-grown (6), solution-grown (27), and melt-grown (27) material prepared in our laboratories. External efficiencies of the vapor-grown diodes have been found to be on the order of 5 to 10 $\times 10^{-4}$ for unencapsulated diodes which emit in the range of 6100-6600Å at room temperature. Brightness values as high as 310 ft-lumens/A-cm^2 were calculated (9) for these diodes. In addition, laser diodes emitting at wavelengths as short as 6105Å with threshold current densities of 4000-6000 A/cm^2 at 80°K have been fabricated (9). Further description and analysis of the luminescence properties of our vapor-grown material as well as a detailed description of the electroluminescent diode characteristics are presented in a companion paper (23).

Summary and Conclusions

An open-tube vapor-growth technique which employs separate transport of the metals as chlorides and PH_3 as the source of phosphorus has been used to deposit single-crystal epitaxial layers of $In_{1-x}Ga_xP$ on GaP substrates. Using precision electronically activated gas-flow controllers, the dependence of composition on deposition temperature and on the relative HCl flows over the metal sources has been determined. Comparison of previously determined kinetic and thermodynamic data with experimental findings in this work show that equilibrium is attained in the metal and deposition zones.

The purity of the vapor-grown layers depends on the growth and reaction temperatures employed. The orientation of the wafer with respect to the gas stream as well as the elimination of ambient gas leaks are found to be important in obtaining large-area macroscopically defect-free epitaxial layers. Evaluation of the photoluminescence half-width, x-ray line broadening, optical transmission, and electron mobility values indicate that alloy homogeneity may be one of the most important parameters governing the perfection and luminescence properties of vapor-grown $In_{1-x}Ga_xP$.

$In_{1-x}Ga_xP$ p-n junctions have been prepared *in situ* by using H_2Se and Zn vapor as the source of donor and acceptor impurities, respectively. Photoluminescence spectra of the as-grown layers consist primarily of an intense near-bandgap peak and a weak low-energy infrared peak which is typically 10-100 times weaker in integrated intensity. Electroluminescence diodes fabricated from the vapor-grown junctions have yielded external quantum efficiencies of up to 0.1% (unencapsulated) and brightness values as high as 310 ft-lumens/A-cm^{-2} for red and orange emission at room temperature.

Acknowledgments

The authors would like to thank E. P. Bertin for the microprobe analyses, R. J. Paff for the x-ray diffraction measurements, W. L. Harrington and E. M. Botnick for the mass spectrometric analyses, and P. Zanzucchi for optical absorption measurements. The technical assistance of J. J. Gannon, J. R. Appert, and H. P. Geyer is greatly appreciated, as also are the many helpful ideas and suggestions made by M. S. Abrahams, V. S. Ban, J. Blanc, M. Ettenberg, I. Kudman, and D. Richman. This research was supported in part by the Office of Naval Research, Arlington, Virginia, under Contract N00014-71-C-0198, and in part by RCA Laboratories, Princeton, New Jersey.

Manuscript submitted Nov. 12, 1972; revised manuscript received March 12, 1973.

Any discussion of this paper will appear in a Discussion Section to be published in the June 1974 JOURNAL.

REFERENCES

1. C. Hilsum and P. Porteous, Ninth International Conference on the Physics of Semiconductors, p. 1214, Nauka, Leningrad (1968).
2. M. R. Lorenz and A. Onton, Proceedings of the Tenth International Conference on the Physics of Semiconductors, p. 444, Cambridge, Mass. (1970).
3. R. J. Archer, *J. Electron. Mater.*, **1**, 128 (1972).
4. B. W. Hakki, Paper 74, presented at Los Angeles Meeting of Electrochem. Soc., May 10-15, 1970.
5. A. Onton and M. R. Lorenz, Proceedings of the Third International Symposium on Gallium Arsenide and Related Compounds, p. 222, Aachen, Germany (1970).
6. C. J. Nuese, D. Richman, and R. B. Clough, *Met. Trans.*, **2**, 789 (1971).
7. H. M. Macksey, N. Holonyak, Jr., D. R. Scifres, R. D. Dupuis, and G. W. Zack, *Appl. Phys. Letters*, **17**, 430 (1970).
8. L. M. Foster and J. E. Scardefield, *This Journal*, **117**, 534 (1970).
9. C. J. Nuese, A. G. Sigai, and J. J. Gannon, *Appl. Phys. Letters*, **20**, 431 (1972).
10. V. Ban and M. Ettenberg, *J. Chem. Phys. Solids*, To be published.
11. C. J. Nuese, J. J. Tietjen, J. J. Gannon, and H. F. Gossenberger, *This Journal*, **116**, 248 (1969).
12. A. G. Sigai, M. S. Abrahams, and J. Blanc, *ibid.*, **119**, 952 (1972).
13. M. Ettenberg, A. G. Sigai, A. Dreeben, and S. L. Gilbert, *ibid.*, **118**, 1355 (1971).
14. D. R. Bosomworth, R. S. Crandall, and R. E. Enstrom, *Phys. Letters*, **28**, 320 (1968).
15. W. G. Oldham, *Electrochem. Technol.*, **3**, 57 (1965).
16. V. S. Ban, *This Journal*, **118**, 1473 (1971).
17. A. E. Blakeslee, *Trans. AIME*, **245**, 577 (1969).
18. M. S. Abrahams, L. R. Weisberg, C. J. Buiocchi, and J. Blanc, *J. Materials Sci.*, **4**, 223 (1969).
19. H. Kressel, C. J. Nuese, and I. Ladany, *J. Appl. Phys.*, To be published.
20. R. E. Enstrom, C. J. Nuese, V. S. Ban, and J. R. Appert, *Trans.* Fourth Int. Symp. on GaAs and Related Compounds, p. 37, Boulder, Colorado (1972).
21. J. C. Sarace, R. H. Kaiser, J. M. Whelan, and R. C. C. Leite, *Phys. Rev.*, **137**, 623 (1965).
22. M. H. Pilkuhn and H. Rupprecht, *Trans. Met. Soc. AIME*, **230**, 282 (1964).
23. C. J. Nuese, A. G. Sigai, M. S. Abrahams, and J. J. Gannon, *This Journal*, **120**, 956 (1973).
24. D. A. Cusano, *Solid-State Commun.*, **2**, 353 (1964).
25. R. C. Clark, B. D. Joyce, and W. H. E. Wilgoss, *ibid.*, **8**, 1125 (1970).
26. J. J. Tietjen and L. R. Weisberg, *Appl. Phys. Letters*, **7**, 261 (1965).
27. I. Kudman and C. J. Nuese, To be published.

Vapor Growth of $In_{1-x}Ga_xP$ for P-N Junction Electroluminescence

II. Luminescence Characteristics

C. J. Nuese, A. G. Sigai,*[1] M. S. Abrahams, and J. J. Gannon

RCA Laboratories, Princeton, New Jersey 08540

ABSTRACT

$In_{1-x}Ga_xP$ epitaxial layers, prepared by an improved vapor-phase growth technique, have been evaluated by photoluminescence measurements and by transmission electron microscopy. Maximum photoluminescence intensities for Se- and Zn-doped $In_{1-x}Ga_xP$ layers ($0.5 \lesssim x \lesssim 0.6$), are observed at carrier concentrations of 1×10^{17} and 3×10^{18} cm^{-3}, respectively. At higher concentrations, a severe degradation in the photoluminescence intensity occurs, concurrent with the appearance (by TEM) of precipitates in concentrations of about 10^{14} cm^{-3}. For Zn-doped $In_{1-x}Ga_xP$, the precipitate has been identified as Zn_3P_2 from its electron diffraction pattern. The luminescence spectra from the vapor-grown layers at 300°K consist of a high-energy peak, attributed to band-to-band recombination, and a low-energy peak, located 0.4 to 0.5 eV less than bandgap. The low-energy peak increases with Se donor concentration and with alloy composition, x, but is typically orders of magnitude less intense than the bandgap peak. Electroluminescent p-n junctions prepared with optimum donor and acceptor concentrations have yielded external quantum efficiencies between 5 and 10×10^{-4} (unencapsulated) for emission between 6150 and 6600Å. From such junctions, laser diodes have been fabricated which emit orange coherent radiation between 6105 and 6150Å with threshold currents as low as 4000 A/cm² (at 77°K).

Visible-light-emitting junctions previously have been prepared (1) in vapor-grown $In_{1-x}Ga_xP$ layers both by Zn-diffusion techniques and by the sequential introduction of donor and acceptor impurities during growth. The performance of the junctions prepared by either technique was poor in the early vapor-grown material (1), as evidenced by low quantum efficiencies of 10^{-5}-10^{-6} and large infrared contributions to the electroluminescence spectra. Nonetheless, the attractiveness of direct energy gaps approaching 2.2 eV (2-4) and a high-brightness capability (5) in this alloy system have prompted a renewed examination of vapor-grown $In_{1-x}Ga_xP$ for electroluminescent diodes.

In the first part of our recent study (6), refinements in the $In_{1-x}Ga_xP$ vapor-growth technology have been described which result in epitaxial layers with significantly improved compositional homogeneity and crystalline perfection, as well as reduced impurity contamination relative to our earlier vapor-grown layers. In the present paper, we treat in detail the optimization of donor and acceptor concentrations used for the vapor-grown p-n junctions, and describe the photoluminescence and electroluminescence characteristics of these structures. We will further show that such optimization can lead to $In_{1-x}Ga_xP$ spontaneous-light-emitting diodes with room-temperature external quantum efficiencies of 10^{-3} between 6100 and 6600Å, and laser diodes which emit coherent orange radiation at 80°K with threshold current densities between 4000 and 6000 A/cm².

Photoluminescence

Although the ultimate objective of our research program has been the fabrication of efficient electroluminescent diodes of $In_{1-x}Ga_xP$, we have relied heavily on a photoluminescence evaluation of both n- and p-type material prior to p-n junction formation, since this simple and rapid technique has been found to reveal a considerable amount of information about the luminescence characteristics of the material. In addition, as we will indicate later in this paper, a strong and consistent correlation has been observed between the "quality" of a particular $In_{1-x}Ga_xP$ layer based on a photoluminescence evaluation and the ultimate performance of similarly prepared junction structures evaluated as electroluminescent diodes.

Our photoluminescence measurements utilize the 5145Å radiation from a pulsed (2W peak power) argon laser, which is focused to a spot size on the order of 0.25 mm. For our apparatus, approximately 0.5W (peak power) of 5145Å radiation is absorbed in the sample after the laser beam is passed through an interference filter and reflected from the shiny surface of the semiconductor. The power absorbed per unit area is about 1000 W/cm², which, for an assumed absorption coefficient of 10^{-4} cm^{-1}, results in a carrier generation rate of 2×10^{25} electron-hole pairs/cm³-sec. For a typical electroluminescent junction, a current density of about 400 A/cm² would be required[2] to generate electron-hole pairs at this rate; hence our pulsed laser source is clearly capable of pumping the semiconductor samples to relatively high excitation levels. A duty cycle of about 0.1% is used to avoid heating effects at this power density.

The as-grown surface condition of the epitaxial layers was found to be sufficient to allow photoluminescence measurements to be taken without first treating the surfaces. In cases where a bromine-methanol-phosphoric etch (6) was used to remove selected portions of the $In_{1-x}Ga_xP$ layers, the photoluminescence characteristics were not altered appreciably by the etching process. This observation is consistent with the relatively low surface recombination velocity previously reported for solution-grown $In_{1-x}Ga_xP$ (7).

Typical photoluminescence emission spectra at room temperature are shown in Fig. 1 for a heavily and lightly doped n-type sample of vapor-grown $In_{1-x}Ga_xP$ with x equal to 0.56 and 0.53, respectively. In both cases, the high-energy near-bandgap peak is shown to dominate the emission spectra, although a broad low-energy infrared peak is also evident at an energy position about 0.4-0.5 eV less than bandgap, especially for the more heavily doped sample. Some of the character-

* Electrochemical Society Active Member.

[1] Present address: Xerox Research Laboratories, Webster, New York 14580.

Key words: $In_{1-x}Ga_xP$, vapor-phase growth, p-n junctions, precipitation, photoluminescence, electroluminescence, lasers.

[2] This estimate assumes a minority carrier diffusion length of 1 μm and a forward voltage of 2V.

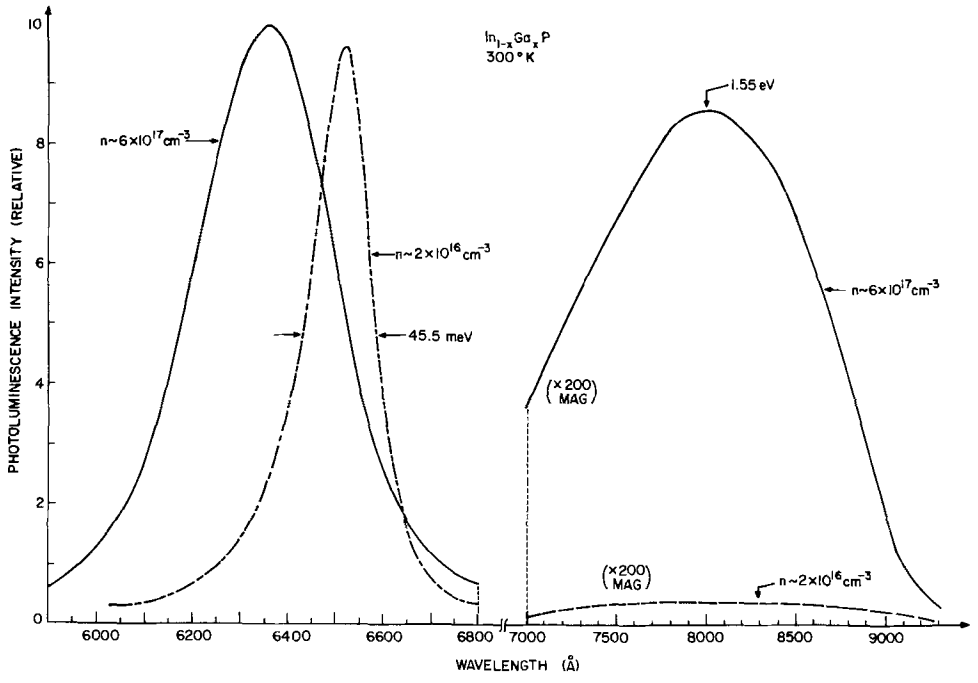

Fig. 1. Typical photoluminescence emission spectra from n-type $In_{1-x}Ga_xP$ vapor-grown layers. Solid curve is for Se-doped sample with $n \sim 6 \times 10^{17}$ cm^{-3} and $x \sim 0.56$. Dashed curve is for undoped sample with $n \sim 2 \times 10^{16}$ cm^{-3} and $x \sim 0.53$.

istics of the near-bandgap peak and the low-energy infrared peak in Fig. 1 are discussed further in a subsequent section of this paper.

Optimization of Donor and Acceptor Concentrations

The refinements in the growth conditions discussed in the first portion of our study (6) would be expected to reduce the introduction of undesired nonradiative recombination centers into the vapor-grown layers. In this section, we describe experiments designed to determine the optimum donor and acceptor concentrations for efficient radiative recombination. The enhancement of the radiative recombination rates which arises due to such an optimization should contribute to a further improvement in the luminescence conversion processes, resulting in brighter electroluminescent diodes.

In order to optimize the impurity concentrations for our vapor-grown $In_{1-x}Ga_xP$, a series of n- and p-type epitaxial layers with selected donor (Se) and acceptor (Zn) concentrations were deposited on single-crystal GaP substrates. For these samples, the alloy composition in the epitaxial layer was graded smoothly between the GaP substrate and the desired final portion of the epitaxy (where $x \sim 0.5$-0.6) at a rate of typically 1-2% InP/μm. The carrier concentrations were determined by standard Hall measurements taken on $In_{1-x}Ga_xP$ layers similarly deposited on semi-insulating Cr-doped GaAs substrates. The manner in which the carrier concentrations were controlled has been described previously (6).

For each of the Se-doped samples, photoluminescence spectra similar to those in Fig. 1 were obtained at room temperature. The relative intensity of the dominant near-bandgap high-energy peak was then plotted as a function of the measured electron concentration, as shown in Fig. 2. For electron concentrations between 10^{16} and 10^{17} cm^{-3}, the photoluminescence intensity increases approximately linearly, as expected. However, for concentrations increasing between 10^{17} and 2×10^{18} cm^{-3}, the photoluminescence intensity falls off by about two orders of magnitude. The maximum intensity occurs at a value of about 1×10^{17} cm^{-3}, which is appreciably lower than the optimum concentrations we have observed for electroluminescence in vapor-grown layers of GaAs (8) or $GaAs_{1-x}P_x$ (9), or that for cathodoluminescence in solution-grown samples of GaAs (10).

The reduction in the photoluminescence intensity at moderately large donor concentrations in Fig. 2 correlates well with a surface degradation observed microscopically, as illustrated in the photomicrographs of Fig. 3a and b. Here, the surface appearance of a Se-doped $In_{1-x}Ga_xP$ layer with a donor concentration of 8×10^{16} cm^{-3} (sample I in the photoluminescence data of Fig. 2) is compared with that for a similarly prepared $In_{1-x}Ga_xP$ layer doped with Se to a concentration of 5×10^{17} cm^{-3} (sample II in Fig. 2). The surface of the more heavily doped sample appears to be decorated orthogonally along <110> directions, although the preponderance of this structure is unidirectional (*i.e.*, lies in the horizontal direction in Fig. 3b). This is in sharp contrast to the unblemished surface of the more lightly doped sample. Surface imperfections such as those apparent in Fig. 3b were observed on n-type vapor-grown $In_{1-x}Ga_xP$ layers only when doped with Se to concentrations greater than about 5×10^{17} cm^{-3}.

Samples I and II of Fig. 2 also were examined by transmission electron microscopy (TEM). For this evaluation, the epitaxial layers were first thinned to 25 μm by chemical-mechanical polishing, after which they were further thinned to about 0.2 μm by an ion plasma etching technique (11). An RCA EMU-3G transmission

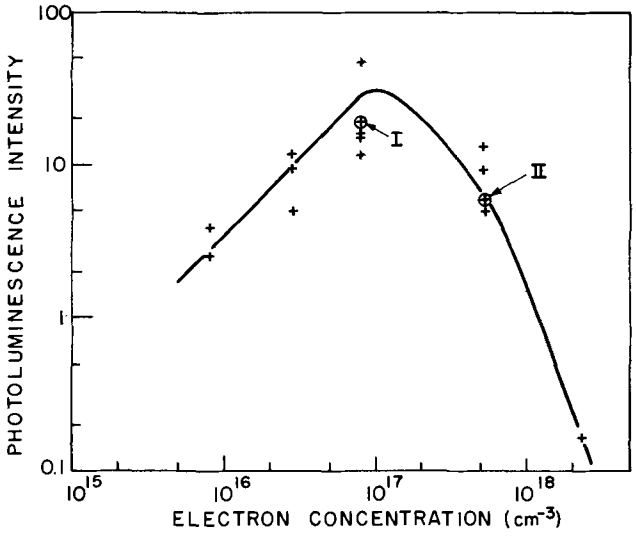

Fig. 2. Room temperature photoluminescence intensity vs. free electron concentration for Se-doped vapor-grown layers of $In_{1-x}Ga_xP$ with $x \sim 0.5$-0.6. Electron concentrations were determined from Hall measurements. Microscope evaluation of samples I and II are illustrated in Fig. 3.

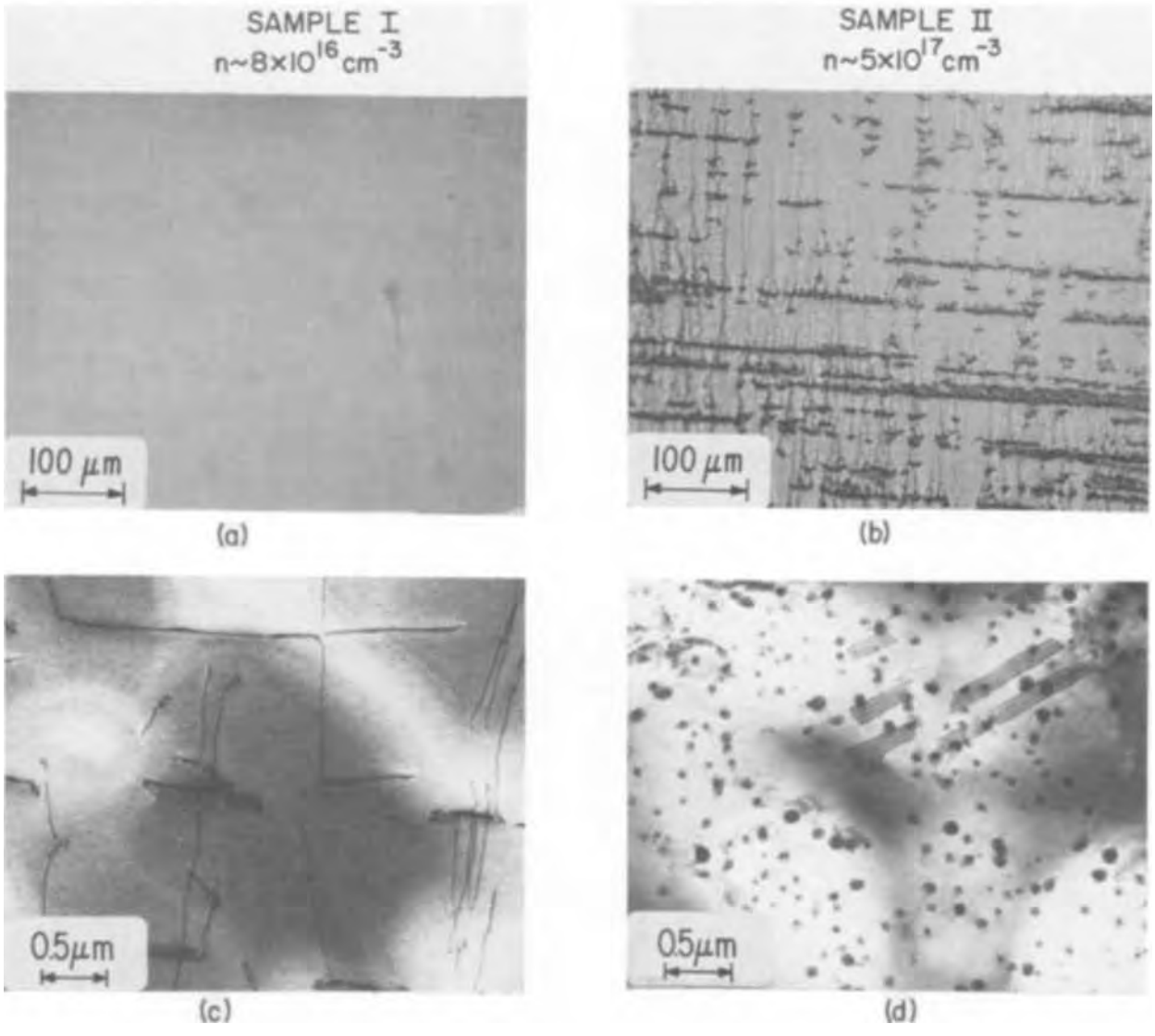

Fig. 3. Optical photomicrographs (a and b) and transmission electron micrographs (c and d) of Se-doped $In_{1-x}Ga_xP$ layers. For sample I, $n \sim 8 \times 10^{16}$ cm^{-3}. For sample II, $n \sim 5 \times 10^{17}$ cm^{-3}. The photoluminescence response of samples I and II are indicated in Fig. 2.

electron microscope was then used to determine the imperfection morphology of the $In_{1-x}Ga_xP$ layers. For each of the samples discussed in this paper, the electron beam was transmitted through the crystal in a direction parallel to the [100] growth direction.

In Fig. 3c we illustrate a transmission electron micrograph taken from sample I ($n = 8 \times 10^{16}$ cm^{-3}). The portion of the epitaxial layer illustrated here was located in the uppermost region of the compositional grading layer (just prior to the junction-containing constant-composition region), which accounts for the expected orthogonal array of "grading" or misfit dislocations (12). More importantly, however, is the fact that there is no evidence of second-phase precipitates in sample I, which is in sharp contrast to the numerous imperfections of this type illustrated in Fig. 3d for the more heavily doped $In_{1-x}Ga_xP$ specimen (sample II). The dark circular particles in Fig. 3d are thought to be precipitates, since their contrast was found to reverse when standard dark-field imaging was employed. The precipitates in Fig. 3d are as large as 700Å and occur with a density of about 10^{14} cm^{-3}. Positive identification of the precipitates could not be made, however, since no extra spots appeared in the electron diffraction pattern for sample II; hence the nature of the precipitates is unknown.

Also shown in Fig. 3d are stacking faults, which occur with a linear density of about 3×10^3 cm^{-1}. The projection of these faults on the (100) plane (as shown in Fig. 3d) was found to be predominantly parallel to one of the two orthogonal [011] directions, much as was the surface structure shown in Fig. 3b.

In previous luminescence studies with other III-V compounds (8-10, 13), a decrease in the luminescence efficiency at high donor concentrations has been attributed to the generation of nonradiative recombination centers associated with precipitation of the dopant impurity. In particular Ga_2Te_3 precipitates have been identified at Te concentrations greater than about 3×10^{18} cm^{-3} in GaAs layers prepared by liquid-phase epitaxy (13). At this stage of our investigation, we cannot conclusively specify whether the precipitates or the stacking faults, or both, in Fig. 3d are responsible for the photoluminescence degradation observed at moderately large Se concentrations. However, based on the presence of stacking faults in three of the four samples ultimately described in this section, even in a lightly doped p-type sample where no photoluminescence or surface degradation was observed, we suspect the precipitates as the primary cause of the degradation found at moderately large Se concentrations. The stacking faults may be related to residual work damage in the substrates.

In order to similarly examine the effects of Zn doping concentrations on the photoluminescence characteristics, a series of eight Zn-doped $In_{1-x}Ga_xP$ layers ($x \sim 0.5$-0.6) with acceptor concentrations between 5×10^{17} cm^{-3} and 1×10^{19} cm^{-3} were deposited epi-

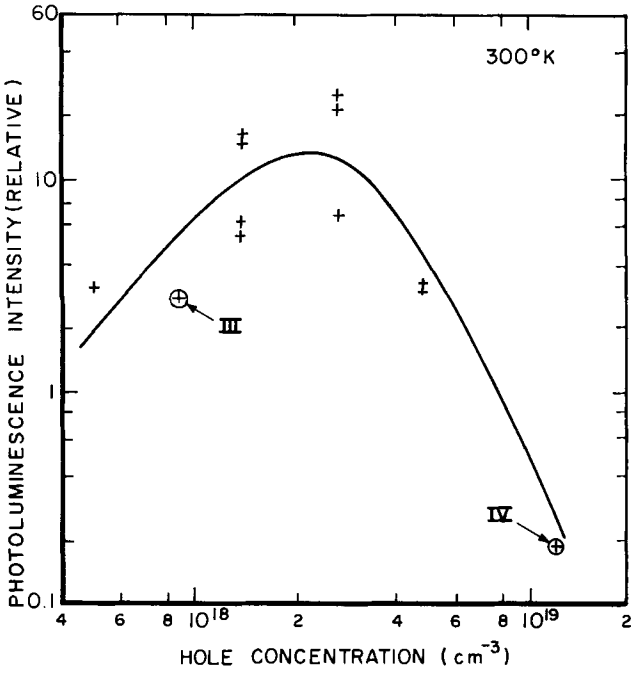

Fig. 4. Room temperature photoluminescence intensity vs. free hole concentration for Zn-doped vapor-grown layers of $In_{1-x}Ga_xP$ with $x \sim 0.5$-0.6. Hole concentrations were determined from Hall measurements. Microscopic evaluation of samples III and IV are illustrated in Fig. 5.

taxially on GaP substrates. The near-bandgap photoluminescence intensity for these samples is illustrated in Fig. 4 as a function of the measured $In_{1-x}Ga_xP$ hole concentrations. As shown here, the photoluminescence intensity increases with increasing Zn concentrations between 5×10^{17} and 3×10^{18} cm^{-3}, but drops by nearly two orders of magnitude for Zn concentrations increased further to values as large as 1.2×10^{19} cm^{-3}. At the optimum acceptor concentration of 3×10^{18} cm^{-3} the photoluminescence intensity was comparable in magnitude to that for the Se-doped $In_{1-x}Ga_xP$ layers doped to the optimum donor concentration of about 1×10^{17} cm^{-3}.

From the photoluminescence data of Fig. 4, it is clear that diffusion conditions which result in large Zn concentrations near the p-n junction should be avoided in vapor-grown $In_{1-x}Ga_xP$. The fact that Holonyak and co-workers (14) have found that improved electroluminescent junctions can be prepared in melt-grown $In_{1-x}Ga_xP$ by utilizing an In(90%)-Zn(10%) source (to reduce the surface concentration of Zn in the diffused wafer) is consistent with our data, and suggests that the doping dependence of the luminescence efficiency shown in Fig. 4 may be applicable to p-type $In_{1-x}Ga_xP$ prepared by other crystal growth techniques.

As was the case for the Se-doped $In_{1-x}Ga_xP$ layers, the fall-off in the photoluminescence intensity at high Zn carrier concentrations was accompanied by a degradation of the surface appearance of the epitaxial layers, as shown in Fig. 5a and b. Here, the surface appearance of a lightly Zn-doped $In_{1-x}Ga_xP$ vapor-grown layer (sample III in the photoluminescence data of Fig. 4) is compared with that for a similarly grown layer doped with Zn to a carrier concentration of about 1×10^{19} cm^{-3} (sample IV in Fig. 4). The surfaces are very similar to those previously illustrated for small and large donor concentrations in Se-doped $In_{1-x}Ga_xP$ layers. Notably, the heavy Zn-doping in Fig. 5b has resulted in an orthogonal array of disturbances which lie parallel to both [011] directions in the (100) planes, but the surface of the sample with lighter Zn doping ($\sim 1 \times 10^{18}$ cm^{-3}) is not perceptibly disturbed.

To determine the cause of the surface deterioration and the photoluminescence degradation at high Zn doping concentrations, the two samples illustrated in Fig. 5a and b also were examined by transmission electron microscopy. A transmission electron micrograph of the Zn-doped constant-composition layer of sample III ($p = 1 \times 10^{18}$ cm^{-3}) is shown in Fig. 5c. The inclined dislocations observed here are typical of a vapor-grown constant composition layer that has been deposited above a compositional grading region. The specimen also was found to contain stacking faults whose density was 1×10^3 cm^{-1} and whose intersections with the (100) specimen surface were parallel to both the [011] and [01$\bar{1}$] directions. In this sample there was no evidence for precipitates, which was also the case for the lightly doped (Se) n-type $In_{1-x}Ga_xP$ layer discussed previously (Fig. 3).

Sample IV was also Zn-doped, but with a carrier concentration of 1×10^{19} cm^{-3}. A transmission electron micrograph of this sample is shown in Fig. 5d. The black circular features are precipitates, which have a diameter of about 500Å and a density of 1×10^{14} cm^{-3}.

The precipitated phase in Fig. 5d was identified as Zn_3P_2 from an electron diffraction pattern obtained from the same region of the specimen as that shown in Fig. 5d. In addition to the normal 100 matrix spot pattern, additional spots (sometimes defining portions of rings) also were seen, due to the presence of the precipitates. The interplanar spacings (d-spacings) of the extra reflections are presented in Table I. Here, we see that the observed values of the d-spacings agree with the reported values for tetragonal Zn_3P_2 to better than 3%. Dark-field imaging of the extra spots and partial rings was observed to cause contrast reversal of the precipitates in Fig. 5d, showing that the extra reflections arise from the precipitates.

It is reasonable to assume that the Zn_3P_2 will be oriented in the $In_{1-x}Ga_xP$ matrix so as to minimize the misfit energy at the interface between the precipitate and the matrix. In order to determine this orientation, we have compared the observed values of d for Zn_3P_2 with the calculated d-spacings for the $In_{1-x}Ga_xP$ sample IV ($x = 0.48$; $a_0 = 5.667$Å). From such a comparison, we find equivalent values for d_{220} of $In_{0.52}Ga_{0.48}P$ and d_{400} of Zn_3P_2: for d_{200} of $In_{0.52}Ga_{0.48}P$ and d_{220} of Zn_3P_2, and for d_{011} of $In_{0.52}Ga_{0.48}P$ and d_{002} of Zn_3P_2. These correspondences indicate that the Zn_3P_2 tetragonal crystals can be incorporated into the $In_{0.52}Ga_{0.48}P$ with minimal misfit strain with one unit cell of Zn_3P_2 replacing four unit cells of $In_{0.52}Ga_{0.48}P$. We should stress, however, that the orientation of the Zn_3P_2 described here is based on the lattice parameter for $In_{1-x}Ga_xP$ at $x = 0.48$, the composition of sample IV. At significantly different alloy compositions, the precipitates could not be expected, *a priori*, to orient identically.

Finally, stacking faults also were seen in sample IV, whose traces on (100) were parallel to both [011] and [01$\bar{1}$]. The faults were observed in approximately

Table I. Reported and measured values of the interplanar spacing for tetragonal Zn_3P_2

hkl	d-values	
	Reported*	Measured
202	3.29	3.35
		2.92
004, 220	2.84	
		2.75
204	2.32**	2.39
400, 224	2.01	2.025
422, 206	1.72	1.76
008	1.42	1.45
426, 602	1.31	1.31
408, 624	1.16	1.17
4210, 646	0.963	0.982
22$\bar{1}$2	0.901	0.921
40$\bar{1}$2	0.859**	0.868
22$\bar{1}$4	0.783**	0.808

* ASTM 2-1264.
** Calculated using a = 8.04Å; c = 11.4Å.

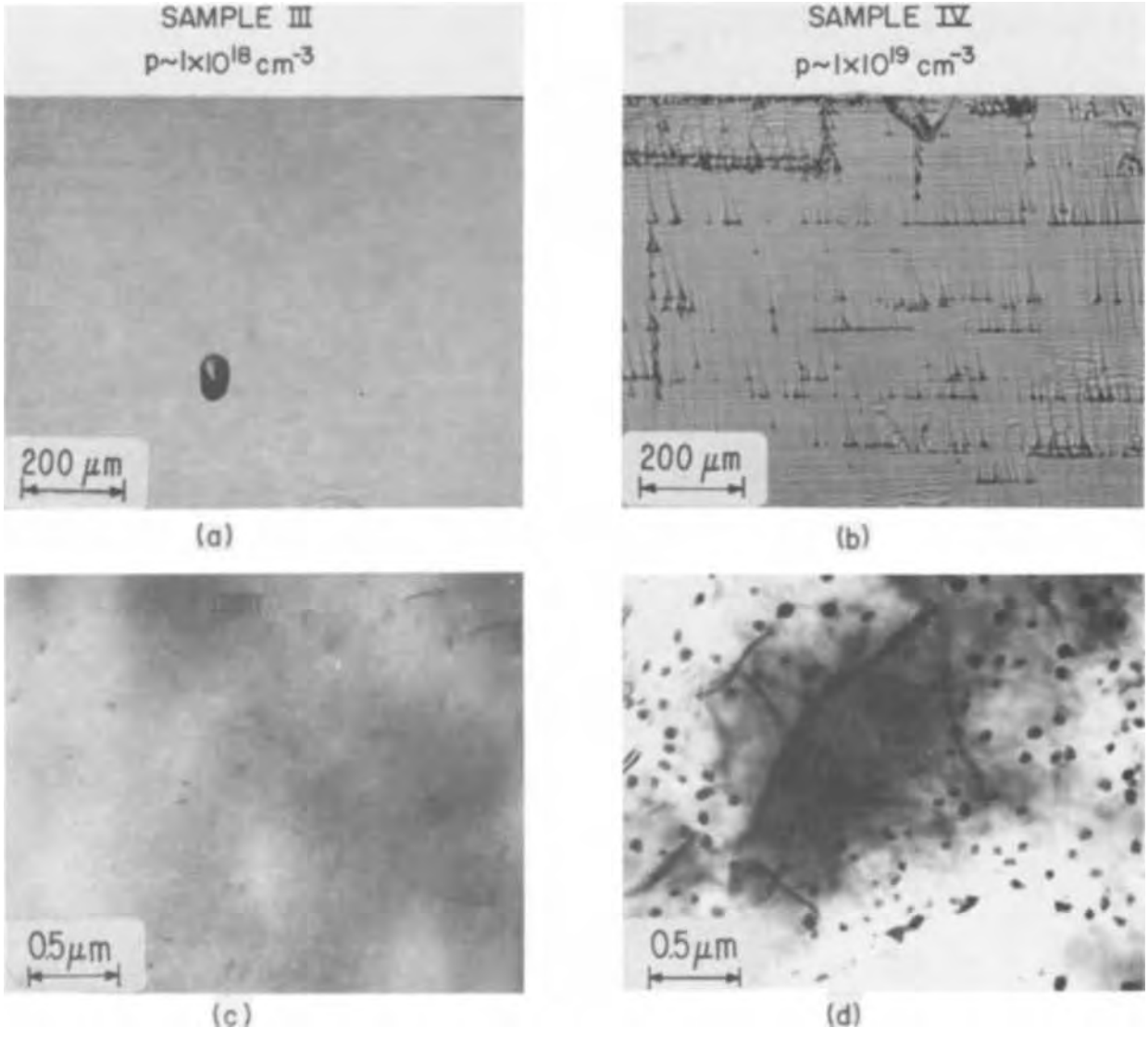

Fig. 5. Optical photomicrographs (a and b) and transmission electron micrographs (c and d) of Zn-doped $In_{1-x}Ga_xP$ layers. For sample III, $p \sim 1 \times 10^{18}$ cm^{-3}; for sample IV, $p \sim 1 \times 10^{19}$ cm^{-3}. The photoluminescence response of samples III and IV are illustrated in Fig. 4.

equal densities (1×10^4 cm^{-1}) in each of these directions.

A summary of the photoluminescence intensity, surface appearance, and TEM evaluation of samples I through IV is given in Table II. From this table (or from Fig. 3 and 5), it is clear that precipitates are formed at moderate-to-large donor and acceptor concentrations in Se- and Zn-doped vapor-grown $In_{1-x}Ga_xP$. Table II also illustrates the strong correlation between the presence of the precipitates and a degradation in the surface appearance and the photoluminescence efficiency of the layers. Since the density of the precipitates for both the Se- and Zn-doped $In_{1-x}Ga_xP$ is about 10^{14} cm^{-3}, the mean separation between precipitates is only 0.2 μm, which is probably much smaller than the minority carrier diffusion lengths. Hence, it is not surprising that the precipitates would have an adverse effect on the recombination processes. It is not clear why these dopants have such adverse effects on the crystalline perfection at the somewhat modest doping concentrations observed here. We speculate that the incorporation of the dopants to date is limited by the relative perfection of the crystalline lattice during vapor-growth. In this regard, the present epitaxial layers are known to be somewhat strained by the observation of bowing in the substrate-epitaxy composite following growth, and by the ease with which the structures cleave on thinning with standard lapping and polishing techniques. Since the radiative recombination lifetime is inversely proportional to the active carrier concentrations, it is important that future efforts be concerned with increasing the

Table II. Evaluation of Se and Zn doping concentrations in $In_{1-x}Ga_xP$

Sample	x	Dopant	n,p (cm^{-3})	Photo-luminescence intensity	Surface appearance	Faults (cm^{-3})	Precipitates (cm^{-3})
I	0.61	Se	8×10^{16}	Normal	Excellent	N.D.*	N.D.
II	0.56	Se	5×10^{17}	Poor	Poor	3×10^3	10^{14}
III	0.58	Zn	1×10^{18}	Normal	Excellent	1×10^3	N.D.
IV	0.48	Zn	1×10^{19}	Poor	Poor	1×10^4	10^{14} (Zn_3P_2)

* N.D. denotes none detected.

donor and acceptor concentrations that can be incorporated into the $In_{1-x}Ga_xP$ layers without adversely affecting their crystalline perfection.

Spectral Characteristics

In an earlier section, we illustrated (Fig. 1) typical photoluminescence spectra for n-type $In_{1-x}Ga_xP$, and showed that the emission contained two spectral peaks, a narrow intense near-bandgap peak in the visible region of the spectrum and a weak but broad infrarad peak located 0.4-0.5 eV less than the bandgap energy. In this section, we examine some of the parameters which have been found to affect the properties of both types of peaks.

Near-bandgap emission.—The dependence of the near-bandgap photoluminescence peak on alloy composition (as determined by x-ray diffraction measurements) for our recent vapor-grown samples is illustrated in Fig. 6. For $In_{1-x}Ga_xP$ layers with x less than about 0.60, the data closely follow the quadratic equation

$$E(x) = 1.35 + 0.735x + 0.70x^2 \quad [1]$$

which was previously obtained by Stringfellow (15) from photoluminescence measurements on $In_{1-x}Ga_xP$ layers prepared by liquid-phase epitaxy. For values of x greater than about 0.6, the peak energy tends to fall below the value given by Eq. [1], in closer agreement to the quadratic dependence noted by Lorenz and Onton (3). The departure from Eq. [1] noted in Fig. 6 near $x = 0.6$ is very similar to that recently observed by McVittie (16) for liquid-phase $In_{1-x}Ga_xP$. A higher energy peak noted by Mabbitt *et al.* (17) when high-purity (six 9's) In and Ga were used as the sources was not observed for our vapor-grown $In_{1-x}Ga_xP$, even though the purity of our metal sources was also as high as can be obtained commercially (six 9's).

The highest energy value observed for our photoluminescence peaks was 2.238 eV at an alloy composition of $x = 0.752$. This data point and another at $x = 0.743$ lie slightly below the curves in Fig. 6, probably

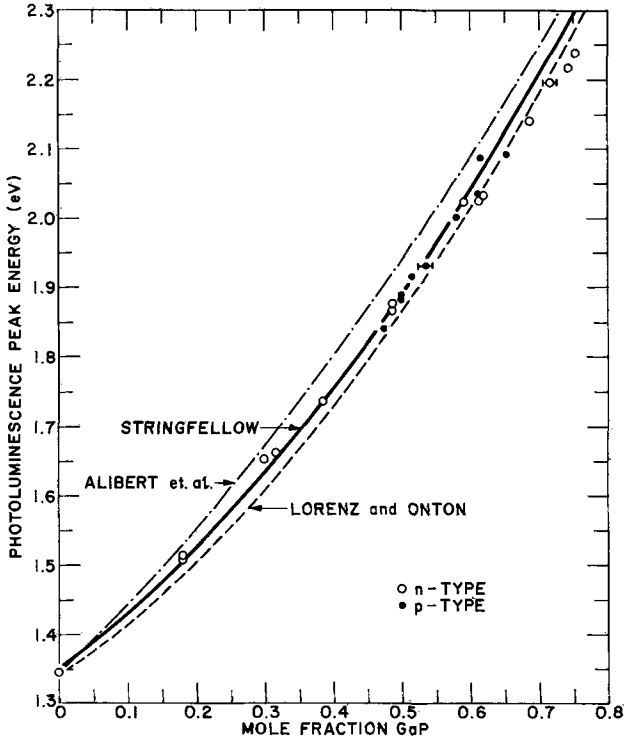

Fig. 6. Photoluminescence emission peak at 300°K for $In_{1-x}Ga_xP$ vapor-grown layers vs. mole fraction GaP in alloy. The solid curve is from photoluminescence measurements on LPE epitaxial $In_{1-x}Ga_xP$ by Stringfellow (15), and is given by Eq. [1] in the text. The upper and lower curves are from Ref. (34) and (3), respectively.

due to distortion caused by the lower energy indirect conduction band minima at these compositions. Direct bandgap recombination has been similarly observed (18, 19) in alloys of $GaAs_{1-x}P_x$ that have compositions slightly on the indirect side of the direct-indirect transition. The phenomenon occurs because of the more efficient recombination from the direct bandgap minimum and the small but finite electron population in the direct conduction band minimum, even when its energy is higher than that of the subsidiary indirect minima.

The fact that the photoluminescence energy at 300°K is approximately the same for both n-type (Se) and p-type (Zn) $In_{1-x}Ga_xP$ is surprising since the donor and acceptor ionization energies in vapor-grown $In_{0.49}Ga_{0.51}P$ have been found to differ substantially (~59 meV for Zn; ~8 meV for Se) (20, 21), and since radiative transitions involving these impurity states would be expected to predominate in extrinsic material. The electroluminescence spectra are indeed shifted to lower energies by typically 30-50 meV relative to the photoluminescence spectra, however, this shift is due to selective high-energy absorption of the junction emission, as evidenced by the fact that photoluminescence peaks on the n- and p-sides of p-n junction structures do not differ substantially in energy, consistent with the trend in Fig. 6. These results suggest that band-to-band or exciton recombination processes (rather than conduction band-acceptor transitions) occur in the p-type vapor-grown layers, perhaps as a result of the relatively light doping concentrations employed here. The fact that the dominant radiative recombination at room temperature is band-to-band in p-type $In_{1-x}Ga_xP$ has been confirmed by Bachrach and Hakki (22) for liquid-phase layers and by Kressel *et al.* (21) for vapor-grown layers.

The emission energy and the spectral half-width of the near-bandgap peak also would be expected to vary significantly with doping concentration due to the interaction of the impurity atoms at high doping concentrations. In a ternary alloy, such as $In_{1-x}Ga_xP$, the dependence of the peak emission energy on doping concentration is difficult to ascertain due to difficulty in precisely controlling the nominal composition of the alloy during crystal growth. However, the spectral broadening which occurs due to the smearing of the conduction or valence band edges with donor or acceptor states, respectively, can be evaluated, even when the alloy composition varies slightly from wafer to wafer. In Fig. 7 we illustrate this dependence for the series of Se-doped (n-type) and Zn-doped (p-type) $In_{1-x}Ga_xP$ vapor-grown layers that were used for the optimization of the photoluminescence intensity on donor and acceptor concentrations (Fig. 2 and 4, respectively). Two effects are apparent here. First, for a given carrier concentration, the half-widths span a range of values (*e.g.*, the half-widths vary between 80 and 100 meV for Se-doped $In_{1-x}Ga_xP$ samples doped to a carrier concentration of 5×10^{17} cm^{-3}). This spread is almost certainly due to fluctuations in the compositional homogeneity of the layers, as discussed in more detail in the first paper (6) of our recent study. Second, for both n- and p-type samples, the spectral half-widths of our vapor-grown $In_{1-x}Ga_xP$ increase more rapidly with doping than do the half-widths previously reported for n- (10, 23) and p-type (10) GaAs at room temperature. At low doping concentrations, the half-widths of our samples are close to those for lightly doped GaAs (40 meV).

Although the GaAs curves in Fig. 7 were taken with electron beam excitation, the difference in penetration depths (2-4 μm for the electron beam excitation, 0.5-1 μm for our laser excitation) for our photoluminescence and the previous cathodoluminescence would not be able to account for the differences illustrated in Fig. 7. To confirm this, photoluminescence measurements also were taken on a series of about 10 vapor-grown Zn-doped GaAs layers for which Hall measurements had

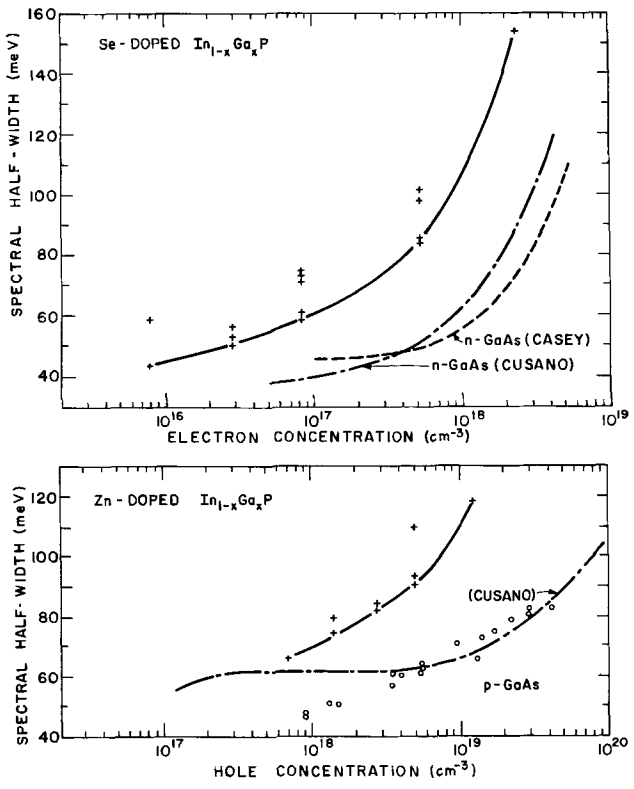

Fig. 7. Spectral half-width at room temperature vs. free carrier concentration for Se-doped (top) and Zn-doped (bottom) $In_{1-x}Ga_xP$ with $x \sim 0.5$-0.6. The dashed curves in the top figure are from cathodoluminescence measurements by Cusano (10) and by Casey and Kaiser (23). The open circles in the bottom figure are from our photoluminescence measurements on Zn-doped vapor-grown GaAs.

been previously taken.[3] As indicated by the round data points in the bottom graph of Fig. 7, photoluminescence measurements taken with the same apparatus as that used for the $In_{1-x}Ga_xP$ show that the disparity in the dependence of spectral half-width on impurity concentration for p-type $In_{1-x}Ga_xP$ and GaAs is genuine. It remains for us to determine whether this difference is fundamentally related to the structure of the energy bands and impurity states in $In_{1-x}Ga_xP$ or to residual inhomogeneity in our present vapor-grown layers.

Low-energy emission.—In an early section of this paper, we illustrated (Fig. 1) that the photoluminescence spectra contained a broad infrared peak located 0.4-0.5 eV below the near-bandgap peak. A low-energy peak such as this is undesirable since the radiation responsible for it is not visible to the eye, and hence does not contribute to the useful brightness of the electroluminescent diode. In addition, the significant breadth of the low-energy peak (~1600Å) magnifies its contribution to the total (integrated) radiative emission. Fortunately, the intensity of the low-energy emission has a sublinear dependence on current density (or incident photon density for the case of photoluminescence) which is characteristic of deep energy states where the recombination rate is proportional to the concentration of a single carrier (rather than both electrons and holes) (24). Hence, the low-energy peak tends to saturate at moderate injection levels.

In our early $In_{1-x}Ga_xP$ vapor-grown material (1), the broad low-energy emission usually dominated the photoluminescence or electroluminescence spectra. However, as the crystalline perfection of the material has improved throughout the course of our recent investigation (6), the peak intensity of the near-bandgap emission has been found to increase by orders-of-magnitude relative to that of the low-energy emission.

[3] The samples were prepared by R. E. Enstrom, J. R. Appert, H. F. Gossenberger, M. Ettenberg, and T. Zamerowski, of RCA Laboratories.

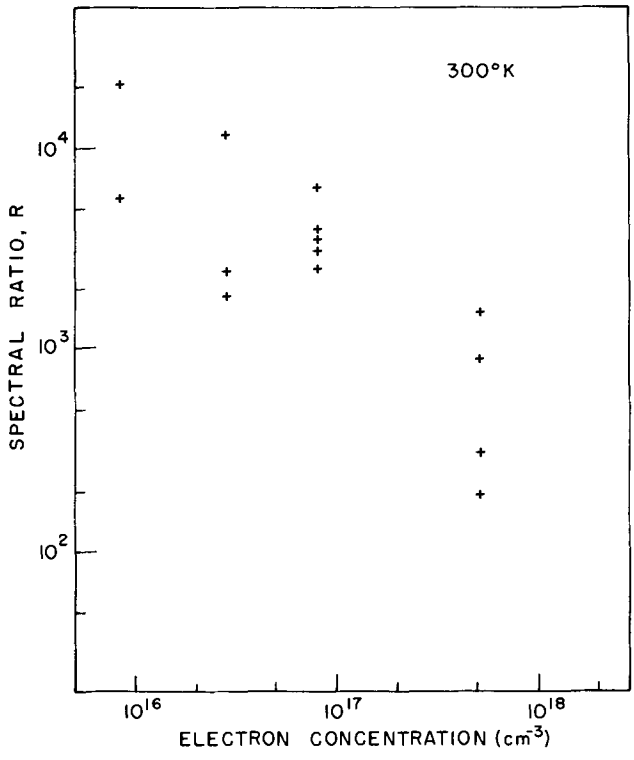

Fig. 8. Photoluminescence spectral ratio R (intensity of near-bandgap peak divided by intensity of low energy peak) vs. free electron concentration for vapor-grown n-type samples of $In_{1-x}Ga_xP$ with $x \sim 0.5$-0.6.

Defining a spectral ratio, R, as the amplitude of the near-bandgap peak divided by the amplitude of the low-energy peak, values of R as large as 20,000 have been observed in the photoluminescence spectra of our recent material. It should be made clear that the spectral ratios used throughout this section do not take into account the integrated response of the two peaks. Ratios based on integrated responses would be about eight times smaller than used here due to the breadth of the low-energy peak.

It is not surprising that the spectral ratio R has increased to some extent with the improvements in crystal quality, since any increase in the radiative efficiency of the material is reflected more strongly in a two-carrier near-bandgap recombination process than in a single-carrier low-energy process (25). However, even a three-order-of-magnitude increase in the radiative efficiency would increase R by only a factor of about 30;[4] hence, the extremely large spectral ratios described above reflect, at least in part, a real reduction in the centers responsible for the low-energy emission relative to those responsible for the near-bandgap emission.

Although we have not conclusively determined the origin of the low-energy emission, several of its predominant characteristics have been established, and are described here. First, from an examination of a large number of n- and p-type vapor-grown samples, we have found that the peak of the infrared emission occurs at about the same energy (at any particular alloy composition) for both conductivity type layers, but that the peak is usually more prominent in the n-type layers. In addition, the magnitude of the low-energy emission (relative to the near-bandgap emission) increases with increasing Se donor concentration, as indicated by the decreasing spectral ratio illustrated in Fig. 8. For the most lightly doped samples here, the low-energy emission was so weak that it was not readily discernible from the background noise. However, ratios of 5000-20,000 were estimated as the mini-

[4] In ref. (25) we show that Mayberg and Black's analysis (24) of band-to-band and low-energy recombination processes result in an expression relating R to the radiative quantum efficiency, η, by an equation R = (constant) η^m, where m is a constant whose value is typically ½.

mum values possible for R, based on the magnitude of the background noise (at the expected wavelength for the low-energy emission) under our most sensitive detection conditions. The data of Fig. 8 show that the spectral ratio varies between a value of about 200 at high Se doping levels to about 20,000 at low donor concentrations. No correlation was observed between the intensity of the infrared peak in p-type material and the Zn acceptor concentration. The dependence of R on the Se concentration strongly suggests that the low-energy emission is the result of a transition between a Se donor state (or a defect related to the incorporation of Se) and a deep-level state which, as yet, is unidentified.

The spectral ratio also was found to vary significantly with alloy composition, as shown in Fig. 9. Although the intensity of both the near-bandgap and the low-energy peaks for these samples varied widely due to differences in their crystalline perfection, the ratio of the intensities, R, decreased monotonically over nearly three orders-of-magnitude for $In_{1-x}Ga_xP$ alloys with x increasing between 0.45 and 0.72. The general trend responsible for this variation was a strong decrease in the near-bandgap peak due to the direct-indirect transition and a relatively unchanging low-energy peak. A similar decrease in R with increasing alloy composition, x, has recently been observed for our melt-grown $In_{1-x}Ga_xP$ samples (26), although for this material much smaller ratios R were observed at any particular value of x (*i.e.*, low-energy peaks were much more intense for the melt-grown material). The stronger low-energy emission for the melt-grown material is consistent with increased contamination (perhaps O_2), since significantly higher growth temperatures (950°-1050°C) and longer growth times (2-4 weeks) are needed for $In_{1-x}Ga_xP$ prepared in this fashion.

It is not clear whether the decrease in R with increasing alloy composition (Fig. 9) is related to the electronic parameters of the $In_{1-x}Ga_xP$ alloy system or to the chemistry of preparing the alloys with differing composition. It should be noted, however, that the low-energy emission also has been observed to become more important for vapor-grown layers of $GaAs_{1-x}P_x$ with GaP-rich alloy compositions (19).

Electroluminescent Diodes

Most of the Zn-doped layers prepared for the optimization of the acceptor concentration were deposited epitaxially as the uppermost layer of a p-n junction structure, so that the junction electroluminescence characteristics could be compared with the photoluminescence from the Zn-doped layers. For electroluminescent diode fabrication, the GaP substrate was thinned to within about 125 μm of the $In_{1-x}Ga_xP$ epitaxial surface by standard lapping and polishing techniques. Ohmic contacts were evaporated to the structure in the form of a Ag-In-Zn film to the p-type epitaxial layer and as an array of Au-Sn, followed by Ag, dots to the n-type GaP substrate. Individual diodes about 1 mm square were cleaved from the wafer and mounted on a TO-5 transistor header with the p-type epitaxial layer adjacent to the header. Au wires 1.5 mils thick were ultrasonically bonded to the Au-Sn, Ag dots to complete device fabrication.

The junction radiation from such structures was directed primarily through the uppermost surface of the GaP substrate. This geometry is particularly attractive for light-emitting diodes since the emission energy from the $In_{1-x}Ga_xP$ junction is much less than the bandgap energy of the GaP substrate, thereby allowing the junction radiation to pass through the substrate with very little absorption. A similar technique, employing a large-energy-bandgap "window," previously was used to enhance the external efficiency of $GaAs_{1-x}P_x$ vapor-grown electroluminescent diodes (9).

For the series of electroluminescent diodes discussed below, the donor concentration was held at about 8×10^{16} cm^{-3}, which was close to optimum for photoluminescence efficiency in the n-type $In_{1-x}Ga_xP$. The thickness of both the n- and p-type vapor-grown layers was held at about 10 μm. The external quantum efficiencies for the series of $In_{1-x}Ga_xP$ diodes were measured with a silicon solar cell placed in close proximity to the uppermost emitting surface of the electroluminescent diodes. A d-c current density between 5 and 10 A/cm^2 was used for the efficiency results described in this paper.

In Fig. 10 the relative electroluminescence efficiency of the vapor-grown p-n junctions is plotted as a function of the Zn doping in the uppermost p-type epitaxial layer. Also shown for comparison is the relative near-bandgap photoluminescence intensity for the p-type layer as a function of the Zn doping concentration

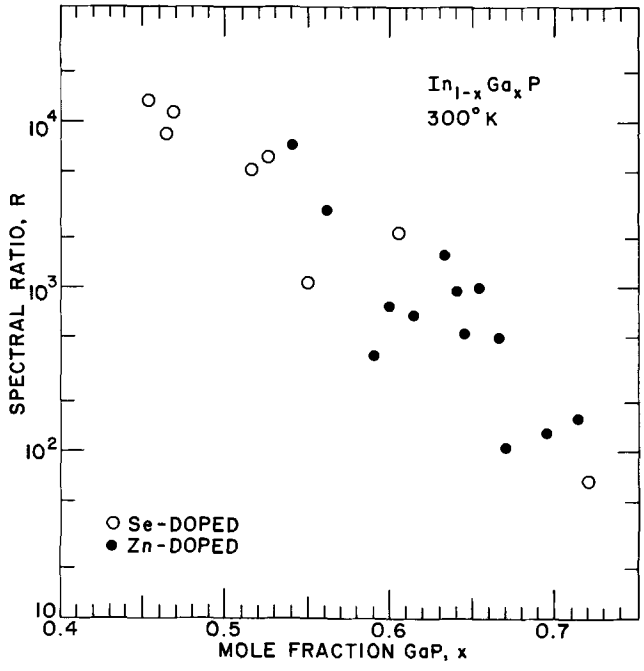

Fig. 9. Photoluminescence spectral ratio R *vs.* mole fraction GaP, x, for n- and p-type $In_{1-x}Ga_xP$ at 300°K.

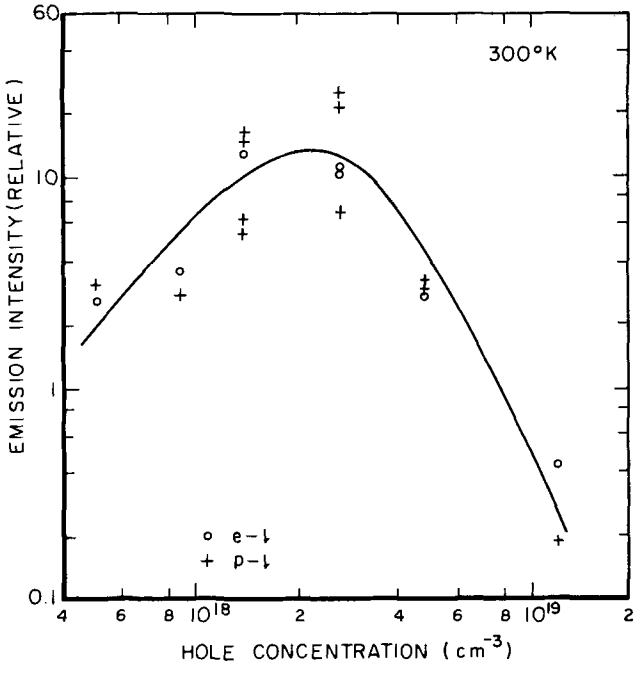

Fig. 10. Photoluminescence intensity of Zn-doped layers (from Fig. 4) and electroluminescence intensity of vapor-grown p-n junctions *vs.* hole concentration in p-type $In_{1-x}Ga_xP$ layers. $x \sim 0.5$-0.6. $T = 300$°K. Emission intensities are relative values.

(previously illustrated in Fig. 4). From Fig. 10 we see that the electroluminescence efficiency has a maximum value at the same Zn acceptor concentration ($\sim 3 \times 10^{18}$ cm^{-3}) as that which results in the maximum photoluminescence intensity. In fact, from the similarity in the shape of the electroluminescence and photoluminescence dependences on the Zn concentration, it is clear that the dominant electroluminescence emission originates on the p-side of the junction, which is the origin of the p-type photoluminescence. In addition, from the manner in which both the photoluminescence and electroluminescence intensities drop off at large Zn concentrations, it is apparent that the deterioration of the surface perfection and the presence of Zn_3P_2 precipitates previously noted also significantly limit the performance of the $In_{1-x}Ga_xP$ p-n junctions.

The p-n junctions prepared with donor (Se) and acceptor (Zn) concentrations that were optimum for maximum photoluminescence intensities also yielded electroluminescent diodes with the highest external quantum efficiencies that we have yet attained for $In_{1-x}Ga_xP$. As illustrated in Table III, external efficiencies of 5 to 10 $\times$ 10^{-4} were obtained for unencapsulated diodes from several different vapor-grown structures that emitted in the range of 6100-6600Å at room temperature. With simple plastic encapsulation, the external efficiencies increased by about a factor of two, as expected, to values of about 10^{-3}. For all of the structures listed in Table III (with the single exception of sample 8-13, DE) the spectral ratio R (near-bandgap to infrared peak intensity) was between 50 and 500 at a d-c current density of 10 A/cm^2, illustrating that the emission spectra consisted primarily of the desired near-bandgap emission. It should be noted, however, that the spectral ratios observed in the electroluminescent diodes and entered in Table III were somewhat smaller than those observed in the photoluminescence spectra of either n- or p-type $In_{1-x}Ga_xP$ (see for example Fig. 7). This probably is due to the fact that the carrier generation levels are higher for the optical excitation than for the junction excitation, and due to the known saturation of low-energy peaks at high excitation levels.

Visually, the brightest diode of those listed in Table III was sample 8-24, D3, for which an estimated brightness (per unit current density) of 317 ft-lumens/A-cm^2 was calculated (27). This value is close to the best reported for an $In_{1-x}Ga_xP$ p-n junction at room temperature [320 ft-lumens/A-cm^{-2}, similarly calculated (5) for a Zn-diffused p-n junction in melt-grown $In_{1-x}Ga_xP$ (28)]. The fact that the vapor-grown diodes are prepared from large-area single-crystal epitaxial layers significantly enhances their ease of fabrication and device yield compared to those prepared infrequently and nonreproducibly from unoriented polycrystalline melt-grown ingots of $In_{1-x}Ga_xP$.

The forward- and reverse-bias I-V characteristics of p-n junction structures prepared with optimum impurity concentrations and the recent refinements described in our vapor-growth process (6) were found to be very free of leakage currents, as shown in Fig. 11. In contrast, the characteristics of most previous melt-grown or vapor-grown junctions were dominated by large leakage currents typically on the order of

Table III. Efficiency values for $In_{1-x}Ga_xP$ vapor-grown electroluminescent diodes

Sample	λ (μm)	Luminescence efficiency (lumens/W)	η_{ext}*	R
8-10, D5	0.6650	31	6.1×10^{-4}	50
8-13, DE	0.6225	239	8.9×10^{-4}	3.0
8-17, D1	0.6185	271	4.0×10^{-4}	50
8-24, D3	0.6170	283	5.9×10^{-4}	200
8-26, D9	0.6650	31	8.1×10^{-4}	500

* Unencapsulated.

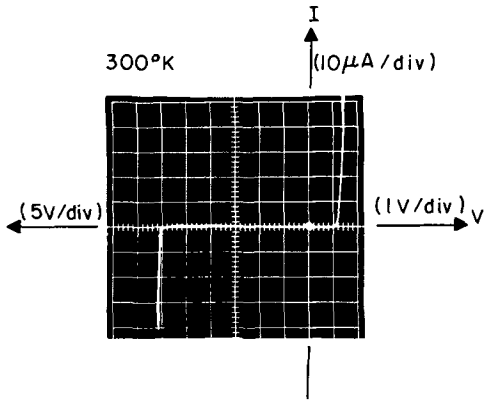

Fig. 11. I-V characteristics at room temperature for vapor-grown $In_{1-x}Ga_xP$ electroluminescent diode (sample 8-24, D3). Diode area is $\sim 10^{-2}$ cm^2. Note that the origin has been displaced three squares to the right of center.

milliamperes at comparable voltages, and "soft" low-voltage reverse breakdown characteristics indicative of junction imperfections. The sharp avalanche breakdown at 30.5V corresponds to a donor concentration of 8.2×10^{16} cm^{-3}, based on Sze and Gibbon's (29) relationship[5] between breakdown voltage, energy bandgap, and doping concentration for an abrupt semiconductor p-n junction. This value is in good agreement with the intended "optimum" donor concentration of Fig. 2, which was used for the fabrication of this series of diodes. At forward-bias currents significantly larger than those of Fig. 11, a series resistance of several hundred ohms was observed, which is attributed primarily to resistive contacts to the GaP substrate. For $In_{0.5}Ga_{0.5}P$ vapor-grown junctions deposited, instead, on GaAs substrates, the series resistance was eliminated, and both the current and the light intensity followed a relationship of the form exp(qV/1kT) at current densities greater than about 10^{-2} A-cm^2. Such a dependence is indicative of classical injection over a junction barrier, and is similar to that observed in our vapor-grown $In_xGa_{1-x}As$ p-n junctions (30).

Injection Laser Diodes

Prior to our investigation, Holonyak and co-workers (31) had demonstrated that melt-grown crystals of $In_{1-x}Ga_xP$ could support laser emission to wavelengths as short as 5800Å at 77°K when the bulk crystals were excited optically. However, only a single report of laser action in $In_{1-x}Ga_xP$ p-n junctions had been made (14), this being for melt-grown material into which a p-n junction was formed by Zn diffusion. For such junctions, the threshold currents were very high (67,000 A/cm^2 at 77°K) even for InP-rich alloys where the emission was in the infrared (at 7600Å). The difficulty in previously obtaining lasers was clearly related to the lack of good crystalline perfection at the semiconductor p-n junction.

The laser diodes that we prepared have been described elsewhere (27). For completeness, we merely note here that the vapor-grown laser diode structures were identical to those described in the previous section, and were prepared with the optimum donor and acceptor concentrations described in this work, after making the improvements in the crystalline perfection discussed in the preceding paper (6). The characteristics of the vapor-grown $In_{1-x}Ga_xP$ lasers are summarized in Table IV, which is taken from Ref. (27). To our knowledge, the emission at 6105Å is the shortest wavelength that has yet been reported from a p-n junction laser diode, and is the first example of orange coherent emission from such a device. The threshold current densities of 4000-6000 A/cm^2 indicated in Table

[5] $V_B = 60\ (E_g/1.1)^{3/2}\ (N_d/10^{16})^{-3/4}$, where V_B is the breakdown voltage, E_g is the energy bandgap, and N_d is the doping concentration on the more lightly doped side of an abrupt semiconductor p-n junction.

Table IV. Emission wavelength and threshold current density at 80°K for short-wavelength-emitting p-n junction lasers

Material	Emission wavelength (A)	J_{th} (A/cm²)	Reference
$In_{1-x}Ga_xP$	6105, 6130, 6145	5.9×10^3	27
$In_{1-x}Ga_xP$	6180	4.1×10^3	27
$Al_xGa_{1-x}As$	6280	$6 \times 10^{3*}$	32
$GaAs_{1-x}P_x$	6350	2.5×10^5	33

* For close confinement heterojunction structure with 2 μm active region.

IV compare favorably with those from $GaAs_{1-x}P_x$ and $Al_xGa_{1-x}As$ at short emission wavelengths, and demonstrate that the 6100Å emission is not limited severely by loss of carriers to the subsidiary indirect conduction band minima. The direct band structure of $In_{1-x}Ga_xP$ should ultimately be capable of providing yellow coherent emission from p-n junctions at wavelengths as short as about 5700Å at 77°K.

Conclusions

A photoluminescence evaluation of Se and Zn doping in $In_{1-x}Ga_xP$ with $x \sim 0.5$-0.6 has been carried out for improved vapor-grown layers deposited epitaxially onto GaP substrates. The near-bandgap photoluminescence intensities at 300°K reach their maximum values at a Se donor concentration of 1×10^{17} cm^{-3} and at a Zn acceptor concentration of 3×10^{18} cm^{-3}. At larger doping concentrations, the photoluminescence intensities decrease drastically due to the introduction of second-phase precipitates. For heavy Zn doping, tetragonal Zn_3P_2 precipitates have been identified, which tend to fit into the lattice of $In_{0.52}Ga_{0.48}P$ by replacing four unit cells.

The near-bandgap photoluminescence emission peak for our vapor-grown layers ($0 \leq x \leq 0.6$) approximately follows the quadratic relationship previously determined by Stringfellow (15). For alloy compositions with $0.6 < x < 0.74$, the peak energy values lie somewhat lower than predicted by the quadratic equation. Spectral broadening of the near-bandgap emission is observed for carrier concentrations larger than about 1×10^{17} cm^{-3} for n-type $In_{1-x}Ga_xP$ and 7×10^{18} cm^{-3} for p-type $In_{1-x}Ga_xP$. The extent of the broadening in the present vapor-grown samples is more severe than it is in GaAs. A low-energy infrared peak located approximately 0.4-0.5 eV less than bandgap is enhanced for alloys with increased GaP concentrations and in n-type material with increased Se donor concentrations, but under all conditions is extremely weak in intensity compared to that of the desired near-bandgap peak.

Vapor-grown p-n junctions prepared with the optimum Se and Zn carrier concentrations yield room-temperature electroluminescence efficiencies between 5 and 10×10^{-4} at wavelengths between 6100 and 6600Å. From the improved $In_{1-x}Ga_xP$ vapor-grown junctions, laser diodes capable of providing coherent orange emission (6105Å at 80°K) with threshold current densities between 4000 and 6000 A/cm² have been fabricated (27).

Acknowledgments

The authors would like to thank C. J. Buiocchi, R. J. Paff, R. W. Snedeker, and T. J. Zamerowski for their assistance in a variety of technical areas. We also would like to acknowledge the helpful discussions and suggestions of J. Blanc, H. Kressel, and D. Richman. The research reported here was supported in part by the Office of Naval Research, Arlington, Virginia, and in part by RCA Laboratories, Princeton, New Jersey.

Manuscript submitted Nov. 10, 1972; revised manuscript received March 12, 1973.

Any discussion of this paper will appear in a Discussion Section to be published in the June 1974 JOURNAL.

REFERENCES

1. C. J. Nuese, D. Richman, and R. B. Clough, *Met. Trans.*, **2**, 789 (1971).
2. C. Hilsum and P. Porteous, Proc. Ninth Int. Conf. on the Physics of Semiconductors, Nauka, Leningrad, 1968, p. 1214.
3. M. R. Lorenz and A. Onton, Proc. of the Tenth Int. Conf. on the Physics of Semiconductors, Cambridge, Mass., 1970, p. 444.
4. H. Rodot, J. Horak, G. Rouy, and J. Bourneix, *Compt. Rend. Paris*, **267B**, 381 (1968).
5. R. J. Archer, *J. Electron. Materials*, **1**, 128 (1972).
6. A. G. Sigai, C. J. Nuese, R. E. Enstrom, and T. Zamerowski, *This Journal*, **120**, 947 (1973).
7. R. D. Burnham, N. Holonyak, Jr., D. L. Keune, and D. R. Scifres, *Appl. Phys. Letters*, **18**, 160 (1971).
8. C. J. Nuese, J. J. Tietjen, J. J. Gannon, and H. F. Gossenberger, *Trans. Met. Soc. AIME*, **242**, 400 (1968).
9. C. J. Nuese, J. J. Tietjen, J. J. Gannon, and H. F. Gossenberger, *This Journal*, **116**, 248 (1969).
10. D. A. Cusano, *Solid-State Commun.*, **2**, 353 (1964).
11. M. S. Abrahams, C. J. Buiocchi, and M. D. Coutts, *Rev. Sci. Instr.*, **39**, 1944 (1968).
12. M. S. Abrahams, L. R. Weisberg, C. J. Buiocchi, and J. Blanc, *J. Mater. Sci.*, **4**, 223 (1969).
13. H. Kressel, F. Z. Hawrylo, M. S. Abrahams, and C. J. Buiocchi, *J. Appl. Phys.*, **39**, 5139 (1968).
14. H. M. Macksey, N. Holonyak, Jr., D. R Scifres, R. D. Dupuis and G. W. Zack, *Appl. Phys. Letters*, **17**, 430 (1970).
15. G. B. Stringfellow, *J. Appl. Phys.*, **43**, 3455 (1972).
16. J. P. McVittie, Tech. Rept. No. 2-KSG-821, Stanford Electronics Labs., Stanford, Calif., July 1972.
17. A. W. Mabbitt, *Solid State Commun.*, **9**, 245 (1971).
18. T. L. Larson, E. E. Loebner, and R. J. Archer, *Bull. Am. Phys. Soc.*, **10**, 388 (1965).
19. A. H. Herzog, W. O. Groves, and M. G. Craford, *J. Appl. Phys.*, **40**, 1830 (1969).
20. R. E. Enstrom, C. J. Nuese, V. S. Ban, and J. R. Appert, Proc. Fourth Int. Symposium on Gallium Arsenide and Related Compounds, Boulder, Colo., p. 37, September (1972).
21. H. Kressel, C. J. Nuese, and I. Ladany, *J. Appl. Phys.*, To be published.
22. R. Z. Bachrach and B. W. Hakki, *J. Appl. Phys.*, **42**, 5102 (1971).
23. H. C. Casey, Jr. and R. H. Kaiser, *This Journal*, **114**, 149 (1967).
24. S. Mayburg and J. Black, *J. Appl. Phys.*, **34**, 1521 (1963).
25. C. J. Nuese and H. E. Schade, Final Report, Contract No. F19628-68-C-0190, Air Force Cambridge Research Labs., Bedford, Mass., Dec. 31, 1970.
26. I. Kudman and C. J. Nuese, To be published.
27. C. J. Nuese, A. G. Sigai, and J. J. Gannon, *Appl. Phys. Letters*, **20**, 431 (1972).
28. A. Onton and M. R. Lorenz, Proc. Third Int. Symposium on Gallium Arsenide and Related Compounds, Aachen, Germany, 1970 (The Inst. of Physics and the Physical Society, London, 1970), p. 222.
29. S. M. Sze and G. Gibbons, *Appl. Phys. Letters*, **8**, 111 (1966).
30. C. J. Nuese and R. E. Enstrom, *IEEE Trans. Electron Devices*, **ED-19**, 1067 (1972).
31. D. R. Scifres, H. M. Macksey, N. Holonyak, Jr., and R. D. Dupuis, *J. Appl. Phys.*, **43**, 1019 (1972).
32. H. Kressel, H. F. Lockwood, and H. Nelson, *J. Quantum Electron.*, **QE-6**, 278 (1970).
33. J. J. Tietjen, J. I. Pankove, I. J. Heygi, and H. Nelson, *Trans. AIME*, **230**, 385 (1967).
34. C. Alibert, G. Pordure, A. Laugier, and J. Chevallier, *Phys. Rev.*, **6B**, 1301 (1972).

Solid-Solid Vacuum Diffusion Processes in Silicon

R. Gereth, A. Kostka, and K. Kreuzer

AEG-Telefunken, Semiconductor Division, Heilbronn, Germany

ABSTRACT

Two diffusion techniques are described making use of doped silicon wafers as the diffusion source. The processes are carried out either in an evacuated capsule or inside a high vacuum furnace. Using the capsule technique, boron and phosphorus layers in silicon have been produced, with sheet resistances ranging from approximately 20-4000 ohms/□, and junction depths between approximately 0.3 and 15 μm. Good uniformity and reproducibility of results were obtained, with relative variations below 3% across one wafer, from wafer to wafer, and from run to run. In a series of boron diffusions, the high vacuum technique yielded results comparable to the capsule technique. It offers more experimental flexibility but requires masking layers other than SiO_2 for the production of planar devices.

The exact and reproducible control of doping profiles is a fundamental requisite for the fabrication of advanced semiconductor devices. Standard diffusion processes in open systems do not always fulfill these requirements. Especially, shallow diffused layers and/or low surface concentrations are extremely difficult to obtain using an open doping system. In addition, during each predeposition step included in open diffusion runs, the semiconductor body is heavily stressed by the rather high impurity concentrations arising from these processes. Crystal structure damage, such as local lattice defects caused by impurity clusters, or dislocation networks caused by partial stress release (1, 2) are the consequences. These defects lead to an appreciably lower electrical quality of the diffused area and its surroundings.

Some of the problems can be overcome by diffusion techniques keeping dopant concentrations well below the saturation value during the high temperature step. Several successful attempts have been made in recent years using capsule diffusion (3, 4), diffusion from doped glasses (5), boron nitride source, or ion implantation (6). This paper deals with two modifications of the sealed capsule process proposed by Armstrong and Duffy (3).

Using doped silicon wafers instead of powder for the diffusion source (4) offers advantages in the handling of the source and the means of surface concentration adjustment by variation of the active source area inside the capsule. Details of this method are reported in the first part of this paper.

Limitations of the capsule diffusion technique arising from insufficient mechanical stability and chemical impurity of the capsule material may be overcome by replacing the capsule with a high vacuum furnace. The features of this technique are described in the second part of this paper.

Sealed Tube Diffusion

Experimental procedure.—Doped silicon source wafers and silicon wafers to be diffused are placed inside an evacuated capsule which is inserted into the diffusion furnace. The basic quartz components employed are shown in Fig. 1. The capsule and the sealing plug are both fabricated from a quartz tube. Typical dimensions of the capsule are 300 mm length, 45 mm diameter, and 2 mm quartz thickness. The quartz wafer carrier exhibits individual grooves approximately 1 mm apart to take up the wafers. All quartz parts are cleaned in an HF-HNO_3-HCl-mixture, rinsed in distilled water, and dried in a furnace of 400°C for 1 hr.

The source wafers are cut, lapped, and polished from a silicon rod doped with the desired material up to the desired level. They may be used for a large number of diffusion processes. During each process, however, doping material concentration is reduced by outdiffusion from a region below the surface. In order to guarantee reproducible source conditions, the source wafers are immersed into a silicon etch to remove the depleted layer before each new diffusion run. As a rule of thumb, a layer thickness twice the produced junction depth is normally etched off. Immediately before capsule loading, both the source wafers and the wafers to be diffused are immersed in a dilute HF etch to remove all traces of surface oxide, because this oxide is able to mask the diffusion resulting in lower surface concentrations and shallower junction depths.

For the diffusion run, the wafers are put into the previously cleaned quartz carrier. The entire assembly is then placed in the quartz tube, which is evacuated to better than 10^{-5} Torr, heated for 30 min at approximately 500°C to drive off all water residues, and sealed by collapsing the outer tube upon the inner one. The whole capsule is put into the diffusion furnace, which must have a thermal flat better than 1°C over the entire length of the capsule. Poor thermal flats result in nonuniform diffusion and in damage to the silicon surface (7).

The geometrical arrangement of the wafers within the capsule has some influence on the diffusion results. A series of experiments revealed the following evidence. If all the wafers are placed at a distance of approximately 1 mm from each other, no variation in results occurs by deliberately changing the positions of the wafers in the capsule. On the other hand, bringing source and test wafers into intimate contact resulted in a certain increase in measured sheet resistances. The observations are in good agreement with the theory of vacuum diffusion processes (8). The transport mechanism in the gas phase is essentially controlled by the total pressure in the sealed tube at

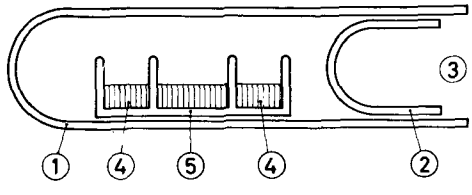

① CAPSULE MADE OF QUARTZ TUBE
② SEALING PLUG
③ PUMP CONNECTION OPENING
④ CONTAINER FOR SOURCE WAFERS
⑤ WAFER CARRIER

Fig. 1. Quartz parts used for sealed capsule diffusions

Key words: silicon diffusion processes, solid source diffusion, closed tube diffusion, high vacuum diffusion.

Table I. Typical diffusion conditions and results of capsule wafer diffusion†

Impurity	T (°C)	t (min)	C_o (cm^{-3})	Φ	ρ_s (ohm/□)	x_j (μm)	C_s^* (cm^{-3})
Boron	1200	600	2×10^{19}	0.85	24	14.5	1.5×10^{19}
		60	5×10^{18}	0.75	313	2.7	4×10^{18}
	1165	120	5×10^{18}	0.75	320	2.7	4×10^{18}
	1100	610	5×10^{18}	0.95	280	2.8	4×10^{18}
		60	5×10^{18}	0.95	1650	0.7	2.5×10^{18}
	1080	300	5×10^{18}	0.75	550	1.9	3×10^{18}
	1050	1020	5×10^{18}	0.95	450	1.5	5×10^{18}
		60	5×10^{18}	0.95	4230	0.3	2×10^{18}
Phosphorus	1200	150	5×10^{18}	0.9	70	4.3	5×10^{18}
		55	5×10^{18}	0.75	185	2.4	3×10^{18}
	1150	180	5×10^{19}	0.9	17	3.5	*
		30	5×10^{19}	0.9	50	1.1	*
	1100	600	5×10^{18}	0.9	155	2.1	5×10^{18}
		60	5×10^{18}	0.9	1100	0.5	2×10^{18}
	1050	1200	5×10^{19}	0.9	44	2.3	*
		270	5×10^{19}	0.9	63	1.2	*

† The terms used are defined: T = diffusion temperature, t = diffusion time, C_o = source concentration, Φ = ratio of source wafer area to total silicon area, ρ_s = diffused sheet resistance, x_j = diffused junction depth, C_s^* = diffused surface concentration, calculated from ρ_s and x_j after Irvin (9) assuming erfc profile, * = no erfc profile because of concentration dependent diffusion coefficient.

the diffusion temperature. In order to achieve a homogeneous mixture of dopant atoms, silicon atoms, and residual gas molecules over all the capsule, the value of the mean free path of all the particles needs to be considerably lower than the distance between the wafers. For the closely stacked arrangement, this condition obviously is not fulfilled. Since the sticking probability of the silicon and dopant atoms on the silicon surfaces is high (4), this geometry results in an impediment of the particle flow out of and into the narrow space between the stacked wafers.

Results.—The capsule wafer diffusion has been applied to diffuse boron and phosphorus into silicon over a wide range of parameters; *i.e.*, source concentration C_o, diffusion temperature T, and diffusion time t. After diffusion, junction depth x_j and sheet resistance ρ_s of the layer in the test wafer were measured. Typical results are shown in Table I. The test wafer surface concentrations C_s^* were calculated from the measured values of x_j and ρ_s using the curves published by Irvin (9) assuming an erfc-profile. The actual surface concentrations C_s may deviate from the calculated values C_s^* becuse of a non-erfc nature of the profile. Theoretical considerations (8), however, show that the difference between the actual and an erfc profile is small provided that the surface concentration is low enough thus allowing the application of a concentration-independent diffusion coefficient, and that the diffusion time is long compared to the duration of the effects mentioned below. For diffusions exhibiting junction depths above 1 μm (deep diffusions), the second condition is fulfilled.

For all experiments with a source concentration $\leq 2.10^{19}$ cm^{-3} we found the relation $C_s^* \leq C_o$. Sealed tube diffusions using a powder source experimentally (3) and theoretically result in $C_s = C_o$ and an erfc profile (*i.e.*, $C_s^* = C_s$). The major reasons for the fact that a wafer source produces results with $C < C_o$ and

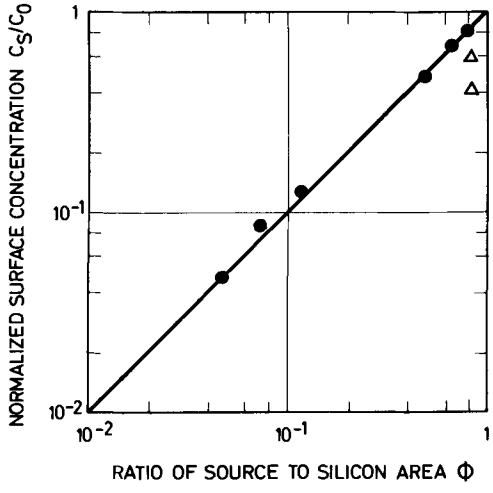

Fig. 2. Normalized surface concentration vs. ratio of source area to total silicon area inside the capsule. C_o = source doping level.

a profile slightly different from erfc (*i.e.*, $C_s^* \approx C_s$) are theoretically analyzed in a separate publication (8) and are shown to be (*a*) the finite area of the source wafers, (*b*) the influence of the capsule walls on the exchange process, and (*c*) the sorption limited rate of exchange during the first stage of the diffusion process.

Effect (*a*) is independent of diffusion time, effect (*b*) and, more rapidly, effect (*c*), vanish with increasing diffusion times. Of course, there are other possible mechanisms that could affect materials exchange in the capsule. The above-mentioned effects, however, are necessarily involved, and their consideration proved to be sufficient for the explanation of our results. This does not exclude minor influences of other processes. As a demonstration of effect (*a*), Fig. 2 shows the results of a couple of diffusion experiments with varying surface area of the source wafers. In all cases, the surface concentration C_s in the test wafer is a certain fraction of the homogeneous source wafer doping C_o. This fraction C_s/C_o has been plotted *vs.* the controlling parameter Φ, denoting the ratio of source wafer area to total Si area in the chamber. Theoretically (8), for deep diffusions, the dependence is linear, $C_s = \Phi C_o$, illustrated by the straight line. The dots are experimental values for deep diffusions. The triangles refer to shallow diffusions. The deviations from the theoretical line may be explained by effects (*b*) and (*c*) and are discussed in detail in the section on Shallow layers below.

The diffused layers produced by the wafer source technique are fully comparable with those produced by the powder source method. In order to examine the uniformity and reproducibility, the series of diffusion runs represented in Table II has been carried out. For

Table II. Repetition tests, wafer capsule diffusion†

Impurity	No.	T (°C)	t (min)	C_o (cm^{-3})	Φ	ρ_s (ohm/□)	x_j (μm)	C_s^* (cm^{-3})	Δ, %
Boron	1	1200	60	5×10^{18}	0.75	314	2.7	4×10^{18}	±1
	2	1200	60	5×10^{18}	0.75	318	2.7	4×10^{18}	±2
	3	1200	60	5×10^{18}	0.75	313	2.7	4×10^{18}	±2.5
Phosphorus	4	1200	55	5×10^{18}	0.75	185	2.4	3×10^{18}	±2
	5	1200	55	5×10^{18}	0.75	180	2.4	3×10^{18}	±2
Boron	6	1165	120	5×10^{18}	0.78	320	2.7	4×10^{18}	±3
	7	1165	120	5×10^{18}	0.78	310	2.7	4×10^{18}	±3
Boron	8	1080	300	5×10^{18}	0.71	550	1.9	3×10^{18}	±2
	9	1080	300	5×10^{18}	0.71	562	1.9	3×10^{18}	±2

† The terms used are defined: Δ = standard deviation of measured sheet resistances from their mean value ρ_s, other symbols defined in Table I.

each series, the source concentration and surface ratio were kept constant. In all cases, the maximal standard deviations from the mean value of the sheet resistances of the diffused layers are below ±3% across one wafer, within the wafers of one diffusion run, and from run to run. This excellent value of uniformity and reproducibility was observed both for blanket diffusions and diffusions into silicon wafers utilizing SiO_2-masked planar structures.

Shallow layers.—The trend in modern devices goes to shallower structures having junction depths below 1μ. Therefore, a series of experiments was performed concerned with the extension of vacuum diffusion processes into the submicron range (10). Of course, this requires either very short diffusion times, which are difficult to control, or relatively low diffusion temperatures, typically 1100°C and below. The first exploratory experiments at 1100°C yielded remarkable deviations from the results expected from the simple model assuming constant surface concentration $C_s = \Phi C_0$. In addition, an influence of the extent of the quartz surface inside the capsule became apparent. For example, doubling the quartz surface inside the capsule yielded a remarkable increase in the diffused sheet resistance. This experiment indicated a direct influence of the inner capsule walls on the material exchange between source and test wafers. In order to evaluate its magnitude under different diffusion conditions, the following series of diffusions has been carried out: phosphorus was diffused at 1100° and 1150°C, boron was diffused at 1050°, 1100°, and 1200°C. For each series, the diffusion time was varied within wide limits. The results are plotted in Fig. 3 and 4. The straight lines indicate the results expected from the constant surface concentration mode. Measured sheet resistances and junction depths (dots) show a systematical deviation from the straight lines, with an increase in the deviation for shorter diffusion times and lower diffusion temperatures.

Qualitatively and quantitatively, the results can be explained through effect (b) mentioned above, an absorption of doping material by the quartz walls of the capsule in the initial stage of the diffusion process. After a certain time saturation of the walls will occur and the exchange of material will no longer be affected.[1] This is the reason for the decrease of the deviation with increasing diffusion time. At higher temperature, saturation of the inner wall surface proceeds faster because of the higher vapor pressures and diffusion constants involved. This is the reason for the decrease of the deviation with increasing temperature. In addition to its time and temperature dependence, the wall coverage effect can be shown to be proportional to the parameter Φ_w denoting the ratio of wall surface to Si surface inside the capsule. Further theoretical details are discussed in a separate paper (8). The experimental conditions of the diffusion series are in accordance with the assumptions on which the theoretical treatment is based. The open circles in Fig. 3 and 4 represent the values calculated by the theory using the set of parameters listed in Table III. The

[1] Radio tracer experiments (11) revealed the expected quantity of phosphorus at the inner quartz walls.

Table III. Parameters used for calculation of sealed tube diffusion results†

Impurity	T (°C)	C_0 (cm^{-3})	ϕ	ϕ_w	$S_{\infty w}$ (cm^{-2})	t_w (min)
Boron	1200	5×10^{18}	0.75	1.6	1.3×10^{13}	0.1
	1100	5×10^{18}	0.93	0.7	4.3×10^{13}	3.0
	1050	5×10^{18}	0.93	0.7	3.0×10^{13}	7.5
Phosphorus	1150	1×10^{20}	0.89	1.1	4.0×10^{14}	1.5
	1100	5×10^{18}	0.91	0.9	3.2×10^{13}	11.6

† The terms used are defined: ϕ_w = ratio of inner capsule wall surface to total silicon area, $S_{\infty w}$ = wall saturation coverage, t_w = rise time for wall coverage effect, and other symbols defined in Table I.

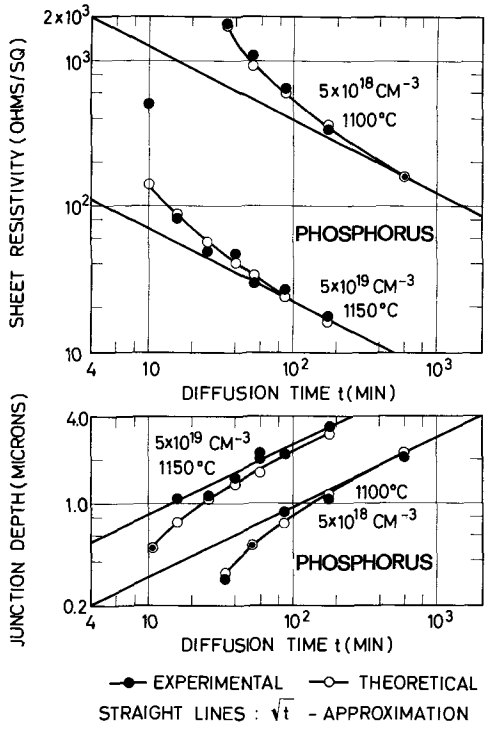

Fig. 3. Results of phosphorus-sealed capsule diffusions

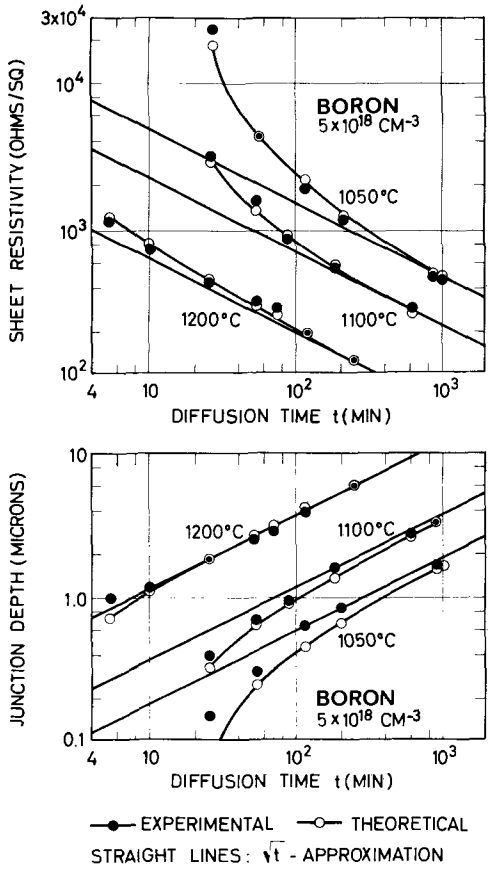

Fig. 4. Results of boron-sealed capsule diffusions

values of sheet resistance have been derived from the concentration profiles using Irvin's (9) relations between concentration and conductance. For the $5 \cdot 10^{19}$ cm^{-2} phosphorus series, the results give only qualitative information since a fictitious value of $1 \cdot 10^{20}$ cm^{-3} for the source doping had to be introduced in order to obtain some accordance with the measurements. This is a consequence of the concentration dependence of the diffusion coefficient which was not accounted for in the theoretical treatment.

In Table III, the quantities $S_{\infty w}$ and t_w denote, respectively, the saturation coverage of the capsule walls and the rise time of the saturation process. The quartz coverage values $S_{\infty w}$ necessary to fit the experimental points all lie well below one monolayer (approximately 10^{15} cm^{-2}). Because of the proportionality to Φ_w, one method to reduce the wall coverage effect for a given diffusion time and temperature is the reduction of Φ_w by increasing the silicon surface inside the capsule. On the other hand, while working under conditions of quartz influence, reproducibility of results can only be guaranteed by keeping Φ_w and $S_{\infty w}$ constant. The first condition is accomplished by using a constant number of wafers in a quartz capsule of definite size for every reproduction run. The second condition may be approximated by using a standardized quartz cleaning procedure that will result in defined quartz surface properties. Minor fluctuations, however, cannot be avoided.

Limitations.—The limitations of the capsule diffusion technique are principally governed by the capsule properties. Maximum operating conditions, such as temperatures and times, are limited by the values quartz can sustain without softening causing a collapse of the capsule. A typical set of values is 20 hr at 1200°C for an industrial grade quartz. Backfilling the capsule with inert atmospheres could extend the range of application. Lower limits in time and temperatures are given by the problematics involved in heating the capsule for a short period of time and by the rapid increase of the quartz adsorption effect for short times and low temperatures. The usable source doping concentration range is limited by the maximum available doping concentration in silicon single crystals for wafer diffusion. The lower concentration limit is set by the impurities always present in the quartz material. During the diffusion step they are partly released from the inner surface of the walls and transported to both test and source wafers, where they cause undesired doping or contamination of the material. Using an industrial grade quartz tube, n-type impurities up to surface concentrations of $2 \cdot 10^{17}$ cm^{-3} were found in test wafers after a test diffusion step without source wafers in the capsule.[2] A high purity quartz material did not show this effect, but mechanical stability of such capsules was insufficient. The limitations arising from quartz material properties may be overcome by replacing the quartz capsule with a high vacuum furnace, as described in the following section.

High Vacuum Diffusion

Experimental procedure.—Doped silicon source wafers to be diffused are placed inside a high vacuum furnace (see Fig. 5) for the diffusion process. The diffusion chamber, 7,[3] is represented by an electrically heated high temperature furnace installed inside the bell jar of a standard high vacuum apparatus. The diffusion chamber has a diameter of 25 cm and a height of 6 cm. It is heated by two meander-shaped carbon plates, 4, each plate located between two quartz disks, 3. Several tantalum sheets, 6, and a water cooling system, 1 + 2, act as heat shields. The wafers are placed in any kind of wafer carrier, 8, suitable for the specific experiment. During the diffusion process both the diffusion chamber and the carrier remain connected to the vacuum system. In this way, a pressure gradient is established which protects the wafers inside the chamber against impurities from the outside.

Source and test wafers cleaned and etched as described in the previous section, are positioned alternately and in direct contact with each other. The sandwich-type arrangement is necessary in the high vacuum furnace in order to avoid thermal etching of the silicon surfaces caused by evaporation and pump-away

[2] Investigations of Fränz and Langheinrich (11) suggest that the n-type doping of the test wafers was caused by an Sb contamination of the quartz material.

[3] Numbers in italic refer to the designations in Fig. 5.

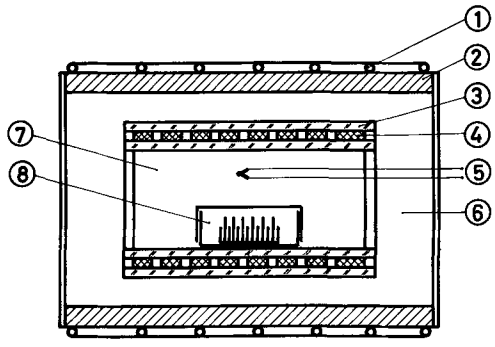

① COOLING COIL
② COPPER PLATE
③ QUARTZ DISC
④ MEANDER SHAPED CARBON PLATE
⑤ THERMOCOUPLE
⑥ TEMPERATURE SHIELD
⑦ DIFFUSION CHAMBER
⑧ WAFER ARRANGEMENT IN QUARTZ BOX

Fig. 5. High temperature furnace for high vacuum diffusions

of the material. A typical diffusion cycle does not require more time than a sealed capsule diffusion run. After evacuating the bell jar (down to approximately $5 \cdot 10^{-7}$ Torr at room temperature, and 10^{-5} Torr at 1200°C) and heating up the diffusion furnace, diffusion temperature is controlled by a variable transformer during the diffusion time. The sensing thermocouple, 5, located inside the black body arrangement easily allows absolute temperature recordings. Cool down is initiated by switching off the furnace supply. In the lower temperature range, a more rapid cooling of the diffusion furnace can be achieved by introducing inert gases (*e.g.*, argon) in the bell jar up to approximately atmospheric pressure.

Material exchange.—In contrast to capsule diffusion processes, high vacuum diffusions are carried out in an open vacuum system. Although a good thermal flat (~±2°C) is maintained inside the symmetrical black body arrangement of the furnace, evaporating material can arrive at and stick to the cooler region of the diffusion furnace, or escape from the diffusion chamber. Because of the steady pump-away of material by maintaining the pressure in the chamber in the high vacuum range, no equilibrium pressure of silicon or dopant is established. Since the mean free path of the evaporating particles exceeds the chamber dimensions, the particles move in straight lines, and the material exchange is defined by the geometrical arrangement of the surfaces. This becomes evident from an experiment illustrated in Fig. 6. Two test wafers are packed together in close contact, one of them covering only half the area of the other. A source wafer is facing them approximately 5 mm apart. After the diffusion cycles only the nonmasked part of the rear test wafer has

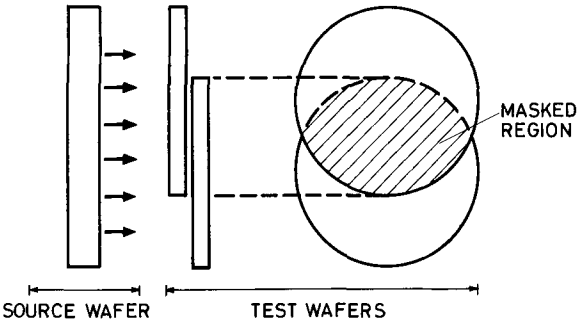

Fig. 6. Straight line material transport during high vacuum diffusion.

Fig. 7. Effect of thermal evaporation from a silicon surface partly covered by another wafer.

been doped. The masked area has been effectively shielded from the source by the front test wafer.

Another consequence of straight line movement and pump-away is thermal etching of open surfaces inside the chamber. Uncovered mirror smooth polished surfaces of Si wafers show heavily damaged surfaces with a strong etch pit pattern after the diffusion step (Fig. 7). Knopp (7) pointed out that the etch pit density of silicon treated in a poor vacuum was much greater than in a high vacuum ($<10^{-6}$ Torr). The enhancement of thermal etching at higher ambient pressure is due to the formation and subsequent evaporation of volatile SiO. This effect is of even greater importance if SiO_2 is used as a localized diffusion mask in high vacuum diffusion processes. At diffusion temperatures, Si and SiO_2 interact forming the rapidly evaporating SiO phase (12, 13). Figure 8 shows the results of such

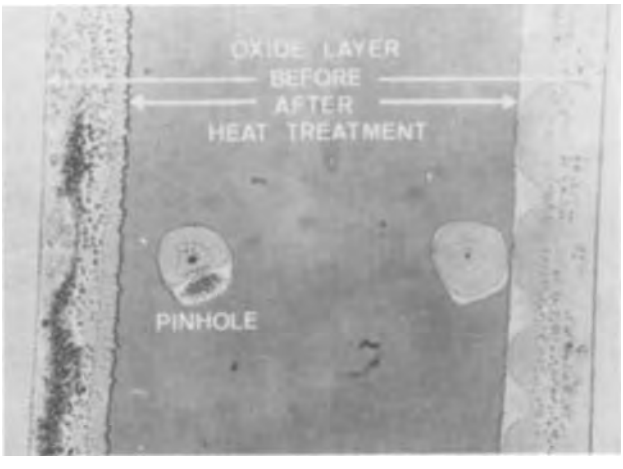

Fig. 8. Effect of silicon monoxide evaporation from silicon-silicon dioxide interfaces.

an experiment at 1200°C for approximately 1 hr. The oxide layer was about 50μ wide, the SiO_2 thickness was 1μ. After diffusion the masking oxide had vanished from the interface between the free silicon surface and the SiO_2 window edges. Because of the same effect, pinholes in the masking oxide lead to widened circles in the middle of Fig. 8.

In order to avoid the silicon evaporation effect, it is necessary to use a closely stacked face-to-face arrangement (sandwich arrangement) of source and test wafers within the high vacuum furnace. The escape probability of the evaporating material from the surfaces directly contacting each other into the outside is greatly reduced. In this way, blanket diffusions applicable, *e.g.*, in the mesa technology, can be carried out resulting in negligible damage to the surfaces, the only exception being a narrow region along the circumference of a wafer. The problem of SiO evaporation from planar device structures may be overcome by using any masking material that does not interact with the underlying silicon, such as Si_3N_4.

Results.—The influence of diffusion temperature on results has been investigated by a series of boron diffusions lasting 1 hr at various temperatures between 1000° and 1200°C. From the theory (8) one gets a value of $\Phi = 0.05$ for the sandwich arrangement of the wafers used, leading to a surface concentration in the test wafer which is half the value of source doping. This result should be independent of temperature if an unhindered material exchange takes place between the facing surfaces. Within experimental error this is indeed the case as can be seen from Table IV. The surface concentration in the test wafers has been evaluated assuming an erfc profile. The maximum deviations from the mean value of measured sheet resistance of the diffused layers are approximately ±4% across one wafer and within the wafers of one run, and approximately ±5% from run to run. These figures are comparable with the results reported for the sealed tube experiments.

Limitations.—Unlike the behavior of capsule diffusion, limitations in the applicability of high vacuum diffusion are not defined by the properties of the material surroundng the gas phase. The principal condition for this is the restriction of material exchange between wafer surfaces directly facing each other in the closely stacked sandwich arrangement.

With the exception of planar devices, which are difficult to handle because of SiO evaporation, limits of the high vacuum diffusion technique arise mainly from the equipment. With the present apparatus, short diffusion times (in order of 10 min) are excluded because of slow cool-down rates. On the other hand, there seems to be no upper limit of diffusion time as encountered with capsule diffusion processes. Diffusion temperatures may be chosen deliberately within the practical range.

Conclusions

Two different diffusion methods employing doped silicon wafers as diffusion source are described, one using an evacuated capsule, the other a high vacuum furnace as the diffusion chamber. Both methods have been proved to be highly reproducible and applicable over a wide range of diffusion parameters. Good control

Table IV. Diffusion results of high vacuum diffusion†

Impurity	T (°C)	t (min)	C_o (cm^{-3})	ρ_s (ohm/□)	x_j (μm)	C_s* (cm^{-3})
Boron	1200	60	2×10^{19}	135	3.9	8.5×10^{18}
	1190			160	3.2	9×10^{18}
	1150			190	2.6	9×10^{18}
	1100			360	1.4	8.5×10^{18}
	1060			720	0.8	8×10^{18}
	1000			1500	0.3	9×10^{18}

† The terms used are defined in Table I.

of results is extended into low concentrations and shallow layers. Doped silicon wafers as diffusion source are attractive because they are readily available in any laboratory or production area dealing with silicon planar technology. The additional equipment for carrying out the diffusion experiments stays within reasonable limits. No extra capital budget has to be allocated for the purchase of an elaborate apparatus.

Acknowledgments

The authors are indebted to Dr. R. Dahlberg who designed the high vacuum diffusion chamber and initiated the high vacuum diffusion experiments. They also acknowledge the contribution of R. Lorenz, who carried out a part of the capsule diffusion experiments. This work has been supported by the German Bundesministerium für Wissenschaft und Forschung.

Manuscript submitted April 21, 1972; revised manuscript received Feb. 19, 1973.

Any discussion of this paper will appear in a Discussion Section to be published in the June 1973 JOURNAL.

REFERENCES

1. M. C. Duffy, F. Barson, J. M. Fairfield, and G. H. Schwuttke, *This Journal*, **115**, 84 (1968).
2. J. M. Fairfield and G. H. Schwuttke, *ibid.*, **115**, 415 (1968).
3. W. I. Armstrong and M. C. Duffy, *Electrochem. Technol.*, **4**, 475 (1966).
4. R. Dahlberg, R. Gereth, A. Kostka, and K. Kreuzer, in "Semiconductor Silicon", pp. 458-468, R. R. Haberecht and E. L. Kern, Editors, The Electrochemical Soc. Inc., New York (1969).
5. M. C. Barry and P. Olofsen, *This Journal*, **116**, 854 (1969).
6. J. D. Macdougall, *Solid State Technol.*, **14**, No. 10, 46 (1971).
7. A. N. Knopp, *This Journal*, **110**, 82 (1963).
8. A. Kostka and K. Kreuzer, *ibid.*, To be published.
9. J. C. Irvin, *Bell System Tech., J.*, **41**, 387 (1962).
10. R. Gereth, A. Kostka, and K. Kreuzer, Paper 123 presented at the Los Angeles Meeting of the Electrochem. Soc., May 10-15, 1970.
11. I. Fränz and W. Langheinrich, Private communication.
12. H. Schäfer and R. Hörnle, *Z. Anorg. Allgem. Chem.*, **263**, 261 (1950).
13. G. Grube and H. Speidel, *Z. Elektrochem.*, **53**, 339 (1949).

A Physical and Mathematical Approach to Mass Transport in Capsule Diffusion Processes

A. Kostka, R. Gereth, and K. Kreuzer

AEG-Telefunken, Semiconductor Division, Heilbronn, Germany

ABSTRACT

A mathematical model based on the various physical processes occurring in a multiphase system is developed to allow the calculation of material exchange in capsule diffusion processes. The influences of three main effects on this exchange are considered: the finite ratio of source to sink surfaces, the limited rate of exchange at the beginning of the process due to the sorption processes at the surfaces, and the disturbance of the exchange process by doping material adsorption at the capsule walls. The first effect is independent of time and offers a simple means of concentration control. The influence of the other two effects on diffusion results is more complicated and may be calculated using a computer program.

Experimental conditions of the early work on capsule diffusion allowed the results to be explained on the basis of diffusion from constant surface concentrations. For capsule diffusion processes using a powder source (1), the constant surface concentration was assumed to be equal to the source doping, which could be verified by experiment. Processes employing doped semiconductor wafers as sources (2, 3) produced surface concentrations appreciably lower than the source doping, especially for short diffusion times or low diffusion temperatures. In order to understand and control these effects, the following work has been carried out. In the first part a review of the various physical processes occurring in the capsule is given. The second part deals with a straight-forward mathematical description for every case and the mass transfer equations resulting from the combination of these different processes. Finally, some characteristic properties of the solution are evaluated.

System Components and Transport Mechanisms

Capsule diffusion processes (1-3) have been carried out in sealed and evacuated quartz tubes loaded with doped and undoped silicon material. The doped source is represented either by a powder (1) or by a wafer (2), the undoped sink is formed by the wafers to be diffused.

Key words: material exchange, solid-gas-solid transport, closed system.

The physical system considered in the present work consists of four components, namely, source, sink, capsule walls, and the gas phase inside the capsule. The treatment, however, is not restricted to the special materials silicon and quartz. It may be easily applied to other semiconductor and capsule materials by switching to the appropriate material constants

The whole system is kept at an over-all constant elevated temperature. During the process, an exchange of all material components existing in the capsule takes place depending on the different surface desorption and readsorption rates. The gas phase, therefore, consists of the gaseous state of each introduced component, together with the residual gas desorbed from the solid components during heat-up.

The material exchange in the described system is controlled by the following mechanisms: (*a*) diffusion inside the solid components, (*b*) sorption (evaporation and condensation) at the solid surfaces, and (*c*) transport in the gas phase. The physics and mathematics of process (*a*) may here be regarded as well known, whereas processes (*b*) and (*c*) require some further considerations.

Sorption effects at solid surfaces generally are rather complex in nature, and the material properties in-

volved in most systems are hardly known. However, a straightforward linear approximation of thermal desorption and physical adsorption reveals the influence of sorption parameters on the capsule diffusion process.

Thermal evaporation of semiconductor and doping atoms from the source and sink crystal surfaces is determined by the temperature and the corresponding activation energy, which is closely related to the binding energy, and has been measured, *e.g.*, for silicon (4).

Condensation rates are mainly controlled by the sticking probability and the particle concentration in the gas phase. The sticking probability is a widely unknown function of material parameters, such as the binding mechanism, surface coverage, and contaminants. Any contaminated or chemically modified surface conditions may effect a drastic reduction of the amount of material exchange caused by a reduction in sticking probability. In order to guarantee process reproducibility, wafer cleaning and capsule evacuation have to be carried out in a way that prevents the wafer surfaces from contamination or reactive gaseous material during the high temperature process.

Under certain circumstances, the inner surfaces of the capsule wall play an important role in the exchange process by adsorbing doping material from the gas phase. The adsorption process will be considered to take place during the initial phase of the diffusion run, lasting until saturation of the walls is achieved.

Material transport in the gas phase is determined by the total pressure. In the high pressure range, realized by an inert gas backfill into the capsule, it has been shown (1) that pressures exceeding 10 Torr result in a restriction of material exchange, presumably by coverage of the surfaces with foreign atoms and reduction of sticking probability. On the other hand, at pressures below 10^{-2} Torr the mean free path of the gas particles exceeds the capsule dimensions. The absence of collisions in the gas phase results in a straight line movement exhibiting shadow effects. A slice shielded from the source by another slice will not be doped (3). Consequently, in order to get a homogeneous mixture in the gas phase independently from the geometrical arrangement of the wafers, the total pressure in the capsule has to be high enough to guarantee at least a couple of collisions for an impurity atom on its way from source to sink. This is roughly the case for pressures exceeding 0.1 Torr. Because of the extremely uniform doping achieved in capsule diffusions, it can be concluded that the total pressure in the capsule will be between 0.1 and 10 Torr, most likely around 1 Torr. Since the vapor pressures of semiconductor, doping, and wall material normally are orders of magnitude smaller (5) than this value, the main part of the gas phase material must be some residual gas desorbed from the surfaces during heat-up of the capsule. It is an interesting feature of capsule diffusion that this overwhelming part of the gas phase does not influence the surface conditions of source and sink in a deleterious manner. One would expect this residual gas to consist of the air components H_2O, O_2, N_2. Nitrogen has been shown to cause no harm up to pressures of 10 Torr (1). Oxygen and H_2O, however, are highly reactant molecules causing silicon oxidation and monoxide evaporation (6) until the saturation pressure is reached.

If the amount of oxidizing material in the capsule exceeds a certain value, *e.g.*, as a result of poor pumping or ineffective water outbake, an oxide layer on the semiconductor surfaces will be formed and will act as a diffusion barrier for the doping atoms. Material exchange is drastically reduced in most of those cases.

Transport Equations and Solution

In this section, a mathematical approach to the different transport processes is made. The transport equations are then summarized and the combined problem is solved. In order to simplify the mathematical treatment, the following idealizations will be made: (*a*) diffusion in the wall material is negligible; (*b*) diffusion in source and sink follows the diffusion equation with a concentration independent diffusion coefficient; (*c*) sorption processes may be described by linear approximations involving constant activation energies and sticking probabilities; (*d*) a homogeneous gas phase transmits the material instantaneously, without taking up a significant part of it; and (*e*) adsorption of doping material at the capsule walls may influence, but not dominate, the exchange process.

All of these assumptions may be verified by a proper choice of capsule material (*a*), doping concentrations in the semiconductor material (*b*), total pressure in the gas phase (*d*), and diffusion time and temperature. For the usual cases with moderately doped silicon in quartz capsules, the validity of assumptions (*a*) through (*e*) may easily be shown (2, 3).

Evaporation.—The particle current density j_e evaporating from a solid surface is dependent on the surface particle density S (per square centimeter) and the activation energy of desorption Q via an Arrhenius formula

$$j_e = SA_0 \exp(-Q/kT) = SA \qquad [1]$$

where A_0 is a material dependent factor of proportionality, k denotes the Boltzmann constant, and T is the absolute temperature. Q is taken to be concentration independent following assumption (*c*). Calculating the dopant evaporation rate from a doped semiconductor surface and relating it to that of the semiconductor atoms (subscript s) results in

$$j_e = ca_sA_s \cdot \frac{A_0}{A_{0s}} \exp(\Delta Q/kT) = ca_sA_s\epsilon \qquad [2]$$

with c being the dopant surface concentration, and a_s the mean atomic distance in the crystal. ΔQ represents the difference of activation energies $Q_s - Q$, which is assumed to be small compared to Q_s since the binding mechanism acting between semiconductor atoms and substitutionally located dopant atoms is essentially the same as between semiconductor atoms themselves. Therefore, ϵ is a factor of proportionality which is only slightly temperature dependent. It denotes the ratio of evaporation probabilities of dopant and semiconductor atoms, respectively.

Condensation.—The particle current density j_c of atoms hitting a surface from the gas phase and sticking to it is

$$j_c = nP(kT/2\pi m)^{1/2} = nPC \qquad [3]$$

with n being the gas phase particle density, P the sticking probability, and m the particle mass. P is taken to be concentration independent following assumption (*c*).

Wall coverage.—The influence of the walls will be described by a process of coverage with dopant atoms following an exponential saturation characteristic

$$S_w = S_{\infty w}(1 - \exp(-t/t_w)) \qquad [4]$$

The wall coverage S_w approaches the saturation value $S_{\infty w}$ with a rise time t_w. The functional dependence of Eq. [4] may only be expected under the condition of constant gas phase dopant particle density. This is the case only in a system free of wall adsorption, or with small adsorption at the walls compared with the total material exchanged between source and sink according to assumption (*e*). Both t_w and $S_{\infty w}$ are regarded as experimental parameters.

Combined problem.—The physical background of the solution is the following: from the laws of sorption and Fick's diffusion laws one gets continuity equations for the dopant material currents at the solid surfaces. Together with a materials balance describing the conservation of the over-all doping material in the system, they form boundary values coupling the system of

partial differential equations for the doping concentrations $c_i(x, t)$ in source ($i = 1$) and sink ($i = 2$). The space and time coordinates are x and t, the surface is situated at $x = 0$, and the diffusion starts at $t = 0$. The diffusion equations are written

$$\dot{c}_i = Dc_i'' \quad (i = 1, 2) \qquad [5]$$

with the point and prime denoting time and space derivation, respectively.

Continuity equations.—At the surfaces of source and sink, material current is described by two different models: diffusion at the bulk side of the surface, and sorption at the gas phase side. In order to find an uncomplicated mathematical expression for the connection of these processes, the assumption is made that every particle at the surface of the semiconductor material takes part in both the diffusion and the sorption processes. This implies that the influence of the ionization process which has to occur before the doping atom will diffuse, or any other electrical influence based on surface space charge layers, may be ignored.

Under these conditions a pile-up of nondiffusing doping material at the surface is prohibited. The particle current densities resulting from diffusion and sorption on both sides of the surface have then to be equal at the surface

$$-Dc_i' = nPC - \epsilon a_s A_s c_i \quad (\text{at } x = 0,\ i = 1, 2) \qquad [6]$$

In Eq. [6], the left-hand term represents the well-known dopant diffusion current density. The right-hand terms represent dopant condensation and evaporation currents after Eq. [2] and [3], respectively.

Materials balance.—The materials balance is based on the assumption that the gas phase does not take up considerable amounts of doping material according to assumption (d) which can be justified for the case of doped silicon in quartz capsules (2). Consequently, the total material currents out of source, sink, and walls sum up to zero

$$F_1Dc_1' + F_2Dc_2' - F_w\dot{S}_w = 0 \quad (\text{at } x = 0) \qquad [7]$$

F denotes the various areas of source (subscript 1), sink (subscript 2), and wall (subscript w). $\dot{S}_w$ represents the time derivative of the wall surface coverage which is equal to the net dopant current density onto the wall.

Initial values.—The initial values depend on the doping conditions of source and sink wafers. For ease of calculation and because of the practical interest we choose the case of homogeneously doped source and undoped sink, that is

$$c_1 = c_o = \text{const} \quad (\text{for all } x \text{ at } t = 0)$$
$$c_2 = 0 \qquad [8]$$

Solution.—The coupled system of Eq. [5]-[8] can be uncoupled and solved under the condition that the term $\dot{S}_w$ in Eq. [7] does not depend significantly on the solution itself. This is the case with Eq. [4] for S_w.

Introduction of the surface ratios $\Phi = F_1/(F_1 + F_2)$ and $\Phi_w = F_w/(F_1 + F_2)$ together with two auxiliary functions

$$d = c_1 - c_2$$
$$m = \Phi c_1 + (1 - \Phi)c_2 \qquad [9]$$

and Eq. [4] into Eq. [5]-[8] results in

$$\dot{d} = Dd''$$
$$d = c_o \quad (\text{at } t = 0)$$
$$d' = \epsilon a_s A_s d/D \quad (\text{at } x = 0) \qquad [10]$$

and

$$\dot{m} = Dm''$$
$$m = \Phi c_o \quad (\text{at } t = 0)$$
$$m' = \Phi_w S_{\infty w} \exp(-t/t_w)/Dt_w \quad (\text{at } x = 0) \qquad [11]$$

The solution of Eq. 10 yields (3, 7)

$$d = c_o(\text{erf}(x/2\sqrt{Dt}) + d^*)$$
$$d^* = \exp(t/t_s + x/\sqrt{Dt_s}) \cdot \text{erfc}(\sqrt{t/t_s} + x/2\sqrt{Dt})$$
$$t_s = D/(\epsilon a_s A_s)^2 \qquad [12]$$

A solution of Eq. [11] is not directly available by using elementary or otherwise tabulated functions. It has to be evaluated numerically from the following integral form

$$m = \Phi c_o - \Phi_w S_{\infty w} m^*$$
$$m^* = \frac{1}{t_w\sqrt{\pi D}} \int_o^t \exp\left(-\frac{\tau}{t_w} - \frac{x^2}{4D(t-\tau)}\right) \frac{d\tau}{\sqrt{t-\tau}} \qquad [13]$$

with help of a computer program. The validity of this solution is verified by insertion. The concentration profiles c_1 and c_2 existing in the source and sink crystals after the diffusion process are now easily achieved by the inversion of Eq. [9] and the introduction of d and m from Eq. [12] and [13]. They are given by

$$c_1 = \Phi c_o + (1 - \Phi)\, c_o(\text{erf}(x/2\sqrt{Dt}) + d^*) - \Phi_w S_{\infty w} m^*$$
$$c_2 = \Phi c_o(\text{erfc}(x/2\sqrt{Dt}) - d^*) - \Phi_w S_{\infty w} m^* \qquad [14]$$

Discussion

The concentration profiles described by Eq. [14] differ from the approximate solution

$$c_1 = c_o$$
$$c_2 = c_o \text{ erfc}(x/2\sqrt{Dt}) \qquad [15]$$

one would get if the sink surface concentration were kept constant and equal to the source doping c_o (diffusion from constant source). One geometrical and two physical effects are responsible for the difference:

(a) The finite surfaces of source and sink limit the maximum concentration achievable at the sink surface to the value Φc_o which is lower than the source doping c_o.

(b) sorption processes at source and sink surfaces limit the rate of material exchange especially in the first stage of diffusion, reducing the concentration in the sink through function d^*.

(c) sorption processes at the capsule wall effect a loss of doping material until saturation of the wall, again reducing the concentration both in source and sink through the term $\Phi_w S_{\infty w} m^*$.

One may note that for the extreme case of a source of infinite surface (powder, $\Phi = 1$) with infinite sorption rates ($d^* = 0$) and negligible wall adsorption ($S_{\infty w} = 0$), Eq. [14] will transform into Eq. [15].

Inserting $x = 0$ into Eq. [14] yields the variation of surface concentrations c_s in source and sink with time. It is determined by the correction functions d^* and m^*, and the relative magnitude of the constants involved. The time dependences of d^* and m^* are illustrated in Fig. 1 for a representative relation between t_s and t_w. For $t > t_w$ and $t > t_s$, both corrections decrease proportionally to the square root of diffusion time. The influence of m^* exhibits a maximum at times around t_w. The corresponding time dependence of surface concentrations is shown in Fig. 2. The dashed lines refer to the case of negligible influence of the walls on the exchange process ($S_{\infty w} = 0$ in Eq. [14]). Because of the sorption limited exchange at times shorter than t_s, the surface concentration in the sink gradually rises from 0 and later saturates at the equilibrium value Φc_o. During the same initial time interval lasting approximately $10t_s$, the surface concentration in the source falls from its initial value c_o down to the equilibrium value Φc_o. The solid lines in Fig. 2 represent the case of considerable adsorption at the capsule walls. The correction term $\Phi_w S_{\infty w}\, m^*$ is also shown for comparison by

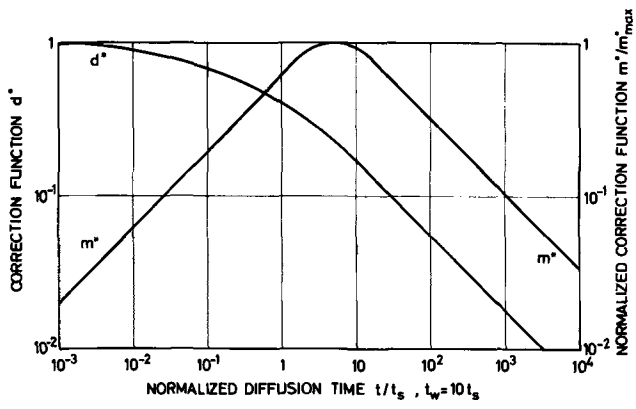

Fig. 1. Variation of the correction functions d^* and m^* with time

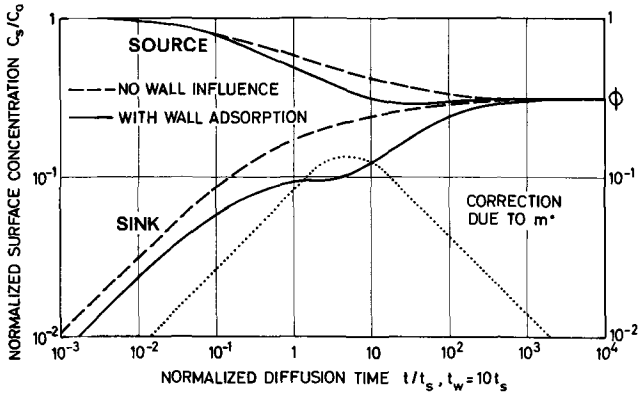

Fig. 2. Variation of normalized surface concentrations in source and sink with time. The correction due to m^* is inserted for comparison.

the dotted line. The result is a marked dip in the concentration curves at times around t_w.

For appreciably longer times, the deviation from Φc_0 rapidly vanishes. Therefore, after diffusion times longer than approximately $10t_w$, a constant surface concentration of the value Φc_0 may be assumed as a boundary condition of the diffusion process, resulting in a nearly undisturbed complementary error function profile.

The absolute values of the characteristic time constants t_s and t_w usually depend on material properties and temperature. The temperature dependence of t_s may be derived from that of D and A_s via the definition of t_s in Eq. 12. For silicon, t_s decreases with temperature, varying from some minutes to some seconds between 1050° and 1200°C. The values of ϵ, which are necessary to calculate t_s, range between 10 and 100 and have been found by fitting the theory to experimental results (3). In the same way, for a quartz capsule t_w is shown to decrease with temperature, with absolute values somewhat higher than t_s mentioned above. For silicon in quartz capsules, therefore, it is possible to avoid deviations from the erfc-solution by using high-temperature, long-time diffusions. For a successive prediction of results achieved by diffusions leading to shallow profiles with junction depths in the submicron range (3), however, the more rigid solutions of Eq. [14] have to be used, since these diffusions are low-temperature and short-time processes.

Acknowledgment

This work was supported by the German Bundesministerium für Wissenschaft und Forschung.

Manuscript submitted April 21, 1972; revised manuscript received Feb. 19, 1973.

Any discussion of this paper will appear in a Discussion Section to be published in the June 1974 JOURNAL.

REFERENCES

1. W. J. Armstrong and M. C. Duffy, *Electrochem. Technol.*, **4**, 475 (1966).
2. R. Dahlberg, R. Gereth, A. Kostka, and K. Kreuzer, in "Semiconductor Silicon," pp. 458-468, R. R. Haberecht and E. L. Kern, Editors, The Electrochemical Society Softbound Symposium Series, New York (1969).
3. R. Gereth, A. Kostka, and K. Kreuzer, *This Journal*, **120**, 966 (1973).
4. R. L. Batdorf and F. M. Smits, *J. Appl. Phys.*, **30**, 259 (1959).
5. R. E. Honig, *RCA Rev.*, **23**, 567 (1962).
6. A. N. Knopp, *This Journal*, **110**, 82 (1963).
7. Ph. Frank and R. v. Mises, "Differentialgleichungen der Physik," Part II, pp. 526 ff., Dover Publications, Inc., New York (1961).

Concentration, Solubility, and Equilibrium Distribution Coefficient of Nitrogen and Oxygen in Semiconductor Silicon

Y. Yatsurugi, N. Akiyama, and Y. Endo

Komatsu Electronic Metals Company, Hiratsuka, Japan

and T. Nozaki

Institute of Physical and Chemical Research, Wako-shi, Saitama, Japan

ABSTRACT

The concentration of nitrogen and oxygen in semiconductor silicon and their solubilities in silicon at its melting point have been measured by charged particle activation analysis and infrared spectrophotometry. It has been found that: (*i*) commercial semiconductor silicon contains less than 1×10^{15} atoms/cm^3 of nitrogen in the un-ionized state; (*ii*) the solubility in solid silicon is $4.5 \pm 1.0 \times 10^{15}$ atoms/cm^3 for nitrogen and $2.75 \pm 0.15 \times 10^{18}$ atoms/cm^3 for oxygen; and (*iii*) the solubility in liquid silicon is about 6×10^{18} atoms/cm^3 for nitrogen and $2.20 \pm 0.15 \times 10^{18}$ atoms/cm^3 for oxygen. Thus, the equilibrium distribution coefficient has been determined to be about 7×10^{-4} for nitrogen and 1.25 ± 0.17 for oxygen. The solubilities of the two elements are compared with those of other elements, especially carbon, and are discussed thermochemically.

After maximum purification of any semiconductor material or metal, carbon, nitrogen, or oxygen almost always constitutes a major portion of the remaining impurity. These light elements are abundant in nature, but a reliable determination of their sub-ppm level cannot be carried out with ease. We reported previously on the concentration and behavior of carbon in semiconductor silicon as studied by charged particle activation analysis (1). Similar studies have been made for nitrogen and oxygen. Infrared spectrophotometry was also used for oxygen, after calibration by activation analysis. As is well known, the activation analysis gives the total oxygen concentration, but the spectrophotometry is sensitive only to oxygen forming the Si-O-Si bonding in silicon crystal. In this paper, (*i*) the concentration range for nitrogen and oxygen in commercial semiconductor silicon is presented, (*ii*) the solubilities of the two elements in solid and liquid silicon at its melting point are given, (*iii*) the physical states of the two elements in solid silicon are discussed, and (*iv*) the solubilities of carbon, nitrogen, and oxygen in silicon are treated thermochemically.

Experimental

Sample preparation.—Commercial semiconductor silicon of various origins and specifications was collected as the sample. In order to obtain polycrystalline silicon rods of anomalous nitrogen contents, monosilane was decomposed thermally in the presence of ammonia. Also, elementary silicon in various stages of the monosilane process at Komatsu Electronic Metals Company was taken to be analyzed. For the measurement of the maximum solubility of the two elements, pure silicon was doped with each of them up to the saturation concentration at the melting point of silicon.

For the measurement of the solid solubility of nitrogen, a silicon rod (30 mm diameter) was cut into hemicylinders and a sufficient quantity of Si_3N_4 was sandwiched between them. A molten zone (10 mm in length) with various velocities was then passed through several parts of the sandwich, in an atmosphere of argon containing several per cent of nitrogen. In the zone-melting, the melt was always covered with small particles of silicon nitride. To determine the solubility of nitrogen in liquid silicon, silicon with Si_3N_4 powder was kept just above its melting point in an evacuated quartz ampoule and was then suddenly cooled to give silicon grains (2-4 mm diameter).

For the oxygen doping, the result of Kaiser and Breslin was used (2). In an atmosphere of oxygen, a molten zone was made, kept immobile for 10 min, and then caused to travel in a part of a silicon rod. Several parts of the same rod were zone melted with various velocities to provide the sample for solubility measurements. Also, the molten zone was cooled suddenly for the measurement of the solubility of oxygen in liquid silicon; the solidification rate was of the order of 100 mm/min.

Activation analysis.—The reactions of $^{14}N(p,\alpha)^{11}C$ and $^{16}O(^3He,p)^{18}F$ were used for the activation analysis of nitrogen and oxygen, respectively. Detailed descriptions of the charged particle activation analysis for carbon, nitrogen, and oxygen in semiconductor silicon are given in a separate paper (3). Careful examination of the accuracy in the oxygen determination, however, showed that the result of the given method involving the chemical separation of ^{18}F should be corrected by a factor of $1.19 + 0.03$. This correction is due mainly to the coprecipitation of $PbCl_2$ with $Pb^{18}FCl$, which results in an overestimation of carrier recovery and thus an underestimation of oxygen content (4). In the present study, oxygen concentrations over 2×10^{17} atoms/cm^3 were usually determined nondestructively, and the correction was applied to the results of the separation-involving method.

This activation analysis has as its lower limit of sensitivity 1×10^{14} atoms/cm^3 for nitrogen and 5×10^{14} atoms/cm^3 for oxygen. Uncertainty in the determination of nitrogen is estimated to be 10 and 30% for concentrations of 1×10^{17} and 1×10^{15} atoms/cm^3, respectively. For oxygen, the accuracy is slightly better than for nitrogen in concentrations over 5×10^{15} atoms/cm^3 but is poorer in those under 2×10^{15} atoms/cm^3.

For granular samples a technique different from that described in Ref. (3) should be used in the charged particle bombardment. A cavity ($30 \times 20 \times 3$ mm) was made in an aluminum block and was covered by a pure silicon plate (200 μm thick). The sample grains were put in the cavity and bombarded by the charged particles through the plate. After the removal of the surface contamination by etching under controlled conditions, the induced annihilation activity was measured nondestructively and its decay followed. This

Key words: solubility, equilibrium distribution coefficient, infrared spectrophotometry of O, phase diagram of N-Si, phase diagram of O-Si, concentration of N and O in Si.

technique gives slightly poorer accuracies than the value described above.

Infrared spectrophotometry of oxygen.—The absorbance of the oxygen absorption peak at 1108 cm^{-1} was measured at room temperature by a popular spectrophotometer of grating type (Japan Spectroscopic Company Model IR-G). After examination of measurement conditions, the spectrophotometer was set as follows: beam cross section, 10 × 5 mm; scanning velocity, 600 cm^{-1}/hr; mechanical slit width, 0.6 mm (observed spectral half-width, 38 cm^{-1}). The sample thickness after a mirror-polishing with the aid of diamond paste was selected to be 2, 5, or 10 mm with uncertainty of ±5 μm. An ultrapure silicon, after being ascertained by activation analysis not to contain more than 3×10^{15} atoms/cm^3 of oxygen, was used as the reference sample. Throughout the present study, care was taken to the possible inhomogeneous distribution of oxygen within a single silicon slice (5).

Since a number of different values have been reported for the absorptivity of oxygen in silicon (5-11), we first examined it using various silicon samples of known histories. Their absorbances were measured and then they were analyzed by activation analysis. [The absorptivity is defined by the relation of $10^{-abc} = 10^{-A} = T/T_0$, where a is the absorptivity, b is the sample thickness, c is the concentration, and T and T_0 are the transmittance for the sample and for the pure matrix itself, respectively, after the correction of multiple reflection. Thus, the absorption coefficient is equal to (ln 10) ac.]

The results for as-grown samples are shown in Fig. 1 (for lower oxygen concentration range) and Fig. 2 (for higher oxygen concentration range), together with the calibration curve used in the present study. Two other calibration curves are also shown in Fig. 2. The ever-reported results for the comparison between infrared absorption and activation analysis (6, 9-11), vacuum fusion (5, 7, 8) of the lithium-diffusion method (9) can be grouped into two categories, one corresponding to an absorptivity of 0.073 ± 0.010 (cm · atomic ppm)$^{-1}$ (5-7) and the other giving considerably lower absorptivities. Our calibration curve belongs to the former. Many of our experimental plots in Fig. 2 lie in the upper side of our own calibration curve, which is the extrapolation from the experimental plots in Fig. 1. A discussion for the justification of our curve and for the explanation of the upward deviation of the experimental plots in Fig. 2 is given in a later section.

As low as 5×10^{15} atoms/cm^3 of oxygen can be detected by this spectrophotometry at room temperature, when a reliable reference sample is available. Its precision is better than activation analysis for concentrations over 2×10^{16} atoms/cm^3. The effect of surface

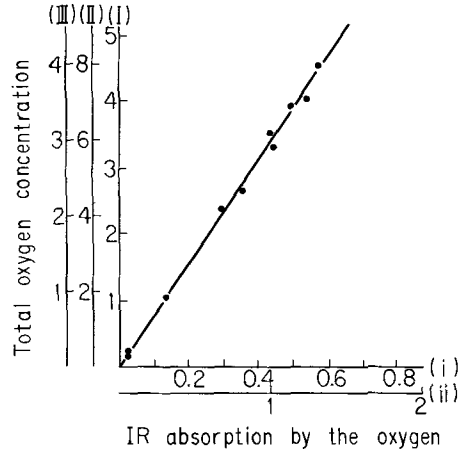

Fig. 1. Infrared absorption vs. total oxygen concentration in lower concentration range. Units of the ordinate I, weight ppm; II, atomic ppm; III, 10^{17} atoms/cm^3. Abscissa: *i*, absorbance for 1-cm sample; *ii*, absorption coefficient (cm^{-1}).

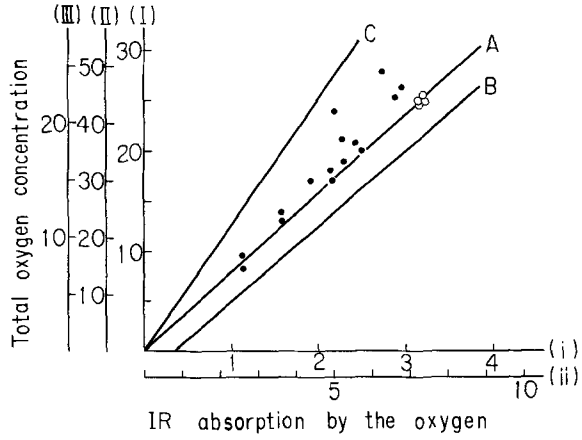

Fig. 2. Infrared absorption vs. total oxygen concentration in higher concentration range. Experimental plots: ●, for ordinary as-grown crystal; ○, for suddenly solidified crystal. Calibration curves: A, present work; B, by Kaiser *et al.* (for single-beam method) (5); C, by Baker (8). Units of the ordinate: I, weight ppm; II, atomic ppm; III, 10^{17} atoms/cm^3. Abscissa: *i*, absorbance for 1-cm sample; *ii*, absorption coefficient (cm^{-1}).

oxygen was examined by treating sample slices with various reagents under 200°C; no notable change of the absorbance has been observed.

Measurement of the effect of nitrogen on conductivity.—The resistivity of semiconductor silicon crystals of various nitrogen contents was measured by the usual method. Nitrogen was then removed from the crystals by three zone passes, and the change in the resistivity was measured. Further, the concentration of phosphorus and boron were determined by the melt-back technique (12), and their contribution to the resistivity of the zone-melted sample was subtracted in order to determine the effect of nitrogen on the resistivity.

Results and Discussion

Nitrogen and oxygen content of semiconductor silicon.—Nitrogen content of commercial semiconductor silicon was found to be always less than 1×10^{15} atoms/cm^3 and usually in the range of 1×10^{14} and 5×10^{14} atoms/cm^3. Oxygen contents of various kinds of semiconductor silicon have already been reported in our previous paper together with the carbon content (1). Most of the float-zone crystals contained from 2×10^{15} to 2×10^{16} atoms/cm^3 and Czochralski crystals usually had from 2×10^{17} to 1×10^{18} atoms/cm^3 of oxygen. It is clear that the oxygen content of the silicon single crystal depends on the condition of the crystal formation but scarcely on the starting material.

Solubility and equilibrium distribution coefficient of nitrogen.—Nitrogen was found to be distributed almost uniformly throughout the entire part of the sample prepared by zone-melting the Si_3N_4-inserted rod, except at its tail-end portion, as is shown in Fig. 3. In the

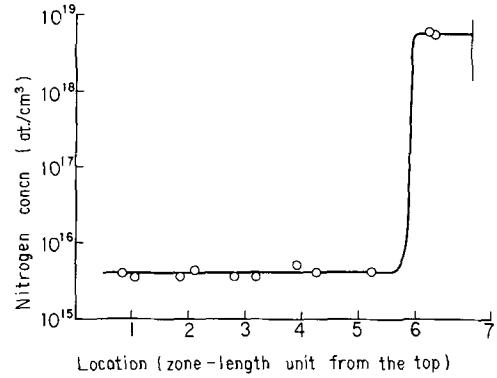

Fig. 3. Nitrogen distribution in a silicon rod after a passage of a nitrogen-saturated molten zone. Zone velocity: 0.4 mm/min.

zone-melting, the liquid phase was always saturated with nitrogen. The resultant solid silicon, however, could contain a slightly higher concentration of nitrogen than its solid solubility at the melting point of silicon, because the solid-liquid boundary might have been dendritic and thus the growing solid phase would have captured a small fraction of the liquid phase. In fact, the nitrogen concentration in the solid was found to depend on the zone-traveling velocity, as is shown in Fig. 4. The solid solubility at the melting point of silicon can be obtained by the extrapolation of the curve in Fig. 4 to zero velocity; it is $4.5 \pm 1.0 \times 10^{15}$ atoms/cm^3.

Nitrogen solubility in liquid silicon at its melting point was determined by the use of the suddenly solidified sample; it was found to be about 6×10^{18} atoms/cm^3. This value agrees fairly well with the value of around 10^{19} atoms/cm^3 reported by Kaiser and Thurmond (13). Almost the same nitrogen concentration was observed at the tail-end portion of the sample from the Si_3N_4-inserted rod when this portion was solidified rapidly. The equilibrium distribution coefficient of nitrogen between solid and liquid silicon, which is equal to the ratio of nitrogen solubility in solid silicon to that in liquid silicon at its melting point, has thus been determined to be about 7×10^{-4}.

From the above information, the phase diagram of the N-Si system in the extremely low nitrogen concentration range can be drawn. It is shown in Fig. 5. The lowering of the melting point (ΔT) was calculated from the relation

$$\Delta T = x(1 - K_{eq})RT_m^2/L \qquad [1]$$

where x is the concentration of the solute in the liquid phase in mole fraction, K_{eq} is its equilibrium distribution coefficient, R is the gas constant, and T_m and L are the melting point and the molar heat of fusion, respectively, of the solvent (for silicon, $T_m = 1683$°K and $L = 12.1 \pm 0.4$ kcal/mol). This equation is an integrated form of Clapeyron's equation and is valid for dilute solutions obeying Raoult's law. Among various silicon nitrides, Si_3N_4 is regarded as the stable form when contacted with silicon at its melting point (13). In the single-crystal formation of silicon, impurity nitrogen is removed very easily, because not only

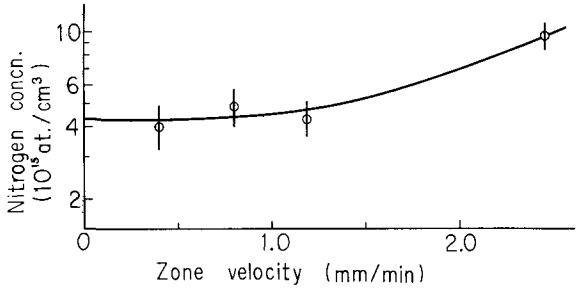

Fig. 4. Nitrogen concentration in silicon solidified from nitrogen-saturated melt with various rates.

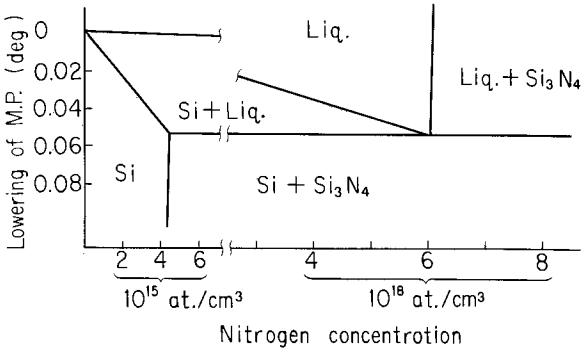

Fig. 5. Phase diagram of N-Si system in extremely low nitrogen concentrations.

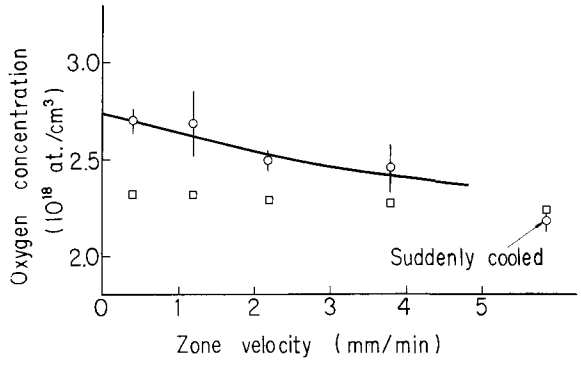

Fig. 6. Oxygen concentration in silicon solidified from oxygen-saturated melt with various rates. ϕ: Result of activation analysis with standard deviation. ⊡: Result of infrared spectrophotometry.

is its distribution coefficient so small but also it evaporates so readily from a silicon melt (14).

Solubility and equilibrium distribution coefficient of oxygen.—The total oxygen concentration in silicon crystals obtained by solidification of the oxygen-saturated melt at various rates is shown in Fig. 6. For each rate, from 4 to 11 wafers were cut out of the zone-melted rods and analyzed by activation; the mean value of the result is indicated in Fig. 6 with standard deviation. The infrared-sensitive oxygen concentration is also shown in Fig. 6, although only the total concentration is necessary for the determination of the solubility. The solubility of oxygen in solid silicon and liquid silicon at its melting point can be given as the total oxygen concentration for the crystals solidified from the oxygen-saturated melt at an infinitely low rate and an infinitely high rate, respectively. Thus, although some arbitrariness may be seen in drawing the smooth curve in Fig. 6, the following constants have been obtained: (*i*) solubility of oxygen in solid silicon at its melting point, $2.75 \pm 0.15 \times 10^{18}$ atoms/cm^3; (*ii*) solubility of oxygen in liquid silicon at its melting point, $2.20 \pm 0.15 \times 10^{18}$ atoms/cm^3; and (*iii*) equilibrium distribution coefficient of oxygen in silicon, 1.25 ± 0.17.

The phase diagram of the O-Si system in the extremely low oxygen concentration range is shown in Fig. 7. The raising of the melting point was calculated by Eq. [1] for K_{eq} equal to 1.25. The stable oxygen silicide in contact with silicon is known to be SiO at the melting point of silicon but to be SiO_2 at somewhat lower temperatures (15). Oxygen in silicon forms a peritectic mixture and cannot be removed by segregation. Oxygen, however, evaporates easily from a silicon melt as SiO, and the oxygen content of the usual float-zone crystals is highly dependent on the conditions of atmosphere in the zone-melting.

Infrared-insensitive oxygen.—As is seen in Fig. 6, silicon crystals made from oxygen-saturated melt usually contained infrared-insensitive oxygen, with its quantity increasing with the decrease of the solidification rate. The upward deviation of the experimental

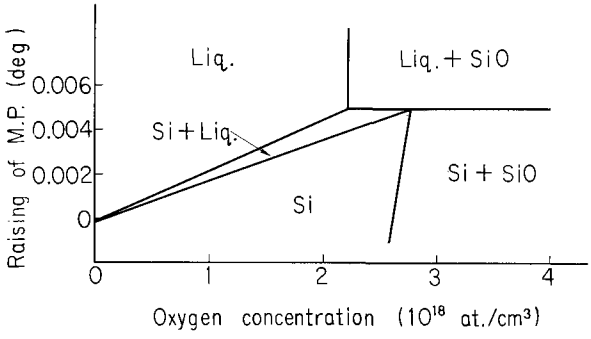

Fig. 7. Phase diagram of O-Si system in extremely low oxygen concentrations.

plots in Fig. 2 can be explained also by the presence of infrared-insensitive oxygen. The nature of this infrared-insensitive oxygen is thought to be aggregates of oxygen (16). The aggregation process and the solid solubility of oxygen in silicon have been studied by many workers (16-18). It has been reported that the aggregation proceeds fairly rapidly over 1000°C and that oxygen in heat-treated silicon is partly aggregated when its concentration is relatively high. Also from our observation on the change of the infrared absorbance in heat-treatment, it can be guessed that the aggregation proceeds to a notable extent after a melt of a relatively high oxygen content is solidified at a usual rate in industrial zone-melting or Czochralski process. Although the rate of aggregation depends on many factors, it is quite natural that the lower the solidification rate and the higher the total oxygen concentration, the larger the aggregated fraction, when other factors are the same. A tendency of the concenration dependence can be observed in Fig. 2.

The experimental relationship between the total and infrared-sensitive oxygen concentration in Fig. 1 is denoted by a straight line, indicating the absence of any notable amount of oxygen aggregate in this low concentration range. This gives a justification of our calibration curve, although many experimental plots in Fig. 2 lie on the upper side of it. The infrared-insensitive fraction, however, has been found mostly to be less than 20% of the total oxygen in as-grown silicon crystals.

Effect of nitrogen on semiconductor property.— The resistivity of an N-type crystal containing nitrogen up to the saturation concentration at the melting point 4.5×10^{15} atoms/cm^3, was found to be 37 ohm-cm, showing the existence of 1.4×10^{14}/cm^3 of free electrons. By the melt-back technique, boron content was found to be about 2×10^{12} atoms/cm^3. Thus, even when the free electrons were entirely due to the nitrogen, the ionization degree of nitrogen should be less than 4%. The phosphorus content of the original crystal was calculated from the measured resistivity of the zone-melted crystal by the use of its reported effective distribution coefficient which was regarded as 0.35 for our solidification rate of about 0.5 mm/min; it was 1.1×10^{14} atoms/cm^3. Therefore, the number of free electrons in the silicon crystal excluding those derived from the phosphorus atoms amounts to only about 1% of the number of nitrogen atoms. When the evaporation of phosphorus in zone-melting is taken into account, the ionization degree of nitrogen should be less than 1%.

A still higher resistivity (7000 ohm-cm) was reported by Kaiser and Thurmond for silicon crystals grown from a nitrogen-saturated melt (13). They calculated the distribution coefficient of nitrogen to be less than 10^{-7} on the assumption that the nitrogen was totally ionized in silicon, although they did not rule out the possibility of the presence of un-ionized nitrogen. Now the existence of un-ionized nitrogen has been proved, and the distribution coefficient of less than 10^{-7} has been shown to be incorrect.

Comparison of the solubility and distribution coefficient.—A summary of the solubilities of carbon, nitrogen, and oxygen in solid and liquid silicon at its melting point (or more correctly at the eutectic or peritectic point) and their equilibrium distribution coefficients is given in Table I. The solubilities of the three elements in liquid silicon are of the same order and are considerably lower than those of many metallic elements, which are soluble up to 10^{20}-10^{22} atoms/cm^3 (19). The solubility in solid silicon, on the other hand, is markedly different among the three elements. Oxygen is more soluble than many refractory metals in solid silicon but less soluble than many metals of low melting points (with a few exceptions such as zinc), and nitrogen is one of the least soluble elements (19). The distribution coefficients of elements within a given group of the Periodic Table have been known to increase with the decrease of atomic number (19). This rule, however, does not hold true for carbon and nitrogen, which have smaller distribution coefficients than silicon and phosphorus.

Explanation of the low solubilities and the small distribution coefficients.—The low solubilities can be explained by the following two properties of the three elements: (*i*) they form stable silicides of vast dissociation energies (SiC, Si_3N_4, and SiO), and (*ii*) they are significantly smaller than silicon in atomic size. The small distribution coefficients of carbon and nitrogen can also be explained by the latter.

As is well known, the solubility in general can be given by the relation of

$$[M] = \exp[\Delta S/R] \exp[-\Delta H/RT] \qquad [2]$$

where $[M]$ is the solubility of a solute M in mole fraction, S is the entropy of solution, R is the gas constant, ΔH is the heat of solution, and T is the absolute temperature. Since H for a solid solution implies the energy necessary for the rupture of its crystal lattice, the following tendency is regarded as existing naturally and has actually been observed (19): the larger the heat of vaporization of the solute substance, the higher its ΔH and consequently the lower its solubility. For the present three elements when dissolved in the atomic state, the heat of dissociation of the stable silicide into silicon bulk, and monatomic gas of carbon, nitrogen, or oxygen should be regarded as equivalent to the heat of vaporization for a usual metallic solute substance. The heats of dissociation calculated by the use of thermochemical tables (15, 20) are shown in Table I. They are as large as the heat of vaporization of a refractory metal (*e.g.*, Zr, 146; Nb, 172; W, 203; Re, 186 kcal/mol at 25°C), and this can be the major reason for the low solubilities. Oxygen in liquid silicon may be in the molecular state of SiO, because its heat of vaporization is about 70 kcal/mol (15). However, this molecule is so different from silicon in atomic size and shape that its solubility should be low, as is shown by the elastic model theory cited just below.

The replacement of an atom in its own crystal by a foreign atom of a different size introduces a strain

Table I. Solubilities of carbon, nitrogen, and oxygen in silicon at its melting point and their equilibrium distribution coefficients and some related values

	Carbon	Nitrogen	Oxygen
Solubility in solid			
Atoms/cm^3	$3.2 \pm 0.3 \times 10^{17}$	$4.5 \pm 1.0 \times 10^{15}$	$2.75 \pm 0.15 \times 10^{18}$
Atomic fraction	$6.5 \pm 0.5 \times 10^{-6}$	$9 \pm 2 \times 10^{-8}$	$5.6 \pm 0.3 \times 10^{-5}$
Solubility in liquid			
Atoms/cm^3	$4.5 \pm 0.5 \times 10^{18}$	6×10^{18}	$2.20 \pm 0.15 \times 10^{18}$
Atomic fraction	$9 \pm 1 \times 10^{-5}$	1.2×10^{-4}	$4.5 \pm 0.3 \times 10^{-5}$
Equilibrium distribution coefficient	0.07 ± 0.01	7×10^{-4}	1.25 ± 0.17
Heat of dissociation,* Kcal/mol	1.9×10^{2}	1.6×10^{2}	1.6×10^{2}
Atomic radius, A	0.77	0.53	0.60
Tetrahedral radius, A	0.77	0.70	0.66

* The heat of reaction for SiC = Si + C, $\frac{1}{4}Si_3N_4 = \frac{3}{4}Si + N$ or SiO = Si + O, with the products being solid Si and monatomic gas of C, N, or O.

energy into the crystal, which is a component of ΔH. The strain energy ($[E^{st}]$) for a substitutional impurity in silicon has been shown to be given by the relation of

$$[E^{st}] = 22 \times 10^{20} (\Delta r)^2 \text{ cal/mol} \quad [3]$$

where Δr is the disparity of tetrahedral radius (in angstroms) between silicon and the impurity (21). Among various theories treating the solubility or alloy formation, the elastic model theory emphasizes the role played by the disparity of atomic size (22). This theory shows that: the greater the disparity, the less the mutual solubility both in liquid and solid solution and also the less the distribution coefficient. The tetrahedral radii and atomic radii of the three elements are shown in Table I. For silicon they are both 1.17Å. Since even thallium, lead, and bismuth are larger than silicon by only about 3Å in tetrahedral radius, the disparity between silicon and the three elements should be considered to be remarkable. Although this theory is regarded as not always reasonable (22), it can explain the small solubilities of the three elements and also the small distribution coefficients of carbon and nitrogen.

Since nitrogen in solid silicon is not ionized, it is probably not substitutional. The much higher ionization potential of nitrogen (14.54 eV) than the ionization potentials of other Group V elements (P, 11.0; As, about 10; Sb, 8.46; Bi, about 8 eV) can be an additional cause of the undetectably low concentration of ionized substitutional nitrogen.

Numerical value of ΔH and ΔS.—It would be worthwhile calculating ΔS in Eq. [2] by the use of the solubility in Table I and of the reported ΔH. For carbon in liquid silicon, Scace gave 59 kcal/mol for ΔH (23); thus ΔS is obtained as about 17 cal mol^{-1} deg^{-1}. For carbon in solid silicon, the value of ΔH reported by Bean and Newman (18) agrees closely with our result (24), the latter being 55 ± 4 kcal/mol. It thus follows that $\Delta S = 88 \pm 2.6$ cal mol^{-1} deg^{-1}. Two different values have been reported for ΔH of oxygen in solid silicon: 22 ± 2 kcal/mol by Hrostowski (17) and 38 ± 4 kcal/mol by Bean and Newman (18). The former and the latter give -6.4 ± 1.5 cal mol^{-1} deg^{-1} and 3.0 ± 2.5 cal mol^{-1} deg^{-1}, respectively, for ΔS. We followed their experiment; our result is closer to the former than to the latter. The smaller ΔH of oxygen than that of carbon makes oxygen more soluble in solid silicon than carbon in spite of its very small ΔS.

Anomalous distribution coefficient of oxygen.—Oxygen in solid silicon is known to be interstitial, forming a Si—O—Si bonding. The small size and the bivalent nature with its own bond angle of oxygen atom are considered favorable for oxygen to be in this state. This can be the reason for the higher solid solubility of oxygen than that of carbon and nitrogen and also of its anomalous distribution coefficient. From the electronic configuration of nitrogen atom, the formation of a Si—N—Si bonding in silicon crystal is regarded as the least probable.

Acknowledgment

The authors would like to express their thanks to the Cyclotron Group of the Institute of Physical and Chemical Research for their bombardment services in the activation analysis.

Manuscript submitted Sept. 28, 1972 revised manuscript received Jan. 30, 1973.

Any discussion of this paper will appear in a Discussion Section to be published in the December 1973 JOURNAL.

REFERENCES

1. T. Nozaki, Y. Yatsurugi, and N. Akiyama, *This Journal*, **117**, 1566 (1970).
2. W. Kaiser and J. Breslin, *J. Appl. Phys.*, **29**, 1292 (1958).
3. T. Nozaki, Y. Yatsurugi, and N. Akiyama, *J. Radioanal. Chem.*, **4**, 87 (1970).
4. T. Nozaki, Y. Yatsurugi, N. Akiyama, Y. Endo, and Y. Makide, *ibid.*, To be published.
5. W. Kaiser and P. H. Keck, *J. Appl. Phys.*, **28**, 882 (1957).
6. E. A. Schweikert and H. L. Rook, *Anal Chem.*, **42**, 1525 (1970).
7. K. Graff, E. Grallath, S. Ades, G. Goldbach, and G. Tölg, *Solid-State Electron.*, To be published.
8. J. A. Baker, *ibid.*, **13**, 1431 (1970).
9. B. Pajot, *ibid.*, **12**, 923 (1969).
10. C. K. Kimm, *Radiochem. Radioanal. Letters*, **2**, 25 (1969).
11. C. Gross, G. Gaetano, T. N. Tucker, and J. A. Baker, *This Journal*, **119**, 926 (1972).
12. F. H. Horn, *ibid.*, **114**, 1307 (1967).
13. W. Kaiser and C. D. Thurmond, *J. Appl. Phys.*, **30**, 427 (1959).
14. T. Nozaki, Y. Makide, Y. Yatsurugi, N. Akiyama, and Y. Endo, *Int. J. Appl. Radiat, Isotopes*, **22**, 607 (1971).
15. O. Kubaschewski, E. Ll. Evans, and C. B. Alcock, "Metallurgical Thermochemistry," p. 226, Pergamon, Oxford (1967).
16. W. Kaiser, H. L. Frich, and H. Reiss, *Phys. Rev.*, **112**, 1546 (1958).
17. H. J. Hrostowski and R. H. Kaiser, *J. Phys. Chem. Solids*, **9**, 214 (1959).
18. A. R. Bean and R. C. Newman, *ibid.*, **32**, 1211 (1971).
19. F. A. Trumbore, *Bell System Tech. J.*, **39**, 205 (1960).
20. *E.G.*, Ref. (15), p. 304; and "JANAF Thermochemical Tables," compiled by D. R. Stull *et al.*, distributed from Clearinghouse, U.S.A. (1965-1967).
21. K. Weiser, *J. Phys. Chem. Solids*, **7**, 118 (1958).
22. R. A. Oriani, *ibid.*, **22**, 335 (1957).
23. R. I. Scace and G. A. Slack, *J. Chem. Phys.*, **30**, 1551 (1959).
24. Y. Endo, Y. Yatsurugi, N. Akiyama, and T. Nozaki, *Anal. Chem.*, **44**, 2258 (1972).

Interface Reactions of B_2O_3-Si System and Boron Diffusion into Silicon

E. Arai, H. Nakamura, and Y. Terunuma

Musashino Electrical Communication Laboratory, Nippon Telegraph and Telephone Public Corporation, Musashino-shi, Tokyo, Japan

ABSTRACT

The interface reactions of the B_2O_3-Si system were studied by infrared spectroscopy, electron and x-ray diffraction, etc.

The compound, which was produced at the B_2O_3-Si interface in the temperature range of 900°-1200°C closely resembled SiB_4 or SiB_6 in the diffraction measurements. The growth rate of silicon oxide, produced in the interface in an oxygen atmosphere, was several times as fast as that in a nitrogen atmosphere. These growth rates are much faster than the ordinary growth rate of silicon oxide in a dry oxygen atmosphere. From these data, the rate constants of growth of silicon oxide were estimated, assuming the relationship of the parabolic oxidation.

Comparing these results with the doping amount of boron in silicon, it was confirmed that the rate-determining step of the transfer of boron into silicon was classified by whether the above Si-B compound was present or not.

Although a number of authors have studied the diffusion of boron into silicon, no detailed measurements concerning the reactions of the glass-silicon interface have been involved (1-4). The purpose of the present work is to study the reactions of the interface.

There are many diffusion sources for diffusion of boron into silicon, *i.e.*, boron tribromide (BBr_3), boron nitride (BN), and diborane (B_2H_6) as the gas phase diffusion sources, and boron doped oxide as the solid or liquid phase diffusion source. By using all of these sources, boron oxide is formed on the silicon surface. It is reduced to elemental boron reacting with silicon as follows

$$B_2O_3 + \frac{3}{2}\,Si \rightleftarrows 2B + \frac{3}{2}\,SiO_2 \qquad [1]$$

and the reduced boron diffuses into silicon.

The two significant problems for diffusion of boron into silicon are the influence of oxygen gas in the atmosphere and the growth condition and the properties of the compound insoluble in a fluoric acid, which is produced in the glass-silicon interface for high boron doping.

This insoluble compound has been studied by Busen *et al.*, using an ellipsometer and it was assumed to be a Si-B phase from the facts that the refractive index of this compound was between 1.6 and 1.7, which was larger than that of boro-silicate glass, and it could be converted to a substance which was removed by standard glass etches by means of a low-temperature oxidation (2, 3). Further, it has been known that the growth rate of this compound is depressed as the oxygen concentration in the atmosphere increases. Therefore, the following reactions are also expected

$$x\mathrm{Si} + y\mathrm{B} \rightleftarrows \text{Si-B compound} \qquad [2]$$

$$\text{Si-B compound} + O_2 \rightleftarrows SiO_2 + B_2O_3 \qquad [3]$$

The doping amount of boron into silicon decreases with increase of the oxygen concentration in the atmosphere and this effect is more marked at a low temperature. Therefore, it is assumed that the silicon surface under the glass is oxidized by the oxygen in the atmosphere, by the reaction

$$Si + O_2 \rightleftarrows SiO_2 \qquad [4]$$

This paper identifies the insoluble compound and reports on a study of its electrical resistivity and its growth condition. Also, measurement was made of the growth rate of silicon oxide at the interface and of the amount of boron doped into silicon by changing the oxygen concentration in the atmosphere and the diffusion sources.

From these measurements the rate-determining step of the transfer of boron into silicon is estimated.

Key words: B_2O_3-Si system, Si-B compound, SiB_4, SiB_6, silicon oxidation, boron diffusion.

Experimental Procedure

BN (source I) and B_2H_6-O_2 gas system (source II) were used as the diffusion sources from gas phase, and boron doped oxide (source III) and pure boron oxide (source IV) were used from the solid or liquid phases. The boron doped oxide (source III) and pure boron oxide (source IV) were deposited on silicon wafers, using the oxidation of SiH_4 and B_2H_6 at 400°C and also that of $(CH_3O)_3B$ at 550°C. The deposition rate of the latter system was about 0.2-0.3 μ/min and the deposition time was 20 min, unless otherwise noted. It should be noted that measurements of the deposition rate of pure B_2O_3 are not satisfactory in accuracy because of a strong tendency to absorb water.

The silicon samples used were 100-200 ohm-cm and 1-2 ohm-cm resistivity, n-type with a mirror-polished (111) surface. The former wafers were used only to measure the infrared absorption spectra.

The insoluble compound produced in the interface was studied by infrared spectroscopy, and electron and x-ray diffraction. To correct for the lattice absorption bands of silicon in an infrared transmission examination, a bare companion wafer of approximately the same thickness was always used in the reference beam of the double beam spectrophotometer. The electrical resistivity of the compound was obtained from the resistance and the thickness of the compound, which were determined by the difference of the sheet resistivity and the weight before and after the removal of the layer, assuming the density of this layer to be 2.55 g/cm^3, which was given by Brosset as that of SiB_4 (5) or to be 2.43 g/cm^3, given by Cline as that of SiB_6 (6).

The growth rate of silicon oxide in the interface during the diffusion of boron into silicon was obtained from the changes of the absorption band of the Si-O at 9.2μ. The sheet resistivity of the diffused layer was measured after removal of the insoluble compound, which was changed to a soluble compound by means of a wet oxygen oxidation (saturated with 95°C water) at 800°C for 5 min. The surface concentration of boron in silicon was determined by differential conductance measurements. The procedure consisted of successively measuring the sheet resistivity of the wafer followed

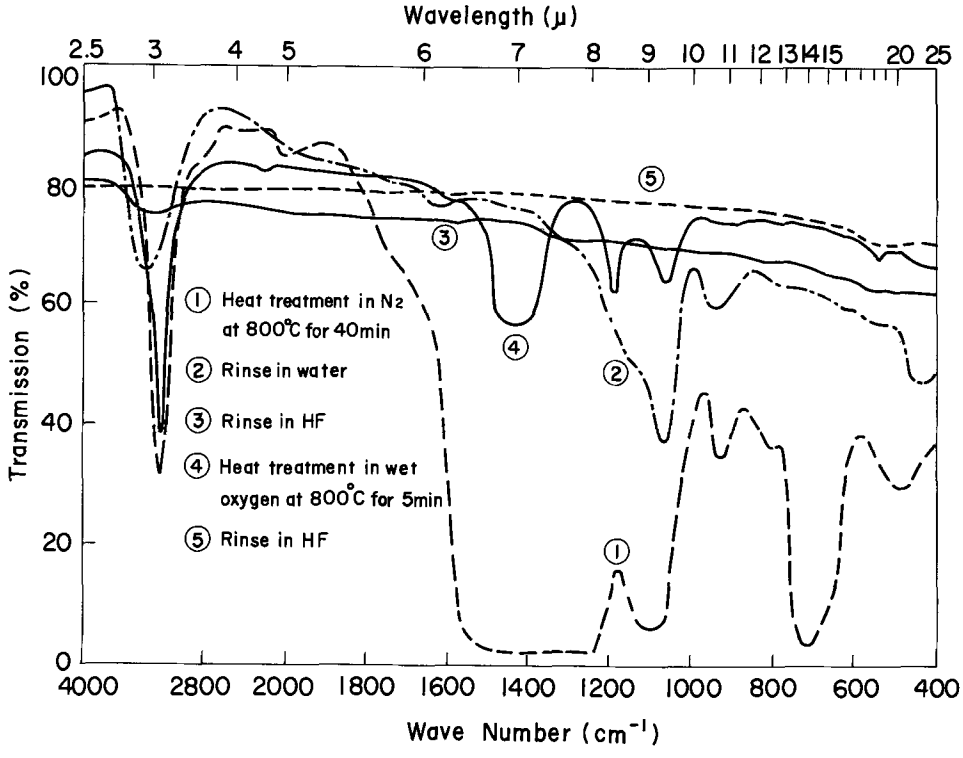

Fig. 1. Changes of absorption spectrum obtained after successive various treatments for source IV.

by the removal of a silicon layer of controlled thickness. Sectioning of the diffused layer was made by anodically growing an oxide of 350Å thickness, corresponding to a consumption of a 140Å silicon layer. The oxide was subsequently removed by etching in a buffered HF solution.

Experimental Results

Identification and properties of the insoluble compound.—The insoluble compound produced in the B_2O_3-Si interface has been assumed to be a Si-B compound by many authors (1, 2) but no direct identification of it has been accomplished. The layer was verified to be a Si-B compound by infrared spectroscopy as follows. Figure 1 shows the infrared absorption spectra for the sample of source IV obtained after successive treatments involving (curve 1) heating in nitrogen gas at 800°C for 40 min, (curve 2) rinse in water to remove the pure B_2O_3 unreacted, (curve 3) rinse in an HF solution to remove the SiO_2 produced in the interface, (curve 4) exposure to wet oxygen at 800°C for 5 min, and (curve 5) rinse in an HF solution to remove the unresolved layer which was oxidized.

Since the spectrum of curve 1 in this figure has the large and broad band of B-O at about 7μ, it is supported that a large amount of B_2O_3 remained unreacted. In the spectrum of curve 2 the band of the B-O disappears completely but the bands of the Si-O at 9.2μ and of the Si-O-B at 10.8μ remained unchanged (7, 8). No absorption band is observed in the spectrum of curve 3 but the insoluble layer is visible on the silicon surface. The absorption bands of the B-O at 7μ, Si-O at 9.2μ, and B-OH at 8.4μ appear again in the spectrum of curve 4. There are no absorption bands in the spectrum of curve 5 and the surface became hydrophobic for the first time. From these experimental results, it is concluded that the insoluble layer is a Si-B compound, which is easily oxidized in a wet oxygen atmosphere at a low temperature and changed to the mixed SiO_2-B_2O_3 system containing water. Since the Si-B compound and SiO_2 are produced by heat-treatment in the interface of the system, which at first consists of a B_2O_3 layer deposited on Si, the system is separated in three successive layers of B_2O_3, SiO_2, and Si-B compound in order on the Si specimen, where SiO_2 contains boron because of the presence of the Si-O-B absorption band.

To identify the Si-B compound, reflection-electron and x-ray diffraction were utilized. X-ray diffraction was carried out with a diffractometer using V-filtered CrKα radiation. Figure 2 shows the electron diffraction patterns of the Si-B compound which were produced by source IV, after heat-treatment at 900°, 1100°, and 1200°C for 4.5 hr and by source II at 1100°C for 10 min. The lattice constants and the relative intensities obtained by the electron and x-ray diffraction are summarized in Table I. The lattice constants were measured in the range from 2θ = 20°-35° for specimens produced below 1100°C and 20°-55° for those at 1200°C in the x-ray diffraction. Table I also shows the data on SiB_4 and SiB_6.

The electron diffraction maxima in Fig. 2 are not sharp and the error due to the broadness of the peaks is 10%. From these broad peaks it is expected that samples never experience the extended heating required to crystallize completely.

Although the measured values in the present work do not always coincide with all maxima of SiB_4 or SiB_6 (orthorhombic and cubic structures) (6, 15) in Table I, the compound produced below 1100°C for source IV is similar to orthorhomic SiB_6, and that produced at 1100°C for source II and at 1200°C for source IV is similar to cubic SiB_6 or SiB_4 in the diffraction maxima.

According to the Si-B phase diagram, reported by Elliot, silicon is in an equilibrium state with SiB_4 below 1269°C and with SiB_6 above 1269°C (9). On the other hand, Brosset *et al.* indicated that SiB_4 can be formed by sintering in the 1200°-1370°C temperature range, although the compound is metastable, only being transitory to the formation of the stable SiB_6 in this temperature range (5). Rizzo and Bidwell reported that B and SiB_4 free of SiB_6 were produced at 1100°C, using the reaction between Si and molten B_2O_3, and the structure of SiB_4 was rhombohedral (16). These experimental conditions are the same as in the present work except for sintering.

From these results and discussions, the Si-B compound obtained in the present work is expected to be SiB_4 and/or SiB_6. More detailed measurements must be carried out to identify the compound completely.

The electrical resistivity of the Si-B compound was measured and was found to be 0.01-0.03 ohm-cm. The samples were prepared at 950°, 1050°, and 1150°C, using source IV. No definite relationship could be

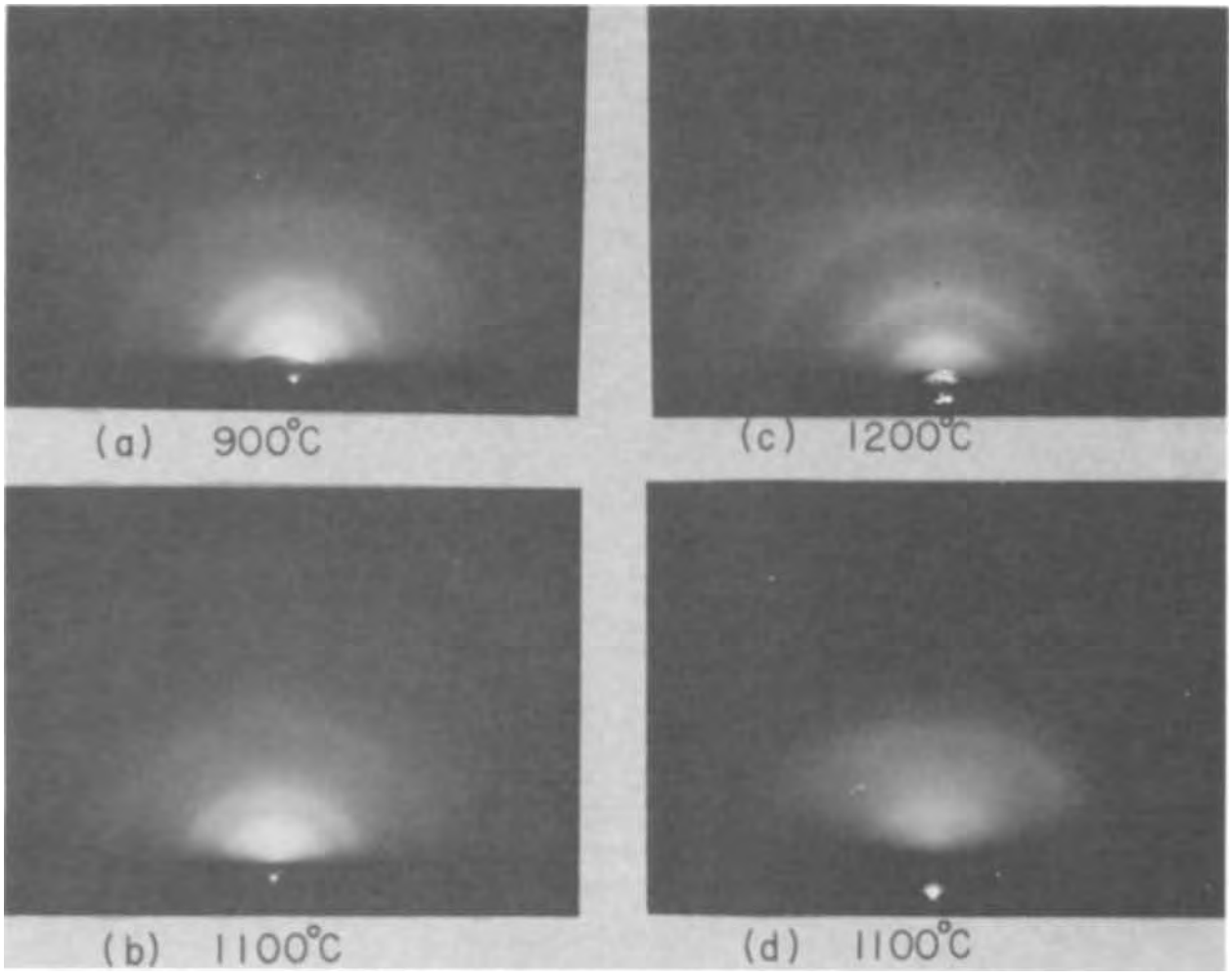

Fig. 2. Electron diffraction patterns of the Si-B compound produced at 900°, 1100°, and 1200°C. (a, b, and c, source IV; d, source II.)

Table I. Electron and x-ray diffraction data for Si-B compound

Source IV								Source II							
900°C		1000°C		1100°C		1200°C		1100°C		SiB_4 [Ref. (16)]		SiB_6 [Ref. (6)]		SiB_6 [Ref. (15)]	
d(Å)	I/I_o	d(Å)	I/I_o	d(Å)	I/I_o	d(Å)	I/I_o	d(Å)	I/I_o	d(Å)	I/I_o	d(Å)	I/I_o	d(Å)	I/I_o
		5.58	11	5.60	14							—			
		5.15	29	5.15	30					5.05	3				
												5.57	10		
		4.85	18	4.86	23					4.16	26				
												4.92	100		
		4.65	100	4.65	100					3.17	21				
												4.62	40		
(4.29)	S			(4.21)	S	(4.06)	M	(4.34)	S	2.76	58				
												4.35	70		
						3.13	40	(3.19)	M	2.69	100			2.93	VS
												4.23	80		
(2.60)	S					2.68	100	(2.63)	S	—				2.40	S
												4.15	50		
										2.05	9	—			
														2.07	MS
						(2.37)	M					3.86	40		
										1.77	6	—			
						(1.91)	W	(1.95)	M					1.85	S
										—		2.85	80		
								(1.67)	M	1.61	18	2.74	50	1.69	MW
				(1.47)	M			(1.46)	S	1.59	7	2.71	60	1.46	MW
(1.37)	M					(1.11)	W			—		2.67	60	1.38	S
						(0.86)	VW			1.512	10	—		1.31	S
												1.71	40		
						(0.75)	VW			1.506	6	—		1.25	M
										1.30	5	1.62	40	1.15	MW
										—		—		1.11	M
														—	
														0.98	MS
														—	
														0.90	MS
														—	
														0.85	VS
														0.81	S
														0.80	MS

Electron diffraction data are shown in parentheses.
VS, very strong; S, strong; MS, mod. strong; M, medium; W, weak; MW, mod. weak; VM, very weak.

found between the electrical resistivity and the time or temperature of heat-treatment. This value is smaller than the electrical resistivity of the SiB_6 single crystal, 0.2 ohm-cm, reported by Cline (6). It is not possible, from these measurements, to conclude a reason for this low resistivity.

Measurements of growth rate of silicon oxide produced at interface.—The growth rate of silicon oxide at the silicon-glass interface was measured by the changes of the infrared absorption band of the Si-O at 9.2μ. Specimens were prepared by heat-treatment at 700°, 800°, and 900°C in a nitrogen and an oxygen atmosphere, using source IV. An example of the changes of infrared absorption spectrum by the heat-treatment at 800°C in an oxygen gas is shown in Fig. 3. From this figure, it is found that the peak height of the Si-O band at 9.2μ and the Si-O-B band at 10.8μ increase with time, but that the broad band at about 7μ hardly changes. Figure 4 shows the changes of the absorption amount of Si-O band at 9.2μ with the time of the heat-treatments in a nitrogen gas at 700°, 800°, and 900°C and in an oxygen gas at 900°C. The absorption amount of the Si-O band and the thickness of the silicon oxide, which was made from the ordinary oxidation of silicon in a dry oxygen gas at 900°C are also shown in this figure. It should be noted that the measured values are the sum of the absorption amount and thickness of the silicon oxide produced in both surfaces of the specimens. From this figure, it can be seen that the silicon oxide produced in an oxygen atmosphere is about 3 times as great as that in a nitrogen atmosphere and 70 times as great as that made from the ordinary oxidation of silicon in a dry oxygen gas at 900°C; the silicon oxide is produced in proportion to the square root of the time of heat-treatment within the time measured.

Influence of Si-B compound on boron diffusion.—The surface concentration and sheet resistivity of the boron

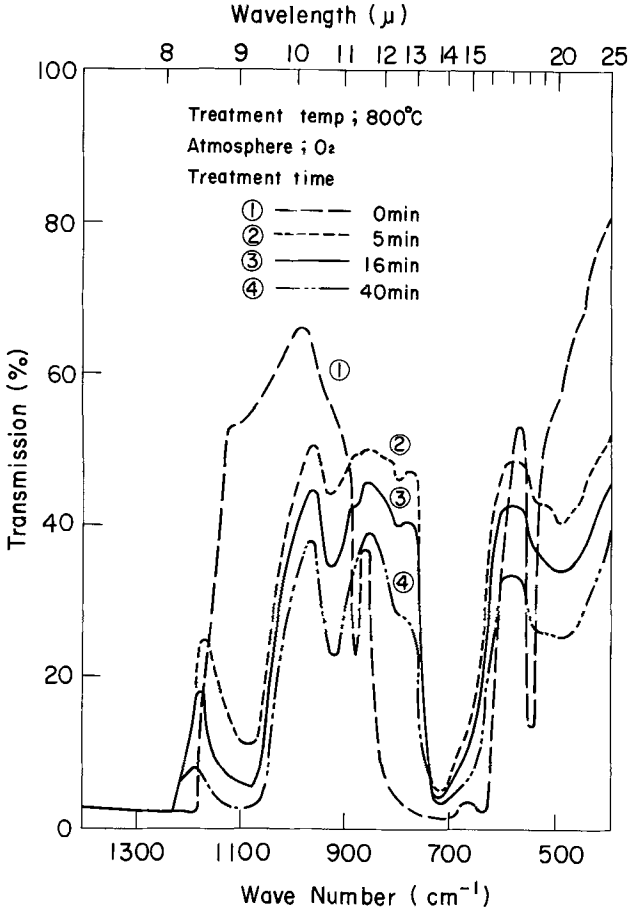

Fig. 3. Changes of absorption spectrum of B_2O_3-Si system in an oxygen atmosphere at 800°C for source IV.

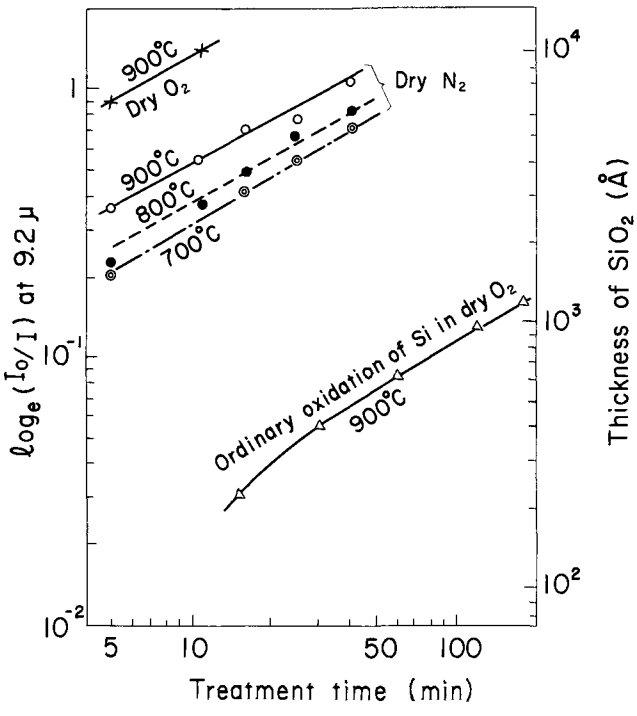

Fig. 4. Dependence of absorption amount of Si-O band at 9.2μ on time of heat-treatment for source IV.

diffused layer in silicon were measured, varying the molar per cent of B_2H_6 in the gaseous reactants for the deposition of the doped oxide (source III and IV). In this measurement, the thickness of the doped oxide was constantly maintained at 0.2μ and the specimens were heated at 1050°C for 15 min in a nitrogen atmosphere. The results are shown in Fig. 5. From this figure, it is found that the surface concentration increases with the molar per cent of B_2H_6 up to about 12%, then it saturates above that, indicating that the solid solubility of boron in silicon at 1050°C is about 2×10^{20} cm^{-3}. This is in good agreement with the experimental value given by Vick and Whittle (1).

Further, it is found that the sheet resistivity decreases with the molar per cent B_2H_6 up to about 12%, then increases gradually. The B_2O_3 content in the doped oxide at 12 mole per cent (m/o) B_2H_6 in the gaseous reactants is expected to be about 12 m/o from the measurements of the ratio of the 7μ B-O and 9μ Si-O infrared absorption peaks, using the data in Ref. (4).

It is interesting that the sheet resistivity at the 100% B_2H_6 (100% B_2O_3) largely depends on the quantities of B_2O_3, *i.e.*, the thickness of B_2O_3 and increases with

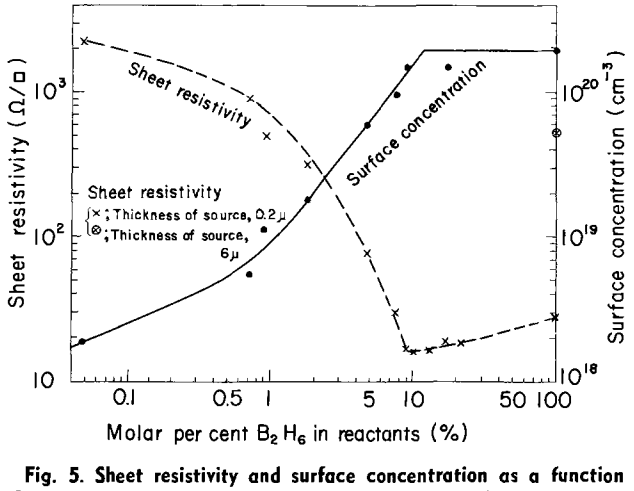

Fig. 5. Sheet resistivity and surface concentration as a function of molar per cent B_2H_6 in reactants Samples were heat-treated at 1050°C for 15 min in a nitrogen atmosphere using sources III and IV.

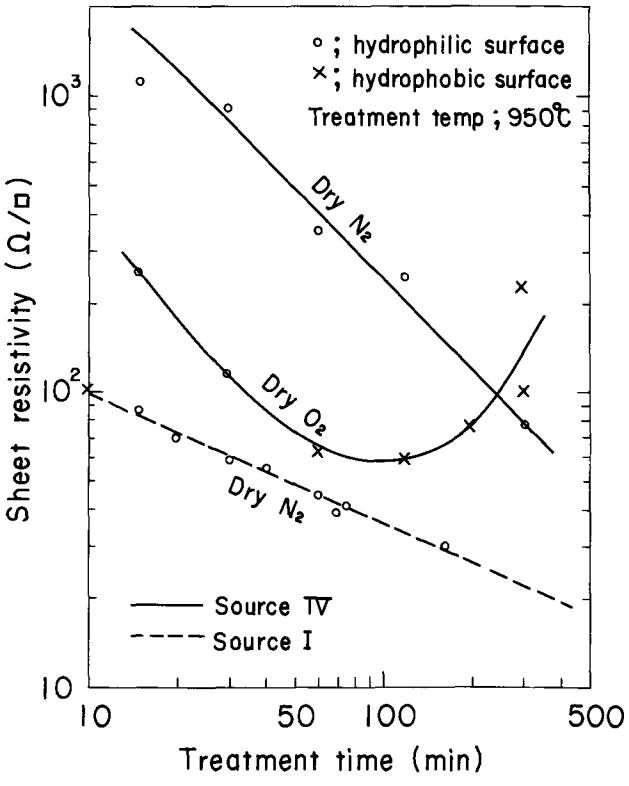

Fig. 6. Dependence of sheet resistivity and presence of the Si-B compound on time of heat-treatment at 950°C for sources I and IV.

it, as shown in the figure. After diffusion and removal of the doped oxide, the hydrophilic nature, characteristic of the presence of the Si-B compound, was observed all over the surface, when the molar per cent B_2H_6 exceeded about 12%. This value coincides with the molar per cent where the surface concentration saturates and the sheet resistivity turns over.

Figure 6 shows the dependences of the sheet resistivity on the time of heat-treatment. Samples were heat-treated at 950°C in nitrogen and oxygen atmospheres for source IV, and in a nitrogen atmosphere for source I. It is also shown in this figure whether the Si-B compound was present or not on the silicon surface, which was determined by the hydrophilic nature of the silicon surface.

In case of source IV, heated in a nitrogen atmosphere, the thickness of the compound increased rapidly with time up to 1 hr and was saturated beyond it, as shown in Fig. 7. These measurements were carried out after oxidizing the Si-B compound in the wet oxygen atmosphere in place of measuring the thickness of the Si-B compound directly. It was impossible to determine the thickness of the Si-B compound for source I in a nitrogen atmosphere and for source IV in an oxygen atmosphere because it was too thin to measure.

From Fig. 5-7 it is found that the doping amount of boron in silicon decreases as the growth rate of the Si-B compound increases and its growth rate is depressed in the oxygen atmosphere. Further, it was also confirmed experimentally that it took more time for the Si-B compound to disappear in the oxygen atmosphere when the quantities of B_2O_3 are increased.

Influence of oxygen on sheet resistivity.—The doping amount of boron into silicon depends markedly on the oxygen concentration in the atmosphere. A comparison was made of the doping amount of boron for source I where a small amount of the Si-B compound is produced in the silicon surface, with that for source IV where a large amount of the Si-B compound is produced. A plot of the sheet resistivity *vs.* the oxygen concentration in the atmosphere is given in Fig. 8. From this figure, it is found that a region of the oxygen concentration, where the sheet resistivity is constant,

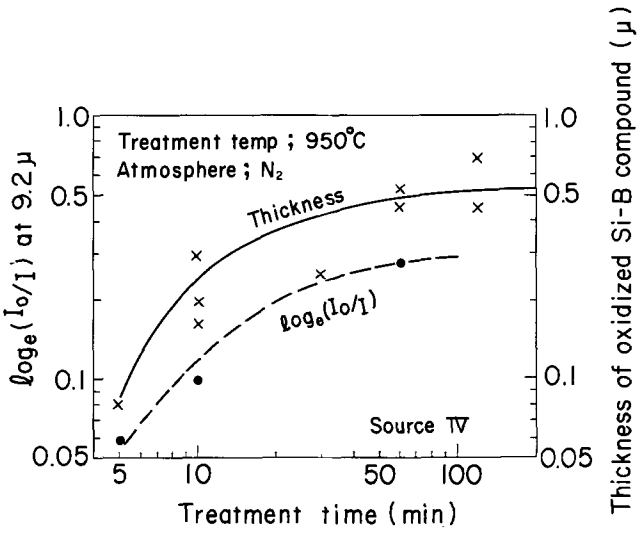

Fig. 7. Growth amount of Si-B compound *vs.* time of heat-treatment at 950°C in a nitrogen atmosphere for source IV. Samples were measured after oxidizing the Si-B compound.

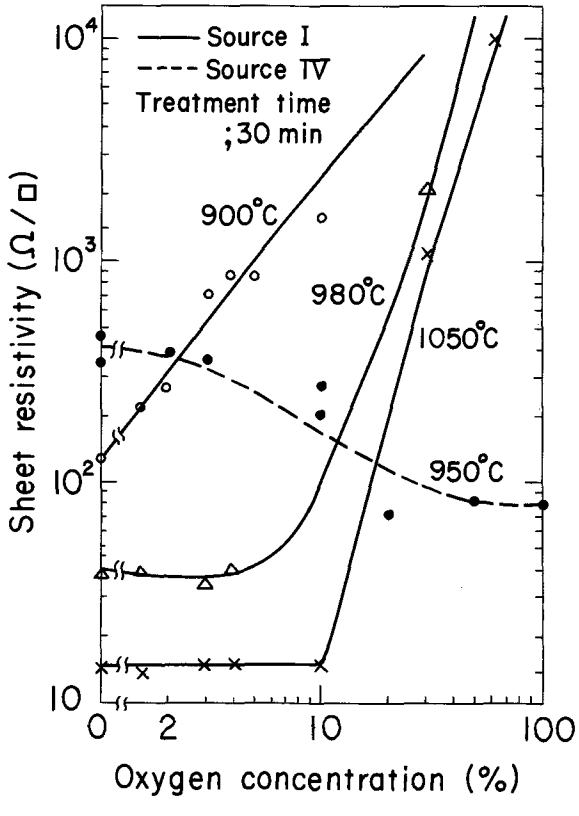

Fig. 8. Dependence of sheet resistivity on oxygen concentration in the atmosphere for sources I and IV.

increases with the temperature of heat-treatment and the sheet resistivity increases with the oxygen concentration rapidly beyond the constant regions for source I. It was confirmed that the surface concentration of the diffused layer coincided with the solid solubility of boron in silicon in these constant regions. On the other hand, it is found in this figure that the sheet resistivity decreases with the oxygen concentration in the case of source IV. In this case, it was also confirmed that the thickness of the Si-B compound decreased with the oxygen concentration and the dependence of the sheet resistivity on the oxygen concentration became similar to that of source I, if the thickness of the deposited B_2O_3 (in source IV) was decreased below 1μ.

To investigate the effect of an oxygen atmosphere upon the diffusion of boron in more detail, the follow-

ing experiment was carried out. Boron was diffused using the B_2H_6-O_2 gas system (source II) where the B_2H_6 and O_2 gases in the atmosphere were removed, leaving N_2 gas only to flow after time t_G, keeping the total diffusion time constant (t = 30 min). The results are shown in Fig. 9a and 9b. As seen in Fig. 9a, only 3 min for t_G is long enough to obtain the largest amount of diffused boron in this system at 800°C and the amount is rather decreased with a longer t_G. If the above data are plotted against time t-t_G, as shown in Fig. 9b, it is found that the sheet resistivity decreases parabolically with time after removal of the doping gases. This fact indicates that the diffusion of boron does not occur when the doping gas stream is flowing. On the other hand, the amount of diffused boron at 900° and 1100°C increases with t_G gradually or is maintained constant, as shown in Fig. 9a.

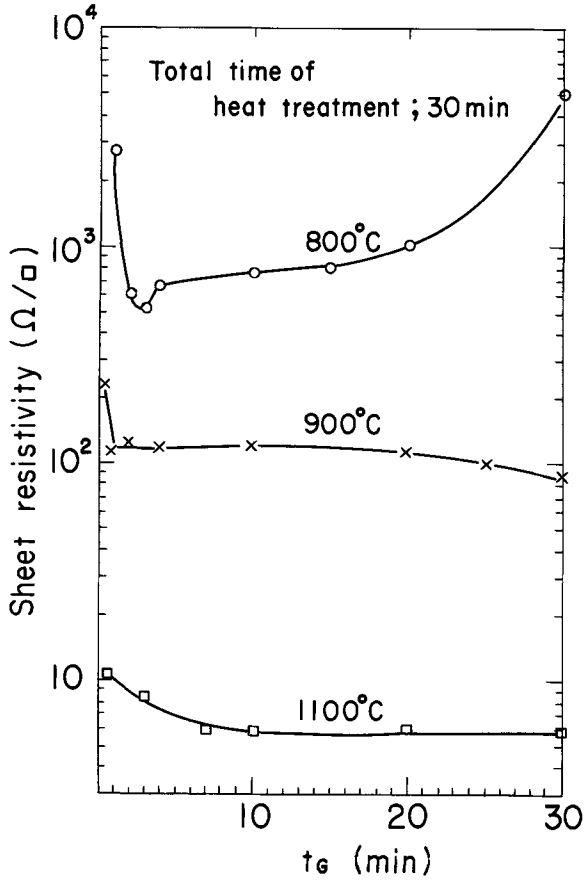

Fig. 9a. Dependence of sheet resistivity on t_G at 800°, 900°, and 1100°C for source II (B_2H_6-O_2 gas system, B_2H_6; 250 ppm, O_2; 0.2%). Total time of heat-treatment, t, is 30 min.

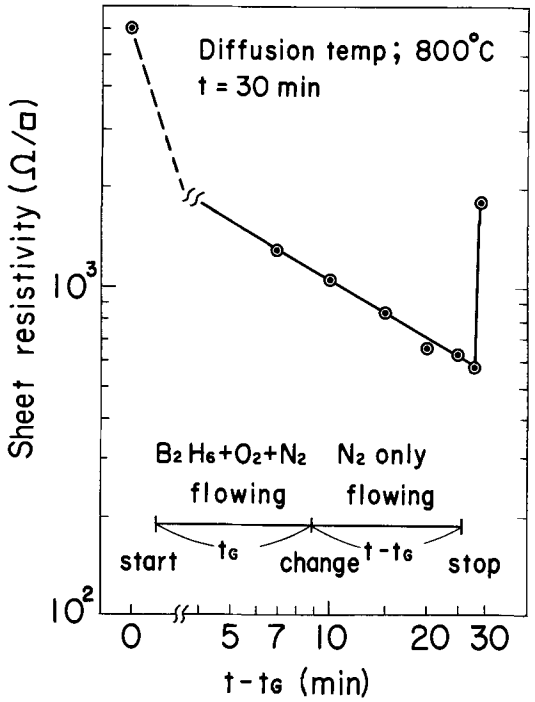

Fig 9b. Sheet resistivity as a function of t-t_G at 800°C for source II, obtained from the data of Fig. 9a.

From these experiments it is assumed that the oxygen in the atmosphere greatly depresses the doping amount of boron into silicon at a low temperature in case of source I or II which supply a small amount of B_2O_3 on the silicon surface.

Discussion

Role of oxygen in interface reaction.—The growth rate of SiO_2 in the silicon-glass interface for source IV is promoted by the oxygen in the atmosphere, as shown in Fig. 4. In order to interpret these results, we must consider the interface reactions of Eq. [1], [3], and [4].

From this figure, it is expected that the growth rate of SiO_2 is limited by the diffusion process resulting in the parabolic relationship

$$w = Kt^{1/2} \qquad [5]$$

where w is the SiO_2 thickness, t is the heat-treatment time, K is the rate constant.

Further, it is expected that the diffusing species which can limit the growth rate of SiO_2 are B_2O_3 in glass in a nitrogen atmosphere, and B_2O_3 and/or oxygen in glass in an oxygen atmosphere. If the growth rate of SiO_2 is given by the sum of the growth rate of SiO_2 as follows, we have

$$w = Kt^{1/2} + K't^{1/2} \qquad [6]$$

instead of Eq. [5] where K and K' are the growth rate constants due to the diffusion of B_2O_3 and oxygen in glass, respectively (*i.e.*, the first term in Eq. [6] corresponds to the reaction of Eq. [1] and the second term to that of Eq. [3] or [4]).

Table II shows the rate constants of the parabolic oxidation calculated by Eq. [6], using the data from Fig. 4. From these data, it is found that K' is about 40 times as much as the ordinary oxidation rate constant for silicon at 900°C and the activation energy of K is about 0.2-0.3 eV. The former result can be explained by the fact that the borate glass presents very little resistance to the diffusion of oxygen, comparing with pure SiO_2 (10). The activation energy of K is expected to be a half of that of the viscosity of a mixed SiO_2-B_2O_3 system, because K is in proportion to the square root of the diffusion coefficient of B_2O_3 in glass and the diffusion coefficient of B_2O_3 is in inverse proportion to the viscosity of the glass. The activation energy of the viscosity of the above glass is 0.65 (B_2O_3: 100%) to 1.3 (B_2O_3:50%) eV (11) and a half of these values is a little higher than the activation energy of

Table II. Relationship of parabolic oxidation rate constants for interface reactions of B_2O_3-Si system

Source	Ambient	Temp. (°C)	Rate const. K (Å)	Rate const. K' (Å)	$K+K'$ (Å)
Source IV	dry N_2	700	761	—	761
Source IV	dry N_2	800	904	—	904
Source IV	dry N_2	900	1225	—	1225
Source IV	dry O_2	900	1225	1837*	3062
Source II		800			~87**
Ordinary oxidation of Si	dry O_2	800	—	17	17
	dry O_2	900	—	45	45

* This value was obtained by substracting the value of K at 900°C in dry N_2 from the total rate constant, $K+K'$ at 900°C in dry O_2.

** This value was calculated from the data of Ref. (14), assuming the parabolic relationship.

K. Thus far, it is not possible to explain the difference between these two values of the activation energy.

If we use diffusion sources such as source I or II the growth of SiO_2 in the silicon surface is not parabolic, as reported by one of the authors (14), and it is expected that the rate-determining step of the interface reaction of Eq. [1] is the deposition of B_2O_3 on silicon, but not the diffusion of B_2O_3 in glass.

Si-B compound growth conditions.—The diffusion current of boron per unit area, $J(t)$, which enters through the surface of the silicon, is given by

$$J(t) = N_0 \sqrt{\frac{D}{\pi t}} \qquad [7]$$

if the diffusion sources are assumed to be infinite (12), where N_0, D, and t are the surface concentration, diffusion coefficient of boron in silicon, and diffusion time, respectively. $J(t)$ decreases in inverse proportion to the square root of the diffusion time and becomes the maximum value, $J_M(t)$, when N_0 reaches the solid solubility of boron in silicon. According to Fig. 6, however, the sheet resistivity decreases more rapidly for source IV than for source I in a nitrogen atmosphere. It is also seen that the sheet resistivity decreases in inverse proportion to the square root of the diffusion time for source I and is lower than that for source IV. Further, the amount of Si-B compound produced in case of source IV was larger than that in case of source I. Considering the composition ratio of Si to B in the Si-B compound and the solid solubility of boron in silicon to be of the order of 10^{20} cm^{-3}, the Si-B compound is expected to be an approximately infinite diffusion source, even if the amount of the compound is very small.

From these considerations, it is expected that the Si-B compound grows under the conditions of Eq. [2] when the production rate of the elemental boron produced under the conditions of Eq. [1] is much more than $J_M(t)$ and it decreases in the opposite case, decomposing it to the diffusion source; the boundary of silicon and the Si-B compound moves to the silicon side in the generation process and to the Si-B compound side in the degeneration process. The production rate of the elemental boron produced in the interface is controlled by the diffusion of B_2O_3 in the vicinity of the interface, as described in the previous section. The liquidus curve in the phase diagram of the B_2O_3-SiO_2 system is fairly flat or very sensitive to the concentration of the SiO_2 at a low temperature (13). Further, the viscosity of this system is very high and becomes higher with the concentration of SiO_2. The samples, therefore, never experience the time required to reach the equilibrium value shown in the phase diagram below liquidus because SiO_2 continues to grow under Eq. [1] and/or [4] during the drive-in process. This effect apparently corresponds to the movement of the liquidus curve of the glass to the side of B_2O_3. From the above discussions, it is expected that the reasons why the growth of the Si-B compound is depressed in an oxygen atmosphere at a low temperature are the promotion of the growth rate of SiO_2 and the high viscosity of this glass.

Boron diffusion rate-determining step.—Based on the above discussions of the growth of SiO_2 and Si-B compound in the interface, the roles of oxygen on the doping amount of boron and the rate-determining step of the transfer of boron into silicon are discussed.

One of the authors reported that boron diffused more quantitatively and more uniformly, and that the growth rate of SiO_2 in the glass-silicon interface was lower in the B_2H_6-CO_2 gas system than in the B_2H_6-O_2 gas system at 800°C. He explained this fact in terms of the oxygen concentration in the atmosphere (14).

From Fig. 8 and 9 (a and b) and Ref. (14) the reason for the doping amount of boron into silicon being depressed in an oxygen atmosphere at a low temperature is expected to be that the temperature dependence of diffusion coefficient of B_2O_3 or oxygen in glass is less than that of the diffusion coefficient of boron in silicon, *i.e.*, the values of the activation energy of Eq. [1], [3], and [4] are smaller than that of the diffusion coefficient of boron in silicon. Therefore, it is concluded that the diffused layer of boron in silicon or the Si-B compound is oxidized and, in case of a small amount of source, such as source I or II, the diffused amount of boron in glass is rapidly decreased with the growth of SiO_2 at a low temperature. On the other hand, in the case of a large amount of source, such as source III or IV, the doping amount of boron is not always depressed if the diffused amount of boron in glass is not decreased with the growth of SiO_2 even at a low temperature, *i.e.*, if the production rate of elemental boron under Eq. [1] is large enough to compensate for the growth rate of SiO_2 under Eq. [3] or Eq. [4].

From the above experimental results and discussions, it is concluded that the rate-determining step of boron into silicon is classified by the presence or absence of the Si-B compound. In the presence of the Si-B compound in the interface, the rate-determining step is the diffusion of boron in silicon, whether the compound is generated or degenerated. In this case, the surface concentration of boron in silicon agrees with the solid solubility of boron.

In the absence of the Si-B compound, the rate-determining step is the diffusion of boron in glass. The diffusion process of boron in B_2O_3-Si system is shown in Fig. 10. The reproducibility and uniformity of boron diffusion into silicon, therefore, depends strongly on the interface reaction, which is controlled by the amount of B_2O_3 and the oxygen concentration in the atmosphere.

Conclusion

1. The compound insoluble in a HF solution produced at the interface in the 900°-1200°C temperature range is supposed to be SiB_4 or SiB_6 from the diffraction measurements. The electrical resistivity of the insoluble compound is 0.01-0.03 ohm-cm.

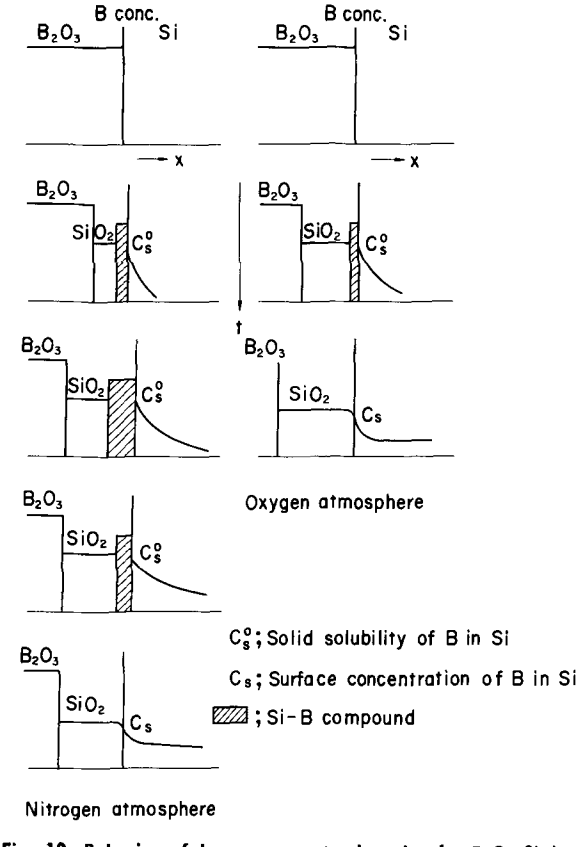

Fig. 10. Behavior of boron concentrations in the B_2O_3-Si interface during heat-treatments.

2. The Si-B compound grows when the production rate of the elemental boron by the interface reaction of Eq. [1] is much more than the maximum diffusion current of boron in the interface and degenerates in the opposite case, decomposing to the diffusion source.

3. The reasons for the growth of the Si-B compound being depressed in an oxidizing atmosphere at a low temperature are due to the increase in the growth rate of SiO_2 and to the high viscosity of the mixed SiO_2-B_2O_3 glass.

4. The growth rate of SiO_2 by Eq. [1] in the silicon-glass interface is rate determined by the diffusion of B_2O_3 in glass in large excess of source, such as source IV, and by the deposition of B_2O_3 on silicon in the case of the diffusion source from gas phase, such as source I or II.

5. The growth rate of SiO_2 by Eq. [3] or [4] in an oxygen atmosphere in the interface of B_2O_3-Si system is very much faster than its ordinary growth rate. This fact is explained by assuming that the diffusion coefficient of oxygen in SiO_2, produced in the interface, becomes larger when the SiO_2 contains boron.

6. The rate-determining step of the transfer of boron into silicon is classified by the presence or absence of the Si-B compound. If the compound is present, it is the boron diffusion in silicon, and if not, it is that in glass.

Acknowledgment

The authors appreciate the helpful discussions held by Dr. M. Yoshida and Dr. K. Ono of the Musashino Electrical Communication Laboratory. Mr. S. Ohyama materially assisted in all phases of the measurements.

Manuscript submitted Nov. 6, 1972; revised manuscript received Jan. 31, 1973.

Any discussion of this paper will appear in a Discussion Section to be published in the June 1974 JOURNAL.

REFERENCES

1. G. L. Vick and K. M. Whittle, *This Journal*, **116**, 1142 (1969).
2. K. M. Busen, W. A. FitzGibbons, and W. K. Tsang, *ibid.*, **115**, 291 (1968).
3. W. A. FitzGibbons, T. Kloffenstein, and K. M. Busen, *ibid.*, **117**, 272 (1970).
4. D. M. Brown and P. R. Kennicott, *ibid.*, **118**, 293 (1971).
5. C. Brosset and B. Magnusson, *Nature*, **187**, 54 (1960).
6. C. Cline, *This Journal*, **106**, 322 (1959).
7. V. R. Bruckner and J. Fernandez, *Glastech. Ber.*, **39**, 283 (1966).
8. D. E. Bethell and N. Sheppard, *Trans. Faraday Soc.*, **51**, 9 (1955).
9. R. P. Elliot, "Constitution of Binary Alloys," McGraw-Hill Book Co., New York (1969).
10. B. E. Deal and M. Sklar, *This Journal*, **112**, 430 (1965).
11. E. F. Rieoling, *J. Am. Ceram. Soc.*, **47**, 478, (1964).
12. W. Jost, "Diffusion in Solids, Liquids, Gases," Academic Press, New York (1960).
13. T. J. Rokett and W. R. Foster, *J. Am. Ceram. Soc.*, **48**, 75 (1965).
14. H. Nakamura; *Japan J. Appl. Phys.*, **11**, 761 (1972).
15. N. N. Zhuravlev, *Soviet Phys. Cryst.*, **1**, 524 (1956).
16. H. F. Rizzo and L. R. Bidwell, *J. Am. Ceram. Soc.*, **43**, 550 (1960).

Flame Emission Analysis of Potassium Contamination in Silicon Slice Processing

William R. Knolle

Bell Telephone Laboratories, Incorporated, Reading, Pennsylvania 19604

ABSTRACT

A study of potassium contamination in semiconductor processing was undertaken to determine its extent and magnitude in processing chemicals and slice-handling tools. Simple methods of preventing contamination of silicon and silicon dioxide from chemicals and tools were investigated. To this end a flame photometric technique has been developed to detect routinely less than one part per billion (ppb) of potassium in solution. Potassium contamination of reagent grade chemicals commonly used in silicon device processing is generally less than 500 ppb which is comparable to levels of sodium contamination. However, Triton X-100 surfactant solution and 30% hydrogen peroxide contain several orders of magnitude more sodium than potassium. Pyrex dishware yields minimal amounts of potassium whereas significant amounts of sodium are leached from Pyrex by chemicals. It is shown that potassium levels on both bare and oxidized silicon slice surfaces from a basic or acidic treatment can be reduced to $<2.3 \times 10^{12}$ atoms/cm^2 by a 10 min overflow rinse of deionized water and by using slice-handling tools and spin drier surfaces which have been rinsed with deionized water for short times immediately prior to use. Potassium is shown to be mobile at high temperatures and presents the same unwanted electrical instability in silicon dioxide as does sodium.

Sodium contamination of semiconductor materials and its deleterious effect on the desired electrical stability of devices is well known. Little attention has been paid to the other alkali elements such as potassium. Potassium is the seventh most abundant element in the earth's crust (sodium is the sixth) (1) and is present in man as is sodium (2). The diffusion coefficient of potassium in silica is about an order of magnitude smaller than that for sodium (3). This is also the case for the diffusion coefficients in silicon at room temperature (4). Possible evidence of potassium contamination of chemically etched silicon has been found (5).

Presented in the following sections are the method of analysis used to detect potassium in the ppb range, sources of potassium contamination of silicon slices due to routine chemical treatment and slice handling, and ways to reduce the potassium contamination. Also pre-

Key words: silicon processing, MOS devices, flame photometry, potassium contamination, sodium contamination.

sented are the results of temperature-bias drift, capacitance-voltage (C-V) measurements made on intentionally potassium-contaminated MOS testers.

Method of Analysis

Trace amounts of potassium in chemicals were determined by emission flame photometry. An Instrumentation Laboratory Model 153 Atomic Absorption Spectrometer was used in the flame emission mode. The grating of the spectrometer has a blaze angle (6) that optimizes the efficiency of the grating at a wavelength of 250 nm; therefore the grating does not efficiently pass light of 766.5 nm—the detection wavelength for potassium. By inserting a 766.5 nm narrow bandpass filter between the flame and the grating, and using the grating as a mirror instead of as a monochromator, the best signal-to-noise ratio was obtained (7). Potassium standards in the ppb range were prepared by successive dilutions of a stock solution. The solutions were contained in polypropylene volumetric flasks that had been soaked in dilute HF for several hours and then finally rinsed with deionized water. The deionized water used in preparing the standards was passed through a set of Barnstead demineralizers and finally a 0.30 μm Millipore filter. The potassium level of this water was less than 1 ppb. See Fig. 1 for the response of the instrument to 3 different potassium standards used to calibrate the instrument's output. A least squares analysis of the instrument's response in Fig. 1 as a function of potassium concentration yields a line with a slope of 9.35 units/ppb and a correlation coefficient of 0.99991.

The silicon slices used in this work for potassium contamination were 10 ohm-cm, n-type, 0.85 in. in diameter, and 0.005 in. thick. Generally, determination of potassium contamination of silicon and silicon-dioxide-covered silicon surfaces was done on several samples and an average value of potassium contamination reported. This averaging over several slices that have received the same chemical treatment was necessary in sodium analyses where accidental contamination of a sample due to a high concentration of sodium was easily possible (8). Therefore the same precaution of averaging data was adopted for the potassium analysis. In order to calculate the minimum amount of potassium detectable under this analytical condition, a procedure according to Gabriels was followed (9). Accordingly, five 2 ml samples of dilute HF were dispensed from the same stock solution and analyzed for potassium. The calculated standard deviation multiplied by a statistical factor yields 1.1 ng of potassium as a workable detection limit in the 2 ml samples. The detection limit for sodium calculated in this way was 0.10 ng of sodium (8).

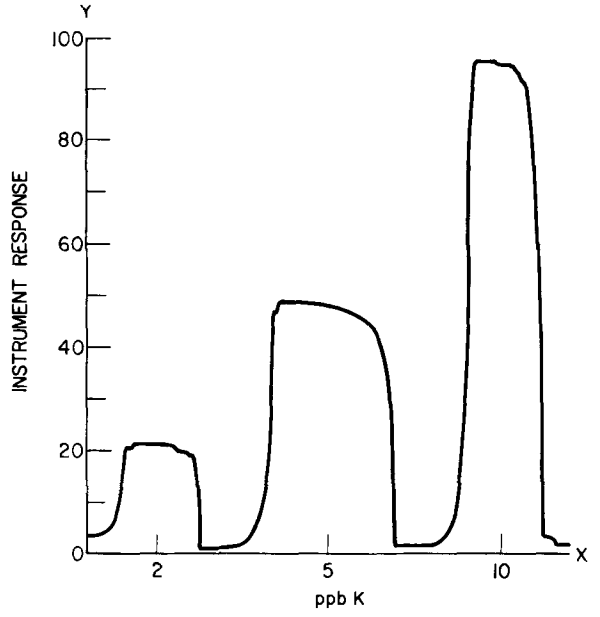

Fig. 1. Strip chart recorder tracing of potassium standards

Potassium in Processing Chemicals

Some chemicals commonly used in silicon semiconductor device processing were checked for potassium. Several of these chemicals were repackaged into polyethylene containers before use. Seven milliliters of each were diluted to 100 ml in a clean polypropylene volumetric flask and the resulting solution aspirated into the flame and analyzed for potassium. The results are presented in Table I. Each value represents the average of measurements on 4 different batches. Also tabulated is the amount of sodium present. The sodium was detected by emission flame photometry with the grating used as a monochromator. Stringent precautions were taken to avoid spurious sodium contamination (8). Hydrochloric acid was very low in both sodium and potassium. A basic peroxide solution used for slice cleaning (1:1:4 by volume of 30% H_2O_2, conc NH_4OH, and H_2O) (10) was high in both sodium and potassium, the sodium coming from the H_2O_2 and the potassium from the NH_4OH.

Contamination of Silicon and Silicon Dioxide by Chemicals

A group of 9 bare silicon slices was treated with hot basic (adjusted to $pH \sim 12$ by addition of NH_4OH) 0.01M KCl solution (~391 ppm potassium) for 20 min and then rinsed in overflowing deionized water. This work was done in a clean bench in order to minimize particulate contamination of the slices. A Fluoroware basket was used to contain the slices. The basket design allowed a flow of solution around the slices sufficient to help prevent any particulate adherence to the silicon slice surface. The flow of water in this work was set at 4 volume changes per min for the Pyrex dish used to contain the Fluoroware basket. Specifying the number of volume changes per min is preferable to specifying only the rinse time since flow rate may vary from process to process. The slices were monitored for residual potassium on their surfaces as a function of rinse time. At periodic intervals a slice was removed from the rinse vessel and placed in 2 ml of dilute HF dispensed from a Nalgene polyethylene automatic constant volume pipettor. The silicon slice and HF were held in a polypropylene container that had been soaked in dilute HF for several days and prior to use was rinsed again in dilute HF followed by copious amounts of deionized water. The dilute HF was allowed to equilibrate with the silicon slice for 5-10 min and at the end of this equilibration time the silicon slice was removed and the solution capped until analysis. This method was found necessary to prevent any spurious sodium contamination during sodium analysis (8) and so was used in the potassium analysis. Similarly, bare silicon slices were treated with hot acidic (adjusted to $pH \sim 3$ by addition of HCl) 0.01M KCl solution and monitored for residual potassium. The data are presented in Fig. 2. Each point represents the average for 3 slices. The results show that potassium contamination from chemicals used to clean the slices may be rinsed from bare silicon slices with overflowing deionized

Table I

Reagent	Sodium ppb	Potassium ppb
H_2O_2	995	9
0.5% Triton X-100*	412	3
H_2SO_4*	220	176
Methanol*	174	74
HNO_3	87	100
HF	19	76
HCl	15	17
NH_4OH*	7	320

* Reagents not repackaged into polyethylene containers.

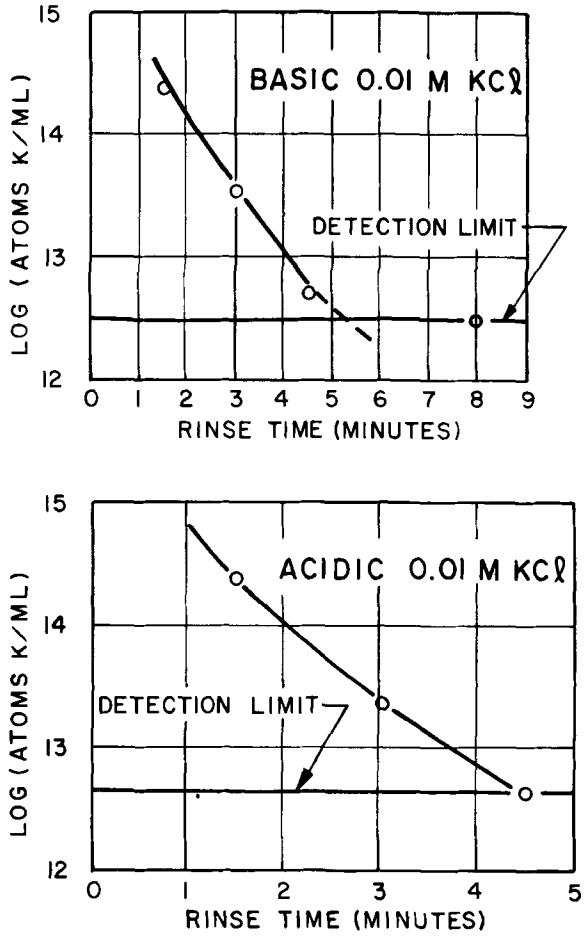

Fig. 2. Desorption of potassium from bare silicon slices. The slices were contaminated by immersion in a hot 0.01M KCl solution for 20 min. Each point represents the average potassium contamination for 3 slices. The overflow water rinse yielded 4 volume changes per minute of the Pyrex dish used to contain the solution.

water. This same result has been found for sodium contamination (8).

A group of silicon-dioxide-covered silicon slices was treated with boiling basic peroxide solution (1:1:4 H_2O_2, NH_4OH, and H_2O by volume) for 15 min and monitored for residual potassium as a function of rinse time. The data is presented in Fig. 3. Similarly, potassium from acidic peroxide solution was rinsed off silicon-dioxide-covered silicon slices within 8 min (to a detection limit of 6×10^{12} atoms of potassium/ml). This is in contrast to sodium from a basic solution on oxidized silicon where an acid rinse prior to overflowing deionized water was necessary to reduce sodium contamination to the detection limit (8).

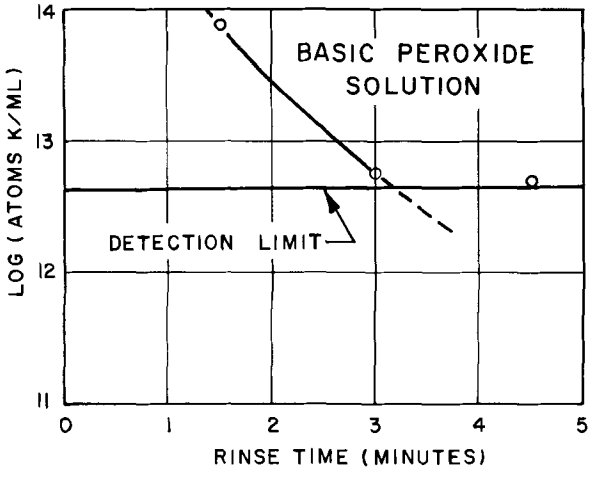

Fig. 3. Desorption of potassium from oxidized silicon slices. The slices were contaminated by immersion in a hot 0.01M KCl solution for 15 min. Each point represents the average contamination for 3 slices .The overflow water rinse yielded 4 volume changes per minute of the Pyrex dish used to contain the solution.

Contamination by Chemicals from Glassware

Two Pyrex beakers were degreased with hot trichloroethylene, rinsed with methanol, and overflow-rinsed with deionized water for 10 min. They were then treated with hot aqua regia for 10 min and finally overflow-rinsed with deionized water for 10 min. This treatment reduced the potassium contamination that may have previously been on the beakers to the detection limit of $<5.7 \times 10^{12}$ atoms of potassium/ml. Then 25 ml of deionized water were placed in each beaker and allowed to stand for 1 hr. At the end of this time the water was analyzed for potassium. No potassium above background level could be detected ($<5.7 \times 10^{12}$ atoms of potassium/ml). In contrast, the amount of sodium leached from Pyrex glass beakers similarly treated was $49 \pm 30 \times 10^{12}$ atoms of sodium/ml (8). The level of potassium contamination of chemicals from glassware is at least an order of magnitude lower than the sodium contamination.

Potassium on Slice-Handling Tools

Several stainless steel vacuum chucks that were routinely used for silicon slice handling were checked for possible potassium contamination. The chucks were dipped into 15 ml of deionized water in a polypropylene container for 15 sec. This treatment is meant to simulate the actual practice of submerging the vacuum chuck into solution in order to remove the silicon slice. Of the 5 chucks checked, only one showed any measurable potassium transferred to 15 ml of deionized water in 15 sec. This was 9.8×10^{14} atoms of potassium compared to 20×10^{14} atoms of sodium for the most sodium-contaminated vacuum chuck found in routine use (8). When a vacuum chuck rinsed with dilute HCl and then deionized water for 30 sec was wiped dry with Twill Jean cloth, no potassium above the detection limit was observed ($<8.6 \times 10^{13}$ atoms of potassium compared with 105×10^{13} atoms of sodium transferred to 15 ml of deionized water in 15 sec) (8).

A stainless steel vacuum chuck cleaned with dilute HCl and deionized water and then touched with 3 ungloved finger tips for 3 sec yielded 311×10^{13} atoms of potassium in 15 ml of deionized water in 15 sec compared with 1680×10^{13} atoms of sodium transferred to deionized water (8). A simple deionized water rinse in flowing water for 30 sec of the finger-touched chuck appeared to remove most of the easily transferrable potassium from the surface of the chuck ($<8.6 \times 10^{13}$ atoms of potassium transferred to deionized water). Again, potassium contamination appears to be an order of magnitude lower than sodium contamination.

MOS Measurements

Electrical instability of semiconductor devices due to potassium contamination of silicon dioxide has not been extensively investigated (11). In order to see if potassium presents any electrical instability similar to sodium, silicon slices with 10,000Å of thermally grown oxide were prepared and purposely contaminated with potassium and MOS capacitance-voltage measurements made.

Seven oxidized silicon slices were immersed in 125 ml of 10 ppm KCl solution whose sodium contamination level was 0.5 ppb above the deionized water reference level. The sodium analysis of the potassium solution was made to assure that there was no inadvertent contamination of the slice by sodium ions. The slices were heated below boiling for 20 min in a quartz beaker and were then spun dry on a clean Teflon-coated spin drier (8). Five of them were analyzed for surface potassium by flame photometry. Each of the 5

slices was immersed in 2 ml of dilute HF in order to etch the first 400Å of oxide considered to be representative of the oxide surface. The first 400Å of oxide yielded a surface concentration of $47 \pm 10 \times 10^{13}$ atoms of potassium/cm^2. In order to differentiate between the temperature-bias drift of potassium and that of the residual sodium contamination, 6 other slices from the same oxidized lot were immersed in a hot 64 ppb sodium solution for 20 min and spun dry. This solution contained over 50 times more sodium than the potassium solution did and so the slices immersed in the 64 ppb sodium solution should have higher mobile charge if potassium is immobile. Five of the 6 sodium-contaminated slices were analyzed for surface sodium by flame photometry. The slices contained less than 7.5×10^{13} atoms of sodium/cm^2 on the surface as detected by flame photometry. As a control, one slice was left untreated and so should have lower mobile charge than the sodium-contaminated slice. The 4 slices then had gold field plates of 0.060 in. diam evaporated onto them.

The MOS testers were temperature-bias-drifted at several temperatures for 5-10 min and $+9 \times 10^5$ V/cm, then cooled quickly to room temperature under bias, and capacitance-voltage measurements made. The results are presented in Fig. 4 where log Q_{FB}/q *vs.* temperature is plotted for the control, the sodium-contaminated, and the potassium-contaminated slices. Each point is the average measurement of 3 or 4 MOS testers.

From Fig. 4 it is apparent that Q_{FB}/q for the potassium-contaminated samples is higher than for the sodium-contaminated samples. The difference between Q_{FB}/q for the control slice and Q_{FB}/q at 275°C for the sodium-contaminated slice (2.3×10^{11} electronic charge/cm^2) is similar to the amount of mobile charge found by Yurash and Deal (12) when oxidized slices were rinsed in 64 ppb sodium solution and blown dry with N_2 gas ($\sim 2.9 \times 10^{11}$ mobile electronic charge/cm^2). The C-V curves for the potassium-contaminated slices resembled those for the sodium-contaminated and control slices except for the much larger flat-band voltage shift. No evidence was found for a thousandfold difference in mobility between sodium and potassium movement in the stressed MOS testers as has been previously reported (11).

It is interesting that the amount of potassium and sodium detected on the contaminated oxide surfaces

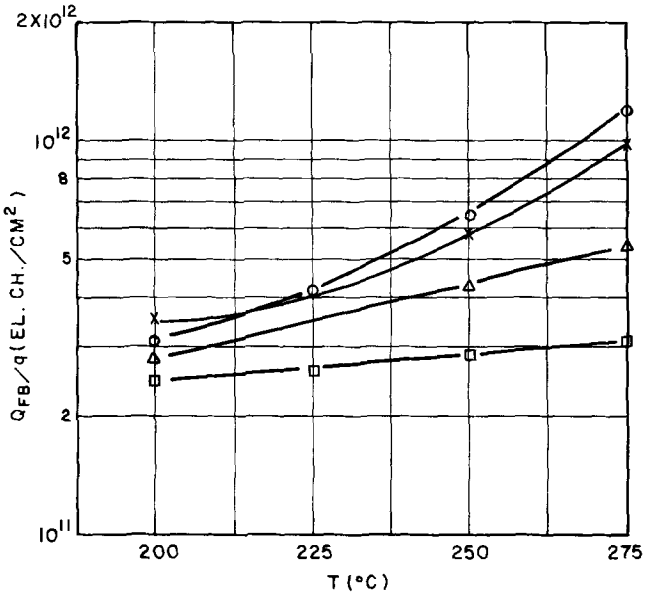

Fig. 4. Plot of Q_{FB}/q *vs.* temperature; 0.060 in. diameter, evaporated-gold field plates bias-drifted at $+9 \times 10^5$ V/cm. X, Potassium-contaminated slice, 5 min drift; ○, potassium-contaminated slice, 10 min drift; △, sodium-contaminated slice, 10 min drift; and □, control slice, 5 min drift.

by flame photometry is greater than the amount of mobile charge calculated from the C-V measurements. A possible explanation for this difference may be the manner in which the contamination is introduced, namely by immersion of the oxidized slices in a solution of the alkali metal salt. While the slice is in solution alkali metal ions may exchange with hydrogen ions that are present in silanol groups (≡Si-OH) on the surface of the oxidized slice, in addition to adsorption of molecules of the alkali metal salt onto the surface. It would not be expected that all of the exchanged alkali metal ions would drift under bias since some may be more tightly bound to the lattice than others. When a slice is contaminated by evaporation of the residue from one drop of a dilute aqueous solution of the alkali metal salt (11), only molecules will be deposited on the slice surface; hence the exchange mechanism for contamination is not possible in this case.

From the MOS tester results it is concluded that at high temperatures potassium contamination of devices will lead to electrical instability similar to that attributed to sodium (13).

Conclusions

Emission flame photometry may be used to routinely detect potassium in concentrations of less than 1 ppb in solution. A practical detection limit of 1.1 ng of potassium in 2 ml of solution is easily achieved when determining potassium contamination of silicon surfaces. For a silicon slice of 0.85 in. diameter, 1.1 ng of potassium corresponds to a detection limit of 2.3×10^{12} atoms of potassium/cm^2.

With respect to silicon slice processing, potassium is found in chemicals to about the same extent as sodium. However, 30% H_2O_2 and 0.5% Triton X-100 surfactant solution are two orders of magnitude lower in potassium than sodium. Potassium contamination of chemicals from Pyrex is minimal whereas significant amounts of sodium are leached out of Pyrex. Potassium can be easily rinsed from bare silicon, oxidized silicon, and stainless steel vacuum chucks with overflowing deionized water. This is in contrast to sodium contamination of oxidized silicon where a dilute acid treatment prior to a deionized water rinse was necessary to reduce sodium contamination to the detection limit (8). Potassium is easily transferred to solutions and slice-handling tools by ungloved hands; to avoid potassium contamination clean gloves are necessary.

Potassium contamination of semiconductor devices is to be avoided since potassium evidently is mobile at high temperatures. By proper handling and treatment the amount of potassium may be kept below the detection limit of 2.3×10^{12} atoms/cm^2.

Acknowledgments

The author thanks R. D. Plummer for helpful discussions about MOS capacitance-voltage measurements and Stanley Smith of Instrumentation Laboratory for help with modifications of the spectrometer.

Manuscript submitted Oct. 27, 1972; revised manuscript received Feb. 5, 1973.

Any discussion of this paper will appear in a Discussion Section to be published in the June 1974 JOURNAL

REFERENCES

1. "Handbook of Chemistry and Physics," R. C. Weast, Editor, 51st ed., The Chemical Rubber Co., Cleveland, Ohio (1970).
2. "Kirk-Othmer Encyclopedia of Chemical Technology," 2nd ed., Vol. 16, p. 385, John Wiley and Sons, Inc., New York (1966).
3. R. H. Doremus, in "Modern Aspects of the Vitreous State," J. D. Mackenzie, Editor, Butterworths, Washington, D.C. (1962).
4. D. L. Kendall and D. B. DeVries, in "Semiconductor Silicon," R. R. Haberecht and E. L. Kern, Editors, The Electrochemical Society Softbound Symposium Series, New York (1969).
5. C. C. Chang, *Surface Sci.*, 23, 283 (1970).
6. "Diffraction Grating Handbook," Bausch and Lomb,

Inc., Rochester, N. Y. (1970).
7. W. R. Knolle, *Appl. Spectr.*, **27**, 142 (1973).
8. W. R. Knolle and T. F. Retajczyk, Jr., To be published.
9. R. Gabriels, *Anal. Chem.*, **42**, 1439 (1970).
10. W. Kern and D. A. Puotinen, *RCA Rev.*, **31**, 187 (1970).
11. J. S. Logan and D. R. Kerr, IEEE Solid-State Device Research Conf., Princeton, N. J., June 1965.
12. B. Yurash and B. E. Deal, *This Journal*, **115**, 1191 (1968).
13. See for example, E. Kooi, *Philips Res. Rept.*, **21**, 477 (1966).

Technical Notes

Electrical Properties of Vapor-Deposited Silicon Nitride Films Measured in Strong Electric Fields

P. K. Chaudhari, J. M. Franz, and C. P. Acker

IBM System Products Division, Essex Junction, Vermont 05452

Recently, silicon nitride films have received considerable attention (1-3), mainly for passivating silicon, constructing diffusion masks, and use as gate insulators. The physical and electrical properties of deposited films have been found to vary with reactant composition during growth, temperature, and method of deposition (4-6).

Studies of the electrical conductivity of silicon nitride films in strong electric fields can give information concerning the mechanism of the increase of conductivity, the existence and location of trap levels, and dielectric constant.

Experimental

The substrates used for this study were mechanically polished 2 ohm-cm, p-type silicon. Just before loading into the reactor, the substrates were chemically etched in fresh, concentrated HF and rinsed in deionized water. An rf-heated, horizontal tube reactor was used for the silicon-nitride deposition.

A 4μ, 2 ohm-cm boron-doped epitaxial layer was deposited at 1135°C by reacting silicon tetrachloride and diborane in hydrogen. The temperature was then reduced to 925°C during the hydrogen purge cycle and silicon nitride was deposited using 150:1 ammonia-silane ratio in a hydrogen ambient. The deposition rate was approximately 100 Å/min. The MIS structures for electrical measurements were formed by evaporating aluminum field plates, 30-mil diam over the silicon nitride through a metal mask. Aluminum was also evaporated on the backside of the silicon for contact. The thickness of the nitride films studied ranged from 175 to 500Å. The thickness and the index of refraction were measured ellipsometrically.

Results and Discussion

Physical Properties.—Optical measurements were made on samples deposited on silicon blanks by the same process as the samples for electrical measurements. Transmittance curves obtained in the range 2.5-40μ using a Beckman Model IR-12[1] spectrophotometer indicate a broad absorption peak in the range 10-12μ with a minimum at 11.6μ. This absorption is due to the Si-N bond and agrees with that reported by Bean *et al.* (6). No peaks due to SiO, SiH, or NH were observed. Etch rates of 0.7 and 1.1 Å/sec were obtained at 50°C for 10:1 and 5:1 buffered etch, respectively, in good agreement with Bean *et al.* The dielectric constant of the silicon nitride films was obtained by measuring the capacitance of MIS structures at 1 MHz, under bias conditions corresponding to strong accumulation of the silicon surface. The electrode area was measured by photographing the electrode with a calibrated scale. The average value of the dielectric constant so determined was 7.

Key words: dielectric, thin film, d-c conductivity, silicon nitride.
[1] Trademark of Beckman Instruments, Incorporated.

High Field Conductivity

The current flow through the silicon nitride films was measured using a Keithley Model 602C electrometer. A hot-stage probe chamber with nitrogen ambient was used for all the measurements in the range 300°-500°K. Special care was taken to ensure that conduction measurements were made under steady-state conditions. The current was measured as a function of bias at various temperatures. Current measurements made on 4 or 5 capacitor dots per wafer indicated a considerable scatter in absolute magnitudes. However, least square fit of the ln σ *vs.* $E^{1/2}$ plots yielded rather consistent values for slope and convergence point (to be discussed below). A representative plot of ln σ *vs.* $E^{1/2}$ at various temperatures for Al-Si_3Ni_4-Si, 324Å thick, 30 mil diam is represented in Fig. 1. Figure 2 shows ln σ against $1/T$ for different field strengths. It is well established (7-9) that for fields in excess of 10^4 V/cm, many dielectric films exhibit current-voltage characteristics of the form

$$\sigma \sim \exp - \left[\frac{q\phi}{K_B T} - \beta_F E^{1/2} \right] \qquad [1]$$

which is evidence of either Schottky or Poole-Frenkel (P-F) effect (10). β_F in Eq. [1] is given by

$$\beta_F = \frac{q}{K_B T} (q/\alpha\pi\epsilon_0\epsilon_n)^{1/2} \qquad [2]$$

where $\alpha = 1$ for P-F effect and 4 for Schottky. Here σ is the conductivity, E is the field in V/cm, ϵ_0 is the vacuum permittivity, K_B is Boltzmann's constant, q is the electronic charge, T is the temperature in degrees Kelvin, ϵ_n is the relative dielectric constant for the insulating film, and ϕ is the potential barrier or the depth of the trap level. In Fig. 1 the curves clearly show that the conductivity obeys Eq. [1]. The slope of

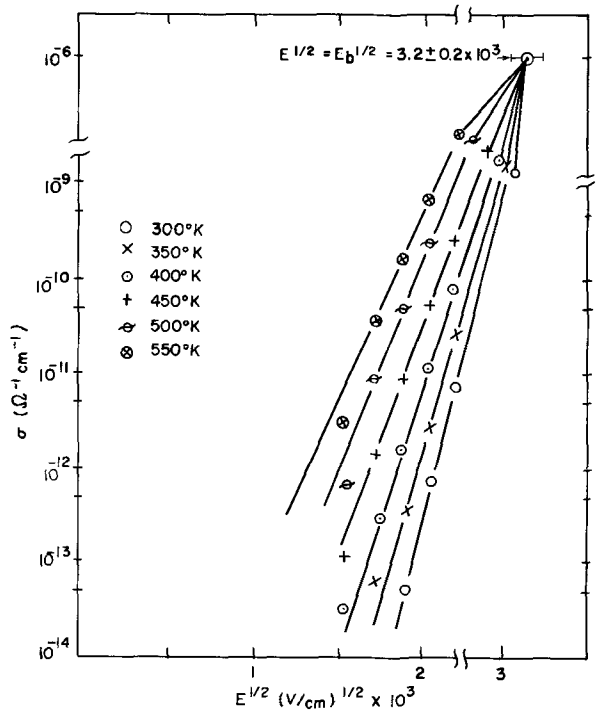

Fig. 1. Conductivity plotted vs. the square root of the electric field for a 324Å thick silicon nitride film, at various temperatures.

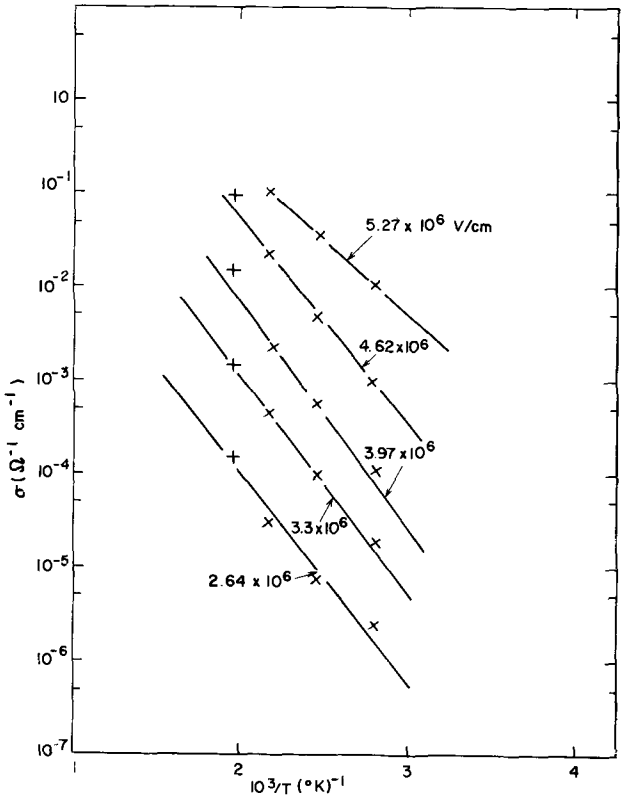

Fig. 2. Conductivity plotted against the inverse of the temperature for a 324Å thick silicon nitride film, at various fields.

the straight lines decreases with increasing temperature, as expected for either of these mechanisms. The slopes β_F obtained from Fig. 1 are plotted against $1/T$ as shown in Fig. 3. Note that not only an increase in β_F with decreasing temperature is observed, but also a rather good proportionality, $\beta_F \sim 1/T$, in the temperature range 300°-500°K, which is in good agreement with Eq. [2]. By equating the slope of Fig. 3 to Eq. [2], $\alpha\epsilon_n = 3.6 \pm 0.2$. The refractive index of the silicon nitride films measured by ellipsometer is $n =$

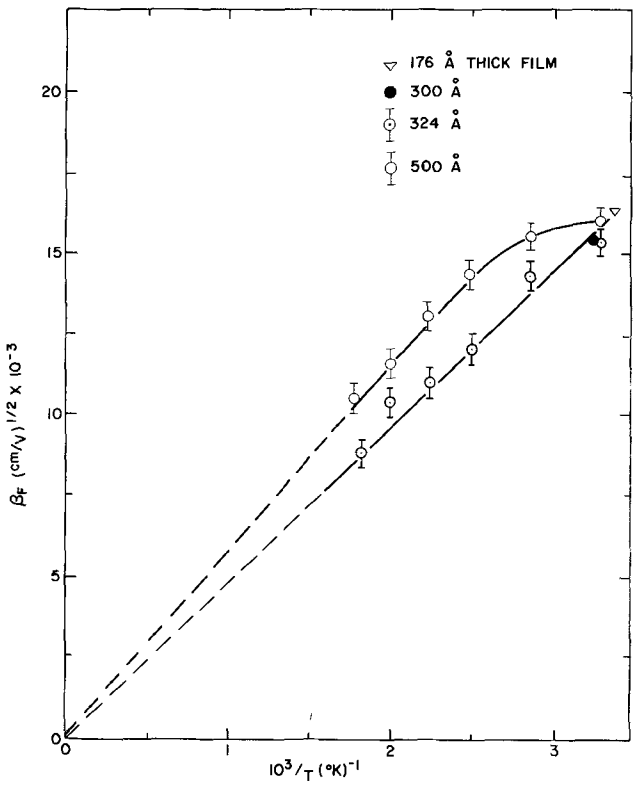

Fig. 3. Temperature dependence of the P-F coefficient β_F obtained from Fig. 1.

1.98 that yields $\epsilon_n = n^2 = 4$, and hence $\alpha = 1$ in Eq. [2]. It therefore appears that Fig. 1 represents a bulk-limited conduction obeying the P-F law. The discrepancy in the value of ϵ_n obtained from the data and that obtained from the ellipsometer measurement is consistent with the concept of an increased effective temperature at high electric fields, as proposed by Jonscher and Ansari (11) and observed experimentally in SiO (11), amorphous carbon films (12), and aluminum-doped SiO (13). Room-temperature data on 176, 300, 324, and 500Å thick films also gave similar values for β_F. However, 500Å films yield higher values of β_F for higher temperatures (see Fig. 3). This anomalous effect has been observed, in scribed silicon nitride samples, by Brown *et al.* (2).

Barrier lowering due to P-F effect.—The ln σ *vs.* $E^{1/2}$ straight lines extrapolated in the high-field region meet at $E^{1/2} = E_B^{1/2}$, indicating a temperature independent conductivity at E_B. This field corresponds to complete removal of the coulombic barrier due to the P-F effect, and is given by $E_B \sim 1 \times 10^7$ V/cm. It is interesting to note that this value agrees with the field strength for electrical breakdown of thicker silicon nitride films (14). Following the same procedure, Fig. 1 of Ref. (2) gave a value of $E_B = 1.05 \times 10^7$ V/cm.

Trap levels.—Consistent with the P-F effect, Eq. [1] is evidence of field-enhanced thermal emission from a localized level or trap level located at ϕ eV below the conduction band. The depth of the trap level is determined by Eq. [3] by equating the exponent to zero and using $E = E_B$. The trap level so determined is found to be $\phi = 1.1 \pm 0.2$ eV below the conduction band. This value also agrees with that obtained from the slope of ln σ *vs.* $1/T$ plot. Kendall (15) reports, from thermally stimulated current work, a definite trapping level in nitride between 0.50 and 0.90 eV. Sze (14) also reports a level located at $\phi = 1.2 \pm 0.3$ eV. ϕ and ϵ_n were calculated from values of E_B and β_F found using computer fit of the data. The uncertainty in E_B and β_F is thus reflected in the uncertainty in ϕ and ϵ_n. These uncertainties in E_B and β_F are indicated in the figures (see Fig. 1 and 3) as error brackets. This

uncertainty includes also a sample-to-sample variation in these parameters.

Data by Kendall (15) indicates the presence of small crystalline regions in his films of silicon nitride and suggests that these regions are responsible for the deep trap levels. However, transmission electron microscopic examination of films similar to those studied here do not show evidence of crystallinity and are found to be essentially amorphous. Hence it is postulated that the origin of the deep-seated traps may be more closely related to structural defects. This is supported by the measured etch rates of about 1 Å/sec at 50°C, indicating the likely presence of excess of silicon.

Acknowledgments

The authors are grateful to Dr. A. LeBlanc for encouragement and support during the early part of this investigation. The authors also wish to acknowledge S. D. Warley and N. R. Rapoport for making many measurements.

Manuscript submitted May 31, 1972; revised manuscript received Feb. 15, 1973.

Any discussion of this paper will appear in a Discussion Section to be published in the June 1974 JOURNAL.

REFERENCES

1. B. E. Deal, P. J. Fleming, and P. L. Castro, *This Journal*, **115**, 300 (1968).
2. G. A. Brown, W. C. Robinette, Jr., and H. G. Carlson, *ibid.*, **115**, 948 (1968).
3. T. L. Chu, J. R. Szedon, and C. H. Lee, *Solid-State Electron.*, **10**, 897 (1967).
4. K. E. Bean, P. S. Gleim, and W. R. Runyan, Paper 147 presented at Electrochem. Soc. Meeting, Philadelphia, Oct. 9-14, 1966.
5. V. Y. Doo and D. R. Nichols, Paper 146 presented at Electrochem. Soc. Meeting, Philadelphia, Oct. 9-14, 1966.
6. K. E. Bean, P. S. Gleim, R. L. Yeakley, and W. R. Runyan, *This Journal*, **114**, 733 (1967).
7. C. A. Mead, *Phys. Rev.*, **128**, 2088 (1962).
8. H. Hirose and Y. Wada, *J. Appl. Phys. (Japan)*, **4**, 639 (1965).
9. T. E. Hartman, J. C. Blair, and R. Bauer, *J. Appl. Phys.*, **37**, 2468 (1966).
10. J. Frenkel, *Tech. Phys. USSR*, **9**, 685 (1938).
11. A. K. Jonscher and A. A. Ansari, *Phil. Mag.*, **23**, 205 (1971).
12. M. Morgan, *Thin Solid Films*, **7**, 313 (1971).
13. M. Deery, J. G. Perkins, and K. G. Stephens, *ibid.*, **8**, R16 (1971).
14. S. M. Sze, *J. Appl. Phys.*, **38**, 2951 (1967).
15. E. J. M. Kendall, *Can. J. Phys.*, **46**, 2509 (1968).

Chemical Vapor Deposition of a TiC Coating on a Cemented-Carbide Cutting Tool

M. Lee and M. H. Richman

Division of Engineering, Brown University, Providence, Rhode Island 02912

Chemical vapor deposition has been used to deposit coatings of titanium carbide on steel and more recently on cemented carbides. The kinetics of the coating process and the coating growth morphology have also been the subject of many earlier reports (1-3). Ever since titanium-carbide-coated, cemented-carbide cutting tools became popular in manufacturing operations, this subject has attracted increased attention from the cutting tool industry.

Direct deposition of the carbide onto a heated surface from a gaseous mixture of volatile titanium tetrachloride, hydrogen, and some hydrocarbon or carbon tetrachloride is a widely used process. Although much is known about the kinetics of this process, some questions still remain unanswered. The most notable problem is the effect of the substrate material and its structure on the growth morphology of the coating. This information must be understood in order to produce consistently satisfactory cutting tools.

While it is generally believed (3) that pyrolysis of the hydrocarbon is the controlling mechanism in the coating process, some questions concerning the growth morphology of the coating remain to be answered. A particularly interesting question is to what extent the hydrocarbon pyrolysis affects the growth morphology of the titanium carbide.

A series of machining experiments relating the performance of the coated cutting tools to the thickness and type of the TiC coating has already been carried out (4) and it is the intent of this paper to present such information regarding the chemical vapor deposition of TiC coatings as may be useful to carbide manufacturers.

Experimental Procedure

The chemical vapor deposition system used in this research is shown schematically in Fig. 1.

Key words: carbide cutting tool, titanium carbide coating, chemical vapor deposition.

Either methane or toluene is used as the hydrocarbon. Gas flow rates are controlled by standard tube-type flow meters equipped with an extrasensitive needle valve, calibrated for each gas species, and corrected for the pressure gradient across the meter. Toluene is carried into the system by hydrogen, and the partial pressure of toluene in hydrogen is controlled by varying the temperature of the liquid toluene bath.

Titanium tetrachloride is introduced into the system by bubbling hydrogen through liquid $TiCl_4$; the concentration of $TiCl_4$ vapor in the system is fixed throughout this research. The total gas pressure inside the coating system is maintained at 1 atm. Any back pressure caused by bubbling the exit gas through an oil trap (depth approximately 2 cm) and a water trap (depth approximately 10 cm) does not signifi-

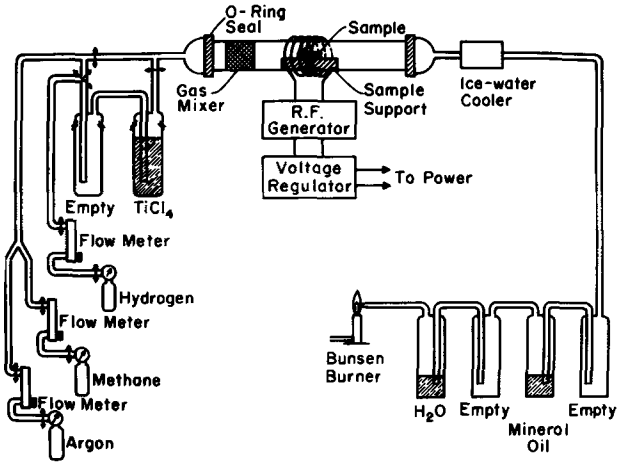

Fig. 1. TiC coating system

cantly increase the total pressure beyond 1 atm. Although the system pressure is an important independent variable in the chemical vapor-deposition process, atmospheric pressure is used throughout this research because of the quality of the coatings which were deposited at this pressure.

Radio-frequency surface heating is used to maintain the tool being coated at the proper temperature. The TiC coating deposited on the surface of the substrate tool changes the heating characteristics of the system, but constant temperature is maintained by continuous adjustment of the power input. A micro-optical pyrometer is used to monitor the substrate temperature, and all necessary corrections are made for the emissivity and the reaction tube wall.

A 32 mm ID Vycor tube equipped at both ends with silicon-rubber o-ring compression seals is used as the reaction chamber. To avoid any influence of the support material on the structure and properties of the coating, the tools to be coated are placed in the center of the chamber on a TiC-coated alumina support. In addition, the tools have a positive rake angle and all metallurgical examinations are performed at the cutting tip which is located at the top of the tool—the face distant from and in no way in contact with the support. While the latter condition would not negate any carbon transport due to eddy currents caused by thermal convection, the former condition would insure a uniform and constant substrate. The tool surface is also deliberately decarburized and η-phase formed before the TiC deposition. Therefore any tendency for η formation where the substrate does not contact the TiC or η suppression where the substrate does contact the TiC would be negligible in this study. A silica-wool trap at the inlet end of the reaction chamber causes the reactant gases to mix and also filters out any dust. A preheating attachment is also used in some cases to bring the temperature of the reactant gas mixture close to the substrate temperature before the gas reaches that point in the chamber. This eliminates the development of a temperature gradient across the tool surface due to any chilling effect of the cold gas on the hot tool. It was also considered that the concentration gradient in the gas mixture across the reaction surface might result in a nonuniform coating but such an effect would be minor. The coating system is baked prior to each run at a temperature over 150°C but below the softening temperature of silicon rubber and purged with argon for at least 1 hr in order to remove air and, especially, water vapor from the system.

Surfaces of the substrate tools are prepared in three different ways: (*i*) cleaning in a highly concentrated bath of boiling KOH; (*ii*) deeply etching the surface with 10% ferricyanide and 10% KOH solution in water which exposes the clean crystalline-carbide grains; and (*iii*) heating the tools in a flow of hydrogen gas which produces a thin silvery white film of continuous η-phase on the surface.

The tools are plated with a thick copper layer and sectioned on a diamond wafering machine. The thickness of the coating is measured metallographically on a section which has been etched with an aqueous solution of 10% potassium hydroxide. Examination of coating and coating-substrate interface structure is performed with an optical metallograph and electron microscopes (JEM 30 and JEM 7). Two-stage carbon replication is used for electron microscopy. All of the coated tools are investigated by x-ray diffraction to identify the crystal structure of the coating and any impurities in it.

Results and Discussion

The dependence of the growth rate on the substrate temperature is shown in Fig. 2. The substrate tool used was WC + 6% Co and the total coating time for each tool was 90 min. The time dependence of the coating growth rate is linear except for a short initial induction period of less than a minute. The waiting

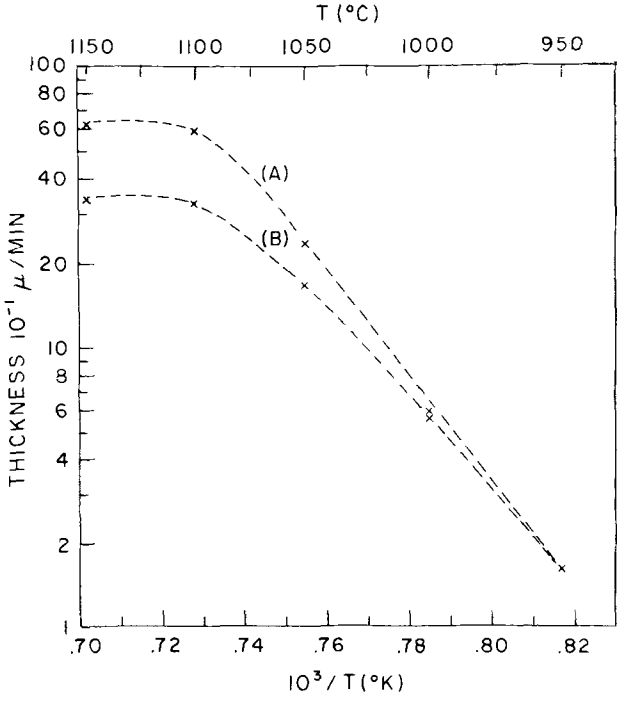

Fig. 2. Arrhenius plot of coating rate. Curve (A), 1500 cm³/min. H_2 saturated with toluene at −18°C; curve (B), 1000 cm³/min. H_2 saturated with toluene at −18°C.

time used for average rate determination is 90 min in each case. The hydrocarbon used for the particular experiment, the results of which are represented in Fig. 2, is toluene carried into the system by hydrogen bubbled through a toluene bath at -18°C. It may be seen from this data that the deposition rate is relatively independent of flow rate when the substrate temperature is below 1100°C, whereas transport of the reactant and the product materials become rate limiting when the temperature exceeds 1100°C.

The growth morphology of the coating is very strongly dependent upon the surface state of the substrate tools. When deeply etched tools with clean crystalline-carbide grains projecting from their surfaces are used as the substrate, three distinct types of deposit structure are observed. (*i*) When the coating temperature and the hydrocarbon concentration in the reactant gas mixture are relatively low, whiskers often form. (*ii*) At an intermediate temperature (*e.g.*, 1050°C) and with a moderate concentration of hydrocarbon, large well-defined crystal growth is often seen. (*iii*) At high temperature, *i.e.*, at the upper edge of the kinetic-controlled (or the transport-restricted) region, a coarse polycrystalline film is formed. The boundaries between these three regions are not definite. There is often considerable overlap because both the temperature and the hydrocarbon concentration are independent variables. At a fixed temperature (*e.g.*, 1050°C), depending on the amount of hydrocarbon in the system, different coating structures can be produced.

When as-ground tools are used after having been cleaned in a bath of boiling KOH, the results are mixed. Sometimes a crystalline form of coarse titanium carbide is deposited, but in most cases a continuous polycrystalline film of fine grain size would form. However, the tool surface is deliberately decarburized to a slight degree by heating in a flow of hydrogen until a thin film of very smooth silvery white η-phase is formed at the surface. The coating deposited on this η-phase layer at a temperature between 950°C and 1150°C with sufficient[1] hydrocarbon in the gas mixture is always a strong continuous film with ultrafine grain size. A typical coating formed under these

[1] About 18% by volume of methane in the total gas mixture is sufficient for the system used here.

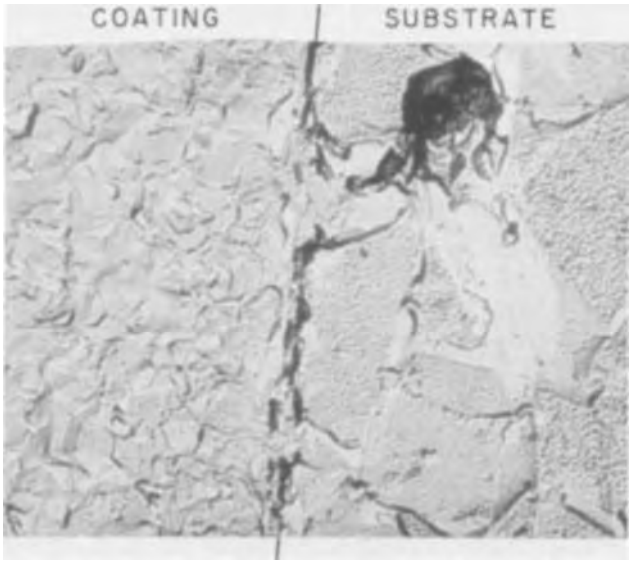

Fig. 3. An electron micrograph of tool-coating interface taken by double-stage carbon replication. Substrate tool: WC + 6% Co; hydrogen reduced surface; coated at 1050°C; rate of $TiCl_4$, saturated H_2 flow, 500 cm^3/min; rate of methane flow, 28 cm^3/min. 14,200×.

conditions is shown in Fig. 3. Although the η-phase is not desirable in cutting tools, it seems to be a necessary condition for good coating.

If a thick coating is deposited at a high rate, the coating consists of an array of large columnar grains oriented normal to the substrate surface. It is also found that the presence of some air or water vapor in the coating system would drastically change both the growth rate and the coating structure. Very fine titanium dioxide (TiO_2) particles which had formed in the gas phase provide extra nucleation sites, increase the growth rate of the coating, and result in a bimodal coating structure. The structure of a thick coating deposited with some air in the system is shown in Fig. 4.

The dependence of the film growth rate on the concentration (Fig. 5) changes with the hydrocarbon content of the reactant gas mixture. This agrees well with previously published reports (3). Along with the coating temperature, the hydrocarbon concentration has a considerable influence on the deposition rate.

An activation energy for the coating process may be estimated from the linear portion of Fig. 2. It varies from 84 ~ 94 kcal/mole depending upon the data obtained. This variation is due to the many sources of possible error mentioned above. It does,

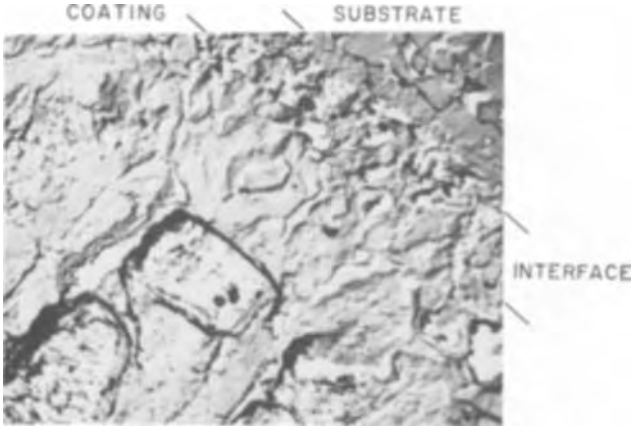

Fig. 4. An electron micrograph of a coating structure with large carbide particles grown from oxide nuclei within a continuous-carbide matrix. 2800×.

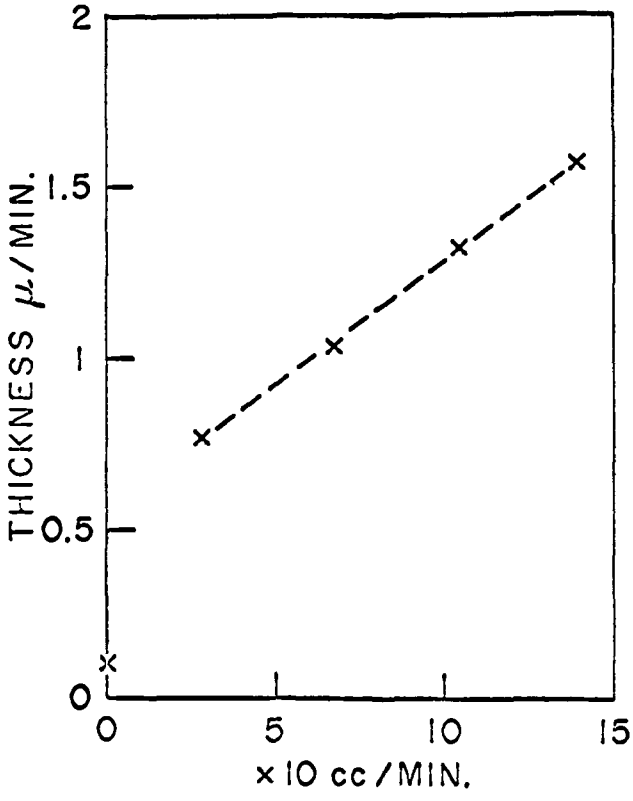

Fig. 5. Coating thickness as a function of hydrocarbon flow rate. Temperature: 1050°C, rate of $TiCl_4$-saturated (at room temperature)-hydrogen flow: 500 cm^3/min.

however, agree reasonably well with the reported activation energy of 90 cal/mole for the deposition of pyrolytic carbon from toluene (5). This may mean that within this surface-controlled region, it is the dissociation of carbon from the hydrocarbon molecules rather than the absorption and desorption of the reactant and the product gases that is the rate-controlling step and that different hydrocarbon gases could show different TiC deposition activation energies equivalent to their dissociation energies. Takahashi *et al.* (1, 2) found from their investigation that the TiC deposition rate changes if different hydrocarbon species are used in the coating process even though all other coating parameters are identical. They reported that methane showed the slowest deposition rate while propane and ethane showed much higher deposition rates. The reported activation energy of pyrolytic graphite deposition from methane is 103 kcal/mole (6). For propane decomposition it is 28 kcal/mole (7) and for ethane, 72 kcal/mole (8). According to these activation energies, methane would be expected to produce TiC at the slowest deposition rate. However Takahashi (1) also reported that the deposition rate is lower with propane than with ethane even though the latter has the higher hydrocarbon dissociation activation energy. It seems that some more study is definitely needed in this area.

It is also quite possible that the morphology of the TiC deposition may be controlled by pyrolytic graphite deposition from the hydrocarbon involved. Takahashi *et al.* (2) have also determined the orientation of their whiskers by the Laue technique and found the <111> axis of the cubic crystal to be the growth direction. They often found a large TiC crystal of hexagonal prism shape. The similarities between Takahashi's TiC whisker growth and the most common type of graphite whiskers indicates that the growth morphology of graphite whiskers may have a direct bearing on the growth morphology of TiC whiskers.

A series of microhardness measurements (Vickers hardness number with a 50g load) was taken on titanium-carbide coatings deposited with different con-

Table I. Microhardness of the coatings and the tools

Materials	Vickers hardness kg/mm²	Remark or Reference
WC + 6% Co	1550-1750	Substrate tools used
WC + 6% Co	1550-1700	Schwarzkopf and Kieffer (10)
Coating 1	2550	CH_4, 140 cm³/min
Coating 2	2350	CH_4, 105 cm³/min
Coating 3	2250	CH_4, 68 cm³/min
Coating 4	2150	CH_4, 28 cm³/min
$TiC_{0.8} \sim TiC_{1.0}$	1900 ~ 2900	William and Lye (9)

The test load used was 50g.

centrations (flow rates) of hydrocarbon in the coating system. The hardness values are listed in Table I for the coating rates shown in Fig. 5 as a function of hydrocarbon flow rate. The microhardness increases as the hydrocarbon concentration in the reactant gas increases. Oxygen or nitrogen impurities in the coating could affect the hardness but the samples were very carefully controlled so that, other than hydrocarbon concentration, all conditions were identical. There are two possible causes for this variation in hardness. (*i*) When the hydrocarbon concentration in the coating system is high, the degree of supersaturation and, therefore, the nucleation rate increases. The coatings deposited under these conditions would have a finer grain size than coatings deposited under other conditions. (*ii*) Titanium carbide usually has some carbon deficiency (as compared to its stoichiometric composition) and according to Williams *et al.* (9), the hardness of the carbide increases linearly as the carbon deficiency decreases.

The hydrocarbon concentration in the coating system is a critical factor which must be understood in order to assure high quality coating production. The coating system must provide the high degree of supersaturation needed to deposit a strong and hard continuous film. However, when the CH_4 flow rate exceeded 35% of the $TiCl_4$-saturated H_2 flow rate, x-ray diffraction analysis indicated the presence of some free graphite in the coating.

A thin layer of TiC could be formed on the surface of the carbide tool without any hydrocarbon in the coating system. In such cases, however, the surface of the tool is degraded (Fig. 6) and the growth rate is very low (Fig. 5).

Conclusions

Each individual coating system will show some difference in the kinetic data due to differences in the gas flow pattern. The following conclusions can serve as a useful reference for coating systems utilizing chemical vapor deposition of titanium carbide from a gas mixture of titanium tetrachloride, hydrogen, and some hydrocarbon.

1. The substrate temperature should not exceed 1200°C. Higher temperature tends to create a grain-growth problem and causes cobalt to diffuse into the coatings and it was observed (4) that coatings of this type do not perform well in cutting applications. At temperatures in excess of 1200°C, the growth rate is too high and control of the coating thickness is difficult.

2. Surface preparation of the substrate tool is very important for good coating production. A slight decarburization and creation of a thin smooth layer of η-phase on the surface insures the optimum coating structure for machining applications with excellent consistency.

3. Control of the hydrocarbon concentration and flow rate is a key to the production of well-coated tools. Selection should be made based on the information regarding the pyrolysis of each hydrocarbon species and an optimum hydrocarbon flow rate must be determined for each coating system. The pyrolysis of hydrocarbon is not only the controlling chemical reaction of the process, but also some evidence tends to indicate that the morphology of the titanium carbide coating depends on the morphology of pyrolitic graphite deposition.

4. It is also noteworthy that deposition of some titanium carbide is possible without any hydrocarbon in the system. Tungsten carbide reacts with $TiCl_4$ and forms double (TiW) carbide but this degrades the substrate tool surface.

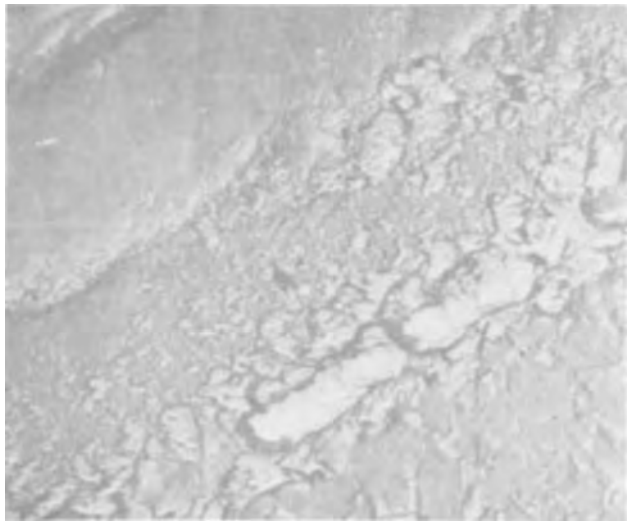

Fig. 6. A tool coated without hydrocarbon in the coating system. The lower right-hand corner is the tool and the upper left-hand corner is a layer of plated copper for preservation of the edge during metallographic preparation. The TiC layer is not very continuous nor does it adhere well to the substrate. 3550×.

Acknowledgments

The authors wish to thank the Materials Science Program at Brown University, supported by NSF and MRL, for the financial support of this research.

Manuscript submitted July 12, 1972; revised manuscript received March 5, 1973.

Any discussion of this paper will appear in a Discussion Section to be published in the June 1974 JOURNAL.

REFERENCES

1. T. Takahashi, K. Sugiyama, and K. Tomita, *This Journal*, **114**, 1230 (1967).
2. T. Takahashi, K. Sugiyama, and H. Itoh, *ibid.*, **117**, 541 (1970).
3. M. L. Pearle and R. W. Marek, *J. Am. Ceram. Soc.*, **51**, 84 (1968).
4. M. Lee, M. H. Richman, and J. Stanislao, Proceedings of 1st Int. Cemented Carbide Conf., SME CCPA, SME Paper FC71-929, Chicago, Feb. 1-3, 1972.
5. M. Blades, A. T. Blades, and E. W. R. Steacie, *Can. J. Chem.*, **32**, 298 (1954).
6. M. B. Palmer and T. J. Hirt, *J. Phys. Chem.*, **67**, 709 (1963).
7. A. R. G. Brown and W. Watt, "Industrial Carbon and Graphite," Society of Chemical Industry, London (1958).
8. R. M. Snow and M. C. Shutt, *Chem. Engr. Progr.*, **53**, 133M (1957).
9. W. S. Williams and R. G. Lye, ML-TDR-64-25, Part I, Air Force Materials Laboratory, R & T DTV., Air Force Systems Command, Wright-Patterson A.F.B., Ohio, 1964.
10. P. Schwarzkopf and R. Kieffer, "Cemented Carbides," Macmillan and Co., New York (1960).

Emission of Eu^{3+} in Some Calcium Germanates

T. J. Isaacs and A. A. Price

Westinghouse Research Laboratories, Pittsburgh, Pennsylvania 15235

In a three-component fluorescent lamp, the optimum Spectral Power Distribution (SPD) for artificial white light consists of spectral colors which emit near 450, 540, and 619 nm when both luminosity and color rendering index are important (1). When Eu^{3+} is used as an activator and substituted into a site having a linear crystal field term (*i.e.*, lacking inversion symmetry), the $^5D_0 \rightarrow {}^7F_2$ transition is allowed and emission at approximately 610 nm is produced (2). Strong emission at this wavelength has been obtained when Eu^{3+} has been substituted in such hosts as Y_2O_3.

We decided to look at Eu^{3+} emission in compounds containing Ca^{2+} in noncentric sites to see if essentially single-line emitting phosphors would be produced. Dicalcium germanate fit our conditions, and it proved to have a very promising spectrum when activated with Eu^{3+}. We then made the other compounds in the system $CaO\text{-}GeO_2$ which have been reported in the literature and studied their spectra when activated with Eu^{3+}. The compounds selected had $CaO:GeO_2$ ratios of 3:1, 2:1, 3:2, 1:1, 2:3, 1:2, and 1:4. A summary of experimental information of other investigators relating to these compounds is as follows:

An olivine-type calcium germanate ($\beta = Ca_2GeO_4$) was probably the first crystalline compound synthesized in the system $CaO:GeO_2$ (3). A high-temperature polymorph (α) was subsequently found which was at first believed to have the olivine structure (4), but was later thought to be similar to the high-temperature Ca_2SiO_4 (5, 6).

Several new compounds in this system (as well as Ca_2GeO_4) were reported and their fluorescence with some activators (Pb, Ti, Mn) given (7). These compounds were $CaGeO_3$, $CaGe_2O_5$, and $Ca_2Ge_3O_8$. The existence of the last mentioned compound was questioned by Eulenberger *et al.* (8) who found that the x-ray diffraction powder pattern which they obtained for a material of this composition was identical to that of their $CaGe_2O_5$ and similar to $CaTiSiO_4$. X-ray diffraction studies of single crystals of $CaGeO_3$ indicated that it has the same structure as β-wollastonite (9).

Eulenberger *et al.* also reported synthesizing $CaGe_4O_9$ (10) and later postulated two modifications with this composition (8).

Tricalcium germanate (Ca_3GeO_5) was synthesized at high temperatures (approximately 1500°C), but this compound was found to be unstable when cooled slowly; it broke down into Ca_2GeO_4 and CaO (5, 8). Polymorphism in this compound was studied by Hahn and Eysel (11), who found two modifications (monoclinic and triclinic) at room temperature. They reported inversion temperatures of 750°, 1030°, and 1160°C. Only one form of Ca_3GeO_5 was observed in a study of the system $CaO\text{-}GeO_2$, and it was found to break down to Ca_2GeO_4 and CaO at 1320°C (12). The compound $Ca_3Ge_2O_7$ was also reported in this work.

Experimental Details

Spectrographic grade starting materials ($CaCO_3$, GeO_2, Eu_2O_3) from Johnson-Matthey were used to make the compounds. The reactions tended to go slowly and, therefore, fluxes were employed. We used Na_2CO_3, B_2O_3, and CaF_2, the last mentioned being one used elsewhere (7). We obtained our best results when we used Na_2CO_3 as the fluxing agent; the reactions were more nearly complete than with the other agents under our conditions of synthesis. Sodium carbonate also served the purpose of being a source of a univalent ion (Na^+) for charge compensation of the Eu^{3+} ion in the Ca^{2+} site. Other charge compensators in this site were K^+ (as K_2CO_3) and Li^+ (as Li_2CO_3), but the best results were obtained with Na, a finding which could be predicted as its ionic radius (1.10Å) is nearer to those of Ca (1.08Å) and Eu^{3+} (1.03Å) than are those of K (1.46Å) and Li (0.82Å) (13).

We also substituted trivalent ions (Al, As, or Sb) for Ge^{4+} to effect charge compensation (instead of substituting a univalent ion in the Ca^{2+} sites) in some of the runs. No improvement in performance was seen, and in fact the Na substituted runs gave the highest intensity of luminescence.

The Eu^{3+} content was varied from 0.25 to 7 mole per cent (m/o) with the optimum amount generally being from 1 to 2%. The amount of compensator was usually the same percentage as the europium.

Samples were fired at temperatures ranging from 1150°C for most of the materials to 1480°C for Ca_3GeO_5 and α-Ca_2GeO_4 as these compounds can only be synthesized at high temperatures and are stable only at these temperatures.

The initial syntheses were done in open boats in air or oxygen atmospheres, but single-phase materials often were not obtained because of volatilization of GeO_2, even when an excess of GeO_2 was used. We also fired mixtures of stoichiometric composition in sealed platinum capsules in our attempts to produce single-phase material, but we often did not obtain the desired compounds. The runs synthesizing Ca_3GeO_5 and α-Ca_2GeO_4 were made with the material in sealed capsules to enable us to quench them quickly in ice water in order to freeze in the high-temperature equilibrium.

X-ray powder diffraction patterns using the Debye-Scherrer method were taken of all the materials, both to identify them and to ascertain that they were essentially single phase. Exposure times were in the order of 9 hr.

Emission spectra were determined at room temperature on a double-beam monochrometer system of the type described by Riedel (14). The relative intensities of the main emission peaks in the different samples were also determined on this instrument. Over-all brightness was measured with a "spectra" brightness meter.

Results and Discussion

The compounds which we were successful in obtaining in a single phase along with the per cent of the total emission in the range 460-730 nm which appeared at 611 nm (in samples containing 1% Eu^{3+}) are given in Table I along with a standard $Y_2O_3:Eu^{3+}$ containing 7% Eu^{3+}. These were the only compounds which we could positively identify as being the materials we sought or as being new single phases.

Results of attempts to make the other compounds mentioned in the literature were at best ambiguous. When we tried synthesizing $CaGe_2O_5$, we obtained a material which had an x-ray powder pattern corresponding to $Ca_2Ge_3O_8$ plus $CaGe_2O_5$ as given in the literature. The same results were seen for materials

Table I

Compound	% of total emission at 611 nm line
$Y_2O_3:Eu^{3+}$	57
β-$Ca_2GeO_4:Eu^{3+}$	58
α-$Ca_2GeO_4:Eu^{3+}$	25
$CaGeO_3:Eu^{3+}$	28
$Ca_3GeO_5:Eu^{3+}$	23

Key words: calcium germanates, emission, europium, phosphor, brightness.

of composition $CaGe_4O_9$. Even the addition of extra GeO_2 to the firing mixture and/or the use of sealed tubes did not produce the materials we sought. These compounds have been made in the past by repeated firings with intermittent grinding and it is possible that there were losses of germania as a result of these treatments which could have led the various authors (7-9, 12) to erroneous conclusions about the compositions of their materials.

The low-temperature (β) form of $Ca_2GeO_4:Eu^{3+}$ proved to be an essentially single line emitter (Fig. 2), with an emission spectrum very similar to that of $Y_2O_3:Eu^{3+}$ containing 7% Eu_2O_3 (Fig. 1). It has its main peak at 611 nm, and approximately 58% of the total Eu^{3+} emission is concentrated in this line. The half-width of this line is approximately 1-3/4 times as wide as that of $Y_2O_3:Eu^{3+}$. The transition producing this peak is assigned to $^5D_0 \rightarrow {}^7F_2$. The brightness, however, was only about 25% that of our standard $Y_2O_3:Eu^{3+}$. We varied the Eu^{3+} concentration from 0.25 to 9% and found that there was little variation in intensity between 0.5 and 7%, with the greatest intensity being at 1%. This was the best of the 5 phosphors we made.

A more complex spectrum was obtained for α-$Ca_2GeO_4:Eu^{3+}$ (Fig. 3). Once again the main peak is at 611 nm, but there are also significant peaks at 700 nm, between 611 and 630 nm, and between 580 and 600 nm. Its brightness is poor compared with Y_2O_3:Eu, and too little of its emission is at 611 nm for it to be a satisfactory red phosphor.

The spectrum for $CaGeO_3:Eu^{3+}$ also shows significant peaks at 600 nm, between 611 and 630 nm, and between 580 and 600 nm as well as its main peak at 611 nm. This material too is not a good red phosphor for the reasons given above.

The spectrum for $Ca_3GeO_5:Eu^{3+}$ shows a number of peaks between 560-700 nm (Fig. 5), and it too is a poor red phosphor.

The spectral energy distribution for β-$Ca_2GeO_4:Eu^{3+}$ is quite good, but its efficiency is poor. Examination of reflectance of this material and of $Y_2O_3:Eu^{3+}$ shows that the reflectivity of $Ca_2GeO_4:Eu^{3+}$ was in the range 40-50% at 254 nm, while that of $Y_2O_3:Eu^{3+}$ was in the range 10-20%. We checked reflectivity to see if the

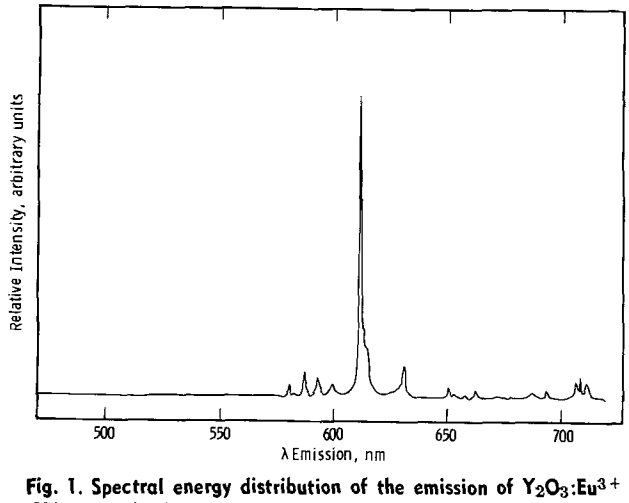

Fig. 1. Spectral energy distribution of the emission of $Y_2O_3:Eu^{3+}$ at 259 nm excitation.

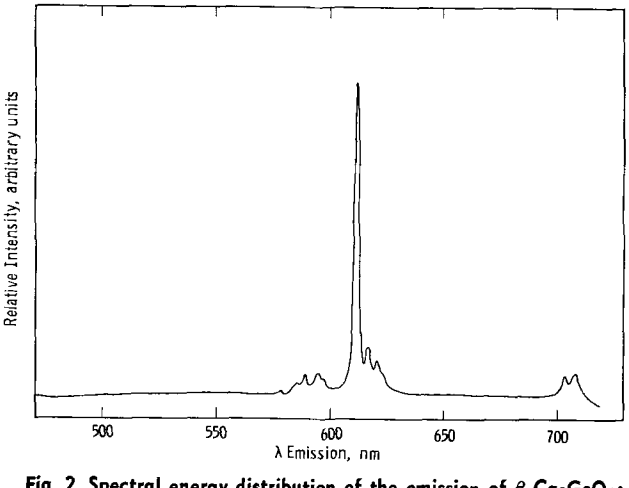

Fig. 2. Spectral energy distribution of the emission of β-$Ca_2GeO_4:Eu^{3+}$ at 259 nm excitation.

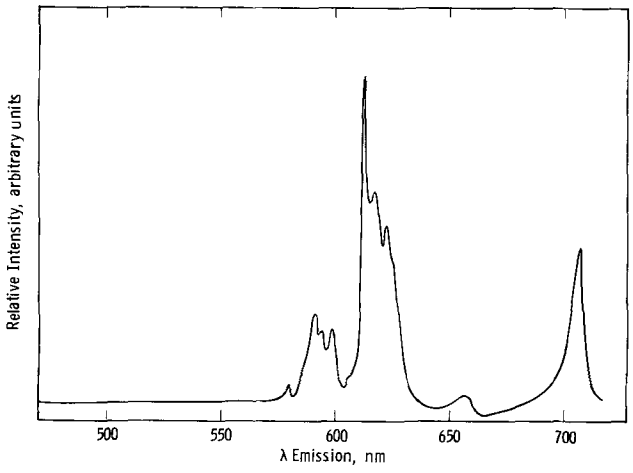

Fig. 3. Spectral energy distribution of the emission of α-$Ca_2GeO_4:Eu^{3+}$ at 259 nm excitation.

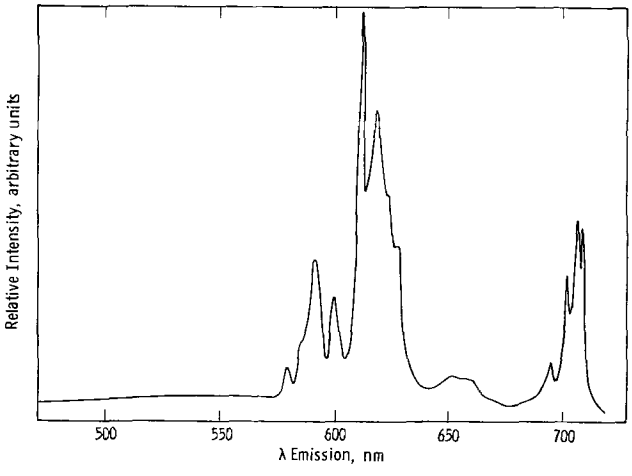

Fig. 4. Spectral energy distribution of the emission of $CaGeO_3:Eu^{3+}$ at 259 nm excitation.

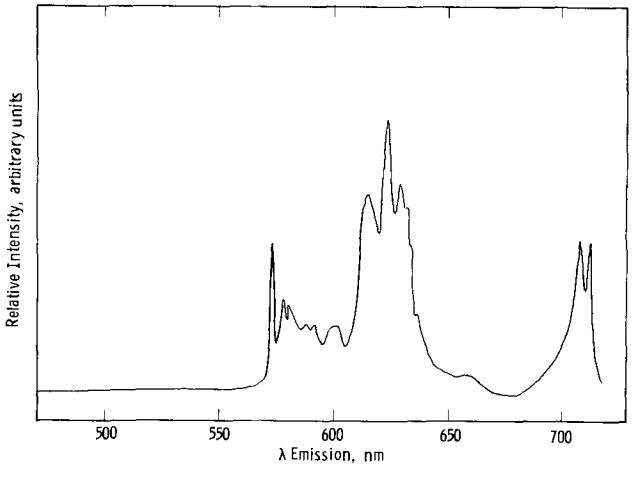

Fig. 5. Spectral energy distribution of the emission of $Ca_3GeO_5:Eu^{3+}$ at 259 nm excitation

low brightness was due to lack of absorption, but the difference in reflectivity was not great enough to explain the much poorer performance of Ca_2GeO_4: Eu^{3+}.

There are two Ca sites in this compound, one of which, ($\bar{1}$), has inversion symmetry, and the other, (m), has no inversion symmetry and has a linear crystal field term. The emission spectrum (Fig. 2) would indicate that much of the Eu^{3+} went into the (m) site, but it is possible that some of the Eu^{3+} may have entered the ($\bar{1}$) site.

If we assume structures analogous to corresponding silicates, then each of the other compounds which we made had one Ca site. It was noncentric and had a linear crystal field term, yet the emission spectra were poor. This result was somewhat unexpected as we expected to find a higher percentage of light in the 610 nm line where there was a single Ca site which was noncentric and had a linear term. A possible explanation for our results could be differences in charge compensation in these materials.

Acknowledgments

We wish to thank R. Williams for taking the emission spectra, and Dr. W. D. Partlow for obtaining reflectance data and, along with Dr. R. Warren, for reviewing the manuscript.

Manuscript submitted Oct. 18, 1972; revised manuscript received Feb. 12, 1973.

Any discussion of this paper will appear in a Discussion Section to be published in the June 1974 JOURNAL.

REFERENCES

1. W. A. Thornton, *J. Opt. Soc. Am.*, **61**, 1155 (1971).
2. G. Blasse and A. Bril, *Philips Tech. Rev.*, **31**, 304 (1970).
3. W. L. W. Ludekens, *J. Inorg. Nucl. Chem.*, **3**, 381 (1956).
4. H. Strunz and P. Jacob, *Neues Jahrb. Mineral. Abhandl.*, **94**, 78 (1960).
5. S. M. Royak and I. A. Prokhratilova, *Dokl. Akad. Nauk SSSR*, **141**, 880 (1961).
6. W. Eysel and Th. Kahn, *Neues Jahrb. Mineral. Abhandl.*, **6**, 137 (1963).
7. H. Koelmans and C. M. C. Verhagen, *This Journal*, **106**, 677 (1959).
8. G. Eulenberger, A. Whittmann, and H. Nowotny, *Monatsh. Chem.*, **93**, 1046 (1962).
9. F. Liebau *Neues. Jahrb. Mineral. Abhandl.*, **94**, 1209 (1960).
10. G. Eulenberger, A. Whittmann, and H. Nowotny, *Monatsh. Chem.*, **93**, 123 (1962).
11. Th. Hahn, and W. Eysel, *Naturwiss.*, **50**, 471 (1963).
12. A. K. Shirvinskaya, R. G. Grebenshchikov, and N. A. Toropov, *Izv. Akad. Nauk SSSR, Neorgan. Materialy*, **2**, 332 (1966).
13. E. J. W. Whittaker and R. Muntus, *Geochim. Cosmochim. Acta.*, **34**, 945 (1970).
14. P. Riedel, *J. Luminescence*, **1**, 197 (1969).
15. N. A. Toropov and A. K. Shirvinskaya, *Zh. Prikl. Khim.*, **36**, 717 (1963).

The Effect of Oxide Thickness on Threshold Voltage of Boron Ion Implanted MOSFET

R. B. Palmer,* C. C. Mai,* and M. Hswe
Mostek Corporation, Worcester, Massachusetts 01606

The greatest interest in the application of ion-implantation to MOS integrated circuit fabrication has been the ability to shift threshold voltages and to produce depletion-mode devices as well as enhancement-mode devices on the same chip (1-3). By applying ion-implantation techniques, the threshold voltage of enhancement-mode devices and the pinch-off voltage or the drain to source current, I_{DSS}, for depletion-mode devices may be adjusted to almost any desired value independent of substrate resistivity, gate dielectric, and metalization.

In the fabrication of MOSFET's by using the ion implantation technique to adjust the threshold voltage, V_T, the impurity ions are usually implanted through a thin oxide layer, *i.e.*, gate oxide. The effect of the oxide thickness on threshold voltage shift, ΔV_T, was studied and is reported in this paper.

Experimental Procedure

N-type silicon slices of 9-15 ohm-cm resistivity and <111> orientation were used as substrates. A standard P-channel MOSFET fabrication process was employed (1). Different thickness of thermally grown SiO_2 in the range of 600-2000Å were used as gates, and boron ions were implanted through these oxide layers. The implantations were carried out at 44 keV with two sets of doses: (*i*) 4×10^{11} ions/cm^2 for enhancement-mode devices and (*ii*) 2×10^{12} ions/cm^2 for depletion-mode devices. During the implantations, one-half of each slice was protected from the boron beam by a thin aluminum strip in order to provide both implanted and unimplanted devices on every slice. The unimplanted devices provide the reference value of V_T so that more accurate determination of the threshold shift may be determined. After implantation the slices were annealed at 950°C for 10 min in order to achieve essentially complete activation of the implanted boron species, and to eliminate the radiation damage.

An MOS test transistor with a channel length of 20 mils and width of 20 mils was used as a vehicle for measuring the threshold voltage (V_T at 1 μA) and drain-to-source current I_{DSS}. The latter was measured with a drain-to-source bias of 10V and 0V bias from gate-to-source. The relatively large values of W and L were chosen in order to minimize the effects of slight variations normally produced during fabrication on the parameters in question.

Effect of Oxide Thickness

Figure 1 shows the threshold voltages of the unimplanted and the implanted enhancement MOSFET's.

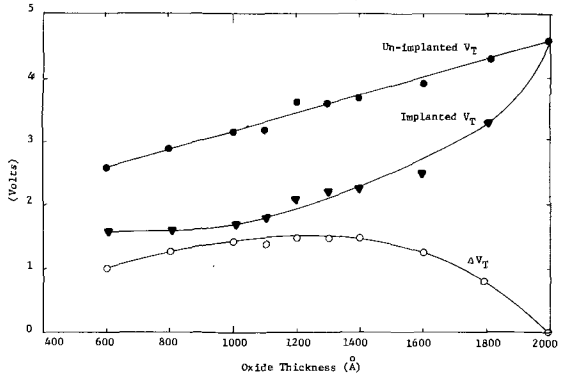

Fig. 1. Threshold voltage as a function of oxide thickness for an implanted dose of 4 X 10^{11} boron ions/cm^2 at 44 keV.

* Electrochemical Society Active Member.
Key words: ion-implantation, threshold voltage, MOSFET.

Also plotted at the bottom of the figure is the shift in threshold voltage as a function of oxide thickness. The boron implantation dose was approximately 4×10^{11} ions/cm^2. The graph shows that ΔV_T equalled 1V for 600Å of oxide and increased with increasing oxide thickness. ΔV_T appeared to remain relatively constant from 1000 through about 1400Å, and then gradually decreased. As the oxides became thicker than 2000Å, ΔV_T was effectively 0, *i.e.*, the additional implantation had no effect on the threshold voltages. The variation of the implanted thresholds with oxide thickness may be explained as follows. For oxides thicker than 2000Å, the implanted boron ions have insufficient energy to penetrate the oxide to reach the SiO_2-Si interface. As the thickness decreases, boron ions begin to reach this interface and counterdope the silicon surface. The channel resistivity is effectively increased, resulting in the reduction in V_T. The number of ions reaching the interface and slightly beyond increases with decreasing gate oxide thickness.

Figure 2 shows the same kind of plot for the more heavily implanted devices. The dose was approximately 2×10^{12} ions/cm^2. All of the MOSFET's became depletion-mode devices with the exception of those having 2000Å thick gate oxides. The pinch-off voltages were determined by extrapolation and the ΔV_T's were calculated. It is interesting to note that the curve of ΔV_T is very similar to that shown in Fig. 1. It may be concluded that for these implantation conditions the effect of implanted boron ions on V_T is essentially the same except for the magnitude of the V_T shifts.

The maximum threshold shift resulting from a given ion dose can be expressed as $V = qN_I/C_o$ (4) where N_I is the implanted dose and C_o is the oxide capacitance. However, V_T's measured in this study were observed to be lower than these maximum values. The percentage ratio of ΔV_T (observed) and ΔV_T max (calculated) is plotted in Fig. 3 as a function of oxide thickness. It is shown that this ratio decreases as oxide thickness increases (curve A). It is interesting to note that for an oxide thickness of 1000Å, the ratio is about 80%, which may be interpreted to mean that at least 80% of the boron ions penetrated the oxide layer and came to rest in the silicon near the SO_2-Si interface. This interpretation is consistent with the data of Swanson and Meindl (5) obtained by computer calculation of the LSS depth-penetration theory.

To calculate the depth distribution of boron in silicon can be very difficult for the SiO_2-Si structure, due to the unknown energy and vector distribution of boron ions at the SiO_2-Si interface (6). For a simple approximation, one can calculate the relative stopping power of SiO_2 and silicon and convert the thickness of SiO_2 into an equivalent thickness of silicon (7, 8). By applying this technique, the projected range of boron at 44 keV has been calculated as a function of oxide thickness, and is plotted (curve B) in Fig. 3. It can be seen that R_p is inversely proportional to

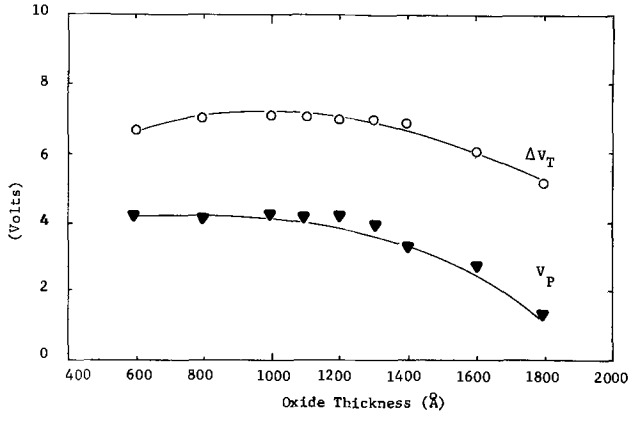

Fig. 2. Threshold voltage as a function of oxide thickness for an implanted dose of 2 X 10^{12} boron ions/cm^2 at 44 keV.

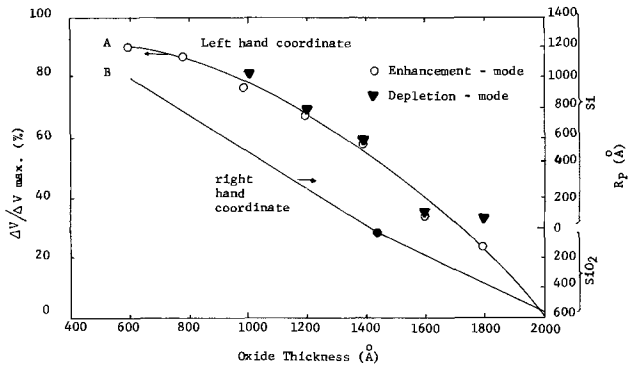

Fig. 3. (A) Left-hand coordinate, the ratio of ΔV to ΔV max as a function of oxide thickness. (B) Right-hand coordinate, R_p as a function of oxide thickness.

oxide thickness, decreasing linearly from 600 to 1440Å where the peak of the distribution is right at the SiO_2-Si interface. The slope then changes slightly and R_p remains in the SiO_2. The difference in slope is due to the small difference in ion stopping power between SiO_2 and Si.

From Fig. 1 it can be seen that at oxide thickness range of 600-800Å the V_T of the implanted devices remained constant at 1.6V regardless of the variation in oxide thickness. Since in this region, V_T changes at the same rate as ΔV_T, they are approximately compensated by each other. At the other extreme, at oxide thickness from 1600-1800Å, V_T is increasing while ΔV_T is decreasing. From a mass production point of view, one wishes to obtain constant V_T irrespective of the small unavoidable variation of oxide thickness. From the above data, we have demonstrated that for any particular energy level, there is an optimum oxide thickness range that can provide better V_T control. For boron ion implantation at 44 keV, the optimum oxide thickness is 600-800Å, which correlated to a R_p of from 900 to 1100Å inside silicon. For different oxide thicknesses, one should change the energy to obtain the same R_p, if constant V_T is desired.

Effect of Boron Projected Range

To demonstrate the importance of boron depth distribution on V_T, another experiment has been done as follows:

A number of slices having gate oxides of 1250Å were implanted with 5×10^{11} ions/cm^2 at energies between 24 and 84 keV. It was found that at 24 keV, ΔV_T was only 0.15-0.2V as shown in Fig. 4. The values of ΔV_T increased with increasing energy until 55 keV. From 55 to 84 keV the value of ΔV_T was essentially constant. This would imply that an energy of 60-70 keV would be most suitable for threshold shifting of devices having 1250Å gate oxides. Similar data have been reported by MacPherson (4).

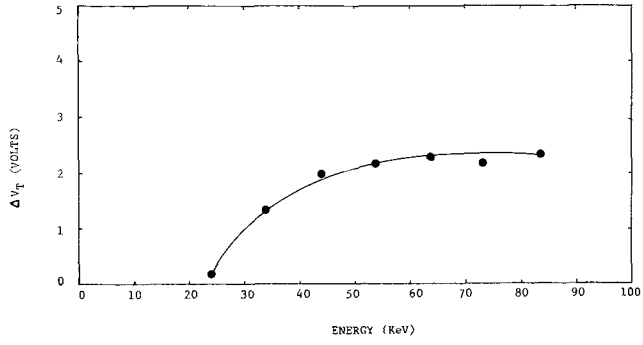

Fig. 4. Threshold shift as a function of implanted energy for an oxide thickness of 1250Å.

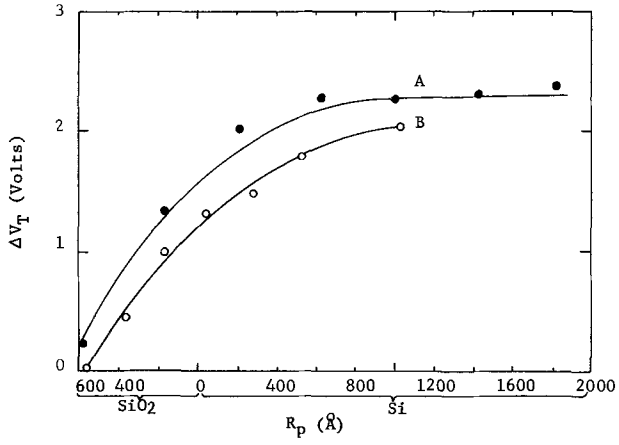

Fig. 5. Threshold shift ΔV_T as a function of boron ion project range R_p: Curve A, for energy of 24-84 keV with fixed oxide thickness of 1250Å; curve B, for fixed energy at 44 keV with oxide thickness from 600 to 2000Å as normalized to 1250Å.

These data are compared to those of Fig. 1 for the boron projected range R_p. ΔV of Fig. 4 and normalized ΔV_T to oxide thickness of 1250Å of Fig. 1 was plotted in Fig. 5 as a function of R_p. It was shown that both curves have the same trend, *i.e.*, ΔV_T increases with R_p and starts to saturate when R_p reaches about 600-800Å inside silicon. This phenomenon can be interpreted as follows. When R_p is deeper than 600-800Å, even though more boron penetrates the silicon dioxide layer, some of the boron ions are situated too far from the SiO_2-Si interface to cause a shift in threshold voltage. From the above study, it can be concluded that to obtain a constant ΔV_T, one can either adjust the oxide thickness with fixed implanted energy, or adjust the energy with fixed oxide thickness to place the R_p in the optimum location.

Summary and Conclusion

The effect of oxide thickness on threshold shifting by ion implantation has been reported. It has been found that for a particular implant energy, there is an optimum oxide thickness range for which a relatively constant V_T can be obtained. It has also been shown that for a given range of oxide thickness, there is an optimum energy which should be used to insure minimum variation in V_T.

Manuscript received Oct. 24, 1972.

Any discussion of this paper will appear in a Discussion Section to be published in the June 1974 JOURNAL.

REFERENCES

1. J. MacDougall, K. Manchester, and R. Palmer, *Electronics*, **43**, 86 (1970).
2. M. R. MacPherson, *Appl. Phys. Letters*, **18**, 502 (1971).
3. V. McKenny, *Electronics*, **44**, 80 (1971).
4. M. R. MacPherson, *Appl. Phys. Letters*, **18**, 502 (1971).
5. R. M. Swanson and J. D. Meindl, *IEEE J. Solid-State Circuits*, **SC-7**, 146 (1972).
6. P. J. Coppen, L. O. Bauer, and H. G. Dill, "Ion Implanted CMOS Technology." Presented at the Western Electronic Show and Convention, August 1972.
7. J. W. Mayer, L. Eriksson, and J. A. Davies, "Ion Implantation in Semiconductor," p. 37, Academic Press, New York (1970).
8. W. S. Johnson and J. F. Gibbons, "Projected Range Statistics in Semiconductors," Stanford University Press, Stanford, California (1969).

Brief Communication

Reliability of NiCr "Fusible Link" Used in PROM'S

R. S. Mo and D. M. Gilbert

Xerox Corporation, El Segundo, California 90245

A fast integrated circuit Programmable Read Only Memory is useful in digital applications not only as a ROM, but as a universal logic element. However, because of its potentially wide usage and the complexity of the device, its reliability is a matter of concern. The usual IC reliability can readily be estimated (1). Some reliability data of the NiCr fusible link is presented in this communication.

The reliability of the NiCr fuses may be treated in two parts: the first part deals with the life of an unblown fuse; the second part deals with the reliability of a blown fuse. The test results reported here are based on six runs of a special test chip from a major vendor as well as samples from other vendors. The test chip is designed such that each fuse is individually accessible. Furthermore, chip temperature is controlled by built in temperature sensor and heater elements. The sample size is approximately 10,000 fuses from kit parts and an equal number from PROM's.

Key words: memory, nichrome, reliability, fuse.

The Fuse

The fuses studied are a NiCr film, approximately 350Å thick, vacuum deposited on a silicon dioxide substrate. Aluminum contacts are deposited over each end of the NiCr film and a 1 μm glass passivation layer covers the resulting structure. The film composition is approximately 65% Ni, 35% Cr with a sheet resistivity of 70 ohms per square.

The Unblown Fuse Life Test

The test fuses are "blown" by stressing with constant current and constant temperatures until they fail. The failure data under each condition was plotted using several distributions. The best fit, however, was obtained using the Weibull distribution (2, 3). The Wei-

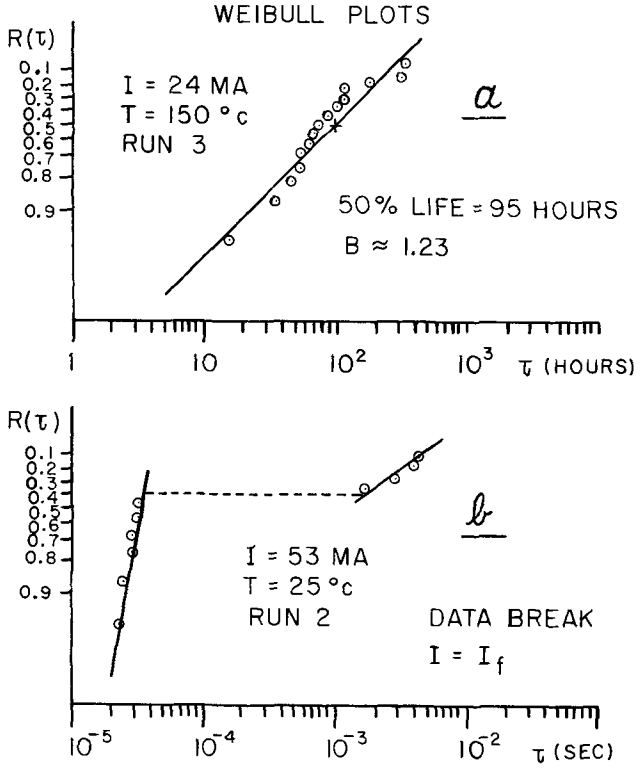

Fig. 1. Weibull plots. (a) For relatively low stresses, where the fuse temperature does not reach melting point, the failure times follow the Weibull distribution. (b) At a high current stress, a data break is observed. This indicates different failure mechanisms. Energy calculations show fuses melt above this break point.

bull density function is

$$f(t) = [\beta(t-\gamma)^{\beta-1}/\alpha] \exp[-(t-\gamma)^{\beta}/\alpha] \quad [1]$$

This expression may be rewritten as

$$\ln\ln[1/R(t)] = \beta \ln(t-\gamma) - \ln\alpha \quad [2]$$

where $R(t) = 1 - \int_0^t f(t)dt = 1 - F(t)$

At each stress level, the failure data was reduced to the form of Eq. [2] and plotted. The resulting "Weibull Plot" was used to estimate the 50% lifetimes. Good fits are obtained with $\gamma \simeq 0$ (time translation factor), and β (shape factor) varies from about 0.7 to 1.5 (Fig. 1a).

The Weibull plots in the very fast blow, high current region show a data break as shown in Fig. 1b. This indicates a different failure mechanism, and from energy calculations, it can be shown to correspond to melting of NiCr. Failure time here is a function of the fuse thermal capacity, thermal time constant, heat of fusion, and input power, and is in the μsec region. Blow times in the region of msec and longer are due to a different mechanism, possibly localized oxidation. By knowing the current at which this data break occurs, the "fusion current" I_f is obtained. I_f is the current required to raise the fuse temperature to the NiCr melting point (~1400°C).

Knowing I_f, the fuse temperature can be calculated at any given stress current I

$$T = [T_c + (I/I_f)^2(1400 - T_{cf})(1 - 1400c)]/$$
$$[1 - c(I/I_f)^2(1400 - T_{cf})] + 273 \quad [3]$$

where T = fuse temperature, T_c = chip temperature, T_{cf} = chip temperature at which I_f is measured, and c = fuse T.C.R. Equation [3] assumes that the T.C.R. is essentially constant throughout the temperature range.

Taking the 50% life estimates at various stress levels from the Weibull plots and comparing these with the calculated fuse temperatures at each of these stress levels, the failure times are observed to obey the Arrhenius equation

$$L = Ae^{\phi/kT} \quad [4]$$

where A = constant, k = Boltzmann constant, ϕ = activation energy, T = calculated fuse temperature, and L = 50% lifetime.

Figure 2 shows the data obtained from four different runs. Run 4 showed abnormally high T.C.R. and low activation energy. The other 3 runs show consistent life projections. Analysis using electron microprobe showed run 4 to have different composition and thickness. It is evidently the result of abnormal process variations. From Fig. 2 the 50% life at 110°C is estimated at 3×10^5 yr. The failure percentage of 1024-bit PROM's in 10 yr may also be estimated: ~1.0% for $\beta = 1$.

The Blown Fuse Reliability

"Healing" or relinking of a blown fuse is found to be possible. The conditions which encourage the heal phenomena are slow blowing and current limited voltage bias across a blown fuse, as well as elevated temperatures.

Figure 3 shows scanning electron micrographs of a fuse blown with a slow ramp voltage source. The "whiskers" are believed to be important in the relinking process, as shown in the figure.

Under normal PROM pulse blowing conditions, the blowing time is usually in the microsecond regions. Tests on fuses blown in this range have never shown healing under normal operating bias voltage (4.5V) and temperature (110°C). Figure 4 is an SEM picture of a fuse blown in that time region. For the marginal cases where the current density at the fuse neck is less than 4×10^7 A/cm^2, and the blowing time is in the region of several milliseconds, the fuses may heal. Heal probabilities as high as 3% have been observed for such fuses at 150°C in 500 hr. Almost all the heals occur in the first two hours. (One fuse healed in ~300 hr.) Healed fuses in these cases have $R \simeq 1K$ and will reblow with $i < 1$ mA.

The evidences so far suggest that unless circuit design takes into account the fuse requirements, healing can definitely occur. The desirable conditions for no healing are: blow current density $\geq 4 \times 10^7$ A/cm^2, such that blow time is <10 μsec; the bias voltage across

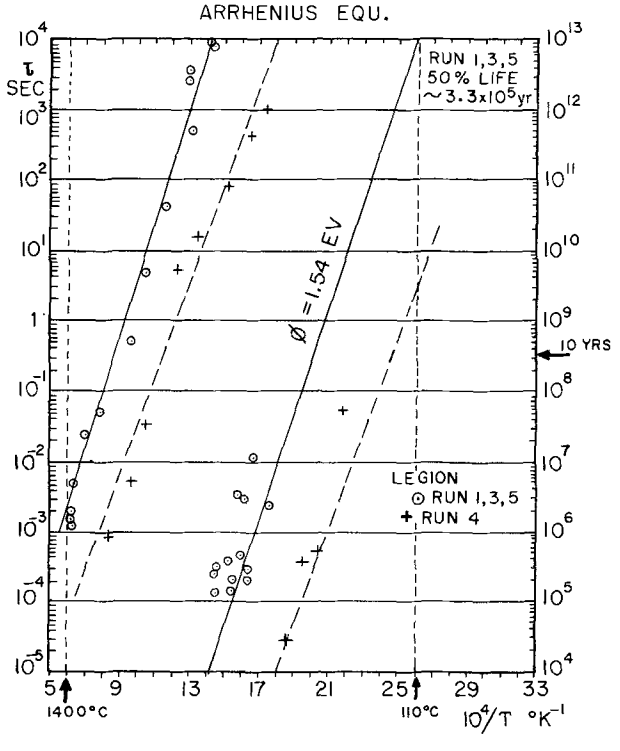

Fig. 2. Arrhenius equation. Fifty per cent life obeys the Arrhenius equation. The life for normal fuses is adequate.

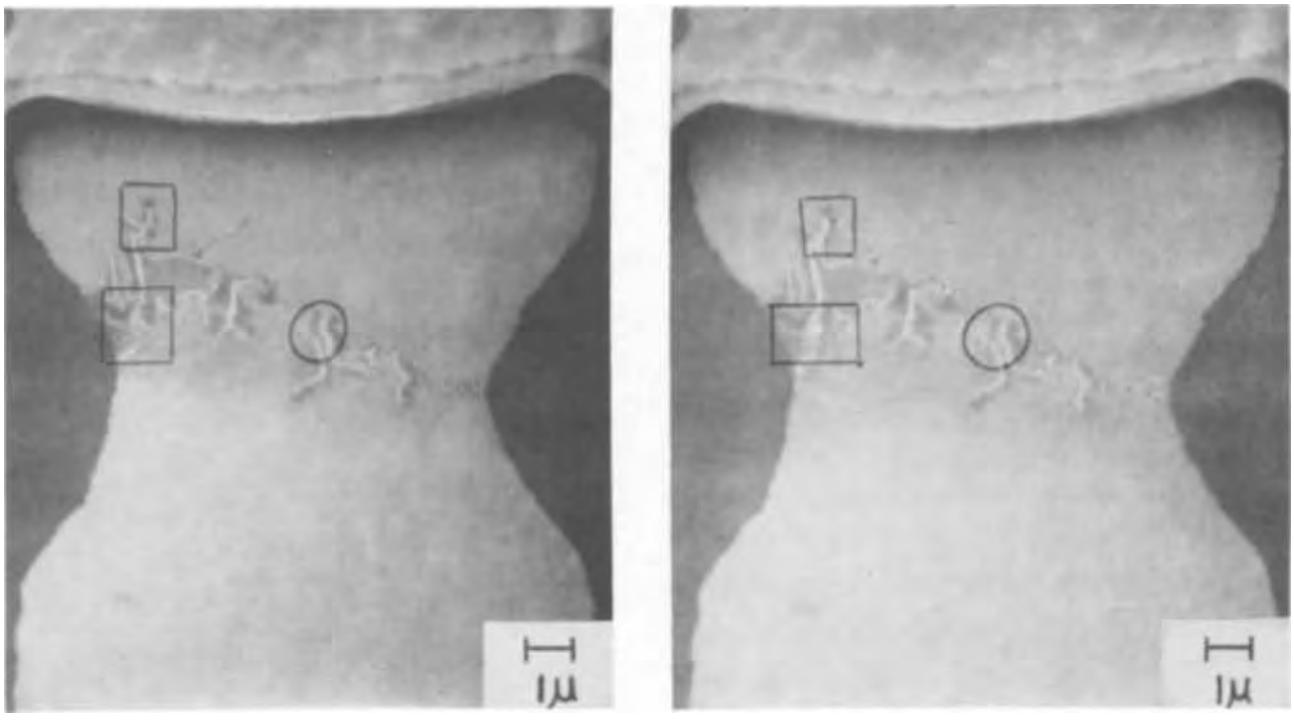

Fig. 3. Fuse blown by slow V-ramp; left, healed fuse; right, same fuse, reblown. The fuse was healed, examined, and then reblown. The marked areas show differences in pattern. Square boxes indicate healed areas reopened by reblowing. Circled area shows growth of conductive strand, though contact was not made.

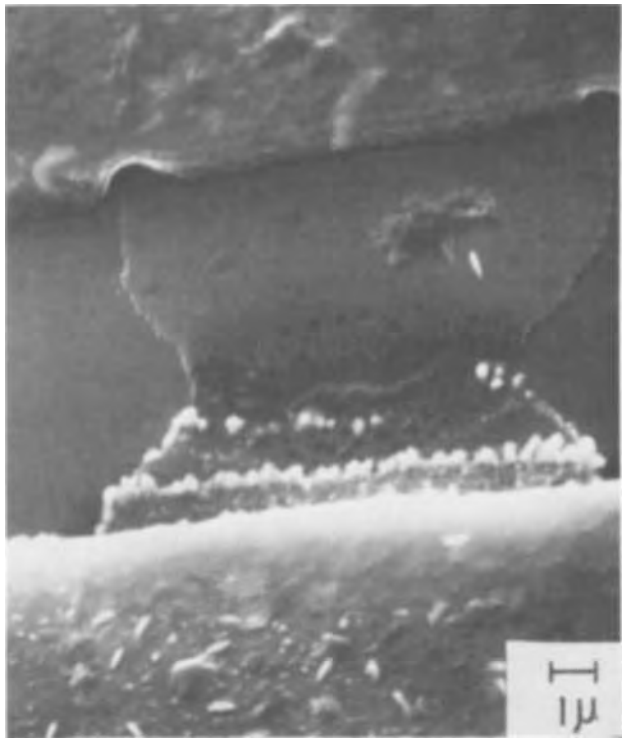

Fig. 4. Fuse blown by fast pulse. This fuse was blown with current density of $\sim 4 \times 10^7$ A/cm^2. Blowing time was < 4 μsec. Such fuses have not been observed to heal.

the blown fuse is low, preferably <1.0V; and the sense circuit has a threshold such that >1 mA conduction through the fuse is needed for detection. The fact that most heals occur quickly also suggests a burn-in after programming may be most useful.

Conclusion

It is shown here that the fuse failure times for a given stress obey the Weibull distribution, and the failure times are temperature dependent, obeying the Arrhenius equation. Excepting for certain grossly abnormal fuse runs, the unblown fuse life is generally adequate though by no means negligible, for a 1024 bit PROM. For the blown fuses, healing can occur. No heal model is available yet. However, it is established that the heal problem can be greatly reduced if proper blowing conditions as well as circuit biasing and sensing conditions are achieved.

Manuscript submitted Nov. 6, 1972; revised manuscript received Feb. 19, 1973. This was Paper 258 presented at the Miami Beach, Florida, Meeting of the Society, Oct. 8-13, 1972.

Any discussion of this paper will appear in a Discussion Section to be published in the June 1974 JOURNAL.

REFERENCES

1. C. M. Ryerson, S. L. Webster, and F. G. Albright, "The Reliability Notebook, Vol. II," *RADC-TR-67-108*, Sept. 1967.
2. Waloddi Weibull, *J. Appl. Mech.*, **18**, 293 (1951).
3. John W. Webb, *ASQC Convention Transactions*, Cincinnati, Ohio (1962).

JOURNAL OF THE ELECTROCHEMICAL SOCIETY

ELECTROCHEMICAL SCIENCE AND TECHNOLOGY

AUGUST 1973

A Model for Discharge of Storage Batteries

Dimitri Gidaspow

Institute of Gas Technology, Chicago, Illinois 60616

and Bernard S. Baker*

Energy Research Corporation, Bethel, Connecticut 06801

ABSTRACT

The common porous electrode model has been rederived to include the transformation of one solid phase into another, for example, lead into lead sulfate. Differential mass balances for the solid porous reactant and the solid product yielded new dimensionless groups which characterize the structural changes that occur during discharge or charge of storage batteries. Effects of fraction of active material, exchange current and molar density ratios on overpotential at a constant current were investigated numerically. The trends agree well with the empirical correlation of Shepherd.

At the present time no comprehensive electrode model exists for batteries of any kind (1-4). Discharge data are related to discharge duration by purely empirical equations of the type $I^n t = C$, where I is current, t is time, and n and C are constants having no physical significance, as for instance in a recent paper on lead-acid batteries (5). A more comprehensive empirical equation is that developed by Shepherd (6). It takes into account the consumption of the active material and in this respect is not purely empirical. Shepherd's equation correctly describes discharge curves for many batteries over a range of current densities. His polarization coefficient and electrical internal resistance, however, have no physical meaning because they are some lumped parameters for two electrodes with at first no electrical resistance in the metal or solution phases (Eq. 7), with an afterthought correction for a resistance (Eq. 8).

The first theoretical attempt at predicting overpotentials as a function of time that can be applied to a single electrode of a battery has recently appeared (7). The authors use the common, steady-state, one-dimensional porous electrode equations combined with a mass transport of an active species given by a mass transfer coefficient that must be determined empirically. To handle time-dependent phenomena Dunning, Bennion, and Newman (7) assume that their mass transfer coefficient is some reasonable function of the amount of active material present in any part of the electrode. Their approach apparently allows them to predict a failure caused by an internal mass transfer limitation with a sparingly soluble reactant, although they do not cite any experimental studies in support of their conclusions. Their model cannot predict failure by blockage of pores that is commonly observed in lead acid batteries (1) and in the recent study of cadmium electrodes (8).

In this paper we are proposing a model that describes the time variation of charge and discharge of a battery for given electrode kinetics and initial structure of electrodes. The structure of the porous electrodes changes with the state of charge or discharge, with pores opening or closing depending on the molar volumes of solid reactants and products. The shape of our calculated overpotential *vs.* fractional capacity utilized curves agree with Shepherd's correlations. A quantitative comparison has not been made, because his discharge data are for two electrodes and because we found that structural parameters that are usually different for the negative and positive electrodes markedly influence the overpotential curves. We present numerical results for constant current operation of a single electrode of a battery.

As in the study of Dunning, Bennion, and Newman (7) we consider the electrode to be one dimensional. We therefore do not consider effects such as shape changes that are two or three dimensional. We also present numerical results only for the case of linear polarization which is claimed to be (9) valid for alkaline nickel-cadmium batteries and should be valid in general at low current densities. The principal contribution of this paper is believed to be the analysis of battery failure by chocking near the front of the electrode.

Description of the Model

Consider generation of current in a porous electrode such as treated by Ksenzhek (10), Pschenichnikov (11), and particularly by Tobias and co-workers (12, 13). However, unlike in the previous studies (7, 13), assume that in the porous electrode a consumable solid-fluid reaction takes place. The reaction could be the formation of lead sulfate in the positive plate of a sulfuric acid lead battery

$$PbO_2 + 2H^+ + H_2SO_4 + 2e \rightarrow PbSO_4 + 2H_2O \quad [1]$$

the reaction of lead in the negative plate

$$Pb + SO_4^{=} - 2e \rightarrow PbSO_4 \quad [2]$$

or the reaction of cadmium to form an insoluble product in the cadmium electrode

$$Cd + 2\,OH^- - 2e \rightarrow Cd(OH)_2 \quad [3]$$

* Electrochemical Society Active Member.

Key words: porous electrode, solid-state reaction, current distribution, pore plugging, molar volumes, integral equation.

In each case, in a well-designed electrode, the solid reagent, be it lead or cadmium, is sufficiently finely dispersed to be accessible to the electrolyte. As the reactions proceed to the right, there is less and less solid reagent to produce current. Furthermore the solid products occupy considerably more space forcing the electrolyte out of the electrode. The ratios of molar volumes of solid products to solid reactants for Eq. [1]-[3] are 1.9, 2.7, and 2.3, respectively (14). This causes a decrease of the effective conductivity of the electrolyte in the pores of the electrode and possible blocking of the pores.

To easily handle this physical reality, assume that at any point in space in the electrode we have the following phases: the solid reactant, called S, the solid product called P, electrolyte, binder, and a metal support that acts as a conductor which is electrically connected to a metal backing. Such a continuum approximation should be valid for a well-designed electrode of a high surface area, as discussed by Gidaspow (15). Then on an inert free basis the volume fractions of S, P, and the electrolyte add up to one

$$\epsilon_S + \epsilon_P + \epsilon = 1 \qquad [4]$$

A current balance on an element of volume $A\Delta x$, as shown in Fig. 1, is

$$[I\epsilon A]_x^{x+\Delta x} = -\int_x^{x+\Delta x} ia\epsilon_S A dx \qquad [5]$$

where i is the rate of production of current per unit area by chemical reaction and a is the surface to volume ratio for the solid reagent. The current flux I is related to the electrical conductivity of the solution, K by Ohm's law

$$I = -K\frac{\partial V_S}{\partial x} \qquad [6]$$

where V_S refers to the voltage in the solution phase as for example in the model of Newman and Tobias (12). Application of the mean value theorems to [5] and the usual limiting process yield the partial differential equation for the solution potential

$$\frac{\partial}{\partial x}\left(K\epsilon\frac{\partial V_S}{\partial x}\right) = ia\epsilon_S \qquad [7]$$

In general i is a function of potential differences and concentrations in the fluid phases of reactants and products. For constant concentrations in the porous electrode a commonly (12) used form is

$$i = i_0\left\{\exp\left[-\frac{n\mathbf{F}}{2RT}(V_m - V_S)\right] - \exp\left[\frac{n\mathbf{F}}{2RT}(V_m - V_S)\right]\right\} \qquad [8]$$

where i_0 is the exchange current density, V_m the metal potential, and the other symbols have their usual meaning. Sometimes (6) for discharge of storage batteries a linear relation seems applicable. For $(V_m - V_S)/(RT/n\mathbf{F}) << 1$ relation [8] becomes

$$i = i_0\left(\frac{n\mathbf{F}}{RT}\right)(V_S - V_m) \qquad [9]$$

Although a specific form of current-polarization relation will be used in this study, the theory presented here is not restricted to any particular electrode kinetics.

It was already shown by Gidaspow (15) that for the reaction

$$A(f)^{-n} + S(s) - n(e) \rightarrow \gamma P(s) \qquad [10]$$

a mass balance on S yields the differential equation for the volume fraction of S

$$\rho_S\frac{\partial\epsilon_S}{\partial t} = -\left(\frac{iM_S a}{n\mathbf{F}}\right)\epsilon_S \qquad [11]$$

when the thickness of the electrode remains constant. Similarly a mass balance on P yielded

$$\rho_P\frac{\partial\epsilon_P}{\partial t} = \left(\frac{iM_P\gamma a}{n\mathbf{F}}\right)\epsilon_S \qquad [12]$$

Since expansion or contraction occurred at the expense of the fluid phase, the volume fraction of liquid is obtained by difference as

$$\epsilon = 1 - \epsilon_S - \epsilon_P \qquad [13]$$

Initial distributions of S and P can be chosen to be functions of electrode thickness. They are ϵ_{SO} and ϵ_{PO}.

Two boundary conditions are needed for the second-order differential Eq. [7]. At the metal backing, solution ends. Therefore at

$$x = L, \quad \frac{\partial V_S}{\partial x} = 0 \qquad [14]$$

To compare calculated results to discharge data, consider the case of constant current discharge. Then for a discharge current density I_0, expressed on an inert free basis, at the solution end we have at

$$x = 0, \quad -K\epsilon\frac{\partial V_S}{\partial x} = I_0 \qquad [15]$$

The electrode overpotential $V_S(t,0) - V_S(t,L)$ is one of the quantities we want to obtain. Note that V_m does not enter into this potential difference.

The case of prescribed potential at $x = 0$, when using the linear relation [9] corresponds exactly to the case of a first-order reaction for concentration obtained by Gidaspow (15). All results presented for concentration are applicable to the potential difference in this case. However, since such operation is uncommon we will proceed only with the constant current case. The model is, of course, applicable to time-dependent operation, as long as changes are slow enough for the double-layer capacity effects to be negligible. Changes in concentration can be accounted for by the use of diffusion equations of the type solved by Gidaspow (15) coupled with the problem presented here. When the metal reagent carries most of the current, an equation for metal potential of the type of Eq. [7] must be added to the system. In this study, however, the conductivity of the metal phase is assumed to be so high that the metal is at the potential of the metal backing plate.

We would like to add that while potentiostatic studies of batteries are rare, as already noted by Sanghi and Fleischmann (16), they provide an excellent means to study rates of electrochemical reactions. Since the rate constants controlling electrochemical reactions are chiefly potential dependent, they can be kept constant during study by this procedure. In this way we obtain an analogy between concentration and potential. We thus expect the rates to behave similarly with potential, as was observed with concentration by Onischak and

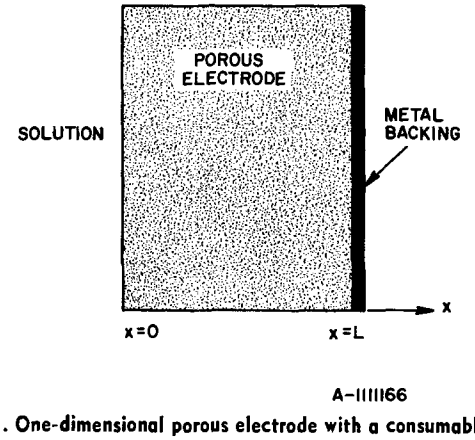

Fig. 1. One-dimensional porous electrode with a consumable solid

Gidaspow (17). Indeed Fleischmann and Thirsk's (18) Equation 1 is analogous to Gidaspow's Equation 12 (15). Furthermore, Fleischmann and Thirsk observed maxima in rates with time for the reverse reaction given by Equation 2 for which pores tend to open up leading to an initial increase in rate. Such limited electrochemical rate studies with consumable solid reactions provide additional support for the form of the rate expression chosen in this study.

Dimensionless Equations

For the case of linear polarization, as expressed by Eq. [9], the potential distribution in the electrode is governed by

$$\frac{\partial}{\partial \bar{x}}\left(\epsilon \frac{\partial Y}{\partial \bar{x}}\right) = \phi^2 \epsilon_S Y \qquad [16]$$

In Eq. [16], Y is the difference of solution minus metal potentials scaled by the current drawn, as shown below

$$Y = \frac{V_S - V_m}{\left(\frac{i_0 L}{K}\right)} \qquad [17]$$

The boundary condition given by Eq. [15] dictated this choice of scale factor.

The group

$$\phi^2 = \frac{i_0 n \mathbf{F} a L^2}{RTK} \qquad [18]$$

is a dimensionless exchange current. It is called ϕ^2 due to its analogy to the Thiele modulus in the concentration problem (15).

The boundary conditions (BC) for Eq. [16] become, in dimensionless form

$$\text{BC 1: } \frac{\partial Y(t,1)}{\partial \bar{x}} = 0 \qquad \text{BC 2: } \epsilon \frac{\partial Y(t,0)}{\partial \bar{x}} = -1 \qquad [19]$$

Equation [11] dictates that the dimensionless time, $\bar{t}$ be expressed as

$$\bar{t} = \left(\frac{i_0 M_S a L}{RTK\rho_S}\right)(I_0 t) = \epsilon_{SO}\phi^2\left(\frac{I_0 t M_S}{\epsilon_{SO} L \rho_S n \mathbf{F}}\right) = \epsilon_{SO}\phi^2 t_f \qquad [20]$$

with

$$t_f = I_0 t / Q$$

where t_f is the fraction of theoretical capacity utilized at time t, since $Q = \epsilon_{SO} L\rho_S n\mathbf{F}/M_S$ is the initial number of coulombs per unit area of electrode on an inert free basis. Discharge data are usually plotted *vs.* $I_0 t$ or *vs.* $I_0 t/Q$.

In Eq. [16], ϵ_S is determined by the integrated form of Eq. [11] which is

$$\epsilon_S = \epsilon_{SO} \exp\left[-\int_0^{\bar{t}} Y dt\right] \qquad [21]$$

and ϵ is given by

$$\epsilon = (1 - E\epsilon_{SO} - \epsilon_{PO}) + (E - 1)\epsilon_S \qquad [22]$$

where E is the ratio of molar volumes of solid product to solid reactant times the stoichiometric coefficient γ.

Integral Equation Representation

To solve this nonlinear system of partial differential equations it is best to reformulate the system in terms of integral equations. Integration of Eq. [16] using boundary condition [2] gives

$$Y = \phi^2 \int_0^x \frac{dz}{\epsilon} \int_0^z Y \epsilon_S dx' - \int_0^x \frac{1}{\epsilon} dz + C_2 \qquad [23]$$

where C_2 is an integration parameter. To obtain C_2 apply an integral of zero to one to Eq. [16]. This procedure gives

$$\epsilon \frac{\partial Y}{\partial x}\Big]_0^1 = \phi^2 \int_0^1 \epsilon_S Y dx' \qquad [24]$$

Then using both boundary conditions we obtain

$$\phi^2 \int_0^1 \epsilon_S Y dx' = 1 \qquad [25]$$

Equation [25] says that we draw current at a constant rate. Using this equation and applying an integral of zero to one to Eq. [23], C_2 is determined to be

$$C_2 = \frac{1}{\int_0^1 \epsilon_S dx'}\left[\frac{1}{\phi^2} - \phi^2 \int_0^1 \epsilon_S dx \int_0^x \frac{dz}{\epsilon} \int_0^z Y \epsilon_S dx' + \int_0^1 \epsilon_S dx \int_0^x \frac{1}{\epsilon} dz\right] \qquad [26]$$

Equation [23] is now a functional equation of the form

$$Y = G(Y) \qquad [27]$$

It is solved simultaneously with the integral Eq. [21] by iteration and marching in time similarly to the procedure already discussed by Gidaspow (15). As a first guess in the iteration procedure the exact analytical solution for zero time, shown in the next section, was used. In this manner the simple iteration

$$Y_{n+1} = G(Y_n) \qquad [28]$$

where the subscripts denote iterates worked for parameters investigated in this study. Improved iteration was only infrequently resorted to.

The fraction of theoretical capacity utilized, t_f, can be obtained from the dimensionless time, $\bar{t}$, using the relation $\bar{t} = \epsilon_{SO}\phi^2 t_f$ derived in the previous section. It can be also obtained by material balance as follows. By definition we have

$$t_f = \int_0^1 \frac{\epsilon_{SO} - \epsilon_S}{\epsilon_{SO}} d\bar{x} \qquad [29]$$

Substitution of Eq. [21] gives

$$t_f = 1 - \int_0^1 \exp\left[-\int_0^{\bar{t}} Y dt\right] d\bar{x} \qquad [30]$$

Such a calculation served as a check on possible accumulation of errors. It was obtained in a natural way from the quantity of solid product formed, given at any x by the equation

$$\epsilon_P - \epsilon_{PO} = E(\epsilon_{SO} - \epsilon_S) \qquad [31]$$

The fractional capacity utilized calculated in this manner always agreed with that calculated from the dimensionless time, $\bar{t}$. To minimize expenditure of computer time, the interval zero to one was divided into only ten or twenty parts, since the computer time increased as the cube of the ratio of subdivisions. With ten subdivisions it took only a few minutes on the small IBM 1130 to generate a complete time profile. For small ϕ^2, results were sufficiently accurate for graphical representation even with such a coarse grid.

Zero Time Solution

At zero time, that is before any capacity of the battery is used up, the system of partial differential equations reduces itself to the simple boundary value problem

$$\frac{d^2Y}{d\bar{x}^2} = \phi^2 \frac{\epsilon_{SO}}{\epsilon_0} Y$$

$$\text{BC 1: } \frac{dY(1)}{d\bar{x}} = 0 \qquad \text{BC 2: } \epsilon_0 \frac{dY(0)}{d\bar{x}} = -1 \qquad [32]$$

where

$$\epsilon_0 = 1 - \epsilon_{SO} - \epsilon_{PO}$$

Its solution is

$$Y = \frac{1}{\phi\sqrt{\epsilon_{SO}\epsilon_0}\tanh\phi\sqrt{\epsilon_{SO}/\epsilon_0}}\cosh\phi x\sqrt{\epsilon_{SO}/\epsilon_0} - \frac{1}{\phi\sqrt{\epsilon_{SO}\epsilon_0}}\sinh\phi x\sqrt{\epsilon_{SO}/\epsilon_0} \quad [33]$$

By Taylor series expansion we can obtain some useful approximations. Equation [33] shows that for small ϕ, that is for thin cells, Y becomes very large. Y is roughly given by $1/\phi^2\epsilon_{SO} - x/\epsilon_0 - x^2/\epsilon_0$. This shows that for small ϕ^2 we must obtain Y correct to a large number of significant figures in order not to lose all accuracy in calculating the potential difference $Y(0) - Y(1)$. This overpotential can be approximated by the formula

$$Y(0) - Y(1) = \frac{1}{2\epsilon}\left(1 - \frac{1}{24}\phi^2\epsilon_{SO}/\epsilon_0\right) \quad [34]$$

for

$$\phi^2\epsilon_{SO}/\epsilon_0 < 1$$

Formula [34] shows that for $\phi^2 < 1$ and reasonable ϵ_{SO}, the overpotential is not a function of the electrode kinetics. Roughly we have

$$\frac{V_S(0,0) - V_S(0,L)}{\left(\frac{I_0 L}{K}\right)} = \frac{1}{2\epsilon_0} \quad [35]$$

The electrode kinetics which appears in the dimensionless exchange current ϕ^2 is only a correction to the dominant behavior which is governed by the conductivity and the structure of the electrode. Values of ϕ^2 much larger than one result in a high localization of the reaction near the solution face and are not desirable. Such cells are much too thick. A value of ϕ^2 near one is not unreasonable as seen from the hypothetical example below. Let

$i_0 = 10^{-5}$ A/cm^2 $\qquad \frac{nF}{RT} = 40$ volts^{-1}

$a = 10^4$ cm^{-1}

$K = 10^{-1}$ mho/cm $\qquad L = 0.1$ cm

Then ϕ^2 becomes equal to 0.4. Note that by having chosen a simplified form of polarization relation we were able to obtain a number of significant conclusions which may have escaped us had we tried to solve a more realistic problem at the start.

Numerical Results and Discussion

Several kinds of information can be derived from the model. In Fig. 2 the distribution of reactant is shown as a function of electrode thickness for different states of discharge starting with zero for reference purposes and rising to 95% discharge. We assumed there was no solid product initially for all cases studied and chose the values of E and ϵ_{SO} such that pores never ultimately close completely. In Fig. 3 the void fraction distribution is indicated by solid lines for this case. The voids are filled with electrolyte in the model and therefore the curves indicate how the electrolyte conductivity changes with depth into the electrode. The dashed curves in Fig. 3 are for such a sufficiently high value of E that pores ultimately close. This leads to incomplete discharge. Only slightly over 56% of the theoretical capacity can be utilized when half the volume of the electrode on an inert free basis is made of the active material. Clearly such an electrode should never be built and those with experience in the field avoid the use of such high percentages of active solid material.

Constant current battery discharge data with respect to a reference electrode can be obtained in the laboratory as a function of discharge time. Figures 4-6 show such overpotentials *vs.* discharge times for various hypothetical electrodes. We note that the plots agree with the empirical correlation of Sheperd (6), as much as one can expect of a correlation that averages the negative and positive electrodes. Specifically Shepherd's Equation 8 can be rewritten in our notation as

$$\frac{V_S(t,0) - V_S(t,L)}{I_0 K_{Sh}} = \frac{1}{1 - \frac{I_0 t}{Q}} + N/K_{Sh} \quad [36]$$

where K_{Sh} is the K used by Shepherd and N is his N. The left side of Eq. [36] corresponds to our dimensionless overpotential in the plots. The independent variable is identical with Shepherd's. Our plots have the basic shape indicated by Eq. [36], except that Shepherd's correlation predicts an infinite overpotential for complete utilization only. Our model predicts high overpotentials for less than complete utilization, for poorly constructed electrodes.

Figure 4 shows the large effect played by the expansion ratio, E. The values indicated are quite realistic, since E for the negative plate of a sulfuric acid

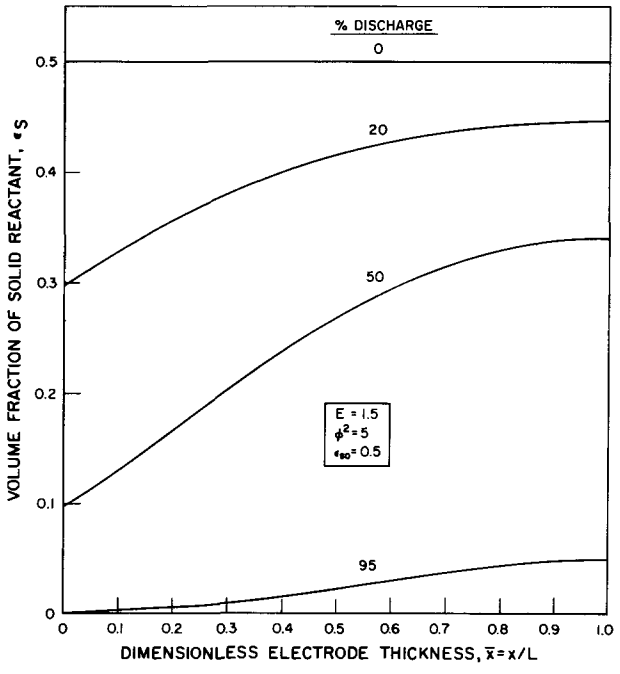

Fig. 2. Distribution of active material during discharge

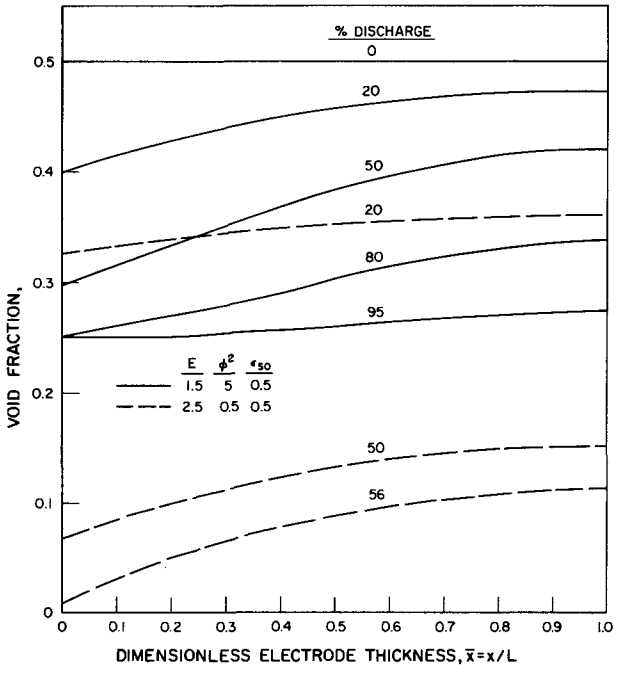

Fig. 3. Distribution of electrolyte with incomplete (——) and complete (– –) pore closing.

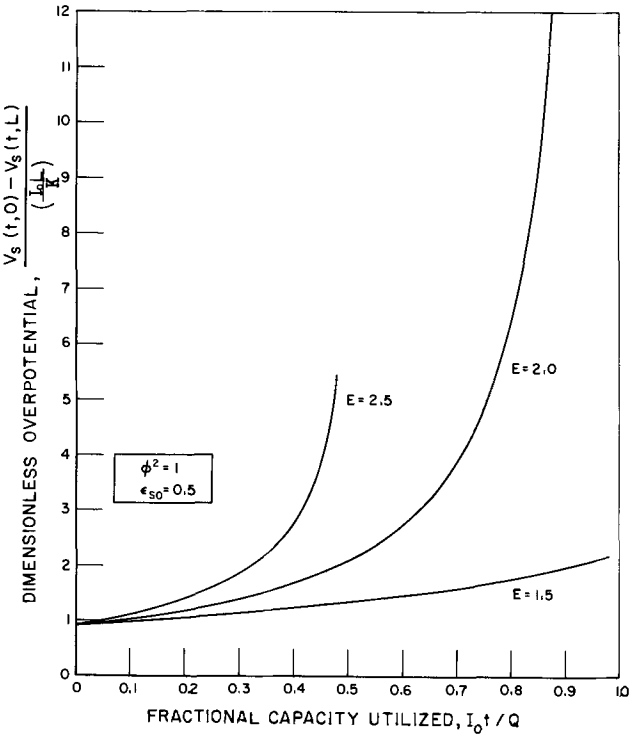

Fig. 4. Effect of expansion ratio on overpotential

battery is 2.7. Thus if half the plate were made of lead ($\epsilon_{so} = 0.5$ in the figure) no more than about 30% of the theoretical capacity could be utilized.

Figure 5 shows the effect of the initial fraction of active material on overpotential. For a uniformly accessible case (15) pores will close completely when the product of ϵ_{so} and E reaches unity. For $E = 2.5$ in Fig. 5 this occurs at $\epsilon_{so} = 0.4$. The performance of the hypothetical battery shown is poor at this value and beyond. No one would build such a plate. Our result, however, has nothing to do with hard won experience. The agreement with the facts shows the validity of the transport phenomena approach.

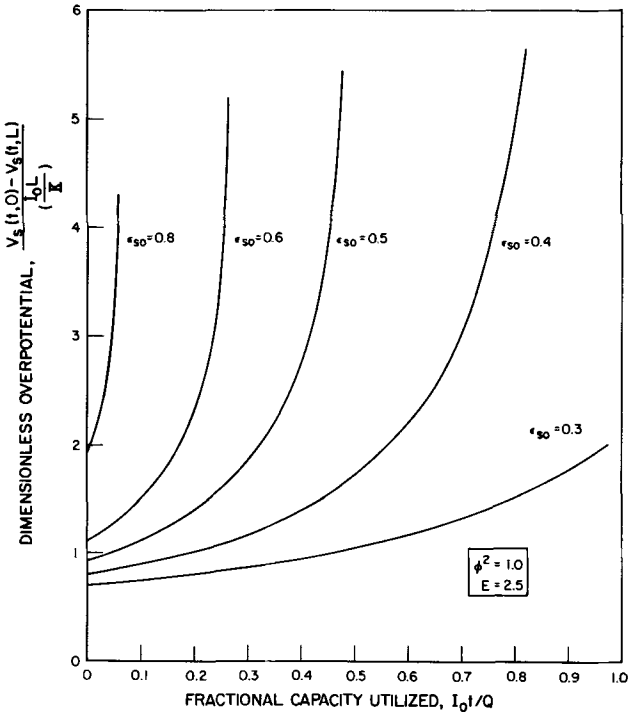

Fig. 5. Effect of initial fraction of active material on overpotential with a high expansion ratio, E, and unit dimensionless exchange current, ϕ^2.

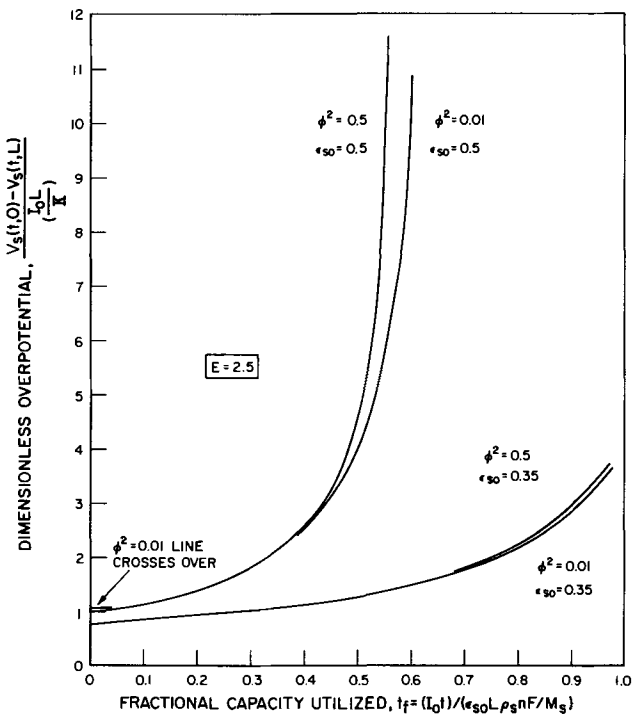

Fig. 6. Effect of dimensionless exchange current, ϕ^2, on overpotential for two initial fractions of active material.

Figure 6 shows the effect of the dimensionless exchange current on overpotential, that is it shows the role played by the electrochemical kinetics. In the linearized polarization curve real kinetics entered only through the exchange current, i_0. In dimensionless quantities it appeared only in ϕ^2. Figure 6 shows that at least for values of ϕ^2 less than one electrochemical kinetics plays only a small role. To verify this surprising conclusion we had developed the approximate solution for zero time presented in the previous section. In view of this result we feel that our model approximates the operation of a real battery.

Operation of the electrode at a constant overpotential, with other assumptions held the same, is described by the results presented by Gidaspow (15) for concentration. The dimensionless problem for a dimensionless overpotential Y is given by his Equations 20 to 23. As shown in his Figure 3, the current will decrease with time exponentially when pores close. We also suggest that kinetic data that are needed for further refinements of our model be obtained potentiostatically on real battery electrodes and analyzed as suggested by the models.

Acknowledgment

Partial support for this study was provided by the Basic Research Program of the Institute of Gas Technology.

Manuscript submitted Oct. 24, 1972; revised manuscript received March 9, 1973. This was Paper 18 presented at the Miami Beach, Florida, Meeting of the Society, Oct. 8-13, 1972.

Any discussion of this paper will appear in a Discussion Section to be published in the June 1974 JOURNAL.

SYMBOLS

- A cross-sectional area of porous electrode, cm²
- a specific surface area of porous electrode (surface to volume ratio) cm²/cm³
- E expansion factor involving a ratio of molar volumes, $\gamma M_{PP}\rho_S/M_{SP}\rho_P$
- F Faraday's constant, 96,500 coulombs/equivalent
- I apparent current density, A/cm²
- I_0 constant current discharge density, expressed on an inert free basis, A/cm²
- i true current density or rate of reaction expression, A/cm²
- i_0 exchange current density, A/cm²

K conductivity of electrolyte (see Eq. [6]), mho/cm
K_{Sh} constant K in Shepherd's correlation
L thickness of electrode, cm
M_P molecular weight of P, gP/mole P
M_S molecular weight of S, gS/mole S
n number of electrons transferred in electrochemical reaction
N constant in Shepherd's correlation
Q initial capacity of electrode per unit inert free area, $\epsilon_{SO}L\rho_S n\mathbf{F}/M_S$, coulombs/cm^2
R ideal gas law constant
T absolute temperature, °K
t time, sec
t_f fraction of theoretical capacity utilized at time t, I_0t/Q
t_m time at which the pore closes, sec
$\underline{t}$ dimensionless time, $i_0M_SaLI_0t/RTK\rho_S = \epsilon_{SO}\phi^2t_f$
V_M potential in the matrix, V
V_S potential in solution, V
x space coordinate in the direction of pores, cm
$\underline{x}$ dimensionless length, x/L
Y dimensionless potential $= (V_S - V_m)/(I_0L/K)$

Greek Letters

γ stoichiometric coefficient in Eq. [10], mole P/mole S
ϵ void fraction, cm^3 fluid/cm^3 total
ϵ_P volume fraction of solid product P, cm^3 P/cm^3 total
ϵ_0 void fraction at zero time, cm^3 fluid/cm^3 total
ϵ_{PO} initial volume fraction of solid product P, cm^3 P/cm^3 total
ϵ_S volume fraction of solid reactant S, cm^3 S/cm^3 total
ϵ_{SO} initial volume fraction of solid reactant S, cm^3 S/cm^3 total
ρ_P void free density of solid product P, gP/cm^3 P
ρ_S void free density of solid S, gS/cm^3 S
ϕ^2 dimensionless exchange current $= i_0n\mathbf{F}aL^2/RTK$ (electrochemical Thiele modulus)

REFERENCES

1. G. W. Vinal, "Storage Batteries," 4th ed., John Wiley & Sons, Inc., New York (1951).
2. Raymond Jasinski, "High-Energy Batteries," Plenum Press, New York (1967).
3. S. Uno Falk and A. J. Salkind, "Alkaline Storage Batteries," John Wiley & Sons, Inc., New York (1969).
4. Jeanne Burbank, A. C. Simon, and Eugene Willihnganz, in "Advances in Electrochemistry and Electrochemical Engineering," Vol. 8, pp. 157-251, Wiley-Interscience, New York (1971).
5. P. E. Baike, M. I. Gillibrand, and K. Peters, *Electrochim. Acta*, **17**, 839 (1972).
6. C. M. Shepherd, *This Journal*, **112**, 657 (1965).
7. J. S. Dunning, D. N. Bennion, and John Newman, *ibid.*, **118**, 1251 (1971).
8. P. Bro and H. Y. Kang, *ibid.*, **118**, 519 (1971).
9. O. G. Malandin, V. N. Kosholkin, A. G. Gerasimov, and O. S. Ksenzhik, 7th Intersociety Energy Conversion Engineering Conference, San Diego, Calif., September 1972.
10. O. S. Ksenzhek, in "Fuel Cells. Their Electrochemical Kinetics," p. 1, Consultants Bureau, New York (1966).
11. A. G. Pshenichnikov, *ibid.*, p. 11.
12. J. S. Newman and C. W. Tobias, *This Journal*, **109**, 1183 (1962).
13. R. C. Alkire, E. A. Grens II, and C. W. Tobias, *ibid.*, **116**, 1328 (1969).
14. R. C. Weast, Editor, "Handbook of Chemistry and Physics," Chemical Rubber Co., Cleveland (1971).
15. Dimitri Gidaspow, 7th Intersociety Energy Conversion Engineering Conference Proceedings, pp. 1159-1168, American Chemical Society, Washington (1972). Also in "Recent Developments in Separation Science," Vol. 2, pp. 59-70, N. N. Li, Editor, Chemical Rubber Co., Cleveland (1972).
16. I. Sanghi and M. Fleischmann, *Electrochem. Acta*, **1**, 161 (1959).
17. Michael Onischak and Dimitri Gidaspow, in "Recent Developments in Separation Science," pp. 71-93, N. N. Li, Editor, Chemical Rubber Co., Cleveland (1972).
18. M. Fleischmann and H. R. Thirsk, *Trans. Faraday Soc.*, **51**, 71 (1955).

The Hydrogen Evolution Reaction on Ti-6Al-4V in Acidic Solutions of NaCl-HCl

Pedro J. Aragon

Facultad de Ciencias, Departamento de Quimica, Universidad de Los Andes, Merida, Venezuela

ABSTRACT

The HER on polycrystalline Ti-6Al-4V in acidic solutions of NaCl-HCl at constant concentration of $Cl^- = 0.5M$, and pH range from 0.65 to 2.5 was studied. Under the present experimental conditions, the reaction was shown to be first order with a Tafel slope of 0.153V. Exchange current densities were in the order of 10^{-8} A-cm^{-2}. An apparent energy of activation of $\Delta E = 45.3$ kcal-mol^{-1} was found. A sharp decrease in potential was observed after reaching about -1.220V (SCE). It is assumed that this effect is due to concentration polarization. Curves corresponding to cathodic polarizations showed a positive deviation from linearity for pH 0.65 and 1.22, presumably due to a second reduction process corresponding to the reduction of a surface oxide film.

The alloy Ti-6Al-4V was investigated because of its excellent corrosion and mechanical properties. Although considerable work has been done on titanium and some of its alloys, only a few papers report on the mechanism of the HER on pure Ti (1, 2) and none on Ti-6Al-4V.

Thomas and Nobe (1) investigated different concentrations of H_2SO_4 as the electrolyte solution. Hackerman and Hall (2), working in approximately neutral solutions of NaCl reported Tafel equations of $E = 1.93 + 0.154 \log i$, and $E' = 1.97 + 0.204 \log i$ for deaerated and aerated solutions.

In this paper the kinetics of the HER on Ti-6Al-4V at 25°C in NaCl-HCl solutions, at constant concentration of Cl^-, and in the pH range 0.65-2.5 is reported.

Key words: hydrogen evolution, kinetics, titanium alloys, corrosion.

Experimental

Several disks of Ti-6Al-4V[1] with an area of 0.363 cm^{-2} and their Teflon holders were polished with

[1] Provided by Titanium Corporation of America, U.S.A.

abrasive paper down to 600 grit. Samples were then polished with diamond powder of 6μ diameter to a mirror finish. Every sample was cleaned with acetone in a soxhlet extractor for at least 3 hr, washed generously in hot conductivity water, and stored in a vacuum desiccator. All solutions were prepared using analytical grade reagents and conductivity water. The pH of 0.5M NaCl solutions was adjusted with 0.5M HCl in order to keep constant concentration of Cl^-. The electrolyses were carried out galvanostatically at 25°C in an H-cell of 500-ml capacity.

Some runs were also made at 20°, 35°, and 40°C using 0.5M HCl. A few experiments using potentiostatic polarizations gave results in agreement with the galvanostatic results reported here. All solutions were deaerated for at least 24 hr before the start of any experiment with N_2 (ultra high purity grade) which was bubbled through a pyrogallol solution before entering the cell. Other details of the experimental procedure have been described previously (3).

Results

Cathodic polarization curves of Ti-6Al-4V in acidic solutions of NaCl are shown in Fig. 1. It can be observed that a positive deviation from linearity appears in the curves corresponding to pH 0.65 and 1.22. These deviations occur at about −1.100V (SCE), apparently due to a second reduction process (1). The results obtained using electrolytes of pH 1.65, 2.2, and 2.5 show a sharp drop in potential after reaching −1.220V. The curves then regain their orginal slope in the linear region B (see Fig. 1) before finally dropping off to a limiting current density. In this linear region (B) the curves regroup closely packed with the same slope as before, showing little or no dependence of the reaction rate on pH. The rest potentials (RP) varied with temperature and pH as shown in Table I.

In all cases a Tafel slope of 0.153V was obtained. The rate of the HER can be written as

$$i = Ka_{H^+}{}^{n}{}_{H^+} \exp\left(-\frac{\alpha F\psi}{RT}\right) \qquad [1]$$

where K = rate constant, a_{H^+} = activity of hydrogen ions, α = over-all transfer coefficient, n = electrochemical reaction order, and ψ = electrode potential.

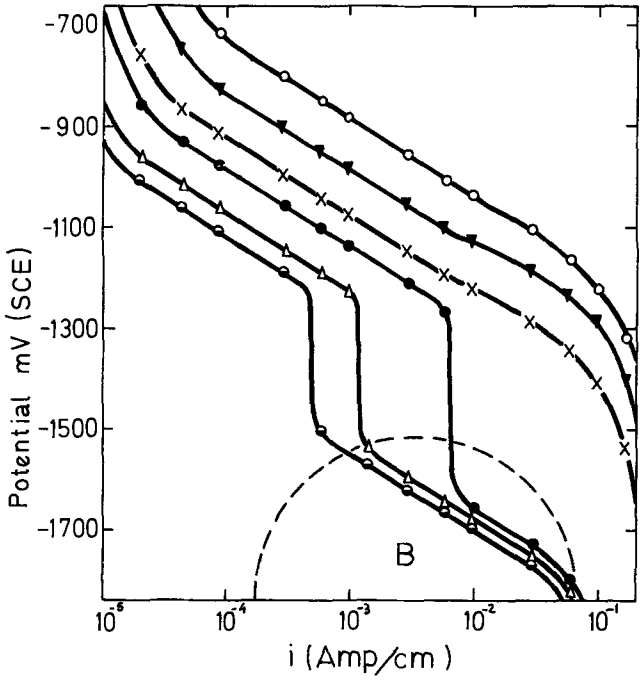

Fig. 1. Cathodic polarization curves of Ti-6Al-4V in NaCl-HCl solutions. For 35°C, ○ = pH 0.65. For 25°C, ▼ = pH 0.65; X = pH 1.22; ● = pH 1.65; △ = pH 2.20; ◒ = pH 2.50.

Table I. Electrochemical data for Ti-6Al-4V in acidic NaCl solutions

Temp, °C	pH	RP (SCE)	Tafel slope	Calculated exchange current (A-cm^{-2})
35	0.65	0.225	0.153	1.4×10^{-7}
25	0.65	−0.290	0.153	2.6×10^{-8}
	1.22	−0.272	0.153	1.1×10^{-8}
	1.65	−0.246	0.153	5.8×10^{-9}
	2.20	−0.194	0.153	2.8×10^{-9}
	2.50	−0.140	0.153	1.8×10^{-9}

According to Eq. [1]

$$\left(\frac{\partial \log i}{\partial pH}\right)_{\psi,T} = -n \text{ (electrochemical reaction order)} \qquad [2]$$

Figure 2 shows the variation of log i with pH, giving for [2]

$$n = 0.98 \cong 1 \qquad [3]$$

At the hydrogen equilibrium potential ψ_o, it follows from Eq. [1] that

$$i_o = K' a_{H^+}{}^{n} \exp\left(-\frac{\alpha F\psi_o}{RT}\right) \qquad [4]$$

Substituting the expression of ψ_o from the Nernst equation[2] into [4] and taking logarithms, yields

$$\log i_o = K''' - pH\,(n - \alpha) \qquad [5]$$

[2] $\psi_o = +\dfrac{2.303\,RT}{F} \log a_{H^+}$.

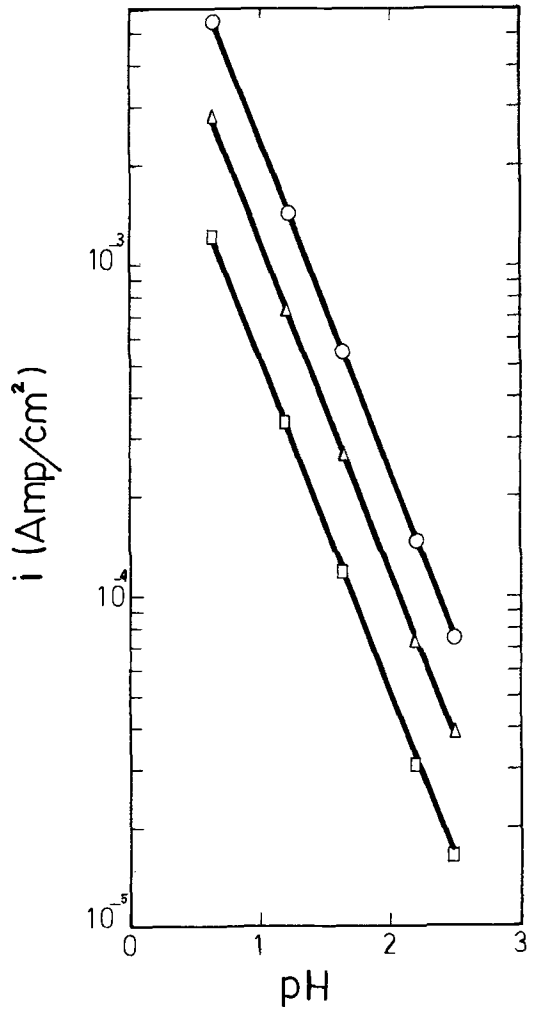

Fig 2. Dependence of the logarithm of i vs. pH in the first Tafel region: ○ 1.000V; △ 1.050V; □ 1.100V.

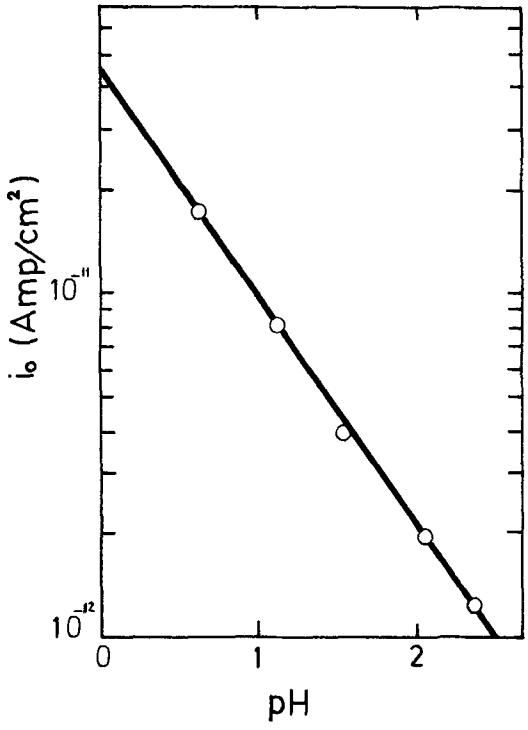

Fig. 3. Dependence of i_0 (exchange current density) on pH

Thus

$$\frac{\partial \log i_o}{\partial \mathrm{pH}} = -(n - \alpha) = -0.60 \qquad [6]$$

which agrees very well with the value obtained from Fig. 3, assuming for α a value of 0.4.

From [1] it can be shown that

$$\left(\frac{\partial \psi}{\partial \mathrm{pH}}\right)_i = -\frac{2.303\,RT}{\mathbf{F}}\frac{n}{\alpha} = -0.148 \qquad [7]$$

(assuming $\alpha = 0.4$ and $n = 1$) which agrees with the experimental values according to the plot in Fig. 4.

Figure 5 is a plot of log K (K = rate constant) as a function of $1/T$ for values of i taken at -1.000V (SCE) and pH 0.65. Since the electrode potential is being referred to a reversible reference electrode maintained outside the thermostatic system, an unknown electrolytic thermal junction potential will be included in the measured emf. Therefore, only an apparent heat of activation ΔE can be measured. The value for ΔE measured in this work was 45.3 kcal/mol.

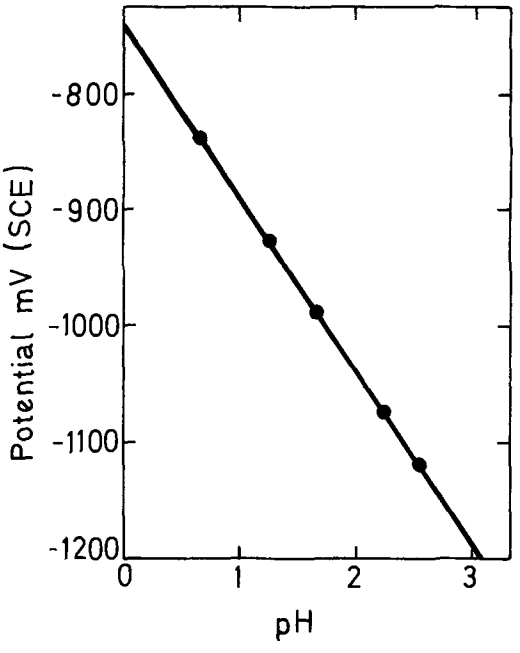

Fig. 4. Plot of potential vs. pH in the first Tafel region. Points correspond to $i = 10^{-4}$ A-cm^{-2}

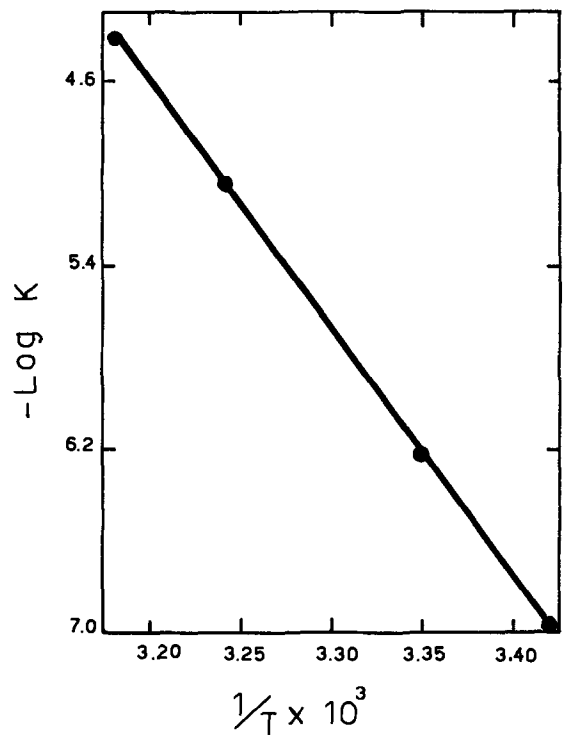

Fig. 5. Arrhenius plot of log K vs $1/T$

It is possible that a limiting current density could be observed at higher cathodic polarization for experiments corresponding to pH 0.65 and 1.22; but, because of equipment limitations it was not possible to increase polarizations beyond the points shown in Fig. 1.

Comparison of the experimental results with those obtained from theoretical derivations show excellent agreement and suggest that the HER on Ti-6Al-4V is a first-order reaction with an over-all transfer coefficient $\alpha = 0.4$.

Discussion

Hackerman and Hall (2) reported a rapid decrease in potential near 0.1 A-cm^{-2} for cathodic polarization of Ti in approximately neutral solutions of NaCl. They explained this behavior assuming the reduction of a small amount of O_2 dissolved in the solution. They interpret the sharp break in their curves as representing the limiting diffusion current density for the oxygen reduction reaction. However, the amount of dissolved oxygen under the present experimental conditions is very low and remains rather constant. Stern (4) found a similar effect for the HER on iron in acidic solutions of NaCl and assumed that the sharp decrease in potential was due to concentration polarization effects. Table II shows the values for i_L (limiting diffusion current) calculated from

Table II. Limiting diffusion current variation with pH

pH	i_L, calculated	i_L, experimental
0.65	3.2×10^{-2}	—
1.22	8.6×10^{-2}	—
1.65	3.2×10^{-3}	6.5×10^{-3}
2.20	9.0×10^{-4}	1.2×10^{-3}
2.50	8.1×10^{-4}	5.0×10^{-4}

$$i_L = \frac{nFD}{\delta} (10^{-3})\, a_{H+} \quad [8]$$

where n = number of electrons taking part in the reaction; F = Faraday constant; δ = thickness of the diffusion layer (= 0.05 cm); D = diffusion coefficient, for $H^+ = 7.39 \times 10^{-5}$ cm^2/sec; and a_{H+} = activity of hydrogen ions.

Except for the first two curves, the agreement between the experimental and calculated values is reasonably good, especially taking into account the uncertainty in the δ values.

The positive deviation from linearity of curves for pH 0.65 and 1.22 in Fig. 1 has been explained before (1) as due to a possible reduction of the thin film oxide attached to the surface of the electrode. For the linear portion of the polarization curves marked B in Fig. 1, it can be assumed that the HER is due to water discharge.

Finally, it is possible that the results published by Thomas and Nobe (1) do not show this type of effect because the electrode was rotated with a certain angular speed, thus, canceling out the diffusional effects.

Acknowledgments

This investigation was supported by a Post-Doctoral Fellowship established by the Bioengineering Program, Clemson University, Clemson, South Carolina. The author is pleased to take this opportunity to thank Dr. S. F. Hulbert for his encouragement throughout this work.

Manuscript submitted June 2, 1972; revised manuscript received Jan. 22, 1973.

Any discussion of this paper will appear in a Discussion Section to be published in the June 1974 JOURNAL.

REFERENCES

1. N. T. Thomas and K. Nobe, *This Journal*, **117**, 622 (1970).
2. N. Hackerman and D. C. Hall, *ibid.*, **101**, 321 (1954).
3. P. J. Aragon and S. F. Hulbert, *J. Biomed. Mater. Res.*, **6**, 155 (1972).
4. N. Stern, *This Journal*, **102**, 609 (1955).

Electrode Reaction Rates on Straining Aluminum-Magnesium Wires in Chloride and Sulfate Solutions

T. P. Hoar* and F. P. Ford

University of Cambridge, Department of Metallurgy and Materials Science, Cambridge, England

ABSTRACT

Electrode reaction rates on aluminum-7 weight per cent (w/o) magnesium wires exposed to chloride and sulfate solutions have been studied as a function of tensile strain rate, electrode potential, solution pH, degree of aeration, and anion concentration. An increase in rate of both anodic and cathodic reactions was observed on application of plastic strain; the increase depends on the strain rate, the anion concentration, and the degree of anodic or cathodic polarization in the chloride or sulfate solution. At electrode potentials remote from the chloride pitting potential, the difference in electrode-reaction rates in chloride or sulfate solutions is relatively minor; as the potential approaches the pitting potential, however, the anodic rate in chloride solution becomes significantly greater than that in sulfate solution. The anodic reaction is primarily dissolution and the cathodic is hydrogen-ion reduction.

There is a relationship between current density on the straining electrode and the rate of passivation found on cessation of plastic deformation. The shape of the current/time transients suggests that the change in reaction rate upon straining is controlled by the rate of oxide rupture (caused by slip-step emergence) and by the subsequent passivation rate of the new bared metal.

Stress-corrosion tests, conducted under potentiostatic control in sulfate and chloride solutions, indicate that the propagation rate of stress-corrosion cracks in isolated metal has the same dependence on pH, anion type and concentration, and degree of aeration, as does the anodic current density of a straining electrode. This suggests that the crack-penetration rate depends on the reaction rate at the crack advancing edge, which is controlled by the rate of oxide rupture and by the subsequent rate of passivation.

The aluminum-magnesium alloy system provides an important series of cold-worked and thermally stabilized commercial alloys that combine a relatively high strength-to-weight ratio with good general corrosion resistance. Unfortunately, there is an increasing susceptibility to intergranular stress-corrosion cracking as the magnesium content is increased, both in neutral and acid chloride solutions (1, 2). It is related (2, 3) to the presence of a discontinuous grain-boundary magnesium rich β-phase. Because of the high chemical activity of this phase in these solutions (4), an initiating notch may be formed, giving stress intensification dependent on the shape and size of the particle. A major problem in understanding the stress-corrosion behavior of these alloys is the mechanism by which a high aspect-ratio crack can propagate from these initiating notches.

Logan (5) suggested that cracks may propagate electrochemically by rupture of passivating oxide films at the crack advancing edge, which is yielding under the high stress there, followed by a high rate of anodic dissolution as compared with that of the crack sides. The high rate of dissolution of bared metal will be modified by passivation, the rate of which is also important.

The object of this paper is twofold: first, to determine the dependence of the anodic and cathodic reaction rates of an aluminum-7 w/o magnesium alloy on applied strain rate for various conditions of anion concentration, solution pH, and electrode potential, and to

* Electrochemical Society Active Member.

Key words: dissolution, passivation, straining, aluminum, alloy.

obtain data on the passivation rate observed when straining is stopped; second, by relating the plastic condition at the crack edge to the macroscopically applied strain rate, to predict the stress-corrosion behavior of the alloy in chloride and sulfate solutions.

Experimental Technique

The specimens used in the electrochemical studies were 0.040 in. diam wires fabricated from a high purity aluminum-7 w/o magnesium ingot.[1] The wet analysis was 7.15 w/o, magnesium, plus a total impurity content of 0.12 w/o, mainly silicon and copper. The wire specimens were transformed to a single-phase condition to simulate the structure at the phase margins, where stress-corrosion cracks propagate, after the final swaging and drawing operation, by annealing at 360°C for 4 hr and water quenching. (Strictly speaking, the composition at the advancing edge of a grain-boundary crack in the heterogeneous alloy is probably nearer 2 w/o, which is the equilibrium composition adjacent to the grain-boundary β-phase; however, preliminary work has indicated (7) that there is no significant difference in the chemical activity of an electrode of aluminum-2 w/o magnesium and aluminum-7 w/o magnesium).

The solutions used were unbuffered 1*N* NaCl and 1*N* Na_2SO_4 at *p*H values of 2.0 ± 0.2 and 5.5 ± 0.2 (adjusted with sulfuric acid); the *p*H values after the experiment remained within the quoted ranges. The solutions were deaerated by saturating with deoxygenated nitrogen (8) in order to confine the cathode reaction to that of hydrogen-ion reduction. However, since stress-corrosion tests are normally conducted in naturally aerated solutions, some straining experiments were made under such conditions in order to determine the effect, if any, of aeration on the anodic reaction rate.

Before each test, the specimens were mechanically polished to a 6 μm diamond finish, masked with Teflon tubing to expose a 1-in. gauge length, inserted into the test cell, Fig. 1, and immersed in deaerated solution for at least 16 hr to allow the surface to reach a pseudostable corrosion potential. Anodic or cathodic polarization to a constant potential was then applied by potentiostat, and the resultant current between specimen and platinum counterelectrode was recorded until a steady value was obtained. Thereupon a steady strain rate was applied by a motorized Hounsfield Tensometer for a time corresponding to 17.5% elongation. The current transient was recorded both during and after straining.

Results

Shape of current transient upon straining.—Figure 2 illustrates the nature of the current/time transient obtained on straining, at two extremes of anodic or cathodic polarization. As will be shown later the shape of the transient between these extremes varies with the anion concentration and *p*H of the solution. Two general observations may be made regarding the shape of these transients. First, there is an incubation period, corresponding to the time to reach the limit of proportionality on the stress/strain curve, before the mean current rapidly rises to a steady value, which will be shown to be dependent on the applied strain rate, electrode potential, solution *p*H, and anion concentration. Second, there is an oscillation superimposed on the current transient which has an amplitude and frequency that increase with applied strain rate. A detail of the net anodic current is shown inset in Fig. 2 for two extremes of strain rate; at the lower strain rate the oscillation can be resolved into a series of current surge and exponential decay events. In general, the oscillation of a net cathodic current is more damped, *i.e.*, the amplitude is lower than that of an anodic current obtained at the same strain rate. This oscillation, which is independent of the occurrence of the Portevin-Le Chatelier discontinuous yielding that occurs in these

[1] Supplied by Olin Corporation, New Haven, Connecticut.

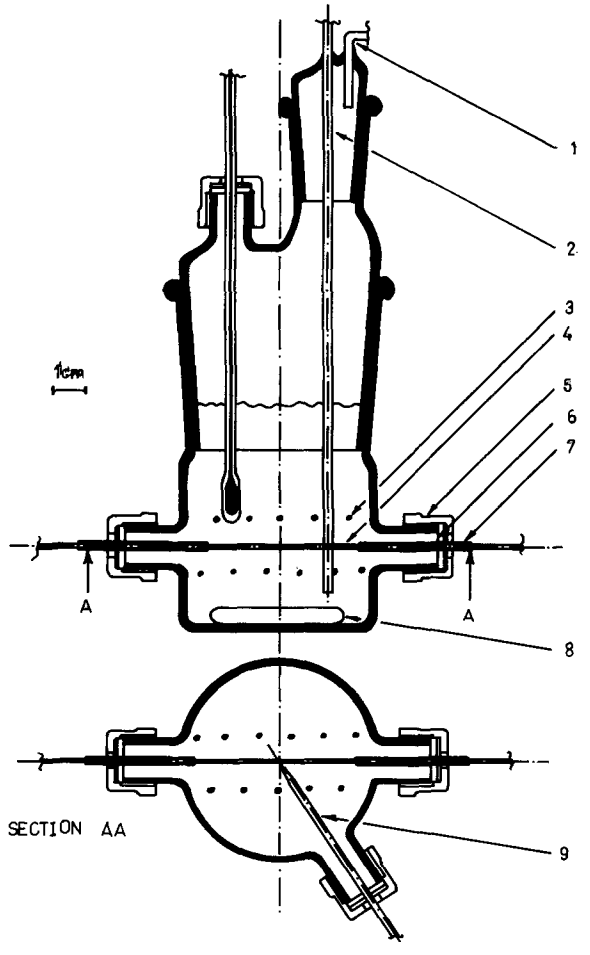

Fig. 1. Test cell. 1, Nitrogen outlet; 2, nitrogen inlet; 3, platinum counterelectrode; 4, wire specimen; 5, threaded joint (SQ.13); 6, Teflon washer; 7, Teflon tubing; 8, magnetic stirrer; 9, Haber-Luggin probe.

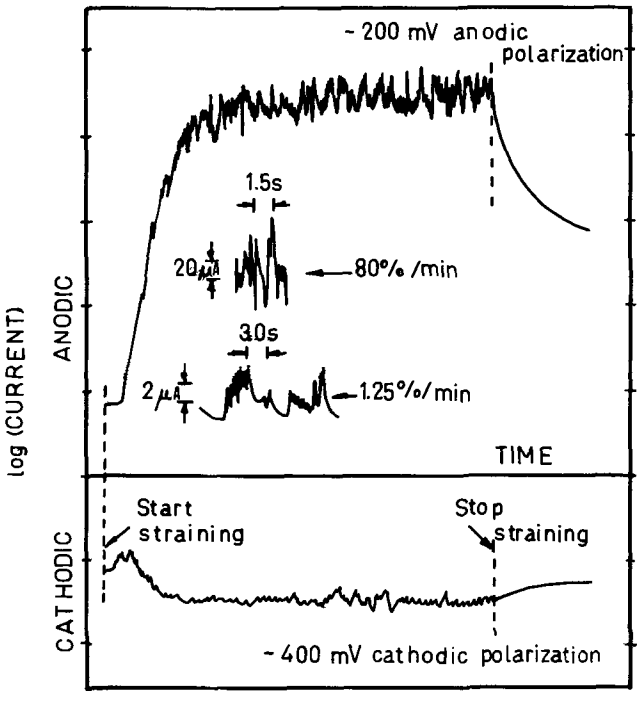

Fig. 2. Typical current/time transients obtained upon straining at extreme values of anodic or cathodic polarization with respect to open-circuit corrosion potential in deaerated solutions. Inset detail indicates nature of superimposed current oscillations at two values of applied strain rate.

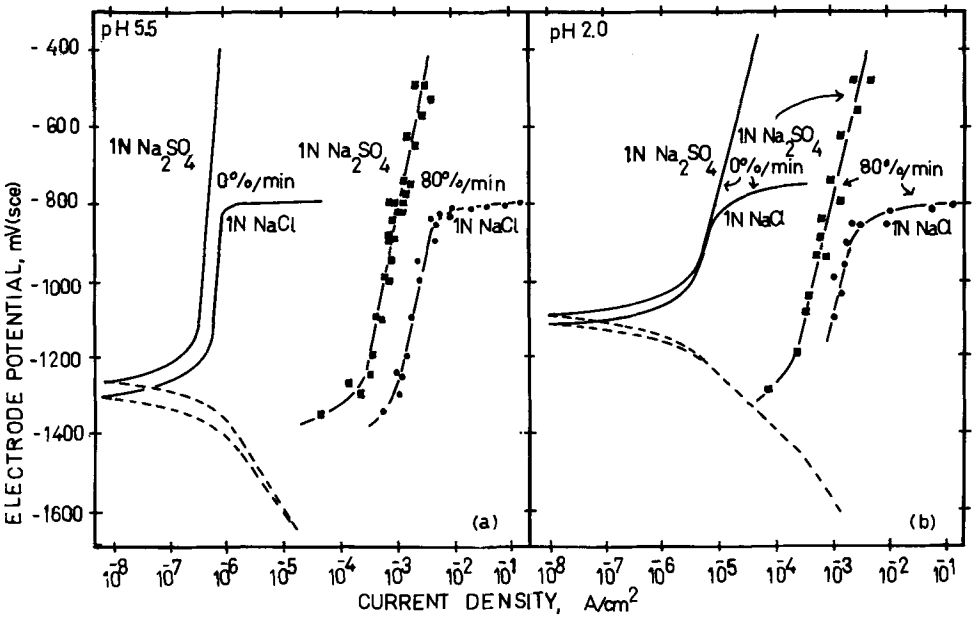

Fig. 3. Variation of steady-state anodic current density with potential in 1N NaCl and 1N Na_2SO_4 at (a) pH 5.5 and (b) pH 2.0. Values are quoted for strain rates of 0 and 80% per min.

alloys, is attributed to successive oxide-rupture and metal-passivation events; work by Grosskreutz (9) indicates that thin film rupture in aluminum alloys occurs at slip steps.

In interpreting the results in terms of current density at the bared metal surface, it might be assumed that the active surface area can be equated to the total slip-step surface area. This area may be calculated from the data of Thomas and Nutting (10), who investigated the slip-step geometries of various binary aluminum-magnesium alloys after different amounts of tensile elongation. The current density on the slip steps could be derived, therefore, from $I - I_o/A$, where I is the steady-state current during straining, I_o the steady-state current before straining, and A the slip-step area. The nonvalidity of this assumption, which is over-naive, is discussed in a later section.

Variation of steady-state anodic current density with electrode potential and strain rate.—The variation of the steady-state current density with electrode potential is illustrated in Fig. 3(a) and (b) for various combinations of anion concentration and pH; the strain rate applied to the specimen was 80% per min. For comparison purposes, the steady-state current density on the unstrained specimens is also shown in the same figures. The over-all mean anodic current density at a given potential increases by several orders of magnitude upon straining; results also indicate that, although the current density on the unstrained specimen at a given electrode potential decreases with increase in pH, the net anodic current density on the straining specimen is slightly lower at pH 2.0 than pH 5.5. At potentials more negative than −900 mV(SCE), the straining electrode current density is slightly higher in the chloride solutions compared to that in the sulfate solutions, but as the potential approaches −800 mV(SCE), this difference rapidly increases.

Figure 4 illustrates the relation between the steady-state anodic current density at −800 mV(SCE) with applied strain rate in acid chloride and sulfate solutions.

Variation of current density during and after straining.—The variation in current density during straining at 80% per min is illustrated in Fig. 5 for various combinations of anion concentration, solution pH, and electrode potential. For the sake of clarity, the superimposed oscillations mentioned previously are not shown. At potentials more positive than −1300 mV(SCE), the current density rises rapidly after an incubation period to a steady anodic value. At potentials more negative than −1300 mV(SCE), however, the current density initially changes in the anodic direction, to be followed by a slower return to cathodic values. In acid solutions the rate of this reaction is fast enough at −1400 mV(SCE) to attain a steady-state cathodic value by the end of the experiment; as might be expected, the reversion in neutral solutions is slower, and a steady-state cathodic value is not reached. At potentials more negative than −1500 mV(SCE), the initial change towards anodic values is suppressed and the current transient is entirely in the cathodic direction.

The current-density decay due to oxide formation that occurs when straining is stopped at 17.5% elongation is shown in Fig. 6 for the various anion-content-pH-electrode-potential combinations illustrated in Fig. 5. Initially the anodic current-density decay may be described by

$$j = j_0 \exp -\beta t^{1.0}$$

However, this simple law does not apply during the whole decay time because of complicating secondary reactions, two of which may be deduced from Fig. 6. The first is the initiation of pitting by straining in

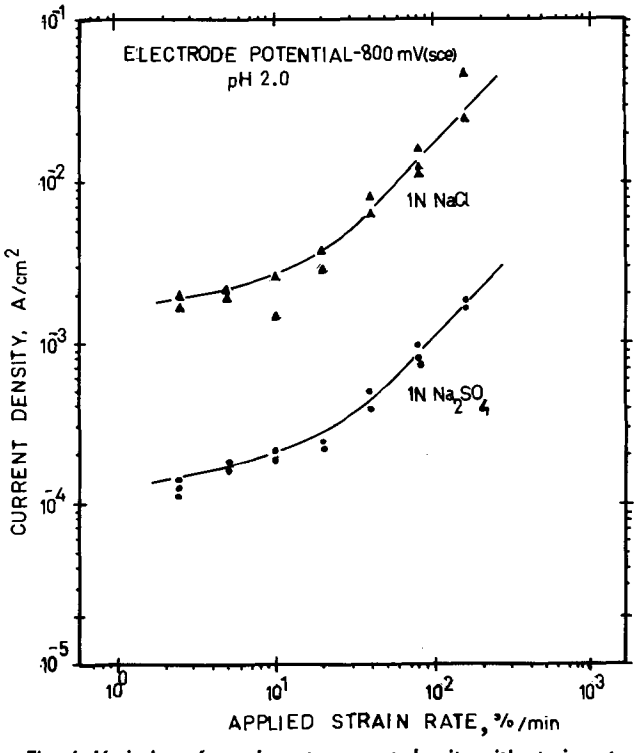

Fig. 4. Variation of steady-state current density with strain rate for 1N NaCl and 1N Na_2SO_4, pH 2.0, at −800 mV(SCE).

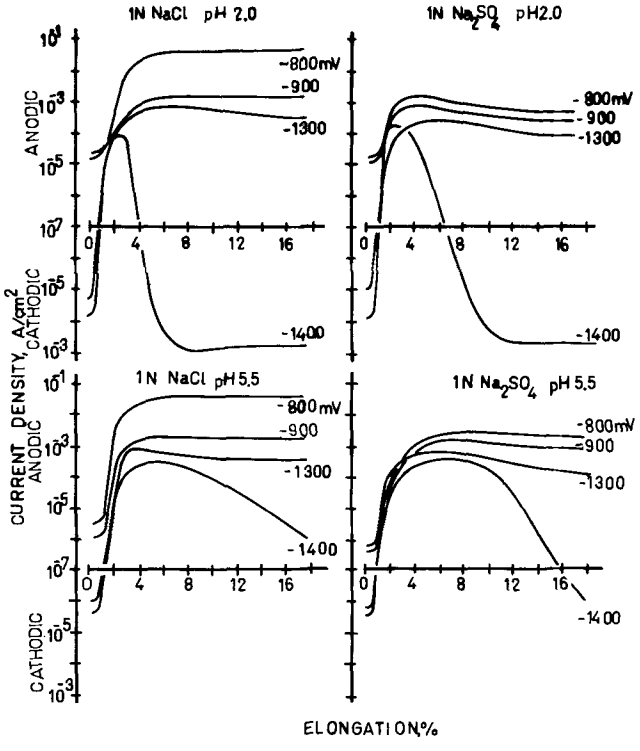

Fig. 5. Current-density/elongation transients obtained during straining at 80% per min. Values for various combinations of electrode potential, anion concentration, and pH.

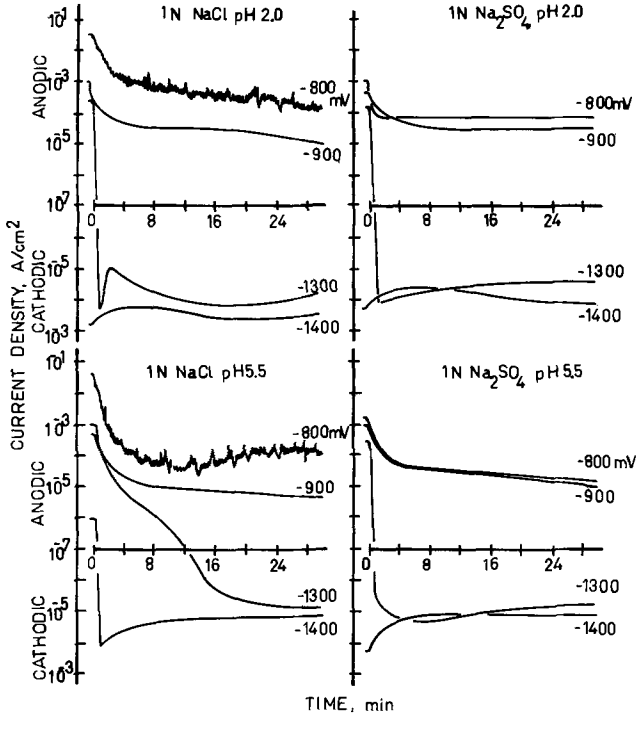

Fig. 6. Current-density-decay curves obtained when straining at 80% per min is stopped. Values for various combinations of electrode potential, anion concentration, and pH.

chloride solutions at potentials between −800 and −950 mV(SCE) as shown by anodic current oscillations and the rise in anodic current after the initial decay, and the second is the effect of the cathodic reaction on the passivating surface, which predominates at potentials more negative than −1300 mV(SCE). In an analogous argument to that suggested from Fig. 5, where it is seen that, upon straining in the potential range −1300 to −1400 mV(SCE), a rapid anodic reaction is followed by a slower cathodic reaction. The

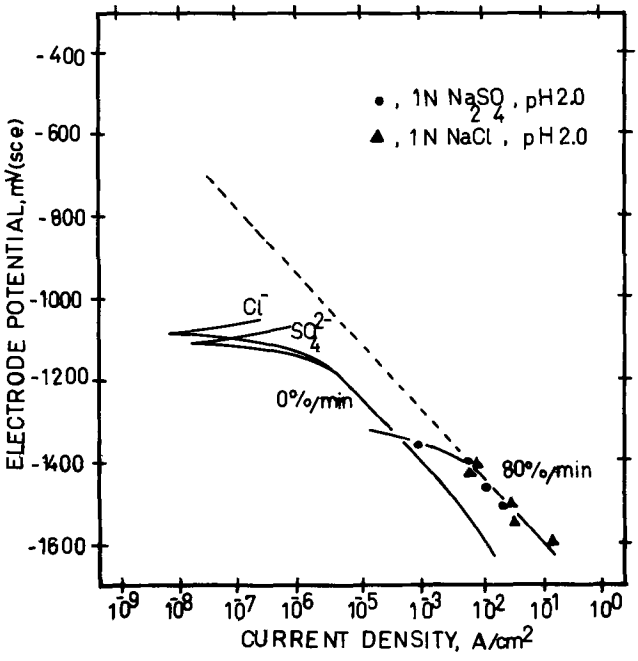

Fig. 7. Variation of steady-state cathodic current density with potential in 1N NaCl and 1N Na_2SO_4 at pH. 2.0. Values for strain rates of 0 and 80% per min.

subsequent decay behavior is dominated in this potential range by rapid anodic passivation followed by a slower cathodic reaction on the passivated surface.

Variation of steady-state cathodic current density with electrode potential.—The variation of the mean steady-state cathodic current density with electrode potential is illustrated in Fig. 7 for acid sulfate and chloride solutions. For comparison purposes, data for the unstrained specimen and a specimen strained at 80% per min are presented on the same graph. The rate of the cathodic reaction, which is observable hydrogen evolution, is increased by a factor of 5 to 6 by straining; this increase is the same in chloride as in sulfate solutions. In addition, there is no significant difference in the slopes of the cathodic polarization curves for strained and unstrained specimens in these acid solutions.

Discussion

Computation of active surface area.—Murata and Staehle (11) have suggested that the net current change observed upon straining a specimen in a film-forming solution can be analyzed in terms of the summation of a series of individual current surge and decay events associated with oxide rupture followed by passivation at emergent slip steps. The analysis predicts that the current will reach a steady-state value during straining through the introduction of new active slip steps and the complete passivation of earlier formed slip steps. The present work qualitatively supports this theory through the presence of an incubation elongation corresponding to oxide rupture at a sufficient number of slip steps to give an observable rapid current rise to an asymptotic value, and the superimposed oscillations suggest that the net effect is made up of a series of current surge and decay events.

The current densities were first calculated (see Results above) on the assumption that, during straining, the active surface area corresponds to the total area created at emergent slip steps. An estimate of this area may be made from the data of Thomas and Nutting (10), who showed that, in the aluminum-7 w/o magnesium alloy, slip steps emerge with a constant step height of 135 nm and with a step separation dependent on the tensile elongation. The assumption that this total slip-step area remains active throughout the time of straining is, however, far from valid, especially in a

system that exhibits fast passivation characteristics. Pagetti and co-workers (12) showed, by using a scratching technique to create a 'bare' surface on an aluminum-7 w/o magnesium alloy, that the anodic current density decay due to passivation at a scratch may fall by several decades within 100 msec in sulfate solutions. Since the experiments described in the present paper last for 20 sec or longer, the assumption that the active surface area on the straining wire corresponds to the total slip-step area grossly overestimates the active surface area in sulfate solution by a factor of around 10^2 for a strain rate of 80% per min, and by correspondingly greater factors at lower strain rates. (In chloride solutions at potentials near the pitting potential, this factor is smaller since the passivation rates are significantly lower than those in sulfate solutions.)

Electrode reactions occurring on the straining electrode.—The hypothesis outlined above concerning the origin of the current transient obtained during straining suggests that the resultant steady-state current density is an average slip-step current density encompassing all conditions from a bare surface to a surface that has just become completely passivated. This average current density should, therefore, be dependent on the passivation rate; as this rate decreases so the proportion of active sites with a higher current density at any given instant will increase. Such a relationship between the average slip-step current density and the passivation rate is noted experimentally and is illustrated in Fig. 8. In this figure the passivation rate is described in terms of the parameters β and n, which appear in the general decay equation $j_a = j_0 \exp -\beta t^n$ used to characterize the current decay when straining is stopped; the values of β and n taken 1 sec after straining is stopped, $\beta(1\text{ s})$ and $n(1\text{ s})$, are used, because the simple equation with β and n constant does not properly describe the j/t transient. The electrode potentials were in the range −1200 mV to −500 mV(SCE).

Figure 8 shows that the slip-step current density during straining has a unique relationship with the passivation parameters $\beta_{(1\text{ s})}$ and $n_{(1\text{ s})}$. This sug-

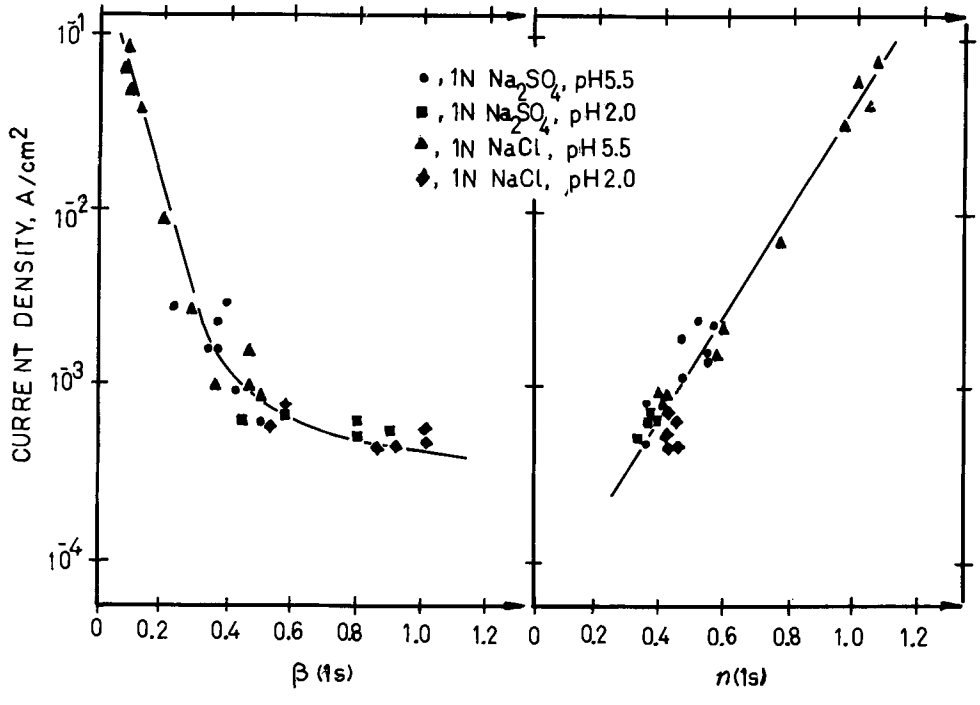

Fig. 8. Correlation between the steady-state anodic current density and the parameters β and n, in the decay equation $j = j_0 \exp -\beta t^n$. The decay characteristics were measured 1 s after straining at 80% per min was stopped.

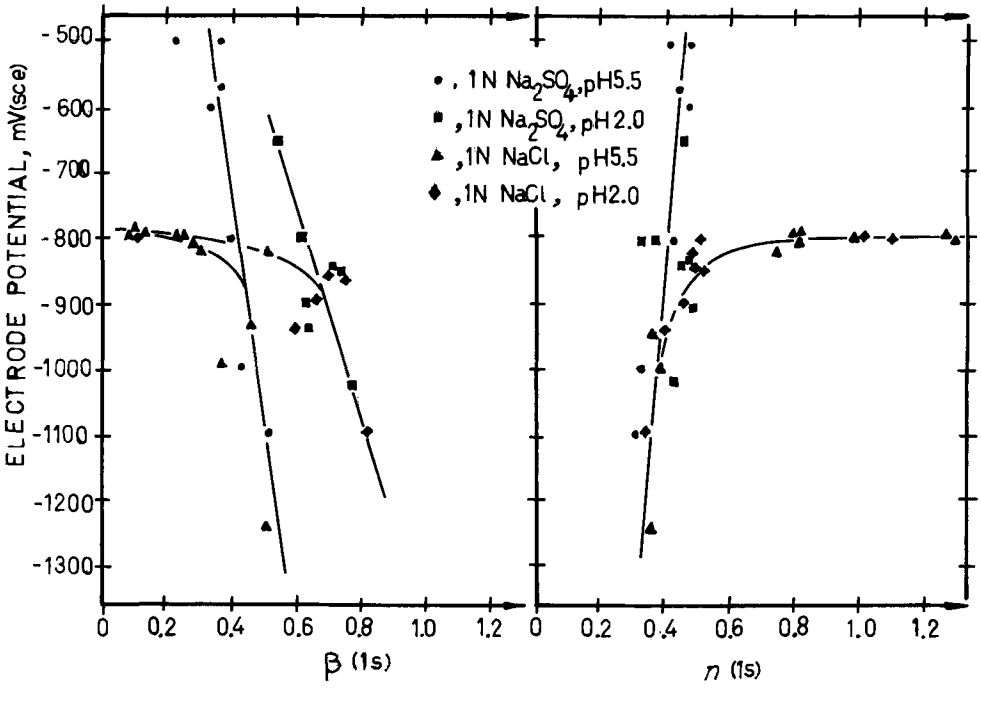

Fig. 9. Variation of the parameters β and n in the decay equation $j = j_0 \exp -\beta t^n$ with electrode potential, for various conditions of anion content and pH.

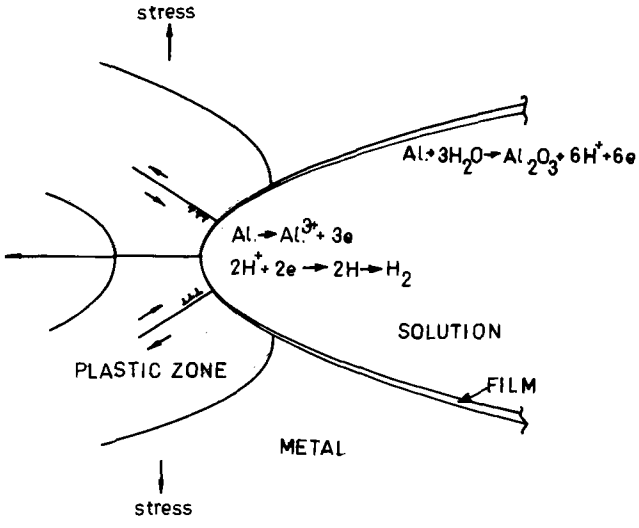

Fig. 10. Schematic representation of the electrode reactions occurring at a crack tip, in neutral and acid solutions.

gests that the dependence of this current density on potential, pH, and anion concentration illustrated in Fig. 3(a) and (b) is controlled primarily by the dependence of the passivation rate on these factors; this latter relationship is indicated in Fig. 9. Further, the fact that the slope of the anodic e/j curve at a strain rate of 80% per min is the same as that given by the unstrained surface in acid solutions confirms that the average is dominated by the current on a partially passivated surface rather than that on the bare slip steps.

From Fig. 7, the average cathodic reaction rate on a specimen being strained at 80% per min in deaerated acid solutions is, by the usual extrapolation, less than 10^{-7} A/cm^2 at potentials more positive than −900 mV(SCE). This is considerably smaller than the observed anodic current on the same specimen at these potentials; consequently, the observed current on the straining electrode is close to the true anodic current. This anodic reaction is presumed to be $Al \rightarrow Al_{aq}^{3+} + 3e$.

The cathodic reaction is evidently the observed hydrogen evolution, in deaerated solutions. Supplementary tests, conducted in aerated chloride solutions at pH 5.5 and −900 mV(SCE), indicated that above a strain rate of 10% per min there was no significant difference in the steady-state current densities obtained in deaerated solutions and those obtained in aerated solutions. Although the presence of oxygen affects the net current density on the unstrained surface, due to the additional oxygen-reduction reaction, the much greater observed current density on the straining surface is overwhelmingly anodic and is essentially the same as that obtained in a deaerated solution at the same potential.

Relationship between average slip-step current density and stress-corrosion cracking.—If the propagation of a stress-corrosion crack is controlled by the anodic dissolution at the crack advancing edge, where protective oxide is continuously undergoing a rupture and formation (passivation) process (see Fig. 10), then the observed propagation rate should have the same dependence on such parameters as pH, electrode potential, and anion concentration as does the steady-state current density observation on a plastically deforming electrode (Fig. 3(a) and (b) and 7).

Stress-corrosion experiments were conducted on specimens fabricated from the same ingot as that used in the straining electrode experiments. The metallurgical condition of the specimen wires was such as to yield a condition susceptible to stress-corrosion cracking in aerated chloride solutions at the corrosion potential: *viz.*, after solution heat-treatment at 360°C for 4 hr and water quenching, the rods were cold swaged a total of 86.5% reduction in area and given a final 110°C, 40 hr sensitization treatment. The specimens were prepared as described in the Results section above, mounted in the experimental cell (Fig. 1), and allowed to attain a pseudostable corrosion potential in the solution. Anodic or cathodic polarization was then applied and the resultant current recorded until a steady value was obtained; thereupon a strain rate of 0.127% per min was applied until failure occurred.

Longitudinal cross sections of the wire specimens were subsequently examined at a magnification of × 500 and the extent of the penetration of grain-boundary cracks was recorded; the average penetration rate was then calculated on the assumption that the longest cracks started propagating at the onset of straining.

The variation of the grain-boundary crack-penetration rate with electrode potential and various anion-concentration–pH combinations is shown in Fig. 11.

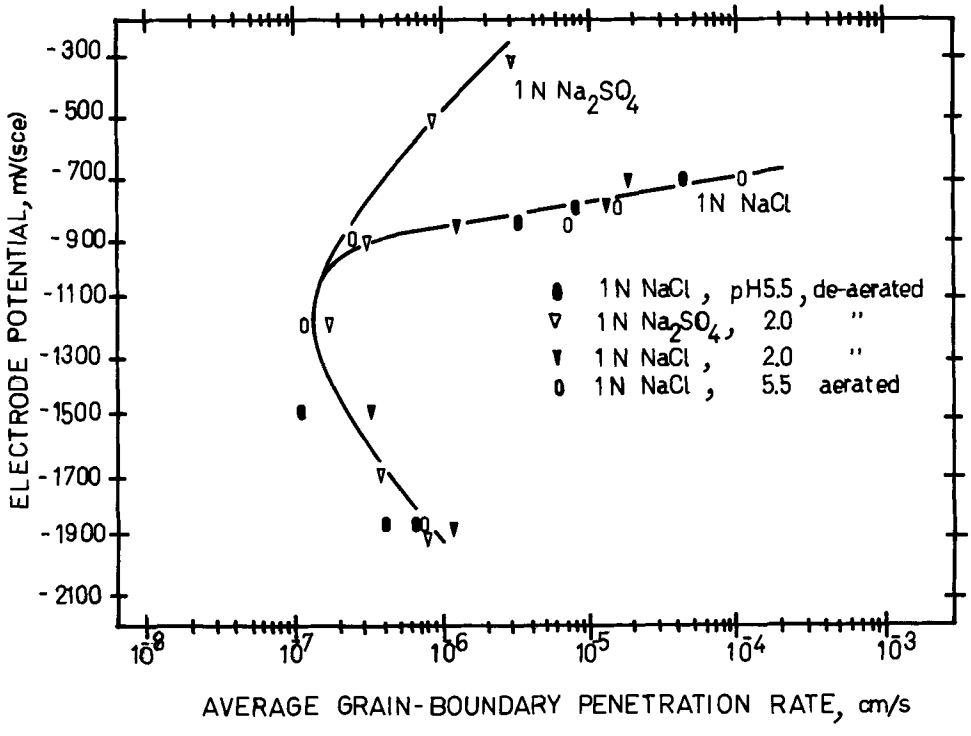

Fig. 11. Variation of the grain-boundary penetration rate in a cold-worked and sensitized aluminum-7 w/o magnesium alloy with electrode potential, for several combinations of anion content, pH, and degree of aeration. Applied strain rate ca. 0.127% per min.

The crack penetration rate is minimal at −1200 mV(SCE) and increases at potentials both more positive and more negative. This suggests that at potentials more positive than −1200 mV(SCE), the penetration rate is caused by an anodic process, presumably dissolution, whereas at more negative potentials, hydrogen-ion reduction controls the penetration by some unknown mechanism. The specificity of chloride anions on crack penetration has significant effect only at potentials more positive than −900 mV(SCE), *i.e.*, at potentials where pitting may be prematurely initiated by straining. This observation may be compared with the markedly greater increase in anodic current density on the straining electrode in chloride solutions as compared to sulfate solutions at these potentials. Changes in *p*H (and oxygen content) have no significant effect on the crack-penetration rate at potentials above −1200 mV(SCE), but there is some evidence in Fig. 11 that at potentials more negative than −1200 mV(SCE) an increase in *p*H may decrease the crack penetration rate.

Stress-corrosion cracking is normally encountered (1, 2) in this alloy when the cold-rolled and heat-treated material is exposed under freely corroding conditions to neutral or slightly acid aerated solutions. The open-circuit corrosion potential in chloride solutions under these condtioins is *ca.* −800 mV(SCE). The results illustrated in Fig. 11 show that the penetration rate may be decreased by the external application of a small amount of cathodic polarization (13) with respect to the open-circuit corrosion potential.

The present results suggest that the crack penetration rate in the aluminum-7 w/o magnesium alloy may be decreased at a given electrode potential by decreasing the over-all reaction rate at the crack edge. Apart from the mild degree of cathodic protection just mentioned, this may perhaps be achieved (6) by decreasing the oxide rupture rate and/or by increasing the passivation rate at the rupture region by attention to possible variations in alloy composition and deformation morphology at the crack edge.

In further experiments, to be reported shortly, we have found that the anodic current densities obtainable at the various potentials on bared, passivating aluminum-alloy surfaces are more than sufficient to account for the measured penetration rates shown in Fig. 11, if the cracks advance solely by electrochemical anodic dissolution.

Manuscript submitted Dec. 20, 1972, revised manuscript received Feb. 26, 1973. This was Paper No. 49 presented at the Miami Beach, Florida, Meeting of the Society, Oct. 8-13, 1972.

Any discussion of this paper will appear in a Discussion Section to be published in the June 1974 JOURNAL.

REFERENCES

1. P. T. Gilbert and S. E. Hadden, *J. Inst. Metals*, **77**, 237 (1950).
2. E. C. W. Perryman and S. E. Hadden, *ibid.*, **77**, 207 (1950).
3. E. H. Dix, Jr., W. A. Anderson, and M. B. Schumaker, *Corrosion*, **15**, 55t (1959).
4. R. B. Mears, R. M. Brown, and E. H. Dix, Jr., in "Symposium on Stress Corrosion Cracking of Metals," p. 323, ASTM-AIME, Philadelphia (1944).
5. H. L. Logan, *J. Res. Nat. Bur. Std.*, **48**, 99 (1952).
6. D. J. Lees, F. P. Ford, and T. P. Hoar, Metals and Materials, **7**, 231 (1973).
7. F. P. Ford, Thesis, Rensselaer Polytechnic Institute (1970).
8. D. Gilroy and J. E. O. Mayne, *J. Appl. Chem.*, **12**, 382 (1962).
9. J. C. Grosskreutz, *This Journal*, **116**, 1232 (1969).
10. G. Thomas and J. Nutting, *J. Inst. Metals*, **85**, 1 (1956/57).
11. T. Murata and R. W. Staehle, Private communication.
12. J. Pagetti, D. J. Lees, F. P. Ford, and T. P. Hoar, *C. R. Acad. Sci., Paris, Ser. C*, **273**, 1121 (1971).
13. H. K. Farmery and U. R. Evans, *J. Inst. Metals*, **84**, 413 (1955/56).

Investigation of the Passivity of Iron by Nuclear Microanalysis Using Stable Oxygen Isotopes

B. Agius and J. Siejka*

Groupe de Physique des Solides de l'Ecole Normale Supérieure, Tour 23; 11 Quai Saint-Bernard, Paris 5ème, France

ABSTRACT

A solution of 0.15*N* sodium borate and 0.15*N* boric acid in O^{18} enriched water was used to study the passivity of iron by means of nuclear microanalysis. It was established that the surface of the sample maintained under cathodic polarization is free of oxygen 18; while in open circuit, the presence of 5×10^{15} atoms/cm^2 of oxygen 18 was detected on the sample which was previously cathodically reduced. Moreover, in the passivity region, the quantity of oxygen 18 fixed on the metal surface varies from $\sim 5 \times 10^{15}$ to $\sim 20 \times 10^{15}$ atoms/cm^2 as a linear function of potential. The value of the apparent electric field of formation was calculated and compared with the literature data deduced from ellipsometric and coulometric measurements. The cathodic reduction of the films was studied by determining the O^{18} losses of the passive films as a function of the charge passed in the circuit and of the temperature. The mechanism of the cathodic reduction is discussed on the basis of the experimental data.

The passive film has been investigated in electrochemistry and metallurgy for many years (1, 2) and several models have been proposed (3-10), pointing out the important role played by oxygen in the mechanism of passive layer formation. Quantitative determination of oxygen contained in passivated films can be expected to provide a useful means for a better understanding of the phenomenon of passivity. Among the various methods, the method of nuclear microanalysis of the 16 and 18 isotopes of oxygen seems to be particularly well suited for this purpose (11, 12).

* Electrochemical Society Active Member.
Key words: iron passivity, nuclear microanalysis, O^{18} tracing, passive film thickness, cathodic reduction.

The present paper describes the use of this method to investigate the passivity of iron in a $pH = 8.4$ buffer solution of 0.15*N* sodium borate and 0.15*N* boric acid in deaerated water of either natural O^{18} isotopic concentration (0.204%) or enriched to 10% in O^{18}. The isotopic composition of hydrogen in the O^{18} enriched water[1] was normalized to natural abundance. By using the enriched solutions, one is able to distinguish the effects of oxygen coming from the solution from those due to atmospheric oxygen which may further oxidize the samples during their transfer from the electrolytic cell to the analytical set-up. Borate solutions were chosen as numerous works referring to such solutions have been published and this will facilitate comparisons. Moreover, borate anions are advantageous in that they isotopically exchange their oxygen with that of the water almost immediately (13), thereby leading to a uniform labeling of the solution. Nagayama and Cohen (5), in an investigation of iron passivity by coulometry and chemical analysis of iron dissolved in the solution, have shown that the thickness of the film varies from 8 to 30Å, depending on the potential of the layer formation. Foley *et al.* (14), by an electron diffraction investigation, have identified the structure of these films after obvious exposure to atmosphere as that of γ-Fe_2O_3. Recent ellipsometric investigations, which may be carried out *in situ*, have shed some new light on certain aspects of the nature of iron oxide films formed in neutral solutions. In particular, Sato and Kudo (15) have found that cathodically reduced iron oxide is characterized by the complex refractive index of the bare metal, and from this, they inferred the total absence of any oxide film. This observation and their measured value of the minimum thickness (9Å) required for passivation to occur led them to the conclusion that the mechanism of passive layer formation is similar to that for anodic films formed on valve metals; this mechanism has been proposed previously in Ref. (1) and (6). On the basis of coulometric measurements, it has been suggested by Frankenthal (9) that adsorption phenomena are responsible for passivation at low values of polarization. Recently, Bockris *et al.* (8) have shown by combining coulometric and ellipsometric methods that a ferrous hydroxide $Fe(OH)_2$ exists in the prepassive region and they assumed that it was transformed into ferric oxide Fe_2O_3 at the beginning of the passivity region and then grew linearly with potential up to 40Å

This short review of the literature shows that the problem of the proper choice of a mechanism of passive film formation still remains open. The purpose of the present work, which is an extension of previous investigations with similar methods on nickel (16, 17), is to obtain new information about the phenomenon of passivity by combining the methods of electrochemical measurements and nuclear microanalysis of the 16 and 18 isotopes of oxygen.

The main objects of the present experiments were to study: (*i*) the effects of polishing on the iron specimens and the definition of a test specimen which exhibits the thinnest surface oxide layer; (*ii*) the determination of the quantity of oxygen coming from the solution and fixed on the metal surface after cathodic reduction and under corrosion potential; (*iii*) the relationship between the potential and the quantity of oxygen fixed on the metal surface in the passivity region; and (*iv*) the measurements of oxygen loss due to the cathodic reduction of these layers. Some of these results have been presented (18).

Experimental Technique

Sample preparation.—The specimen (substrate) was a pure iron electrode (99.9% or 99.99% purity, see Table II) of 10 × 10 mm with an iron wire electrowelded to it to give the electric contact. Polishing of the specimen surface was carried out in a mixture of glacial acetic and perchloric acids (20:1) at a current density of 450 mA/cm², with intense mechanical stirring (19). All potentials are expressed on the standard hydrogen scale. Most of the experiments were carried out at 23° ± 1°C, while some of them were performed at −3° and 50°C.

After rinsing and drying, the specimens were stored in a vacuum of the order of 10^{-2} mm Hg. Immediately before the experiments, the samples were repolished for 1 min.

Experimental procedure.—First the samples were put in the solution and left unpolarized while their potential stabilized around a value of about −250 mV. They were then pretreated by cathodic reduction (10 μA/cm²) to remove any existing oxide from the surface (5). This brought a decrease in the potential to about −650 mV (ϕ_c). Polarization was then switched off. In 5 min, the potential rose to about −510 mV (ϕ_{s2}). After this pretreatment (summarized in Table I) samples were oxidized potentiostatically and analyzed following the proceedings and precautions described in Ref. (16, 17) where oxygen desorption was carefully studied. The possible losses were minimized here in the same way.

Nuclear microanalysis of O^{16} and O^{18}.—Nuclear microanalysis, by the observation of nuclear reactions, yields the number N_O16 (reaction $O^{16}(d,p)O^{17*}$) or N_O18 (reaction $O^{18}(p,\alpha)N^{15}$) of oxygen atoms per square centimeter fixed on the specimen surface (20, 21). The number of oxygen atoms coming from the solution, $\hat{N}_O18$, can be obtained by dividing N_O18 by the solution enrichment (ratio of O^{18} to the total oxygen in the solution), *i.e.*, by normalizing the results.

Results and Interpretation

Analysis of the state of the sample surface.—The quantity of oxygen present at the metal surface was determined before and after polishing for specimens of different purities supplied by different manufacturers.

Figures 1 and 2 show the spectra of the $O^{16}(d,p)O^{17*}$ reactions of oxygen obtained under identical experimental conditions for 99.9 and 99.99% iron before and after polishing. The spectrum for 99.9% purity iron (Fig. 1a) shows a tail on the lower energy side which tends to disappear after polishing (Fig. 2a), while the over-all oxygen quantity near the surface drops by a factor of 100. The depth scale of Fig. 1 is only illustrative; in fact, to deduce the concentration profile, $C(x)$, from the spectrum, one has to take into account the variation of cross section with depth (21). From this, it may be inferred that, in addition to the surface oxide layer, there exists some oxygen buried in the metal matrix which can be removed by polishing (12, 16, 21, 22). This component may be shown to extend to a depth of some microns. In the case of the 99.99% purity iron, practically no bulk oxygen was observed, even before polishing (Fig. 1b).

The results obtained from these spectra are shown in Table II, where the number of O^{16} atoms is given for various iron surfaces along with, for comparison, the

Table I. Successive steps of sample treatment

Polished iron sample, 99.99% purity*	Time	Current	Equilibrium potential (NHE)
Without any polarization	5 min	—	$\phi_{s1} = -250$ mV
Under cathodic polarization (galvanostatic method)	5 min	10 μA/cm²	$\phi_c = -650$ mV
Without any polarization	5 min	—	$\phi_{s2} = -510$ mV
Anodic polarization (potentiostatic method)	150 sec 60 sec	Final current: 5 μA/cm²	$V_{ox} = +940$ mV $V_{ox} = +140$ mV
Without any polarization**	120 sec	—	$V_{ox} = -60$ mV

* Supplied by Materials Research Corporation.
** Potential of passive samples in open circuit.

[1] Normalized O^{18} enriched water produced at the Weizmann Institute, Rehovot, Israel.

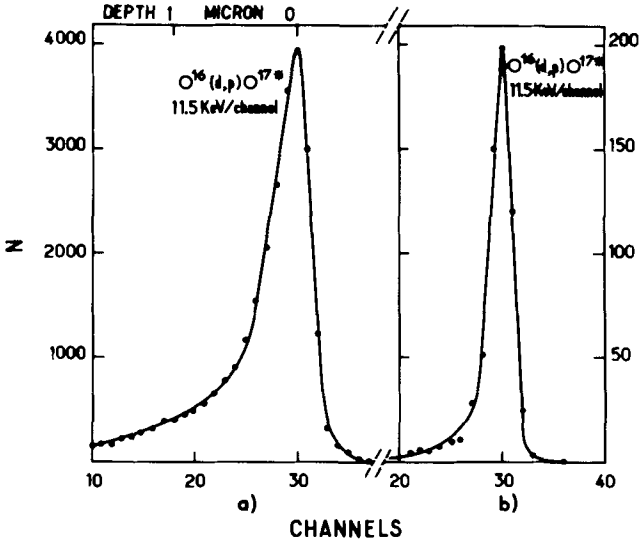

Fig. 1. Proton energy spectra for the reaction $O^{16}(d,p)O^{17*}$ observed on unpolished iron samples: (a) 99.9% purity (Armco), (b) 99.99% purity (MRC).

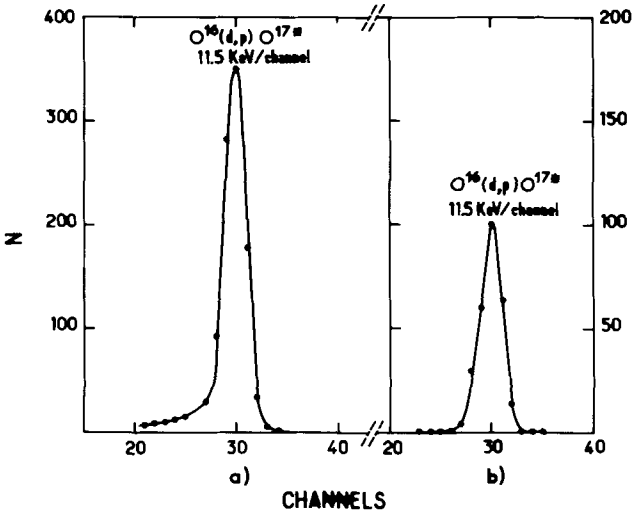

Fig. 2. Proton energy spectra for the reaction $O^{16}(d,p)O^{17*}$ observed on polished iron samples: (a) 99.9% purity (Armco), (b) 99.99% purity (MRC).

corresponding results for nickel (16). With reference to the data for unpolished specimens, Table II only indicates their order of magnitude, as the corrections for deep penetration were not taken into consideration, these results presenting a marked irreproducibility.

It is seen that the three iron specimens of different origin and purity are characterized by different amounts of surface oxygen, expressed as the number of oxygen atoms per square centimeter, after polishing.

Table II. Characteristic of the surface layers on iron and nickel

Metal	Surface preparation	$N_O^{16} \times 10^{15}$ atoms/cm²
Iron 99.99% (Johnson Matthey)	Unpolished	~80
	Polished*	23
Iron 99.99% (Materials Research Corporation)	Unpolished	~25
	Polished*	10
Iron 99.9% (Armco)	Unpolished	~500
	Polished*	30
Nickel 99.99% (16) (Materials Research Corporation)	Unpolished	~100
	Polished**	6

* In a mixture of glacial acetic and perchloric acids (20:1) at a current density of 450 mA/cm², during 2 or 10 min for 99.99 or 99.9%, respectively.
** In 54.5% sulfuric acid at 400 mA/cm².

This could be explained by: (*i*) the roughness factor which would vary from one specimen to another; and (*ii*) the presence of oxygen atoms in the bulk which may be located within the first few thousand angstroms of the metal, in particular in grain boundaries. It should be noted that the finite depth resolution of our measurements [0.20 μm (21, 22)] does not allow one to distinguish between surface oxygen atoms and those situated in the volume up to 0.20 μm from the surface.

Of these two explanations, the second seems to us the most probable, as discussed below.

As the Materials Research Corporation (M.R.C.) 99.99% iron seems to have a lower surface oxygen level than that of Johnson and Matthey, the first named brand was used in all the following experiments on 99.99% purity iron.

Nature and equivalent thickness of the passive layer.—The quantity of oxygen fixed on the iron surface was studied as a function of the polarization potential V_{ox}. Following Ref. (16), it was thought necessary to stop the oxidation at a constant final current (5 μA/cm²) and to withdraw the specimens while maintaining their potential.

Oxygen content of films present in the prepassive and passive regions at 23°C.—First, we investigated the formation of the passive layer in a solution of natural isotopic O^{18} concentration, *i.e.*, practically only O^{16}. In the passive region, the function $N_O16 = f(V_{ox})$ is approximately a straight line, the slope of which is difficult to determine given the poor reproducibility of the measurements. In fact, the amount of oxygen fixed on the sample surface varies from about 12×10^{15} atoms/cm² at a potential $\phi_1 = -300$ mV, at the beginning of passivation, to about 25×10^{15} atoms/cm² at a potential $\phi_2 = +900$ mV, at the end of the passivation period. Furthermore, it should be noted that the quantity measured at potential ϕ_1 is of the same order as that determined after cathodic treatment of the specimen, about 12×10^{15} atoms/cm². This would imply that approximately 12×10^{15} atoms/cm² remain on the surface of specimens which have been cathodically polarized and exposed to air. Such a large quantity of oxygen, which is equivalent to an oxide layer 20Å thick if one assumes a γ-Fe_2O_3 structure with a roughness factor equal to unity, could be explained by two reasons: an oxidation due to atmospheric oxygen during transfer of the specimen from the electrochemical cell to the vacuum chamber of the accelerator, or an insufficient cathodic reduction in that it did not completely remove the surface film covering the polished specimen. However, this oxygen content seems to be essentially due to an oxidation in air during the transfer of samples from the electrochemical cell to the scattering chamber of the accelerator. This effect has been already observed in the case of nickel (17).

These results clearly show that the O^{18} tracing techniques are indispensable for obtaining further information; in particular, they should permit the effect of atmospheric oxygen to be distinguished from that of oxygen coming from the solution. All the oxygen 18 thus measured must come from the solution. Nevertheless, one cannot exclude the possibility of an exchange taking place by spontaneous oxidation when the sample is removed from the electrolytic cell. This would have the effect of decreasing the amount of O^{18} measured at the surface. In what follows this effect has been considered as negligible. This assumption has been confirmed by comparing our results with those obtained using other methods like ellipsometry and coulometry. Furthermore, nuclear microanaylsis measurements cannot be carried out *in situ*. After each oxidation, the specimens are withdrawn from the solution and immediately plunged into triple-distilled water of natural isotopic composition. Thus the nonpolarized specimen is in contact with a layer of enriched solution for the few seconds preceding immer-

sion in distilled water and is therefore under open-circuit potential of ~−60 mV (see Table I). Following literature data (7, 10), we may associate the quantity of oxygen fixed on the surface with the maximum value of the potential applied to the specimen. Thus it can be noticed that in the case of cathodically polarized specimens in an open circuit the potential increases, whereas it decreases when a potential greater than ~−60 mV is applied. In conclusion, this manipulation would not appear to affect the measurements except for cathodic polarization.

Cathodic pretreatment of the specimen before polarization was investigated in order to determine the state of the specimen at a potential $\phi_c = -650$ mV (Table I), *i.e.*, to determine whether oxygen from the solution fixes on the metal surface at the end of this period when it is still under cathodic potential. The following experiment was carried out: the specimen was cathodically polarized at 10 μA/cm^2 for 5 min and then, instead of withdrawing it from the solution [which, as we have described above, induces an oxidation by the layer of solution attached to the surface of the metal, about 3×10^{15} atoms/cm^2 of oxygen 18 (Fig. 3)], the 10 cm^3 of solution was diluted ten times with a deaerated solution having natural isotopic composition. Thus, the percentage of O^{18} enrichment was decreased by a factor of ten. During this dilution in a neutral atmosphere, the potential of the specimen was maintained at the previous level $\phi_c = -650$ mV. The specimen was then withdrawn from the cell and analyzed. No O^{18} was found fixed at the surface. This indicates that there is no oxygen from the solution at the surface of the specimen for $\phi_c = -650$ mV. However, from this experiment alone it cannot be determined whether the cathodic reduction completely removed the film at the surface of the polished specimen. Following literature data deduced from ellipsometric (8, 15, 23) and coulometric (5, 9) measurements, the specimen was assumed to be free of oxygen under these experimental conditions.

In a further experiment, before passivation of the specimen, the polarization was switched off for 5 min, causing an immediate increase of potential from $\phi_c = -650$ mV to a final value stabilizing at about −510 mV (ϕ_{s2}). This increase may be attributed to the process of oxidation at the surface and to the effect of hydrogen there. This intermediate stage before passivation was deliberately chosen to provide the experimental conditions under which the hypothesis recently proposed by Bockris *et al.* (8) could be studied. Bockris postulated the presence of an iron hydroxide $Fe(OH)_2$ in the prepassive region, which at the beginning of the passive region is transformed by the applied voltage into ferric oxide Fe_2O_3. The results obtained at this intermediate stage are discussed below.

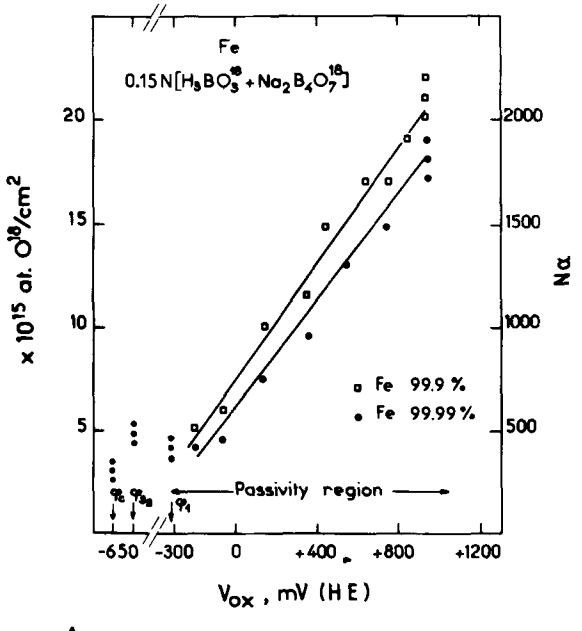

Fig. 3. $\hat{N}_{O18}$ as a function of applied potential V_{ox} for Fe 99.9% purity (□) and Fe 99.99% purity (●).

Then and only after this pretreatment, film formation was studied in the potential region, from −310 to +900 mV. Figure 3 shows the number of O^{18} atoms as a function of potential for 99.9% and 99.99% purity iron specimens. It should be noted that the error indicated between brackets is related to the irreproducibility of the formation of the passive films on several samples. It also should be remembered that the error of individual measurements only referring to the relative statistical precision of the counting rate is much lower than that previously mentioned. The results may then be summarized as follows:

1. The relationship between the number of oxygen atoms and the potential is approximately linear in the passive region.

2. For the iron of 99.9% purity, the slope of the line $\hat{N}_{O18} = f(V_{ox})$ is about 15% greater than that for 99.99% purity. This may be attributed to the different roughness factor of the 99.9% and 99.99% iron. One is now in a position to chose between the two hypothesis previously advanced to explain the presence of different quantities of oxygen at the surface of polished specimens of different origins (Table II). If this spread were due to varying roughness factors, then in the case of the polished 99.9% and 99.99% purity specimens this variation should be less than 15%, which is clearly not the case since this same variation calculated from the quantity of oxygen measured by the nuclear reaction is equal to 300% (see Table II). Consequently, it would seem reasonable to explain the above differences by the presence of traces of bulk oxygen, probably situated at the grain boundaries.

3. The maximum amount of oxygen coming from the solution and fixing on the surface does not exceed $(18 \pm 2) \times 10^{15}$ atoms/cm^2 for the 99.99% purity specimen. This corresponds to an oxide layer of about 35Å if one assumes a γ-Fe_2O_3 structure for the oxide, as suggested by Foley *et al.* (14) on the basis of electron diffraction experiments, and by Sato and Kudo (15) who reached the same conclusion using ellipsometric measurements.

4. The quantity of oxygen coming from the solution and fixing on the surface of iron speciments which have been subjected to cathodic reduction and have attained the corrosion potential ϕ_{s2}(−510 mV) is $(5 \pm 1) \times 10^{15}$ atoms/cm^2.

5. The quantity of oxygen present at the beginning of passive layer formation ($\phi_1 = -310$ mV) is $(5 \pm 1) \times 10^{15}$ atoms/cm^2. Thus, the difference in the quantity of oxygen (coming from the solution) at potentials ϕ_{s2} and ϕ_1 is statistically zero to within 2×10^{15} atoms/cm^2 (maximum value of error obtained by direct sum of errors). This is equivalent to about a monoatomic oxygen layer.

The above results referring to the passivity region agree satisfactorily with the corresponding data taken from the literature (7, 9) (Fig. 4), if one assumes a passive film with a γ-Fe_2O_3 structure and a roughness factor equal to unity. On the basis of this agreement, we shall deduce, in the following section, the apparent parameters of the passive film. However, at the corrosion potential $\phi_{s2} = -510$ mV, there is complete disagreement with regard to the presence [established in Ref. (8) and in this work] or the absence of oxygen [according to certain data in the literature (15)]. We have therefore taken great care to investigate the presence of oxygen at ϕ_{s2} and the following experiment was designed to exclude any oxidation effect caused by removal of the specimen from the electrolytic cell.

The iron specimen, subjected to the usual cathodic treatment, was stabilized for 5 min at the potential ϕ_{s2}. Instead of withdrawing the specimen from the O^{18} enriched solution, the 10 cm^3 of this solution were, as

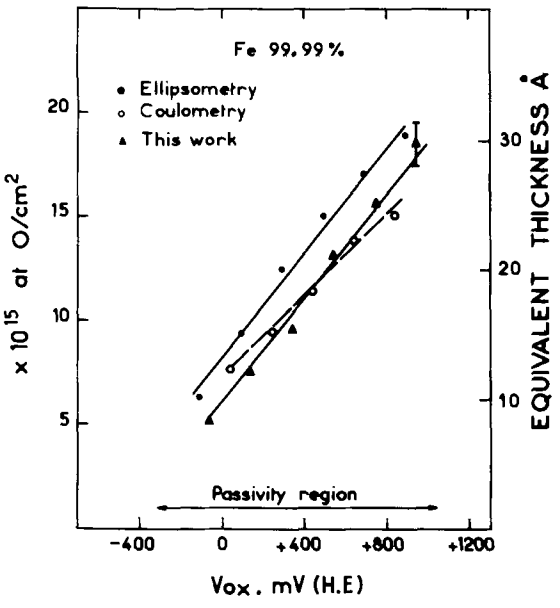

Fig. 4. Comparison between nuclear measurements and literature data for iron 99.99%. ● Foley *et al.* (14), ellipsometric measurements; ○ Frankenthal (9), coulometric measurements; ▲ This work.

previously, diluted with 100 cm³ of the same solution which was also deaerated but had a natural isotopic composition. During this transfer in a neutral atmosphere, the potential of the specimen was maintained at the previous level ϕ_{s2}. If the presence of oxygen at the spontaneous potential ϕ_{s2} were due to some oxidation caused by oxygen of the solution during removal of the specimen from the electrolyte cell, the quantity of oxygen 18 would be expected to be decreased by a factor of 10. However, this is not the case and thus the oxygen 18 adsorbed on the specimen surface originates from a real process of fixation of oxygen, between the moment when the specimen is no longer held at cathodic polarization and that when it reaches its spontaneous potential ϕ_{s2}. It should be noted that the corrosion potential ϕ_{s2} measured under the present experimental conditions, −510 mV, is closely consistent with the thermodynamic data for certain types of iron oxide or hydroxide (24). This constitutes further evidence, in agreement with Kruger and Calvert (7), for the presence of oxygen on the iron specimen at this potential. This question will be further developed in the section on Discussion.

Apparent electric field of formation.—Nuclear microanalysis allows one to determine the oxygen content of the passive layer as a function of the potential. Growth of passive layers at high potentials is generally accepted to be due to the transport of ions across a barrier layer as in the case of anodic oxides of valve metals. Thus, the growth laws established for anodic oxides like those of aluminum and tantalum (25) may also be valid for oxides forming a passive layer at high potentials; accordingly, we attempted to calculate some apparent parameters of these oxides and essentially the apparent electric field of formation.

The values of the field of formation E_{ox} were deduced from the slope of the curve $\hat{N}_{O}18 = f(V_{ox})$ for $J =$ const. Such a calculation, following (25), is possible provided this curve is linear, i.e., E_{ox} and the sum of the overpotentials $\Sigma\eta$ at the interfaces must be constant given the condition that the nature and structure of the oxide do not change. In fact, see Ref. (26), these physical parameters are connected through the following equation

$$V_{ox} - V_{eq} = E_{ox} \cdot l + \Sigma_{\eta} \qquad [1]$$

where l is the oxide thickness. If one assumes the stoichiometry, the density of the oxide, and the roughness factor to be constant, l is proportional to the oxygen content, $\hat{N}_{O}18$, of the compact passive film

$$l = a\,\hat{N}_{O}18 \qquad [2]$$

With reference to Eq. [1], if Σ_{η} is constant, as might be expected (25), is appears that V_{eq}, which corresponds to the thermodynamic potential V_{Th} of oxide formation, does not depend very much on the choice of one of the types of oxide or hydroxide which can be expected to occur (24).

The physical meaning of the calculation of the electric field E_{ox} depends on the condition that V_{eq}, Σ_{η}, and a be constant in the passivity region moreover, if V_{eq} and Σ_{η} vary only little for the different types of oxide, there must be a linear relationship between V_{ox} and $\hat{N}_{O}18$ under the condition that all the oxygen fixed on the specimen surface contributes to the formation of a barrier-type layer. This fact has indeed been observed in the present work (Fig. 3). The values of the fields E_{ox}, deduced from the slopes of the straight lines $\hat{N}_{O}18 = f(V_{ox})$ as obtained by nuclear microanalysis, have been calculated assuming, in agreement with the findings of other workers (5, 7, 8, 15), that the oxide has a structure of Fe_2O_3, a density ρ of 5, and a roughness factor equal to unity.

The values obtained for 99.99% purity Fe are $E_{ox} = 5.1 \times 10^6$ V/cm and 4.4×10^6 V/cm for 99.9% purity Fe. Values of E_{ox} calculated from various investigations are shown in Table III. These values refer to a potential region, ranging from + 100 to + 900 mV, in which there is a general agreement among all workers with regard to the structure of the thin oxide layers, *i.e.*, Fe_2O_3.

Our results obtained for $J = 5\ \mu A/cm^2$ are compared with those found in the literature for much smaller currents (Fig. 4). However, since for the system under investigation E_{ox} depends only slightly on the final current, our values recalculated with the densities indicated by the other authors are shown in brackets. Besides, the physical meaning of the quite small variation of E_{ox} with J has been analyzed by Kruger and Calvert (7).

Except for the large value of E_{ox} obtained by Nagayama and Cohen, it appears from the results obtained by the other workers that the slope of the $\hat{N}_{O}18 = f(V_{ox})$ curve depends apparently on the purity of the specimen. All we can say is that for a same degree of purity the results obtained by three different methods (coulometry, ellipsometry, and nuclear microanalysis) agree well.

Cathodic reduction.—Studies of oxygen loss during cathodic reduction were carried out at 23°C; for the iron specimen used, the rate of dissolution of the passive films was previously measured and found to be smaller than 7×10^{10} atoms/cm² sec (27). The passivation films formed at +940 mV in O^{18} solution were cathodically reduced in the same solution at a constant current density of 10 $\mu A/cm^2$. Figure 5 shows the variation of the number of oxygen 18 atoms fixed on the sample surface and the corresponding drop in potential during the cathodic reduction, as a function

Table III. Electric field of formation E_{ox} x 10^6 V/cm

Investigator(s)	Material	J, $\mu A/cm^2$	ρ	$E_{ox} \times 10^6$ V/cm
Nagayama and Cohen (5)	Fe 99.95%	0.1	5·18	6.25
Foley *et al.* (14)	Fe 99.99%	0.1	5	5
Frankenthal (9)	Fe 99.99%	0.1	5	5.4
Sato and Kudo (15)	Fe 99.9%	0.1	5·18	4.4
This work	Fe 99.9%	5	5	4.4 (4.6)*
	Fe 99.99%	5	5	5.1 (5.3)*

* Calculated for $\rho = 5{\cdot}18$.

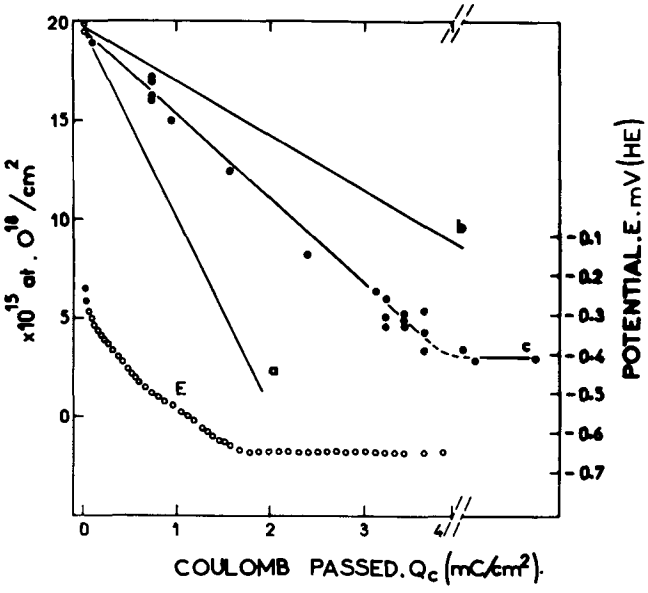

Fig. 5. Change in $\hat{N}_{O}18$ and in potential (*E*) of iron during the galvanostatic-cathodic reduction at 10 μA/cm^2 and 23°C for the passive films formed in 3 min. (I_{final} = 5 μA/cm^2) at +940 mV. (a) n = 2/3e (theoretical value), (b) n = 2e (theoretical value), and (c) n = 1.38e (experimental value).

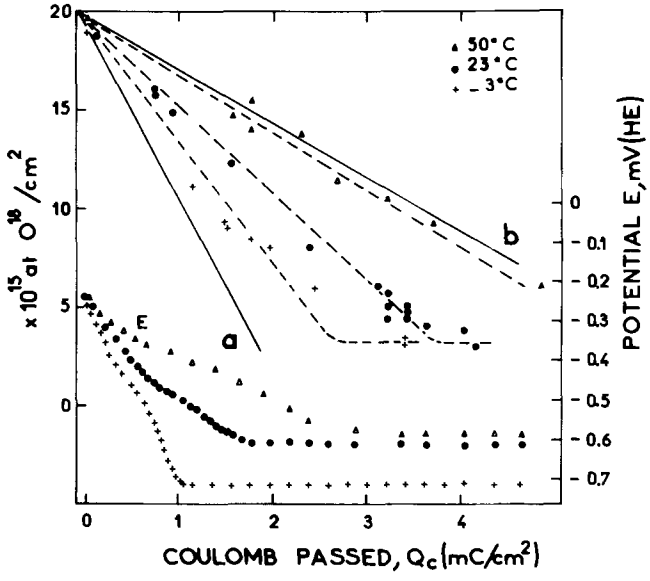

Fig. 6. Change in $\hat{N}_{O}18$ and in potential (*E*) of iron during the galvanostatic-cathodic reduction at 10 μA/cm^2 for the passive films formed in 3 min. (I_{final} = 5 μA/cm^2) at + 940 mV and at different temperatures.

of time, *i.e.*, as a function of the charge Q which has been passed. The slope of the curve $\hat{N}_{O}18 = f(Q_{mC/cm^2})$ gives the number n of electrons associated with an oxygen ion entering the solution. It should be mentioned that the nuclear microanalysis allows us to measure n directly, in contrast to other methods where n can only be deduced from changes of electrical or optical parameters of the film.

The problem of cathodic reduction has been studied for a long time (5, 10). Based on the mechanisms proposed in the literature, two slopes may be deduced theoretically relating $\Delta\hat{N}_{O}18$ to Q, (see Fig. 5). The first gives a value of 2/3e (electronic charge) associated with each oxygen ion passing into the solution. This is represented by curve a of Fig. 5 and was derived from the following mechanism

$$(a)\quad Fe_2O_3 + 6H^+ + 2e^- = 2Fe^{2+}{}_{(sol)} + 3H_2O$$

The second slope corresponding to curve b of Fig. 5 gives a value of 2e and corresponds to the mechanism

$$(b)\quad Fe_2O_3 + 6H^+ + 6e^- = 2Fe^\circ + 3H_2O$$

The experimental results gave us a value of 1.38 ± 0.07 electronic charge per oxygen ion passing into the solution. Our measurements were not precise enough to be able to distinguish between the first and second reduction stages; the existence of these two stages was deduced from ellipsometric measurements (6, 10).

To gain some insight into this problem, we have carried out the same cathodic reduction experiments at −3°C and +50°C. The passive films have been formed at this temperature, according to the process used at 23°C (see Table I) and we have shown that the rate of the oxygen losses, in open circuit, were negligible and smaller than 7 × 10^{10} atoms/cm^2 sec. Figure 6 shows the variation of the number of oxygen 18 fixed on the sample surface and the corresponding decrease in potential as a function of the charge passed. From Fig. 6, we deduce the value of n for two temperatures

$$n = 1.88 \pm 0.08e \text{ for } t = 50°C$$
$$n = 1.04 \pm 0.08e \text{ for } t = -3°C$$

This number n cannot be smaller than 2/3e [mechanism (a)]. Greater values of n could be obtained only with current efficiency smaller than 100% or if mechanism (b) also contributes to the cathodic reduction. In any case, it is not possible that the reaction takes place solely following mechanism (b). The value of the average charge cannot pass from 1.38 (at 23°C) to 2e since we have shown at the beginning of the paragraph that the chemical dissolution of the film is negligible. The ratio of the minimum theoretical slope to experimental slope is the minimum current efficiency for each temperature; it is equal to 66 and 35% at −3°C and +50°C, respectively.

Discussion

Presence of oxygen in the prepassive and post-passive regions.—The above results, *i.e.*, the presence of 5 × 10^{15} oxygen 18 atoms/cm^2 at the potential ϕ_1 and a maximum deviation of 2 × 10^{15} atoms/cm^2 between ϕ_1 and ϕ_{s2}, give rise to a question which may be stated as follows: does the passivation phenomenon result from oxygen fixed on the metal surface at a potential ϕ_{s1} or is it due to the oxygen corresponding to the difference between the two values at potentials ϕ_{s2} and ϕ_{s1}, *i.e.*, to the quantity of oxygen corresponding to the maximum deviation?

These two alternative interpretations may be formulated in the following manner: (*i*) passivation requires the presence of a monoatomic oxygen layer (~2 × 10^{15} atoms/cm^2); this would confirm the theory of adsorbed oxygen layers proposed by Uhlig (3) and Frankenthal (9); with increasing potentials in the passivity region, further formation of an oxide layer occurs on top of this monoatomic layer; and (*ii*) on the contrary, the onset of passive layer formation is associated with the presence of 5 × 10^{15} oxygen atoms/cm^2, as suggested by Sato and Bockris; this quantity of oxygen atoms would result from the transformation of the oxygen fixed at ϕ_{s2} into an oxide.

Presently, our results do not allow us to distinguish between these two mechanisms. However, we intend to obtain new information about this important problem by associating ellipsometric measurements to the results obtained from nuclear microanalysis with O^{18} tracing.

Cathodic reduction.—The results of nuclear microanalysis indicate, at 23°C, an electronic charge of 1.38e associated with each ion of oxygen passing into the solution. However, at the present moment, the precision of our experiments is insufficient due to the irreproducibility of the initial passive layers and thus cannot reveal the existence of two different slopes for

the rate of decrease of oxygen atoms as a function of the charge passed, as have been observed by Sato and Kudo (15).

If one takes for the current efficiency of the cathodic reduction a value of 50% at 23°C, then this value of $1.38e$ is reduced to nearly $2/3e$, which would imply that the cathodic reduction takes place essentially by mechanism (a). This value of 50% is the same as that proposed by Sato and Kudo (50%) for the over-all reduction process (two stages) but smaller than that proposed by Nagayama and Cohen (70%). One should notice that our experimental conditions were slightly different from those of the latter workers. The differences concerned are: (*i*) the conditions of preparation: 3 min in the present work instead of 1 hr anodic polarization; and (*ii*) the presence of dissolved iron in our solutions, since this is not changed after each cathodic reduction in O^{18} enriched solution; however, the quantity of dissolved iron is never greater than 10^{-5} mole/liter.

We are endeavoring to determine the influence of each one of these factors on the experimental slope of the curve $\hat{N}_O 18 = f(Q)$. The results should then enable us to decide whether or not the cathodic reduction takes place essentially according to mechanism (a). In the literature, Sato *et al.* (10) have suggested that reaction (b) takes place in two stages, the first one leading to the formation of an hydroxide $Fe(OH)_2$, while the subsequent step consists in the reduction of the hydroxide and the formation of the metal. The mechanism proposed by Nagayama and Cohen (5) is different (reduction of Fe_2O_3) but would also ensure a slope corresponding to an electronic charge of 2.

In the light of our results, it would appear that the temperature has a great influence on the cathodic reduction: at low temperatures, the curves $\hat{N}_O 18 = f(Q)$ imply that the cathodic reduction takes place in accordance with mechanism (a), while at higher temperatures mechanism (b), with two electrons associated with each oxygen atom, predominates. This, however, contradicts what one could reasonably deduce from the phenomenon of the decrease in potential, which is generally comprising two stages (5, 10). The first one would correspond to the reduction from Fe^{3+} to Fe^{2+}, while the second step indicates the formation of metallic iron from Fe^{2+}.

By determining the value of the current efficiency and by combining the results of ellipsometric measurements with those of nuclear microanalysis, carried out on the same samples, we are attempting to establish the detailed mechanism of the cathodic reduction.

Acknowledgments

The authors wish to thank Dr. G. Amsel for his numerous comments and suggestions during this work. The help of Mr. A. Laurent for his technical assistance was much appreciated. This work was supported by the Centre National de la Recherche Scientifique, (RCP No. 157), the DRME, and the DGRST.

Manuscript submitted Nov. 22, 1972; revised manuscript received March 15, 1973.

Any discussion of this paper will appear in a Discussion Section to be published in the June 1974 JOURNAL.

REFERENCES

1. U. R. Evans, "The Corrosion and Oxidation of Metals," Edward Arnold Publishers Ltd, London (1960).
2. T. P. Hoar, in "Modern Aspects of Electrochemistry," Vol. 2, Chap. IV, Butterworth Scientific Publications, New York (1959).
3. H. H. Uhlig, *Z. Electrochem.*, **62**, 626 (1958).
4. K. J. Vetter, *This Journal*, **110**, 597 (1963).
5. H. Nagayama and M. Cohen, *ibid.*, **109**, 781 (1962); **110**, 670 (1963).
6. N. Sato and M. Cohen, *ibid.*, **111**, 512 (1964); **111**, 519 (1964); **111**, 624 (1964).
7. J. Kruger and J. P. Calvert, *ibid.*, **114**, 43 (1967).
8. J. O'M. Bockris, M. A. Genshaw, V. Brusic, and H. Wroblowa, *Electrochim. Acta*, **16**, 1859 (1971).
9. R. P. Frankenthal, *ibid.*, **16**, 1845 (1971).
10. N. Sato, K. Kudo, and T. Noda, *ibid.*, **16**, 1909 (1971); **10**, 785 (1970).
11. G. Amsel, C. Cherki, M. Croset, G. Feuillade, J. P. Nadai, C. Ortega, S. Rigo, and J. Siejka, *Collection Czech. Chem. Commun.* **36**, 883 (1971).
12. G. Amsel, "Physics of Electrolytes," Vol. *1*, J. Hladik, Editor, Academic Press, London (1972).
13. T. C. Hoering and J. W. Kennedy, *J. Am. Chem. Soc.*, **79**, 56 (1957).
14. C. L. Foley, J. Kruger, and C. J. Bechtoldt, *This Journal*, **114**, 994 (1967).
15. N. Sato and K. Kudo, *Electrochim. Acta*, **16**, 447 (1971).
16. J. Siejka, C. Cherki, and J. Yahalom, *ibid.*, **17**, 2371 (1972).
17. J. Siejka, C. Cherki, and J. Yahalom, *This Journal*, **119**, 991 (1972).
18. B. Agius and J. Siejka, Proc. 5th Intern. Congr. Metallic Corrosion, Tokyo, Japan, May 21-27, 1972.
19. P. B. Sewell, C. D. Stockbridge, and M. Cohen, *Can. J. Chem.*, **37**, 1813 (1959).
20. G. Amsel and D. Samuel, *Anal. Chem.*, **39**, 1689 (1967).
21. G. Amsel, J. P. Nadai, E. D'Artemare, D. David, E. Girard, and J. Moulin, *Nucl. Instr. Methods*, **92**, 481 (1971).
22. G. Amsel, G. Beranger, B. De Gelas, and P. Lacombe, *J. Appl. Phys.*, **39**, 2246 (1968).
23. C. L. McBee and J. Kruger, *Surface Sci.*, **16**, 340 (1969).
24. M. Pourbaix, "Atlas of Electrochemical Equilibria in Aqueous Solutions," Pergamon Press, New York (1966).
25. J. Siejka, J. P. Nadai, and G. Amsel, *This Journal*, **118**, 727 (1971).
26. L. Young, "Anodic Oxide Films," Academic Press, New York (1961).
27. B. Agius and J. Siejka, 22nd Meeting of C.I.T.C.E., Dubrovnik, September 1971, p. 31.

Solution-Side Transport Processes in the Electropolishing of Copper in Phosphoric Acid

K. Kojima and C. W. Tobias*

Inorganic Materials Research Division, Lawrence Berkeley Laboratory, and Department of Chemical Engineering, University of California, Berkeley, California 94720

ABSTRACT

The unsteady-state anodic dissolution of copper in 5-10*M* phosphoric acid was carried out in the absence of convection, under galvanostatic and potentiostatic conditions. At a given bulk concentration of H_3PO_4, the product of current density, i, and the square root of the time (t_s) of onset of sharp potential rise (or abrupt decline of current) is nearly constant in the active dissolution range. $i\sqrt{t_s}$ decreases with increasing acid concentration. The transition times found are in substantial agreement with those reported by Elmore and Edwards. By using the most reliable diffusivity data available for phosphoric acid and for anodically formed copper phosphate, it is shown that the rate-limiting step in the active dissolution regime is the transport of copper phosphate from the electrode surface into the bulk solution. The potential jump in galvanostatic dissolution, or the peak current phenomena reported by numerous authors for steady-state potentiostatic dissolution can be best interpreted by assuming rapid increase of coverage of the anode surface with solid reaction product after the critical solubility limit of copper phosphate is reached at the surface. The concentration of phosphoric acid at the surface up to and including the peak current density where the critical solubility of copper phosphate is exceeded, remains finite. The magnitude of the peak current density can be predicted by considering the transport of copper phosphate away from the surface to be the limiting transport process.

Electropolishing of copper in concentrated phosphoric acid occurs under diffusion control (1, 2). Although the constancy of the product of current density and square root of transition time in galvanostatic unsteady-state dissolution has been confirmed (3-6), identification of the rate-determining species at the current plateau (2-4, 7, 8) has remained a controversial problem. Edwards (3) and Wagner (9) proposed that transport of one of the reactants from the bulk electrolyte to the anode surface is the rate-limiting process. The role of diffusion of water on the limiting current was discussed by Petit (8). On the other hand, Elmore (4, 10) claimed that without significant increase of applied cell voltage the current begins to decrease when the concentration of the dissolved copper species at the anode surface reaches the solubility limit. Hickling and Higgins (7) found that the limiting current decreases proportionally to the decrease of concentration difference of cupric ions between the anode surface and the bulk electrolyte. However, Hickling and Higgins' test was performed in dilute phosphoric acid (2*M*/1), where electropolishing is not possible.

In the decades that have passed since the two essentially opposite transport mechanisms have been proposed by Elmore and Edwards, a great deal of information has been developed on properties of the phosphoric acid-copper phosphate-water system. It appears therefore timely and worthwhile to undertake a reexamination of the question of the transport mechanism responsible for the smoothing and brightening action during electropolishing. Optical observations (11) of the copper surface undergoing dissolution, surface impedance measurements (12), ellipsometric studies (13), and wetting characteristics (mercury test) (1), all point to the fact that visible as well as invisible surface layers play an important role in the polishing process. In a qualitative study, preliminary to the present investigation, the present authors have found that in the unsteady-state active dissolution of copper in phosphoric acid the surface is free of solids. In steady-state electropolishing, however, solid material exists on and near the surface. These findings corroborate the observations reported earlier among others by Lorking (11) and Hoar *et al.* (1).

In the following, unsteady-state dissolution experiments are described, which were conducted deliberately under conditions similar to those used by Elmore and Edwards. Transition times in the active dissolution regime are interpreted using the best available transport property values.

The transport mechanism proposed on the basis of these unsteady-state experiments is then subjected to critical test using the peak current density data obtained by Hoar and Rockwell under steady-state potentiostatic conditions.

Dissolution of Copper under Galvanostatic Conditions

Experimental apparatus and procedure.—The experimental cell is shown schematically in Fig. 1. This simple cell was purposely designed to resemble the cell geometry employed by both Elmore (4, 10) and Edwards (3). The straight wall of the cylindrical anode compartment parallel to the direction of electric cur-

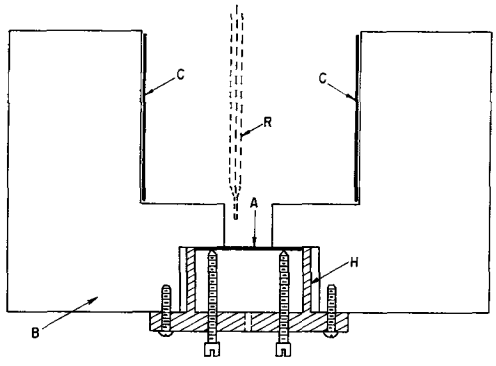

Fig. 1. Side view of the experimental cell. A, anode disk 1.27 cm diam exposed; B, Plexiglas cell body; C, 5 cm diam copper cathode ring. Anode compartment, 1.2 cm high; cathode compartment, 2.4 cm. H, Plexiglas anode holder; R, 0.06 cm OD reference capillary junction. The reference electrode is a copper wire set in the capillary tube.

* Electrochemical Society Active Member.

Key words: electropolishing of copper; mass transport; anodic dissolution of copper; phosphoric acid, role of, transport, in electropolishing of copper.

rent flow and the ratio of the height of the anode compartment to its diameter provide a geometry that gives a reasonably uniform current density distribution over the entire surface of the portion of the anode exposed to the electrolyte. The apparent area of the portion of the anode exposed to the electrolyte is 1.46 cm^2 and the inside area of the cylindrical cathode exposed to the electrolyte is 38 cm^2. During cell operation, the anode disk was in a horizontal position, facing upward. Since a more dense solution is forming upon anodic dissolution of copper, this configuration assures absence of convection during experimental runs. The laminar free convection occurring at the vertical cathode did not disturb the immobile solution in the anode compartment within the relatively short time spans (0.2-100 sec) involved in these experiments.

Analytical grade phosphoric acid (Baker, 85.9%) was diluted to desired concentrations (5 or 10*M*) for each experiment. The cathode was made from 99.9% polycrystalline copper; the anodes were prepared either from the same material, or cut from single crystals parallel to the (111) plane. Anode specimens were mechanically polished, washed with water and acetone, and subsequently anodically etched in concentrated H_3PO_4. In a few instances chemical polish was used in a HNO_3:H_3PO_4:HAc = 2:1:1 volume solution. Dissolution experiments were carried out at 22° ± 1°C.

After the current was cut off, anodes were immediately removed, washed with water and acetone, and dried at room temperature for weight loss measurements, or for microscopic observation of the surface. Anode surfaces were also observed *in situ* during dissolution under relatively low (10-45×) magnification. Constant current experiments were carried out by using external control of current (*a*) or, by potentiostatic control of the anode potential (*b*), involving approximately 2-7 ohm resistance between reference capillary tip, and anode surface.

(*a*). Constant current supply was provided by an Electronic Measurements Model C 621 power supply. The cell voltage was recorded by Sargent Model MR recorder. This technique was used for transition times of over 25 sec. This range allowed observation of the surface *in situ* under low level (10-45×) magnification.

(*b*). Anotrol Model 4100 potentiostat was employed to provide a constant potential between a reference electrode and the anode surface. In the active dissolution region the resistance between capillary tip and surface was sufficiently large compared to the impedance associated with the electrode reaction, so that potential control in this case corresponded to controlling current, at least up to the transition time. The current *vs.* time behavior was obtained by passing the cell current through a calibrated resistor and recording the resulting potential drop on a Tektronix Model 531 oscilloscope. Transition times in the range of 0.2-5 sec could be obtained with good reproducibility.

Visual observation of the anode surface during dissolution.—Typical cell voltage *vs.* time behavior in externally controlled constant current runs is illustrated in Fig. 2. After closing the circuit the cell voltage abruptly rises to a plateau and then increases only slightly (40-60 mV) to point A, at transition time t_s, after which the increase is quite sharp (the first voltage jump[1]). Visual observation under 10-45× magnification reveals, that at point A blue solid particles (probably copper phosphate) begin to form at the anode. As point E is reached (the second voltage jump) the number of particles becomes quite large; the blue color is spread over the entire surface. The onset of formation of small particles of blue color at point A becomes less distinct at higher applied current densities (above 0.05 A/cm^2). At the highest current density employed in these experiments, at i = 0.0676 A/cm^2, identification of two separate potential breaks was no longer possible.

[1] The first voltage jump is probably caused both by solid copper phosphate deposits and by the formation of copper oxides (18).

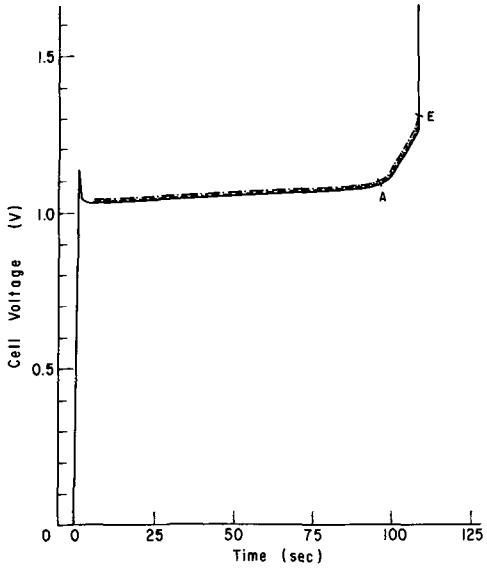

Fig. 2. Cell voltage change with time for polycrystalline copper in 10.0 M/liter H_3PO_4, i = 0.0362 A/cm^2 (six repeated runs are indicated by solid —, and dashed - - lines). The apparent valence is 2.0. Time elapsed to point A: transition time, t_s.

Valence of dissolution.—Weight loss measurements were carried out in runs extended up to the transition point A. The apparent valence of dissolution n' was obtained from

$$n' = \frac{M \cdot I \cdot t}{\mathbf{F} \cdot \Delta W}$$

where I is total current (A), t is time (sec), M is molecular weight of copper (g/g-mole), $\mathbf{F}$ is the Faraday, and ΔW is weight loss (g). From eight measurements, up to i = 0.038 A/cm^2, n' = 2.0 was obtained. In the following we shall assume that in the active dissolution regime, copper anodically dissolves in phosphoric acid with a valence of 2. Visual identification of the appearance of solid blue particles at the time when the voltage begins to rise rapidly in galvanostatic experiments suggests that the latter event is caused by the formation of solid copper phosphate at the anode surface. The change of concentration of reactants, or of reaction products at the anode surface is obtained by solving the diffusion equation with the appropriate initial and boundary conditions. Neglecting migration effects, we obtain (see Appendix B)

$$|C(t) - C(0)|_{x=0} = \frac{2i}{n\mathbf{F}} \left(\frac{t}{\pi D} \right)^{1/2} \qquad [1]$$

wheres $C(0)$ and $C(t)$ are the concentration of a reactant, or of a product at the surface, respectively, and n is the number of electrons transferred in the electrode process per g-mole (or g-ion) of the participating species considered. The concentration of a reactant or a reaction product at the anode surface at the transition time $t = t_s$ has some characteristic value, solely determined by the bulk composition, and temperature, independent of applied constant current density.

Figure 3 includes results from about 90 individual experiments obtained by current control (0.031-0.0676 A/cm^2) and potential control (0.16-0.6 A/cm^2) in 10.0*M* H_3PO_4. In this range of current densities, $i\sqrt{t_s}$ = 0.36 ± 0.015. Similar experiments conducted in 5*M* H_3PO_4 yielded $i\sqrt{t_s}$ = 0.73 ± 0.04, again indicating that the transition time t_s, as defined by the time of onset of the first voltage jump, is controlled by transport of one of the reactants or products.

Discussion

Comparison of present work with previous results.—Figure 3 shows that $i\sqrt{t_s}$ is nearly independent of cur-

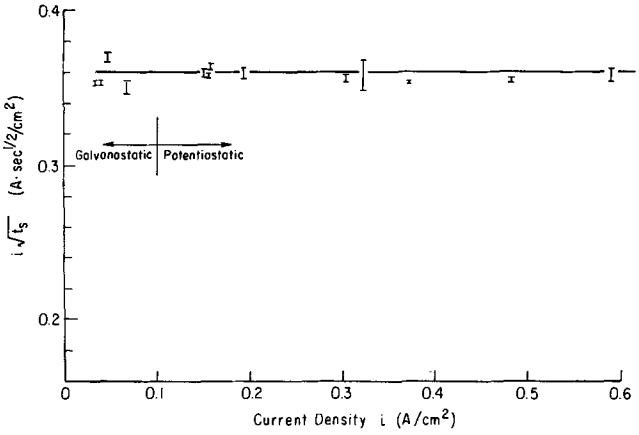

Fig. 3. Relation between $i\sqrt{t_s}$ and i in 10.0$_5$M H_3PO_4. (111) face of a single crystal (99.999%) was employed in runs at i = 0.308, 0.485, and 0.591 A/cm². All others involved were 99.9% polycrystalline copper. Number of experiments at a given current density: 3-10.

rent density in the range of 0.03-0.6 A/cm². This is in good agreement with the results obtained by Elmore (4), Edwards (3), Krichmar (5), and Vozdvishensky *et al.* (6). In 10M H_3PO_4 the values of $i\sqrt{t_s}$ obtained by interpolation from Elmore's and Edward's work are 0.36_8 (at 23.5°-24°C) and 0.37_4 (at 25°C), respectively, very close to the value of 0.36 obtained in this research.

The apparent valence of dissolved copper obtained in this work, 2.0 for the active dissolution of copper, is in good agreement with the value 2.00 reported by Petit and Schmitt (15).

Relation between $i\sqrt{t_s}$ and the concentration of phosphoric acid.—If the values of $i\sqrt{t_s}$ are characteristic of the properties of the electrolyte, it follows that they should be unique functions of the concentration of aqueous phosphoric acid at a given temperature. In Fig. 4, $i\sqrt{t_s}$ is plotted against the concentration of phosphoric acid. The values obtained by Elmore, Edwards, and by the present authors, are in good agreement with one another; $i\sqrt{t_s}$ decreases with increasing acid concentration. It is to be noted that the significance of this pattern of behavior was not recognized by the authors mentioned above.

Diffusion kinetics.—The reactants and reaction products in the active dissolution of copper move to or away from the anode by migration and diffusion. The diffusion layer is built up corresponding to the applied current density, time, diffusivity, and transference number of a species participating in the process.

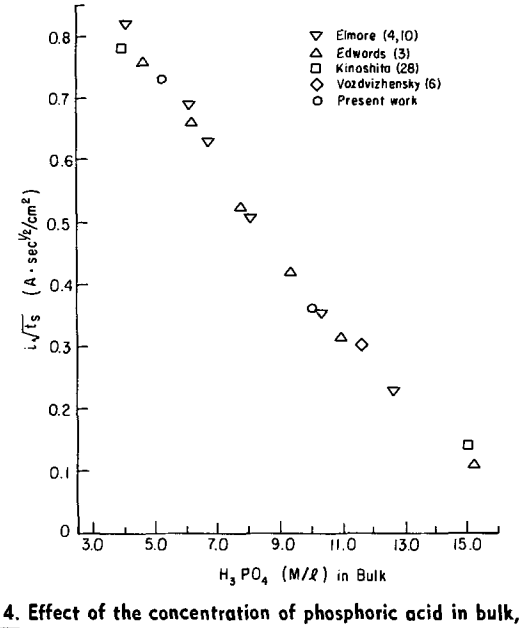

Fig. 4. Effect of the concentration of phosphoric acid in bulk, C_{rb}, on $i\sqrt{t_s}$

According to Laforgue-Kantzer (16), copper dissolves in concentrated phosphoric acid along the following over-all reaction scheme

$$Cu + H_3PO_4 + H_2O = (CuOH)^+(H_2PO_4)^- + 2H^+ + 2e^- \quad [I]$$

Krichmar and Galushko (17), on the other hand, claim that the copper dissolution reaction may be described by

$$Cu + 2H_3PO_4 = Cu^{++}(H_2PO_4)_2^- + 2H^+ + 2e^- \quad [II]$$

The first cell voltage jump may be expected to result (*a*) from the strong depletion of one of the reactants, that is, H_3PO_4 or H_2O in reaction [I] and H_3PO_4 in reaction [II], and (b) from the solubility limit of one of the reaction products (copper phosphate[2]) being exceeded and a high resistive film being formed on the anode.

In case (*a*), the concentration of a reactant C_r at the anode surface decreases with time and reaches $C_r \to 0$ at $t = t_s$, causing a sharp increase of the concentration overpotential. Here at $t = t_s$, the concentration of the reaction product is assumed to be below its solubility limit. In case (b), the concentration of the reactant at the anode surface does not reach $C_r \to 0$ at $t = t_s$.

Assuming that copper dissolution occurs with 100% current efficiency, the following relations [for derivation, see Appendix and also Ref. (18)] are applicable at the anode surface in reaction [I]

$$i = \frac{2F}{1 - t_{CuOH+}} D_p \left| \frac{\partial C_p}{\partial x} \right| \quad \text{for copper phosphate} \quad [3]$$

$$i = \frac{F}{t_{H+} - \frac{1 - t_{CuOH+}}{2}} D_r \left| \frac{\partial C_r}{\partial x} \right| \quad \text{for phosphoric acid} \quad [4]$$

In reaction [II]

$$i = \frac{2F}{1 + t_{Cu++}} D_p \left| \frac{\partial C_p}{\partial x} \right| \quad \text{for copper phosphate} \quad [5]$$

and

$$i = \frac{F}{t_{H+}} D_r \left| \frac{\partial C_r}{\partial x} \right| \quad \text{for phosphoric acid} \quad [6]$$

i, t_{Cu++}, t_{H+}, D_p, and D_r are applied current-density, transference number of Cu^{++}, that of H^+, diffusivity of copper phosphate, and that of phosphoric acid, respectively. Calculations of limiting current density in terms of water or H^+ concentration are not convenient because the necessary experimental data are not available. The diffusivity of phosphoric acid in the H_3PO_4-H_2O system has been measured at 25°C by Edwards and Huffman (19) and that of the anodic dissolution product of copper in phosphoric acid at 20°C by Krichmar *et al.* (20).

We now choose phosphoric acid as the reactant and copper phosphate as the reaction product in our diffusion calculations.

Case (*a*): If the first cell voltage jump is caused by the strong depletion of phosphoric acid at the anode surface, because of $C_r(t_s) = 0$ we get (see Appendix B)

$$i\left(\frac{t_s}{D_r}\right)^{1/2} = \frac{F}{2} \cdot \frac{\sqrt{\pi}}{t_{H+} - \frac{1 - t_{CuOH+}}{2}} \cdot C_{rb}$$

for reaction [I] [7]

and

[2] We use the terminology "copper phosphate" to denote the dissolution product of copper in phosphoric acid.

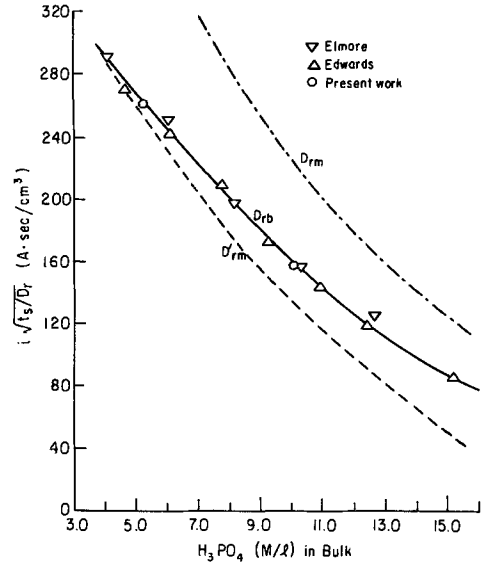

Fig. 5. Relation between $i\sqrt{t_s/D_r}$ and the concentration of phosphoric acid, C_{rb}. $i\sqrt{t_s/D_r}$ was obtained from Elmore, Edwards, and the present work. - - - curve indicates approximate pattern of experimental results of arithmetic mean diffusivity $D'_{rm} = \frac{1}{2}(D_{rb} + D_{ro})$. $D_{ro} \to D_r$ for $(H_3PO_4) \to 0$. —·—·— curve indicates qualitative behavior for $D_{rm} = \frac{1}{2}(D_{rb} + D_{rs})$, where D_{rs} denotes the value of D_r at the critical solubility of copper phosphate. Because copper phosphate increases considerably the viscosity of electrolyte $D_{rb} >> D_{rs}$ is assumed.

$$i\left(\frac{t_s}{D_r}\right)^{1/2} = \frac{\mathbf{F}}{2} \cdot \frac{\sqrt{\pi}}{t_{H+}} \cdot C_{rb} \text{ for reaction [II]} \quad [8]$$

Assuming that the transference number of H^+ or $CuOH^+$ is constant, the term $i\sqrt{t_s/D_r}$ should be proportional to C_{rb}, the concentration of phosphoric acid in the bulk of the electrolyte, the driving force for the diffusion of phosphoric acid. The relation between $i\sqrt{t_s/D_{rb}}$ and the concentration of phosphoric acid is shown by the solid curve in Fig. 5, where the values of $i\sqrt{t_s}$ measured by Elmore, Edwards, and the present authors are plotted. As shown, $i\sqrt{t_s/D_{rb}}$ decreases sharply as the bulk concentration of phosphoric acid increases. A sharper decline of $i\sqrt{t_s/D_r}$ with bulk H_3PO_4 concentration would be obtained, if we were to use some average value of diffusivity between bulk and interface (D'_{rm}). This would correct upward the effective diffusivities. The correction would be proportionally larger, the higher bulk concentration, because $D'_{rm} = (1/2)(D_{rb} + D_{ro})$ and the diffusivity of H_3PO_4 at the interface, D_{ro}, has the same (highest) value irrespective of C_{rb}.

Qualitatively the reverse situation arises if we take into consideration the effect of copper phosphate at the anode surface on the diffusivity of phosphoric acid (case of D_{rm}): because of the presence of copper phosphate the viscosity is higher at the interface than in the bulk. Consequently the relationship between $i\sqrt{t_s/D_{rm}}$ [3] and H_3PO_4 concentration would be described by a curve lying above the one obtained by assuming $D_r = D_{rb}$. As a further test of the hypothesis involving phosphoric acid as the limiting reactant, the ratio of calculated *vs.* experimentally obtained $i\sqrt{t_s}$ values are plotted in Fig. 6. For reaction [II] the calculated values were obtained by

$$i(t_s)^{1/2}_{calc} = \frac{\mathbf{F}}{2}(\pi D_r)^{1/2} C_{rb} \quad [9]$$

For diffusivities of phosphoric acid, the bulk values, D_{rb}, were employed, and the transference number of hydrogen ion, t_{H+}, was assumed to be unity. It should

[3] $D_{rm} = (\frac{1}{2})(D_{rb} + D_{rs})$.

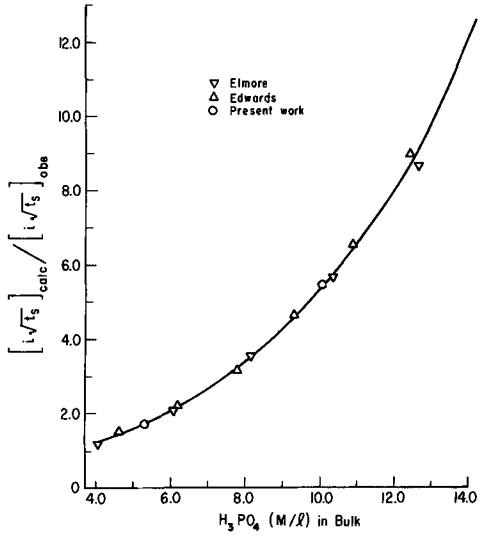

Fig. 6. Relation between $i\sqrt{t_s}_{calc}/i\sqrt{t_s}_{obs}$ and the concentration of H_3PO_4 for strong depletion of H_3PO_4 at the anode surface (reaction [II]). $i\sqrt{t_s}_{calc}$ was obtained by Eq. [9] with D_{rb}.

be noted that both the use of arithmetic mean values of diffusivities between bulk and surface, as well as the assumption of lower transference number for the hydrogen ion causes the ratios plotted in Fig. 6 to increase, *i.e.*, to depart further from correspondence of calculated *vs.* experimental values. Similarly, the discrepancy becomes larger, if we assume that the reaction stoichiometry is represented by reaction [I]. Lowering of t_{H+} at the anode surface due to large interfacial concentration of copper phosphate and low interfacial concentration of phosphoric acid could be expected when the bulk concentration of phosphoric acid is low. In reaction [II] the calculated value of $i\sqrt{t_s}$ increases inversely proportional to the value of t_{H+}. As shown in Fig. 6 the calculated $i\sqrt{t_s}$ obtained with $t_{H+} \approx 1$ in dilute phosphoric acid are, however, of the same order of magnitude as those of the measured $i\sqrt{t_s}$. [4] The analysis of transition time data presented above, indicates that available experimental evidence is incongruent with a model in which the transport limitation of phosphoric acid is responsible for reaching the limiting condition at the anode surface. If the transport of the reactant solute (*i.e.*, H_3PO_4) were to be limiting, $i\sqrt{t_s/D_r}$ should increase rather than strongly decline with bulk concentration.

We conclude therefore, that the transport of phosphoric acid is not directly responsible for the limiting phenomena in the anodic dissolution of copper.

Case (b): We will now proceed and assume that the interfacial concentration of H_3PO_4 is not approaching zero at the anode surface, rather it will have some finite value. The transference number of hydrogen ions, t_{H+}, then, will be close to unity,[5] and that of copper ions, t_{Cu++}, will approach zero. For $C_p(0) = 0$ and $C_p(t_s) = C_{ps}$ we get

$$i\left(\frac{t_s}{D_p}\right)^{1/2} = \frac{\mathbf{F}(\pi)^{1/2}}{1 - t_{CuOH+}} C_{ps} \quad \text{reaction [I]} \quad [10]$$

or

$$i\left(\frac{t_s}{D_p}\right)^{1/2} = \frac{\mathbf{F}(\pi)^{1/2}}{1 - t_{Cu++}} C_{ps} \quad \text{reaction [II]} \quad [11]$$

Assuming $t_{CuOH+} \to 0$ and $t_{Cu++} \to 0$, we obtain the

[4] When the bulk concentration of H_3PO_4 is high (6-15*M*), its interfacial concentration is also quite appreciable (approximately 4-10*M*), while that of copper phosphate is much lower (1-2*M*) (18). For this reason t_{H^+} should be not far from unity at the interface. However, even if we assumed $t_{H^+} = 0.5$, $i\sqrt{t_s/D_r}_{calc}/i\sqrt{t_s/D_r}_{obs}$ strongly increases with bulk acid concentration, rather than approaching unity.

[5] According to Kerker and Espenscheid (21) t_{H^+} in 4*M* H_3PO_4 is 0.89. In Chapman's critical review of transport properties (22) the range of $t_{H^+} = 0.93 \to 1.0$ is given for $4 \to 12M$ H_3PO_4.

simplified relation

$$i\left(\frac{t_s}{D_p}\right)^{1/2} = \mathbf{F}(\pi)^{1/2} C_{ps} \qquad [12]$$

for both reactions [I] and [II]. If the first cell voltage jump is caused by reaching the solubility limit of copper phosphate, followed by the formation of a resistive film, $i\sqrt{t_s/D_p}$ should be proportional to the solubility of copper phosphate, C_{ps}. For purposes of this calculation we employ Hickling and Higgins' experimental values (7) for the solubility of Cu^{++} in phosphoric acid at 20°C. Diffusivities of anodically formed copper phosphate were measured by Krichmar *et al.* (20). Because of the complex way in which the concentration dependent diffusivity influences t_s, values of $i\sqrt{t_s/D_p}$ in Fig. 7 have been evaluated using two different diffusivities: (*i*) D_{po}, the diffusivity of Cu^{++} at very low concentration (*i.e.*, corresponding to conditions in the bulk), and (*ii*) D'_{pm}, the arithmetic mean of D_{po} and D_{ps} (diffusivity at critical solubility). As shown in Fig. 7, in the range of phosphoric acid concentration (4-15*M*) the value of $i\sqrt{t_s/D_{po}}$ or $i\sqrt{t_s/D'_{pm}}$, in fact, increases approximately directly proportionally with the solubility of copper phosphate (1.3-2.4 *M*/l).

Another test can be made by examining the relation between $i\sqrt{t_s/D_p}$ and $(C_{ps} - C_{pb})$ for a fixed C_{ps} and a variable C_{pb}. Edwards (3) found that for a given phosphoric acid concentration the value of $i\sqrt{t_s}$ decreases with the increase of C_{pb}. However, because of lack of diffusivity data of copper phosphate the relation between $i\sqrt{t_s/D_p}$ and $(C_{ps} - C_{pb})$ was not investigated. This relation as evaluated by the present authors is shown in Fig. 8. $i\sqrt{t_s}$ and C_{pb} were obtained from Edwards (3). For the diffusivity of copper phosphate its

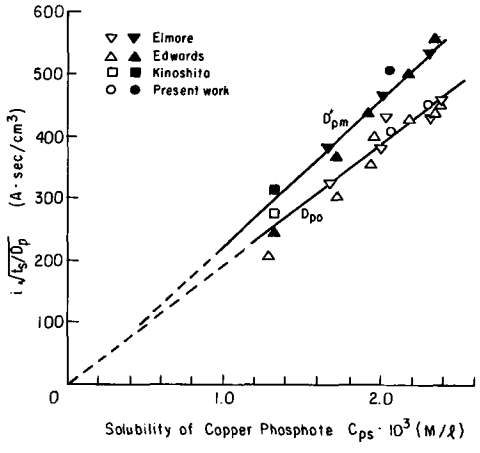

Fig. 7. Relation between $i\sqrt{t_s/D_p}$ and the critical solubility of copper phosphate. $D_{po} \rightarrow D_p$ at $C_p \rightarrow 0$, $D_{pm} = (1/2)(D_{po} + D_{ps})$.

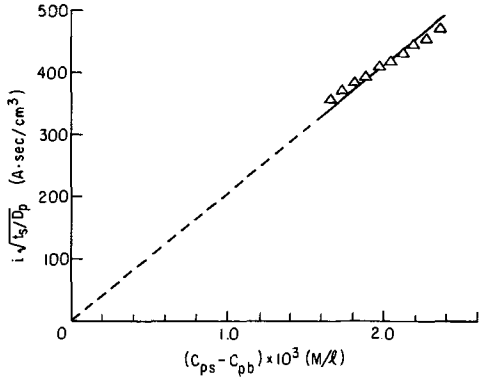

Fig. 8. Relation between $i\sqrt{t_s/D_p}$ and the concentration difference of copper phosphate between anode surface and bulk electrolyte. $i\sqrt{t_s}$ and C_{pb} data were taken from Edwards (3).

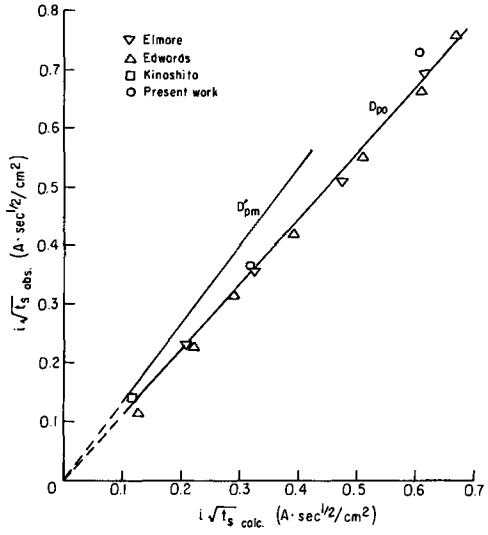

Fig. 9. Relation between $i\sqrt{t_s}$ calc and $i\sqrt{t_s}$ obs in the case of the reaction product control. $i\sqrt{t_s}$ calc was obtained by Eq. [12']. Ronge of bulk concentration of H_3PO_4: $4 < C_{rb} < 15M$. The slope of $i\sqrt{t_s}$ obs *vs.* $i\sqrt{t_s}$ calc line is about 1.1 for D_{po} and 1.3 D'_{pm}, respectively.

value in the bulk phosphoric acid (50%) is used. Direct proportionality of $i\sqrt{t_s/D_p}$ to $(C_{ps} - C_{pb})$ is again demonstrated. Thus, in contrast to the interpretation of Edwards, his data on the effect of presence of Cu^{++} in the bulk electrolyte indicate that the onset of voltage rise is caused not by the depletion of H_3PO_4, but rather by the accumulation of copper phosphate at the anode surface.

It remains to be tested whether the proportionality constant is in good agreement with the constant theoretically obtained. For the purpose of this test, the experimental values of $i\sqrt{t_s}$ are plotted against

$$i(t_s)^{1/2}{}_{calc} = \mathbf{F}(\pi D_p)^{1/2} C_{ps} \qquad [12']$$

Figure 9 shows that for D_{po} the calculated values are over a wide range in reasonable agreement with the measured values of $i(t_s)^{1/2}$. The ratios of calculated to measured values are about 1.1 for D_{po} and 1.3 for D'_{pm} respectively.[6] The above argument gives strong support to the view that the first cell voltage jump is caused by reaching the solubility limit of copper phosphate followed by the formation of a resistive film (18, 23). If the first cell voltage jump is really caused by the critical solubility of copper phosphate, the concentration of phosphoric acid at the anode surface at $t = t_s$, C_{rs}, is higher than zero. In Fig. 10, values of C_{rs}, calculated by using Eq. [7] or [8] are compared to those obtained by chemical analysis[7] (17, 24). The calculated C_{rs} values are in fairly good agreement with the measured concentrations of free phosphoric acid in the anolyte. The concentration of free phosphoric acid at the interface increases with the increase of the concentration of phosphoric acid in the bulk of the electrolyte.

When copper phosphate deposits on the anode surface the interfacial concentration of phosphoric acid, C_{rs}, is higher for reaction [I] and lower for reaction [II]. Simultaneous occurrence of both reactions would lead to intermediate values of C_{rs}.

The result obtained from the foregoing diffusion-kinetic study as well as the evidence for the formation of copper oxides at the current plateau (18) conclu-

[6] If we were to take into account the possible contribution of migration of Cu^{++} (or $CuOH^+$) to the mass flux, the agreement between experimental and calculated values would be further improved.

[7] The following assumptions are made:

total concentration of phosphoric acid $\cong$ free phosphoric acid concentration + concentration of phosphoric acid combined with Cu^{++}

and

$$\left[\text{total concentration of phosphoric acid}\right]_{x=0} \cong \left[\text{total concentration of phosphoric acid}\right]_{x=\infty}$$

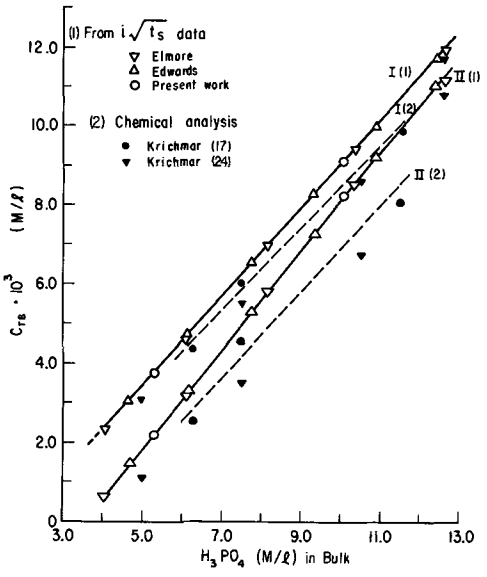

Fig. 10. Concentration of phosphoric acid at the anode surface, C_{rs}, as the function of bulk phosphoric acid concentration, C_{rb}. Lines I(1) and I(2) for reaction [I] and lines II(1) and II(2) for reaction [II] were obtained from measured values of $i\sqrt{t_s}$ and from chemical analysis.

sively support the view that the first cell voltage jump in galvanostatic experiments or the current decrease in potentiostatic experiments is caused by reaching the critical solubility of copper phosphate followed by the formation of a resistive film on the anode surface.

Peak Current Density

In the active dissolution of copper, the anodic current density increases with the increase of anode potential according to the Tafel relation (18). Under given hydrodynamic conditions, the concentration of copper phosphate increases with the increase of anode potential, and finally reaches the critical solubility. It is important to evaluate whether the onset of sharp potential rise in galvanostatic (unsteady-state diffusion) experiments (3, 4, 18) is caused by the same mass transport mechanism as the occurrence of the peak current density[8] phenomenon in steady-state anodic polarization runs obtained in forced convection (1).

In laminar forced convection, the correlation (26, 27)

$$\mathrm{Nu} = 1.85 \left(\mathrm{Re\ Sc} \frac{d}{L} \right)^{1/3} \qquad [13]$$

can be used as an accurate representation of mass transfer to an electrode in a flat duct, when the concentration of a reactant of a reaction product is kept constant over the whole surface of the electrode. Nu, Re, Sc, d, and L are Nusselt number, Reynolds number, Schmidt number, equivalent duct diameter, and electrode length, respectively.

For the particular electrode configuration in a horizontal rectangular channel such as the one used by Hoar and Rothwell,[9] the limiting current is difficult to estimate. However, the proportionality

$$\frac{i_{pk}}{F} \propto D^{2/3} V^{1/3} \Delta C \qquad [14]$$

is still expected to be valid (i_{pk} is the peak current density and V is the center line velocity of flow in the duct). For a given phosphoric acid concentration, we have $(i_{pk}/F) \propto V^{1/3}$. Examination of Hoar and Rothwell's data shows indeed proportionality of i_{pk} to $V^{1/3}$ for the entire range of H_3PO_4 concentration employed (6-10M). This suggests that the peak current densities are greatly affected by the hydrodynamic conditions near the anode surface.

If the peak current densities are caused by the strong depletion of phosphoric acid, the values of $i_{pk}/D_r^{2/3}V^{1/3}$ should be proportional to the concentration of phosphoric acid in the bulk electrolyte, the driving force for mass transfer.

The viscosity of the electrolyte saturated with copper phosphate at the anode surface is several times higher than that of the bulk electrolyte (18, 24). This should cause lowering of the diffusivity of phosphoric acid in the diffusion layer. Since there is no information available on the effect of Cu^{++} concentration on the diffusivity of phosphoric acid, two cases are considered: (a) the effective diffusivity of phosphoric acid in the diffusion layer is assumed to be equal to the diffusivity of phosphoric acid in the bulk electrolyte, D_{rb}, and (b) the effective diffusivity is same as the one corresponding to the concentration at the surface. Using either of these diffusivity estimates, the ratio $i_{pk}/D_r^{2/3}V^{1/3}$ decreases with increasing bulk concentration of H_3PO_4. This result indicates that the peak current cannot be explained by the limiting transport of phosphoric acid.

If on the other hand the peak current phenomenon is caused by the attainment of the critical solubility of copper phosphate followed by the coverage of the surface by solid deposits we should expect that

$$\frac{i_{pk}}{V^{1/3}} \propto D_{pm}^{2/3} (C_{ps} - C_{pb})\ ^{10} \qquad [15]$$

A reasonable confirmation of this proportionality is demonstrated in Fig. 11, in which the experimental peak current densities are those by Hoar and Rothwell (1). Again, as in the analysis of data obtained under galvanostatic conditions in pure diffusion, we conclude that the controlling step in the active dissolution range and up to the peak current is the transport of copper phosphate from the surface to the bulk electrolyte. For purposes of comparison, values of $i/V^{1/3}$ calculated with the current density at the polishing plateau, i_{pol}, as obtained by Hoar and Rothwell, are also shown in Fig. 11. The behavior demonstrated by i_{pol} is also consistent with the controlling role of the transport of copper phosphate from the surface into the bulk electrolyte.

Concluding Remarks

In the foregoing we have compared new results of unsteady-state experiments on the anodic dissolution of

[10] Because of a narrow range of the critical solubility of copper phosphate in the concentration range of 6M H_3PO_4 to 10M H_3PO_4, proportionality of $i_{pk}/V^{1/3}$ to $D_{pm}^{2/3}$ $(C_{ps} - C_{pb})$ is tested. $D_{pm} = (1/2)(D_{ps} + D_{pb})$.

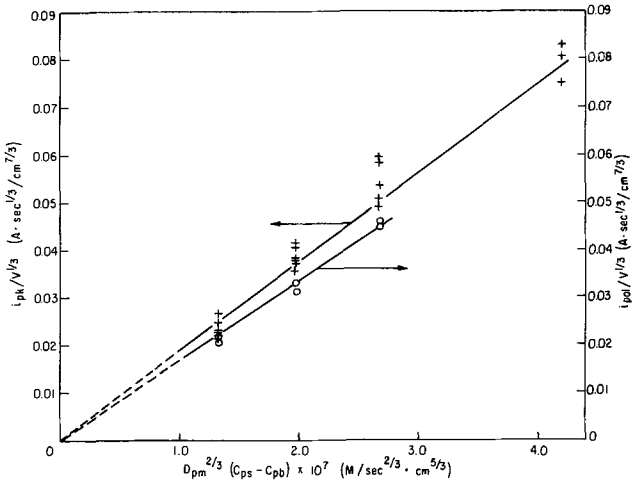

Fig. 11. Relation between $i_{pk}/V^{1/3}$ or $i_{pol}/V^{1/3}$ and $D_{pm}^{2/3}$ $(C_{ps} - C_{pb})$. Data from Hoar and Rothwell (1). $D_{pm} = (1/2)(D_{pb} + D_{ps})$.

[8] Using the analysis developed by Selman (25), we find that the potential scan velocities employed by Hoar and Rothwell indeed allow reaching the steady state.

[9] The velocity boundary layer in this cell is not fully developed at the leading edge of the electrode. Further, because of the circular geometry of the anode, the mass transfer boundary layer thickness varies across the anode, not only in the direction of flow, but also in a direction normal (90°) to it.

copper in phosphoric acid in the active dissolution regime with those obtained earlier by Elmore and Edwards. Transition times in 5 and 10*M* H_3PO_4 agree very well with those reported by the above authors. Analysis of transition times by using the best available diffusion coefficient and solubility data leads to the conclusion that in the limiting current phenomenon characteristic of the electropolishing of copper, transport of phosphoric acid is not the limiting process. The solubility limit if copper phosphate is exceeded while the concentration of phosphoric acid is still quite appreciable at the anode surface. This interpretation is congruent with the peak current density values reported by Hoar and Rothwell for electropolishing of copper in steady-state laminar flow. A more precise and definitive description of the controlling transport mechanism will only be possible when more extensive information becomes available on the properties of the ternary system Cu^{++}-H_3PO_4-H_2O.

APPENDIX

A. Derivation of Eq. [3]-[6]

Reaction I.—

$$Cu + H_3PO_4 + H_2O = [CuOH]^+[H_2PO_4]^- + 2H^+ + 2e^- \text{ (over-all)}$$

$$H_3PO_4 \rightleftarrows H^+ + H_2PO_4^-$$

$$Cu + H^+OH^- = CuOH^+ + H^+ + 2e^-$$

$$(t_{H+}) + (t_{H_2PO_4-}) + (t_{CuOH+}) = 1 \qquad [A\text{-}1]$$

in which $t_{HPO_4=}$, $t_{PO_4\equiv}$, t_{Cu++}, and t_{OH-} are neglected. The increase[11] of $[CuOH]^+[H_2PO_4]^-$ and decrease of H_3PO_4 per unit time at the anode surface may be calculated as follows

$$CuOH^+: \quad \frac{i}{2F}(1 - t_{CuOH+})$$

$$H_2PO_4^-: \quad \frac{i}{F}t_{H_2PO_4-}$$

$$\frac{i}{F}t_{H_2PO_4-} = \frac{i}{2F}(1 - t_{CuOH+}) - \frac{i}{F}t_{H+} + \frac{i}{2F}(1 - t_{CuOH+}) \qquad [A\text{-}2]$$

$$H^+: \quad -\left(\frac{i}{F}t_{H+} - \frac{i(1 - t_{CuOH+})}{2F}\right)$$

The first term on the right-hand side of Eq. [A-2] expresses the increase of $[CuOH]^+[H_2PO_4]^-$ and the second and third terms express the decrease of $[H_3PO_4]$. From this the rate of increase of $[CuOH]^+[H_2PO_4]^-$ by electrochemical reaction minus its decrease by migration away from the anode is

$$\frac{i}{2F}(1 - t_{CuOH+})$$

and the rate of decrease of $[H_3PO_4]$ is

$$\frac{i}{F}t_{H+} - \frac{i}{2F}(1 - t_{CuOH+})$$

Assuming that the increase in $[CuOH]^+[H_2PO_4]^-$ and the decrease in $[H_3PO_4]$ is a result of diffusion away from the anode surface or to it from the bulk of the electrolyte, we obtain the relations

$$\left.\begin{aligned} &\frac{i}{2F}(1 - t_{CuOH+}) = -D_p\frac{\partial C_p}{\partial x} \\ &\text{or} \\ &i = \frac{2F}{1 - t_{CuOH+}}D_p\left|\frac{\partial C_p}{\partial x}\right| \end{aligned}\right\} \text{ for } [CuOH]^+[H_2PO_4]^- \qquad [A\text{-}3]$$

and

$$\left.\begin{aligned} &\frac{i}{F}t_{H+} - \frac{i}{2F}(1 - t_{CuOH+}) = D_r\frac{\partial C_r}{\partial x} \\ &i = \frac{F}{t_{H+} - \frac{1 - t_{CuOH+}}{2}}D_r\left|\frac{\partial C_r}{\partial x}\right| \end{aligned}\right\} \text{ for } H_3PO_4 \qquad [A\text{-}4]$$

Reaction [II].—

$$Cu + 2H_3PO_4 = Cu(H_2PO_4)_2 + 2H^+ + 2e^- \text{ (over-all)}$$

$$H_3PO_4 \rightleftarrows H^+ + H_2PO_4^-$$

$$Cu = Cu^{++} + 2e^-$$

$$(t_{H+}) + (t_{H_2PO_4-}) + (t_{Cu++}) = 1 \qquad [A\text{-}5]$$

The increase of $[Cu(H_2PO_4)_2]$ and decrease of $[H_3PO_4]$ per unit time at the anode surface may be calculated in the same way as for reaction [I]

$$Cu^{++}: \quad \frac{i}{2F}(1 - t_{Cu++})$$

$$H_2PO_4-: \quad \frac{i}{F}t_{H_2PO_4-} = \frac{i}{F}(1 - t_{Cu++}) - \frac{i}{F}t_{H+} \qquad [A\text{-}6]$$

$$H^+: \quad -\frac{i}{F}t_{H+}$$

The first term on the right-hand side of Eq. [A-6] describes the increase of $[Cu(H_2PO_4)_2]$ and the second term the decrease of $[H_3PO_4]$. The net rate of increase of $[Cu(H_2PO_4)_2]$ is

$$\frac{i}{2F}(1 - t_{Cu++})$$

and the decrease of H_3PO_4

$$\frac{i}{F}t_{H+}$$

In the same manner, we obtain the relations

$$i = \frac{2F}{1 - t_{Cu++}}D_p\left|\frac{\partial C_p}{\partial x}\right| \quad \text{for } Cu(H_2PO_4)_2 \qquad [A\text{-}7]$$

and

$$i = \frac{F}{t_{H+}}D_r\left|\frac{\partial C_r}{\partial x}\right| \quad \text{for } H_3PO_4 \qquad [A\text{-}8]$$

B. Derivation of Eq. [7]-[12]

Solution of the diffusion equation in one dimension

$$\frac{\partial C}{\partial t} = D\frac{\partial^2 C}{\partial x^2} \qquad [A\text{-}9]$$

with initial and boundary conditions

Initial condition: $C = C(0)$ at $t = 0$

Boundary condition 1: $i = -\frac{nFD}{k}\left(\frac{\partial C}{\partial x}\right)_{x=0}$ at $x = 0$

Boundary condition 2: $C = C(0)$ at $x = \infty$

and assuming that D, n, and k are constants, yields (14)

$$C(t) - C(0) = 2k\frac{i}{nF}\left(\frac{t}{D\pi}\right)^{1/2}\exp\left(\frac{-x^2}{4Dt}\right) - k\frac{ix}{nFD}\operatorname{erfc}\left(\frac{x}{2(Dt)^{1/2}}\right) \qquad [A\text{-}10]$$

At the anode surface

$$[C(t) - C(0)]_{x=0} = 2k\frac{i}{F}\left(\frac{t}{D\pi}\right)^{1/2} \qquad [A\text{-}11]$$

For phosphoric acid transport controlling [case (*a*)], $C_r(t_s) = 0$ at $x = 0$, $C_r(0) = C_{rb}$, $n = 1$; $k = t_{H+} - (1/2)(1 - t_{CuOH+})$ for reaction [I], and $k = t_{H+}$ for reaction [II].[12]

[11] Increase is shown by positive sign.

[12] For a rigorous treatment of migration effects in Nernst boundary layers see Ref. (28).

At $t = t_s$ we obtain for reaction [I]

$$i\left(\frac{t_s}{D_r}\right)^{1/2} = \frac{\mathbf{F}}{2} \cdot \frac{\sqrt{\pi}}{t_{H+} - \frac{1 - t_{CuOH+}}{2}} \cdot C_{rb} \quad [A\text{-}12]$$

and for reaction [II]

$$i\left(\frac{t_s}{D_r}\right)^{1/2} = \frac{\mathbf{F}}{2} \cdot \frac{\sqrt{\pi}}{t_{H+}} \cdot C_{rb} \quad [A\text{-}13]$$

For copper phosphate controlling [case (b)], $C_p(t_s) = C_{ps}$ at $x = 0$, $C_p(0) = 0$, $n = 2$; $k = 1 - t_{CuOH+}$ for reaction [I], and $k = 1 - t_{Cu++}$ for reaction [II].

At $t = t_s$

$$i\left(\frac{t_s}{D_p}\right)^{1/2} = \frac{\mathbf{F}(\pi)^{1/2}}{1 - t_{CuOH+}} C_{ps} \text{ for reaction [I]} \quad [A\text{-}14]$$

and

$$i\left(\frac{t_s}{D_p}\right)^{1/2} = \frac{\mathbf{F}(\pi)^{1/2}}{1 - t_{Cu++}} C_{ps} \text{ for reaction [II]} \quad [A\text{-}15]$$

NOMENCLATURE

d	equivalent duct diameter (cm)
i	apparent current density (A/cm²)
i_{pol}	current density in good electropolishing region (A/cm²)
i_{pk}	peak current density (A/cm²)
n	number of electrons transferred in the electrode process
n'	apparent valence of a dissolved anode
t	time (sec)
t_s	time required for the onset of an anode potential jump (sec)
t_{H+}, t_{Cu++}, t_{CuOH+}	transference number
x	rectangular coordinate
$C(t)$	concentration at $t = t$ (mol/cm³)
C_p	concentration of copper phosphate (mol/cm³)
C_{pb}	concentration of copper phosphate in the bulk solution (mol/cm³)
C_{ps}	solubility of copper phosphate (mol/cm³)
C_r	concentration of phosphoric acid (mol/cm³)
C_{rb}	concentration of phosphoric acid in the bulk solution (mol/cm³)
D	diffusion coefficient (cm²/sec)
D_p	diffusion coefficient of copper phosphate (cm²/sec)
D_{po}	diffusion coefficient of copper phosphate at $C_p = 0$ (cm²/sec)
D_{pb}	diffusion coefficient of copper phosphate in the bulk solution (cm²/sec)
D_{pm}	$(1/2)(D_{ps} + D_{pb})$ (cm²/sec)
D'_{pm}	$(1/2)(D_{ps} + D_{po})$ (cm²/sec)
D_{ps}	diffusion coefficient of copper phosphate at the anode surface (cm²/sec)
D_r	diffusion coefficient of phosphoric acid (cm²/sec)
D_{ro}	diffusion coefficient of phosphoric acid at $C_r \rightarrow 0$ (cm²/sec)
D_{rb}	diffusion coefficient of phosphoric acid in the bulk solution (cm²/sec)
D_{rs}	diffusion coefficient of phosphoric acid at the anode surface (cm²/sec)
D_{rm}	$(1/2)(D_{rb} + D_{rs})$ (cm²/sec)
D'_{rm}	$(1/2)(D_{rb} + D_{ro})$ (cm²/sec)
$\mathbf{F}$	Faraday's constant (96,500 coul/g equiv.)
I	total current (A)
L	electrode length (cm)
M	molecular weight of a dissolved metal (g/mol)
V	center line velocity of flow in a rectangular channel (cm/sec)
ΔW	weight loss of an anode specimen (g)

Dimensionless numbers

Nu	Nusselt number
Re	Reynolds number
Sc	Schmidt number

Acknowledgment

This work was supported by the United States Atomic Energy Commission.

Manuscript submitted Aug. 29, 1972; revised manuscript received March 21, 1973.

Any discussion of this paper will appear in a Discussion Section to be published in the June 1974 JOURNAL.

REFERENCES

1. T. P. Hoar and G. P. Rothwell, *Electrochim. Acta*, **9**, 135 (1964).
2. Z. Zembura, *Bull. Acad. Polon. Sci.*, **C1. X1**, No. 5, 271 (1963).
3. J. Edwards, *This Journal*, **100**, 223C (1953).
4. W. C. Elmore, *J. Appl. Phys.*, **11**, 797 (1940).
5. S. I. Krichmar, *Proc. Acad. Sci.* USSR, Phys. Chem. Sect, (*English Transl.*), **114**, 303 (1957).
6. G. S. Vozdvizhensky and A. I. Turashev, *Dokl. Akad. Nauk. SSSR*, **114**, 358 (1957).
7. A. Hickling and J. K. Higgins, *Trans. Inst. Metal Finishing*, **29**, 274 (1953).
8. M. C. Petit, *Electrochim. Acta*, **8**, 217 (1963).
9. C. Wagner, *This Journal*, **101**, 225 (1954).
10. W. C. Elmore, *J. Appl. Phys.*, **10**, 724 (1939).
11. K. F. Lorking, *Electrochim. Acta*, **7**, 101 (1962).
12. K. Ohashi, T. Murakawa, and S. Nagaura, *J. Electrochem. Soc. Japan*, **30**, 165 (1962).
13. M. Novak, A. K. Reddy, and H. Wroblowa, *This Journal*, **117**, 733 (1970).
14. H. S. Carslaw and J. C. Jaeger, "Conduction of Heat in Solids," 2nd ed., Oxford (1959).
15. Marie-Claude Petit and M. Roger Schmitt, *Compt. Rend.*, **254**, 2569 (1962).
16. D. Laforgue-Kantzer, *ibid.*, **233**, 547 (1951).
17. S. I. Krichmar and V. P. Galushko, *Russ. J. Inorg. Chem.*,(*English Transl.*), **1**, No. 10, 2422 (1956).
18. K. Kojima, Ph.D. Thesis, Univ. of California, Berkeley (1972).
19. O. W. Edwards and E. O. Huffman, *J. Phys. Chem.*, **63**, 1830 (1959).
20. S. I. Krichmar, A. Ya. Pronskaya, and K. F. Afendik, *Soviet Electrochem.* (*English Transl.*), **2**, No. 8, 896 (1966).
21. M. Kerker and W. F. Espenscheid, *J. Am. Chem. Soc.*, **80**, 776 (1958).
22. T. W. Chapman, Ph.D. Thesis, Univ of California, Berkeley (1967).
23. K. Kojima and C. W. Tobias, IMRD Annual Report, UCRL-18735, p. 35 (1968).
24. S. I. Krichmar, *Russ. J. Phys. Chem.*, (*English Transl.*), **39**, No. 4, 433 (1965).
25. J. R. Selman, Ph.D. Thesis, Univ. of California, Berkeley (1971).
26. R. H. Norris and D. D. Streid, *Trans. Am. Soc. Mech. Engrs.*, **62**, 525 (1940).
27. R. G. Hickman, Ph.D. Thesis, Univ. of California, Berkeley (1963).
28. J. S. Newman, "Electrochemical Systems," 473 pp., Prentice-Hall, Inc., Englewood Cliffs, N. J. (1973).

Change in *pH* near the Cathode During the Electrodeposition of a Bivalent Metal. Analysis

Lee B. Harris*

Xerox Corporation, Rochester Research Center, Webster, New York 14580

ABSTRACT

An important factor in the cathodic electrodeposition of a base metal (M) is the increase in pH ("alkalization") of the electrolyte near the cathode.

Chemical equilibria and transport processes in the cathodic diffusion layer are analyzed by numerical integration of the transport equations. The analysis shows that alkalization is caused by the production of OH^- at the cathode and is prevented when the hydroxyl ions so produced react to form a soluble species (*e.g.*, MOH^+ or H_2O).

When complex ions are not formed, alkalization occurs if $i_W\delta > \mathbf{F}D_{H^+}[H^+]_o$, where i_W is the hydrogen reduction current, δ is the thickness of the diffusion layer, $[H^+]_o$ is the bulk hydrogen ion concentration, and D_{H^+} is the ionic diffusion coefficient for hydrogen. Formation of metal-hydroxy or metal-anion complexes can prevent alkalization even when this limit is exceeded. This is illustrated by specific numerical examples.

It has been well established by numerous experimental studies (1-5) that during the electrolytic deposition of nickel, the layer of electrolyte immediately adjacent to the cathode ("diffusion layer") is more alkaline than the bulk of the electrolyte. The degree of "alkalization" is strongly dependent on temperature and stirring as well as bulk pH and current density. Under some conditions precipitation of basic nickel salts may occur near the cathode (6-9), sometimes to such an extent as to be visible to the naked eye (9). It is likely that alkalization and precipitation are significant factors in determining the appearance, structure, and properties of electrodeposited nickel (10).

Although this problem has been discussed many times in the electrochemical literature, much of the discussion is qualitative and some is misleading. For example, scattered through the literature are statements that seem to imply alkalization is caused by the dissociation of water in the liquid phase near the cathode (in response to depletion of the hydrogen ion population by reduction of H^+ at the cathode). The present analysis indicates that this is not the case. To understand the mechanism of alkalization, and to determine the conditions under which precipitation is to be expected, it is necessary to analyze in some detail the transport and chemical equilibria of the various species present in the electrolyte near the cathode, including soluble complexes and complex ions. The analysis reported here shows that alkalization has its origin in the production of OH^- at the cathode, and can be moderated or prevented when the hydroxyl ions so produced can react to form a soluble species (*e.g.*, MOH^+). The formation of a soluble complex between the metal and its counterion can also play a significant (though less direct) role.

Method

Let us consider the very simplest model having the most essential features of the actual physical system: an aqueous solution of a bivalent metal ion M^{+2} that can form a hydroxy complex MOH^+ and/or a soluble one-to-one complex $MA^{+(2-Z)}$ with its counterion A^{-Z} ($Z = 1$ or 2).

The relative concentrations of these four species (and the concentrations of hydrogen ions and hydroxyl ions) are assumed to be governed by the same equations that hold in thermodynamic equilibrium. In other words, the rates of formation and dissociation of the complex species are assumed to be fast enough to establish equilibrium in less time than it takes for any of the reacting species to travel through an appreciable fraction of the diffusion layer.

Convective-diffusion determines the degree to which bulk concentrations are maintained near the cathode (11, 12). To describe this facet of the problem accurately would require that the convective-velocity field be known (as for the rotating disk electrode) and that it be included in the transport equations (11-13), thus making them very difficult to integrate. To avoid this problem, the following analysis makes use of the customary Nernst approximation in which the diffusion layer near the electrode is assumed to be stagnant. The stagnant layer is assumed to be separated from the well-mixed bulk of the electrolyte by a well-defined boundary plane (the "Nernst boundary") at which all species are present at concentrations characteristic of the bulk. The transport equations are formulated for the stagnant region, and the bulk concentrations comprise a boundary condition. The effect of convection is then reduced to a single parameter, the thickness of the stagnant diffusion layer. Starting at the Nernst boundary, one may, for a specified set of conditions (*e.g.*, total current density, hydrogen evolution current density, bulk pH, temperature, etc.) integrate the transport equations to calculate the concentrations and flux densities[1] of the various species as functions of distance from the boundary.

To apply these results to a particular case, one may then imagine the electrode to be at a particular distance from the boundary; the chosen distance is equal to the specified thickness of the diffusion layer for the particular case under consideration. The calculated concentrations and flux densities at that distance from the Nernst boundary are those that must (under the assumptions of the calculation) prevail at the electrode surface when the thickness of the diffusion layer, the bulk concentrations, the current densities, etc., are equal to the values specified for the particular case.

Analysis

Figure 1 shows all the species considered and the reactions among them, including the dissociation of H_2O. The circled number next to any species will be used in the text as a subscript to identify any variable associated with that species. From Fig. 1 it follows that the rate of formation of M^{+2} must be equal to sum of the rates at which $MA^{+(2-Z)}$ and MOH^+ are disappearing, *i.e.*, equal to the negative of the sum of their

* Electrochemical Society Active Member.
Key words: catholyte, alkalization, electrodeposition.

[1] I use "flux density" to denote normalization to unit area, *i.e.*, flux density = flux per unit area (mole/cm² sec).

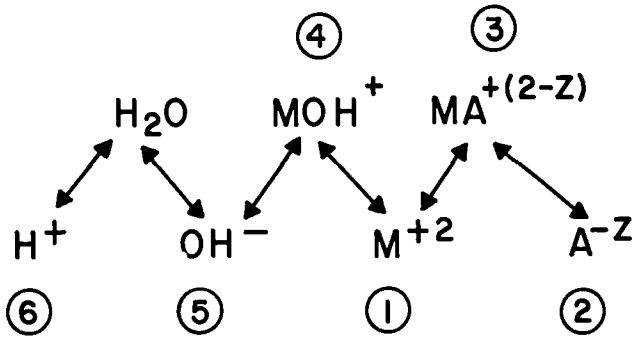

Fig. 1. Schematic diagram showing reactions among the various species. Circled numbers are used as subscripts in the text.

rates of production. In steady state[2] this condition yields the partial differential equation

$$\nabla \cdot j_1 + \nabla \cdot j_3 + \nabla \cdot j_4 = 0 \qquad [1]$$

where j_i is the flux density of the i^{th} species (mole/cm² sec). Similar considerations yield the equations

$$\nabla \cdot j_2 + \nabla \cdot j_3 = 0 \qquad [2]$$

$$\nabla \cdot j_4 + \nabla \cdot j_5 - \nabla \cdot j_6 = 0 \qquad [3]$$

In addition to Eq. [1-3] we have the three equilibrium conditions governing the concentrations C_i (mole/cm³); namely

$$C_3 = K_3 C_1 C_2 \qquad [4]$$

$$C_4 = K_4 C_1 C_5 \qquad [5]$$

$$C_5 C_6 = K_W \qquad [6]$$

and finally, there is the electroneutrality approximation[3]

$$\Sigma n_i C_i = 0 \qquad [7]$$

where n_i is the number of electronic charges (including sign) carried by the i^{th} species. The flux density of the i^{th} species is given by[4]

$$j_i = -\{D_i \text{ grad } C_i + \mu_i C_i \text{ grad } \Phi\} \qquad [8]$$

where μ is the electrical mobility (cm²/V sec), D the diffusion[5] coefficient (cm²/sec), and Φ the electrical potential (V). For this analysis we assume the Nernst-Einstein relationship between the electrical mobility and the diffusion coefficient; namely

$$\mu_i = n_i (\mathbf{F}/RT) D_i \qquad [9]$$

where $(\mathbf{F}/RT)$ is expressed in reciprocal volts. Substituting Eq. [8] and [9] into Eq. [1–3] and integrating once, we obtain the following three first-order differential equations

$$D_1C_1' + D_3C_3' + D_4C_4' + [2D_1C_1 + n_3D_3C_3 + D_4C_4]\phi' = -j_M \qquad [10]$$

$$D_2C_2' + D_3C_3' + [n_2D_2C_2 + n_3D_3C_3]\phi' = -J_A \qquad [11]$$

$$-D_4C_4' - D_5C_5' + D_6C_6' + [D_5C_5 - D_4C_4 + D_6C_6]\phi' = -j_W \qquad [12]$$

In these equations the divergence is replaced by simple differentiation (denoted by a prime) with respect to the position variable x; and ϕ is the dimensionless potential

$$\phi = (\mathbf{F}/RT)\,\Phi \qquad [13]$$

j_M is the total flux density (mole/cm² sec) of metal atoms in all forms, *i.e.*, as metal ions or contained in the anionic or the hydroxy complex. It is proportional to the electrodeposition current density i_M, *i.e.*

$$i_M = 2\mathbf{F}\, j_M \qquad [14]$$

Similarily, j_A is the total flux density of counterions A^{-Z} [as simple anions or associated into the complex $MA^{+(2-Z)}$]. In the present (cathodic) case it is assumed that the net combined flux of counterions in both these forms is zero. In other words, the flux of counterions moving toward the cathode in the form of $MA^{+(2-Z)}$ is balanced by an equal flux of A^{-Z} moving away from the cathode. This must be true if no reaction at the cathode either removes any counterions or adds to their total number. With this assumption, $j_A \equiv 0$.

j_W is proportional to the combined current density i_W carried by hydroxyl groups (either alone or contained in the hydroxyl complex) and hydrogen ions (i_W is the "hydrogen evolution" current), *i.e.*

$$i_W = \mathbf{F}\, j_W \qquad [15]$$

It is possible, by means of a change of independent variable in Eq. [10–12], to replace j_W and j_M by a single constant. For our present purpose it is convenient to use the dimensionless variable (see next section for physical significance)

$$y = x/L_H \qquad [16]$$

where

$$L_H = \mathbf{F} D_6 (C_6)_0 / |i_W| \qquad [17]$$

In terms of y, Eq. [10–12] are then changed slightly, by the substitutions

$$-j_W \rightarrow \pm D_6 (C_6)_0 \qquad [18]$$

and

$$-j_M \rightarrow \pm D_6 (C_6)_0 / 2(i_W/i_M) \qquad [19]$$

The positive x-direction is defined so that x increases with increasing distance from the electrode. With this convention j_W and j_M are negative and the upper signs in Eq. [18] and [19] are valid when the electrode is operating cathodically. The position origin ($x = 0$) is taken to be at the Nernst boundary; and the subscript zero refers to values at that boundary. (Within the diffusion layer, x is negative.)

To solve Eq. [10–12] (with the substitution of Eq. [18] and [19]) subject to the conditions of Eq. [4-7], the latter conditions were differentiated to yield four additional first-order linear differential equations. The whole set of seven equations was then integrated numerically by means of the Runge-Kutta method, using a double-precision Gaussian elimination to compute the derivatives from the values of the seven dependent variables and the specified value of (i_W/i_M).[6] The starting point for the integration is the Nernst boundary, at which the hydrogen ion concentration $(C_6)_0$ is chosen to correspond to a selected value of pH, and the other concentrations are adjusted to satisfy Eq. [4–7] and to fix the total amount of metal in solution at a specified value, namely, 10^{-3} mole/cm³ (*i.e.*, 1M) for all cases considered in this paper.

Results and Discussion

Figure 2a shows a plot of concentration profiles as a function of y for a particular case.[7] The curve labeled

[1] Steady state means that all concentrations are independent of time. Any gradual depletion or accumulation of constituents in the bulk is assumed to be insignificant. Initial transients in the diffusion layer itself are assumed to have died out.

[3] This approximation can be used whenever the actual space charge is so small it can be produced by concentrations that deviate insignificantly (by say less than 1%) from those calculated using the constraint of Eq. [7]. This is true for cases discussed in this paper.

[4] Whereas Eq. [1–3] hold everywhere in the electrolyte Eq. [8] applies only to the stagnant diffusion layer, since convective transport is not included in it.

[5] Diffusion coefficients are assumed to be constants in order to simplify the calculations. This assumption may not be too bad in view of Newman's finding (13a) that in solutions of moderate ionic strength (~0.01M) concentration dependence of the D's causes only very minor changes in the transport of H^+.

[6] The ratio i_W/i_N does not take on arbitrary values in real experiments. My approach is to calculate conditions in the diffusion layer when i_W/i_M has some reasonable value that corresponds roughly to an actual situation. The major advantage of this approach is that boundary conditions imposed by electrode kinetics need not be considered. The price we pay is that i_W/i_M must be measured in order to correlate theory with the experiment.

[7] The following values were used for all calculations. At 300°K, $D_1 = D_3 = D_4 = 1.0 \times 10^{-5}$; $D_2 = 2.0 \times 10^{-5}$; $D_5 = 6.0 \times 10^{-5}$; $D_6 = 1.0 \times 10^{-4}$ (cm²/sec) (14-15). At other temperatures, $D_i(T) = D_i(300°K)\ (T/300.)\ [\eta(300°)/\eta(T)]^{p_i}$ where η is the viscosity of water and $p_1 = p_2 = \ldots\ldots p_5 = 1$; $p_6 = 0.63$ (14). The dissociation constant for water was calculated from the formula given by Kortum (16), namely, $-\log K_W = 4471.99/T - 6.0846 + 0.017053T$.

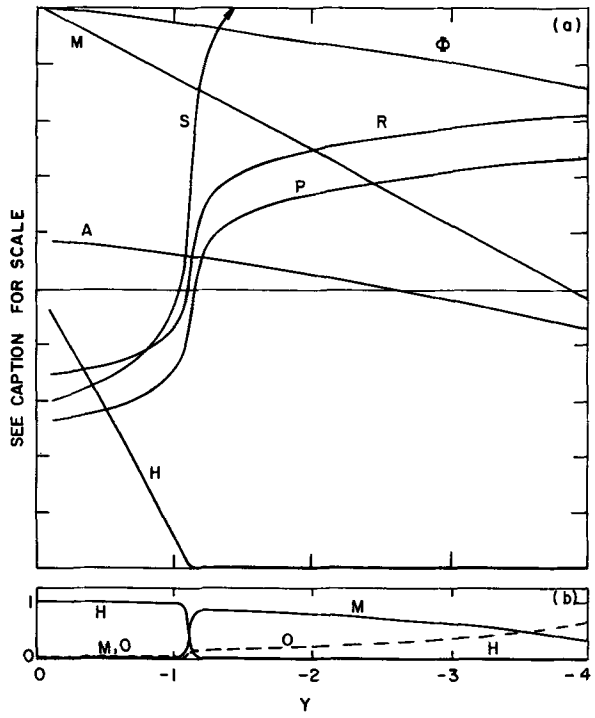

Fig. 2. (a) Curve *M*, total metal concentration normalized to bulk (scale: 0 to 1). curve *A*, fraction of metal complexed with counterion (scale: 0 to 1); curve *H*, hydrogen ion concentration normalized to bulk (scale: 0 to 2); curve *P*, ratio of hydroxyl ion concentration to hydrogen ion concentration (log scale: −10 to +10); curve *R*, ratio of metal-hydroxy complex to hydrogen ion concentration (log scale: −10 to +10); curve *S*, product corresponding to solubility product of $M(OH)_2$ (log scale: −30 to −20); Φ, electrical potential (scale: −200 mV to 0V). (b) *H*, fraction of hydrogen evolution current carried by hydrogen ions; *O*, fraction of hydrogen evolution current carried by hydroxyl ions; *M*, fraction of hydrogen evolution current carried by metal-hydroxy complex. Conditions: $Z = 1$, $T = 340°K$, pH = 4.0, $i_W/i_M = 10^{-3}$, $K_3 = 10^3$, $K_4 = 10^5$ (cm^3/mole).

M is the total concentration of metal (in all three forms) plotted on a scale from zero to one as a fraction of the bulk value (*i.e.*, 10^{-3} mole/cm^3 at the Nernst boundary). The curve labeled *H* is the hydrogen ion concentration, also normalized to the bulk value but with the scale compressed by a factor of two. *S* is the product $C_1(C_6)^2$ (*i.e.*, $[M^{+2}]\,[OH^-]^2$) plotted on a log scale running from −30 to −20 ($mole^3/cm^9$). *A* is the fraction of the total metal concentration that is tied up in the complex $MA^{+(2-Z)}$ (scale from zero to one). *R* is the ratio C_4/C_6 (*i.e.*, $[MOH^+]/[H^+]$) plotted on a log scale running from −10 to +10; and *P* is the ratio C_5/C_6 (*i.e.*, $[OH^-]/[H^+]$) on the same log scale. If we take the solubility constant for $M(OH)_2$ to be 10^{-25} ($mole^3/cm^9$) then the critical value y_c of the dimensionless position variable at the point where curve *S* crosses the horizontal midline $[C_1(C_6)^2 = 10^{-25}]$ corresponds to the thickness δ_c of the thickest diffusion layer for which no precipitation will occur under the other specified conditions. From the definition of y (Eq. [16] and [17] it follows that[8]

$$\delta_c = |y_c|\mathbf{F}D_6(C_6)_0/|i_W| \qquad [20]$$

or

$$|i_W\delta|_c = |y_c|\mathbf{F}D_6(C_6)_0 \qquad [21]$$

If the magnitude of the product of i_W and δ exceeds this critical product then precipitation of metal hydroxide is predicted. Of course, if that should be the case, the transport equations would be greatly modified by the formation, migration, and subsequent reactions of the precipitate. In this paper, we restrict ourselves to determining the margin of conditions that just avoids this possibility.

The form of curve *H* conforms almost exactly to Nernst's simplified description of transport in the diffusion layer. Near the Nernst boundary both the hydroxyl ion and the hydroxy complex are present only in small concentrations relative to the hydrogen ion, and do not contribute appreciably to i_W. Since the flux of hydrogen ions is almost constant in this region (there is no appreciable net recombination or dissociation), and since transport is primarily due to diffusion, the concentration gradient is nearly constant and is almost just sufficient to carry the current, *i.e.*

$$|i_W| \simeq \overline{|\text{grad } C_6|}\mathbf{F}D_6 \qquad [22]$$

(*cf.* Eq. [8] and [15]) where $\overline{\text{grad } C_6}$ is the average concentration gradient in this region. The distance required for the concentration to drop to nearly zero is

$$L = (C_6)_0/\overline{|\text{grad } C_6|} \qquad [23]$$

When the diffusion layer is this thick (*i.e.*, $\delta = L$) Eq. [22] and [23] yield the familiar Nernst relationship between the "limiting current" and the thickness of the diffusion layer, namely

$$\delta = \mathbf{F}D_6(C_6)_0/|i_W| \qquad [24]$$

Comparing Eq. [24], [17], and [16] it is clear that the dimensionless variable y gives the distance from the Nernst boundary in multiples of that critical diffusion layer thickness that would just support a diffusion-limited hydrogen ion current equal to i_W. If the diffusion layer is thicker than that, then in the region in which the hydrogen ion concentration is essentially zero (*i.e.*, $|y| \gtrsim 1$ in Fig. 2a) the current i_W must be carried by hydroxyl groups moving away from the cathode. Beyond $|y| \simeq 1$ the solution becomes more alkaline (see curve *P* in the figure) and precipitation will occur for thicker layers. The most important point here is that when alkalization occurs, the "hydrogen evolution" current exceeds the Nernst "limiting current" (*i.e.*, the maximum current that could be carried by hydrogen ions diffusing all the way across the stagnant layer). The two things are simply different manifestations of the same causative factor, namely, the production of OH^- at the cathode, either due to the decomposition of water according to one of the reactions[9]

$$e^- + H_2O \rightarrow OH^- + 1/2\,H_2 \qquad [25]$$

$$e^- + H_2O + M^{+2} \rightarrow MOH^+ + 1/2\,H_2 \qquad [26]$$

or due to the reduction of dissolved oxygen, *e.g.*, according to one of the reactions[10]

$$e^- + 1/4\,O_2 + 1/2\,H_2O \rightarrow OH^- \qquad [25a]$$

$$e^- + 1/4\,O_2 + 1/2\,H_2O + M^{+2} \rightarrow MOH^+ \qquad [26a]$$

Proof of this is shown in Fig. 2b, in which are plotted the relative fractions of j_W carried by H^+ (curve *H*), OH^- (curve *O*) and MOH^+ (curve *M*). In the vicinity of $|y| = 1$, the flux of hydrogen ions moving toward

[8] Because distance is measured positive away from the electrode and x is zero at the Nernst boundary, x and y are negative in the diffusion layer. And since positive current is equivalent to positive charge moving away from the electrode, cathodic current is negative. Hence, the absolute value signs used from here on.

[9] This and all other electrode reactions are written to show only what is felt by the transport system. Reaction [25] may actually occur as (*i*) $H^+ + e^- \rightarrow \frac{1}{2}H_2$, (*ii*) $H_2O \rightleftarrows H^+ + OH^-$; but when more H^+ is annihilated than can be supplied by diffusion the balance must be supplied by (*ii*) or else reaction [25] must occur directly. In any case the transport system sees only reaction [25], assuming electrode reactions occur within a few angstroms of the surface.

[10] If reaction [25a] or [26a] (or, say $e^- + \frac{1}{2}O_2 + H_2O \rightarrow \frac{1}{2}H_2O_2 + OH^-$) plays a significant role, then i_W cannot truly be called a hydrogen evolution current, since the net result of [25a] and [27] (or [26a] and [28]) is simply $e^- + H^+ + \frac{1}{4}O_2 \rightarrow \frac{1}{2}H_2O$.

Reactions such as [25a] or [26a] can, under ordinary ambient conditions, be the source of alkalization only for pH $\gtrsim$ 3.5. In more acid baths, because of the relatively low concentration of dissolved atmospheric oxygen ($< 2 \times 10^{-4}$M) and its relatively low diffusion coefficient $\sim 2 \times 10^{-5}$ cm^2/sec), the flux of molecular oxygen diffusing across the stagnant layer to the cathode cannot produce at the cathode a flux of hydroxyl ions greater than the flux of hydrogen ions that can diffuse from the bulk to the cathode across the stagnant layer.

the cathode (H) drops sharply with increasing $|y|$, and the flux of hydroxyl groups moving away from the cathode increases correspondingly. In the particular case shown in the figure, the total flux of hydroxyl groups is shared by the flux of hydroxyl ions (O) and the flux of hydroxyl complex (M). (The relative share is carried by each of these changes from point-to-point and is determined by their concentrations and concentration gradients as well as the electric field.) If we consider a region surrounding the transition zone in which the sharpest changes occur, it is apparent that the flux of H^+ entering the region on the left is much greater than that leaving on the right; whereas this picture is reversed for OH^- and MOH^+. Within the transition region the recombination reaction[11]

$$H^+ + OH^- \rightarrow H_2O \qquad [27]$$

$$H^+ + MOH^+ \rightarrow H_2O + M^{+2} \qquad [28]$$

remove equal quantities of hydrogen ions entering from the left and hydroxyl groups entering from the right. (The equality of production or removal of these two species is true for any region; that is the meaning of Eq. [3].) The important point is that to the right of the transition zone, most of the hydrogen evolution current is carried by hydroxyl groups, which must be produced at the cathode.

The particular case shown in Fig. 2 is of the simplest type, in which neither the hydroxy complex nor the complex $MA^{+(2-Z)}$ plays a dominant role. In that simple situation $|y_c| \simeq 1$ and Eq. [20] is essentially identical to the Nernst relationship, Eq. [24]. There is a very sharply defined critical diffusion layer thickness. For thinner layers i_W is carried almost entirely by hydrogen ions diffusing all the way across, but if this thickness is even slightly exceeded, alkalization must occur in order to produce the same value of i_W.

Figure 3 shows what happens when K_4 is increased by three orders of magnitude to 10^8 (cm^3/mole), a realistic value consistent with those listed for $NiOH^+$ in Bjerrum's compilation (17) of stability constants. The hydroxyl ion concentration (curve P) changes much more slowly than in Fig. 2 and is greatly exceeded (by five orders of magnitude) by the concentration of MOH^+ (curve R). The causative factor here is the greater tendency for metal ions to associate with OH^- thus removing the hydroxyl ions from the reaction scheme. The dynamics of the situation can be seen in Fig. 3b which shows that no significant part of the hydrogen evolution current is carried by OH^-.

This means that the production of OH^- at the cathode must take place according to the over-all reaction given in Eq. [26] or [26a]. The actual mechanism is not important for the present argument. The net result, however, must be that practically all of the hydroxyl groups generated at the cathode associate with cathode-bound metal ions within a very short distance of the cathode. The resulting high concentration of hydroxy complex produces a concentration gradient that actually causes (by diffusion) a net flux of this positively charged species away from the cathode against the electric field. Eventually these hydroxy ions recombine with hydrogen ions according to reaction [28]; however, since MOH^+ (as opposed to OH^-) can exist at relatively high concentrations even in somewhat acid solution, this recombination process occurs over a relatively wide transition zone in which the hydrogen evolution current is shared by H^+ and MOH^+ moving in opposite directions. As a result, $|y_c|$ is considerably greater than unity. (See Fig. 2a where curve S crosses the horizontal midline.) In other words, the diffusion layer thickness can be greater (as much as 70% greater) than that thickness which would allow i_W to be carried by the diffusion of H^+ to the cathode; and despite this thicker stagnant layer no precipitation of hydroxide will occur.

[11] Reaction [28] probably proceeds through the dissociation of MOH^+, but here again only the over-all reaction is shown.

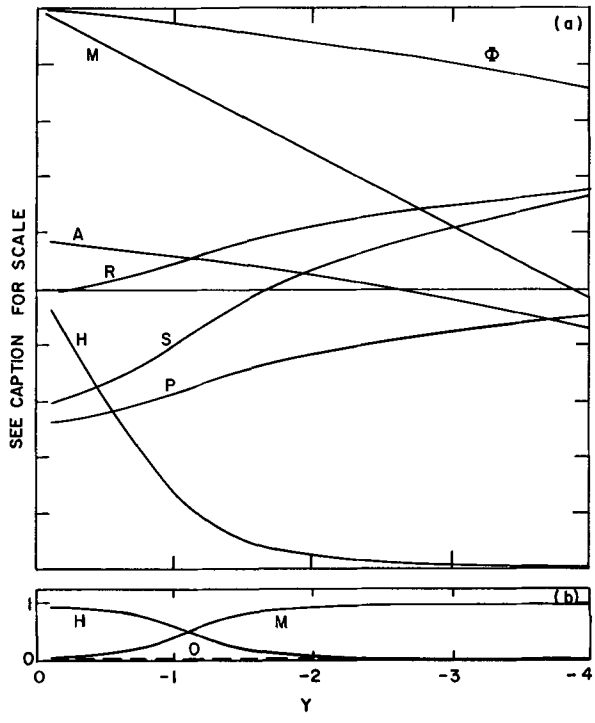

Fig. 3. (a) Curve M, total metal concentration normalized to bulk (scale: 0 to 1); curve A, fraction of metal complexed with counterion (scale: 0 to 1); curve H, hydrogen ion concentration normalized to bulk (scale: 0 to 2); curve P, ratio of hydroxyl ion concentration to hydrogen ion concentration (log scale: -10 to $+10$); curve R, ratio of metal-hydroxy complex to hydrogen ion concentration (log scale: -10 to $+10$); curve S, product corresponding to solubility product of $M(OH)_2$ (log scale: -30 to -20); Φ, electrical potential (scale: -200 mV to 0V). (b) H, fraction of hydrogen evolution current carried by hydrogen ions; O, fraction of hydrogen evolution current carried by hydroxyl ions; M, fraction of hydrogen evolution current carried by metal-hydroxy complex. Conditions: $Z = 1$, $T = 340°K$, $pH = 4.0$, $i_W/i_M = 10^{-3}$, $K^3 = 10^3$, $K_4 = 10^8$ (cm^3/mole).

An equally interesting but entirely different effect is shown in Fig. 4 and 5, which illustrate what may happen when the complex $MA^{(2-Z)}$ plays a significant role. The two cases differ in the value of K_3 (10^4 cm^3/mole in Fig. 4; 1.5×10^5 cm^3/mole in Fig. 5). The anion is divalent in both cases and all other conditions are equal.[12]

The electrical potential Φ is plotted on a scale running from -200 mV to 0V, and can be seen to drop much more sharply in Fig. 5 than in Fig. 4. The correspondingly higher electric field assists the movement of hydrogen ions, permitting them to penetrate the stagnant layer more deeply. The higher electric field is required to maintain i_M because of two closely related factors, both due to the higher value of K_3.[13] First of all, with 90% of the metal ions (and counterions) tied up in the neutral complex MA (see curve A) the conductivity is correspondingly lower; in fact, more than half the nickel ion flux is carried by diffusion of the neutral complex toward the cathode. This leads to the second related factor: the high flux of MA toward the cathode must be balanced by an equal, oppositely directed, flux of counterions away from the cathode, since $j_A \equiv 0$. The electric field must be sufficient to sustain this countercurrent against a concen-

[12] The reader may note that the slope of curve M is steeper in Fig. 4 and 5 than in Fig. 2 and 3. This is related to the fact that for Eq. [10] and [11] alone (no species present except M^{+2} and A^{-Z}) the concentrations of these two species drop linearly to zero over a characteristic distance

$$L_M = 2(2 + Z)\, FD_1(C_1)_0/Z|i_M|$$

This distance depends on Z in a manner quite independent of the other complications of the model. L_M corresponds to the maximum diffusion layer thickness for which i_M is not transport limited. For all cases considered in this paper, $L_H < \delta_c < L_M$.

[13] Note that this higher value is quite realistic. The values listed by Bjerrum (17) for $NiSO_4$ generally lie between 10^5 and 10^6.

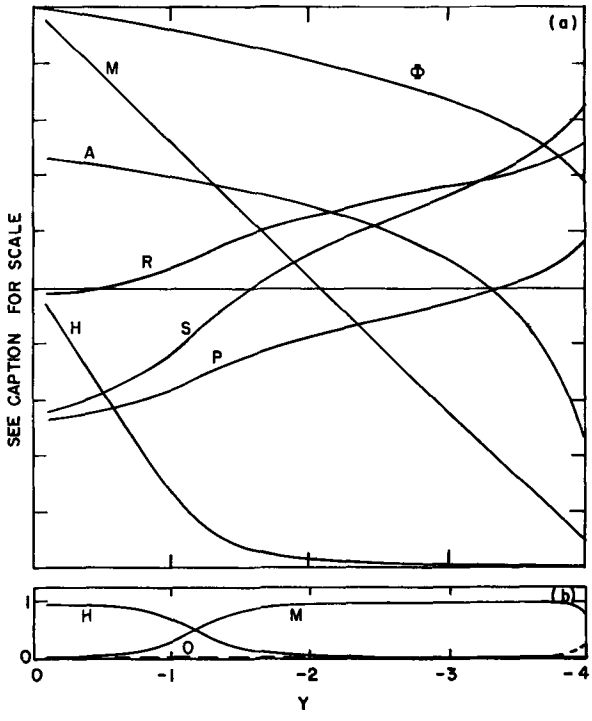

Fig. 4. Curve *M*, total metal concentration normalized to bulk (scale: 0 to 1); curve *A*, fraction of metal complexed with counterion (scale: 0 to 1); curve *H*, hydrogen ion concentration normalized to bulk (scale: 0 to 2); curve *P*, ratio of hydroxyl ion concentration to hydrogen ion concentration (log scale: −10 to +10); curve *R*, ratio of metal-hydroxy complex to hydrogen ion concentration (log scale: −10 to +10); curve *S*, product corresponding to solubility product of $M(OH)_2$ (log scale: −30 to −20); Φ, electrical potential (scale: −200 mV to 0V). (b) *H*, fraction of hydrogen evolution current carried by hydrogen ions; *O*, fraction of hydrogen evolution current carried by hydoxyl ions; *M*, fraction of hydrogen evolution current carried by metal-hydroxy complex. Conditions: $Z = 2$, $T = 340°K$, pH = 4.0, $i_W/i_M = 10^{-3}$, $K_3 = 10^4$, $K_4 = 10^8$ (cm^3/mole).

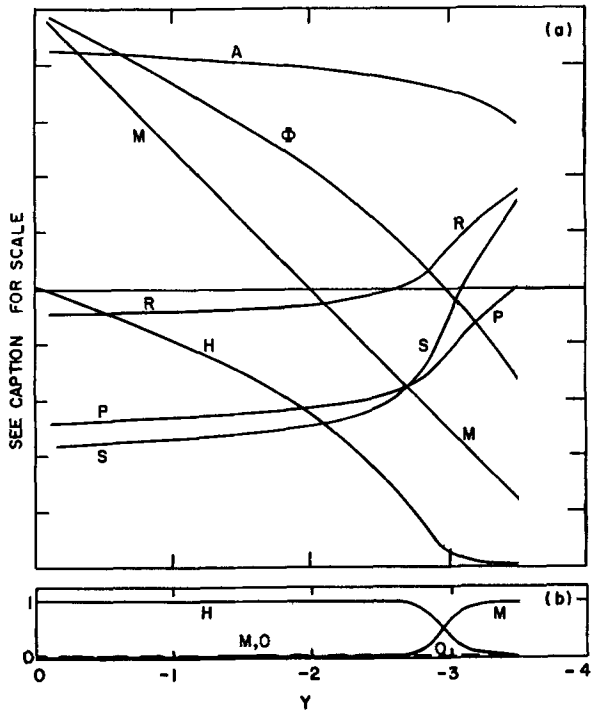

Fig. 5. (a) Curve *M*, total metal concentration normalized to bulk (scale: 0 to 1); curve *A*, fraction of metal complexed with counterion (scale: 0 to 1); curve *H*, hydrogen ion concentration normalized to bulk (scale: 0 to 2); curve *P*, ratio of hydroxyl ion concentration to hydrogen ion concentration (log scale: −10 to +10); curve *R*, ratio of metal-hydroxy complex to hydrogen ion concentration (log scale: −10 to +10); curve *S*, product corresponding to solubility product of $M(OH)_2$ (log scale: −30 to −20); Φ, electrical potential (scale: −200 mV to 0V). (b) *H*, fraction of hydrogen evolution current carried by hydrogen ions; *O*, fraction of hydrogen evolution current carried by hydroxyl ions; *M*, fraction of hydrogen evolution current carried by metal-hydroxy complex. Conditions: $Z = 2$, $T = 340°K$, pH = 4.0, $i_W/i_M = 10^{-3}$, $K_3 = 1.5 \times 10^5$, $K_4 = 10^8$ (cm^3/mole).

tration gradient and in spite of the relatively low concentration of counterions. Note that under these conditions more than half of the electrodeposition at the cathode is accounted for by the over-all reaction

$$2e^- + MA + A^{-2} \qquad [29]$$

the remainder being effected by the reaction[14]

$$2e^- + M^{+2} \rightarrow M \qquad [30]$$

Interestingly, the effect shown in Fig. 5 does not occur for a univalent counterion if only the one-to-one complex MA^+ is formed. Figure 6 illustrates this. The conditions are the same as in Fig. 3 except that K_3 is increased by three and one half orders of magnitude. Comparison of Fig. 2, 3, and 6 shows that this increase simply removes the effect of the hydroxy complex (*cf.* Fig. 2) by tying up almost all of the metal in the complex MA^+. Even though more than 99% of the metal is tied up this way, the electrical conductivity is not drastically affected since first of all, MA^+ is positively charged and secondly, more than half of the counterions are available to move in the other direction. It is likely that formation of the neutral complex MA_2 would have the same effect in the case of the univalent counterion as does the formation of the neutral complex MA in the case of the divalent counterion, but this still remains to be verified by calculation.

[14] Reaction [29] may actually occur at $MA \rightarrow M^{+2} + A^{-2}$ followed by reaction [30], but under the specified conditions the over-all result must be simply a weighted combination of Eq. [29] and [30], with weights proportional to the transport to the cathode of MA and M^{+2}, respectively.

Additional Comments

With the help of Eq. [24] a partial answer can be obtained as to whether alkalization and precipitation of hydroxide occur under ordinary plating conditions. For example, consider a nickel electroplating bath operating at pH = 4.0, plating current density ≃ 100 A/ft² ($i_M \simeq 10^{-1}$ A/cm²), $i_W/i_M = 10^{-2}$ (*i.e.*, current efficiency = 99% and $i_W = 10^{-3}$ A/cm²). Equation [24] yields $\delta = 10^{-3}$ cm. This is approximately the diffusion layer thickness that would be achieved by laminar flow at a rotating disk at 100 rps (11). Whether this degree of stirring is usually achieved is a moot point; if not, then i_W exceeds the Nernst limit. Since the assumed conditions are not unusual, it may be that precipitation of hydroxide usually occurs and plays an important role in the plating process as is often stated (18).

It has been reported that in concentrated chloride baths at temperatures above 80°C, hydrogen evolution is inhibited (19) and concurrently, macroscopic crystals of nickel are formed at the cathode (19, 20). At the other extreme, hydrogen evolution, alkalization, and precipitation may sometimes occur to such an extent as to interfere with the production of good nickel plate (9). Since neither of these extremes is a suitable situation for electroplating, it is necessary to maintain the proper balance, and it is not hard to imagine that this requirement plays a significant part in determining the carefully chosen combination of plating current, temperature, and pH that characterizes industrial nickel plating baths. The rate of electrolytic reduction of water (*i.e.*, i_W) is determined in part by the cathode potential required to achieve a specified plating current. This potential depends

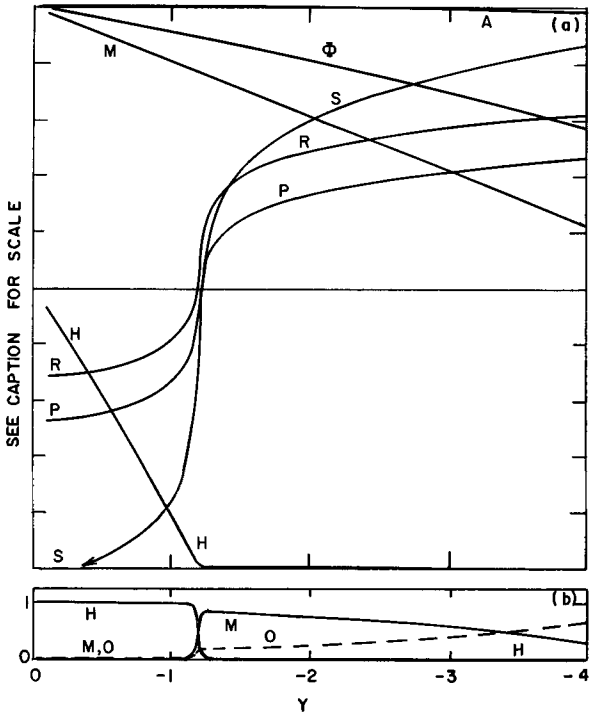

Fig. 6. (a) Curve *M*, total metal concentration normalized to bulk (scale: 0 to 1); curve *A*, fraction of metal complexed with counterion (scale: 0 to 1); curve *H*, hydrogen ion concentration normalized to bulk (scale: 0 to 2); curve *P*, ratio of hydroxyl ion concentration to hydrogen ion concentration (log scale: −10 to +10); curve *R*, ratio of metal-hydroxy complex to hydrogen ion concentration (log scale: −10 to +10); curve *S*, product corresponding to solubility product of $M(OH)_2$ (log scale: −30 to −20); Φ, electrical potential (scale: −200 mV to 0V). (b) *H*, Fraction of hydrogen evolution current carried by hydrogen ions; *O*, fraction of hydrogen evolution current carried by hydroxyl ions; *M*, fraction of hydrogen evolution current carried by metal-hydroxy complex. Conditions: $Z = 1$, $T = 340°K$, pH = 4.0, $i_W/i_M = 10^{-3}$, $K_3 = 3.0 \times 10^6$, $K_4 = 10^8$ (cm^3/mole).

strongly on temperature. Whether and to what extent precipitation occurs depends on the extent to which alkalization is moderated by the supply of hydrogen ions from the bulk (*i.e.*, pH) and by buffering reactions in the diffusion layer.

The role played by the hydroxy complex in preventing or moderating alkalization is important, not only *per se*, but also because of the hint it yields as to mechanisms by which other buffers may operate. In the region in which the hydroxy complex plays an important role, the fraction of metal ions tied up in this complex is very small (less than 1%). This means that an additive present in equally low concentration could still assist in preventing alkalization. For example, consider an additive species B^- that associates efficiently with M^{+2} to form a stable intermediate MB^+ which then reacts with OH^- to form a soluble complex. If the rate constant and equilibrium constant for this second reaction are high enough, (*i.e.*, $K \gtrsim 10^{10}$ cm^3/mole) then its effect may rival or exceed in efficiency the previously described process involving MOH^+. Reduced to simplest terms what is suggested here is a process in which B^- "hitchhikes" toward the cathode with M^{+2} (as MB^+) and then further combines with OH^- to form a soluble complex that can migrate back to a region of lower pH where it releases the OH^-. MB^+ then repeats the cycle.

With regard to the cause of alkalization, statements are frequently encountered in the literature implying it is caused by dissociation of water in a region near the cathode (in response to depletion of the hydrogen ion population by cathodic reduction). If this were true, the hydrogen ions produced by dissociation would add to the hydrogen ion flux, which would therefore become larger upon moving toward the cathode into the region of dissociation. Figures 2b-5b show that for all cases presented here this is not so. Nor is it so for any of the other cases studied in this investigation, covering a range of pH from 3 to 6 and with equilibrium constants ranging over many orders of magnitude. The presumption is therefore very strong that alkalization is not caused by dissociation of water in the liquid phase, but by production of OH^- at the cathode. This is not surprising if one considers that the electric field (the primary driving force in the liquid) is not likely to cause an increase in alkalinity toward the cathode since on the average it will tend to move OH^- away from the cathode.

Finally, I should again remind the reader that the detailed results of this analysis depend on the assumption of "fast" reactions. One referee pointed out that for nickel complexes this assumption may not hold. To explore in detail the implications of this possibility would be an interesting project, but probably is not justified until more experimental data is available to test the simpler model. However, a few comments and speculations may be *à propos*. Slow formation of MOH^+ would probably shift the transition zone (between the alkali and acid regions) toward the Nernst boundary and slow dissociation of MOH^+ would broaden this zone. However, the shift will not necessarily lower the threshold for precipitation if (as is likely) MOH^+ is usually an intermediate in the formation of the hydroxide. And broadening the zone will just cause some excess undissociated MOH^+ to be carried into the bulk where it will hardly be noticed as it dissociates while mixing. In connection with precipitation, I should also mention that supersaturation can be expected to delay the onset of precipitation unless the rise in alkalinity is quite abrupt (as in Fig. 2 and 6). If the reaction $M^{+2} + A^{-2} \rightarrow MA$ were slow, then (for example in the case of Fig. 5) there would be an excess concentration (*vis-à-vis* equilibrium) of free metal ions and counterions near the cathode. However, only a population excess that persists all the way across the diffusion layer can contribute to i_M. Slow dissociation of MA entering the diffusion layer would probably not appreciably affect the ion population near the Nernst boundary, in which case its effect would be mild.

Conclusions

1. "Alkalization" of the electrolyte near the cathode will occur only if OH^- is produced at the cathode (*e.g.*, due to the electrolytic decomposition of water). In the simplest case the criterion for precipitation is the same as the Nernst criterion for diffusion-limited hydrogen ion reduction; namely

$$i_W \delta > \mathbf{F} D_{H^+} [H^+]_o \qquad [31]$$

where i_W is the "hydrogen evolution" current density, δ the thickness of the diffusion layer, and $[H^+]_o$ the concentration of hydrogen ions in the bulk.

2. Precipitation is prevented when the hydroxyl ions produced at the cathode can immediately react to form some species (*e.g.*, MOH^+ or H_2O) other than an insoluble metal salt. In the absence of "buffers," precipitation is controlled by the ease of formation of the metal-hydroxy complex and by the depth of penetration of hydrogen ions into the diffusion layer. The latter can be significantly affected by the presence of a neutral metal-anion complex. If the equilibrium constant for the formation of the metal-hydroxy complex is greater than about 10^5 liter/mole (consistent with Bjerrum's list of values for say $NiOH^+$) then the limit on the right of Eq. [31] may be increased by a factor of two in some cases. If the equilibrium constant for the formation of the neutral complex MA (for a bivalent anion) is greater than about 10^5 liter/mole (consistent with Bjerrum's list of values for say $NiSO_4$) the limit may in some cases be increased severalfold (*vis à vis* Eq. [31]).

3. The results of this study indicate that to pin down the mechanism of alkalization experiments should be conducted in which the thickness of the diffusion layer is controlled, the "hydrogen evolution current" measured, and the onset of precipitation detected.

LIST OF SYMBOLS

A	Atomic species of counterion
C	Concentration, mole/cm^3
D	Diffusion coefficient, cm^2/sec
F	Faraday constant, coulomb/mole
i	Electrical current density, A/cm^2
j	Molecular flux density, mole/cm^2 sec
K	Equilibrium constant
L	Characteristic length, cm
M	Metal atom
n	Ionic charge number
R	Gas constant, joule/mole degree
T	Temperature, °K
x	Distance, cm
y	Dimensionless distance variable (see Eq. [16], [17])
δ	Thickness of diffusion layer, cm
μ	Electrical mobility, cm^2/V sec
Φ	Electrical potential, V
ϕ	Dimensionless potential (see Eq. [13])

Subscripts

A	Pertaining to the counterion
c	"Critical" in the sense that higher values may cause alkalization
i (or 1, 2, . . .)	Pertaining to the different species shown in Fig. 1
H	Pertaining to hydrogen ions
M	Pertaining to the metal
0	Pertaining to the Nernst boundary or the bulk electrolyte
W	Pertaining to water or its ionic substituents

Superscripts

+	Indicates a single positive electronic charge
−	Indicates a single negative electronic charge
± 2, 3, etc.	Indicates specific charge of ionic species

Acknowledgment

I would like to thank Dr. M. L. Hair for his encouragement and interest in this work, Dr. H. Scher for his thorough reading of the manuscript and constructive suggestions, and Dr. A. Damjanovic for valuable discussions and suggestions.

Manuscript submitted Dec. 11, 1972; revised manuscript received March 23, 1973. This was Paper 253 presented at the Chicago, Illinois, Meeting of the Society, May 13-18, 1973.

Any discussion of this paper will appear in a Discussion Section to be published in the June 1974 JOURNAL.

REFERENCES

1. S. I. Berezina and G. S. Vozdvizhenskii, *Zh. Prikl. Khim.*, **24**, 832 (1951).
2. A. Brenner and G. S. Wranglen, *Svensk Kem. Tidskr.*, **67**, 81 (1955).
3. N. T. Kudryavtsev, M. M. Yarlykov, and M. M. Mel'nikova, *Zh. Prikl. Khim.*, **38**, 545 (1965).
4. A. Knodler and K. W. Neugebohren, *Metalloberflaeche*, **24**, 78 (1970).
5. S. I. Berezina, G. A. Gorbachuk, and A. N. Kurenkova, *Elektrokhimiya*, **7**, 467 (1971).
6. A. L. Rotinyan and V. Ya. Zeldes, *J. Appl. Chem. USSR*, **23**, 757 (1950); *ibid.*, **24**, 675 (1951).
7. S. I. Berezina, G. A. Gorbachuk, and A. N. Kurenkova, *Elektrokchimiya*, **7**, 1058 (1971).
8. A. G. Ives, J. W. Edington, and G. P. Rothwell, *Electrochim. Acta*, **15**, 1797 (1970).
9. S. K. Verma and H. Wilman, *J. Phys. D: Appl. Phys.*, **4**, 2051 (1971).
10. V. S. Kublanovskii V. N. Belinskii, and D. P. Zosimovich, *Ukr. Khim. Zh.*, **37**, 713 (1971), (Ass. Tech. Serv. Transl.)
11. V. G. Levich, "Physicochemical Hydrodynamics," pp. 286ff Prentice Hall, New Jersey (1962).
12. L. L. Bircumshaw and A. C. Riddiford, *Quart. Rev. (London)*, **6**, 157 (1952).
13. J. Newman, *Ind. Eng. Chem.*, **60**, 12 (1968).
13a. J. Newman and L. Hsueh, *Ind. Eng. Chem., Fundamentals*, **9**, 677 (1970).
14. R. A. Robinson and R. H. Stokes, "Electrolyte Solutions," 2nd ed. (revised), Butterworths, London (1965).
15. M. Breiter and K. Hoffman, *Z. Elektrochem.*, **64**, 462 (1960).
16. G. Kortum, "Treatise on Electrochemistry," p. 317, American Elsevier Publishing Co., Inc., New York (1965).
17. "Stability Constants of Metal Ion Complexes," Revised ed., Compiled by L. Sillen *et al.*, ACS Spec. Pub. No. 17 (1964).
18. H. Brown, *Plating*, **50**, 1047 (1963).
19. S. Tajima and M. Ogata, *Electrochim. Acta*, **13**, 1845 (1968).
20. A. T. Vagramyan, M. A. Zhamagortsyan, L. A. Ukarov, and A. A. Yavich, *Electrokhimiya*, **6**, 755 (1970).

Potential Distribution in Axisymmetric Mercury-Pool Electrolysis Cells at the Limiting Current

John Newman*

Inorganic Materials Research Division, Lawrence Berkeley Laboratory, and Department of Chemical Engineering, University of California, Berkeley, California 94720

and J. E. Harrar

General Chemistry Division, Lawrence Livermore Laboratory, University of California, Livermore, California 94550

ABSTRACT

An expression has been obtained and graphs are presented for the potential distribution at a disk working electrode located at the bottom of a cylindrical cell, with the counterelectrode separator taken to be a uniform-current disk placed concentrically at the solution level. The condition of maximum working electrode potential variations, *i.e.*, when the working electrode current density is uniform, is examined in detail. For cells of typical size, the most sensitive geometrical parameter in determining the potential distribution is the height of the counterelectrode separator above the pool. Recommendations on the placement of the reference electrode probe are given.

Uniformity of potential at the working electrode has become an important criterion in the design of cells for controlled-potential electrolysis and coulometry. Deviations of the actual electrode potential from the desired control potential may cause significant errors in coulometry (1-4) and unwanted product distributions in electro-organic syntheses (4-7).

Because deviations of the working electrode potential are minimized, the preferred configuration of a mercury-pool type cell is the axisymmetric arrangement in which the counterelectrode separator is placed concentrically above the pool. When the separator is parallel to the pool, and of nearly the same diameter, a virtually uniform potential distribution should be achieved, and this has been experimentally realized in several instances (1, 7-10). Use of a large-diameter separator, however, complicates the placement of the other cell components and renders the design of an efficient cell more difficult. For cells whose separators are significantly smaller in diameter than the working electrode, [see, for example, Ref. (6, 10-15)] a means for estimating the possible electrode potential deviations would be useful. Since the potential within the electrode material is uniform, attention is to be focused on the variation of potential within the adjacent solution.

Stouffer and Richardson (16) considered the boundary-value problem represented by this configuration and derived an equation [given in Ref. (2)] for the potential difference arising in the solution adjacent to the working electrode under worst case conditions, *i.e.*, when the cell is operating at the limiting current and a uniform current density prevails at the working electrode. However, none of the useful predictions afforded by the theory, *e.g.*, the relative influence of various geometrical parameters on the potential distribution, were explored by these authors in their brief treatment. This fact, the somewhat unwieldy form of the Stouffer-Richardson equation, and our recent need for a numerical evaluation of this potential distribution have prompted us to re-examine this problem. Graphical representations are presented that facilitate design calculations and provide insight to the properties of axisymmetric cells in general.

The basic problem is formulated for the geometry shown in Fig. 1, where the working electrode is assumed to be a uniform-current disk of radius r_w at the bottom of a cylindrical cell, and the counterelectrode separator is taken to be a uniform-current disk of radius r_c placed concentrically at the solution level, *i.e.*, in an insulating plane. This model does not take into account the typical experimental conditions of nonuniform mass transport at the working electrode, curvature of the mercury pool at its periphery, and deviations of the counterelectrode separator from the assumed uniform-current source, but these characteristics are expected to be of secondary influence on the potential distribution.

In cylindrical coordinates r and z, Laplace's equation for the potential Φ in the solution reads

$$\frac{1}{r}\frac{\partial}{\partial r}\left(r\frac{\partial \Phi}{\partial r}\right)+\frac{\partial^2 \Phi}{\partial z^2}=0 \qquad [1]$$

and the boundary conditions stated above can be expressed explicitly as

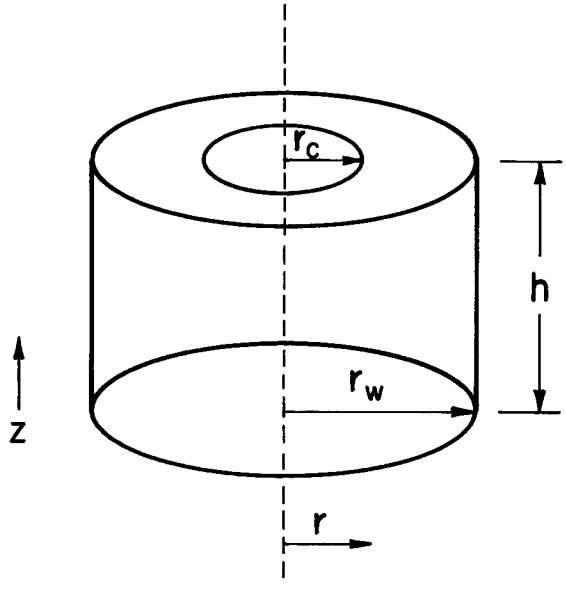

Fig. 1. Axisymmetric cylindrical cell. The working electrode (mercury pool) is at the bottom and the counterelectrode or counterelectrode separator is at the top. The term "very small counterelectrode" will refer to limiting expressions where r_c approaches zero.

* Electrochemical Society Active Member.

Key words: current distribution, electro-organic synthesis, controlled-potential electrolysis, controlled potential coulometry.

$$\frac{\partial \Phi}{\partial z} = \frac{i}{\kappa} \text{ at } z = 0 \text{ at the working electrode} \quad [2]$$

$$\frac{\partial \Phi}{\partial r} = 0 \text{ at } r = r_w, \text{ at the cell wall} \quad [3]$$

$$\frac{\partial \Phi}{\partial z} = \frac{i}{\kappa} \frac{r_w^2}{r_c^2} \text{ at } z = h,\ r \leq r_c \quad [4]$$

$$\frac{\partial \Phi}{\partial z} = 0 \text{ at } z = h,\ r > r_c \quad [5]$$

where i is the uniform current density at the working electrode and κ is the conductivity of the solution.

By the method of separation of variables (17), the appropriate solution of Laplace's equation is

$$\Phi = \frac{iz}{\kappa} + \frac{ir_w}{\kappa} \sum_{n=1}^{\infty} c_n \cosh\left(\lambda_n \frac{z}{r_w}\right) J_0\left(\lambda_n \frac{r}{r_w}\right) \quad [6]$$

where J_0 is the Bessel function of the first kind of order zero, and λ_n is one of a sequence of eigenvalues. The first term on the right represents a uniform current density i on the working electrode. Each of the terms in the sum is a solution of Laplace's equation having zero current density on the working electrode and also on the cylindrical wall of the cell. This latter condition is assured by choosing the eigenvalues λ_n so that the derivative of $J_0(x)$ is zero at $x = \lambda_n$. Since the derivative of $J_0(x)$ is $-J_1(x)$, the Bessel function of the first kind of order one, this means that the eigenvalues λ_n are the zeros of J_1. These are tabulated along with the values of $J_0(\lambda_n)$ in Ref. (18).

The coefficients c_n can then be chosen to yield the specified current-density distribution at the top of the cell: a uniform current density for $r < r_c$ and a zero current density elsewhere. Equation [6] is differentiated with respect to z, and then z is set equal to h, the height of the cell. Multiplication by $rJ_0(\lambda_m r/r_w)$ and integration from $r = 0$ to $r = r_w$ give for the coefficients

$$c_n = \frac{2\frac{r_w}{r_c} J_1\left(\lambda_n \frac{r_c}{r_w}\right)}{\lambda_n^2 [J_0(\lambda_n)]^2 \sinh(\lambda_n h/r_w)} \quad [7]$$

The expression for the potential distribution at the pool then is

$$\Phi_0 = \frac{2I}{\pi\kappa r_w} \sum_{n=1}^{\infty} \frac{\frac{r_w}{r_c} J_1\left(\lambda_n \frac{r_c}{r_w}\right) J_0\left(\lambda_n \frac{r}{r_w}\right)}{\lambda_n^2 [J_0(\lambda_n)]^2 \sinh(\lambda_n h/r_w)} \quad [8]$$

where I is the total cell current. Because the metal of the working electrode is of uniform potential, Φ_0 also defines the "electrode potential" gradient. Numerical evaluation of this equation for a range of typical cell parameters yields the curves shown in Fig. 2 and 3. The working electrode potential, relative to the adjacent solution, is most cathodic for a reduction process and most anodic for an oxidation process at the center of the cell.

Important in many design calculations would be the maximum potential difference, $\Delta\Phi_{max}$, between the center of the cell and its periphery. Figure 4 shows how this quantity varies with I, h/r_w, and r_c/r_w, as well as the over-all cell size as represented by r_w. Figure 5 emphasizes the effect of changing the size of the counterelectrode separator and provides a means for interpolating on Fig. 4. These figures demonstrate that one must increase the size of the counterelectrode separator considerably in order to obtain appreciable improvement over the potential distribution for $r_c = 0$. Changes in h affect the potential distribution more profoundly, and this design parameter can be adjusted

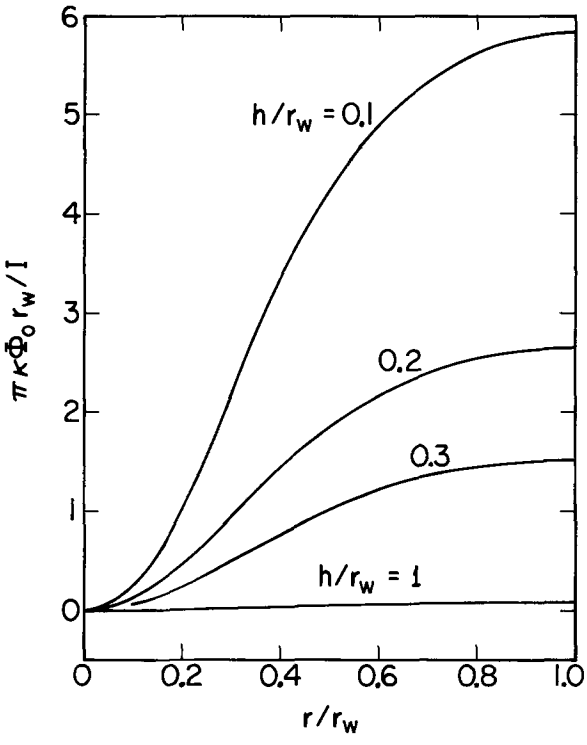

Fig. 2. Potential distribution in the solution at the pool for the limiting current, with $r_c/r_w = 0.3$. The lowest curve also appears on Fig. 3 with an expanded scale.

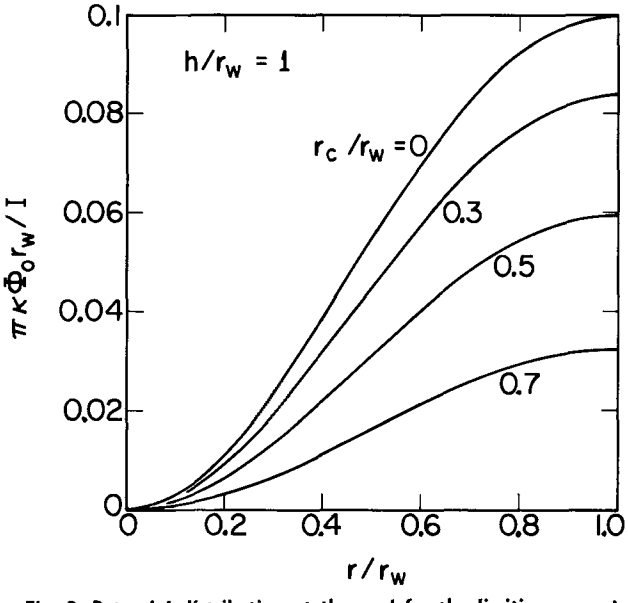

Fig. 3. Potential distribution at the pool for the limiting current, with $h = r_w$.

to render $\Delta\Phi_{max}$ negligible. However, increasing h for this geometry also would increase the volume of the solution and hence the time of the electrolysis, unless the rate of stirring were also increased.

The order of magnitude of expected electrode potential gradients is indicated by numerical evaluation of a typical case. For a cell in which $r_w = h = 3$ cm, $r_c = 1$ cm, and $I = 100$ mA, $\Delta\Phi_{max}$ would be 200 mV for a 0.1M solution of tetrabutylammonium perchlorate in DMF ($\kappa \approx 0.0045$ ohm^{-1} cm^{-1}) and 4 mV for 0.5M H_2SO_4 ($\kappa \approx 0.2$ ohm^{-1} cm^{-1}). The latter difference would be negligible in most work; note, however, that if h is decreased to 1 cm, $\Delta\Phi_{max}$ would then become 70 mV.

The dashed line on Fig. 4 indicates the potential variation for the two-dimensional rectangular geometry of Fig. 6, in which the counterelectrode separator is

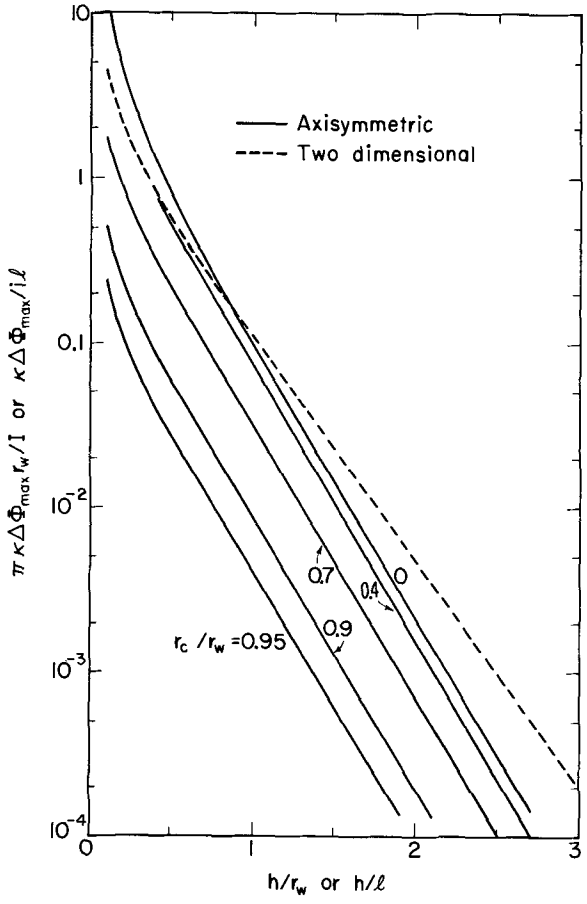

Fig. 4. Maximum potential difference in the solution adjacent to an electrode with a uniform current density.

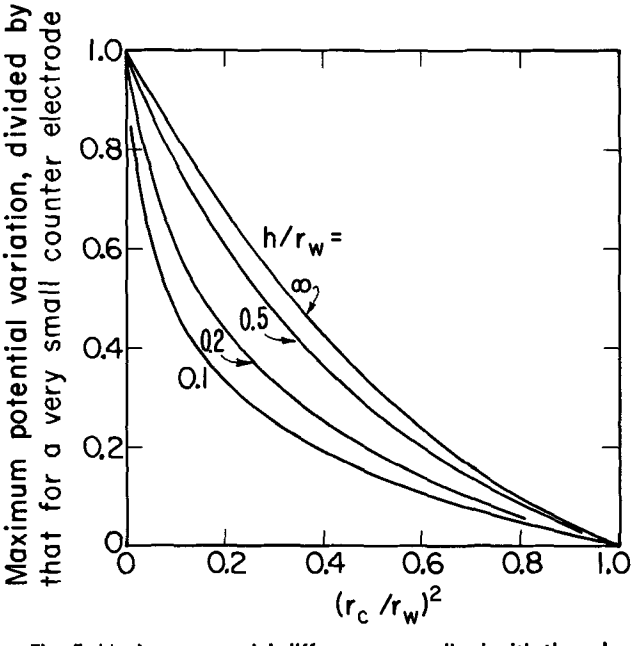

Fig. 5. Maximum potential difference, normalized with the value for a small counterelectrode ($r_c = 0$), showing the dependence on the size of the counterelectrode.

regarded as being a line at the upper edge of the cell. This configuration is thus a two-dimensional analogue of the axisymmetric geometry for $r_c = 0$.

Placement of the Reference Electrode

The position of the reference electrode probe within the controlled-potential electrolysis cell can be chosen on the basis of the known potential distribution at the working electrode and the specific purpose of the

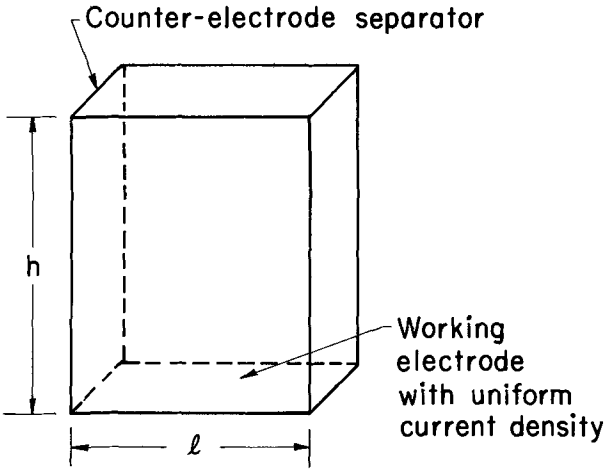

Fig. 6. Two-dimensional cell with counterelectrode separator reduced to a line at the upper edge of the cell.

electrolysis. In most analytical coulometry and separations, the optimum location for the probe is the center of the cell, because exceeding the desired control potential may cause the coelectrolysis of interferences or the supporting electrolyte (2). This configuration also ensures that the cell transfer function will have a minimum phase shift, which facilitates attaining good control system response (10). The probe should of course also be placed close to the working electrode to minimize the uncompensated resistance.

On the other hand, when controlled-potential electrolyses are utilized for the elucidation of electrode reaction pathways via coulometry and the analysis of current-time curves, or the technique is used as a tool for organic synthesis, it would usually be desirable to minimize the maximum difference between the actual electrode potential and the control potential. Such potential control in the axisymmetric cell could be established by positioning the reference electrode probe off center, at an appropriate location selected on the basis of the known potential gradient. The actual electrode potential would then deviate both above and below the nominal control potential. This configuration would result in increased phase shift in the cell transfer function, but in most cases this could be neutralized by adjustment of the phase compensation in the potentiostat.

LIST OF SYMBOLS

c_n	coefficient in series for potential
h	height of cell solution and counterelectrode separator, cm
i	normal current density at working electrode surface, A/cm^2
I	total cell current, A
$J_0(x)$, $J_1(x)$	Bessel functions of the first kind of order zero and one, respectively
l	length of rectangular cell, cm
n	index
r	radial position coordinate
r_c	radius of counterelectrode separator, cm
r_w	radius of working electrode and cell, cm
x	argument of Bessel function
z	normal distance from working electrode surface, cm
κ	solution conductivity, ohm^{-1} cm^{-1}
λ_n	zeroes of $J_1(x)$
Φ	potential of the solution, V
Φ_0	potential of solution adjacent to working electrode surface relative to value at center of electrode, V
$\Delta\Phi_{max}$	maximum potential difference in the solution at the working electrode between the center of the cell and its periphery, V

Acknowledgment

This work was supported by the United States Atomic Energy Commission.

Manuscript submitted Oct. 24, 1972; revised manuscript received March 12, 1973.

Any discussion of this paper will appear in a Discussion Section to be published in the June 1974 JOURNAL.

REFERENCES

1. G. L. Booman and W. B. Holbrook, *Anal. Chem.*, **35**, 1793 (1963).
2. J. E. Harrar and I. Shain, *ibid.*, **38**, 1148 (1966).
3. L. Meites, *Pure Appl. Chem.*, **18**, 35 (1969).
4. L. Meites, in "Techniques of Chemistry," Vol. 1, Part IIA, A. Weissberger and B. W. Rossiter, Editors, pp. 664, 673, Wiley-Interscience, New York (1971).
5. D. Peltier and C. Moinet, *Bull. Soc. Chim. France*, 2657 (1968).
6. M. M. Baizer, J. P. Petrovich, and D. A. Tyssee, *This Journal*, **117**, 173 (1970).
7. E. Kirowa-Eisner and E. Gileadi, *J. Electroanal. Chem.*, **38**, 191 (1972).
8. S. Karp and L. Meites, *ibid.*, **17**, 253 (1968).
9. C. Moinet and D. Peltier, *Bull. Soc. Chim. France*, 690 (1969).
10. J. E. Harrar and C. L. Pomernacki, *Anal. Chem.*, **45**, 57 (1973).
11. I. Bergman and J. C. James, *Trans. Faraday Soc.*, **50**, 60 (1954).
12. P. E. Iversen and H. Lund, *Acta Chem. Scand.*, **19**, 2303 (1965).
13. L. Eberson and H. Schäfer, "Organic Electrochemistry," p. 35, Springer-Verlag, New York (1971).
14. P. K. Das, H. A. O. Hill, J. M. Pratt, and R. J. P. Williams, *J. Chem. Soc., A*, 1261 (1968).
15. J. Chang, R. F. Large, and G. Popp, in "Techniques of Chemistry," Vol. 1, Part IIB, A Weissberger and B. W. Rossiter, Editors, pp. 70-72, Wiley-Interscience, New York (1971).
16. J. C. Stouffer and R. L. Richardson, in U.S. Atomic Energy Comm. Rept. HW-80365, Richland, Washington (1964).
17. John Newman, in "Electroanalytical Chemistry," Vol. 6, pp. 187-352, A. J. Bard, Editor, Marcel Dekker, Inc., New York (1973). Chapt. 3.
18. M. Abramowitz and I. A. Stegun, Editors, "Handbook of Mathematical Functions," p. 409, National Bureau of Standards, Washington, D.C. (1964).

Separation of Isotopes by Electromigration

Theory of Steady-State Enrichment at the Low Concentration Range

A. S. Roy*

Department of Chemical Engineering, University of the Negev, Beer-Sheva, Israel

ABSTRACT

The general differential equation for isotope separation by countercurrent electromigration is derived, normalized for the general case independent of properties of any particular liquid system, and solved for steady-state enrichment of an isotope of low abundance. Two primary process parameters are defined, the reduced reflux ratio, ρ, and reduced number of plates, ν, in terms of which the process is specified. The ranges within which the reflux ratio and number of plates may vary are determined. Minimum $\rho\nu$ is established as a criterion for preferred operation and a general solution is derived to comply with this criterion. The general solutions of the differential equations provide easy application of the results for any system of any particular properties.

Reviews of previous work on isotopic enrichment by electromigration in liquids have been published (1-3). Many of the investigations involve experimental derivation of the elementary process separation coefficient α (Eq. [14] below) and theories dealing with the functional relationships between α and the material properties, such as diffusivity, composition, and temperature. Given, however, the coefficient α and other properties of the system, the question may then arise as how to design an electromigration cell to obtain a selected isotope at a desired level of enrichment and a steady rate of production. A solution of such a problem has been given by Westhaver (4) with respect to a particular system. In the present work, a general solution to the problem in the low concentration range is obtained in a form which enables it to be easily applied to all systems and which facilitates interpretation of results.

The Countercurrent Velocity

Figure 1 illustrates a model cell for continuous isotope separation by electromigration, made of a U-tube containing two electrode compartments, cathodic and anodic, and two packed sections. The packing ("diaphragm") is a uniformly porous medium providing resistance towards pressure flow of liquid. This impedes turbulence and free convection in the liquid and also equalizes the velocity of the liquid at the full cross-sectional area of the tube. For simplicity, let the ionic liquid in the cell be a pure monovalent fused salt of the type MX in which M represents a metallic element consisting of two different isotopes, 1 and 2, while X is a halogen, such as chlorine.

By applying a voltage difference between the electrodes, the ionic liquid in the cell undergoes electrolysis. The prominent process responsible for isotope separation by electromigration is the specific (electro) migration velocity that each liquid constituent possesses in an electrostatic potential gradient. Within wide limits the migration velocity is proportional to the field strength and its magnitude in a unit field strength is known as the typical mobility of the particular constituent. The respective different migration velocities, w_1 and w_2 [cm/sec] of the two isotopes are shown in the packed section, directed towards the cathode. The migration velocity of the halogen, w_3, has an opposite direction (not shown). The main treatment here will deal with the transport in the cathodic packed section of the cell where velocities will have positive values for actual displacements towards the cathode, according to the positive z direction.

The other significant process that takes place in the cell is the faradaic electrodic reaction, which entails the reduction of neutral halogen at the cathode, as is formulated by the equation (from left to right)

$$1/2\ X_2 + e = X^- \qquad [1]$$

where e is an electron and X^- is a negatively charged halogen atom in the liquid, such as Cl^-. To provide for

* Electrochemical Society Active Member.

Key words: electromigration, isotope separation, ionic transport.

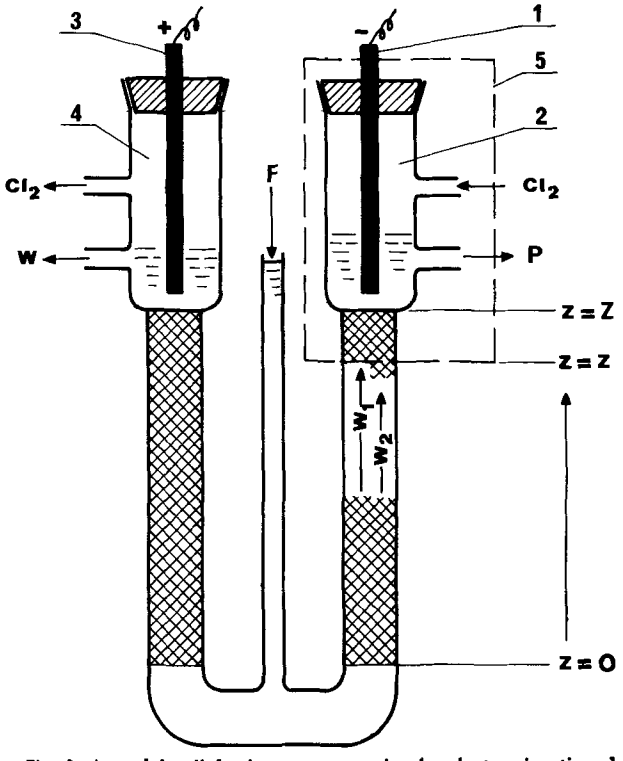

Fig. 1. A model cell for isotope separation by electromigration. 1, Cathode; 2, cathode compartment; 3, anode; 4, anode compartment; 5, material balance envelope around the catholyte.

this reaction, excess halogen gas is circulated at the cathode. At the anode, a reaction of an opposite direction of Eq. [1] takes place. In contradistinction to the halogen, the metallic isotopes M do not undergo any faradaic reaction and they permanently remain within the liquid phase-boundaries with no fluxes in or out of the (liquid) system.

The combination of the two distinct processes, the migration and the faradaic processes, results in a material flux into the catholyte (the liquid in the cathode compartment) as follows (streams F, P, W of Fig. 1 are considered zero now). By Faraday's law

$$\text{Flux of } X^- \text{ by cathodic formation} = i/\mathbf{F}[\text{mol/sec/cm}^2] \quad [2]$$

where $\mathbf{F}$ is the Faraday constant [96,500 coulombs/equiv.], and i is the current density (A/cm^2). The area to which fluxes and current density relate is the total cross-sectional area of the packed tube. For the current density we have

$$i = \mathbf{F}\,\Sigma_j z_j c_j w_j \quad [3]$$

where z_j is the valence (or charge number, *i.e.*, +1 for M and −1 for X), and c_j is the concentration of species j [mol/cm^3 (of packed volume)], and the summation is for all the constituents in the liquid. Substitution of Eq. [3] into Eq. [2] gives for our system

$$\text{Flux of } X^- \text{ by cathodic formation} = \Sigma z_j c_j w_j = c_1 w_1 + c_2 w_2 - c_3 w_3 \quad [4]$$

Drawing a material balance line around the catholyte (the dashed line, Fig. 1), the total flux of X^- into the catholyte is the addition of the separate fluxes originating from the two different mechanisms: one by migration, which is $c_3 w_3$, and the other by cathodic reduction, which is according to Eq. [4]. Summing these two fluxes results in

$$\text{Total flux of } X^- \text{ into catholyte} = c_1 w_1 + c_2 w_2 \quad [5]$$

Simultaneously, there are also fluxes of isotopes 1 and 2 into the catholyte. These, however, originate from migration alone and are given by

$$\text{Flux of } M^+ \text{ into catholyte} = c_1 w_1 + c_2 w_2 \quad [6]$$

Equations [5] and [6] state that the electrolysis (migration plus electrodic reaction) creates an equal molar flux into the catholyte of both M^+ and X^-, namely a flux of neutral salt MX (electroneutrality is preserved), and the magnitude of this flux is $c_1 w_1 + c_2 w_2$.

Concurrently, a flux of the same magnitude but of opposite sign goes into the anolyte. This brings the liquid-level higher at the cathode and lower at the anode (2), creating a hydrostatic pressure difference which causes a pressure flow of liquid of velocity v_h with an actual direction opposite to that of isotopes 1, 2; hence it is a "hydrodynamic back-flow" or "countercurrent flow." Because of this flow, the catholyte level will stop rising at some height which depends on the electric current density, liquid viscosity and the hydrodynamic permeability of the porous packing. For constant electric current and temperature and if the overall molar density of the catholyte is unchanged, then the liquid level, hence also the volume of the catholyte and the total number of moles it contains, will reach a steady state and stay constant. In order to have the catholyte at constant molar density, one of the following conditions has to hold: nonchanging concentration, equal molar volume of the isotopes, or a concentration profile (along the z-axis) that does not change in time (steady-state enrichment). If one of these is valid, then, because the molar content of the catholyte is unchanged, the total molar flux across level z into the catholyte should sum up to zero

$$c\,v_h + c_1 w_1 + c_2 w_2 = 0 \quad [7]$$

where $c = c_1 + c_2$, the total molar concentration of MX. In terms of mole fractions x_j of the isotopes, Eq. [7] gives

$$v_h = -x_1 w_1 - x_2 w_2 \quad [8]$$

The mole fractions fulfill

$$x_1 + x_2 = 1 \quad [9]$$

Consequently, the observed (over-all) velocity of isotope 1 (with respect to stationary axes), v_1, at any location z of the tube is, in fact, obtained by the superposition of the countercurrent velocity v_h on the migration velocity w_1 and (by using Eq. [8] and [9]) is equal to

$$v_1 = w_1 + v_h = w_1 - x_1 w_1 - x_2 w_2 = (w_1 - w_2) x_2 \quad [10a]$$

and similarly, for isotope 2,

$$v_2 = w_2 + v_h = w_2 - x_1 w_1 - x_2 w_2 = -(w_1 - w_2)\, x_1 \quad [10b]$$

For $w_1 > w_2$ these (over-all) velocities of the isotopes involve a net positive flux of isotope 1 towards the cathode, which will cause the enrichment of isotope 1 in a catholyte (and depletion of isotope 2) (2, 4, 5). The countervelocity v_h thus acts as the reflux in distillation for inducing separation, and the cathodic packed section, as a rectifying column.

All the above can be made true also for aqueous solutions and other ionic liquid mixtures, provided that a controlled countercurrent flow and material adjustments at the electrodes are accomplished to make Eq. [7] valid (4). In the case of the simple fused salt of the type MX, this countercurrent flow is formed automatically, thanks to the very interesting and fortunate combination of electrodic and migration fluxes, as shown above.

Now that isotopic enrichment can proceed, a continuous feed stream F (a pressure flow) can be added to the system from the outside in order to obtain a product stream P enriched with isotope 1, and a depleted stream, W, as shown in Fig. 1. However, for fixed migration velocities (namely, electric current density), length of column, and enrichment desired,

no more than a limited production rate can be obtained, otherwise the enrichment level will not hold. The solution of the problem lies in formulating and solving the appropriate differential equation in which the important process parameters will be interrelated.

The General Differential Equation

The total flux N_1 (mol/sec/cm^2) of isotope 1 in the enriching column is the sum of fluxes originating from the following origins: migration plus countercurrent flow (Eq. [10]), diffusion, and imposed production flow

$$N_1 = c\,x_1\,(w_1 - w_2)\,x_2 - D\frac{d}{dz}(cx_1) + c\,x_1\,v_p \qquad [11]$$

where D is the binary effective diffusion coefficient between isotopes 1 and 2 (cm^2/sec), "effective" meaning the over-all longitudinal coefficient of remixing by both pure diffusion, including the effect of the tortuous void passage in the porous medium (6) and also of some convective remixing (4). The velocity v_p (cm/sec) is an additional velocity component (by mechanism of pressure flow) resulting from stream F (Fig. 1).

As there is no generation of any isotope in the liquid phase, the material balance for a small volume element leads to the differential conservation law

$$\frac{\partial c_j}{\partial t} = -\nabla \cdot N_j \qquad [12]$$

where t is time (sec). For isotope 1 in our column of unidirectional and uniform velocity across the tube, the differential equation determining the distribution of concentrations is (by Eq. [11] and [12])

$$-\frac{\partial c_1}{\partial t} = \frac{\partial[c\,x_1\,x_2\,(w_1 - w_2)]}{\partial z} - \frac{\partial}{\partial z}\left(D\frac{\partial c x_1}{\partial z}\right) + \frac{\partial(c\,x_1\,v_p)}{\partial z} \qquad [13]$$

We limit our treatment to systems of constant c, v_p, D, and α, independent of isotopic concentration. The elementary process separation coefficient α is defined by

$$\alpha \equiv w_1/w_2 \qquad [14]$$

For low concentrations of isotope 1, the constancy of α implies also constancy of w_1 and w_2. Integrating Eq. [13] for steady state ($\partial c_1/\partial t = 0$) gives

$$(w_1 - w_2)\,x_1x_2 + v_p\,x_1 - D\frac{dx_1}{dz} = \text{constant} \qquad [15]$$

By comparison to Eq.[11], the constant is identified with N_1/c. At the steady state, N_1 is the constant net flux of isotope 1 which is independent of location z and therefore is equal also to the flux at $z = Z$ where x_1 is designated by x_p, the mole fraction of isotope 1 in the product stream P. Hence

$$\text{constant} = x_p\,v_p \qquad [16]$$

Defining the reflux ratio, R

$$R \equiv w_2/v_p \qquad [17]$$

and the height of an equivalent theoretical plate, h

$$h \equiv D/w_2 \qquad [18]$$

and replacing x_1 by x, Eq. [14-18] yield the equation (4)

$$-\frac{dx}{dz} + \frac{\alpha - 1}{h}x(1 - x) + \frac{1}{Rh}(x - x_p) = 0 \qquad [19]$$

or

$$\frac{dx}{d\xi} - (\alpha - 1)nx(1 - x) - \frac{n}{R}(x - x_p) = 0 \qquad [20]$$

where n is the number of plates

$$n \equiv Z/h \qquad [21]$$

and ξ, the reduced distance on the column

$$\xi \equiv z/Z \qquad [22]$$

Defining new parameters, ρ, the reduced reflux ratio

$$\rho \equiv R\,(\alpha - 1) \qquad [23]$$

and ν, the reduced number of plates

$$\nu \equiv n\,(\alpha - 1) \qquad [24]$$

Equation [20] takes the new form of

$$\frac{dx}{d\xi} - \nu\,x\,(1 - x) - \frac{\nu}{\rho}(x - x_p) = 0 \qquad [25a]$$

By using the reduced nondimensional parameters ρ and ν (rather than R and n), Eq. [25a] becomes the general differential equation for steady-state isotope separation by electromigration independent of any particular liquid system, and thus the solution of Eq. [25a] will be easily applicable for various ionic liquid systems. It is also worthy of notice that in order to determine the coefficients of Eq. [19], the values of four parameters, α, u, R, x_p, have to be given. However, by using ρ and ν (Eq. [23] and [24]) the three parameters ρ, ν, and x_p are sufficient to determine the coefficients of either Eq. [19] or [25a]. Needless to say, the number of parameters cannot be reduced to less than three.

The nondimensional parameters, the reduced reflux ratio, ρ, and the reduced number of plates, ν, are model parameters which express the effort necessary for separating the isotope. For instance, the case of $\nu = 1$ means that the number of plates in the column is (by Eq. [24]) $n = 1/(\alpha - 1)$. A larger ν or a smaller $\alpha - 1$ value involves a larger number of plates, *i.e.*, a longer column. Similarly, by Eq. [23], a larger ρ or a smaller $\alpha - 1$ value indicate a larger reflux ratio, namely, a smaller fraction of the migration velocity becomes useful for production. More specifically, by Eq. [14], [17], and [23]

$$v_p = (w_1 - w_2)/\rho \qquad [26]$$

Thus, a value of ρ equal to unity means that all the difference between the migration velocities of the two isotopes is utilized as the production velocity v_p. The larger the value of ρ, the less we utilize the migration difference for production. However, a larger ρ, as well as a larger ν, helps to produce a higher enrichment, as results from the solution of the differential equation [25a], as is shown below.

Solution for the Low Abundance Range

The problem of enriching isotopes available in nature at low abundance is of great interest. For this case $x << 1$, and the differential equation [25a] can be modified to

$$\frac{dx}{d\xi} - \nu\,x - \frac{\nu}{\rho}(x - x_p) = 0 \qquad [25b]$$

Let an "enrichment factor" E'_p be defined

$$E'_p = x_p/x_0 \qquad [27]$$

where x_0 is the mole fraction of the isotope at $\xi = 0$. For the low concentration range, this factor is an adequate approximation of the enrichment factor E_p of the column, generally defined as $[x_p/(1 - x_p)]$ $[x_0/(1 - x_0)]$. Solving the differential equation [25b] for the boundary conditions of $x(0) = x_0$ and $x(1) = x_p$, results in

$$E_p = \frac{1 + \rho}{1 + \rho\,e^{-\omega}} \qquad [28]$$

where the parameter ω is defined by

$$\omega \equiv \nu\frac{\rho + 1}{\rho} \qquad [29]$$

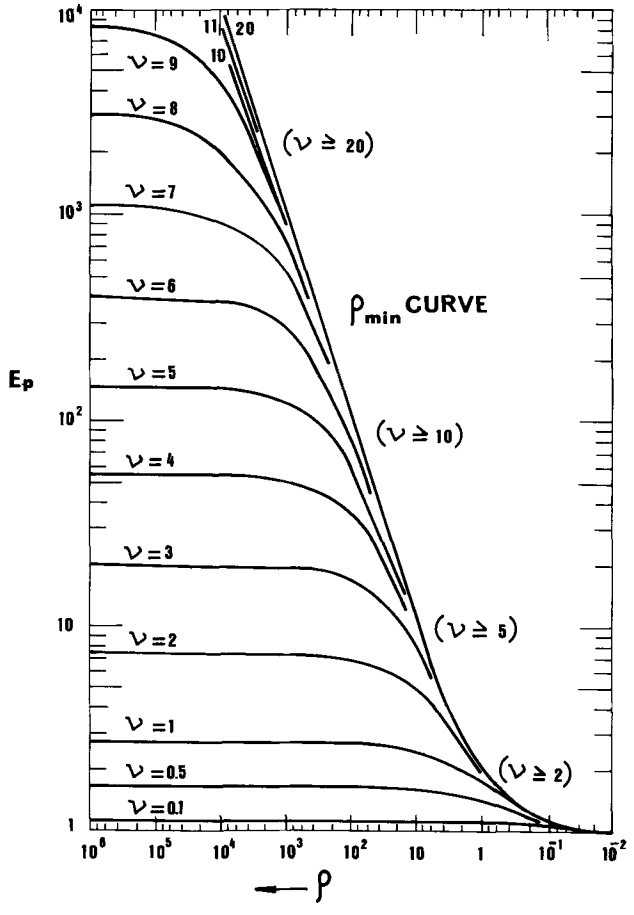

Fig. 2. E_p as a function of ρ and ν (Eq. [28])

Assigning numerical values to ρ and ν explicitly determine E_p. The same E_p, however, can be obtained from an unlimited number of different (ρ, ν) pairs, as can also be recognized from Fig. 2 which represents Eq. [28]. In Fig. 2, E_p is presented as a function of ρ on the abscissa (notice that ρ increases from right to left, $1/\rho$ from left to right), and ν is a parameter. The shape of the resulting curves resemble those given for the general case of isotope separation for square cascades (7).

The ranges in which ρ and ν may vary are limited. For obtaining a certain E_p, Eq. [28] indicates that ρ decreases as ν increases. For $\nu = \infty$, the smallest ρ value will be reached

$$\rho_{min} = E_p - 1 \qquad [30]$$

Namely, given E_p, then $E_p - 1$ is the minimum (reduced) reflux ratio. It requires however an infinitely long column. For a column of finite length

$$\rho > E_p - 1 \qquad [31]$$

The range of permissible ρ is, therefore

$$\infty > \rho > E_p - 1 \qquad [32]$$

The value of ρ_{min} for any E_p value can be ascertained graphically from Fig. 2 by drawing a horizontal line from the assigned E_p point on the ordinate until it intersects the steep line, the ρ_{min} curve, at the extreme right of the curve family, where the value of $E_p - 1$ is obtained for ρ, *e.g.*, for $E_p = 10$, $\rho_{min} = 9$. For $E_p = 2$, $\rho_{min} = 1$, etc. The ρ_{min} curve represents $\nu = \infty$. For the purpose of locating ρ_{min} the condition of $\nu = \infty$ is substantially realizable for quite finite ν-values, as is apparent from Fig. 2, *e.g.*, for $E_p \leq 2$, a $\nu \geq 2$ is practically infinity, for $E_p \leq 10$, $\nu \geq 5$, etc.

It is interesting to note in Fig. 2 the rise of E_p with the increase of ρ. There is a steep rise and then it levels to a plateau. For low ν values, the rise of E_p is slight. This represents short columns having a small number of plates. In this case, back-transport by diffusion controls the process and enrichment is very limited even at a high reflux. At large ν values, ionic transport overrides diffusion and a very high enrichment can be reached as ρ increases. However, with any ν value there is a limit to the enrichment (E_p) possible even for very high ρ-values, as is indicated by the plateaus. For $\rho = \infty$, *i.e.*, total reflux (no product withdrawal, $v_p = 0$), one obtains from Eq. [24], [28], and [29]

$$E_p = e^{\nu} = e^{n(\alpha-1)} \qquad [33]$$

As in general (except for H-D isotopes) $\alpha - 1 << 1$, hence $\alpha = e^{\alpha-1}$, and Eq. [33] takes the form of

$$E_p = \alpha^n \qquad [34]$$

This equation elucidates the concept of number plates, n, by identifying the height of a theoretical plate, h, (Eq. [21] and [18]) as the incremental length of the column over which the enrichment (concentration at low abundance) increases by a factor of α when the column is under total reflux. This also explains Eq. [18]: the higher the diffusivity D, the longer becomes such an incremental length of column.

By Eq. [28], in order to obtain a certain E_p, ν decreases as ρ increases, and for $\rho = \infty$, ν has a minimum value, which (by Eq. [33]) is

$$\nu_{min} = \ln E_p \qquad [35]$$

For any magnitude of E_p the corresponding ν_{min} value is identified in Fig. 2 as the parameter ν of the curve, the asymptotically horizontal part of which, intersects the ordinate at the prescribed E_p, *e.g.*, $\nu_{min} = 1$ for $E_p = 2.7$, $\nu_{imn} = 2$ for $E_p = 7.4$, etc. The ν_{min} is thus the lowest ν value for which an E_p (of value of e^{ν}) will be asymptotically reached as ρ increases infinitely. For low ν values the condition of infinite ρ is already realized at quite low ρ values (*e.g.*, 1 for $\nu = 0.1$ and 10 for $\nu = 0.5$, etc.)

In practice, for finite production rate, $\rho < \infty$, hence, in general

$$\nu > \ln E_p \qquad [36]$$

The range of permissible ν is, therefore

$$\infty > \nu > \ln E_p \qquad [37]$$

The permissible ranges for ν and ρ (Eq. [32] and [37]) still leave open the question of choice of a pair of ν and ρ out of their wide ranges in order to produce a liquid product of a certain enrichment factor E_p. Either infinite ν or ρ are impractical and the reasonable choice should be somewhere in between, governed by economic criteria.

The Preferred ρ and ν Values

As the cost of electrical energy is a major factor in the process of electromigration, it should be advantageous to search for a ρ and ν combination (as a function of E_p) that would minimize the electrical energy required for producing a unit quantity of enriched product. The energy per unit product is obtainable by dividing the electrical power $I^2 2Z/\kappa A$ (J/s) by the production rate $P = cv_p A$ (mol/sec), where I is the electric current (A), A the column cross section (cm^2), and κ the conductivity (mho/cm) of the column content (liquid plus packing). By Eq. [17], [21], [23], and [24] (and $i = I/A$), this ratio becomes

$$\frac{\text{joules}}{\text{mole}} = \frac{2\nu\rho i h}{c\, u_2 (\alpha - 1)^2} \qquad [38]$$

where u_2 is the mobility of isotope 2 (cm/sec per V/cm), or

$$u_2 = \frac{w_2}{i/k} \qquad [39]$$

It is interesting to note that the parameters appearing in the denominator of Eq. [38], c, u, and $\alpha - 1$, are all

properties of matter, whereas those in the numerator, ν, ρ, i, and h are operational. The parameter h is operational both because of w_2 (Eq. [18]), the magnitude of which is determined by the voltage we apply, and because D is not a pure property of the liquid as it includes also convective mixing effects. In fact, achieving a small h measures the degree of experimental accomplishment.

For a liquid of definite properties (c, u_2, $\alpha - 1$) and for operation at a selected current density (i) and a fixed height of a plate (h), the minimum energy consumption [joule/mol] will be achieved according to Eq. [38] when $\rho\nu$ is minimum. Minimization of $\rho\nu$ is required based on Eq. [28]. From Eq. [28] and [29] we obtain

$$\rho\nu = \frac{\rho^2}{\rho + 1} \ln \frac{\rho E_p}{\rho - (E_p - 1)} \qquad [40]$$

Differentiating $\rho\nu$ with respect to ρ and equating to zero yields the expression for minimum $\rho\nu$

$$\nu = \frac{\rho}{\rho + 2} \cdot \frac{E_p - 1}{\rho - (E_p - 1)} \qquad [41]$$

Values of ρ and ν complying with both Eq. [41] and Eq. [28] constitute the minimum $\rho\nu$ values for any chosen E_p. Direct solution of these two equations leads to a transcendental equation. Instead, ρ, E_p, and ν can all be expressed as functions of ω (Eq. [29]) consistent with both Eq. [41] and [28], to yield the E_p, ρ, and ν relationships for minimum $\rho\nu$. The expressions are

$$\rho = \frac{e^\omega - 1}{\omega} - 2 \qquad [42]$$

$$E_p = \left(\frac{e^\omega - 1}{\omega} - 1 \right) \Big/ \left[1 + \left(\frac{e^\omega - 1}{\omega} - 2 \right) e^{-\omega} \right] \qquad [43]$$

$$\nu = \omega \left(\frac{e^\omega - 1}{\omega} - 2 \right) \Big/ \left(\frac{e^\omega - 1}{\omega} - 1 \right) \qquad [44]$$

The results obtained from Eq. [42-44] are plotted in Fig. 3. The preferred ρ and ν for minimum $\rho\nu$ are shown *vs.* $E_p - 1$ in terms of $\rho/(E_p - 1)$ and $\nu/\ln E_p$. These ratios are in fact ρ/ρ_{min} and ν/ν_{min}, respectively, (by Eq. [30] and [35]). It is very interesting to note how little these preferred ratios vary even at an enormously wide $E_p - 1$ range. For extremely low enrichments, the two ratios start at values around 1.4 and 1.8, respectively, and change no more than to about 1.1 and 1.2 for extremely high enrichments.

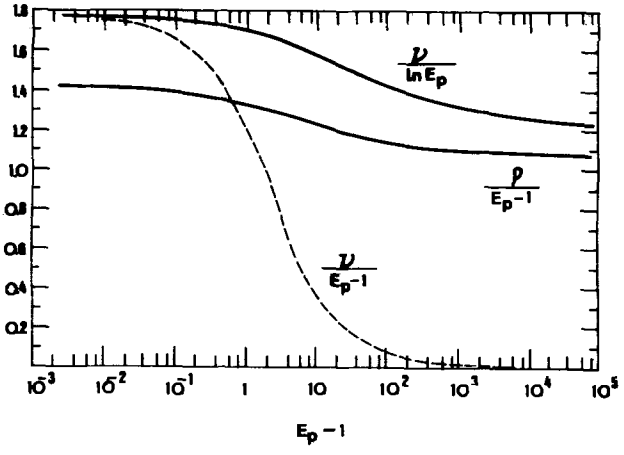

Fig. 3. Preferred ρ and ν for minimum $\rho\nu$ (Eq. [42-44])

It has been pointed out above (Eq. [26]) that ρ signifies the inverse "useful" fraction of $(w_1 - w_2)$ that is utilized as v_p for production. As, according to Fig. 3, $\rho/(E_p - 1)$ is nearly constant, this means that at the preferred conditions, this "useful" fraction is approximately inversely proportional to $E_p - 1$. For instance, the "useful" fraction is $\sim$ 10/1.4 for $E_p - 1 = 0.1$ (700% utilization of $w_1 - w_2$), going down to $\sim$1/1.4 for $E_p - 1 = 1$ (70% utilization), and to $\sim$0.1/1.4 for $E_p - 1 = 10$ (7%). For higher enrichments, the production velocity decreases further. This is very reasonable and is explainable even by the material balance alone, made around the whole enriching column (cathodic packing).

A different trend is shown by the curve of the reduced number of plates, ν. A constant $\nu/\ln E_p$ means, in fact, a very slow increase of ν with the increase of E_p (or $E_p - 1$). This is made more apparent by the curve $\nu/(E_p - 1)$ (dashed line) included in Fig. 3. The diminishing growth of ν with the increase of $E_p - 1$ (for $E_p > 1$) can be illustrated by the following figures

$E_p - 1$:	1.2	9.3	140	2,000	12,000	80,000
ν :	1.4	3.7	7	10	12	14

Figure 3 (Eq. [42-44]) gives the answer for the question of how to decide upon the basic parameters that define the electromigration column for steady-state isotope separation. The approximate constancy of $\rho/(E_p - 1)$ and of $\nu/\ln E_p$ constitute an interesting result.

The General Applicability of the Results

It has been shown how the enrichment is determined (Eq. [28], Fig. 2), based on the model parameters ρ (Eq. [23]) and ν (Eq. [24]). The ranges of these parameters have been derived (Eq. [32] and [37]). The minimum $\rho\nu$ relationship (Eq. [42-43], Fig. 3), has been established as a preference criterion.

Application of these results for any particular ionic liquid in the low abundance range is simple. For instance, given α and h of a particular system, the preferred ρ and ν are easily determined as a function of any enrichment E_p required, by use of Fig. 3. Non-preferred conditions can be obtained from Fig. 2. The length of column needed, Z, is easily obtainable from Eq. [24] and [21], and the reflux ratio R, from Eq. [23]. The relationship between v_p, w_2, i, and κ is given by Eq. [17] and [39].

Acknowledgment

Thanks are due to Dr. Y. Ilamed for helpful discussions.

Manuscript received Nov. 6, 1972. This was Paper 262 presented at the Chicago, Illinois, Meeting of the Society, May 13-18, 1973.

Any discussion of this paper will appear in a Discussion Section to be published in the June 1974 JOURNAL.

REFERENCES

1. A. Klemm and K. Heinzinger, *Advan. Chem. Ser.*, **89**, 246 (1969).
2. A. Lunden, Doctoral Thesis, Chalmers Institute of Technology, Goteborg, Sweden (1956).
3. M. Gasith and A. Roy, *J. Electrochem. Technol.*, **2**, 85 (1964).
4. J. W. Westhaver, *J. Res. Natl. Bur. Std.*, **38**, 169 (1947).
5. V. A. Klemm, *Z. Naturforsch.*, **7a**, 417 (1952).
6. R. B. Bird, W. E. Stewart, and E. N. Lightfoot, "Transport Phenomena," pp. 542-544, John Wiley and Sons, New York (1960).
7. K. Cohen, "The Theory of Isotope Separation as Applied to Large-Scale Production of U^{235}" G. M. Murphy, Editor, pp. 33, Fig. 2.1, McGraw-Hill Book Co., New York (1951).

Electrical Conductance of Molten Alkali Carbonate Binary Mixtures

P. L. Spedding

Department of Chemical and Materials Engineering, The University of Auckland, Auckland, New Zealand

ABSTRACT

The electrical conductances are reported for molten lithium, sodium, and potassium carbonate binary mixtures over the complete composition range. Molar concentration-equivalent conductance isotherms exhibit a negative deviation from ideal behavior. Attempts to handle the results by using conduction theories proved unsuccessful except in the case of the Markov equation. Calculations with the Markov equation gave values for the conduction of dissimilar interacting cations that indicated that the temperature dependence of the conduction is governed by the anion environment present, while the absolute value of conductance gives an indication of the ease of movement of the dissimilar interacting cations.

The alkali metal carbonates have been subjected to extensive study over recent years primarily because of their possible practical application in electrochemistry. This present study was undertaken as part of an integrated fuel cell research program aimed at obtaining a better understanding of the actual processes taking place in the molten carbonate-type cell.

Experimental

Methods which are used for measurement of electrical conduction of molten salts have been reviewed by a number of workers (1-5) who have concluded that the most accurate technique which is available for corrosive media is the capillary cell with the actual capillaries formed in noncorrosive insulating material (6-8). The technique therefore was used in this study. The actual apparatus employed is detailed in Fig. 1 and is similar to that of Janz and co-workers (9-10). Care was taken with the design and construction of the apparatus to ensure that the conduction path was entirely confined to the capillaries and the melt between their two immersed extremities. The capillaries were ultrasonically drilled in two single crystals of magnesium oxide. The salt bath was held in a Palau crucible (80% Au-20% Pd) in a controlled carbon dioxide atmosphere, in order to ensure the melt composition was unchanged during experimentation. The over-all details of the control and operation of the system have been presented elsewhere (11, 12). Temperature was better than ± 0.1° at 800°C.

The capillary cell was calibrated with aqueous KCl solution at 25°C using standard techniques (13). Coefficient of expansion data (14) then were applied to the particular cell geometry employed to give the operating cell constant. The calibration was checked against molten KCl data (15) at intervals during the entire work and was found to agree within ± 0.002%. The cell constants for the various cells used during the determination were approximately 370^{-1} cm in the operating temperature range used. Measurements were taken at approximately 20°C intervals at increasing and then at decreasing temperatures. During an actual measurement the furnace was switched off to avoid errors which arise because of interference from the furnace windings. The Jones bridge-oscillator-oscilloscope combination used to measure the conductance virtually eliminated any capacitance effects. Readings were taken over a frequency range of 2,000-40,000 Hz, so that the conductance value at infinite frequency could be determined thus eliminating any effect of polarization which may occur at the electrodes. One of the major sources of error with the capillary cell is caused by the presence of bubbles within the capillaries during a reading. Drying of the salt at 120°C and premelting under carbon dioxide eliminated the possibility of the formation of any water vapor bubbles on the internal surfaces of the capillaries. Raising and lowering the salt bath into the capillaries several times removed any possibility of mechanically formed bubbles adhering to the internal surface of the capillary cell.

Key words: conductance, molten alkali carbonates.

Results

The conduction data were presented as specific conductance, κ, expressed in the form

$$\kappa = A_\kappa \exp(-\Delta E_\kappa / RT) \quad [1]$$

The equivalent conductance, Λ was calculated from the specific conductance and melt density (12), via the equation

$$\Lambda = \kappa(\Sigma x_i E_i)/\rho \quad [2]$$

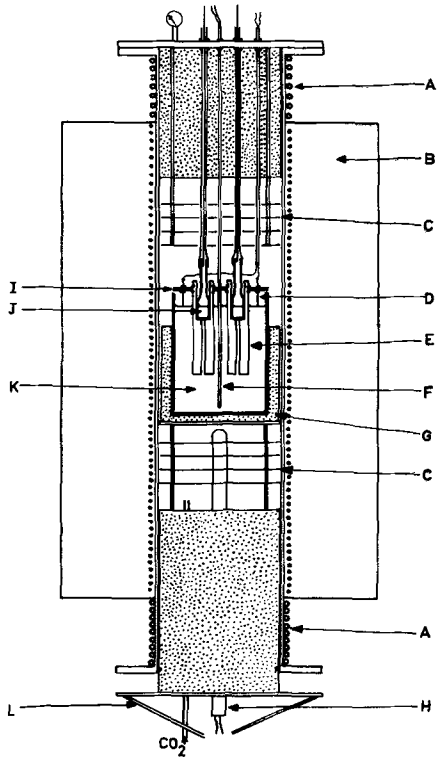

Fig. 1. Conductivity cell and furnace: A, cooling coils; B, furnace; C, heat shields; D, height senser; E, MgO capillaries; F, measuring thermocouple; G, pyrophyllite insulation; H, control thermocouple; I, capillary holder; J, Palau electrodes; K, salt bath; L, laboratory jack.

where x_i and E_i are the mole fraction and equivalent weight of the component, i, in the melt.

The equivalent conductance was expressed as the Arrhenius equation

$$\Lambda = A_\Lambda \exp(-\Delta E_\Lambda / RT) \quad [3]$$

The data exhibit a departure from the Arrhenius relation about the eutectic composition in the temperature range immediately above the melting point as shown by Fig. 2 and 3. This departure is in agreement with the findings of other workers (15). However, in each of these cases there is a region in a higher temperature range in which the Arrhenius relations of Eq. [1] and [3] satisfactorily fit the data. The constants of Tables I and II were calculated for this region alone using the method of least squares (16).

Discussion

Janz and co-workers (9, 10) determined the specific conductivities of the pure alkali metal carbonates and their eutectic mixtures and resolved most of the anomalies which existed in previous work (17-20). The present data show good agreement with that of Janz and co-workers except in the case of the $LiKCO_3$ eutectic where this work gave a smooth graduation in the magnitude of the conductance as the composition was varied, in contrast to Janz's data which showed correspondence with the K_2CO_3 values.

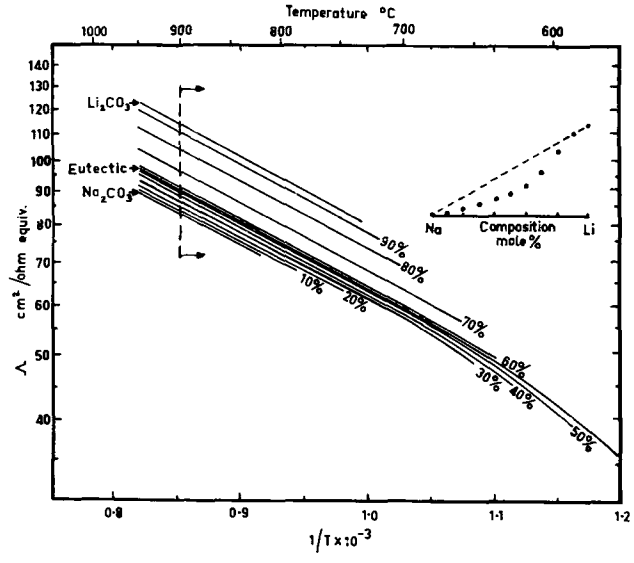

Fig. 2. Equivalent conductances of lithium carbonate-sodium carbonate binary mixtures.

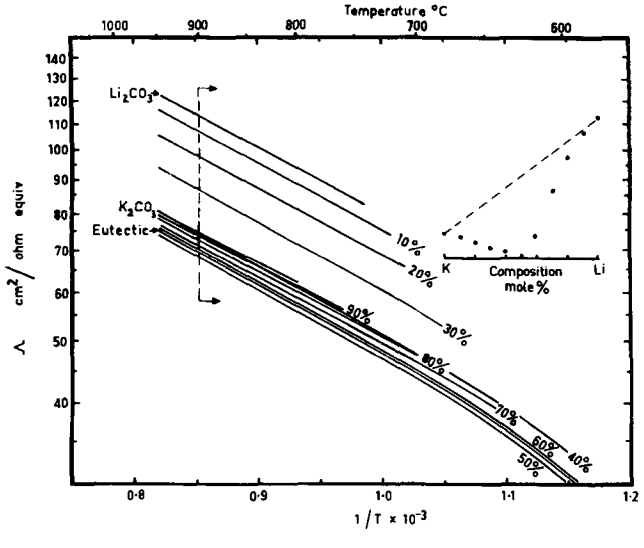

Fig. 3. Equivalent conductances of lithium carbonate-potassium carbonate binary mixtures.

Table I. Specific conductances of molten alkali metal carbonate mixtures expressed as the constants of Eq. [1]

Media*	A_κ, ohm cm	ΔE_κ, kcal/gmole	Temperature range, °C**
Li_2CO_3	29.22 ± 0.67	3.94 ± 0.04	740-880
90% Li_2CO_3	28.00 ± 0.23	3.98 ± 0.06	734-928
80% Li_2CO_3	25.05 ± 0.55	3.93 ± 0.05	700-925
70% Li_2CO_3	23.21 ± 0.21	4.00 ± 0.05	664-923
60% Li_2CO_3	21.74 ± 0.47	4.05 ± 0.06	(591-) 680-930
53.3% Li_2CO_3	20.84 ± 0.39	4.05 ± 0.03	(523-) 640-947
50% Li_2CO_3	20.36 ± 0.30	4.03 ± 0.03	(589-) 660-939
40% Li_2CO_3	18.85 ± 0.46	3.94 ± 0.04	(562-) 710-966
30% Li_2CO_3	17.29 ± 0.30	3.82 ± 0.04	(658-) 710-961
20% Li_2CO_3	15.88 ± 0.47	3.71 ± 0.07	(730-) 740-951
10% Li_2CO_3	14.71 ± 0.67	3.62 ± 0.08	804-959
Na_2CO_3	14.12 ± 0.31	3.59 ± 0.05	872-965
90% Na_2CO_3	13.95 ± 0.17	3.70 ± 0.03	870-981
80% Na_2CO_3	13.65 ± 0.09	3.80 ± 0.02	813-963
70% Na_2CO_3	13.20 ± 0.17	3.91 ± 0.03	798-949
60% Na_2CO_3	12.98 ± 0.11	3.99 ± 0.02	800-957
58% Na_2CO_3	12.38 ± 0.18	3.91 ± 0.03	(742-) 770-953
50% Na_2CO_3	12.20 ± 0.21	3.90 ± 0.04	771-957
40% Na_2CO_3	11.79 ± 0.50	3.86 ± 0.09	774-973
30% Na_2CO_3	11.49 ± 0.53	3.87 ± 0.07	803-964
20% Na_2CO_3	11.32 ± 0.34	3.88 ± 0.08	875-985
10% Na_2CO_3	10.85 ± 0.34	3.85 ± 0.07	884-977
K_2CO_3	10.52 ± 0.30	3.83 ± 0.07	905-1008
90% K_2CO_3	10.85 ± 0.31	3.84 ± 0.06	723-863
80% K_2CO_3	11.41 ± 0.28	3.89 ± 0.05	699-892
70% K_2CO_3	13.32 ± 0.20	4.18 ± 0.03	(640-) 700-920
60% K_2CO_3	14.49 ± 0.32	4.32 ± 0.04	(600-) 730-924
57.3% K_2CO_3	14.56 ± 0.59	4.32 ± 0.08	(588-) 740-950
50% K_2CO_3	14.96 ± 0.62	4.33 ± 0.07	(562-) 740-949
40% K_2CO_3	16.63 ± 0.29	4.24 ± 0.03	(597-) 720-954
30% K_2CO_3	20.27 ± 0.30	4.18 ± 0.03	(681-) 728-966
20% K_2CO_3	23.37 ± 0.64	4.11 ± 0.06	761-973
10% K_2CO_3	26.46 ± 0.86	4.03 ± 0.06	860-987
Li_2CO_3	29.22 ± 0.67	3.94 ± 0.04	740-880

* Mole per cent composition.
** Bracketed values not included in the determination of constants.

Table II. Equivalent conductances of molten alkali carbonate mixtures expressed as the constants of Eq. [3]

Media*	A_Λ, cm²/ohm equiv.	ΔE_Λ, kcal/gmole	Temperature range, °C**
Li_2CO_3	799.8 ± 24.9	4.56 ± 0.06	740-880
90% Li_2CO_3	784.4 ± 9.6	4.57 ± 0.03	734-928
80% Li_2CO_3	720.1 ± 13.7	4.52 ± 0.04	700-925
70% Li_2CO_3	693.6 ± 19.6	4.63 ± 0.06	664-923
60% Li_2CO_3	678.2 ± 4.3	4.70 ± 0.02	(591-) 680-930
53.3% Li_2CO_3	652.5 ± 6.3	4.66 ± 0.03	(523-) 640-947
50% Li_2CO_3	640.0 ± 11.0	4.63 ± 0.04	(589-) 660-939
40% Li_2CO_3	604.6 ± 11.5	4.52 ± 0.04	(562-) 710-966
30% Li_2CO_3	566.8 ± 12.0	4.41 ± 0.05	(658-) 710-961
20% Li_2CO_3	515.2 ± 15.8	4.24 ± 0.07	(730-) 740-951
10% Li_2CO_3	498.6 ± 24.7	4.19 ± 0.12	804-959
Na_2CO_3	490.5 ± 11.1	4.16 ± 0.05	872-965
90% Na_2CO_3	517.2 ± 19.9	4.35 ± 0.09	870-981
80% Na_2CO_3	519.0 ± 13.3	4.43 ± 0.06	813-963
70% Na_2CO_3	516.0 ± 27.0	4.53 ± 0.12	798-949
60% Na_2CO_3	525.8 ± 21.0	4.62 ± 0.09	800-957
58% Na_2CO_3	503.0 ± 26.4	4.53 ± 0.15	(742-) 770-953
50% Na_2CO_3	506.0 ± 15.6	4.52 ± 0.07	771-957
40% Na_2CO_3	498.4 ± 17.5	4.47 ± 0.07	774-973
30% Na_2CO_3	502.0 ± 6.7	4.48 ± 0.03	803-964
20% Na_2CO_3	511.2 ± 13.4	4.49 ± 0.06	875-985
10% Na_2CO_3	516.1 ± 17.2	4.52 ± 0.08	884-977
K_2CO_3	508.2 ± 12.9	4.48 ± 0.06	905-1008
90% K_2CO_3	484.6 ± 11.7	4.42 ± 0.05	723-863
80% K_2CO_3	499.8 ± 11.2	4.53 ± 0.05	699-892
70% K_2CO_3	545.8 ± 14.2	4.79 ± 0.06	(640-) 700-920
60% K_2CO_3	571.1 ± 19.5	4.92 ± 0.07	(600-) 730-924
57.3% K_2CO_3	571.3 ± 20.8	4.93 ± 0.07	(588-) 740-950
50% K_2CO_3	566.2 ± 17.6	4.94 ± 0.06	(562-) 740-949
40% K_2CO_3	591.7 ± 17.3	4.86 ± 0.05	(597-) 720-954
30% K_2CO_3	676.5 ± 14.3	4.78 ± 0.04	(681-) 728-966
20% K_2CO_3	725.2 ± 14.5	4.69 ± 0.04	761-973
10% K_2CO_3	763.1 ± 29.5	4.59 ± 0.08	860-987
Li_2CO_3	799.8 ± 24.9	4.56 ± 0.06	740-880

* Mole per cent composition.
** Bracketed values not included in the determination of constants.

The effect of frequency, f, on the measured resistance, R, of the melt followed the relation (21)

$$R = R_\infty + a/\sqrt{f} \quad [4]$$

for each salt for the frequency range of 2,000-40,000 Hz. No satisfactory correlation with the value of the constant, a, and melt composition could be obtained.

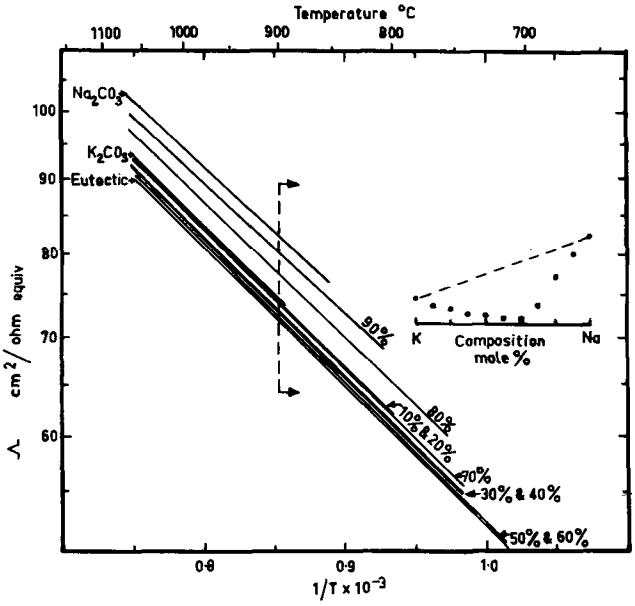

Fig. 4. Equivalent conductances of sodium carbonate-potassium carbonate binary mixtures.

There are a number of theories which have been advanced to explain conduction in melts. Most of these were inapplicable to the present discussion for one reason or another. Lack of data just above the melting point and in the high-temperature region precluded using the reduced volume concept developed by Angell (22) and the approach of Grantham (23), respectively. Furthermore, the frictional formalism has not yielded sufficient insight into the mechanisms of transport to warrant its inclusion in this discussion (24). Lack of necessary fundamental data for these salts did not allow the formal application to these data of the hole model as developed by Bockris *et al.* (25) or the free volume approach of Laidler *et al.* (26). However, estimates of the ionic radius (12), ion vibration (4), and jump distance for the pure alkali metal carbonates have allowed approximate calculations to be performed for the hole model, the results of which gave conductances of similar accuracy as those for univalent salts; that is the calculated Arrhenius coefficients were in reasonable agreement with experimental values but the absolute values were not. In the case of the binary mixtures the hole model predicted ideal behavior which is far from the actuality shown in Fig. 2-4. The possible reasons for these discrepancies between theory and experiment are enumerated by Brummer and Hills (27).

The equivalent conductance-molar composition isotherms exhibit the usual negative deviation from ideality even for Na_2CO_3-K_2CO_3 melts which possess ideal molar volume behavior (12). For ideal binary melt mixtures Markov (28) developed the equation

$$\Lambda_m = x_1^2 \Lambda_{11} + x_2^2 \Lambda_{22} + 2x_1x_2 \Lambda_{12} \qquad [5]$$

for the calculation of conductances and has discussed its importance as far as providing insight into the nature of the melt and its transport mechanisms. The equation has yielded predicted values of conductances for $PbCl_2$-$PbBr_2$ and KNO_3-$NaNO_3$ melts which are within ± 2% of experimental data (28). The Markov equation follows directly from a consideration of the probability of interaction between pure salts in the mixture and the electrical conductance of such an arrangement within the melt. Thus the probability of the interactions M_1X-M_1X, M_2X-M_2X, and M_1X-M_2X are, respectively, x_1^2, x_2^2, and $2x_1x_2$, where x is the mole fraction of the appropriate component. Strictly the Λ_{12} conductance in a mixture having only M_1X-M_2X type interactions, is a hypothetical concept. Markov avoided this issue and simplified the equation by replacing the conductance Λ_{12} by that of the pure salt with the larger Arrhenius coefficient. The reason for this procedure is obscure and calculations on the pure alkali metal carbonate eutectic melts (Table III) show the procedure to be unsatisfactory.

Actually the predictions of the Markov equations are improved considerably in this instance by taking the value of the Λ_{12} conductance as that component in the melt which possesses the smaller, more mobile ion. Accepting the M_1X-M_2X type interactions at face value, there is no good reason to suppose that the Λ_{12} conductance has not got a specific value which is completely dissimilar in magnitude from either of the pure components. Calculation back from experimental data using Eq. [5] confirms that the Λ_{12} conductances for each of the binary melts are different to those of pure melts

$$\Lambda Li,Na = 615 \exp(-4700/RT) \qquad [6]$$

$$\Lambda Na,K = 540 \exp(-4700/RT) \qquad [7]$$

$$\Lambda Li,K = 475 \exp(-4700/RT) \qquad [8]$$

The similarity of the Arrhenius coefficients for the Λ_{12} conductance for each binary melt suggests that the temperature dependence of conductance is influenced primarily by the anion environment which obviously is similar for each system. Rice (29) came to the same conclusion from theoretical considerations of melt transport. The pre-exponential term, on the other hand, exhibits a definite trend which may well reflect the ability of the interacting ion to move through the melt in a similar manner to that which has been suggested for other transport phenomena (30). Resubstitution of the Λ_{12} conductance values given by Eq. [6]-[8] back in the Markov equation leads to the predicted values given in the final column of Table III for the eutectic melts. The over-all error in these calculated values over the complete composition range is within ± 3.5%, ± 3.2%, and ± 14% for the Li_2CO_3-Na_2CO_3, Na_2CO_3-K_2CO_3, and Li_2CO_3-K_2CO_3 melts, respectively.

Closer examination of the data indicates that a significant difference between the calculated and experimentally determined values only occurs when the systems depart from ideal molar volume behavior (12). This is particularly noticeable with the Li_2CO_3-K_2CO_3 melt where satisfactory predictions (± 1.8%) are obtained in the ideal molar volume region up to 25% mole and beyond 67% mole lithium carbonate concentration. In the intervening region where nonideality is marked there is a significant difference between experimental and calculated conductances. Such behavior could be interpreted in terms of the formation of a complex in the region of the eutectic of the general type suggested by Bockris and Reddy (37). That is an entity is formed in which a certain num-

Table III. Electrical conductance calculations cm²/ohm equiv.

System	Experimental 900°C	Experimental 1000°C	Ideal 900°C	Ideal 1000°C	Markov $\Lambda_{12} = \Lambda_{22}$ 900°C	Markov $\Lambda_{12} = \Lambda_{22}$ 1000°C	Markov Λ_{12} calculated 900°C	Markov Λ_{12} calculated 1000°C
Li_2CO_3	113.0	131.8	—	—	—	—	—	—
Na_2CO_3	82.3	94.7	—	—	—	—	—	—
K_2CO_3	74.5	86.7	—	—	—	—	—	—
Li-$NaCO_3$	88.0	103.0	98.0	113.5	105.6	122.8	89.9	104.5
Na-KCO_3	72.5	84.7	78.0	90.5	76.0	88.5	74.7	87.0
Li-KCO_3	69.0	81.5	95.0	110.3	104.5	121.5	78.5	91.6

ber of ligand ions participate in the random walk of the ion for a period that is at least several orders of magnitude longer than the time required for a single vibration. These suggestions are at the best qualitative and it is not obvious how unequivocal conclusions about complex formation in the melts can be drawn from the data. Presumably Raman spectra studies are the only way to resolve the point unambiguously.

Acknowledgments

Grateful acknowledgment is made to the U.G.C. of New Zealand for a research grant and to the Reserve Bank of Australia for a fuel cell research grant which have been used partly to finance this study. Thanks are due to Dr. R. Mills of the Australian National University for helpful discussions.

Manuscript submitted Dec. 27, 1972; revised manuscript received March 23, 1973.

Any discussion of this paper will appear in a Discussion Section to be published in the June 1974 JOURNAL.

REFERENCES

1. J.O'M. Bockris, J. L. White, and J. D. Mackenzie, "Physico-Chemical Measurements at High Temperatures," p. 247, Butterworth, London (1959).
2. M. Blander, "Molten Salt Chemistry," p. 559, John Wiley & Sons, Inc., New York (1964).
3. B. R. Sundheim, "Fused Salts," p. 208, McGraw Hill Book Co., New York (1964).
4. G. J. Janz, "Molten Salt Handbook," p. 517, Academic Press, New York (1967).
5. C. J. Janz and R. D. Reeves, *Advan. Electrochem. Eng.*, **5**, 147 (1967).
6. E. W. Yim and M. Feinleib, *This Journal*, **104**, 622 (1957).
7. H. R. Bronstein and M. A. Bredig, *J. Am. Chem. Soc.*, **80**, 2077 (1958).
8. G. J. Janz and M. R. Lorenz, *Rev. Sci. Instr.*, **32**, 130 (1961).
9. G. J. Janz and M. R. Lorenz, *This Journal*, **108**, 1052 (1961).
10. A. T. Ward and G. J. Janz, *Electrochim. Acta*, **10**, 849 (1965).
11. P. L. Spedding and R. Mills, *This Journal*, **112**, 594 (1965); **113**, 599 (1966).
12. P. L. Spedding, *ibid.*, **117**, 177 (1970).
13. R. A. Robinson and R. H. Stokes, "Electrolyte Solutions," p. 87, 2nd edition, Butterworth, (1959).
14. P. L. Spedding, *J. Less-Common Metals*, **7**, 395 (1964).
15. E. R. Van Artsdalen and I. S. Yaffe, *J. Phys. Chem.*, **59**, 118 (1955); **60**, 1125 (1956).
16. H. Margenau and G. M. Murphy, "The Mathematics of Physics and Chemistry," 2nd edition, p. 519, John Wiley & Sons, Inc., New York (1957).
17. F. Braun, *Pogg. Ann.*, **154**, 190 (1875).
18. K. Arndt, *Z. Elektrochem.*, **12**, 337 (1906).
19. E. Ryschkewitsch, *ibid.*, **39**, 531 (1933).
20. G. V. Vorobev, S. V. Karpachev, and S. F. Palguev, *Izv. Anal. Inst. Obs. Neorg. Khim. Akad. Nauk SSSR Sekt Fiz Khim*, **26**, 164 (1955).
21. H. Bloom, *Rev. Pure Appl. Chem.*, **9**, 139 (1959).
22. C. A. Angell, *J. Phys. Chem.*, **68**, 218, 1917 (1964); **69**, 399 (1965).
23. L. F. Grantham and S. J. Yosim, *J. Phys. Chem.*, **67**, 2506 (1963); **72**, 762 (1968); **38**, 1671 (1963); **45**, 1192 (1966).
24. R. W. Laity, *Ann. N.Y. Acad. Sci.*, **79**, 997 (1960).
25. J.O'M. Bockris, E. M. Crook, H. Bloom and N. E. Richards, *Proc. Roy. Soc.*, **255A**, 558 (1960).
26. W. A. Adams and K. J. Laidler, *Can. J. Chem.*, **46**, 1990 (1968).
27. S. B. Brummer and G. J. Hills, *Trans. Faraday Soc.*, **57**, 1816, (1961).
28. Yu. K. Delimarskii and B. F. Markov, "Electrochemistry of Fused Salts," p. 32, Sigma, Washington, D.C. (1961).
29. S. A. Rice, *Trans. Faraday Soc.*, **58**, 499 (1962).
30. P. L. Spedding, *Rev. Pure Appl. Chem.*, **21**, 1 (1971).
31. J.O'M. Bockris and A. K. N. Reddy, "Modern Electrochemistry," Vol. I, p. 589, Plenum Press, New York (1970).

The Triangular Voltage Sweep Method for Determining Double-Layer Capacity of Porous Electrodes

II. Porous Silver in Potassium Hydroxide

E. G. Gagnon*

Electrochemistry Department, Research Laboratories, General Motors Corporation, Warren, Michigan 48090

ABSTRACT

One major problem in measuring the double-layer capacity of a porous electrode is the effect of distributed reactions. Ohmic resistance of the electrolyte makes it easier to charge or discharge the outer surface of the electrode, while the interior lags behind. Triangular voltage sweep results obtained with porous silver in 31 weight per cent KOH agreed well with predicted values obtained using a mathematical model which considers the physical properties of the electrode and electrolyte.

The surface area of a porous electrode may be determined by a number of techniques (*e.g.*, from weight/size distribution of particles, or BET measurements), but measurement of the double-layer capacity (DLC) of an electrode gives the best indication of internal area available for electrochemical reaction. One major problem in the measurement of the DLC of a porous electrode is the effect of distributed capacity. Ohmic resistance of the electrolyte within the pores of the electrode makes it easier to charge or discharge the outer surface of the electrode while the back of the electrode lags behind (1). This paper will compare experimental results with data obtained using a mathematical model proposed earlier (2, 3). The model considers the triangular voltage sweep technique and shows the effect of distributed capacity in the absence of faradaic current. The system investigated was porous silver in potassium hydroxide.

* Electrochemical Society Active Member.

Key words: double-layer capacity, porous electrode, silver electrode.

Theory

Assumptions and model.—The physical situation considered is illustrated in Fig. 1. The Luggin capillary of a reference electrode is positioned a distance, d, from the surface of the electrode having a thickness, L. One face of the electrode is exposed to the electrolyte and current collection takes place at the back of the electrode. It is assumed that (*a*) the porous system is so highly interlinked that the concentration of electrolyte in the pores of the electrode is constant over plane x in the electrode, (*b*) the electrode potential is constant over plane x, (*c*) transport gradients

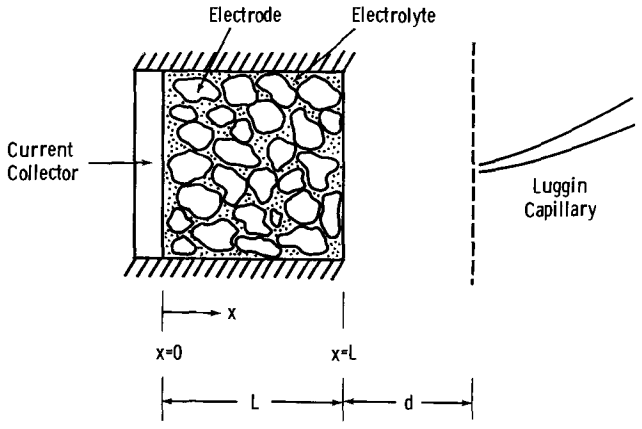

Fig. 1. Illustration of a Luggin capillary positioned a distance, *d*, from a porous electrode of thickness, *L*.

are one dimensional across x, (*d*) electronic conductivity of the electrode material is large compared to the ionic conductivity of the electrolyte within the pores, and (*e*) diffuse double-layer effects are negligible because the electrolyte used is concentrated.

Working equations.—The electrical double-layer between electrode and electrolyte has, in concentrated electrolytes, a thickness of only a few angstroms, and therefore follows the micro-contours of the surface. The DLC of an electrode is proportional to the electrode-electrolyte phase boundary and hence to the area available for electrochemical reaction. The DLC is defined by

$$i_c = C|dV/dt| \qquad [1]$$

where i_c is the capacitative current (A), C is the capacity (farads), V is the potential (V) between the electrode material and electrolyte near the phase boundary, and t is time (sec).

For the case where faradaic current effects are negligible, distributed capacity effects give rise to the behavior illustrated in Fig. 2 during a triangular voltage sweep (TVS) experiment (solid line); in the absence of distributed capacity effects, a square wave is seen (dashed line) which is what one would expect with a solid electrode. Elsewhere (2), it was shown that the current density at the face of a porous electrode (at $x = L$) may be predicted from

$$i(L) = \beta_1 kC' \qquad [2]$$

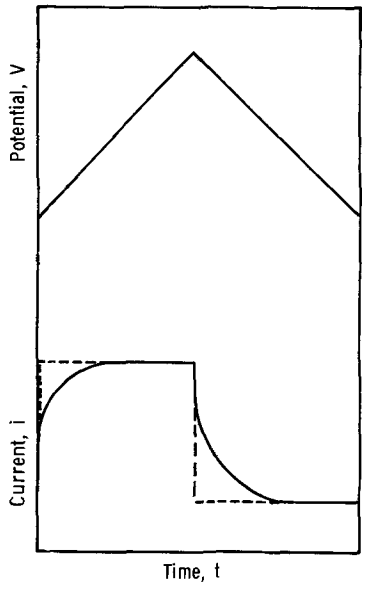

Fig. 2. Illustration of triangular voltage sweep results in the absence of faradaic currents: dashed line, negligible distributed capacity effects; solid line, significant distributed capacity effects.

where

$$\beta_1 = 1 - \sum_{n=1}^{\infty} \exp\left[-M_n^2 \frac{t}{\rho_e C' L}\right] \cdot \left[\frac{2\psi^2}{M_n^2(\psi^2 + M_n^2 + \psi)}\right] \qquad [2A]$$

$$\psi = \frac{L\lambda}{d} = \frac{\rho_e}{R_e A} = M_n \tan M_n \qquad [3]$$

$$\rho_e = \rho\lambda \qquad [4]$$

and k is sweep rate (mV/sec); C' is capacity (farads/cm^2) based on the geometric area, A (cm^2), of the electrode; L is electrode thickness (cm); t is time (sec); ρ is the specific resistance (ohm-cm) of the bulk electrolyte; ρ_e is the specific resistance (ohm-cm) of the electrolyte in the pores of the electrode; R_e is the resistance (ohms) of the bulk electrolyte; and λ is the labyrinth factor. For each value of ψ, values of M_n can be found from tables (4) listing the various roots of the transcendental equation $M_n \tan M_n = \psi$. Clearly, as time decreases, as the electrode thickness increases, or as the specific resistance of the electrolyte increases, distributed capacity effects become much more significant.

At the reversal point of the TVS, the current density at the face of the porous electrode was predicted (3) from

$$i(L) = \gamma kC' \qquad [5]$$

where

$$\gamma = \beta_1 - \beta_2$$

and

$$\beta_2 = \sum_{n=1}^{\infty} \exp\left[-M_n^2 \frac{t}{\rho_e C' L}\right] \cdot \left[\frac{2(\psi^2 + M_n^2)}{M_n^2(\psi^2 + M_n^2 + \psi)}\right] \sin^2 M_n \qquad [5A]$$

Experimental

Test cell.—The electrochemical cell used in this study was a 1000 ml beaker with a U-shaped side arm. A coil of platinum, which was used as the counterelectrode, was sealed into a ground glass joint and was placed in the side arm of the cell. A top made from acrylic sheet, with holes to admit the test and reference electrodes, was used to cover the main compartment of the cell. The electrolyte was 31 w/o (weight per cent) aqueous KOH, prepared from 45 w/o reagent grade KOH and distilled water.

The test electrodes were punched from a sheet of sintered, porous silver (99.8% purity). The electrodes were disk shaped, had a thickness of 0.127 cm, a diameter of 3.5 cm, a geometric area of 9.65 cm^2, a porosity of 62%, and a BET area of 0.18 m^2/g. They were inserted into an electrode holder similar to that used in a previous study (2). The test electrode was butted against a nickel current collector and current collection took place at the back of the electrode. The holder exposed one face of the electrode to the electrolyte.

All measurements were performed using a Hg/HgO (31 w/o KOH) reference electrode with a Luggin capillary. The tip of the Luggin was positioned close to the surface of the test electrode.

The cell was assembled in a constant temperature chamber which was used to control the temperature of the electrolyte (± 1°F).

Measurements.—Constant current measurements were made using a d-c power supply and a power resistance decade box. A Hg-wetted relay was used to switch on or interrupt the cell current. A storage oscilloscope with a dual trace amplifier and a time base was used to record potential-time traces. A high impedance vacuum tube voltmeter monitored the elec-

trode potential. Ohmic polarization, η_{ir}, was obtained using the vertical, blanked-out portion of the potential-time oscilloscope trace when current was switched on or off.

Triangular voltage sweep (TVS) measurements were performed using a potentiostat in conjunction with a signal generator. A dual trace recorder was used to record the potential (test *vs.* reference electrodes) and current (between test electrode and counterelectrode) as a function of time. From both traces, plots of current and/or capacity as a function of potential or time were obtained.

Results and Discussion

Figure 3 shows typical data obtained at room temperature when the potential of the test electrode *vs.* Hg/HgO was varied cathodically from 0 to −0.140V at a sweep rate of 56.5 mV/sec and then anodically back to 0V at the same rate. The curve shows the current flowing between the test electrode and counterelectrode as a function of time (top abscissa) and also potential (bottom abscissa). As the sweep begins, the cathodic current rises in region *ab* and reaches a plateau of short duration at c before passing through a peak at *d*. After the peak, the current starts to decrease again and at the reversal point of the sweep, the current becomes anodic. Some attempt will be made to explain the nature of the various regions in the cathodic portion of the curve.

Region abc.—To test whether the delay time observed in region *abc* is the result of a distributed capacity effect which can be predicted by Eq. [2], estimates of the parameters ψ, λ, d, and ρ_e were made to calculate β_1, since $\beta_1 = f(\psi, t/\rho_e C'L)$. The first parameter required was $\psi = L\lambda/d$.

The distance between the test electrode and tip of the Luggin capillary, d, was determined from η_{ir} measurements which were performed between 71° and −50°F. Figure 4 shows the variation of the effective resistance, R_e, as a function of temperature, for an undisturbed position of the Luggin capillary. Also shown is the specific resistance of the electrolyte, ρ (solid line). The results indicate that for the experimental set-up used, $R_e \simeq 1/10\rho$. Thus, the mean path length, d, can be calculated from $d = R_e A/\rho = (0.1\rho)(9.65/\rho = 0.965$ cm; A being the geometric area of the electrode.

An initial estimate of the labyrinth factor, λ, was made by curve fitting a set of experimental points found in region *abc* with calculated values using Eq. [2]. In this way, a value of $\lambda = 2$ was found. Since the porosity of the electrode, θ, was determined from porosimeter data to be 0.62, the tortuosity factor, q, was estimated (5) using $\lambda = q/\theta$, to be 1.24. This value

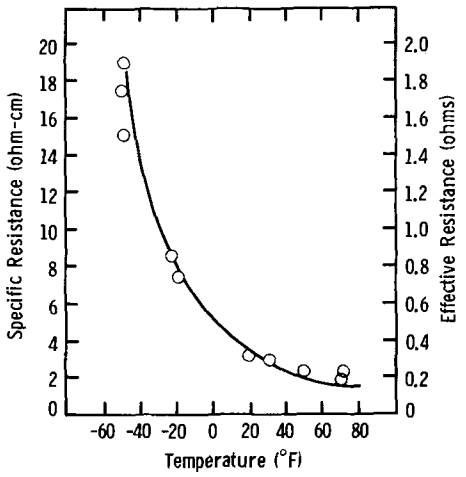

Fig. 4. Specific reistance of 31 w/o KOH (solid) and effective resistance (points) of electrolyte between the test electrode and tip of the Luggin capillary.

is in reasonable accord with values close to $\sqrt{2}$ found for electrodes in fuel cell and battery studies. It will be shown later that the determined value of λ holds quite well for other test conditions (*e.g.*, variations in sweep rate and temperature). De La Rue and Tobias (6), in their studies on the conductivity of dispersions, found that $\lambda = 1/\theta^n$, where $n = 1.5$. Using $\theta = 0.62$, a value of $\lambda = 2.05$ is obtained which is in good agreement with the value determined experimentally.

The value of ψ estimated using Eq. [3] has a value of 0.27. Taking $L = 0.13$ cm, $\lambda = 2$, $q = 1.24$, $d = 0.965$ cm, ρ_e (see Fig. 4) $= 1.9 \times 2 = 3.8$ ohm-cm, C (from the plateau region at c in Fig. 3) $= 0.45$ farads, values of $t/\rho_e C'L$ were calculated using the values corresponding to the experimental conditions. Thus, values of β as a function of ψ and $t/\rho_e C'L$ were obtained and the current, i, was predicted from $i = \beta_1 kC$. Figure 5A shows predicted *vs.* experimental results (region *abc*, Fig. 3) obtained using a sweep rate, k, of 56.5 mV/sec.

As a cross check on the capacity, C, used in the calculations, galvanostatic measurements performed from an open-circuit potential of −0.038V, using a current density of 31 mA/cm², gave an apparent capacity $C = 0.46$ farads, which is in good agreement with the 0.45 farads obtained using the TVS technique. The oscilloscopic potential-time trace was linear in the potential range of interest indicating that effects due to faradaic current in region *abc* were negligible.

Figures 5B, 5C, and 6 show similar results obtained using sweep rates of 27.1, 5.6, and 534 mV/sec, where the predicted values were based upon a C value of

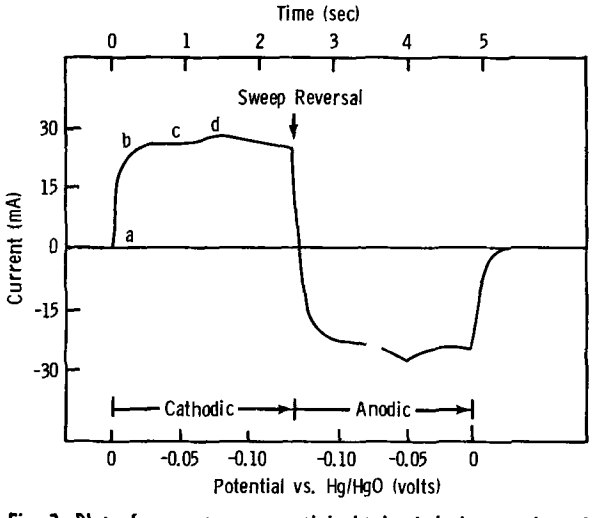

Fig. 3. Plot of current *vs.* potential obtained during a triangular voltage sweep at room temperature: $k = 56.5$ mV/sec.

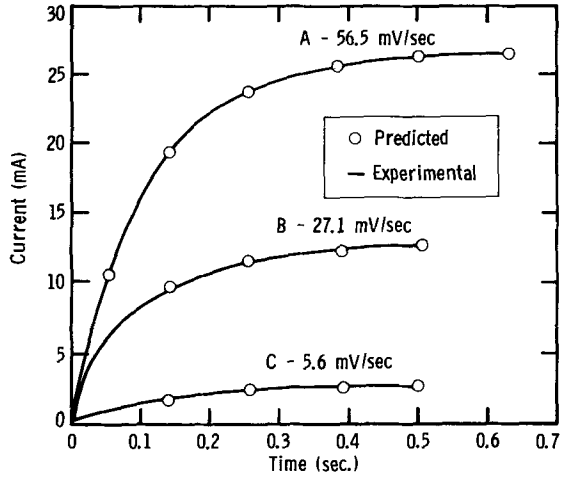

Fig. 5. Experimental *vs.* predicted results obtained in region *abc* at 71°F: A, 56.5 mV/sec; B, 27.1 mV/sec; C, 5.6 mV/sec.

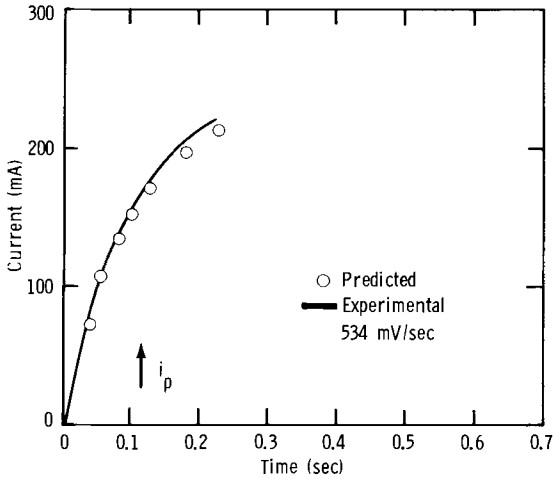

Fig. 6. Experimental *vs.* predicted results obtained using a sweep rate of 534 mV/sec at 71°F.

0.45 farads; in all the calculations, $\lambda = 2$ was used. For the two lower sweep rates, the agreement between the predicted and experimental results is good. For the results obtained using the fastest sweep rate, $k = 534$ mV/sec, the experimental results deviate from the predicted values at about 0.11 sec, which in this case corresponds to the appearance of i_p (region *d* in Fig. 3). For the lower sweep rates, the plateau region at c is reached well before i_p (region *d*) occurs.

Region d.—In this region a cathodic current peak, i_p, appears at about −0.070V *vs.* Hg/HgO. Plots of i_p *vs.* sweep rate at 71° and −19°F are shown in Fig. 7. The plots are linear and have the form

$$i_p = C^{\dagger}\,(dV/dt)$$

where $C^{\dagger}$ is a pseudocapacity which is potential and temperature dependent. Results obtained at higher sweep rates are not available because effects due to distributed reactions, as shown in Fig. 6, gave spurious results. The anodic peak was about 30 mV more positive than the cathodic peak indicating the possibility of a reversible process where the number of electrons transferred in the over-all process is equal to 2. McMullen (7) found that with Ag in 1*N* Na_2SO_4, a "hump" occurred in the same potential region reported here. Veselovsky (8) reported that for silver in 0.1*N* KNO_3, the point of zero charge occurs in the vicinity of these peaks. Bockris (9) has explained the "hump" generally in terms of a simple-lateral-repulsion model of contact adsorbing ions within the inner Helmholtz plane.

Figure 8 shows a composite of seven different cathodic sweeps where the start of each sweep was at a different potential, but each was run at the same sweep rate of 56.5 mV/sec. Included in Fig. 8 are apparent capacities, *C*, calculated using Eq. [1] and capacities, *C**, based on the BET area of the electrode. It appears that capacity decreases to a minimum value

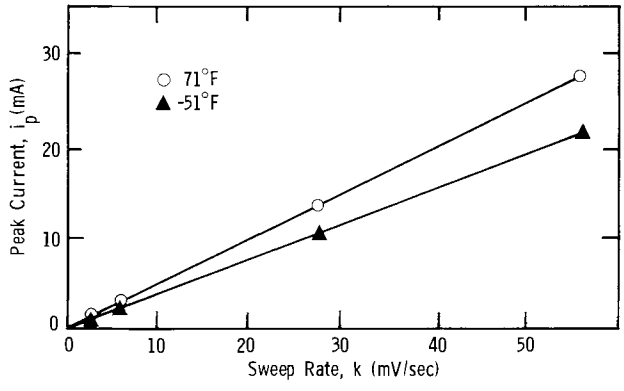

Fig. 7. Effect of sweep rate on peak current (region *d*)

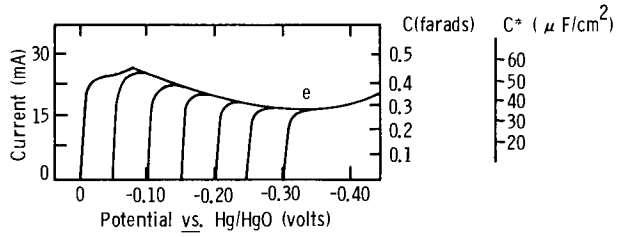

Fig. 8. Plot of capacity *vs.* potential for porous Ag in KOH at 71°F.

at *e*, before starting to increase again; the capacity based on a BET area varies from a peak value of 55 μF/cm² at −0.07V to a minimum value of 35 μF/cm² at about −0.33V. This is in reasonable agreement with results found in the literature for solid silver. It was found that capacities for solid Ag in 1*N* Na_2SO_4 ranged from 45 to 58 μF/cm² (7) and in 30 w/o KOH varied from 36 to 49 μF/cm² (10).

Low-temperature effects.—The theory predicts that, in the absence of faradaic current, distributed capacity effects will give rise to behavior illustrated in Fig. 2, where the upsweep and downsweep results are predicted using Eq. [2] and [5], respectively. The room temperature results in Fig. 5A, 5B, and 5C predicted the upsweep results quite well, but the downsweep results could not be easily checked because of interference by i_p in region *d*. To test the model, measurements were performed entirely in a region of minimum DLC (region *e*) by using a smaller potential excursion of 50 mV. Also, the test temperature was −51°F, where the specific resistance of the electrolyte was 19/1.9 = 10 times greater than that at room temperature, thus making the distributed capacity effects more severe.

Except for $k = 20$ mV/sec, $\rho = 19$ ohm-cm (see Fig. 4), and $C = 0.20$ farads (obtained experimentally), all of the parameters used in Eq. [2] and [5] were the same as before, including $\lambda = 2$. The predicted *vs.* experimental results are shown in Fig. 9. The agreement is seen to be good.

The results also indicate that the capacity of Ag decreases with temperature; in the region of minimum DLC, the capacity has a value of 0.20 farads or 21 μF/cm² (based on BET area) compared to a value of about 35 μF/cm² at room temperature.

Summary and Conclusions

With porous silver electrodes, distributed reactions in the absence of faradaic currents give rise to electrode behavior which is complex, but which can be quantitatively treated using a mathematical model previously developed (2, 3). Experimental results obtained with porous Ag in KOH agreed well with predicted values at temperatures between 71° and −51°F. The model considers the thickness, porosity, labyrinth, and tortuosity factors of the porous electrode, the distance be-

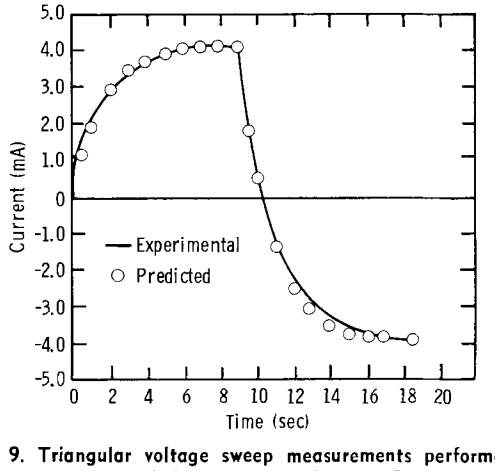

Fig. 9. Triangular voltage sweep measurements performed in a region of constant DLC (region e, Fig. 8) at −51°F.

tween the surface of the test electrode and the tip of the Luggin capillary, and the resistivity of the electrolyte in the pores of the porous electrode.

The capacity of porous Ag was potential dependent, and the values ranged from a peak value of 55 μF/cm^2 at -0.07V to a minimum value of 35 μF/cm^2 at about -0.33V. At -51°F, the capacity in the region of minimum DLC was found to be about 21 μF/cm^2.

The model enables one to select the proper experimental conditions to determine DLC free from distributed capacity effects.

Acknowledgments

The author expresses his appreciation to Professor L. G. Austin, The Pennsylvania State University, for helpful discussions during the course of this study.

Manuscript submitted Jan. 23, 1973; revised manuscript received March 28, 1973. This was Paper 242 presented at the Chicago, Illinois, Meeting of the Society, May 13-18, 1973.

Any discussion of this paper will appear in a Discussion Section to be published in the June 1974 JOURNAL.

REFERENCES

1. L. G. Austin and E. G. Gagnon, *Am. Inst. Chem. Engrs. J.*, **17**, 1057 (1971).
2. E. G. Gagnon and L. G. Austin, HDL-065-4, Harry Diamond Laboratories, Washington, D.C., September 1971.
3. L. G. Austin and E. G. Gagnon, *This Journal*, **120**, 251 (1973).
4. H. S. Carslaw and J. C. Jaeger, "Conduction of Heat in Solids," p. 491, Oxford at the Clarendon Press (1959).
5. L. G. Austin, "Handbook of Fuel Cell Technology," p. 178, C. Berger, Editor, Prentice Hall, Englewood Cliffs, N. J. (1968).
6. R. E. De La Rue and C. W. Tobias, *This Journal*, **106**, 827 (1959).
7. J. J. McMullen and N. Hackerman, *ibid.*, **106**, 341 (1959).
8. V. I. Veselovsky, *Acta Physicochim. URSS*, **11**, 815 (1939).
9. J. O'M. Bockris and A. K. N. Reddy, "Modern Electrochemistry," Vol. 2, p. 777, Plenum Press, New York (1970).
10. J. McCallum, R. W. Hardy, and R. F. Redmond, AFAPL-TR-66-31, Battelle Memorial Institute, Columbus, Ohio, April 1966.

Anodic Polarization Study of Mild Steel in NaCl Solution During Electrochemical Machining

Kao-Wen Mao*

Electrochemistry Department, Research Laboratories, General Motors Corporation, Warren, Michigan 48090

ABSTRACT

A current interruption technique was used to study the anode potential of mild steel during electrochemical machining (ECM) in NaCl solution. The results show that in the turbulent region the iron dissolution process is not affected by flow rate, but is influenced by NaCl concentration. Anodic film effects were observed when the electrolyte flow is in the transition region.

Since 1959, when the first commercially available electrochemical machining (ECM) device was announced (1), considerable effort has been expended in studying this process. However, because of experimental difficulty, a meaningful anodic polarization study under actual ECM conditions is still lacking. Anode potentials of iron dissolution in NaCl at current densities less than 8 A/cm^2 have been determined by extrapolating the distance between the working and the reference electrode to zero (2). Landolt, Muller, and Tobias (3) used a galvanostatic-pulse method to study high-rate dissolution of copper. The results concerning active dissolution at current densities between 0.01 and 100 A/cm^2 were analyzed. Recently, Landolt (4) measured both anode and cathode potentials during ECM of nickel at current densities up to 15 A/cm^2 using a current interruption technique.

In this work, a current interruption technique was employed to study the anode potentials during ECM of mild steel in NaCl solutions at current densities from 5 to 100 A/cm^2.

Experimental

Flow cell apparatus.—The ECM experiments were carried out in an electrochemical cell operated at controlled fluid dynamic conditions. The flow cell apparatus is shown in Fig. 1. The electrolyte was continuously circulated by means of a stainless steel turbine pump. The pump was electrically insulated from the motor to avoid a complicated grounding system for the cell. The electrolyte flow rate was measured by a stainless steel rotameter. Stainless steel diaphragm pressure gauges were employed to measure the electrolyte pressures at various positions. All pipes, fittings, and valves were made of either stainless steel or PVC. The electrolyte reservoir had a capacity of 8 liters and was made of acrylic sheet.

The electrochemical cell consisted of a rectangular electrolyte flow channel 0.0508 cm deep (the distance between the two electrodes)[1] $\times$ 0.714 cm wide $\times$ 16.5 cm long formed between two acrylic plates. The cell was sealed by means of O-rings and toggle clamps. The rectangular mild steel[2] anode and the brass cathode 0.0635 cm (in the flow direction) $\times$ 0.254 cm, was cast into an epoxy cylinder 0.635 cm in diameter. The electrodes were located 14 cm, or 148 hydraulic diameters,[3] from the inlet of the cell to provide fully developed velocity profiles at the electrodes (5). Teflon fittings were used for the purpose of sealing and positioning the electrodes. The reference electrode compartments were connected to the cell through capillary holes (0.0254 cm diameter) which were positioned near and upstream from the electrodes. A calomel reference electrode saturated with NaCl was used to measure the anode potential. In the present work, the cathode potential was not measured.

* Electrochemical Society Active Member.
Key words: current interruption, dissolution, IR drop, potential decay, salt film.

[1] The cell was designed so that the distance between the two electrodes could be increased by inserting a plastic spacer.
[2] Composition (other than Fe) of the mild steel anode: C, 0.07%; Mn, 0.4%; P, 0.008%; S, 0.018%; Ni, 0.005%; Si, 0.005%; Co, <0.003%.
[3] The hydraulic diameter is defined by four cross section/wetted perimeter.

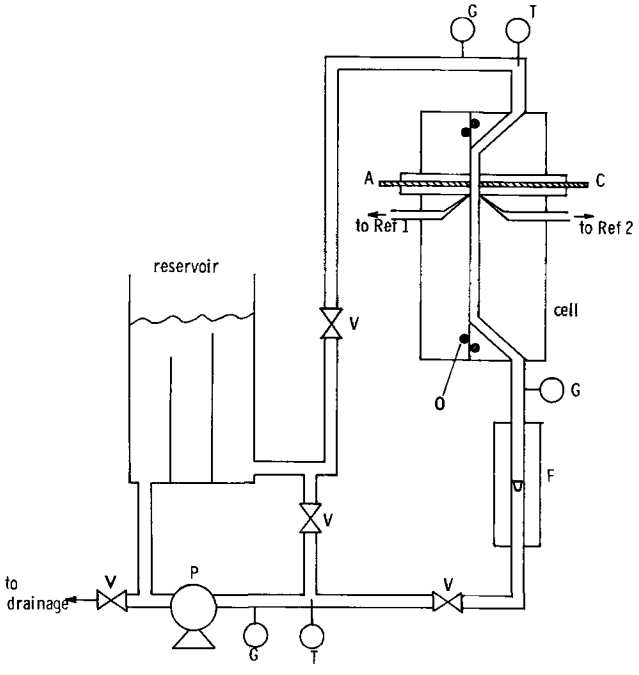

Fig. 1. Schematic of flow cell apparatus. A, anode; C, cathode; F, rotameter; G, pressure gauge; O, O-ring; P, turbine pump; Ref. 1, anode reference electrode compartment; Ref. 2, cathode reference electrode compartment; T, thermometer; V, needle valve.

The mild steel (or brass) electrode was degreased, washed, and dried before it was cast into the epoxy cylinder. The electrode was polished with a 600-grit wet grinding paper and, before a run, it was treated with 6*N* HCl for 30 sec followed by rinsing with distilled water. Reagent grade NaCl and distilled water were used to prepare the solutions. The electrolyte was frequently changed to avoid any accumulation of sludge. Experiments were conducted at 26° ± 2°C.

Polarization measurements.—A current interruption technique was used to measure the *IR*-free anodic potential. Figure 2 shows the electrical circuit for the measurements. A constant current was applied to the cell by a Sorensen DCR 150-5A constant voltage/constant current d-c power supply. Before the circuit was closed, the current passed through a variable resistor with a resistance comparable to that of the cell. A Weston milliammeter (Model 901) or ammeter (Model 931) was used to measure the current. A Clare HGS5018 mercury-wetted contact relay was employed to control the cell circuit. The changes of the anode potential and the cell current were observed on a Tektronix 555 dual-beam oscilloscope with

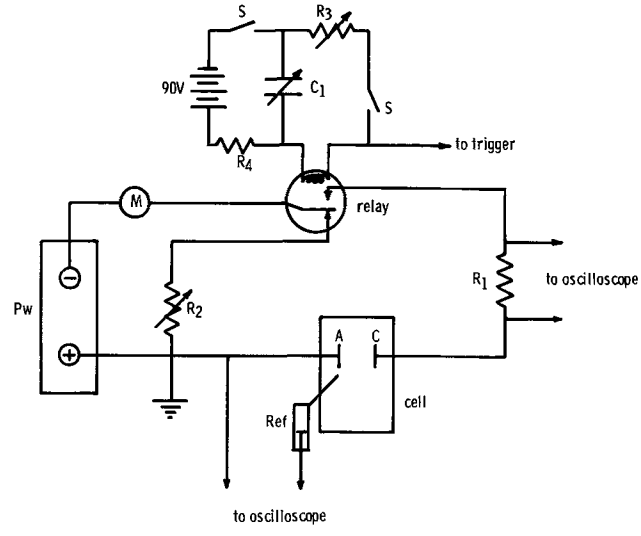

Fig. 2. Diagram of the electrical circuit. A, anode; C, cathode; C_1, variable capacitor (removable); M, ammeter; Pw, constant current power supply; R_1, 1 ohm precision resistor; R_2, R_3, variable resistors; R_4, resistor; S, switch.

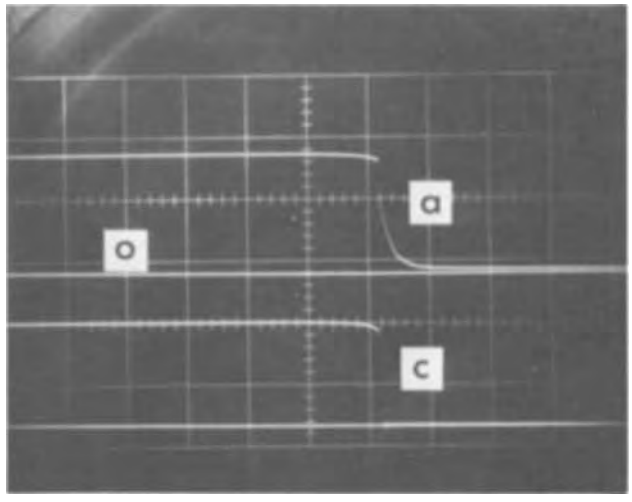

Fig. 3. Typical results obtained with 4M NaCl at Re = 15,500 and 100 A/cm^2; time scale, 20 μsec/div; curve a, anodic potential transient, 5 V/div; curve O, open-circuit potential; curve c, current transient, 1 V/div.

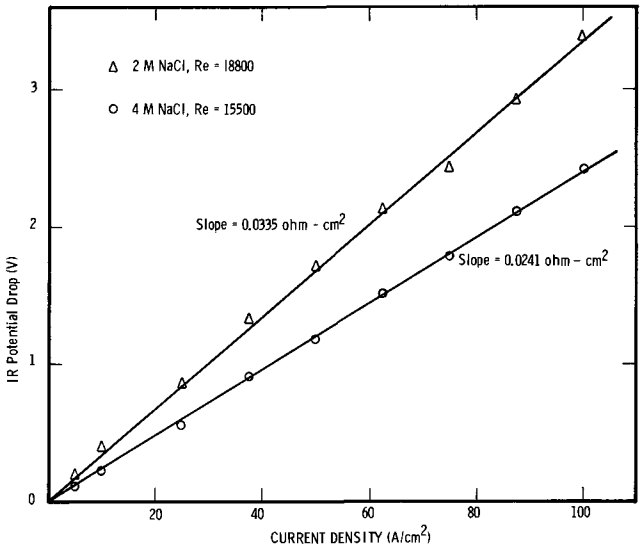

Fig. 4. *IR* potential drop vs. current density

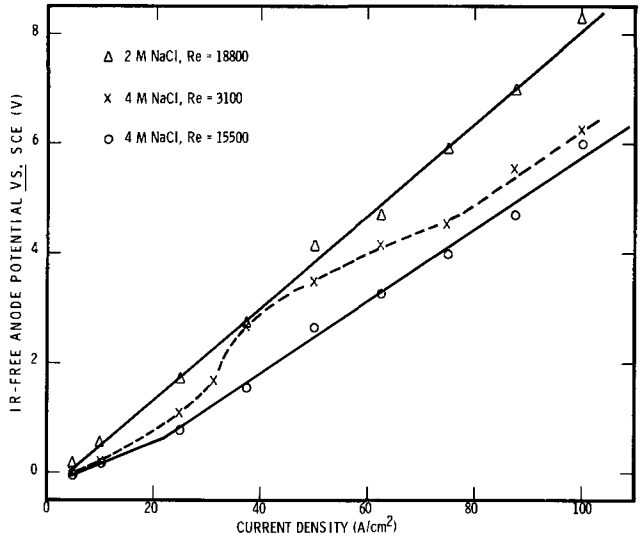

Fig. 5. *IR*-free anode potential vs. current density

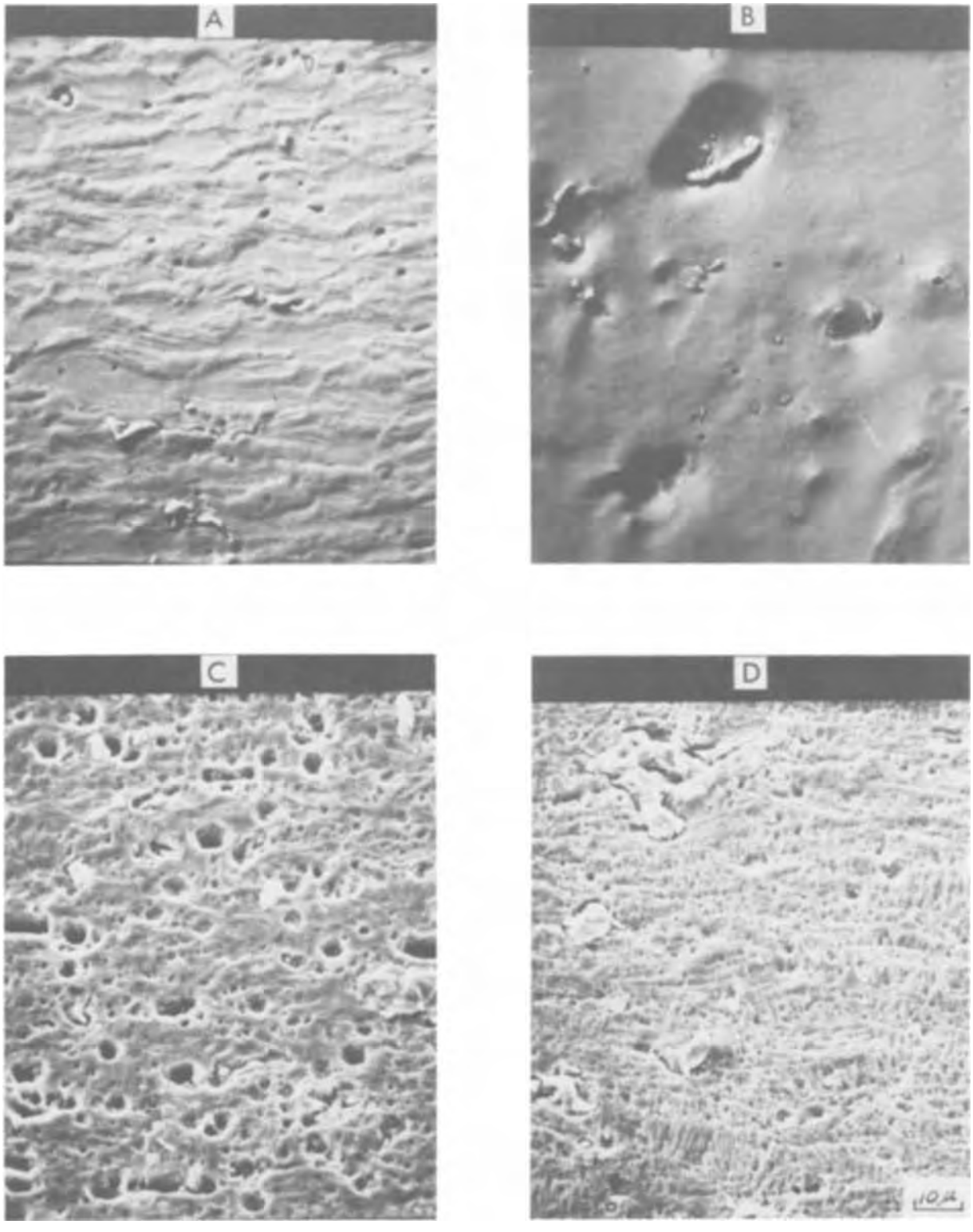

Fig. 6. Scanning electron micrographs of the machined surface obtained by ECM. A, 4M NaCl, 75 A/cm^2, Re = 15,500; B, 4M NaCl, 75 A/cm^2, Re = 3100; C, 4M NaCl, 10 A/cm^2, Re = 15,500; D, 2M NaCl, 75 A/cm^2, Re = 18,800; flow direction ↑.

Type G preamplifiers and a time scale of 20 μsec/cm, and were recorded on photographic film. The current, measured by the voltage drop across a precision 1 ohm resistance, was interrupted after it had passed through the cell for 0.6-2.0 sec, depending upon the current density used.[4] The photographic picture was enlarged ten times to determine the initial slope (dV/dt) of the anodic decay curve after the current was interrupted. The IR potential drop between the anode and the reference electrode was determined by linear extrapolation of the decay curve to zero time ($t = 0$) since the drop is assumed to be instantaneous.

[4] By using a different trigger mode and slower oscilloscope time scale, it was found that, in the present system, a steady state was reached in less than 0.5 sec.

Results and Discussion

Figure 3 shows typical experimental results. Curve a represents the change of the anode potential due to the current interruption. The current transient is given by curve c. From curve c, it was noted that there was a slight decrease in the current before it was completely interrupted. This may result from a higher resistance of the relay due to the presence of a thin mercury filament. Various power supplies and relays have been tested for this work. So far, the

present combination provided the best results. In this report, the experimental data are analyzed using the steady-state currents and the small changes in current before interruption are neglected.

All data presented in this report represent average values of two or more runs. The maximum difference between the results of different runs is less than 10%.

Figure 4 shows the *IR* potential drops measured in the present cell in 4M NaCl at Re = 15,500[5] (flow velocity u = 2000 cm/sec) and in 2M NaCl at Re = 18,800 (u = 2000 cm/sec). The solid straight lines which pass through the zero point were determined by the method of least squares. Since the ratio of the two slopes (or apparent resistances), 0.0335/0.0241 = 1.39, is comparable to the ratio of the resistivities of the solutions, ρ (2M NaCl)/ρ(4M NaCl) = 6.69/4.37 = 1.53 (6), it is believed that the *IR* drop determinations made in this work are reasonably accurate. Similar results were obtained at different flow rates.

If one assumes that at the beginning of the open-circuit transient the electrode self-discharge process has the same rate as that corresponding to the steady-state current density (7, 8), then the double layer capacitance, C, can be determined by

$$C = -\frac{i}{(dV/dt)|_{t=0}} \qquad [1]$$

where i is the steady-state current density before the current interruption. Based on Eq. [1], it is observed that in the present system the capacitance does not vary with current density and average values are C = 73.4 ± 7.7 μF/cm² in 4M NaCl at Re = 15,500 and C = 49.4 ± 4.8 μF/cm² in 2M NaCl at Re = 18,800.

The *IR*-free anode potentials measured in 2 and 4M NaCl solutions at the flow rates mentioned above are shown in Fig. 5. Apparently, the anode potential is linearly related to the current density. The straight lines in Fig. 5 were drawn using the method of least squares. In 4M NaCl, the polarization data can be represented by two straight lines with slopes of 0.042 ohm-cm² from 5 to 22.5 A/cm², and 0.0665 ohm-cm², from 22.5 to 100 A/cm². In the case of 2M NaCl, a single straight line with slope of 0.0839 ohm-cm² is used to fit all the data. Experiments were also carried out in 2 and 4M NaCl solutions at Re = 4700 (u = 500 cm/sec for 2M NaCl and u = 600 cm/sec for 4M NaCl); the results are similar to those obtained at higher flow rates.

[5] Re represents the Reynolds number which is defined as the hydraulic diameter × flow velocity/kinematic viscosity.

Electrochemical machining of mild steel in NaCl solutions has been studied using a closed cell system (9). It was found that the anodic current is mainly consumed in iron dissolution ($Fe \rightarrow Fe^{++} + 2e$) although there is a slight decrease in current efficiency as the current density increases. Based on the results of this study, it is suggested that in the turbulent flow region (say Re > 4700), the ECM iron dissolution process in NaCl solutions is not affected by the electrolyte flow, but is influenced by NaCl concentration. It should be pointed out that the measured potentials shown in Fig. 5 bear no resemblance to common electrode potentials of a single interface. At the present time, there is no evidence which explains the linearity of the relationships between the *IR*-free anode potential and the current density under ECM conditions. However, it has been suggested (10) that during ECM the process of transfer of ions in the layer near the anode under the influence of a strong electric field is perhaps important; an activation control is not likely because of such high overpotentials. The dependence of potential on electrolyte concentration seems to reflect the change in conductivity of the solution.

In Fig. 5, the broken line shows the results obtained with 4M NaCl at Re = 3100 (u = 400 cm/sec). The anode potentials are apparently higher than those found at the higher flow rate, and a linear relationship between the *IR*-free potential and the current density is not observed. It was also noticed that at this low flow rate the data were less reproducible than at higher flow rates. This change in potential behavior may be caused by the presence of an anodic film resulting from the precipitation of the anode product (11) which, in turn, was caused by the reduction of the flow rate to a value in the turbulent/laminar transition region (12). By studying the surface finish, it was found that the surface obtained at R = 3100 (Fig. 6B) is brighter than that obtained at Re = 15,500 (Fig. 6A), both at 75 A/cm².

It is of interest to note that at this low flow rate (Re = 3100) the anodic potential always exhibited an arrest after the initial rapid decay (Fig. 7A). Such an arrest may be caused by the presence of an anodic film. Compared with the result at Re = 15,500 (Fig. 7B), the arrest potential at Re = 3100 is significantly higher. The difference between the two arrest potentials was found to be proportional to the difference between the two *IR*-free anode potentials which are shown in Fig. 5.

During ECM of steel in 4M NaCl at Re = 15,500, no arrest was observed at current densities lower than

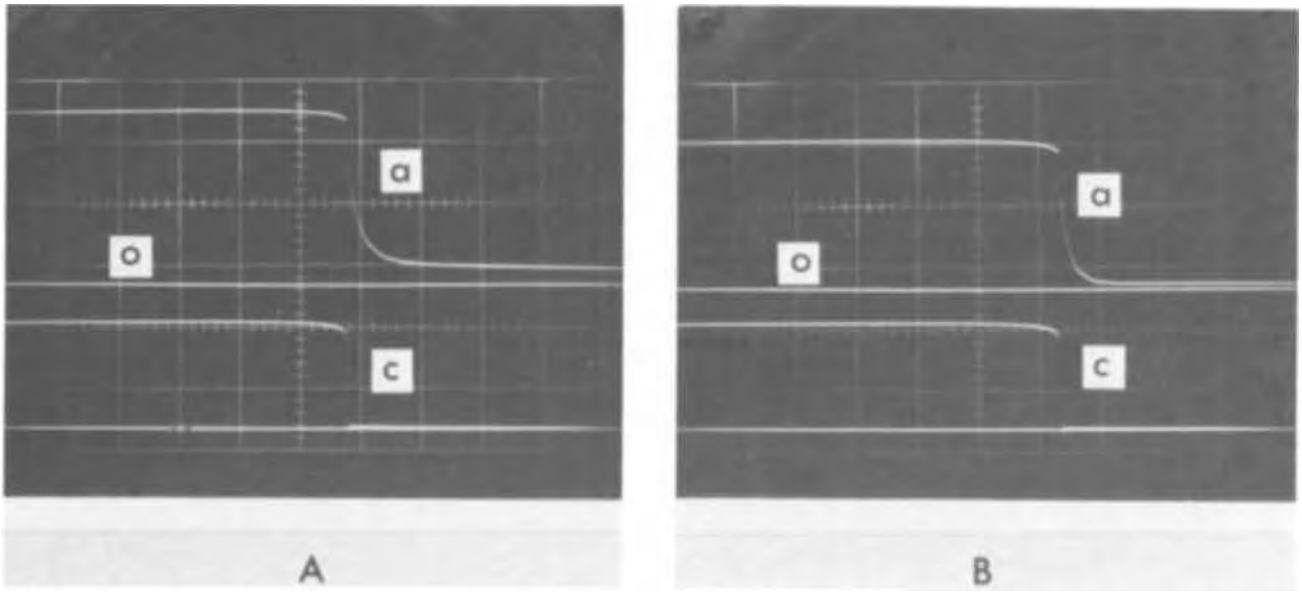

Fig. 7. Anodic potential decay in 4M NaCl at 50 A/cm². A, Re = 3100; B, Re = 15,500; time scale, 20 μsec/div; curve a, anodic potential transient, 2 V/div; curve o, open-circuit potential; curve c, current transient, 0.5 V/div.

25 A/cm², and the arrest potential becomes higher as the current density increases above 25 A/cm². This indicates that the change of the slope of the polarization curve shown in Fig. 5 may be caused by an anodic film. Figure 6C shows that the surface obtained at 10 A/cm² is sponge-like,[6] and is less smooth than that obtained at 75 A/cm² (Fig. 6A). The sponge-like surface is believed to be caused by a high rate of etching process. In the case of ECM in 2M NaCl at Re = 18,800, the arrest potential is significantly lower and, in most cases, is not observed. Hence, the anodic film effect is not significant, and the polarization curve can be represented by a straight line (Fig. 5). Figure 6D shows that the surface obtained in 2M NaCl at 75 A/cm² is still etched and is rougher than that obtained in 4M NaCl at the same current density (Fig. 6A).

From the above discussion it is apparent that during ECM of mild steel in NaCl solutions the presence of an anodic film, which can affect the surface finish, is influenced by the current density, the electrolyte flow rate, and the concentration. However, once in the turbulent region (Re > 4700) the flow rate has little effect on the anodic film. The *IR*-free anode potential is linearly related to the current density, and the iron dissolution process is mainly affected by NaCl concentration.

[6] By x-ray fluorescence analysis the white particles seen protruding from the surface in Fig. 6C and 6D were found to be rich in manganese.

Manuscript submitted Nov. 6, 1972; revised manuscript received March 9, 1973.

Any discussion of this paper will appear in a Discussion Section to be published in the June 1974 JOURNAL.

REFERENCES

1. Anonymous, *Am. Machinist*, **103**, 99 (1959).
2. A. D. Davydov, V. D. Kashcheev, and B. N. Kahanov, *Elecktrokhimiya*, **5**, 221 (1969).
3. D. Landolt, R. H. Muller, and C. W. Tobias, *This Journal*, **118**, 40 (1971).
4. D. Landolt, *ibid.*, **119**, 708 (1972).
5. D. Landolt, R. H. Muller, and C. W. Tobias, *ibid.*, **116**, 1384 (1969).
6. G. J. Janz, B. G. Oliver, G. R. Lakshminarayanan, and G. E. Mayer, *J. Phys. Chem.*, **74**, 1285 (1970).
7. H. B. Morley and F. E. W. Wetmore, *Can. J. Chem.*, **34**, 359 (1956).
8. B. E. Conway, E. Gileadi, and M. Dzieciuch, *Electrochim. Acta*, **8**, 143 (1963).
9. K. W. Mao, *This Journal*, **118**, 1876 (1971).
10. T. P. Hoar, Private communication, (1972).
11. D. T. Chin, *This Journal*, **118**, 174 (1971).
12. D. Landolt, *Rev. Sci. Instr.*, **43**, 592 (1972).

Natural Convection Within Porous Electrodes During Electrolysis

Richard Alkire* and Roman Plichta**

Department of Chemical Engineering, University of Illinois, Urbana, Illinois 61801

ABSTRACT

Depletion of reactive solute species from interior regions of a porous electrode during electrolysis can result in a density difference between the electrolyte within the porous electrode and the bulk solution. The density difference which may thus arise can in some cases provide the driving force necessary for natural convection flow of electrolyte through the porous electrode. A one-dimensional steady-state theoretical model has been developed to investigate system conditions under which density-driven flows may be anticipated and to what extent these flows can enhance reaction rates. Calculations were conducted for three aqueous electrolyte systems: potassium hydroxide, sulfuric acid, and copper sulfate in excess sulfuric acid. The theoretical results predict conditions under which volumetric reaction rates may be increased significantly by the occurrence of natural convection. The results indicate that double-porosity high-rate porous electrodes may be designed within which electrochemical reaction would occur primarily in the fine, high surface area, pores while natural convection of electrolyte would take place in the larger pore structure.

The widespread usage of porous electrodes has come about in order to achieve large reaction rates per unit volume. Although the interfacial surface area of porous electrodes can be exceedingly large, a number of dilemmas arise in the design of these systems. For example, upper limitations on the effectiveness of the large reactive surface can be encountered, such as through ohmic resistance of the electrolyte in the pores, or through mass transfer limitations on the supply of reactants to the porous region. In the latter case of mass transport limitations, it seems clear that convection of reactants into the porous electrode is superior to diffusion as a mode of supply. Many practical systems, however, cannot afford the price or weight of a pumping system. The following investigation evaluates conditions under which mass-transport limitations may be substantially relieved by the occurrence of natural convection flow within porous electrodes during electrolysis.

The porous electrode structure consists of a connected matrix of electrically conductive solid material interspersed with connected pores totally filled with electrolyte. Electrode reactions take place within this porous matrix. Species may be removed or supplied to the porous region either by mass transport or by generation (or consumption) of species owing to reaction. When the availability of reactive species is hindered by slow transport in the electrolyte within the pore, concentration gradients arise during extended electrolysis. As a result of these concentration gradients, density gradients may occur within the electrode. Hydrodynamic instabilities may thus ensue so that electrolyte from the bulk would enter the pore, sweeping with it "fresh" reacting species. Natural convection would render the concentrations within the pore more uniform than would be observed under pure diffusion operation.

* Electrochemical Society Active Member.
** Electrochemical Society Student Associate.
Key words: porous electrode, natural convection, mathematical model.

Natural convection owing to density differences has received widespread attention. Previous investigations indicate that the nature of the fluid motion depends strongly on the orientation of the reactive solid surface which bounds the fluid undergoing convection. Near vertical surfaces, the fluid motion takes on a boundary layer type of structure while near horizontal surfaces, the flow is usually cellular in nature and can exhibit multiple steady states (1-7). Multi-dimensional natural convection within an inert porous media has also received attention, both near vertical and horizontal solid reactive surfaces (8-10). The study presented below differs from previous studies in that the porous electrode, throughout which natural convection of electrolyte takes place, is reactive and thus contributes to the densification process. Moreover, the fluid passes through the electrode and returns to the upstream face through an external path.

The purpose of this work is to develop a theoretical basis for predicting the effect on electrode behavior of natural convection flow within the porous media, and to evaluate conditions under which operation of diffusion-limited porous electrodes may be enhanced by the occurrence of these flows.

Mathematical Development

A schematic diagram of the porous electrode system under consideration is shown in Fig. 1. The porous electrode is completely flooded with liquid electrolyte, and the reactive species diffuse into the porous region from both sides of the electrode. There is no mass transport resistance external to the porous electrode. Further, the porous electrode is positioned in a large well-stirred bath whose composition changes by negligible amounts during the period of electrolysis. Thus the solute concentration is the same on either side of the porous electrode and remains constant during the duration of electrolysis. Additional details of the cell geometry have not been included in the figure since they do not enter into this simple analysis of natural convection effects. The counterelectrode may be positioned either above or below the porous electrode; current does not flow around the sides of the porous electrode and enter from the rear. Figure 1 illustrates two possible situations for the case where the counterelectrode is above the porous electrode. If, owing to density changes during electrolysis, the fluid within the porous electrode becomes lighter than the bulk electrolyte, convective flow will tend to occur toward the counterelectrode as indicated in Fig. 1A. If, on the other hand, electrolyte within the porous electrode becomes heavier than the bulk solution, convection away from the counterelectrode will tend to occur as shown in Fig. 1B. Similar diagrams could be drawn for the situation where the counterelectrode is below the porous electrode.

Since rigorous calculations are not justifiable for a preliminary evaluation of natural convection effects, the following assumptions have been introduced:

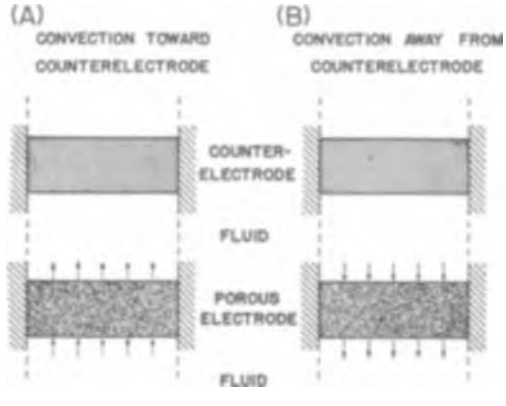

Fig. 1. Electrolysis cell configuration for natural convective flow in porous electrodes.

1. The pore structure is uniform and is sufficiently fine that the electrode behaves in a one-dimensional manner. The porous electrode is isopotential and isothermal; no appreciable structural changes of the solid phase occur during operation.
2. The electrolyte is sufficiently dilute that the transport parameters are constant, and activities can be replaced by concentrations. Diffusion resistances external to the porous electrode are negligible.
3. Density differences in the fluid are important only in the buoyancy effect which is the sole driving force for convection. Hydrodynamic motion occurs in plug flow and encounters resistance to flow only within the porous electrode.
4. A single electrochemical reaction occurs which obeys the Butler-Volmer rate equation.
5. Operation in the steady state prevails.

The preceding assumptions have been chosen in order to focus attention squarely on the influence of one type of natural convection on porous electrode behavior.

The region representing the porous electrode extends from $y = 0$, near the counterelectrode, to $y = L$, far from the counterelectrode. Within this region electrochemical reaction occurs with the stoichiometric form

$$\sum_i \nu_i M_i^{z_i} = ne^- \qquad [1]$$

The movement of solute species in the electrolyte occurs by diffusion, migration, and convection

$$N_i = -D_i \nabla c_i - z_i u_i c_i \mathbf{F} \nabla \phi + v c_i \qquad [2]$$

Under steady-state operation, a material balance for each solute species yields

$$\frac{dN_i}{dy} = -\frac{A\nu_i}{n\mathbf{F}} j \qquad [3]$$

where j is the local reaction rate for species i, given by the Butler-Volmer rate equation

$$j = i_o \left[\frac{c_a}{c_a^o} e^{-\frac{\alpha n\mathbf{F}(\phi - \phi_e)}{RT}} - \frac{c_c}{c_c^o} e^{\frac{(1-\alpha) n\mathbf{F}(\phi - \phi_e)}{RT}} \right] \qquad [4]$$

With use of the Nernst-Einstein equation

$$u_i = \frac{D_i}{RT} \qquad [5]$$

one may combine Eq. [2], [3], and [4] to find

$$D_i \frac{d^2 c_i}{dy^2} + \frac{z_i D_i \mathbf{F}}{RT} \frac{d}{dy}\left(c_i \frac{d\phi}{dy} \right) - v \frac{dc_i}{dy} = \frac{A\nu_i i_o}{n\mathbf{F}} \left[\frac{c_a}{c_a^o} e^{\frac{-\alpha n\mathbf{F}(\phi - \phi_e)}{RT}} - \frac{c_c}{c_c^o} e^{\frac{(1-\alpha) n\mathbf{F}(\phi - \phi_e)}{RT}} \right] \qquad [6]$$

Equation [6] states that solute species within the porous electrode move about owing to diffusion, migration, convection, and electrochemical reaction. The potential ϕ represents the potential in the solution phase under the prevailing (local) concentration, while ϕ_e represents the potential in the solution that would be observed under equilibrium conditions at bulk concentration. The potential ϕ therefore includes both concentration and activation overpotential.

The movement of charged solute species is restricted in accord with the requirement of electroneutrality

$$\sum_i z_i c_i = 0 \qquad [7]$$

The convective velocity within the porous electrode is based on an empirical balance between buoyancy

forces and viscous forces encountered during flow through packed beds (11), as derived in the Appendix

$$v = 0.24 \frac{g_c \epsilon r_H^2}{\mu} \Delta\rho \qquad [8]$$

The density driving force, $\Delta\rho$, is the difference between the density of the bulk electrolyte and the average density of the electrolyte within the porous region as determined from the solute concentration distributions (12).

Equations [6], [7], and [8] are sufficient in number for determining the velocity, potential, and solute concentrations throughout the electrode provided that sufficient boundary conditions are provided. At the external surface near the counterelectrode ($y = 0$) the potential and solute concentrations have known values

$$c_i = c_i^o$$
$$\phi = \phi_a \qquad [9]$$

At the rear surface ($y = L$) the concentrations have known values and the current density in the solution is zero

$$c_i = c_i^o$$
$$-F^2 \frac{d\phi}{dy} \sum_i z_i^2 u_i c_i - F \sum_i z_i D_i \frac{dc_i}{dy} = 0 \qquad [10]$$

Analysis of the foregoing set of equations is rendered more convenient if the variables are transformed to dimensionless quantities by defining

$$Y = \frac{y}{L}$$
$$C_i = \frac{c_i}{c_r}$$
$$\Phi = \frac{F}{RT}(\phi - \phi_e)$$
$$V = \frac{vL}{D_r}$$
$$J = \frac{jAL^2}{nFc_rD_r} \qquad [11]$$

Equations [6], [7], and [8], which serve to define the model, then take the forms

$$\pi_i \frac{d^2C_i}{dY^2} + z_i\pi_i \frac{d}{dY}\left(C_i \frac{d\Phi}{dY} \right) - V\frac{dC_i}{dY} = \nu_i\xi \left[\frac{C_a}{\gamma_a} e^{-\alpha n\Phi} - \frac{C_c}{\gamma_c} e^{(1-\alpha)n\Phi} \right] \qquad [12]$$

$$\sum_i z_i C_i = 0 \qquad [13]$$

$$V = 0.24\zeta \frac{\Delta\rho}{\rho} \qquad [14]$$

Upon transformation to dimensionless form, boundary conditions [9] and [10] become

at $Y = 0$: $C_i = \gamma_i$, $\Phi = \Phi_a$

at $Y = 1$: $C_i = \gamma_i$

$$\sum_i \left(z_i\pi_i C_i \frac{d\Phi}{dY} + z_i\pi_i \frac{dC_i}{dY} \right) = 0 \qquad [15]$$

The dimensionless parameters which appear in the foregoing model are

$$\xi = \frac{i_o AL^2}{nFc_rD_r}$$
$$\zeta = \frac{r_h^2 g_c \epsilon \rho L}{\mu D_r}$$
$$\gamma_i = \frac{c_i^o}{c_r}$$
$$\pi_i = \frac{D_i}{D_r} \qquad [16]$$

The two most important parameters which arise from the analysis are ξ and ζ. The quantity ξ denotes the ratio of diffusion resistance to charge-transfer resistance insofar as it contains the ratio i_o/D_r. The absolute value of the parameter ζ denotes the ease with which fluid can pass through a porous bed under a given hydrostatic head. The sign of ζ depends on both the cell geometry and the direction of flow as indicated in Table I. The role which these two parameters play in determining electrode behavior will be discussed carefully in the results which follow.

Once the potential and concentration distributions are determined, the local reaction rate may be calculated from the dimensionless form of Eq. [4]

$$\beta J = \xi \left(\frac{C_a}{\gamma_a} e^{-\alpha n\Phi} - \frac{C_c}{\gamma_c} e^{(1-\alpha)n\Phi} \right) \qquad [17]$$

where

$$\beta = \frac{i^* L}{nFc_rD_r}$$
$$J = \frac{ALj}{i^*}$$

Method of Solution

The central problem in the calculational procedure was that the convective velocity can be determined only if the concentration profiles are known, while the concentrations can be calculated only if the convective velocity is known. An iterative procedure was therefore utilized in order to converge on a solution. First, Eq. [12] and [13] were solved simultaneously with the convective velocity arbitrarily set equal to zero. Based on these results, the average density of the solution within the porous electrode was calculated (12) and a new estimate of the convective velocity was obtained by Eq. [14]. With use of the revised velocity, new calculations of concentrations and potential were obtained by solving Eq. [12] and [13]. Once again, the concentration distributions were used to generate a buoyancy force and thereby to obtain a new estimate of the velocity. The procedure was repeated until two successive calculations of convective velocity agreed within 0.001 dimensionless velocity units. The typical number of "outer loops" required for velocity convergence was seven.

At each stage in the iterative process, it was necessary to solve the nonlinear conservation equations along with the electroneutrality condition. These coupled equations were first linearized about an approximate solution and then put into finite difference form. The resulting set of tridiagonal matrices was inverted with the use of a computer-implemented numerical technique (13). The solution of the nonlinear problem was then obtained by iteration of the approximate solution. Convergence on the solution of the nonlinear problem was defined by the criterion that

Table I. Interpretation of the sign of ζ

Placement of counterelectrode	Direction of convective flow: Upward	Downward
Above porous electrode	$\zeta < 0$	$\zeta > 0$
Below porous electrode	$\zeta > 0$	$\zeta < 0$

Table II. Properties of systems under study

Species	z_i	ν_i	γ_i	π_i
	(a) Acidified copper sulfate: $n = 2$			
Cu^{++}	+2	−1	0.10	0.7188
H^+	+1	0	4.0	9.312
$SO_4^=$	−2	0	2.1	1.065
	(b) Sulfuric acid: $n = 2$			
H^+	+1	0	5.0	9.312
$O_4^=$	−2	1	2.5	1.065
	(c) Potassium hydroxide: $n = 2$			
K^+	+1	0	6.87	2.075
OH^-	−1	2	6.87	4.15

two successive calculations of the potential in the solution with the convective velocity set equal to zero, agreed to within 0.01%. In typical cases, four iterations were usually sufficient. It was found that equally spaced mesh points of size $\Delta y = 0.01$ gave results which were essentially independent of mesh spacing. The calculations were conducted with an IBM 360 computer. A single calculation typically took 4000 centiseconds of processor time and cost $1.20 per run.

Results

Calculations have been conducted in order to illustrate conditions under which natural convection effects may be anticipated. Three types of electrochemical systems have been considered:

(a) Cathodic deposition of copper from an acidified sulfate electrolyte, a system for which the physical properties are known with accuracy, has the electrode reaction

$$Cu^{++} + 2e^- = Cu \qquad [18]$$

(b) Anodic operation of a secondary battery electrode with sulfuric acid electrolyte has the reaction

$$M + SO_4^= = MSO_4 + 2e^- \qquad [19]$$

(c) Anodic operation of a secondary battery electrode with potassium hydroxide electrolyte has the reaction

$$M + 2\,OH^- = M(OH)_2 + 2e^- \qquad [20]$$

The dimensionless parameters which have been used in describing these three systems, shown in Table II, should permit evaluation of a wide variety of actual systems.

Consider first the acidified copper sulfate system. In the complete absence of convection ($\zeta = 0$), the steady-state current distribution depends primarily on the parameter ξ as illustrated in Fig. 2. For electrode reactions having large exchange current densities (large ξ), reactant species are consumed primarily near the pore entrance so that the reaction rate distribution is highly nonuniform. Even though the counterelectrode is positioned on only one side of the porous electrode (toward the left of Fig. 2), the reaction distribution is nearly symmetric about $Y = 0.5$ since ohmic losses in the solution phase are small with respect to the concentration overpotentials which arise. For reactions having low exchange current densities (low ξ), current tends to be transferred more uniformly throughout the pore since diffusional limitations are less severe.

The results given in Fig. 2 will be altered when natural convection occurs. Of course, the convection effect will depend on the orientation of the system with respect to the gravitational field. For the cathodic copper reaction, flow of the copper-depleted solution occurs in the upward direction. In accord with Table I, positive values of ζ therefore imply that the counterelectrode is below the porous electrode so that flow is directed away from the counterelectrode. Conversely, negative values of ζ indicate that the counterelectrode is above the porous electrode and flow is toward the counterelectrode. Figure 3 illustrates the cupric ion distribution throughout the porous electrode for various values of ζ. For the value $\zeta = 0$, the concentration

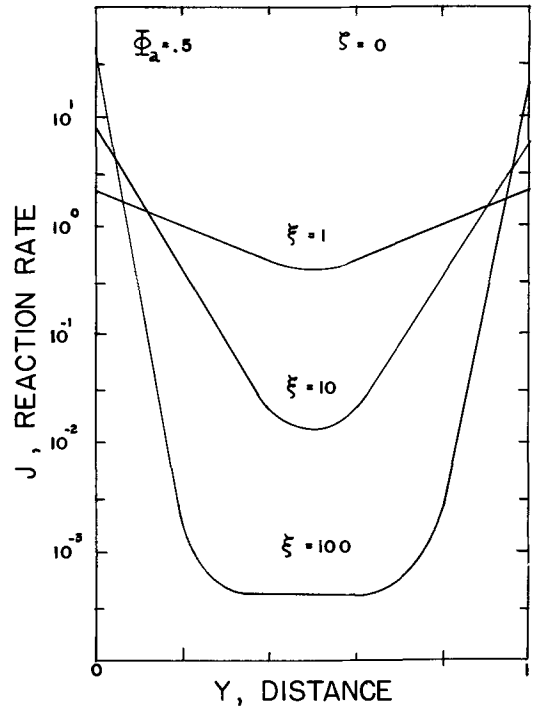

Fig. 2. Current density distributions for various values of ξ, acidified copper sulfate electrolyte.

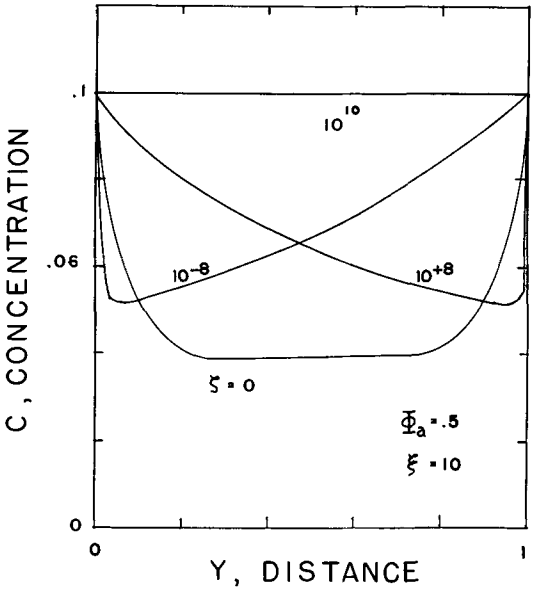

Fig. 3. Concentration distribution of cupric ions during natural convection with several values of ζ.

distribution corresponds to the results of Fig. 2. For positive values of ζ, the convective flow sweeps the cupric ions downstream, away from the counterelectrode, thereby shifting the minimum concentration toward the back of the electrode. "Fresh" electrolyte is swept in the upstream side, nearest the counterelectrode, and thereby increases the concentration of reactive species in that region. With sufficiently large values of ζ, the concentration distribution becomes nearly uniform; that is, only negligible concentration differences are sufficient to overcome viscous resistance and thus cause convective flow. For negative values of ζ, flow is directed toward the counterelectrode so that the minimum in the concentration distribution shifts toward $Y = 0$.

The effect of convection on the current distribution is illustrated in Fig. 4 for flow away from the counterelectrode. As ζ increases, the reaction rate distribution becomes more uniform since concentration overpoten-

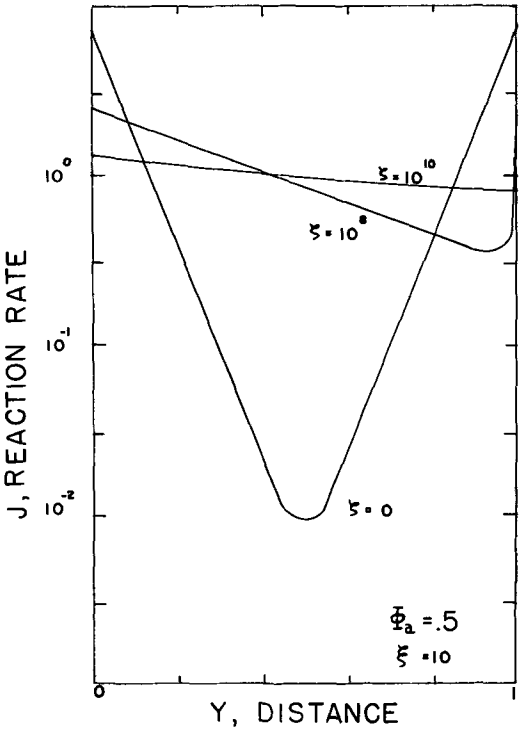

Fig. 4. Dependence of current density distribution on convective flow rate in acidified copper sulfate electrolyte.

tial restrictions are relieved. For extremely large values of ζ (negligible concentration overpotential), activation overpotential tends to force the current deeper into the electrode so that the reaction distribution is nearly uniform.

For the acid copper sulfate system, Fig. 5 gives two sets of current-potential curves which correspond to the complete absence of concentration gradients ($\zeta = \infty$), and to the complete absence of natural convection ($\zeta = 0$). These two sets of curves provide the boundaries within which natural convection can enhance current output. For example when $\Phi = 2.5$ and $\xi = 1$, the diffusion-restricted current (lower graph) has the value $\beta = -2$; it is seen from the upper graph that the value $\beta = -16$ could be obtained if concentration gradients would be relieved. For this example, natural convection could be expected to increase the diffusion-restricted current by a factor of $\Psi = -16/(-2) = 8$. For $\Phi_a = 2.5$ and $\xi = 100$, the convective effect could increase total current by a factor of $\Psi = -250/(-20) = 12.5$. The ratio Ψ is called the enhancement factor

$$\Psi = \frac{\beta_{\text{with convection}}}{\beta_{\text{diffusion restricted}}} \qquad [21]$$

The compilation of many calculations is provided in Fig. 6 for the acid copper sulfate system. The effect of Φ_a and ζ on the enhancement factor is shown for two values of ξ. It is seen that enhancement of performance is to be expected when Φ_a and ξ are large (large applied potentials, diffusion restricted operation) and when ζ is large (low resistance to flow). When Φ_a and ξ have small values, electrode operation is not diffusion controlled so that concentration gradients do not arise. When ζ has a small value, the viscous resistance to flow is so high that convection is impeded. It is also seen that the enhancement factor increases from unity to an upper value over a range of ζ which is about two orders of magnitude wide.

It was found that under identical conditions of operation, convection away from the counterelectrode resulted in a larger total current than convection toward the counterelectrode. With flow away from the counterelectrode, fresh reactants are swept into the highly reactive zone nearest the counterelectrode. When flow is in the opposite direction, on the other hand, reactants tend to be somewhat depleted by the time the solution reaches the (downstream) regions near the counterelectrode; that is, the electrode regions near the counterelectrode suffer concentration overpotential so that the total current is less. Under the conditions $\Phi_a = -5$, and $\xi = 100$, flow away from the counterelectrode yielded β values of 619, 715, and 791 for $\zeta = 10^3$, 10^4, and 10^5, respectively. Under the identical conditions but with flow toward the counterelectrode (negative ζ), β took on the values 571, 624,

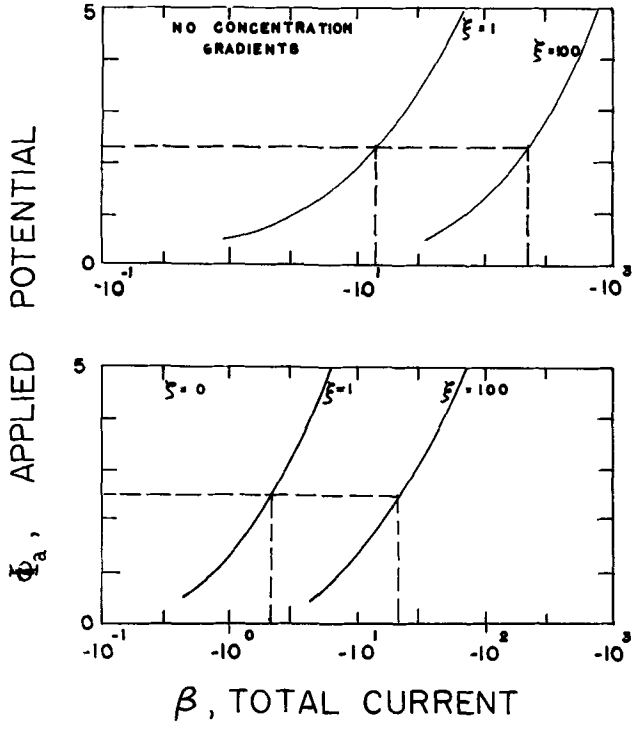

Fig. 5. Predicted current-potential behavior for the acidified copper sulfate system. Lower graph, diffusion-limited operation; upper graph, operation without diffusion restriction.

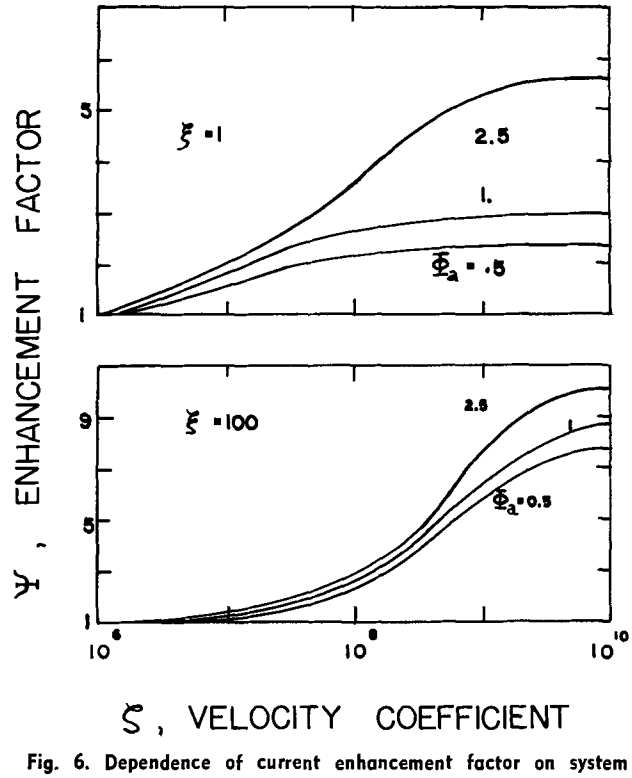

Fig. 6. Dependence of current enhancement factor on system parameters for acidified copper sulfate system.

and 757. That is, for flow toward the counterelectrode, the current was 92, 87, and 95% of the current for flow away from the counterelectrode with $\zeta = 10^3$, 10^4, and 10^5, respectively. For the range of parameters considered in this work it was found that the maximum effect of flow direction on total current was less than 5% for $\xi = 1$, and ranged between 10 and 30% for $\xi = 100$. All enhancement factor data reported in this study are for positive ζ and therefore represent the maximum enhancement with respect to flow direction. From these results it is recognized that direction of convective flow is inconsequential both for low values of ζ (no appreciable convection) and for high values of ζ (no appreciable concentration variation). However, for intermediate values of ζ, corresponding to the inflection points in Fig. 6, the direction of flow may influence electrode behavior significantly.

Let us apply the foregoing results to a copper sulfate system consisting of an electrode of thickness 5 mm and specific surface area of 775 cm^2/cm^3 void volume. Since $n = 2$ g-equiv./g-mole, $\mathbf{F} = 96{,}500$ coul/g-equiv., $D_r = 10^{-5}$ cm^2/sec, $c_r = 10^{-3}$ g-mole/cm^3, and $i_0 = 10^{-3}$ A/cm^2, one finds $\xi = 100$. Now proceed to calculate how large the pores would need to be in order that natural convection occur to an appreciable extent. Under an applied potential of 62.5 mV ($\Phi_a = 2.5$), Fig. 6 indicates that a three-fold enhancement of total current would be observed if the parameter ζ has the value 10^8. For an electrode of 35% porosity, $\mu = 1.3 \times 10^{-2}$ g/cm sec, $\rho = 1.1$ g/cm^3, one calculates that the hydraulic radius necessary to achieve the desired enhancement is $r_h = 0.0106$ cm. This value is similar to that found in industrial reactors containing, for example, graphitized pellets, but is orders of magnitude larger than the pore structure of present-day batteries.

Figure 7 shows how the current enhancement factor varies with several system parameters for reaction [19], anodic operation with sulfuric acid electrolyte. Although a severalfold enhancement may occur under proper conditions, the enhancement is not nearly so great as may occur for the acidified copper sulfate system. The transference number of the reacting ion is larger in reaction [19] than in reaction [18] with the result that concentration differences tend to be smaller in the binary system. If the transference number of the reacting ion were one, concentration differences would not arise at all. Even though natural convection may occur in the sulfuric acid system, the concentration overpotential tends to be a smaller portion of the total overpotential so that enhancement is limited. Figure 8 provides current enhancement data for reaction [20], anodic operation of a metal in potassium hydroxide. Enhancement of diffusion operation by only 40% may be expected owing primarily to the large transference number of the reacting ion.

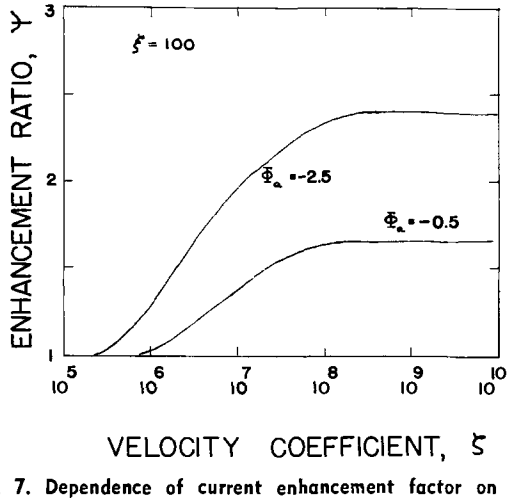

Fig. 7. Dependence of current enhancement factor on system parameters for sulfuric acid system.

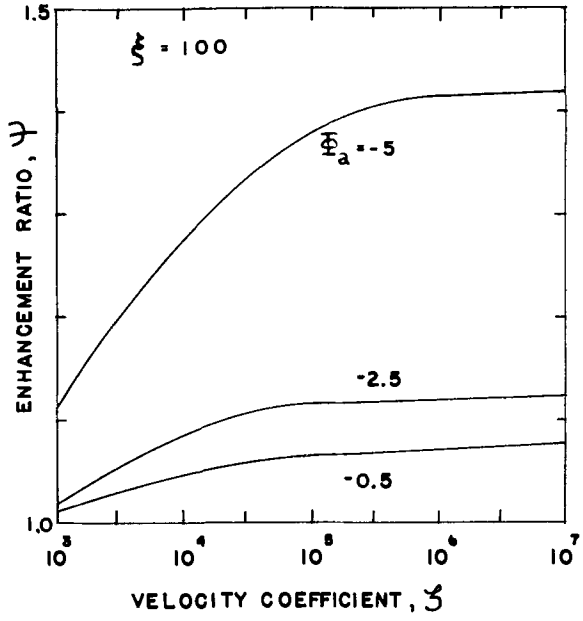

Fig. 8. Dependence of current enhancement factor on system parameters for potassium hydroxide system.

Conclusions

The central emphasis in the foregoing development has been in demonstrating operating conditions under which natural convection may arise within porous electrode structures. The predictions of the model are naturally restricted by the suitability of the assumptions which were invoked. In order to deal with specific systems, however, several of the assumptions can be substantially modified without complicating the overall computational method. For example, alternative forms of the reaction rate equation could be employed with ease. Also, flux equations for concentrated electrolytic solutions could be used instead of the dilute solution equations. On the other hand, if the flow resistance of the electrolyte "return loop" is appreciable, more complex modes of natural convection may set in within, or near, the porous electrode which could not be accounted for by simple modification of the present model.

Similarily, different boundary conditions could be investigated. For example, the electrolyte at the downstream exterior face of the porous electrode may not be well-stirred with the result that the concentration there would be the same as that emanating from the porous electrode, but not the same as the bulk solution. Thus by ignoring back-diffusion at the downstream end of the electrode, one would have the condition

$$\frac{dc_1}{dy} = 0 \quad \text{at } y = L \qquad [22]$$

By neglecting diffusion at the downstream end, the use of Eq. [22] would result in greater concentration differences within the porous electrode, thus larger buoyancy forces, than with use of boundary conditions [9] and [10] used in this study. Therefore it may be recognized that the predictions made in this investigation represent conservative estimates of reactivity enhancement by natural convection. That is, mass transfer restrictions external to the porous electrode (not considered in the present model) will always act to increase the natural convection effect above that estimated here.

Enhancement of diffusion-restricted operation by natural convection was found to occur in each system studied. The extent of enhancement was highest for the acidified copper sulfate system and lowest for the potassium hydroxide system. In general, one may conclude that natural convection effects would tend to arise more easily in those systems in which the trans-

ference number of the reacting ion is low. Under identical conditions of operation, larger currents were predicted when the convective flow was directed away from the counterelectrode than toward the counterelectrode.

Although natural convection occurs most readily in electrodes of high permeability, there exists an upper permeability above which further enhancement will not be obtained. On the other hand, efforts directed toward increasing electrode permeability can be generally expected to result in a concomitant lowering of the specific surface area. As a consequence, diffusional restrictions would become reduced, so that the buoyancy driving force for natural convection would be suppressed. One may therefore anticipate the need for careful electrode design in order to achieve a desirable balance between high specific surface area and high permeability.

The foregoing results indicate that attention should be directed toward development of high-rate double porosity battery electrodes within which electrochemical reaction would take place primarily in the fine, high surface-area pores, while natural convection would occur in the larger pore structure. The present theoretical framework could be easily extended toward such double porosity systems.

APPENDIX

The friction factor for flow through a packed bed [Eq. 6.4-1 of Ref. (11)] is defined as

$$f = \frac{D_p (\mathcal{P}_o - \mathcal{P}_L)}{4L(1/2)\rho v_o^2} \qquad [A\text{-}1]$$

where D_p = bed particle diameter, $(\mathcal{P}_o - \mathcal{P}_L)$ = pressure drop across bed, and v_o = superficial velocity of fluid, external to the bed.

Experimental measurements indicate that over the range $(D_{p\rho}\, v_o/\mu)(1 - \epsilon)^{-1} < 10$, the friction factor is

$$f = \frac{(1-\epsilon)^2}{\epsilon^3} \frac{75}{D_{p\rho}\, v_o} \qquad [A\text{-}2]$$

where ϵ = volume of voids per volume of bed.

The pressure difference which leads to flow is due to the difference in density of the fluid within the pores and that outside the pores

$$(\mathcal{P}_o - \mathcal{P}_L) = g_c \epsilon L\, (\rho^{bulk} - \rho^{avg}) \qquad [A\text{-}3]$$

In addition, the particle diameter D_p is related to the hydraulic radius [Eq. 6.4-4, 5, and 6 of Ref. (11)] by

$$D_p = 6 r_h \frac{(1-\epsilon)}{\epsilon} \qquad [A\text{-}5]$$

By combining the four equations, one obtains for the superficial velocity

$$v_o = 0.24 \frac{g_c\, \epsilon^2\, r_h^2}{\mu} \Delta p \qquad [A\text{-}6]$$

The fluid velocity in the interstices is related to the superficial velocity by $v = v_o/\epsilon$.

SYMBOLS

A specific surface area of porous electrode, cm^{-1}
c_a concentration of anodic reactant, g-mole/cm^3
c_c concentration of cathodic reactant, g-mole/cm^3
c_i concentration of species i, g-mole/cm^3
c_i^o Bulk concentration of species i, g-mole/cm^3
C_i concentration of species i, c_i/c_r, dimensionless
c_r reference concentration, g-mole/cm^3
D_i diffusion coefficient of species i, cm^2/sec
D_r reference diffusion coefficient, cm^2/sec
$\mathbf{F}$ Faraday's constant, 96,500 coulombs/g-equiv.
g_c gravitational constant, 980 cm/sec^2
i_o exchange current density, A/cm^2
i^* current density at pore mouth, A/cm^2
j local reaction rate density, A/cm^2
J local reaction rate density, ALj/i^*, dimensionless
L thickness of porous electrode, cm
M_i chemical symbol of species i
N_i flux of species i, g-mole/cm^2-sec
n number of electrons taking part in electrode reaction
r_h hydraulic radius of electrode pores, cm
T temperature, °K
u_i mobility of species i, cm^2 g-mole/joule-sec
v hydrodynamic velocity, cm/sec
V hydrodynamic velocity, vL/D_r, dimensionless
y spatial variable, cm
Y spatial variable, y/L, dimensionless
z_i valence of species i

Greek Characters

α transfer coefficient in reaction rate equation
β current at $y = 0$, $i^*L/n\mathbf{F}c_rD_r$, dimensionless
γ_i bulk concentration of species i, c_i^o/c_r, dimensionless
ϵ electrode porosity
ζ hydrodynamic permeability factor, $g_c\epsilon\rho L/a^2\mu D_r$, dimensionless
μ electrolytic solution viscosity, g/cm-sec
ν_i stoichiometric coefficient for species i
ξ electrode kinetic factor, $i_oAL^2/n\mathbf{F}c_rD_r$, dimensionless
π_i diffusion coefficient of species i, D_i/D_r, dimensionless
ρ electrolytic solution density, g/cm^3
ϕ potential in solution, V
ϕ_e potential in the solution under equilibrium conditions, V
Φ potential, $\mathbf{F}(\phi - \phi_e)/RT$, dimensionless

Acknowledgment

This study constituted partial fulfillment of requirements for a Master of Science degree in the Department of Chemical Engineering, University of Illinois at Champaign-Urbana. The authors appreciate the financial support of the University of Illinois Research Board which sustained computer charges. The junior author (R. P.) conducted these studies under sponsorship of a Minnesota Mining and Manufacturing Company Industrial Fellowship.

Manuscript submitted Dec. 7, 1972; revised manuscript submitted March 14, 1973.

Any discussion of this paper will appear in a Discussion Section to be published in the June 1974 JOURNAL.

REFERENCES

1. C. Wagner, *J. and Trans. Electrochem. Soc.*, **95**, 161 (1949).
2. C. R. Wilke, M. Eisenberg, and C. W. Tobias, *This Journal*, **100**, 513 (1953); *Chem. Eng. Progress*, **49**, 663 (1953).
3. U. Böhm, N. Ibl, and A. M. Frei, *Electrochim. Acta*, **11**, 412 (1966); **13**, 891 (1968).
4. C. W. Tobias and E. J. Fenech, *ibid.*, **2**, 311 (1960).
5. G. Schütz, *Intern. J. Heat Mass Transfer*, **6**, 873 (1963).
6. A. Acrivos, *Am. Inst. Chem. Engrs. J.*, **6**, 584 (1960); *Chem. Eng. Sci.*, **21**, 343 (1966).
7. J. R. Selman and J. S. Newman, *This Journal*, **118**, 1070 (1971).
8. R. A. Wooding, *Proc. Roy. Soc. (London)*, **A252**, 120 (1959); *J. Fluid Mech.*, **15**, 527 (1963).
9. C. S. Yih, "Dynamics of Nonhomogeneous Fluids," MacMillan, New York (1965).
10. D. R. Westbrook, *Phys. Fluids*, **12**, 1547 (1969).
11. R. B. Bird, W. E. Stewart, and E. N. Lightfoot, "Transport Phenomena," pp. 187, 196-200, John Wiley & Sons, Inc., New York (1960).
12. S. K. Arapkoske and J. R. Selman, Lawrence Radiation Laboratory Report UCRL-20510, University of California, Berkeley, 1971.
13. J. S. Newman, *Ind. Eng. Chem., Fundamentals*, **7**, 514 (1968).

Technical Notes

Surface Effects in the Measurement of Range Profiles by Oxide Dissolution

D. Phillips and J. P. S. Pringle*

Chalk River Nuclear Laboratories, Atomic Energy of Canada Limited, Chalk River, Ontario, Canada

Range profiles in anodic tantalum oxide have recently been surveyed (1) by means of a sectioning technique (2). Originally, radioactive $^{198}Au^+$ was chosen as an example of a very heavy ion implant, but the results proved anomalous; the survey was therefore completed with $^{204}Tl^+$ and $^{222}Rn^+$. The anomaly with $^{198}Au^+$ was however investigated further, with the results described below.

Gold-198 was implanted at 40 keV by means of a mass separator, and the oxide sectioned by slow dissolution in concentrated HF almost saturated with NH_4F, according to the procedure described elsewhere (1, 2). Since the range profile for a species implanted in amorphous tantalum oxide depends only on its mass and energy, the range profile for 40 keV $^{198}Au^+$ was expected to be very similar to those for 40 keV $^{204}Tl^+$ and 40 keV $^{222}Rn^+$. The latter indicated that only about 10% of the initial $^{198}Au^+$ activity should remain after the removal of 200Å of oxide, yet the fraction observed experimentally was over 90%. Since thickness measurements and interference colors both indicated that the oxide was dissolving normally, the only possible conclusion was that the gold was not dissolving in the HF-NH_4F reagent. If it was not dissolving, it could only be present on the surface of the remaining oxide.

To prove this, the oxide was exposed for 30 sec to a reagent, aqua regia, known to dissolve gold, whereupon the activity fell to the expected 10%. (Fig. 1). This interpretation is only valid, however, if the oxide does not itself dissolve in the aqua regia, and this was established in separate experiments. No change (< 5Å) in oxide thickness was detected on prolonged contact, and when the surface layer was labeled with $^{24}Na^+$ implanted at the very low energy of 1 keV, no significant fraction of the activity was lost (1). Continued sectioning in HF-NH_4F, alternating with 30 sec treatments in aqua regia, gave the results shown in Fig. 1, from which it was obvious that the range profile had the expected form.

Integrated range profiles for implanted $^{198}Au^+$ were therefore obtained by means of this two-stage technique, and analyzed as error function complements using the least squares fitting procedure described in Ref. (1). The modal range at 40 keV was found to be 119.5 ± 2Å, and the standard deviation 66.5 ± 0.5Å; the errors quoted are standard errors of the fit, rounded to the nearest 0.5Å. For comparison, the modal range with 40 keV $^{204}Tl^+$ was 109.5 ± 2Å and the standard deviation 59.5 ± 1Å; the agreement is probably as good as can be expected (3). Two range measurements for 5 keV $^{198}Au^+$ gave 33 ± 2Å and 39.5 ± 1.5Å as the modal ranges, and 17 ± 1Å and 21.5 ± 0.5Å as the standard deviations, again in reasonable agreement with the 33 ± 2Å (mode) and 19 ± 1Å (standard deviation) observed with 5 keV $^{204}Tl^+$.

It is clear, therefore, that implanted ^{198}Au exposed by the dissolution of the oxide has a much greater affinity for the retreating oxide surface than for dissolution in the stripping agent. Unless this factor be taken into account, the measured ranges will be spuriously large. Phenomena of this kind have actually been observed with the rather similar sectioning technique for aluminum.

In this technique (4), a thin layer of the metal is converted to oxide via anodic oxidation, and the oxide is then dissolved in a mixture of chromic and phosphoric acids; the metal surface is thus re-exposed, and the process can be repeated. Extensive range profile measurements (5) and channeling studies (6) have been performed with this technique, using alkali metal or noble gas implants, and the results were in all cases excellent. Experience at this and other laboratories has shown, however, that the same is not always true for other implants. Thus the range of certain fission products, notably ^{111}Ag, appears to be anomalously large (7) when determined by this technique, and more detailed studies (8) have confirmed that this is because very little of the ^{111}Ag present in each aluminum layer is actually stripped from the specimen.

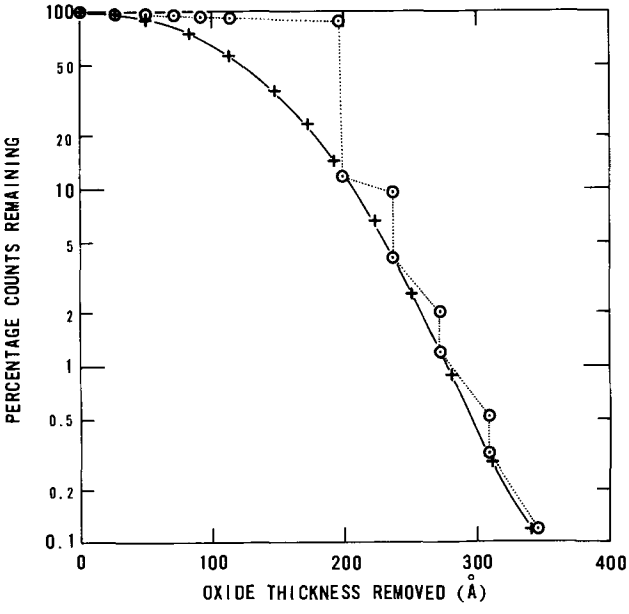

Fig. 1. Integrated range profiles for $^{198}Au^+$ implanted at 40 keV into anodic tantalum oxide. The dotted line connects points obtained with a specimen sectioned in the HF-NH_4F reagent until approximately 200Å of oxide had been removed; then alternately in aqua regia and HF-NH_4F. The crosses connected by the continuous line are experimental points for the specimen analyzed in the text; each point was obtained by treatment in HF-NH_4F, followed by 30 sec in aqua regia.

* Electrochemical Society Active Member.
Key words: tantalum, anodic oxide, ion implantation, impurity dissolution.

In the case of an anodizing and stripping technique, two explanations are possible for the retention of a particular implant. The implant may fail to dissolve in the stripping agent, and hence remain on the specimen surface, as described here. Alternatively, it could fail to enter the oxide at all during the anodization process, and thus be segregated on the metal side of the metal/oxide interface. Rutherford scattering experiments by W. D. Mackintosh are currently underway in these laboratories to distinguish between these possibilities.

Very similar observations have been reported recently (9) in the silicon/silicon oxide system. Gold-198 dissolved in 10% HF was found to deposit on silicon surfaces; after subsequent thermal oxidation to 1100°C, part of the gold occurred at the oxide surface.

Manuscript received Jan. 15, 1973.

Any discussion of this paper will appear in a Discussion Section to be published in the June 1974 JOURNAL.

REFERENCES

1. J. P. S. Pringle, *This Journal*, Submitted for publication.
2. J. P. S. Pringle, *ibid.*, **119**, 482 (1972).
3. J. P. S. Pringle, To be submitted for publication.
4. J. A. Davies, J. Friesen, and J. D. McIntyre, *Can. J. Chem.*, **38**, 1526 (1960).
5. See for example, B. Domeij, F. Brown, J. A. Davies, and M. McCargo, *Can. J. Phys.*, **42**, 1624 (1964).
6. See for example, G. R. Piercy, M. McCargo, F. Brown, and J. A. Davies, *ibid.*, **42**, 1116 (1964).
7. N. K. Aras, M. P. Menon, and G. E. Gordon, *Nucl. Phys.*, **69**, 337 (1965).
8. M. Hollstein and H. Munzel, *Radiochim. Acta*, **5**, 195 (1966). An English translation of what appears to be this paper is available as M. Hollstein, *URCL Trans.*, 1253 (L).
9. T. A. O'Shaughnessy, H. D. Barber, D. A. Thompson, and E. L. Heasell, Paper 155 presented at Electrochem. Soc. Meeting, Chicago, Illinois, May 13-18, 1973.

Porous Anodic Aluminum Oxide Membrane

Alan W. Smith

Boeing Aerospace Company, Seattle, Washington 98124

Anodization of aluminum in certain acids causes the formation of an oxide nearly penetrated by pores whose diameter (in angstroms) is about ten times the forming voltage (in volts) (1). Such porous oxides might be interesting membranes for ultrafiltration or reverse-osmosis applications. Burwell and May studied such membranes (2). However, they did not remove the thin barrier layer formed during anodization, and so their membranes had low permeabilities. In the work presented here, the barrier layer has been removed and interesting membranes produced.

The method used was to place an aluminum foil between two o-rings such that it formed a barrier between two chambers. Different solutions could be placed in either chamber for anodizing, etching, sealing, or measuring osmotic flow. For flow measurements a lid, containing conductivity electrodes to measure salt flow and capillaries to measure liquid flow, was placed over the chambers.

Foils of 0.0005 and 0.002 in. were used. Anodization was carried out from one side in various chromic and sulfuric acid solutions. The most uniform membranes were obtained in a 10% chromic acid-1% sulfuric acid solution. Voltages between 10 and 130V were used. Penetration of the foil by pits was apt to occur unless anodization was first carried out at a low voltage, 1V, until the as-received oxide was removed. Uniform membranes were rarely produced if the anodizing was allowed to proceed completely through the foil. The best membranes were produced by anodization part way through and then removing the unanodized aluminum by etching from the other side in a 50% HCl, 10^{-1}M $CuCl_2$ solution until the metal is just removed. Such membranes had low values of water and salt permeability.

To obtain high permeability membranes it was necessary to remove the barrier layer which is formed next to the metal interface during anodization. Since the thickness of the oxide between the pores is only about twice that of the barrier layer (1), it is not possible to etch away the barrier layer from the porous side without destroying the whole membrane. To remove the barrier layer, either an acid or basic solution was put into the chamber on the barrier layer side, while a buffered solution was placed on the porous side.

Figure 1 is a plot of the water flow to salt flow ratio *vs.* the water flow for a number of samples. These measurements were of the osmotic flow of water into a 1M NaCl solution and the counterflow of salt into the pure water. These samples were prepared in a variety of conditions in an attempt to obtain good salt rejection and high water flow. No correlations were found between parameters such as anodizing voltage. Only the kind of etching and sealing was significant. Samples were etched with acid solutions

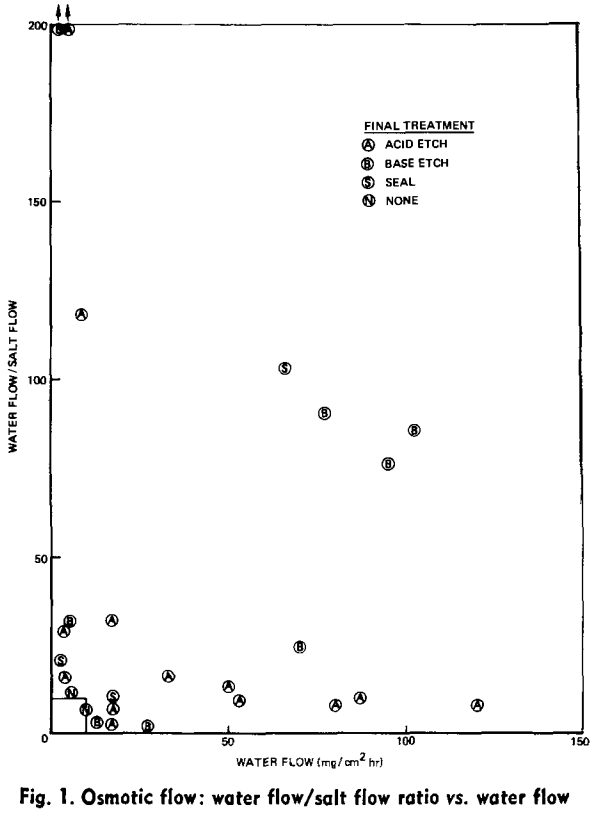

Fig. 1. Osmotic flow: water flow/salt flow ratio *vs.* water flow

Key words: membrane, anodic, aluminum, oxide, porous.

of various strengths and base solutions below 0.05M. In some cases the samples were partially sealed in 60°C water for 1 hr.

The thing to note about Fig. 1 is that the acid etch did not result in membranes with substantial water flows and good salt rejection (high values of water to salt flow). The good salt rejection in some cases of acid etch was for treatments not expected to remove the barrier layer completely.

Good salt rejection and substantial water flow were obtained when the samples were given an alkaline etch or when the samples were partially sealed after etching. Since the pores of the membrane are too large to reject salt it is not surprising that sealing which partially closes the pores increases the salt rejection. It is believed that the alkaline etch which dissolves the oxide rapidly and allows a hydrous oxide to reprecipitate also partially closes the pores. It seems likely that the membrane is similar to those formed by depositing hydrous oxides in porous solids (3).

It is believed that the upper limit of water flow in these measurements is due to concentration polarization so that the numbers given in Fig. 1 for the higher flow rates are presumably on the low side.

The acid etch should produce membranes useful for ultrafiltration. Pores of 100-1300Å in diameter should be formed under anodization conditions used here. For reverse osmosis desalination applications, an alkaline etch or partial seal is necessary.

Manuscript submitted Feb. 1, 1973; revised manuscript received March 16, 1973.

Any discussion of this paper will appear in a Discussion Section to be published in the June 1974 JOURNAL.

REFERENCES

1. G. C. Wood and J. P. O'Sullivan, *Electrochim. Acta*, **15**, 1865 (1970).
2. R. L. Burwell, Jr. and T. P. May, *This Journal*, **94**, 195 (1948).
3. A. J. Shor, K. A. Kraus, W. T. Smith, Jr., and J. S. Johnson, Jr., *J. Phys. Chem.*, **72**, 2200 (1968).

Electrolytic Synthesis of Some Heavy Metal Tellurides

M. H. Miles*

Department of Chemistry, Middle Tennessee State University, Murfreesboro, Tennessee 37130

and W. S. McEwan

Chemistry Division, Naval Weapons Center, China Lake, California 93555

The binary semiconductors $Pb_{1-x}Sn_xTe$ and $Hg_{1-x}Cd_xTe$ have special interest due to their composition-dependent energy gaps (1). Preparations of these alloy semiconductors often utilize the individual compounds of PbTe and SnTe or HgTe and CdTe (1-3). The use of these telluride compounds in the preparation of infrared detectors prompted further investigation into the electrolytic method of synthesis. Previous work has defined the conditions for the electrochemical preparation of small quantities of the compounds (4, 5). This work shows that specific problems become apparent when larger preparations are attempted. Methods for minimizing these problems are discussed.

Experimental

All preparations were performed in a controlled-atmosphere (N_2 + 3% H_2) glove box system to minimize unwanted reactions with oxygen (4, 5). Oxygen concentrations are claimed to be less than 1 ppm in this system. Electrical contact was made directly to both the tellurium cathode and the selected metal used as the anode. The geometrical electrode areas exposed to the solutions were usually between 5 and 15 cm^2. The two electrodes, along with a reference electrode (SCE), were positioned in a vessel containing the ammonium acetate-acetic acid *p*H 4.5 buffer solution. The anode and cathode were always placed as far apart as the vessel permitted; the usual separation being at least 10 cm. The passage of a constant current of 100 mA was used to generate the ions of the desired compound, which combine and precipitate from the solution. The rate of stirring was controlled magnetically.

* Electrochemical Society Active Member.
Key words: cadmium, lead, mercury, tin.

Results

Table I presents a summary of results for electrolytic synthesis of tellurides. A critical factor in large-

Table I. Summary of results for electrolytic syntheses of tellurides

Preparation attempted	V_{sol}/A_{Te}	Coulombs passed	Electrode weight loss (% of theoretical)	X-ray pattern
PbTe[a]	~50	450	103% (Pb) 102% (Te)	PbTe lines only
PbTe	50	2060	101% (Pb) 57% (Te)	—
PbTe	50	3500	104% (Pb) 45% (Te)	Pb and PbTe lines
PbTe	250	5000	101% (Pb) 97.8% (Te)	PbTe lines only
CdTe[b]	~100	801	101% (Cd) 97.1% (Te)	—
CdTe	250	4060	102% (Cd) 99.7% (Te)	CdTe lines only
HgTe	250	5700	— 96.7% (Te)	HgTe lines only
SnTe[a]	~50	450	98.9% (Sn) 97.3% (Te)	SnTe lines only
SnTe	50	7400	89% (Sn) 6.1% (Te)	Mainly Sn lines
SnTe[c]	250	7300	98.3% (Sn) 55.8% (Te)	SnTe, SnO_2, Te lines
SnTe	500	5700	94.7% (Sn) 35.4% (Te)	—
SnTe[d]	500	7300	99.0% (Sn) 63.8% (Te)	—

[a] Data taken from Ref. (4).
[b] Average of data from Ref. (5).
[c] Reaction was observed when the dried sample was exposed to air. Apparently the Sn present was oxidized to SnO_2.
[d] Stirring was minimized to the slight agitation required to prevent the tellurium electrode from becoming heavily coated with precipitate.
All other solutions were vigorously stirred at nearly equal rates except for data taken from Ref. 4 where the rate of stirring was not mentioned.

scale preparations of PbTe and CdTe was found to be the ratio of the volume of the solution used to the surface area of the tellurium electrode exposed to the solution (V_{sol}/A_{Te}). For example, a preparation of PbTe where $V_{sol}/A_{Te} = 50$ showed less than 60% of the theoretical weight loss at the tellurium electrode. This experiment involved the passage of a constant current of 100 mA for 20,600 sec or 2060 coulombs. Upon increasing the V_{sol}/A_{Te} ratio to 250 by increasing the solution volume, the weight loss at the tellurium cathode increased to 98% of the theoretical. In this second experiment 5000 coulombs were used. In both experiments the weight loss at the lead anode was 101% of the theoretical weight. Analyses of the products by x-ray diffraction showed that free, crystalline lead was present in the first preparation, while the powder pattern for the second preparation, with $V_{sol}/A_{Te} = 250$, showed only the PbTe diffraction lines. Obviously, some of the Pb^{++} ions produced at the anode fail to find partners for precipitation as PbTe and, instead, become reduced to the free metal at the tellurium cathode. The extent of this contamination of the PbTe product by the free metal depends upon the V_{sol}/A_{Te} ratio and upon the total coulombs passed.

Results for the preparations of CdTe were similar to those found for PbTe. When a large V_{sol}/A_{Te} ratio is used, the x-ray powder pattern shows only the CdTe diffraction lines. However, the absence of foreign lines in such x-ray analyses indicates only that any contamination of the product by the free metal is small but not, necessarily, completely absent. It should be noted that the systematic error source found in this work was indicated by the statistical tests of preparations of small quantities of CdTe reported previously (6).

Mercury (II) telluride was conveniently prepared in large quantities by simply using a mercury pool, which is slowly stirred to expose fresh mercury, as the anode. Although Hg_2^{++} is produced initially, the reaction $Hg_2^{++} + Te^{--} \rightarrow Hg + HgTe$ produces the desired product (5). Most of the excess mercury was removed from the HgTe by centrifuging. The x-ray diffraction pattern corresponded to that of HgTe. Although the effect of the V_{sol}/A_{Te} ratio was not specifically investigated, using a ratio of about 250 gave a weight loss at the tellurium cathode which was 97% of the theoretical result for the 5700 coulombs used.

All attempts to prepare large quantities of SnTe resulted in a product highly contaminated with free tin. Even for V_{sol}/A_{Te} ratios as large as 500, low weight losses at the tellurium electrode and large amounts of free tin in the product were found. Using Te and Sn metals with purities exceeding 99.999% gave no significant improvement. Although a successful electrolytic preparation of SnTe in small quantities is reported by Panson (4), it is apparent that eventually the cathodic reaction becomes essentially the reduction of Sn^{++} ions to free tin.

Discussion

The probability of a metal ion, such as Pb^{++}, contacting the tellurium cathode and becoming reduced to the free metal is related to the V_{sol}/A_{Te} ratio. A larger ratio results in a smaller probability and allows a longer average time for the metal cation to find a Te^{--} partner. The Te^{--} ions, however, being a soft base, will tend to adsorb strongly to the tellurium metal surface (6, 7), thus relatively few Te^{--} ions reach the anode and become oxidized to free tellurium. Experimentally, most of the precipitation of the metal telluride is observed to occur near the cathode. Increasing the area of the tellurium electrode will increase the number of Te^{--} ions adsorbed, hence the probability of Pb^{++} ions coming close enough to the cathode for the charge-transfer reaction to occur will also increase.

The problems encountered in the attempt to prepare large quantities of SnTe could possibly result from the gradual formation of a tin plate or film on the tellurium electrode. Such a film would result in the cathodic reaction becoming essentially the reduction of Sn^{++} ions. Other metals such as Pb, Cd, and Hg are possibly less efficient in forming a film on the tellurium cathode. A possible solution to this problem would be to periodically reverse the current to oxidize the tin or other metals deposited on the tellurium electrode.

Another possibility is that a reaction such as

$$H^+ + SnTe + 2e^- \rightarrow Sn + HTe^- \quad [1]$$

may occur with the SnTe product. The calculated $E^\circ = -1.13$V (SHE) for this reaction suggests that such a reaction is thermodynamically possible for the experimental potentials of the cathode. However, the standard potential for the PbTe reduction reaction is only slightly more negative ($E^\circ = -1.18$V) while the standard potential for the HgTe reaction is less negative ($E^\circ = -1.03$V); yet both the PbTe and HgTe preparations, unlike the SnTe preparation, gave close to the theoretical weight loss for the tellurium cathode.

Some stirring of the solutions during the synthesis of the telluride compounds is desirable to remove the product which tends to form and collect at the tellurium cathode. Stirring also provides efficient use of the entire volume of the solution. However, rapid stirring will increase the motion of the metal cation and will, therefore, likely increase the probability of this ion contacting the cathode and becoming reduced to the free metal.

The free metal present in the telluride products could be removed by utilizing the differences in physical and chemical properties. For example x-ray diffraction studies showed that adding 1M HNO_3 to PbTe contaminated with free Pb dissolved the Pb and left the PbTe unchanged. Free mercury could likely be removed from HgTe by utilizing their different boiling points. Impurities other than the free metals will be controlled by the purity levels of the metals used as the electrodes and by purity levels in the ammonium acetate-acetic acid buffer solution used. Some electrolytic purification in this synthesis is possible. A highly pure, single crystalline telluride product could likely be produced from the electrolytic product by using liquid tellurium as the solvent for crystal growth (8).

Acknowledgment

A summer position in 1972 as a visiting professor for M.H.M., at the Naval Weapons Center at China Lake, California, is gratefully acknowledged.

Manuscript submitted Dec. 11, 1972; revised manuscript received March 30, 1973.

Any discussion of this paper will appear in a Discussion Section to be published in the June 1974 JOURNAL.

REFERENCES

1. R. K. Willardson and A. C. Beer, Editors, "Semiconductors and Semimetals," Vol. 5, Chap. 4 and 5, Academic Press, New York (1970).
2. E. Z. Dziuba, *This Journal*, **116**, 104 (1969).
3. R. Ueda, O. Ohtsuki, K. Shinohara, and Y. Ueda, *J. Cryst. Growth*, **13**, 668 (1972).
4. A. J. Panson, *Inorg. Chem.*, **3**, 940 (1964).
5. M. H. Miles and W. S. McEwan, *This Journal*, **119**, 1188 (1972).
6. M. H. Miles and P. M. Kellett, *ibid.*, **117**, 60 (1970).
7. S. A. Awad, *J. Phys. Chem.*, **66**, 890 (1962).
8. R. O. Bell, N. Hemmat, and F. Wald, *IEEE Trans. Nucl. Sci.*, **17**, 241 (1970).

Electrochemical Machining of High-Temperature Alloys in $NaClO_3$ Solutions

James P. Hoare,* Armand J. Chartrand, and Mitchell A. LaBoda*

Electrochemistry Department, Research Laboratories, General Motors Corporation, Warren, Michigan 48090

It has been shown in a series of recent reports (1-6) that an understanding of the electrochemistry of the processes occurring during the electrochemical machining (ECM) operation is desirable for obtaining a commercially finished product. Good control of dimensions and geometry, which is required for commercial exploitation, is obtained if a potential-dependent, protective, anodic film is formed on a given metal in a given electrolyte (1, 2, 6). For a given metal in a passivating electrolyte, the ECM process takes place in the transpassive region (1-3). If, in the transpassive region, the anodic film is reduced to a very thin, uniform, porous layer on the anode surface, an electropolishing or brightening of the surface will be realized (4-6). It was found (7) that $NaClO_3$ electrolytes gave superior results for the machining of steel by ECM, and that the behavior of the actual ECM of a metal on a laboratory ECM machine using $NaClO_3$ solutions correlated very well with the results of steady-state polarization curves obtained on soft iron (8), mild steel (2), and fully hardened steel (6) in terms of a potentially dependent, protective, anodic film.

Where ECM holds the greatest advantage is in the machining of high-strength, high-temperature alloys. Since these alloys contain large amounts of elements other than iron, it is important to determine how these elements influence the properties of the anodic film which, in turn, influence the quality of the finished product. It is the purpose of this report to describe the results of polarization studies made on seven high-temperature alloys and the machining behavior of these alloys in a $NaClO_3$ electrolyte.

Experimental

Small slugs or pegs were trepanned with the laboratory plunge-cut ECM machine shown in Fig. 1 from samples of the seven high-temperature alloys reported in Table I in which the composition of each alloy is listed. The composition of a mild (Type 1020) steel and of a fully hardened (Type 5160H) steel is also included. In all cases, the electrolyte (350g $NaClO_3$/liter) was pumped through the hollow, copper-tube cathode (0.25 in. or 0.64 cm, OD) at a rate of 0.5 gpm (0.031 liter/sec) and the cell voltage remained constant at 18.5V during the course of the plunge cut. The feed rate recorded was the highest value which could be obtained without tripping the cutoff switch.

After these slugs were degreased in trichlorethylene, washed in acetone, rinsed in distilled water, and dried, they were imbedded in polyethylene so that only the tip of the slug was exposed. The geometrical area of the exposed tip of the slug was determined from the dimensions obtained with a magnifier and calipers. For each run, three such electrodes as checks were mounted

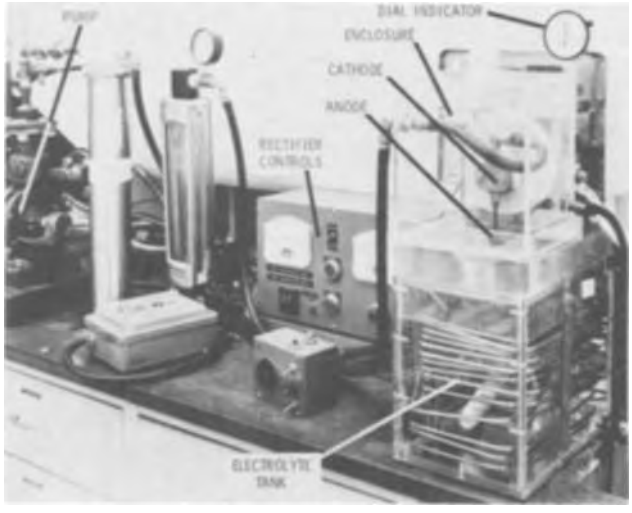

Fig. 1. Laboratory ECM plunge-cut machine

in one side of a two-compartmented Teflon cell (9). A saturated calomel reference electrode (SCE) was mounted in the other side which was separated by a fine glass frit from the first. After the cell was filled with the $NaClO_3$ solution (350 g/liter), the system was sealed with molten polyethylene.

Steady-state anodic polarization measurements were carried out on the slugs in O_2-stirred $NaClO_3$ electrolyte with a 61R Wenking potentiostat. Correction for the solution *IR*-drop was not made in the polarization data points because current interrupter measurements indicated that at current densities up to about 10 mA/in.^{2} (1.5 mA/cm^2) the *IR*-drop had values less than 1 mV. When the current output of the potentiostat became virtually steady, the potentiostat was disconnected mechanically from the circuit, and a constant-current stripping pulse was applied to the electrode by means of a mercury-wetted relay (10). The resulting transient was displayed on an oscilloscope and recorded photographically similarly to the methods used before (2). From the determination of the transition time of the arrests on the trace (11) and the knowledge of the value of the constant current, the amount of charge associated with the anodic film formed at the given potential could be calculated. In this way, the amount of film associated with the surface of the anode could be determined as a function of potential.

The plunge-cut samples were sawed in half to expose the sides of the plunged-cut hole so that an assessment of the quality of the machined surface could be made. The trace obtained from the stylus of the

* Electrochemical Society Active Member.

Key words: ECM, alloys, $NaClO_3$, electrolytes, steel.

Table I. Composition of the alloys investigated in weight per cent

Alloy	% C	% Mn	% Fe	% Si	% Cr	% Mo	% V	% Ti	% Al	% Ni	% Nb	% B	% Co	% W
1020	0.23	0.3	bal.	—	—	—	—	—	—	—	—	—	—	—
5160H	0.65	1.0	bal.	0.35	0.9	—	—	—	—	—	—	—	—	—
H13	0.4	0.4	bal.	1.2	5.5	1.75	1.2	—	—	—	—	—	—	—
Inco 901	0.05	0.5	bal.	0.35	13	6.0	—	2.5	2.0	40	—	—	—	—
Inco 713C	0.12	0.15	1.0	0.4	13	4.5	—	0.6	6.0	bal.	2.25	—	—	—
GMR 235	0.15	0.25	10	0.6	15.5	5.25	—	2.0	3.0	bal.	—	0.06	—	—
A 286	0.05	1.35	bal.	0.5	15	1.25	0.3	2.0	2.0	26	—	—	—	—
HS 31	0.5	0.5	1.5	0.5	25	—	—	—	—	10	—	—	bal.	8
410	0.15	1.0	bal.	1.0	13.5	—	—	—	—	—	—	—	—	—

Proficorder[1] shows not only the peak-to-valley roughness of the surface but also the profile of the cut. Scanning electron micrographs (SEM) of these machined surfaces were obtained at several magnifications.

All potentials are recorded with respect to the SCE, and the temperature at which the data were recorded was ambient.

Results

For each alloy, the experimental data are presented in a single figure with part (a) containing the steady-state polarization data averaged from three different runs on three different anode samples and part (b) showing a plot of the charge, Q, associated with the anodic film as a function of potential. Because of the difficulty of determining a true area due to the repeated formation and stripping of the anodic film during a given run, the polarization data are plotted as a function of the apparent current density, and a roughness factor of 10 was assumed in the calculation of values of Q. Included in each figure are SEM micrographs taken on the side of the plunge-cut hole at two or three magnifications depending on the complexity of the pattern. Finally, the Proficorder trace obtained along the side of the plunge-cut hole is reproduced at the top of each figure. The data for H13 tool steel are given in Fig. 2; for Inco 901 nickel-iron alloy in Fig. 3; for Inco 713C nickel-based alloy in Fig. 4; for GMR 235 nickel-based alloy in Fig. 5; for A286 nickel-chromium stainless steel in Fig. 6; for HS31 cobalt-based alloy in Fig. 7; and 410 stainless steel in Fig. 8. A plot of the cutting rate (feed rate), surface roughness, and weight per cents of Cr, Ni, and Fe for the seven alloys together with Type 1020 mild steel and 5160H fully hardened steel is presented in Fig. 9. From Fig. 9, it is seen that Fig. 2-8 are arranged in the order of alloys of increasing machining difficulty.

The rms roughness of the surface recorded in Fig. 9 was estimated from the Proficorder trace by calculating 1/3 of the peak-to-valley value. As noted in Fig. 2-8, the micropattern of peaks is superimposed on a macroundulation or long waviness reflecting the surface profile. The large amount of long waviness is caused by wobble in the cathode of the laboratory ECM machine and could be greatly reduced or eliminated in a more rugged machine.

[1] Gould, El Monte, California.

Discussion

For an alloy which is low in Cr- but high in Fe-content, such as H13 tool steel (Fig. 2), the polarization curve is similar to that obtained on soft iron (7) or mild steel (2, 6). In such cases, the metal is active at low potentials but a protective film is formed on the anode surface at potentials of about 0.8V. This film begins to dissolve at the beginning of the transpassive region at about 1.5V. Such a metal can be machined by ECM at high-metal removal rates with good dimensional control and low surface roughness. For those

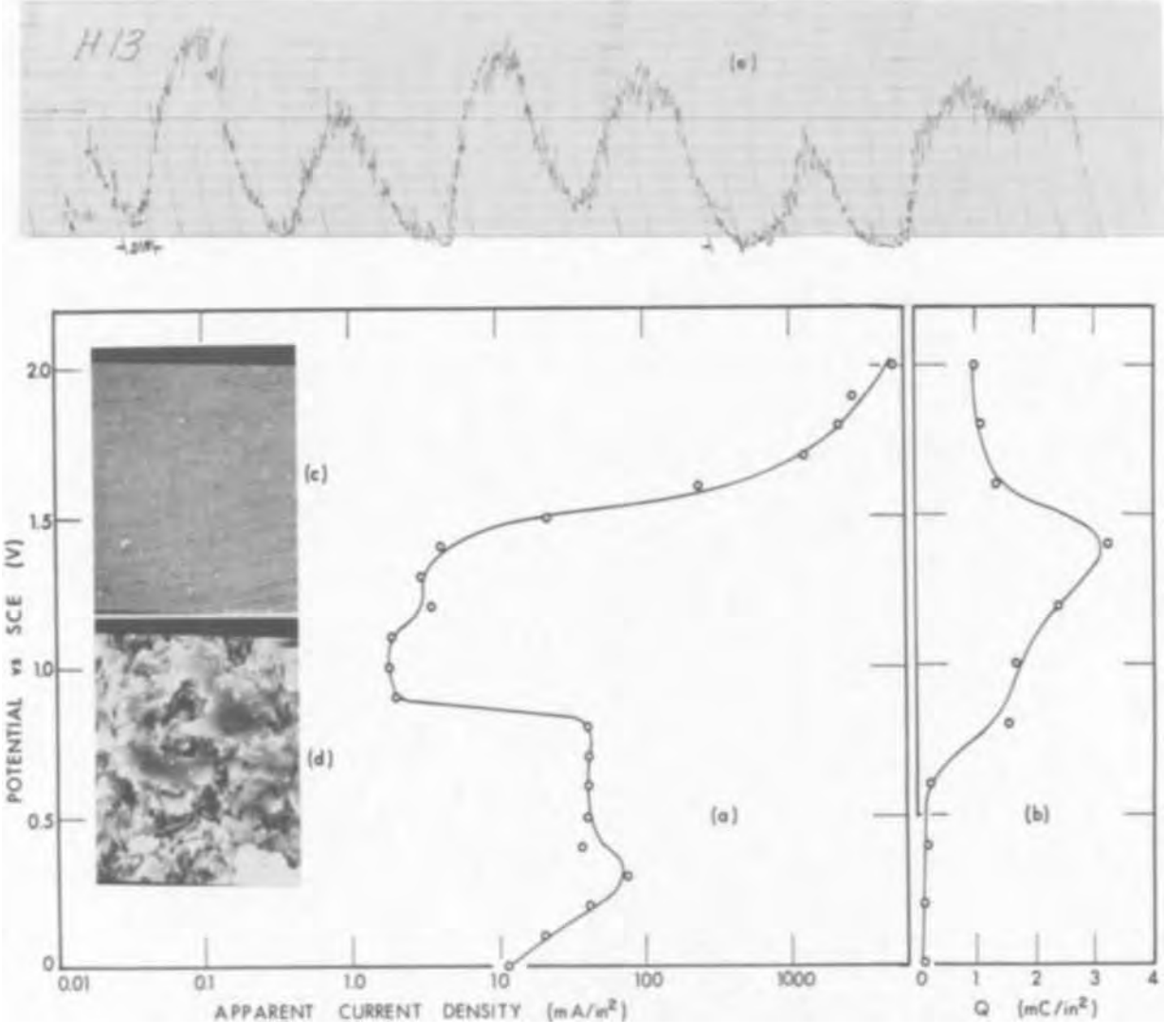

Fig. 2. a, Steady-state polarization curve for H13 tool steel in O_2-saturated $NaClO_3$ (350 g/liter) solution; b, charge Q, associated with the surface film as a function of potential; SEM micrographs at (c) 100X magnification and 30° angle of incidence and (d) 5000X at 30°; e, Proficorder trace, x-axis is 0.010 in./div., y-axis is 25 μin./div.

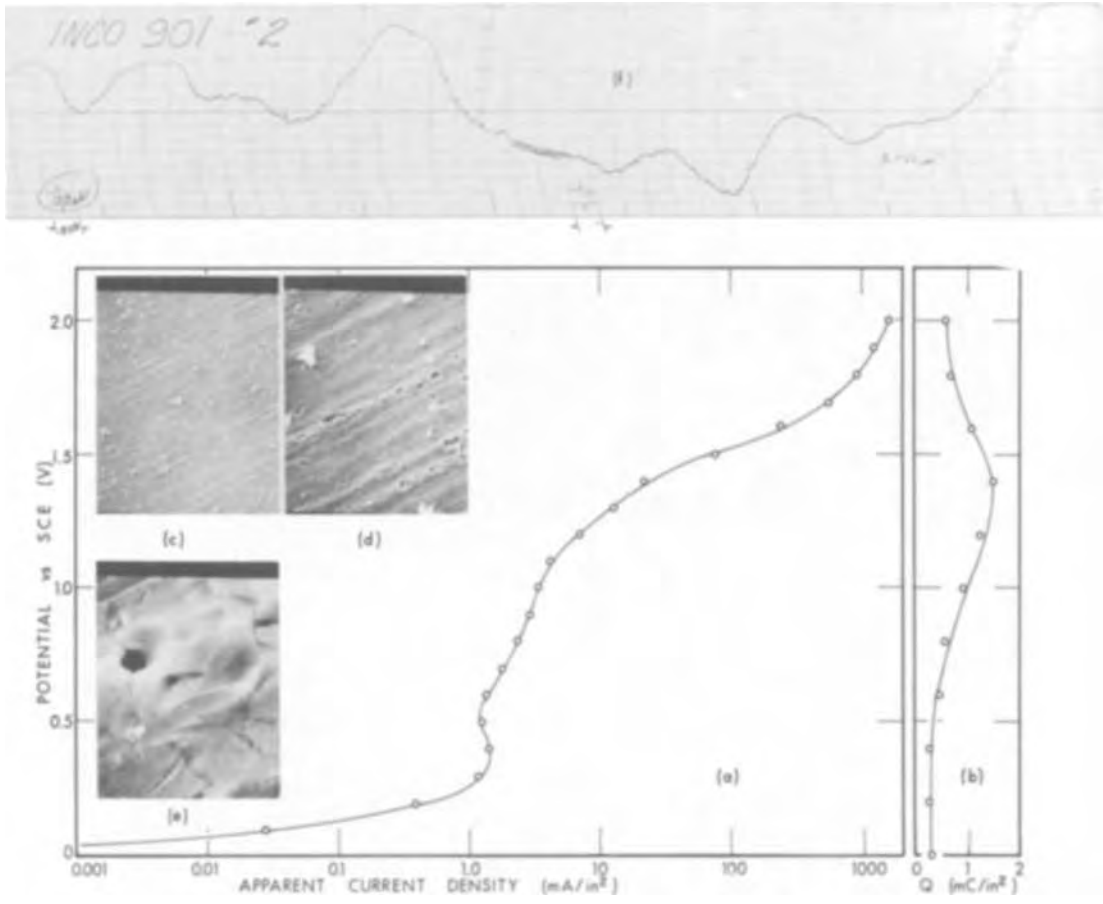

Fig. 3. a, Polarization curve for Inco 901 Ni-Fe alloy; b, Q as f (potential); SEM micrographs at c, 100X; d, 1000X, and e, 10,000X at 30°; f, Proficorder trace with x-axis, 0.010 in./div. and y-axis, 100 μin./div.

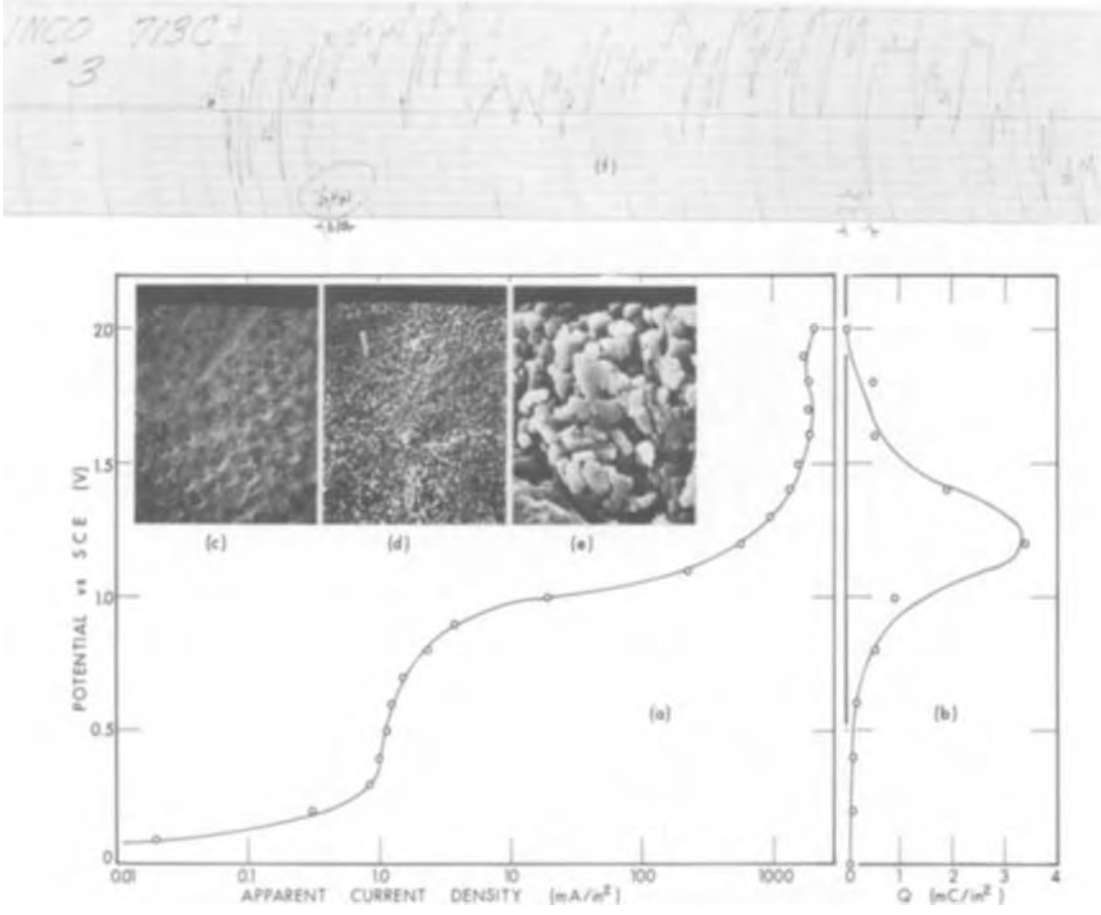

Fig. 4. a, Polarization curve for Inco 713C Ni-based alloy; b, Q as f (potential); SEM micrograph at c, 100X; d, 1000X, and e, 10,000X at 30°; f, Proficorder trace with x-axis, 0.010 in./div. and y-axis, 100 μin./div.

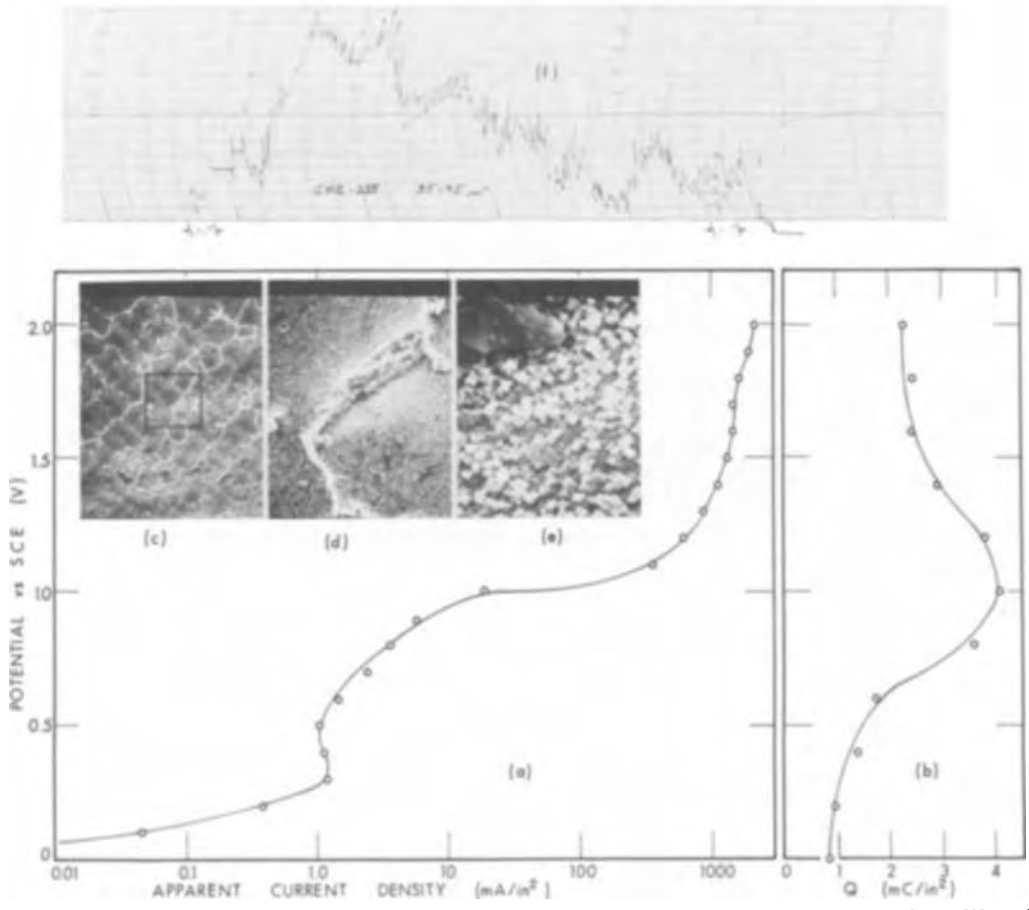

Fig. 5. a, Polarization curve for GMR 235 Ni-based alloy; b, Q as f (potential); SEM micrographs at c, 100X, d, 1000X, and e, 10,000X at 30°; f, Proficorder trace with x-axis, 0.020 in./div. and y-axis, 100 μin./div.

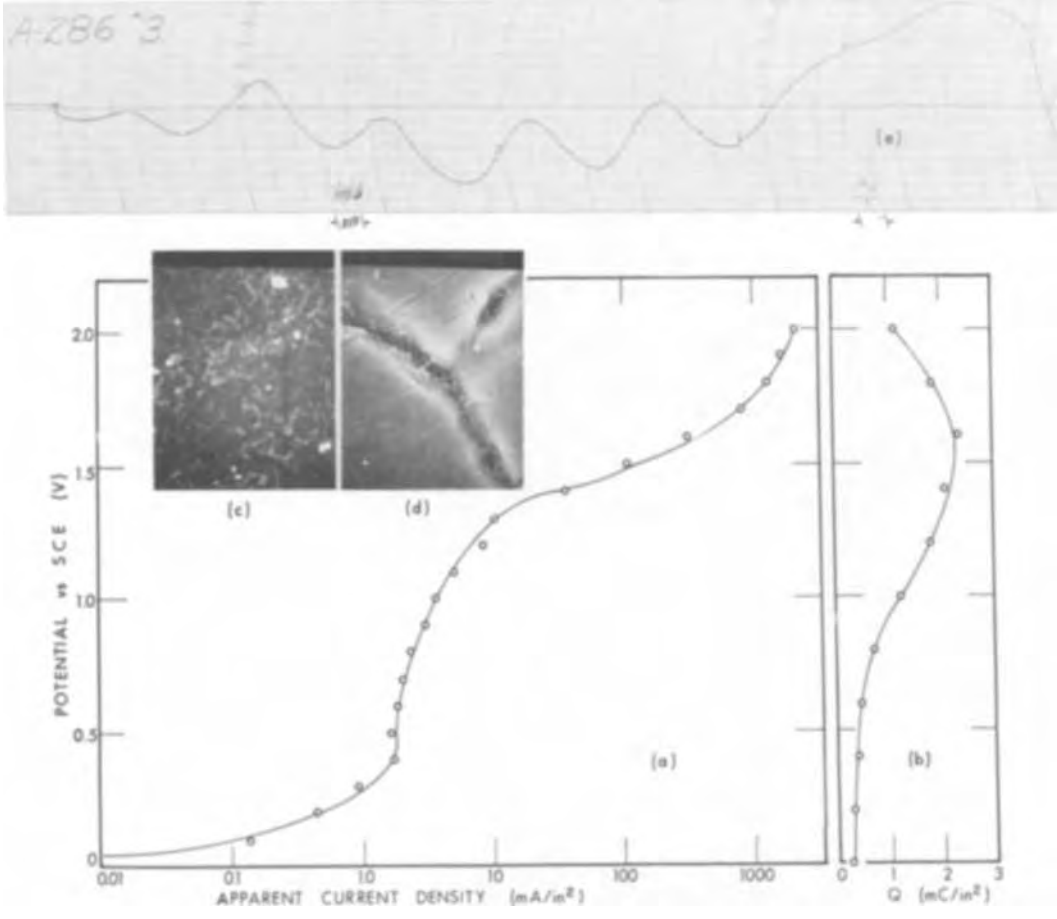

Fig. 6. a, Polarization curve for A286 Ni-Cr stainless steel; b, Q as f (potential); SEM micrographs at c, 500X and d, 10,000X at 30°; e, Proficorder trace with x-axis, 0.010 in./div. and y-axis 100 μin./div.

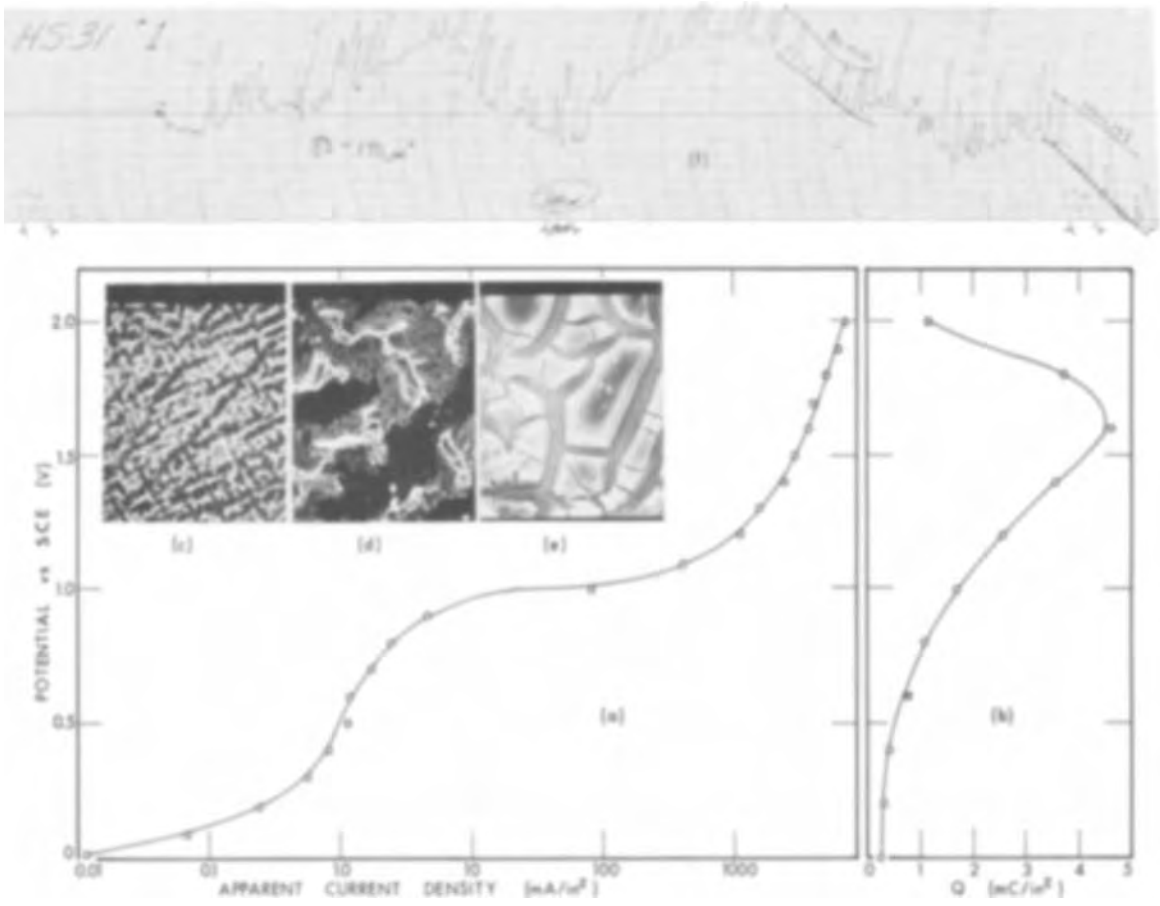

Fig. 7. a, Polarization curve for HS31 Co-based alloy; b, Q as f (potential); SEM micrographs at c, 100X, d, 500X, and e, 5000X at 30°; f, Proficorder trace with x-axis, 0.010 in./div. and y-axis 100 μin./div.

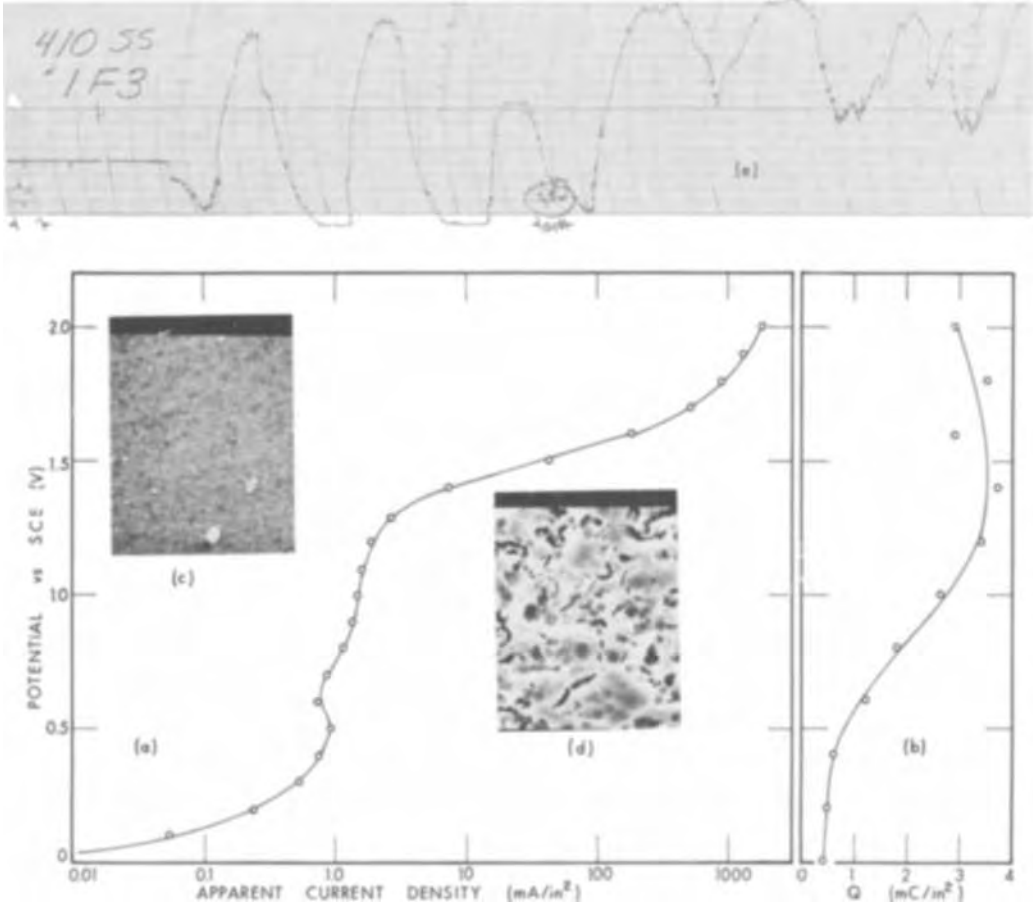

Fig. 8. a, Polarization curve for 410 Cr stainless steel; b, Q as f (potential); SEM micrographs at c, 300X and d, 5000X at 30°; e, Proficorder trace with x-axis, 0.010 in./div. and y-axis, 25 μin./div.

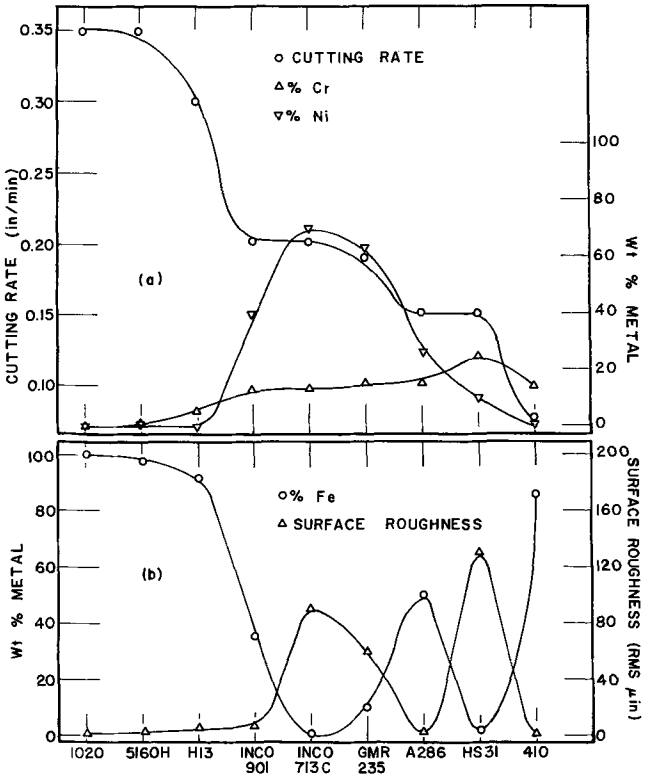

Fig. 9. A plot of the cutting rate in in./min, the peak to valley surface roughness in rms μin., and the weight per cent of Ni, Cr, and Fe for the seven alloys studied along with 1020 and 5160H steel.

alloys rich in Ni but poor in Fe content, such as Inco 713C and GMR 235, the polarization curve is similar to that found (12) on Ni. Here, the metal is passive even at low potential values (Fig. 4 and 5), and the transpassive region begins at about 1.0V. The machining rate of these high Ni content alloys is low and the surface finish poor. With an alloy rich in both Fe and Ni, the experimental results lie between those for soft iron and for pure nickel. An example is A286 stainless steel (Fig. 6) which is passive at low potentials but the transpassive region begins at 1.5V. The machining rate is low but the surface finish is very good. Apparently, the electrochemical properties of the anode surface are a function of the electrochemical properties of the major metallic components of the anode material.

From the data in Fig. 9 it is seen that the machining rate falls, in general, as the Cr content of the alloy increases. The polarization curves for the high Cr content alloys do not have an active-passive transition but rather reach a sort of limiting current until the transpassive region sets in. This behavior can be interpreted in terms of an anodic film possessing good electronic conductivity since photomicrographs of the surface in this region show little or no attack of the metal surface and the solution was not colored.

As $CrO_4^=$ ion was added to a solution of KCl, Hoar and Evans (13) found that the passivating film on iron became thinner and more protective as the $CrO_4^=$ content of the electrolyte increased. From tracer studies, the composition of the protective film on iron in solutions containing $CrO_4^=$ ions may be as high as 25% Cr_2O_3 (14). It is possible that the anodic film on Cr containing alloy anodes becomes richer in Cr as the Cr content of the alloy increases thus imparting a higher degree of passivity to the protective film. Because of the high electronic conductivity of these films, the anodic current is consumed more in O_2 evolution and less in metal dissolution; and, consequently, the machining rate would diminish with the increased Cr content of the alloy.

In the presence of a high Cr content, the data of Fig. 9a indicate that the machining rate of the alloy in $NaClO_3$ is increased as the Ni content of the alloy is increased. Possibly, the presence of Ni in the anodic film lowers the electronic conductivity of the film. In such a case the current from O_2 evolution would be reduced and more metal would be dissolved for the passage of a given number of coulombs.

In the data shown in Fig. 9b, alloys with a high iron content are machined in $NaClO_3$ with very low values of surface roughness but those with a low iron content are machined with high values of surface roughness. It is possible that the high Fe content alloys (H13, 901, A286, 410) are more homogeneous in composition, and the surface grains or domains are more evenly dissolved across the surface as noted in Fig. 2c, 3c, 6c, and 8c where only a slight grain-boundary attack is evident.

In passing, the data of Fig. 6 and 8 are interesting because they point out the lack of correlation between reflectivity and surface roughness. The surface roughness of both A286 and 410 stainless steel is very low (between 2 and 5 μin. rms). However, the machined surface of A286 is mirror bright whereas that of 410 is dull. The SEM micrographs offer an explanation. On a microscopic scale (Fig. 8d), the machined surface of 410 has a sponge-type appearance and light becomes trapped in these cavities. Consequently, the surface appears dull to the unaided eye. On the other hand, the machined surface of A286 (Fig. 6d) suffers only from a mild grain-boundary attack which does not trap the light; and, as a result, the surface appears mirror bright.

For those alloys with low Fe content (713C, GMR235, HS31), the surface roughness is very high, and the SEM micrographs exhibit a high degree of heterogeneity in the metal removed from various parts of the surface. In the case of 713C [Fig. 4 (c-e)], there is evidence that one phase is dissolved more rapidly than another leaving a rock-pile appearance to the surface. The material at the grain boundaries is more resistant to attack than the material of the grains for GMR235 [Fig. 5 (c-e)] machined in $NaClO_3$. This situation results in a raised network of strands of material spread randomly over the metal surface. Preferential attack of one phase with respect to others is indicated in the micrographs (Fig. 7) of the machined surface of HS31 in $NaClO_3$, giving a cross-hatched appearance to the surface and a very high degree of surface roughness.

These data demonstrate that high-temperature alloys high in Fe content can be machined in $NaClO_3$ electrolytes with excellent surface finish but the machining rate may be low if the Cr content is high. The machining of low Fe content alloys in $NaClO_3$ yields high metal removal rates if the Ni content is high but the surface finish is poorer due to preferential phase attack. Consequently, no single universal electrolyte exists which will produce acceptable machining of all metals because the ECM properties depend on the properties of the anodic film formed in the given system. Since properties of the anodic film formed in a given electrolyte differ from metal to metal, one must choose or tailor the proper electrolyte for the given material which is to be electrochemically machined.

Acknowledgments

The authors are indebted and offer their thanks to T. L. Davis for assistance in sample preparation and to C. Eib for the Proficorder tracing, both of the Processing Department of Research Laboratories, General Motors Corporation, and to R. L. Adams of the Electrochemistry Department of Research Laboratories, General Motors Corporation, for making the SEM micrographs.

Manuscript submitted Oct. 25, 1972; revised manuscript received Feb. 12, 1973. This was Paper 216 presented at the Chicago, Illinois, Meeting of the Society, May 13-18, 1973.

Any discussion of this paper will appear in a Discussion section to be published in the June 1974 JOURNAL.

REFERENCES

1. J. P. Hoare, M. A. LaBoda, M. L. McMillan, and A. J. Wallace, *This Journal*, **116**, 199 (1969).
2. J. P. Hoare, *ibid.*, **117**, 142 (1970).
3. M. A. LaBoda, J. P. Hoare, and S. E. Beacom, *Collection Czech. Chem. Commun.*, **36**, 380 (1970).
4. J. P. Hoare, K-W. Mao, and A. J. Wallace, *Corrosion*, **27**, 211 (1971).
5. K-W. Mao, *This Journal*, **118**, 1870, 1876 (1971).
6. K-W. Mao, M. A. LaBoda, and J. P. Hoare, *ibid.*, **119**, 419 (1972).
7. M. A. LaBoda and M. L. McMillan, *Electrochem. Technol.* **15**, 340 (1967).
8. J. P. Hoare, *Nature*, **219**, 1034 (1968).
9. J. P. Hoare, *This Journal*, **109**, 858 (1962).
10. J. P. Hoare, *Electrochim. Acta*, 9, 599 (1964).
11. R. Thacker and J. P. Hoare, *J. Electroanal. Chim.*, **30**, 1 (1971).
12. J. P. Hoare, A. J. Chartrand, and M. A. LaBoda, *Electrochim. Acta*, Submitted for publication.
13. T. P. Hoar and U. R. Evans, *Trans. Electrochem. Soc.*, **134**, 2476 (1932).
14. M. Cohen and A. F. Beck, *Z. Electrochem.*, **62**, 696 (1958).

JOURNAL OF THE ELECTROCHEMICAL SOCIETY

SOLID-STATE SCIENCE AND TECHNOLOGY

AUGUST 1973

Partial Substitution of Oxygen in the Surface Layer of Vapor-Deposited Lead Monoxide Crystallites by Chemisorption of Hydrogen Chloride

A. H. Boonstra and R. M. A. Sidler

Philips Research Laboratories, Eindhoven, The Netherlands

ABSTRACT

The reaction of HCl with the surface molecules of vapor-deposited PbO layers was investigated at different temperatures. Below about −150°C only a surface reaction was measured. This reaction causes a marked decrease of the surface area of such layers. Taking this decrease into account, the chemisorption of HCl results in a coverage of a monolayer, forming the surface compound Pb_2OCl_2. As a result of the chemisorption of H_2S at room temperature on such layers, two sulfur compounds with the formulas $Pb_8O_3S_3Cl_4$ and $Pb_4S_3Cl_2$ are formed having optical absorption edges of, respectively, 1.70 and 1.30 eV.

It has been shown previously (1) that the adsorption of H_2S on vapor-deposited PbO layers, at adsorption temperatures below −120°C, leads to the replacement in steps of the oxygen atoms by sulfur atoms. This results in a coverage of the PbO surface of about 0.25, 0.5, and 1 monolayer, forming surface compounds with bandgaps of, respectively, 1.45, 1.05, and 0.80 eV.

With chemisorption of HBr on vapor-deposited PbO layers at −160°C, it was found that half of the oxygen surface atoms were replaced by twice the number of bromine atoms, resulting in the formation of the surface compound Pb_2OBr_2 (2). The oxygen atoms in this compound could be replaced not only by other bromine atoms but also by sulfur atoms. In the latter case the surface compound $Pb_8O_3S_3Br_4$ was formed.

In this paper the results are given of investigations concerning the behavior of HCl on the surface of vapor-deposited PbO layers and of H_2S on layers previously treated with HCl.

Experimental Techniques

The adsorption of HCl at the surface of tetragonal lead monoxide was investigated on vapor-deposited PbO layers, prepared in the usual way (1, 3).

These layers consist of crystallites in the form of platelets and are oriented perpendicular to the substrate surface (4). The structure of tetragonal PbO can be described, according to Dickens (5), as a sandwich structure containing a plane of oxygen atoms flanked by two planes each containing half the number of Pb atoms. The lone pairs of electrons of the lead atoms hold the sandwiches together by van der Waal forces. Assuming that this also occurs in our vapor-deposited PbO layers, the surface density of lead and of oxygen atoms is $1.25 \cdot 10^{15}$ cm^{-2} (6, 7). On an adsorption apparatus the surface area of the PbO layers was determined at −195°C using krypton with the well-known BET method (8). These layers have a specific area of about 50 m^2 g^{-1} and a porosity of 50%. The mean space between the crystal plates is 5 nm. The dimensions of the platelets are approximately $2 \times 0.5 \times 3.5 \cdot 10^{-3}$ μm. These properties of the layer make it possible for the gas molecules to penetrate readily into the spaces throughout the entire thickness of the layer.

After the determination of the surface area, adsorption experiments were carried out at different temperatures. Some PbO layers were treated with HCl at room temperature, and the adsorption of HCl was found by measuring the change of the HCl pressure as a function of the adsorption time. The water liberated during this reaction was frozen out by cooling part of the system to −95°C with melting acetone.

During the adsorption of HCl at very low temperatures, as for example −160°C, there was a physical adsorption of HCl in addition to a fast chemisorption. The amount of physically adsorbed HCl could be readily desorbed by cooling another part of the system with liquid nitrogen. The change in surface area as a result of the HCl chemisorption and the reactivity of H_2S for these layers were also investigated.

For optical measurements on these layers, the windows with the PbO layers were separated from the tubes. The optical absorption spectra were determined with the aid of a Beckman Instruments, Incorporated DK 2 A spectrophotometer using a special integrating sphere accessory. The total (diffuse and specular) reflection spectra, R, and total transmission spectra, T, were measured, illuminating the layers with normal incident light.

After fracturing the PbO layers the depth of penetration of the HCl and the H_2S into the PbO layers was investigated under a microscope. This was possible because as a result of the H_2S adsorption the color of the PbO layer was changed.

Adsorption Results

The chemisorption of HCl on a PbO layer was measured as a function of the adsorption time at different

Key words: chemisorption, surface compound formation, photoconductivity, adsorption, phosphors, lead monoxide.

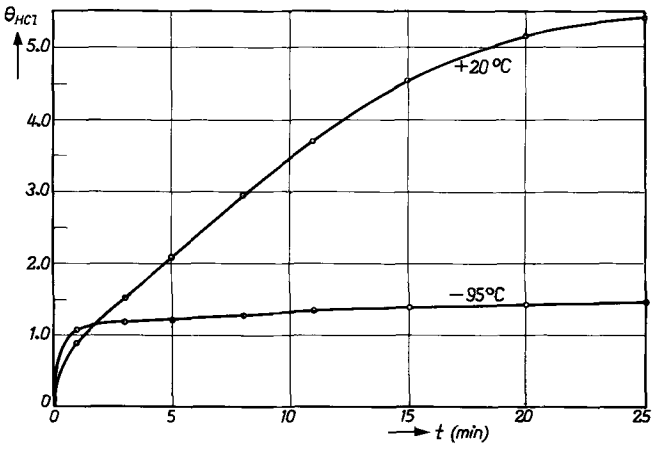

Fig. 1. Chemisorption of HCl on the surface of a PbO layer at +20°C and at −95°C, expressed in terms of monolayers (θ_{HCl}), as a function of the adsorption time.

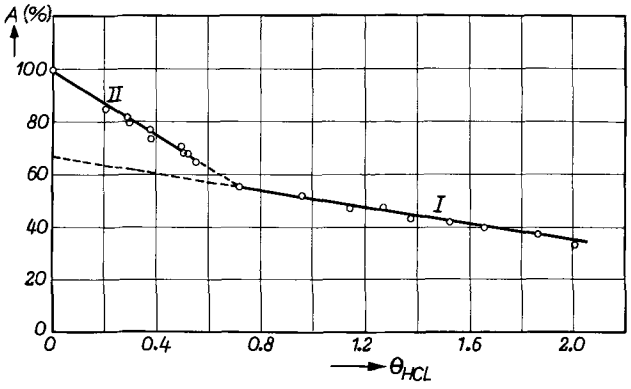

Fig. 3. Total surface area of PbO layers expressed in percentage of the total original surface area, plotted vs. the total amount of adsorbed HCl for: I, a PbO layer treated several times with HCl at −160°C and after each treatment warming up to room temperature, and II, PbO layers after one adsorption step of HCl and with a coverage less than 0.75.

temperatures. The results of these measurements are given in Fig. 1 for two temperatures. It is seen from this figure that, after an adsorption time of 25 min, an HCl adsorption at +20°C gives rise to a coverage of more than 5 monolayers, whereas at −95°C a coverage of only 1.5 monolayers is obtained in the same time. The initial rate of adsorption at 20°C is slower than at −95°C as a result of the desorption of water vapor at 20°C, through which the supply of HCl in the pores is hindered. Monolayer adsorption is understood as an adsorption of one gas molecule per PbO surface molecule. After the adsorption of about one monolayer the adsorption velocity strongly depends on the adsorption temperature. At room temperature the pressure of the HCl decreased from 1 Torr to about 10^{-1} Torr as a result of the adsorption.

At −160°C both a fast chemisorption and a physical adsorption were measured. The HCl pressure now decreased to less than 10^{-4} Torr. The amount of physically adsorbed HCl could be readily desorbed by cooling part of the system with liquid nitrogen. The chemisorption resulted in a coverage of about 0.75 of a monolayer, independent of the excess of HCl. This value of the coverage was also found with a chemisorption at −183°C.

It appeared that a PbO layer treated with HCl at −160°C to produce a coverage of 0.75 of a monolayer could adsorb a new quantity of HCl at −160°C, if the tube was first warmed up to room temperature and then cooled again to −160°C. This procedure could be repeated several times, as is represented in Fig. 2 in which the dots on the graph indicate the result of such a procedure. These coverages were calculated on the basis of the original surface area.

The results of these measurements suggest an interchange of chlorine ions from the surface layer with the oxygen of the underlying layers during the warming up of the tube to room temperature. At the next adsorption step at −160°C, the HCl can react again with the PbO surface molecules thus newly formed.

The surface area was also measured after each adsorption step. The results of these measurements are given in Fig. 3. In our opinion the small decrease of the surface area is caused by a recrystallization as a result of the diffusion process. Extrapolation of the straight line (I) in Fig. 3 to zero coverage suggests that at low degrees of coverage another recrystallization process occurs. Therefore the change of surface area was measured on a number of PbO layers treated at −160°C with less than 75% of a monolayer HCl. The results are also given in Fig. 3. With these coverages, we see a strong decrease of the surface area, which is linearly dependent on the coverage of the chemisorbed HCl. This decrease in surface area already occurs during chemisorption and not during the warming up of the tube to room temperature. This was determined by cooling some tubes to −195°C, directly after the chemisorption of HCl at −160°C, at which temperature the surface area was measured once again.

To find out if the HCl was built up homogeneously or inhomogeneously across the layer, the following experiments were made.

A number of PbO layers were treated at −160°C with different quantities of HCl. Then, H_2S was added to each of these layers at room temperature. After this the layers were broken and examined under a microscope. We see that as a result of the chemisorptions the first part of the layer was deep-red colored, followed by a black part, while the remaining part retained its original yellow-orange color. A photograph of such a layer is given in Fig. 4.

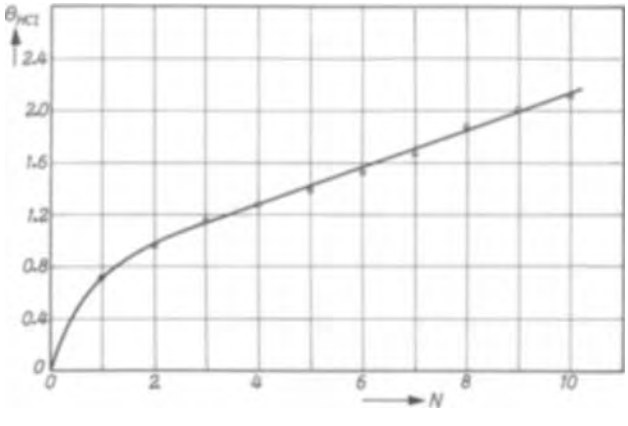

Fig. 2. Chemisorption of HCl on the surface of a PbO layer at −160°C vs. the number of processes (N). Each process consists of cooling to −160°C, adsorbing HCl, and warming up the layer to room temperature.

Fig. 4. Photograph of a PbO layer in which the large light-colored part is treated with HCl to a coverage of 0.60 and with H_2S to a coverage of 0.60, the dark part being treated with a monolayer of H_2S only, the small light part being the uncovered part of the layer.

It is known that a PbO layer treated with H_2S at room temperature becomes black colored (1). So we conclude that the red color is caused by the successive adsorption of HCl and H_2S, and that the HCl was built up inhomogeneously across the PbO layer.

To get an impression about the coverage of the HCl (θ_{HCl}) as a function of the depth of penetration into the PbO layer, and of the coverage of the H_2S on a thus treated layer ($\theta_{H_2S}^{HCl}$) a number of PbO layers were treated in the above described way. The amount of H_2S (Q_{H_2S}) was such each time that the depth of penetration of the H_2S into the PbO layer (D_{H_2S}) was greater than that of the HCl (D_{HCl}). During the H_2S adsorption water was liberated. No desorption of HCl or Cl_2 was measured in any of the H_2S processes.

The θ_{HCl} was calculated from these data as well as the known values of the adsorbed amounts of HCl.

From previous experiments (1) we know that the θ_{H_2S} of a PbO layer is about 0.90, therefore the coverage of H_2S on the part of the layer covered with HCl could also be calculated using the formula

$$Q_{H_2S} = Q_1 + Q_2 \qquad [1]$$

where Q_1 is the amount H_2S adsorbed on the part of the layer previously covered with HCl and Q_2 is the amount of H_2S used for the part covered with H_2 S only.

When Q is the amount of H_2S to cover the whole PbO layer with one monolayer then

$$\frac{Q_{H_2S}}{Q} = \theta_{H_2S}^{HCl}\frac{D_{HCl}}{D} + \theta_{H_2S}\frac{D_{H_2S} - D_{HCl}}{D} \qquad [2]$$

or

$$\theta_{H_2S}^{HCl} = \frac{D}{D_{HCl}}\frac{Q_{H_2S}}{Q} - \frac{D_{H_2S} - D_{HCl}}{D_{HCl}}\theta_{H_2S} \qquad [3]$$

where D is the total layer thickness.

The results are given in Table I. We see that the θ_{HCl} is independent of the depth of penetration and is about 0.60, and that the $\theta_{H_2S}^{HCl}$ is about 0.60. This θ_{HCl} is different from the coverage found by adding at −160°C an excess of HCl at which the coverage is about 0.75. This means that the chemisorption of HCl on PbO layers at −160°C takes place in two steps, the first resulting in a coverage of 0.60 and the second making the coverage up to 0.75.

The change in surface area of the part of the layer covered with HCl ($\theta_{HCl} = 0.60$) can be calculated, assuming that the uncovered part does not undergo a change in surface area.

We can now calculate also the coverage of HCl on the basis of the newly formed area. This calculation results in a θ_{HCl}' of about 1.0, assuming the same density of Pb atoms/cm². The results are given in Table II, in which A'/A (column 4 of Table II) is the ratio between the surface area of the covered part of the layer (A') and that of the same part of the layer before HCl had been adsorbed (A).

These results suggest that half of the amount of oxygen from the PbO surface molecules is replaced by chlorine, forming Pb_2OCl_2 according to the reaction equation

$$2PbO + 2HCl \rightarrow Pb_2OCl_2 + H_2O$$

To get a more accurate determination of the adsorption of H_2S as a function of the depth of penetration into a PbO layer covered with HCl, a number of PbO layers were treated with HCl to a coverage of 0.60 at −160°C. Different quantities of H_2S were then added to each of these layers at +20°C. The depth of penetration of H_2S into these layers was determined under a microscope after the layers had been fractured. This procedure of determining the depth of penetration is possible because of the sharp color boundary in the layer owing to the deep-red color of that part of the layer which is treated with HCl and H_2S while the rest of the layer, which is treated with HCl only is yellow colored. Figure 5 is a photograph of such a layer. The results of these measurements are given in Table III and Fig. 6. It is seen that the mean coverage of H_2S ($\bar{\theta}_{H_2S}^{HCl}$) of a PbO layer treated in this way is greater the deeper the depth of penetration.

From a determination of the surface area of layers treated in this way it was found that the further decrease of the surface area of the part that was treated with H_2S was about 10%.

Table I. Coverage of H_2S of part of PbO layer covered with HCl

Sample No.	Amount of HCl adsorbed at −160°C in % of a monolayer	Amount of H_2S adsorbed at +20°C in % of a monolayer	Depth of penetration HCl (%)	θ_{HCl}	Depth of penetration of H_2S (%)	$\theta_{H_2S}^{HCl}$
1	10.3	31.0	18	0.59	41	0.58
2	14.9	30.3	25	0.60	43	0.58
3	22.6	28.9	41	0.55	48	0.55
4	29.5	39.5	54	0.55	65	0.55
5	35.3	44.6	61	0.58	72	0.57

Table II. Change of surface area of PbO layer on which HCl is absorbed

Sample No.	Amount of HCl adsorbed at −160°C in % of a monolayer	Total surface area after HCl adsorption, in % of the original surface area	$\frac{A'}{A}$ (%)	θ_{HCl}'
1	20.6	85.2	57.1	1.05
2	29.5	81.9	63.0	0.95
3	29.6	79.5	59.0	1.02
4	38.0	76.8	62.5	0.96
5	38.1	73.0	58.0	1.03
6	49.4	71.2	64.5	0.93
7	50.4	66.9	63.7	0.94
8	52.2	67.7	63.0	0.95
9	55.5	64.0	61.2	0.98

Table III. Depth of penetration of H_2S on HCl-covered PbO layer

Sample No.	Amount of HCl adsorbed at −160°C in % of a monolayer	Amount of H_2S adsorbed at +20°C in % of a monolayer	Depth of penetration of H_2S (%)	$\bar{\theta}_{H_2S}^{HCl}$
1	53.1	5.5	13	0.41
2	44.5	11.6	27	0.43
3	52.4	15.2	35	0.44
4	54.4	20.1	43	0.46
5	53.1	25.5	53	0.48
6	53.8	30.0	61	0.49
7	55.5	35.7	69	0.52
8	52.2	41.4	78	0.53
9	54.4	43.2	81	0.53

Optical Results

The results of the adsorption measurements suggest that, in the case of H_2S chemisorption at +20°C on a PbO layer covered with about 60% HCl at −160°C, more than one surface compound is formed. To obtain more information about this matter we carried out some optical measurements. Special care had to be taken to ensure that the depth of penetration of the H_2S was not larger than that of the HCl, for otherwise we would have measured the optical absorption spectra of a surface compound created by a reaction of PbO with H_2S only (1).

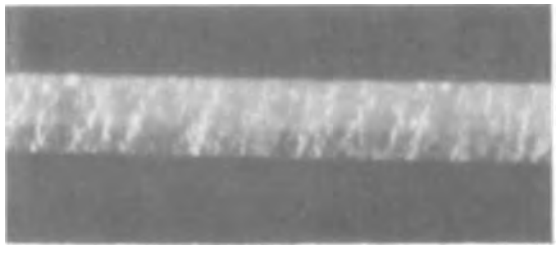

Fig. 5. Photograph of a PbO layer in which the dark part is treated with HCl to a coverage of 0.60 and with H_2S to a coverage of 0.50. The rest of the layer is only treated with HCl to a coverage of 0.60 of a monolayer.

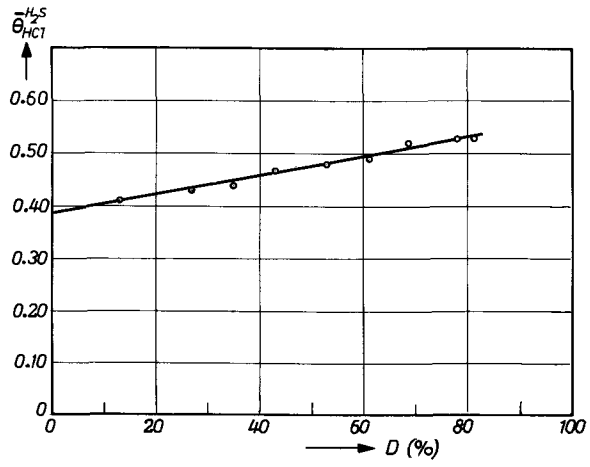

Fig. 6. Coverage of H_2S adsorbed at +20°C on a PbO layer previously treated with HCl at −160°C, *vs.* the depth of penetration (*D*) of H_2S into the PbO layer, expressed in percentages.

What interests us particularly is the wavelength at which the optical absorption of these layers becomes small and ultimately drops to zero.

In determining the absorption spectra one has to bear in mind that these vapor-deposited PbO layers scatter the incident light rather strongly. The form of the crystallites makes it impossible to handle the scattering rigorously. Therefore one has to fall back on the phenomenological reflection theory of Kubelka and Munk (9), on the basis of which Matzinger (10) shows that the optical absorption (A) in the bandgap region can be approximated by

$$1\text{-}R\text{-}T = A = \frac{\alpha D\left(1 + \frac{1}{2}\alpha D + \sigma D\right)}{1 + \left[\alpha + \sigma + \frac{1}{3}\alpha D(\alpha + 2\sigma)\right] D} \quad [4]$$

where R is the total reflection spectrum, T the total transmission spectrum, D the layer thickness, α the absorption coefficient, and σ the Kubelka-Munk scattering coefficient. Expression [2] is valid for $\alpha D(\alpha D + 2\sigma D)$ not exceeding one.

The product σD can be estimated from the reflection spectrum. For our layers it is generally somewhat smaller than one. Therefore, in the region of the bandgap ($\alpha D << 1$) the term $\alpha D(\alpha D + 2\sigma D)$ is also $<< 1$. Hence expression [2] reduces to simply

$$A = \alpha D \frac{1 + \sigma D}{1 + \sigma D} = \alpha D \quad [5]$$

The optical absorption as a function of the wavelength can be calculated from the total reflection and total transmission spectra. In Fig. 7 the total reflection and total transmission spectra are given for a PbO layer treated with HCl to a coverage of 0.55 at −160°C (curves 1), for a PbO layer treated with HCl to a coverage of 0.55 at −160°C and with H_2S to a coverage of 0.25 at +20°C (curves 2), and for a PbO layer treated with HCl to a coverage of about 0.60 at −160°C and with H_2S to about 0.10 at −125°C (curves 3).

The deviation of the reflection curve of 3 is caused by the difference in substrate temperature during the preparation of the layers. The dimensions of the crystallites of layer 3 are smaller than those of layers 1 and 2 because the specific area of this layer is 75 $m^2\ g^{-1}$. Figure 8 shows the superimposed spectra ($T + R$) of these layers, while Fig. 9 gives the square root of the absorption of these layers *vs.* $h\nu$. An $A^{1/2}$ which is linearly dependent on photon energy is characteristic of indirect energy gap media. For very small values of A deviations from the straight line show up. This absorption tail is always found in our vapor-deposited PbO layers and is probably caused by impurities. After subtraction of this tail from the absorption curve a square root dependence of the absorption on the photon energy is shown in Fig. 9b for samples 1 and 3. In the case of H_2S adsorption at room temperature on an HCl-covered PbO layer, the absorption spectrum consisted of two branches. After linear subtraction the square root of the values of the absorption was plotted against the photon energy, as is shown in Fig. 9b for sample 2.

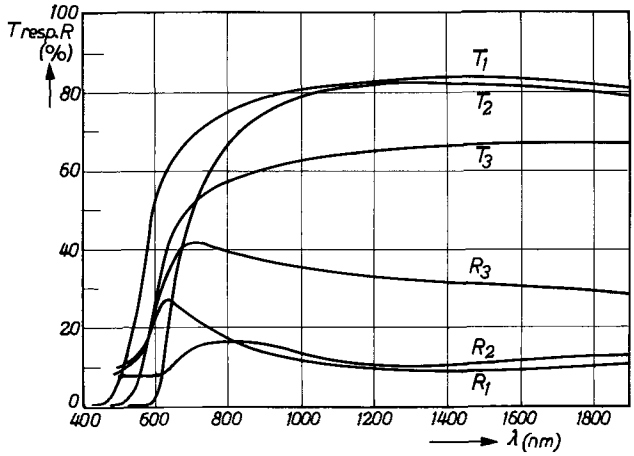

Fig. 7. Total reflection spectra (*R*) and total transmission spectra (*T*) as a function of the wavelength of the incident light, denoted by 1, for a PbO layer treated with HCl to a coverage of 0.55 (sample 1 of Table IV), by 2, for a PbO layer treated with HCl to a coverage of 0.55 and H_2S to a coverage of 0.25 (sample 6 of Table IV), and by 3, for a PbO layer treated with HCl to a coverage of 0.60 and H_2S to a coverage of 0.10 (−125°C), (sample 9 of Table IV).

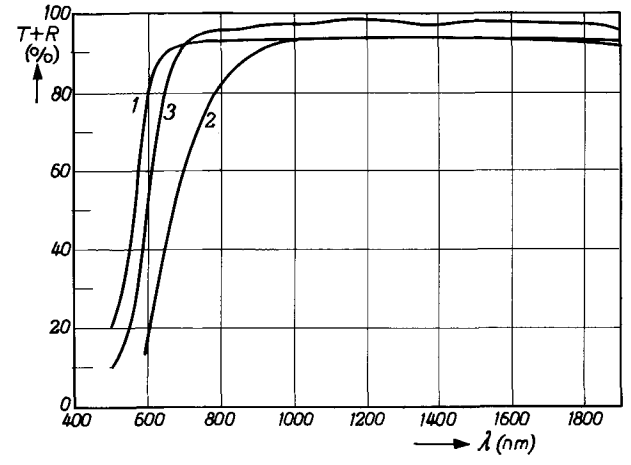

Fig. 8. Superposition of the total transmission and total reflection spectra ($T + R$) as a function of the wavelength of the incident light, 1 being used to denote sample 1, 2 to denote sample 6, and 3 to denote sample 9 given in Table IV.

Table IV gives the results for a number of layers treated in the normal way, and for the ones subjected to an H_2S treatment at low temperatures. All the layers treated with HCl and H_2S were found to have a bandgap of about 1.70 eV; besides this bandgap the layers treated in the normal way showed a bandgap of about 1.30 eV. The latter value was not found if the H_2S treatment took place at temperatures below −80°C. In the case of an HCl treatment only, an absorption edge of 1.91 eV was found. Compared with measurements on single crystals of tetragonal PbO, which gives an absorption edge of 1.94 eV (11), these results suggest that the value of 1.91 eV has to be ascribed to tetragonal PbO.

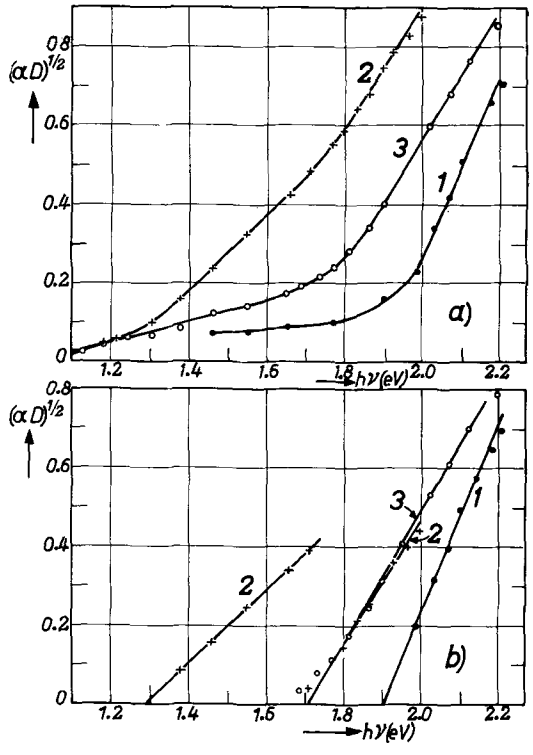

Fig. 9. a. The absorption spectra of sample 1 (curve 1) sample 6 (curve 2), and sample 9 (curve 3) of Table IV, vs. $h\nu$. b. The above absorption spectra after subtraction of an absorption tail always found in vapor-deposited PbO layers and probably caused by impurities.

Conclusions

From the adsorption measurements of HCl on a PbO layer at −160°C we found a θ_{HCl} of 0.75; the same value of the coverage was found at liquid oxygen temperature. At higher temperatures this value was not constant but depended on the HCl pressure during the reaction and on the adsorption time. We may conclude that at temperatures below −150°C there is only a surface reaction, whereas at higher temperatures there is in addition a reaction of the HCl with the underlying PbO layers. However, it was possible to chemisorb more HCl at −160°C by repeating this chemisorption process after warming up the sample to room temperature. So there must be an interchange of the chlorine of the first layer with the oxygen of the second layer. From surface area measurements we may conclude that this process is accompanied by surface recrystallization.

From the adsorption measurements of H_2S on PbO layers treated with different amounts of HCl at −160°C, we may conclude that $\theta_{HCl} = 0.60$, which is independent of the depth of penetration of HCl. If the whole layer is covered to a degree of 0.60, the chemisorption of HCl at −160°C increases to a coverage of 0.75. So chemisorption of HCl on PbO layers at −160°C takes place in two steps.

Table IV. Bandgap energy of PbO layer

Sample No.	Amount of HCl adsorbed at −160°C in % of a monolayer	Amount of adsorbed H_2S in % of a monolayer	Adsorption temperature of H_2S (°C)	E_{e_1} (eV)	E_{e_2} (eV)	E_{e_3} (eV)
1	55.0	—	—	1.91	—	—
2	29.6	10.3	+20	—	1.72	1.32
3	29.7	10.4	+20	—	1.70	1.25
4	50.1	19.0	+20	—	1.70	1.32
5	70.1	20.0	+20	—	1.68	1.32
6	55.1	25.2	+20	—	1.70	1.30
7	55.5	30.0	+20	—	1.69	1.30
8	61.3	20.6	−80	—	1.72	—
9	57.5	11.1	−125	—	1.72	—
10	53.6	7.7	−158	—	1.75	—

Surface area measurements on PbO layers treated at −160°C with HCl to a maximum of 0.60 of a monolayer showed a strong decrease of the surface area. Assuming that the surface area of the uncovered part of the layer had not changed, we see that the surface area of the part of the layer covered with a θ_{HCl} of 0.60 diminished to 60% of the original surface area. From surface area measurements before the sample was warmed up to room temperature we may conclude that the surface recrystallization was caused by the energy liberated during the chemisorption of HCl.

Assuming the same density of Pb atoms/cm², we see a θ_{HCl}' of 1.0 on the basis of the newly formed surface area. This means that half of the oxygen atoms of the surface molecules were replaced by chlorine atoms. In this process two chlorine atoms were necessary to replace one oxygen surface atom. This resulted in the formation of a new surface molecule with the formula Pb_2OCl_2.

The chemisorption of H_2S at +20°C on a layer treated with HCl resulted in a coverage of H_2S varying from 0.40 to 0.60, dependent on the depth of penetration. These values are based on the original surface area. Taking into account the decreases of the surface area caused by the chemisorption of HCl and that of H_2S of 40 and 10%, respectively, the values are 0.75 and 1.10. Our explanation is that a fast chemisorption to a θ_{H_2S}' of 0.75 was followed by a slower one which, in our conditions, reached a value of 1.10. This means that in the fast chemisorption process oxygen atoms amounting to 1.5 times the number of oxygen atoms present in the Pb_2OCl_2 surface layer were replaced by sulfur atoms. Thus, even during the fast chemisorption, part of the oxygen atoms of the second layer must also be replaced by sulfur atoms.

In our opinion the first and the second layer interact to form a new surface layer, consisting of a complex compound with the formula $Pb_8O_3S_3Cl_4$. As a result of the slower chemisorption process of H_2S the rest of the oxygen in this surface layer was also replaced by sulfur, forming a compound with the formula $Pb_4S_3Cl_2$. This hypothesis was confirmed by the optical results.

From the optical measurements on PbO layers treated with HCl to a coverage of 0.60 at −160°C and H_2S at +20°C we found two bandgaps, namely 1.70 and 1.30 eV. This second branch was not found if the H_2S adsorption took place at temperatures below about −80°C, where the slower chemisorption step is suppressed. So the bandgap of 1.70 eV belongs to the compound $Pb_8O_3S_3Cl_4$ and the value of 1.30 eV to the compound $Pb_4S_3Cl_2$.

The partial replacement of the oxygen atoms of the PbO surface molecules by atoms of another element, as described above, had already been found in the case of the elements sulfur (1), selenium (1), and bromine (2). It is known that the oxygen atoms in tetragonal PbO have an identical surrounding, so we may conclude that as a result of the replacement of a surface oxygen atom by that of another element the bond of the neighboring oxygen atoms with lead atoms becomes stronger.

At this stage of the investigations it is impossible to make more definite statements concerning the structure and types of bond of these surface compounds. In our opinion this must be possible by making selective use of the exising surface techniques and extending the investigations to other metal-oxygen compounds.

Acknowledgment

We are indebted to Mr. C. G. A. Kregting for his assistance in our experiments.

Manuscript submitted Dec. 22, 1972; revised manuscript received March 23, 1973.

Any discussion of this paper will appear in a Discussion Section to be published in the June 1974 JOURNAL.

REFERENCES
1. A. Netten and A. H. Boonstra, *Surface Sci.*, **27**, 77 (1971).
2. A. H. Boonstra and R. M. A. Sidler, *This Journal*, **119**, 1193 (1972).
3. L. Heijne, *Philips Res. Repts. Suppl. 4* (1961).
4. A. van der Drift, *Philips Res. Rept.*, **21**, 289 (1966).
5. B. Dickens, *J. Inorg. Nucl. Chem.*, **27**, 1503 (1965).
6. *Structure Reports*, **11**, 237 (1947-1948).
7. J. Leciejewicz, *Acta Cryst.*, **14**, 1304 (1961).
8. S. Brunauer, P. H. Emmett, and E. Teller, *J. Am. Chem. Soc.*, **60**, 309 (1938).
9. P. Kubelka and F. Munk, *Z. Techn. Physik*, **12**, 592 (1931).
10. B. H. Matzinger, To be published.
11. J. van den Broek, *Philips Res. Rept.*, **22**, 36 (1967).

Piezoelectricity Induced by Charge Injection in Thin Polymer Films

G. Dreyfus and J. Lewiner

Laboratoire d'Electricité Générale, Ecole Supérieure de Physique et de Chimie, 75231 Paris Cedex 05, France

ABSTRACT

The vibrations produced in the electrodes surrounding a polypropylene foil in a three-layer capacitive microphone under an a-c field are analyzed. These vibrations can be due either to the electrostatic pressure acting on the electrodes (direct excitation) or to the vibrations of the central dielectric foil itself transmitted to the electrodes (transmitted excitation). Experimental evidence is given showing the separation between these two types of excitations. In the case of transmitted excitation, electrostriction of the central dielectric layer was to be ruled out as an explanation of the observed effects. They were interpreted in terms of piezoelectricity and were proved to be due, in this case, not to a high field effect, but to charge injection, even in the absence of macroscopic space charge.

Piezoelectricity has been reported to occur in various polymeric or biological substances, in either bending, elongational, or compressional conditions, leading to different and sometimes conflicting interpretations (1-3). Most of the experimental techniques use electrodes evaporated or deposited on the surface of the sample. In the case of elongational piezoelectricity, the samples are vibrated in a direction parallel to the plane of the electrodes, and the induced alternating voltage between the electrodes is studied (4-8). Experiments are also carried out on polymer films that have been "poled" by heating and subsequent cooling under high static electric field (9, 10) and piezoelectricity has been reported to exist in various conditions. To observe compressional piezoelectricity, an a-c field is applied and the vibration of the whole sample (polymer plus electrodes) is recorded (10). Inverse piezoelectricity has also been reported to be induced by a d-c field in untreated polyethylene (11).

The results of the above experiments have been interpreted in terms of the crystalline symmetry of the materials (1, 3, 5, 6, 8), in terms of surface charges appearing during the manufacturing process (12), or in terms of dipole orientation during heating or manufacturing (7, 11).

Generally speaking, one considers that piezoelectricity occurs when a linear dependence exists between the voltage or current induced in the electrodes and the stress or strain applied to the system, or reciprocally. However, two types of excitations, which are basically different in nature, may lead to a similar apparent effect. These two different situations are perfectly illustrated by two classical systems: (*i*) When an a-c voltage is applied across a piezoelectric transducer, the transducer itself vibrates and this vibration can be transmitted to the adjacent electrode, through a bonding agent, if the acoustic impedances are matched. (*ii*) When an a-c voltage is applied across an electrostatic transducer (for instance, a capacitive transducer), the electrodes are directly vibrated by the electric forces acting on them.

Key words: transducer, electrets, polypropylene, ultrasonics.

In the general case of transmitted excitation one still has to be careful before assuming piezoelectricity; the vibration of the material could also be due to electrostriction. In the present work we have used a capacitive ultrasonic transducer to investigate the mechanical vibrations produced in the electrodes surrounding a 10 μm thick polypropylene foil, in order to separate the above mentioned two types of excitations.

In the next section we shall describe the general principle of operation of our transducer. The section following will present the experimental setup and the analysis of the observed effects.

Principle of Operation of the Transducer

In order to analyze the vibrations produced by the polypropylene foils, we have used them as the central medium of an ultrasonic transducer.

Let us assume, for the time being, that the foil has no piezoelectric properties. Consider first that it is provided with two plane contacting electrodes, as shown in Fig. 1; the pressure exerted on each electrode is

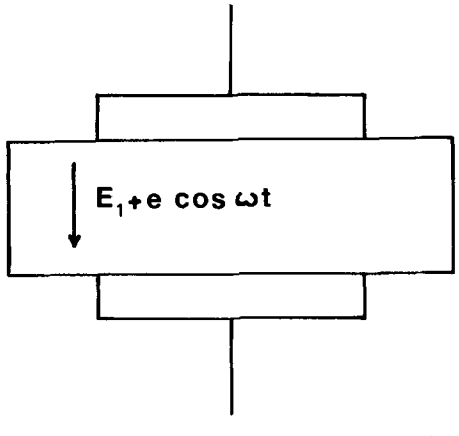

Fig. 1. Sample provided with two contacting electrodes. The field $E_1 + E \cos \omega t$ exerts an electrostatic pressure on the electrodes and vibrates them.

$p = \epsilon \frac{E^2}{2}$, where ϵ is the permittivity of the plate and E the field between the electrodes. Assuming that the field has a d-c component E_1 and an a-c component $E \cos \omega t$, the pressure is

$$p = \frac{\epsilon}{2}\left(E_1^2 + \frac{E^2}{2} + 2E_1 E \cos \omega t + \frac{E^2}{2}\cos 2\omega t\right) \quad [1]$$

If $E_1 >> E$, the component of p at frequency ω is much greater than that at 2ω; it is proportional to e, as would be the case if the dielectric plate were piezoelectric.

It must be pointed out that d-c field is the relevant parameter; it may be due either to an external voltage applied across the plate or to a distribution of charges within the dielectric or to both.

Let us now consider, as shown in Fig. 2, that the dielectric plate of permittivity ϵ and thickness d_2 is separated from two noncontacting electrodes of area S by layers 1 and 3, of permittivity ϵ_0 and thicknesses d_1 and d_3. If V is the voltage applied to the electrodes and if we assume that there exist, in the dielectric plate, surface charge densities σ_1 and σ_2 and a volume charge density $\rho(z)$, the field E_1 in layer 1 is given by

$$LE_1 = -V - \left(\frac{d_2 - \langle z\rangle}{\epsilon} + \frac{d_3}{\epsilon_0}\right)\frac{Q}{S} - \sigma_2 \frac{d_3}{\epsilon_0} - \sigma_1\left(\frac{d_2}{\epsilon} + \frac{d_3}{\epsilon_0}\right) \quad [2]$$

where $L = d_1 + \frac{\epsilon_0}{\epsilon} d_2 + d_3$. Q is the total volume charge in the dielectric plate, and $\langle z\rangle$ is the mean penetration depth of the charges, defined by

$$\langle z\rangle = \frac{\int_0^{d_2} z\rho(z)\,dz}{\int_0^{d_2} \rho(z)\,dz}$$

We have assumed z to be the only spatial variable. Relation [2] may be stated more briefly as

$$LE_1 = V_0 - V \quad [3]$$

In this expression V_0 is called the equivalent voltage of the electret. It only depends on the charge distribution and on the geometry of the system, assuming the charges to be independent of the applied voltage, which is the case if the electret is stable and if no discharge occurs through layers 1 and 3. If an a-c field is added, relation [1] still holds and the electrodes are vibrated. Conversely, if one of the electrodes is mechanically vibrated, an a-c current arises in the external circuit; it is proportional to E_1. It must be pointed out that the superiority of the assembly of Fig. 2 over that of Fig. 1 lies in the fact that the electric field E_1 can be canceled without canceling the field in the foil, by applying an external voltage equal to the equivalent voltage of the electret ($V = V_0$). If we assume now that the foil exhibits piezoelectric properties, the assembly of Fig. 1 is such that, with an a-c voltage applied, the electrodes will be vibrated, whatever the value of the applied voltage V. The assembly of Fig. 2 would exhibit a similar behavior provided that the medium filling layers 1 and 3 achieve proper acoustic impedance matching between the foil and the electrodes.

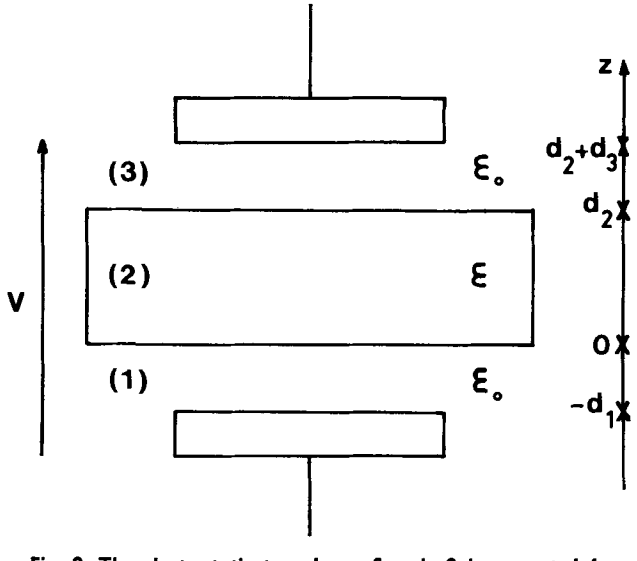

Fig. 2. The electrostatic transducer. Sample 2 is separated from the electrodes by gas layers 1 and 3.

Experimental Setup and Discussion of the Results

The dielectric under study was a 10 μm thick, highly isotactic, polypropylene foil, that had been corona-charged through gas layers 1 and 3. The maximum applied voltage was 4 kV; V_0 ranged from 0 to 2000V. A standard pulse echo ultrasonic technique was used combined with a high voltage supply for the electrostatic transducer (14). A block diagram of the system is shown in Fig. 3. The a-c voltage, at 10 mHz, was supplied by a pulsed oscillator; the lower, grounded electrode was an aluminum single crystal in which the ultrasonic pulses created by the transducer were propagated, and then received by an X-cut quartz crystal transducer at the other end of the crystal. The pulses were amplified, detected, and displayed on an oscilloscope. The detected pulses were also passed through a gated amplifier and integrated and the resulting d-c voltage was recorded on a strip-chart recorder. The voltage thus recorded was a function of the amplitude of the ultrasonic pulses, and, consequently, was directly related to the module of the electric field E_1. Assuming that the transducer operates as an electrostatic transducer, the dependence of the amplitude A of an ultrasonic echo as a function of applied voltage V is given by relation [2] and shown in Fig. 4a. In our experiments, no ultrasonic pulses could be observed under zero applied voltage before charging the foils. This shows that the foils which were used did not exhibit observable "natural" piezoelectricity. Figure 4b is the experimental dependence of A *vs.* V; the important feature is that, for most foils, A does not come exactly to 0 when $V = V_0$. This can be due either to some unexpected phenomenon related to the above process (since $E_1 = 0$ for $V = V_0$) or to the vibration of the polymer foil itself, transmitted to the aluminum crystal through layer 1. In the latter case, and for a given amplitude of vibration of the foil, the impedance mismatch between layers 1, 2, and the metal, would cause the transmitted vibrations to be so small that they would be seen only when the vibrations due to direct

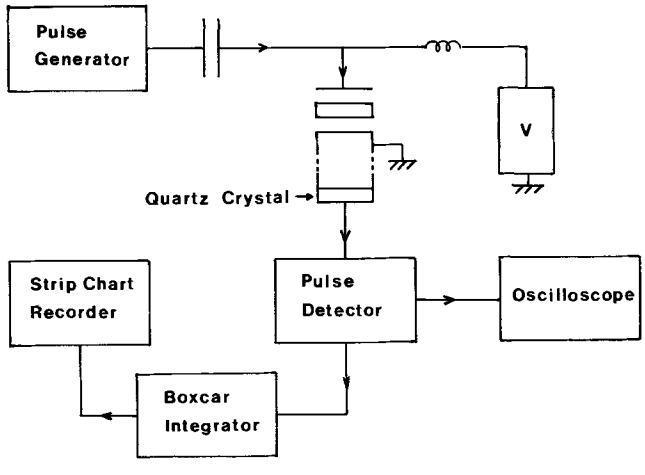

Fig. 3. Block diagram of the apparatus

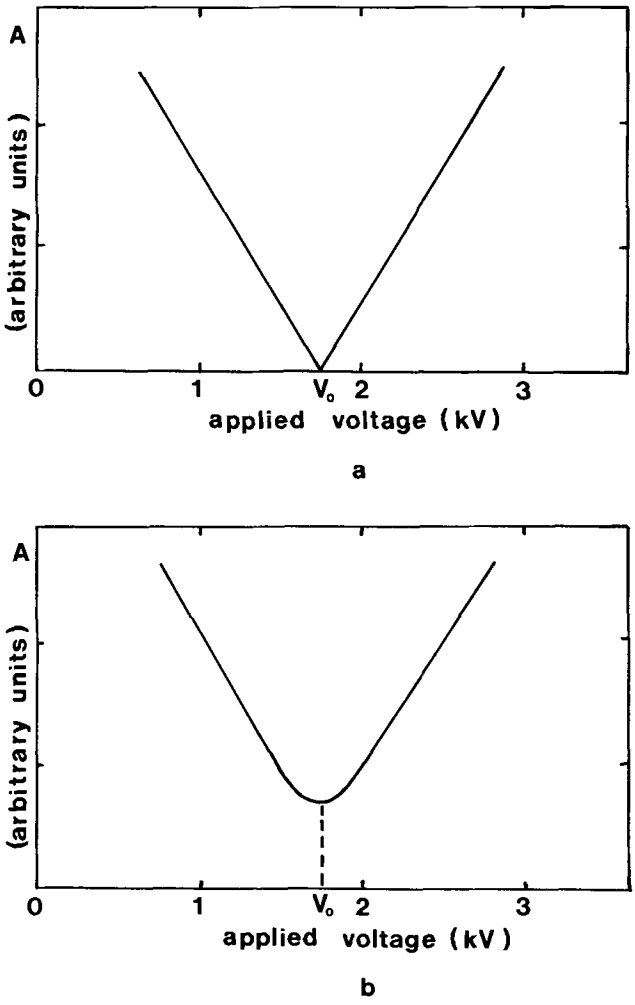

Fig. 4. a) Theoretical dependence of the amplitude of the ultrasonic pulses at frequency ω *vs.* applied voltage. Pulses cancel for $V = V_0$, as results from relations [1] and [3]. b) Experimental dependence of the amplitude of the ultrasonic pulses at frequency ω *vs.* applied voltage. Pulses do not cancel for $V = V_0$.

excitation of the metal are 0, *i.e.*, when $V \neq V_0$. If we assume this latter hypothesis, *i.e.*, that the foil itself vibrates, two synchronous vibrational waves should exist in the electrodes for V different from V_0. One of them is due to the direct excitation of the electrode and the other is due to the vibration transmitted from the foil to the electrode. Two experimental evidences support this hypothesis; first, we could measure a difference in the phases of the two types of waves; second, we were able to observe interferences between these 2 waves.

As to the first evidence, the shape of an echo was recorded on an XY recorder by sweeping linearly in time the position of the gate of the gated amplifier first for $V = V_0$, then for $V \neq V_0$. In order to scale the X axis the markers delivered by a quartz-crystal stabilized pulse generator were similarly recorded. It was observed that the echo produced at $V = V_0$ was delayed from that obtained at $V \neq V_0$ by 0.10 ± 0.03 μsec. Similar phase differences have been reported (15) to occur between directly excited waves and transmitted waves from conventional piezoelectric transducers.

As to the second evidence, the sample and sample holder were slowly cooled down to liquid nitrogen temperature. The mechanical properties of the assembly being a function of temperature, the phase of the pulses due to the polymer foil varied during cooling relative to that of the directly excited pulses, so that, when both systems of pulses were present (*i.e.*, $V \neq V_0$), the amplitude of the detected signal was modulated in time (and consequently in temperature) as shown in Fig. 5. This is due to the interference of the two systems; when the two waves are just in phase they add and the detected voltage is maximum; when they are out of phase the detected voltage is minimum. This oscillatory behavior of the detected signal as a function of temperature disappeared at $V = V_0$, *i.e.*, when only one type of wave was emitted.

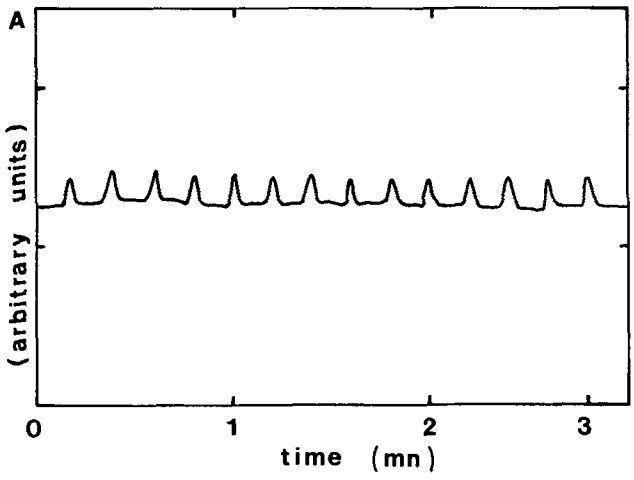

Fig. 5. Interferences between the wave emitted by direct excitation of the electrodes and that due to the vibration of the foil, transmitted to the electrodes.

The two experiments just described allow us to differentiate between the wave emitted by what we called the direct excitation and that produced by the vibration of the foil itself transmitted through layer 1.

Since the polymer foil itself vibrates, it seems desirable to know whether it is caused by electrostriction or piezoelectricity. The following experiments support the latter hypothesis. First, the electret was Corona-charged by applying a high positive voltage to the foil, so that it became negatively charged on the lower side, and positively charged on the upper side; a negative voltage was then applied, so that the inverse process took place: negative charges were injected on the upper side, positive ones on the lower side. The equivalent voltage was then measured, and, if it was still positive, more inverse charges were injected. This process was carried on until V_0 equaled zero. Considering relation [2], and taking into account the symmetry of the geometry and of the process, it can be seen that this implies that

$$\sigma_1 = \sigma_2 = \rho(z) = 0$$

The vibration of the foil due to an electrostrictive effect is described by a similar relation as relation [1], in which field E_1 is replaced by the field $E_2(z)$ within the dielectric foil. Since under the above assumptions on the symmetry of the process, we have $\rho(z) = 0$, then $E_2(z)$ is uniform. When no external voltage is applied, the field E_2 is 0 since $\sigma_1 = \sigma_2 = 0$. No signal at frequency ω should be observed if the relation between stress and electric field were quadratic. Such was not the case in our experiments, which proves that the relation between stress or strain and total electric field is linear. Finally the occurrence of piezoelectricity was proved by the following observation of the direct piezoelectric effect: ultrasonic pulses emitted by the quartz transducer were received by the upper transducer, in the same conditions as previously mentioned where fields E_1 and E_2 are canceled, leaving no other possibility for the conversion than piezoelectricity. Since the polymer foil did not exhibit any piezoelectricity prior to being corona-charged, we had to determine whether the origin of the observed piezoelectricity was related to the high field applied during the charging process (1 to 4 $\times$ 10^6 V/cm), or to the injection of the charges. To answer this question the foil was submitted to as strong an electric field as mentioned above, but without injecting charges. In order

to prevent electric discharges in layers 1 and 3, the sample was very slightly electrified by gentle rubbing; and thus adhered to the upper electrode, which was raised. The sample holder was placed in a vacuum chamber which was pumped until the pressure was about 10^{-5} Torr; the upper electrode was then lowered in vacuo and the electric field turned on. Fields as high as 2×10^6 V/cm were reached without charging the sample and without the foil becoming piezoelectric. The pressure was then raised, the voltage being kept constant, until the disruptive field was reached, according to Paschen's law. The foil was charged and became piezoelectric.

Conclusion

We have analyzed systematically the possible origin of an observed vibration of the electrodes surrounding a polypropylene foil, under an a-c excitation.

The deductive path that has been followed is summarized in Fig. 6. First we have separated the direct excitation from the transmitted excitations. In this latter case electrostriction of the central dielectric had to be ruled out to explain the observed effects. Finally the observed piezoelectricity was proved to be due, not to a high field effect, but to charge injection; this is in agreement with the fact that polypropylene is a nonpolar material. The foil becomes piezoelectric when equal quantities of positive and negative charges have been injected into it; since the penetration depth of such charges is generally small compared to the thickness of the sample (16, 17), we may assume that the piezoelectricity is due to two near-surface layers in which quantities of opposite charges are embedded. We know from Furukawa *et al.* (12) that the component in the direction α of the polarization created by a distribution of charges is

$$P_\alpha = \sum_\beta (u_{\alpha\beta})_0 \sum_i q_i x_{\beta i} + \sum_\beta \sum_\gamma \frac{\partial u_{\alpha\beta}}{\partial x_\gamma} \sum_i q_i x_{\beta i} x_{\gamma i}$$

α, β, γ stand for cartesian coordinates; $(u_{\alpha\beta})_0$ is the macroscopic strain under uniform conditions; q_i is the charge of the i^{th} electric charge; $x_{\beta i}$ is the coordinate of the i^{th} charge in direction β; and $\sum_i q_i x_{\beta i}$ is the dipole moment of the distribution. The second term is the quadrupole moment of the distribution. Since in our case the dipole moment is 0 ($V_0 = 0$), the observed effect is not first order piezoelectricity (*i.e.*, piezoelectricity due to uniform strain). We can infer that in polypropylene the location of traps for positive and negative charges is not completely random, and assume that charges are probably not trapped in the highly disordered surface region, but in the crystalline parts of the polymer foil (18). With this assumption the observation of piezoelectrity should be a powerful tool in order to get information on the symmetry of the crystallites, taking into account the symmetry required by piezoelectricity.

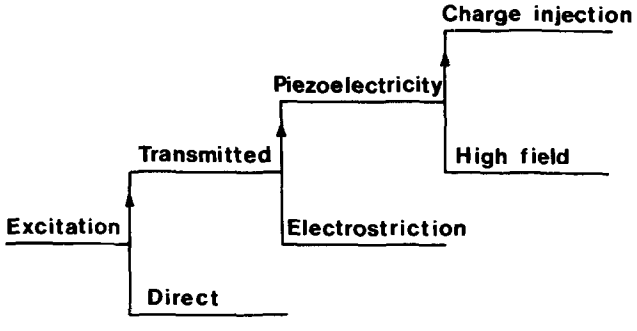

Fig. 6. Logical path followed in the analysis of the vibrations observed in the electrode.

Acknowledgment

This work was supported in part by the C.N.R.S. and the D.G.R.S.T.

Manuscript submitted Oct. 3, 1972; revised manuscript received Jan. 3, 1973. This was Paper 155 presented at the Miami Beach, Florida, Meeting of the Society, Oct. 8-13, 1972.

Any discussion of this paper will appear in a Discussion Section to be published in the June 1974 JOURNAL.

REFERENCES

1. E. Fukada, *Ultrasonics*, 229 (1968).
2. M. H. Shamos and L. S. Lavine, *Nature*, **213**, 267 (1967).
3. E. Fukada, *Biorheology*, **5**, 199 (1968).
4. J. Cohen and S. Edelman, *J. Appl. Phys.*, **42**, 893 (1971).
5. M. Date, S. Takashita, and E. Fukada, *J. Polymer Sci., A2*, **8**, 61 (1970).
6. E. Fukada, M. Date, and K. Hirai, *Nature*, **5083**, 1079 (1966).
7. J. Cohen and S. Edelman, *J. Appl. Phys.*, **42**, 3072 (1971).
8. E. Fukada, M. Date, and K. Hara, *J. Appl. Phys. (Japan)*, **8**, 151 (1969).
9. S. Edelman, L. R. Grisham, S. C. Roth, and J. Cohen, *J. Acoust. Soc. Am.*, **48**, 1040 (1970).
10. H. Kawai, *J. Appl. Phys. (Japan)*, **8**, 975 (1969).
11. R. W. Greaves and D. R. Lamb, *J. Mater. Sci.*, **6**, 74 (1971).
12. T. Furukawa, Y. Uematsu, K. Asakawa, and Y. Wada, *J. Appl. Polymer Sci.*, **12**, 2675 (1968).
13. W. C. Cady, "Piezoelectricity," p. 234. Dover Publications Inc., New York.
14. D. Legros and J. Lewiner, *J. Acoust. Soc. Am.*, To be published.
15. W. C. Overton, Jr. and J. Gaffney, *Phys. Rev.*, **98**, 969 (1955).
16. G. M. Sessler, *J. Appl. Phys.*, **43**, 408 (1972).
17. R. A. Creswell and M. M. Perlman, *ibid.*, **41**, 2365 (1970).
18. L. Mandelkern, *J. Phys. Chem.*, **75**, 3909 (1971).

Fabrication of GaAsP MIS Capacitors Using a Thermal-Oxidation Dielectric-Growth Process

D. H. Phillips, W. W. Grannemann, L. E. Coerver, and G. J. Kuhlmann

The University of New Mexico, Albuquerque, New Mexico 87106

ABSTRACT

Heterogeneous insulating films were grown on $GaAs_{1/2}P_{1/2}$ by thermal oxidation at atmospheric pressure. Good insulating and passivating properties of the films resulted from inert-atmosphere annealing. A processing temperature upper limit of 710°C on a minimum of 90 min annealing time are required. Evidence that the film is a mixture of β-Ga_2O_3 and $GaPO_4$ is presented.

Capacitance *vs.* voltage data for metal insulator semiconductor (MIS) capacitors are presented, and surface-state density instabilities are discussed. Use of thermal cycling and chromium doping to obtain stable MIS capacitors is described.

$GaPO_4$ is physically similar to SiO_2. Thermally grown SiO_2 on silicon is fundamental to the MIS integrated circuit technology. The results presented here suggest similar possibilities for GaAsP.

One of the important aspects of the technology of any new semiconductor material is the question of thermal oxidation of the semiconductor surface, both for surface passivation (1) and as the insulator for possible metal insulator semiconductor (MIS) structures. The thermal oxidation of GaAs and GaP have both been studied previously (2, 3). This paper reports the successful thermal oxidation of $GaAs_{1-x}P_x$ to create good, pinhole-free dielectric films suitable for use as insulators in MIS structures.

The goal of the research was to define an open-tube process for growing an insulating film suitable for use as the insulator in an MIS structure. It was evident that surface damage would be an important limitation on the process. Growth rate and dielectric constant of the grown film would also be important film properties to be determined.

Experimental

All experiments were performed on 100 × 100 mil chips using commercially available[1] (100) $GaAs_{1-x}P_x$ material with a phosphorus mole fraction of $x = 50 \pm 2\%$. The 4 mil thick GaAsP epitaxial layer was tellurium doped to a donor concentration of 2.0×10^{15} atoms/cm^3. This material represents the median between GaAs and GaP whose oxidation properties are better known. The epitaxial layer was grown on a 15 mil thick GaAs substrate. The tellurium-doped substrate had a resistivity of 0.003 ohm-cm.

There was a graded region (1-2 mil thick) between the epitaxial layer and the substrate in which the phosphorus mole fraction varied from 0% at the GaAs substrate to 50% at the epitaxial layer.

The growth of the insulating layer on this material was done by open-tube oxidation. Before introduction into the furnace, the chips were lapped and polished to a mirror surface. They were then degreased in trichloroethylene, cleaned in acetone, and chemically etched in a cold mixture of 5:1:1 H_2SO_4:H_2O_2:H_2O for several minutes. The total lapping, polishing, and chemical etch steps removed no more than 38μ of the $GaAs_{1/2}P_{1/2}$ material. The chemical etch was always performed immediately before introducing the chips into the furnace. The oxidation was accomplished by passing atmospheric pressure dry oxygen at a flow rate of from 0.2-1.0 liters/min over the GaAsP chips on a quartz boat in the center section of a Lindberg Diffusatron Mk II style M-50 furnace.

It was quickly discovered that an anneal step was necessary when measurements were made on MIS capacitors. Capacitors made on an unannealed insulator layer almost invariably showed metal semiconductor characteristics with the continuously decreasing capacitance *vs.* voltage (C-V) of a metal semiconductor junction. However, if the chips were put back in the furnace at a temperature no higher than 700°C in a 0.3-1.0-liter/min stream of argon or nitrogen for periods of greater than 1½ hr, most of the pinhole shorts disappeared, and MIS capacitors formed on the annealed insulator film showed capacitor characteristics rather than diode behavior. Consequently, the anneal in an inert atmosphere was always part of the film growth process.

MIS capacitors were formed on the chips by vacuum evaporation of either Al or Cr metal through a metal mask, leaving approximately 10 mil diameter capacitors. Metal contacts were applied immediately after removing the chips from the furnace after annealing. Aluminum was evaporated at pressures less than 2×10^{-5} Torr, and Cr at pressures less than 5×10^{-8} Torr.

After oxidation and annealing there was often some oxide on the GaAs substrate which had to be lapped off before making ohmic contacts on the substrate side.

Ohmic contacts were made on the GaAs by vacuum evaporation of elemental silver at a pressure of less than 2×10^{-6} Torr. This was followed by a microalloying step. The silver dots were alloyed at 650°C for 6 min in an argon flow of about 1 liter/min.

Results and Discussion

A large number of time and temperature experiments were run. An experiment consisted of growing and annealing a film, evaporating metal dots on the surface, and lapping off the oxidized surface of the GaAs substrate. The C-V curve of the device was examined. Experiments were evaluated on the basis of whether they showed MIS capacitor or metal semiconductor diode characteristics.

Figure 1 is a graphical presentation of the results of these experiments with dry oxygen. The dashed lines indicate general regions and are not intended to be exact demarcation lines.

Figure 2 shows four photomicrographs of the oxidized surfaces. Under no circumstances does the film grown look like a single crystal or a completely unstructured glass; it always shows a small crystallite structure. In Fig. 2a, which shows a film grown at 700°C in dry O_2 for 675 min, the film crystallites appear to be considerably less than 1μ in diameter. The background, as always, carries with it the character-

Key words: oxidation, semiconductor devices, dielectric films, $GaPO_4$, Ga_2O_3.

[1] Supplied by Monsanto Company, St. Louis, Missouri.

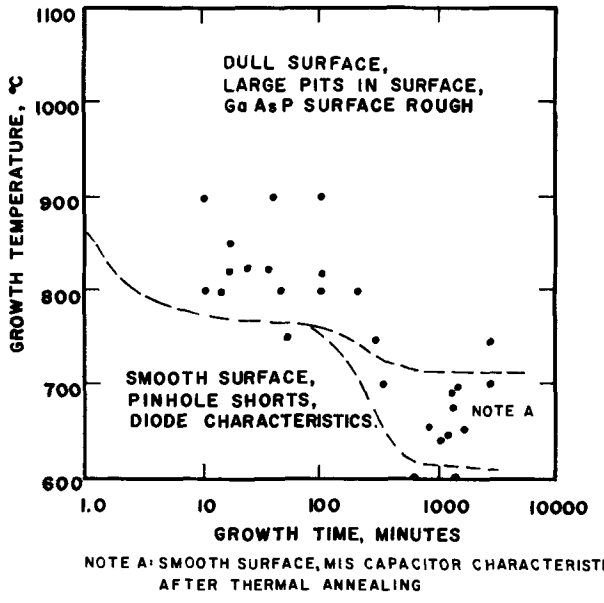

Fig. 1. Temperature-time plot of oxidation experiments on $GaAs_{1/2}P_{1/2}$ in dry oxygen. Flow rate is 1 liter/min.

istic color of the film, which goes through the same color sequence as other insulator films on a reflecting semiconductor surface. In all four figures, there are many small white crystallites interspersed in the characteristic color matrix.

Crystallite size grows with increasing temperature, as can be seen by comparing Fig. 2b, c, and d with Fig. 2a.

The film grown at 875°C had varicolored patches on it; the photomicrograph (Fig. 2c) shows a boundary between two such patches. In order to show the structure, the microscope magnification had to be reduced for the 875° and 950°C films. At 950°C a pronounced growth of a white amorphous layer begins to cover considerable areas of the film. The increasing heterogeneity of the films with increasing temperature explains why the MIS structures grown at high temperatures show pinhole shorts and diode characteristics. For increasing temperatures, the crystallites are better defined and the grain boundaries show less tendency to be changed by annealing.

Figure 3, a and b, show the GaAsP surface after the insulating layer has been etched off. Figure 3a shows a chip on which a film had been grown in oxygen for 341 min at 660°C. Later the chip was photomasked and part of the film was etched off with NH_4F. The light part of Fig. 3a is the bare GaAsP surface after etching; the dark part is the unetched film. Small pits can be observed on the surface. Figure 3b shows a similar chip on which a film had been grown for 251 min at 740°C with a subsequent anneal. On this chip, the insulating layer was subsequently removed with NH_4F. It can be seen that there is much more surface

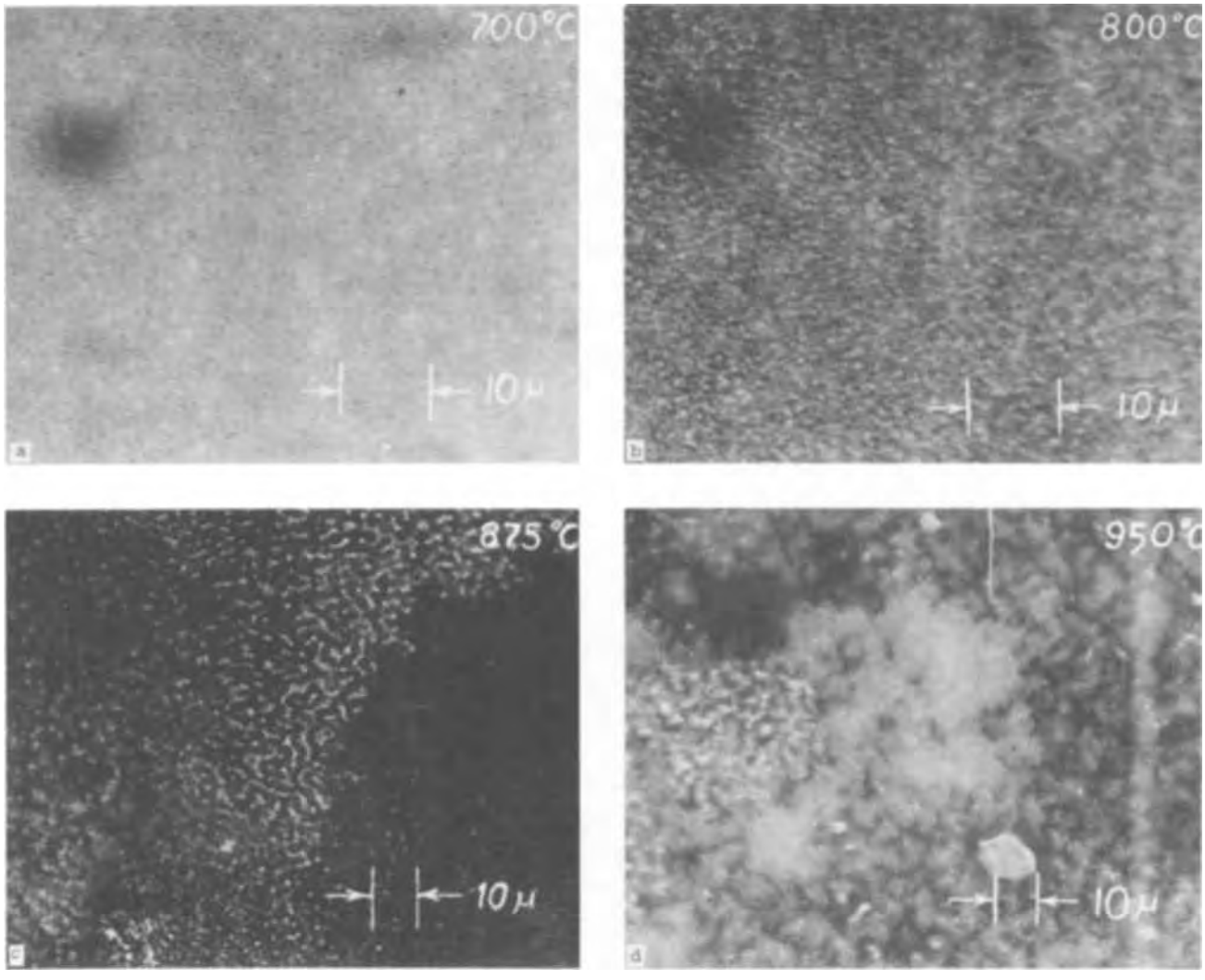

Fig. 2. Photomicrographs of insulating film grown on $GaAs_{1/2}P_{1/2}$ in dry oxygen for various temperatures. Note increasing grain size with temperature. a, 700°C for 675 min (X1000); b, 800°C for 630 min (X1000); c, 875°C for 630 min (X500); d, 950°C for 630 min (X500).

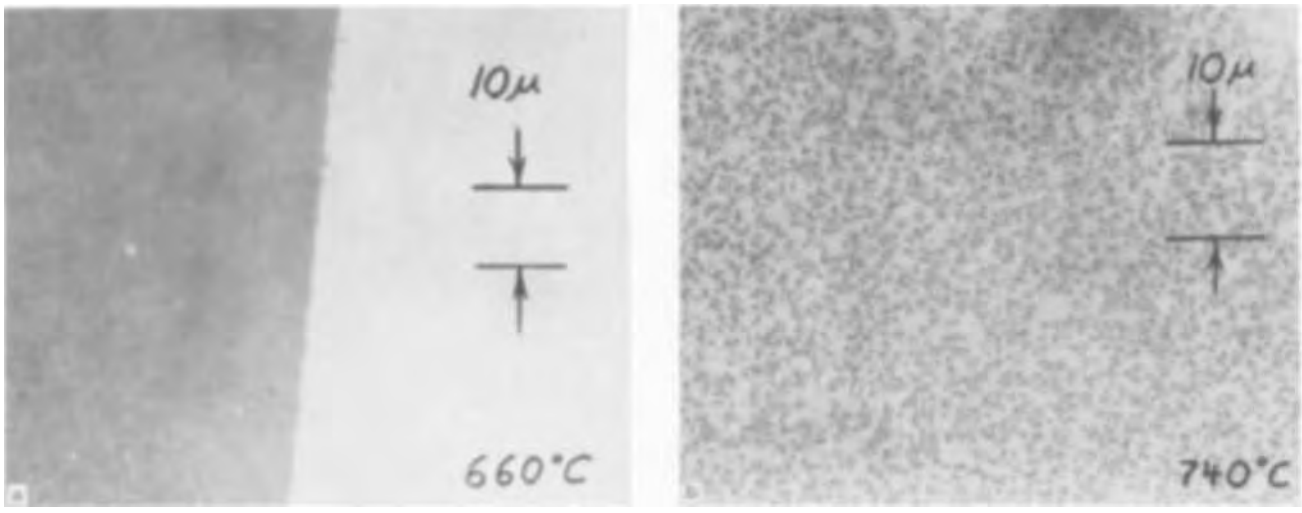

Fig. 3. Photomicrographs of surface of $GaAs_{1/2}P_{1/2}$ after thermal oxidation and etching off of film showing surface damage resulting from oxidation process. a, Partially etched (left-hand side is insulator) at 660°C for 341 min; b, completely etched surface at 740°C for 251 min. Note increase in pit size and density.

pitting and individul pits are larger. It is for this reason that film growth at temperatures higher than 700°C is not recommended.

Figure 3a also indicates the type of edge which can be obtained by photomasking. The edge definition is expected to be limited by the crystallite size, which is about ½μ or less. To check the effects of NH_4F on the surface, a freshly polished $GaAs_{1/2}P_{1/2}$ chip was placed in NH_4F for over 3 days and re-examined. Some slight etching at irregular points about 10μ apart could be seen, and these widely separated etch pits were all aligned along two directions at right angles to each other. The very slow etch rate and pronounced alignment of etch pits to crystallographic planes on a fresh surface indicate that the surface damage of Fig. 3 is due to the oxidation step.

Since the surface pitting dictated such a low oxidation temperature, the growth rate was measured. A number of chips oxidized for various times were selectively etched and the oxide thickness was measured by interferometry. In the process of etching the samples, many etches were tried: NaOH was very fast; NH_4OH very slow; buffered HF, hot HNO_3, and hot H_2SO_4 all etched the film with varying speeds. Hardened negative photoresist was successfully removed in J-100 at temperatures less than 65°C for up to 15 sec. Hot J-100 was also an etch if it was used at the recommended temperature of 80°C.

The most successful etch used was full strength NH_4F. It was slow enough for easy monitoring and did not undercut the photoresist as badly as HF did.

The growth rates for temperatures of 660° and 690°C are shown in Fig. 4. Although this seems slow, it is actually slightly faster than SiO_2 growth on Si at these temperatures. A color chart giving approximate thicknesses of the insulator, provided the order of the reflection is known, is also included in the figure.

There has been some work on the identification of the films but it is not conclusive. From the temperature at which growth must take place and the appearance of the film as a mass of submicron-sized crystallites, it appeared likely that the constituents are separate crystallites of different compounds. The most likely compounds are Ga_2O_3, $GaPO_4$, and $GaAsO_4$ with perhaps some As_2O_3 and/or P_2O_5 trapped in the interstices, although both of the latter are volatile at 700°C.

The very thin layers of insulator make ordinary x-ray crystallographic techniques difficult. One experiment has been performed using a low-energy electron beam to generate K-shell x-rays characteristic of Ga, As, and P. The beam was scanned over a region of the surface generating an x-ray count. The three counts give relative proportions of the three elements. The beam, although of low energy, still penetrated below the film, and the count was representative of the underlying substrate as well as of the film. After applying corrections for electron range, ionization cross section, and x-ray absorption, the results indicated that the arsenic count was much less than that of gallium or phosphorus. If the gallium and phosphorus are assumed to be present as $GaPO_4$ and Ga_2O_3, then the results indicated approximately 60% by volume of $GaPO_4$ and about 30% by volume of Ga_2O_3 with the remainder probably $GaAsO_4$ or As_2O_3. There must be some loss of phosphorus as well as most of the arsenic in order to account for these compounds simply.

If this result is legitimate, it is to be expected that the anneal step could be a process of removal of trapped volatile compounds from a substantial volume of grain boundary and the adjustment of grain boundaries between adjacent submicron crystallites.

If one compares the thickness between two adjacent orders of interference an index of refraction can be calculated. This is more accurate than calculating an index of refraction for a single color, since there are unknown phase shifts at the interfaces which will be subtracted out when a difference and the same color are used (4). Using the mean thickness of two blues and the wavelength of light for which this path length is an integer half-wavelength in Si_3N_4 and SiO_2, an index of refraction of about 1.6 is obtained. This compares with published indices of refraction for $GaPO_4$

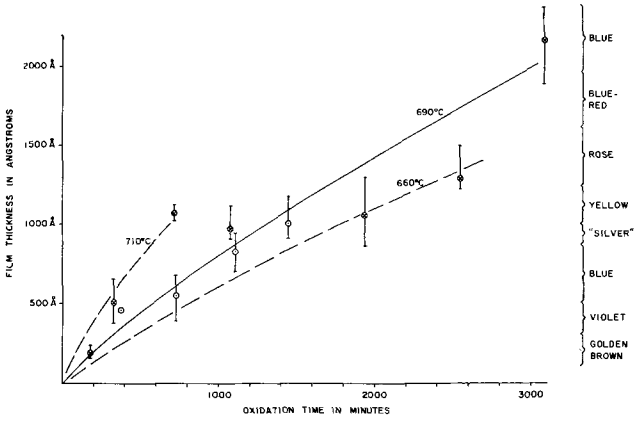

Fig. 4. Growth rate curves for $GaAs_{1/2}P_{1/2}$ oxidized in O_2 at 660°, 690°, and 710°C vs. oxidation time.

of 1.603 and 1.93 for Ga_2O_3 (5) and is taken as evidence that the crystallites carrying the film color are more likely $GaPO_4$ than Ga_2O_3.

Dielectric constant data were not conclusive. The dielectric constant was calculated from data obtained by incorporating thickness data, as described above, with accurate capacitance and area measurements. The MIS capacitors were formed as described above using chromium dots. Ohmic contacts were alloyed silver with a layer of indium soldered to the silver dots for more positive contact. Capacitance measurements were made on a Boonton Model 75C capacitance bridge at a frequency of 500 kHz. MIS capacitors were forward biased to minimize the effect of depletion in the semiconductor. No measurable parallel conductance like that seen with reverse-biased p-n junctions was seen during these measurements.

The thicker films (1500-2000Å thick) had dielectric constants as high as 2.9 with an average at 2.5. The thinner films (600-1200Å thick) had lower dielectric constants with the average at 1.8 and numbers between 1.4 and 2.0. This disparity could be due to a change in the proportions of the compounds in the film or a lower effective density of the film in the case of thinner growths compared with a more dense layer when the growth time was longer. Probably both effects are present.

The main evaluation of the films was the measurement of capacitance-voltage curves of MIS capacitors. The capacitance was measured with a Boonton Model 71A capacitance meter. Voltage was applied by means of an HP 202A low-frequency function generator operating in the triangular wave mode for a period of 50 sec. Provision for applying d-c offset voltage was also incorporated in the measurement system. Normally the offset voltage was set to provide a bias which was swept from +4 to −18V in 25 sec. C-V curves were plotted on a Houston Corporation X-Y plotter.

The original MIS structures used aluminum metalization. The C-V curves showed very bad instability. When the C-V curve was plotted on both the increasing and decreasing values of the triangular wave from the function generator, flatband voltage [see, for instance, Ref. (6), p. 279] shifted in an irregular manner indicating changes in the "fast" surface-state density as the bias was slowly varied from +8 to −10V.

Considerable improvement was obtained by thermal cycling of the MIS structure. A thermal cycle consisted of placing the chips on a quartz boat in the Lindberg furnace for 5 min and then withdrawing the boat to the furnace mouth for 5 min. This process comprised one thermal cycle. Ten such cycles gave adequate bias stability of the C-V curves except for the initial C-V trace. [This result was described in some detail by the authors in Ref. (1).]

Further improvement was obtained when chromium was used as the metal in the MIS structure in place of aluminum. The process was as described in the experimental procedure above except that the MIS structure was sintered, after chrome metalization, by heating the MIS capacitor at 600°C for 45 min or at 700°C for 5 min in an argon stream with a flow rate of about 0.5 liter/min. No bias stress shifts in the flatband voltage were observed.

The final shape of the C-V curves now being obtained is shown in Fig. 5. The insulator film was grown for about 10 hr at 700°C on n-type $GaAs_{1/2}P_{1/2}$ material with a tellurium doping of 5.36×10^{15} atoms/cm^3. An anneal of 285 min at 700°C in argon (0.3 liter/min) followed the oxidation. From the color, the thickness was determined to be approximately 1100Å. Evaporated 10 mil chromium dots formed the metal top of the structure. The capacitor area was 5.0×10^{-4} cm^2. Ohmic contact to the GaAs was made with a pattern of silver 10 mil dots which were pulse alloyed to break down residual metal semiconductor barriers.

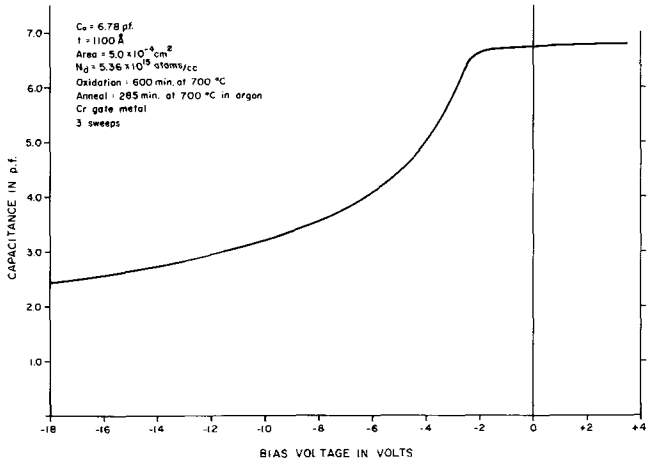

Fig. 5. Capacitance vs. voltage of typical MIS capacitor showing the continuous decrease in differential capacitance and the displacement of flatband voltage in the negative direction which is characteristic of positive surface charge density.

These MIS capacitors exhibit very good short and long-term bias stress stability. The flatband voltages of devices of this kind now exhibit the same positively charged surface-state densities which are common in silicon MIS capacitor structures.

The continuous depletion observed in the curves under steady-state (slow bias sweep) conditions is not fully explained. The effect is believed to be caused by the much lower generation rate in $GaAs_{1/2}P_{1/2}$, which has a 2.0 eV bandgap and intrinsic carrier concentration of about 10^3 carriers/cm^3. In silicon, with its 1.1 eV bandgap and intrinsic carrier concentration of 1.2×10^{10} carriers/cm^3, this effect does not occur under steady-state conditions.

In silicon, the inversion layer is formed by thermal generation of minority carriers in the depletion region. Under transient (nonequilibrium) conditions, such as when a rapid voltage pulse is applied, an inversion layer cannot build up rapidly enough at the surface to follow the voltage, and a continuously decreasing capacitance results (7, 8). This essentially means that the thermal generation rate is not high enough for minority carriers to respond to the applied bias voltage.

In $GaAs_{1/2}P_{1/2}$ the thermal generation of minority carriers in the semiconductor depletion region may not be sufficient to invert the semiconductor-insulator interface. This would result in a steady-state depleted region in $GaAs_{1/2}P_{1/2}$ similar to that observed under transient conditions in silicon. The depletion width will increase with increasing negative bias, and a depletion-type curve similar to that shown in Fig. 5 would result.

Conclusions

The work reported in this paper allows the following conclusions to be drawn.

Dry thermal oxidation of $GaAs_{1/2}P_{1/2}$ will result in a heterogeneous growth of an insulating layer of sufficient integrity to be used as the insulator for MIS structures provided the rigid temperature constraints are not violated and the film is annealed in an inert atmosphere.

MIS structures which have stable, reproducible electrical properties can be fabricated using sintered chromium as the gate metal, the mixture of compounds as the gate insulator, and the $GaAs_{1/2}P_{1/2}$ as the semiconductor.

Acknowledgments

The authors wish to thank Sgt. Harniman at the Materials Science Laboratory, Technology Division, Air Force Weapons Laboratory, Kirtland Air Force Base, for providing the scanning electron microscope

data. They also wish to thank Dr. Harold Southward, Director of the Bureau of Engineering Research at The University of New Mexico, for his assistance and encouragement.

This work was supported by the Office of Naval Research.

Manuscript submitted March 21, 1972; revised manuscript received Dec. 24, 1972. This was Paper 51 presented at the Houston, Texas, Meeting of the Society, May 7-11, 1972.

Any discussion of this paper will appear in a Discussion Section to be published in the June 1974 JOURNAL.

REFERENCES

1. L. E. Coerver, D. H. Phillips, W. W. Grannemann, and G. J. Kuhlmann, Paper No. 8.6, presented at the International Electron Devices Meeting, Washington, D. C., Oct. 12, 1971.
2. H. T. Minden, *This Journal*, **109**, 733 (1962).
3. M. Rubenstein, *ibid.*, **113**, 540 (1966).
4. F. Reisman and W. Van Gelder, *Solid State Electron.*, **10**, 625 (1967).
5. E. C. Shafer and R. Roy, *J. Am Ceram. Soc.*, **39**, 333 (1956).
6. A. S. Grove, "Physics and Technology of Semiconductor Devices," John Wiley and Sons, Inc., New York (1967).
7. M. Zerbst, *Z. Angew. Phys.*, **22**, 30 (1966).
8. J. Grosvalet, C. Jund, C. Motsch, and R. Poirier, *Surface Sci.*, **5**, 49 (1966).

Etch Rates of Doped Oxides in Solutions of Buffered HF

A. S. Tenney*,[1] and M. Ghezzo*

General Electric Corporate Research and Development, Schenectady, New York 12301

ABSTRACT

The dependence of the etch rates of vapor-deposited binary borosilicate, phosphosilicate, and arsenosilicate glasses on glass composition and per cent buffered HF (1 part 48% HF to 10 parts 40% NH_4F) in water are presented. The etch rates of these doped glasses generally increase with increasing dopant oxide concentration, the exception being those of borosilicate glasses in concentrated buffered HF which exhibit minima at about 18 mole per cent (m/o) B_2O_3. The use of these and similarly gathered results to infer new etchants is demonstrated.

The use of doped oxides as dielectric materials, passivation layers, diffusion masks, diffusion sources, etc. has become increasingly important to semiconductor device technology. The employment of these materials frequently demands a knowledge of their rate of dissolution in some convenient etching solution. Selective etchants—solutions which etch glasses at rates dependent upon the glass composition—have been employed extensively (2, 3, 5-7, 10, 14-16, 19, 25, 27). Particularly useful would be a general relation between etch rate and chemical composition in light of recent work allowing the nondestructive determination of borosilicate (18, 20, 21), phosphosilicate (12, 28), and arsenosilicate (22) glass compositions.

Usually, the composition of the doped glass, and thus its etch rate in a given solution, is dictated by the application planned for the glass. Frequently the resulting etch rate is either inconveniently slow or uncontrollably fast in familiar etchants. However, the isothermal etch rate of a glass may depend not only on the composition of the glass but also on that of the etchant. The effect of the systematic variation of etchant composition on the etch rate of SiO_2 has been studied (17). With the glass composition fixed, desirable etching characteristics may still be achieved by varying the etchant composition.

Thus the processing of these glasses can be facilitated with knowledge of the dependence of their etch rates not only on glass composition but also on etchant composition.

In the present work, the effect of dilution in water on the etch properties of buffered HF (10 parts 40% NH_4F solution to 1 part 48% HF solution by volume) is studied. Presented in this paper are the etch rates of borosilicate, phosphosilicate, and arsenosilicate glasses as functions of glass composition and dilution of buffered HF in water. Results for all these glasses after heat-treatment (simulating conditions often used to achieve dopant diffusion into silicon) and for phosphosilicate glasses as-deposited at 350°C are shown.

Experimental

The doped oxides were deposited on chemically polished 10 ohm-cm P-type silicon wafers 1 in. in diameter by the reaction of Ar-diluted mixtures of O_2, SiH_4, and B_2H_6, PH_3, or AsH_3 at 300°-500°C. The chemical vapor deposition system employed is identical to that described by Brown and Kennicott (16). The films were generally about 7000Å thick.

The glass compositions were calculated from their *IR* spectra, as obtained with a Perkin-Elmer double beam recording spectrophotometer, Model 457-A, employing calibration curves relating glass composition to the *IR* spectra of these glasses. Compositions were determined within an estimated ± 0.5 to 1% for borosilicate glasses (21), ±1.5% for phosphosilicate glasses (28), and ±1% for arsenosilicate glasses (22).

Heat-treatments were performed in an open tube furnace flushed with argon.

Etching solutions were prepared by adding distilled water in the desired proportion to buffered HF solution (10 parts 40% NH_4F: 1 part 48% HF by volume) prepared from Mallinckrodt Transist AR-grade chemicals. All etchings were performed at room temperature (26°±1°C).

The etch rate was defined as the decrease in film thickness per unit time in the etchant. Film thicknesses were determined from the interference colors observed perpendicularly to the film surface under a fluorescent "daylight" lamp employing the color chart of Pliskin

* Electrochemical Society Active Member.
[1] Present address: General Electric Solid State Lamp Project, Chesterland, Ohio 44026.
Key words: borosilicate glass, phosphosilicate glass, arsenosilicate glass.

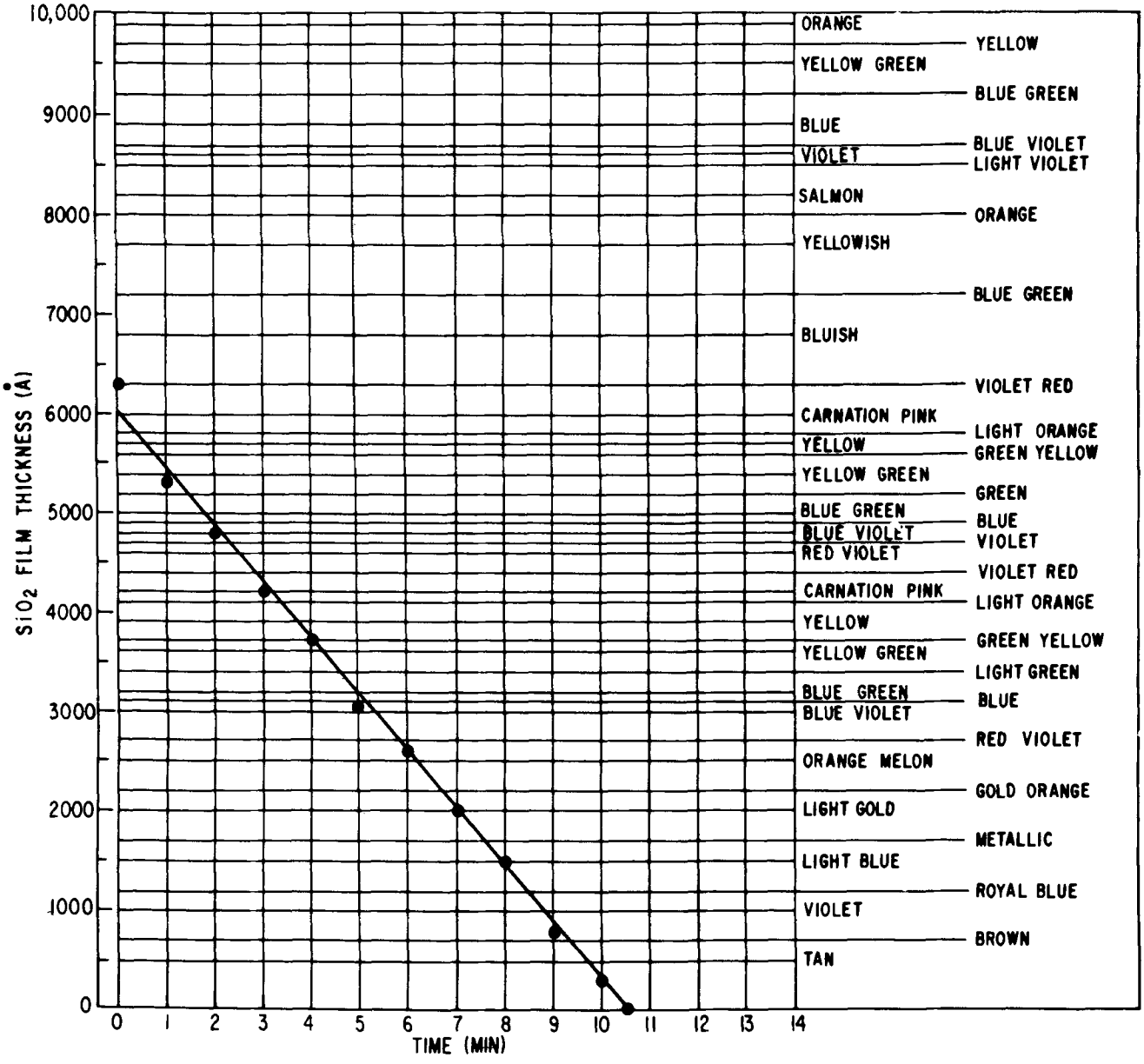

Fig. 1. Graphical representation of the interference color chart of Pliskin and Conrad (1). The data shown are for a heat-treated SiO_2 film etched in 50% BHF. The slope of the plot of residual thickness vs. etching time gives an etch rate of 570 Å/min.

and Conrad (1). It was determined ellipsometrically that the refractive indices of the doped oxides are close enough to that of pure SiO_2 to allow the use of this chart with the introduction of an uncertainty smaller than the experimental one. Figure 1 shows a graphical arrangement of this interference color chart which allows a direct plot of the residual film thickness *vs.* etching time. The slope of this plot is the etch rate.

Except for heat-treated borosilicate glasses [for which a hydrophilic, boron-rich phase may form at the silicon-glass interface (8, 9, 16, 29)], the complete removal of the oxide film is easily detected by observing a reversal of the meniscus formed by the etching solution with the partially immersed wafer held perpendicularly to the liquid surface (11). The oxide film is hydrophilic while the silicon surface is hydrophobic. The precise determination of this point is reflected in its agreement with the rest of the data plotted in Fig. 1.

Results

Borosilicate glass.—The etch rates of four glasses (0, 16.5, 23.5, and 30 mole per cent (m/o) B_2O_3] in four etchants buffered HF (BHF = 1 part 48% HF to 10 parts 40% NH_4F by volume), 50 volume per cent (v/o) BHF in H_2O, 10% BHF and 1% BHF) were determined. These glasses were heat-treated for 15 min at 1000°C.

In Fig. 2, the etch rates of these glasses in these four etchants are shown as functions of glass composition. Both 1% BHF and 10% BHF etch glasses of increasing B_2O_3 concentration at increasing rates while 50% BHF and BHF show minima in their etch rates at about 18 m/o B_2O_3. Brown and Kennicott (16) and Kern and Heim (15) have observed similar minima in the etch rate of borosilicate glasses in BHF.

The etch rates of these four glasses are plotted in Fig. 3 as functions of the concentration, in volume per cent, of BHF in water. As can be seen from either Fig. 2 or Fig. 3, the etch rate of SiO_2 decreases with decreasing BHF concentration, while borosilicate glasses with $16 < \text{m/o } B_2O_3 < 30$ exhibit etch rates which first increase then decrease with decreasing BHF concentration.

Phosphosilicate glass.—The etch rate of five glasses (0, 0.5, 3.0, 6.0, and 8.2 m/o P_2O_5) in six etchants (BHF, 50% BHF, 25% BHF, 10% BHF, 3% BHF, and 1% BHF) were determined. Both glasses as-deposited at 350°C and after heat-treatment for 2 hr at 1100°C were studied.

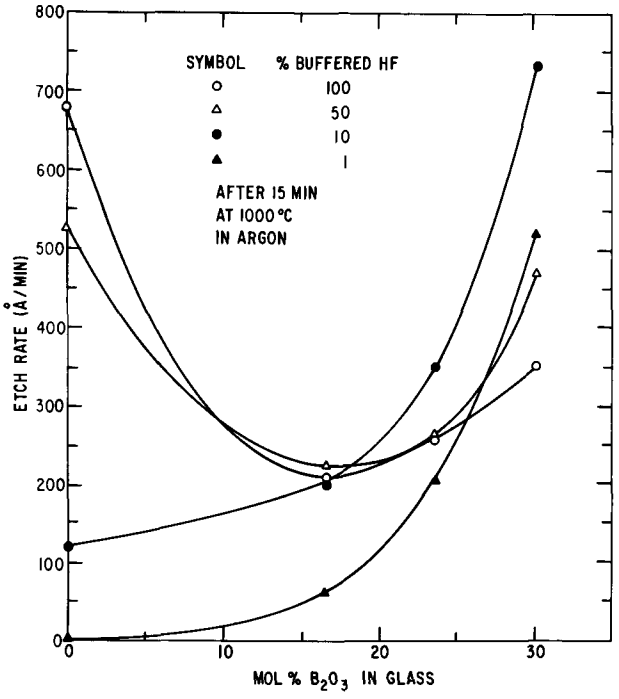

Fig. 2. Etch rates of heat-treated borosilicate glasses in buffered HF(BHF), 50% BHF, 10% BHF, and 1% BHF *vs.* mole per cent B_2O_3.

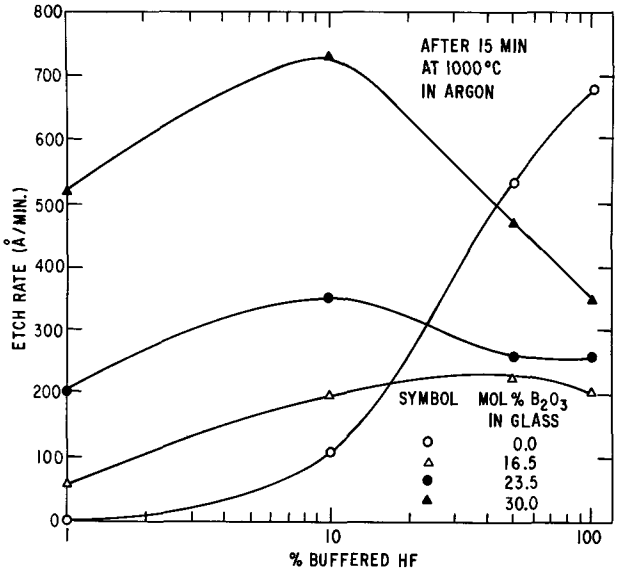

Fig. 3. Etch rates of heat-treated borosilicate glasses 0, 16.5, 23.5, and 30.0 m/o in B_2O_3 *vs.* per cent BHF.

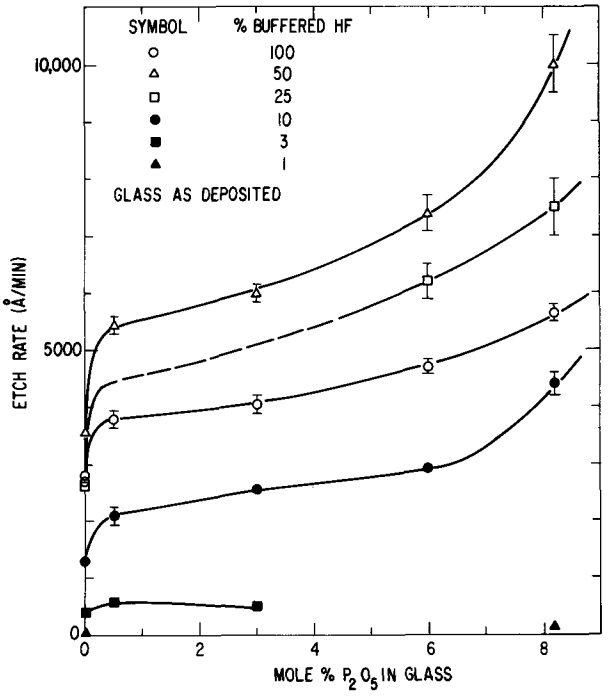

Fig. 4. Etch rates of as-deposited phosphosilicate glasses in BHF, 50% BHF, 25% BHF, 10% BHF, 3% BHF, and 1% BHF *vs.* mole per cent P_2O_5.

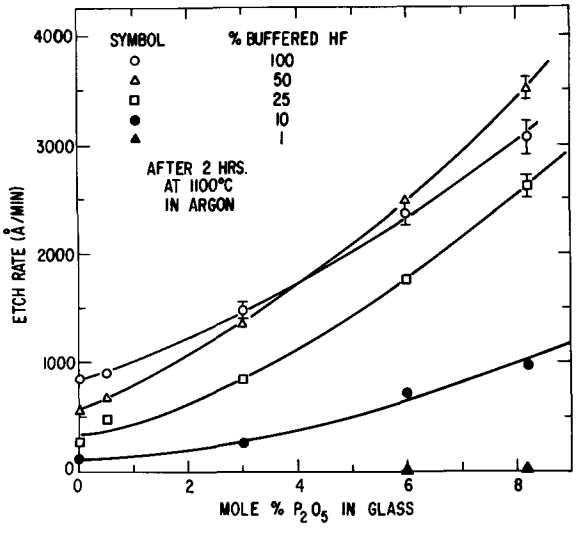

Fig. 5. Etch rates of heat-treated phosphosilicate glasses in BHF, 50% BHF, 25% BHF, 10% BHF, and 1% BHF *vs.* mole per cent P_2O_5.

The addition of an initial 1 m/o P_2O_5 to pure SiO_2 appears to cause a marked increase in the etch rate of as-deposited glasses (Fig. 4) which is not observed in that of heat-treated glasses (Fig. 5). The heat-treatment employed causes a decrease in the etch rates of the phosphosilicate glasses studied by a factor of three to five. Similar decreases in etch rates of borosilicate (15, 16), phosphosilicate (15), and arseno-silicate (25) glasses have been observed upon heat-treatment.

The etch rates of these glasses as-deposited and after heat-treatment, respectively, are shown in Fig. 6 and 7 as functions of per cent BHF. It is seen in Fig. 6 that the etch rates of all phosphosilicate glasses studied, and of pure SiO_2 as well, as-deposited exhibit maxima at about 50% BHF. After heat-treatment, however, only glasses greater than 6.0 m/o in P_2O_5 exhibit maxima in their etch rates while increasingly smaller shoulders are observed in the 50% BHF region for glasses of decreasing P_2O_5 content, as seen in Fig. 7.

Arsenosilicate glass.—The etch rates of four glasses (0, 0.5, 2.2, and 4.8 m/o As_2O_3) in four etchants (BHF, 50% BHF, 10% BHF, and 1% BHF) were determined after heat-treatment for 5 hr at 1100°C. These etch rates increase approximately linearly with increasing As_2O_3 concentration over the range $0 \leq$ m/o $As_2O_3 < 5$ as seen in Fig. 8. Although no maximum is observed in the dependence of etch rate on per cent BHF as seen in Fig. 9, the shoulder, increasingly prominent in this plot with increases in As_2O_3 concentration, suggests that glasses richer in As_2O_3 than those studied here may exhibit maxima. Such a determination was obviated by the fact that arsenosilicate glasses of more than about 7 m/o As_2O_3 are damaged on heat-treatment (27). The results for arsenosilicate glasses shown in Fig. 8 and 9 are remarkable only in their similarity, both in characteristics and in absolute values, to those for heat-treated phosphosilicate glasses, over the same concentration range, shown in Fig. 5 and 7.

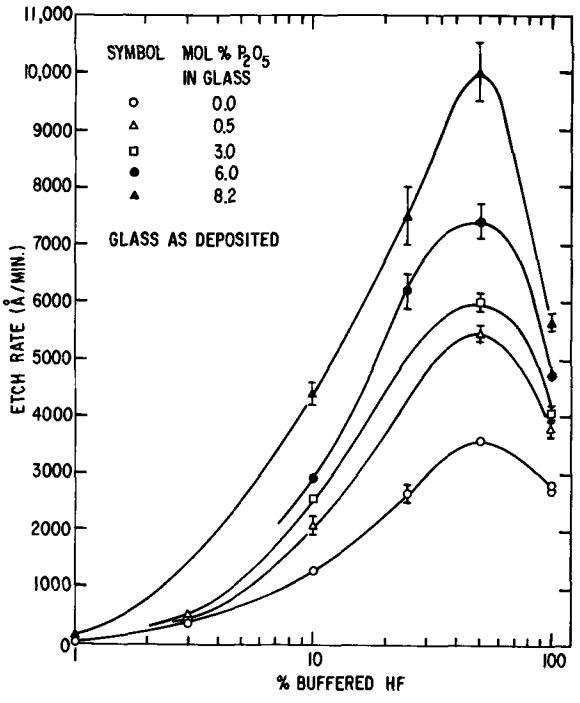

Fig. 6. Etch rates of as-deposited phosphosilicate glasses 0, 0.5, 3.0, 6.0, and 8.5 m/o in P_2O_5 vs. per cent BHF.

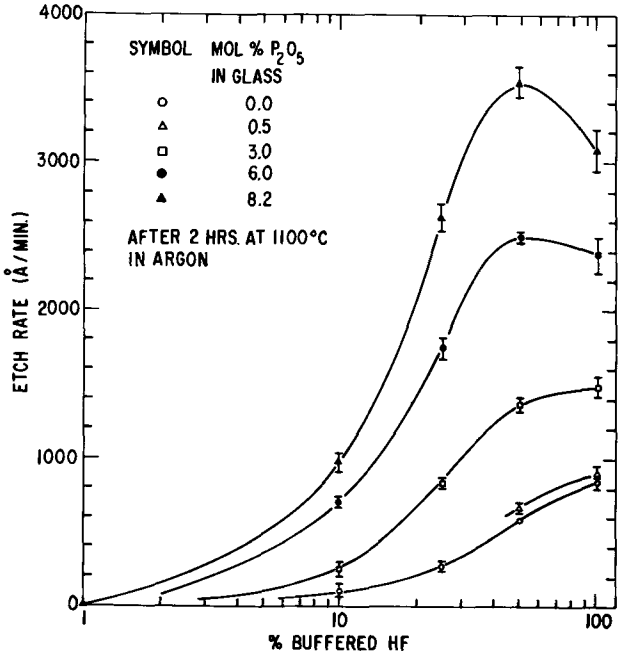

Fig. 7. Etch rates of heat-treated phosphosilicate glasses 0, 0.5, 3.0, 6.0, and 8.5 m/o in P_2O_5 vs. per cent BHF.

Discussion

Etch rate results such as those shown in Fig. 2-9 are helpful in semiconductor device processing. For instance, suppose that there were interest in etching a pattern in 30% B_2O_3 glass deposited over pure SiO_2. Forty-two per cent BHF will etch both glasses at about the same rate (as seen by the intersection of the 30% B_2O_3 and 0% B_2O_3 lines in Fig. 3) while 1% BHF will etch the 30% B_2O_3 glass at a reasonable rate (500 Å/min) leaving the SiO_2 beneath essentially unetched. Thus, either selective or nonselective etches may be inferred from these or similar results.

The monotonic increase in etch rate with increases in dopant concentration observed for borosilicate glasses in dilute BHF solutions and for phosphosilicate and arsenosilicate glasses in all concentrations of BHF

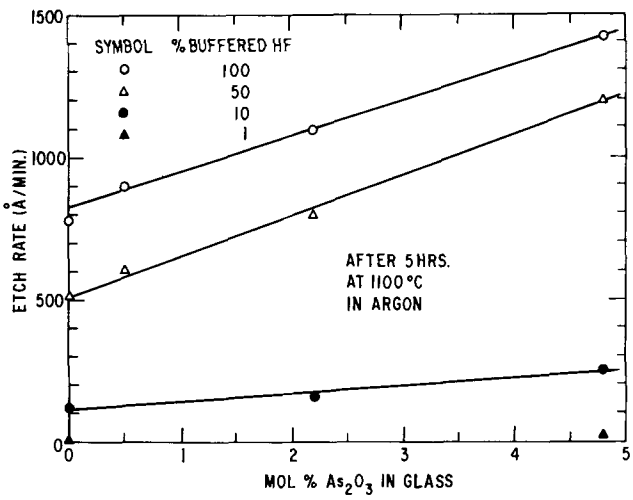

Fig. 8. Etch rates of heat-treated arsenosilicate glasses in BHF, 50% BHF, 10% BHF, and 1% BHF vs. mole per cent As_2O_3.

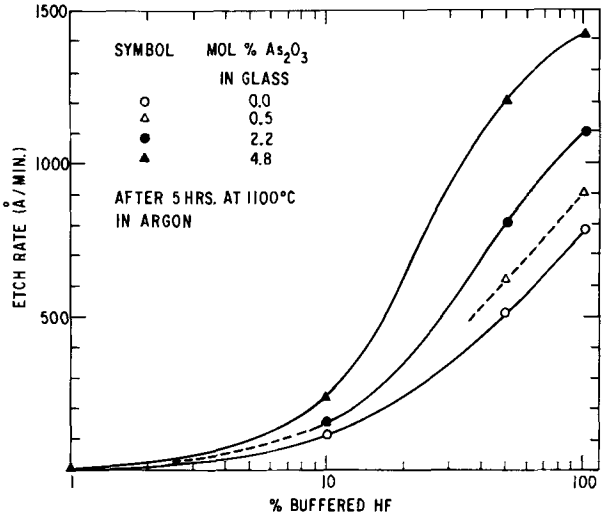

Fig. 9. Etch rates of heat-treated arsenosilicate glasses 0, 0.5, 2.2, and 4.8 m/o in As_2O_3 vs. per cent BHF.

suggests that these etch rates are controlled primarily by the dissolution of the SiO_2 in the glass. Adding dopant oxide essentially dilutes the SiO_2 facilitating its dissolution. Implicit in this description of the etching process is the assumption that the dopant tends to be removed from the glass more rapidly than SiO_2 does. Assuming further that the dopant is removed primarily by its dissolution in the water present in the etching solution is consistent with two observations: (*i*) there is an initial increase in the etch rates of heavily doped glasses with increasing water concentration and (*ii*) the etch rate maximum shifts to increasingly dilute solutions of BHF with increases in dopant concentration.

Thus the etching process may be seen most simply as a combination of the dissolution of the SiO_2 by BHF-originated species[2] and that of the dopant oxide by water.

Extension of this description to the etching of borosilicate glass in solutions concentrated in BHF requires the further assumption that the initial dopant species formed on addition of boron oxide to SiO_2 is not strongly soluble in water. This is not inconsistent with previous results for these glasses; for while B_2O_3 itself is soluble in water, it has been shown that the B—O—B bonds present in pure B_2O_3 are present only at very low concentrations in borosilicate glasses dilute in boron oxide (24).

The effect of boron oxide present at low concentrations in borosilicate glass appears to be to protect the

[2] J. S. Judge (17) has shown these to be HF_2^- and HF.

SiO_2 from the BHF, thus lowering the etch rate in concentrated solutions of BHF. As the B_2O_3 is increased in concentration, its solubility in water becomes a more important factor and the etch rate increases (see Fig. 2). The etching characteristics of borosilicate glass in BHF have been described similarly by Brown and Kennicott (16). As stated above, the etch rates of borosilicate glasses in dilute solutions of BHF appear to be limited for all B_2O_3 concentrations by the ability of this dilute BHF to dissolve the SiO_2.

The relative etching characteristics of borosilicate and phosphosilicate glasses appear to be related to the relative solubilities of B_2O_3 and P_2O_5, respectively, in water. This difference manifests itself in the fact that the etch rates of phosphosilicate glasses increase much more rapidly with increasing dopant concentration than do those of borosilicate glasses (compare Fig. 2 and 5). Also, phosphosilicate glasses exhibit maxima in their etch rates at BHF concentrations less than 100% for much lower dopant oxide concentrations than do borosilicate glasses (compare Fig. 3 and 7).

This relationship between etching characteristics and dopant oxide solubility does not extend to arsenosilicate glasses. These exhibit etching characteristics which are very similar to those of phosphosilicate glasses of similar dopant concentration in spite of the fact that the solubility of As_2O_3 is quite similar to that of B_2O_3—far less than that of P_2O_5. Such etching characteristics would be expected only if the dopant species in arsenosilicate glasses were As_2O_5, which has been shown not to be the case (22).

It should be pointed out that a direct comparison of the borosilicate phosphosilicate, and arsenosilicate glass etch rates is complicated by the fact that these glasses were subjected to different heat-treatments after deposition: 15 min at 1000°C for the borosilicate glasses, 2 hr at 1100°C for the phosphosilicate glasses, and 5 hr at 1100°C for the arsenosilicate glasses. It is clear that the thermal "history" of a glass can have a measurable effect on such properties as vibrational spectra (4, 7, 13, 15, 18, 20, 21, 24, 28, 30), strain density and damage (4, 7, 13, 22, 23, 26, 27), and, specifically, etch rates (4, 15, 16, 25).

Summary and Conclusion

The etch rates of vapor-deposited borosilicate, phosphosilicate, and arsenosilicate glasses have been determined as functions of glass and etchant compositions. Given is a qualitative explanation of these results based on the assumption that each oxide component of the binary mixture is preferentially etched by only one component of the etchant solution. Specifically, it is assumed that SiO_2 is dissolved by BHF and dopant oxide principally by water. A simple correlation between etching characteristics and dopant oxide aqueous solubility was not found in terms of this model.

The use of these results to infer the optimum BHF concentration for a specific processing situation has been demonstrated. Of more general interest, however, is the fact that the principle employed—the gathering of results for a few different substrate and etchant compositions followed by the interpolation of the results to new compositions—may be applied to the etching of any multicomponent system for which etchants which preferentially etch each component may be found (and mixed).

Finally, the graphical representation of Pliskin and Conrad's interference color chart (1) provides a convenient method for gathering etch-rate data and calculating the results.

Acknowledgment

The authors take the opportunity for thanking Dr. D. M. Brown for use of his chemical vapor deposition equipment and his continuing interest in this work.

Manuscript submitted Oct. 19, 1972; revised manuscript received Feb. 1, 1973.

Any discussion of this paper will appear in a Discussion Section to be published in the June 1974 JOURNAL.

REFERENCES

1. W. A. Pliskin and E. E. Conrad, *IBM J. Res. Develop*, **8**, 43 (1964).
2. W. A. Pliskin and R. P. Gnall, *This Journal*, **111**, 872 (1964).
3. H. Osafune, Y. Matukura, S. Tanaka, and Y. Miura, Paper 110 presented at Electrochem. Soc. Meeting, Buffalo, New York, Oct 10-14, 1965.
4. W. A. Pliskin and H. S. Lehman, *This Journal*, **112**, 1013 (1965).
5. E. H. Snow and B. E. Deal, *ibid.*, **113**, 263 (1966).
6. S. Nishimatsu and T. Tokuyama, Paper 170 presented at Electrochem. Soc. Meeting, Chicago, Illinois, Oct 15-19, 1967.
7. W. A. Pliskin in "Measurement Techniques for Thin Fiims," B. Schwartz and N. Schwartz, Editors, p. 280, The Electrochemical Society Softbound Symposium Series, New York (1967).
8. K. M. Busen, W. A. Fitzgibbons, and T. Kloffenstein, *Electrochem. Technol.*, **6**, 256 (1968).
9. K. M. Busen, W. A. Fitzgibbons, and W. K. Tsang, *This Journal*, **115**, 291 (1968).
10. J. M. Eldridge and P. Balk, *Trans. Met. Soc. AIME*, **242**, 539 (1968).
11. W. Kern, *RCA Rev.*, **29**, 557 (1968).
12. R. P. Esch, J. M. Eldridge, P. Balk, and W. A. Pliskin, Paper 95 presented at Electrochem. Soc. Meeting, Detroit, Michigan, Oct 5-9, 1969.
13. E. Arai and Y. Terunuma, *Japan. J. Appl. Phys.*, **9**, 691 (1970).
14. A. H. El-Hoshy, *This Journal*, **117**, 158 (1970).
15. W. Kern and R. C. Heim, *ibid.*, **117**, 568 (1970).
16. D. M. Brown and P. R. Kennicott, *ibid.*, **118**, 293 (1971).
17. J. S. Judge, *ibid.*, **118**, 1772 (1971).
18. W. Kern, *RCA Rev.*, **32**, 429 (1971).
19. R. O. Schwenker, *This Journal*, **118**, 313 (1971).
20. E. A. Taft, *ibid.*, **118**, 1985 (1971).
21. A. S. Tenney, *ibid.*, **118**, 1658 (1971).
22. J. Wong and M. Ghezzo, *ibid.*, **118**, 1540 (1971).
23. M. Ghezzo, *ibid.*, **119**, 1428 (1972).
24. A. S. Tenney and J. Wong, *J. Chem. Phys.*, **56**, 5516 (1972).
25. J. Wong, *This Journal*, **119**, 1071 (1972).
26. J. Wong and M. Ghezzo, *ibid.*, **119**, 1413 (1972).
27. M. Ghezzo and D. M. Brown, *ibid.*, **120**, 110 (1973).
28. A. S. Tenney and M. Ghezzo, *ibid.*, Accepted for publication.
29. A. S. Tenney, Unpublished results.
30. J. Wong, *This Journal*, **120**, 122 (1973).

The Use of Rutherford Backscattering to Study the Behavior of Ion-Implanted Atoms During Anodic Oxidation of Aluminum: Ar, Kr, Xe, K, Rb, Cs, Cl, Br, and I

F. Brown and W. D. Mackintosh

Chalk River Nuclear Laboratories, Atomic Energy of Canada Limited, Chalk River, Ontario, Canada

ABSTRACT

It is shown that from the energy spectra of He ions backscattered from aluminum, recorded before and after anodic oxidation, the thickness of the oxide films and the positions of ion-implanted foreign atoms within the films can be determined. Information on the composition and uniformity of the films is also obtained. The scope, limitations, and precision of the method are predictable and are discussed. As model experiments the behavior of ion-implanted noble gases was studied. The results agree with previous work and can be interpreted to show that, as expected, both aluminum and oxygen are mobile during the oxidation. The behavior of ion-implanted alkali metals and halogens was also studied. These species were found to be mobile during oxidation and behaved in a manner consistent with their expected ionic charges.

Background.—Radio-tracer techniques for studying the migration of metal and oxygen during anodic oxidation have been described in several publications (1-5). In these methods a very thin surface layer is tagged with radioactive marker atoms and after oxidation the position of the marker relative to the surface, *i.e.*, its depth, is determined. In one method (1-3) ^{125}Xe was used as the marker and its depth determined by β-ray spectrometry; the energy loss suffered by the low energy conversion electrons in traveling to the surface is a measure of the depth of the emitting marker atoms. In a second modification (4), ^{222}Rn was used as marker and its depth determined by measuring the energy loss of the emitted α-particles. In a third method (5), chemical sectioning combined with radio-assay was used to determine the positions of ^{222}Ra, ^{125}Xe, ^{85}Kr, and ^{41}Ar. All these experiments are interpreted by assuming that the noble gas markers are immobile during anodic oxidation, whereby transport numbers for metal and oxygen can be derived. Evidence for immobility of noble gas markers, in experiments on anodic oxidation of tantalum, has been discussed in detail by Pringle (5).

Direct observation of oxygen migration during anodic oxidation has been achieved by Amsel (6) and for thermal oxidation, by Ollerhead, Almqvist, and Kuehner (7) and by Cox and Roy (8). In these studies, isotopically enriched oxygen was located by means of nuclear reactions promoted by accelerated ions.

Whitton (9) has used radio-tracer and sectioning techniques to study the behavior of Rb, Kr, and Br during the anodic oxidation of zirconium and tantalum.

In this paper we describe a method for determining marker position using Rutherford scattering which requires neither radioactive tracers nor sectioning techniques. For the present we describe experiments to establish some of the advantages and disadvantages of the method, choosing systems that should serve as simple models. We have extended earlier work with noble gases in the anodic oxidation of aluminum, using a single technique to study the behavior of Ar, Kr, and Xe under identical oxidation conditions. In addition, since the argument for the immobility of noble gas markers is founded, in part, on the concept that they are uncharged, we have, following Whitton (9), studied the behavior of potentially charged species. The alkali metals and the halogens were used to find whether a consistent behavior could be observed.

Key words: anodic oxidation, Rutherford backscattering, aluminum, noble gases, alkali metals, halides.

In performing and interpreting the experiments we have attempted to cover the following points.

(*i*) The technique has been tested generally to confirm that practical results for sensitivity, resolution, and precision are in line with expectations and to indicate the types of systems that are amenable to practical investigation.

(*ii*) The behavior of a foreign atom during anodic oxidation might well be different according to whether it was initially in the metal or in a layer of oxide already formed. Experiments were therefore done with the markers both in the metal and in preformed anodic oxide of about 10 $\mu g/cm^2$ thickness.

(*iii*) Rutherford scattering requires more marker atoms than radio-tracer methods. It was therefore necessary to establish whether the amount of marker required for the analysis interferes with the anodizing process. To this end a series of specimens were used containing different amounts of marker.

(*iv*) Experiments were also carried out to establish whether or not markers were affected by an electric field under such conditions that the oxide was not growing.

(*v*) We have established that limited, but useful information can be obtained on the widths of marker distributions.

(*vi*) In addition to studying marker positions the technique gives useful information on the uniformity, thickness, and stoichiometry of the oxide films.

Principles of marker methods.—These principles, especially as applied to the use of noble gas markers, have been discussed in papers already cited. If the marker is regarded as immobile it forms a reference point from which the transport numbers of the metal and oxygen can be calculated. Given this reference point the movement of another species can, in principle, be established. In the case of a mobile species we have calculated a migration number, defined as the ratio of the distance moved (from the immobile reference point) to the thickness of oxide grown. This, of course, implies that the immobile reference point must be established or assumed for the particular system being studied.

Location of markers by Rutherford scattering.—The principles and analytical applications of Rutherford scattering have been reviewed by Mackintosh and

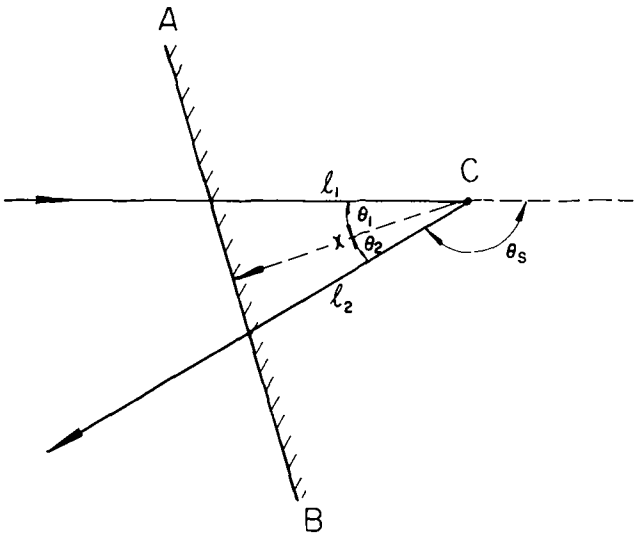

Fig. 1. Schematic diagram showing the geometric relationships of the angles involved in Eq. [1] and [2]. l_1 is the ingoing trajectory of the particles making an angle θ_1 to the normal to the surface AB. l_2 is the outgoing trajectory making an angle θ_2 to the normal. x is the depth of the target atom C below the surface. θ_S is the laboratory scattering angle.

Davies [(10) and references therein]. We reiterate here only those principles necessary for understanding marker location.

When a beam of monoenergetic ions strikes a surface some will be scattered from the surface atoms, losing energy in an amount dependent on the mass of the atom struck and the scattering angle. The energy of the reflected particle is given by

$$E_1 = k^2 E_0$$

where

$$k = \frac{M_1 \cos\theta_S}{M_1 + M_2} + \left[\frac{(M_1 \cos\theta_S)^2}{(M_1 + M_2)^2} + \frac{M_2 - M_1}{M_1 + M_2} \right]^{1/2} \quad [1]$$

M_1 is the mass of the incident ion, M_2 the mass of the struck atom, and θ_S is the laboratory scattering angle (Fig. 1). If the incident particle does not suffer scattering in the surface layer, it will lose energy as it penetrates to lower layers. Thus, just before being scattered, it will have an energy of E_0^1. The scattered particle will also be slowed down on its way back to the surface and will emerge with an energy E_1^1. If the rate of energy loss is given by the stopping power $S(E)$, then the energy of a particle emerging from a depth x below the surface is expressed by

$$E_1^1 = k^2 \left[E_0 - \int_0^{l_1 = x\sec\theta_1} S(E)\,dl \right] - \int_{l_2 = x\sec\theta_2}^{0} S(E)\,dl \quad [2]$$

The first and second integrals are, respectively, the energy losses along the ingoing and outgoing trajectories l_1 and l_2. The angles the trajectories make with the normal to the surface are θ_1 and θ_2; thus $l_1 = x\sec\theta_1$ and $l_2 = x\sec\theta_2$ (Fig. 1). $S(E)$, the stopping power, depends on the energy of the particle.

In the present work a beam of 2 MeV He^+ ions was used, with a solid-state detector and pulse height analyzer to record the energy spectra of backscattered ions. The spectra were then interpreted using Eq. [1] and [2] to obtain depth profiles.

Experimental

Preparation of samples.—The aluminum specimens were 0.9 cm diameter disks 0.5 mm thick. Surfaces were first prepared by mechanical and vibratory polishing (11). This was followed by four cycles in which the specimen was anodized and the oxide stripped with a solution of phosphoric and chromic acid at 95°C. Marker ions were implanted in the surface layers with an isotope separator (12) at energies of 20 keV and over an area of 0.7 cm diameter. The number of ions of each species implanted is given in Tables I and II.

Following implantation most specimens were anodized in a saturated solution (~5%) of ammonium pentaborate in water at a temperature of 23°C. The current was kept constant at 2 mA/cm² until the chosen voltages were reached. Supplementary anodizing and stripping experiments were carried out using much larger foils which could be weighed to obtain a linear calibration of voltage *vs.* oxide thickness. The ratio of weight gain to weight loss agreed with the value expected for the stoichiometry of Al_2O_3 within the experimental error (relative standard deviation 3.0%). The thickness values for the disk specimens shown under "calibration" in Tables I and II were obtained by reference to this calibration. In order to make direct comparison with earlier work (3) a few specimens were anodized in a solution of 50 g/liter of sodium tetraborate in 95% ethylene glycol, 5% water.

Backscattering experiments.—The specimens were bombarded with He ions at a nominal energy of 2 MeV, using a Van de Graaff accelerator. The actual energy in each run was obtained by calibration against

Table I. Data from experiments with noble gas implants into preformed oxide films

Sample number	Implanted species	Implant dose (ions/cm²)	Oxide thickness from calibration (μg/cm²)	Oxide thickness determined (μg/cm²)	Marker depth (μg/cm²)	Aluminum transport number
1	Xe	2×10^{15}	95	95	38	0.43
				90	35.5	0.44
				94.5	35	0.40
				92.5	33.5	0.39
		Average of four determinations:		93	35.5	0.42
						Std. dev.: 0.02
2	Xe	5×10^{13}	95	95	30	0.34
3	Xe	2×10^{14}	112	101	35	0.39
4	Xe	4×10^{14}	112	115	40	0.37
5	Xe	5×10^{14}	95	90	30.5	0.37
6	Xe	1×10^{15}	112	115	47	0.42
7	Xe	7×10^{15}	95	90	38	0.46
8	Xe	1×10^{16}	95	95	38	0.44
9	Xe	1×10^{16}	95	90	39	0.48
		Average of samples 2-9:	113.3	110.8		0.41
						Std. dev.: 0.05
10*	Ar	2×10^{15}	95	95	38	0.44
	Xe	2×10^{14}			32.5	0.36
11*	Ar	1×10^{16}	95	91.5	38	0.45
	Xe	2×10^{14}			35.5	0.42
		Average of all measurements:	97.2	95.3		0.41
						Std. Dev.: 0.04

* Both implants were in the same specimen.

Table II. Data from experiments with noble gas implants into metal

Sample number	Implanted species	Implant dose (ions/cm²)	Oxide thickness from calibration (μg/cm²)	Oxide thickness determined (μg/cm²)	Marker depth (μg/cm²)	Aluminum transport number
1	Xe	5×10^{13}	49	49.5	16	0.35
2	Xe	5×10^{13}	93	97.5	36	0.37_5
3	Xe	5×10^{13}	47	49.5	19.5	0.42
4	Xe	5×10^{13}	93	93.5	36	0.38
5	Xe	2×10^{14}	47	49.5	15	0.32
6	Xe	2×10^{14}	93	96.5	33	0.35
7	Xe	2×10^{14}	47	49.5	17	0.36
8	Xe	2×10^{14}	93	93.5	32.5	0.35
9	Xe	1×10^{15}	47	49.5	17	0.36
10	Xe	1×10^{15}	93	93.5	35.5	0.38
11	Xe	1×10^{15}	47	49.5	20.5	0.44
12	Xe	1×10^{15}	93	95.5	33	0.35
13	Xe	7×10^{13}	47	47	19	0.43
14	Xe	7×10^{13}	93	93.5	39.5	0.43
15	Xe	7×10^{13}	47	47	19.5	0.44
16	Xe	7×10^{15}	93	91.5	41.5	0.46
17	Xe	2×10^{14}	47	47	17	0.38
18	Xe	2×10^{14}	93	92	33	0.36_5
19	Xe	2×10^{14}	47	47	16.5	0.37
20	Xe	2×10^{14}	93	94.5	30.5	0.33
21	Kr	5×10^{14}	56	61	20	0.39
22	Kr	5×10^{14}	112	115	45	0.43
						Average: 0.38
						Std. dev.: 0.08

the 5.486 MeV α-particles from an ^{241}Am source. Target and counting arrangements are shown in Fig. 2. The aperture defined an area of 1 mm² on the target. The target holder could be moved both vertically and horizontally without breaking the vacuum so that various parts of one specimen could be examined and several targets could be examined. The surface barrier silicon detector had a resolution [full width at half maximum, (FWHM)] of 17 keV at 2 MeV. The target was connected to circuitry which stopped the pulse height analyzer at any preset integrated beam current, chosen to give the best statistics consistent with available time. The beam current was sufficiently low (20-30 nA) to prevent excessive dead-time losses in the counting system. The targets were tilted so their faces made an angle of 15° to the beam ($\theta_1 = \theta_2 = 15°$) and the detector was placed 30° ($\theta_s = 150°$) to the beam.

Interpretation of spectra.—A spectrum of backscattered He ions is shown in Fig. 3; the scattering material was Al with ^{134}Xe implanted at 20 keV. The depth of the implant is about 5 μg/cm² (~200Å) and the width of its distribution (FWHM) is about half its depth. The energy losses of the ions in traversing these distances is small (1 μg/cm ~2.0 keV). Thus scattering from the Xe produces the peak at the right-hand side of the figure, having an energy given by Eq. [1] less 2.0 keV for each μg/cm² of depth. The bombarding He ion energy in this case was 1.975 MeV; k^2 for Xe is 0.894, hence the peak occurs just below 1.766 MeV. The width of the peak is determined by the detector resolution (17 keV). The sharp step terminating the plateau at 1165 keV in Fig. 3 occurs at the energy given by Eq. [1] for He^+ scattering from surface atoms of Al. The counts recorded at lower energies are derived from ions scattered from progressively greater depths. As x increases the energy E_1^1 decreases according to Eq. [2].

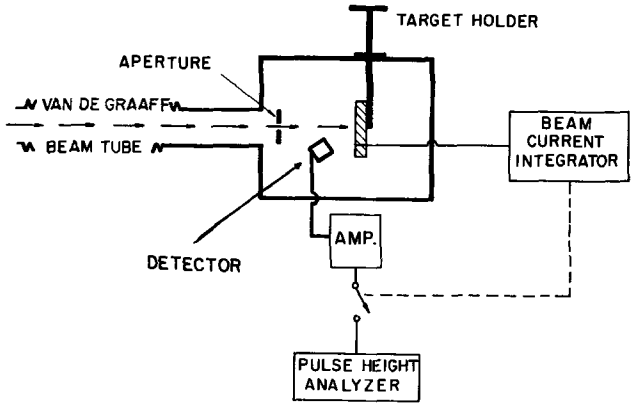

Fig. 2. Schematic diagram of the target chamber arrangements

Figure 4 is a spectrum obtained under the same conditions as Fig. 3 except that the Al specimen had been anodized after implantation and thus had ~100 μg/cm² of oxide on the surface and the thin layer of Xe was buried in the oxide. The Al edge occurs at the same energy as before. However, the continuum has a marked step. The height of the spectrum at any particular energy is proportional to the number of Al atoms contributing to the scattering at the depth corresponding to that energy. In the oxide layer this number is considerably less than that in the underlying metal, consequently, there is a reduced height until particles backscattered from the Al atoms in the metal are recorded in the spectra. This will occur at an energy E_1^1 given by Eq. [2] where the stopping power is that for Al_2O_3, k is that for Al, and x is the total thickness of the oxide (x_o). The width of the oxide step is thus a measure of the oxide thickness; its height reflects the stoichiometry. The Xe peak is displaced relative to its position in Fig. 3 because it is buried deeper beneath the surface. The energy of the peak is given by Eq. [2] where the stopping power is for Al_2O_3, k is for Xe, and x is now the depth of Xe below the oxide surface (x_m).

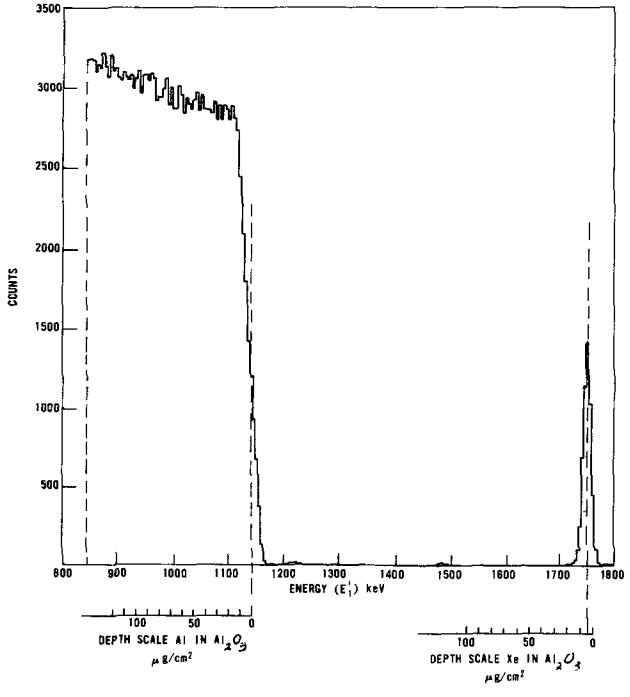

Fig. 3. Spectrum from 7×10^{15} Xe atoms implanted in Al. The incident energy of the He^+ was 1975 keV.

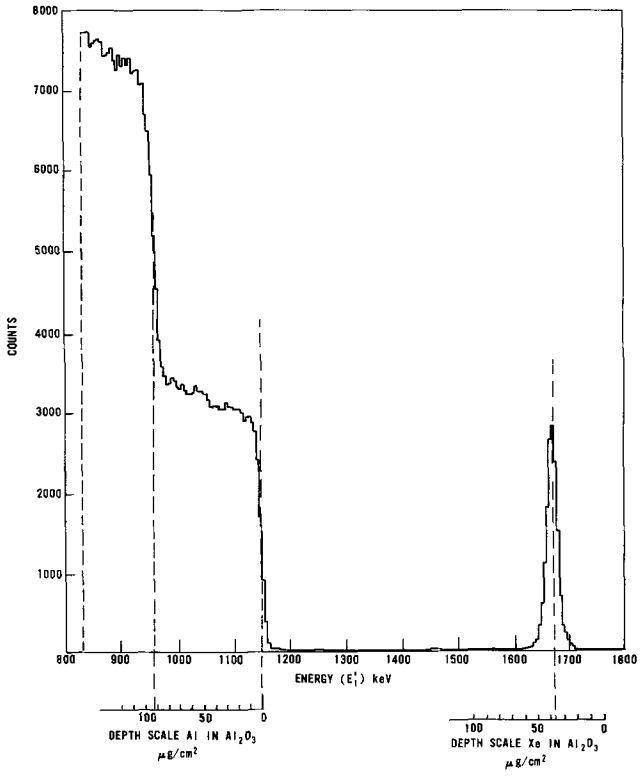

Fig. 4. Spectrum from 7 x 10^{15} Xe atoms buried in an oxide layer (95 μg/cm² thick) on the surface of Al. Incident energy of the He^+ was 1975 keV.

The transport number required from the experiments is the ratio of x_m to x_o. To obtain this ratio from the spectra two computer programmes were used. The first of these established a tabulation of the values of E_1^1 for small, successive x intervals (1 μg/cm²) using Eq. [2] when E_o, θ_1, θ_2, and k^2 were given appropriate values for the initial energy and geometric arrangements of the particular experiment. As the value of $S(E)$ is continually changing as E changes with depth, the programme included a tabulation of stopping power as a function of energy. This was obtained by the Bragg additivity rule using published data (13, 14) for oxygen and aluminum and assuming stoichiometric Al_2O_3. This input data is given in micrograms per square centimeter and since the unit of distance was also in the same terms it was not necessary to know the density of the oxide. The tabulations for the specific examples of Fig. 3 and 4 have been reproduced as scales on these figures. The scale for Xe differs from that for Al as a consequence of the difference in the value of k^2 for these two atoms. The scales are not linear since stopping power varies with energy.

The second computer programme produced values of E_1^1 for the Al(oxide) edge, the Al(metal) edge, and the implant from the raw data. These could then be read in terms of thicknesses and depths from the first tabulation. The programme smoothed the data by a least square fitting routine, then extracted the position of edges and implants, assuming that the peaks were Gaussian and that the edges were integrated Gaussians. Output was given directly in energy by inputing a calibration curve for the pulse height analyzer.

In these experiments with Al experimentally determined, values for the stopping power of Al and O_2 were available and as will be shown later the assumption of stoichiometric Al_2O_3 were justified. However the experimental technique can be extended to systems where good data are not available and the stoichiometry is unknown, with some loss in accuracy. The tabulations of depths of Xe and Al in Al_2O_3 differ from each other by less than 10% and differ from linearity by less than 5% over the range 0-100 μg/cm². As an approximation one could assume that the stopping power is independent of energy. In this case the ratio of x_m to x_o is simply the ratio of the energy shift of the marker to the energy width of the oxide step and can be obtained directly from the number of channels in the spectra. This approximation is good to about 10% under the conditions of the present experiment since the stopping power does not vary rapidly with energy.

In Rutherford scattering experiments it is possible, within limits, to determine the width of the marker distribution. Before anodizing (*e.g.*, Fig. 3), the width of the Xe peaks are determined, for all practical purposes, by the detector resolution (FWHM = 17 keV). After anodizing (*e.g.*, Fig. 4) the width of the Xe peaks (FWHM) are found to be typically 24 keV. The edges, or steps, in the spectra also have widths. The shape of these edges is, to a good approximation, an integrated Gaussian and hence these widths can also be expressed as a FWHM. In an anodized specimen (with approximately 100 μg/cm² of oxide) the width of the higher energy edge (outer surface) was typically 18 keV which is, as expected, identical for practical purposes with the detector resolution. The width of the lower energy edge (metal-oxide interface) was typically 23 keV. A brief discussion of widths and their significance is given in the discussion of results, below.

Since the areas of the peaks in the backscattering spectra are proportional to the number of marker atoms, the incident ion fluence and the scattering cross section, possible loss of marker atoms during anodizing could be detected. In comparing markers at the same depth it was merely necessary to normalize for the ion fluence. Another normalization was necessary if the markers were at different depths because the ion energies at the point of scattering would then differ, resulting in a difference of cross section proportional to $1/E^2$. Integration of the peak areas was included in the computer programme used to determine the energy.

One last piece of information can be gleaned from the spectra obtained in these experiments; it is possible to establish whether or not the anodic films are stoichiometric Al_2O_3. First, the ratio of the counts in any chosen channel of the Al(metal) step to a chosen channel of the oxide step that should be obtained for stoichiometric Al_2O_3 is calculated. The ratio of Al atoms/microgram of Al to Al atoms/microgram of Al_2O_3 is modified by (*i*) the ratio of the thickness represented by the energy interval of one channel in the Al to one channel in the oxide, and (*ii*) the inverse ratio of the squares of the energy of the He^+ particles at the instant they reach the depth represented by the chosen channels. For these purposes it is not only necessary to use the tabulations already described but to provide an additional one for Al in Al (as shown in Fig. 3) and one of E_o^1 *vs.* depth, where E_o^1 is the initial energy less losses in traversing depth x. These calculated ratio were then compared with the actual ratio in the spectra. The channels chosen were taken to be those indicated as the edges in the computer programme. The number of counts was extracted by a programme after smoothing the data and extrapolation of the plateau curves to the edge channels. Agreement of the calculated and experimental ratios indicates stoichiometric Al_2O_3. If there were disagreement the actual stoichiometry could be obtained by recording spectra which include the backscattered particles from O (they have been biased out in our spectra) and the Al:O ratio calculated in the manner described in Ref. (15, 16).

Results and Discussion

Table I lists results obtained from experiments with the inert gases implanted into preformed oxide films (30V = 11 μg/cm²) and Table II those obtained with the implants in metal beneath the natural airformed oxide (~0.7 μg/cm²). The tables indicate the implanted species and the number of atoms implanted.

Oxide thickness, stoichiometry, precision.—The thicknesses of the anodized oxide layers were determined

from the energies of the particles backscattered from the Al at the metal-oxide interface, *i.e.*, from the width of the oxide step (Fig. 4). These values are listed under "determined" in Tables I and II. Taking all of the results, Tables I and II, we find that a comparison of each individual thickness "determined" with its corresponding "calibration" value shows a relative standard deviation of 6.3%. The average of all determined thicknesses differs from the average of all calibration values by only +0.3%, suggesting that the absolute value used for the stopping power of Al_2O_3 is substantially correct. On comparing calculated values for the ratio of heights in chosen channels of the metal and oxide steps it was found that the average value obtained from 22 spectra differed from the value calculated for stoichiometric Al_2O_3 by 3.8%. The relative standard deviation for the 22 spectra was 2.0%. The difference of 3.8% cannot be considered significant in view of the limited accuracy of the stopping power data. More important is the fact that the relative standard deviation of 2.0% is entirely consistent with the statistical accuracy of the counting data, confirming that the techniques used can yield precise verification of film composition.

Sample 1 was measured four times to demonstrate the reproducibility of the thickness determination (relative standard deviation from the mean 3%) and the marker depth measurement (6%).

Noble gases.—In calculating the transport numbers for aluminum small corrections (3) have been made for (*i*) the finite initial depths of the marker in metal and in preformed oxide films, (*ii*) the fact that with implants in metal, oxidation of the metal lying above the implant will take place without either Al or O traversing the implant layer, and (*iii*) the small amount of Al that dissolves during anodizing. The amount dissolving is about 2% of the total Al converted to oxide (17).

The lower limit of dose is set by the practical limit of sensitivity of the technique, which for Xe is about 5×10^{13} atoms/cm^2. In the experiments with a dose of 1×10^{16} atoms/cm^2 more than half the Xe disappeared during anodizing, although the remainder behave normally, *i.e.*, as though the dose had been 5×10^{15} atoms/cm^2. It is suspected (but not established) that the heavy radiation damage results in some loosening of the oxide film which peels off at the start of anodizing. The somewhat higher transport number is consistent with this contention as the calculations would contain too great a correction for implant depth. Hence, in this case at least, there is an upper limit to the useful dose. In all the other experiments, with lower doses, no loss of marker was detectable.

There appears to be a tendency for the transport number to increase with dose. It is difficult to decide whether or not this is real. If it is, a possible explanation can be offered; the larger doses must have associated greater radiation damage to the outer layers which conceivably alters the anodization process. The implants in preformed oxides would be most affected; they do show the trend most clearly. Doses below 5×10^{14} do not show this tendency, consequently it is concluded that marker atoms do not significantly alter the results when the number implanted is no greater than 5×10^{14}.

All completely immobile markers should give the same value for transport numbers. Since the Rutherford scattering cross section varies as Z^2 the minimum useful dose for Ar was 2×10^{15} atoms/cm^2 and for Kr, 5×10^{14} atoms/cm^2. Bearing in mind the small dose effect already noted, the tables show that within experimental error Ar, Kr, and Xe do give the same value for the aluminum transport number. It should be noted however that Pringle (5), employing more sensitive techniques applicable to Ta_2O_5, has detected small differences for Ar, Kr, and Xe markers.

As far as the transport number is concerned there was no real difference between the behavior of implants made into metal and those made into preformed anodic oxide (30V $\approx$ 11 μg/cm^2), except for the slightly greater spread in results. As discussed in more detail later, the distribution of the implant atom tends to broaden in the "metal" case. This broadening is not reproducible from specimen to specimen and leads to more variation in the determination of the peak position.

The value for the cationic (aluminum) mobility obtained by taking a simple average of all the individual values listed in Table I is 0.39. The best value obtained by β-ray spectrometry (3) for anodic oxidation in tetraborate-glycol solutions at a current density of 1 mA/cm^2 was 0.6. The value obtained from the ^{222}Rn experiment (4) using aqueous ammonium citrate solution, was approximately 0.3. However, Table III shows that transport numbers depend on the electrolyte. Samples 1 and 2 (metal implants) were anodized in sodium tetraborate-ethylene glycol solution. These results agree quite well with those of Ref. (3) in which the specimens were similarly treated. The preformed oxide in samples 3 and 4 were formed in the aqueous electrolyte, the subsequent anodizing was in the glycol solution. The intermediate value of the transport numbers substantiates the conclusion that oxidation proceeds differently in the two electrolytes.

Halogens and alkali metals.—In the experiments with halogens and alkali metals it was immediately obvious that these species are mobile during anodizing. Hence, to formulate the results in Table IV we have calculated a migration number. To do this we calculated the position of an immobile reference point, using the transport number of Al. The transport number used was the average of all values given in Table I. Given this reference point we then calculated how far the marker had moved from this point. Finally, we took the ratio of this distance to the thickness of oxide grown. Corrections for the finite initial depth of the marker and for Al dissolution were made as before. Bearing in mind the limited number of experiments, the following comments can be made.

The direction of motion is consistent with the halogens and alkali metals moving as ions. Size appears to be one factor since we find the mobility of Cl > Br > I and of K > Rb > Cs. It is not the only factor, however, since all the alkali metal ions are smaller than the halogen ions but the alkali metals taken in a group, do not move faster than the halogens.

As far as the migration numbers are concerned there is no significant difference established between implants into metal and into preformed oxide. Nor is there any obvious dependence of the mobility on the thickness of oxide grown.

In two cases (I and Cs) the anodized specimen was returned to the electrolyte and a voltage equal to the original anodizing voltage was applied until the current had decayed to about 0.01 mA/cm^2 ($\approx$10 min). During this period a small additional amount of oxide

Table III. Data from experiments using ethylene glycol electrolyte (Xe implants)

Sample number	Implanted layer	Implant dose (ions/cm^2)	Oxide thickness determined (μg/cm^2)	Marker depth (μg/cm^2)	Aluminum transport number
1	Metal	2×10^{14}	40	25.5	0.68
2	Metal	2×10^{14}	35	21.5	0.66
3	Oxide	2×10^{14}	45	17	0.48
4	Oxide	2×10^{14}	39.5	14	0.46

Table IV. Data from experiments with halogens and alkali metals

Sample number	Implanted layer	Implanted species	Implanted dose (ions/cm²)	Oxide thickness from calibration (μg/cm²)	Oxide thickness determined (μg/cm²)	Marker movement (μg/cm²)	Migration number
14	Metal	Cl	2×10^{15}	35	40	32.5 (in)	0.35
15	Metal	Br	5×10^{14}	56	61	12.5 (in)	0.21
16	Metal	Br	5×10^{14}	112	116	20.9 (in)	0.18
17	Oxide	I	2×10^{14}	112	112	7.0 (in)	0.08
18	Oxide	I	2×10^{14}	112	121	12.7 (in)	0.11
19	Metal	I	2×10^{14}	112	101	14.3 (in)	0.14
20	Metal	I	2×10^{14}	112	104	11.1 (in)	0.11
			2×10^{14}			23.0 (out)	0.22
21	Oxide	Cs	2×10^{14}	112	112	18.6 (out)	0.18
22	Oxide	Cs	2×10^{14}	112	121	22.3 (out)	0.20
23	Metal	Rb	5×10^{14}	56	61	15.2 (out)	0.25
24	Metal	Rb	5×10^{14}	112	117	32.3 (out)	0.27
25	Metal	K	2×10^{15}	112	100	34.3 (out)	0.34
			Average:	96.3	97.2		

formed and allowing for this, the positions of the markers were unchanged. Similar specimens were returned to the electrolyte and held at a voltage slightly below the original voltage for 15 min, during which time the current was, as expected, essentially zero, no oxide formed and the markers did not move. Thus the markers have measurable mobility only when the oxide is growing.

For the implant doses used there was no detectable loss of implanted ions to the electrolyte nor any suggestion of the implant penetrating from the oxide into the metal. In fact, as seen in Table IV, the mobility of the implanted anions used in the present experiments was always less than that of oxygen and the mobility of the implanted cations always less than that of aluminum. This is not to be taken as a generalization applying to foreign atoms other than the ones mentioned in this paper.

Taking the results for the noble gases, the alkali metals and the halogens all together we can say that the picture is consistent with the assumption that the noble gases are immobile. It does not, of course, provide a complete proof of this assumption.

Peak widths.—The spectra for all specimens having approximately 100 μg/cm² of anodic oxide were analyzed to determine the widths of the upper energy edge (outer surface) and the lower energy edge (metal-oxide interface). For the outer surface the width (FWHM) was 18.3 keV with a standard deviation of 1.8 keV. For the metal-oxide interface the width was 22.8 keV with a standard deviation of 2.1 keV. The width from outer surface is composed of the detector resolution together with possible contributions from accelerator energy drifts and electronic gain changes. The observed width of 18 keV is clearly in agreement with the detector resolution of 17 keV. The width from the metal-oxide interface contains an added contribution from the energy straggling of the He ions in passing into and out of the oxide layer, together with possible contributions from nonuniformity of the oxide or diffusiveness at the interface. The straggling contribution is impossible to obtain exactly since there is no experimental data for the exact system in question. However, Hvelplund (17) has published data for 500 keV He ions in air and in Ne. An extrapolation of his data, admittedly very approximate, suggests that the whole of the difference between 23 and 18 keV can be accounted for by He ion energy straggling.

The spectra for the Xe implanted into preformed oxide and then anodized were analyzed to find the width (FWHM) of the Xe peaks. The average width was 24.0 keV with a standard deviation of 1.1 keV. Since the Xe is buried to the extent of about four-tenths of the oxide thickness its peak width contains, besides the detector resolution, a contribution from the He ion energy straggling. If allowance is made for these contributions the remainder is 12 keV, or 6 μg/cm²; however, in view of the corrections and errors this number has scarcely any significance. In the case of Ta_2O_5, Pringle (5), using a more sensitive technique, has detected small broadening of inert gas markers. If his results are applicable to Al_2O_3 they would suggest a broadening of about 2 μg/cm² in our experiments.

The number of experiments in preformed oxides using species other than Xe is limited. For the cases studied, Ar, Cs, and I, there is no evidence that the peak widths after anodizing are any different from those observed for Xe; see Table III.

The situation for implants made into metal, rather than preformed oxides, is quite different. The number of samples for each implant is not large; however, for all cases studied, Kr, Xe, K, Rb, Cs, Cl, Br, and I the peak width after anodizing was very obviously broadened. Widths (FWHM) ranged from 27.4 keV (potassium) to 39.2 keV (bromine) with no obvious correlation as to type of implant; see Table V. It appears therefore that the major factor contributing to broadening is the phase change in the region of the implant and not the behavior of the implant once it has become incorporated into the oxide.

Assessment of Method

An important advantage of the method is its generality, subject to the limitation that the foreign atoms be heavier than the matrix atoms. Clearly, of the noble gases, Xe is the most practical to use; the sensitivity is good (because of the Z^2 dependence of the scattering cross section) and it can be used in fairly heavy matrix. For example application of Eq. [1] and [2] shows that Xe atoms buried to a depth of 25 μg/cm² in ZrO_2 could just be resolved from the Zr continuum. In any particular case the behavior of the marker will also be important. In our experiments, potassium could be studied in films of 100 μg/cm² since it remains close to the outer surface. Chlorine, which moves inward, could be studied only in films that were <50 μg/cm² since it becomes deeply buried and the chlorine peak can be lost under the aluminum continuum.

Small quantities of foreign atoms, as listed in the tables, can be studied only if they lie in a depth distribution narrow enough to give a sharp peak in the spectrum. Obviously the ideal condition is when the width of the depth distribution is small compared to the detector resolution, *i.e.*, in the present case, small compared to 17 keV which corresponds to about 8 μg/

Table V. Widths (keV, FWHM) of edges and implant peak after anodizing to 300V

Average width from outer surface: 18.29 ± 1.82
Average width from metal-oxide interface: 22.84 ± 2.14

Peak widths for implants made into preformed oxide		Peak widths for implants made into metal	
Xe (8 expt.)	24.03 ± 1.13	Xe	33.11
Ar	22.64	Kr	35.15
Cs (2 expt.)	20.35 ± 0.58	K	27.40
I (2 expt.)	23.57 ± 0.39	Rb	29.09
		Cs	38.90
		Cl	~40
		Br	39.21
		I (2 expt.)	36.32 ± 3.88

cm^2. Ion implantation is especially useful since it produces a narrow distribution, gives the choice of incorporating the marker in metal or preformed oxide and offers an almost unlimited choice of marker species and matrix. However, the method could be applied to markers adsorbed on surfaces and with limitations, to species incorporated from solution or present as additives in the metal being oxidized.

At the other extreme, foreign atoms distributed uniformly through the matrix will produce a continuum and larger amounts of material will be required to maintain the statistical significance of the spectrum. Similar, but more extreme, considerations apply to studying atoms that are lighter than the matrix; the oxygen in Al_2O_3 film can easily be detected but oxygen as a minor constituent in aluminum would not be.

The quantity of marker required thus depends on several factors but in any case the sensitivity of the method is not as high as that obtainable with radiotracer methods and the quantity of marker is, by necessity, larger. This might be a serious disadvantage in some cases; we have noted that the amount of Xe implanted might have a small influence on the observed transport numbers. In these particular experiments the over-all behavior during anodizing was not affected, *i.e.*, the oxide had the expected thickness and was uniform and adherent. Similarly, the over-all behavior of specimens implanted with alkali metals or halogens, at the doses used, appeared normal. Nevertheless, there remains the obvious possibility that, in general, the presence of foreign atoms can influence the anodizing behavior and that the behavior of a mobile foreign atom will itself be influenced by its concentration.

A second major advantage of the method is that it measures the position of the marker and the thickness of the film simultaneously. Useful information can be obtained, if necessary, without any knowledge of the film composition, density, or stopping power. Indeed, spectra obtained in a suitable way can be used to measure the stoichiometry and to detect changes in stoichiometry with depths, *e.g.*, in duplex films (15, 16). The uniformity of the film throughout its thickness is automatically checked. These factors are of special advantage in studying more complex film forming processes, *e.g.*, anodic or thermal oxidation of compounds and alloys or the formation of intermetallic films, where information on the nature of the films is often minimal.

The presence of impurities, especially surface contaminants, will also be revealed under suitable conditions discussed above. For example, it is known (19) that aluminum that has been anodized and stripped in chromic-phosphoric acid retains a thin oxide containing Cr and P. All our specimens so treated give spectra that showed very clearly the presence of Cr at the surface; phosphorus was also detectable, although poorly resolved from the Al.

It is possible, by judicious selection, to use two or three markers in a single experiment, thus comparing their behavior under absolutely identical conditions. For example, in Table I, specimens 12 and 13 were implanted with both Ar and Xe. By the same methods it would be possible to check for the possible interference of one species with another.

The precision of the method, as found in practice, is consistent with expectations based on the detector resolution and counting statistics. The expected resolution (FWHM) corresponds to 8 $\mu g/cm^2$; in the four measurements made on sample No. 1, Table I, the standard deviation for oxide thickness was 2.0 $\mu g/cm^2$ and for the Xe depth 1.6 $\mu g/cm^2$. The stoichiometry of the oxide could be verified with a precision ($\pm 2\%$) consistent with the counting statistics.

Acknowledgments

It is a pleasure to acknowledge the assistance of O. M. Westcott for mass separator operations, C. W. Sitter for anodic oxidations. G. R. Bellavance for Van de Graaff irradiations, G. A. Sims for Van de Graaff operation, and H. H. Plattner for oxidations, irradiations, and computer calculations.

Manuscript submitted Sept. 13, 1972; revised manuscript received March 26, 1973.

Any discussion of this paper will appear in a Discussion Section to be published in the June 1974 JOURNAL.

REFERENCES

1. J. A. Davies, J. P. S. Pringle, R. L. Graham, and F. Brown, *This Journal*, **109**, 999 (1962).
2. R. L. Graham, F. Brown, J. A. Davies, and J. P. S. Pringle, *Can. J. Phys.*, **41**, 1686 (1963).
3. J. A. Davies, B. Domeij, J. P. S. Pringle, and F. Brown, *This Journal*, **112**, 675 (1965).
4. J. A. Davies and B. Domeij, *ibid.*, **110**, 849 (1963).
5. J. P. S. Pringle, *ibid.*, **119**, 482 (1972).
6. G. Amsel and D. Samuel, *J. Phys. Chem. Solids*, **23**, 1707 (1962).
7. R. W. Ollerhead, E. Almqvist, and J. A. Kuehner, *J. App. Phys.*, **37**, 2440 (1966).
8. B. Cox and C. Roy, *Electrochem. Technol.*, **4**, 121 (1966).
9. J. L. Whitton, *This Journal*, **115**, 58 (1968).
10. W. D. Mackintosh and J. A. Davies, *Anal. Chem.*, **1**, 26A (1969).
11. J. L. Whitton, *J. Appl. Phys.*, **36**, 3917 (1965).
12. J. A. Davies, F. Brown, and M. McCargo, *Can. J. Phys.*, **41**, 829 (1963).
13. P. D. Bourland, W. K. Chu, and D. Powers, *Phys. Rev.*, **B3**, 3625 (1971).
14. W. K. Chu and D. Powers, *ibid.*, **187**, 478 (1969).
15. O. Meyer, J. Gyulai, and J. W. Mayer, *Surface Sci.*, **22**, 263 (1970).
16. I. V. Mitchell, M. Kamoshida, and J. W. Mayer, *J. Appl. Phys.*, **42**, 4378 (1971).
17. J. A. Davies, Chalk River Nuclear Laboratories, Atomic Energy of Canada Limited, Private communication, 1972.
18. P. Hvelplund, *Mat. Fys. Medd. Dan. Vid. Selsk.*, **38**, 4 (1971).
19. J. E. Lewis and R. C. Plumb, *Intern. J. Appl. Radiation Isotopes*, **1**, 36 (1956).

Charge in SiO_2-Al_2O_3 Double Layers on Silicon

J. A. Aboaf* and D. R. Kerr*

IBM System Products Division, East Fishkill Laboratory, Hopewell Junction, New York 12533

and E. Bassous*

IBM T. J. Watson Research Center, Yorktown Heights, New York 10598

ABSTRACT

The negative charge in Al-Al_2O_3-SiO_2-Si double layers was found to be located at the insulator-insulator interface. This charge is independent of the thickness of the Al_2O_3 and inversely dependent on the SiO_2 thickness. Evidence for a constant voltage drop across the SiO_2 during Al_2O_3 deposition was found for polycrystalline Al_2O_3, N_2-deposited and O_2-deposited amorphous Al_2O_3. It is suggested that the traps at the interface Al_2O_3-SiO_2 are due to oxygen vacancies.

Double layer insulators are becoming more and more common in semiconductor technology. One system of particular recent interest is the Al_2O_3-SiO_2 structure. Aluminum oxide films provide a barrier to sodium ions (1) and are also more radiation resistant than thermal oxide films (2). It is well known that thermal oxide on silicon tends to make the surface of silicon more n-type; Al_2O_3, on the contrary, makes the surface more p-type (3).

Aluminum oxide films have been deposited on silicon by various methods: by chemical vapor deposition from $AlCl_3$, CO_2, and H_2 at high temperature (1); from pyrolysis of alkoxydes of aluminum (3), by sputtering (4, 5), and by electron beam evaporation (6-8). The characteristics of the insulator charge and in particular the location of the resulting charges in metal-Al_2O_3-SiO_2-Si structures have been studied by several workers but there is still no complete agreement on this subject. Using polycrystalline Al_2O_3, Nigh (9) interprets his results for double layers Al_2O_3-SiO_2 on silicon to one or more of the following: a sheet of negative charge at the insulator-insulator interface, a positive contact potential of approximately +1.1V, and a change in the metal-insulator barrier energy when Al_2O_3 is substituted for SiO_2. Kalter *et al* (10), studying the same system, report a +1.5V potential step at the insulator-insulator interface but no interface charge. Nishimatsu *et al.* (11), using amorphous Al_2O_3, report the presence of a constant negative charge (3.5×10^{11} charges/cm^2) at the Al_2O_3-SiO_2 interface and a distributed negative charge in the Al_2O_3 but no contact potential. Gosney (8) finds a negative single layer of charge (7×10^{11} charges/cm^2), no contact potential and no bulk charge; he reports also that the effective charge is positive when Al_2O_3 is deposited directly on silicon. Salama (4) reports a single layer of positive charge at the interface and a contact potential of about +1V in his double layer structures; both positive and negative charge can be observed in the Al_2O_3-Si structure depending on the sputtering conditions and the annealing conditions (4, 5).

In this paper, the magnitude and location of the charge in Al-Al_2O_3-SiO_2-Si structures was studied for both amorphous and polycrystalline Al_2O_3.

Experimental

Aluminum oxide films, both amorphous and polycrystalline, were used in this study.

Amorphous Al_2O_3.—Low-temperature amorphous Al_2O_3 films were deposited from the pyrolysis of aluminum triisopropoxide at 425°C in either nitrogen or oxygen ambient. Details of the process have already been described (3). The deposition rate is 60 Å/min; the index of refraction is 1.6; and dielectric constant is 7.7.

Polycrystalline Al_2O_3.—High-temperature Al_2O_3 films were deposited by chemical vapor deposition from $AlBr_3$ + NO at 910°C in a resistance heated furnace in a forming-gas atmosphere. This process (12) is very similar to that developed by Rand (13) for depositing SiO_2 films from $SiBr_4$ + NO + H_2. Films were deposited at 70 Å/min; the index of refraction is 1.75; the etch rate, in hot phosphoric acid (150°C), is 150 Å/min, and the dielectric constant is 9.5.

Metal-insulator-semiconductor capacitor structures were used in the electrical evaluation. Capacitance-voltage (C-V) characteristics at 1 MHz were obtained to measure the charge stored in the double layers.

The metal-insulators-silicon structures were obtained as follows: Silicon wafers <100>, p-type 2 ohm-cm were thoroughly cleaned and oxidized in dry oxygen at 1050°C for various periods of time. Annealing at 1050°C was done in nitrogen for 30 min. The measured flat-band voltage for these oxides (300-1000Å thick) was (after evaporating aluminum electrodes and annealing again at 420°C in a forming-gas atmosphere for 30 min) −0.8 to −0.9V and the mobile charge (after biasing MOS dots for 30 min, at 200°C, at $\pm 2 \times 10^6$ V/cm) in the low 10^{10} charges/cm^2 range. Al_2O_3 films, approximately 3000Å thick, were subsequently deposited on the SiO_2 films. No annealing of the Al_2O_3 film was done immediately after deposition.

Depending on the Al_2O_3 film deposited, further processing was made as follows: *i*) For the amorphous Al_2O_3, steps of approximately 5 mm in width and approximately 500Å depth were made on the Al_2O_3 film. A first step was done by covering most of the wafer with tape and etching in buffered HF for a certain period of time. By decreasing successively the area of the wafer taped, several etching steps could be obtained. *ii*) For the polycrystalline Al_2O_3, a film of high-temperature SiO_2 was deposited on the Al_2O_3 film. A step was then etched in buffered HF as above for a certain period of time in hot phosphoric acid. Repeat of the same procedure several times resulted in a wafer with 5 or 6 steps, of about 5-6 mm width.

Finally 12 mil diam aluminum dots were evaporated on the structure and annealed at 420°C for 30 min in a forming-gas atmosphere. Aluminum was also evaporated on the bare backside of the silicon for contact. A cross section of the experimental structure is given in Fig. 1.

Results and Discussion

The flat band voltage of the metal-insulator structures is shown in Fig. 2 and 3 as a function of the Al_2O_3 thickness for various constant thickness SiO_2 films. The results for amorphous Al_2O_3 films are qualitatively

* Electrochemical Society Active Member.

Key words: Al_2O_3, aluminum oxide, double layer insulators, metal-insulator-semiconductor, trapping centers, insulator charge.

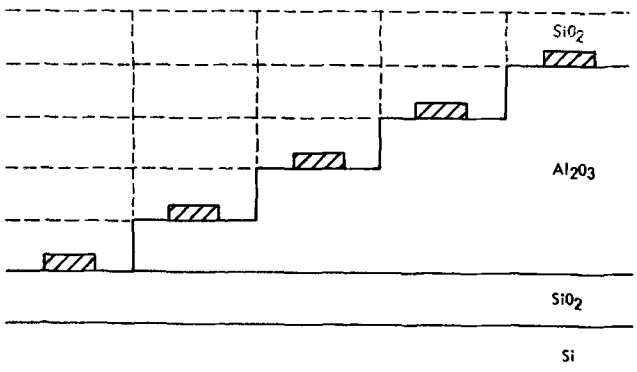

Fig. 1. Cross section of structures tested (see text for dimensions)

similar to those for polycrystalline Al_2O_3. The bars on the lines show that the spread in flatband voltage on each step is about ±0.1V (typically 5 devices measured). Thickness of the Al_2O_3 films were obtained by comparison of the color of the film with a predetermined color scale similar to that of Pliskin and Conrad (14). The error would probably be within 10% of the exact thickness.

The results obtained for N_2-deposited and O_2-deposited amorphous Al_2O_3 films on SiO_2-Si are compared in Fig. 4 for a constant SiO_2 thickness of 230Å.

In all cases, the flatband voltage of the Al_2O_3-SiO_2 structures increases fairly linearly with the increase of the Al_2O_3 film thickness for a constant SiO_2 thickness and reaches about −0.8V for zero Al_2O_3 thickness. The flatband voltage of the N_2-deposited Al_2O_3 structure is much more positive than that for the O_2-deposited one.

If we postulate sheet charges Q_{ox} and Q_{int} at the Si-SiO_2 and the SiO_2-Al_2O_3 interfaces, respectively, the flatband voltage will be given by

$$V_{FB} = -Q_{ox}\frac{t_o}{K_o} - (Q_{ox} + Q_{int})\frac{t_A}{K_A} + \phi_{ms} \quad [1]$$

where t_o and K_o are the thickness and dielectric constant of the SiO_2 film, t_A and K_A are the thickness and dielectric constant of the Al_2O_3 film, and ϕ_{ms} is the metal-to-silicon work-function difference. The fact that V_{FB} reaches the expected ϕ_{ms} value (−0.8V for aluminum and p-type silicon) for $t_A = 0$ indicates that Q_{ox} is essentially zero for our samples. This is not unreasonable for well-annealed oxides on <100> oriented silicon. Equation [1] then reduces to

$$V_{FB} = -Q_{int}\frac{t_A}{K_A} + \phi_{ms} \quad [2]$$

Table I. SiO_2-Al_2O_3 interface charge N_{int} (in units of 10^{11} charges/cm^2) for varied SiO_2 thickness and Al_2O_3 processes

SiO_2 thickness	Amorphous Al_2O_3 (O_2-deposited)	Amorphous Al_2O_3 (N_2-deposited)	Polycrystalline Al_2O_3
230Å	−2.1	−5.9	—
315Å	—	—	−5.3
425Å	—	—	−3.5
560Å	−1.1	−2.2	−3.0
1000Å	—	−1.4	−1.9

The data of Fig. 2-4 display the linear dependence of V_{FB} on t_A predicted by Eq. [2] and indicate in all cases a layer of negative charge at the SiO_2-Al_2O_3 interface. Values of $Q_{int}/q = N_{int}$ obtained from the slopes of the best straight-line fits to the V_{FB} *vs.* t_A data are shown in Table I. Note that the charge densities thus determined fall in the range 1-6 × 10^{11} electronic charges/cm^2, with an apparent inverse dependence of N_{int} on SiO_2 thickness for any particular type of Al_2O_3. This relationship becomes more obvious in Fig. 5, in which all the data of Table I is plotted as a function of SiO_2 thickness. It is seen that all the data can be well fit to parallel lines of −1 slope on the log-log plots, thus indicating that N_{int} is proportional to t_o^{-1}.

We subscribe to the mechanism proposed recently by Labuda *et al.* (15), which postulates that the Al_2O_3 is conductive enough during deposition to maintain internal fields within the Al_2O_3 at zero and, further, that the silicon and Al_2O_3 are in thermal equilibrium (equal Fermi levels). As shown in Fig. 6, a fixed voltage V_{ox} will then be dropped across the SiO_2 during deposition, which will be determined by the Fermi levels in the Si

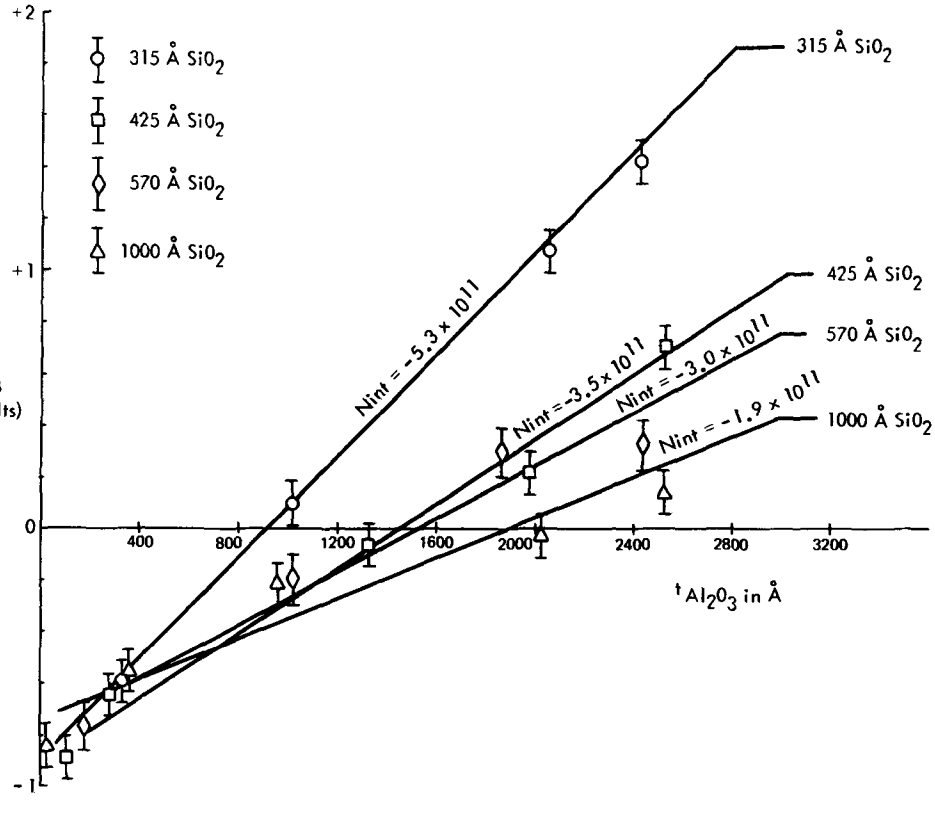

Fig. 2. Flatband voltage of structure Si-SiO_2-Al_2O_3 (polycrystalline)-Al as a function of aluminum oxide thickness.

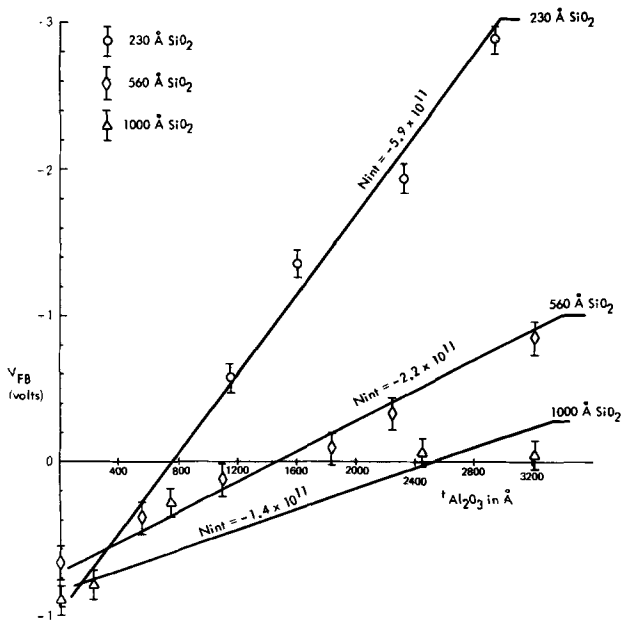

Fig. 3. Flatband voltage of structure Si-SiO_2-N_2 deposited Al_2O_3 (amorphous)-Al as a function of aluminum oxide thickness.

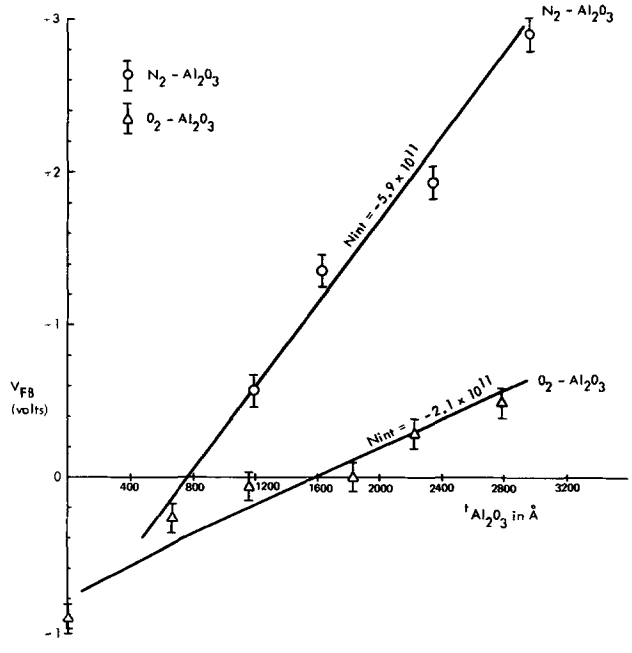

Fig. 4. Flatband voltage of structure Si-230Å SiO_2-Al_2O_3 (amorphous)-Al as a function of aluminum oxide thickness.

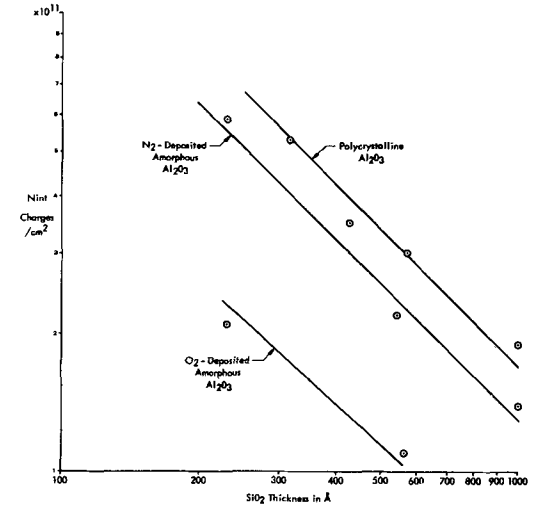

Fig. 5. Log-log plot of the interface charge vs. SiO_2 thickness for various polycrystalline and amorphous Al_2O_3 films.

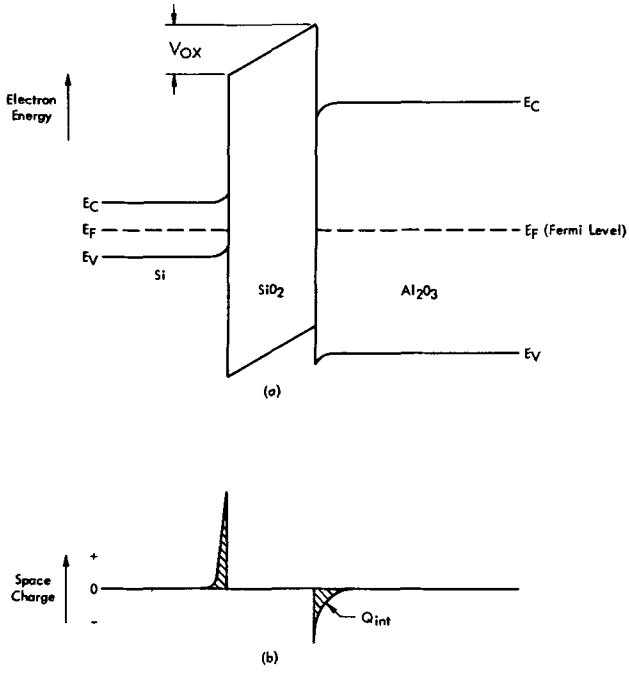

Fig. 6. Schematic picture of proposed energy-band diagram (a) and space-charge distribution (b) during Al_2O_3 deposition. Our measurements indicate V_{ox} values of 0.75V for polycrystalline Al_2O_3, 0.6V for N_2-deposited amorphous Al_2O_3, and 0.25V for O_2-deposited amorphous Al_2O_3.

and the Al_2O_3 and by the Si-SiO_2 and Al_2O_3-SiO_2 potential barriers, but should be independent of SiO_2 or Al_2O_3 thicknesses. An electronic charge K_oV_{ox}/t_o will be associated with V_{ox} and will reside in the Al_2O_3 close to the SiO_2-Al_2O_3 interface. This charge is assumed to remain in traps at this interface as the sample is cooled to room temperature to give Q_{int}. Calculating the voltage drop V_{ox} for the three types of Al_2O_3 gives values of 0.75V for the polycrystalline Al_2O_3, 0.6V for N_2-deposited amorphous Al_2O_3, and 0.25V for O_2-deposited amorphous Al_2O_3. Labuda *et al.* (15) used a 900°C $AlCl_3$ process for Al_2O_3 deposition and found a V_{ox} of 0.76V.

The Fermi level within the Al_2O_3, which in turn determines V_{ox}, will be sensitive to the density and energy distribution of traps within the Al_2O_3. The V_{ox} difference between N_2-deposited and O_2-deposited Al_2O_3 could be explained by a decrease in trap density when the Al_2O_3 is deposited in oxidizing conditions. This would suggest that the traps in the Al_2O_3 are oxygen vacancies and that an excess oxygen during deposition will reduce them. Balk (16) in his studies of metal-Al_2O_3-SiO_2-Si structures found that charge injection under negative bias is not observed in polycrystalline Al_2O_3, which was oxygen annealed at 900°C for 1 hr, and suggested that the trapping centers could be oxygen vacancies. From the electron microprobe analysis of N_2-deposited and O_2-deposited amorphous Al_2O_3 and polycrystalline Al_2O_3 (see Table II), it was not possible to differentiate the variation of the aluminum or oxygen content in the bulk of the film. An excess of aluminum is found in all deposited films in respect to single crystal sapphire. The data obtained for polycrystalline Al_2O_3 confirms the data reported earlier by Nigh (9).

Conclusions

It has been shown that negative charges are observed in double layers Al_2O_3-SiO_2 structures on silicon. The negative charge was found to be located at the interface Al_2O_3-SiO_2. This charge is independent of the thickness of the Al_2O_3 film and dependent on the

Table II. Electron microprobe analysis of aluminum oxide films

	Weight fraction of Al in film	Weight fraction of O in film
Amorphous Al_2O_3		
420°C—N_2-deposited	0.534	0.466
420°C—O_2-deposited	0.534	0.466
Polycrystalline Al_2O_3		
910°C as deposited	0.547	0.453
O_2 anneal 4 hr 1000°C	0.543	0.457
4 hr 1100°C	0.546	0.454
Single crystal sapphire	0.529 ± 0.008	0.471

SiO_2 thickness. A constant voltage drop across the SiO_2 during Al_2O_3 deposition was found for polycrystalline Al_2O_3 (0.75V), N_2-deposited amorphous Al_2O_3 (0.6V), and O_2-deposited amorphous Al_2O_3 (0.25V). It is suggested that the traps in the Al_2O_3 are due to oxygen vacancies.

Acknowledgments

The authors would like to thank J. Kuptsis for his microprobe analysis and J. Hollis for his technical assistance. Thanks are also due to J. Gardner for the use of his testing equipment.

Manuscript submitted June 19, 1972; revised manuscript received March 16, 1973.

Any discussion of this paper will appear in a Discussion Section to be published in the June 1974 JOURNAL.

REFERENCES

1. S. K. Tung and R. E. Caffrey, *This Journal*, **114**, 275C (1967).
2. A. Waxman and K. H. Zaininger, *Appl. Phys. Letters*, **12**, 109 (1968).
3. J. A. Aboaf, *This Journal*, **114**, 9 (1967).
4. C. A. T. Salama, *ibid.*, **117**, 7 (1970).
5. M. C. Chen, *ibid.*, **118**, 4 (1970).
6. D. Hoffman and D. Leibowitz, *J. Vacuum Sci. Technol.*, **8**, 107 (1970).
7. R. A. Abott and T. I. Kamina, *Solid State Electron*, **13**, 565 (1970).
8. W. M. Gosney, Ph.D. thesis, University of California, Berkeley, March, 1970.
9. H. E. Nigh, Proceedings of the International Conf. on Properties and Use of MIS Structures, Grenoble, France, June 17-20, 1969, pp. 77-88.
10. H. Kalter, J. J. H. Schartorje, and E. Kooi, *Philips Res. Rept.*, **26**, 181 (1971).
11. S. Nishimatsu, T. Tokuyama, and M. Matsushita, *This Journal*, **115**, 239C (1968).
12. J. A. Aboaf, Paper 604RNP presented at Electrochem. Soc. Meeting, Montreal, Oct. 6-11, 1968.
13. M. J. Rand, *This Journal*, **114**, 3, 274 (1967).
14. W. A. Pliskin and E. E. Conrad, *IBM J. Res. Develop.*, **8**, 43 (1964).
15. E. F. Labuda, J. T. Clemens, and C. N. Berglund, IEEE Device Research Conf., University of Michigan, Ann Arbor, June 28-July 1, 1971.
16. P. Balk and F. Stephany, *This Journal*, **118**, 1634 (1971).

Monitoring Sodium Contamination in Silicon Devices and Processing Materials by Flame Emission Spectrometry

William R. Knolle and Theodore F. Retajczyk, Jr.

Bell Telephone Laboratories, Incorporated, Murray Hill, New Jersey 07974

ABSTRACT

Sources of sodium contamination found in routine chemical treatment and handling of silicon slices have been identified and quantitatively measured using a flame photometric technique. Common processing chemicals generally contain less than 500 ppb of sodium. Ways to reduce the level of sodium contamination during silicon device processing have been determined. Sodium may generally be rinsed off silicon and silicon-dioxide-covered silicon slices with a dilute acid rinse followed by a deionized water rinse. Subsequent handling and contact with the slices should be done with freshly cleaned handling tools to prevent recontamination.

Sodium contamination of silicon devices and its adverse effect on the electrical properties of these devices is well known. In an effort to minimize sodium contamination of silicon slices, the sources and extent of sodium contamination found in routine silicon-slice processing were investigated. Because the level of sodium contamination is very small, *i.e.*, generally less than 0.1 ng (nanogram) of sodium on the surface of a clean silicon slice, sensitive methods of analysis are necessary. Emission flame photometry has been shown to be a sensitive and facile method for detecting sodium on silicon, silicon dioxide, and in processing chemicals (1, 2). Presented here is a discussion of the method used to detect trace amounts of sodium in the 100 part per trillion range, the sources and extent of sodium contamination found in routine processing, and ways to reduce this contamination.

Method of Analysis

An Instrumentation Laboratory Model 153 atomic absorption spectrometer was used in the flame emission mode with a Boling burner head. The rotary beam chopper was eliminated in order to increase signal intensity and an RCA 1P21 photomultiplier tube operated at 1200V was used for detection of the signal. A black anodized aluminum shield was placed around the top of the flame and the fume exhaust duct in order to minimize flame instability due to air currents.

The response of the instrument was calibrated with sodium standards prepared by dilution of an aqueous stock solution. The solutions were contained in polypropylene volumetric flasks that had been leached of sodium with frequent changes of a dilute solution of HF for several days prior to use. The flasks were then equilibrated for several weeks by frequent changes of the given standard. The deionized water used to prepare the solutions was first passed through a set of demineralizers and finally a 0.2 μm filter. The sodium content of this water was typically less than 2 ppb. Prior to an analysis, the instrument response was calibrated with several of these standards. The response was recorded on a Varian Model G-14A-2 strip chart recorder. Figure 1 is a typical curve.

Sodium analysis of water-soluble reagents was generally done on a sample diluted at least ten-fold with deionized water and stored in a polypropylene volu-

Key words: flame photometry, sodium analysis, silicon device processing.

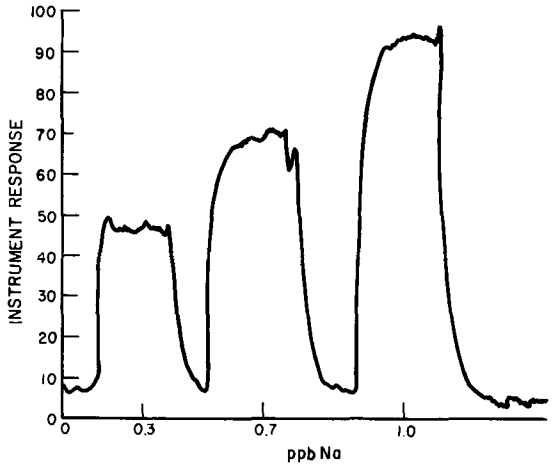

Fig. 1. Recorder tracing of sodium standards near maximum sensitivity.

metric flask for analysis on the same day. Analysis of sodium on silicon and silicon dioxide was done by placing a wafer in a preleached polyethylene sample vial and adding 2 ml of dilute HF dispensed from a preleached Nalgene automatic constant-volume pipette.

Rubber gloves freshly rinsed in deionized water were used to handle the samples during preparation and aspiration into the flame. All samples were prepared in a clean bench and capped until ready for analysis. Samples of deionized water that were carried uncapped through room ambient to the instrument had very large variations in the amounts of sodium measured.

Manipulation of the wafer with a pair of polyethylene tweezers in order to remove the wafer from the vial after etching proved to be another source of sodium contamination presumably arising from a mutual abrasion of the polyethylene surfaces which exposed fresh surfaces containing sodium. Substitution of a specially designed polyethylene holder in place of the tweezers so that the wafer might be readily transferred from vial to vial with a minimum amount of manipulation and contact with surfaces reduced the sodium level in the blank solutions. Figure 2 is a drawing of the wafer in this holder just prior to insertion into the vial containing the etching solution. Even with all of the above-mentioned precautions the chance of inadvertent sodium contamination during sample preparation and analysis was high and so generally several samples were analyzed and an average value of sodium on the wafer was reported.

A realizable working detection limit for sodium in solution when analyzed as above may be determined according to Gabriels (3). This detection limit for five, 2-ml samples of dilute HF was 0.10 ng of sodium. A detection limit of 0.10 ng of sodium in solution corresponds to 3.6×10^{11} atoms of sodium/cm^2 on the slice surface. The silicon slices used in this study were 10 ohm-cm, 2.16 cm in diameter, chemically etched on the back, and Syton-polished on the front side.

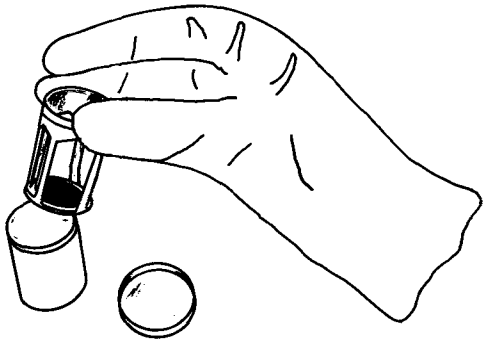

Fig. 2. Sample holder and etching receptacle

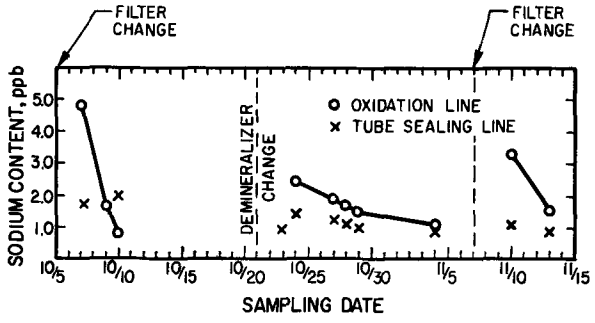

Fig. 3. Variation in sodium content of water from oxidation and tube sealing lines vs. time.

Sodium in Reagents

Deionized water.—Deionized water at two particular processing stations was monitored for sodium content over a period of 39 days. The data is presented in Fig. 3. The large values of sodium contamination in the oxidation line water were traced to filter changes and a demineralizer change in the water line prior to the sodium analyses. The manipulation required to make these changes plus any residual sodium on the new filters contributed to an initially high sodium content in the water that took several days to be reduced. No filter changes were made at the other processing line and the fluctuation of sodium content in the water was less.

Chemicals.—The typical sodium content of some common reagents used in silicon device processing are presented in Table I. Each value represents the average of measurements on four different samples. Some of these reagents are repackaged from bulk containers into polyethylene containers. The Triton X-100 surfactant solution and unstabilized 30% hydrogen peroxide solution are very high in sodium contamination. Most of the reagents contain less than 500 ppb of sodium.

Sodium Contamination of Reagents from Glassware

Pyrex glass contains about 4 w/o (weight per cent) Na_2O or 7×10^{20} atoms of sodium/g of Pyrex glass (4). Pyrex dishware is often used to contain hot or boiling reagents used to clean silicon wafers. To investigate the effect of dishware on reagents, the sodium content of reagents contained in Pyrex and quartz beakers was measured. Pyrex and quartz beakers were degreased with trichloroethylene followed by methanol and water rinses. The beakers were then cleaned with boiling aqua regia for 10 min and overflow-rinsed with deionized water for 10 min. Mere specification of time of rinse and not flow rate is meaningless since flow rates may vary from process to process. Throughout this work the flow rate was set to yield 40 volume changes in a 10-min rinse time. The acid treatment of the beakers removes any surface sodium that is not due to sodium in the glass. The deionized water rinse removes any sodium left on the beakers from the aqua regia. Fifty milliliters of deionized water was placed in each of the two Pyrex and two quartz beakers just cleaned. After standing covered for 1 hr, the sodium in the water

Table I. Average value of sodium found in reagents

Reagent	Sodium, ppb
H_2O_2	995
0.5% Triton X-100*	412
H_2SO_4*	220
Methanol*	174
HNO_3	87
HF	19
HCl	15
NH_4OH*	7
Trichloroethylene*	~1
Acetone*	~1

* Not repackaged into polyethylene containers.

Table II. Amount of sodium found in identical solutions held in various containers

Volumetric flask	Reagent: Aqua regia	NH_4OH, H_2O_2, H_2O	HCl, H_2O_2, H_2O
Polypropylene			
Atoms of Na/ml	28×10^{13}	360×10^{13}	400×10^{13}
ppb Na	11	140	150
Pyrex			
Atoms of Na/ml	82×10^{13}	490×10^{13}	505×10^{13}
ppb Na	31	187	193
Quartz			
Atoms of Na/ml	33×10^{13}	360×10^{13}	400×10^{13}
ppb Na	13	140	150

leached from the Pyrex was 2.7 and 7.1 $\times 10^{13}$ atoms/ml whereas the quartz beakers yielded 0.34 and 0.39 $\times 10^{13}$ atoms of sodium/ml.

The results of similar tests with various chemicals substituted for the water at room temperature are presented in Table II. Tabulated is the amount of sodium present in the reagents. Ten milliliters of the reagent were placed in the clean beaker and after 25 min were diluted to 100 ml and the solution analyzed. In all cases the sodium content of the reagents was much higher when contained in the Pyrex glass.

The effect of heating the reagents on the amount of sodium leached from the Pyrex was ascertained by heating 75 ml of water for 15 min in a Pyrex beaker. After cooling 15 min, the amount of sodium in the water had increased to 66 $\times 10^{13}$ atoms/ml. Water that was allowed to stand 14 days in a covered Pyrex dish at room temperature had an additional 50 $\times 10^{13}$ atoms of sodium/ml. From this it may be concluded that special low-sodium reagents should not be used with Pyrex containers for them.

Sodium Contamination of Glassware from Reagents

It is possible that glassware may become contaminated with sodium found in the reagents. To investigate this, Pyrex dishes were treated with boiling aqua regia or NH_4OH, H_2O_2, H_2O (1:1:4 by volume) for 10 min each, and overflow-rinsed for various times with deionized water. At the end of the rinse, the desorption of sodium from the glass into the still water within a 15-min interval was analyzed. The amount of sodium attributable to the Pyrex after 1 min of rinsing after treatment with the acidic solution was 8 $\times 10^{13}$ atoms/ml. See Fig. 4. After five more minutes of overflow rinsing, the sodium in the water attributable to the Pyrex had fallen to 1.35 $\times 10^{12}$ atoms/ml. For the dish treated with the basic solution, after a total of 16 min of rinsing 9 $\times 10^{12}$ atoms of sodium/ml was contributed by the container walls. Only after another treatment of the dish with aqua regia and a 5-min deionized water rinse did the sodium level in the water reach 1.35 $\times 10^{12}$ atoms/ml. Quartz beakers generally rinsed clean after treatment with both reagents without the lag that was observed for the basic peroxide solution in Pyrex.

These results indicate that a Pyrex dish, after a basic peroxide treatment and water rinse, will retain more sodium than after an acid treatment. Therefore silicon slices should not be allowed to sit very long in rinse water after a basic peroxide treatment. If slices must stand for any length of time in water, then quartz or polyethylene dishware is recommended unless subsequent treatments in the cleaning process are used to desorb the accumulated sodium.

Sodium Contamination of Silicon from Reagents

Silicon wafers that had been treated with hot dilute HCl, rinsed with overflowing deionized water, and finally pulled out of a dilute HF solution in a hydrophobic condition, were then analyzed for surface sodium. This treatment generally reduced sodium contamination of the silicon surface below the detection limit of 3.6 $\times 10^{11}$ atoms/cm^2. Slices cleaned in this manner were then placed in solutions of differing *p*H and known sodium concentration, added to the solutions in the form of NaCl. After 10 min in the solution, the slice was pulled out, blown dry with filtered dry nitrogen, and analyzed immediately for sodium content. The results are presented in Fig. 5. As expected, sodium adsorption onto silicon was found to be proportional to the sodium concentration in solution. Adsorption is greatest in the 0.1*N* NH_4OH and least in the acidic solutions. Adsorption of sodium from water is seen to be slightly greater than from acid solution. Adsorption from 0.1*N* HF is approximately the same as from 0.1*N* HCl, indicating that sodium adsorption on a bare silicon surface is about the same as on a silicon surface containing a native oxide, at least in acidic solution. Extrapolation of the data in Fig. 5 suggests that the sodium content of reagents should be well below 0.1 ppm in order to have sodium contamination levels on a slice below 10^{11} atoms/cm^2 if no subsequent desorption occurs later in the process.

The effect of *p*H on sodium adsorption onto silicon is more clearly shown in Fig. 6 where the sodium content of silicon slice surfaces is plotted *vs.* the *p*H of the adsorbing solution at a constant ionic strength of 0.1 and a constant sodium concentration of 10 ppm. Adsorption increased exponentially with *p*H. Although it was not practical to obtain data beyond the *p*H range indicated due to the difficulty of obtaining reagents with a low residual-sodium content, the curve suggests that sodium adsorption can become substantial at higher *p*H's.

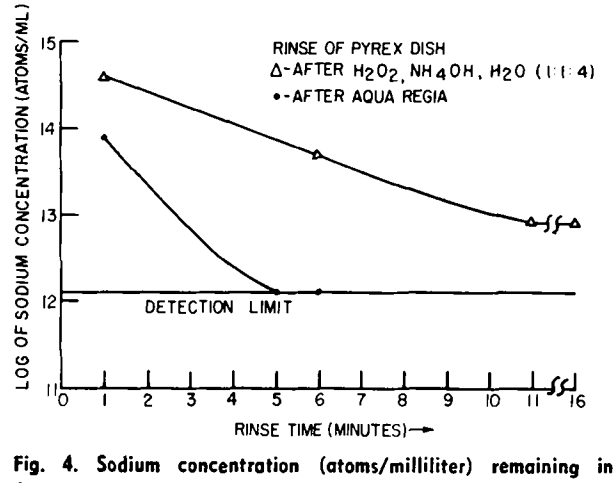

Fig. 4. Sodium concentration (atoms/milliliter) remaining in water.

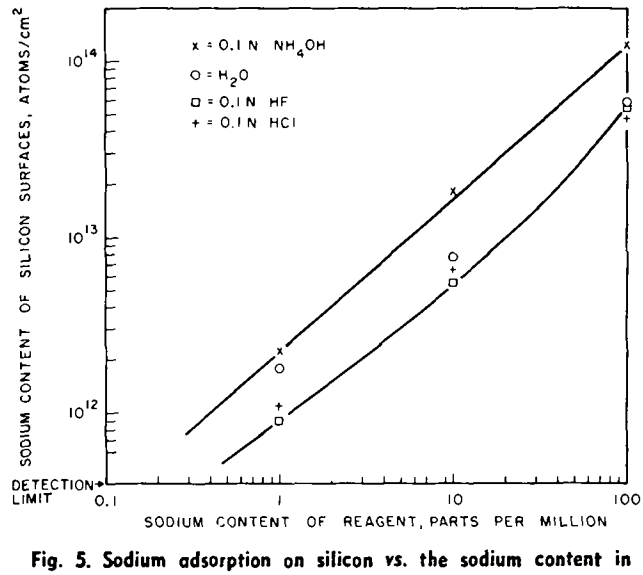

Fig. 5. Sodium adsorption on silicon *vs.* the sodium content in solution.

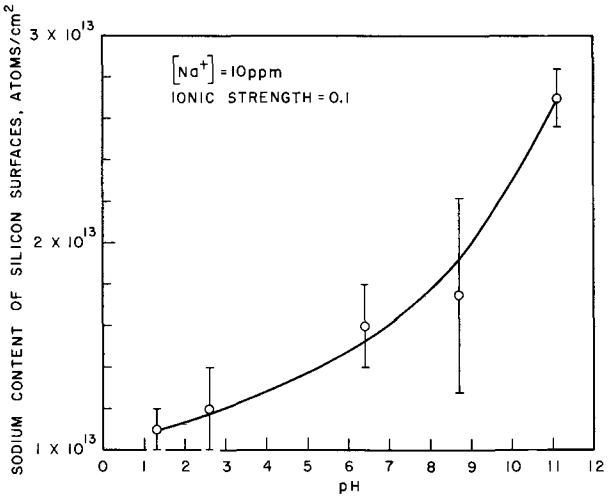

Fig. 6. Sodium adsorption on silicon vs. pH

Experiments were conducted to determine the efficiency of a deionized water rinse in removing sodium from slices. Slices were placed in a Fluoroware basket whose design allows for a laminar flow of water about the slice surface. For a surface sodium coverage of up to 3×10^{13} atoms of sodium/cm², the sodium on the slice surfaces was reduced to below the detection limit within 1 min of rinsing when the sodium was initially adsorbed onto the slice from neutral or acidic solutions. When sodium was adsorbed from a basic solution of 10% NH_4OH, the rate of removal was not so fast. It required several minutes rather than one minute to bring the sodium levels below the detection limit of 3.6×10^{11} atoms/cm². The rapid removal of sodium from slice surfaces suggests that most of the sodium is physically rather than chemically adsorbed. Increasing the *p*H increases the degree of dissociation of surface silanol groups ($\equiv Si-OH$) and thus the number of negatively charged $\equiv Si-O^-$ sites, thereby causing some sodium to become chemisorbed. This explains why it takes longer to remove sodium which was initially adsorbed from a more basic solution.

Sodium Contamination of Silicon-Dioxide-Covered Silicon Slices

Oxidized slices were checked to determine the influence of various chemicals on sodium contamination of their surfaces. A group of five slices was placed in a Fluoroware basket and rinsed for 5 min with overflowing deionized water. The slices were then treated with boiling aqua regia for 15 min and a slice immediately removed and placed in 2 ml of dilute HCl in a preleached polypropylene container and after 10 min the solution was analyzed for sodium. Then after 1.5, 3, 4.5, and 8 min of rinsing, slices were removed for analysis. See Fig. 7a. Initially 2.3×10^{13} atoms of sodium/cm² on the silicon dioxide were detected. After 8 min the sodium contamination was down to $4.7 \pm 3.3 \times 10^{11}$ atoms/cm². Slices treated with the acidic peroxide solution were rinsed of sodium in a similar manner. See Fig. 7b. Oxidized slices treated with the basic peroxide solution and checked for sodium as above did not reproducibly rinse free of acquired sodium on their surfaces. Plotted in Fig. 7c is the sodium content found on slices for two different trials. It appears that after a basic solution which has an initially high sodium content (probably greater than 480×10^{13} atoms of sodium/ml, the majority of which comes from the H_2O_2) a deionized water rinse is not sufficient to controllably remove the sodium from oxidized slices to as low a level as that observed after an acid treatment and water rinse.

A group of oxidized slices was treated with hot 0.01M NaOH (6×10^{18} atoms of sodium/ml) for 1 min, then treated with hot aqua regia for 10 min and finally overflow-rinsed with deionized water for 10

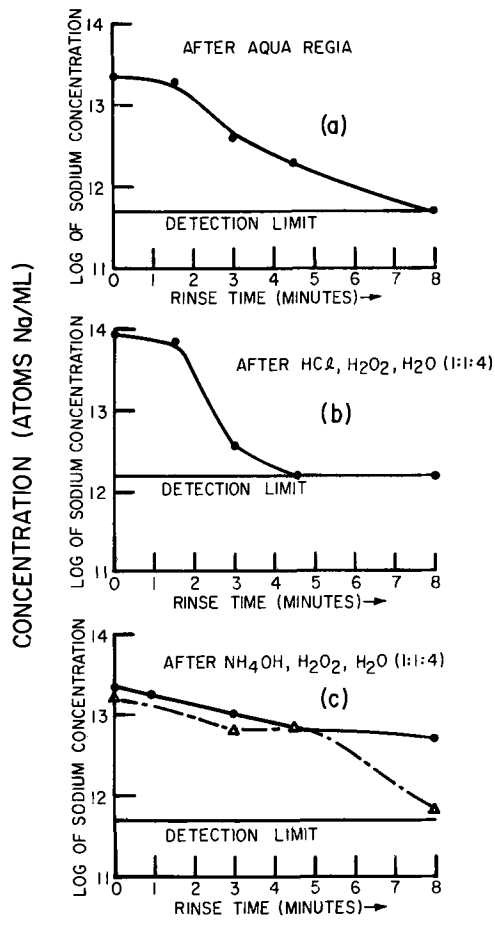

Fig. 7. Surface sodium concentration (atoms/milliliter) on oxidized silicon slices.

min. The sodium content of the first 400Å (taken to represent the surface) and the remaining bulk SiO_2 was not significantly different from the sodium content of the group of five slices not given the NaOH treatment (see Table III). It seems that an acid treatment is able to reduce sodium contamination of the surface from such a drastic treatment with NaOH. It is interesting to note that within experimental error the average bulk oxide sodium content was not affected.

Contamination of Silicon from Slice-Handling Tools

Since it was found that a high-purity water rinse is effective in removing adsorbed sodium, silicon cleaning processes that use this rinse as a final step should yield slices that are "sodium-free." That this is generally not the case is due to the fact that the slices must be handled after the water rinse.

Stainless steel vacuum chucks.—A group of four stainless steel vacuum chucks that were in routine use for handling of slices were checked for sodium contamination. See Table IV for the amount of sodium transferred from four different chucks into 15 ml samples of deionized water in 15 sec. This procedure is meant to simulate the actual practice of retrieving silicon slices from solution by submerging the chuck into the water in order to contact the slice. A simple deionized water rinse of the vacuum chuck for 30 sec prior to use reduced the amount of easily trans-

Table III. Sodium found on oxidized silicon slices treated with 0.01*N* NaOH

	Slices treated with 0.01*N* NaOH, then properly rinsed, atoms of Na	Control group, atoms of Na
Surface	$5.0 \pm 4.0 \times 10^{13}$/cm²	$4.9 \pm 4.4 \times 10^{13}$/cm²
Bulk	$1.6 \pm 2.3 \times 10^{17}$/cm³	$1.2 \pm 0.9 \times 10^{17}$/cm³

Table IV. Amount of sodium transferred from stainless steel vacuum chucks to 15 ml of deionized water in 15 sec

Chuck number	Atoms of Na $\times 10^{-14}$	% Increase of Na in water
1	0.44	13
2	3.22	91
3	16	460
4	20	570

ferrable sodium on its surface by a factor of 20. Touching the stainless steel vacuum chuck for 3 sec with three gloved fingers increased the sodium level by 310% while with ungloved fingers the increase was 4800%. Wiping dry a clean vacuum chuck with Twill-Jean cloth increased the sodium level by 300%. Similar results were obtained with stainless steel tweezers. If a dry vacuum chuck is necessary then a deionized water rinse and stream of dry filtered nitrogen gas just prior to use minimizes the amount of surface sodium ($<5 \times 10^{12}$ atoms of sodium transferred to 15 ml of water in 15 sec).

Spin dryer.—A standard procedure often found as a last step in slice cleaning just prior to loading oxidized silicon slices into a furnace is to spin dry them. To investigate the amount of sodium a slice might experience from the dryer, 2 ml of deionized water was placed on the anodized aluminum surface of a spinner that was in routine use and after 5 sec the water was removed with a polypropylene eyedropper. Appropriate controls of 2 ml of deionized water transferred with the eyedropper from one vial to another were run as a check of inadvertent sodium contamination. It was found that the sodium level was generally very high in the water (182 to 366 $\times 10^{13}$ atoms of sodium/ml for the two determinations). The amount of easily transferrable sodium on the anodized aluminum spinner was reduced after a dilute HCl and deionized water rinse to between 30 and 39 $\times 10^{13}$ atoms/ml. The HCl should not be spun off the surface of the spinner since it may damage the spinner mechanism of the dryer.

Five oxidized slices were treated with boiling HCl for 10 min and then given an overflow water rinse for 15 min (a treatment that reproducibly yields surface concentration of sodium near the detection limit of 3.6×10^{11} atoms/cm^2). The anodized aluminum spinner was wiped with a wet Twill-Jean cloth which raised the sodium concentration in the water on the spinner to 148×10^{13} atoms/ml. The five cleaned slices after spin drying had an average surface concentration of $38 \pm 30 \times 10^{11}$ atoms of sodium/cm^2. After a dilute HCl and water rinse the spinner surface yielded 6×10^{13} atoms of sodium/ml and five slices treated as before showed a surface concentration of $6.5 \pm 3.5 \times 10^{11}$ atoms of sodium/cm^2. Evidently a dirty spinner head can account for a large amount of surface contamination of the slices as well as a very large fluctuation in the amount of surface sodium from slice to slice.

Spinner heads that are ribbed so that the wet slice does not make full contact with the spinner surface and heads that are covered with an inert material such as Teflon would be an improvement over anodized aluminum. Such a spinner also in routine use had one-tenth as much sodium on its surface as did the aluminum head.

From this it can be concluded that metal spinner plates should be cleaned prior to use with dilute HCl and water to minimize sodium contamination of the slices. Spinner heads should be designed so that they are easily removed for cleaning prior to each use.

It should be made clear that the above cleaning procedures for slice-handling tools apply only for the removal of sodium. The stainless steel vacuum chucks and tweezers probably need a thorough degreasing to remove organic compounds that may be present on the surface. It should be recognized that other contaminants may be added to the silicon slice from the handling equipment, if they have not been previously removed.

Clean bench environment.—While most handling of silicon slices is done in vertical laminar flow hoods to minimize stray particle contamination, the possibility of sodium contamination of the slices during exposure to the filtered, partly recirculated air is possible. A 3.2-cm diameter polypropylene container with 20 ml of water was allowed to stand uncovered in such a hood for 5 min. Next to it a similar container of water stood covered. The sodium content of the uncovered water increased by $1.0 \pm 0.2 \times 10^{13}$ atoms/ml whereas no change was detected in the covered water. If a corresponding amount of sodium had adhered to the surface of a slice exposed to the ambient for 5 min, then $9.2 \pm 1.8 \times 10^{13}$ atoms of sodium/cm^2 would be measured as the average sodium concentration on the silicon surface. This indicates that slices even in a clean bench should be exposed to as little ambient as possible.

Rubber gloves.—A new pair of rubber gloves was put on with bare hands and rinsed in a stream of deionized water for 40 sec. The gloved index finger was dipped into 10 ml of water for 15 sec. The contamination attributable to the glove was 2×10^{13} atoms of sodium/ml. With three rinses of the glove in dilute HCl, a rinse in a stream of deionized water, and finally dry filtered N_2 gas to remove the water, the sodium contamination was down to 0.65×10^{13} atoms/ml or about one-third that of the uncleaned glove. All of these levels are high compared to the sodium levels attainable in properly treated dishes and on silicon slices. While rubber gloves are certainly better than bare hands, they should by no means be considered clean to the extent that they may contact chemical reagents, baskets, the working end of slice-handling equipment, or the interiors of containers used for critical sodium contamination reduction steps. Again, it should not be construed that rubber gloves need merely a dilute HCl rinse to be clean. The dilute HCl rinse removes easily transferrable sodium and not necessarily other contaminants.

Conclusions

Any handling or exposure to ambients increases the chance of sodium contamination of the silicon slice. Vacuum chucks used for handling slices should be rinsed at least with deionized water prior to use. Spin dryers of anodized aluminum have been shown to increase surface sodium content on silicon slices. Although a dilute HCl and water rinse will reduce sodium contamination, a better spinner head would be coated with an inert material such as Teflon and the head would be easily removable for cleaning with deionized water prior to each use.

Chemicals that come into contact with the silicon slice do not have to be especially low in sodium content. What is more important is that the high sodium content reagents be followed with an acidic solution for silicon-dioxide-covered slices. Then a water rinse is sufficient to reduce sodium contamination below 3.6×10^{11} atoms/cm^2. The solution of ammonium hydroxide, hydrogen peroxide, and water should not be used for sodium removal from oxidized silicon surfaces. It was not designed for sodium removal (5), and if sodium removal is desired, the basic peroxide solution should be followed by an acid treatment prior to final rinsing.

Either pulling a bare Si slice with an hydrophobic surface from dilute HF or spinning off water from an adequately rinsed (acidic solution plus overflow rinse) oxidized surface of silicon yields equally low levels of surface sodium contamination. This obtains provided the vacuum chuck and spinner head are clean, *i.e.*, rinsed free of easily transferrable sodium prior to use

and that recontamination is avoided by proper care in handling of them. Slices that must stand in water for any length of time prior to drying should not be contained in Pyrex dishes since sodium leaches out of the Pyrex. Quartz or Teflon dishes are viable alternatives. Low-sodium reagents should not be used with Pyrex and those reagents packaged in glass should either be used immediately or repackaged into clean polyethylene containers to minimize sodium pick-up from the glass.

Acknowledgment

The authors are pleased to thank J. R. Mathews for helpful discussions and encouragement during the course of this work.

Manuscript submitted Dec. 1, 1972; revised manuscript received March 5, 1973.

Any discussion of this paper will appear in a Discussion Section to be published in the June 1974 JOURNAL.

REFERENCES

1. B. Yurash and B. E. Deal, *This Journal*, **115**, 1191 (1968).
2. J. E. Barry, H. M. Donega, and T. E. Burgess, *ibid.*, **116**, 257 (1969).
3. R. Gabriels, *Anal. Chem.*, **42**, 1439 (1970).
4. "Kirk-Othmer Encyclopedia of Chemical Technology," 2nd edition, Vol. 10, p. 542, John Wiley & Sons, Inc., New York (1966).
5. W. Kern and D. A. Puotinen, *RCA Rev.*, **31**, 187 (1970).

Mass Spectra Analyses of Impurities and Ion Clusters in Amorphous and Crystalline Silicon Films

Charles Feldman

Applied Physics Laboratory, The Johns Hopkins University, Silver Spring, Maryland 20910

and Frank G. Satkiewicz

GCA Technology Division, Bedford, Massachusetts 01730

ABSTRACT

Vacuum-deposited amorphous and crystallized silicon films were studied by sputter-ion source mass spectrometry. Crystallization was carried out in both argon and vacuum environments. Positive impurity ions and polyatomic ions (clusters) were examined. Impurities which arose from the crucible, residual atmosphere, substrate, and structural components in the system are described. Films crystallized in the vacuum generally contained more impurities than those crystallized in an inert atmosphere. Cluster distributions or relative amount of Si_n^+ (n = 1-6) *vs.* m/e for amorphous and crystallized samples are essentially the same. However higher order cluster peaks ($n \geq 6$) appear to be slightly lower in amorphous samples. The relation between cluster distribution and atomic nearest neighbor environment is discussed.

The study and application of vacuum-deposited amorphous and crystalline silicon films has been severely handicapped by the lack of information available on their impurity content and atomic structure. The grain size and total amount of material in the sample are usually too small for detailed spectrograph, chemical, or structural diffraction analysis. Electron microprobe x-ray fluorescence analysis has limited sensitivity (<100 ppm) and activation analysis is only suitable for specific impurities (1). The problem is further complicated by the fact that silicon films, as normally deposited, are amorphous and the characterization of their structure is somewhat speculative (2). Their structure furthermore depends on preparation conditions (3).

The sputter-ion source mass spectrometer (sometimes termed the ion microprobe mass spectrometer), which has recently become available, has the potential of providing much of the required analytical information on impurity content, and perhaps structure, in the films (4, 5). In this paper, an analysis of amorphous and crystalline silicon films using this mass spectrometer will be described. As far as known, this is the first study of this nature ever carried out.

The mass spectrometer records positive ion spectra of single atomic species (*e.g.*, Si^+), polyatomic species or clusters[1] (*e.g.*, Si_4^+) as well as complexes (*e.g.*, SiO^+). The impurity spectra and the cluster spectra will be dealt with separately. The two types of spectra are related, however, in that the cluster distribution is altered by the presence of impurities.

Impurities in both the amorphous phase and the crystalline phase, which is obtained by heating the amorphous phase, will be described. Every impurity will not be discussed in detail here, but a table of sample preparation conditions (Table I) and the resulting major impurities (Tables II-IV) will enable the reader to infer the origin of a particular impurity.

Mass clustering, which represents groups of atoms that leave the surface of the solid together, was first observed by Honig in the vapor of Group IV elements (6). Honig reported that the cluster distribution showed departures from a smooth curve. Using a spark-source mass spectrometer, Chupakhin *et al.* (7) reported differences in cluster spectra when silicon crystals were heavily doped. Chupakhin has suggested that this cluster distribution is related to the parent structure. Baun *et al.* (8) have similarly reported differences in the carbon cluster distribution from amorphous and crystalline carbon.

In view of the reported sensitivities of the cluster distribution to atomic structure, cluster spectra from silicon films were examined in an attempt to observe differences between the amorphous and crystalline phases. While it is well known from x-ray diffraction studies that both amorphous and crystalline silicon are four-fold coordinated and have similar first atomic nearest neighbor environments (9), their cluster dis-

Key words: silicon films, mass analysis, amorphous semiconductors, impurities, ion clusters.

[1] These clusters, found in the vapor phase, should not be confused with the clusters or aggregates sometimes used to describe amorphous structure in the solid phase (2).

tributions may be different, due to the presence of dangling bonds, voids, low density, and differences in second and third nearest neighbors in the amorphous phase (2, 3, 10).

During the course of this study, the silicon cluster spectra from amorphous SiO and SiO_2 were examined and will be reported here for the first time. A brief report of this study was presented at The International Conference on Thin Films, 1972 (11).

Silicon Sample Preparation

The deposition of silicon was carried out in a 12-in. diameter vacuum chamber using either a stainless steel or a Pyrex bell jar. The bell jar and feedthrough ring employed a Viton gasket; all other seals employed copper gaskets. Water-cooling coils were used to maintain low temperatures in the Viton gaskets. In the interest of cleanliness, only supports absolutely necessary were in the chamber. The pumping system consisted of a fast mechanical pump (130 cfm), an oil diffusion pump (2400 liters/sec) using DC 705 oil, and a titanium getter pump (550 liters/sec). A zeolite trap was located between the mechanical pump and the diffusion pump, and a liquid nitrogen trap was located directly above the diffusion pump. The titanium getter pump, located just below the chamber and baffled from it, employed a liquid-nitrogen-cooled surface. Titanium was not deposited during the deposition. The system contained a residual gas analyzer which was used extensively during the study. Predeposition pressures of less than 5×10^{-9} Torr were obtained. The substrates were outgassed at about 500°C by quartz, tungsten-filament, halogen-filled lamps.

Water-cooled crucibles, of various materials, about 1½-in. internal diameter, were used. As the study progressed, the cooling of the evaporation source crucible was improved. The source crucible used in series 42 through 82 and series 89 consisted of a heavy copper crucible cooled by ¼-in. diameter copper tubing which was brazed with Cu-Ag eutectic. In series 52, the entire assembly was silver plated. In series 86, a similar design was employed, but the crucible was molybdenum with stainless steel tubing. The design was changed in series 96 to a stainless steel, internally cooled, double-wall construction with a molybdenum liner. Zone-refined, 500 ohm-cm, silicon contained in these crucibles was melted by a focused electron beam with a power between 1 and 2 kW. Care was taken not to allow molten silicon to contact the walls of the crucible.

Silicon films, as normally deposited on substrates held at temperatures less than 300°C, are amorphous and must be heated to develop their crystalline structure. This crystallization process is a function of both time and temperature. A minimum temperature of 700°C for 30 min is required to crystallize the samples (12). Temperatures greater than 700°C were used in this study to insure good crystal growth and for future reference for processing at higher temperatures. The higher crystallization temperature also increased the introduction of impurities. Heating was performed either in the vacuum chamber or in tube furnaces flowing with high-purity argon gas. The conditions under which the samples were deposited are listed in Table I.

Sputter-Ion Source Mass Spectrometer

The sputter-ion source mass spectrometer (13) employed a 10 keV argon ion beam which was generated in a duoplasmatron. The ion beam ejected from the target atomic and polyatomic fragments of which a fraction was ionized. The beam could be focused for maximum resolution in performing trace analyses in bulk materials, but in this study the beam was defocused to provide the appropriate sputtering rate and, more importantly, uniform sputtering from surface to depth. The uniform sputtering rate eliminated the need for crater geometry corrections.

The sputtered positive ions were directed to a double focusing mass spectrometer and were detected by an ion multiplier. A compensation electron emitting filament was used to overcome charge-up in the samples on insulating substrates. The filament temperature was kept as low as possible to avoid heating the sample and introducing impurities. The instrument has an "energy window" feature which provides a means of selecting ions in a narrow energy range, enhancing either the polyatomic spectrum (zero energy window) or the atomic spectrum (100 eV window). Thus in the energy distribution curve of the sputtered species, the intensity of the polyatomic peaks falls off more rapidly at higher energies (100 eV) than the monoatomic peaks (5). The use of the 100 eV window thus reduced interference from the polyatomic ions. The spectra were recorded on an x-y chart recorder.

Polyatomic Ion Cluster Spectra

A typical mass spectrum using zero-energy window is shown in Fig. 1. The silicon positive ion intensities and their isotopes ($^{28}Si^+$, $^{29}Si^+$, $^{30}Si^+$) for Si_1^+, $Si_2^+ \ldots Si_6^+$ can clearly be observed. The ion intensities were normalized according to

$$Si_n^+ = \frac{I_{Si_n^+}}{\Sigma I_{Si_n^+}} \qquad n = 1\text{-}6$$

where $I_{Si_n^+}$ is the recorded silicon ion current for a cluster containing n atoms. Plots of the normalized intensities in per cent for each ion cluster *vs.* the number of atoms in each cluster (or the cluster mass) are shown in Fig. 2-4. The points to be observed in these figures are the fall off as the clusters become large and the structure in each individual plot.

Figure 2 shows typical distributions for amorphous and crystalline films. As can be seen, there are only

Table I. Silicon film preparation conditions

Sample No.	Crucible	Deposition pressure (Torr)	Sub. temp, °C	Substrate	Rate (A/min)	Deposit time (min)	Bell jar	Post-treatment
42	Cu	1.3×10^{-6}	160	Silica	440	20	Pyrex	As deposited
52	Cu/Ag	2.5×10^{-7}	800	Silica	760	10	Pyrex	As deposited
63A	Cu	2.4×10^{-6}	200	Silica	1080	6	Pyrex	As deposited
63C	Cu	2.4×10^{-6}	200	Silica	1080	6	Pyrex	Vacuum, 850°C, 2 hr
63F	Cu	2.4×10^{-6}	200	Silica	1080	6	Pyrex	Vacuum, 975°C, 1 hr
77E	Cu	2.7×10^{-6}	−50	Silica	520	14	Pyrex	As deposited
82C	Cu	3.0×10^{-6}	160	Silica	210	20	S.S.*	As deposited
86F	Mo	7.9×10^{-7}	300	Silica	400	14	S.S.	As deposited
86E	Mo	7.9×10^{-7}	300	Tantalum	400	14	S.S.	As deposited
86B	Mo	7.9×10^{-7}	300	Silica	400	14	S.S.	Argon, 900°C, ½ hr
89A	Cu	2.0×10^{-6}	290	Silica	400	15	S.S.	Argon, 900°C, ½ hr
89B-1	Cu	2.0×10^{-6}	290	Suprasil	400	15	S.S.	As deposited
89B-2	Cu	2.0×10^{-6}	290	Suprasil	400	15	S.S.	Argon, 900°C, ½ hr
93C	Mo	5.2×10^{-6}	200	Silica	660	10	S.S.	As deposited

* Stainless steel Type 304.

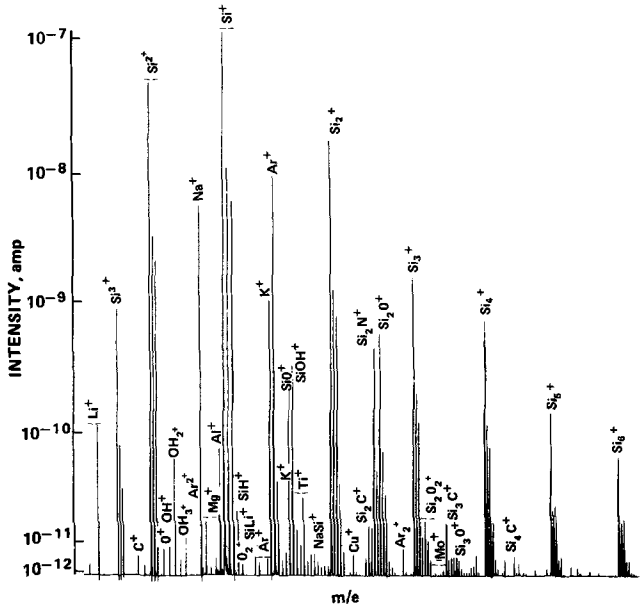

Fig. 1. Sputter-ion source mass spectra, 0 eV window, from silicon film No. 52.

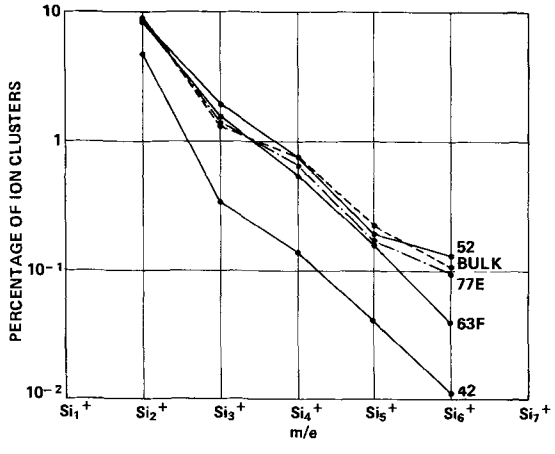

Fig. 2. Positive silicon ion cluster distribution in various samples (see Table I for information on samples).

small differences between the amorphous sample, 77E, deposited at a substrate temperature of −50°C, and a crystalline sample deposited at a substrate temperature of 800°C. Both samples have essentially the same cluster distribution as the bulk single crystal. For clusters greater than Si_2^+, the relative number of clusters in the amorphous sample (77E) remains less than those in the crystalline samples. However it is difficult to determine, at present, whether this slight deviation is significant. A deviation at Si_6^+ will be

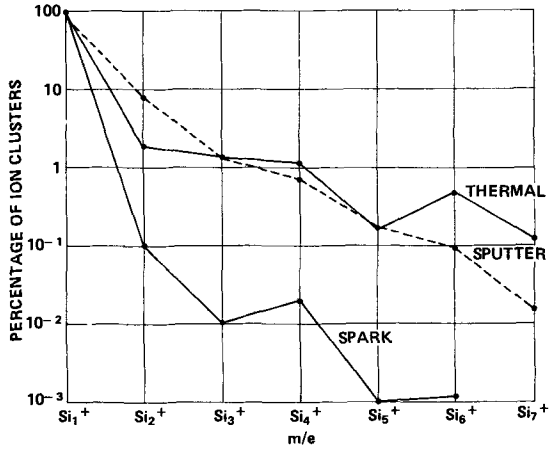

Fig. 3. Silicon ion cluster distribution from bulk samples. (a) Sputter-ion source, (b) thermal source [Honig (4)], and (c) vacuum spark source [Chupakhin (5)].

discussed in the next section. Differences in fall off and structure appear in samples 42 and 63F but this is believed due to the large amount of impurities present. Sample 42 contains 1.2% oxygen and 63F, 8.47% chromium. The impurity analyses of these samples are given in Table II.

The cluster distribution observed by Honig (6) for thermal sources and by Chupakhin (7) for vacuum spark sources, along with that obtained here, are shown in Fig. 3 for comparison. Note the characteristic Si_4^+ and Si_6^+ peaks in all these curves. The relative heights of the Si_4^+ and Si_6^+ peaks in the case of the sputter-ion source are lower than either the thermal or spark source. A change in bombarding ion mass could, however, change the sputter-ion source cluster distribution.

Cluster spectra from bulk fused SiO_2 (substrate), a deposited SiO film on fused silica, bulk crystalline SiC, and bulk crystalline Si for comparison, are shown in Fig. 4. Note the rapid fall off and lack of structure in SiO_2.

Discussion of Cluster Spectra

If one assumes that clusters represent groups of atoms ejected from the target in one piece, then their distribution should give an indication of the nearest neighbor environment in the material. This was pointed out in the beginning of the paper. In SiO_2, for example, there are ideally no Si-Si bonds and the clustering of Si atoms should be relatively small compared to pure silicon. This is observed in Fig. 4. There is no particular reason to expect a peak at Si_4^+ in SiO_2. The clusters that one observed in SiO_2 may be due to recombination on or near the surface or to a few Si-Si bonds that may exist. SiO, on the other hand, contains some fraction of Si-Si bonds and thus

Table II. Major impurities in silicon films (ppm)

(Zero energy window)

Species	Yield	Bulk	42	52	63A	63C	63F	77E	82C
Li	100	9	15	81	110	380	60	21	27
B	260	ND*	15	12	3.6	8.5	18	1.2	1.5
C	50	0.9	100	22	150	270	2,400	63	67
O	2.3	<200	12,000	<100	<200	<100	4,600	1,800	<100
Na	940	0.9	530	6	320	1,000	24	660	300
Mg	150	0.3	2,900	ND	9	33	250	24	15
Al	1,000	2	8	2	10	49	19	5	4
Cl	14	14	175	15	90	73	70	97	28
K	4,500	0.9	73	3	110	300	3	75	39
Cr	150	ND	<10 (I)†	1.8	6	72	84,000	120	<10(I)
Cu	8	21	39	54	2,000	200	950	140	70
Ag	15	7	55	81	110	64	I	74	19
Si	10	—	—	—	—	—	—	—	—

* ND = Not detected.
† I = Interference between peaks.

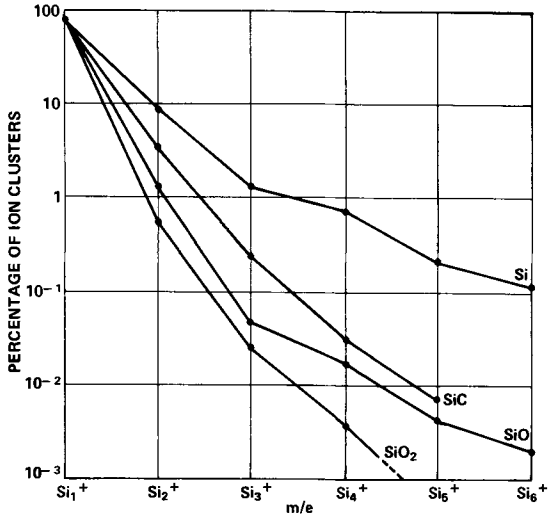

Fig. 4. Cluster distribution from solid silicon compounds

a higher percentage of clusters is obtained. Furthermore a peak appears at Si_4^+ in SiO samples.

The peak at Si_4^+ in silicon probably results from the large number of four-bonded nearest neighbors. If the number of nearest neighbors is changed, one would expect, by these arguments, a change in the cluster distribution. Baun *et al.* (8) have, in fact, observed large differences in cluster distribution between amorphous carbon, diamond, and graphite corresponding to changes in nearest neighbor structure. Similar unreported results on carbon have been observed with the sputter-ion source mass spectrometer at GCA. Impurities in silicon which serve to break the Si-Si bond should then alter the polyatomic ion distribution. This is observed in samples 42 and 63F in Fig. 2.

The similarity in cluster distribution between the amorphous and crystalline phase is thus a consequence of their similar nearest neighbor environments. The slight diminution of clusters, particularly the Si_6^+ peak in the sample deposited at low temperature, may be significant. Curves, not shown here, carried out to Si_8^+ confirm this diminution of higher order clusters in amorphous samples. The amorphous samples studied here are about 8% less dense than the corresponding crystallized samples (12). The diminution of the higher order cluster peaks may thus be due to the presence of voids or to changes in the second and third nearest atomic neighbor distances.

The influence of the defocused bombarding argon beam on film structure and consequently cluster distribution is believed to be small in view of the cluster changes observed in the carbon system and the cluster sensitivity to impurities in silicon.

Impurity Spectra

Analysis of the atomic impurity fraction (f_X^+) was obtained from spectra such as shown in Fig. 1, and spectra using the 100 eV window shown in Fig. 5. The absence of the polyatomic peaks is evident in Fig. 5 Quantitative data is obtained according to the following relation

$$f_X^+ = \frac{I_{X+}/Y_{X+}}{I_{X+}/Y_{X+} + I_{Y+}/Y_{Y+} \ldots I_{Z+}/Y_{Z+}}$$

where I_{X+}, I_{Y+}, and I_{Z+} represent the ion peaks of species X, Y, and Z, and Y_{X+}, Y_{Y+}, ... Y_{Z+} their respective sputter yields. In dealing with pure silicon, the following approximate relation was used

$$f_{X+} = \frac{I_{X+}\ Y_{Si+}}{I_{Si+}\ Y_{X+}}$$

where I_{Si+} and Y_{Si+} are the measured silicon peak ion current and yield, respectively.

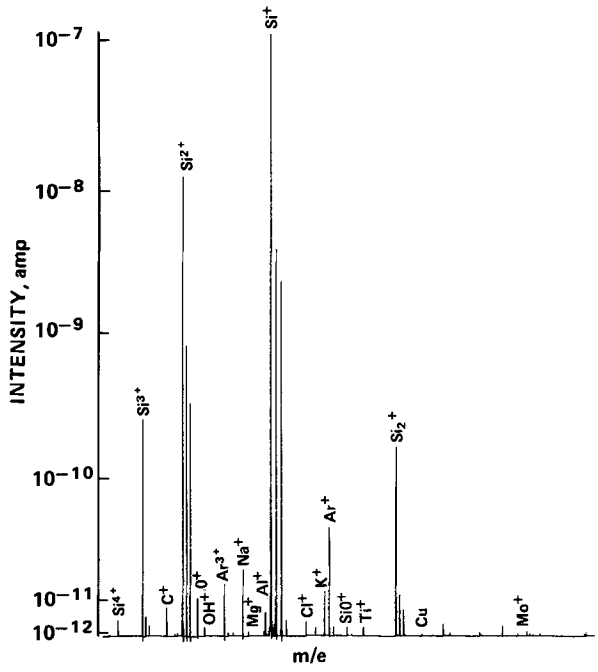

Fig. 5. Sputter-ion source mass spectra, 100 eV window, silicon film No. 93C.

A knowledge of the yields for each ion is thus necessary in order to obtain quantitative results. A specific calibration of impurity yields from the silicon matrix has not yet been made. Approximate yields based on prior work on elements and compounds (14) were therefore used in the present study. The yield figures, based on impurities being present in the oxidized state, are indicated in Tables II and III. Yields on a relative basis for 0 eV energy window are different in some cases from those for the 100 eV window. Comparison among samples does not, of course, depend on accurate yield values.

The impurities in representative silicon films are given in Tables II, III, and IV. The impurities present in quantities greater than approximately 1 ppm are listed. The spectrometer sensitivity to each impurity depends, of course, on the sputtering yields. The amount of oxygen present is probably the most questionable figure in the tables. Oxygen is present in the spectrometer background and in the substrates (SiO_2) as well as in the sample.

Discussion of Origins of Impurities

On comparing the data in Tables II, III, and IV with the fabrication conditions (Table I), one may infer the sources of impurities in the samples. In Table III, for example, the large quantity of tantalum and oxygen in sample 86E arose from the use of a tantalum substrate. The Ag and Cu impurities in sample 52

Table III. Major impurities in silicon films (ppm)

(Energy window 100 eV)

Species	Yield	86F	86E	86B	93C
Li	20	7	ND	100	150
B	260	ND	ND	ND	ND
C	50	150	75	100	30
O	2.3	<100	19,000	2,500	<100
F	6	400	100	ND	ND
Na	190	130	180	110	28
Mg	150	ND	14	ND	2
Al	330	4	6	20	4
Cl	14	50	<50	140	60
K	920	3	3	4	3
Ti	550	ND	ND	2	1
Cr	150	7	ND	5	ND
Mn	30	ND	ND	<1	ND
Fe	29	40	ND	ND	ND
Cu	8	8	ND	14	6
Ta	1	ND	19,000	ND	ND
Mo	30	<1	<1	<1	6
Si	10	—	—	—	—

Table IV. Influence of substrate on crystallized (fired) silicon films

Energy window 100 eV (impurities in ppm)

	Fused silica	Suprasil	Unfired 89B-1 (Sup)	Fired 89A (Sil)	Fired 89B-2 (Sup)
Li	34	ND	ND	7,000	ND
B	0.2	ND	ND	13	ND
C	200	10	30	700	30
O	—	—	<100	3,300	3,500
F	60	10	150	ND	ND
Na	4	1.5	90	180	80
Mg	3	0.3	2	35	0.6
Al	70	0.3	4	1,200	6
Cl	6	20	<6	20	ND
K	2	190	9	20	4
Ti	40	0.2	1	600	30
Cr	4	0.3	2	40	2
Mn	I ($AlSi^+$)*	1	ND	I ($AlSi^+$)	ND
Fe	I (Si_2^+)	10	ND	I (Si_2^+)	20
Cu	I (TiO^+)	10	60	I (TiO^+)	40

* I = Interference with the peaks.

came from the use of a silver-plated crucible. Samples 63C and 63F were heated at 850° and 975°C, respectively, in the vacuum and may be compared with the unheated film 63A. One sees that lithium, sodium, and potassium impurities were picked up at 850°C but were lost (re-evaporated) at 975°C. The carbon, oxygen, magnesium, chromium, and boron content increased, however, with firing temperatures. Chromium was present in extremely large quantities at 975°C and probably arose from the stainless steel supports, etc., in the system.

On examining samples 86F and 86B in Table III, it can be seen that lithium and oxygen were picked up in sample 86B during the firing in argon. There was little change in sodium or potassium content. In comparing series 63 and 86, one sees that firing in argon resulted, in general, in purer films than firing in vacuum. Somewhat more boron seemed to be present when the Pyrex bell jar was used than when the stainless steel one was used. The Pyrex bell jar was not water cooled and became warm during the vacuum heating. This may account for the large boron concentration in sample 63F. Na and K content appeared to be lower when the deposition was carried out on hot substrates as in sample 52. In all samples, the impurities introduced from the crucible material (Cu, Ag, Mo) were small and may, with proper precautions (*e.g.*, cooling as in series 89), be kept to a minimum (< 1 ppm). Since the titanium pump was not operated during the deposition, the small amount of Ti present may come from the substrate.

In order to ascertain the extent of the impurities introduced from fused silica substrates, depositions were made on "semiconductor" grade fused-silica[2] and Suprasil[3] fused-silica substrates. Results are shown in Table IV. Impurities listed in 89A and 89B-2 were those found close to the substrate. Impurity concentrations in the films and substrate were determined using yields listed in Table III. As can be seen from Table IV, Suprasil substrates introduced generally less impurities than the fused-silica substrate. The sample on fused silica contained very high quantities of Li, C, Al, and Ti, conforming to the higher quantity of these impurities in the substrate. Oxygen diffused in from both substrates.

Impurities that were occluded in the layer from the residual gases during deposition may be estimated in the usual fashion from the partial pressures of the residual gas during deposition and the deposition rate (15). The partial pressures during deposition of sample 89 are listed in Table V for those gases which may contribute O, C, and Cl impurities to the sample. Total hydrocarbons were estimated from the 43 ($C_3H_7^+$) peak (17). Note that the CO_2 partial pressure accounts

[2] Silica was obtained from U.S. Fused Quartz Company, Inc., Fairfield, New Jersey.
[3] Suprasil was obtained from Amersil, Inc., Hillside, New Jersey.

Table V. Residual gasses during deposition (Sample 89)

Gas	Mass	Partial pressure during deposition, Torr	ν molecules striking substrates, cm^{-2} sec^{-1}	$\frac{\nu_g}{\nu_{Si}} \times 100$
CH_4	16	1×10^{-7}	5×10^{14}	13
H_2O	18	9×10^{-9}	4×10^{13}	1.1
$CO + N_2$	28	5×10^{-7}	2×10^{15}	51
O_2	32	9×10^{-10}	3×10^{12}	0.086
HCl	36	2×10^{-9}	7×10^{12}	0.18
C_nH_m	43	6×10^{-9}	2×10^{12}	0.049
CO_2	44	1×10^{-6}	3×10^{15}	81
Si	—	—	4×10^{15}	—

for a large portion of the pressure increase from 5×10^{-9} to 2×10^{-6} Torr during deposition. The ratio of gas atoms (ν_g) striking the substrates per square centimeter/second to silicon atoms (ν_{Si}) being deposited per square centimeter/second is listed in the table. As can be seen, this ratio easily accounts for the O, C, and Cl impurities shown in sample 89B-1 (Table IV). The results indicate that the sticking coefficients for the residual gases at the substrate temperature of 290°C were small.

Ordinary laboratory dust contains 5% (weight) or more of O, Mg, Al, Si, C, and Fe; many other impurities are present in the 1-5% range such as Na, P, and Pb (13). If the sample is fired some of these impurities, in spite of precautions, may diffuse into the interior. Contaminants may also be picked up during handling and transferral from APL to GCA for the mass analysis. Some surface contaminants are removed during the initial sputtering process. Particles too large to be sputtered away contribute, however, to the film impurity analysis. The impurities quoted in this paper unless stated otherwise, were those found below the surface layer of the samples.

In summary, one may divide the major impurities found in the interior of the Si films into the following broad categories: (*i*) residual gas related: O, C, Cl, F; (*ii*) bell jar and system related: B, Cr; (*iii*) crucible related: Cu, C, Ag, Mo; (*iv*) substrate related: Li, B, C, Na, Mg, Al, Ti, Fe, Cu, O; and (*v*) tube furnace related: Li. Impurities in categories (*ii*), (*iv*), and (*v*) are found primarily in crystallized or fired samples.

Conclusions

Sputter-ion source mass spectrometry has provided a great deal of information on the nature of thin silicon films. Both the cluster spectra and the impurity spectra were useful in analyzing samples. There appeared to be little difference in the cluster distribution fall off or structure between amorphous and crystalline samples. This is believed due to the fact that the nearest neighbor environment in both phases was essentially the same. In order to determine possible effects of voids, dangling bonds, and more distant neighbors, cluster regions of Si_6^+ to Si_8^+ must be carefully examined using extremely pure samples. As in the case of the spark source, the sputter-ion source cluster distribution is sensitive to impurities.

The silicon cluster spectra of amorphous SiO and SiO_2 showed large differences in both fall off and structure. This suggests the possibility of distinguishing between SiO, SiO_x, and SiO_2 layers. This is a difficult task by other techniques.

The impurity spectra provided a great deal of information on techniques for fabricating pure silicon that may have only been suspected in the past. The purest films were fabricated at elevated temperatures (~500°C). This temperature limits the introduction of high vapor pressure impurities. Processing the films for annealing or crystallization purposes in the vacuum chamber at high temperatures (>700°C) brings about the introduction of impurities unless suitable precautions are taken, such as avoiding hot stainless steel supports. Crystallization of the films in an inert gas atmosphere in a fused silica tube furnace generally

appears preferable to vacuum heating. The use of ultra-pure fused silica substrates is important in limiting impurities in crystallized samples.

As a result of this study, vacuum-deposited silicon films on fused-silica substrates have been crystallized and doped n- or p-type in a standard diffusion furnace with considerable success. This work will be described in a subsequent report.

Acknowledgment

The authors wish to thank K. Hoggarth for his valuable aid in depositing the silicon samples. The project was supported by Naval Ordnance Systems Command Contract N00017-72-C-4401, Task A13B.

Manuscript submitted Nov. 10, 1972; revised manuscript received March 8, 1973.

Any discussion of this paper will appear in a Discussion Section to be published in the June 1974 JOURNAL.

REFERENCES

1. P. F. Kane and G. B. Larrabee, "Characterization of Semiconductor Materials," McGraw-Hill Book Co., New York (1970).
2. See, for example, D. Turnbull and D. E. Polk, *J. Non-Crystalline Solids*, **8-10**, 19 (1972).
3. N. J. Shevchik and W. Paul, *ibid.*, **8-10**, 381 (1972); D. Henderson and F. Herman, *ibid.*, **8-10**, 359 (1972).
4. A. J. Socha, *Surface Sci.*, **25**, 147 (1971).
5. H. J. Biebl and R. F. K. Herzog, *J. App. Phys.*, **34**, 2893 (1963); A. E. Barrington, R. F. K. Herzog, and W. O. Poschenrieder, "Progress in Nuclear Energy, Series IX, Analytical Chemistry 7," Pergamon Press, New York (1966); R. F. K. Herzog, W. P. Poschenrieder, W. P. Ruedenauer, and F. Satkiewicz, Proceedings of 15th Annual Conference Mass Spectrometry, Denver, Colorado, p. 306 (May 1967).
6. R. E. Honig, *J. Chem. Phys.*, **22**, 1610 (1954).
7. M. S. Chupakhin, *J. Analytical Chem., USSR*, **22-23**, 325 (1967).
8. W. L. Baun, F. N. Hodgson, and M. Desjardins, *J. Chem. Phys.*, **38**, 2787 (1963).
9. R. Grigorovici, *J. Non-Crystalline Solids*, **1**, 303 (1969).
10. S. C. Moss and J. F. Graczyk, *Phys. Rev. Letters*, **23**, 1167 (1969).
11. C. Feldman and F. G. Satkiewicz, *Thin Solid Films*, **12**, 217 (1972).
12. N. Blum and C. Feldman, *J. Non-Crystalline Solids*, **11**, 242 (1972).
13. GCA Ion Microprobe Solids Analytical Mass Spectrometer (IMS 101B).
14. F. G. Satkiewicz, Proceedings of 19th Annual Conference on Mass Spectrometry, Atlanta, Georgia, p. 276 (1971).
15. D. S. Allam, Proceedings of Symposium on Mass Spectrometry, Enfield College of Technology, England, p. 139, July 5, 1967.
16. R. D. Craig and E. H. Harden, *Vacuum*, **16**, 67 (1966).

Current Gain Mechanism in Arsenic Emitter Transistors

R. D. Lillard, J. L. Saltich, and C. E. Volk*

Motorola, Inc., Semiconductor Products Division, Phoenix, Arizona 85008

ABSTRACT

The effect of arsenic and arsenic-phosphorous mixed emitters on current gain in bipolar transistors is discussed. Experimental data for doping profiles and output admittance tests are correlated with emitter efficiency. It is conclusively shown that emitter efficiency is greater for arsenic-type devices, and that base recombination limits the gain when arsenic is used as the emitter dopant.

The use of arsenic as an emitter dopant in bipolar transistors has received considerable attention during the past year (1-3). The primary advantages of arsenic over phosphorus for emitter diffusions are the steeper doping gradient at the emitter-base junction and the absence of the "push ahead" or "emitter dip" effect. The published work on arsenic emitters during the past year has treated the diffusion characteristics of arsenic in silicon and the resulting improved high-frequency performance of arsenic emitter devices.

In the previous work, the limiting gain mechanism in an arsenic emitter bipolar transistor has been assumed to be emitter efficiency. Ghosh *et al.* (1) have demonstrated that the emitter efficiency is higher when arsenic is used as the emitter dopant. This paper will present data showing that the limiting gain mechanism in arsenic emitter structures is base region recombination, whereas for phosphorus emitter devices, emitter injection efficiency limits the gain. Moreover, the emitter efficiency increases as the concentration of arsenic increases in phosphorus-arsenic mixed emitters. Thus, as the concentration of arsenic increases, the emitter efficiency becomes greater and base recombination plays a more dominant role in limiting the transistor's current gain.

* Electrochemical Society Active Member.

Key words: output admittance test, lifetime, arsenic, phosphorus, dopant profiles.

Experimental

The emitter diffusions employed in this study were made from solid sources of arsenic, phosphorus, and arsenic-phosphorus mixtures to a depth of 1 μm. The doping profiles of these emitter diffusions were analyzed by the anodic oxidation technique with a NH_4NO_3-$OCH_2CH_2CHCH_2OH$ (tetrahydrofurfuryl alcohol) anodizing solution. The concentration of NH_4NO_3 was 3.34 g/liter. The thickness of oxide grown in this manner was determined from calibrated color charts. After oxide removal with HF, the resistivity was measured with a four-point resistivity bridge.

The depth-resistivity data were then analyzed with a computer program to obtain a concentration *vs.* depth profile. The computer program simply performs the calculation

$$\frac{d\,(\rho_s^{-1})}{dx} = N_x\,\mu_x\,q \qquad [1]$$

to find the concentration N_x at the depth x. In Eq. [1], ρ_s is the sheet resistivity, q is the electron charge, and μ_x is the electron mobility at the depth x. The mobility values used were from the compilation by Irvin (4).

The transistors used to study the limiting current gain mechanism of the various emitters were devices with emitter and base areas of 1.8×10^{-4} cm^2 (28 milli-in.^{2}) and 18×10^{-4} cm^2 (280 milli-in.^{2}), respec-

tively. The transistors were built on <111>, n^+ substrates with 10 μm of 3-5 ohm-cm epitaxially deposited silicon.

Two sets of transistors were fabricated. The first set had current gains of 30 and were used for the output admittance comparison discussed below. These transistors were fabricated with the same prebase-getter and base cycles. Emitters with varying arsenic-phosphorus concentrations were then diffused to a depth of 1.0μ from a solid source. Because the different emitters required varying temperature-time cycles to obtain a depth of 1.0 μm, the base depths and consequently the integrated base doping varied somewhat from transistor to transistor.

The second set of transistors were fabricated with arsenic and phosphorus emitters. With these transistors, the same prebase-getter cycle was employed. However, the base and emitter cycles were adjusted so as to obtain the same emitter depth, base width, and integrated base doping for the arsenic and phosphorus emitter devices. The final base and emitter depths were 3.5 and 1.8 μm, respectively. The current gains were 80 and 40 for the arsenic and phosphorus devices, respectively.

The recombination mechanism dominating the current gain in these transistors was determined using the output admittance test of George and Clark (5). Briefly, they found that for emitter efficiency limited devices

$$\left.\frac{\partial I_C}{\partial V_C}\right|_{I_B} = \left.\frac{\partial I_C}{\partial V_C}\right|_{V_{BE}} \qquad [2]$$

whereas for base recombination limited gain

$$\left.\frac{\partial I_C}{\partial V_C}\right|_{I_B} \approx 2\left.\frac{\partial I_C}{\partial V_C}\right|_{V_{BE}} \qquad [3]$$

These relationships enable the determination of the mechanism limiting current gain from simple curve-tracer measurements. The result of the experiments will now be discussed.

Results and Discussion

The doping profiles obtained for arsenic, phosphorus, and a 1P:3As mixed source are shown in Fig. 1. From these profiles, the grade constants at the junction were measured as 5.7×10^{22}, 2×10^{22}, and 3.6×10^{22} cm^{-4} for the arsenic, phosphorus, and mixed source, respectively. These values are lower than those of Ghosh *et al.* (1), who observed a value of 10^{24} cm^{-4} for a sealed ampoule arsenic diffusion, and a value of 2-3 $\times 10^{23}$ cm^{-4} for open-tube $POCl_3$ and PH_3 diffusions. The emitters studied by Ghosh, however, were 0.5 μm deep, whereas the emitters of this work are 1.0 μm deep. In fact, values comparable to those of Ghosh are observed in this laboratory for 0.5 μm diffusions. A very important result, shown in Fig. 1, is the variation of the grade constant with arsenic concentration. This makes possible the tailoring of the emitter profile for specific applications.

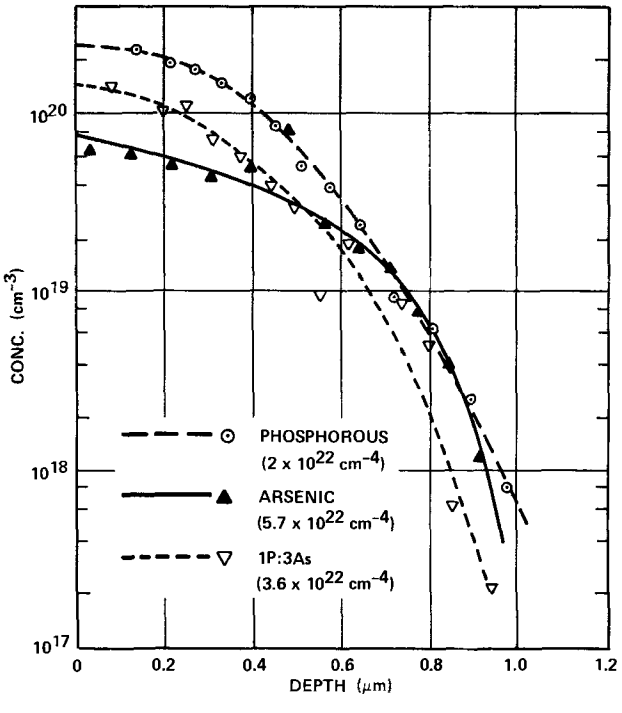

Fig. 1. Doping profiles obtained for diffusions from solid sources of arsenic, phosphorus, and a 1P:3As mixed source.

Table I. Comparison of transistors with mixed arsenic-phosphorous emitters

Emitter dopant	β_{d-c}	I_C(600 mV) [$\Rightarrow Q_b$] (μA)	ρ_e[$\Rightarrow Q_e$] (ohm/□)	g_{out}/I_B / g_{in}/V_{BE}
Phosphorus	30	44	10	1.0
1P:1As	30	40	12	1.5
1P:2As	30	36	13.5	1.65
1P:3As	30	32	15	1.87
As	30	28	20	2.0

Q_b, integrated base doping; β_{d-c}, peak d-c current gain; Q_e, integrated emitter doping; I_C(600 mV), collector current at V_{BE} = 600 mV.

The results of output admittance tests on transistors with various emitter dopants are tabulated in Table I, along with data for other important device parameters. The output admittance comparison and emitter sheet resistance are plotted in Fig. 2 as functions of the arsenic concentration in the emitter. From the figure, it is seen that the phosphorus device has an admittance ratio of 1 and is therefore (by the previously described test) emitter efficiency limited; the admittance ratio of the arsenic device is 2, implying base recombination limited gain. For mixed arsenic-phosphorus emitters, the ratio varies from 1 to 2 with increasing arsenic concentration. For these mixed emitters, base recombination becomes more dominant as the arsenic concentration is increased. Alternatively, one can say that emitter efficiency is increasing as the arsenic concentration is increased. In fact, increased emitter efficiency is necessary in order to realize the gain in the mixed emitter devices, because the integrated base doping is monotonically increasing as the arsenic concentration is increased. This increased emitter efficiency is occurring in spite of the lower net doping in the emitter as evidenced by the emitter sheet resistances.

To demonstrate the increased emitter efficiency of arsenic emitters, transistors were carefully processed to have identical base widths, identical integrated base

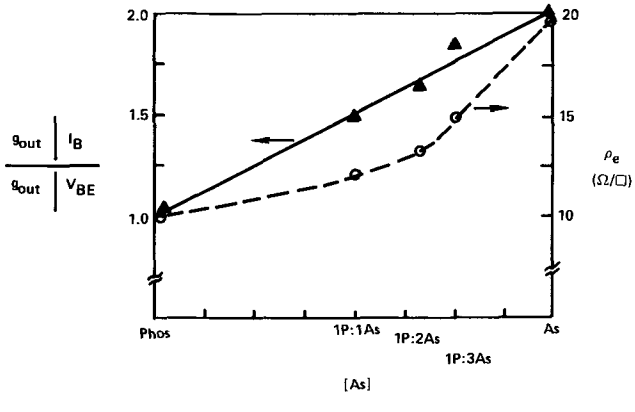

Fig. 2. Output admittance test and emitter sheet resistance as a function of arsenic concentration in mixed phosphorous-arsenic emitters.

Table II. Comparison of transistors with arsenic and phosphorus emitters

Parameter	Arsenic emitter	Phosphorus emitter
ρ_{sbe} [= > Q_b] sheet resistance of base under emitter	2350 ohm/□	2300 ohm/□
I_C (600 mV) [= > Q_b] collector current at V_{BE} = 600 mV	87 μA	84 μA
I_t (CB) [= > τ] forward biased collector base current at V_{BC} = 600 mV	1.60 mA	1.52 mA
β_{d-c} peak d-c gain	80	40
x_{je} emitter depth	1.83 μm	1.83 μm
W_B base width	1.80 μm	1.80 μm
g_{out}/I_B / g_{in}/V_{BE}	2	1

Q_b, integrated base doping; τ, minority carrier lifetime in collector.

doping, and comparable minority carrier lifetimes. Both arsenic and phosphorus emitter structures were fabricated. Some important device parameters are shown in Table II. The sheet resistance under the emitter, ρ_{sbe}, and the collector current at V_{BE} = 600 mV, I_C (600 mV), are identical for the arsenic and phosphorus devices. Series resistance effects are assumed negligible as I_C is increasing one decade for each 60 mV of applied V_{BE} from V_{BE} = 480 mV to V_{BE} = 660 mV. Both these results indicate that the integrated base doping is the same in each device. It should also be noted that the emitter depth and base widths are identical for these devices. Finally, the minority carrier lifetime is comparable for both devices, as can be inferred from the forward biased collector-base I-V data.

Equivalence of minority carrier lifetime in the emitter, base, and collector, is desirable when comparing the efficiency of different emitters in bipolar transistors. Consideration of gain controlling mechanisms implies identification of the various sources of base current. For an emitter efficiency limited device, the dominant mode of base current is the minority carriers injected into the emitter. Some of the factors important in determining the magnitude of minority carriers injected into the emitter are: (*i*) base doping, Q_B; (*ii*) emitter doping, Q_E; (*iii*) emitter-base profile; and (*iv*) minority carrier lifetime in the emitter. Thus, when comparing the effect of doping profile on emitter efficiency it is necessary to control all other parameters, such as Q_B, Q_E, and lifetime. Unfortunately, no techniques are available for directly measuring minority carrier lifetime in the emitter. The assumption has been made that collector lifetime and emitter lifetime will "track." That is, equivalent values for collector lifetime imply equivalent values for emitter minority carrier lifetime; of course, the absolute value of emitter lifetime is not known, but is much lower than the value for collector lifetime.

The significant difference between these devices is the high current gain, 80, exhibited by the arsenic emitter transistor. Because all other process parameters are identical for these devices, it is evident that the increased gain of the arsenic transistor is a direct result of increased emitter efficiency.

The arsenic emitter devices, however, are base recombination limited, as shown above. Therefore, the emitter efficiency of the arsenic emitter device has increased to such an extent that base recombination limits the gain. In the phosphorus emitter transistor, with the same base width and minority carrier lifetime, emitter efficiency limits the gain.

Increased emitter efficiency with arsenic emitters has been suggested several times in the literature (1, 2), but has not been demonstrated. These results demonstrate that emitter efficiency is greater for arsenic emitter devices, and that base recombination limits the gain when arsenic is used as the emitter dopant.

Summary

Small-signal bipolar transistors have been fabricated using arsenic, phosphorus, and mixed arsenic-phosphorus solid sources for the emitter dopant. The emitter profiles, emitter efficiency, and current gain mechanism were studied in these structures. The results are as follows.

Dopant profiles.—The grade constants for phosphorus, arsenic, and 1P:3As sources were 2×10^{22}, 5.7×10^{22}, and 3.6×10^{22} cm^{-4}, respectively. The grade constant increases as the arsenic concentration is increased.

Emitter efficiency.—The emitter efficiency increases as the concentration of arsenic in the emitter is increased.

Current gain mechanism.—Transistors fabricated with phosphorus emitters are emitter efficiency limited, whereas arsenic emitter devices are base recombination limited. For mixed arsenic-phosphorus emitter devices, base recombination becomes more dominant as the arsenic concentration is increased.

Acknowledgments

The authors wish to thank R. E. Hunt, R. P. Arnold, and W. L. George for their suggestions and stimulating discussions.

This work was supported in part by the Electronic Systems Division, Air Force Systems Command. Contract No. F19628-71-C-0157-P00001.

Manuscript submitted Dec. 11, 1972; revised manuscript received March 16, 1973. This was Paper 263 presented at the Miami Beach, Florida, Meeting of the Society, Oct. 8-13, 1972.

Any discussion of this paper will appear in a Discussion Section to be published in the June 1974 JOURNAL.

REFERENCES

1. H. N. Ghosh, A. S. Oberai, J. J. Chang, and M. B. Vora, *IBM J. Res. Develop.*, **15**, 472 (1971).
2. J. A. Archer, *Solid-State Elecron.*, **15**, 249 (1972).
3. Y. Nakajima, S. Ohkawa, and T. Fukano, *Fujitsu Sci. Tech. J.*, **8**, 93 (1972).
4. J. C. Irvin, *Bell System Tech. J.*, **41**, 387 (1962).
5. W. George and L. Clark, *IEEE Trans. Nucl. Sci.*, **NS-18**, 387 (1971).

Experimental Approach to the Quantitative Determination of Dopant Segregation During Crystal Growth on a Microscale: Ga Doped Ge

A. F. Witt,* M. Lichtensteiger, and H. C. Gatos*

Department of Metallurgy and Materials Science and Center for Materials Science and Engineering, Massachusetts Institute of Technology, Cambridge, Massachusetts 02139

ABSTRACT

An experimental approach was developed combining differential etching, rate striations, and spreading resistance measurements. This approach permitted the direct determination of dopant concentrations and growth rates on a microscale in gallium-doped germanium. Compositional inhomogeneities as revealed by differential etching were quantitatively related to dopant concentration variations. Rotational striations were identified as dopant concentration maxima associated with decreasing growth rates. Dopant concentration variations up to 50% were found within rotational cycles. The experimental results were subjected to a Burton, Prim, and Slichter analysis on a microscale. It was found that steady-state segregation is encountered only during increasing growth rates within each rotational cycle; the dependence of dopant segregation on growth rate became weaker in the presence of remelting. In all instances the effective diffusion layer thickness was smaller than that computed on the basis of the Cochran analysis.

Compositional inhomogeneities are encountered in virtually all solids and are the result of nonsteady-state conditions prevailing during growth from the melt, solution, or vapor phase. Thus the effective segregation of solute elements (dopants) is a complex function of experimental growth parameters. Dopant inhomogeneities have been intensively investigated (1) because of their adverse effects on materials properties and also because they reflect the conditions at the growth interface, and thus, can be used to study growth and segregation phenomena. However, both the nature and origin of dopant inhomogeneities have been the subject of controversial interpretations (2) primarily because the experimental methods available for their investigation have been limited in sensitivity and/or resolution. The use of various etching techniques has led to the identification of several types of impurity inhomogeneities (3) (striations), but the lack of quantitative correlations between etching rates and dopant concentration has limited the value of these investigations. The recently developed method of introducing rate striations permitted the determination of the microscopic growth behavior and established unambiguously the origin of certain compositional inhomogeneities (4). However, this method, based on high resolution etching, could not establish quantitative cause and effect relationships regarding compositional inhomogeneities.

The present investigation is concerned with the development of an experimental approach which permits simultaneously the quantitative determination of dopant inhomogeneities and the corresponding growth rates on a microscale by combining the rate striation technique with spreading resistance measurements (5). This approach is applied to the study of the segregation behavior of gallium in germanium grown by the Czochralski technique. The results are analyzed on the basis of the Burton, Prim, and Slichter (BPS) theory (6) on effective dopant segregation.

Experimental Procedure

Crystal growth.—The crystal used for the present investigation was grown in the <111> direction by the Czochralski method from a melt charge of 73g Ge doped with Ga (9.8×10^{19}/cm^3) at pulling rates of 7.6 and 3.0 cm/hr, with and without seed rotation. Rate striations (4) were introduced during growth by transmitting current pulses (20 A/cm^2) of 0.03 sec duration across the crystal-melt interface at a repetition rate of 0.5 sec (current direction melt to crystal). The crystal sections analyzed were 2 mm thick slices obtained by cutting the crystal along the axis of rotation (see sketch in Fig. 1).

Spreading resistance measurements.—The spreading resistance associated with a metal-semiconductor point contact has been extensively investigated (5). It has been shown that the point contact resistance for lapped germanium surfaces of moderate resistivities is predominantly given by its spreading resistance with an insignificant contribution from surface resistance due to a potential barrier. Accordingly, measurements of spreading resistance, R_s, can be used to obtain local values of resistivity. The local resistivity, ρ, of a volume element of approximately 10^{-9}/cm^3 associated with the point contact of an effective diameter, D, is given by $\rho = 2DR_s$ for a large sample with a large second ohmic contact at a relatively long distance (other side of specimen). In practice it is found that D is a complex function of several parameters and cannot readily be determined. However, R_s can be converted to ρ through calibration based on samples of known resistivity.

The apparatus (commercially available) used in the present investigation is equipped with an air-operated probe descent mechanism which gives reproducible point contacts with the specimen mounted on a traversing stage. The spreading resistance was determined by measuring the current flow through the point contact at an applied constant voltage of 10 mV.

All spreading resistance measurements were performed with the single point configuration, referred to above, on samples soldered onto a backing plate with an indium-tin alloy (large ohmic contact). Calibration of spreading resistance *vs.* carrier concentration was obtained from two gallium-doped germanium samples which exhibited the best dopant homogeneity (see nonrotated segment of curve b in Fig. 2). The resistivity and carrier concentration of the sections with the most uniform spreading resistance ($\Delta R_s < \pm 3\%$) were determined with Hall effect measurements at room temperature in the Van der Pauw configuration. The values obtained (Table I) are in excellent

* Electrochemical Society Active Member.
Key words: dopant segregation, spreading resistance, growth rates.

Table I. Spreading resistance calibration data

Spreading resistance, R_s [ohm]	Resistivity $\times 10^{-3}$, ρ [ohm · cm]	Carrier concentration, N [cm^{-3}]	Calculated mobility, μ [cm^2 V^{-1} sec^{-1}]
4.50	13.05	8.54×10^{17}	563
1.96	2.18	1.43×10^{19}	201

agreement with earlier published results of ρ as a function of carrier concentration (7).

Surface preparation.—In view of the observed sensitivity of spreading resistance on surface preparation, several procedures were investigated. It was found that measurements on Ge surfaces prepared by "chemical lapping" with Lustrox and Syton on Polytex pads are reproducible to better than ±1%. However, since chemically polished surfaces do not reveal dopant inhomogeneities and rate striations, differential etching procedures were studied. It was observed that spreading resistance data obtained on differentially etched surfaces are completely reproducible and in quantitative agreement with measurements on chemically polished surfaces. Thus, compositional inhomogeneities, microscopic growth rates, and carrier concentrations could be determined directly on the identical surface.

The adopted surface preparation procedure was as follows: The cut Ge slices were lapped with 10 μm Al_2O_3 abrasive and subsequently polished unidirectionally with Linde "A" and Linde "B" abrasive (0.03μ). After removal from the polishing block, the samples were transferred into distilled H_2O and while still wet were subjected to etching (10 sec) in a solution of 1 part H_2O_2, 1 part HF, and 1 part CH_3COOH. After drying the etched specimens were soldered with an In-Sn alloy onto brass support blocks.

Experimental Results and Discussion

The photomicrograph in Fig. 1 (obtained with interference contrast) shows a part of the etched "off-core" region of a germanium crystal (see sketch in Fig. 1). The following features can be distinguished: (*a*) rotational striations (3) propagating from top to bottom (from the center to the periphery in the crystal with a spacing of about 0.023 cm), (*b*) rate striations, faint dark lines, introduced during growth by Peltier cooling at time intervals of 0.5 sec, and (c) equally spaced (10 μm), impact traces of the spreading resistance probe (bottom of microphotograph).

The part of the crystal shown (0.068 cm long) was pulled at a rate of 21.2 μm/sec (7.6 cm/hr) with seed-rotation (6.16 rpm). The actual growth rate and its variations, as obtained from the spacing of the rate striations with a time resolution of 0.5 sec, is shown in curve a. It is seen that the average growth rate was 26 μm/sec; the difference between the pulling and the average growth rate (in the absence of remelting) reflects the continuous lowering of the melt level at a rate of 4.8 μm/sec. During each rotational cycle the growth rate varies continuously and reaches maximum and minimum values of about 39 and 15 μm/sec, respectively. The growth rate changes are somewhat irregular and do not exhibit the generally assumed sinusoidal behavior observed in InSb crystals (3).

It is of interest to note that the rotational striations do not coincide with the location of the three growth rate minima; rather they appear under conditions of decelerating growth rate and precede the actual rate minima. It can also be seen that irregularities of the microscopic growth rate in the vicinity of their minima are not reflected as compositional inhomogeneities. The carrier concentration (Ga concentration) and its variations is recorded in curve b with a linear resolution of 10 μm obtained from spreading resistance measurements (probe impact traces are seen on the

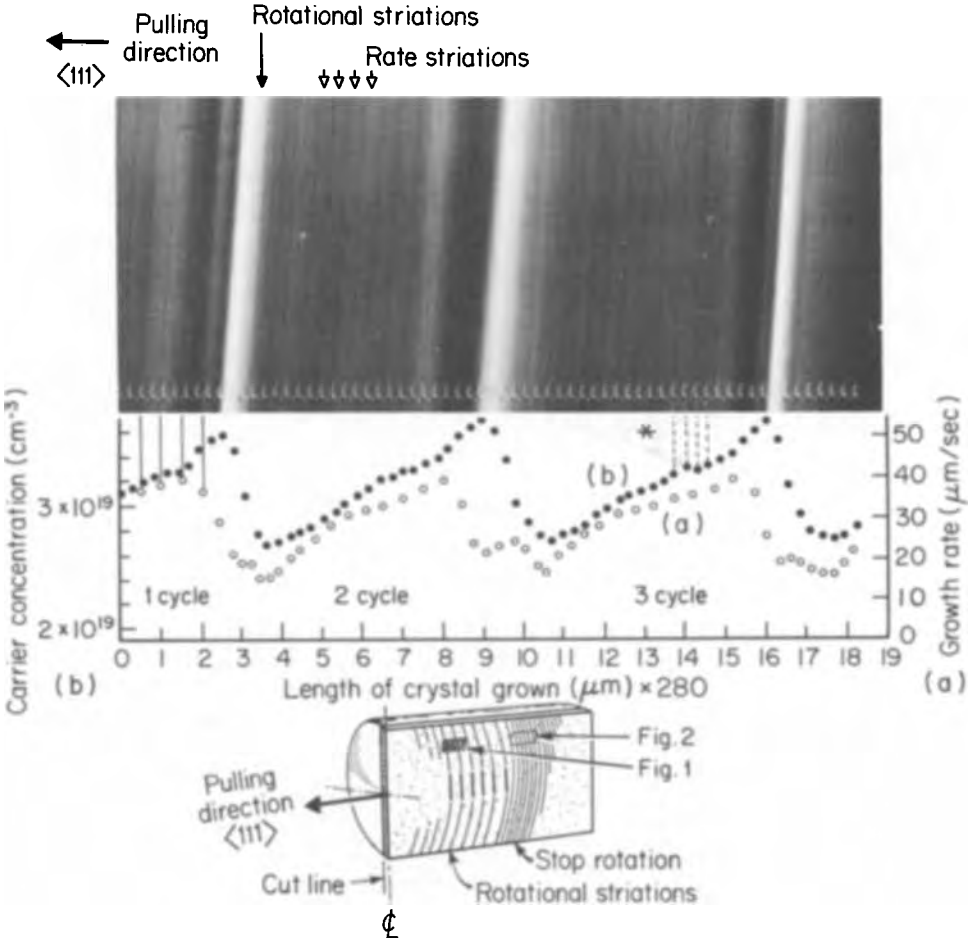

Fig. 1. Differentially etched segment of gallium-doped germanium single crystal pulled with seed rotation and dopant distribution analysis: curve (a) microscopic growth rates as obtained from the spacings of rate striations introduced at 0.5 sec intervals, curve (b) carrier (dopant) distribution as obtained from spreading resistance measurements at spacings of 10 μm. The location of the depicted crystal segment is shown on the sketch. (Magnification 98X.)

photomicrograph). It can be seen that segregation on a microscale undergoes continuous changes with the average dopant concentration of $3.1 \times 10^{19}/cm^3$ fluctuating between 2.6 and $3.7 \times 10^{19}/cm^3$. Curve b, together with the photomicrograph, gives the first confirmation of the generally assumed direct correspondence between topographic features resulting from etching and dopant concentration on a microscale. Abrupt compositional fluctuations as low as about 2% (to the left of the center of the rotational striations) can be unambiguously detected on the photomicrograph; on the other hand, the gradual compositional changes between successive rotational striations are not revealed by interference contrast. It is important to point out that the rotational striations (as revealed by etching) are pronounced dopant concentration maxima. Thus, earlier reports for example on InSb (4a), which attributed rotational striations to compositional minima coinciding with growth rate minima, cannot be generalized.

The outstanding feature of the present approach lies in the inherent superposition of curves a and b: dopant concentration data, together with the precisely corresponding microscopic growth rates, permit now the experimental investigation of the growth rate dependence of segregation on a microscale.

As seen from curves a and b, the generally assumed dependence of segregation on growth rate is observed only in the segments of "increasing" growth rates with each rotational cycle. The dopant concentration continues to increase beyond the growth rate maxima and reaches pronounced peak values (rotational striations) under steadily decreasing growth rates. Segregation minima on the other hand, coincide in all instances with growth rate minima.

The growth and segregation behavior of another segment of the same crystal (see sketch in Fig. 1) pulled at a rate of 8.5 μm/sec (3.0 cm/hr) is shown in Fig. 2. The left part of this crystal segment was pulled with seed rotation (6.2 rpm) whereas the right part was pulled without seed rotation. The growth rate data (curve a) reveal a pronounced effect of rotation at this reduced pulling rate. Because of extensive remelting, the average microscopic growth rate in the rotated segment increased to about 30 μm/sec and thus became larger, by a factor of 3.5, than the pulling rate. This rate is higher than that in Fig. 1 although the pulling rate was here reduced by a factor greater than two. The spreading resistance measurements at spacings of 5 μm (curve b) indicate an average carrier concentration of $3.4 \times 10^{19}/cm^3$ ranging from 2.9 to $3.7 \times 10^{19}/cm^3$. The rotational "remelt" striations are readily identified as abrupt transitions of high to low dopant concentrations confirming the conclusions of earlier qualitative studies (4a). Comparing the effective segregation behavior in Fig. 1 and 2 it is seen that its growth rate dependence in the presence of remelting is noticeably decreased.

The average growth rate in the nonrotated segment is 9 μm/sec and, thus, less than expected from the applied pulling rate and the corresponding lowering of the melt level. This discrepancy is attributed to a gradual relocation of the crystal melt interface resulting from the changes in thermal conditions associated with the arrest of seed rotation.

Analysis of Segregation Behavior on the Microscale

The following analysis of microsegregation associated with rotational crystal pulling should be considered as preliminary and is primarily intended to demonstrate the potential of the present approach; *i.e.*, no special attempt was made to grow the crystals at any particular doping levels, nor were the experimental growth conditions varied in any systematic way.

Nonequilibrium segregation has been the subject of several theoretical treatments (6, 8) among which that by Burton, Prim, and Slichter has been applied with partial success to actual growth systems (9). Discrepancies between theory and experiment (tested on a macroscale) have not been as yet resolved since some of the experimental parameters could not be determined with the required accuracy. Thus, in all reported investigations the segregation controlling microscopic growth rate has been equated with the macroscopic growth rate; as was recently shown, the two rates may differ by a factor of up to 30 or more (4).

To carry out an analysis of microsegregation according to the BPS theory, it is necessary to obtain the effective segregation coefficients ($k_{eff} = C_S/C_L$). Since the exact dopant concentration in the melt (C_L) for the segments presently investigated was not known, the linear growth rate dependence of k_{eff} (and thus of C_S), indicated in the BPS theory for small growth rates under steady-state growth conditions, was used for its determination. The growth rate dependence of C_S for the third rotational cycle in Fig. 1 (curve a) is plotted in Fig. 3. The expected linear rate depen-

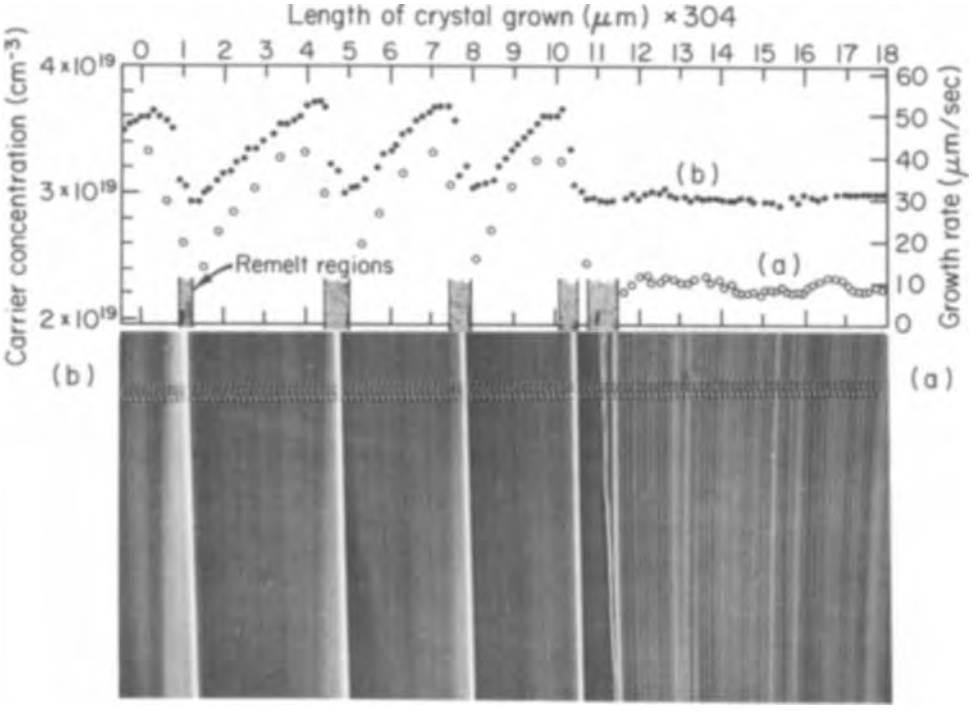

Fig. 2. Differentially etched segment of gallium-doped germanium single crystal pulled with seed rotation (left part) and without seed rotation (right part) and dopant distribution analysis. Curve (a) growth rates as obtained from the spacings of the rate striations introduced at 0.5 sec intervals. Growth rate analysis could not be carried out in the immediate vicinity of the remelt striations (remelt regions). Curve (b) carrier (dopant) distribution as obtained from spreading resistance measurements at spacings of 5 μm. The location of the depicted crystal segment is given in the sketch in Fig. 1. (Magnification 90X)

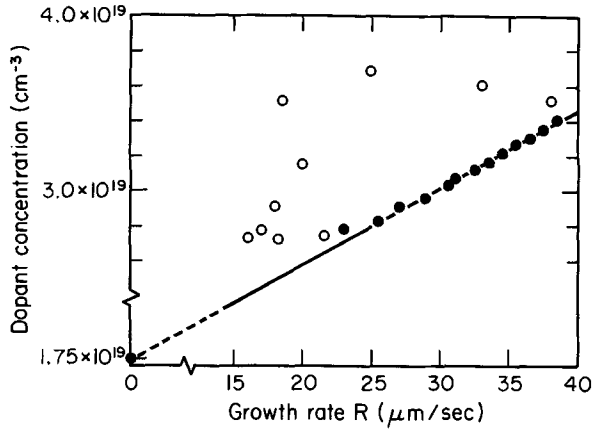

Fig. 3. Growth rate dependence of dopant concentration for the third rotational cycle of crystal segment in Fig. 1. ● dopant concentrations associated with increasing growth rates; ○ dopant concentrations associated with decreasing growth rates. Note that the linear dependence is observed only for the segment of the rotational cycle with increasing growth rates.

dence is observed only in the segment of steadily increasing growth rate. The segregation behavior in the segment of decreasing growth rate cannot at present be explained. Assuming that the linear portion in Fig. 3 reflects steady-state segregation the extrapolated value of C_{S_0}, at zero growth rate, is found to be $1.75 \times 10^{19}/cm^3$. Taking the generally accepted value for the equilibrium segregation coefficient of Ga in Ge (10) ($k_0 = C_{S_0}/C_L = 0.087$), C_L was found to be 1.97×10^{20}. This value of C_L agrees reasonably well (within about 20%) with that computed for directional solidification of 30% of the melt at an average rate of 20 μm/sec (assuming a boundary layer thickness of 0.04 cm).

To test the applicability of the BPS theory, the relationship

$$k_{eff} = \frac{k_0}{k_0 + (1 - k_0)e^{-\delta R/D}} \qquad [1]$$

is converted to the convenient form

$$\ln\left(\frac{1}{k_{eff}} - 1\right) = \ln\left(\frac{1}{k_0} - 1\right) - \frac{R\delta}{D} \qquad [2]$$

where R is the growth rate, δ the thickness of the "diffusion layer," and D the diffusion coefficient of gallium in germanium, 1.9×10^{-4} cm²/sec.

A plot of $\ln(1/k_{eff} - 1)$ against the microscopic growth rate for the third rotational cycle of Fig. 1 is shown in Fig. 4. It is seen that dopant segregation with constant "effective diffusion layer thickness" (δ/D = 180 sec/cm) takes place only during the segment of increasing microscopic growth rate within the rotational cycle. The diffusion layer thickness thus computed is 0.0342 cm. The value of δ obtained for the applied rotational rate from Cochran's analysis (11)

$$\delta = 1.8\, AD^{1/3}\nu^{1/6}\omega^{-1/2} = 0.0412 \text{ cm} \qquad [3]$$

where $A = 0.87$ (11), $\nu = 0.0025$ cgs units (11), $\omega = 0.645$ sec^{-1}.

The microsegregation behavior in the presence of "remelting" during rotation (Fig. 2) is analyzed in Fig. 5. It is seen that the "effective diffusion layer thickness" (δ/D = 90 sec/cm; δ = 0.017 cm) remains constant for all three cycles. A comparison with the segregation behavior in Fig. 1 shows that "back melting" (a result of the decreased pulling rate) leads to a reduction of the diffusion layer thickness by a factor of two and thus to a significantly weaker dependence of dopant segregation on growth rate. It is also of interest to note that the dopant concentration associated with the growth rate minima ($2.9 \times 10^{19}/cm^3$) is virtually identical with that observed for nonrotational pulling.

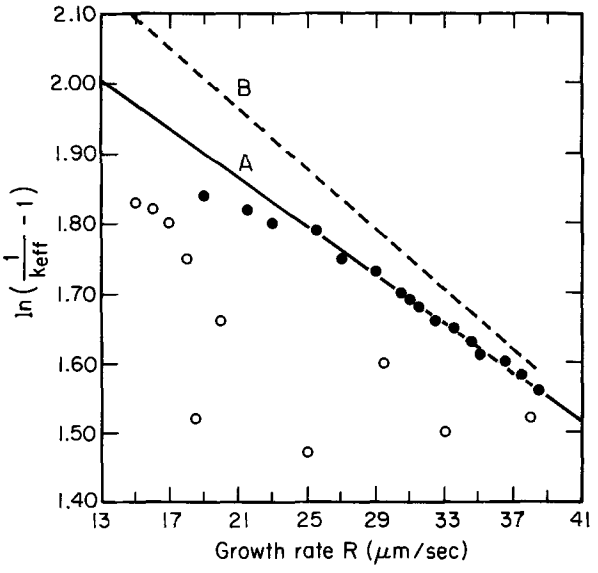

Fig. 4. Analysis of growth rate dependence of dopant segregation according to the BPS theory for the third rotational cycle shown in Fig. 1. ● dopant segregation associated with increasing growth rates; ○ dopant segregation associated with decreasing growth rates. Steady-state segregation (slope δ/D = 180 sec/cm) is indicated only for the segment of the rotational cycle with increasing growth rates (curve A). δ/D obtained from a Cochran analysis is 217 sec/cm (curve B).

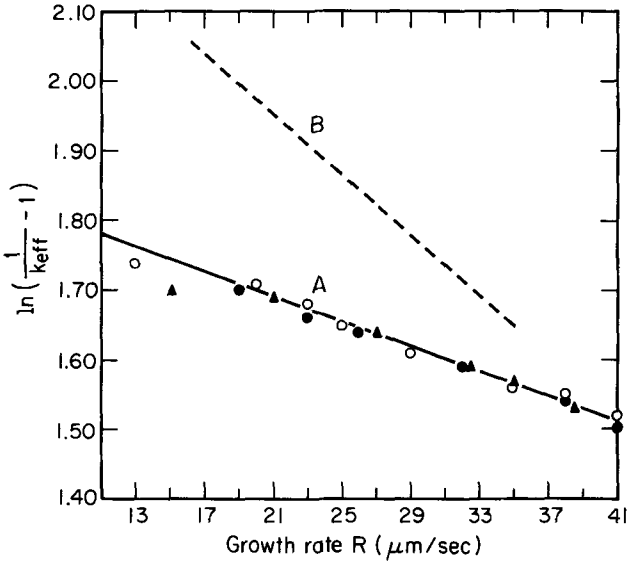

Fig. 5. Analysis of growth rate dependence of dopant segregation under remelt conditions according to the BPS theory for the three rotational cycles (○, ●, ▲, respectively) of the crystal segment shown in Fig. 2. Steady-state segregation is indicated for all three rotational cycles. The growth rate dependence of dopant segregation (δ/D = 90 sec/cm) is significantly weaker than in the case of Fig. 4. Curve B represents the growth rate dependence on the basis of a Cochran analysis (δ/D = 217 sec/cm).

Summary

An analytical approach was developed for the quantitative determination of dopant segregation and the precisely corresponding growth rates on the microscale. The approach is based on the use of rate striations in conjunction with spreading resistance measurements on differentially etched specimens. A preliminary analysis of germanium crystals pulled by the Czochralski technique from a gallium-doped melt revealed the following growth and segregation behavior: at a pulling rate of 7.6 cm/hr and seed rotation of 6.16 rpm the microscopic growth rate exhibits continuous

periodic changes (ranging from 15 to 39 μm/sec) which, however, are not sinusoidal, as generally assumed. The associated dopant segregation varies continuously (by more than 45%). Rotational striations, as revealed by etching, are identified as pronounced dopant concentration maxima which do not coincide with the growth rate maxima. Pulling at a reduced rate, 3.0 cm/hr, results in pronounced "remelt" rotational striations and an average microscopic growth rate (31 μm/sec) which exceeds the pulling rate by a factor of more than three. An analysis of the effective dopant segregation according to the BPS theory indicates the presence of steady-state conditions (constant δ/D) only for the segments of increasing growth rates within each rotational cycle. The effective diffusion layer thickness (δ) is found to be smaller than that computed from a Cochran analysis and decreases noticeably in the presence of remelting.

Acknowledgments

The authors are indebted to the National Science Foundation for financial support and continued encouragement. The skillful assistance of Miss A. S. Carlstein with the sample preparation is gratefully acknowledged.

Manuscript submitted Jan. 10, 1973; revised manuscript received March 26, 1973.

Any discussion of this paper will appear in a Discussion Section to be published in the June 1974 JOURNAL.

REFERENCES

1. For example: P. R. Camp, *J. Appl. Phys.*, **25**, 459 (1954); H. Ueda, *J. Phys. Soc. Japan*, **16**, 61 (1961); A. Müller and M. Wilhelm, *Z. Naturforsch.*, **19A**, 254 (1964); J. C. Brice and P. A. C. Whiffin, *Brit. J. Appl. Phys.*, **18**, 581 (1967).
2. For example: H. C. Gatos, A. J. Strauss, M. C. Lavine, and T. C. Harmon, *J. Appl. Phys.*, **32**, 2057 (1961); M. G. Milvidskii and A. V. Berkova, *Soviet Phys.-Solid State*, **5**, 517 (1963); K. Lehovec, *Surface Sci.*, **1**, 165 (1964); J. R. Carruthers, *Can. Met. Quart.*, **5**, 55 (1966).
3. A. F. Witt and H. C. Gatos, *This Journal*, **113**, 808 (1966).
4. (a) A. F. Witt and H. C. Gatos, *ibid.*, **115**, 70 (1968); (b) K. M. Kim, A. F. Witt, and H. C. Gatos, *ibid.*, **119**, 1218 (1972).
5. For example: F. L. Jones, "Physics of Electrical Contacts," Oxford University Press (1957); R. G. Mazur and B. H. Dickey, *This Journal*, **113**, 255 (1966); R. G. Mazur, *ibid.*, **114**, 255 (1967); D. C. Gupta and J. Y. Chan, *Rev. Sci. Instr.*, **41**, 176 (1970); D. C. Gupta, J. Y. Chan, and P. Wang, *This Journal*, **117**, 1611 (1970).
6. J. A. Burton, R. C. Prim, and W. P. Slichter, *J. Chem. Phys.*, **21**, 1987 (1953).
7. F. A. Trumbore and A. A. Tartaglia, *J. Appl. Phys.*, **29**, 1511 (1958); D. B. Cuttriss, *Bell System Tech. J.*, **40**, 509 (1961).
8. W. A. Tiller, K. A. Jackson, J. W. Rutter, and B. Chalmers, *Acta Met.*, **1**, 428 (1953); C. Wagner, *Trans. AIME*, **200**, 154 (1954); R. N. Hall, *J. Phys. Chem.*, **57**, 836 (1953); A. Trainor and B. E. Bartlett, *Solid State Electron.*, **2**, 106 (1961).
9. J. A. Burton, E. B. Kolb, W. P. Slichter, and J. D. Struthers, *J. Chem. Phys.*, **21**, 1991 (1953); U. Merten, K. D. Voss, and A. P. Hatcher, *J. Phys. Chem. Solids*, **30**, 627 (1969).
10. F. A. Trumbore, *Bell System Tech. J.*, **39**, 669 (1959).
11. J. A. Burton and W. P. Slichter, in "Transistor Technology," Vol. I, p. 71, H. E. Bridgers, J. H. Scaff, and J. N. Shive, Editors, Van Nostrand (1959).

Diffusion from a Thin Layer into a Semi-Infinite Medium with Concentration Dependent Diffusion Coefficient. Part II

M. Ghezzo*

General Electric Corporate Research and Development, Schenectady, New York 12301

ABSTRACT

A formal solution of the diffusion equation is presented for a redistribution case with an initial diffusant concentration represented by a delta function and a diffusion coefficient proportional to the concentration elevated to an integer power. The time dependence of the surface concentration and of the distance of the diffusion front from the surface is discussed and shown to be different from the familiar square root law or its inverse. An example of application of this theory is provided by the high concentration diffusion of arsenic into silicon from a finite source, for which numerical data are computed.

In a recent article (1) a transformation similar to Boltzmann's transformation was applied in the mathematical treatment of impurities redistribution in a semi-infinite medium with a diffusion coefficient dependent only on the ratio of impurities concentration to surface concentration. This case was presented more for illustrative purposes than for solving actual diffusion problems, because in a redistribution of impurities the surface concentration is changing with time and therefore the diffusion coefficient as specified above would not be truly concentration dependent. This paper is the result of further work on this subject for extending the application of the transformation method to physically meaningful cases, such as those occurring for example in the dopant diffusion into semiconductors for the formation of PN junctions.

* Electrochemical Society Active Member.

Key words: diffusion theory, Boltzmann's transformation, concentration dependent diffusion coefficient, arsenic diffusion.

Theory

Following the same terminology of the previous article (1) we assume a more general transformation for the expression of the impurity concentration, N, given by

$$N(x,t) = f(t) \cdot F(xf(t)) \qquad [1]$$

where f and F are analytical functions to be determined in such a way that N will satisfy the boundary conditions and the diffusion equation.

In the redistribution case considered here the boundary conditions are

$$N(x,t) \to \infty \text{ for } x = 0,\ t = 0 \qquad [2a]$$

$$N(x,t) = 0 \quad \text{for } x > 0,\ t = 0 \qquad [2b]$$

$$N(x,t) = 0 \quad \text{for } x \to \infty,\ t \geq 0 \qquad [2c]$$

Furthermore as the initial concentration profile is assumed to be represented by a delta function

$$Q = \int_0^\infty N(x,t)\,dx \qquad [3]$$

where Q is the total amount of impurities per unity of surface in the indiffused medium and is constant.

Let us assume that the diffusion coefficient, D, depends on the concentration, N, according to the expression

$$D = D_0\,(N/N_0)^m \qquad [4]$$

with m a positive integer including zero and D_0 the value of the diffusion coefficient at the reference concentration N_0. As both D_0 and N_0 are constants, it is convenient to conglobate them in a new constant, K, defined by

$$K = D_0/N_0{}^m \qquad [4a]$$

so that D becomes

$$D = KN^m \qquad [4b]$$

Substitution of Eq. [1] and [4b] in the diffusion equation

$$\frac{\partial N}{\partial t} = \frac{\partial}{\partial x}\left[D\,\frac{\partial N}{\partial x} \right] \qquad [5]$$

and a change of coordinates from (x,t) to (η,t), where

$$\eta = xf(t) \qquad [6]$$

yields

$$f'(t)\cdot\left[\eta\,\frac{\partial F(\eta)}{\partial \eta} + F(\eta) \right] = f(t)\,\frac{\partial}{\partial \eta}\left[Kf^m(t)F^m(t)f^2(t)\,\frac{\partial F(\eta)}{\partial \eta} \right] \qquad [7]$$

which simplifies to

$$f'(t)\,\frac{d}{d\eta}[\eta F(\eta)] = f(t)\,\frac{\partial}{\partial \eta}\left[Kf^{(m+2)}(t)F^m(\eta)\,\frac{dF(\eta)}{d\eta} \right] \qquad [8]$$

After variable separation, Eq. [8] is set equivalent to the system of equations

$$f'(t) = -Kf^{(m+3)}(t) \qquad [9]$$

$$\frac{d}{d\eta}[\eta F(\eta)] = -\frac{d}{d\eta}\left[F^m(\eta)\,\frac{dF(\eta)}{d\eta} \right] \qquad [10]$$

A simple integration of Eq. [9] subject to the boundary condition [2a] yields

$$f(t) = \frac{1}{[K(m+2)t]^{1/(m+2)}} \qquad [11]$$

As for Eq. [10], integration between η and ∞ results in

$$\eta F(\eta) = -F^m(\eta)\,\frac{dF(\eta)}{d\eta} \qquad [12]$$

because, for satisfying the boundary conditions [2c] and [3], $F(\eta)$ must be of order greater than one in $1/\eta$ and therefore

$$\lim_{\eta\to\infty}(\eta F(\eta)) = \lim_{\eta\to\infty}\left(F^m(\eta)\,\frac{dF(\eta)}{d\eta} \right) = 0 \qquad [13]$$

Integration of Eq. [12] between 0 and η finally yields

$$F(\eta) = \left[F^m(0) - \frac{\eta^2}{2}m \right]^{1/m} \qquad [14]$$

when $m \geq 1$, and

$$F(\eta) = F(0)\,\exp(-\eta^2/2) \qquad [15]$$

when $m = 0$, that is $D = D_0$.

While $F(\eta)$ as expressed by Eq. [15] is always a real positive number assuming that $F(0)$ is the same, the value of $F(\eta)$ given by Eq. [14] may be a positive real number only if the argument under the m-root sign is positive, that is for η limited to the interval

$$0 \leq \eta < \sqrt{\frac{2}{m}F^m(0)} \qquad [16]$$

Therefore for $m \geq 1$ the impurity concentration profile must be represented by a composite function as specified below

$$N(x,t) = \frac{1}{[K(m+2)t]^{1/(m+2)}}\left\{ F^m(0) - \frac{mx^2}{2[K(m+2)t]^{2/(m+2)}} \right\}^{1/m} \qquad [17]$$

for

$$0 \leq x < X(t) \qquad N(x,t) = 0 \text{ for } X(t) \leq x < \infty$$

where

$$X(t) = \sqrt{\frac{2}{m}F^m(0)}\cdot[K(m+2)t]^{1/(m+2)} \qquad [18]$$

is the transition point between the significant solution of the diffusion equation and the solution identically zero. The obvious discontinuity of $\partial N/\partial x$ for $x = X(t)$ is acceptable, because the impurities flux $J = -D\,\dfrac{\partial N}{\partial x}$ is continuous and equal to zero when computed from both sides of the transition point $X(t)$, as $D = 0$ for $N = 0$ with $m \geq 1$. A similar combination of a significant solution with the zero solution was also found by Wagner (2) to represent the concentration profile in the case of a diffusion from an infinite source with constant surface concentration and diffusion coefficient proportional to the concentration.

It is easy to verify that Eq. [17] gives an expression of N, which satisfies the boundary conditions represented by Eq. [2] and [3]. Indeed as a check and for finding the relationship between Q and $F(0)$, we substitute in Eq. [3] the expression of N given above

$$Q = \int_0^\infty N(x,t)\,dx = \int_0^{X(t)} f(t)\left[F^m(0) - \frac{m}{2}x^2f^2(t) \right]^{1/m} dx = \int_0^{\sqrt{\frac{2}{m}F^m(0)}} \left[F^m(0) - \frac{m}{2}\eta^2 \right]^{1/m} d\eta \qquad [19]$$

The independency of the integration limits from any variable is a further proof that Q is constant, as required by the boundary conditions. A formal verification that Eq. [17] satisfies the diffusion equation is given in the Appendix.

Applying the transformation

$$\eta = \xi\cdot\sqrt{\frac{2}{m}F^m(0)} \qquad [20]$$

to Eq. [19], the relationship between Q and $F(0)$ is easily found

$$Q = \sqrt{\frac{2}{m}}\cdot F(0)^{(m/2+1)}\cdot\int_0^1 (1-\xi^2)^{1/m}d\xi \qquad [21]$$

or else, by explicating $F(0)$

$$F(0) = \left[\frac{Q\sqrt{\frac{m}{2}}}{\int_0^1 (1-\xi^2)^{1/m} d\xi} \right]^{2/(m+2)} \quad [22]$$

In many applications it is useful to express the concentration profile in a normalized form, which can be obtained combining Eq. [17], [18], and [22]. The result is

$$\frac{N(x,t) \cdot X(t)}{Q} = \left\{ 1 - \left[\frac{x}{X(t)} \right]^2 \right\}^{1/m} \Big/ \int_0^1 (1-\xi^2)^{1/m} d\xi \quad [23]$$

where, using Eq. [4a] for expressing K

$$X(t) = \left\{ 2\left(\frac{m+2}{m}\right) \left[\frac{Q}{N_0 \int_0^1 (1-\xi^2)^{1/m} d\xi} \right]^m D_0 t \right\}^{1/(m+2)} \quad [24]$$

The surface concentration, N_s, decreases with time and its expression is found by setting $x = 0$ in Eq. [23]

$$N_s(t) = Q \Big/ \left[X(t) \cdot \int_0^1 (1-\xi^2)^{1/m} d\xi \right] \quad [25]$$

Plots of normalized concentration profiles are shown in Fig. 1 for different values of m, while the values of the definite integral appearing in Eq. [23], [24], and [25] are tabulated in Table I for values of m between 1 and 10.

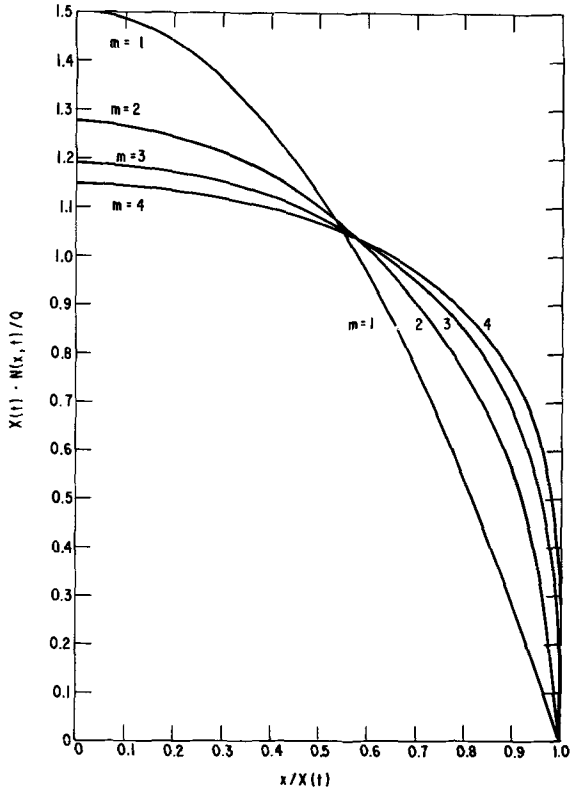

Fig. 1. Plots of normalized concentration profiles for the diffusion coefficient $D = D_0(N/N_0)^m$, with $m = 1, 2, 3, 4$, in a redistribution case with initial concentration represented by a delta function.

Table I. Values of $\int_0^1 (1-\xi^2)^{1/m} d\xi$ for m between 1 and 10

m	$\int_0^1 (1-\xi^2)^{1/m} d\xi$
1	0.6666
2	0.7852
3	0.8409
4	0.8734
5	0.8947
6	0.9098
7	0.9211
8	0.9299
9	0.9368
10	0.9425

From Eq. [24] we observe that a diffusion front advances with the $(m+2)$-root of the diffusion time and that only in the case of a constant diffusion coefficient we obtain the familiar square root law dependence. It is also important to point out that for x larger than $X(t)$ and $m \geq 1$, $N(x,t)$ is identically zero, while for $m = 0$, $N(x,t)$ is represented by an exponential function and is therefore larger than zero for any positive x at any time t after the beginning of the diffusion process. In particular for $m = 1$ and using linear scales the concentration profile is represented between 0 and $X(t)$ by a branch of a parabola, symmetrical with respect to the ordinate axis and with the concavity pointing down, while outside this interval it is coincident with the abscissa axis. As the time increases, the vertex of this parabola, which corresponds to the surface concentration at time t, decreases by a factor inversely proportional to the cubic root of time, while its curvature also decreases shifting its intersection with the abscissa axis at progressively higher x values, which are directly proportional to the cubic root of time, as seen from Eq. [24].

Often the diffusion of impurities into a semiconductor is used for the formation of PN junctions and therefore it is of paramount importance the determination of the diffusion time, τ, required for achieving a desired junction depth, x_j, when besides Q and D the background concentration, N_B, is known. For this purpose we rewrite Eq. [23] in the form

$$\frac{N(x,t) \cdot x}{Q} = \left[\frac{x}{X(t)} \right] \cdot \left\{ 1 - \left[\frac{x}{X(t)} \right]^2 \right\}^{1/m} \Big/ \int_0^1 (1-\xi^2)^{1/m} d\xi \quad [26]$$

and we plot the corresponding family of curves for the first four values of m in Fig. 2. When in Eq. [26],

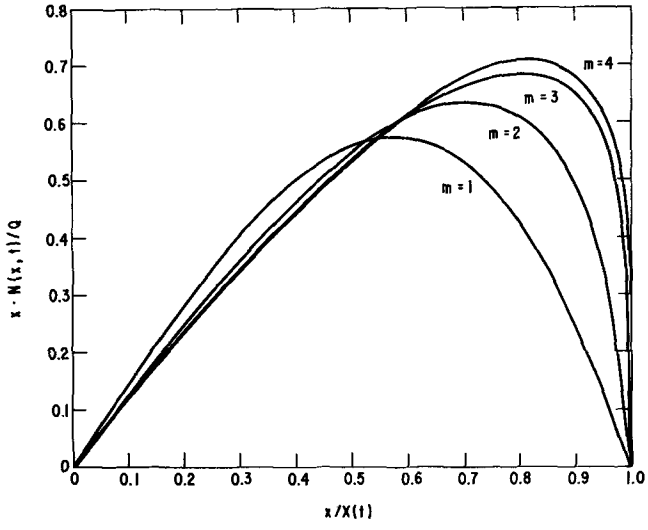

Fig. 2. Plots of $(x \cdot N(x,t))/Q$ vs. $x/X(t)$ for $m = 1, 2, 3, 4$, used in the determination of the diffusion time required for obtaining a desired junction depth, x_j.

$N(x,t)$ is replaced by N_B and x by x_j, two solutions for $x_j/X(\tau)$ are found at the intersection of the appropriate plot of Fig. 2 with the horizontal line of ordinate $(N_B \cdot x_j)/Q$. They both are physically meaningful, because as the diffusion time increases the concentration profile spreads at the expense of its peak height and therefore its intersection with a reference concentration, like N_B, occurs twice at a junction depth x_j at two different times, τ_1, and τ_2.

These two solutions coincide when $(x_j \cdot N_B)/Q$ is equal to the maximum of the plot of Fig. 2 for the corresponding value of m. This means that there is a maximum junction depth, x_{jm}, achievable for any chosen ratio (Q/N_B) and that it can be obtained only with one diffusion time, τ_m.

Equating to zero the derivative of the right-hand member of Eq. [26] we find that the relative maximum occurs at

$$\frac{x_{jm}}{X(\tau_m)} = \sqrt{\frac{m}{m+2}} \qquad [27]$$

and therefore by substituting in Eq. [26] $x/X(t)$ with its expression given by Eq. [27] we obtain x_{jm}

$$x_{jm} = \frac{Q}{N_B} \cdot \sqrt{\frac{m}{m+2}} \cdot \left(\frac{2}{m+2}\right)^{1/m} \Big/ \int_0^1 (1-\xi^2)^{1/m} d\xi \qquad [28]$$

The time τ_m is easily computed from Eq. [24], [27], and [28]

$$\tau_m = \frac{m}{4D_o} \cdot \left(\frac{2}{m+2}\right)^{2(m+1)/m} \cdot \left[\frac{Q}{N_B \int_0^1 (1-\xi^2)^{1/m} d\xi}\right]^2 \cdot \left(\frac{N_o}{N_B}\right)^m \qquad [29]$$

while the corresponding surface concentration, N_{sm} is derived from Eq. [25], [27], and [28]

$$N_{sm} = N_B \cdot \left(\frac{m+2}{2}\right)^{1/m} \qquad [29a]$$

Example

Masters and Fairfield (3) have shown that the diffusion coefficient of As in Si conforms with the relationship

$$D = D_i(n/n_i) \qquad [30]$$

where (n/n_i) is the ratio of the free electron concentration in the extrinsic sample to that of intrinsic silicon at the diffusion temperature.

In Table II the values of n_i and D_i are presented as a function of the diffusion temperature T, having used for their computation the formulas of Ref. (3). Calling N the As concentration, we write following Equation 4 of Ref. (3)

$$\frac{n}{n_i} = \frac{N}{2n_i} + \left[1 + \left(\frac{N}{2n_i}\right)^2\right]^{1/2} \qquad [31]$$

which clearly shows that

Table II. Values of intrinsic carrier concentration in Si, n_i, and intrinsic arsenic diffusion coefficient in Si, D_i, at different diffusion temperatures, T [computed from formulas in Ref. (3)]

T (°C)	n_i (cm^{-3})	D_i (cm^2/sec)
900	4.923×10^{18}	5.505×10^{-17}
1000	9.360×10^{18}	1.437×10^{-15}
1100	1.648×10^{19}	2.333×10^{-14}
1200	2.729×10^{19}	2.594×10^{-13}

$$\frac{n}{n_i} \simeq \frac{N}{n_i} \quad \text{for} \quad N >> 2n_i \qquad [32a]$$

$$\frac{n}{n_i} \simeq 1 \quad \text{for} \quad N << 2n_i \qquad [32b]$$

Therefore the theory developed for the impurity redistribution with concentration dependent diffusion coefficient is only approximate in the As case and its results are reliable in the profile region where the As concentration is larger than $2n_i$ at the diffusion temperature.

Considering for example a diffusion temperature of 1100°C we find from Eq. [24] that

$$X(t) = (9QD_it/n_i)^{1/3} = 2.335 \times 10^{-11} \times Q^{1/3}t^{1/3} \qquad [33]$$

where $X(t)$ is expressed in centimeters, Q in cm^{-2}, and t in seconds. Equation [33] shows that the high concentration region of the diffusion front is advancing in first approximation with the cubic root of the diffusion time instead of with the square root, as in the familiar case of constant diffusivity.

The profile as computed from Eq. [23] is

$$N(x,t) = \frac{3}{2}\frac{Q}{X(t)} \cdot \left\{1 - \left[\frac{x}{X(t)}\right]^2\right\} \quad \text{for } 0 \leq x < X(t) \qquad [34]$$

$$N(x,t) = 0 \quad \text{for} \quad X(t) \leq x < \infty$$

which is a parabola with the concavity facing the negative ordinate direction and with its maximum represented by the surface concentration, followed by the zero solution for values of x larger than the intersection of the parabola with the abscissa axis.

Assuming a P-type background concentration, N_B, larger than 3.296×10^{19} cm^{-3} ($= 2n_i$ at 1100°C), Eq. [28] shows that the maximum junction depth, x_{jm}, achievable for a chosen Q is

$$x_{jm} = \frac{Q}{\sqrt{3}\,N_B} = 0.578 \times \frac{Q}{N_B} \qquad [35]$$

while the time, τ_m, required for obtaining this junction depth with an As diffusion at 1100°C is according to Eq. [29]

$$\tau_m = \frac{Q^2 n_i}{9D_i N_B^3} = 7.848 \times 10^{31} \times \frac{Q^2}{N_B^3} \qquad [36]$$

where τ_m is expressed in seconds, Q in cm^{-2}, and N_B in cm^{-3}.

According to Eq. [29a] the surface concentration for this profile is

$$N_{sm} = 1.5\,N_B \qquad [36a]$$

For carrying on in more detail this example, let us further assume that $N_B = 6 \times 10^{19}$ cm^{-3} and $Q = 1.8 \times 10^{16}$ cm^{-2}, corresponding to an initial box distribution profile 0.1μ deep and with a uniform As concentration of 1.8×10^{21} cm^{-3}, that is equal to the solid solubility of As in Si at 1100°C (4). Substituting these values into Eq. [33], [34], [35], and [36] and using the same units as before unless otherwise specified, we obtain the following results

$$X(t) = 6.1 \times 10^{-6} \times t^{1/3} \qquad [37]$$

$$N(x,t) = \frac{4.42 \times 10^{21}}{t^{1/3}} \times [1 - 2.7 \times 10^{10} \times (x/t^{1/3})^2] \qquad [38]$$

for

$$0 \leq x < X(t)$$

$$x_{jm} = 1.74\mu \qquad [39]$$

$$\tau_m = 1.18 \times 10^5 \text{ sec} = 32.8 \text{ hr} \qquad [40]$$

$$X(\tau_m) = 3.00\mu \qquad [41]$$

$$N_{sm} = 9 \times 10^{19} \text{ cm}^{-3} \qquad [42]$$

It is interesting to observe that due to the small discrepancy between the actual initial distribution and the delta function assumed in the theory, Eq. [37] and [38] are not valid for very small diffusion times. This observation is more of academic interest than of practical importance, because the errors introduced in the profile calculations by random changes in the heat-up times are more relevant. Nevertheless this observation was felt necessary to avoid the impression that Eq. [38] contemplates surface concentrations larger than the solid solubility limit. Indeed a short calculation shows that this happens only in the first 15 sec according to Eq. [38], while the time errors due to the heat-up are usually larger.

Furthermore, the large diffusion time (32.8 hr) required for achieving a junction depth of only 1.74μ operating at 1100°C is somewhat surprising. This is partially due to the high background concentration (6×10^{19} cm^{-3}) assumed in this example, so as in Eq. [41] it is given also the corresponding value of the diffusion front penetration, that is 3μ, which is about twice as large as x_{jm}. But the main reason for this seemingly slow diffusion is the cubic root dependence of $X(t)$ on t, which is more effective in reducing the penetration rate of the diffusion front with time than the familiar square root law.

Summary

A formal solution of the diffusion equation was found for a redistribution of impurities from a thin layer into a semi-infinite medium with an impermeable boundary and a diffusion coefficient proportional to the concentration elevated to an integer power. This solution is represented by a combination of a significant function and by the function identically zero, so as a rigorous definition of the diffusion front is possible. The advancement in depth of the diffusion front with time is following a law, which is different from the square root law and is represented by the $(m + 2)$-root of time for D proportional to N^m. Likewise the surface concentration decreases as the reciprocal of the $(m + 2)$-root of time for a similar diffusion coefficient. Therefore the value of m can be easily inferred from redistribution experiments.

An example of application of this theory is provided by the high concentration diffusion of arsenic into silicon, for which formulas are given and numerical data are computed.

APPENDIX

Verification that $N(x,t)$ given by Eq. [17] is a formal solution of the diffusion equation when $D = KN^m$ and $m \geqq 1$.

Let us assume

$$S(x,t) = \left\{ F^m(0) - \frac{mx^2}{2[K(m+2)t]^{2/(m+2)}} \right\}^{1/m} \quad [A\text{-}1]$$

so as

$$N(x,t) = \frac{S(x,t)}{[K(m+2)t]^{1/(m+2)}} \text{ for } 0 \leqq x < X(t) \quad [A\text{-}2]$$

Therefore

$$\frac{\partial N}{\partial t} = \left(-\frac{1}{m+2}\right)[K(m+2)t]^{-\left(\frac{m+3}{m+2}\right)} K(m+2) \cdot S(x,t) + \frac{1}{[K(m+2)t]^{1/(m+2)}} \cdot \frac{1}{m} \cdot S(x,t)^{(1-m)} \left(-\frac{mx^2}{2}\right) \cdot \left(-\frac{2}{m+2}\right) \cdot [K(m+2)t]^{-\left(\frac{m+4}{m+2}\right)} K(m+2)$$

$$= \frac{KS(x,t)^{(1-m)}}{[K(m+2)t]^{\left(\frac{m+3}{m+2}\right)}} \cdot \left\{ -F^m(0) + \frac{mx^2}{2[K(m+2)t]^{2/(m+2)}} + \frac{x^2}{[K(m+2)t]^{2/(m+2)}} \right\} = \frac{KS(x,t)^{(1-m)}}{[K(m+2)t]^{\left(\frac{m+3}{m+2}\right)}} \cdot \left\{ -F^m(0) + \left(\frac{m+2}{2}\right) \frac{x^2}{[K(m+2)t]^{2/(m+2)}} \right\} \quad [A\text{-}3]$$

$$\frac{\partial N}{\partial x} = \frac{1}{[K(m+2)t]^{1/(m+2)}} \cdot \frac{1}{m} \cdot S(x,t)^{(1-m)} \cdot \left(-\frac{m}{2}\right) \cdot \frac{1}{[K(m+2)t]^{2/(m+2)}} \cdot 2x$$

$$= -\frac{xS(x,t)^{(1-m)}}{[K(m+2)t]^{3/(m+2)}} \frac{\partial}{\partial x}\left(KN^m \frac{\partial N}{\partial x}\right)$$

$$= \frac{\partial}{\partial x}\left\{ -K \frac{S^m(x,t)}{[K(m+2)t]^{m/(m+2)}} \cdot \frac{xS(x,t)^{(1-m)}}{[K(m+2)t]^{3/(m+2)}} \right\}$$

$$= -\frac{K}{[K(m+2)t]^{\left(\frac{m+3}{m+2}\right)}} \cdot \frac{\partial}{\partial x}[xS(x,t)]$$

$$= -\frac{K}{[K(m+2)t]^{\left(\frac{m+3}{m+2}\right)}} \cdot \left\{ S(x,t) + x\frac{1}{m} S(x,t)^{(1-m)} \cdot \left(-\frac{m}{2}\right) \frac{2x}{[K(m+2)t]^{2/(m+2)}} \right\}$$

$$= \frac{KS(x,t)^{(1-m)}}{[K(m+2)t]^{\left(\frac{m+3}{m+2}\right)}} \cdot \left\{ -S^m(x,t) + \frac{x^2}{[K(m+2)t]^{2/(m+2)}} \right\} = \frac{KS(x,t)^{(1-m)}}{[K(m+2)t]^{\left(\frac{m+3}{m+2}\right)}} \cdot \left\{ -F^m(0) + \left(\frac{m+2}{2}\right) \frac{x^2}{[K(m+2)t]^{2/(m+2)}} \right\} \quad [A\text{-}4]$$

The right-hand members of Eq. [A-3] and [A-4] are identical, as required for proving that Eq. [A-1] and [A-2] represent a formal solution of the diffusion equation with the diffusion coefficient specified above.

Manuscript received Oct. 6, 1972.

Any discussion of this paper will appear in a Discussion Section to be published in the June 1974 JOURNAL.

REFERENCES

1. M. Ghezzo, *This Journal*, **119**, 977 (1972).
2. C. Wagner, *J. Chem. Phys.*, **18**, 1229 (1950).
3. B. J. Masters and J. M. Fairfield, *J. Appl. Phys.*, **40**, 2390 (1969).
4. F. A. Trumbore, *Bell System Tech. J.*, **39**, 205 (1960).

Vapor-Doped Multislice LPE for Efficient GaP Green LED's

R. H. Saul and D. D. Roccasecca

Bell Laboratories, Murray Hill, New Jersey 07974

ABSTRACT

A single-step liquid phase epitaxy process has been developed for the growth of efficient GaP green light-emitting diodes (LED's), in which all doping is accomplished from the vapor phase. The use of vapor-phase doping increases the flexibility of the LPE process since junction formation and control of doping profiles is accomplished by regulating the composition and flow rates of the doping gases. This method has been applied to multislice growth on large area substrates (up to 38 mm in diameter). Thin melts and nearly complete utilization of the GaP initially dissolved in the melt minimize the gallium usage. Encapsulated LED's with efficiencies in the 0.10-0.15% range at 7 A/cm^2 are obtained routinely. These efficiencies are comparable to the highest values reported to date for low current (~10 mA) operation. Efficiencies as high as 0.2% have been obtained at 7 A/cm^2 using this method. The short deposition time for this single-step method, reproducibility, multislice capability, and minimum gallium consumption make this method economically attractive for the high level production of efficient green LED's.

Efficient green junction luminescence in nitrogen-doped GaP has been demonstrated for p-n junctions grown by liquid phase epitaxy (LPE) (1-3). The commercial interest in this material for display devices and discrete light emitting diodes (LED's), has stimulated interest in developing inexpensive high capacity LPE systems, capable of producing efficient p-n junctions. In this paper we report on a single-step LPE technique for green LED's which employs vapor-phase doping for p-n junction formation and control of doping profiles. The vapor-doping method has been applied to growth from thin melts and a multislice system capable of producing reproducibly efficient, green LED material is discussed. The single-growth step, high production capability, and minimum Ga consumption make this method economically attractive for commercial applications. A more comprehensive account of the growth procedures and material characteristics will be given elsewhere (4).

Green LED Structure

The LED structure, schematically illustrated in Fig. 1, is similar to that described by Logan and co-workers (1). The recombination and injection processes and their relation to quantum efficiency are discussed elsewhere (5). The p-n junction is formed by LPE on {111}-oriented, n-type, liquid encapsulated Czochralski (LEC) substrates which are doped with the Se donor at a level of $N_D - N_A = 0.3\text{-}1.0 \times 10^{18}$ cm^{-3}. The n-type LPE material is doped with S typically at $N_D - N_A = 1 \times 10^{17}$ cm^{-3}, and the p-type material is doped with Zn at a level of $N_A - N_D \sim 8 \times 10^{17}$ cm^{-3}. The isoelectronic nitrogen center from which the efficient green recombination originates (6), is present in both LPE layers at a concentration of $\sim 7 \times 10^{18}$ cm^{-3}, as determined by optical absorption measurements (1). Previous studies have shown that for these doping levels, the external luminescence is generated equally in the n- and p-regions for operating current densities of 5-10 A/cm^2 (5).

Key words: crystal growth, junction formation, electroluminescence.

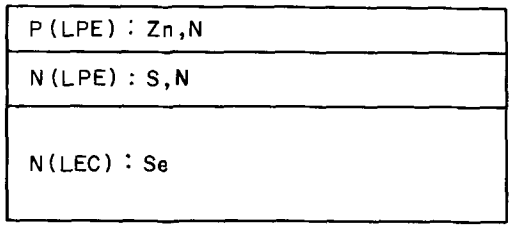

Fig. 1. Schematic representation of the p$^+$-n-n green LED structures.

Junction Formation and Control of Doping Profiles

The high efficiency junctions described by Logan and co-workers (1) were formed by a two-step LPE process involving consecutive growth of the n- and p-layers in separate growth systems. Ladany and Kressel (2) accomplished this in a single-growth system by employing a slider boat containing separate compartments for the n- and p-melts. Recently, Lorimor and co-workers (3) have successfully applied the method of overcompensation (7) to form the p-n junction. This was achieved in a vertical dipping system by growing an n-layer from a S- or Te-doped melt and then adding a pellet of metallic Zn to the melt (via a drop tube) to produce an overcompensated (*i.e.*, p-type) layer on further cooling. The single-step nature of this method and that of Ladany (2) is expected to improve reproducibility, however, the doping profiles are not readily controlled (especially for the overcompensation method) as discussed below.

In Fig. 2 we show the doping profile, variation of doping level along the growth direction, for a p-n

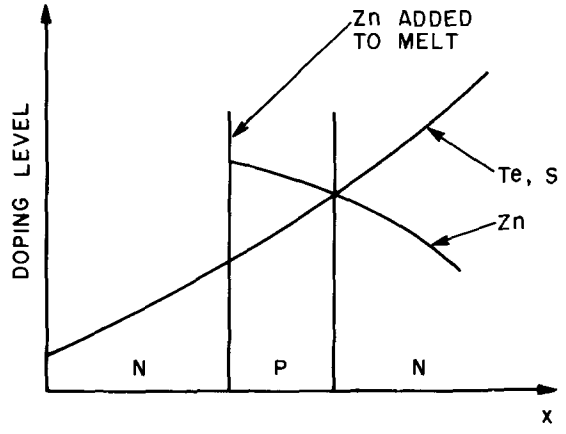

Fig. 2. Variation of doping level along the growth direction for the overcompensation method employing direct melt additions. The N concentration (not shown) is essentially constant. The substrate is located at $x = 0$.

junction formed by overcompensation employing direct melt additions. The Te (or S) concentration increases along the growth direction as a result of the increasing distribution coefficient with decreasing temperature (8). On the other hand, the Zn concentration decreases as a result of the decreasing distribution coefficient with decreasing temperature (9, 10) and volatilization of Zn from the melt in open flow systems. As shown in Fig. 2, these effects result in an increasingly compensated p-layer. Eventually, the donor concentration exceeds the acceptor concentration and the material reverts back to n-type giving a n-p-n structure. The increased compensation and formation of an n-skin will also result without intentional donor additions because of the net donor concentration associated with residual impurities (10, 11). To provide low voltage LED's, growth must be terminated not only prior to the formation of the n-skin, but before the net acceptor concentration in the p-layer is reduced to levels $N_A - N_D \lesssim 1 \times 10^{17}$ cm^{-3}, where low voltage ohmic contacts are difficult to form. These considerations become more important for growth from thin melts (next section) where a wide temperature range is required to grow layers of sufficient thickness (~25-40μ).

In this work, we have employed vapor-phase doping for both junction formation and control of doping profiles in the grown layers. Since all doping is done from the vapor phase, the geometry of the LPE system can be relatively simple and the method is readily adapted to growth from thin melts (12, 13). The donor S is introduced by passing H_2S over the growth solution, the acceptor Zn is obtained from an evaporating elemental source, and N is introduced in the form of NH_3. All constituents are added using palladium-diffused H_2 as a diluent carrier gas and controlled doping is achieved by regulating the respective gas flow rates.

The doping profile obtained using vapor-phase doping is shown in Fig. 3. In a typical growth run, the n-layer is first grown from a S,N-doped melt. The increasing S concentration along the growth direction can be maintained constant by reducing the H_2S flow rate during cooling; in practice, the normally obtained gradient is not detrimental so this adjustment is not made. When growth is terminated by interrupting the cooling, the H_2S is purged from the reactor tube using H_2 and the dissolved S is transformed back to H_2S. Simultaneously Zn vapor is introduced into the gas flow. After an equilibration period, cooling is continued to grow the p-layer. The overcompensation of the p-layer is virtually eliminated by the effective removal of S from the melt.

The incorporated Zn level, C^S_{Zn}, is determined by the distribution coefficient, viz.

$$C^S_{Zn} = k(T, C^l_{Zn})C^l_{Zn} \quad [1]$$

where, as discussed earlier, k decreases with decreasing T. For ideal solutions ($\gamma^l_{Zn} \approx 1$), the liquid concentration C^l_{Zn} is given by

$$C^l_{Zn} \simeq p_{Zn}(f, T_s)/p^o_{Zn}(T) \quad [2]$$

where p_{Zn}, the Zn partial pressure over the melt, is determined by the relative flow rate f over the evaporating elemental source maintained at temperatures T_s. The quantity $p^o_{Zn}(T)$ is the vapor pressure over elemental Zn at the growth temperature T. Combining Eq. [1] and [2], C^S_{Zn} is given by

$$C^S_{Zn} = [k(T, C^l_{Zn})/p^o_{Zn}(T)]p_{Zn}(f, T_s) \quad [3]$$

The Zn distribution can therefore be readily controlled by varying f or T_s during cooling. For the case of constant f and T_s, the Zn distribution in the solid is determined by the bracketed term in Eq. [3]. Using Jordan's (9) values of k and p^o_{Zn} obtained from Ref. (14), the equilibrium Zn distribution can be shown to be essentially invarient, as verified experimentally. This produces the desirable result of moderate surface doping levels ($N_A - N_D \sim 6 \times 10^{18}$ cm^{-3}) for application of ohmic contacts and minimization of current crowding under the top contact. (Free carrier absorption at these doping levels is negligible compared to the A-line self-absorption). When the p-layer is partially compensated by residual S, the same surface (net) doping level can be achieved by increasing f during cooling.

The requirements for producing the abrupt changes in doping levels needed for junction formation and control of doping profiles are: (*a*) a reactor tube which minimizes incorporation of previously used dopants (so-called memory effect); and (*b*) appropriate design of the LPE boat to permit rapid communication between the melt and (doping) vapor phase.

Reactor tube design.—In Fig. 4 we show a schematic representation of the reactor tube. The tube consists of (*i*) an active zone in which the crystal growth and doping takes place, and (*ii*) a passive zone which provides the vapor source of Zn. The two zones are isolated by a connecting capillary tube. This restriction also increases the flow velocity of the Zn vapor to the active zone when the flow of carrier gas (H_2) is initiated. All dopants are introduced in the hot zone using independent delivery tubes. This has been found to be essential to reduce system memory effects. An LPE slider boat rests on a quartz ramp of rectangular cross section and is accurately positioned in the hot zone by a depression in the ramp. The transverse motion of the slider is accomplished using a push rod fed through a Teflon O-ring seal. Loading is accomplished within a nitrogen-filled chamber and is countercurrent to the gas flow to minimize entrance of contaminants into the system. The active zone is contained in a modified diffusion furnace. The Zn boat in the passive zone is maintained at $T_s \sim 600$°C, using a

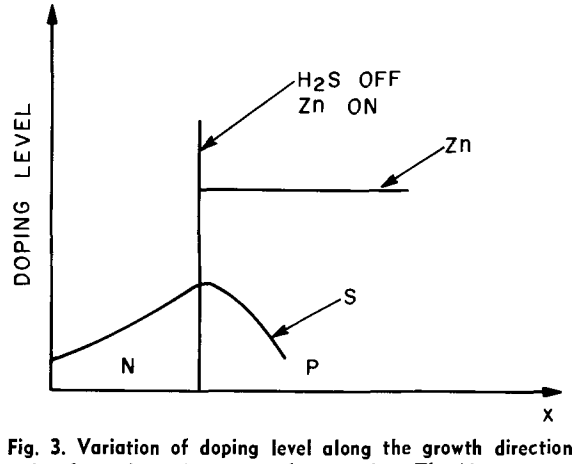

Fig. 3. Variation of doping level along the growth direction for junction formation using vapor-phase doping. The N concentration (not shown) is essentially constant.

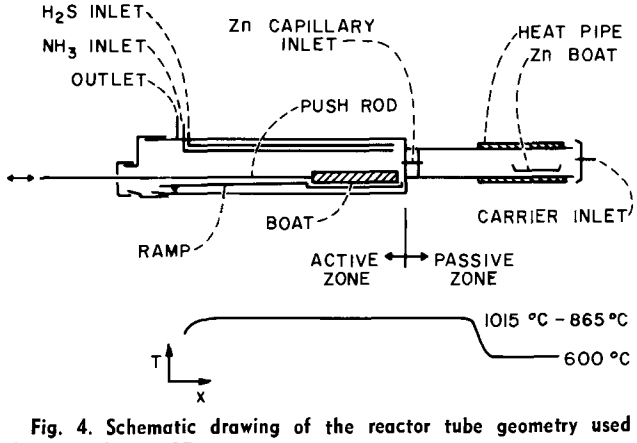

Fig. 4. Schematic drawing of the reactor tube geometry used for vapor-doped LPE.

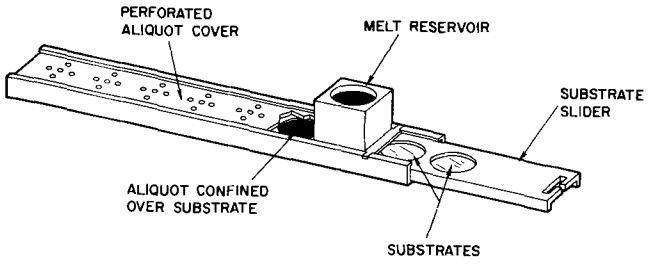

Fig. 5. Perspective drawing of multislice LPE system as described in the text.

separately controlled furnace. An evaporating sodium heat pipe is used to provide a constant temperature zone T_s (±5°C) which is independent of the active zone, as the temperature of the latter varies during the growth cycle.

LPE system.—A thin melt LPE apparatus is used for growth of the GaP layers. As in earlier (13, 15) double slider boats, the thin melts are produced by sectioning a reservoir melt into increments (aliquots) of equal thickness. The multislice LPE boat which we are currently using is schematically illustrated in Fig. 5. Six substrates up to 38 mm in diameter can be accommodated in this prototype system. The carbon boat utilizes 1-2 mm aliquot melts which are sequentially formed by passing a slider containing the substrates under the reservoir melt. The formation of thin aliquots is aided by the wetting action of the substrates and the use of a nonwetting (carbon) cover plate which confines the aliquot (13). The aliquot thickness is determined by the depth of the substrate well. As shown in Fig. 5, the aliquot cover plate is perforated to maximize communication with the gas phase. Previous double-slider boats (13, 15) utilized a second slider to confine the aliquot and to terminate growth (by wiping the melt from the substrate) for control of the surface doping levels. In the present case, the former is achieved with a stationary cover plate and the surface doping levels are controlled from the gas phase. Approximately 90% of the GaP in solution is deposited on the substrates, owing to the high deposition efficiency from thin melts (13) and cooling to low temperatures where melt depletion is nearly complete.

Discussion

The growth conditions which are most widely used are summarized in Table I. The partial pressures of H_2S and Zn are appropriate for achieving the desired doping levels (see section on Junction Formation and Control of Doping Profiles) while the NH_3 pressure is maintained below the level where solid GaN becomes an equilibrium phase (16). (The NH_3 purification as described in Ref. (1) was not utilized in this work, however extreme care was taken to eliminate air leaks and other sources of oxygen.) Growth of the n-layer occurs over the indicated temperature interval after a suitable equilibration period. Termination of the n-growth is achieved by interrupting the cooling during which time the H_2S is purged from the system and the carrier flow is started over the hot Zn source. Approximately 30-60 min are required to equilibrate the gas dopants. The p-layer is then grown by cooling to low temperatures (<865°C) where the melt is essentially depleted. A total growth time of less than 2 hr is possible, independent of the number of substrates. After completion of a run, Ga adhering to the substrates is readily removed by mechanical swabbing and/or aqueous etching. Since the melt is depleted when growth of the p-layer is terminated, the smoothness of the as-grown surface is not dictated by the effectiveness of the Ga removal, as in the usual case where growth is terminated at elevated temperatures.

Table I. Summary of growth conditions

	Partial pressure of dopants (atm)*			Growth interval (°C)**	
	H_2S	NH_3	Zn	$T_{initial}$	T_{final}
N-layer	~6 × 10⁻⁷	8 × 10⁻⁴	—	1015°	950°
P-layer	—	8 × 10⁻⁴	1.8 × 10⁻³	950°	<865°

* A hydrogen carrier gas is used for all dopants.
** The cooling rate is 3°/min.

This system has been extensively operated according to the schedule given in Table I using from one to six 25-35 mm substrates in a given run to produce a total of ~80 p-n junction slices. [During the latter stages of this work, the growth process was automated so that the entire junction formation sequence was executed without operator assistance (17).] The doping levels were found to be reproducible with no indication of memory effects even after 50 consecutive runs with the same reactor tube. The excellent surface quality and layer thickness uniformity ($\lesssim$10%) is typical of slider-grown LPE material. The green[1] electroluminescence efficiency was determined using a calibrated close-couple cavity (18) for both slurry-cut die and abrasive-honed mesas which were wire bonded and mounted on TO-18 headers, the former being used for rapid material evaluation. Measurements were made at a forward current density of ~7 A/cm² (10 mA for a 0.015 × 0.015 in. die). In a given multislice run, variations of ~±10% in slice-to-slice average efficiency have been observed, which probably represent the reproducibility of the measuring technique. The efficiencies of epoxy-coated diodes in the mesa configuration routinely ranged between 0.10-0.15%, for both d-c and pulsed measurements. These efficiencies compare favorably with the 0.09-0.14% reported by Logan (1) (using LEC substrates), Ladany (2) and Lorimor (3), for mesa diodes at this current density. Several encapsulated die mounted (without reflectors) on TO-18 headers had efficiencies of 0.2% at 7 A/cm². This is the highest efficiency reported to date for low current operation. Although extensive measurements have not been performed at high current densities where pulsed excitation is required to avoid device heating, the increase in efficiency per decade of current density is roughly a factor of two less than that indicated by Ladany (2). This difference may be associated with the higher donor concentrations and the presence of N in the p-layers for our structures.

Summary

We have described a single-step LPE process for GaP green LED's which utilizes vapor-phase doping. Vapor-phase doping substantially increases the flexibility of the LPE process since junction formation and the control of doping profiles are achieved by regulating the flow of doping gases. Termination of growth is not required to control surface doping levels as with conventional doping methods (*i.e.*, direct additions to the melt) and thus ~90% of the GaP initially dissolved in the melt is grown on the substrate. This method has been applied to multislice growth from thin (1-2 mm) melts by providing access holes so that the melt, which is confined over each substrate, can communicate with the gas ambient. The prototype LPE system described here accommodates six substrates up to 38 mm in diameter, and yielded LED's which routinely were in the 0.10-0.15% range at 7 A/cm². A total growth time (n-layer plus p-layer) of less than 2 hr is possible, independent of the number of substrates. The speed of this single-step technique, its multislice capability and its minimal Ga consumption make this method economically attractive for high level production of efficient green LED's.

[1] The measurement apparatus incorporates a filter to provide a 30:1 red to green rejection ratio. It should be noted also that the integrated green to red ratio for typical diodes is 10:1.

Acknowledgments

The authors are indebted to W. H. Hackett, Jr. and R. Z. Bachrach for providing the efficiency and N-level determinations. We also thank P. Garbinski for fabrication of the mesa diodes. We especially acknowledge the skillful assistance of C. R. Paola in designing the LPE apparatus, and helpful discussions with numerous colleagues.

Manuscript submitted Feb. 15, 1973; revised manuscript received March 30, 1973.

Any discussion of this paper will appear in a Discussion Section to be published in the June 1974 JOURNAL.

REFERENCES

1. R. A. Logan, H. G. White, and W. Wiegmann, *Solid-State Electron.*, **14**, 55 (1971).
2. I. Ladany and H. Kressel, *Proc. IEEE*, **60**, 1101 (1972).
3. O. G. Lorimor, W. H. Hackett, Jr., and R. Z. Bachrach, *This Journal*, **119**, 303C (1972).
4. R. H. Saul and D. D. Roccasecca, To be published.
5. P. D. Dapkus, W. H. Hackett, Jr., O. G. Lorimor, G. W. Kammlott, and S. E. Haszko, *Appl. Phys. Letters*, **22**, 227 (1973).
6. D. G. Thomas, J. J. Hopfield, and C. J. Frosch, *Phys. Rev. Letters*, **15**, 857 (1965).
7. K. K. Shih, J. M. Woodall, S. E. Blum, and L. F. Foster, *J. Appl. Phys.*, **39**, 2962 (1968).
8. R. H. Saul and W. H. Hackett, Jr., *ibid.*, **41**, 3554 (1970).
9. A. S. Jordan, *This Journal*, **118**, 781 (1971).
10. R. H. Saul and W. H. Hackett, Jr., *ibid.*, **117**, 971 (1970).
11. I. Ladany, *ibid.*, **116**, 993 (1969).
12. J. A. Donahue and H. T. Minden, *J. Crystal Growth*, **7**, 221 (1970).
13. A. A. Bergh, R. H. Saul, and C. R. Paola, Paper presented at Electrochemical Society Meeting, Miami Beach, Oct. 8-13, 1972.
14. R. A. Honig and D. A. Kramer, *RCA Rev.*, **30**, 285 (1969).
15. R. H. Saul and D. D. Roccasecca, *J. Appl. Phys.*, To be published.
16. C. D. Thurmond and R. A. Logan, *This Journal*, **119**, 622 (1972).
17. R. H. Saul, O. G. Lorimor, and D. D. Roccasecca, Unpublished.
18. J. M. Ralston, *Rev. Sci. Instr.*, **43**, 876 (1972).

Technical Notes

Reduction of Carrier Concentration in $Pb_{1-x}Sn_xTe$ by Cd Diffusion and Doping with Zn

K. J. Linden

Infrared and Optical Research Laboratory, Special Microwave Devices Operation, Raytheon Company, Waltham, Massachusetts 02154

The compounds PbTe and SnTe form a complete series of pseudobinary solid solutions ($Pb_{1-x}Sn_xTe$, where $0 \leq x \leq 1$) characterized by the rock-salt crystal structure. These alloys have received considerable attention because they can be used to prepare high performance infrared detectors, operating at 77°K and above, that are sensitive in the 8-14 μm atmospheric window region of the infrared spectrum (1). The alloys of particular interest for this application are those with compositions in the range $0.18 < x < 0.25$, since their energy gaps lead to detector responsivities peaking in this region.

As is the case for PbTe and SnTe, as-grown crystals of $Pb_{1-x}Sn_xTe$ obtained from stoichiometric source materials by either melt-growth or vapor-growth techniques are strongly p-type, with carrier concentrations typically in the range between 10^{18} and 10^{19} cm^{-3}. The acceptors responsible for these high hole concentrations are native point defects that are present because the crystals are Te-rich with respect to the stoichiometric composition (2). In order to obtain material for device applications, annealing can be used to decrease the hole concentration by reducing the amount of excess Te or to convert the crystals to low concentration n-type by making them slightly Pb rich.

Reduced carrier concentrations in $Pb_{1-x}Sn_xTe$ with $x \approx 0.2$ have generally been obtained by an isothermal annealing technique (1, 3). The crystals are typically annealed in an ampoule containing a metal-rich, solid-liquid $(Pb_{1-x}Sn_x)_yTe_{1-y}$ mixture with the same x value as that of the crystals, but with y (typically 0.51) outside the homogeneity range of $Pb_{1-x}Sn_xTe$. The crystals change their composition by solid-state diffusion until they reach equilibrium with the vapor phase by becoming metal saturated. At equilibrium, their deviation from stoichiometry is therefore determined by the location of the metal-rich solidus for their particular x-value at the specific annealing temperature used.

The metal-rich solidus lines for $Pb_{1-x}Sn_xTe$ alloys with $x \approx 0.2$ cross the stoichiometric composition line, where the conductivity changes from p- to n-type, so that in principle the isothermal annealing technique could be used to obtain exactly stoichiometric material if the proper annealing temperature were used. However, near the crossover point the carrier concentration along the solidus line varies so strongly with annealing temperature that concentrations below 10^{16} cm^{-3} have not been reproducibly obtained, although a concentration of 1.8×10^{15} cm^{-3} has been reported for an n-type sample of $Pb_{0.83}Sn_{0.17}Te$ (4). Furthermore, for certain alloy compositions (namely those associated with smaller energy gaps) the lower isothermal annealing temperatures required to obtain reduced carrier concentrations necessitate the use of long annealing times.

Since as-grown $Pb_{1-x}Sn_xTe$ is normally p-type, the introduction of donor impurities can be expected to result in carrier concentration reductions. Elements from Group III of the periodic table (*e.g.*, Al and Ga) are capable of acting as donor impurities in PbTe in that when substituted for the Pb atom they provide an extra electron. These impurities may also increase the ratio of metal to nonmetal atoms and thereby lead to reduced carrier concentrations. The Group V atoms, Bi and Sb, behave in a similar manner in PbTe (5). The Group II impurities Zn and Cd have also been

Key words: lead tin telluride, infrared detectors, photoconductors, chalcogenides, ternaries.

shown to act as donor impurities, and low carrier concentrations have been achieved in $Pb_{0.83}Sn_{0.17}Te$ by annealing in the presence of these elements (6). Since these atoms have the same number of available electrons as Pb and Sn, their donor behavior is presumably the result of their increasing the metal to nonmetal ratio.

By the diffusion of vapor-grown samples of $Pb_{1-x}Sn_xTe$ with Zn and Cd, Antcliffe and Wrobel (6) obtained n-type material with carrier concentrations of 1.3×10^{17} cm^{-3} and mobilities up to 5×10^5 cm^2 V^{-1} sec^{-1} at 4.2°K. Using radioactive tracer methods, these authors found the Zn concentrations to be of the same order of magnitude as the excess hole concentrations in the material prior to diffusion, and therefore postulate that the Zn solubility is controlled mainly by the concentration of Pb vacancies. In the experiments reported here, diffusion experiments were performed on p-type vapor-grown crystals of $Pb_{1-x}Sn_xTe$ under various Cd vapor pressures. The results of attempts to incorporate Cd and Zn impurity atoms into $Pb_{1-x}Sn_xTe$ crystals during the vapor-growth process are also reported.

Cadmium diffusion experiments.—Cadmium diffusion experiments were carried out on $Pb_{0.76}Sn_{0.24}Te$ crystals grown from a stoichiometric source by a closed-tube vapor-growth technique similar to the one described by Calawa *et al.* (3). Such crystals were used since they generally have crystallographic and electrical properties superior to those of crystals obtained by melt-growth techniques such as the Bridgman method. This has been verified by cleavage experiments performed in this laboratory in which near-identically shaped and oriented samples of both Bridgman-grown and vapor-grown $Pb_{1-x}Sn_xTe$ were subjected to cleavage tests. It was found that the vapor-grown samples were characterized by cleavage faces with considerably fewer defects than those observed in the cleaved faces of Bridgman-grown samples. It was also found that photodiodes fabricated from vapor-grown material generally had higher quantum efficiencies than those fabricated from Bridgman-grown material.

Two different diffusion techniques were used: a single-zone method with elemental Cd as the source, and a two-zone technique in which the $Pb_{0.76}Sn_{0.24}Te$ crystals were held at one temperature and a Cd-In alloy source was at a lower temperature.

In the single-zone method, three to five crystals of $Pb_{0.76}Sn_{0.24}Te$ were sealed in an evacuated quartz capsule together with a weighed amount of Cd. Typical hole concentrations in the as-grown crystals varied from approximately 10^{18} to 10^{19} cm^{-3} at 77°K. Diffusions were carried out for 3 days at 600°C. Different Cd partial pressures were obtained by varying the amount of Cd in the capsule, which had a volume of about 35 cm^3. After diffusion, the capsule was removed from the furnace in such a manner that the Cd vapor condensed on one end of the capsule rather than on the crystals (which radiate efficiently and can therefore cool rapidly). The crystals were removed from the capsule, lapped to thicknesses of about 0.75 mm, polished, and etched. The resistivity and Hall coefficient of each crystal were then measured at 77°K by the van der Pauw method (7).

While it was not practical to remeasure the electrical characteristics of a given sample after repeated runs under the same diffusion conditions (since the effect of the soldered contacts at elevated temperatures would introduce an additional unknown), experiments showed that the length of the annealing times used (3 days) was sufficient to produce equilibrium for even the largest samples. This was demonstrated by annealing some samples for longer periods, and others for shorter periods. Samples annealed for longer times did not exhibit further changes in carrier concentration and mobility, but samples annealed for less than 2 days did not appear to have reached equilibrium.

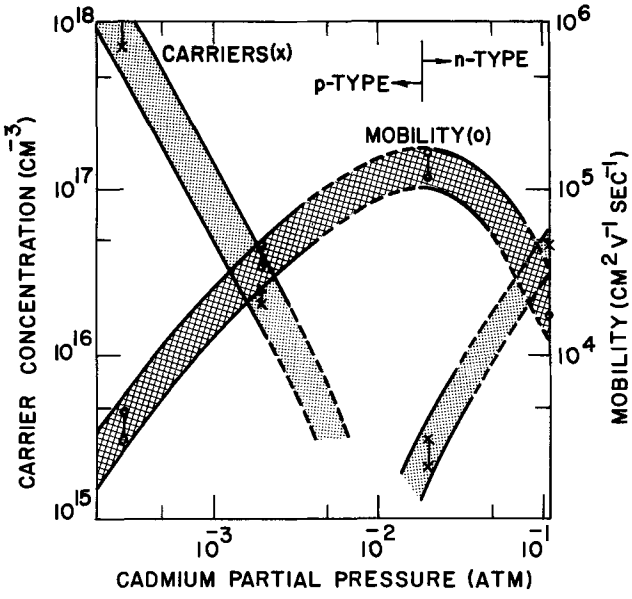

Fig. 1. Carrier concentration and mobility of $Pb_{0.76}Sn_{0.24}Te$ doped with cadmium by postgrowth diffusion using a single-zone method.

The results of the single-zone diffusion experiments are given in Fig. 1, which shows the carrier types, concentrations, and mobilities of crystals annealed under Cd partial pressures between about 3×10^{-4} and 1.1×10^{-1} atm. The pressure values were calculated by the perfect gas law from the amount of Cd introduced into each capsule. At the lowest Cd partial pressures shown in Fig. 1, the observed carrier concentrations and mobilities were similar to those of nonannealed material. As higher partial pressures were used, reduced carrier concentrations and increased mobility values were observed until, at partial pressures in excess of approximately 10^{-2} atm, the material converted from p- to n-type. The lowest carrier concentration attained by this single-zone diffusion method was 2.3×10^{15} cm^{-3}, n-type, with an accompanying mobility of 1.95×10^5 cm^2 V^{-1} sec^{-1}. From the slope of the curves in Fig. 1 it is clear that the attainment of carrier concentrations much below this value can be expected to be increasingly difficult. Further increases in Cd partial pressure lead to increased electron concentrations and reduced mobility values. Surface alloying of the Cd with the $Pb_{0.76}Sn_{0.24}Te$ was observed at the highest Cd pressure used (1.1×10^{-1} atm). At this pressure, the amount of Cd in the capsule was sufficiently large to cause condensation on the samples. In these experiments, it was assumed that the Pb-Sn ratio of the annealed crystals was the same as the ratio prior to annealing, this ratio having been initially determined by microprobe analysis.

The spread in data indicated in Fig. 1 is probably due to a combination of factors such as a variation in the carrier concentration of the as-grown crystals and differences in the total weight of the $Pb_{0.76}Sn_{0.24}Te$ crystals from one capsule to the next. The data points for a given annealing temperature were generally obtained for crystals grown in separate runs, although those at 2×10^{-3} atm were obtained for crystals from the same growth run. Each data point represents a different annealing run.

Assuming a linear relationship between density of states effective mass and energy gap, which is supported by $Pb_{1-x}Sn_xTe$ laser emission data, Melngailis and Harman (1) have calculated the intrinsic carrier concentrations for various temperatures as a function of energy gap. For material with a bandgap of approximately 0.09 eV at 77°K, the calculated intrinsic carrier concentration at 77°K is approximately 8×10^{13} cm^{-3}. Thus the lowest carrier concentration achieved in the above series of Cd diffusions was from one to two orders of magnitude larger than the cal-

culated intrinsic carrier concentration. It should be noted that, while $Pb_{0.76}Sn_{0.24}Te$ has been made n-type by annealing at 600°C in a Cd atmosphere, this cannot be achieved by isothermal annealing at this temperature in the absence of impurities since, for this composition, even metal-saturated crystals are p-type at 600°C (3).

The homogeneity of the annealed samples was studied by electron-microprobe analysis using a 1 μm diameter electron beam to scan the wafer surfaces. This analysis did not reveal any compositional inhomogeneities or precipitates to within the accuracy of the instrument (1-2%). However such microprobe analysis is incapable of revealing the presence of any microprecipitates which are considerably smaller than 1 μm in dimension or microprecipitates located more than an electron beam absorption length (on the order of a few micrometers) below the sample surface. It has been shown by Wolfe, Stillman, and Rossi (8) that inhomogeneities in semiconductors can result in anomalously high mobility values. It is therefore possible that the high value of mobility observed here could be due to the presence of some microprecipitates or microinhomogeneities in the samples.

In a second type of Cd diffusion experiment, $Pb_{0.76}Sn_{0.24}Te$ crystals and a Cd source were sealed into an evacuated quartz capsule which was then placed in a two-zone furnace. The crystal temperature was held at 500°C, while in different runs the source temperature was varied from approximately 120° to 265°C. In order to reduce the possibility of surface alloying as well as the dependence of Cd partial pressure on source quantity, an infinite alloy source of 1% Cd in In weighing approximately 0.2g was used. Since the vapor pressure of In is eight orders of magnitude less than that of Cd, and Cd readily alloys with In to form a soft, dilute mixture, the 1% Cd in In alloy proved to be a convenient diffusion source. The results of this second series of Cd diffusion experiments are summarized in Fig. 2. As in the first series of experiments, measurements on samples in the van der Pauw configuration were used to determine carrier concentrations and mobilities. As the diffusant source temperature was increased from 120°C, the hole concentration decreased and the mobility increased until, at approximately 200°C, the material converted from p- to n-type. The lowest carrier concentration achieved by this two-zone diffusion technique was 1.4×10^{15} cm^{-3} with an accompanying mobility of 1.85×10^5 $cm^2\ V^{-1}\ sec^{-1}$. This concentration is somewhat lower than the lowest obtained by the single-zone diffusion method. In connection with the high mobility value observed here, the same comments regarding the possibility of microinhomogeneities causing anomalous mobility values as noted above are relevant, even

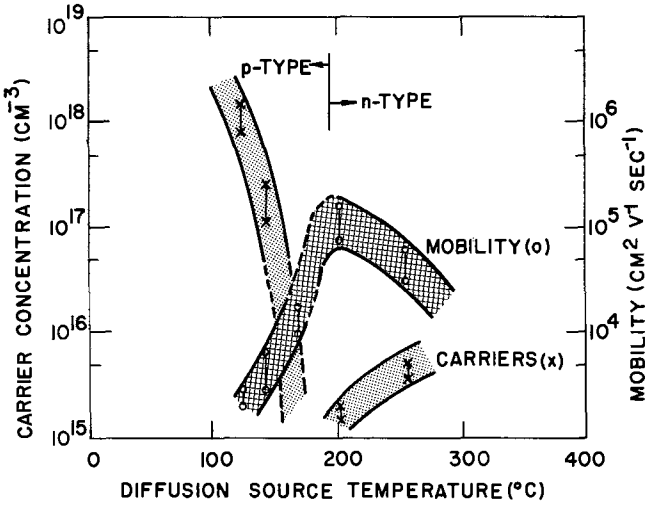

Fig. 2. Carrier concentration and mobility of $Pb_{0.76}Sn_{0.24}Te$ diffused from a 1% Cd in In source using a two-zone method.

though electron-microprobe scans of these samples revealed no inhomogeneities.

In order to determine whether any significant outdiffusion of Cd from $Pb_{1-x}Sn_xTe$ would occur under elevated-temperature vacuum conditions (such as might occur during the vacuum Dewar packaging of devices), Cd-diffused van der Pauw samples were baked at 125°C for 8 days under a dynamic vacuum of approximately 10^{-8} Torr. As might be expected for a temperature so low compared to the in-diffusion temperature, no changes in either the carrier concentrations or the mobilities were observed.

Cadmium and zinc incorporation into $Pb_{1-x}Sn_xTe$ during vapor growth.—Experiments were also performed to determine whether a reduction in carrier concentration could be achieved by incorporating Cd or Zn into $Pb_{1-x}Sn_xTe$ during crystal growth from the vapor phase. Either elemental Cd or Zn was introduced into the vapor-growth capsules, which were maintained in a horizontal position to prevent alloying of the metal with the $Pb_{1-x}Sn_xTe$. This technique is inherently less versatile than the methods described previously since the impurity can be incorporated into the crystals only at the growth temperatures, which typically range from 700° to 800°C. On the other hand, the method is in principle convenient since the impurities are introduced during growth and no postgrowth annealing is required. A range of impurity partial pressures was obtained by introducing amounts of Cd or Zn varying from 10^{-5} to 10^{-3}g into the growth capsules, which had volumes between 100 and 300 cm^3. With increasing Cd or Zn pressure the as-grown crystals changed from p- to n-type, and carrier concentrations as low as 4.4×10^{16} cm^{-3} were obtained. However, the results were so irreproducible that this method does not appear to be feasible for obtaining low carrier concentrations.

Conclusion

Experiments were carried out to explore possible methods of reducing carrier concentrations in $Pb_{1-x}Sn_xTe$ vapor-grown crystals. A significant reduction in carrier concentration accompanied by an increase in mobility has been achieved by using one-zone and two-zone annealing techniques for the diffusion of Cd into vapor-grown crystals of $Pb_{0.76}Sn_{0.24}Te$. The reduction in carrier concentration should make it possible to fabricate efficient photoconductive detectors and potentially to produce low capacitance photodiodes.

Acknowledgments

The author is indebted to L. Thurber for crystal growth and diffusion and to L. Sicotte for sample fabrication and testing. Useful discussions with L. Cameron of the U.S. Army Electronics Command's Night Vision Laboratory, T. C. Harman of M.I.T. Lincoln Laboratory, P. P. Debye and C. A. Kennedy of this laboratory are also acknowledged. The electron beam microanalysis of the van der Pauw samples was carried out by O. J. Guentert of the Raytheon Research Division. Finally, the author is indebted to A. J. Strauss for illuminating comments and suggestions incorporated in the introduction and text of this paper.

This work was funded, in part, by the Far Infrared Technical Area, U.S. Army Electronics Command's Night Vision Laboratory, Ft. Belvoir, Virginia.

Manuscript submitted Sept. 11, 1972; revised manuscript received Dec. 21, 1972.

Any discussion of this paper will appear in a Discussion Section to be published in the June 1974 JOURNAL.

REFERENCES

1. I. Melngailis and T. C. Harman, in "Semiconductors and Semimetals," R. K. Willardson and A. C. Beer, Editors, Vol. 5, p. 111, Academic Press, New York (1970).
2. R. F. Brebrick, in "Progress in Solid State Chemis-

try," H. Reiss, Editor, Vol. 3, pp. 217-220, Pergamon Press, New York (1966).
3. A. R. Calawa, T. C. Harman, M. Finn, and P. Youtz, *Trans. Met. Soc. AIME*, **242**, 374 (1968).
4. T. C. Harman, in "The Physics of Semimetals and Narrow-Gap Semiconductors," D. L. Carter and R. T. Bate, Editors, p. 363, Pergamon Press, Oxford, England (1971).
5. Yu. I. Ravich, B. A. Efimova, and I. A. Smirnov, "Semiconducing Lead Chalcogenides," p. 34, Plenum Press, New York (1970).
6. G. A. Antcliffe and J. S. Wrobel, *Mater. Res. Bull.*, **5**, 747 (1970).
7. L. J. van der Pauw, *Philips Res. Rep.*, **13**, 1 (1958).
8. C. M. Wolfe, G. E. Stillman, and J. A. Rossi, *This Journal*, **119**, 250 (1972).

The General Problem of Rediffusion in Semiconductor Devices

M. A. Fullenwider*,[1]

Institute for Inorganic, Analytic, and Physical Chemistry, University of Bern, Bern, Switzerland

The problem of rediffusion (solution for the flux out of precharged specimens and the resulting concentration profiles) has been solved for many cases. Two cases of particular importance have been solved (1) for semi-infinite specimens. They are (*i*) the case of the uniform initial condition and (*ii*) the case of the error function complement initial condition. The expressions for the flux (J_t) at the surface are, respectively

$$J_t = C_o\left(\frac{D}{\pi t}\right)^{1/2}\left[1 - 2\sum_{n=0}^{\infty}(-1)^n e^{-(n+1)^2L^2/Dt}\right] \quad [1]$$

an equation applying to a finite specimen, with the approximation for semi-infinite specimens

$$J_t = C_o\left(\frac{D}{\pi t}\right)^{1/2} \quad [1a]$$

Note that Eq. [1] as it appears in Ref. (1) is in error by a factor of 2. And

$$J_t = \frac{D^{1/2}C_o}{\pi^{1/2}}\left[\frac{1}{t^{1/2}} - \frac{1}{(t+t_o)^{1/2}}\right] \quad [2]$$

and for the concentration profiles, $C(x, t)$, during the rediffusion process, respectively

$$C(x,t) = C_o - C_o\sum_{n=0}^{\infty}(-1)^n \operatorname{erfc}\frac{(2n+1)L - x}{2(Dt)^{1/2}} - C_o\sum_{n=0}^{\infty}(-1)^n \operatorname{erfc}\frac{(2n+1)L - x}{2(Dt)^{1/2}} \quad [3]$$

and

$$C(x,t) = C_o\left[\operatorname{erf}\frac{x}{2(Dt)^{1/2}} - \operatorname{erf}\frac{x}{2(Dt_o + Dt)^{1/2}}\right] \quad [4]$$

where: C_o is the maximum concentration within the specimen at the time rediffusion starts; D, the diffusion coefficient; t, the time of rediffusion after the surface concentration has been made zero; t_o, the time that the specimen is allowed to charge with the diffusing species; x, the distance into the specimen; and L, the thickness of the specimen.

These expressions have been of great utility. For example, Eq. [2] was used (1) to extend the evaluation of D for hydrogen in metals by a factor of approximately 10^5.

The error function complement profile is one of the two types of profiles commonly found in semiconductor devices, corresponding to a constant quantity of the impurity at the surface of a semi-infinite specimen during diffusion into the semiconductor. The other case, the problem of rediffusion, to be discussed here since it does not appear in the literature, is that of a Gaussian concentration profile, corresponding to a finite quantity of the impurity at the surface of the semiconductor. The solutions to these problems of rediffusion should be of interest to solid-state scientists since, by varying the two quantities, (*i*) time of diffusion into the specimen and (*ii*) time of rediffusion out of the same specimen, quite a variety of known profiles can be easily prepared.

The expression for the initial condition of the problem to be discussed here is (2)

$$C(x, t_o) = C_o e^{-x^2/4Dt_o} \quad [5]$$

where the symbols have the same definition as previously. Also

$$C_o = \frac{Q}{(\pi Dt_o)^{1/2}} \quad [6]$$

where Q is the amount of diffusing substance at the surface initially. To obtain a solution to the problem of rediffusion in this case we use the Green's function representation of the diffusion equation. Thus we have in one dimension (3)

$$C(x,t) = \int (u)_{\tau=0} f(x')\,dx' + D\int_o^t \phi(\tau)\frac{\partial u}{\partial n_i}\,d\tau \quad [7]$$

where $f(x')$, is the initial distribution; $\phi(\tau)$, the surface distribution; $\partial/\partial n_i$, the differentiation along the inward drawn normal to the surface; and u, the Green's function, is the concentration at x' and time t due to a unit instantaneous source at x and time τ. In this case we have (3)

$$u = \frac{1}{[4\pi D(t-\tau)]^{1/2}}\{e^{-(x-x')^2/4D(t-\tau)} - e^{-(x+x')^2/4D(t-\tau)}\} \quad [8]$$

also

$$\phi(\tau) = 0 \quad [9]$$

Thus

$$C(x,t) = \frac{C_o}{(4\pi Dt)^{1/2}}\int_o^{\infty} e^{-x'^2/4Dt_o}\, e^{-(x-x')^2/4Dt}\,dx' - \frac{C_o}{(4\pi Dt)^{1/2}}\int_o^{\infty} e^{-x'^2/4Dt_o}\, e^{-(x+x')^2/4Dt}\,dx' \quad [10]$$

and by a known definite integral we have for the concentration profile

$$C(x,t) = C_o\left(\frac{t_o}{t+t_o}\right)^{1/2} e^{-x^2/4D(t+t_o)} \operatorname{erf}\left\{x\left[\frac{t_o}{4D(t^2+tt_o)}\right]^{1/2}\right\} \quad [11]$$

and since

* Electrochemical Society Active Member.
[1] Present address: 2970 MacArthur Road, White Hall, Pennsylvania 18052.
Key words: rediffusion, concentration profiles.

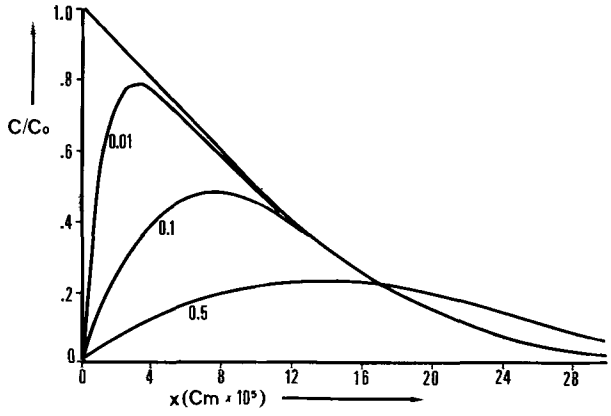

Fig. 1. Error function complement initial condition, surface concentration zero during rediffusion.

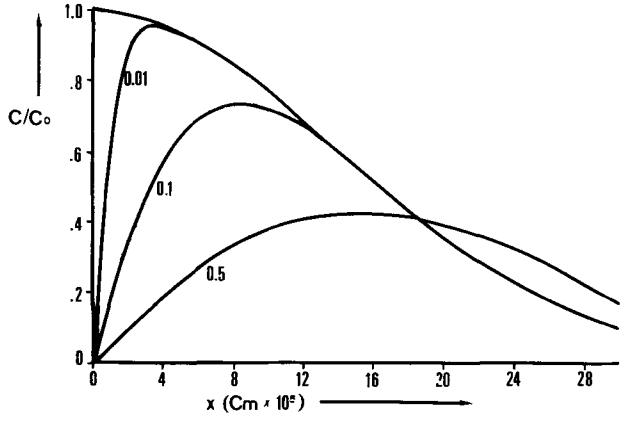

Fig. 2. Gaussian initial condition, surface concentration zero during rediffusion.

$$J_t = -D\left(\frac{\partial C}{\partial x}\right)_{x=0} \qquad [12]$$

we have for the flux at the surface

$$J_t = \frac{D^{1/2} C_o}{\pi^{1/2}}\left[\frac{t_o}{t^{1/2}(t + t_o)}\right] \qquad [13]$$

Also putting Eq. [6] into Eq. [13] we have an interesting expression involving only J_t, Q, t, and t_o

$$J_t = \frac{Q}{\pi}\left[\frac{t_o^{1/2}}{t^{1/2}(t + t_o)}\right] \qquad [14]$$

Now Eq. [4] and Eq. [11] hold only for the case of zero surface concentration during the rediffusion process. To obtain solutions for cases where the surface concentration has some constant nonzero value it is only necessary to add to these solutions the quantity (from Eq. [7] and Eq. [8] with $f(x') = 0$ and $\phi(\tau) = C_1$, the concentration at the surface during rediffusion)

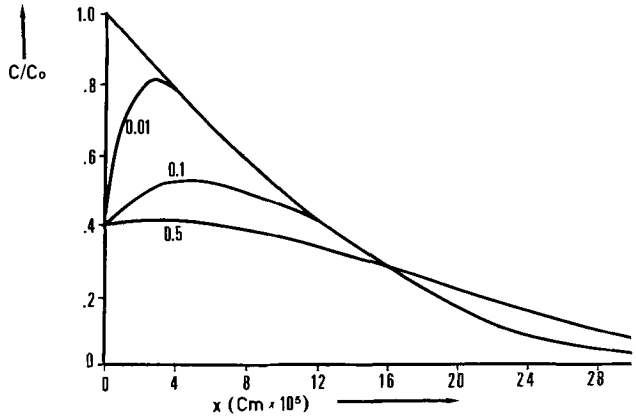

Fig. 3. Error function complement initial condition, $C_1/C_o = 0.4$ during rediffusion.

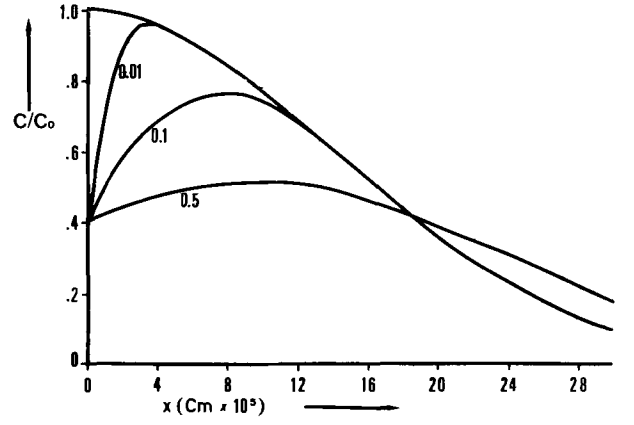

Fig. 4. Gaussian initial condition, $C_1/C_o = 0.4$ during rediffusion

$$C(x, t)_{f(x')=0} = \frac{C_1 x}{(4\pi D)^{1/2}}\int_o^t \frac{e^{-x^2/4D(t+\tau)}}{(t - \tau)^{3/2}}\, d\tau \qquad [15]$$

which is simply

$$C(x, t)_{f(x')=0} = C_1 \operatorname{erfc}\frac{x}{2(Dt)^{1/2}} \qquad [16]$$

Figures 1-4 illustrate some typical concentration profiles. The numbers on the curves are the ratios of t to t_o.

Manuscript submitted July 17, 1972; revised manuscript received March 8, 1973.

Any discussion of this paper will appear in a Discussion Section to be published in the June 1974 JOURNAL.

REFERENCES

1. J. O'M. Bockris, M. A. Genshaw, and M. Fullenwider, *Electrochim. Acta*, **15**, 47 (1970).
2. R. M. Barrer, "Diffusion in and through solids," p. 44, Cambridge University Press, New York (1934).
3. H. S. Carslaw and J. C. Jaeger, "Conduction of Heat in Solids," p. 356, Oxford University Press, London (1959).

Impurity Atom Distribution Resulting from Thermal Redistribution of an Implanted Impurity Source

David S. Perloff

Research and Development Laboratory, Signetics Corporation, Sunnyvale, California 94086

The diffusion into silicon of impurities introduced by implantation is acquiring increasing significance in device and circuit fabrication (1-4). An important advantage of this method is that the implanted impurities may be thermally redistributed without concurrent oxidation if the implantation is carried out

Key words: diffusion, ion implantation, oxide, semiconductor, silicon.

through an existing oxide layer of sufficient thickness (1, 5). For such a case, a general solution of the diffusion equation may be obtained which describes the distribution of impurities within the semiconductor and, under a rather unrestrictive assumption, within the oxide layer. A related problem has been treated by Kennedy and Murley (6) for the two-step diffusion process traditionally employed for transistor fabrication.

In certain MOS applications, a significant fraction of the implantation dose is deposited within the oxide layer (7). The net transfer of impurities from oxide to semiconductor must then be considered to predict doping profiles accurately. The results of the following mathematical treatment should be found useful for determining the significance of the oxide layer as a secondary source of impurities in such cases. As an example, the behavior of boron as the implanted diffusant is treated.

Mathematical Treatment

The impurity distribution resulting from the implantation will be approximated by (8)

$$N(x) = \frac{\phi}{\sqrt{2\pi}\,\Delta R_p} \exp - \left(\frac{x + w - R_p}{\sqrt{2}\,\Delta R_p} \right)^2 \quad t = 0 \qquad [1]$$

where $N(x)$ is the impurity concentration at a distance x from the oxide-semiconductor interface, w is the thickness of the oxide layer, R_p and ΔR_p are, respectively, the projected range and standard deviation of the implanted impurity (assumed to be the same in both oxide and semiconductor), and ϕ is total implantation dose expressed in ions/cm^2.

The impurity atom distribution in the oxide (diffusion constant D_1) is then obtained by solving the diffusion equation

$$\frac{\partial^2 N_1}{\partial x^2} = \frac{1}{D_1} \frac{\partial N_1}{\partial t} \quad -\infty < x < 0 \qquad [2]$$

and that in the semiconductor (diffusion constant D_2) by solving

$$\frac{\partial^2 N_2}{\partial x^2} = \frac{1}{D_2} \frac{\partial N_2}{\partial t} \quad 0 < x < \infty \qquad [3]$$

The boundary conditions, in addition to Eq. [1], are

$$D_1 \frac{\partial N_1}{\partial x} = D_2 \frac{\partial N_2}{\partial x} \quad x = 0, \quad t > 0 \qquad [4]$$

$$N_2 = mN_1 \quad x = 0, \quad t > 0 \qquad [5]$$

$$N_1 = 0 \quad x = -\infty \qquad [6]$$

$$N_2 = 0 \quad x = \infty \qquad [7]$$

Strictly speaking, Eq. [1] is valid only when the stopping power associated with each medium is identical and effects such as channeling and enhanced diffusion are neglected. Nevertheless, a simple Gaussian distribution should provide an adequate representation of the initial distribution of impurities in many cases of practical interest.

Equation [6] implies that the external boundary of the oxide layer is sufficiently far from the oxide-semiconductor interface that it can be neglected when considering the distribution of impurities inside the semiconductor. This assumption is reasonable when the diffusion length of the impurity within the oxide is small compared with the thickness of the oxide. (For both boron and phosphorous in silicon, this condition is satisfied over a wide range of implantation and diffusion conditions for oxide thicknesses greater than 1000A.)

Solutions to Eq. [2] and [3], subject to the boundary conditions, are obtained by employing integral representations for N_1 and N_2 in the manner described by Boltaks (9). The impurity distribution in the semiconductor ($x \geq 0$) is given by

$$N_2(x,t) = \frac{1}{2\sqrt{\pi}} \frac{\phi}{\gamma_2} \left\{ \left[\exp - \left(\frac{x - \lambda}{\gamma_2} \right)^2 \cdot \operatorname{erfc} - \left(\frac{\alpha_2^2 x + \alpha_0^2 \lambda}{\sqrt{\alpha_0^2 + \alpha_2^2}} \right) + \exp - \left(\frac{x + \lambda}{\gamma_2} \right)^2 \cdot \operatorname{erfc} \left(\frac{\alpha_2^2 x - \alpha_0^2 \lambda}{\sqrt{\alpha_0^2 + \alpha_2^2}} \right) \right] - \frac{2r}{r+m} \left[\exp - \left(\frac{x + \lambda}{\gamma_2} \right)^2 \cdot \operatorname{erfc} \left(\frac{\alpha_2^2 x - \alpha_0^2 \lambda}{\sqrt{\alpha_0^2 + \alpha_2^2}} \right) - m \frac{\gamma_2}{\gamma_1} \exp - \left(\frac{rx - \lambda}{\gamma_1} \right)^2 \operatorname{erfc} \left(\frac{\alpha_1^2 rx + \alpha_0^2 \lambda}{\sqrt{\alpha_0^2 + \alpha_1^2}} \right) \right] \right\} \qquad [8]$$

where the following parameters have been introduced

$$r = \sqrt{D_1/D_2}; \quad \lambda = R_p - w$$

$$\alpha_0 = 1/\sqrt{2}\,\Delta R_p; \quad \alpha_1 = 1/2\sqrt{D_1 t}; \quad \alpha_2 = 1/2\sqrt{D_2 t}$$

$$\gamma_1 = \sqrt{1/\alpha_0^2 + 1/\alpha_1^2}; \quad \gamma_2 = \sqrt{1/\alpha_0^2 + \alpha_2^2} \qquad [9]$$

The impurity distribution in the oxide ($x \leq 0$), subject to the assumption already discussed, may be obtained by interchanging indices 1 and 2 and setting $x = -x$, $\lambda = -\lambda$, $r = 1/r$, and $m = 1/m$ in the right-hand side of Eq. [8].

Equation [8] has been structured to emphasize the influence of the oxide-semiconductor interface on the distribution of impurities in the semiconductor. The first half of Eq. [8] is the distribution of impurities when the oxide-semiconductor interface is impermeable ($-D_2\,\partial N_2/\partial x = 0$ at $x = 0$). The second half of Eq. [8] therefore describes the incremental distribution of impurities due to the segregation of impurities at the oxide-silicon interface (Eq. [5]) and the requirement that the flux of impurities be continuous at the interface (Eq. [4]).

The impurity concentration at the oxide-semiconductor interface, gotten by substituting $x = 0$ in Eq. [8], is given by

$$N_2(0,t) = \frac{\phi}{\sqrt{\pi}} \frac{m}{r+m} \left[\frac{\exp - (\lambda/\gamma_2)^2}{\gamma_2} \cdot \operatorname{erfc} - \left(\frac{\alpha_0^2 \lambda}{\sqrt{\alpha_0^2 + \alpha_2^2}} \right) + r \frac{\exp - (\lambda/\gamma_1)^2}{\gamma_1} \cdot \operatorname{erfc} \left(\frac{\alpha_0^2 \lambda}{\sqrt{\alpha_0^2 + \alpha_1^2}} \right) \right] \qquad [10]$$

$N_1(0,t)$ is immediately obtained by using the condition $N_2(0,t) = mN_1(0,t)$ specified in Eq. [5].

The impurity content of the silicon, as a function of time, is determined by evaluating the integral $\phi_2(t) = \int_0^\infty N_2(x,t)\,dx$, in which $N_2(x,t)$ is given by Eq. [8] and, by definition, $\phi_1(t) + \phi_2(t) = \phi$. Using the fact that the fractional impurity content at $t = 0$ is given by

$$\frac{\phi_2(0)}{\phi} = \frac{1}{2}\left[1 + \operatorname{erf}(\alpha_0 \lambda)\right] \qquad [11]$$

the following expression may be shown to describe the fractional impurity content at any later time t

$$\frac{\phi_2(t)}{\phi} = \frac{\phi_2(0)}{\phi} + \frac{1}{2}\frac{\exp -(\alpha_0\lambda)^2}{r+m}\left\{ r\left[\frac{\tan^{-1}(\alpha_2/\alpha_0)}{\pi/2} - \frac{\alpha_2}{\alpha_0}F(-\alpha_2)\right] - m\left[\frac{\tan^{-1}(\alpha_1/\alpha_0)}{\pi/2} - \frac{\alpha_1}{\alpha_0}F(\alpha_1)\right] - (r-m)\right\} \quad [12]$$

where, for $i = 1$ or 2

$$F(a_i) = \frac{2}{\sqrt{\pi}}\int_0^{\pi/2} a_i^3 \exp(a_i^2) \cdot \operatorname{erfc}(a_i)\frac{d\theta}{(\alpha_0\lambda\sin\theta)^2} \quad [13]$$

and

$$a_i(\theta) = \frac{\alpha_0^2\lambda\sin\theta}{\sqrt{\alpha_0^2\sin^2\theta + \alpha_i^2(1+\sin 2\theta)}} \quad [14]$$

The definite integrals in Eq. [12] represented by the functions $F(a_1)$ and $F(-a_2)$ may be numerically evaluated by routine application of Simpson's rule.

Example

As an example, the case of boron implanted through an oxide layer into an underlying silicon substrate will now be considered. In Fig. 1, the net change of impurity content of the silicon is plotted as a function of the dimensionless quantity $|R_p - w|/2\sqrt{D_2 t}$ for various values of the parameter $\phi_2(0)/\phi$. The values $m = 0.33$ and $r^2 = D_1/D_2 = 2.5 \times 10^{-4}$ used for these calculations are typical of those encountered for the diffusion of boron over the temperature range 1150°-1250°C (10, 11). In general, when $m < 1$, impurity transfer occurs first out of the silicon (to correct for the nonequilibrium distribution of impurities at the interface at $t = 0$), then into the silicon (to replenish impurities which rapidly diffuse away from the silicon interface), and finally out of the silicon (when the oxide has become depleted of impurity to the extent that Eq. [5] can no longer be satisfied). In many practical applications in device and circuit fabrication involving boron as the diffusant, the oxide will therefore behave as a secondary source of impurities. The extent to which this occurs will of course depend on the location of the implanted distribution relative to the oxide-silicon interface.

In Fig. 2, the net change of impurity content of the silicon for the case $\phi_2(0)/\phi = 0.5 (R_p = w)$ is plotted as a function of the dimensionless parameter $\alpha_2/\alpha_0 = \sqrt{2}\,\Delta R_p/2\sqrt{D_2 t}$ for $r^2 = 2.5 \times 10^{-4}$ and various values of the segregation coefficient m. According to Eq. [12]-[14], when $R_p = w$ ($\lambda = 0$)

$$\frac{\phi_2(t)}{\phi} = \frac{1}{2}\left\{1 + \frac{1}{r+m}\left[r\frac{\tan^{-1}(\alpha_2/\alpha_0)}{\pi/2} - m\frac{\tan^{-1}(\alpha_1/\alpha_0)}{\pi/2} - (r-m)\right]\right\} \quad [15]$$

As $\alpha_2/\alpha_0 \to 0$, $\phi_2(t)/\phi_2(0) \to (m-r)/(m+r)$ and consequently $\phi_2(t)/\phi_1(t) \to m/r$, a result which may also be obtained using the qualitative argument employed by Wagner (12). This behavior is illustrated in Fig. 2 for $\alpha_2/\alpha_0 \sim 10^{-4}$. Evidently, for the smaller values of the segregation coefficient m, significant transfer of impurity from the silicon to the oxide will take place when $\alpha_2/\alpha_0 \gtrsim 0.05$.

In Fig. 3 the normalized impurity concentration $N_2(x,t)/\tilde{N}_2(0,t)$ (for the case $R_p = w$) is plotted as a function of the dimensionless parameter x/γ_2 for various values of the parameter α_2/α_0. The quantity $\tilde{N}_2(0,t) = \phi/\sqrt{\pi}\gamma_2$ represents the surface concentration when the interface is impermeable, obtained by setting $r = \lambda = 0$ in Eq. [10]. For this case, $N_2(x,t) = (\phi/\sqrt{\pi}\gamma_2)\cdot\exp -(x/\gamma_2)^2$, which describes a Gaussian distribution of impurities for which the standard deviation is $\gamma_2/\sqrt{2}$ and the total impurity content $\phi/2$. The departure from a Gaussian distribution for the case of a permeable interface ($r \neq 0$) becomes quite significant when $\alpha_2/\alpha_0 \lesssim 0.05$, as suggested also in Fig. 2. It is easily shown that as $\alpha_2/\alpha_0 \to 0$, both $\phi_2(t)/\phi_2(0)$ and $N_2(0,t)/\tilde{N}(0,t)$ approach a limiting value of $2r/(m+r)$ which, for $r^2 = 2.5 \times 10^{-4}$ and $m = 0.33$, is equal to 1.91 (Fig. 2 and 3).

The curves of Fig. 1-3 are expected to provide a reasonable description of the diffusion behavior only as long as the diffusion length of boron in silicon dioxide does not exceed the oxide thickness. The parameter $|R_p - w|/2\sqrt{D_2 t}$ must, therefore, be greater than $r|R_p/w - 1|$ for each of the curves of Fig. 1. For example, according to Eq. [11], when $\phi_2(0)/\phi = 0.60$, $R_p/w = 1.065$ (assuming $R_p = 4\Delta R_p$). Thus the range of validity for the curve labeled 0.60 should be restricted to that portion of the abscissa for which $|R_p - w|/2\sqrt{D_2 t} \gtrsim 1 \times 10^{-3}$. A similar restriction applies to the use of the curves in Fig. 2 and 3. In this case, $\sqrt{2}\,\Delta R_p/2\sqrt{D_2 t}$ must be greater than or equal to $r \cdot \sqrt{2}\,\Delta R_p/R_p$. Since $R_p \approx 4\Delta R_p$ for practical applica-

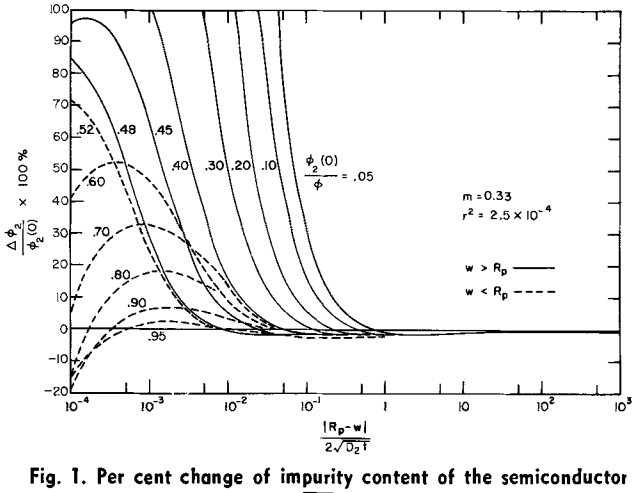

Fig. 1. Per cent change of impurity content of the semiconductor as a function of $|R_p - w|/2\sqrt{D_2 t}$ for various values of the parameter $\phi_2(0)/\phi$.

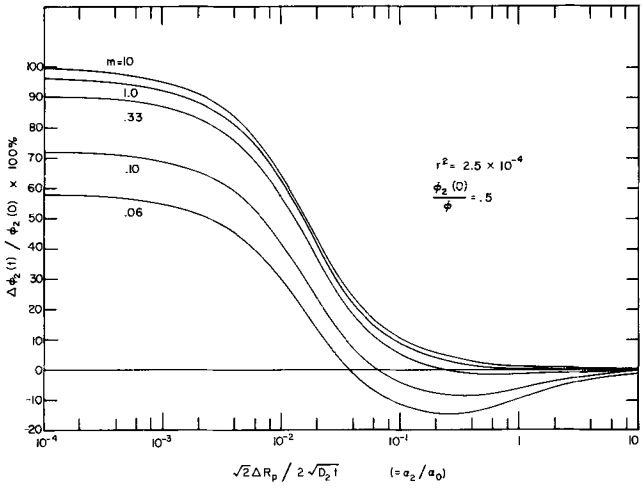

Fig. 2. Per cent change of impurity content of the semiconductor as a function of $\sqrt{2}\Delta R_p/2\sqrt{D_2 t}$ for the case $\phi_2(0)/\phi = 0.5$ ($R_p = w$). Curves are plotted for various values of the segregation coefficient m.

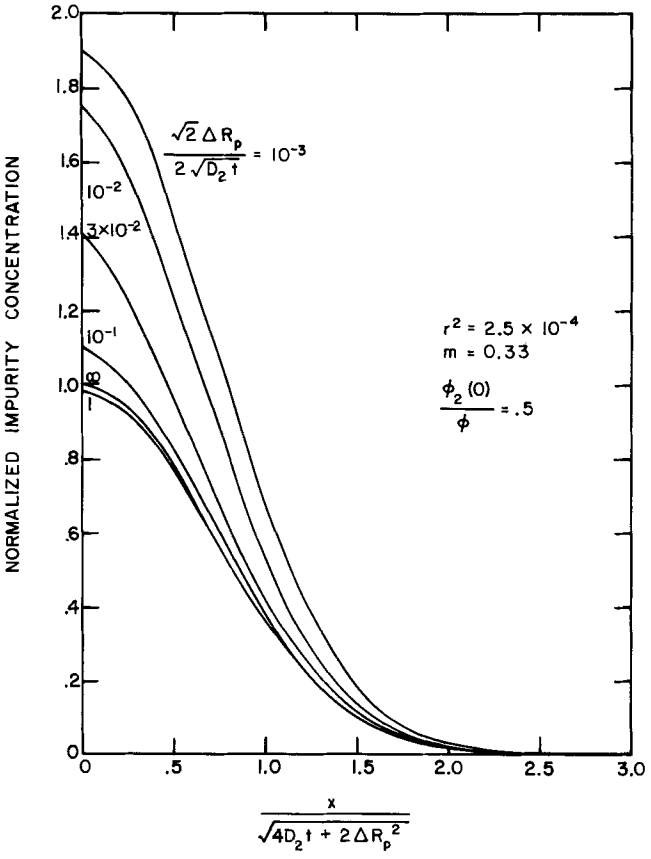

Fig. 3. Normalized impurity concentration as a function of $x/\sqrt{4D_2t + 2\Delta R_p^2}$ ($= x/\gamma_2$) for the case $\phi_2(0)/\phi = 0.5$ ($R_p = w$). Curves are plotted for various values of the parameter $\sqrt{2}\Delta R_p/2\sqrt{D_2 t}$. The curve labeled ∞ represents the normalized distribution of implanted impurities at $t = 0$, exp $- (x/\sqrt{2}\Delta R_p)^2$.

tions involving implanted boron, it follows that the range of validity for the parameter $\sqrt{2}\,\Delta R_p/2\sqrt{D_2 t}$ does not extend below values $\sim 5 \times 10^{-3}$. In order to accurately treat the diffusion behavior for those cases for which $2\sqrt{D_1 t} \gtrsim w$, it would be necessary to consider the influence of the SiO_2-ambient interface, as has been done for conventional doped-oxide diffusion sources (13).

Conclusion

An exact solution of the diffusion equation has been obtained for the impurity atom distribution which results from thermal redistribution of an ion implanted impurity source. It was assumed that the implantation was through an existing oxide layer of thickness at least comparable to the diffusion length of the impurity in the oxide. As an illustration, the behavior of a boron implanted impurity source in silicon was examined, assuming diffusion parameters typical of the temperature range 1150°-1250°C.

Manuscript submitted Jan. 15, 1973; revised manuscript received March 23, 1973.

Any discussion of this paper will appear in a Discussion Section to be published in the June 1974 JOURNAL.

LIST OF SYMBOLS

α_0	reciprocal of the standard deviation of the implanted Gaussian distribution, cm^{-1}
α_1	reciprocal of the diffusion length of the impurity in the oxide, cm^{-1}
α_2	reciprocal of the diffusion length of the impurity in the semiconductor, cm^{-1}
D_1	diffusion coefficient of impurity in oxide, cm^2 sec^{-1}
D_2	diffusion coefficient of impurity in semiconductor, cm^2 sec^{-1}
λ	distance between peak of the implanted Gaussian distribution and oxide-semiconductor interface, cm
m	segregation coefficient of impurity between oxide and semiconductor
N_1	concentration of impurity in oxide, cm^{-3}
N_2	concentration of impurity in semiconductor, cm^{-3}
ϕ	total implanted dose, cm^{-2}
$\phi_1(t)$	density of impurities in the oxide after time t, cm^{-2}
$\phi_2(t)$	density of impurities in the semiconductor after time t, cm^{-2}
$\Delta\phi_2(t)$	net change of density of impurities in the semiconductor after time t, cm^{-2}
R_p	projected range of impurity, cm
ΔR_p	standard deviation of the implanted Gaussian distribution of impurities, cm
r	ratio of diffusion length in oxide to diffusion length in semiconductor
t	elapsed time, sec
w	thickness of oxide layer, cm
x	distance from oxide-semicondutcor interface, cm

REFERENCES

1. J. Stephen, Semicon Symp. Internepcon, Brighton, Eng. (1971).
2. A. V. MacRae, *Radiation Effects*, **7**, 59 (1971).
3. R. A. Moline and G. F. Foxhall, *IEEE Trans. Electron Devices*, **ED-19**, 268 (1972).
4. P. J. Coppen, K. G. Aubuchon, L.-O. Bauer, and N. E. Moyer, *Solid-State Electron.*, **15**, 165 (1972).
5. R. W. Bower in "Ion Implantation in Semiconductors," Ch. 6, Mayer, Eriksson, and Davies, Editors, Academic Press, New York (1970).
6. D. P. Kennedy and P. C. Murley, *Proc. IEEE*, **52**, 520 (1964).
7. F Kashkooli, Signetics Corp., Private communication (1972).
8. J. F. Gibbons, *Proc. IEEE*, **56**, 295 (1968).
9. B. I. Boltaks, "Diffusion in Semiconductors," Academic Press, New York (1963).
10. A. S. Grove, O. Leistiko, and C. T. Sah, *J. Appl. Phys.*, **35**, 2695 (1964).
11. K. V. Anand, H. D. McKell, and D. C. Northrop, *J. Phys. D: Appl. Phys.*, **4**, 1722 (1971).
12. S. Wagner, *This Journal*, **119**, 1570 (1972).
13. M. L. Barry and P. Olofsen, *ibid.*, **116**, 854 (1969).

Brief Communications

On the Statistics Governing the Defect Density Determination in SiO_2 Films

N. J. Chou* and J. M. Eldridge*

IBM Thomas J. Watson Research Center, Yorktown Heights, New York 10598

In a paper by Meek and Braun that appeared in the November 1972 JOURNAL (1), reference was made to the statistical method first employed by Fritzsche (2) and then by Chou and Eldridge (3) to determine the defect density in the SiO_2 films on Si in their assessment of the oxide quality in terms of dielectric strengths. It was contended that the defects in SiO_2 films ought to be regarded as indistinguishable, and that Bosse-Einstein rather than Boltzmann statistics should have been used in deriving the functional relationship among the defect density ρ [or σ in Ref. (1)], the electrode area, F, and the fraction, P, of the MOS capacitors exhibiting primary breakdown when tested for dielectric strengths.

A parallel was drawn between the fraction of primary breakdown and the yield of integrated circuits (IC). The work of Price (4) was cited to show that different expressions for the IC yield could be obtained depending on the choice of statistics. For distinguishable defects, for which Boltzmann statistics are appropriate, the IC yield, P, [or Y_1 in Ref. (4)], is given by

$$P = \exp(-F\rho)$$

or

$$\rho = -\frac{\ln P}{F} \qquad [1]$$

where F now denotes the active area of the IC devices. In the case of indistinguishable defects, where Bose-Einstein statistics are applicable, the IC yield, P [or Y_2 in (4)], is expressed by

$$P = \frac{1}{1 + \rho F}$$

or

$$\rho = \frac{1}{F}\left(\frac{1 - P}{P}\right) \qquad [2]$$

Consequently Eq. [2] was considered to be more appropriate for determining the defect density from the breakdown distribution of the SiO_2 films. [See footnote 2, p. 1539, Ref. (1).]

In this short communication, we shall discuss why Boltzmann statistics are preferred in the evaluation of defects in SiO_2 films.

It is perhaps instructive to note that in determining the IC yield, the device failure due to various types of defects is evaluated on a "go or no go" basis. Such a proposition makes the defects statistically indistinguishable provided they are sufficiently small in relation to the active area of the devices. Be it pinholes, misalignments, or diffusion faults, they contribute equally to the device failure. The situation with dielectric strength measurements in SiO_2 films is quite different. Even though the defects in the SiO_2 films may be of a single type,[1] they should be regarded as distinguishable for the following reasons:

i) In deriving these functional relationships we have applied a two-dimensional statistical model to the three-dimensional reality. Since the defects are comparable in size to the third dimension, *i.e.*, the oxide thickness, their dimensional variation in that direction can be taken implicitly into account only when they are considered distinguishable. To be more specific, let us assume that the defects responsible for nonprimary breakdowns are devitrified spots containing crystallites of various dimensions (1-3). If the crystallite has associated with it a well-defined breakdown strength, then the spots containing crystallites of varied lengths should be distinguishable in the two-dimensional model on account of their variable dielectric strengths. A simple argument can be advanced. When the crystallite in a defective spot does not occupy the entire oxide thickness, the dielectric strength of this particular spot will be that of the composite material, *i.e.*, the crystallite plus the amorphous SiO_2 with their respective dielectric constants and breakdown strengths, and should therefore assume an apparent value between the dielectric strengths of these two materials. Considering the frequently observed zigzag paths of electrical breakdown (5), this is obviously an oversimplified picture since the interactive effect of defects in various depths of the oxide film has been completely ignored. However, it does underscore the necessity of treating the defects as distinguishable in our two-dimensional model. In fact, recent refinement in the experimental technique has shown that defect-related breakdown field in SiO_2 films can indeed assume any value between 2 mV-cm^{-1} (secondary) and 9 mV-cm^{-1} (primary). As pointed out by Osburn (6), the measuring circuit used by Chou and Eldridge (3) did not have a sufficiently fast response to detect all the "self-healing" breakdowns; therefore their breakdown strength distributions were distorted in favor of low- and high-field events. While peaks at low fields ($\sim$2 mV-cm^{-1}) were also observed with an improved measuring circuit, the defect-related breakdown events were found to constitute more than often a continuous spectrum of dielectric strengths [see Fig. 2, Ref. (6)]. Using a different form of mathematical treatment, Osburn arrived at essentially the same functional relationship as obtained by Boltzmann statistics (compare Eq. [1] with Eq. [7] in Ref. (6)).

ii) In actual defect density computations, the fraction of primary breakdowns is usually determined by arbitrarily setting a threshold field value, above which the breakdown events are considered to occur in the primary mode. This procedure is warranted by the fact that the primary breakdown strength is not a well-defined quantity. The variability of the primary breakdown strength and the spread of dielectric strengths near its peak have been frequently observed in the MOS capacitors fabricated under various conditions [see, for example, Fig. 2 and 3 in Ref. (3)]. Obviously, the said procedure differs from the "go or no go" proposition in the IC yield determinations.

* Electrochemical Society Active Member.

Key words: dielectric breakdown, silicon dioxide, reliability, statistics.

[1] For ease of discussion we shall ignore the presence of pinhole-type defects (tertiary breakdowns).

Table I. Fitting of experimental breakdown data to statistical models

Data set No.	Experimental data: Electrode area, F, mm²	Fraction of primary breakdown, P, %	$-\ln P$	$(1-P)/P$	Results of least square fitting: Defect density, ρ, defects/cm²	Intercept, c	Standard deviation, σ	Correlation coefficient, K	Reference
1	0.05	96	0.04	0.041					(3)
	0.5	72.5	0.32	0.38					
	1.3	62.3	0.47	0.60					
		Boltzmann statistics (Eq. [1]):			33	0.08	0.06	0.95	
		Bose-Einstein statistics (Eq. [2]):			43	0.08	0.06	0.96	
2	0.05	85.7	0.15	0.167					(6)
	0.5	65	0.43	0.54					
	1.3	31.9	1.14	1.94					
		Boltzmann statistics (Eq. [1]):			80	0.08	0.04	0.99	
		Bose-Einstein statistics (Eq. [2]):			146	−0.01	0.12	0.98	
3	0.05	50	0.69	1.0					(3)
	0.5	5	3.0	1.9					
	1.3	1.5	4.2	6.57					
		Boltzmann statistics (Eq. [1]):			265	0.99	0.49	0.94	
		Bose-Einstein statistics (Eq. [2]):			462	0.31	0.51	0.98	

Having advanced our argument in favor of Boltzmann statistics, it would appear appropriate, at this time, to present some experimental evidence in its support. Unfortunately, the experimental breakdown data currently available for SiO_2 films do not permit us to make a confident choice between the two statistical models. As pointed out by Meek and Braun (1), Eq. [1] and [2] yield essentially the same results at low-defect densities (or at large P's), since for $P \geq \frac{1}{2}$, $(1-P)/P$ in Eq. [2] is the first term in the series expansion of $-\ln P$ in Eq. [1]:

$$-\ln P = \frac{1-P}{P} - \frac{1}{2}\left(\frac{1-P}{P}\right)^2 + \frac{1}{3}\left(\frac{1-P}{P}\right)^3 \cdots \quad [3]$$

Thus, for $P \geq 90\%$, the difference between the calculated ρ is indeed less than 5%.

As P decreases, however, the difference becomes substantial and reaches as high as 45% at $P = 50\%$. In order to differentiate between the two models, one should therefore rely on the data for highly faulted SiO_2 films. Such data are understandably meager because defective films are neither reproducible nor of practical interest. Nevertheless, three sets of experimental data with $P \leq 0.7$ have been collected from Ref. (3) and (6). Using F as a variable, these data have been least-square fitted to Eq. [1] and [2]. The results are shown in Table I. Since $P = 100\%$ for $F = 0$, the straight lines representing Eq. [1] and [2] should both pass the origin (0,0) in a $-\ln P$ *vs.* F and a $(1-P)/P$ *vs.* F plot. For this reason, the intercepts (C's) are included as a criterion for comparison; the smaller the intercept, the better fit the model gives.

As can be seen from the tabulated results, the experimental data fit both models equally well except, perhaps, for the third set which appears to be slightly in favor of the Bose-Einstein model on account of its smaller intercept. It is clear, therefore, that much more data are needed to settle the problem experimentally.

Manuscript submtted Jan. 2, 1973; revised manuscript received April 2, 1973.

Any discussion of this paper will appear in a Discussion Section to be published in the June 1974 JOURNAL.

REFERENCES

1. R. L. Meek and R. H. Braun, *This Journal*, **119**, 1538 (1972).
2. C. Fritzsche, *Z. Angew. Phys.*, **24**, 48 (1967).
3. N. J. Chou and J. M. Eldridge, *This Journal*, **117**, 1287 (1970).
4. J. E. Price, *Proc. IEEE*, **58**, 1290 (1970).
5. See, for example, S. Whithead, "Dielectric Breakdown of Solids," p. 104, Oxford University Press, New York (1951).
6. C. M. Osburn and D. W. Ormond, *This Journal*, **119**, 591 (1972).

Ellipsometry of Multilayered Dielectrics on Silicon, Applied to MNOS Structures

Leif Lundkvist

Research Laboratory of Electronics III, Chalmers University of Technology, Gothenburg, Sweden

In a recent paper, Maguire and Augustus (1) reported on the detection of a thin silicon oxynitride layer on top of silicon nitride layers fabricated by pyrolysis of silane at about 800°C. In the present communication, we want to point out that the interpretation of their ellipsometer measurements needs some modification. As ellipsometer measurements are used routinely in much solid-state device work, the results presented have a general applicability.

Maguire and Augustus used nitride layers which were originally 610Å and 1010Å thick and had refractive indices of 1.88 and 1.95, respectively. After heating in vacuum at 1140°C for up to 2 hr, the layers had decreased in thickness by about 30Å and had a refractive index of just over 2. This was interpreted to mean that the removed oxide (oxynitride) layer had had a thickness of 30Å and that the removal of 30Å oxide with a refractive index of 1.46 had increased the refractive index of the remaining layer to just over 2, a value that is characteristic of the nitride layer alone.

This interpretation is incorrect both with regard to the refractive index and the thickness for reasons given below. We believe that the refractive index increases mainly because of sintering and not oxide removal.

Key words: ellipsometry of multilayers, silicon nitride, MNOS.

Interpretation of Ellipsometer Measurements of MNOS Multilayers

In order to clearly show the correct way of interpreting the data by Maguire and Augustus (1), the two cases studied by them have been analyzed and subsequently checked by separate experiments on similar wafers. The theory of ellipsometry of multilayered di-

electrics has been treated earlier, [see for example Ref. (2) and (3)]. The problem is that knowledge of refractive indices and thicknesses of the dielectric layers makes it possible to calculate the ellipsometer readings Δ and Ψ (4), but not the inverse.

Figure 1 shows calculated ellipsometer readings for monolayers of various thicknesses and refractive indices around those found in silicon nitride [cf. Fig. 1 and 4 in Ref. (4)]. The points measured by Maguire and Augustus (1) are shown as open circles, with an arrow indicating the direction of change upon heating at 1140°C for 2 hr. The dashed line starting at the first of these points shows the direction and magnitude the change should have had if the heat treatment had resulted in removal of oxide ($n = 1.46$) from the top of the sample. This line is given by a computer program used to calculate ellipsometer readings of multilayered dielectrics, just by taking as the first layer the measured refractive index and thickness (for example $n = 1.95$ and 1010Å) and on that a layer of oxide ($n = 1.46$) with negative thickness. This method is approximate but it is simple and can be used if the oxide is not too thick (<100Å). In this case the error is always less than 0.5° for the sum of Δ and Ψ. It is important to note that removal of oxide increases the apparent refractive index on the 610Å sample, while it reduces the apparent refractive index on the 1010Å sample.

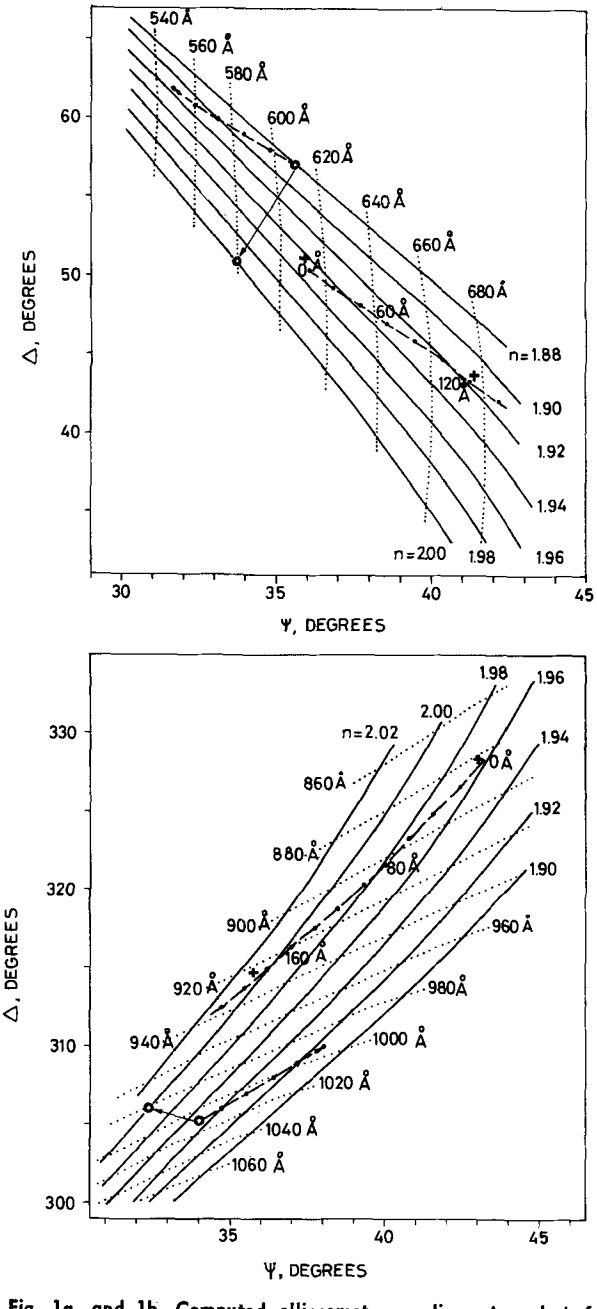

Fig. 1a. and 1b. Computed ellipsometer readings Δ and ψ for dielectric layers on silicon. The solid lines are computed for single layers with some different refractive indices. The dotted lines are lines of constant thickness. The dashed lines are computed for multiple layers, where the layer on top is oxide ($n = 1.46$) of variable thickness. These lines have a dot for each 20Å of oxide. Points measured by Maguire and Augustus (1) are marked ○. Experimental points from the present work are marked +. Angle of incidence is 70°.

Figure 2 shows that when oxide ($n = 1.46$) is added to nitride ($n = 1.96$), the apparent refractive index reduces when the nitride is 0-800Å thick, but increases when the nitride is 800-1600Å thick. The curves for oxide on nitride starts on the nitride curve and continues with an oxide branch more or less parallel with the oxide curve. A diagram similar to Fig. 2 can be drawn for other combinations of dielectrics to get the direction of change in other cases.

The correct thicknesses of the two layers are now found at the intersection of the dashed line and the line of refractive index of the nitride (see Fig. 1). Consequently, the value of the refractive index of the nitride by itself used by Maguire and Augustus, assuming identical nitride on both samples, must have been 1.915, half way between the two values found, 1.88 and 1.95. Adding 100Å (not 30Å as assumed by Maguire and Augustus) of oxide on top of both samples would then give the values found by Maguire and Augustus, as indicated in Fig. 1a and 1b by circles at the starting point of the arrows. Removal of the oxide layer by heating in vacuum, as done by Maguire and Augustus, would then give values of refractive index and thickness as indicated in Fig. 1 by dashed lines, the end points of which would correspond to complete removal of oxide. If the layer on top was oxynitride with a refractive index between that of oxide and that of nitride, removal of oxynitride would give a point on a line between the one for oxide (dashed line) and the one for nitride ($n =$ constant). This is in disagreement with the values after vacuum heating found by Maguire and Augustus as indicated in Fig. 1 by circles at the end point of the arrows. Thus a different explanation as discussed later is required.

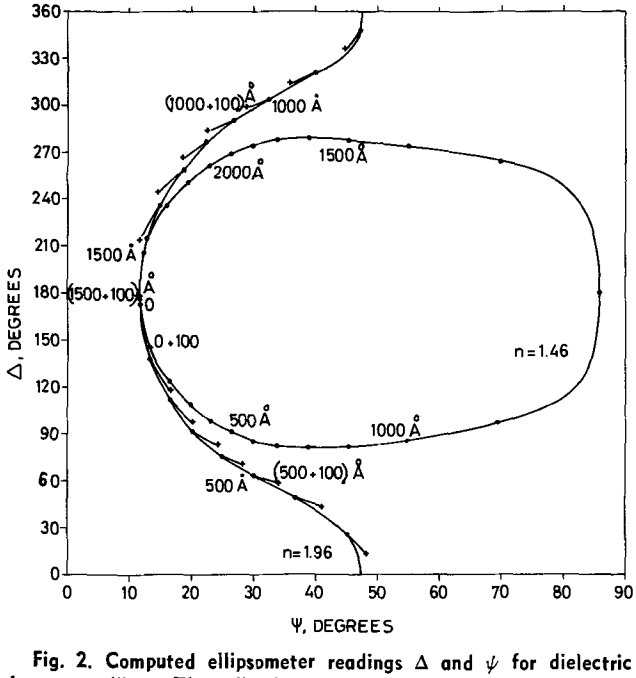

Fig. 2. Computed ellipsometer readings Δ and ψ for dielectric layers on silicon. The solid dots are for oxide ($n = 1.46$) and nitride ($n = 1.96$) on 20Å of oxide. Crosses are for 20Å of oxide + nitride + 100Å oxide. When the nitride is 0-800Å thick, the crosses are at a lower refractive index than that of the nitride, but when the nitride is 800-1600Å they are at a higher refractive index.

Table I. Present experimental results—comparison of multilayers evaluated as if they were single layers

	Sample No. and Fig. No. 1a	1b
Two layers		
Apparent refractive index	1.945	1.965
Apparent thickness, Å	610	880
Three layers		
Apparent refractive index	1.91	2.01
Apparent thickness, Å	680	920
Apparent thickness difference, Å	+70	+40
Real thickness difference = thickness of third layer (on control slice), Å	120	220

Experimental Test of the Analysis

In order to test that the analysis presented is correct, two silicon wafers were made with a nitride thickness of 590Å and 865Å. This nitride was made by pyrolysis of SiH_4 in NH_3 at about 700°C. After ellipsometer measurements, the wafers were covered by oxide made by pyrolysis of SiH_4 in O_2 at about 400°C. The thickness of the oxide was measured on clean slices of silicon on which the oxide was deposited at the same time. The ellipsometer readings before and after deposition of oxide are shown as crosses in Fig. 1 and the results are summarized in Table I. A computer program was used to calculate theoretical curves for the two slices. The parameters used for the calculation were: Fig. 1a, first a layer of oxide ($n = 1.46$) 20Å thick, then nitride ($n = 1.96$) 590Å thick, and finally oxide ($n = 1.46$) 0-140Å thick; Fig. 1b, first a layer of oxide ($n = 1.46$) 20Å thick, then nitride ($n = 1.96$) 865Å thick, and finally oxide ($n = 1.46$) 0-220Å thick. These calculated ellipsometer readings are shown in Fig. 1 as dashed lines. The experimental points correspond very closely to theory. The first layer of 20Å of oxide used in the calculations is an approximation of the oxide always left on the slice after cleaning. The effect of this layer is to change the apparent refractive index in the same direction as for the oxide layer on the top, but the apparent thickness is very close to the sum of the nitride thickness and the oxide thickness.

Conclusion and Discussion

When analyzing multilayers of dielectrics on silicon, single layer evaluation does not give a correct result. The large change in refractive index seen by Maguire and Augustus (1) cannot be explained by removal of oxide, but must have some other explanation. Our nitride, which has only a very thin oxide on the top (if any), also shows an increase in refractive index when heated at temperatures higher than the deposition temperature. This heating also reduces the etch rate, just as higher deposition temperatures do. We believe that the change in both cases is due to densification or rearrangement of the nitride. To ensure that no such changes occur, all treatments must be performed at low temperature, for example, by stepwise chemical etching of the oxide (or oxynitride) layer combined with ellipsometry.

The difference in refractive index on the samples used by Maguire and Augustus also needs some explanation. If there is 20Å of oxide under the nitride, the oxide on the top must be about 60Å if the nitride has the same refractive index on both samples. It is not probable that that much oxide can be created by oxidation of nitride during the cooldown period, as Maguire and Augustus (1) suggested. Fränz and Langheinrich (5) show that the oxidation rate of silicon nitride is lower than that of silicon, and that the result of the reaction is oxide, not oxynitride. If the oxygen content in the carrier gas is high enough to give appreciable oxidation of the nitride, it must also be high enough to give oxynitride as the result of the deposition of nitride, as this process is very sensitive to oxygen impurities. The result is an oxynitride film with refractive index lower than for nitride and with variations due to variations in oxygen impurity content from deposition to deposition. This may be the explanation of parts of the variation observed by Maguire and Augustus.

Acknowledgments

The author is indebted to G. H. B. Hansson who has initially written the computer program, and to Professor J. T. Wallmark and Dr. J. Maserjian for helpful discussions.

Manuscript received Jan. 15, 1973.

Any discussion of this paper will appear in a Discussion Section to be published in the June 1974 JOURNAL.

REFERENCES

1. H. F. Maguire and P. D. Augustus, *This Journal*, **119**, 791 (1972).
2. G. A. Bootsma and F. Meyer, *Surface Sci.*, **14**, 52 (1969).
3. H. Yokota, M. Nishibori, and K. Kinosita, *ibid.*, **16**, 275 (1969).
4. R. J. Archer, *J. Opt. Soc. Am.*, **52**, 970 (1962).
5. I. Fränz and W. Langheinrich, *Solid-State Electron.*, **14**, 499 (1970).

JOURNAL OF THE ELECTROCHEMICAL SOCIETY

ELECTROCHEMICAL SCIENCE AND TECHNOLOGY

SEPTEMBER 1973

EST

A Novel Electrolyte System: Solutions of Diethyl Ether in Concentrated Aqueous HCl + $ZnCl_2$ Mixtures

A. J. Easteal[1] and C. A. Angell

Department of Chemistry, Purdue University, West Lafayette, Indiana 47907

ABSTRACT

Electrolyte solutions with novel characteristics are formed by dissolution of ether in $ZnCl_2$ + hydrochloric acid solutions of high concentration. At 0°C ether is only slightly soluble in the "solution" $ZnCl_2 + 4H_2O$, but dissolves in the solution $HCl + 4H_2O$ until moles Et_2O:moles $H_2O \approx 1:2.8$. Its solubility increases markedly in mixtures of these solutions, reaching a maximum near the mole ratio corresponding to the formation of $ZnCl_4^=$, when moles Et_2O: moles $H_2O \approx 1:1.3$. Furthermore, the solubility in this mixture increases with decreasing temperature, down to the glass transition temperature at −124°C. Although ionic mobilities appear to increase with increasing ether content the electrical conductance at 0°C decreases, evidently due to the disruption of an efficient proton transfer mechanism in the chlorozincate acid. The strongly proton conducting solutions may have useful low temperature electrolyte applications, since the conductivity is not necessarily limited by the ionic and molecular transport mechanisms which determine the fluidity.

The extraction, with various ethers, of complex metal halide ions and/or halo acids of the form HMX_n from acidified solutions of metal halides is a well-established experimental procedure (1). We have attempted to use this procedure with diethyl ether (Et_2O), to characterize species existing in concentrated aqueous solutions of $ZnCl_2$ + HCl. From the results of a study of concentrated aqueous $ZnCl_2$ + LiCl solutions (2) it was concluded that formation of a tetrachlorozincate species has a profound effect on a variety of properties of these electrolytes. It seemed feasible that from aqueous $ZnCl_2$ + HCl electrolytes the acid H_2ZnCl_4 (probably with associated water molecules) might be extractable with Et_2O, particularly at low temperatures.

The extraction experiments did not achieve this objective for reasons which form the subject of this communication because they have led us to a study of a class of electrolytes which seem not to have been previously investigated in detail.

Experimental

In the experiments described below an aqueous electrolyte, E (0.6 HCl, 0.4 $ZnCl_2$, $4H_2O$), of fixed composition was used. When a mixture containing 20 mole per cent (m/o) E and 80 m/o Et_2O is shaken at room temperature, two liquid phases result. This was expected on the basis of analogous experiments described in the literature. When the two-phase mixture is cooled with agitation in liquid nitrogen, a single homogeneous liquid phase is formed. This was an unexpected result and was the basis of our subsequent experiments. The homogeneous solution becomes turbid and eventually completely separates into two phases on warming.

Variation of the relative proportions of E and Et_2O showed that the saturated solution of Et_2O in E at 0°C contained 74.3 ± 0.2 m/o Et_2O, while mixtures containing more than *ca.* 81 m/o Et_2O could not be induced to form a single phase on cooling in liquid nitrogen. The solubility of Et_2O in E at 23.9° ± 0.2°C was measured as 65.8 ± 0.3 m/o Et_2O. From the solubilities at 0° and 23.9°C the average heat of solution[2] of Et_2O in E between these two temperatures was calculated as $\Delta H = -2.78 \pm 0.05$ kcal mole^{-1} (and the dissolution is thus exothermic).

Electrolyte E can be regarded as a mixture of the two components

electrolyte E_H: HCl, $4H_2O$
electrolyte E_Z: $ZnCl_2$, $4H_2O$

in the mole ratio 0.6 E_H, 0.4 E_Z. At 0°C the saturated solution of Et_2O in E_H contains 59.4 ± 0.2 m/o Et_2O, and in E_Z approximately 5.8 m/o. The dissolution of Et_2O in E_Z is endothermic since the saturated solution at about 25°C contains approximately 7.5 m/o Et_2O.

A portion of the phase diagram (at 0°C) for the ternary system $Et_2O/E_H/E_Z$ is shown in Fig. 1, which has been constructed from the solubility measurements at 0°C. Qualitative experiments indicated that the maximum solubility of Et_2O, at a given temperature, should occur for mixtures of E_H with E_Z in which the Zn:Cl ratio is 1:4.

The solubilities of Et_2O in electrolytes E_H, E, and E_Z at 0°C are 1.46, 2.89, and 0.05_8 moles per mole of electrolyte, respectively. In electrolyte E this mole ratio increases to 4.27 at the lowest temperatures studied (see below). The latter ratio corresponds to 7.1 moles of Et_2O for each proton present in the solution. Since there are 4 moles of H_2O for each mole of E_E, this low temperature saturated solution contains Et_2O and H_2O

[1] Permanent address: Department of Chemistry, University of Auckland, Auckland, New Zealand.

Key words: low temperature electrolytes, glass transition temperature, electrical conductance, complex ions, protonic conduction.

[2] The heat of solution measured was the differential heat of solution, defined as the heat absorbed when 1 mole of solute is dissolved in a solution which is already practically saturated.

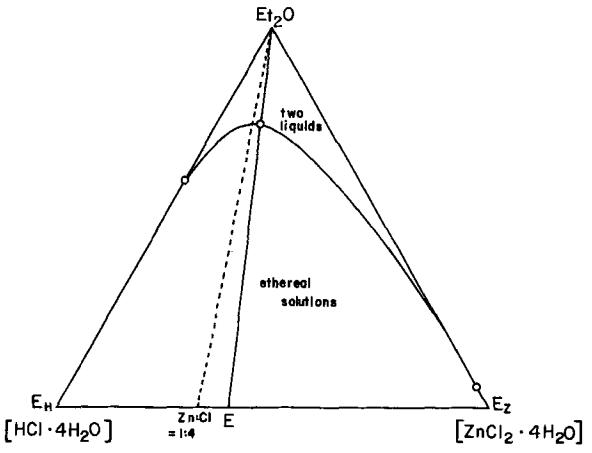

Fig. 1. Part of the phase diagram (at 0°C) for the pseudoternary system Et_2O/E_H $(HCl \cdot 4H_2O)/E_Z(ZnCl_2 \cdot 4H_2O)$. The open circles indicate experimental compositions derived from solubility measurements.

in approximately equal proportions ($Et_2O:H_2O$ = 4.27:4 = 1.07).

The homogeneous solutions of Et_2O in E are resistant without crystallization: when cooled in liquid nitrogen they form glasses which do not crystallize on warming. The solutions (especially those most concentrated in Et_2O) appear to have relatively high fluidity down to very low temperatures (*e.g.*, of the order −100°C) and for this reason may have some practical value as low temperature electrolytic media.

We have measured glass transition temperatures (denoted T_g) of vitrified solutions containing up to 70.6 m/o Et_2O, using in essence the differential thermal analysis method described previously (3). T_g decreases slowly and linearly (within experimental precision) from 0 to 70.6% Et_2O: the rate of change of T_g is −0.13°C (mole per cent $Et_2O)^{-1}$. T_g for pure Et_2O has been measured as −175°C ± 2°C.

To further characterize the ethereal solutions we have measured their electrical conductance as a function of composition at 0°C. For these measurements a simple U-shaped Pyrex glass capillary cell was used, with platinized platinum electrodes, in conjunction with a Wayne-Kerr Type B331 impedance bridge. The cell constant was 175.0 ± 0.2 cm^{-1} (measured using 0.1 demal aqueous KCl). Specific conductances, κ ohm-cm^{-1}, are listed in Table I as a function of composition.

In Fig. 2, T_g and log κ are plotted *vs.* composition expressed as mole per cent ether (lower scale), and as moles water: moles ether (R, upper scale).

Discussion

The propensity of $ZnCl_2$, a strong Lewis acid, for coordinating chloride ions to yield $ZnCl_4^{2-}$ tetrahedral complexes, is well known. The stoichiometry of the 2:1 mixture of electrolytes E_H and E_2 (Fig. 1) corresponds to $(H_3O^+)_2$ $ZnCl_4^{2-}$ diluted with 12 moles of water, while the 6:4 mixture (electrolyte E) corresponds to $(H_3O^+)_3Zn_2Cl_7^{3-}$ diluted with 16 moles of water. Although competition of water for positions in the Zn^{++} first coordination sphere will undoubtedly lead to some complicated distribution of chloro- and chlorohydrate species, it is certain that free chloride ions will not be present, and that the protons in the solution will be particularly free from anion binding interactions.

Table I. Specific conductance at 0°C of solutions of diethyl ether in the electrolyte 0.6 HCl, 0.4 $ZnCl_2$. $4H_2O$

Mole fraction ether	κ (ohm^{-1} cm^{-1})
0.000	0.3075
0.020	0.2912
0.030	0.2825
0.040	0.2732
0.050	0.2548
0.074	0.2461
0.125	0.2021
0.167	0.1776
0.286	0.1171
0.351	0.08556
0.444	0.05385
0.545	0.02972
0.615	0.01723
0.667	0.01398
0.706	0.01163

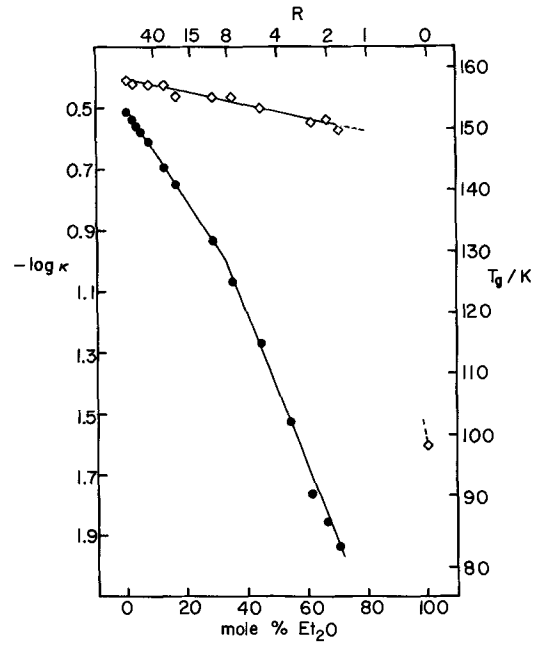

Fig. 2. Variation of glass transition temperature (T_g, unshaded diamonds) and log (specific conductance) (κ in $ohm^{-1}cm^{-1}$, shaded circles) with ether content of the pseudobinary system Et_2O/E (0.6 HCl, 0.4 $ZnCl_2$, $4H_2O$). *R* is the mole ratio H_2O: Et_2O corresponding to given solution compositions.

The increase in Et_2O solubility in electrolyte E over that in aqueous $HCl(E_H)$ is presumably to be associated with this increase in proton activity, although the extent to which ether molecules are protonated, rather than just coordinated to hydrated proton complexes, is unknown.[3] However, some rather specific structuring must be involved since the properties of the pseudobinary solutions E + Et_2O vary with composition in a highly nonideal fashion (which eventually leads to the phase separation commencing at ~70% Et_2O). In particular the cohesive energy density, indicated by the glass transition temperature, changes very slowly with ether content when viewed against the very low value of T_g characteristic of ether itself (Fig. 2).

By contrast, ether addition has a severe effect on the conductance of E. The addition to E of only 1 Et_2O molecule per 10 H_2O molecules reduces the conductance by more than 60% of its initial value. In view of the decrease in T_g with ether additions, which implies an increase in particle mobilities at constant temperature $T > T_g$ (3), the sharp decrease in conductance is best interpreted in terms of a decrease in efficiency of some Grotthus-like proton transfer mechanism which makes a major contribution to the conductance of electrolyte E. The existence of such a contribution would be expected on general grounds, and would be consistent with recent experience (5) that this substance yields a protonic semiconducting glass with conductance several orders of magnitude greater than expected from ionic mobilities alone.

Figure 2 shows that the conductance decreases exponentially with mole per cent ether, *i.e.*, the proton jump probability *P* is of the form

[3] It is noteworthy that Clark *et al.* (4) have recently isolated the anhydrous ethereal acids $[H(Et_2O)_n]^+[MCl_4]^-$ where *M* = Al(III), Fe(III), Ga(III), or In(III), and *n* can take values from 1.5 to 8.

$$P = P_o \exp(-X_{ether}) = P_o \exp\left(\frac{1}{1 + cR}\right)$$

where X_{ether} is the ether mole fraction, R is the water: ether mole ratio, and c is a constant. This form presumably reflects the probability of an ether molecule interceding between water molecules otherwise favorably orientated for a proton transfer process, but until further data on solutions of this type are available the development of a detailed model for this effect is unwarranted. The apparent break between low and high ether content behavior occurs at about $R = 8$, which corresponds to the presence of one ether molecule per $H^+(H_2O)_4$, or ($H_9O_4^+$). This is the water: proton ratio in the Pr_2O extract from $FeCl_3$-HCl-H_2O solutions suggested by Friedman (6), so the break in this plot is probably significant. Simple dilution effects must also contribute to the decrease in specific conductance with ether additions.

In two respects these solutions deserve further attention. In the first place, an electrolyte which exists at normal temperatures as a combination of highly conducting and poorly conducting layers at normal temperatures, but a single highly conducting phase at low temperatures could be useful for low temperature-activated electrolytic systems. Secondly, electrolytes in which the proton conduction mechanism is very efficient offer an in-principle method of overcoming otherwise fundamental limitations on low temperature operations of liquid electrolyte systems (7) imposed by the loss of ionic mobility approaching the glass transition temperature for the solution.

Acknowledgment

The authors gratefully acknowledge support of this research by a grant from the Office of Saline Water, U. S. Department of the Interior.

Manuscript submitted Nov. 20, 1972; revised manuscript received Feb. 26, 1973.

Any discussion of this paper will appear in a Discussion Section to be published in the June 1974 JOURNAL.

REFERENCES

1. See for example, M. J. Taylor, *Inorg. Nucl. Chem. Letters*, **4**, 33 (1968) and references cited therein.
2. A. J. Easteal, E. J. Sare, C. A. Angell, and C. T. Moynihan, To be published.
3. C. A. Angell, E. J. Sare, and R. D. Bressel, *J. Phys. Chem.*, **71**, 2759 (1967); C. A. Angell and E. J. Sare, *J. Chem. Phys.*, **52**, 1058 (1970).
4. R. J. H. Clark, B. Crociani, and A. Wasserman, *J. Chem. Soc. (A)*, 2458 (1970)
5. I. M. Hodge, Private communication; C. A. Angell, P. M. Gammell, and R. D. Bressel, *J. Non-Cryst. Solids*, **7**, 295 (1972).
6. H. L. Friedman, *J. Phys. Chem.*, **66**, 1595 (1962).
7. C. A. Angell, *This Journal*, **112**, 1224 (1965).

Computer Simulation of Full-Size, High-Drain, AgCl-Mg Sea Water-Activated Batteries

Duane W. Faletti*[1]

Applied Physics Laboratory, University of Washington, Seattle, Washington 98105

ABSTRACT

The predictions of a computer simulation for high-drain, AgCl-Mg batteries are compared to the observed performance of four full-size AgCl-Mg batteries: the Mk 61 (Mod 0 and Mod 2), Mk 64, and Mk 67. The Mk 61 Mod 0, like the Mk 64 and Mk 67 batteries, uses AZ61 magnesium anodes; the Mk 61 Mod 2 uses the high-voltage magnesium alloy, AP65. These four batteries differ sufficiently in their configurations and were discharged over a wide enough range of operating conditions to constitute a valid test of the capabilities of the computer simulation. The simulation gave voltage predictions accurate to within 7% for over 90% of the discharge. Predictions for other useful parameters, such as electrolyte temperature, are also given. This simulation can eliminate the need for most of the "cut and try" effort presently required in AgCl-Mg battery development and should be helpful in system studies of this battery.

Present design techniques for high-drain, sea water-activated, AgCl-Mg batteries require considerable experimentation involving the construction and testing of subassemblies as well as full-size prototypes. The operating conditions for such batteries often encompass a wide range of temperature, salinity, and pressure conditions. Because of limited discharge facilities and the expense of in-water tests, it is not feasible to test sea water-activated batteries over their entire operating range.

A computer simulation, which was developed as an aid to the design of AgCl-Mg water-activated batteries, has been described (1). Here we will compare the agreement between the predictions of that simulation and the observed behavior of four full-size, high-drain batteries. Three of these batteries, the Mk 61 Mod 0, Mk 64, and Mk 67, use AZ61 magnesium alloy for their anodes; the Mk 61 Mod 2 uses a high-voltage magnesium alloy, AP65. They differ sufficiently in their configurations and were discharged over a wide enough range of operating conditions to constitute a valid test of the capabilities of the simulation.

* Electrochemical Society Active Member.
[1] Present address: Naval Torpedo Station, Keyport, Washington 98345.

Key words: AgCl-Mg batteries, sea water-activated batteries, high-drain batteries, AZ61 magnesium alloy, AP65 magnesium alloy, computer simulations, modeling, AgCl, Mg, simulations.

Characteristics of the Mk 61, Mk 64, and Mk 67 Batteries

The Mk 61, 64, and 67 are high-drain, sea water-activated batteries which use a compact, rugged, lightweight, pile-type construction (Fig. 1). Glass beads embedded in the cathodes act as separators, permitting electrolyte to pass between the electrodes of the cell. Metal foil is placed between adjacent cells to prevent unwanted electrochemical reactions and to provide electrical contact.

In the pile-type construction parasitic currents flow between cells of different potential because the cells are immersed in a continuous electrolyte. The parasitic currents act as a load in parallel to the external load, causing lower battery voltage and a reduced discharge life. The magnitude of the parasitic currents

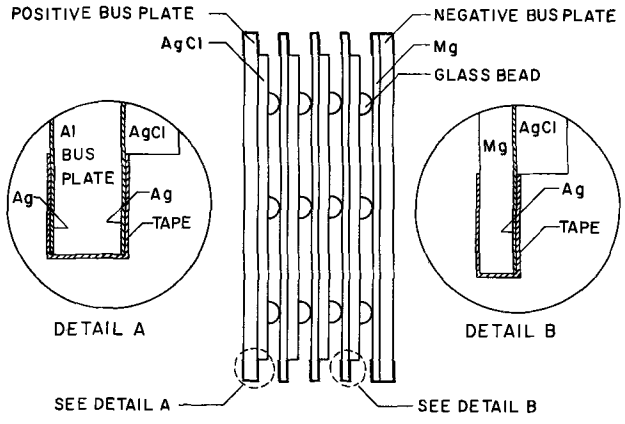

Fig. 1. Four-cell series-connected section. Current is transferred to the load by bus rods (not shown). Glass beads imbedded in the AgCl provide interelectrode spaces through which the electrolyte passes. Silver foil provides electrical contact between cells while acting as a barrier to chemical reactions between AgCl and Mg. The edges of magnesium-silver foil assemblies are taped to prevent electrolyte from reaching the back of the anodes.

increases with the conductivity and volume fraction of the electrolyte, the area of the flow passages above and below the battery, and the cross-sectional area of the flow passages within the cells.

Of the three batteries, the Mk 64 operates at the highest current density and has a parasitic-to-external current ratio of less than 0.05. The Mk 61 battery, which has the same flow passage area and cell configuration but operates at about half the current density, has a ratio near 0.08. The Mk 67 battery operates with a voltage control system which has the effect of increasing the conductivity of the electrolyte as the discharge progresses; thus, its parasitic-to-external current ratio increases during the discharge and, depending on the temperature and composition of the entering electrolyte, ranges from 0.19 to 0.25 in the early portions of the discharge, 0.25 to 0.33 when the discharge is 90% complete, and 0.67 to 0.85 at the completion of the discharge.

The cells of the battery may be connected in series as in Fig. 1, or they may be divided into two series-connected sections which are connected in parallel to the load as in Fig. 2. The Mk 64 battery has 169 cells connected electrically in series; the Mk 61 Mod 0, Mk 61 Mod 2, and Mk 67 batteries each have two sections connected electrically in parallel, each section containing 118, 104, and 230 cells, respectively.

The Mk 61 and Mk 64 batteries have cells and flow passages of the same size and shape (Table 1 and Fig. 3) and are designed to operate at near the same power level. Since the Mk 64 has a single section and the Mk 61 has two, the current density is nearly twice as high and the discharge period is correspondingly shorter for the former.

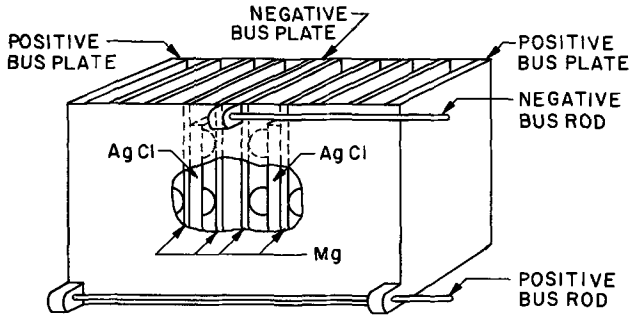

Fig. 2. Battery composed of two series-connected sections, containing four cells each, which are connected in parallel. Cell assembly is of same construction as that in Fig. 1, but there is symmetry about the negative bus plate.

Table I. Summary of battery configurations

	Mk 61 Mod 0	Mk 61 Mod 2	Mk 64	Mk 67
No. of cells	236	208	169	460
No. of parallel-connected sections	2	2	1	2
Cathode area, cm²	396	393	396	1097
Cathode thickness, cm	0.038	0.037	0.038	0.055
Anode thickness, cm	0.028	0.028	0.028	0.033
Electrode separation, cm	0.058	0.058	0.058	0.058
Area of flow passages, cm²	10.24	10.24	10.24	67.25

The cells of the Mk 67 battery are rectangular in shape (Table I and Fig. 3) and are about two and one-half times larger than the Mk 61 and Mk 64 cells. The Mk 67 cathodes have about one-third greater capacity per unit area than those of the Mk 61 and Mk 64 batteries.

The Mk 61 and Mk 64 batteries operate with an entering electrolyte of constant flow rate. This produces battery voltages which are strongly dependent on electrolyte composition and temperature, and which fall continuously as the discharge progresses.

The Mk 67 battery is designed to operate within a few per cent of 245V over the range of sea water temperature and composition found in the world's oceans. This is accomplished by a voltage control system that recirculates a constant flow rate of effluent back into the lower flow passage and adjusts the flow rate of entering sea water to achieve the desired voltage (Fig. 4).

These particular batteries were chosen for this study because (*a*) their physical dimensions and method of manufacture and testing were well documented, and (*b*) the three batteries differed sufficiently in operating conditions and physical configurations to provide a good test of the capabilities of the computer simulation.

Results

The predictions of the computer simulation are compared to observed battery voltages, effluent electrolyte temperatures, and (for the case of the Mk 67 battery) electrolyte flow rates in Fig. 5-16. The observed values

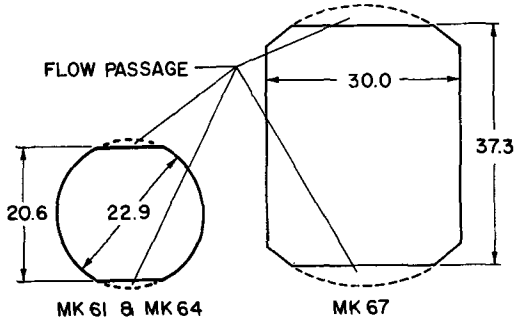

Fig. 3. Configuration of Mk 61, 64, and Mk 67 cells (dimensions in centimeters).

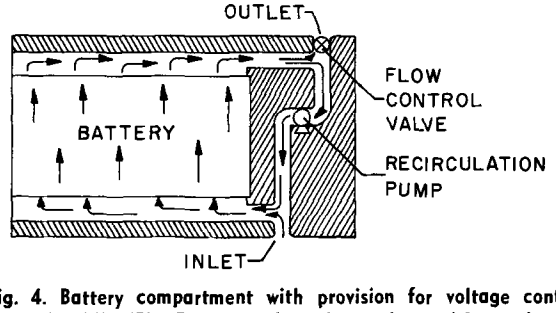

Fig. 4. Battery compartment with provision for voltage control (as in the Mk 67). Entering electrolyte mixes with portion of battery effluent recycled by recirculation pump before entering flow passage under battery. Intake flow of new electrolyte is adjusted by flow control valve located at exit.

lie within the crosshatched areas on the figures and were obtained from discharges conducted by the Quality Evaluation Laboratory of the Naval Torpedo Station, Keyport, Washington.

The manufacturing tolerances, and to a lesser extent the test tolerances of these batteries, allow a significant spread in battery performance. A measure of the maximum possible spread in performance was obtained by making three computer simulations for each test condition studied. These were (*a*) for the case where the battery was built according to the nominal specified dimensions and tested according to the nominal specified test conditions, (*b*) for the case where the battery was built with the most favorable set of dimensions allowed by the specifications and tested according to the most favorable set of operating conditions permitted by the test specifications, and (c) for the case of the least favorable set of dimensions permitted and the least favorable set of operating conditions permitted. These three conditions are referred to as the nominal, best, and poorest performance predictions, respectively, and are represented by the solid lines in Fig. 5-16.

For the sake of brevity, the computer inputs for battery dimensions and discharge conditions are given only for the Mk 67 battery (Table II). Reference (2) gives a complete listing of all computer inputs. Two other computer inputs warrant discussion. The computer simulation makes use of numerical analysis to account for spatial and temporal variations within these batteries. This is done by dividing the cells into a sufficiently large number of subcells so that spatial variations in operating conditions within any subcell are small, and by dividing the discharge period into short time intervals so that temporal variations within a time interval are small. For this study we chose 25 subcells and a 10-sec time interval. This was shown to be adequate by making checks in which the number of subcells was increased to 100 and the time intervals decreased to 1 sec. Only negligibly small changes in the computer predictions were observed.

Mk 61 battery.—The Mk 61 battery is tested under four discharge conditions which encompass four levels of temperature (0.8, 12.8, 15.6, and 31.1°C), as well as two levels of salinity (31 and 38°/₀₀), pressure (15 and 45 psig), and resistance (0.72 and 0.58 ohm). Figures 5-8 present comparisons between the predicted and observed voltages that are typical for all test conditions encountered by the Mk 61 Mods 0 and 2.

The computer simulation predicts low voltages, *i.e.*, discharge periods which are too long for both the Mk 61 Mod 0 (AZ61 anodes) and for the Mk 61 Mod 2 (AP65 anodes).

A significant number of the batteries performed better than the highest predictions of the computer simulations in all four test conditions. Thus, unless the batteries were built or tested outside of the allowed tolerances, it must be concluded that the voltage predictions for the Mk 61 battery are intrinsically low. However, the magnitude of this discrepancy is not large, especially in view of the 6% spread in observed voltages and the 5-20% spread in the observed discharge time to a cutoff voltage of 100V (0.85 V/cell). The predicted voltages are within 7% of the observed voltages (taken to be the center line of the observed voltage envelope) for 100% of the discharge period to a cutoff voltage of 100V for the low-temperature discharges, for 92% of the two sets of discharges near 15°C, and for 97% of the high-temperature discharges.

Table II. Battery dimensions and test conditions for the Mark 67 battery simulation

	Performance		
	Low	Nominal	High
Battery dimensions			
Number of cells	460	460	460
Number of sections	2	2	2
Cathode area, cm²	1086.13	1097.48	1108.77
Cathode thickness, cm	0.05207	0.05461	0.05715
Anode thickness, cm	0.03048	0.03302	0.03556
Silver foil thickness, cm	0.00127	0.00190	0.00254
Electrode separation, cm	0.06604	0.05842	0.05334
Cell thickness, cm	0.1397	0.1480	0.1562
Width of bottom and top opening of cells, cm	22.9387	22.8473	22.7558
Width of tape at top and bottom of cells, cm	0.1359	0.2649	0.3937
Thickness of tape at top and bottom of cells, cm	0.0025	0.0025	0.0025
Area of flow passage above (or below) the battery, cm²	67.84	67.25	66.67
Test tolerances			
Load resistance, ohms	0.435	0.438	0.441
Pressure, atm	3.72	4.06	4.40
New electrolyte flow rate, gal/min			
Maximum	122.0	120.0	118.0
Minimum	17.0	15.0	13.0
Recirculation flow rate, gal/min	32.0	36.0	40.0
Electrolyte temperature, °C			
High temperature	29.4	30.8	32.2
Ambient temperature	10.0	12.8	15.6
Low temperature	0.0	0.0	0.56
Electrolyte salinity, °/₀₀			
High temperature	35.0	37.5	40.0
Ambient temperature	30.0	35.0	40.0
Low temperature	7.5	10.0	12.5

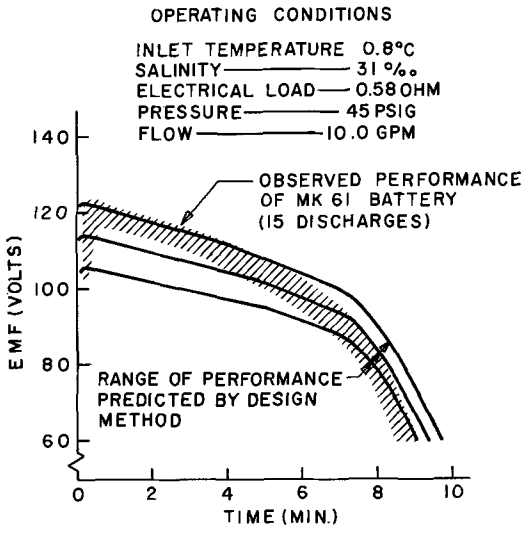

Fig. 5. Comparison of predictions of computer simulation to performance of Mk 61 Mod 0 battery when discharged at low temperature.

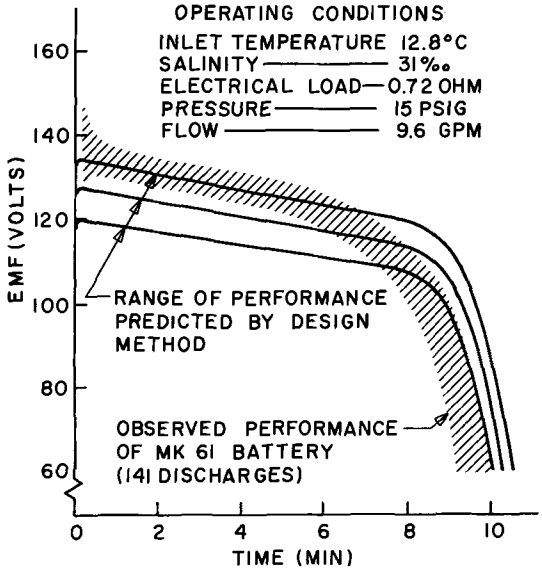

Fig. 6. Comparison of voltage predictions of computer simulation to observed performance of Mk 61 Mod 0 battery when discharged at 12.8°C.

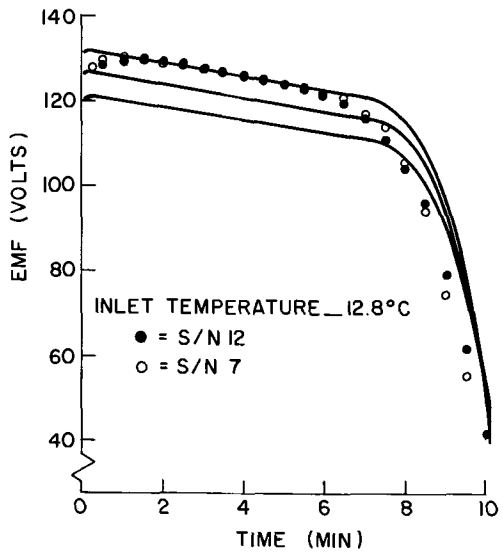

Fig. 7. Comparison of voltage predictions of computer simulation to performance of Mk 61 Mod 2 battery when discharged at 12.8°C.

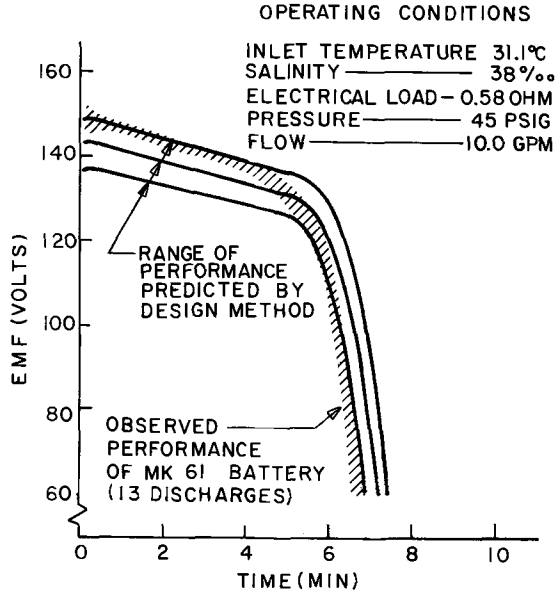

Fig. 8. Predicted voltage and observed voltages of Mk 61 Mod 0 when discharged at high temperature.

Except for starting transients caused mainly by the limitations of the test facility, the observed and predicted temperatures are in good agreement. The predicted and observed Mk 61 effluent temperatures for the discharges at 12.8°C, which are typical of all four test conditions, are compared in Fig. 9 and 10. The predicted temperatures would have to be about 1°-2°C higher to be consistent with the voltage predictions. However, this is not much larger than the uncertainties in temperature measurement and is well within the accuracy required for battery design.

Mk 64 battery.—The Mk 64 battery is designed to operate at the same power level as the Mk 61 but for a shorter period of time. Since it has only one section compared to the Mk 61's two, and since the cells are the same size (Table I), the current density is roughly twice as high.

The observed voltages (taken to be the center line of the observed voltage envelope) are within 2% of the nominal predicted voltage until the observed voltage drops to 100V (0.59 V/cell) at 3.7 min (Fig. 11). The accuracy of the simulation decreases between 3.7 and 5.2 min with a maximum error of +15% occurring at 4.5 min. The low predictions of the simulation beyond 5.4 min are the result of the higher predicted exhaustion rate during the 3.7-5.2-min period.

The errors at or below 100V result from the limitations of the semiempirical model on which the simulation is based (1, 3). Fortunately, enough is known about these limitations that the operating regions where serious errors might be expected can be identified. In practice this is not a serious consideration since the model works well over the range of operating conditions of interest in modern battery design.

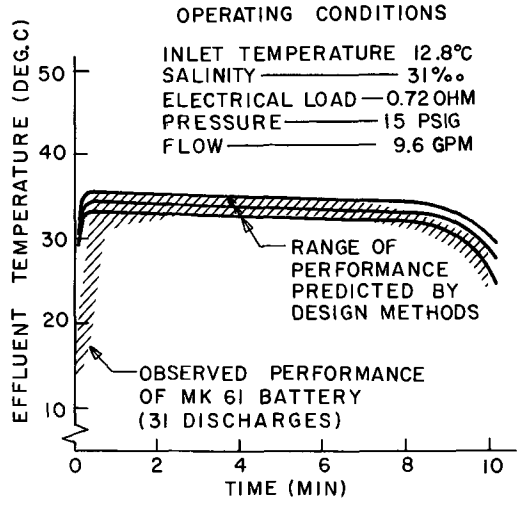

Fig. 9. Predicted and observed effluent temperatures of Mk 61 Mod 0 when discharged at 12.8°C.

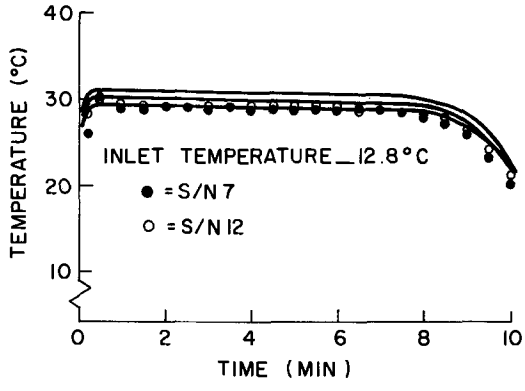

Fig. 10. Predicted and observed effluent temperatures of MK 61 Mod 2 when discharged at 12.8°C.

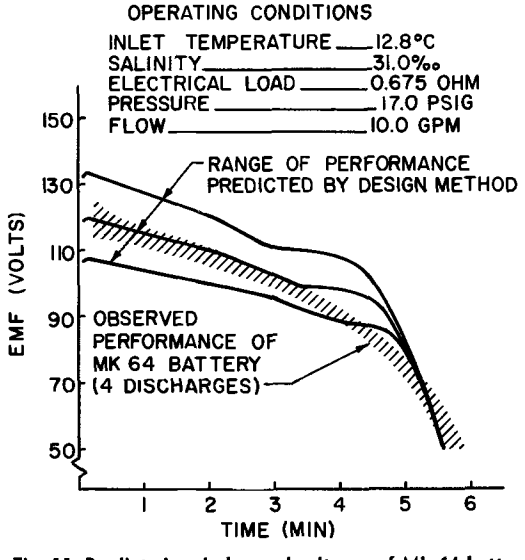

Fig. 11. Predicted and observed voltages of Mk 64 battery

Observed and predicted effluent temperatures are in excellent agreement. The slightly high temperature predictions of the computer simulation are consistent with the slightly high voltage predictions.

Mk 67 battery.—The Mk 67 battery was tested for three conditions: (*a*) high temperature, high salinity, (*b*) ambient temperature, normal salinity, and (c) low temperature, low salinity (Table II). The high-temperature, high-salinity discharges will be discussed first.

Although the Mk 67 battery is designed to operate at 245V, the performance of the battery is such that even at its maximum flow rate of 120 gal/min the voltage does not fall to 245V until the 7-9 min mark for the high-temperature, high-salinity discharge condition (Fig. 12). This permitted us to determine the adequacy of the computer simulation for the Mk 67 battery when discharged at constant flow rate. The agreement is excellent, with the simulation predicting voltages accurate to better than 1% for the first 5 min and to within 2% until the 8-min mark.

At the 8-min mark the observed voltages begin to fall approximately 0.8 min earlier than that predicted by the "low performance" predictions of the simulation. An examination of the flow rate data for this condition shows that the experimental reductions in flow rate lag behind those of the simulation. This lag in flow reduction, which is caused by equipment limitations, explains much of the discrepancy found after 8 min. Another possible source of low observed voltage, especially at low flow rates, is that significant amounts of H_2 are quite likely recirculated into the lower flow passage by the recirculation pump (4). This is most likely to occur near the end of the discharge when flow rates are low because of the increasing volume fraction of H_2 at low flow rates. In spite of this, the predicted and observed discharge life agreed to 5%, based on the "nominal" computer predictions and the average observed time to 160V (0.7 V/cell).

The predicted and observed temperatures are in excellent agreement (within about a degree centigrade) for the first 4 min of the discharge where the flow is constant at 120 gal/min. Thereafter, the observed temperatures were lower than the predicted temperatures, reflecting the high observed flow rates responsible for the low observed voltages described above.

The comparisons between the predicted and observed voltages, temperatures, and flow rates when the Mk 67 battery is discharged at 12.8°C are presented in Fig. 13, 14, and 15, respectively. The nominal voltage predictions are within a few per cent of the observed voltages for 96% of the discharge period to a cutoff voltage of 160V (0.7 V/cell).

The temperature and flow predictions are in good agreement with the observed results over most of the discharge (Fig. 14 and 15). During this period, which ends at about 7½-8 min, the computer predictions imply that the Mk 67 battery is performing between the nominal and the best expected of it. Thereafter, the observed flow rates decrease and the observed temperatures rise faster than the predictions of the computer simulation. This apparent decrease in the intrinsic voltage capabilities of the Mk 67 battery could be the result of H_2 recirculation.

Figure 16 presents the agreement between the simulation and the observed voltages for the case of low temperature and low salinity. The voltage predictions of the simulation are excellent between the 1½ and 7-min marks.

The discrepancies in the first 1½ min of the discharge are caused by starting transients. The battery is filled at a flow rate of 120 gal/min until the system pressure reaches 45 psig, whereupon the flow rate is

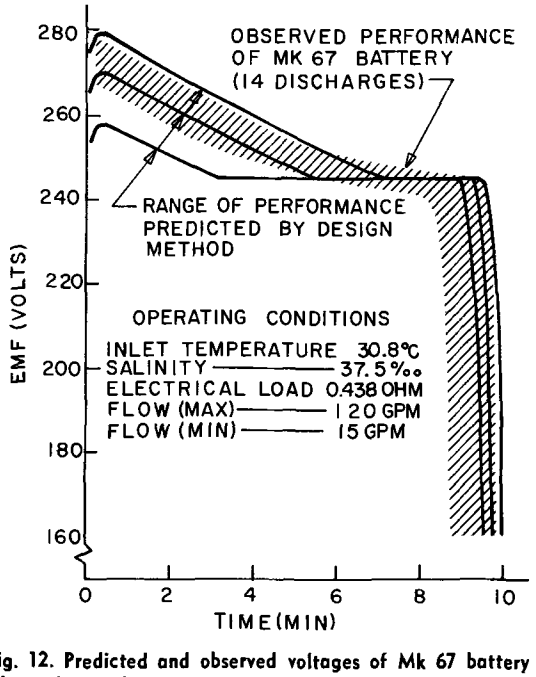

Fig. 12. Predicted and observed voltages of Mk 67 battery when discharged at high temperature.

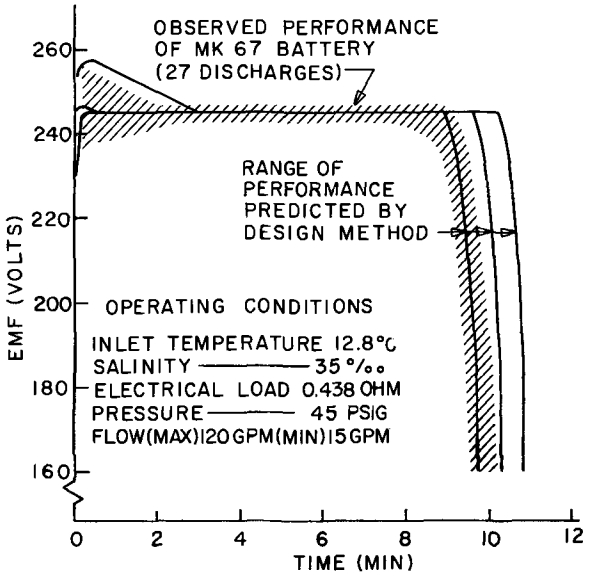

Fig. 13. Predicted and observed voltages of Mk 67 battery when discharged at 12.8°C.

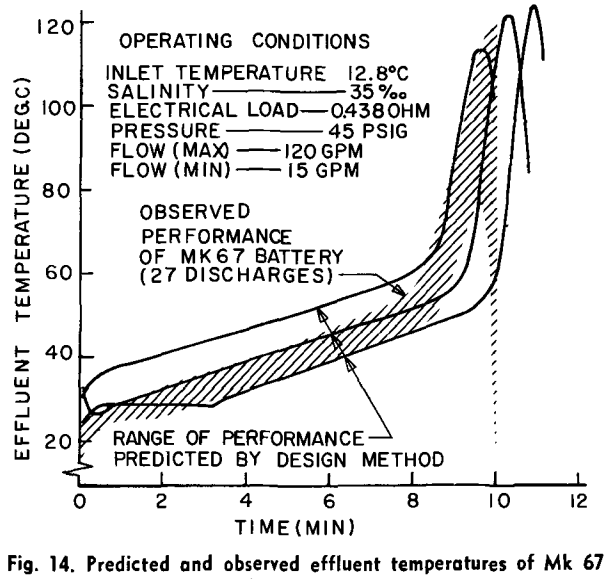

Fig. 14. Predicted and observed effluent temperatures of Mk 67 battery when discharged at 12.8°C.

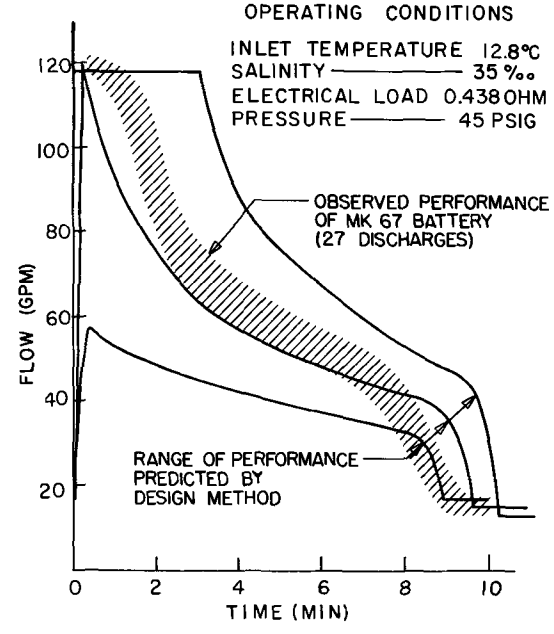

Fig. 15. Predicted and observed flow rates of sea water entering Mk 67 battery when discharged at 12.8°C.

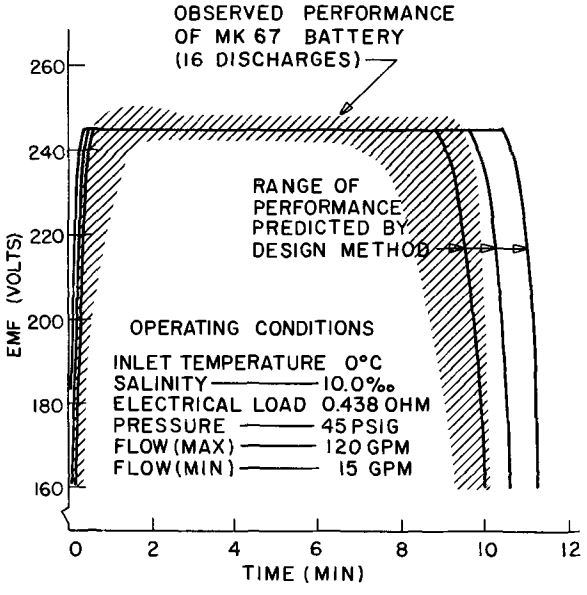

Fig. 16. Predicted and observed voltages of Mk 67 battery when discharged at 0°C.

reduced to the 30-40 gal/min required to bring the battery voltage up to the desired 245V. The wide range of observed voltages found in the first 1½ min (Fig. 16) results from variations in the time it takes to accomplish this task. In contrast, the computer simulation simulates operation in which the filling time is very short with a flow control valve with infinitely fast and accurate response. This condition is best approached by the battery behavior given by the "leading edge" of the observed voltage envelope. It is significant that the agreement between the simulation and the leading edge is excellent.

Low-temperature, low-salinity discharges of the Mk 67 battery are frequently marked by clogging and electrical arcing within the battery in the period beyond 7½ min. This, along with the probable recirculation of H_2, accounts for the poor performance during this period. Since the simulation assumes that no voltage losses from undesired effects such as arcing or clogging occur, a valid comparison during the latter portion of the discharge would be that of the trailing edge of the voltage envelope and the nominal predicted voltage line. These two lines are in good agreement, reaching the cutoff voltage of 160V (0.7 V/cell) within 0.5 min of each other.

Thus, the nominal voltage predictions of the simulation are in excellent agreement for 95% of the discharge time to a cutoff voltage of 160V if the leading edge of the voltage envelope is used during the first 1½ min of the discharge to compensate for the effects of start-up procedures and if the trailing edge of the voltage envelope is used beyond the 8-min mark to compensate for the effects of arcing and clogging.

Discussion

When limitations of the test facility and the effects of clogging and arcing are taken into account, the voltage, flow, and temperature predictions of the computer simulation are in good-to-excellent agreement with the observed performance of the Mk 61 Mods 0 and 2, Mk 64, and Mk 67 batteries. The configurations of the four batteries used in this study are sufficiently diverse that these results are applicable to all high-drain AgCl-Mg battery configurations known to this author. Furthermore, the temperature and salinity of the electrolytes used in the discharges reported here cover the extremes found in the world's oceans with the exception of a few small regions such as those at the bottom of the Red Sea where extremely warm concentrated brines are found. On this basis we conclude that the simulation is more than adequate for use in carrying out parametric studies or for the design of high-drain, sea water-activated batteries which use AZ61 magnesium alloy, the most common alloy for such batteries today.

The computer cost of simulating a battery discharge ranges from $15-$30. The cost of discharging a full-size battery ranges from $2,000 to $30,000 (1). In addition to the advantage of low cost, the simulation gives information on the spatial and temporal distributions of such quantities as temperature, electrolyte composition, and current density that are difficult or impossible to obtain from battery discharges. A further advantage of the simulation is that the range of operating conditions which can be studied is not limited by the availability of discharge facilities or by the practicality of tests conducted at sea. This latter is a significant problem, not only because of the high costs of field operations and instrumentation problems but because of the unpredictable occurrence of many of the test conditions which are of interest.

Thus, the computer simulation permits rapid and inexpensive determinations of the behavior of competing battery configurations permitting a large reduction or even the complete elimination of the "cut and try" effort previously required to design batteries. This ability to evaluate the performance of candidate battery configurations for any desired operating condition considerably reduces the technological risks of battery development. These comments apply with equal force to system studies involving the application of high-drain AgCl-Mg batteries.

Acknowledgment

Dr. William R. Davis, Associate Director of the Applied Physics Laboratory, and staff, Mr. William Felton, Mr. Rodney Lipp, Mrs. Linda Rines, and Mr. Robert Van Valkenburgh contributed to the success of this effort. Their contributions are gratefully acknowledged.

This work was supported by the Naval Ordnance Systems Command, United States Department of the Navy, under Contract NOw 65-0207-d.

Manuscript submitted April 26, 1971; revised manuscript received April 23, 1973.

Any discussion of this paper will appear in a Discussion Section to be published in the June 1974 JOURNAL.

REFERENCES
1. D. W. Faletti, Applied Physics Laboratory APL-UW 7116, University of Washington, Sept. 1, 1972.
2. D. W. Faletti, Applied Physics Laboratory, APL-UW 7112, University of Washington, Sept. 15, 1971.
3. D. W. Faletti and M. A. Gackstetter, *This Journal*, **115**, 1210 (1968).
4. George Perkons, General Electric Co., Pittsfield, Mass., Personal communication.

The Ag/KCN-4AgI/2 Perylene · $3I_2$ Solid-State Battery System

D. V. Louzos,* W. G. Darland,* and G. W. Mellors

Union Carbide Corporation, Consumer Products Division, Cleveland, Ohio 44101

ABSTRACT

A solid-state battery system using a powdered silver anode, a charge transfer iodine complex cathode of 2 perylene · $3I_2$, and an electrolyte of ionically conductive solid KCN-4AgI has been developed. The open-circuit voltage of single cells is 0.64V. Being totally solid, the system enjoys long shelf life and freedom from electrolyte leakage. Cell construction is such that the thickness of the highly conductive (1.4×10^{-1} ohm^{-1} cm^{-1}) KCN-4AgI electrolyte layer can be as low as 0.004 in. without sacrificing useful shelf life. This coupled with the high electronic conductance of both anode and cathode results in low impedance cells capable of delivering continuous currents as high as 50 mA/in.^{2} and pulse currents up to 1.0 A/in.^{2}. Successful operation under conditions of severe rotational spin has been demonstrated. Cell performance over the wide temperature range of $-40°$ to $+250°$F has been shown.

Solid electrolyte batteries enjoy inherent advantages over their liquid electrolyte counterparts in that the absence of a liquid extends the temperature range over which the battery is operable and permits the construction of a leakproof system. Anode corrosion and loss of solvent by drying out constitute two of the important limitations of shelf life in aqueous batteries and it is reasonable to expect that solid-state systems should show improved behavior in these respects. Solid-state batteries should also be capable of pressure packaging or hard encapsulation to yield rugged assemblies that would be capable of withstanding shock and vibration.

Within the last 20 years attempts have been made to use solid ionic conductors as battery electrolytes. Work done before 1950 was mainly of theoretical interest and consisted of measurement of single-cell potentials. During the 1950's a flurry of activity occurred within the battery industry with the resultant development of a number of solid electrolyte systems. However, the most conductive ionic solid known at that time was silver iodide whose specific conductance at 25°C was about 10^{-6} ohm^{-1} cm^{-1}.

Because of this, very thin electrolyte layers had to be employed in order to minimize internal resistance and permit the delivery of current even in the microampere range. During the period 1957-1960 pilot plant production techniques were developed usually under Industrial Preparedness Study Contracts to study design and production problems. The development work conducted by five major battery companies during this period confirmed the advantages predicted for solid electrolyte batteries (1). Miniaturization approaching 100V/cm was achieved, and shelf life was estimated at 10 years. Manufacturing techniques were amenable to a high degree of mechanization. Some of the battery systems were operational and apparently unharmed at temperatures approaching 100°C Packaging could be made exceptionally sturdy and rugged and the batteries were able to withstand shock and vibration.

The development work indicated that there were also limitations inherent in solid-state systems. All exhibited very high internal resistance and high polarization losses during discharge at room temperature. No system could be considered a useful power source for drains in excess of 10 μA/cm^2. Recently a revival of interest in solid-state systems has occurred mainly as a result of the discovery of new conducting compounds. Reuter and Hardel (2) reported Ag_3SI to have conductance of 10^{-2} ohm^{-1} cm^{-1}, and cells of the type $Ag/Ag_3SI/I_2$ built by Takahashi and Yamamoto (3) yielded currents of 1 mA/cm^2 at 25°C. Since Ag_3SI, when slightly off stoichiometry, possesses appreciable electronic conductance and reportedly reacts with iodine to form silver iodide and sulfur (4), further work to clarify the stability of this system is required.

Materials of the general formula MAg_4I_5 (where M = K, Rb, or NH_4) were described almost simultaneously by Bradley and Greene (5) and Owens and Argue (6). Ionic conductances in the region of 2×10^{-1} ohm^{-1} cm^{-1} were reported for the best of these materials, and later papers described cells in the system $Ag/RbAg_4I_5/RbI_3$ (7). Other cathodes used were iodine and the reaction product of iodine and tetrabutylammonium iodide (8). Currents in the milliampere region may be drawn continuously from these batteries.

Recent work (9, 10) has described the preparation and properties of a family of cyanide-iodide solids whose conductance is essentially ionic and again differs but little from that of aqueous battery electrolytes. For example, the specific conductance of KCN-4AgI is 1.4×10^{-1} ohm^{-1} cm^{-1} while that of the aqueous electrolyte of Leclanché cells is 2.0×10^{-1}.

The present paper describes the development of a solid-state battery (11) based on these cyanide-iodide materials and a perylene-iodine cathode. Of necessity, since these solids conduct by silver ion transport, the anode was silver metal. A large number of inorganic and organic iodine complexes were evaluated as potential cathode materials, however, the charge transfer complex of perylene-iodine was used in all cells described here.

Experimental

Materials.—The materials that were used in the cell fabrications were generally Reagent Grade or ACS grade purity chemicals. The preparation of the solid electrolytes of the KCN-AgI and RbCN-AgI systems has been previously described (10).

Cell construction.—In its simplest form the cell consists of an anode layer, an electrolyte layer, and a

* Electrochemical Society Active Member.

Key words: solid electrolyte battery, silver/perylene iodine battery system, potassium cyanide-silver iodide electrolyte, shelf life, perylene-iodine.

cathode layer. The anode can be merely a thin sheet of silver foil or a thin layer of silver metal deposited on one side of the electrolyte layer, or a silver powder-electrolyte composition. This is mechanically separated from the cathode by a thin layer of the compressed KAg_4I_4CN electrolyte. The cathode is also a pressed powder disk formed from the iodine-containing complex, 2 perylene · $3I_2$. The three layers are held together in intimate contact obtained by compression of the respective powders during cell fabrication, the cell thereafter functioning without any applied external pressure.

Figure 1 shows a partial cutaway view of a typical cell construction that utilizes an electrolyte layer that even if as thin as 0.004 in. does not shorten the useful shelf life of the cell and which at the same time results in more efficient utilization of cell volume. The anode subassembly consists of a pressed disk containing silver powder adjacent to the electrolyte layer and an anode collector that serves as an electronic contact to the anode situated on the outside surface of the anode as shown. The cathode subassembly is a disk containing the 2 perylene · $3I_2$ powder and a metallic cathode collector, for example, a thin sheet of nickel. The entire cell assembly is compressed during manufacture to establish intimate physical bonding between the various layers. A standard Adolph Buehler metallographic mounting press may be used for these molding operations in the laboratory. The cell is thereafter encapsulated in plastic, for example, Lucite or Kel-F. Cells have been made whose diameter varied between 0.4 to 1.25 in. In a cell encapsulated in plastic, holes may be drilled through the plastic at either end, filled with conductive silver epoxy cement in which are embedded lead wires, the latter serving as contacts. In a hermetically sealed (metal case) system, one electrode may be brought out through a Stupakoff seal (glass-metal) and the other may be the metal case, or both may be brought out through glass-metal seals.

Electrodes.—In general the choice of anode for a solid-state battery is dependent on the nature of the conducting ion. In the present electrolytes, one must use silver and while the anode metal may be present as a flat, thin metal foil, it is preferable for optimized performance that a large surface area of silver be provided in the anode in contact with solid electrolyte. This is accomplished by the physical blending of mixtures of silver powder and electrolyte powder. The resulting pressed powder compact not only has a large area of interfacial contact between anode and electrolyte but also provides intimate contact between the anode and the electrolyte layers when these are subsequently pressed together. A third component of the anode may be finely divided carbon black which further improves cell performance.

In all cells described here the charge transfer complex of perylene-iodine (2:3) was used as active cathode material. For a battery to possess good, high-temperature shelf life it is desirable that the iodine exert a low vapor pressure; the data of Fig. 2 obtained in this laboratory (12) shows the variation with temperature of the vapor pressure of I_2 over perylene-iodine (2:3) and over solid iodine. In addition the perylene-iodine materials are particularly well suited for use as solid-state battery cathodes because of their high electronic

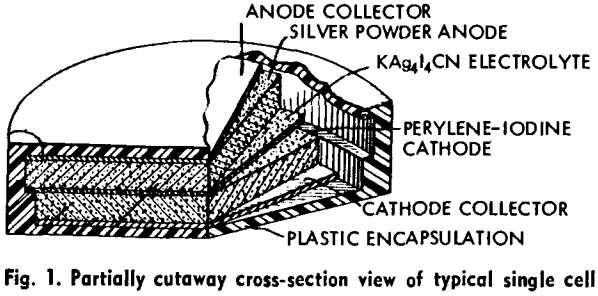

Fig. 1. Partially cutaway cross-section view of typical single cell

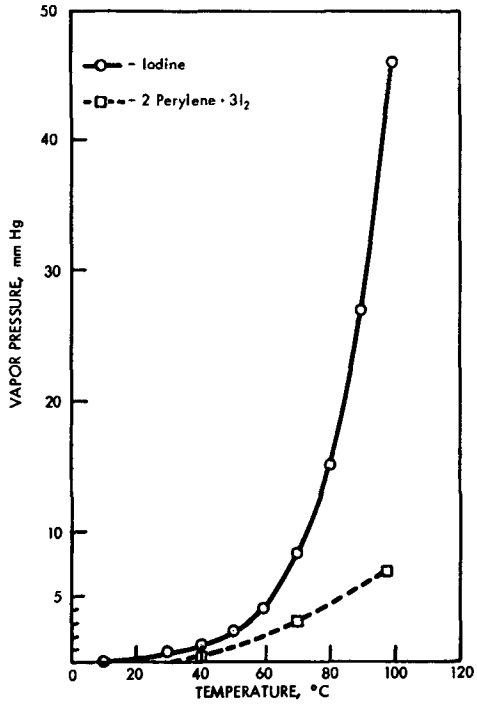

Fig. 2. Variation of iodine vapor pressure with temperature for iodine and 2 perylene · $3I_2$.

conductivities. For example, the specific resistivity of a pressed pellet of 2 perylene · $3I_2$ is 8 ohm-cm. The complex is prepared by reacting the components in a closed tube at 200°C for several hours. While in the open, iodine evaporates slowly and leaves golden-yellow perylene behind, in the sealed environment of the cell the complex is stable.

The 2 perylene · $3I_2$ complex may be powdered and compressed alone as the useful cathode, but preferably it is compounded in much the same manner as the anode, *i.e.*, starting with the dried powder form of the active cathode material, electrolyte, and carbon and physically mixing these together. Drying is again accomplished by storing the respective powders in an argon atmosphere over P_2O_5.

In Table I are shown typical electrode formulations together with capacities and silver and iodine utilizations.

While the charge transfer complex, 2 perylene · $3I_2$, was used as the active cathode material for the cells whose performance is described herein, a number of other organic and inorganic iodine-containing materials were also evaluated. A number of cell systems resulting from this work are shown in Table II.

Electrolyte.—A number of solid compositions prepared in the KCN-AgI and RbCN-AgI system have been used as the solid electrolyte. Of these, the KCN-4AgI solid (KAg_4I_4CN) is preferred because of the

Table I. Typical electrode formulations

	Anodes					
	Formulation, %			Capacity,	Capacity,	Silver
Designation	Silver	Electrolyte	Carbon	mA-hr/g mix	mA-hr/g Ag	utilization, %
1A	44.6	41.0	14.4	33	74.0	30
2A	71.9	27.4	0.7	73	101.5	40
3A	67.5	30.0	2.5	100	148.5	60

	Cathodes						
					Capacity		
Designation	Perylene-iodine, %	I_2 only, %	Electrolyte, %	Carbon, %	mA-hr/g mix	mA-hr/g I_2	Utilization, %
1C	22.0	13.2	56.4	21.6	9	67.2	32
2C	50.0	30.0	37.5	12.5	45	150.0	71
3C	87.0	52.1	0.0	13.0	90	172.5	82

Table II. Open-circuit voltages for selected systems

Cell system	Open-circuit voltage
$Ag/KAg_4I_4CN/2$ perylene · $3I_2$	0.64
$Ag/RbAg_4I_4CN/2$ perylene · $3I_2$	0.64
$Ag/KAg_4I_4CN/2$ phenothiazine · $3I_2$	0.64
$Ag/RbAg_4I_4CN/2$ phenothiazine · $3I_2$	0.64
Ag/KAg_4I_4CN/pyrene · I_2	0.64
$Ag/RbAg_4I_4CN$/pyrene · I_2	0.64
$Ag/KAg_4I_4CN/(CH_3)_4NI_3$	0.65
$Ag/KAg_4I_4CN/RbI_3$	0.67

Table III. Comparison of electrolyte conductances

Type of system	Electrolyte	Specific conductance at 25°C, ohm^{-1} cm^{-1}
Solid state		
Ag/2 perylene · $3I_2$	KAg_4I_4CN	1.4×10^{-1}
Aqueous		
Leclanché		
Zn/MnO_2	$NH_4Cl + ZnCl_2$	2×10^{-1}
Alkaline		
Zn/MnO_2 Zn/Ag_2O Zn/HgO Cd/NiOOH	KOH	5×10^{-1}
Lead acid		
Pb/PbO_2	H_2SO_4	7×10^{-1}

lower cost of potassium salts as compared to rubidium salts. This material was ground to a fine powder in a dry argon atmosphere before being used in the compression molding of cells. The powdered solid electrolyte layer is intimately compressed into both the powdered anode and cathode layers to form a good continuous cell structure. The conductance of KCN-4AgI has been reported in an earlier publication (10) and it may be noted that the conductance is adequate, even at −80°C, to permit use in cells. A comparison of the specific conductance of this material with those of the aqueous electrolytes used in commercial systems is presented in Table III.

Results

In the following section data are reported on single cells and on batteries having a number of cells connected in series or in series-parallel.

Single-cell discharge data.—Continuous discharge data at nominal drains of 50, 150, and 300 μA are shown in Fig. 3, 4, and 5, respectively, over the temperature range of −40° to 160°F. Pulse discharge at 1A for 5

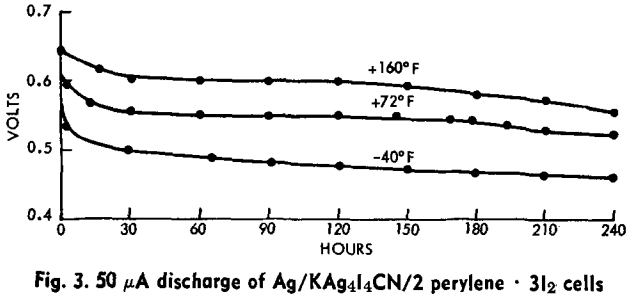

Fig. 3. 50 μA discharge of $Ag/KAg_4I_4CN/2$ perylene · $3I_2$ cells

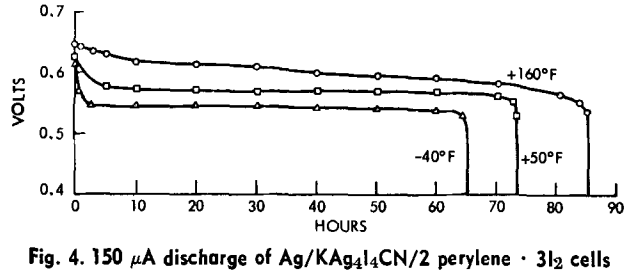

Fig. 4. 150 μA discharge of $Ag/KAg_4I_4CN/2$ perylene · $3I_2$ cells

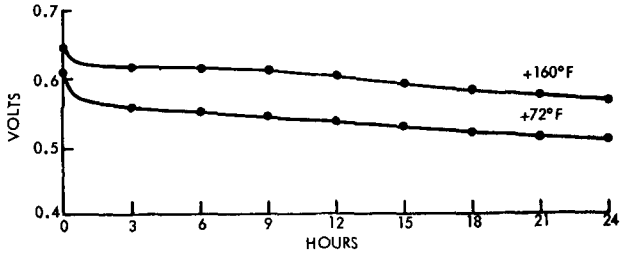

Fig. 5. 300 μA discharge of $Ag/KAg_4I_4CN/2$ perylene · $3I_2$ cells

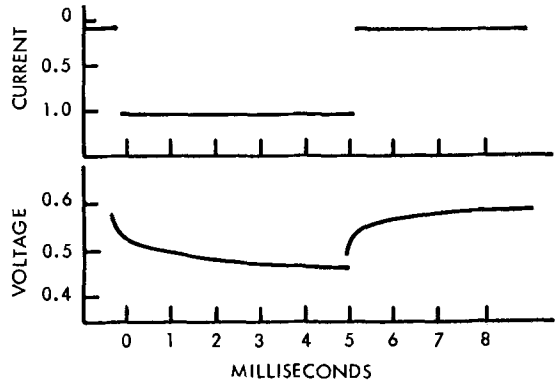

Fig. 6. 1 Ampere discharge for 5 msec $Ag/KAg_4I_4CN/2$ perylene · $3I_2$ cell.

msec is shown in Fig. 6. The ratio of silver to iodine in the electrodes was 4:1 and the formulations 1A and 1C (Table I) were used. The open-circuit potential was 0.64-0.66V and the cells were 1 in. in diameter with a nominal electrode cross-sectional area of 0.75 in^2.

In Fig. 7 is shown a photograph of a hermetically sealed single cell, where the steel container is one contact and the other lead was brought out through a glass to metal (Stupakoff) seal. This construction permitted continuous operation at the 5-6 mA level at up to 250°F in an oil bath (Fig. 8). Polarization scans at 72° and 250°F are shown in Table IV.

Another smaller size of single cell was developed and tested for a low drain-extended service application. This was 0.5 in. in diameter, used electrode formulations 2A and 2C (Table I), and the silver to iodine ratio in the electrodes was 1:1. Performance at room temperature at average currents of 12.6 and 28.3 μA are shown in Fig. 9. Other cells were made in this size with identical anodic silver:cathodic iodine ratios but using the 3A-3C combinations of electrode formulations.

A typical variation of open-circuit potential with temperature for a single cell consisting of 3A-3C elec-

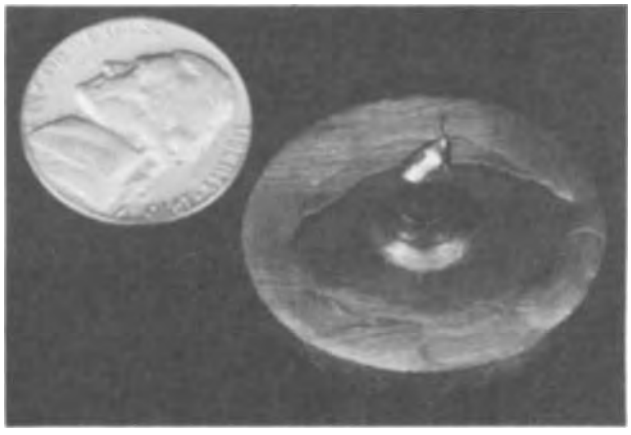

Fig. 7. Hermetically sealed $Ag/KAg_4I_4CN/2$ perylene · $3I_2$ cell

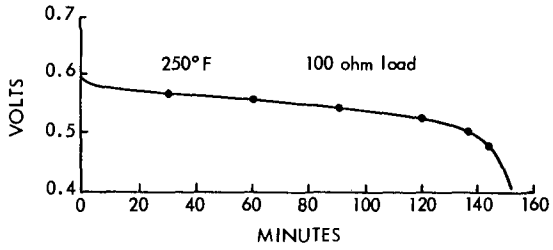

Fig. 8. Discharge of hermetically sealed Ag/KAg_4I_4CN/2 perylene · $3I_2$ cell.

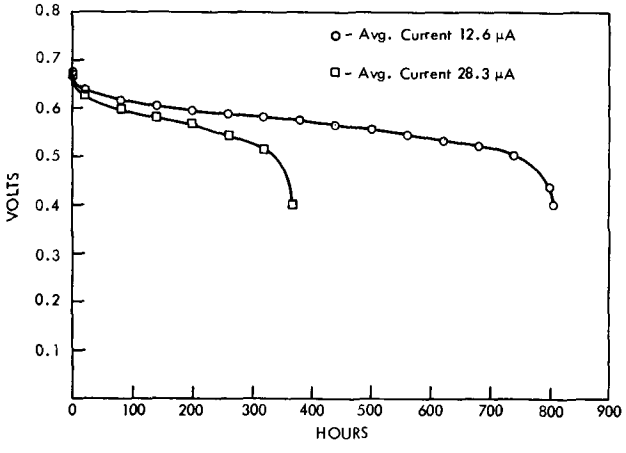

Fig. 9. Performance of 0.5-in. diameter cells using 2A and 2C electrode formulations.

trodes is shown in Table V and the performance of such a cell at room temperature and at −40°C is shown in Fig. 10.

The capability of the cell is much reduced at low temperatures but, by employing a silver reference electrode built into the cell, it was found that under these conditions the anode polarized severely and thus, by increasing the amount of anode (*i.e.*, increasing silver:iodine ratio), improved performance at low temperatures could be obtained. However, this improvement was at the expense of performance at room temperature and 160°C. Data for +23° and −40°C are shown in Fig. 10 and it was decided that the best compromise was an Ag:I_2 ratio of 4:1. One may note that, in cells that are anode-limited, the anode efficiency falls from 58% at room temperature to 12% at −40°F, while

Table IV. Polarization scans of Ag/KAg_4I_4CN/2 perylene · $3I_2$ cells

Load, ohms	Volts	Calc., mA	mA/in.²
	72°F		
1000	0.58	0.58	0.77
500	0.58	1.16	1.55
300	0.57	1.90	2.53
100	0.55	5.44	7.39
50	0.53	10.7	14.2
10	0.48	48.2	64.3
	250°F		
1000	0.60	0.60	0.80
500	0.60	1.19	1.59
300	0.59	1.98	2.64
100	0.59	5.85	7.80
50	0.57	11.4	15.2
10	0.49	49.0	65.3

Table V. Variation of open-circuit voltage with temperature

Cell No.	Electrodes	Temperature (°C)	OCV
1242	3A-3C	−64	0.636
		−20	0.641
		0	0.643
		22	0.645
		44	0.648
		60	0.650

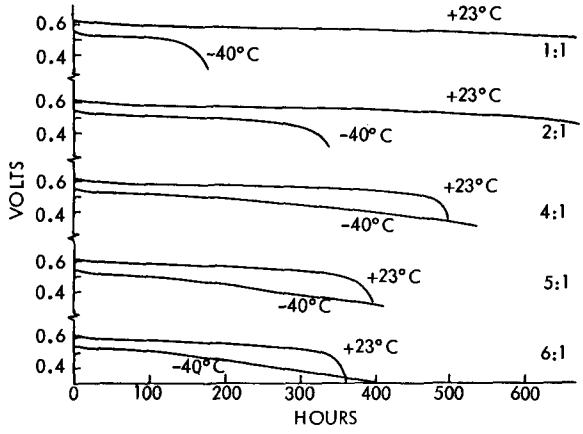

Fig. 10. Performance of 0.5-in. diameter cells with 3A and 3C electrode formulations including −40°C data (20,000-ohm load) as a function of anode:cathode ratio.

in a cell designed to be cathode-limited the figures are 83% at room temperature and 74% at −40°F based on iodine utilization.

Multiple cell batteries.—Batteries have been made with single cells connected in series, or in parallel, or in combination. A hermetically sealed four-cell battery (two parallel pairs of two cells in series) designed to operate over the temperature range −40° to 160°F is shown in Fig. 11a while a 3.25V battery (five cells in series) is shown in Fig. 11b. The latter was intended to supply a pulse of 1A for 5 msec. A discharge curve for a single cell under these load conditions has been shown in Fig. 6.

Figure 12a shows a variety of single cells and stacks made from these cells, while Fig. 12b shows encapsu-

Fig. 11a. Hermetically sealed 4-cell battery Ag/$RbAg_4I_4CN$/2 perylene · $3I_2$.

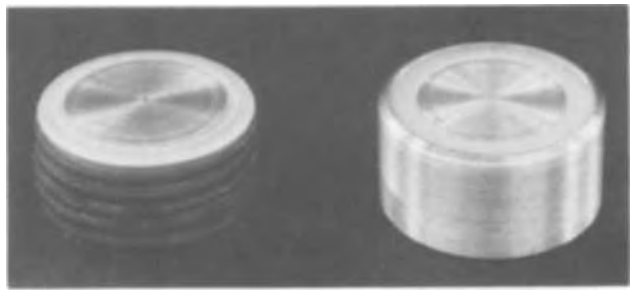

Fig. 11b. 3.25V battery consisting of five Ag/KAg_4I_4CN/2 perylene · $3I_2$ cells in series.

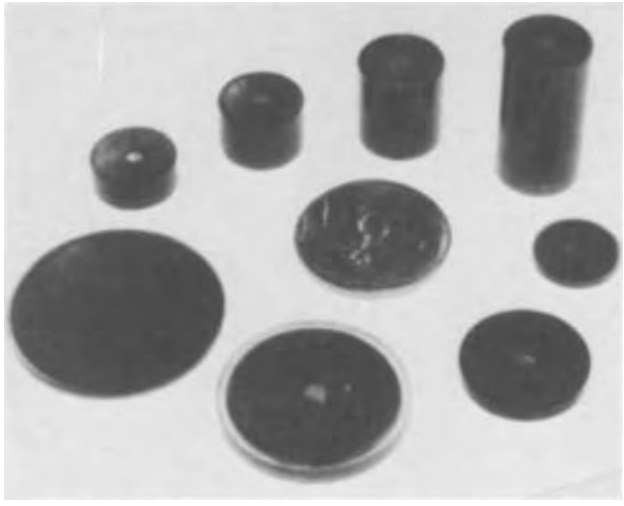

Fig. 12a. Variety of single cells and stacks

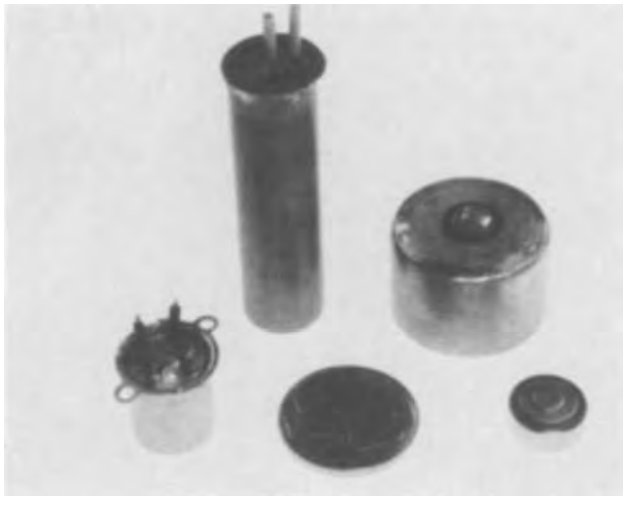

Fig. 12b. Hermetically sealed encapsulations of above cells and stacks.

lations in hermetically sealed containers of some of those batteries.

Performance of three and seven cell stacks of 1/2 in. OD cells is shown in Fig. 13 with loads as indicated (anode:cathode ratio 1:1, 3A and 3C formulation). Figure 14 shows the discharge of seven cell batteries at three different temperatures.

Performance of a series-parallel battery is shown in Fig. 15. Curve A is for a battery having two cells in

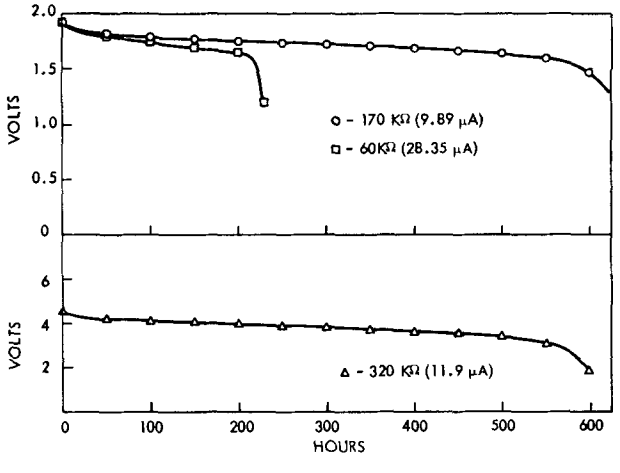

Fig. 13. Performance of 3- and 7-cell stacks (0.5-in. diameter)

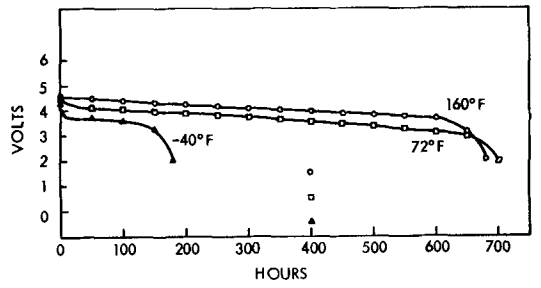

Fig. 14. Discharge of 7-cell batteries at three temperatures (20,000-ohm load).

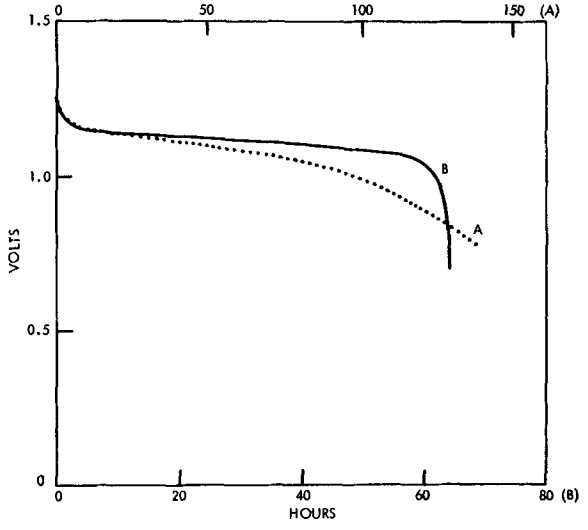

Fig. 15. Performance of a series-parallel battery. Curve A: 2 cells in series, paralleled three times; Curve B: 2 cells in series, paralleled four times. Average current: 1.0 mA.

series, paralleled three times, while Curve B has four series pairs in parallel. Curve A was obtained by discharging at a 500-ohm load 15 msec on, 30 msec off. The average current was 0.70 mA and the capacity 104 mA-hr to 0.8V cut-off. Curve B was obtained with an 1100-ohm load, 1.0 mA average current with capacity 64 mA-hr to 0.8V cut-off.

Impedance.—Since the electronic conductance of the anode and cathode and the ionic conductance of the electrolyte are all high, it is not surprising that at room temperature single cells of 1-in. diameter have an impedance of about 0.3 ohm. In addition after 12 months storage at 160°F, only a small increase to 0.7 ohm occurred. At −40°F, single-cell impedance is 2.1 ohms fresh and 2.5 ohms after storage. Cell discharge also results in additional small impedance increases as can be seen from Table VI.

The impedance of equivalent cells made with $RbAg_4I_4CN$ electrolyte in place of KAg_4I_4CN is essentially identical. The variation of impendance with temperature for a four-cell (series-parallel) battery using $RbAg_4I_4CN$ electrolyte (see photograph of cell, Fig. 11a) is shown in Fig. 16. The temperature coefficient is 2.9×10^{-3} ohm/°F (5.2×10^{-3} ohm/°C).

Table VI. 1000 Hz impedance of single cells. 1-in. diameter, 0.75 in.^{2} apparent area

Discharge	Temperature of discharge, °F	Impedance (ohms)	
		Fresh cells	After 12 months storage at 160°F
Before	70	0.3	0.7
After	70	0.5	1.2
Before	−40	2.1	2.5
After	−40	—	4.6

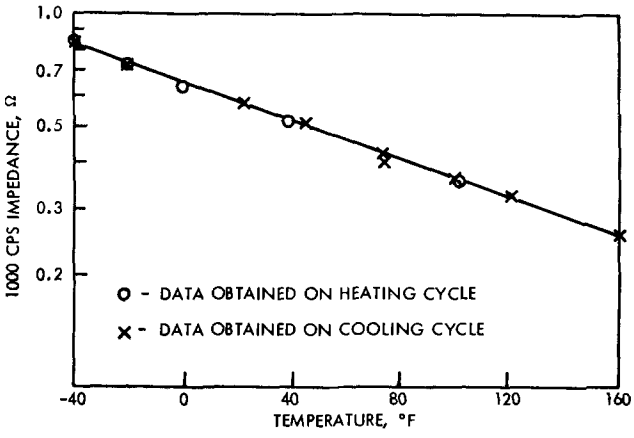

Fig. 16. Variation of impedance with temperature (for 4-cell [series parallel] battery of Ag/RbAg$_4$I$_4$CN/2 perylene · 3I$_2$ system).

Some typical values (also at 1000 cycles) of impedance for 3-, 5-, and 7-cell batteries are shown in Table VII.

Depending on the components and on the amounts of material used for example, high capacity necessitates thick electrodes and hence higher than normal impendance, the figures given in Table VIII can be quoted for impedance for single cells.

Shelf life.—Shelf-life studies were conducted with 1-in. diameter cells under conditions designed to minimize any variabilty caused by seals and moisture ingress. These cells were built as described in previous sections utilizing the design of the single cell shown in Fig. 1, with the 1A-1C electrode formulation (4:1 silver-iodine ratio). Cells were encapsulated in Lucite plastic with an additional second layer of epoxy plastic placed over the Lucite not normally placed over cells destined for hermetic battery sealing. The cells were further stored in a desiccator over P_2O_5 so as virtually to eliminate the possibility of moisture ingress during the storage period. The experimental conditions chosen for this shelf-life study simulate those that exist in the hermetically sealed construction used in later designs of this battery. The shelf-life capability of the system is evaluated by discharge of cells that have been stored for six months at 160°F and then tested over the temperature range of −40° to +160°F. A comparison of the capacities obtained under these conditions with those obtained from fresh cells may be found in Fig. 17. While some decrease in capacity was noted after prolonged 160°F storage (accelerated shelf test), a substantial and certainly useful cell capacity is obtained, and a rule of thumb common in battery technology suggests that one month of storage at 160°F is approximately equivalent to one year at room temperature.

Table VII. Battery impedance at 1000 cycles

Battery type and nominal area	Electrodes (see Table I)	Time	1000 Cycle a-c resistance (ohms)
3-cell, 0.11 in.²/cell	3A-3C	Fresh	3.68
		4 months	4.5
		1 year	4.6
5-cell, 0.11 in.²/cell	3A-3C	Fresh	5.7
		1 month	5.9
7-cell, 0.11 in.²/cell	3A-3C	Fresh	7.3
		3 months	8.3

Table VIII. Impedance of single cells

Area (in.²)	Impedance (ohms)
0.11	0.9 ~ 2.5
0.28	0.5 ~2.0
0.60	0.25 ~ 1.0

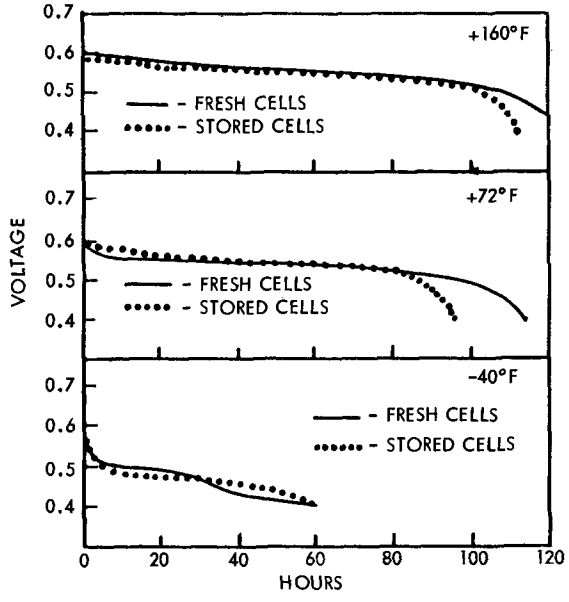

Fig. 17. Shelf-life study (capacity retention of Ag/KAg$_4$I$_4$CN/2 perylene · 3I$_2$ system) (4000-ohm load).

Storage experiments with 0.5-in. diameter cells (3A-3C electrode formulations, 1:1 silver to iodine ratio) are shown in Fig. 18. After six months storage at room temperature virtually no loss in capacity was observed on discharging at room temperature. On the other hand, some loss was observed in the room temperature capability after storage at 160°F for six months.

A loss of open-circuit voltage is seen upon storage and an attempt has been made to determine the magnitude of this decay. An examination of data from several sources indicates a continuously decreasing rate of open-circuit decay. The rate of decay is defined as the total loss in voltage from the time of manufacture divided by the number of days during which the loss occurred. Over a long period of time the loss becomes very small, as is demonstrated in Fig. 19; for example, after storage at room temperature for about one year the average decay is 0.028 mV/day.

Spin testing.—Ag/KAg$_4$I$_4$CN/2 perylene · 3I$_2$ cells have been subjected to discharge loads ranging from 47 to 10,000 ohms while being rotated at speeds of 360 rps (21,600 rpm). The cells operate essentially the same while being rotated at 360 rps as they do under normal static conditions.

Summary

Solid-state battery systems were developed using either KCN-4AgI or RbCN-4AgI as the solid electrolyte, and the charge transfer complex, 2 perylene · 3I$_2$ as cathode. This material provided iodine for electrochemical reduction at a low vapor pressure thus pre-

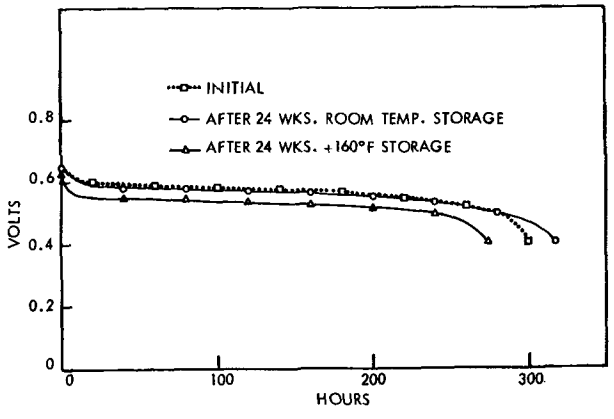

Fig. 18. Storage data with 3A-3C electrode formulations (20,000-ohm load).

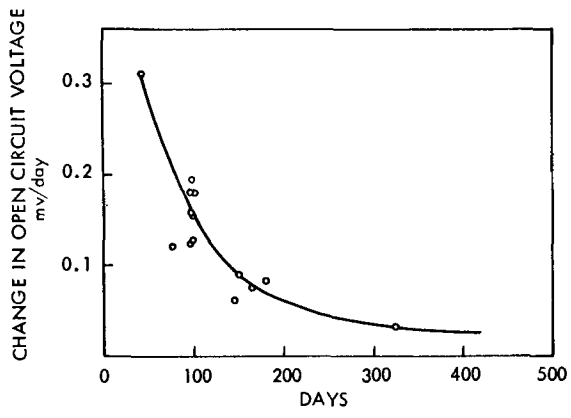

Fig. 19. Loss of open-circuit voltage on storage over extended periods at room temperature.

serving high-temperature shelf life, and was well suited for use as a cathode because of its high electronic conductivity. The use of a silver anode was dictated by faradaic experiments which established the conductance of the solid electrolytes as being due to the movement of Ag^+ ions. In its simplest form, the equation of cell discharge may be written as

at the anode

$$Ag \rightarrow Ag^+ + e^-$$

at the cathode

$$\tfrac{1}{2}I_2 \text{ (perylene complex)} + e^- \rightarrow I^- + \text{perylene}$$

over-all

$$Ag + \tfrac{1}{2}I_2 \text{ (perylene complex)} \rightarrow AgI + \text{perylene}$$

Cell construction and molding techniques were developed that permitted electrolyte thickness as low as 0.004 in. to be used without sacrificing useful shelf life. $Ag/KAg_4I_4CN/2$ perylene $\cdot$ $3I_2$ cells of 1-in. diameter (0.75-in.^{2} apparent electrode cross section) were made whose 1000 Hz impedance is only 0.3 ohm at room temperature. Useful cell discharge was demonstrated over the temperature range of $-40°$ to $+250°$F.

Acknowledgments

The authors would like to express their thanks to M. S. Soldat, R. L. Johnson, and J. T. Marshall who performed much of the experimental work.

Manuscript submitted Nov. 8, 1972; revised manuscript received April 6, 1973. This was Paper 12 presented at the Miami Beach, Florida, Meeting of the Society, Oct. 8-13, 1972.

Any discussion of this paper will appear in a Discussion Section to be published in the June 1974 JOURNAL.

REFERENCES

1. J. N. Mrgudich and D. V. Louzos, "The Primary Battery," Vol. 1, chap. 11, pp. 385-398, G. W. Heise and N. C. Cahoon, Editors, John Wiley & Sons, Inc., New York (1971).
2. B. Reuter and K. Hardel, *Naturwiss.*, **48**, 161 (1961).
3. T. Takahashi and O. Yamamoto, *Electrochim. Acta*, **11**, 911 (1966).
4. B. Owens, G. R. Argue, I. J. Groce, and L. D. Hermo, *This Journal*, **116**, 312 (1969).
5. (a) J. N. Bradley and P. D. Greene, *Trans. Faraday Soc.*, **62**, 2069 (1966); (b) **63**, 424 (1967); (c) **63**, 1023 (1967); (d) **63**, 2516 (1967); (e) Brit. Pat. No. 1, 140, 398 (1969).
6. (a) B. B. Owens and G. R. Argue, *Science*, **157**, 308 (1967); (b) U. S. Pat. No. 3,443,997 (1969).
7. B. Owens, G. R. Argue, and I. J. Groce, (a) *Proc. 22nd Annual Power Sources Conf.*, **103**, May 14-16 (1968); (b) *Proc. 6th Intern. Power Sources Symposium*, Brighton, England, chap. 24, p. 89 (1968).
8. M. DeRossi, G. Pistoia, and B. Scrosati, *This Journal*, **116**, 1642 (1969).
9. G. W. Mellors, U. S., Pat. No. 3,582,291, June 1, 1971.
10. G. W. Mellors and D. V. Louzos, *This Journal*, **118**, 846 (1971).
11. D. V. Louzos, U. S. Pat. No. 3,653,968, April 4, 1972.
12. J. Kommandeur and F. R. Hall, *J. Chem. Phys.*, **34**, 129 (1961).

The Silver/Silver Iodide/Silver Thermocell

Herbert F. Hunger*

Power Sources Technical Area, Electronics Technology and Devices Laboratory, United States Army Electronics Command, Fort Monmouth, New Jersey 07703

ABSTRACT

Various thermodynamic expressions for the thermoelectric effects in solid electrolytes, including silver iodide, have been reported in the literature. No attempt has been made so far to account for the contraction phenomenon occurring in γ, β silver iodide during temperature increase. Considering that we are dealing actually with a thermomechanical electrical effect, a novel equation for the thermoelectric power of silver iodide was developed which appears to account quantitatively for the experimental data.

The equation contains two terms. Discussion of the nature of these terms and their numerical values lead us to believe that the first term is identical with the heterogeneous thermoelectric effect and the second term with the homogeneous thermoelectric effect. These two effects were postulated and discussed by earlier investigators.

The equation permits computation of both effects as well as computation of the total thermoelectric power as a function of impurity ion concentration and temperature from 0° to 140°C. It appears that the heterogeneous thermoelectric effect is a function of the impurity ion concentration level. The levels in a commercial product of powdered silver iodide from which the sensor pellets were prepared were 4.95×10^{17} and 8.65×10^{17} impurity ions per cm^3. These levels correspond to an averaged thermoelectric power of 7.5×10^{-4} V/°K at room temperature.

A thermocell composed of two identical silver electrodes in intimate contact with opposite faces of a pellet made of compressed silver iodide powder can sense a temperature gradient across the cell by development of a potential difference. Thereby the warmer electrode assumes a negative potential *vs.* the cooler, positive electrode.

* Electrochemical Society Active Member.

Key words: thermomechanical electrical effect, homogeneous thermoelectric effect, heterogeneous thermoelectric effect, strain-potential effect.

The thermoelectric effect of silver iodide and of other solid electrolytes was first studied in 1928 by Reinhold (1). He reported measurements of thermovoltages of various modifications of silver iodide and developed empirical equations describing the observations.

A series of fundamental publications pertinent to the effect followed. Eastman contributed fundamentally with a thermodynamic treatment of stationary states in nonisothermal systems (2). The key to the treatment was the introduction of the heat of transfer and of the entropy of transfer. Wagner's and Reinhold's work led to the separation of the thermoelectric effect into two effects, one homogeneous and one heterogeneous (3, 4). Reinhold expected that in a system consisting of a homogeneous solid electrolyte in a nonisothermal arrangement there would be a potential difference and termed it the homogeneous thermoelectric effect. According to the theory of Wagner, the homogeneous thermoelectric effect can be related to the "elemental heat of transport." This elemental heat of transport differs from Eastman's heat of transfer (of a specie, i, in a mixture) in that only one component of a system participates in the transportation process. The heat of this migrating component is equal to its elemental heat of transport. The heterogeneous thermoelectric effect is equal to the temperature coefficient of the potential difference at the phase boundary between the two electrodes and the solid electrolyte. Reinhold computed the heterogeneous effect from thermal data.

A general theory of the homogeneous thermoelectric effect was developed by Lidiard both for the intrinsic region where Frenkel or Schottky defects prevail and also for the region of impurity-controlled conductivity at lower temperatures (5). The theory suggests that the homogeneous effect is independent of the impurity ion concentration.

In this paper, a mechanistic treatment of the Ag/AgI/Ag thermocell is presented, with the homogeneous thermoelectric effect assumed to be due to Ag^+ transport and the heterogeneous thermoelectric effect to Ag^+ concentration differences (strain-induced) at the electrodes.

Results and Discussion

Movement of ionic charge carriers in a simultaneous electrical and thermal diffusion field.—The current density I_i of an ionic specie, i, in a simultaneous diffusion and electrical field is

$$I_i = I_D + I_E = Z_i F D_i \left(\frac{-\partial c_i}{\partial X} + \frac{Z_i F}{RT} c_i \frac{\partial V}{\partial X} \right) \quad [1]$$

This equation is valid if no temperature gradient is present in the system, or in other words, if the system is isothermal. In a nonisothermal system where $\partial T/\partial X \neq 0$, a current density I_T due to the temperature gradient will be observed (5). We derived an expression for I_T, the thermal current density, from the thermal diffusion equation (6)

$$I_T = -Z_i F \Delta_i \frac{q_i c_i N_L}{C_p T^2} \left(\frac{\partial T}{\partial X} \right) \quad [2]$$

where Δ_i is the thermal diffusivity and q_i the heat of transport of a single charge carrier i.

The sign convention for the partial currents (Eq. [1] and [2] and Fig. 1) has been introduced by Lidiard (5) and has been adopted in our basic considerations. The total current density of charge carriers in a simultaneous electrical and thermal diffusion field is

$$I_i = I_D + I_E + I_T = 0 \quad [3]$$

Looking at the scheme in Fig. 1, which represents a silver iodide crystal with a thermal gradient ΔT across it, we can give proper signs to the various currents. Due to the negative thermal expansion coefficients of γ and β silver iodide, contraction, $-\Delta l$, of the crystal occurs on the warmer side. It is postulated that depletion of silver ions at the compression side causes the negative potential. The movement of silver ions to the cooler side provides ionic heat and mass transport across the crystal.

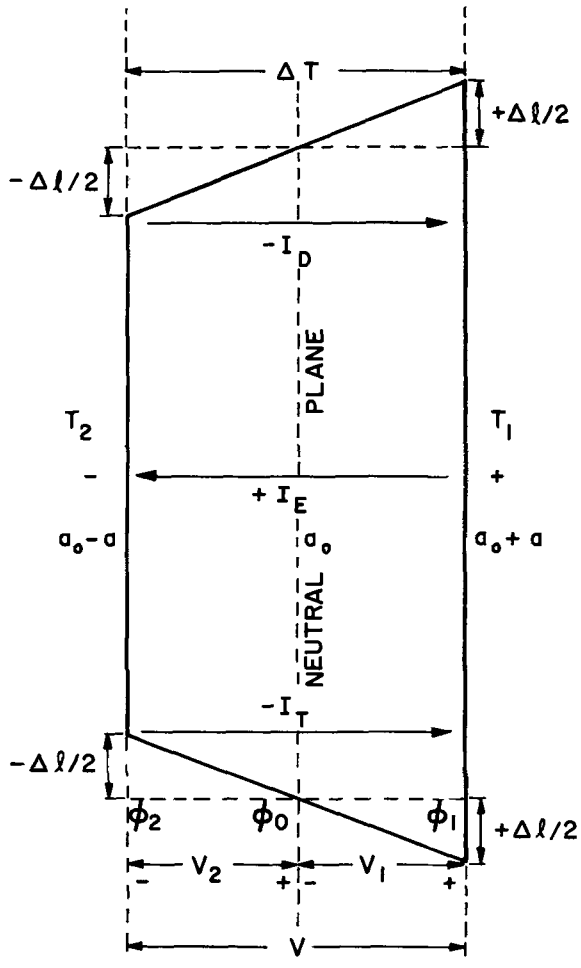

Fig. 1. Scheme of thermoelectric effect in silver iodide

The cooler side assumes a more positive potential. The increasing potential difference across the crystal causes some of the cations to move in the opposite direction, providing for the component I_E. In steady state, I_i has to become zero.

Thermoelectric power equation.—From Eq. [3] the thermoelectric power can be derived. Rearranging we obtain

$$\left(\frac{\partial V}{\partial X} \right) = \frac{RT}{Z_i F} \frac{1}{c_i} \left(\frac{\partial c_i}{\partial X} \right) + \frac{RT}{ZF} \frac{\Delta_i}{Z_i F} \frac{q_i}{C_p T^2} N_L \left(\frac{\partial T}{\partial X} \right) \quad [4]$$

Making $q_i N_L = Q_i$, and multiplying both sides with $(\partial X/\partial T)$, we obtain for the thermoelectric power θ

$$\theta = \left(\frac{\partial V}{\partial T} \right) = \frac{RT}{Z_i F} \frac{\partial \ln c_i}{\partial T} + \frac{Q_i}{Z_i f F T} \frac{\Delta_i}{D_i} \quad [5]$$

This equation contains two terms; the dimension of the two terms is measured in (g-cm^2 sec^{-2} grad^{-1} coulomb^{-1}). The first term describes the temperature dependence of the thermocell voltage caused by the change in mobile silver ion concentration with temperature. This is formally the temperature coefficient of the voltage of a concentration cell with ionic transport (cation transference number = 1) in which the concentration changes with temperature. The second term is proportional to the heat of transfer. Q_i is the elemental heat of transfer of 1 mole of charge carriers

as defined in the works of Eastman, Wagner, and Reinhold (2-4). Δ_i/D_i is the thermal diffusion ratio, whereby Δ_i is the thermal diffusion coefficient and D_i is the mass diffusion coefficient.

The thermoelectric power of silver iodide is negative in sign (1). The first term of Eq. [5] should carry a negative sign since it expresses, in the case of γ-β silver iodide, a decrease in positive electrode potential caused by a decrease in mobile silver ion concentration with increasing temperature. According to Reinhold the second term is also negative (4). Therefore, Eq. [5] can be expressed in its negative form; however, for convenience sake, we are avoiding negative signs in the following.

Thermomechanical electrical effect.—Analysis of the thermoelectric effect shows, in analogy to the pyroelectric and piezoelectric effect, that we are dealing with a thermomechanical electrical effect (7). Our effect is analogous to the "false" pyroelectric effect which is due to the deformation which accompanies a change in temperature and which is, therefore, of piezoelectric origin.

The "true" thermopotential effect, which follows path $T \rightarrow V$, could only be measured if $-\Delta l = 0$ (6). The "false" thermopotential effect, which is a secondary effect, is a sequence of the thermal contraction effect and the strain-potential effect and follows the path $T \rightarrow -\Delta l \rightarrow V$ (6). Consequently, the mechanical electrical part of the effect can be treated formally like the strain-potential effect (8, 9). The first term of the thermoelectric power Eq. [5] can be developed further by applying strain-potential calculations to the effect. The strain potential difference V_s is directly proportional to the strain (6, 8, 9)

$$V_s = 2\frac{RT}{Z_i\mathbf{F}}\frac{b \cdot \epsilon}{a_o} \qquad [6]$$

b is a constant and a_o is the original mobile ion concentration before deformation.

Since $\epsilon = \Delta l/l$, we have to relate $-\Delta l$, the contraction of the crystal, to $\Delta T = T_2 - T_1$. This can be done by using the negative thermal expansion coefficient α of γ-β silver iodide (10-14).

Equation [6] thus changes to

$$V_s = 2\frac{RT}{Z_i\mathbf{F}}\frac{b}{a_o}\alpha T \qquad [7]$$

Differentiation of V_s by T gives a new equation which corresponds to the first term in Eq. [5]

$$\frac{dV_s}{dT} = \frac{4RT}{Z_i\mathbf{F}}\frac{b\alpha}{a_o} \qquad [8]$$

The new term takes material parameters into account, such as the negative thermal expansion coefficient α and the original mobile ion concentration a_o, which was found to be practically identical with the impurity ion concentration (8, 9)

$$\theta = A + B = \frac{4R}{Z_i\mathbf{F}}\frac{b}{a_o}\alpha T_2 + \frac{q_i N_L}{Z_i f \mathbf{F} T_1}\frac{\Delta_i}{D_i} \qquad [9]$$

A and B are the heterogeneous and homogeneous components of the thermoelectric power, respectively. Equation [9] considers that the temperatures in the two terms are different, T_2 being the high temperature on the contraction side and T_1, the original lower temperature of the system, now the temperature of the heat sink.

Numerical evaluation of the thermoelectric power equation.—Equation [9] can be numerically evaluated if we rearrange the B term. The heat of transfer q_i can be estimated (6)

$$q_i = \frac{c_p \cdot \rho \cdot \overline{T}}{c_i} \qquad [10]$$

c_p is the specific heat, ρ the density, and c_i the mobile charge carrier concentration.

Since α, c_p, ρ, and consequently c_i are in themselves functions of the temperature which we can estimate, we can improve Eq. [9] to

$$\theta = A + B = \frac{4R}{Z_i\mathbf{F}} b\,\alpha_T \frac{T_2}{a_o} + \frac{1}{Z_i f \mathbf{F}}\frac{\Delta_i}{D_i} N_L \frac{(c_p)_T \cdot \rho_T}{2(c_i)_T}\left(1 + \frac{T_2}{T_1}\right) \qquad [11]$$

By our definition $T_1 = T_2 - 1$, and a_o and T_2 are real variables. The following are constants: $4R/Z_i\mathbf{F} = 3.355 \times 10^{-4}$; $b = 3.28 \times 10^{20}$; $1/Z_i f\mathbf{F} = 7.25 \times 10^{-6}$; $N_L = 6.02 \times 10^{23}$. Δ_i/D_i, the thermal diffusion ratio, is unknown and will be estimated. α_T, $(c_p)_T$, ρ_T, and $(c_i)_T$ are, within the range of temperatures considered, linear functions of T_2 or $\overline{T}$, respectively (6). $\overline{T}$ is the average bulk temperature of the electrolyte.

$$\alpha_T = 4.0 \times 10^{-6} + \frac{2.215 \times 10^{-8}}{11}(T_2 - 273) \qquad [12]$$

$$(c_p)_T = 4.48 \times 10^{-2} + 2.669 \times 10^{-4}(\overline{T} - 273) \qquad [13]$$

$$\rho_T = 5.5984 + 2.82 \times 10^{-3}(\overline{T} - 273) \qquad [14]$$

$$(c_i)_T = 1.438 \times 10^{22} + 7.07 \times 10^{18}(\overline{T} - 273) \qquad [15]$$

The thermal diffusion ratio Δ_i/D_i in the B term of Eq. [11] is unknown for the solid-state system under consideration. We are, however, able to estimate it from Eq. [11] by using experimental theta data.

A Fortran program was used to compute the thermal diffusion ratio from Eq. [11] utilizing an experimental theta value of 7.5×10^{-4} measured by Catz (15). For 274°K and experimental impurity ion concentrations a_o ranging from 4.95×10^{17} to 8.65×10^{17} ions/cm^3 in Malinchrodt silver iodide samples (9), we obtain ratio values of 7.98 and 6.61, respectively. These values are physically reasonable (6).

Another Fortran program was prepared in order to compute the first term A and the second term B of Eq. [11], and further their sum theta as a function of a_o and T_2. We varied a_o irregularly. T_2 varied from 274° up to 414°K in steps of 10°K. The upper limit was chosen to be 420°K. The data of the computer program are presented in Fig. 2. The logarithm of the thermoelectric power theta is plotted *vs.* the absolute temperature T_2 as a function of a_o. The a_o range of interest is 10^{17}-10^{20}. In the figure, the computed theta values are compared with experimental data given by Catz and Reinhold (15, 1). Over 80% of these data fall

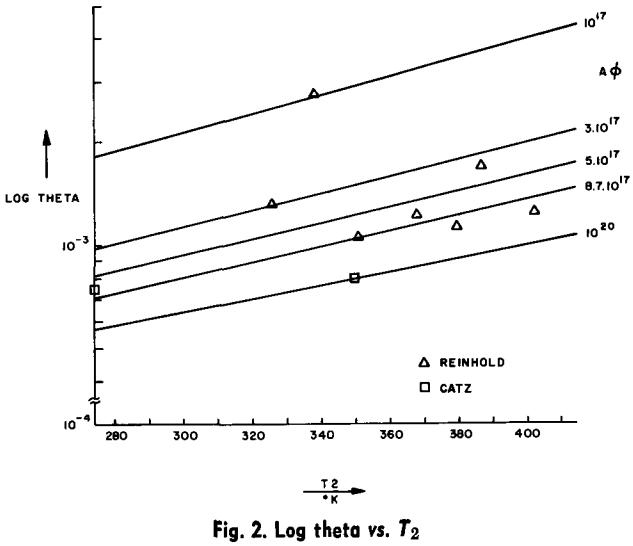

Fig. 2. Log theta *vs.* T_2

Table I. Heterogeneous and homogeneous thermoelectric effect in silver iodide

T°K	$(\partial V/\partial T)\cdot 10^3$ (V/°K)	$(\partial V/\partial T)\cdot 10^3$ hetero	$(\partial V/\partial T)\cdot 10^3$ homo
400°K (16, 17))	−1.24	−0.11	−1.13
400°K (our data, $a_0 = 10^{18}$)	−1.296	−0.31	−0.99

within the range of experimentally observable impurity ion concentrations.

In the next two figures (Fig. 3 and 4), log theta, log A, and log B are plotted *vs.* the absolute temperature T_2 for $a_0 = 10^{17}$ and 10^{18}, respectively. We can see from Fig. 3 and 4 that at $a_0 = 10^{17}$, the A effect dominates the theta data both in absolute value and slope. At $a_0 = 10^{18}$, however, the situation becomes reversed and the B effect dominates.

A more comprehensive presentation is given by a log theta, log A, and log B *vs.* log a_0 plot (Fig. 5). The two full curves, designated 274° and 414°K represent log theta *vs.* log a at the given temperatures. The interrupted lines A274 and A414 show the A effect at the two temperatures, and B274 and B414 the B effect. Figure 5 shows the influence of both T_2 and a_0 on the different terms of the thermoelectric power equation. It can be seen that the major effect can be either the

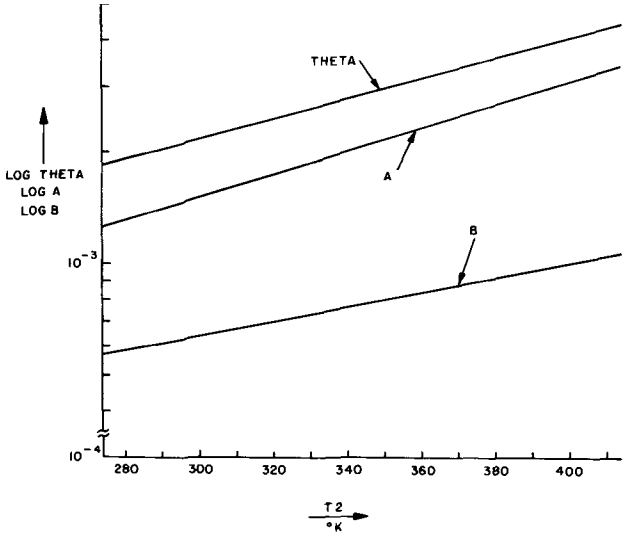

Fig. 3. Log theta, log A, and log B *vs.* T_2; $a_0 = 10^{17}$

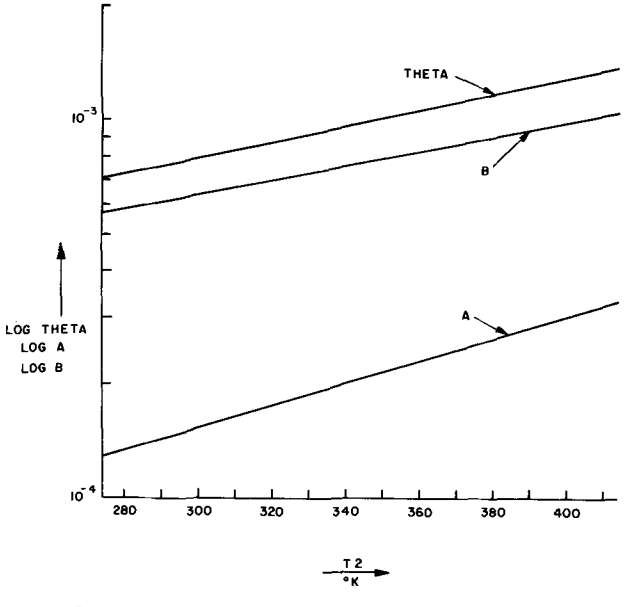

Fig. 4. Log theta, log A, and log B *vs.* T_2; $a_0 = 10^{18}$

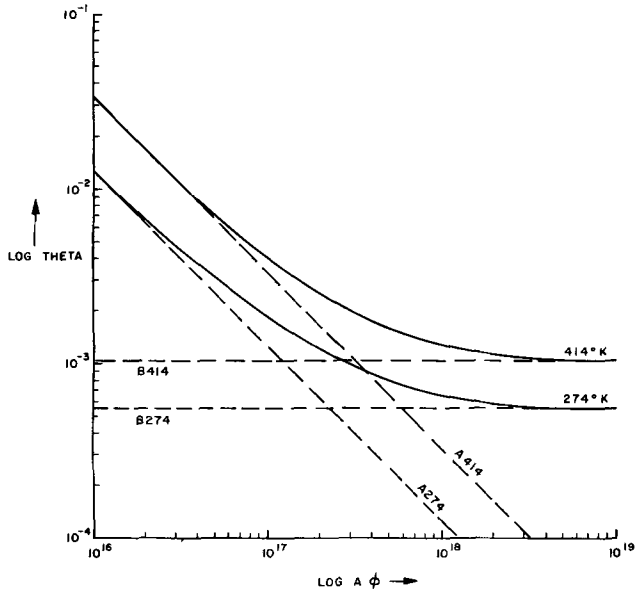

Fig. 5. Log theta, log A, and log B *vs.* log a_0

A or B effect depending upon the order of magnitude of the impurity ion concentration. An increase in thermoelectric power can be expected in silver iodide material with low impurity ion concentration.

We have found in the work of Reinhold and Blachny, summarized by Hauffe, thermodynamic treatment and estimates of the homogeneous and heterogeneous thermoelectric effects (16, 17). The data given there for the thermocell Ag/βAgI/Ag are summarized in Table I and compared with our data for the A and B effect. Reinhold and Blachny derived the homogeneous effect as the difference between the experimental thermal power and the heterogenous effect which was computed from thermal data. From the data given in Table I, it appears that our A effect is practically identical with the heterogeneous thermoelectric effect. The numerical difference can be accounted for by a slight difference in the impurity ion concentration of the two silver iodide samples. The B effect is in excellent numerical agreement with the homogeneous thermoelectric effect.

Manuscript submitted Nov. 5, 1971; revised manuscript received April 6, 1973.

Any discussion of this paper will appear in a Discussion Section to be published in the June 1974 JOURNAL.

LIST OF SYMBOLS

A	heterogeneous thermoelectric effect
a	mobile ion concentration of specie i
a_0	original mobile ion concentration, impurity ion concentration
B	homogeneous thermoelectric effect
b	constant in strain-potential equation
C_p	heat capacity per mole
c_i	concentration of ionic specie i
$(c_i)_T$	temperature function c_i
c_p	specific heat
$(c_p)_T$	temperature function c_p
D_i	mass diffusion coefficient of ionic specie i
F	Faraday constant
f	C_p/R
I_D	diffusion current density
I_E	current density in electrical field
I_i	current density of an ionic specie i
I_T	thermal current density
l	length
$-\Delta l$	contraction
N_L	Loschmidt's number
n	number of moles
Q_i	elemental heat of transfer of one mole of charge carriers i
Q_i/T	molar entropy of heat transfer process
q_i	heat of transport of a single charge carrier i
R	universal gas constant

T absolute temperature
$\overline{T}$ average bulk temperature of electrolyte
t time
V potential difference
V_s strain-induced potential difference
X direction of x
Z_i valency of ionic specie i
α thermal expansion coefficient
Δ_i thermal diffusivity of a single charge carrier i
Δ_i/D_i thermal diffusion ratio
ΔT temperature difference
e strain
Θ thermoelectric power
ρ density
ρ_T temperature function ρ
ϕ local potential (in Fig. 1)

REFERENCES

1. H. Reinhold, *Z. Anorg. Allgem. Chem.*, **171**, 181 (1928).
2. E. D. Eastman, *J. Am. Chem. Soc.*, **48**, 1482 (1926); *ibid.*, **50**, 283 (1928).
3. C. Wagner, *Ann. Physik*, **5**, 629 (1929); *ibid.*, **6**, 370 (1930).
4. H. Reinhold, *Z. Physik Chem.*, **(B) 11**, 321 (1931).
5. A. B. Lidiard, "Encyclopedia of Physics," Vol. 20, Electrical Conductivity II, pp. 324-349, Springer, Berlin (1957).
6. H. F. Hunger, Research and Development Technical Report ECOM-3418 (1971).
7. W. G. Cady, "Piezoelectricity," Vol. 2, p. 39, Dover Publications, Inc., New York, (1964).
8. H. F. Hunger, Abstract No. 17, p. 51, Electrochem. Soc. Extended Abstracts, Fall Meeting, Atlantic City, N. J., Oct. 4-8, 1970.
9. H. F. Hunger, Research and Development Technical Report ECOM-3360 (1970).
10. H. Fizeau, *Ann. Phys.*, **208**, (1867); *Pogg. Ann.*, **132**, 292 (1867).
11. J. Rodwell, *Chem. News*, **31**, 5 (1875).
12. G. Jones and F. C. Jelen, *J. Am. Chem. Soc.*, **57**, 2532 (1935).
13. K. H. Lieser, *Z. Phys. Chem.*, **9**, 302 (1956).
14. A. Bienenstock and G. Burley, *J. Phys. Chem. Solids*, **24**, 127 (1963).
15. J. Catz, Final Report, Contract No. DAAB07-68-C-0444, Mechanical Engineering Dept., University of Miami, Coral Gables, Florida (1969).
16. K. Hauffe, "Reaktionen in und an Festen Stoffen," p. 113, Springer Verlag, Berlin-Göttingen-Heidelberg (1955).
17. H. Reinhold and A. Blachny, *Z. Electrochem.*, **39**, 290 (1933).

Cathodic Discharge of Graphite Intercalation Compounds in Organic Electrolytes

Herbert F. Hunger* and George J. Heymach

Power Sources Technical Area, United States Army Electronics Technology and Devices Laboratory (ECOM), Fort Monmouth, New Jersey 07703

ABSTRACT

A survey of graphite intercalation compounds with cathodic depolarizer capability showed that two groups, graphite fluorides and graphite oxides, offer theoretically 900-1500 W-hr/lb of cell reactants in lithium batteries. The attractiveness of these compounds is further enhanced by their practical insolubility in the electrolytes of interest. Mechanically stable cathodes were prepared from tetracarbon monofluoride, carbon monofluoride, and graphite oxide. Galvanostatic current-potential curves of the cathodes in 1M $LiClO_4$–propylene carbonate electrolyte were measured at 30°C. The current-potential curves of the intercalation compounds were compared with that of cathodes prepared in the same fashion but containing manganese dioxide as the depolarizer. Galvanostatic discharge curves showed that 100% reduction of the cathodic depolarizers can be achieved. This is followed by solvent reduction which led to an apparent increase in utilization over 100%. By graphical integration of the cathodic and cell discharge curves, a comparison of the energy content (watt-hour/pound of depolarizer and watt-hour/pound of cell components) of the depolarizers as a function of rate, per cent utilization, electrolyte anion, and solvent was made. Considering the essential cell component weights, up to about 150 W-hr/lb of battery components can be expected in practical lithium/carbon monofluoride batteries.

There has been recent interest in the use of graphite intercalation compounds, primarily graphite fluorides, as cathodic depolarizers in organic electrolyte batteries.

Carbon monofluoride was first synthesized by Ruff and Bretschneider (1) by direct fluorination of coarse graphite in the temperature range of 420°-460°C.

Tetracarbon monofluoride, a compound with lower fluorine content, was prepared by Ruedorff and Ruedorff (2) by reacting fluorine in a fluorine-hydrogen fluoride mixture with graphite at room temperature.

The first report of utilization of graphite intercalation compounds in batteries comes from Brown (3, 4). He reports to have used and tested graphite oxides as depolarizer in Leclanché cells.

Braeuer (5-8) was the first to demonstrate and report the feasibility of lithium organic electrolyte batteries using a graphite intercalation compound, tetracarbon monofluoride, as the cathodic depolarizer. In comparing his cell with the best organic electrolyte batteries available, there appeared promise in graphite intercalation compounds as cathodic depolarizers.

Fukuda *et al.* (9, 10) have shown the usefulness of carbon monofluoride as cathodic depolarizer in experimental lithium organic electrolyte batteries. The use of intercalation compounds in a secondary, nonaqueous solvent battery was reported by Bennion (11).

The objective of this paper is to compare various potential depolarizers for primary lithium organic

* Electrochemical Society Active Member.

Key words: graphite oxide, carbon monofluoride, tetracarbon monofluoride, manganese dioxide, dimethyl sulfite.

electrolyte batteries with each other and to cite their relative merits.

After a survey of all known graphite intercalation compounds (12, 13), the following two groups of graphite intercalation compounds were considered in our experimental study as potential cathodic depolarizers: graphite oxides and graphite fluorine compounds.

In Table I a comparison is made of the theoretical energy contents of various depolarizers in lithium organic electrolyte batteries. The first three depolarizers are transition metal oxides; the next two are copper halides; the last three are graphite intercalation compounds. In computing the faradaic capacities, the following assumptions were made. In the case of V_2O_5, the reduction is assumed to occur from the +5 valency state to the +4 valency state, in the case of MnO_2 from the +4 to the +3, and in the case of MoO_3 from the +6 to the +4 state. The figures for $CuCl_2$ and CuF_2 were given by Jasinski (14). The faradaic capacities for tetracarbon monofluoride, carbon monofluoride, and graphite oxide were calculated by assuming LiF and Li_2O as end products. The emf's in Table I were computed from thermodynamic data (15, 16). In the case of CF and C_4F, emf data calculated from the free energy of the cell reaction were used (17). The measured open-circuit voltages of Li/CF and Li/C_4F cells are considerably lower than the theoretical emf's. This discrepancy could be due to the establishment of a mixed potential, CF reduction being the cathodic reaction and solvent oxidation the anodic reaction involved. The mixed potential would lie between the two corresponding redox potentials. In the fourth column of Table I, experimentally observed open-circuit voltages are recorded. It has been found that the open-circuit voltages in the cases of MnO_2 and MoO_3 exceed the theoretical emf's considerably (18). Unknown electrode processes other than those assumed in the computations must be responsible for the experimentally observed data. From the table, a theoretical watt-hour/pound ratio, ranging from 918 to 1505, can be expected for the graphite intercalation compounds. This high ratio combined with their practical insolubility in the organic electrolytes of interest makes these compounds promising candidates for depolarizers in lithium-nonaqueous electrolyte batteries.

Table II shows a comparison of theoretical energy densities of cathodic depolarizers in lithium batteries.

Table I. Comparison of theoretical energy contents of various depolarizers in lithium organic electrolyte batteries

T = 25°C

Depolarizer	A-hr/lb[a]	EMF	Open-circuit voltage	W-hr/lb[b]
V_2O_5	62.1	2.34	3.5	217
MnO_2	129.5	2.69	3.48-3.98	349
MoO_3	154.0	1.93	2.9-3.0	297
$CuCl_2$	164.0	3.06	3.1	502
CuF_2	211.0	3.55	3.3	749
C_4F	175.8	5.23	3.14-3.32	918
CF	320.0	4.66	3.14-3.3	1491
C_2O	451.4	—	3.34	1505

[a] Ampere-hour/pound of reactants.
[b] Watt-hour/pound of reactants.

Table II. Comparison of theoretical energy densities of cathodic depolarizers in lithium batteries

T = 25°C

Electrochemical couple	A-hr/cm³ of reactants	W-hr/cm³ of reactants
Zn/HgO	1.19	1.59
Li/CF	1.11	5.17
Li/C_2O	1.11	3.71
Li/CuF_2	1.07	3.80
Li/$CuCl_2$	0.81	2.48
Li/C_4F	0.59	3.08

For comparison purposes, the data for a Zn/HgO cell are added. It can be seen from the table that the theoretical enery densities to be expected from graphite intercalation compounds look highly attractive.

Experimental

Most of the experimental work was performed in a dry lab (Dri-Lab/Dri-Train/Vacuum/Atmospheres Corporation, North Hollywood, California) in pure, dried argon atmosphere.

Purification of solvents.—The solvent mainly used in this study was propylene carbonate, PC, (Eastman Kodak Company, T_B = 121°-123°C at 17 mm pressure). It was chosen because it has been widely studied and most of its data of interest are reported in the literature (19). Its purification procedures are also well described (20). After drying the PC with 5A molecular sieves, the solvent was submitted to vacuum fractionation at 7 mm Hg. The first fraction of 300 ml was discarded.

Dimethylsulfite, $DMSO_3$, (Eastman Kodak Company), was the other solvent used in the study. It was chosen because electrolytes prepared with this solvent have only about 40% of the viscosity of those containing PC. $DMSO_3$ was purified by treatment with 5A molecular sieves.

Preparation of electrolytes.—Three types of electrolytes were prepared: 1M $LiClO_4$-PC, 1M $LiAsF_6$-PC, and 1M $LiClO_4$-$DMSO_3$. Lithium perchlorate, anhydrous, (Alfa Inorganics, Inc., Beverly, Massachusetts) was vacuum dried at 150°C and 1M solutions were prepared in the dry lab; 1M solutions with $LiAsF_6$, electrochemical grade, (U.S. Steel Corporation) were prepared in a similar manner. The use of 1M $LiAsF_6$-PC electrolytes presented no problem in measuring the characteristics of the depolarizers *vs.* a lithium reference electrode; they appeared, however, to be of questionable value as practical electrolytes since the lithium anode showed random passivation phenomena in this medium.

Depolarizer materials.—The following depolarizer materials were used in the study:

1. Tetracarbon monofluoride with the actual composition $C_{5.54}F$ (Ozark-Mahoning Company, Tulsa, Oklahoma).

2. Carbon monofluoride $CF_{1.007}$ (Ozark-Mahoning Company, Tulsa, Oklahoma). Spectroscopic analysis detected further the following metals in percentage of total weight. Ni 0.01, Fe 0.1, Al 0.005, Mg 0.0005, and Cu 0.0005. The metals are probably present as fluorides.

3. Graphite oxide could not be obtained commercially and had to be prepared in-house by partial oxidation of graphite (21). In this preparation, graphite is treated with an anhydrous mixture of concentrated sulfuric acid, sodium nitrate, and potassium permanganate, followed by washing and drying procedures (P_2O_5). An analysis gave the following data: C = 54.43%, H = 2.46%, O = 40.35%, or $C_8O_{4.4}$, $H_{4.36}$. Considering the "ideal formula" of graphite oxide, $C_8O_2(OH)_2$, proposed by Hofmann (22), we recognize that our sample has a too high hydrogen content. This could mean that it contains water. Thus, we arrive from our analytical data at a composition of $C_8O_{1.48}(OH)_{1.48}\cdot 1.44\ H_2O$. Our graphite oxide thus reached about 75% of its maximum oxidation state and contains about 1.1 molecule of water per each C_6 arrangement.

4. Manganese dioxide, Type M (Manganese Chemical, Baltimore, Maryland).

5. Graphite, Microcrystalline Graphite 1651 (Southwestern Graphite Company, Burnet, Texas).

Preparation of electrodes.—*Cathodes.*—The preparation method described by Braeuer (7) was first considered, but soon discarded, since it was found that no good adherence of the cathodic mix to the copper grid

could be maintained after submersion of the electrodes in propylene carbonate.

Another preparation method, described by Watanabe and Fukuda (9), which consists in pasting a mix of the depolarizer with carbon (or graphite), Teflon powder, and propylene carbonate onto a nickel-screen, did not result in a mechanically stable electrode during discharge.

Consequently, a method was devised which resulted in mechanically stable cathodes. In this method, a cathodic mix was prepared from 1g depolarizer, 0.2g graphite, and 0.2g Teflon powder; 0.25 ml Teflon emulsion 41 BX (Du Pont)), containing 0.8g Teflon per ml, was added to 2g of the cathodic mix. Distilled water was added to form a sludge under stirring. The total Teflon content of the cathodes was 21.8%. Then, a generous amount of acetone was added. Current collectors (3.2 × 3.2 cm plus a tab) made from copper grid (Exmet 3-10) were placed on a glass plate and covered with acetone. The sludge was smeared with a spatula on the grids and rolled on with a glass tube. The product was brought between two filter papers and Teflon sheets and pressed to remove the major amount of liquid and to compact the electrodes. Pressure applied per electrode varied, but was usually around 10,000 psi for 1 min. The compressed electrodes were vacuum dried in a dessicator. In the case of the graphite fluorides, the cathodes were further dried in a vacuum oven at 140°C until the weight became constant. In the case of graphite oxide, however, it became necessary to dry the finished electrodes in a vacuum dessicator over P_2O_5, because of the low decomposition temperature of the compound (starting 70°C). The rubberlike consistency of graphite oxide also led to bending of the cathodes after drying. Careful pasting of each side and twice compressing, however, eliminated that problem. The electrodes containing MnO_2 were also vacuum dried over P_2O_5. In one experiment, graphite was used as the sole depolarizer. In this case, the mix did not form a sludge in water-acetone as in the case of the intercalation compounds. The suspension had to settle and was decanted from the liquid and then carefully pasted on the copper screen. Its adherence was extremely poor before compression.

Lithium electrodes.—A commercial lithium ribbon (4 × 0.015 in.) stored in decahydronaphthalene, was cut to size (5 × 2.5 in.) and pressed into a nickel screen (Exmet 2/0; 5 × 6 in.). Pressing was performed between two stainless steel plates greased with petrolatum (Fisher, snow white, U.S.P.). The pressure applied for a minute was 1000 psi per electrode. Then, eight electrodes were cut out. Their dimensions were about 3.2 × 3.2 cm with an attached nickel screen tab of 1.5 × 4.0 cm. Lithium anodes thus prepared contained about 0.16g lithium metal each, which corresponds to about 0.617 A-hr per electrode. The finished electrodes were stored in decahydronaphthalene. Before use, they were thoroughly washed several times in petrol ether.

Electrochemical cell.—The electrochemical cell case used was essentially of the design described by Braeuer (7) and fabricated completely from Teflon. The cathode was held in position by the center groove of the cell case, thus separating the cell in two electrolyte compartments. A U-fold paper separator (3.2 × 6.6 cm) was put around the cathode to protect against eventual flaking off of the cathodic material. The paper separator was made of Genuine Whatman Filter Paper No. 1 (W & R Balston Ltd., England). The lithium anode and the lithium reference electrode, which were identical in design to the lithium anode, were held in position by the two outside grooves in the cell case. These lithium electrodes were thus pressed with one surface against the walls of the case so that only one surface was exposed to the electrolyte. The geometrical surface areas of anode and reference electrode in contact with the electrolyte were thus about 10 cm^2 each. The anode and reference electrodes were arranged parallel to the cathode each at a distance of 5 mm from the latter. Since there were two separate electrolyte compartments, the active geometrical surface area of the cathode *vs.* the anode was about 10 cm^2. The cell temperature was monitored. The electrolyte resistance between each lithium electrode and the cathode was about 10.2 ohms.

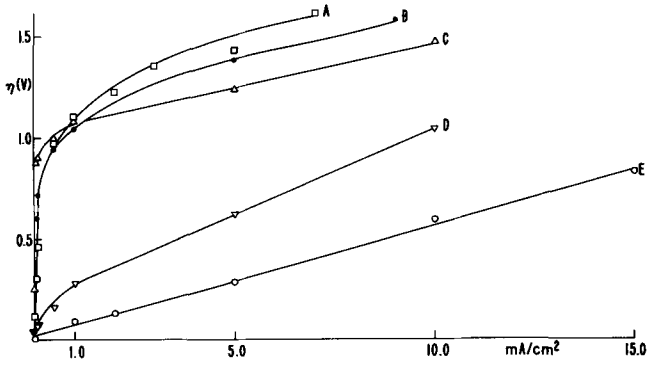

Fig. 1. Polarization curves of cathodes and anodes in Li/1M $LiClO_4$-PC/depolarizer cells. A, $C_{5.54}F$; T = 29.8°C. B, $C_xO_yH_z$; T = 29.5°C. C, CF_x; T = 29.0°C. D, MnO_2; T = 26.0°C. E, Li anode; T = 32.5°C.

Electrochemical measurements.—The open-circuit voltage of the cells was measured with a 610B electrometer, Keithley Instruments, after at least 1 hr of equilibrium in the electrolyte. In order to measure the current-voltage relationship of the total cell and of an individual electrode *vs.* the reference electrode, galvanostatic steps were applied to the cell with a precision current source, Model CS-12, North Hills Electronics, Inc., Glen Cove, New York. Voltage readings were taken with the 610B electrometer until steady state was reached. For practical purposes, steady state was defined as voltage change $\leq$ 10 mV/5 min. Since the conductance of 1M $LiClO_4$ in propylene carbonate is $\sigma = 4.9 \times 10^{-3}$ ohm^{-1} cm^{-1}, the iR drop within the electrolyte to the reference electrode $\simeq 1.5 \times 10^{-15}$V for the highest potential measured and can be neglected.

Galvanostatic discharge curves at various current densities were measured to determine the cathode utilization. Electrode potential and cell voltage readings were taken during continuing discharge mainly with a Hewlett-Packard Strip-Chart Recorder, Model 7100B, with two 1750A Input Modules.

Results and Discussion

Current-voltage relationship.—Table III compares experimentally observed open-circuit voltages of various Li/organic electrolyte/depolarizer cells with theoretical emf's. It can be seen from the table that all graphite intercalation compound-electrolyte combinations show open-circuit voltages ranging from 2.85 to 3.34V. In case of CF, data are about 1.44V lower than those thermodynamically expected. One exception occurs in the case of 1M $LiAsF_6$-PC electrolyte, where an even lower open-circuit voltage was observed.

Figure 1 shows the polarization, η, of $C_{5.54}F$, CF, graphite oxide $C_xO_yH_z$, and MnO_2 cathodes and also of a lithium anode, measured *vs.* the lithium reference electrode as a function of current density. By definition

Table III. Comparison of open-circuit voltages of various Li/organic electrolyte/depolarizer cells with emf's

Cell	Open-circuit voltage	EMF	T, °C
Li/1M $LiClO_4$-PC/$C_{5.54}F$	3.32	—	29.5
Li/1M $LiClO_4$-PC/CF	3.14	4.66	29.0
Li/1M $LiClO_4$-PC/$C_xO_yH_z$	3.34	—	28.0
Li/1M $LiClO_4$-PC/MnO_2	3.51	2.69	24.2
Li/1M $LiClO_4$-PC/C graphite	3.00	—	30.0
Li/1M $LiAsF_6$-PC/CF	2.85	4.66	30.0
Li/1M $LiClO_4$-$DMSO_2$/CF	3.22	4.66	30.0

the polarization is composed of activation polarization, concentration polarization, and internal electrode resistance polarization (*e.g.*, due to a nonconducting film, or in this specific case, due to contact resistance between graphite and the intercalation compounds or MnO_2, respectively). The curves were measured up to the current density where the voltage between lithium anode and cathode reached zero volt and started to reverse. No limiting currents were observed in that current density region. The limiting current density of a lithium anode in 1M $LiClO_4$-PC electrolyte at room temperature is around 40 mA/cm² (19).

All three graphite intercalation compounds show a polarization larger than 1V at a relatively low current density of 1 mA/cm². The kinetic reason for this behavior is unknown at the present time. Polarization-current density curves of similar shapes, however, have been observed in cases of high activation polarization due to low exchange current densities (23). One step in the reduction mechanism of the depolarizer will be rate limiting, *e.g.*, in the case of carbon monofluoride it could be

$$(CF)_n + ne^- \longrightarrow nC + nF^- \qquad [1]$$

The breaking of the covalent C—F bond and/or formation of an activated complex could be connected with a high activation energy resulting in a low exchange current density. No severe concentration polarization can be recognized in any of the three curves over the measured current density range.

It has to be noted that manganese dioxide is kinetically superior to the graphite intercalation compounds. It does not exhibit the high polarization effect. The comparison between manganese dioxide and the intercalation compounds also shows that the common slow kinetic of the latter is not a consequence of the electrode preparation or potential measurement technique since manganese dioxide cathodes were prepared and measured in the same manner.

The cathodic reaction [1] will be followed by [2]

$$F^- + Li^+ \longrightarrow LiF_s \qquad [2]$$

leading to the formation of solid lithium fluoride within the cathode. The solubility of lithium fluoride in pure propylene carbonate is less than 5×10^{-6} molar (24). Addition of lithium perchlorate to form a one molar solution should decrease the solubility of lithium fluoride further.

Cathodic depolarizer utilization.—From coulometric analysis of galvanostatic discharge curves, the utilization of graphite intercalation compounds could be determined.

Graphite fluorides.—Galvanostatic discharge curves for CF (curve A), $C_{5.54}F$ (curve C), and a graphite cathode (curve E) in 1M $LiClO_4$-PC electrolytes are shown in Fig. 2. The current density is 1 mA/cm². The cathode potentials are measured *vs.* the lithium reference electrode. The interrupted lines of curves B and D represent the corresponding cell discharge curves. The amounts of CF and $C_{5.54}F$ in the cathodic mix used at the electrodes correspond to 0.26 and 0.065 A-hr, respectively. The corresponding points on discharge curves A and C, which should give, in the absence of any side reactions, the potentials at which 100% utilization of the depolarizer has been reached, are shown. Visible gas evolution at the cathodes, marked in the figure with arrows, can be observed around these potentials and continues on further discharge.

Since utilization efficiencies above 100% can be obtained by discharging to lower potentials, another reduction process must account for a utilization exceeding 100%. It is highly probable that this is solvent reduction [3]

$$C_4H_6O_3 + 2e^- \longrightarrow CH_3 - CH = CH_2 + CO_3^{2-} \qquad [3]$$

Reaction [3] could occur simultaneously with the reduction of the graphite fluorides or successive to it. The strong bend in the CF discharge curve, just above 1.1V, suggests a change in the discharge mechanism. Electrochemical reduction of propylene carbonate at graphite rods in 1M $LiClO_4$-PC electrolyte to propylene gas and carbonate ions has been described in the literature (25). Curve E (Fig. 2) shows the potential change of a graphite cathode at 1 mA/cm².

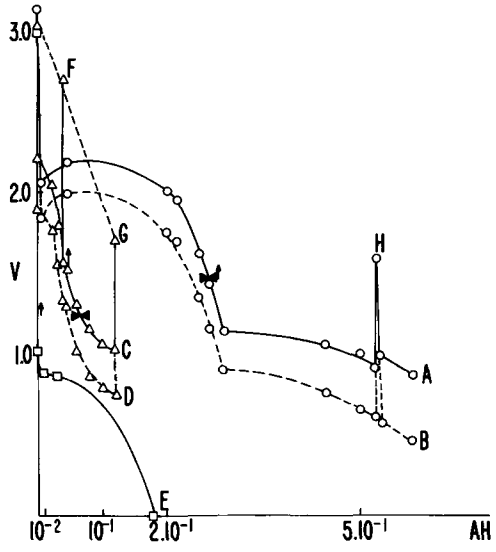

Fig. 2. Galvanostatic discharge curves of graphite fluorides in Li/1M $LiClO_4$-PC/C_xF cells. $I = 1$ mA/cm². A, CF cathode *vs.* lithium reference electrode; $T = 29°C$. B, Li/1M $LiClO_4$-PC/CF cell; $T = 29°C$: C, $C_{5.54}F$ cathode *vs.* lithium reference electrode; $T = 31°C$. D, Li/1M $LiClO_4$-PC/$C_{5.54}F$ cell; $T = 31°C$. E, Graphite cathode *vs.* lithium reference electrode; $T = 30°C$. F,G,H, Open-circuit potentials after partial or complete discharge. ↑, Gas evolution at cathode. ⋈, 100% utilization.

The discharge of $C_{5.54}F$ was interrupted and the open-circuit potential after partial discharge was measured. It can be seen that point F lies considerably below the original open-circuit potential and point G, after theoretically complete discharge, is still lower. There appears to exist a linear relationship between these "rest" potentials and the ampere-hours passed. CF showed a similar behavior (point H).

Graphite oxide.—The composition of the graphite oxide under study was $C_8O_{1.48}(OH)_{1.48} \times 1.44\ H_2O$. The following reaction was assumed to occur during its cathodic discharge

$$C_8O_{1.48}(OH)_{1.48} \times 1.44H_2O + 4.44e^- \longrightarrow C_8 \times 1.44H_2O + 1.48\ O^{--} + 1.48\ OH^- \qquad [4]$$

O^{--} and OH^- react further with lithium ions to form lithium oxide and lithium hydroxide.

Figure 3 shows the galvanostatic discharge curves of a Li/1M $LiClO_4$-PC/$C_xO_yH_z$ cell. Curve A shows the cathode potential during discharge at a current density of 1 mA/cm² and curve B the corresponding cell voltage.

The amount of depolarizer in the cathode corresponds to 0.262 A-hr. Again a utilization above 100% can be observed if the discharge is continued to lower potentials. Gas evolution at the cathode is observed just prior to 1.1V. The discharge was interrupted several times in order to measure the open-circuit potentials after partial or complete discharge (curve C). These potentials were attained after resting the electrodes overnight. It can be seen that curve C shows a linear behavior up to about 100% theoretical utilization, followed by a marked break and change in slope.

Manganese dioxide.—The cathodic reduction of manganese dioxide at 1 mA/cm² is presented in Fig. 4. Assuming a reduction of Mn^{4+} to Mn^{3+}

$$2MnO_2 + 2e^- \longrightarrow Mn_2O_3 + O^{--} \qquad [5]$$

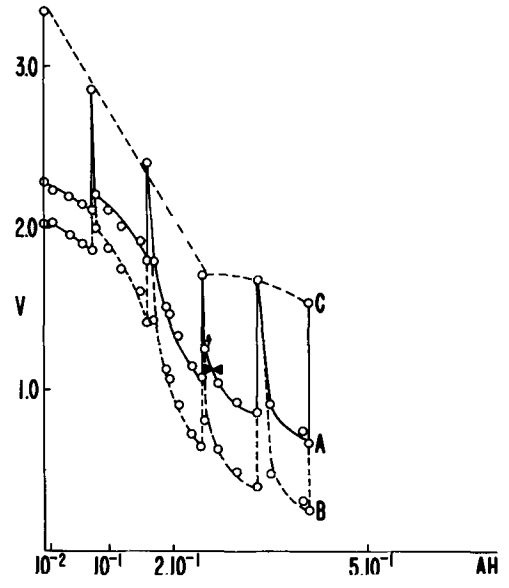

Fig. 3. Galvanostatic discharge curves of graphite oxide in Li/1M $LiClO_4$-PC/$C_xO_yH_z$ cells. $I = 1$ mA/cm^2; $T = 29.2$°C. A, $C_xO_yH_z$ cathode vs. lithium reference electrode. B, Li/1M $LiClO_4$-PC/$C_xO_yH_z$ cell. C, Open-circuit potential after partial or complete discharge. ↑, Gas evolution at cathode. ⋈, 100% utilization.

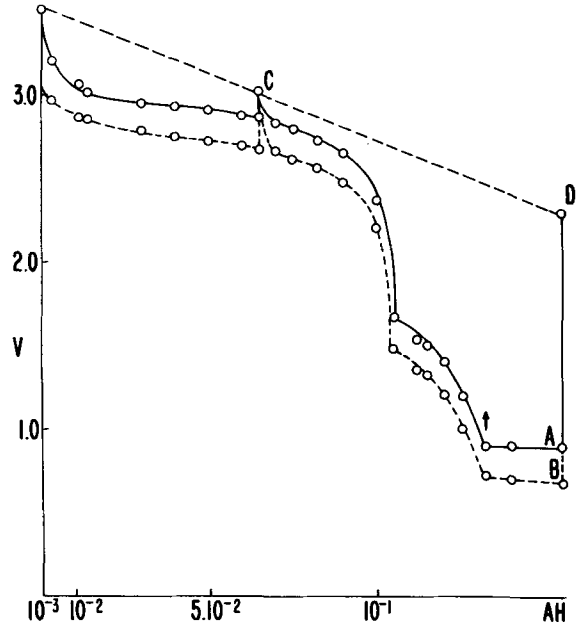

Fig. 4. Galvanostatic discharge curve of manganese dioxide in Li/1M $LiClO_4$-PC/MnO_2 cells. $I = 1$ mA/cm^2; $T = 29.2$°C. A, MnO_2 cathode vs. lithium reference electrode. B, Li/1M $LiClO_4$-PC/MnO_2 cell. C, D, Open-circuit potentials after partial discharge. ↑, Gas evolution at cathode.

the depolarizer would yield 0.194 A-hr, however, only about 0.13 A-hr are obtained, corresponding to a utilization of about 68% by discharge down to 0.9V.

The open-circuit potential and the major part of the discharge curve lies above the theoretical, reversible potentials of the assumed cell reaction

$$2Li + 2MnO_2 = Li_2O + Mn_2O_3; \quad E_o^{298} = 2.69V \quad [6]$$

The reversible potential for a 4+ and 3+ reduction lies at the end of the first plateau. A second reduction region can be recognized between 1.7 and 0.9V *vs.* lithium. Since strong gassing is observed at the cathode at the latter potential, it is probable that solvent reduction occurs at 0.9V and at lower potentials.

The disagreement between the discharge potentials and reversible potential (Eq. [6]) suggests that other unknown electrode reactions are responsible for the behavior on discharge. The open-circuit potentials after partial discharge (points C and D) exhibit again a linear relationship *vs.* time.

Comparison of cathodic depolarizers.—The depolarizers investigated were compared with each other, using the galvanostatic discharge curves in Fig. 2, 3 and 4. By graphical integration of the discharge curves from open-circuit potential to a cathode potential corresponding theoretically to 100% utilization, except in the case of manganese dioxide, a comparison was made of the energy content and the kinetics of the depolarizers. Relating this data to the grams of depolarizer used, the watt-hour/pound ratio could be computed. The results are shown in Table IV. It can be seen that carbon monofluoride yields the highest watt-hour/pound ratio under the given experimental conditions. Its $\bar{V}$ value is the highest one of the three intercalation compounds investigated, being surpassed only by the more reactive manganese dioxide.

Comparison of the energy content of Li/1M $LiClO_4$-PC/CF and Li/1M $LiClO_4$-PC/MnO_2 cells during discharge at a rate of 1 mA/cm^2.—From the results of Table IV, two depolarizers appear to be of interest. Carbon monofluoride was chosen for its high energy content and manganese dioxide because of its somewhat better kinetic characteristics. Consequently, a comparison was made of these two on the basis of their cell discharge curves and the essential component weights involved. For this purpose, curves B in Fig. 2 and 4 were graphically integrated from cell open-circuit voltage to a chosen end (cut off) voltage. The watt-hours obtained were related to essential component weights. In case of CF, the cut off voltages chosen were 1.8, 1.5, and 0.9V. The area under the curve to 1.8V was 0.344 W-hr, to 1.5V was 0.44 W-hr, and to 0.9V was 0.494 W-hr.

The actual component weights within the experimental cell in grams were:

CF cathode + Cu grid	0.467 + 0.528 = 0.995
Li anode + Ni grid	0.163 + 0.419 = 0.582
Separator (4.2 × 4.2 ×3.2 cm)	0.230
Electrolyte (10 ml) (26)	12.590
Total experimental component weight =	14.397g

Table V lists improvements in component weights that can be made in the experimental cells. It can be seen that the electrolyte accounts for about one half of the component weight. The influence of the cathode characteristics in practical cells will, therefore, not be as marked as in Table IV. No consideration was given during the conceptual redesign of the experimental cell to any changes in the ohmic cell resistance

Table IV. Comparison of cathodic depolarizers discharged in Li/1M $LiClO_4$-PC/depolarizer cells at 1 mA/cm^2 and $\bar{T} = 29.7$°C

Depolarizer	(W-hr/lb) theoretical[a]	(W-hr/lb) maximum[b]	(W-hr/lb) experimental[c]	% Theoretical[d]	% Maximum[e]	$\bar{V}$[f]	η[g]
$C_{5.54}F$		471	263		55.8	1.85	100
CF	1491	1020	804	54.0	78.8	2.05	100
$C_8O_{1.48}(OH)_{1.48}$		1500	590		39.3	1.87	100
MnO_2	349	451	241	69.0	53.5	2.52	68.3

[a] (W-hr/lb) theoretical are based on emf values computed from thermodynamic data and pounds of total cell reactants.
[b] (W-hr/lb) maximum are based on experimental open-circuit voltage and pounds of total cell reactants.
[c] (W-hr/lb) experimental are based on graphical integration of the discharge curves, up to the utilization efficiency η, and on pounds of depolarizer only. A comparison of this data with *a* or *b* gives the loss in theoretical energy content given by the cathodic polarization at the given rate. In case of CF, *e.g.*, this loss amounts to 46.0%.
[d] % theoretical = (W-hr/lb) experimental/(W-hr/lb) theoretical.
[e] % maximum = (W-hr/lb) experimental/(W-hr/lb) maximum.
[f] The average discharge potential $\bar{V}$ = (W-hr/g) experimental/(A-hr/g) theoretical.
[g] η depolarizer utilization in %.

Table V. Improvements in component weights

CF cathode + Cu grid 0.467 + 0.2[a] =	0.667	(29.0%)
Li anode + Ni grid 0.069[b] + 0.2[c] =	0.269	(11.7%)
Separator	0.100[d]	(4.4%)
Electrolyte	1.259[e]	(54.9%)
Essential component weight (in grams)	2.295	(100.0%)

[a] Shorter tab area 0.528 → 0.404g and half the copper weight by using a more open grid.
[b] 0.617 A-hr/0.16g lithium electrode yields 61.7 hr of operation at 10 mA. CF depolarizer amount, however, requires only 26.4 hr. Therefore, only 0.069g lithium metal are required at the anode.
[c] Shorter tab area and half the nickel weight by using a more open grid.
[d] Separator thinned by 50%.
[e] Electrolyte spacing decreased from 5 to 0.5 mm → 1 ml electrolyte. Practical experimental cell configurations with two lithium anodes on each side of a depolarizer cathode required about 3.06g electrolyte (27).

which would be reflected in the cell discharge characteristics. An increase in ohmic resistance due to a smaller collector-depolarizer interface will certainly be upset by a considerable decrease in electrolyte resistance due to decreased electrolyte spacing.

A comparison between cells using carbon monofluoride and manganese dioxide is given in Table VI. From these data, it can be seen that CF has a higher W-hr/lb ratio than manganese dioxide, especially at lower cut off voltages. A proper preselected cut off voltage is of greater significance in the operation of practical batteries of this type. According to Eq. [3], the cathodic reduction of propylene carbonate is accompanied by evolution of propylene gas. Although propylene shows some solubility in the electrolyte (25), continued gas evolution will lead to a pressure buildup in sealed batteries. This problem can be eliminated if the proper cut off voltage is chosen.

Energy content and depolarizer utilization as a function of discharge rate, electrolyte anion, and electrolyte solvent.—The next point of interest in this study was the influence of factors, such as rate, electrolyte anion, and electrolyte solvent, on the energy content and depolarizer utilization.

For this purpose, the following additional cell compositions were prepared and discharged at a given rate at about 30°C:

Li/1M $LiAsF_6$, PC/CF	0.46 mA/cm² to vary rate and electrolyte anion
Li/1M $LiClO_4$, PC/CF	0.50 mA/cm² to vary rate
Li/1M $LiClO_4$, $DMSO_3$/CF	1.00 mA/cm² to vary solvent
Li/1M $LiClO_4$, PC/CF	1.88 mA/cm² to vary rate

During the discharge, the cathode potential *vs.* a lithium reference electrode plus the total cell voltage were monitored.

The rate changes did not produce anything new in the discharge behavior (Fig. 5). The discharge curves are similar in shape to that in Fig. 2 with a somewhat different position in the V-A-hr plot. The open-circuit potential after partial discharge up to full discharge follows a straight line. The steep slope of the discharge curves diminishes after reaching a theoretically 100% utilization.

Table VI. Comparison of W-hr/lb of cell components[a] during discharge of Li/1M $LiClO_4$-PC/depolarizer cells at 1 mA/cm² and T = 29.7°C

	Cutoff voltage			
	0.9V		1.8V	
Depolarizer	W-hr/lb	% Utilization	W-hr/lb	% Utilization
CF	97.7	100	68.0	65.5
MnO_2	58.7	67.2	52.6	53.7

[a] Based on essential component weights.

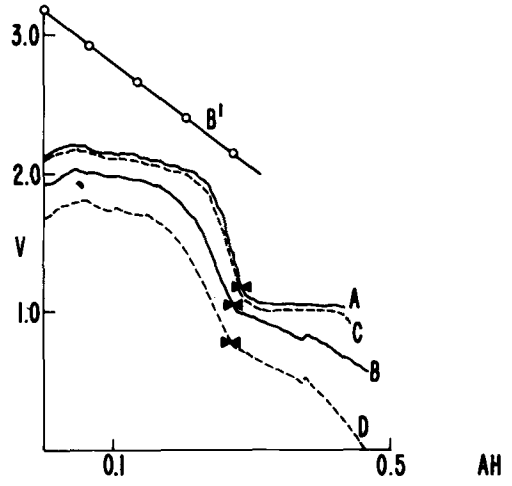

Fig. 5. Galvanostatic discharge curves of carbon monofluoride in Li/1M $LiClO_4$-PC/CF cells at different current densities. $T \simeq$ 30°C. A, CF cathode *vs.* lithium reference electrode; I = 0.5 mA/cm². B, CF cathode *vs.* lithium reference electrode, I = 1.88 mA/cm². B', Corresponding open-circuit potential after partial discharge. C, Li/1M $LiClO_4$-PC/CF cell; I = 0.5 mA/cm². D, Li/1M $LiClO_4$-PC/CF cell. I = 1.88 mA/cm². ⋈, 100% utilization.

Changing the electrolyte anion from ClO_4^- to AsF_6^- presented experimental problems with the lithium anode. After operating the cell for about 0.165 A-hr, the voltage between anode and cathode changed polarity to −2.5V. After about 15 min at this voltage level, it returned again to a positive reading. A similar phenomenon occurred after about 0.28 A-hr. The cell voltage, however, remained from then on reversed while under discharge. The first observation at the anode had the characteristics of a film formation-film removal phenomenon. The second had that of permanent passivation at the anode. The potential of the cathode *vs.* the lithium reference electrode remained always positive and showed no unusual behavior with time (Fig. 6).

In Fig. 6, we compare the discharge curves in electrolytes with different anions at about the same current density. Initially, the curves appear to be practically identical. Prior to 100% utilization, curve B exhibited a higher potential. There are marked differences, however, in the open-circuit potentials after partial and complete discharge. The initial open-circuit potential

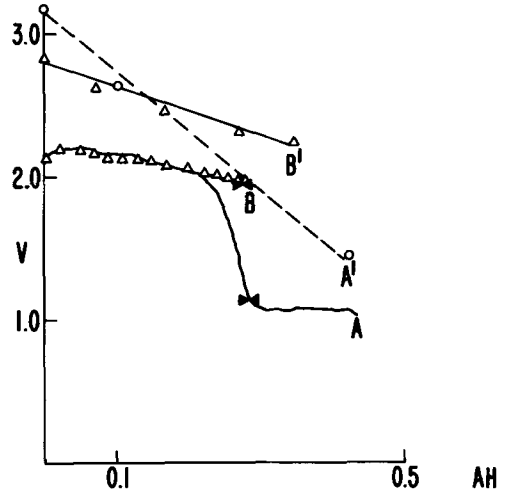

Fig. 6. Galvanostatic discharge curves of carbon monofluoride in Li/1M solute-PC/CF cells with different solutes; $T \simeq$ 30°C. A, CF cathode vs. lithium reference electrode; I = 0.5 mA/cm²; $LiClO_4$ as solute. B, CF cathode vs. lithium reference electrode; I = 0.46 mA/cm²; $LiAsF_6$ as solute. A', B', Corresponding open-circuit potentials after partial or complete discharge. ⋈, 100% utilization.

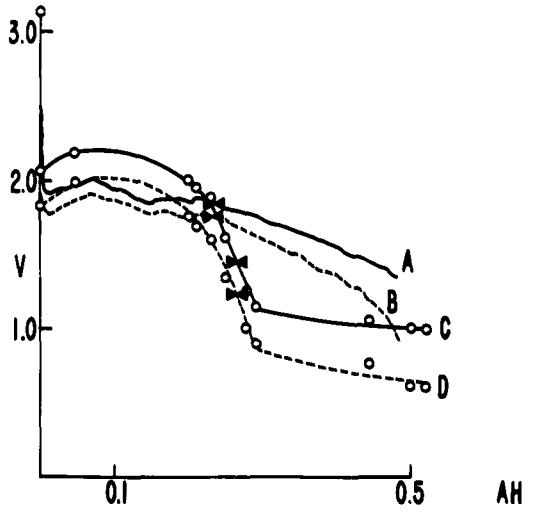

Fig. 7. Galvanostatic discharge curves of carbon monofluoride in Li/1M $LiClO_4$-solvent/CF cells with different solvents; $T \simeq 30°C$; $I = 1$ mA/cm². A, CF cathode vs. lithium reference electrode; $DMSO_3$ as solvent. B, Li/1M $LiClO_4$-$DMSO_3$/CF cell. C, CF cathode vs. lithium reference electrode; PC as solvent. D, Li/1M $LiClO_4$-PC/CF cell. ⋈, 100% utilization.

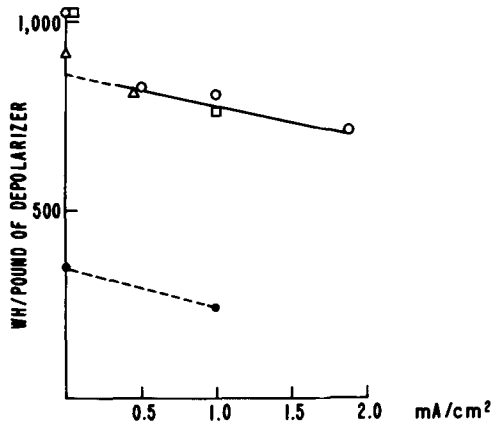

Fig. 8. Watt-hour/pound of depolarizer ratio as a function of current density, electrolyte anion, and solvent; $T \simeq 30°C$. ○, CF in 1M $LiClO_4$-PC, $\eta = 100\%$. △, CF in 1M $LiAsF_6$-PC; $\eta = 100\%$. □, CF in 1M $LiClO_4$-$DMSO_3$; $\eta = 100\%$. ●, MnO_2 in 1M $LiClO_4$-PC; $\eta = 68.3\%$.

in $LiAsF_6$-PC is lower (~2.8V) than in $LiClO_4$-PC. The open-circuit potential in $LiAsF_6$-PC after complete discharge, however, is higher than that in $LiClO_4$-PC.

The influence of solvent on the discharge is shown in Fig. 7. Propylene carbonate and dimethylsulfite are compared. A markedly different discharge behavior is observed. The open-circuit potentials are both above 3.0V. While CF in $LiClO_4$-PC shows a strong potential drop before 100% theoretical utilization, followed by a flat PC reduction curve, CF in $LiClO_4$-$DMSO_3$ continues at a higher potential level even after complete utilization. The resulting apparent utilization efficiency above 100% can be explained as in the case of propylene carbonate by solvent reduction.

Graphical integration of the discharge curves in Fig. 2, 4-7 (cathode potential *vs.* lithium reference electrode) led to a comparison of the energy content of the depolarizers as a function of discharge rate, electrolyte anion, and solvent. The results are compared in Table VII.

From Table VII it can be seen that neither a strong anion nor solvent effect on the energy density exists at 100% theoretical utilization. The average discharge potential, $\overline{V}$, shows also that neither the anion nor solvent effect is a marked one. The experiment with $DMSO_3$, however, indicates that a remarkable increase in the W-hr/lb depolarizer ratio could be obtained if solvent reduction can be utilized.

In the column of $V_{reference}$, the cathode potential at the given rate and utilization is shown. The last column contains the per cent of theoretical energy that can be obtained on discharge. The maximum theoretical value computed from thermodynamic data is 1491 W-hr/lb of depolarizer.

In Fig. 8, the W-hr/lb of depolarizer ratio is plotted as a function of current density, electrolyte anion, and

Table VII. Galvanostatic discharge of CF and MnO_2 cathodes in various 1M organic electrolytes at 30°C

Depolarizer, electrolyte	mA/cm²	W-hr/lb depolarizer	$\overline{V}$	% Theoretical utilization	$V_{reference}$	% Theoretical energy
CF, $LiAsF_6$-PC	0.46	812	2.07	100[a]	1.98	54.5
CF, $LiAsF_6$-PC	0.46	804	2.04	90	2.00	53.8
CF, $LiClO_4$-PC	0.50	825	2.10	100	1.14	55.3
CF, $LiClO_4$-PC	1.00	804	2.05	100	1.12	53.8
CF, $LiClO_4$-$DMSO_3$	1.00	760	1.94	100	1.87	51.0
CF, $LiClO_4$-$DMSO_3$	1.00	1437[b]	1.78[b]	206[b]	1.35[b]	96.4[b]
MnO_2, $LiClO_4$-PC	1.00	241	2.52	68.3	0.92	69.0
CF, $LiClO_4$-PC	1.88	713	1.81	100	1.05	47.8

[a] Extrapolated value.
[b] Apparently additional solvent reduction.

Table VIII. Galvanostatic discharge of Li/1M organic electrolyte/depolarizer cells at various current densities at $\simeq 30°C$

Depolarizer electrolyte	mA/cm²	Cutoff voltages (V)				
		1.98	1.8	1.5	1.0	0.9
CF, $LiAsF_6$-PC	0.46	113 (100)	—	—	—	—
CF, $LiClO_4$-PC	0.50	—	95 (84)	101 (32)	112 (100 + 9)[a]	137 (100 + 54)
CF, $LiClO_4$-$DMSO_3$	1.00	—	64 (76)	118 (100 + 48)	149 (100 + 122)	—
CF, $LiClO_4$-PC	1.00	—	68 (66)	87 (84)	—	98 (100)
MnO_2, $LiClO_4$-PC	1.00	—	53 (54)	53 (54)	—	59 (67)
CF, $LiClO_4$-PC	1.88	—	0.0 (0.0)	68 (73)	—	83 (96)

[a] Utilization efficiency of, *e.g.*, (100 + 9) means that theoretically 100% CF discharge has occurred plus additional solvent reduction equivalent to 9% CF discharge.

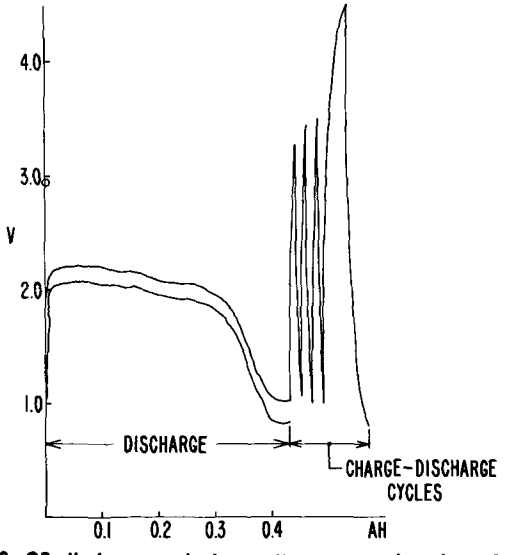

Fig. 9. CF discharge and charge-discharge cycles; $I = 1$ mA/cm^2; $T \simeq 30$°C.

solvent. It can be seen that the data points are arranged around a straight line. Neither a strong anion nor solvent effect can be noted.

By graphical integration of the cell discharge curves in Fig. 2, 4-7 and from the essential component weights, the W-hr/lb of cell components were estimated. The W-hr/lb of cell components and in parenthesis the per cent utilization efficiency for various cut off voltages are given in Table VIII.

The table shows that the approximate limit for a lithium carbon monofluoride battery, using anodes and cathodes made according to our preparation procedures, operating in the given current density range at about 30°C, would be somewhere in the range between 85 and 113 W-hr/lb of cell components at about 100% theoretical CF utilization. If additional solvent reduction can be tolerated (discharge to 1.0-0.9V cut-off voltage), then far higher energy densities can be envisioned probably even above 150 W-hr/lb. A reduction in energy density of about 20% should be considered if a battery case is included in the component weights.

Feasibility of electrically recharging the Li/LiClO$_4$-PC/CF cells.—Limited experimentation was performed to explore the feasibility of electrically recharging the Li/1M LiClO$_4$-PC/CF cells. A platinum grid was used instead of the copper grid at the cathode since the latter disintegrated during charge/discharge cycles. After regular discharge of the CF at 1 mA/cm^2, the cell was charged at the same current density. Although the cell appeared to charge and discharge well for short periods, the charge voltage was increasing and the discharge voltage was decreasing with cycles (Fig. 9). The cell was unable to hold a charge for a longer period of time. At both 4.5 and 0.9V, gas bubbles were noted at the cathode, probably connected with oxidation and reduction of the solvent.

Acknowledgment

The authors wish to thank Captain Burt Strasser for performing the preparative experimentation required to synthesize graphite oxide, one of the depolarizers investigated, and Mr. J. W. Mellichamp for performing the spectrochemical analysis of CF.

Manuscript submitted Oct. 20, 1972; revised manuscript received April 11, 1973. This was Paper 5 presented at the Miami Beach, Florida, Meeting of the Society, Oct. 8-13, 1972.

Any discussion of this paper will appear in a Discussion Section to be published in the June 1974 JOURNAL.

REFERENCES

1. O. Ruff and O. Bretschneider, *Z. Anorg. Allgem. Chem*, **217**, 1 (1934).
2. W. Ruedorff and G. Ruedorff, *Chem. Ber.*, **80**, 417 (1947).
3. B. K. Brown, *Trans. Am. Electrochem. Soc.*, **53**, 113 (1928).
4. B. K. Brown and O. W. Storey, *ibid.*, **53**, 129 (1928).
5. K. Braeuer, Abstract No. 210, p. 495, Electrochem. Soc. Extended Abstracts, Spring Meeting, Boston, Mass., May 5-9, 1968.
6. K. Braeuer, Abstract No. 64, p. 401, Electrochem. Soc. Extended Abstracts, Spring Meeting, New York, N. Y., May 4-9, 1969.
7. K. Braeuer, "Feasibility Study of the Lithium/C_xF Primary Cell," R&D Technical Report ECOM-3322, August 1970.
8. K. Braeuer and K. R. Moyes, U.S. Pat. 3,514,337, May 1970.
9. N. Watanabe and M. Fukuda, *C. A.*, **72**, No. 8, Feb. 23, 1970, p. 549, No. 38270n.
10. M. Fukuda and T. Iijima, Abstract No. 41, p. 100, Electrochem. Soc. Extended Abstracts, Fall Meeting, Cleveland, Ohio, Oct. 3-7, 1971.
11. J. S. Dunning, W. H. Tiedemann, L. Hsueh, and D. M. Bennion, *This Journal*, **118**, 1886 (1971).
12. W. Ruedorff, in "Advances in Inorganic Chemistry and Radiochemistry," Vol. 1, pp. 223-265, H. J. Emeleus and A. G. Sharpe, Editors, Academic Press, New York (1959).
13. G. R. Hennig, in "Progress in Inorganic Chemistry," Vol. 1, F. A. Cotton, Editor, Interscience Publishers, Inc., New York (1959).
14. R. Jasinski, "High-Energy Batteries," Plenum Press, New York (1967).
15. W. M. Latimer, "The Oxidation State of Elements and Their Potentials in Aqueous Solution," Prentice-Hall, Inc., New York (1961).
16. JANAF, Thermodynamic Data, Thermal Research Laboratory, The Dow Chemical Co., Midland, Michigan, June 30, 1970.
17. J. L. Wood, A. J. Valerga, R. B. Badachhape, and J. L. Margrave, Final Report, Contract DAAB07-72-C-0105, Nov. 1973; Second Monthly Progress Report, Contract DAAB07-73-C-0056, Dec. 1972, Rice University, Houston.
18. L. Campanella and G. Pistoia, *This Journal*, **118**, 1905 (1971).
19. R. Jasinski, "Advances in Electrochemistry and Electrochemical Engineering," Vol. 8, p. 253, Wiley-Interscience, New York (1971).
20. J. N. Butler, "Advances in Electrochemistry and Electrochemical Engineering," Vol. 7, p. 151, Wiley-Interscience, New York (1970).
21. W. S. Hummers and R. E. Offemann, *J. Am. Chem. Soc.*, **80**, 1339 (1958).
22. A. Clauss, R. Plass, H. P. Boehm, and U. Hofmann, *Z. Anorg. Chem.*, **291**, 205 (1957).
23. G. J. Young, "Fuel Cells," p. 42, Reinhold Publishing Corp., New York (1960).
24. R. Keller *et al.*, Fourth Quarterly Report, Contract NAS 3-8521, July 1967.
25. A. N. Dey and B. F. Sullivan, *This Journal*, **117**, 222 (1970).
26. R. Jasinski, P. Malachesky, and B. Burrows, Final Report, Contract N00019-67-C-0680, Tyco, July 1968.
27. R. Rinaldi, Unpublished research and development, personal communication.

Evaluation of the Ferric Ion Sensitive Chalcogenide Glass Electrode

Raymond Jasinski* and Isaac Trachtenberg*

Texas Instruments Incorporated, Dallas, Texas 75222

ABSTRACT

Further information is presented on the preparation, composition, performance, and ferric ion sensing mechanism of the chalcogenide glass $Fe_nSe_{60}Ge_{28}Sb_{12}$ (where n falls between 1.3 and 2). Properly prepared and activated electrodes respond to changes in ferric ion concentration in perchlorate, chloride, and nitrate solutions with an average Nernstian slope of 57.6 ± 2.9 mV/decade, over the concentration range of 10^{-2}-10^{-5}M ferric iron (based on 16 electrodes). Useful response is found down to at least 10^{-6}M Fe^{+3}. Details are presented on the activation and operating procedures. Although a complete evaluation of the sensing mechanism has not been made, it has been established that the activation process involves both an oxidation of the fresh surface as well as a chemical interaction of this surface with ferric iron from solution. The sensing process then involves exchange of ferric iron with this modified surface.

It has been shown (1) that electrodes formed from the chalcogenide glass, $Fe_nSe_{60}Ge_{28}Sb_{12}$, hereafter designated as Fe-1173, will develop potentials relatable to the free, uncomplexed ferric ion concentration of aqueous solutions. This effect is of practical interest in the monitoring of some process effluents and waste waters for ferric iron; application of these electrodes has also been made to the determination of sulfate ion in natural and waste waters (2, 3). This response is of scientific interest in that (*a*) the electrode potential is independent of the ferrous ion content of the solution, while (*b*) the potential response to ferric ion is a nominal 60 mV/decade concentration change, indicative of a one-electrode process rather than the expected three-electron process (20 mV/decade).

Further information is therefore presented on the preparation and composition of this unique material, its electrochemical performance, and the ion sensing mechanism.

Experimental

The iron glasses were prepared by fusing the appropriate amount of iron wire at 900°-1000°C with the glass, $Se_{60}Ge_{28}Sb_{12}$, previously synthesized directly from the pure elements. To form electrodes, disks, 1.1-1.2 cm diameter and 0.1-0.2 mm thick were cut from the melt; gold was then evaporated onto one side of the glass disk; a platinum wire lead made contact to the gold via silver micropaint; the lead side of the glass was isolated from the test solutions by sealing the glass disk into a Plexiglas[1] tube.

Resistivity and potential measurements were made as described previously (1). Potentiostatic measurements were made with a Wenking Model 6343R potentiostat. All potentials are reported with respect to the commercial Ag/AgCl electrode used as reference. In those experiments concerned with the possible influence of chloride ion on the measured potentials, this electrode was replaced with an Orion double junction Ag/AgCl reference electrode containing a potassium nitrate solution in the outer junction. All measurements were made at ambient room temperature.

Four Fe-1173 electrodes were generally immersed in the specific solutions under test, so as to separate out spurious electrode effects from the particular parameter being studied. For simplicity of presentation, only the data from one of the set will be discussed.

In order to obtain a reproducible surface, independent of the previous history of the electrode, the sensor was etched periodically in 10% KOH for 30 sec, rinsed with supporting electrolyte, re-etched, and rerinsed. The electrodes were then stored in 10^{-3}M Fe^{++} overnight before use. The significance of these etchings and equilibration steps will be discussed.

The supporting electrolytes used in this study were 1M KCl and 0.1*N* $NaClO_4$. Chloride forms weak complexes with ferric iron; perchlorate shows little tendency to complex (4). The responses in nitrate were discussed previously (1).

A motor-driven paddle stirrer was used in the experiments concerned with the effect of stirring on response time. Magnetic stirrers were avoided to obviate any possible complications from the heat so produced.

The analytical method for determining the total iron content of the various slices of Fe-1173 glasses was based on dissolution of the sample in aqua regia, followed by measurement with an atomic absorption spectrometer.

Results and Discussion

The surface of an electrode prepared as described is visibly heterogeneous, containing islands of one phase imbedded in a matrix phase. Portions of this electrode material were ground to a powder and an x-ray (Fe radiation) pattern taken under prolonged exposure. In no case could a detectable pattern be found. It must therefore be concluded that neither phase of the electrode material is crystalline.

The Fe-1173 electrodes are opaque to infrared radiation; the parent 1173 glass is transparent. It must therefore be concluded that neither phase is the original 1173 glass. It was not possible to withdraw portions of either phase individually for chemical analysis.

The homogeneity of the melts prepared as previously described (1) is indicated by the data shown in Table I for the iron contents of slices taken along the length of two melts (slice 1 is the top of the melt). There are significant variations in composition from slice to slice and it is not possible to infer the composition of slice x from that of slice $x \pm 1$. No trend in iron content could be established from the position of the slice within the melt; crushing and remelting the slices did not improve the homogeneity of melt composition.

It had been shown previously (1) that there was a dependence of resistivity on the iron concentration of the melt. The existence of a critical iron concentration, above which the resistivity decreased from the order of 10^3 ohm-cm down to the order of 50 ohm-cm, was confirmed with chemical analysis of the individual slices on which the resistivity measurements had been made. This was necessary in view of the compositional

* Electrochemical Society Active Member.

Key words: ion-selective electrodes, chalcogenide glass, ferric ion sensor, potentiometry, selective ion electrode activation.

[1] Registered trademark of Rohm and Haas Company.

Table I. Iron content along the melts

Slice No.	Weight per cent total iron Melt 39 (1.0 w/o Fe added)	Melt 23 (1.4 w/o Fe added)
1	0.97	1.27
2	0.91	1.29
3	—	1.27
4	1.02	1.18
5	0.95	1.29
6	0.76	—
7	0.94	1.29
8	0.84	1.30
9	0.82	1.22
10	0.80	—
11	0.76	—
12	0.78	—
13	0.84	—
14	0.84	—

variations shown in Table I. As a result of improved analyses, the critical concentration found was 1.3 a/o (atomic per cent) iron rather than the approximate 2.3% value previously reported.

Shown in Table II are the electrochemical performances of three high-resistance electrodes; here performance is discussed in terms of the potential-log concentration slopes between the specified concentration limits. All the high-resistance glasses showed less than the expected Nernstian slope to changes in iron concentration at low net ferric ion contents. Shown in Table III are the steady-state Nernstian slopes for 16 low-resistivity (≤50 ohm-cm) electrodes over the concentration range of 10^{-5}-10^{-2}M ferric chloride in 1M KCl, pH 2. All electrodes had iron concentrations of approximately 1.3 a/o Fe. Included in the table are the standard deviations of slope as calculated from a least squares fit of the data for each electrode. (The numbering system is such that the first number refers to a particular melt; the second number refers to a particular slice within the melt.) The average slope computes as 57.6 mV/decade with a net standard deviation of ±2.9 mV/decade. This then is a measure of the reproducibility with which electrodes can be prepared. No correlation could be found with iron content and performance, except as determined by the resistivity of the glass. Unless otherwise specified, all data discussed below were taken with low-resistance electrodes.

Shown in Fig. 1 are the response times of one such electrode to small changes in iron concentration. Steady state was achieved within 2-4 min; response time to increasing iron concentration appeared to be

Table II. Potential change vs. Fe^{+3} concentration change Δ potential (mV)

Electrode resistivity (ohm-cm)	Concentration range 10^{-5}-10^{-4}	10^{-4}-10^{-3}	10^{-3}-10^{-2}	10^{-2}-10^{-1}
10^7	16.7	28.2	45.8	59.0
2×10^3	37.8	57.4	61.0	60.0
4×10^3	28.4	41.2	56.5	60.0

Table III. Nernstian slopes for low resistance electrode response to Fe^{+3}

Electrode	Slope, mV/decade	Standard deviation, mV
30-1	62.1	1.9
30-2	61.3	1.8
30-4	59.3	1.4
30-7	59.9	2.2
30-8	60.3	2.9
30-11	58.3	2.3
32-4	52.5	1.4
32-7	56.2	2.9
32-8	55.2	1.4
32-9	58.5	1.3
32-11	54.9	1.3
32-15	55.5	0.6
46-2	52.1	0.8
46-11	58.2	2.5
49-2	58.6	2.2
49-12	57.3	1.7

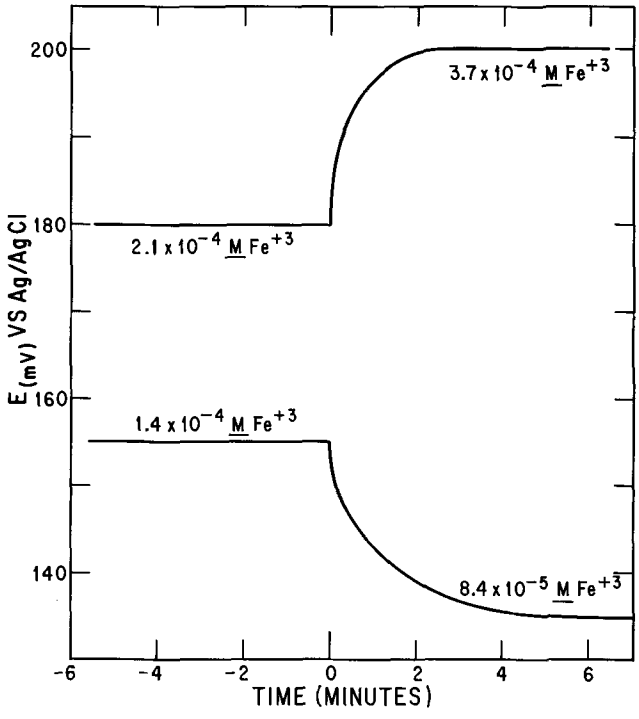

Fig. 1. Response times for a 2.39 mole per cent Fe°-1173 glass electrode to changing ferric ion concentration.

somewhat faster than responses to decreasing concentrations.

Response time increased significantly, however, (*a*) when the concentration changes were increased to order-of-magnitude increments, and (*b*) when the ambient ferric iron concentration was decreased below 10^{-4}M ferric iron. With stirring, steady state at 10^{-5}M was achieved within 20-30 min; without stirring, steady-state responses at 10^{-5}M were always quite long, taking up to 60 min to reach steady state (here steady state is defined as an electrode potential stable to within 0.1 mV/min). At steady state the electrode potentials were independent of stirring rate, over the range of 0-275 rpm. At 10^{-4}M ferric ion, steady state was achieved within 10-20 min with stirring.

This trend of decreasing response time with increasing iron concentration did not persist above 10^{-3}M; generally 20 min were required to reach steady state, as defined, and stirring had little effect. Response times were the same in perchlorate and in chloride solutions.

During the preliminary studies of electrode behavior, it was often observed that the potential changes measured at and below 10^{-3}M Fe^{+++} were smaller than expected (from a Nernstian slope of about 59 mV/decade) if the electrodes had been first exposed to 10^{-1} or 10^{-2}M ferric iron for prolonged periods of time. Furthermore, the equilibrium potentials themselves were higher than had been observed after the electrodes had been first exposed to 10^{-4}M ferric iron. This effect was found in both chloride and perchlorate solutions. The phenomenon can be illustrated and explained by the following experiment. A thoroughly washed electrode was equilibrated in 100 ml of 10^{-3}M ferric chloride after exposure for 10 min to 10^{-1}M Fe^{+++}; a steady potential of +355.7 mV was observed. The electrode was then rinsed with supporting electrolyte and the test solution was replaced with a second sample of the same 10^{-3}M concentration but which had not been exposed previously to an Fe-1173 electrode; a steady-state potential of +341.7 mV was recorded. Not only is this potential lower, but it is what was anticipated from Nernstian behavior and the potential observed at 10^{-2}M ferric iron. Placing the electrode back into the original 10^{-3}M solution restored the potential reading to its original value. This indicates that the potential difference between the two millimo-

lar iron solutions was not an artifact or electrode drift but was indeed representative of the ferric iron contents of the solutions. It would appear then that ferric ion was transferred from the surface of the electrode, previously exposed to high iron content solutions, into the first millimolar iron solution.

Thus when measuring the potential of a solution more than an order-of-magnitude different in ferric iron content than the solution previously monitored, the electrodes had to be equilibrated for at least 30 min in the test solution and then placed in a fresh portion of the test solution. This provided the most accurate representation of potentials characteristic of the ferric iron content of the particular solution under study.

A more classical source of contamination was also found with a number of the supporting electrolytes used in the study, specifically the presence of a small amount of residual iron impurity in the salt itself. The KCl and $NaClO_4$ electrolytes were analyzed for total soluble iron via an atomic absorption spectrometric method (5). The 0.1*N* $NaClO_4$ solution used contained 1.7×10^{-5}M Fe; the 1M KCl solution contained 2×10^{-7}M Fe. It was found that the KCl solutions did vary in soluble iron content according to the particular batch of KCl used; most samples contained residual iron in the 10^{-7}M range.

The lower limits-of-detection of the Fe-1173 electrodes were therefore estimated as follows. Equilibrium potentials were first measured for a KCl solution with a known, large concentration of added iron. Sufficient EDTA (at the same pH) was added to complex all iron present; potentials were recorded after 15 min. The results of one such experiment in 1M KCl are shown in Table IV. Comparing the potentials at 10^{-5}M Fe^{+3} with those of the KCl + EDTA solution (*i.e.*, no iron), it would appear that the electrodes are sensitive down to approximately 10^{-6}M ferric iron in 1M KCl.

The same experiment was carried out in perchlorate solution with substantially the same result, *i.e.*, the electrode is capable of measuring soluble ferric ion above a concentration of 10^{-6}M.

Also of interest were the observations that exposure of the electrode to EDTA did not adversely affect activity, in fact exposure may well have improved electrode performance. An example of this is shown in Table V. Listed are the steady-state potentials at 10^{-4} Fe, (*a*) initially, (*b*) after exposure to 10^{-1} Fe, and (*c*) after exposure to EDTA. (The significance of the 10^{-1} exposure will be discussed below in more detail; suffice it to say that such an exposure has a deactivating effect for subsequent exposure of the electrode to 10^{-4} solutions.)

In order to generate electrodes which showed these Nernstian responses to varying ferric ion concentrations, it was necessary to activate the sensor surface

Table IV. Determination of limit-of-detection

Solution	Electrode		
	32-5, mV	32-5, mV	32-8, mV
10^{-5}M Fe + KCl	+216	+235	+232
10^{-6}M Fe + KCl	+165	+203	+198
KCl	+147	+188	+184
KCl + EDTA	+145	+182	+180

Table V. Effect of EDTA on equilibrium potentials

Electrode	Potentials (for 10^{-4}M Fe)*		
	Initial	After 10^{-1}	After EDTA
5	231.7	223	230
6	210.8	204	211
7	232.6	208.9	230
8	226.6	209.9	227

* Obviously, there is good agreement between the "Initial" and "After EDTA" potentials.

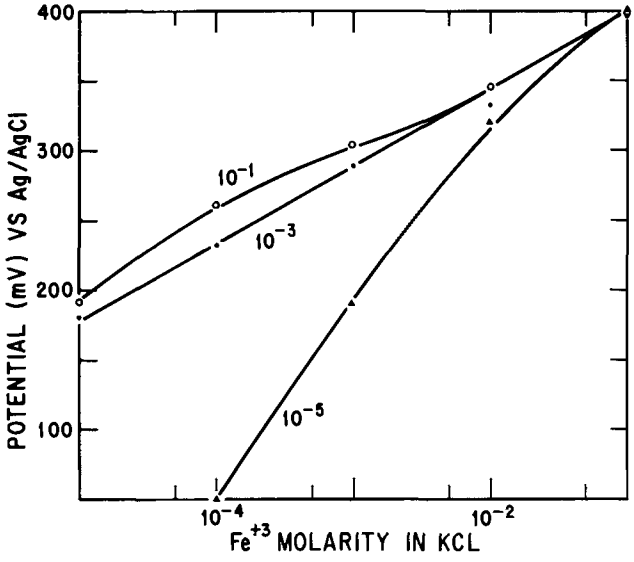

Fig. 2. Response of an Fe-1173 electrode to varying ferric ion concentrations after equilibration overnight in ferric iron solutions of the concentrations indicated.

by exposing a freshly etched electrode to a solution high in ferric ion concentration ($\geq 10^{-3}$M). This phenomenon is illustrated by the data shown in Fig. 2, in which are plotted the responses of a freshly etched electrode after equilibration overnight in three different iron solutions. In each case, measurements were first made at the 10^{-5}M concentration level and then for successively increasing iron concentrations. Chloride was the supporting electrolyte, but similar results were obtained with perchlorate ion.

Consider first the response of the electrode equilibrated in the 10^{-5}M iron solution: (*a*) potential readings were abnormally low below 10^{-3}M and (*b*) the response above 10^{-4}M was super-Nernstian, *i.e.*, greater than ~58 mV/decade change in iron concentration. After exposure to 10^{-1}M ferric ion, this electrode showed the normal Nernstian responses as obtained with properly activated electrodes (data not shown in the figure).

Consider next the electrode equilibrated overnight in 10^{-3}M ferric ion. Response was Nernstian, and little hysteresis was observed in potential on increasing and decreasing the iron concentration (data not shown in the figure). Similar behavior was observed after equilibrating a freshly etched electrode for 1 hr in 10^{-1}M ferric ion solution.

Finally consider the plot for the electrode equilibrated overnight in 10^{-1}M ferric iron. The subsequent performance at and above 10^{-3}M is normal; response below 10^{-3}M was less than would be expected from Nernstian behavior. Furthermore the potentials showed considerable long term drift. In many cases such treatment with 10^{-1}M ferric ion resulted in electrodes completely nonresponsive to changing ferric ion concentration below 10^{-4}M ferric ion.

To confirm that this deactivation involved exposure time as well as ferric iron concentration, an active electrode was exposed to 10^{-3}M ferric ion for 87 hr rather than overnight as described above. Subsequent measurements of the concentration-potential responses indicated a decrease in sensitivity of the electrode to low concentrations of ferric ion, *e.g.*, a potential change of only 35 mV was observed from 10^{-5} to 10^{-4}M iron and 53 mV from 10^{-4} to 10^{-3}, rather than the previously observed 58 mV/decade. Above 10^{-3}M ferric ion the response was still Nernstian. This result has obvious implications relative to the use of this sensor for the continuous monitoring of process streams. As with other ion-selective electrode, the best performance is obtained when the electrode is used to measure less

than order of magnitude changes in concentration around a constant ambient concentration.

In order to avoid, or at least minimize, such deactivation of the electrode when the sensor is not in use, consideration was given to storing the electrodes in the dry state, without etching and chemical reactivation between applications. Accordingly a series of four electrodes were activated overnight in 10^{-3}M ferric ion and then operated. After demonstration of the expected sensitivity to ferric ion, the electrodes were washed with supporting electrolyte, washed with distilled water, dried, and left overnight in air. The electrodes were then exposed to solutions of varying iron content and the steady-state potentials were recorded. The greatest divergence between the two sets of potentials was 20 mV; the average divergence was 10 mV. Two conclusions can be made. First dry storage does not deactivate the electrode, and, second, as with all ion-selective electrodes, recalibration is a desirable precaution.

The operational effects discussed above raise significant questions regarding the electrode mechanism for sensing ferric ion concentration. In particular it is necessary to rationalize the 58 mV/decade Nernstian slope, *i.e.*, a one-electron process, with the following: (*a*) the electrode activation phenomenon, (*b*) the electrode deactivation process, (*c*) the autocontamination of the test solutions, and (*d*) the variation in response times with the magnitude of concentration change and concentration level.

One possible explanation, consistent with previously discussed redox behavior, is that the electrode sees only the oxidation potential of the ferric ion (the reduced half of the equilibrium couple is in the electrode), but to function properly the electrode surface must first be oxidized, *e.g.*, to a potential approximating that of 10^{-1}M ferric chloride. The autocontamination effect could indicate that the solubility of the electrode material is potential dependent. Similarly the deactivation process could be explained by a competing slow and irreversible oxidation of the surface by ferric ion at potentials equal to or greater than +400 mV *vs.* Ag/AgCl.

The following experiment was carried out in an attempt to evaluate the effect of oxidation potential (this study was done in replicate, but for simplicity of presentation we will discuss the data for only one run). An electrode was etched, washed with supporting electrolyte, and placed in 1M KCl, *p*H 1.7 but with no added iron. The potential of the electrode was set to +400 mV with the potentiostat and held for 3 hr. This is approximately the potential the electrode would have reached if exposed to 10^{-1}M ferric chloride in 1M KCl, *p*H 1.7. A current flow of 2 mA anodic was observed initially, decreasing within 15 min to 0.003 mA anodic. Thus, a chemical oxidation of the electrode surface does take place during the electrode activation step.

After the anodic current had definitely fallen to zero (3 hr), the applied potential was removed and the electrode was exposed to varying concentrations of ferric ion in the same supporting electrolyte, starting with 10^{-5}M and proceeding to higher concentrations in order of magnitude increments. The potential-log concentration response so obtained was substantially identical to that shown in Fig. 2 for the freshly etched electrode exposed to 10^{-5}M ferric chloride. At 10^{-5}M Fe^{+3}, the electrode potential was of the order of 150 mV below its equilibrium Nernstian value and only slowly increased toward this potential (at ~5 mV/hr). This rate of approach to equilibrium was much slower than observed during operation of the chemically activated electrode at this concentration level. Varying the solution Fe^{+3} concentration generated a super-Nernstian response. As concentration increased, the potentials more closely approximated their "true" equilibrium values and the rate-of-approach to equilibrium increased.

It can thus be concluded that oxidation of the electrode surface does occur during the activation step, but, in itself, is not sufficient to provide an electrode responsive to changing iron concentrations in the supporting electrolyte solution. Exposure to high concentrations of ferric iron is indeed required. Since the phenomenon is observed in perchlorate solution, the important species involved in this process is ferric ion and not a chloride complex.

It had been determined previously that exposure of the electrode to 10^{-1}M ferric iron for 3 hr, *i.e.*, the time period used in the potentiostatic treatment discussed above, was sufficient to deactivate the electrode response to low concentrations of ferric iron in the solution. However, the potentiostatic treatment did not adversely affect the electrode performance. To further confirm this, a freshly etched and chemically activated electrode was put on the potentiostat at +400 mV for 3 hr. Subsequent potentiometric response to varying iron content in solution was unchanged, *i.e.*, the electrode was not detectably deactivated. Thus it can be concluded that electrode deactivation also does not solely involve surface oxidation, *i.e.*, high potential, but that high concentrations of ferric ion are required.

The next point to establish is the nature of the chemical interaction between the ferric iron in solution and the surface of a chemically, or electrochemically oxidized Fe-1173 electrode. The most likely reaction is that of equilibrium (rather than irreversible) chemisorption of Fe^{+3}. The specificity of such a process would account for the selectivity of the electrode material. The equilibrium exchange of the adsorbed iron with ferric ion in solution would account for the autocontamination effect, as the electrode is severely shifted from equilibrium by, for example, reducing the solution iron content more than an order of magnitude. The initial adsorption of ferric iron would, of course, be expected to produce a potential change and indeed after potentiostatic oxidation, the addition of ferric ions subsequently does lead to an increase in potential which, as described, is super-Nernstian, *i.e.*, is greater than expected from the effect of concentration change alone.

A series of experiments was therefore carried out in an attempt to elucidate the chemistry involved in this electrode-ferric ion interaction. The specific measurement techniques used were: (*i*) free ferric iron analysis of the equilibration solutions with an activated Fe-1173 electrode, (*ii*) total iron analysis of the equilibration solution via atomic absorption spectrometric analysis, and (*iii*) Fe^{+3}/Fe^{+2} ratio monitoring via a platinum screen electrode.

Accordingly an electrode was freshly etched and placed in a 10^{-5}M $FeCl_3$ solution (*p*H 1.7, 1M KCl) which was equilibrated with the active Fe-1173 electrode. The potential of the active electrode decreased by 7.8 mV in 60 min. Atomic absorption analysis indicated no change in total iron content. These results are rationalized by noting that a freshly etched electrode is in a reduced state (at approximately −400 mV) and is thus capable of reducing ferric ion to ferrous ion. Potentiostating such an electrode at +400 mV did result in an anodic current flow as described above.

The test electrode was therefore re-etched, potentiostated at +400 mV, for 2.5 hr, and then exposed to 10^{-5}M ferric chloride solution. The active Fe-1173 electrode again indicated a decrease in ferric iron content, but the potential change was much smaller, *i.e.*, of the order of a millivolt; the platinum screen electrode indicated a decrease in potential of 4.6 mV. Thus there is indeed a change in the composition of the equilibrating electrolyte, but it is small. Atomic absorption analysis of the solution showed no change in the total iron content. However the changes indicated by the electrodes are at the limit of reproducibility of the atomic absorption analytical method. Complicating matters, however, was the observation that in no case

during the replicate atomic absorption analysis of replicate solutions was there indicated a lower concentration of total iron in the equilibration solution compared to that for the original electrolyte.

Nevertheless it is possible to conclude that very little, if any, reduced species come off the electrode during the activation step. The potential change noted for the platinum electrode, if due solely to ferrous iron or a similar reduced specie, would be of the order of 10^{-7}M (0.006 ppm Fe). The same conclusion applied to a chemically activated electrode during ferric iron sensing. The platinum electrode was placed in a 10^{-5}M ferric chloride solution until steady state was achieved. An active Fe-1173 electrode was placed in this solution; no change in potential of the platinum electrode was observed.

These observations then are consistent primarily with the adsorption of ferric iron onto the electrode surface during the activation step. The quantities involved are proportional to solution ferric ion concentration and hence are small at low ambient concentrations of ferric iron. (At higher concentrations there would be the problem of detecting small differences between large numbers.)

However, with available data it is not possible to exclude rigorously, the desorption or dissolution of material from the electrode surface which would form a stable complex ion with Fe^{+3}, and thereby reduce the electrode potentials of the monitoring electrodes as described. Such a mechanism would be consistent with the atomic absorption results on total iron content of the solutions. However (*a*) such dissolution would have to take place only in the presence of ferric iron (or the process would have been completed during the potentiostating step), (*b*) such dissolution could not expose fresh Fe-1173 surface (or steady state would not have resulted), and (c) the Fe^{+3} complex would have to have a low equilibrium constant (log *K* of the order of 2 or 3) or the changes in ferric iron concentration would be greater than observed; this in turn would imply a solubility product not strongly influenced by the Fe^{+3} concentration and condition (*a*) would not apply.

Thus the most likely interaction is adsorption of ferric iron on the fresh electrode surface.

If the deactivation process proceeds via an irreversible, slow adsorption of ferric iron species, which may or may not be potential dependent, then it would be expected that, if the potential of the electrode were reduced, it would be possible to displace ferric iron from the electrode surface or it would be possible to reduce this adsorbed ferric iron to ferrous iron. Since ferrous iron does not evoke an electrode response, it can be assumed that it is not adsorbed onto the electrode. In both cases, soluble iron should appear in the supporting electrolyte. Accordingly, a deactivated electrode was potentiostated at +120 mV for 10 min in 1M KCl, *p*H 1.7, containing no added iron. Current flow was cathodic, but less than 0.001 mA. The solution was then analyzed for soluble iron via a sensitive atomic absorption spectrometric method (5); 0.34 mg/liter (6×10^{-6}M) iron was found. Although small, the value is nevertheless real, *i.e.*, in excess of the residual iron content found in the particular KCl solution used in this experiment. This then is evidence in support of deactivation via irreversible, but slow, adsorption of ferric iron onto the electrode surface. Consistent with such a mechanism is the fact that inactive electrodes always read high, i.e., give potentials in excess of what is expected for equilibrium with the solution being measured. Such would be the case for an electrode with an excess of iron on the surface.

We are therefore left with the following conclusion regarding the activation and sensing mechanism of Fe-1173 electrodes. A properly activated electrode will show Nernstian responses to solutions varying in ferric iron content with a slope of approximately 58 mV/decade concentration change, *i.e.*, a one-electron change process. However to function properly, a freshly etched surface must first be exposed to ferric iron solution of moderately high concentration, of the order of 10^{-3}M or higher. During this step, the electrode surface is first oxidized, after which a chemical interaction takes place between the electrode and ferric iron in the solution. It is this modified surface which is involved in the sensing of ferric iron content of solutions. This sensing mechanism does not involve the injection of reduced species into the electrolyte. This interaction of the electrode with ferric iron in solution is most likely one of specific adsorption, although the quantity of ferric iron so involved is low, at least at low ambient iron concentrations. The operational effects discussed imply that the subsequent ferric ion sensing mechanism involves the exchange of ferric ions in solution with the electrode surface.

Electrode deactivation is rationalized in terms of a slow, irreversible adsorption of ferric iron taking place simultaneously with the faster adsorption process which forms the basis of the sensing mechanism. In any event the involvement of ferric iron in the deactivation process is strongly indicated. The rate of deactivation is proportional to the average Fe^{+3} concentration seen by the electrode thus further supporting the idea of dry storage to prevent deactivation.

The remaining problem is to account, at least qualitatively, for the one-electron Nernstian slope with such a mechanism. Obviously the electrode mechanism is more complex than that originally proposed, *i.e.*, a redox couple Fe^{+3}/M^{+2}, where M^{+2} is contained in the electrode surface. That the electrode responds to oxidizing agents such as Ce^{+4} and peroxides, there is little doubt (1). However there may well be more than one mechanism depending on the species involved; work in progress is consistent with such a conclusion. To be consistent with the information discussed above relative to Fe^{+3} sensing, it is necessary to postulate a surface adsorption or chelation which involves a potential determining ion exchange with Fe^{+3} in solution. The over-all process of generating an active surface and sensing ferric iron may be represented as follows

$$\text{Fe-1173} + Fe^{+3}\ (\text{sol}) \rightarrow \text{oxidized Fe-1173} + Fe^{+2}\ (\text{sol})$$
$$\text{Fe-1173 (ox)} + Fe^{+3} \rightarrow M^*$$
$$M^* + Fe^{+3}\ (\text{sol}) \rightleftarrows M^*Fe$$

The freshly etched Fe-1173 on exposure to ferric iron in solution is first oxidized. This surface then interacts chemically with further ferric iron to form the active centers (M*) involved with the subsequent ferric iron sensing. (This process is inferred from the extremely slow approach of the oxidized electrode to true equilibrium when exposed to low concentrations of ferric ion in solution.) The active site (M*) now establishes its potential via fast, reversible adsorption-desorption equilibrium with Fe^{+3} in solution and that adsorbed on the surface. At the same time a much slower irreversible adsorption-deactivation process takes place which is dependent on the concentration of ferric ion in solution.

Summary

Properly prepared, activated and operated Fe-1173 electrodes show Nernstian responses to changing ferric ion concentration between 10^{-5} and approximately 10^{-1}M Fe^{+3}, with a nominal slope of 58 mV/decade ferric iron concentration. This slope is reproducible from electrode to electrode within ± 3 mV (1σ level). The same slopes were found in chloride and in perchlorate media. Ferrous ion is not seen by the electrode.

As presently prepared, slices of sensor material taken from a given melt can vary $\pm 10\%$ in total iron content. Fe-1173 glasses containing less than 0.9% (weight) are higher in resistivity ($\geq 10^{+3}$ ohm-cm). Electrodes of this material while responding to changes in ferric iron content in solution, are less sensitive to low ($\leq 10^{-4}$M) concentrations of Fe^{+3}. Low resistivity ($<10^{3}$ ohm-cm and preferably $<10^{2}$ ohm-cm) material

results in electrodes that are sensitive to concentrations as low as 10^{-6}M Fe^{+3} (0.06 ppm) in chloride and perchlorate solutions.

Electrode response time decreases with decreasing increment of concentration change, increasing ambient concentration of ferric iron, and with stirring. Exposure of the electrodes to strong chelating agents such as EDTA does not adversely affect subsequent electrode response.

In order to develop an active sensor for monitoring ferric ion concentration, the electrode surface must be etched in a caustic and exposed to high ($\geq 10^{-3}$M) concentration of ferric iron. This activation process involves the oxidation of the surface as well as further chemical reaction with ferric iron. The activation process is different from the sensing process in that the latter involves a fast, reversible exchange between solution ferric ions and adsorbed ferric ions. A slow chemical deactivation of the surface takes place which involves at least in part the irreversible adsorption of ferric ion. Electron life can be prolonged by dry storage and deactivated electrodes are readily reactivated by etching and exposure to ferric ion.

Acknowledgments

Financial support of this work by the Office of Saline Water, United States Department of the Interior is gratefully acknowledged.

Manuscript submitted March 12, 1973; revised manuscript received April 27, 1973.

Any discussion of this paper will appear in a Discussion Section to be published in the June 1974 JOURNAL.

REFERENCES

1. C. Baker and I. Trachtenberg, *This Journal*, **118**, 571 (1971).
2. R. Jasinski and I. Trachtenberg, *Anal. Chem.*, **44**, 2373 (1972).
3. R. Jasinski and I. Trachtenberg, *ibid.*, **45**, 1277 (1973).
4. L. Sillén and A. Martell, "Stability Constants of Metal-Ion Complexes," Special publ. No. 17, The Chemical Society, London (1964).
5. J. Jones and R. Eddy, *Anal. Chim. Acta*, **43**, 165 (1968).

Electrochemical Behavior of Sodium Tungsten Bronze Electrodes in Acidic Media

J. P. Randin,* A. K. Vijh,* and A. B. Chughtai*

Hydro-Quebec Institute of Research, Varennes, P.Q., Canada

ABSTRACT

The electrochemical behavior of sodium tungsten bronze electrodes (Na_xWO_3, with x between 0.58 and 0.89) has been examined in helium-saturated 1*N* H_2SO_4. Several techniques have been employed, *e.g.*, steady-state polarization, potentiodynamic scanning, galvanostatic charging, and open-circuit decay of electrode potential. New data involving potential-*p*H, rotating-disk, and thermogravimetric measurements on the sodium tungsten bronze electrode are also reported.

The results indicate that the surface layer of a strongly anodized bronze electrode is depleted of sodium and its composition may approach WO_3. On a strongly (cathodically) reduced Na_xWO_3, formation of sodium-hydrogen tungsten bronze ($Na_xH_zWO_3$) is indicated. The reduction of a preoxidized (and hence sodium-depleted) sodium tungsten bronze electrode produces hydrogen tungsten bronze H_zWO_3.

Sodium tungsten bronzes have been proposed as electrocatalysts for the oxygen reduction reaction. Although their electrocatalytic activity has been the subject of numerous studies (1-9), relatively little information is available on the electrochemical stability of these materials.

It has been hypothesized (5-8) that on anodization the sodium diffuses out of the bronze surface, leaving a semiconducting layer of very low sodium content. Ion probe microanalysis has confirmed this hypothesis (10). The formation of hydrogen tungsten bronze and the oxido-reduction of the surface layer has been proposed (7). Finally, a model based on the existence of a nonstoichiometric, hydrated tungsten oxide-like layer at the surface has been proposed (11).

In the present study, the effect of electrode potential on the surface composition of sodium tungsten bronzes will be presented. The nature of the processes taking place on the surface layer of the bronze electrode in acidic media will be discussed. Several different techniques such as steady-state polarization, potentiodynamic scanning, galvanostatic charging, and open-circuit electrode potential decays have been applied. New data involving potential-*p*H, rotating-disk, and thermogravimetric measurements on the sodium tungsten bronze electrode will also be reported. A detailed a-c impedance investigation of the bronze-electrolyte interface, with particular emphasis on the Mott-Shottky behavior in relation to the electrode pretreatment, has been reported elsewhere (12).

Sodium tungsten bronzes are nonstoichiometric compounds of general formula Na_xWO_3 where x is a variable <1. For Na_xWO_3 in the approximate composition range $0.49 < x < 0.93$, a cubic structure is found which is intermediate between the hypothetical $NaWO_3$ and undistorted WO_3 structures and in which a fraction $(1 - x)$ of sodium atoms are missing from the cube corners of the $NaWO_3$ unit cell. The limiting structure of "$NaWO_3$" is that of the perovskite (ABO_3). The unit cell has a tungsten atom at the center of a cube octahedrally surrounded by 6 oxygen atoms at the face centers; there are 8 "interstitial" sites occupied by sodium atoms at the corners of the cube. The structure of WO_3 is a distorted version of the ReO_3 structure in which tungsten atoms are slightly off-center in adjacent unit cells such that the W-W distances are alternately long and short. As the sodium content of the bronze decreases, the cubic symmetry of the lattice is lowered and the structure passes through two tetragonal phases and one orthorhombic to the monoclinically distorted phase of pure WO_3.

* Electrochemical Society Active Member.

Key words: electrochemical stability, sodium tungsten bronze, anodization, oxidation, hydrogen tungsten bronze.

Sodium tungsten bronzes with $x > 0.25$ behave as metallic conductors between 4° and 800°K. Detailed consideration of the Hall and Seebeck effects reveals that there is one free electron per metal atom in the host lattice and that the carrier mobility is comparable with that of free electrons in the conduction band of a typical metal (13, 14). The different models (15-18) for the conduction band of bronzes have been reviewed recently (19, 20). In the preferred model (18), the conduction band is made up predominantly of the overlap of W, 5*d* (t_{2g}) and O, $2p_{(\pi)}$ orbitals.

Rather little information is available on the electrical properties of low x values Na_xWO_3. It seems that below $x = 0.25$ sodium tungsten bronzes are semiconductors (21). For a single crystal of $Na_{0.025}WO_3$, semiconductor-type behavior has been established (22). The low sodium content Na_xWO_3 exhibits n-type semiconductivity with an energy gap expected to be about 0.5 eV (15) due to a localization of the π electrons in isolated cation-anion pairs or clusters (18). For pure WO_3, the conduction band is empty and the energy gap, *i.e.*, about 2.5 eV (23), is sufficiently large that at room temperature very few electrons are found in the conduction band.

The sodium tungsten bronzes are very resistant towards acids but are readily oxidized to tungstate in the presence of alkali and oxygen (or oxidizing agents). The chemical inertness of the tungsten bronzes is perhaps associated either with the high energy of activation for the diffusion of sodium ions in the oxide matrix [51.8 kcal/mole for Na in $Na_{0.78}WO_3$ (24)] or with the formation of a protective layer of WO_3 (25).

Experimental

The sodium tungsten bronzes were prepared by electrolysis of molten mixtures of sodium tungstate and tungsten trioxide as will be described elsewhere. Sodium tungsten bronze samples with an x value from 0.58 up to 0.89, and platinum content between 1 and 1450 ppm were investigated in the present work.

The crystals of sodium tungsten bronze were mounted in electrodes by compression moulding within a Kel-F holder. Apparent surface area of each of the electrodes used in the present study was about 0.2 cm^2. All data are given with respect to the apparent surface area of the electrode. Prior to the electrochemical measurements, the bronze electrode was mechanically polished using different particle sizes of alumina (Buehler Ltd.) down to 0.3 μm and subsequently washed thoroughly with triple distilled water.

The electrochemical cell used for linear sweep voltammetry, open-circuit potential decays, and galvanostatic charging experiments consisted of the main compartment which contained the sodium tungsten bronze electrode, and separate compartments for both the reference and the counterelectrodes. The counter compartment was separated from the main part of the cell by a solution-sealed stopcock whereas the reference compartment was connected to the main one through a coarse fritted disk via a Luggin capillary, whose tip was located approximately 3 mm below the working electrode. Gas outlets with water bubblers were used in the main and counter compartments. All connections from gas lines to the cell were made by means of glass-to-glass ground joints. A Teflon plate mounted in the rotating disk electrode assembly served as a gas tight cover when the Teflon O-ring located at the top of the cell was firmly seated against the plate. The electrode shaft seal was provided by a centrifugally induced unidirectional gas flow within the small gap between the Teflon disk on the electrode shaft and the horizontal Teflon cover plate during rotation. The volume of the electrolyte used in the main compartment was about 300 cm^3. An Hg/Hg_2SO_4 (1*N* H_2SO_4) reference electrode was used and the counterelectrode in the separate compartment was sodium tungsten bronze with a surface area of about 1 cm^2. This cell was used on an ESB Depack XLR-2 model rotating electrode system.

An all-glass three-compartment cell was used for other electrochemical measurements. Hydrogen electrode (in the same solution) and Hg/Hg_2SO_4 (1*N* H_2SO_4) were used as reference electrodes. All electrode potentials are given with respect to NHE. The counterelectrode in a separate compartment was sodium tungsten bronze or spectroscopic grade graphite (Union Carbide Corporation).

The hydrogen gas used for the reference electrode was purified by a palladium diffusion processor (Model HPD 050, Engelhard Industries, Newark, New Jersey). Helium gas used for deaeration and to provide an inert atmosphere inside all the electrochemical cells before and during all measurements was purified by passing it through a train, which included a BTS catalyst (BASF, Ludwigshafen-am-Rhein, Germany), maintained at 180°C to remove oxygen and CO, and Linde Type 3A and 13X molecular sieves to remove other impurities.

Sulfuric acid solutions were prepared by diluting H_2SO_4 (ULTREX, J. T. Baker Chemical) in deionized and doubly distilled water, both distillations being over alkaline permanganate. No pre-electrolysis was conducted in the present work since it was noted in some preliminary runs that pre-electrolysis tends to produce impurities, especially from the anode. It was observed that pre-electrolysis conducted with two platinum gauze electrodes (3 × 10 cm) at 1 mA for 48 hr in 100 cm^3 of helium-saturated 1*N* H_2SO_4 brought 10^{-6}g platinum into the electrolyte.[1] Sodium tungsten bronze and spectroscopic graphite were also found unsuitable. Although the problem of trace impurities may, in general, be of crucial importance in a kinetic study, the results of the present work have not been found to depend strongly on the impurity level; this statement excludes, of course, highly catalytic impurities such as traces of Pt.

In some potentiostatic measurements, the tungstate concentration in the electrolyte was measured spectrophotometrically (Spectrophotometer Perkin-Elmer, Coleman, Model 124D) using the thiocyanate method (26).

The potentiostats used were a Wenking Model 68TS3 or a Tacussel Type Bipad. A linear potential-time input was obtained from a Tacussel Electronic Function Generator, Type GSTP 2, or a Servovit 9, also from Tacussel. A Wenking Scanning Potentiometer Model SMP 69 was used to control and program the potentiostat in the automatic recording of steady-state current-potential curves (27). Constant current d-c power supplies (Kepco, Type CC 100-0.2M, and Hewlett-Packard, Model 6177B) were used for charging curves with mercury-wetted-contact vacuum relays for current inversion and open-circuit potential decay measurements.

Experiments were carried out at room temperature unless otherwise specified.

The thermogravimetric measurements[2] were performed in helium at a linear heating rate of 4°/min using a Thermoanalyser Mettler I (Mettler Instrumente AG, CH 8606 Greifensee-Zurich, Switzerland).

Results

Linear sweep voltammetry.—A typical voltammetry curve for sodium tungsten bronze electrodes with low platinum content in He-saturated 1*N* H_2SO_4 is shown in Fig. 1. A well-defined oxidation-reduction peak occurs around 0.2V. The effect of increasing the sweep rate on the voltammetry curve in the vicinity of the peak is illustrated in Fig. 2. The potentials of current maxima for the anodic and cathodic peaks are more separated at the higher sweep rates than at the lower ones and their difference approaches a constant value,

[1] Amount of platinum determined by spark-source mass spectroscopy by the National Research Council, Chemistry Division, Ottawa, Ontario, Canada.

[2] Performed by the "Centre de Thermoanalyse," Ecole Polytechnique, Montréal, P.Q., Canada.

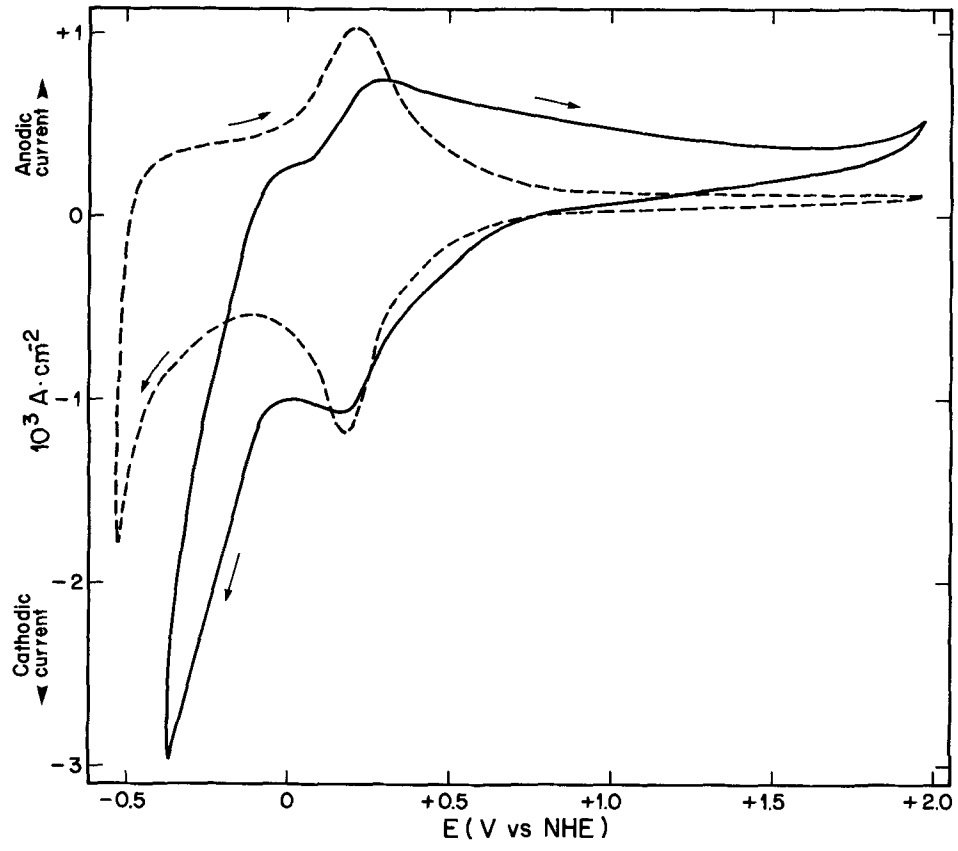

Fig. 1. Linear sweep voltammetry curve at 0.017 V/sec for $Na_{0.68}WO_3$ with 1 ppm Pt (dashed line) and 255 ppm Pt (solid line) in He-saturated 1*N* H_2SO_4. Direction of sweep indicated by arrows.

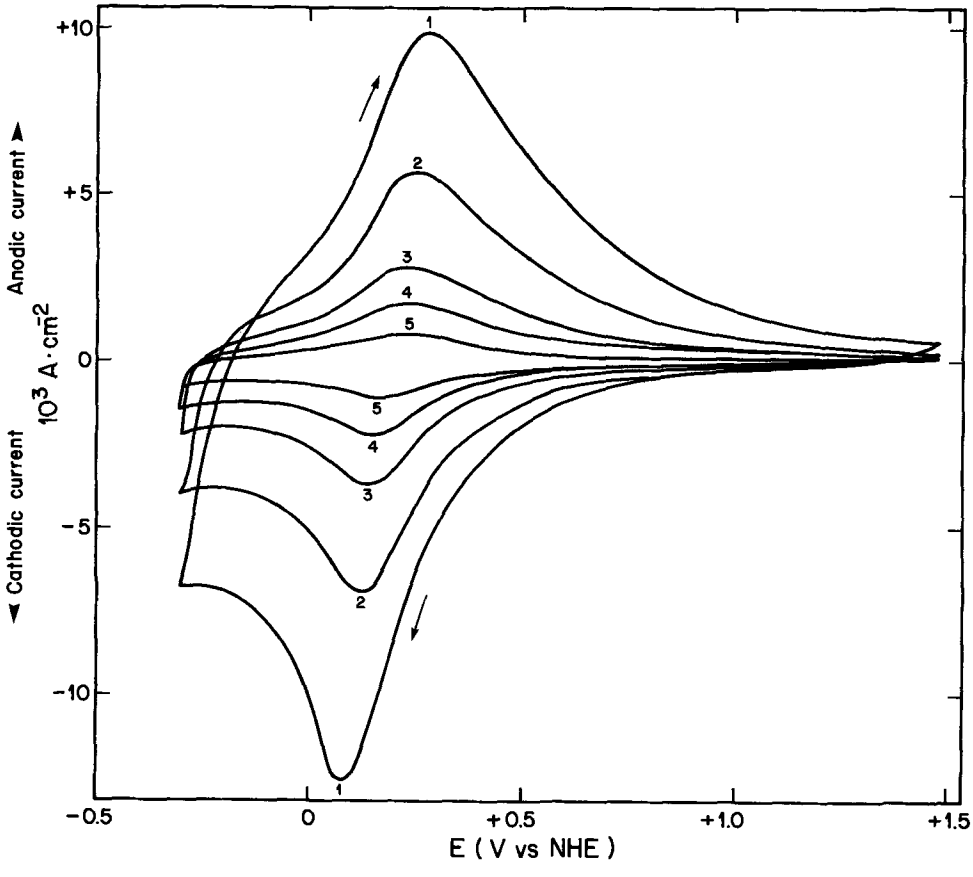

Fig. 2. Linear sweep voltammetry at various sweep rates for $Na_{0.68}WO_3$ (1 ppm Pt) electrode in He-saturated 1*N* H_2SO_4. 1, 0.720; 2, 0.360; 3, 0.180; 4, 0.090; 5, 0.036 V/sec.

i.e., about 60 mV, as the sweep rate is decreased. The 60 mV potential difference between the anodic and cathodic peaks is typical of a reversible process (28). A plot of the peak currents *vs.* the square root of the voltage scan rate, or, the voltage scan rate, shows that no linear relation passing through the origin is obtained, either in the anodic or in the cathodic direction of sweep.

This same general behavior was found for all the samples studied. The x value in the range 0.58-0.89 has no significant effect on the voltammetry curves. Samples with high platinum content exhibit some dif-

ferences with respect to samples containing only a low concentration of platinum (Fig. 1); the peak around 0.2V is still present, but it is now much broadened and overlaps the hydrogen evolution region on the cathodic sweep.

Steady-state current-potential relationships.—A typical steady-state current-potential relationship between −0.5 and 1.0V is shown in Fig. 3. Background anodic currents of the order of 10 μA cm^{-2} (apparent area), accompanied by a characteristic inhibition inflection (peak at 0.2V), a long transition region on anodic potentials, and a significant cathodic background current are the main features of the curve. The hydrogen evolution region is also shown in Fig. 3 and will not be examined in detail here. A Tafel line for the oxygen evolution reaction is observed around 2V (Fig. 4). A passivation region at potentials more anodic than 2.5V is usually quite characteristic of profound surface changes suffered by the electrode material on anodic polarization (Fig. 4).

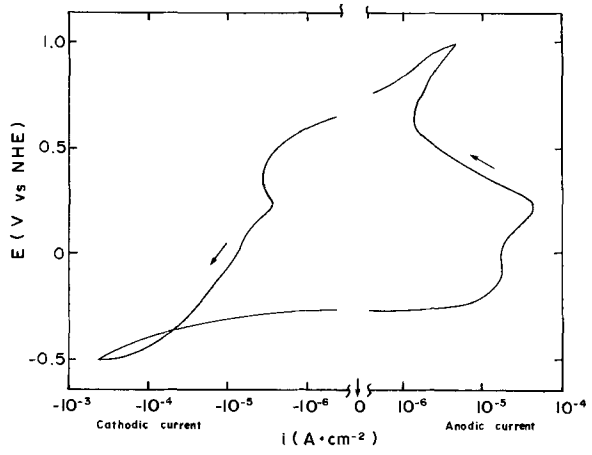

Fig. 3. Steady-state, potentiostatic polarization curve on $Na_{0.65}WO_3$ (1 ppm Pt) electrode in He-saturated 1*N* H_2SO_4. Direction of sweep indicated by arrows. Point by point measurements, 10 mV step per 2 min.

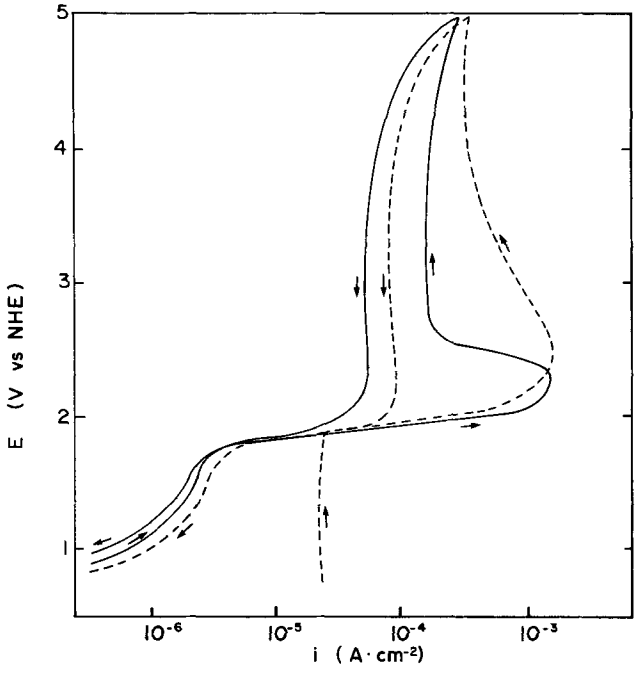

Fig. 4. Steady-state, potentiostatic polarization curve on a $Na_{0.65}WO_3$ (1 ppm Pt) electrode in He-saturated 1*N* H_2SO_4. Direction of sweep indicated by arrows. Point by point measurements, 10 mV step per 2 min. – – – first scan, ——— second (and following) scan.

Galvanostatic charging curves.—Anodic and cathodic galvanostatic charging curves were studied over a wide range of $i \times \tau$, where i is the charging current density and τ the duration of the transient. Normal surface conditioning performed before each galvanostatic charging curve involved a cathodic prepolarization at about 20 mA cm^{-2} for 200 sec. In a typical charging curve (Fig. 5), an arrest is obtained below 1V, followed by a plateau corresponding to the oxygen evolution reaction at about 2.3V. At low charging currents, typically 5 mA cm^{-2}, this potential remains almost constant over a long period of time. When the charging current was greater than 5 mA cm^{-2}, the voltage increased rapidly following a period during which it remained constant at about 2.3V. This transition time, τ, is shorter, the higher the applied current density. At a still higher current density, a voltage build-up as high as 40V is reached during anodization, which is an indication that some electrically limiting layer is formed on the electrode surface. It has been shown in a previous publication (29) that most likely the electrically limiting layer was an oxide. The kinetics of the oxide growth were also examined previously (29).

The transient observed at potentials below 1V was studied in detail as a function of the charging current density and the prepolarization conditions. The reverse curve was also examined and compared with the forward one.

On a freshly polished electrode, the analysis of the charging curve aimed at establishing the relative roles of diffusion and activation-controlled processes gives ambiguous relationships between the current density and $\tau^{-1/2}$ or τ^{-1}.

It was noted that a prior electrochemical treatment, especially an oxidation, had a significant effect on the shape of the galvanostatic charging curve, as well as on the charging current density *vs.* τ relationship. A preoxidized electrode gave a linear relationship between i and τ^{-1}, indicating an activation-controlled process (Fig. 6), whereas a prereduced electrode gave an i *vs.* $\tau^{-1/2}$ linear relationship, characteristic of a diffusion-controlled reaction (Fig. 7). These two different relationships have been taken as criteria of an "oxidized" and a "reduced" electrode surface, respectively.

An oxidized electrode was usually obtained after charging at about 20 mA cm^{-2} for 20 min. The reduced state of the electrode surface was much more difficult to obtain. An overnight reduction at about 20 mA cm^{-2} was sometimes not sufficient to attain the reduced state. Whereas the platinum content of the bronze had no significant effect on the time required to obtain the oxidized bronze surface, it was easier to reduce a bronze electrode containing platinum than one deprived of it. Between each series of measure-

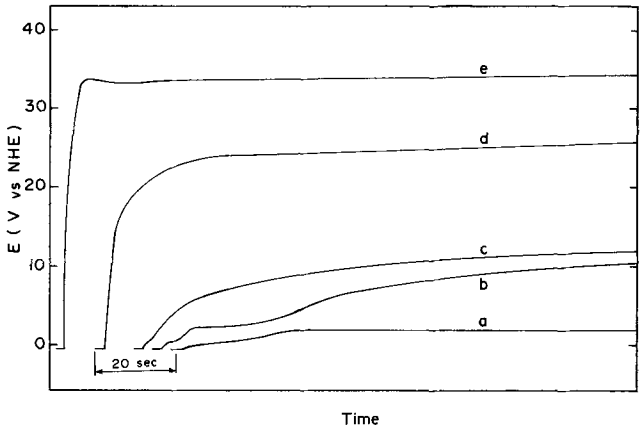

Fig. 5. Effect of current density on anodic charging curves for a $Na_{0.65}WO_3$ (1 ppm Pt) electrode following normal electrode surface preparation, in He-saturated 1*N* H_2SO_4. New surface preparation done for every charging current density: a, 4.25; b, 8.50; c, 12.8; d, 59.6; and e, 183 mA cm^{-2}.

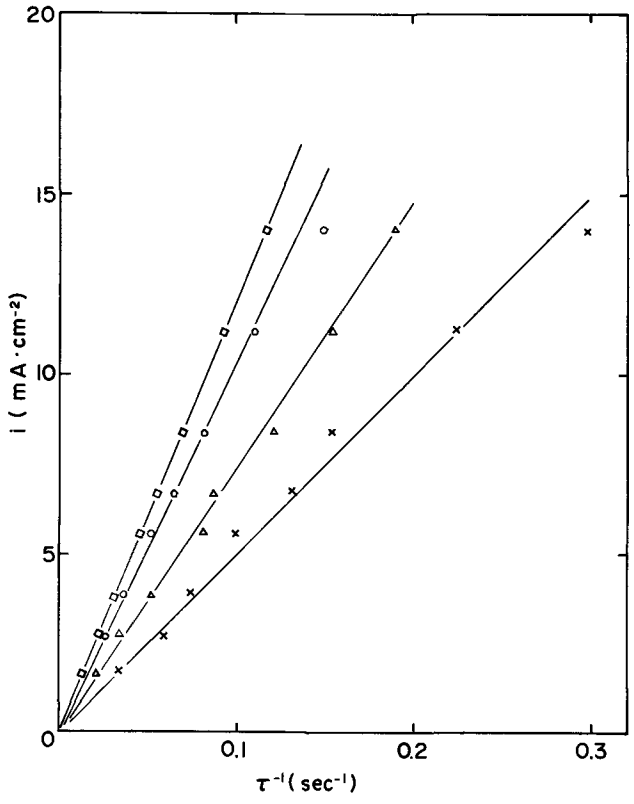

Fig. 6. Current density vs. τ^{-1} relationship for the galvanostatic charging curves carried out on a $Na_{0.65}WO_3$ (1 ppm Pt) electrode preoxidized at 20 mA cm^{-2} for 30 min in He-saturated 1*N* H_2SO_4. x $\tau_{ox(1)}$, Δ $\tau_{ox(2)}$, □[$\tau_{ox(1)} + \tau_{ox(2)}$], and ○ τ_{red}

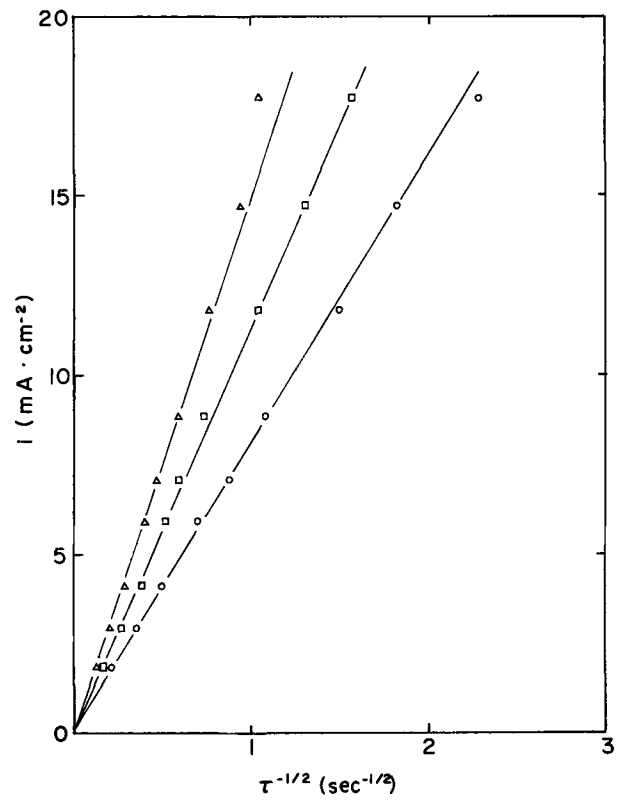

Fig. 7. Current density vs. $\tau^{-1/2}$ relationship for the galvanostatic charging curves carried out on a $Na_{0.65}WO_3$ (1 ppm Pt) electrode prereduced at −20 mA cm^{-2} for 18 hr in He-saturated 1*N* H_2SO_4. Δ τ_{ox}, measured as defined in Fig. 9; □ τ_{ox}, measured by the tangent method (Fig. 8); and ○ τ_{red}, measured by the tangent method (Fig. 8).

ments the electrode surface was usually polished. If a reduced bronze electrode was subsequently oxidized without polishing, the typical behavior of an oxidized electrode was obtained. On the contrary, it was not possible to obtain the behavior of a reduced electrode with a previously oxidized electrode without polishing it thoroughly.

Typical galvanostatic charging curves obtained with strongly prereduced and preoxidized electrodes are shown in Fig. 8. At a given current density, the transition time is longer with an oxidized electrode than with a reduced one. This trend is more pronounced at higher current densities than at low ones. The anodic charging curves performed on a reduced electrode with a current density smaller than about 5 mA cm^{-2} exhibit a plateau at about 2.2V corresponding to the oxygen evolution reaction. The same measurements carried out on an oxidized electrode show only a small break at the oxygen evolution potential, followed by a rapid increase of the potential. This behavior is characteristic of an oxidized surface layer (Fig. 5). The transition times depend slightly on the extent of the pretreatment.

The transition times, τ, used in the current *vs.* τ relationship were taken from the beginnng of the transient to the minimum of the capacity-potential profile calculated from the anodic charging curve (Fig. 9). The transition time was also measured using the time between the beginning of the transient and the intersection of the tangent traced in the transition region with the continuation of the linear section of the charging curve between 1 and 2V (30). Both τ values gave the same trend in the current *vs.* τ relationship (Fig. 7.) The transition time determined by the tangent method was usually preferred to that given by the minimum of the capacity-potential profile because of the broad shape of this latter curve at potentials between 1 and 2V.

On a preoxidized electrode surface, the capacity-potential profile calculated from the anodic charging curve exhibits two maxima, suggesting the occurrence

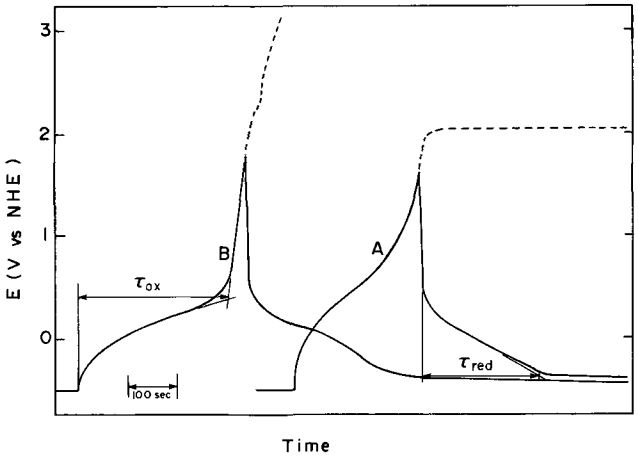

Fig. 8. Current-reversal galvanostatic charging curves for a $Na_{0.65}WO_3$ (1 ppm Pt) electrode in He-saturated 1*N* H_2SO_4. The dashed lines indicate the form of the charging curve if the current had not been reversed. $i = \pm$ 0.85 mA cm^{-2} after normal surface preparation. A, electrode prereduced at 21 mA cm^{-2} for 18 hr; and B, electrode preoxidized at 21 mA cm^{-2} for 30 min.

of two different processes (Fig. 10). These two capacity peaks overlap broadly, however, and the capacity-potential curve calculated from the cathodic charging measurements exhibits only one peak. The transition times of the two processes defined by the capacity-potential profile from the anodic charging curve have been called $\tau_{ox(1)}$ and $\tau_{ox(2)}$ and defined as indicated in Fig. 10. A linear relationship is obtained between the current density and $\tau_{ox(1)}^{-1}$, $\tau_{ox(2)}^{-1}$, $(\tau_{ox(1)} + \tau_{ox(2)})^{-1}$ and τ_{red}^{-1} (Fig. 6).

The capacitance-potential curves calculated from the galvanostatic charging curves exhibit a very high max-

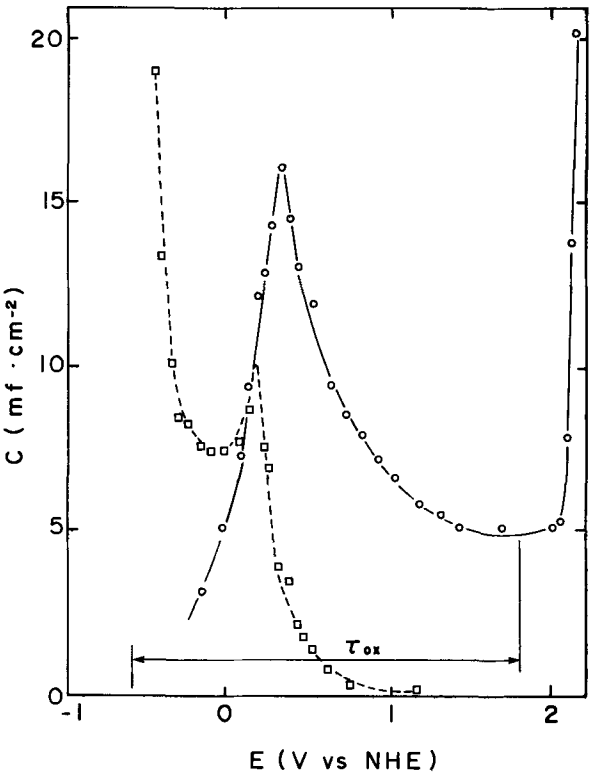

Fig. 9. Capacity-potential profile calculated from the anodic (○) and cathodic (□) charging curves for a $Na_{0.65}WO_3$ (1 ppm Pt) electrode prereduced at -27 mA cm^{-2} for 18 hr in He-saturated 1*N* H_2SO_4. Current density $i = 1.66$ mA cm^{-2} following normal surface preparation.

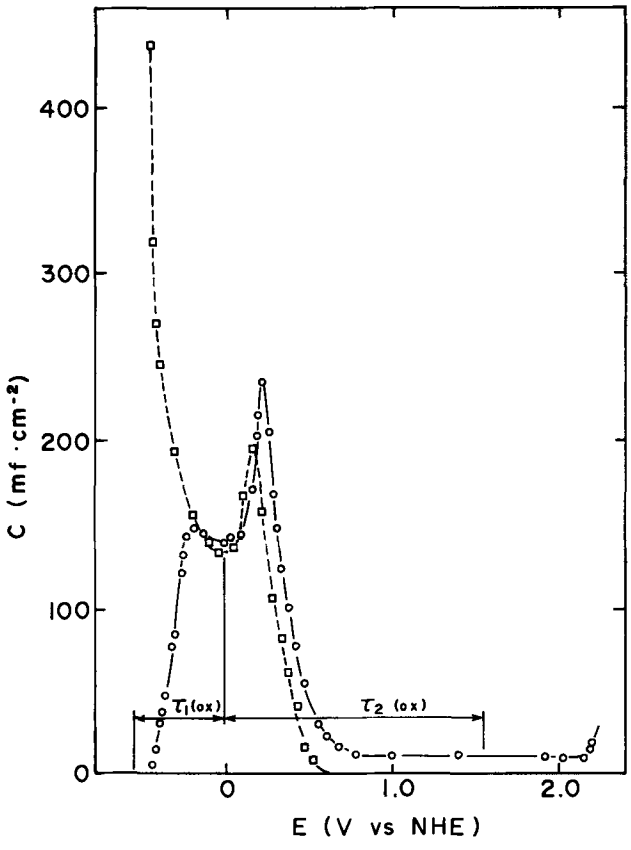

Fig. 10. Capacity-potential profile calculated from the anodic (○) and cathodic (□) charging curves for a $Na_{0.65}WO_3$ (1 ppm Pt) electrode preoxidized at 27 mA cm^{-2} for 30 min in He-saturated 1*N* H_2SO_4. Current density $i = 1.66$ mA cm^{-2} following normal surface preparation.

imum pseudocapacity. The capacitance is higher with an oxidized electrode than with a reduced one (Fig. 9 and 10). The value of the total charge given by the average slope of the anodic charging current *vs.* τ^{-1} in Fig. 6 is equal to about 120 millicoulomb cm^{-2}, whereas the charge corresponding to the cathodic charging current is equal to about 100 millicoulomb cm^{-2}.

A comparison of the ratio $\tau_{oxidation}$ to $\tau_{reduction}$ deduced from the data in Fig. 6 and 7 gives a value of about 1.2-1.3. The value of $\tau_{reduction}$ depends only slightly on the potential at which the current was reversed, *i.e.*, $\tau_{reduction}$ from a cathodic curve triggered at 1.3V (anodic) is about 15% smaller than that from a curve triggered at 2.0V (anodic) on an oxidized electrode. According to the diagnostic criteria defined by Reinmuth (31) for a diffusion controlled process, the equivalence of τ_{ox} and τ_{red} is observed only when the reduced species involved in the process is insoluble.

The general behavior of the galvanostatic charging curves has been found not to depend, significantly, on either the x value in Na_xWO_3 (for x between 0.58 and 0.89) or the platinum content of the bronze electrode (platinum content ranging from a few ppm up to 1450 ppm). The effect of platinum to achieve a reduced surface has already been pointed out.

Measurements with a rotating disk assembly.—The rotation of the electrode has no significant effect on the potentiodynamic and galvanostatic measurements carried out at intermediate potentials, *i.e.*, between -0.5 and 2V. These results indicate that diffusion in the electrolyte plays no major role in the process (es) under investigation. The electrode was sometimes rotated at low speed (about 1000 rpm) to help remove the gas bubbles from the bronze surface.

Open-circuit potential decay.—Open-circuit potential decay curves were recorded following polarizations at 1.0, 1.5, and 2.0V for times varying between 30 and 1800 sec. Each run was preceded by a prepolarization at about 5 mA cm^{-2} for 240 sec. In a given series of measurements from one particular value of the anodic electrode potential, the electrode surface was polished only before the first measurement. Three regions of potential can be distinguished (Fig. 11). First, at highly anodic potentials, a region of slow decay is observed in curves triggered after long oxidation times; this is perhaps associated with a solid-state diffusion process. Second, a more rapid region is observed whose slope, dE/d log t, is a function of both the time of polarization at a given potential (Fig. 11) and the value of the polarization potential. The more anodic the polarization potential and the longer the time of polarization, the steeper is the potential decay. This behavior is characteristic of an oxide-covered surface (32). Third, a slow potential decay is observed in the region of the rest potential, which is possibly due to a slow attainment of the equilibrium mixed potential. Neither the x value in Na_xWO_3 nor the platinum content of the electrode have a significant effect on the open-circuit potential decay.

Potential-pH relationship.—The potentials were measured in 1*N* H_2SO_4, then NaOH was progressively added to increase the pH, and inversely in NaOH with increasing amount of H_2SO_4. The rest potentials in acidic solution have low reproducibility and a long time was needed to reach a stable value. In alkaline solutions the reproducibility is better and the stable potential was reached after a shorter time than in acidic solution. Each potential-pH point was measured after allowing sufficient time (at least 24 hr) for the equilibrium to take place and the potential to stabilize.

Typical results are shown in Fig. 12. At pH values lower than about 3, the potential seems to be independent of pH, although some uncertainties exist due to the lack of reproducibility of the measurements and the long time needed to reach a stable potential. A potential-pH relationship with a slope close to 60 and

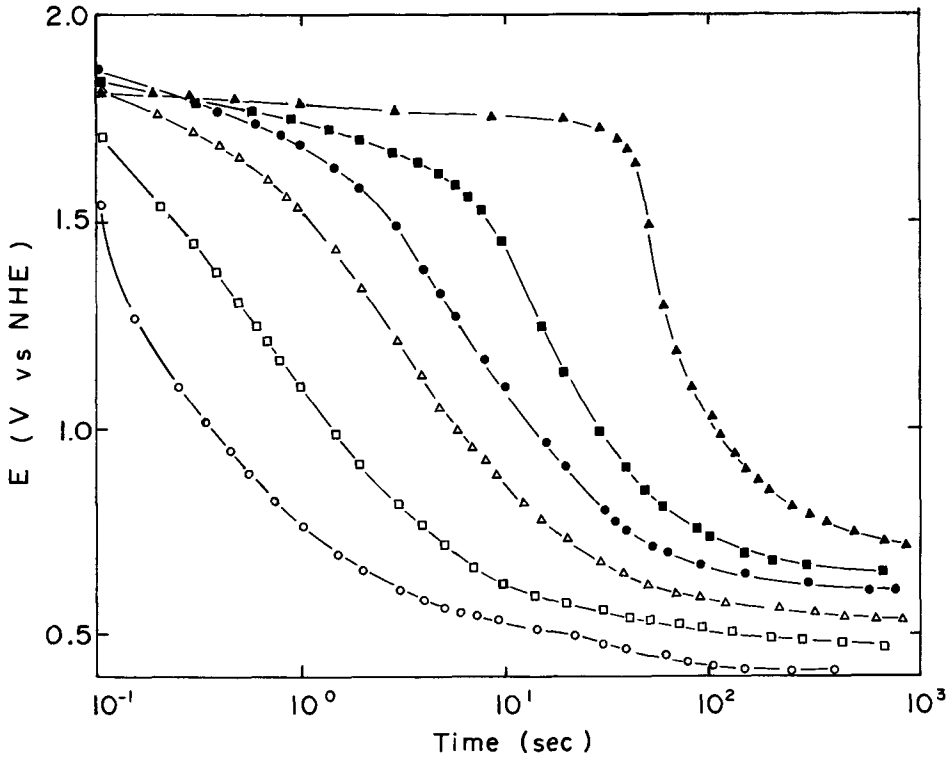

Fig. 11. Open-circuit potential decay for a $Na_{0.65}WO_3$ (1 ppm Pt) electrode in He-saturated 1*N* H_2SO_4. Galvanostatic prepolarization at −5 mA cm^{-2} for 240 sec followed by potentiostatic polarization at 2V vs. NHE for 30 sec (○), 60 sec (□), 120 sec (△), 240 sec (●), 480 sec (■), and 1800 sec (▲).

120 mV/pH in acidic and alkaline media, respectively, is indicated in Fig. 12. However, a 180 mV/pH slope in strongly alkaline solutions cannot be entirely ruled out. The presence of tungstate ions in the sulfate solution has no significant effect on the potential-pH relationship.

Tungstate dissolution upon potentiostatic polarization.—Potentiostatic polarizations at 2V were carried out on a 0.17 cm^2 polished bronze electrode in 100 cm^3 in 1*N* H_2SO_4 in the presence of He or O_2 bubbling. The amount of tungstate dissolved and the integrated charge as a function of the polarization time are given in Fig. 13. Despite scatter in these results, some general conclusions may be drawn. Roughly linear relations are obtained between the charge or the tungstate dissolved and the polarization time. However, the ratio of the tungstate dissolved to the charge passed is very low, *i.e*, of the order of 2×10^{-3}. It was also observed that this relatively low corrosion, under anodic polarization, of the bronze electrode is not appreciably enhanced by the presence of oxygen.

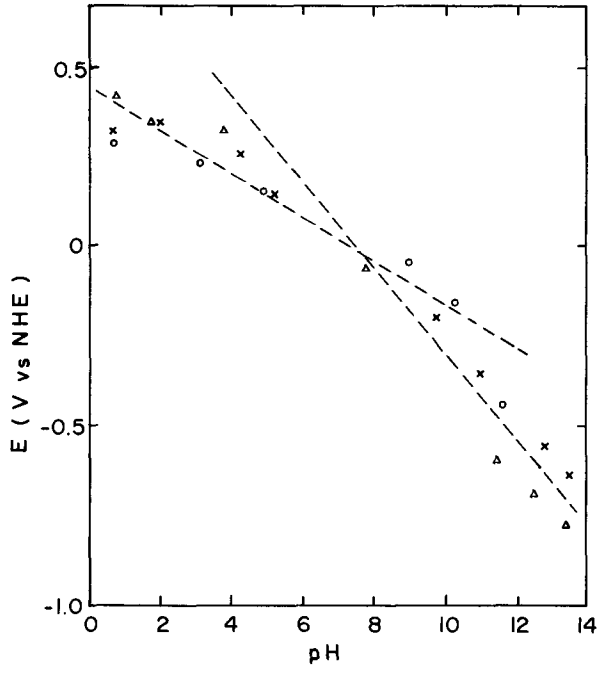

Fig. 12. Electrode potential-pH plot for a $Na_{0.65}WO_3$ (1 ppm Pt) electrode in He-saturated 1*N* H_2SO_4-Na_2SO_4 solutions [measured by going towards alkaline media (x) and towards acidic media (○)] and in 1*N* H_2SO_4 — Na_2SO_4 + 0.2 *M* Na_2WO_4 solutions [measured by going towards acidic media (△)].

The amount of tungstate dissolved at open circuit is very low, almost at the detection limit of the analytical method used, *i.e.*, 2.3×10^{-8} and 0.8×10^{-8} mole, respectively, after 170 hr in oxygen and helium saturated 1*N* H_2SO_4. These values fit reasonably well with those given by Pourbaix (33) for WO_3, *i.e.*, 10^{-8} mole/liter at pH = 3 and 25°C. These results point out the relative insolubility of the bronze in 1*N* H_2SO_4. As expected from the insolubility of tungstate in acidic media, the oxidation of W(V) into a W(VI) species does not give rise to a soluble compound since only a thousandth of the current is used for the dissolution of tungstate. It cannot be ruled out that a part of the tungstate analyzed in the electrolyte is in fact an insoluble species, such as WO_3, which erodes from the electrode surface and drops down in the electrolyte as a colloidal particle and is subsequently analyzed as a "soluble" species.

Thermogravimetric analysis.—A thermogravimetric diagram obtained with a $Na_{0.65}WO_3$ powdered sample previously immersed in water and subsequently dried at 120°C, is shown in Fig. 14. The weight loss between 100° and 400°C is only about 0.02% and a weight gain is recorded at temperatures higher than 400°C.

Discussion

The results of the present study indicate that the surface of the bronze electrode changes significantly upon electrochemical treatment. Steady-state polarization curves exhibit a significant background current in both the anodic and the cathodic direction. Potentiodynamic and galvanostatic measurements show the existence of a pseudofaradaic process at about 0.3V, which exhibits high pseudocapacitance. High pseudocapacitance values are also observed in the a-c impedance measurements (12). Steady-state potentiostatic measurements reveal a passivation region at po-

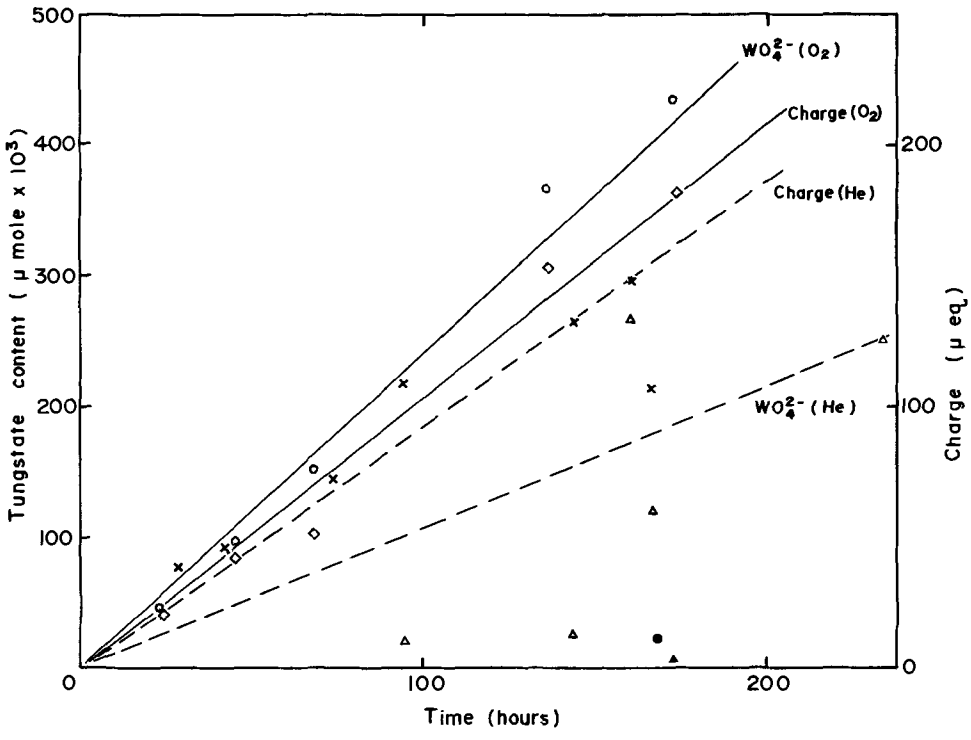

Fig. 13. Amount of tungstate dissolved in 100 cm^3 of 1*N* H_2SO_4 and integrated charge vs. the polarization time at 2.0V vs. NHE. $Na_{0.65}WO_3$ (1 ppm Pt) electrode with 0.17 cm area. △, dissolved tungstate in He-saturated H_2SO_4; x, charge during runs in He-saturated H_2SO_4; ○, dissolved tungstate in O_2-saturated H_2SO_4; ◇, charge during runs in O_2-saturated H_2SO_4; ●, dissolved tungstate in O_2-saturated H_2SO_4, open circuit; and ▲, dissolved tungstate in He-saturated H_2SO_4, open circuit.

tentials more anodic than about 2.5V. Galvanostatic charging curves obtained at high current densities show a voltage build-up as high as 40V (Fig. 5). Previous work also shows capacitative behavior associated with the presence of a semiconducting surface oxide (12, 29).

Irreversibility possibly due to sodium depletion of the surface layer.—Indirect evidence described in the present study and elsewhere (6-11) indicates that the sodium tungsten bronze electrode undergoes some kind of irreversible process when anodically treated. The a-c impedance measurements reveal the presence of a semiconducting layer (10, 12). The sodium content of this surface layer is very low, *i.e.*, corresponds roughly to $x < 0.01$ in Na_xWO_3, as compared to the bulk concentration (12). McHardy and Bockris (10) have presented the only direct evidence of sodium depletion of the surface layer. This is based on ion probe analysis. The decrease, at anodic potential, of the sodium content in the surface layer can result from either the sodium depletion of the bronze surface or the growth of a sodium-free oxide on the bronze surface.

The anodic reaction for sodium depletion may be described as

$$Na_xWO_3 \rightarrow Na_yWO_3 + (x - y)Na^+ + (x - y)e^- \quad [1]$$

The occurrence of this reaction to an appreciable depth into the electrode is in contradiction with the high activation energy for the diffusion of sodium in Na_xWO_3, *i.e.*, 51.8 kcal/mole for $Na_{0.78}WO_3$ (24). [A recent study (34) indicates that sodium in tetragonal Na_xWO_3 ($x = 0.4$) diffuses much more easily than in the cubic structure. This result, however, may not be relevant to our work since it has been shown that the cubic symmetry can be extended to considerably lower x values (0.23) than the normal composition range ($0.49 < x < 0.93$) by diffusing sodium from a crystal initially in the normal cubic composition range (22)]. With such a high activation energy the diffusion of sodium is expected to occur over a few lattice dimensions only, whereas the typical depth for the sodium depleted layer found by McHardy and Bockris (10) by means of ion probe mass spectroscopy is between 500 and 2000Å for a platinum-free crystal of $Na_{0.7}WO_3$ and between 200 and 400Å for a crystal of the same bulk sodium content but containing platinum.

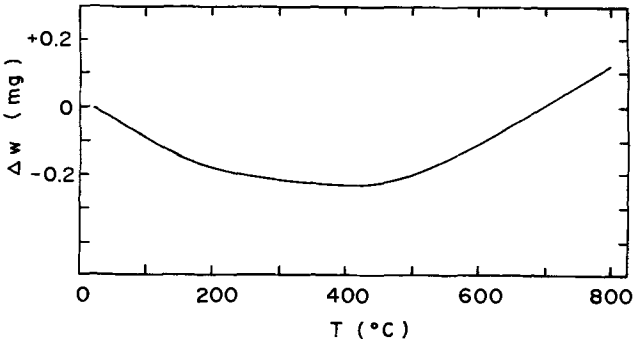

Fig. 14. Thermogravimetric diagram for $Na_{0.65}WO_3$ previously dried at 120°C. Heating rate 4°C/min, initial weight 0.60543g, He-atmosphere at 10 liter/hr.

It has been mentioned above that another possible reason for the decrease of the sodium content in the surface layer was the growth of a sodium-free oxide on the bronze surface. This alternative will be discussed below and found to be in contradiction with the experimental results.

The surface composition of a reduced electrode.—The formation of hydrogen tungsten bronzes by reduction of WO_3 with hydrogen at room temperature (35) or with zinc in boiling hydrochloric acid (36) is well documented. A synergistic effect due to platinum has been found when platinized WO_3 is reduced by hydrogen (35). The highest degree of reduction obtained at 25°C corresponds to the formula $H_{0.44}WO_3$ (35). Single crystals of H_xWO_3 in the composition range $0.3 < x < 0.6$ behave as metallic materials analogous to the corresponding sodium tungsten bronzes. The H_xWO_3 are structurally analogous to Na_xWO_3. The electronic properties of H_xWO_3 are compatible with a model in which H atoms enter the host lattice WO_3 as protons and donate electrons to a fairly wide conduction band formed from the overlapping of W_{5d} and O_{2p} orbitals (36-38). No thermodynamic data could be found for H_xWO_3.

Hence, the composition of the surface layer of the electrode during electrochemical reduction is believed to change according to the following reaction

$$Na_xWO_3 + yH^+ + ye^- \rightleftharpoons Na_xH_yWO_3 \quad [2]$$

This reaction agrees well with the conclusions drawn from the analysis of the impedance data at cathodic potential, especially the frequency dispersion of the capacitance and resistance (12).

The reaction [2] is preferred to a reaction in which the oxygen of the bronze is removed by reaction with protons, such as

$$Na_xWO_3 + 2yH^+ + 2ye^- \rightleftharpoons Na_xWO_{3-y} + yH_2O \quad [3]$$

This is because reaction [3] would require the breaking of a tungsten-oxygen bond which is expected to be energetically less probable than the introduction of a proton with the valence adjustment of tungsten.

Surface composition of an oxidized electrode.—Sodium tungsten bronze with low sodium concentration ($x < 0.25$) is known to be an n-type semiconductor with an energy bandgap of about 0.5 eV (22, 16). The a-c impedance study (12) revealed the presence of an n-type semiconducting layer with a low equivalent x value.

The injection of negative charge carriers O^{2-} into the bronze, giving a compound with an excess of anion, has been proposed recently (10, 29). This hypothesis, however, is not sustained because such a nonstoichiometric compound would exhibit a p-type semiconductivity, which is in contradiction with the experimental results. In general interstitial oxygen excess is not found in nonstoichiometric oxides because of the large size of the oxygen anion. So far, only UO_{2+x} (39) has been found to correspond to a nonstoichiometry associated with an excess of interstitial anions. A deficiency of tungsten ions would have the same effect and is also ruled out.

An alternative explanation could involve the injection of negative charge carriers into the bronze lattice whose sodium has not been completely depleted, even after a prolonged oxidation treatment. The negative charge injected as an interstitial oxygen anion should be compensated by a valence adjustment of the tungsten cations. This process could occur as long as the sodium ion is still in the lattice; *i.e.*, only half the mole content of sodium could neutralize the mole content of oxygen injected. In this process, however, the carrier concentration should decrease on going to high anodic potential; this is in contradiction with the experimental results (12).

The similarity between the a-c impedance data obtained on WO_3 single crystal electrodes by Baticle *et al.* (40) and those reported in a related study on strongly oxidized Na_xWO_3 (12) suggests that both surface layers have a similar composition. Tungsten trioxide is known to be an n-type semiconductor with a bandgap of 2.5 eV and a donor concentration equal to $2\text{-}4 \times 10^{18}$ donor-cm^{-3} (41). This compound can have various stoichiometries, due to the regular interruption of the octahedral structure by planes of discontinuity where octahedra share edges rather than corners, and not, as might be supposed, to the loss of oxygen with the concomitant ordering of vacant sites (42).

Perovskites with an oxygen deficiency (ABO_{3-x}) are also known, for example $BaNiO_{2.67}$, $BaCoO_{2.23}$ (42). However, an oxygen deficiency does not correspond to the accepted stoichiometry of the bulk Na_xWO_3. As a matter of fact, the oxygen stoichiometry in the as-grown Na_xWO_3 has been the subject of some discussion. Ingold and deVries (43) found that sodium tungsten bronzes prepared by electrolysis of molten mixture of Na_2WO_4 and WO_3 can exist with a O/W ratio as high as 3.5. More careful chemical analyses of Na_xWO_3 performed by Raby and Banks (44) indicate that the O/W ratio is 3.0. However, these data are not necessarily representative of the surface composition. The latter has not yet been analyzed.

On the basis of the preceding discussion, the most likely reaction for the oxide growth is reaction [1], which leads, in the case of strong oxidation, to a pronounced sodium depletion resulting in a very thin surface layer composed almost entirely of WO_3, *i.e.*, y in Eq. [1] is very small.

Nature of the quasi-reversible redox process at intermediate potentials.—On an electrode that has not been extensively oxidized or reduced, a quasi-reversible process occurs around 0.3V. This process is neither purely activation-controlled nor purely diffusion-controlled.

On an electrode subjected to a prolonged reduction, the quasi-reversible process is purely diffusion-controlled. Since the rotation of the electrode has no significant effect on the transition time, the diffusion is expected to occur in the solid state. The pseudocapacitance associated with this process is high and only one peak is observed in the capacity-potential profiles.

If anodic galvanostatic charging curves triggered from cathodic potentials exhibit an arrest, this would indicate that desorption of hydrogen, surface hydride formation, or hydrogen bronze formation (reaction [2]) has occurred during the cathodization. The latter process is expected to be reversible, diffusion-controlled, with diffusion occurring in the solid state. Thus the quasi-reversible reaction occurring at intermediate potentials on a reduced electrode is believed to be the hydrogen bronze formation. The potential range at which this reaction occurs, *i.e.*, about 0.2V, corresponds to the potential of the adsorption-desorption peaks for hydrogen on platinum (45).

Galvanostatic charging curves obtained with strongly oxidized electrodes reveal the occurrence of a more complex surface redox process since the capacity-potential profile calculated from the anodic charging curves exhibits two peaks. Although the process probably involves two or more steps, it can reasonably be discussed as one reaction since the reduction curve has only one peak in the capacity-potential profile (Fig. 10). On the strongly oxidized electrode the process is activation-controlled in contrast with that occurring on the reduced electrode, which appears to be diffusion-controlled. The potential of the maximum capacitance in the capacitance-potential curve is roughly the same on both the reduced and the oxidized electrodes, *i.e.*, about 0.2V. Consequently, the redox process is believed to be the same on both the pretreated electrodes; *i.e.*, the hydrogen bronze formation. On a strongly oxidized electrode the reaction may be written as

$$WO_3 + zH^+ + ze^- \rightleftharpoons H_zWO_3 \quad [4]$$

In this reaction, and in the following discussion, the composition of the oxidized electrode will be formulated as WO_3, although it is understood that a small amount of sodium may still be present in the surface layer.

The fact that the same reaction is controlled by activation on an oxidized surface and by diffusion on a reduced surface may be explained in the following way. According to Vijh (46), a rough correlation is obtained between the rate of a reaction taking place on an oxide covered electrode and the energy bandgap of that oxide. Hence, on a wide bandgap oxide such as WO_3, the electron transfer may be the rate determining step (rds) and the reaction may hence be activation-controlled. On a surface layer with a much smaller energy bandgap, such as $Na_xH_yWO_3$, the electron transfer is no longer the rds and the reaction may consequently be diffusion-controlled, as is indeed observed.

It was mentioned above that a strongly oxidized electrode subsequently reduced without polishing did not exhibit diffusion-controlled behavior typical of a reduced electrode in the galvanostatic charging curves. This fact does not necessarily imply that, once oxidized, the electrode cannot be reduced, but rather that the behavior of this reduced state does not correspond to that observed on an electrode reduced immediately after polishing. According to the preceding discussion the surface composition of an oxidized electrode may be taken as WO_3. An extensive reduction

carried out on such an electrode is expected to produce a surface layer corresponding to the composition H_zWO_3. On the other hand, an electrode reduced immediately after polishing will have a surface layer corresponding to $Na_xH_zWO_3$. The proposed explanation involves the occurrence of the same redox process in each case proceeding with different rds, depending on the composition of the surface layer. The reaction is diffusion-controlled only on a surface layer containing sodium ($Na_xH_zWO_3$). On a surface layer without sodium (WO_3 or H_zWO_3) the process is activation-controlled. The proposed reason for this behavior is that the diffusion of protons in Na_xWO_3 is hindered by the presence of sodium at the corners of the lattice, these sites being those of hydrogen in the hydrogen tungsten bronze. This interpretation is supported by the high activation energy for the diffusion of sodium in Na_xWO_3 (24). On WO_3 the interstitial sites are vacant and, consequently, protons can move easily into the canals of the octahedra. Hence, it is not surprising that the diffusion in the solid state is not the rds of the process taking place on H_zWO_3 or WO_3.

The only significant effect of platinum on the behavior of Na_xWO_3 noted in the present study involves its enhancement of the reduction process to form a hydrogen tungsten bronze. Similar enhancement has been described by Hobbs and Tseung (35) for the anodic oxidation of hydrogen. A mechanism explaining the effect of platinum to achieve a reduced surface is the following

$$x\text{Pt} + x\text{H}^+ + xe^- \rightleftharpoons x\text{Pt (H)}_{ads} \quad [5]$$

$$x\text{Pt (H)}_{ads} + Na_xWO_3 \rightleftharpoons Na_xH_zWO_3 + \text{Pt} \quad [6]$$

The rate of the over-all reaction of sodium hydrogen bronze formation would be limited by the electron transfer step on the platinum. However, it should be noted in Eq. [6] that platinum has an effect only on the forward process and not on the backward one. This is because the Pt can act only as a porter of hydrogen by providing catalytic sites for forming Pt-H during cathodization.

The foregoing discussion may be schematically represented as follows

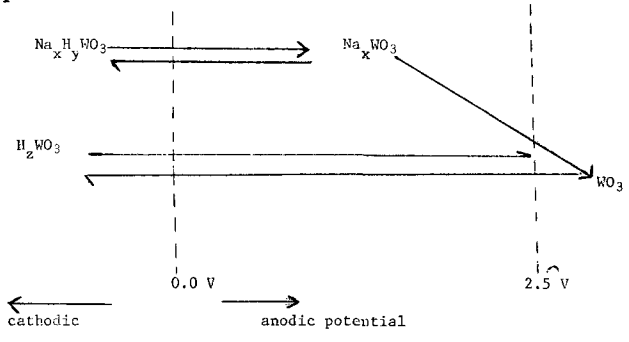

The rate determining step for the hydrogen bronze formation is the electron transfer on a sodium-depleted electrode (WO_3 or H_zWO_3). On an electrode containing sodium ($Na_xH_yWO_3$) the process is controlled by the diffusion of protons in the solid state.

Sodium tungsten bronze electrodes as pH indicator.—Several studies on the use of bronzes in pH and other related measurements have been published recently (47-48). Koksharov *et al.* (47) report a slope of about 60 mV/pH between pH 1.5 and 13.5 for a sodium tungsten bronze ($Na_{0.8}WO_3$) prepared by the solid-state method. Tetragonal bronze ($Na_{0.3}WO_3$) and melted bronze gave no definite slope in acidic media and responded to changes in pH only in a narrow interval of pH in alkaline solutions. Wechter *et al.* mentioned (48) that the potential-pH response of sodium tungsten bronze electrodes deviates from linearity but reported no data.

Thus, it appears from the present work, as well as from the earlier studies (47), that in strongly acidic media (pH < 3) no definite equilibrium potential is reached. At intermediate pH (between about 3 and 10), a 60 mV/pH slope is suggested from Fig. 12. Such behavior is predicted from any one of the following reactions (33, 11)

$$W_2O_5 + H_2O \rightleftharpoons 2\,WO_3 + 2H^+ + 2e^-, \quad E_o = -0.029\text{V} \quad [7]$$

$$WO_2 + H_2O \rightleftharpoons WO_3 + 2H^+ + 2e^- \quad [8]$$

$$2\,WO_2 + H_2O \rightleftharpoons W_2O_5 + 2H^+ + 2e^-, \quad E_o = -0.031\text{V} \quad [9]$$

$$W_6O_{11}(OH)_8 \rightleftharpoons W_6O_{17}(OH)_2 + 6H^+ + 6e^- \quad [10]$$

In alkaline media, a 120 mV/pH slope is suggested by Fig. 12, and it may be attributed to the following reaction

$$NaWO_3 + H_2O \rightleftharpoons WO_4^{2-} + Na^+ + 2H^+ + e^- \quad [11]$$

The lack of dependence of the potential of the bronze electrode on tungstate concentration is a behavior similar to that found for a ReO_3 electrode for which no dependence of potential on ReO_4^- concentration was indicated (49). These results may be contrasted with those obtained with MnO_2 electrodes for which Mn^{+2} concentration influences the potential-pH relationship (50).

Hydration characteristics of the sodium tungsten bronze electrode.—Vojnovic, Sepa, and Ovcin (11) have recently proposed a model of the surface of the bronzes in acidic solution based on the existence of a nonstoichiometric hydrated tungsten oxide-like layer at the surface. This model is based mainly on the findings of Spitzin and Kaschtanoff (51) concerning the bonding of water at the bronze surface. These authors (51) claim that a bronze sample previously dried at 120°C releases water below 300°C. This result is in contradiction with the more recent thermogravimetric measurements in which Polaczkova (52) has shown that a $Na_{0.11}WO_3$ sample gains about 0.2% weight upon heating between 200° and 300°C and the weight remains stable between 300° and 800°C.

If the structurally bonded water is removed from the surface sites upon heating as claimed by Vojnovic *et al.* (11), a sudden weight loss should be recorded around 300°C. The DTG diagram is devoid of such a peak. The small weight loss between 100° and 400°C followed by a small increase in weight between 400° and 800°C shown in Fig. 14 may be due to some gas adsorption or desorption. Thus the results of Polaczkowa (52) and those of the present study put in serious doubt the earlier work of Spitzin *et al.* (51) and would, consequently, invalidate the model proposed by Vojnovic *et al.* (11) for the surface of bronzes in acidic solution.

Acknowledgments

The authors thank Mr. R. Bellemare for his assistance in the experimental work, Dr. G. Bélanger for helpful discussions, and Dr. P. Lenfant for his interest and encouragement. The cooperation of the Materials Science and Electronics Departments of the Hydro-Quebec Institute of Research is gratefully acknowledged. One of the authors (A.B.C.) thanks the Canadian International Development Agency, Ottawa, for the award of a training fellowship.

Manuscript submitted Feb. 12, 1973; revised manuscript received April 11, 1973.

Any discussion of this paper will appear in a Discussion Section to be published in the June 1974 JOURNAL.

REFERENCES

1. D. B. Sepa, A. Damjanovic, and J. O'M. Bockris, *Electrochim, Acta*, **12**, 746 (1967).
2. A. Damjanovic, D. Sepa, and J. O'M. Bockris, *J. Res. Inst. Catal. Hokkaido Univ.*, **16**, 1 (1968).
3. B. Broyde, *J. Catalysis*, **10**, 13 (1968).

4. J. M. Fishman, J. F. Henry, and S. Tessore, *Electrochim. Acta*, **14**, 1314 (1969).
5. J. O'M. Bockris, A. Damjanovic, and J. McHardy, "Proc. 3rd Int. Symp. Fuel Cells, Brussels, Belgium, June 16-20, 1969," p. 15, Press. Acad. Européennes, Brussels (1969).
6. R. A. Fredlein and J. McHardy, "24th Power Sources Symp.," p. 175, P.S.C. Publications Committee, Red Bank, N. J. (1970).
7. R. D. Armstrong, A. F. Douglas, and D. E. Williams, *Energy Conversion*, **11**, 7 (1971).
8. J. McHardy and J. O'M. Bockris, in "From Electrocatalysis to Fuel Cells," G. Sanstede, Editor, p. 109, University of Washington Press, Seattle (1972).
9. J. O'M. Bockris and J. McHardy, *This Journal*, **120**, 61 (1973).
10. J. McHardy and J. O'M. Bockris, *ibid.*, **120**, 53 (1973).
11. M. V. Vojnovic, D. B. Sepa, and D. S. Ovcin, *Croat. Chem. Acta*, **44**, 89 (1972).
12. J. P. Randin, *Electrochim. Acta.*, Submitted for publication.
13. L. D. Muhlestein and G. C. Danielson, *Phys. Rev.*, **158**, 825 (1967).
14. L. D. Muhlestein and G. C. Danielson, *ibid.*, **160**, 562 (1967).
15. A. R. Mackintosh, *J. Chem. Phys.*, **38**, 1991 (1963).
16. R. Fuchs, *J. Chem. Phys.*, **42**, 3781 (1965).
17. M. J. Sienko, in "Non-Stoichiometric Compounds," *Advan. Chem. Ser.*, **39**, 224 (1963).
18. J. B. Goodenough, *Bull Soc. Chim. France*, 1200 (1965).
19. P. Hagenmuller, *Progr. Solid State Chem.*, **5**, 71 (1971).
20. P. G. Dickens and M. S. Whittingham, *Quart. Rev.*, **22**, 30 (1968).
21. H. R. Shanks, P. H. Sidles, and G. C. Danielson, in "Non-Stoichiometric Compounds," *Advan. Chem. Ser.*, **39**, 237 (1963).
22. W. McNeill and L. E. Conroy, *J. Chem. Phys.*, **36**, 87 (1962).
23. M. J. Sienko, *J. Am. Chem. Soc.*, **81**, 5556 (1959).
24. J. F. Smith and G. C. Danielson, *J. Chem. Phys.*, **22**, 266 (1954).
25. M. E. Straumanis, *J. Am. Chem. Soc.*, **71**, 679 (1949).
26. E. B. Sandell, "Colorimetric Determination of Traces of Metals," 3rd ed., p. 896, Interscience Publishers, Inc., New York (1959).
27. G. Bélanger, *This Journal*, **118**, 583 (1971).
28. P. Delahay, "New Instrumental Methods in Electrochemistry," p. 137, Interscience Publishers, Inc., New York (1954).
29. J. P. Randin, *This Journal*, **120**, 378 (1973).
30. W. H. Reinmuth, *Anal. Chem.*, **33**, 485 (1961).
31. W. H. Reinmuth, *ibid.*, **32**, 1514 (1960).
32. R. E. Meyer, *This Journal*, **107**, 847 (1960).
33. M. Pourbaix, "Atlas d'Equilibres Electrochimiques," p. 283, Gauthier-Villars, Paris (1963).
34. M. S. Whittingham and R. A. Huggins, *J. Chem. Phys.*, **54**, 414 (1971).
35. B. C. Hobbs and A. C. C. Tseung, *This Journal*, **119**, 580 (1972).
36. P. G. Dickens and R. J. Hurditch, *Chem. Extended Defects Non Metals Solids, Proc. Inst. Advanc. Study*, p. 555 (1969).
37. P. G. Dickens and R. J. Hurditch, *Nature*, **215**, 1266 (1967).
38. B. C. Hobbs and A. C. C. Tseung, *Nature*, **222**, 556 (1969).
39. L. Lynds, W. A. Young, J. S. Mohl, and G. G. Libowitz, in "Non-Stoichiometric Compounds," *Advan. Chem. Ser.*, **39**, 58 (1963).
40. A. M. Baticle, P. Lemasson, F. Perdu, P. Vannereau, and J. Vernière, *C. R. Acad. Sci. Paris*, **268B**, 1203 (1969).
41. J. M. Berak and M. J. Sienko, *J. Solid State Chem.*, **2**, 109 (1970).
42. A. D. Wadsley, in "Non-Stoichiometric Compounds," L. Mandelcorn, Editor, p. 98, Academic Press, New York (1964).
43. J. H. Ingold and R. C. deVries, *Acta Met.*, **6**, 736 (1958).
44. B. A. Raby and C. V. Banks, *Anal. Chem.*, **36**, 1106 (1964).
45. B. E. Conway, "Theory and Principles of Electrode Processes," Ronald Press, New York (1965).
46. A. K. Vijh, *This Journal*, **119**, 1498 (1972).
47. A. G. Koksharov and V. F. Ust-Kachkintsev, *Uch. Zap. Permsk. Gos. Univ.*, **111**, 63 (1964); *C. A.*, **64**, 1617g (1966).
48. M. A. Wechter, H. R. Shanks, G. Carter, G. M. Ebert, R. Guglielmina, and A. F. Voigt, *Anal. Chem.*, **44**, 850 (1972).
49. P. Chartier and R. Poisson, *C. R. Acad. Sci. Paris*, **265 C**, 1353 (1967).
50. P. Benson, W. B. Price, and F. L. Tye, *Electrochem. Technol.*, **5**, 517 (1967).
51. V. Spitzin and L. Kaschtanoff, *Z. Anal. Chem.*, **75**, 440 (1928).
52. E. Polaczkowa, *Bull. Acad. Polon. Sci., Ser. Sci. Chim.*, **17**, 445 (1969).

Thermal Effects During the Formation and Dissolution of Anodic Tantalum Oxide

J. P. S. Pringle*

Chalk River Nuclear Laboratories, Atomic Energy of Canada Limited, Chalk River, Ontario, Canada

ABSTRACT

Anodic films formed on tantalum at 10 mA/cm² were found to be thicker at the top of the specimen than at the bottom. The effect has been traced to a temperature difference resulting from the presence of convection currents in the electrolyte; these currents are powered by the heat released during anodization. The oxide thickness is thus very sensitive to changes in the anodizing temperature, and this sensitivity has been used to determine the temperature rise within the film itself. Convection currents during the dissolution of the oxide in buffered HF give rise to similar thickness variations, from which it has been concluded that the oxide dissolves exothermically.

A highly precise sectioning technique (1) has recently been developed for the purpose of measuring concentration profiles in anodic tantalum oxide (2, 3). The technique is based on slow dissolution of the oxide in HF almost saturated with NH_4F, and its extreme precision is due to the uniformity of the dissolution. In verifying this precision (1), it was shown that the anodization kinetics must necessarily give rise to oxide films of uniform thickness. Measurements showing that the oxide film was thicker at the top of a specimen than at the bottom therefore came as a surprise!

* Electrochemical Society Active Member.
Key words: tantalum, anodic oxidation, oxide dissolution, convection currents.

Fortunately, the explanation was soon apparent. The film thickness depends, *inter alia*, on the anodizing temperature; the higher the temperature, the greater the thickness formed. A greater thickness at the top of the specimen implies a higher anodizing temperature, and this could be due to convection currents in the electrolyte. Since the anodization of tantalum proceeds with the evolution of heat (4), such convection currents will inevitably be present unless action is taken to eliminate them. The observed thickness variations therefore act as a sensitive thermal probe, and some additional investigations were suggested thereby. In particular it seemed reasonable to suppose that if thickness variations resulted from thermal changes during anodization, they might also result from thermal changes during the dissolution of the oxide in buffered HF; appropriate experiments showed that this was indeed the case.

Anodization

Consequences of the anodization kinetics.—At constant temperature, the anodization kinetics may be represented approximately by

$$i = C \cdot \exp(DV/h) \qquad [1]$$

where i is the current density and V the potential across the oxide film of thickness, h; C and D are positive constants. Suppose that at a certain point on the surface the oxide thickness is less than h; then from Eq. [1], the current density at that point will be greater than i. If the current density is greater than i, the oxide will thicken more rapidly, and so the thickness irregularity will disappear as anodizing is continued. The oxide thickness must therefore remain extremely uniform throughout the anodizing process (1).

This argument is valid even though the anodization kinetics are much more complex than indicated by Eq. [1]; in particular, they vary with temperature. The best description (5) appears to be Young's (6) equation

$$i = i_o \cdot \exp[-(W - A \cdot (V/h) - B \cdot (V/h)^2)/kT] \qquad [2]$$

where i_o, W, A, and B are constants, k is the Boltzmann constant, and T the absolute temperature. This equation may be rearranged thus

$$h/V = 2B/[-A + \sqrt{(A^2 - 4B \cdot (-W + kT \cdot \ln(i_o/i)))}] \qquad [3]$$

On inserting appropriate values obtained from a least squares fit of Eq. [2] to the original data of Ref. (6)

$$h/V = 9.851/[1 - \sqrt{(0.001091T - 0.2056)}] \quad [\text{Å/V}] \qquad [4]$$

where i is taken as 10 mA/cm², the current density used in the present experiments. The left-hand side defines the "angstrom/volt" parameter, which measures the oxide thickness formed per volt of anodizing potential at the specified current density; the right-hand side shows that this value increases with the anodizing temperature, T°K.

Angstrom/volt values can easily be calculated from measurements of applied voltage and oxide thickness, but the results obtained here agreed only qualitatively with those computed from Eq. [4]. The reason for this is obscure, but it may perhaps be due to idiosyncracies in the apparatus used; the present anodizing apparatus (7) was intended merely to control the process, not to make accurate measurements on the kinetics.

On differentiating [4] with respect to temperature

$$d(h/V)/dT = 0.0363 \quad [\text{Å/V/°C}] \qquad [5]$$

for 25°C, the temperature at which the present experiments were performed. Hence if two tantalum specimens are anodized by 10 mA/cm² to 200V, and at temperatures close to 25°C but 1°C apart, the oxide thicknesses formed will differ by approximately 7Å. Such a difference can readily be detected by the spectrophotometric method for measuring oxide thickness (1, 8).

Thus although [4] could not be applied satisfactorily to measure the anodizing temperature itself, it was possible to apply [5], with good confidence, to measure differences in anodizing temperature. Fortunately, it was these differences that were of the greatest interest.

Heat liberated during anodic oxidation.—The resistive heat generated by the current flow is given by $V \cdot i/4.2$ cal/cm²/sec, where V is the potential across the oxide film in volts, and i is the current density in amperes/square centimeter. If V is 100V and i is 10 mA/cm², the heat liberated is 0.24 cal/cm²/sec, which is very large in relation to the small volume in which it is generated; the heat generation per unit volume is in fact of the order of 50 kW/cm³. Unless this heat is dissipated very quickly, therefore, the temperature of the oxide will rise substantially.

This problem has been considered by Young (4), who noted that while some of the heat would be dissipated by conduction to the underlying tantalum, most of it would be lost by convection currents in the electrolyte. He concluded, on both theoretical and experimental grounds, that the temperature rise would be appreciable only at current densities greater than a few milliamperes/square centimeter; and then only if the metal specimen were thin, the stirring of the electrolyte inefficient, and the anodization carried out continuously to high voltages. These general conclusions have been confirmed by others (9, 10) and also by experience in these laboratories.

Experimental results and discussion.—Rectangular coupons, 35 mm long by 10 mm wide, were cut from 0.37 mm (0.015 in.) tantalum sheet supplied by the Fansteel Metallurgical Corporation. A tantalum wire, 1.25 mm (0.050 in.) in diameter, was spot welded on one corner to provide electrical contact, and the coupons were then cleaned and chemically polished as described elsewhere (1). All anodizations were performed in 0.1M H_2SO_4 electrolytes maintained at 25°C by means of a water bath, using the apparatus devised by Walker (7). Oxide thicknesses were measured with a precision of 2Å or 0.15% of the thickness, whichever was greater (1), by means of the spectrophotometric method due to Young (8).

Four coupons were set in unstirred electrolyte with their long axes vertical, and anodized to 55, 110, 165, and 220V, respectively, at 10 mA/cm². Average oxide thicknesses over areas 8 × 2 mm (1) running across the coupons were then measured for the mean positions listed in Table I. The anodic films were all found to

Table I. Effect of thermal convection currents in the electrolyte on the thickness of the anodic oxide formed on rectangular tantalum coupons, 35 mm long by 10 mm wide. Temperature differences calculated from [5]. Anodizing conditions: 10 mA/cm², 0.1M H_2SO_4, 25°C

Distance from bottom or end of foil, mm	Oxide thickness, Å					
	Vertical orientation				Horizontal orientation	
					Upper side	Lower side
29.5	872	1750	2633	3549	3563	3566
17.5	871	1743	2628	3531	3574	3584
5.5	869	1734	2609	3498	3570	3574
Maximum potential applied (V)	55	110	165	220	220	220
Maximum temperature difference across coupon (°C)	1	4	4	6	1	2
Temperature increase at mid point relative to first coupon (°C)	—	0	2	6	11	12

be thicker at the top of the coupons than at the bottom, exactly as predicted from the convection current hypothesis. Angstrom/volt values were calculated for each end of the coupons, and the difference divided by 0.0363 [5] to obtain the maximum temperature differences. These are also listed in Table I, from which it can be seen that they increase with final anodizing voltage.

As already noted, the heat generated during anodization is proportional to $V \cdot i$, and therefore increases linearly with voltage under the constant current conditions used here. More heat is generated at the larger voltages, and, because the anodization takes longer, there is more time in which the convection currents can be set up. Increased temperature differences at the larger voltages are thus readily explained. By the same token, the average temperature of the electrolyte in contact with the coupon will increase, and so the mean anodization temperature will also be greater. Temperature differences calculated from the angstrom/volt values at the midpoints of the various coupons confirm this hypothesis also.

Further proof that convection currents are responsible for these nonuniformities was provided by changing the orientation of the coupons in the electrolyte. When a coupon was aligned horizontally, the results shown on the right-hand side of Table I were obtained. The greatest thickness now occurred in the middle of the coupon, as might be expected from the nature of the convection currents set up. The latter would, however, be so much weaker than for the vertical orientation that the temperature differences across the coupon would be less, and the electrolyte in contact with it would heat up more. The result in Table I shows that this is indeed what happens.

A convection current can be destroyed by stirring the electrolyte, and so the following experiment was performed. Two coupons, oriented with their long axes vertical, were placed in different anodizing cells immersed in the same water bath. The electrolyte was well stirred in one cell, but not at all in the other, and both coupons were anodized simultaneously to 220V at 10 mA/cm^2. Film thicknesses on the coupon in the unstirred cell were within 10Å of those for the similar specimen in Table I, which illustrates the reproducibility attained in these experiments; those in the stirred cell averaged 3398Å, with no significant variation across the foil. From the corresponding angstrom/volt values, the temperature difference at the midpoints was no less than 16°C, so that the way in which the heat is dispersed in the electrolyte has significant consequences for the anodizing process.

This ability to measure small temperature differences suggested that it might be possible to detect an effect when only one side of a coupon was anodized. A suitable specimen was prepared by masking one side with Apiezon N grease (1), and then anodizing the other to 170V at 1 mA/cm^2. On dissolving the Apiezon N in trichlorethylene, the first side was available for further anodization, while the second was protected by the anodic film already formed. The specimen was then anodized to 150V at 10 mA/cm^2 in a well-stirred electrolyte; simultaneously, an ordinary specimen was anodized in the same well-stirred electrolyte on both sides. The thickness of the film formed on the one side was 2290 ± 2Å (range of three measurements), while that formed on both sides was 2299 ± 2Å (range of six measurements, three on each side); repetition of the experiment gave exactly the same results. There is no doubt, therefore, that a temperature difference does exist under these conditions, and that its magnitude is of the order of 1.5°C.

If the presence of the second anodizing film raises the temperature of the first by 1.5°C, this implies that the first is already 1.5°C above the ambient electrolyte temperature; always assuming that the temperature gradient in the metal is negligible, as has been demonstrated theoretically (10). Such a result is of some significance for precise measurements on the anodization kinetics [*e.g.*, Ref. (6)] Obviously, the temperature increase will depend on the conditions of the experiment, and will be greater at larger current density and final voltage.

Dissolution

As discussed in Ref. (1), the dissolution of anodic tantalum oxide in concentrated HF almost saturated with NH_4F is normally just about as uniform as the anodization. Thus a tantalum coupon of the usual size was anodized at 220V at 1 mA/cm^2 and the thickness measured at 4 mm intervals across each face, starting 5.5 mm from one end. The fourteen measurements thus obtained ranged from 3588 to 3592Å, with a mean of 3590Å. The specimen was then stripped, with agitation, in 200 ml 48% HF + 80g NH_4F for four 10-min periods, being washed in water and acetone at the end of each period (1). Remeasurement of the oxide thickness at the same fourteen positions gave results ranging from 1907 to 1914Å, with a mean of 1911Å. A layer of oxide 1679 ± 2Å (rms deviation) thick had therefore been removed from every part of the specimen surface.

A second specimen was anodized and measured in exactly the same way, the fourteen thicknesses ranging from 3595 to 3597Å. This specimen was then placed in the same sample of stripping reagent and held stationary, with its long axis vertical, for 40 min. After washing and drying, remeasurement of the oxide thicknesses on one side gave 1811, 1812, 1814, 1818, 1820, 1827, and 1831Å for 4 mm intervals starting 5.5 mm from the bottom; the corresponding positions on the second side gave 1808, 1812, 1815, 1821, 1819, 1826, and 1829Å. More oxide had been dissolved from the bottom than the top, and more oxide had been removed overall, compared with the agitated sample. Convection currents were obviously present.

To establish the nature of these convection currents, two additional pieces of information were needed. As in anodization, the influence of temperature had to be established. Three anodized specimens were stripped in the same sample of reagent at three different temperatures (3.1°, 26.4°, and 46.9°C) whereupon the stripping rates were found to be 17, 81, and 479 Å/min, respectively. The dissolution rate therefore increases very markedly with temperature.

Second, the dissolution of oxide presumably weakens the reagent's ability to dissolve further oxide. To confirm this, approximately 1g of tantalum metal was dissolved in 20 ml concentrated HF, and then 8g of NH_4F added to make up the reagent; simultaneously, another 8g of NH_4F were added to 20 ml of the same concentrated HF to act as a standard. After equilibrating to the same temperature, the stripping rates were found to be 35 and 47 Å/min respectively, so that the presence of the dissolved tantalum had indeed decreased the stripping rate.

The convection currents can then be interpreted as follows. The oxide dissolves exothermically in the HF-NF_4F reagent, and the solution in contact with the surface becomes warmer. As it warms, it starts to rise; and as it dissolves the oxide, so its ability to dissolve further oxide is reduced. The two effects are in opposition, and hence the observed result depends on the outcome of the competition between them. The faster over-all dissolution is obviously a consequence of the temperature effect, while the slower dissolution at the top of the specimen is due to the weakening of the dissolving agent. The alternate possibility, that the oxide dissolves endothermically, can be dismissed, for the two effects would then reinforce one another to leave the greatest thickness at the bottom of the coupon.

Duplicate experiments confirmed these observations and showed that they were surprisingly reproducible, apart from the single occasion, noted in Ref. (1), when the interference colors indicated spots of thinner oxide. To study the formation of the convection currents, four specimens were anodized simultaneously at 1 mA/cm^2 to a thickness of 3565Å, and then stripped in a sta-

tionary vertical position for 10 × 4, 5 × 8, 2 × 20, and 1 × 40 min, respectively; after each strip, the specimens were washed and dried in the usual way (1). All four specimens were thus stripped for the same total time, and in the same sample of reagent at the same temperature; the effect of the convection currents was expected to become greater as the stripping periods lengthened. This was precisely what was observed. The thicknesses at the midpoints were found to be 1058, 1011, 942, and 950Å, respectively, which demonstrates the increase in dissolution rate due to local heating of the reagent. At the same time, the oxide thickness at the top was found to be 7, 13, 20, and 14Å greater than that at the bottom, thus demonstrating the onset of the convection currents.

Conclusions

1. Tantalum coupons anodized at 10 mA/cm² in unstirred electrolytes developed a greater oxide thickness at the top than at the bottom. These thickness variations have been related via the known kinetics of anodization, to differences in anodizing temperature.
2. The differences in anodizing temperature have been attributed to the presence of a convection current resulting from the heat liberated during the anodic oxidation.
3. The relation between oxide thickness variations and anodizing temperature differences has been used to measure the temperature rise in an oxide film during anodization in well-stirred electrolyte. For anodization at 10 mA/cm² to 150V, it was found to be about 1.5°C.
4. Thickness variations that developed when the oxide was dissolved in concentrated HF almost saturated with NH_4F were also attributed to convection currents.
5. From the nature of these currents, the oxide must dissolve exothermically.

Acknowledgments

The author expresses his appreciation to D. Phillips for taking the experimental measurements, to T. A. Eastwood for reviewing the manuscript, and to L. Young for supplying the original data of Ref. (6).

Manuscript submitted Jan. 15, 1973; revised manuscript received March 29, 1973.

Any discussion of this paper will appear in a Discussion Section to be published in the June 1974 JOURNAL.

REFERENCES

1. J. P. S. Pringle, *This Journal*, **119**, 482 (1972).
2. J. P. S. Pringle, *ibid.*, **120**, 398 (1973).
3. J. P. S. Pringle, Accepted for publication in *This Journal*.
4. L. Young, *Trans. Faraday Soc.*, **53**, 229 (1957).
5. M. J. Dignam, and D. B. Gibbs, *J. Phys. Chem. Solids*, **30**, 375 (1969).
6. L. Young, *Proc. Roy. Soc.*, **A258**, 496 (1960).
7. D. Walker, Atomic Energy of Canada Limited Report, AECL-2502 (1965).
8. L. Young, *Proc. Roy. Soc.*, **A244**, 41 (1958).
9. F. R. Applewhite, J. S. L. Leach, and P. Neufeld, *Corrosion Sci.*, **9**, 305 (1969).
10. J. Zahavi and J. Yahalom, *Electrochim. Acta*, **16**, 89 (1971).

Magnetic Plating on Nonconductors

John R. DePew*

General Products Division, International Business Machines Corporation, Boulder, Colorado 80302

ABSTRACT

Thin magnetic films of Co-P were autocatalytically deposited on two different plastic substrates. A polycarbonate and a polyimide plastic were chosen as the nonconductive substrates because of their thermal stability and flatness. The conditioning, sensitization, activation, and autocatalytic deposition of these nonconductors are described. A citrate hypophosphite bath was used with variations in the ratio of cobalt salts to citrate salts. The magnetic properties (coercive force, remanence, and squareness) of the thin (250-4000Å) films were analyzed, and the most promising concentration ratio and substrate were chosen for further experimentation. Variations in reductant concentrations were made at a constant ratio of cobalt to citrate. For each concentration of reductant, films of different thicknesses were prepared, and the effects of composition and thickness on the crystallographic and magnetic properties of the deposits were studied.

With the coming of the computer age, magnetic recording media consisting of thin films of magnetic material on substrates such as tape, drums, disks, or loop surfaces became indispensable to the complete data processing system. The most extensively used magnetic coating over the last ten years or so has been a finely divided ferric-oxide dispersion in a thermoplastic binder. In recent years, considerable effort has been spent on developing autocatalytic metal deposition. This technique deposits thin ferromagnetic metal films on conducting and nonconducting substrates by catalytic reduction of metal salts from aqueous baths. The thin films used are particularly suitable for very high-density digital magnetic recording because of their thinness, high coercivity, and high magnetic-moment density.

This paper deals with autocatalytically plating a thin cobalt-phosphorus magnetic film from a citrate-hypophosphite bath onto polycarbonate and polyimide nonconductive substrates. The effect of metal-ion concentration to citrate-ion concentration on the respective substrates (relative to magnetic properties) was evaluated in order to choose the optimum ratio for varying the reductant concentration. The resulting crystallographic and magnetic properties were examined.

Experimentation

The substrates chosen to receive an autocatalytic deposit of cobalt-phosphorus had to meet the following criteria: thermal stability, smoothness or flatness, nonconductivity, and flexibility (plasticity). These criteria are dictated by the requirements of the magnetic recording medium and its application in the computer industry.

Some previous work has been reported in which Mylar[1] was used as a substrate. Although somewhat more expensive than Mylar (a polyester), Kapton[1]

* Electrochemical Society Active Member.

Key words: plating, autocatalytic deposition, Co-P deposition, magnetic films, nonconductive substrates.

[1] Registered trademark, E. I. du Pont de Nemours Company.

(a polyimide) and Lexan[2] (a polycarbonate) were the substrates chosen for the experiments described in this report.

The following procedures were developed to obtain good coverage and adhesion by the metal. The Lexan and the Kapton were first ultrasonically cleaned in a detergent and a chlorinated solvent. Next the Lexan was soaked for 1 min in N, N dimethyl foramide, and then for 10 sec in a dichromate solution at 95°C (1, 2). The Kapton was soaked for 15 sec in a dichromate solution at 95°C, followed by a 15-sec dip in a 4M solution of NaOH at 90°C. The substrates were then given the usual sensitization (stannous chloride) and activation treatment (palladium chloride) (1). After each step, the substrate was rinsed in distilled water. The substrates were then ready for the autocatalytic deposition of the magnetic coating.

The deposition was carried out in a one-liter beaker. The general and the experimental formulations for the baths are given in Table I (3, 4). An expanded-scale pH meter was used to constantly monitor the pH. An ammonium-hydroxide solution was added to the bath to raise the pH as needed. The temperature of the bath was maintained by a thermostatically controlled hot plate. The agitation of the solution during deposition was kept at a level merely sufficient to ensure uniformity of temperature and concentration.

A fresh bath was prepared for each set of experimental conditions. To minimize the effects of the gradual depletion of the solution, only six samples were plated in each bath.

Photomicrographs were obtained by using an optical microscope and a scanning electron microscope. The percentages of cobalt and phosphorus in the films were determined by x-ray fluorescence. Standards of Co-P films that had been previously analyzed by wet chemical means were used to establish a graph of counts *vs.* mass per unit area (milligrams/square centimeter).

The percentage of phosphorus in the deposits was calculated by using the mass-per-area values of cobalt and phosphorus obtained by fluorescence. The thicknesses of the films were calculated by using the bulk density of cobalt (about 8.9 at 20°C) and assuming that the cobalt was the main constituent of the deposit. A diffractometer was used to trace the x-ray diffraction patterns of select plated samples to establish the particle size and the cobalt orientation in the experimental films.

Orientation with respect to the substrate of the films can be predicted from the intensity ratio of planes

$$\frac{I_{(0002)}}{I_{(10\bar{1}0)}}$$

Cullity (5) holds that a ratio of less than one indicates a preferred orientation of the (0002) planes to the surface of the substrate, whereas a ratio greater than one indicates (0002) planes, or c-axis, normal to the substrate. Values close or equal to one after normalization indicate a random c-axis orientation in the films.

All plated samples were placed on a vibrating sample magnetometer in order to measure the magnetic hysteresis. The two magnetic parameters measured were the coercivity and the squareness. A nickel standard of five-nines purity, accurately weighed, was used to calculate the saturation moment and the remanent moment. A calibrated x-axis on the recorder was used to calculate the coercivity of all samples.

[2] Registered trademark, General Electric Company.

Table I. Formulations

General	Experimental Series 1 (g/liter)	Experimental Series 2 (g/liter)
$CoSO_4 \cdot 7H_2O$ (35 g/liter)	2.5-35.0	17.5
$Na_3C_6H_5O_7 \cdot 2H_2O$ (35 g/liter)	35.0	35.0
$NaH_2PO_2 \cdot H_2O$ (20 g/liter)	20.0	10.0-30.0
$(NH_4)_2SO_4$ (66 g/liter)	66.0	66.0
Temperature = 178° ± 4°F		
pH = 8.6 ± 0.1		

Results

As was previously noted, the first experiments were done on Lexan and Kapton substrates. The first plating bath (series 1) used to deposit a magnetic coating on these substrates was a modified Brenner bath that had been used by others (4, 5). The pH, temperature, reductant concentration, buffer concentration, and complexing agent concentration of the bath were held constant. The only variables were time and the cobalt-ion concentration. Since the ratio of the cobalt ion to the complexing agent controls the amount of free cobalt available for reduction, it was this relationship that was examined and represented graphically in Fig. 1 for the Lexan and the Kapton substrates. Since the requirements for high-density media for digital recording are high coercivity, high squareness, and reasonable plating rates, the graphic results were examined to determine the optimum substrate and concentration ratio.

Figure 1 also shows that the squareness is quite linear and high over most of the range for Kapton, whereas the coercivity is somewhat erratic except in the range of 15-35 g/liter. The plating rate appears flat and reasonable (1250 Å/min) in the same range.

The results obtained by using Lexan as the substrate show very low coercivities and high squareness, initially. A peak in coercivity is reached at a concentration of 27.5 g/liter, but corresponding low squareness makes it unsatisfactory for high-density media. Adhesion between the deposits and the Lexan became very poor with thicknesses above 1700Å. The deposit blistered and tended to flake off in the bath.

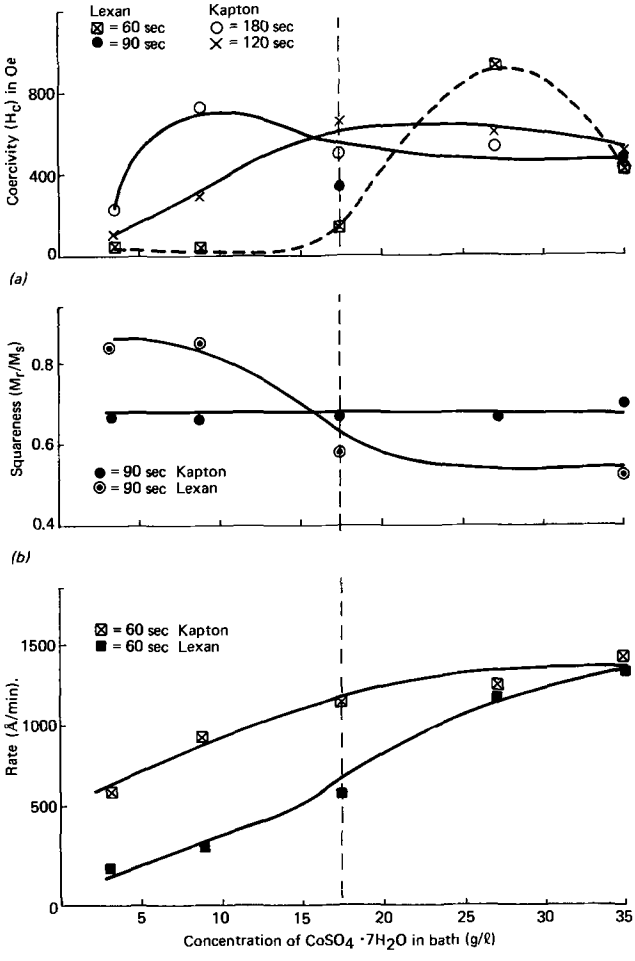

Fig. 1. Properties of deposit at different cobalt-ion concentrations on Kapton/Lexan substrates. (a) Coercivity, (b) squareness, (c) rate.

The reasons for choosing the 0.50 concentration ratio (represented by the vertical broken line) for further study become more apparent on examination of Fig. 1. The unusual relationship between the coercivity and the cobalt-ion concentration is an extension of the work disclosed by Wright (6), but contradicts his conclusion that the coercivity increases with decreasing cobalt-cation concentration.

After the initial experimental results were examined, further efforts were centered on the Kapton substrate, using a bath concentration ratio of 0.50. The pH, temperature, buffer concentration, complexing agent concentration, and cobalt-ion concentration were kept constant. The time and the reductant concentration were the only independent variables in this phase of the experiment (series 2). The reductant was chosen as the main variable since it had pronounced effects [discussed by others (7)] on rates of deposition, the amount of phosphorus in the deposit, and the crystallography, coercivity, and squareness.

The weight of the cobalt and the phosphorus deposited, determined by x-ray fluoresence, is shown in Fig. 2 as a function of deposition time with the reductant concentration as a variable. The total weight of the deposit is a linear function of the deposition time for each concentration of reductant; hence the deposition rate must be constant for each composition. If we assume a bulk density for cobalt (the main constituent of all deposited films) of 8.9 g/cm^3, we can calculate the dependence of the plating rate on the reductant concentration from Fig. 2. The average rate of deposition is a linear function of the reductant concentration over the range covered, and is probably the result of the optimum ratio of the cobalt ion to the complexing agent (0.50). Figure 3 supports the conclusion that the thickness of the deposit is a linear function of time and the reductant concentration.

The phosphorus in the films greatly influences their crystallographic and magnetic properties. The structure-sensitive property of hysteresis (and hence the coercivity and squareness) is greatly determined by phosphide-forming elements and particle size. According to Amendola *et al.* (8), the phosphorus content of a film is also a criterion for resistance to wear; cobalt thin films containing more than 2% phosphorus are abrasion-resistant.

The weight of the phosphorus deposited depends on the total weight of the deposit. There is no apparent change in the percentage of phosphorus over this thickness range in which the average percentage of phosphorus is independent of the weight of the deposit. The average phosphorus content remained quite constant throughout the concentration range of the reductant. Another noteworthy influence of increased film thickness is a decrease in the phosphorus content of the

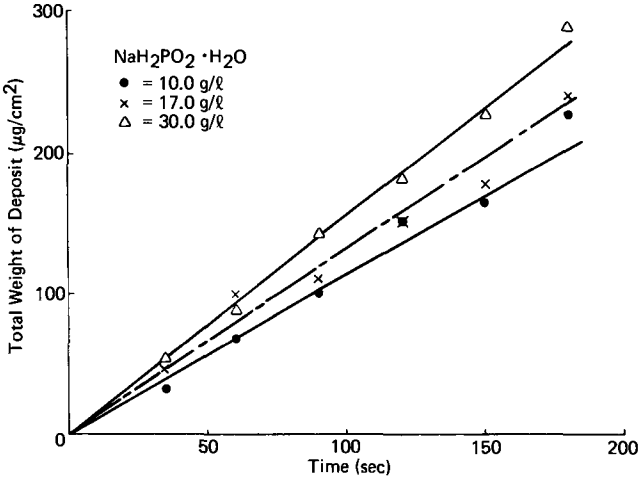

Fig. 2. Total weight of cobalt and phosphorus deposit vs. plating time.

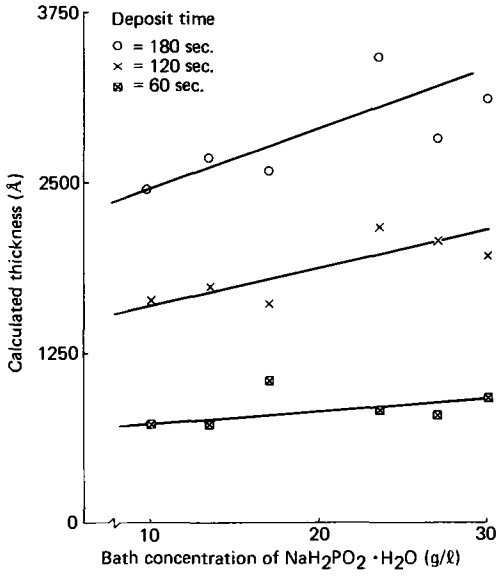

Fig. 3. Calculated thickness vs. reductant concentration in bath

deposits (see Fig. 4). Much of the phosphorus is co-deposited in the initial stages of the autocatalytic reaction. Some deposits in the lower thickness range achieved a phosphorus content of nearly 10%.

The effects of these varied amounts of phosphorus on the relative smoothness of the deposit are shown in Fig. 5. This figure shows the results obtained by examining various film samples with a scanning electron microscope. The film with 0.6% phosphorus appeared to have a crevice pattern; it also appeared less bright to the naked eye. The film with 6.5% phosphorus was cracked through to the substrate, probably because of the high stress associated with the high phosphorus content. Even though it contains twice as much phosphorus as the film with 3.1%, it looks only slightly smoother. All these effects have been observed by others (8, 9) except that no one has reported the cracking with high percentages of phosphorus, no doubt because only films containing up to 3% of phosphorus were studied.

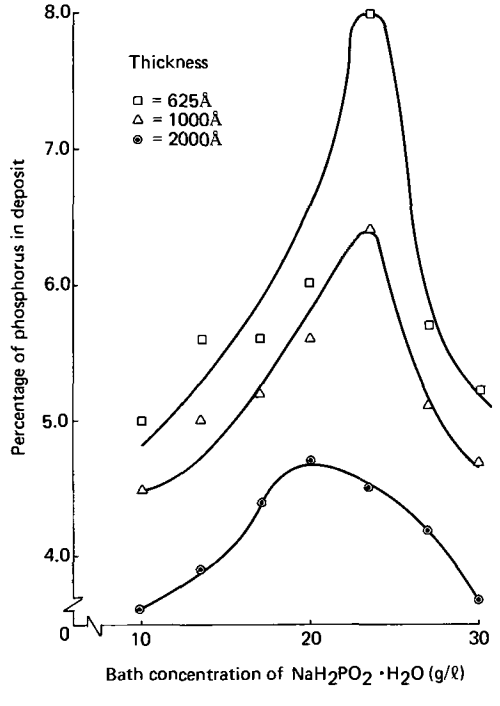

Fig. 4. Percentage of phosphorus vs. reductant concentration in bath.

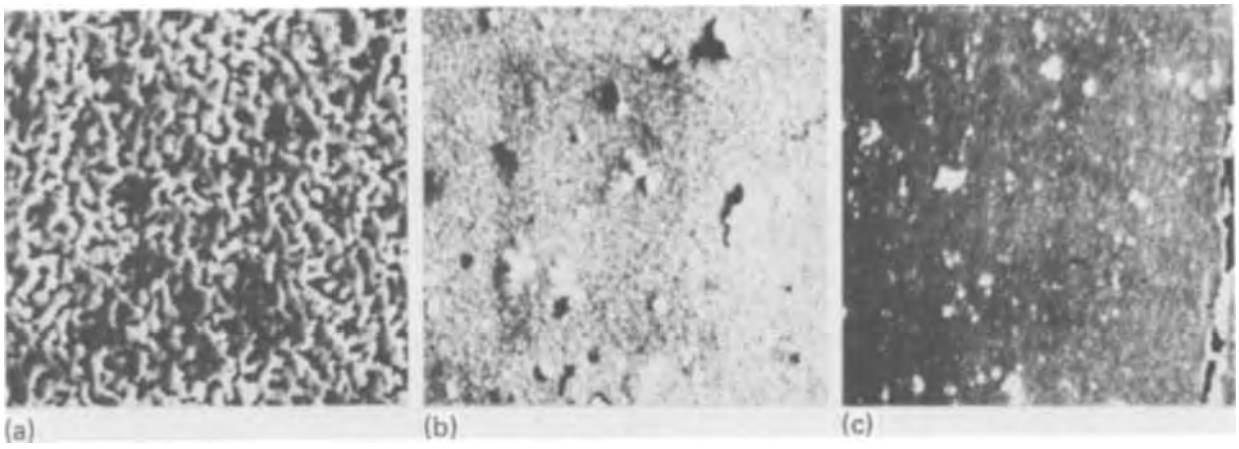

Fig. 5. Scanning electron micrographs of Co-P plated surfaces over a range of phosphorus content (4000×). (a) 0.6% phosphorus, (b) 3.1% phosphorus, (c) 6.5% phosphorus.

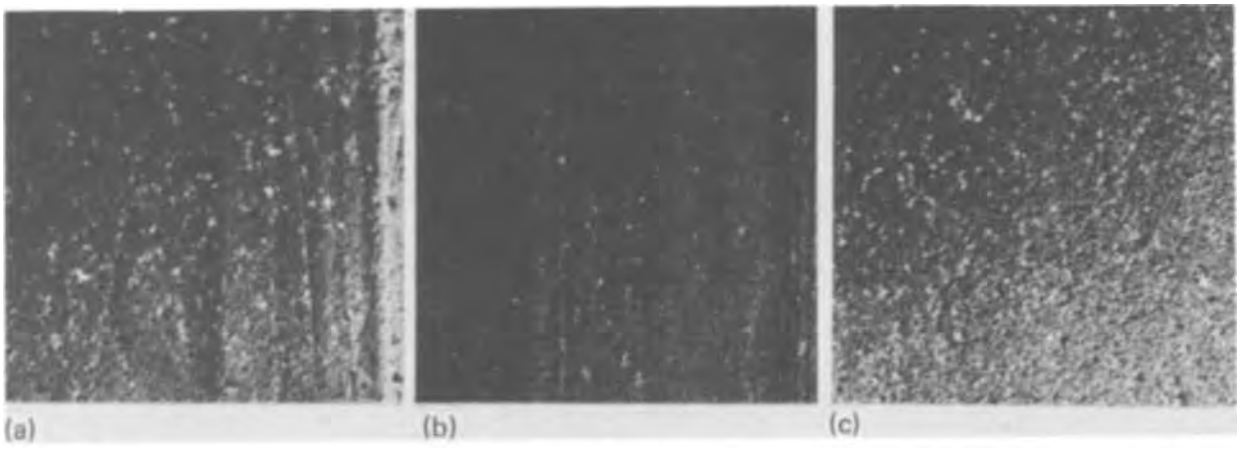

Fig. 6. Photomicrographs of Co-P plated surfaces at various hypophosphite concentrations (800×). (a) 10 g/liter, 3.6% phosphorus, (b) 17.0 g/liter, 4.8% phosphorus, (c) 30.0 g/liter, 4.0% phosphorus.

Figure 4 shows that the percentage of phosphorus in the deposit depends on the hypophosphite content of the bath. Note that the phosphorus content of the deposits reaches a peak and then decreases as the reductant content of the bath increases. Note also that there are large variations in the percentage of phosphorus in the thinner deposits, whereas linearity is approached in the thickest deposit. Films approximately equal in thickness and in phosphorus content were examined for relative surface roughness. As Fig. 6 shows, the films containing a bit more phosphorus than others were only slightly smoother. No deposits that contained medium amounts of phosphorus were cracked.

The saturation magnetic moments of the deposits were measured with a vibrating sample magnetometer, relative to a five-nines-purity nickel standard that was accurately weighed. The moments so obtained were dependent on deposit thickness but only slightly affected by hypophosphite concentration (Fig. 7). The saturation magnetic moment density (σ_s) of the films, calculated from the slope of the line, was 128 electromagnetic units/g. If we assume that the phosphorus exists as nonferromagnetic Co_2P, an average weight of 4.2% P would correspond to about 18% by volume of Co_2P. Therefore, a theoretical calculation of σ_s is about 132 electromagnetic units/g. Although phosphorus was quantitatively detected by x-ray fluorescence, its presence as Co_2P was never conclusively shown. At any rate, the nonmagnetic diluents in the deposits are assumed to be Co_2P and other phases of cobalt and phosphorus. These other phases may account for the discrepancy between the experimental and the theoretical values of σ_s.

For the two extreme reductant concentrations, the squareness of the deposits decreased with increasing thickness and tended to level off in thicker deposits, as is shown in Fig. 8. The median concentration of hypophosphite tended to give a linear relationship between squareness and thickness throughout the range covered.

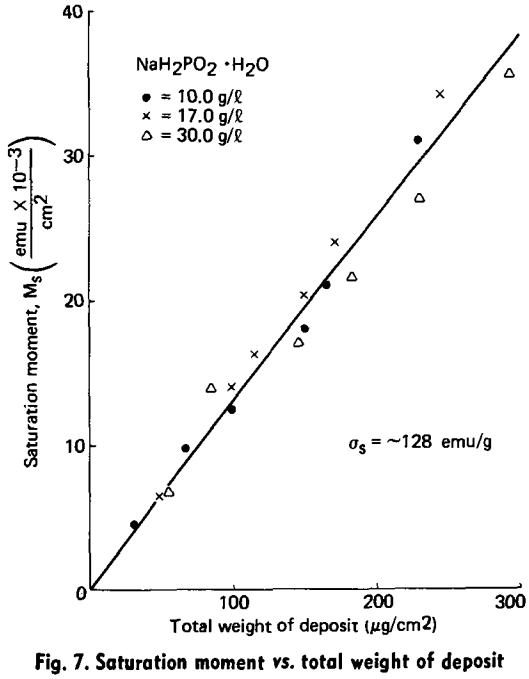

Fig. 7. Saturation moment vs. total weight of deposit

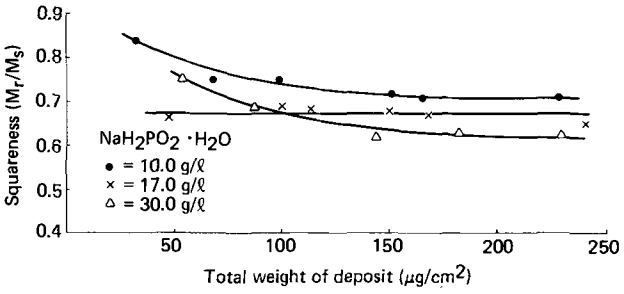

Fig. 8. Squareness vs. total weight of deposit

This finding is in direct conflict with earlier work (5, 10) in which a ratio of 0.3 cobalt to 1.0 citrate ion in the bath was used. The apparent discrepancy can be explained by observing the linear relationship that gives an average of 4.2% phosphorus, independent of thickness and hypophosphite concentration. The content of phosphorus, and therefore the occurrence of single-domain regions, are presumably constant throughout the deposits.

The structure-sensitive property of coercivity is a complicated function of many variables. One of these variables, thickness, is plotted against coercivity in Fig. 9. Here we see that thickness greatly influences the coercivity of the deposited film, particularly with lower concentrations of reductant, say 10.0 g/liter. This curve follows the usual relationship of monotonically decreasing coercivity with increasing thickness (7, 11, 12). However, the high concentration of reductant monotonically increases with thickness and tends to level off to 700 oe at 2300Å. This is about the same level of coercivity at which the 17.0 g/liter concentration of reductant levels off after decreasing from 1000 oe. The linearity of the coercivity at thicknesses greater than 2000Å is further substantiated by the results obtained with 23.5 g/liter of hypophosphite in the bath. At this concentration, coercivity is independent of thickness.

Attempts to induce anisotropy in the films were made in the early experiments by autocatalytically plating in a strong field. These attempts were unsuccessful as were those of previous investigators. All deposited films were isotropic in the film plane.

The influence of the sodium hypophosphite in the bath on the coercivity of the film is shown in Fig. 10. With short deposit times (and hence thin deposits), the coercivity decreased very rapidly with increasing hypophosphite. With longer deposit times, no sharp

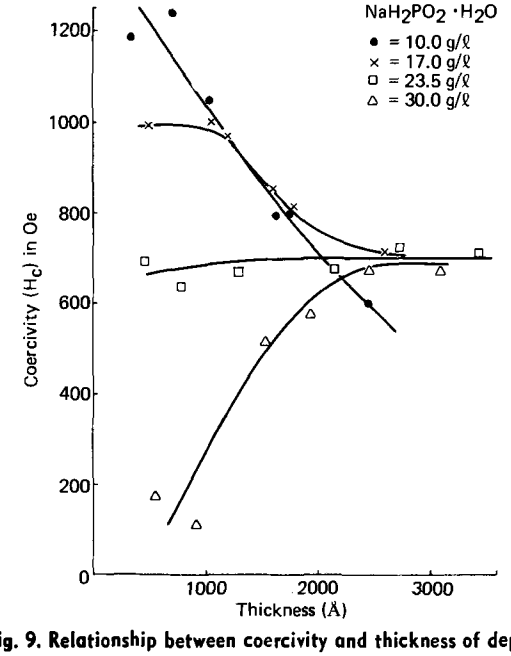

Fig. 9. Relationship between coercivity and thickness of deposit

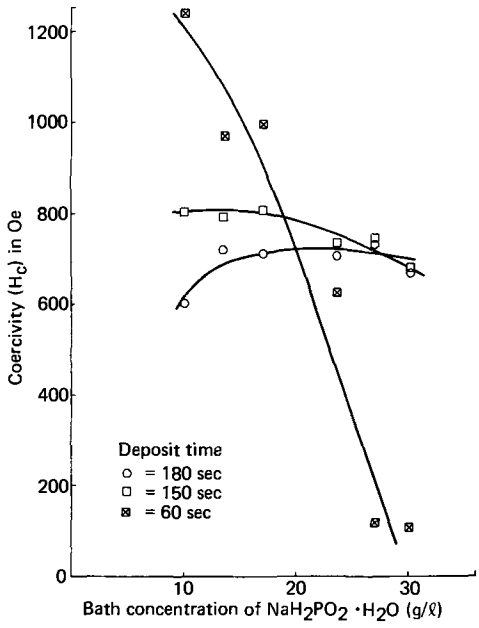

Fig. 10. Coercivity vs. hypophosphite in bath

changes in coercivity were observed. Linearity was approached at 700-800 oe. Figure 10 represents two different effects: film thickness and concentration of reductant. Therefore the changes in coercivity shown seem to be the results of increases in film thickness caused by the reductant concentration, as shown in Fig. 3. The similarity of Fig. 9 and 10 further substantiates the conclusion that the true influence of the reductant concentration on coercivity is masked by the thickness of the deposit. Figure 11 is included merely to show the effect of the reductant concentration in the bath on the coercivity of the deposit at two different ratios of cobalt ions to citrate ions in the solution. The reductant concentration has a larger effect on coercivity at the 1.0 ratio than at the 0.5 ratio, even though a linear relationship is evident in both cases. This relationship indicates that coercivity is more reproducible in the 0.5-ratio bath because the slope approaches zero.

X-ray diffraction revealed that all deposits were predominantly hexagonal-close-packed (hcp) cobalt.

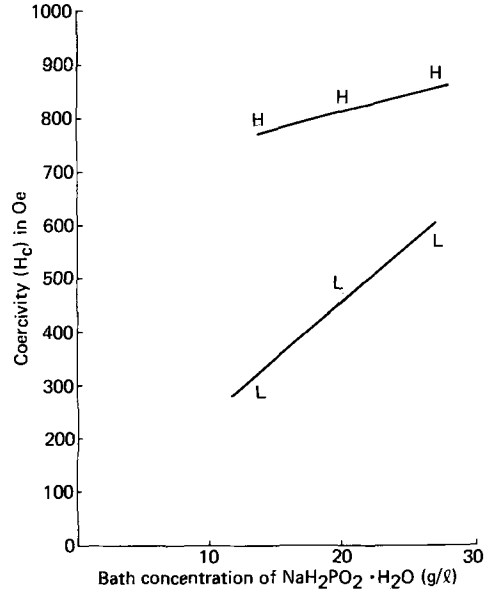

Fig. 11. Coercivity vs. hypophosphite at different concentration ratios. *H* = 0.5 ratio, (high citrate) at 2100Å; *L* = 1.0 ratio, (low citrate) at 2500Å.

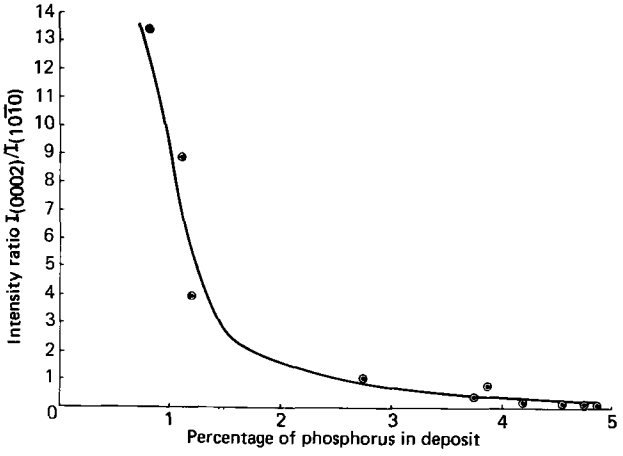

Fig. 12. Intensity ratio vs. percentage of phosphorus in deposit

X-ray line broadening was used to estimate the crystallite sizes in the deposits. Most estimates were from 200-400Å. A few films appeared to have either very small crystallites (20-60Å) or an amorphous structure. However, these estimates of crystallite size are actually the lower limit, since the stresses and faults in the deposit also contribute to the line broadening. In most cases, the estimates of crystallite sizes showed no correlation with thickness, phosphorus content, or magnetic properties. Figure 5 shows an example of a change in crystallite size with a change in phosphorus concentration; (b) and (c) are 300Å, whereas (a) is only about 50Å. Figure 6, on the other hand, maintains the same crystallite size in the range of 3.6-4.8% of phosphorus. Films with coercivities of 200-800 oe had the same relative crystallite size, whereas the samples with coercivities greater than 800 oe tended to have smaller crystallites. It appears that since most of the crystallite sizes were in the 200-400Å range, the magnetic properties of the experimental thin films were a result of single-domain behavior.

Diffracted x-ray intensities of the (0002) and the $(10\bar{1}0)$ planes of the deposits were measured. Calculating the normalized value of these ratios

$$\frac{I_{(0002)}}{I_{(10\bar{1}0)}}$$

enables us to predict the c-axis orientation in the films. If the intensity ratios are plotted against the percentage of phosphorus in the films, as in Fig. 12, a clear relationship can be shown between crystal orientation and phosphorus content. The plot nearly duplicates that of Amendola *et al.* (8), except that it shows the percentage of phosphorus from less than 1.0 to more than 5.0. Since the films under study here contain an average of 4.2% phosphorus, it is apparent that these deposits exhibited a preferred orientation of the c-axis in the plane of the substrate. The raw data imply no relationship between coercivity and intensity ratios.

Summary and Conclusion

Preliminary experiments were made on two kinds of nonconductive substrates. The magnetic and physical properties of the deposits were examined in order to formulate an autocatalytic solution to improve these properties. Kapton, the most promising substrate on the basis of adhesion and appearance, was chosen for further study. The independent variables of time and reductant concentration were examined, and the resulting physical and magnetic properties of the deposits were evaluated. The average plating rate was linear, increasing with increasing reductant concentration. The average amount of phosphorus in the deposits remained constant over the range of reductant concentrations, and had little effect on the roughness or the coercivity of the deposit. The saturation magnetic moment density for the deposits agreed closely with the theoretical value. This led to the conclusion that the nonmagnetic diluent was chiefly Co_2P. The squareness was high and linear throughout the range; the coercivity depended greatly on thickness and hypophosphite concentration. Crystallite sizes of 200-400Å were found in most of the films, independent of phosphorus content, with smaller crystallites appearing in the films with coercivities above 800 oe. Intensity-ratio calculations showed that most of the films had their c-axes oriented in the plane of the substrate.

Others have shown that in the autocatalytic deposition of a magnetic film, the thickness and the hysteresis of the film can be controlled by varying the deposition time, the *p*H of the bath, the temperature, and the reductant concentration. Proper combination of these variables will produce a coating that has excellent properties for recording. One such combination has been given in this paper. It is a bath with a 0.50 ratio of cobalt ion to citrate ion (with other conditions as previously given), and a reductant concentration of about 23 g/liter of sodium hypophosphite. Metal deposition is carried out on a specially prepared Kapton substrate for approximately 2.5 min. The resulting deposit is an excellent reproducible medium for high-density digital magnetic recording.

Acknowledgments

The author expresses his appreciation to the International Business Machines Corporation for its financial support of this program, to Mr. Harry D. McCabe for his assistance in determining the physical properties of the deposits, and to Mr. Pete Larson for editing this paper. Special thanks to Dr. Malcolm Hepworth for the many helpful discussions of the program.

Manuscript submitted May 8, 1972; revised manuscript received April 2, 1973. This was Paper 221 presented at the Miami Beach, Florida, Meeting of the Society, Oct. 8-13, 1972.

Any discussion of this paper will appear in a Discussion Section to be published in the June 1974 JOURNAL.

REFERENCES

1. H. Narcus, "Metallizing of Plastics," Reinhold Publishing Co., New York (1960).
2. H. Koretsky, U. S. Pat. 3,142,582, 1964.
3. G. Bate, *J. Appl. Phys.*, **37**, 1164 (1966).
4. J. S. Judge, J. R. Morrison, D. E. Speliotis, and G. Bate, *This Journal*, **112**, 681 (1965).
5. B. D. Cullity, "Elements of X-ray Diffraction," p. 276, Addison-Wesley, Reading, Mass. (1959).
6. R. H. Wright, *IBM Tech. Disclosure Bull.*, **8**, 1175 (February 1966).
7. J. S. Judge, J. R. Morrison, and D. E. Speliotis, *This Journal*, **113**, 547 (1966).
8. A. Amendola, G. W. Brock, and R. Travieso, *J. Am. Soc. Lub. Eng.*, **26**, 22 (January 1970).
9. M. G. Miksic, R. Travieso, A. Arcus, and R. H. Wright, *This Journal*, **113**, 360 (1966).
10. J. S. Judge, J. R. Morrison, D. E. Speliotis, and J. R. DePew, *Plating*, **54**, 533 (1967).
11. M. A. Foley, U. S. Pat. 3,138,479, 1964.
12. J. R. DePew and D. E. Speliotis, *Plating*, **54**, 705 (1967).

Electrochemical Studies of Titanium in Molten Fluorides

F. R. Clayton and G. Mamantov*

Department of Chemistry, University of Tennessee, Knoxville, Tennessee 37916

and D. L. Manning

Analytical Chemistry Division, Oak Ridge National Laboratory, Oak Ridge, Tennessee 37830

ABSTRACT

The electrochemical reduction of Ti(IV) in molten LiF-NaF-KF [46.5-11.5-42.0 mole per cent (m/o)] at 500°C was studied by means of linear sweep voltammetry, chronopotentiometry, and chronoamperometry. The reduction of Ti(IV) to Ti(III) was found to proceed reversibly at both platinum and pyrolytic graphite electrodes; further reduction of Ti(III) to the metal was shown to be a reversible process involving alloy formation with the platinum electrode. Standard electrode potentials for the processes, Ti(IV) + e = Ti(III) and Ti(III) + $3e$ = Ti, are −0.058 and −1.798V, respectively (both *vs.* a unit mole fraction Ni(II)/Ni electrode).

The electrochemical oxidation of Ti(III) at unsheathed platinum and sheathed glassy carbon electrodes was studied in molten LiF-BeF_2-ZrF_4 (65.6-29.4-5.0 m/o) at 500°C. Evidence for a reversible electrode reaction was obtained from voltammetric and chronopotentiometric studies. A standard potential of +0.197V (*vs.* a unit mole fraction Ni(II)/Ni electrode) was determined for the process Ti(III) = Ti(IV) + e.

The more anodic value of the standard potential of the Ti(IV)/Ti(III) couple in LiF-BeF_2-ZrF_4 in comparison to LiF-NaF-KF reflects the higher acidity (Lewis concept) of the LiF-BeF_2-ZrF_4 melt.

In this paper we describe electrochemical studies of titanium solute species in molten LiF-NaF-KF [46.5-11.5-42.0 mole per cent (m/o)] and LiF-BeF_2-ZrF_4 (65.6-29.4-5.0 m/o). Interest in molten fluorides stems from their importance in nuclear reactor technology and use in production of aluminum and fluorine, electrodeposition of refractory metals, formation of corrosion-resistant diffusion coatings, and preparative electrochemical fluorination.

Most of the studies of electrode reactions in molten fluorides have been rather recent. The status of this subject through 1968 has been summarized by Mamantov (1). Recent reviews of molten salt electrochemistry (2-4) contain much more information pertaining to molten fluorides than did earlier reviews on the same topic (5-8).

The electrochemistry of titanium has been studied to a much greater extent in molten chlorides than in any other molten halide system. The usual solvent is LiCl-KCl eutectic. The results of voltammetric studies in this solvent have been summarized in two reviews (6, 7). In polarographic studies of the reduction of Ti(III) in molten LiCl-KCl eutectic at 400°-550°C, two reduction steps, Ti(III) to Ti(II) and Ti(II) to Ti, were observed.

Baboian, Hill, and Bailey (9) have reported $E°$ values for the reversible couples, Ti(III)/Ti(II) and Ti(II)/Ti, *vs.* the Pt(II)/Pt reference electrode in the LiCl-KCl eutectic at 450° and 550°C. Flengas (10) was able to measure the standard potential of the Ti(IV)/Ti(III) couple in addition to the above two couples in NaCl-KCl at 700°C.

Senderoff (11) has reviewed the methods of obtaining titanium metal by electrolysis of molten halide solutions. Barksdale (12) has discussed the commercial production of titanium including the electrolytic methods in fused salt baths. However, little information exists regarding the nature of the electrode reactions involved in these electrolytic processes. Nevertheless, the two reviews (11, 12) serve to point out the importance of lower-valent species to the over-all current efficiency, the nature of deposits obtained, and the cell design considerations. Most of the electrolytic methods employ a fluoride-chloride process with tetravalent titanium as solute (K_2TiF_6 in LiCl-KCl, NaCl-KCl, or NaCl) or an all-chloride process with reduced titanium ($TiCl_3$ or $TiCl_2$) as solute (12). One all-fluoride process was described by Stetson (13) in which coherent titanium deposits were obtained at 850°C on selected substrates from a fluoride bath (NaF-KF) containing K_2TiF_6. It was noted that a layer of insoluble lower-valent titanium salts remained in contact with the cathode during the entire operation. This coating proved to be advantageous in preventing attack of the deposited titanium by the Ti(IV) solution and by the anode gases. The lower-valent salts so described were likely composed of Ti(III) since, according to Wurm, Gravel, and Potvin (14), the formation of insoluble Ti(III) double fluorides of sodium and potassium always precedes the production of metallic titanium during electrolysis of molten NaCl-KCl mixtures containing K_2TiF_6 or Na_2TiF_6. These double fluorides of Ti(III) were identified as K_2NaTiF_6, K_3TiF_6, and Na_3TiF_6 by Bright and Wurm (15). Furthermore, no divalent titanium compounds were detected by chemical analysis in the chloride melts where fluoro complexes of titanium were present (14).

Thus, previous work indicates that there are differences in behavior between the two solvent systems, chlorides and fluorides, notably the nonexistence of an intermediate reduction step involving Ti(II) in fluoride or chloride-fluoride melts.

Experimental Section

Materials

Two fluoride salt mixtures were used as solvents in this investigation. Their compositions and melting points are as follows: (*i*) LiF-NaF-KF (46.5-11.5-42.0 m/o, eutectic temperature 454°C) (16); and (*ii*) LiF-BeF_2-ZrF_4 (65.6-29.4-5.0 m/o, liquidus temperature 434°C) (17). The LiF-NaF-KF and LiF-BeF_2-ZrF_4 solvents and anhydrous nickel(II) fluoride were obtained from the Reactor Chemistry Division of the Oak Ridge National Laboratory (18).

High-purity K_2TiF_6 was prepared by D. E. LaValle of the Oak Ridge National Laboratory. TiF_3 was used as received from Research Inorganic Chemicals. The single crystals of LaF_3 used to fabricate reference elec-

* Electrochemical Society Active Member.

Key words: titanium, molten fluorides, voltammetry, chronopotentiometry, melts.

trode compartments (19, 20) were obtained from Optovac, Incorporated. ATJ graphite was used for container fabrication.

All salts and active metals were stored in an inert-atmosphere dry box prior to their use.

Apparatus and Procedure

Electrolytic cell assembly.—The experimental setup employed for these studies is similar to that described earlier (21). The melts were contained in a graphite or platinum cell approximately 2 in. diam and 4½ in. long. To maintain a vacuum or controlled atmosphere, the cell was enclosed in a Pyrex outer jacket approximately 2½ in. diam and 10 in. long. The top of the Pyrex jacket was sealed to a removable Pyrex cap by means of a 102/75 O-ring joint. The joint was secured with an adjustable clamp; Viton or Teflon O-rings were employed. On the cap were located six ¼-in. Cajon Ultra-Torr fittings which provided access to the melt for the various electrodes, thermocouples, and helium bubbling line. Vacuum and inert atmosphere connections were through a three-way vacuum stopcock located on the side of the cap. The lower part of the cell assembly was heated in a 3-in. ID resistance furnace (725W Hoskins Model). The temperature of the furnace was controlled to about ±2°C by means of a Wheelco Model 407 temperature controller. The actual temperature of the melt was monitored with a shielded Chromel-Alumel type thermocouple inside a platinum sheath.

The metal wire electrodes (platinum and nickel) consisted of 2-in. long wires (1 mm diam or less) which were arc-welded to the end of ⅛ × 12 in. nickel rods. The tops of the nickel rods were fitted with ¼-in. Teflon sleeves (about 3 in. long) to provide a leak-tight connection when the electrodes were inserted through the adjustable Cajon fittings. The platinum indicator electrodes (0.5 and 0.8 mm diam) were immersed to depths of 6-8 mm (typical electrode area 0.08-0.12 cm^2). Platinum quasi-reference electrodes (22, 23) (1.0 mm diam) were adjusted to depths of 1-2 in. as were larger diameter (⅛ in.) platinum or graphite counterelectrodes.

The pyrolytic graphite indicator electrode (1 mm diam) consisted of an unsheathed pyrolytic graphite rod (prepared by the Metals and Ceramics Division of the Oak Ridge National Laboratory) which was attached to the ⅛-in. nickel rod by means of a threaded connection. Details of the construction of this type of electrode have been given previously (24). The glassy carbon indicator electrode was sheathed in boron nitride. A description of the fabrication of a similar type of sheathed planar electrode is available (25). Since the entire surface of the glassy carbon is immersed below the melt, a more accurate determination of the electrode area is possible. The area of the glassy carbon electrode used was 0.08 cm^2.

The reference electrode used in the three-electrode measuring system consisted of a $NiF_{2(sat.)}$/Ni couple contained in a single-crystal lanthanum fluoride compartment for isolation from the bulk melt. The utility of the Ni(II)/Ni couple as a reference electrode in molten fluorides was demonstrated earlier (26, 27). A reference electrode for molten fluorides employing a single-crystal LaF_3 membrane for separation has been described recently (19, 20).

Instrumentation.—The controlled potential-controlled current cyclic voltammeter used in this study has been described in detail (28). With this instrument, scan rates from 0.01 to 500 V/sec are available and cell currents up to 100 mA can be measured. In the controlled current mode, currents from a few microamperes to 500 mA can be passed through the electrolytic cell. The built-in time base allows the measurement of transition times from 400 sec to 4 msec.

Cyclic voltammograms and chronopotentiograms were recorded either on a Moseley Autograph X-Y recorder (Model 2D-2A) or on a Tektronix Type 549 storage oscilloscope equipped with a Tektronix Type C-12 camera attachment. Photographs were made using Type 42 Polaroid film (ASA 200 speed).

The details of the experimental procedure are described elsewhere (20).

Results and Discussion

Electrochemical Studies of Titanium(IV) in Molten LiF-NaF-KF

Voltammetric studies.—Initial voltammetric studies of the reduction of titanium(IV) in molten LiF-NaF-KF (46.5-11.5-42.0 m/o) at 500°C were carried out in a graphite beaker using platinum and pyrolytic graphite (PG) working electrodes, a large Pt wire counterelectrode, and a platinum wire quasi-reference electrode (QRE). However, it became apparent that Ti(IV) could not be kept in solution for more than one to two days in the graphite beaker and all subsequent experiments on titanium were done in a platinum crucible. In the platinum container, Ti(IV) solutions were found to be stable; no appreciable change in concentration was observed voltammetrically during a three-week period. Ti(IV) was added to the melt as K_2TiF_6 in all cases. Potentials were measured with respect to a Ni(II) (saturated)/Ni reference electrode (LaF_3 membrane type) unless otherwise stated. Concentrations are expressed in terms of molarity. Conversion to mole fraction, X, can be made by use of the following equations (27): in LiF-NaF-KF (46.5-11.5-42.0 m/o) at 500°C, M(molarity) = $52.6X$; in LiF-BeF_2-ZrF_4 (65.6-29.4-5.0 m/o) at 500°C, M = $62.2X$.

Linear sweep voltammograms (scan rate = 0.1 V/sec) obtained at a Pt electrode prior to the addition of K_2TiF_6 are shown in Fig. 1. Two small reduction waves occur at −0.55 and −0.85V [*vs.* Ni(II) (saturated)/Ni reference electrode]. Similar reduction waves were also obtained at the PG electrode. These waves are probably due to residual amount of iron and chromium impurities, respectively, which are commonly found in the LiF-NaF-KF eutectic (21). A larger wave was observed at the Pt electrode at −1.70V, which was very broad and irreversible in nature. Although this wave was not identified, it is probably caused by the predeposition of alkali metal as a result of alloy formation with the platinum electrode (6). The cathodic limit at about −2.0V corresponds to the reduction of alkali metal cations (probably potassium ions); the anodic limit at ~+1.5V is due to oxidation of platinum (21).

Additions of K_2TiF_6 resulted in a well-defined, peak-shaped reduction wave [$E_p \approx +0.01$V *vs.* Ni(II) (saturated)/Ni reference electrode] at both Pt and PG electrodes. A typical linear sweep voltammogram for Ti(IV) reduction at a Pt electrode is shown in Fig. 2. A similar voltammogram was obtained at the PG electrode. At the Pt electrode a second reduction wave, larger and steeper than the first one, was observed with

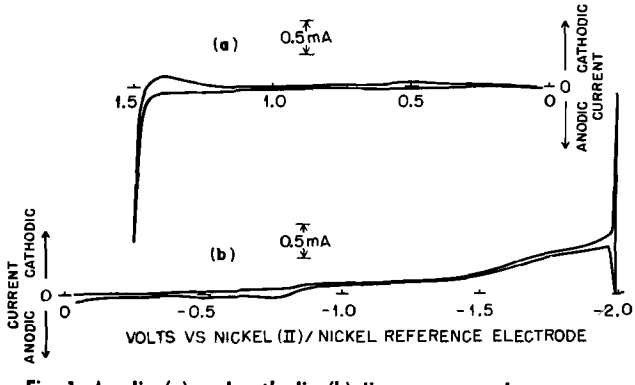

Fig. 1. Anodic (a) and cathodic (b) linear sweep voltammograms of the LiF-NaF-KF melt at 500°C. Platinum electrode area: 0.10 cm^2; scan rate: 0.1 V/sec; Ni(II)(saturated)/Ni reference electrode (LaF_3 membrane type).

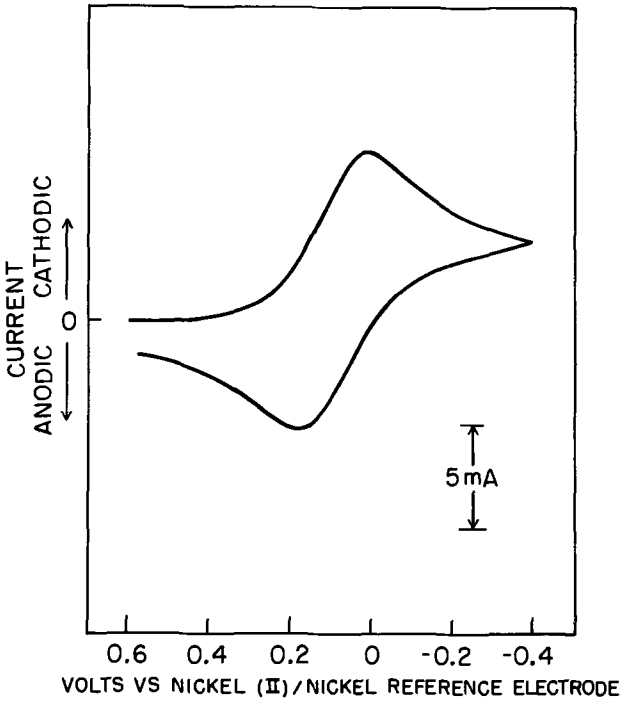

Fig. 2. Linear sweep voltammogram at platinum electrode for the reduction of Ti(IV) to Ti(III) in molten LiF-NaF-KF at 500°C. Scan rate: 1.0 V/sec; electrode area: 0.10 cm².

a well-defined peak located at about −1.69V. On the reverse cycle an anodic stripping peak clearly associated with this second wave was observed at −1.18V. A linear sweep voltammogram for the second reduction step at Pt electrode is shown in Fig. 3. The voltage span extended from +0.6 to −2.0V *vs.* the Ni(II) (saturated)/Ni reference electrode; however, only the potential region of interest is shown since no other reduction waves [other than Ti(IV) to Ti(III) wave] were observed. The second wave could not be studied at a PG electrode because with this electrode a large reduction peak at about −1.2V *vs.* the Ni(II) (saturated)/Ni reference electrode is observed in LiF-NaF-KF (1); this peak is probably caused by the predeposition of potassium and the formation of a graphite-potassium intercalation compound (29).

The voltammograms for the two-step charge transfer process observed in the reduction of Ti(IV) can be treated as independent waves since the separation between the half-wave potentials is greater than the minimum value required, $(T/298)(118/n)$ mV (true for reversible waves) (30). The data for half-wave potentials, anodic to cathodic peak potential separation ($\Delta E_p = E_{ap} - E_{cp}$), and half-peak to peak potential separation ($\Delta E = E_{p/2} - E_p$) are given in Table I. The $E_{1/2}$ values were measured at potentials corresponding to 0.85 i_p (31). The expected values for peak potential separation and half-peak to peak potential separation are 2.22 $RT/n\mathbf{F}$ and 2.20 $RT/n\mathbf{F}$, respectively, (31) for the first wave. Half-peak to peak potential

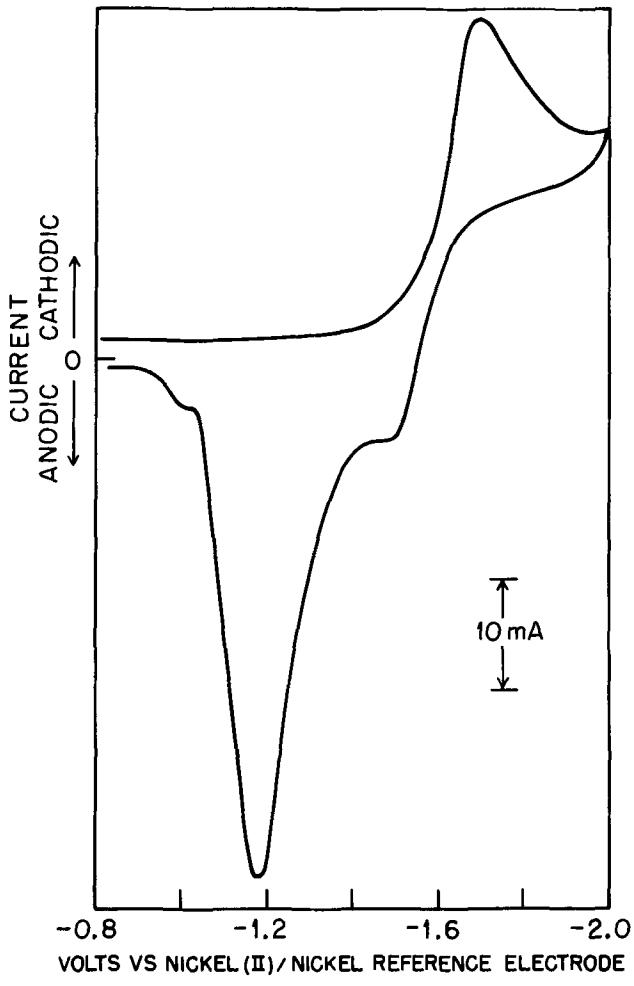

Fig. 3. Linear sweep voltammogram at platinum electrode for the reduction of Ti(III) to Ti in molten LiF-NaF-KF at 500°C. Scan rate: 0.5 V/sec; electrode area: 0.10 cm².

separation ΔE for the second wave should be 2.2 $RT/n\mathbf{F}$ (31), if the product of the reversible electrode reaction (presumably titanium metal) is soluble in the electrode, and 0.77 $RT/n\mathbf{F}$ (32), if reversible deposition of an insoluble product occurs. The experimental ΔE obtained (Table I) clearly favors formation of a soluble product (assuming that the electrode reaction is reversible).

The ratio of anodic to cathodic peak current (i_{ap}/i_{cp}) calculated using Nicholson's semiempirical formula (33) is 0.95 for the first wave. A ratio of one is expected for simple reversible electron transfer (31). A plot of log $(i_p - i)/i$ *vs.* potential for the first reduction wave was linear in the approximate range 0.35-0.70 i_p. The expected (32) slope of the line for a reversible charge transfer where both reactants and products are soluble is 0.58 $n\mathbf{F}/RT$. An n value of one was calculated from the slope. A plot of log $(i_p - i)/i$ *vs.* potential for the second wave resulted in a slope corre-

Table I. Half-wave potentials, anodic to cathodic peak potential separation, and half-peak to peak potential separation (theoretical values in parentheses) for the processes Ti(IV) + e = Ti(III) (process I) and Ti(III) + 3e = Ti(process II) at platinum electrode at 500°C.

Process	Melt	Concentration (M)	$E_{1/2}$ (V)[a]	$\Delta E_p = E_{ap} - E_{cp}$ (mV)	$\Delta E = E_{p/2} - E_p$ (mV)
I	LiF-NaF-KF	0.339	+0.080 ± 0.005	150 ± 5 (148)	143 ± 5 (147)
I	LiF-BeF_2-ZrF_4	0.510	+0.380 ± 0.010	160 ± 10 (148))	150 ± 10 (147)
			E_p (V)[a]		
II	LiF-NaF-KF	0.339	−1.685 ± 0.005		60 ± 5 (49[b], 17[c])

[a] Versus Ni(II) (saturated)/Ni reference electrode (LaF_3 membrane type).
[b] For reversible reduction yielding a soluble product.
[c] For reversible deposition of an insoluble product.

sponding to $n = 3$. The solubility of titanium metal in the Pt electrode is probably responsible for the agreement of this type of plot with that expected for a three-electron reversible reaction involving soluble reactants and products.

The peak current i_p for the first wave was found to be directly proportional to concentration of Ti(IV) in the range 8.97×10^{-3} to 3.39×10^{-1} M and to the square root of the scan rate v (up to ~2.0 V/sec) at the Pt electrode. The variation of i_p with $v^{1/2}$ at a Pt electrode for a given concentration of Ti(IV) is shown in Fig. 4. According to Nicholson and Shain (31) the parameter $i_p/v^{1/2}$ is independent of the scan rate for a simple reversible charge transfer reaction. The nonlinear increase of i_p with $v^{1/2}$ in Fig. 4 starting at ~5 V/sec indicates weak adsorption of the reactant (24, 30).

A scan rate study of the second reduction wave which is believed to be due to Ti(III) reduction to the metal, resulted in a linear plot of i_p *vs.* $v^{1/2}$. The results indicate that, at the scan rates studied, diffusion is the predominant mass transfer process since the Randles-Sevcik equation (34) is obeyed. The Randles-Sevcik equation at 500°C becomes

$$i_p = 1.67 \times 10^5 n^{3/2} A D^{1/2} v^{1/2} C \qquad [1]$$

The diffusion coefficient of Ti(IV) in molten LiF-NaF-KF at 500°C was calculated from Eq. [1] using the slope of the linear portion of the i_p *vs.* $v^{1/2}$ plot (Fig. 4). Because of the uncertainty in the area of the unsheathed platinum wire electrode employed, the value of D, is reported as approximately $2.6 \pm 0.5 \times 10^{-6}$ cm²/sec.

These voltammetric results indicate that the two reduction waves at platinum for Ti(IV) in LiF-NaF-KF correspond to one-electron and three-electron reversible charge transfer processes involving the reduction of Ti(IV) to Ti(III) and Ti(III) to the metal, respectively. Similar voltammetric behavior at pyrolytic graphite was observed for the reduction of Ti(IV) to Ti(III) in LiF-NaF-KF at 500°C; however, no reduction of Ti(III) could be observed at pyrolytic graphite in this melt.

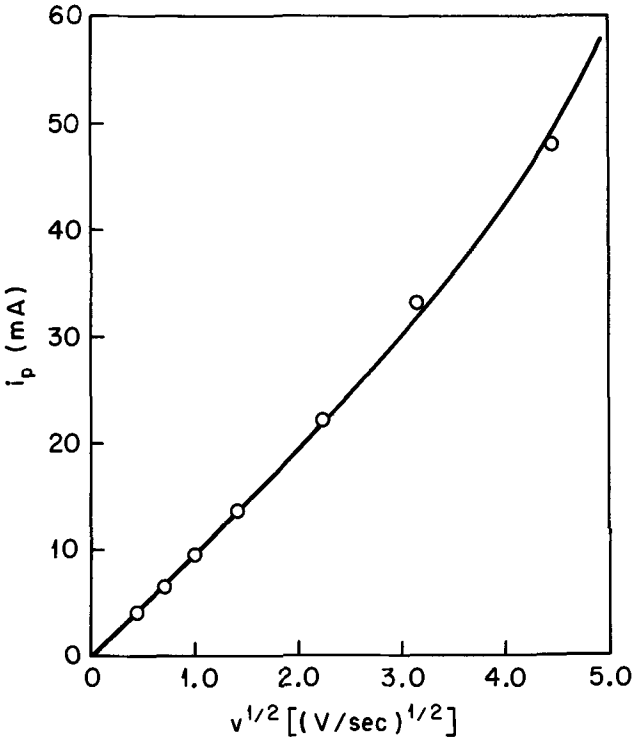

Fig. 4. Plot of i_p *vs.* $v^{1/2}$ for the first wave, Ti(IV)→ Ti(III), in molten LiF-NaF-KF at 500°C. Ti(IV) concentration: 0.339M; Pt electrode area: 0.10 cm².

Polarographic analysis using current-time curves.—The polarogram constructed from current-time curves for the reduction of Ti(IV) in molten LiF-NaF-KF at a Pt electrode is shown in Fig. 5. This polarogram has been corrected for the residual currents measured from current-time curves obtained prior to addition of K_2TiF_6 at the same electrode. Two cathodic waves with a limiting current ratio of 2.9 were obtained. The corresponding log $(i_d - i)/i$ *vs.* potential plots (35) were straight lines with the theoretical slopes, 2.3 $RT/n\mathbf{F}$ (35), for a one-electron and three-electron reversible process, respectively.

Thus, the polarographic results support voltammetric evidence that the reduction of Ti(IV) at platinum in LiF-NaF-KF proceeds reversibly to Ti(III) which in turn is reduced to the metal alloying with the platinum electrode.

Chronopotentiometric studies.—Chronopotentiograms were obtained for the reduction of Ti(IV) in LiF-NaF-KF at 500°C at both Pt and PG electrodes using a platinum quasi-reference electrode. The definition of the potential-time curves was reasonably good for the first step; however, the poor definition and reproducibility of the second step (seen only at platinum) prevented any meaningful analysis of this subsequent reduction reaction. The variation of $i\tau^{1/2}$ with current for chronopotentiograms at platinum is shown in Fig. 6. The observed increase of the product $i\tau^{1/2}$ with increasing current is generally indicative of adsorption (24, 36, 37), in agreement with the voltammetric i_p *vs.* $v^{1/2}$ plot (Fig. 4) at higher scan rates. No attempt was made to arrive at a theoretical model for adsorption since the limited utility of chronopotentiometry for the study of adsorption has been pointed out (38).

The diffusion coefficient for Ti(IV) in LiF-NaF-KF at 500°C calculated using the Sand equation (34) is $1.9 \pm 0.4 \times 10^{-6}$ cm²/sec, in fair agreement with the value obtained from voltammetry. The value of $i\tau^{1/2}$

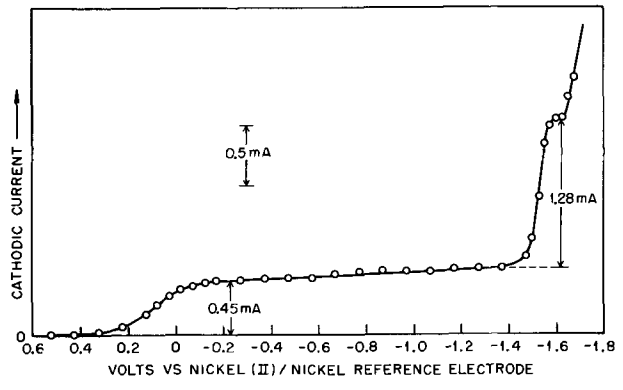

Fig. 5. Polarogram constructed from current-time curves for the reduction of Ti(IV) at platinum electrode in molten LiF-NaF-KF at 500°C. Ti(IV) concentration: 7.62×10^{-2}M; electrode area: 0.12 cm²; time at which current was measured: 5 sec.

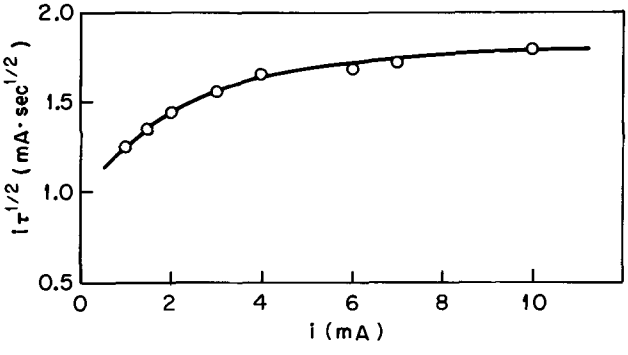

Fig. 6. Plot of $i\tau^{1/2}$ *vs.* current for the chronopotentiometric reduction of Ti(IV) in LiF-NaF-KF at 500°C. Ti(IV) concentration: 7.62×10^{-2}M; platinum electrode area: 0.12 cm².

used in the calculation was obtained from the intercept of a plot of $i\tau^{1/2}$ *vs.* $1/\tau^{1/2}$ using the data shown in Fig. 6. Such a plot has been proposed (39) as a semiempirical correction for the effects of charging of the double layer, oxidation or reduction of the electrode, and adsorption of the electroactive species on the electrode. Transition times were in the range 0.03-1.5 sec.

Excellent verification of $n = 1$ for the first Ti(IV) reduction step in LiF-NaF-KF was achieved from the ratio of voltammetric $i_p/v^{1/2}$ to chronopotentiometric $i\tau^{1/2}$. For this determination of n, concentration, diffusion coefficient, and electrode area do not need to be known. The ratio is obtained by dividing Eq. [1] by the Sand equation (34) and is given by the following expression

$$\frac{i_p/v^{1/2}}{i\tau^{1/2}} = 1.96\, n^{1/2} \qquad [2]$$

Using values for $i_p/v^{1/2}$ and $i\tau^{1/2}$ determined under identical experimental conditions, n is calculated to be 1.01.

Standard electrode potentials of the titanium(IV)/titanium(III) and titanium(III)/titanium couples.—The half-wave potential $E_{1/2}$ for a reversible process $O + e \rightleftarrows R$ may be taken as the voltammetric equivalent of the standard electrode potential $E°$, assuming that diffusion coefficients and activity coefficients for O and R are equal (31). $E_{1/2}$ for the reversible process Ti(IV) + $e \rightarrow$ Ti(III) was found to be +0.080V with respect to a Ni(II) (saturated)/Ni reference electrode (Table I). By extrapolating the Nernstian plot for the Ni(II)/Ni couple in LiF-NaF-KF (20) to unit mole fraction of nickel(II), $E°$ for the Ti(IV)/Ti(III) couple is estimated to be −0.058V.

A similar estimate of the standard electrode potential for the Ti(III)/Ti couple in LiF-NaF-KF can be made assuming that Ti is soluble in the platinum electrode. Experimental evidence for titanium solubility in platinum is obtained from the fact that the peak potential for the Ti(III) reduction wave is independent of concentration as predicted for a reversible electrode reaction yielding a soluble product (31). In the case of reversible deposition of insoluble (unit activity) titanium metal, ΔE should decrease by about 0.05V for a ten-fold change in concentration (34).

Other experimental evidence in favor of titanium solubility in the platinum electrode is (*i*) the observed adherence of the polarographic wave [Ti(III) + $3e \rightleftarrows$ Ti] to the Heyrovsky-Ilkovic equation (40), (*ii*) the half-peak to peak potential separation for the Ti(III) voltammetric reduction wave (Table I), and (*iii*) the unusually large separation between the anodic and cathodic peak potentials for the Ti(III) + $3e \rightleftarrows$ Ti process (Fig. 3). It is also of interest to note that titanium is known to form several alloys with platinum, such as $TiPt_3$, TiPt, and Ti_3Pt (41). Thus, on the basis of titanium metal solubility in platinum, an $E_{1/2}$ for the Ti(III) + $3e \rightleftarrows$ Ti process can be calculated from the following expression (31)

$$E_p = E_{1/2} - 1.11\, RT/nF \qquad [3]$$

using the experimental E_p given in Table I. An $E_{1/2}$ of −1.660V [*vs.* Ni(II)(saturated)/Ni reference electrode] is obtained which corresponds to an $E°$ of −1.798V [*vs.* a unit mole fraction Ni(II)/Ni electrode] for the Ti(III)/Ti couple in molten LiF-NaF-KF at 500°C.

Electrochemical Studies of Titanium(III) in Molten LiF-BeF_2-ZrF_4

Voltammetric studies.—Initial voltammetric studies of titanium in molten LiF-BeF_2-ZrF_4 (65.4-29.6-5.0 m/o) at 500°C were undertaken using K_2TiF_6 as the solute. However, these studies of titanium(IV) reduction were greatly complicated by the observed instability of Ti(IV) in the melt. White deposits were found to collect in the cooler part of the electrolytic cell after K_2TiF_6 was added to the melt. The volatilization of titanium tetrafluoride from the melt was confirmed in a separate experiment in a closed stainless steel vessel provided with a cold trap; the volatile product collected was identified as TiF_4 by x-ray diffraction. These observations are not too unexpected since the formation of TiF_4 may occur in this fluoride-deficient melt at 500°C by virtue of the following reactions

$$TiF_{6(l)}^{2-} + 2ZrF_{x(l)}^{4-x} \rightleftarrows 2ZrF_{x+1(l)}^{3-x} + TiF_4(g) \qquad [4]$$

$$TiF_{6(l)}^{2-} + ZrF_{x(l)}^{4-x} \rightleftarrows ZrF_{x+2(l)}^{2-x} + TiF_4(g) \qquad [5]$$

Since TiF_4 volatilizes at 284°C (42), its removal from the melt serves as a driving force to shift the above equilibrium reactions to the right even if TiF_4 were to be a stronger Lewis acid than ZrF_x^{4-x}.

Preliminary results indicated the presence of a single reduction wave for Ti(IV) at about −0.2V (*vs.* a platinum quasi-reference electrode); however, the continuously changing wave height prevented a meaningful study of this wave. Voltammetric studies of the oxidation of titanium(III) in molten LiF-BeF_2-ZrF_4 at 500° were then initiated since TiF_3 was expected to be stable in the melt at this temperature. The sublimation point of TiF_3 is 930° *in vacuo* (42).

Linear sweep voltammograms for molten LiF-BeF_2-ZrF_4 containing Ti(III) at a sheathed glassy carbon electrode are shown in Fig. 7. Similar but less well-defined waves were obtained at an unsheathed platinum electrode. This was the only wave observed upon addition of TiF_3 within the potential limits of the melt, +1.5 to −1.5V, measured at platinum *vs.* the nickel(II)(saturated)/nickel reference electrode (LaF_3 membrane type). These potential limits correspond to anodic dissolution of platinum and the reduction of Zr(IV), respectively. The plot of i_p *vs.* $v^{1/2}$ is also shown in Fig. 7. The resulting straight line is indicative

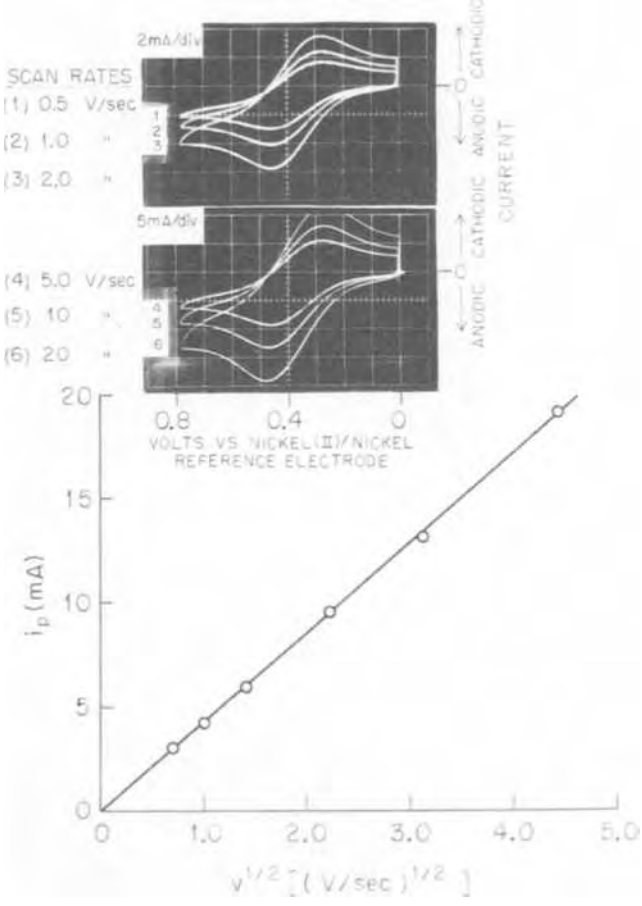

Fig. 7. Voltammograms for the oxidation of titanium(III) at glassy carbon electrode in molten LiF-BeF_2-ZrF_4 at 500°C; plot of i_p *vs.* $v^{1/2}$ for the voltammograms shown. Ti(III) concentration: 0.319M; electrode area: 0.08 cm².

of a simple charge transfer reaction. The concentration dependence of i_p is linear in the concentration range 0.05-0.32*M*.

The data for half-wave potential, peak potential separation, and half-peak to peak potential separation for the Ti(III) oxidation wave are given in Table I; theoretical values are given in parentheses. The value of i_{ap}/i_{cp} (33) for the wave at a scan rate of 1.0 V/sec is 0.98. The plots of log $(i_p - i)/i$ *vs.* potential for the wave at several scan rates are linear for the range $i = 0.35\text{-}0.70\ i_p$ and yield a slope in the same region corresponding to an n value of 1.

The diffusion coefficient of Ti(III) in molten LiF-BeF_2-ZrF_4 at 500°C obtained from the slope of the straight-line i_p *vs.* $v^{1/2}$ plot of Fig. 7 is $1.0 \pm 0.1 \times 10^{-6}$ cm²/sec. A more precise value of D was obtained in this case since a planar glassy carbon electrode ($A = 0.08$ cm²) sheathed in boron nitride was used.

Chronopotentiometric studies.—Chronopotentiograms for the oxidation of Ti(III) at a sheathed glassy carbon electrode in LiF-BeF_2-ZrF_4 at 500°C were reasonably well-defined. The product $i_o\tau^{1/2}$, essentially constant in the current density range 0.025-0.100 A/cm², was found to be 0.038 ± 0.002 A·sec$^{1/2}$·cm^{-2}. Transition times were in the range 0.1-2.3 sec. The diffusion coefficient for Ti(III) was calculated to be $1.9 \pm 0.2 \times 10^{-6}$ cm²/sec. No explanation is available for the poor agreement with the value obtained by voltammetry.

Verification of $n = 1$ for Ti(III) oxidation was accomplished using the ratio of voltammetric $i_p/v^{1/2}$ to chronopotentiometric $i\tau^{1/2}$. The n value determined by this method was 0.90.

In chronopotentiometry the half-wave potential for a reversible electrode reaction corresponds to the potential at one-fourth of the transition time (34). Thus, the value of $E_{1/2}$ obtained from chronopotentiograms for the oxidation of Ti(III) in LiF-BeF_2-ZrF_4 at 500°C is +0.40V *vs.* the nickel(II)(saturated)/nickel reference electrode. This chronopotentiometric $E_{1/2}$ compares well with the corresponding $E_{1/2}$ obtained from voltammetry (see Table I).

Standard electrode potential of the titanium(IV)/titanium(III) couple.—The standard electrode potential $E°$ for the Ti(IV)/Ti(III) couple may be estimated from the $E_{1/2}$ for the process Ti(III) $\rightleftarrows$ Ti(IV) + e in molten LiF-BeF_2-ZrF_4 at 500°C. The $E_{1/2}$ is given as +0.380V with respect to the Ni(II)(saturated)/Ni reference electrode in Table I. By extrapolating the Nernstian plot for the Ni(II)/Ni couple in LiF-BeF_2-ZrF_4 (20) to unit mole fraction of the nickel(II), $E°$ for the Ti(IV)/Ti(III) couple is estimated to be +0.197V.

The difference between $E°$ values in LiF-NaF-KF and in LiF-BeF_2-ZrF_4 is a good indication of the greater stability of Ti(III) relative to Ti(IV) in the latter solvent. In LiF-BeF_2-ZrF_4, the standard potential of the Ti(IV)/Ti(III) couple is 0.255V more anodic than its value in LiF-NaF-KF. Thus, Ti(III) is 0.255V or 5.81 kcal more stable relative to Ti(IV) in LiF-BeF_2-ZrF_4 than in LiF-NaF-KF. Such an effect may be caused by the formation of stable BeF_4^{2-} and ZrF_x^{4-x} complexes which would make LiF-BeF_2-ZrF_4 a more acidic solvent (using the Lewis concept) than LiF-NaF-KF by the reduction of the activity of the basic species, free F^-. Acidic solvents tend to stabilize lower oxidation states as pointed out previously (43). A similar acid-base effect was observed for the Fe(III)/Fe(II) couple (27) on the basis of measured electrode potentials in LiF-NaF-KF (46.5-11.5-42.0 m/o) and LiF-BeF_2-ZrF_4 (65.6-29.4-5.0 m/o).

Acknowledgments

This work was supported by the U.S. Atomic Energy Commission under contract with the Union Carbide Corporation and Contract AT-(40-1)-3518. Thanks are due D. E. LeValle, ORNL, for preparation of K_2TiF_6 and H. W. Dunn, ORNL, for x-ray diffraction analyses of samples. This work is in partial fulfillment of the requirements for the Ph.D. degree from the University of Tennessee for F. R. Clayton.

Manuscript submitted Feb. 22, 1973; revised manuscript received May 3, 1973.

Any discussion of this paper will appear in a Discussion Section to be published in the June 1974 JOURNAL.

REFERENCES

1. G. Mamantov in "Molten Salts: Characterization and Analysis," pp. 529-561, G. Mamantov, Editor, Marcel Dekker, New York (1969).
2. D. Inman, A. D. Graves, and R. S. Sethi, in "Electrochemistry," Vol. 1, A Specialist Periodical Report, pp. 166-222, The Chemical Society, London (1970).
3. D. Inman, A. D. Graves, and A. A. Nobile, in "Electrochemistry," A Specialist Periodical Report, Vol. 2, pp. 61-116, The Chemical Society, London (1972).
4. K. W. Fung and G. Mamantov, in "Advances in Molten Salt Chemistry," Vol. 2, J. Braunstein, G. Mamantov, and G. P. Smith, Editors, Plenum Press, New York (1973).
5. Yu. K. Delimarskii and B. F. Markov, "The Electrochemistry of Fused Salts," Sigma Press, Washington, D.C. (1961).
6. C. H. Liu, K. E. Johnson, and H. A. Laitinen in "Molten Salt Chemistry," pp. 681-733, M. Blander, Editor, Interscience Publishers, New York 1964).
7. H. A. Laitinen and R. A. Osteryoung in "Fused Salts," pp. 255-300, B. R. Sundheim, Editor, McGraw-Hill Book Co., New York (1964).
8. D. Inman and S. H. White, *Ann. Reports*, **62**, 106 (1965).
9. R. Baboian, D. L. Hill, and R. A. Bailey, *Can. J. Chem.*, **43**, 197 (1965).
10. S. N. Flengas, *Ann. N.Y. Acad. Sci.*, **79**, 853 (1960).
11. S. Senderoff, *Met. Rev.*, **11**, 97 (1966).
12. J. Barksdale, "Titanium: Its Occurrence, Chemistry, and Technology," pp. 162-170, The Ronald Press, New York (1966).
13. A. R. Stetson, *Mater. Design Eng.*, **57**, 81 (1963).
14. J. G. Wurm, L. Gravel, and R. J. A. Potvin, *This Journal*, **104**, 301 (1957).
15. N. F. H. Bright and J. G. Wurm, *Can. J. Chem.*, **36**, 615 (1958).
16. W. D. Powers, S. I. Cohen, and N. D. Greene, *Nucl. Sci. Eng.*, **71**, 200 (1963).
17. B. J. Sturm and R. E. Thoma, USAEC Report ORNL-3789, 83 (1965).
18. W. R. Grimes, D. R. Cuneo, F. F. Blankenship, G. W. Keilholtz, H. F. Poppendiek, and M. T. Robinson, in "Fluid Fuel Reactors," p. 584, J. A. Lane, H. G. MacPherson, and F. Moslan, Editors, Addison-Wesley, Reading, Mass. (1958).
19. H. R. Bronstein and D. L. Manning, *This Journal*, **119**, 125 (1972).
20. F. R. Clayton, Ph.D. Dissertation, The University of Tennessee, Knoxville, Tennessee, 1972.
21. D. L. Manning, *J. Electroanal. Chem.*, **6**, 227 (1963).
22. G. Mamantov and D. L. Manning, *Anal. Chem.*, **38**, 1494 (1966).
23. D. J. Fisher, W. L. Belew, and M. T. Kelley, in "Polarography 1964," Vol. 2, pp. 1043-1059, G. J. Hills, Editor, Macmillan, London (1966).
24. D. L. Manning and G. Mamantov, *J. Electroanal. Chem.*, **17**, 137 (1968).
25. D. L. Manning and G. Mamantov, *ibid.*, **7**, 102 (1964).
26. H. W. Jenkins, G. Mamantov, and D. L. Manning, *ibid.*, **19**, 385 (1968).
27. H. W. Jenkins, G. Mamantov, and D. L. Manning, *This Journal*, **117**, 183 (1970).
28. T. R. Mueller and H. C. Jones, *Chem. Instrum.*, **2**, 65 (1969).
29. W. Rudorff, in "Advances in Inorganic Chemistry and Radiochemistry," Vol. 1, p. 223, H. J. Emeleus and A. G. Sharpe, Editors, Academic Press, New York (1959).
30. R. H. Wopschall and I. Shain, *Anal. Chem.*, **39**, 1514 (1967).
31. R. S. Nicholson and I. Shain, *ibid.*, **36**, 706 (1964).
32. G. Mamantov, D. L. Manning, and J. M. Dale, *J. Electroanal. Chem.*, **9**, 253 (1965).
33. R. S. Nicholson, *Anal. Chem.*, **38**, 1406 (1966).

34. P. Delahay, "New Instrumental Methods in Electrochemistry," pp. 412, 17, 119, 124, 184, Interscience Publishers, New York (1954).
35. I. M. Kolthoff and J. J. Lingane, "Polarography," Vol. 1, pp. 192-194, 24, Interscience Publishers, New York (1952).
36. S. V. Tatwawadi and A. J. Bard, *Anal. Chem.*, **36**, 2 (1964).
37. H. A. Laitinen and L. M. Chambers, *ibid.*, **36**, 5 (1964).
38. P. J. Lingane, *ibid.*, **39**, 485 (1967).
39. A. J. Bard, *ibid.*, **35**, 340 (1963).
40. J. J. Lingane, "Electroanalytical Chemistry," 2nd ed., p. 28, Interscience Publishers, New York (1958).
41. R. P. Elliott, "Constitution of Binary Alloys, First Supplement," pp. 751-752, 586, 649, 584, 648, 676, McGraw-Hill Book Co., New York (1965).
42. R. J. H. Clark, "The Chemistry of Titanium and Vanadium," pp. 25, 40, Elsevier Publishing Co., Amsterdam (1968).
43. J. D. Corbett in "Preparative Inorganic Reactions," Vol. 3, pp. 1-33, W. L. Jolly, Editor, Interscience Publishers, New York (1966).

Electrochemical Studies of Titanium in Molten Sodium Tetrafluoroborate

F. R. Clayton and G. Mamantov*

Department of Chemistry, University of Tennessee, Knoxville, Tennessee 37916

and D. L. Manning

Analytical Chemistry Division, Oak Ridge National Laboratory, Oak Ridge, Tennessee 37830

ABSTRACT

The electrochemical reduction of Ti(IV) in molten $NaBF_4$ at 420°C was studied by voltammetry, chronopotentiometry, and chronoamperometry. The process, Ti(IV) + e = Ti(III), at both platinum and pyrolytic graphite electrodes was found to be reversible. No further reduction steps were observed. A standard electrode potential for this couple of −0.358V (*vs.* a unit mole fraction Fe(II)/Fe electrode) was obtained.

Use of molten fluoroborates as solvents for electrochemical investigations has been quite limited. Fluoroborates have been used as electrolytes for the electrodeposition of boron metal (1) and boron-silicon alloys (2) and for the preparation of KBF_4 (2). Although their potential use as coolants for molten-salt nuclear reactors (3) has necessitated a number of fundamental studies of these systems (4-8), electroanalysis in molten fluoroborates apparently has not been explored previously. The relatively nonhygroscopic nature, the convenience of high-purity preparation (4), and the low melting points of alkali-metal tetrafluoroborates (5) make fluoroborates attractive as molten salt solvents; unfortunately, slow decomposition of fluoroborates in the molten state produces boron trifluoride (6), creating certain experimental problems in containment and handling (7, 8).

An iron(II)/iron reference electrode utilizing a single-crystal lanthanum trifluoride membrane was recently employed by us (9) for potential measurements in molten $NaBF_4$ at 420°C. In this paper, we report on the use of the above reference electrode to study the electrochemistry of titanium in molten $NaBF_4$ at 420°C by means of linear sweep voltammetry, chronopotentiometry, and chronoamperometry. The electrochemical behavior of titanium in this medium is of particular interest because titanium is the least noble constituent of the Hastelloy N alloy used to contain the coolant in molten salt reactors.

Experimental

Reagent grade $NaBF_4$ was obtained from the Harshaw Chemical Company and was further purified by a recrystallization procedure described previously (4). The procedure involved a double recrystallization from 0.12M HF (aqueous) solution, air-drying at 110°C, crushing, and redrying. All-plastic ware was used throughout.

The electrolytic cell assembly and the instrumentation employed for this study was the same as that used in our previous electrochemical study (10) of titanium in molten fluorides. The Fe(II)/Fe reference electrode contained in a lanthanum fluoride compartment was described recently (9).

Results and Discussion

Background voltammograms of the $NaBF_4$ melt at platinum and pyrolytic graphite electrodes are shown in Fig. 1. The residual currents observed are reasonably low within the potential range of interest. A small impurity wave (25-30 μA) located at about −0.1V *vs.* Fe(II) (saturated)/Fe reference electrode (LaF_3 membrane type) is due to the presence of iron(II) at a concentration of about 200 ppm ($M = 7.16 \times 10^{-3}$). Its

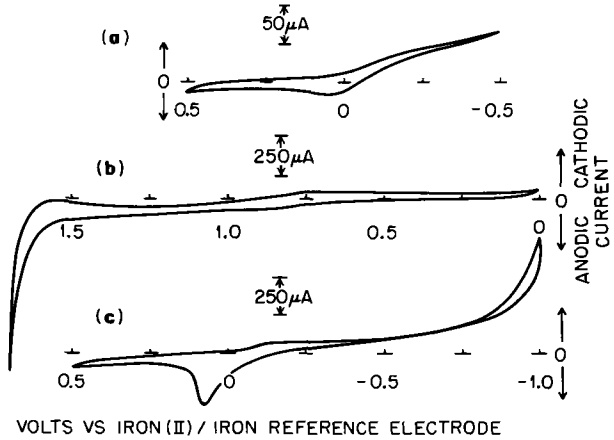

Fig. 1. Typical linear sweep voltammograms of the $NaBF_4$ melt at 420°C showing (a) iron impurity wave at platinum, (b) anodic potential limit at platinum, and (c) cathodic potential limit at pyrolytic graphite. Electrode areas: both 0.12 cm^2; scan rate: 0.1 V/sec.

* Electrochemical Society Active Member.

Key words: titanium, molten fluoroborates, voltammetry, chronopotentiometry, melts.

identity was confirmed by additions of FeF_2 to the melt which resulted in proportionate increases in the height of this wave. The anodic stripping wave for the iron impurity was more pronounced at the pyrolytic graphite electrode. The anodic and cathodic potential limits are believed to be due to anodic dissolution of the platinum electrode and reduction of boron(III), respectively. A small unidentified wave was observed at about +0.8V. The possibility of an extraneous metallic impurity was excluded on the basis of emission spectroscopic analyses of the melt. However, the wave may be due to oxidation of oxide impurities since chemical analyses (performed by General Analyses Laboratory, Oak Ridge National Laboratory) revealed a total oxygen content of about 200 ppm.

Linear sweep voltammograms for Ti(IV) (added as K_2TiF_6) in molten $NaBF_4$ at a platinum electrode are shown in Fig. 2. The plot of i_p *vs.* $v^{1/2}$ for those voltammograms is linear as is also shown in Fig. 2. Peak currents at the Pt electrode were observed to increase linearly with increasing concentration of Ti(IV) in the range 1.01×10^{-3} to 1.59×10^{-1}M. Similar well-defined voltammograms were obtained at a pyrolytic graphite electrode. No other reduction waves were obtained in this system.

The half-wave potential, peak potential separation, and half-peak to peak potential separation for the Ti(IV) reduction wave are −0.150 ± 0.01 (*vs.* an Fe(II)saturated/Fe reference electrode), 0.140 ± 0.01, and 0.130 ± 0.01V, respectively. The log $(i_p - i)/i$ *vs.* E plot yielded a straight line of theoretical slope (11) corresponding to an n value of 1. Further evidence for a simple reversible electrode reaction is provided by the semi-empirically calculated (12) value of i_{ap}/i_{cp} equal to unity in agreement with the theoretical value (13).

The diffusion coefficient for Ti(IV) in molten $NaBF_4$ was determined from the Randles-Sevcik equation (14) which at 420° is given by

$$i_p = 1.77 \times 10^5 n^{3/2} A D^{1/2} C v^{1/2} \quad [1]$$

Using the slope of the i_p *vs.* $v^{1/2}$ plot (Fig. 2), $A = 0.12$ cm², $C = 0.140$M, D was calculated as $2.6 \pm 0.5 \times 10^{-6}$ cm²/sec.

The polarogram constructed from current-time curves for the reduction of Ti(IV) at a platinum electrode is shown in Fig. 3. The corresponding log $(i_d - i)/i$ *vs.* potential plot is shown in Fig. 4; the straight line drawn through the data points has the theoretical slope for a one-electron reversible process.

A series of chronopotentiograms for the reduction of Ti(IV) in molten $NaBF_4$ is shown in Fig. 5. The value of $i_o\tau^{1/2}$ of 13.7 ± 0.3 mA · cm^{-2} · sec$^{1/2}$ obtained from these chronopotentiograms was reasonably constant over the current density range studied. Transition times were in the range 0.06-0.52 sec. From the $i_o\tau^{1/2}$ value, D was calculated as $1.3 \pm 0.3 \times 10^{-6}$ cm²/sec. As in the case of Ti(III) in $LiF\text{-}BeF_2\text{-}ZrF_4$ (10), the agreement between D values obtained by voltammetry and chronopotentiometry was not good. Additional evidence for the electrode reaction being simple and re-

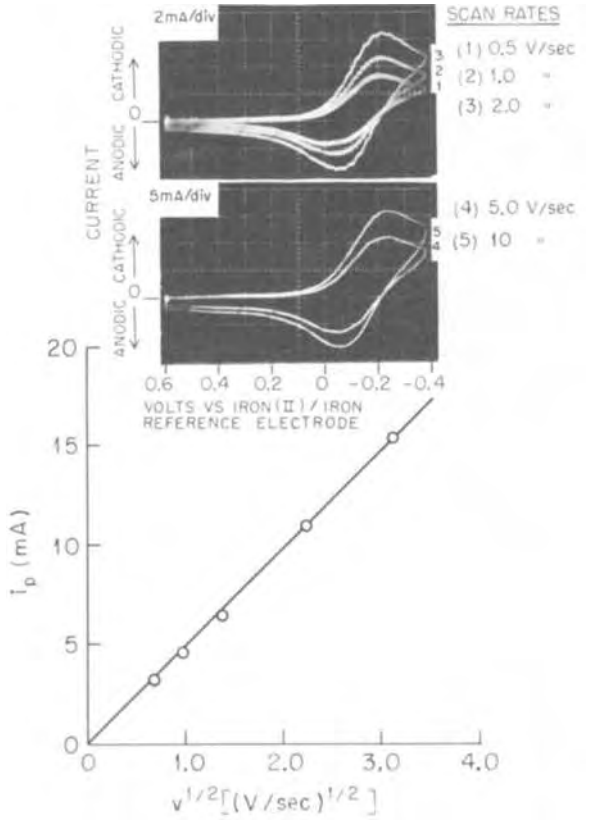

Fig. 2. Voltammograms for the reduction of Ti(IV) at platinum electrode in molten $NaBF_4$ at 420°C; plot of i_p *vs.* $v^{1/2}$ for the voltammograms shown. Ti(IV) concentration: 0.140M; electrode area: 0.12 cm².

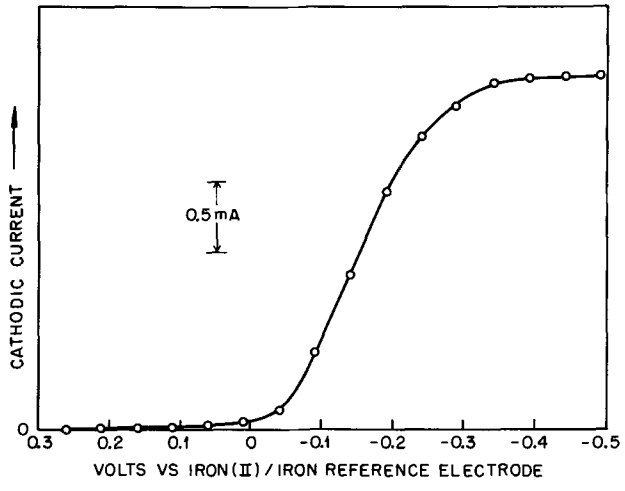

Fig. 3. Polarogram constructed from current-time curves for the reduction of Ti(IV) at platinum electrode in molten $NaBF_4$ at 500°C. Ti(IV) concentration: 0.178M; electrode area: 0.20 cm²; current measured at 5 sec.

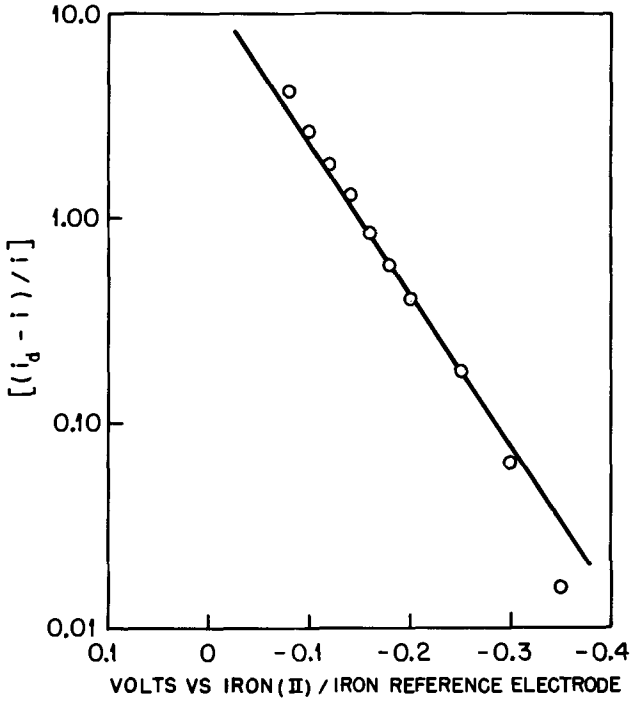

Fig. 4. Plot of log $(i_d - i)/i$ *vs.* potential for the polarographic wave of Fig. 3.

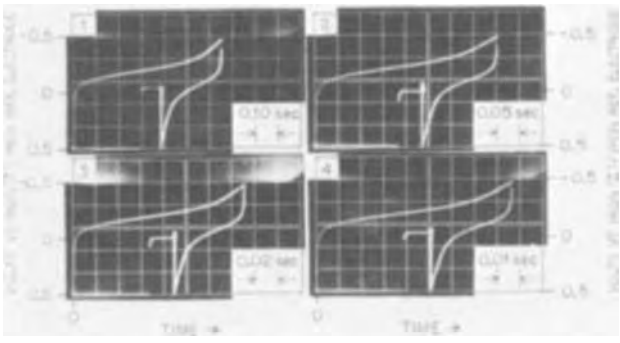

Fig. 5. Chronopotentiograms for the reduction of Ti(IV) in molten $NaBF_4$ at 420°C. Platinum electrode area: 0.08 cm^2; Ti(IV) concentration: 0.140M; currents: 1, 1.5 mA; 2, 2.0 mA; 3, 3.0 mA; 4, 4.5 mA.

versible was obtained from measurement of the reverse transition time τ_r for the chronopotentiograms in Fig. 5. According to Reinmuth (15), τ_r should be equal to one-third of the forward transition time τ for a simple reversible electron transfer. The experimentally determined ratios of 0.35 to 0.37 were in good agreement with theory.

Direct comparison of the chronopotentiometric $E_{1/2}$ with the voltammetric $E_{1/2}$ for the Ti(IV) reduction wave can be made since the same iron(II) (saturated)/iron reference electrode (LaF_3 membrane type) was used in both measurements. From Fig. 5 an $E_{1/2}$ (determined from the potential at $\tau/4$) of -0.15 ± 0.01V was obtained, in excellent agreement with the voltammetric $E_{1/2}$.

The half-wave potential for the reversible process $Ti(IV) + e \rightleftarrows Ti(III)$ of -0.150V [*vs.* the Fe(II) (saturated)/Fe reference electrode] was used to estimate the standard electrode potential of the Ti(IV)/Ti(III) couple. Extrapolation of the Nernstian plot for the Fe(II)/Fe couple in molten $NaBF_4$ (9) to unit mole fraction of iron(II) gives an $E°$ for the Fe(II)/Fe couple which is about 0.208V more anodic than the potential of the Fe(II) (saturated)/Fe reference electrode. Thus, $E°$ for the Ti(IV)/Ti(III) couple in $NaBF_4$ at 420°C is estimated to be -0.358V (with respect to a unit mole fraction Fe(II)/Fe electrode).

Acknowledgments

The authors would like to acknowledge the support of this work by the U.S. Atomic Energy Commission under contract with the Union Carbide Corporation and Contract AT-(40-1)-3518. We also thank D. E. LaValle and J. A. Carter of the Oak Ridge Natonal Laboratory for preparation of K_2TiF_6 and spectroscopic analysis of $NaBF_4$, respectively. This work was done in partial fulfillment of the requirements for the Ph.D. degree from the University of Tennessee for F. R. Clayton.

Manuscript submitted Feb. 22, 1973; revised manuscript received May 3, 1973.

Any discussion of this paper will appear in a Discussion Section to be published in the June 1974 JOURNAL.

REFERENCES

1. A. E. Newkirk in, "Boron, Metallo-Boron Compounds and Boranes," R. M. Adams, Editor, pp. 239-242, Interscience Publishers, New York (1964).
2. G. J. Janz, "Molten Salt Handbook," pp. 265-286, 433, 437, 414, Academic Press, New York (1967).
3. M. Shaw, J. W. Landis, R. V. Laney, M. Rosenthal, and W. H. Layman, *Nucl. Eng.*, **15**, 899 (1970).
4. C. J. Barton, L. O. Gilpatrick, J. A. Bornmann, H. H. Stone, T. N. McVay, and H. Insley, *J. Inorg. Nucl. Chem.*, **33**, 338 (1971).
5. S. Cantor and L. O. Gilpatrick, USAEC Report ORNL-4449, 122 (1969).
6. S. Cantor, C. E. Roberts, and H. F. McDuffie, USAEC Report ORNL-4229, 55 (1967).
7. A. S. Quist, *Appl. Spectry.*, **25**, 80 (1971).
8. S. Cantor, D. P. McDermott, and L. O. Gilpatrick, *J. Chem. Phys.*, **52**, 4600 (1970).
9. F. R. Clayton, G. Mamantov, and D. L. Manning, *High Temp. Sci.*, In press.
10. F. R. Clayton, G. Mamantov, and D. L. Manning, *This Journal*, **120**, 1193 (1973).
11. G. Mamantov, D. L. Manning, and J. M. Dale, *J. Electroanal. Chem.*, **9**, 253 (1965).
12. R. S. Nicholson, *Anal. Chem.*, **38**, 1406 (1966).
13. R. S. Nicholson and I. Shain, *ibid.*, **36**, 706 (1964).
41. P. Delahay, "New Instrumental Methods in Electrochemistry," pp. 412, 17, 119, 124, 184, Interscience Publishers, New York (1954).
15. W. H. Reinmuth, *Anal. Chem.*, **32**, 1514 (1960).

Interpretation of the Impedance Properties of the Anode-Surface Film in the Electropolishing of Copper in Phosphoric Acid

K. Kojima and C. W. Tobias*

Inorganic Materials Research Division, Lawrence Berkeley Laboratory, and Department of Chemical Engineering, University of California, Berkeley, California 94720

ABSTRACT

The frequency dispersion of the impedance measured by Ohashi *et al.*, between a vertical copper anode and a reference electrode during electropolishing in concentrated phosphoric acid, is analyzed in terms of linear combinations of resistors and capacitors. The frequency dependence of the anode under electropolishing conditions may be satisfactorily represented by an analogue circuit consisting of a resistor and a capacitor connected in parallel. The resistivity is in the range of 4.5-5 ohm · cm^2 while the capacitance is 5-8 $\mu F/cm^2$. The contribution of the solution-side resistance to the total impedance is small. Assuming that the solid film layers on the anode surface are composed of oxides of copper, depending on actual composition, the measured impedances are consistent with a thickness range of 13-124Å.

The question of the presence of an invisible anode solid film during copper electropolishing in concentrated phosphoric acid has been a subject of investigation by many researchers in recent years. The mercury test by Hoar and his co-workers (1, 2) and an ellipsometric study of the anode *in situ* by Novak *et al.* (3) provide strong evidence of the existence of a solid film on the surface.

Electrical properties of the anode-electrolyte interface during electropolishing have been explored by Ohashi, Murakawa, and Nagaura (4) by means of a-c impedance measurements. A reinterpretation of these experimental impedance data allow inferences about the nature of the invisible solid film.

Impedance of Anode Film in Electropolishing Region[1]

The a-c impedance between a vertical anode and a reference electrode during electropolishing was measured by Ohashi *et al.* (4) in the frequency range of 400 Hz to 10 kHz. They have interpreted their experimental results in terms of a resistor, R_s, and a capacitor, C_s, connected in series. The series resistance R_s decreases sharply while C_s decreases only slightly with increase of frequency. However, for this analogue to represent the experimental impedance values, both the series resistance, R_s, and capacitance, C_s must be independent of frequency. Obviously, the series connection of a resistor and a capacitor does not represent the measured impedance properly.

The wavelength range of a.c. used by Ohashi *et al.* (400 Hz to 10 kHz) is many orders of magnitude larger than the dimensions of the anode specimen. This allows an equivalent circuit to be represented by linear elements. We exclude here nonlinearity caused by roughness of the surface on the microscale. One of the equivalent circuits to be considered for nonporous films of uniform properties along the anode surface is shown in Fig. 1. It is assumed that there is no special adsorption of ions affecting the anode impedance. The Warburg impedance is probably negligible in the high frequency range.

Assuming that either the solid side or the solution side is the controlling factor of the over-all anode impedance, one greatly simplified equivalent circuit is the parallel connection of a resistor and a capacitor with series resistors as shown in Fig. 2.

The total impedance across points A and R, Z_{ar}, for the equivalent circuit shown in Fig. 2 is given by

$$Z_{ar} = \frac{R_x}{1 + \omega^2 R^2{}_x C^2{}_x} + R_{ar} + R_{sc} - j\frac{\omega R^2{}_x C_x}{1 + \omega^2 R^2{}_x C^2{}_x} \quad [1]$$

in which ω is the angular frequency. For the series connection of a resistor and a capacitor, used by Ohashi, the following relation holds

$$Z_{ar} = R_s - j\frac{1}{\omega C_s} \quad [2]$$

Comparing Eq. [1] with Eq. [2], we get

$$R_s = R_{ar} + R_{sc} + \frac{R_x}{1 + \omega^2 R_x{}^2 C_x{}^2} \quad [3]$$

and

$$\frac{1}{\omega C_s} = \frac{\omega R_x{}^2 C_x}{1 + \omega^2 R_x{}^2 C_x{}^2} \quad [4]$$

From these equations we obtain [5]

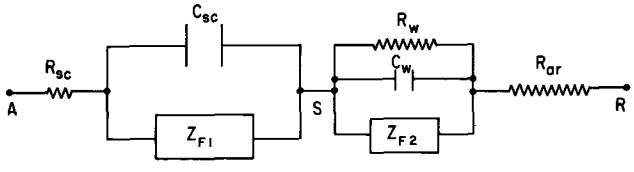

Fig. 1. Analogue circuit representing the electrical characteristics of the copper/solid film/solution system. R_{sc}, series resistance of the solid film; C_{sc}, capacitance of the solid barrier layer; R_w, double layer resistance; C_w, double layer capacitance; R_{ar}, resistance due to the electrolyte between the anode and reference electrode; Z_{F1}, Faradaic impedance on the solid side; Z_{F2}, Faradaic impedance on the solution side; point A, copper; point S, solid film/solution interface; point R, reference electrode.

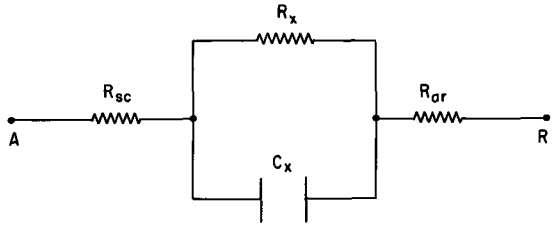

Fig. 2. Simplified analogue circuit

* Electrochemical Society Active Member.
Key words: anodic films, electropolishing, impedance of surface films, anodic dissolution of copper in phosphoric acid.
[1] Section of the current plateau below the onset of the transpassive region.

$$\left(\frac{R_x}{1+\omega^2R_x^2C_x^2}-\frac{R_x}{2}\right)^2+\left(\frac{\omega R_x^2C_x}{1+\omega^2R_x^2C_x^2}\right)^2=\left(\frac{R_x}{2}\right)^2 \quad [5]$$

or

$$\left(R_s-R_{ar}-R_{sc}-\frac{R_x}{2}\right)^2+\left(\frac{1}{\omega C_s}\right)^2=\left(\frac{R_x}{2}\right)^2 \quad [6]$$

Equation [6] is the equation of a circle which is centered at $(R_x/2,0)$ with radius $R_x/2$, if the measured reactance, $1/\omega C_s$, is plotted against resistance, $R_s - R_{ar} - R_{sc}$. The values of R_{ar} and R_{sc} have been estimated in two ways: (*i*) from extrapolating the measured values of R_s *vs.* $1/f$ [Ref. (4)] to infinite frequency, and (*ii*) from the measured values of the resistance between the anode and the reference electrode when the anode dissolves in the active region.

Figure 3 shows the impedance loci of the Cu/solid film/solution/reference electrode system, when the anode potential is $1.0V < E_n < 1.3V$ and the frequency is in the range of 400 Hz to 10 kHz. The experimental data points fall close to a circle of 16-ohm diameter. This suggests that the analogue circuit of a parallel resistor and a parallel capacitor is approximately correct. In Fig. 4 and 5, the parallel resistance $R_{x,o}$ (ohm · cm²) and parallel capacitance $C_{x,o}$ (μF/cm²) of the analogue circuit per unit area of the apparent surface are plotted as functions of frequency. $R_{x,o}$ is nearly independent of frequency, although it slightly decreases with the increase of anode potential. Figure 5 shows that $5\ \mu F/cm^2 < C_{x,o} < 8\ \mu F/cm^2$.

The foregoing analysis indicates that the impedance of the anode surface under electropolishing conditions can be satisfactorily represented by the parallel connection of a resistor and a capacitor, instead of the series combination suggested by Ohashi *et al.* (4).

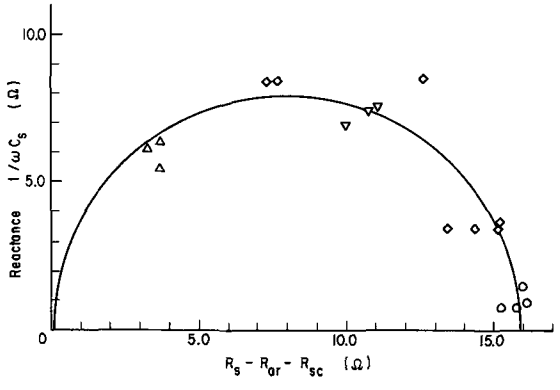

Fig. 3. Impedance loci of the copper/solid film/solution/reference electrode system (calculated by Eq. [6]). $1.0V < E_h < 1.3V$. Data by Ohashi *et al.* (4). ○, 400 Hz; ▽, 3 kHz; ◇, 1 kHz; △, 10 kHz.

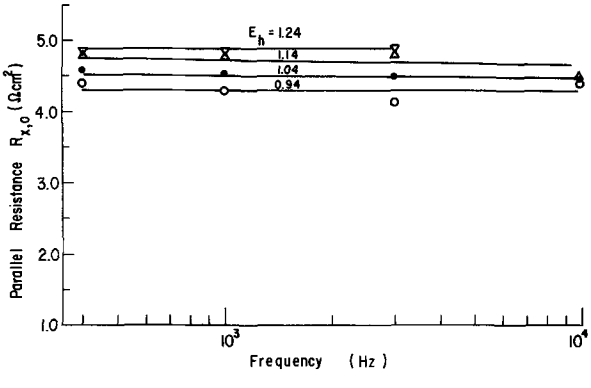

Fig. 4. Effect of frequency on the parallel resistance $R_{x,o}$ (this work). Data by Ohashi *et al.* (4).

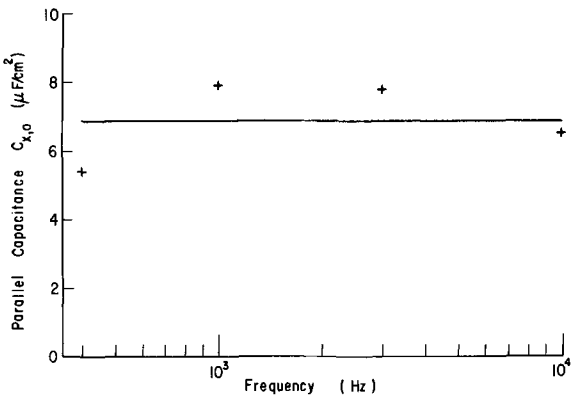

Fig. 5. Effect of frequency on the parallel capacitance $C_{x,o}$. $E_h = 1.04$-$1.24V$ (this work).

Effect of Solution-Side Impedance

We shall now examine whether the impedances, R_x and C_x, are predominantly determined by the solution-side impedance, R_w, C_w, and Z_{F2}. The fact that $R_{x,o}$ and $C_{x,o}$ are nearly independent of frequency suggests that under Ohashi's experimental conditions the effect of the diffusion impedance on the over-all impedance is small.

Assuming the diffusion impedance to be negligible, we get

$$\frac{1}{R_x}\simeq\frac{1}{R_w}+\frac{1}{R_T} \quad [7]$$

and

$$C_x\simeq C_w \quad [8]$$

The reaction resistance R_T may be calculated by the following relation (6)

$$R_T=\left(\frac{\partial E_h}{\partial i}\right)_{i=i_l}\simeq\frac{RT}{\alpha_a F i_l} \quad [9]$$

in which the Tafel relation [$i = i_o \exp(\alpha_a\eta_a F/RT)$] is assumed to be applicable. If we assume that for the anodic transfer coefficient, α_a, in Eq. [9] we can use the value obtained for the active dissolution of copper [$\alpha_a = 1.44$ (7)], we obtain for $i_l = 0.018$ A/cm²[2] at 30°C

$$R_T\simeq 1\ \text{ohm}\cdot\text{cm}^2$$

This leads to $R_{x,o} < 1$ ohm · cm². As shown in Fig. 6, in the electropolishing region the observed $R_{x,o}$ is of

[2] The current density used in Ohashi *et al.*'s experiments (4).

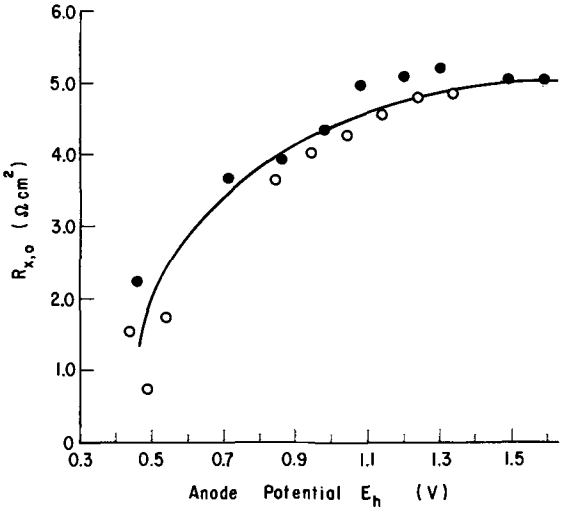

Fig. 6. Effect of anode potential on the parallel resistance $R_{x,o}$ at $f = 1$ kHz (this work). Data by Ohashi *et al.* (4). Best electropolishing region: $1.0 < E_h < 1.6V$. Active dissolution occurs when $E_h < 0.4V$ (7).

the order of 4.5-5.0 ohm · cm². $R_{x,o}$ in the active dissolution of copper is probably much smaller than that in the electropolishing region (Fig. 6). Considering R_T to be the slope of the anodic polarization curve at a given current density, it is evident under electropolishing conditions the observed $R_{x,o}$ does not represent the solution-side resistance.

We now turn our attention to the behavior of capacitance. From Ohashi's experimental data the parallel capacitance, $C_{x,o}$, in active dissolution of copper is of the order of 200-800 μF/cm². According to Bockris and Conway (8), Hoey (9), Noguet *et al.* (10), at $E_h > 0.3V$ [3] the double-layer capacitance of copper electrodes is of the order of 100 μF/cm² or higher. Even after a correction for surface roughness is made, the double-layer capacitance is still too large compared to the values of $C_{x,o}$ under electropolishing conditions.

It is concluded that the parallel resistance and capacitance obtained under the conditions of electropolishing do not represent the impedance at the anode/solution interface. This is in agreement with the results obtained with respect to the electrode reactions at the current plateau (1, 7). It should be mentioned that according to Hoey (9) the effect of the solution-side impedance on the over-all impedance of the $Cu/Cu_2O/$ aqueous solution system may be neglected when no direct current passes, and the frequency is larger than 10^3 Hz.

Solid Film Properties

We now examine the second extreme case, in which the impedance of the solid film is represented by parallel resistor and capacitor (R_x, C_x). The order of magnitude of the solid film thickness θ_f, then, may be estimated by

$$\theta_f \simeq \frac{\epsilon_0 \epsilon_f f}{C_{x,o}} = 8.854 \times 10^{-14} \frac{\epsilon_f}{C_{x,o}} f \qquad [10]$$

in which ϵ_f and f are the dielectric constant of the solid film and the roughness factor of the film, respectively. A study of the rest potential of copper anodes at the current plateau (7, 11), as well as electron diffraction studies (12-17) of electropolished copper, indicates that the anode during electropolishing is covered with copper oxides. According to Noguet *et al.* (10) and Heltemes (17) the dielectric constant of Cu_2O is 7.5-7.6, while that of CuO is 18 [Ref. (18)]. On the other hand, Hoey (9) has found that a film of the multilayer structure composed of Cu_2O, CuO, and an unidentified higher copper oxide has a dielectric constant of the order of 46-70, much higher than that of pure Cu_2O or CuO (7). Assuming that the possible range of the dielectric constant of the anode solid film is 7.5-70 and that for well-electropolished surfaces the roughness factor f is 1.3 (19), we obtain from Eq. [10]

$$\theta_f \simeq 13\text{-}124\text{Å}$$

If any portion of the solid film functions as a series resistor, the film thickness should be larger than 13-124Å.

According to Hoar (20) the film thickness estimated from impedance data is of the order of 6-60Å. Using an ellipsometric technique, Novak *et al.* (3) have found recently that the film thickness is of the order of 40-120Å at a limiting current density close to that in Ohashi's impedance experiments.

If the film thickness is really of the order of magnitude mentioned above, copper ions will transfer through the solid film under the electric field of 10^6-10^7 V/cm. Under this high field, the current density passing through an anode film is approximately given by the following form (21, 22)

$$i = A_2 \exp(BE) \qquad [11]$$

in which the apparent field strength, E, is given by $E = \Delta\eta_f/\theta_f$, where $\Delta\eta_f$ is the apparent overvoltage at the anode. The value of B may be estimated from the relation

$$R_{x,o} = \left(\frac{\partial E_h}{\partial i}\right)_{i_l} = \frac{\theta_f}{i_l B} \qquad [12]$$

Equation [12] yields $B = (1.5 - 14) \times 10^{-6}$ cm/V for $\theta_f = 13\text{-}124$Å and $i = 0.018$ A/cm². It is interesting to note that the value of B is 6.8×10^{-6} cm/V for a 60Å film, which is proposed to be the probable value of the film thickness by Novak *et al.* The fact that the value of B for a 60Å film is of the same order of magnitude as that for anodic oxide films formed on Ta, Al, Zr, Nb, InSb, etc. (22) under a high electric field strength gives strong support to the view that copper ions transfer through the anode film under the high electric field. For this reason, $R_{x,o}$ should be interpreted as the over-all reaction resistance of the solid film.

Finally, it is necessary to consider to what degree our interpretation of impedance measurements may be affected by nonisothermal conditions. When large current densities pass through the resistive film, the rate of heat generation by the Joule effect may be considerable. A temperature rise of the film may cause flow of electrolyte near the anode, causing a nonuniform current-density distribution. Assuming that in Ohashi's experiments the heat generated in the solid film was transferred to the electrolyte primarily by natural convection, we can estimate the order of magnitude of the average film temperature, T_e, at steady state

$$T_e - T_{soln} \approx \frac{0.24\, i_l^2}{h_m}\left(R_{x,o} \sim \frac{\Delta\eta_f}{i_l}\right) \qquad [13]$$

in which T_{soln}, i_l, and h_m are the temperature of the electrolyte in immediate contact with the anode, the limiting current density, and heat-transfer coefficient, respectively. The heat-transfer coefficient has been estimated (7) using the well-established correlation between Nu and Gr·Pr for heated vertical plates (23). Nu, Gr, and Pr are the Nusselt number, the Grashof number, and the Prandtl number, respectively. For the thermal conductivity and the thermal coefficient of volumetric expansion, the respective physical properties of water have been used. The calculated temperature difference, $(T_e - T_{soln})_{calc}$ is of the order of 1°C or smaller. Since in fact heat is also lost by thermal conduction through the back of the anode the temperature difference, $T_e - T_{soln}$, is probably smaller than 1°C.

Concluding Remarks

The impedance of the anode under electropolishing conditions may be approximately represented by the parallel connection of a resistor and a capacitor. The resistance of the parallel resistor starts to increase in the anode-potential region in which the passivation of copper by cuprous oxide takes place (7). The parallel resistance is nearly constant in the electropolishing potential region. Lowering of limiting current in the electropolishing region shows that the parallel resistance affects the over-all transport resistance of copper ions.

The generally accepted exponential form for ion transport under high field may be applicable for the transport of copper ions through the solid film.

Acknowledgment

This work was supported by the United States Atomic Energy Commission.

Manuscript received Aug. 29, 1972.

Any discussion of this paper will appear in a Discussion Section to be published in the June 1974 JOURNAL.

REFERENCES

1. T. P. Hoar and G. P. Rothwell, *Electrochim. Acta*, **9**, 135 (1964).
2. T. P. Hoar and T. W. Farthing, *Nature*, **169**, 324 (1952).

[3] Anode potential region in which active dissolution of copper occurs.

3. M. Novak, A. K. Reddy, and H. Wroblowa, *This Journal*, **117**, 733 (1970).
4. K. Ohashi, T. Murakawa, and S. Nagaura, *J. Electrochem. Soc. Japan*, **30**, 165 (1962).
5. C. A. Desoer and E. S. Kuh, "Basic Circuit Theory," McGraw-Hill Book Co., New York (1966).
6. B. E. Conway, "Electrode Processes," Ronald Press Co., New York (1965).
7. K. Kojima, Ph.D. Thesis, University of California, Berkeley (1972).
8. J. O'M. Bockris and B. E. Conway, *J. Chem. Phys.*, **28**, 707 (1958).
9. G. R. Hoey, *This Journal*, **108**, 387 (1961).
10. C. Noguet *et al.*, *J. Phys. (Paris)*, **26**, (6), 317, 321 (1965).
11. A. Sh. Valeev and G. I. Petrov, *Soviet Electrochem.*, **3**, No. 5, 553 (1967).
12. H. R. Nelson, *Phys. Rev.*, **57**, 559 (1940).
13. W. Kranert, K. H. Leise, and H. Raether, *Z. Physik*, **122**, 248 (1944).
14. J. A. Allen, *Trans. Faraday Soc.*, **48**, 273 (1952).
15. Yu. I. Sozin and G. A. Gorbachuk, *Russ. J. Phys. Chem.*, **37**, 463 (1963).
16. G. P. Deziderev, G. A. Gorbachuk, and Yu. I. Sozin, *ibid.*, **39**, 27 (1965).
17. E. C. Heltemes, *Phys. Rev.*, **141**, (2), 803 (1966).
18. F. Ochme, *Chemiker Ztg.*, **88**, (17), 657 (1964).
19. S. Toshima and I. Uchida, *J. Electrochem. Soc. Japan*, **36**, 20 (1968).
20. T. P. Hoar, in "Modern Aspects of Electrochemistry," No. 2, p. 313, J. O'M. Bockris, Editor, Butterworths, London (1959).
21. L. Young, "Anodic Oxide Films," Academic Press, New York (1961).
22. D. A. Vermilyea, in "Advances in Electrochemistry and Electrochemical Engineering," Vol. 3, p. 211, C. W. Tobias, Editor, Interscience Publishers, Inc., New York (1963).
23. R. B. Bird, W. E. Stewart, and E. N. Lightfoot, "Transport Phenomena," p. 414, John Wiley & Sons, Inc., New York (1960).

Theory of Successive Electron Transfer Steps in Cyclic Voltammetry: Application to Oxygen Pseudocapacitance on Platinum

A. J. Appleby*

Laboratoire d'Electrolyse, C.N.R.S. Bellevue, 92-Bellevue, France

ABSTRACT

Previous work on the theory of the cyclic voltammetric (potential sweep) method is reviewed. In cases where a multielectron reaction occurs, it is shown that simple kinetic assumptions (that all electrons are transferred in a single step or that all steps save one are in pseudoequilibrium) are likely to lead to erroneous interpretations. The most fundamental parameter is (in the irreversible case) the variation of the peak maximum potential with log sweep rate. This will enable the rate-determining step to be located in the reaction sequence. The transfer coefficient and Temkin parameters determined from the peak shape are not necessarily those of the rate-determining step, but those of the potential-determining step. Results are applied to adsorbed oxygen film formation and reduction on platinum. It is shown that a two-stage reaction occurs, with the rate constant of the first anodic step (—OH formation) falling exponentially with coverage. This is associated with a rearrangement of the surface phase, accompanied by very rapid —O formation. In the cathodic direction, the position and shape of the peak is governed by the kinetic parameters of —O reduction, whereas —OH reduction is rate-determining. There is evidence that the heterogeneity factor and the free energy of the —O reduction step depend on coverage [cf. Ref. (6)]. The same mechanism may apply to palladium and rhodium and perhaps also to gold.

Since its inception by Will and Knorr (1) in 1960, the linear potential scan (triangular sweep) technique has received a great deal of attention from electrochemists who have desired an experimentally simple and rapid method of gathering information on processes involving adsorption and desorption at interfaces under nondiffusion-controlled conditions. Most instances of its application have involved studies of hydrogen and oxygen submonolayer films on the noble metals, generally from the qualitative point of view—*i.e.*, as demonstrations of irreversibility or of the existence of non-Langmuirian adsorption isotherms (2). In general, attempts to derive information of kinetic value from these studies have been few, although a number of attempts have been made to analyze peak parameters in kinetic terms (3-6). The reason for this paucity of analytical data is clear when it is realized that, in the potential sweep method, overpotential, current, reactant and product concentration, and ohmic potential drop change simultaneously, which results in mathematical analyses that are very much more difficult than, for example, in steady-state techniques. A further important point is that the universal assumption of the steady-state hypothesis, a normal situation for work involving reactions occurring in several stages in conventional kinetics, cannot be applied at all.

As a consequence of these problems, all kinetic analyses to date have involved a study of reactions that proceed in a single step under irreversible conditions (3-6). When the kinetics of all steps are considered to be sufficiently rapid for equilibrium to be maintained at the experimental scan rates under study, general equations may be derived in a straightforward way (3). In this paper, some of the assumptions and conclusions of earlier kinetic work are examined, and extensions of the equations to irreversible cases involving multiple stage reactions are described. The equations are applied to the formation and reduction of adsorbed oxygen films on platinum in acid solution, and the conclusions thus obtained are compared with earlier interpretations.

* Electrochemical Society Active Member.
Key words: adsorbed oxygen, platinum, cyclic scans, rate equations.

Previous Analyses of the Potential Sweep Method

Pseudoequilibrium case.—The pseudoequilibrium case was discussed by Srinivasan and Gileadi in 1966 (3) though the potential dependence of adsorption pseudocapacitance for various postulated isotherms had been previously calculated by Conway and Gileadi (7) and other authors (8, 9). In the pseudoequilibrium case, it is assumed that the adsorption-desorption steps are sufficiently rapid that equilibrium is maintained throughout the potential scan. In such a case, we can write a very generalized equilibrium

$$\frac{\theta}{(1-\theta)^m} = A_i \exp \frac{n\mathbf{F}}{RT}(E' - E_o + ct) \qquad [1]$$

where m is the reaction order for metal sites, A_i is the product of the activities of reactants in solutions, and n is the over-all number of electrons transfered in the over-all process

$$A_i + m\,S \rightleftharpoons X + ne^- \qquad [2]$$

where S represents the number of metal sites, and X the adsorbate, whose coverage is θ. E_o is the standard potential of the process, E' is the potential at the start of the linear sweep, whose scan rate is c. t is time in seconds. If S is the saturation coverage of X (in coulombs/cm^2), then it is clear that

$$S\frac{d\theta}{dt} = i \qquad [3]$$

where i is the current in amperes. Differentiation of Eq. [1] shows that

$$i = \frac{\theta(1-\theta)}{1 + (m-1)\theta}\left(\frac{Sn\mathbf{F}c}{RT}\right) \qquad [4]$$

where θ is the equilibrium coverage at the potential in question. The potential and current maximum is obtained from the second derivative of Eq. [1] in the usual way. We therefore find that

$$i_{max} = (1 + m^{1/2})^{-2}\left(\frac{Sn\mathbf{F}c}{RT}\right) \qquad [5]$$

$$\theta_{max} = (1 + m^{1/2})^{-1} \qquad [6]$$

When $m = 1$, the peaks are therefore symmetrical (*i.e.*, $\theta_{max} = \frac{1}{2}$), as shown by Srinivasan and Gileadi (3), whereas for large values of m (*e.g.*, adsorbates requiring several adjacent surface sites), the peaks are asymmetrical and flatter. If a coverage-dependent (*e.g.*, Temkin-type) isotherm is considered to operate, Eq. [1] must contain an exp $-r\theta/RT$ term, where r is the change in free energy of adsorption as θ moves from limitingly low to limitingly high values. The same procedure shows that i is then given by[1]

$$i = \frac{\theta(1-\theta)}{1 + (m-1)\theta + r\theta(1-\theta)/RT}\left(\frac{Sn\mathbf{F}c}{RT}\right) \qquad [7]$$

where θ_{max} is given by the same value as before. i_{max} is therefore given by

$$i_{max} = [(1 + m^{1/2})^2 + r/RT]^{-2}\left(\frac{Sn\mathbf{F}c}{RT}\right) \qquad [8]$$

Peaks under Temkin adsorption conditions are therefore lower and flatter than under Langmuir conditions. It is clear that if Eq. [6] is substituted in Eq. [1], then the potential of the peak maximum, $E' - E_o + ct_{max}$, where t_{max} is the elapsed time to the peak maximum, is constant, and is thus independent of c, the sweep rate. This is the practical criterion of reversibility. The above equations are all perfectly general and may be applied to a range of reversible systems provided that the over-all reaction is or can be written in the same form as Eq. [2]. The conclusions do not depend on any assumptions with regard to reaction mechanism.

Totally irreversible case.—For irreversible processes, it is necessary to consider the rate-determining step of the over-all reaction. If the back reaction is sufficiently slow to be ignored, we can in principle write (for a cathodic process), under Langmuir conditions

$$-S\frac{d\theta}{dt} = i = n\mathbf{F}k\,\theta^m \exp - \alpha n\mathbf{F}\,(E' - E_o + ct)/RT \qquad [9]$$

where k is the backward (cathodic) rate constant, α is the "transfer coefficient," and where the other symbols are as discussed previously. Such an equation was used by Ohashi *et al.* in 1966 (4) and Stonehart in 1968 (5). Srinivasan and Gileadi (3), on the other hand, considered the simple case of a one-electron process (H^+ discharge to give an adsorbed H atom), where both n and m are unity. A solution of Eq. [9] corresponding to the peak maximum is easily obtained by putting its time derivative equal to zero in the usual way. We thus obtain:

$$-i_{max} = \frac{S\alpha n\mathbf{F}c\theta_{max}}{mRT} \qquad [10]$$

If, on the other hand, the free energy of adsorption of the reactant is coverage-dependent and may be represented by a Temkin isotherm, then the expression for i (Eq. [9]) must be multiplied by exp $\alpha r\theta/RT$, where r is the change in free energy of adsorption as θ moves from limitingly low to limitingly high values. In such cases, a calculation shows that i_{max} is then given by an expression of the form

$$-i_{max} = \frac{S\alpha n\mathbf{F}c}{RT}\left(\frac{m}{\theta_{max}} + \frac{\alpha r}{RT}\right)^{-1} \qquad [11]$$

θ_{max} is found by integrating Eq. [9] (for the Langmuir case) with the boundary condition $\theta = \theta_o$ at $t = 0$, where θ_o is the starting coverage on the electrode. i_{max} (from Eq. [10]) is then substituted for i in the integrand, and the assumption is made that i is negligible when $\theta = \theta_o$ and $t = 0$. We then obtain for the general case, $m \neq 1$

$$\theta_{max} = \theta_o\left(\frac{m-1}{m}\right)^{\frac{1}{m-1}} \quad (m \neq 1) \qquad [12]$$

and for the special case, $m = 1$

$$\theta_{max} = \theta_o/e \quad (m = 1) \qquad [13]$$

The peak maximum therefore occurs at $\theta = 0.37\theta_o$ if $m = 1$, *i.e.*, the peaks are therefore asymmetrical, and the ratio of reversible to irreversible (with θ_o taken to be 1) peak heights is $e/4\alpha$. As θ_{max} is independent of c, then, from Eq. [9], we can write

$$-i_{max} = \text{const. exp} - \alpha n\mathbf{F}E_{max}/RT \qquad [14]$$

where E_{max} is the potential of the peak maximum. Thus, using Eq. [10]

$$dE_{max}/d\ln c = -RT/\alpha n\mathbf{F} \qquad [15]$$

Thus a Tafel-type shift of the peak potential with ln sweep rate should be observed. This may be taken as a criterion of the totally irreversible case.

For the Temkin case, integration of the rate equation to give a simple analytical solution for θ_{max} is not possible. However, we can write

$$-\int_{\theta_o}^{\theta_{max}} \theta^{-m} \exp - \alpha r\theta/RT\, d\theta = n\mathbf{F}k \exp - \alpha n\mathbf{F}(E' - E_o)/RT \int_0^t \exp - \alpha n\mathbf{F}ct/RT\, dt \qquad [16]$$

[1] Expressions similar to Eq. [4]-[8] were derived in Ref. (7) for the case $m = 1$.

where t is the elapsed time to the peak maximum. For $\exp - \alpha nFct/RT >> 1$ (*i.e.*, assuming the rate of reduction at $t = 0$ to be negligible), we obtain (using Eq. [11])

$$\left(\int_{\theta_o}^{\theta_{max}} \theta^{-m} \exp - \alpha r\theta/RT \, d\theta \right) (\theta_{max})^m \exp \alpha r\theta/RT = \left(\frac{RT}{\alpha nFc} \right) i_{max}/S = \left(\frac{m}{\theta_{max}} + \frac{\alpha r}{RT} \right)^{-1} \quad [17]$$

It is clear from Eq. [17] that θ_{max} is independent of sweep rate; thus the relationship between E_{max}, c, and αn (Eq. [15]) should also be valid in the Temkin case.

Intermediate cases.—Srinivasan and Gileadi (3) examined a first-order one-electron discharge process for different combinations of forward and backward rate constants and concluded that the general case (*i.e.*, where both forward and back reactions are important) applied only over a limited range of sweep rate (about two decades). A series of numerical analyses by Stonehart, Kozlowska, and Conway (6) for cases where a Temkin-type adsorption behavior occurs indicate a similar conclusion. The same workers point out that in totally irreversible cases peak symmetry is a function of the Temkin factor r [in addition to the effect of m (4)]. Thus, under Temkin conditions, with $m = 1$, increasing r produces broader but more symmetrical peaks; *i.e.*, it has in some degree a similar effect to increasing m (4, 6).

Stonehart and co-workers (6) write a rate equation of the form

$$i = nF \left(\vec{k}(1 - \theta) \exp (1 - \alpha)[nF(E' - E_o + ct)/RT] \exp - r\theta/RT - \overleftarrow{k} \theta^m \exp - \alpha[nF(E' - E_o + ct)/RT] \exp - r\theta/RT \right) = S \frac{d\theta}{dt} \quad [18]$$

where α is again the cathodic transfer coefficient, and $\vec{k}$ and $\overleftarrow{k}$ are the forward and backward rate constants. They apply numerical solutions of this equation to the reduction of noble metal oxide films. A discussion of the basic hypotheses underlying the use of this equation, together with a summary of their conclusions, is presented in the next section.

Adsorbed Oxygen Film Formation on Noble Metals

Cyclic voltammetric scans for the formation and reduction of the adsorbed oxygen layer on platinum are by now (1, 2) so familiar that they almost constitute the leitmotiv of recent electrochemistry. Scans on rhodium and palladium in acid solution are similar to those on platinum under the same conditions (1, 2, 6), whereas similar scans on iridium (1, 2), osmium (10), and ruthenium (11) show different characteristics. Only scans on platinum (and, by extension, those on rhodium and palladium) will be considered here.

Scans on platinum have been the subject of study by a large number of authors (1, 2, 4-6, 12, 13). In all cases, a considerable irreversibility between anodic and cathodic scans has been noted, except at low coverages [*i.e.*, when the anodic triangular sweep is terminated at low potentials (6, 12)]. It is of interest to enumerate some of the other characteristics of the anodic and cathodic pseudocapacitance peaks.

1) The anodic sweep is considerably broader and flatter than that in the cathodic direction. This suggests the operation of a Temkin-type isotherm, as discussed by Böld and Breiter (2) for the oxygen adsorption process.

2) The cathodic peaks show much hysteresis and are essentially symmetrical and quite narrow. They thus appear to be closer to the Langmuir case, though this is inconsistent with their symmetry, unless (*cf.*, Eq. [12]), the reduction reaction is second order ($m = 2$), when symmetrical peaks would be expected.

3) An important characteristic parameter, $dE_{max}/d \ln c$ (see Eq. [15]), has been examined by Will and Knorr (1) in both the anodic and cathodic directions in acid solution and in rather more detail by Gilroy and Conway (13), again in acid solution but in the cathodic direction only. In the anodic direction, Will and Knorr's conclusions, which refer to a sweep rate range greater than that required for Srinivasan and Gileadi's irreversibility-reversibility criterion (3), show that, although the fine structure of the peak is dependent on sweep rate, the position of the peak as a whole is virtually independent of ln sweep rate. Under irreversible conditions, the numerical analyses of Srinivasan and Gileadi and Stonehart *et al.* (6) show that the whole peak should be translated bodily without any change in shape; *i.e.*, for any current value on the peak (not only for i_{max}), the $dE/d \ln c$ relationship should be that given by Eq. [15]. This is not observed; the implication is, therefore, that at least the initial anodic process takes place under reversible conditions. Under cathodic conditions, the results of Will and Knorr indicate (with some scatter) $dE_{max}/d \ln c \simeq 50$ mV/decade. The results of Gilroy and Conway, conducted over a much wider sweep rate range (including some results from differentiated galvanostatic charging curves—*i.e.*, the equivalent of scans at extremely low sweep rates) show $dE_{max}/d \ln c$ in the region of 40 mV/decade. This fact indicates that the cathodic sweeps represent an irreversible process.

4) The i_{max}/peak width ratio (the "aspect ratio" of the peak) in the cathodic direction increases with increasing coverage (13).

It is generally accepted that the Pt-O adsorption reduction process occurs in at least two stages [*cf.* Böld and Breiter (2)]. The experimental results of Will and Knorr (1) and Gilroy and Conway (13) reinforce this idea. In both cases, for the cathodic sweep the value of $-RT/\mathbf{F}(d \ln c/dE_{max})$ was determined to be somewhat greater than unity. It should be noted that this term will always be equal to α for a totally irreversible reaction, even if r and α are θ-dependent, so long as the initial coverage on the electrode at the start of each cathodic scan is the same, and provided that the scanning rate has no effect on peak symmetry. This should be generally true and is supported by Gilroy and Conway's experimental results of peak form as a function of ln sweep rate. A general equation for the cathodic transfer coefficient, assuming that one step is rate-determining with all preceding steps in pseudoequilibrium, is given by the equation (14)

$$\alpha = x/\nu + \beta n' \quad [19]$$

where α in Eq. [19] is the equivalent of αn in Eq. [9] (*i.e.*, $-RT/\mathbf{F}(d \ln c/dE_{max})$ and where x is the number of electrons transferred per unit of the over-all reaction before the rate-determining step, whose stoichiometric number is ν. n' is the number of electrons transferred per unit rate-determining step, and β is the symmetry factor for electron transfer in the rate-determining step. There is compelling theoretical evidence to suggest that n' will not exceed unity, on the grounds that the total rearrangement energy of the system will be much greater in a simultaneous multielectron transfer than for a series of single electron transfers (15). Multielectron transfers can therefore be eliminated on activation energy grounds. In addition, the transition probability for a bi-(or other multi-)electron combination undergoing a Landau-Zener-type transition mechanism will be lower than for a single electron transfer—*i.e.*, such processes will be anadiabatic, and thus the pre-exponential term, as well as the activation energy, will be highly unfavorable to multielectron transfers. Consequently, we may confidently state that n' will be unity. The corresponding expression in the anodic direction is given by

$$(1 - \alpha) = x'/\nu + (1 - \beta) \quad [20]$$

where n' is taken to be unity and x' is the number of

electrons transferred before the rate-determining step in the anodic direction. Thus, in general, if n is the number of electrons involved in the over-all reaction, then

$$x + x' + \nu = n \qquad [21]$$

as ν is the number of times the one-electron rate-determining step occurs in the over-all process.

Kinetic data obtained from the use of Eq. [18], which implies a two-electron transfer with $x = x' = 0$, are thus likely to be illusionary. Although, formally, the value of the transfer coefficient αn may be used as a representative convention for the true physical meaning of the transfer coefficient (Eq. [19] for the cathodic process), conclusions drawn from its use are not likely to have any mechanistic meaning. It should be noted that the sum of the transfer coefficients in Eq. [19] and [20] is equal to n/ν, whereas the sum of the corresponding values as they appear in the formalism of Eq. [18] is simply n.

The sweep rate dependence results of Will and Knorr (1) and Gilroy and Conway (13) give us a possibility of determining the rate-determining step of the cathodic reduction process. The latter data are probably the more reliable, and indicate $dE_{max}/d \ln c$ values $\simeq$ 40 mV/decade, *i.e.*, at 25°C, $\alpha \sim 3/2$. Thus, from Eq. [19], with $\beta = \frac{1}{2}$ and $n' = 1$, $x/\nu = 1$. The most logical reaction sequence is an over-all two-electron transfer with $\nu = 1$ of the form (2)

$$Pt + H_2O \rightarrow PtOH + H^+ + e^- \qquad [A]$$

$$PtOH \rightarrow PtO + H^+ + e^- \qquad [B]$$

in which the second electron transfer step in the cathodic direction (*i.e.*, relation [A]) is rate-determining. The pH dependence of such a process would be $-RT/F$, which is consistent with that experimentally observed (2). In the anodic direction, the reaction is effectively at equilibrium, as discussed above. Again, in such a case a pH dependence of $-RT/F$ would be expected, as is observed (2). If, however, the anodic process were under kinetic control from the reaction that is rate-determining in the cathodic direction (reaction [A]), a pH dependence of zero would be expected. These observations reinforce the idea that a considerable change in reaction rate constant has occurred between the processes in the anodic and cathodic directions. A reaction taking place in more than two electron transfer steps to any great extent in the potential range of interest is not probable, as maximum coverages observed correspond to a monolayer whose coulombic area is twice that for adsorbed hydrogen. A two-electron over-all reaction taking place in two one-electron steps is therefore indicated.

Ohashi *et al.* (4), who used an equation of type [9] in their investigations of the cathodic reaction, attempted to determine the cathodic reaction order and the value of r (*cf.* Eq. [11]) by a series of plots of $1/i_{max}$ as a function of $1/\theta_{max}$ (to determine r from Eq. [11] and of $\ln i - m \ln \theta$ against potential (using Eq. [9]) to establish the value of m. Their plot of $1/i_{max}$ against $1/\theta_{max}$ indicates that r approaches zero as θ increases. They therefore assume (as would be expected in conventional kinetics) that r is constant and negligible. This conclusion leads them to obtain a value of $\alpha n \simeq 0.52$ and a value of m (from $\ln i - m \ln \theta$ against potential, assuming $r = 0$) equal to 2. However, it is quite clear that if r is a function of θ (say $\propto 1/\theta$) in Eq. [11], the results can be explained equally well in terms of $m = 1$. This however fails to account for the surprising symmetry of the adsorbed oxygen reduction peaks, which would be expected to be unsymmetrical (*cf.* Eq. [13]) when r is negligible (*i.e.*, at large θ_o). Their αn value, obtained in several different ways (4), is also quite inconsistent with that obtained from the sweep rate dependence of the peak potential (1, 13).

Stonehart *et al.* (6) determined some of the properties of the peaks that result from numerical integration of Eq. [18]. They examined the effect of the Temkin factor r on peak symmetry, and concluded that, for the irreversible case, a substantial increase in apparent symmetry takes place for comparatively small values of r. They therefore conclude that the changing "aspect ratio" of essentially symmetrical peaks with θ_o is due to the coverage (or time) dependence of r, but they find it necessary to propose at the same time a rising value of αn with increasing θ_o. Their αn values are in the range 0.52-0.96. The effect of an increase in αn is an increase in the slope of the peak leading edge—this numerical adjustment is necessary as r decreases so that symmetry is maintained. A numerical demonstration of this effect will be given below. Again, the major difficulty with the interpretation of Stonehart *et al.* is that αn values obtained by peak profile analysis are inconsistent with those resulting from sweep rate experiments (1, 13), which give αn values of about 1.5. The varying value of αn with coverage is also difficult to accommodate on any physical model. It will be shown that such inconsistencies result from a failure to take into account a two-stage reaction sequence.

Investigation of the Oxygen Adsorption-Reduction Process on Platinum as a Two-Stage Reaction

Formally, we can write the rate equations for steps A and B for adsorption and removal of adsorbed —O on Pt in the following forms (at constant pH, and ignoring diffuse double-layer effects)

Reaction [A]

$$S\frac{d\theta_1}{dt} = Sc\frac{d\theta_1}{dV} = k_1F\Big((1-\theta_1-\theta_2) [\exp(1-\beta)FV/RT \exp -(1-\beta)r_1(\theta_1+\theta_2-\tfrac{1}{2})/RT] - \theta_1 [\exp -\beta FV/RT \exp \beta r_1(\theta_1+\theta_2-\tfrac{1}{2})/RT] \Big) - Sc\frac{d\theta_2}{dV} \qquad [22]$$

Reaction [B]

$$S\frac{d\theta_2}{dt} = Sc\frac{d\theta_2}{dV} = k_2F\Big(\theta_1 [\exp(1-\beta')F(V-V_d)/RT \exp -(1-\beta')r_2(\theta_1+\theta_2-\tfrac{1}{2})/RT] - \theta_2 [\exp -\beta'F(V-V_d)/RT \exp \beta' r_2(\theta_1+\theta_2-\tfrac{1}{2})/RT] \Big) \qquad [23]$$

so that the total current flowing is given by the expression $Sc(d\theta_1/dV + 2d\theta_2/dV)$, where θ_1 is the coverage in —OH, θ_2 is that in —O r_1 and r_2 are the Temkin constants for each rate equation, and V is potential measured on a scale relative to the reversible potential under standard conditions (standard state taken to be $\theta = \frac{1}{2}$) for reaction [A]. V_d is then the (negative) potential difference between the standard potentials of reactions [A] and [B]. Fk_1 and Fk_2 are the appropriate exchange currents in each case.

A certain difficulty exists in defining the manner in which the free energy (Temkin) terms depend on total coverage. Generally speaking, this term is not necessarily linear with coverage—however, it will be seen that a linear dependence gives a sufficiently good account of the experimental data. From the "induced heterogeneity" model of Boudart (16), it is reasonable to suppose that these terms will depend on the total coverage of all similar species (*i.e.*, species with similar bonding characteristics and electronegativity) on the surface of the electrode (7). Because —O is essentially a double bonded species, whereas —OH is single bonded, it may well be that the former has a more substantial effect on the bonding characteristics of neighboring oxygen dipoles than the latter. There is indeed some evidence for this (17). Consequently, it may be more exact to write Temkin terms of the form $r(\theta_1 + p\theta_2 - \frac{1}{2})/RT$, where p is a weighting factor characteristic of the bonding difference between —OH and —O. In the numerical calculations this has been disregarded, for the simple reason that the predominant species on the electrode is always —O, with θ_1 playing

a minor role. Consequently, the r values as determined from numerical analysis refer to the change in —O coverage (θ_2). In order to cut down the number of variables in the two above simultaneous equations, a simplifying assumption that the two symmetry factors, β and β', were both equal to ½ was made.

Numerical Computations

Solutions of the simultaneous equations [22] and [23] were obtained for various postulated k_1, k_2, r_1, r_2, and V_d values as a function of sweep rate and starting potentials and coverages using the Runge-Kutta method and an IBM 1800 computer. Rate constant values used were dimensionless; *i.e.*, all numerical values were expressed as k/c, and thus in themselves contain the variation in the sweep rate parameter. The facts that had to be explained were as follows: (*i*) In the cathodic direction, reaction [A] is rate determining. At all potentials of interest, reaction [B] is therefore considerably faster than reaction [A]. (*ii*) In the anodic direction, at least at low coverage, the rate-determining step (*i.e.*, reaction [A]) is sufficiently rapid to be regarded as a quasi-equilibrium.

Anodic Process

A straightforward numerical integration of Eq. [22] for reaction [A] indicates that the classical flat-topped pseudocapacitance peak for oxygen adsorption on platinum can be approximated by the assumption that r_1/RT is about 40. The second oxidation step (reaction [B]) is assumed to be in pseudoequilibrium. A plot of the current-potential curve, with $k_1/c = 10$, and with current expressed on a nominal scale, is shown in Fig. 1. A k_1/c value of 10 is sufficient for reversibility (Fig. 2). The difficulty with this interpretation is that the calculated peak shape does not exactly reproduce that experimentally observed, which shows a dip following an initial peak and, more importantly, it provides no explanation for the change in dimensionless rate constant from the initial value of 10 to a much lower value (so that total irreversibility is exhibited) in the cathodic direction. This may be remedied by introducing the simple concept that the rate constant k_1 is coverage dependent. This will satisfactorily explain the change in rate constant in the cathodic direction, and it gives a more satisfactory account of the observed shape of the experimental peak. As $k_1\mathbf{F}$, the standard exchange current of reaction [A], is determined by exp $- f\lambda/RT$, where $f\lambda$ is a fraction of the reorganizational energy of the system [the energy required to change the ground state of reactants or products to a corresponding product or reactant state in the same nuclear configuration (18)], then it is reasonable to suppose that it will be exponentially affected by the bonding character of the adsorbate, if this should change with θ or time. If the surface rearranges to give a different adsorbed phase [for example, *via* a place exchange mechanism (6)], and if subsequent growth of the film takes place in the configuration prevailing at that particular time and θ value, then a simple model for the k_1 dependence on θ can be suggested. For example, initial adsorption of oxygenated species may be in a random manner, and this may be followed by the formation of a surface phase (not necessarily a phase oxide) as coverage rises. The maximum coverage that will not involve nearest neighbor sites on a close-packed plane is $\theta = 0.3$. After this coverage is exceeded, new oxygenated radicals will have to be accommodated in nearest-neighbor sites. A place exchange mechanism that reduces energy may then be favored, which at the same time reduces the net film growth rate. Further addition of oxygen radicals will then be to the edges of "islands" of surface phase, which will take on a uniform character. The degree of rearrangement, hence the reorganizational energy, can then be considered to be proportional to θ, and k_1 may be put equal to k_1° exp $- q(\theta_1 + \theta_2)$ at constant temperature, where q is a constant.

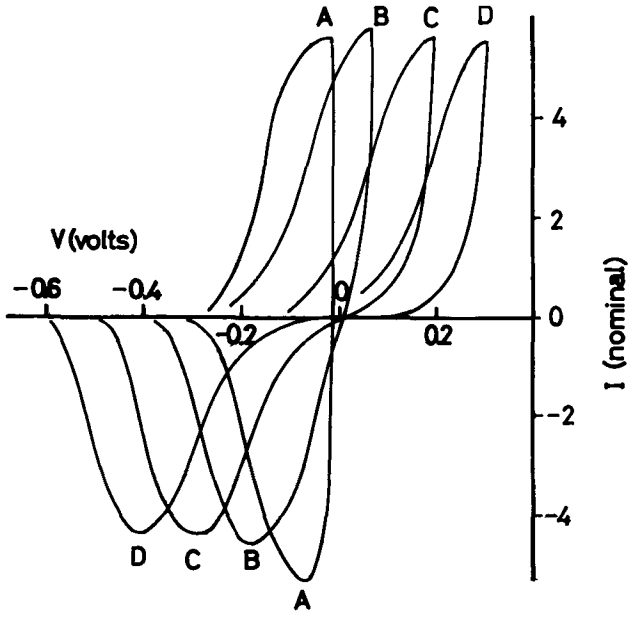

Fig. 2. Effect of changing k_1/c (invariant) for partial anodic coverages, second oxidation step (reaction [B]) ignored. $r_1/RT = 13$; A, $k_1/c = 10$; B, $k_1/c = 1.0$; C, $k_1/c = 0.1$; D, $k_1/c = 0.01$.

An examination of the effect of such a term is shown in Fig. 3 for $k_1^\circ/c = 10$ (to ensure initial reversibility, cf. Fig. 2). It has been postulated that k_1 changes by 3 orders of magnitude as $\theta_1 + \theta_2$ moves from low to high coverage to ensure sufficient irreversibility in the cathodic direction, so that q has been put equal to 6.9. r_1/RT has been taken to be 13, with reaction [B] as a quasiequilibrium (discussed in next section). It can be seen that the resulting anodic peaks show many of the features of experimental scans on platinum, for example, the initial rise followed by a dip. In practice, a further rise is noted after the dip, which may be attributed to the appearance of molecular oxygen on the surface.

Cathodic Process

Effect of V_d.—In the cathodic direction, it is postulated that the rate constant k_1 for reaction [A] corresponds to that for the highest value of θ reached in the anodic process and remains constant during the scan.

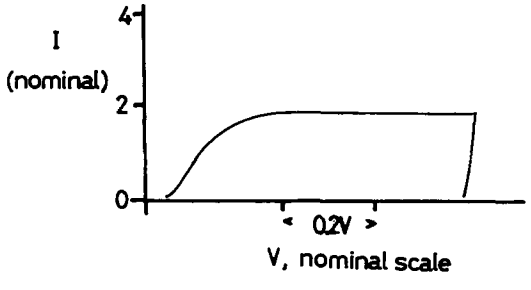

Fig. 1. Calculated anodic scan: $k_1/c = 10$ (invariant), $r_1/RT = 40$, reaction [B] in pseudoequilibrium.

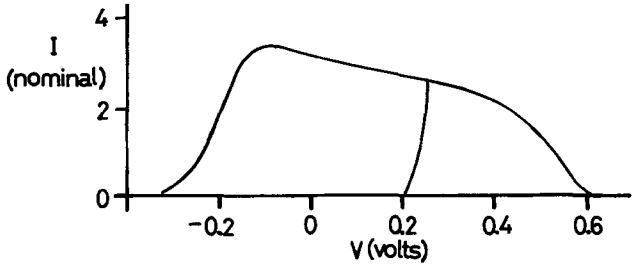

Fig. 3. Calculated anodic scans: $k_1^\circ/c = 10$, $q = 6.9$, $r_1/RT = 13$.

It is therefore the rate constant for an adsorbate with the degree of rearrangement corresponding to the initial value of θ. In order that reaction [A] should be rate-determining in the cathodic direction, it is necessary that $k_2 \exp \beta' \mathbf{F} V_d/RT$ should be much greater than k_1. To avoid the appearance of two cathode peaks, corresponding to two single-electron steps, it is clear therefore that the standard potential for the second oxidation step (reaction [B]) should be more cathodic than that for reaction [A]. For this reason, and because of the high k_2 value, reaction [B] must be a pseudoequilibrium in the anodic direction. The effect of changing V_d is shown for a hypothetical case in Fig. 4, where $r_1/RT = r_2/RT = 13$, and $\theta_2^o = 1$. V_d is taken to be 300, 400, and 500 mV. It can be seen that the effect of a 100 mV change in V_d is a translation of the peak by about 70-80 mV, with little change in the general form of the peak as a whole. In the case of platinum, the peak maximum in the anodic direction occurs at about 1000 mV *vs.* hydrogen in the same electrolyte, indicating a standard potential about 100 mV higher (see Fig. 3). The cathodic peak occurs in practice at about 800 mV *vs.* hydrogen. A rough estimate, therefore, for the value of V_d is about 300 mV.

Effect of r_2—The effect of changing r_2/RT is shown in Fig. 5. V_d is taken to be 300 mV, with $k_2/c = 80$ and $k_1/c = 0.02$. (k_2/k_1) $(\exp \beta' \mathbf{F} V_d/RT)$ is therefore about 30. r_1/RT is taken, as for the anodic direction, to be 13, and r_2/RT is given values of 13, 6, and 2. It can be seen that peaks with a good degree of visual symmetry result, whose shape (*i.e.*, "aspect ratio") is essentially controlled by the non-rate-determining reaction step (reaction [B]). They are quite different in form from the "totally irreversible" peaks, as reproduced in Ref. (3) and (6), because reaction [B] takes place under conditions of fast reduction close to its reversible potential. However, it is important to note that a simple assumption of reversibility for reaction [B], *i.e.*, if the relationship (from Eq. [23])

$$\theta_1 = \theta_2 \exp - \mathbf{F}(V - V_d)/RT \exp r_2(\theta_1 + \theta_2 - \tfrac{1}{2})/RT \quad [24]$$

is substituted directly for θ_1 in Eq. [22] (in the cathodic direction under totally irreversible conditions), is not a valid approximation for a calculation of the over-all peak shape. This is illustrated by the calculated shape for a pseudoequilibrium situation (potential on a nominal scale) for a totally irreversible reaction [A], using Eq. [24] with $r_1/RT = 13$ and $r_2/RT = 6$ illustrated in Fig. 6 (cf. curve B in Fig. 5). The shape of such a peak is much broader than that in Fig. 5, *i.e.*, it reflects a peak whose Temkin term is equal to $\beta r_1 + r_2$, rather than βr_2. The pseudoequilibrium assumption cannot be used because Eq. [24] is invalid in practice; on reduction of $-O$, the $-OH$ produced is immediately converted to H_2O under irreversible conditions and thus is removed from the reversible system. The steady-state assumption, implicit in Eq. [24], cannot therefore be applied, and the peak shape must be calculated directly from the appropriate rate equations (Eq. [22] and [23]).

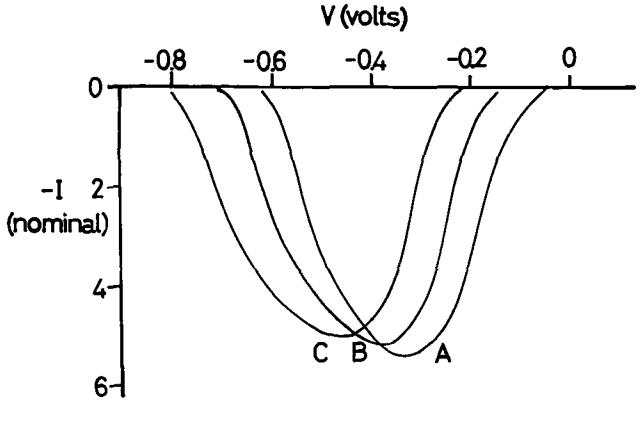

Fig. 4. Effect of changing V_d (cathodic scans): $k_1/c = 0.02$, $k_2/c = 8.0$, $r_1/RT = r_2/RT = 13$. Curves A, B, C: $V_d = 0.3$, 0.4, and 0.5V, respectively.

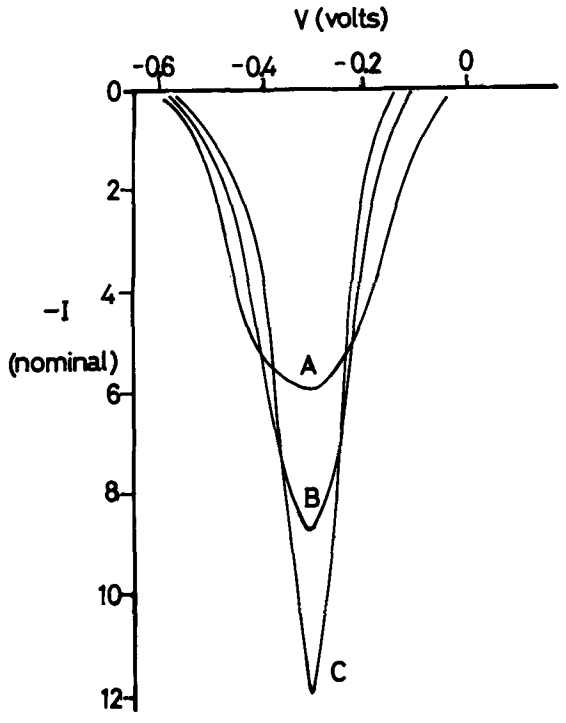

Fig. 5. Effect of changing r_2 (cathodic scans): $k_1/c = 0.02$, $k_2/c = 80$, $r_1/RT = 13$, $V_d = 0.3$. Curves A, B, C: $r_2/RT = 13$, 6, and 2, respectively.

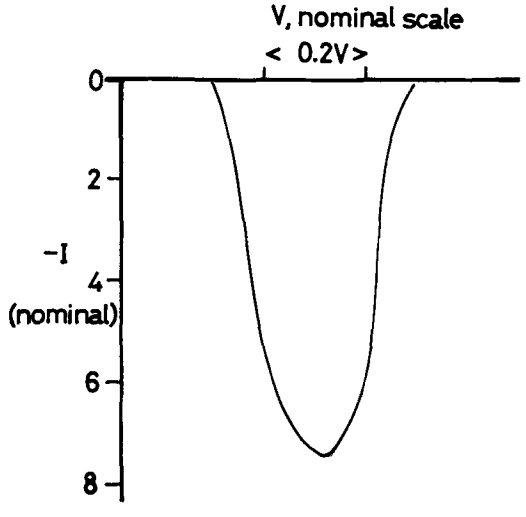

Fig. 6. Cathodic curve calculated using pseudoequilibrium assumption (Eq. [24]) for reaction [B]. $k_1/c = 0.02$, $r_1/RT = 13$, $r_2/RT = 6$.

Effect of k_1 *and* k_2*; effect of sweep rate.*—In Fig. 7 k_2/c is taken to be 80 and 8, representing a tenfold change in sweep rate. k_1/c is assumed to be 0.2, 2.0, and 20 for $k_2/c = 80$, and 10% of these values for $k_2/c = 8$, reflecting the sweep rate change. The ratio k_2/k_1 $(\exp \beta' \mathbf{F} V_d/RT)$ is therefore about 3.0, 0.3, and 0.03, respectively (for $V_d = 300$ mV). r_1/RT is assumed to be 13, and r_2/RT, 6. It can be seen that an increase in the $k_2/k_1 \exp \beta' \mathbf{F} V_d/RT$ ratio results in more symmetrical, less blunt peaks, and that $dV_{max}/d \log_{10} c$ decreases with increase in this ratio. The corresponding values are about 120, 90, and 60 mV, respectively (*i.e.*, from Eq. [15], $\alpha n = 0.5$, 0.75, and 1.0, respectively).

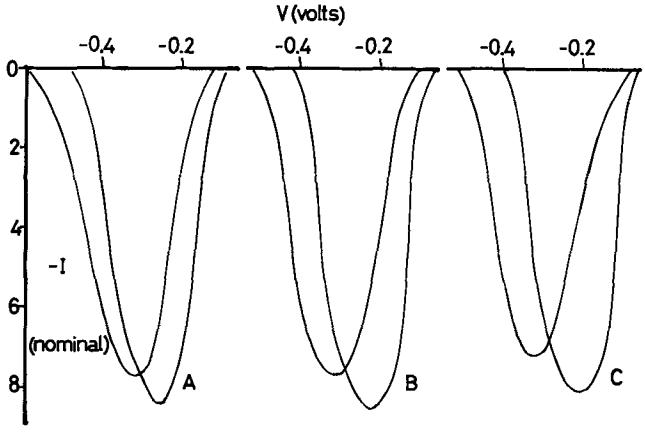

Fig. 7. Effect of one decade increase in sweep rate (cathodic scans). $r_1/RT = 13$, $r_2/RT = 6$, $V_d = 0.3$. k_2/c for slower sweep equal to 80 in each case. Curves A, B, C: $k_1/c = 0.2$, 2.0, and 20, respectively, for slower sweep.

In Fig. 8, the ratio of $k_2/k_1 \exp \beta' \mathbf{F} V_d/RT$ is assumed to be one decade greater than the maximum in Fig. 7 (*i.e.*, 30, as in Fig. 5). A sweep rate change of 2 decades is considered here, taking $k_2/c = 800$, 80, and 8, with $k_1/c = 0.2$, 0.02, and 0.02, respectively. As in Fig. 7, $r_1/RT = 13$ and $r_2/RT = 6$. $dV_{max}/\log_{10}c$ is now 50 mV, close to the experimental value (1, 13). High sweep rates produce a broadened, though still sharp, peak, as is experimentally noted (13).

Figure 9 shows the effect of changing k_2/c at constant k_1/c and *vice versa*. Assuming $k_2/c = 80$, the peaks corresponding to k_1/c values of 20, 2.0, 0.2, and 0.02 in Fig. 7 and Fig. 8 are superposed to show the corresponding change in peak shape and potential of the maximum. Similarly, k_1/c is kept constant at 0.02 and k_2/c is varied through 3 decades from 80 to 0.08 using the same r_1/RT and r_2/RT values. The latter shown a change to the typical "totally irreversible" peak form [cf. Ref. (3) and (6)] at small k_2/c values, corresponding to $k_2/k_1 \exp \beta' \mathbf{F} V_d/RT$ values in the 0.3-0.03 range. The second peak appearing at the lowest k_2 value is a computer artifact and represents reduction of —OH (which would not be present in practice). In solving the simultaneous differential equations [22] and [23], a nonzero value (about 0.05) for θ_1 must be assumed in order to obtain meaningful solutions.

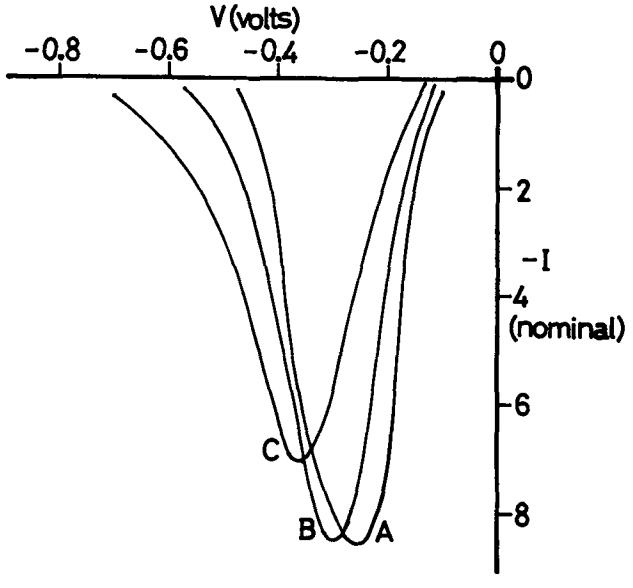

Fig. 8. Effect of sweep rate with reaction [A] rate-determining (cathodic scans). $r_1/RT = 13$, $r_2/RT = 6$, $V_d = 0.3$. Curve A: $k_1/c = 0.2$, $k_2/c = 800$. Curves B and C represent a tenfold and hundredfold increase in c.

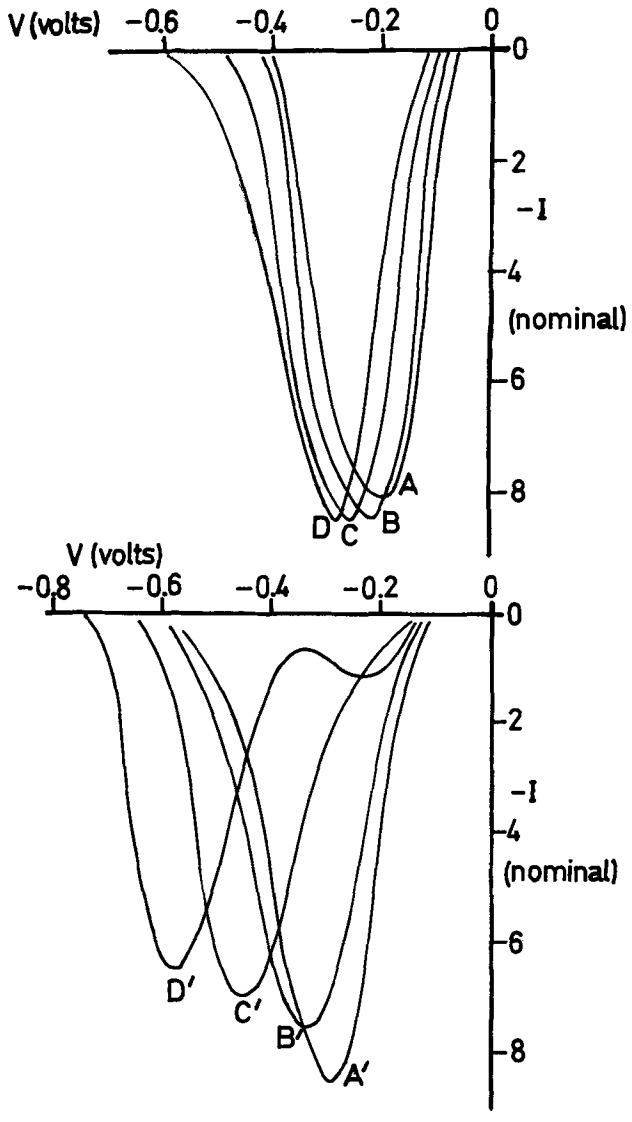

Fig. 9. Effect of relative changes in k_1 and k_2 (cathodic scans). $r_1/RT = 13$, $r_2/RT = 6$, $V_d = 0.3$. Curves A-D: $k_2/c = 80$, $k_1/c = 20$, 2.0, 0.2, and 0.02, respectively. Curves A'-D': $k_1/c = 0.02$, $k_2/c = 80$, 8.0, 0.8, and 0.08, respectively.

General Conclusions

The above calculations demonstrate that symmetrical peaks closely resembling those for a single electron process with a low heterogeneity factor result from a two-stage two-electron reduction process in which the second stage is rate-determining. The criterion for this condition is that the rate of the first stage near the potential of the peak maximum should be at least 1½ orders of magnitude greater than that of the second stage under the same conditions. The peak maximum occurs close to the reversible potential for the first step (assumed to be more cathodic than that for the second step, otherwise two separate peaks result). The general shape of the peak is determined by the heterogeneity factor of the first step, with that for the second, rate-determining step, even though it may be greater, having little effect. Attempts to explain peak symmetry by the occurrence of reactions whose orders are higher than unity (4) are therefore unnecessary. The value of $dV_{max}/d \log_{10} c$, where V_{max} is the potential of the peak maximum, is in the region of 50 mV, in good agreement with the experimental value (1, 13). This corresponds to a value of the transfer coefficient of about 3/2, which is consistent with a rate-determining primary charge transfer (with $\beta = ½$) (13). The use of a simple pseudoequilibrium assumption (*i.e.*, the substitution of Eq. [24] in the cathodic reaction of Eq. [22]), which results in a transfer coefficient equal to $1 + \beta$

($\simeq$3/2) in a numerical evaluation leads to peaks that differ considerably in shape from those determined from a solution of the simultaneous rate equations. On this basis, it is suggested that transfer coefficient values obtained by fitting leading edge slopes or other peak parameters to those expected from simple models involving multielectron transfer steps may be completely erroneous. There is no question that the most useful parameter that can be obtained from a study of potentiodynamic scans under irreversible conditions is the dV_{max}/d ln c value. This should be measured over at least two decades to ensure that the irreversible condition applies. In all cases, it should be possible to derive a true kinetic transfer coefficient value from this parameter, and thus the number of pseudoequilibrium steps preceding the rate-determining charge transfer may be determined. Studies of multielectron steps by the potential sweep method must use a numerical computation based on the rate equations for the discrete single electron steps to find best fits for rate parameters. Parameter values will generally have to be supplemented by other studies, for example, rates at constant current or rates at constant potential as a function of time.

For the special case of the adsorption and reduction of the oxygen layer on platinum, examined here as a model, no attempt has been made to fit exact values of parameters in the rate equations. However, results may be summarized as follows:

1) Initial adsorption under anodic conditions is sufficiently fast as to be reversible and consists of the formation of —OH after a one-electron transfer, with a second very rapid step whose reversible potential is lower by about 300 mV[2] (standard state, $\theta = \frac{1}{2}$), which consists of —O formation.

2) The rate constant for the first anodic step (—OH formation) falls exponentially with coverage. This superficially gives the effect of a large Temkin term. The true value of the Temkin term in this step is 6-9 kcal/equivalent ($r/RT \simeq$ 10-15). Such an explanation gives a general peak shape in agreement with experiment. As the second anodic stage is in pseudoequilibrium, it is not possible to determine its Temkin parameter.

3) The exponential fall of the rate constant of the first reaction step with coverage results from surface rearrangement. This probably occurs as a consequence of, or alongside, the second oxidation step. A place-exchange mechanism is probably involved (6).[3] The net result is a uniform surface phase with a "fossilized" rate constant in the cathodic direction for the first anodic (second cathodic) reaction step. It is not possible to determine whether the rate of the second anodic step is coverage-dependent.

4) The rate-determining step in the cathodic direction is the second electron transfer (*i.e.*, —OH reduction). However, the shape and position of the cathodic peak are determined by the standard potential and r value of the primary (—O) reduction step.

This model gives rise to essentially symmetrical peaks with the correct dV_{max}/d log c dependence. A typical computed plot for a medium coverage case ($k_1^\circ/c = 10$, $q = 6.9$, $r_1/RT = 13$, $r_2/RT = 6$, $k_2 = 80$) is shown in Fig. 10. In practice, r_2/RT is probably lower than 6, and V_d rather more than 300 mV to agree with the correct shape and position of the cathodic peak. At high anodic potentials a further process starts to intervene: that of evolution of molecular oxygen. This is reflected in an extension of the leading edge of the cathodic peak close to the voltage axis, which represents reduction of adsorbed oxygen molecules. The over-all process, however, is undoubtedly not so simple as indicated above. This is illustrated by the plot in Fig. 11, which shows the variation in position of computed cathodic scans as a function of

[2] At least for coverages greater than about 0.2. See Appendix.

[3] It is not a rate-determining place exchange (19), which is inconsistent with the experimental dE_{max}/d log c value [see, however, Appendix and Ref. (23)].

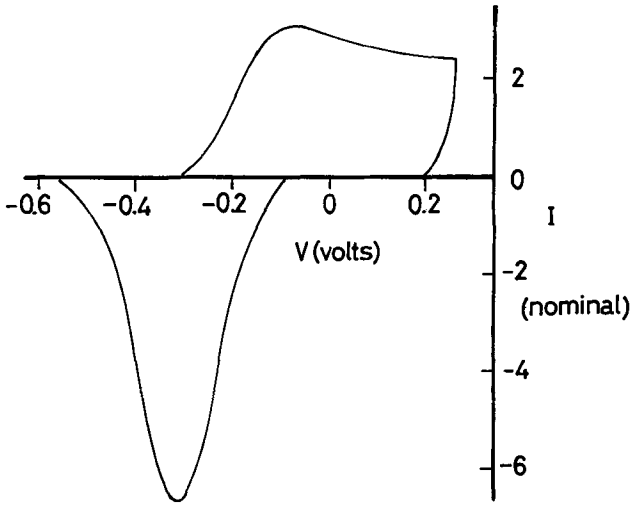

Fig. 10. Calculated anodic and cathodic scan for partial coverage case $r_1/RT = 13$, $r_2/RT = 6$, $V_d = 0.3$. $k_1^\circ/c = 10$, $q = 6.9$, $k_2/c = 80$.

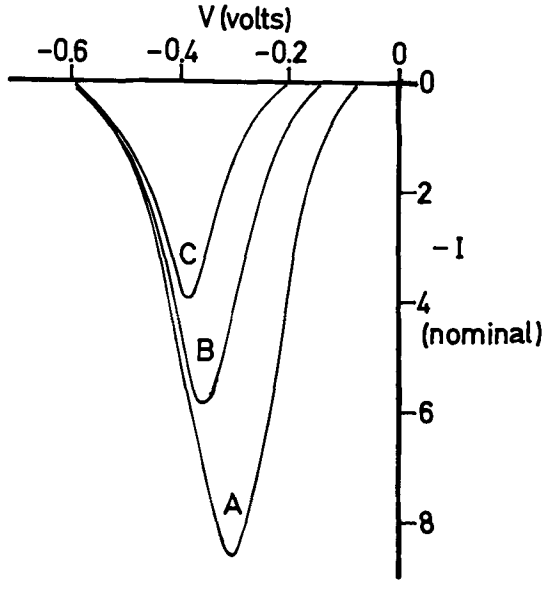

Fig. 11. Effect of partial initial coverage on cathodic scans. $r_1/RT = 13$, $r_2/RT = 6$, $V_d = 0.3$. $k_1/c = 0.02$, $k_2/c = 80$. Curves A, B, C: θ_2 initial = 0.90, 0.50, 0.25, respectively.

coverage ($k_1/c = 0.02$, $k_2/c = 80$, $r_1/RT = 13$, $r_2/RT = 6$, $V_d = 300$ mV). Initial θ_2 values of 0.9, 0.5, and 0.25 are considered. It can be seen that the peaks stack with their trailing edges together, but narrow appreciably with decreasing coverage. In practice, this is not observed—on platinum, peaks at low coverage are as broad (or broader) than those at higher coverage, though their trailing edges do approximately stack together (6). On palladium, however, where the same process may apply, trailing edges are shifted cathodically as a function of increasing coverage (6). This argues that r_2/RT and V_d are coverage dependent (6), though this effect is of comparatively small order compared with the major change of k_1 with coverage. If standard potentials are expressed using $\theta = 0$ (rather than $\theta = \frac{1}{2}$) as a standard state, then trailing edges of peaks with differing r values (in the cathodic direction) stack together (*i.e.*, $E_0^{\theta=0} = E_0^{\theta=1/2} - r/2F$). This is illustrated (reading cathodically) by Fig. 2 in Ref. (6). Expressed on this convention V_d (representing the change in free energy of the —O deposit at low coverage) is therefore not strongly θ-dependent on Pt, but apparently is on Pd.

Recently, certain authors (20) have argued that the oxygen compound on the surface of platinum and other

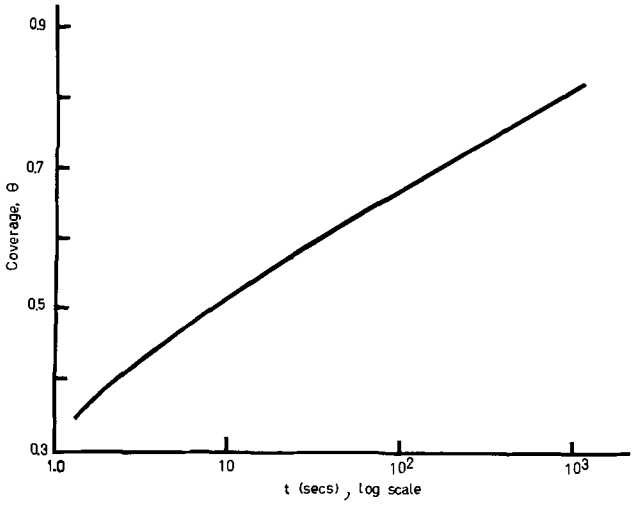

Fig. 12. Calculated potentiostatic film growth curve. $V = 0.1$ (1.2V vs. hydrogen), $k_1 = 10$, $r_1/RT = 13$, θ initial $= 0.3$. Reaction [B] in pseudoequilibrium.

Pt group metals and gold is entirely in a superficially adsorbed form until a coverage corresponding to 2 —O groups/Pt atom is reached. As a result of the present analysis, and of previous work (6), this would appear to be an oversimplification. This idea is also supported by recent ellipsometric work (21) under cyclic scanning conditions, which demonstrate that irreversible surface changes perhaps connected with place-exchange occur (6). It may well be that the equivalent of 2 adsorbed —O atoms/Pt atom represents only the first monolayer of unit cells of an epitaxial surface phase, whereas formation of a true phase oxide, involving rearrangement of deeper platinum layers, requires considerably more energy. Such conclusions, however, require further investigation for confirmation.

Several authors have shown that film growth on Pt in the submonolayer region is logarithmic with respect to time (22, 13). This concept is easily explained if film growth is considered to be totally irreversible under Temkin adsorption conditions, ignoring pre-exponential θ terms (*i.e.*, the $(1 - \theta)$ metal site term in Eq. [22]) (22). Gilroy and Conway (13), on the other hand, argue that an inverse logarithmic growth would be expected if pre-exponential θ terms are taken into account, based on the analytical solution of the integral of an equation of the same type as Eq. [22] under Langmuirian conditions ($r = 0$). Accordingly, a numerical integration of Eq. [22] under Temkin conditions at constant potential has been carried out, using $k_1^\circ = 10$, $q = 6.9$, and $r_1/RT = 13$, at $V = 0.1$V (*i.e.*, taking the reversible potential to be about 1.1V *vs.* hydrogen as previously discussed, at about 1.2V). As before, reaction [B] is assumed to be a pseudoequilibrium. The calculated curve (assuming $\theta_2 \simeq 0.3$ at $t \simeq 0$ as an initial boundary condition) is shown in Fig. 12. The initial rapid rise, followed by a slower logarithmic growth, is characteristic of experimental curves. This lends additional support to the ideas discussed above. However, it must be admitted that such experimental curves show no tendency to go to a limit at $\theta = 1$, indicating that bulk oxidation (place exchange) occurs at higher coverages—*i.e.* the concept of an active site $(1 - \theta)$ term is probably meaningless at high coverages.

Acknowledgment

This work was carried out as part of the basic research program of the Institute of Gas Technology, Chicago, Illinois. The author wishes to express his thanks to the Director and members of the computer staff for the valuable aid that made this study possible.

Manuscript submitted March 13, 1972; revised manuscript submitted Aug. 14, 1972.

Any discussion of this paper will appear in a Discussion Section to be published in the June 1974 JOURNAL.

APPENDIX

Since this paper was prepared for publication, two important sets of experimental data on the platinum oxidation-reduction process have become available, namely those of Vetter and Schultze (23), and Koslowska, Conway, and Sharp (24). In many ways, they confirm the major suppositions used above, in particular, the initial reversibility of the anodic peak (in terms of low or negligible Tafel slopes) and the value of the Tafel slope for the cathodic process at medium to high coverages, in addition to the fall in the rate constant for oxidation by several orders of magnitude as a function of coverage (in terms of the intersection point of the anodic and cathodic Tafel lines (23).

Above, the anodic peak was considered to consist only of a single phase material, initially —OH, converted very rapidly to —O. Rearrangement of the surface caused the —OH rate constant to fall with coverage, so that an irreversible cathodic peak, kinetically controlled by —OH reduction occurs at the surface redox potential for the rapid —O → —OH process (about 0.8V *vs.* hydrogen in the same solution). The results reported in Ref. (24) show that the assumption of a single surface phase needs modification. Two initially reversible phases occur at low coverages ($\theta <$ ~0.2, based on —O coverage), and at least part of these surface compounds persists along with the rearranged surface phase [see also Ref. (12)], especially at low temperatures. These peaks occur between 0.8 and 1.0V and are normally partially masked by solution impurities [see for example the integrated cyclic scans of Böld and Breiter (2), compared with a steady-state θ-V curve obtained under high purity conditions, shown by Damjanovic and Brusic (25)]. The existence of a reversible phase at low coverage, followed by a progressively irreversible phase above 1.0V, is supported by capacitance measurements (23), and has been suggested as an explanation of oxygen reduction Tafel slopes (25, 17) and rest potentials of Pt oxygen electrodes (17). These initial phases represent adsorption not involving nearest neighbor sites (*i.e.*, where rearrangement is not possible, as discussed above).

In the analysis given in the text, it was proposed that the reversible potential of the —O → —OH reaction changes with coverage. This explains the cathodic translation of the reduction peak at increased coverage (6) and the broadened quasi-reversible peak at low coverage (12, 24), where the peak aspect ratio is controlled by r_1/RT (see Fig. 9), owing to the relative change in the rates of the two steps at the same potential. This change in reversible potential is confirmed by the translation of the cathodic Tafel lines as a function of coverage (23). Thus the initial reversible phase peaks may consist of —OH rather than —O [as suggested in Ref. (24)], if the surface redox potential for the process —O → —OH is sufficiently anodic at low coverage. The rearranged ($\theta > 0.2$) phase, due to its different free energy of formation, exhibits a lower (~0.8V) surface redox potential for this reaction.

It thus seems clear that the majority of the adsorbed oxygen on the surface at coverages greater than $\theta = 0.2$ behaves according to the mechanism described in the text, with the participation of small amounts of nonrearranged phases whose reduction peaks are hidden in the leading edge of the cathodic peak. The irreversible phase formed at high anodic potentials would be expected to have a limiting Tafel slope of $2RT/F$ at constant θ. This appears in the experimental results of Vetter and Schultze (23). The latter authors, however, give a very different mechanism of oxide formation and reduction from that given here, based on a place-exchange mechanism. It does not seem likely that place exchange can be involved in the reduction rate-determining step—an electron plus proton transfer must occur to explain the potential-pH dependence of the cathodic peak.

The author wishes to thank Professor Conway for his unpublished data (24) and for helpful discussions.

REFERENCES

1. F. G. Will and C. A. Knorr, *Z. Elektrochem.*, **64**, 258, 270 (1960).
2. W. Böld and M. Breiter, *Electrochim. Acta*, **5**, 145, 169 (1961).
3. S. Srinivasan and E. Gileadi, *ibid.*, **11**, 321 (1966).

4. K. Ohashi, K. Sasaki, and S. Nagaura, *Bull. Chem. Soc. Jap.*, **39**, 2066 (1966); K. Sasaki and K. Ohashi, *Electrochim. Acta*, **12**, 366 (1967).
5. P. Stonehart, *ibid.*, **13**, 1789 (1968); P. Stonehart and F. P. Portante, *ibid.*, **13**, 1805 (1968).
6. P. Stonehart, H. A. Kozlowska, and B. E. Conway, *Proc. Roy. Soc. (London)*, **A310**, 541 (1969).
7. B. E. Conway and E. Gileadi, *Trans. Faraday Soc.*, **58**, 2493 (1962).
8. A. Eucken and B. Weblus, *Z. Elektrochem.*, **55**, 114 (1951).
9. J. O'M. Bockris and H. Kita, *This Journal*, **108**, 676 (1961).
10. J. Llopis and M. Vazquez, *Anales Real Soc. Espan. Fis. Quim. (Madrid)*, **63**, 273 (1967).
11. J. Llopis, I. M. Tordesillas, and J. M. Alfayate, *Electrochim. Acta*, **11**, 623 (1966).
12. V. L. Tikhomirova, A. I. Oshe, V. S. Bagotskii, and V. I. Luk'yanycheva, *Dokl. Akad. Nauk. SSSR.*, **159**, 644 (1964).
13. D. Gilroy and B. E. Conway, *Can. J. Chem.*, **46**, 875 (1968).
14. R. Parsons, in T. P. Hoar, Proc. 8th. Meeting CITCE, Madrid (1956), p. 439, Butterworths, London (1958).
15. M. A. Vorotynsev and A. M. Kuznetsov, *Elektrokhimiya*, **6**, 208 (1970).
16. M. Boudart, *J. Am. Chem. Soc.*, **72**, 1531, 3556 (1952).
17. A. J. Appleby, *J. Electroanal. Chem.*, **35**, 193 (1972).
18. R. A. Marcus, *J. Chem. Phys.*, **43**, 679 (1965).
19. A. K. N. Reddy, M. A. Genshaw, and J. O'M. Bockris, *ibid.*, **48**, 671 (1968).
20. T. Biegler and R. Woods, *J. Electroanal. Chem.*, **20**, 73 (1968); T. Biegler, D. A. J. Rand, and R. Woods, *ibid.*, **29**, 269 (1971); and D. A. J. Rand and R. Woods, *ibid.*, **31**, 29 (1971).
21. F. Chao, M. Costa, and A. Tadjeddine, *Bull. Soc. Chim. France*, **1971**, 2466.
22. H. A. Laitinen and C. G. Enke, *This Journal*, **107**, 773 (1960); S. W. Feldberg, C. G. Enke, and C. E. Bricker, *ibid.*, **110**, 826 (1963); see also, K. H. Pool, J. G. Smith, and A. L. Crittenden, *Anal. Chem.*, **38**, 1242 (1966).
23. K. J. Vetter and J. W. Schultze, *J. Electroanal. Chem.*, **34**, 131, 141, (1972).
24. H. Angerstein-Koslowska, B. E. Conway, and W. B. A. Sharp, *ibid.*, **43**, 9 (1973).
25. A. Damjanovic and V. Brusic, *Electrochim. Acta*, **12**, 615 (1967).

Technical Notes

Cathode Reactants in High Energy Density Aprotic Battery Systems

The Metallic Borosulfides

Frank M. Kimmerle* and Gaétan Giasson

Chemistry Department, Université de Sherbrooke, Quebec, P. Q., Canada

The choice of cathodic materials in aprotic battery systems represents a compromise between high cell type voltage, low equivalent weight, and compatibility with electrolyte solvent and anode material, *i.e.*, low self-discharge leading to a long shelf life. Among the several transition metal sulfides and halides evaluated (1), only one, the couple CuS/Li, seems to have been exploited commercially (2).

This exploratory work was undertaken in order to investigate the utility of other sulfur compounds. Boron trisulfide has a very high energy of formation and a low equivalent weight and thus an energy density in excess of 2000 Whr kg^{-1} for the reaction

$$B_2S_3 + 6Li \rightarrow 2B + 3Li_2S$$

Its very hygroscopic nature, its high solubility and chemical reactivity with various aprotic solvents, and its high degree of polarization render it, however, totally unsuitable as an electrode material. Although the synthesis and x-ray diffraction patterns of some transition metal borosulfides have been reported in the literature (3, 4) very little is known about their physical characteristics or chemical behavior. We suspected that these compounds, intermediate between the sulfides of the transition metals and boron, might combine the chemical inertness of the former with the high energy density of the latter.

Experimental

Synthesis of the transition metal borosulfides was most conveniently carried out by heating stoichiometric mixtures of elemental boron, sulfur, and metal in an evacuated sealed quartz or Vycor tube (2). Heating at temperatures from 600° to 1200°C was continued for 2-4 weeks depending on sample size to ensure equilibrium conditions. The synthesis using B_2S_3 and or metal sulfides yielded identical compounds but had the inconvenience that mixing of the reagents in an inert atmosphere was mandatory. Four compounds have definitely been identified from chemical analysis and comparison of their x-ray diffraction patterns with those reported in the literature. Their compositions are given as AgBS, CuBS, $Pb_2B_2S_5$, and MnB_2S_4. The latter two correspond to a 2:1 and 1:1 ratio of metal sulfide and boron trisulfide which may be regenerated by thermolysis decomposition. Further analysis of the structure was not attempted with these polycrystalline materials.

The borosulfides were found to be very stable in air, water, caustic solutions, and most mineral acids with the exception of MnB_2S_4 which decomposed slowly in water to yield MnS and boric acid. Analysis by gas chromatography (GC) after 30 days contact with three aprotic solvents, propylene carbonate (PC), dimethylformide (DMF), and dimethylsulfoxide (DMSO), at room temperature did not indicate significant solvent decomposition. The solubilities of the borosulfides (monitored by chemical analysis and atomic adsorption over a 60 day period) also indicated little variation (<5%), followed the order PC < DMF <DMSO, and were approximately equal to those of the corresponding sulfides.

Cathode disks of about 1 mm thickness and 1¼ in. diam were fabricated in the following manner. After

* Electrochemical Society Active Member.
Key words: aprotic batteries, borosulfides, lithium.

mortarizing the borosulfide, it was intimately mixed with 10-20% graphite (Fisher grade No. 38), powdered polypropylene (Du Pont), and compacted at 800 kg cm^{-2} for several minutes at 150°C onto a copper wire mesh. The porosity could be varied by including some electrolyte salt (*e.g.*, $LiClO_4$, LiBr) which was subsequently leached out. For evaluation purposes we preferred this type of electrodes: rugged, quite flexible, and uniformly smooth without cracks or imperfections. A lower polypropylene content caused a certain fragility, unevenness, and a tendency for the electrodes to flake off but it also resulted in material having higher current densities and might therefore be preferred for practical work. The prototype cells used in these studies consisted essentially of three disks: the depolarizer, a fiber glass separator saturated with electrolyte, and a thin lithium anode, pressed lightly together at the bottom of a small cylinder. Although assembled in an Argon filled glovebox, they were dipped in hot wax or covered with a layer of epoxy and kept for up to four months in the laboratory. A third electrode, consisting of a lithium ribbon plunged into the same electrolyte and connected to the cell by a Luggin capillary, was occasionally used as a reference electrode. Although its potential is without precise thermodynamic significance, it does facilitate a simple separation of the overpotentials into anodic and cathodic polarization effects.

The aprotic solvents were twice redistilled from material equilibrated for one week with activated 4A Linde Molecular Sieves. The water content (Karl Fisher Analysis) was less than 50 ppm (PC), 60 ppm (DMF), and 150 ppm (DMSO). The electrolyte solutes $LiClO_4$ and LiBr, although dried in a vacuum oven, at 150°C for 48 hr, contributed some additional moisture but further purification was not deemed necessary for evaluation purposes. All cell discharges were carried out at 3 mA with 1¼-in. disks or at current densities of 0.4 mA cm^{-2} of geometric area at 23°C. We confirmed Dey's observation (5) that PC itself constitutes a cathode reactant and will sustain 1V *vs.* the lithium electrode for several days, forming propylene (GC analysis) and Li_2CO_3 (x-ray diffraction analysis). Analogous behavior was observed with mixtures of acetonitrile (AN) and PC with LiBr electrolyte, while DMSO formed a thio ether (6). In DMF however a rapid decay of the discharge potential occurred and the initial current can be attributed to impurities from the solvent or graphite.

Thus, despite the fact that DMF displays a lower dielectric constant, lower specific conductance, and higher solubilities of the borosulfides, that it polymerizes to yield a gel in the presence of Li metal, and that lithium has not been successfully plated from Li solutions (*i.e.*, that the reaction is irreversible) (7), we chose to use a 1.4M $LiClO_4$ solution of DMF as an electrolyte since it allows us to follow the complete discharge of cathode reactant. Typical discharge curves are given in Fig. 1. For AgBS plateaus corresponding to two one electron changes can clearly be discerned and close to 100% current efficiency is observed, although not at useful potentials. The potential decreases gradually for CuBS and $Pb_2B_2S_5$ but two regions are again clearly distinguishable. MnB_2S_4 which has the highest solubility also gives the poorest performance yielding only about 15% useful discharge. The polarization of the lithium electrode remained below 0.5V during the first part of the discharge increasing slightly when the second plateau was reached.

Figure 2 indicates that the performance is significantly improved using PC or PC-AN electrolytes. For AgBS, as incidently for Ag_2S, Cu_2S, and CuS, the improvement is due almost entirely to a decrease of the polarization of the lithium anode. The CuBS now shows a distinctive plateau at 1.6V and about 50% utilization before the decomposition of the electrolyte becomes evident. Mixtures of PC and AN having a lower freezing point gave almost identical results and significant improvements in performance should be sought by changing the physical characteristics of the electrodes such as porosity, optimum thickness, etc.

An evaluation of these cathodic materials is made in Table I. Apparent current densities, electrode preparation, cell design, etc., were kept as identical as possible and thus, although arbitrarily, established a basis of comparison. Column 2 indicates that the open-circuit voltages of the transition metal borosulfides are lower than the respective sulfides and a modest 2V.

Table I. Cathodic reactant materials

Couples, Li/X	$E^{25°C}$, Volts	ΔG_f, kcal/mole	$C_{calc.}$, A-hr/g	$W_{calc.}$	$W_{pract.}$, Whr/kg DMF	PC
S	2.64		1.67	3080	—	—
CuBS	1.99	−30	0.504	890	190	440
Cu_2S	2.40		0.337	740	310	—
CuS	2.33		0.561	1140	230	—
AgBS	2.07	−26	0.355	670	200	290
Ag_2S	2.71		0.216	560	100	—
$Pb_2B_2S_5$	2.18	−106	0.449	880	140	140
PbS	2.25		0.224	480	50	—
MnB_2S_4	2.09	−100	1.05	1720	90	90
MnS	1.92		0.616	1020	40	—

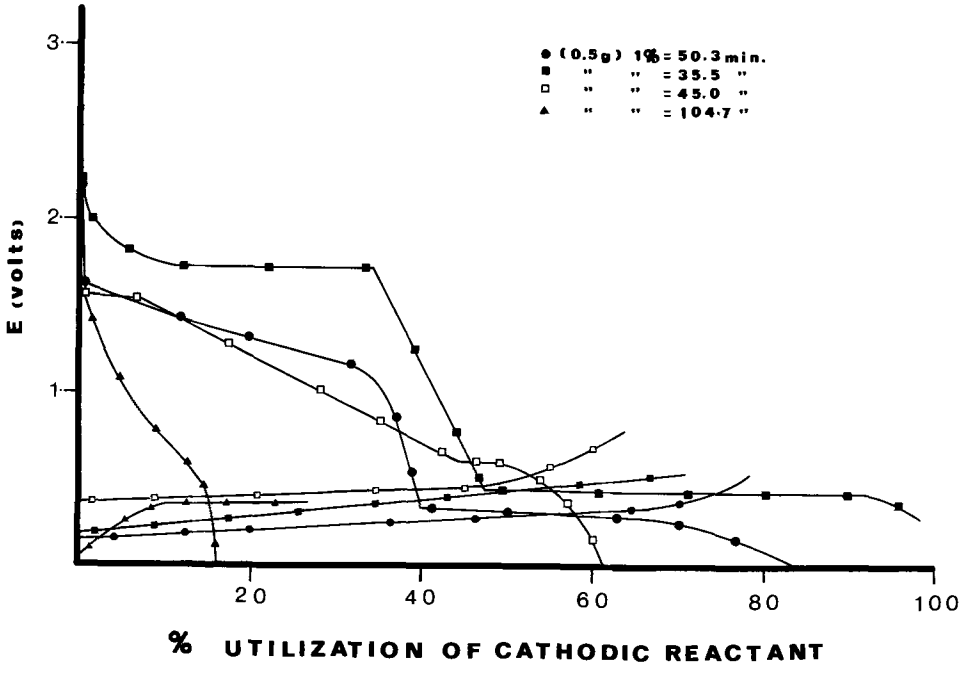

Fig. 1. Discharge characteristics of metallic borosulfide. Cathode and anode potentials vs. Li reference electrode in DMF (1.4M $LiClO_4$). ● ● CuBS; ■ ■ AgBS; □ □ $Pb_2B_2S_5$; ▲ ▲ MnB_2S_4.

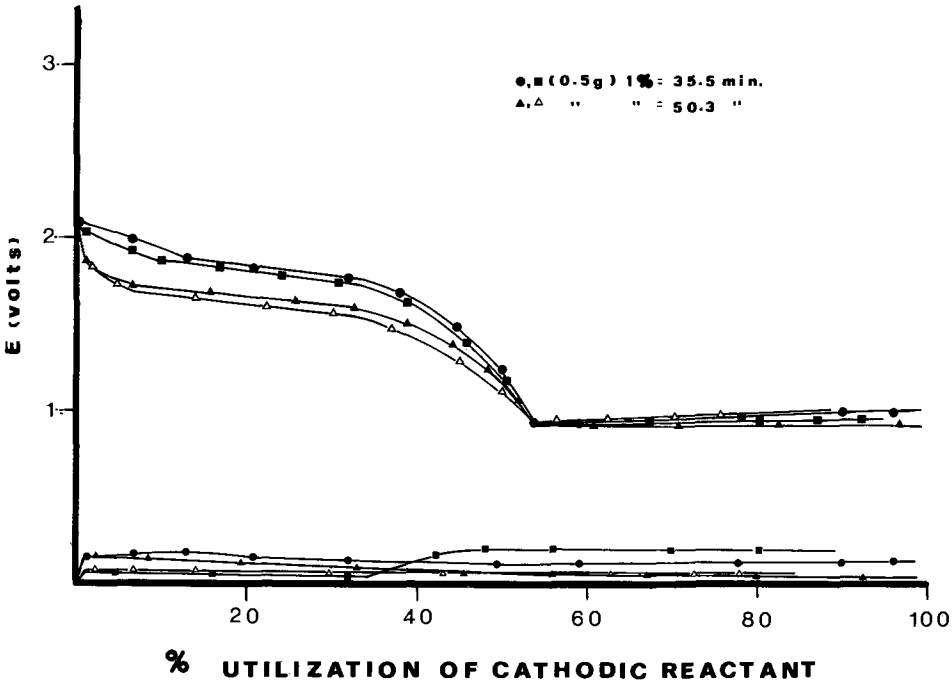

Fig. 2. Discharge characteristics. Cathode and anode potentials vs. Li reference electrode. PC + AN: volume ratio 3:1, ● ● AgBS in PC (1.0M $LiClO_4$); ■ ■ AgBS in PC + AN (LiBr saturated); ▲ ▲ CuBS in PC (1.0M $LiClO_4$); △ △ CuBS in PC + AN (LiBr saturated).

However, the lower equivalent weight and hence C (column 4) indicate the reason for the comparatively high theoretical energy density (column 5). The free energy of formation of the four new depolarizers (column 3) were calculated from the electrode potentials of the couples Li/S and Li/X and the ΔG_f for the metallic sulfides and may include an uncertainty of up to 10%. The practical energy density was established by integrating the area between anode and cathode potentials of graphs such as Fig. 1 and 2 up to the end of the first discharge plateau.

The highest energy density was obtained for CuBS exceeding that of the copper sulfides, and the other three borosulfides also show striking improvements with respect to their sulfide analogs.

Preliminary results indicate further that the CuBS and AgBS will support current densities of up to 5 mA cm^{-2} for short periods and that 50% discharged electrodes may be recharged several times although at low power efficiencies.

Conclusion

The discharge curves obtained at room temperature indicate clearly that with optimization of electrode porosity, electrolyte, and cell configuration, performance in excess of the insoluble metal sulfides can be realized. The synthesis of the metal borosulfides employed is far too expensive to warrant practical interest. Nevertheless the projected cell performance is sufficiently competitive to encourage us to establish discharge efficiencies at low temperatures and storage life at high temperatures using prototype batteries.

Acknowledgment

Support of this work by a research grant from the Defence Research Board, Ottawa, Ontario, Canada, is gratefully acknowledged.

Manuscript submitted Feb. 22, 1973; revised manuscript received April 12, 1973.

Any discussion of this paper will appear in a Discussion Section to be published in the June 1974 JOURNAL.

REFERENCES

1. F. Conté and G. Pistoia, *J. Appl. Chem. Biotechnol.*, **21**, 77 (1971).
2. J. P. Gabano, V. Déchenaux, G. Gerbier, and J. Jammet, *This Journal*, **119**, 459 (1972).
3. J. Flahaut, L. Domange, and J. Kamsu Kom, *C. R. Acad. Sc. Paris*, **255**, 701 (1962); **254**, 299 (1962).
4. D. Thomas and G. Tridot, *ibid.*, **259**, 2854 (1964); **258**, 2587 (1967).
5. A. N. Dey and B. P. Sullivan, *This Journal*, **117**, 222 (1970).
6. Tech. Bulletin, DMSO Crown Zellerbach Corp., Chem. Prod. Div., Camas, Wash.
7. Raymond Jasinski, "High Energy Batteries," Plenum Press, New York (1967).

The Kinetics of $Fe^{2+}/FeCl_2^+/HCl(aq)$ on Pyrolytic Graphite Electrodes

B. G. Ateya* and L. G. Austin**

Department of Materials Science, Fuel Science Section, Pennsylvania State University, University Park, Pennsylvania 16802

Silverman and Dodson (1) have shown that the homogenous electron-exchange reaction of iron in strong hydrochloric acid solutions involves the ions $FeCl_2^+$ and Fe^{2+} and they give activation energies and entropies of 9.7 kcal/mole and −20 cal/deg mole for this exchange. The corresponding ferrous-ferric electrode reaction is

$$FeCl_2^+ + e^- \rightleftarrows Fe^{2+} + 2Cl^-; \quad E^\circ = 0.700V \text{ (1f HCl)}$$

* Electrochemical Society Student Associate.
** Electrochemical Society Active Member.
Key words: exchange current, activation energy.

where $FeCl_2^+$ is the predominant ferric species in concentrated hydrochloric acid solutions.

We have determined transfer coefficients, exchange currents, and the activation energy for this reaction on the edge atom and basal plane faces of pyrolytic graphite, using the rotating disk technique.

Experimental

The pyrolytic graphite electrode used was obtained from the General Electric Company and had a theoretical density of 2.223 g/cm³ and a measured density of 2.21 g/cm³, indicating negligible porosity. It was machined to a cylinder of 1/8 in. diam, with edge atom face at the ends. The electrode was fitted with shrinkable Teflon tubing over the immersed region. It was found necessary to spray a thin Teflon layer over the rod, fit and heat-shrink the shrinkable tubing, and then reinforce the tightness at the end by shrinking another short piece of tubing over the first. This technique prevented slow creep of electrolyte between the tubing and the electrode cylindrical surface. The electrode end was then machined, perpendicular to its axis, and polished, using 0.3 and 0.05μ alumina powder, to a mirror-like finish; the polished surface had a double layer capacity of about one-tenth of the machined surface. After rinsing, the surface was cleaned by briefly evolving first oxygen and then hydrogen. The same procedure was used to prepare electrodes of 0.6 cm diam, used in the transition time measurements.

No precautions were taken to ensure ultra-high purity conditions, since the rate of the redox reaction is sufficiently high to dominate over any impurity reaction. The electrode was used in a rotating disk assembly capable of a range of speeds up to 12,000 rpm, measured by a stroboscope; the electrode assembly weighed about 2g and the system gave no observable vibrations. All tests were run in 4*N* HCl which is strong enough (2) to make $FeCl_2^+$ the major oxidized species. Electrode potentials were measured using a Luggin capillary and a saturated calomel reference electrode. The junction potential was estimated to be 30 mV, giving a theoretical reversible potential for equal concentrations of ferrous and ferric iron of 0.425V *vs.* the reference electrode. The open-circuit potential observed for 0.093*N* ferrous and 0.096*N* ferric was 0.433V *vs.* the reference electrode. The counterelectrode was an inch-long platinum wire bent in a circle around the axis of the test electrode and positioned well below it: movement of the counterelectrode did not affect the results.

A blank test with no dissolved iron gave residual currents of less than 0.3 mA/cm² over the potential range −0.2 to +1.0V *vs.* the reference; the effect of residual current was negligible under all test conditions. The resistance between the test electrode and Luggin tip was estimated by the blanked-out portion on an oscilloscope trace on current interruption using a mercury-wetted relay interruptor circuit. Double-layer capacity was measured in 0.5M K_2SO_4 using a triangular voltage sweep method, so that the relative area of different electrodes could be compared. Potassium sulfate gave a wide voltage range in which double-layer capacity was constant, whereas pseudocapacity was present in 4*N* HCl as the electrode went toward the chlorine evolution potential.

Results

Using the formation constants of 30.0, 4.0, and 0.1 (3), the equilibrium ratios of ferric iron species at room temperature were calculated to be $FeCl^{2+} = 0.04$, $FeCl_2^+ = 0.68$, and $FeCl_3 = 0.27$. To test whether slow chemical steps were contributing to the rate expressions, galvanostatic transition times were measured for both anodic and cathodic currents. Over a range of transition times from 0.3 sec to nearly 30 sec, $i\tau^{1/2}$ was constant within ±3% for each current direction, giving values of diffusion coefficients of (5.7) (10^{-6}) and (5.5) (10^{-6}) cm²/sec, anodic and cathodic respectively, based on total iron concentrations. It was concluded that chemical steps did not affect the rate at the high current density used, almost 40 mA/cm². Calculations of the diffusion layer thickness showed edge effects to be negligible.

From the theory of the rotating disk electrode (4)

$$i_L = 0.62nFD^{2/3}\gamma^{-1/6}\omega^{1/2}R_b \text{ A/cm}^2 \qquad [1]$$

For the range of Reynold's numbers used, the Newman correction (5) to Eq. [1] is less than 0.1%. Figure 1 shows a typical set of data. It is seen that the equation is obeyed both for oxidation and reduction directions. Using a mean value of kinematic viscosity of 10^{-2} stokes, the measured values of D as a function of temperature are shown in Fig. 2. Thus, for the oxidized and reduced species

$$D = (5)(10^{-6})\exp\left[\frac{4500}{2}\left(\frac{T-298}{298T}\right)\right]$$

$$\pm 20\% \text{ cm}^2/\text{sec}$$

over the range $T = 273°$-$320°$K. It is evident that within the experimental error of the tests the difference between the diffusion coefficients of the oxidized and the reduced species is too small to be detected.

If the reaction is a simple, first-order, one-electron transfer reaction, the net anodic current is

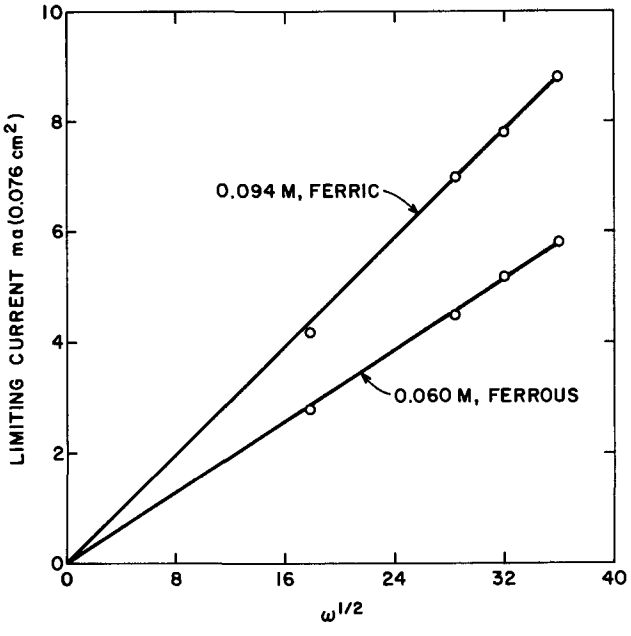

Fig. 1. Test of Levich rotating disk equation for ferrous (cathodic) and ferric (anodic) ions in 4*N* HCl.

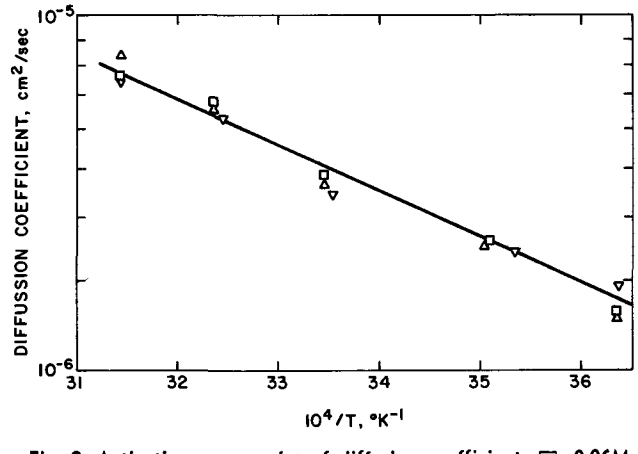

Fig. 2. Activation energy plot of diffusion coefficient. □, 0.06M ferrous; △, 0.094M ferric; ▽, 0.10M ferric.

$$i = i_o[(R_S/R_b) \exp(\alpha\eta/b) - (P_S/P_b) \exp(-\beta\eta/b)] \quad [2]$$

where subscripts S and b refer to surface and bulk concentrations. Since the rotating disk gives a uniform diffusion layer thickness

$$R_S/R_b = 1 - i/i_{La}$$
$$P_S/P_b = 1 + i/i_{Lc} \quad [3]$$

where i_{La} and i_{Lc} are limiting anodic and cathodic currents, which are readily measured at a given rpm. Then

$$\eta = 2.3(b/\alpha) \log q - 2.3(b/\alpha) \log i_o$$

where

$$q = \frac{1}{\left(\frac{1}{i} - \frac{1}{i_{La}}\right) - \left(\frac{1}{i} + \frac{1}{i_{Lc}}\right) \exp(-\eta/b)} \quad [4]$$

The measured polarization, η_m, was corrected for ir between the electrode and Luggin tip using the resistance r measured as described above, $\eta = \eta_m - ir$. The relative magnitude of the ir correction depended on conditions but was always less than 30%. Figure 3 shows some typical plots of η *vs.* log q.

It is concluded that the simple kinetic expression of Eq. [2] adequately describes the experimental results, at least up to currents of about 0.7 of the limiting current. The values of the transfer coefficients α and β determined from the slopes of the lines are $\alpha = 0.4 \pm 0.04$, anodic, and $\beta = 0.6 \pm 0.04$, cathodic, so that $\alpha + \beta = 1.0$. The concentrated electrolyte used makes diffuse double-layer effects fairly small (6), so that these values are significantly different from one half. From the slope and intercepts the values of exchange current density are obtained. Figure 4 shows i_o as a function of temperature; hence the apparent activation energy, $E^{\ddagger}$, is estimated to be 11.5 kcal/mole, with true values (7) of 18.0 kcal/mole anodic, 1.8 kcal/mole cathodic. The double-layer capacity was estimated to be 35 ± 3 μf/cm^2, in the potential region 0.1-0.5V (*vs.* standard calomel reference) where residual current and surface adsorption are a minimum.

The experiments were repeated using the basal plane of the pyrolytic graphite as the reacting face. A 0.3 cm thick disk containing a 0.15 by 0.15 cm hole was fitted to a corresponding stud on a cylinder of the graphite cut to give edge atom face contacting basal plane face, thus acting as a current collector. The double-layer capacity was 32 ± 3 μf/cm^2 both for unpolished and polished basal plane face. However,

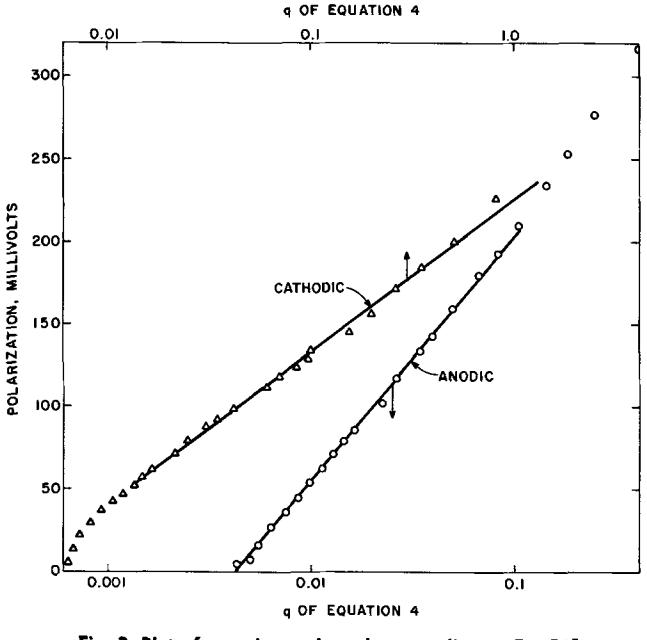

Fig. 3. Plot of experimental results according to Eq. [4]

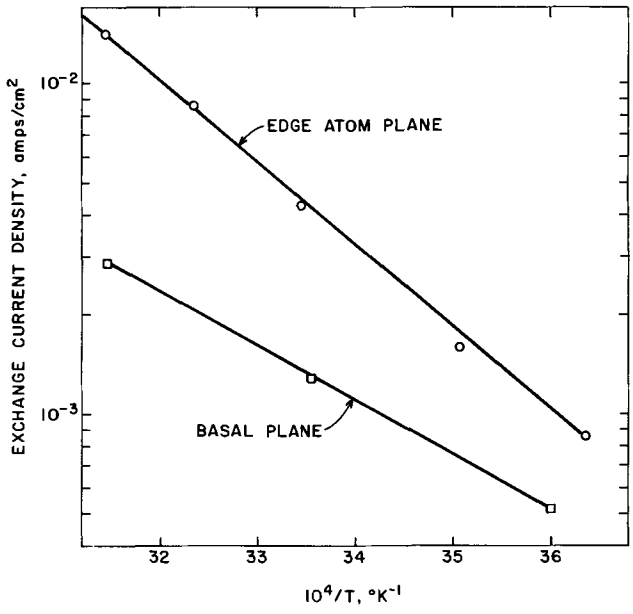

Fig. 4. Activation energy plot of exchange current

because the pyrolytic carbon is an approximation to a single crystal of graphite, the electronic conductivity normal to the basal plane is lower and somewhat higher ir effects were observed via the blanked-out portion on current interruption. The exchange current density for the basal plane face was three to four times smaller than that on the edge atom face, depending on the temperature, as it also appeared to have a slightly lower activation energy (see Fig. 4).

Conclusions

By rotating disk electrode measurements it is concluded that the diffusion coefficients of both iron species in 4N HCl are about (5) (10^{-6}) exp [4500/2 (T − 298/298T)] ± 20% cm^2/sec. The kinetics of the reaction

$$FeCl_2^+ + e^- \rightleftarrows Fe^{2+} + 2Cl^-$$

on the edge atom and basal plane surfaces of pyrolytic graphite, in the presence of excess H^+ and Cl^-, appear to be first order in iron species with one-electron transfer. The transfer coefficients are α(anodic) = 0.4 ± 0.04 and β(cathodic) = 0.6 ± 0.04. These values are in good agreement with transfer coefficient values on platinum in different media (8). Exchange current density at 25°C is (4) (10^{-3}) A/cm^2 for concentrations of 0.094N ferric, 0.06N ferrous, or k = (5.2) (10^{-4}) cm/sec, assuming unit activity coefficients. This agrees with the value of 2.29 × 10^{-4} cm/sec reported by Galus and Adams (9) for the same reaction at carbon paste electrode. The apparent activation energy over the temperature range 273°-320°K is 11.5 kcal/mole. This is slightly larger than the value of 9 kcal/mole on platinum in 1N $HClO_4$ reported by Randles (10). The rate parameters are based on unit polished surface area, with double-layer capacity in 0.5M K_2SO_4 of 35 ± 3μf/cm^2. The rate constant on basal plane of the same reactive area as the edge atom plane is (1.5) (10^{-4}) cm/sec at 25°C, and the activation energy is 9.5 kcal/mole. The Newman J factor (11) for these exchange currents is roughly 0.05, so that correction for the position of the Luggin capillary is negligible.

Acknowledgments

We gratefully thank the National Science Foundation for financial support under Grant GK-11689.

Manuscript submitted Jan. 8, 1973; revised manuscript received April 16, 1973.

Any discussion of this paper will appear in a Discussion Section to be published in the June 1974 JOURNAL.

LIST OF SYMBOLS

b	RT/F
D	diffusion coefficient, cm^2/sec
$E^{\ddagger}$	apparent activation energy of the electrode reaction
k	standard rate constant at the reversible potential, cm/sec
F	Faraday, 96,500 coulomb/g equivalent
i_o	exchange current density, A/cm^2
i_{La}	anodic limiting current, A/cm^2
i_{Lc}	cathodic limiting current, A/cm^2
R_S, R_b	reactant concentration at electrode surface and in the bulk of electrolyte
P_S, P_b	same as above for product concentrations
q	a current function defined by Eq. [4]
R	gas constant
T	temperature in °K
α	anodic transfer coefficient
β	cathodic transfer coefficient
γ	kinematic viscosity in stokes, cm^2/sec
η_m	measured total polarization
ω	angular velocity, radians/sec
τ	transition time, sec

REFERENCES

1. J. Silverman and R. Dodson, *J. Phys. Chem.*, **56**, 846 (1952).
2. E. Rabinowich and W. Stockmayer, *J. Am. Chem. Soc.*, **64**, 335 (1942).
3. H. Freiser and Q. Fernando, "Ionic Equilibria in Analytical Chemistry," pp. 147, 306, John Wiley & Sons, New York (1963).
4. V. G. Levich, "Physicochemical Hydrodynamics," p. 69, Prentice-Hall, Englewood Cliffs, N. J. (1962).
5. W. H. Smyrl and J. Newman, *This Journal*, **118**, 1079 (1971).
6. L. G. Austin, in "Handbook of Fuel Cell Technology," p. 64, C. Berger, Editor, Prentice-Hall, Englewood Cliffs, N. J. (1968).
7. K. J. Vetter, "Electrochemical Kinetics," p. 115, Academic Press, New York (1967).
8. N. Tanaka, and R. Tamamushi, *Electrochim. Acta*, **9**, 963 (1964).
9. Z. Galus and R. N. Adams, *J. Phys. Chem.*, **67**, 866 (1963).
10. J. E. B. Randles and K. W. Somerton, *Trans. Faraday Soc.*, **48**, 937 (1952).
11. W. H. Tiedemann, J. Newman, and D. N. Bennion, *ibid.*, **120**, 256 (1973).

Brief Communication

Vapor-Deposited Gold Electrodes: Effects of Undercoatings

Radoslav Adzic,[1] Jean Horkans,† B. D. Cahan,* and Ernest Yeager*

Department of Chemistry, Case Western Reserve University, Cleveland, Ohio 44106

Vapor-deposited metal-film electrodes on smooth glass substrates are attractive for optical reflectance studies of electrochemical systems because of the high optical quality of the surface and a ratio of true to apparent area relatively close to unity. With gold, the double layer capacity of the vapor-deposited films has been found by the authors to be approximately one-half that observed on mechanically polished electrodes of the bulk metal at the same potentials. Metals such as gold, however, do not adhere well when deposited directly on a glass substrate, and some kind of undercoating generally has been used by various authors (1-4) in order to obtain adherence, *e.g.*, Paik *et al.* (3) used glass Ta-Pt-Au. A number of substances yield adherent vapor-deposited gold films. The purpose of this note is to call attention to the fact that these undercoats can seriously interfere with the optical and electrochemical measurements.

Four undercoats on glass have been examined for gold films: a sputtered tantalum underlayer, a platinum over tantalum layer, a sputtered titanium underlayer, and a sputtered niobium layer. Only the niobium was found to be a satisfactory undercoating.

The glass substrate (microscope slide) was cleaned by ultrasonic treatment first in Alconox solution and then in distilled water and finally vapor degreased in isopropanol. After the vacuum chamber was pumped down to a pressure of $\sim 10^{-6}$ Torr, the substrates were heated to ~200°C to drive off any residual volatile impurities and then maintained at ~100°C during the course of vapor deposition. The Nb is presputtered for ~1 hr before the shutter is opened and a film of approximately 10-50Å thickness is deposited on the substrate. A thick (2000-5000Å) film of Au is evaporated on this undercoating in the same vacuum system without exposing the Nb layer to air.

A much better vacuum than the 10^{-6} Torr available for the present work is required for the vapor deposition of most metals to avoid oxide formation. Fortunately, gold does not oxidize and hence high quality films could be deposited even with this poor vacuum.

The current-potential behavior in the double layer region of such an Au electrode in 1*N* $HClO_4$ is shown in Fig. 1. The squareness of the voltammogram indicates that the primary process occurring in this po-

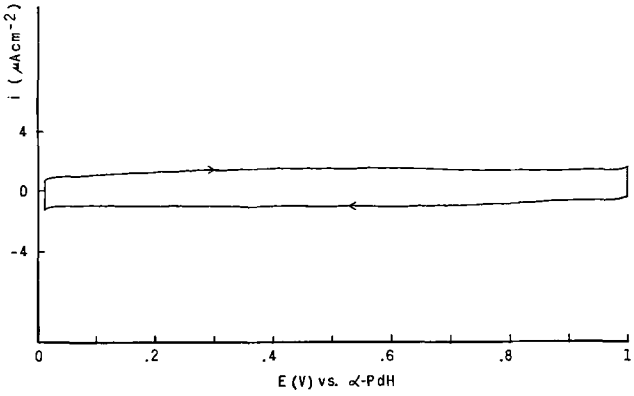

Fig. 1. Voltammetry curve for evaporated gold film with a niobium undercoating in 1M $HClO_4$. Sweep speed 20 mV/sec at ~25°C.

* Electrochemical Society Active Member.
† Electrochemical Society Student Member.
[1] Permanent address: Institute of Chemistry, Technology and Metallurgy, Belgrade, Yugoslavia.

Key words: specular reflectance of electrodes, gold electrodes, vapor-deposited electrodes.

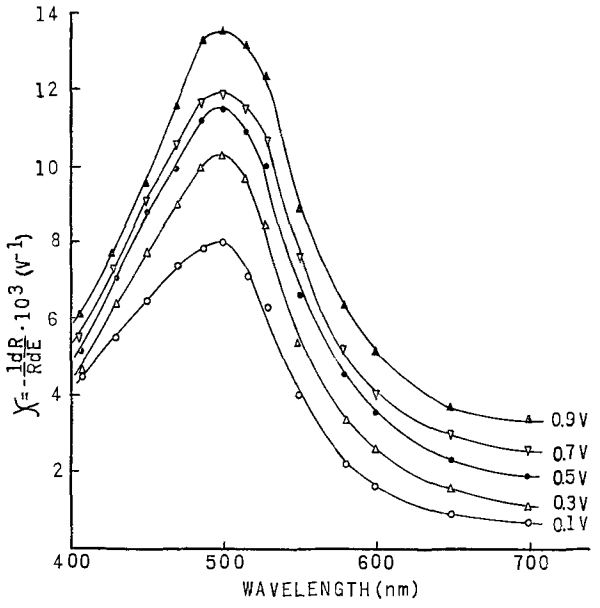

Fig. 2. Wavelength dependence of the electromodulation coefficient, $\chi = -\frac{1}{R}\frac{dR}{dE}$, at different potentials, α-Pd-H reference electrode, for evaporated gold electrode with a niobium undercoating in 1M $HClO_4$. Angle of incidence = 45°, parallel polarization.

tential region is double layer charging. No small peaks are observed which would indicate the presence of impurities or interference from the undercoat.

The electroreflectance was measured at various electrode potentials using an a-c potential modulation (35 mV rms) with a phase sensitive detection system and a single reflection. In Fig. 2 the in-phase portion of the electromodulation coefficient, $\chi = R^{-1}dR/dE$, measured at 45 Hz is shown; under these conditions, the out-of-phase portion of the signal is very small compared to the in-phase portion. The magnitude of χ increases with increasing electrode potential. The position of the peak at 500 nm is independent of potential. The electrochemical and optical behavior of the Au electrode with a Nb undercoat are in good agreement with results obtained using bulk Au either electropolished or mechanically polished.

Substantial complications have been encountered with other undercoatings. The use of Ta directly under Au has been found to be unsatisfactory because of apparent formation of a Ta-Au alloy or compound with considerably different spectral properties than pure Au. A Ta-Pt-Au sandwich was tried with the intermediate Pt layer to isolate the Ta from the Au. The Pt, however, interfered considerably with both the electrochemical and optical measurements. The voltammetry curves showed evidence of hydrogen peaks involving platinum and the wavelength and potential dependence of χ was changed as can be seen from a comparison of Fig. 2 with corresponding figures in earlier publications (1, 2). The changes in the electroreflectance are believed to have been caused by partial exposure of Pt or a Pt-Au alloy.

Titanium was also investigated as a possible undercoat. Effects due to Ti were evident in the voltammetry curves with the appearance of an additional peak at ~0.95V *vs.* α-PdH reference electrode. The addition of titanium sulfate to the solution was found to intensify this peak, thus indicating that titanium probably entered the solution from the substrate layer. During cyclic voltammetry studies with halide ions present in solution, the Ti undercoat was attacked sufficiently rapidly that the disappearance of the undercoat could be seen from the reverse side through the glass after a few hours. This raises questions concerning the use of Ti as an undercoat for gold [see, for example, Ref. (4)].

Niobium appears to be a satisfactory undercoat material, showing good agreement with bulk Au electrodes in both the voltammetry and optical measurements. The only difficulty so far encountered is in unbuffered aqueous NaF solutions, where some attack of the undercoat occurs. The authors advocate the use of an Nb undercoat in studies involving metal-film electrodes.

Acknowledgment

Research partially supported by the Office of Naval Research and a fellowship from the National Steel Corporation to one of the authors (J. H.).

Manuscript received April 26, 1973.

Any discussion of this paper will appear in a Discussion Section to be published in the June 1974 JOURNAL.

REFERENCES

1. B. D. Cahan, J. Horkans, and E. Yeager, *Symp. Faraday Soc.*, **4**, 36 (1970).
2. B. D. Cahan, J. Horkans, and E. Yeager, *This Journal*, **118**, 1322 (1971).
3. W.-K. Paik, M. A. Genshaw, and J. O'M. Bockris, *J. Phys. Chem.*, **74**, 4266 (1970).
4. J. D. E. McIntyre and D. M. Kolb, *Symp. Faraday Soc.*, **4**, 99 (1970).

JOURNAL OF THE ELECTROCHEMICAL SOCIETY

SOLID-STATE SCIENCE AND TECHNOLOGY

SEPTEMBER 1973

Nonstoichiometry and Thermodynamics of Chromium Sulfides

D. J. Young, W. W. Smeltzer,* and J. S. Kirkaldy

Department of Metallurgy and Materials Science, McMaster University, Hamilton, Ontario, Canada

ABSTRACT

The composition-equilibrium sulfur pressure isotherm at $T = 700°C$ for the system CrS_x with $1.000 < x < 1.500$ is reported. The phases CrS, Cr_7S_8, Cr_5S_6, Cr_3S_4, Cr_2S_3 (trigonal), and Cr_2S_3 (rhombohedral) were found and their existence ranges determined. Cr_3S_4 has a wide range of homogeneity and deviations from stoichiometry within this range can be described with the aid of a Wagner-Schottky model. The phase changes between adjacent sulfides are first order and the free energies of these reactions are reported.

The present-day use of Ni-Cr alloys at high temperatures in sulfur containing atmospheres points up the current paucity of knowledge of the system Ni-Cr-S. Its phase diagram is, of course, essential to the understanding of chemical reactions between the components. In a companion study (1) to the present work, isothermal sections of this diagram are reported. They indicate that the lowest free energies are reached in the region of the chromium sulfide phases, this factor controlling the behavior of the ternary system. The thermodynamics of the Cr-S binary system are therefore of considerable interest. To date, however, structural, thermodynamic, and kinetic studies have failed to yield a complete and self-consistent picture.

Jellinek (2) has determined the structures and existence ranges of the chromium sulfides which are reproduced in Table I. All sulfides were synthesized at 1000°C and x-ray powder patterns determined at room temperature. Cr_7S_8 and higher sulfides were found to be stable at room temperature. On the other hand, it appeared that the homogeneity range of CrS is narrower at room temperature than at the temperature of preparation. Thus, quenching led to disproportionation. The compositional ranges were estimated from the results of synthesizing sulfides from known amounts of the elements. Therefore, they are imprecise.

More recently, Igaki *et al.* (3) studied the Cr-S system by determining the sulfur partial pressure (P_{S_2}) in equilibrium with sulfides of known stoichiometry. In contrast to Jellinek, they conclude that CrS_x in the range $1.200 \leq x < 1.390$ is homogeneous. This observation is difficult to understand as symmetry arguments (4) predict that the phase change $Cr_5S_6 \rightarrow Cr_3S_4$ is first order. Trigonal Cr_2S_3 and rhombohedral Cr_2S_3 were found to have existence ranges of, respectively, $1.420 \lesssim x \lesssim 1.463$ and $1.463 \lesssim x \lesssim 1.480$. Thus, both phases are metal excess with respect to Cr_2S_3.

Igaki *et al.* also determined the standard free energy of the reaction

$$2Cr_3S_{4+(s)} + 1/2\, S_{2(g)} \rightleftarrows 3Cr_2S_{3-(s)}$$

as

$$\Delta G^\circ = -5.90 \times 10^4 + 38.6T \text{ cal}$$

for $1270°K < T < 1370°K$. Here Cr_3S_{4+} represents the sulfur rich limit of the phase and Cr_2S_{3-} represents the metal rich limit of the trigonal phase. The only other thermodynamic information available for the system is the determination by Hager and Elliot (5) of the free energy of formation of the lowest stable chromium sulfide in equilibrium with chromium metal. They found $\Delta G^\circ = -48{,}400\ (\pm 1100) + 13.4\ (\pm 0.8)T$ cal for $1375°K < T < 1570°K$ referred to 1 atm sulfur atoms. The identification of the sulfide phase was, however, equivocal.

Despite the discrepancies between the results of Jellinek and Igaki *et al.*, it is clear that some at least of the chromium sulfides are nonstoichiometric over considerable ranges. The nature of the lattice defects responsible for these deviations from stoichiometry is of interest but no investigations in this field have been reported. Indirect evidence may, however, be found from kinetic studies of the sulfidation of chromium metal and chromium alloys by invoking the Wagner-Hauffe theory (6, 7).

* Electrochemical Society Active Member.
Key words: defects, solid-state, phase changes.

Table I. Properties of CrS_x

Phase	Symmetry	Existence range: Jellinek (2)	Existence range: Igaki *et al.* (3)	Existence range: Present work
CrS	Monoclinic	Narrow		
Cr_7S_8	Trigonal	$1.136 < x < 1.149$		$1.130 < x < 1.142$
Cr_5S_6	Trigonal	Narrow		$1.190 < x < 1.203$
			$1.200 < x < 1.390$	
Cr_3S_4	Monoclinic	$1.265 < x < 1.316$		$1.286 < x < 1.377$
Cr_2S_3(tr)	Trigonal	Narrow	$1.420 < x < 1.463$	$1.423 < x < 1.463$
Cr_2S_3(rh)	Rhombohedral	Narrow	$1.463 < x < 1.480$	$1.463 < x < 1.500$

Mrowec *et al.* (8) found that the rate of sulfidation of chromium with minority additions of nickel was lower than that of pure chromium. In both cases the sulfide product was Cr_2S_3. If the nickel is assumed to be incorporated as Ni^{2+}, then the kinetic effect may be explained if Cr_2S_3 is a metal-deficit material. Thus, the introduction of cations having a lower charge reduces the number of cation vacancies and hence the cation diffusivity. This conclusion is in conflict with the observation of Strafford and Hampton (9) that the addition of molybdenum lowers the sulfidation rate of chromium. If the alloying element is incorporated as Mo^{4+}, then a metal excess structure for Cr_2S_3 must be invoked to explain the kinetic effect.

In the present study the composition-equilibrium sulfur pressure isotherm at $T = 700°C$ was constructed. From it are deduced the nature of phase transitions (first order or otherwise), the free energies of these transitions, and the existence ranges of the various sulfides. The Wagner-Schottky model (10) of nonstoichiometry is employed in a discussion of the probable point defects responsible for deviations from stoichiometry.

Experimental

Chromium sulfide of initial composition $CrS_{1.500\pm0.003}$ was equilibrated at 700°C with controlled partial pressures of sulfur. Equilibrium was judged to be attained when the sample weight was constant to within one part in 10^4 over a period of 8 hr. The composition of the sulfide was calculated from the weight loss of the sample assuming chromium to be involatile. At selected compositions, the sample was analyzed for sulfur by combustion and subsequent iodometric determination of the product SO_2. Results obtained in this way were always in agreement [to within the analytical error of ±0.1 weight per cent (w/o)] with those calculations from weight losses.

As the equilibration process is slow, the same sample was brought to equilibrium at successively lower values of P_{S_2} until a composition of approximately CrS was obtained. Reproducibility of the resulting set of P_{S_2} *vs.* x values was checked by equilibrating the CrS at a few successively higher values of P_{S_2} until a composition of $CrS_{1.50}$ was regained. It was found in this way that the error in x was ±0.003.

Sulfur pressures were controlled by mixing known proportions of H_2S and H_2 and flowing the resultant mixture over the sample at 700°C. The flow rates of the individual gases were measured with flowmeters calibrated by the soap bubble method. Gas mixtures were analyzed for H_2S by the method of Dunicz and Rosenqvist (11) and P_{S_2} was calculated from the thermodynamic data of Lewis and Randall (12). A "once-through" gas flow system was chosen in preference to a circulating gas system for the reasons enumerated by Hager and Elliott (5). Tests with argon and nitrogen showed that gas adsorption on the sample gave rise to no detectable weight change.

The temperature of the chromium sulfide sample was measured to within ±2°C and controlled at 700° ± 4°C.

Phase identification was accomplished by comparing Debye-Scherrer powder patterns with those obtained by Jellinek (2).

Materials.—Matheson ultrahigh purity hydrogen (<10 ppm total impurities) and Matheson C. P. grade H_2S were employed. For very low sulfur pressures, Matheson premixed H_2-0.5% H_2S was further diluted with hydrogen. Chromium sulfide was supplied by Atomergic Chemetals as nominally 99.995% Cr_2S_3. Its analysis is given in Table II.

Table II. Analysis of Cr_2S_3 starting material

Element	Ni	Co	Cu	Fe	Ca	Mg	Mn	V
Concentration (ppm)	<10	<20	20	110	100	18	~3	—

Results

The P_{S_2}-composition isotherm at $T = 700°C$ is shown in Fig. 1. Also shown in this figure are the results of x-ray structure determinations. All phases found by Jellinek (2) were detected. Existence ranges for the sulfides are summarized in Table I. Owing to the large uncertainty in P_{S_2} in the region $1.0 < x < 1.1$ it is not possible to state the existence range of CrS. It would appear from the results of Jellinek (2) that CrS is in fact closely stoichiometric. According to our observations Cr_7S_8 and Cr_5S_6 have quite narrow existence ranges, the results for the former being in close agreement with those of Jellinek.

All phase changes are first order with the possible exception of trigonal $Cr_2S_3 \rightarrow$ rhombohedral Cr_2S_3. The data are not sufficiently precise to determine the nature of this transition. The transition $Cr_5S_6 \rightarrow Cr_3S_4$ is clearly first order whereas Igaki *et al.* find no discontinuity in their x *vs.* P_{S_2} plot in this region.

Free energies at $T = 700°C$ for the various phase equilibria may be calculated directly from the equilibrium P_{S_2} values. Referred to 1 atm $S_{2(g)}$ they are

$$2Cr + S_{2(g)} \rightleftarrows 2CrS \qquad \Delta G°_{973} \simeq -67 \pm 4 \text{ kcal}$$

$$14CrS_{1+} + S_{2(g)} \rightleftarrows 2Cr_7S_{8-} \qquad \Delta G°_{973} = -60.1 \pm 0.4 \text{ kcal}$$

$$5Cr_7S_{8+} + S_{2(g)} \rightleftarrows 7Cr_5S_{6-} \qquad \Delta G°_{973} = -57.4 \pm 0.4 \text{ kcal}$$

$$3Cr_5S_{6+} + S_{2(g)} \rightleftarrows 5Cr_3S_{4-} \qquad \Delta G°_{973} = -55.7 \pm 0.8 \text{ kcal}$$

$$4Cr_3S_{4+} + S_{2(g)} \rightleftarrows 6Cr_2S_{3-(trig)} \qquad \Delta G°_{973} = -37 \pm 1 \text{ kcal}$$

$$xCr_2S_{3+(trig)} + S_{2(g)} \rightleftarrows yCr_2S_{3-(rhom)} \qquad \Delta G°_{973} = -32.5 \pm 0.8 \text{ kcal}$$

If Hager and Elliott's free energy of formation for the lowest sulfide is extrapolated to $T = 700°C$ a value of -70 ± 2 kcal results. The agreement between this value and the one obtained in the current work for the first reaction above indicates that the sulfide formed by Hager and Elliott was indeed CrS. Extrapolation of free energy data (3) for the phase change $Cr_3S_{4+} \rightarrow Cr_2S_{3-}$ leads to $\Delta G°_{973} = -43$ kcal, in poor agreement with the present results.

Nonstoichiometry in the phase field of Cr_3S_4 may be defined in terms of a quantity, Δ, such that the composition of the material is given by $Cr_3S_{4+\Delta}$. The logarithm of $|\Delta|$ is plotted against $\log_{10} P_{S_2}$ in Fig. 2. The slopes

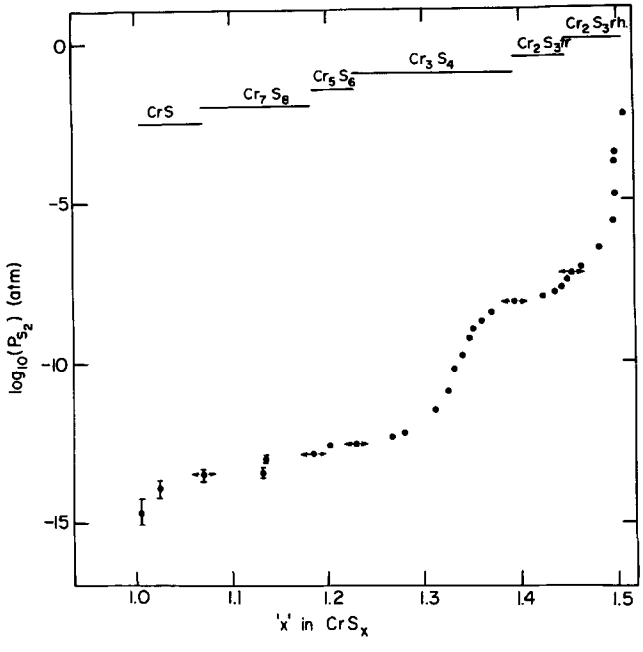

Fig. 1. P_{S_2}-composition isotherm at 700°C. Results of powder pattern phase identifications are shown in upper part of figure. Points with horizontal arrows are in two-phase fields.

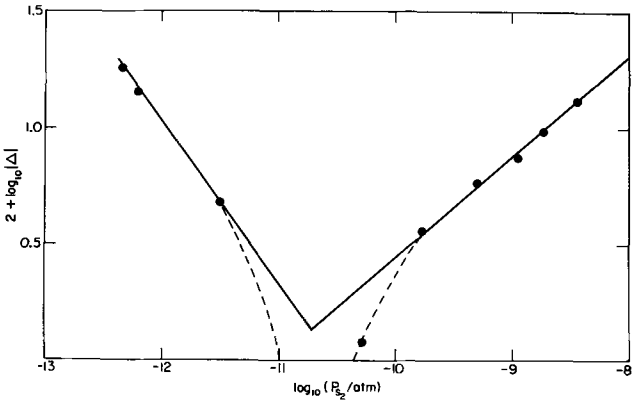

Fig. 2. Dependence of nonstoichiometry in $Cr_3S_{4+\Delta}$ on P_{S2}

of the linear portions of this plot are such that

$$\Delta \propto P_{S_2}^{1/2} \quad \Delta > 0$$

and

$$-\Delta \propto P_{S_2}^{-2/3} \quad \Delta < 0$$

This behavior is discussed in the following section.

The two forms of Cr_2S_3 both display metal excess type nonstoichiometry. The precision of our data is insufficient to deduce a pressure dependence. Strafford and Hampton (13) also find Cr_2S_3 to be metal excess.

Discussion

A defect reaction model for nonstoichiometry must not only explain the experimentally observed pressure dependence but must also be consistent with the known crystal structures of the compounds. The extraordinarily wide existence range of Cr_3S_4 and the frequent appearance of this material as a result of sulfidation of Cr and Ni-Cr alloys (1, 14) make the defect structure of Cr_3S_4 a subject of some interest. Pertinent considerations are the crystal structure of Cr_3S_4 and the adjacent phases $Cr_2S_{3(trig)}$ and Cr_5S_6.

The NiAs type structure in which all the sulfides crystallize may be visualized as consisting of approximately hexagonally close-packed sulfide ions in the octahedral interstices of which structure the metal ions reside. The sublattice of octahedral sites is, however, fully occupied only in the case of CrS. The cation sublattice in sulfides higher than Cr_7S_8 consists of alternately filled and partialy filled layers at right angles to the c axis. The partially filled layers have, in Cr_5S_6, every third site vacant, in Cr_3S_4, every second site vacant, and in trigonal Cr_2S_3, two in every three sites vacant. The rhombohedral modification of Cr_2S_3 is slightly less well ordered than the trigonal form.

It is to be emphasized that the vacancies mentioned above are characteristic of the pure stoichiometric compounds. They therefore bear no charge but are, of course, available for occupancy by other species.

According to Jellinek (2), the bonding in chromium sulfides is best regarded as consisting of ionic Cr-S bonds and metallic Cr-Cr bonds. In fact, Cr_3S_4 shows metallic conductivity (15). Whilst a purely ionic picture is undoubtedly an oversimplification it is useful in formulating defect reactions and will be employed in this discussion.

It has been suggested (15) that the half-filled metal layers in Cr_3S_4 are occupied by Cr^{2+} ions while the completely filled layers are occupied by Cr^{3+} ions. (The metallic conduction of Cr_3S_4 can be rationalized within the framework of this model.) If the sulfide ions form a truly close-packed hexagonal array, then taking the radius of S^{2-} as 1.84Å, the radius of an octahedral site is 0.76Å and that of a tetrahedral site is 0.41Å. It is therefore improbable that S^{2-} will occupy any site other than its normal hexagonal one. The radii of Cr^{2+} and Cr^{3+} are respectively 0.84Å and 0.69Å indicating a preference for octahedral sites. This tendency is reinforced by the greater crystal field stabilization energy afforded by such sites for d^4 and d^3 cations. Supernumerary (defect) cations are therefore expected to occupy octahedral rather than tetrahedral sites.

It will be convenient in the discussion which follows to distinguish three different types of octahedral sites: those normally occupied by trivalent cations; those normally occupied by divalent cations; and those sites which, in a perfect stoichiometric crystal, are vacant. A defect notation particularly well-suited to this purpose is that proposed by Rees (16) in which sites are represented by squares, □, and the real charge of the species normally occupying the site by a subscript. Thus, for example, a trivalent cation on its normal site is represented by $Cr^{3+} \mid \square_{3+}$, a vacancy where a divalent cation is expected by $\square_{2+}$, and a stoichiometric vacancy by $\square_0$. Note that the latter two species are quite different, the first having an effective charge and the last having none. Similarly $S^{2-} \mid \square_{2-}$ represents a divalent sulfur anion on its normal lattice site.

From the preceding discussions it is reasonable to suppose that the incorporation of excess sulfur into Cr_3S_4 results in disorder only in the already partially vacant metal layers. We therefore propose as the nonstoichiometric reaction

$$\begin{gathered} 1/2\ S_{2(g)} \rightleftarrows S^{2-} \mid \square_{2-} + \square_{2+} + 2h \\ 2h + 2Cr^{2+} \mid \square_{2+} \rightleftarrows 2Cr^{3+} \mid \square_{2+} \\ 2Cr^{3+} \mid \square_{2+} + \square_{2+} \rightleftarrows (2Cr^{3+} \mid \square_{2+}, \square_{2+}) \end{gathered} \qquad [1]$$

Here the expression in parentheses represents a defect complex. The incipient nucleation of the new Cr_2S_3 phase is readily apparent. Thus, equilibrium [1] is consistent with the phase change reaction

$$2Cr_3S_{4(s)} + 1/2\ S_{2(g)} \rightarrow 3Cr_2S_{3(s)} \qquad [2]$$

The equilibrium expression for [1] is readily obtained. Let n_v be the concentration of vacant sites, $\square_{+2}$, and N be the concentration of sites in the divalent cation sublattice. Then

$$n_v = N K_x P_{S_2}^{1/2} \exp(-w_v/kT \qquad [3]$$

where K_x is the partition function for $S^{2-} \mid \square_{2-}$, w_v is the internal energy change involved in the creation of a divalent cation vacancy, and $n_v << N$ has been assumed. The pressure effect noted for $\Delta > 0$ in Fig. 2 is explained. Assignment of positive holes to localized sites in equilibrium [1] is not really necessary as Cr_3S_4 is a metallic conductor (15) and the concentration of free carriers formed in the defect reaction is negligible compared to that of the intrinsically available carriers.

When deviation from stoichiometry in Cr_3S_4 occurs in the metal excess (sulfur deficit) direction, the structure is moving towards that of Cr_5S_6. Thus vacancies must be filled in the divalent cation sublattice. Since the metal atoms required to fill these sites can come only from the trivalent cation sublattice, the defect reaction must involve both metal sublattices. The following reaction is proposed

$$\begin{gathered} 20Cr^{3+} \mid \square_{3+} + 10Cr^{2+} \mid \square_{2+} + 10\ \square_0 + 40S^{2-} \mid \square_{2-} \\ \rightleftarrows 18Cr^{3+} \mid \square_{3+} + 9Cr^{2+} \mid \square_{2+} + 3Cr \mid \square_0 + 6\ \square_0 \\ + 36S^{2-} \mid \square_{2-} + 2S_{2(g)} + (2\ \square_{3+} \\ + \square_{2+} + \square_0 + 4\ \square_{2-}) \end{gathered} \qquad [4]$$

The left-hand side of Eq. [4] is equivalent to $10Cr_3S_4$ and the terms in parentheses sum to the absence of one Cr_3S_4 unit, *i.e.*, they are equivalent to zero. Again, the ionization state of Cr | $\square_0$ need not be specified as the material is metallic. However, the precipitation of the new Cr_5S_6 phase may be visualized in terms of an ionization of these species

$$\begin{gathered} 18Cr^{3+} \mid \square_{3+} + 9Cr^{2+} \mid \square_{2+} + 3Cr \mid \square_0 \\ + 6\ \square_0 + 36S^{2-} \mid \square_{2-} \rightleftarrows 12Cr^{3+} \mid \square_{3+} + 6Cr^{2+} \mid \square_{3+} \\ + 9Cr^{2+} \mid \square_{2+} + 3Cr^{2+} \mid \square_0 + 6\ \square_0 + 36S^{2-} \mid \square_{2-} \end{gathered}$$

The right-hand side of the equation is equivalent to $6Cr_5S_6$ and involves a vacancy at every third site in the divalent sublattice as required.

To obtain an equilibrium expression for [4], let n_i be the concentration of the Cr $|$ $\square_0$ species and w_i the internal energy change involved in their creation. Then, assuming $n_i << N$

$$n_i = N K_x^{-4/3} P_{S_2}^{-2/3} \exp(-w_i/kT) \quad [5]$$

The pressure dependence of deviations from stoichiometry in the metal excess range (Fig. 2) is explained.

It is of interest to relate Δ and P_{S_2} with the intrinsic, or stoichiometric, disorder and sulfur pressure, $P_{S_2(o)}$, at which $\Delta = 0$. From [1] and [4]

$$\Delta = (n_v - 4/3\, n_i)/4N \quad [6]$$

An intrinsic disorder reaction consistent with [1] and [4] is

$$2Cr^{3+} \mid \square_{3+} + 9Cr^{2+} \mid \square_{2+} \rightleftarrows 3Cr \mid \square_0 + 4(2Cr^{3+} \mid \square_{2+}, \square_{2+}) \quad [7]$$

whence

$$\frac{n_i}{N}\left(\frac{n_v}{N}\right)^{4/3} = \exp(-E_f/kT) \quad [8]$$

where E_f is the internal energy required to create a defect pair of the type (Cr $|$ $\square_0$ + 4/3 $\square_{2+}$) and therefore equals (w_i + 4/3 w_v). Putting $n_f = n_i = 3/4\, n_v$ leads to the definition of intrinsic disorder

$$\delta = n_f/N \quad [9]$$

Combination of Eq. [3], [5], [6], [8], and [9] leads, after some algebra, to the result

$$\Delta = \frac{\delta}{3}\left(\frac{P_{S_2}^{1/2}}{P_{S_{2(o)}}^{1/2}} - \frac{P_{S_2}^{-2/3}}{P_{S_{2(o)}}^{-2/3}}\right) \quad [10]$$

Curve fitting the data to [10] leads to estimates of $\delta = (3.27 \pm 0.04) \times 10^{-2}$ and $P_{S_{2(o)}} = (3.16 \pm 0.05) \times 10^{-11}$ atm. The success of the fit may be judged from the linearized plot in Fig. 3.

The high concentration of intrinsic defects in Cr_3S_4 and the consequently wide existence range of the material indicate that the cationic diffusion coefficient of this material should be large. Such a conclusion is supported by the observation of wide zones of Cr_3S_4 in various diffusion couple experiments (1). Studies of cation self-diffusion as a function of stoichiometry would be of interest in this context.

The metal excess type nonstoichiometry observed in Cr_2S_3(tr) and Cr_2S_3(rh) is in agreement with the findings of Igaki *et al.* (3) and Strafford and Hampton (9). Mrowec *et al.* (8), however, deduced a metal deficit structure for Cr_2S_3. The fact that these latter authors used a much higher sulfur pressure (P_{S_2} = 1 atm) may account for this apparent anomaly.

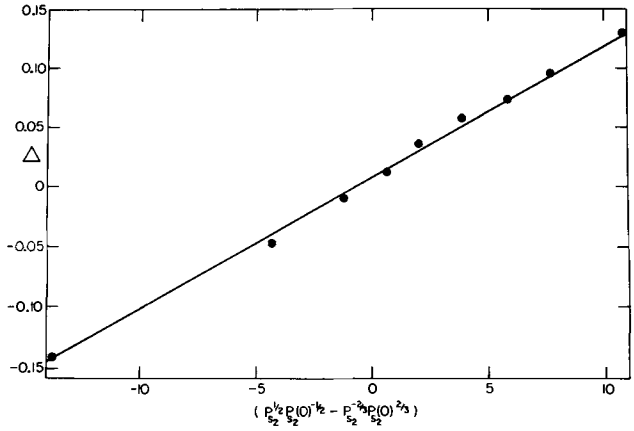

Fig. 3. Nonstoichiometry in $Cr_3S_{4+\Delta}$ plotted according to Eq. [10].

Acknowledgments

The authors are grateful to Falconbridge Nickel Mines, Limited, for financial support of the program.

We are indebted to the following persons from the above company: M. J. Lavigne and L. A. Morris, for their advice and encouraging discussions, and A. V. Campbell for several chemical analyses.

Manuscript submitted Oct. 10, 1972; revised manuscript received March 23, 1973.

Any discussion of this paper will appear in a Discussion Section to be published in the June 1974 JOURNAL.

REFERENCES

1. J. S. Kirkaldy, G. M. Bolze, D. McCutcheon, and D. J. Young, *Met. Trans.*, **4**, 1519 (1973).
2. F. Jellinek, *Acta Cryst.*, **10**, 620 (1957).
3. K. Igaki, N. Ohashi, and M. Mikami, *J. Phys. Soc. Japan*, **31**, 1424 (1971).
4. C. Haas, *Solid State Commun.*, **4**, 419 (1966).
5. P. Hagar and J. F. Elliott, *Trans. AIME*, **239**, 513 (1967).
6. C. Wagner and K. E. Zimens, *Acta Chem. Scand.*, **1**, 574 (1947).
7. K. Hauffe and C. Gensch, *Z. Physik. Chem.*, **195**, 116 (1950).
8. S. Mrowec, T. Werber, and M. Zastawnik, *Corrosion Sci.*, **6**, 47 (1966).
9. K. N. Strafford and A. F. Hampton, *J. Less-Common Met.*, **21**, 305 (1970).
10. W. Schottky and C. Wagner, *Z. Physik. Chem.*, **B11**, 163 (1930).
11. B. H. Dunicz and T. Rosenqvist, *Anal. Chem.*, **24**, 404 (1952).
12. G. N. Lewis and M. Randall, "Thermodynamics," p. 173, McGraw-Hill Book Co., New York (1961).
13. K. N. Strafford and A. F. Hampton, Private communication.
14. A. U. Seybolt, *Trans. AIME*, **242**, 1955 (1968).
15. R. J. Bouchard and A. Wold, *J. Phys. Chem. Solids*, **27**, 591 (1966).
16. A. L. G. Rees, "Chemistry of the Defect Solid State" Methuen, London (1954).

Properties of Anodic Oxide Films Formed in the Anodization of Silicon Nitride

C. J. Dell'Oca*

Research and Development Laboratory, Fairchild Camera and Instrument Corporation, Palo Alto, California 94304

ABSTRACT

The anodization of silicon nitride films on silicon has been characterized using ellipsometry. Calculations made indicate that the sensitivity of ellipsometry to the anodization depends on the initial silicon nitride thickness. Ellipsometry data obtained during stepwise anodization are consistent with a model of two layers on silicon where the anodic oxide layer grows at the expense of the silicon nitride. The thickness ratio of oxide produced to silicon nitride used falls within ±0.25 of the theoretically expected value, 1.81, and depends to some extent on anodization conditions. The refractive index and growth ($\log_{10} J$ *vs.* E) properties of the oxide are similar to those of anodic oxides of silicon. Stepwise etchback studies on the oxide give results which are consistent with the anodization data and which indicate an abrupt silicon nitride-anodic oxide interface.

Anodization of silicon nitride is of practical importance because it converts silicon nitride to a more soluble form and thus can be used in the localized etching of silicon nitride films passivating semiconductor devices (1). Areas can be selectively anodized while the remaining area is protected from anodization usually by a greater dielectric thickness in the form of silicon dioxide. One direct application of silicon nitride anodization has been to silicon bipolar transistors where silicon nitride is added to the existing thermally grown silicon dioxide passivation to provide protection from ionic contaminants. Here, the anodization was used to open windows in the silicon nitride to facilitate electrical contact to the active device area (2).

Because of its insulating properties, the anodization must be studied with thin silicon nitride films deposited on more conducting substrates. This poses certain difficulties in determining the properties of the oxide produced. In the past, the conversion of silicon nitride to anodic oxide has been qualitatively followed by infrared interferometry (1), and the oxide thickness has been measured by destructive techniques (3). More recently, nuclear microanalysis has been used to determine the constituents of the oxide (4). In the present investigation, ellipsometry was employed to nondestructively study the anodization of silicon nitride.

Experimental

The specimen used in these studies is shown in Fig. 1. The substrate was a chemically mechanically polished silicon slice which was thermally oxidized to provide electrical insulation. An opening cut in the insulation by photolithography and etching exposed the underlying silicon surface and precisely defined the anodization area of the subsequently deposited silicon nitride. The anodization area was kept small, about 0.13 cm^2, primarily to keep the power dissipated during anodization small; but it also served to minimize effects resulting from small thickness gradients which may occur in the silicon nitride. A substrate was accepted for deposition of Si_3N_4 if the exposed silicon surface was covered by less than 20Å of oxide. Calculations indicate that the effect of this layer on optical measurements may be neglected. Silicon nitride films were grown by chemical vapor deposition employing the reaction of $SiCl_4$ and NH_3 in H_2. The indices of refraction of the silicon nitride films were within 1.98 ± 0.02.

The anodizations were carried out at constant current[1] in a closed glass vessel containing a solution of 0.04M KNO_3 in ethelene glycol which was stirred and maintained at 25°C. In some cases, 2% water was added to the solution. The water content of the solution was periodically determined by the Karl Fisher method.

Electrical contact to the silicon was made using mercury through a window cut in the backside oxide and was facilitated by an "O" ring vacuum chuck (2). The chuck was rigidly attached to a ground glass joint through which a glass tube facilitated both vacuum and electrical connection to the chuck. The entire assembly was fitted into the anodization vessel through a mating joint. A similar mating joint on the ellipsometer held the assembly for ellipsometric measurements.

During anodization the voltage between the mercury contact and a platinized platinum cathode was monitored by a Keithley 610C electrometer and its output recorded on one channel of a Hewlett Packard 7100 BM strip chart recorder. The other channel monitored the cell current through a small precision resistor. A Cimroon 7400A digital voltmeter was used to give precise voltage readings and to hold the final voltage value at the end of each anodization.

Anodizations were carried out in a stepwise fashion. After each anodization step the anodized surface was rinsed with a spray of isopropyl alcohol, blown dry with nitrogen gas, and measured with a Rudolph ellipsometer. Unless otherwise stated, all thickness and refractive index measurements were made by ellipsometry at an angle of incidence of 70° and employing an He-Ne laser light source of 6328Å wavelength.

[1] Electronic Measurements Model C636K constant-current power supply.

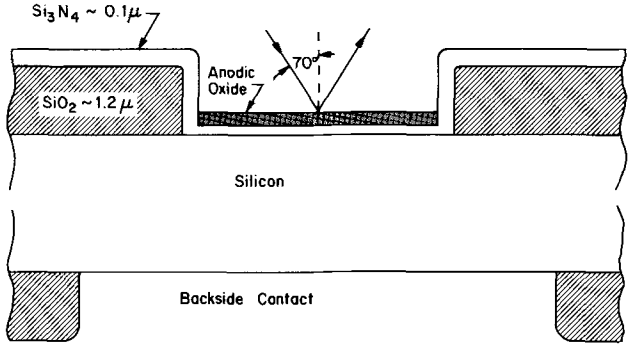

Fig. 1. Schematic representation of anodization specimen in the vicinity of the anodization area, showing optical model of partially anodized Si_3N_4 film (not to scale).

* Electrochemical Society Active Member.
Key words: ellipsometry, refractive index, growth kinetics.

Calculations

Based on prior evidence (1, 3), the expected optical model consists of two layers on silicon where the outer layer, presumably anodic silicon dioxide, grows at the expense of the silicon nitride layer during anodization (Fig. 1). Ellipsometry of such a model can best be understood by first considering the case of a single nonabsorbing homogeneous film on silicon. In ellipsometry the growth of such a film is characterized by an ellipsometry curve (a plot of Δ vs. ψ, which are quantities measured in ellipsometry) with film thickness as a parameter along the curve. Within rather wide limits, this curve is unique to the index of refraction,[2] n, of the film (5). Thus, in the anodization of Si_3N_4 it is expected that the ellipsometry measurements would begin at a point representing its thickness on the silicon nitride ellipsometry curve. As anodization proceeds, the ellipsometry curve obtained would eventually approach and end on the curve for oxide when anodization of the silicon nitride is complete. This general behavior can be seen in Fig. 2 which presents some representative calculated conversion curves. In this graph, the solid curve to the left represents a portion of the ellipsometry curve covering the range from 400 to 1500Å of only a silicon nitride layer on silicon. Similarly, the upper and lower solid curves are portions of the curve for only a silicon dioxide film on silicon. The dashed lines are the conversion curves for various initial thicknesses of Si_3N_4 calculated using indices of refraction of 1.46, 2.00, and $3.862-0.0335j$ respectively for the oxide, nitride, and silicon substrate, and a conversion ratio of 1.75. The conversion ratio (CR) is the thickness ratio of oxide produced to silicon nitride consumed in the anodization.

Several points can be made from these calculations. First, ellipsometry will have the highest sensitivity to conversion if the Si_3N_4 is about 900Å prior to anodization. Other thicknesses give rise to smaller Δ-ψ loops. Second, ellipsometry points must be obtained away from the parent curve if they are to be useful. This is because, *e.g.*, in the conversion of 1000Å of Si_3N_4,

[2] The index of refraction is written as $N = n - jk$.

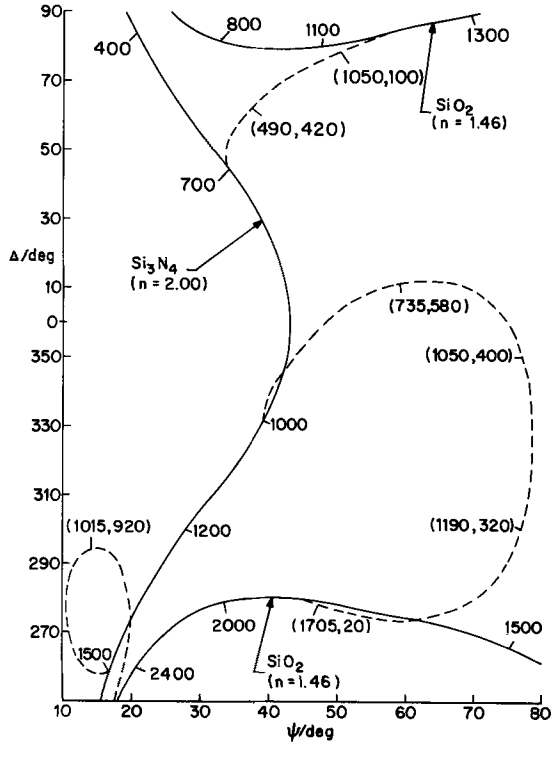

Fig. 2. Calculated conversion curves (broken curves) for Si_3N_4 films of 700, 1000, and 1500Å. Numbers in brackets respectively indicate thickness of oxide produced and Si_3N_4 remaining in angstroms.

initially during the anodization the composite film (the two layers treated as one) still looks much like a thinner silicon nitride film when in fact the oxide plus nitride is thicker than the original film. In fact, although it might be normal to expect that as conversion occurs the index of refraction of the composite film gradually changes from that of Si_3N_4 to that of the oxide, this is not always the case. For example, the far left point of the 1500Å conversion curve represents a composite film with an apparent index of refraction of about 3. On the other hand, in the conversion of 1000Å of Si_3N_4, there is a region immediately after conversion begins where the composite film has a higher index of refraction than Si_3N_4, while near the end of the conversion the composite film has a lower index of refraction than SiO_2. Therefore, the composite film may appear optically more or less dense than either of its constituents.

Results

Ellipsometry of anodization and etchback.—General agreement was found between calculated and experimental ellipsometry conversion curves for silicon nitride films ranging from 500 to 1500Å; but, because of greater sensitivity, the study was centered around films between 910 and 950Å. In order to illustrate the characteristics of the ellipsometry results and the analyses used to arrive at the properties of the oxide, two examples are discussed. One represents an anodization (Fig. 3) while the other represents a different anodization followed by an etchback (Fig. 4).

Figure 3 shows an ellipsometry curve typical of anodization. The experimental points were obtained at intervals in the stepwise anodization of 916Å Si_3N_4 film at a current density of 20 mA/cm^2. These results were curve fitted with the aid of a computer which, when given the initial thickness (916Å) and index of refraction (1.98) of the Si_3N_4 layer, varied the index of refraction of the oxide produced and the conversion ratio until the mean square deviation between the experimental points and the calculated curve was minimized. The layers were assumed to be nonabsorbing. The dashed line represents the best fit to the data and yielded a conversion ratio of 1.81 and an index of refraction, n, of 1.45 for the oxide. The thickness of

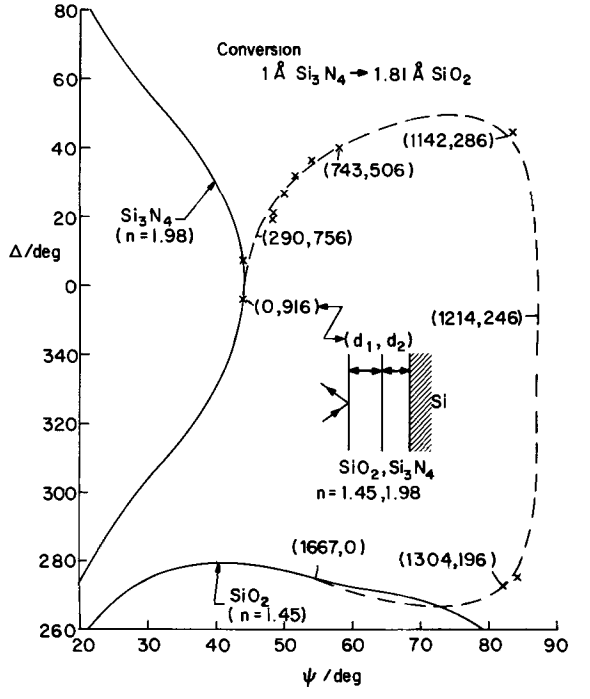

Fig. 3. Ellipsometry results from anodization of a 916Å Si_3N_4 film at 20 mA/cm^2. Dashed line is computed from the model and values given in the figure. Curves for Si_3N_4 and SiO_2 are also shown (solid lines).

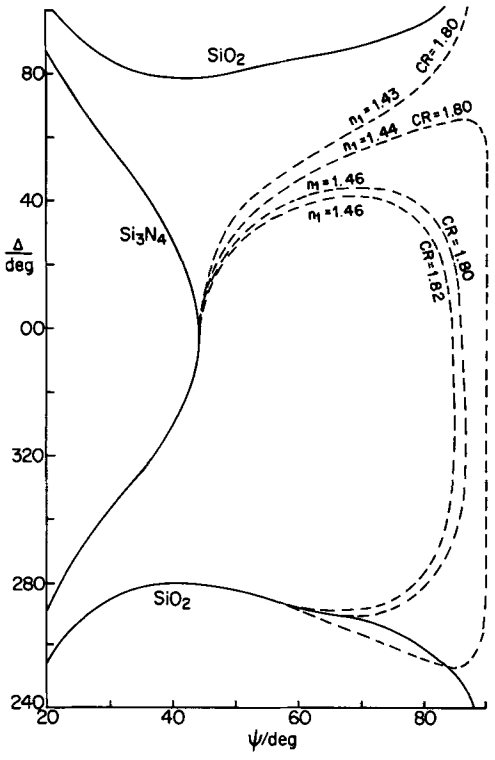

Fig. 4. Calculated conversion curves for small independent variations in *CR* and index of refractions of oxide (n_1).

each layer at each experimental point was also determined.

It is difficult to show how *CR* and n_1 enter into the curve fitting; however, an indication of the sensitivity of ellipsometry to separate variations in these quantities is given in Fig. 4. Quite distinct curves are calculated for small changes in these quantities. Therefore, determination of these quantities can be accurately made.

A typical etchback ellipsometry curve is shown in Fig. 5. Here, a 929Å silicon nitride film was first partially anodized and then etched back. The etchback points (open circles) trace out a curve which, as expected, eventually approaches the ellipsometry curve

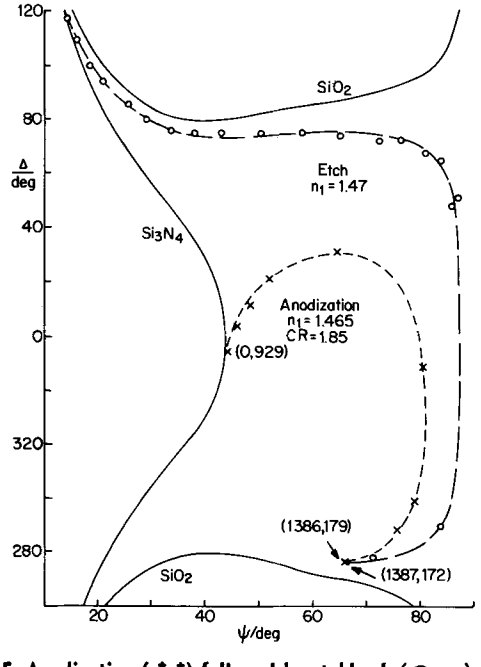

Fig. 5. Anodization (-*-*) followed by etchback (○ —) ellipsometry results. Broken lines computed from $n_2 = 1.98$ and n_1 and *CR* as shown.

for silicon nitride as the oxide is removed. These points were fitted using essentially the same computer program as in fitting the anodization results. In this case, however, the index of refraction of the oxide and thickness of the silicon nitride remaining after anodization were varied to obtain the best fit. The refractive index of the silicon nitride was known. The best fitting curve to the etchback results is given in the figure and indicates that the oxide has a refractive index of 1.47.

Since the approach to fitting the anodization and etchback results are independent of each other, the parameters determined may be directly compared for consistency. That is, the refractive index of the oxide and the thickness of each layer after anodization or prior to etchback may be compared. In Fig. 5, a refractive index, for the oxide, of 1.47 determined from etchback compares favorably with 1.465 from anodization. (More comparisons will be given later in the discussion of the oxide properties.) In Fig. 5 the final thicknesses of the oxide and silicon nitride as determined from anodization were 1386 and 179Å, respectively, which compares favorably with 1387 and 172Å prior to etchback as determined from the etchback results. The consistency of the thickness measurement observed in all the anodization and etchback experiments will now be discussed. The agreement was generally better for the oxide thickness, usually within about 10Å, while that of the remaining nitride was within about 25Å. The higher value for the latter occurs because in curve fitting the etchback results the ability to determine the remaining silicon nitride thickness decreases with its thickness and becomes very poor for very thin films (~100Å). At this point small changes in this thickness do not appreciably affect the etchback curve. However, the remaining silicon nitride can also be measured after all the oxide is removed and it turns out that, except for the very thin films, this value and that determined from anodization and etchback were all within 25Å. The consistency of these results indicates a precision of better than 2% in measuring total film thickness.

A summary of the anodization characteristics as determined by ellipsometry is given in Table I and these will be discussed in greater detail in the following sections.

Conversion ratio.—The conversion ratio expected theoretically on the basis of densities for converting Si_3N_4 (3.1 g/cm³) to SiO_2 (2.2 g/cm³) is 1.81. Experimentally, the observed values range from 1.55 to 2.1 and appear to depend on anodization conditions. In order to ascertain that such a range was real and not a result of the measurement technique, the conversion ratio was determined by an independent method. In this method part of the oxide was masked and retained during some of the etchback ellipsometry experiments. Because the silicon nitride has an etch rate about two orders of magnitude lower than that of the oxide, the oxide can be completely removed with insignificant reduction in silicon nitride thickness. The silicon nitride thickness was then determined precisely by ellipsometry and the oxide step was measured by the Tolanski interference technique. The *CR* measured in this way is considered accurate to the first decimal place. The *CR* determined from anodization, etchback, and the

Table I. Summary of anodization characteristics*

Formation current (mA/cm²))	2	5	10	20	50**
CR with 2% H_2O**		1.56	1.60	1.68	
<*CR*> with no H_2O	1.72	1.81	1.88	1.86	1.83
Oxide properties					
$\langle dx_1/dt \rangle$ (A/sec¹)	0.072	0.38	0.85	2.10	5.6
<Growth efficiency> (%)	0.5	1.1	1.2	1.5	1.6
<Electric field> $\times 10^{-7}$ (V/cm¹)	1.82	1.93	2.00	2.11	2.06
<Etch rate> (A/sec⁻¹ in 0.5% HF)		4.7	4.6	5.0	
<Index of refraction>	1.46	1.47	1.44	1.45	1.46

* < > denotes average values.
** Results from single ellipsometry curve, not average value.

Table II. Conversion ratios from ellipsometry of anodization and etchback, and other techniques

Specimen	Anodization	Etchback	Other*
A	1.60	1.60	1.5_8
B	1.64	1.65	1.6_8
C	1.70	1.73	1.7_5
D	1.93	1.85	1.8_8
E	1.98	1.94	2.0_4

* Oxide height by Tolanski interference, remaining Si_3N_4 by ellipsometry.

independent method are consistent (Table II) and it must be concluded that the observed spread in conversion ratios is real.

The dependence of *CR* on anodiation conditions is not completely clear (first two lines of Table I). With 2% water intentionally added to the electrolyte the conversion ratio increases with current density of formation. However, this is based on a singe anodization curve at each formation. The values are somewhat higher and the dependence on current density opposite to that previously found for this particular solution (3). With water not intentionally added to the solution, the *CR* is higher and on the average closer to the theoretically expected value. However, the dependence on current density is less clear. The results appear to be tempered by the Si_3N_4 deposition conditions since samples from the same deposition gave more consistent *CR*'s, although the water content which varied between 0.1 and 0.3%, could also be a factor. The average *CR*'s given in Table I have a standard deviation less than 0.04.

Properties of the oxide.—The oxide is rapidly attacked by even dilute HF. In a 0.5% HF solution the ellipsometry results indicate that the first 100Å or so etch more rapidly than the rest of the oxide which etches at a constant rate. Some curves showing the removal of oxide with time are given in Fig. 6. The etch rate is about 5Å/sec with no apparent dependence on current density of oxide formation. The average etch rates from two etchback curves at each current density is shown in Table I. These etch rates are appreciably higher than that of thermal oxides of silicon. The etch solution was renewed for each etch step to reduce effects of depletion. On reaching the Si_3N_4 interface, the etch rate changes almost abruptly and an abrupt silicon nitride oxide interface is indicated in agreement with previous infrared transmission results (1). The break in the etch curves (Fig. 6) signifies the point where all the oxide is removed, and this is an indication of the ability of ellipsometry to determine the interface position from fitting etchback results. That is, the break in the curve should occur when the oxide thickness is zero. In most cases (5 out of 8) the interface was predicted within 10Å, one of these and the three worst cases 20, 30, and 50Å are shown in this figure.

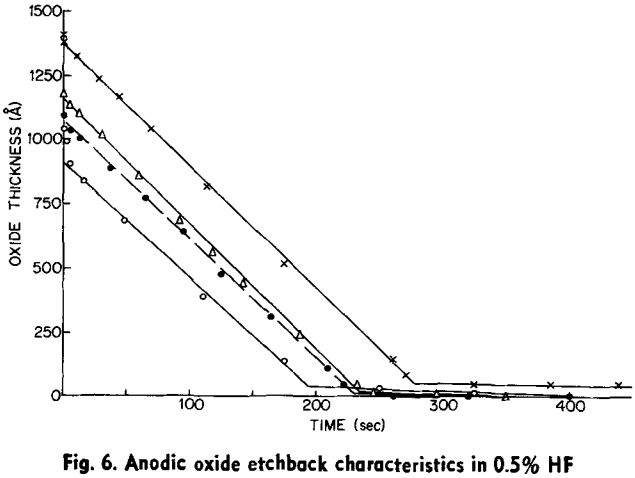

Fig. 6. Anodic oxide etchback characteristics in 0.5% HF

Table III. Refractive index

J (mA/cm²)	Anodization	Etchback
5	1.460	1.472
	1.476	1.475
10	1.440	1.480
	1.443	1.470
20	1.460	1.454
	1.456	1.470
	1.443	1.470

The index of refraction of the anodic oxide has a value falling within 1.45 ± 0.02 (last line Table I) and is within experimental error the same as that of thermal and anodic oxides on silicon (7). As shown in Table III, the index of refraction was generally somewhat larger when determined from curve fitting etchback results than from anodization results. At times a small change in ellipsometry measurements was found between the final anodization and the measurements prior to etchback indicating that perhaps small adjustments occur in the film with time. In general there was no noticeable dependence of refractive index on current density or water in the electrolyte. The latter has an effect on anodic oxides of silicon (7).

Kinetics of oxide growth.—Figure 7 shows a typical time development of the various layers as determined from ellipsometry during constant current formation. As expected, a linear time dependence is observed. From the rate of change of oxide thickness it is possible to calculate the efficiency of oxide formation if it is assumed that the oxide is SiO_2 with a density of 2.2 g/cm³. The efficiencies are low, in the order of 1%, and increase slightly with current density as has been found previously (3) (average values are given in Table I). Figure 8 shows a typical dependence of cell voltage on film thickness. Although there is some scatter in the data, the voltage dependence on film thickness can be described as linear within the precision of the present experiments. Of interest is the rate of change of voltage with total thickness, dV/dx, because with certain justifiable assumptions it leads to the electric field, E_1, in the oxide during growth. The cell voltage can be written as $V = E_1 x_1 + E_2 x_2 + V_o$, which is respectively the sum of the voltage in the outer and inner layers plus a constant voltage which, at a given current density, takes into account *IR* drops, contact voltage, etc. This constant is generally difficult to determine and drops out when dV/dx is taken. Two

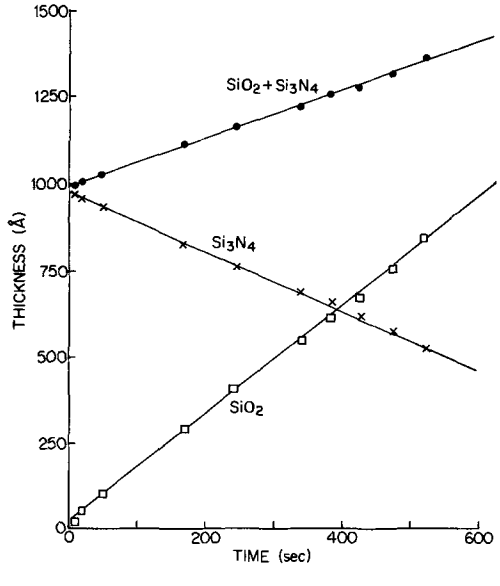

Fig. 7. Typical thickness development with time for anodization at 20 mA/cm².

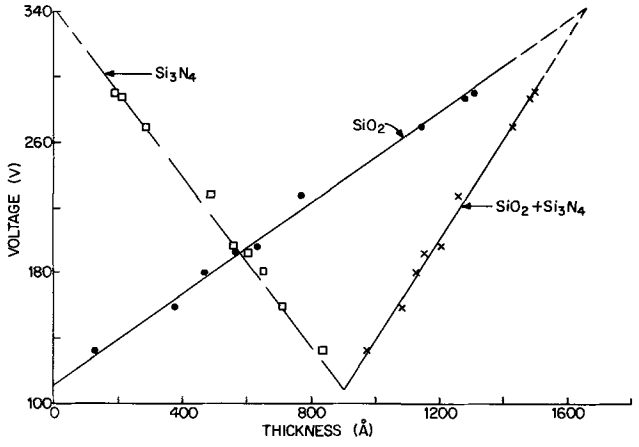

Fig. 8. Typical voltage dependence on thickness at 20 mA/cm²

assumptions are made. First, the electric field in each layer is independent of its thickness and there appears to be support for this (3, 8). Secondly, during anodization at a given current density the electric field in the silicon nitride is assumed to be the same as that determined from conductivity measurements on MNS (metal/silicon nitride/semiconductor) structures. The second assumption should be a direct consequence of the first, except that MNS measurements are usually made at constant voltage whereas the present experiments are at constant current. Spot checks indicated that in MNS structures the conductivities determined by the two methods are essentially the same as long as sufficient time for current stabilization is allowed in the constant voltage case.

Figure 9 gives the oxide growth rate on a logarithmic scale as a function of electric field. If the density of the oxide were known, this could then be transformed to the more familiar ionic current density ($\log_{10} J$) *vs.* electric field plot. The points to the right on this figure represent dV/dx determined from the voltage *vs.* total thickness data using the method of least squares. The applied current density, J_{total}, is given opposite each cluster of results. The curve to the left represents the electric field in the silicon nitride which was arrived at in the following manner. The electric field value for each J_{total} was obtained from previous

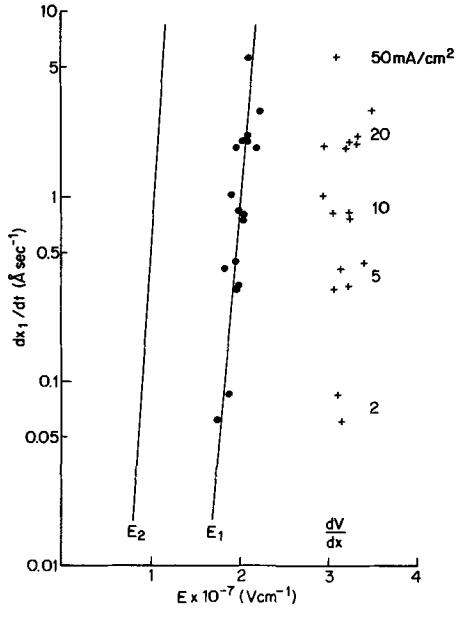

Fig. 9. Oxide growth rate as a function of electric field in the inner (far left curve) and the outer (center curve) layer and in the total film. The latter is denoted by +'s, and the formation current density is noted to the right of these points.

measurements made at this laboratory on MNS structures (9). These values were then plotted on this figure at points corresponding to the average dx_1/d_t for that J_{total}. The curve in the center is drawn through points representing the calculated electric field in the oxide. The horizontal scatter in these points is much less than that observed in dV/dx. This reduction in scatter occurs by the way CR enters into the expression for the electric field. Surprisingly, if an oxide density of 2.2 g/cm³ is assumed it turns out that the line drawn through these points is coincident with the line drawn by Young and Zobel through their results obtained from the anodization of silicon (10).

From comparisons wih previous anodizations of silicon nitride, Tripp (3) calculated, from the point where all the silicon nitride was anodized, an electric field of 1.93×10^7 V cm^{-1} for an oxide growth rate of 27.4 Å/min^{-1}. At this growth rate, our results are in agreement.

Having determined the electric field in the oxide, it is now possible to determine V_0 by extrapolation from results such as are given in Fig. 8. Here the extrapolated intersection of the oxide and oxide plus nitride curves gives the cell voltage and oxide thickness at the point when all the silicon nitride is anodized. Then the product of this oxide thickness and its electric field gives a voltage which differs by V_0 from the extrapolated voltage. Generally the values of V_0 found were not significant (1-6V) when compared to the experimental accuracy, uncertainty of extrapolation, and the magnitude of the voltage used in the anodizations. This result supports the idea that ionic conduction is controlled by the oxide bulk and not the interfaces.

Discussion

One of the questions raised in the anodization of silicon nitride concerns the nature of the silicon nitride oxide interface. In the original work, Schmidt and Wonsidler concluded that the interface was abrupt from infrared absorption evidence (1). Later Tripp corroborated this evidence but, claiming that the *IR* method was insensitive, opted for a graded oxy-nitride interface on the basis of oxide solubility data (3). That is, he found a significant difference in oxide thickness between the point where the entire film became easily soluble in HF and the point where the conversion of silicon nitride was complete, the latter being coincident with the point where the silicon began to anodize. This result was interpreted in terms of a graded interface. If this is the case then the interface extends over a significant distance, and it would be expected that the etch rate decreases across the interface. The present etch experiments employing very dilute HF did not detect such a dependence and indicate that if a graded interface exists it must be very thin (less than about 30Å). A similar conclusion has also recently been reached on the basis of micronuclear analysis (4). Re-examining Tripp's data it appears that a large portion of the difference in oxide thickness indicating a graded interface can be accounted for within the experimental uncertainties quoted. Although, as pointed out by one of the reviewers, it is possible, but not likely, that the transition region is as insoluble as Si_3N_4 in dilute HF.

The anodization of silicon nitride is similar to the anodization of silicon. The oxide produced has the same index of refraction, the efficiency of oxide growth is low, and the electric field causing oxide growth is very high. In fact it appears that the log J *vs.* E curve is the same as that found previously by Young and Zobel for the anodization of silicon (10); however, there is scatter in both sets of data. Although it was assumed in calculating this curve that the anodic oxide of silicon nitride had the same density as that of thermal oxides of silicon, this value is not critical. Some variation from this value would not significantly effect the curve because of the steep exponential dependence of ionic current on electric field in the

oxide. Similar log J *vs.* E curves may *a priori* be expected for silicon nitride and silicon anodization if the nitrogen atoms liberated in the anodization of silicon nitride do not electrically interact in the oxide, and if ionic conduction is principally controlled by the oxide and not the interfaces. Such behavior may be taken in support of the original postulate that gaseous nitrogen is liberated during the anodization (1). Recently it has been found that at low current densities about 0.1 nitrogen per oxygen atom remains in the oxide (4). Such a high concentration of impurities would be expected to affect the film properties as is the case with phosphates in anodic oxides of tantalum (6). However, the present experiments were at current densities where incorporation of nitrogen was not found (4).

In summary, the properties of silicon nitride anodization have been studied using ellipsometry. The anodic oxides produced in the anodization of silicon nitride have growth characteristics which are similar to those of anodic oxides of silicon. The refractive index is also the same except that, within the accuracy of these experiments, no dependence on water concentration was resolved for anodic oxides of silicon nitride. The present experiments indicate that the ionic conduction is largely controlled by the oxide and not by the interfaces.

Acknowledgment

The author wishes to express his gratitude to M. L. Barry and B. E. Deal for their encouragement during this work.

Manuscript submitted Sept. 15, 1972; revised manuscript received April 26, 1973. This was Paper 81 presented at the Cleveland, Ohio, Meeting of the Society, Oct. 3-7, 1971.

Any discussion of this paper will appear in a Discussion Section to be published in the June 1974 JOURNAL.

REFERENCES

1. P. F. Schmidt and D. R. Wonsidler, *This Journal*, **114**, 603 (1967).
2. C. J. Dell'Oca and M. L. Barry, *Solid State Electron.*, **15**, 659 (1972).
3. T. B. Tripp, *This Journal*, **117**, 157 (1970).
4. M. Croset, S. Rigo, and G. Amsel, Abstract No. 82, Electrochemical Society Extended Abstracts, Fall Meeting, Cleveland, Ohio, Oct. 3-7, 1971.
5. R. J. Archer, *J. Opt. Soc. Am.*, **52**, 970 (1962).
6. C. J. Dell'Oca and L. Young, *This Journal*, **117**, 1545 (1970).
7. E. F. Duffek, E. A. Benjamini, and C. Mylroie, *Electrochem. Technol.*, **3**, 75 (1965).
8. S. M. Sze, *J. Appl. Phys.*, **38**, 2951 (1967).
9. V. Rodriquez, E. MacKenna, and P. J. Fleming, Unpublished data.
10. L. Young and F. Zobel, *This Journal*, **113**, 277 (1966).

The Electrical Conductivity of CaO-Doped Nonstoichiometric Cerium Dioxide from 700° to 1500°C

R. N. Blumenthal, F. S. Brugner, and J. E. Garnier

Metallurgy and Materials Science, College of Engineering, Marquette University, Milwaukee, Wisconsin 53233

ABSTRACT

The electrical conductivity of sintered specimens of CaO-doped CeO_2 [0.1-16.0 m/o (mole per cent)] was measured over the temperature range 700°-1500°C and from 1 to 10^{-22} atm of oxygen. All specimens of CaO-doped CeO_2 exhibited mixed conduction. Two limiting case regions were observed. At low temperatures and high oxygen pressures, the conductivity is predominantly ionic. In this region the conductivity is independent of P_{O_2} and between approximately 1 and 8 m/o CaO is proportional to mole per cent CaO. The following equation for ionic conductivity

$$\sigma_i \simeq 6.0[\text{m/o CaO}] \exp -0.62/kT$$

was obtained by fitting the conductivity data in this region to an expression derived on the basis of an oxygen vacancy model. An approximate expression for the diffusion coefficient for oxygen vacancies

$$D_{V_O^{\cdot\cdot}} \simeq 3.7 \times 10^{-3} \exp -0.62/kT$$

was calculated from the above expression and the Nernst-Einstein relation. At high temperatures and low oxygen partial pressures and for lower CaO contents the conductivity is predominantly electronic. In this region the magnitude and P_{O_2} dependence of σ is similar to "pure" CeO_2. A thermodynamic argument is also presented which favors oxygen vacancies as the nonstoichiometric defect in both pure and CaO-doped CeO_2.

Only a limited number of studies (1-4) have been reported on the electrical conductivity of CaO-doped nonstoichiometric cerium dioxide. Kevane *et al.* (2) measured the electrical conductivity as a function of temperature (250°-1500°C), oxygen pressure (1-10^{-4} atm), and CaO content (0.03-0.86% Ca). They reported mixed conduction, electronic and ionic. The electronic conductivity was predominately n-type at elevated temperatures; at lower temperatures p-type behavior was observed. A recent electrical conductivity study of solid electrolytes in air by Meyer and Marincek (4) indicates that a 15 m/o (mole per cent) CaO-doped CeO_2 specimen is predominantly an ionic conductor. Ionic transference measurements in air by Yushina and Pal'guev (5) confirm the ionic conductivity of CeO_2 doped with 5-15 m/o CaO in the temperature range 700°-1100°C.

The solubility of CaO in CeO_2 based on an x-ray study has been reported to be 15 m/o CaO at 1600°C (6). Although no thermodynamic study on CaO-doped CeO_2 has been reported, the range of oxygen pressure over which the fluorite structure is stable should be large because CeO_{2-x} is thermodynamically stable (7-9) over a wide range of P_{O_2} and temperature. For

Key words: oxygen vacancy, diffusion, electrical conductivity, calcia-doped cerium dioxide, activation energy.

example, the fluorite structure of CeO_{2-x} is stable to values of P_{O_2} as low as 10^{-20} atm at 1023°C.

The above conductivity studies on CaO-doped CeO_2 have been made over only a rather limited range of oxygen pressures and CaO content. The results of a recent electrical conductivity study (10) on cerium dioxide over a wide range of oxygen pressures (1-10^{-21} atm) and temperatures (800°-1500°C) have been interpreted in terms of a nonstoichiometric defect model involving triply and quadruply ionized cerium interstitials and localized electrons. This defect model was based on a comparison of the isothermal oxygen pressure dependence of the electrical conductivity and a theoretically derived expression for the conductivity using the law of mass action.

The purpose of this study was (*i*) to measure the electrical conductivity over a wide range of temperature, oxygen pressure, and CaO content and (*ii*) to characterize the electronic and ionic conductivity by a comparison of the data with proposed defect models for CaO-doping and oxygen nonstoichiometry.

Theory

Defect model for ionic conductivity.—It is generally assumed that doping CeO_2 with CaO produces oxygen vacancies (2). In order to test the oxygen vacancy model, a room temperature study (11) was made in this laboratory comparing the true density and calculated values of the density based on lattice parameter data. The true density was determined using a water pycnometric technique. The measurements were made on powder obtained by crushing and grinding the sintered CaO-doped CeO_2 specimens in an alumina mortar and pestle. With this procedure the problem associated with pores in the density measurements was eliminated. The results of this study, for specimens in the stoichiometric condition with CaO contents between 0.1 and 16 m/o, are shown in Fig. 1. Curves A and B corresponding to Eq. [1] and [2],[1] respectively

$$CaO \rightarrow Ca_i^{\cdot\cdot} + O_i'' \qquad [1]$$

$$CaO \rightarrow Ca_i^{\cdot\cdot} + 1/2\, V_{Ce}'''' + O_o^x \qquad [2]$$

were calculated assuming calcium ions occupy cerium interstitial sites and the formation of charge-compensating defects which can be oxygen interstitials or cerium vacancies. Curves B and C corresponding to Eq. [3] and [4], respectively

$$1/2Ce_{Ce}^x + CaO \rightarrow Ca_{Ce}'' + 1/2Ce_i^{\cdot\cdot\cdot\cdot} + O_o^x \qquad [3]$$

$$CaO \rightarrow Ca_{Ce}'' + V_o^{\cdot\cdot} + O_o^x \qquad [4]$$

were calculated assuming calcium ions occupy cerium sites and the formation of charge-compensating defects

[1] The notation used to identify defects in this paper is the same as used by Kröger (22).

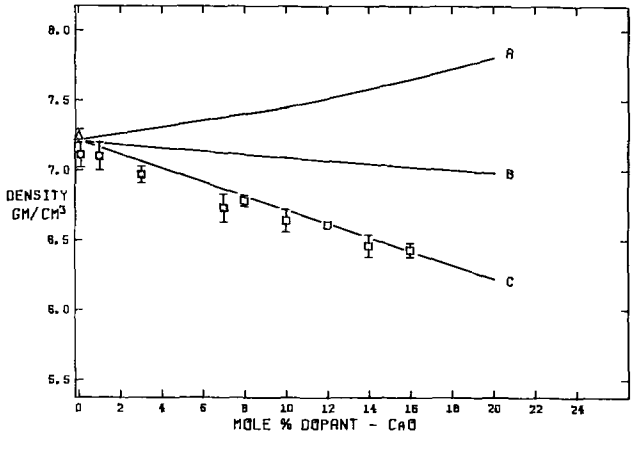

Fig. 1. Comparison of pycnometric density and calculated values of the density based on lattice parameter data for specimens of CeO_2 doped with CaO between 1 and 16 m/o.

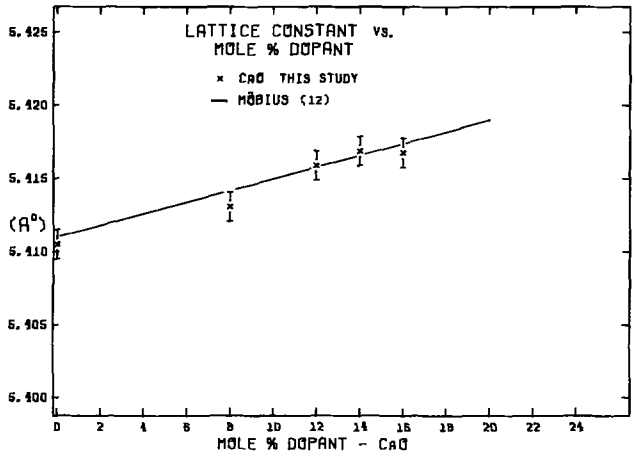

Fig. 2. Room temperature lattice parameter of CaO-doped CeO_2 vs. mole per cent CaO. The data points represented by the average values and the error bars were determined in this study (11). The solid line represents the reported results of Mobius (12).

which can be cerium interstitials or oxygen vacancies. The lattice parameter data used in these calculations is shown in Fig. 2. The data points shown in Fig. 1 correspond to the room temperature true density measurements made on the CaO-doped specimens used in this conductivity study. The agreement between the experimental data and curve C confirms the existence of oxygen vacancies in CaO-doped CeO_2.

The simplest model for ionic conduction in CaO-doped CeO_2 is to assume that the ionic conduction occurs by the migration of oxygen vacancies with only one state of ionization, $V_o^{\cdot\cdot}$. For this case the ionic conductivity, σ_i, may be represented by the expression

$$\sigma_i = 2B[V_o^{\cdot\cdot}]e\mu_{V_o^{\cdot\cdot}} \qquad [5]$$

where the bracketed term represents the number of a given species divided by the number of sites available for that species, B is a parameter which relates the concentration in site fraction to number/cubic centimeter, e is the charge on an electron, and $\mu_{V_o^{\cdot\cdot}}$ is the mobility of doubly ionized oxygen vacancies. If the oxygen vacancies are isolated point defects randomly distributed and the concentration of nonstoichiometric defects is small, then

$$[V_o^{\cdot\cdot}] = \frac{(\text{m/o CaO})}{200} \qquad [6]$$

In addition, if $\mu_{V_o^{\cdot\cdot}}$ is assumed to be a function of temperature only

$$\mu_{V_o^{\cdot\cdot}} = \mu'_{V_o^{\cdot\cdot}} \exp(-E_i/kT) \qquad [7]$$

Combining Eq. [5], [6], and [7] the relation for ionic conductivity is

$$\sigma_i = A(\text{m/o CaO}) \exp(-E_i/kT) \qquad [8]$$

where

$$A = B\,\mu'_{V_o^{\cdot\cdot}}\, e/100$$

Equation [8] may be tested in a region near stoichiometry where the ionic conduction predominates (*i.e.*, $\sigma \simeq \sigma_i$) by observing if σ is directly proportional to the CaO content in this region. In the region of this limiting case, σ should also be independent of P_{O_2}.

Defect models for electronic conductivity.—In a previous study on "pure" nonstoichiometric CeO_2 the isothermal dependence of σ on P_{O_2} was rationalized in terms of a defect model involving triply and quadruply ionized cerium interstitials and localized electrons (10). However, as discussed above the predominate defects produced by doping CeO_2 with CaO are oxygen vacancies. Based on thermodynamic considerations it can be shown that for both pure and CaO-doped CeO_2 the concentration of cerium interstitials is dependent on the concentration of oxygen vacancies.

For example applying the law of mass action to the defect reaction

$$1/2Ce_i^{\cdots\cdot} = 1/2Ce_{Ce}^{x} + V_o^{\cdot\cdot} \quad [9]$$

obtained by subtracting Eq. [3] from Eq. [4] yields

$$K \simeq \frac{[V_o^{\cdot\cdot}]}{[Ce_i^{\cdots\cdot}]^{1/2}} \quad [10]$$

Since the free energy change for Eq. [4] is more negative than Eq. [3], ΔG, for the defect reaction described by Eq. [9] is negative and $K > 1$.

Then according to Eq. [10]

$$[V_o^{\cdot\cdot}] > [Ce_i^{\cdots\cdot}]$$

because $[V_o^{\cdot\cdot}]$ and $[Ce_i^{\cdots\cdot}]$ are < 1. On the basis of the above thermodynamic argument it appears that if the addition of CaO to CeO_2 produces oxygen vacancies then the nonstoichiometric defects in pure CeO_2 are oxygen vacancies. Of course this argument would be invalidated if significant defect interaction occurs because of the addition of CaO to CeO_2 or as a result of large departures from stoichiometry.

Assuming the oxygen vacancies are doubly ionized, the nonstoichiometric defect reaction in CeO_2 may be characterized by the following reaction

$$O_o^x + 2Ce_{Ce}^x = 2Ce_{Ce}' + V_o^{\cdot\cdot} + 1/2\,O_2(g) \quad [11]$$

Electron transport is assumed to occur by a "hopping" type process (13, 14). Applying the law of mass action to Eq. [11] yields

$$K_1 = \frac{[Ce_{Ce}']^2\,[V_o^{\cdot\cdot}]\,P_{O_2}^{1/2}}{[O_o^x]\,[Ce_{Ce}^x]^2} \quad [12]$$

If the appropriate electroneutrality expression is

$$[Ce_{Ce}'] = 2[V_o^{\cdot\cdot}] \quad [13]$$

and $[O_o^x]$ and $[Ce_{Ce}^x] \simeq 1$ then

$$[Ce_{Ce}'] \propto P_{O_2}^{-1/6} \quad [14a]$$

or

$$\sigma_e \propto P_{O_2}^{-1/6} \quad [14b]$$

if μ_e is temperature dependent only.

It should be noted that under isothermal conditions and over a range of oxygen pressures the electrical conductivity of pure CeO_2 was observed (10) to be proportional to $P_{O_2}^{-1/5}$ (*e.g.*, between $P_{O_2} = 10^{-6}$ and 10^{-9} at 1100°C). However, at lower oxygen pressures (*i.e.*, large departure from stoichiometry) the dependence of σ_e on P_{O_2} involves a more complicated relationship (10). Thus the above analysis is inconsistent with the behavior of the oxygen pressure dependence of σ, which would seem to imply that either or both the mass action approach or the defect reaction given in Eq. [11] are incorrect.

Greener *et al.* (15) discussed a defect model proposed by Bevan involving a simple divacancy, $(V_o - V_o)^{\cdots\cdot}$, to explain the $P_{O_2}^{-1/5}$ dependence of σ in pure CeO_2. However, because of electrostatic repulsion between the negatively charged vacancies this model does not appear to be physically reasonable.

With the addition of CaO to CeO_2, the electroneutrality relation is

$$2[Ca_{Ce}''] + [Ce_{Ce}'] = 2[V_o^{\cdot\cdot}] \quad [15]$$

for the doubly ionized oxygen vacancy model.

Two interesting limiting cases may be readily deduced for this defect model. At low CaO contents and where the departures from stoichiometry are sufficiently large that

$$[Ce_{Ce}'] >> 2[Ca_{Ce}''] \quad [16]$$

the equation derived for CaO-doped CeO_2 would be the same as Eq. [14] which was derived for pure CeO_2.

However for near-stoichiometric conditions, where the CaO content is sufficiently large that

$$[Ce_{Ce}'] << 2[Ca_{Ce}''] \quad [17]$$

then the concentration of electron carriers, $[Ce_{Ce}']$, is given by Eq. [18] for the doubly ionized oxygen vacancy model

$$[Ce_{Ce}'] = \frac{K_1^{1/2}}{[Ca_{Ce}^{\cdot\cdot}]^{1/2}}\,P_{O_2}^{-1/4} \quad [18]$$

According to Eq. [18] for a given temperature and P_{O_2}, $[Ce_{Ce}']$ should decrease with increasing CaO content. On the basis of these simple limiting case models for CaO-doped CeO_2 the P_{O_2} dependence of σ_e, under isothermal conditions, might be expected to vary between $P_{O_2}^{-1/4}$ and $P_{O_2}^{-1/6}$ over a limited region of nonstoichiometry and CaO content. Since $\sigma \propto P_{O_2}^{-1/5}$ for pure CeO_2 over a range of oxygen pressures (10), it would be expected that both pure and CaO-doped CeO_2 should exhibit a similar isothermal dependence of σ_e on P_{O_2}, at least over a limited range of oxygen pressures.

Experimental

Conductivity specimens of CeO_2 doped with CaO (0.1-16.0 m/o CaO) were prepared by dry mixing the appropriate proportions of CeO_2 and $CaCO_3$ powder. The chemical analysis of CeO_2 and $CaCO_3$ powders are shown in Tables I and II, respectively. These mixtures were calcined for 12 hr at 1000°C in air. The calcined material was ground in an alumina mortar and pestle to an approximate particle size of 20μ or less. These powders were then pressed into bars 2 × 1/4 × 1/4 in. with a pressure of 20,000 psi. The bars were placed in an alumina boat and completely covered with CaO-doped CeO_2 powder of the same composition to avoid loss of CaO during sintering. A molybdenum-wound resistance furnace was used to sinter the bars at 1650°C for 3 1/2 hr in an argon atmosphere. Conductivity specimens were cut from the sintered bars to an average length of 2 cm. The bulk density measurements were determined from the mass of the specimen and the volume which was obtained from the external dimensions of the specimen. The nominal calcia content, the ratio of bulk density to true density, and the results of the chemical analysis on several of these specimens are shown in Table III. The nominal calcia content specimens, 0.3, 2.0, 5.0, and 7.0 m/o CaO, agree with

Table I. Mass spectrographic analysis of CeO_2

Element*	CeO_2,** ppmw
Ca	200
F	30
Fe	10
K	600
Li	20
Mg	10
Na	300
P	200
Pb	10
S	100
Si	20
Th	40
Ti	20
Zr	10

* Seventy-three elements were present, most in traces; only major impurities are listed.
** American Potash and Chemical Corporation CeO_2 (code 217.91).

Table II. Impurity analysis of Fisher F. W. 100.091 Certified Reagent $CaCO_3$

Impurity*	Percentage
SO_4	0.009
Ba	0.001
Cl	0.0005
Fe	0.0005
Pb	0.001
Sr	0.0
Mg	0.005
K	0.00

* 0.004% insoluble in HCl ond 0.001% insoluble in NH_3OH.

Table III. Nominal mole per cent CaO, density, and chemical analysis of the CaO content of the conductivity specimens used in this investigation

Nominal m/o CaO	XRF,* m/o CaO	AAS,** m/o CaO	% Bulk density/ true density
0.10	—	—	72.2
0.30	0.367	—	72.3
1.00	1.43	—	67.0
2.00	1.82	—	86.5
5.00	4.93	5.10	79.0
7.00	7.30	7.10	71.0
8.00	—	—	88.6
10.00	—	—	83.1
12.00	—	—	71.5
14.00	—	—	82.7
16.00	—	—	100

* X-ray fluorescence.
** Atomic absorption spectrometry.

the results of the x-ray fluorescence and the atomic absorption analysis within the reported experimental error of these analyses ±10%. With the exception of the 1 m/o CaO specimen, the nominal values of mole per cent CaO of all specimens analyzed were within the reported experimental accuracy of the x-ray fluorescence and atomic absorption analysis. Thus, in this study the nominal mole per cent CaO values will be used to identify the calcia content of each specimen.

The electrical conductivity measurements on the above CaO-doped cerium dioxide specimens as a function of P_{O_2} in the temperature range 700°-1500°C were made in a molybdenum-wound resistance furnace. A standard four-probe d-c technique was employed for the electrical conductivity measurements. The experimental apparatus employed was essentially the same as that described in an earlier publication (16). Four-probe conductivity specimens were prepared from sintered bars of CaO-doped CeO_2 by wrapping with 0.01-in. diameter platinum wire. Two current leads were wrapped near the ends of the specimen and two potential leads were wrapped closer to the center with a spacing of approximately 1 cm. An Altair Model C2 constant current source with a continuously variable range from 1 to 50 μA was used to supply the current. The d-c conductivity measurements were found to be independent of the applied field and time in this study. In addition a-c measurements in the frequency range 10-1000 Hz were found to be in agreement with the d-c measurements. These results indicate that ohmic behavior was achieved and that polarization was not a problem in these measurements.

Oxygen partial pressures were achieved by means of two methods. For pressures from 1 to 10^{-4} atm, premixed and analyzed O_2-Ar mixtures at 1 atm total pressure were used in the study. Controlled oxygen partial pressures in the low-pressure region were obtained by introducing known mixtures of CO and CO_2 at 1 atm total pressure. The well-known free energy values for the CO/CO_2 reaction were used to calculate the oxygen partial pressure. A linear flow rate of 0.7 cm/sec was maintained for all gas mixtures used in this investigation to avoid errors arising from thermal diffusion (17). However, no flow dependence was noted when the flow rate was increased or decreased within 50% of this value. Electrical conductivity measurements were made at various temperatures between 700° and 1500°C for a fixed gas mixture for both increasing and decreasing temperature. Data were taken in 200°C increments, starting at 700°C and proceeding to 1500°C while heating. During cooling from 1400° to 800°C data was recorded at 200°C intervals. Since the composition of calcia-doped nonstoichiometric ceria has a unique value for each CaO content, oxygen partial pressure, and temperature, the above technique insured the measurement of equilibrium conductivity because the nonstoichiometric equilibrium state was approached from both higher and lower compositions of oxygen. In addition some isothermal conductivity measurements were made. The conductivity data obtained from both techniques were found to be in good agreement.

Results and Discussion

The electrical conductivity of sintered specimens of calcia-doped nonstoichiometric cerium dioxide (0.1-16.0 m/o CaO) was measured as a function of temperature (*i.e.*, 700°-1500°C) and oxygen pressure ($1-10^{-21}$ atm). Typical behavior of the conductivity as a function of the reciprocal absolute temperature in Ar-O_2 and CO-CO_2 mixtures is illustrated in Fig. 3 for a nonstoichiometric cerium dioxide specimen doped with 1.0 m/o CaO. The measured values of the conductivity, σ_{meas}, for the sintered specimen have been corrected for porosity using the relation (18)

$$\sigma = \sigma_{meas} \frac{\rho_{theor}}{\rho_{meas}} \qquad [19]$$

where ρ_{theor} is the theoretical density and ρ_{meas} is the bulk density of the sintered specimen. For all of the CaO-doped specimens two distinct types of behavior are observed as illustrated in Fig. 3. At lower temperatures and high oxygen pressures (*i.e.*, Ar-O_2 mixtures), the conductivity is independent of oxygen partial pressure and exponentially dependent on temperature. At higher temperatures and low oxygen pressures, the conductivity exhibits n-type behavior. Based on the simple limiting case defect models discussed in the theory section, the ionic conductivity should be proportional to mole per cent CaO and independent of P_{O_2}; whereas the electronic conductivity of Ca-doped CeO_2 should exhibit a dependence on P_{O_2} similar to pure CeO_2. Isothermal plots of log σ *vs.* log P_{O_2} were made for each of the CaO-doped specimens to test these simple models (13). Typical plots are shown in Fig. 4-6 for 1, 5, and 12 m/o CaO, respectively. For comparative purposes the conductivity (10) of a pure CeO_2 specimen is shown as a dashed line in these figures.

A qualitative explanation of the observed electrical conductivity data may be given in terms of three regions as follows:

Region 1: At high temperatures and particularly at low oxygen pressures, the σ of the CaO-doped specimens exhibits a similar P_{O_2} dependence as pure CeO_2.

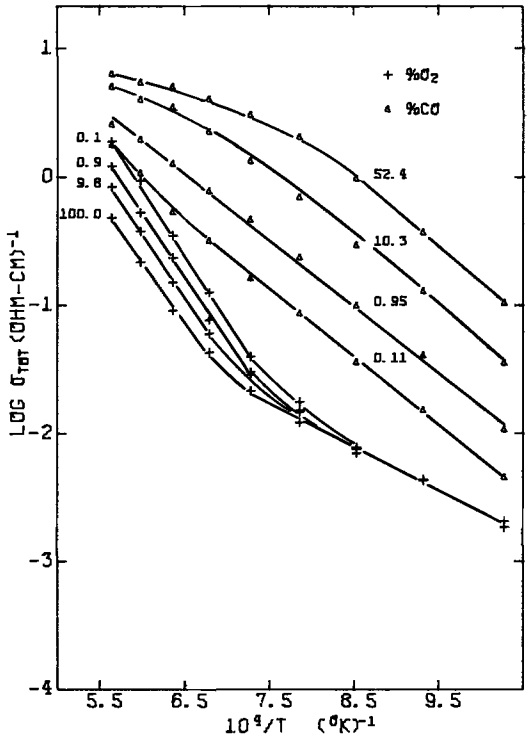

Fig. 3. Log σ vs. $1/T$ for 1 m/o CaO-doped CeO_2 in Ar-O_2 and CO-CO_2 mixtures.

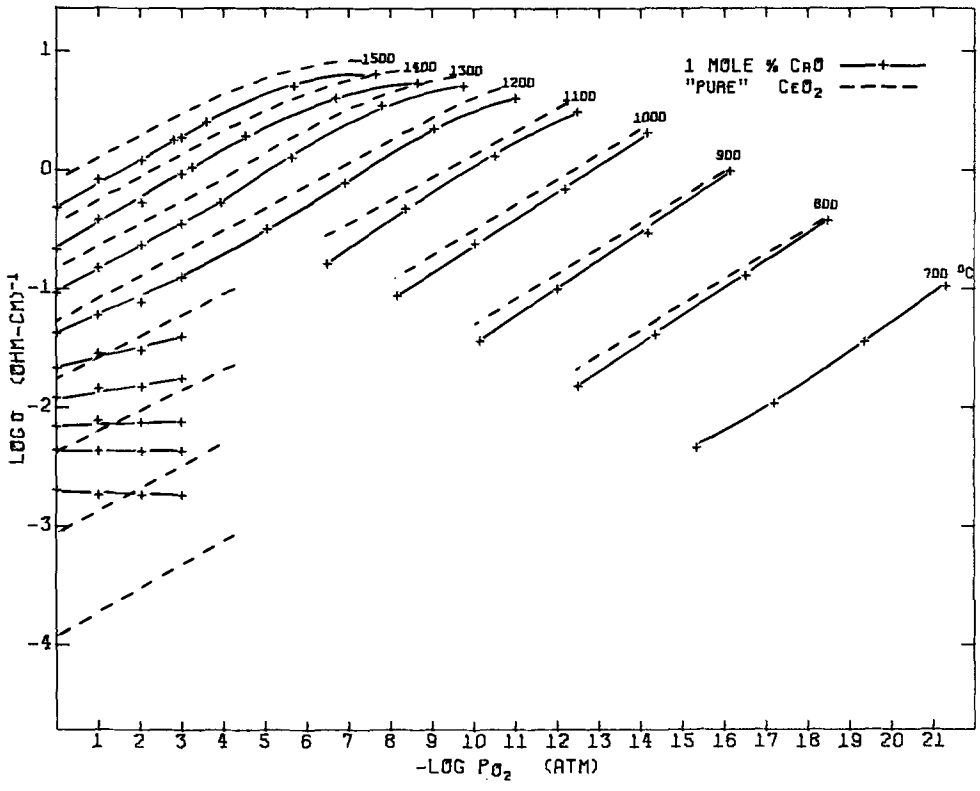

Fig. 4. Comparison of isothermal plot of log σ vs. log P_{O2} for pure nonstoichiometric cerium dioxide and 1.0 m/o CaO-doped CeO_2 sintered specimens.

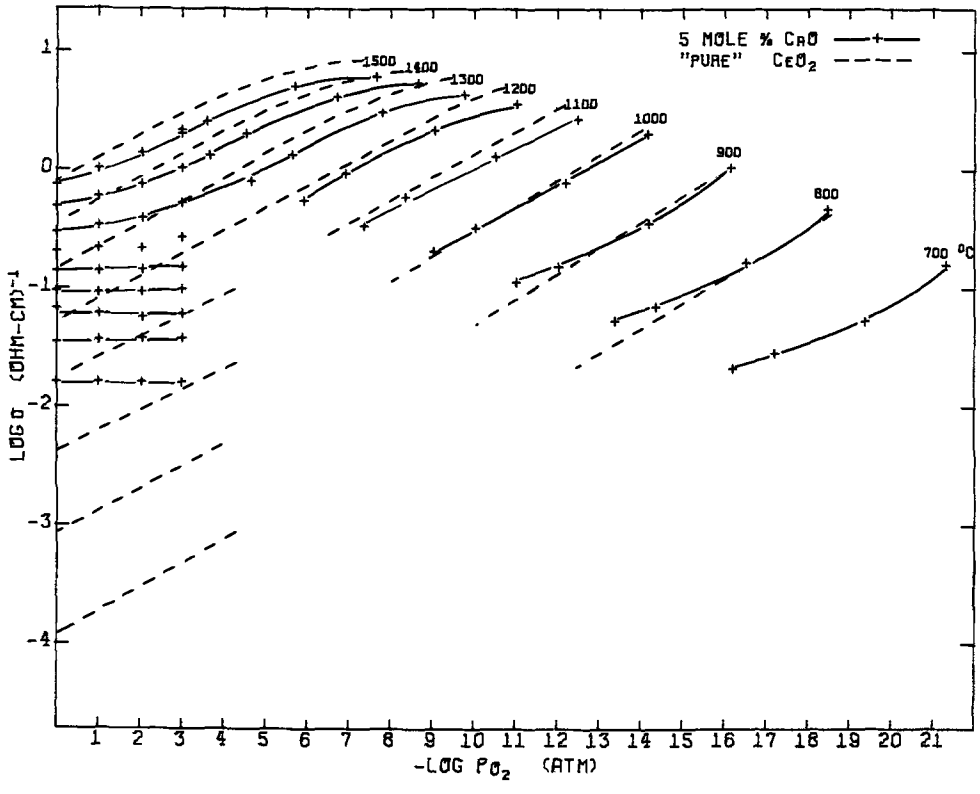

Fig. 5. Comparison of isothermal plot of log σ vs. log P_{O2} for pure nonstoichiometric cerium dioxide and 5.0 m/o CaO-doped CeO_2 sintered specimens.

The conductivity in this region appears to be predominantly electronic (*i.e.*, $\sigma \simeq \sigma_e > \sigma_i$) and is probably controlled by the same nonstoichiometric defects as in pure CeO_2. As the CaO content increases, lower oxygen pressures (*i.e.*, a higher concentration of nonstoichiometric defects) are required to "mask" out the effect of the CaO.

Region II: For low temperatures and high oxygen partial pressures (*i.e.*, near stoichiometric conditions), the conductivity of the CaO-doped specimen is independent of oxygen partial pressure. The σ is also much larger than that of pure CeO_2. Since σ_i is to a first-order approximation independent of the oxygen pressure, this observation is consistent with a conduction process which is primarily ionic (*i.e.*, $\sigma \simeq \sigma_i > \sigma_e$).

Region III: For all oxygen pressures and temperatures intermediate to regions I and II, the conductivity appears to be mixed, *i.e.*, where σ_e and σ_i are of the same order of magnitude.

As discussed in the Theory section, the simple limiting case defect models for electronic conduction predict that the concentration of electronic defects should decrease with increasing CaO content. However, based on the defect model for CaO doping, the ionic conductivity is directly proportional to the CaO content. As a test of these models, isothermal plots were made of

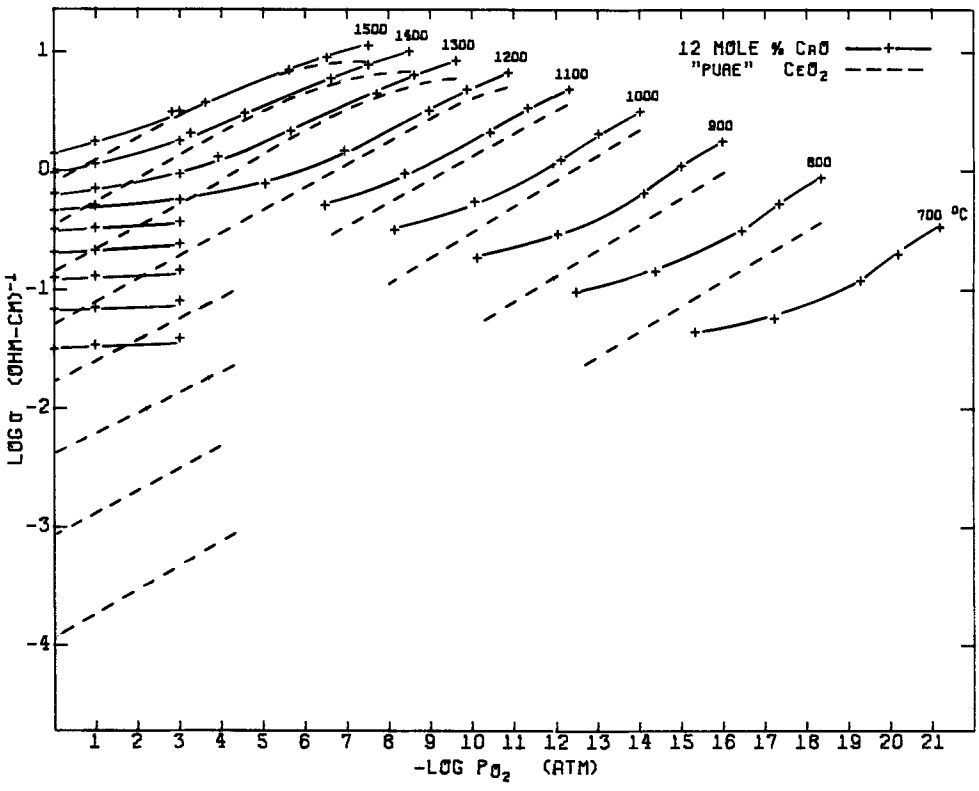

Fig. 6. Comparison of isothermal plot of log σ vs. log P_{O_2} for pure nonstoichiometric cerium dioxide and 12 m/o CaO-doped CeO_2 sintered specimens.

log σ *vs.* log mole per cent CaO for all of the gas mixtures used in this study (11, 13). Typical plots of log σ *vs.* log mole per cent CaO are shown in Fig. 7, 8, and 9 for atmospheres containing 100% O_2, 0.1% CO, and 48.1% CO, respectively. The same three regions of behavior discussed above may be observed. In region I (*i.e.*, $\sigma \simeq \sigma_e$) the magnitude of the conductivity of pure and CaO-doped CeO_2 are similar. This region extends to higher CaO compositions and lower temperatures in more reducing gas mixtures (*i.e.*, lower oxygen partial pressures). In region II (*i.e.*, $\sigma \simeq \sigma_i$) the slope of log σ *vs.* log per cent CaO is approximately one. This region is observed primarily at lower temperatures and higher oxygen pressures. For example, in an atmosphere of 100% O_2 (Fig. 7) this region extends from approximately 1 to 8 m/o CaO in the temperature range 700°-1100°C, whereas in a strongly reducing atmosphere (48.1% CO, Fig. 9) this region is barely detectable at 700°C. At high oxygen pressures, low temperatures, and low CaO contents (0.1 m/o CaO, Fig. 7) a curvature in the line is observed. This effect is probably due to impurities in CeO_2. For example,

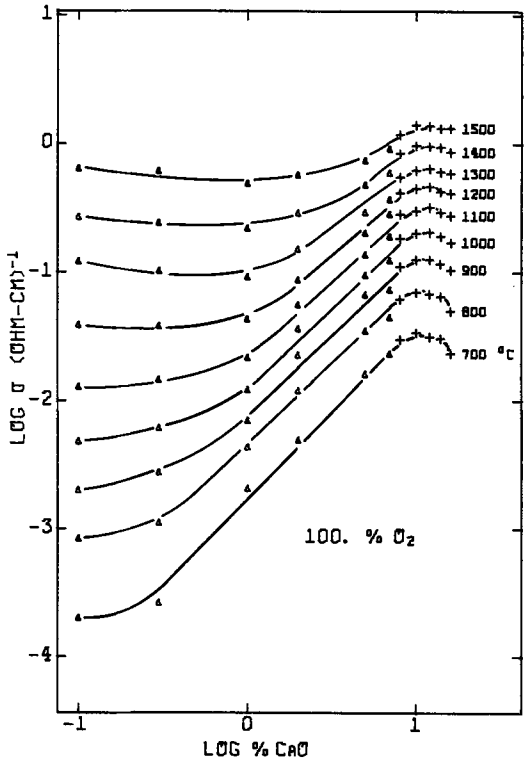

Fig. 7. Isothermal plot of log σ vs. log mole per cent CaO in CeO_2 in 100% O_2.

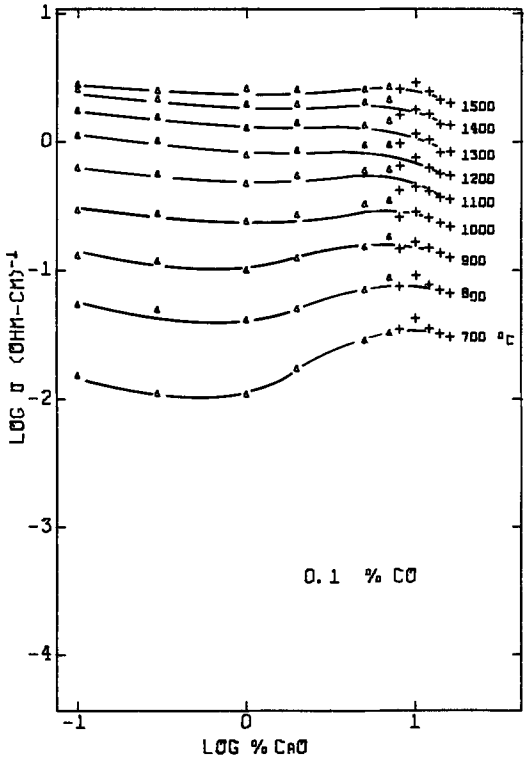

Fig. 8. Isothermal plot of log σ vs. log mole per cent CaO in CeO_2 in 0.1% CO.

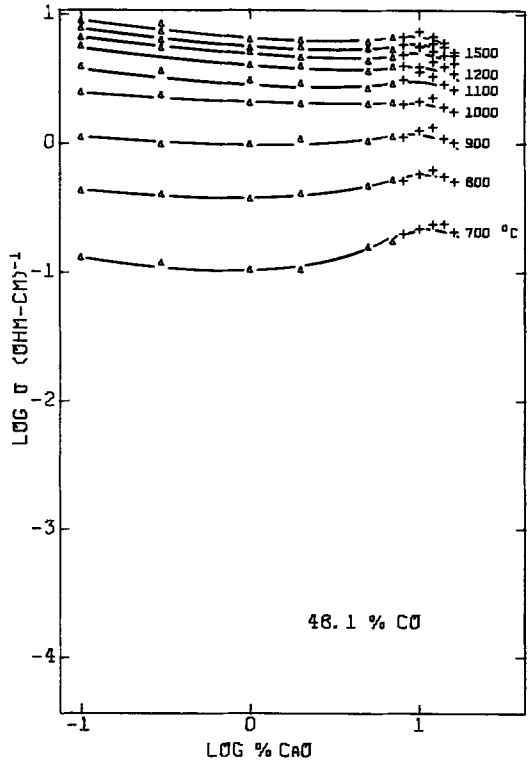

Fig. 9. Isothermal plot of log σ vs. log mole per cent CaO in CeO_2 in 48.1% CO.

the conductivity for pure CeO_2 has been reported (10) to be influenced by impurities in this temperature and oxygen pressure region (*i.e.*, in the near stoichiometric condition). Thus, it appears that a dopant concentration of $>$ 0.3 m/o CaO is required to produce a sufficient number of defects to completely swamp out the effect of impurities in near stoichiometric CeO_2. Region III is a region of mixed conduction. Another interesting observation from Fig. 7-9 is that at high CaO compositions the conductivity appears to exhibit a maximum with increasing CaO content. This behavior also appears to be relatively independent of temperature and oxygen partial pressure. Similar behavior has been reported for other fluorite oxide systems doped with lower valent cations. Two different models have been used to explain the maximum in σ observed in CaO-doped ZrO_2 (19). One model is based on a clustering of defects and the other on synthetic zones of composition. In both of these models the activation energy increases with increasing CaO content. In contrast to the predictions of these models, the activation energy for CaO-doped CeO_2 determined from a plot of log σ *vs.* $1/T$ at 1 atm of O_2 is independent of CaO content. Also in the vicinity of the σ maximum only a very small variation in the magnitude of the conductivity with CaO content is observed. Although the reported solubility (6) is 15 m/o CaO in air at 1600°C, the dependence of temperature and oxygen pressure on the solubility limits of CaO-doped CeO_2 is not known. Thus the question of whether the concentration of CaO in this region exceeds the solubility of CaO in CeO_2 cannot be easily ascertained. Because of these considerations no attempt has been made to analyze the maximum in the conductivity of CeO_2 doped with CaO.

The qualitative interpretation of the electrical behavior of CaO-doped CeO_2 observed in this study may be summarized as follows. CaO-doped CeO_2 exhibits both electronic and ionic conductivity. Two, limiting case regions were observed. At low temperatures and high oxygen pressures, and CaO contents of approximately 1-8 m/o CaO, the conductivity is proportional to mole per cent CaO and is predominately ionic. Whereas at high temperatures and low oxygen partial pressures and lower CaO contents the conductivity is predominately electronic.

The qualitative predictions of the limiting case defect models for electronic conduction (*i.e.*, similar magnitude and P_{O_2} dependence as pure CeO_2) in CaO-doped CeO_2 appear to be consistent with the observed behavior of the conductivity in this limiting case region. It should be noted that the limiting case models for oxygen vacancies would be expected to apply only in the oxygen pressure region where $\sigma \propto P_{O_2}^{-1/5}$ in pure CeO_2. However, for oxygen pressures below this region, the conductivity of pure and CaO-doped CeO_2 are actually in closer agreement. This implies that the same defects are responsible for the nonstoichiometric behavior in pure and CaO-doped CeO_2. In the Theory section the inconsistencies of the previously proposed cerium interstitial defect model for pure CeO_2 and CaO-doped CeO_2 have been discussed. The problem with the mass action interpretation of the doubly ionized oxygen vacancy model has also been discussed. In addition information on the transference number should be available in order to determine a more exact dependence of σ_e on temperature, oxygen pressure, and CaO content. Because of these considerations no attempt has been made in this paper to analyze quantitatively the conductivity data in terms of the above defect models.

In order to analyze quantitatively the proposed oxygen vacancy model for ionic conductivity, Eq. [8], the conductivity in the region where ionic conductivity predominated was plotted as a function of CaO. These results are shown in Fig. 10 at $P_{O_2} = 1$ atm for 700°-1000°C and for CaO contents between 1 and 16 m/o. A direct proportionality was observed for specimens with CaO contents between approximately 1 and 8 m/o CaO. The parameter E_i in Eq. [8] was obtained from the plot shown in Fig. 11 of log σ *vs.* $1/T$ at $P_{O_2} =$ 1 atm for several different CaO contents. The average value of E_i determined from a least square analysis was 0.62 $\pm$ 0.03 eV for compositions from 1.0 to 14.0 m/o CaO. A value of $A = 6.0 \pm 0.5$ was determined by curve fitting Eq. [8] to the data shown in Fig. 11. Thus if the proposed limiting case defect model for ionic conductivity is correct and ionic conductivity predominates in the composition region, 1-8 m/o CaO, (*i.e.*, $t_i \simeq 1$), σ_i may be approximated by the relation

$$\sigma_i \simeq [6.0 \pm 0.5]\ [\text{m/o CaO}] \exp -0.62/kT \qquad [20]$$

An approximate expression for the diffusion coefficient of oxygen vacancies, $D_{V_O^{\cdot\cdot}}$, in CaO-doped CeO_2

$$D_{V_O^{\cdot\cdot}} \simeq 3.7 \times 10^{-3} \exp -0.62/kT \qquad [21]$$

was determined in this study from the above data and the Nernst-Einstein relation. It is interesting to note that the diffusion coefficient for oxygen vacancies in

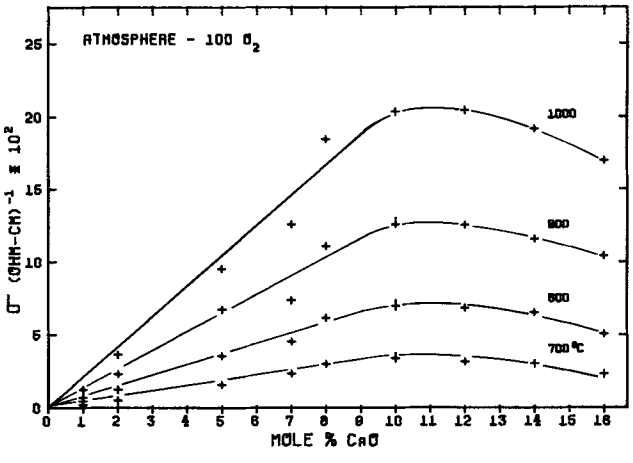

Fig. 10. Isothermal plot of σ vs. mole per cent CaO in CeO_2 at 1 atm O_2.

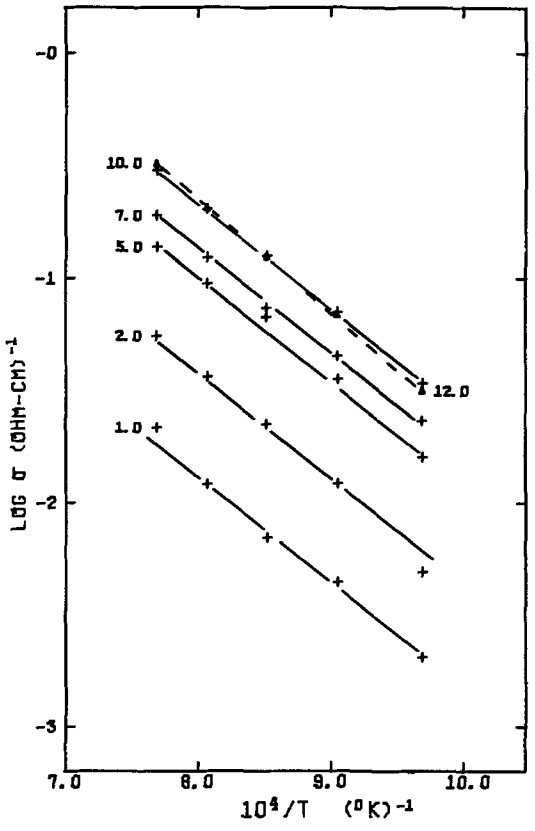

Fig. 11. Log σ vs. 1/T for 1, 2, 5, 7, 10, and 12 m/o CaO-doped CeO_2 at 1 atm O_2.

CaO-doped CeO_2 is larger than in CaO-doped ZrO_2 (20).

A recent study of oxygen self-diffusion (21) in ceria-yttria solution at $P_{O_2} = 1$ atm in the temperature range 850°-1150°C indicates that the activation energy, approximately 20 kcal/mole, is essentially independent of yttria composition (*i.e.*, for x between 0 and 0.2 in the formula $Ce_{1-2x}Y_{2x}O_{2-x}$). The activation energy obtained in this study (~14 kcal/mole) for diffusion of oxygen vacancies produced by CaO is in relatively good agreement with the self-diffusion of oxygen in $Ce_{1-2x}Y_{2x}O_{2-x}$). It is also interesting to note that the reported (21) activation energy for oxygen self-diffusion in pure ceria varied from about 24 kcal/mole in near stoichiometric ceria to about 4 kcal/mole for $CeO_{1.8}$. Thus it might be expected that the activation energy for oxygen diffusion in CaO-doped CeO_2 would decrease in the presence of a large concentration of nonstoichiometric defects (*i.e.*, at low oxygen pressures).

A study of transference measurements on CaO-doped CeO_2 has been initiated in this laboratory to determine t_i as a function of temperature, P_{O_2}, and CaO content. These data when combined with the above σ data should allow the determination of the T, P_{O_2}, and CaO dependence of the electronic and ionic conductivity. The combined results of these studies should permit a more quantitative test of the simple limiting case defect models for ionic and electronic conductivity.

Acknowledgment

This work was supported by the United States Atomic Energy Commission, Division of Research. This is AEC Report COO-1441-16. This paper is based in part on theses submitted in partial fulfillment of the requirements for the Ph.D. degree and M.S. degree, Marquette University, by F. S. Brugner (August 1971) and J. E. Garnier (December 1972), respectively.

Manuscript submitted Nov. 24, 1971; revised manuscript received Feb. 21, 1973.

Any discussion of this paper will appear in a Discussion Section to be published in the June 1974 JOURNAL.

REFERENCES

1. E. L. Holverson, Ph.D. Dissertation, Arizona State University, Tempe, Ariz. (1964).
2. C. J. Kevane, E. L. Holverson, and James B. Armstrong, Paper presented at the Fifth Rare Earth Research Conference, Ames, Iowa (Aug. 1965).
3. R. N. Blumenthal and B. A. Pinz, *J. Appl. Phys.*, **38**, 2376 (1967).
4. E. Meyer and B. Marincek, *Schweizer Archiv.*, **36**, 194 (1970).
5. L. D. Yushina and S. F. Pal'guev, "Electrochemistry of Molten and Solid Electrolytes," Vol. 11, p. 74, M. V. Smirnov, Editor, Consultants Bureau, New York (1969).
6. E. K. Keler, N. A. Godina, and A. M. Kalinina, *Zh. Neorgan. Khim., Moscow*, **1**, 2557 (1956).
7. G. Brauer and K. A. Gingerich, *J. Inorg. Nucl. Chem.*, **16**, 87 (1960).
8. F. A. Kuznetsov, V. I. Beliy, and T. N. Rezukhina, *Dokl. Akad. Nauk SSR, Fiz-Khim.*, **139**, No. 6, 1405 (1961).
9. D. J. M. Bevan and J. Kordis, *J. Inorg. Nucl. Chem.*, **26**, 1509 (1964).
10. R. N. Blumenthal, P. W. Lee, and R. J. Panlener, *This Journal*, **118**, 123 (1971).
11. J. E. Garnier, M. S. Thesis, Marquette University, Milwaukee, Wisc., 1972.
12. H. H. Mobius, *Z. Chem.*, **4**, 81 (1964).
13. F. S. Brugner, Ph.D. Dissertation, Marquette University, Milwaukee, Wisc., 1971.
14. R. N. Blumenthal and R. J. Panlener, *J. Phys. Chem. Solids*, **31**, 1190 (1970).
15. E. H. Greener, J. M. Wimmer, and W. M. Hirthe, "Rare Earth Research," Vol. 2, pp. 539-554, K. S. Vorres, Editor, Gordon and Breach, Science Pub., New York (1964).
16. R. N. Blumenthal, J. Coburn, J. Baukus, and W. M. Hirthe, *J. Phys. Chem. Solids*, **27**, 643 (1966).
17. L. S. Darken and R. W. Gurry, *J. Am. Chem. Soc.*, **67**, 1398 (1945).
18. F. S. Brugner and R. N. Blumenthal, *J. Am. Ceram. Soc.*, **54**, 57 (1971).
19. R. E. Carter and W. L. Roth, in "Electromotive Force Measurement in High Temperature Systems," C. B. Alcock, Editor, pp. 125-144, American Elsevier Publishing Co., Inc., New York (1968).
20. C. E. Birchenell, "Mass Transport in Oxides," NBS Special Publ. 296, p. 119 (1968).
21. B. C. H. Steele and J. M. Floyd, *Proc. Brit. Ceram. Soc.*, **19**, 55 (1971).
22. F. A. Kröger, "The Chemistry of Imperfect Crystals," North-Holland Publishing Co., Amsterdam (1964).

D-C Conduction and Electroluminescence in Dielectric-Embedded ZnS:Mn,Cu,Cl

John M. Fikiet[1] and John L. Plumb[2]

Department of Electrical Engineering, University of Connecticut, Storrs, Connecticut 06268

ABSTRACT

The effect of binder on the d-c characteristics of electroluminescent ZnS:Mn,Cu,Cl phosphor powder dispersed in a plastic (polymethylmethacrylate) binder was investigated. A plot of the current-voltage characteristic showed that $I = I_0 \exp \sqrt{V/V_I}$, where I_0 and V_I are constants for a given sample, suggesting current limited by Schottky emission from Cu-rich lines in the phosphor. As the phosphor concentration in the binder is increased, V_I decreases to a nearly constant value much smaller than calculated for a uniform electric field in an insulator. This result indicates that Schottky emission occurs at points of field concentration, such as at the ends of Cu-rich lines.

Electroluminescence in Mn-activated ZnS is enhanced by the incorporation of Cu (1), and the resulting doubly activated phosphor is electroluminescent to both a-c and d-c excitation (2-4). High efficiency and brightness in ZnS:Mn,Cu,Cl powder dispersed in an insulating binder and excited with a d-c voltage have been reported by Vecht, *et al.* (5-6). Two different methods of phosphor activation were used, one being post activation by the conventional slurrying technique (7) which resulted in a quantum efficiency as high as 170% and the other being simultaneous activation followed by copper coating of the phosphor which resulted in a brightness as high as 1000 ft-L. Close control of the ZnS purity and the Mn and Cu additions was described, but little information regarding the current-voltage characteristic or the effect of binder on cell properties was reported.

In the case of a-c excitation of activated ZnS powder dispersed in an insulating binder, a purpose of the binder is to avoid discharges and breakdown (7), and the only apparent effect on electroluminescence is to modify the electric field distribution (8, 9). The brightness with a-c excitation has been reported not to depend on binder material or proportion of binder to phosphor (10). The brightness and efficiency with d-c excitation, however, should depend significantly on proportion of binder to phosphor.

Electroluminescence with d-c excitation has been observed and studied in ZnS phosphor crystals and films as well as embedded powder. Light emission from the cathode region has been observed in Cu-activated and Mn-activated crystals relatively free of internal barriers (11), and this electroluminescence is most readily ascribed to impact excitation by injected electrons accelerated in a high-field region adjacent to the cathode (12). This mechanism is also consistent with data obtained for Mn-activated ZnS films made d-c electroluminescent by converting a surface layer of ZnS to Cu_2S (13).

Electroluminescence in both crystals and embedded powders has been observed as originating at the tips of striations or lines within the crystal or powder particle (14, 15). These lines are believed to be a separate phase of Cu_2S existing at crystal imperfections (16). Electrons can be injected into the ZnS from this separate conducting phase at points of electric field concentration. Electroluminescence in ZnS:Mn,Cu,Cl films has been observed to originate at the anode (17). The current-voltage characteristics of the films indicate that electron injection occurs at the ends of Cu or Cu_2S lines that extend from the cathode to the vicinity of the anode (18).

Vecht *et al.* (6) have investigated the brightness-current and brightness-voltage characteristics of the electroluminescent ZnS:Mn,Cu,Cl powder-binder system and the effect of varying the concentration of Cu and Mn in the phosphor powder. The present paper describes the current-voltage characteristics and the effect of varying the concentration of phosphor powder in the insulating binder.

Electroluminescent Cell Preparation and Characteristics

Electroluminescent cells were made by dispersing ZnS:Mn,Cu,Cl phosphor powder in polymethylmethacrylate (PMMA) and sandwiching this mixture between Al and transparent, conducting, tin oxide electrodes. The phosphor was prepared by the post-activated slurry technique described by Vecht *et al.* (6). Aqueous solutions of Cu and Mn acetates and HCl solution were added to luminescent grade ZnS. The mixture was dried, pulverized, and fired at 900°C for 1 hr in a nitrogen atmosphere. The powder was sifted through a 320-mesh sieve and mixed with PMMA[2] in a solvent. This mixture was spread with a sharp edge (at constant height) onto a tin-oxide-coated glass substrate[3] and allowed to dry a few minutes at room temperature and finally at 65°C. To form a top electrode Al was deposited by evaporation.

The phosphor powder was analyzed for Cu and Mn content by atomic absorption film spectrometry and for Cl content by coulometric titration. The thickness and roughness of each phosphor film were measured with a Zeiss light section microscope and the cell fabrication was completed only if the film was flat and 30 to 35 μm thick.

The tin oxide layer was contacted with a Ag paint. The d-c voltage producing average electric fields ranging from 70 to 280 kV/cm in the phosphor/binder layer were applied between the Ag and Al. The cell current was measured with a Keithley 103 microvolt-ammeter and the luminance with an RCA 4473 photomultiplier.

In two cells, no phosphor was dispersed in the PMMA binder. Varying voltage was applied to the cell and the current at each voltage was measured after the charging component had decayed to a negligible value. There was no significant difference between ascending and descending data. The logarithm of the current is plotted *vs.* the square root of the voltage in Fig. 1. The current-voltage characteristic is seen to follow the relation

$$I = I_0 \exp \sqrt{V/V_I} \qquad [1]$$

where I_0 and V_I are constants for the cell. This current-voltage characteristic can be explained as the result

[1] Present address: American Embassy, Peace Corps, Caracas, Venezuela.
[2] Present address: Transitron Electronic Corporation, Wakefield, Massachusetts 01880.
Key words: carrier injection, insulator, polymethyl methacrylate, zinc sulfide.

[2] Rohm and Haas Acryloid A 101.
[3] Corning IRR 7420.

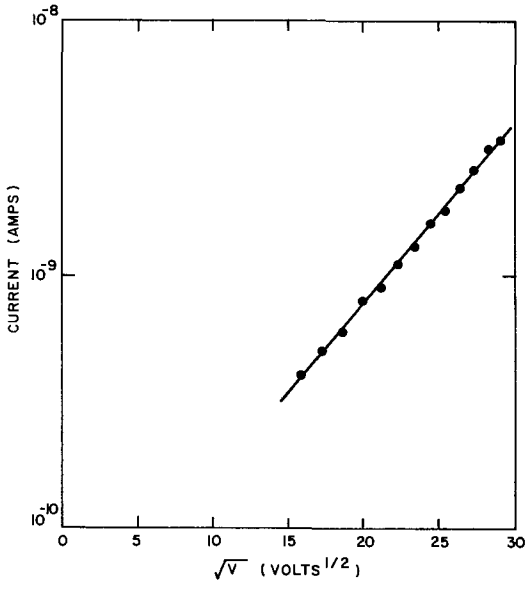

Fig. 1. Current-voltage characteristic for a 30-μm thick polymethylmethacrylate binder film without phosphor plotted as logarithm of current *vs.* square root of voltage.

of a thermal process such as Schottky emission, *i.e.*, field-enhanced thermal injection from a metal electrode caused by image-force lowering of the barrier (19).

The factor V_I in the exponent of Eq. [1] is related to the slope of the curve in Fig. 1. Theoretically, for Schottky emission

$$I = AT^2 \exp\left[-e(\phi_0 - \sqrt{eV/4\pi K\epsilon_0 d})/kT\right] \quad [2]$$

where A is Richardson's constant and ϕ_0 is the contact barrier height (20). The constant V_I of Eq. [1] is therefore

$$V_I = 4\pi K\epsilon_0 dk^2T^2/e^3 \quad [3]$$

where K is the high-frequency dielectric constant of the PMMA, ϵ_0 is the free-space permittivity, and d is the PMMA thickness. Here it is assumed that the electric field is uniform and equal to V/d.

Cells with phosphor dispersed in the PMMA binder were electroluminescent immediately on application of d-c voltage. The brightness for a given current was not as high as that reported by Vecht *et al.* (6), but the voltage required to produce a given brightness was less. The electroluminescent cells prepared by Vecht *et al.* (6), from phosphor simultaneously activated and copper-coated also exhibited lower luminance for a given current and higher luminance for given voltage than those prepared from post-activated powder, but these required a forming step after preparation. In cells prepared in the present work, the current decreases slowly with time, as also does the luminescence. The voltage was set at the maximum value for 5 min and then a voltage-current-luminescence characteristic was recorded.

In Fig. 2 are plotted log I *vs.* $\sqrt{V}$ for a cell with pure ZnS (cell A) and another with ZnS:Mn,Cu,Cl dispersed in the binder (cell B). The phosphor concentration is 0.5g of phosphor per cubic centimeter of binder. The Mn concentration is 0.40%, the Cu concentration is 0.09%, and the Cl concentration is 0.005% by weight, in the ZnS. The curves are linear and the slopes are greater than in Fig. 1. (Note the change in the vertical scale.) The slope is greater for cells with ZnS:Mn,Cu,Cl than those with pure ZnS dispersed in the PMMA binder.

A number of cells were fabricated with varying phosphor binder ratio. The relation of Eq. [1] was obeyed by the d-c current-voltage characteristic of each cell, and only the constants I_0 and V_I varied. I_0 and V_I are plotted *vs.* phosphor concentration in Fig. 3. Also plotted are I_0 and V_I for zero phosphor concentration, *i.e.*, with no phosphor dispersed in the binder. It is seen that I_0 falls on introduction of the phosphor and then increases rapidly as the phosphor concentration is increased. V_I decreases sharply and then becomes relatively independent of phosphor concentration.

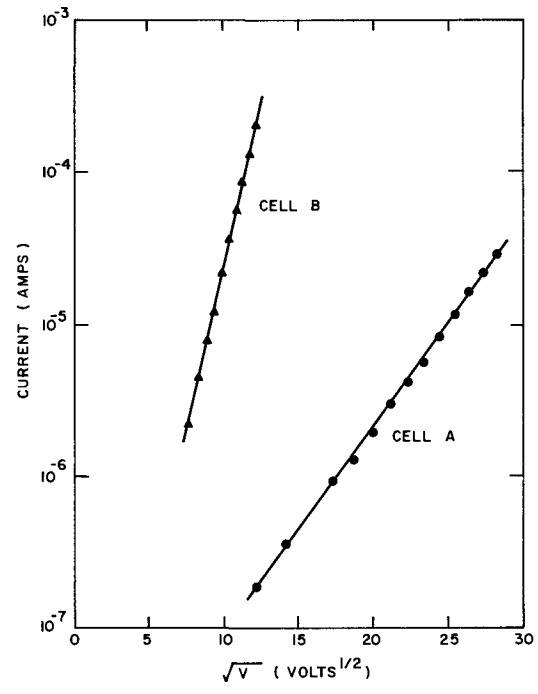

Fig. 2. Current-voltage characteristics for films with pure ZnS (cell A) and ZnS:Mn,Cu,Cl phosphor (cell B) mixed into binder.

The luminance-voltage characteristic for each cell obeyed reasonably the relation

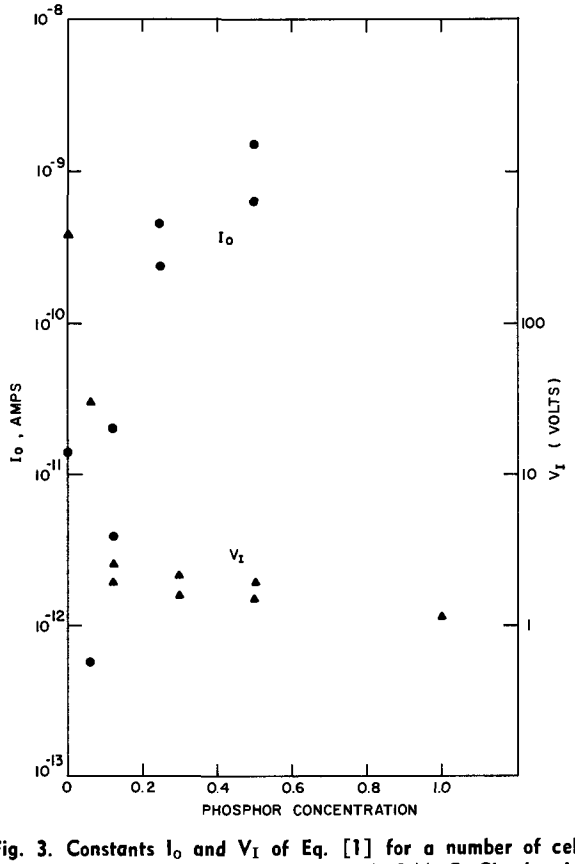

Fig. 3. Constants I_0 and V_I of Eq. [1] for a number of cells with electroluminescent films of various ZnS:Mn,Cu,Cl phosphor concentrations.

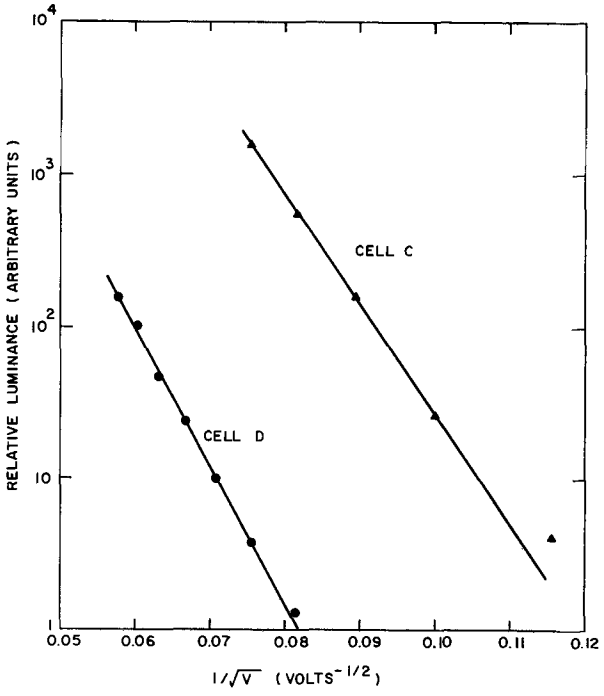

Fig. 4. Typical luminance-voltage characteristics plotted as logarithm of luminance *vs.* reciprocal square root of voltage. In cell C the phosphor concentration is 1.0 g/cm^3 of binder. In cell D the phosphor concentration is 0.25 g/cm^3 of binder.

$$L = L_0 \exp \sqrt{V_L/V}$$

for higher voltages. Log L is plotted *vs.* $1/\sqrt{V}$ for two cells of different phosphor binder ratios in Fig. 4. In cell C the phosphor concentration is 1g of phosphor per cubic centimeter of binder, and in cell D it is 0.25g of phosphor per cubic centimeter of binder. Log L is plotted *vs.* log I for the same cells in Fig. 5. In general, the luminance at constant voltage increased as the phosphor concentration was increased. The luminance at constant current seemed to increase with decreasing phosphor concentration to about 0.25g of phosphor per cubic centimeter of binder and then become relatively independent of phosphor concentration.

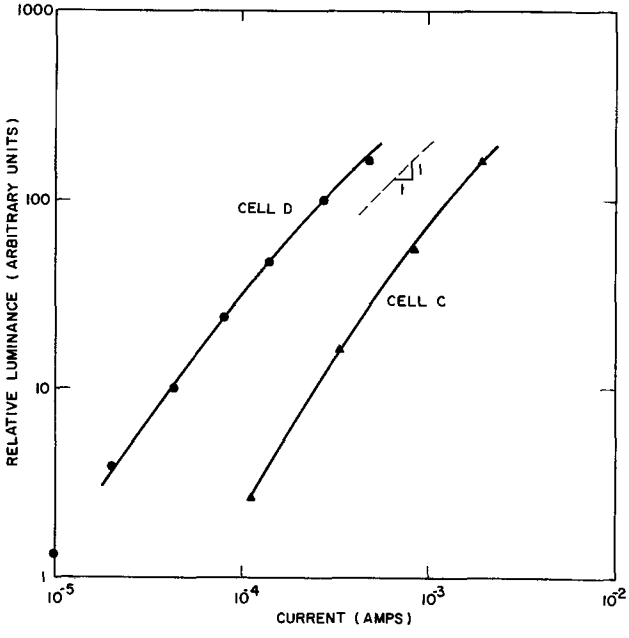

Fig. 5. Luminance-current characteristic for same cells as in Fig. 4. Unity slope is approached at higher luminances.

Discussion

Polymethylmethacrylate is an atactic polymer and amorphous (21). Optical transmittance is constant for wavelengths longer than 3500Å, which corresponds to an optical bandgap of 3.55 eV. The a-c conduction and loss in polymers is generally attributed to rotation of polar groups not directly attached to the main polymer chain. The d-c conduction in polymer films has also been assumed ionic (22, 23). The d-c conduction in other insulating films at high fields and room temperature has been found to be normally Schottky emission from electrodes, or field-enhanced release of electrons from traps in the insulator, the Poole-Frenkel effect (19). Schottky emission has been reported, however, for 1-mm thick PMMA (24) 1-mil thick Mylar (25), and 2-mil thick polyvinyl formal (25). Current-voltage characteristics appropriate for Poole-Frenkel conduction have been reported for 1-mil thick Mylar (26) and polymerized thin films of silicone oil (27) and styrene (28). The thickness of the PMMA films studied in the present work is 1.4-1.6 mils.

The dielectric constant of PMMA is given as 3.3-3.9 at 60 Hz and decreases as frequency is raised (29). It passes through a broad minimum of approximately 2.5 at 10^7 Hz and is approximately 2.6 at 10^9 Hz. A high-frequency value can be calculated from the slope of the curve in Fig. 1. Assuming Schottky emission to be dominant and using Eq. [3], the experimental value for K is 2.7 and compares well with published values.

The large increase in the slope of the log I *vs.* $\sqrt{V}$ curves on addition of ZnS or ZnS:Mn,Cu,Cl can be attributed to a nonuniform field, *i.e.*, a field much greater in value than V/d at ends of ZnS particles or at tips of conducting Cu-rich lines. If ZnS particles in the binder are assumed to provide conduction paths from one electrode to another, it is possible for conduction to be controlled by Schottky emission of electrons from conducting lines or from an electrode into ZnS. Assuming the high-frequency dielectric constant of ZnS to be 5.7 (30), insulator thicknesses d were calculated from Eq. [3]. These are effective insulator thicknesses since the field is in this case not uniform. For the two cells whose characteristics are plotted in Fig. 2 the effective ZnS thickness is 3.7 μm in cell A and the effective ZnS:Mn,Cu,Cl thickness is 0.7 μm in cell B as compared to binder-phosphor thicknesses of 30 and 35 μm, respectively, in the two cells. This indicates a greater concentration of field in the activated ZnS, likely at the tips of Cu-rich lines, than in unactivated ZnS.

The sharp decrease that is observed in the constant V_I of Eq. [1] as the phosphor is introduced into the binder can therefore be explained. As conduction in the phosphor becomes much greater than conduction in the binder, V_I approaches a constant value. The constant I_0 falls as the phosphor is introduced, and then rises as the phosphor concentration is increased.

A linear log I *vs.* $\sqrt{V}$ dependence of current on voltage has also been observed in evaporated electroluminescent films of ZnS:Mn,Cu,Cl contacted with Al and tin oxide electrodes (18). For these films an effective phosphor film thickness of 0.13 μm, for example, was calculated for a phosphor film with an actual thickness of 5.6 μm.

In Fig. 5, the slope of the curves of luminance *vs.* current appears to approach unity at high luminances. A linear dependence of luminance on current can be attributed to direct excitation of Mn luminescence centers without ionization, and Vecht and Werring (31) have proposed collision-excitation of Mn centers by conduction electrons to be the dominant process. In d-c electroluminescence current injection into the phosphor from electrodes or binder must occur. The results described above indicate that injection is essentially from electrodes. The mixing of electroluminescent phosphor with a plastic binder facilitates the spreading of the material into a layer of uniform thickness. The effect on the d-c characteristics of changing

the electroluminescent layer thickness and phosphor particle size were not investigated and may be important.

Manuscript submitted Dec. 4, 1972; revised manuscript received April 18, 1973.

Any discussion of this paper will appear in a Discussion Section to be published in the June 1974 JOURNAL.

REFERENCES

1. H. C. Froelich, *J. Opt. Soc. Am.*, **43**, 320 (1953).
2. W. A. Thornton, *Bull. Am. Phys. Soc.*, **3**, 233 (1958).
3. V. N. Favorin and G. S. Kozina, *Opt Spectry.*, **10**, 43 (1960).
4. O. N. Kazankin, F. M. Pekerman, and L. M. Petoshina, *ibid.*, **7**, 458 (1959).
5. A. Vecht, N. J. Werring, and P. J. F. Smith, *Brit. J. Appl. Phys.*, **1**, 134 (1968).
6. A. Vecht, N. J. Werring, R. Ellis, and P. J. F. Smith, *ibid.*, **2**, 953 (1969).
7. H. F. Ivey, "Electroluminescence and Related Effects," Academic Press, New York (1963).
8. W. W. Piper and F. E. Williams, in "Solid State Physics," Vol. 6, p. 96, F. Seitz and D. Turnbull, Editors, Academic Press, New York (1958).
9. V. E. Solodkin and T. V. Eremeeva, *Lakokrasochnye Materialy Primenenie (USSR)*, **1**, 19 (1967).
10. S. Roberts, *J. Opt. Soc. Am.*, **42**, 850 (1952).
11. D. Frankl, *Phys. Rev.*, **111**, 1540 (1958).
12. F. F. Morehead, in "Physics and Chemistry of II-VI Compounds," p. 613, M. Aven and J. S. Prener, Editors, John Wiley & Sons, Inc., New York (1967).
13. D. A. Cusano, in "Luminescence of Organic and Inorganic Materials," p. 494, H. P. Kallman and G. M. Spruch, Editors, John Wiley & Sons, Inc., New York (1962).
14. J. L. Gillson and F. J. Darnell, *Phys. Rev.*, **125**, 149 (1962).
15. A. G. Fischer, *This Journal*, **109**, 1043 (1962).
16. A. G. Fischer, *ibid.*, **110**, 773 (1963).
17. P. Goldberg and J. W. Nickerson, *J. Appl. Phys.*, **34**, 1601 (1963).
18. J. L. Plumb, *Jap. J. Appl. Phys.*, **10**, 326 (1971).
19. W. Schottky, *Physik. Z.*, **15**, 872 (1914).
20. J. G. Simmons, in "Handbook of Thin Film Technology," Chap. 14, L. I. Maissel and R. Glang, Editors, McGraw-Hill Book Co., New York (1970).
21. J. A. Brydson, "Plastics Materials," D. van Nostrand Co., Inc., Princeton (1966).
22. H. O. Spauschus, in "Plastics for Electrical Insulation," p. 37, P. F. Bruins, Editor, John Wiley-Interscience, New York (1968).
23. R. W. Warfield and M. C. Petree, *Soc. Plastics Engineers Trans.*, Apr. 1961, p. 80.
24. R. J. Munick, *J. Appl. Phys.*, **28**, 1302 (1957).
25. G. Lengyel, *ibid.*, **37**, 807 (1966).
26. A. C. Lilly and J. R. McDowell, *ibid.*, **39**, A1 (1968).
27. R. H. Colburn and R. W. Christy, *ibid.*, **40**, 3958 (1969).
28. B. Ai, H. Carchano, and D. Sanchez, *ibid.*, **43**, 3794 (1972).
29. C. A. Harper, in "Handbook of Materials and Processes for Electronics," Chap. 1, C. A. Harper, Editor, McGraw-Hill Book Co., New York (1970).
30. M. Neuberger, "II-VI Semiconducting Compound Data Tables," Electronic Properties Information Center, Hughes Aircraft Co., Culver City, Calif. (1969).
31. A. Vecht and N. J. Werring, *J. Phys. D.*, **3**, 105 (1970).

Silicon Surface Contamination: Polishing and Cleaning

R. L. Meek,* T. M. Buck, and C. F. Gibbon

Bell Laboratories, Murray Hill, New Jersey 07974

ABSTRACT

A Rutherford backscattering study using 2 MeV He^+ ions has shown that the principal contaminants heavier than Si remaining on silica-sol polished silicon surfaces are S (10^{14} cm^{-2}), Cl (10^{13} cm^{-2}), Ca (10^{14} cm^{-2}), Cu (10^{14} cm^{-2}), and a heavy metal in the range Pt-Au-Pb (10^{12} cm^{-2}). Preoxidation cleaning using HNO_3 and HF was found to be erratic in the ability to yield surfaces free of Ca and Cu and always left heavy metal contaminants. Cleaning with H_2O_2:HCl and H_2O_2:NH_4OH solutions always removed all elements heavier than chlorine to below the level of detectability. Both cleaning treatments left S and Cl at levels $\sim 10^{13}$ cm^{-2}. Breakdown voltage measurements indicated that junction quality was not predominantly controlled by surface impurities present after preoxidation cleaning, although the diode quality on cleaned wafers was much higher than on as-polished wafers.

Fabrication of silicon integrated microelectronic devices typically begins with sawing, etching, polishing, and cleaning of wafers before thermal oxidation. Impurities, particularly the fast diffusing heavy metals, left on the surface after these steps may be diffused into junction regions where they can degrade device properties. Determination of the identity and amount of these impurities on polished and cleaned surfaces is particularly amenable to the ion scattering technique (1-4).

Several workers (5-14) have investigated the absorption of metal cations onto silicon, germanium, and other semiconductor surfaces, usually using radiochemical techniques, and studied the consequent deleterious effects on junction properties. Kern (15) has recently reviewed the radioactive tracer work on semiconductor surface contamination. Typically, it is found that contact with solutions contaminated with ~1 ppm of heavy metal ions may leave on the order of monolayers of surface contamination (6, 12, 13). In this work we have determined the surface contamination levels actually introduced by typical processing operations.

* Electrochemical Society Active Member.

Key words: contamination, soft junctions, silicon surfaces, polishing, cleaning, ion backscattering.

Experimental

Polishing.—Mendel (16) has recently reviewed the methods for polishing silicon. The conclusion is that the most satisfactory surfaces for device fabrication, that is those most nearly perfect (16-18), can be ob-

tained with the silica-sol polishing method (19). The silica-sol polishing medium is a colloidal suspension of silica gel in aqueous sodium hydroxide solution having a *p*H of 9.9. The suspension is about 30% silica having a particle size range of 100-400Å.

The results of a semiquantitative spectrographic analysis of the silica-sol solution are presented in Table I. The principal contaminants are Mg, Ca, Al, Ti, Fe, Cu, and Pb. The solution as it comes off the polishing pad has also been analyzed. In that solution the concentration of Mg, Ca, and Cu has increased and K appears. We have polished wafers with an iron ring deliberately placed on the pad in an attempt to increase iron contamination since earlier work (17) had indicated that iron might be a significant polishing-introduced contaminant. Of equal interest is the list of elements sought but not found in either the new or used solutions since these include Pt, Au, and Tl. We have quite often found a surface contaminant in the mass range Pt-Pb (*i.e.* Pt, Au, Hg, Tl, or Pb).

Cleaning.—In various polishing facilities a variety of ways of treating the silicon wafers in removing them from the polishing block have evolved. Those we have examined are given in Table II and range from the very simple method of simply rinsing off the wafers and block in flowing water, heating to remove, and rinsing off the mounting wax in acetone (WFF1) to much more involved procedures involving several organic solvents, HF and HNO_3 (ROM2).

Two basic final preoxidation cleanings have been considered and are summarized in Table III. The first of these uses HNO_3 and HF (NHF), while the second is based on use of solutions (20) of H_2O_2:NH_4OH and H_2O_2:HCl (PNH). We have also examined a slight modification of the NHF procedure (NHFA) which adds a final HCl dip in an attempt to remove Cu and the Pt-Pb mass range quite often found after the basic NHF cleaning.

Table I. Contaminants in silica-sol polishing solution as determined by qualitative spectrographic analysis* (parts per million by weight)

	Unused solution	Solution off pad	Solution off pad with Fe ring
Mg	1	10	10
Al	100	100	100
K	†	10	10
Ca	10	1000	1000
Ti	100	100	100
Fe	10	10	10
Cu	1	10	10
Pb	1	1	1

Elements sought but not found: Li, V, Cr, Mn, Co, Ni, Zn, Ga, Ge, As, Rb, Sr, Zr, Nb, Mo, Pd, Ag, Cd, In, Sn, Sb, Cs, Ba, Ta, W, Pt, Au, Tl, Bi.

* Lucius Pitkin, Inc., New York.
† Not detected.

Table II. Summary of slice demounting (preclean) procedures

RDCP
1. Rinse with DI water, blow dry.
2. Heat to remove from block.
3. Scrub with Triton-X 100.
4. Rinse with trichloroethylene.

ROM 1
1. Scrub under tap water, rinse DI water, blow dry.
2. Heat to remove from block.
3. Boil 5 min in trichloroethylene.
4. Acetone rinse, swab with methanol.

ROM 2
1. Flood with DI water, blow dry.
2. Heat to remove from block.
3. Boil in trichloroethylene, rinse acetone, methanol.
4. 1:1 HF:H_2O, DI rinse.
5. HNO_3, DI rinse, methanol rinse, blow dry.

WFF 1
1. Scrub with detergent under flowing tap water, blow dry.
2. Heat to remove from block.
3. Rinse in acetone.

WFF 2
Same as WFF 1 but no detergent.

Table III. Summary of preoxidation cleaning procedures

NHF
1. Rinse, trichlor, acetone, H_2O.
2. Superoxol boil, rinse H_2O, HF dip, rinse H_2O.
3. HNO_3, 80°C, 10 min, rinse H_2O.
4. HF dip, rinse H_2O, blow dry.

NHFA
1-4. Same as NHF.
5. Dip in HCl 2 min.

PNH
1. Scrub with Triton-X100, rinse H_2O, ethanol.
2. NH_4OH: $4H_2O$: H_2O_2, 80°C, 10 min, rinse H_2O.
3. HF dip, rinse H_2O.
4. 4HCl: H_2O_2: H_2O, 80°C, 10 min, rinse H_2O.
5. HF dip, rinse H_2O, spin dry.

Ion scattering.—The MeV Rutherford ion backscattering technique (1-4) has proven to be an excellent tool for identification and quantitative determination of silicon surface contaminants. A schematic of the basic experimental arrangement is shown as Fig. 1. A beam of 2 MeV He^+ ions is collimated through two Ta collimators 1 mm in diameter about 2m apart. The backscattered (177°) He ions were detected in a 50 mm^2 surface barrier detector having an energy resolution of 16 keV. Secondary electron suppression and pile up rejection electronics were used. The silicon samples were surrounded by a baffle cooled to liquid nitrogen temperature and were mounted in a two axis goniometer which allowed the sample to be aligned with a <110> axis parallel to the beam. This channeling combining with pile-up rejection allows maximum sensitivity since pile-up counts beyond the silicon edge, which would tend to obscure true surface impurity counts, can be virtually eliminated, while still maintaining a sufficient total beam current to give reasonable measurement times (typically 30 min). The scattering chamber was maintained at 10^{-6} Torr and the He ion fluence was typically 10^{16} cm^{-2}.

MeV He^+ ions are known to closely obey the Rutherford scattering law. The scattered ion yield per unit solid angle is given by

$$\frac{dn}{d\Omega} = \frac{n_o N b^2}{16} \sin^{-4}\left(\frac{\theta_c}{2}\right) \quad [1]$$

where

$$b = \frac{Z_1 Z_2 e^2}{\frac{1}{2}\left(\frac{M_1 M_2}{M_1 + M_2}\right) V^2} \quad [2]$$

and Z_1 and Z_2 are the atomic numbers of incident particle and target atom, M_1 and M_2 are the respective masses, and θ_c is the center of mass scattering angle; e is the electronic charge, V is the velocity of the incident ion, n_o is the number of incident ions, and N is the number of target atoms cm^{-2}. The center of mass and laboratory scattering angles are related by

$$\sin(\theta_c - \theta_L) = \frac{M_1}{M_2} \sin\theta_L \quad [3]$$

Since the scattering is elastic, ions scattered from a target atom of given mass at a given θ_L have a characteristic energy, E, given by

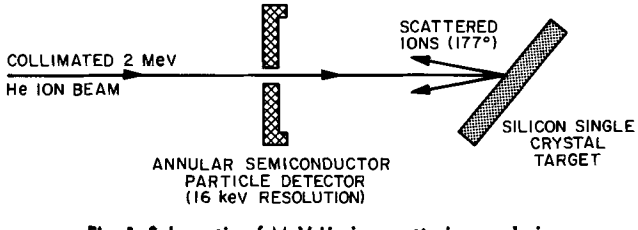

Fig. 1. Schematic of MeV He ion scattering analysis

$$\frac{E}{E_o} = \frac{M_1^2}{(M_1 + M_2)^2}\left\{\cos\theta_L + \left(\frac{M_2^2}{M_1^2} - \sin^2\theta_L\right)^{1/2}\right\}^2 \quad [4]$$

where E_o is the ion energy before the scattering event.

It is convenient to define a sensitivity factor α, which depends on the scattering cross section, such that

$$n = \alpha N_c/F \quad [5]$$

where n is the impurity concentration (atom cm^{-2}), N_c is the number of counts at an energy corresponding to that impurity, and F is the incident ion fluence in microcoulombs. This sensitivity factor is plotted, for our experimental conditions, in Fig. 2. For a few tens of microcoulombs and peaks of a few counts, the sensitivity is then $\sim 10^{12}$ cm^{-2} for masses near Cu and $\sim 10^{11}$ cm^{-2} for masses near Au.

The mass resolution decreases with increasing mass since the detector energy resolution is constant. Near Cu the mass separation is about 6 keV/atomic mass units and near Au is only 1 keV/atomic mass units so that we are not able to definitively identify the heaviest mass species, but rather only a mass range.

Diode formation.—After surface characterization as described above, a masking oxide was grown on the wafers at 1050°C in steam, a pattern of 1 × 2 mil openings cut, a 8 × $(10)^{14}$ cm^{-2} boron diffusion source implanted, and diodes formed by diffusing for 40 min at 1130°C in pure O_2. After a light etch, the breakdown voltages of 15 diodes on each wafer were determined.

Results

Typical experimental data.—In Fig. 3 is the spectrum obtained from a typical silica-sol polished, WFF1 precleaned, surface of <111> 10 ohm-cm, n-type silicon. The impurities detected on this sample are sulfur, chlorine (the two isotopes are clearly resolved, especially for somewhat larger total fluence), calcium, perhaps titanium, and copper. The absence of pulse pile-up is evident from the absence of background counts at high energy. Somewhat longer counting times reveal a slight contamination in the Pt-Pb mass range (about $3(10)^{11}$ cm^{-2}). Figure 4 is the spectrum

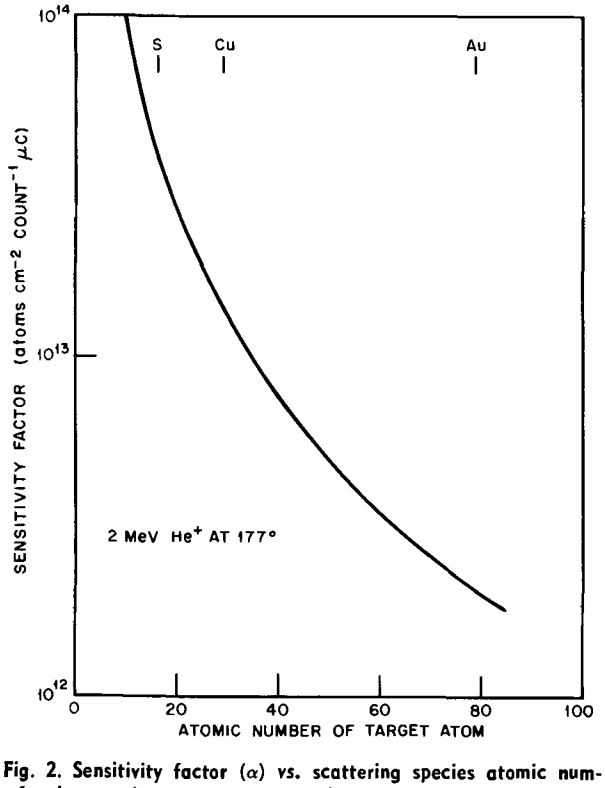

Fig. 2. Sensitivity factor (α) *vs.* scattering species atomic number for the experimental geometry used.

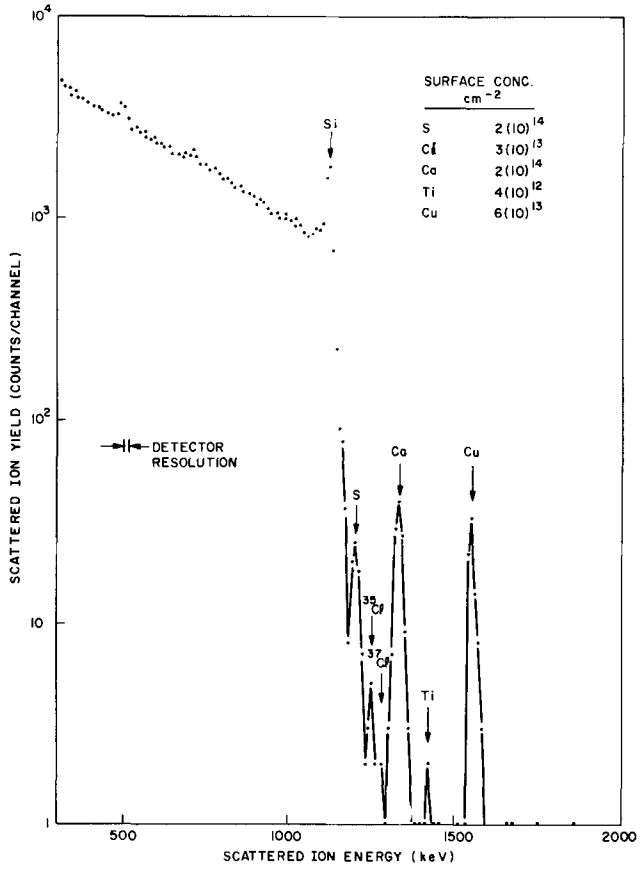

Fig. 3. Typical scattered ion spectrum from a silica-sol polished surface. The He ion dose is $(10)^{16}$ cm^{-2}.

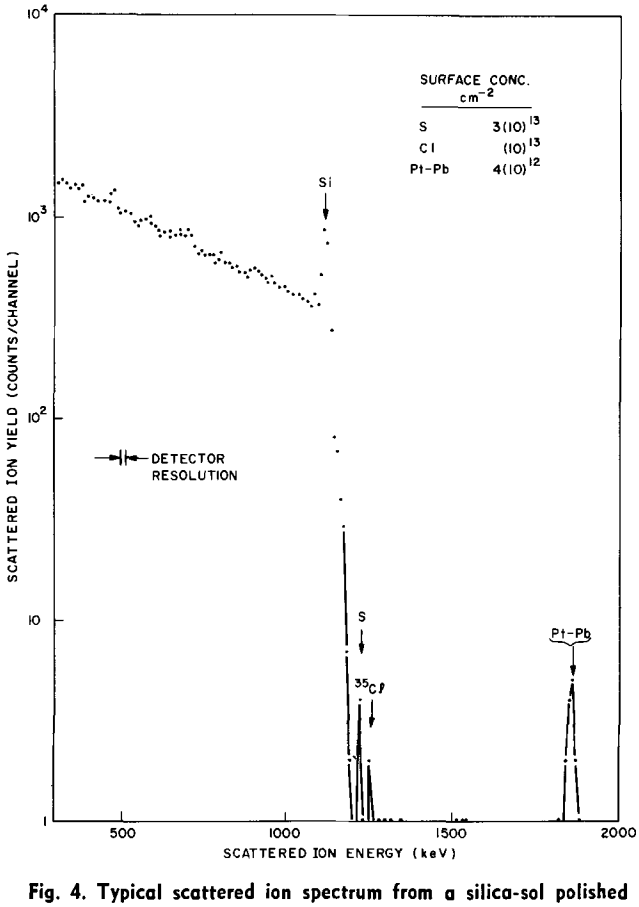

Fig. 4. Typical scattered ion spectrum from a silica-sol polished and $HF:HNO_3$ (NHF) cleaned surface.

Table IV. Silicon surface contamination levels (atom cm^{-2}) after sawing and etching

	Sawed	Sawed plus HCl dip	Etched[a]
S	$3(10)^{14}$	$(10)^{14}$	$(10)^{14}$
Cl	$2(10)^{14}$	[c]	$4(10)^{13}$
K	[b]	$2(10)^{13}$	$(10)^{13}$
Ca	$2(10)^{14}$	$2(10)^{13}$	$(10)^{13}$
Ti	$4(10)^{13}$	—	—
Cr	$2(10)^{13}$	—	$7(10)^{12}$
Fe	$4(10)^{13}$	$9(10)^{12}$	$7(10)^{12}$
Cu	$2(10)^{14}$	$(10)^{13}$	—
Ga	$5(10)^{13}$	—	—
Mo-Ba	$7(10)^{13}$[d]	—	$(10)^{13}$[e]
Pt-Pb	$4(10)^{12}$	—	—

[a] Etch composition; $5H_3COOH$: $4HNO_3$: 1HF with 3g I_2/liter.
[b] Not discerned due to magnitude of neighboring peaks.
[c] Not detected.
[d] Mostly Ag, I, Ba.
[e] Iodine.

Table V. Silicon surface contamination levels (atom cm^{-2}) after dipping in silica-sol polishing solution.

	Unused solution	Solution off pad	Solution off pad with Fe ring
S	$4(10)^{13}$	$2(10)^{13}$	$2(10)^{13}$
Cl	$2(10)^{13}$	$(10)^{13}$	$(10)^{13}$
K	$4(10)^{12}$	$3(10)^{12}$	$4(10)^{12}$
Ca	$4(10)^{12}$	$3(10)^{12}$	$2(10)^{12}$
Ti	$6(10)^{12}$	*	$3(10)^{12}$
Fe	$3(10)^{12}$	$2(10)^{12}$	$2(10)^{12}$
Cu	*	$6(10)^{12}$	$6(10)^{12}$
Pt-Pb	*	$2(10)^{11}$	$2(10)^{11}$

* Not detected.

for a sample which had been NHF cleaned after polishing. Here sulfur, chlorine, and a species in the mass range Pt-Pb remain on the surface.

Sawed and etched surfaces.—Wafers for polishing are produced by ID sawing from silicon ingots and etching to remove surface damage (17, 21). We have examined the surface contamination on the sawed and etched wafers; the results are tabulated in Table IV. Numerous contaminants are seen. Sulfur and chlorine are first detected after sawing, and, as will be seen, persist throughout the polishing and cleaning. A rather broad peak is found in the mass range Mo-Ba, the structure of which suggests it is mostly Ag, I, and Ba. Ba and S are thought to originate from the $BaSO_4$ used as a filler in the wax used to hold the ingot during sawing. K and Ca probably come from the water used during cutting and the metals from the steel ID blade and the Cu-Ni alloy used to bond the diamond grit to the blade. Results after etching are shown in the third column of Table IV. Of particular interest are the facts that S and Cl remain and that Cu and species in the Pt-Pb mass range are not detected.

Contamination of clean surfaces in contact with polishing solution.—As will be discussed subsequently, it is possible to prepare clean silicon surfaces free of contaminants heavier than chlorine. The contamination levels introduced on such clean silicon surfaces left in contact for 30 min with unused and used silica-sol polishing solutions are given in Table V. The S and Cl levels are typical of the cleaned surface, and K, Ca, Ti, Fe, Cu, and something in the Pt-Pb range are each found at $\sim 10^{12}$ cm^{-2}. The level of impurities is fairly independent of whether the solution was new or used except that Cu and Pt-Pb are found only after immersion in the used solution. It will be recalled from Table I that the Cu concentration is an order of magnitude greater in the used solution.

There are at least two reasons to suppose that the contamination found on as-polished surfaces will be different. The first is that as the surface is being polished its adsorption-desorption characteristics may be different than a clean silicon surface with its native oxide. The second is that the treatment (preclean) which the slice receives during removal from the polishing block may introduce or remove some surface impurities.

Polished surfaces.—Table VI summarizes the data for polished samples treated in various ways. S ($\sim 10^{14}$ cm^{-2}), Cl ($\sim 5(10)^{13}$ cm^{-2}), and K ($\sim 10^{13}$ cm^{-2}) are found on all as-polished samples. Ca is not present on RDCP precleaned surfaces but appears at $\sim 10^{13}$ cm^{-2} on ROM1 or ROM2 surfaces and at $\sim 10^{14}$ cm^{-2} on WFF1 or WFF2 surfaces. This seems reasonable since the latter involve scrubbing with tap water. Cu is present at roughly $\sim 10^{14}$ cm^{-2} on all as-polished samples except that which had the ROM2 treatment. This is explicable since the nitric acid involved in ROM2 should remove Cu.

Species in the Pt-Pb mass range are present at 10^{11}-10^{13} cm^{-2} except on samples which had the ROM1 or ROM2 preclean. Finally we note that placing

Table VI. Silicon surface contamination levels (atom cm^{-2}) after silica-sol polishing and cleaning

Preclean	Clean	S	Cl	K	Ca	Fe	Cu	Pt-Pb
RDCP	None	$9(10)^{13}$	$3(10)^{13}$	10^{13}	—	$2(10)^{12}$	$3(10)^{14}$	$(10)^{13}$
RDCP	NHF	$2(10)^{13}$	$2(10)^{13}$	[a]	—	—	—	$2(10)^{13}$
RDCP	NHFA	$(10)^{13}$	$4(10)^{13}$	$3(10)^{12}$	—	$4(10)^{13}$	$3(10)^{13}$	$3(10)^{13}$
RDCP	PNH	$2(10)^{13}$	$3(10)^{13}$	—	—	—	—	—
ROM1	None	$6(10)^{13}$	$5(10)^{13}$	[b]	$4(10)^{13}$	$3(10)^{12}$	$7(10)^{12}$	—
ROM1	NHF	$5(10^{13}$	$2(10)^{13}$	—	—	—	—	$7(10)^{12}$
ROM1	NHFA	$(10)^{13}$	$4(10)^{12}$	—	—	$2(10)^{12}$	—	—
ROM1	PNH	$6(10)^{13}$	$4(10)^{13}$	—	—	—	—	—
ROM2	None	$6(10)^{13}$	$5(10)^{13}$	$5(10)^{13}$	$3(10)^{13}$	—	—	—
ROM2	NHF	$8(10)^{13}$	$2(10)^{13}$	—	$2(10)^{13}$	—	—	—
ROM2	NHFA	$7(10)^{13}$	$4(10)^{12}$	—	—	$3(10)^{12}$	—	—
ROM2	PNH	$4(10)^{12}$	$4(10)^{12}$	—	—	—	—	—
WFF1	None	$2(10)^{14}$	$3(10)^{13}$	[b]	$2(10)^{14}$	—	$6(10)^{13}$	$3(10)^{11}$
WFF1	NHF	$6(10)^{13}$	$5(10)^{13}$	$3(10)^{12}$	$3(10)^{12}$	$(10)^{13}$	$8(10)^{13}$	$2(10)^{12}$
WFF1	NHFA	$4(10)^{12}$	$3(10)^{12}$	—	—	$5(10)^{12}$	—	—
WFF1	PHN	$(10)^{13}$	$(10)^{13}$	—	—	—	—	—
WFF2	None	$4(10)^{14}$	$9(10)^{13}$	[b]	$4(10)^{14}$	—	$2(10)^{14}$	$(10)^{12}$
WFF2	NHF	$6(10)^{13}$	$2(10)^{13}$	—	—	—	—	$2(10)^{12}$
WFF2	NHFA	$5(10)^{12}$	$(10)^{13}$	—	—	—	—	—
WFF2	PNH	$6(10)^{13}$	$2(10)^{13}$	—	—	—	—	—
WFF1[c]	None	$2(10)^{14}$	$4(10)^{13}$	[b]	$2(10)^{14}$	—	$2(10)^{14}$	$3(10^{11}$
WFF1[c]	NHF	$2(10)^{13}$	10^{13}	—	$2(10)^{12}$	—	—	$5(10)^{11}$
WFF1[c]	NHFA	$3(10)^{13}$	—	—	$4(10)^{12}$	—	$(10)^{12}$	—
WFF1[c]	PNH	$3(10)^{13}$	10^{13}	—	—	—	—	—
WFF2[c]	None	$2(10)^{14}$	$8(10)^{13}$	[b]	$2(10)^{14}$	—	$2(10)^{14}$	$6(10)^{11}$
WFF2[c]	NHF	$5(10)^{13}$	$5(10)^{13}$	—	—	—	—	$2(10)^{12}$
WFF2[c]	NHFA	$2(10)^{13}$	$6(10)^{12}$	—	$2(10)^{12}$	—	—	—
WFF2[c]	PNH	$4(10)^{12}$	$4(10)^{12}$	—	—	—	—	—

[a] Not detected.
[b] Not discerned due to magnitude of neighboring peaks.
[c] Iron ring on polishing pad.

the Fe ring on the polishing pad had no effect and that Fe is only rarely found, and then at very low levels, $\sim 10^{12}$ cm^{-2}. Based on the cleanliness of the as-polished surface one would tend to prefer the most complicated demounting procedure (ROM2). However, as will be shown, equally clean surfaces can be prepared regardless of the preclean used, even when the sample is simply rinsed with tap water (WFF2) so that extensive effort at the preclean stage is probably not justified.

The results for cleaned surfaces are also given in Table VI and summarized in more tractable form in Table VII. The NHF cleaning leaves S and Cl at $2(10)^{13}$ and 10^{13} cm^{-2}, respectively. Ca is found at various levels from undetectable to 10^{12} cm^{-2} and Cu at levels from undetectable to 10^{14} cm^{-2}. The mass range Pt-Pb is found at levels from 10^{11} to 10^{13} cm^{-2}, increasing for increasing levels on the as-polished sample but in every case being greater on the cleaned sample than on the as-polished surface. This very likely indicates that some species in this mass range is actually introduced by the cleaning.

Adding a HCl dip to the NHF cleaning (NHFA) reduces all contamination levels. In particular it removes Ca and Cu and markedly reduces the Pt-Pb mass range. However, Fe is quite often found after this HCl dip, even when it was not detectable on the as-polished surface. Subsequent work has shown that Fe is in fact a contaminant in HCl.

The PNH cleaning on the other hand reduces S and Cl to $\sim 10^{13}$ cm^{-2} and no impurities heavier than Cl are ever found on PNH cleaned surfaces.

Diode quality.—Two sets of wafers from different parts of the same ingot were polished, WFF1 precleaned, and then preoxidization cleaned in various ways before diode formation as described previously. The results are summarized in Table VIII. One observes:

1. The as-polished wafers give the poorest results for both sets, as expected; comparison with Table VII suggests that this may be related to the retention of copper on the surface.

2. The two groups of wafers, although processed through diode formation simultaneously in one batch, show a very large difference in diode formation properties. The surface contamination was similar in both cases so this does not appear to be a surface contamination-related effect. The wafers in each group were from different parts of the same ingot and one might conjecture that some bulk contaminant was nonuniformly distributed through the ingot.

Table VII. Polished and cleaned surfaces (surface concentration, cm^{-2})

	Polished	NHF	NHFA	Peroxide ammonia
S	$(10)^{14}$	$2(10)^{13}$	$(10)^{13}$	$(10)^{13}$
Cl	$(10)^{13}$	$(10)^{13}$	$3(10)^{12}$	$(10)^{13}$
Ca	$(10)^{14}$	N.D. to $(10)^{12}$	N.D.	N.D.
Fe	N.D.*	N.D.	N.D. to $(10)^{12}$	N.D.
Cu	$(10)^{14}$	N.D. to $(10)^{14}$	N.D.	N.D.
Pt-Pb	$(10)^{11}$-$(10)^{13}$	$(10)^{11}$ to $(10)^{13}$	N.D. to $(10)^{12}$	N.D.

* N.D. = not detectable.

Table VIII. Diode formation results for polished and cleaned surfaces

	As polished	NHF	NHFA	PNH
Group I				
BV range	~0V	~1V	~1V	~1V
Diode quality (on 10 μA scale)	All very soft	All soft	All soft	All soft
Group II				
BV range	20-110	102-116	100-108	100-118
Diode quality (on 10 μA scale)	80% soft	All hard	All but one hard	All hard

Furthermore we have found when gettering processed material to produce hard diodes (22) that typically 10^{15} cm^{-2} of Cu and Fe and 10^{13} cm^{-2} of Au are gettered. On the other hand, gettering of control wafers (23) indicates that impurities of this concentration are not usually present in the starting material. We have also examined the back sides of the wafers of Table VIII to see if impurities had already been "self-gettered" to the back side of the wafers as has been found to be the case with other wafers which formed hard diodes as processed (22). No such effect was found for either group. Identification of the steps in processing responsible for impurity introduction is under investigation but it appears from the present work that impurities introduced by polishing and preoxidation cleaning are not significant contributors to soft diode formation. This is emphasized by the case of the PNH ($HCl:H_2O_2$ and $NH_4OH:H_2O_2$) cleaning procedure since these metal surface impurities are not detected, yet in one case all the diodes are hard and in the other they are all soft.

Conclusions

The conclusions of the present work may be summarized as follows:

1. The manner in which polished wafers are treated (precleaned) in removing them from the polishing block is not an important factor in the final observed surface contamination of cleaned wafers.
2. Fe is not an important surface contaminant after silica-sol polishing.
3. S and Cl are present at $\sim 10^{13}$ cm^{-2} after all cleaning procedures studied.
4. Other major contaminants are Ca, Cu, and some species in the Pt-Pb range.
5. The peroxide-ammonia, peroxide-hydrochloric acid cleaning eliminates Ca and Cu much more reliably than does the $HF:HNO_3$ cleaning.
6. $HF:HNO_3$ cleaning leaves a heavy mass impurity in the Pt-Pb range. An added HCl dip reduces it.
7. The peroxide-ammonia cleaning procedure removes all surface impurities heavier than Cl to below the level of detectability.
8. Impurities left after silica-sol polishing and preoxidation cleaning do not appear to control diode quality.

Acknowledgments

The authors would like to recognize the contribution of E. I. Povilonis in the processing and measurement of the diodes, and thank W. F. Flood and R. O. Miller for polishing samples.

Manuscript submitted Dec. 19, 1972; revised manuscript received March 12, 1973. This was Paper 243 presented at the Miami Beach, Florida, Meeting of the Society, Oct. 8-13, 1972.

Any discussion of this paper will appear in a Discussion Section to be published in the June 1974 JOURNAL.

REFERENCES

1. J. A. Davies, J. Denhartog, L. Eriksson, and J. W. Mayer, *Can. J. Phys.*, **45**, 4053 (1967).
2. E. Bφgh, *ibid.*, **46**, 653 (1968).
3. J. A. Davies, *J. Vacuum Sci. Tech.*, **8**, 487 (1971).
4. T. M. Buck, J. M. Poate, K. A. Pickar, and C-M Hsieh, *Surface Sci.*, In press.
5. D. Keiler, *Solid-State Electron.*, **6**, 605 (1963).
6. V. S. Sotnikov and A. S. Belanovskii, *Russ. J. Phys. Chem.*, **34**, 1001 (1960).
7. V. S. Sotnikov and A. S. Belanovskii, *ibid.*, **35**, 249 (1961).
8. G. M. Krembs and M. M. Schlacter, *This Journal*, **111**, 417 (1964).
9. A. G. Petrova and A. V. Rakov, *Soviet Phys.-Semicond.*, **4**, 591 (1970).
10. I. M. Kuleshov and A. F. Naumova, *Russ. J. Phys. Chem.*, **32**, 65 (1958).
11. H. C. Theuerer, J. M. Whelan, H. E. Bridgers, and E. Buehler, *This Journal*, **104**, 721 (1957).
12. G. B. Larrabee, *ibid.*, **108**, 1130 (1961).
13. D. A. Thompson, H. D. Barber, and W. D. Mackintosh, *Appl. Phys. Letters*, **14**, 102 (1969).

14. P. F. Kane and G. B. Larrabee, "Characterization of Semiconductor Materials," p. 203, McGraw-Hill Book Co., New York (1970).
15. W. Kern, *Solid State Technol.*, **15**, 34 (1972).
16. E. Mendel, *ibid.*, **10**, 27 (1967).
17. T. M. Buck and R. L. Meek, "Silicon Device Processing," p. 419, C. P. Marsden, Editor, NBS Special Publ. 337 (1970).
18. A. C. Adams and R. H. Kaiser, Paper 134 presented at Electrochem. Soc. Meeting, Los Angeles, May 10-15, 1970.
19. R. J. Walsh and A. H. Herzog, U. S. Pat 3,170,273 (Jan. 10, 1963).
20. W. Kern and D. A. Puotinen, *RCA Rev.*, **31**, 187 (1970).
21. R. L. Meek and M. C. Huffstutler, *This Journal*, **116**, 893 (1969).
22. R. L. Meek and C. F. Gibbon, To be published.
23. T. E. Seidel and R. L. Meek, 3rd Int. Conf. on Ion Impl., To be published.

$Ga_{1-x}Al_xAs$-GaAs P-P-N Heterojunction Solar Cells

H. J. Hovel* and J. M. Woodall*

IBM Thomas J. Watson Research Center, Yorktown Heights, New York 10598

ABSTRACT

Solar cells consisting of $pGa_{1-x}Al_xAs$-pGaAs-nGaAs have been fabricated by the liquid phase epitaxial growth of Zn-doped $Ga_{1-x}Al_xAs$ on n-type GaAs substrates. The spectral response of the cells has been used to calculate the absorption coefficient of the alloy layer; the coefficient varies as $(h\nu - Eg)^{1/2}$, and indirect bandgaps of 2.071 and 2.094 eV for compositions of $x = 0.73$ and $x = 0.86$, respectively, are indicated. The solar cell characteristics were measured in sunlight at Air Masses of 0.9 and 1.3 and in simulated sunlight at Air Mass 0; the open-circuit voltages ranged from 0.97 to 1.0V, the short-circuit currents from 20 to 22.5 mA/cm^2, and the efficiencies (corrected for contact area) from 11.7 to 12.8% at Air Mass 0 and a temperature of 80°F. The short-circuit current and open-circuit voltage increase and decrease, respectively, linearly with temperature. The efficiency has a maximum at around −75°C, and decreases at a rate ($\Delta\eta/\Delta T$) of 0.022% per °C up to 200°C and at over twice that rate above 200°C. Efficiencies of almost 6% at 300°C and over 3% at 350°C were measured using a quartz-halogen light source that simulates Air Mass 1.

It has long been recognized that GaAs solar cells would be preferable to Si solar cells if the costs were equal. Some advantages of GaAs over Si include a higher theoretical efficiency [24% for GaAs compared to 21% for Si (1)], the ability to operate at higher temperatures, and a superior resistance to degradation from particle radiation. In fact, however, the highest measured efficiency for GaAs (13%) (2) has not equaled the value for Si (15%) at Air Mass 1, and the cost of GaAs cells greatly exceeds that for Si cells (Air Mass is a term which quantifies optical absorption and scattering in the earth's atmosphere). Therefore the major interest in the past few years has been in Si cells rather than GaAs, and the situation seems likely to remain that way due to the high level of technology developed for Si, its abundance as an element, its relatively low cost, and its excellent solar cell behavior.

Recently, however, GaAs solar cells have been reported (3, 4) with higher efficiencies produced by the addition of a thin, epitaxial layer of p-type $Ga_{1-x}Al_xAs$ on the GaAs p-n junction surface. Efficiencies of over 16% at Air Mass 1 and 19-20% at Air Mass 2 have been measured. This enhances the outlook for GaAs cells in particular satellite applications where cost is not the limiting factor. The improvement in efficiencies can be attributed to five factors: (*i*) the close lattice match between $Ga_{1-x}Al_xAs$ and GaAs, which results in a low surface recombination velocity at the GaAs p-n junction surface (which is now the interface); (*ii*) a reduction in the series resistance, since the heavily doped, transparent, p-type $Ga_{1-x}Al_xAs$ alloy layer acts as the electrical contact to the p-type GaAs; (*iii*) longer diffusion lengths in the GaAs p-region due to the lower doping allowed there as a result of the highly doped alloy layer; (*iv*) the optical transparency of the alloy layer which allows light over much of the solar spectrum to reach the GaAs; and (*v*) the presence of a barrier at the interface which prevents minority carriers from the p-type GaAs region from entering the alloy layer, and which therefore improves the collection of these carriers.

This paper describes the fabrication of the heterojunction solar cells by liquid phase epitaxy and the technology of contacting, etching, and applying antireflective coatings. The absorption coefficient of the alloy layer as a function of wavelength has been calculated for various compositions by an analysis of the spectral response of the cells. Finally, the electrical and optical properties of the devices are discussed, as well as the effect of temperature on the device behavior.

Fabrication

The solar cell consists of an n-type GaAs substrate, a p-type GaAs surface region of the order of a micron wide, and a p-type $Ga_{1-x}Al_xAs$ alloy layer on the pGaAs surface, with compositions ranging from $x = 0.27$ to $x = 0.86$ and thicknesses from 2 to 20μ. In form, the solar cell is similar to the heterojunction lasers reported by a number of authors (5, 6), except that the compositions and doping levels are different, and is similar to the $pGa_{1-x}Al_xAs$-nGaAs cells reported by Alferov *et al.* (7) (the latter had no pGaAs region). The cells are fabricated by a vertical liquid phase epitaxy technique in a system described previously (8); the main features of this apparatus are shown in Fig. 1. For most of the experiments n-type (100) GaAs substrates (~1 cm^2 surface area) doped with either 1-2 × 10^{17} Si atoms/cm^3 or 1-2 × 10^{18} Sn atoms/cm^3 were used. Preparation of the substrate was accomplished by: (*i*) lapping with 2μ grit; (*ii*) etching with 2% bromine-methanol solution for 2 min; (*iii*) etching with 1:3:4, $HF:HNO_3:H_2O$ for 15 sec; (*iv*) etching with 1:1:2 $NH_4OH:H_2O_2:H_2O$; and (*v*) rinsing with deionized water and drying in air. The substrate is placed in the recess located in the carbon substrate

* Electrochemical Society Active Member.
Key words: photovoltaic devices, optical properties.

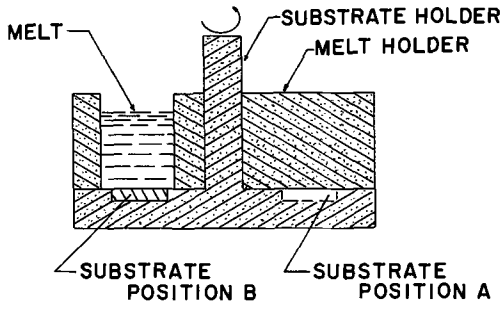

Fig. 1. Melt and substrate holder arrangement used in the liquid phase epitaxial growth of $Ga_{1-x}Al_xAs$-GaAs structures.

holder. A mixture of Ga, Al, GaAs chunks, and Zn is placed in the melt chamber located in the carbon melt holder; typical proportions consist of 5.0g of Ga, 0.03g of Al, >0.5g of bulk GaAs, and 0.03g of Zn, although both the Al proportions and Zn content can be changed in order to vary the alloy composition and junction depth, respectively. The apparatus of Fig. 1 is placed in a quartz growth tube which is evacuated and flushed with palladium-purified hydrogen. The system is then heated to 900°C and maintained at that temperature for a period of 1/2 hr to allow the melt to equilibrate. The substrate is initially enclosed by the high purity carbon (position A) to prevent any appreciable loss of As from the surface during the equilibration period; similarly, the melt chamber is capped to minimize loss of Zn due to the high Zn vapor pressure. At the end of the equilibration period the substrate holder is rotated with respect to the melt holder until the substrate is covered by the melt (position B), and the system is cooled from 900° to 890°C at a rate of 0.1°C/min, after which the sample is rotated away from the melt once more. Since the substrate thickness is nearly equal to the depth of the recess in the carbon holder, the melt is "wiped off" the substrate surface at this point, preventing spurious growth during cooling to room temperature.

During the growth of the Zn-doped $Ga_{1-x}Al_xAs$ layer, Zn diffuses into the n-type substrate to form the p-type GaAs region. For the high Al compositions ($x = 0.86$) and for the high substrate doping levels (2×10^{18} cm^{-3}) it was sometimes found that the Zn content in the melt was not sufficient to counterdope the substrate and no pGaAs region was produced, while the same Zn content with a $x = 0.7$ composition would produce the pGaAs region, indicating that the segregation coefficient in the alloy layer decreases somewhat with increasing Al content. For a given alloy layer composition and substrate doping level, the junction depth (width of the pGaAs region) is controlled by varying the Zn content in the melt as shown in Fig. 2. The junction depth appears to obey a 0.59 power law dependence on the Zn concentration as suggested by previous studies of Zn diffusion into GaAs (9, 10). For the device studies, the junction depth was varied between 0.2 and 7.0μ, but most of the units were made with depths of 0.6-1.0μ since analysis showed (4) that the highest efficiencies are expected in this range.

To reduce the sheet resistivity of the alloy layer and facilitate making ohmic contact to it, Zn was diffused into the layer at 700°-720°C for 10-20 min using a sealed quartz ampule and $ZnAs_2$ as the diffusion source, raising the Zn concentration at the surface to greater than 10^{19} cm^{-3}. The reverse side of the substrate is then lapped until the total sample thickness is around 0.2 mm. A contact pattern is applied to the $Ga_{1-x}Al_xAs$ surface either by electroless plating of Au-Zn followed by electroplated In, or by evaporating Au-Zn through a metal mask with the sample at about 300°C. Contact to the back side of the cell was made by electroless Au-Sn plating followed by In electroplating, or by evaporation of Au-Ge-Ni. In general, evaporation was

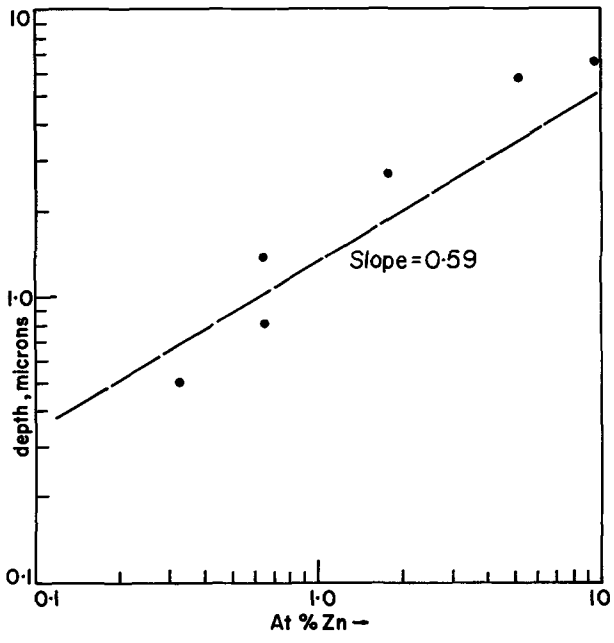

Fig. 2. Junction depth vs. zinc concentration in the melt for a substrate doping of 2 x 10^{17} cm^{-3} and an alloy composition of 0.7.

preferred because it left the sample surfaces in a cleaner state and seemed to produce lower contact resistances.

In order to perform a variety of experiments and to facilitate mounting, the wafers were diced into four to six cells of 0.18-0.10 cm^2 surface area, and the units were mounted onto TO-5 headers with gold wires thermocompression bonded between the contact stripes and the header posts. The surfaces were then masked with Apiezon wax and the devices were etched for about 5 min in $9H_3PO_4$-$1HNO_3$ to reduce the reverse leakage current to between 0.5 and 5 nanoA at −1V. After removal of the wax and careful cleaning of the surface, a layer of SiO was evaporated onto the devices as an antireflection coating. The SiO coating is about 750Å thick, designed for a reflection minimum at 5200-5500Å, and was evaporated with the sample at 150°C.

In general, when the wafer was uniform in appearance after the growth of the alloy layer, the four to six cells cut from the wafer were very similar in their behavior, *i.e.*, the voltage and current output and efficiencies were about the same for all the units. When nonuniformities (such as excess growth on the sample surface due to small amount of melt left on the sample after "wiping") were present several of the units would behave better than the others.

It was also occasionally noticed that the thermocompression bonding of Au wires to the contact stripes caused degradation in some of the cells, and it was concluded that thermocompression bonding is not a good way to contact these devices.

Spectral Response and Absorption

The energy band diagram of a $pGa_{1-x}Al_xAs$-pGaAs-nGaAs solar cell, both in equilibrium and with light incident, is shown in Fig. 3. Light with energy less than E_{g1} but more than E_{g2} passes through the alloy layer and is absorbed in the GaAs, generating hole-electron pairs which can be separated by the junction electric field and will then give rise to photocurrent and photovoltage. Since there is no appreciable barrier in the valence band at the alloy-GaAs interface, the upper layer acts as a transparent ohmic contact in this range of photon energies, while the energy barrier

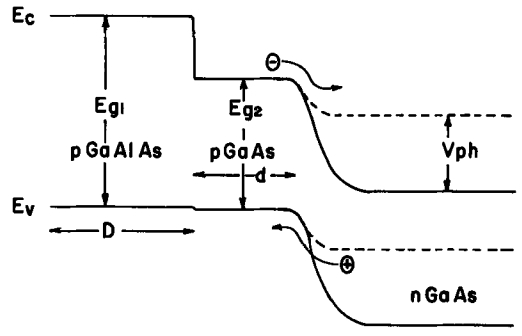

Fig. 3. Energy band diagram of a $Ga_{1-x}Al_xAs$-GaAs solar cell showing photocurrent and photovoltage generated by incident light.

in the conduction band[1] at this interface prevents photogenerated electrons in the pGaAs region from entering the $Ga_{1-x}Al_xAs$ and being lost. Incident light with photon energies greater than E_{g1} is attenuated by the alloy layer in accordance with its absorption coefficient. The generation rate of hole-electron pairs at a distance y into the GaAs from the alloy-GaAs interface is given by

$$g = F(\lambda) \exp(-\beta D)\, \alpha(\lambda) \exp(-\alpha y) \qquad [1]$$

where $F(\lambda)$ is the number of incident photons at wavelength λ, β and D are the absorption coefficient and thickness of the alloy layer, respectively, and α is the absorption coefficient of GaAs. Using this generation term, the minority carrier continuity equations can be solved to find the densities of electrons in the pGaAs region, holes in the nGaAs substrate, and hole-electron pairs in the depletion region, and the spectral response can be obtained by solving for the short-circuit current and dividing by the input flux, $F(\lambda)$. The result can be written as (4)

$$R(\lambda) = \exp(-\beta(\lambda)D) \cdot R'(\lambda) \qquad [2]$$

where $R(\lambda)$ is the spectral response of the device and $R'(\lambda)$ is the response of the underlying GaAs p-n junction alone. The assumptions involved in [2] are that the recombination velocity at the alloy-GaAs interface, the drift fields in the GaAs regions outside the depletion region, the collection of carriers generated in the alloy layer, and the reflection of light incident on the cell are all negligible.

Equation [2] was evaluated by computer for the same combinations of junction depths, diffusion lengths, and alloy layer thicknesses and compositions as expected in the experimental devices. When the $Ga_{1-x}Al_xAs$ thickness is taken as zero, the response $R(\lambda) = R'(\lambda)$ of the GaAs p-n junction rises sharply at 1.4 eV, increases slowly from 1.5 to 1.8 eV, and becomes constant for photon energies above 1.8 eV. The measured spectral response of the heterojunction cells (with the $Ga_{1-x}Al_xAs$ layer included) can therefore be used to compute the absorption coefficient β of the $Ga_{1-x}Al_xAs$ for any alloy composition having a bandgap energy above 1.5 eV [since the function $R'(\lambda)$ is known].

The spectral response (number of carriers collected/number of incident photons at a given wavelength) was measured by illuminating the device with monochromatic light from a Perkin-Elmer prism spectrometer. The light was "chopped" at 13 Hz, and the short-circuit current of the cell was fed into a lock-in amplifier which was used to drive an x-y recorder. The result was a plot of short-circuit current per unit incident power as a function of wavelength, which becomes short-circuit current per photon after dividing by the photon energy.

The normalized spectral responses of several $Ga_{1-x}Al_xAs$-GaAs solar cells of various compositions are shown in Fig. 4; these cells all have about the same junction depths and doping levels (and therefore about the same diffusion lengths). The response rises rapidly at the GaAs band edge, becomes flat above 1.7 eV, and remains fairly constant with increasing energy until the alloy layer begins to attenuate the light. The absorption coefficient of the alloy layer is found from [2] after including the effects of the reflection of light from the surface as a function of wavelength

$$\beta(\lambda_2) - \beta(\lambda_1) = \frac{1}{D} \ln \frac{R(\lambda_1)R'(\lambda_2)[1-\pi(\lambda_2)]}{R(\lambda_2)R'(\lambda_1)[1-\pi(\lambda_1)]} \qquad [3]$$

where $\beta(\lambda_2)$, $R(\lambda_2)$, $R'(\lambda_2)$, and $\pi(\lambda_2)$ are the absorption coefficient, total response, response of the GaAs p-n junction alone, and reflection from the device surface at wavelength λ_2, and $\beta(\lambda_1)$, etc., are the same quantities at λ_1. Since λ_1 can be chosen before cut-off begins [$\beta(\lambda_1) = 0$] and since the GaAs junction response can be taken as constant, [3] simplifies to

$$\beta(\lambda_2) = \frac{1}{D} \ln \frac{R(\lambda_1)[1-\pi(\lambda_2)]}{R(\lambda_2)[1-\pi(\lambda_1)]} \qquad [4]$$

The reflection $\pi(\lambda)$ from an SiO-coated GaAs sample as a function of energy is shown in Fig. 4, and the $Ga_{1-x}Al_xAs$ absorption coefficients (plotted as $\beta^{1/2}$ *vs.* energy) calculated from [4] are shown in Fig. 5.

From the steepness of the plots for the two lower compositions, it can be inferred that the direct band edges are being measured, with bandgap values of 1.69 and 1.99 eV, respectively. [The lowest bandgap for the $x = 0.23$ composition is, indeed, believed to be direct (12, 13), but it cannot be inferred from Fig. 5 that the lowest bandgap for the $x = 0.46$ compositions is direct, since this composition is very near the crossover point (12, 13) and an indirect edge at a slightly lower energy would be hidden in Fig. 5.] For the $x = 0.73$ and 0.86 compositions, the slow rise in absorption indicates that the bandgap is indirect, and the absorption coefficient behaves as

$$\beta \propto (h\nu - Eg)^{1/2} \qquad [5]$$

for $\beta^{1/2} \leq 18\ \text{cm}^{-1/2}$, with intercepts (bandgaps) of 2.071 and 2.094 eV, respectively. These values are in good agreement with those reported by Onton *et al.* (12) but slightly higher (by 0.1 eV) than those reported by Casey and Panish (13) for compositions

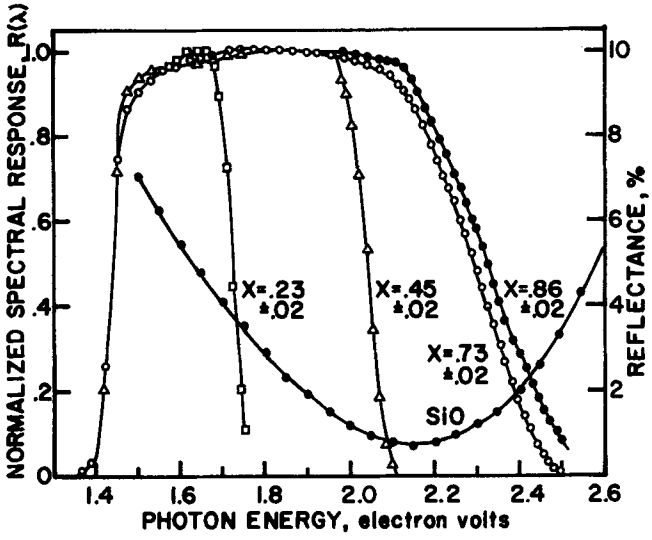

Fig. 4. Normalized spectral response for various alloy compositions. The $Ga_{1-x}Al_xAs$ thicknesses range from 11-16μ The reflection of incident light from a SiO-coated GaAs surface is also shown.

[1] It is probable that some grading in composition takes place between the $Ga_{1-x}Al_xAs$ and the GaAs due to the nature of the liquid phase epitaxial method of growth for these two materials. The distances over which this grading is expected to take place should be relatively small at these growth temperatures, and the diagram in Fig. 3 should be a reasonable approximation to the actual situation. [See Womac and Rediker (11).]

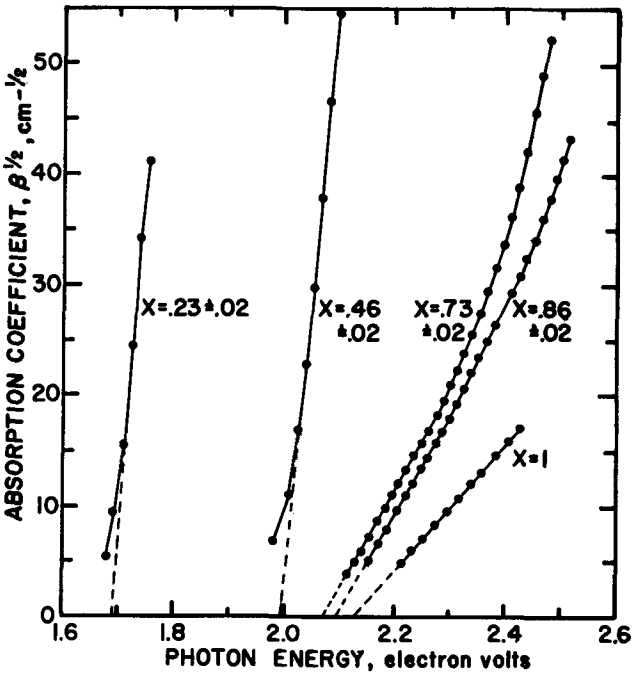

Fig. 5. Calculated absorption coefficients for $Ga_{1-x}Al_xAs$. The bandgaps indicated by the intercepts are 1.69, 1.99, 2.071, and 2.094 for the $x = 0.23$, 0.46, 0.73, and 0.86 compositions, respectively. The absorption coefficient in AlAs is also shown [after Lorenz *et al.* (14)].

with $x > 0.23$. The onset of direct band absorption is suggested by the steeper rise above 2.4-2.5 eV.

The absorption coefficient of AlAs ($x = 1$) as reported by Lorenz *et al.* (14) is shown in Fig. 5 for comparison. A bandgap of 2.125 eV is indicated for this material.

The method outlined above for computing the absorption of the $Ga_{1-x}Al_xAs$ layer from the spectral response slightly underestimates the absorption coefficient because it neglects any contribution to the measured response from the collection of carriers generated in the alloy layer. The error should be relatively small, however, as long as the thickness of the layer is three or more times larger than the electron diffusion length in the layer. (For the devices of Fig. 4 and 5, the thicknesses D ranged from 11 to 16μ, while the diffusion length in the alloy should be less than 2μ at the high doping levels present after the Zn diffusion step.) For photon energies where β is small, the total number of carriers generated in the alloy layer is small, and although the carriers are generated fairly uniformly throughout the layer, only those are collected which are about a diffusion length or less away from the $Ga_{1-x}Al_xAs$-GaAs interface. At higher photon energies where β is large, most of the carriers will be generated near the surface and not collected for large D. The largest error probably occurs when $\beta \approx 1/D$ ($25 < \beta^{1/2} < 30$ for these devices) and probably does not exceed 10%.

Solar Cell Characteristics

The current-voltage characteristics of a typical $Ga_{1-x}Al_xAs$-GaAs solar cell, both in the dark and during illumination, are shown in Fig. 6. As a first approximation, the current obeys the familiar relationship

$$J = J_o (\exp (qV/AKT) - 1) - J_{sc} \qquad [6]$$

where J_{sc} is the short-circuit photocurrent density and the modifying factor A varies from 1.4 to 2.1 from growth run to growth run with no discernable correlation with growth parameters. The short-circuit current density J_{sc} and the open-circuit voltage V_{oc} are determined from the intercepts of the characteristic with the current and voltage axes, respectively. In

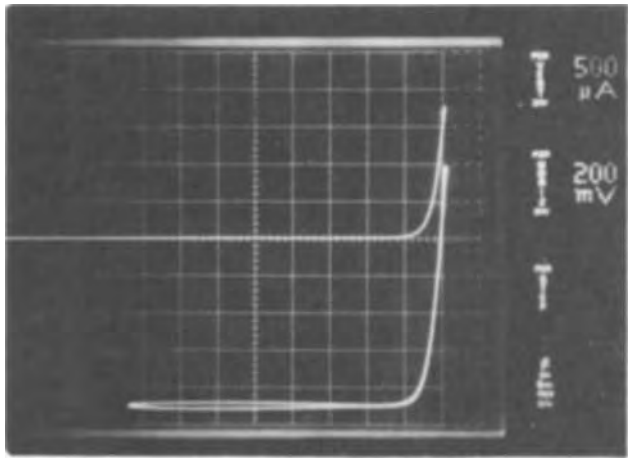

Fig. 6. Voltage-current characteristic with and without light for cell 298. The zero of the axes is at the center of the graph. The power output is equal to the maximum value of $V \times I$ in the fourth quadrant.

keeping with standard solar cell theory, the maximum power ($V_{mp}J_{mp}$) that can be obtained from the cell is equal to the greatest value of $V \times J$ in the fourth quadrant, and the ratio of the maximum power to the product of J_{sc} and V_{oc} is known as the "usage factor" (or "fill factor").

The open-circuit voltage, short-circuit current, and maximum power output were measured in sunlight on cloudless days at around noontime. The power input/square centimeter was measured with an Eppley thermopile. The device parameters for several cells of various junction depths, alloy thicknesses, and alloy compositions are shown in Table I, where the measurements were made at sea level, with an Air Mass of around 1.3 and a temperature of 65°F. (The Air Mass, which is the ratio of the optical path length of sunlight through the atmosphere to the path length when the sun is at the zenith, was determined by measuring the sun's angle and modifying the result by the altitude compared to sea level.) Table II lists the same solar cell parameters measured at an altitude of 12,800 ft, with an Air Mass of around 0.9 and a temperature of 45°F [values for several of these cells at Air Mass 1 and 2 were given earlier (3)]. The short-circuit current has been corrected for the contact area of 5-7% and both the uncorrected and corrected efficiencies are given. Around Air Mass 1, the short-circuit currents are of the order of 18-21 mA/cm² and the open-circuit voltages usually range from 0.97 to 1.0V (300°K). The usage factors vary from growth run to growth run, apparently due to differences in series

Table I. Cell behavior (AM 1.3) in sunlight at sea level. Input power was 90-91 mW/cm². $T = 65°F$

Cell	J_{sc}, mA/cm²	V_{oc}, V	U.F.	P_{out}, mW/cm²	η_u, %	η_c, %
287	19.94	0.971	0.779	14.13	15.7	16.7
288	18.41	0.975	0.8118	13.77	15.25	16.13
298	18.09	1.003	0.811	13.83	15.23	16.2
289	18.94	1.000	0.743	13.20	14.6	15.6
323	19.69	0.982	0.783	14.54	16.25	16.9

Table II. Cell behavior (AM 0.9) in sunlight at 12,800 ft. Input power was 114 mW/cm². $T = 45°F$

Cell	J_{sc}, mA/cm²	V_{oc}, V	U.F.	P_{out}, mW/cm²	η_u, %	η_c, %
287	21.81	1.002	0.780	15.96	14.00	14.95
288	19.93	1.001	0.8124	15.32	13.44	14.2
298	19.43	1.029	0.8115	15.24	13.37	14.22
289	20.42	1.025	0.7435	14.59	12.8	13.64
323	21.00	1.007	0.790	16.04	14.07	14.65

resistance when the doping in the alloy layer is too low and the significant sheet resistivities or contact resistances are present (it has been discovered recently that "firing-in" the Au-Zn contacts to the alloy layer and the Au-Ge-Ni contact to the substrate at temperatures in excess of 400°C for several minutes in a H_2 atmosphere is an important step in achieving negligible contact resistance). The usage factors are generally between 0.74 and 0.82 with 0.79-0.80 being typical, and the voltage output at the maximum power point, V_{mp}, is usually in the range of 0.79-0.84V. The output power and the over-all efficiency are functions of the Air Mass value, *i.e.*, functions of the atmospheric conditions (3, 4), since the spectral distribution of sunlight reaching the earth's surface is substantially modified by atmospheric absorption and scattering (15, 16); the higher the Air Mass value is, the greater is the degree to which ultraviolet and near-infrared radiation are lost in the atmosphere, and sunlight effectively becomes channeled into the visible range of wavelengths where the highest response of the cells is obtained. The efficiency therefore increases with increased Air Mass value.

Table III lists the solar cell parameters measured using an Air Mass 0 (outer space) simulator at the Jet Propulsion Laboratories in Pasadena, California. Since the major difference between AM0 and AM1 sunlight is the ultraviolet content, the efficiency drops sharply from AM1 to AM0 (the alloy layer for these thicknesses attenuates light of all energies greater than 2.5 eV). Nevertheless, these efficiencies are equal to most of the present-day silicon values, and higher efficiencies are expected (4) as the $Ga_{1-x}Al_xAs$ layer is made thinner.

Table IV lists the alloy thickness and composition and the junction depths for these cells. By comparing the short-circuit currents of the units in Tables I-III with their fabrication parameters in Table IV, it can be seen that higher currents are obtained for thinner alloy layers of a given composition, as expected from the reduced absorption in the $Ga_{1-x}Al_xAs$. Increasing the Al composition in the alloy has the same effect. The data also implies that higher currents are obtained for junction depths of around a micron, as predicted from computer evaluations of the spectral response integrated with the solar spectrum (4), than for junction depths greater than 1μ; that is due to a maximum in the sum of the photogenerated electrons collected from the surface p region and the photogenerated holes collected from the base (n region) at a junction depth of around 0.6-0.8μ. However, the collection is quite high for the devices of Tables I-IV even when the junction depth is 3μ, which indicates that the minority carrier diffusion length of electrons in the pGaAs region is 4μ or greater (4), in agreement with the results of Hayashi and Panish (5) for diffusion lengths in heterojunction lasers.

Table III. Cell behavior in simulated AM0 sunlight. Input power was 134.8 mW/cm². $T = 80°F$

Cell	J_{sc}, mA/cm²	V_{oc}, V	U.F.	P_{out}, mW/cm²	η_a, %	η_c, %
287	22.46	0.967	0.771	15.67	11.63	12.37
288	20.19	0.969	0.799	14.79	11.0	11.7
298	19.98	0.997	0.810	15.18	11.3	12.0
289	21.08	0.994	0.757	14.89	11.0	11.7
323	21.84	0.976	0.798	16.35	12.1	12.8

Table IV. Alloy layer composition and thickness, and junction depth, for the devices of Tables I-III

Cell	$x(Ga_{1-x}Al_xAs)$	$D(\mu)$	$d(\mu)$
287	0.73	5.5	0.8
288	0.73	13.8	0.8
298	0.73	11.1	3.5
289	0.86	15.8	2.7
323	0.78	2-4	2.8

The effect on the device behavior of varying the input power and the temperature was observed with the use of collimated light from a quartz-iodine lamp operating at about 3200°K; the light was shown through a 2-mm thick wafer filter onto the sample. Although this system does not duplicate the solar spectrum by any means, it does result in efficiency values (uncorrected for contact area) that are nearly the same as those measured in sunlight at Air Mass 1 (after the contact area correction is made). For convenience, therefore, this system will be referred to as an Air Mass 1 simulator.

The short-circuit current is proportional to the intensity (input power) of the incident light over at least three orders of magnitude, provided that the spectral distribution of the incident light remains constant as the intensity varies. This can be seen in Fig. 7, where neutral density filters (which attenuate light of wavelengths from 0.4-0.9μ equally) have been used to vary the input power from the Air Mass 1 simulator. The open-circuit voltage is proportional to the log of the input power, while the usage factor drops at low intensities and saturates above 10 mW/cm².

Temperature

The solar cell behavior as a function of temperature in the range of −190° to +150°C was measured by placing the unit in a vacuum of 1×10^{-5} Torr and illuminating it through a sapphire window with the Air Mass 1 simulator. For temperatures above 150°C, the devices were measured in air. The power input to the devices was 100 mW/cm².

The short-circuit current increases linearly with increasing temperature as can be seen in Fig. 8. The increase in J_{sc} could be partly due to a shift in the absorption edge (17) of the GaAs to lower energies as temperature increases, and partly due to an increase in the diffusion lengths. The shift in the GaAs absorption edge is only large enough to account for about 5% of the 50% variation in J_{sc} that occurs from 100° to 420°K, and it is probably offset to some degree by a shift in the $Ga_{1-x}Al_xAs$ absorption edge to lower energies as the temperature increases. Therefore the increase in J_{sc} is most likely due to improved collection efficiency resulting from increased diffusion lengths at higher temperatures. Higher diffusion lengths in turn could result from either larger diffusion coefficients or

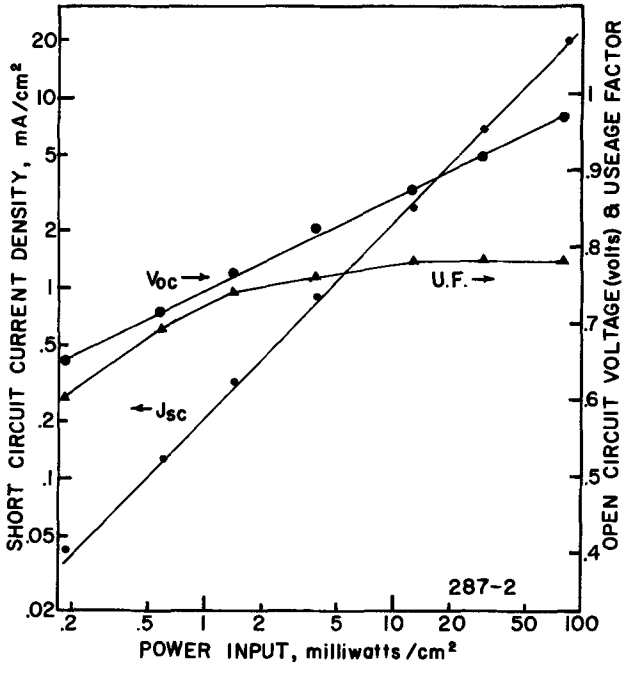

Fig. 7. Short-circuit current density (uncorrected for contact area), open-circuit voltage, and usage factor as functions of input power with the spectral distribution of the light held constant.

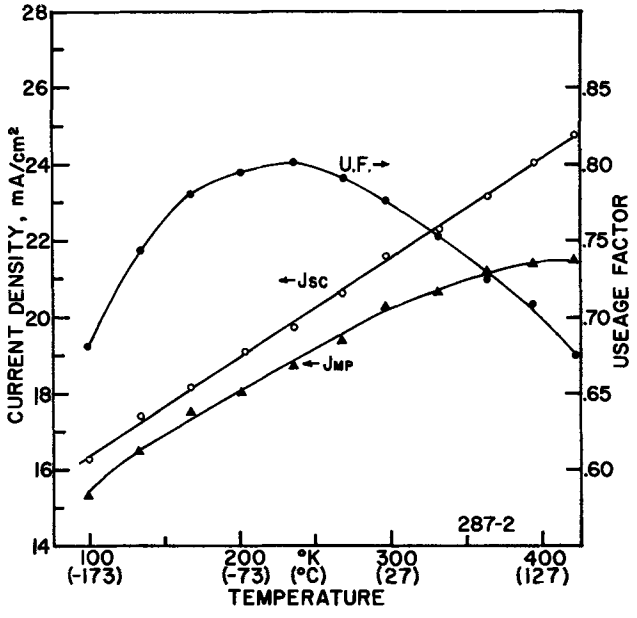

Fig. 8. Short-circuit and maximum power current densities (uncorrected for contact area) and the usage factor as functions of temperature. The unit was measured in vacuum with the Air Mass 1 simulator and a power input of 100 mW/cm².

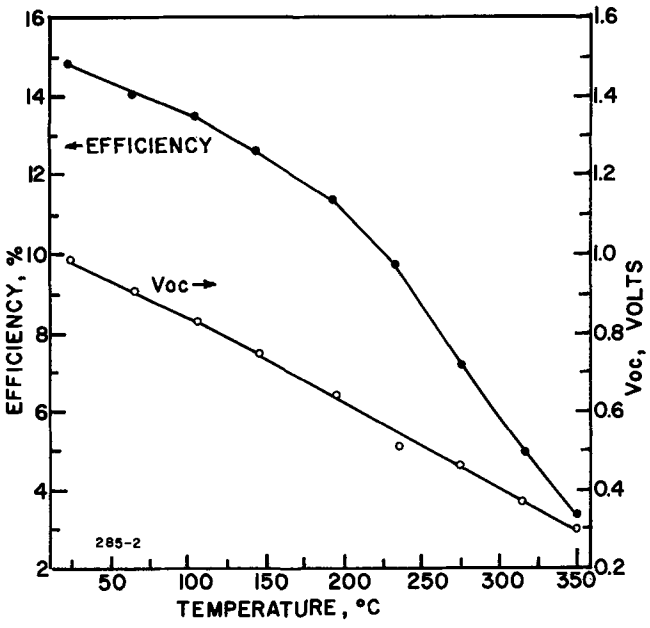

Fig. 10. Open-circuit voltage and efficiency (uncorrected for contact area) for a device measured in air with the Air Mass 1 simulator. The power input was 100 mW/cm².

higher lifetime. The current at maximum power, J_{mp}, follows the increase in short-circuit current up to about 0°C, then levels off and even decreases above 200°C. This behavior of J_{mp} can be attributed to the increasing "softness" of the "knee" in the I-V characteristic (Eq. [6]) as temperature increases. This "softness" is also the probable cause of the decreasing usage factor above −25°C as shown in Fig. 8.

The open-circuit voltage decreases linearly with increasing temperature, as seen in Fig. 9; the rate of decrease is around 2 mV/°C. The voltage at maximum power, V_{mp}, is proportional to V_{oc} above 0°C but saturates for temperatures below about −75°C. Both the efficiency and usage factor go through a maximum as a function of temperature at around −70° and −25°C, respectively, and decrease as the temperature is reduced below these values. The reasons for these variations are not clear at this time.

The open-circuit voltage and efficiency for a unit measured in air from 24° to 350°C with the Air Mass 1 simulator are shown in Fig. 10. The voltage decreases linearly as in Fig. 9, while the efficiency drops gradually at a rate (change in efficiency/change in temperature) of 0.022%/°C to about 11% at 200°C and more rapidly (0.059%/°C) for temperatures above 200°C. The efficiency is nearly 6% at 300°C and over 3% at 350°C. (This measurement, however, was a destructive one due to oxygen attack of the In contact at 350°C, although the device itself was not affected. There was no effect on the device or contact when the unit was cycled from −190° to +150°C in vacuum or up to 230°C in air.)

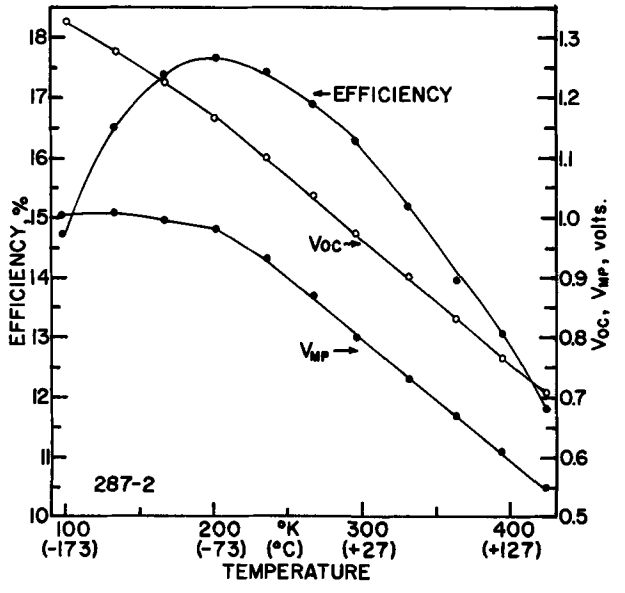

Fig. 9. Open-circuit and maximum power voltages and the efficiency (uncorrected for contact area) under the same conditions as in Fig. 8. The efficiency goes through a maximum at around −75°C.

Conclusions

Highly efficient solar cells can be fabricated using GaAs p-n junctions with a thin $Ga_{1-x}Al_xAs$ alloy layer on the GaAs surface. The alloy layer is grown by liquid phase epitaxy, and serves the purposes of reducing surface recombination and reducing series resistance. The $Ga_{1-x}Al_xAs$ is transparent to photons with energies up to about 2.1 eV and cuts off the light gradually in the range 2.1-2.6 eV due to the indirect bandgap. This high energy cut-off in the spectral response can be used to determine the absorption coefficient of the $Ga_{1-x}Al_xAs$ as a function of wavelength and composition, as long as the thickness of the layer exceeds about 6μ.

The behavior of the cells in sunlight at around Air Mass 1 was determined; typical devices have open-circuit voltages from 0.97 to 1.0V, short-circuit currents (corrected for contact area) of 18-21 mA/cm², and efficiencies (corrected for contact area) of 15 to 16%. At Air Mass 0, using a solar simulator, the currents were in the range of 20 to 22 mA/cm², and the efficiencies from 11.7 to 12.8%. The highest short-circuit currents are obtained with thin alloy layers of high Al composition and with junction depths of 0.8μ. Substantial short-circuit currents are obtained for junction depths of 3μ however, indicating electron diffusion lengths of 4μ or more in the p-type GaAs (doping level around 10^{18} cm^{-3}).

The short-circuit current and open-circuit voltage increase and decrease, respectively, linearly with increasing temperature. The efficiency has a maximum at around −75°C; it decreases gradually up to about 200°C, then decreases at twice the rate for higher temperatures. Efficiencies of nearly 6% at 300°C and over 3% at 350°C have been measured (using an Air Mass 1 simulator).

It is important to note, of course, that the efficiencies of these cells with 0.2 cm^2 area cannot be compared directly with the efficiencies of Si cells of 2 cm^2 area. However, it was the purpose of this work to demonstrate the soundness of the ideas involved and the feasibility of obtaining high efficiency GaAs cells, not to compete with Si on a 1:1 area basis. Presumably, the problems associated with scaling up these devices to larger areas should be no different than the problems associated with the scaling-up of other materials, and it is expected that $Ga_{1-x}Al_xAs$-GaAs cells with 1 or 2 cm^2 areas exhibiting similar or better efficiencies will be obtained in the near future.

Acknowledgments

The authors would like to express their appreciation to Dr. W. E. Howard for many helpful comments and suggestions. They would also like to thank Mr. R. M. Potemski, Mr. S. Renick, and Miss A. Benoric for their assistance during portions of the work. Finally, the services of the Jet Propulsion Laboratories in making the AM0 solar simulator measurements possible were greatly appreciated.

Manuscript submitted Jan. 4, 1973; revised manuscript received April 23, 1973. This was Paper 65 presented at the Houston, Texas, Meeting of the Society, May 7-11, 1972.

Any discussion of this paper will appear in a Discussion Section to be published in the June 1974 JOURNAL.

REFERENCES

1. P. Rappaport and J. J. Wysocki, *Acta Electronica*, **5**, 364 (1961).
2. A. R. Gobat, M. F. Lamorte, and G. W. McIver, *IRE Trans. Military Electron.*, **6**, 20 (1962).
3. J. M. Woodall and H. J. Hovel, *Applied Phys. Letters*, **21**, 379 (1972).
4. H. J. Hovel, J. M. Woodall, and W. E. Howard, 1972 Symposium on GaAs, Boulder, Colorado, Sept. 25-27, 1972, p. 205.
5. I. Hayashi and M. B. Panish, *J. Appl. Phys.*, **41**, 150 (1970).
6. H. Kressel, H. Nelson, and F. Z. Hawrylo, *ibid.*, **41**, 2019 (1970).
7. Zh. I. Alferov, V. M. Andreev, M. B. Kagan, I. I. Protasov, and V. G. Trofim, *Soviet Phys. Semicond.*, **4**, 2047 (1971).
8. J. M. Woodall, *J. Crystal Growth*, **12**, 32 (1972).
9. L. L. Chang, *Solid-State Electron.*, **7**, 853 (1964).
10. H. C. Casey, Jr., M. B. Panish, and L. L. Chang, *Phys. Rev.*, **162**, 660 (1967).
11. J. F. Womac and R. H. Rediker, *J. Appl. Phys.*, **43**, 4129 (1972).
12. A. Onton, M. R. Lorenz, and J. M. Woodall, *Bull. Am. Phys., Soc., Ser. II*, **16**, 371 (March 1, 1971).
13. H. C. Casey, Jr., and M. B. Panish, *J. Appl. Phys.*, **40**, 4910 (1969).
14. M. R. Lorenz, R. Chicotka, G. D. Pettit, and P. J. Dean, *Solid State Commun.*, **8**, 693 (1970).
15. P. Moon, *J. Franklin Inst.*, **230**, 583 (1940).
16. J. V. Dave and J. Gazdag, *Appl. Opt.*, **9**, 1457 (1970).
17. M. D. Sturge, *Phys. Rev.*, **127**, 768 (1962).

Phosphorus Isoconcentration Diffusion Studies in Silicon

J. S. Makris* and B. J. Masters

IBM System Products Division, East Fishkill Laboratory, Hopewell Junction, New York 12533

ABSTRACT

^{32}P-concentration profiles were obtained of diffusions conducted in intrinsic and extrinsic silicon, employing isoconcentration conditions for the latter. All diffusions were conducted in evacuated closed quartz capsules at diffusion temperatures ranging from 950° to 1200°C. The temperature dependence of phosphorus diffusivity in intrinsic and extrinsic silicon is described by the empirical equations $D_{int} = 5.3 \exp(-3.69\ eV/kT)$ cm^2/sec and $D_{ext} = 0.39 \exp(-3.12\ eV/kT)$ cm^2/sec, respectively.

The phosphorus diffusivity is seen to increase about a factor of 10 over the value obtained in intrinsic silicon for the highest phosphorus concentration employed. The results are explained by assuming the diffusion process of phosphorus into silicon is primarily controlled by monovacancies in the single negative charged state.

This is the fourth in a series of investigations (1-3) dealing with the diffusion of substitutional atoms in the silicon lattice. Throughout this series particular attention has been focused on the diffusion coefficient dependencies upon background doping level and upon diffusant concentration. In order to explain the observations, a general mechanism of diffusion has been proposed (3), in which the existence of negatively charged, neutral, and positively charged vacancies is assumed, and in which the diffusion of ionized substitutional impurities is considered to be controlled primarily by the concentration of vacancies of charge type opposite to that of the diffusing impurity.

The present investigation was undertaken in order to extend the measurements of diffusivity dependence upon concentration and upon background doping level to include phosphorus as the diffusant impurity, as well as to provide a further test of the proposed diffusion mechanism.

Experimental Procedure

For the entire investigation Czochralski grown silicon single crystals cut in the <100> direction with a boron background concentration of 1.6×10^{16} atoms B/cm^3 ($\rho = 1$ ohm-cm) were used. Crystal dimensions were 1.25 in. in diameter and 0.007 in. thick. Dislocation density was less than 4×10^3 lines/cm^2. The crystals were chemically mechanically polished to eliminate surface damage.

All diffusions were conducted employing the evacuated sealed quartz capsule technique and appropriate Si(P) source powders. To obtain the phosphorus diffusivities in intrinsic silicon as a function of temperature, a phosphorus-doped silicon powder source with a concentration of $\sim 4 \times 10^{18}$ atoms P/cm^3 was used. To obtain the diffusivities in extrinsic silicon as a function of temperature, a high phosphorus concentration silicon source powder, 4.5×10^{20} atoms P/cm^3, was used. For determining the diffusivities as a function of background doping at a constant diffusing temperature, 1000°C, the concentrations of Si(P) powder sources ranged from 4×10^{18} to 4.5×10^{20} atoms P/cm^3. Phosphorus contents in all Si(P) source powders were determined by neutron activation techniques.

For phosphorus diffusions into intrinsic silicon, the crystals were cleaned in hydrofluoric acid, rinsed in deionized water, and dried in hot nitrogen. The cleaned crystals were placed erect in a quartz boat containing

* Electrochemical Society Active Member.
Key words: phosphorus, isoconcentration, diffusion.

2.5 g of the Si(P) source powder, 4×10^{18} atoms P/cm^3, and the boat and crystals placed in a quartz capsule sealed at one end. (All quartzware was previously etched in $3HNO_3$-1HF, rinsed in deionized water, and baked out under vacuum at 1200°C.) Each capsule containing the silicon crystals and source powder was baked out at 450°C for 0.5 hr under vacuum of 6×10^{-6} Torr and then sealed. Diffusions were conducted in furnaces which were controlled to ± 1°C and had a constant temperature zone of at least 10 in. Diffusion temperatures and times employed were: 950°C for 24 hr, 1000°C for 4 hr, 1050°C for 3 hr, 1100°C for 1 hr, and 1200°C for 1/2 hr. After each diffusion the hot quartz capsules were quenched in running cold tap water.

^{32}P-concentration profiles in intrinsic silicon were obtained by neutron activating the phosphorus diffused wafers to produce a fraction of ^{32}P which has a half life of 14.3 days. The ^{31}Si also produced has a half life of 2.6 hr and this was allowed to decay at least 48 hr before the crystals were further processed. Mesas of known diameter were made on the neutron-activated diffused crystals by etching away several microns of silicon from the edge regions, and autoradiograms were made to ensure lateral homogeneity of the diffusion and to ensure that the silicon had decayed below detection levels. Sectioning of the crystals was done by successively oxidizing and removing layers of silicon of predetermined thickness using the anodic oxidation technique (4). Each dissolved layer removed was captured and placed into a vial. A "cocktail" was made containing the dissolved layer and appropriate scintillation solution.

Counting was done using a liquid scintillation counter. Each cocktail was counted and corrected for decay against a standard similarly prepared. Extreme precautions were taken to ensure a low statistical counting error of the cocktails having a very low ^{32}P-concentration by counting for a long time. Sectioning was carried out until near background counting rate was reached.

Diffusions into extrinsic silicon crystals were conducted employing the isoconcentration technique (2). In this technique, all electrical and elastic effects of concentration gradients are eliminated. First a long time prediffusion is done using Si(P) source powder and then a second diffusion is done using a neutron-activated portion of the same source powder. The prediffusion is designed to produce a relatively flat phosphorus concentration profile several microns deep into the crystal. Prediffusion and the second (sequential) diffusion are done at the same diffusion temperature in order to ensure equilibrium conditions of the diffusing species at the silicon crystal surface. The crystals and the quartz capsules were prepared as described above for the phosphorus diffusions in intrinsic silicon. Prediffusion times ranged from 2.3 hr at 1200°C to 250 hr at 950°C. Sequential diffusion times employed were the same as those used for the intrinsic silicon diffusions. In the sequential diffusion an intrinsic silicon crystal was included in the capsule for comparison. The ^{32}P-concentration profiles from the sequential diffusion were obtained using the same sectioning and counting techniques as described above. For all the sequential diffusions into extrinsic silicon the radiophosphorus profiles were much shallower than the prediffusion profiles.

Results

Radiophosphorus profiles for diffusions conducted at 1200°C are shown in Fig. 1. Profiles shown are typical of ones obtained for other diffusion temperatures. Concentration profile I is of the diffusion conducted into intrinsic silicon using the low source concentration. Profile II is of the prediffusion conducted into silicon using the highest source concentration. This profile was obtained by neutron activating the crystal after prediffusion. Only a portion of the profile was obtained to show the flatness of the concentration gradient. Actually the concentration profile of the prediffusion extends much deeper into the crystal than is shown. Concentration profiles III and IV are of the sequential diffusion conducted into extrinsic (isoconcentration condition) and intrinsic silicon, respectively. Only profiles I and III, obtained under intrinsic and isoconcentration diffusion conditions, conform to the complementary error function (5)

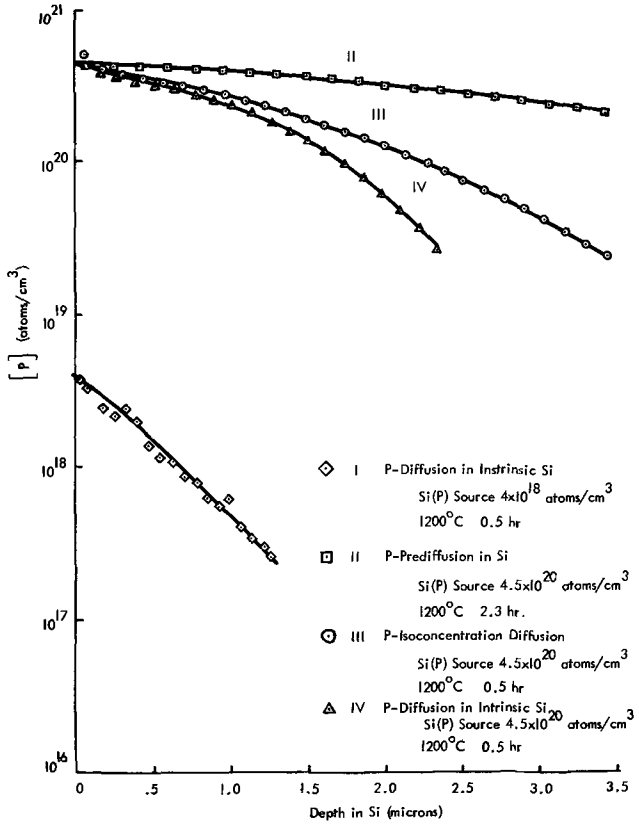

Fig. 1. Phosphorus concentration profiles in silicon for diffusions conducted at 1200°C.

$$C_x = C_o \operatorname{erfc} [x/2\ (Dt)^{1/2}] \qquad [1]$$

The diffusivities calculated for intrinsic and isoconcentration conditions, as well as diffusion temperatures and times employed, are listed in Table I. In Fig. 2, diffusivities *vs.* the reciprocal of absolute temperature for the present investigation, as well as the intrinsic or near intrinsic data of others (6-9) are plotted. A least squares fit of the combined data of Maekawa, Mackintosh, and our intrinsic diffusion data is well represented by the relationship

$$D_{\text{int}} = 5.30 \exp (-3.69\ \text{eV}/kT)\ \text{cm}^2/\text{sec} \qquad [2]$$

The diffusion coefficient as a function of temperature for the highest phosphorus concentration employing isoconcentration diffusion conditions is

$$D_{\text{ext}} = 0.39 \exp (-3.12\ \text{eV}/kT)\ \text{cm}^2/\text{sec} \qquad [3]$$

In Table II the results of phosphorus diffusivity measurements at 1000°C for various background doping levels, N_D, are summarized. The free electron concentration was determined using the equation

$$n = \tfrac{1}{2}[N_D + (N_D^2 + 4n_i^2)^{1/2}] \qquad [4]$$

in which n_i is the intrinsic electron concentration, which was calculated using Morin and Maita's empirical

Table I. Intrinsic and extrinsic (0.9 atom per cent P-doped) diffusion data

Temp. (°C)	Time (hr)	$D_{\text{intrinsic}}$ (cm^2/sec)	$D_{\text{extrinsic}}$ (cm^2/sec)
950	24	3.27×10^{-15}	4.83×10^{-14}
1000	4	1.45×10^{-14}	1.76×10^{-13}
1050	3	4.12×10^{-14}	5.5×10^{-13}
1100	1	1.49×10^{-13}	1.36×10^{-12}
1200	0.5	1.13×10^{-12}	8.55×10^{-12}

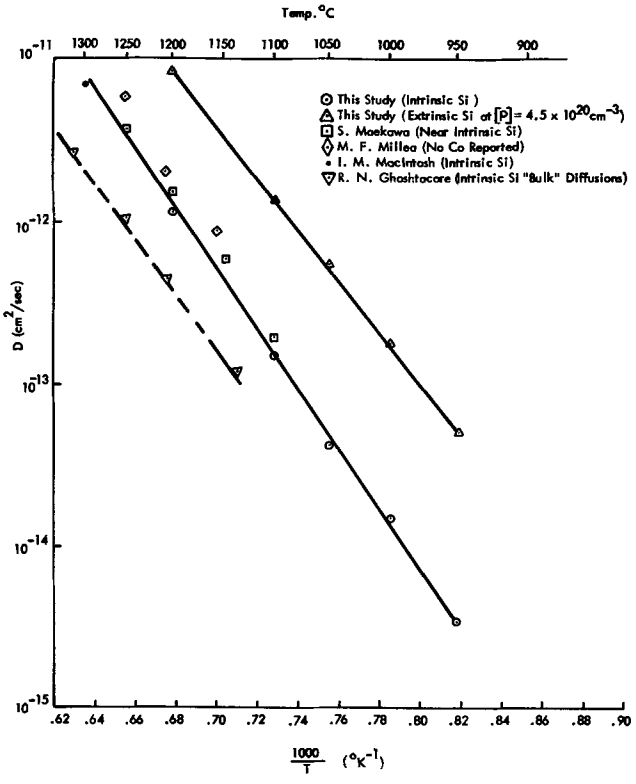

Fig. 2. Temperature dependence of phosphorus diffusivity in intrinsic silicon. Phosphorus diffusivity data for intrinsic and near intrinsic silicon of other investigations are also included.

relations (10)

$$n_i = 3.87 \times 10^{16} T^{3/2} \exp - (1.21 + \Delta Eg)/2kT \quad [5]$$

$$\Delta Eg = - 7.1 \times 10^{-10} (n_i)^{1/2} T^{-1/2} \quad [6]$$

The use of the equations above imply the common assumptions of nondegeneracy, charge neutrality in the crystal, and complete ionization of the background dopant at the diffusion temperature.

In Fig. 3, phosphorus diffusivities as a function of background electron concentration for diffusions conducted at 1000°C are plotted. The arsenic data (2) for diffusions conducted at 950°C are also shown for comparison. Phosphorus is observed to have the same behavior as arsenic. That is, phosphorus diffusion into silicon appears to increase almost linearly with increasing free electron concentration.

Discussion

From Fig. 2 it is apparent that the intrinsic diffusion measurements obtained in the present study are in good agreement with the data of Mackintosh (8), Maekawa (6), and Millea (7), but not with the "bulk diffusivity" values reported by Ghoshtagore (9, 11).[1] This discrepancy has been attributed by Ghoshtagore to a depth dependence of diffusivity arising from higher vacancy concentrations near the free surface than in the bulk. Neither in the present study nor in any other profiling experience of this laboratory has an intrinsic

[1] Note added in proof: Since the preparation of this paper, new data on the "surface limited" intrinsic diffusivity of phosphorus have been published by R. N. Ghoshtagore [*Solid State Electron.*, 15, 1113 (1972)], and these values are in good agreement with the intrinsic diffusivities reported in the present study.

Table II. Phosphorus diffusivity at 1000°C as a function of electron concentration

Background conc. (atoms/cm³)	n (electrons/cm³)	D (cm²/sec)
Intrinsic	9.27×10^{18}	1.45×10^{-14}
[P] 1.95×10^{19}	2.31×10^{19}	2.21×10^{-14}
[P] 4.4×10^{19}	4.58×10^{19}	2.71×10^{-14}
[P] 2.8×10^{20}	2.8×10^{20}	1.95×10^{-13}
[P] 4.5×10^{20}	4.5×10^{20}	1.76×10^{-13}

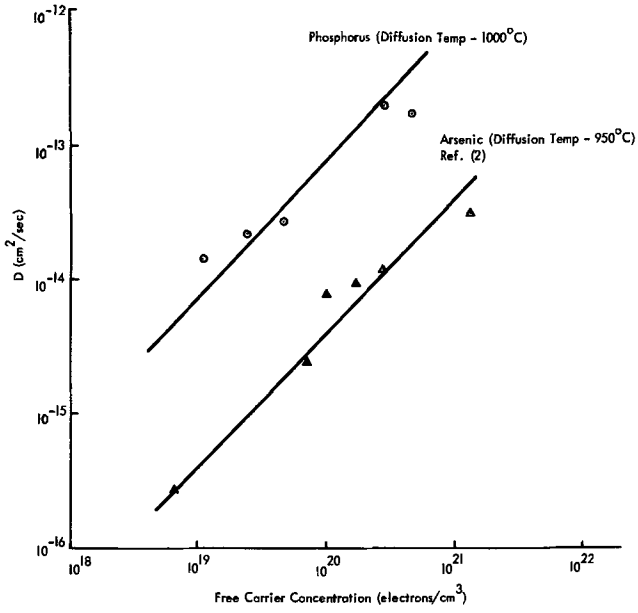

Fig. 3. Phosphorus diffusivity as a function of free carrier concentration for diffusions conducted at 1000°C. Arsenic diffusivity data of Masters and Fairfield (2) for diffusions conducted at 950°C.

diffusion coefficient decrease with increasing depth, in confirmation of Ghoshtagore's observations, been observed. However, it must be recognized that our experimental conditions have differed considerably from those employed by Ghoshtagore, and further investigations of this effect would be highly desirable.

The diffusivity measurements obtained under extrinsic isoconcentration diffusion conditions are in qualitative agreement with the concentration dependencies indicated in previous studies (6-8), and owing to the absence of steep concentration gradients, are capable of a much more quantitative interpretation. The very significant increase in phosphorus diffusivity with doping level, accompanied by decreased activation energy and entropy of diffusion under extrinsic conditions, is reminiscent of the results encountered for arsenic isoconcentration diffusion (2). This similarity is further evidenced in Fig. 3, in which the phosphorus diffusivity dependence upon free electron concentration obtained at 1000°C is compared with the previously reported 950°C arsenic data. In both instances, an approximately first-order dependence is observed, and it appears likely that similar mechanisms of diffusion are operating in the two cases.

In a previous study of gallium diffusion in boron-doped silicon (3), a general model for the migration of substitutional ionized impurities in silicon was developed. In this model, the diffusion of donor impurities is presumed to be controlled primarily by the local concentration of singly ionized acceptor monovacancies, with a negligibly small contribution from the un-ionized vacancy population. The model further assumes the existence of a vacancy acceptor level located near the middle of the forbidden gap, a matter which is discussed in more detail elsewhere (12).

For such an acceptor level, the negative vacancy concentration is approximated by (13)

$$[V^-] \simeq [V^\circ](n/n_i) \quad [7]$$

in which $[V^\circ]$, the neutral vacancy concentration, is estimated (1) to be

$$[V^\circ] \simeq 5 \times 10^{25} \exp(-3.4 \text{ eV}/kT)/\text{cm}^3 \quad [8]$$

This simplified model predicts that the ratio of phosphorus diffusivities for extrinsic to intrinsic silicon should be equal to the ratio of the corresponding charged vacancy concentrations

$$D_{ext}/D_{int} \simeq [V^-]_{ext}/[V^-]_{int} \quad [9]$$

From the above equations the ratio of phosphorus diffusivities should have the following dependence

$$D_{ext}/D_{int} \simeq n/n_i \quad [10]$$

The solid line in Fig. 3 shows the first-order dependence which is in reasonable agreement with observed results. It appears that the phosphorus concentration dependency observed in the present study is well accounted for in terms of this simplified model.

Summary

Phosphorus diffusivity in intrinsic silicon was found to be in good agreement with most investigators and in disagreement with Ghoshtagore's results. To a first approximation, a first-order phosphorus concentration dependency was observed at fixed diffusion temperature. The results are explained by assuming phosphorus diffusion in silicon to be primarily controlled by monovacancies in the negative charged state. The results are consistent with the previous investigations (1-3) and provide further support that the mechanism for substitutional atom diffusion in silicon is primarily controlled by monovacancies opposite in charge to the diffusing species.

Acknowledgment

The authors wish to thank Dr. R. H. Kastl for his assistance in the radiochemical procedures and Dr. H. S. Rupprecht for his encouragement in this work.

Manuscript submitted Nov. 21, 1972; revised manuscript received March 16, 1973.

Any discussion of this paper will appear in a Discussion Section to be published in the June 1974 JOURNAL.

REFERENCES

1. J. M. Fairfield and B. J. Masters, *J. Appl. Phys.*, **38**, 3148 (1967).
2. B. J. Masters and J. M. Fairfield, *ibid.*, **40**, 2390 (1969).
3. J. S. Makris and B. J. Masters, *ibid.*, **42**, 3750 (1971).
4. E. Tannenbaum, *Solid State Electron.*, **2**, 123 (1961).
5. P. G. Shewmon, "Diffusion in Solids," p. 14, McGraw-Hill Book Co., New York (1963).
6. S. Maekawa, *J. Phys. Soc. Japan*, **17**, 1592 (1962).
7. M. F. Millea, *J. Phys. Chem. Solids*, **27**, 315 (1966).
8. I. M. Mackintosh, *This Journal*, **109**, 392 (1962).
9. R. N. Ghoshtagore, *Phys. Rev. Letters*, **25**, 856 (1970).
10. F. J. Morin and J. P. Maita, *Phys. Rev.*, **96**, 28 (1954).
11. R. N. Ghoshtagore, *Appl. Phys. Letters*, **17**, 137 (1970).
12. B. J. Masters, *Solid State Commun.*, **9**, 283 (1971).
13. R. L. Longini and R. F. Green, *Phys. Rev.*, **102**, 992 (1956).

Undercut Isolation—A Technique for Closely Spaced and Self-Aligned Metalization Patterns for MOS Integrated Circuits

C. N. Berglund, J. T. Clemens, and E. H. Nicollian*

Bell Laboratories, Murray Hill, New Jersey 07974

ABSTRACT

A new technique for achieving electrically isolated, closely spaced, and self-aligned metalization patterns on thin insulating films for integrated circuit applications is described. This scheme takes advantage of the shadowing effect of an undercut area etched in a two-layer insulator sandwich. A pattern first etched in the upper insulator delineates and acts as an etch mask for undercutting and thinning down the second insulator on the semiconductor substrate. The major requirement is that the first insulator be weakly or not at all affected by the etch for the second insulator. Because of the masking effect of undercutting, a thin metal evaporation will be discontinuous at all undercut edges resulting in electrically isolated metalization patterns with virtually zero lateral spacing between them. The silicon dioxide-alumina double insulator system with titanium-palladium-gold metalization was used and the details of the technique, including methods of selectively connecting isolated metal patterns, are described. Experimental data are presented to show that undercut isolation can be achieved with high reliability, undercut edges several centimeters in length being typically observed between unintentional shorts. Advantages and utility of the technique are illustrated by describing the design of a charge-coupled device.

One of the well-known problems in integrated circuit fabrication is undercutting which occurs when one attempts to etch through multiple layers of different materials on a semiconductor wafer. If the upper layer either etches slower or not at all in the etchant required for the lower layer, there will be a ledge of the upper material formed when the lower layer is etched. When the two layers are insulators, for example, this leads to serious difficulty in making reliable electrical connections on an integrated circuit. Recently there have been several successful attempts to make use of undercutting effects like this to simplify device fabrication (1-3). Advantages cited include the fact that undercutting can be used to achieve a self-aligned metalization pattern with virtually no lateral spacing between adjacent metal lines. Most of the work has been directed towards fabrication of Schottky-barrier field-effect transistors (2), with the lower metal usually being deposited directly onto the semiconductor substrate. In this paper we shall show that the undercutting effect also can be used to isolate metal patterns on two different thicknesses of insulators and that reliable and selective contact can be made between the two patterns or between either pattern and semiconductor substrate (4). In this way, the attractive features of the technique, such as the fact that it is self-aligning and has virtually no lateral spacing between adjacent metal lines, are combined with the additional versatility arising from having both levels of metalization on top of insulating films. This makes the undercutting isola-

* Electrochemical Society Active Member.
Key words: charge-coupled devices, silicon devices, thin insulator films.

tion scheme of general interest for integrated circuit semiconductor device fabrication.

In describing the undercut isolation technique, we shall restrict ourselves to one specific material system, the silicon-silicon dioxide-alumina (Si-SiO_2-Al_2O_3) double insulator system (5) with titanium-palladium-gold (Ti-Pd-Au) metalization (6). It is evident that other materials systems will work equally well and in some cases may have important advantages.

We will first describe the essential structure of the undercut isolation scheme and report on experimental results with respect to its fabricational feasibility and associated defects that can potentially reduce integrated circuit yield. Secondly, we will describe the design of a charge coupled device (CCD) shift register employing undercut isolation to illustrate its utility.

Undercut Isolation Scheme

Fundamental structure.—The standard procedure used in Si planar technology to isolate, electrically, adjacent metalization lines is to etch away a metal region, thus forming an isolation gap. This technique, however, possesses a major drawback, namely that the gap width is limited in minimum size by photoresist and metal etching technology. A possible way to reduce (or eliminate) this lateral gap is to transfer it to the vertical position. Using a stepped insulator structure, it is possible to visualize the lateral gap approaching zero dimension. However, to fabricate experimentally such a structure one must rely upon a shadowing effect during vacuum deposition of metal to provide the necessary discontinuity of metal over the insulator step. In practice, one will rarely find complete electrical isolation at such a step because: (*i*) oxide steps are never completely vertical, and (*ii*) incident metal vapor during deposition, originating from a spatially extended source, never can be purely vertical to the spatially extended sample.

A possible method of overcoming these two deleterious effects is to form a ledge (or overhang) at the insulator step, so that a desired shadowing effect will occur and form an isolation gap. In the next section, we shall describe a specific two material insulator system that may be used to construct the desired physical geometry.

Al_2O_3-SiO_2 insulator system.—This double insulator system has a disjoint etching characteristic (*i.e.*, Al_2O_3 may be patterned or etched in phosphoric acid, H_3PO_4, but is inert in hydrofluoric acid, HF; conversely, SiO_2 may be patterned with HF, but is essentially inert in H_3PO_4). Using this fact, we will now describe a technique by which one may fabricate a double insulator MOS structure electrically isolated by means of the proposed overhang structure.

The important cross-sectional views of the MOS structure during fabrication are illustrated in Fig. 1. A silicon wafer is thermally oxidized and a thin layer of Al_2O_3 is deposited along with a layer of SiO_2 [Fig. 1(a)]. This deposited layer of SiO_2 will be used as an etch mask for the Al_2O_3, because standard photoresist materials are severely attacked by the 180°C boiling aqueous solution of phosphoric acid used to etch Al_2O_3. The SiO_2 is patterned by standard photolithography techniques and then the Al_2O_3 is patterned [Fig. 1(b)].

In the next step, the desired undercut ledge is formed. This is accomplished by etching the structure in an aqueous HF solution possessing a calibrated etch rate (nominal etch = 10 parts by volume H_2O and 1 part by volume conc HF). This process step thins the thermal oxide in the exposed area to a predetermined thickness and undercuts the Al_2O_3 film forming the desired overhang [Fig. 1(c)]. A second film of Al_2O_3 is now deposited over the entire structure, thereby passivating it [Fig. 1(d)]. This step is included to assure a completely passivated structure.

Finally, a titanium-palladium (Ti-Pd) metalization film of thickness less than the overhang gap in Fig. 1(d) is vacuum deposited over the wafer, yielding the undercut isolated double insulator MOS structure shown in Fig. 1(e).

Experimental Results and Discussion

Fabricational aspects.—To explore the feasibility of the previously described technique, we fabricated 20 mil² undercut isolated MOS capacitors on n-type <100> Si wafers. Figure 2 is a cross section of the test structure with critical dimensions indicated. Figure 3 is a scanning electron microscope (SEM) photomicrograph of the first Al_2O_3 overhang immediately after the thermal oxide thinning step where the oxide has been deliberately overetched to expose the Si substrate (for dimensional reference) and to illustrate the rigidity of overhang.

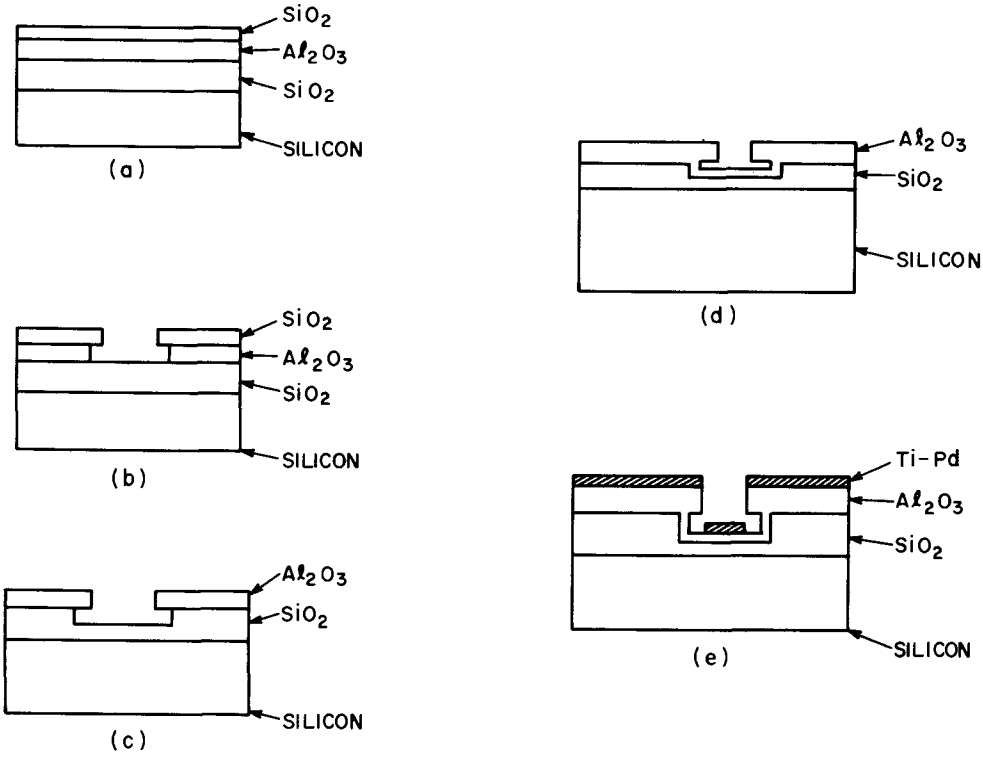

Fig. 1. Steps illustrating the basic undercut isolation scheme described in the text.

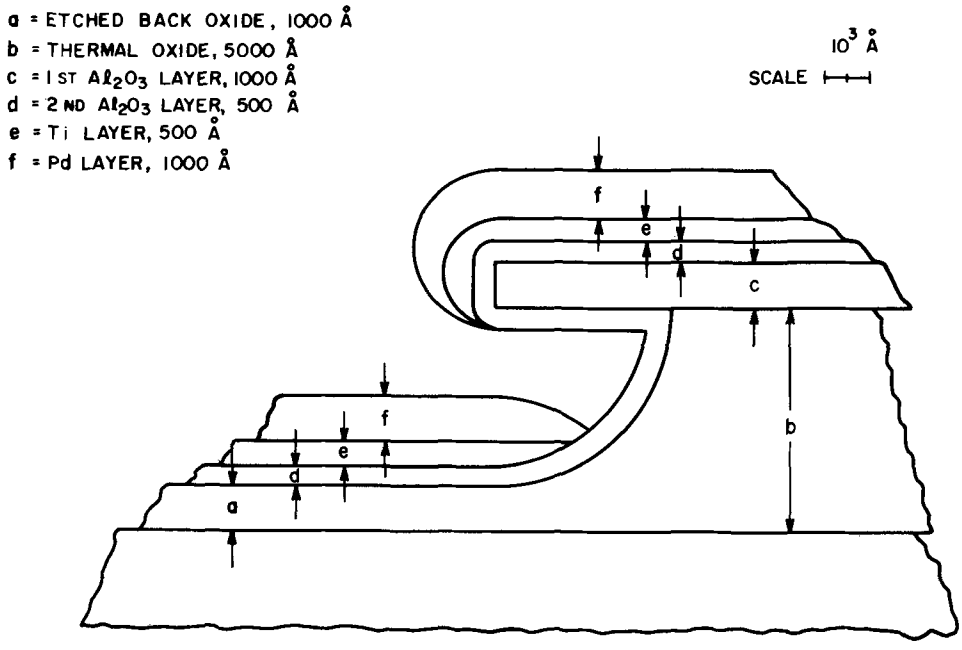

Fig. 2. Sectional drawing of undercut edge of an experimental structure.

To check the passivation character of the second Al_2O_3 deposition, samples were soaked in buffered HF to decorate pinholes at the overhang edge. No significant pinholes or voids were observed in the passivated layer. Figure 4 (a) and (b) is a photomicrograph of a finished experimental sample at the stage shown in Fig. 1(e) which shows the final desired isolation gap in the metalization layer.

Electrical characteristics.—All important electrical characteristics of the undercut isolation technique [namely: (*i*) isolation yield per unit length (or equivalent linear defect density); (*ii*) MOS characteristics; and (*iii*) insulator and isolation gap breakdown strength and stability] may be measured with the capacitor structure. Let us consider each separately.

(*i*) *Isolation yield per unit length.*—Several hundred MOS structures were checked for vertical shorts on each test wafer fabricated. Typically, less than 10% of the structures were shorted, one wafer in particular yielding only 2% shorts. Scratches, due to handling, were often observed on the shorted MOS pads, and a large fraction of shorted pads were located in the immediate vicinity of the edge of the wafer. To ascertain the failure mechanism in shorted unscratched MOS pads, SEM photomicrographs of those pads were obtained. Figure 4(c) illustrates the observed failure mode, particulate matter causing metallic bridging between metalization levels.

In order to obtain a quantitative figure for unintentional shorts useful for circuit/device design, assume that spatial location of a short occurring between lower metalization and upper metalization levels is a random variable. The probability of a short occurring per unit length of isolation edge then may be easily characterized. It is straightforward to show that probability, $P(l)$, of finding no shorts in a length l of isolation edge is given by

$$P(l) = \exp(-l/l_0) \qquad [1]$$

where l_0 is average distance between shorts. An estimate of l_0 may be obtained from previously described yield data. Recalling that each MOS pad is a 20 mil^2 (0.20 cm perimeter), a 10% probability of shorting corresponds to l_0 (10%) = 2 cm; while a 2% probability corresponds to l_0 (2%) = 10 cm.

(*ii*) *MOS characteristics.*—MOS characterization of both isolated (thin insulator) and field (thick insulator) capacitors indicated that their electrical characteristics are essentially identical to those found on standard double insulator (Al_2O_3-SiO_2) capacitors. The midgap interface state density was approximately 2.0×10^{10} cm$^{-2} \times$ eV^{-1}; and flatband voltage for the thin insulator pad was approximately 0.3V.

(*iii*) *Insulator breakdown strength and stability.*—Breakdown electric field strength in the etch-back insulator region was found to be approximately 5.2×10^6 V/cm. This means that the insulator breakdown strength is not seriously degraded by thinning of the thermal oxides. Additionally, breakdown electric field strength associated with the undercut isolated edge, measured by destructive breakdown between metal levels, was found to be approximately 6.5×10^6 V/cm.

Stability measurements under bias-temperature aging were also performed. The isolated thin insulator MOS pads, under a bias of -1.0×10^6 V/cm at 350° for 30 min, exhibited a shift in flatband voltage of 0.10V and an increase in interface state density at mid-bandgap from 2.0×10^{10} cm$^{-2} \times$ eV^{-1} to 5.5×10^{10} cm$^2 \times$ eV^{-1}. Similar results, except for a correspondingly larger shift in flatband voltage (a factor of 3-5 larger), were obtained on the field capacitors. Such results indicate that double insulator MOS characteristics and Si-SiO_2 interface properties obtained from the undercut isolation process are essentially equal to those obtained from the standard double insulator (Al_2O_3-SiO_2) process and that additional Al_2O_3 deposition does not degrade usually observed characteristics of the SiO_2-Al_2O_3 system.

Undercut Isolation Charge-Coupled Device

In the preceding sections, we have demonstrated feasibility of a metalization isolation scheme that possesses, in addition to a zero lateral isolation gap, excellent MOS characteristics. Such a scheme may have many applications in integrated circuit design. However, an immediate application lies in the area of CCD's.

Several studies have indicated that operational ability and charge transfer efficiency of this device depends critically upon absolute magnitude of interelectrode spacing (7, 8). In this section, we will describe how the overhang technique may be used to fabricate a two-phase p-channel CCD with zero interelectrode spacing. In addition to this primary device feature, the undercutting technique will also yield the structure for attaining charge propagation directionality, *i.e.*, a stepped electrode configuration formed by different insulator thicknesses (9). The processing procedure outlined here is only one of many possibilities considered. It was chosen because it is similar to one first used to fabricate a CCD using undercut isolation (4).

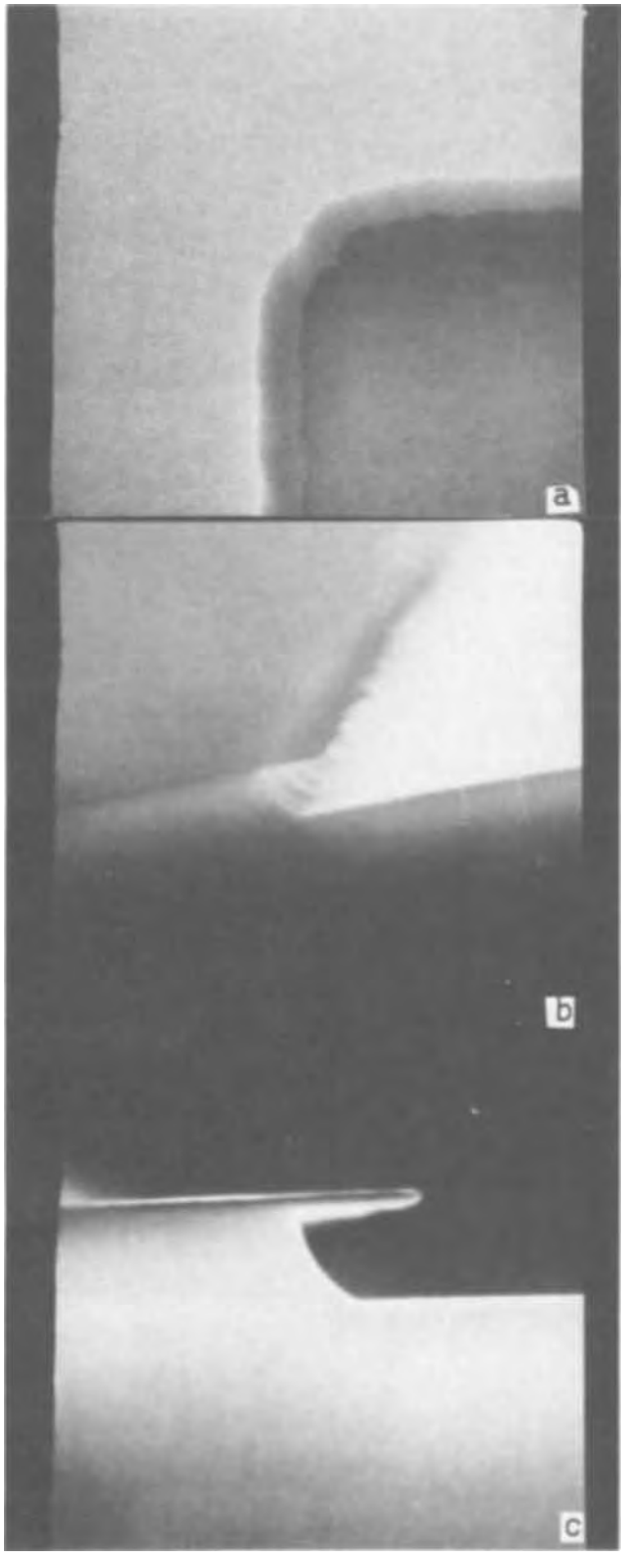

Fig. 3. Several electron microscope views of an undercut isolated edge before second Al_2O_3 deposition.

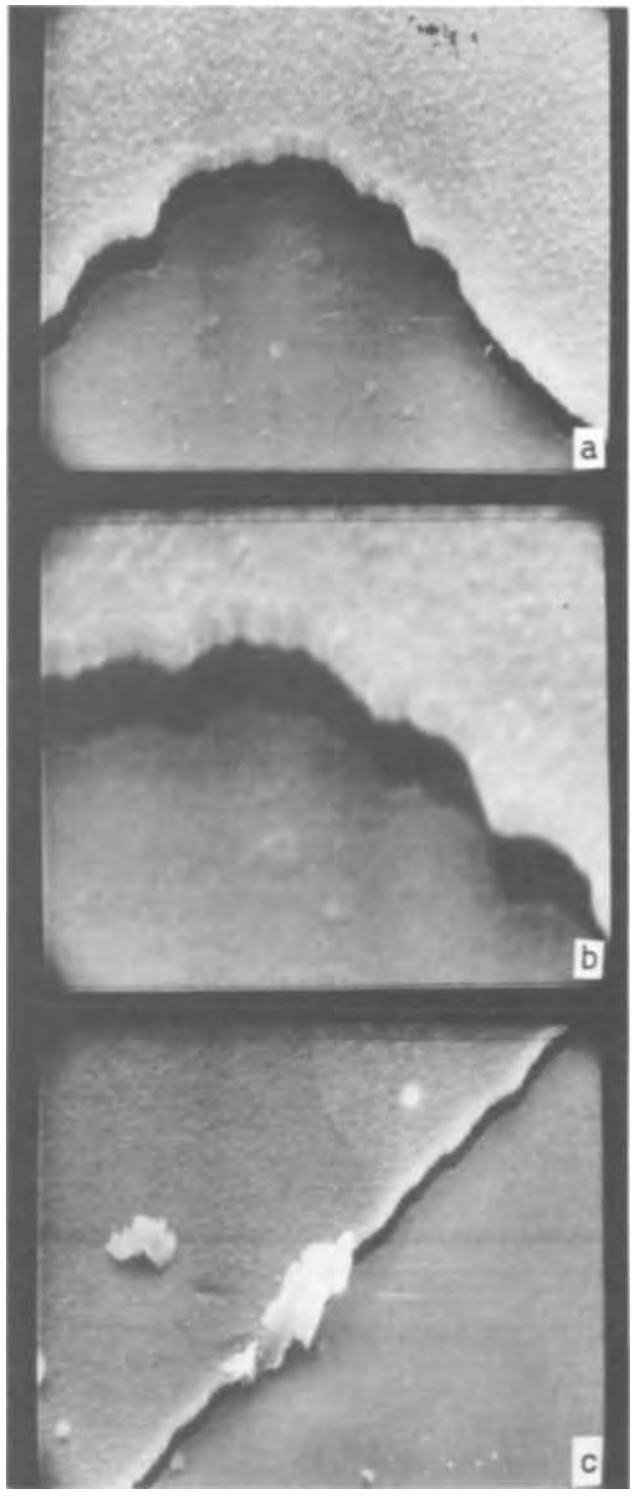

Fig. 4. An undercut isolated edge after titanium-palladium deposition.

Fabrication scheme.—Figures 5-8 illustrate the important steps and features in the CCD fabrication. Initially, appropriate p-type diffusions for input-output circuitry are performed and are followed by growth of a thick field oxide [Fig. 5(a)]. Charge transfer channels and contact regions are defined in the field oxide using a sloped oxide technique; and a thinner SiO_2 layer (~1000Å) is deposited and defined by the previously described technique. Patterned Al_2O_3 is left only in those regions where isolation overhangs are desired [Fig. 5(c)]. Exposed oxide is thinned (to 1000Å in transfer regions) and the overhang ledge is produced. The second layer of Al_2O_3 (~500Å) is deposited for passivation and contact windows defined. Figure 6 depicts final insulator structure immediately prior to metalization.

Metalization of the CCD can be achieved by one of several approaches previously described. Here we will describe only one possible scheme. First, a Pd silicide is formed in the contact windows and, then, a Ti (~500Å) and Pd (~1000Å) layer is evaporated over the wafer. Photoresist is now applied for selective gold plating (Fig. 7), and gold is plated to a thickness of approximately one micron. When the gold plate is as thick as the isolation gap, shorting (or bridging) will

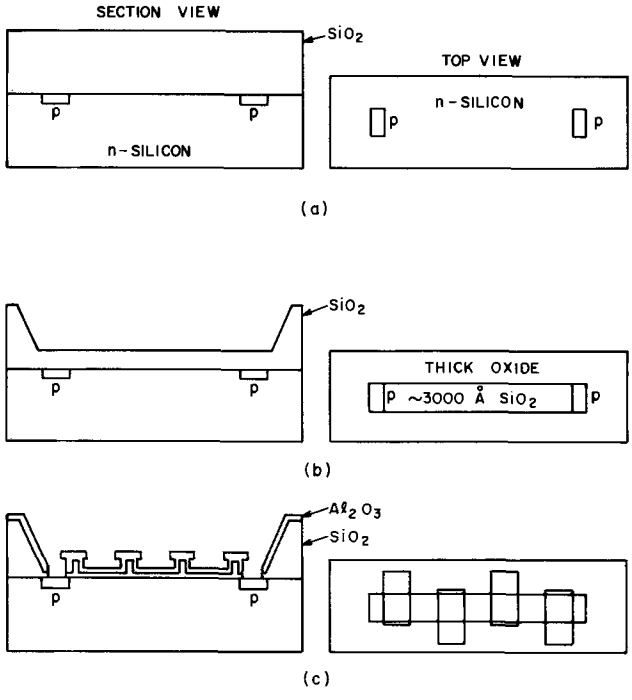

Fig. 5. Illustration of CCD fabrication steps prior to metalization.

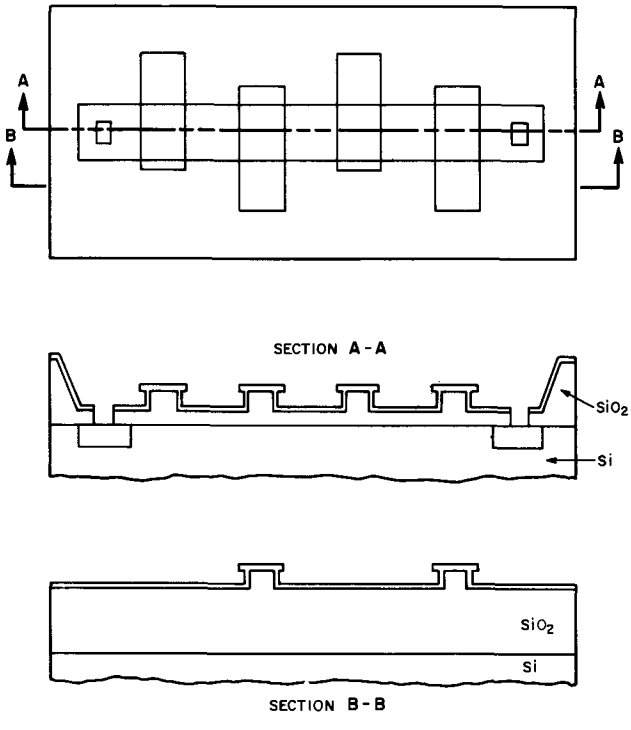

Fig. 6. Further details of CCD fabrication procedure prior to metalization.

occur between isolated and field regions, thereby yielding the selective interconnection desired. Necessary electrode structure for the two-phase CCD, an isolated overhang pad electrically connected to an adjacent metalization pad on the thinned insulator region is generated by selective etching of the Pd and Ti layer. Final device structure is illustrated in Fig. 8. A CCD has been fabricated along lines described here and is reported elsewhere (4).

Electrical characteristics.—Area per bit for the desired CCD structure is determined by minimum linewidths and spacings associated with photoresist technology. If a set of parallel CCD's is designed, then area per bit is given by

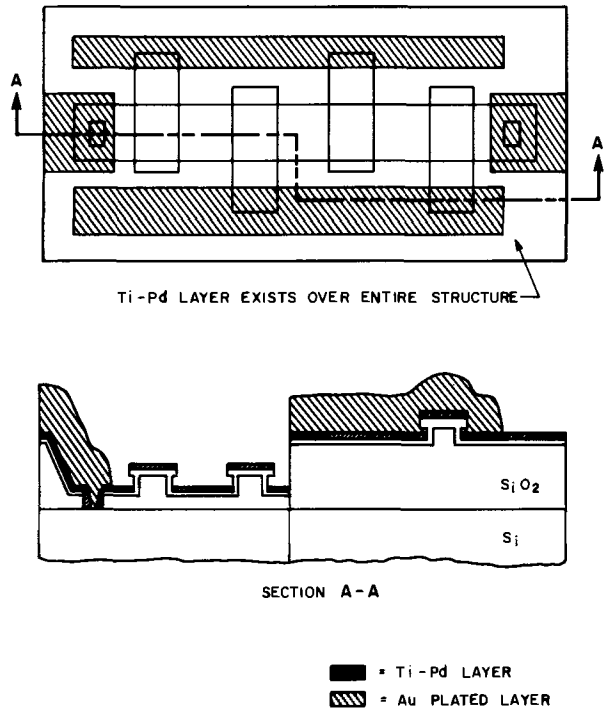

Fig. 7. Illustration of gold plating for selective electrical connection of isolated regions.

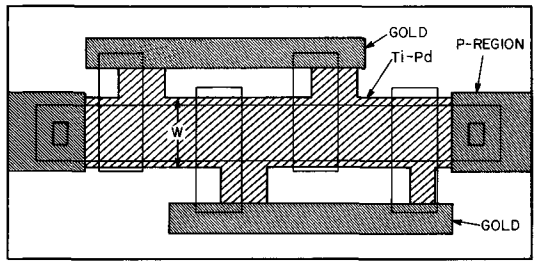

Fig. 8. Finished CCD

$$\text{Area/Bit} = (2/L)(W + F) \quad [2]$$

where L = minimum electrode width; W = minimum transfer channel width; and F = minimum field oxide width between adjacent channels. Assuming a standard 10.0μ (0.40 mil) photoresist technology, an 800μ^2 (1.28 mils^2) area/bit is realizable. This quantity compares favorably with various proposed CCD structures (10).

The most significant advantages of this device, however, are two fold. It is a completely self-aligned structure, which implies, with respect to its electrical characteristics: (*i*) the structure possesses maximum ratio of active signal storage area to total bit area obtainable; and (*ii*) performance of the basic CCD cell itself is not a function of, or sensitive to, photolithography realignment.

Device yield and manufacture considerations.—The contribution to process yield associated with the isolation overhang technique may be estimated for an n-bit CCD. Total isolated edge length per bit is given by $2(W + F)$. Consequently, probability of producing n good bits $P(n)$ is from Eq. [1] and [2] given by

$$P(n) = \exp[-2n(W + F)/l_o] = \exp(-n \cdot 10^{-3}) \quad [3]$$

where we have assumed a 10.0μ technology and l_o = 4.0 cm, (1024 bit CCD = >37% yield of CCD's with no metalization shorts at the undercut edge).

Conclusions

We have shown, using the (Al_2O_3-SiO_2) double insulator undercut system and titanium-palladium metalization, that reproducible electrical isolation between

adjacent metal patterns can be achieved. Using a simple MOS capacitor pattern, it has been possible to answer the important questions about the technique. It has been found that the excellent and reliable MOS properties of the (Al_2O_3-SiO_2) double insulator system have not been compromised by additional processing necessary for undercut isolation and that very high breakdown voltages exist between adjacent isolated metalization levels. One of the potential problems with the technique, unintentional shorts between adjacent metal lines, has been characterized and shown to be relatively unimportant.

The undercut isolation technique can and does possess many potential applications in integrated circuit design. As an immediate example, we have illustrated use of the technique for fabrication of a CCD. The described device has an area/bit smaller than, or equal to, any competing CCD and should possess superior electrical characteristics.

Manuscript submitted Nov. 30, 1972; revised manuscript received April 12, 1973.

Any discussion of this paper will appear in a Discussion Section to be published in the June 1974 JOURNAL.

REFERENCE

1. T. O. Mohr, *IBM J. Res. Develop.*, **14**, 142 (1970).
2. M. C. Driver, H. B. Kim, and D. L. Barrett, *Proc. IEEE*, **59**, 1244 (1971).
3. J. A. Appels and M. M. Paffen, *Philips Res. Rept.*, **26**, 157 (1971).
4. See for example, Y. Okinaka, R. Sard, W. H. Craft, and C. Wolowodiuk, Abstract No. 206, p. 509, Electrochem. Soc. Extended Abstracts, Fall Meeting, Miami Beach, Florida, Oct. 8-13, 1973; Y. Okinaka, R. Sard, W. H. Craft, and H. A. Waggener, Abstract No. 207, p. 512, *ibid.*; and C. N. Berglund, R. J. Powell, E. H. Nicollian, and J. T. Clemens, *Appl. Phys. Letters*, **20**, 413 (1972).
5. S. K. Tung and R. E. Caffrey, *Trans. Met. Soc. AIME*, **233**, 572 (1965).
6. M. P. Lepselter, *Bell System Tech. J.*, **45**, 233 (1966).
7. G. F. Amelio, W. J. Bertram, Jr., and M. F. Tompsett, *IEEE Trans. Electron Devices*, **ED-18**, 986 (1971).
8. R. H. Krambeck, *Bell System Tech. J.*, **50**, 3169 (1971).
9. D. Kahng and E. H. Nicollian, Patent No. 3651349, issued March, 1972.
10. C. N. Berglund and R. J. Strain, *Bell System Tech. J.*, **15**, 655 (1972).

Growth of High Purity CdTe Single Crystals by Vertical Zone Melting

R. Triboulet and Y. Marfaing

Laboratoire de Physique des Solides, C.N.R.S. (92) Meudon-Bellevue, France

ABSTRACT

The synthesis of CdTe in a Bridgman furnace, under determined vapor pressure of cadmium, and its purification by the vertical zone melting technique is described. The influence of the thermodynamic state of the crystals after synthesis on the conductivity type of the zone-melted purified material is shown. Purity, homogeneity, and compensation of the material, as determined by electrical measurements, photoluminescence, and spectrographic trace analysis, are presented and discussed.

The different applications of CdTe, as solar cells, electrooptic modulators, or γ-ray detectors, necessitate a carefully characterized pure material. On the other hand, the identification of native defects in CdTe, which is not a clearly solved problem, requires a material in which the foreign impurity concentration is lower than the native lattice defects concentration. Therefore, the preparation of a high purity material is of prime importance. For that purpose, different methods have been used: synthesis and crystallization from highly purified cadmium and tellurium (1); horizontal zone melting under vapor pressure of cadmium (2, 3); sublimation of the compound (4-6); crystal growth from Te solution, for instance by T.H.M. (7); and vertical zone melting by the Heumann method (8) applied to CdTe (9-11). It is this last method that we have used.

The preparation of the quartz tubes, the synthesis of the compound, and the zone-melting process will be successively described. The results concerning the purity, the time changes of the characteristics and the homogeneity will then be given. The segregation profiles will be finally studied by electrical measurements and photoluminescence.

Preparation and Purification of the Compound

Preparation of the tubes.—Metals generally react with silica to form silicates. With cadmium, at high temperature, there is formation of cadmium metasilicate $CdSiO_3$. This reaction is more intense when traces of cadmium oxide are present and, because the material sticks on the quartz walls, brings about, in addition to a contamination by the impurities included in silica, the breakage of the tubes. Consequently, it is of prime importance to avoid all direct contact of the silica with the material and to reduce any oxides. This is partly ensured by coating the inner surface of the quartz tubes with graphite.

For this purpose the tube is preliminarily cleaned for some minutes with a 25% aqueous solution of HF, rinsed in ultra pure water, and evacuated to 10^{-6} Torr for about twenty hours at 1150°C. It is then connected for some seconds with a container filled with ultra pure benzene, the vapors of which are drawn in and, by cracking, deposit graphite on the walls. The injection of benzene vapors is followed by fore-vacuum pumping. This process is repeated several times to deposit successive thin layers of graphite up to the desired thickness. The adhesive coating is then backed out under 10^{-6} Torr, at 1150°C, for several hours. After cooling, the rupture of vacuum is achieved by connecting the tube with a bag of very pure argon or hydrogen.

The elements, Cd and Te (99.9999% from Koch Light), are used in bars to limit their surface of contact with air during the manipulations. Cadmium is etched in a solution of 4% HNO_3 in ethanol, and tellurium is etched in diluted HCl. One hundred and sixty grams of Cd + Te are loaded into the 15 mm ID tube

Key words: Bridgman crystallization, electron mobility, photoluminescence, resistivity.

which includes a small container of cadmium in its upper part. The tube is sealed under 10^{-6} Torr. Its total length is then 30 cm. Two liquid nitrogen traps are inserted between the tube and the diffusion pump to avoid contamination by oil.

Synthesis of the compound.—The CdTe is synthesized, under a controlled vapor pressure of cadmium (3), in a Bridgman furnace, constituted by three superposed furnaces A, B, and C, as shown in Fig. 1. The temperature of the upper furnace A controls the vapor pressure of cadmium and allows one to use the solid-liquid vapor equilibrium to adjust the deviation from stoichiometry of the compound. A determined pressure of cadmium gives a determined composition of the compound. The temperature of this furnace is regulated by means of a thermocouple which is fastened to the top of the synthesis tube. Thus, this end remains always, for any position inside the furnace, at a constant temperature. The central furnace B is formed of six piled up refractory pancakes surrounding circular spiral resistances in Kanthal A1. These resistances are arranged so as to obtain, with a 20 cm high furnace, a temperature plateau of 12 cm at ±10°C. The temperature gradient at the solid-liquid interface is around 50°C/cm.

For the synthesis, the temperature of furnace B is progressively raised to about 800°C while the top of the tube is maintained at 500°C. Near 800°C the exothermic reaction of formation of the compound takes place. The temperature of furnace B can then be rapidly raised to 1120°C, while the temperature of furnace A is simultaneously adjusted to give the desired vapor pressure. The temperature of furnace C is set at 850° ± 20°C. The tube is subsequently slowly lowered into the furnace at a rate of 0.3 cm/hr. After this normal freezing, which gives an impurity segregation along the ingot, the lower furnace C is slowly cooled to room temperature, in 24 hr, by a controlled program, to limit the dislocation density in the material.

For temperatures of the upper furnace higher than 820°C, the obtained crystals are generally n-type, while for temperatures lower than 800°C, the crystals are generally p-type. The intermediate temperature range corresponds to high resistivity material. These data, in agreement with those of Ref. (1), are notably influenced by the nature and the concentration of impurities.

Zone melting.—After synthesis the thickness of the graphite layer has diminished as consequence of reaction with oxides. The ingot is taken out of the tube which, for this procedure, has been chosen slightly conic. The same tube is cleaned, backed out, and graphitized again as described above. This new layer prevents, as much as possible, the CdTe from being in contact with silica, although diffusion can probably exist between silica and CdTe across this stratified layer. The best results have been obtained with the Heraeus "Heralux" quality tubes. The tube is then loaded with the ingot, evacuated to 10^{-6} Torr, and sealed with a quartz plug positioned to rest on the ingot.

The tube is then placed in the zoning apparatus (Fig. 2). The temperature of the graphite susceptor ring is regulated with a precision of ±0.5°C and controlled by a thermocouple. The temperature is adjusted by substituting for the zone melting tube a thermal analysis tube of the same dimensions, with a thermocouple. We have chosen a temperature of about twenty degrees above the melting point of CdTe: the molten zone is then approximately one centimeter wide.

As a consequence of the reaction of oxides with graphite, the periphery of the ingot presents small gas pockets, hence a first pass is performed at 4 cm/hr for a better filling of the tube. The following passes (10-20 generally) are carried out at rates between 2.5 and 0.25 cm/hr and stopped at 2 cm from the top of the ingot. The vapors of Cd and Te produce a self-sealing of the end of the ingot which completely isolates it

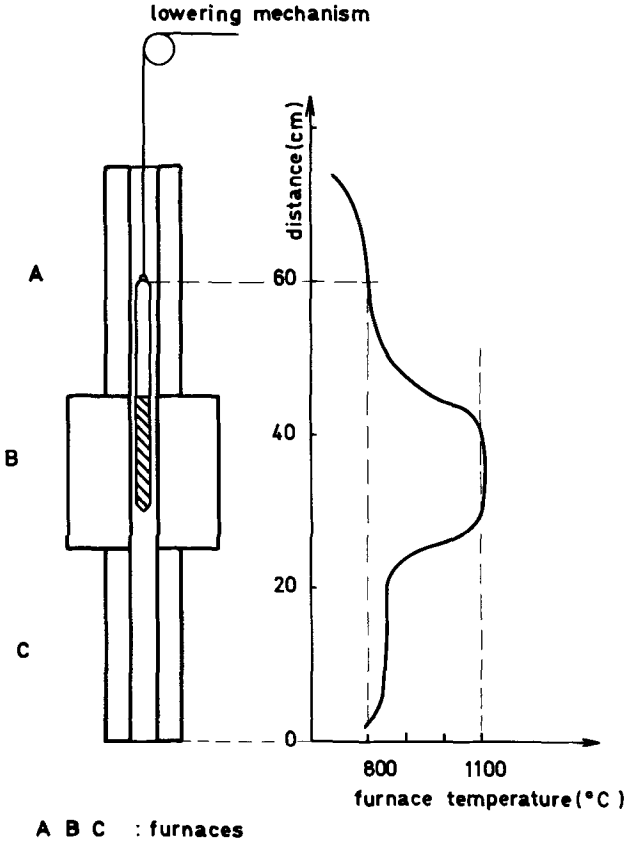

Fig. 1. Schematic diagram of the Bridgman furnace and of its temperature profile.

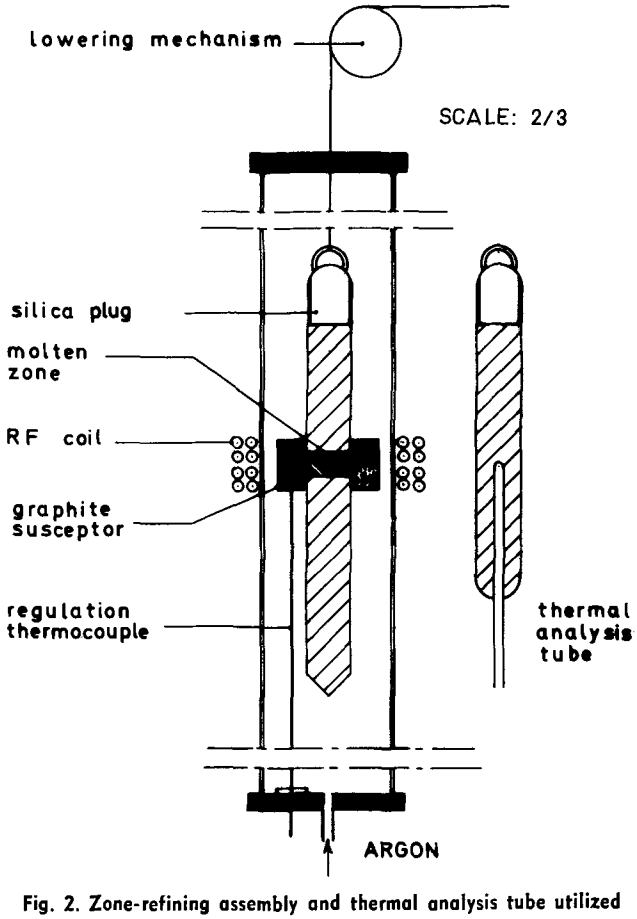

Fig. 2. Zone-refining assembly and thermal analysis tube utilized to adjust the molten zone temperature.

from the small void space at the upper part of the tube. The ingots so obtained contain large single crystals, about 2-3 cm^3 in size.

Results

Conductivity type of the crystals.—Woodbury and Lewandowski (11) have found a relation between the susceptor temperature and the conductivity type of the crystals: for temperatures higher than 1200°C, the crystals are p-type, and for temperatures lower than 1160°C, n-type. They do not find any obvious correlation between resistivity and susceptor temperature in the intermediate range.

Our zone melting has always been carried out at a liquid temperature of about 1115°C (susceptor temperature 1170°C). Under these conditions, the characteristics of the material, after zone melting, seem to depend on the initial state of the material, *i.e.*, the vapor pressure of cadmium during the Bridgman growth. Thus, for vapor pressures of cadmium lying between 2 and 2.8 atm (upper Bridgman furnace temperature 820°-850°C), the material is n-type with a resistivity between 10-500 ohm-cm, and an electron concentration between 1.5×10^{13} to 8×10^{14} cm^{-3} at room temperature. A vapor pressure of one atmosphere (upper furnace temperature 760°C) corresponds after zone melting to a high resistivity p-type material. So, although the equilibrium reached during zone melting tends to reduce the departure from stoichiometry, the history of the material, *i.e.*, the thermodynamic conditions of its synthesis, should be taken into consideration. As a matter of fact, according to our experimental process, it is possible to get a material of very reproducible characteristics.

Purity.—Emission spectrography was used to follow the segregation of impurities. The amounts of Si, Ca, and Mg do not vary along the ingots while Cu, Fe, and Ag segregate to the end of the ingots. These impurities were the only ones detected by this method.

Qualitative analysis by means of ionic probe reveals the presence of Al, Na, Cl, F, K, Co, Fe, and Si, depending on the samples.

Mass spectrometry analysis was conducted; for most of the elements the limit of detection was around 0.5 ppm. Numerous elements could not be measured because of associations and interferences. One found a large concentration of C (a few ten ppm) and small amounts (around one ppm) of S, Na, and K.

One of the most typical results of trace analysis is that distribution profiles of impurities along the ingots are not clearly seen if the analyzed samples are of a larger size. This suggests the presence of inhomogeneities and the coexistence of pure and impure regions at short distance. The main acceptor impurities seem to be copper and sodium and the residual donor impurities could be the halogens and aluminum.

Because of the sensitivity limitations of spectrographic methods and the difficulties of bringing them into play, electrical measurements were currently used to determine purity.

The electrical measurements data for some of the purest samples are summarized in Table I.

Mobilities of $\sim 10^5$ cm^2/V sec at 32°K—the maximum of the mobility curve, probably located at about 20°K, is not still reached at this temperature—are the highest mobilities measured until now in cadmium telluride.

Some curves of mobility *vs.* temperature are plotted on Fig. 3. Curve 1 corresponds to one of our purest

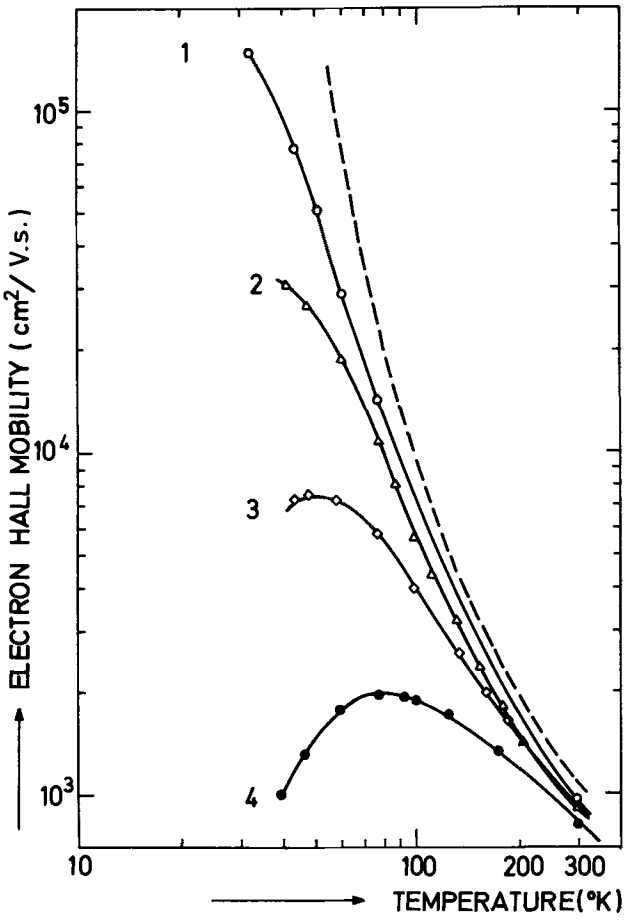

Fig. 3. Electron mobility *vs.* temperature for samples cut from the head (1) to the end (4) of vertical zone melted ingots.

samples (24A5) with $\mu_{32°K} = 1.46 \times 10^5$ cm^2/V sec.[1] The dashed curve represents the theoretical curve calculated for a scattering by LO phonons by Segall *et al.* (12). The following curves, 2, 3, and 4, are related to samples of decreasing purity, *i.e.*, samples taken in less pure parts of an ingot. The maximum of the mobility curve shifts towards higher temperatures when the purity decreases.

Figure 4 represents the photoluminescence spectrum of a pure sample (16A12). This spectrum is characteristic of a high purity and uncompensated sample.

The intensity of the free exciton line (1.596 eV), which is self-absorbed in the crystal, is remarkably high. The one and two LO phonon replicas are at 1.575 and 1.554 eV. The line at 1.594 eV is attributed to excitons trapped on neutral hydrogenic donors at $E_c - 0.011$ eV (13, 14). By comparison, the line at 1.591 eV, which is associated to a neutral acceptor-exciton complex, with $E_A = E_V + 0.05$ eV, is very weak. Only a weak line at 1.540 eV emerges in the 1.550 eV region, generally rich in impurity transitions (15).

This spectrum shows also a line at 1.605 eV which probably corresponds to the radiative band-to-band transition and its first phonon replica at 1.584 eV. These lines, never seen before, constitute another proof of

[1] On such samples, a total concentration of electrically active centers around 10^{14} cm^{-3} has been determined by M. Caillot (Private communication).

Table I

Name	$n_{300°K}$, cm^{-3}	$\rho_{300°K}$, ohm-cm	$\mu_{300°K}$, cm^2/V sec	$n_{32°K}$, cm^{-3}	$\rho_{32°K}$, ohm-cm	$\mu_{32°K}$, cm^2/V sec
16A2	1.45×10^{13}	390	1100	7.4×10^{12}	8.3	1.03×10^5
17A6	2.7×10^{13}	279	830	1.5×10^{13}	4.59	9×10^4
24A7	4.95×10^{13}	123	1020	1.65×10^{13}	3.36	1.13×10^5
24A5	5.1×10^{13}	130	950	1.65×10^{13}	2.6	1.46×10^5
15A3	7.2×10^{13}	81	1075	4.6×10^{13}	1.58	8.6×10^4
14A13	5.8×10^{14}	10	1080	2.16×10^{14}	0.32	9.1×10^4

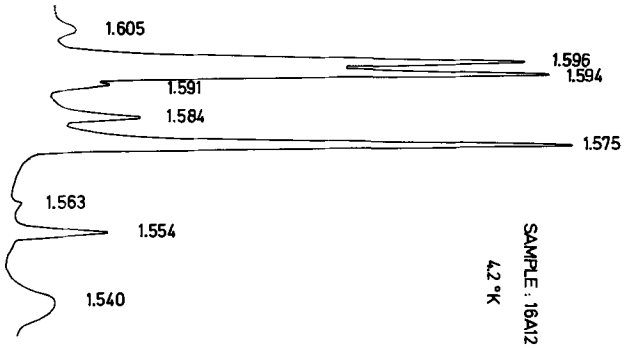

Fig. 4. Photoluminescence spectrum of a high purity sample at liquid helium temperature.

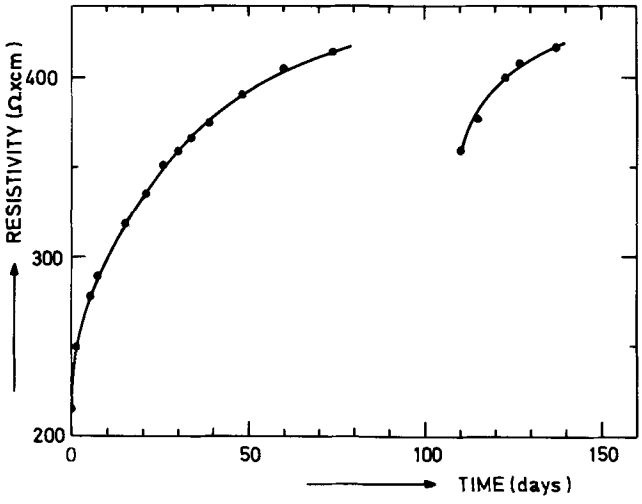

Fig. 5. Change of the resistivity with time of a sample kept under vacuum during the first 0-80 day period, in the atmosphere during the following 80-110 day period, and put again under vacuum during the last period.

the high quality of the crystals and permit a direct measurement of the cadmium telluride bandgap at 4.2°K.

By comparison, the spectra of less pure samples present the following characteristics: the band-to-band transition is not seen; the free exciton line is weak or absent; the bound exciton line at 1.591 eV, which may be related to the presence of shallow acceptor impurities, is very strong; while in the 1.550 eV region, intense broad lines emerge corresponding to donor acceptor-pair transitions.

Instability of the sample characteristics.—We have observed a shift, with time, of the characteristics of the purest zone-melted samples of low electron concentration, corresponding to an increase in compensation (11): both the electron mobility and concentration decrease. These changes are very accelerated by heating even at moderate temperatures. As an example, the dependence of the resistivity at room temperature *vs.* time t for a sample first kept under static vacuum (10^{-2} Torr) after contact soldering has been plotted on Fig. 5. For the first 80 days the resistivity increases with time. During the subsequent period (80-110 days) the sample is exposed to air and its resistivity decreases. When the sample is put again under vacuum its resistivity tends to recover the high values measured at the end of the first stage. This experiment shows the strong influence of the ambient conditions on the electrical properties. The variation of electron concentration during the first period follows the law: $n = A - B \log t$, which could be interpreted in terms of a chemisorption phenomenon (16).

Homogeneity.—The statistical dispersion of the electrical characteristics of samples cut in the pure part (2 cm) of an ingot has been studied. In Fig. 6 is presented the statistical distribution of mobilities at 35°K and of carrier concentrations at room temperature for about fifteen samples.

The mobilities at 35°K, which are close to the maximum of the mobility curve, have more scattered values than the room temperature carrier concentrations. $n_{300°K}$ is equivalent to $N_D - N_A$ while the low temperature mobility is limited by the total concentration $N_D + N_A$. It appears that $N_D + N_A$ can largely fluctuate from one sample to another, while $N_D - N_A$ changes weakly. This can be explained by self-compensation between impurities and native defects.

Some samples present an abnormally low mobility at room temperature. These effects have been attributed by different authors (17, 18) to the existence of microinhomogeneities in the material. The electronic mobility at room temperature, *vs.* the ratio of the carrier concentrations at 300°-35°K, has been plotted in Fig. 7. The greater this ratio, the lower is the mobility. This is an indication that microhomogeneities are to be related to the presence of trapping levels in which electrons freeze out when temperature decreases.

Impurities Segregation, Results and Discussion

The distribution profiles of impurities in ingots obtained after 2, 10, and 20 passes, have been studied by means of electrical measurements and photoluminescence.

Figure 8 gives the electron mobility at 35°K *vs.* the distance along the ingot axis for ingots grown with 2,

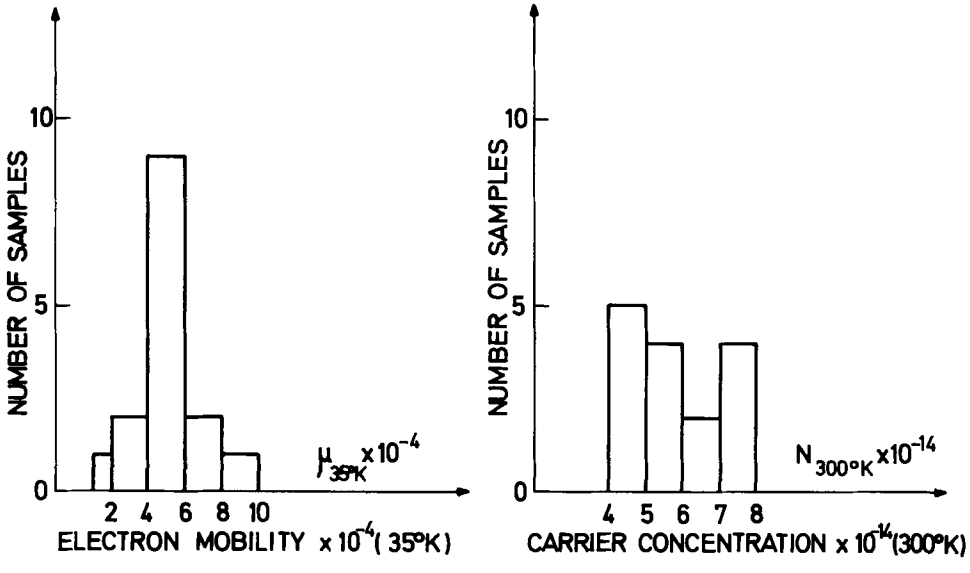

Fig. 6. Statistical distribution of the electron mobilities at 35°K and of the carrier concentrations at room temperature for 15 samples cut in the purest part of a vertical zone melted ingot.

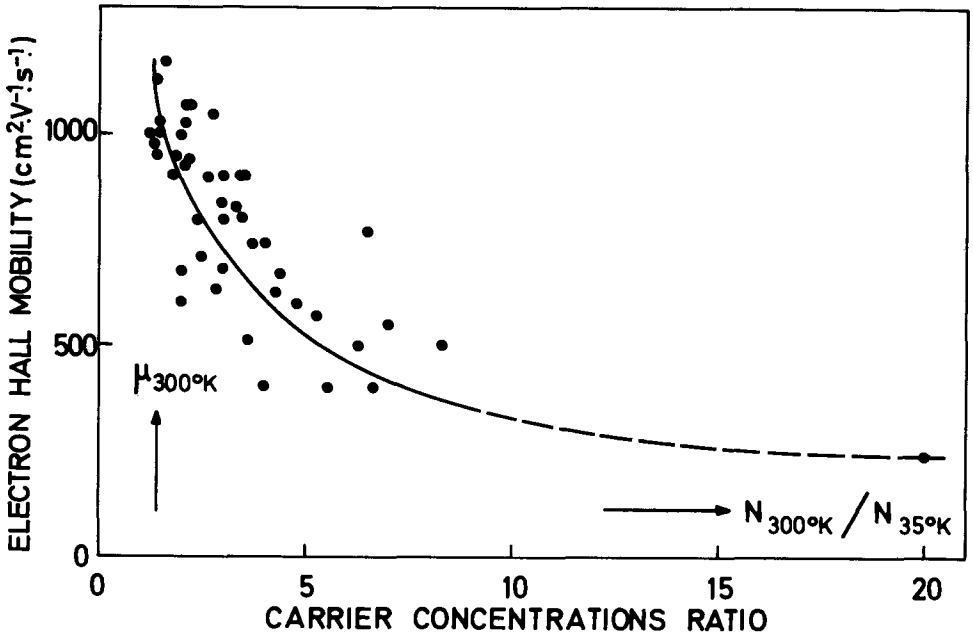

Fig. 7. The room temperature electron mobility vs. the carrier concentrations ratio at 300° and 35°K.

10, and 20 passes. These profiles cannot be directly compared to the classical impurities distributions obtained after zone melting. They are in fact the result of zone melting superposed upon normal freezing for the whole distribution of impurities. High mobilities are rapidly reached in the first part of the ingots. Some ingots, after 10 passes, already present mobilities up to 10^5 cm²/V sec. The increase in the number of passes has more the effect of increasing the length of the purest part of the ingot (2/3 of the ingot after 20 passes) rather than of improving the purity which seems to reach a limit value probably depending on a contamination-purification equilibrium.

Considering the impurities distribution coefficient values in CdTe (generally ranging between 0.2 and 0.5), zone-melting purification is not sufficient to explain the fairly high mobilities measured after only 2 passes, whereas our Bridgman-grown material does not present mobilities higher than 5×10^3 cm²/V sec at low temperatures. One can think that, in these samples, impurities assemble to form highly compensated microinhomogeneities, which explain the high mobilities found at low temperatures. On the other hand the additional scattering, brought about by these heterogeneities, causes small mobility values at room temperature (between 240 and 700 cm²/V sec). Thus the low temperature mobility would be significant of purity only if the theoretical mobility value is observed at room temperature ($\sim 10^3$ cm²/V sec).

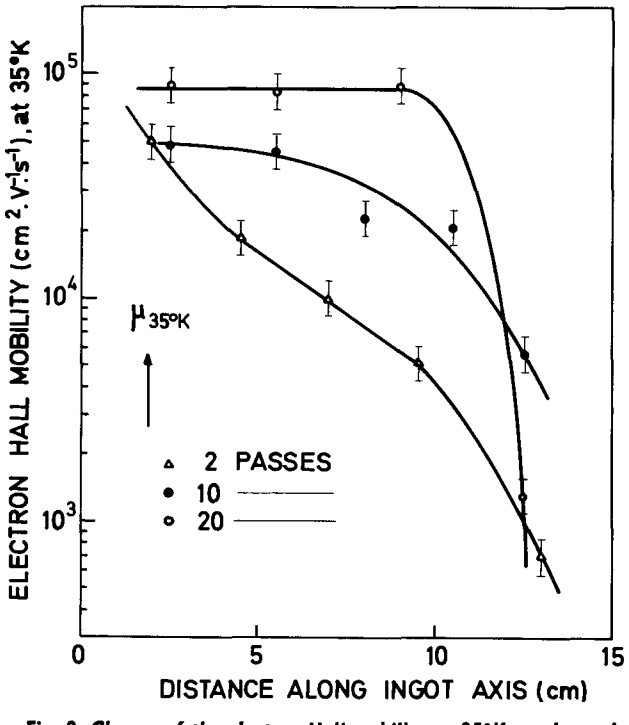

Fig. 8. Change of the electron Hall mobility at 35°K on the position of the samples along the ingot growth axis.

Another marked effect on low temperature mobilities is probably the departure from stoichiometry which can be high in CdTe: $\sim 10^{20}$ at cm^{-3} from each side of the stoichiometric composition (19, 20). In fact, some observations suggest that, due to the particular equilibrium reached during the process, the material approaches the stoichiometric composition: indeed, it is habitual to find some cadmium—or tellurium as the case may be—around the zone-melted ingots.

The carrier concentration *vs.* the position of the samples along the ingot is plotted in Fig. 9. The variation range is not very important. However a rather strong dispersion is observed, which reflects the fluctuations in compensation.

The ratio between the intensity of the two impurities-bound exciton lines at 1.594 and 1.591 eV, seen in photoluminescence, *vs.* the distance along the ingot axis is plotted in Fig. 10. This ratio is very sensitive to purity. The intensity of the line at 1.594 eV is related to the concentration of the donors which are neutralized under light excitation at helium temperature, *i.e.*, N_D, while the intensity of the 1.591 eV line is for the same reason related to the acceptor concentration, N_A. The variations of the 1.594 eV line follow roughly these of $n_{300°K}$ as it is observed: in the ingots grown with 10 and 20 passes its intensity varies little with sample position. On the contrary, the line at 1.591 eV is multiplied by a factor 25-250 from the tip to the top of the ingots, depending on the ingots. This line is associated to a compensating acceptor center probably involving impurities.

The ratio $I_{1.594}/I_{1.591}$ is thus close to the ratio N_D/N_A and characterizes the compensation state of the material.

Conclusion

Very pure crystals have been prepared by the vertical zone melting method, as confirmed by electrical and photoluminescence measurements; low temperature electron mobilities above 10^5 cm²/V sec were found, while in photoluminescence the band-to-band radiative transition is seen at low temperature.

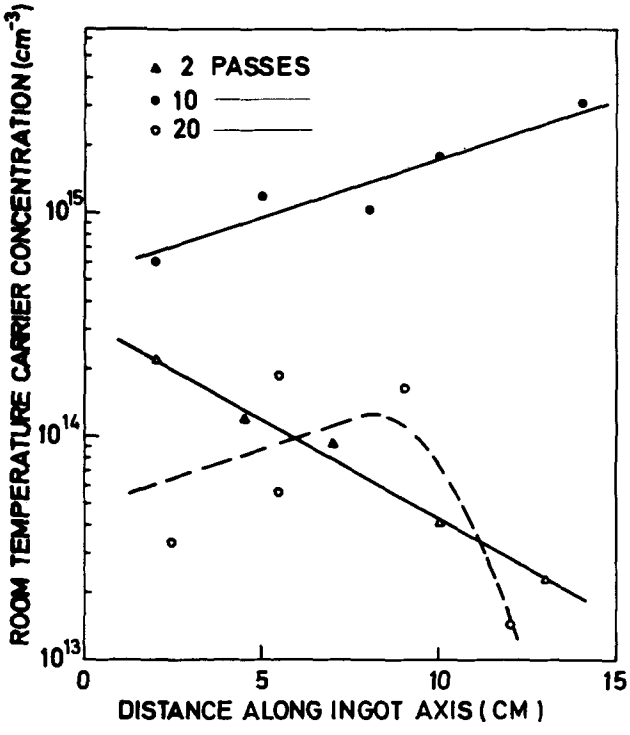

Fig. 9. The room temperature carrier concentration vs. the position of the samples along the ingot growth axis.

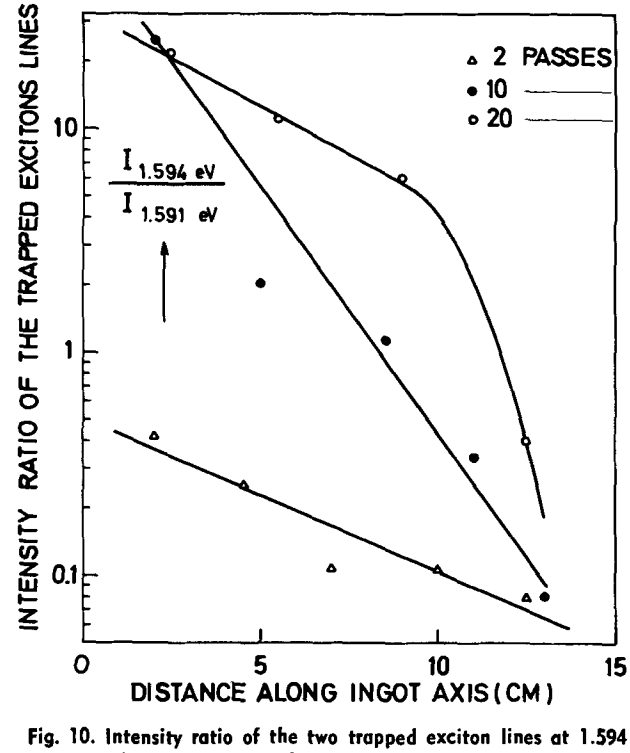

Fig. 10. Intensity ratio of the two trapped exciton lines at 1.594 and 1.591 eV vs. the position of the samples along the ingot axis.

The following points seem to be determinative in the results of our purification: the particular care taken in the preparation of the quartz tubes; the synthesis and Bridgman crystallization performed under determined thermodynamic conditions; all the operations, from synthesis to zone melting, achieved in the same quartz tube (the manipulations, always corresponding to pollution, are thus reduced to the minimum); and the temperature of the melted zone fixed and known with precision.

We suggest that the purity reaches a limiting value depending on a contamination-purification equilibrium and that microinhomogeneities can explain, in some materials, the simultaneous occurrence of low mobilities at room temperature and abnormally high mobilities at low temperature. Thus low temperature mobility is indicative of purity only when the theoretical room temperature mobility is observed.

The ratio of the intensity of two exciton lines at 1.594 and 1.591 eV is shown to characterize the compensation state of the material.

The conductivity type of the zone-melted samples depends on the thermodynamic state of the material after synthesis. This state is controlled by the vapor pressure of cadmium during the preliminary Bridgman growth.

Thus it appears possible, by the vertical zone melting method, to obtain a high resistivity material suitable for different applications, by a correct adjustment of this vapor pressure.

However, this material brings up problems of stability, compensation, and inhomogeneities which need further studies.

Acknowledgments

The authors wish to thank G. Didier for his skillful assistance in the preparation of the crystals. We also thank S. Godefroy of C.N.E.T. and J. Rioux for the spectrographic traces analysis.

Manuscript submitted Jan. 22, 1973; revised manuscript received March 30, 1973.

Any discussion of this paper will appear in a Discussion Section to be published in the June 1974 JOURNAL.

REFERENCES

1. C. A. Medvedev, C. N. Maximovsky, U. V. Klevkov, and P. V. Chapkine, *Tellurid Kadmiya, Izd. Nauka, Moscou*, 7 (1968).
2. D. de Nobel, *Philips Res. Rept.*, **14**, 361 (1959).
3. R. Triboulet and H. Rodot, *Compt. Rend.*, **266**, 498 (1968).
4. P. Hoschl and C. Konak, *Czech. J. Phys. B.*, **13**, 785 (1963).
5. W. Akutagawa and K. Zanio, *J. Cryst. Growth*, **11**, 191 (1971).
6. N. R. Kyle, Proc. International Symp. on CdTe, P. Siffert and A. Cornet, Editors, Strasbourg, France, 1971.
7. R. O. Bell, N. Hemmat and F. Wald, *Phys. Status Solidi (a)*, **1**, 375 (1970).
8. F. K. Heumann, *This Journal*, **109**, 345 (1962).
9. M. R. Lorenz and R. E. Halsted, *ibid.*, **110**, 343 (1963).
10. A. Cornet, P. Siffert, and A. Coche, *J. Cryst. Growth*, **7**, 329 (1970).
11. H. H. Woodbury and R. S. Lewandowski, *ibid.*, **10**, 6 (1971).
12. B. Segall, M. R. Lorenz, and R. E. Halsted, *Phys. Rev.*, **129**, 2471 (1963).
13. J. P. Noblanc, J. Loudette, and G. Duraffourg, *Phys. Status Solidi*, **32**, 281, (1969).
14. J. P. Noblanc, J. Loudette, and G. Duraffourg, Proc. Conf. Luminescence, Newark, N. J. (1969).
15. R. Triboulet, Y. Marfaing, and M. E. Burgos, *Phys. Status Solidi (a)*, **2**, 851 (1970).
16. P. Mark, *RCA Rev.*, **26**, 461 (1965).
17. L. R. Weisberg, *J. Appl. Phys.*, **33**, 1817 (1962).
18. M. V. Alekseenko, E. N. Arkad'eva, and O. A. Matveev, *Soviet Phys.-Semicond.*, **4**, 349 (1970).
19. S. A. Metvedev, K. V. Kiseleva, N. N. Senturina, S. N. Maximovsky, and Y. V. Kleykov, Proc International Symp. on CdTe, P. Siffert and A. Cornet, Editors, Strasbourg, France, 1971.
20. R. F. Brebrick, *This Journal*, **118**, 2014 (1971).

Oxidized Boron Nitride Wafers as an *In-Situ* Boron Dopant for Silicon Diffusions

David Rupprecht*,[1] and Joseph Stach**

Solid State Device Laboratory, Electrical Engineering Department, The Pennsylvania State University, University Park, Pennsylvania 16802

ABSTRACT

Hot-pressed 93% boron nitride wafers when properly oxidized and used as an *in situ* boron dopant in open-tube silicon diffusions are capable of providing sheet resistance tolerances of ±1-2% across a silicon wafer and ±4% within a run and from run to run. Although for the experimental conditions studied silicon sheet resistance variations were not expected to be a function of diffusion ambient, ambient flow rate, or source to silicon spacing the contrary was found to be true and the relationships opposite to that intuitively expected. By correlating sheet resistance, impurity profiles, and ellipsometric measurements the observed dependence of sheet resistance *vs.* ambient, ambient flow rate, and source to silicon spacing is explained in terms of Si-B phase formation.

The use of boron nitride (BN) wafers as a diffusion source for p-n junctions in silicon has been investigated by Goldsmith *et al.* (1) in view of efficient manufacturing techniques and employed by Nicholas (2) as a boron source for the study of anomalous diffusion in silicon. In review, Goldsmith *et al.* (1) have indicated that boron nitride wafers when oxidized and employed as in Fig. 1 provide (*a*) equal impurity mass transfer to all silicon wafers regardless of position within diffusion boat, (*b*) equal impurity mass transfer to all portions of a silicon wafer, (c) low temperature diffusion capabilities, and (*d*) the absence of carrier gas mixing or composition problems. Nicholas (2) was primarily concerned with the anomalous diffusion mechanism and considered his results not specific to the use of a BN source. It is the purpose of this report to contribute additional data and to further discuss the consequences of a boron nitride wafer source on diffusion.

* Electrochemical Society Student Associate.
** Electrochemical Society Active Member.
[1] Present address: AMI, Santa Clara, California 95050.
Key words: boron nitride, *in-situ* dopant, Si-B phase.
[2] The Carborundum Company, Niagara Falls, New York.

Table I. Important physical properties of grade A BN

Physical products	Grade A
Chemical composition	
Boron	41.50%
Nitrogen	52.00
Oxygen	4.0-6.0
Boric oxide	5.0-8.0
Carbon	<0.05
Calcium	<0.20
Chloride	<0.10
Other	<0.20
Silica	—
Density, g/cm³	2.08
Maximum use temp.	
Inert atmosphere	>275°C
Oxidizing atmosphere	985°C
Water absorption	
% wt gain in 168 hr, 25°C, 80% RH	1.1

Experimental

The material employed in this investigation was Carborundum Grade A boron nitride (ABN) wafers[2] and the important physical properties are as outlined in Table I. The material as received is chemically stable and requires an oxidation step prior to sourcing (1). Cleaning and oxidation procedures to prepare ABN wafers as a boron source were decided upon after several depositions were performed with wafers as received. Poor cosmetic appearance of the ABN after high-temperature deposition coupled with erratic silicon sheet resistance readings indicated a need for more precise control of the ABN's history prior to deposition.

The cleaning procedure chosen is outlined in Table II and was based on the following goals: (*a*) degreasing of an ABN wafer and (*b*) development of a virgin surface. Methanol treatments were avoided in cleaning because of loss of wafer physical strength due to the solvation of the boric oxide binder material used in hot pressing the ABN wafers (3).

Simultaneous development of the source during deposition was deemed imprudent after a review of potentially analogous BBr_3 reaction rate problems as discussed by Parekh and Goldstein (4), and a separate oxidation step preceding deposition was initiated in which precise control of a volatile boron source could

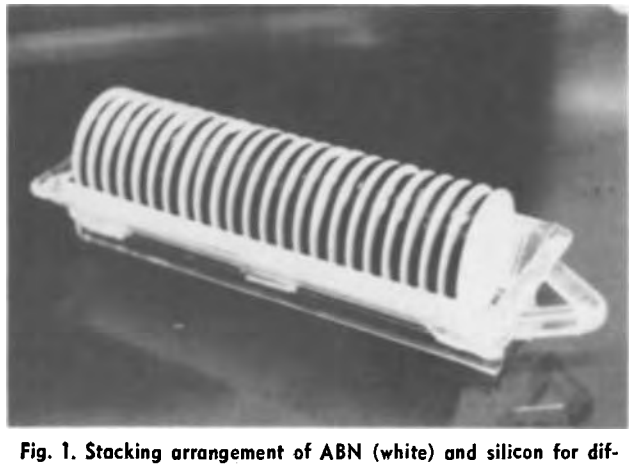

Fig. 1. Stacking arrangement of ABN (white) and silicon for diffusion.

Table II. Preparation and maintenance of ABN

Cleaning	a. Degreasing: Trichlorethylene, 60°C, 3 min; acetone, 40°C, 3 min; DI H_2O rinse, 3 min b. Prep. of virgin surface: Conc HF, 23°C, 1 min; DI H_2O rinse, until rinse water 10 megohm; dry at 345°C, 30 min
Oxidation	a. Temperature: at desired deposition temperature b. Time: 15 min c. Ambient: 0.5 to 1.0 lpm dry O_2
Storage	a. When: when not using material as a source b. Where: vestibule of furnace if capped
Reoxidation	a. When: 15 min daily b. How: follow oxidation; no additional cleaning required.

be obtained. The oxidation procedure was based on thermogravimetric data, TGA, (5) compiled at 950°C, Fig. 2. The TGA data is presented as a log-log plot of net weight increase (decrease) of the ABN wafer as a function of time and gaseous ambient.

The slope (m) of the oxidation curve equals 0.86. The two controlling extremes, reaction rate limitation of oxide growth, $m = 1$, and diffusion rate limitation, $m = 0.5$, are also plotted. Comparison of the experimental slope to these extremes suggests a reaction rate limited oxide growth for BN in dry O_2[3] for the time and temperature studied. Evaluation of the data yields the following mathematical representation of oxidation of BN and volatilization of oxidized BN in dry N_2 at 950°C

$$W_I = 0.35t^{+0.86} \quad [1]$$

$$W_D = 0.25t^{-0.40} \quad [2]$$

where W_I = per cent weight increase of BN in dry O_2, W_D = per cent weight decrease of oxidized BN in dry N_2, and t = time in hours.

Extrapolating from the volatilization in dry N_2 data, reoxidation of source should not be required until after 2000 hr of continuous usage (approximately 80 days). No attempt was made to verify this sourcing life-time.

Assuming ideal gas behavior and applying a straight line approximation to the weight loss data, the dynamic vapor pressure of the volatilizing species, assumed to be B_2O_3, can be obtained from the following equation

$$P_{BN} = \frac{N_{BN}}{N_G} P_T \quad [3]$$

where P_{BN} = dynamic vapor pressure of oxidized BN, N_{BN} = moles of oxidized BN vaporized per unit time, N_G = moles of gas passing sample per unit time, and P_T = total pressure. For values obtained from weight loss data, $N_{BN} = 4.73 \times 10^{-6}$ moles/hr, $N_G = 9.6 \times 10^{-2}$ moles/hr

$$P_{BN} = 4.93 \times 10^{-5} \text{ atm}$$

Comparison of this value to extrapolated values of B_2O_3 vapor pressure obtained from Speiser *et al.* (7) and Soulen *et al.* (8) suggests that the volatile species is not totally composed of B_2O_3 vapor pressure at 950°C of 3×10^{-7} atm.

Work by Randall and Margrave (6) on vapor equilibrium in the B_2O_3-H_2O system indicates significant increases in vapor pressure of B_2O_3 for ambients containing 1% H_2O. Extrapolation from their work at 1000°C indicates that for approximately 300 ppm H_2O the observed vapor pressure of hydrated B_2O_3 in the form of HBO_2 is approximately 5×10^{-5} atm. Spectrographic analysis of the volatilized vapor confirms that the significant vapor species is HBO_2. The expected oxidation and deposition reactions from this information are proposed as follows:

$$\text{Oxidation: } 2BN + 3O_2 \rightarrow 2B_2O_3 + 2N_2 \quad [4a]$$

$$B_2O_3 + H_2O \rightarrow 2HBO_2 \quad [4b]$$

$$\text{Deposition: } 2HBO_2 + 2Si \rightarrow 2SiO_2 + 2B + H_2 \quad [5]$$

Elevated temperature storage of the ABN wafers after oxidation is necessary because of boric oxide's great affinity for water vapor (9). No reasonable degree of tolerance with respect to sheet resistance could be obtained with ABN wafers stored at room temperature and room humidity. As such the ABN wafers when not in use were stored in the mouth of the diffusion tube with dry N_2 flushing the diffusion tube at all times. Figure 3 schematically represents ABN wafers after oxidation and their relationship to silicon wafers.

Table II summarizes preparation of ABN as a diffusion source. While the extrapolated time between reoxidation of source is long, the authors chose to reoxidize daily for 15 min. Recent work by Assour (10) suggests that potential purity problems associated with ABN can be minimized with frequent reoxidations.

Experimental conditions pertaining to deposition work are as follows. All depositions were performed with 1.5 in. BN and silicon wafers in a 60 mm ID quartz tube, three-zone furnace capable of ±1.0°C, and 15 in. flat zone. The silicon consisted of a 3-7 ohm-cm arsenic-doped, 8-10μ thick epitaxial layer on (111) 0.013 ohm-cm maximum arsenic-doped substrate. Deposition performance was ascertained with sheet resistance measurements, ρ_s, and profiles. The four-point probe employed consisted of a linear array tungsten carbide probe of 0.04 mm ±10% tip radius, 1.00 mm spacing, 200g ± 2% loading, and a resistivity tester consisting of a 0.001-10 mA ±0.1% of full scale current source, and 0-20 mV ±0.5% of full scale digital voltmeter. Sheet resistance data, ρ_s, was generated by probing the diffused silicon in five areas, (top, bottom, left, right, and center) and then averaging these values. Where the symbol $\bar{\rho}_s$ appears, several ρ_s's have been averaged. To adequately characterize the BN deposition system in terms of process variables the following tests

[3] Air Products brand of bottled O_2, consisting of less than 0.5 ppm total hydrocarbon content; other constituents such as water vapor not provided.

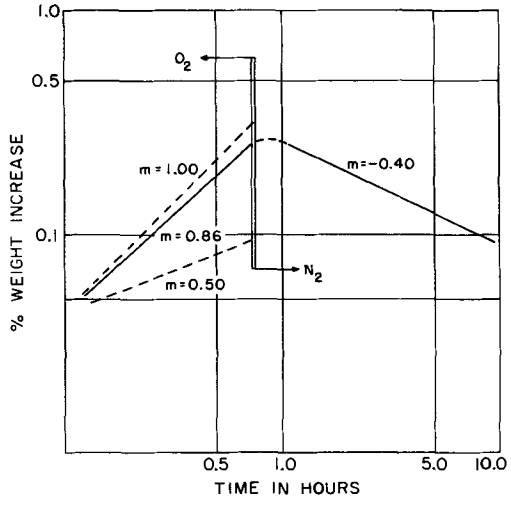

Fig. 2. Log-log plot of TGA data at 950°C

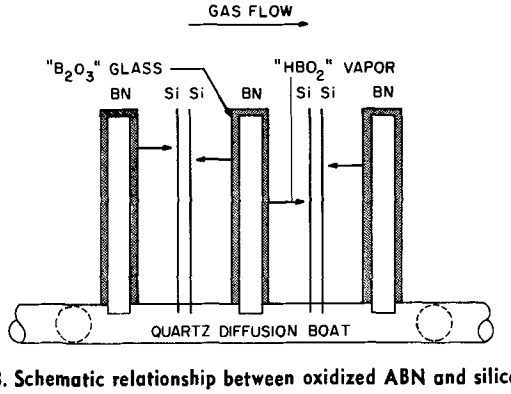

Fig. 3. Schematic relationship between oxidized ABN and silicon

were performed: (*a*) ρ_s *vs.* flow rate, (*b*) ρ_s *vs.* spacing, (*c*) ρ_s *vs.* ambient, (*d*) doping concentration *vs.* penetration, (*e*) ρ_s *vs.* run number, and (*f*) ρ_s *vs.* time, temperature; except where noted all diffusions were performed with the stacking arrangement depicted in Fig. 1, temperature = 950°C, diffusion time = 30 min, dry N_2 ambient at 0.45 standard liters/min, and silicon to BN spacing nominally 125 mils center to center.

Results and Discussion

To better understand the mechanism of mass transport of HBO_2 from BN to silicon the following process variables were investigated: (*a*) $\bar{\rho}_s$ *vs.* flow rate, Fig. 4; (*b*) $\bar{\rho}_s$ *vs.* BN to silicon spacing, Fig 5; and (*c*) $\bar{\rho}_s$ *vs.* ambient, Fig. 6. The data contained in these figures are

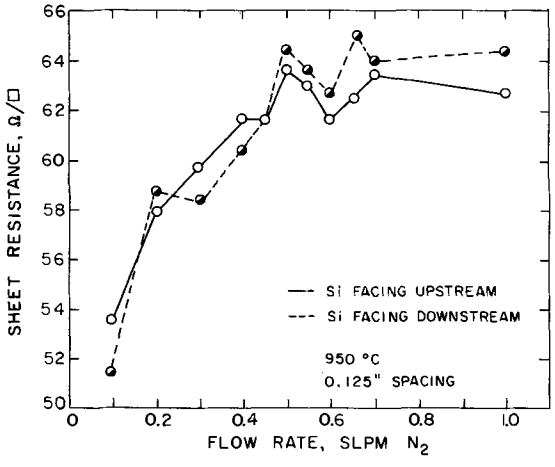

Fig. 4. Sheet resistance vs. flow rate

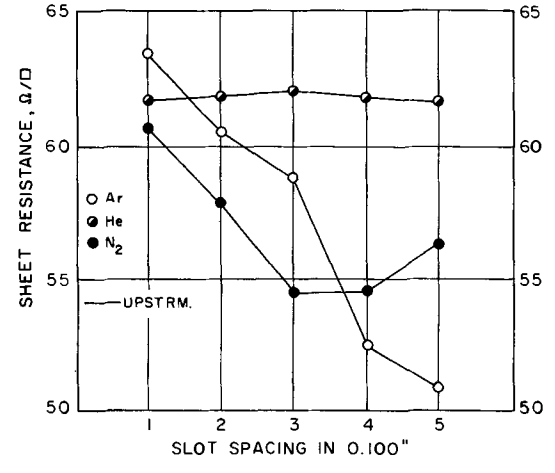

Fig. 5. Sheet resistance vs. ABN to silicon spacing

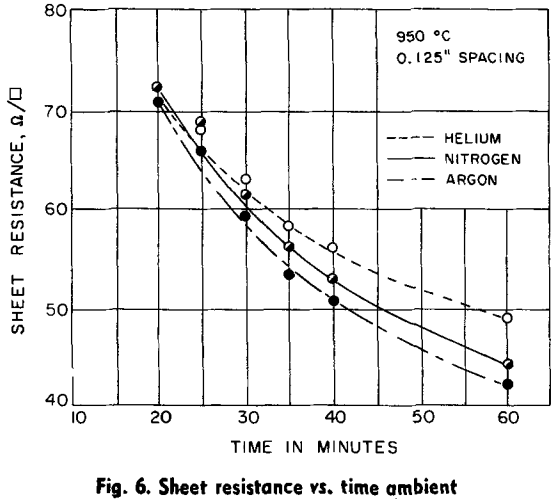

Fig. 6. Sheet resistance vs. time ambient

the average values of at least three distinct data. Briefly, the contents of the figures are as follows. Figure 4 indicates that $\bar{\rho}_s$ increases as flow rate increases between 0.1-0.6 standard liters/min and is relatively constant for flow rates between 0.6-1.0 standard liters/min. Figure 5 indicates that for increasing silicon to boron spacing $\bar{\rho}_s$ decreases for argon and nitrogen ambients and remains constant for helium ambients. Figure 6 indicates that for longer diffusion times differences in $\bar{\rho}_s$ as a function of ambient increase.

For the data collected a paradox intuitively exists. For the particular stacking arrangement and flow rates considered, the calculated Reynolds number, Re, for flow through an angular ring is approximately 1. Characteristically, turbulence does not onset until Re $\geq$ 2000 (11), and as such it is to be expected that mass transport of HBO_2 to be governed by Fick's law of concentration gradient diffusion rather than turbulent transport. For the temperatures considered diffusivities of HBO_2 are on the order of 1-5 cm^2/sec and it would be expected that an equilibrium concentration of HBO_2 be established in the volume between BN and silicon wafer in a fraction of a second. For these conditions, one would expect $\bar{\rho}_s$ to be constant with flow rate, spacing, and ambient.

A review of the literature indicates that for other liquid and gaseous diffusion systems high doping levels have produced films not easily etched in HF (12). Busen and co-workers, (13-15) have considered such films as a Si-B phase necessary to uniform processing control. The appearance of HF unetchable films on Si wafers processed in He ambient suggest the presence of a Si-B phase and the possibility of this phase dictating the data observed. Following the example of Busen *et al.* (13), ellipsometry as described by Vedam *et al.* (16) was employed to identify the presence and relative thickness of a Si-B phase.

Argon and helium ambient samples for $\bar{\rho}_s$ *vs.* spacing data were scribed in halves and one set of halves subjected to ellipsometry while the other set of halves was profiled using anodic oxidation (17) and four-point probe measurements (18). To insure that a minimum of oxide was present when ellipsometric measurements were performed, the silicon wafers and an undiffused control wafer were stripped of any oxide by immersion in concentrated HF for 1 min. Measurements obtained with the ellipsometer were compared to measurements made on the undiffused silicon wafer and data obtained by Vedam and So (19). Ellipsometric measurements are extremely accurate in determining thin films on the order of a monoatomic layer (20) and even small deviations in Ψ, amplitude ratio, and Δ, relative phase change, from the true values are indicative of a thin oxide layer or phase. Ψ and Δ measurements differing from that obtained for the control silicon were interpreted as indicative of various thicknesses of a Si-B phase.

Before discussing the implications of these measurements it is instructive to compare typical diffusion profiles obtained for argon and helium ambients to the ideal complementary error function profile, Fig. 7. Reference to Fig. 7 indicates the differences in calculated and experimental junction depths and the deviation of experimental profiles from erfc. Following the work of Joshi and Dash (21) the deviation in profiles from theoretical can be explained in terms of dislocations if the associated areas under the respective curves are equal. The basic premise for this test is that dislocations do not change the flux entering the surface but cause only a redistribution of the solute in the bulk. Calculation of the number of solute atoms per square centimeter, Q, for the profiles of Fig. 7 reveal that Q(erfc) = 1.75×10^{15} atoms/cm^2, Q(argon) = 2.27×10^{15} atoms/cm^2, and Q(helium) = 1.83×10^{15} atoms/cm^2. While Q(helium) is within 4% of Q(erfc), Q(helium) is less than the minimum Q and 3×10^{15} atoms/cm^2 required to generate dislocations as calculated by Schokley (22).

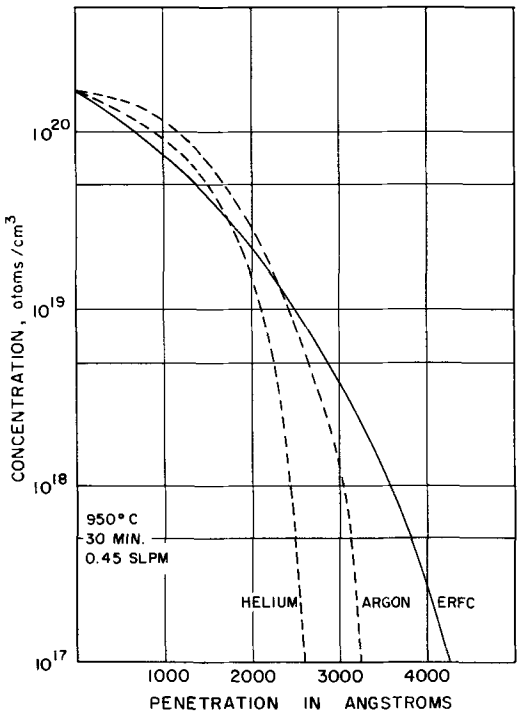

Fig. 7. Argon and helium ambient profiles compared to complementary error function profile.

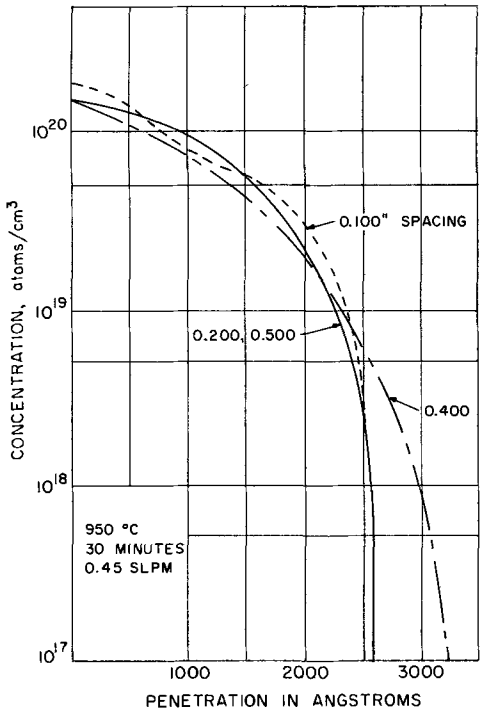

Fig. 8. Helium ambient profiles as a function of ABN to silicon spacing.

From this data it is unlikely that the observed ABN diffusion phenomena are primarily the result of dislocations but rather as previously suggested the result of phase formation.

As described by Boltaks (23) the formation of a new phase during diffusion, assumed in this case to be the Si-B phase described by Busen and co-workers (13-15), invariably leads to diffusion retardation.

Inspection of Table III, $\bar{\rho}_s$, x_j — Ψ, and Δ data, reveals two trends: (*i*) for the nitrogen ambient deposition, as spacing between BN and silicon decreases $\delta\Psi$ and $\delta\Delta$ increase (indicating an increase in Si-B phase thickness) along with an increase in $\bar{\rho}_s$ and a decrease in x_j; (*ii*) for the helium ambient, all $\delta\Psi$ and $\delta\Delta$ are larger than those for N_2 ambient and as spacing decreases $\delta\Psi$ and $\delta\Delta$ increase while $\bar{\rho}_s$ and x_j remain constant. The junction depth measurements of Table III were obtained from impurity profiles of Fig. 8 and 9. A few additional comments concerning these profiles are in order.

For the helium ambient profiles, Fig. 8, 100-, 200-, and 500-mil spacings, the profiles are approximately the same while the ellipsometric data varies significantly. It is felt that in all cases the thickness of a Si-B phase is above a critical thickness necessary to reach a saturated diffusion coefficient. The profile for 300-mil spacing is deleted from Fig. 8 because the silicon wafer was damaged during profiling; the 400-mil spacing profile is felt to be experimentally incorrect because of the discrepancy between calculated sheet resistance $\bar{\rho}_s$ cal = 55 ohms/□, and measured sheet resistance, $\bar{\rho}_s$ = 61 ohms/□.

For the argon ambient profiles, Fig. 9, the spacing increases, junction depth increases, and Ψ and Δ measurements correspondingly approach that of the undiffused silicon indicating a decrease in Si-B phase formation; the 500-mil spacing was deleted because of damage during profiling. It can be hypothesized from the data of Table III and Fig. 8 and 9 that (*a*) as the Si-B phase increases above a specific thickness its effect becomes diminished and the average diffusion coefficient of boron in silicon becomes independent of any increase in thickness (in reality it may become slowly varying function) and (*b*) below this thickness the diffusion coefficient of boron in silicon becomes dependent on the thickness of the Si-B phase, and in such a manner that increasing Si-B phase thickness retards diffusion and increases sheet resistance.

Although additional ellipsometric data must be gathered and correlated, it will be assumed that the phenomena of Fig. 4-6 can be interpreted in terms of a Si-B phase with it implied that increasing Si-B thickness is due to increasing mass transport and reaction of HBO_2 at the silicon surface. As such for Fig. 4, increasing $\bar{\rho}_s$ with flow rate indicates the presence of an Si-B phase and the enhanced transport of HBO_2. At present it is unresolved whether this enhanced mass transport occurs as the result of (*i*) an increase in the drift component of the volatilizing species due to an increase in gas flow rate or (*ii*) an increase in the

Table III. $\bar{\rho}_s$, x_j — ψ, Δ data

Spacing	Argon				Helium			
	$\bar{\rho}_s$, ohms/□	x_j, A	ψ	Δ	$\bar{\rho}_s$, ohms/□	x_j, A	ψ	Δ
0.100	65.6	3200	12.11	167.63	65.5	2600	20.56	100.91
0.200	59.0	3300	**	**	61.7	2600	16.38	119.11
0.300	58.7	3500	12.03	169.99	62.9	3300	13.56	140.92
0.400	55.4	3750	11.97	172.29	61.3	**	13.48	143.44
0.500	58.5	**	12.10	169.61	60.5	2600	13.81	137.97
Control	—	—	12.01	173.92	—	—	12.01	173.92
True*	—	—	11.83	172.48	—	—	11.83	172.48

* As determined by Ref. (19).
** Sample broke.

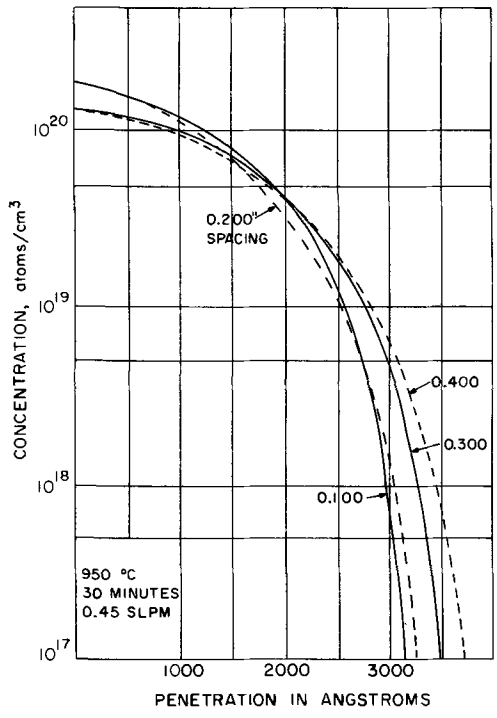

Fig. 9. Argon ambient profiles as a function of ABN to silicon spacing.

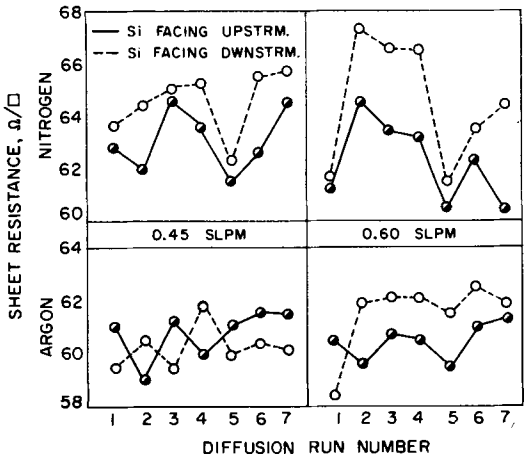

Fig. 10. Sheet resistance vs. run number for argon, nitrogen ambient, and 0.45, 0.60 standard liters/min flow rates.

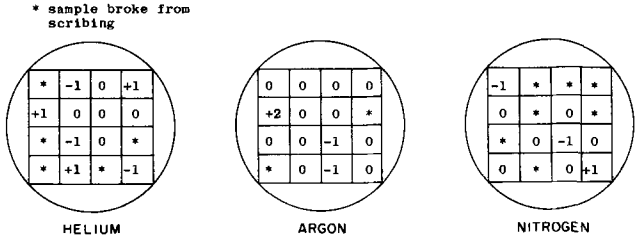

Fig. 11. Per cent sheet resistance deviation vs. x, y position on silicon wafer.

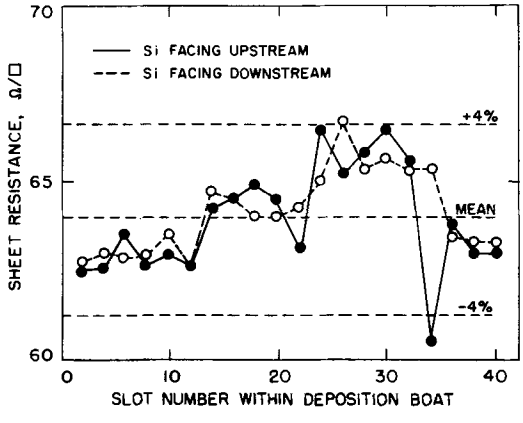

Fig. 12. Sheet resistance vs. slot number in deposition boat

vapor pressure of the volatilizing species due to an increase in flow rate of a hydrated ambient gas and the corresponding increase in dynamic conversion of B_2O_3 to HBO_2. While it is unlikely that mechanism (*i*) is reasonable for the flow rate considered the occurrence and degree of B_2O_3 hydrated during (*a*) the BN oxidation step, (*b*) loading and unloading of silicon for diffusion, and (c) during diffusion must be determined before supporting experiment results can be attributed entirely to mechanism (*ii*).

Reference to Fig. 5 suggests that differences in diffusion coefficients for HBO_2 in Ar, He, and N_2 are significant and except for the He ambient an equilibrium concentration of HBO_2 in the volume separating BN and Si is not established during diffusion. As indicated by $\bar{\rho}_s$ and ellipsometric data for the nitrogen and argon ambients, as the source to silicon distance decreases $\bar{\rho}_s$ and Si-B phase thickness increases. Only for the helium ambient was the diffusivity of HBO_2 large enough to establish an HBO_2 concentration at all source to silicon spacings sufficient for critical Si-B phase thickness. The data of Fig. 6 is interpreted as follows. Differences in $\bar{\rho}_s$ *vs.* time for various ambients reflect differences in time to reach a critical Si-B phase thickness above which the diffusion coefficient is relatively constant. Considering stagnant ambient diffusion coefficients and assuming that for the flow conditions considered the relationship for the time-averaged diffusion coefficients are the same, the time-averaged diffusion coefficient of HBO_2, $\bar{D}$, in helium, argon, and nitrogen has the following relationship: $\bar{D}_{He} > \bar{D}_{N_2} > \bar{D}_{Ar}$. In turn, it is expected that the time to establish the critical Si-B thickness, $\bar{t}$, follows the inverse relationship, $\bar{t}_{Ar} > \bar{t}_{N_2} > \bar{t}_{He}$. Therefore, it is expected as depicted in Fig. 6 that $\bar{\rho}_{sHe} > \bar{\rho}_{sN_2} > \bar{\rho}_{sAr}$.

To determine the reliability and general performance of the BN deposition system the following tests were performed: (*a*) ρ_s *vs.* run number for argon, nitrogen ambient, 0.45, 0.60 standard liters/min, Fig. 10; (*b*) ρ_s per cent deviation *vs.* x, y position on silicon wafer, Fig. 11; and (*c*) ρ_s *vs.* slot number in deposition boat, Fig. 12. Examination of Fig. 10 suggests improved sheet resistance tolerance for 0.45 standard liters/min flow rate and Ar ambient while Fig. 10 shows no appreciable across wafer ρ_s variation (1-2%) for any of the wafers mapped. The mappings were performed on Si randomly chosen from wafers processed at 0.45 standard liters/min and obtained by scribing the Si wafers into 250 mil squares and four-point probing. Data presented in Fig. 12 are of one of three large scale depositions performed. No significant pattern as a function of position was observed. The results of all three depositions are plotted in Fig. 13 in terms of frequency of occurrence *vs.* sheet resistance. As indicated by $\pm 2s$ limits (s = standard deviation) 95% of all measurements fell within ±4% of the 64 ohms/□ norm. In Fig. 14, sheet resistance data for 0.125-in. spacing runs 3-11% higher for temperatures less than 1000°C than that reported by Goldsmith *et al.* (1) for a furnace with fast recovery time. While the data of Fig. 14, 0.125-in. spacing, agrees well with data by Goldsmith *et al.* (1) for a furnace with slow recovery time, the furnaces used in obtaining the above presented data are of the tight tolerance, fast recovery type, and it is assumed that the differences and similarities observed are due to other experimental differences.

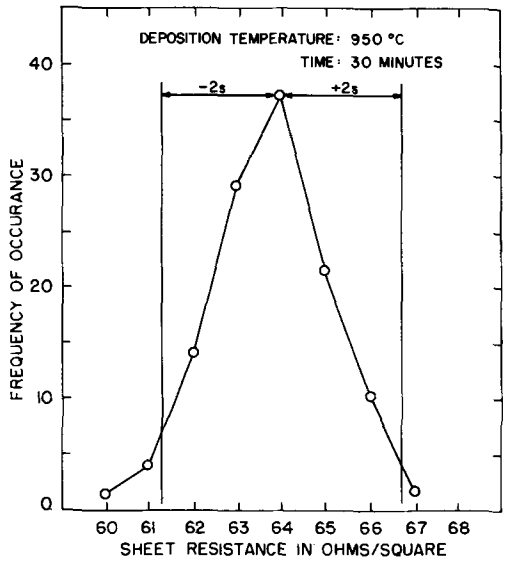

Fig. 13. Sheet resistance standard deviation for 120 silicon wafers

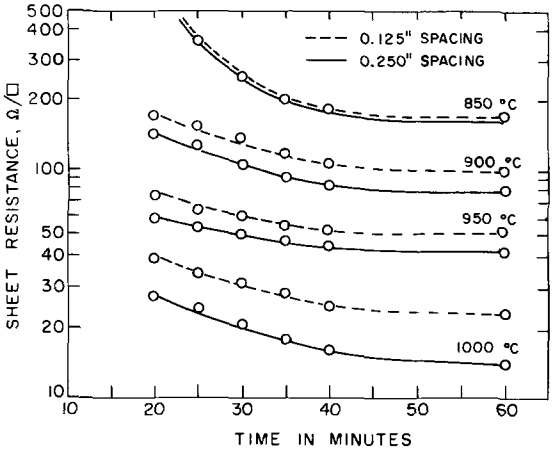

Fig. 14. Sheet resistance vs. time, temperature, and spacing; nitrogen ambient.

Summary and Conclusions

The presented work supports claims by Goldsmith *et al.* (1) but with the additional qualifications: (*i*) the oxidized material is hygroscopic and the vapor pressure of the species changes with water vapor absorption such that if the care in storage is not exercised reproducibility of ρ_s is difficult; and (*ii*) ρ_s values are affected by gas ambient, flow rate, and source to silicon spacing and ρ_s reproducibility may also be a function of these parameters. However, for the studied experimental conditions, the BN deposition system is capable of $\pm$1-2% ρ_s variation across a silicon wafer, $\pm$4% ρ_s variation from run to run.

The mechanism to explain the observed experimental profiles is suspected to be due to reactive diffusion and it has been tentatively demonstrated that the observed phenomena can be explained in terms of Si-B phase thickness: below a specific thickness, increasing Si-B phase thickness decreases junction depth while above a specific thickness, increasing Si-B phase thickness has negligible effect on junction depth. Additional work is needed before the complete consequences of a Si-B phase on device processing and electrical performance can be obtained.

Acknowledgments

The authors would like to thank Mr. D. Ott of the Carborundum Company for providing ample ABN samples and technical support and Dr. K. Vedam and M. Mallin for their assistance with ellipsometric data. Part of the research presented was supported by contract DAAB07-71-Q0299 sponsored by United States Army Electronics Command Post, Fort Monmouth, New Jersey.

Manuscript submitted Dec. 7, 1971; revised manuscript received March 19, 1973. This was Paper 176 presented at the Cleveland, Ohio, Meeting of the Society, Oct. 3-7, 1971.

Any discussion of this paper will appear in a Discussion Section to be published in the June 1974 JOURNAL.

REFERENCES

1. N. Goldsmith, J. Olmstead, and J. Scott, Jr., *RCA Rev.*, **28**, 344 (1967).
2. K. H. Nicholas, *Solid-State Electron.*, **9**, 35 (1966).
3. T. Miles, Private communication.
4. P. C. Parekh and D. R. Goldstein, *Proc. IEEE*, **57**, 1507 (1969).
5. A. W. Coats and J. P. Redfern, *Analyst*, **88**, 906 (1963).
6. S. P. Randall and J. L. Margrave, *J. Inorg. Nucl. Chem.*, **16**, 29 (1960).
7. R. Speiser, S. Naiditch, and H. L. Johnston, *J. Am. Chem. Soc.*, **72**, 2578 (1950).
8. J. R. Soulen, P. Sthapitanonda, and J. L. Margrave, *J. Phys. Chem.*, **59**, 132 (1955).
9. W. A. Weyl and E. C. Marboe, "The Constitution of Glasses," Vol. 1, p. 142, Interscience Publishers, Inc., New York (1962).
10. J. M. Assour, *This Journal*, **119**, 1270 (1972).
11. R. B. Bird, W. E. Stewart, and E. N. Lightfoot, "Transport Phenomena," p. 54, John Wiley & Sons, Inc., New York (1960).
12. W. R. Runyan, "Silicon Semiconductor Technology," p. 149, McGraw-Hill Book Co., New York (1965).
13. K. M. Busen, W. A. Fitzgibbons, and W. K. Tsang, *This Journal*, **115**, 291 (1968).
14. K. M. Busen, W. A. Fitzgibbons, and T. Kloffenstein, *Electrochem. Technol.*, **6**, 256 (1968).
15. W. A. Fitzgibbons, T. Kloffenstein, and K. M. Busen, *This Journal*, **117**, 272 (1970).
16. K. Vedam, W. Knaunsenberger, and F. Lukes, *J. Opt. Soc. Am.*, **59**, 64 (1969).
17. E. Tannebaum, *Solid-State Electron.*, **2**, 123 (1961).
18. R. P. Donovan, *ibid.*, **10**, 155 (1967).
19. K. Vedam and S. S. So, *Surface Sci.*, **29**, 379 (1972).
20. R J. Archer and G. W. Gobeli, *J. Phys. Chem. Solids*, **26**, 343 (1965).
21. M. L. Joshi and S. Dash, *IBM J. Res. Dev.*, **10**, 446 (1966).
22. H. J. Queisser, *J. Appl. Phys.*, **32**, 1776 (1961).
23. B. I. Boltaks, "Diffusion in Semiconductors," p. 66, Academic Press, New York (1963).

Crystal Growth and Characterization of Gadolinium Gallium Garnet

D. F. O'Kane,* V. Sadagopan,* and E. A. Giess

IBM Thomas J. Watson Research Center, Yorktown Heights, New York 10598

and E. Mendel*

IBM Components Division, East Fishkill, New York 12533

ABSTRACT

Single crystals of $Gd_3Ga_5O_{12}$ with dislocation and inclusion levels below 5/cm^2 were grown in a nitrogen atmosphere with an infrared television system of computer controlled Czochralski crystal growth. Coring was prevented by a high crystal rotation rate and a slow pull rate during growth, although striations occurred in the crystal at high rotation rates. Dislocations were avoided by good crystal diameter control during growth and low thermal gradients in the crystal puller. Etching and polishing techniques were developed to reveal defects.

$Gd_3Ga_5O_{12}$ (GGG) has attracted interest as a substrate material for the epitaxial growth of rare earth iron garnet films (1, 2). The crystal growth of GGG by the Czochralski method has been reported (3-5). Some questions still remain on the growth conditions necessary to eliminate inclusions of iridium, which come from the crucible, and other defects. This paper describes the growth conditions necessary to produce crystals with less than five dislocation and iridium inclusion type defects per cm^2. Also, the sources of defects and methods for revealing them are described.

Experimental

The starting materials, Ga_2O_3 and Gd_2O_3, were either 99.9 or 99.99% purity and were prereacted by sintering at 1400°C to give $Gd_3Ga_5O_{12}$. The sintered powder was melted in nitrogen atmosphere in a 77 cm^3 tapered iridium crucible which held about 400g of GGG. The crucible had a 57 mm ID at the top and a height of 60 mm; the outside was flame sprayed with zirconia. Zirconia crucibles and powder were used to insulate the iridium crucible in the crystal puller. An iridium tube with one end sealed and openings at the side was inserted in the lower half of the iridium crucible to dampen the convective temperature fluctuations (6). The gas atmosphere in the crystal puller was either pure nitrogen or 1% O_2-99% N_2. All crystals were grown along the [111] axis with an oriented seed crystal.

An infrared television system for computer controlled Czochralski crystal growth (7) was adapted to the growth of GGG (8) as shown in Fig. 1. The silicon diode array type TV camera supplied information which enabled the computer to calculate the crystal diameter throughout the crystal growth process and to regulate the power to the puller to control the diameter. Figure 1 shows the TV camera focused on the growing crystal and the image displayed on the TV monitor. The marker pulse was positioned manually on the TV monitor to indicate to the computer the location of the center of the crystal and the melt interface. The logic control circuit (9) was used to sample the TV voltage at the points necessary to determine the crystal diameter. Every 15 sec, the computer calculated the crystal diameter and the rate of change of diameter per unit length of pulled crystal. The Tektronix storage scope provided a display of the variables, such as crystal diameter, rate of change of crystal diameter, rf power to the puller, and length of pulled crystal, as cal-

* Electrochemical Society Active Member.

Key words: gadolinium gallium garnet, Czochralski crystal growth, low defect level crystals.

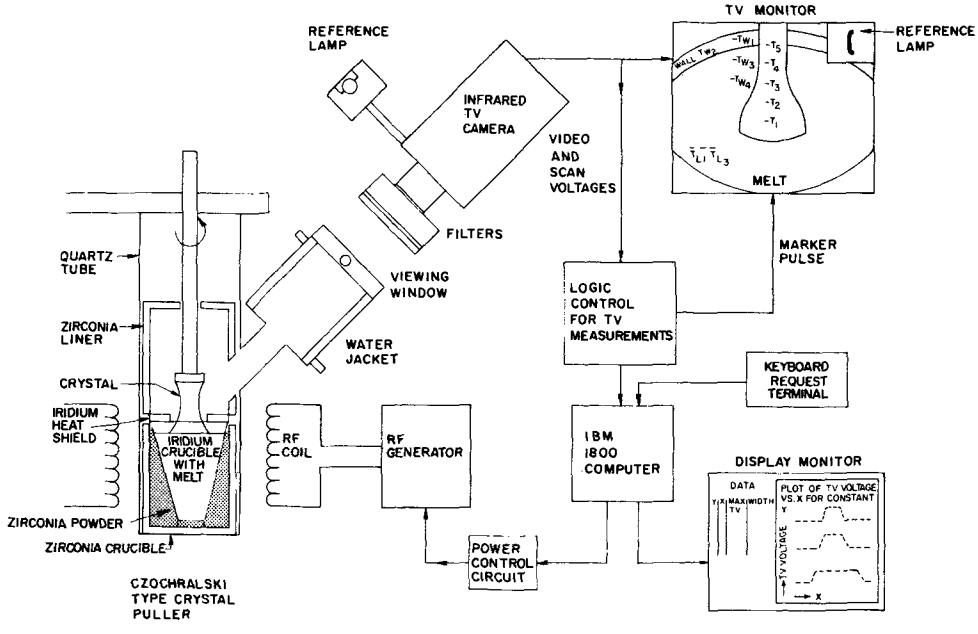

Fig. 1. Infrared television system for the computer controlled crystal growth of $Gd_3Ga_5O_{12}$.

culated by the remotely located IBM 1800 computer. The keyboard was used to enter new commands to the computer. The computer adjusted the power output of the rf generator to keep the crystal diameter or the rate of change of diameter within specified limits. The computer program for crystal growth was divided into four sequential sections: (*i*) crystal diameter reduction after dipping the seed crystal in the melt; (*ii*) growth at a small diameter (3 mm); (*iii*) increase of crystal diameter to the final size; and (*iv*) growth of the main body of the crystal at a constant diameter. In adapting the computer process to the growth of GGG, the most significant changes were made in the computer program which provided better control of the crystal diameter and the rate of change of diameter per unit length of pulled crystal. Also, the GGG required an iridium crucible.

The crystals were grown at rates of 3-6 mm/hr with rotation rates of 60-80 rpm. The higher pull rate was used before growth of the main body of the crystal. The most usual crystal diameter was 15 mm; however, crystals up to 22 mm diam were grown. A 15 mm diameter was a convenient size for GGG wafers to be used in liquid phase epitaxy experiments. The length of the main body of a crystal was usually 6 cm and the weight of a 15 mm diam crystal was about 100g. A typical crystal required 26 hr to grow and 6 hr to cool.

Some crystals pulled along the [111] axis were examined for striations normal to the direction of growth by taking 1 mm thick longitudinal slices midway between the centers and edges of the crystals, polishing them with 3μ diamond paste, and then inspecting them on a polarizing microscope. The appearance of the striations was not influenced by the radial position used for the longitudinal slice. The remainder of the crystals were oriented and sliced normal to the growth direction. A multiple blade cutter with 30μ SiC abrasive slurry was used to produce 28 mil wafers which were lapped with a 30μ resin-bonded diamond disk to remove saw damage and produce a flat surface. Two mils of material were removed from each side during this operation. This was followed by 9, 6, 3, and 1μ diamond paste polishing and then chemical polishing (500Å silicon dioxide in alkaline medium). Final wafer thickness was 20 mils. In many cases, the wafers were suitable for defect examination after a 6μ polish. Dislocation etch pits were revealed by a 10 min etch in a 1:1 mixture of H_2SO_4 and H_3PO_4 at 140°C. Wafers used as substrates for the deposition of magnetic films were cleaned in organic solvents after chemical polishing and dried in warm nitrogen. Over 20 crystals pulled from stoichiometric melts were cut entirely into wafers. Each wafer was examined on a polarizing microscope for coring, strain, dislocations, and iridium inclusions.

Crystals of GGG were grown from melts containing excesses of Ga_2O_3 or Gd_2O_3 to determine the affect of nonstoichiometry on the lattice parameter. Also, high purity (99.999%) GGG powders with excesses of Ga_2O_3 and Gd_2O_3 were heat-treated and used for lattice parameter measurements. One set of samples was annealed in air at 1650°C for 9 hr and another set was annealed at 1400°C for four periods of 16 hr each with grinding between each annealing period. X-ray measurements were made on a Guinier focusing camera with monochromatic CuK_α radiation and a silicon internal standard. Lattice constants were determined from a least squares reduction of film data for Bragg reflections in the range $25 < 2\theta < 75°$ and are accurate to a standard deviation of $< \pm 0.01\%$.

Results

Figure 2 shows two crystals of GGG. The first crystal, G-36, was grown under computer control during the diameter reduction, diameter increase, and the initial 10 mm growth of the main body of the crystal. The remainder of the crystal was grown with constant power to the crystal puller. The diameter reduction was used to remove dislocations (10) which were present in the seed crystal. The diameter of crystal G-36 was increased slowly from 3 to 14 mm by the computer to avoid introducing strain in the crystal. The second crystal, G-57, was grown under manual rather than computer control. It shows a rapid diameter increase, which can occur with manual control, producing strain in the main body of the crystal. The principle advantage of the computer controlled growth process was the improved crystal diameter control, which resulted in better crystal quality. Under computer control, the crystal diameter was more easily reduced to 3 mm to remove dislocations and could be increased gradually without introducing new strain and dislocations. Under manual control, there was a tendency for the crystal diameter to increase too rapidly when the diameter was being increased from about 3 to 14 mm. This was found to cause strain and dislocations.

Initially, the crystals were grown in a 99% N_2-1% O_2 atmosphere to avoid the gallium oxide vaporization problem described (3) for inert atmospheres. This resulted in attack on the iridium crucible walls (oxidation and vaporization of the iridium), a build-up of iridium on the melt surface, and condensation of iridium particles on the pulled crystal. The presence of oxygen in the puller atmosphere resulted in a rougher crystal surface. This latter point is illustrated by the difference in surface appearance of crystal G-36 (Fig. 2) grown in 99% N_2-1% O_2 and crystal G-57 which was grown in pure nitrogen. Repeated use of the seed crystals caused a build-up of iridium deposits on their surfaces. This accounts for the dark regions near the top of each crystal in Fig. 2.

Generally crystals grown under computer control with a nitrogen atmosphere in the puller had less than 5 defects (dislocations and iridium inclusions) per cm^2 and some crystals had a high percentage of wafers free of these and all other defects. The nitrogen atmosphere did not cause gallium suboxide inclusions from the decomposition of Ga_2O_3. Also, no significant loss of Ga_2O_3 was observed with either atmosphere. Crystals could be pulled overnight (16 hr) at constant power with only the expected small decrease in crystal diameter as the liquid level was lowered and the additional radiant heat came from the crucible wall. A sizable loss of Ga_2O_3 would have caused a lowering of the melting point and a large decrease in crystal diameter.

The principal defects in GGG were due to iridium inclusions and coring. Gallium suboxide inclusions were rarely observed. The triangular and hexagonal shapes of the iridium inclusions are shown in Fig. 3. These inclusions were identified as iridium by electron microprobe analysis. The 1:1 H_2SO_4:H_3PO_4 etch was used to reveal the dislocation pattern around the iridium inclusion in Fig. 3b. This source of dislocation has been described (11). Dislocation density and iridium inclusions could not be related to the position of the wafer along the length of the crystal from the data available on more than 20 crystals.

Dislocations were also observed from strain produced by rapid crystal diameter increases during growth and in a few crystals by severe temperature gradients above the melt which were produced by directing an inert gas flow near the crystal-melt interface.

Striations present in GGG are illustrated in Fig. 4. These striations occur normal to the direction of pulling and were usually spaced between 10 and 45 μm. The spacings corresponded to time periods of 9-40 sec without any direct correlation with rotation rate. They disappeared when the rotation was reduced from 70-60 rpm. The striations are believed to result from temperature fluctuations which produce growth rate changes. We have observed melt temperature fluctuations caused by high rotation rates during the growth of other high melting materials. An attempt was made to relate the striations to a variation in Ga_2O_3 or Gd_2O_3 concentrations. However, electron microprobe analysis across a 200 μm region of striated GGG in steps of

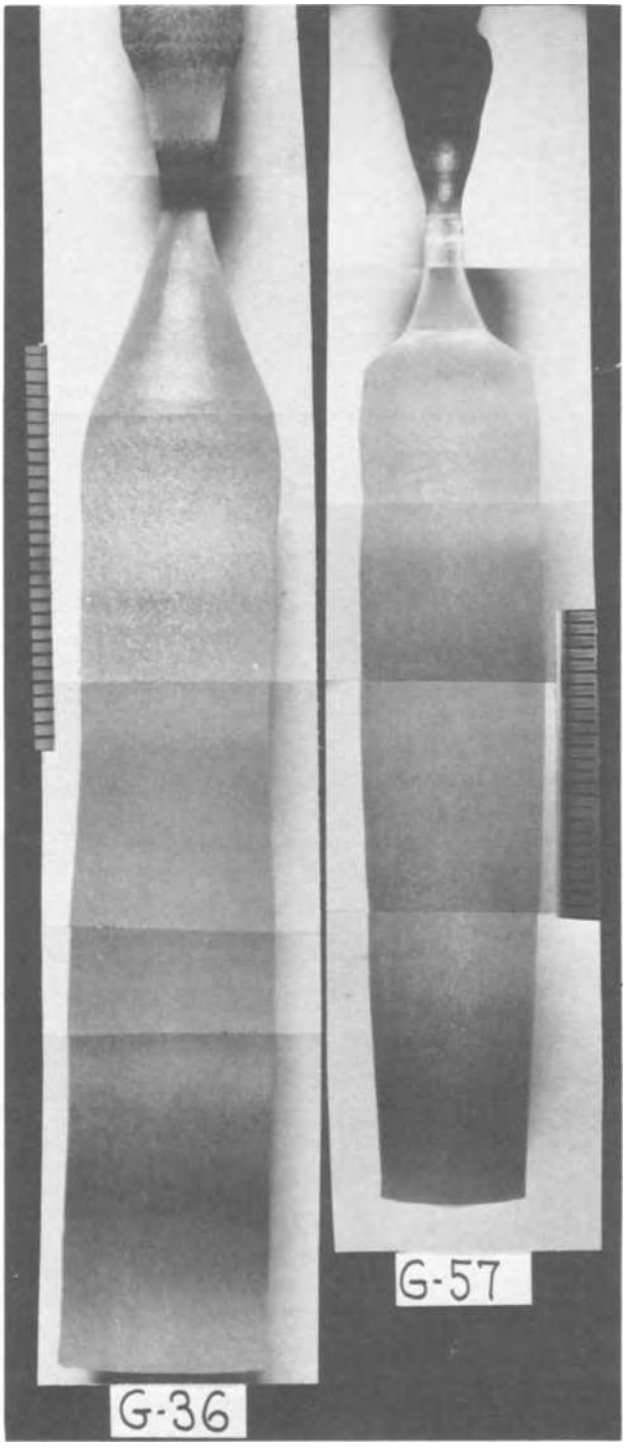

Fig. 2. Two single crystals of $Gd_3Ga_5O_{12}$. Crystal G-36 was grown under computer control and crystal G-57 was grown with manual control of the power. Scale shows 1 mm divisions.

2 μm failed to detect any changes in gallium or gadolinium concentrations. The limit of detection for these elements was about 1 weight per cent (w/o). The only impurity detected was silicon below 200 ppm and its concentration had no relation to the striations.

The striations were not caused by thermal asymmetry in the melt or by departure of the rotation axis from the thermal center of the melt. This type of striation is dependent on the amount of crystal grown per revolution. In the case of GGG, the vertical travel per revolution was about 1 μm, whereas the actual striations were 10 μm or larger.

Strain associated with (211) facets on the growth interface has been reported (4) for GGG. This strain can impede the motion of magnetic bubbles in films

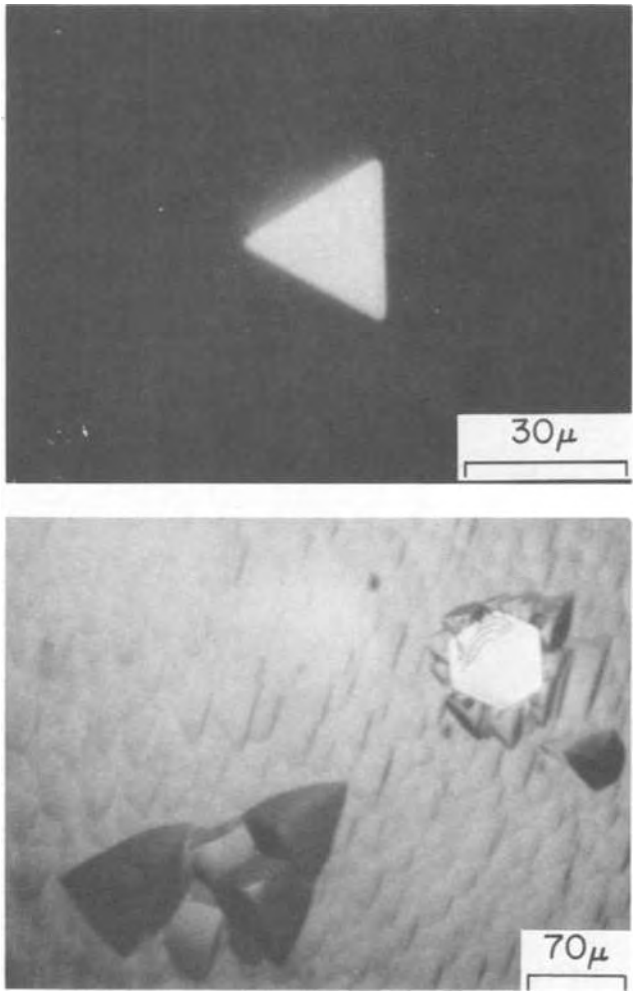

Fig. 3. Top photograph shows triangular shaped iridium inclusion. Lower photograph shows hexagonal iridium inclusion on etched surface of $Gd_3Ga_5O_{12}$.

grown on GGG substrates. In other garnets (12), high rotation rates have prevented this coring effect by producing a flat growth interface. In our crystal puller, high rotation rates (80 rpm) and slow growth rates (3 mm/hr) prevented coring. These conditions were used to grow the low defect (less than 5/cm^2) crystals. The 80 rpm rotation rate did cause striations; however, the motion of the magnetic bubbles in the epitaxial film was not influenced by the striations in the substrate wafer.

Table I shows the lattice parameter data on a flux grown GGG single crystal, Czochralski pulled GGG crystals grown from melts containing either excess Ga_2O_3 or excess Gd_2O_3, and powder samples sintered at 1400° and 1650°C. The compositions indicated in the

Table I. Influence of composition and temperature on the lattice parameter of $Gd_3Ga_5O_{12}$

Composition	Lattice parameter a_o, Å
Flux grown $Gd_3Ga_5O_{12}$	12.376
Czochralski grown crystals of $Gd_3Ga_5O_{12}$	
4 w/o excess Ga_2O_3	12.382
$Gd_3Ga_5O_{12}$	12.382
2 w/o excess Gd_2O_3	12.388
Samples sintered at 1650°C	
1 w/o excess Ga_2O_3	12.377
$Gd_3Ga_5O_{12}$	12.380
1 w/o excess Gd_2O_3	12.390
Samples sintered at 1400°C	
1 w/o excess Ga_2O_3	12.376
$Gd_3Ga_5O_{12}$	12.375
1 w/o excess Gd_2O_3	12.377

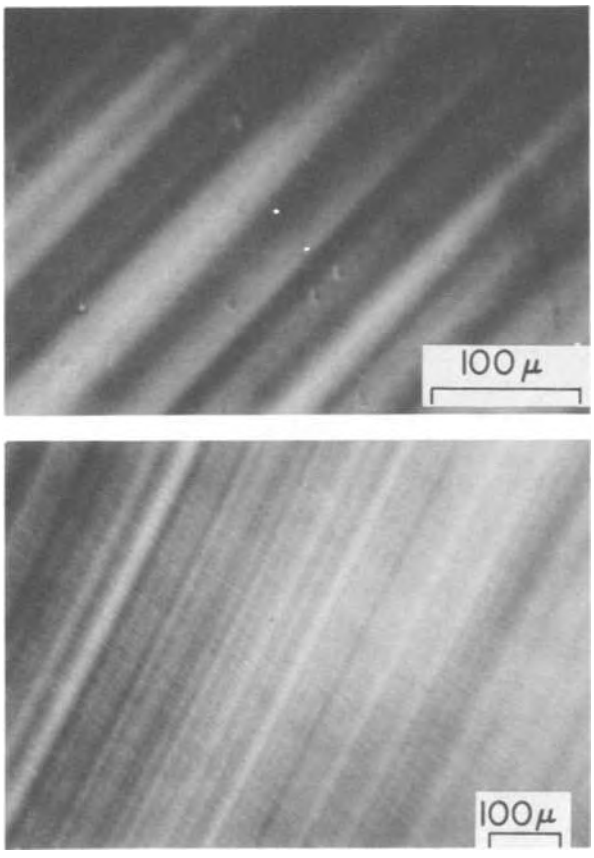

Fig. 4. Striations normal to the growth axis of $Gd_3Ga_5O_{12}$

table are the melt compositions from which the crystals were grown and the initial composition of the powder samples which did not show a significant weight change after annealing. The flux grown crystal was obtained from a melt containing PbO and excess Ga_2O_3 by cooling below 1250°C. The flux crystal and the 1400°C sintered samples had the smallest lattice parameters. The largest lattice parameters were obtained from the 1650°C sintered samples of GGG with excess Gd_2O_3 and the crystal pulled from a melt of 2 w/o excess Gd_2O_3. The lattice parameter of the pulled crystals was more strongly influenced by excess Gd_2O_3 than excess Ga_2O_3.

No significant difference in lattice parameter was observed between the initial and final section of a pulled crystal that was grown from a stoichiometric melt in a 24 hr period. A sizable loss of Ga_2O_3 by evaporation would have resulted in an increase in lattice parameter during growth. The wider range of lattice parameters obtained with the sintered compositions at 1650°C was not observed in the pulled crystals and the 1400°C annealed compositions. This suggests that the range of solid solubility is smaller near the melting point (1750°C) and at 1400°C; therefore retrograde solubility may occur. Also, an order-disorder effect may influence the lattice parameter since the pycnometric densities of the two stoichiometric Czochralski pulled crystals that were measured (7.100 and 7.068 g/cm^3) were lower than the density calculated (7.113 g/cm^3) from x-data for a stoichiometric crystal with a lattice constant of $a_o = 12.385$Å. Geller (13) has reported other cases of rare earth oxide solubility in gallium and aluminum garnets.

Summary

Single crystals of GGG with less than 5 defects/cm^2 from iridium inclusions and dislocations were obtained with a TV system of computer controlled Czochralski crystal growth. A pure nitrogen atmosphere in the crystal puller was successful in reducing iridium inclusions in the pulled crystals. Coring was prevented by a high crystal rotation rate and a slow pull rate during growth; striations in the crystal were observed at such high rotation rates. Dislocations were avoided by good crystal diameter control during growth. An etching procedure was developed to reveal dislocations. The lattice parameter of GGG did not vary during the 26 hr period required for growth. Excess Ga_2O_3 in the melt caused only a slight decrease in lattice parameter while excess Gd_2O_3 raised the lattice parameter significantly.

Acknowledgments

The authors wish to thank P. C. S. Yin for assistance in the crystal growth, J. D. Kuptsis for electron microprobe analysis. C. Guerci for x-ray measurements, W. Kateley and A. R. Ciarfella for crystal polishing, Dr. A. L. Bednowitz for computer programming support, and T. W. Kwap and L. Gulitz for the electronics support on the computer controlled crystal growth system.

Manuscript submitted Sept. 27, 1972; revised manuscript received Feb. 15, 1973. This was Paper 9 presented at the Houston, Texas, Meeting of the Society, May 7-11, 1972.

Any discussion of this paper will appear in a Discussion Section to be published in the June 1974 JOURNAL.

REFERENCES

1. H. J. Levenstein, S. Licht, R. W. Landorf, and S. L. Bland, *Appl. Phys. Letters*, **19**, 486 (1971).
2. E. A. Giess, J. D. Kuptsis, and E. White, *J. Cryst. Growth*, To be published.
3. R. C. Linares, *J. Cryst. Growth*, **3/4**, 443 (1969).
4. C. D. Brandle and A. J. Valentino, *J. Cryst. Growth*, **12**, 3 (1972).
5. C. D. Brandle, D. C. Miller, and J. W. Nielsen, *J. Cryst. Growth*, **12**, 195 (1972).
6. P. A. C. Whiffin and J. C. Brice, *J. Cryst. Growth*, **10**, 91 (1971).
7. D. F. O'Kane, T. W. Kwap, L. Gulitz, and A. L. Bednowitz, *J. Cryst. Growth*, **13/14**, 624 (1972).
8. D. F. O'Kane, A. L. Bednowitz, T. W. Kwap, and L. Gulitz, 2nd Natl. Conf. on Crystal Growth, Princeton, N. J., July, 1972.
9. T. W. Kwap, D. F. O'Kane, and L. Gulitz, 5th Symp. on Temperature, Washington, D. C., June, 1971.
10. W. C. Dash, *J. Appl. Phys.*, **30**, 459 (1959).
11. J. W. Matthews, E. Klokholm, V. Sadagopan, T. S. Plaskett, and E. Mendel, *Acta Met.*, To be published.
12. B. Cockayne, M. Chesswas, and D. B. Gasson, *J. Mater. Sci.*, **3**, 224 (1968).
13. S. Geller, *Z. Krist.*, **125**, 1 (1967).

Composition of Phosphosilicate Glass by Infrared Absorption

A. S. Tenney*,[1] and M. Ghezzo*

General Electric Corporate Research and Development, Schenectady, New York 12301

ABSTRACT

The ratio of the intensity of the P=O absorbance band at ~1325 cm^{-1} to that of the Si-O band at ~1050 cm^{-1} has been correlated with the composition of vapor-deposited phosphosilicate glasses over the range 0-20 mol per cent P_2O_5. While the ratio of the linear absorbances of these bands depends somewhat on deposition temperature as well as on film composition, the ratio of the areas of these bands is uniquely related to film composition over the range of deposition temperature studied. The deposition rates and compositions of these films (for a constant flow of reactant gases) were found to be relatively weakly dependent on deposition temperature. These results for phosphosilicate glass combined with previously published calibration curves for borosilicate and arsenosilicate glasses allow the rapid, nondestructive determination of the compositions of all three doped glasses commonly used as sources for impurity diffusion into silicon.

Properties of phosphosilicate glass (PSG) make it useful in a variety of applications in semiconductor technology. It serves as a source for the diffusion of phosphorus into silicon (1), as a general "getter" of sodium and other metal ions (2, 3), and, more specifically, as a diffusion mask allowing the selective diffusion of zinc into III-V compounds (4-7).

Since the properties of PSG which make it useful in a given application may depend on the PSG composition, it is important to be able to control and determine this composition. Composition control is frequently achieved by controlling temperature and reactant gas composition during the chemical vapor deposition of the PSG film (8). In many applications, the chemical composition need not be known as long as the dependence of the property of interest on the deposition conditions (reactant flows, temperature, etc.) is known. However, it has been shown that films of dissimilar composition may be deposited in different deposition systems under nominally identical deposition conditions (9). Thus, results determined for one deposition system are not unequivocally transferable to other systems. It is usually more convenient, therefore, to know the film composition and in quality control applications a rapid, nondestructive determination is often desirable. Finally, a detailed understanding of the processes involving these films requires knowledge of the film composition.

Composition determinations based on the IR spectra of vapor-deposited borosilicate (9-11) and arsenosilicate (12) glasses have proven useful. The IR reflectance spectra of silicate glasses have been employed as a qualitative test for the presence of phosphorus oxide (13).

The P=O absorbance value at 1330 cm^{-1} has been employed to determine the composition of layers of PSG formed by passing P_2O_5 vapors over thermally oxidized silicon wafers (25). This method requires an accurate knowledge of the PSG thickness and also that the integrated absorptivity (absorption per atom of phosphorus) be independent of PSG composition.

The etch rates of phosphosilicate glasses in selective etchants have proved to be a useful means of determining PSG compositions particularly in light of the fact that little instrumentation is required (3, 21-24, 28). However, this method is destructive and is complicated by the fact that the etch rate of a glass generally depends on its "history" as well as on its composition.

In the present work, the ratio of the absorbance of the P=O band at 1325 cm^{-1} to that of the Si-O band at 1050 cm^{-1} was determined for vapor-deposited phosphosilicate glasses as a function of composition over the range 0-20 m/o (mole per cent) P_2O_5. This method is nondestructive. The employment of absorbance ratios obviate the need to know the film thickness. Since the relationship between absorbance ratio and composition is empirical, the integrated absorptivity need not be independent of PSG composition.

Experimental

Glasses were deposited by passing Ar-diluted mixtures of SiH_4, PH_3, and O_2 over 10 ohm-cm p-type chemically polished <100> silicon wafers heated to 300°-700°C in a previously described vertical deposition system (14). For instance, with flow rates of 3800 cm^3 min^{-1} Ar, 40 cm^3 min^{-1} O_2 ,150 cm^3 min^{-1} SiH_4 (1% in Ar), and 13 cm^3 min^{-1} PH_3 (1% in Ar), a 1.0μ thick film 4.9 m/o in P_2O_5 was deposited in 35 min at 400°C. Although similar films may be deposited by the oxidation of SiH_4 and $POCl_3$, these become damaged on heating to the temperatures usually employed to achieve phosphorus diffusion in silicon and, therefore, were not included in this work (15).

The vibrational spectra of these films were determined over the range 4000 to 250 cm^{-1} employing a Perkin-Elmer Model 457 double-beam recording spectrophotometer with scan rates of 1000 and 500 cm^{-1} per min over the ranges 4000-2000 and 2000-250 cm^{-1}, respectively. A silicon wafer of the same resistivity and type as those of the substrate was placed in the reference beam.

Film thicknesses were determined within an uncertainty of ±100-200Å from the interface colors employing the color chart of Pliskin and Conrad (16) after determining ellipsometrically that the refractive index of these films was 1.45 ± 0.03. Deposition rates were determined by recording film color *vs.* time during the deposition. A graphical arrangement of Pliskin and Conrad's color chart facilitates the recording of these data and the calculation of the deposition rate (17).

The compositions of these films were determined by microprobe analyses for silicon and phosphorus using high-purity, undoped samples of silicon and gallium phosphide, respectively, for reference. The PSG films were generally about 1μ thick and the electron beam was kept low enough in energy (~6 keV) to assume no penetration to the Si substrate (26, 27). From the phosphorus to silicon atomic ratio, the phosphosilicate glass composition was calculated assuming that phosphorus is present in these films as P_2O_5 and silicon as

* Electrochemical Society Active Member.
[1] Present address: General Electric Company, Miniature Lamp Products Department, Chesterland, Ohio 44026.
Key words: doped oxides, infrared peak ratio, chemical vapor deposition.

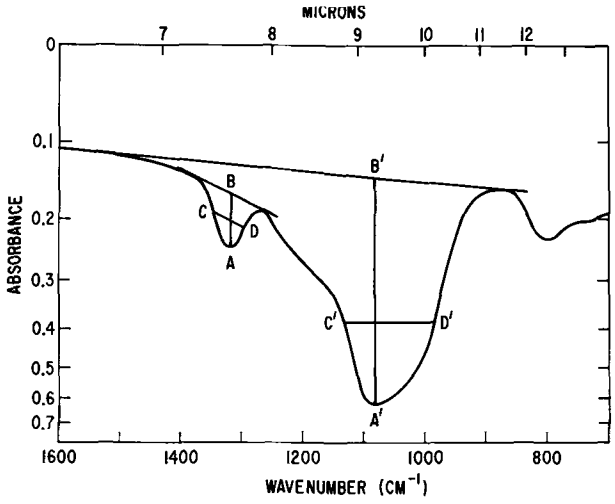

Fig. 1. Calculation of linear absorbance and approximated band areas for vapor-deposited phosphosilicate glasses. The spectrum shown is that of a glass approximately 15 m/o P_2O_5.

SiO_2. The uncertainty in the values of mol per cent P_2O_5 thus determined is estimated to be less than 1 m/o.

Results and Discussion

The phosphosilicate glass composition may be related to the ratio of the absorbance of the P-O band at about 1325 cm^{-1} to that of the Si-O band at about 1050 cm^{-1}. However, these bands are not so well resolved as those of the borosilicate (8, 9) and arsenosilicate (12) binary mixtures. The absorbance of the Si-O band is significant at 1325 cm^{-1}. A calibration curve based on the ratio of the total absorbance at 1325 cm^{-1} to that at 1050-1100 cm^{-1} [2] would indicate a value of about 0.045 for this ratio for pure SiO_2. Much more important is the fact that the uncertainty in absorbance introduced in drawing the base line (see Fig. 1), while negligible in the calculation of Si-O absorbance, is significant in the P=O absorbance calculation for glasses low in phosphorus concentration.

It has been found more reproducible to calculate the linear absorbance ratios as follows. The base line for the Si-O band is drawn as shown in Fig. 1. The Si-O absorbance in the 1325 cm^{-1} region is largely corrected for by drawing the P=O base line as the straight line tangent to the absorbance curve at points on either side of the P=O absorbance at 1325 cm^{-1}. The absorbances of the two bands are taken to be the maximum differences in absorbance units between their respective base lines and the absorbance curve (A-B and A'-B' for the P=O and Si-O bands, respectively, in Fig. 1). For the P=O band this is not necessarily at the frequency of maximum total absorbance. The linear absorbance ratio for the glass whose spectrum is shown in Fig. 1 is thus

$$R = (\text{A-B})/\text{A'-B'})$$

This ratio is shown in Fig. 2 as a function of glass composition for several deposition temperatures. The curve is drawn to represent results for glasses deposited at 400°C only. There appears to be a small but systematic dependence of the linear absorbance ratio on temperature. Glasses of similar compositions exhibit increasing linear absorbance ratios with increases in deposition temperature. A similar (although opposite) temperature dependence was observed for borosilicate glasses; but it was further established that the ratio of band areas (approximated by the product of the linear absorbance times the half-width) was uniquely related to the glass composition (9).

A similar approximation for the P=O band area is complicated by the fact that the base line for this band

[2] The frequency of maximum absorbance of the Si-O band varies somewhat with composition (20).

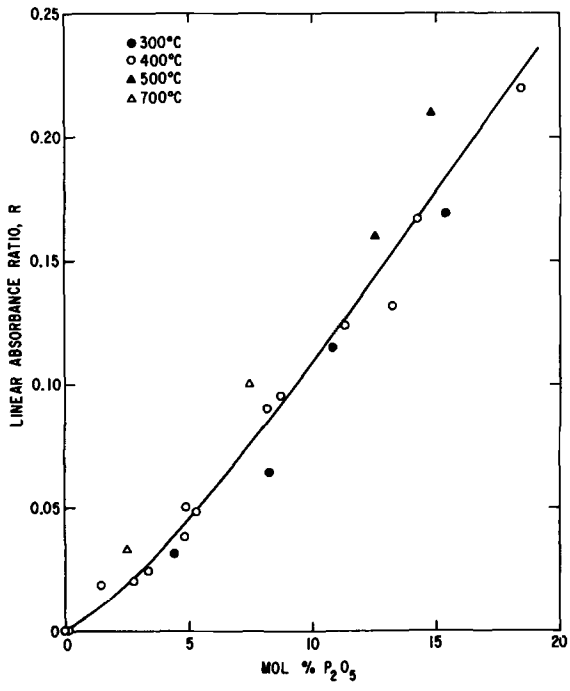

Fig. 2. Linear absorbance ratio vs. mole per cent P_2O_5 for phosphosilicate glasses vapor-deposited at temperatures ranging from 300° to 700°C.

is generally far from horizontal. However, the half-width of this band may be constructed by drawing the line parallel to the base line through the point half way (in absorbance units) between the base line and the point on the absorbance curve farthest from the base line. The line C-D in Fig. 1 represents this construction. The projection of C-D on the horizontal axis, (C-D)p, is taken to be the half-width of the P=O band in cm^{-1}. The half-width of the Si-O band is taken to be the width of the band (in cm^{-1}) at half the maximum absorbance (C'-D' in Fig. 1).

Thus the band area ratio for the glass whose spectrum is shown in Fig. 1 is[3]

$$R^* = \frac{(\text{A-B}) \times (\text{C-D})\text{p cm}^{-1}}{(\text{A'-B'}) \times (\text{C'-D'}) \text{ cm}^{-1}}$$

The composition dependence of the band area ratio is shown in Fig. 3. Employing this calibration curve, the compositions of phosphosilicate glasses 0-20 m/o in P_2O_5 vapor deposited at temperatures ranging from 300° to 700°C may be determined from the IR spectra of these glasses. The scatter of 1-2 m/o observed in these results is too large to be attributed to the uncertainty of the microprobe analysis. It is due primarily to the fact that, for all concentrations studied, the P=O band is relatively weak and its area is difficult to calculate with less than about 10% uncertainty.

Employing the band area ratio in lieu of the linear absorbance ratio may appear to reduce the temperature dependence in the resulting calibration curves much less dramatically than in the borosilicate glass case (9). [Thus, PSG compositions may be determined from the more simply calculated linear absorbance ratio (Fig. 2) with little loss of precision.] It must be pointed out, however, that the highest P_2O_5 compositions included are about 20 m/o. The dependence of the linear

[3] It would be more nearly correct to construct C'-D' parallel to the base line as C-D is constructed. The Si-O base line is so nearly horizontal, however, that the correction introduced is negligible. Even more nearly correct would it be to draw C-D and C'-D' parallel to their respective base lines not geometrically but logarithmically. Finally, for a true representation of the integrated intensity, of these bands, the spectra should be recorded in linear absorbance units and the area ratios determined with a planimeter. However, all of these refinements have an effect on the relationship between the area ratio as calculated above and the chemical composition which is insignificant when compared to the uncertainties introduced in determining the absorbance and half-width of the P=O band.

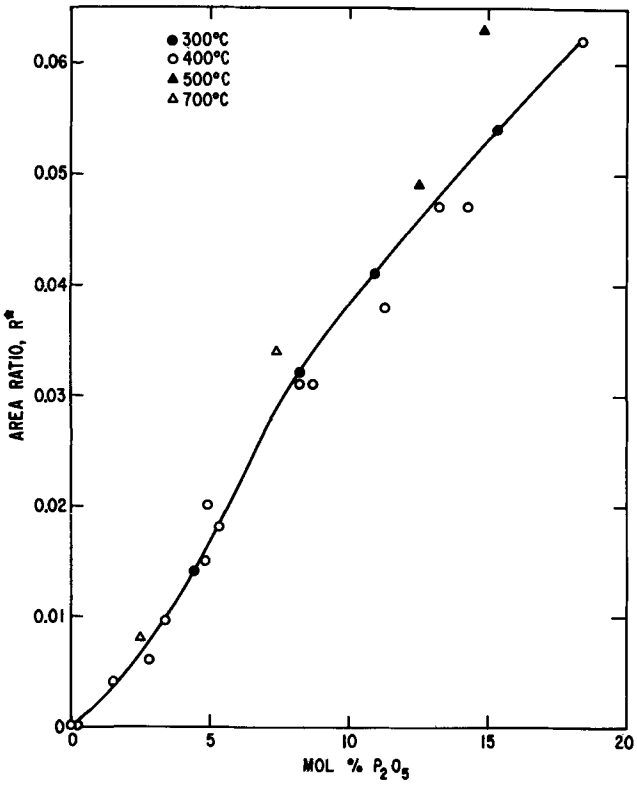

Fig. 3. Band area ratio vs. mole per cent P_2O_5 for phosphosilicate glasses vapor-deposited at temperature ranging from 300° to 700°C.

absorption ratio on temperature was not detected in borosilicate glasses less than about 25 m/o in B_2O_3.

Extension of the calibration curves shown in Fig. 2 and 3 to glasses of more than 20 m/o P_2O_5 is made difficult by the fact that at about this composition the 1325 cm^{-1} band begins to broaden and decrease in intensity with increases in P_2O_5 concentration while new bands begin to appear at frequencies closer to that of the 1050 cm^{-1} Si-O band. These trends are seen in Fig. 4 where the spectra of four glasses of different composition are shown. Except for the absence of significant absorption at ~3000 cm^{-1} (18), the spectrum of the glass 15 m/o in P_2O_5 is in good agreement with previously published results for similarly deposited glasses (18, 20, 22).

The dependence of deposition rate and of glass composition on deposition temperature is shown in Fig. 5 and 6, respectively, for three different reactant gas compositions. N_{PH_3} is defined to be the PH_3 flow rate divided by the total hydride flow rate. Except for the results at 300°C for the hydride mixture where $N_{PH_3} = 0.31$, neither the deposition rate nor the composition of the film appears to be a strong function of deposition temperature. Similar results were found by Kern and Heim who concluded that the deposition rate and composition of phosphosilicate films are less dependent on deposition conditions than are those of borosilicate films (19).

The rate of deposition from hydride mixtures dilute in PH_3 ($N_{PH_3} < 0.15$) increases monotonically with increases in temperature while increasingly prominent maxima are observed in the temperature dependence of the deposition rate with increases in PH_3 concentration over the range $0.2 < N_{PH_3} < 0.3$ (see Fig. 5). (The absolute values of the deposition rates for the different gas mixtures shown in Fig. 5 are not directly comparable because different total hydride flow rates were employed for each gas mixture. The apparent equality of these values at 500°C is coincidental.)

The P_2O_5 concentration in glasses deposited from a given reactant composition decreases monotonically with increases in deposition temperature as shown in Fig. 6.

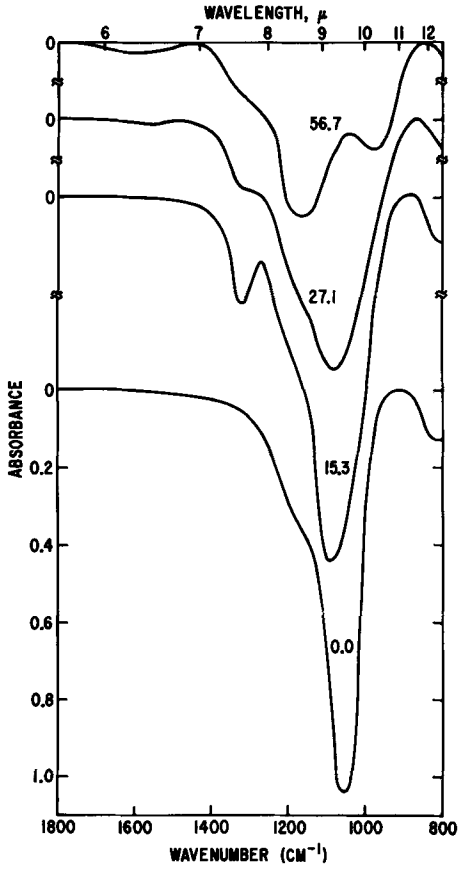

Fig. 4. Vibrational spectra of vapor-deposited phosphosilicate glasses 0, 15.3, 27.1, and 56.7 m/o in P_2O_5.

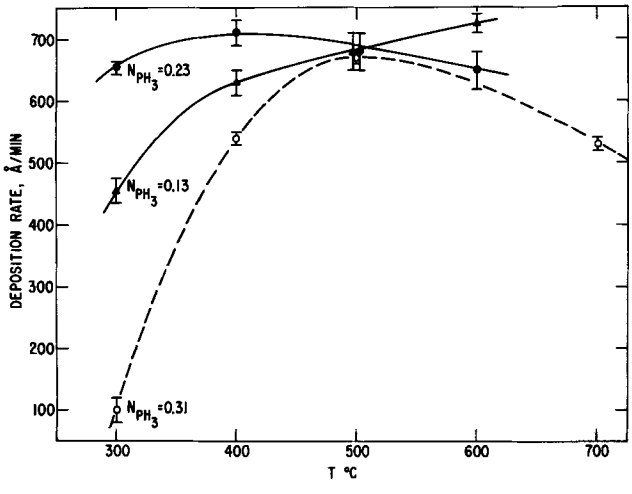

Fig. 5. Temperature dependence of the rate of deposition of phosphosilicate glasses from the indicated hydride mixtures.

If it is assumed that these films are the stoichiometric products of the reaction of SiH_4 and PH_3 with excess O_2, the composition of the film may be calculated from that of the hydride mixture by the relation

Table I. Mole per cent P_2O_5 observed at high deposition temperatures and calculated by Eq. [1]

N_{PH_3}	Mole per cent P_2O_5	
	Calculated	Observed (Fig. 6) (600°-700°C)
0.13	7.0	7 ± 1
0.23	11.5	11 ± 1
0.31	18.4	14 ± 1

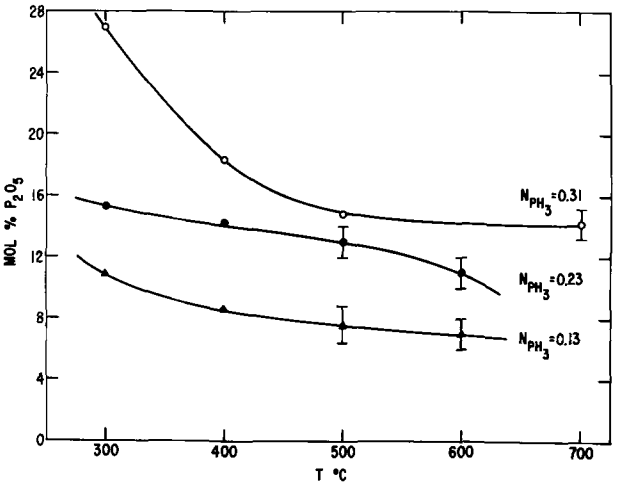

Fig. 6. Temperature dependence of the composition of phosphosilicate glasses deposited from the indicated hydride mixtures.

$$\text{mol per cent } P_2O_5 = 100N_{PH_3}/(2 - N_{PH_3}) \quad [1]$$

A comparison of the PSG compositions thus calculated with those observed at high deposition temperatures is made in Table I.

While the P_2O_5 concentration calculated assuming stoichiometry is about 4 m/o higher than that observed for glasses deposited at high temperatures from a hydride mixture of $N_{PH_3} = 0.31$, the calculated and observed compositions are in good agreement for glasses deposited (at high temperatures) from glass mixtures lower in PH_3 concentration. It has been reported that glasses up to 5 m/o in P_2O_5 ($N_{PH_3} \sim 0.095$) are the stoichiometric products of the oxidation of SiH_4 and PH_3 at 400°C while further increases in N_{PH_3} are not accompanied by proportionate increases in P_2O_5 concentration (19). The present results suggest that increases in deposition temperature cause increases in the values of N_{PH_3}, for which the reaction proceeds stoichiometrically to about 0.23 at 600°-700°C. For higher values of N_{PH_3} the reaction product is still less than stoichiometric in P_2O_5.

Acknowledgments

We thank M. F. Ciccarelli for performing the microprobe analyses of the phosphosilicate glasses and R. B. Bolon and E. Lifshin, as well as Mr. Ciccarelli, for many useful discussions concerning the analytical aspects of this work.

Manuscript submitted Nov. 17, 1972; revised manuscript received April 3, 1973.

Any discussion of this paper will appear in a Discussion Section to be published in the June 1974 JOURNAL.

REFERENCES

1. M. L. Barry, *This Journal*, **117**, 1405 (1971).
2. D. R. Kerr, J. S. Logan, P. J. Burkhardt, and W. A. Pliskin, *IBM J. Res. Develop.*, **8**, 376 (1964).
3. E. H. Snow and B. E. Deal, *This Journal*, **113**, 263 (1966).
4. D. Flatley, N. Goldsmith, and J. Scott, *ibid.*, **111**, 61C (1964).
5. W. T. Lynch and R. A. Furnage, *IEEE Trans. Electron. Devices*, **ED-14**, 705 (1967).
6. B. J. Baliga and S. K. Ghandi, *ibid.*, **ED-19**, 761 (1972).
7. A. S. Tenney, Unpublished results.
8. A. S. Tenney and J. Wong, *J. Chem. Phys.*, **56**, 5516 (1972).
9. A. S. Tenney, *This Journal*, **118**, 1658 (1971).
10. W. Kern, *RCA Rev.*, **32**, 429 (1971).
11. E. A. Taft, *This Journal*, **118**, 1985 (1971).
12. J. Wong and M. Ghezzo, *ibid.*, **118**, 1540 (1971).
13. E. A. Corl, S. L. Silverman, and Y. S. Kim, *Solid-State Electron.*, **9**, 1009 (1966).
14. D. M. Brown and P. R. Kennicott, *This Journal*, **118**, 293 (1971).
15. M. Ghezzo, *ibid.*, **119**, 1428 (1972).
16. W. A. Pliskin and E. E. Conrad, *IBM J. Res. Develop.*, **8**, 43 (1964).
17. A. S. Tenney and M. Ghezzo, *This Journal*, **120**, 1091 (1973).
18. W. Kern and R. C. Heim, *ibid.*, **117**, 568 (1970).
19. W. Kern and R. C. Heim, *ibid.*, **117**, 562 (1970).
20. W. A. Pliskin, *Appl. Phys. Letters*, **7**, 158 (1965).
21. W. A. Pliskin and R. P. Gnall, *This Journal*, **111**, 872 (1964).
22. H. Osafaune, Y. Matukura, S. Tanaka, and Y. Miura, Abstract No. 110, Vol. 14, No. 2, Electrochemical Soc., Extended Abstracts, Fall Meeting, Buffalo, N. Y., Oct. 10-14, 1965.
23. S. Nishimatsu and T. Tokuyama, Abstract No. 170, p. 24, J-4, Electrochemical Soc. Extended Abstracts, Fall Meeting, Chicago, Ill., Oct. 15-20, (1967).
24. W. A. Pliskin, in "Measurement Techniques for Thin Films," B. Schwartz and N. Schwartz, Editors, p. 280, The Electrochemical Society Softbound Symposium Series, New York (1967).
25. R. P. Esch, J. M. Eldridge, P. Balk, and W. A. Pliskin, Abstract No. 95, page 265, Electrochemical Soc. Extended Abstracts., Fall Meeting, Detroit, Mich., Oct. 5-9, 1969.
26. S. J. B. Reed, in "X-Ray Optics and Microanalysis," R. Castaing, P. Deschamps, and J. Philibert, Editors, p. 339, Hermann, Paris (1966).
27. C. A. Anderson, in "The Electron Microprobe," T. D. McKinley, K. F. J. Heinrich, and D. B. Wittry, Editors, p. 58, John Wiley & Sons, Inc., New York (1966).
28. J. M. Eldridge and P. Balk, *Trans. Met. Soc. AIME*, **242**, 539 (1968).

The Composition of Oxides Formed on Electroless Ni-P Deposits

S. T. Pai and J. P. Marton

Welwyn Canada Limited, London, Ontario, Canada

The initial state of electroless Ni-P deposits varies with the composition of the chemical solution employed and with the deposition conditions (1, 2). The initial state of Ni-P deposits prepared from nickel sulfate solution and deposited at 25°C is known to be a single phase, fine polycrystalline material of Ni and P, in which the P atoms are dissolved in the Ni lattice, forming a solid solution (3). Upon heating the deposit in an oxygen environment up to 400°C, an oxide layer will form. Some previous work (4-6) has been done on the electrical, optical, and other properties of the Ni-P oxide layer. However, little is known about the exact composition. Knowledge of the composition is important for a better understanding of the optical and electrical properties. The present investigation is an attempt to find the nature of the oxides formed on Ni-P deposits by reflection electron diffraction.

In this work we used two types of Ni-P deposits. One type was made at the over-all composition of 16 atomic per cent (a/o) of P and the other at 30 a/o. They were prepared from acid solution of nickel sulfate and hypophosphate at pH = 5.3 and 3.3, respectively. The substrates used were activated borosilicate glass. The details of deposition process were reported elsewhere (7). Heat-treatment of these samples was carried out in vacuum, inert gases (Ar and He), oxygen, and open air environments. Reflection electron diffraction results revealed that all samples heated in vacuum or inert gases have either Ni or Ni + Ni_3P structures only (8), whereas samples heated in oxygen or open air showed NiO structure with a few additional weak rings appearing in the diffraction pattern. The results were obtained by employing an AEI EM6G electron microscope and are shown in Fig. 1. The diffraction patterns were taken at 100 kV.

In Figure 2 are microdensitometer traces of the diffraction patterns. Curve (a) is the diffraction pattern obtained from a sample containing about 30 a/o P,

Key words: oxides, electroless Ni-P deposits.

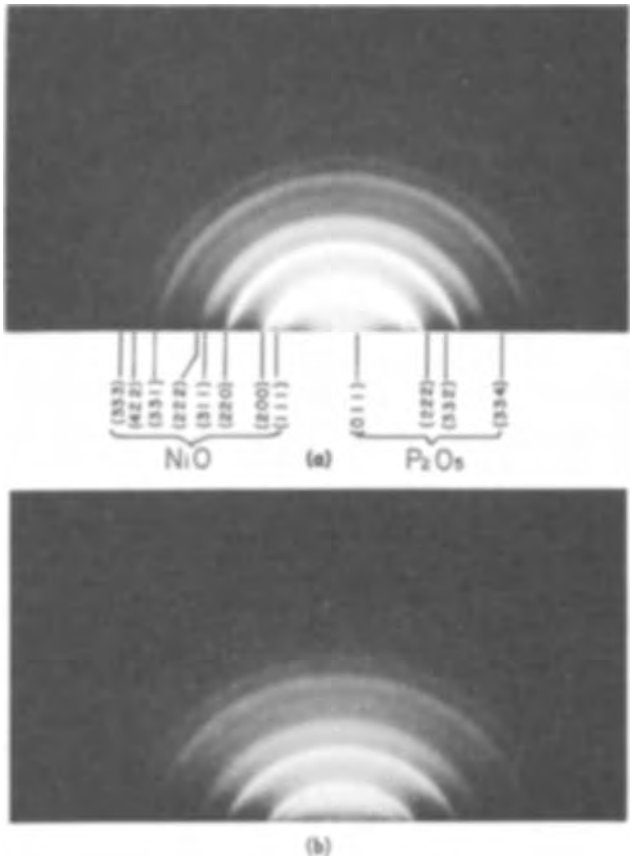

Fig. 1. Reflection electron diffraction patterns of Ni-P oxides taken at 100 kV for two phosphorous concentrations. (a) P content, 30 a/o (b) P content, 16 a/o.

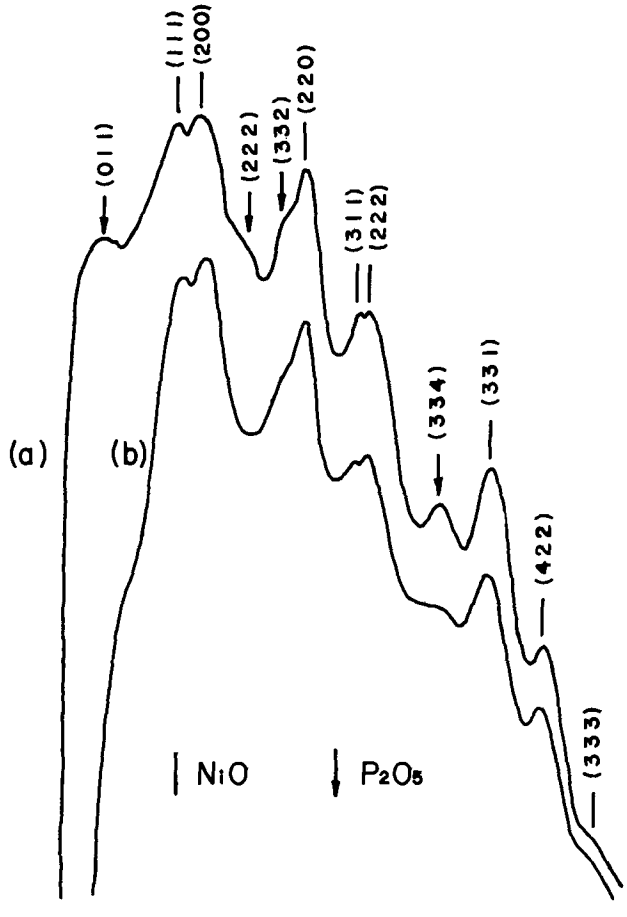

Fig. 2. Microdensitometer traces of plates in Fig. 1(a) and (b). The structure corresponds to NiO and to P_2O_5. The peaks for P_2O_5 at higher P concentration in (a) are easily discernible. At lower P concentration in (b) the peaks are weaker.

and curve (b) is that from a sample containing about 16 a/o P. From the figure, we can see that as the P content increases, so do the intensities of the additional rings. Their positions are marked by vertical arrows. The pattern indicates that the additional rings have a direct connection with the P content in the deposits. Upon close examination of the diffraction patterns, the rings were identified to be due to orthorhombic P_2O_5 crystallites within a 1% experimental error using lattice constants (9) $a = 9.23$Å $b = 7.18$Å, and $c = 4.94$Å.

The present finding suggests that the surface oxides of Ni-P deposits contain both NiO and P_2O_5 and that the P_2O_5 crystallites are dispersed in the NiO matrix, forming a crystalline mixture. As pointed out before, the optical constants and the electrical properties are related to the composition of the material under study, so the present findings may furnish some useful information for investigations of the optical and other properties of oxidized Ni-P surfaces.

Manuscript submitted April 12, 1973; revised manuscript received May 7, 1973.

Any discussion of this paper will appear in a Discussion Section to be published in the June 1974 JOURNAL.

REFERENCES

1. "Electroless Nickel Plating," ASTM Special Technical Publication No. 265 (1959).
2. S. T. Pai and J. P. Marton, *J. Appl. Phys.*, **43**, 4836 (1972).
3. S. T. Pai, J. P. Marton, and J. D. Brown, *ibid.*, **43**, 282 (1972).
4. S. T. Pai and J. P. Marton, *ibid.*, **43**, 4972 (1972).
5. J. P. Marton and E. C. Chan, *ibid.*, **43**, 1681 (1972).
6. E. C. Chan and J. P. Marton, *ibid.*, **43**, 4027 (1972).
7. J. P. Marton and M. Schlesinger, *This Journal*, **115**, 16 (1968).
8. S. T. Pai and J. P. Marton, 23rd Proc. Electron. Components Conf., p. 233 (1973).
9. C. H. MacGillavry, H. C. J. de Dicker, and L. M. Nijiland, *Nature*, **164**, 448 (1949).

Localized Plastic Deformation of GaP and GaAs Generated by Thermocompression Bonding

W. A. Brantley and D. A. Harrison[1]

Bell Laboratories, Murray Hill, New Jersey 07974

Thermocompression (TC) bonding is employed in the assembly of a variety of devices fabricated from the compound semiconductors GaAs, GaAlAs, and GaP, such as IMPATT's, lasers, and LED's. In this technique the semiconductor chip is heated to temperatures around 300°-400°C, and pressure is applied for bonding to heat sinks or contact wires. Recent evidence (1) indicates that dislocations may be generated in <111> oriented GaAs at 380°C by TC bonding at loads exceeding ~7.5 kg/mm².[2] Although the detailed experimental investigations have not been performed to date on compound semiconductor devices, dislocations may affect device characteristics and long-term reliability directly or, perhaps more likely, indirectly by serving as rapid "pipe" diffusion regions for impurities or as sites for enhanced dopant diffusion and precipitation (2). Accordingly, it is important in general to determine the conditions of stress and temperature for which dislocations may be generated in compound semiconductors during device processing.

This paper presents the results of low temperature stressing experiments performed on GaP and GaAs specimens having typical device dimensions of the order of 10 mils. The TC bonding station was employed solely as a mechanical loading apparatus to achieve combined stresses and temperatures which might be encountered during device processing. Subsequently, the stressed specimens and unstressed controls were immersed in various etchants which have previously been demonstrated to reveal dislocations. The results for both GaAs and GaP demonstrate that nonuniform loading conditions often prevail during TC bonding and that localized plastic deformation, *i.e.*, the introduction of dislocations, is possible at temperatures as low as 200°C. Moreover, the extent of deformation is strongly dependent on the hardness of the medium in contact with the semiconductor.

A variety of compound semiconductor device materials was employed for the stressing experiments: (*i*) GaP p-n junction material for green light-emitting diodes (LED's) consisting of n- and p-type liquid-phase epitaxial (LPE) layers, each approximately 1 mil thick, grown on an n-type liquid encapsulated Czochralski (LEC) GaP substrate (3); (*ii*) a GaP slice consisting of only the n-type LPE layer on an n-type LEC substrate; (*iii*) S-doped bulk GaAs grown by the LEC technique (4); and (*iv*) a GaAs slice with an n-type layer about 8 μm thick grown by vapor-phase epitaxy (VPE) on an n^+ substrate (5), similar to slices presently being fabricated into IMPATT's. Slice (*iv*) was grown in the <100> orientation whereas the remaining material was <111> oriented.

The GaP specimens were in the form of dice approximately 15 mils square and 10 mils in height, prepared by lapping and chemically polishing the starting slice followed by slurry cutting. The GaAs specimens were in the form of mesas having approximately 8 mils top diameter and 6 mils height, prepared by lapping and chemically polishing one side of the starting slice followed by Au ball masking and sandblasting for the other side. Individual specimens were placed on a Au-plated Cu stud and stressed by the TC bonding station at 300° or 400°C using a sapphire ram and loads of 30, 100, or 300g with several specimens per condition. The stressing temperatures were measured with a thermocouple placed in contact with the top of the stud, and these temperatures were in good agreement (temperature difference <20°C) with values obtained with the aid of temperature-indicating markers painted on top of the studs.

Gershenzon and Mikulyak have reported that bulk plastic deformation of GaP does not occur below 900°C (6) although experimental evidence for dislocation generation in GaP at 600°C has been obtained (7). Therefore, a 5 mil (hexagonal cross section) loading ram was initially utilized in order to increase the applied stress on the 15 mil square dice; the 5 mils correspond to the distance between opposite hexagonal faces. Etched p($\sim 1 \times 10^{18}$ Zn/cm³, $\sim 1 \times 10^{19}$ N/cm³) layers of the p/n/n GaP specimens are illustrated in Fig. 1 for (a) the unstressed condition and after stressing at 300°C by the TC bonding station with (b) 30, and (c) 300g

[1] Present address: Research Devices, Incorporated, Berkeley Heights, New Jersey 07922.

Key words: compound semiconductors, mechanical properties, semiconductor device processing, dislocations.

[2] 1 kg/mm² = 9.8 × 10^7 dyn/cm² = 1.42 × 10^3 psi.

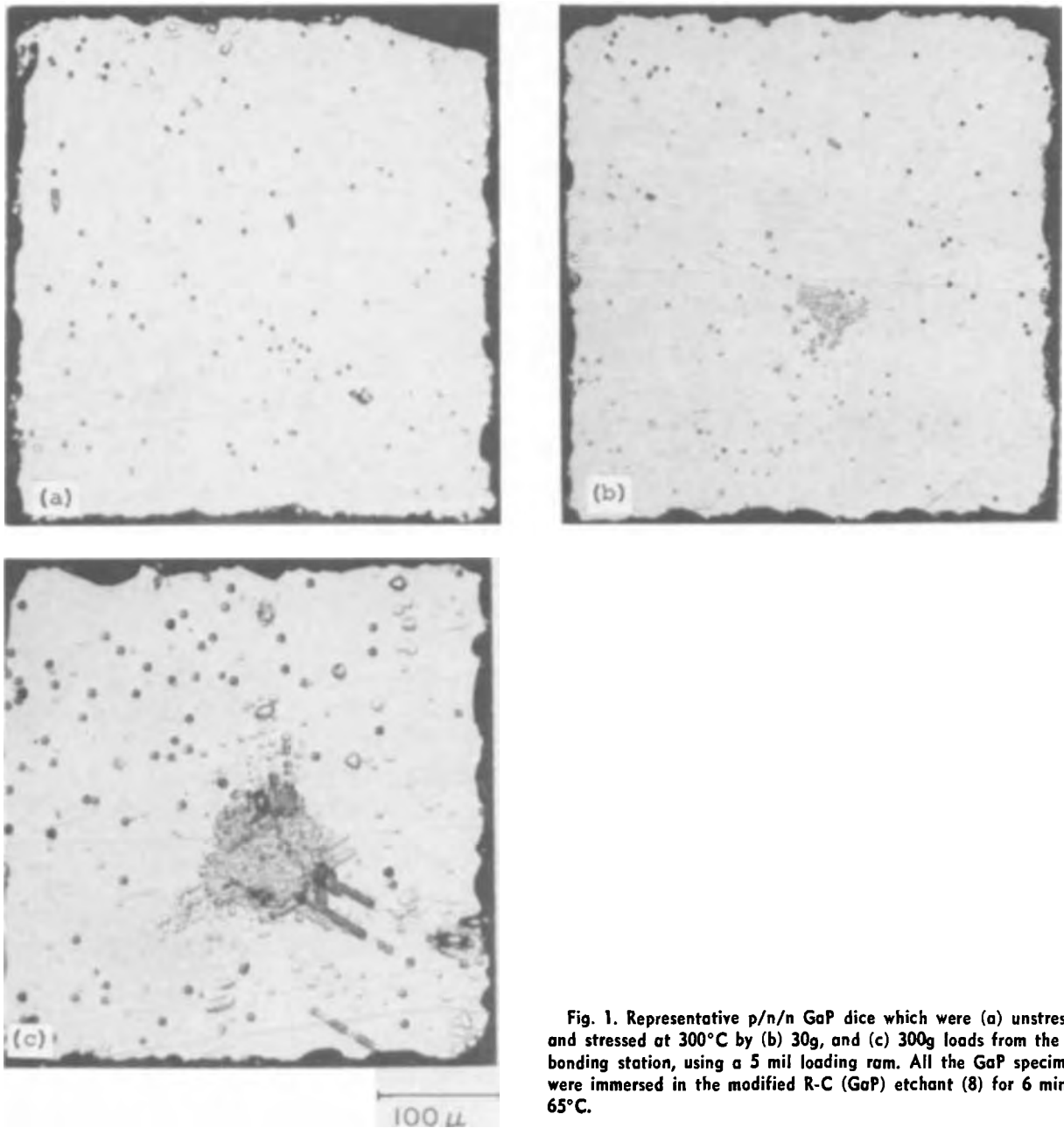

Fig. 1. Representative p/n/n GaP dice which were (a) unstressed and stressed at 300°C by (b) 30g, and (c) 300g loads from the TC bonding station, using a 5 mil loading ram. All the GaP specimens were immersed in the modified R-C (GaP) etchant (8) for 6 min at 65°C.

loads. All GaP specimens were immersed in the modified R-C etchant (8) for approximately 6 min at 65°C to reveal emergent dislocations.

The clusters of small etch pits in the center of Fig. 1 (b and c) are due to fresh dislocations generated by the mechanical stressing. This interpretation follows immediately from the increasing dislocation density with applied load, the similar appearances for the small pits and the larger sharp-bottomed pits corresponding to old, grown-in dislocations, and the existence of numerous small etch pits in rows lying along one of the three <110> directions corresponding to traces of oblique {111} slip planes. (The sides of the dislocation etch pits produced by the R-C etch lie along <110> directions.) The prominent etch grooves in Fig. 1(c) are not observed for unstressed specimens and may be traces of stacking faults (8) or twinned regions generated by the applied stress. However, diffraction contrast experiments would be required for precise identification of these defects. The dislocation density increases from 1 to 2 $\times$ 10^5 cm^{-2} for unstressed specimens to values exceeding 10^7 cm^{-2} in the regions of localized deformation. Thus, localized plastic deformation of GaP can occur at temperatures as low as 300°C. In all cases, the mechanical deformation behavior for the n-type LPE layers of the n LPE/n LEC GaP dice was similar to that for the p-type LPE layers of the p/n/n specimens subjected to the same stressing conditions.

The effect of stressing temperature on deformation behavior is evident from comparison of Fig. 1(c) and 2(a). These two p/n/n GaP specimens were stressed with 5 mil rams, the latter by a 100g load at 400°C and the former by a 300g load at 300°C. The extent of localized deformation is conspicuously greater at 400°C compared to 300°C, even though a smaller load was utilized at 400°C. Dislocations also were generated in the 15 mil square GaP dice at 400°C when a 20 mil ram was employed, for loads exceeding ~30g. An etched p/n/n specimen subsequent to stressing at 400°C with the larger ram and a 100g load is illustrated in Fig. 2(b). It is apparent that nonuniform loading near the specimen periphery occurred with the 20 mil ram. Dislocation generation in GaP was even observed at 200°C for a 600g load. A different stressing apparatus was utilized, having a weighted stainless steel piston larger than the die surface confined within a nearly tight-fitting sleeve (2). However, the similar appearance of the deformed area to Fig. 2(b) indicated that nonuniform loading occurred, with the local stress consider-

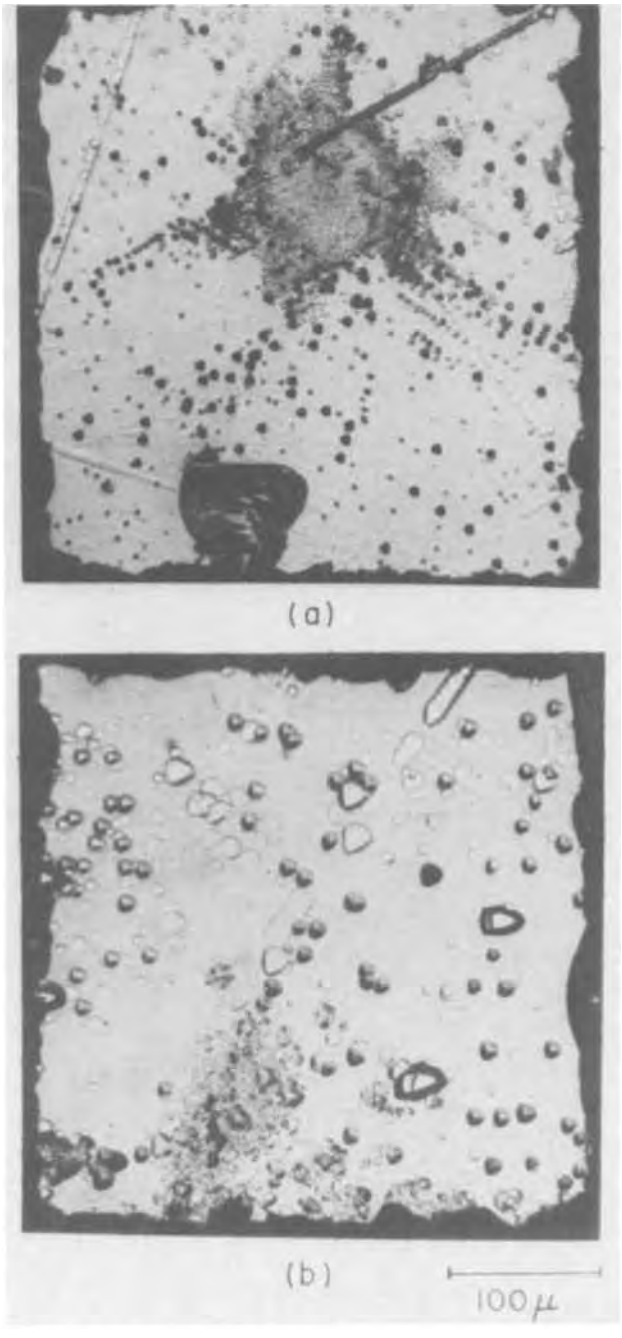

Fig. 2. Additional p/n/n GaP specimens which were stressed at 400°C by a 100g load: (a) 5 mil ram and (b) 20 mil ram. The prominent fracture in the lower portion of (a) occurred during the course of the chemical etching and the microscopic observation.

ably exceeding the nominal value of ~4 kg/mm² corresponding to the 600g load.

Additional experiments established that under appropriate conditions dislocation generation in the GaP specimen dice could be prevented for stressing in the 300°-400°C temperature range with the thermocompression bonding station. Localized plastic deformation was not observed in specimens gripped and loaded peripherally by a specially designed collet or in specimens centrally stressed with a Au loading tip. The absence of dislocation generation in these two cases is evidently due, respectively, to the applied stress being well distributed and to deformation of the softer Au loading tip in contact with the GaP specimens in comparison to the sapphire loading ram.

For GaAs mesas from the <111> oriented, bulk-grown ($n \sim 4 \times 10^{17}$ cm^{-3}) material the onset of macroscopic dislocation generation occurred for loads between 30 and 100g at 300°C and below 30g at 400°C. The loading ram utilized was larger than the top surface of the GaAs mesas, and the 30g load corresponds to a nominal compressive stress of ~1 kg/mm². Complementary results were obtained with the Schell (9, 10), modified (11) R-C (12), and A-B (13) etchants. For mesas fabricated from the {100} GaAs and having the VPE layer ($n \gtrsim 1 \times 10^{16}$ cm^{-3}) for the top surface, similar deformation behavior was found at 400°C, the only temperature investigated. Experiments with the weighted piston apparatus demonstrated that localized deformation in GaAs also is possible at 200°C, for ~300g loads on 14 mil square dice prepared by sawing (2). No evidence of dislocation generation was observed at room temperature for loads up to ~1000g on the 8 mil mesas, above which fracture generally occurred.

No mechanical deformation data are available for GaP to permit comparison with the present stressing experiments. The present investigations have demonstrated that under the proper loading conditions dislocation generation is possible in GaP at temperatures as low as 200°C, considerably below the values previously reported. The likelihood of localized deformation is greatly enhanced by utilization of a stressing medium (such as the sapphire ram) harder than GaP and by loading over an area smaller than the specimen which is expected to produce stress concentration effects (particularly at corners of the hexagonal ram). In addition, the greater lateral extent of the deformation bands in Fig. 1(c) and 2(a), compared to the 5 mil ram size, demonstrates that not only dislocation generation but also some dislocation mobility is possible for GaP in the 300°-400°C temperature range.

For GaAs, limited information concerning bulk deformation behavior is available. Previous studies (14-16) have indicated that the initial generation of large numbers of fresh dislocations in n-type, <111> oriented GaAs requires a compressive yield stress exceeding 20 kg/mm² at 400°C. Extrapolation of curves for the temperature dependence of the yield stress suggests that stresses over an order of magnitude greater (possibly ~400 kg/mm²) may be required at 300°C. (For GaP, dislocation generation and mobility are more difficult.) Moreover, dislocations in GaAs evidently possess considerable mobility in this temperature range since dislocation motion is possible at 300°C for stresses of the order of 1 kg/mm² (17).

However, nonuniform loading conditions can exist for TC stressing of specimens with dimensions of the order of 10 mils; *cf.*, Fig. 2(b). Under these circumstances, high local stresses which greatly exceed nominal computed values can arise and induce dislocation generation at temperatures considerably less than predicted from bulk deformation behavior. The very limited amount of plastic flow at room temperature previously reported (18) for GaAs deformed by indentation, where an extremely high stress is expected, appears to be an extreme example of this behavior.

Acknowledgment

The authors gratefully acknowledge the assistance of W. L. Boughton, C. Waters, and N. J. Engelmann with the TC bonding experiments. Helpful comments and encouragement from R. H. Saul and J. R. Patel are appreciated. The GaAs material for these experiments was grown by M. E. Weiner and L. C. Luther, and the GaP material was grown by O. G. Lorimor. The assistance of R. A. Furnanage in having the slurry cutting of the GaP specimens performed is also appreciated.

Manuscript submitted March 6, 1973; revised manuscript received April 26, 1973.

Any discussion of this paper will appear in a Discussion Section to be published in the June 1974 JOURNAL.

REFERENCES

1. F. Hasegawa and H. Ito, *Appl. Phys. Letters*, **21**, 107 (1972).

2. W. A. Brantley and D. A. Harrison, *Proc. IEEE Reliability Physics Symposium*, April 1973, To be published.
3. O. G. Lorimor, W. H. Hackett, Jr., and R. Z. Bachrach, *This Journal*, **119**, 303C (1972).
4. M. E. Weiner, D. T. Lassota, and B. Schwartz, *ibid.*, **118**, 301 (1971).
5. J. V. DiLorenzo and G. E. Moore, Jr., *ibid.*, **118**, 1823 (1971).
6. M. Gershenzon and R. M. Mikulyak, *J. Appl. Phys.*, **35**, 2132 (1964).
7. R. H. Saul, Unpublished research.
8. R. H. Saul, *This Journal*, **115**, 1184 (1968).
9. H. A. Schell, *Z. Metallk.*, **48**, 158 (1957).
10. M. S. Abrahams and L. Ekstrom, in "Properties of Elemental and Compound Semiconductors," H. C. Gatos, Editor, Interscience Publishers, Inc., New York (1960).
11. M. S. Abrahams, *J. Appl. Phys.*, **35**, 3626 (1964).
12. J. L. Richards and A. J. Crocker, *ibid.*, **32**, 611 (1960).
13. M. S. Abrahams and C. J. Buiocchi, *ibid.*, **36**, (1965).
14. N. P. Sazhin, M. G. Mil'vidskii, V. B. Osvenskii, and O. G. Stolyarov, *Soviet Phys.—Solid State*, **8**, 1223 (1966).
15. H. Alexander and P. Haasen, *Solid State Phys.*, 27 (1968).
16. I. N. Shershakova, V. B. Osvenskii, and O. G. Stolyarov, *Neorg. Mater.*, **6**, 457 (1970).
17. S. K. Choi and M. Mihara, *J. Phys. Soc. Japan*, 1154 (1972).
18. M. S. Abrahams and L. Ekstrom, *Acta Met.*, **8**, 654 (1960).

Colorimetric Determination of Boron in Aqueous Solutions and in Borosilicate Glass by Solvent Extraction

A. S. Tenney*,[1]

General Electric Corporate Research and Development, Schenectady, New York 12301

Boron has been determined in steel (1), in soils (2), and in natural waters (3) colorimetrically by extracting methylene blue fluoroborate with 1, 2 dichloroethane. Recently (4) a modification of this method was employed to determine boron in thin films of pyrolytically deposited borosilicate glass. The details and short discussion of the procedure are presented here.

Sample Preparation

(*i*) If necessary, the boron-containing sample is dissolved in a measured amount of H_2O and diluted to the range 1-4 μg B/ml.

(*ii*) To a 30 ml polyethylene dropping bottle (A. H. Thomas, No. 2247-S) 2.0 ml of the solution made in step (*i*), 2.0 ml dilute HF (DHF: 50 ml 50% HF/1 H_2O), and 3.0 ml 0.001M methylene blue solution (MBS: approximately 374 mg/liter) are added. The bottle is then shaken and allowed to stand at least 1 hr.

Standards are stored as aqueous solutions of H_3BO_3. Standard samples are prepared by mixing 2.0 ml standard solution, 2.0 ml DHF, and 3.0 ml MBS as in step (*ii*). Blanks consist of 2.0 ml DHF, 2.0 ml H_2O, and 3.0 ml MBS.

(*iii*) To samples, standard samples, and blanks, 10.0 ml 1,2 dichloroethane are added. The mixture is shaken and allowed to stand overnight (about 16 hr).

Absorbance Measurement

The bottles are inverted so that the organic phase may be squeezed into 1 cm cells. Absorbance is determined in the range 4000-7000Å with a double beam recording spectrophotometer (Perkin-Elmer Model 202) using a blank as reference and drawing a base line with a blank in both beams.

The spectra of the boron-containing samples appear to have three absorbance peaks relative to the base line: a minor one at about 4900Å and major ones at 6050-6300Å and at 6750Å as shown in Fig. 1 (the exact positions of the latter two peaks being more or less dependent on the boron concentration). Actually, the two major peaks result from the fact that the blank exhibits a relatively sharp band while the boron-containing samples display broader bands with maxima at about 6600Å.

Calibration curves of absorbance of these three peaks *vs.* boron concentration in micrograms per milliliters (in the original sample, not in the organic phase) are shown in Fig. 2. The standard deviation for determinations on standard samples was 0.01 absorbance indirating that boron may be determined in the range 0-5 μg/ml with an uncertainty of $\pm$0.05 to 0.1 μg/ml using results from the two major peaks. Since 2.0 ml of solution are used, the limit of detectability is about $\pm$0.1 μg boron.

The calibration curve of the minor peak absorbance at 4900Å may be extended to boron concentrations of at least 20 μg/ml. However, it was found easier and more precise to dilute the boron-containing samples to less than 5 μg B/ml and employ the major peak absorbances. Nevertheless, the minor peak may be employed to estimate the boron present should a sample contain enough boron that the major peak absorbances are too large to be determined.

The absorbance is quite sensitive to the HF concentration (1) so at least three standard samples were always analyzed with a batch of samples.

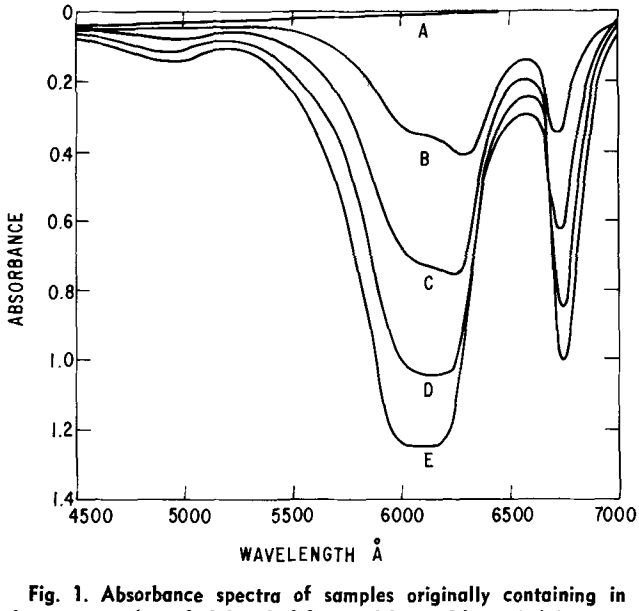

Fig. 1. Absorbance spectra of samples originally containing in the aqueous phase 0, 1.0, 2.0, 3.0, and 4.0 μg of boron/ml (spectra A through E, respectively) *vs.* wavelength.

* Electrochemical Society Active Member.
[1] Present address: General Electric Company, Miniature Lamp Products Department, Chesterland, Ohio 44026.
Key words: boron analysis, methylene blue, doped oxides.

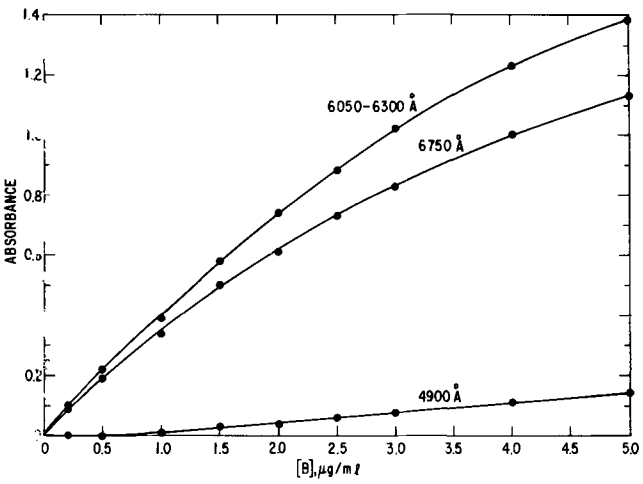

Fig. 2. Absorbance at 4900, 6050-6300, and 6750Å vs. concentration of boron in μg/ml of aqueous solution.

The procedure described here is simpler than those employed previously (1-3), firstly because of the use of a double beam recording spectrophotometer which automatically subtracts the significant absorbance of the bl nk, and secondly because no procedure is employed to eliminate interfering ions such as NO_3^-, As-V, and Cr-VI (2). Nevertheless, this procedure should be generally useful in the determination of microquantities of boron in aqueous solutions in the absence of these ions.

To determine boron in glass, only a slight modification of the above procedure is required. The sample is dissolved in a measured amount of DHF and diluted in DHF to 1-4 μg B/ml. Two milliliters of this dilution are mixed with 2.0 ml H_2O and 3.0 ml MBS and treated as described above. Because of the interference of arsenic (2), this procedure may not be used to determine boron in arsenic-containing glasses.

This procedure was combined with an atomic absorbance analysis for silicon to determine the composition of thin films of borosilicate glass pyrolytically deposited on silicon wafers (4).

Manuscript submitted Sept. 6, 1972; revised manuscript received Jan. 12, 1973.

Any discussion of this paper will appear in a Discussion Section to be published in the June 1974 JOURNAL.

REFERENCES

1. L. Pasztor, J. D. Bode, and Q. Fernando, *Anal Chem.*, **32**, 277 (1960).
2. R. E. Stanton and Alison J. McDonald, *Analyst*, **91**, 775 (1966).
3. S. Utsumi and A. Dsozaki, *Nippon Kagaku Zasshi*, **88**, 545 (1967).
4. A. S. Tenney, *This Journal*, **118**, 1658 (1971).

Distribution of Sodium in Sputtered SiO_2 as Determined by Neutron Activation and U.V. Spectrographic Analyses

Satish Kumar*,[1] and L. V. Gregor*

IBM System Products Division, East Fishkill, Hopewell Junction, New York 12533

Neutron activation techniques have been applied to epitaxial silicon (1) to measure the impurity concentration in the outer layer of epitaxial films. Kern (2) investigated semiconductor surface contamination by radioactive tracer techniques. Lunde (3) applied nondestructive neutron activation analysis on single-crystal silicon for different impurities. Yon *et al.* (4) studied the sodium distribution in thermal SiO_2 on silicon by radiochemical and MOS analysis.

Contamination in sputtered SiO_2 films can cause an increase in MOS surface leakage current due to surface inversion. Sodium ion is one of the major contaminants that cause this problem. Neutron activation and u.v. spectrographic techniques have been rarely applied to sputtered SiO_2 films. The purpose of this work was to investigate the presence and distribution of sodium in sputtered SiO_2 and to determine the source of the sodium.

Experimental Methods

Wafer Preparation

Silicon wafers (2-ohm cm, p-type 2.25 in. diam) were thermally oxidized to a SiO_2 thickness of 500 ± 30Å. Oxidation was done in dry oxygen in an all-quartz system at 1000° ± 2°C for 50 min. The wafers were annealed to 1050°C for 15 min in N_2.

* Electrochemical Society Active Member.
[1] Present address: National Cash Register (NCR), Microelectronics Division, Miamisburg, Ohio 45342.
Key words: sodium, sputtering, SiO_2, MOS.

Sputtering Technique

Sputtered SiO_2 was deposited by rf sputtering of a commercial fused silica target at a frequency of 13.56 MHz. Gallium-indium alloy (75:25) was applied to the back of the wafers, taking care that no alloy touched the front side. SiO_2 deposition was accomplished by placing wafers in a parallel plate sputtering system so that they were electrically and thermally connected to the anode plate by Ga-In.

A turbomolecular pump was used to eliminate pump oil back-streaming. After 2 μm of SiO_2 was deposited, excess Ga-In was removed by Freon, and the remaining Ga-In was removed by dipping the wafers in hot H_2SO_4 + HNO_3 (1:1) for 5 min at 100°C. The wafers were then rinsed in deionized water and dried with N_2.

After 2.0 μm of sputtered SiO_2 was deposited over the wafers, they were annealed to decrease the oxide charge level created during sputtering.

Aluminum dots 0.060 in. diam were deposited by use of a metal mask, at ambient temperature, to a thickness of 1.0 ± 0.1 μm. The wafers were annealed again to decrease the surface state density.

CV Measurement

MOS capacitance/voltage characteristics were measured (2) with a Boontoon 1 MHz capacitance bridge after oxide was removed from the back of the wafer.

Neutron Activation Analysis

Dissolution technique.—The wafers to be analyzed by neutron activation analysis were cut into strips ¾ × 2

in. and packed along with the standard in an evacuated quartz capsule for activation. The neutron irradiation was carried out for 24 hr at a thermal flux of 3×10^{13} neutron/cm^2/sec.

After activation, the wafer samples were scrubbed in deionized water, dried, and stripped in 48% HF. The solution containing the dissolved oxide was then assayed for radioactive Na^{24}. The results of this analysis are shown in Runs 1 and 2 of Table I.

The high activity of Si^{31} was allowed to decay about one day (nine half lives) to avoid interference.

Nondestructive analysis.—Six wafers with 2 μm of sputtered SiO_2 were also analyzed by neutron activation analysis. They were accompanied by a set of untreated wafers to establish a sodium blank for the silicon.

Samples ½ × 1 in. were cut from each wafer containing sputtered SiO_2. The "flat" of each wafer served as reference, and samples were cut parallel to the flat. The control wafer samples were cut to slightly larger dimensions to serve as spacers in packaging the samples for neutron bombardment. Zirconium foil was used to encapsulate the samples.

The neutron flux for the irradiation was 1×10^{13} neutron/cm^2/sec. Exposure time was approximately 40 hr. Irradiated samples were initially surveyed for impurities by gamma ray spectroscopy, which permitted resolution of the 1.38 meV photopeak of Na^{24}. The integrated counts comprising this photopeak were compared for samples and comparator standards. The sodium in parts per million by weight is shown in Run 3, Table I.

Analysis of quartz target by neutron activation.—An 8.3g piece of sputtering target was subjected to analysis by using the instrumental neutron activation analysis (INAA) technique. The sample and Br, P, and Na standards were irradiated for 24 hr in a thermal neutron flux of 3×10^{13} neutron/cm^2/sec.

After irradiation, the sample was etched for 30 min in 48% HF, rinsed, and mounted for counting on the multichannel pulse height analysis system.

Gamma spectral analysis showed the presence of 16 peaks, which could be assigned to Br^{82} and Na^{24}, and β^- particles produced bremsstrahlung which was assigned to P^{32} by half-life measurement. The results of the analysis are shown in Table II. No other elements were observed, but some may have been present in the range masked by the sodium.

U.V. Spectrographic and Flame Photometric Analysis

Gallium-indium alloy.—A sample of the alloy was dissolved in concentrated nitric acid. After evaporation to dryness, the resulting nitrate was converted to oxide over a Meker burner. The sample was run in duplicate against a Ga_2O_3 standard, by using a 20A d-c arc in an oxygen-argon atmosphere (1:3).

For flame photometric analysis, a sample was weighed in a plastic beaker and dissolved with high-purity nitric acid. The sample was diluted and analyzed relative to solution standards for alkali elements, by using a flame photometric technique.

Stainless steel shield.—A sample of stainless steel used as the sputtering shield was dissolved in aqua regia and heated to dryness over a Meker burner to convert the sample into oxide. This oxide was run against Fe_2O_3 standards. A d-c arc in an oxygen-argon atmosphere (1:3) was used for excitation.

For flame photometry, the sample was etched, rinsed in deionized water, dried, and weighed on a microbalance. The sample was dissolved with aqua regia and diluted and then analyzed relative to solution standards by using a flame photometric technique for sodium and potassium.

Sulfuric and nitric acid.—A 50-ml amount of each acid was placed in platinum dishes and dried over a hot plate. Ten milligrams of graphite were added to each residue and compared against graphite standards. A d-c arc in a 1:3 oxygen-argon atmosphere was used for excitation.

Discussion

Neutron activation analysis was used to determine the amount of sodium present in sputtered SiO_2 films. Neutron activation analysis by the dissolution technique was used on the wafers of Runs 1 and 2, and neutron activation analysis by the nondestructive technique was used on Run 3.

The three sputtering runs were made under the same conditions. All the wafers, including controls, had gone through precleaning steps to remove any surface contamination. Generally, control wafers showed a sodium content of less than 1 ppm, except for Run 3 in which it was 6.8 ppm because of contamination. The sodium content on blank wafers is comparable to that obtained by Lunde (3) by neutron activation on single-crystal silicon slices. Run 1 had the highest amount of sodium in the wafers (32 ppm), and Run 2 had the lowest, probably because the sputtering system had been cleaned just before the run.

In Run 1, two wafers went through all the processing steps except for sputtering. The average amount of sodium was only 0.4 ppm, which indicates that sodium is picked up only during the sputtering process.

The nondestructive neutron activation technique was applied to Run 3. Three wafers of this run with the highest sodium content were selected and etched with dilute hydrofluoric acid (HF). Neutron activation analysis then showed that the average amount of Na in the three wafers was 5.5 ppm, as compared with 21 ppm originally. This significant reduction in Na can take place only if the Na is concentrated near the surface of the sputtered quartz film.

In order to find the source of sodium in the sputtered quartz films, the materials shown in Table III were analyzed by neutron activation and u.v. spectrographic analyses. The highest amount of sodium present (8 ppm) came from the stainless steel shield. This comparatively high amount of sodium could be resputtered into the SiO_2 thin film. The amount of sodium coming from other sources was relatively small.

Table I. Analysis of sputtered SiO_2 films by neutron activation technique

Run 1 Wafer number	Run 1 Na in weight (ppm)	Run 2 Wafer number	Run 2 Na in weight (ppm)	Run 3 Wafer number	Run 3 Na in weight (ppm)	After etch
1	35	1	2.4	1	15.3	
2	29	2	2.7	2	15.9	
3	42	3	2.0	3	16.8	
4	48	4	2.8	4	19.4	} 5.5 ppm
5	12	5	1.9	5	21.4	
6	17	6	1.4	6	22.7	
7	20					
8	57					
Control	0.8	Control	0.7	Control	6.8[b]	
NS control[a]	0.4	Control	0.7			

[a] Wafers received all processing except sputtering.
[b] Wafer became contaminated.

Table II. Amount of sodium and flatband voltage

	Run 1	Run 2	Run 3
Amount of Na (average ppm)	32	2.2	18.6
N_{FB}/cm^2	1.8×10^{12}	5.6×10^{11}	9.2×10^{11}

Table III. Amount of sodium in materials

Material	Amount of Na (ppm)	Analytical technique
Fused silica sputtering target (SiO_2)	0.36	Neutron activation
Ga-In (75:25)	<1	U.V. spectrographic
Stainless steel shield	8	U.V. spectrographic
Sulfuric acid	0.01	U.V. spectrographic
Nitric acid	0.1	U.V. spectrographic

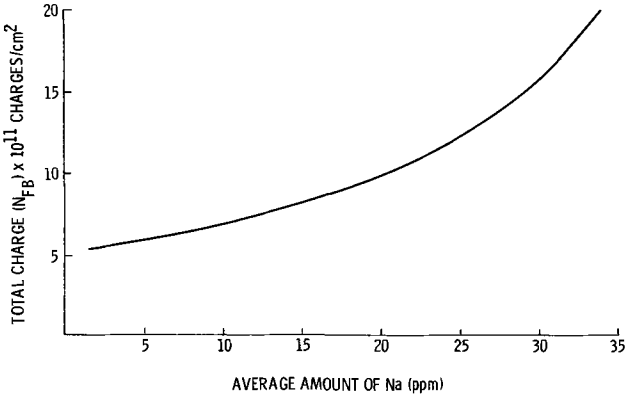

Fig. 1. Average amount of sodium *vs.* total charge

Figure 1 shows the correlation between Na in films *vs.* N_{FB} for 2.0 μm thick sputtered SiO_2 on oxidized monitor wafers. Table II shows the average amount of Na for each of the three sputtering runs and the corresponding N_{FB} charge.

Conclusions

1. Most of the sodium appears concentrated on the top surface of the sputtered SiO_2, because the amount of sodium decreases to a relatively small level upon etching. This finding was checked by neutron activation analysis.

2. The materials that commonly come in contact with sputtered SiO_2 were analyzed by uv spectrographic, flame photometry, and neutron activation techniques. The stainless steel shield contained the largest amount of sodium (8 ppm) of all the materials examined. This sodium could be incorporated into films as a result of resputtering.

Acknowledgment

The authors are indebted to Mr. R. Kastl and Mr. J. E. Lewis for experimental assistance and gratefully acknowledge the help given by Mr. B. G. Smith and Mr. C. J. Ekblom. They also wish to thank Mr. C. P. Hayunga for his encouragement to write this paper.

Manuscript submitted Nov. 16, 1972; revised manuscript received April 3, 1973. This was Paper 349RNP presented at the Miami Beach, Florida, Meeting of the Society, Oct. 8-13, 1972.

Any discussion of this paper will appear in a Discussion Section to be published in the June 1974 JOURNAL.

REFERENCES

1. G. B. Larrabee and J. A. Keenan, *This Journal*, **118**, 1351 (1971).
2. W. Kern, *Solid State Technol.*, **15**, 34 (1972).
3. G. Lunde, *ibid.*, **11**, 32 (1968).
4. E. Yon, W. H. Ko, and A. B. Kuper, *IEEE Trans. Electron Devices*, **ED-13**, 276 (1966).

JOURNAL OF THE ELECTROCHEMICAL SOCIETY

ELECTROCHEMICAL SCIENCE AND TECHNOLOGY

OCTOBER 1973

Conduction Characteristics of the Lithium Iodide-Aluminum Oxide Solid Electrolytes

C. C. Liang*

P. R. Mallory and Company, Incorporated, Laboratory for Physical Science, Northwest Industrial Park, Burlington, Massachusetts 01803

ABSTRACT

The conduction characteristics of the polycrystalline lithium iodide containing aluminum oxide were studied. It was found that the incorporation of aluminum oxide substantially increased the conductivity of lithium iodide. Lithium iodide containing 33-45 mole per cent (m/o) aluminum oxide exhibited conductivities in the order of 10^{-5} ohm^{-1} cm^{-1} at 25° ± 2°C. Inasmuch as no substantial amount of aluminum oxide was found soluble in the lithium iodide under the experimental conditions, the increase in conductivity could not be explained by the classical doping mechanism. The electronic conductivity of the lithium iodide-aluminum oxide solid was negligible compared to the ionic conductivity. Therefore, it is suitable as a solid electrolyte in solid-state battery systems.

The use of lithium iodide as a solid electrolyte material in the solid-state battery systems was reported previously (1-4). Lithium iodide is chemically compatible with such an active anode material as lithium and has extremely low electronic conductivity. Therefore, it is suitable as a solid electrolyte for high voltage cells. However, the relatively low ionic conductivity of lithium iodide (10^{-7} ohm^{-1} cm^{-1} at 25°C) limits the rate capability of the solid electrolyte cells. In an attempt to increase the ionic conductivity of lithium iodide Schlaikjer and Liang (5, 6) studied the conduction characteristics of lithium iodide doped with various calcium compounds. They found that the freshly quenched lithium iodide containing 1 mole per cent (m/o) of calcium iodide showed a conductivity of 10^{-5} ohm^{-1} cm^{-1} at room temperature. However, the conductivity would decrease with time and reach 10^{-6} ohm^{-1} cm^{-1} after about 500 hr. Further investigations on the polycrystalline lithium iodide revealed that the conductivity of the lithium iodide based solid electrolyte can be stabilized at 10^{-5} ohm^{-1} cm^{-1} at room temperature by the incorporation of aluminum oxide. The results of these investigations are discussed in this report.

Experimental

Material pretreatment.—Anhydrous lithium iodide was prepared from dehydrating Foote Mineral LiI · $3H_2O$ under vacuum. The dehydration process was similar to that reported previously (5). The hydrated lithium iodide was heated at about 120°C in a vacuum oven for about 48 hr. After the dehydration, the solid lithium iodide could be fused in a helium-filled Vacuum Atmosphere dry box (less than 15 ppm H_2O and O_2) without decomposition or discoloration. Analyses of the lithium iodide showed that the iodide content was as expected and no excess of alkali was found in the sample.

Fisher adsorption grade aluminum oxide and Alcoa F-1 activated aluminum oxide were dried in an oven at 600° ± 50°C for at least 24 hr. They were transferred to the helium-filled dry box and heated at 600° ± 50°C again for 4 hr. Both types of aluminum oxide were used in the preparation of the solid electrolytes.

Solid electrolyte preparation.—Powder mixtures of the anhydrous lithium iodide and the 600°C dried aluminum oxide in various mole ratios were blended, heated at 550°C for about 17 hr, quenched to ambient temperature, and pulverized. All processes were carried out in the helium-filled dry box. The H_2O and O_2 content in the dry box was maintained at less than 15 ppm.

Conductivity measurement.—The conductivity cell was made by the procedures described as follows. A weighed amount of lithium iodide-aluminum oxide powder was pressed into a pellet in a 0.6 in. diameter steel die under a pressure of 100,000 psi. The geometric area of the pellet was calculated from the diameter and the thickness of the pellet was measured with a micrometer while the pellet was still in the die. Lithium electrodes with steel current collectors were pressed on both sides of the pellet under 50,000 psi. The resistance of the conductivity cell was measured by means of a General Radio conductance bridge at 1000 Hz. It was also determined from the potential drop between the two lithium electrodes upon passing a direct current. The conductivity of the pellet was calculated from the measured resistance and the physical dimensions of the pellet.

Debye-Scherrer powder pattern.—Debye-Scherrer powder patterns of the anhydrous lithium iodide, the 600°C dried aluminum oxide, and the lithium iodide-aluminum oxide electrolyte were obtained at room temperature using the conventional techniques with CuKα radiation.

Cell fabrication and evaluation.—Li/LiI(Al_2O_3)/PbI_2, Pb; Li/LiI(Al_2O_3)/CuI,Cu; and Li/LiI(Al_2O_3)/AgI,Ag

* Electrochemical Society Active Member.

Key words: solid electrolyte, lithium iodide, ionic conductivity, solid electrolyte cells, solid-state batteries.

solid electrolyte cells were fabricated. The cathodes were well blended mixtures of the metal iodide [40 weight per cent (w/o)], the parent metal powder (30 w/o), and the electrolyte (30 w/o). The anodes were thin lithium metal disks and the current collectors were steel disks for the anodes, and lead, copper, or silver disks for the cathodes. The metal iodides and the metal powders were dried in a vacuum oven at about 100°C for about 16 hr. The solid electrolyte cells were fabricated by pressing the cathode, the electrolyte, and the anode in a 0.6 in. diameter steel die under a pressure of 100,000 psi.

The open-circuit voltages of the solid electrolyte cells were measured by means of a Tacussel Aries 10,000 digital voltmeter (internal impedance $> 10^{12}$ ohms). The voltages under constant current were measured by means of a Keithley 610B electrometer and recorded by a Varian 14A strip chart recorder.

Results

During the 550°C treatment of the lithium iodide and aluminum oxide mixture, a slurry was obtained. Presumably lithium iodide was melted whereas aluminum oxide remained solid.

The inclusion of aluminum oxide caused a substantial increase in the conductivity of the polycrystalline lithium iodide. Figure 1 shows the conductivity of the lithium iodide-aluminum oxide electrolyte as a function of the aluminum oxide content at 25° ± 2°C. It was noted that the maximum conductivity, about 10^{-5} ohm^{-1} cm^{-1}, occurred at 35-45 m/o aluminum oxide. Furthermore, the conductivity did not change with time. The lithium iodide-aluminum oxide powder which had been stored in a covered brown glass bottle in the dry box for 6 months exhibited the same pellet conductivity as the freshly prepared powder.

The apparent activation energy of the conduction process for the lithium iodide-aluminum oxide electrolytes in the temperature range of −40°-100°C was found to be 10 kcal/mole (Fig. 2). This is in good agreement with the value obtained for both single crystal (7) and polycrystalline (5) lithium iodide.

In order to determine the suitability of the lithium iodide containing aluminum oxide as a solid electrolyte material, the open-circuit voltages of the Li/LiI(Al_2O_3)/PbI_2,Pb; Li/LiI(Al_2O_3)/CuI,Cu; and Li/LiI(Al_2O_3)/AgI,Ag cells were measured at 25° ± 2°C by means of a high internal impedance (greater than 10^{12} ohms) digital voltmeter. The results of these measurements agreed extremely well with those calculated from the Gibbs free energies of formation (8, 9) as shown in Table I. Furthermore, not only no change in the open-circuit voltage was observed after 2 years storage on the Li/LiI(40 m/o Al_2O_3)/PbI_2,Pb cells, but the discharge characteristics of these cells were also found to be similar to those of the freshly fabricated cells (Fig. 3). It was noted further that a 100% discharge efficiency was obtained on the 5 mA-hr/cm^2 Li/Li(40 m/o Al_2O_3)/PbI_2,Pb cells under a current of 75 $\mu A/cm^2$ or less at room temperature (Fig. 4).

The x-ray diffraction patterns of the LiI(Al_2O_3) electrolytes and the anhydrous LiI and Al_2O_3 used for the preparation of the LiI(Al_2O_3) electrolytes are shown in Table II. Both LiI and Al_2O_3 lines were found in the LiI(Al_2O_3) patterns.

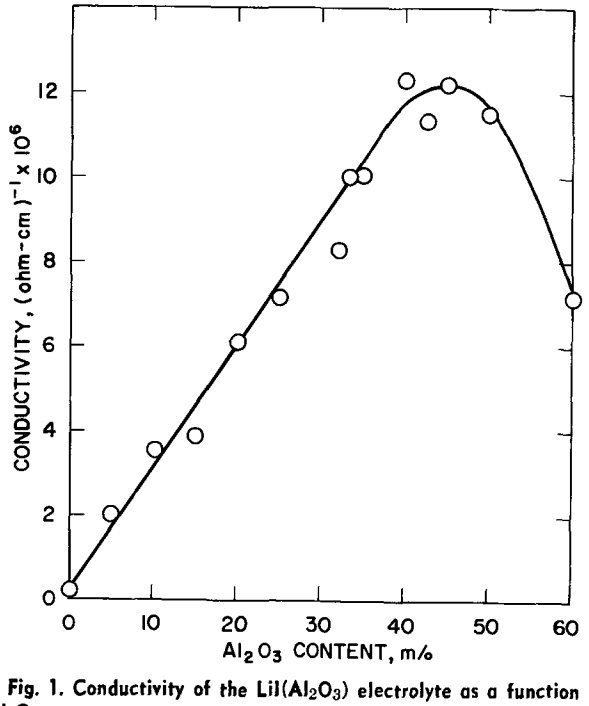

Fig. 1. Conductivity of the LiI(Al_2O_3) electrolyte as a function of Al_2O_3 content

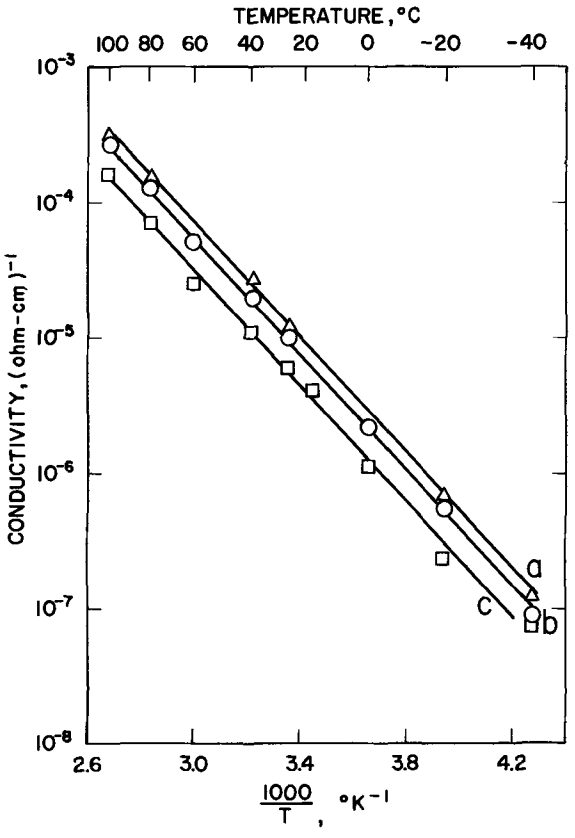

Fig. 2. The effect of temperature on the conductivity of the LiI(Al_2O_3) electrolyte (a) LiI(40 m/o Al_2O_3); (b) LiI(33 m/o Al_2O_3); and (c) LiI(20 m/o Al_2O_3).

Discussion

It is noted that the conductivity of the lithium iodide-aluminum oxide electrolyte can reach 10^{-5} ohm^{-1} cm^{-1} at room temperature at an aluminum oxide content ranging between 35 and 45 m/o. Furthermore, the conductivity remains constant even after a long storage period. In addition to these findings, the following conclusions can be reached from the experimental results.

1. The electronic conductivity of the lithium iodide-aluminum oxide is insignificant compared to its ionic conductivity.

The Li/LiI(Al_2O_3)/PbI_2,Pb; Li/LiI(Al_2O_3)/CuI,Cu; and Li/LiI(Al_2O_3)/AgI,Ag solid electrolyte cells ex-

Table I. The open-circuit voltages of various solid electrolyte cells at 25°C

Cell	Open-circuit voltage (V) Calculated	Observed
Li/LiI(Al_2O_3)/PbI_2,Pb	1.896	1.905 ± 0.010
Li/LiI(Al_2O_3)/CuI,Cu	2.075	2.080 ± 0.010
Li/LiI(Al_2O_3)/AgI,Ag	2.109	2.105 ± 0.010

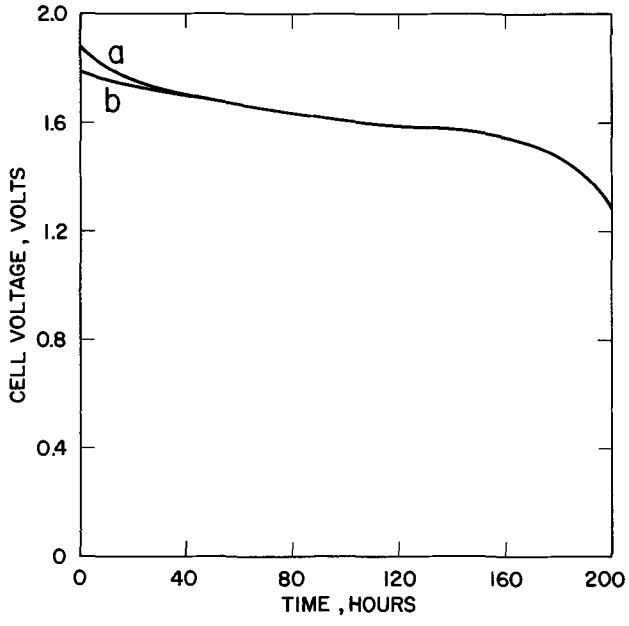

Fig. 3. Discharge curves of the Li/LiI(40 m/o Al_2O_3)/PbI_2, Pb solid electrolyte cells (a) before storage (b) after storage. Geometric area of the electrode: 1.8 cm^2; capacity: 5 mA-hr/cm^2 (cathode limiting); discharge current: 25 $\mu A/cm^2$; discharge temperature: 25° ± 2°C; storage: (a) freshly made and (b) stored at room temperature for 2 years.

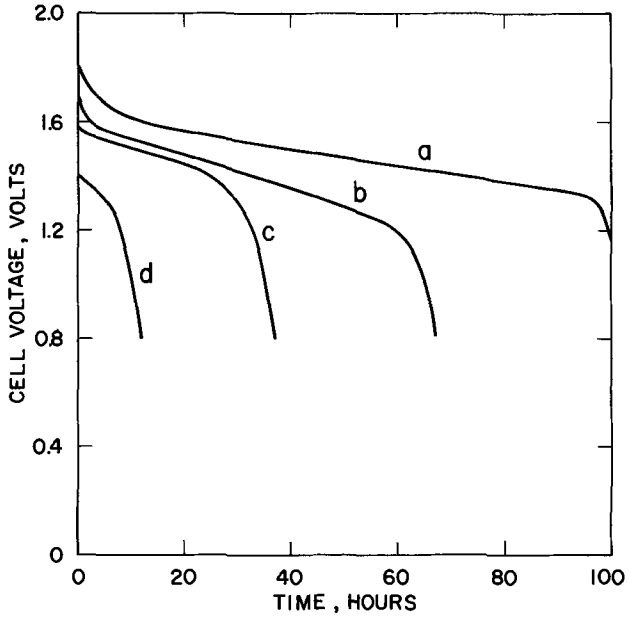

Fig. 4. Discharge curves of the Li/LiI(40 m/o Al_2O_3)/PbI_2, Pb solid electrolyte cells under various constant currents. Geometric area of the electrode: 1.8 cm^2; capacity: 5 mA-hr/cm^2; discharge current: (a) 50 $\mu A/cm^2$, (b) 75 $\mu A/cm^2$, (c) 100 $\mu A/cm^2$, and (d) 200 $\mu A/cm^2$; discharge temperature: 25° ± 2°C.

hibit open-circuit voltages as expected according to thermodynamics. This clearly indicates that the LiI(Al_2O_3) electrolytes have low electronic conductivity (5). Furthermore, after a 2 year storage period, the Li/LiI(Al_2O_3)/PbI_2,Pb cells exhibit not only the same open-circuit voltage, but also the same discharge characteristics as the freshly made cells. Therefore, one concludes that the electronic conductivity is indeed insignificant and the lithium iodide-aluminum oxide solid is suitable as a solid electrolyte material.

2. The conduction mechanism of the lithium iodide-aluminum oxide electrolytes is identical with that of lithium iodide. The cation vacancies are the principal mobile species.

Table II. X-ray diffraction data on (a) anhydrous LiI; (b) γ-Al_2O_3 (600°C dried); and (c) LiI (40 m/o Al_2O_3) electrolyte

(a) This experiment		LiI ASTM Card 1-0592		
d (A)	*RI**	*d* (A)	*I/I*$_o$	*hkl*
3.43	S	3.47	100	111
2.96	S	3.00	75	200
2.11	S	2.12	40	220
1.80	VS	1.81	40	311
1.72	W	1.73	10	222
1.50	W	1.50	6	400
1.36	M	1.38	15	331
1.34	M	1.34	15	420
1.22	W	1.23	8	422
1.15	W	1.16	8	333, 511
1.06	VW	1.06	1	440
1.02	W	1.02	6	531
1.00	VW	1.00	2	600, 442
0.95	VW	0.95	2	620
0.92	VW	0.92	1	533

* *RI* = visually observed relative intensities. VS = very strong; S = strong; M = medium; W = weak; VW = very weak.

(b) This experiment**		γ-Al_2O_3 ASTM Card 10-425		
d (A)	*RI*	*d* (A)	*I/I*$_o$	*hkl*
		4.56	40	111
2.77	W	2.80	20	220
2.39	VS	2.39	80	311
2.28	S	2.28	50	222
1.98	VS	1.977	100	400
1.52	M	1.520	30	511
1.39	VS	1.395	100	440
1.14	W	1.140	20	444
1.00	W	1.027	10	731
0.99	W	0.989	10	800
0.88	W	0.884	10	840
0.81	W	0.806	20	844

** All lines are diffuse indicating small particle size.

(c) This experiment***		LiI ASTM Card 1-0592			γ-Al_2O_3 ASTM Card 10-425		
d (A)	*RI*	*d* (A)	*I/I*$_o$	*hkl*	*d* (A)	*I/I*$_o$	*hkl*
3.45	VS	3.47	100	111			
3.01	VS	3.00	75	200			
2.40	W				2.39	80	311
2.28	W				2.28	50	222
2.13	VS	2.12	40	220			
1.97	W				1.977	100	400
1.81	M	1.81	40	311			
1.71	W	1.73	10	222			
1.50	S	1.50	6	400			
1.39	M	1.38	15	331	1.395	100	440
1.34	S	1.34	15	420			
1.23	M	1.23	8	422			
1.16	M	1.16	8	333, 511			
1.06	W	1.06	1	440			
1.02	M	1.02	6	531			
1.00	W	1.00	2	600, 442			
0.95	W	0.95	2	620			
0.92	W	0.92	1	533			

*** The diffraction patterns of the LiI (20 m/o Al_2O_3) and LiI (60 m/o Al_2O_3) electrolytes are similar to that of Table II, part (c).

Inasmuch as the lithium iodide-aluminum oxide electrolytes are practically pure ionic conductors, the fact that only ohmic behavior was observed during the d-c measurements on the Li/LiI(Al_2O_3)/Li conductivity cells indicates the reversibility of the lithium electrodes with respect to the LiI(Al_2O_3) electrolyte. Furthermore, the activation energy for the conduction process in the studied temperature range was found to be identical with that of lithium iodide in the extrinsic region (5, 7). Therefore, we conclude that the conduction mechanism of the lithium iodide-aluminum oxide is identical with that of lithium iodide and that the lithium ion vacancies are the principal mobile species (5, 7).

3. No chemical reaction was observed between the lithium iodide-aluminum oxide electrolyte and the electrodes. The electrolyte is suitable for high-energy solid-state battery systems using lithium anodes.

The Li/LiI(Al_2O_3)/PbI_2,Pb cells which were stored for 2 years exhibited identical open-circuit voltage and

similar discharge characteristics as the freshly made cells (Fig. 3). If the aluminum oxide in the electrolyte were reduced by the metallic lithium, both the open-circuit voltage and the discharge characteristics would have changed significantly due to the formation of Li_2O and Al. Figure 4 shows the discharge curves of the Li/LiI (40 m/o Al_2O_3)/PbI_2,Pb cells under various constant currents. It is noted that a 100% discharge efficiency may be realized at 75 $\mu A/cm^2$ or less indicating that the LiI(Al_2O_3) solid electrolytes can be used in practical solid-state battery systems.

4. The increase in the ionic conductivity by the incorporation of aluminum oxide in lithium iodide cannot be explained by the classical doping mechanism.

The x-ray diffraction patterns of the LiI(Al_2O_3) electrolytes showed both the lithium iodide and the aluminum oxide lines indicating insignificant solubility of aluminum oxide in the lithium iodide lattice and *vice versa*. Furthermore, no new lines were present in the diffraction pattern to show the formation of a solid complex between the two starting compounds.

It is conceivable that Li^+ vacancies are created by the dissolution of Al_2O_3 molecules in the lithium iodide lattice (2 Al^{3+} replaces 2 Li^+ and 3 O^{2-} replace 3 I^- creating 1 Li^+ vacancy to balance the charge). However, if this were the mechanism for the increased conductivity, one would expect that a few mole per cent of Al_2O_3 would be sufficient to reach the equilibrium concentration of the vacancies. Indeed, it was observed during the electrolyte formation at 550°C that at least a substantial amount of the aluminum oxide remained solid even at 2 m/o indicating a less than 2 m/o solubility of aluminum oxide in lithium iodide. Since it was known (5) that 1 m/o of vacancies would result in an ionic conductivity of about 10^{-5} ohm^{-1} cm^{-1} at room temperature, the fact that about 40 m/o undissolved Al_2O_3 is required to attain the 10^{-5} ohm^{-1} cm^{-1} conductivity suggests that the classical doping mechanism is not valid in the present case.

The mechanism of the conduction enhancement will be discussed in a subsequent publication.

Acknowledgments

The author wishes to express his appreciation to Dr. G. Wallis and Dr. C. Schlaikjer for their helpful discussion, and to L. Barnette for his assistance in part of the experimental work.

Manuscript submitted April 2, 1973; revised manuscript received June 5, 1973.

Any discussion of this paper will appear in a Discussion Section to be published in the June 1974 JOURNAL.

REFERENCES

1. C. C. Liang and P. Bro, *This Journal*, **116**, 1322 (1969).
2. C. C. Liang, J. Epstein, and G. H. Boyle, *ibid.*, **116**, 1452 (1969).
3. C. C. Liang, Proc. 1971 Intersoc. Energy Conv. Eng. Conf., p. 673 (1971).
4. B. Scrosati, *J. Appl. Electrochem.*, **2**, 231 (1972).
5. C. R. Schlaikjer and C. C. Liang, *This Journal*, **118**, 1447 (1971).
6. C. R. Schlaikjer and C. C. Liang, in "Fast Ion Transport in Solids," W. van Gool, Editor, pp. 685-694, North-Holland Publishing Co., Amsterdam (1973).
7. B. J. H. Jackson and D. A. Young, *J. Phys. Chem. Solids*, **30**, 1973 (1969).
8. JANAF Thermochemical Tables, 2nd ed., National Bureau of Standards, Washington, D. C., June 1971.
9. "Selected Values of Chemical Thermodynamic Properties," National Bureau of Standards Technical Note 270-4, May 1969.

Some Aspects of Sodium-Sulfur Cell Operation

Jacques Fally, Claude Lasne, Yvon Lazennec, and Pierre Margotin

Compagnie Générale d'Electricité, Marcoussis, Essonne, France

ABSTRACT

An experimental sodium-sulfur cell using a beta-alumina electrolyte is described. The cell uses carbon felt as a cathode current collector with molybdenum wires as terminals and with a beta-alumina tube. At temperatures between 300° and 350°C and at a current density of 0.2 A/cm^2 lifetime is about 200 cycles with a 30-35% depth of discharge and a power density of 0.3 W/cm^2 at the working potential. Experiments at greater depth of discharge are described.

The great interest in the sodium-sulfur storage battery using beta-alumina as the electrolyte is due to the fact that the characteristics of the anodic and cathodic reactants allow one to expect batteries with an energy density higher than 150 W-hr/kg, under satisfactory economic conditions (1-5). This fact makes the sodium-sulfur battery one of the most promising power sources for urban electric vehicles when comparison is made with other conventional electrochemical systems.

As for any electrochemical cell, correct optimization of each component (anode, cathode, separator) is of great importance in determining over-all performance.

In the sodium-sulfur case, the beta-alumina ceramic separator represents a major performance-determining component. It will be discussed in a separate article.

The present paper is only concerned with the aspects connected with cell operation: experimental cell technology, cathode study, long-term cycling behavior, influence of electrolyte composition, and certain operating conditions on lifetime.

Key words: sodium-sulfur cells, beta-alumina, high-temperature cells.

Technology and Results

A schematic and a photographic representation of an experimental glass cell are shown in Fig. 1. The glass-ceramic technology was chosen because it presented no difficulty of construction and permitted the study of fundamental problems related to battery operation in the laboratory.

The two-block beta-alumina electrolyte is a closed-end tube of 8 mm OD and approaching a wall thickness of 600μ. The active surface is about 10 cm^2. The anodic compartment consists of a glass tube sealed off under vacuum and sealed to the beta-alumina tube. A molybdenum wire (2 mm diameter) is used as the terminal. The anode compartment filling is achieved by molten sodium nitrate bath electrolysis; this procedure avoids all the difficulties of handling metallic sodium and provides a high-purity reactant. Initial contact between

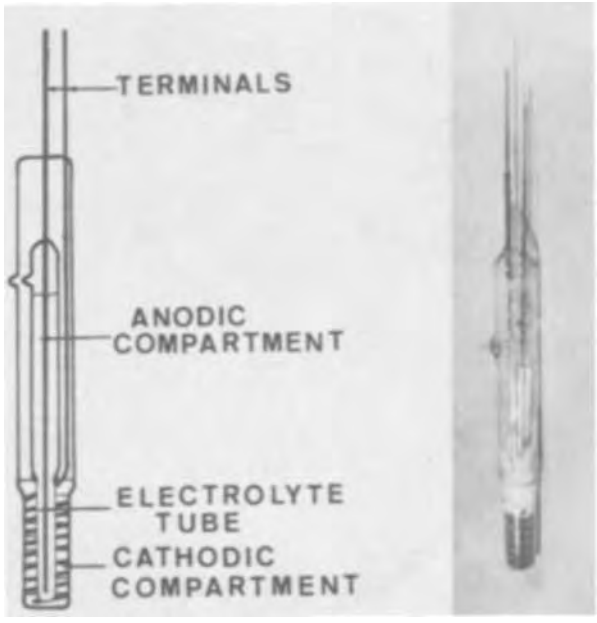

Fig. 1. Sodium-sulfur experimental glass cell using beta-alumina closed-end tube as electrolyte

the beta-alumina and the molybdenum current collector is made by a small molybdenum spring.

The cathode compartment consists of a sealed outer glass vessel surrounding the anode reservoir and electrolyte, containing graphite felt rings and a molybdenum spiral as the terminal. The sulfur thickness is 5 mm. Because of the larger volume of sodium polysulfide reaction product it is necessary to put into the cell about 30% less sulfur than the theoretical absorption capacity of graphite felt. Before sealing the compartment, a low pressure of inert gas is admitted to prevent boiling off of sulfur at the testing temperature.

The theoretical capacity of such a cell, limited by the sulfur electrode, is about 6 A-hr.

Cycling runs were carried out on these cells under the following conditions at 330°C: *(i)* 1 hr discharge at 200 mA/cm² (power produced 300-350 mW/cm² depending on the cell resistance); *(ii)* 3 hr charge at 67 mA/cm²; and *(iii)* depth of discharge being 35%.

The initial cell specific resistance, in the range 1.6-2.0 ohm-cm² yielded a maximum power of 600-700 mW/cm². In order to increase the specific power, a few runs were carried out under the same cycling conditions as above with thinner electrolytes (200-300μ in thickness). These were unsuccessful, probably because of a higher mechanical fragility when the tube thickness decreases.

Cathode Study

Because of the very low conductivity of sulfur, it is necessary to use an electronically conductive material in the cathode reactant. Graphite felt is very suitable for this application, but its cost is still too high for a practical power source. Accordingly, other cathodic collectors were tried, in particular graphite powder with a grain size smaller than 300μ. The optimum composition for sulfur-graphite powder mixtures is in the range 70-80 weight per cent (w/o) sulfur and 20-30 w/o graphite. Figure 2 shows that the resistance of mixtures containing more sulfur are too high and vary rapidly with sulfur content, while mixtures containing more graphite are insufficiently fluid. It is also apparent that cathode thickness has an important influence on cell resistance. These data indicate that construction of high capacity sodium-sulfur cells with graphite powder cathodes is not practical. For instance, with the same cell geometry, and at a temperature of 330°C, the part of the cell resistance due to the cathode is 4.6 ohm-cm² of active electrolyte surface for a 20 w/o suspension of graphite powder in molten sulfur, while a felt cathode only represents 0.5 ohm-cm² and contains 5 w/o graphite. Runs have also been carried out with graphite cloth, the absorption capacity of which was too low, and with stainless steel felts, which presented the same disadvantage. In addition, with stainless steel considerable corrosion problems occurred.

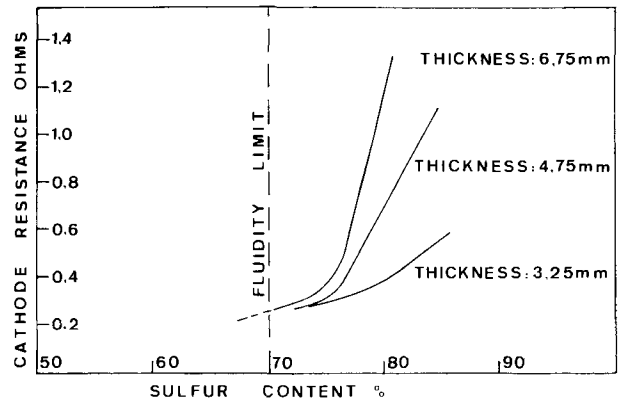

Fig. 2. Relation between graphite powder-sulfur cathode resistance and sulfur content for various cathode thicknesses

In view of these observations, graphite felt was finally chosen as the cathode current collector.

With the glass cells described above, the depth of discharge was limited to 40%, corresponding to the polysulfide composition range Na_2S_5 to Na_2S_3. During charge, when the catholyte composition reaches the sulfur-pentasulfide two-phase region of the sodium-sulfur phase diagram (6), the cell resistance increases considerably and the applied voltage often rose to values higher than 3V, above which electrolytic decomposition of beta-alumina may occur. This rise is probably forming an insulating layer due to free sulfur formation at the cathode-electrolyte interface. However, it was found that if a thin (1 mm) layer of insulating mineral felt (Kaowol) was interposed between the electrolyte and the graphite felt cathode, more than 70% depth discharge can be attained. An improvement in depth of discharge was also noted when the glass wall and molybdenum spiral were replaced by a metallic-walled cathode.

Time Behavior of Experimental Cells

Cells exhibited two kinds of phenomenology during cycling.

Firstly, a progressive increase in internal resistance occurred, which results in a decrease in power. In Fig. 3 a series of current-voltage characteristics is plotted at various stages of a cell's lifetime. After a life of 82 A-hr/cm², power at the working point decreased by 10%. Figure 4 shows the same degradation in a different plot; it can also be seen that the behavior was

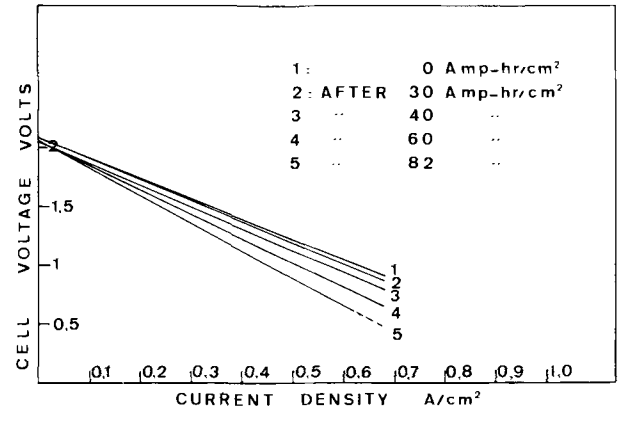

Fig. 3. Performance of a cell in continuous operation at 200 mA/cm² during discharge and 67 mA/cm² during charge

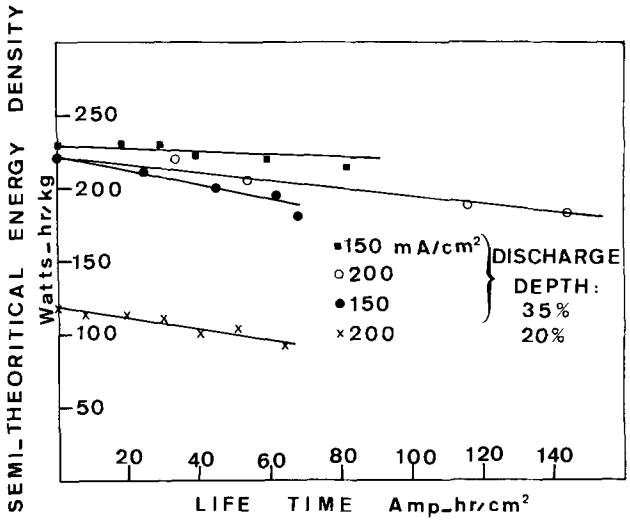

Fig. 4. Cell energy density under various conditions of current density and discharge depth

slightly different at 150 and at 200 mA/cm². The lower "semitheoretical" energy density in one of the runs is caused by a low discharge depth voluntarily limited to 20%. (For the "semitheoretical" energy density only the weight of the reactants, but not of the container and other components, is taken into account.) Secondly, between 1000 and 1500 hr of cycling, the electrolyte rather suddenly develops electronic conductivity, which quickly renders the cell useless.

Influence of Electrolyte Composition

The appearance of electronic conductivity in the electrolyte is connected either with metallic sodium precipitation in beta-alumina or with crack formation. Metallic sodium precipitation is probably a result of the presence of foreign ions in the electrolyte lattice, such as Mg^{++}, since beta-alumina behavior during filling of the anodic compartments by molten sodium nitrate electrolysis is strongly influenced by magnesia additions as indicated below.

No difficulties have been encountered in filling beta-alumina tubes with a 0.8 w/o magnesia content of total beta-alumina using the electrolytic process. However, no cell with a magnesia content of 3 or 6 w/o could be filled by electrolysis. In such cases, metallic sodium appears in the electrolyte in the form of black dendritic accumulations as seen in Fig. 5. This phenomenon, which is thought to be caused by internal discharge of sodium ions, is first initiated at the sodium-beta-alumina interface, then progresses through the whole ceramic producing a short circuit. The impossibility of filling beta-alumina tubes with a high magnesia content by the electrolytic method is probably due to the same phenomenon. Indeed, filling has been shown in the present work to be possible if electrolytes containing only 0.8% magnesia are used. From the data in Table I it may be seen that the lifetime of experimental cells greatly depends on beta-alumina composition. Thus, from a practical point of view, the lifetime improvement obtained by using additive-free electrolytes compensates the small decrease in specific power due to an increase in resistivity. In addition, it may be concluded that high impurity levels are the

Table I. Correlation between chemical composition and lifetime

Electrolyte composition	Lifetime (A-hr/cm²)	Remarks
Commercial β-alumina	17	High impurities level (3000 ppm)
8.5 Al_2O_3, Na_2O + 0.8 w/o MgO	31.5	
8.5 Al_2O_3, Na_2O + 3 w/o MgO	—	Damaged during filling
8.5 Al_2O_3, Na_2O + 6 w/o MgO	—	Damaged during filling
8.5 Al_2O_3, Na_2O	90	Low impurities level (70 ppm)

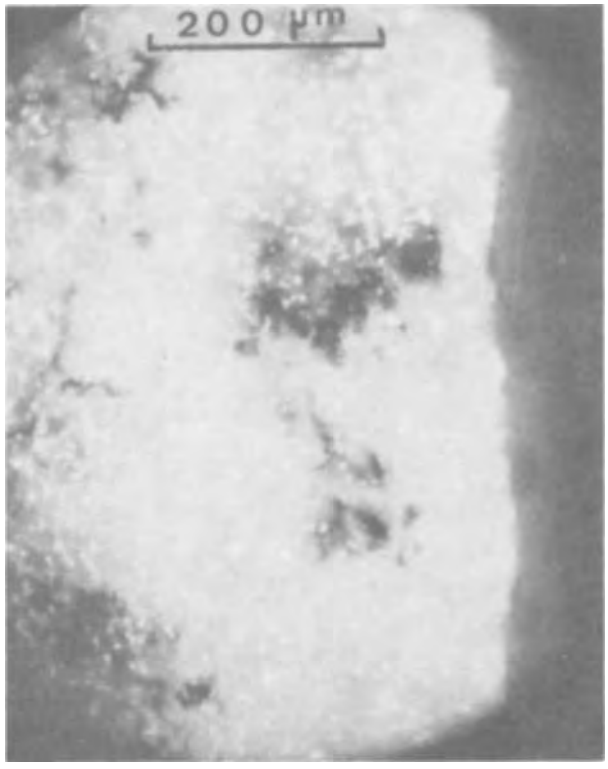

Fig. 5. Metallic sodium precipitation in beta-alumina containing 3 w/o magnesia during filling of electrolyte tubes by molten sodium nitrate electrolysis

cause of the poor results obtained with commercial beta-alumina.

Other evidence of the importance of impurities is shown by the fact that potassium and silicon (etched from the glass by molten sodium) penetrate into beta-alumina during cycling to give levels higher than 1%. Figure 6 is an electron microprobe photograph show-

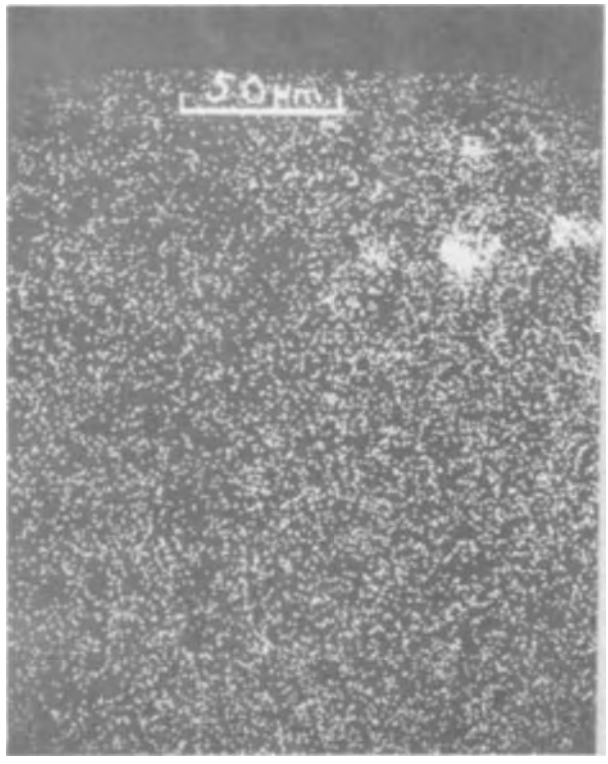

Fig. 6. Beta-alumina contamination by potassium from glass corrosion as seen by electron microprobe examination

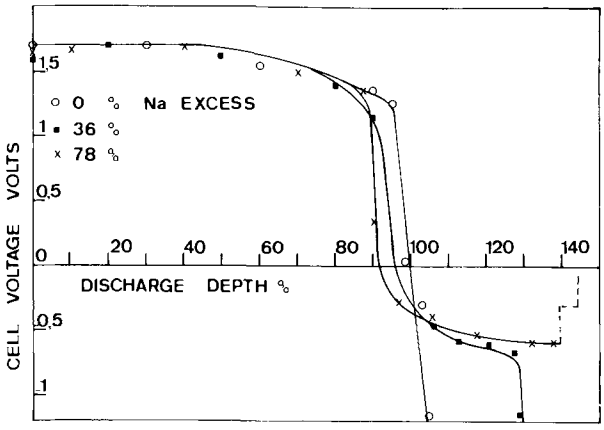

Fig. 7. Discharge curves of three cells with different amounts of excess sodium (compared with Na_2S_3 stoichiometry)

ing the potassium distribution in the electrolyte. It is possible that these impurities also have effect on lifetime.

Effect of Operating Conditions

As already indicated no significant influence of current density in the 150-200 mA/cm^2 range on cell lifetime is observed.

Nevertheless, polarity reversal experiments on some cells (by prolonging discharge beyond Na_2S_3) seem to show another possible cause of cell degradation. Cell life may also be limited by mechanical strains due to solid reaction products. Prolonged discharge curves of three sodium-sulfur cells are shown on Fig. 7. These cells differ by the sodium amount available in their anodic compartment compared with that required for Na_2S_3 stoichiometry.

Those data indicate that: (*i*) inversion of cell polarity occurs as soon as the catholyte composition reaches Na_2S_3; (*ii*) a voltage plateau occurs at an overpotential of about −0.6V; (*iii*) a second voltage drop occurs corresponding to sodium depletion in cases where it is not in great excess (*cf.* curve for 36% excess in Fig. 7); and (*iv*) the electrolyte ruptures at a composition of about Na_2S_2 if there is a sufficient excess of sodium. This rupture seems to be induced by the presence of solid sodium polysulfides. During normal operation this occurs despite control of the total faradaic balance, indicating the total cathode composition. It is possible that such solid reaction products locally occur at the cathode-electrolyte interface, and break the ceramic. Such a point of view is supported by Fig. 8 which is a scanning electron microscope photograph of beta-alumina which has received normal cycling. Superficial grains show conchoidal fractures. Polysulfide solidification during cooling of discharged cells can probably cause the same effect.

Conclusion

The detrimental influence of magnesia additions on cycle life (and probably of a number of other impurities introduced during electrolyte preparation or cycling) resulted in the use of only beta-alumina electrolytes, without additives, and of rigidly controlled purity (<70 ppm) in the sodium sulfur cell. Contamination of beta-alumina by potassium and silicate (or silicide) ions from glass seals can, however, only be

Fig. 8. View of beta-alumina surface after operation in sodium-sulfur cell (scanning electron microscope)

avoided by a new experimental cell technology. Control of catholyte composition (*i.e.*, the working range on the discharge curve) also seems to be an important factor in cell longevity.

The average lifetime obtained to date is 90 A-hr/cm^2, with an upper limit of 150 A-hr/cm^2. It seems necessary to us to double this figure before a battery in the range of few hundred watts can be constructed.

Acknowledgment

This work was sponsored by the "Direction des Recherches et Moyens d'Essais" of the French Army.

Manuscript submitted June 30, 1972; revised manuscript received May 17, 1973. This was Paper 172 presented at the Houston, Texas, Meeting of the Society, May 7-11, 1972.

Any discussion of this paper will appear in a Discussion Section to be published in the June 1974 JOURNAL.

REFERENCES

1. Y. F. Yao and J. T. Kummer, *J. Inorg. Nucl. Chem.*, **29**, 2453 (1967).
2. R. H. Radzilowski, Y. F. Yao, and J. T. Kummer, *J. Appl. Phys.*, **40**, 4716 (1969).
3. M. S. Whittingham and R. A. Huggins, *J. Chem. Phys.*, **54**, 414 (1971).
4. I. Wynn Jones and L. J. Miles, *Brit. Ceram. Soc. Proc.*, **19**, 161 (1971).
5. J. T. Kummer and N. Weber, *S.A.E.* Jan. 1967; "Proc. 21st Annual Power Sources Conference," May 1967.
6. E. G. Bunzel and E. J. Kohlmeyer, *Z. Anorg. Allgem. Chem.*, **254**, 1 (1947).

Study of a Beta-Alumina Electrolyte for Sodium-Sulfur Battery

Jacques Fally, Claude Lasne, Yvon Lazennec, Yves Le Cars, and Pierre Margotin

Compagnie Générale d'Electricité, Marcoussis, Essonne, France

ABSTRACT

The structural properties of sodium aluminates (beta-aluminas) as ionic conductors have been studied. The Al_2O_3-Na_2O diagram for Al_2O_3 above 84 mole per cent between 1100° and 1600°C is described. The fabrication of closed-end tubes (for use as battery electrolyte) by electrophoretic deposition is shown to give a useful and reproducible product. Finally, the physical and electrical properties of sodium-conducting ceramics prepared in this way are evaluated.

As shown in a preceding paper, studies of sodium-sulfur batteries have indicated the strong influence of the β-alumina electrolyte on cell operation. It has accordingly been necessary to study the structural properties of sodium aluminates as electrolytes for optimization of cell performance.

Pure β-alumina electrolyte closed-end tubes, with and without additives, have been prepared. The chemical, physical, and electrical properties of these tubes have been determined in relation to optimum cell operation.

Phase Diagram and Structural Properties Study

Al_2O_3-Na_2O phase diagram.—Recent work in this laboratory has examined the Al_2O_3-Na_2O system (1) for alumina concentrations higher than 84 mole per cent (m/o). The method used a sodium oxide vapor loss. Phases were identified by x-ray diffraction. It has been shown that depending on temperature the phases present have β-alumina structure (generally accepted $Na_2O \cdot 11Al_2O_3$) (2) and β″-alumina structure (with the theoretical formula $Na_2O \cdot 5.33Al_2O_3$) (3-5). Beta″-alumina prepared by solid-state reaction between α-alumina and sodium carbonate above 1050°C is always present with β-alumina. Above 1400°C, the proportion of β-alumina in the mixture increases and at 1550°C the transformation $\beta'' \rightarrow \beta$ is complete.

This transformation is not reversible. It would appear that only the β-phase is stable.

As shown in Fig. 1, the domain of the β-phase extends up to 1400°C from $Na_2O \cdot 5.33Al_2O_3$ to $Na_2O \cdot 8.5Al_2O_3$. The zone represents the coexistence domain of β and β″. By extrapolation of the obtained domain boundaries to melting, we get a peritectic point, the composition of which is about $Na_2O \cdot 8.5Al_2O_3$. It is remarkable that $Na_2O \cdot 11Al_2O_3$ β-alumina is outside the domain. The results obtained confirm those of other workers for the temperature range above 1700°C (6, 7), and extend the Na_2O-Al_2O_3 diagram to lower temperatures.

Structure.—As β and β″ phases always coexist, crystallographic aspects of their juxtaposition were studied.

Crystals of composition corresponding to the zone described above were grown using a lead oxide (PbO) evaporation flux method, (6). Weissenberg and oscillating crystal patterns were obtained and compared with those corresponding to pure β-alumina. Figure 2 represents patterns obtained around $\vec{c}$ axis on β and on β + β″. Both photographs show that all β-alumina reflections satisfy the $P6_3/mmc$ space group whose parameters for a hexagonal lattice are $a = 5.50$Å and $c = 22.52$Å.

For the β + β″ pattern a second reflecting system appears, located at about the third from pair planes of β-alumina. The systematic extinctions and the different symmetry elements identify without ambiguity β″-alumina (whose space group is $R\bar{3}m$) in a hexagonal multiple cell description, yielding the parameters $a'' = 5.58$Å and $c'' = 33.95$Å where the $\vec{a}''$ and $\vec{c}''$ directions are in perfect coincidence with the $\vec{a}$ and $\vec{c}$ directions of β-alumina.

Hence we may assume that hexagonal β-alumina (stable phase) and rhombohedral β″-alumina (metastable phase) coexist in epitaxy.

Electrolyte Preparation

Taking into account the above results, only hexagonal β-alumina was used for electrolyte preparation. This is a two-step process, *viz.*, synthesis of β-alumina by fusion and fabrication of closed-end tubes.

Synthesis of β-alumina by fusion.—Beta-alumina has been obtained by induction melting of a mixture of α-alumina and sodium carbonate in a water-cooled copper crucible. The initial mixture compositions used varied between $Na_2O \cdot 5.33Al_2O_3$ and $Na_2O \cdot 11Al_2O_3$. In some cases additions of magnesia and zirconia were incorporated in the mixtures before melting.

The fused mass was in each case first crushed, then milled in a stainless-steel ball mill. Metallic impurities introduced during milling were leached out by hydrochloric acid, which also eliminates the sodium aluminate sometimes present. This method gives powders

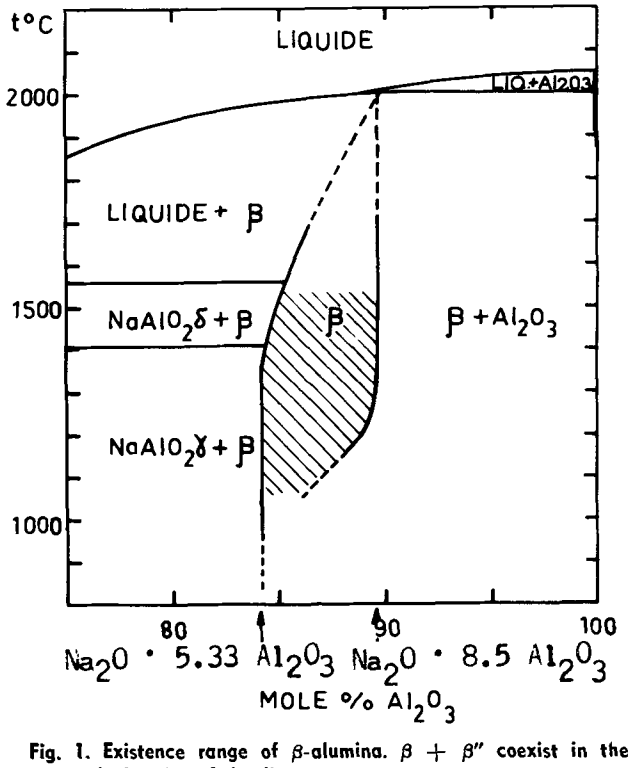

Fig. 1. Existence range of β-alumina. β + β″ coexist in the cross hatched region of the diagram.

Key words: beta-alumina, solid electrolyte, sodium sulfur battery.

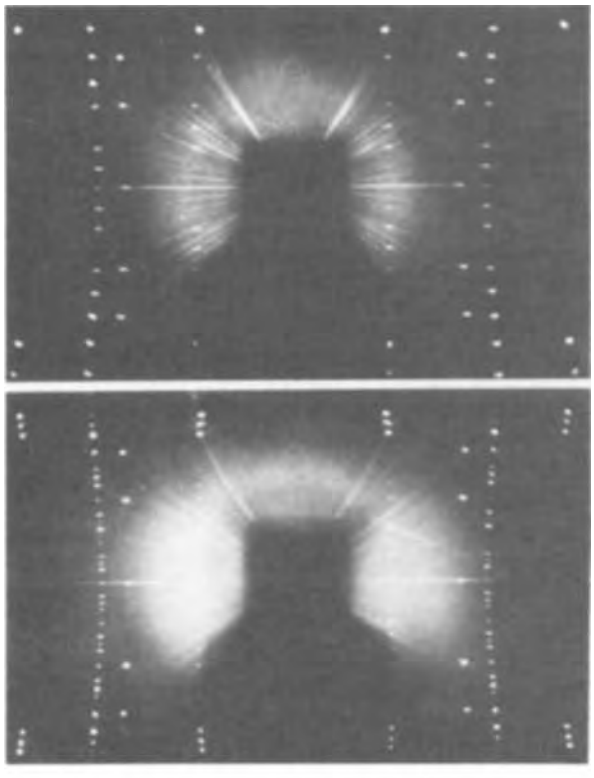

Fig. 2. Oscillating crystal patterns around c axis of hexagonal lattice (β- and β + β″-aluminas).

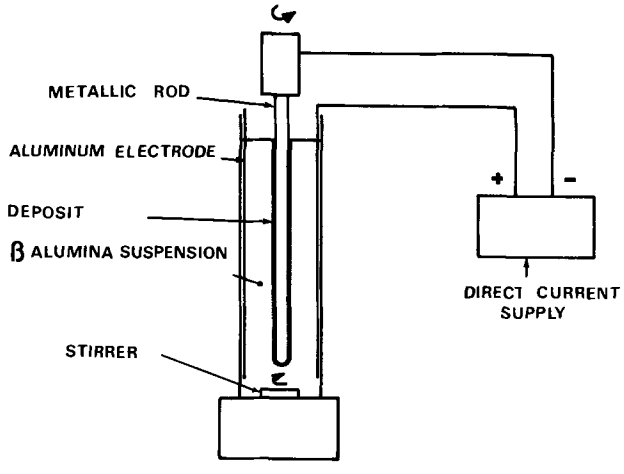

Fig. 3. Schematic view of electrophoretic deposition apparatus

with a low level of metallic impurities as shown in Table I. Their specific surface area is about 2 m^2/g.

Fabrication of closed-end tubes.—Tubes were formed by electrophoretic deposition of β-alumina on a metallic rod. (Figure 3 is a schematic view of the electrophoretic deposition apparatus.) The powder was suspended in an organic solvent and electrically charged by adsorption of positive charges from dissociation of a dissolved organic acid. Using this method, homogeneous tubes of wall thickness between 200 and 2000 μm may be obtained. In general, tubes used in experimental cells had a wall thickness of about 600 μm.

Table I. Spark mass spectrometry analysis of β-alumina samples

Elements	Mg	Si	K	Cr	Fe	Cu	Ga
Powder	10	8	13	5	15	2	3
Tube before working	1.5	20	20	—	16	1	7
Tube after working	10	>150	>760	5	17	2	7

Sintering was carried out at about 1850°C in air with a propane-oxygen furnace. Beta-alumina crucibles are used to prevent sodium loss from the tubes, which becomes important at 1500°C. Their sodium oxide content automatically determines the final content of the tubes. We have established that the firing temperature may be lowered to 1700°C by using a 1 w/o zirconia addition. Magnesia, however has no effect on sintering.

Analysis and Characterization of Electrolytes

Analysis and physical characterization were performed to obtain reproducible electrolytes and to obtain correlations between their properties and their electrochemical behavior.

Chemical analysis.—The sodium content of the β-alumina was determined by atomic absorption after dissolution of β-alumina in lithium borate. The error of this method is $\leq \pm 5\%$. The sodium content of the majority of electrolytes was about 6.2 ± 0.2 w/o.

The impurity content of the tubes and the powder were measured by spark-source mass spectrometry. Table 1 shows that the β-alumina powders obtained are of high purity and that the manufacturing process does not substantially contaminate the electrolytes.

Ion and electron microprobe examinations were used for impurity distribution determinations. This method showed that zirconium is localized at grain boundaries, while magnesium is found in the β-alumina lattice.

Figure 4 is a scanning electron microscope photograph of a fractured β-alumina tube showing cleavage.

Physical characterization.—Crystalline structures were determined by x-ray diffraction. The density of the tubes measured by the hydrostatic method in tetrabromoethane was between 3.15 and 3.20 cm^3/g.

Micrographic examinations were carried out on polished samples etched with pure boiling orthophosphoric acid. They showed the distribution of porosity near

Fig. 4. Fracture scanning electron microscope examination of a β-alumina tube showing cleavage.

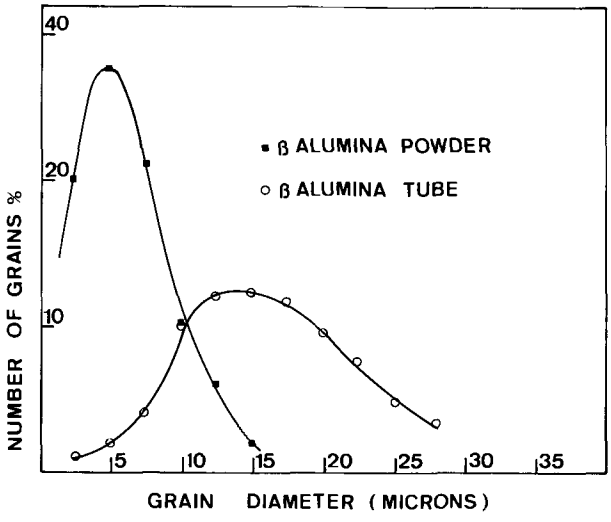

Fig. 5. Grain size distribution of powder and of β-alumina tube

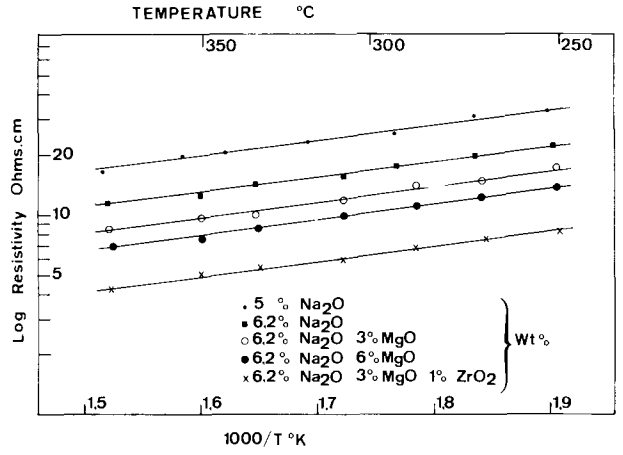

Fig. 6. Variation of log resistivity of β-alumina tubes vs. reciprocal temperature

grain boundaries, the possible presence of a second phase (perhaps α-alumina), and the grain size distribution. Figure 5 shows that the average grain size is about 15 μm. Comparison with the grain size distribution of the powder shows that the grain growth during sintering is low.

The sintering process used represents a compromise between the conditions for small grain size and low residual porosity.

Electrical characterization.—A four-probe a-c technique at 1000 Hz enabled electrolyte resistivity to be measured directly on tubes. Accuracy of the method is ±1 ohm-cm at 350°C and is independent of the frequency (in the range 200-100,000 Hz). Electrical contacts were made with platinum wire and platinum or silver paste.

Resistivity of low soda content samples containing α-alumina reaches 20 ohm-cm. On the other hand, magnesia additions decrease the resistivity to 8 ohm-cm. Values of 5 ohm-cm are obtained by use of zirconia additives.

These values are the lowest for β-alumina compared to the literature (8-10).

Discussion

The above characterizations of the different electrolytes studied lead to evident correlations between their electrochemical behavior and their properties. In particular, magnesia additions which decrease the resistivity are undesirable with regard to experimental cell lifetime (11). A resistivity of 13 ohm-cm at 350°C of the pure β-alumina electrolyte seems sufficiently low for its use in a high-power battery.

A considerable incorporation of impurities in the electrolyte, especially of potassium and silicon, took place during cycling in our glass cells. This may be explained by the corrosion of the glass by molten sodium, and can perhaps account for a substantial part of battery aging. In addition, sodium analysis of electrolytes after cycling indicates a sodium oxide content of about 6.2 w/o. This corresponds to the original composition, which is therefore not modified by electrochemical cycling.

Lifetime is also a function of tube wall thickness, thicker tubes giving a longer lifetime (11).

Conclusions

A study of the structural properties of β-aluminas, and the correlations discussed above, demonstrates that the electrolyte developed in this work is β-alumina, without additions and with a low impurity level.

In addition, the manufacturing process produces electrolyte tubes with reproducible chemical, physical, and electrical properties.

The average lifetime of experimental cells using these tubes (600 μm wall) is about 90 A-hr/cm² (current density 200 mA/cm² during discharge) as discussed previously (11).

It would appear that a very long lifetime may be obtained with such electrolytes. For this it is necessary to avoid any contamination of the electrolyte during operation. A thorough knowledge of the degradation mechanism is also necessary. This is the subject of current work.

Acknowledgment

This work was sponsored by "Direction des Recherches et Moyens d'Essais" of the French Army.

The study by one of the authors (Y. L. C.) was carried out in collaboration with Professor R. Collongues and Miss J. Thery, Laboratoire de Chimie Appliquée de l'Etat Solide, CECM Vitry-sur-Seine, France.

Manuscript submitted June 30, 1972; revised manuscript received May 17, 1973. This was Paper 173 presented at the Houston, Texas, Meeting of the Society, May 7-11, 1972.

Any discussion of this paper will appear in a Discussion Section to be published in the June 1974 JOURNAL.

REFERENCES

1. W. L. Bragg, C. Gottfried, and J. West, *Z. Krist*, **77**, 255 (1931).
2. C. A. Beevers and M. A. Ross, ibid., **97**, 59 (1937).
3. J. Thery and D. Briancon, *Compt. Rend.*, **254**, 2782 (1962).
4. J. Thery and D. Briancon, *Rev. Hautes Temp. Réfractaires*, **1**, 221 (1964).
5. G. Yamaguchi and K. Suzuki, *Bull. Chem. Soc. Japan*, **41**, 93 (1968).
6. M. Harata, *Mat. Res. Bull.*, **6**, 461 (1971).
7. C. Peters, M. Bettman, J. W. Moore, and M. D. Glick, *Acta Cryst.*, **B27**, 1826 (1971).
8. J. T. Kummer and N. Weber, Automotive Engineering Congress, Detroit, Michigan, 1967.
9. D. S. Demott and P. Hancock, *Proc. Brit. Ceram. Soc.* (1971).
10. I. W. Jones and L. J. Miles, *ibid.* (1971).
11. J. Fally, C. Lasne, Y. Lazennec, and P. Margotin, *This Journal*, **120**, 1292 (1973).

Transient Response of the System Ta/Ta_2O_5/Electrolyte

I. Ion Current Transients

D. F. Taylor *,[1] **and M. J. Dignam***

Department of Chemistry, University of Toronto, Toronto 181, Ontario, Canada

ABSTRACT

The dielectric relaxation model for ion current transients is tested against both new data obtained under potentiostatic conditions and data obtained by Dewald under galvanostatic conditions. A single set of system constants reproduces both sets of data. As has been already shown for the system Al/Al_2O_3/electrolyte, some of the system constants appear to vary slightly with film formation conditions, a possible consequence of minor structural or compositional changes. The results of a-c impedance measurements made during steady-state film growth were also reproduced by the same set of system constants for frequencies below 1 kHz. Above 1 kHz, an anomalous increase in a-c conductance with increasing frequency was observed.

The purpose of this paper (Parts I and II[2]) is to test the dielectric relaxation model for ion current transients (1-8) against a variety of forms of data for the valve metal-oxide system Ta/Ta_2O_5/electrolyte ($0.2N$ H_2SO_4). In Part I, the model is first presented in greater mechanistic detail than heretofore, incorporating the substantial modifications which have been made (2-8) since its inception (1). Equations relevant to ion current transients are then derived and compared against new and published data.

Other models which have been proposed to account for ion current (faradaic current) transients in connection with the anodic oxidation of the valve metals (principally Ta, Nb, Al, and Bi) are the high field Frenkel defect model (9, 10) due to Bean *et al.* and the ionic avalanche model (11-13) due to Young. It was Young who first showed that the form of potentiostatic ion current transients for the tantalum system could not be accounted for, even qualitatively, by the high field Frenkel defect model (11). Subsequently, Dignam and Ryan showed the same was true for the aluminum system (14).

Young proposed the ionic avalanche model specifically to account for potentiostatic transients, which it does do qualitatively. The fit achieved, however, is not very good and the fitting parameter varies with field strength. Since the mechanism underlying the equations has not been set out in any detail, it is neither possible to make an independent estimate of the fitting parameter nor even to predict the form of its dependence on field strength. Furthermore, the model has not been developed to the point where it can be tested against data for any other form of transient.

Finally, Adams, van Rysselberghe, and Willis [ref. (15), sec. 20.5] have proposed a mechanism in which the rate-controlling step is injection of interstitial metal ions at the metal/oxide interface, with the number of sites at which injection can take place being controlled by the concentration of step sites at the interface, which in turn is assumed to depend on the rate of oxide formation through, for example, the properties of screw dislocations. The model has not been set forth in mathematical terms and hence cannot be tested against the results of kinetic measurements.

For the reasons outlined, only the dielectric relaxation model is tested in this paper.

Theory

The principal postulates on which the dielectric relaxation model is based are:

1. Defect injection at one of the interfaces constitutes the rate-controlling step for ion conduction through the oxide film.
2. Dielectric relaxation processes occur within the oxide phase and are responsible for ion current transients.

In order to derive analytic expressions relating the current density, field strength in the oxide film, and time, these postulates require considerable amplification. A difficulty arises, however, since within the framework provided by postulates 1 and 2, a number of models can be proposed which ultimately predict the same form for the transient response of the system. We have chosen to handle this problem by developing a very specific model, indicating in the process, however, the alternatives which exist.

Before a model for the interfacial process can be presented we require a mechanism for ion transport within the oxide film. In the remainder of this section, a description of mobile ionic defects is presented following which postulates 1 and 2 are amplified in turn.

Nature of mobile defects.—The dielectric relaxation model of ion current transients can be developed from almost any model for the mobile defects. Only the transport mechanism due to Dignam (16, 2, 4, 8) however appears to be consistent with the unusual transport number values found for the valve metal-oxide systems (8). We proceed, therefore, on the basis of this mechanism, which is summarized briefly below. [For further details see ref. (8).]

The model is directly applicable to odd valent (M_2O_3 and M_2O_5) vitreous metal oxides only, although it can be extended to cover some mixed vitreous oxides. Using the random network model of the vitreous state due to Zachariasen, a "network" defect pair can be imagined to be formed by the rupture of one of the metal-oxygen bonds in an ionic fashion, followed by separation of these "ionized dangling bonds" through a series of partner exchanges. Alternatively, one may imagine forming such a defect pair by transferring the molecular ionic group TaO_2^+ from one region of the vitreous oxide to another, then allowing the structure to relax in the two perturbed regions. In either case the defect pair may be described as one region with a stoichiometric excess of one-half an oxygen ion, and another with a stoichiometric excess of one-fifth of a tantalum ion. The properties of these defects of importance in the present study are that they bear a charge of $-e$ and $+e$, respectively, where e is the charge on the proton, and that defect migration occurs via a cooperative motion of both the metal atoms and the oxygen atoms in the neighborhood of the moving defect, such motion constituting irreversible displacement of the atoms, no single atom, however, being displaced as far as one interatomic distance.

* Electrochemical Society Active Member.
[1] Present address: General Electric Company, Research and Development Center, Schenectady, New York 12301.
Key words: anodic oxidation of Ta, transient response, anodic films, thin films, anodic oxides, tantala films, a-c impedance of anodic tantala films.
[2] See pp. 1306-1310 of this issue.

In addition to accounting for transport number data, this transport mechanism predicts the correct value for the activation energy for ionic conduction in bulk vitreous B_2O_3 (8).

Model for interfacial control.—The postulate that defect injection at one of the interfaces constitutes the rate-controlling step for ion transport through valve metal oxide films was first proposed by Mott and Cabrera (17). The justification for this postulate in the case of the valve metal-oxide systems follows.

In general, a space charge region must exist near the interface (or interfaces) at which the ionic defects enter the film (15, 8). Space charge effects have been investigated for the tantalum system by both Young (18, 19) and Vermilyea (20-22), the results limiting the thickness of the characteristic space charge length for the system either to the order of 10Å or less, or to very much larger than the film thickness, *i.e.* $\gtrsim 10^5$Å. If the former is the case (which corresponds to bulk control) the concentration of mobile ionic defects must be of the order of the lattice ion concentration, which is improbable. If the latter is the case, then the rate will be controlled at one or both of the interfaces.

There is no very convincing evidence upon which a decision between control at one or the other interface can be made. Thus lack of dependence of the kinetics of film growth on the crystallographic orientation of the metal surface (18, 23) does not preclude rate control at the metal-oxide interface, as noted in ref. (8), p. 217. As electrolyte composition does appear to have a small effect on the interfacial kinetics [see ref. (8), p. 229] we have chosen to develop the model on the basis of control at the oxide/electrolyte interface. It is fair to say, however, that at present no generally accepted model of the oxide-solution double layer exists. The details of the following development are accordingly in considerable doubt. Fortunately, the forms of the resulting equations, Eq. [5] and [7], are preserved on altering many of the details of the interfacial processes, including the interface at which the rate is assumed to be controlled. The following should therefore be considered only as one example of a model for the interfacial processes which leads to [5] and [7].

Equilibrium is assumed to be maintained with respect to reactions of the following type

$$\left(\begin{array}{c} M \\ \diagdown \\ \quad O \\ \diagup \\ M \end{array}\right)_{\text{surface}} + H_2O \rightleftharpoons \left(\begin{array}{c} M\text{—}OH \\ \\ M\text{—}OH \end{array}\right)_{\text{surface}} \qquad [1]$$

with the interfacial electrochemical reaction being represented by

$$(M\text{—}OH)_{\text{surface}} \rightarrow (M\text{—}O^-)_{\text{surface}} + H^+_{aq} \qquad [2]$$

[For further details see ref. (8).] Vermilyea (24) has demonstrated that rapid proton exchange takes place between the surface region of anodically formed Ta_2O_5 and the electrolyte. We assume, therefore, that [2] and its reverse are in equilibrium, giving

$$m = (M_p - m)\frac{1}{X(H^+)}\exp -\left[\frac{\Delta G^\circ_{pa} - edE_d}{kT}\right] \qquad [3]$$

where M_p is the total number of surface hydroxyl groups and O^- groups per unit area at the film/double-layer interface, m the number of excess negative charges per unit area at this interface arising from proton abstraction, $X(H^+)$ the mole fraction (or Raoult law activity) of hydrogen ions at the outer Helmholtz plane, ΔG°_{pa} the standard free energy change for proton abstraction, and edE_d the electrical energy term for proton abstraction with E_d the field strength in the double layer of effective thickness d, and e the charge on the proton. We have used the convention of choosing the sign of E_d to be positive for anodic film growth, which differs from that used in ref. (8).

Assuming now that each site of excess negative charge acts as a site for injection of an anion network defect bearing a charge $-e$ into the oxide film, we have for high field strengths (17)

$$i = em\nu_o \exp\left[-(Q_o - ebE_d)/kT\right] \qquad [4]$$

where ν_o, Q_o, and b are the kinetic frequency term, activation energy, and activation distance, respectively, for defect injection, and i the ion current density or faradaic current density. In writing [4], it has been assumed that the field assisting defect injection is that in the double layer, E_d, rather than that in the bulk of the film, say.

For $M_p >> m$, elimination of m between [3] and [4] and setting $\Delta G^\circ_{pa} = \Delta H^\circ_{pa} - T\Delta S^\circ_{pa}$ yields

$$i = i_o \exp\left[-W(E_d)/kT\right] \qquad [5]$$

where

$$i_o = e\nu_o\left[\exp\left(\Delta S^\circ_{pa}/k\right)\right]/X(H^+)$$

and

$$W(E_d) = (\Delta H^\circ_{pa} + Q_o) - e(d + b)E_d \qquad [6]$$

If a quadratic field term is included in Eq. [3] and/or Eq. [4] (5, 8), Eq. [6] takes the form

$$W(E_d) = Q_e - u^*E_d(1 - u^*E_d/CQ_e) \qquad [7]$$

where the effective activation energy at zero field strength, $Q_e = \Delta H^\circ_{pa} + Q_o$, and the effective activation dipole at zero field strength, $u^* = e(d + b)E_d$, while C is a dimensionless constant, the value for which is determined by the mechanism or mechanisms leading to the quadratic field term (5, 8).

Assuming that space charge within the oxide film is negligible, a condition which must apply if ion transport is controlled entirely at an interface, the field strength in the film, E, is related to that in the double layer, E_d through the equation

$$\epsilon_o K_d E_d + me = \epsilon_o E + P \qquad [8]$$

where ϵ_o is the permittivity of free space, K_d the effective dielectric constant of the double-layer region, and P the polarization of the oxide film. Equation [8] is simply the continuity condition on the normal component of the electric displacement (allowing for surface charge) applied to the oxide/double-layer interface.

It can be shown [ref. (8) p. 174] that $\epsilon_o K_d E_d$ will be very much larger than the surface charge density, me, for the Ta/Ta_2O_5/electrolyte system provided that $\Delta G^\circ_{pa} \gtrsim 0.8$ eV, whereas it would appear that ΔG°_{pa} has a value of about 1.3 eV [ref. (8), p. 235]. Accordingly, me will be neglected in comparison with $\epsilon_o K_d E_d$.

P may be written in terms of a fast component, P_1, which follows the field in the normal manner, *i.e.*, $P_1 = \epsilon_o \chi_1 E$, and one or more slow components P_k, $k = 2,3\ldots$, viz.

$$P = \epsilon_o \chi_1 E + \sum_{k=2,3\ldots} P_k \qquad [9]$$

so that [8] becomes, on neglecting me

$$\epsilon_o K_d E_d = \epsilon_o K_1 E + \sum_{k=2,3\ldots} P_k \qquad [10]$$

where $K_1 = 1 + \chi_1$ and is the dynamic dielectric constant of the film.

Under steady-state conditions of constant E and i, the polarization components P_k, $k = 2,3\ldots$ will ultimately take up their equilibrium (or steady-state) values, *i.e.*, $P_k = \epsilon_o \chi_k E$, $k = 2,3\ldots$, in which case [10] reduces to

$$K_d E_d = K_s E_{ss} \qquad [11]$$

where the subscript ss denotes steady-state conditions, and $K_s = 1 + \chi_1 + \chi_2 + \chi_3\ldots$ is the static dielectric constant of the oxide. Equation [11], with [5] to [7] gives

$$i_{ss} = i_o \exp [-W_{ss}(E)/kT] \quad [12]$$

$$W_{ss}(E) = Q_e - u^*_{ss}E(1 - u^*_{ss}E/CQ_e)$$

where $u^*_{ss} = u^*K_s/K_d$ and is the effective steady-state activation dipole. Young (25, 26) has shown that the inclusion of a quadratic field term in $W_{ss}(E)$ can account for the kinetics of steady-state film growth on Ta and Nb, while Dignam *et al.* (27, 28) have shown the same to be the case for Al.

Equation [12] may be written

$$i_{ss} = \alpha \exp \beta_{ss}E \quad [13]$$

where $\beta_{ss} = u^*_{ss}$ (1-2 $u^*_{ss}E/CQ_e)/kT$ and is the differential steady-state field coefficient, while

$$\alpha = i_o \exp [-(Q_e - (u^*_{ss}E)^2/CQ_e)/kT]$$

For a series of measurements made at a fixed temperature, since E varies by only a few per cent for several decades change in i_{ss}, β_{ss} and α may be treated as essentially independent of E. Similarly [5] may be written

$$i = \alpha \exp \beta E_d \quad [14]$$

where

$$\beta/K_d = \beta_{ss}/K_s \quad [15]$$

For conditions in which the applied field strength is changing very rapidly, [10] gives $K_d dE_d/dt = K_1 dE/dt$, which with [14] gives

$$\lim_{dE/dt \text{ large}} \frac{d \ln i}{dE} = \beta_t E \quad [16]$$

where the transient differential field coefficient, β_t, is given by

$$\beta/K_d = \beta_t/K_1 = \beta_{ss}/K_s \quad [17]$$

The ratio of the steady-state to the transient field coefficient is thus equal to the ratio of the static to the dynamic dielectric constant for the film. [For further and more detailed discussion relating to the field coefficients, see ref. (8).] Vermilyea (29) was the first to note that two field coefficients are required to characterize the behavior of many of the valve metal-oxide systems.

Kinetics of polarization.—To complete the development of the model we require expressions describing the time dependence of the "slow" polarization components. The form chosen for these kinetics dictates the form of the transient kinetics predicted. The rate of change of a thermally activated polarization process is often expressed as (15)

$$(dP_j'/dt) = (1/\tau_j)(\epsilon_o\chi_j'E - P_j'), \; j = 2,3 \ldots \quad [18]$$

Equation [18] predicts ion current transients for a constant field, and field transients for a constant ion current, that decay with a characteristic time or times which are simply related to the τ_j and hence independent of i. Experimentally, however, the characteristic time for decay of the transients is found to be proportional to $1/i$ (3, 7, 10, 14). To obtain this result, the polarization kinetics for sufficiently high ion current, i, must take the form

$$\lim_{i \text{ large}} \frac{dP_k}{dt} = B_k i(\epsilon_o\chi_k E - P_k), \; k = 2,3 \ldots \quad [19]$$

If network defects are responsible for ion transport through vitreous oxide films their passage through the film will be accompanied by local irreversible structure changes, such changes constituting in general polarization changes. For large enough ion current, this could constitute the principal mechanism whereby the "slow" polarization components decay to their equilibrium (or steady-state) values, and would lead to Eq. [19] with eB_k being a measure of the interaction cross-sectional area for the moving network defects in relation to the kth polarization component; *i.e.*, if the passage of a network defect through the film is assumed to bring about equilibrium polarization for the polarization component P_k within a distance r_k of the defect, then $B_k = \pi r_k^2/e$.

The total rate of change of P, including thermally activated processes, is now obtained on combining [9], [18], and [19], viz.

$$\frac{dP}{dt} = \epsilon_o\chi_1 \frac{dE}{dt} + \sum_{k=2,3\ldots} B_k i(\epsilon_o\chi_k E - P_k) + \sum_{j=2,3\ldots} (1/\tau_j)(\epsilon_o\chi_j'E - P_j') \quad [20]$$

Note that we are not entitled to set $P_2 = P_2'$, $\chi_2 = \chi_2'$ etc., since P is divided into components P_2', $P_3' \ldots$ on the basis of the activation energies for the polarization processes, whereas it is divided into the components P_2, $P_3 \ldots$ on the basis of structural features and their association with the mechanism of network defect migration. It must be true, however, that $\Sigma P_k = \Sigma P_j'$, and $\Sigma\chi_k = \Sigma\chi_j'$.

In summary, the set of kinetic equations for this model are given by [10], [14], and [20].

Experimental

Potentiostatic ion current transients.—The apparatus used for forming the tantala films and for the measurement of the transients has been described (6). In a typical run, anodic oxidation of a Ta electrode was carried out galvanostatically in 0.2*N* aqueous H_2SO_4 at 2.39×10^{-4} A · cm^{-2} and 22.6°C, up to a potential of 45.18V *vs.* $Hg/Hg_2SO_4/H_2SO_4$ (0.2*N*). Following careful rinsing in distilled water, they were then stored at room temperature in air for a period of at least one month before being used for potentiostatic ion current transient measurements. This long waiting period was to ensure that the "slow" polarization components had decayed substantially prior to initiating the potentiostatic transient measurements. The transient measurement was effected by returning the electrode to the cell and applying potentiostatically a potential in the neighborhood of 41V *vs.* $Hg/Hg_2SO_4/H_2SO_4$ (0.2*N*), the precise potential being varied somewhat from specimen to specimen to test the influence of the field strength used for the experiment on the kinetic parameters.

Data points from a typical run are shown in Fig. 1. They fall on a curve of the same form as those reported earlier by Young for the Ta/Ta_2O_5/electrolyte system (11) and by Dignam and Ryan for the Al/Al_2O_3/electrolyte system (14).

A-C impedance measurements under conditions of steady-state film formation.—The procedure employed for these measurements is essentially that used by Goad and Dignam (30). The apparatus used for the

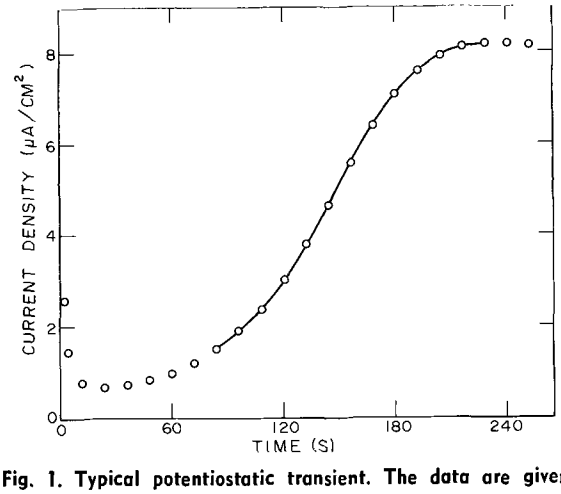

Fig. 1. Typical potentiostatic transient. The data are given by the open circles.

present studies, however, was a considerable refinement on the original in that the process of data aquisition was automated and recorded in digital form for subsequent analysis. This led to a substantial improvement in measurement accuracy.

The technique involves superimposing a small, constant amplitude a-c current onto the constant d-c formation current. The d-c electrode potential, and the components of the a-c electrode potential which are respectively in and out of phase with the a-c current are then recorded as a function of time. The data so obtained can then be processed to give the parallel-circuit-equivalent effective a-c conductivity, $\sigma_{a\text{-}c}$, and effective dielectric constant, K_{eff} (30).

Oxide films were grown galvanostatically to a final cell potential of approximately 95V with a small a-c current superimposed on the d-c current. The amplitude of this a-c component was constant and equal in magnitude to approximately 1% of the d-c current. Before and after each run, both the d-c and a-c voltages appearing across a standard shunt resistance were measured and recorded.

Frequencies in the range 3-7771 Hz were combined with current densities of 233 ± 2 μA/cm^2 (768-7771 Hz) and 1.16 ± 0.01 mA/cm^2 (3-768 Hz) to provide a wide range of (ω/i_{ss}) values. The variations in the current densities arose only from variations in electrode area; the actual current flowing during any given run was constant to within 0.02%.

The d-c cell potential was measured between anode and reference electrode, but the in- and out-of-phase a-c voltage components were measured at the anode with respect to ground, as a much cleaner and more stable a-c signal was then obtained. Since both components of the a-c voltage (measured against ground) appearing at the reference electrode were found to be independent of time, no measurable error was introduced in this way.

The a-c voltage components were measured using a phase sensitive detector combined with automatic alternate switching between reference signals which were respectively in and out of phase with the a-c cell current. At the end of each interval, the d-c voltage, and the magnitude, polarity, and identification (in or out of phase) of one a-c voltage component, were recorded automatically on paper tape.

Both the d-c electrode potential, V_o, and the two a-c components, V_{in} and V_{out}, were observed to increase linearly with time, so that the data could be presented in the form of the parallel equivalent a-c conductivity, $\sigma_{a\text{-}c}$, and effective dielectric constant, K_{eff} as was done in a recent publication from this laboratory (30). These are related to the observables through the equations (30)

$$\sigma_{a\text{-}c} = I_\omega \dot{V}_{in}\dot{V}_o/E_o(\dot{V}_{in}^2 + \dot{V}_{out}^2) \quad [21]$$

$$\omega\epsilon_o K_{eff} = -I_\omega \dot{V}_{out}\dot{V}_o/E_o(\dot{V}_{in}^2 + \dot{V}_{out}^2) \quad [22]$$

where $\dot{V}_{in}$ is the time derivative of the amplitude of the component of the a-c electrode potential which is in phase with the impressed a-c current density of amplitude, I_ω, etc., while V_o and E_o are the d-c components of the electrode potential and field strength, respectively. The d-c current density, I_o, and field strength, E_o, as well as the electrode area (and hence I_ω) were calculated from V_o and the d-c cell current using the steady-state data of Young (25). In reduced form, the results therefore take the form $\sigma_{a\text{-}c}$ and K_{eff} as functions of I_o and angular frequency, ω. In Fig. 2 and 3, $\sigma_{a\text{-}c}/I_o$ and K_{eff} are plotted against log (ω/I_o), the points in each case falling on a smooth curve despite the fact that different values for I_o have been used. This same behavior has been noted previously (30) for the system Al/Al_2O_3/electrolyte, and as noted there is a natural consequence of the fact that ionic transients for these systems appear to involve the charge passed per unit area, (*i.e.*, $\int_0^t Idt$) as the variable characterizing the decay of the transient rather than time ($\sigma_{a\text{-}c}/I_o$, K_{eff}, and ω/I_o are all dimensionally independent of time). The large negative values of K_{eff} occurring for small ω/I_o are noteworthy since they reflect the large contribution of the ion current transients to the current component which is out of phase with the field (30).

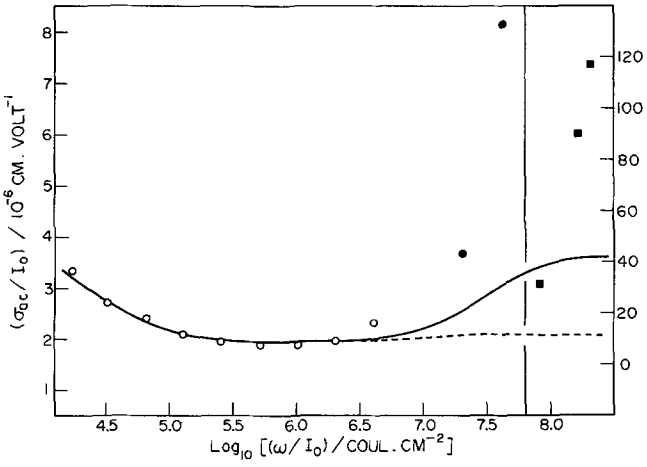

Fig. 2. Dependence of ($\sigma_{a\text{-}c}/I_o$) on (ω/I_o). The open circles represent data obtained for I_o = 0.233 mA/cm^2, the filled symbols data for I_o = 1.16 mA/cm^2. The change in symbols emphasizes the change in scale past the vertical line. This scale change does not apply to the computed curves.

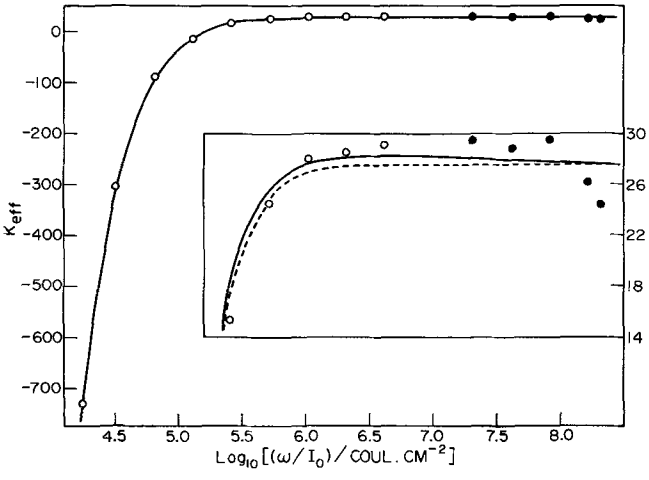

Fig. 3. Dependence of K_{eff} on (ω/I_o). Data point identification as in Fig. 2.

Analysis and Discussion

Galvanostatic transients.—It is convenient to begin with an analysis of the galvanostatic transient measurements of Dewald (10) on the system Ta/Ta_2O_5/0.1*N* H_2SO_4, as these provide, without difficulty, values for the constants χ_k and B_k. The experiments were performed by forming tantala films under steady-state conditions ($I_{ss} \sim 10^{-4}$ A/cm^2, room temperature) then increasing abruptly the current density by a factor of 2. The field strength was observed to increase rapidly initially, go through a maximum, then decay more slowly to the steady-state field strength corresponding to the new impressed current. Goad and Dignam (7) have shown that the data beyond the maximum can be fitted within experimental error by an equation of the form

$$\frac{E - E_2}{E_2 - E_1} = M_1 \exp(m_1 q) + M_2 \exp(m_2 q) \quad [23]$$

where E_1 and E_2 are the steady-state field strengths corresponding to the formation and final current densities, respectively, and M_1, M_2, m_1, m_2 are constants.

Goad and Dignam (7) derive an equation of the same form as [23] from the equations for the dielectric relaxation model and the following approximations

$$\sum_k B_k i(\epsilon_0\chi_k E - P_k) >> \sum_j (1/\tau_j)(\epsilon_0\chi_j' E - P_j') \quad [24]$$

$$I >> i_c \quad [25]$$

where $I = i + i_c$ is the total current density, and $i_c = \epsilon_0 dE/dt + dP/dt$ is the charging current density. The second approximation is shown to be valid beyond the maximum in $(E - E_2)/(E_2 - E_1)$ while the first is simply assumed to be valid, since i is substantial ($\sim 10^{-4}$ A/cm^2) throughout the transient. The analysis leading to [23] requires only two ion current driven polarization terms and has been published (7). Following an identical procedure, Taylor (31) has extended the analysis to include three terms, the result being given in the Appendix. Including only two terms, χ_2, B_2, χ_3, B_3 are related to M_1, m_1, M_2, m_2 through the following equations: B_2 and B_3 are the roots of the equation

$$x^2 + c_1 x + c_2 = 0 \quad [27]$$

where

$$c_1 = \frac{m_1(1 + M_2) + m_2(1 + M_1)}{1 + M_1 + M_2}$$

and

$$c_2 = \frac{m_1 m_2}{1 + M_1 + M_2}$$

while

$$\chi_j = (c_3 + c_4 B_k)/(B_k - B_j) \quad [27]$$

where

$$c_3 = K_1 \frac{(m_1 M_1 + m_2 M_2)}{(1 + M_1 + M_2)}$$

and

$$c_4 = K_1(M_1 + M_2)$$

These equations, with Dewald's results and $K_1 = 27.6$ (15) give (7)

$$\chi_2 = 36.0,\ B_2 = 0.657 \times 10^{-4}\ \text{cm}^2/\text{coulomb}$$

$$\chi_3 = 16.4,\ B_3 = 4.34 \times 10^{-4}\ \text{cm}^2/\text{coulomb} \quad [28]$$

These values for B_2 and B_3 correspond to interaction-cross-sectional radii for the network defects of 1.82 and 4.69, respectively, values which appear to be of the correct magnitude. One may also calculate $K_s = K_1 + \chi_2 + \chi_3 = 80.0$ and hence the ratio of the steady-state to transient field coefficient, $\beta_{ss}/\beta_t = K_s/K_1 = 2.9$ (see [17]) which is in good agreement with independent estimates (8). The dielectric relaxation model provides, therefore, an entirely satisfactory account of galvanostatic transients. To be acceptable, however, the model, with the same values for the constants, must account for other forms of transient.

Potentiostatic ion current transients.—An exact analysis of the data of Fig. 1 on the basis of the equations for the dielectric relaxation model and over the entire range of the data is beyond our present capabilities, as the equations are in fact incomplete. One would require a knowledge of the relaxation times, τ_j, and of the equations relating the set of polarization components $\{P_j'\}$ to the set $\{P_k\}$. Dignam and Ryan (14) have attempted such a complete analysis of potentiostatic transients for the system Al/Al_2O_3/electrolyte by making a number of simplifying approximations. The result was qualitative agreement over the entire curve. On the basis of this partial success, the initial current decay is interpreted as a decrease in charging current density, i_c associated with the approach of the slow polarization components, P_j', toward their equilibrium values via thermal activation, *i.e.*, in this region i is very small so that

$$\sum_j (1/\tau_j)(\epsilon_0\chi_j' E - P_j') >> \sum_k B_k i(\epsilon_0\chi_k E - P_k) \quad [29]$$

(see Eq. [20]). As P increases, however, so does E_d (see Eq. [10]) and hence i (see Eq. [14]) so that ultimately the total current density, I, begins to increase. Furthermore, as i increases, a point is reached at which the inequality [29] is no longer valid. In fact for i large enough, based on the results for the galvanostatic transients, the inverse of [29], namely [24], must apply. Under conditions in which [24] is satisfied, the kinetics of the transients are effectively independent of polarization mechanisms involving thermal activation, making the analysis relatively easy.

Accordingly, for [24] and [25] valid approximations (which will only be true for times greater than some value lying beyond the minimum in I) and making the further approximation that E is constant during the potentiostatic transient, [20] integrates to give

$$P = \epsilon_0(K_s - 1)E + \sum_k (P_k^0 - \epsilon_0\chi_k E)\exp(-B_k q) \quad [30]$$

where $q = \int_0^t I dt$ and is the charge passed per unit electrode area, while P_k^0, is the value of P_k for $q = 0 = t$. Eliminating P from [30] using [10], and E and E_d from the resulting equation using [13] and [14] and the approximation $(\partial\beta/\partial E)_T \simeq 0 \simeq (\partial\alpha/\partial E)_T$, gives

$$\ln(I/I_{ss}) = \sum_{k=2,3} A_k \exp(-B_k q) \quad [31]$$

where $A_k = (P_k^0 - \epsilon_0\chi_k E)B_k/\epsilon_0 K_d$ and is independent of time (and q) for E constant.

Extrapolation of the data in Fig. 1 from the region beyond the minimum in I to time zero (in an attempt to estimate the ion current density in the region up to the minimum) and integrating, gives on the basis of the values for the constants obtained in the previous section, $B_3 q >> 1$ and hence $A_3 \exp(-B_3 q) << A_2 \exp(-B_2 q)$ for values of q lying beyond the minimum. Under these conditions (which are the only ones in which [31] is a valid approximation) [31] reduces to

$$\ln(I/I_{ss}) = \ln[I(t = 0)/I_{ss}] \exp(-B_2 q) \quad [32]$$

where the time $t = 0$ is chosen to lie sufficiently beyond the minimum in I so that [23] and [24] are valid.

The solid line in Fig. 1 is calculated from [32] with $B_2 = 6.14 \times 10^3$ cm^2/coulomb and is typical of the fit achieved in a total of five determinations. The value of B_2 was chosen in each case to minimize the variance in I, the mean of the five determinations being given by $B_2 = (6.6_3 \pm 0.3_6) \times 10^3$ cm^2/coulomb in excellent agreement with the value obtained from Dewald's galvanostatic transient data, 6.57×10^3 cm^2/coulomb. No variation of B_2 with the final steady-state current, I_{ss}, was observed.

Using Young's data (11), obtained for a tantala film formed at 100V (constant potential) for 3.5 hr then annealed by immersion in boiling water for 5 min, Dignam and Ryan (14) calculate a value for B_2 of 8.0×10^3 cm^2/coulomb. Furthermore, good agreement with the data was achieved. That this value differs somewhat from those reported above is undoubtedly due to the fact that the films in this instance were formed in an entirely different manner than were those giving rise to the values near 6.6×10^3 cm^2/coulomb. A similar slight dependence of B_2 on film formation conditions (but not on measuring conditions) has already been noted for the system Al/Al_2O_3/electrolyte (14, 8). Since the constants B_2 and B_3 must be dependent on the detailed structure and composition of the oxide film, then if this structure and/or composition varies somewhat with formation current density, say, then B_2 and B_3 will vary with formation current density. For both the aluminum and tantalum systems, B_2 decreases slightly with increasing formation current density, the rate being about 10% per decade of current density for the aluminum system (14).

In a recent paper (12) Young attempted to fit [32] to his potentiostatic data and while he achieved a reasonably good fit, it was not the excellent fit achieved here and previously in this laboratory (14). The reason for this appears to lie in Young's failure to ap-

preciate the approximations inherent in [32] (*i.e.*, conditions [24] and [25]) which restrict its application to the region of the curve lying well beyond the minimum in I.

A-C impedance measurements.—Expressions for $\sigma_{a\text{-}c}/I_0$ and K_{eff} as functions of (ω/I_0) and the system constants (β_t, β_{ss}, K_1 and χ_k, B_k for $k = 2,3$) have been derived by Goad and Dignam (30) from the equations for the dielectric relaxation model on the assumption that inequality [24] is valid. This will be the case for the measurements presented herein since the smallest value of I_0 was 2.33×10^{-4} A/cm^2. The analysis has been extended to include an additional ion-current-driven polarization term by Taylor (31), the result being given in the Appendix. The dashed lines in Fig. 2 and 3 have been calculated from these equations using the values for the parameters obtained from Dewald's data and the values for β_{ss} calculated from Young's steady-state data (25). For frequencies below about 1 kHz, the agreement between the experimental and calculated curves is excellent. At the high frequency end, however, while K_{eff} shows no significant discrepancy, the calculated value for $\sigma_{a\text{-}c}/I_0$ is too low by a factor of about 50. The solid line was calculated from essentially the same set of constants but including an additional set of polarization parameters with the following values: $\chi_4 = 0.52_6$, $B_4 = 3.33 \times 10^7$ cm^2/coulomb. The significance of this particular choice for χ_4, B_4 is covered in Part II of this paper. At this point we simply note that the inclusion of an additional set of polarization parameters with these values does not reduce the high frequency discrepancy in $\sigma_{a\text{-}c}/I_0$ significantly. It appears likely that some new process is responsible for the rapid rise in $\sigma_{a\text{-}c}$ with increasing frequency. We are, however, unable to offer by way of explanation any mechanism which would lead to such a dramatic increase in $\sigma_{a\text{-}c}$ with increasing frequency. If the phenomenon occurs as well during the galvanostatic and potentiostatic transients, then from the value of (I_0/ω) or of ω at which it appears, we calculate that it will make a negligible contribution over the regions of the transient curves which we have analyzed. Thus while the anomalously high values for $\sigma_{a\text{-}c}$ are not accounted for by this model, neither are they in conflict with it.

Other forms of ion current transient.—Young (32) has published data on the tantalum system obtained in the following way. A film was grown galvanostatically until a certain voltage, V', was reached, at which time the voltage was reduced suddenly to zero. The voltage was held at zero for time t' (differing from experiment to experiment) then the voltage V' was re-applied. The so called "instantaneously" observed ionic current, obtained by an extrapolation procedure, was found to be less than the formation current density and to decrease with increasing t'.

In a recent paper (12) Young claims to have analyzed the results of the above measurements on the basis of the dielectric relaxation model obtaining qualitative agreement only. The analysis, however, was based implicitly on the assumption that inequality [24] is valid for the conditions of zero applied potential, whereas it is easily shown from the parameters reported herein and the form of the observed potentiostatic transients that [29] is the correct inequality. The data may be fitted exactly if this correction is made and the τ_j and χ_j' treated as disposable parameters (since one has in effect an infinite number of disposable parameters and the general behavior predicted by the model is correct). Such an exercise is, however, without merit. A test of the model against this or similar data must await independent information on the kinetics of polarization via mechanisms involving thermal activation. Under the high field conditions frequently encountered when dealing with the valve metal oxide systems, these kinetics may not even be in accord with [18]. Measurements relating to charging current made at low field strength will not necessarily give useful information about high field polarization kinetics.

Dell'Oca and Young (33) report a-c impedance measurements on the Ta/Ta_2O_5/electrolyte system made during the course of a potentiostatic transient experiment of the same kind reported herein. They claimed their results to be opposed to the predictions based on the dielectric relaxation model for ion current transients. This claim has already been shown to be incorrect by Dignam and Taylor (34). However, it appears necessary to state our position once again, since the same claim has been repeated in a recent review by Dell'Oca, Palfrey, and Young (13). In this review, no mention is made of our rebuttal.

The argument presented originally by Dell'Oca and Young, and repeated in the review mentioned above, is based on an improper analysis of the data. They fail to consider the contribution to the out of phase a-c current component arising from ion current relaxation phenomena (34). This contribution can be very large (see, *e.g.*, Fig. 3). Most important, however, the model that they discredit is in fact one of their own making, although they claim it to be an extension of the dielectric relaxation model, expected "... on the logic of Dignam's theory..." [ref. (13), p. 17]. In effect they assume that $P_j' = P_j$, $\chi_j' = \chi_j$, and $(1/\tau_j) \propto B_j$ for all j (see [20] and following). We are unable to conceive of any mechanism, reasonable or otherwise, which would lead to such relations. The model presented herein certainly does not, as noted already, nor does the original outdated model (1) which leads to equations substantially of the same form as those for the present model. Furthermore, the experimental results are contrary to these relations, since apparently only two B_k values are required to account for ion current transients, while a large range of τ values appears to be necessary to account for dielectric behavior in the absence of ion current (15).

Summary and Conclusions

The dielectric relaxation model has been shown to give an accurate and self-consistent account of several kinds of ion current transient, the parameters being in every case of the expected magnitude (8). Certain kinds of transients cannot at present be used to provide a quantitative test for the model since information on the kinetics of polarization at high field strengths via mechanisms involving thermal activation is not available.

We are aware of no data which are in conflict with the dielectric polarization model, though a large number of phenomena are not encompassed by it (*e.g.*, the high value observed for $\sigma_{a\text{-}c}$ at high frequencies, see Fig. 2). The crucial test of the theory, however, is to look for direct evidence of polarization changes which are in accord with [19], and test whether or not the kinetics which describe these changes are consistent with those deduced indirectly through the study of ion current transients. The first part of this test has already been reported (6), the results being consistent with the dielectric relaxation model. In Part II of this paper, a quantitative investigation of the ion current driven polarization processes is undertaken.

Acknowledgments

The authors are grateful to the National Research Council of Canada for supporting this research and for a scholarship (D.F.T.).

Manuscript submitted Oct. 3, 1972; revised manuscript received May 8, 1973.

Any discussion of this paper will appear in a Discussion Section to be published in the June 1974 JOURNAL.

APPENDIX

Galvanostatic transients.—Using the identical procedure given in ref. (7), Eq. [9] to [11], [13] to [15], [17], and [20], with the inequalities [24] and [25], lead to the following equations for galvanostatic transients when a total of three polarization components

which are driven by the passage of ion current are included. [For details see ref. (31).]

$$\frac{E - E_2}{E_2 - E_1} = M_1 e^{m_1 q} + M_2 e^{m_2 q} + M_3 e^{m_3 q} \qquad [A\text{-}1]$$

where the constants M_j, m_j are related to the system parameters, χ_k, B_k, through the following equations. The parameters B_2, B_3, B_4 are the roots of the equation

$$x^3 + c_1'x^2 + c_2'x + c_3' = 0 \qquad [A\text{-}2]$$

where

$$c_1' = \frac{m_1(1 + M_2 + M_3) + m_2(1 + M_1 + M_3) + m_3(1 + M_1 + M_2)}{(1 + M_1 + M_2 + M_3)}$$

$$c_2' = \frac{m_1m_2(1 + M_3) + m_2m_3(1 + M_1) + m_3m_1(1 + M_2)}{(1 + M_1 + M_2 + M_3)}$$

$$c_3' = m_1m_2m_3/(1 + M_1 + M_2 + M_3)$$

while the parameters χ_k are given by

$$\chi_j = \frac{c_4' + B_kB_lc_5' + c_6'(B_k + B_l)}{(B_k - B_j)(B_l - B_j)} \qquad [A\text{-}3]$$

where $j = 2,3,4$; $k = 3,4,2$; $l = 4,2,3$, and the constants c_4', c_5', and c_6' are given by

$$c_4' = K_1\left[\frac{m_1^2M_1 + m_2^2M_2 + m_3^2M_3}{1 + M_1 + M_2 + M_3} - \left(\frac{m_1M_1 + m_2M_2 + m_3M_3}{1 + M_1 + M_2 + M_3}\right)^2\right]$$

$$c_5' = K_1(M_1 + M_2 + M_3)$$

$$c_6' = K_1\frac{(m_1M_1 + m_2M_2 + m_3M_3)}{(1 + M_1 + M_2 + M_3)}$$

For $\chi_3 = 0$, one obtains by the same process [26] and [27], which in turn are equivalent to those presented in ref. (7).

A-C impedance under conditions of steady-state film formation.—The parallel-equivalent, effective a-c conductivity, $\sigma_{a\text{-}c}$, and effective dielectric constant, K_{eff}, are defined by the equations

$$\sigma_{a\text{-}c} = I_{in}/E_\omega \qquad [A\text{-}4]$$

$$K_{eff} = I_{out}/E_\omega\epsilon_0\omega \qquad [A\text{-}5]$$

where I_{in} and I_{out} are the amplitudes of the a-c current components which are respectively in and out of phase with the a-c field of amplitude E_ω. Equations [A-4] and [A-5] are equivalent to [21] and [22] [see ref. (30)].

Using Eq. [9] to [11], [13] to [15], [17], and [20] with the inequality [24] and the identical procedure given in ref. (30), the following expressions for $\sigma_{a\text{-}c}$ and K_{eff} can be obtained (31)

$$K_{eff} = \frac{\left[\left(K_sT_1 - \frac{\beta_{ss}}{\epsilon_0K_s}T_2\right)I_o^6 + \left(T_3 - \frac{\beta_{ss}}{\epsilon_0K_s}T_4\right)I_o^4\omega^2 + \left(T_5 - \frac{\beta_{ss}}{\epsilon_0K_s}T_6\right)I_o^2\omega^4 + K_1\omega^6\right]}{(T_1I_o^6 + T_7I_o^4\omega^2 + T_8I_o^2\omega^4 + \omega^6)} \qquad [A\text{-}6]$$

$$\frac{\sigma_{a\text{-}c}}{I_o} = \frac{\left[\beta_{ss}T_1I_o^6 + \left(\frac{\beta_{ss}}{K_s}T_3 + \epsilon_0T_2\right)I_o^4\omega^2 + \left(\frac{\beta_{ss}}{K_s}T_5 + \epsilon_0T_4\right)I_o^2\omega^4 + \left(\frac{\beta_{ss}K_1}{K_s} + \epsilon_0T_6\right)\omega^6\right]}{(T_1I_o^6 + T_7I_o^4\omega^2 + T_8I_o^2\omega^4 + \omega^6)} \qquad [A\text{-}7]$$

$$T_1 = B_2^2B_3^2B_4^2$$

$$T_2 = B_2B_3B_4(\chi_4B_2B_3 + \chi_3B_2B_4 + \chi_2B_3B_4)$$

$$T_3 = B_2^2B_3^2(K_1 + \chi_2 + \chi_3) + B_2^2B_4^2(K_1 + \chi_2 + \chi_4) + B_3^2B_4^2(K_1 + \chi_3 + \chi_4)$$

$$T_4 = B_2B_3(\chi_2B_3 + \chi_3B_2) + B_2B_4(\chi_2B_4 + \chi_4B_2) + B_3B_4(\chi_4B_3 + \chi_3B_4)$$

$$T_5 = B_2^2(K_1 + \chi_2) + B_3^2(K_1 + \chi_3) + B_4^2(K_1 + \chi_4)$$

$$T_6 = \chi_2B_2 + \chi_3B_3 + \chi_4B_4$$

$$T_7 = B_2^2B_3^2 + B_2^2B_4^2 + B_3^2B_4^2$$

$$T_8 = B_2^2 + B_3^2 + B_4^2$$

Equations [A-6] and [A-7] reduce to Eq. [10] and [11] of ref. (30) on setting $\chi_4 = 0$.

REFERENCES

1. M. J. Dignam, *This Journal*, **112**, 722 (1965).
2. M. J. Dignam, Abstract No. 36, pp. 33, Electrochem. Soc. Extended Abstracts, Vol. 4, No. 1, Spring Meeting, Dallas, Texas, May 7-12, 1967.
3. M. J. Dignam and P. J. Ryan, *Can. J. Chem.*, **46**, 535 (1968).
4. M. J. Dignam, Extended Abstracts, Dielectric and Insulation Division, Electrochem. Soc. Meeting, New York, May 4-9, 1969, Vol. 6, No. 1., p. 11.
5. M. J. Dignam and D. B. Gibbs, *J. Phys. Chem. Solids*, **30**, 375 (1969).
6. M. J. Dignam and D. F. Taylor, *Can. J. Chem.*, **48**, 1971 (1970).
7. D. G. W. Goad and M. J. Dignam, *ibid.*, **50**, 3250 (1972).
8. M. J. Dignam, in "Oxides and Oxide Films," Vol. I, Chap. 2, J. W. Diggle, Editor, Marcel Dekker, Inc., New York (1972).
9. C. P. Bean, J. C. Fisher, and D. A. Vermilyea, *Phys. Rev.*, **101**, 551 (1956).
10. J. F. Dewald, *J. Phys. Chem. Solids*, **2**, 55 (1957).
11. L. Young, *Proc. Roy. Soc.*, **A263**, 395 (1961).
12. L. Young, *Can. J. Chem.*, **50**, 574 (1972).
13. C. J. Dell'Oca, D. L. Pulfrey, and L. Young, in "Physics of Thin Films," Vol. 6, Chap. 1, Academic Press, London and New York (1971).
14. M. J. Dignam and P. J. Ryan, *Can. J. Chem.*, **46**, 549 (1968).
15. L. Young, "Anodic Oxide Films," Academic Press, London (1961).
16. M. J. Dignam, Extended Abstracts, Chemical Institute of Canada Symposium on Physical Chemistry of Solids, Univ. of Montreal, Quebec, 1966, p. 35.
17. N. Cabrera and N. F. Mott, *Rept. Prog. Phys.*, **12**, 163 (1948).
18. L. Young, *Trans. Faraday Soc.*, **50**, 153 (1954).
19. L. Young, *Proc. Roy. Soc.*, **A244**, 41 (1958).
20. D. A. Vermilyea, *Acta Met.*, **3**, 106 (1955).
21. D. A. Vermilyea, *This Journal*, **102**, 655 (1955).
22. D. A. Vermilyea, *ibid.*, **104**, 140 (1957).
23. D. A. Vermilyea, *ibid.*, **103**, 690 (1956).
24. D. A. Vermilyea, *Surface Sci.*, **2**, 444 (1964).
25. L. Young, *Proc. Roy. Soc.*, **A258**, 496 (1960).
26. L. Young and F. G. R. Zobel, *This Journal*, **113**, 277 (1966).
27. M. J. Dignam, D. Goad, and M. Sole, *Can. J. Chem.*, **43**, 800 (1965).
28. M. J. Dignam and D. Goad, *This Journal*, **113**, 381 (1966).
29. D. A. Vermilyea, *ibid.*, **104**, 427 (1957).
30. D. Goad and M. J. Dignam, *Can. J. Chem.*, **50**, 3267 (1972).
31. D. F. Taylor, Ph.D. Thesis, University of Toronto, 1970.
32. L. Young, *This Journal*, **111**, 1289 (1964).
33. C. J. Dell'Oca and L. Young, *Appl. Phys. Letters*, **13**, 228 (1968).
34. M. J. Dignam and D. F. Taylor, *ibid.*, **15**, 198 (1969).

Transient Response of the System $Ta/Ta_2O_5/Electrolyte$

II: Investigation of Faradaic-Current-Driven Polarization Processes

D. F. Taylor*,[1] and M. J. Dignam*

Department of Chemistry, University of Toronto, Toronto 181, Ontario, Canada

ABSTRACT

Voltage pulse experiments were carried out on the system $Ta/Ta_2O_5/0.2N$ H_2SO_4 to test for the presence of polarization processes which are driven toward their equilibrium (or steady-state) values by the passage of faradaic current. Such processes were observed, their behavior being in quantitative accord with that predicted by the dielectric relaxation model using the system constants determined from measuremens of ion current transients (see Part I). In addition, an "anomalous" effect was observed which appears to be related to the anomalous a-c conductance effect reported in Part I, but is otherwise unexplained. It is believed that these experiments constitute a crucial test of this model, and one that it has passed successfully.

In Part I of this paper (1), the dielectric relaxation model for ion current transients has been outlined and tested successfully against galvanostatic and potentiostatic transient data as well as a-c impedance data obtained during steady-state film formation. However, none of these experiments show directly the presence of a polarization process whose rate is proportional to the ion-current density, such processes being required by the theory.

The problem may be stated as follows. From the values for the constants determined in Part I, the extraordinary polarization current is predicted to be at most a few per cent of the ion current producing it. Even the calculated contribution to the effective dielectric constant made by the ion-current-driven polarization processes during ion-current transients is negligible (2). All attempts to detect the extraordinary polarization current in the presence of ion current are consequently bound to be unsuccessful. It is therefore necessary to observe the effect in the absence of ion current. Equation [20] of Part I, reproduced below for convenience, holds the key to this apparent paradox.

$$dP/dt = \epsilon_0 K_1 dE/dt + \sum_k B_k i(\epsilon_0 \chi_k E - P_k) + \sum_j (1/\tau_j)(\epsilon_0 \chi_j' E - P_j') \quad [1]$$

When ion current is flowing, both types of polarization mechanism operate to produce a change in the polarization of the film on making a sudden change in the field. For a sufficiently small ion current density, all changes in the polarization will be thermally activated. Thus when a square-wave voltage pulse of sufficient amplitude to induce a significant flow of ion current is applied potentiostatically across a preformed film, the polarization of the oxide will be driven upward during the pulse by both the ion-current and thermal mechanisms. After the pulse, however, the polarization must return to its original equilibrium value by thermal relaxation alone, since the ion current is then negligibly small.

The time integral of the capacitive discharge current is a measure of the total polarization induced during the pulse. An increase in the ion current which flows during the pulse should polarize the oxide layer to a greater extent, and this in turn should manifest itself as a larger discharge current. In this paper, the total charge passed during the discharge period, q_-, is measured as a function of the faradaic charge passed during the voltage pulse, q_f, and the results compared with those predicted from the dielectric relaxation model.

Experimental Procedures

A description of the apparatus and materials has been published (3). In a typical run, anodic oxidation of the electrode blade was carried out galvanostatically at 22.6°C with a current density of 2.39×10^{-4} A-cm^{-2}, and film growth was halted at 45.18V (Hg/Hg_2SO_4 reference electrode). A number of pulse measurements were made on each fresh electrode by switching the cell potential sequentially from V_1 to V_2 to V_1. $(V_2 - V_1)$ was held constant at 25.01V for all the experiments, while V_1 ranged between 0 and 25.01V. These values were chosen so that significant ion current would flow only during the charging pulse.

In our earlier investigation (3), the voltage drop across a current-measuring resistor in the potentiostat circuit was monitored by an oscilloscope and camera, and four pictures with different time scales and baseline positions were required for each selected value of V_1. In the present series of experiments, electronic integration of the current-time curves improved the accuracy considerably. The current-measuring resistor was fixed at a value of 20 ohms, and the oscilloscope and camera recorded net charge passed as a function of time. A suitable constant bias voltage was applied to the second input terminal of the oscilloscope just after switching to V_2, and was removed immediately following the return of the cell voltage to V_1. This signal in effect subtracted out the contribution to the total charge made by the fast polarization processes, and allowed the use of a very sensitive scale on the oscilloscope. Electronic integration prohibited a change in measuring resistor midway through the period of interest, but the increase in sensitivity achieved with the biasing voltage more than compensated for this loss.

The polarizing pulse width was varied between 10.6 and approximately 26 msec, but remained constant for the entire set of measurements carried out on a given electrode. Only one voltage pulse and resulting oscilloscope trace were required for each value of V_1. For the first set of experiments, a minimum of 1 hr was allowed between successive pulses and V_1 was changed by no more than 2V between such successive measurements.

In a second series of voltage-pulse experiments, a different approach was used. Rather than waiting for "equilibrium polarization" at each value of V_1, the pulse switching circuit was triggered at 1-min intervals for 10 or 15 min, with only the last charge-time curve being recorded. In all other respects, the experimental procedure for the two series was the same.

Two experimental difficulties were encountered with these measurements, which were not eliminated completely. The first was the appearance of a false charge

* Electrochemical Society Active Member.
[1] Present address: General Electric Company, Research and Development Center, Schenectady, New York 12301.
Key words: dielectric properties of anodic tantala, polarization processes in anodic tantala, anodic films, thin films, anodic oxides, tantala films.

component at the output of the integrator, arising presumably from circuit transients during the rapid voltage changes from V_1 to V_2 and from V_2 to V_1. Studying the effect in the absence of a cell (*i.e.*, with only the 20-ohm measuring resistance present) it was found that slowing down the switching speed substantially reduced this effect, but did not eliminate it entirely. The residual effect appeared as small, false, charge components, introduced during the two switching intervals, but remaining constant at other times. The false charge components were found to be dependent on load conditions and on $V_2 - V_1$, but not on V_1.

The second experimental difficulty appeared as a short duration anodic voltage pulse superimposed on V_2 and introduced on switching from V_1 to V_2. This meant that significant ion current flowed even for values of V_2 which would otherwise have led to negligible ion current. The amount was small, however, corresponding to the order of 10 nanocoulombs/cm², so that it introduced no difficulties in data analysis.

Results

Figure 1 shows a typical charge-time curve obtained directly from an oscilloscope trace. The position of the curve lying within the field pulse has been reduced by 7.70 μcoulombs/cm² by the application of the bias voltage to the oscilloscope terminals, as described earlier. Thus if it were not for the problem of false charges discussed earlier, the total charge passed per unit electrode area associated with the charging process, q_+, would be given by $Q_+ + 7.70$ μcoulombs/cm². Similarly, that associated with the complete discharge, q_-, would be given by $Q_- - 7.70$ μcoulomb/cm² provided that the discharge is complete within 0.2 sec. Again, assuming that the discharge process is complete within 0.2 sec, then the total faradaic charge passed during the field pulse

$$q_f = q_+ + q_- \qquad [2]$$

would be given by $Q_f = Q_+ + Q_-$.

For a series of measurements performed on a given electrode system and for a fixed value of $V_2 - V_1$, the effect of the false charges is simply to displace the origin of the graph of Q_- *vs.* Q_f a small amount from its correct position. Thus provided that the discharge process is complete within 0.2 sec, the graph of Q_- *vs.* Q_f for a given series of measurements will differ from that of q_- *vs.* q_f only by a shift in origin.

Figure 2 is a superposition of the results of the measurements obtained by the first procedure in which the electrode was held at V_1 for at least 1 hr before applying the voltage pulse. The individual origins have been shifted to obtain maximum coincidence of the data for the different runs. The choice of origin in Fig. 2 can be considered as essentially arbitrary, but corresponds to setting $Q_- = 0$ at $Q_f = 0$.

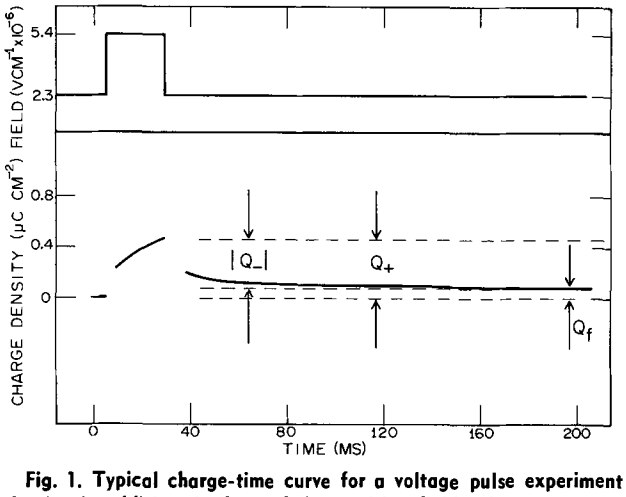

Fig. 1. Typical charge-time curve for a voltage pulse experiment showing in addition the form of the resulting field pulse.

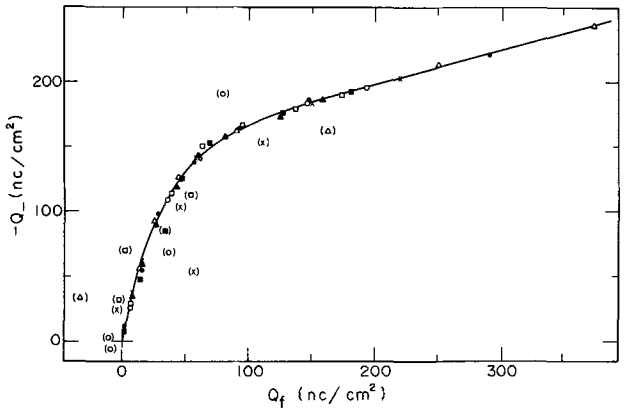

Fig. 2. Dependence of the observed charge passed for the discharge process, Q_-, on the observed faradaic charge passed during the voltage pulse, Q_f, on allowing ~1 hr between pulses. The origin is chosen so that $Q_- = 0$ when $Q_f = 0$. For all runs, $E_2 - E_1 = \Delta E = 3.20 \times 10^6$ V/cm; for runs designated by ▲, ○, and □, pulse width, $t' = 10.6$ msec, E_1 changing from 0.19 to 2.30×10^6 V/cm in steps of $0.26_4 \times 10^6$ V/cm; X, ■, and ●, $t' = 25.9$ msec, $E_1 = 0.19$-2.30 for X, to 1.77×10^6 V/cm for ■ and ●; for △, $t' = 25.9$ msec, $E_1 = 0.72$-2.04×10^6 V/cm plus 2.56 and 2.82×10^6 V/cm. Bracketed points are considered spurious.

Not all of the data obtained have been included in Fig. 2. For values of Q_f larger than about 0.4 μcoulomb/cm², the discharge current decayed over a period substantially greater than 0.2 sec, making the measurement of the total charge for the discharge process effectively impossible due to integrator drift. Data for such runs fall below the extrapolated curve in Fig. 2 as expected.

The results for the second set of experiments, in which voltage pulses were applied at the rate of one per minute for 10 to 15 min before recording the charge are shown in Fig. 3. Again the origins for the individual runs have been shifted to produce maximum coincidence between the runs, and the origin again selected so that $Q_- = 0$ for $Q_f = 0$.

For values of V_1 corresponding to $Q_f > 0.4$ μcoulomb/cm², Q_f and Q_+ were found to decrease initially with successive pulses, reaching ultimately steady-state values. Analysis of these data led to points falling below the extrapolated curve of Fig. 3, as was observed for the first set of measurements, presumably for the same reason.

Analysis and Discussion

Qualitatively, the results of Fig. 2 and 3 confirm our earlier findings (3) that $-Q_-$ is an increasing function of Q_f, as expected on the basis of the dielectric relaxation model for ion current transients. A more detailed analysis of the data follows, the symbols and equations of Part I being used without redefinition.

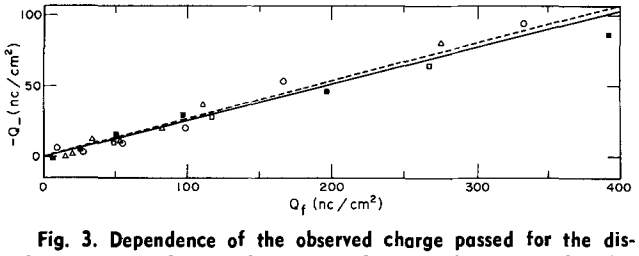

Fig. 3. Dependence of the observed charge passed for the discharge process, Q_-, on the observed faradaic charge passed during the voltage pulse, Q_f, when the repetitive pulsing technique is used. The origin is chosen so that $Q_- = 0$ when $Q_f = 0$. Pulse height and pulse widths as per Fig. 2; ■, E_1 from 3.09 to 1.77×10^6 V/cm in steps of $-0.26_4 \times 10^6$ V/cm; ○, $E_1 = 3.09$-2.04×10^6 V/cm plus 1.51×10^6 V/cm; □, $E_1 = 3.09$-2.56×10^6 V/cm; △, $E_1 = 3.09, 2.82$-2.16×10^6 V/cm in steps of $-0.13_2 \times 10^6$ V/cm.

For a voltage (or field) pulse of sufficiently short duration such that the polarization components P_j' and P_k change very little, the different polarization mechanisms may be treated as operating independently. Thus for such a pulse, the equation describing the time dependence of the component P_k, (Eq. [19], Part I) may be integrated over the duration of the pulse to give

$$q_k = \epsilon_0 \chi_k \Delta E[1 - \exp(-B_k q_f)] \quad [3]$$

where $\Delta E = E_2 - E_1$ is the height of the field pulse, q_f is the time-integral over the pulse duration of the ion current density, q_k is the time integral of the charging current density component, dP_k/dt, over the pulse duration, and the boundary condition $P_k(t = 0) = \epsilon_0 \chi_k E_1$ has been used. Since [3] will in general only be a valid approximation for ΔP_k small, *i.e.*, for $B_k q_f << 1$, we introduce this approximation in [3] to obtain

$$q_k = \epsilon_0 \Delta E \chi_k B_k q_f \quad [4]$$

Using the values of B_k, χ_k, $k = 2,3$ given in Part I, the condition $B_k q_f << 1$, $k = 2,3$ is satisfied for all the voltage pulsing experiments.

In the same way, the equation describing the time dependence of the component P_j' (Eq. [18], Part I) may be integrated over the duration of the pulse to give

$$q_j' = \epsilon_0 \chi_j' \Delta E[1 - \exp(-t'/\tau_j)] \quad [5]$$

where t' is the duration of the pulse, q_j' the time integral of the charging current component, dP_j'/dt, over the pulse duration, and the boundary condition $P_j'(t = 0) = \epsilon_0 \chi_j' E_1$ has been used. Note that for fixed ΔE and t', q_j' is constant; in particular it is independent of E_1 and q_f. This will be the case for any assumed form for the kinetics of a thermally activated polarization process so long as dP_j'/dt is a function of the displacement of the polarization component from its equilibrium value, but not of the polarization state itself. Thus kinetics in accord with $dP_j'/dt \propto \sinh[(\epsilon_0 \chi_j' E - P_j')/c_j'']$ satisfy this condition, whereas those in accord with $dP_j'/dt \propto [(\epsilon_0 \chi_j' E)^2 - (P_j')^2]$ do not. In the following development, we assume that this condition is satisfied and hence that q_j' is a function of ΔE and t' only.

Using this result and Eq. [4], the following expression for the total charge passed per unit area during the charging pulse is obtained

$$q_+ = q_0 + \epsilon_0 \Delta E q_f \sum_k \chi_k B_k + q_f \quad [6]$$

where $q_0 = \epsilon_0 K_1 \Delta E + \sum_j q_j'$ and is a function of ΔE and t' only. Equations [6] and [2] then give

$$-q_- = q_0 + \epsilon_0 \Delta E q_f (\chi_2 B_2 + \chi_3 B_3) \quad [7]$$

Since for all the experiments ΔE had the same value, namely 3.20×10^6 V/cm, while for any given set of measurements, t' was held constant, Eq. [7] predicts that for each set of measurements, $-q_-$ will be a linear function of q_f, with slope $\epsilon_0 \Delta E(\chi_2 B_2 + \chi_3 B_3)$. Thus for data obtained from runs in which the discharge process is complete within 0.2 sec, $-Q_-$ should be a linear function of Q_f with slope $\epsilon_0 \Delta E(\chi_2 B_2 + \chi_3 B_3)$. Furthermore, there should be no difference between the results obtained for the runs involving repetitive pulsing and those for the other runs, since the repetition period is greater than 0.2 sec. From Fig. 2 and 3, this clearly is not the case.

Setting aside this difficulty for the moment, the slope divided by $\epsilon_0 \Delta E$ for the four runs comprising the data of Fig. 3 is given by

$$[\text{Slope of Fig. 3}]/\epsilon_0 \Delta E = (9.3_0 \pm 0.4) \times 10^5 \text{ cm}^2/\text{coulomb} \quad [8]$$

On the basis of Eq. [7] and following, however, we have

$$[\text{Slope (Eq. [7])}]/\epsilon_0 \Delta E = (\chi_2 B_2 + \chi_3 B_3)$$
$$= (2.37 + 7.12) \times 10^5 \text{ cm}^2/\text{coulomb}$$
$$= 9.4_9 \times 10^5 \text{ cm}^2/\text{coulomb} \quad [9]$$

where the values for χ_k, B_k calculated from Dewald's data have been used in [9] (see Part I). The agreement between the observed and calculated slope is excellent. The solid line in Fig. 3 represents the least squares regression line, while the dashed line is drawn in accord with [9].

A similar analysis of that portion of the data in Fig. 2 which appears to fall on a straight line gives

$$[\text{Slope of linear part of Fig. 2}]/\epsilon_0 \Delta E = (9.6_5 \pm 0.6) \times 10^5 \text{ cm}^2/\text{coulomb} \quad [10]$$

again in excellent agreement with the theoretical value.

An explanation for the initial curved portion of Fig. 2 which occurred to us originally was that yet a further polarization component which changes via ion current flow must be present which has a "charge constant," $1/B_k$, of the order of 50 nanocoulombs/cm^2 (see Fig. 2). Including such a term in the analysis, adds to [7] a term of the form of [3], *i.e.*

$$-q_- = q_0 + \epsilon_0 \Delta E q_f (\chi_2 B_2 + \chi_3 B_3) + \epsilon_0 \Delta E \chi_4 [1 - \exp(-B_4 q_f)] \quad [11]$$

The solid line in Fig. 2 is the result of a nonlinear least squares analysis of the data according to [11], with $(\chi_2 B_2 + \chi_3 B_3) = 9.65 \times 10^5$ cm^2/coulomb (see [10]) and B_4, χ_4 chosen to minimize the variance in $-Q_-$. This gave $\chi_4 = 0.53$ and $B_4 = 3.3_3 \times 10^7$ cm^2/coulomb ($1/B_4 = 30$ nanocoulombs/cm^2). Despite the good fit achieved in this way, the explanation must be rejected for a number of reasons. First, the value of B_4 required for the fit corresponds to an interaction radius for the mobile ionic defect of 130Å, which is too large to be physically meaningful. Second, this explanation would not account for the absence of the "anomalous effect" when the experiments are performed by repetitive pulsing. Finally, on noting that the "charge constant" for this anomalous effect (30 nanocoulombs/cm^2) corresponds very closely to that for the anomalous a-c conductance effect noted in Part I (*i.e.*, the rapid rise of $\sigma_{a\text{-}c}/I_0$, Fig. 2, Part I, occurs in the region $I_0/\omega \sim 30$ nanocoulombs/cm^2) it is reasonable to assume that the same process or processes give rise to both anomalous effects. However, the anomalous a-c conductance effect cannot be accounted for simply by introducing the additional parameters χ_4, B_4, with the values given above, as noted in Part I.

As with the anomalous a-c conductance effect, we are unable to account for the anomalous charging process other than to suggest that the two are probably related. Again, however, and for the same reason, the present effect is not contrary to the dielectric relaxation model, but simply not encompassed by it.

Finally, we comment briefly on the observations that for $Q_f \lesssim 0.4$ μcoulomb/cm^2, the polarization induced by the ion current during the voltage pulse can apparently decay via thermally activated mechanisms in a time $\lesssim 0.2$ sec, while for $Q_f > 0.4$ μcoulomb/cm^2, a time greater than 0.2 sec is required for the decay. It would seem that small amounts of ion-current-induced polarization can dissipate via thermally activated mechanisms having small relaxation times, but that with progressively increasing ion-current-induced polarization, thermally activated relaxation mechanisms involving progressively larger relaxation times are involved. This illustrates the complex relationships which apparently exist between the polarization components divided on the basis of their relaxation times under thermal activation, and those divided on the basis of their interaction with the mobile ionic defects. In particular, the relationship $B_j \propto 1/\tau_j$ is clearly invalid. (See Part I for further discussion of this point.)

Criticism of the Dielectric Relaxation Model for Ion Current Transients

As noted in Part I, the authors are aware of no data which are contrary to the dielectric relaxation model for ion current transients. Some criticisms of the model of a more general nature have, however, been offered and we now direct our attention to these.

In a recent review (4) Dell'Oca, Pulfrey, and Young outline a model due to one of us (M.J.D.) and offer criticism of it. As the version of the model they present (5) is out of date, some of the criticism they offer is no longer relevant. The argument which they offer as being "Perhaps the main objection to Dignam's theory . . . . " [p. 17, ref. (4)] is, however, equally applicable to the current version of the model as it is to the original. Their point is that the value of K_s required to account for ion current transients is unreasonably large in relation to K_1. For both the tantalum and aluminum systems, one must set the ratio of the static to dynamic dielectric constant, K_s/K_1, to about 3 to account for the ratio of β_{ss}/β_t. (Note that K_1 is not defined as the dielectric constant at optical frequencies but rather that at a frequency ω' such that $1/\omega'$ is small compared with the times involved for ion current transients to decay.) Their criticism in this regard is based on an extrapolation of the value for the dielectric constant from 1 kHz to 0.01 Hz, from which they conclude that K_s is not expected to be more than 3.5% larger than K_1 (*i.e.*, K at 1 kHz).

A lower bound on K_s may be obtained in the following way which involves neither extrapolation nor assumptions concerning polarization mechanisms, kinetics, or the structural changes corresponding to the polarization changes. It involves simply the integration of the total charge passed following the application of a potential to a preformed specimen, the potential being large, but not so large as to lead to significant ion current. To illustrate the method, the data obtained by Dignam and Ryan (6) on the system Al/Al_2O_3/(glycol-borate electrolyte) will be used, as data for the tantalum system are not available in quite such a convenient form.

The experiments were performed as follows. Aluminum electrodes were formed at a constant current density of about 0.2 mA/cm² up to an anodic overpotential of 41.8V. The anode potential was then dropped to zero and the electrode removed from the cell and immersed in mineral oil at 60°C for 2 hr (to reduce the oxide polarization to zero). Following washing, they were returned to the cell and a linear ramp voltage was applied to the Al electrode in an anodic direction until about 80% of the formation voltage was reached, following which the potential was held constant. The results from one such measurement are reproduced in Fig. 4.

Following the application of the ramp voltage, the "fast polarization processes" will contribute a constant charging current component, $\epsilon_0 K_1(dE/dt)$, which will go to zero once the voltage rise ceases. The total charge corresponding to the area element A_1 in Fig. 4 is therefore the charge associated with the fast polarization processes on charging the electrode system from 0 to 33.8V. Since the steady-state ion current calculated for a field corresponding to 33.8V is negligible compared to the measured current, as is apparently the leakage current (the current is still falling after 400 msec) it is reasonable to assume that essentially all of the measured current is charging current, in which case

$$K_s/K_1 \gtrsim (A_1 + A_2 + A_3)/A_1 \simeq 2 \qquad [12]$$

where A_1, A_2, and A_3 refer to area elements in Fig. 4. This lower bound value for K_s is already impossibly large according to the argument advanced by Dell'Oca *et al.*, but is entirely consistent with a value for $K_s/K_1 \sim 3$. Although experiments of this form have not been performed on tantalum, estimates of K_s/K_1 from the charging currents observed initially in potentiostatic ion current transient measurement (see Fig. 1, Part I) give a value for the ratio approximately the same as that for aluminum.

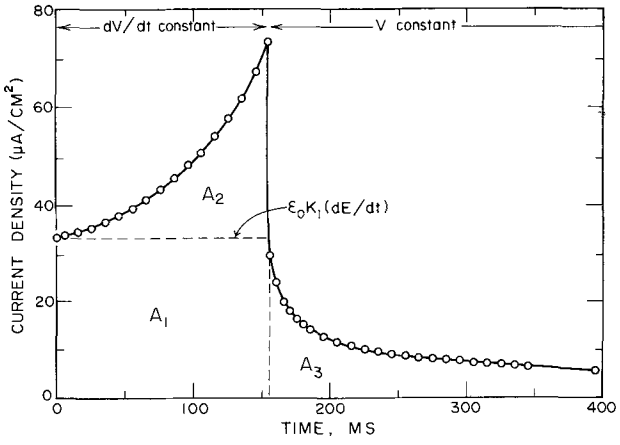

Fig. 4. Charging current transient for the system Al/Al_2O_3/(glycol-borate electrolyte) on reapplication of anodic overpotential at the rate of 209.4 V/sec to 33.8V, to an electrode formed at 0.2 mA/cm² to 41.8V. The data are according to Dignam and Ryan [Fig. 3, ref. (6)].

If most of the thermally activated polarization processes obey kinetics, say, of the following form

$$dP_j'/dt = (C_j''/\tau_j) \sinh [(\epsilon_0 \chi_j' E - P_j')/C_j''] \qquad [13]$$

then they would be active only at high field strengths. This in turn would account for the discrepancy between the estimate of K_s given by Dell'Oca *et al.* and that obtained here.

Reservations concerning certain features of the dielectric relaxation model have been expressed by one of us [M. J. D., ref. (7)]. One concerns the reasonableness of postulating two ". . . polarization mechanism(s) involving ion-current induction" [ref. (7), p. 272]. We now feel that this is not in fact an accurate statement of the postulate which is required to fit the data. Only a single mechanism need be postulated. However, the "slow" polarization components must be assumed to be divided into two classes, each class being characterized by an electric susceptibility parameter, χ_k, and a "relaxation charge density," $1/B_k$. This division could be based on local structure variations, variations in the detailed processes involved in the partner exchange steps required for network defect migration (see Part I), variations in the paths followed by the network defects, etc.

The other reservation expressed in (7) concerns the details of the proposed interfacial reactions. In particular, Siejka, Nadai, and Amsel (8), using nuclear methods of analysis for oxygen 16 and 18 appear to have shown that the contribution of the oxide-solution double-layer to the overpotential during film formation is zero within experimental error for both tantalum and aluminum anodized in an aqueous solution of 5 weight per cent ammonium citrate of pH 6. The implication of this result is that the outer Helmholtz plane and the "oxide surface" essentially coincide. If this is correct, the details of the interfacial model presented in Part I are not. Even if it is not correct, the details of the interfacial model are almost certainly incorrect, at least in part, as already noted (Part I). In any event, rate control by defect injection at one of the interfaces is not precluded, and this assumption is essentially all that is required to develop the model.

Summary and Conclusions

In this investigation, two sets of experiments have been carried out in an attempt to obtain confirmation for the existence of polarization processes which follow equations of the form of Eq. [19], Part I, *i.e.*

$$dP_k/dt = B_{ki}(\epsilon_0 \chi_k E - P_k) \qquad [14]$$

Equation [14] predicts that the presence of ion current during the application of a voltage pulse to an electrode system will lead to a greater polarization increase than would occur in its absence. Such an effect has definitely been observed. Furthermore, one of the sets of measurements (those involving repetitive pulsing) are in quantitative agreement with the behavior predicted on the basis of [14] and the values for χ_2, B_2, χ_3, B_3 determined from ion current transient measurements using the dielectric relaxation model. The other set of measurements also shows the effect predicted by [14], the agreement again being quantitative, but in addition another effect is observed which can be accounted for neither by [14] nor by any other process known to the authors. It appears likely, however, that the same process gives rise to both the anomalous charging effect and the anomalous increase in the a-c conductivity (Part I). While these effects are not encompassed by the dielectric relaxation model for ion current transients, neither are they in conflict with it.

We believe that these experiments constitute a crucial test of the model, and one which it has passed successfully. No other model proposed to date approaches the success achieved here by this model, yet much remains unexplained.

Acknowledgments

The authors are grateful to the National Research Council of Canada for supporting this research and for a scholarship (D.F.T.).

Manuscript submitted Oct. 3, 1972; revised manuscript received May 8, 1973.

Any discussion of this paper will appear in a Discussion Section to be published in the June 1974 JOURNAL.

REFERENCES

1. D. F. Taylor and M. J. Dignam, Part I of this paper, *This Journal*, **120**, 1299 (1973).
2. M. J. Dignam and D. F. Taylor, *Appl. Phys. Letters*, **15**, 198 (1969).
3. M. J. Dignam and D. F. Taylor, *Can. J. Chem.*, **48**, 1971 (1970).
4. C. J. Dell'Oca, D. J. Pulfrey, and L. Young, "Anodic Oxide Films," in "Physics of Thin Films," Vol. 6, chap. 11, Academic Press, London and New York (1971).
5. M. J. Dignam, *This Journal*, **112**, 722 (1965).
6. M. J. Dignam and P. J. Ryan, *Can. J. Chem.*, **46**, 549 (1968).
7. M. J. Dignam, in "Oxides and Oxide Films," Vol. I, chap. 2, J. W. Diggle, Editor, Marcell Dekker, Inc., New York (1972).
8. J. Siejka, J. P. Nadai, and G. Amsel, *This Journal*, **118**, 727 (1971).

Pitting of Titanium

I. Titanium-Foil Experiments

T. R. Beck*

Flow Research, Inc., Kent, Washington 98031

ABSTRACT

Experiments were conducted in which pitting occurred at the edges and on the circumference of holes in titanium foil in chloride, bromide, and iodide solutions under potentiostatic conditions. Valence of dissolution was approximately 4. The effect of potential, temperature, concentration, pH, and solution flow on current density and pitting potential was determined. Very complex behavior not fitting a single kinetic, mass transport, or ohmic limitation was observed. A model combining a salt film on the metal surface with events in the electrolyte diffusion layer qualitatively fits the data.

Pitting attack of titanium alloys was recently reviewed (1), and thus the literature is not discussed to any extent here. Relatively little experimental work has been reported on pitting corrosion of titanium as compared to aluminum and iron alloys. The present series of papers presents a detailed experimental study of pitting of titanium and a proposed model.

Much of the pitting literature describes work at open circuit in which cathodic reactions on the same specimen provide the corrosion current. While valuable for relating to conditions in the field, such experiments are of limited value in formulating quantitative mechanisms.

Experimental conditions in this work were therefore idealized in order to make measurements that were directly applicable to the pitting surfaces. Specimens were potentiostated so that anodic dissolution currents could be directly measured as a function of potential. Specimen configurations were such that the active corrosion area could be measured and current densities could be determined. Pitting corrosion at the edges of a thin foil is described in this paper. In the following paper the system was further idealized by using artificial pits propagated at the ends of thin rods embedded in insulating material.

* Electrochemical Society Active Member.

Key words: titanium, corrosion, pitting, pitting potential, pitting model.

Experimental

Pitting experiments were conducted with strips of titanium foil in beakers of chloride, bromide, or iodide solutions. The 0.0038 cm thick by approximately 1 cm wide × 5 cm long titanium foil anodes were suspended in the solutions. The analysis of the commercially pure foil is given in Table I. Bakers reagent-grade chemicals and distilled water were used to make up electrolyte solutions. A platinum counterelectrode and a saturated calomel reference electrode were used together with a Wenking potentiostat. All potentials are referred to the saturated calomel electrode (SCE) in this paper. Current measurements were displayed on an x-y plotter or strip-chart recorder. Open-circuit potentials of the foil specimens were measured with a Keithley electrometer. Fast potential transients were displayed on a Tektronix oscilloscope and photographed with a Polaroid camera.

Table I. Analysis of titanium foil (Titanium Metals Corporation)

	Weight per cent
Fe	0.05
C	0.014
N	0.009
H	0.007
O	N.A.

Results

Most of the experiments were conducted in bromide solutions because pitting occurs rather readily and could easily be observed. A high potential is required to initiate and sustain pitting in chloride solutions and the current densities are extremely high. Pitting is somewhat more difficult to maintain in iodide solutions than in bromide and the simultaneously formed iodine obscured visibility.

Current vs. time.—Corrosion occurred at the edge of a foil specimen when it was potentiostated between the steady-state pitting potential of about 0.9V (SCE) and a potential of about 1.4V in neutral bromide solution. At potentials above about 1.4V, oxygen bubbles initially formed on the surface and a pit nucleated under each bubble. The pits were initially hemispherical but soon penetrated the foil and the corrosion then occurred at the circumferences of radially growing holes. A continuous transition from hemispherical pits to corrosion on the edges of the foil in the holes indicates that the same basic phenomenon is occurring. Corrosion at the foil edges, at the circumferences of the holes, and at the outer edges of specimens are considered to be a form of pitting in this paper. Examples of such pitting are illustrated in Fig. 1. In general the edge corrosion surface was more or less planar and at right angles to the foil faces.

Relations of corrosion current to time under potentiostatic conditions are shown in Fig. 2. At 1.2V applied potential the current increased rapidly, passed through a maximum, and then slowly declined. The initial rapid increase can be attributed to growth of cusps along the edge from the points of nucleation. The decline is due in part to uniting of individual cusps to form a smooth front and to decrease in area as the perimeter of the specimen decreases. Current density can be calculated from

$$i = \frac{I}{t\Sigma l} \qquad [1]$$

where I = current, t = foil thickness, and Σl = corroding length. The corroding length can be measured on the edges of the specimen or calculated from the number and the average circumference of the holes.

At a potential of 1.9V, which gives holes, the current increased linearly with time until oscillations set in. Initial penetration of the hemispherical pits through the foil occurs rapidly before the linear increase. Once a group of holes is initiated, they tend to grow in preference to nucleation of new pits. Thus there is a limited range in hole sizes. For the case of n holes growing at a constant current density on their circumferences it can be shown that

$$i = \left[\frac{zF\rho}{2\pi ntM}\,(dI/d\tau)\right]^{1/2} \qquad [2]$$

where ρ = density, M = molecular weight of Ti, and τ = time. The observed linear increase in total current indicates a constant current density at the circumferences of the holes. A reasonable agreement is observed for current densities calculated from Eq. [1] and [2] in Table II for 0.6M KBr solutions.

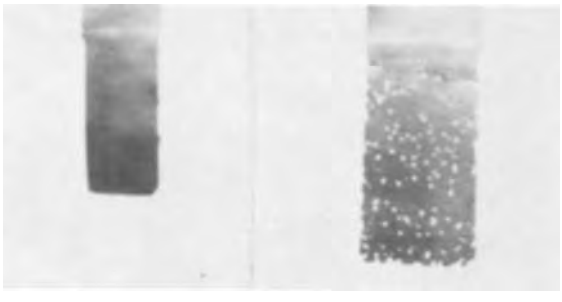

Fig. 1. Examples of pitting corrosion of titanium foil in 0.6M KBr solution. Left, 1.2V; right, 1.9V.

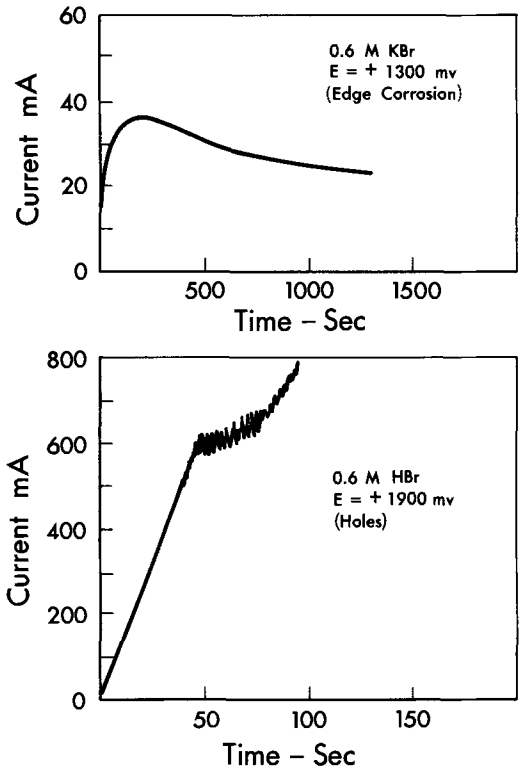

Fig. 2. Current vs. time plots in which corrosion was predominantly at the foil edge or on the circumference of holes.

Valence.—The valence for dissolution of the titanium foil was determined from weight loss of the specimens and an integration of current over the course of the experiments. Data shown in Table III in chloride and bromide solutions indicate a valence of about 4, consistent with results of other workers (2, 3). Iodide solutions were not used because of the observed oxidation to iodine on the foil faces. The experiments were not precise for a number of reasons: halide ion discharge, metal particles, and current oscillations.

Essentially, no valence 3 titanium was produced as there was no trace of the violet Ti^{3+} color produced in solution. Ti^{3+} salts can be readily detected from uniform dissolution in the active region in strong acid solutions well below the pitting potential. During pitting in acid halide solutions a colorless solution can be seen streaming down from the corroding areas. Observed in a 35× microscope, this stream contains small white particles. In neutral or basic solutions a floccu-

Table II. Current density in holes in foil with 0.6M KBr solution

Potential	Current density (A/cm²) Eq. [1]*	Eq. [2]**
Initiated at 1.8V		
Propagated at 1.2V	1.6	1.4
Propagated at 1.8V	4.1	3.1

* Based on final current and Σl.
** For valence, $z = 4$.

Table III. Observed valence for corrosion of titanium foil under pitting conditions

Run	Salt	Δw (g)	z
1	0.6M KBr	0.038	3.56
2	0.6M KBr	0.038	4.22
4	0.6M KCl	0.020	4.21
8	0.6M KBr	0.280*	4.02
15	4M KBr	0.025	3.87

* Large sheet of foil.

lent white precipitate can be seen streaming down from the corroding areas. These observations are consistent with formation of TiO^{++} or TiO_2 to be expected from Ti(IV) under acid and neutral to basic conditions respectively (4) at high anodic potentials.

Current density.—Current density in 0.6M KBr and 0.6M HBr varied with applied potential as shown in Fig. 3. The steady-state pitting potential is about 0.9V in these solutions. All of the pitting potentials given in this paper were determined by starting with specimens corroding at steady state and decreasing potential slowly until corrosion stopped. There is considerable scatter in the data so that it is not clear what relationship of current density to potential gives the best fit. Arrows are drawn from the experimental points indicating the direction of corrections that should be made. An arrow pointing down indicates roughness of the corroding surface and therefore a lower actual current density. An arrow pointing up indicates either that oscillations or a maximum in current occurred as illustrated in Fig. 2. Oscillations may indicate that not all of the corroding surface is active simultaneously.

Effect of concentration.—The relationship of current density to concentration is shown in Fig. 4 for an applied potential of 1.4V. Below a concentration of 0.02M no pitting occurred. At 0.02M the current was very unstable. The best straight line drawn by eye through the log-log plot from 0.06 to 4M has a slope of about 0.27.

Figure 5 shows steady-state pitting potential as a function of concentration for foil in HBr and KBr solutions. The data are rather scattered but show a decreasing trend in pitting potential with increased concentration. The average slope appears to be about −110 mV per decade of concentration on the semilog plot and independent of bulk *p*H in neutral to acid solutions.

Effect of temperature.—The effect of temperature on the pitting corrosion current density is shown in Fig. 6 for 0.6M KBr at potentials of 1.2 and 1.6V. From the slopes of the straight line segments of the log *i* *vs.* 1/T plots, activation energies at 1.2 and 1.6V are 12.2 and 10.0 kcal, respectively. Current density fell off from the straight line relationship at 15°C and pitting corrosion ceased altogether below about 15°C.

Steady-state pitting potential in 0.6M bromide solutions as a function of temperature is given in Fig. 7.

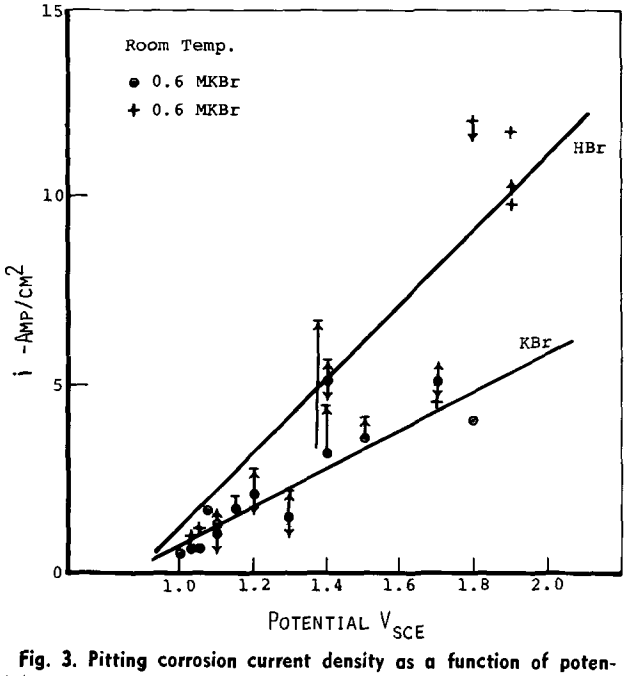

Fig. 3. Pitting corrosion current density as a function of potential.

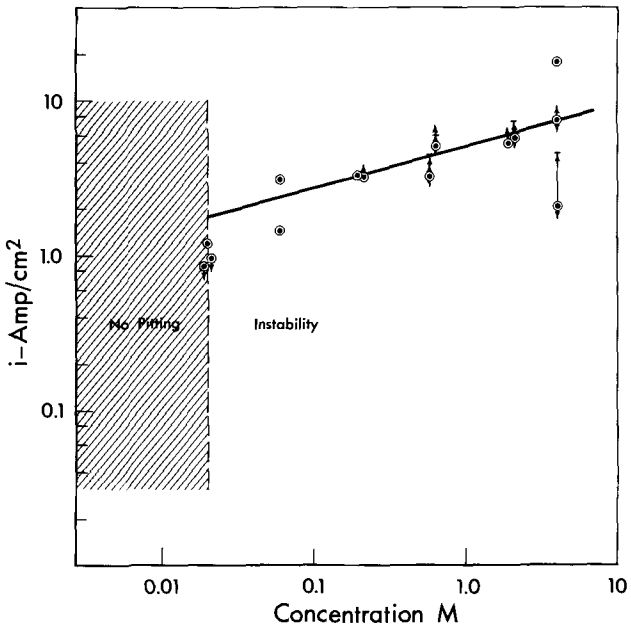

Fig. 4. Relationship of pitting corrosion current density to concentration of KBr at a potential of +1.4V.

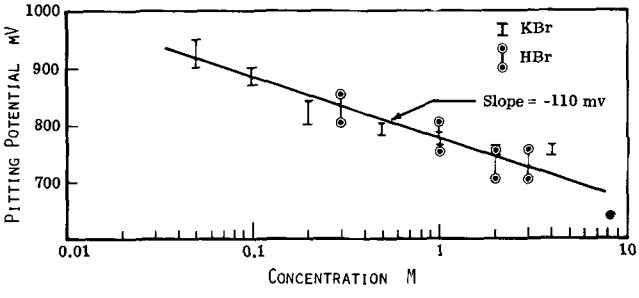

Fig. 5. Effect of concentration on steady-state pitting potential

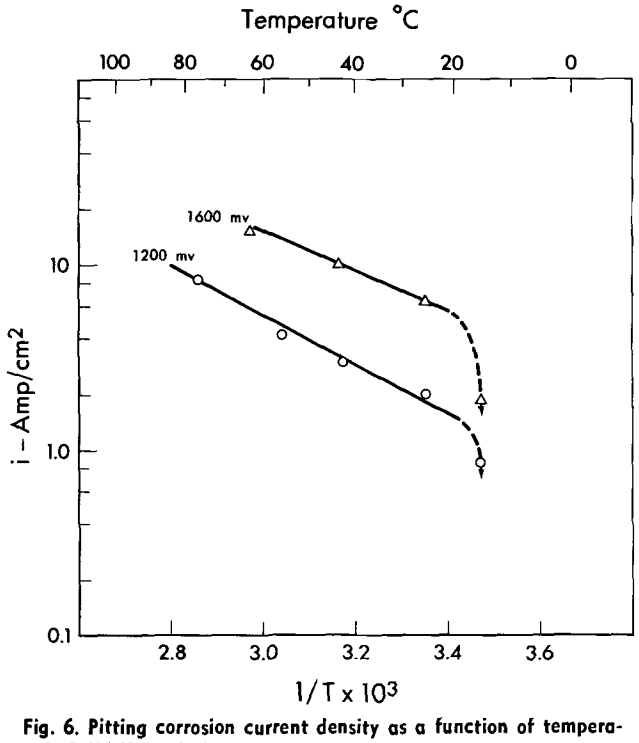

Fig. 6. Pitting corrosion current density as a function of temperature in 0.6M KBr solution.

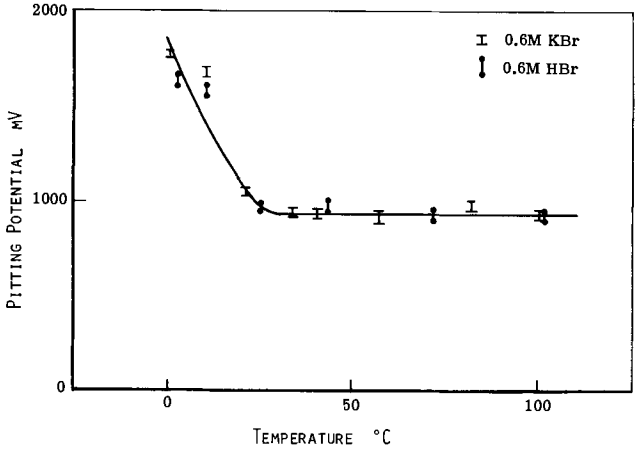

Fig. 7. Effect of temperature on steady-state pitting potential in KBr and HBr solutions.

At room temperature and above, the pitting potential appears to be constant at about 0.9V. Below room temperature the pitting potential rises sharply. This rise in the pitting potential is consistent with pitting corrosion not observed in bromide solution below 15°C in Fig. 6. Experiments conducted in a beaker inside a closed stainless steel pressure vessel gave a constant steady-state pitting potential of about 0.9V up to temperatures above 150°C.

Steady-state pitting potential in 0.6M iodide solutions, given in Fig. 8, increased with temperature and it appeared to be slightly higher in KI as compared to HI solutions. Pitting was very difficult to initiate above room temperature, *e.g.*, it would not initiate at a potential of greater than 10V at 50°C. The points above room temperature were obtained by initiating at room temperature at a high potential (2-5V), increasing the temperature, and then decreasing the potential slowly until pitting stopped. Pitting in iodide was accompanied by iodine formation on the faces of the foil.

An interesting phenomenon sometimes observed above room temperature is the occurrence of "red headed worms." Instead of forming a flocculent precipitate of titanium oxide in solution as is obtained below room temperature in iodide solution or in chloride and bromide solutions, the oxide sometimes forms a more compact wormlike body that is extruded from the pits. The oxide is reddish brown near the pit from tetraiodide or simultaneously formed iodine but the color is removed from the "body" by the solution. The result is a white-bodied "red headed worm" which appears to be gnawing into the edge of the foil.

Heating iodide solutions to near boiling gives readily initiated pitting and a lower steady-state pitting potential of 0.45V. Flocculent precipitated titanium oxide is also formed. As the temperature is lowered the oxide again clings to the surface and below 50°C pitting becomes difficult to sustain. The steady-state pitting potential appears constant between 50° and 100°C in iodide solution.

The effect of temperature on the steady-state pitting potential in bromide and iodide solutions is summarized in Fig. 9. Data of Posey and Bohlmann (5) for 1M sodium chloride solution over a wide range of temperature are also shown. Data obtained in 0.6M chloride solution in this work from room temperature to 100°C are in agreement with that of Posey and Bohlmann. The threshold current density to sustain pitting in chloride solution is greater than 20 A/cm^2 at room temperature.

Transient behavior.—Potential sweep measurements were made to test if a diffusion-limited process is involved in pitting. A diffusion-limited process initially at steady state should have no increase in current density with a rapid potential increase. This was found to be true for high sweep speeds (31,200 mV/min) for potentials below about 1.5V as shown in Fig. 10. Above this potential the current increased even with high sweep speed, indicating initiation of a new process.

Oscillations at a frequency of 1-4 Hz occurred on the downsweep above 1.4V. Below 1.4V the current decreased approximately linearly with potential, characteristic of a process controlled by an ohmic resistance. The extrapolated zero-current intercept potential decreased with higher sweep speed.

When a specimen of titanium undergoing pitting corrosion is suddenly open circuited its potential rapidly decays over the first 10^{-2} sec, goes through a minimum between 10^{-2} and 10^{-1} sec, and then increases to the normal passive potential of about zero volt. The open-circuit potentials were measured with the electrometer and oscilloscope. The minimum potential could be attributed to that of the corroding surface or a mixed potential established thereafter. Minimum potentials for specimens initially corroding at 1.2V in 0.6M chloride, bromide, and iodide solutions are shown in Fig. 11. The minimum potential appears to be relatively insensitive to the potential applied during pitting. In the case of chloride the minimum potential is close to the calculated (6) reversible potential for

$$Ti + 4X^- \rightarrow TiX_4 + 4e$$

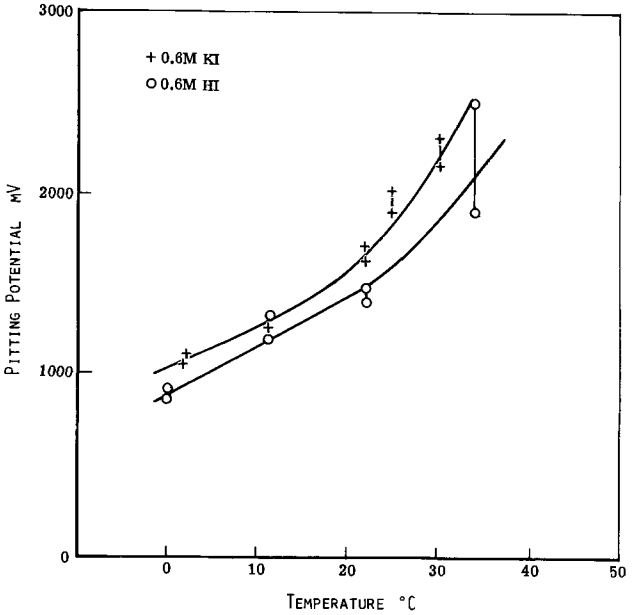

Fig. 8. Effect of temperature on steady-state pitting potential in 0.6M KI and HI solutions.

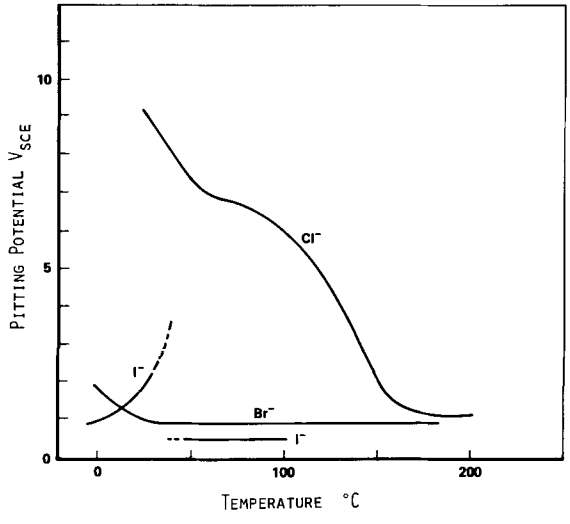

Fig. 9. Effect of temperature on steady-state pitting potential of C.P. titanium in 0.6-1M halide solutions [chloride from Posey and Bohlmann (5)].

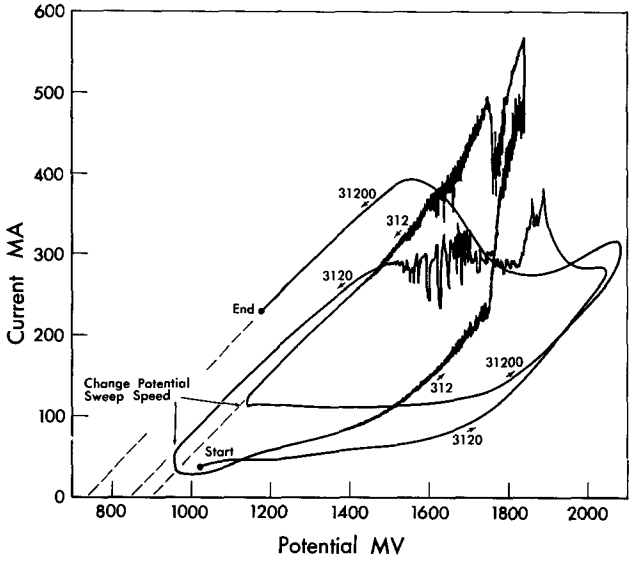

Fig. 10. Potential sweep experiments in 0.6M KBr (parameter in millivolts per minute).

but it is higher for bromide and iodide. Within the experimental error the minimum in bromide solutions was constant with concentration from 0.1 to 6M and with temperature from 0° to 100°C.

The intercepts from Fig. 10 and the minimum potential from Fig. 11 are plotted *vs.* time to reach that potential in Fig. 12. It appears that repassivation of a pitting titanium surface is very rapid below the pitting potential.

Effect of solution flow.—A hydrodynamic flow experiment was designed to verify if a diffusion-limited process is present. The experiment is illustrated in Fig. 13. A pit was initiated in the titanium foil diaphragm by piercing it with the sharpened titanium probe that was connected electrically through a current-limiting resistor to the cell cathode. Once initiated, pitting was controlled potentiostatically. The saturated calomel reference electrode was connected through a salt bridge having a porous Vicor end that has a high flow resistance without an excessive electrical resistance. Solution could be made to flow through the orifice-shaped pit by raising the level of a reservoir of solution connected by rubber tubing. Solution was collected in a graduated cylinder for determining the flow rate. Thus pitting current could be determined as a function of flow rate past the corroding surface under potentiostatic conditions.

Results in bromide and iodide solutions are shown in Fig. 14. The ratio of the current with solution flow to

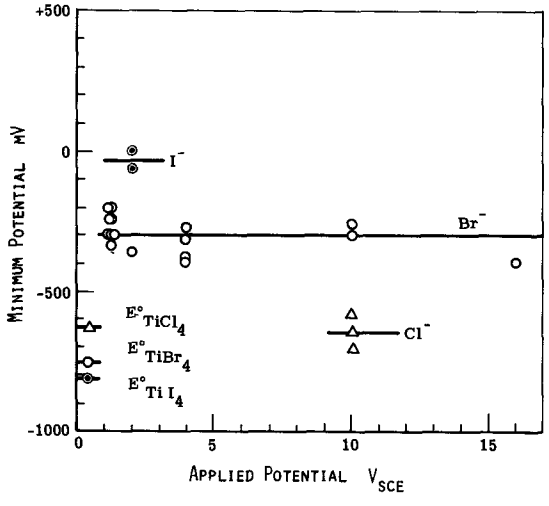

Fig. 11. Initial open-circuit potential during pitting of titanium in 0.6M halide solutions.

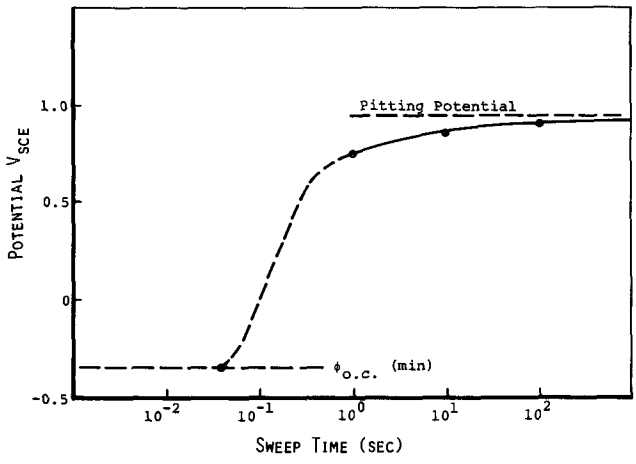

Fig. 12. Potential intercept as a function of sweep time

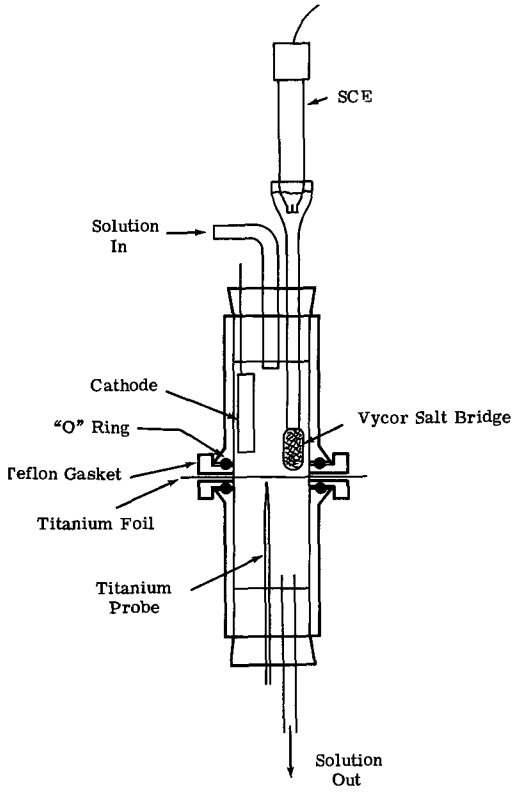

Fig. 13. Apparatus for flow experiment

the current at no flow is plotted against the flow rate. The current increased with flow rate in iodide and decreased with flow in bromide. The effect of flow was greater with the more dilute bromide solution. Pitting corrosion was completely stopped by flow in chloride solutions. Only a qualitative treatment has been made on the effect of flow because quantitative treatment is difficult with the technique used.

Great care was required to initiate pits in chloride solution. The potential was slowly increased to 10V prior to piercing the foil. When a potential of 10V was suddenly applied to a fresh foil in chloride solution, pits initiated at the periphery at the edge of the Teflon gasket.

Discussion

The experimental data make it evident that some rather complex events occur during pitting of titanium. The reaction is not under simple kinetic, mass-transport, or ohmic control. There is apparently a diffusion-limited current density on the upsweep in Fig. 10 but the current density either increases or decreases with fluid velocity in Fig. 14 depending on the

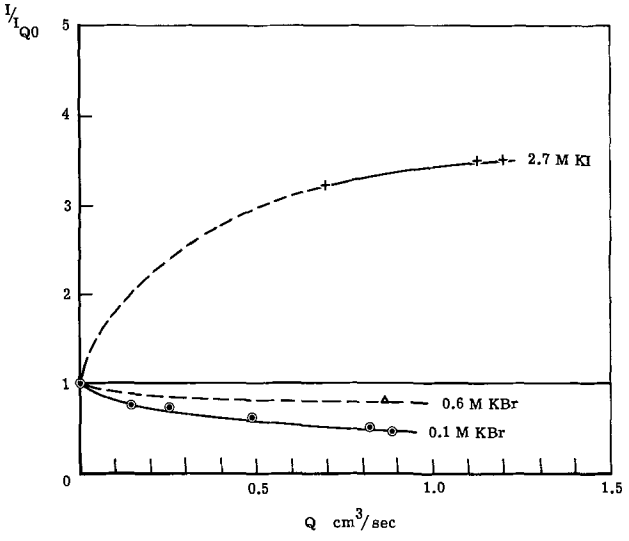

Fig. 14. Results of flow experiments for bromide and iodide solutions.

halide ion. The corrosion current density has a small dependence on halide ion concentration in Fig. 4, but increases appreciably with temperature in Fig. 6. On the other hand, the current density appears to be ohmically controlled on the downsweep in Fig. 10.

Pitting potential for titanium in solutions of the three halide ions exhibits some peculiar increases and decreases in Fig. 9. The zero-current potential intercept decreases with increasing negative sweep speed in Fig. 12 to a value that is to a first approximation independent of initial applied potential, halide concentration, or temperature.

How can these apparently diverse experimental observations be rationalized? A model will be put forth in qualitative form without proof here. Different aspects of it will be mathematically modeled and quantitatively tested in subsequent papers.

Model.—The essence of the model is presented in Fig. 15. It is assumed that a titanium tetrahalide (or oxyhalide) film is formed at the metal surface. On the solution side is a diffusion layer in which the halide dissolves and is transported away. Simultaneously, hydrolysis of the covalent tetrahalide occurs to give TiO^{++} or TiO_2 (depending on the bulk pH) and H^+ and halide ions. Current density at steady state is controlled by diffusion of either water to the salt film surface to dissolve it at a limiting rate or of halide ion to form the tetrahalide. The former is the charge acceptor concept considered by Wagner (7) in electropolishing. The latter would require that the dissolved tetrahalide is completely covalent, giving essentially no halide ions by dissociation.

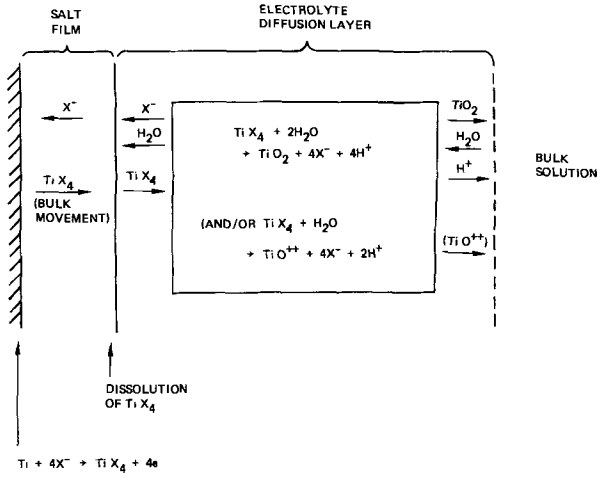

Fig. 15. Model for reactions in pit

The salt film grows to a thickness required to develop a potential drop across it corresponding to the potential applied and the current density. The metal to salt interface is assumed to be approximately the minimum open-circuit potential which is near the calculated reversible potential for the reaction

$$Ti + 4X^- \rightarrow TiX_4 + 4e$$

as indicated in Fig. 11.

The ohmic drop in solution appears to be only a small part of the total difference between the applied potential and the metal-to-salt interface potential in moderately concentrated solutions. Ohmic resistance of the solution can be approximated by

$$R(\text{soln}) = \frac{t \ln (\pi r_2/t)}{\pi\kappa} \text{ ohm-cm}^2 \qquad [3]$$

for hemicylindrical condition in electrolyte with conductivity, κ, between the position of the reference electrode, r_2, and an equivalent half cylinder with half circumference equal to the foil thickness, t. Calculated solution iR drop is 0.22 and 0.57V, respectively, for 0.6M HBr ($\kappa = 0.18$ ohm^{-1}-cm^{-1}) and 0.6M KBr ($\kappa = 0.07$ ohm^{-1}-cm^{-1}) for a current density of 5 A/cm^2. Total potential drops for these two solutions at 5 A/cm^2 *from* Fig. 3 are 1.4 − (−0.6) = 2.0V and 1.9 − (−0.6) = 2.5V, respectively. The differences between the total and solution potential drops can be attributed to the resistance of the salt film.

A rapid decrease in potential from a steady-state condition (Fig. 10) therefore gives a decreasing current density. The active pitting surface apparently passivates rapidly because the minimum open-circuit potential lasts for only a few tenths of a second before a rise to the normal steady-state open-circuit potential for passive titanium. The faster the potenial sweep in the negative direction, the less passivation occurs and thus the more negative the intercept as shown in Fig. 12.

The small dependence of pitting current density on concentration (Fig. 4) is consistent with diffusion of water through the electrolyte being the limiting rate. Regeneration of halide ion within the diffusion layer could also make the limiting diffusion rate of halide ion to the salt surface relatively independent of bulk halide concentration.

It appears from the experiments that a minimum current density of about 1 A/cm^2 is required to sustain pitting at the edge of the foil in bromide solution. The threshold concentration for pitting observed in Fig. 4 could be attributed to too high a solution resistance by Eq. [3] to maintain the required minimum current density.

Hydrolysis within the diffusion layer requires a limited range of the hydrolysis rate constant. If the hydrolysis is too slow it will occur outside of the diffusion layer resulting in no halide ion, oxyhalide, or oxide build-up in it. A large rate constant would give oxide close to the salt film surface which could cause blockage of dissolution.

Some aspects of pitting behavior in iodide solution could be attributed to oxide blockage. Increased current density with electrolyte flow in iodide solution shown in Fig. 14 could be attributed to decrease in diffusion layer thickness and faster removal of the blocking oxide. The lower pitting potential in HI as compared to KI in Fig. 8 could be attributed to a shift to soluble TiO^{++} in more acid solution. Decrease in pitting potential below room temperature in iodide solution could be attributed to slower hydrolysis and less blockage. The lower pitting potential above 50°C in iodide is consistent with increased rate of nucleation and growth of TiO_2 particles in solution as observed in TiO_2 pigment technology (8).

Pitting behavior in bromide and chloride solutions is consistent with a slower hydrolysis rate expected for the respective tetrahalides based on larger tita-

nium-halogen bond energies (6). Decreased current density with flow for bromide solutions as observed in Fig. 14 could be attributed to decrease in concentration of hydrolysis products which may be necessary to maintain the salt film and prevent passivation. The relative decrease in current with flow is greater in the more dilute solution which would have the smaller build-up of hydrolysis products at a lower current density. Complete cessation of pitting with flow in chloride solution could be attributed to cooling as well as decreasing concentration in the diffusion layer. Heat flux at a pitting surface in chloride is high enough to cause boiling, *i.e.*, a 9V drop at the surface and 20 A/cm^2 gives 180 W/cm^2 which is considerably greater than the heat flux required for boiling (9). Pitting in chloride solution is accompanied by an intense local agitation at the surface which may be attributed to local boiling.

Pitting potential.—Presence of a salt layer and very rapid passivation below the pitting potential suggests a new mechanism for the steady-state pitting potential. It is the potential at which the salt film thickness is such that a passivating species can be transported through it and cover the surface faster than the salt-forming reaction occurs. Two passivating compounds could be considered for titanium; oxide or hydride. Oxide is considered to be the more likely based on observations to be presented in subsequent papers.

This mechanism for pitting potential is related to one proposed by Vetter (10) except that he based the replacement of salt by oxide on thermodynamics rather than mass transport. Quantitative treatment of the present model will be presented in a subsequent paper.

Conclusions

The following conclusions are based on experiments conducted with edge pitting of titanium foil in chloride, bromide, and iodide solutions.

1. The valence for dissolution appears to be approximately 4.
2. At constant potential, current density in the corroding area appears to be approximately constant as edge pitting propagates in bromide solutions.
3. Current density in the corroding area increases with potential above the steady-state pitting potential in bromide solutions.
4. Current density at constant potential varies only as about the ¼ power of bulk concentration of bromide above a threshold level.
5. Current density at constant potential increases with temperature above a threshold level in bromide solution.
6. Steady-state pitting potential decreases logarithmically with bromide concentration, independent of pH.
7. Steady-state pitting potential bears a complex relation to temperature: it decreases in chloride solution from about 10V at room temperature to about 1V at 200°C, it decreases from about 1.7V at 0°C to 0.9V at room temperature and remains constant to above 100°C in bromide, and increases from about 1V at 0°C to over 10V at 50°C in iodide then drops to 0.45V from 50°C to at least 100°C.
8. With rapid potential transients between 1.0 and 1.5V in bromide solution the current density appeared to be constant on the upsweep as for a diffusion-controlled reaction but decreased linearly on the downsweep as with an ohmic controlled reaction.
9. Repassivation is very rapid below the pitting potential, *e.g.*, about 10^{-1} sec.
10. Hydrodynamic flow past corroding surfaces caused increased current in iodide, decreased current in bromide, and stopped pitting in chloride.
11. A model for the reactions in a pit consisting of a salt film plus electrolyte diffusion layer qualitatively fits the data presented.

Acknowledgment

This work was performed in part under NASA Headquarters Contract NAS 7-489 and in part under Air Force Office of Scientific Research Contract F44620-72-C-0070. This paper was based on work done at Boeing Scientific Research Laboratories, Seattle, Washington 98124.

Manuscript submitted March 2, 1973; revised manuscript received May 9, 1973. The experimental results were presented in part as Paper 76 at the Chicago, Illinois, Meeting of the Society, Oct. 15-19, 1967.

Any discussion of this paper will appear in a Discussion Section to be published in the June 1974 JOURNAL.

REFERENCES

1. T. R. Beck, "A Review: Pitting Attack of Titanium Alloys," Proceedings of International Conference on Localized Corrosion, Dec. 6-10, 1971, Williamsburg, Va., NACE, In press.
2. O. Rüdiger and W. R. Fischer, *Z Elektrochem.*, **62**, 803 (1958).
3. J. Dugdale and J. B. Cotton, *Corrosion Sci.*, **4**, 397 (1964).
4. M. Pourbaix, "Atlas of Electrochemical Equilibria," pp. 213-222, Pergamon Press, New York (1966).
5. F. A. Posey and E. G. Bohlmann, *Desalination*, **3**, 269 (1967).
6. W. M. Latimer, "Oxidation Potentials," p. 267, Prentice Hall, Englewood Cliffs, N. J. (1956).
7. C. Wagner, *This Journal*, **101**, 225 (1954).
8. J. Barksdale, "Titanium, its Occurrence, Chemistry and Technology," 2nd Ed., Chap. 14 and 18, Ronald Press, New York (1966).
9. J. H. Perry, "Chemical Engineers Handbook," 2nd Ed., p. 992, McGraw Hill Book Co., New York (1941).
10. K. J. Vetter, *Ber. Bunseng. Physik. Chem.*, **69**, 683 (1965).

Pitting of Titanium

II. One-Dimensional Pit Experiments

T. R. Beck*

Flow Research, Inc., Kent, Washington 98031

ABSTRACT

Experiments were conducted with pitting corrosion of the ends of titanium rods insulated on the sides with epoxy resin. The rods were potentiostated in the anode-facing-up position in chloride, bromide, and iodide solutions. After a small depth of corrosion a uniform current density was obtained characteristic of one-dimensional mass transport and conduction. Current density is mass-transport limited in the electrolyte and it appears that a salt film forms on the metal surface to absorb most of the potential applied.

In prior studies on pitting of titanium (1) it was observed that pits grown on foil were initially approximately hemispherical as observed for other metals (2-4). After the pits penetrated the foil, corrosion continued at the circumference of the holes with no apparent change in mechanism. The new corroding areas were nearly cylindrical and at right angles to the foil faces. A further simplification from a cylindrical to a planar surface would allow a one-dimensional analysis of the mass-transport phenomena.

In the present work, planar corrosion was obtained on the ends of small diameter rods or rectangular prisms of titanium which were cast in epoxy resin like the lead in a pencil. This technique of insulated cylinder has been reported by Edwards (5) with larger diameter specimens of copper in studies of electropolishing. A related technique was used by Pickering and Frankenthal (6) in which they did single-pit experiments through a hole drilled in a Lucite plate bonded to a steel surface.

Experimental

General.—Commercially pure, A-75, titanium from Titanium Metals Corporation was used for the experiments. Cross sections of three different size specimens were 0.163 cm diameter, 0.1 × 0.1, and 0.16 × 0.32 cm with lengths of 3-6 cm. The specimens were cast in epoxy resin with an outside diameter of 0.6 cm. The working end of each titanium "pencil" was ground flat with silicon carbide paper on a belt sander before each experiment. The initial surface was not critical as the corrosion reaction shortly established its own configuration of the surface.

All experiments were conducted with the titanium in the anode-facing-up position. Most of the experiments were done in an inverted cut-off polyethylene bottle with the titanium pencil mounted in a rubber stopper similar to the arrangement in Ref. (5). Electrolyte filled the cell to a level about 1 cm above the end of the pencil. Events in the "pit" formed at the working end of the pencil were observed through a B&L binocular zoom microscope at 7 to 35X. The cell was potentiostated using a Wenking Model 66TSI with platinum counterelectrode and saturated calomel electrode (SCE) reference. All potentials cited in this paper are in respect to the SCE. Most of the potential drop in the cell was within the pit, so the location of the counter and reference electrodes was not important electrically and they could be located at the side of the cell out of the way of the microscope. All experiments were conducted at room temperature (~21°C) unless otherwise specified. All chemicals used were Bakers reagent grade without further purification. Solutions were made with commercially supplied distilled water.

Cell current and electrode potential were displayed on a Hewlett-Packard strip chart recorder and X-Y plotter. Fast transients were displayed on a Tektronix oscilloscope and photographed with a Polaroid camera.

* Electrochemical Society Active Member.
Key words: titanium, corrosion, pitting, pitting potential, pitting model.

Potential vs. pit depth.—A cell illustrated in Fig. 1 was designed to measure the potential drop in the pit electrolyte. The cell was made of Plexiglas pieces cemented together. The titanium pencil was fitted in the bottom of the cell with a threaded Teflon sleeve. An annular platinum disk counterelectrode was axial to the titanium pencil. The titanium pencil was potentiostated in respect to a calomel reference electrode mounted in the cell.

A scale drawing of the Luggin capillary in the artificial pit showing the important dimensions is given in Fig. 2. The cross-sectional area of the tip was 2.4% of the area of the pit. Measurements of potential *vs.* position were made over a range of pit depths from 0.07 to 0.12 cm. At a distance above the pit the capillary flared out to a shaft diameter of 0.1 cm that fitted into a Plexiglas bushing mounted on split titanium leaf springs. A sliding fit sealed with stopcock grease was used in order to avoid breaking the capillary tip when it hit the electrode at the bottom of the pit.

The Plexiglas bushing mounted on split leaf springs of titanium maintained axial alignment of the Luggin capillary. The bushing and capillary were forced down against the spring by a micrometer head mounted on top of the cell. A Teflon tube filled with electrolyte connected the Luggin capillary-bushing assembly to a second calomel electrode in a reservoir outside of the cell. The signal from this calomel electrode was fed into Keithley Model 610B electrometer.

A Helipot connected as a voltage divider across a mercury cell provided an electrical analog signal of the Luggin capillary position. The Helipot was attached to the cell through a leaf spring which allowed axial movement but prevented rotation, and the shaft was connected to the micrometer. The signals from the Helipot and from the electrometer connected to the

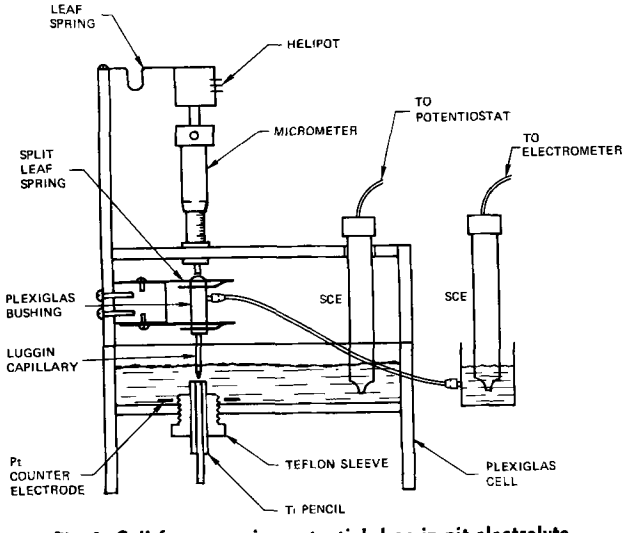

Fig. 1. Cell for measuring potential drop in pit electrolyte

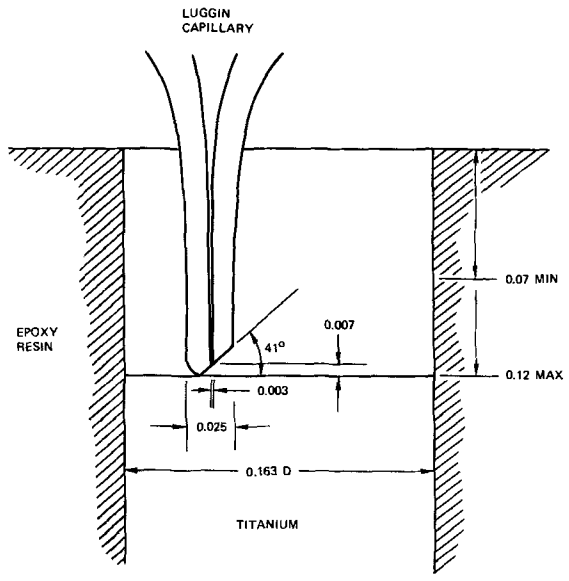

Fig. 2. Scale drawing of Luggin capillary in artificial pit. Dimensions in centimeters.

SCE from the Luggin capillary were displayed on the X-Y plotter. The Helipot signal, which was linear with Luggin capillary position, was calibrated with the micrometer. During the experiments periodic checks of Luggin capillary position and pit depth (seen through the epoxy resin) were made with a cathetometer.

Open-circuit potential transients.—The pattern of decay of potential of a working electrode with time after open circuiting is diagnostic in determining the type of potential drop, *e.g.*, electrolyte ohmic drops should disappear immediately while activation overvoltage should decay with log time (7).

A titanium pencil was potentiostated in a polyethylene cell. The circuit was opened by a Stevens Arnold, Inc. millisecond relay on the counterelectrode side. The signal from a separate calomel electrode in the cell was fed into a Tektronix Model 510 oscilloscope for short-time transients and through the electrometer to the strip chart to record longer period transients.

For each applied potential to the specimen a series of open-circuit transients was photographed on the oscilloscope screen at sweep speeds a decade apart from 10 μsec/cm to 100 msec/cm. The strip chart was used to obtain data out of 10 sec or more. This procedure gave some overlap for each scale when the data were replotted on a semilog graph.

Identification of gas from pits.—A small amount of gas was observed to emanate continually from the pits. An experiment was devised to determine if the gas was hydrogen or oxygen. The gas was collected in a section of 1 ml burette with a flared end filled with water and inverted over an artificial pit. After a few tenths of a milliliter of gas were collected, either hydrogen or oxygen were introduced. The gas mixture was sparked with platinum electrodes at the top of the burette and change in volume was determined.

Photographs.—Photographs of the corroded surfaces were taken with an Ultrascan Model SM-2 scanning electron microscope (SEM). All of the surfaces were prepared by corroding at constant potential. The total charge passed was 1000-2400 coulombs/cm^2 at 2.0-6.0V, 750 at 1.5V, 490 at 0.98V, and 120 at 0.94V.

Results

Current-potential curves.—A typical series of current-potential curves is shown in Fig. 3 for pitting of the 0.1 × 0.1 cm titanium pencil in 1M KBr. These curves obtained with a sweep rate of about −20 V/min, were taken at various times during propagation of a pit at a potential of 6.0V. Amount of charge passed up to the time of the measurement is the parameter.

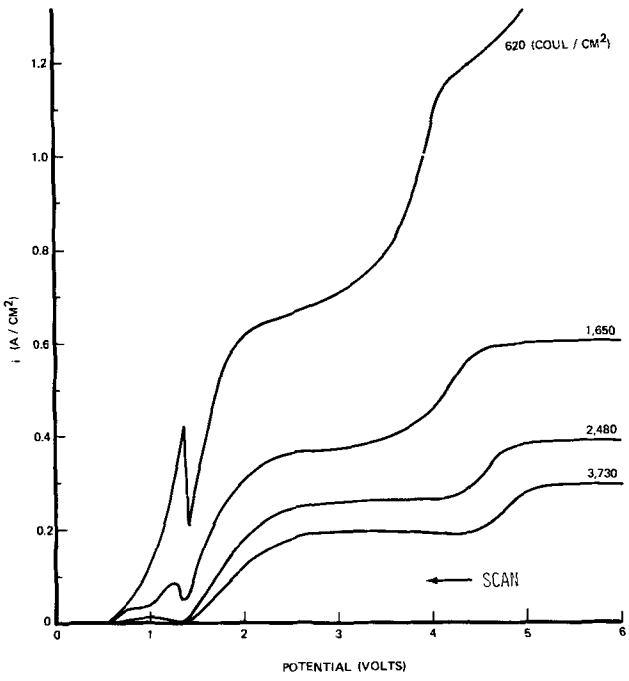

Fig. 3. Transient current density-potential curves for 10^{-2} cm^2 titanium electrode in 1M KBr. Parameter is amount of charge passed.

Three regions are observed: a hump between the pitting potential and 1.4V, a plateau between about 2.0V and 3.5-4.5V, and a second plateau about 4.0-5.0V, at least out to 17V. These will be referred to as the hump, the lower plateau, and the upper plateau, respectively. At slower sweep speeds the maximum of the hump occurs at a potential of about 0.98V and the steady-state pitting potential is 0.9V. With elapsed time or charge passed the current density in all three regions decreases and the half-wave potential between the lower and upper plateaus increases. The minimum between the hump and the lower plateau tends to remain constant at 1.4V. A positive sweep rate gives similar shape curves except that a second hump in current density occurs on the lower plateau at 1.8V.

Current-potential curves for more nearly steady-state conditions for 0.16 × 0.32 cm titanium pencils in 4.4M HBr are shown in Fig. 4. These curves were constructed from the constant-potential experiments from which the SEM photographs were taken. Interpolations were made for three charge densities. The current density decreased in these runs in a range of 0 to −1.7 power of the cumulative charge density depending on potential and charge density. The large nega-

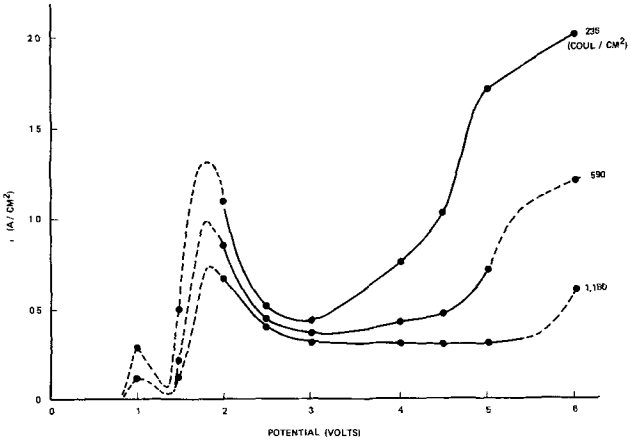

Fig. 4. Steady-state current density-potential curves for 0.05 cm^2 titanium electrode in 4.4M HBr. Parameter is amount of charge passed.

tive slope was related to the change from the upper to the lower plateau.

Above room temperature (50°-77°C) strong oscillations occurred between 0.9 and 1.5V in 4.4M HBr solution. The frequency was about 10 cycles/min.

The character of the corroding surface was different in the three regions. At the hump and up to a potential somewhere between 1.5 and 2.0V the pit was covered with what looked like a layer of compact gray mud. The metal surface after cleaning ultrasonically or by cathodic hydrogen evolution was very porous as can be seen for 0.94, 0.98, and 1.5V in the SEM photograph at 1000X in Fig. 5a, 5b, 5c.

On the lower plateau an orange-to-white precipitate was formed and extruded from the pit. The outer surface was chunky and white and the chunks slowly dissolved in the HBr solution. Deeper in the pit the material was orange and appeared to be somewhat gelatinous. Most of the material was easily removed with a jet of water after the experiments except for a thin film that adhered to the surface. After washing this film with acetone and drying it usually cracked and pealed off. The underlying metal surface appeared bright and crystallographically etched under the 35X binocular microscope. The SEM photograph in Fig. 5f shows the faceting and what looks like terraces. The transition to the terraced condition at 2.0 and 2.5V is shown in Fig. 5d and 5e.

On the upper plateau, a viscous orange solution covered the bottom of the pit and the shiny metal surface could be seen through it. With time the solution became translucent and the metal surface could no longer be seen. In washing out the pit material as above a salt film adhering to the metal was also observed. The underlying metal was polished as can be seen in the SEM photograph in Fig. 5g and 5h. In spite of being polished, it can be seen that there remained some differential metal removal between different grain faces. Some round bumps also covered the surface. Frankenthal and Pickering (8) also observed porous crystallographic and polished surfaces during the pitting of iron.

Good leveling of the titanium surface, as opposed to the above microtexture, occurred in bromide solution at all potentials as the pits deepened. Initially, when a potential above 2.5V is applied to a sanded pencil end the corrosion starts at the circumference of the titanium. The gelatinous corrosion product then spreads inwardly until the whole surface is active. Corrosion is initially greater at the circumference of the titanium as would be expected for primary current distribution. As the pit deepens, the surface becomes very level and at right angles to the epoxy resin walls. The surfaces were usually rougher in chloride and iodide solutions.

Stirring the precipitate in the pits with a glass microstirring rod always caused the current to increase in all three regions. Sometime the small gas bubbles (0.001-0.01 cm diameter) agglomerated into a larger bubble that filled the pit and forced out the precipitate. Current decreased during the growth of these bubbles and increased on their release. In switching from the upper plateau to 1.5V such a conglomerate bubble always formed. As it pushed up the precipitate a layered structure could be observed. Typically there was a compact layer about 10^{-3} cm thick that was next to the metal surface with a columnar layer about 10^{-2} cm thick above it.

In the prior paper (1) it was found that flow of electrolyte past the corroding surface in chloride solution stopped pitting. This was attributed to decreasing the diffusion layer thickness and removing hydrolysis products essential to the pitting process as well as decreasing temperature which appears to be at boiling in chloride solutions. Increasing the diffusion layer thickness in chloride solution should therefore promote pitting. An experiment was conducted with a titanium pencil in the anode-facing-up position in 6M HCl to test this idea. As corrosion propagated and depth increased, the potential to sustain pitting increased as shown in Table I, and the threshold current density, shown in Fig. 6, decreased as expected. The depth was calculated from the charge passed for valence (IV) titanium produced and checked with measured depth at the end of the experiment. Apparent electrolyte conductivity in the pit, calculated from the threshold current density, potential, and pit depth in Table I is seen to decrease exponentially with depth.

Generation of gas.—Volumetric measurements with the gas burette during pitting of titanium pencils in chloride solutions are given in Table II. Chloride solutions were used because the higher current density therein gave sufficient gas generation rate for measurement, whereas the gas generation rate was very low in bromide solutions. Only three possible gases, hydrogen, oxygen, or chlorine, could be generated in the pit under these conditions and the experiments were designed to determine which one.

Column 1 of Table II gives data for the gas collected from pitting in 1M HCl. The gas was sparked after collection, giving a decrease in volume indicating a combination of part of the gases. Hydrogen was then added from a platinum wire cathode in the same solution. No change in volume occurred on sparking, indicating that there was no residual oxygen (or chlorine) in the gas after the first sparking. The gas burette was then transferred without spilling to a cell with 1*N* H_2SO_4 electrolyte and oxygen was collected from a platinum wire anode. After sparking, the volume decreased as noted in column 1a. These results show that the gas from the pit was predominantly hydrogen but some oxygen (or chlorine) was also present.

Column 2 gives data for gas collected from an alkaline chloride solution in order to eliminate the possibility of chlorine being present. The solution was boiled in a flask to remove dissolved air and then cooled and poured into the cell with a minimum of agitation to minimize further air dissolution. A decrease in volume of the collected gas occurred on sparking showing that again a mixture of combustible gases were present. The burette was then transferred without spilling to a preboiled and cooled 0.3M NaOH solution in which oxygen was collected from a platinum wire anode. The gas was sparked during collection of oxy-

Table I. Threshold potential, current density, and apparent electrolyte conductivity as function of pit depth in 6M HCl

Depth (cm)	i (A/cm²)	ϕ (V)	κ^* (ohm^{-1} cm^{-1})
0	~20	9	—
0.1	10	6	0.15
0.18	7.5	7	0.18
0.25	5.0	10	0.12
0.45	3.0	16	0.08
0.65	1.6	26	0.04
0.80	1.0	30	0.026

* $\kappa = \dfrac{it}{(\phi + 0.6)}$.

Table II. Volumetric measurements with gas burette

	Gas volume (cm³)			
	1*	1a	2	3
Gas from pit (or cathode)	0.100	—	0.210	0.165
Loss on sparking	0.020	—	0.050	0.010
Remaining	0.080	—	0.160	0.155
H_2 added	0.027	—	—	—
Total	0.107	—	—	—
After sparking	0.107	—	—	—
O_2 added	0.031	0.025	—	—
Total	0.138	0.105	—	—
After sparking	0.080	0.047	—	—
Remaining at H_2-O_2 equivalence point for simultaneous O_2 addition and spark	—	—	0.095	0.070

* Notes: 1. Pitting in 1M HCl; H_2 generated in 1M HCl; O_2 generated in 1*N* H_2SO_4.
2. Pitting in 1M NaCl + 0.1M NaOH, preboiled; O_2 generated in 0.3M NaOH, preboiled.
3. H_2 and O_2 generated in 0.3M NaOH, preboiled.

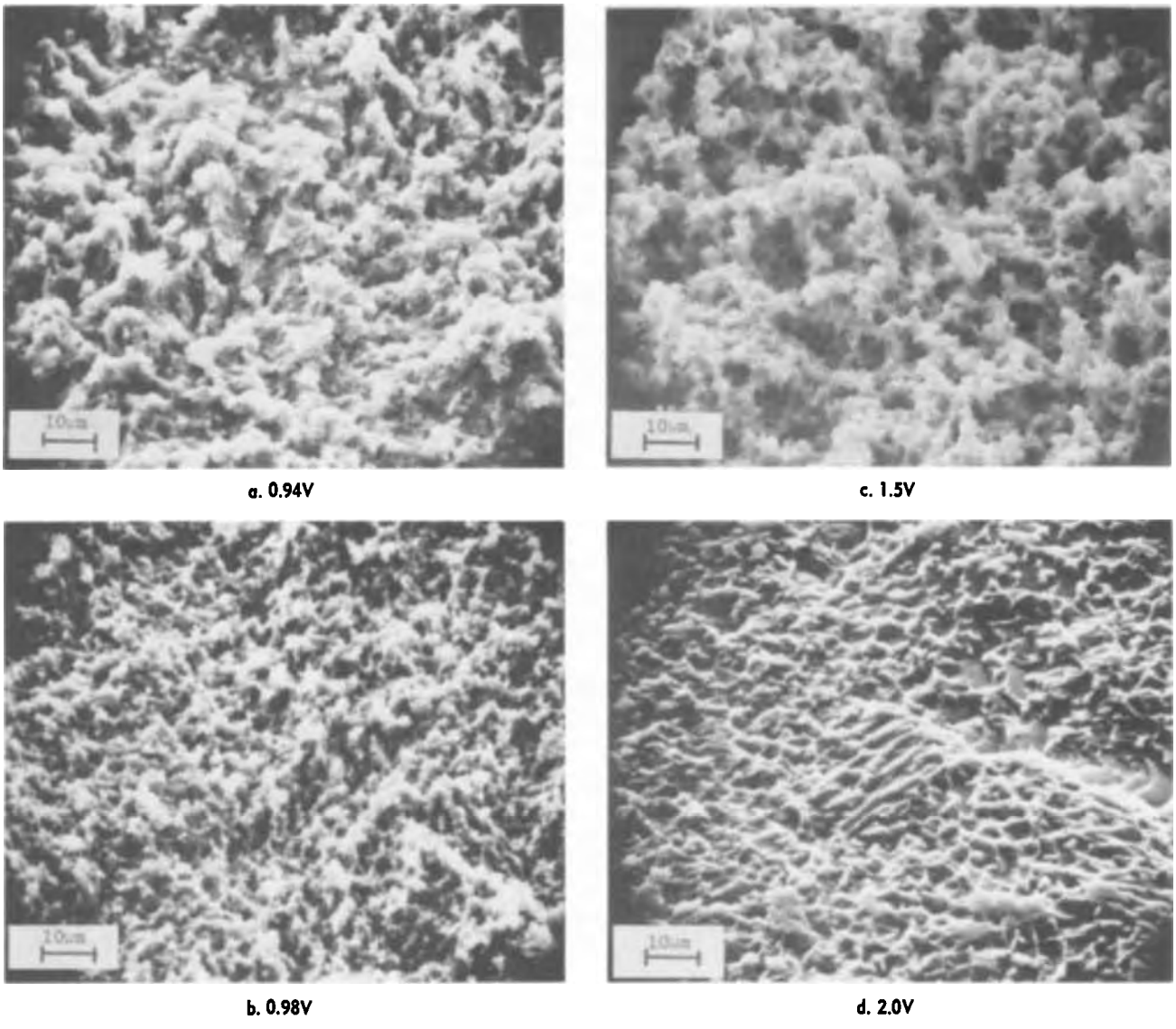

Fig. 5a-d. SEM photographs of titanium surfaces corroded at various constant potentials

gen and the volume decreased linearly with time then increased linearly at the same rate. An amperometric equivalence point was thereby obtained at a residual volume of 0.095 cm^3. The residual gas is assumed to be nitrogen from air that redissolved in the solutions.

Column 3, Table II, shows the results of an experiment in which hydrogen was collected from a platinum wire cathode in preboiled 0.3M NaOH solution. Sparking again caused a slight decrease in volume. Addition of oxygen from a platinum wire electrode in the same solution with simultaneous sparking gave a linear decrease in volume followed by a linear increase with an equivalence point at a residual volume as above. In this case, there can be no doubt that the residual gas was nitrogen from dissolved air. A calculation of mass transfer rates of gases from bubbles to solutions (9) confirms that the experimental observations are reasonable. A more sophisticated gas analysis method might have been used but it would have been subject to the same problems of mass transfer in solution.

It appears that hydrogen is the dominant gas, and probably the only gas issuing from these pits. A rough estimate of the amount from the above experiments and counts of bubbles gave an estimated coulombic equivalent between 0.01 and 0.07 that of the anodic current in chloride and in bromide solutions. In general, there appeared to be a greater gas evolution rate at lower potentials and higher temperature.

Potential traverse in pit.—A typical potential traverse for the Luggin capillary is shown in Fig. 7. Calibrations for potential and position are shown. The potential varied smoothly until the tip of the capillary hit the bottom of the pit as noted by the discontinuity followed by a smaller slope. The length of this region of smaller slope is assumed to be the displacement of the Luggin capillary into the Plexiglas bushing (Fig. 1) because the summation of these displacements from each run agreed with measurements made with the cathetometer. The potential on the outward traverse was slightly lower for a given tip position presumably due to disturbing the precipitate with the capillary. The pit current usually also increased during the outward traverse indicating a slight decrease in resistance.

Eleven usable traverses were obtained for the lower and upper plateau between 2.0 and 8.5V applied. Five other runs were rejected because they were taken below 2.0V, had an inadequate sensitivity, or the curve was erratic. Slopes were determined for each usable curve and the electrolyte conductivity was calculated as a function of position by Ohm's law

$$\kappa = -\frac{i}{d\phi/dl} \qquad [1]$$

using the current density i at the time of measurement. Values of κ were averaged as a function of position from the pit bottom and plotted in Fig. 8 with their standard deviations. Values for capillary-opening positions outside of the pit mouth were rejected

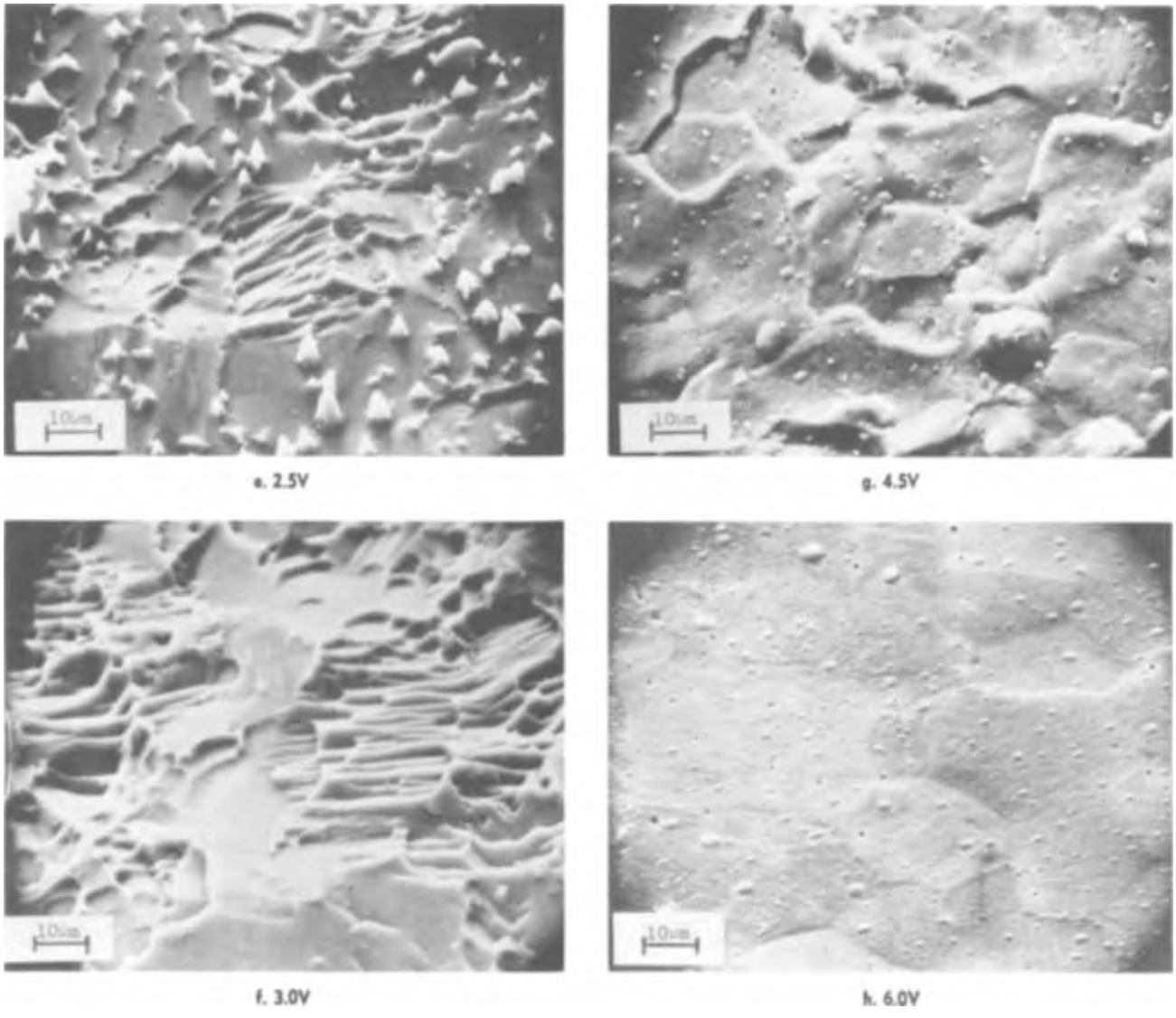

Fig. 5e-h. SEM photographs of titanium surfaces corroded at various constant potentials

from the averages. It is seen that conductivity decreases considerably within the pit and appears to become linear with distance from the bottom for small distances. The straight-line portion extrapolates to zero conductivity at a position equal to the distance of the capillary opening above the tip (Fig. 2) and has the equation

$$\kappa = 2.6l \qquad [2]$$

No significant correlation was found between calcu-

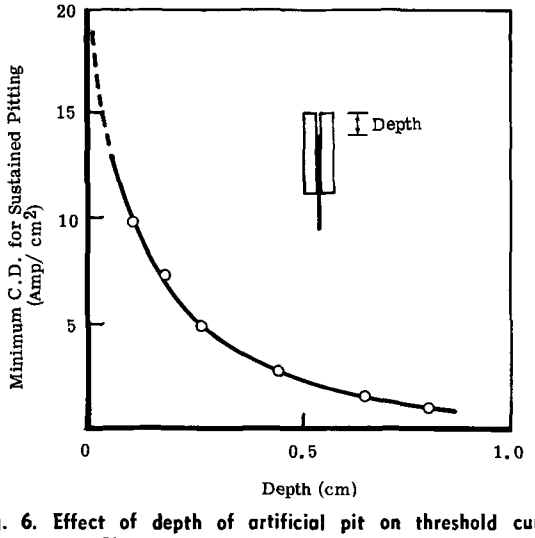

Fig. 6. Effect of depth of artificial pit on threshold current density in 6M HCl.

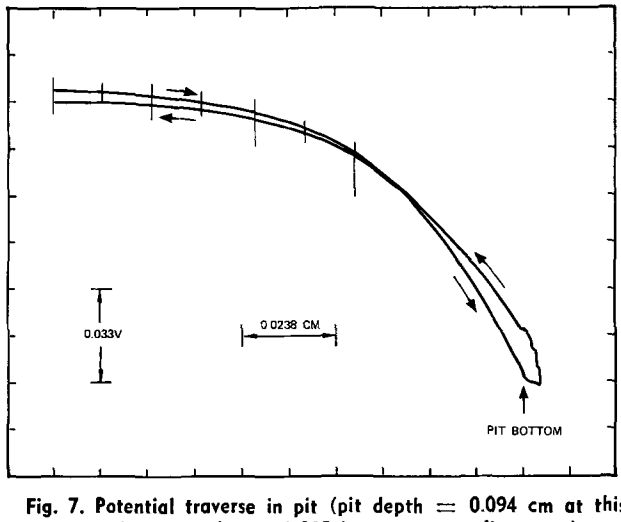

Fig. 7. Potential traverse in pit (pit depth = 0.094 cm at this measurement). Tic marks are 0.005 in. apart according to micrometer.

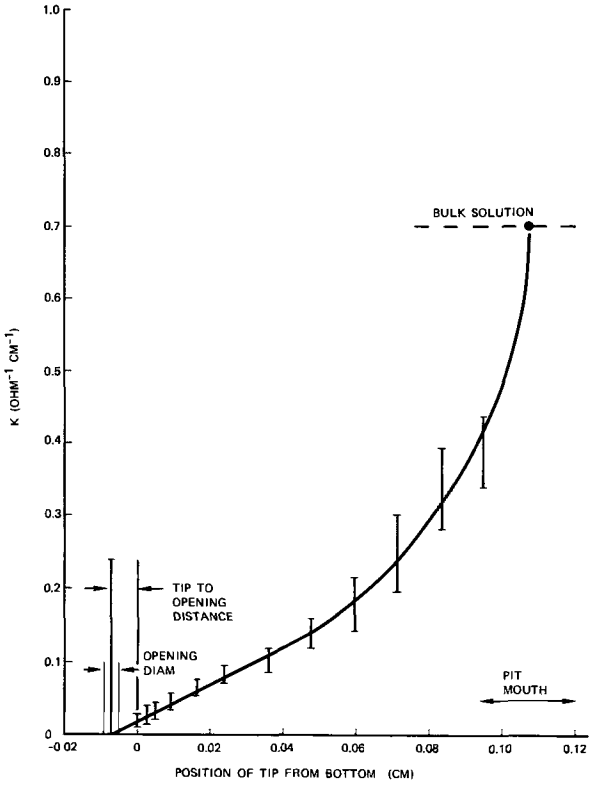

Fig. 8. Electrolyte conductivity in pit

lated conductivities and current density or pit depth within the ranges used.

Open-circuit potential transients.—Potential transient data replotted from oscilloscope photographs and strip chart records are shown in Fig. 9. For applied potentials at 2.0 through 5.0V a linear relationship was obtained between open-circuit potential and logarithm of time from 10^{-6} to 10^{-2} sec. At 7.0V applied the linear region extended only about two decades of time. Below 2.0V there did not appear to be any linear region.

A minimum occurred at about 10^{-1} sec from open circuit for all applied potentials. Values of this minimum are shown in Fig. 10 for pits in 4.4M HBr and 5M HI. These were determined by visually observing the oscillosope screen for repeated open-circuit transients. The minimum could be interpreted as either the potential of the corroding surface or a mixed potential established at open circuit.

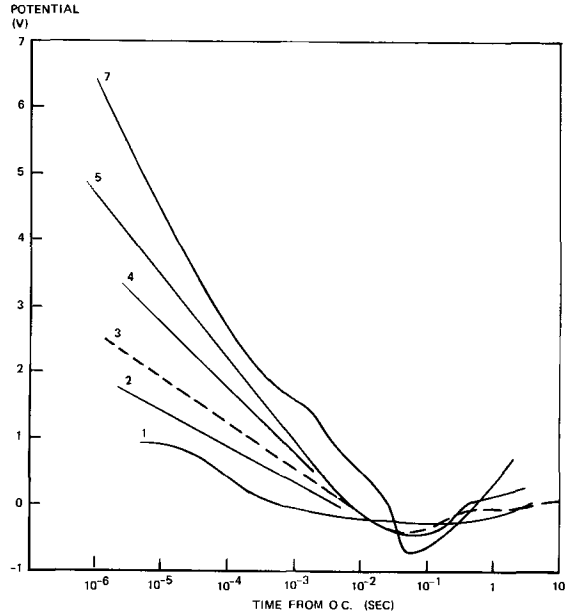

Fig. 9. Open-circuit potential transients for titanium pits in 4.4M HBr. Numbers on curves are initial applied potential (volts).

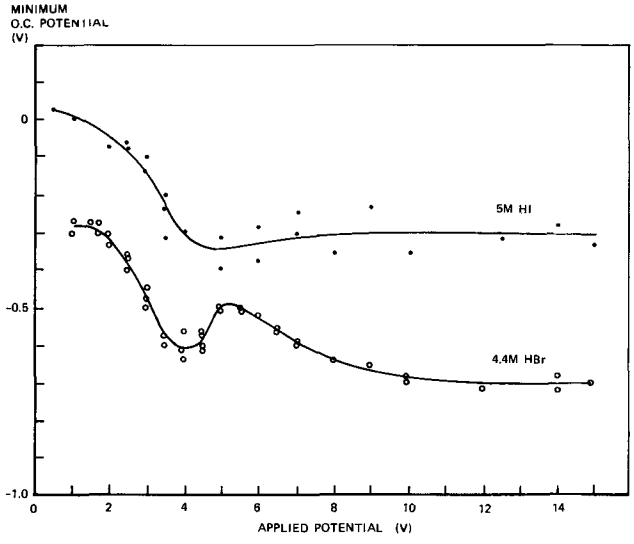

Fig. 10. Minimum open-circuit potentials for titanium pits in HBr and HI.

Discussion

Potential distribution.—The first task is to account for the potential distribution in and around a pit. The ohmic potential drop outside of the pit approximated by hemispherical conduction from an infinite distance to the pit mouth

$$\Delta\phi_{oo} = \frac{ir}{\kappa} \qquad [3]$$

is on the order of tens of millivolts for the current densities, pit radii, r, and conductivity, κ, for the concentration (4.4M HBr) used in the experiments. Measurements with the probe cell (Fig. 1) were in agreement with the low values predicted by this calculation. The metal surface is at a potential negative to the hydrogen electrode as demonstrated by hydrogen gas issuing from the pits in agreement with the minimum open-circuit potentials of −0.3 to −0.7V in HBr (Fig. 10). Therefore, nearly all of the difference between the applied potential and this negative potential must be accounted for within the boundaries of the pit.

An approximation for the ohmic potential drop inside the electrolyte of the pit is made by integrating Eq. [1], using the linear conductivity relationship of Eq. [2]

$$\Delta\phi_{ol} = \frac{i}{2.6} \ln (l/l_o) \qquad [4]$$

For a pit depth, $l = 0.1$ cm and a lower bound distance of molecular dimensions, $l_o = 10^{-7}$ cm, $\Delta\phi_{ol} = 5.3i$. This is, of course, a gross extrapolation down to molecular dimensions but it will serve as a first approximation. Values of Eq. [4] are shown in Table III, together with applied potentials and current densities from the potential-traverse experiments. It is seen

Table III. Calculation of potential drops in pit

ϕ_p (V)	i (A/cm^2)	ϕ_{oc} (V)	$\Delta\phi_{oo}$ (V)	$\Delta\phi_{ol}$ (V)	Unaccounted $\Delta\phi_u = \phi - \phi_{oc} - \Delta\phi_{oo} - \Delta\phi_{ol}$ (V)
1	0.005	−0.28	—	0.03	1.25
1.5	0.06	−0.28	—	0.32	1.46
2	0.11	−0.40	0.01	0.58	1.81
3	0.12	−0.48	0.01	0.64	2.47
4	0.11	−0.62	0.01	0.58	4.03
5	0.18	−0.50	0.02	0.95	4.53
8.5	0.25	−0.65	0.03	1.33	7.79

that the largest component of potential by difference $\Delta\phi_u = \phi - \phi_{oc} - \Delta\phi_{oo} - \Delta\phi_{oi}$, is unaccounted.

The unaccounted potential could either be due to error in the conductivity extrapolation or to potential drop in a thin salt film. A high surface activation overpotential can be excluded because hydrogen gas is produced.

Potential decay.—The potential decay experiments are diagnostic in that a linear relationship of potential with log time is characteristic of discharge of the electrical double layer by a reaction following Tafel kinetics (7, 10) or to discharge of capacitance across a film by high-field conduction (11). The former gives a constant Tafel slope independent of the initial potential, whereas the latter gives a variable slope which is a function of the film thickness.

A plot of the decay slopes as a function of applied potential from 2 to 5V is shown in Fig. 11. The data appear to be linear and the least squares line has a slope of −0.20 and an intercept of −0.55V. The potential-decay data are therefore consistent with high-field conduction through a salt film, the intercept being the potential for zero salt film thickness.

Presence of a salt film is in accord with the observations of Frank (12) and Vetter and Strehblow (13) for pitting of iron.

Paradox.—An apparent paradox exists in that the steady-state polarization data (Fig. 3 and 4) indicate a diffusion-limited process whereas the potential decay experiments indicate high-field conduction controlling. It will be assumed that both operate simultaneously and that they are series processes, *e.g.*, a salt film that maintains a thickness to use up, by high-field conduction, the potential applied and the rate of dissolution of this film is controlled by diffusion of water to the electrolyte-salt interface.

Model.—A qualitative model to describe the events in a pit has already been presented (1). A salt film is assumed to form on the metal surface. The simplest composition, TiX_4, is chosen although it could also be $TiOX_2$ or some other oxy-halide salt of Ti(IV). The halide ion is transported by high-field conduction through the salt to metal surface. The X^- ion occurs at a high concentration in the electrolyte next to the salt film because it is regenerated within the diffusion layer by hydrolysis of TiX_4. The salt is transported away from the metal-salt interface by bulk flow. (The alternative of high-field conduction of Ti^{4+} outward does not change the arguments presented here.)

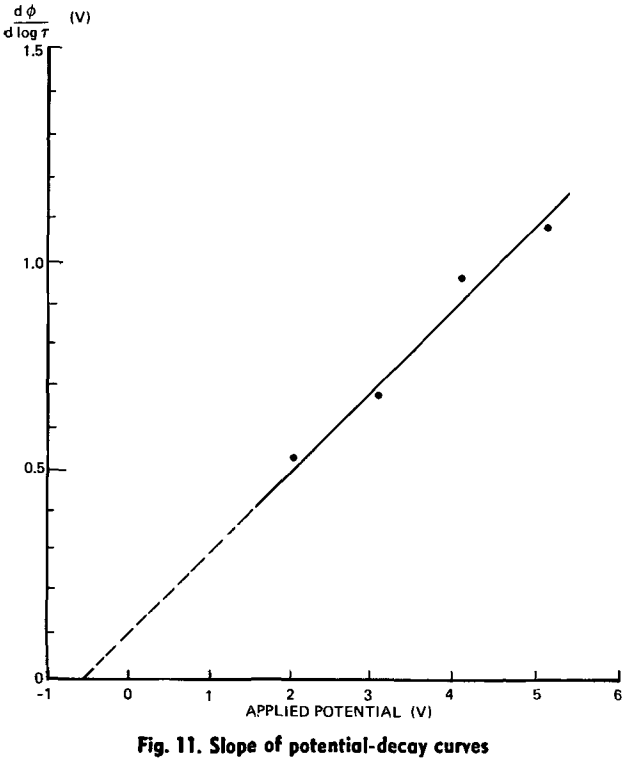

Fig. 11. Slope of potential-decay curves

At the salt-electrolyte interface the TiX_4 dissolves covalently in the water which has diffused to the interface. Within the diffusion layer, hydrolysis of TiX_4 to TiO_2 and/or TiO^{++} occurs, generating halide and hydrogen ions which make the solution acidic regardless of the *p*H of the bulk solution outside of the pit. If the hydrolysis goes to completion within the pit, the overall pit reactions are

$$Ti + 2H_2O \rightarrow TiO_2 + 4H^+ + 4e$$

or

$$Ti + H_2O \rightarrow TiO^{++} + 2H^+ + 4e$$

and only TiO_2, TiO^{++}, and H^+ are transported out. Water is then the only species transported into the pit from the environment at steady state.

Areas of agreement of the experimental data and the model can now be discussed, starting with the diffusion layer.

The orange viscous material deep in the pits in bromide solutions is consistent with the color of $TiBr_4$ or $TiOBr_2$ which would be an expected intermediate in the hydrolysis. White precipitate, at the outer part of the pits, and dense colorless liquid streaming out of the pits, are consistent with TiO_2 and TiO^{++} ion, respectively, expected from valence IV titanium.

Decrease in conductivity with distance into a pit may be attributed to an increase in viscosity due to high concentration of TiO_2 and TiO^{++}. Valence IV titanium has a known tendency to polymerize (14). The linear form of the decrease in conductivity with distance is yet to be understood quantitatively, however. Decrease in conductivity could not be attributed to concentration of conducting species in the model because both H^+ and X^- are generated in the diffusion layer and therefore should be at high concentration.

According to the model, the only species entering a pit at steady state is water. If this is the diffusion-limited species the current density would decrease with depth or thicker viscous layer. That the current density decreased in a variable way from 0 to −1.7 power of depth indicates a complex nature of the viscous layer. Increase in current density with stirring of the viscous layer is in accord with a diffusion-limited species in it.

The rapidly increasing current density with temperatures above 50°C for the lower plateau in iodide solution (1) can only be speculated upon at this time. It is known from TiO_2 pigment technology that nucleation and growth of TiO_2 particles from chloride or sulfate solutions occur above a temperature of 50°-60°C (15) and are arrested below this temperature. Growth of TiO_2 particles in a pit could decrease the concentration of TiO^{++} and thus avoid the viscous polymeric gel.

The requirement for a salt film has already been discussed but the points will be summarized here. The fact that hydrogen gas issues from the pits is the strongest argument that the metal surface is at a negative potential. Hydrogen generation can be attributed to diffusion of hydrogen ions through the salt film. Electric migration tends to carry them out. The observation of increased hydrogen gas rate when the potential was decreased is consistent with a greater diffusion flux of hydrogen ions through a thinner salt film.

Faceting and terraces observed on the metal surface at the lower plateau and the residual differences between grains indicates that the metal is reacting at close (tens of millivolts) to the reversible potential. The reversible potential for the reaction

$$Ti + 4Br^- \rightarrow TiBr_4 + 4e$$

is −0.76V (SCE) according to thermodynamic data in Latimer (16). The minimum in the open-circuit potential (Fig. 10) and the extrapolated intercept of the slopes of the potential decay curves (Fig. 11) are in approximate agreement with a mixed potential from this reaction and hydrogen ion reduction.

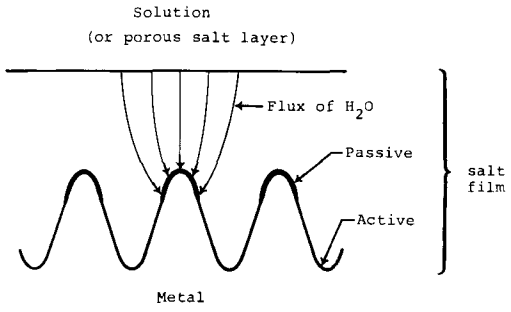

Fig. 12. Mechanism for initiating porous metal surface

Most of the potential drop in a pit cannot be accounted for in any other way than by resistance of a salt film. The potential decay (Fig. 9) and the constant double derivative of open-circuit potential to log time and applied potential (Fig. 11) are in accord with a salt film concept.

Although the model qualitatively is in accord with the experimental observations, several questions remain. The composition of the salt film is not known; whether it is TiX_4, $TiOX_2$, or other. The explanation of two plateaus in current density is unknown. The ratio of current densities of the upper to the lower plateau in eight experiments was 1.53 with standard deviation of ± 0.04. More work would have to be done to resolve which term in the diffusion equation changes by this amount.

Pitting potential.—The same value of pitting potential was obtained for the titanium pencils as was earlier determined for pitting on titanium foil (1), using the same technique of decreasing the potential of a propagating pit until the current decayed to zero. Pitting potential in an artificial pit at the end of a titanium pencil cannot be attributed to an equilibrium between a salt layer and a pre-existing oxide at the boundary of a pit (17) as there is no pre-existing oxide layer present after corrosion has progressed for a period of time.

The porous surface, Fig. 5a, 5b, and 5c, bearing no relation to the metal grains at potentials between the pitting potential and 1.5 to 2.0V needs explanation. Dissolution of a metal under mass-transport limiting conditions should produce electropolishing (18) as was observed on the upper plateau. In order to have preferential dissolution in holes or pores, the peaks must be passivated. A way to accomplish this would be to have diffusion of a passivating agent through the salt layer to reach the peaks at a sufficient rate for passivation but to reach the bottom of the pores at an insufficient rate as illustrated in Fig. 12. This is related to the concept of smoothing agents in electroplating (19) where the agents diffuse to peaks at a sufficient rate to block deposition but do not reach and block deposition in the valleys.

Two possible passivating agents are TiO_2 and TiH_2 layers. A number of considerations point to the oxide as being more likely. Mansfeld (20), for example, found that addition of water to methanol-1*N* HCl (anhydrous) caused the pitting potential to change approximately as

$$\phi_p = -0.4 + 0.15X \qquad \text{V (SCE)}$$

where X is weight per cent of water. Methanol-HCl would have hydrogen ions that could react and form hydride at -0.4V (SCE). Titanium does not passivate in this anhydrous solution (20, 21). Oxide is the only new passivating species expected with the addition of water. A quantitative treatment will be made in a later paper.

Conclusions

The following conclusions are based on experiments conducted with one-dimensional pits at the ends of insulated titanium pencils in the anode-facing-up position in chloride, bromide, and iodide solutions.

1. Current density is uniformly distributed and is mass-transport limited in a viscous solution in the pits.
2. Steady-state pitting potential for the titanium pencil in bromide solution is about 0.9V (SCE) as for earlier experiments with edge pitting of titanium foil.
3. Detailed microstructure of the corroding metal surface is related to the potential applied and varies from a sponge structure through a terraced crystallographic etch to electropolished surface between the pitting potential and about 6V applied.
4. The corroding metal surface is at a potential negative to hydrogen evolution. Hydrogen evolved is equivalent to about 1-10% of the anodic current.
5. Only a small part of the difference between the applied potential and that of the metal surface can be attributed to potential drop in the electrolyte, although the electrolyte conductivity decreases toward the metal surface.
6. It appears that a salt film on the metal surface absorbs the potential applied by high-field conduction.
7. Results observed with the titanium pencils are qualitatively and semiquantitatively in agreement with the dual layer salt-film-diffusion-layer model previously presented.

Acknowledgment

This work was performed in part under NASA Headquarters Contract NASW-2245 and in part under Air Force Office of Scientific Research Contract F44620-72-C-0070. The scanning electron microscope photographs were made by Mr. Al Curtis of the Boeing Company. This paper was based on work done at Boeing Scientific Research Laboratories, Seattle, Washington 98124.

Manuscript submitted March 15, 1973; revised manuscript received May 9, 1973. This was Paper 72 presented at the Miami Beach, Florida, Meeting of the Society, Oct. 8-13, 1972.

Any discussion of this paper will appear in a Discussion Section to be published in the June 1974 JOURNAL.

REFERENCES

1. T. R. Beck, *This Journal*, **120**, 1310 (1973).
2. H. J. Engell and N. D. Stolica, *Z. Physik. Chem.*, **215**, 167 (1960).
3. U. F. Frank, *Werkstoffe Korrosion*, **9**, 504 (1958).
4. H. Kaesche, *Z. Physik. Chem. NF*, **26**, 138 (1960).
5. J. Edwards, *This Journal*, **100**, 189C (1953).
6. H. W. Pickering and R. P. Frankenthal, *ibid.*, **119**, 1297 (1973).
7. B. E. Conway, "Electrode Processes," p. 155, Ronald Press, New York (1965).
8. R. P. Frankenthal and H. W. Pickering, *This Journal*, **119**, 1304 (1972).
9. R. B. Bird, W. E. Steward, and E. N. Lightfoot, "Transport Phenomena," p. 541, John Wiley & Sons, Inc., New York (1960).
10. J. A. V. Butler and G. Armstrong, *Trans. Faraday Soc.*, **29**, 1261 (1933).
11. L. Young "Anodic Oxide Films," p. 33, Academic Press, New York (1961).
12. U. F. Frank, 1st Int. Congr. on Metallic Corrosion, London 1961, p. 120, Butterworths, London (1962).
13. K. J. Vetter and N. N. Strehblow, Paper No. 14, U. R. Evans Intl. Conference on Localized Corrosion, Williamsburg, Va., Dec. 1971.
14. F. A. Cotton and G. Wilkinson, "Advanced Inorganic Chemistry," Interscience, New York (1966).
15. J. Barksdale, "Titanium, Its Occurrence, Chemistry and Technology," 2nd Ed., Chap. 14 and 18, Ronald Press, New York (1966).
16. W. M. Latimer, "Oxidation Potentials," 2nd Ed., Prentice Hall, Englewood Cliffs, N. J. (1952).
17. K. J. Vetter, *Ber. Bunseng. Physik. Chem.*, **69**, 683 (1965).
18. C. Wagner, *This Journal*, **101**, 225 (1954).
19. O. Kardos and D. G. Foulke, in "Advances in Electrochemistry and Electrochemical Engineering," Vol. 2, P. Delahay and C. W. Tobias, Editors, John Wiley & Sons, Inc., New York (1962).
20. F. Mansfeld, *This Journal*, **118**, 1412 (1971).
21. T. R. Beck, Submitted to *Electrochimica Acta*.

Electrochemical Deposition of Sodium Tungsten Bronzes

Jean-Paul Randin*

Hydro-Quebec Institute of Research, Varennes, Province of Quebec, Canada

ABSTRACT

The electrochemical deposition of sodium tungsten bronzes (Na_xWO_3) from Na_2WO_4/WO_3 melts has been studied between 700° and 900°C. The relation between the x-value in Na_xWO_3 and the concentration of WO_3 in the melt is linear between 2 and 10 mole/liter WO_3. Extrapolation of the linear section gives $x = 1.0$ at zero concentration of WO_3. The current efficiency of the bronze deposition depends on both the applied current and the melt temperature. This dependence is attributed to the occurrence of simultaneous chemical dissolution of the bronze. A transition temperature has been found below which Na_xWO_3 is deposited, and above which W (or W + Na_xWO_3) is obtained. The nature of the deposit is a function of the melt composition and temperature. The slope of the $(i)_{\eta=\text{const.}}$ *vs.* T^{-1} plot shows no break at, or near, the transition temperature, indicating that the rate-determining step for the deposition of Na_xWO_3 is the same as that for the deposition of W. The tungsten formation occurs most likely by decomposition of the previously deposited bronze. The content of platinum in a platinum-containing bronze is favored by a high temperature. The amount of platinum codeposited in the bronze is small compared to the amount of platinum dissolved from the anode. A relatively high concentration of platinum in the melt inhibits the bronze deposition. A nonelectrochemical reaction is believed to be responsible for the codeposition of platinum.

The sodium tungsten bronzes are nonstoichiometric compounds of the general formula Na_xWO_3, where $0 < x \leq 1$. They are chemically inert and have semimetallic properties, in particular, metallic luster and good electrical conductivity. Their properties have been reviewed recently (1-3).

Two methods have been extensively used for the preparation of these bronzes. The first method involves a solid-state reaction between a mixture of fine powders of sodium tungstate, tungsten trioxide, and metallic tungsten, the latter acting as a reducing agent, at a temperature between 500° and 1000°C in a nonoxidizing atmosphere. This reaction may be written as

$$3xNa_2WO_4 + (6 - 4x)\ WO_3 + xW \rightleftharpoons 6Na_xWO_3 \quad [1]$$

The bronzes produced by this technique are in the form of fine powders (4, 5).

The second method involves the electrolysis of a molten mixture of sodium tungstate and tungsten trioxide; it is essential when large single crystals are required. Crystal growth occurs at the cathode and oxygen evolution takes place at the anode, according to the over-all reaction

$$\frac{x}{2}Na_2WO_4 + \left(1 - \frac{x}{2}\right)WO_3 \rightarrow Na_xWO_3 + \frac{x}{4}O_2 \quad [2]$$

The growth of tungsten bronzes by fused salt electrolysis has been used by a number of investigators [see, for example (6-11)], but virtually no details about the actual growth method were reported until very recently. Banks, Fleischmann, and Meites (12) performed polarographic experiments which revealed a polymeric character of the WO_3 species reduced at the cathode for a melt concentration between 10 and 60 m/o (mole per cent) WO_3 and a temperature of 750°C. This work confirmed an earlier Raman spectroscopic investigation in which the formation of polyions in a Na_2WO_4/WO_3 melt at 710°C was suggested (13). Meites *et al.* (14) studied the voltammetric behavior of polytungstate melts. Potentiostatic investigation of reaction kinetics at the growing and dissolving sodium tungsten bronze electrode allowed Fredlein and Damjanovic (15) to propose two probable mechanisms of the process. Finally, Shanks (6) reported on the parameters for the growth of Na_xWO_3 crystals with predictable compositions and established the phases obtained as a function of melt composition and temperature.

Sodium tungsten bronzes containing platinum[1] have recently been claimed to exhibit a high electrocatalytic activity for the oxygen reduction reaction (16-18) and have attracted attention as possible electrocatalysts in fuel cells and energy storage devices.

The present work deals with the effect of the melt composition and temperature on the bronze composition and the nature of the phases obtained. The effect of current density and temperature on the current efficiency has also been studied, as well as the incorporation of platinum into the bronze crystal. The effect of platinum on the current efficiency and the process of platinum codeposition are discussed.

Experimental

The depositions were carried out in a recrystallized alumina crucible (Coors AD 99) placed in a top-fed furnace purged with purified helium. The helium was purified by passing it through a train, wihch included a BTS catalyst (BASF, Ludwigshafen-am-Rhein, Germany) maintained at 180°C to remove oxygen and CO, and Linde Type 3A and 13X molecular sieves to remove other impurities.

Molten mixtures were prepared by fusing reagent-grade Na_2WO_4 (A and C, American Chemical) and H_2WO_4 (Baker Analyzed Reagent). Both reagents were previously dried at 200°C. A typical charge was about 600g of the mixture $Na_2WO_4 + WO_3$. A new crucible was used for each new melt composition.

WO_3 concentrations were calculated as mole per cent or mole per liter of the melt (molarity) and were based on the weights of the reagents and corrected for the consumed quantities, according to reaction [2], if necessary. The molarities of the melts were calculated using density data reported by Morris and Robinson (19).

The temperature was monitored with a Chromel-Alumel thermocouple placed on the side of the crucible. This value was corrected by means of a calibration curve relating the temperature in the melt to that on the side of the crucible and determined at the end of a set of experiments in order to prevent contamination of the melt by the thermocouple sheath. The melt temperature, held constant by means of a proportional

* Electrochemical Society Active Member.

Key words: electrodeposition, tungsten bronzes, crystal growth, platinum codeposition.

[1] Called "platinum doped bronzes" by some authors (17, 18). As the term "doped" may not be strictly applicable in the normal semiconductor sense, "platinum-containing bronze" better described the unknown distribution of the platinum impurities.

Table I. Growth of sodium tungsten bronzes on gold electrodes

Crystal No.	Melt composition (m/o WO_3)	(mole/liter)	Temp (°C)	Average current (mA)	Composition x in Na_xWO_3	Crystal faces formed	Pt content (ppm)	Yield (%)
87	10	1.38	735	8.87	0.89*	100	2	68
89	10	1.38	735	15.1	0.89*	100	1	79
69	15	2.14	786	21.8	0.87	100	—	81
20	20	2.95	786	9.23	0.81	100	3	88
93	25	3.80	735	9.65	0.81	100	1	92
94	25	3.80	786	14.1	0.81	100	1	85
95	25	3.80	750	11.9	0.81	100	1	91
97	25	3.80	750	15.1	0.81	100	1	92
12	39	6.40	792	6.67	0.67	100	2	76
77	40	6.59	786	9.15	0.63	100	2	69
78	40	6.59	786	16.9	0.63	100	—	80
81	38	6.20	786	14.3	0.65	100	0.5	69
44	50	8.97	786	12.4	0.58	110	—	94
45	50	8.97	786	8.92	0.58	110	2	74
42	60	11.42	807	10.4	0.34*	Tetragonal	—	63

* Determined by chemical analysis.

control system (Thermolyne, Sybron Corporation), did not fluctuate more than 3°C.

The bronzes were grown at the end of a gold wire. The anode consisted of a gold wire or sheet (99.99% purity). In some experiments the gold wire used as the anode was placed within a porcelain crucible whose bottom had a 1 mm slit to provide ionic conduction between the compartments. The porcelain tube inside the cell acted as a chimney for the evolved oxygen and, therefore, prevented oxygen from going to the catholyte. However, no noticeable difference in the current efficiency was found with or without this device. A platinum sheet (99.99% purity, 1.5 × 1.0 × 0.01 cm) was used as the anode in electrolyses in which platinum incorporation was sought. The concentration of platinum in the melt was therefore maintained by anodic dissolution of the metal.

A bronze crystal grown in the same melt as the working bath was used as the reference electrode (15) in the activation energy measurements. A constant current d-c power supply (Hewlett-Packard, Model 6177B), an electronic coulometer (Koslow Scientific Company, Model 541), and a potentiostat (Wenking, Model 68TS3) were used.

X-ray diffraction angles and relative intensities of diffracted beams were determined on powdered samples (Philips Diffractometer, Ni-filtered CuK_α radiation). The sodium concentration of cubic bronzes was determined from the x-ray measurements of the lattice parameter using Brown and Banks (7) relation between lattice parameter and sodium content. High ($x > 0.85$) and low ($x < 0.5$) x-values were determined by wet chemical analysis.[2]

Spark-source mass spectrographic analysis[3] was used to determine the concentrations of trace elements, including platinum and gold. Concentrations of platinum higher than about 50 ppm were determined by optical emission spectroscopy.[3] Standard platinum samples were prepared for calibration of both the above methods.

Results

Growth of Na_xWO_3

Crystal characterization.—Crystal characterization and yield for different conditions of growth are summarized in Table I. Cubic phase material was obtained for all melt compositions with less than 50 m/o WO_3. The sodium tungsten bronzes grown in a melt containing 40 m/o WO_3 or less were of a cubic habit ({100} faces), while those grown in a 50 m/o WO_3 melt were dodecahedral ({110} faces). The bronzes grown in a 60 m/o WO_3 melt were tetragonal. These results are in agreement with the recent studies by Fredlein and Damjanovic (15) and Shanks (6).

The temperature of deposition has no significant effect on the crystal habit of the bronze except in a 50 m/o WO_3 melt from which needle-shape crystals are deposited above 850°C. The side faces of the needles are the {100} planes and the end faces the {110} planes.

The x-values vs. melt composition.—The relation between the x-values of the bronzes and the melt composition is given in Fig. 1. The results of the present study fit well with those previously reported (6, 8, 11, 15, 20). In Fig. 1, the melt composition is given in mole of WO_3 per liter, rather than in mole per cent WO_3 as in previous studies (6, 15), since the molarity of the melt is a more significant quantitative measure of the proportionality of the amount of reactant than the mole fraction.

The relation between the x-value in Na_xWO_3 and the concentration of WO_3 in the melt is linear between 2 and 10 mole/liter WO_3. Extrapolation of the linear section gives $x = 1.0$ at zero concentration of WO_3. The deviation from linearity at low concentrations of WO_3 is believed to be due to an activity effect of WO_3. A possible reason for the deviation from linearity at high WO_3 concentrations may be the change in the crystal structure of the bronzes (from cubic to tetragonal).

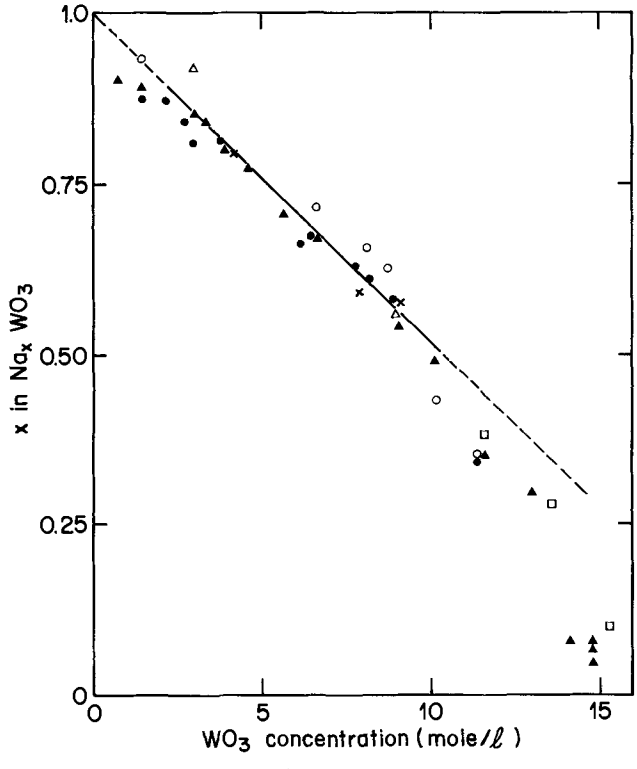

Fig. 1. Bronze composition, i.e., x in Na_xWO_3, vs. melt composition. ● Present work, ▲ Shanks (6). ○ Fredlein and Damjanovic (15), X Hauck, Wold, and Banks (11), △ Vest, Griffel, and Smith (8), □ Magneli and Blomberg (20).

[2] Performed by Technitrol Limited, Montreal, Province of Quebec, Canada.

[3] Performed by the National Research Council, Chemistry Division, Ottawa, Ontario, Canada.

Platinum contamination.—Since the bronze crystals were prepared for subsequent electrocatalysis studies, platinum contamination was an important matter. In the preparation of pure bronzes, *i.e.*, without purposely added platinum, the aim was to keep the platinum contamination at a minimum level. It was thought that the first crystal grown in a freshly prepared melt would act as a scavenger in which most of the impurities would accumulate. The subsequently grown crystals were expected to have a much lower impurity concentration. Surprisingly, the platinum concentration found in crystal No. 77, deposited out of a freshly prepared melt, and that found in crystal No. 81 (Table I), deposited out of the same melt but after four bronze crystals had already been grown, are almost within the experimental error of the spark-source mass spectrograph (±50% at a few ppm level). In crystals No. 93-97, all deposited from the same freshly prepared melt, the platinum content did not vary from the first crystal to the sixth.

The platinum content of the reagents, also determined mass spectrographically, was found to be 2 ppm in Na_2WO_4 (A and C, American Chemical), and <0.2 ppm in H_2WO_4 (Baker Analyzed Reagent). Any other source of the platinum contamination of the melt is unlikely since gold used as the anode is a 99.99% purity material and does not dissolve significantly during the electrolysis.

Pre-electrolyses with large gold electrodes were carried out in an attempt to decrease the residual platinum concentration in the melt. These experiments were performed at high temperatures and high current densities since these experimental conditions will be shown later to favor platinum incorporation from an intentionally contaminated melt. Pre-electrolysis was first carried out in Na_2WO_4 at 930°C with a cathodic current density of 100 mA-cm^{-2} for 72 hr. Tungsten trioxide was then added and a second pre-electrolysis was performed. The crystals deposited in such a pre-electrolyzed melt exhibited a platinum concentration similar to that found in crystals deposited in a melt that had not previously been pre-electrolyzed.

Gold contamination.—Contamination of the bronze crystals by gold is also relevant to this study since gold was used as an anode in the deposition of pure crystals. Gold is more noble in the melt than platinum but nevertheless dissolves slowly during prolonged use as the anode. The typical gold concentration determined by spark-source mass spectrography is between 30 and 80 ppm. Crystals deposited from a melt pre-electrolyzed for a long time with gold electrodes contain up to 700 ppm gold. In the crystals deposited with a platinum anode the gold content is at the ppm level.

Other impurities present in the bronze samples at the ppm level are: Al, Si, Ti, S, Mo, Cl, Ca, P, Fe, Co, Ni, Cr, Y, V, Mg, and K.

Effect of current and temperature on efficiency.—The yields (coulombic efficiency) were determined by weighing and analyzing the bronze formed after the passage of an accurately measured amount of electricity and were found to depend on both current density and melt temperature (Table I). High current densities and low temperatures tend to favor high yields. In the depositions summarized in Table I, the applied current was increased during growth in order to take into account the increase in surface area. At the beginning of the deposition the gold wire area was about 0.2 cm^2 and cubic crystals as large as 1 cm in linear dimensions were easily grown. Typical currents used were from 3 to 30 mA.

In another set of measurements reported in Fig. 2 and 3 the current was held constant during the entire deposition. Since the surface area of the crystal increases with deposition time by about one order of magnitude, the following results are useful only from the point of view of crystal growth; no mechanistic conclusion can be drawn from them.

The yield of bronze as a function of applied current at different temperatures in a 50 m/o WO_3 melt are reported in Fig. 2. The first series of depositions was carried out at 840°C in a freshly prepared melt. The temperature of the melt was then decreased to 746°C and the second series of depositions was performed at this temperature at different constant currents. The next experiments were carried out at regularly increasing temperatures. The coulombic efficiency depends on both the melt temperature and the applied constant current. In addition, the deposition yield in a freshly prepared melt also depends on the first melt temperature. The efficiency of depositions carried out at 840°C in a freshly prepared melt containing 50 m/o WO_3 were only in the 20% range, whereas 80% efficiency was reached in the same but used (at lower temperatures) melt, at the same temperature.

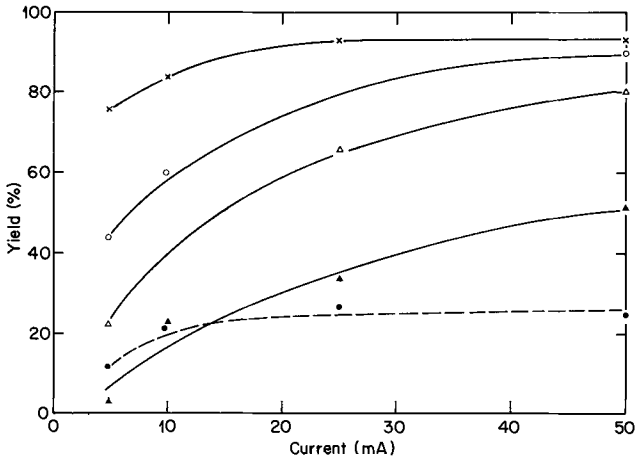

Fig. 2. Effect of current on the yield of deposition of Na_xWO_3 in a 50 m/o WO_3 melt. Total charge consumed 13.4 meq. First series of depositions in a fresh melt at 840°C (●), followed by depositions at 746°C (X), 792°C (○), 840°C (△), and 884°C (▲).

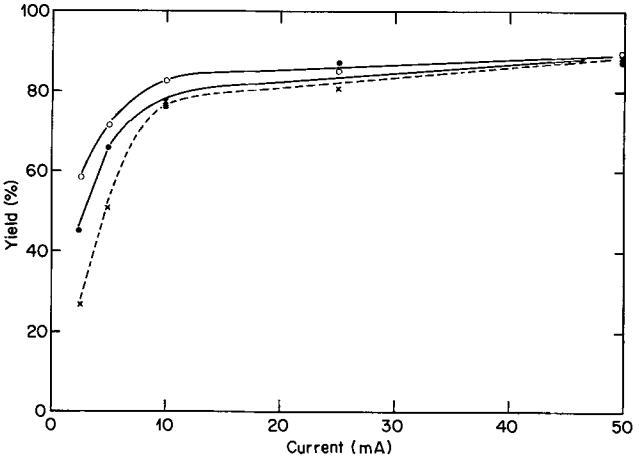

Fig. 3. Effect of current on the yield of deposition of Na_xWO_3 in a 20 m/o WO_3 melt. Total charge consumed 7.5 meq. First series of depositions in a fresh melt at 786°C (X), followed by depositions at 735°C (○), and 786°C (●).

In a 20 m/o WO_3 melt, the deposition efficiency depends on both the applied current and the melt temperature (Fig. 3) in a manner similar to that described for a 50 m/o WO_3 melt.

Effect of temperature on composition of deposit.—The deposition efficiency decreases with increasing temperature from the melting point to some higher temperature where the amount of bronze deposited suddenly decreases to zero and tungsten metal is recovered instead. The transition temperature between the deposition of Na_xWO_3 and metallic tungsten (or a mixture of W and Na_xWO_3) depends on the melt composition as shown in Fig. 4. Two phase domains can be distinguished: one at high temperatures where tungsten is the major constituent of the deposit, and the other at low temperatures where sodium tungsten

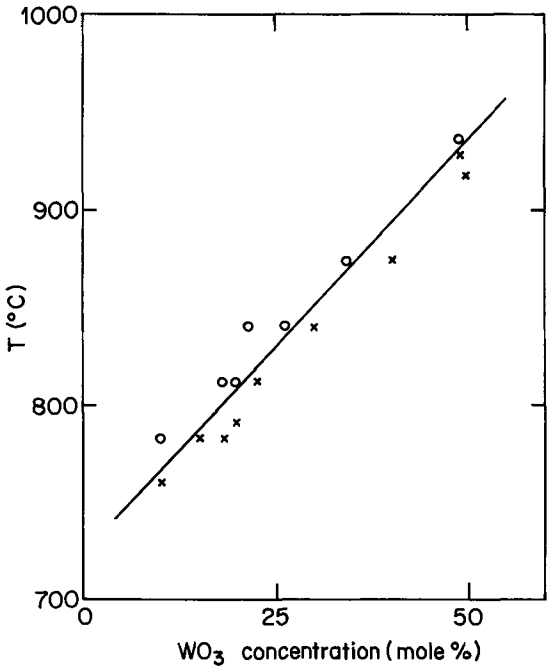

Fig. 4. Composition of the cathodic deposit as a function of the melt temperature and composition. X Na_xWO_3 deposit, ○ W (or mixture W + Na_xWO_3) deposit.

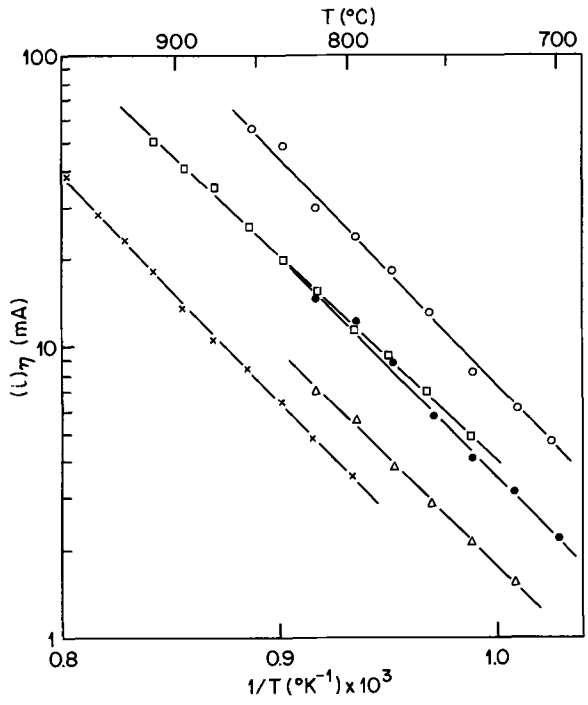

Fig. 5. Current at a constant potential vs. temperature relationship in a 20 m/o WO_3 melt at $\eta = -8.4$ mV (△), $\eta = -14.4$ mV (●), $\eta = -31.2$ mV (○), in a 40 m/o WO_3 melt at $\eta = -20.0$ mV (□), and in a 50 m/o WO_3 melt at $\eta = -10.0$ mV (X).

bronze is deposited. The transition temperature is well defined, *i.e.*, it ranges over only about 10°C. The results in Fig. 4 confirm those recently given in a more qualitative way by Shanks (6).

Within the bronze deposition domain the x-value does not depend significantly on the deposition temperature.

Heat of activation.—The bronze deposition reaction proceeds very fast and, consequently, the exchange current density, i_o, is difficult to measure since the Tafel region is inaccessible. For this reason, the deposition current at a constant over-potential has been taken as a measure of the deposition rate. These experiments were performed on a bronze crystal grown in the same melt for 15 hr at 10 mA. No significant growth of the bronze electrode occurred during these experiments. The maximum temperature at which the measurements can be performed is limited by the dissolution rate of the bronze reference electrode. In Table IV, it is shown that in a 20 m/o WO_3 melt a 65% weight loss is measured after 20 min at 863°C. This duration is roughly the stabilization period of the furnace to reach a constant temperature when changed from one temperature to another. The results reported in Fig. 5 for 20, 40, and 50 m/o WO_3 melts show no change of the slope $\partial \log (i)_{\eta=\text{const.}} \partial/(1/T)$ at, or near, the transition temperature. The activation energy varies between 32 and 35 kcal/mole between 700° and 900°C.

Growth of Na_xWO_3 Containing Platinum

Table II summarizes the platinum concentration, x-value, crystal faces formed, and yields obtained for different conditions of growth. The platinum content of Na_xWO_3 increases with increasing melt temperature, although there are some exceptions (crystals No. 55 and 104). High current densities also favor high platinum concentrations in the bronze.

The amount of platinum dissolved was determined from the weight loss of the anode during the deposition and compared to the amount of platinum incorporated in Na_xWO_3 during the same experiment. The ratio of deposited platinum to dissolved platinum is very low, *i.e.*, about 0.02 (Table III). It follows that the amount of platinum in the melt increases with the number of crystals prepared. After about 10 depositions, the melt contains about 1.5g of platinum [0.2 w/o (weight per cent)]. The observation and analysis of the solidified melt after such a series of depositions show the presence of metallic platinum segregated at the bottom of the crucible.

The coulombic efficiency of the deposition decreases with increasing temperature (Table II), as would be

Table II. Growth of platinum containing sodium tungsten bronzes (gold cathode, platinum anode)

Crystal No.	Melt composition (m/o WO_3)	Temp (°C)	Average current (mA)	Composition x in Na_xWO_3	Crystal faces formed	Pt content (ppm)	Yield (%)
51	47	786	20.9	0.58	110	100	86
52	47	786	20.9	—	110	120	82
54	46	786	19.6	0.61	110	200	75
55	46	830	21.3	—	110	165	74
56	45	830	23.3	—	110	500	55
57	45	878	59.6	0.63	110	1200	50
59	42	878	61.2	—	110	—	33
60	42	878	69.0	0.66	110	1450	13
98	18	750	18.5	0.84	100	80	87
99	18	786	13.9	0.84	100	210	85
101	23	812	13.5	0.81	100	200	68
104	30	840	23.3	0.77	100	120	70
106	40	875	24.5	0.68	100	250	43
107	42	875	16.4	0.67	100	270	46
108	41	745	23.6	0.69	100	74	85
8*	36	800	8.6	0.68	100	255	25

* In a Pt crucible with two gold electrodes.

Table III. Comparison of dissolved and deposited platinum during growth of Na_xWO_3 containing platinum

Crystal No.	Platinum content in bronze (ppm)	Dissolved Pt (mg)	Deposited Pt (mg)	Ratio $Pt_{dep.}/Pt_{dis.}$
51	100	31.3	0.63	0.020
52	120	54.6	0.72	0.013
54	200	79.0	3.0	0.038
55	165	66.8	0.86	0.013
56	500	131.3	4.35	0.033
59	—	210.5	≈10	≈0.050
60	1450	496.7	12.5	0.025

expected from the results obtained without platinum incorporation. In the presence of platinum, however, there is an additional effect presumably associated with the platinum. Under similar experimental conditions the yield decreases sharply from one sample to the next (crystals No. 57-60 in Table II). It is believed that the increasing amount of platinum in the melt inhibits the deposition of the bronze.

The presence of platinum in the range from 1 to 1450 ppm has no significant effect on either the x-value in Na_xWO_3 (Tables I and II) or the crystal habit of the bronzes.

Discussion

Efficiency of deposition.—The current efficiency of the bronze deposition depends both on the applied current and the melt temperature. The shape of the yield *vs.* current curves can be explained by the occurrence of a side reaction, the most likely being the occurrence of simultaneous chemical dissolution of the bronze. Because of the high yield in the low temperature range and the continuous increase in efficiency with increased current, the bronze deposition reaction is the predominant one. The secondary process, *i.e.*, the reaction that lowers the yield, increases with both temperature and time of contact of the crystal with the melt (lower applied current).

The open-circuit dissolution of a bronze crystal in the melt in which it has been grown occurs at a rate which depends on the temperature (Table IV). In the range of temperatures between 750° and 790°C, a 10% weight loss is recorded after 19 hr (Table IV). Under similar experimental conditions the deposition efficiency is about 90 or 80% for a 50 or 20 m/o WO_3 melt, respectively (Fig. 2-3). The agreement between the efficiency decrease and the weight loss is reasonable. Thus simultaneous chemical dissolution explains satisfactorily the dependence of the deposition efficiency on temperature and current.

It is difficult to explain why a bronze deposited at high temperature in a freshly prepared melt is deposited with a much lower yield than a bronze at the same temperature in a melt previously used at a lower temperature (Fig. 2). One possibility is that the tetramer of WO_3, which has been shown to be the reducible species (12, 13), forms at the lower temperature.

Effect of temperature on composition of deposit.—At temperatures lower than the transition temperature defined in Fig. 4, the dissolution reaction is most likely the reverse of the deposition reaction. At temperatures higher than the transition temperature the reaction product is metallic tungsten (or a mixture of W and Na_xWO_3). Van Liempt (21) has proposed that the tungsten originates from the decomposition of sodium tungsten bronze according to the reaction

Table IV. Open-circuit dissolution of bronzes

Melt composition (m/o WO_3)	Temp (°C)	Dissolution time (hr)	Initial bronze weight (g)	Weight loss (%)
20	766	19.00	2.669	10.7
20	816	7.00	4.455	11.1
20	863	0.33	4.367	64.8
50	786	19.00	4.346	10.2
50	927	6.37	3.903	32.1
50	927	16.00	≈2.5	100

$$6Na_xWO_3 \rightleftarrows xW + 3xNa_2WO_4 + (6 - 4x)WO_3 \quad [3]$$

The first product of electrolysis is the sodium tungsten bronze, irrespective of the melt temperature. When the temperature is higher than the transition temperature the bronze decomposition, (reaction [3]) gives rise to a metallic tungsten deposit.

The activation energy measurements reported in Fig. 5 support the above reaction for the tungsten deposition. The slope of the $(i)_{\eta=const.}$ *vs.* T^{-1} plot shows no break at, or near, the transition temperature, indicating that the rate determining step for the deposition of Na_xWO_3 is the same as that for the deposition of W. Therefore, the deposition of Na_xWO_3 is a prerequisite for the W deposition.

The reversibility of reaction [3] was tested by putting a bronze crystal, grown at a temperature lower than the transition temperature in the melt at a temperature higher than that of the transition. The bronze crystal dissolved completely after a short time (Table IV) leaving a gray powder at the bottom of the alumina crucible. The analysis of the remaining powder after washing the frozen melt shows that it contained metallic tungsten (along with Na_xWO_3). The gray powder left at the bottom of the crucible after dissolution of the bronze at high temperature becomes gold colored on decreasing the melt temperature.

Codeposition of platinum.—The following observations tend to indicate a nonelectrochemical process for the platinum codeposition but do not constitute final evidence: (*i*) platinum is always present in a pure bronze at the ppm level, even in a carefully pre-electrolyzed melt; (*ii*) the amount of platinum incorporated in the bronze is small compared to the amount of platinum dissolved (or eroded) from the anode and does not depend significantly on the temperature (Table III).

McHardy (18) has recently proposed an electrophoretic mechanism on the basis that most of the platinum occurs in the alumina inclusion particles. He suggests that a colloidal alumina particle eroded by the melt from the crucible acquires a negative charge by the equilibrium

$$Al_2O_3 + WO_4^{-2} \rightleftharpoons Al_2O_4^{-2} + WO_3 \quad [4]$$

and, hence, attracts cations to its surface. Collisions among colloid particles will bring about coagulation and, eventually, the particles will be large enough to settle out. Particles that settle out onto the growing crystal will be discharged, and the platinum ions will be reduced to the metal. If this hypothesis is correct, the final concentration of platinum in the crystal will depend on the concentration both of platinum ions and of colloid particles in the melt.

Following this argument, a crystal deposited in a melt which has never been in contact with alumina should not contain any significant amount of platinum. On the contrary, crystal No. 8 (Table II) grown in a freshly prepared melt contained in a platinum crucible using two gold wires as cathode and anode exhibits 255 ppm Pt. Moreover, the amount of alumina removed from the crucible by etching would be expected to increase with the aging of the crucible. Hence, if alumina takes part in the platinum incorporation, as suggested by McHardy, a bronze deposited in an alumina crucible used for a long time should be richer in platinum than a sample prepared in a new alumina crucible, provided that the platinum concentration in the melt is the same in both experiments. Contrary to this expectation, crystals No. 98 and 108 (Table II) deposited at roughly the same temperature and in the same melt contained in an alumina crucible incorporate the same amount of platinum. It is therefore unlikely that the colloidal reaction advanced by McHardy is the only operative process for the platinum codeposition.

The electrophoresis explanation may be a valid one when both the alumina and the platinum contents are high. When one of these concentrations is low, or zero, another mechanism is obviously involved. At high platinum concentrations a purely electrolytic

deposition process cannot be ruled out. However, the measurements reported in the present study (Table III) suggest another explanation. The amount of platinum deposited is low compared to the amount dissolved or eroded (Table III). At room temperature, the platinum contained in the melt has been shown to be present as a metallic deposit. One may assume that platinum (and not platinum ion) is also present in the melt at its high operating temperature. Metallic platinum may come from the reduction of the ionic platinum (arising from oxidation of the anode) at the cathode. The reduction may occur at a high current density which tends to deposit a powder that does not adhere to the cathode but drops down through the melt as colloidal particles. Another possibility is the mechanical erosion of the anode during the oxygen evolution reaction.

If colloidal platinum particles are present in the melt, their codeposition may occur through: (*i*) electrophoretic transport arising from the high potential gradient in the diffusion layer, (*ii*) transportation of the particle as a complex ion to the cathode layer, and (*iii*) mechanical trapping.

Codeposition of gold was also shown to arise during the growth of bronze, especially when a gold anode was used A mechanism similar to that occurring for the platinum incorporation is likely to be operative in the case of the gold codeposition.

In a platinum-containing melt, the current efficiency decreases sharply with the amount of platinum dissolved from the anode. One possible explanation for the decrease in the yield in the presence of platinum is the occurrence of reduction of platinum ions at the cathode giving rise to colloidal platinum along with the platinum incorporation in the bronze. This would not, however, account for the entire current consumed in the side-reaction (87% of the total current for crystal No. 60). Another likely explanation is the formation of a polymer between platinum and tungsten oxide, which would undergo preferential charge transfer. If this polymeric species does not deposit, little or no bronze is formed, but the species can presumably undergo further charge transfer, and very much more charge would then be required to reduce it to metal. A similar explanation has been proposed by Fredlein and Damjanovic (15) to account for the complete inhibition of bronze formation by the addition of 0.1% of a rhenium oxide to the Na_2WO_4/WO_3 melt.

Acknowledgments

Grateful acknowledgment is made to Dr. A. K. Vijh for numerous critical discussions and suggestions throughout the course of this work. The author is indebted to Drs. G. Bégin, G. Dionne, E. Dancy, G. Bélanger, and P. Lenfant for helpful discussions. The author thanks Mr. R. Bellemare for his assistance in the experimental work and Mr. R. Dubuc for the x-ray analysis. Special acknowledgments are due to Dr. D. S. Russell, Chemistry Division, National Research Council, Ottawa, for the careful determination of platinum and the authorization to publish the results.

Manuscript submitted Dec. 20, 1972; revised manuscript received May 7, 1973.

Any discussion of this paper will appear in a Discussion Section to be published in the June 1974 JOURNAL.

REFERENCES

1. P. Hagenmuller, in "Progress Solid State Chemistry," Vol. 5, p. 71, H. Reiss, Editor, Pergamon Press, New York (1971).
2. E. Banks and A. Wold, in "Preparative Inorganic Reactions," Vol. 4, p. 237, W. L. Jolly, Editor, Interscience Publishers Inc., New York (1968).
3. P. G. Dickens and M. S. Whittingham, *Quart. Rev.*, **22**, 30 (1968).
4. A. S. Ribnick, B. Post, and E. Banks, in "Advances in Chemistry," No. 39, p. 246, American Chemical Society, Washington, D.C. (1963).
5. M. F. Straumanis, *J. Am. Chem. Soc.*, **71**, 679 (1949).
6. M. R. Shanks, *J. Crystal Growth*, **13-14**, 433 (1972).
7. B. W. Brown and E. Banks, *J. Am. Chem. Soc.*, **76**, 963 (1954).
8. R. W. Vest, M. Griffel, and J. F. Smith, *J. Chem. Phys.*, **28**, 293 (1958).
9. L. D. Ellerbeck, H. R. Shanks, P. H. Sidles, and G. C. Danielson, *ibid.*, **35**, 298 (1961).
10. P. F. Weller, B. E. Taylor, and R. L. Mohler, *Mater. Res. Bull.*, **5**, 465 (1970).
11. C. T. Hauck, A. Wold, and E. Banks, *Inorg. Synth.*, **12**, 153 (1970).
12. E. Banks, C. W. Fleischmann, and L. Meites, *J. Solid State Chem.*, **1**, 372 (1970).
13. J. Vallier, *J. Chim. Phys.*, **63**, 1530 (1966).
14. L. Meites, E. Banks, and C. W. Fleischmann, *Anal. Chem.*, **44**, 1133 (1972).
15. R. A. Fredlein and A. Damjanovic, *J. Solid State Chem.*, **4**, 94 (1972).
16. D. B. Sepa, A. Damjanovic, and J. O'M. Bockris, *Electrochim. Acta*, **12**, 746 (1967); A. Damjanovic, D. Sepa, and J. O'M. Bockris, *J. Res. Inst. Catalysis, Hokkaido Univ.*, **16**, 1 (1968); B. Broyde, *J. Catalysis*, **10**, 13 (1968); J. H. Fishman, J. F. Henry, and S. Tessore, *Electrochim. Acta*, **14**, 1314 (1969); J. O'M. Bockris, A. Damjanovic, and J. McHardy, Proc. 3rd Int. Symp. Fuel Cells, Brussels, Belgium, June 16-20, 1969, Press Acad. Européennes, Brussels, p. 15 (1969).
17. R. A. Fredlein and J. McHardy, 24th Proc. Power Sources Symp. P.S.C. Pub. Committee, Red Bank, N. J., p. 175 (1970).
18. J. McHardy, Ph.D. Thesis, University of Pennsylvania, (1972), see also, J. McHardy and J. O'M. Bockris, *This Journal*, **120**, 53, 61 (1973).
19. K. B. Morris and P. L. Robinson, *J. Chem. Eng. Data*, **9**, 444 (1964).
20. A. Magneli and B. Blomberg, *Acta Chem. Scand.*, **5**, 372 (1951).
21. J. A. M. van Liempt, *Z. Elektrochem.*, **31**, 249 (1925).

The Drum-activated Graphite Ribbon Electrode

John T. Stock* and Joseph P. Sapio

Department of Chemistry, University of Connecticut, Storrs, Connecticut 06268

ABSTRACT

Film formation by products in oxidative electrosyntheses, with consequent cessation of current, can sometimes be alleviated by mechanical reactivation of the anode. A composite anode that consists of a graphite ribbon in contact with a rapidly rotating perforated graphite drum is described. This provides both high flow rate and continuous reactivation.

Anodic organic electrosyntheses often require quite long periods of electrolyses. Possible causes are low current efficiency, deactivation of the anode by products or by-products, or inefficient design or operation of the cell. The utility of graphite cloth electrodes in coulometry and in preparative-scale electrolyses has recently been pointed out (1). Bobbitt *et al.* (2-4) have made extensive use of graphite cloth or graphite felt anodes in their studies of the preparative-scale oxidative coupling of certain heterocyclic phenols. As in voltammetric studies (5-7), the attempted anodic electrolysis of aqueous alkaline solutions of these compounds sometimes results in a rapid fall in current due to deactivation of the anode. On the microscale associated with voltammetry, this effect can often be prevented or minimized by intermittent electrolysis (8) or by continuous reactivation of the electrode by a rotating drum (6, 7). Attempts were therefore made to extend the drum method to the preparative scale.

The essentials of the apparatus are shown in Fig. 1, (a) and (b). Ribbon A (see Fig. 1), which is of graphite cloth,[1] is 2.5 cm wide and approximately 10 cm long. One end carries polyethylene stretcher B (see Fig. 1), which is cut from the spine of a transparent report cover.[2] This stretcher is sprung over one end of the ribbon and heat-sealed to it. The tension thread, C, of nylon radio dial cord, is attached to the middle of the stretcher, passes up the glass guide tube, D, and is gripped in a binding post at the end of the brass strip spring, E. After passing around the graphite drum, F, the ribbon terminates at the post, G. This is a 12 mm diameter hardwood rod which has received several coats of waterproof varnish after having been grooved longitudinally. The free end of the ribbon is gripped by the glass rod, H, which lies in the groove and is secured by two collars of rubber tubing, as shown enlarged in Fig. 1 (c). Electrical connection to the ribbon is made by a length of 26 gauge platinum wire, one end of which runs along the bottom of the groove beneath the ribbon.

A sewing machine motor provided with a controller drives the plastic-coated steel shaft, I, at an essentially constant speed. This shaft carries the drum, F, but is insulated from it. Four rows of twelve 1.5 mm diameter holes, are drilled in the periphery of the drum, as shown in the horizontal cross section in Fig. 1 (d). These holes terminate in the 10 mm diameter central hole that is drilled from the underside of the drum. Rotation of the drum causes the cell solution to be drawn into this central hole, thrown out through the radial holes, and thus forced through the interstices of the ribbon.

The electrolyses with this drum-activated graphite ribbon electrode (DAGRE) were carried out with 250 ml portions of solution. For runs with $K_4Fe(CN)_6$, the platinum foil counterelectrode was isolated in a tube, J, the lower end of which carried a fritted-glass septum. In other runs, the counterelectrode was simply immersed in the cell solution. Power was supplied by a Beckman Electroscan 30 that was operated in the potentiostat mode. An asbestos-thread type junction, K, located close to the ribbon as shown in Fig. 1 and leading to a saturated calomel electrode (SCE), enabled the potential of the ribbon to be controlled.

Preliminary experiments with $K_4Fe(CN)_6$ in 0.01*M* $HClO_4$ showed that the current, which increased with drum speed, was both large and not very sensitive to drum speed when this reached approximately 1400 rpm. All of the subsequent runs were made at this rate of rotation. Figure 2 compares the rate of oxidation of $K_4Fe(CN)_6$ under these conditions with the considerably lower rate observed in a similar run in which the drum was stationary but the solution was vigorously agitated by a magnetic stirrer.

The high rotation rate results in slight abrasion of drum and ribbon, so that the solution may become gray during the run. However, the useful running life of a ribbon is in excess of 50 hr. This small but definite wear provides a degree of surface renewal, and hence

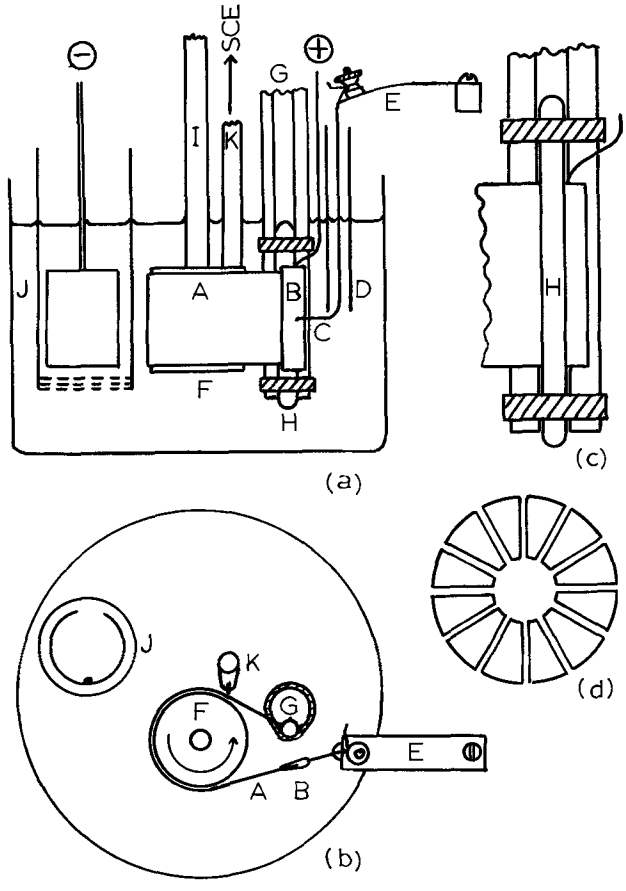

Fig. 1. Drum-activated graphite ribbon electrode. (a) Side view; (b) plan view; (c) detail of ribbon post; (d) horizontal cross section of drum.

* Electrochemical Society Active Member.

Key words: electro-oxidation, electrosynthesis, graphite electrode, electrode activation, ultrasonics.

[1] Type WCB, Carbon Products Division, Union Carbide Corporation, New York, N.Y. 10017.

[2] E-Z Slide, Cook's Inc., Blackwood, N.J. 08012; Kleer-Vu Industries, Inc., New York, N.Y. 10016.

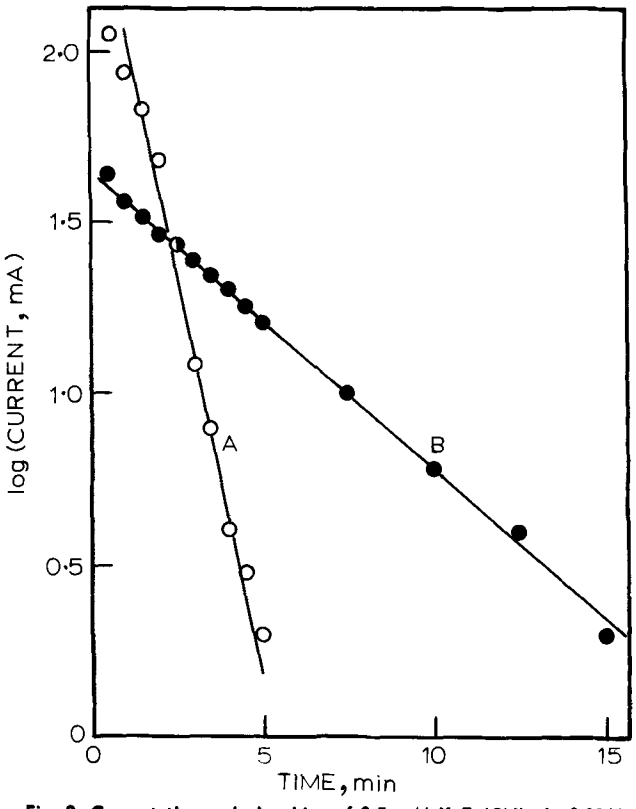

Fig. 2. Current-time relationships of 0.5 mM $K_4Fe(CN)_6$ in 0.01M $HClO_4$ at 0.06V vs. SCE. Curve A, rotating drum; curve B, drum stationary but solution vigorously stirred.

of electrode reactivation. The current-time curves, shown in Fig. 3 and obtained with the strongly deactivating system tyramine in alkaline solution (7), illustrate this effect. These curves were obtained under deliberately restricted conditions where only the rubbing portions of the ribbon and drum were exposed to the solution. The outer surface of the ribbon was heat-sealed to a polyethylene sheet and the top and bottom of the drum were varnished.

A series of preparative oxidative couplings of 0.5g portions of corypalline (1,2,3,4-tetrahydro-7-hydroxy-6-methoxy-isoquinoline) in 0.1*M* borax gave results similar to those reported by Kirkbright *et al.* (5), who used a platinum gauze anode. Although the anode-deactivating properties of corypalline are quite mild, those of isocorypalline (1,2,3,4-tetrahydro-6-hydroxy-7-methoxy-isoquinoline) are pronounced (7). In fact, when the oxidation of an aqueous alkaline solution of isocorypalline was attempted at a platinum gauze anode, the current fell rapidly to zero and no products could be detected (2). Electrolysis at a DAGRE potential of +0.35V of 0.5g of isocorypalline in 0.1*M* borax gave a 6% (actual) yield of the pure oxygen-linked coupling product [compound 18, see Ref. (2)]. The current fell from approximately 20 to 5 mA during the 5 hr run, after which approximately 30% of the starting material was recovered. A DAGRE with a 7 cm diameter drum is now being constructed, so that larger quantities can be subjected to electrolysis.

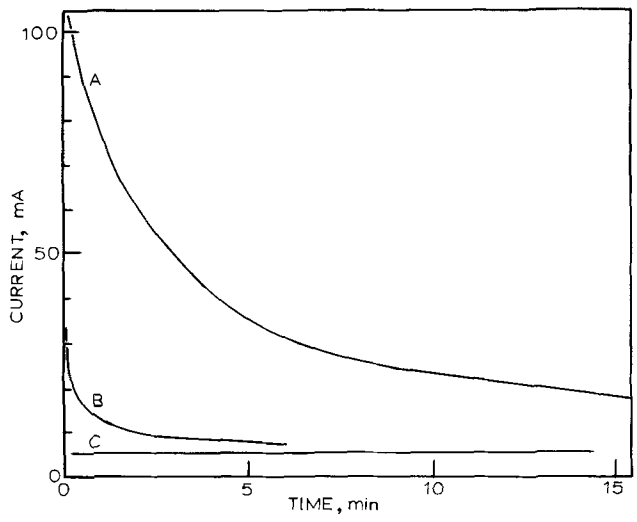

Fig. 3. Current-time relationships of 5.0 mM tyramine in 0.1M $NaHCO_3$ at 0.35V vs. SCE. Curve A, ribbon under tension; curve B, ribbon slack; curve C, residual current only.

Preliminary experiments with solutions of $K_4Fe(CN)_6$ and of corypalline have shown that the quite large electrolysis currents can be further augmented by mounting the cell in the bath of an 80-kHz ultrasonic generator. In view of a report that the anodic oxidation of certain inorganic ions such as iron(II) is more rapid at a frequency of 25 kHz than at higher or lower frequencies (9), the generator is now being rebuilt in variable frequency form.

Acknowledgments

We thank Professor J. M. Bobbitt of this Department both for supplies of corypalline and isocorypalline and for many helpful suggestions. This work was carried out with the partial support of the National Science Foundation (Grant No. GP-30574X).

Manuscript received Feb. 16, 1973.

Any discussion of this paper will appear in a Discussion Section to be published in the June 1974 JOURNAL.

REFERENCES

1. R. Hand, A. K. Carpenter, C. J. O'Brien, and R. F. Nelson, *This Journal*, **119**, 74 (1972).
2. J. M. Bobbitt, H. Yagi, S. Shibuya, and J. T. Stock, *J. Org. Chem.*, **36**, 3006 (1971).
3. J. M. Bobbitt, I. Noguchi, H. Yagi, and K. H. Weisgraber, *J. Am. Chem. Soc.*, **93**, 3551 (1971).
4. J. M. Bobbitt and R. C. Hallcher, *Chem. Commun.*, **1971**, 543.
5. G. F. Kirkbright, J. T. Stock, R. D. Pugliese, and J. M. Bobbitt, *This Journal*, **116**, 219 (1969).
6. J. T. Stock, *Microchem. J.*, **15**, 564 (1970).
7. J. T. Stock, *Anal. Chem.*, **43**, 289 (1971).
8. J. T. Stock and R. D. Pugliese, *ibid.*, **41**, 198 (1969).
9. E. Kowalska and J. Mizera, *Ultrasonics*, **9**, 81 (1971).

Reduction of Crotonic Acid with Hydrogen on a Slurry Electrode

D. N. Baria[1] and Hugh M. Hulburt*

Department of Chemical Engineering, Northwestern University, Evanston, Illinois 60201

ABSTRACT

A slurry electrode system consisting of a suspension of metal or a supported metal powder in an electrolyte in contact with a gold foil electrode was studied as a hydrogen electrode for the reduction of crotonic acid in a supporting electrolyte of sodium p-toluene sulfonate. Current-voltage curves and current efficiency were studied. Effects of suspension concentration, crotonic acid concentration, butyric acid concentration, pH, and temperature were studied for platinum black and palladium-on carbon slurries. The results are consistent with the view that the potential-determining reaction is the discharge of hydrogen atoms adsorbed on the catalyst. Olefin competes for adsorbed hydrogen and this modifies the observed potential. Very low anodic limiting currents were observed in the presence of olefin, suggesting that it is strongly adsorbed on the anodic hydrogen electrode. The following electrokinetic expressions were established for cathodic currents: (*i*) for 5% Pd on C

$$\log i = \log k + 0.42 \log C_{H+} - 0.013 \log C_R - 0.49 \log C_{RH_2} + 0.23 \log W_{cat} - 0.22\, EF/RT$$

and (*ii*) for Pt black

$$\log i = \log k + 0.52 \log C_{H+} + 0.077 \log C_R + 0.028 \log C_{RH_2} + 0.45 \log W_{cat} - 0.30\, EF/RT$$

where i is the current, k is a constant, C_{H+} is hydrogen ion concentration, C_R is crotonic acid concentration, C_{RH_2} is butyric acid concentration, W_{cat} is catalyst concentration, E is the electrode potential, F is Faraday's constant, R is universal gas constant, and T is the absolute temperature.

A slurry electrode system consists of a suspension of a metal or a supported metal powder catalyst in an electrolyte in contact with an inert collector electrode. It has a larger surface area on which the electrode reaction can take place than plain plate-type electrodes or porous electrodes made of the same material.

Muller and Schwabe (1, 2) first measured the potential of suspended metallic powders in an electrolyte. Later Sokol'skii and Druz (3, 4) showed that it was possible to transfer the potential of a powdered metal catalyst suspended in an electrolyte onto a stationary electrode. Boutry, Bloch, and Balaceau (5) showed that a catalyst powder, suspended in an electrolyte in the presence of a conducting collector electrode, had all the properties and uses of a classical compact electrode.

Gerischer and Held (6, 7) showed that it was possible to draw considerably higher currents from a suspension of catalyst when hydrogen was oxidized or oxygen reduced. They followed the transport of current by individual catalyst particles by means of an oscillograph. Schwabe and Satsko (8) found that the current drawn by a suspension of platinized carbon was independent of catalyst concentration, whereas the currents obtained with Raney nickel and platinum black were appreciably greater and proportional to the catalyst concentration.

Fasman, Sokol'skii, and Shurov (9) studied polarization curves of moving powder electrodes by circulating the catalyst suspension through a polarized nickel screen. They determined the quantitative relations between catalyst potential and the collector electrode potential using the concepts of equivalent circuits. Lazorenko and Ushakov (10) derived relationships between the current drawn and the applied potential for slurry electrodes and showed that they behaved as normal compact electrodes with increased exchange current. Eyring (11) studied the effect of different catalysts, catalyst concentrations, and the effect of agitation on the polarization curves for the oxidation of hydrogen on slurry electrodes. He attempted the reduction of benzaldehyde and ethylene on slurry electrodes. Beck (12) studied the hydrogenation of substances with a triple bond on slurry electrodes.

The aim of the present work was to study the behavior of the slurry electrode for the electrochemical reduction of crotonic acid and to analyze the data obtained from it by the conventional steady-state methods known for compact electrodes. An over-all empirical equation was obtained for the current in terms of concentrations, pH, and temperature and potential for platinum black and 5% palladium on carbon catalyst powders using steady-state methods. The reaction mixture was analyzed to determine the products of the reaction and to obtain the coulombic efficiency.

Crotonic acid was chosen because it has an olefinic double bond which can easily be reduced. Also it is soluble in water and so presents no problems in preparing aqueous solutions of crotonic acid using sodium p-toluene sulfonate as supporting electrolyte.

Experimental

The electrolytic cell, shown in Fig. 1, consisted of a 300 ml glass round bottom flask, called the measuring or working electrode compartment, A, into which the catalyst and the electrolyte were charged. The measuring or the working electrode, C, was a smooth 24 carat gold strip, 8.9 by 1.3 cm, with a thickness of 0.025 cm. It was formed into a circle 2.5 cm in diameter such that the ends of the strip were 0.5 cm apart. The glass stirrer, E, was concentric with the circular measuring electrode. The stirrer rod, D, and the glass bearing, F, were ground to a precision fit. The counter or the opposing electrode, I, was a perforated bright platinum strip, 1.3 cm square and 0.013 cm thick, placed in the counterelectrode compartment, G, and separated from the measuring electrode compartment by a sintered glass disk, H. Gas could be bubbled from the bottom of the cell through a sintered glass sparger, B. The reference electrode was a Hg/HgO electrode. The capillary tip of the reference electrode, J, was kept at a distance of about 0.5 cm from the measuring electrode. The cell was kept at a constant temperature, within ±0.1°C, in a water bath.

* Electrochemical Society Active Member.

[1] Present address: Ames Laboratory, USAEC, Iowa State University, Ames, Iowa 50010.

Key words: slurry electrode, electrocatalysis, hydrogenation, olefin reduction.

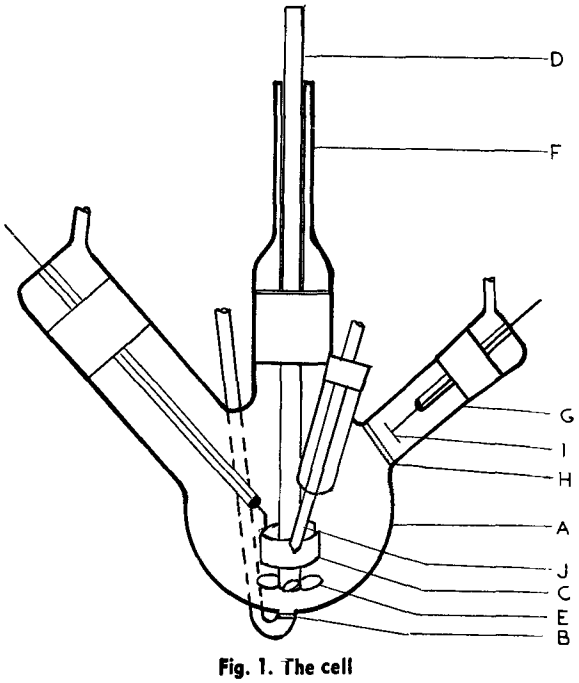

Fig. 1. The cell

Sodium p-toluene sulfonate and crotonic acid were purified by recrystallization before use. Three hundred milliliters of the electrolyte solution were prepared by dissolving 40g sodium p-toluene sulfonate, the required amounts of crotonic acid, butyric acid, and previously standardized sulfuric acid in deionized water. Sulfuric acid was used to control the pH of the solution. The cell was filled with the electrolyte and the required amount of the catalyst powder. The electrodes and the stirrer were put in place. The stirrer speed was always kept at a constant 1400 rpm, since earlier experiments had shown that higher speeds had no effect on the current drawn by the cell (13). The system was purged with nitrogen gas for 20 min to get rid of oxygen in the system. Then hydrogen gas was bubbled through the sparger at a flow rate of 2.5 ml/sec. It took about 15-20 min for the open-circuit potential to reach a steady value.

A Wenking Potentiostat 61TRS was used to measure and control the potential between the reference and measuring electrodes and to measure the current flowing between the counter and measuring electrodes. The current flowing in the cell attained a constant value in about 5 min for each potential setting.

The pH effect was studied by varying the pH of the electrolyte from 1.42 to 2.32; the crotonic acid effect was studied by varying crotonic acid concentration from 66.7 g/liter (0.7748M) to 6.667 g/liter (0.0775M); the butyric acid effect was studied by varying its concentration from 9.58 g/liter (0.1087M) to 23.95 g/liter (0.2718M); the catalyst concentration effect was studied by varying its concentration from 5.0 to 0.313 g/liter; and the temperature effect was studied by varying temperature from 20° to 40°C.

An Aerograph Hy-Fi Model A-600C gas chromatograph with an isothermal temperature controller and a hydrogen flame ionization detector was used to identify and determine the butyric acid formed.

Theory

Mechanism.—The probable course of the electrochemical reduction of crotonic acid is proposed as following the adsorption mechanism

$$S + H^+ + e \underset{k_{-1}}{\overset{k_1}{\rightleftarrows}} H \qquad \text{[step 1]}$$

$$H_{ads} \underset{k_{-2}}{\overset{k_2}{\rightleftarrows}} \tfrac{1}{2}H_2 + S \qquad \text{[step 2]}$$

$$S + R \underset{k_{-3}}{\overset{k_3}{\rightleftarrows}} R_{ads} \qquad \text{[step 3]}$$

$$R_{ads} + H_{ads} \underset{k_{-4}}{\overset{k_4}{\rightleftarrows}} RH_{ads} \qquad \text{[step 4]}$$

$$RH_{ads} + H_{ads} \underset{k_{-5}}{\overset{k_5}{\rightleftarrows}} RH_{2ads} \qquad \text{[step 5]}$$

$$RH_{2ads} \underset{k_{-6}}{\overset{k_6}{\rightleftarrows}} RH_2 + S \qquad \text{[step 6]}$$

where R stands for $CH_3CH = CHCOOH$, RH stands for $CH_3CH - CH_2COOH$, RH_2 stands for $CH_3CH_2CH_2COOH$, and S stands for surface of the catalyst.

Although the exact mode of action in the slurry electrode is not fully understood, it is probable that the hydrogen ions, dissolved hydrogen gas, and crotonic acid in the electrolyte solution are adsorbed on the catalyst surface. As the slurry is agitated, the catalyst particles come in contact with the collector electrode. At cathodic polarization, the collector electrode is more negative than the particles and when the particles touch the electrode, electrons are transferred from the electrode to the particles, which reduce the adsorbed hydrogen ions to hydrogen atoms. They can either desorb to form hydrogen gas or react with the adsorbed crotonic acid to form butyric acid. The catalyst particle moves away from the collector electrode. The butyric acid formed then desorbs from the catalyst surface into the solution. As room is made, more reactants are adsorbed on the particle and the cycle is repeated.

In preliminary work (13) it was established that butyric acid is formed both for cathodic and anodic polarization of the working electrode. It would seem unlikely that a direct electrochemical reduction of the double bond would occur under cathodic polarization. This possible alternative to step 1 has therefore been omitted. Moreover, addition of crotonic acid to a hydrogen saturated solution enhances the cathodic current but inhibits the anodic current, suggesting that adsorption of crotonic acid and the competitive reaction with adsorbed hydrogen dominate the direct electron transfer to the double bond.

If it is assumed that steps 4, 5, and 6 go in the forward direction only, making use of the steady-state approximation for the surface concentrations of the adsorbed species, one finds

$$\theta_{RH} = \frac{k_4}{k_5}\theta_R \qquad [1]$$

$$\theta_R = \frac{k_3 C_R(1 - \theta_H - \theta_{RH} - \theta_{RH_2})}{k_{-3} + k_3 C_R + k_4\theta_H} \qquad [2]$$

$$\theta_H = \frac{k_1 C_{H^+}(1 - \theta_R - \theta_{RH} - \theta_{RH_2})\, e^{-\beta\eta F/RT} + k_{-2}p_{H_2}^{1/2}(1 - \theta_R - \theta_{RH} - \theta_{RH_2})}{k_1 C_{H^+} e^{-\beta\eta F/RT} + k_{-1}e^{(1-\beta)\eta F/RT} + k_2 + k_{-2}p_{H_2}^{1/2} + k_4\theta_R + k_5\theta} \qquad [3]$$

where C_{H^+} = concentration of hydrogen ion; p_{H_2} = partial pressure of hydrogen gas; C_R = concentration of crotonic acid; θ_m = fractional coverage of the surface of the catalyst by species, m; and β = symmetry factor.

The current passing through the cell is proportional to the rate of step 1

$$i = k_{-1}\theta_H e^{(1-\beta)\eta F/RT} - k_1 C_{H^+}(1 - \theta_T)e^{-\beta\eta F/RT} \qquad [4]$$

where

$$\theta_T = \theta_H + \theta_R + \theta_{RH} + \theta_{RH_2}$$

At high cathodic overvoltage ($\eta \to -\infty$), Eq. [4] reduces to

$$i = -k_1 C_{H^+}(1 - \theta_T)e^{-\beta\eta F/RT} \qquad [5]$$

The fraction of bare surface, $(1 - \theta_T)$, is very small (nearly zero) at higher overvoltages. It should not vary much relative to the other fractional coverages and can be assumed to be constant. Under these conditions

$$\frac{\partial \ln i}{\partial \eta} = -\frac{\beta \mathbf{F}}{RT} \quad [6]$$

At high anodic overvoltages, the second term in Eq. [4] tends to zero. Using Eq. [3] and [4], one finds

$$i = k^2{}_{-1} \quad [7]$$

Equation [7] indicates that the current should reach a limiting value for high anodic overvoltages.

Over-all empirical equation.—The over-all cathodic reduction of crotonic acid can be represented by the following reaction

$$CH_3CH{=}CHCOOH + 2H^+ + 2e \rightarrow CH_3CH_2CH_2COOH$$

Using the concept of electrochemical reaction orders, the observed cathodic current can be expressed as

$$i_c = K_c C_R{}^{a_1} C_{H^+}{}^{b_1} C_{RH_2}{}^{d_1} \exp(-\beta \mathbf{F}E/RT) \quad [8]$$

Similarly for anodic polarization

$$i_a = K_a C_R{}^{a_2} C_{H^+}{}^{b_2} C_{RH_2}{}^{d_2} \exp((1 - \beta)\mathbf{F}E/RT) \quad [9]$$

At high cathodic overvoltages, the anodic partial current density may be neglected and the reaction orders can be obtained from the cathodic current-voltage curves.

$$\left.\frac{\partial \log |i|}{\partial \log C_R}\right|_{C_{H^+}, C_{RH_2}, E} = a_1 \quad [10]$$

$$\left.\frac{\partial \log |i|}{\partial \log C_{H^+}}\right|_{C_R, C_{RH_2}, E} = b_1 \quad [11]$$

$$\left.\frac{\partial \log |i|}{\partial \log C_{RH_2}}\right|_{C_{H^+}, C_R, E} = d_1 \quad [12]$$

The reaction orders for the anodic region can be obtained similarly from the anodic partial current density.

Effect of temperature and activation energy.—The effect of temperature on the current density is very similar to its effect on the rate of a heterogeneous chemical reaction. Hence the energy of activation can be studied by studying the effect of temperature on the current at constant potential.

The charge-transfer reaction associated with the cathodic current takes place in the direction

$$H^+ + e \rightarrow H_{ads} \quad [13]$$

The cathodic current density corresponding to this reaction is

$$i_c = n\mathbf{F}r_c \quad [14]$$

where n = number of electrons taking part and r_c = reaction rate for the cathodic process in the charge-transfer reaction.

According to Eq. [5], at constant potential, the rate constant k_1 must be proportional to the Boltzmann factor, $\exp(-E_c/RT)$, which expresses the apparent cathodic activation energy. Therefore

$$i_c = k_c C_{H^+}(1 - \theta_T) \exp(-E_c/RT) \quad [15]$$

where k_c = constant and E_c = apparent cathodic activation energy. Similarly, the anodic current density is given by

$$i_a = k_a \theta_H \exp(-E_a/RT) \quad [16]$$

where k_a = constant and E_a = apparent anodic activation energy. Therefore from Eq. [15] and [16] at constant potential and concentrations

$$\left.\frac{\partial \log i_c}{\partial (1/T)}\right|_{E,pH} = -\frac{E_c}{2.303R} \quad [17]$$

$$\left.\frac{\partial \log i_a}{\partial (1/T)}\right|_{E,pH} = -\frac{E_a}{2.303R} \quad [18]$$

The apparent activation energies E_c and E_a depend on the electrode potential E. These relationships have been derived by Vetter (14) and Delahay (15) for large excess of supporting electrolyte as

$$E_c = E^\circ{}_c + \beta \mathbf{F}E \quad [19]$$

$$E_a = E^\circ{}_a - (1 - \beta)\mathbf{F}E \quad [20]$$

Results

The current *vs.* potential plots for Pt black and Pd on C catalysts for varying pH, crotonic acid, butyric acid, and catalyst concentrations and temperature revealed a straight line relationship at high cathodic overvoltages, whereas they reached a rather low limiting current of about 3.5 mA for Pt black catalyst and 0.25-0.45 mA for Pd on C catalyst for low anodic overvoltages. Figures 2, 3, and 4 are typical current *vs.* potential graphs for Pt black slurry electrodes for varying pH, crotonic acid, and butyric acid concentrations, respectively. Figures 5 and 6 are typical current *vs.* potential graphs for Pd on C slurry electrodes for varying catalyst concentrations and temperature, respectively. All the data, except the ones at varying temperature, were taken at 20°C. The reaction orders with respect to pH, crotonic acid, and butyric acid were obtained using a linear least square fit of Eq. [8] and are tabulated in Table I for Pt black and for Pd on C catalysts. The activation energies calculated are shown in Table II. The coulombic efficiency based on butyric acid was calculated as 84.8 and 78.8% for two separate runs for Pd on C catalyst systems using gas chromatograph techniques for determining butyric acid.

Discussion

It was shown in preliminary experiments that the blank current, *i.e.*, the current when no catalyst is present, was less than 5% of the current obtained when

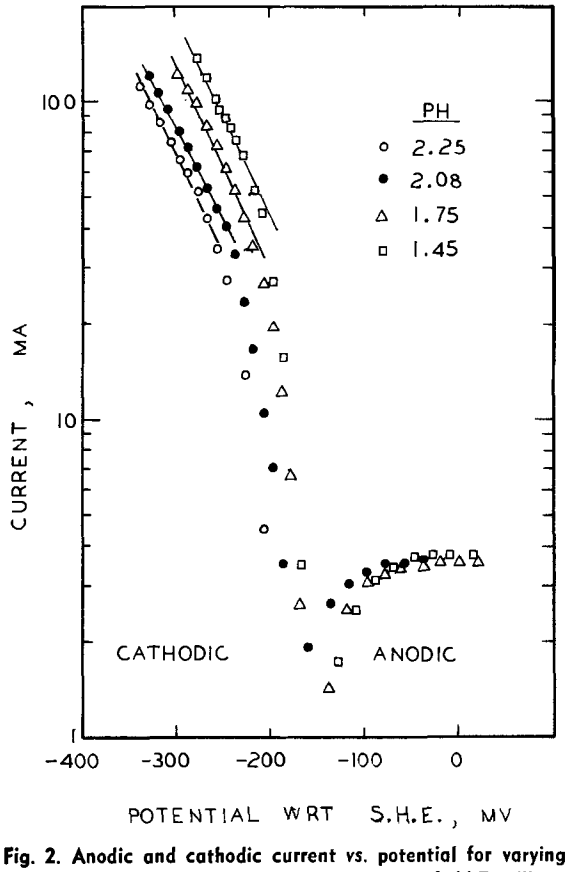

Fig. 2. Anodic and cathodic current *vs.* potential for varying pH values at constant crotonic acid concentration of 66.7 g/liter and Pt black catalyst concentration of 1.25 g/liter.

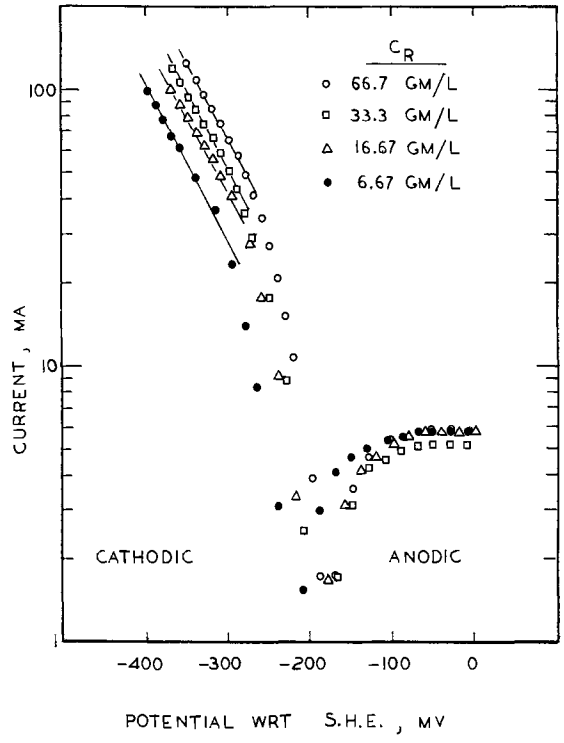

Fig. 3. Anodic and cathodic current vs. potential for varying crotonic acid concentrations at constant Pt black catalyst concentration of 1.25 g/liter.

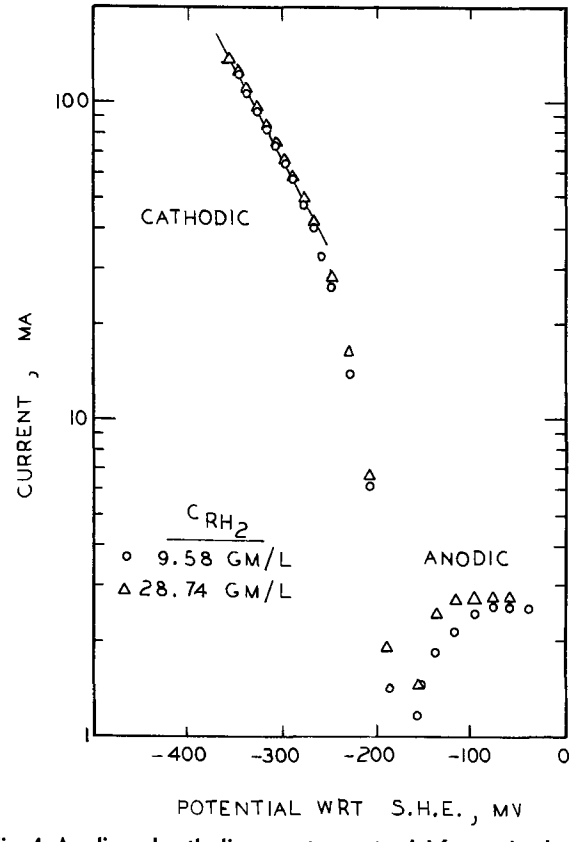

Fig. 4. Anodic and cathodic current vs. potential for varying butyric acid concentrations at constant crotonic acid concentration of 66.7 g/liter and Pt black catalyst concentration of 1.25 g/liter.

the catalyst was present. Hence this blank current was neglected and the observed current was taken as due to the slurry electrode alone. It was also shown that the pH effect was the same at two different crotonic acid concentration levels and it was hence assumed that each effect was independent of the other.

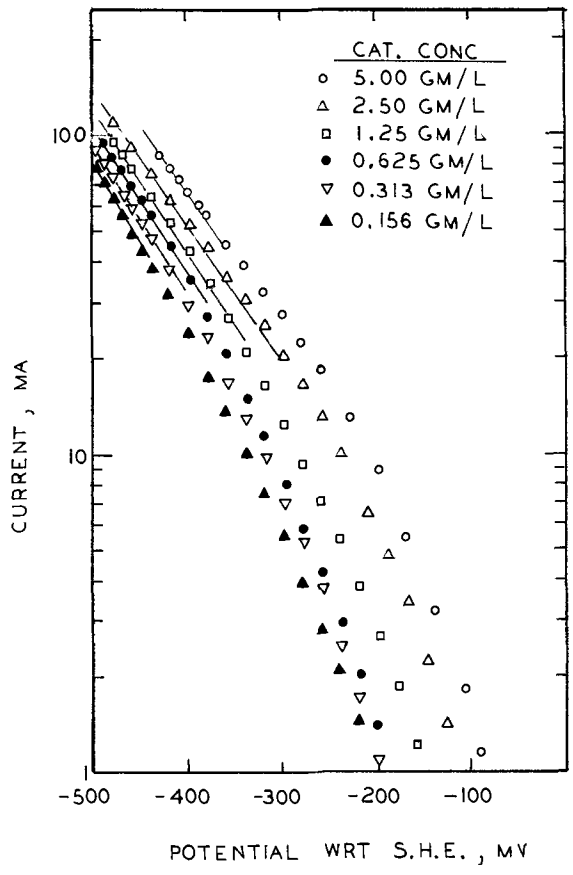

Fig. 5. Cathodic current vs. potential for varying concentrations of 5% Pd on C catalyst at constant crotonic acid concentration of 66.7 g/liter.

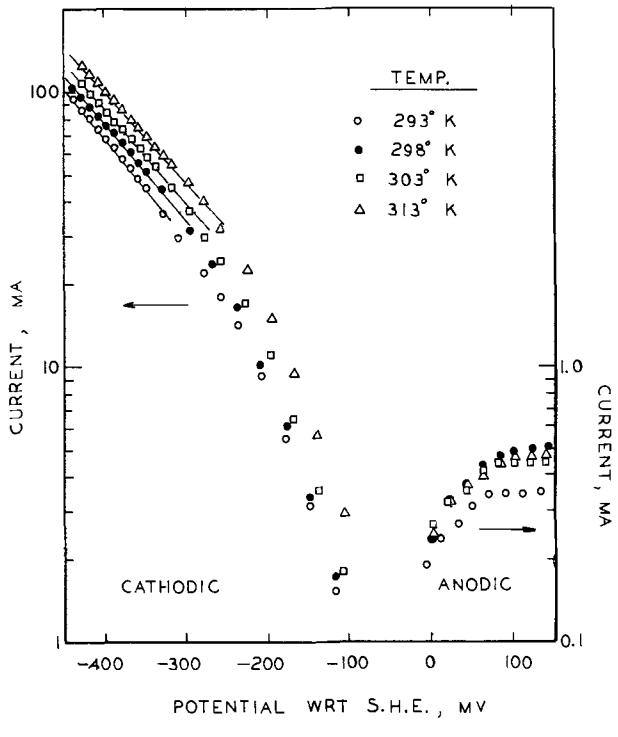

Fig. 6. Cathodic and anodic current vs. potential for varying temperatures at constant crotonic acid concentration of 66.7 g/liter and 5% Pd on C catalyst concentration of 5 g/liter.

Effect of pH.—The reaction order with respect to pH for both 5% Pd on C and Pt black catalysts was found to be around 0.5. This seems qualitatively correct, in that the higher the hydrogen ion concentration the

Table I. Kinetic parameters for crotonic acid reduction

Catalyst: 5% Pd on C

Effect	Cathodic		
	Reaction order	Tafel slope $\beta F/2.3\,RT$	β
Hydrogen ion (1st set)	0.389	0.00383	0.222
Hydrogen ion (2nd set)	0.443	0.00331	0.192
Crotonic acid	−0.013	0.00306	0.178
Butyric acid	−0.490	0.00370	0.215
Catalyst: Pt-Black			
Hydrogen ion	0.522	0.00577	0.335
Crotonic acid	0.077	0.00524	0.305
Butyric acid	0.028	0.00542	0.316

Table II. Temperature effects

Catalyst	Energy of activation	$\frac{d \log i_c}{d\,(1/T)}$	Tafel slope $\beta F/2.3\,RT$
5% Pd on C	−3.65 kcal/mole	−800	0.0026
Pt black	−3.82 kcal/mole	−850	0.0045

larger will be the rate of the charge-transfer step and hence the current, independent of the catalyst used.

Equation [5] can be rewritten in terms of the potential, E, by substituting in it $\eta = E - E^o$

$$i = -kC_{H^+}(1 - \theta_T)e^{-\beta FE/RT} \qquad [21]$$

where

$$k = k_1 e^{-\beta FE^o/RT} = \text{constant} \qquad [22]$$

Equation [21] predicts a reaction order of unity with respect to hydrogen ion concentration, whereas the observed order is around 0.5. A similar situation in the oxidation of hydrocarbons was explained by Bockris *et al.* (16, 17), who proposed that there is a penetration of hydrogen atoms into the platinum lattice of the electrode and that a charged double layer exists within that electrode due to dipoles generated. The observed potential difference is the potential difference between the bulk of the solution and the interior of the electrode and does not take into account the potential drop through the double layer due to the dioples within the electrode. Hence, to make use of Eq. [21], the potential difference, E, has to be replaced by the observed potential difference, E_S, plus the potential of zero charge, E_{PZC}

$$E = E_S + E_{PZC} \qquad [23]$$

Experimental observations by Bockris *et al.* (16, 17) have shown that PZC changes with pH on a clean Pt foil by RT/F per unit pH unit as expressed by the following equation

$$E_{PZC} = E^o_{PZC} + (RT/F) \ln a_{H^+} \qquad [24]$$

where E^o_{PZC} = constant and a_{H^+} = activity of hydrogen ion.

This equation was obtained experimentally for a highly purified Pt electrode and has no theoretical basis. Hence it is reasonable to multiply the pH effect by a factor α to take into consideration that the system being considered in this study had a different electrode and different electrolyte from that studied by Bockris *et al.*

Therefore we write

$$E_{PZC} = E^o_{PZC} + (\alpha RT/F) \ln a_{H^+} \qquad [25]$$

and Eq. [21] can be written as

$$i = -ka_{H^+}{}^{(1-\alpha\beta)}(1 - \theta_T) \exp(-\beta F(E_S + E^o_{PZC})/RT) \qquad [26]$$

Therefore

$$\left.\frac{\partial \ln i}{\partial \ln a_{H^+}}\right|_{E_S} = 1 - \alpha\beta \qquad [27]$$

The fractional order $(\partial \ln i/\partial \ln a_{H^+})_{E_S}$ observed was 0.42 for Pd on C catalyst and 0.52 for Pt black catalyst (Table I). Since the experimental value of β was found to be 0.2 for Pd on C and 0.3 for Pt black, the value of α is calculated to be 2.9 for Pd on C and 1.6 for Pt black. The value of α different from unity is to be expected, since the present system is quite different from the one for which Eq. [24] was obtained.

Effect of crotonic acid concentration.—The reaction order with respect to crotonic acid concentration was found to be −0.05 for Pd on C and 0.07 for Pt black, and hence can be assumed to be zero for both the catalysts. A similar observation has been made in the electrochemical reduction of maleic acid (19). This zero order with respect to crotonic acid may be explained by reference to Eq. [21]. If it is assumed that the catalyst surface is saturated with adsorbed crotonic acid so that the fraction of crotonic acid adsorbed on the catalyst θ_R is constant for varying concentrations of crotonic acid, one finds for the apparent order

$$\left.\frac{\partial \ln i}{\partial \ln C_R}\right|_{E,pH} = 0 \qquad [28]$$

Effect of butyric acid concentration.—The observed effect of butyric acid concentration was different for the two catalysts studied. The reaction order is −0.48 for Pd on C and nearly zero for Pt black.

This would seem to imply that the adsorption of butyric acid is markedly weaker on Pd on C than on Pt black. However, more detailed data on the competitive adsorption of crotonic acid and butyric acid and their effects on the rate-limiting step would be necessary for fuller understanding of the apparent orders for crotonic and butyric acids. In the absence of data, speculation on this point seems highly inconclusive.

Anodic effects.—The anodic reaction orders with respect to pH, crotonic acid concentration, and butyric acid concentration were found to be negligible or zero, within limits of reproducibility.

The anodic limiting current that was observed in all cases is probably due to mass-transfer limitations. The reaction steps for the anodic current can be written as follows

$$H_2 \rightarrow 2H_{ads} \qquad [\text{step 1}]$$

$$H_{ads} \rightarrow H^+ + e \qquad [\text{step 2}]$$

$$CH_3CH{=}CHCOOH + 2H_{ads} \rightarrow CH_3CH_2CH_2COOH \qquad [\text{step 3}]$$

Mass-transfer limitation occurs when the hydrogen transfer from the solution to the catalyst surface becomes limited in the step prior to the charge-transfer reaction. Therefore increasing the potential does not increase the rate of step 2 and a limiting current is observed. A low limiting current would be observed if the crotonic acid were adsorbed tightly on most of the catalyst sites, leaving only a few sites available for hydrogen adsorption.

This was checked by obtaining the anodic current-potential curves with a Pd on C catalyst, but no crotonic acid, as shown in Fig. 7. A limiting current of 16 mA was reached as compared to 0.5 mA when crotonic acid was present. To check the effect of butyric acid, the anodic current-potential curve was obtained for a solution containing 9.5 g/liter butyric acid and Pd on C catalyst as shown in Fig. 7. This had a limiting current of 16.5 mA. The two curves, with and without butyric acid, were very similar except that the curve for the one without butyric acid rose at first more slowly with increasing potential than the curve with butyric acid. At higher potentials they were very alike. There was also a potential shift observed at open circuit. Since the pH of the solution with butyric acid (pH = 2.8) was much lower than the pH of the solution without it, the anodic current-potential curve was obtained for a solution without butyric acid containing Pd on C catalyst at pH = 2.8 made by adding sulfuric acid. As shown in Fig. 7, this curve can be superimposed exactly on the curve taken when butyric acid was present at the same pH. Hence the shift was due to pH effect and not to butyric acid *per se*.

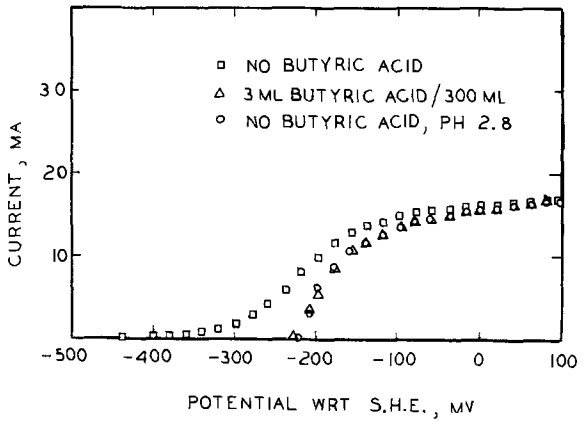

Fig. 7. Anodic current vs. potential, with and without butyric acid and no crotonic acid, and 5 g/liter 5% Pd on C catalyst.

The above experiments confirmed that addition of butyric acid did not inhibit the current when crotonic acid was absent. The current was inhibited when crotonic acid was present. Hence crotonic acid must be strongly adsorbed on the catalyst sites.

Effect of catalyst concentration.—The current was proportional to a fractional power of the catalyst concentration at constant potential for both Pd on C and Pt black catalysts at high overvoltages. It was presumed initially that since the charge is transferred during the collisions of the catalyst particles with the collector electrode, increasing the number of catalyst particles should increase the current proportionately at constant overvoltage and not constant potential. This was observed for oxidation of hydrogen on Pd on C and Pt black (11, 13). But it was not true for the present system studied, where the current was found to be independent of catalyst concentration for both the catalysts at constant overvoltage. This can be seen in Fig. 8 which is the graph of current-overvoltage for Pd on C catalyst. The catalyst concentration appeared to affect only the open-circuit potential.

Since the catalyst particles are around 0.5μ in diameter, they are at an average distance of 20 diameters or more apart in the solution for the range of concentrations used. Hence the assumption that the particles interfered with one another is hard to maintain.

Calculations to check the diffusion rate of hydrogen through the pores formed by a cluster of the catalyst particles revealed there was no limitation to the diffusion.

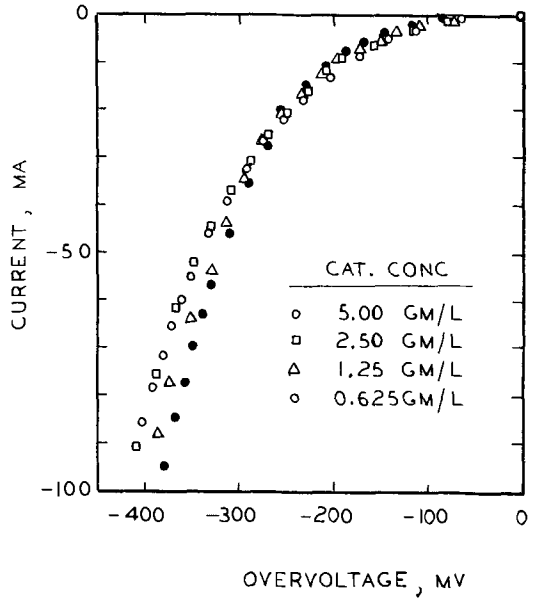

Fig. 8. Cathodic current vs. overvoltage for varying 5% Pd on C catalyst concentrations at constant crotonic acid concentration of 66.7 g/liter.

The decrease of the open-circuit potential with increased catalyst concentration could not be explained by the hypothesis that the pH of the solution increased due to adsorption of hydrogen ions from the solution on the catalyst particles since the pH of the solution with varying amounts of the catalysts was found to be constant at 2.45 in separate measurements.

A possible explanation is that since the clusters of the particles are loosely held together by a film of electrolyte, the electrical resistance is not the same throughout the cluster. When the cluster comes in contact with the collector electrode, only the hydrogen ions near the surface pick up the discharged electrons, whereas the ones further away cannot because of relatively higher resistance. As the catalyst concentration increases, the size of the clusters may increase, but only the same number of particles near the surface can discharge, and hence increased catalyst concentration has no effect on the total current.

In the absence of a fully satisfactory explanation, the cathodic current was expressed empirically as

$$i_c = kw^f e^{-\beta FE/RT} \qquad [29]$$

The values of f and β are 0.23 and 0.24, respectively, for Pd on C and 0.45 and 0.31 for Pt black.

Effect of temperature.—The cathodic activation energy values (Table II) represent activation energy not for the over-all reduction of crotonic acid, but only for the charge-transfer step. They are in agreement with those between —3 and —7 kcal/mole observed by Conway and MacKinnon (20) for the hydrogen ion reduction on metals. These low values of the activation energies are expected of atomic reactions like the hydrogen ion reduction where there is no breaking of chemical bonds.

The Tafel slope was found not to be a function of temperature in the range studied, but was constant (Table II). Conway *et al.* (20, 21) have noted that the Tafel slope given by $\beta F/RT$ is rarely found experimentally to be of that form, but is far less temperature dependent than is implied by that relation and is usually independent of temperature.

For the anodic polarization, no temperature effect was noticed, possibly because it was smothered by mass-transfer limitations evident from the low limiting anodic current.

Current efficiency.—Since the hydrogen formed could either desorb to form hydrogen gas or react with crotonic acid to give butyric acid, the reaction efficiency of around 80% meant that 80% of the hydrogen reacted with crotonic acid to give butyric acid, and that only 20% was desorbed to form hydrogen gas. Hence Pd on C catalyst was rather selective for the hydrogenation path and the current could be used as a measure of the reaction rate. This would be equally true of Pt black catalyst.

Manuscript submitted Sept. 29, 1972; revised manuscript received May 10, 1973.

Any discussion of this paper will appear in a Discussion Section to be published in the June 1974 JOURNAL.

REFERENCES

1. E. Muller and K. Schwabe, *Z. Elektrochem.*, **34**, 179 (1928).
2. E. Muller and K. Schwabe, *Kolloid-Z.*, **52**, 163 (1930).
3. D. V. Sokol'skii and V. A. Druz, *Dokl. Akad. Nauk SSSR*, **73**, 949 (1950).
4. D. V. Sokol'skii and V. A. Druz, *Zh. Fiz. Khim.*, **26**, 364 (1952).
5. P. Boutry, O. Bloch, and J. C. Balaceanu, *Compt. Rend.*, **254**, 2583 (1962).
6. H. Gerischer, *Ber. Bunsenges.*, **67**, 164 (1963).
7. J. Held and H. Gerischer, *ibid.*, **67**, 921 (1963).
8. K. Schwabe and A. Satsko, *J. Electroanal. Chem.*, **11**, 308 (1966).
9. A. B. Fasman, D. V. Sokol'skii, and K. A. Schurov, *Dokl. Akad. Nauk SSSR*, **153**, 653 (1966).

10. R. M. Larorenko-Manevich and A. V. Ushakov, *ibid.*, **161**, 156 (1965).
11. W. M. Eyring, M. S. Thesis, Northwestern University, Evanston, Ill. (1965).
12. F. Beck, *Ber. Bunsenges Physik. Chem.*, **69**, 199 (1965).
13. D. N. Baria, M.S. Thesis, Northwestern University, Evanston, Ill. (1967).
14. K. J. Vetter, "Electrochemical Kinetics," p. 111, Academic Press, New York (1967).
15. P. Delahay, "Double Layer and Electrode Kinetics," p. 156, Interscience Publishers, Inc., New York (1966).
16. J. O'M. Bockris and S. Srinivasan, "Fuel Cells: Their Electrochemistry," p. 396, McGraw-Hill Book Co., New York (1969).
17. J. O'M. Bockris, S. D. Argsde, and E. Gileadi, *J. Phys. Chem.*, **70**, 2044 (1966).
18. V. L. Kheifets and B. S. Krasikov, *Zh., Fiz. Khim.*, **31**, 1992 (1957).
19. L. N. Ivanovskaya, I. V. Kudryashov, and S. A. Kolesnikova, *Elektrokhimiya*, **5**, 760 (1969).
20. B. E. Conway and D. J. MacKinnon, *This Journal*, **116**, 1665 (1969).
21. B. E. Conway, K. J. MacKinnon, and B. V. Tilak, *Trans. Faraday Soc.*, **66**, 1203 (1970).

The Transient Response of a Disk Electrode

Kemal Nişancioğlu* and John Newman**

Inorganic Materials Research Division, Lawrence Berkeley Laboratory and Department of Chemical Engineering, University of California, Berkeley, California 94720

ABSTRACT

A mathematical model is proposed to treat the transient response of a disk electrode to a change in the applied current. The analysis reduces to a well-defined boundary value problem, which yields solutions in terms of newly defined eigenfunctions. The results allow the determination of time constants characteristic of decay due to an electrode reaction and due to a redistribution of charge within the double layer during the transient process.

The transient behavior of electrochemical cells has been of interest since the development of the commutator method for the assessment of electrode overpotentials (1). The subsequent invention of the more accurate interrupter technique (2) and its perfection in the last couple of decades (3, 4) have provided a reliable tool for the measurement of the uncompensated ohmic drop in the solution. The presence of a nonuniform current distribution at the electrode surface [such as in the case of a disk electrode below the limiting current (5-7)], however, appears to complicate the interpretation of interrupter data, as this subject has already received ample thought and experimentation (4, 8-12).

Newman (8) has shown that the step change in potential at interruption corresponds to the primary current distribution (5) and discussed the time constants for decay of the double-layer capacity due to a faradaic reaction and redistribution of charge within the double layer. A more complete mathematical study will be presented here in order to determine the transient response of a disk electrode to step changes in the cell current.

The problem was originally conceived for an ideally polarizable electrode with the purpose of calculating the transients one would observe during the charging and decay of the double-layer capacity. However, the effect of a faradaic reaction can be incorporated into the formulation without any added difficulty in the analysis. The more general case will therefore be analyzed with due notice of the mathematical subtleties relevant to an ideally polarizable electrode. [According to Grahame (18), an ideally polarizable electrode is one for which no steady current flows at any potential in the range of potentials of interest.]

The following assumptions are made in the treatment of the problem:

(*i*) The disk electrode is embedded in an infinite, insulating plane, and the counterelectrode is placed at infinity.

(*ii*) The diffusion layer is neglected. This is a fairly good assumption when the rate of stirring is high (high rotation speeds), and the current density at the electrode surface is considerably below the limiting current (13).

(*iii*) Linear kinetic relationships govern the electrode reaction. This situation is encountered for high reaction rate constants and sufficiently small current densities such that $|i| << i_o$, where i_o is the exchange current density (6).

(*iv*) The double-layer capacity is regarded to be independent of the potential. This is a reasonable approximation for small changes in the electrode potential, especially for cathodic polarizations with respect to the electrocapillary maximum.

The last three assumptions are stated for the sake of simplicity so that the phenomena which directly influence the transient behavior of an electrode can be singled out for investigation with a minimum number of complicating factors. The effect of steady-state mass transfer on the current distribution below the limiting current has been discussed elsewhere for various geometries with the consideration of nonlinear electrode kinetics (6, 7, 14, 15). Newman has treated the mass transfer problem in rapid double-layer charging at an ideally polarizable electrode (16). Some attention has been directed to the proper treatment of the capacitive effect of the diffuse double layer in transient problems in the presence of concentration and sizable potential variations, and the reader is directed to the pertinent literature (19-21). More discussion is also in order in a later section concerning the validity of the above assumptions in practical application.

Mathematical Model

The potential in the solution satisfies Laplace's equation

$$\nabla^2 \Phi = 0 \qquad [1]$$

The boundary conditions are

$$\frac{\partial \Phi}{\partial z} = 0 \qquad \text{at } z = 0, r > r_o \qquad [2]$$

** Electrochemical Society Student Member.
* Electrochemical Society Active Member.
Key words: interrupter, double-layer capacity, time constant, ideally polarizable electrode.

$$\Phi \to 0 \qquad \text{as } r^2 + z^2 \to \infty \qquad [3]$$

and the potential is well behaved on the axis of the disk. Furthermore, the normal component of the current density at the electrode surface is given by (13)

$$i_z = C\frac{\partial \eta_s}{\partial t} + (\alpha_a + \alpha_c)\frac{i_o F}{RT}\eta_s = -\kappa\frac{\partial \Phi}{\partial z}$$

$$\text{at } z = 0, r \leq r_o \qquad [4]$$

where

$$\eta_s = V - \Phi_o \qquad [5]$$

is the surface overpotential associated with the faradaic reaction, V is the electrode potential, Φ_o is the potential in the solution adjacent to the electrode, κ is the conductivity of the solution, C is the double-layer capacity, and $(\alpha_a + \alpha_c)\ i_o\ \mathbf{F}/RT$ is the kinetic coefficient for the faradaic reaction.

We would like to have our model simulate the transient response of a disk electrode for the charging or decay of the double-layer capacity immediately after the current is turned on or off, respectively. The potential in solution for the charging period can then be represented as the difference of a steady-state and a transient contribution

$$\Phi = \Phi^{ss} - \Phi^t \qquad [6]$$

such that each part satisfies Laplace's equation by itself. The electrode potential V can similarly be expressed as the difference of a steady-state and a transient part. The steady-state part of the potential includes the contribution of the total cell current, while the transient part contains no net current. Once the current is turned off, therefore, the steady-state part vanishes, and the decay period is represented by only the transient part: $\Phi = \Phi^t$.

Steady-State Part of the Potential

The solution of Laplace's equation for the potential distribution in a disk electrode system is well known for various steady-state boundary conditions at the electrode surface (5, 6, 9). A solution for the steady-state part of the potential will be presented here to meet the purposes of this analysis.

In rotational elliptic coordinates (5) η and ξ, the solution for the steady-state part of the potential satisfying the conditions [2] and [3] can be expressed as (6)

$$\frac{\Phi^{ss}}{\Phi_o^p} = \sum_{n=0}^{\infty} B_n^{ss} P_{2n}(\eta)\, M_{2n}(\xi) \qquad [7]$$

where $P_{2n}(\eta)$ is the Legendre polynomial of order $2n$, $M_{2n}(\xi)$ is a Legendre function with known properties (7), and Φ_o^p is the uniform potential in the solution just outside the double layer corresponding to the primary current distribution (5). This quantity, in fact, is the ohmic drop which is normally measured by interrupter methods (8) and is identical to $I/4\kappa r_o$ in this work. The choice of Φ_o^p as the scaling factor in Eq. [7] is mathematically convenient since this normalizes the numerical value of B_o^{ss} to unity regardless of the electrode conditions. Substitution into the boundary condition [4] yields

$$-\frac{1}{\eta}\frac{\partial \Phi^{ss}}{\partial \xi}\bigg|_{\xi=0} = J\,(V^{ss} - \Phi_o^{ss}) \qquad [8]$$

where J is the dimensionless exchange current density given by

$$J = \frac{i_o r_o F}{RT\kappa}(\alpha_a + \alpha_c) \qquad [9]$$

Combining Eq. [7] and [8] and employing the orthogonality property of the Legendre polynomials (6) gives

$$\frac{V^{ss}}{\Phi_o^p} = 1 + \frac{4}{\pi J} + 2\sum_{n=1}^{n_{max}} a_{o,n} B_n^{ss} \qquad [10]$$

and

$$\sum_{n=1}^{n_{max}}\left[a_{m,n} - 2a_{o,m}a_{o,n} - \delta_{m,n}\frac{M'_{2m}(0)}{(4m+1)J}\right]B_n^{ss} = \frac{4}{\pi J}a_{o,m} \quad (m = 1, 2, \ldots, n_{max}) \qquad [11]$$

where

$$a_{m,n} = \int_0^1 \eta\, P_{2m}(\eta)\, P_{2n}(\eta)\, d\eta \qquad [12]$$

$$a_{o,m} = \int_0^1 \eta\, P_{2m}(\eta)\, d\eta = -\frac{P_{2m}(0)}{2(2m-1)(m+1)} \qquad [13]$$

$$\delta_{m,n} = \begin{cases} 0 \text{ if } m \neq n \\ 1 \text{ if } m = n \end{cases} \qquad [14]$$

The series in Eq. [10] and [11] are truncated at n_{max} for the purposes of numerical calculation. The accuracy of calculation hence depends on the number of terms taken into consideration. The coefficients B_n^{ss} for the first 10 terms in the series are listed in Table I for various J values. The quantity V^{ss}/Φ_o^p, which can directly be calculated from Eq. [10] once B_n^{ss} are obtained from Eq. [11], is identified as the dimensionless effective d-c resistance (17) $4r_o\kappa R_{eff}$ for the disk system with the reference electrode at infinity.

For an ideally polarizable electrode it is possible to express the coefficients B_n^{ss} explicitly. Since for large charging times the ideally polarizable electrode surface attains a uniform current distribution, we can replace the condition [8] with

$$-\frac{1}{\eta}\frac{\partial \Phi^{ss}}{\partial \xi}\bigg|_{\xi=0} = \frac{I}{\pi r_o \kappa} \qquad [15]$$

which yields

$$B_n^{ss} = -4a_{o,n}(4n+1)/\pi M'_{2n}(0) = -\frac{(4n+1)\,[P_{2n}(0)]^3}{(2n-1)(n+1)} \qquad [16]$$

An Eigenvalue Problem

The transient part of the potential can be expressed by a series expansion of the form

$$\frac{\Phi^t}{\Phi_o^p} = \sum_{i=1}^{\infty} C_i e^{-t/\tau_i} U_i(r, z) \qquad [17]$$

where U_i is a characteristic dimensionless potential defined here to be independent of time, and τ_i is a time constant for decay corresponding to the potential U_i. The analysis can be pursued conveniently in terms of two additional dimensionless quantities, *viz.* the

Table I. D-C resistance V^{ss}/Φ_o^p and coefficients in the series for the steady-state potential

n	$J = 0$	$J = 0.1$	$J = 1$	$J = 10$
0	1.00000	1.00000	1.00000	1.00000
1	0.31250	0.30731	0.26863	0.13306
2	−0.05273	−0.05446	−0.06568	−0.07356
3	0.01984	0.02040	0.02491	0.04037
4	−0.00993	−0.01019	−0.01232	−0.02324
5	0.00580	0.00594	0.00713	0.01423
6	−0.00373	−0.00382	−0.00455	−0.00926
7	0.00256	0.00262	0.00312	0.00636
8	−0.00185	−0.00189	−0.00224	−0.00456
9	0.00139	0.00142	0.00168	0.00339
10	−0.00107	−0.00110	−0.00130	−0.00260
V^{ss}/Φ_o^p	—	13.81194	2.34368	1.16459

dimensionless eigenvalue

$$\Lambda_l = \frac{r_o C}{\kappa \tau_l} - J \qquad [18]$$

and the dimensionless time

$$\theta = \frac{\kappa t}{r_o C} \qquad [19]$$

Equation [17] then transforms to the form

$$\frac{\Phi^t}{\Phi_o^p} = \sum_{i=1}^{\infty} C_l e^{-\theta(\Lambda_l + J)} U_l(\eta, \xi) \qquad [20]$$

The transient part of the electrode potential can analogously be expressed as

$$\frac{V^t}{\Phi_o^p} = C_o e^{-\theta J} + \sum_{i=1}^{\infty} C_l e^{-\theta(\Lambda_l + J)} v_l \qquad [21]$$

where v_l is a constant which will henceforth be taken to be unity, thus providing a normalization for the eigenfunctions U_l.

The functions U_l satisfy Laplace's equation

$$\nabla^2 U_l = 0 \qquad [22]$$

and the conditions

$$\left.\begin{aligned} &\frac{\partial U_l}{\partial \eta} = 0 \quad \text{at } \eta = 0 \\ &U_l = 0 \quad \text{as } \xi \to \infty \\ &U_l \text{ well behaved at } \eta = 1 \end{aligned}\right\} \qquad [23]$$

The solution can therefore be given by

$$U_l = \sum_{n=1}^{\infty} B_{n,l} P_{2n}(\eta) M_{2n}(\xi) \qquad [24]$$

The zeroeth term is excluded from the summation since U_i includes no contribution to the net current. The boundary condition [4] now reduces to

$$\left.\frac{\partial U_i}{\partial \xi}\right|_{\xi=0} = \Lambda_i \eta (1 - U_{i,o}) \qquad [25]$$

Combining Eq. [24] and [25] and invoking the orthogonality property of the Legendre polynomials yield

$$\sum_{n=1}^{n_{max}} a_{o,n} B_{n,l} = \frac{1}{2} \qquad [26]$$

$$\sum_{n=1}^{n_{max}} \left[a_{m,n} + \frac{\delta_{m,n}}{\Lambda_l} \frac{M'_{2m}(0)}{4m+1} \right] B_{n,l} = a_{o,m}$$

$$(m = 1, 2, \ldots, n_{max}) \qquad [27]$$

The above set of equations can be solved simultaneously for Λ_l and $B_{n,l}$. Some results are given in Table II, and the first three eigenfunctions are plotted in Fig. 1.

Each term in Eq. [17], and the corresponding term in Eq. [21], describes a potential distribution and a state of charge in the electric double layer which can decay with a single time constant and involves no net current flow to the counterelectrode at infinity. The state of charge is proportional to $V - \Phi_o$ or to $1 - U_{i,o}$ for a particular eigenfunction. If this state of charge is nonuniform, it will have associated with it a flow of current through the solution in a direction which tends to make even the charge distribution across the electrode. At the same time, the double-layer charge may be decaying through the faradaic reaction (if $J > 0$).

If each eigenfunction is to represent a single time constant, the amount of current flowing through the solution (related to $\partial U_i/\partial \xi$ at $\xi = 0$) must be proportional, over the surface of the electrode, to the rate of change of the double-layer charge. Equation [25] represents this state of affairs. Only for certain characteristic decay constants Λ_l is it possible to find consonant current and charge distributions which decay with a single time constant, and these eigenvalues are not known in advance. The lowest eigenvalue, either $\Lambda_o = 0$ or $\Lambda_1 = 4.12130$, is the most important because its effect can most readily be observed experimentally after the other eigenfunctions have decayed to negligible values.

It is a further consequence of boundary condition [25] (current in solution is proportional to surface charge for each eigenfunction) that the eigenfunctions U_i satisfy the unusual orthogonality relationship

$$\int_0^1 U_{i,o}(1 - U_{j,o})\, \eta d\eta = \begin{cases} \dfrac{1}{\Lambda_l} \displaystyle\sum_{n=1}^{\infty} \frac{M'_{2n}(0)}{4n+1} B^2_{n,l} & \text{if } i = j \\ 0 & \text{if } i \neq j \end{cases} \qquad [28]$$

Table II. The first five eigenvalues and the related coefficients $B_{n,l}$ of the eigenfunctions

	Λ_1	Λ_2	Λ_3	Λ_4	Λ_5
	4.12130	7.34208	10.5171	13.6773	16.8308
n	$i = 1$	$i = 2$	$i = 3$	$i = 4$	$i = 5$
1	4.56973	3.77405	3.44403	3.25860	3.13835
2	3.58511	−3.70789	−4.65165	−4.79056	−4.75592
3	0.51738	−7.51662	−0.26793	2.76530	4.12700
4	0.10883	−2.89555	9.61986	5.38647	1.50528
5	−0.03142	−0.67828	6.80910	−8.19370	−8.96687
6	0.02274	−0.02899	2.44679	−10.7732	3.13094
7	−0.01587	−0.03991	0.44950	−5.76314	12.7102
8	0.01161	0.02427	0.11317	−1.72889	10.1185
9	−0.00879	−0.01882	−0.02225	−0.42934	4.33793
10	0.00684	0.01470	0.02444	−0.02855	1.34839

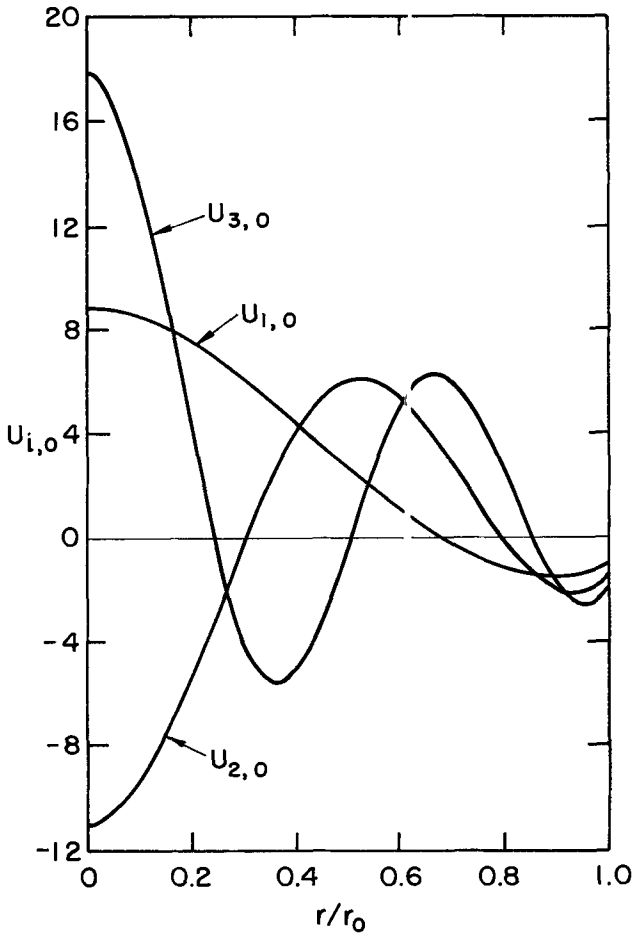

Fig. 1. The first three eigenfunctions for the transient solution

This has much the same meaning; the potential at the surface for one eigenfunction is in a sense orthogonal to the current density for another eigenfunction.

One can study the eigenfunctions in Fig. 1 to visualize how the current flows through the solution. The potential is nonuniform for a given eigenfunction because the state of charge is nonuniform. The current density in the solution is proportional to $1 - U_{i,o}$ and flows from a region of high charge to a region of low charge. The higher order eigenfunctions have more minima and maxima in the curves. The current need, therefore, flow a shorter distance in order to even up the charge, and the time constants are correspondingly shorter.

Transient Potential Distribution

In order to be able to calculate the values of C_i and thereby complete the analysis, we need to specify suitable initial conditions for the problem. Let us assume that the current is switched on as a step at $\theta = 0+$ and kept constant until $\theta = \theta_{ch}$, at which instant it is turned off. The time scale for the decay period can be defined as

$$\theta' = \theta - \theta_{ch} \qquad [29]$$

Therefore, for the charging period

$$V = \Phi_o = \Phi_o^p \quad \text{at} \quad \theta = 0+, \quad \xi = 0 \qquad [30]$$

and for the decay period

$$\left.\begin{aligned} V &= V(\theta_{ch}) - \Phi_o^p \\ \Phi_o &= \Phi_o(\theta_{ch}) - \Phi_o^p \end{aligned}\right\} \text{at} \quad \theta' = 0+, \quad \xi = 0 \qquad [31]$$

Application of the initial condition [30] for the charging period to Eq. [6] gives

$$\frac{\Phi_o^{ss}}{\Phi_o^p} - 1 = \sum_{i=1}^{\infty} C_i U_{i,o} \qquad [32]$$

Multiplication by $(1 - U_{j,o})\eta$ and integration with respect to η yields

$$C_j = \frac{\int_0^1 \frac{\Phi_o^{ss}}{\Phi_o^p}(1 - U_{j,o})\,\eta d\eta}{\int_0^1 U_{j,o}(1 - U_{j,o})\,\eta d\eta} = \frac{\sum_{n=1}^{\infty} \frac{M'_{2n}(0)}{4n+1} B_n^{ss} B_{n,j}}{\sum_{n=1}^{\infty} \frac{M'_{2n}(0)}{4n+1} B^2_{n,j}} \qquad [33]$$

Application of the corresponding initial condition for the electrode potential gives

$$C_o = \frac{V^{ss}}{\Phi_o^p} - 1 - \sum_{i=1}^{\infty} C_i = \frac{4}{\pi J} \qquad [34]$$

For the decay period where $\Phi = \Phi^t$ (the negative of the transient part for charging), the same results, summarized by Eq. [32]-[34], also apply as long as θ_{ch} is large enough so that the steady state has been reached right before interruption. If this is not the case, the equations for decay become

$$\frac{\Phi}{\Phi_o^p} = \sum_{i=1}^{\infty} C_i \left[1 - e^{-\theta_{ch}(\Lambda_i + J)}\right] e^{-\theta'(\Lambda_i + J)} U_i \qquad [35]$$

for the potential in the solution, and

$$\frac{V}{\Phi_o^p} = C_o(1 - e^{-\theta_{ch} J})\, e^{-\theta' J} + \sum_{i=1}^{\infty} C_i \left[1 - e^{-\theta_{ch}(\Lambda_i + J)}\right] e^{-\theta'(\Lambda_i + J)} \qquad [36]$$

for the electrode potential. The coefficients C_i are the same as for the charging period, given by Eq. [33] and [34].

For an ideally polarizable electrode ($J = 0$) the same relationships hold to express the potential in the solution, both for charging and for decay. The electrode potential, however, increases indefinitely once the current is turned on and decays to a nonzero value after the interruption of current. This is because of the fact that the net double-layer charge has no means for decay in the absence of an electrode reaction; it can only redistribute by flow of current through the solution in order to attain a final uniform state. Hence, for the charging period we have

$$\frac{V}{\Phi_o^p} = \frac{4}{\pi}\theta + D - \sum_{i=1}^{\infty} C_i e^{-\Lambda_i \theta} \qquad [37]$$

The constant term can be obtained by integrating condition [4] over the electrode surface for the total period of charging to obtain the net charge added to the double layer

$$2\pi C \int_0^{r_o}\int_0^{t_{ch}} \frac{\partial(V - \Phi_o)}{\partial t}\, dtrdr = 2\pi \int_0^{r_o}\int_0^{t_{ch}} i_z\, dtrdr = It_{ch} \qquad [38]$$

Substitution of Eq. [6] and [37] into the left side and integration lead to the result

$$D = 2\sum_{n=0}^{\infty} B_n^{ss} a_{o,n} = 1.08076 = 32/3\pi^2 \qquad [39]$$

Finally, the electrode potential for the decay period is

$$\frac{V}{\Phi_o^p} = \frac{4}{\pi}\theta_{ch} + \sum_{i=1}^{\infty} C_i e^{-\Lambda_i \theta'}(1 - e^{-\Lambda_i \theta_{ch}}) \qquad [40]$$

The analysis at this point can readily be extended to account for arbitrary changes in the cell current by a straightforward application of the superposition integral. If the time dependent cell current is given by $I(\theta)$, the electrode potential can be expressed as

$$4r_o\kappa V = I(\theta) + C_o J e^{-\theta J}\int_0^{\theta} I(\theta) e^{\theta J} d\theta + \sum_{i=1}^{\infty} C_i(\Lambda_i + J) e^{-\theta(\Lambda_i + J)} \int_0^{\theta} I(\theta) e^{\theta(\Lambda_i + J)} d\theta \qquad [41]$$

in the presence of an electrode reaction, and

$$4r_o\kappa V = I(\theta) + \frac{4}{\pi}\int_0^{\theta} I(\theta)\, d\theta + \sum_{i=1}^{\infty} C_i \Lambda_i e^{-\Lambda_i \theta} \int_0^{\theta} I(\theta) e^{\Lambda_i \theta} d\theta \qquad [42]$$

for an ideally polarizable electrode. One application of these equations would be for an a-c situation, where the frequency dispersion of the measured impedance is of interest. A more rigorous and accurate calculation has been performed by Newman (17) for this particular case. The present equations were used to compute the frequency dispersion in capacity measurements at a disk electrode and compared to Newman's results (17). The agreement is good for small frequencies, but a large number of terms is required in the series to attain any reasonable accuracy at high frequencies. The same numerical problem is encountered in calculating the short-time response of the potential to a step change in the current since the series do not converge very fast. An asymptotic

solution, applicable to small charging and decay periods, may therefore be desirable.

Results and Discussion

Figure 2 depicts a typical potential trace for double-layer charging and decay in the presence of a faradaic reaction, and Fig. 3 shows potential decay curves after the interruption of current for various values of the kinetic parameter J. For both representations, the current is interrupted after the double layer is charged to steady-state conditions. For large decay periods, the slope of each curve approaches the corresponding J value on a semilogarithmic scale as can be inferred from Eq. [36]. Curves similar to Fig. 2 could be constructed for different J values by making use of the information contained in Fig. 3 and by remembering that the ohmic drop is given by the primary distribution Φ_0^p and that the charging and decay portions of each curve are symmetric.

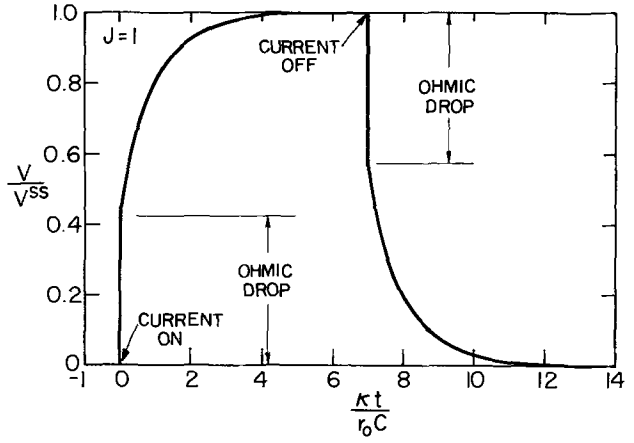

Fig. 2. Double-layer charging and decay in the presence of a faradaic reaction.

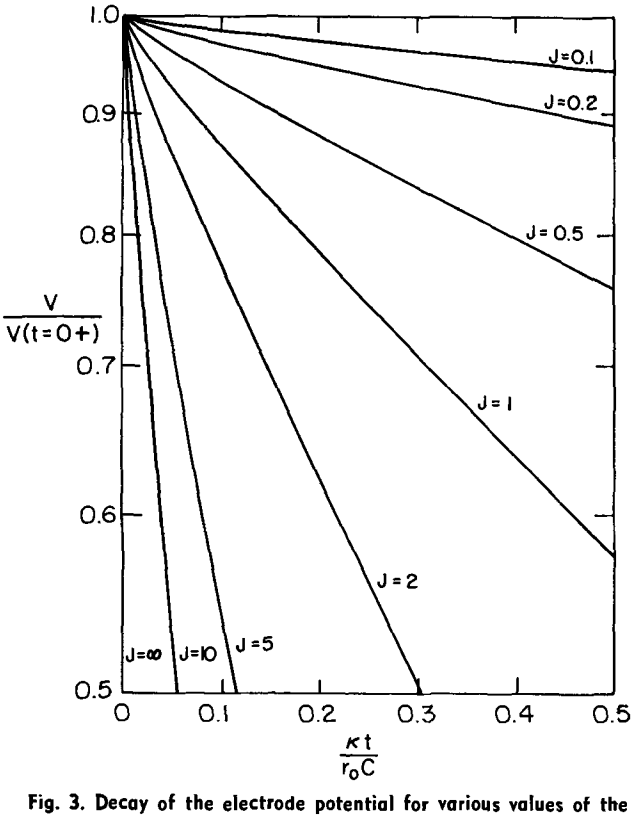

Fig. 3. Decay of the electrode potential for various values of the kinetic parameter J. A steady condition was attained before interruption of the current.

The fact that the instantaneous potential step immediately preceding both the charging and decay portions of Fig. 2 corresponds to the primary current distribution (8) is implicit in the present analysis by virtue of the particular initial conditions (Eq. [30] and [31] employed. Nanis and Kesselman (9) have expressed the contrary view in this regard. We would like to stress that the same criterion would hold for the ohmic drop even if the diffusion layer were taken into consideration. An experimental verification along these lines has been provided by Miller and Bellavance (12).

The transient response of an ideally polarizable electrode to step changes in the current is depicted in Fig. 4. The step portions again correspond to the primary distribution. The differences in comparison to Fig. 2 are obvious. The potential-time relationship becomes linear for sufficiently large charging periods as the surface current density attains a uniform distribution. After the interruption of current, the electrode potential decays to a nonzero value, given by $4\theta_{ch}/\pi$. Decay curves for various charging periods are sketched in Fig. 5 to show the effect of short charging times on the potential decay. The same effect is also discernable when J is greater than zero, but the dependence on the charging period was not of prime interest in constructing Fig. 3 and was suppressed by allowing a steady state to develop before current interruption.

An important result of the present analysis is the assessment of an accurate time constant for the decay of the double-layer capacity in the absence of concentration gradients at the electrode surface. From Eq. [18], we obtain

$$\tau_1 = \frac{1}{\Lambda_1 + J} \frac{r_0 C}{\kappa} \qquad [43]$$

When an electrochemical reaction is possible, the dominant time constant at long times is

$$\tau = \frac{r_0 C}{\kappa J} \qquad [44]$$

as identified by Newman (8). When an electrochemical reaction is not possible (the ideally polarizable electrode), this time constant becomes infinite, and the potential decays to a nonzero constant. The dominant time constant then is

$$\tau = \frac{r_0 C}{\Lambda_1 \kappa} = \frac{1}{4.12} \frac{r_0 C}{\kappa} \qquad [45]$$

also suggested in the same context (8) but without the determination of the numerical factor. The present analysis amplifies the roles and interrelationship of these two quantities and the processes they describe.

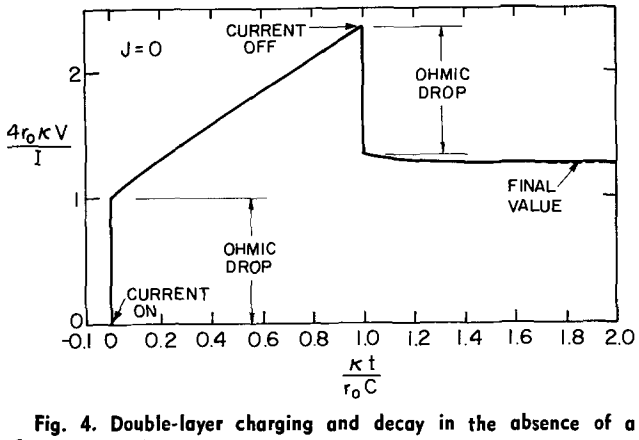

Fig. 4. Double-layer charging and decay in the absence of a faradaic reaction.

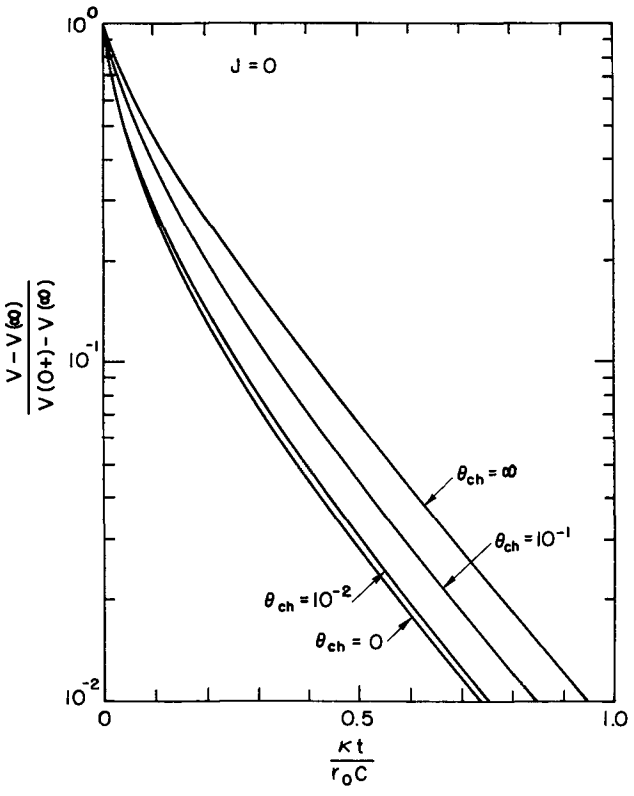

Fig. 5. Decay of the electrode potential for various charging periods in the absence of a reaction. The slope here is related at long times to the first eigenvalue Λ_1.

A direct experimental test of these time constants may be performed with the utility of an original reference electrode system designed by Miller and Bellavance (12). This consists of two probes positioned coaxially with the disk in the solution, so that the potential drop between two distinct locations in the solution could be measured. If linear electrode kinetics and finite exchange current densities are ensured, and concentration gradients near the surface of the disk are avoided, the time constant so measured should correspond to Eq. [43] for $i = 1$.

Validity and Significance of Theoretical Results in Practical Application

The reference electrode was assumed to be positioned at infinity relative to the working electrode in obtaining all our results. In practical situations, the reference electrode has to be placed at a finite distance from the disk, and if this is not accounted for in the evaluation of experimental data, serious errors may result (11). The necessary correction is rather simple to accomplish; since one can assume without significant error that the primary distribution (5) prevails in the bulk of the solution, the reading on the reference electrode can be extrapolated to infinite distance from the disk (12).

A possible application of the present results might be in the study of the double-layer structure at solid surfaces. Difficulties are encountered in the measurement of differential capacities at solid electrodes due to the frequency dispersion effect (17), except when it is feasible to construct and employ spherical electrodes (22, 23). Such difficulties may be overcome by attempting to measure relaxation times in interrupter experiments; in the absence of mass transfer, these relaxation times are related to the differential capacity of the disk electrode as shown in previous sections.

In practice, one first investigates the structure of the double layer in the presence of supporting electrolyte alone. If currents due to gas evolution and reduction of impurities are avoided, the working electrode is an ideally polarizable electrode. In this way, one finds out about the relationship between the electrode potential and the surface charge density (18). One may then add a small amount of reactant and assume that the same charge-potential dependence prevails. Investigations along these lines appear to be successful in depicting qualitatively the influence of the double-layer structure on faradaic reactions, as reviewed by Parsons (24).

Let us consider an ideally polarizable disk system where $r_0 = 0.635$ cm, $C = 30\ \mu f/cm^2$, $\kappa = 0.036$ $ohm^{-1}\text{-}cm^{-1}$, and the ohmic drop is 11 ohms. The current is interrupted after charging the electrode for 1 msec at $I = 5$ mA. The characteristic time constant for decay can be calculated from Eq. [45] as $\tau = 128\ \mu sec$. We can further compute

$$\Phi_0^p = 55\ \text{mV}$$

$$\Delta V \equiv V(\theta = 0+) - V(\theta = \infty) = 0.08076\,\Phi_0^p = 4.44\ \text{mV}$$

If the reference electrode is placed along the axis of the disk, we have

$$\Delta\Phi_0\,(r = 0) \equiv \Phi_0\,(r = 0,\ \theta = 0+) - \Phi_0\,(r = 0,\ \theta = \infty)$$

$$= \Phi_0\,(r = 0,\ \theta = 0+) = \Phi_0^{ss}\,(r = 0) - \Phi_0^p$$

$$= \Phi_0^p \left[\sum_{n=0}^{\infty} B_n^{ss} - 1 \right] = \Phi_0^p \left(\frac{4}{\pi} - 1 \right)$$

$$= 15\ \text{mV}$$

$$\Delta(V - \Phi_0) = \Delta V - \Delta\Phi_0\,(r = 0) = -10.6\ \text{mV}$$

$$V - \Phi_0\,(\theta = \infty) = V\,(\theta = \infty) = \frac{It_{ch}}{\pi r_0^2 C} = 132\ \text{mV}$$

It is interesting to note that $\Delta\Phi_0\,(r = 0)$ is larger than ΔV and can be detected with relative ease with a double-probe reference electrode (12). The negative value of $\Delta(V - \Phi_0)$ indicates that this quantity (which we would have called the electrode overpotential if a faradaic reaction were present) actually increases at the center of the disk as the charge redistributes itself in the double layer to effect a final uniform and nonzero charge distribution. The change in $V - \Phi_0$ during the transient process is also moderately small compared to its absolute value, so that the double-layer capacity C can be assumed to be independent of the potential in this range without much error.

In reality, it is impossible to have a perfect ideally polarizable electrode. One can approximate it by maintaining its potential by an external source (18). The transient response of a disk electrode under potentiostatic control has been treated elsewhere (25). If the current is interrupted, the potential of a real electrode will decay more or less slowly to its open-circuit potential due to the reduction of impurities present in the solution (18). Thus if an electrode reaction is possible either owing to the presence of impurities or a reactant in the solution, the characteristic times for decay are

$$\tau_e = \frac{r_0 C}{\kappa J} \qquad [46]$$

for the electrode potential, and

$$\tau_s = \frac{1}{4.12 + J} \frac{r_0 C}{\kappa} \qquad [47]$$

for the potential in the solution. Even if Tafel kinetics

might govern the electrode reaction soon after interruption, linear kinetics will take over at large times as the overpotential decays, and the above time constants will become prevalent. Thus, if J is small, let us say 0.005, then the electrode potential will decay with a time constant $\tau_e = 106$ msec whereas the potential in the solution will decay much more rapidly, with the time constant $\tau_s = 0.13$ msec.

If however, J is of order unity or larger, this effect is rather appreciable and has to be accounted for. One possibility is to measure τ_s and τ_e simultaneously by a disk electrode-double probe reference electrode setup appropriately hooked up to a dual-beam oscilloscope. By subtracting the reciprocals of the two time constants, we obtain

$$\frac{1}{\tau_s} - \frac{1}{\tau_e} = \frac{4.12\kappa}{r_o C} \qquad [48]$$

which is independent of the exchange current density.

If the electrode reaction is mass-transfer controlled, the characteristic times depend on additional parameters such as the diffusion coefficient of active species and the diffusion-layer thickness. For the situation where one is concerned about the reduction of impurities at the disk after the interruption of current, a reasonable estimate of the faradaic current can be obtained from

$$i_f = nFD\frac{c_\infty - c_o}{\delta} \qquad [49]$$

where δ is the Nernst diffusion layer thickness. Assuming a highly reversible reaction controlled by diffusion and the capacitive effect of the double layer, the capacitive current is

$$i_c = C\frac{\partial \eta_c}{\partial t} \qquad [50]$$

where η_c is the concentration overpotential (13), given by

$$\eta_c = \frac{RT}{n\mathbf{F}}\ln\frac{c_\infty}{c_o} \qquad [51]$$

Since the net current is zero

$$i = i_f + i_c = 0 \qquad [52]$$

When we combine these four equations and integrate, we obtain a characteristic time constant for this case

$$\tau_D = \frac{CRT\delta}{n^2\mathbf{F}^2 D c_\infty} \qquad [53]$$

τ_D thus depends inversely on the concentration of impurities, which has to be kept as small as possible. Consider the reduction of a bivalent ion ($n = 2$) with $D = 10^{-5}$ cm^2/sec, $\delta = 10^{-3}$ cm, and $c_\infty = 10^{-9}$ mole/cm^3. Then, $\tau_D = 0.2$ msec.

In case the capacitive effect can be ignored, and a purely mass-transfer-controlled electrode process is considered, the appropriate time constant is proportional to δ^2/D, or more exactly

$$\tau_D = \frac{3.26\,Sc^{1/3}}{\Lambda_D\,\Omega} \qquad [54]$$

where Ω is the angular frequency of rotation of the disk and Λ_D is a constant characteristic of the diffusion process. Determination of this constant requires a detailed analysis of the transient mass transfer problem at a disk electrode. With the simplifying assumption of a radially independent concentration distribution, Selman (26) obtained $\Lambda_D = 7.216$ for a step change of concentration. Using this value for Λ_D, $Sc = 1000$, and $\Omega = 250$ radians/sec, we obtain $\tau_D = 18$ msec. The characteristic decay time for a current step is always larger than that for a concentration step for the same system, according to the review by Selman (26). Nanis and Klein (27) report experimental relaxation times (defined as the time required for the overpotential to decay to 99 per cent of its initial value) of 50-0.5 sec for rotational Reynolds numbers between 130 and 8500, respectively, in 0.005M ferrocyanide-ferricyanide redox system in 2M KOH solution.

The above discussion suggests that the effects of the double layer and mass transfer can be controlled according to the needs of the experimenter by proper design of the electrochemical system and the experimental method. It is possible to reduce mass transfer effects by choosing a system where the relaxation times due to mass transfer are of a much larger scale than the relaxation times associated with the diffuse double layer. The magnitude of the effect is also important as well as its duration. Note that while the time constant in Eq. [54] becomes smaller as Ω increases, the amplitude of the corresponding concentration disturbance would decrease. In other words, the other extreme where the concentration effects would become negligible is the well-stirred solution case, one of our assumptions in treating the theoretical problem.

Conclusions

The transient behavior of a disk electrode for a step change in the applied current has been worked out theoretically in the absence of mass transfer effects. The analysis leads to a boundary value problem, which yields analytic solutions in terms of a new set of eigenfunctions U_i. These equations can be extended to account for arbitrary variations in the applied current by employing the superposition integral.

The results demonstrate (*i*) the effects of a faradaic reaction, (*ii*) the nonuniform primary current distribution on the double-layer charging and decay at a disk electrode, and (*iii*) the interaction of these phenomena to determine the resultant electrode behavior. The over-all treatment of the problem allows the determination of accurate time constants for each of these effects.

Acknowledgment

This work was supported by the United States Atomic Energy Commission.

Manuscript submitted Aug. 7, 1972; revised manuscript received April 10, 1973.

Any discussion of this paper will appear in a Discussion Section to be published in the June 1974 JOURNAL.

LIST OF SYMBOLS

$a_{o,m}$	see Eq. [12]
$a_{m,n}$	see Eq. [11]
B_n^{ss}	coefficients in sereis for Φ^{ss}
$B_{n,i}$	coefficients in series for U_i
c_o	concentration at the electrode surface (mole/cm^3)
c_∞	concentration in the bulk (mole/cm^3)
C	double-layer capacity (f/cm^2)
C_i	coefficients in series for Φ^t and V^t
D	1.08076 (Eq. [39])
D	diffusion coefficient (cm^2/sec)
$\mathbf{F}$	Faraday's constant (coulomb/equiv.)
i_z	component of current density normal to the plane of disk (A/cm^2)
i_o	exhange current density (A/cm^2)
I	total current (A)
J	dimensionless exchange current density
M_{2n}	Legendre function discussed in Ref. (6)
n	number of electrons transferred per mole of reaction
P_{2n}	Legendre polynomial of order $2n$
r	radial position from axis of disk (cm)
r_o	radius of disk electrode (cm)
R	universal gas constant (joule/mole-deg)
R_{eff}	effective d-c resistance (ohm)
t	time (sec)
t_{ch}	total period of charging (sec)

T absolute temperature (°K)
U_i eigenfunctions in series for Φ^t
$U_{i,o}$ value of U_i at the electrode surface
V electrode potential (V)
V^{ss} steady-state part of the electrode potential (V)
V^t transient part of the electrode potential (V)
z distance from plane of disk (cm)
α_a, α_c parameters in the kinetic coefficient
δ Nernst diffusion layer thickness (cm)
$\delta_{m,n}$ Kronecker delta
η rotational elliptic coordinate
η_s surface overpotential (V)
κ conductivity of the solution (ohm^{-1}-cm^{-1})
Λ_i dimensionless eigenvalue
Λ_D eigenvalue characteristic of diffusion
Φ potential in the solution (V)
Φ_o value of Φ at the electrode surface (V)
Φ^{ss} steady-state part of potential in the solution (V)
Φ^t transient part of potential in the solution (V)
Φ_o^p potential in the solution adjacent to the disk corresponding to the primary current distribution (V)
ξ rotational elliptic coordinate
τ_i time constants for decay (sec)
θ dimensionless time for the charging period
θ' dimensionless time for the decay period
θ_{ch} dimensionless total period of charging
v_i constants in the series for V^t (normalized to unity)
Ω angular frequency of rotation (radians/sec)

REFERENCES

1. S. Glasstone, *J. Chem. Soc.*, **123**, 2926 (1923).
2. A. Hickling, *Trans. Faraday Soc.*, **33**, 1540 (1937).
3. S. Schuldinger and R. E. White, *This Journal*, **97**, 433 (1950).
4. J. D. E. McIntyre and W. F. Peck, Jr., *ibid.*, **117**, 747 (1970).
5. J. Newman, *ibid.*, **113**, 501 (1966).
6. J. Newman, *ibid.*, **113**, 1235 (1966).
7. J. Newman, *ibid.*, **114**, 239 (1967).
8. J. Newman, *ibid.*, **117**, 507 (1970).
9. L. Nanis and W. Kesselman, *ibid.*, **118**, 454 (1971); and *ibid.*, **118**, 1967 (1971).
10. J. Newman, *ibid.*, **118**, 1966 (1971).
11. W. Tiedemann, J. Newman, and D. N. Bennion, *ibid.*, **120**, 256 (1973).
12. B. Miller and M. I. Bellavance, *ibid.*, **120**, 42 (1973).
13. J. Newman, *Intern. J. Heat Mass Transfer*, **10**, 983 (1967).
14. W. R. Parrish and J. Newman, *This Journal*, **116**, 169 (1969).
15. W. R. Parish and J. Newman, *ibid.*, **117**, 43 (1970).
16. J. Newman, *J. Phys. Chem.*, **73**, 1843 (1969).
17. J. Newman, *This Journal*, **117**, 198 (1970).
18. D. C. Grahame, *Chem. Rev.*, **41**, 441 (1947).
19. E. Levart and D. Schuhmann, *J. Electroanal. Chem.*, **24**, 41 (1970).
20. A. M. Johnson and J. Newman, *This Journal*, **118**, 510 (1971).
21. J. Newman, "Electrochemical Systems," p. 58, Prentice-Hall, Inc., Englewood Cliffs, N. J. (1973).
22. E. Mattsson and J. O'M. Bockris, *Trans. Faraday Soc.*, **55**, 1586 (1959).
23. D.-T. Chin, *This Journal*, **118**, 1434 (1971).
24. R. Parsons, *Advan. Electrochem. Electrochem. Eng.*, **1**, 1 (1961).
25. K. Nisancioğlu and J. Newman, *This Journal*, **120**, 1356 (1973).
26. J. R. Selman, Ph.D. Thesis (UCRL-20557), University of California, Berkeley, June, 1971.
27. L. Nanis and I. Klein, *This Journal*, **119**, 1683 (1972).

Electrochemical Reduction of Molybdenum(VI) Compounds in Molten Lithium Chloride-Potassium Chloride Eutectic

B. N. Popov

Faculty of Technology and Metallurgy, University Kiril and Metodij, Skopje, 91000, Yugoslavia

and H. A. Laitinen*

Roger Adams Laboratory, School of Chemical Sciences, University of Illinois, Urbana, Illinois 61801

ABSTRACT

Molybdenum(VI) oxide reacts with molten LiCl-KCl eutectic at 450° to form MoO_2Cl_2, which probably is present as an anion $MoO_2Cl_4^=$, and pyromolybdate, $Mo_2O_7^=$. Both of these species are electrochemically reduced to MoO_2, which can be reoxidized to MoO_2Cl_2 by current reversal. A second reduction step, observed whether MoO_3 or $Mo_2O_7^{2-}$ is added to the melt, can be attributed to the reduction of $MoO_4^=$, formed as a secondary reaction product in the first step. The reduction of molybdate proceeds in two steps, the first at −0.85V and the second at −1.75V *vs.* the 1M Pt(II)/Pt reference electrode. The first step shows an abnormally short transition time, attributable to a slow equilibrium. The second step corresponds to a diffusion-controlled reduction with $n = 0.5$, yielding a product of the empirical formula $Li_5Mo_2O_8$.

The literature contains very little fundamental information on the behavior of molybdenum compounds in molten systems. Stavenhagen and Engels (1) described a sodium molybdenum bronze in the form of a dark bluish-grayish powder formed by electrolytic reduction of fused sodium molybdate. Cannery (2) reported the preparation of lithium, sodium, and potassium molybdenum bronzes using the same method. However, the next year Burgers and van Liempt (3) showed that the bronzes mentioned by Cannery were mixtures consisting of molybdenum(IV) oxide and molybdenum blue. According to Magneli, only molybdenum oxides were obtained by Hagg in similar experiments (4, 5). Wold, Kunmann, Arnot, and Ferretti (6) prepared pure MoO_2 crystals by electrolytic reduction of MoO_3-Na_2MoO_4 mixtures at 675°C. In addition, both sodium molybdenum bronze and potassium molybdenum bronze crystals were grown from molybdenum(IV) oxide-alkali molybdate melts under carefully controlled conditions. Senderoff and Brenner (7, 8) have investigated the reduction of molybdate dissolved in molten alkali halides. They found that the bulk of the reaction product was dispersed throughout

* Electrochemical Society Active Member.
Key words: molybdenum, molybdenum(VI) oxide, molybdenum oxychloride, lithium pyromolybdate, lithium molybdate, molten salts, electrochemistry.

the melt as a black, water insoluble powder containing about 77% molydenum, corresponding to MoO_2 (75% Mo).

The present investigation was undertaken in order to study the reduction of molybdenum(VI) compounds and to characterize any reduction products observed. It was also considered possible that some aspects of molybdenum chemistry and interactions between molybdenum(VI) compounds and chloride melt could be deduced.

Experimental

Apparatus.—The instrumentation and equipment used in this study have been previously described (9-11).

Electrodes.—Platinum microelectrodes for voltammetry were prepared from 26B and S gauge platinum wire as described earlier (10). Indicator electrodes for chronopotentiometric measurements were made by sealing 26 gauge platinum wire into Pyrex glass and then spot welding a piece of 0.5 cm^2 platinum foil to the end of the wire extending from the platinum glass seal. The cathodes used for the preparation of the electrode deposits were constructed from 52-mesh platinum gauze. The counterelectrode was a ⅛-in. diameter graphite rod. All potentials are referred to the 1M Pt(II)/Pt reference electrode. Details on the generation and use of this reference electrode in LiCl-KCl have been described previously (11, 12).

Chemicals.—All chemicals used in this study were reagent grade. Those chemicals containing water of hydration were vacuum dried at 110°C before being added to the melt.

The LiCl-KCl eutectic was obtained from Anderson Physics Laboratories, Inc., Urbana, Illinois. The method of purification has been described (11). All experiments in the melt were carried out at 450°C unless otherwise noted.

Solid chemicals were added to the melt by means of a small glass spoon. A blanket of argon was kept over the melt at all times to exclude oxygen and water vapor. The purification train used in purifying the argon has been described (13).

Techniques for preparation and analysis of electrode deposits.—Before their insertion in the melt solution, the gauze electrodes were cleaned in boiling, concentrated HNO_3, rinsed with distilled water, and dried at 130°C for 20 hr. After the material had been deposited on the electrode, the electrode was allowed to cool, washed with deionized water, and dried at 120°C. The deposits were then dissolved in 5 ml of concentrated nitric acid by heating on a hot plate. The molybdenum content of the deposit was determined by addition of an excess of Pb^{2+} which was back-titrated with EDTA using xylenol orange as the indicator. The total molybdenum was also obtained by amperometric titration with lead, a procedure developed by Aylward (14). The amount of reduced molybdenum in the sample was determined by the method developed by Bourret (15). Lithium was quantitatively determined by flame photometry. Chloride was determined by the Volhard method.

Results and Discussion

MoO_3-LiCl-KCl system.—Preliminary steady-state voltammetric experiments (Fig. 1) showed that MoO_3 exhibits two reduction waves in LiCl-KCl at 450°. The half-wave potentials are approximately −0.3 and −1.75V. The voltammetric curves were not highly reproducible because of the formation of an insoluble product which rapidly increases the surface area of the electrode. Upon prolonged electrolysis at the limiting plateau, a brown-violet film formed on the electrode, and the current increased with time. Chronopotentiometric experiments with proper choice of concentration and current density circumvented the difficulty due to film formation. Two transitions, at −0.35 and −1.75V, respectively, were observed, in agreement with the voltammetric observations. The Sand equation was checked for the first reduction step

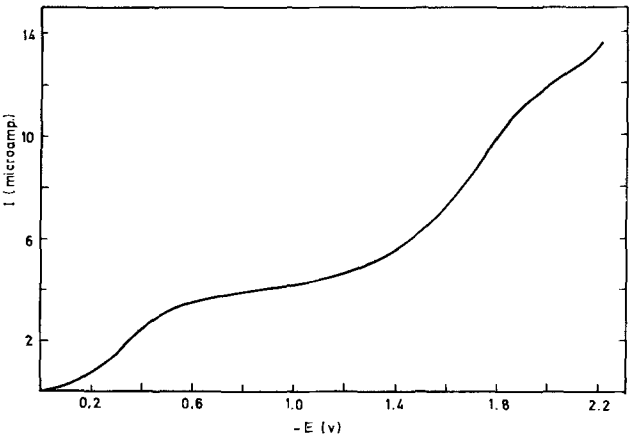

Fig. 1. Current-voltage curve for the reduction of MoO_3. Electrode area = $2.2 \cdot 10^{-3}$ cm^2; MoO_3 = $3.63 \cdot 10^{-3}$ M.

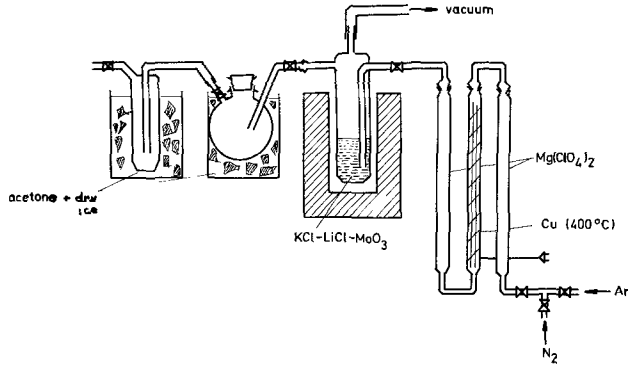

Fig. 2. Apparatus used to study acid-base reaction of MoO_3 and chloride melt.

using four to six current densities at three different MoO_3 concentrations (Table I). Constancy of the quantity $I\tau^{1/2}/C$ indicated diffusion-controlled reaction. However, it was observed during the measurements that a volatile product was slowly evaporating from the melt. Therefore, owing to the uncertain concentration it was not possible to calculate a valid diffusion coefficient from the data.

To establish the nature of the volatile product, the apparatus shown in Fig. 2 was used. Previously dried MoO_3 was added to the melt, air was excluded, and the volatile product was displaced by inert gas into a weighed trap cooled with acetone and dry ice. The product was yellow in color, very volatile, and soluble in water. Analysis for Mo and Cl^- by the methods described above showed that the sample weight could be completely accounted for in terms of the compound MoO_2Cl_2. To determine the product formed from the

Table I. Chronopotentiometric data for the first reduction step of MoO_3

C_{MoO_3} (M)	I (mA)	$I\tau^{1/2}$ (A-$sec^{1/2}$)	$I\tau^{1/2}/C$ (A-$sec^{1/2}$ cm^3 mol^{-1})
$3.63 \cdot 10^{-3}$	1.540	$0.784 \cdot 10^{-3}$	210
	1.050	$0.715 \cdot 10^{-3}$	197
	0.550	$0.671 \cdot 10^{-3}$	185
	0.680	$0.664 \cdot 10^{-3}$	183
	0.596	$0.660 \cdot 10^{-3}$	183
	0.630	$0.680 \cdot 10^{-3}$	187
		Avg $0.679 \cdot 10^{-3}$	Avg 187
$9.84 \cdot 10^{-3}$	2.500	$1.802 \cdot 10^{-3}$	183
	2.000	$1.780 \cdot 10^{-3}$	181
	1.670	$1.734 \cdot 10^{-3}$	176
	1.430	$1.770 \cdot 10^{-3}$	181
		Avg $1.770 \cdot 10^{-3}$	Avg 181
$2.3 \cdot 10^{-2}$	10.000	$4.250 \cdot 10^{-3}$	185
	6.670	$4.200 \cdot 10^{-3}$	183
	5.550	$4.350 \cdot 10^{-3}$	189
	4.540	$4.140 \cdot 10^{-3}$	180
		Avg $4.230 \cdot 10^{-3}$	Avg 184

reaction of the oxide ion, the melt was extracted from the product with ethanol and acetone to yield $Li_2MO_2O_7$, which accounted completely for the sample weight. Accordingly the reaction between MoO_3 and the melt can be written

$$3MoO_3 + 2Cl^- \rightarrow MoO_2Cl_2 + Mo_2O_7^=$$

A phase diagram study of MoO_3 and Li_2MoO_4 was carried out to verify further the existence of $Li_2Mo_2O_7$. Phase transition temperatures were determined for eight samples ranging in composition from 42 to 55 m/o (mole per cent) MoO_3. The experiments were done by the visual polythermal method in which the temperature of the first crystals was measured by a Pt-Rh thermocouple. From Table II it is evident that a local maximum exists for the molar ratio $MoO_3/Li_2MoO_4 = 1$, implying the formation of a solid compound $Li_2Mo_2O_7$. An x-ray powder pattern of the 1:1 sample is described in Table III. No lines for MoO_3 or Li_2MoO_4 were found in the diffraction pattern, thus precluding the possibility that the material is a mixture of MoO_3 and Li_2MoO_4.

To determine whether the acid-base reaction occurs completely before the electrolysis experiments, the data of Table I were examined for a chemical reaction preceding charge transfer by plotting $I_o\tau^{1/2}/C$ *vs.* I_o and I_o/C. The plots showed no discernible downward slope, but only a scatter that could be attributed to uncertainties in concentration owing to volatility of the oxychloride, and perhaps to variation in electrode area with the formation of solid deposit.

Plots of E *vs.* log $(\tau^{1/2} - t^{1/2})$ were linear as shown in Fig. 3. This function would be expected to yield linear plots either for a totally irreversible charge transfer process or for a reversible process with the formation of a solid product of constant activity. Current reversal chronopotentiometry showed an anodic transition upon reversal of the current at the inflection point (Fig. 4): ratios of the coulombs of charge in the forward to backward electrolysis varied between 0.985 and 1.025, indicating the quantitative formation of a solid product that can be reoxidized. If the slope of the log plot is equated to $2.3\ RT/\alpha n_a F$, we calculate

Table II. Melting points of MoO_3-Li_2MoO_4 system

Mole per cent MoO_3	Mole per cent Li_2MoO_4	Melting point, °C
42	58	550
45	55	520
48	52	495
49	51	526
50	50	534
51	49	515
53	47	535
55	45	555

Table III. X-ray powder diffraction pattern of $Li_2Mo_2O_7$

d (A)	I/I_o
6.4241	10
5.3679	10
4.1385	30
3.7824	10
3.6820	10
3.5199	80
2.9809	50
2.9780	50
2.8823	10
2.8331	10
2.7136	50
2.5074	10
2.3659	10
2.1917	100
2.1396	50
2.0064	60
1.9012	80
1.8398	5
1.8294	5
1.8030	5
1.7697	5
1.7323	5
1.6937	70
1.6161	10
1.5900	20
1.5522	90
1.5043	40

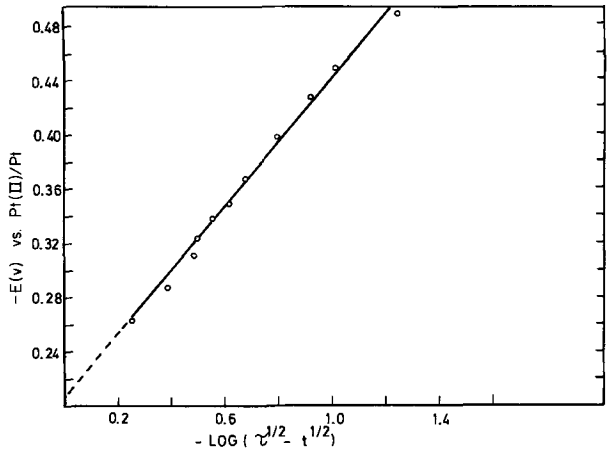

Fig. 3. Potential-time curve for the first reduction step of MoO_3.

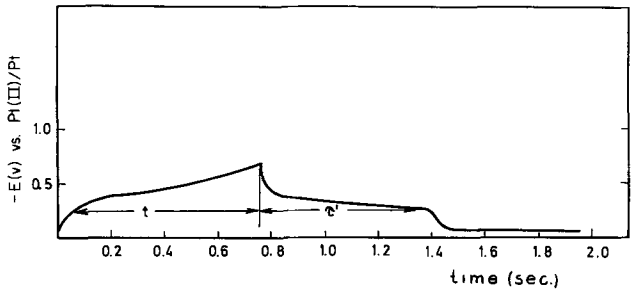

Fig. 4. Typical reverse current chronopotentiogram for the first reduction step of MoO_3. $I_f = I_r = 2.0$ mA/cm^2.

$\alpha n_a = 0.56$ rather than 2 for a reversible process. Neglecting the back-reaction, the value of $k_{f,h}$ at -0.208V, the starting potential, is calculated to be 3.18×10^{-3} cm-sec^{-1}.

Analysis of the reduction products of MoO_3.—Samples of the first reduction product, prepared coulometrically from 0.35M MoO_3 solution using a platinum gauze cathode, in the form of a homogeneous, brown-violet solid, were boiled in distilled water to remove chlorides and soluble molybdates and dried at 130°. Analysis revealed only MoO_2, and the x-ray powder pattern agreed in d-spacings and approximate relative densities with the ASTM files for MoO_2.

Attempts were also made to prepare the second reduction product, by holding the potential of the working electrode at -1.75V. A product showing x-ray lines of MoO_2, plus several weak lines, and containing Li but not K was formed, corresponding to a mixture of the first and second reduction products. The composition could not be completely accounted for in terms of MoO_2 and Li_2O or Mo_2O_5 and Li_2O. It is possible that the second reduction product is partially soluble in the melt.

MoO_2Cl_2-LiCl-KCl-system.—The solubility of MoO_2Cl_2 in the melt was determined at three temperatures, 400°, 450°, and 500°, by saturating an argon gas stream with the vapor and bubbling the dilute stream (heated to 120° to avoid crystallization from the vapor) through the melt for at least 2 hr, and analyzing the melt for molybdenum. The solubility was found to be 2.60 ± 0.12, 2.75 ± 0.14, and $2.78 \pm 0.09 \times 10^{-5}$ moles MoO_2Cl_2/cm^3 at the three temperatures. The relatively high solubility and low vapor pressure over the melt indicates a strong interaction between MoO_2Cl_2, probably to form an anion $MoO_2Cl_4^=$ with the chloride ion of the melt.

Chronopotentiometry indicated a single wave, occurring at a potential of -0.35V, in agreement with the postulated interaction between MoO_3 and melt. From the value of $I_o\tau^{1/2}/C = 560 \pm 10$ A-sec$^{1/2}$ cm mol^{-1}, $n = 2$, the diffraction coefficient was calculated to be 1.08×10^{-5} cm^2/sec.

Table IV. Chronopotentiometric data for the first reduction step of $Li_2Mo_2O_7$

$C_{Mo_2O_7^=}$ (millimolar)	I_o (mA)	$I_o\tau^{1/2}$ (mA-sec$^{1/2}$/cm^2)	$I_o\tau^{1/2}/C$ (A-sec$^{1/2}$ cm^3 mole^{-1})
3.48	1.60	1.92	552
	2.00	1.82	524
	2.44	1.81	520
	3.00	1.77	509
			Avg 526
10.80	6.00	4.97	460
	7.00	4.85	449
	7.50	4.77	442
	8.00	4.55	421
			Avg 443
21.23	6.00	8.15	383
	8.00	7.84	369
	9.00	7.74	364
	10.00	7.80	366
			Avg 371
95.40	28.00	33.05	348
	30.00	31.20	327
	34.00	31.28	331
	36.00	30.96	324
			Avg 332

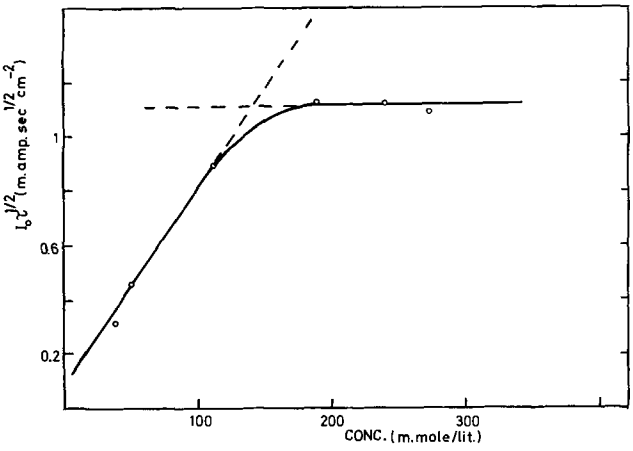

Fig. 5. Variation of $I_o\tau^{1/2}$ with Li_2MoO_4 concentration for the first reduction step.

Constant current electrolysis carried out at potentials never more negative than −0.35V, of a solution of MoO_2Cl_2 prepared by bubbling the vapor through the melt for 2 hr produced a brown-violet deposit. Comparison of the micromoles of molybdenum with the microfaradays of current consumed indicated a consumption of two electrons per molybdenum atom. The x-ray powder pattern agreed with that of the first reduction product of MoO_3 and with the ASTM pattern of MoO_2. The electrode reaction at −0.35V can thus be described as

$$MoO_2Cl_2 + 2e^- \rightleftarrows MoO_2 + 2Cl^-$$

or

$$MoO_2Cl_4^= + 2e^- \rightleftarrows MoO_2 + 4Cl^-$$

$Li_2Mo_2O_7$-LiCl-KCl system.—The chronopotentiometric behavior of $Li_2Mo_2O_7$ was found to be quite similar to that of MoO_3. Two waves were observed, one at −0.44V and the other at approximately −1.75V. The transition time data for the first reduction process (Table IV) were somewhat scattered, showing a trend to decrease with concentration and with increasing current density. When both MoO_3 (3.55 mM) and $Li_2Mo_2O_7$ (2.15 mM) were present, two waves were once again observed, one at −0.37V and the other at −1.75V. It is concluded that the first wave of MoO_3 is actually the sum of the first waves of MoO_2Cl_2 and $Mo_2O_7^=$.

The first reduction product of $Li_2Mo_2O_7$ was characterized as before, and identified as MoO_2. Accordingly, the first reduction process can be written

$$Mo_2O_7^= + 4e^- \rightarrow 2MoO_2 + 3\,O^=$$

with a following acid-base reaction, no doubt

$$3Mo_2O_7^= + 3\,O^= \rightarrow 6MoO_4^=$$

The complexity of this process presumably accounts for the lack of diffusion control in the over-all process.

$MoO_4^=$-LiCl-KCl system.—Chronopotentiograms were recorded over a concentration range of 8.03×10^{-3}M to 0.2725M Li_2MoO_4. At current densities below 2 mA/cm^2, two waves were discerned, one at −0.85V and the other at −1.75V. The first wave increased with concentration until the concentration reached 1.12×10^{-2}M, and leveled off at higher concentrations (Fig. 5). The slope of the plot at low concentrations yielded $I_o\tau^{1/2}/C = 9.87 \pm 0.6$ A-sec$^{1/2}$ cm mol^{-1}, corresponding to $nD^{1/2} = 1.45 \times 10^{-4}$ cm-sec$^{-1/2}$. Such an abnormally low transition time constant suggests an equilibrium such as

$$MoO_4^= + 2Cl^- \rightleftarrows MoO_3Cl_2^= + O^=$$

in which $MoO_3Cl_2^=$ exists as a minority component responsible for the first reduction step. If such an equilibrium exists, it must be relatively slow, because $I_o\tau^{1/2}$ was not found to decrease with increasing current density as would be expected for a prior chemical step with appreciable interconversion during the time of electrolysis.

With a molybdate concentration of 5.35×10^{-2}M and with a current density of 16 mA/cm^2 only the second transition was observed. The Sand equation was tested for four to five current densities at five different molybdate concentrations (Table V). The average value of $I_o\tau^{1/2}/C$ calculated from these data is 174 ± 6 A-sec$^{1/2}$ cm mol^{-1}, corresponding to $D = 1.64 \times 10^{-5}$ cm-sec^{-1} at 450°, taking $n = 0.5$ from the analytical data given below.

Attempts to prepare the first reduction product by constant current electrolysis were unsuccessful. Using 0.85M Li_2MoO_4, even with current densities lower than 100 μA/cm^2, the electrode potential rapidly rose beyond that corresponding to the first reduction step. Using current densities of 100 μA, 5 mA, and 10 mA/cm^2, deposits were prepared by electrolyzing at −1.18 to −1.2V, at −1.5V, and at −1.75V, respectively. Examination of the cathodes showed only one type of solid product, an adherent dark brown-black solid with a metallic luster. The samples were washed with distilled water, dried at 130°, and analyzed for Li and Mo with the results given in Table VI. The deposit was found to contain an average of 54.0% Mo and 9.85% Li but no K or Cl. The ratio Li/Mo is 2.52. No appreciable trend of composition with current density was observed. If it is assumed that the deposit contains only Li, Mo, and O, the empirical formula $Li_{2.49}MoO_{3.96}$ is obtained indicating an average oxidation state of 5.5 for molybdenum.

Additional preparations produced at −1.75V were analyzed for oxidation state, with the results listed in Table VII. The sum of Li_2O, Mo_2O_5, and MoO_3 is very close to 100%, confirming the absence of K and Cl, and indicating once more that the product is $Li_{2.5}MoO_4$ or $Li_5Mo_2O_8$. To ascertain whether the product is a single compound or a mixture, an x-ray powder pattern was obtained for the products prepared at −1.2, −1.5, and −1.75V. The d spacing along with relative intensities are given in Table VIII. No lines for LiCl or Li_2MoO_4 were found in the diffraction pattern. The diffraction data do not correspond with any known molybdenum compound listed in the ASTM files or with other deposits obtained by reduction of Mo(VI) compounds.

Table V. Chronopotentiometric data for the second reduction step of lithium molybdate

Molybdate conc. (millimolar)	$I_o\tau^{1/2}$ (mA-sec$^{1/2}$/cm^2)	Range of I_o (mA/cm^2)
8.03	1.29 ± 0.08	2.5-4.0
20.80	3.46 ± 0.06	6.0-10.0
53.50	9.72 ± 0.09	24.0-20.0
110.02	20.04 ± 0.18	24.0-44.0
178.05	31.00 ± 0.90	26.0-34.0

Table VI. Typical analysis of Li_2MoO_4 deposit prepared at constant current

Sample	A	B	C	D	E	F
Current density, mA/cm²	5	5	5	10	10	10
Sample weight, mg	73.5	129.9	112.5	150.6	148.2	134.5
Li, mg found	7.17	12.7	11.0	15.2	14.7	13.2
Per cent weight Li	9.7	9.8	9.8	10.1	9.9	9.9
Mo, mg found	39.6	70.6	61.1	81.2	80.23	72.2
Per cent weight Mo	53.9	54.4	54.1	53.8	54.0	53.6
Per cent weight O= to 100%	36.3	35.8	36.1	36.1	36.1	36.5
Li found, μmoles	1035	1830	1585	2200	2120	1910
Mo found, μmoles	412	736	636	846	835	753
O calculated, μmoles	1670	2920	2520	3380	3320	3065
Empirical formula	$Li_{2.51}MoO_{3.95}$	$Li_{2.46}MoO_{3.96}$	$Li_{2.49}MoO_{3.95}$	$Li_{2.59}MoO_{3.99}$	$Li_{2.55}MoO_{3.96}$	$Li_{2.54}MoO_{4.07}$

Table VII. Determination of the empirical formula of Li_2MoO_4 deposit prepared at constant potential

Sample	A	B	C	D
Milliliters 0.05*N* $Na_2S_2O_8$	6.29	7.42	8.54	9.40
Milligrams $NaIO_3$ calculated	25.9	29.8	35.2	38.7
Milligram total Mo calculated	50.7	60.7	67.7	78.2
Average valence of Mo	5.50	5.51	5.49	5.52
Micromoles Li	1320	1600	1730	2010
Milligrams Li_2O	19.8	23.8	25.9	30.1
Total Mo, mg	50.7	60.7	67.5	78.2
Micromoles Mo	528	632	702	815
Milligrams Mo(V)	25.0	29.8	34.2	37.8
Milligrams Mo_2O_5	35.6	42.2	48.5	53.6
Milligrams Mo(VI)	25.7	31.0	33.3	40.4
Milligrams MoO_3	38.4	46.2	50.0	60.6
Total mg found	93.8	112.3	124.3	144.4
Sample weight, mg	92.6	113.5	123.1	143.3
Per cent weight found	101.9	99.2	101.0	100.5
Empirical formula	$Li_{2.50}MoO_{4.00}$	$Li_{2.52}MoO_{4.02}$	$Li_{2.48}MoO_{3.98}$	$Li_{2.47}MoO_{3.99}$

To study the stability of the product, one sample was heated at 300° under vacuum. No change in diffraction pattern was observed. The deposit was further boiled in distilled water 3 hr and dried at 200°. The boiled product exhibited a different x-ray pattern as shown in Table IX. The analytical data indicated Li/Mo to be 4.43/2 and the sum of the weight percentages of Li_2O + MoO_3 to be 97.66, indicating the presence of water in the sample or partial oxidation of Mo_2O_5.

The electrode reaction of molybdate can be written

$$2MoO_4^{=} + e^- \rightarrow Mo_2O_8^{-5}$$

The mechanism of this reaction is unclear. There is no evidence for dimerization of molybdate prior to reduction, and the diffusion coefficient is consistent with our expectation for a monomer. The simplest mechanism would be the formation of the anion MoO_4^{3-}, with the incorporation of equimolar amounts of MoO_4^{2-} with lithium ions to form the crystalline compound $Li_5Mo_2O_8$.

Table VIII. X-ray powder diffraction pattern of $Li_5Mo_2O_8$

d (A)	I/I_o
4.9130	60
2.4661	60
2.3659	20
2.0740	100
1.9125	20
1.4912	40
1.4443	40
1.3882	40

Table IX. X-ray powder diffraction pattern of boiled deposit

(A)	I/I_o
3.6302	60
3.2785	30
2.9568	10
2.6727	100
2.5510	10
2.2046	30
2.0279	30
1.8845	10
1.8345	10
1.7172	20
1.6752	20

Acknowledgment

One of the authors (B. N. P.) is indebted to the University of Illinois for the support in the form of research assistantship. Financial support of this research was provided by the United States Army Research Office-Durham and by the Center for Application of Radioisotopes in Industry, Skopje, Yugoslavia.

Manuscript submitted March 30, 1973; revised manuscript received May 18, 1973.

Any discussion of this paper will appear in a Discussion Section to be published in the June 1974 JOURNAL.

REFERENCES

1. A. Stavenhagen and E. Engels, *Ber.*, **28**, 2281 (1895).
2. C. Cannery, *Gazz. Chim. Ital.*, **60**, 113 (1930).
3. W. G. Burgers and J. A. M. Van Liempt, *Z. Anorg. Allgem. Chem.*, **302**, 325 (1931).
4. A. Magnéli, *N. Acta Reg., Sc. Upsaliensis*, **14**, No. 816 (1939).
5. G. Hagg, *Z. Physik. Chem.*, **B29**, 192 (1935).
6. A. Wold, W. Kunnmann, R. J. Arnott, and A. Ferretti, *Inorganic Chem.*, **3**, 545 (1964).
7. S. Senderoff and A. Brenner, *This Journal*, **101**, 16 (1954).
8. S. Senderoff and A. Brenner, *ibid.*, **101**, 31 (1954).
9. H. A. Laitinen and J. H. Propp, *Anal. Chem.*, **38**, 644 (1969).
10. H. A. Laitinen and B. N. Popov, *This Journal*, **117**, 482 (1970).
11. H. A. Laitinen and K. W. Hanck, *ibid.*, **118**, 1123 (1971).
12. H. A. Laitinen and K. R. Lucas, *ibid.*, **12**, 553 (1966).
13. H. A. Laitinen and D. R. Rhodes, *ibid.*, **10**, 413 (1962).
14. G. H. Aylward, *Anal. Chim. Acta*, **14**, 386 (1956).
15. P. Bourret, J. M. Lecure, and K. Weis, *Chim. Anal. (Paris)*, **52**, (1) 48 (1970).

The Electrochemical Response of a Disk Electrode to Angular Velocity Steps

Stanley Bruckenstein[*,1], **Maria I. Bellavance, and Barry Miller**[*]

Bell Laboratories, Murray Hill, New Jersey 07974

ABSTRACT

An experimental study has verified the prediction that the establishment of a boundary layer at the surface of an impulsively started disk is complete in less than three tenths of a rotation. A similar result was found for a rotating disk electrode whose speed was stepped between two values. The current transient produced by a step change of the rotation speed of a disk electrode held in the convective-diffusion limiting current region of some electroactive species has been derived. Studies of the reduction of Ag^+, Fe^{3+}, and Hg_2^{2+} are in good agreement with theory and show that the relaxation process is limited by the convective-diffusion of the electroactive species rather than the hydrodynamic relaxation phenomenon.

Heretofore, nonsteady-state studies using the rotating disk electrode have been carried out at constant angular velocity by perturbing the potential and measuring the time-dependent current response, or vice versa. Recently, angular velocity programming of rotating (ring) disk electrodes has become feasible (1, 2) and is being used to advantage in electrochemical studies (2, 3). However, it became apparent that electrochemical transients could be produced by rapidly scanning or applying a step change to the angular velocity of a disk electrode.

In most disk electrode angular velocity studies, experimental problems such as adsorption of impurities from solution, growth of dendrites during metal deposition, or surface roughening by electrode dissolution can be minimized if rapid angular velocity programming is used. However, in such situations, appreciable deviation from steady-state flow conditions is unacceptable since the ultimate data treatment assumes a hydrodynamic steady-state. Hence, a quantitative treatment of the electrochemical transient resulting from an angular velocity perturbation would be of considerable utility.

In this paper, we consider one of the many possible situations, namely, the time-dependent current response obtained under potentiostatic conditions on application of an angular velocity step. To avoid electrochemical kinetic complications, the potential chosen in all the examples was sufficient to produce complete concentration polarization of the diffusing species. It will be shown that little change in current occurs during the time required for the new hydrodynamic "steady-state" to be attained, and the current-time transient results primarily from the relaxation of the (convective-) diffusion layer thickness.

Theoretical

Benton (4) investigated the time-dependence of fluid flow near an impulsively started disk ($\omega = 0$ at $t = 0$, $\omega = \omega_2$ at $t > 0$) using a series expansion technique. He found that the time dependence of the normal fluid velocity, w, could be represented, to a good approximation, by

$$w(\eta, \Phi) = -4(\nu\omega_2)^{1/2}\Phi^{3/2}\,[h_1(\eta) + h_2(\eta)\Phi^2 + h_3(\eta)\Phi^4 + \ldots] \quad [1]$$

where values of the functions $h_1(\eta)$, $h_2(\eta)$, and $h_3(\eta)$ were given in tabular form, and

$$\Phi = \omega_2 t \quad [2]$$

$$\eta = z/2(\nu t)^{1/2} \quad [3]$$

ν is the kinematic viscosity of the solution and z the normal distance coordinate, where $z = 0$ on the electrode.

A complete description of the electrochemical response of an impulsively started disk electrode would require that Eq. [1] be applicable for $0 \leq \Phi \leq \infty$. However, as Benton has pointed out, the third term in the series has outlived its usefulness by $\Phi = 2$ radians and Eq. [1] is a reliable description only in the range $0 \leq \Phi \sim 2$. This result was satisfactory for Benton's purposes, since the asymptotic steady-state is approached. Since no other work on this problem appears to have been done, and lacking an analytical description of the behavior of $w(\eta,\Phi)$ for $2 \sim \Phi < \infty$, the combined electrochemical/hydrodynamic problem was examined in the range $0 \leq \Phi \sim 2$. The details are given in the Appendix, and it was found that only a negligible fraction of the total electrochemical response took place by $\Phi = 2$. Thus it appeared justifiable to simplify the problem by assuming that the hydrodynamic relaxation was instantaneous compared to the electrochemical response. We have performed experiments, described below, that confirm this assumption.

No studies, describing the nonsteady-state fluid flow when the angular velocity of a disk is stepped from one value to another, ω_1 to ω_2, appear to have been made. However, our experiments indicate that the relaxation times of the electrochemical transient in this case were quite similar to those for the impulsively started disk. Thus, it seemed reasonable to assume again that the hydrodynamic relaxation would be instantaneous on the time scale of the electrochemical transient. Again, experiments reported below support this assumption.

Potentiostatic condition.—Consider the electrochemically reversible reaction

$$Ox + ne \rightleftarrows Red$$

where Ox exists at a bulk concentration C^b, and the electrode potential of the disk is held constant. At a certain instant in time, the velocity of a disk electrode is changed instantaneously. We distinguish between the impulsively started stationary disk problem and the situation in which the velocity step is applied to a rotating disk only in the way in which we describe the concentration profile at $t = 0$. For obvious reasons, the first problem is referred to as a Cottrell-Levich experiment and the second as a Levich-Levich experiment. In either experiment, the instantaneous diffusion layer thickness existing at $t = 0$, as determined by the Cottrell equation in one case, and by the Levich equation in the other, begins to change on applying the angular velocity step in a way governed by the nonsteady-state fluid flow and the convective-diffusion equation. Ultimately the diffusion layer thickness reaches a value governed by the new angular velocity.

* Electrochemical Society Active Member.
[1] Permanent address: Department of Chemistry, State University of New York at Buffalo, Buffalo, New York 14214.
Key words: rotating electrode, hydrodynamic relaxation, boundary layer, convective-diffusion, potentiostatic control.

The time-dependent convective-diffusion equation for the rotating disk electrode may be written

$$\frac{\partial C}{\partial t} = D\frac{\partial^2 C}{\partial z^2} - w(z,t)\frac{\partial C}{\partial z} \quad [4]$$

Applying the Method of Moments as was done previously (5), Eq. [4] may be integrated with respect to z from 0 to ∞, thereby obtaining a gross mass balance

$$\int_0^\infty \frac{\partial C}{\partial t}dz = -D\frac{\partial C}{\partial z}\bigg|_{z=0} - \int_0^\infty w(z,t)\frac{\partial C}{\partial z}dz \quad [5]$$

Assuming that a simple time-dependent Nernst diffusion layer provides an adequate description of the problem, the upper limit of the integrals in Eq. [5] may be replaced by δ. Also, under potentiostatic conditions for the reversible electrochemical case, the concentration distribution of the electroactive species may be approximated by

$$C(z,t) = \begin{cases} C^s + (C^b - C^s)z/\delta & 0 \leq z \leq \delta \\ C^b & \delta < z < \infty \end{cases} \quad [6]$$

Hence

$$\frac{\partial C}{\partial t} = \begin{cases} \dfrac{-(C^b - C^s)z\dot{\delta}}{\delta^2} & 0 \leq z \leq \delta \\ 0 & \delta < z < \infty \end{cases} \quad [7]$$

and

$$\frac{\partial C}{\partial z} = \begin{cases} \dfrac{C^b - C^s}{\delta} & 0 \leq z \leq \delta \\ 0 & \delta < z < \infty \end{cases} \quad [8]$$

Thus, Eq. [3] becomes

$$\frac{\dot{\delta}}{2} = \frac{D}{\delta} + \int_0^\delta \frac{w(z,t)}{\delta}dz \quad [9]$$

Finally

$$w(z,t) = \begin{cases} w_1(z) & \text{at } t = 0 \\ w_2(z) & t \to \infty \end{cases} \quad [10]$$

and

$$\delta(t) \to \delta_L \qquad \text{as } t \to \infty \quad [11]$$

By assuming that $w(z,t) = w_2(z)$ at $t > 0$ for the reasons discussed earlier and remembering that $w(z) = 0.51\ (\omega^3/\nu)^{1/2}\ z^2$ (6), we can then substitute Eq. [12]

$$w(z,t) = w_2(z) = -0.51\left(\frac{\omega_2^3}{\nu}\right)^{1/2} z^2 = Kz^2 \quad [12]$$

into Eq. [9] and integrate to obtain

$$\Phi = \frac{A}{Q}\int_L^Y \frac{\theta d\theta}{(1-\theta^3)} \quad [13]$$

where

$$A = 1.3125 \quad [14]$$

$$Q = 0.8058\left(\frac{D}{\nu}\right)^{1/3} \quad [15]$$

$$Y = \delta/\delta_L = (i)_{t=\infty}/(i)_t \quad [16]$$

$$\delta_L = 1.6116\left(\frac{D}{\nu}\right)^{1/3}\left(\frac{\nu}{\omega_2}\right)^{1/2} \quad [17]$$

$$L = (i)_{t=\infty}/(i)_{t=0} \quad [18]$$

The lower limit of the integral in Eq. [13] is the ratio of the steady-state current reached after the angular velocity step to the current existing just prior to the velocity step. The upper limit corresponds to the ratio of the final steady current to the instantaneous current. δ_L is the steady-state convective-diffusion layer thickness attained at angular velocity ω_2.

Since Eq. [13] can be integrated in closed form, we obtain

$$\Phi = F(Y) - F(L) \quad [19]$$

where

$$F(\theta) = \frac{A}{3Q}\left\{ \tfrac{1}{2}\ln\frac{1-\theta^3}{(1-\theta)^3} - \sqrt{3}\tan^{-1}\left(\frac{2\theta+1}{\sqrt{3}}\right)\right\} \quad [20]$$

Equation [19] predicts that, for a given redox couple, a plot of Y (or Y^{-1}) *vs.* Φ for data obtained in experiments with the same L-values will yield a single curve. Also, from Eq. [19], we see that for data obtained in experiments involving different L-values, *e.g.*, L_1 and L_2, the plots of Y^{-1} *vs.* Φ will have the same shape and be displaced from each other on the Φ-axis by $F(L_1) - F(L_2)$.

Intercomparisons between different redox couples are best made by plotting Y^{-1} *vs.* $Q\cdot\Phi$. The new variable, $Q\cdot\Phi$, is independent of all species and solution parameters, as can be seen from Eq. [13], [19], and [20]. Hence, data obtained for any species at the same L-value should fall on the same curve when Y^{-1} is plotted *vs* $Q\cdot\Phi$.

Experimental

Chemicals.—The materials and general techniques used have been described elsewhere (2, 7). A 2.17 mM Fe^{3+}-1.0M H_2SO_4 solution was used in the Cottrell-Levich experiments and in one of the Levich-Levich experiments. The other Levich-Levich experiments used a 2.0 mM Ag^+-1.0M $HClO_4$ solution and a 4.0 mM Hg_2^{2+}-1.0M $HClO_4$ solution. Solutions were purged with nitrogen to remove oxygen and blanketed with nitrogen during all experiments.

Electrodes.—A platinum disk electrode, $r = 0.239$ cm, was used for the reduction of Fe^{3+} and Ag^+. An amalgamated gold disk electrode, $r = 0.238$ cm, was used for the reduction of Hg_2^{2+}.

Speed control.—A description of the motor speed apparatus and associated electronics has been given earlier (7).

Impulsively started disk experiment.—Three function generators were required to perform this experiment. The first function generator (Wavetek Model 114) changed the motor speed, and the second (General Radio Model 1340) was triggered by the first to produce a square wave pulse of variable duration. At the end of the square wave pulse, an oscilloscope (Tektronix Model 564 storage oscilloscope) was triggered simultaneously with the third function generator (Tacussel GSTP2), which provided the control signal to the potentiostat for the potential jump. The time between the motor speed step and the potential step was varied between 2 μsec and 2 sec in the experiments reported below. Effectively, 2 μsec was treated as zero time delay.

Cottrell-Levich experiment.—In these experiments, a potential step was applied to a stationary disk electrode. The initial potential was chosen so that no faradaic process was occurring, while the final potential was selected to lie on the limiting (convective-) diffusion current region for the reduction of Fe^{3+}. After a predetermined time, the angular velocity was stepped to the desired value. The Wavetek function generator provided the control signal for the angular velocity step, and the Tacussel function generator provided the potential step control signal to the disk electrode potentiostat (8). Current-time curves were recorded oscilloscopically. Triggering was accomplished by appropriate use of the two function generators.

Levich-Levich experiment.—The disk electrode potential was set to give the convective-diffusion limiting current for the reduction being studied and the

angular velocity set at the desired initial value. Using the Wavetek function generator as the control signal for the angular velocity step and oscilloscope trigger, the rotation speed was stepped to the desired final value and the current-time curve recorded.

Results and Discussion

Time of hydrodynamic relaxation.—Impulsively started disk.—Benton (4) concluded that boundary layer displacement thickness for an impulsively started disk would be close to the steady-state value two radians after the angular velocity step. In principle, the potential step method is capable of estimating the evolution time for the flow and thus testing Benton's conclusion. Consider the following experiment. At time $t = 0$, the disk is stepped from $\omega = 0$ to some constant value. The electrode potential is held so that the current at the disk electrode is zero. At $t = \tau$, the electrode potential is jumped to a value in the convective-diffusion limiting region, and the current transient recorded. If $\tau = 0$, both the rotation speed and potential change at the same time. If $\tau >> 0$, the potential step occurs after the new boundary layer has become established. Hence, by varying τ, it should be possible to detect, by comparison of i-t curves, whether the hydrodynamic steady state has been reached by a particular value of τ. An experiment of this sort is shown in Fig. 1.

Curve A of Fig. 1 represents the motor speed as determined from the motor tachometer voltage. The subscripts refer to the τ values in seconds for the experiments that were performed. Curve B is the current transient produced in a potential step at a stationary platinum disk electrode in a 2.17 mM Fe^{3+}-1M H_2SO_4 solution, and has all the characteristics of a situation very nearly approximating semi-infinite linear diffusion. Curve C is the superposition of current transients for $\tau = 0$ and $\tau = 2$ sec. In this, and in other experiments in which the i-t curves were magnified as they are for curves B′ and C′, all values of $\tau \geq 0$ produced current transients that superimposed on curves C and C′.

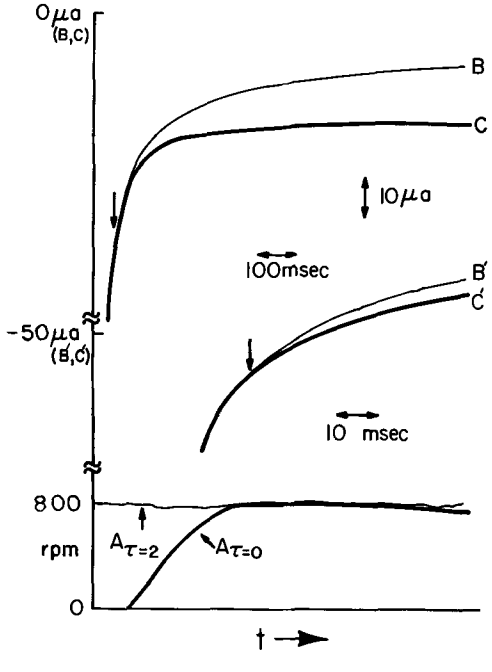

Fig. 1. Effect of time delay between a rotation speed step and a potential step on an i-t curve. 2.17 mM Fe^{+3}-1M H_2SO_4 solution. Speed step. 0→800 rpm (curve A: delay time indicated for subscript τ in seconds). Curve B: potential step at stationary disk electrode, 0.60 to 0.00V. Curves C and C′: potential step at rotating disk electrode, 0.60 to 0.00V, $\tau = 0$ sec. A delay time of two seconds produces curves that exactly superimpose on curves C and C′.

It is clear that the evolution time for the flow is less than the rise time of the motor speed, 0.027 sec. At the speed used, 800 rpm, this corresponds to 2.3 radians of rotation. The response characteristic of the motor system precludes making measurements at shorter times.

Despite the failure of this experiment to produce evidence for a hydrodynamic relaxation, it is possible to conclude that Benton's predicted value of two radians is not too large. In addition, the results in Fig. 1 indicate that a problem exists with the simplified boundary condition given by Eq. [12], where it was assumed that $\omega = \omega_2$ at $t > 0$. Because the motor speed rise time is greater than the evolution time of the flow, the early stages of the i-t response will not agree with theory.

ω-Stepped rotating disk.—Experiments analogous to those in the previous section were performed by stepping the rotation speed of the disk electrode from 100 to 400 rpm in the same solution used for Fig. 1. No evidence for a hydrodynamic relaxation was found for $\tau \geq 0$ for times as short as 0.065 sec, *i.e.*, 2.7 radians. Benton did not treat this case, but as assumed in the theoretical section, the evolution time for the flow is not longer than for an impulsively started disk.

The rise time for the motor speed was 0.020 sec, *i.e.*, 1.3 radians. Thus it was possible to compare i-t curves for varying τ values at times corresponding to an angular rotation larger than 1.3 radians, and it was found that all τ-values yielded identical i-t curves. However, data in the region 0.8 to 2.7 radians (0.020 to 0.065 sec) are without significance in this experiment because no difference can be detected between the i-t curves for a stationary electrode and one rotating at 400 rpm in this time interval. Hence, the relaxation of the boundary layer could not produce any detectable electrochemical effect.

Generally, in these sorts of experiments, the response of the motor speed, in terms of angular rotation, varied over a considerable range. The actual value depended on the initial and final rotation speed, and such data are given below where they are relevant.

Cottrell-Levich experiment.—Figure 2 shows a typical result obtained for the reduction of a 2.17 mM Fe^{3+}-1.0M H_2SO_4 solution. Curve A represents the oscilloscopically recorded i-t curve for the reduction of Fe^{3+} while curve B shows the time dependence of the motor speed. As can be seen, the change in motor speed occurs in a time that appears short compared to the current-time relaxation. Values of Y^{-1} (Eq. [16]) and Φ were calculated from curve A, assuming that

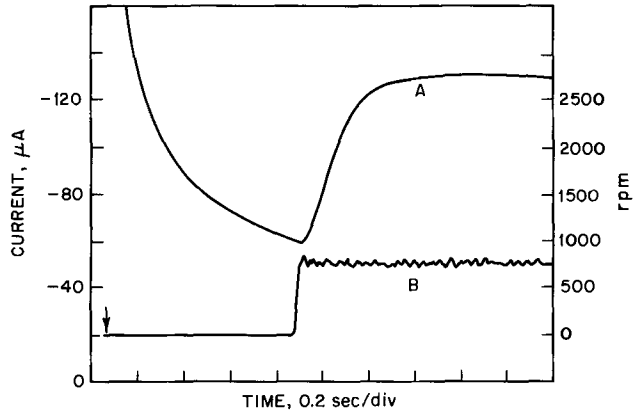

Fig. 2. Oscilloscope traces of a Cottrell-Levich experiment. Trace A: disk current, microamperes. Trace B: disk speed, rotations per minute. Horizontal sensitivity 0.2 sec/division, with vertical arrow on trace B indicating triggering time for both sweep and for disk potential step from +0.60 to 0.00V vs. SCE. Speed step 0-800 rpm. Minimum in trace A is $i_{Cottrell}$; plateau at upper right is i_{Levich}. Solution 2.17 mM Fe^{3+} in 1M H_2SO_4, Pt disk.

the minimum in the current-time curve corresponded to the instant the electrode speed changed.

Figure 3 presents the results of four such experiments corresponding to L-values between 1.546 and 2.870. The dashed line has been drawn through the experimental values obtained for $L = 2.870$. The initial flat region that exists cannot result either from the hydrodynamic relaxation process or the motor response time, since both processes are completed in much less than this time. We ascribe this delay to the change over from semi-infinite linear diffusion to convective-diffusion. At the time of the angular velocity step, the current at the disk is proportional to $t^{-1/2}$ (δ is proportional to $t^{1/2}$). During the 2 radians required to establish the boundary layer and for some time thereafter, i tends to decrease because of the existing diffusion process and to increase as a result of convective processes, thus producing a flat region until the convective-diffusion process predominates. These processes produce the equivalent of a time lag in the start of the experiment after the motor has reached the new rotation speed.

The solid lines in Fig. 3 represent the theoretical curves calculated from Eq. [19] for the experimental L-values. The points on these curves are the experimental Y^{-1}-values, shifted by the number of radians specified in the legend to Fig. 3. Excellent agreement exists between the Φ-shifted experimental points and the theoretical curves.

Levich-Levich experiments.—Reduction of Fe^{3+}.— Curve A of Fig. 4 represents the current transient produced in a 2.17 mM Fe^{3+}-1.0M H_2SO_4 solution on changing the rotation speed of a rotating platinum disk electrode from 144 to 1211 rpm. Curve B represents the time dependence of the motor speed. In these and in some of the other experiments that are described below, the angular rotation equivalent to the motor speed transient varied from 2 to 7 radians, and was not insignificant as compared to the current transient. Thus, an uncertainty arose in the time to be taken as the start of the current-time curve. We have arbitrarily used the intersection of the two linear segments of the motor speed-time curve to define the start of the experiment.

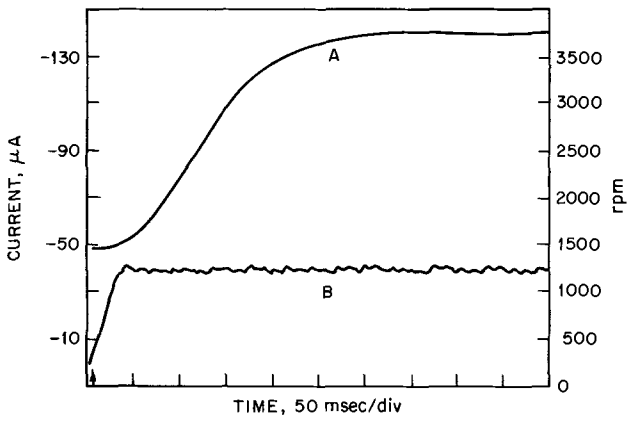

Fig. 4. Oscilloscope traces of a Levich-Levich experiment. Trace A: disk current, microamperes. Trace B: disk speed, revolutions per minute. Horizontal sensitivity 50 msec/division with vertical arrow indicating triggering time for programmed speed step from 144 to 1211 rpm. Disk potential 0.0V vs. SCE throughout. Solution and electrode of Fig. 2.

The results of five experiments for L-values between 1.512 and 3.848 are shown in Fig. 5. The dashed line is drawn through the current-time data obtained in jumping from 100 to 1600 rpm. In this data set, as in some of the others, a time delay occurs before the current begins to change. This delay is considerably less than that found in the Cottrell-Levich experiments.

All data sets can be made to coincide with the theoretical curves calculated from Eq. [19] (solid lines) by Φ-shifts in the range of -1.2 to -3.8 radians. Since the uncertainty in the time to be taken as the start of the experiment must be an appreciable fraction of the rotation required for the motor to reach speed (Φ_M in legend of Fig. 5), no significance can be attributed to the differences between these radian shifts and their absolute magnitudes. Hence, the agreement between theory and experiment is satisfactory.

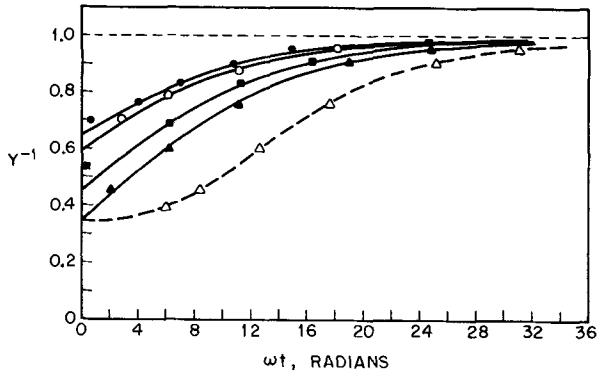

Fig. 3. Comparison of theoretical and experimental Cottrell-Levich curves for ferric reduction. Solid curves are calculated (see text). Experimental points are $Y^{-1} = i(t)/i_{\text{Levich}}$ vs. ωt, radians, where $t = 0$ is the point at which the tachometer reaches rated output in Fig. 2 data (same solution and electrode). Values of L, i_{Cottrell}, ω_2, and $\Delta\Phi$ shifts in the horizontal direction (see text) are as follows:

	L*	i_{Cottrell} (μA)	ω_2 (rad/sec)	$\Delta\Phi$ (rad)
●	1.546	58.2	41.89	—5.3
○	1.676	40.8	20.94	—5.6
■	2.200	60.0	83.78	—6.4
▲	2.870	46.0	83.78	—6.3
△	2.870	46.0	83.78	0.0

* Calculated from $i_{t=\infty}/i_{t=0}$.

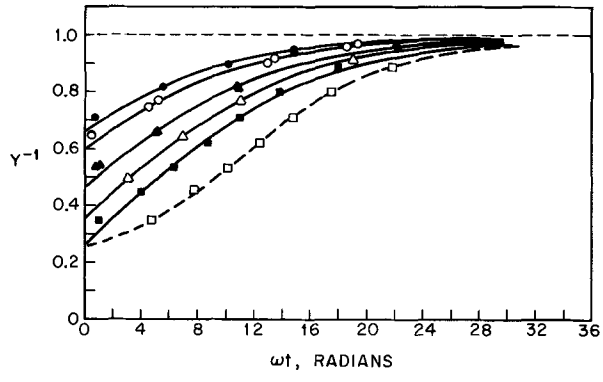

Fig. 5. Compression of theoretical and experimental Levich-Levich curves for ferric reduction. Solid curves are calculated (see text). Experimental points are $Y^{-1} = i(t)/i_{\text{Levich}}$ vs. ωt, radians, where $t = 0$ is the point at which tachometer reaches rated output in Fig. 4 data. Solution and electrode of Fig. 2. Values of L, final speed ω_2, $\Delta\Phi$ shifts, and Φ_M are as follows:

	L*	ω_2 (rad/sec)	$\Delta\Phi$ (rad)	Φ_M (rad)
●	1.512	94.25	—1.2	1.8
○	1.678	94.25	—2.4	2.0
▲	2.155	114.04	—3.0	3.4
△	2.820	126.81	—3.6	4.4
■	3.848	167.55	—3.8	6.9
□	3.848	167.55	0.0	6.9

* Calculated from $i_{t=\infty}/i_{t=0}$.

Reduction of Ag^+.—Figure 6 gives the results obtained for the reduction of a 2.0 mM Ag^+-1.0M $HClO_4$ solution at a rotating platinum disk. L-values between 1.514 to 3.966 were used. The radian shifts required to match the experimental Y^{-1}-Φ data to the theoretical curves are given in the legend to Fig. 6 and do not differ significantly from zero. Within the experimental error in determining the start of the experiment, all curves have been shifted the same amount and the shifts hardly differ from zero.

Intercomparison of current-time transients for different couples.—As was pointed out at the end of the theoretical section, a plot of Y^{-1} *vs.* $Q\cdot\Phi$ should be independent of redox couple, provided the same L-value is used. Figure 7 shows the results of such a plot using some of the data previously described. Also, a set of data for the reduction of 4.0 mM Hg_2^{2+} in a 1.0M $HClO_4$ solution at an amalgamated gold disk electrode is included. The slight differences in the L-values, 2.118 (Hg_2^{2+}), 2.148 (Ag^+), and 2.151 (Fe^{3+}), may be ignored.

The dashed curve in Fig. 7 passes through the data for Fe^{3+} reduction before any radian shift has been used. The three sets of Y^{-1}-t data required different radian shifts in order to have the experimental points fall on the theoretical Y^{-1} *vs.* $Q\cdot\Phi$ plot (solid curve, Fig. 7). All these shifts are within the experimental error and comparable to the radian shifts in the preceding experiments.

Conclusion

The relaxation time for the hydrodynamic boundary layer is short compared to the diffusion layer relaxation time at a rotating disk electrode. At a constant potential, the current transient produced by a step change in rotation speed is a function of only the initial and final rotation speeds and the Schmidt number. The Levich equation should accurately predict the time-dependent limiting convective-diffusion current at a rotating disk electrode if the square root of the angular velocity is modulated sinusoidally (7), provided the frequency of modulation (a few Hertz) and the amplitude of modulation do not exceed the limits implied by these relaxation studies.

Manuscript received April 19, 1973.

Any discussion of this paper will appear in a Discussion Section to be published in the June 1974 JOURNAL.

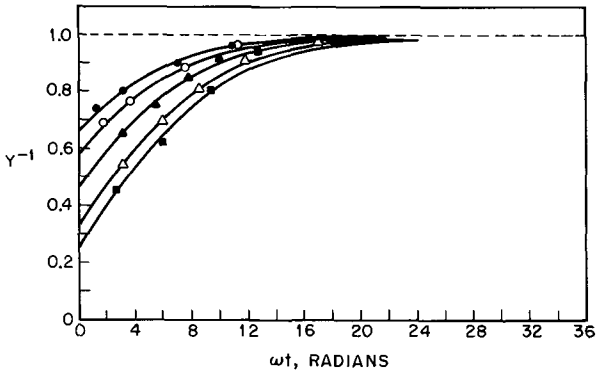

Fig. 6. Comparison of theoretical and experimental Levich-Levich curves for silver reduction. Data treatment and calculations follow those of Fig. 5. Solution 2 mM Ag^+ in 1M $HClO_4$, Pt disk.

	L^*	ω_2 (rad/sec)	$\Delta\Phi$ (rad)	Φ_M (rad)
●	1.514	94.75	−0.6	1.9
○	1.726	94.75	0.0	2.3
▲	2.148	113.42	−0.5	2.7
△	2.967	212.70	+0.6	10.0
■	3.966	166.35	0.0	5.4

* Calculated from $i_{t=\infty}/i_{t=0}$.

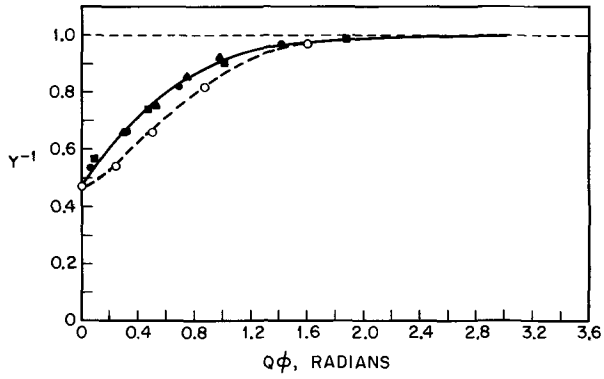

Fig. 7. Comparison of normalized theoretical and experimental Levich-Levich curves for Fe^{3+}, Hg_2^{2+}, and Ag^+ reductions. Solid curves are computer calculated (see text). Experimental points are plotted as Y^{-1} *vs.* $Q\cdot\Phi$ for normalization (see text) and have been shifted horizontally by $Q\cdot\Delta\Phi$. Values of L, final speed ω_2, $(D/\nu)^{1/3}$, and $Q\cdot\Delta\Phi$ are as follows:

	Species	L^*	ω_2 (rad/sec)	$(D/\nu)^{1/3}$	$Q\cdot\Delta\Phi$ (rad)
■	Hg_2^{2+}	2.118	114.26	0.102	−0.18
▲	Ag^+	2.148	113.42	0.121	−0.04
●	Fe^{3+}	2.151	114.03	0.079	−0.18
○	Fe^{3+}	2.151	114.03	0.079	0.0

* Calculated from $i_{t=\infty}/i_{t=0}$.

The respective solutions and disk surfaces were: 4 mM Hg_2^{2+} in 1M $HClO_4$ (amalgamated gold), 2 mM Ag^+ in 1M $HClO_4$ (Pt), and 2.17 mM Fe^{3+} in 1M H_2SO_4 (Pt).

APPENDIX

As was pointed out in the text, the potentiostatic problem in the region $\Phi < 2$ can be treated using Benton's results (4). His tabulated values of $h_1(\eta)$, $h_2(\eta)$, and $h_3(\eta)$ of Eq. [1] were fitted by a third order Newton-Gregory interpolation formula (9) in the range $0 \leq \eta \leq 0.3$. The results are of the form of Eq. [A-1]

$$h_i(\eta) = A_{i1}(\eta) + A_{i2}(\eta)^2 + A_{i3}(\eta)^3 \qquad [A\text{-}1]$$

where the values of A_{i1}, A_{i2}, and A_{i3} are given for $i = 1$, 2, and 3 in Table I.

Substituting Eq. [A-1] into Eq. [1] yields

$$w(\eta, \Phi) = -4(\nu\omega_2)^{1/2}\Phi^{3/2}\{\beta_1\eta + \beta_2\eta^2 + \beta_3\eta^3\} \qquad [A\text{-}2]$$

where

$$\beta_j = A_{1j} + A_{2j}\Phi^2 + A_{3j}\Phi^3 \qquad [A\text{-}3]$$

The potentiostatic problem is described, as before, by Eq. [4] through [11], but Eq. [12] is now replaced by Eq. [A-2]. It is necessary that Eq. [9] be expressed in terms of the variables Q, Y, Φ, and η by substitution of Eq. [2], [3], [15], and [16], respectively, into it. This yields

$$\frac{dY}{d\Phi} = \frac{0.95563}{Y} + \frac{2\Phi^{1/2}}{w_2\delta_L QY}\int_0^{QY/\Phi^{1/2}} w(\eta, \Phi)\,d\eta \qquad [A\text{-}4]$$

If Eq. [A-2] is substituted in Eq. [A-4], and the integration performed, the result is

$$\frac{dY}{d\Phi} = \frac{0.95563}{Y} - \frac{4}{Q}\left[\frac{\beta_1}{2}QY\Phi + \frac{\beta_2}{3}Q^2Y^2\Phi^{1/2} + \frac{\beta_3}{4}Q^3Y^3\right] \qquad [A\text{-}5]$$

Table I. Newton-Gregory coefficients of $h_i(\eta)$

i	A_{i1}	A_{i2}	A_{i3}
1	1.73×10^{-3}	3.75×10^{-1}	-4.43×10^{-1}
2	-1.48×10^{-4}	2.835×10^{-2}	-1.77×10^{-2}
3	-1.37×10^{-5}	2.875×10^{-3}	-1.18×10^{-3}

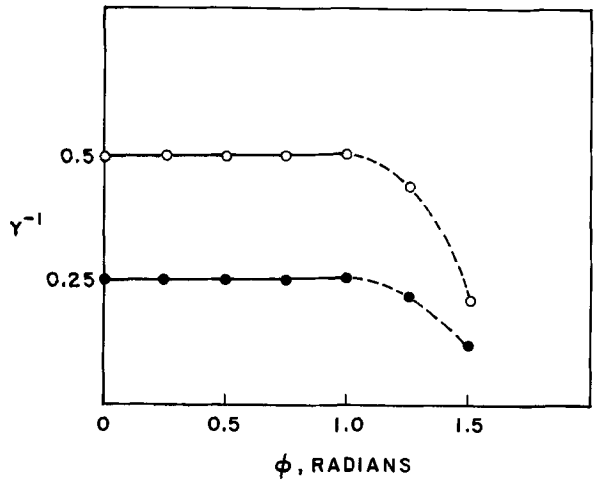

Fig. 8. Theoretical plot of Y^{-1} vs. Φ in the Benton region. Calculated for Fe^{3+} in 1.0M H_2SO_4 from Eq. [A-5]. $D = 4.52 \times 10^{-6}$ cm²/sec, $\nu = 9.18 \times 10^{-3}$ cm²/sec. ○: $L = 2.0$. ●: $L = 4.0$.

The variables in Eq. [A-5] are not separable, and DESUB (10) was used to obtain a numerical solution.

Two plots of Y^{-1} *vs.* Φ in the range $0 \leq \Phi \leq 1.5$ for L-values of 2.0 and 4.0 are shown in Fig. 8. The value of D/ν corresponded to that for Fe^{3+} in 1.0M H_2SO_4. As can be seen, little change in Y^{-1} occurs during the time that it takes for the new hydrodynamic steady state to be established, after the step change in angular velocity. The rapid decrease of Y for $\Phi > 1$ appears to be related to difficulties arising from the use of Eq. [1] to represent the time dependence of the axial fluid flow velocity at longer times. Benton (4) estimated that Eq. [1] would have outlived its usefulness before 2.0 radians. Hence, considering the time scale of our experiments, the assumption that $\omega = \omega_2$ at $t > 0$ is a reasonable one. This assumption is also supported by the results obtained in the experiment shown in Fig. 1.

LIST OF SYMBOLS

C^b bulk concentration
C^s surface concentration
D diffusion coefficient, cm²/sec
$(i)_t$ disk current at time t
L defined in Eq. [18]
Q defined in Eq. [15]
t time after rotation speed step, sec
Y defined in Eq. [16]
w time dependent normal fluid velocity (see Eq. [1])
z normal distance from disk
δ time dependent diffusion layer, cm
δ_L steady-state Levich diffusion layer thickness, cm
η similarity variable, defined in Eq. [3]
ν kinematic viscosity, cm²/sec
τ time between angular velocity step and potential step, sec
Φ angle of rotation after rotation speed step, radians (see Eq. [2])
Φ_M motor speed rise time, radian
$\Delta\Phi$ radian shift applied to Φ to fit Y^{-1} *vs.* Φ data to Eq. [19]
ω angular velocity, rad/sec
ω_1 initial angular velocity
ω_2 final angular velocity

REFERENCES

1. S. C. Creason and R. F. Nelson, *J. Electroanal. Chem.*, **27**, 189 (1970).
2. B. Miller and S. Bruckenstein, *This Journal*, **117**, 1032 (1970).
3. B. Miller, M. I. Bellavance, and S. Bruckenstein, *ibid.*, **118**, 1082 (1971).
4. E. R. Benton, *J. Fluid Mech.*, **24**, 781 (1966).
5. S. Bruckenstein and S. Prager, *Anal. Chem.*, **39**, 1161 (1967).
6. W. G. Cochran, *Proc. Cambridge Phil. Soc.*, **30**, 365 (1934).
7. B. Miller, M. I. Bellavance, and S. Bruckenstein, *Anal. Chem.*, **44**, 1983 (1972).
8. B. Miller, *This Journal*, **116**, 1117 (1969).
9. G. A. Korn and T. M. Korn, "Mathematical Handbook for Scientists and Engineers," p. 654, McGraw-Hill Book Co., New York (1961).
10. P. C. Crane and P. A. Fox, DESUB, in "Numerical Mathematics Computer Programs," Vol. 2, Issue 1, Feb. 6, 1969, Bell Laboratories, Murray Hill, N. J.

The Transient Response of a Disk Electrode with Controlled Potential

Kemal Nişancioğlu* and John Newman**

Inorganic Materials Research Division, Lawrence Berkeley Laboratory and Department of Chemical Engineering, University of California, Berkeley, California 94720

ABSTRACT

A mathematical treatment is given for the transient behavior of a disk electrode when the potential is varied. The characteristic time constant for decay of the double-layer capacity is assessed.

The authors have recently treated the transient response of a disk electrode to a step change in the applied current (1). The present paper reports a mathematical analysis developed for the same model but with the electrode potential put under control instead of the current. The results could be relevant to some electroanalytical applications of the disk electrode, *e.g.*, interrupter methods under potentiostatic control are already in common use (2).

* Electrochemical Society Student Member.
** Electrochemical Society Active Member.
Key words: current distribution, time constant, double-layer capacity.

The problem was formulated with certain assumptions in the earlier paper (1) and will not be repeated here. The only difference in the present formulation lies in the fact that the electrode potential is set at zero time as a step to a given value V and is maintained at that value thereafter. Our purpose here is therefore to simulate the transient decay of the cell current from an initial value I_0 corresponding to the primary distribution (3, 4) to a final steady-state value I_∞.

Analysis

The potential in the solution can be expressed in terms of a steady-state and a transient contribution

$$\Phi = \Phi^{ss} - \Phi^{t} \qquad [1]$$

Detailed analyses for the steady-state problem have been given elsewhere (1, 5). Earlier treatment of the ideally polarizable electrode (1), however, does not apply for the present situation; Φ^{ss} vanishes in the absence of an electrode reaction since no net current is associated with the working electrode at steady state when the potential is fixed.

In terms of rotational elliptic coordinates (3) η and ξ, the transient part of the potential can be expressed as

$$\frac{\Phi^{t}}{V} = \sum_{i=0}^{\infty} G_i e^{-\theta(\lambda_i + J)} T_i(\eta,\xi) \qquad [2]$$

where T_i is a dimensionless potential independent of time, λ_i is an eigenvalue characteristic of the potential T_i, and θ and J are the dimensionless time and exchange-current density (1), respectively. Since Φ^{t} satisfies Laplace's equation, the functions T_i also satisfy

$$\nabla^2 T_i = 0$$

The boundary conditions associated with T_i are

$$\left.\begin{aligned} &\frac{\partial T_i}{\partial \eta} = 0 \quad \text{at} \quad \eta = 0 && \text{(on the insulating portion of the disk)}\\ &T_i = 0 \quad \text{as} \quad \xi \to \infty && \text{(far from the disk)}\\ &T_i \text{ well behaved at} \quad \eta = 1 && \text{(on the axis of the disk)} \end{aligned}\right\} \qquad [4]$$

and

$$\frac{\partial T_i}{\partial \xi} + \lambda_i \eta\, T_i = 0 \quad \text{at} \quad \xi = 0 \qquad \text{(on the disk electrode)} \qquad [5]$$

which is obtained by a direct substitution of Eq. [2] into the boundary condition on the disk electrode (1).

Equations [3] and [5] constitute an eigenvalue problem, which can be solved in a straightforward fashion (1). The solution to Eq. [3] satisfying the conditions [4] is

$$T_i = \sum_{n=0}^{\infty} \mathcal{B}_{i,n} P_{2n}(\eta) M_{2n}(\xi) \qquad [6]$$

where $P_{2n}(\eta)$ is the Legendre polynomial of order $2n$ and $M_{2n}(\xi)$ is a Legendre function with known properties (5). Substitution into Eq. [5] for each i and inversion of the resulting set of linear equations with the normalization condition, $\mathcal{B}_{i,o} = 1$, yield the numerical values of the eigenvalues λ_i and the coefficients $\mathcal{B}_{i,n}$ (see Table I). The first four eigenfunctions are plotted with respect to the radial position on the surface of the disk in Fig. 1.

The functional behavior of $T_{i,o}$ has much the same significance as the corresponding eigenfunctions $U_{i,o}$ of the galvanostatic problem (1) in depicting the nonuniform state of charge and the pattern of local current flow on the surface of the disk during the transient process. One may note, in fact, that $T_{i,o}$ in Fig. 1

Table I. The first six eigenvalues and the related coefficients $\mathcal{B}_{n,i}$ of the eigenfunctions

n	λ_0 1.15777 $i=0$	λ_1 4.31680 $i=1$	λ_2 7.46018 $i=2$	λ_3 10.6023 $i=3$	λ_4 13.7441 $i=4$	λ_5 16.8858 $i=5$
0	1.0	1.0	1.0	1.0	1.0	1.0
1	0.39451	−3.30704	−3.20144	−3.08673	−3.00260	−2.94030
2	−0.01974	−3.09447	2.69232	3.87544	4.20749	4.29990
3	0.01259	−0.52802	6.45944	0.65745	−2.15584	−3.53764
4	−0.00657	−0.10223	2.64610	−8.32547	−5.09803	−1.69133
5	0.00393	0.02410	0.63787	−6.16121	7.06426	8.21141
6	−0.00256	−0.01843	0.03554	−2.27051	9.75697	−2.49615
7	0.00178	0.01289	0.03502	−0.43176	5.33233	−11.5222
8	−0.00129	−0.00946	−0.02056	−0.10618	1.62964	−9.36731
9	0.00097	0.00718	0.01605	0.01863	0.40730	−4.07287
10	−0.00075	−0.00559	−0.01255	−0.02158	0.02998	−1.27763

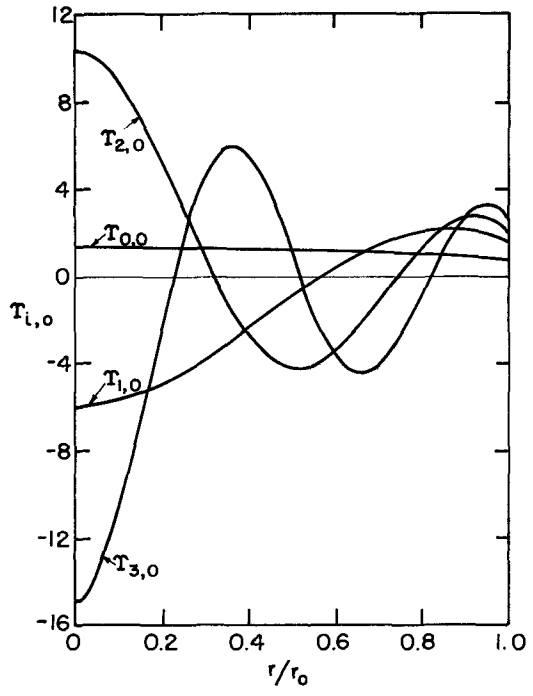

Fig. 1. Behavior of the first four eigenfunctions on the surface of the disk electrode.

are quite similar to the corresponding curves for $U_{i,o}$ given in Ref. (1) for $i > 0$. The eigenvalues λ_i also become more similar in numerical value to Λ_i of the galvanostatic series with increasing i.

An important departure from the galvanostatic case is clearly that Φ^{t} does include a net current in the present situation. This additional contribution is contained, for example, in the first eigenfunction T_o, which unlike U_o is nonzero. the fact that $T_{o,o}$ exhibits no extrema nor any zeroes suggests that it persists the longest during the decay process and is therefore associated with the largest time constant.

The eigenfunctions $T_{i,o}$ satisfy the orthogonality relationship

$$\int_0^1 \eta T_{i,o} T_{j,o}\, d\eta = \begin{cases} 0 & \text{if } i \neq j \\ -\dfrac{1}{\lambda_i} \displaystyle\sum_{n=0}^{\infty} \frac{M'_{2n}(0)}{4n+1} \mathcal{B}^2_{n,i} & \text{if } i = j \end{cases} \qquad [7]$$

From the initial condition

$$\Phi = V \quad \text{at} \quad \theta = 0+, \quad \xi = 0 \qquad [8]$$

the coefficients G_i can now be calculated from the equation

$$G_i = \frac{2\lambda_i}{\pi(\lambda_i + J) \displaystyle\sum_{n=0}^{\infty} \frac{M'_{2n}(0)}{4n+1} \mathcal{B}^2_{n,i}} \qquad [9]$$

The current is given by

$$I = -2\pi r_o \kappa \int_0^1 \left.\frac{\partial \Phi}{\partial \xi}\right|_{\xi=0} d\eta = I_o \left[\frac{I_\infty}{I_o} - \sum_{i=0}^{\infty} G_i e^{-\theta(\lambda_i + J)}\right] \qquad [10]$$

where r_o is the radius of the disk electrode and κ is the solution conductivity. The ratio I_∞/I_o is a known quantity once the value of J is specified and can be obtained directly from the steady-state analysis. Some calculated values are given in Ref. (1) (reciprocal of $V^{ss}/\Phi_o{}^{p}$). Figure 2 shows current *vs.* time traces for

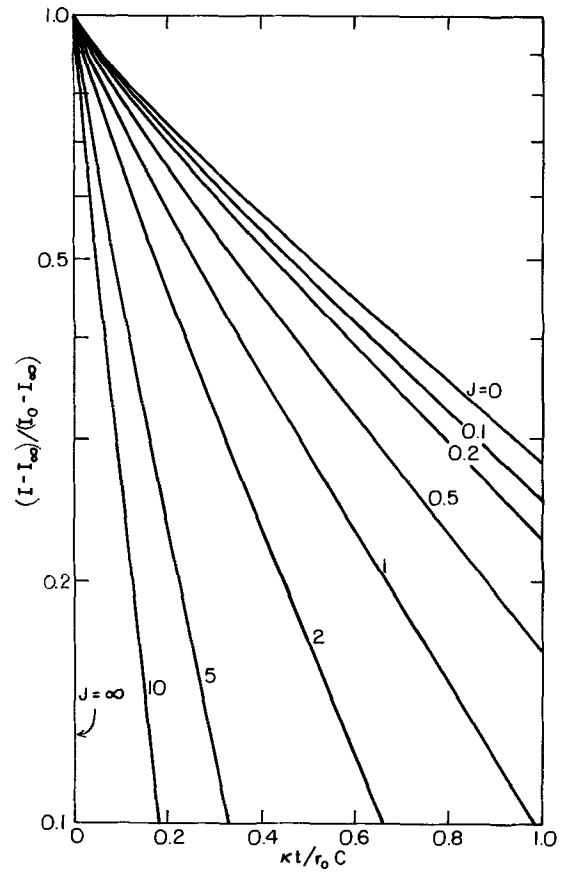

Fig. 2. Current traces at various J values for decay (or charging) of the double-layer capacity. The slope of each curve at large times is related to $\lambda_1 + J$.

various J values. Each curve is characterized by a time constant for decay given by

$$\tau = \frac{1}{1.16 + J} \frac{r_0 C}{\kappa} \qquad [11]$$

where C is the double-layer capacity.

The analysis can be generalized by superposition to incorporate an arbitrary time dependence of the applied potential $V(\theta)$. The current is then given by

$$\frac{I}{4r_0\kappa} = V(\theta) + \sum_{i=0}^{\infty} G_i(\lambda_i + J)e^{-\theta(\lambda_i+J)} \times \int_0^{\theta} e^{\theta(\lambda_i+J)}V(\theta)\,d\theta \qquad [12]$$

The present results should apply for large and moderately small times without much difficulty in the numerical calculations. For very short times, however, numerical difficulties are inevitable because the current distribution is equal to the primary distribution everywhere on the disk except in a small region near the edge. A large number of terms are thus required in the summation in both Eq. [2] and [6]. The same problem is encountered for large J values (5). A separate treatment of the edge region for short times or large J values overcomes these difficulties. The authors have formulated this problem, and the results should be published shortly.

Conclusions

The transient response of a disk electrode to step changes in the applied potential has been formulated to yield a well-defined eigenvalue problem, which can readily be solved to give solutions in terms of a series of characteristic potential functions. Each function is related to a certain mode of decay of the double-layer capacity and is associated with a characteristic time constant, the first being the dominant one in determining the system behavior at large times. These time constants can accurately be calculated from the eigenvalues of the boundary-value problem. The results can be generalized for arbitrary changes in the applied potential with time by a straightforward application of the superposition integral.

Acknowledgment

This work was supported by the United States Atomic Energy Commission.

Manuscript received Nov. 6, 1972.

Any discussion of this paper will appear in a Discussion Section to be published in the June 1974 JOURNAL.

LIST OF SYMBOLS

$\mathcal{B}_{n,i}$	coefficients in series for T_i
C	double-layer capacity, f/cm^2
G_i	coefficients in series for Φ^t
I	total current, A
I_0	total current at $t = 0+$ $(= 4\kappa r_0 V)$, A
I_∞	total current at $t = \infty$, A
J	dimensionless exchange-current density $= i_0 r_0 \mathbf{F}(\alpha_a + \alpha_c)/RT\kappa$ [see Ref. (1)]
M_{2n}	Legendre function discussed in Ref. (5)
P_{2n}	Legendre polynomial of order $2n$
r	radial position from axis of disk, cm
r_0	radius of disk electrode, cm
t	time, sec
V	electrode potential, V
η	rotational elliptic coordinate
κ	conductivity of the solution, ohm^{-1}-cm^{-1}
λ_i	eigenvalue
Φ	potential in the solution, V
Φ^{ss}	steady-state part of Φ, V
Φ^t	transient part of Φ, V
ξ	rotational elliptic coordinate
τ	characteristic time constant for decay, sec
θ	$r_0 C/\kappa t$, dimensionless time
T_i	eigenfunctions in series for Φ^t
$T_{i,0}$	value of T_i at the electrode surface

REFERENCES

1. K. Nişancioğlu and J. Newman, *This Journal*, **120**, 1339 (1973).
2. J. D. E. McIntyre and W. F. Peck, Jr., *ibid.*, **117**, 747 (1970).
3. J. Newman, *ibid.*, **113**, 501 (1966).
4. J. Newman, *ibid.*, **117**, 507 (1970).
5. J. Newman, *ibid.*, **113**, 1235 (1966).

Technical Note

A Spectroelectrochemical Study of Mixed-Valence μ-Pyrazine-decaamminediruthenium(II,III) Complex

V. S. Srinivasan[1] and F. C. Anson*

Arthur Amos Noyes Laboratory of Chemical Physics, California Institute of Technology, Pasadena, California 91109

Much of the recent interest (1-4) in the redox behavior of the complex [Ru(II) N⊜N Ru(III)]$^{5+}$, first described by Creutz and Taube (5), focuses on the absorption band in the near infrared that is displayed by the mixed-valence complex but not by its one electron oxidation or reduction products. In this note we describe a thin-layer electrochemical cell with which the visible and near infrared spectrum of the mixed-valence complex could be monitored while it was being electrochemically generated by oxidation of the corresponding diruthenium(II) complex in an aqueous solution (D_2O). The spectra obtained matched those reported for the same complex prepared by chemical oxidations.

The cell employed resembles some previously described thin-layer cells for spectroelectrochemical studies (6-10). Its design shares with certain of the earlier cells (7) the desirable features of low ohmic potential drops and ready applicability at wavelengths from the ultraviolet to the near infrared.

Experimental

The design of the optically transparent thin-layer electrode cell assembly is shown in Fig. 1 and 2. A thin layer of the solution is trapped between a conducting transparent electrode (a thin deposit of platinum on quartz) and a quartz window. The window is part of the innerside of an annular cell, with a Teflon ring to contain the test solution. The Teflon ring and the quartz window were precision made. The Teflon ring was made a few hundred microns longer than the inner tube which contained the window. A platinum gauze was wrapped around the cylindrical window to serve as the auxiliary electrode. A salt bridge connected to a reference electrode (nonisolated) made contact with the solution through a small hole in the top of the Teflon ring. The size of the cell allowed it to be introduced into the sample compartment of the spectrophotometer.

The whole cell assembly, including the demountable, transparent electrode, the tubular window, and the Teflon ring were held together by a set of machined aluminum cell holders. A pair of neoprene O-rings held in the groove of the Teflon ring prevented

* Electrochemical Society Active Member.
[1] Present address: Department of Chemistry, Bowling Green State University, Bowling Green, Ohio 43402.
Key words: spectroelectrochemistry, ruthenium, complex, pyrazine.

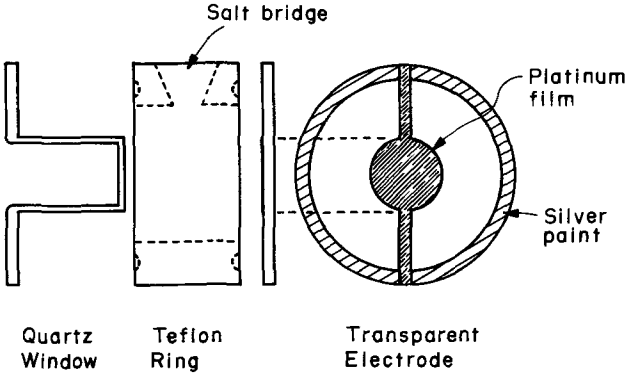

Fig. 1. Exploded view of the optical thin-layer cell assembly

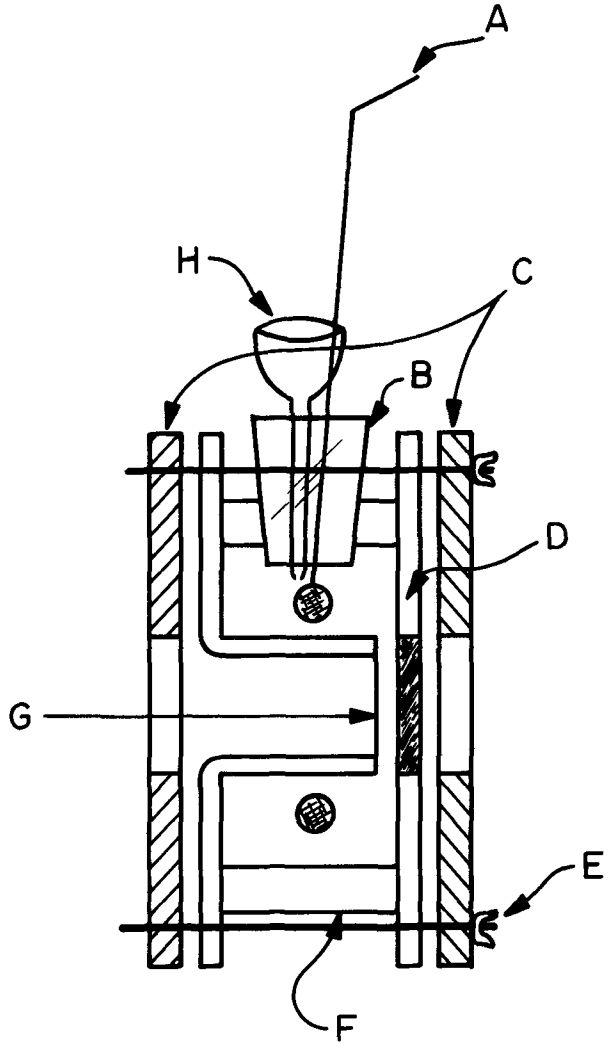

Fig. 2. Cross section of the assembled thin-layer cell. A, Pt wire connecting to Pt gauze auxiliary electrode; B, connector; C, aluminum holders; D, transparent platinum film electrode; E, threaded stock with wing nut; F, Teflon body; G, quartz window; and H, salt bridge.

direct contact between the hard Teflon and glass surfaces. The neoprene rings could be squeezed gently by exerting pressure on the aluminum holders so that the thickness of the thin layer could be varied. The average thickness of the thin layer was *ca.* 300μ, as determined from the absorbance of the diruthenium(II) complex. A matching quartz plate with a platinum deposit was used in the reference compartment of the spectrophotometer.

The conducting electrode was a thin deposit of platinum vacuum deposited on spectrosil quartz, with a large circle of deposit in the center and two channels for electrical connections to silver paint around the rim. The areas of the channels were very small compared to the area of the circle that trapped the thin layer of liquid. Platinum deposition was done after cleaning the surface of the quartz with a glow discharge achieved by exposing the surface to a nitrogen atmosphere (100 Torr) and initiating a radio frequency discharge. For deposition of the platinum a metallic mask was used to produce the desired geometry and the platinum was evaporated from a tungsten filament in a metal deposition apparatus.

A Cary XIV-R Spectrophotometer was used with the sample compartment lid modified to permit electrical connections to be made to the cell.

The chemicals used were of reagent grade. μ-Pyrazine-decaamminediruthenium(II) *p*-toluenesulfonate was synthesized according to Ref. (1). The purity was checked spectrophotometrically. The tosylate anions were removed by ion exchange to produce the trifluoroacetate salt in D_2O. The solutions used for the experimental measurements were 0.6 mM in the complex and 0.2M in trifluoroacetic acid. Oxygen was removed from the solutions before they were introduced into the cell by bubbling with prepurified argon.

Results and Discussion

Cyclic voltammograms for solutions of Ru N⬭N Ru^{4+} in the thin-layer cell showed two clear oxidation and corresponding reduction peaks, but the peak potentials at low sweep rates, *e.g.*, several millivolts/second, were shifted by about 50 mV from the values obtained previously in conventional cells, *i.e.*, E_p(anodic) = 140 and 535 mV; E_p(cathodic) = 76 and 465 mV *vs.* SCE (4). These shifts were in the direction to be expected from the small ohmic potential drops likely to be present in the thin-layer cell, and the potentials used for the controlled potential electrochemical oxidations were adjusted accordingly.

With the electrode potential at 0V *vs.* SCE in a solution of Ru N⬭N Ru^{4+} there is no current flow, and the visible and near infrared spectra given in curves A of Fig. 3 were obtained. The value of λ_{max} (557 nm) agrees with value of Creutz and Taube (1) as does the absence of the band at 1570 nm.

When the electrode potential is changed to 400 mV *vs.* SCE, anodic current flows and the spectra obtained after *ca.* 5 min of electrolysis are shown in curves B of Fig. 3. Both the shift in λ_{max} and the decrease in absorption intensity of the visible peak correspond to those reported by Creutz and Taube (1), and the band that develops at 1570 nm agrees with their reports. The spectra could be shifted back and forth between the two cases by alternately reducing and oxidizing the solution at 0 or 400 mV, respectively. Thus the same mixed valence species, Ru N⬭N Ru^{5+}, results from both the chemical and electrochemical oxidation of Ru N⬭N Ru^{4+}.

In a second experiment the absorbance at 1570 nm was monitored continuously when the electrode potential was stepped from 0 to 640 mV *vs.* SCE. At this potential the oxidation product at the electrode is Ru N⬭N Ru^{6+} which does not absorb at 1570 nm.

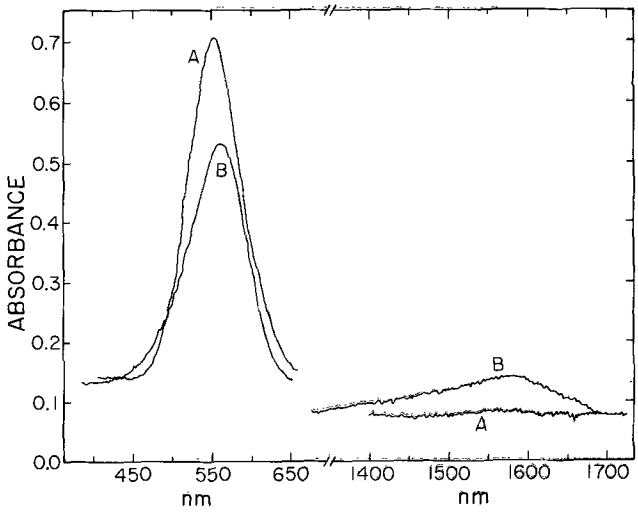

Fig. 3. Visible and near infrared spectra of Ru N⬭N Ru^{4+}, curves A, and Ru N⬭N Ru^{5+}, curves B, generated in the thin-layer cell.

However, the electrode reaction product diffuses back into the thin solution layer where it can react with the unoxidized Ru N⬭N Ru^{4+} that has not had time to reach the electrode surface. The product of this reaction is the Ru N⬭N Ru^{5+} ion which does absorb at 1570 nm. As expected, the measured absorbance at 1570 nm increases during the first 2–3 min of electrolysis, reaches a maximum, and then decreases to zero after *ca.* 10 min. At this point the spectrum of the solution matched that reported for Ru N⬭N Ru^{6+} (1).

These results illustrate the utility of the cell for spectral observation of electrode reaction products in the visible and near infrared and demonstrate the identity of the chemical and electrochemical oxidation products of Ru N⬭N Ru^{4+}.

Acknowledgment

This work was supported in part by the National Science Foundation. Acknowledgment is also made to the donors of the Petroleum Research Fund, adminstered by the American Chemical Society for partial support.

Manuscript submitted May 14, 1973; revised manuscript received June 7, 1973.

Any discussion of this paper will appear in a Discussion Section to be published in the June 1974 JOURNAL.

REFERENCES

1. C. Creutz and H. Taube, *J. Am. Chem. Soc.*, **95**, 1086 (1973).
2. S. A. Adeyemi, J. N. Braddock, G. M. Brown, J. A. Ferguson, F. J. Miller, and T. J. Meyer, *ibid.*, **94**, 300 (1972).
3. E. B. Fleischer and D. K. Lavallee, *ibid.*, **94**, 2599 (1972).
4. H. S. Lim, D. J. Barclay, and F. C. Anson, *Inorg. Chem.*, **11**, 1460 (1972).
5. C. Creutz and H. Taube, *J. Am. Chem. Soc.*, **91**, 3988 (1969).
6. R. W. Murray, W. R. Heineman, and G. W. O'Dom, *Anal. Chem.*, **39**, 1666 (1967).
7. W. R. Heineman, J. N. Burnett, and R. W. Murray, *ibid.*, **40**, 1970 (1968); **40**, 1974 (1968).
8. A. Yildiz, P. T. Kissinger, and C. N. Reilley, *ibid.*, **40**, 1018 (1968).
9. C. N. Reilley, *Rev. Pure Appl. Chem.*, **18**, 137 (1968).
10. I. Piljac and R. W. Murray, *This Journal*, **118**, 1758 (1971).

Brief Communication

Induction Periods in Anodization of Aluminum

S. Ikonopisov* and L. Andreeva

Department of Physical Chemistry, Higher Institute of Chemical Technology, Sofia 56 (Darvenitza), Bulgaria

Two different kinetics are generally observed in galvanostatic anodization of valve metals. The first, in electrolytes with little tendency to dissolve the oxide, is characterized by a linear increase of the potential drop, U_f, across the film with the charge passed, Q. In the second, where the film is rather soluble in the anodizing solution, the slope dU_f/dQ decreases continuously with time, thus with Q. A third type of kinetics, *viz.*, a retarded anodization, has recently been observed with Bi (1), Mo (2), W (3), and Sb (4). Under appropriate conditions the process begins with an induction period (IP) during which U_f remains close to its initial value, followed by a more or less linear potential rise up to high voltages[1] (several tens or hundreds volts). It is the purpose of this communication to point out that an IP can be developed in the anodic film formation on aluminum also.

Specimens (99.99% Al) with an exposed surface area of 10 cm^2 were annealed for 4 hr at 550°C, electropolished, and brightened as previously described (5). The cell was a four neck glass flask, with glass stoppers supporting the anode, a glass stirrer furnished with a hydraulic gate, a thermometer, and a back flow condenser assembled with the counter and reference electrodes. The electrolyte was a 2.5% aqueous solution of H_3BO_3 adjusted with NH_4OH to the required pH. The anodization was carried out under automatic galvanostatic and thermostatic regulation and stirring of the electrolyte.

In galvanostatic anodization of aluminum IP's proved to appear only within narrow limits of appropriate anodizing conditions. This can explain why this phenomenon has not been observed so far, although the anodic oxidation of Al has been subject to extensive kinetic investigations. The appearance and prolongation of the IP requires an almost neutral anodizing electrolyte and is favored by high temperatures and lower current densities. In a borate solution with pH = 6 which is known to cause a "normal" anodization with 100% efficiency at temperatures below 40°C (6), a well-expressed IP appears at a sufficiently high temperature and low current density (*e.g.*, 90°C and 0.3 mA/cm^2), as shown in Fig. 1. The increase of the current density causes a sharp decrease or disappearance of IP (Fig. 1). All described features of the IP with Al seem similar to those with the above-mentioned metals and quite different from those with zirconium (7), where the IP is caused by the surface roughness and is absent with chemically polished Zr.

In solutions of simple H_3BO_3 (without addition of NH_4OH, pH = 3.5) IP's were not observed. The attempts to reveal a retarded anodization by increasing *pH* at decreased temperatures also failed. The known (8) accelerated dissolution of the film, increased electronic conduction, and decreased dielectric constant were only found at low current density under these conditions.

* Electrochemical Society Active Member.

Key words: anodic films, aluminum, induction period.

[1] The appearance of an induction period in the low-voltage passivation has been well known for a long time.

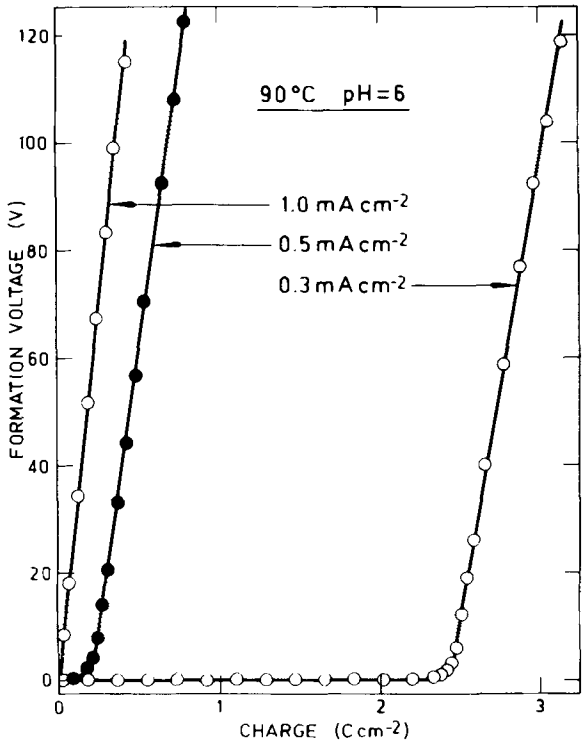

Fig. 1. Galvanostatic anodization curves for three current densities

In conclusion, an IP with Al can be observed under strictly defined conditions only. Yet the existence of IP's in the anodic oxidation, not only of the aforementioned metals but also of such a typical true film former as Al, suggests that a retarded film formation is a much more general phenomenon in the anodization at high voltages than it was supposed.

Manuscript received May 2, 1973.

Any discussion of this paper will appear in a Discussion Section to be published in the June 1974 JOURNAL.

REFERENCES

1. S. Ikonopisov and Ts. Nikolov, *This Journal*, **119**, 1544 (1972).
2. S. Ikonopisov, *J. Electroanal. Chem.*, **35**, App. 1 (1972); *Electrodepos. Surface Treat.*, **1**, 305 (1972/73).
3. I. A. Ammar and R. Salim, *Corrosion Sci.*, **11**, 591 (1971).
4. S. Ikonopisov, A. Girginov, and V. Tsochev, *Compt. Rend. Acad. Bulgare Sci.*, **25**, 653 (1972); I. A. Ammar and A. Saad, *J. Electroanal. Chem.*, **34**, 159 (1972).
5. S. Ikonopisov, *Electrochim. Acta*, **14**, 761 (1969).
6. L. Andreeva and S. Ikonopisov, *Elektrokhimiya*, **6**, 1070 (1970).
7. L. Young, "Anodic Oxide Films," p. 259, Academic Press, London (1961); O. Flint and J. H. O. Varley, *J. Phys. Chem. Solids*, **6**, 213 (1958).
8. S. Ikonopisov and L. Andreeva, *Elektrokhimiya*, **5**, 1358 (1969); S. Ikonopisov, L. Andreeva, and C. Vodenicharov, *Electrochim. Acta*, **15**, 421 (1970).

JOURNAL OF THE ELECTROCHEMICAL SOCIETY

SOLID-STATE SCIENCE AND TECHNOLOGY

OCTOBER 1973

Sulfidation Properties of a Nickel-20 w/o Chromium Alloy at 700°C and Low Sulfur Pressures

J. A. Chitty[1] and W. W. Smeltzer*

Department of Metallurgy and Materials Science, McMaster University, Hamilton, Ontario, Canada

ABSTRACT

The sulfidation kinetics and the morphological development of the reaction product for a Ni-20 weight per cent Cr alloy have been determined at 700°C and sulfur pressures below 5×10^{-10} atm. The kinetics were observed to be parabolic; the parabolic sulfidation rate constant was found to vary as a semilogarithmic function of the sulfur pressure. The reaction product consisted of an external scale identified mainly as Cr_3S_4 with dissolved nickel up to 5 atomic per cent, and a chromium sulfide subscale with morphological breakdown of the alloy/external scale interface. Approximate determinations for the diffusion rates of chromium in the scale and sulfur in the alloy were made. Tentative mechanisms are proposed to explain the diffusion-controlled reaction and the stabilization of the external scale by dissolved nickel.

An increased interest in sulfur corrosion has developed in recent years due to the natural occurrence of sulfur and its compounds in fuels and the difficulty of purifying these fuels. The behavior of Ni-Cr alloys of various compositions in sulfidizing gaseous environments has been fundamentally investigated by several workers (1-7). Romeo *et al.* (5) studied the diffusional growth of the duplex scale containing chromium and nickel sulfides on a Ni-20 w/o (weight per cent) Cr alloy at 700°C in H_2-H_2S atmospheres with sulfur partial pressures ranging from 8×10^{-10} to 2×10^{-2} atm. The present study is a continuation of this work using the same alloy composition and temperature, but under conditions of extremely low sulfur potentials ($P_{S_2} < 5 \times 10^{-10}$ atm). It is known that under these conditions chromium sulfide is the only reaction product, both externally and internally (7). Our purpose, accordingly, was to precisely establish the morphology of the scale and to ascertain the dependence of the nature of the chromium sulfide and the reaction kinetics on sulfur pressure.

Experimental

A Ni-20 w/o Cr alloy exists as a solid solution over a broad temperature range (8). The impurity contents of the alloy used in the investigation are recorded in Table I. Formation of a liquid phase in the Ni-Cr-S system is possible at temperatures above 600°C when the sulfur pressure is less than 10^{-8} atm (9). Preliminary experiments at 700°C with $P_{S_2} < 5 \times 10^{-10}$ atm showed, nevertheless, that the reaction is of the gas-solid type. Thermodynamic considerations show that only chromium sulfide formation is possible at these sulfur pressures and this influence is experimentally supported by the work of Lifshin *et al.* (7).

The sulfur pressures used were obtained by controlling the H_2/H_2S ratio of the atmosphere obtained by passing hydrogen through molten sulfur according to the method described by Rosenqvist and Dunicz (10) and by Brigham *et al.* (11). The H_2/H_2S ratio varies with temperature of the molten sulfur which is controlled in turn by a constant-temperature oil bath. This apparatus which yields atmospheres at sulfur potentials as low as 2×10^{-12} atm is shown in Fig. 1. Measurement of the H_2/H_2S ratio was determined from the sulfur analyses using the iodide titration method (12).

Alloy plates, 1.5 × 0.5 × 0.1 cm, metallographically polished to 1μ diamond abrasive as previously described were used as test specimens (5).

The assembly for the sulfidation experiments is shown schematically in Fig. 1. For measurement of the reaction kinetics the specimen was suspended in the reaction chamber from a McBain balance. The balance spring was manufactured from a Ni-span-C wire and the weight gain of a specimen was measured by following the spring elongation with a cathetometer (13). The assembly was evacuated to 10^{-2} Torr while the furnace was brought to temperature, and it was flushed with helium prior to passing the reaction gas. A specimen was then lowered into the reaction zone and the weight gains followed for suitable periods of time. At the end of each run, the specimen was winched into the upper portion of the column where the temperature drop was sufficient for quenching it.

Table I. Analysis of the nominal Ni-20 w/o Cr alloy. Actual Cr content: 19.9 w/o

Element	Analysis (ppm)
Si	500
Mn	10
Co	50
Fe	50
Al	100
C	22
S	6

* Electrochemical Society Active Member.
[1] Present address: Atomic Power Division, Westinghouse Canada Ltd., Hamilton, Ontario, Canada.
Key words: Ni-Cr alloy, sulfidation kinetics, chromium sulfide scale.

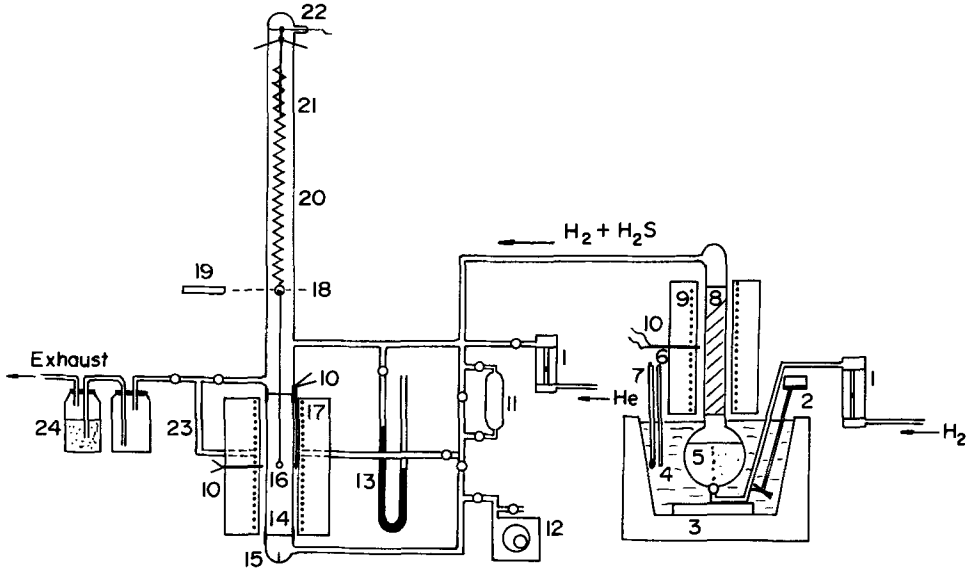

Fig. 1. Schematic of kinetic assembly: 1, rotameter; 2, stirrer; 3, heating element; 4, constant temperature oil bath; 5, sulfur bath; 6, temperature control; 7, thermometer; 8, porcelain packing; 9, furnace 500°C; 10, thermocouple; 11, gas sampler; 12, vacuum pump; 13, manometer; 14, mullite tube; 15, alignment spike; 16, specimen; 17, furnace 700°C; 18, target; 19, cathetometer; 20, spring chamber; 21, marker; 22, winch and forks for positioning specimen; 23, gas bypass; 24, ballast and absorption flask.

Specimens at various stages of scale growth were obtained by replacing the spring chamber with a column containing four winches and quartz rods for lowering and raising specimens from the reaction zone held at 700°C.

Cross sections of the sulfidized specimens were examined metallographically. The scales were protected for polishing by nickel plating of the specimens before their mounting in epoxy resin. Scale thicknesses and subscale penetration were measured with an optical microscope and the volume fraction occupied by the subscale was measured by point counting. Features of the scales were also examined with a scanning electron microscope. X-ray analysis by the powder technique was used to identify the sulfide constituents. Nickel-filtered copper radiation at low intensity was found to give the best resolution of the lines on the x-ray film. An electron microprobe was used to collect information about phase compositions and the diffusion profiles of the elements in the alloy and across the scale. Nickel, chromium, and sulfur counts were analyzed with respect to standards (the metals, NiS, Cr_7S_8) mounted with the specimens and the results were corrected for atomic number and mass absorption.

Results

Kinetics and scale morphology.—The results of the kinetic measurements at sulfur potentials in the range 5.5×10^{-12}-2.3×10^{-10} atm are shown in Fig. 2. After an induction period of 1-2 hr parabolic kinetics were observed. The values of the parabolic rate constants, K_p, determined from the slopes of the reaction curves are given in Table II.

The reaction product when observed microscopically appeared as a single-layer scale combined with a subscale. Morphological breakdown of the alloy interface was also observed which appeared to increase with increasing sulfur potential and time. A photomicrograph of a typical cross section is shown in Fig. 3.

In all cases the depth of subscale penetration appeared as approximately double the external scale thickness. Both increased parabolically with time as shown in Fig. 4. Subscale penetration was initially irregular but became regular with increasing time. The subscale particle size was finer with increasing penetration. A grain boundary etch showed that the sulfide particles occurred at inter- and transgranular sites in the alloy and that morphological breakdown of the alloy/scale interface was particularly severe at alloy grain boundaries.

Light colored stringers were observed in several of the external scales obtained after long sulfidation times. Two cases are shown in Fig. 5. The stringers, which became coarser with increasing sulfur potential, were observed to occur at grain boundaries within the sulfide scale. They extended from the peaks of the alloy at the broken down interface. Most of the stringers penetrated through the external scale although a few ended within the layer or hooked back on themselves. There was no evidence of stringers in the scale formed at the lowest sulfur pressure (5.5×10^{-12} atm) for the longest exposure periods. The scales formed in all other atmospheres did exhibit stringers, their occurrence being observed after 8 and 6 hr for specimens exposed in the atmospheres corresponding

Table II. Parabolic rate constants as a function of gas composition and the sulfur pressure

P_{H_2S}/P_{H_2}	Sulfur pressure, P_{S_2}	Parabolic rate constant, k_p ($g^2 \cdot cm^{-4} \cdot sec^{-1}$)
4.45×10^{-4}	5.5×10^{-12}	2.7×10^{-11}
7.56×10^{-4}	1.6×10^{-11}	1.43×10^{-10}
1.52×10^{-3}	6.5×10^{-11}	2.76×10^{-10}
2.85×10^{-3}	2.3×10^{-10}	3.75×10^{-10}

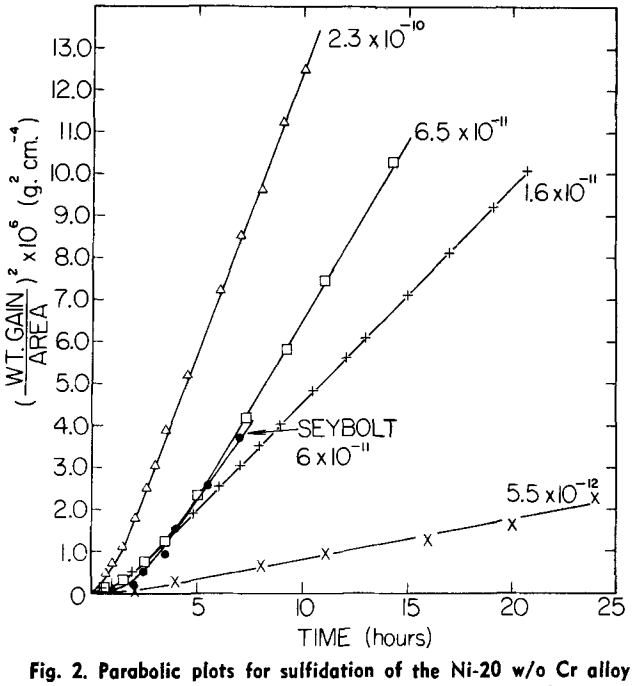

Fig. 2. Parabolic plots for sulfidation of the Ni-20 w/o Cr alloy in H_2-H_2S atmospheres at different sulfur pressures. The curve designated Seybolt is from ref. (4).

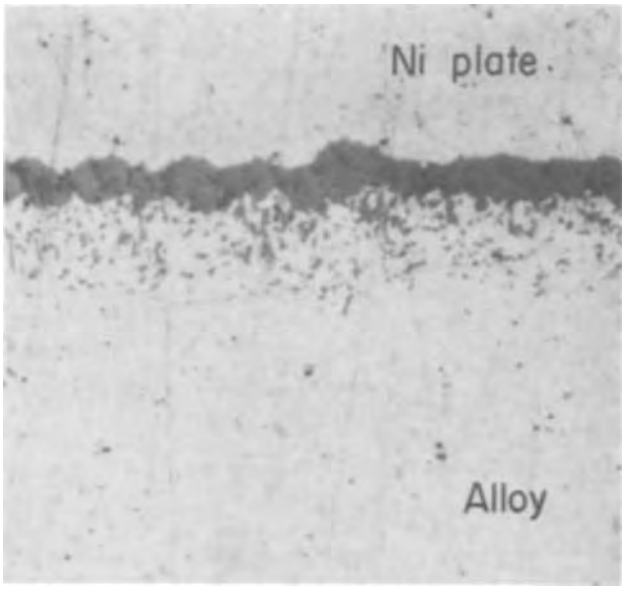

Fig. 3. Micrograph of a Ni-20 w/o Cr alloy sulfidized at a sulfur pressure of 2.3×10^{-10} atm for 2 hr. Magnification × 1800.

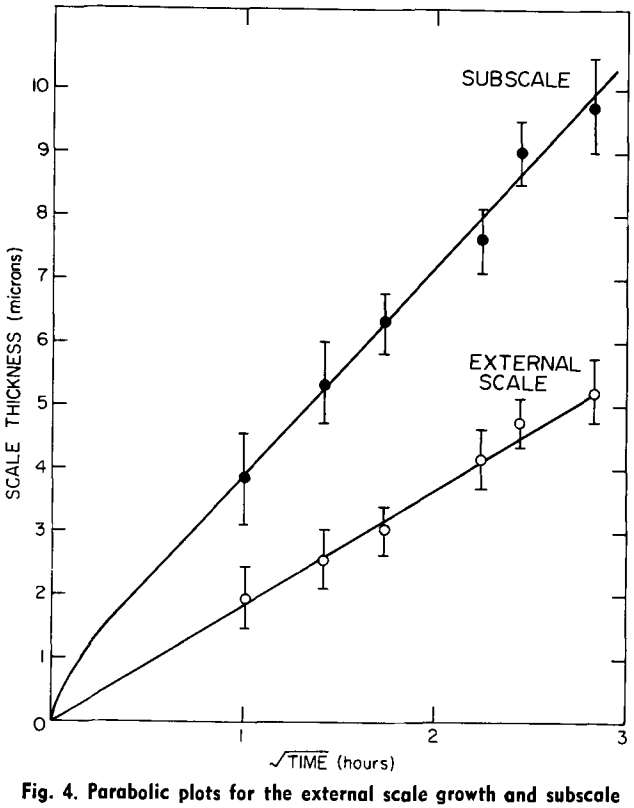

Fig. 4. Parabolic plots for the external scale growth and subscale penetration into the Ni-20 w/o Cr alloy at a sulfur pressure of 6.5×10^{-11} atm.

to $P_{S_2} = 1.6 \times 10^{-11}$ and 2.3×10^{-10} atm, respectively.

Phase identification.—Three techniques were employed to identify the phases present in an external scale. Due to the inherent difficulty in identifying the various forms of chromium sulfide the results from each technique alone are insufficient but when combined certain conclusions can be made.

Electron microprobe scans were made from the alloy interior across the subscale and through the external scale. Point counts at various distances were also obtained. The electron beam spot is about 2μ which is the same order of magnitude as a scale thickness and larger than the sulfide particle size in the subscale. As a consequence the probe results can only be considered as a qualitative representation of the concentration profiles, especially at the alloy/external scale interface where there is morphological breakdown. Typical composition distance profiles are shown for specimens exposed at the lowest and intermediate sulfur potential atmospheres in Fig. 6 and 7. It appears that much of the chromium in the subscale region was consumed in chromium sulfide formation and that the alloy was extremely nickel-rich at its interface.

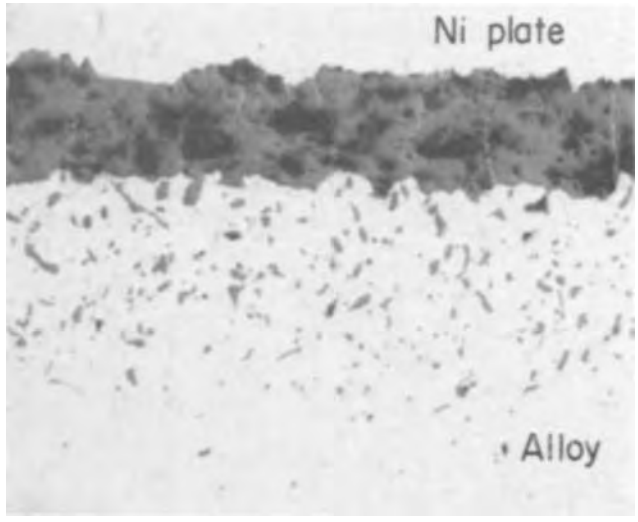

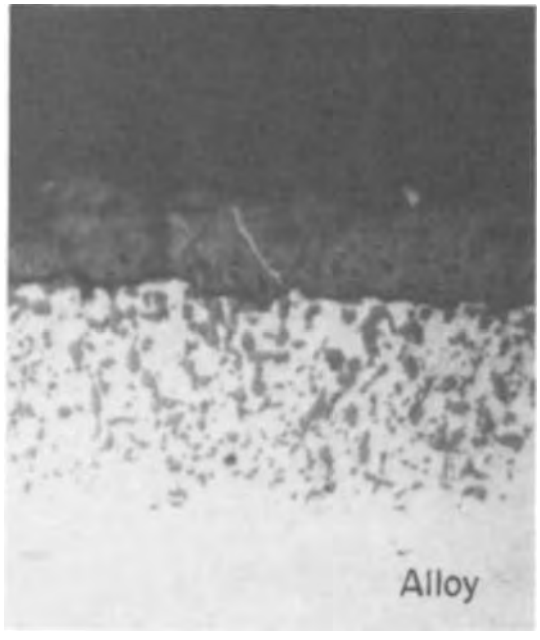

Fig. 5. Micrographs of Ni-20 w/o Cr alloy specimens sulfidized at different sulfur pressures. Magnification × 1650. (a, top) Exposure for 15.5 hr at $P_{S_2} = 1.6 \times 10^{-11}$ atm, (b, bottom) exposure for 8 hr at $P_{S_2} = 2.3 \times 10^{-10}$ atm.

The phase compositions identified in the external scale by the electron microprobe are summarized in Table III. The powder x-ray analyses are also included. There are problems in analyzing for chromium sulfides using ASTM x-ray cards since the six phases existing in the range CrS to Cr_2S_3 yield similar patterns (14). The x-ray technique identified the scale as mainly Cr_3S_4 with lines that could be assigned to Cr_2S_3. The probe technique also identified compositions near $(CrNi)_3S_4$ but other compositions nearer to $(CrNi)_5S_6$ and $(CrNi)_2S_3$ were also observed.

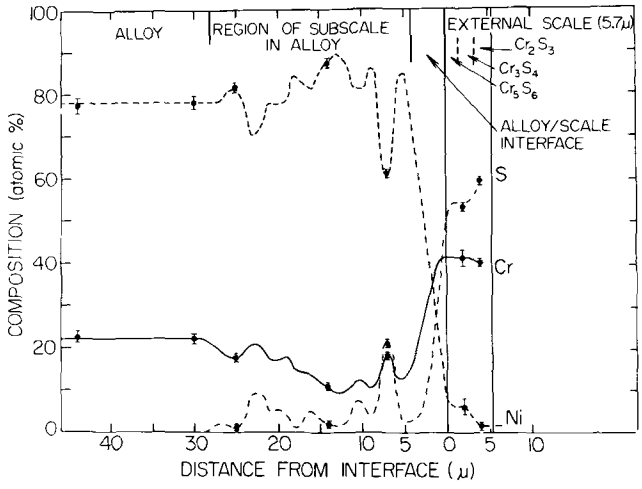

Fig. 6. Composition profiles of Cr, Ni, and S in a Ni-20 w/o Cr alloy specimen exposed for 24 hr in an H_2-H_2S atmosphere at a sulfur pressure $P_{S_2} = 5.5 \times 10^{-12}$ atm.

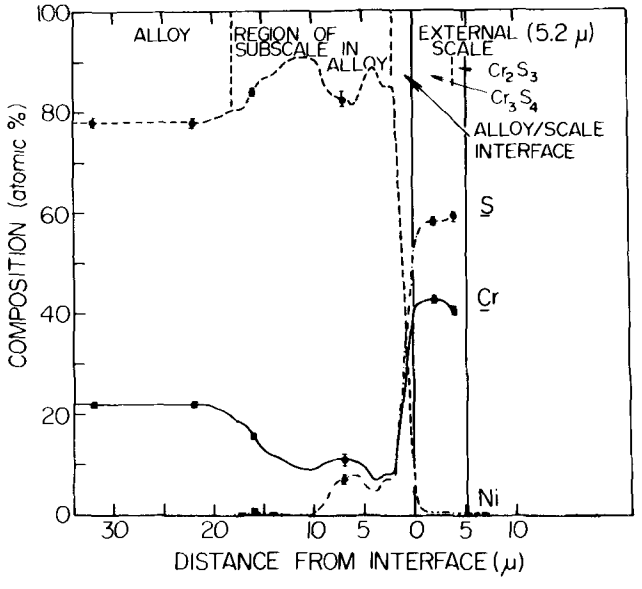

Fig. 7. Composition profiles of Cr, Ni, and S in a Ni-20 w/o Cr alloy specimen exposed for 8 hr in an H_2-H_2S atmosphere at a sulfur pressure $P_{S_2} = 6.5 \times 10^{-11}$ atm.

An attempt was made to positively identify the stringers using a x-ray microdetector mounted on the scanning electron microscope. Figure 8 shows SEM micrographs of stringers traversing the scale by three grain boundaries and compositional maps of the scale at regions of these stringers. This mapping demonstrates that the stringers in comparison to the scale are nickel-rich and depleted of sulfur. Actual counts obtained at points in a stringer and the scale are recorded in Table IV. These counts also show that the stringers are enriched in nickel and depleted of sulfur with respect to the adjacent scale. Although the electron beam possibly penetrates through stringers, since its intensity could not be reduced below 15 keV for effective counting of nickel, the metal/sulfur ratios based on the point counts vary from 1.01 within the stringer to 0.65 in the scale far from the stringer. The sulfide compositions, accordingly, correspond closely to the phases (NiCr)S and $(CrNi)_2S_3$ at these respective regions.

Discussion

The parabolic kinetics observed demonstrate that the reaction processes are diffusion controlled. Marker measurements have previously shown that metal is

Table III. Phase analysis of the external scale by x-ray and electron microprobe techniques

Sulfur potential (atm)	Electron microprobe analysis of external scale			X-ray analyses
	Inside		Outside	
5.5×10^{-12}	$Cr_{0.41}Ni_{0.05}S_{0.54}$ Cr_3S_6	Cr_3S_4	$Cr_{0.39}Ni_{0.02}S_{0.59}$ Cr_2S_3	Cr_3S_4
1.6×10^{-11}	$Cr_{0.42}Ni_{0.02}S_{0.56}$ Cr_3S_4		$Cr_{0.39}Ni_{0.02}S_{0.59}$ Cr_2S_3	$Cr_3S_4(Cr_2S_3)$
6.5×10^{-11}	$Cr_{0.42}Ni_{0.01}S_{0.57}$ Cr_3S_4		$Cr_{0.40}N_{0.01}S_{0.59}$ Cr_2S_3	$Cr_3S_4(Cr_2S_3)$
2.3×10^{-10}	$Cr_{0.39}Ni_{0.02}S_{0.59}$ Cr_2S_3			$Cr_3S_4(Cr_2S_3)$

* Bracketed compound refers to the scale constituent in minor proportions.

Table IV. Point counts and phase analyses of the external scale by x-ray microdetector mounted on a scanning electron microscope

Position	Ni(Kα1)	Cr(Kα1)	S(Kα1)	Composition
Scale far from stringer	1,225	15,229	25,400	$(CrNi)_{1.95}S_3$
Scale close to stringer	3,701	13,111	21,228	$(CrNi)_{3.19}S_4$
Inside stringer	6,469	9,944	16,213	$(CrNi)_{1.01}S$

the diffusing species in the chromium sulfide scale (5). A requirement to be met for concurrent subscale formation accompanied with morphological breakdown of the alloy interface is that the chromium diffusivity in the scale be several orders of magnitude larger than its diffusivity in the alloy. Thus, diffusion of chromium in these phases and sulfur in the alloy play fundamental roles in the formation of chromium sulfide on and in the alloy.

The external scale was identified as consisting mainly of $(CrNi)_3S_4$ although both lower and higher sulfide phases were present. An analysis of the nonstoichiometry and thermodynamics of the various binary forms of the chromium sulfides at 700°C has been made by Young *et al.* (15). All the sulfides approximate to the NiAs structure which may be described as hexagonally close-packed with the cations in the octahedral interstitial positions of the sulfide anion structure. Full occupation of these octahedral sites is found only in the case of CrS. The sulfides higher than Cr_7S_8 have a cation sublattice consisting of alternately filled and partially filled layers and, it has been proposed (16), that the partially filled layers are occupied by Cr^{+2} ions while the completely filled layers are occupied by Cr^{+3} ions. Cr_3S_4 has the largest nonstoichiometry ranging over the metal-excess and metal-deficiency sides of the stoichiometric formula ($1.286 < x < 1.377$ at 700°C when Cr_3S_4 is expressed as CrS_x and the intrinsic defect density is $\delta = 3.3 \times 10^{-2}$ at $P_{S_2} = 3.2 \times 10^{-11}$ atm).

According to this description of chromium sulfide, formation of the scale is expected to be controlled by metal diffusion via vacancies in the Cr^{+2} sublattices. The relationship between the parabolic rate constant and sulfur pressure is semilogarithmic as shown in Fig. 9. The significance of this relationship can be assessed from equations derived by Wagner (17) to describe the diffusion of metal from a binary alloy through its scale consisting of a ternary solid solution undergoing parabolic growth in terms of the metal diffusivities, the composition, and the activity gradients. His first-order differential equation expressing these parameters in terms of the parabolic rational rate constant for growth of a Ni-Cr-S solid solution layer exhibiting ideal or Henrian solution behavior would be (18)

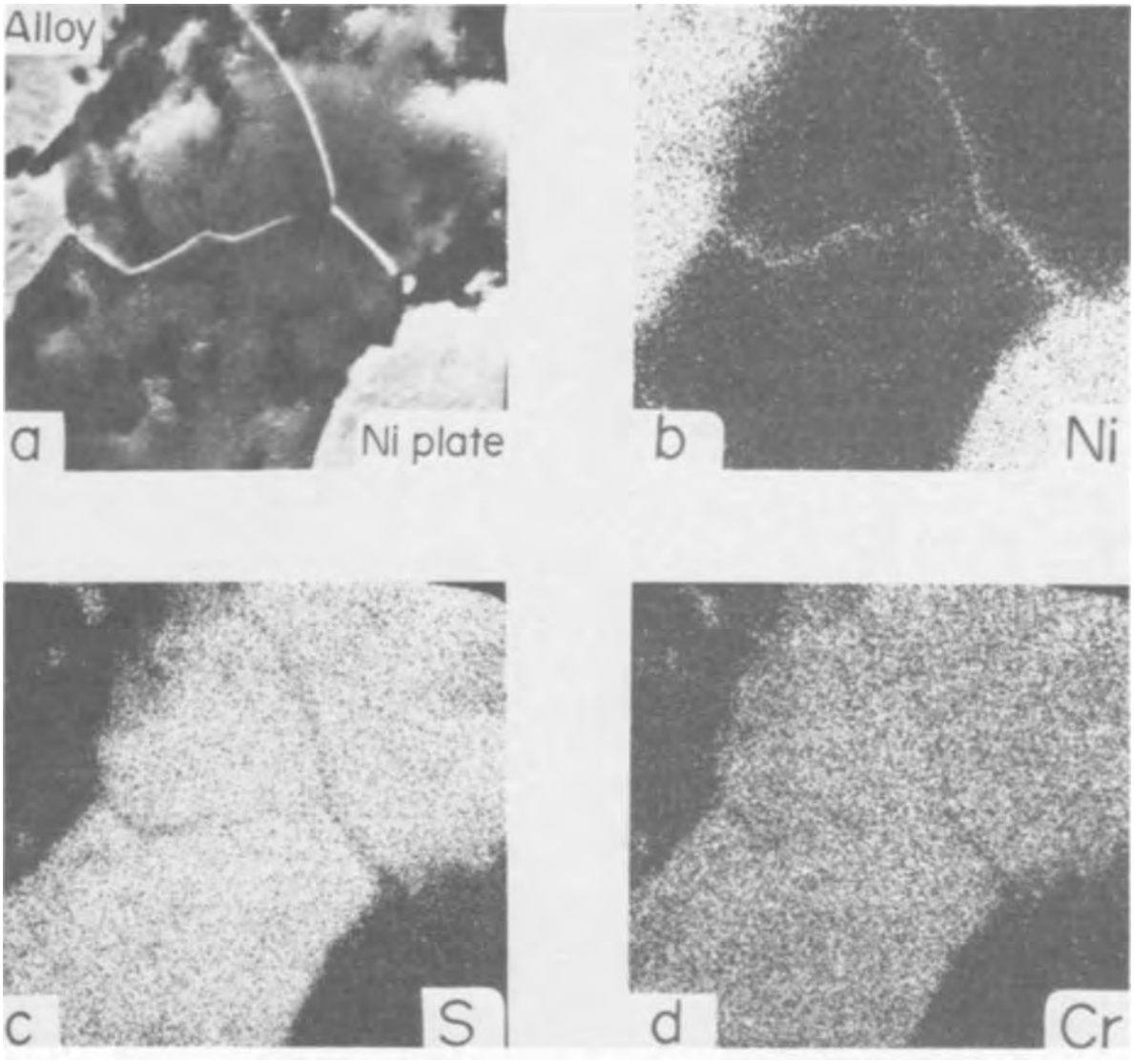

Fig. 8. SEM micrographs of the external scale in the region of stringers showing the stringers at grain boundaries and the Ni, S, and Cr composition maps. Magnification × 3500.

$$D_{Ni}(1-\epsilon)\left(-\frac{d\ln a_{Ni(S)}}{\partial\epsilon}\frac{d\epsilon}{dy}+\frac{z_{Ni}}{Z_S}\frac{d\ln a_S}{dy}\right)$$
$$+D_{Cr\epsilon}\left(-\frac{d\ln a_{Cr(S)}}{\partial\epsilon}\frac{d\epsilon}{dy}+\frac{z_{Cr}}{Z_S}\frac{d\ln a_S}{dy}\right)=k_r \quad [1]$$

where D_{Cr} and D_{Ni} are the metal self-diffusion coefficients, $1-\epsilon$ and ϵ are the local concentrations of nickel and chromium cations in equivalents, Z and a represent an appropriate valency and activity, y is the fractional distance x/x_s where x_s is the total scale thickness, and k_r is the parabolic rate constant in eq./cm sec. This equation can be applied to the present results by assuming that the chromium sulfide scale is a phase exhibiting continuous activity gradients for the diffusing species and that the above-expressed metal self-diffusivities act as appropriate average self-diffusion coefficients for total scale growth.

Certain assumptions can be made about several of the parameters in Eq. [1] from the scale compositions. First, the compositions and hence the activity gradients for the nickel and chromium sulfide constituents of a scale exhibit very little variation with respect to the much larger sulfur activity gradient. Second, the nickel concentration in the scale is very small [<5 a/o (atom per cent)] so that the value of ϵ can be approximated to unity. Equation [1] may then be written as

$$k_r \simeq D_{Cr\epsilon}\frac{z_{Cr}}{|Z_S|}\frac{d\ln a_S}{dy} \quad [2]$$

which corresponds to the expression for the parabolic rational rate constant describing growth of a binary sulfide layer on a pure metal (19).

Equation [2] is placed in the form

$$\frac{dk_r}{d\ln P_{S_2}}=\frac{\epsilon}{2}\frac{z_{Cr}}{|Z_S|}D_{Cr} \quad [3]$$

since the slope of the plot for the parabolic rate constant *vs.* $\ln P_{S_2}$ is proportional to the chromium diffusion coefficient. This slope (Fig. 9) gives a value of 1.5×10^{-11} cm²/sec for the diffusivity of chromium in the chromium sulfide scale.

The above analysis is but a first approximation to a complex reaction. It enables one, nevertheless, to obtain an evaluation for an average chromium self-diffusivity in the scale for comparison to that for the alloy. Since the phase changes between chromium sulfides are first order (15), the composition profiles at the phase boundaries are discontinuous. Unfortunately the resolving power of the electron probe was insufficient to define these compositional changes. The constant value obtained for the chromium diffusivity over the sulfur pressure range examined demon-

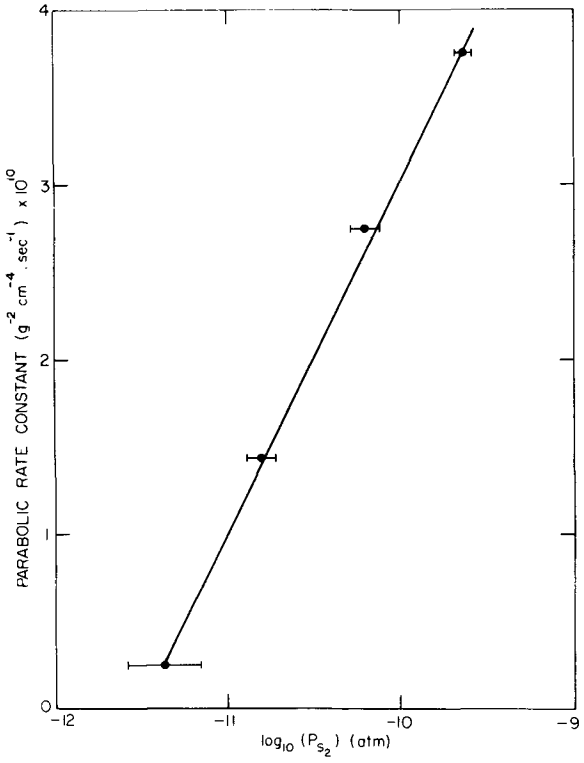

Fig. 9. Semilogarithmic plot of the parabolic sulfidation constants vs. the sulfur pressure in the H_2-H_2S atmospheres.

strates that this metal gradient and consequently the cation vacancy gradient across the scale was not strongly dependent on sulfur activity. This finding is consistent with the observations that $(CrNi)_3S_4$ was the fastest growing phase since pure Cr_3S_4 possesses an intrinsic disorder ($\delta = 3.3 \times 10^{-2}$) equal to one-third of its total possible nonstoichiometric disorder.

The diffusivity of chromium in a Ni-19.9 w/o Cr alloy has been investigated by Monma and co-workers (20) and at 700°C a value of 1.5×10^{-15} cm²/sec has been obtained. This is four orders of magnitude smaller than the value estimated for chromium diffusivity of the scale. These diffusion results can be used to examine the theoretical instability criteria for a planar interface of a binary alloy during its sulfidation advanced by Wagner (21). He established that the necessary but insufficient condition for instability is given by

$$\frac{X_{Cr}\,(D_{Cr}/V)_{alloy}}{1 - X_{Cr}\,(D_{Cr}/V)_{sulfide}} < 1 \qquad [4]$$

where X_{Cr} is the chromium mole fraction in the bulk alloy, and the terms in parentheses refer to the diffusivities and molar volumes of the alloy and chromium sulfide phases. The value of the above ratio from the results of this investigation is $\sim 10^{-5}$ which demonstrates as was found that morphological development of the external scale led to a very irregular alloy interface.

Since subscale penetration also obeyed parabolic kinetics, the diffusivity of sulfur in the alloy can be estimated from a relationship deduced by Wagner (22) between the volume fraction of the internal precipitates and the diffusivities. If the depth of subscale penetration and the distribution of the chromium sulfide particles are determined by outward diffusion of chromium and inward diffusion of sulfur, the volume fraction of chromium sulfide ϕ is given to a limiting approximation by

$$\phi = \frac{2}{\tilde{\pi}} \frac{X_{Cr}}{X_S^{o}} \left(\frac{\tilde{D}}{D_S}\right)_{alloy} \qquad [5]$$

Here, $\tilde{D}$ and D_S are the metallic interdiffusion coefficient and the sulfur diffusivity in the alloy, respectively, and X_S^{o} is the sulfur solubility in the alloy taken to be equal to that for pure nickel. The volume fraction was approximately 30% and the solubility of sulfur is the order of 30 ppm (11). This treatment yields $D_S \sim 10^{-11}$ cm²/sec which can be compared to the value of chromium diffusivity quoted previously $\sim 10^{-15}$ cm²/sec. Thus sulfur diffusion in the alloy is several orders of magnitude faster than the counter diffusion of chromium which meets the condition for internal precipitation of chromium sulfide. Since the subscale has a vague dendritic appearance with the formation of large irregular particles at the alloy grain boundaries, these boundaries acted as preferred sites for nucleation and growth of chromium sulfide.

A study of the scale compositions shows that the stoichiometry of the ternary chromium sulfides obtained exist at lower sulfur pressures than expected from the binary equilibrium study (15). The compositions nearest to the outer edge of the scales as obtained by the microprobe were used for this comparison since these values are most closely related to those for equilibrium with the determined sulfur pressures in the H_2-H_2S atmospheres. It appears that the presence of nickel in the scales in quantities up to 5 a/o has the effect of stabilizing the chromium sulfides by lowering their dissociation pressures. It is known that the presence of chromium in nickel sulfide has this effect (5). In order to illustrate this behavior, the Ni-Cr-S isothermal phase diagram for 700°C due to Kirkaldy and co-workers (9) has been converted into a tentative phase diagram of sulfur pressure *vs.* metal composition. The result is given in Fig. 10. In this diagram, the terminal phase compositions are known to a good degree of certainty from

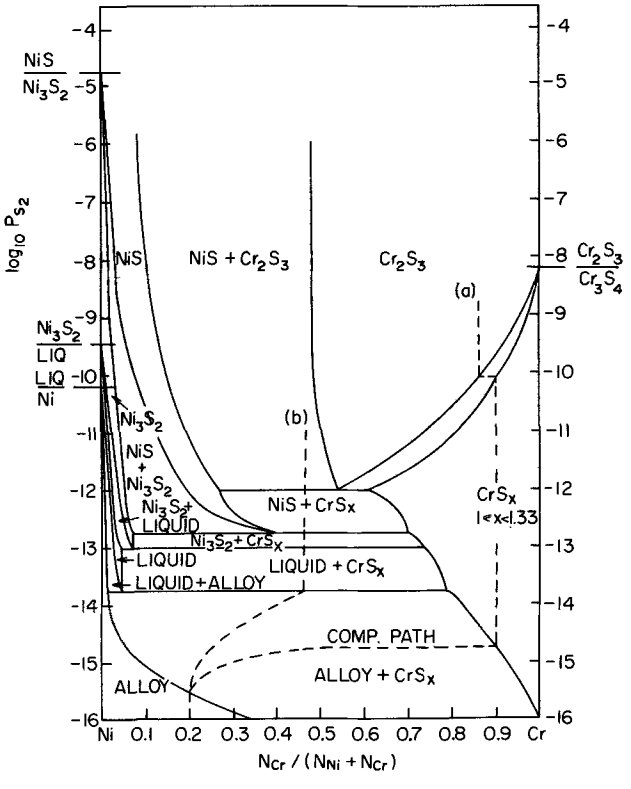

Fig. 10. Plot of the logarithm of the sulfur pressure vs. the metal atom fraction in the alloy and nickel-chromium sulfide phases to yield a tentative phase diagram representation of the Ni-Cr-S system at 700°C. The compositional paths (a) and (b) refer to the compositions within the alloy and the scale at the main regions of the scale and the regions of the scale boundaries containing nickel-rich sulfide stringers, respectively.

the phase diagram study but the sulfur pressures for stability of the phases are only of qualitative significance since they are approximations from the compositions of the chromium sulfide found in the scales at the different sulfur pressures under kinetic growth conditions. It would appear therefore that nickel solubility in a chromium sulfide phase, or vice-versa, decreased the sulfur pressures at which the various ternary sulfide phases are stable relative to those pressures for the pure binary compounds.

This representation of phase equilibria at 700°C suggests several compositional factors relevant to the morphological development of the reaction product. It has been found that the scales consisted essentially of chromium sulfide except at several grain boundaries where an additional phase as stringers extended from the tips of the irregular alloy interface. Representative compositional paths are shown in Fig. 10 which are in qualitative accordance with the electron microprobe results for compositions at these regions of the scale and subscale. Path (a) corresponds to compositions in the major regions of a scale. This path is shown to cut the (alloy + CrS_x) phase field at increasing sulfur pressure in order to account for the internal formation of chromium sulfide particles as a subscale. A large sulfur activity gradient subsequently occurs across the chromium sulfide phase fields of the external scale. Formation of the (NiCr)S stringers, however, implies that this compositional path at the regions of these stringers would be displaced toward the nickel side of the diagram. If the alloy tips could be depleted of chromium to approximately 1 a/o, a compositional path for these regions would possibly pass through the (liquid + CrS_x), (Ni_3S_2 + CrS_x), (NiS + CrS_x), and (NiS + Cr_2S_3) phase fields. This behavior which is shown by the compositional path (b) would account for stringers which, at the reaction temperature, would exist as liquid in contact with the solid alloy and they would extend directly from the alloy tips. This latter consideration appeared to be the case. The stringers, however, did not measurably increase the sulfidation rate because they existed as solid at the higher sulfur activities within the major portion of the external scale. A more detailed account cannot be given for these phenomena due to the limitations of the techniques for chemical analyses of the phases of small spatial extent. It has been possible to demonstrate, notwithstanding, that this behavior of the stringers is different than in a sulfidation example at the higher temperature of 850°C where it was found that the formation of completely liquid nickel sulfide stringers was associated with enhanced sulfidation and rapid degradation of a Ni-Cr alloy (6).

The results from this investigation may be compared to those previously obtained upon exposing a Ni-20 w/o Cr alloy to H_2-H_2S atmospheres supporting higher sulfur pressures at 700°C (5). At pressures greater than 8×10^{-8} atm a superficial layer of nickel sulfide was formed on the chromium sulfide layer. Both of these layers grew by parabolic kinetics without subscale formation and development of an irregular alloy interface. Consequently these latter features can be avoided in the sulfidation of a Ni-20 w/o Cr alloy when there is an outermost layer of nickel sulfide to act as a sink for nickel and subsequent rapid inward displacement of the alloy-scale interface.

Summary

Sulfidation of a Ni-20 w/o Cr alloy at 700°C in H_2-H_2S atmospheres supporting sulfur pressures for formation of chromium sulfide proceeded by parabolic kinetics. Chromium sulfide appeared as an external scale and subscale accompanied by morphological development of an irregular alloy interface. The parabolic rate constant varied semilogarithmically with sulfur pressure and the reaction processes were governed by the diffusion rates of chromium in both the external scale and alloy and sulfur in the alloy. The average self-diffusivity of chromium in the scale, 1.5×10^{-11} cm²/sec, was of the same magnitude as the sulfur diffusivity in the alloy, $\sim 10^{-11}$ cm²/sec, but four orders of magnitude larger than the chromium diffusivity in the alloy. These relative values for the diffusivities satisfied theoretical considerations for formation of a scale and subscale with simultaneous development of an irregular alloy interface. An explanation was also given for the formation of (NiCr)S stringers at grain boundaries in the chromium sulfide scale by reference to the thermodynamic stabilities of the various ternary metal sulfide phases.

Acknowledgments

This paper is based on the thesis submitted by J. A. Chitty to McMaster University in partial fulfilment of the requirements for the M.Eng. degree. The authors are grateful to L. A. Morris, M. J. Lavigne, and D. J. Young for useful and encouraging discussions, and to Falconbridge Metallurgical Laboratories for providing materials. This research was supported by grants from Falconbridge Nickel Mines Ltd. to J. S. Kirkaldy and from the National Research Council of Canada to W. W. Smeltzer.

Manuscript submitted Jan. 2, 1973; revised manuscript received May 3, 1973.

Any discussion of this paper will appear in a Discussion Section to be published in the June 1974 JOURNAL.

REFERENCES

1. S. Mrowec, T. Werber, and M. Zastawnik, *Corrosion Sci.*, **6**, 47 (1966).
2. P. Hancock, First International Conference on Metallic Corrosion, London, 1961, p. 193 (1962).
3. A. Davin, D. Coutsouradis, M. Urbain, and L. Habraben, *Ind. Chem. Belge*, **30**, 340 (1965).
4. A. U. Seybolt, *Trans. AIME*, **242**, 1955 (1968).
5. G. Romeo, W. W. Smeltzer, and J. S. Kirkaldy, *This Journal*, **118**, 740 (1971); **118**, 1336 (1971).
6. G. Romeo and W. W. Smeltzer, *ibid.*, **119**, 1268 (1972).
7. E. Lifshin, A. U. Seybolt, and J. B. Hudson, General Electric Co., Report No. 70-C-134 (April 1970).
8. C. J. Bechtold and H. C. Vacher, *Trans. AIME*, **221**, 14 (1961).
9. J. S. Kirkaldy, G. Bolze, D. McCutcheon and D. J. Young, *Met. Trans.*, **4**, 1519 (1973).
10. T. Rosenqvist and B. L. Dunicz, *Trans. AIME*, **194**, 604 (1952).
11. R. J. Brigham, H. Neumayer, and J. S. Kirkaldy, *Can. Met. Quart.*, **9**, 525 (1970).
12. B. L. Dunicz and T. Rosenqvist, *Anal. Chem.*, **24**, 404 (1952).
13. L. A. Morris and W. W. Smeltzer, *Acta Met.*, **15**, 1591 (1967).
14. F. Jellinek, *Acta Cryst.*, **10**, 620 (1957).
15. D. J. Young, W. W. Smeltzer, and J. S. Kirkaldy, *This Journal*, In press.
16. R. J. Bouchard and A. Wold, *J. Phys. Chem. Solids*, **27**, 591 (1966).
17. C. Wagner, *Corrosion Sci.*, **9**, 91 (1969).
18. Ref. 17, Eq. [11], p. 94.
19. C. Wagner, "Atom Movements," ASM, Cleveland, p. 153 (1951).
20. K. Monma, H. Suto, and H. Oikawa, *J. Japan. Inst. Metals*, **28**, 188 (1964).
21. C. Wagner, *This Journal*, **103**, 571 (1966).
22. C. Wagner, *Z. Elektrochem.*, **63**, 772 (1959).

The Effect of Mobile Sodium Ions on Field Enhancement Dielectric Breakdown in SiO_2 Films on Silicon

C. M. Osburn*

IBM Thomas J. Watson Research Center, Yorktown Heights, New York 10598

and S. I. Raider*

IBM System Products Division, East Fishkill Facility, Hopewell Junction, New York 12533

ABSTRACT

The presence of mobile sodium ions in SiO_2 films, thermally grown on silicon, can lead to time-dependent conduction and subsequent dielectric breakdown. When this occurs, it will be shown that anomalously high (ten orders of magnitude) electronic currents can result, presumably because of a modification of the shape of the injecting barrier, due to the high electric field created by the presence of the uncompensated positive charge. The time (t) required to break down the SiO_2 film under an applied field (E) was found to approximate the empirically known Peek's law relationship, *i.e.*, $E \propto t^{-1/4}$. Moreover, it will be demonstrated that field enhancement in the oxide due to space charge effects provides the fundamental breakdown mechanism. Capacitance-voltage measurements of the silicon flatband voltage were used to determine the internally created field, and thereby to demonstrate that breakdown occurred when the total field reached the breakdown strength of the film. It will be seen that the limiting time before breakdown, with sodium-contaminated samples, correlates with the kinetics of ionic motion, *e.g.*, it exhibits the same activation energy and varies roughly as the square of the oxide thickness. The other statistical variations in breakdown times can be quantitatively attributed to defects present in the starting oxide films.

Despite the high reliability of solid-state semiconductor devices, increasing reliability requirements, particularly for large MOSFET memory arrays, make a thorough understanding of any time-dependent deterioration mechanism necessary. Since the gate oxide region of an FET is normally subjected to electric fields approaching one-fourth of the intrinsic breakdown strength of SiO_2 (*i.e.*, $\sim$ 9 mV/cm), it is subject to dielectric breakdown. It has been known for some time that mobile ions (1) can be responsible for threshold voltage shifts over a period of time; nevertheless, little work has focused on the influence of mobile ions on the dielectric integrity of thermally grown SiO_2 films. Recently, Raider (2) found that mobile ions can be responsible for time-dependent dielectric breakdown.

Several recent papers (3-9) have been concerned with the dielectric breakdown of SiO_2 layers on thermally grown Si. Wide variabilities in breakdown strength across a Si wafer were usually observed and attributed to oxide defects. Various materials and processing parameters were tested to determine their influence on defects. For example, sodium contamination was introduced during oxide growth in one study (7), but it did not increase the defect density although it did lower the maximum breakdown strength. Unfortunately, however, very little attention has been directed in the earlier work to the time dependence of breakdown in relatively defect-free SiO_2 films, such as would be present in high quality MOSFET devices. Worthing (5) reported a time-dependent breakdown mechanism in MOS structures for silicon biased negatively and an intrinsic, time-independent mechanism for silicon positive. The breakdown time for Si(−) followed an empirical Peek's law relationship, *i.e.*, $E \propto t^{-1/4}$, where t is the time to breakdown at field E; this time dependence is the same as that observed earlier by Raider (2) in sodium contaminated SiO_2 films. Other work (4, 6-8) has failed to find this Peek's law behavior in high quality oxides. A second time-dependent breakdown mechanism, (*i.e.*, one that could not be described with Peek's law) was first observed experimentally by Raider (2). It was later described by DiStefano (9) in terms of a barrier-height lowering which leads to breakdown as a result of Na ion buildup at the Si/SiO_2 interface. This barrier lowering is similar to work-function lowering which occurs with Cs on Si [see Ref. (9)] and leads to breakdown triggered by excessively high current in SiO_2.

This paper focuses more extensively on the effect of sodium ions on the time dependence of SiO_2 breakdown as well as the breakdown mechanism. Primary consideration is given to the high internal fields (10) that can be associated with uncompensated charge in the SiO_2. It is shown that Worthing's results can be explained by the motion of ions in the oxide.

Experimental Procedure

Metal-oxide-semiconductor capacitors were fabricated on 2 ohm-cm, p- and n-type, <100>-oriented silicon wafers. The wafers were ultrasonically cleaned using NH_4OH-H_2O_2, HCl-H_2O_2 (11), and HF solutions, while the quartz glassware was etched with HNO_3-HF. Oxides were grown from 200 to 2000Å thick at 1000°C in dry oxygen; the oxide thicknesses were measured ellipsometrically.

Contamination was introduced by evaporating a small amount of NaCl onto the freshly oxidized surface. To complete the capacitors, 3000Å thick aluminum dots (32 mil diam) were evaporated through metal masks in a clean evaporation system, and the wafers were then annealed for 30 min at 400°C in dry nitrogen. Samples prepared in this fashion had mobile charge densities from 10^{11} to $10^{15}/cm^2$, as measured by the charge-time (Q-t) technique (12). Although films having such high mobile Na contamination levels are not acceptable for technological applications, locally high sodium concentrations may be present even though the average level is low. Control wafers typically had mobile ion concentrations less

* Electrochemical Society Active Member.

Key words: dielectric breakdown, silicon dioxide, sodium contamination, electrical conduction, field enhancement.

than $5 \times 10^{10}/cm^2$ as determined by the capacitance-voltage flatband shift method (1).

Measurements were made of both the time to breakdown and the time dependence of the capacitance-voltage flatband voltage for stressed samples. In the first measurement, a constant voltage was applied to an MOS capacitor dot with the aluminum dot biased positively. Breakdown was identified by an almost instantaneous jump in the current density to well over 10 mA/cm². Often current spikes occurred which were generally correlated with the appearance of small black specks or holes in the capacitor (seen with 500X magnification) in the aluminum electrode and were attributed to self-healing breakdown events (2). The times at which each breakdown event occurred were recorded. Usually the MOS capacitor would finally short out; this time was also recorded. Capacitance-voltage measurements for monitoring ionic drift have been described previously (1, 12), are straightforward, and are not discussed further here.

Results and Discussion

Conduction.—When a high field (4-8 MV/cm) is applied to a contaminated MOS capacitor with the metal electrode biased positively, the current is observed initially to increase with time. If the contamination level or the applied field is high enough, breakdown occurs after a given period of time has elapsed. When the applied field is low enough so that breakdown does not occur, the current reaches a maximum and then decays with time as shown in Fig. 1. Current densities up to 150 mA/cm² have been observed in 1000Å thick films. The current observed here is much too large to be explained by ionic motion and is attributed to enhanced electron injection into the oxide as a result of the high internal field created by the ions. The time at which the current maximum occurs as well as the maximum current density are shown as functions of applied field in Fig. 2.

The time dependence of this current through an SiO_2 film contaminated with sodium ions (viz., Fig. 1) can be explained by the variation of the tunneling distance with the position of the sodium sheet (13)

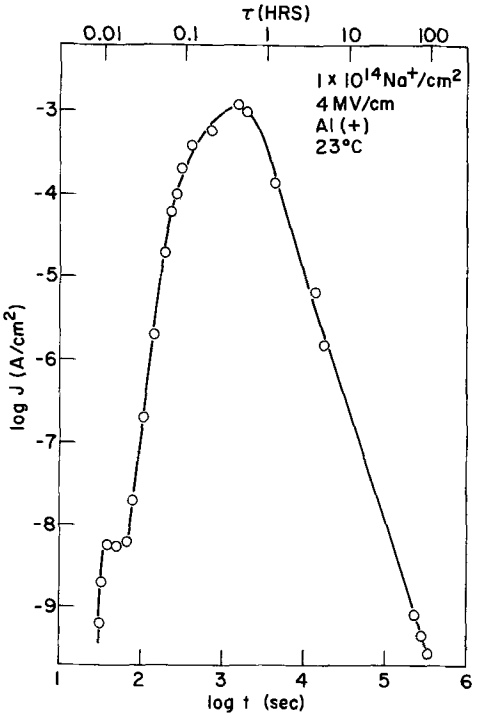

Fig. 1. Current through a Na^+-contaminated, 2000Å SiO_2 film as a function of time.

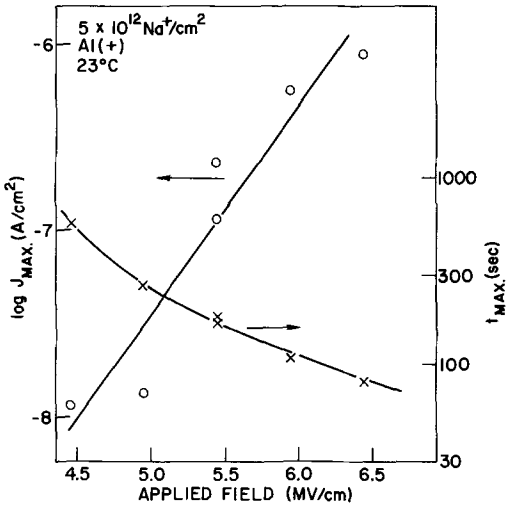

Fig. 2. Dependence of the maximum current and the time at which the current peak occurs on applied field.

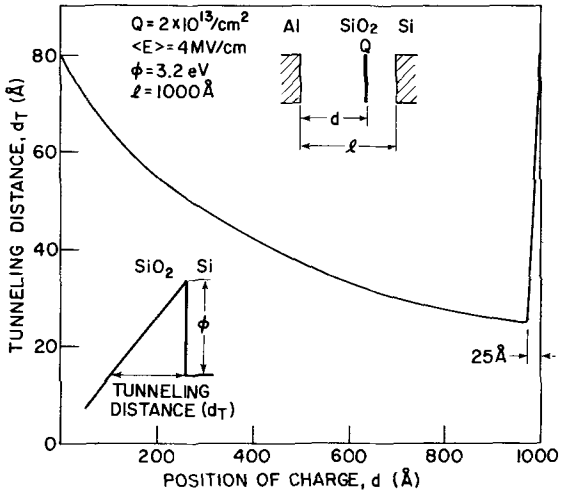

Fig. 3. Variation of tunneling distance with position of charge inside oxide.

(Fig. 3). In the absence of ionic effects, room temperature conduction through SiO_2 has been shown (8, 14) to take place via a Fowler-Nordheim tunneling mechanism in which conduction electrons from the injecting electrode (silicon in the case of Fig. 1) tunnel through a triangular-shaped potential barrier into the oxide conduction band. The slope of the oxide conduction band forming the barrier is given by the internal electric field. The tunneling distance (d_T) is determined by the barrier height (ϕ) and the applied field (E) when no charge is present in the film. The effect of the electrically uncompensated sheet of positive charge in the oxide is to reduce the tunneling distance by increasing E internal near the Si. As seen in Fig. 3, the F-N barrier thickness becomes progressively smaller as the charge sheet penetrates the oxide until it is almost to the Si/SiO_2 interface (25Å away, estimated using the system parameters for the case considered here). Once the charge is located less than the tunneling distance away from the silicon, further charge motion actually increases the tunneling distance. When all of the charge is at the Si/SiO_2 interface, the tunneling distance is the same as if the charge were at the metal/SiO_2 interface. Calculations (10) (neglecting strain energy) do show that the equilibrium position for sodium ions (10^{13}/cm²) under even low bias (1 MV/cm) is less than 5Å from the silicon. Accordingly, the shape of the current-time plot (Fig. 1) can be now understood: the

small peak (at ~ 30 sec) is caused by ion motion; the large maxima at 1000 sec is developed as the tunnel distance minima is reached; and, the slow current decay at longer times take place as the charge sheet reaches the SiO_2/Si interface. The rapid current increase followed by a slow decrease must then reflect rapid motion of charge through the bulk of the film followed by slower motion near the interface.

It should be noted that although high (0.1 A/cm^2) current densities have been observed in these contaminated capacitors, the current levels expected with a space-charge limited mechanism are much higher (~ 10^5 A/cm^2 assuming an electron mobility of 1 cm^2/V-sec), and electrode-limited conduction is still seen here. Samples that were immersed in liquid nitrogen at the peak of the current time curve (Fig. 1) continued to show the very high conduction level. The current was reduced by only a factor of five which would correspond to an activation energy less than 0.02 eV. From this unreasonably low energy it can be concluded that the conduction mechanism at the highest current levels remains Fowler-Nordheim tunneling which is only weakly temperature dependent (8, 14). Thermal runaway leading to breakdown was not observed although runaway would be likely for current densities above 1 A/cm^2.

Dielectric breakdown.—When the field is high and breakdown does occur, the time to breakdown is determined by the field applied, the contamination level, the oxide thickness, and the measuring temperature. Figures 4 and 5 give typical breakdown field *vs.* breakdown time characteristics; the data reasonably describe the equation $E_{BD} = E_o + \alpha t^{-1/4}$. This Peek's law dependence for SiO_2 films on Si was empirically observed first by Worthing (5) and was attributed to conduction and thermal instability rather than mobile ions at that time. It should be noted that each point in Fig. 4 or 5 represents the longest time observed when a reasonably large sampling, 10-20, of identically prepared and stressed capacitors are allowed to break down. Often breakdown would occur earlier if a defect were present in the oxide; accordingly, thin metal electrodes were used so that these randomly occurring, early breakdown events would recover by the well-known self-healing breakdown process (3). The rate of these breakdown events would increase with time until final shorting occurred, with total destruction of the capacitor. The times for final shorting (in Fig. 4 and 5) are the maximum ones that will elapse before breakdown, and are believed to be representative of uniform, defect-free SiO_2 films. An actual FET device would suffer a failure in less time. The early breakdowns are scattered, of course, but they do generally follow the same behavior as the limiting times shown in Fig. 4. A correlation of the limiting or longest time to breakdown was made to the time for the current maxima (viz., Fig. 1). Actual breakdowns were seen both before the peak (*i.e.*, when the current was increasing with time) was reached and after the peak. However, the limiting breakdown time was seldom greater than the time for the current maximum. It should be emphasized that the field-enhancement type of breakdown occurred before all the sodium drifted to the Si/SiO_2 interface.

The effect of oxide thickness on the time-to-breakdown relationship is shown in Fig. 4 while the effect of measuring temperature is given in Fig. 5. In each case we find a common intercept, that is a field below which breakdown does not occur regardless of the temperature or oxide thickness. The time to breakdown varies almost as the square of the oxide thickness while Fig. 6 indicates that it is also thermally activated in the temperature range studied.

These results can be explained in terms of the internal field created by the presence of the charged ions. The electric field in the oxide at the SiO_2-Si interface (E_{Si}) at any time is given by

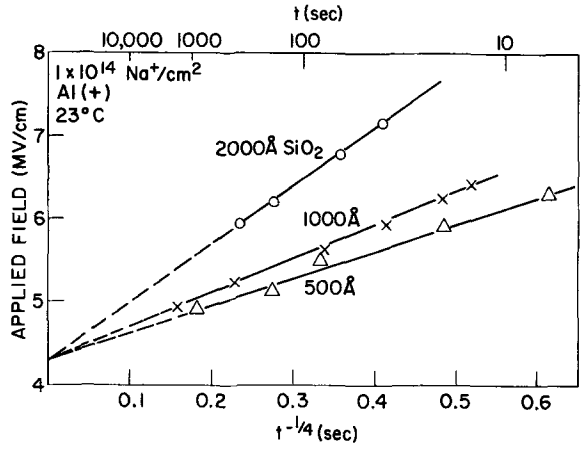

Fig. 4. Effect of oxide thickness on time interval before breakdown.

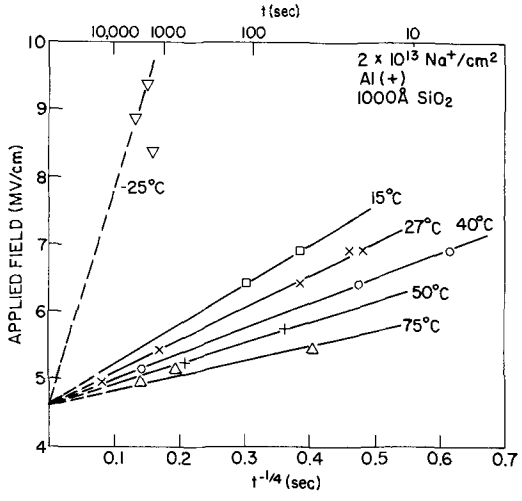

Fig. 5. Effect of temperature on breakdown time

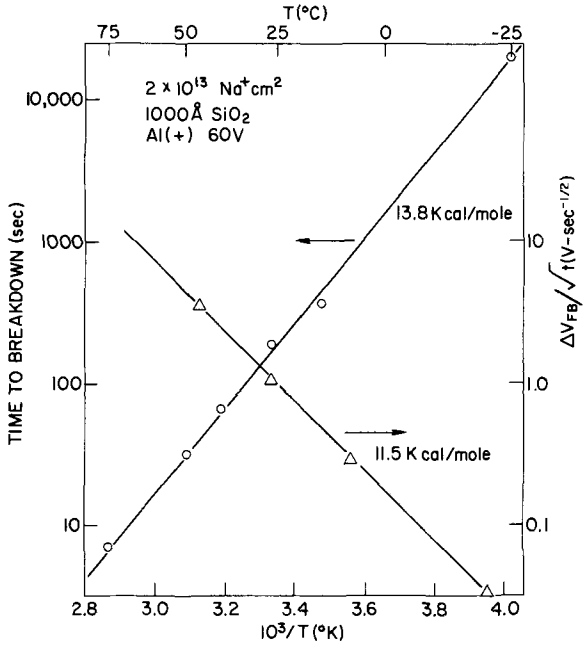

Fig. 6. Temperature dependence of time to breakdown and of C-V shift.

$$E_{Si}(t) = E_{appl} + \frac{\Delta V_{FB}(t)}{d_{ox}} \quad [1]$$

where E_{appl} is the applied field, $\Delta V_{FB}(t)$ is the Si flatband voltage shift at time t, and d_{ox} is the oxide thickness. The term $\Delta V_{FB}(t)$ is seen to be (1)

$$\Delta V_{FB}(t) = \frac{1}{\epsilon}\int_{x=0}^{x=d_{ox}} q(x, t)\, x\, dx \quad [2]$$

where ϵ is the oxide dielectric constant and $q(x)$ is the charge density at the position x in the oxide. The point $x = o$ corresponds to the oxide surface, and $x = d_{ox}$ corresponds to the silicon-SiO_2 interface. If only positive charge is present in the oxide, the maximum internal field is that at the Si/SiO_2 interface and is given by E_{Si} in Eq. [1].

An applied field can shift the mobile charge even at room temperature. As the sodium ions drift under the applied field toward the silicon, the flatband voltage becomes larger, resulting in an increase in the oxide field near the silicon. When E_{Si} exceeds the maximum breakdown strength of the oxide (E_{max}), breakdown occurs [see Ref. (7) for the dependence of E_{max} on oxide thickness and Si doping]. The maximum field enhancement occurs when all of the sodium is near the silicon in which case Eq. [2] reduces to

$$\Delta V_{FB} = \frac{Q d_{ox}}{\epsilon} \quad [3]$$

where Q is the total amount of sodium/cm^2 present. Breakdown will not occur at all with this model when the maximum breakdown strength (E_{max}) satisfies

$$E_{max} > E_{appl} + \frac{Q}{\epsilon} \quad [4]$$

As an example when Q is 10^{13} Na^+/cm^2, Q/ϵ becomes 4.6 MV/cm; for a 1000Å SiO_2 film E_{max} is 9 MV/cm[7]. Thus breakdown should not occur for applied fields less than $9 - 4.6 = 4.4$ MV/cm.

Based on the above findings, the essential condition needed to cause breakdown in these systems can be written as

$$E_{max} = E_{appl} + \frac{\Delta V_{FB}(t_{BD})}{d_{ox}} \quad [5]$$

where E_{max} is a function of oxide thickness and Si doping. This relationship was verified, within experimental error, for a wide range of controlled sodium levels from 10^{12}/cm^2 to 10^{15}/cm^2, over the temperature interval from −25° to +75°C, and SiO_2 thicknesses from 200 to 2000Å. For example, by using a contamination concentration of 2×10^{13} Na^+/cm and a 1000Å thick SiO_2 film stressed with a nominal 60V potential, it was seen that the dependencies of the flatband voltage shift and of the time to breakdown activation energies for Na^+ drift and oxide breakdown are essentially the same. See Fig. 6. In light of the sample-to-sample variability of most breakdown results which will be discussed shortly, this agreement to within 2 kcal/mole must be considered quite good.

Although the experimental data fit the empirical Peek's law relationship well, the fundamental relationship governing the above behavior is given actually by Eq. [5]. The flatband voltage shift is a complicated function of the initial sodium concentration, temperature, and the field. Furthermore, the rate of flatband voltage shift is subject to considerable changes over a period of time and is still not completely understood. In view of this complexity it is not possible to obtain a simple E_{appl} *vs.* t equation. The simplest expression arises when log $\Delta V_{FB}/\sqrt{t}$ is proportional to the field as seen in one segment of Fig. 8 and is more fully explained in the section on Sodium drift. With this proportionality, it can be shown that the limiting time to breakdown, t_{BD}^{max}, is given by

$$t_{BD}^{max} = \left[\frac{E_{max} - E_{appl}}{K \cdot \exp(kE_{appl})}\right]^2 \quad [6]$$

where K and k come from the intercept and slope, respectively, of the log $\Delta V_{FB}/\sqrt{t}$ *vs.* E plot. Although Eq. [6] is too restrictive and complex to be very useful, it is more fundamental than Peek's law.

A considerable amount of variability in the results was observed. As mentioned earlier, breakdown events do occur at times considerably shorter than the limiting times presented here and these short time failures are the most important ones for actual devices. Only the process of self-healing, whereby the electrode above weak spots is vaporized, allows us to determine the limiting time. If the electrode metalization is too thick or if an oxide defect is large, shorting occurs during a breakdown and gives a time which is shorter than the limiting time. This phenomenon made it difficult to obtain data that had little scatter. Because of it, minor, but expected, deviations from an exact Peek's law behavior could not be seen.

Although the occurrence of breakdown after the current has reached a maximum is rare, *i.e.*, in about 1% of the capacitors tested, it is significant in formulating the details of the breakdown model. Electronic breakdown in SiO_2 has been postulated previously (8) to occur via collision ionization: injected electrons gain sufficient energy from the electric field to ionize centers in the oxide. With Fowler-Nordheim injected electrons, the first possible ionizing collision occurs at a distance of about $\lambda + d_T$ where λ is the mean free path and d_T is the tunneling distance. (Note: the electrons do not gain energy during tunneling.) For breakdown to occur the high field region must extend that far into the oxide; thus the centroid of the mobile ions must be at least $\lambda + d_T$ away from the silicon. To first order, the tunneling distance is given by the barrier height, ϕ, divided by the field E and is minimized when the centroid of the mobile charge is located at d_T and thereby results in the current maxima. Thus it is argued that ionization and breakdown from Fowler-Nordheim injected electrons would occur before the current peak was reached. Electrons injected over the top of the barrier (Schottky emission), on the other hand, do not have this restriction. If the mean free path of these electrons is less than the tunneling distance, then breakdown can take place after the current peak has occurred. Our data indeed show that the conditions required for breakdown to be substantially later than the current peak also results in a Fowler-Nordheim tunneling distance (given by the barrier height divided by the field) that is 35-50Å and hence longer than the reported mean free path of 34Å (15).

When the aluminum was biased negatively no time dependent conduction or breakdown was observed. The sodium contamination was introduced just before metalization. Negative bias would keep the Na in place where it would not enhance the applied field. If the contamination was uniformly distributed through the oxide, a time dependence would be expected.

Sodium drift.—The breakdown time dependence can be explained from the kinetics of the flatband voltage shift. Mobile ion drift in SiO_2 films has been extensively examined (1, 16-20); however, a complete characterization of the drift process has never been presented, particularly at room temperature and for high applied fields. Figure 7 presents a typical plot of the capacitance-voltage flatband shift as a function of time and applied field at room temperature. When the flatband voltage shift is small compared to the total possible flatband shift, the voltage shift varies

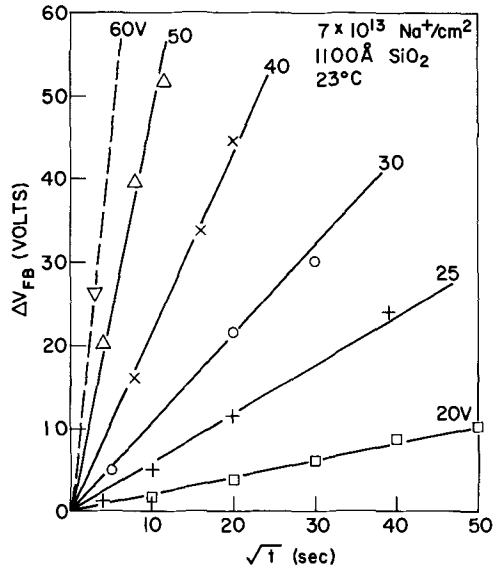

Fig. 7. Capacitance-voltage flatband shift as a function of time and applied voltage.

as the square root of time. Snow *et al.* (1) attributed their kinetic results to a field-free boundary layer while Hofstein (16-17) showed that the drift could better be explained in terms of sodium emission from interfacial traps. If the trapping band is less than few kT wide, then a linear ΔV_{FB} *vs.* $\sqrt{t}$ plot would be expected for short times. Other work has supported the model of sodium release from traps (18-19). Figure 8 gives the slope of the ΔV_{FB} *vs.* $\sqrt{t}$ curves as a function of applied field. Eldridge and Kerr (20) have explained the field dependence of the flatband shift due to Na^+ ions drifting through phosphosilicate glass-SiO_2 films in terms of the lowering of the barrier of a potential well. They found

$$\Delta V_{FB}(t) \propto \sqrt{t} \exp\{(-\phi + qEW/2)/kT\} \quad [7]$$

where ϕ is the depth of the potential well and W is its width. The field dependence seen in SiO_2 films without PSG does show log $\Delta V_{FB}/\sqrt{t} \propto E$ over a segment of the data but not over the entire field range.

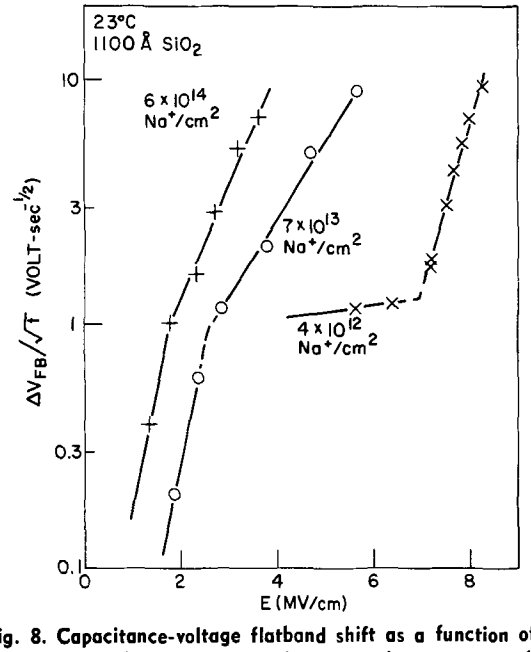

Fig. 8. Capacitance-voltage flatband shift as a function of field for different Na^+ contamination levels showing apparent changes in Na^+ drift mechanism.

As Fig. 8 shows, two line segments do a reasonable job of approximating the data. Thus these drift data might be interpreted in terms of sodium emission at the electrode from two (or more) different trap levels. It should be noted that plots of $\Delta V_{FB}/\sqrt{t}$ *vs.* E (*i.e.*, replacing E by $\sqrt{E}$ in Eq. [7] for the case where the barrier lowering is proportional to $\sqrt{E}$) also show two line segments. With two trapping levels one would expect a higher slope of the plot log $(\Delta V_{FB}/\sqrt{t})$ *vs.* E at higher fields. When the total sodium concentration is small, ($<5 \times 10^{12}/cm^2$) this expected change in slope is seen (Fig. 8).

However at the high fields required for breakdown to occur in lightly contaminated films, the kinetics of Na drift become nearly identical for drift in either direction (2) suggesting that it may well be at least partially controlled by the bulk rather than the interfaces. When sufficient amounts of Na are released from interface traps, one might expect motion to be diffusion limited. This hypothesis is further supported by the observation that the breakdown time increases nearly as the square of the oxide thickness.

The highly contaminated samples ($> 10^{13}/cm^2$) on the other hand, show slope changes (Fig. 8) in the opposite direction and cannot readily be explained by a dual trap level model. The case of high doping is particularly interesting since the internal field due to the ions can be significantly greater than the applied field. In addition for these high contamination levels it has been observed that the breakdown times vary nearly as the square of the oxide thickness (see Fig. 4) suggesting a bulk-limited diffusion. A substantial concentration of ions in the oxide could even reverse the direction of the field and probably cause ion drift to cease. Here the rate-limiting step for sodium ion motion is probably not emission from traps but rather the necessity for maintaining a positive electric field. Only a minor sodium concentration dependence of the drift would be expected above $10^{13}/cm^2$ since that concentration could be sufficient to reverse the direction of the field. When the amount of diffusing sodium is limited by the applied field, the internal field is small and the concentration gradient could become the driving force for motion; thus it is likely that kinetics of sodium motion should be similar to those for bulk-limited diffusion. Breakdown data further support the model of field-limited drift and will be considered later. In light of the present data for high sodium concentrations it seems possible then to account for the two slopes of the log $\Delta V_{FB}/\sqrt{t}$ *vs.* E plot (7×10^{13} and 6×10^{14} Na^+/cm^2 curves of Fig. 8): one segment (at low applied field) being electrode emission-limited and the other (at high fields) being field-limited. It is apparent, however, that the problem of sodium drift in SiO_2 films is more complicated than previously realized and that considerably more work needs to be done to understand the ion motion.

For each point on the time-to-breakdown plot (Fig. 4-5) the flatband voltage shift can be determined from the flatband voltage *vs.* time curve or a plot similar to Fig. 7 for the wafer under consideration at the temperature of interest. When the flatband shift term is added to the applied voltage to determine the internal field, E_{Si}, at the interface as in Fig. 9, it is found that in the region where breakdown occurs rapidly (*i.e.*, <1000 sec), the internal field at breakdown is equal to the maximum dielectric strength of thick SiO_2. For longer times (>>1000 sec) before breakdown, the internal field is even higher. These phenomena can be qualitatively accounted for by realizing that the high field region near the Si/SiO_2 interface ultimately becomes very narrow as the Na^+ ions reach the SiO_2/Si interface. In an earlier paper (7), one of the present authors had already established

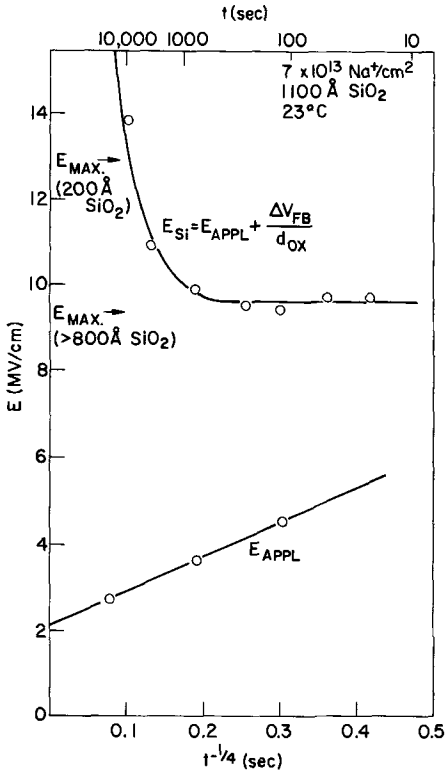

Fig. 9. Internal and applied fields in SiO_2 at breakdown as functions of time. The lower curve gives measured breakdown time as a function of applied field; the upper curve gives the oxide field at the silicon as calculated using C-V data. The maximum dielectric strength of thick (> 800Å) and thinner (200Å) SiO_2 are included for reference.

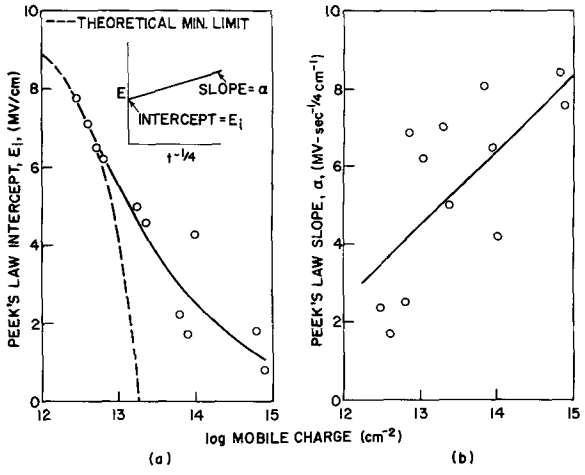

Fig. 10. Sodium ion concentration dependence of Peek's law plot. (a) intercept, (b) slope.

that the maximum dielectric strength increases very rapidly with decreasing oxide thickness for films $\lesssim$400Å thick. Thus the internal field required to cause breakdown increases as the time to breakdown increases because the oxide thickness of the high field region decreases. In Fig. 9 the maximum dielectric strengths of 200Å thick and >800Å thick SiO_2 films are included for reference. Apparently after 10,000 sec of mobile ion drift, the effective thickness of the high field region is about 200Å.

Variability was seen in the rate of Na^+ drift. Measurements made on different days gave results that differed by a factor of two or three. Although this behavior remains unexplained, it is surmised that if the diffusion of Na^+ is limited by emission from the interface (that is, controlled by the release of sodium from traps at the electrode interface) rather than bulk diffusion limited, changes in humidity, thermal history, and previous stressing might result in large variations in the data.

The effect of total sodium concentration on breakdown characteristics was recorded during this work. Figure 10 shows the concentration dependence of the intercept and the slope of a Peek's law plot. The dotted line in Fig. 10(a) represents the expected theoretical intercept as computed from Eq. [5] where $\Delta V_{FB}/d_{ox}$ is replaced by Q/ϵ (Q is the total sodium density) and the thick oxide limit of E_{max} (9.2 MV/cm) was used. For large sodium concentrations, the intercept was higher than expected. This observation supports the conclusion that the internal field in the oxide can be very high without causing breakdown if this high-field region is narrow. A field of 500 MV/cm results from 10^{15} Na^+/cm^2 inside the oxide; nevertheless, it is indeed possible to move this amount of charge through the film without causing breakdown. Apparently the sodium can be concentrated into a narrow region even though coulombic repulsion and stress effect do not favor a high concentration. If the high-field region is to be narrow during biasing, it must be argued that the transit time through the SiO_2 should be short compared to the time of release from traps at the electrode. Otherwise the distance from the silicon to the center of charge and hence the width of the high-field region becomes substantial and results in breakdown.

The high intercept in Fig. 10 also supports the field-limiting model for sodium ion motion. Above 10^{13} ions/cm^2, the number of sodium ions that can move through the oxide (and hence the magnitude of the field enhancement) without reversing the direction of the internal field is controlled more by the applied field than by the surface ion concentration. Calculations with a simple model assuming uniform and sheet ion injection into the oxide and a uniform ion velocity show that the maximum charge injection into the film should contribute three to four times the applied field; hence, a minimum intercept of about 2 MV/cm would be expected. A more precise treatment would require knowledge of the exact ion profiles as a function of time. Data are too limited to even attempt such calculations; nevertheless, this elementary consideration provides a qualitative explanation of the seemingly high intercepts of Peek's law plots.

A phosphosilicate glass layer (400Å, 7% P_2O_5) was added to one oxide film (1000Å total thickness) prior to sodium evaporation (10^{14}/cm^2) and the breakdown time-voltage relationship was determined from room temperature to 300°C. The improvement with the PSG was quite dramatic. Breakdowns that occurred in a few seconds at room temperature in the samples without PSG took several hours or did not occur at all even at 300°C. The intercept of the Peek's plot was about 2 MV/cm for the control sample at room temperature and 5 MV/cm for the PSG sample at 300°C; at room temperature the PSG sample had an intercept of over 7 MV/cm. The temperature dependence of the breakdown time at a fixed field was found to be considerably less than that of sodium drift seen earlier (20). The improvement in breakdown times seen with a PSG layer is believed to be more accentuated than is the retardation of the flatband shift. In the extreme case of emission-limited ion motion (where, for all practical purposes, the sodium is either trapped at the metal interface or is at the Si-SiO_2 interface), no breakdown should occur. As shown earlier, breakdown only occurs when a substantial amount of charge is at least 30Å away from the Si-SiO_2 interface. When the sodium is at the interface, breakdown must occur via a mechanism other than simple field enhancement. The discrepancies between control- and

PSG-sample intercepts as well as the different temperature dependencies of sodium drift and breakdown time in PSG samples are evidence that the ion motion through a PSG layer is a better approximation to a completely emission-limited process than is ion motion in a pure SiO_2 film.

Effect of defects.—Statistical measurements of the times to the first breakdown at constant voltage of an array of capacitors in a heavily contaminated sample are shown in Fig. 11 where the fraction of MOS capacitors is plotted as a function of breakdown time [Fig. 11(a)]. A very considerable spread in the times was observed. When the breakdown fraction of the same data is plotted as a function of $t^{-1/4}$ [Fig. 11(b)], a well-defined peak is seen with a tail at larger values of $t^{-1/4}$. By using the Peek's law plot to transform the ordinate from increments of $t^{-1/4}$ to increments of voltage and by determining the absolute internal field at breakdown for one sample, it was possible to calculate the voltage distribution of breakdown [Fig. 11(c)]. Details of the transformation are given in the Appendix. This calculated distribution was nearly identical to a breakdown distribution on a control wafer [Fig. 11(d)]. No significant difference could be discerned between voltage distributions either as calculated from the time distribution of breakdown or as measured with a voltage ramp on a control wafer [note the differences between Fig. 11(c) and 11(d) reflect normal variations in distributions as a consequence of using discrete intervals and do not reflect any substantial difference between the two]. The large variations in time to breakdown are indeed surprising in light of the tightly clustered voltage distribution. It is fortunate that the time and the voltage distributions are equivalent; nevertheless, it is obvious that the time distribution is much more sensitive to sample variations than is the voltage distribution.

Summary

Mobile Na ions are seen to be responsible for one type of time dependent dielectric breakdown in MOS structures. Breakdown occurs because of the high internal field associated with the presence of ions in the oxide film. As mobile Na ions drift through the oxide, the electric field strength at the Si-SiO_2 interface increases. When the field becomes as large as the breakdown strength of the oxide, breakdown occurs. The capacitance-voltage flatband shift is a direct measure of the field enhancement at the Si-SiO_2 interface.

The time lapse before breakdown in a Na-contaminated MOS was found to depend on the applied field, the contamination level, the oxide thickness, and the temperature. The breakdown time-applied field relationship was found to approximate the empirical Peek's law ($E \propto t^{-1/4}$) although its more fundamental theoretical form is much more complex than Peek's law. The contamination level, the oxide thickness, and the temperature dependence of the breakdown time correlated with the rate of flatband shift. Higher contamination reduced the time to breakdown. The breakdown time varied almost as the square of the oxide thickness and was exponentially activated by temperature (14 kcal/mole from −25° to +75°C, 2×10^{13} Na^+/cm^2).

As sodium ions moved through the oxide film of an MOS capacitor, the electronic conduction varied with time. Electronic current density increases up to 150 mA/cm^2 were observed. If the sample did not break down, the current would reach a maximum and then decay slowly. An analysis (13) showed that the Fowler-Nordheim tunneling distance decreased and then increased as ions moved from the metal to the silicon. The minimum tunneling distance (maximum in current) occurred when the ions were about 25Å from the silicon.

The kinetics of sodium drift were measured in the process of verifying that the sum of the applied voltage plus the flatband voltages shift must equal the breakdown voltage for breakdown to occur. The rate of flatband voltage shift ($d\Delta V_{FB}/d\sqrt{t}|\ t = 0$) was found to vary exponentially with the applied field over the range of the data. Such a field dependence was reported earlier (20) for sodium emission and motion from traps in phosphosilicate glass-SiO_2 structures. To account for all of the data, however, it was necessary to consider at least two exponential field dependencies. In some cases the results could be accounted for by consideration of two distinct trapping levels for the sodium. The heavily contaminated case could not be explained in terms of multiple trap levels. Evidence was seen in this case for a field-limiting injection where injection is limited by the necessity of having the field remain in the same direction throughout the sample.

Statistical measurements of the time to breakdown of contaminated capacitors were made. The previously established relationship between breakdown time and voltage was used to convert the time-based distribution to a voltage-based one. This voltage-based distribution was then compared to a statistical distribution of the breakdown voltages of uncontaminated capacitors. Quantitatively, the distributions were essentially the same showing that the capacitors that broke down early were those capacitors that had low breakdown strengths to begin with.

The results obtained in this work are very similar to those of Worthing (5): with Al(−) no time dependence of breakdown was seen, and with Al(+) a Peek's law type of behavior was recorded. In view of these facts, it may be possible to attribute his results to the presence of mobile ions. Ion concentrations of $10^{13}/cm^2$ (at least locally) could account for Worthing's results.

A second breakdown process, which was suggested (9) to be the result of barrier lowering due to sodium contamination at the Si/SiO_2 interface, requires times considerably longer than the transit time of the sodium through the SiO_2. At such long times all of the sodium should be near the Si/SiO_2 interface and

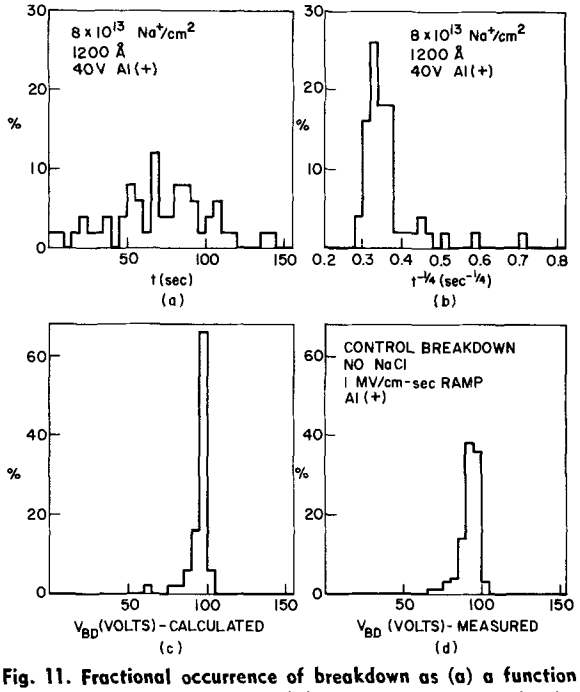

Fig. 11. Fractional occurrence of breakdown as (a) a function of time, (b) a function of (time)$^{-1/4}$, (c) as a function of voltage, V_{BD}, (calculated from the time dependence), and (d) as a function of voltage, V_{BD}, on a control wafer.

should not cause field-enhancement breakdown since the enhanced field region is too narrow to sustain an avalanche.

Acknowledgments

The authors would like to thank Drs. A. Berman, N. Chou, J. Eldridge, D. Kerr, and W. Pliskin for stimulating conversations, access to unpublished data and calculations, and samples. Measurements and sample preparation were skillfully done by D. Ormond, E. Vishnesky, and E. Weitzman.

APPENDIX

Relationship of Breakdown Time to Ramp Breakdown Field

Transforming a distribution of breakdown times to a distribution of breakdown fields requires information about (*a*) the time *vs.* field dependence of breakdown and (*b*) the nature of the oxide defects. In the case of field-enhancement breakdown, Peek's law provides an adequate empirical description of breakdown time as a function of field. Two limiting cases of oxide defects can be considered: Case 1 in which the oxide is locally thin (*i.e.*, oxide pinholes, or a rough silicon surface) and case 2 in which the defect is electrical in nature. The internal field, E_{int}, in each case is greater than the applied field, E_{appl}, and is given by

$$E_{int} = kE_{appl} \quad \text{Case 1}$$
$$E_{int} = E_{appl} + E_{enhance} \quad \text{Case 2} \qquad [A\text{-}1]$$

where k is the ratio of the nominal oxide thickness to the minimum oxide thickness at the defect, and $E_{enhance}$ is the magnitude of the field enhancement due to the electrical defect. The parameters k and $E_{enhance}$ give the magnitude of the physical or electrical defect. Associated with the higher internal field is a shorter time to breakdown. Since Peek's law empirically holds, then

$$E_{int} - E_{appl} = (dE/dt^{-1/4})\,(t^{-1/4} - t_m^{-1/4}) \qquad [A\text{-}2]$$

where $dE/dt^{-1/4}$ is the Peek's law slope, t_m is the limiting breakdown time at a field E_{appl}, and t is the breakdown time of a capacitor with a defect.

Breakdown under a ramp voltage occurs when the internal field equals the maximum breakdown field, E_{max}. Thus

$$\left.\begin{aligned} E_{BD} &= \frac{E_{max}}{k} \quad \text{Case 1} \\ E_{BD} &= E_{max} - E_{enhance} \quad \text{Case 2} \end{aligned}\right\} \text{at breakdown} \qquad [A\text{-}3]$$

Once a Peek's law plot is determined, each breakdown time of a distribution of times can be inserted into Eq. [A-2] to obtain the corresponding field enhancement. Equation [A-1] gives the parameters describing the defect magnitude. Equation [A-3] is then used to compute the ramp breakdown field associated with each defect size. Thus a series of breakdown times t_i (obtained at a field E_{appl}) can be transformed to a series of breakdown fields, $(E_{BD})_i$, by

$$(E_{BD})_i = \frac{E_{max} \cdot E_{appl}}{E_{appl} + (de/dt^{-1/4})\,(t_i^{-1/4} - t_m^{-1/4})} \quad \text{Case 1}$$
$$(E_{BD})_i = E_{max} - (dE/dt^{-1/4})\,(t_i^{-1/4} - t_m^{-1/4}) \quad \text{Case 2} \qquad [A\text{-}4]$$

An illustration of this transformation is seen in Fig. 11. Part (a) gives the distribution of t_i's, part (b) the $t_i^{-1/4}$'s, and part (c) the field-based distributions. The assumption of an electrical defect (case 2) is given in Fig. 11; nevertheless, the assumption of a geometrical defect (case 1) gives similar results. Of course, the general case would include both electrical and geometrical defects.

Manuscript submitted Jan. 15, 1973; revised manuscript received May 23, 1973.

Any discussion of this paper will appear in a Discussion Section to be published in the June 1974 JOURNAL.

REFERENCES

1. E. H. Snow, A. S. Grove, B. E. Deal, and C. T. Sah, *J. Appl. Phys.*, **36**, 1664 (1965).
2. S. I. Raider, *Appl. Phys. Letters*, **23**, 34 (1973).
3. N. Klein, *IEEE Trans. Electron Devices*, **ED-13**, 788 (1966).
4. C. Fritzsche, *Z. Angew. Phys.*, **24**, 43 (1967).
5. F. L. Worthing, *This Journal*, **115**, 88 (1968).
6. N. Chou and J. Eldridge, *ibid.*, **117**, 1287 (1970).
7. C. M. Osburn and D. W. Ormond, *ibid.*, **119**, 591 (1972); **119**, 597 (1972).
8. C. M. Osburn and E. J. Weitzman, *ibid.*, **119**, 603 (1972).
9. T. H. DiStefano, *Appl. Phys. Letters*, **19**, 280 (1971), *J. Appl. Phys.*, **44**, 527 (1973).
10. N. Chou, To be published.
11. W. Kern and D. A. Puotinen, *RCA Rev.*, **31**, 187 (1970).
12. W. A. Pliskin, D. R. Kerr, and J. A. Perri, "Physics of Thin Films," Vol. 4, pp. 257-324, Academic Press, Inc., New York (1967).
13. D. R. Kerr, Private communication.
14. M. Lenzlinger and E. H. Snow, *J. Appl. Phys.*, **40**, 278 (1968).
15. C. N. Berglund and R. J. Powell, *ibid.*, **42**, 573 (1971).
16. S. R. Hofstein, *IEEE Trans. Electron Devices*, **ED-13**, 222 (1966).
17. S. R. Hofstein, *ibid.*, **ED-14**, 749 (1967).
18. D. R. Kerr, Reliability Physics Symposium, Las Vegas, April 7-10, 1970.
19. M. Kuhn and D. J. Silversmith, *This Journal*, **118**, 966 (1971).
20. J. M. Eldridge and D. R. Kerr, *ibid.*, **118**, 986 (1971).

Accelerated Dielectric Breakdown of Silicon Dioxide Films

C. M. Osburn* and N. J. Chou*

IBM Thomas J. Watson Research Center, Yorktown Heights, New York 10598

ABSTRACT

The time dependent, dielectric breakdown of thermally grown SiO_2 films in metal-SiO_2-Si structures was studied as a function of oxide thickness and growth conditions, stressing temperature and electric field, and electrode material. With no field applied, thermal annealing of Al-SiO_2-Si capacitors markedly increased the measurable defect density. In the range 200°-350°C, the time required to form 20 defects/cm^2 is proportional to $d_{ox}^{1.7}e^{-\Delta H/RT}$ where d_{ox} is the oxide thickness and ΔH is 14 kcal/mole. The degradation without bias was much less, comparatively, when Mo, Pt, and polycrystalline-Si electrodes were used, as well as when a phosphosilicate glass film was formed on the SiO_2 surface. Under electrothermal stressing, the breakdown time decreased almost exponentially with applied field and, in films over 200Å thick, was thermally activated with an energy 1.4 ± 0.2 eV. The oxide thickness dependence of the wear-out under bias varied according to the applied field and ranged from the 2.1 power of the thickness at 2 MV/cm to the 5.5 power at 7 MV/cm. A model is described according to which the generation of the interface states, leading to a decrease of the injecting barrier height and attendant large increases in current, is probably responsible for the subsequent dielectric breakdown.

In order to practically assess the long term reliability of the gate insulator in MOSFET devices, it is necessary to determine failure rates under accelerated stress conditions (*e.g.*, using temperatures and electric fields higher than would be encountered during normal device operation) and then to extrapolate these rates to the usual operating conditions. As a result of extensive testing in many laboratories, it is quite clear that the dielectric breakdown of the thin (typically 1000-1500Å) thermally grown SiO_2 film on silicon, used for the gate dielectric, constitutes a major FET failure mode. Already several authors (1-6) have observed that the dielectric breakdown strength of SiO_2 films can be significantly dependent on the duration of the applied field, while others (7-8) have reported that the oxide can be degraded by the so-called "post-metalization anneal" in the 400°-500°C range, in the absence of an applied field.

Since some ions have been observed (9, 10) to be mobile in metal oxide semiconductor structures, much of the early work (3-5) dealing with time dependent breakdown has focused on the influence of such ions. Two models of mobile ion induced degradation have been proposed: field intensification due to charged ions (4, 11) and barrier height lowering (5, 12). In the field intensification model, charged ions within the oxide film enhance the internal electric field as described by Gauss's law. As ions move through the oxide it is possible for the internal field to equal the dielectric strength of the film and thereby cause breakdown. Worthing (2) first reported a Peek's law dependence of the breakdown time, t, of MOS capacitors with the silicon biased negatively, *i.e.*, $t^{-1/4} \propto E$ where E is the applied field; he found no time-dependent breakdown when the metal electrode was biased negatively. More recently (3-4) similar breakdown characteristics were attributed to field intensification associated with sodium. In the absence of any complicating mechanism such as ion trapping, the field intensification mechanism (4) was found to be very rapid (~ 1 hr) and required a very high contamination level (~ 10^{13} ions/cm^2); as such this mechanism is probably not responsible for long term device failures. The barrier height lowering model (5, 12) proposes that breakdown occurs as a result of the lowering of the barrier between the silicon and SiO_2 conduction bands. The barrier lowering occurs because of the dipole set up when contaminant ions are near the Si-SiO_2 interface. Both electrical (13) and photoemission (12) measurements have exhibited this lowering after tens or hundreds of hour's stressing. Many questions remain unanswered about this model and it is not possible to definitely assess the importance of this failure mode.

In addition to mobile ions, many different electrochemical processes have been reported that could influence breakdown. High temperature annealing in a N_2 ambient was previously shown (7-8) to result in a degradation of breakdown strength as statistically measured on arrays of MOS capacitors. Chou and Eldridge (7) found that the edge of a capacitor electrode attacked the underlying SiO_2 and Si. Crystallization of SiO_2 films has been observed both at room temperature (14-16) as well as after high temperature processing in the presence of impurities such as sodium (15-18). Crystallization might be expected to produce microcracks, interfacial charge, and electric field inhomogeneities and thereby promote breakdown; Meek and Braun report a correlation between crystallization and breakdown (19). Reaction of the electrode metal with the SiO_2 has been reported at elevated temperatures for Al (20-22), Pt (21), Si (23), and Cr (24-25) electrodes. Such reaction leads to ion injection and possibly filament formation and therefore might account for dielectric failure. Furthermore, interface state and oxide charge generation and trapping have been seen (6, 26-29) as a function of bias-temperature (B-T) stressing. This type of charge generation should lead to field enhancement and barrier lowering just as mobile ions. Finally, Jorgensen (30) has studied the solid-state electrolysis of SiO_2 in MOS samples, and asserts that Si^{+4} in the oxide can be reduced to elemental silicon. The silicon formation, either uniformly or in dendrites, should make the dielectric film thinner and more susceptible to breakdown.

This study was initiated to gain a more complete understanding of the mechanism responsible for long term wear-out (by dielectric breakdown) of SiO_2 films such as those employed in MOSFET devices. It was also undertaken in part to obtain a sufficient data

* Electrochemical Society Active Member.

Key words: dielectric breakdown, reliability, silicon dioxide, electrical conduction, interface state.

base in order to make reliability predictions for MOS structures from data obtained under accelerated testing conditions. Electrical measurements were made up to the time of breakdown to help determine which, if any, of the previously observed electrochemical processes are responsible for the degradation.

Experimental Procedure

Sample preparation.—Silicon wafers, as received from Semimetals and Monsanto were cleaned sequentially in solutions of NH_4OH-H_2O_2, HCl-H_2O_2 (31), HF, and thoroughly rinsed in deionized H_2O, just prior to the oxidation step. Each processing step was closely controlled and transistor grade reagents were used to optimize the quality of the films. The resistivity and the dopant of the silicon were varied, although 2 ohm-cm, p-type <100>-oriented material wafers were used in most of this work. The so-called "standard SiO_2" films were grown at 1000°C in dry oxygen. Some oxide films were grown at 1000°C in an ambient of 3 volume per cent HCl, 97 volume per cent O_2 in order to further upgrade the SiO_2 quality. Mobile charge was found to be less than $10^{10}/cm^2$ by the triangular-voltage-sweep (TVS) technique (23). Phosphosilicate glass (PSG) layers were added to a few films by depositing P_2O_5 onto SiO_2, followed by a drive-in at 975°C.

One hundred electrode contacts (10-50 mil diam) were added to each wafer by depositing metal through masks, using an electron beam heated source. The resulting capacitors were then annealed in nitrogen to remove radiation damage, sustained during metalization. Aluminum was the most widely used electrode metal although Al-4% Cu (32), Mo, Pt, and polycrystalline-Si electrodes were also employed. The polycrystalline-Si electrodes were doped with a deposition and drive-in of P_2O_5 at 975°C to ensure a low resistance contact.

Electrical measurements.—Breakdown characterization studies fell into two categories: the determination of statistical distribution of breakdown voltages of large numbers of identically prepared capacitors; and the time to break down a capacitor under fixed stress conditions. Statistical distributions are determined by applying a slowly varying ramp voltage to an array of capacitors and measuring the voltages at which each capacitor breaks down (7, 8, 33). A histogram giving the number of failures as a function of applied voltage can then be constructed.

In order to evaluate the effects of the well-known postmetalization annealing process, wafers were annealed for various times in dry N_2 at temperatures in the 200°-500°C range, and the resultant breakdown voltage distributions were then measured at room temperature. The combined effects of field and temperature on breakdown were determined by stressing capacitors in a high temperature biasing cell filled with dry N_2. In these experiments, the current flowing through the capacitor was monitored until breakdown occurred, and the breakdown time was recorded. In testing large numbers of identically prepared capacitors, the time to breakdown under stressing was found to vary from sample-to-sample in a statistical manner. In the present paper, only the longest or limiting time to breakdown results are discussed since they are believed to be representative of the effects of field and temperature on the breakdown time of uniform defect-free SiO_2 films, and as such were easier to analyze. A detailed study of the influence of oxide defects on breakdown is underway also, and the results will be published elsewhere.

Additional measurements were used to supplement breakdown data. Capacitance voltage, C(V), curves giving the silicon flatband voltage were used to monitor the fixed charge at the SiO_2-Si interface and also oxide polarization (9), while the Gray and Brown method (34) (*i.e.*, comparison of C-V curves at 77° and 300°K) gave a measure of the fast surface state density. Room temperature current-voltage characteristics (35) were observed in order to determine the height of the injecting barrier during testing.

Results and Discussion

Oxide degradation in the absence of electric fields.—Breakdown voltage distributions of capacitor arrays can be altered by the annealing process (7, 8). As an example of this effect, Fig. 1 gives the distribution or breakdown fields of identically prepared Al-SiO_2-Si capacitors before and after a 350 hr anneal at 250°C. Extended annealing clearly shifts the breakdown distribution to lower fields. The rate of this degradation depends on the annealing temperature and electrode metal, and could be markedly reduced by the presence of a phosphosilicate glass layer. In order to manageably handle the large volumes of statistical data, a single defect density was computed from each statistical breakdown distribution. More precisely, the fraction of capacitors which break down at electric fields $< 0.8\ E_{max}$ (where E_{max} is the maximum dielectric strength and is a function of oxide thickness and Si doping) has been shown (7, 8) to be proportional to the capacitor area, and the defect density can be calculated from the proportionality constant. By using this approach, changes in the oxide defect density (ρ) could be quantitatively followed as a function of annealing time and temperature. In assessing annealing effects in a study involving the use of a wide range of material and processing parameters, it is also convenient to determine the conditions needed to produce a given but arbitrary increase in ρ. Thus, Fig. 2 illustrates both the SiO_2 thickness and temperature dependences of the time necessary for ρ to increase by 20 defects/cm^2 (τ). The data indicate that two thermally activated processes are present: one degradation mechanism has an activation energy of 55 kcal/mole and predominates above 350°C while the other has an energy of 14 kcal/mole from 200°-350°C. Excessively long testing times prohibited measurements below 200°C; such low temperature measurements would be helpful because of the danger inherent in extrapolating data to lower temperatures. Chou and Eldridge (7) found that the capacitor degradation after 500°C annealing resulted from electrode attack at the edge of the capacitor. Presumably this edge attack is responsible for the high temperature failures seen here;

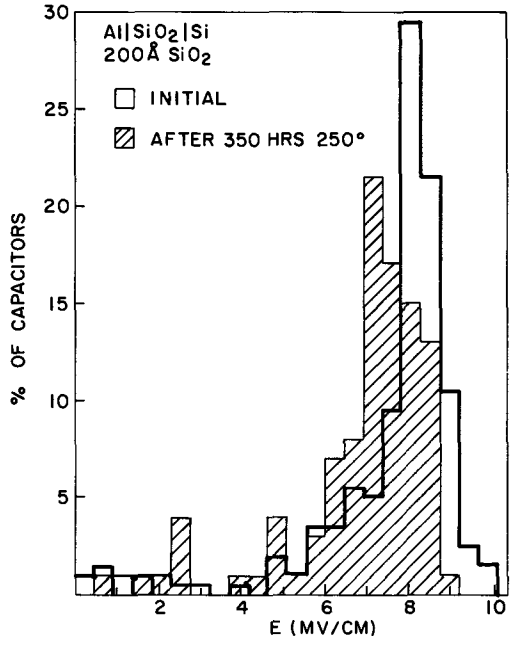

Fig. 1. Shift in breakdown distributions after high-temperature annealing without bias.

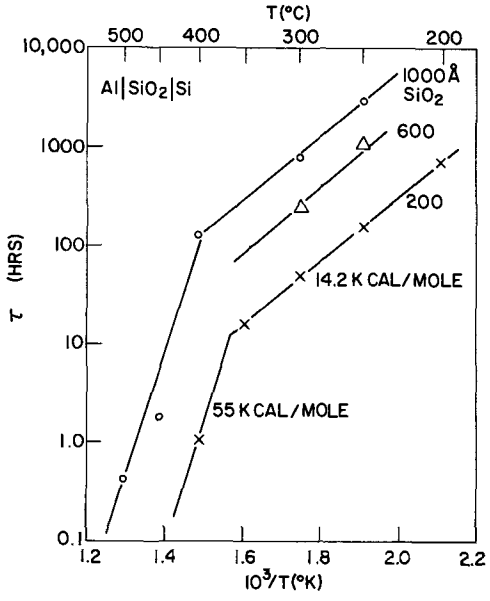

Fig. 2. Temperature dependence of annealing-induced degradation for 200, 600, and 1000Å films.

nevertheless the basic mechanism remains obscure. These results are replotted in Fig. 3 in order to dramatize the strong thickness dependence of the lower temperature degradation process where

$$\tau \propto [\text{oxide thickness}]^{1.7} \qquad [1]$$

The defect generation rate depends on the electrode material and can be retarded markedly by the presence of a thin, dilute phosphosilicate glass layer of the type used to block Na^+ drift effects on the FET threshold (36). Table I summarizes the time for the defect density to increase by 20/cm² for a variety of electrode metals and PSG. It was seen that an addition of 4% Cu to the aluminum did not influence the deteriorization process while a substantial PSG layer gave very significant improvements. The copper was added to make the electrodes more resistant to electromigration (32). Platinum, molybdenum, and polycrystalline Si electrodes also increased the lifetime. Poly-Si gave the most substantial improvement, while molybdenum was only a factor of about two better than aluminum. It was noted in several instances that polycrystalline Si

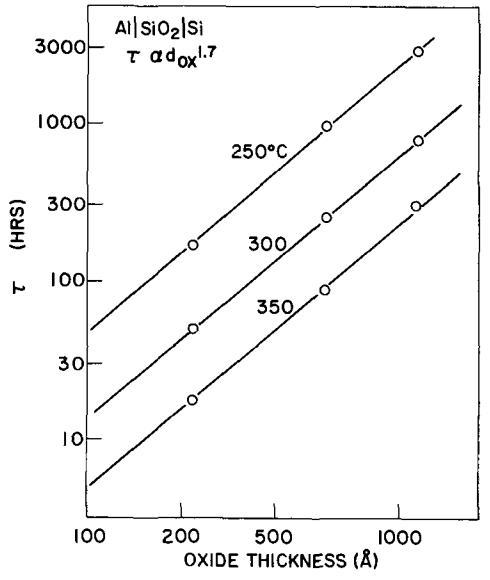

Fig. 3. Oxide thickness dependence of annealing-induced degradation.

Table I. Effect of electrode metal and oxide thickness on long-term degradation under no bias conditions

Metal	d_{ox} (A)	T (°C)	Time for defect density to increase by 20/cm² (hr)
Al	200	300	50
Al	600	300	150
Al	1000	300	800
Al	1000	500	0.4
Al-Cu	200	300	50
Al-Cu	1000	500	0.3
Al	250 PSG (4.3% P_2O_5)	300	>1000
Al	1000 (with 400A PSG, 7% P_2O_5)	300	>2000
		500	1
Pt	200	300	>1000
Pt	1000	300	>1500
Mo	200	300	80 (variable)
Mo	1000	300	>1000
Si (poly)	1000	500	>200

electrodes had abnormally high initial defect levels despite their long term resistance to wear-out. Presumably this was a consequence of the high temperature processing needed to dope the poly-Si in order to obtain low electrode resistance. After deposition of the poly-Si, the electrodes are exposed to temperatures as high as 1000°C. Hence it is not surprising that these capacitors have high initial defect levels but are resistant to further degradation at 500°C.

Oxide degradation in the presence of electric fields.— Under sufficiently high electric fields and temperatures, breakdown will obviously occur. Just as the breakdown voltage of capacitors can vary from sample to sample when a slowly increasing, or ramp voltage, is applied, the time to breakdown for capacitors held for long times at elevated temperatures under a fixed field can exhibit a wide distribution of values. Nevertheless, upon testing an array of identically prepared specimens under a given set of stressing conditions, a well-delineated, maximum breakdown time could be obtained in the same way as a maximum breakdown strength is found using the ramp breakdown technique. A typical statistical distribution of breakdown times, under a constant field, is presented in Fig. 4, and the maximum breakdown time is taken as the time required to cause 100% failures of all devices. When thin (*e.g.*, $\lesssim$ 1000Å) electrodes are used so that defected oxide regions are eliminated by the well-known nonshorting (or self-healing) breakdown mechanism (37), the time at which final shorting occurred agreed very closely with the statistically determined t_{max} value. Many samples must be tested to accurately establish t_{max}; in this study, five to twenty capacitors were measured for each set of experimental conditions. As can be seen in Fig. 4, the time required for 80-90% failures are factors of two to three

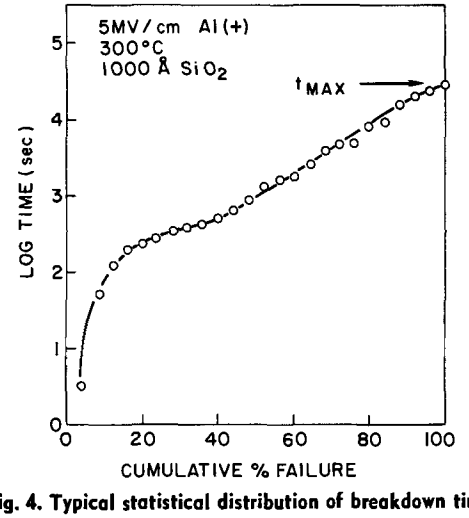

Fig. 4. Typical statistical distribution of breakdown time

lower than t_{max}. Thus the error associated with measuring t_{max} from five to ten capacitors is only a factor of two to three which is small compared to the wide range of failure times observed under varying conditions. Maximum times to breakdown of several hundred hours have been observed under moderate fields; all evidence points to the existence of a maximum breakdown time even when quite modest fields are applied, although these times are prohibitively large to measure.

Values of the maximum time to breakdown were used extensively since they should be representative of wear-out times for uniform SiO_2 films free of significant structural and/or impurity defects. It must be emphasized at this point, however, that the earlier failures are much more germane for making MOSFET device reliability projections than are the t_{max} ones. In other words, the oxide lifetime results discussed here are representative of essentially ideal MOS structures. Presumably the same wear-out mechanisms will be operative, in varying degrees, in SiO_2 films of lesser perfection.

Proceeding with this approach, it was then found that t_{max} is a strong function of the applied field, as seen in Fig. 5 and 6 for 1000 and 200Å films of SiO_2, respectively. The time for the defect density to increase by 20 defects/cm^2 (τ) as determined from Fig. 2 and 3 for degradation with no bias are given for reference. It is seen that the t_{max} times vary over seven orders of magnitude and extrapolate slightly above the τ time value at zero bias. Since τ represents the time for a partial wear-out only, such a value should be less than t_{max} at zero applied field. The polarity dependence of t_{max} is also evident in Fig. 5 and 6 where the breakdown times are considerably shorter for the Al(+) bias than for Al(−). Furthermore, the intercepts of the Al(+) and the Al(−) curves should coincide at zero field. In addition, higher temperatures shorten the life of capacitors. At high applied fields, the breakdown times decrease roughly exponentially with increasing field but this dependence is less at smaller E. These observations suggest that both field-dependent and field-independent wear-out mechanisms are operative.

Oxide film thickness is a very important parameter, as already seen by comparing Fig. 5 and 6, and illustrated more fully in Fig. 7 for Al/SiO_2 (100-1000Å)/Si structures. At constant field, it can be seen that t_{max}

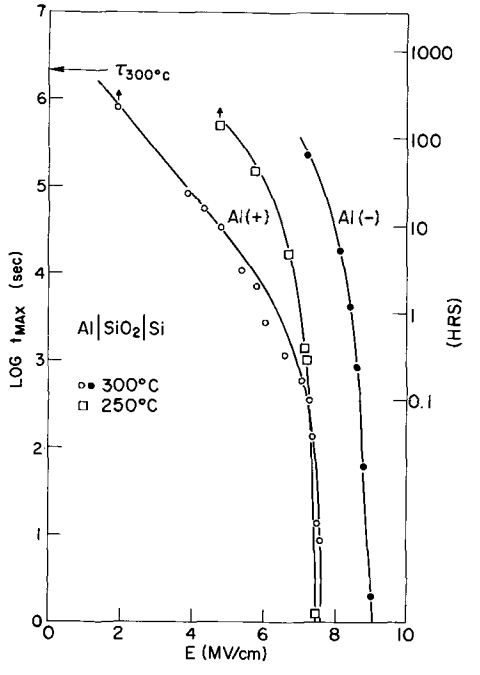

Fig. 5. Maximum breakdown time as a function of applied field in 1000Å SiO_2 films.

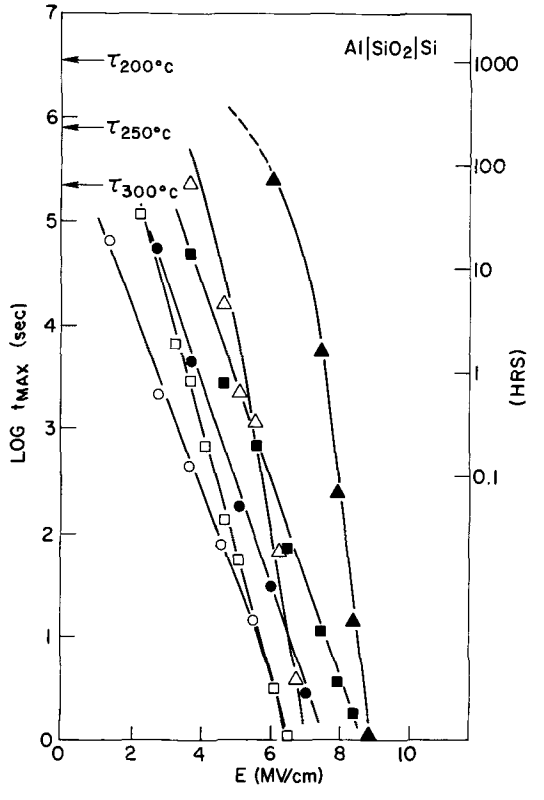

Fig. 6. Maximum breakdown time in 215Å SiO_2 films as a function of applied field at ○, 300°C; □, 250°C; and △, 200°C. Open symbols represent Al(+) bias and closed ones Al(−).

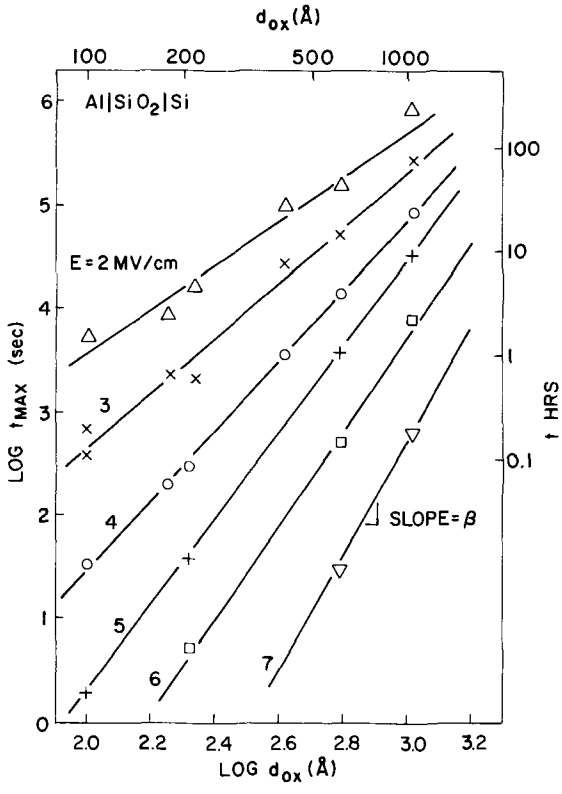

Fig. 7. Oxide thickness dependence of limiting breakdown time for 300°C Al(+) biasing.

$\propto (d_{ox})^{\beta}$. The thickness dependence power (β) increases linearly with increasing E, going from 2.1 at 2 MV/cm to 5.5 at 7 MV/cm, as shown in Fig. 8. From the linear relationship of Fig. 8, one can write

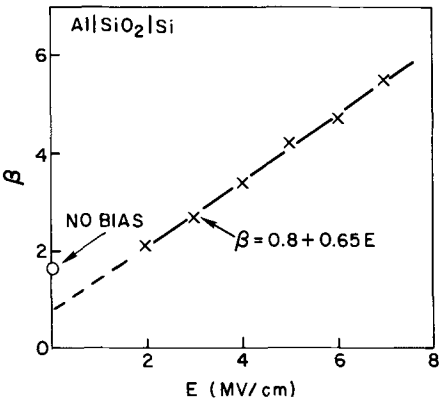

Fig. 8. Electric field *vs.* β, the power of the oxide thickness dependence for 300°C Al(+) biasing.

$$t_{max} \propto d_{ox}^{(0.8+0.65E)} \quad [2]$$

where E is given in megavolts per centimeter.

The temperature dependence of t_{max} is shown in Fig. 9, over the range 100°-400°C. The limiting time is thermally activated with a reasonably well-defined energy of 1.4 ± 0.2 eV, as calculated from the slopes of the log t_{max} *vs.* T^{-1} plots. The same energy was observed for both biasing polarities with 200Å films although failure times were considerably longer in the Al(−) case. Silicon dioxide films up to 1000Å thick also exhibit a 1.4 ± 0.2 eV activation energy with Al(+) (Fig. 10). For 100Å SiO_2 films, however, the activation energy is 1.1 ± 0.2 eV at 6 MV/cm at ~250°C, and appears to fall to 0.9 ± 0.3 eV at 2 MV/cm near 300°C.

Many other parameters influence the breakdown time of MOS capacitors. For example, Fig. 11 shows that samples stressed in a moist N_2 ambient (17 Torr H_2O) broke down in much less time than those biased in dry N_2. Presumably MOSFET devices that have been heavily glassed during packaging would not be as moisture sensitive. In addition, an effective post-metalization annealing treatment (*e.g.*, 5 min in N_2 at

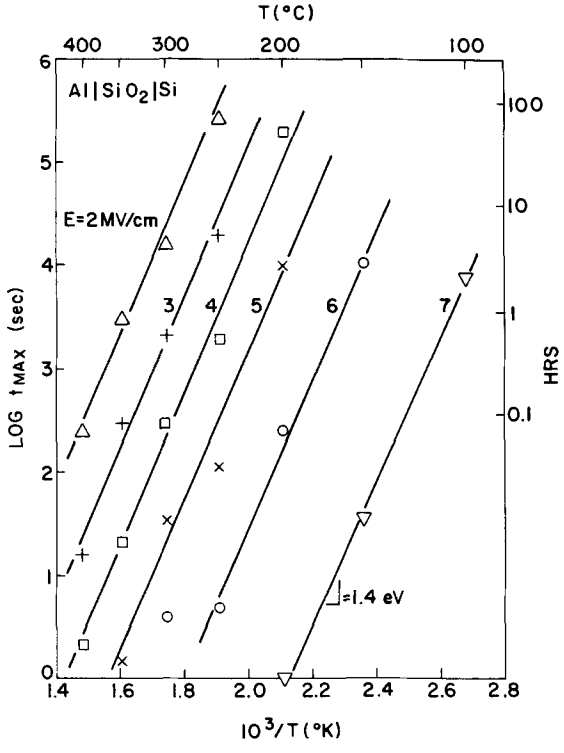

Fig. 9. Temperature dependence of limiting breakdown time in 200Å SiO_2 films for Al(+) stress.

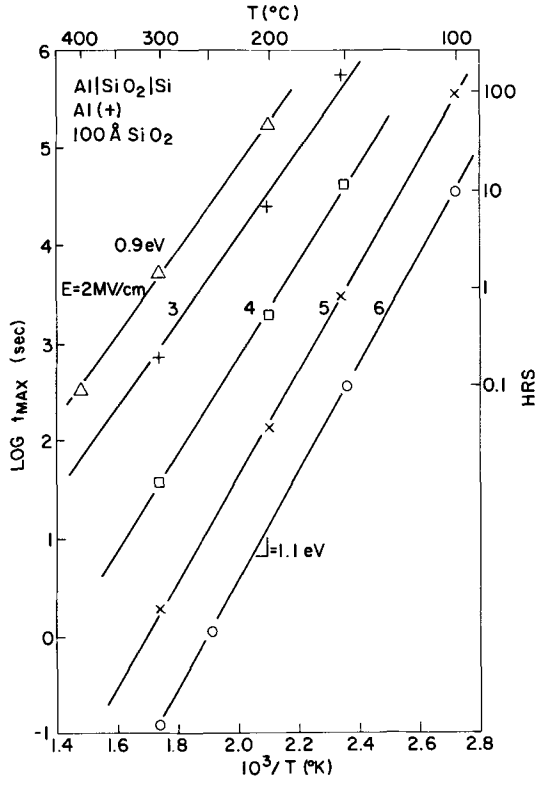

Fig. 10. Temperature dependence of limiting breakdown time in 100Å SiO_2 films for Al(+) stress.

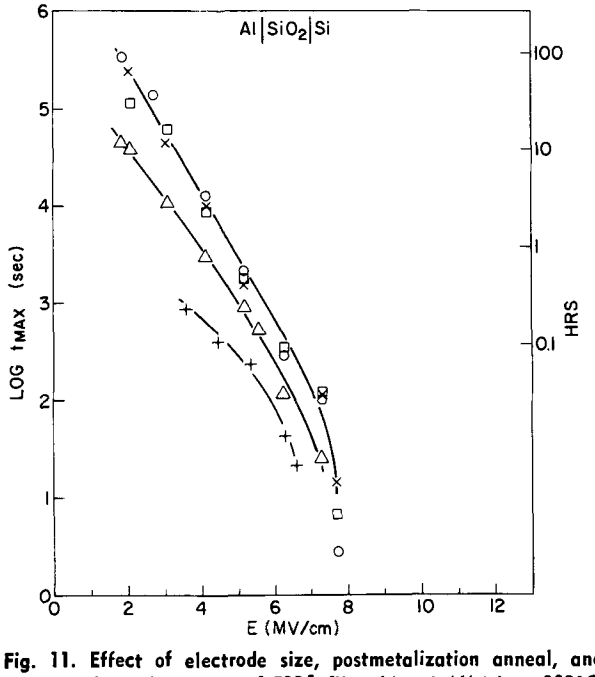

Fig. 11. Effect of electrode size, postmetalization anneal, and ambient on breakdown time of 500Å films biased Al(+) at 300°C. □, 0.05 mm²; X, 0.5 mm²; and ○, 1.25 mm² electrodes measured in dry N_2 ambient; △, measured in N_2 containing 17 Torr H_2O; +, without postmetalization anneal.

500°C) in nitrogen is also necessary to insure maximum reliability. This may be accounted for by the fact that annealing reduces the oxide conduction (35), eliminates surface states at the Si-SiO_2 interface, and improves over-all statistical breakdown distributions (8). It should be emphasized that t_{max} is area independent since capacitors from 10 to 50 mil diam gave identical t_{max} values (see Fig. 11). This area independence suggests that this time is characteristic of defect free SiO_2 films because any deterioration process

involving the presence of randomly occurring oxide defects would presumably scale with the electrode area.

Significant effects attributable to the electrode material are seen in Fig. 12, where aluminum electrodes gave longer life than platinum or molybdenum ones. Most important technologically are the findings that t_{max} can be substantially improved with a phosphosilicate glass addition or by growing the SiO_2 in 97% O_2-3% HCl.

Degradation mechanism and discussion.—In order to better understand the degradation mechanisms, some studies were made in which the currents through the oxide films were continuously monitored until breakdown occurred. See Fig. 13, where the current densities are plotted against time for both polarity cases. The initially low currents increase by several orders of magnitude in a relatively short time under these severe stressing conditions and current noises increase until breakdown occurs. The same sort of current enhancement occurred with both polarities although a longer time was required to see the Al(−) enhancement. The current density, as averaged over the entire electrode area, immediately prior to breakdown was usually less than 10^{-2} A/cm^2; this value is less than would be expected were the final breakdown process to take place via a uniform thermal runaway mechanism. The same kind of conduction enhancement occurs under smaller fields but the current is more likely to remain constant for even hundreds of hours before the onset of current enhancement noise preceding breakdown. In addition, the current changes are typically more steplike in appearance of J *vs.* t plots, rather than the gradual changes indicated in Fig. 13.

Once current enhancement had taken place due to prolonged stressing, the enhancement persists even at room temperature provided the capacitor is quenched under bias, at a rate fast enough to avoid breakdown during cooling. Such enhanced room-temperature conduction can be obtained for both bias polarities, after which the capacitors will last many hours without breakdown under the same bias at room temperature.

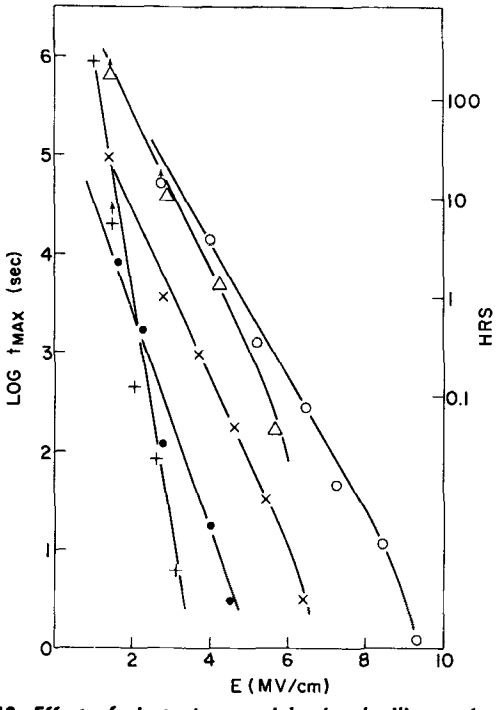

Fig. 12. Effect of electrode material, phosphosilicate glass, and HCl-oxidation on breakdown time of 250Å films biased Si(—) at 300°C. ○, Al electrode, 4% P_2O_5 film; △, Al electrode, oxide grown in 3% HCl/97% O_2; X, Al electrode, standard oxide; ●, Pt electrode, standard oxide; +, Mo electrode, standard oxide.

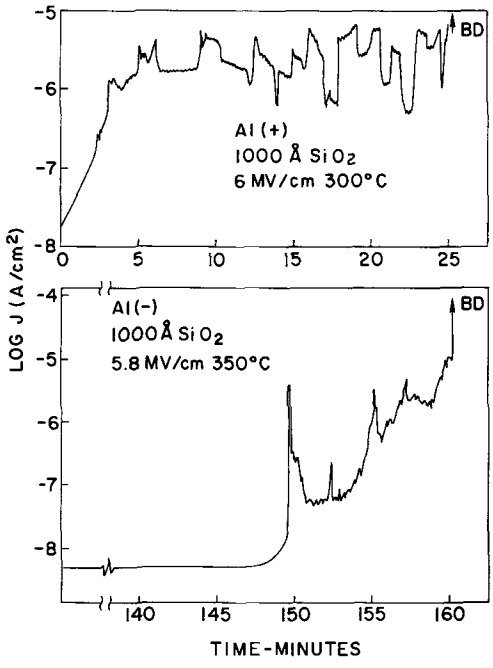

Fig. 13. Current enhancement after accelerated stressing

The enhanced current level depends more or less on the rate of cooling as well as the current level prior to quenching and may vary by several orders of magnitude. Under comparable conditions, the enhancement is usually greater for the capacitors with larger electrodes although it is not proportional to either the area or the perimeter of the electrode. The enhanced conduction cannot be removed by reheating the capacitor up to 300°C under a field of reversed polarity, but can be readily eliminated by moist ambients. While hydrogen, oxygen, and forming gas did not affect the enhanced conduction process, monochromatic illumination from a xenon source was found to be capable of reducing the conduction at low enhancement levels only.

The effect of moisture and light exposure on the enhancement is demonstrated in Fig. 14, where the current in an Al-SiO_2-Si capacitor (0.35 cm^2 in area) had been enhanced to a level of 10^{-6} A at 6.5 MV-cm^{-1}, Al(+) at room temperature. After a 2-min exposure

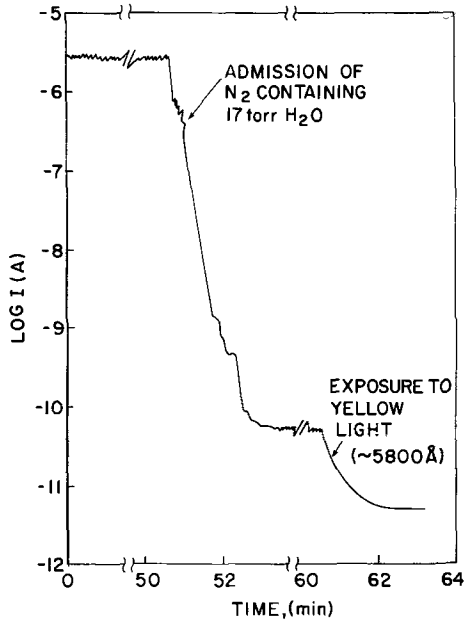

Fig. 14. Moisture and light sensitivity of conduction enhancement

to wet nitrogen (containing 17 Torr water vapor) the current dropped five orders of magnitude to 10^{-10} A. At this level the current was further reduced to 10^{-11} A by monochromatic radiation with wavelengths shorter than 5800Å. It should be noted at this point that, while a longer exposure to moisure can always completely remove the room-temperature enhancement, monochromatic irradiation is ineffective at high conduction levels (10^{-6} A in this particular example) even in the uv region ($\geqq$ 2000Å). Furthermore, the moisture effect can also be nullified if a moderate field of reversed polarity is applied to the capacitor during the exposure. Finally, and most importantly, the removal of current enhancement is not permanent in the sense that when the capacitor is restressed, the current enhancement and subsequent breakdown will occur in a much shorter duration than that observed in the first treatment.

Typical, room-temperature *I-V* characteristics of capacitors, in which enhancement had occurred, are shown in Fig. 15. The normal conduction in SiO_2 was previously shown (35, 38) to be via Fowler-Nordheim tunneling through a 3.2 eV barrier. A similar analysis of the sample curve in Fig. 15 showed a high-field conduction identical (within experimental error) to the control conduction. At low fields, however, a very low barrier height (0.3 eV) was obtained. A large polarity (*i.e.*, electrode) dependence and only a minor temperature dependence of this low-field conduction was observed and was similar to that found in control oxides and shows that the conduction mechanism was Fowler-Nordheim. Such a low barrier height would result in extremely high current densities ($>>$ 1 A/cm^2) and could be expected to ultimately result in thermal runaway and breakdown. The apparent current density as shown in Fig. 15, while considerably enhanced from the normal conduction, is still not of the order of that expected if the enhancement were uniform. Thus it can be inferred from these data that the conduction is localized. The ratio of the measured current to that expected with the lowered barrier could be used to estimate the area of the conducting channel. In this manner, the conduction was found to occur through extremely small channels having a diameter on the order of 20-1000Å. At very low barrier heights, Schottky conduction could be expected to predominate over Fowler-Nordheim conduction; nevertheless this alternate mechanism does not radically alter either the calculated local current density or the size of the conducting channel.

The fact that breakdown can be arrested during the B-T treatment by rapid cooling is another indication that the mode of dielectric failure in the degraded SiO_2 films now occurs not by electronic, but by thermal breakdown. Such contention is also supported by the observation that specimens with enhanced conduction can last many hours under the same bias at room temperature, since the critical field for thermal breakdown increases with decreasing temperature (39).

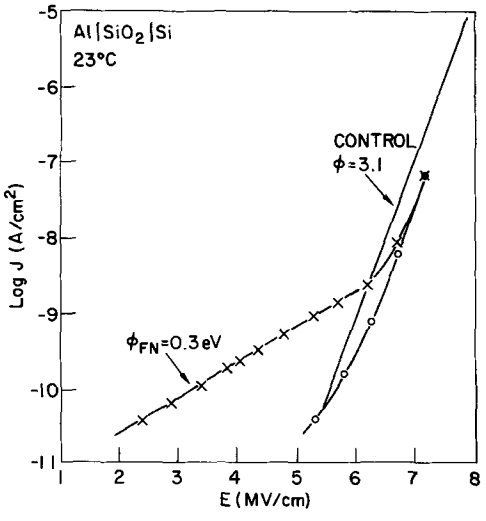

Fig. 15. Barrier height lowering as a result of stressing a 1000Å film at 6 mV/cm, Al(+) at 300°C for 1 hr. X, after stressing; ○, after stressing and subsequent exposure to moisture.

Capacitance-voltage flatband measurements were made on selected capacitors during the interval prior to breakdown. When the aluminum electrode was biased positively under high B-T stressing (5 MV/cm at 300°C for 2 hr) voltage shifts corresponding to 10^{11} positive charges/cm^2 were monitored. Since this flatband voltage shift could be attributed to mobile charge, the direction of the bias was reversed to drive any mobile species away from the Si-SiO_2 interface. The reverse bias did not reduce the flatband voltage; instead, the flatband often became even more negative implying the presence of additional positive charge. Annealing the stressed capacitors for 5 min at 500°C in N_2 was effective in reducing the flatband voltage to its original value. The fact that this charge is removed by annealing but not by reverse bias suggests that it is not due to mobile ions but rather is a result of stressing.

The method of Gray and Brown (34) was used to measure fast state densities after Al(+) stressing in order to eliminate the possible ambiguity in the interpretation of flatband voltage shifts. Figure 16 shows the increase in fast state density, N_{ss}, as a function of biasing time. This density was calculated from room temperature and liquid nitrogen *C-V* measurements by

$$N_{ss} = \frac{C_{ox}}{q}\left[V_{FB}\ (\text{room temp}) - V_{FB}\ (\text{liq. } N_2\ \text{temp})\right] \quad [3]$$

where C_{ox} is the oxide capacitance and V_{FB} is the flatband voltage. Over 10^{11} states/cm^2 were generated by positive B-T stressing. Deal *et al.* (28) found the same behavior with negative bias stressing. It should be emphasized that capacitance measurements reflect the average charge levels and are not useful in measuring localized buildup of charge particularly of the degree inferred from the electrical conduction measurements in Fig. 15.

Measurements with aluminum negative repeatedly showed the generation of positive charge in the oxide as previously reported (26-29). This negative-bias type of instability, although widely observed, is generally not given as much attention as the mobile ion instability. Different models have been proposed to account for this instability. Hofstein (26) considered trapping of holes by donor states near the Si valence band; Deal *et al.* (28) have proposed silicon ion injection; and Miura and Matukura (29) examined the generation of positively charged oxygen vacancies at the Si-SiO_2 interface. Despite the uncertainty as to the species responsible for the instability, all observations point to an electrochemical generation or transport of a species intrinsic to the MOS system.

It thus appears that the deterioration of SiO_2 films during the accelerated testing is a consequence of lo-

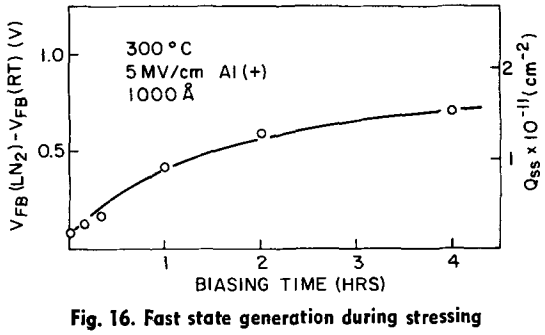

Fig. 16. Fast state generation during stressing

calized barrier lowering which has developed chemically or electrochemically at an unspecified number of spots under the electrode in the otherwise defect-free films. The localized barrier lowering can be attributed to the pile-up of positively charged centers of yet unknown species, which have been generated or mobilized and transported to the electronically injecting electrode during the biasing treatment. It can be also ascribed to the dendritic growths during the solid-state electrolysis of the SiO_2 film (30), whose pointed tips are undoubtedly the sites of intense field, which in turn can generate positively charged centers in their vicinity by high-field ionization (35).

The experimental data accumulated so far do not allow us to differentiate between the two alternate degradation mechanisms. Either mechanism can be invoked to explain qualitatively the observed field, temperature, and thickness dependencies of the accelerated breakdown; and, either mechanism can result in the formation of charge centers and interface states which have been observed after the B-T treatment by $C(V)$ techniques, and thus account for the ambient sensitivity and nonpermanent removal of enhanced conduction. It is evident that much work has to be done before one can discuss the degradation mechanism in quantitative terms.

Summary

Time-dependent breakdown of thermally grown SiO_2 films representative of those employed in the gate region of MOSFET's was investigated under accelerated conditions using MOS capacitors with various oxide thicknesses, electrode metals, and growth conditions. Extended heating in the absence of an electric field resulted in an increase in the defect density in Al-SiO_2-Si capacitors. In the temperature range from 200° to 350°C, the time required to form 20 defects/cm^2 (τ) was found to be thickness dependent, and can be ascribed empirically by the relationship

$$\tau \propto d_{ox}^{1.7}\ e^{-\Delta H/kT}$$

where d_{ox} is the oxide thickness and $\Delta H = 0.6$ eV. The formation of defects in the absence of bias was also found to be slower with Mo, Pt, and polycrystalline-Si electrodes and retarded by a PSG film on the oxide. The degradation without bias thus seems to originate from the reaction between the oxide and the electrode metal.

Under high-temperature biasing conditions, the limiting time for breakdown exhibited a nearly exponential decrease with increasing applied field. Its oxide thickness dependence was empirically an increasing function of the field

$$t_{max} \propto d_{ox}^{(0.8+0.65E)}\ e^{-\Delta H/kT}$$

where ΔH is 1.4 eV for 200 to 1000Å films. These results demonstrate that reliability will become more of a problem in thinner oxides.

The mechanism for the degradation under bias appears to be of electrochemical origin. The results of various $I(V)$ and $C(V)$ measurements suggest that the emergence of charge centers near the injecting electrode causes localized barrier lowering and formation of highly conductive channels which eventually lead to thermal instability and dielectric breakdown.

The fact that a single thermal activation energy is observed between 100° and 400°C is evidence that a single wear-out mechanism is operative and that the data possibly could be extrapolated even further to room temperature. With such an extrapolation, the acceleration factor between 300°C and room temperature becomes 10^{11}. Since defect-related breakdowns are most important to device reliability, statistical measurements under accelerated conditions are required to obtain a complete room-temperature characterization.

Acknowledgment

The authors would like to thank Dr. J. Eldridge, for discussions during this work. Dr. T. Light provided x-ray diffraction patterns prior to their publication elsewhere. Measurements and sample preparation were performed by R. Hammer and D. Ormond.

Manuscript submitted Jan. 15, 1973; revised manuscript received May 23, 1973.

Any discussion of this paper will appear in a Discussion Section to be published in the June 1974 JOURNAL.

REFERENCES

1. G. L. Schnable, H. J. Ewald, and E. S. Schlegel, *IEEE Trans. Reliability*, **R21**, 12 (1972).
2. F. L. Worthing, *This Journal*, **115**, 88 (1968).
3. S. I. Raider, *Appl. Phys. Letters*, **23**, 34 (1973).
4. C. M. Osburn and S. I. Raider, *This Journal*, **120**, 1369 (1973).
5. T. H. DiStefano, *J. Appl. Phys.*, **44**, 527 (1973).
6. M. H. Woods and J. W. Tuska, Reliability Physics Symposium, Las Vegas, April 1972.
7. N. J. Chou and J. M. Eldridge, *This Journal*, **117**, 1287 (1970).
8. C. M. Osburn and D. W. Ormond, *ibid.*, **119**, 591 (1972).
9. E. H. Snow, A. S. Grove, B. E. Deal, and C. T. Sah, *J. Appl. Phys.*, **36**, 1664 (1965).
10. D. R. Kerr, Reliability Physics Symposium, Las Vegas, April 7-10, 1970.
11. N. J. Chou, Private communication.
12. T. M. DiStefano, *Appl. Phys. Letters*, **19**, 280 (1971).
13. C. M. Osburn and D. W. Ormond, To be published.
14. J. Drobek, Private communication reported in *This Journal*, **118**, 325 (1971).
15. T. B. Light, C. M. Osburn, and N. J. Chou, To be published.
16. R. L. Meek and R. H. Braun, *This Journal*, **119**, 92C (1972).
17. T. Sugano, K. Hoh, K. Kudo, and N. Hishimura, *Jap. J. Appl. Phys.*, **7**, 715 (1968).
18. N. Nagasima and H. Enari, *ibid.*, **10**, 441 (1971).
19. R. L. Meek and R. H. Braun, *This Journal*, **119**, 1538 (1972).
20. P. J. Burkhardt, *IEEE Trans. Electron Devices*, **ED-13**, 268 (1966).
21. N. J. Chou, *This Journal*, **117**, 260C (1970).
22. S. R. Hofstein, *IEEE Trans. Electron Devices*, **ED-13**, 222 (1966).
23. N. J. Chou, *This Journal*, **118**, 601 (1971).
24. R. J. Kriegler and R. Bartnikas, *IEEE Trans. Electron Devices*, **ED-17**, 1010 (1970).
25. D. J. Silversmith, *This Journal*, **119**, 121 (1972).
26. S. R. Hofstein, *Solid State Electron.*, **10**, 657 (1967).
27. A. Goetzberger and H. E. Nigh, *Proc. IEEE*, **54**, 1454 (1966).
28. B. E. Deal, M. Sklar, A. S. Grove, and E. H. Snow, *This Journal*, **114**, 266 (1967).
29. Y. Miura and Y. Matukura, *Jap. J. Appl. Phys.* **5**, 180, 582 (1966).
30. P. J. Jorgensen, *J. Chem. Phys.*, **49**, 1594 (1968).
31. W. Kern and D. A. Puotinen, *RCA Rev.*, **31**, 187 (1970).
32. I. Ames, F. M. d'Heurle, and R. Horstmann, *IBM J. Res. Develop.*, **14**, 461 (1970).
33. C. Fritzsche, *Z. Angew. Phys.*, **24**, 43 (1967).
34. P. V. Gray and D. M. Brown, *Appl. Phys. Letters*, **8**, 31 (1966).
35. C. M. Osburn and E. J. Weitzman, *This Journal*, **119**, 603 (1972).
36. J. M. Eldridge and D. R. Kerr, *ibid.*, **118**, 986 (1971).
37. N. Klein, *IEEE Trans. Electron Devices*, **ED-13**, 788 (1966).
38. M. Lenzlinger and E. H. Snow, *J. Appl. Phys.*, **40**, 278 (1969).
39. See, for example, J. J. O'Dwyer, *This Journal*, **116**, 239 (1969).

The Anodic Oxidation of GaAs in Aqueous H_2O_2 Solution

R. A. Logan, B. Schwartz,* and W. J. Sundburg

Bell Laboratories, Murray Hill, New Jersey 07974

ABSTRACT

The characteristics of GaAs anodization at constant applied voltage, V, in a concentrated (30%) H_2O_2 electrolyte are examined in detail. Uniform oxides, with a refractive index of 1.8 and oxide thickness, t, proportional to V, are grown over the pH range 1-6. The pH can be adjusted by the addition of NH_4OH or H_3PO_4 to the electrolyte but the presence of other common acids at concentrations of a few parts per million can transform the anodization process into an etching procedure. In 10 min anodizations at $p\text{H} = 2$, 18 Å/V of oxide are grown and 12 Å/V of GaAs are consumed on chemically polished surfaces (for $V \leq 225$V). The resistance of the electrolyte causes significant voltage drops in the electrolyte at all pH values and limits the initial current flow. Most of the oxide is grown during the initial anodization (typically in the first minute) where the current is decreasing rapidly with time and the voltage drop across the oxide is increasing. The oxide is insoluble in the HNO_3 but is soluble in most other acids and bases. Limited MOS measurements yield a dielectric constant of 5.4 and a breakdown field of 3×10^6 V/cm. The use of the oxide as a mask for chemical etching was demonstrated by forming passive optical waveguides in GaAlAs-GaAs-GaAlAs epitaxial layers.

The growth of a native oxide on a semiconductor surface is an essential factor in the utilization of the semiconductor in many device applications. Native oxides have been grown on GaAs by galvanic techniques (1) and on GaP by both galvanic and anodic techniques (2) using concentrated (30%) H_2O_2 as the electrolyte. Galvanically grown oxides have been shown to be useful in passivating the surface of electroluminescent GaP p-n junctions (3) and GaAs-GaAlAs heterojunction lasers (4). It has also been noted that the oxides are useful as masks for the selective etching of local areas of these semiconductors (5) since the oxides are soluble in most acids and bases (permitting windows to be cut through the oxidized surface) and yet insoluble in common semiconductor etchants involving halogens dissolved in alcohols (*e.g.*, bromine-methanol).

The properties of the GaAs anodization process, at constant voltage, are examined in detail in the present studies. The oxide thickness is shown to depend upon the anodization voltage, the time of anodization, and upon the impurity content and the pH of the concentrated H_2O_2 electrolyte bath. The latter can be adjusted by the addition of either NH_4OH or H_3PO_4 to the electrolyte. However the adjustment of the pH with HCl or HNO_3 causes the anodization procedure to transform into an etching process, and intermediate results were obtained using H_2SO_4.

In addition, a description is given of some other factors which characterize the anodization of GaAs at constant bias: the voltage drop in the electrolyte as a function of pH of the bath; the role of surface imperfections (occlusions, surface preparation, etc.); the time dependence of the layer thickness and anodization current at fixed bias; the anodization voltage range over which uniform oxides can be grown; and the amount of GaAs consumed during anodization.

Limited measurements on MOS structures indicate an oxide dielectric constant of 5.4, and a breakdown field of 3×10^6 V/cm with low prebreakdown currents ($\sim 10^{-5}$ A/cm^2) at room temperature.

The application of oxide masking with photoresist techniques to selectively etch local areas of GaAs is described. While the definition achieved in surface oxide protected regions with standard photoresist techniques shows dimensional fluctuations of $\pm 0.5\mu$, the subsequent chemical etching to develop mesas can reduce these fluctuations by more than an order of magnitude. To illustrate the device applications that can be achieved using these techniques, a description is given of the etching of mesas, 0.5 cm long, $\sim 5\mu$ wide, and 10-30μ deep, in GaAlAs-GaAs-GaAlAs epitaxial layers to form passive optical waveguides.

* Electrochemical Society Active Member.

Key words: gallium arsenide, anodization, native oxide.

Experimental Procedure

The anodic oxidation of GaAs at room temperature in concentrated H_2O_2 was studied using a cell previously described for similar studies of the anodization of GaP (2); the electrolyte was contained in a quartz beaker with a platinum cathode. The GaAs sample was immersed in the bath to a depth such that the platinum clamp holding the sample did not contact the bath. Since accumulation of gas bubbles on the test sample would cause nonuniform anodization, the bath was vigorously stirred and a quartz baffle was inserted between the sample and the cathode where most of the bubbles originated. The anodization was performed at constant voltage and the current flow was monitored during the process.

The pH of the bath was measured before and after use and was found to be stable in time. The pH of concentrated (30%) H_2O_2 (J. T. Baker Chemical Company, electronic grade) is typically 3.6, and was decreased or increased by the addition of small quantities of H_3PO_4 or NH_4OH, respectively. In addition, some baths were prepared with the addition of both of these additives. The effect of common acid contaminants (HCl, HNO_3, and H_2SO_4) on the anodization process was investigated by adding to the bath a drop of the test acid diluted in 30 cm^3 of deionized water with sufficient NH_4OH added to produce a solution with a pH ~ 7. In this way, about 2 ppm of the test acid could be added to the bath without changing the pH of the bath.

The anodization studies were generally performed on undoped, (100)-oriented GaAs with a net donor concentration of $\sim 10^{17}$ cm^{-3} and with limited studies performed on similarly oriented p-type samples containing a net Zn acceptor concentration of $\sim 10^{18}$ cm^{-3}. The samples were chemically mechanically polished (6) with 0.075% bromine-in-methanol solution using a PAN-W polishing cloth. One set of experiments was performed to evaluate the oxide growth on (100)-oriented GaAs polished with Tizox-6500 abrasive (Tizon Chemical Corporation, Flemington, New Jersey 08822). The abrasively polished samples were both undoped n-type GaAs and p-type GaAs with a net acceptor concentration of $\sim 3 \times 10^{18}$ cm^{-3}. The MOS

structures were made on n-type, $N_D - N_A \sim 10^{17}$ cm^{-3}, (111)-oriented GaAs etched in chlorine-methanol.

Following procedures developed in similar studies with GaP (2), the samples were routinely dried in air after anodization by heating for 1 hr at 95°C followed by heating for 2 hr at 250°C.

The thickness and index of refraction of the oxide were measured with an ellipsometer using procedures described for similar studies of the oxidation of GaP (2). The layer thickness was also measured with a Talystep (Taylor-Hobson Company) by measuring the step height formed where the oxide was locally dissolved in HCl.

The initial attempt to determine the amount of GaAs consumed during anodization was made by waxing a portion of the polished sample surface with Apiezon wax, anodizing the exposed surface, dissolving the oxide in HCl ,and measuring the step height developed in the surface after removing the wax. Because of undercutting of wax in the anodization process, it was found necessary to use the following procedure: (*i*) anodize the entire surface of the test sample; (*ii*) apply the wax mask; (*iii*) dissolve the exposed oxide in HCl; (*iv*) anodize the exposed surface; and (*v*) remove the wax in organic solvents and then dissolve the oxide in HCl. In this way, a well-defined step due to the GaAs consumed in the second anodization was developed; the step height formed in this way was measured using a Talystep.

The electrical properties of the oxide were determined by making simple MOS structures. After alloying a Sn ohmic contact to one end of the n-type sample, the sample was anodized while contacted in the region of the alloyed Sn and then dried. Metal field plates were obtained by evaporation of Pb through a mask with 0.030 in. diameter openings. Since a thin Pb film crept over the surface during the evaporation, this excess Pb was removed by dipping the samples in HNO_3 (in which the oxide is insoluble) and rinsing the samples in water prior to measurement. Similar procedures using Au evaporation were unsuccessful. The current voltage characteristics of the Au barriers appeared to be regular Schottky barriers (rather than the high impedance MOS structures), suggesting that at the high temperatures required for Au evaporation, this metal penetrated the oxide.

Results and Discussion

Anodization process.—For a given time of anodization the oxide thickness, t, varied with the anodization voltage, V, and the pH of the H_2O_2 electrolyte. The current of anodization, I, decreased with time at constant V. Typical data are shown in Fig. 1 where the logarithm of I is plotted against time for samples 2 cm^2 in area, using a bath with a pH = 2.0 and for several values of V. After the rapid initial decrease in current, I decreases linearly with time.

With a platinum anode of 2 cm^2 area (equal to that of the test sample) the bath resistance was observed to be 2.0 k-ohms, independent of current. The voltage drop across the oxide is thus less than the applied bias during the initial growth at large I and approaches V as I decreases. The growth of the oxide thickness with time at 100V and pH = 2.05 is shown in Fig. 2. The rapid initial oxide growth is followed by a slower increase with time. It is apparent that after rapid initial growth the resistance of the oxide limits the current flow, retarding the layer growth. The resistivity of the as-grown oxide on GaAs is apparently much higher than that in GaP where only the exponential decrease of I with V was observed in the first 10 min of anodization (2).

All thickness measurements reported here were performed on samples which were dried by heating in air for 1 hr at 95°C, followed by heating for 2 hr at 250°C. This procedure was developed in similar studies in GaP (2) where it was designed to remove water from the oxide layers where measurements indicated that

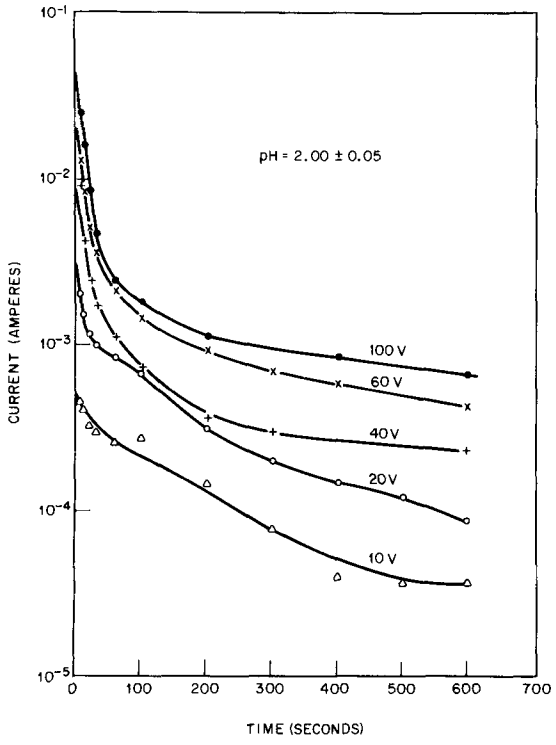

Fig. 1. A semilogarithmic plot of the variation of anodization current with time for a series of anodization voltages. The pH of the bath is 2.00 ± 0.05 and the area of the GaAs sample is ~2 cm^2 with faces in the <100> directions.

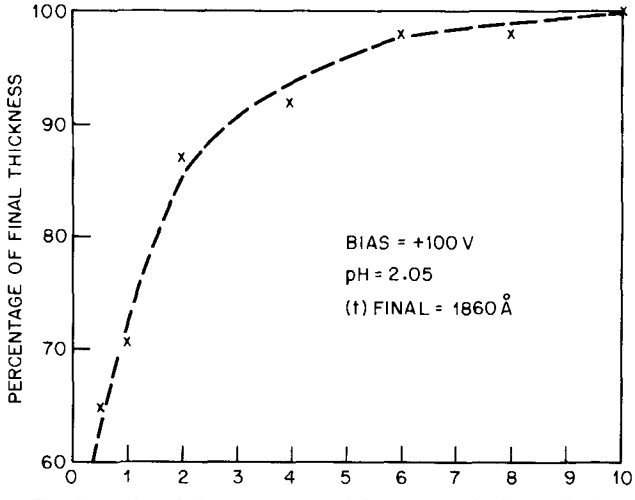

Fig. 2. A plot of the percentage of final oxide thickness obtained vs. time of anodization in a bath with pH = 2.05 and with anodization voltage of 100V. The anodization time was standardized at 10 min in this work and the final thickness of the oxide was 1860Å in this case.

the drying procedure reduced the layer thickness ~20%. The layer thickness, t, and the index of refraction, n, of the as-grown layer on GaAs were often indistinguishable from those of dried layers but occasionally were both 10% greater in t and lower in n. Due to the reproducible results obtained using the dried oxide layers the drying procedure was routinely followed in obtaining the results described here.

The dependence of oxide thickness, t, upon the anodization voltage, V, is shown in Fig. 3 for chemically (Br-methanol) and abrasively (Tizox) polished (100)-oriented GaAs samples, using an H_2O_2 bath with a pH = 2.0 ± 0.05. The oxide thicknesses are linear in V, with 18 Å/V on the chemically polished surface and 20 Å/V on the abrasively polished surface. The excellent reproducibility of the oxide growth is shown

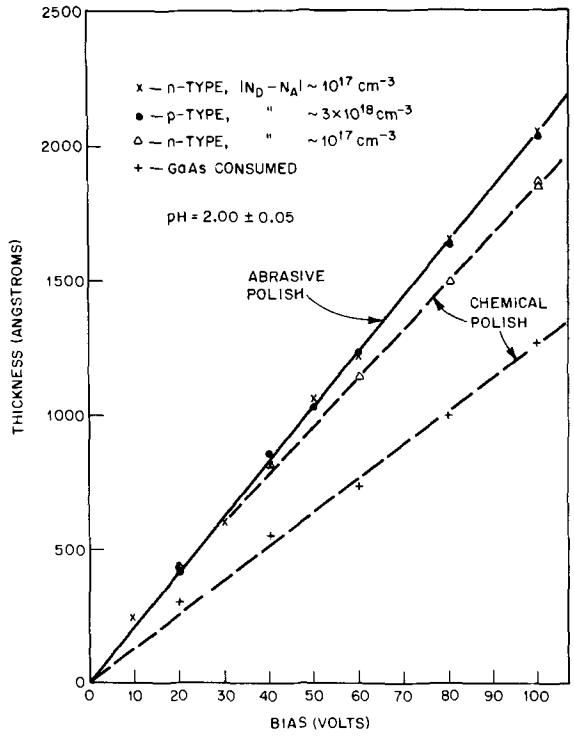

Fig. 3. The oxide thickness plotted against anodization voltage (for 10 min anodization) for (100)-oriented samples with doping levels indicated and using a bath with a pH = 2.00 ± 0.05. The linear dependence of thickness upon bias is 20.6 Å/V on the abrasively polished samples and 18.6 Å/V on the chemically polished samples. In the latter case, GaAs was consumed during the anodization at a rate of 12.5 Å/V.

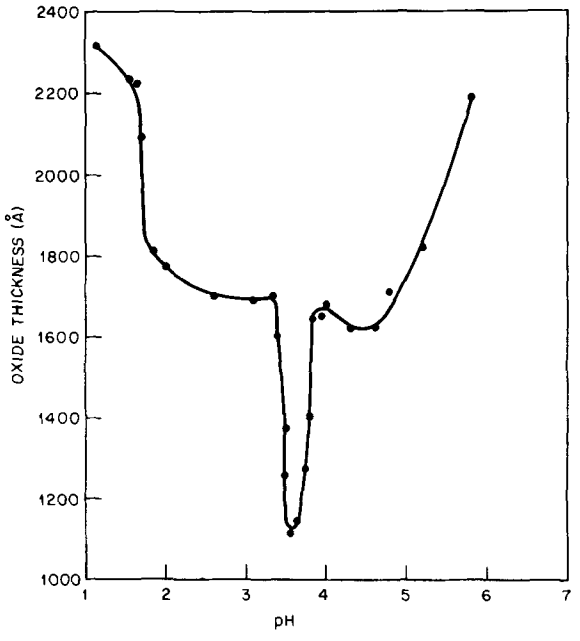

Fig. 4. The oxide thickness obtained in 10 min anodizations at 100V as a function of the pH of the electrolyte (H_2O_2). At higher pH values (~6.5) the oxide became nonuniform in thickness.

for the two sets of data on p- and n-type abrasively polished GaAs. The refractive index, n, of the oxide was 1.8 in all cases. The oxide growth rate is sensitive to surface perfection and the oxidation is, in fact, a useful tool (7) to examine surfaces for scratches, compositional or doping inhomogeneity, occlusions, etc.

The dependence of t upon V remained linear to 150V. The oxide layers produced at 175 and 200V were uniform in color and the ellipsometer measurements of t and n were 1030Å, 2.2 and 500Å, 2.7, respectively. To confirm this decrease in t and increase in n the oxide was locally removed by waxing and etching in HCl, and from the step-height measurement with the Talystep the linear relationship between t and V was found to hold for $V \leq 225$V. Thus the ellipsometry measurement technique fails in oxides formed at the higher anodization voltages where some nonuniformities apparently occur in the oxide. With $V > 225$V, the oxide was gray and granular in appearance and the portions of the original GaAs surface from which the oxide was dissolved were discolored. Using the procedures of oxidization, masking, and dissolving the oxide as described above, and then reanodizing and dissolving the exposed oxide in HCl, the measurement of the step developed in the surface of the sample indicated the amount of GaAs consumed in the anodization. For chemically polished GaAs, the GaAs consumed in anodization was linear in V, with the value 12 Å/V (compared to the oxide thickness of 18 Å/V).

While basic solutions of H_2O_2 are etchants, uniform oxidation occurs over a wide range of pH values in acidic solutions of H_2O_2. The pH of concentrated (30%) H_2O_2 is typically 3.6 and was decreased (or increased) by the addition of very small amounts of phosphoric acid (or ammonium hydroxide). The results of anodization at 100V for 10 min are shown in Fig. 4 where t is plotted against the pH of the bath.

The pH dependence of t shows two general features: an increase in t towards each end of the pH range and a decrease in t, near pH = 3.6, where the concentration of additives in the bath is minimal. The decrease in I during anodization exhibited the normal dependence of Fig. 1 except near pH = 3.6 where I decreased linearly to a value of only ~50% of the initial I. The initial and final anodization currents at 100V as a function of pH are shown in Fig. 5. The dependence of the initial current flow upon pH is due to the variation of the bath conductivity with pH as shown by the plot in Fig. 5 of the current flow through the bath at 100V, with the test sample replaced by a platinum anode of

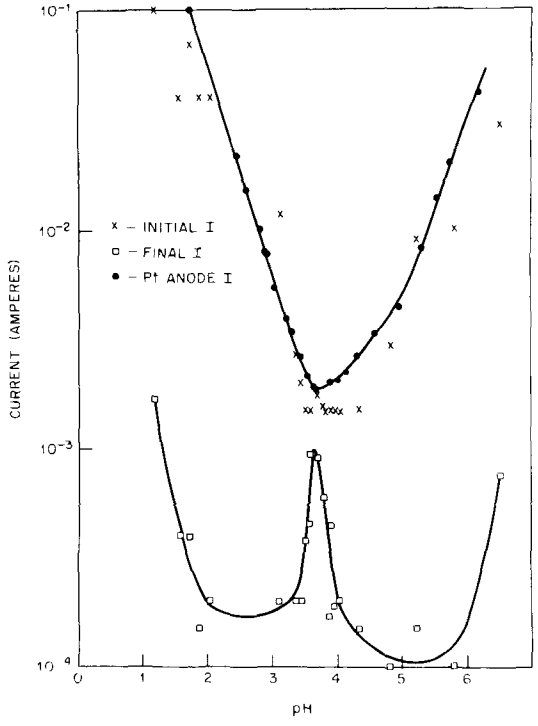

Fig. 5. A semilogarithmic plot of the initial and final current of anodization at 100V for 10 min as a function of the pH of the electrolyte (H_2O_2) for (100)-oriented samples of GaAs, ~2 cm^2 in area. Also shown is the current flow as a function of pH obtained with a platinum anode of 2 cm^2 area replacing the test sample.

equal area (~2 cm²). The bath conductivity, measured with two platinum electrodes, was linear in I. The initial and final voltages across the oxide for anodization at 100V are plotted in Fig. 6 as a function of the bath pH. It is evident that near pH = 3.6, the pH range of reduced oxide growth is much narrower than that of the broad conductivity minimum centered about the same pH value.

The importance of the amount of additives in the bath rather than the value of the adjusted pH of the electrolyte is shown by the anodization results obtained with both NH_4OH and H_3PO_4 added to the bath. For example, if the pH of the bath is increased to ~6 by the addition of NH_4OH, and afterwards is decreased to 2, then the dependence of t, the initial and final currents, and the bath conductivity are all insensitive to further increases of pH by the addition of NH_4OH (with no discontinuities near pH = 3.6). In this case, the bath resistance is only ~750 ohms and the initial and final voltages across the oxide are ~60 and ~100V, respectively.

However, as described above for anodization at $V >$ 150V (pH = 2), the ellipsometry measurements on these layers indicate low values of t (~1000Å) and high values of n (~2.8). The determination of t using the Talystep technique showed that t = 1900 ± 100Å for 2 < pH < 5.5. Ellipsometry measurements, on oxides formed by anodization in this compensated bath with $V \lesssim 60$V, gave values of t and n in agreement with those obtained at pH = 2 with only H_3PO_4 added to the bath (Fig. 3). For $V > 60$, the ellipsometry measurements again failed to give the correct t (and presumably n value also) of oxides formed in the doubly compensated bath. Hence while the conductivity of the bath can be increased, and the dependence of t upon pH can be reduced by adding both H_3PO_4 and NH_4OH, the properties of the oxide films with $V > 60$V ($t > 1000$Å) cannot be determined by ellipsometry measurements.

Electrical properties.—MOS structures were formed by evaporation of Pb through a mask containing 0.030 in. diameter holes onto anodized n-type, $N_D - N_A$ ~10^{17} cm^{-3}, samples of GaAs. These (111)-oriented samples had been polished by immersion into chlorine-methanol etchant. An ohmic contact was then formed by alloying Sn in a hydrogen atmosphere at ~500°C in a brief heating cycle. Samples were then anodized at 30, 50, 70, and 100V, respectively, (pH = 2.0) and dried. After the Pb evaporation the surfaces were cleaned of a thin film of Pb between the 0.030 in. diameter islands by dipping the samples into concentrated HNO_3 (in which the oxide is insoluble) and then rinsing them in water. At room temperature, the pre-breakdown currents were in the 10^{-8}-10^{-9}A range, independent of bias and the reverse bias breakdown field was 3 ± 0.5 × 10^6 V/cm in all units. From the limiting value of the capacitance in forward bias and using the known oxide thicknesses, the dielectric constant was evaluated on two metal barriers per sample. From the eight measurements, the average dielectric constant and mean deviation were found to be 5.4 ± 0.2.

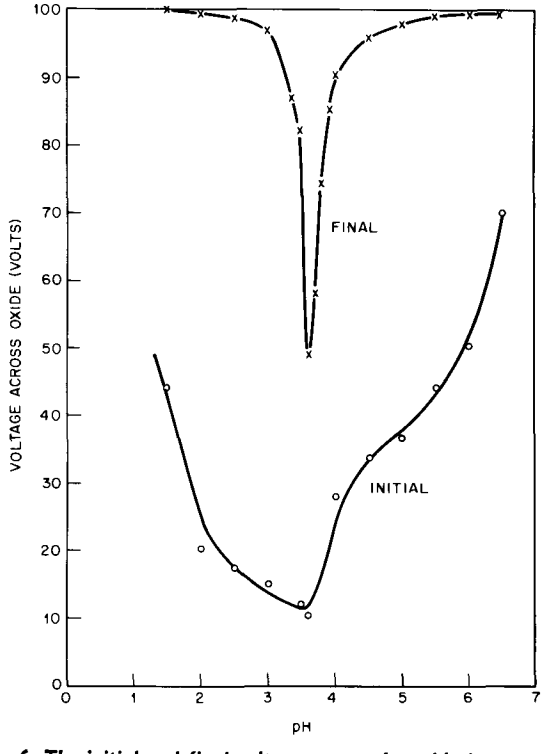

Fig. 6. The initial and final voltage across the oxide layer on the anodized sample as a function of the pH of the electrolyte (H_2O_2) for anodization at 100V for a period of 10 min.

Effects of contaminants on anodization.—Uniform oxides have been grown (with V selected as 100V), using electrolytes of concentrated H_2O_2 with or without the addition of either H_3PO_4 or NH_4OH to adjust the pH in the range from 1 to 6. The effect of contaminants on this process was revealed in one instance when the pH of pure H_2O_2 (pH = 3.52) was increased slightly to pH = 3.65 by the addition of a drop of NH_4OH diluted in distilled water in a well-rinsed beaker which had previously contained HNO_3. While uniform anodization had previously been achieved over a wide pH range, this bath produced an etching of the sample instead of anodization. It was therefore decided that it would be of interest to those applying the anodization process to make some assessment of the effects of contaminants. The common acids HCl, HNO_3, and H_2SO_4 were selected as contaminants. By dilution of one drop of these acids in 30 cm³ of water and then by adding enough NH_4OH so as to form a contaminant solution with a pH ~7, it was estimated that one drop of this dopant solution added 2 ppm of the selected contaminant acid to the electrolyte bath without changing the bath pH. Using baths with a pH of ~3.5, 2 ppm of HCl or HNO_3 caused etching instead of anodization while fairly uniform anodization occurred with the bath containing H_2SO_4. Using baths with a pH ~2 (adjusted with H_3PO_4), the addition of 2 ppm of the contaminant acid did not disturb the anodization process. Adjustment of the bath pH to 2 with H_2SO_4 instead of H_3PO_4 also produced fairly uniform anodization. The behavior of the contaminants is rather complex since the oxide is insoluble in HNO_3 (which severely affects the anodization), soluble in H_3PO_4, NH_4OH, and H_2SO_4 (which assist the oxide growth in H_2O_2 solutions), and soluble in HCl which also severely affects the anodization.

Oxide masking in device fabrication.—Native oxides form ideal etching masks on many of the III-V compound semiconductors (5) since they are insoluble in common etchants (halogen-alcohol solutions); and because of their growth on the semiconductor surface, there is no separation of the mask from the surface during the etching. Native oxide masking is obviously useful in any device application where mesas have to be formed on a processed semiconductor wafer. To demonstrate the properties of this procedure a description is given of the etching procedures used to form mesa stripes, 0.5 cm long, ~5-30μ wide, and 3-40μ high, on GaAs and on GaAlAs-GaAs-GaAlAs epitaxial layers grown on GaAs. The ability to develop mesas on the latter structures has obvious uses in fabricating GaAs, GaAlAs heterojunction lasers (8), and optical waveguides.

To etch mesas on the surface of samples, the surface is first oxidized and dried and then treated with photo-

resist AZ111 and exposed through a mask containing opaque stripes of the desired dimensions (9). The regions protected by the opaque portions of the mask remain oxidized after the photoresist treatment with the unprotected oxide dissolved in the caustic photoresist developer solution. With a bromine-methanol polished (100) GaAs sample and a mask containing 30μ wide stripes, 1 cm in length, the surface oxide stripes remaining after the photoresist process are shown in Fig. 7(a). It is noted that the edge dimensional fluctuations are $\sim \pm 0.5\mu$. After etching for 1.5 hr in a stagnant solution of 0.1% bromine in methanol the top view of the mesa (after dissolving the oxide in HCl) is shown in Fig. 7(b) and the cross-section view, obtained by cleaving in a (110) plane, is shown in Fig. 7(c). The etching to a depth of 3μ has reduced the edge dimension fluctuations by at least an order of magnitude. The flat sides of the etched mesas are (111) planes. To permit observation of the cross section of the mesa, the direction of the oxide stripes is made normal to a (110) cleavage plane. With the stripes in the [110] direction in the (100) surface of the GaAs sample, the flat mesa sides are (111) planes.

Application of the same procedures to GaAlAs-GaAs-GaAlAs epitaxial layers grown upon a GaAs (100) substrate produced the structures shown in cross section in Fig. 8. These mesas extend about 0.5 cm in length and are passive optical waveguides for infrared radiation which is confined in the GaAs middle layer due to the decreased index of refraction in the adjacent Al rich layers ($X_{Al} \sim 10\%$) and air interface on the sides. It is noted that the etched sides in Fig. 8(a) are smooth curves but are (111) planes in Fig. 8(b). While both waveguides lie in <110> directions in the (100) plane they are mutually perpendicular. Thus the cleavage planes are $(0\bar{1}\bar{1})$ in Fig. 8(a) and $(01\bar{1})$ in Fig. 8(b). The straight sides of the mesas in Fig. 8(b) are (111) and $(1\bar{1}\bar{1})$ planes which etch more slowly (10) than the corresponding {111} planes in Fig. 8(a) where the mesa sides are curved. The bright line at the top of the surface of the crystal in Fig. 8(b) is the oxide and shows that the depth of etching can be monitored by noting that it is about double that of the oxide overhang which is visible under microscopic inspection of the top of the structure.

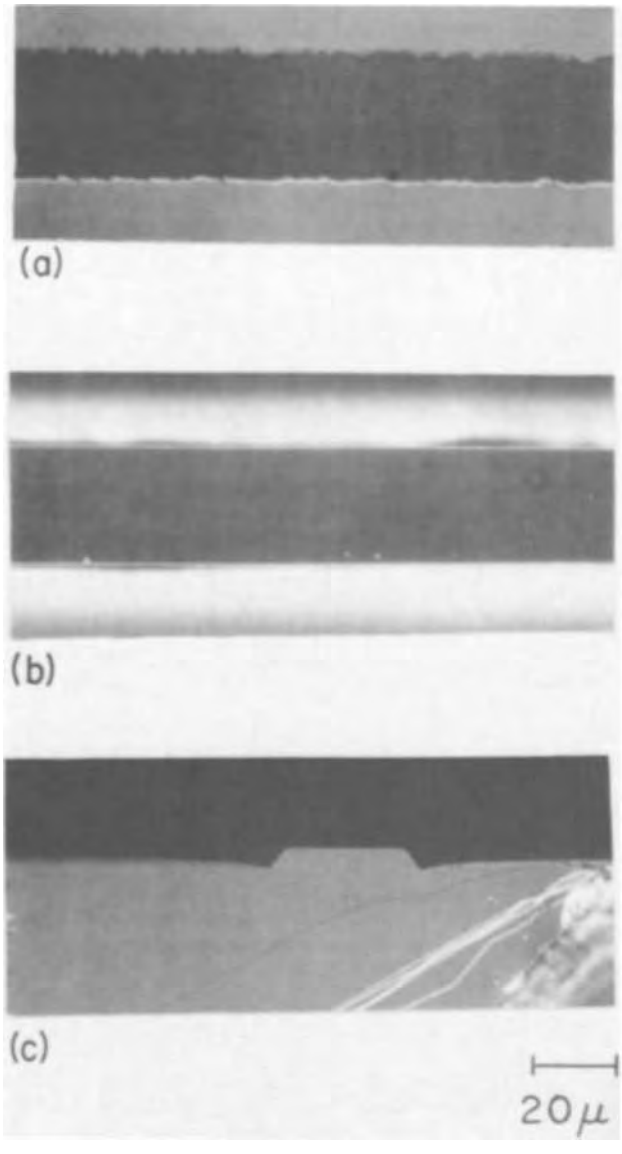

Fig. 7. (a) A 30μ wide stripe of oxide on a GaAs surface defined with photoresist techniques. (b) The same region after developing a mesa by etching in Br-methanol (and dissolving the oxide in HCl). (c) Cross-section view of (b).

Summary

These studies describe many of the factors which influence the anodic growth of a native oxide on GaAs in an aqueous H_2O_2 electrolyte at constant anodization voltage and may be summarized as follows:

1. Uniform oxide layers, with a refractive index equal to 1.8 and with layer thickness proportional to the anodization voltage, may be grown over extended ranges of anodization voltages and pH of the electrolyte. The pH of the electrolyte may be increased (or decreased) by the addition of NH_4OH (or H_3PO_4). The oxide layer thickness is sensitive to surface imperfections as evidenced by an oxide growth of 20 Å/V on an abrasively polished surface and 18 Å/V on a chemically polished surface (with a bath pH = 2 and $V \leq 225$V). In the latter case the growth of the oxide consumed 12Å of GaAs per volt of anodization voltage.
2. Since the oxide is of high resistivity the anodization current (and the voltage drop in the electrolyte) decrease as the oxide is grown at constant bias. The voltage drop across the oxide becomes essentially equal to the applied bias after about 1 min of anodization.
3. The resistance of the electrolyte causes significant voltage drops in the electrolyte at all pH values and limits the initial current flow during anodization.
4. Most of the oxide is grown during the initial anodization (typically in the first minute) when the current is decreasing rapidly with time (and the voltage drop across the oxide is increasing). For example at pH = 2 and 100V applied, 70% of the oxide is grown during the first minute of anodization of a 10 min cycle.
5. As-grown oxides were often indistinguishable from those which were air dried at temperatures of 95°-250°C. The reproducibility of the layer properties is improved by drying, but the effects are less severe than in similar oxides on GaP where t decreased by 20% using the same drying procedure.
6. For $1 < pH < 6$, the pH dependence of t (at fixed V) shows a small increase in t towards each end of the pH range and a decrease in t near pH = 3.6. The reduced oxide growth near pH = 3.6 correlates with the absence of additives (NH_4OH or H_3PO_4) in the bath rather than with the broad conductivity minimum of the electrolyte centered about the same pH value.
6. At pH = 2 and $V > 150$V, the oxide properties cannot be characterized by ellipsometry measurements, but Talystep measurements of t showed the linear relationship between t and V extended to $V \leq 225$V.
7. Contaminants such as HCl and HNO_3 at concentrations of a few parts per million in the bath can cause the anodization process to transform into an etching process.
8. The oxide is insoluble in HNO_3 but is soluble in most other acids and bases.

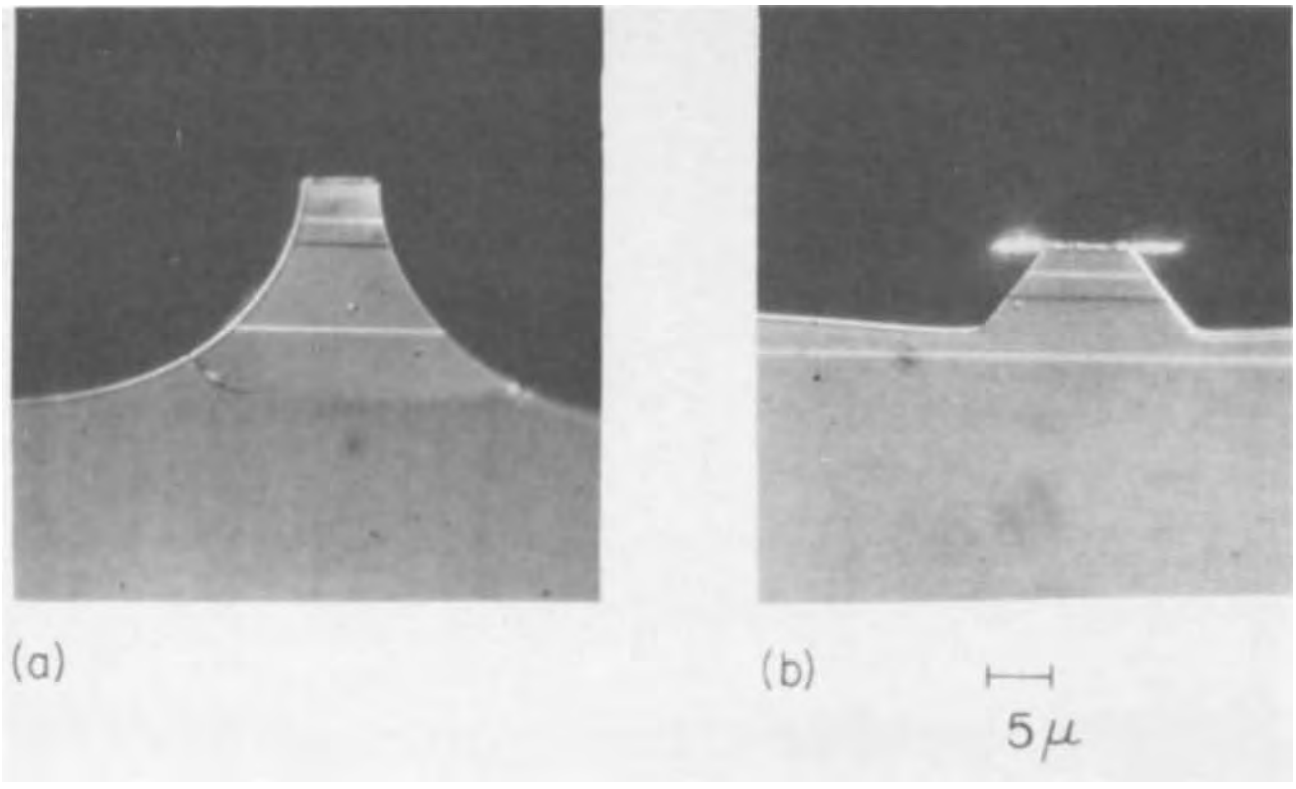

Fig. 8. The cross-section view of mesas formed in GaAlAs-GaAs-GaAlAs epitaxial layers grown on a GaAs substrate using the technique of masking by growth of a native oxide, defining area by photoresist techniques, and etching in Br-methanol. The mesas lie in the <110> directions in the (100) plane and are viewed on cleavage planes: (a) in the [01$\bar{1}$] direction and (b) in the (01$\bar{1}$) direction. The straight sides of the mesas in (b) are (111) and (1$\bar{1}$1) planes which etch more slowly (10) than the corresponding {111} planes in (a) where the mesa sides are curved.

9. Limited measurements on MOS structures suggest the oxide should be useful in such applications.

10. The use of the oxide as a mask for chemical etching was demonstrated by describing the formation of passive optical waveguides by the etching of mesas, 0.5 cm long, 5μ wide, and 10-30μ deep in GaAlAs-GaAs-GaAlAs epitaxial layers.

11. Anodization, followed by dissolving the oxide, is a useful etching procedure to remove a small, predetermined thickness of the crystal. The amount of GaAs consumed in anodization is linear in V. This procedure should be useful in diffusion studies and as a general cleaning procedure for cleaning crystal surfaces while maintaining geometrical control.

12. These anodization procedures should extend directly to other III-V compound semiconductors; for example, an anodic oxide has been grown on InSb. In addition, an oxide has been grown on silicon by this technique.

While many of the properties and applications of the anodization process have been described, it is apparent that there is little understanding of the kinetics of the process. Anodization at constant bias can produce uniform oxides with predetermined properties but the kinetics are obscured since most of the oxide is grown in the initial anodization where there are rapid changes in the anodization current and the voltage across the oxide. Impurities play an important role in the kinetics since the rate of oxide growth depends upon the concentrations of H_3PO_4 and NH_4OH in the electrolyte rather than only on the pH of the bath. Moreover, some additives, such as HNO_3 and HCl, can transform the anodization process into an etching procedure.

Measurements are now being attempted to directly measure the oxide composition; only then can firm models be proposed to explain the observed results. It is presently assumed that the oxidation proceeds via the hydrated forms of gallium oxide and arsenious oxide (*i.e.*, $Ga_2O_3 \cdot mH_2O$ and $As_2O_3 \cdot nH_2O$) which are both generated on the GaAs surface. However, if the conditions in the solution are such as to cause the removal of either of these products (*e.g.* the pH effect on the dissolving of arsenious oxide to form arsenious acid or the influence of nitrates or chlorides on the rate of oxide formation) then the kinetics can be drastically altered.

Acknowledgments

We appreciate the assistance of R. C. Manz and A. J. Sayko with the chemically polished samples and of S. Bortas with the abrasively polished samples. The Talystep measurements were obtained by F. B. Alexander and the photoresist procedures were applied by D. L. Deppen.

Manuscript submitted March 5, 1973; revised manuscript received May 3, 1973.

Any discussion of this paper will appear in a Discussion Section to be published in the June 1974 JOURNAL.

REFERENCES

1. B. Schwartz, *This Journal*, **118**, 657 (1971).
2. B. Schwartz and W. J. Sundburg, *ibid.*, **119**, 241C (1972).
3. R. L. Hartman, B. Schwartz, and M. Kuhn, *Appl. Phys. Letters*, **18**, 304 (1971).
4. B. Schwartz, J. C. Dyment, and S. E. Haszko, IV International Conference on GaAs and Related Compounds, Boulder, Colorado, Sept. 25-27, 1972.
5. B. Schwartz and R. C. Manz, Submitted to *This Journal*.
6. M. V. Sullivan and G. A. Kolb, *ibid.*, **110**, 585 (1963).
7. B. Schwartz, S. E. Haszko, and D. R. Wonsidler, *ibid.*, **118**, 1229 (1971).
8. I. Hayashi and M. B. Panish, *J. Appl. Phys.*, **41**, 150 (1970); T. Tsukada, H. Nakashima, J. Umeda, S. Nakamura, N. Chinone, R. Ito, and O. Nakada, *Appl. Phys. Letters*, **20**, 344 (1972).
9. R. L. Field, Private communication.
10. Y. Tarui, Y. Komiya, and Y. Harada, *ibid.*, **118**, 118 (1971).

The Migration of Oxygen during the Anodic Oxidation of Tantalum

J. P. S. Pringle*

Chalk River Nuclear Laboratories, Atomic Energy of Canada Limited, Chalk River, Ontario, Canada

ABSTRACT

Oxygen-18 concentration profiles in thin oxide films have been measured by combining a sectioning technique for locating the isotope with a nuclear method for detecting it. The system studied was the anodic oxidation of tantalum, and the oxide was sectioned by slow dissolution in concentrated HF almost saturated with NH_4F; the ^{18}O present was detected by bombarding the oxide with 3.042 MeV protons and counting neutrons emitted in $^{18}O(p,n)^{18}F$ reaction. On anodizing first in ^{16}O electrolyte and then in ^{18}O electrolyte, the ^{18}O incorporated last was found outside the ^{16}O layer incorporated first. There was, however, a small mixing of the populations at the boundary between them, and the degree of mixing was found to be proportional to the square root of the thickness added in the ^{18}O electrolyte. The results could be analyzed very well in terms of forced diffusion (under the influence of the electric field during anodization) from a constant source (the electrolyte) into a semi-infinite medium (the oxide), thus confirming that oxygen indeed migrates during the anodic oxidation of tantalum.

The sectioning technique described in previous papers (1, 2) has been combined with a least squares fit analysis (3) and used to study transport processes in the anodic oxidation of tantalum (4). Radioisotopes of the noble gases were found to approximate quite closely to the inert immobile markers required for transport number experiments, and it was then possible to show that the oxide thickens largely by oxygen migration. The next step, therefore, was to find out how the individual oxygen atoms moved through the oxide film, and this required a tracer for the oxygen itself. Results obtained in such experiments are described below.

The configuration of a tracer experiment depends on the methods used to incorporate, detect, and locate the tracer species. Thus the noble gas atoms used in the previous study (4) were incorporated by ion implantation, detected by means of their radioactivity, and located using the sectioning technique. No long-lived radioisotopes of oxygen exist, and so one of the rare stable isotopes, ^{17}O or ^{18}O, must be used instead. These can be detected either by means of nuclear reactions (5, 6) or by mass spectrometry (7), but the detection efficiency of these methods is much less than that for radioactivity. Accordingly, much more tracer is required, and since implantations at high fluence alter the properties of the anodic oxide (2), this was an undesirable method for the incorporation of the oxygen isotopes. The only alternative was to anodize in water enriched with the appropriate isotope.

In their pioneering study on the migration of oxygen during anodic oxidation, Amsel and Samuel (6) incorporated ^{18}O tracer by anodizing in $H_2{}^{18}O$, detected it by counting α particles emitted from the nuclear reaction $^{18}O(p,\alpha)^{15}N$, and located it by taking advantage of the extremely narrow 1165 keV proton resonance in this reaction. Such nuclear methods of location depend on measuring the energy lost by charged particles in traversing the solid, and the resolution is limited by the energy straggling that occurs. This straggling is quite sufficient to mask the effect of small variations in the concentration profile, so that gross changes alone can be observed (8). Using specimens prepared in these laboratories, Evans and Pemsler (7) have detected and located ^{18}O tracers by means of ion microprobe mass spectrometry, in which the oxide is gradually sputtered away with 2 keV argon ions. By feeding the sputtered atoms to a mass spectrometer, the ^{18}O isotope could be detected and located as a function of the sputtering time. The resolution is, of course, limited by the uniformity of the sputtering and appears to be little better than that for the nuclear method.

In the present experiments, ^{18}O was incorporated by anodizing in $H_2{}^{18}O$ electrolyte, detected by counting neutrons from the $^{18}O(p,n)^{18}F$ reaction, and located by means of the sectioning technique described in previous papers (1, 2). The use of separate techniques for detection and location improved the resolution by about an order of magnitude.

The Principle of the Tracer Experiments

As in the previous paper (4), an ideal oxidation system will be assumed; one in which the oxide is homogeneous, of uniform thickness, and grown on a plane metal surface. The experiments were performed by anodizing to an initial thickness, h_i, in ordinary $H_2{}^{16}O$ electrolyte, and then to a final thickness, h_f, in identical electrolyte made up with $H_2{}^{18}O$. Under these circumstances, three basic possibilities for the ^{18}O profile exist, as illustrated in Fig. 1.

I. If the oxide thickens entirely by metal migration, the ^{18}O atoms will be incorporated on top of the ^{16}O atoms, and populations will not mix. Since the ^{16}O layer is of extremely uniform thickness (1), the ^{18}O concentration will fall abruptly to the natural abundance at the boundary between the layers.

If the oxide thickens entirely by oxygen migration, there are two extreme possibilities.

II. The oxygen atoms could move in succession as space becomes available, thus preserving their order in queues. Due to the statistical nature of the motion, some queues will move faster than others, and so some of the leading ^{18}O atoms will overtake some of the trailing ^{16}O atoms. The population mixing that results serves to distinguish this possibility from the previous one.

III. The other extreme is to suppose that once the oxygen atoms are incorporated in the oxide, they move right across until they are stopped at the metal/oxide interface. Under these conditions, the oxygen order will be reversed, since the ^{18}O atoms incorporated last will be found underneath the ^{16}O layer formed first.

* Electrochemical Society Active Member.

Key words: tantalum, anodic oxidation, oxygen tracer, nuclear microanalysis, oxygen migration.

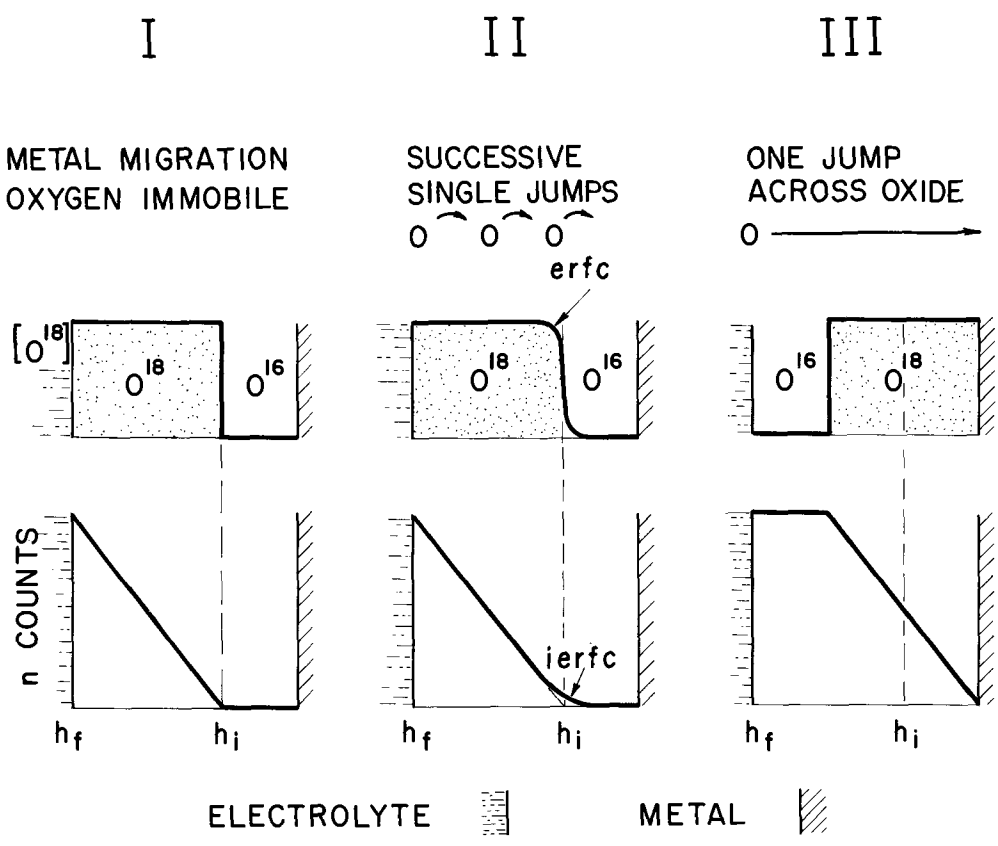

Fig. 1. The three basic ^{18}O concentration profiles in anodic tantalum oxide when the oxide is formed initially to a thickness, h_i, in $H_2{}^{16}O$, and then to h_f in $H_2{}^{18}O$. The lower curves show the corresponding neutron count profiles when the films are analyzed by the $^{18}O(p, n)^{18}F$ method described in the text.

These three profiles are the simplest and most easily interpretable, but many others are possible. Thus, profiles intermediate to II and III will occur if the atoms move several interatomic distances at a time, instead of one as assumed in II, or all as in III. When both metal and oxygen move, with a new oxide being formed at the interfaces, the ^{18}O distribution will be a combination of I with II or III, or some intermediate thereof. If a new oxide is formed within the existing oxide, the ^{18}O profile will depend on the location of this new oxide as well. Certain types of profile could, therefore, be rather difficult to interpret.

Fortunately, most of these possibilities can be eliminated by the evidence already available. Transport number measurements (4) show that both tantalum and oxygen migrate, and that the new oxide is formed at the metal/oxide and oxide/electrolyte interfaces only. The possible profiles, therefore, are those in which I is combined with II or III, or with some intermediate between II and III.

Measurement of the ^{18}O Concentration Profiles

Incorporation of the ^{18}O.—Tantalum foils, 35 × 10 × 0.37 mm³, were cut from 0.015 in. sheet supplied by the Fansteel Metallurgical Corporation. The middle 28 mm on each side was divided into seven areas, each 4 × 10 mm, by means of scratches running across the foil. A 0.5 mm (0.020 in.) diameter tantalum wire was spot welded on one corner, and the foils were then chemically polished as described previously (1). After a 2 min dip in the NH_4F-HF stripping solution to remove any film left by the polishing (9), the foils were anodized to the desired initial thickness using 0.01M KI in ordinary water as the electrolyte. This particular electrolyte was chosen to avoid dilution of the enriched oxygen electrolytes; the anion contains no oxygen, and the salt does not crystallize with water of hydration.

Two $H_2{}^{18}O$ samples were obtained from YEDA, Israel, and KI, dried at 150°C for 2 hr, was dissolved in them to make up approximately 0.01M solutions; 26.10 mg were dissolved in 15 ml of 11.43% $H_2{}^{18}O$ (0.0105M), and 2.60 mg in 2 ml of 97.56% $H_2{}^{18}O$ (0.0087M). The tantalum foils were then reanodized to the final thickness in one or other of these electrolytes, using specially designed Lucite cells. A platinum wire served as cathode, and because the anodizing circuit (10) required a reference electrode, a silver wire was added for the purpose. The intended Ag/AgI electrode, however, did not have the necessary impedance, and so the other end of the silver wire was electrically connected to the usual glass electrode by dipping both in a beaker of ordinary 0.01M KI.

Anodization behavior with this arrangement was normal, as determined from angstroms/volt and seconds/volt measurements. The use of 0.01M KI in place of 0.1M H_2SO_4 did not noticeably affect the thickness calibration (1) for the tantalum oxide. No temperature control was provided for the anodizing cell, with the result that the heat liberated during anodization raised the temperature of the small quantity of electrolyte present; indeed, the temperature rose sufficiently to produce considerable condensation on the walls of the cell above the electrolyte. At 10 mA/cm², the heating was so pronounced that the final thickness was very much greater than that intended, and so much hydrogen was discharged at the cathode that the specimen was anodized in a froth.

Detection of the ^{18}O.—Several charged particle nuclear reactions can be used for the detection of ^{18}O. If the reaction product is itself a charged particle, as in the case of the $^{18}O(p, \alpha)^{15}N$ reaction used by Amsel and Samuel (6), the detector must be placed inside the vacuum system of the accelerator. Such apparatus was not available at the time these experiments were performed, and so reaction products that would pass through the accelerator wall were needed. These could only be neutrons or γ rays, and neutrons from the $^{18}O(p, n)^{18}F$ reaction were in fact used. The other product of this reaction, radioactive ^{18}F, has been employed by Thompson (11) to measure the ^{18}O content of natural anodic oxide on tantalum.

The $^{18}O(p, n)^{18}F$ reaction has a proton threshold energy of 2.574 MeV (12), above which there are a series of resonances (13). To optimize the conditions

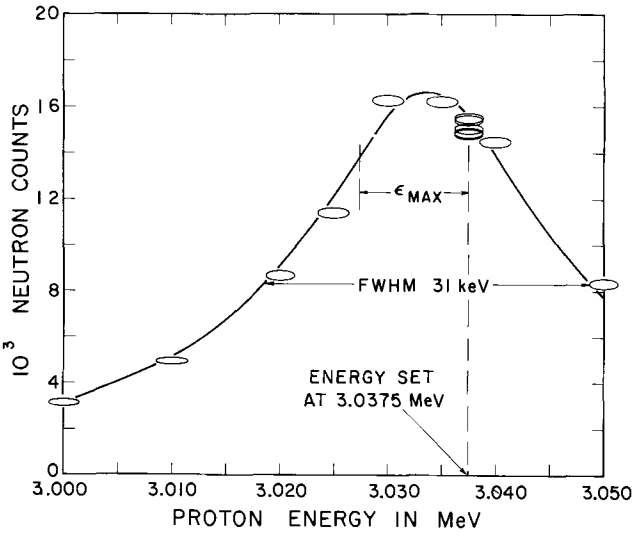

Fig. 2. The 3.037 MeV resonance in the $^{18}O(p, n)^{18}F$ reaction measured with an anodic $Ta_2{}^{18}O_5$ sample 490Å thick in proton bombardment ii; 3 MeV protons lose approximately 2 keV in traversing this thickness of oxide. The scale along the abscissa is a working scale, which has been calibrated only approximately; it appears to be about 5 keV low. The random standard error in each energy measurement is known to be about 1 keV, and the standard error in each count is 2.1 times $\sqrt{}$ (observed count). Error ellipses have been drawn at two standard errors from the points actually measured to show the 95% confidence limits. The maximum energy lost in an oxide film during the course of these experiments is indicated by ϵ_{max}.

for neutron counting, it was necessary to consider three factors.

First, neutrons can be produced by p, n reactions on nuclei other than ^{18}O. In this respect, it was fortunate that the p, n threshold for ^{16}O is 17.4 MeV, and that ^{181}Ta, with its high Z, has a large coulomb barrier. Tests with chemically polished tantalum showed that the background count decreased by an order of magnitude for every MeV reduction in the proton energy below 5.5 MeV; this observation is in agreement with published data for the $^{181}Ta(p, n)^{181}W$ cross section (14). To keep the background down, therefore, the proton energy had to be as small as possible.

The second requirement was to maximize the neutron yield from the ^{18}O, and this meant using a resonance in the $^{18}O(p, n)^{18}F$ reaction. According to the literature (13), the lowest resonance occurs at 2.649 ± 0.005 MeV; when tested here, this gave acceptable neutron counting rates. It was not used for the actual experiments, however, because it could not meet the third requirement; that the p, n cross section be constant at all points in the oxide film.

The maximum thickness of the ^{18}O profiles studied here was about 2700Å. From energy loss data (15), it can be calculated that 3 MeV protons lose approximately 13 keV in traversing this thickness of tantalum pentoxide, so that a proton incident on one side with an energy 6.5 keV above resonance would emerge from the other with an energy 6.5 keV below resonance. The third requirement meant, therefore, that the p, n cross section had to be approximately constant for 6.5 keV on either side of the resonance peak. Since the full width at half maximum for the 2.649 MeV resonance was only 8 keV, this resonance was obviously much too narrow.

The next resonance in the $^{18}O(p, n)^{18}F$ reaction occurs at 3.037 MeV, with an FWHM reported as 33 ± 3 keV (13); the latter was confirmed here, as demonstrated in Fig. 2. This resonance is the broadest available below 3.5 MeV (13), and therefore had to be used in the present experiments. The incident proton energy was fixed at 3.042 MeV, 5 keV above resonance, to keep the average cross section for any oxide film up to 2700Å in thickness as constant as possible; the residual variation was estimated to lie within a range of 4%.

Location of the ^{18}O.—The anodized foils were thinned by means of the sectioning technique (1) in such a way as to leave a series of steps in the oxide surface, as indicated schematically in Fig. 3. The area of each step, 4 × 10 mm, was defined by the scratch marks on the tantalum surface, and the oxide thickness at each step adjusted to a preselected value by controlling the time spent in the NH_4F-HF stripping solution. Once the desired thickness had been reached,

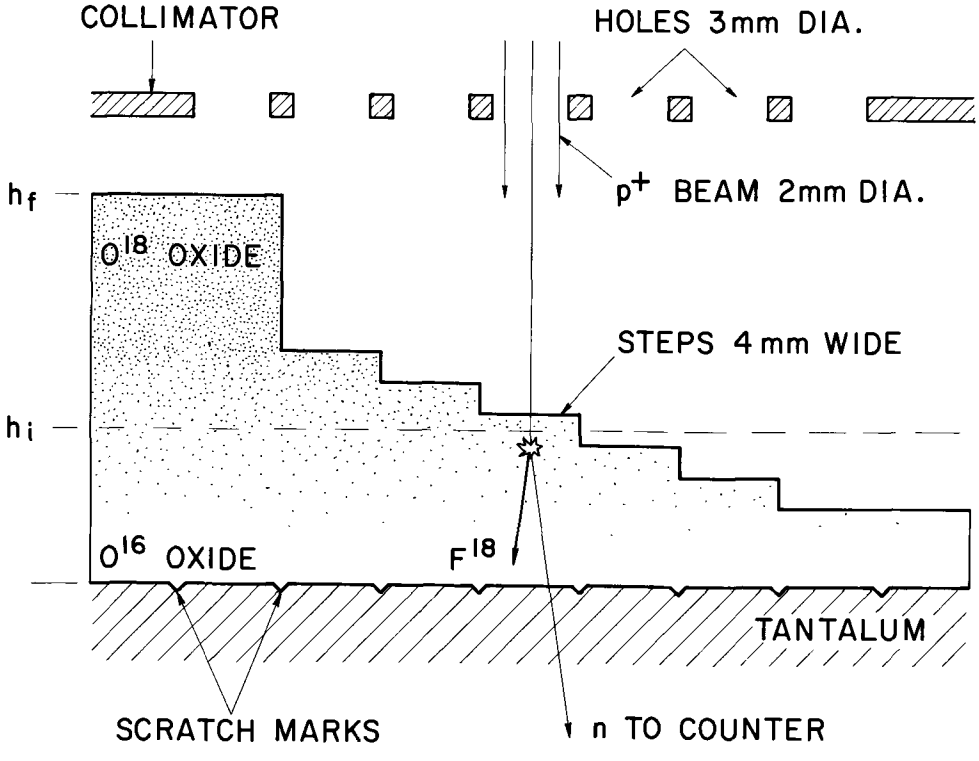

Fig. 3. Schematic diagram illustrating the measurement of an ^{18}O concentration profile by means of the $^{18}O(p, n)^{18}F$ reaction. The film was anodized initially to h_i in $H_2{}^{16}O$, and then to h_f in $H_2{}^{18}O$; one step was left at h_f, and the others stripped back to give a series of thicknesses about h_i. The scratch marks on the tantalum surface defined the area of each step.

the step was covered with Apiezon N grease to prevent further attack as thinning continued elsewhere; the grease was subsequently dissolved in trichlorethylene. Comparison of the intended thicknesses with those actually measured by the spectrophotometric technique showed that the difference was rarely more than 10Å and frequently less than 5Å. The uniformity of the thinning and the errors in the thickness measurements have been discussed elsewhere (1, 3, 4).

Two types of oxide samples were prepared for the present study. Those intended to investigate the gross features of the ^{18}O concentration profile were anodized first to 880Å in ^{16}O electrolyte, and then to more than 3000Å in ^{18}O electrolyte; steps of 150Å or more were then placed in the oxide surface to cover the whole range of thicknesses from 3000 to about 700Å. These samples showed that the ^{18}O profile was of the form II in Fig. 1, and so the second type of sample was designed to measure the mixing at the $^{16}O/^{18}O$ boundary. They therefore required much smaller steps of 10-20Å, centered about the initial thickness, normally 880Å, of ^{16}O oxide. This thickness was chosen as standard because it is close to the bottom of the range that can be continuously measured with spectrophotometer (1).

The composite $^{16}O/^{18}O$ oxides were thus thinned down, as illustrated in Fig. 3, to leave seven different thicknesses on each side of the tantalum foil, for a total of fourteen different thicknesses in all. By bombarding each thickness with the same dose of 3.042 MeV protons, the relative amount of ^{18}O beneath a given depth in the composite oxide could be determined. The results, in the form of neutron counts *vs.* oxide thickness remaining, described the integrated concentration profile, from which the ^{18}O profile itself could be obtained by differentiation.

Proton bombardments.—Four tantalum foils prepared as above were mounted longitudinally in an aluminum target holder. The latter was electrically insulated, so that the proton charge deposited in the tantalum foils could be passed to a current integrator as a measure of the proton dose. Collimating plates were placed about a centimeter away on each side of the foils, and twenty-eight 3 mm diameter holes bored in each plate at positions opposite the individual steps on each foil (Fig. 3). The whole assembly was then inserted into the target chamber of a High Voltage Engineering EM Van der Graaff accelerator.

To make a measurement, the proton beam was first focused to a spot 2 mm in diameter on a quartz viewing screen placed in front of the target assembly. By means of a rack and pinion, the target assembly could be moved so that any one of the twenty-eight positions could be selected for bombardment; the quartz was then removed, and the protons passed through the collimating holes to strike the oxide surface. Neutrons emitted in the $^{18}O(p, n)^{18}F$ reaction peak strongly in the forward direction, and were detected by means of a conventional long counter placed as close as possible behind the target chamber. The amount of material between the oxide film and the long counter was minimized to reduce neutron scattering; neutrons knocked out of the ^{18}O nuclei passed first through the underlying tantalum foil 0.015 in. thick, and then through the 1/16 in. aluminum end plate of the Van de Graaff vacuum system. The scattering was in any case small; on one occasion a 1/2 in. steel plate was inadvertently left under the end plate, and reduced the neutron counting rate by about 10%.

Measurements on a series of foils were made as follows. A standard sample, containing 490Å of 97.56% ^{18}O oxide, was bombarded first to establish the position of the resonance with respect to the energy scale of the accelerator; this sample was about 2 keV "thick" to 3.042 MeV protons. The energy region about 3.037 MeV was scanned in 10 keV steps, and, once the peak had been located, the proton energy was fixed 5 keV above, as illustrated in Fig. 2. The oxide steps on the prepared targets were then bombarded successively, going down one side of the target holder, rotating it through 180°, and back up the other side. The target assembly was then removed and replaced by its twin, carrying a new load of targets which were measured in the same way. Finally, when all positions on all prepared targets had been bombarded, the standard sample was again inserted in the proton beam to make sure that conditions had not changed in the course of the experiments; no significant discrepancies were in fact observed.

The proton dose was 150 μcoulombs at a beam current of about 1 μA; this corresponds to an implantation fluence of about 3×10^{16} $^1H^+/cm^2$ over the area implanted. A single dose of this magnitude had no discernible effect on the appearance of the foils, but the repeated doses applied to the standard changed the interference colors in such a way as to indicate a thickening. This thickening has been attributed to the deposition of carbon from traces of pump oil in the vacuum system (2), and had no effect on the neutron counting rate.

The total neutron count varied from a background of about 100 to a maximum of 90,000, and was subject to the following errors: (*i*) the usual statistical error, equal to the square root of the number of counts; (*ii*) inaccuracies in the measurement of the proton dose, due partly to contamination of the proton beam by other ions or by neutral hydrogen atoms, and partly to fluctuations in secondary electron emission by the target oxides; (*iii*) fluctuations in the efficiency of the neutron counter; (*iv*) fluctuations in the average proton energy and/or the energy spread, leading to fluctuations in neutron yield; and (*v*) variation of the beam position within the collimator holes, leading to variations in the number of neutrons generated in the foils, and also in the collimator itself. The collimator material was therefore of some importance, and originally gold was chosen on the ground that it is the only metal of high atomic number which does not support a surface oxide at room temperature. Experience showed, however, that the gold collimator gave a rather high background, and so it was replaced with one made of tantalum. The latter was chemically polished, and then treated with the $HF-NH_4F$ reagent to remove as much surface oxide as possible (9). This tantalum collimator gave a much lower neutron background, and proved satisfactory.

Duplicate measurements on several different samples showed that the average error was 2.1 times the statistical error [see (*i*) above] and so the former was taken as the standard error for the purposes of least squares fit analysis. There was, however, considerable variation between individual samples, due presumably to the effects of (*ii*)–(*v*).

Originally, it had been intended to bombard one side of the foils only. When the holder was modified to allow bombardment of both sides, the two orientations presented different geometries to the neutron counter. By bombarding the seven steps of a particular oxide film in both orientations, a conversion factor of 0.825 ± 0.006 (standard error) could be calculated. Since the oxide film was thinned alternately on each side of the foil, two seven-point samples could in principle be obtained; by applying the conversion factor, these could be combined in a single fourteen-point sample, which proved more suitable for analysis. On reversing the foil in the target holder, a second fourteen-point sample was obtained for comparison with the first; within experimental error, two such samples agreed.

Results

The experimental results were obtained as a series of neutron counts *vs.* oxide thickness remaining, their general form being illustrated in Fig. 4 and 5. These plots correspond to the integrated ^{18}O distribution in the oxide, and reference to Fig. 1 will show that they are most closely related to condition II or a combination of I and II. In order to eliminate the possibility of condition I alone, it is necessary to show that the mixing of the ^{16}O and ^{18}O populations in Fig. 5 is real, and not just an artifact due to uneven stripping of the oxide layers. The uniformity of the oxide stripping process has been studied in detail (1), and the magnitude of the irregularities is definitely not great enough (4) to account for the effects observed. Migration of the oxygen is therefore confirmed, and it most probably occurs via mechanism II; that is, the oxygen atoms all migrate in succession as space becomes available, so that their order is largely conserved. The system can then be regarded as a form of bulk diffusion, and has been analyzed mathematically in the Appendix.

The analysis predicts that the ^{18}O concentration profile should be an error function complement (erfc), and hence that the neutron count profile actually observed should be an integrated error function complement (ierfc). As indicated in Fig. 6, these functions involve five parameters, whose individual significance is as follows:

C(1), expressed in neutron counts/angstrom of oxide/150 μcoulombs of proton charge, is a proportionality constant relating neutron counts to ^{18}O enrichment.

C(2), measured in angstroms from the metal/oxide interface, defines the midpoint, or mode of the error function complement within the oxide film.

C(3), also in angstroms, is the standard deviation associated with the error function complement, and measures its dispersion about the mode.

C(4), in the same units as C(1), relates neutron counts to the natural ^{18}O background.

C(5), in neutron counts/150 μcoulombs of proton charge, are those due to impurities in the oxide and the underlying tantalum.

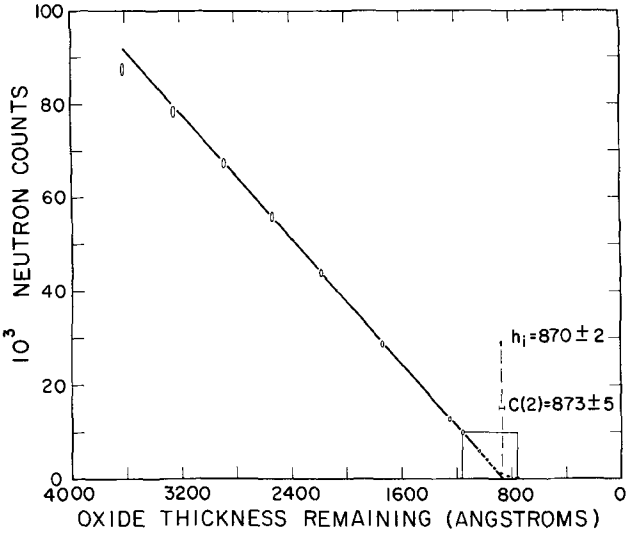

Fig. 4. Neutron counting profile obtained with the trial specimen in the first set of proton bombardments. Initial anodization to 870Å in $H_2{}^{16}O$, final anodization to 3622Å in $H_2{}^{18}O$, both at 1 mA/cm² in 0.01M KI. The error ellipses define the 95% confidence limits around the measured points, and the straight line has been fitted through the five points from 1254 and 2893Å. The small square in the lower right hand corner defines the area covered by Fig. 5.

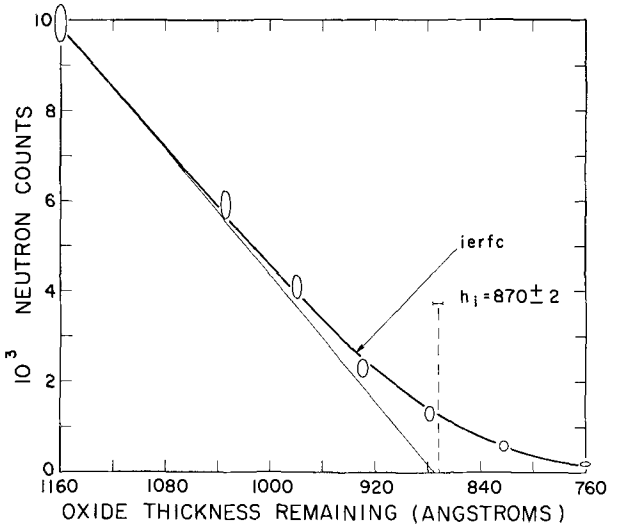

Fig. 5. Ten times magnification of the $^{16}O/^{18}O$ boundary region in Fig. 4, illustrating the fit of an integrated error function complement (ierfc) to the data points in the vicinity of h_i.

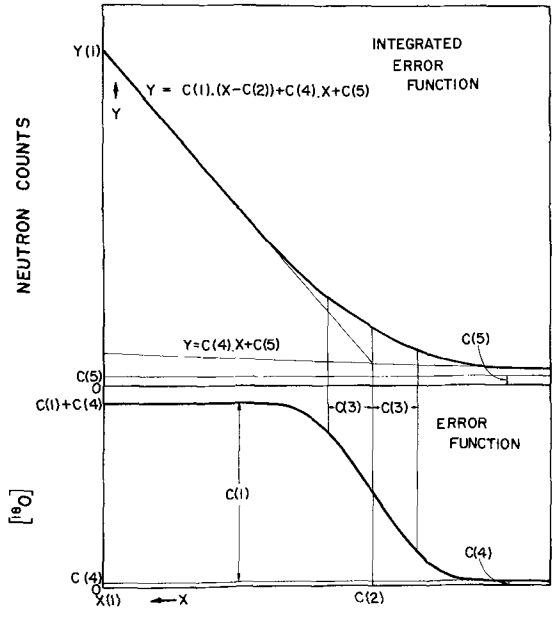

Fig. 6. The relationship between the error function complement

$$Y = (C(1)/\sqrt{2})\cdot\mathrm{erfc}[-(X-C(2))/\sqrt{2}\cdot C(3)] + C(4)$$

and its integral

$$Y = (C(1)\cdot C(3)/\sqrt{2})\cdot\mathrm{ierfc}[-(X-C(2))/\sqrt{2}\cdot C(3)] + C(4)\cdot X + C(5)$$

The relationships between these parameters are defined by a series of equations ([A-1]–[A-19]) in the Appendix, and these were tested experimentally in three sets of proton bombardments. The first set, i, was used to establish the best conditions for the experiments, which were then reproduced in sets ii and iii. The reproduction was not, however, completely accurate; the bombardment energy in set ii appeared to be slightly different, while the neutron counts in set iii were all 10% low due to the presence of the ½ in. steel plate.

The relationships tested were as follows:

(i) The neutron counts obtained from an oxide film formed entirely in ordinary water should be proportional to the oxide thickness remaining (Eq. [A-16]).

A sample of this kind was bombarded twice during set i, and once during set iii when, to save time,

Table I. Least squares fit of the straight line $Y_b(I) = C(4) \cdot X(I) + C(5)$ to the neutron counts vs. oxide thickness data for anodic tantalum oxide formed entirely in ordinary aqueous electrolyte (natural ^{18}O abundance 0.204%). Same sample used in both runs.

Run	Parameter C(4) (counts/Å)	Parameter C(5) (counts)	Number of data points fitted N	Fitting probability $p(\chi^2)_{N-2}$
i	0.061 ± 0.006	64 ± 10	28	0.084
iii	0.047 ± 0.013	66 ± 24	9	0.008

only nine of the fourteen positions were bombarded; the results are given in Table I. In view of the uncertainty in the calculation of the fitting probabilities (see Appendix), no good evidence against a linear relationship has been obtained, and so this has been assumed. In subsequent tests, these values of $C(4)$ and $C(5)$ have been used to correct the observed data for background, those for set ii being assumed identical to those for set i.

(*ii*) For an oxide formed first in ordinary water, and then in $H_2{}^{18}O$, the neutron counts due to the enrichment should, for oxide thicknesses much greater than the initial ^{16}O thickness, be linearly dependent on the oxide thickness remaining (Eq. [A-18]).

(iii) Furthermore, this linear relationship should extrapolate to zero counts when the remaining oxide thickness equals the initial thickness of ^{16}O oxide (Eq. [A-14] and [A-18]).

A trial specimen was prepared for the first set of proton bombardments by anodizing a tantalum foil to 870 ± 2Å in ordinary aqueous electrolyte, and then to 3622 ± 6Å in 97.56% $H_2{}^{18}O$. One side was stripped in approximately 400Å steps to leave seven thicknesses between 3622 and 1254Å, while the other was stripped to leave a series of thicknesses about 870Å. The observed neutron counting profiles for the two sides are illustrated in Fig. 4 and 5.

After correction for background, a straight line was fitted to the seven points on the first side, and the fitting probability found to be well below 0.001. The fit was therefore decidedly not acceptable, and reference to Fig. 4 shows why; the two points at the largest oxide thickness fall below an extension of the straight line drawn through the other five. The same sample was re-analyzed twice more in set ii, when this decrease in the neutron counts at the largest oxide thicknesses was not observed; all seven points could now be fitted to a straight line (fitting probabilities 0.041 and 0.064). The phenomenon was therefore peculiar to set i, and was almost certainly due to an erroneous setting for the incident proton energy. If this is too low, protons nearing the end of their track in a thick ^{18}O oxide will have an energy substantially below resonance, and so the neutron yield from these protons will be reduced.

Within experimental error, therefore, the results were consistent with a linear relationship between neutron counts and oxide thickness, and it but remained to obtain estimates for $C(1)$ and $C(2)$. Due to the variation in the average (p, n) cross section with oxide thickness, it was decided to fit a straight line repeatedly to the experimental data, dropping the point with largest oxide thickness between each fit, and to take $C(1)$ and $C(2)$ from that fit which gave the greatest fitting probability. "Best" estimates for $C(1)$ and $C(2)$ thus obtained are listed in Table II, from which it can be seen that $C(2)$ is, within twice the combined individual standard errors, identical to the initial ^{16}O oxide thickness, h_i. Similar but

Table II. Least squares fit of the straight line $Y_c(I) = C(1) \cdot (X(I) - C(2))$ to the neutron counts vs. oxide thickness data for an oxide film formed first in ordinary water (^{18}O abundance 0.204%) to h_i and then in water enriched with ^{18}O to an abundance of 97.56%. Neutron counts due to the enrichment (97.36%) were fitted only at oxide thicknesses greater than $h_i + 3 \cdot C(3)$; see Appendix for details.

Proton bombardment	Parameter C(1) (counts/Å)	Parameter C(2) (Å)	Number of data points fitted N	Fitting probability $p(\chi^2)_{N-2}$
First specimen with h_i = 870 ± 2Å				
i	33.53 ± 0.16	873 ± 5	5	0.835
ii	33.03 ± 0.34	865 ± 11	5	0.288
ii[a]	33.11 ± 0.23	868 ± 8	5	0.622
Average	33.2 ± 0.2			
Second specimen with h_i = 904 ± 2Å				
iii	30.16 ± 0.34	923 ± 10	10	0.078

[a] Configuration in specimen holder reversed.

less accurate results were obtained using the ^{18}O enrichment of 11.23%.

Predictions (*ii*) and (*iii*) are thus verified.

(*iv*) For oxide thicknesses approximately equal to the original ^{16}O thickness, the neutron counting profile should have the form of an integrated error function complement (Eq. [A-17]).

(*v*) This ierfc function should have its mode at h_i (Eq. [A-14] and [A-17]).

For the purpose of fitting Eq. [A-17], $C(1)$ was taken from Table II as 33.2 ± 0.2 (standard error) for sets i and ii, and 30.2 ± 0.3 for set iii; $C(2)$ was taken as h_i with standard error $\sqrt{[(\epsilon(h_i))^2 + (0.00144\ h_i)^2]}$, where $\epsilon(h_i)$ is the random measurement error in h_i (1), while $(0.00144\ h_i)$ is the standard error due to the uncertainty in the refractive index (1,4). Reference to Table III will show that all but two of the twenty separate data samples had fitting probabilities greater than 0.025, and that the two exceptions were duplicated by acceptable fits. Within experimental error, therefore, the ierfc function, with $C(2) = h_i$, does adequately fit the experimental data, and so predictions (*iv*) and (*v*) have been confirmed experimentally.

(*vi*) The standard deviation of the ierfc function should be proportional to the square root of the thickness added in the $H_2{}^{18}O$ electrolyte, provided that the latter is not too small (Eq. [A-19] and discussion in the Appendix).

In testing for the relation between $C(3)$ and $(h_f - h_i)$, three of the eighteen acceptable fits in Table III were eliminated from consideration. The sample anodized by 26Å in the ^{18}O electrolyte was eliminated because $(h_f - h_i) < 5.C(3)$; and both samples from the specimen anodized between 256 and 1041Å were eliminated because the thickness measurements were atypical, for reasons described in the next section. A least squares fit of Eq. [A-19] to the remaining fifteen samples gave the constant of proportionality, β, as 1.725 ± 0.026Å$^{1/2}$ (standard error), with $p(\chi^2)_{14}$ as 0.845. The latter is more than adequate, and so prediction (*vi*) is established.

(*vii*) The standard deviation of the ierfc function should be independent of h_i provided h_i is not too small (Eq. [A-19] and discussion in Appendix).

This follows from the fit of Eq. [A-19] to the data in Table III, section B.

The oxide thicknesses for the first sample in section B had to be measured in first order. As noted elsewhere (1), first order minima are rather broad and

Table III. Least squares fit of the integrated error function complement $Y_e(I) = (C(1)\cdot C(3)/\sqrt{2})\cdot \text{ierfc}\ [-(X(I)-C(2))/\sqrt{2}\cdot C(3)]$ to the neutron counting profile with $C(2) + 2\cdot C(3) > X(I) > C(2) - 2\cdot C(3)$. The variation of $C(1)$ and $C(2)$ was restricted as described in the Appendix. When two results are quoted for the same specimen, the second was obtained by reversing the orientation in the target holder. Unless otherwise stated, the anodizing conditions were 1 mA/cm² in 0.01N KI at about room temperature.

Final $^{18}O + {}^{16}O$ thickness h_f (Å)	Initial ^{16}O thickness h_i (Å)	Thickness added in ^{18}O electrolyte $(h_f - h_i)$[a] (Å)	Standard deviation $C(3)$ (Å)	Number of data points fitted N	Fitting probability $p(\chi^2)_{N-3}$
A. Dependence on thickness added in ^{18}O electrolyte					
907	881	26	14 ± 6	10	0.089
949	881	68 ± 4	14 ± 6	9	0.197
989	881	108 ± 4	23 ± 9	8	0.126
1093	881	212 ± 4	31 ± 6	9	0.114
1345	882	463 ± 4	40 ± 3	11	0.849
1795	879	916 ± 4	53 ± 3	11	0.866
2227	880	1347 ± 5	65 ± 4	11	0.793
2732	877	1855 ± 5	76 ± 6	11	0.242
3506	908	2597 ± 6[b]	85 ± 8	11	0.083
3753	892	2863 ± 6[b]	85 ± 6	12	0.337
3757	893	2863 ± 6[b]	88 ± 4	12	0.858
			87 ± 9	12	0.003
5734	904	4830 ± 9	121 ± 6	12	0.250
			122 ± 12	12	0.000
B. Dependence on initial thickness formed in ^{16}O electrolyte					
1041	256	785	39 ± 5[c]	11	0.197
			45 ± 6	10	0.531
1795	879	916 ± 4	53 ± 3	11	0.866
2706	1762	944 ± 5	50 ± 8	11	0.097
3680	2645	1034 ± 7[b]	55 ± 7	11	0.408
C. Dependence on current density					
10 mA/cm² (with heating)					
4161	881	3281 ± 6[b]	109 ± 6	10	0.232
1 mA/cm²					
3506	908	2597 ± 6[b]	85 ± 8	11	0.083
0.1 mA/cm²					
3633	872	2761 ± 7	88 ± 6	11	0.558

[a] Errors quoted only for those samples used to calculate the broadening parameter, β.
[b] Figures not additive because individual values have been rounded to the nearest angstrom.
[c] First figure obtained from thickness measurements in first order, the second using thickness measurements converted from second order; see text for details.

difficult to measure accurately; furthermore, the range of thicknesses that can be measured in the satisfactory 300-400 mμ region is limited to 197-330Å. As an added check, therefore, the oxide steps were incorporated from the starting thickness of 1041Å, so that their magnitude could be measured in second order. The stepped oxide was then thinned down in such a way as to place the middle step as close as possible to 256Å. If the oxide thins uniformly, the step heights measured in second order can be combined with the measured first order thickness for the middle step to calculate the final thickness for all the other steps. The estimates for $C(3)$ obtained from the two sets of measurements do not differ significantly from each other, or from those in the rest of section B, Table III.

All six relationships involving the ^{18}O tracer have thus been confirmed experimentally. Three additional factors were considered.

(*viii*) Current density.

From Eq. [A-4] and [A-5], the standard deviation of the ierfc function would appear to vary as the reciprocal of the current density, i. However, it also varies directly as the diffusion constant, D, and if D is linearly proportional to i, the ratio D/i will be constant. In that case, the standard deviation, $C(3)$, would be independent of the current density during the anodization process.

The data in Table III, section C, were used for the fit of Eq. [A-19], and the adequacy of the fit shows that $C(3)$ does not vary significantly with current density.

(*ix*) Isotopic ratios in oxide and electrolyte.

If there is no isotope effect during the incorporation of oxygen, the isotopic ratio in the oxide should be the same as that in the electrolyte.

From Eq. [A-14] and [A-15], $C(1)$ and $C(4)$ are proportional to the ^{18}O enrichment and the natural ^{18}O abundance, respectively. A comparison of neutron counting rates *vs.* ^{18}O enrichment of the electrolyte is given in Table IV. Least squares fits of straight lines passing through the origin gave a slope of 0.34 for sets i and ii, and 0.32 for set iii, but $p(\chi^2)_2$ was far less than 0.025 in both cases. The best that can be said, therefore, is that the isotopic ratios are approximately proportional.

(*x*) Kirkendall Effect.

The differing masses of ^{16}O and ^{18}O might lead to a difference in migration rate, and hence to a type of Kirkendall effect (16). This would be manifest as a neutron count profile significantly different from an ierfc function, for which there is no evidence.

Discussion

Nature of the oxygen migration.—The experimental results show quite clearly that the oxygen atoms move, and that they all move. Since the analysis is based on a statistical system in which a large number of atoms all make a series of small jumps, it follows that the mean distance traveled by each oxygen atom during each charge transfer event must be small compared to the total distance migrated. Just how small can be estimated, very crudely, from the following analysis.

Suppose that the mean distance between adjacent oxygen sites is a, and that the "high field approximation" (17) applies. It follows that the oxygen jumps will cluster about the axis of the field and in the forward direction; that is, towards the metal/oxide interface. The average distance jumped in the direction of the field will then be close to a; for simplicity, it will be assumed constant and equal to a. If the oxide thickens by an amount $(h_f - h_i)$, the leading ^{18}O atoms travel a distance $t_o\cdot(h_f - h_i)$, in an average of n jumps so that

$$n\cdot a = t_o\cdot(h_f - h_i)$$

A second equation including these quantities can be obtained by considering the standard deviations. That of the left hand side is $a\cdot\sqrt{n}$, as discussed for the derivation of Eq. [19] in Ref. (4); that of the right hand side is in fact $C(3)$, because it can be shown (18) that Eq. [A-11] describes the broadening of an infinitesimally thin layer of ^{18}O. Substituting for $C(3)$ by means of Eq. [A-19]

$$a\cdot\sqrt{n} = \beta\cdot\sqrt{(h_f - h_i)}$$

Solving for a

$$a = \beta^2/t_o = 3.9\text{Å}$$

Nearest neighbor oxygen distances in the crystalline forms of tantalum oxide range from 2.02 (19) to 3.19Å (20) with an average that appears to be about 2.7Å; the observed figure is therefore somewhat greater. Considering the crudity of the analysis, however, the agreement is quite reasonable. On this basis, then, it would appear that oxygen migrates by jumping from one site to the next.

Table IV. Comparison of neutron counting rates per angstrom of anodic oxide with the ^{18}O enrichment of the electrolyte, as quoted by the supplier (YEDA)

^{18}O enrichment e(%)	Runs i and ii $C(1)$ or $C(4)$	Run iii $C(1)$ or $C(4)$
0.204	0.061 ± 0.006	0.047 ± 0.013
11.23	4.15 ± 0.08	3.69 ± 0.04
97.36	33.2 ± 0.2	30.2 ± 0.3

The real situation is, however, much more complex. Results reported elsewhere (4) show that implanted noble gases behave in a very similar fashion to oxygen; that is, the noble gas atoms move, and it may reasonably be inferred that they all move. When the preceding analysis was applied to them, however, the results were absurd, and it was then concluded that their movement was a form of Brownian motion (4). If so, the migration of the oxygen may well proceed by two processes: the forced directional migration discussed so far, and a more or less random diffusion due to a Brownian-type motion.

This second process will have little or no effect on the ^{18}O profile mode, but it will contribute to the standard deviation. An estimate for this contribution may be obtained by assuming that the broadening parameter, β, associated with the motion of the noble gases varies with mass. Extrapolation of the data in Table III of Ref. (4) to oxygen of average mass 17 gives β as 1.37Å½, which may be compared with the observed value of 1.725 ± 0.026Å½. If the forced migration and Brownian motion are completely independent processes, the square of the observed β will be equal to the sum of the squares of its components; β for the forced migration alone will then be 1.05Å½, so that a would be 1.46Å. This calculation is, however, probably not justified, since the Brownian process is almost certainly a consequence of the forced migration, and therefore not independent of it.

The nature of the oxygen migration is thus rather obscure, but the present results are not inconsistent with the hypothesis put forward in the previous paper (4), that charge is transferred during the anodic oxidation of tantalum via the simultaneous movement of a group of atoms, both tantalum and oxygen. Such a process would require some mixing of the ^{16}O and ^{18}O populations, but would generally conserve their order, as is observed.

Conclusions

1. Concentration profiles for oxygen isotopes in anodic tantalum oxide can be measured with excellent precision by combining the sectioning technique for locating the isotope with a nuclear method for detecting it.

2. This scheme requires that the detection efficiency shall be independent of the oxide thickness. Oxygen-18 was detected by means of neutrons produced in the $^{18}O(p, n)^{18}F$ reaction; bombardment with 3.042 MeV protons ensured that the detection efficiency was sensibly constant.

3. On anodizing first in ^{16}O electrolyte and then in ^{18}O, it was found that the oxygen order was largely, but not completely, conserved.

4. The mixing of the ^{16}O and ^{18}O populations across the boundary between them could be analyzed very well in terms of forced diffusion from a constant source into a semi-infinite medium, thus confirming that oxygen migrates under the influence of the electric field.

5. The jump distance associated with the oxygen migration was found to be of the order of 4Å, which is little more than the expected nearest neighbor oxygen distance.

Acknowledgments

The author is grateful to J. Butler for advice on neutron counting, to J. Denhartog and G. Hearn for assistance with the proton bombardments, and to T. A. Eastwood and W. D. Mackintosh for reviewing the manuscript.

Manuscript submitted Dec. 20, 1972; revised manuscript received May 28, 1973.

Any discussion of this paper will appear in a Discussion Section to be published in the June 1974 JOURNAL.

APPENDIX

Theory of the migration.—The oxide film may be regarded as a semi-infinite medium, bounded by a plane corresponding to the oxide/electrolyte interface but otherwise extending to infinity. This concept is valid in discussing the ^{18}O migration provided that the metal/oxide interface is sufficiently far from the $^{16}O/^{18}O$ boundary that it does not influence the mixing of the populations; this would appear true for the experiments reported here. Arguments presented elsewhere (4) suggest that thermal diffusion is negligible at room temperature, and hence that the oxygen moves solely under the influence of the electric field present during anodization; that is, it is a forced migration, with the electrolyte acting as a constant source of ^{18}O. The diffusion system is one, therefore, of forced diffusion from a constant source into a semi-infinite medium.

The kinetics of forced diffusion have been discussed in detail by Boltaks (18), who treats the problem as free diffusion coupled with a superimposed drift velocity due to the applied field. For forced diffusion from a constant source into a semi-infinite medium, he cites the following equation

$$C(x,t) = \frac{C_o}{2}\left[\left(1 - \text{erf}\left(\frac{x - vt}{\sqrt{2}\sqrt{(2Dt)}}\right)\right) + \exp\left(\frac{vx}{D}\right)\cdot\left(1 - \text{erf}\left(\frac{x + vt}{\sqrt{2}\sqrt{(2Dt)}}\right)\right)\right] \quad [A\text{-}1]$$

where C is the concentration of the diffusing species at time t and distance x into the medium, C_o is the steady-state concentration of the diffusing species at the boundary plane $x = o$, v is the average velocity of the diffusing particles in the direction of the applied field, and D is the diffusion constant of the free component that arises in consequence of the concentration gradient set up by the forced migration.

The second term of Eq. [A-1] is effectively a perturbation due to the presence of the boundary plane; as t increases, it tends to zero. Computations were made to find out how rapidly it approached zero, using appropriate values of v and D calculated from the experiments. It turned out that the second term was considerably less than 1% of the first for all values of x once vt was greater than $5\cdot\sqrt{(2Dt)}$; that is, once the mean distance traveled by the leading particles, vt, was more than five times their standard deviation, $\sqrt{(2Dt)}$, about that mean. This condition was met in the present experiments, and so Boltaks equation reduces to

$$C(x,t) = \frac{C_o}{2}\left[1 - \text{erf}\left(\frac{x - vt}{\sqrt{2}\sqrt{(2Dt)}}\right)\right] \quad [A\text{-}2]$$

Application of Eq. [A-2] to the migration of oxygen in anodic oxides requires some changes in format, and these are illustrated schematically in Fig. 7. Suppose the reanodization in $H_2{}^{18}O$ be performed for a time, t, at constant current density, i, and that the oxide thickens from an initial thickness, h_i, to a final thickness, h_f. If the current efficiency is 100% (17), the charge passed will be related to the oxide formed by Faraday's law; that is

$$it = (\rho\mathbf{F}/Q)\cdot(h_f - h_i) \quad [A\text{-}3]$$

where ρ is the oxide density, $\mathbf{F}$ the Faraday constant, and Q the equivalent weight of Ta_2O_5. The factor $\sqrt{(2Dt)}$ in the error function of Eq. [A-2] can then be replaced by $\beta\sqrt{(h_f - h_i)}$ where β is given by

$$\beta = \sqrt{(2D\rho\mathbf{F}/iQ)} \quad [A\text{-}4]$$

Examination of Fig. 7 will show that by changing the reference plane from the oxide/electrolyte interface to the metal/oxide interface, and reversing the sense of the axes, the quantity $(x - vt)$ in Eq. [A-2] can be replaced by $-(h - h_i)$, where h is a variable measured relative to $h = o$ at the metal/oxide interface.

Equation [A-2] then becomes

$$C(h, h_f - h_i) = \frac{C_o}{2}\left[1 - \text{erf}\left(\frac{-(h - h_i)}{\sqrt{2}\cdot\beta\sqrt{(h_f - h_i)}}\right)\right] \quad [A\text{-}5]$$

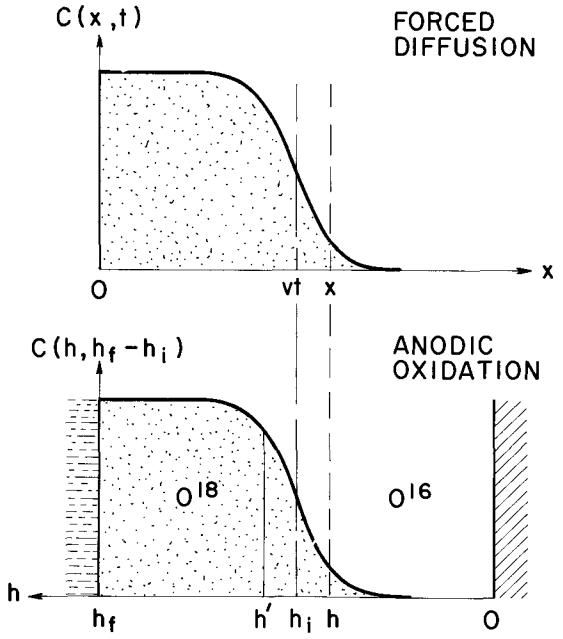

Fig. 7. Diagram illustrating the relation between the quantities used in the theory of forced diffusion and those used in the anodic oxidation.

Substituting

$$\sigma = \beta\sqrt{(h_f - h_i)} \qquad [A\text{-}6]$$

Eq. [A-5] becomes

$$C(h, h_f - h_i) = (C_o/2)\cdot\mathrm{erfc}(-(h - h_i)/\sqrt{2}\cdot\sigma) \qquad [A\text{-}7]$$

Equation [A-7] describes the ^{18}O profile to be expected if the oxygen migrates by forced diffusion. The neutron counts actually observed, however, will be proportional to the integral of this equation; thus if the oxide is thinned from h_f to a certain thickness h', the neutron counts, K, will be given by

$$K(h') = \int_o^{h'} P\cdot(C_o/2)\cdot\mathrm{erfc}(-(h - h_i)/\sqrt{2}\cdot\sigma)\cdot dh \qquad [A\text{-}8]$$

where P is a constant of proportionality, determined by the cross section for the $^{18}O(p, n)^{18}F$ reaction and the efficiency of the neutron counter. The integration is taken from the metal/oxide interface at $h = o$ to the existing oxide surface at h' (Fig. 7). If the ^{18}O concentration in the metal is assumed zero, the lower limit may be changed to $-\infty$ without affecting the value of $K(h')$. Replacing $-(h - h_i)/\sqrt{2}\cdot\sigma$ by y, and making the appropriate substitutions, Eq. [A-8] becomes

$$K(h') = \int_\infty^{-(h'-h_i)/\sqrt{2}\cdot\sigma} P\cdot(C_o/2)\cdot\mathrm{erfc}(y)\cdot(-\sqrt{2}\cdot\sigma)\cdot dy \qquad [A\text{-}9]$$

Reversing the limits of the integration

$$K(h') = (\sigma P\, C_o/\sqrt{2})\cdot\int_{-(h'-h_i)/\sqrt{2}\cdot\sigma}^{\infty}\mathrm{erfc}(y)\cdot dy$$

$$= (\sigma P\, C_o/\sqrt{2})\cdot\mathrm{ierfc}(-(h' - h_i)/\sqrt{2}\cdot\sigma) \qquad [A\text{-}10]$$

Equation [A-10] describes the expected variations in neutron counts as a function of distance, h', from the metal/oxide interface. For reasons given in the discussion of Eq. [A-1], neither Eq. [A-7] nor [A-10] is strictly correct when $(h_f - h_i)$ is small, for then the perturbing effect of the oxide/electrolyte boundary cannot be ignored. There must also be a perturbing effect due to the metal/oxide boundary when h_i is very small, and although no calculations have been made, it seems reasonable to suppose that the two perturbations would be similar. Equations [A-7] and [A-10] should therefore be valid provided both $(h_f - h_i)$ and h_i are greater than about $5\beta\cdot\sqrt{h_f - h_i}$.

Least squares fitting procedure.—These erfc and ierfc functions are the first and second integrals of a normal distribution. Using the nomenclature of previous papers (3, 4) the parent normal distribution may be written

$$Y(I) = C(1)/(\sqrt{(2\pi)}\cdot C(3))\cdot\exp[-(-(X(I) - C(2))/\sqrt{2}\cdot C(3))^2] \qquad [A\text{-}11]$$

where the parameter $C(1)$ is a normalizing constant, $C(2)$ the modal value, and $C(3)$ the standard deviation. Integration of this equation gives

$$Y(I) = (C(1)/2)\cdot\mathrm{erfc}[-(X(I) - C(2))/\sqrt{2}\cdot C(3)] + C(4) \qquad [A\text{-}12]$$

where $C(4)$ is a constant of integration. On integrating again

$$Y(I) = (C(1)\cdot C(3)/\sqrt{2})\cdot\mathrm{ierfc}[-(X(I) - C(2))/\sqrt{2}\cdot C(3)] + C(4)\cdot X(I) + C(5) \qquad [A\text{-}13]$$

where $C(5)$ is another constant of integration. The relationship between Eq. [A-11] and [A-12] has been illustrated in Fig. 5 of Ref. (3), while that between Eq. [A-12] and [A-13] is illustrated in Fig. 6 of the present paper.

Equation [A-13] is the function that must be fitted through the experimental points $I = 1, 2, \ldots\ldots N$. The first term on the right hand side corresponds to Eq. [A-10], so that

$$\begin{aligned} C(1) &\equiv P\cdot C_o \\ C(2) &\equiv h_i \\ C(3) &\equiv \sigma \\ X(I) &\equiv h' \end{aligned} \qquad [A\text{-}14]$$

$C(4)$ accounts for the ^{18}O present in natural abundance, C_n, in the ^{16}O layer, so that

$$C(4) = P\cdot C_n \qquad [A\text{-}15]$$

while $C(5)$ accounts for neutrons produced from the underlying tantalum and any impurities that may be present.

Equation [A-13] contains five adjustable parameters, which is too many to be characterized successfully with a maximum of only fourteen points per sample. Fortunately, two of them, $C(4)$ and $C(5)$, can readily be eliminated. If a tantalum specimen is anodized solely in ordinary water, the neutron counting profile due to the natural ^{18}O will be

$$Y_b(I) = C(4)\cdot X(I) + C(5) \qquad [A\text{-}16]$$

The least squares fit of a straight line through the experimental points from such a sample will then provide estimates for $C(4)$ and $C(5)$, so that by subtracting Eq. [A-16] from Eq. [A-13]

$$Y_e(I) = Y(I) - Y_b(I) = (C(1)\cdot C(3)/\sqrt{2})\cdot\mathrm{ierfc}(-(X(I) - C(2))/\sqrt{2}\cdot C(3)) \qquad [A\text{-}17]$$

where the $Y_e(I)$ are the neutron counts due to the ^{18}O enrichment.

When $X(I) << C(2)$, ierfc $[-(X(I) - C(2))/\sqrt{2}\cdot C(3)]$ tends to zero, and so $Y_e(I)$ also tends to zero. When $X(I) >> C(2)$, however, ierfc $[-(X(I) - C(2))/\sqrt{2}\cdot C(3)]$ tends to $2\cdot(X(I) - C(2))/\sqrt{2}\cdot C(3)$, so that Eq. [A-17] becomes

$$Y_e(I) = C(1)\cdot(X(I) - C(2)) \qquad [A\text{-}18]$$

which is a straight line. For least squares fitting purposes, Eq. [A-18] was indistinguishable from [A-17] once $X(I) > C(2) + 3\cdot C(3)$. If Eq. [A-18] is fitted to the appropriate data, estimates for $C(1)$ and $C(2)$ can be obtained; the latter is expected, from Eq. [A-14], to equal the initial ^{16}O oxide thickness, h_i.

In making the least squares fit of a function with several parameters, it frequently happens that information on some of the parameters is already available, as in the case of $C(2)$ above. Such information is wasted if the least squares fit is used to obtain

additional estimates for these parameters; *i.e.*, if the parameters are allowed to vary freely. By fixing the parameters at known values, or by allowing them to vary within limits dictated by known standard errors, such information can be incorporated in the least squares fitting program. The more the variation of the parameters is restricted, the less accommodating does the procedure become, and the greater the difficulty in obtaining a satisfactory fit. The most stringent goodness-of-fit test, therefore, is obtained by restricting the variation as much as possible.

This principle has been applied in the least squares fit of Eq. [A-17]. It was assumed that $C(2)$ should be equal to h_i, and this assumption was then incorporated in the fitting procedure by restricting the variation of $C(2)$ about h_i to the standard error in h_i. Values of $C(1)$ together with their errors were obtained from least squares fits of Eq. [A-18], and these were incorporated in similar fashion. Equation [A-17] was fitted to data with $C(2) + 2 \cdot C(3) > X(I) > C(2) - 2 \cdot C(3)$, while Eq. [A-18] was fitted only to data with $X(I) > C(2) + 3 \cdot C(3)$; the information used to obtain $C(1)$ was not therefore used again in fitting Eq. [A-17].

Operationally, the least squares fitting was performed as described in Ref. (4), with the error, $EX(I)$, in $X(I)$ taken proportional to 0.067 times the difference between the "kick" wavelengths (1), and the error, $EY(I)$ in $Y(I)$ as 2.1 times the statistical counting error. As noted earlier, the multiplication factor in $EY(I)$ tends to vary from sample to sample, and since the fitting probabilities are extremely sensitive to the magnitudes of the experimental error, their correct values are in some doubt. Furthermore, the use of restricted parameters raises a prob'em in connection with the number of degrees of freedom, which is of importance for calculating the χ^2 probability (3). Since there is no obvious answer to this, the most unfavorable case was assumed; that is, the number of degrees of freedom in the fit of Eq. [A-17] was reduced to a minimum by treating $C(1)$ and $C(2)$, for this purpose only, as varying freely. The actual magnitude of the individual χ^2 probabilities is fortunately not of great significance; what does matter is whether they are, in general, greater or less than the chosen acceptance level of 0.025 (3). And for that purpose, the present computations were good enough.

By combining Eq. [A-6] and [A-14]

$$C(3) = \beta\sqrt{(h_f - h_i)} \qquad [A\text{-}19]$$

so that $C(3)$ is expected to be proportional to the square root of the oxide thickness formed in the ^{18}O electrolyte.

REFERENCES

1. J. P. S. Pringle, *This Journal*, **119**, 482 (1972).
2. J. P. S. Pringle, Submitted to *This Journal*.
3. J. P. S. Pringle, Accepted for publication in *This Journal*.
4. J. P. S. Pringle, *ibid.*, **120**, 398 (1973).
5. R. W. Ollerhead, E. Almqvist, and J. A. Kuehner, *J. Appl. Phys.*, **37**, 2440 (1966).
6. G. Amsel and D. Samuel, *J. Phys. Chem. Solids*, **23**, 1707 (1962).
7. C. A. Evans and J. P. Pemsler, *Anal. Chem.*, **42**, 1060 (1970).
8. C. Ortega and J. Siejka, Abstract No. 86, page 221, Electrochem. Soc. Extended Abstracts, Fall Meeting, Cleveland, Ohio, Oct. 3-7, 1971.
9. B. Maurel, D. Dieumegard, and G. Amsel, *This Journal*, **119**, 1715 (1972).
10. D. Walker, Atomic Energy of Canada Ltd. Report AECL-2502, Chalk River, Canada, 1965.
11. B. A. Thompson, *Anal. Chem.*, **33**, 583 (1961).
12. R. O. Bondelid and J. W. Butler, *Nucl. Phys.*, **53**, 618 (1964).
13. H. A. Hill and J. M. Blair, *Phys. Rev.*, **104**, 198 (1956).
14. L. F. Hansen, R. C. Jopson, H. Mark, and C. D. Swift, *ibid.*, **30**, 389 (1962).
15. W. Whaling, "Handbuch der Physik," S. Flugge, Editor, Vol. 34, pp. 193-217, Springer-Verlag, Berlin (1958).
16. E. O. Kirkendall, *Trans. Am. Inst. Mining Met. Engrs.*, **147**, 104 (1942).
17. L. Young, "Anodic Oxide Films," Academic Press, London and New York (1961).
18. B. I. Boltaks, "Diffusion in Semiconductors," Academic Press, New York (1963).
19. N. C. Stephenson and R. S. Roth, *J. Solid State Chem.*, **3**, 145 (1971).
20. N. C. Stephenson and R. S. Roth, *Acta Cryst.*, **B27**, 1037 (1971).

The Choice and Evaluation of Phosphors for Application to Lamps with Improved Color Rendition

J. J. Opstelten, D. Radielović, and W. L. Wanmaker*

N. V. Philips' Gloeilampenfabrieken, Eindhoven, The Netherlands

ABSTRACT

The optimum color rendering index was calculated both for low- and high-pressure mercury vapor lamps by adding spectral lines or emission bands of various wavelengths to the relevant mercury spectrum. The optimum wavelengths were calculated. In fluorescent lamps they depend both on the type of lamp and on the luminous efficacy. In high-pressure mercury-vapor lamps it is desirable to add both a blue and a red emission to the mercury spectrum. From these specifications a certain choice of phosphors to be used can be made. The merits of these phosphors are evaluated and some suggestions are given concerning the design of lamps with an improved color rendition.

The choice of the phosphors to be used in fluorescent lamps with improved color rendition can be made by constructing lamps with various phosphor blends and evaluating the color rendering indices. This is a rather complicated and time-consuming method, however. Accordingly, when fluorescent lamps with improved color rendition were introduced in an early stage, calculations were carried out with "theoretical" lamps (1, 2). For instance Kruithof and Ouweltjes (1) studied the color rendition (using both the spectral band method and the behavior of test samples as a criterion) of mixtures of calcium halophosphate, magnesium arsenate, and willemite phosphors. When using these phosphor blends they found from their calcula-

* Electrochemical Society Active Member.

Key words: color rendition, fluorescent lamps, phosphors.

tions that it is useful for the emission of the violet and blue mercury emission lines (404.7, 407.8, and 435.8 nm) to be partially absorbed. In another paper, Ouweltjes (2) describes the way in which the spectral power distribution of lamps can be computed and their color rendition with respect to test color samples evaluated by starting with various mixtures of three phosphors.

Several papers have been published in recent years in which the optimization of the spectral power distribution of lamps is reported, in order to achieve improved color rendition. For instance, Koedam *et al.* (3), Thornton (4), and Koedam *et al.* (5) calculated the optimum combinations of three spectral lines or emission bands for light sources of different correlated color temperatures. For fluorescent lamps, Walter (6) calculated the optimum for two emission bands to which the low-pressure mercury-vapor spectrum was added. Koedam *et al.* (5) calculated the General Color Rendering Index (R_a) for fluorescent lamps, using the emission bands of existing phosphors.

In the present optimization study the spectrum of the mercury discharge was taken as a starting point, both for low- and high-pressure mercury-vapor lamps. Optimum combinations of the mercury spectrum and spectral lines or emission bands were calculated. These calculations permit conclusions to be drawn about the required emission characteristics of the phosphors to be used. This leads to a choice of certain phosphors, the merits of which can be evaluated by using the same computer program as used for the optimization study.

Experimental

Optimization of the Color Rendition of Fluorescent Lamps

The work on fluorescent lamps was restricted to the three current types, viz., Warm White, Cool White, and Daylight. The optimization was carried out by adding two or three spectral lines or emission bands to the visible spectrum of the 40W low-pressure mercury-vapor discharge as it is found in a fluorescent lamp. The relative spectral power distribution in the visible part of this spectrum is given in Table I. It corresponds to chromaticity co-ordinates: x; $y = 0.221$; 0.208. The exciting power (P_e) of the mercury discharge appears to be: $P_{e(253.7\ nm)} = 45 \times P_{(435.8\ nm)}$ (7). P_e determines the number of ultraviolet photons available for the excitation of the phosphor.

The General Color Rendering Index (R_a) was calculated in accordance with the C.I.E. Publication 13 (8). For this purpose the visible wavelength region was divided in 5 nm intervals, the centers of these intervals lying at 382.5, 387.5, . . . 742.5 nm.

Optimization by adding two spectral lines.—Two spectral lines of varying wavelengths were added to the visible mercury spectrum of the fluorescent lamp. The wavelengths of the lines were varied in steps of 5 nm. As the chromaticity co-ordinates of the total spectrum are given, it follows from colorimetric principles that the intensities of the two lines with respect to that of the mercury spectrum are fixed by their chromaticity co-ordinates. The luminous efficacy of the resulting spectrum can be calculated by considering the lumen contribution of the added lines.

Optimization by adding three spectral lines or emission bands.—The relative intensity of three spectral lines or emission bands added to the mercury spectrum of the fluorescent lamp are not defined entirely by the prescribed chromaticity co-ordinates of the lamp under consideration.

In a 40W fluorescent lamp about 200 lumens stem from the mercury spectrum. Since commercial fluorescent lamps with an improved color rendition rates at about 50 lm/W, we have assumed in most calculations that the lumen contribution of the added light (either spectral lines or emission bands) is nine times that of the mercury spectrum. This leads to 2000 lm (50 lm/W) for a 40W fluorescent lamp. It can also be calculated which fraction (we called this the quantum-conversion fraction: Q) of the ultraviolet photons available is converted into visible light. When applying a phosphor in a lamp a reasonable value of Q is 0.80, since this value corresponds to an absorption of the exciting radiation of 90% and a quantum efficiency (254 nm excitation) of 90%. If in a calculation a Q value lower than 0.80 is found, it means that a theoretical lamp can be made with a higher efficacy than 50 lm/W.

In the case of emission bands being added to the mercury spectrum, the form of the bands was taken as Gaussian when the number of emitted photons was plotted *vs.* photon energy, following the method used by Walter (6).

Table I. Relative spectral power distribution of the low-pressure mercury-vapor discharge in the visible part of the spectrum

Wavelength (nm)	Power P (rel. units)
404.7	382
407.8	27
435.8	1000
546.1	483
578.1	153

Optimization of the Color Rendition of the Color-Corrected High-Pressure Mercury-Vapor Lamp

In the optimization of the color-corrected high-pressure mercury-vapor lamp we started from the visible spectrum of a 400W lamp. The optimum color rendering index was calculated by adding one or two spectral lines or emission bands with varying wavelengths to this spectrum.

The exciting ultraviolet radiation of a high-pressure mercury-vapor lamp consists of both line and continuum radiation which extend to 400 nm. This implies that phosphors with a broad excitation spectrum will be most suitable.

In the calculations it was assumed that all ultraviolet photons available (emitted between 200 and 310 nm) are used for conversion into visible light, *i.e.*, $Q = 1$. In contrast to the fluorescent lamps the chromaticity co-ordinates of the color-corrected high-pressure mercury-vapor lamp have not been standardized. Therefore the spectral lines or emission bands were added at constant Q value.

Results and Discussion

Fluorescent Lamps

The results of the optimization study by adding two and three spectral lines are given in Tables II and III, respectively. In these tables the optimum wavelengths of the spectral lines are given, together with the General Color Rendering Index (R_a), the R_9, . . . R_{14} values, and the value of Q. The first solution of Table II gives the optimum R_a value, yielding however a very low R_9 value. As in practice the color rendering of saturated red object colors (R_9) is important, and in fact is often one of the most important criteria in color rendition. A second solution is also given in Table II. This is a kind of compromise solution yielding a higher R_9 and a somewhat lower R_a value.

It follows from Table II that in the case of the addition of two spectral lines to the low-pressure mercury-vapor spectrum an optimum color rendition can only be reached with an incomplete utilization of the ultraviolet photons available (*i.e.*, Q has a low value). This leads to a low lumen/watt value.

Table III, however, shows that both a higher efficacy and a much better color rendition can be achieved by adding three spectral lines instead of two. Since in our calculations the mercury spectrum of the fluorescent lamp has been included, a better color rendition is achieved than in the case of only three spectral lines (3, 4). Comparing the optimum wavelengths of Table

Table II. Results of the optimization study of a fluorescent lamp, with the addition of two spectral lines to the mercury spectrum

Type of lamp	λ_1 (nm)	λ_2 (nm)	Color Rendering Indices R_a	R_9	R_{10}	R_{11}	R_{12}	R_{13}	R_{14}	Q^*	η(lm/W)
Warm White	527.5	602.5	70	−184	80	39	60	86	89	0.31	36
	537.5	612.5	67	30	49	52	34	64	44	0.32	36
Cool White	522.5	602.5	73	−135	80	29	48	87	90	0.17	23
	527.5	612.5	64	77	69	16	45	66	60	0.18	23
Daylight	512.5	602.5	75	−98	88	26	30	92	93	0.11	15
	517.5	612.5	67	92	84	7	36	78	80	0.10	15

$$^*Q = \frac{\text{number of photons emitted}}{\text{number of ultraviolet photons available}}$$

Table III. Results of the optimization study of a fluorescent lamp, with the addition of three spectral lines to the mercury spectrum. Calculated with $\eta = 50$ lm/W.

Type of lamp	λ_b (nm)	λ_g (nm)	λ_r (nm)	Color Rendering Indices R_a	R_9	R_{10}	R_{11}	R_{12}	R_{13}	R_{14}	Q^*
Warm White	497.5	557.5	617.5	92	90	91	78	70	90	86	0.50
Cool White	482.5	557.5	617.5	84	89	66	10	85	85	87	0.51
Daylight	472.5	542.5	612.5	81	89	59	67	59	74	61	0.52

$$^*Q = \frac{\text{number of photons emitted}}{\text{number of ultraviolet photons available}}.$$

III with those of a pure three-line spectrum it appears that the addition of the mercury spectrum shifts the added blue line to longer wavelengths, viz., a shift of 10-30 nm being observed. This is due to the presence of the blue mercury lines.

It can be seen from Table III that the value of Q is low, viz., about 0.50. Therefore calculations were carried out with a lumen contribution of the added light (as a percentage of the total light output) above 90% (as used in Table III). The result is that in the case of a Warm White fluorescent lamp an efficacy of 75 lm/W can be reached with $R_a = 90$, but the color rendering of the yellow-green saturated color is somewhat decreased ($R_{11} \sim 40$).

The color rendition of a fluorescent lamp can be further improved by adding spectral emission bands instead of spectral lines to the mercury spectrum. It can be seen from Table IV that in the case of three emission bands with the same bandwidth the color rendition of both Daylight and Cool White fluorescent lamps increases by broadening the emission bands. With Warm White fluorescent lamps, however, such a broadening of the emission bands leads to a decrease of the color rendition. This is due to the fact that with the use of broad-emission bands the required blue-green emission band is located at a longer wavelength. As a result a gap in the spectrum of the theoretical lamp exists between this added blue-green band and the blue mercury line leading to a decrease of the color rendition. When absorbing a part of the blue mercury emission lines, however, this gap is narrowed and as a consequence the color rendition improves (see Table

Table IV. Results of the optimization study of a fluorescent lamp, with the addition of three emission bands (with varying bandwidths) to the mercury spectrum. Calculated with $\eta = 50$ lm/W

	Type of lamp: Daylight									Cool White					
	Bandwidth (50%) (nm)			Wavelength at peak (nm)						Wavelength at peak (nm)					
No.	Blue	Green	Red	Blue	Green	Red	R_a	$\overline{R_{14}}$**	Q^*	Blue	Green	Red	R_a	$\overline{R_{14}}$	Q^*
1	10	10	10	476.0	544.5	612.0	82	78	0.54	485.0	554.0	616.5	87	83	0.53
2	30	30	30	475.0	543.5	613.5	89	86	0.55	486.5	554.0	616.5	91	89	0.54
3	70	70	70	472.0	540.0	618.0	96	94	0.60	487.0	549.0	623.5	96	95	0.60
4	100	100	100	472.0	530.5	626.5	96	95	0.67	494.0	539.0	626.5	96	95	0.67
5	100	30	30	483.5	559.5	617.5	96	94	0.56	500.5	566.5	620.0	96	94	0.53
6	30	100	30	462.5	525.0	618.5	95	94	0.56	474.0	542.5	621.5	96	94	0.54
7	30	30	100	468.5	524.5	605.5	95	93	0.63	476.5	531.5	614.0	95	93	0.64
8	100	100	10	472.0	551.0	618.5	95	93	0.56	484.0	554.5	620.0	92	91	0.52
9	100	10	100	486.5	540.5	614.0	96	95	0.65	502.0	545.0	621.5	96	95	0.66
10	10	100	100	457.5	510.0	623.0	96	94	0.65	475.0	527.5	629.0	96	95	0.68

	Type of lamp: Warm White									Warm White; suppression of blue mercury lines 30%					
	Bandwidth (50%) (nm)			Wavelength at peak (nm)						Wavelength at peak (nm)					
No.	Blue	Green	Red	Blue	Green	Red	R_a	$\overline{R_{14}}$	Q^*	Blue	Green	Red	R_a	$\overline{R_{14}}$	Q^*
1	10	10	10	499.0	561.5	619.5	96	92	0.52	490.5	560.5	619.5	93	89	0.53
2	30	30	30	501.5	562.5	620.5	96	94	0.54	492.5	561.5	621.5	96	94	0.55
3	70	70	70	515.0	557.0	622.5	92	90	0.61	499.5	565.0	629.5	96	95	0.65
4	100	100	100	517.5	538.0	636.5	90	89	0.75	515.0	537.5	624.0	95	93	0.70
5	100	30	30	529.5	571.5	623.5	90	89	0.53	510.0	562.5	619.5	93	90	0.53
6	30	100	30	492.5	558.0	623.5	93	91	0.55	484.5	558.0	623.5	95	94	0.56
7	30	30	100	497.5	542.5	621.0	94	92	0.70	488.5	540.5	622.0	96	95	0.72
8	100	100	10	510.5	559.0	621.5	88	86	0.51	494.5	563.0	621.5	91	90	0.53
9	100	10	100	528.5	531.5	629.0	90	87	0.71	515.0	530.5	627.0	96	94	0.72
10	10	100	100	493.5	546.0	637.0	95	93	0.76	481.5	538.5	634.0	97	95	0.75

$$^*Q = \frac{\text{number of photons emitted}}{\text{number of ultraviolet photons available}}.$$

** $\overline{R_{14}}$ means the average of $R_1 - R_{14}$.

IV). When adding emission bands of varying bandwidths, the following picture can be deduced from Table IV. When using a broad-emission band and two narrower ones (see Table IV, No. 5, 6, and 7) nearly the same color rendition can be obtained as in the case with three broad-emission bands. If the broad-emission band is a blue or a green one, the calculated Q value is lower than in the case of a broad, red-emission band, due to the relatively low luminous efficacy of the latter band. For the same reason the combination of a broad, blue- and a broad, green-emission band with a very narrow, red-emission band is most favorable for obtaining both good color rendition and a high efficacy (see No. 8, 9, and 10 from Table IV).

Since the Q values calculated for an efficacy of 50 lm/W are lower than 80%, lamps with higher efficacies might be made.

Summarizing the results of Table IV the combination of a good color rendition and a high efficacy in a fluorescent lamp can be reached with a narrow-band red-emitting phosphor combined with blue- and green-emitting phosphors with both or either having a broad-emission band (see cases 5 and 6 in Table IV). The location of the bands depends on the type of fluorescent lamps, the required peak wavelengths shifting to longer wavelengths as the color temperature decreases. The location of the bands not only depends on their own widths but also on the widths of the neighboring bands. Finally it may be remarked that it follows from our calculations that the location of a band becomes more critical as the width of the band decreases.

A more detailed discussion of the results obtained by this optimization study will be given elsewhere (9).

Choice and evaluation of the phosphors required.—The requirements of the phosphors to be used in fluorescent lamps can be deduced from the data of Table IV.

When we make a choice among the existing phosphors, we should also keep in mind that Table IV applies to single Gaussian bands. In practice in many cases the spectral power distribution of phosphors covers either several separate bands (No. 7-9 from Table V) or partly overlapping bands (No. 10 from Table V). About 30 phosphors were evaluated. The phosphors giving the best results are tabulated in Table V. Only numbers 2, 9, and 10 are conventional lamp phosphors, the others being recently discovered new phosphors, such as Tb-activated $CaNaBO_3$ (10), showing a poor performance in lamps. $SrWO_4$-Tb,Na (11) is also a new phosphor, which should give a good maintenance in lamps. $(Ba,Mg)Al_2Si_2O_8$-Eu^{2+} is a blue-emitting phosphor with a high quantum efficiency (12).

The merits of various phosphor blends were evaluated by means of the same computer programmes as used in the optimization study.

Red phosphor.—The required emission peak is located at 618-624 nm. Therefore the $Y(P,V)O_4$-Eu^{3+} (phosphor No. 9 from Table V) is well suited.

Green phosphor.—Using a narrow-band phosphor the maximum wavelength is located at about 560-570 nm (see No. 5 from Table IV) and in the case of a broad-band phosphor at 525-560 nm depending on the type of the fluorescent lamps involved. Up until now we have not found any suitable narrow-band green-emitting phosphor at the required wavelength. The Tb-activated phosphors (No. 7 and 8 from Table V) have their emission peaks at too short a wavelength. As far as the broad-band-emitting phosphors are concerned, no good choice is available. The emission peak of the Tb-phosphors matches the requirements but their emission bands are too narrow.

Blue phosphor.—Using a narrow-band phosphor the maximum required wavelength lies at 460-490 nm and with a broad-band phosphor at 480-530 nm. No narrow-band blue-emitting phosphors of the right wavelength peak are available. $BaZrSi_3O_9$-Eu^{2+} fulfills the location of the emission band, but it has a broad-emission band. $(Ba,Sr)Si_2O_5$-Eu^{2+} (No. 6 from Table V), however, fulfills the requirements of a broad-band green-emitting phosphor (required wavelength 505 nm).

From the foregoing it might be concluded that there is some need for a narrow-band blue-emitting phosphor ($\lambda_{max} \sim$ 460-490 nm), a narrow-band green-emitting phosphor ($\lambda_{max} \sim$ 560-570 nm), and a broad-band-emitting one ($\lambda_{max} \sim$ 525-560 nm).

Evaluation of various phosphor blends.—Cool White fluorescent lamps (Table VI).—According to the cal-

Table V. List of phosphors giving the best results in the optimization study of fluorescent lamps with improved color rendition

No.	Phosphor	Emission		C.I.E. Color Co-ordinates		250-270 nm		Reference number
		λ_{max} (nm)	Bandwidth (50%) (nm)	x	y	Quant. effic., %	Reflection, %	
1	$(Ba,Mg)Al_2Si_2O_8$-Eu^{2+}	444	96	0.153	0.136	73	7	12
2	$Sr_2P_2O_7$-Sn	455	128	0.148	0.150	82	12	13
3	$BaZrSi_3O_9$-Eu^{2+}	475	74	0.132	0.201	68	15	14
4	Sr-chlorsilicate-Eu^{2+}	485	70	0.129	0.297	80	15	15
5	$Mg(Ga,Al)_2O_4$-Mn	505	30	0.067	0.644	68	12	16
6	$(Ba,Sr)Si_2O_5$-Eu^{2+}	505	100	0.221	0.406	80	14	17
7	$CaNaBO_3$-Tb	545	12	0.362	0.591	80	15	10
8	$SrWO_4$-Tb,Na	545	12	0.307	0.606	76	13	11
9	$Y(P,V)O_4$-Eu^{3+}	619	2	0.679	0.321	70	5	18
10	$(Sr,Mg)_3(PO_4)_2$-Sn	625	136	0.541	0.423	83	5	19

Table VI. Evaluation of various phosphor blends for application in Cool White fluorescent lamps with improved color rendition

Composition of phosphor blend numbers[a]	Calculated efficiency, 50 lm/W								Calculated efficiency, 75 lm/W							
	Color Rendering Indices								Color Rendering Indices							
	R_a	R_9	R_{10}	R_{11}	R_{12}	R_{13}	R_{14}	Q*	R_a	R_9	R_{10}	R_{11}	R_{12}	R_{13}	R_{14}	Q*
3, 7, 9	92	83	71	73	80	94	71	0.48	92	94	84	79	94	89	99	0.73
4,7,9	91	95	83	92	87	89	82	0.49	86	80	90	95	88	80	87	0.75
3,6,10	96	84	89	98	90	94	98	0.70	—[b]	—	—	—	—	—	—	—

* $Q = \dfrac{\text{number of photons emitted}}{\text{number of ultraviolet photons available}}$.

[a] The numbers refer to the list of phosphors given in Table V.

[b] — means: lamp cannot be made, since a Q value above unity is required.

culations the combination of phosphors 3, 7, and 9 gives quite a satisfactory result. The same applies to the combination of phosphors 4, 7, and 9. Both combinations are broad-band blue-, narrow-band green-, and narrow-band red-emitting phosphors. Although the emission of the $(Sr,Mg)_3(PO_4)_2$-Sn (No. 10) not only consists of a red band but also contains an emission peak at about 550 nm, the combination of phosphors 3, 6, and 10 (giving a very high R_a) illustrates the aforementioned results that a combination of a high R_a and a high luminous efficacy can only be reached when using a narrow-band red-emitting phosphor.

Daylight fluorescent lamps (Table VII).—Here again the evaluation corresponds to the foregoing calculations. Since $SrWO_4$-Tb,Na contains more blue radiation than phosphor No. 7 ($CaNaBO_3$-Tb), the combination of phosphors 1, 8, and 9 is more favorable than 1, 7, and 9. Combination of phosphors 2, 6, and 10, containing three broad emission band phosphors, is also quite a good one, but as discussed earlier, with the broad red emission band the luminous efficacy is too low (see Q-value = 0.95 at a calculated efficacy of 75 lm/W). Combination of phosphors 3, 7, and 9, consisting of a broad blue emission band and both a narrow green emission band and a red one is also suitable.

Warm White fluorescent lamps (Table VIII).—In this case also the expectations are fulfilled, *e.g.*, combination of phosphors 3, 7, and 9 is a good one. When using phosphor No. 10 as a broad-band red emitter, the combination of a high luminous efficacy and an excellent color rendition could only be reached by the partial absorption of the blue radiation of the mercury lines.

In order to substantiate the afore-mentioned theoretical calculations some test lamps were made. The properties of the lamps were consistent with the calculations: *e.g.*, it was calculated for a Warm White fluorescent lamp that a Color Rendering Index of 94 should be reached by using a mixture of a broad red-emitting phosphor ($\lambda_{max} \sim 625$ nm) and a narrow green-emitting one ($\lambda_{max} \sim 505$ nm). Making fluorescent lamps (color temperature 3000°K) with a mixture of 86 w/o (weight per cent) of $(Sr, Mg)_3(PO_4)_2$-Sn (phosphor No. 10 of Table V) and 14 w/o of $Mg(Ga, Al)_2O_4$-Mn (phosphor No. 5 of Table V) with a Color Rendering Index of 92 and an efficacy of 52 lm/W could be reached.

Color-Corrected High-Pressure Mercury-Vapor Lamps

Adding spectral lines to the mercury spectrum.—In general, it is desirable for the color point of the high-pressure mercury-vapor lamp to be located close to the Black Body Locus. It follows from Fig. 1 that this can be realized by adding to the spectrum of a 400W HPMV lamp a red spectral emission line with a wavelength between 595 and 625 nm. A longer wavelength is both unnecessary and undesirable, since it lowers the lumen output of the lamp too much. The color point of the high-pressure mercury-vapor lamp is also located close to the Black Body Locus when a blue spectral line with a wavelength between 460 and 470 nm has been added to the mercury spectrum (see Fig. 1). This will lead, however, to a high color temperature, which is unacceptable in practice due to the poor color rendering of red objects. Figure 2 shows that the color rendition of a HPMV lamp can be improved by adding to the mercury spectrum either a red spectral line ($\lambda_{max} \sim 620$ nm) or a blue spectral line ($\lambda_{max} \sim 480$ nm). Figure 3 shows the color rendition of HPMV lamps in which both a blue spectral line (with varying wavelength) and a red spectral line ($\lambda_{max} \sim 622.5$ nm) are added to the mercury spectrum. The conclusion can be drawn that about 30% of the red spectral line has to be replaced by a blue or bluish-green one ($\lambda_{max} \sim 485$ to ~ 520 nm), in accordance with the results of Thornton (23). Since the color point of the lamp should lie near the Black Body Locus, a blue emission of about 480-495 nm is to be preferred as is illustrated in Fig. 4.

Evaluation of phosphors.—In evaluating phosphors for color-corrected high-pressure mercury-vapor lamps one should not only consider the spectral requirements of the phosphor (as discussed above) but also its suitability for use in these lamps. The special requirements for a phosphor to be used in this type of lamp are: (*i*) high brightness at elevated temperature (see Fig. 5 for the brightness at elevated temperature of some blue-emitting phosphors); (*ii*) an efficient excitation at both 254 nm and 365 nm radia-

Table VII. Evaluation of various phosphor blends for application in Daylight fluorescent lamps with improved color rendition

Composition of phosphor blend numbers[a]	Calculated efficiency, 50 lm/W								Calculated efficiency, 75 lm/W							
	Color Rendering Indices								Color Rendering Indices							
	R_a	R_9	R_{10}	R_{11}	R_{12}	R_{13}	R_{14}	Q*	R_a	R_9	R_{10}	R_{11}	R_{12}	R_{13}	R_{14}	Q*
1,7,9	75	37	33	55	52	75	67	0.53	78	44	40	57	59	78	70	0.79
1,8,9	84	76	48	73	65	91	78	0.54	86	83	53	76	71	91	81	0.81
3,7,9	91	89	88	76	94	88	93	0.54	86	74	78	78	85	83	96	0.81
2 6,10	96	88	89	98	88	95	94	0.66	96	94	89	97	90	95	97	0.95

* $Q = \frac{\text{number of photons emitted}}{\text{number of ultraviolet photons available}}$.

[a] The numbers refer to the list of phosphors given in Table V.

Table VIII. Evaluation of various phosphor blends for application in Warm White fluorescent lamps with improved color rendition

Composition of phosphor blend numbers[a]	Calculated efficiency, 50 lm/W								Calculated efficiency, 75 lm/W								Suppression of the blue mercury lines (%)
	Color Rendering Indices								Color Rendering Indices								
	R_a	R_9	R_{10}	R_{11}	R_{12}	R_{13}	R_{14}	Q*	R_a	R_9	R_{10}	R_{11}	R_{12}	R_{13}	R_{14}	Q*	
3,7 9	91	89	88	76	94	88	93	0.54	90	64	66	76	69	95	75	0.70	0
3,7,10	90	63	64	75	66	96	74	0.46	83	54	48	68	45	94	69	0.69	0
3,7,10	93	72	80	83	84	89	79	0.52	90	66	67	78	71	94	75	0.71	30
3,7,10	91	78	89	88	90	85	81	0.56	92	74	80	84	85	89	78	0.73	50

* $Q = \frac{\text{number of photons emitted}}{\text{number of ultraviolet photons available}}$.

[a] The numbers refer to the list of phosphors given in Table V.

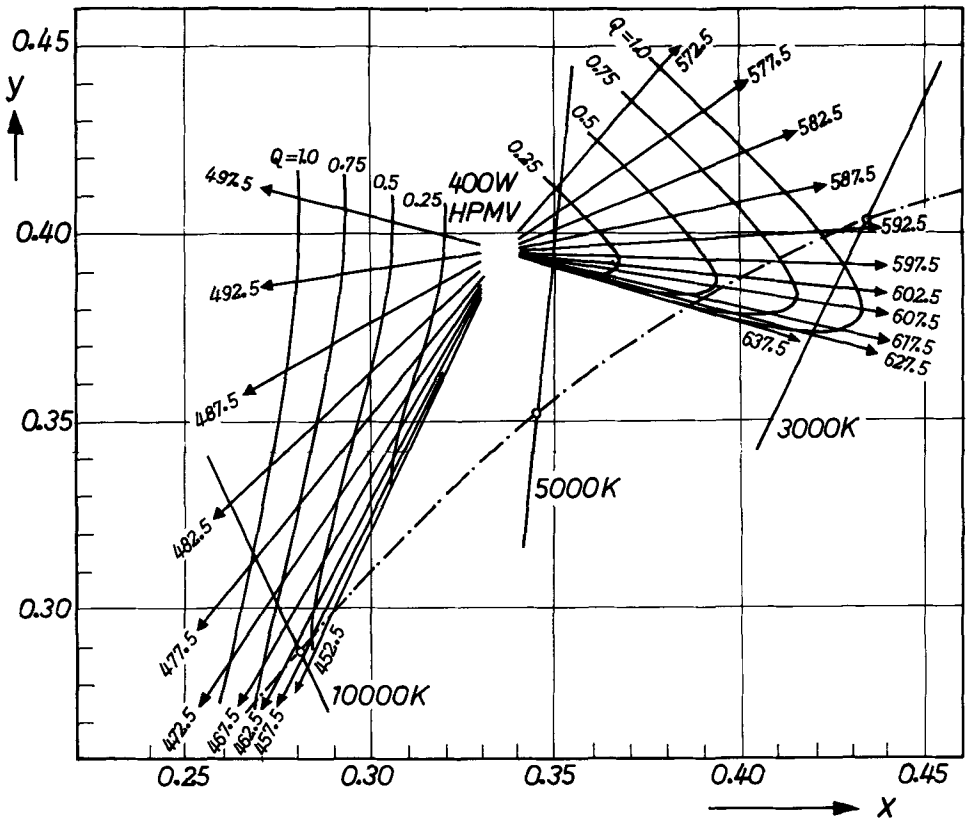

Fig. 1. Effect of addition of one spectral line on the chromaticity co-ordinates of a 400W HPMV lamp.

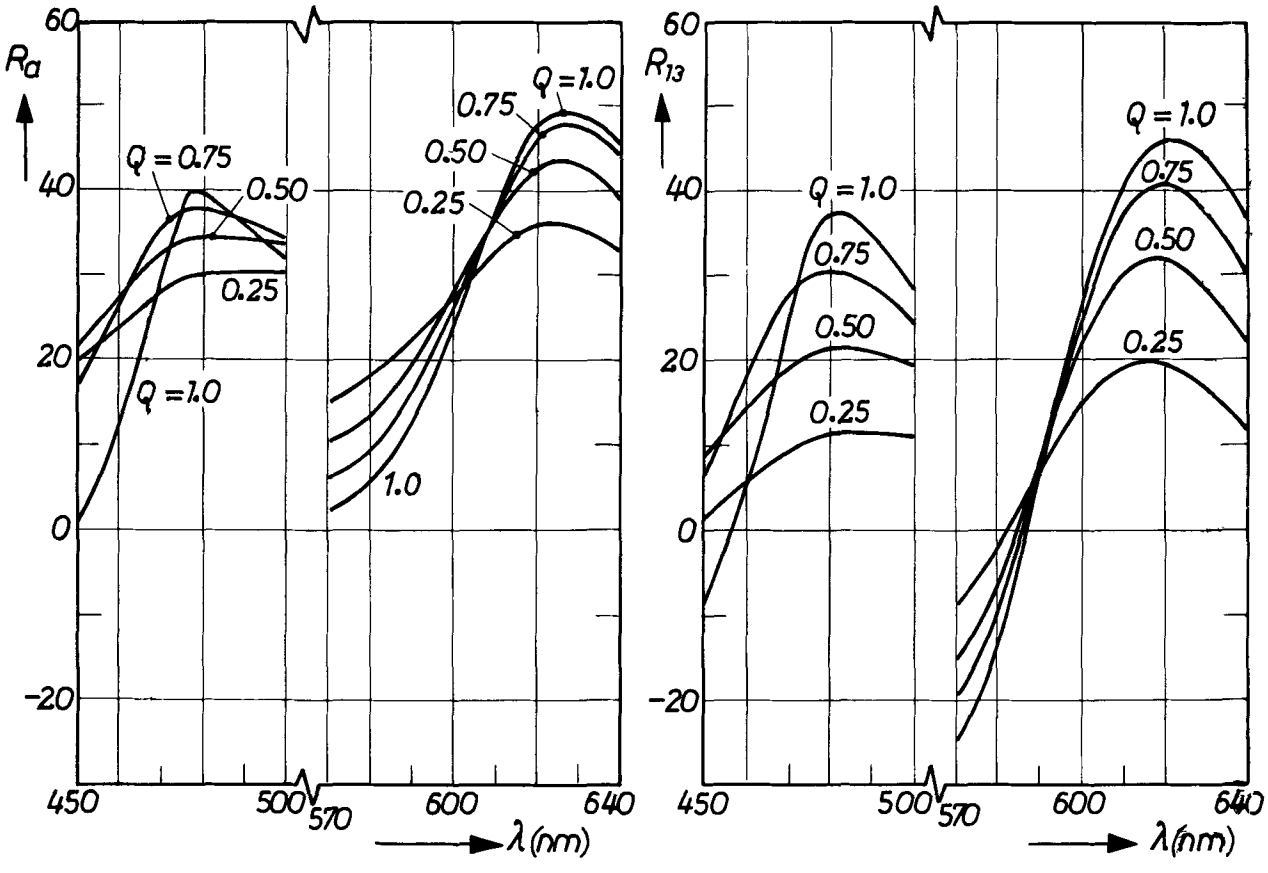

Fig. 2. Effect of addition of one spectral line on the color rendition of a 400W HPMV lamp

tion; and (*iii*) good stability against the intense ultraviolet radiation.

It was shown in Fig. 2 that the most pronounced improvement in color rendition can be achieved by adding a red spectral line to the mercury spectrum. In accordance herewith it has been common practice for several years to coat the outer bulb of the HPMV lamp with a red-emitting phosphor, such as $Y(P,V)O_4$-Eu (17, 18). Since Fig. 3 showed that a further (although rather small) improvement can be achieved by adding also a blue emission, the merits of mixtures of $Y(P,V)O_4$-Eu with some blue-emitting phosphors

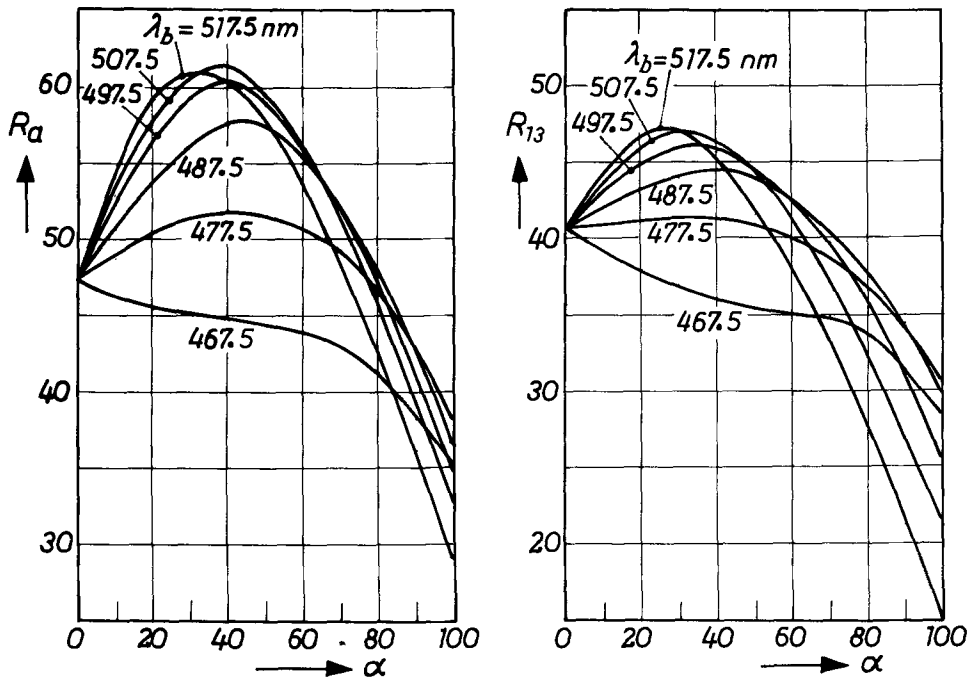

Fig. 3. Effect of addition of (1 — α) per cent of a red spectral line (λ ~ 622.5 nm) and α per cent of blue spectral lines of various wavelengths on the color rendition of a 400W HPMV lamp. All calculations: Q = 0.75.

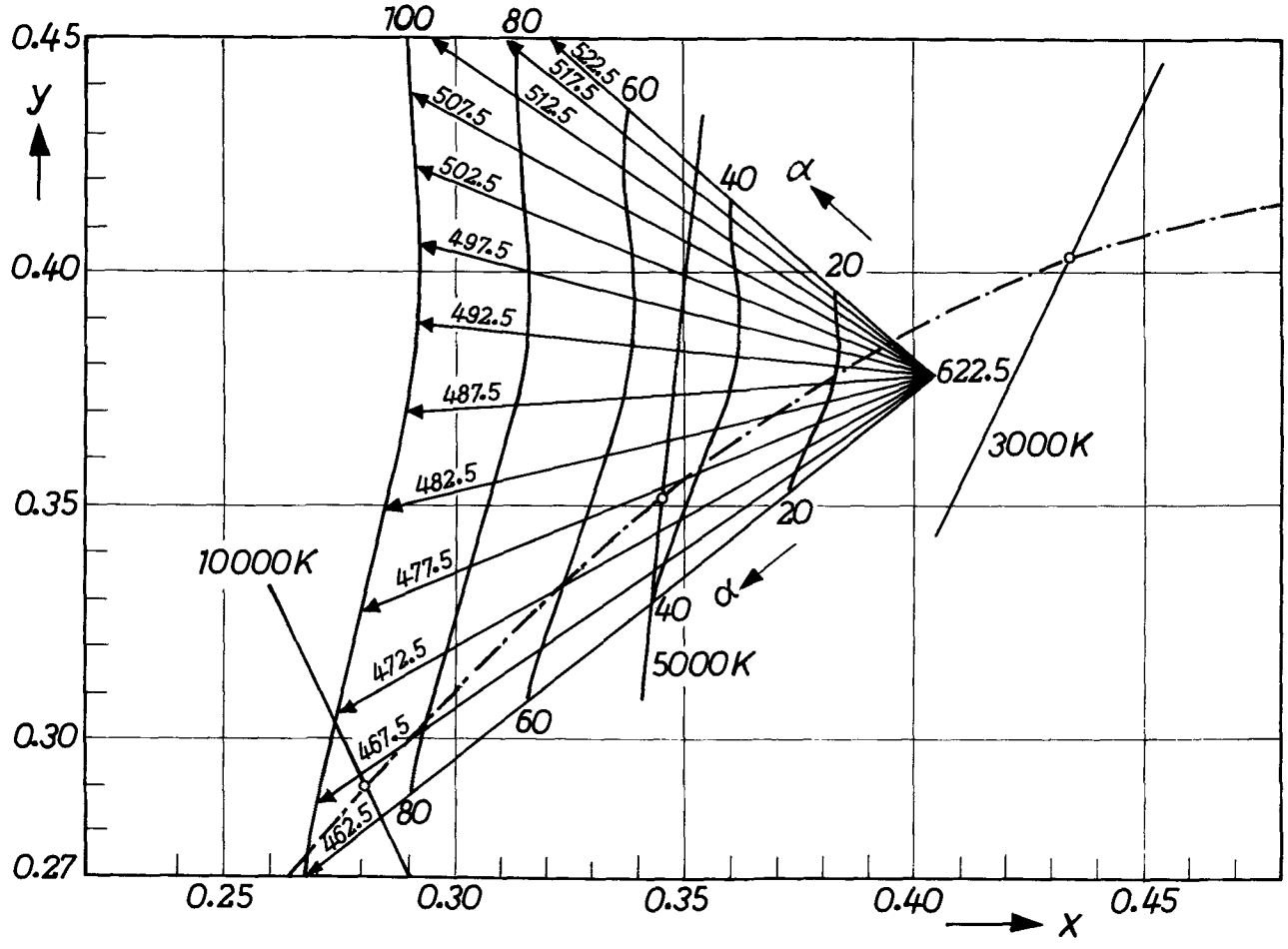

Fig. 4. Chromaticity co-ordinates of a 400W HPMV lamp to which a red (λ ~ 622.5 nm) spectral line of (1 — α) per cent and blue spectral lines of α per cent of various wavelengths are added. All calculations: Q = 0.75.

have also been evaluated. Phosphors were chosen having a high brightness at elevated temperatures, as shown in Fig. 5.

The Y(P,V)O_4-Dy phosphor of Fig. 6 was made with the addition of boric acid (in the same way as the corresponding Eu-activated phosphor). This preparation method gives a higher intensity of the 484 nm emission line with 254 nm excitation, viz., intensity ratio of the 484 and 573 nm emission line in our phosphor 0.65-0.70, whereas a ratio of about 0.40 was reported by Faria and Palumbo (24).

The merits of europium-activated strontium chlorapatite (22) were also evaluated, since Thornton (23) reported that a better color rendering of the human complexion and an R_a value of 67 can be reached with this phosphor (λ_{max} ~ 450 nm). The results of the calculations are given in Fig. 6 and Table IX. It follows from these data that the best results, as far as color

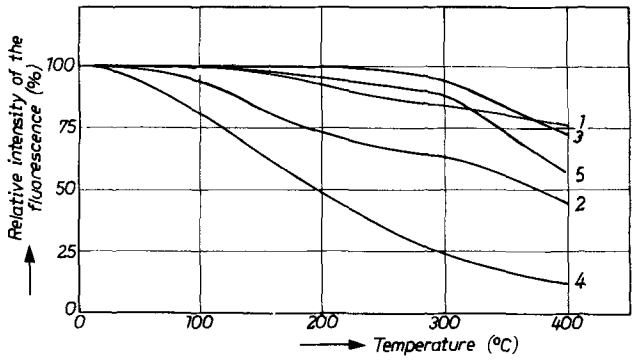

Fig. 5. Variation of fluorescent intensity with temperature for various blue-emitting phosphors.

x/y	Curve	Phosphor	λ_{max} (nm)	Half-width (nm)
0.129/0.297	1	Sr-chlorsilicate-Eu^{2+}	485	70
0.148/0.150	2	$Sr_2P_2O_7$-Sn^{2+}	455	128
0.153/0.136	3	$(Ba,Mg)Al_2Si_2O_8$-Eu^{2+}	444	96
0.154/0.023	4	$Sr_{10}(PO_4)_6Cl_2$-Eu^{2+}	449	34
0.217/0.382	5	$(Sr,Mg)_3(PO_4)_2$-Cu^{+}	490	80

nearly the same. The former phosphor has the advantage of being excited more efficiently (giving a higher quantum conversion fraction) by the long wavelength ultraviolet radiation (365 nm) of the HPMV lamp. When using a blend with a phosphor strongly absorbing the 365 nm radiation of the HPMV lamp, however, the absorption of this radiation by the second phosphor is of minor importance.

The importance of a high quantum conversion fraction (Q) is illustrated in Table IX, showing that in mixtures of $Y(P,V)O_4$-Eu and strontium chlorsilicate-Eu an increase of the Q-value from 0.7 to 1.0 not only results in an increase of the luminous efficacy by about 6%, but also in an improved color rendition.

When comparing the quality of a 125 and a 400W lamp, it should be remembered that the mercury spectra of these lamps are not the same, due to differences in lamp constructions (arc length, pressure, etc.). For instance, with a given phosphor blend the best color rendition can be achieved with a 125W HPMV lamp (see Table IX).

Summarizing the data concerning the color rendition of HPMV lamps, it may be concluded that the partial substitution (about 30%) of a blue-green emitting phosphor for a red-emitting one will yield very useful results.

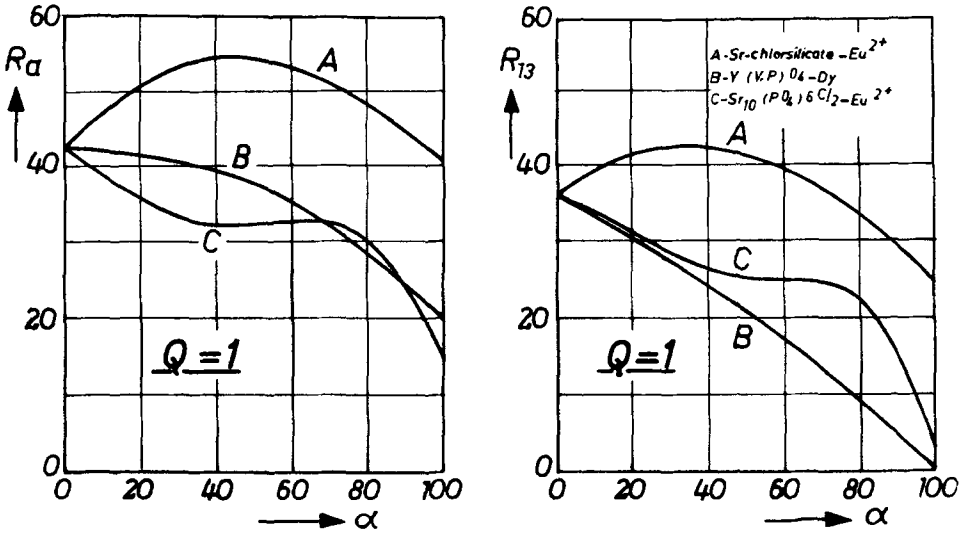

Fig. 6. Effect of addition of (100 — α) per cent of the red-emitting phosphor $Y(P,V)O_4$-Eu^{3+} and of α per cent of various blue-emitting phosphors on the color rendition of a 400W HPMV lamp. Curve A, Sr-chlorsilicate-Eu^{2+}; curve B, $Y(P,V)O_4$-Dy; curve C, $Sr_{10}(PO_4)_6Cl_2$-Eu^{2+}.

rendition is concerned, are reached with mixtures of europium-activated $Y(P,V)O_4$ and strontium chlorsilicate-Eu. We have found a lower color rendition than Thornton, however. This difference can be ascribed to the use of a different reference source. Thornton used the D_{65} Daylight reference, whereas in our study reference sources were used, as recommended in the C.I.E. Publication 13, with a color temperature corresponding to that of the lamp to be evaluated.

The poor performance as regards color rendition of $Y(P,V)O_4$-Dy is due to the strong emission at 573 nm. It can be seen from Table IX that the merits of strontium chlorsilicate-Eu and $(Sr,Mg)_3(PO_4)_2$-Cu (21) are

Manuscript submitted Dec. 21, 1972; revised manuscript received April 9, 1973. This was Paper 75 presented at the Houston, Texas, Meeting of the Society, May 7-11, 1972.

Any discussion of this paper will appear in a Discussion Section to be published in the June 1974 JOURNAL.

REFERENCES

1. A. A. Kruithof and J. L. Ouweltjes, *Philips Tech. Rev.*, **18**, 249 (1956/1957).
2. J. L. Ouweltjes, *Farbe*, **9**, 207 (1960).
3. M. Koedam and J. J. Opstelten, *Lighting Res. Technol.*, **3**, 205 (1971).
4. W. A. Thornton, *J. Opt. Soc. Am.*, **61**, 1155 (1971).
5. M. Koedam, J. J. Opstelten, and D. Radielović, *J.*

Table IX. Evaluation of mixtures of 70% of $Y(P,V)O_4$-Eu and 30% of various blue-emitting phosphors in 125W and 400W HPMV lamps, respectively

	125W HPMV lamp						400W HPMV lamp					
	Q = 0.7			Q = 1.0			Q = 0.7			Q = 1.0		
Phosphor[a]	R_a	R_{13}	η^*	R_a	R_{13}	η^*	R_a	R_{13}	η^*	R_a	R_{13}	η^*
1	39	30	104	38	34	109	35	24	112	34	28	117
2	51	38	110	58	49	117	46	32	117	53	42	125
3	49	37	111	57	48	118	45	32	118	51	41	126

* η = relative efficiency; HPMV lamp without phosphor: η = 100.
[a] Phosphor 1, strontium chlorapatite-Eu. Phosphor 2, strontium chlorsilicate-Eu. Phosphor 3, strontium magnesium orthophosphate-Cu.

Ill. Eng. Soc., **1**, 285 (1972).
6. W. Walter, *Appl. Opt.*, **10**, 1108 (1971).
7. M. Koedam, Private communication.
8. C.I.E. Publication No. 13 (1965).
9. J. J. Opstelten, To be published.
10. W. L. Wanmaker, A. Bril, and J. W. ter Vrugt, *This Journal*, **112**, 1147 (1965).
11. German "Auslegeschrift," 2,024,408 (Dec. 10, 1970).
12. J. M. P. J. Verstegen, J. W. ter Vrugt, and W. L. Wanmaker, *J. Inorg. Nucl. Chem.*, **34**, 358 (1972).
13. A. H. McKeag, British Pat. 680,846 (1952).
14. G. Blasse and A. Bril, *J. Solid State Chem.*, **2**, 105 (1970).
15. H. L. Burrus and K. P. Nicholson, *J. Luminescence*, **3**, 467 (1971).
16. W. L. Wanmaker, J. W. ter Vrugt, and J. G. C. M. de Bres, *Philips Res. Rept.*, **22**, 304 (1967).
17. W. L. Wanmaker and J. W. ter Vrugt, *Lighting Res. Technol.*, **3**, 147 (1971).
18. W. L. Wanmaker, A. Bril, J. W. ter Vrugt, and J. Broos, *Philips Res. Rept.*, **21**, 270 (1966).
19. H. Koelmans and A. P. M. Cox, *This Journal*, **104**, 442 (1957).
20. S. S. Trond, J. S. Martin, J. P. Stanavage, and A. L. Smith, *ibid.*, **116**, 1047 (1969).
21. W. L. Wanmaker and C. Bakker, *ibid.*, **106**, 1027 (1959).
22. C. R. J. Leete and A. H. McKeag, British Pat. 1,087,655 (1967).
23. W. A. Thornton, I.E.S. 1971, Conference Preprint No. 3.
24. S. Faria and D. T. Palumbo, U.S. Pat. 3,555,337 (Jan. 12, 1971).

Replication of Relief-Phase Holograms for Prerecorded Video

R. A. Bartolini, N. Feldstein,*[1] R. J. Ryan

RCA Corporation, David Sarnoff Research Center, Princeton, New Jersey 08540

ABSTRACT

This paper describes the replication process used for the HoloTape® system. HoloTape is a clear plastic tape that has relief-phase holograms embossed on its surface, each hologram corresponding to a frame of a color-encoded motion picture. The replication process is based on the electroforming of a metal master and on the embossing of a transparent thermoplastic film.

Prerecorded video systems have created intense interest in the electronics industry within the last few years with the announcement of a variety of tape and disk systems for use in the home (1-3). These include the magnetic tape and photographic film systems, several disk systems based on mechanical and optical pickup, and the HoloTape[2] system. HoloTape is a clear plastic tape that has relief-phase holograms embossed on its surface, each hologram corresponding to a frame of color-encoded motion picture.

There are many ways to encode picture information so that it can be stored as a relief pattern. Eidophor projections (4) utilize a scanning electron beam to deform a special liquid. Similar systems have been developed that employ thermoplastic material instead of liquids (5). The advent of holography, coupled with the development of lasers, has led to a new method for encoding picture information which offers the following advantages:

(*i*) Scratch and dirt resistance. Highly redundant holograms (6) can be scratched, obscured by dirt and otherwise mutilated without serious image degradation.

(*ii*) Image immobilization. Fraunhofer holograms (7) produce stationary images even though the holograms are continuously moving through the readout beam. Flicker-free images can be produced at any tape speed with no need for servo control between tape speed and television scan rate, intermittent tape transport, or moving shutters.

(*iii*) Low cost replication. Relief-phase holograms can be replicated onto a metal master using electroless and electrolytic processes and embossed into a low cost thermoplastic tape. The processes involved in replication are the basis for this paper.

Relief-Phase Holograms

Replication of holograms has attracted attention since the laser was first successfully used in the making of holograms (8). To date, most attempts at replication have been with amplitude holograms (9-13). This paper describes an inexpensive and reliable method of relief-phase hologram replication.

Holography is an imaging process in which one records not an image of the object, but rather the wave pattern of the light that emanates from the object. The record (hologram) is thus in the form of an interference pattern which exists when the diffraction pattern of the object is made to interfere with a coherent reference beam.

If this interference pattern is stored in photographic film by changes in density of the film, an amplitude hologram is produced. To replicate this type of hologram, contact printing techniques are necessary. The film required for this type of replication is expensive due to the need for high-resolution capability (1000-2000 cycles/mm). A high degree of precision is also needed to minimize diffraction effects. A vacuum chuck hold-down is usually necessary in this case (14).

When the interference pattern is stored in the recording medium by changes in the surface structure, a relief-phase hologram results. The information in a relief-phase hologram is stored in the amplitude and periodicity of the surface corrugation. This type of hologram modulates the phase of the playback beam on transmission because of the variations in the optical path introduced by the relief pattern.

A common material for recording relief-phase holograms is photoresist. Both positive and negative photoresists can record relief-phase holograms. The positive photoresist has the advantage that only the exposed portions are removed, so that most of the material remains on the substrate, maintaining good bonding between the two. Negative photoresists remain after development only where they are exposed sufficiently to be hardened all the way to the substrate. The hologram therefore consists of very fine lines of photoresists that tend to detach from the substrate.

Shipley AZ-1350,[3] a commercial positive photoresist, was found to be an acceptable recording medium for the HoloTape system. The HoloTape processing se-

* Electrochemical Society Active Member.
[1] Present address: Surface Technology, Inc., Princeton, New Jersey 08540.
Key words: relief patterns, photoresists electroforming, embossing.
[2] Trademark RCA Corporation.
[3] Shipley Company, Incorporated, Newton, Massachusetts 02612.

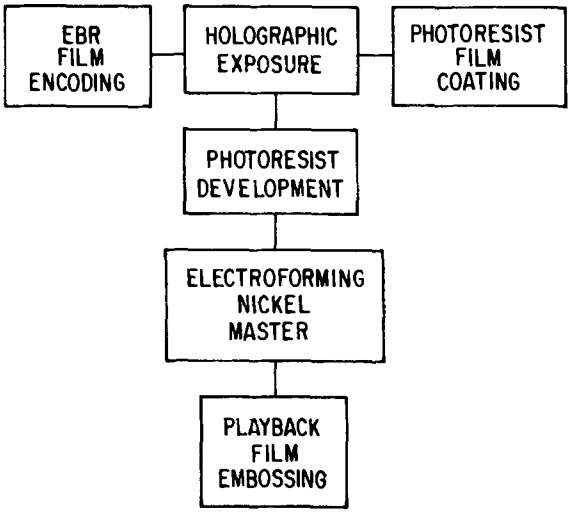

Fig. 1. HoloTape processing sequence

quence is shown schematically in Fig. 1 and typical processing equipment in Fig. 2.

For the HoloTape system, AZ-1350 photoresist is coated onto a polyester tape such as Cronar[4] to provide a dry-film thickness in the order of 1 μm. Contact roller coating off a grooved steel wheel in a clean room (class 100 hood within a class 10,000 room) has been found to produce a photoresist layer of adequate cleanliness and uniformity. The photoresist is applied directly to the polyester base as the AZ-1350 type photoresist interreacts with most resin-subbing layers to reduce its effective sensitivity. An antireflection layer absorbing greater than 95% of the transmitted light is coated onto the back side of the tape to prevent fringes in the recording due to back reflections from the tape/air interface.

[4] Trademark, E. I. du Pont de Nemours and Company, Incorporated.

Discussion of Process

Hologram recording.—For the recording of color holograms, monochrome transparencies spatially encoded (by means of an electron beam recorder) with the color information serve as the object. The holographic recording system includes a He-Cd laser, photoresist tape and object film transports, the usual beam expanders, pinholes, mirrors, and beam splitters, and a special optical pinhole array which enables highly redundant holograms to be recorded (6, 7). The recording system functions automatically, recording a sequence of holograms on photoresist tape, each hologram corresponding to a frame of the color-encoded motion picture. After exposure, the photoresist-coated tape is passed through a developing machine in which the areas exposed to more intense light are etched away, leaving the surface corrugations which form the relief-phase holograms.

Exposure characteristics of a positive photoresist for holography are much different than those normally encountered in photolithographic applications. In holographic exposure, the photoresist layer is exposed in an analog fashion due to the interference of the reference and object beams. In the simplest case, two plane waves of equal intensity create a sine-wave exposure pattern in the photoresist with amplitude proportional to the first order Bessel function, J_1. Maximum grating efficiency can be achieved with exposures of approximately 10 mJ/cm^2 corresponding to a very low reaction level of the photoresist sensitizer. (Full reaction of the sensitizer in a 1.2 μm layer requires an exposure of approximately 300 mJ/cm^2.)

The mechanism for positive photoresist development involves dissolving away the exposed areas of the photoresist while leaving the unexposed areas essentially intact. This is essentially a binary process which is ideal for applications such as the fabrication of in-

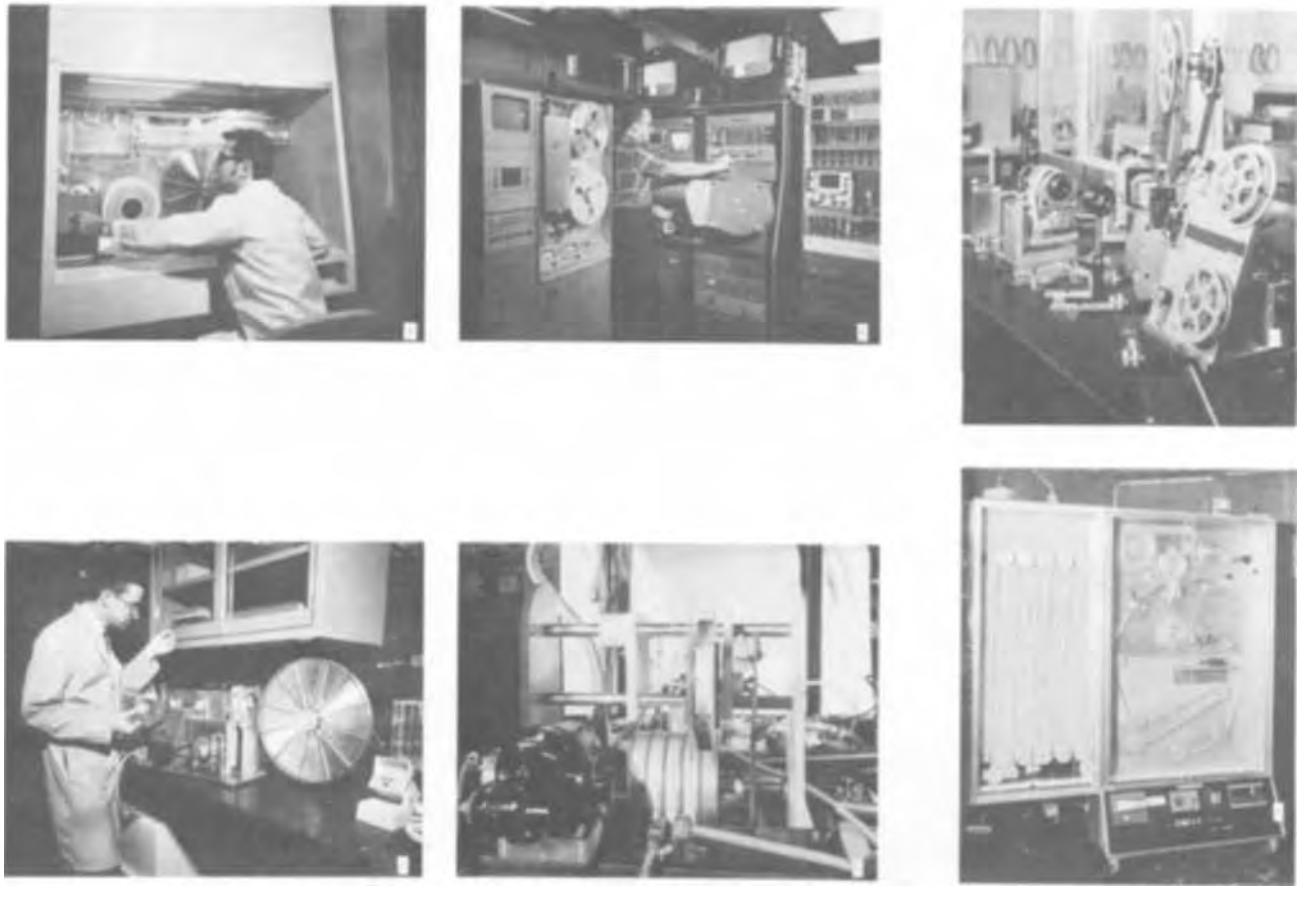

Fig. 2. Laboratory equipment used to manufacture experimental HoloTape. a, Coating; b, encoding; c, recording; d, developing; e, plating; and f, replicating.

tegrated circuits. However, for holographic recording, an analog process is desired. Moreover, to avoid nonlinear distortion, it is desirable to have a depth *vs.* exposure characteristic which is approximately linear over a wide exposure range. When using AZ-1350 developer, as is normally used with AZ-1350 photoresist, the photoresist appears to act nonlinearly; the hologram diffraction efficiency for a given intermodulation distortion is limited to a greater degree by this material nonlinearity than by the intrinsic nonlinearity of thin-phase holograms. It has been found that the use of the more alkaline AZ-303 developer with the AZ-1350 photoresist relieves the photoresist nonlinearity, thereby allowing higher image readout efficiencies and a net increase in material sensitivity (15).

Maximum average usable hologram efficiency is restricted, by intermodulation effects from the intrinsic nonlinearity, to approximately 5% which is equivalent to a peak-to-peak corrugation depth of approximately 0.1 μm. Photomicrographs of simple and Fraunhofer hologram relief patterns recorded in AZ-1350 photoresist and developed in AZ-303 developer are shown in Fig. 3. The line spacing (periodicity) of the contour structure is approximately 1 μm (1000 cycles/mm). The sinusoidal grating pattern produced by the interference of two simple plane waves is shown in Fig. 3(a). Figure 3(b) is the interference pattern of a complex object (such as a film transparency) and a plane reference wave. These SEM photographs were taken at an angle of 80° from the perpendicular and at a 7500× magnification. Faithful replication of this fine pattern in the subsequent plating and embossing steps requires proper choice and control of all materials and processes.

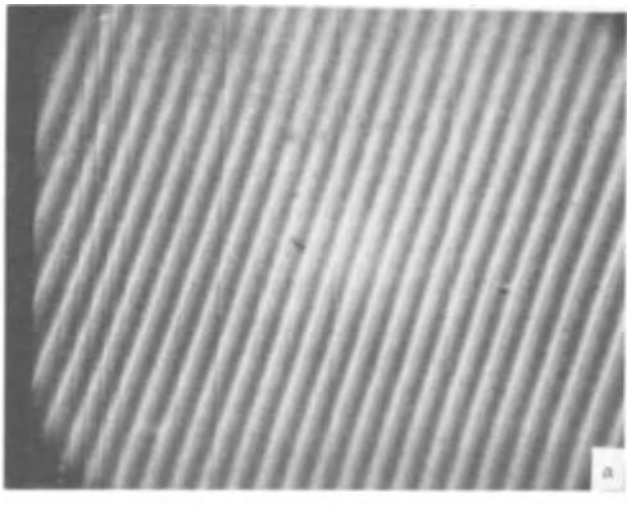

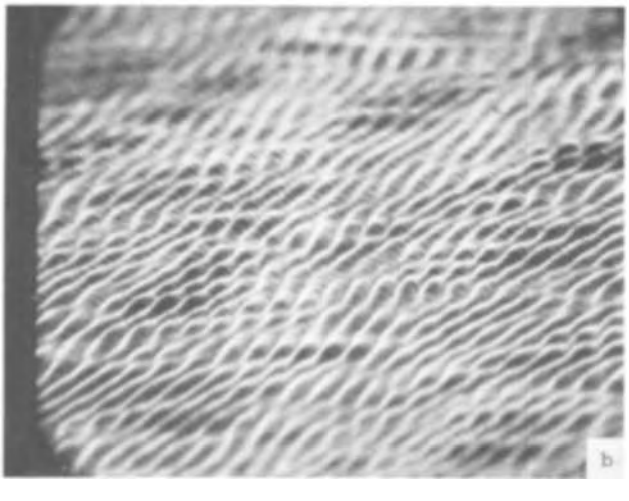

Fig. 3. Photomicrographs of relief patterns in photoresist (1000 cycles/mm carrier frequency). a, Simple interference pattern; b, Fraunhofer hologram.

Processing of metal embossing masters.—Replication is accomplished by a two-step process: (*i*) electroforming a metallic stamper master and (*ii*) embossing this stamper into a transparent flexible thermoplastic to produce replicas. The electroforming process involves electroless nickel plating of a thin conductive layer and electrolytic nickel plating to a metal thickness of 2.5 mils. The over-all process is similar to that used in the production of audio record stampers. Equipment and control conditions are unique, however, due to the high resolution of the holographic information and the tape format. The use of an all nickel process has the advantage of producing a hard, corrosion-resistant master requiring no additional surface treatments.

Figure 4 shows the highlights of the electroforming sequence. In this sequence, two new developments facilitated a good reproducible process; (*i*) an improved sensitizer composition (16, 17) which ensures uniform sensitization of hydrophobic surfaces such as photoresists and (*ii*) a room temperature, electroless, nickel plating formulation (18) which provides continuous and conductive surfaces, ready for subsequent electrolytic buildup.

Electroless plating.—The electroless nickel layer forms the surface of the final master and determines the quality and faithfulness of the hologram replication. Properties required of the nickel deposit include fine grain size, good hardness and corrosion resistance, uniform coverage, and no adverse effects of processing solutions on the photoresist surface. Other chemically deposited metals such as Cu or Ag are softer and more corrosive and are generally deposited from high alkaline baths. The electroless plating sequence involves four main steps as shown in Fig. 4. All steps are followed by double 1 min rinses in deionized water. Plating is normally carried out under yellow light conditions to insure uniformity of the photoresist surface. Variable exposure of the positive photoresist layer could alter the layer characteristics during subsequent processing.

Surface preparation is important to insure removal of any particulate matter or films from the surface of the photoresist recording tape due to prior processes. Generally a 1-2 min rinse cycle with mild agitation in a neutral detergent solution is sufficient. It has been found, however, that residual films can be carried over from the photoresist development cycle which appear as microroughness in the electroformed surface. These are effectively removed by prerinsing in a mild alkaline solution for 15-30 sec prior to detergent cleaning. An alkaline solution is chosen which does not affect further development of the photoresist layer.

The sensitization step is most important in determining coverage and uniformity of the subsequent

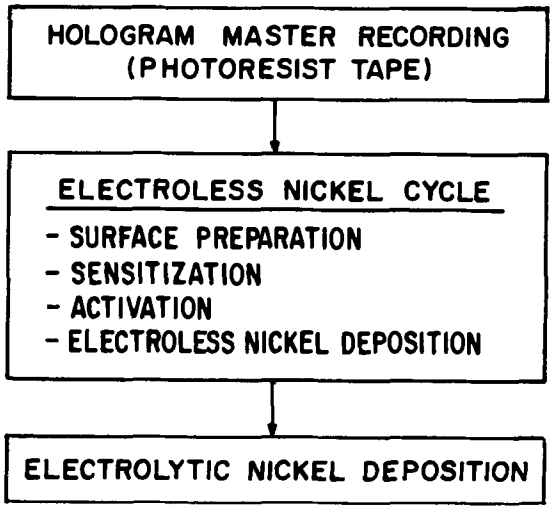

Fig. 4. Plating sequence in the electroforming of HoloTape metal embossing masters.

nickel deposition. Shipley AZ-1350 photoresist is inherently hydrophobic and nonwetting in most commercial sensitizing solutions or in colloidal catalytic solutions. Sensitizing solutions (16, 17) in which tin (II) and aged tin (IV) are incorporated produce complete wetting of tape surfaces and the formation of an absorbed layer of tin (II) on the surface during a 1 min immersion. A typical composition of sensitizer is given in Table I. The aged tin (IV) component has been properly conditioned prior to its incorporation into the solution.

Activation is accomplished in an acidic palladium chloride solution such as listed in Table I by immersion for 1 min. This step requires only the normal maintenance associated with electroless activating solutions. During the immersion, palladium nuclei are formed on the surface of the tape by reduction with absorbed tin (II) ions and provide catalytic sites for initiation of the electroless nickel deposition.

The electroless nickel cycle must provide a thin conductive layer of fine grain nickel uniformly over the entire tape surface with sufficient adhesion to with stand the subsequent electroplating cycle. A room temperature bath described previously (18) and based on the nickelpyrophosphate ammonia system with dimethylamine borane (DMAB) as a reducing agent was found to provide the necessary properties. Bath composition is shown in Table I. Although the bath is alkaline in nature, no adverse effects are observed on the AZ-1350 photoresist surface. The adherence of the nickel layer is dependent on the stress levels in the deposit and layer thickness. Control of the stress level is critical due to possible lifting from the flexible tape surface during subsequent processing. Since total stress of the deposit is a function of the deposition rate and layer thickness, rates must be maintained to provide a suitable low stress level and reproducible thickness of nickel. Rates are controlled by maintaining the dimethylamine borane reducing agent content to produce a nickel thickness of approximately 150Å in 7 min. Sheet resistivity at this thickness is on the order of 250 ohms/□ and is adequate for the subsequent electroplating step.

Curves showing deposition rate as a function of DMAB concentration are shown in Fig. 5. The data were determined from Cronar tape samples plated in freshly prepared baths under equivalent plating conditions. The amount of nickel deposited for a given time and tape area was analyzed by colorimetric methods. Standard curves were also plotted relating nickel deposition to light transmission. This provides an easy method of analysis for thin nickel deposits on transparent substrates. For batch type work, rates are controlled by addition of DMAB daily based on analysis. Continuous type plating would require replenishment on a more frequent or continuous basis. Good bath life is achieved by controlling carry-over of chemicals from the activation step with thorough rinsing in deionized water and by maintaining levels of DMAB, Ni, NH_4OH, and pH through analysis. Apparatus for electroless nickel plating of HoloTape masters has been developed as a batch immersion type which provides tape masters up to 50 ft in length (equivalent to 100 sec of video playback) and as continuous in-line steps for longer time programs.

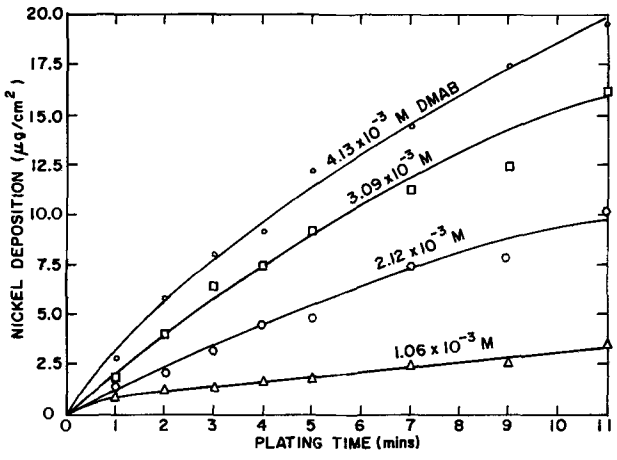

Fig. 5. Electroless nickel deposition as a function of plating time and reducing agent concentration.

Electrolytic nickel plating.—The electroforming step consists of a continuous, two-stage nickel sulfamate bath similar to those used in record stamper processing. Bath makeup data is given in Table II. Rolled depolarized nickel anodes in Dynel bags are used in both baths. A wetting agent such as Duponal WA[5] is generally used in the preplate bath and controlled to produce a solution surface tension of 37±2 dynes/cm. The baths are continuously filtered with 10μ filters. Ion exchange cartridges are used with both baths and a carbon cartridge included with the high-speed bath off an inlet manifold.

Typically, nickel deposits from these baths show a tensile stress of 5000-10,000 psi, a tensile strength of 80,000-90,000 psi, and an elongation of 15-20%. Plating rates are ample for practical production schedules.

Laboratory continuous plating apparatus is shown in Fig. 6. In the first stage, the electroless plated tape is fed onto metal cathode contact wheels partially immersed in the bath. Approximately 0.05 mil of nickel is deposited on both sides of the tape at a current density of 2.5 A/dm². The second stage is designed as a series of loops to increase the deposition area in the bath and to provide suitable through-put rates. Cathode contact is made out of solution to the back of the tape via metal contact wheels. The wheels are designed either as direct drive or with a slip pressure plate to compensate for tape expansion at the elevated temperature. The bottom wheels immersed in the bath are plastic. The tape is shielded in the solution by baffle plates to direct the plating to the front of the tape. Current density is controlled at approximately 4 A/dm². The tape is electroformed to a uniform thickness

[5] E. I. du Pont de Nemours and Company, Incorporated.

Table I. Chemical makeup of electroless solution

Sensitizing solution		Electroless nickel	
$SnCl_2$	1.3×10^{-1}M	Nickel stock solution A:	
$SnCl_4$*	7.5×10^{-3}M	$NiSO_4 \cdot 6H_2O$	50 g/l
HCl	4.7×10^{-1}M	$Na_4P_2O_7 \cdot 10H_2O$	100 g/l
		NH_4OH (58%)	22 cm³/l
Activating solution		**Bath makeup:**	
$PdCl_2$	2.5×10^{-3}M	Solution A	1 part
HCl	1.0×10^{-2}M	Deionized H_2O	11 parts
		$(CH_3)_2NHBH_3$	0.16 g/l
		NH_4OH	To adjust pH to 10.1

* Preconditioned prior to use.

Table II. Electrolytic nickel sulfamate bath makeup

Preplate bath	
Ni (from nickel sulfamate)	75-80 g/l
$NiCl_2$	7-12 g/l
H_3BO_3	37-42 g/l
pH	3.5
Operating temp.	100°-110°F
Current density	1-3 A/dm²
High-speed bath	
Ni (from nickel sulfamate)	75-80 g/l
$NiCl_2$	18-20 g/l
H_3BO_3	37-42 g/l
pH	3.5
Operating temp.	110°F
Current density	4-7 A/dm²

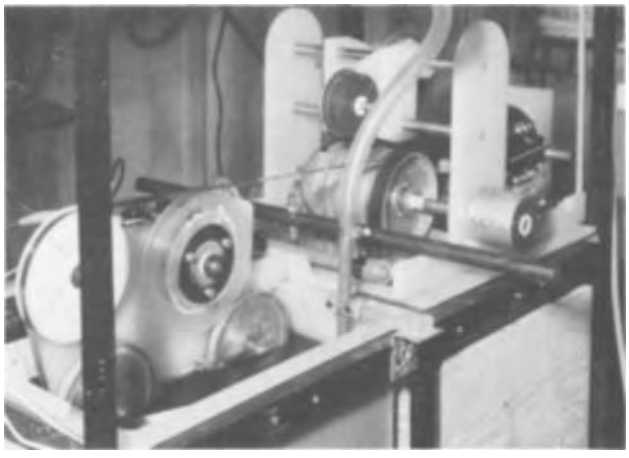

Fig 6. Experimental HoloTape electroplating apparatus

of 2.5 mils in a continuous manner and reeled up at the exit end of the plating line at a through-put rate of 2.5 in./min. Production type equipment of 34 loops has been constructed and operated at speeds of 15 in./min.

The electroformed nickel master is completed by separating the nickel tape from the photoresist tape. To provide good edges on the master, the thin nickel layer on the back of the photoresist tape is spray etched prior to separation. Tapes are generally separated in a hot cleaner solution to avoid mechanical distortion. The nickel master is then cleaned, dried, and wound, interleaved with a plastic tape to prevent abrasion of the hologram surface.

In order to determine performance of the electroforming process in replicating the hologram surface, a series of sine-wave grating patterns of various efficiencies were recorded in the photoresist and processed. Diffraction efficiency was measured on the photoresist tapes and the completed nickel master. Surface studies were also run using scanning electron microscopy. No significant difference in efficiency or surface structure was found. These studies also show that no deterioration of the positive photoresist surface occurs with use of the alkaline electroless Ni bath at a pH of 10.2

Embossing of holographic masters.—Replication of the recorded holographic information is completed by thermal mechanical embossing of a clear thermoplastic film. The process is shown schematically in Fig. 7. During the embossing cycle, a 1-2 mil thick thermoplastic film is placed in contact with a heated nickel holographic master and passed between pressure rollers, thus impressing relief patterns identical to the phase holograms into the softened plastic surface. After passing through the pressing station, the tapes are cooled, and the embossed plastic film is separated from the nickel master. The process provides a simple inexpensive method for the replication of holographic films. Important material and process considerations are presented below.

The important material requirements include: high optical quality, controllable thermosoftening behavior, and good stability for playback and storage. This confines the choice of materials to the clear thermoplastic films, such as, vinyls, polyesters, acetates, polycarbonates, and polyolefins.

The optical quality of a thermoplastic film is dependent upon the method of polymer preparation, compounding, and the film fabrication process. Ideally, the polymer should have a narrow molecular weight distribution and be free of reactants or reaction by-products. Additives required for compounding should be completely miscible with the polymer and not produce any significant scattering with coherent light transmission (less than 1%).

Calendering, extrusion, and casting are the principal methods of plastic film fabrication. Of these, casting methods have been shown to produce the highest quality films. The film fabrication process has a marked effect on optical quality and determines the surface flatness and parallelism. In general, these types of defects far outshadow those due to bulk film nonuniformities. Abrupt changes in the surface will result in variation in color or shading of the reproduced image on playback. Wedge effects produce image displacement.

Embossing is a thermomechanical process in which the surface of a plastic film is molded by compression in contact with a patterned master. In order to reproduce faithfully the patterned information in the plastic film, the temperature of the film surface must be above the glass transition point for the material. Vinyl materials, for example, fall in a range of 60°-90°C. In practice, sufficient heat is required to raise the temperature above this point and to a sufficient depth that is greater than the maximum depth of the patterned information. This implies that with holograms, the

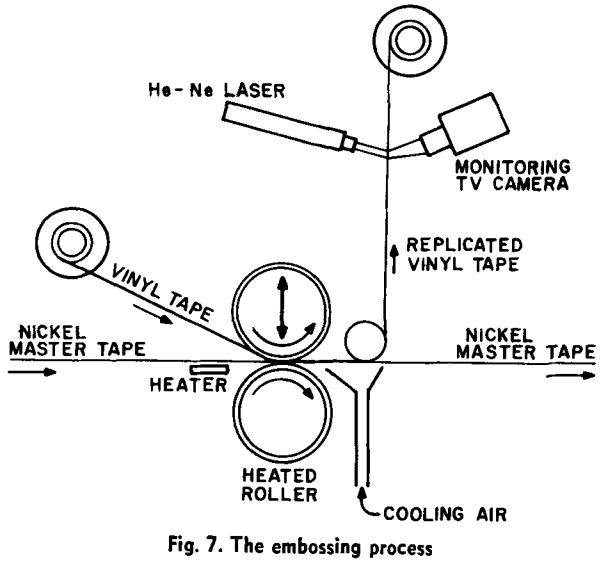

Fig. 7. The embossing process

Fig. 8. Embossing apparatus

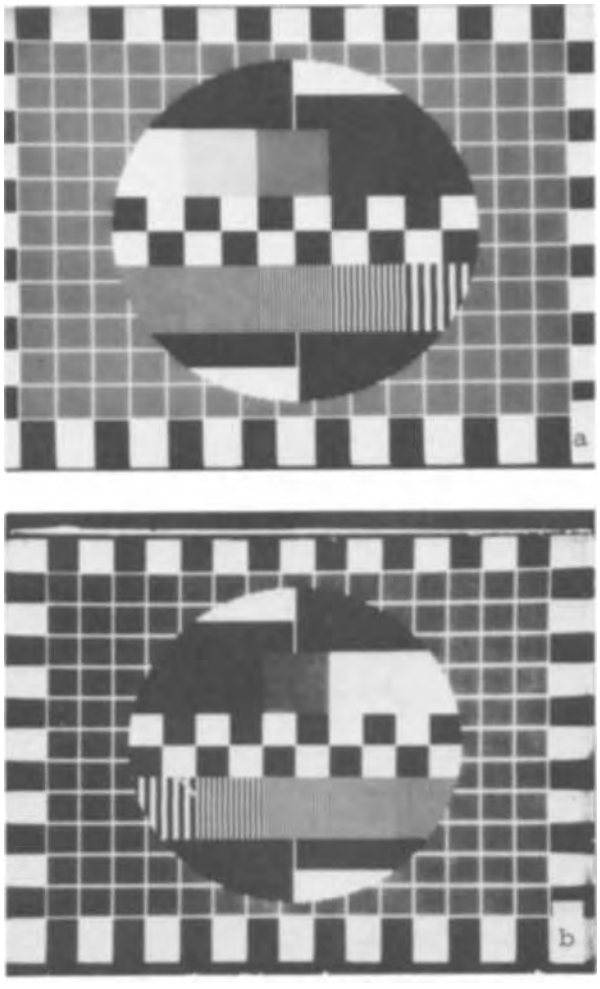

Fig. 9. Resolution of embossed hologram in vinyl film. a, High resolution silver-halide object film; b, vinyl hologram replica.

plastic surface must be heated to a depth beyond the maximum grating amplitude in order to achieve exact replication.

The mechanical aspects of the embossing process are equally important to the thermal cycle in producing distortion-free replicated films. Tape guiding, roller alignment, and tape windup must be adjusted to prevent edge distortion in the film in order to provide a flat film during holographic readout. The compression roller is coated with a uniform smooth resilient elastomer to equalize pressure at the nip between the plastic film and nickel master surface. Experimental apparatus for replication speeds up to 10 in./sec is shown in Fig. 8. Vinyl tapes have been replicated with this equipment which exhibit no change in signal-to-noise ratio or efficiency of embossed holograms between the initial replica and the 5000th copy. Comparison of Fraunhofer hologram test patterns, recorded in photoresist, with film embossed from equivalent electroformed nickel masters show no significant loss in efficiency, resolution, or signal-to-noise ratio. A comparison between an image from an original hologram and an embossed film replica hologram is shown in Fig. 9. Other equipment has been designed for high speed embossing using RF heating of the nickel master and demonstrations have been given at replication speeds up to 60 in./sec.

Acknowledgments

The HoloTape program at RCA Laboratories was carried out under the direction of W. J. Hannan. The authors wish to thank the following for their technical assistance: R. P. Borchardt, R. R. Demers, L. A. DiMarco, J. R. Frattarola, A. Sabo, and H. G. Scheible.

Manuscript submitted Nov. 27, 1972; revised manuscript received March 30, 1973.

Any discussion of this paper will appear in a Discussion Section to be published in the June 1974 JOURNAL.

REFERENCES

1. R. A. Bartolini, W. J. Hannan, D. Karlsons, and M. J. Lurie, *Appl. Opt.*, **9**, 2283 (1970).
2. O. Doyle, *Electronics*, **42**, 108 (1969).
3. R. E. Flory, "Video Recording and Playback," 1972 McGraw-Hill Yearbook of McGraw Hill Encyclopedia of Science and Technology, McGraw-Hill Book Co., New York (1972).
4. R. Kingslake, "Applied Optics and Optical Engineering," Vol. II, pp. 305-306, Academic Press, New York and London (1965).
5. W. E. Glenn, *J. Soc. Motion Picture Television Engrs.*, **74**, 663 (1965).
6. A. H. Firester, E. C. Fox, T. Gayeski, W. J. Hannan, and M. J. Lurie, *RCA Rev.*, **33**, 131 (1972).
7. R. A. Bartolini, J. Bordogna, and D. Karlsons, *ibid.*, **33**, 170 (1972).
8. E. N. Leith and J. Upatnicks, *J. Opt. Soc. Am.*, **52**, 1123, (1962).
9. F. S. Harris, Jr., G. C. Sherman, and B. H. Billings, *Appl. Opt.*, **5**, 665 (1966).
10. M. J. Landry, *Appl. Phys. Letters*, **9**, 303 (1966).
11. D. B. Brumm, *Appl. Opt.*, **5**, 1946 (1966).
12. G. C. Sherman, *ibid.*, **6**, 1749 (1967).
13. M. J. Landry, *ibid.*, **6**, 1947 (1967).
14. D. B. Brumm, *ibid.*, **6**, 588 (1967).
15. R. A. Bartolini, *ibid.*, **11**, 1275 (1972).
16. N. Feldstein and J. A. Weiner, *Plating*, **59**, 140 (1972).
17. N. Feldstein and J. A. Weiner, *This Journal*, **119**, 668 (1972).
18. N. Feldstein, *RCA Rev.*, **31**, 317 (1970).

Optically Erasable Cathodochromic Coloration in Sodalites Containing Sulfate

Takeshi Takeda and Akinori Watanabe

Matsushita Research Institute Tokyo, Incorporated, Ikuta, Kawasaki, Japan

ABSTRACT

Optically erasable cathodochromic coloration was studied in sodalite of which halogen ions were partially substituted by sulfate radicals. The materials were prepared by a solid-state sintering method in air. The achievable contrast ratio, decay time, optical erasability, and color changed considerably depending on the substitution amount of sulfate radicals. The composition $Na_6Al_6Si_6O_{24}\cdot 1.2NaCl\cdot 0.4Na_2SO_4$ showed the best compromise among these properties. In this composition the maximum contrast ratio 7.7 was achieved at 20 kV without a significant residual coloration. The peak wavelength of induced absorption spectrum was 553 nm and the thermal decay time was about 30 min.

Photochromic and cathodochromic properties of sodalite have been widely investigated for the purpose of storage-display applications (1-15). Especially, dark trace tubes using cathodochromic sodalite as a screen material are under current development (13-15), since they give improved features over the early KCl tubes (16).

Sodalite has the chemical formula $Na_6Al_6Si_6O_{24}\cdot 2NaX$, where X = halogen. Photochromic and cathodochromic sodalites are colored by ultraviolet and electron-beam irradiation, respectively. The induced coloration is bleached upon exposure to visible light or by heating the material.

Photochromic sodalites have usually been doped with sulfur (2, 4, 13) or iron (6), since these ions were found to aid photochromic coloration. As-grown materials are not photochromic and must be sensitized by a heat-treatment in a hydrogen or an inert atmosphere. Photochromic sodalites are also cathodochromic.

To induce only the cathodochromism, S- or Fe-doping is not necessary and these ions have been reported (11, 13, 15) to degrade the cathodochromic performance in some cases. Several variations of synthesis and sensitization processes have been reported. Williams *et al.* (4) reported high-temperature hydrothermal synthesis after which the products were sensitized by heat-treatment in a reduction atmosphere. This process has been used by several workers (5-8). Recently, Schipper *et al.* (9) reported a modified solid-state sintering method and a low-temperature hydrothermal method. The products by these methods were found to show optimum cathodochromic properties when they were treated in an oxidizing atmosphere rather than in a reducing one.

The induced coloration, which is the result of F center absorption, can usually be classified into two categories. One is the "optical-erase mode" coloration that can be erased by light, and the other is the "thermal-erase mode" coloration that can only be perfectly erased by heating to about 200°C. At low levels of electron-beam irradiation, the former mode of coloration is much more efficient, but at high levels of irradiation saturation tends to occur, whereas, in the latter mode, coloration continues to increase with irradiation. The relative sensitivity of these two coloration modes is a strong function of both the composition of sodalite and of the method of preparation. In bromo-sodalite, Faughnan *et al.* (15) succeeded in improving the sensitivity of thermal-erase mode coloration to such an extent that the device applications for this mode of coloration look very promising. Several attempts to reduce the thermal-erase mode coloration also have been performed, since, when the materials are used in the optically reversible dark trace tubes, this mode occasionally gives rise to a residual coloration. Iodo-sodalite was reported to be the most suitable composition for this purpose (6). Some success also has been obtained by firing the products with extra sodium halide (9, 11) or by annealing them in fused sodium halide (6).

The present paper is also concerned with the attempt to reduce the sensitivity of thermal-erase mode coloration, and the results for sodalites in which halogen ions are partially replaced by sulfate radicals will be described.

Key words: color center, absorption spectrum, display, storage.

Crystal Structure and Material Preparation

The crystal structure of sodalite is built up from aluminosilicate cages formed of (AlO_4) and (SiO_4) tetrahedra linked together by their oxygen atoms. The cages are stacked together to form a crystal with over-all cubic symmetry (17). In the center of the cage, there exists a halogen ion surrounded by four Na^+ ions as shown in Fig. 1. Many variations can be synthesized by changing the contents of the cage; for example, instead of sodium halide in sodalite, the mineral noselite contains Na_2SO_4, and the pigment ultramarine contains Na_2S_x.

The sodalites studied in the present work contain sulfate radicals which partially replace the halogen

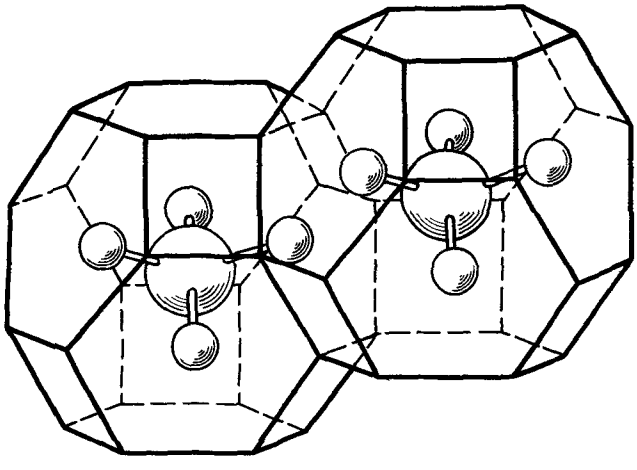

Fig. 1. Cage structure of sodalite [see Ref. (15)]. Large circles on the center of the cage represent halogen ions. The smaller circles represent Na ions. The Al, Si, and O ions forming the aluminosilicate cage are not shown for the sake of clarity.

ions. Chloro- and bromo-sodalites are especially dealt with and the formula can be written as $Na_6Al_6Si_6O_{24}\cdot 2(1 - x)NaX\cdot xNa_2SO_4$, where $0 \leq x \leq 1$.

The materials were prepared by the solid-state sintering method. The reagent grade chemicals Na_2CO_3, Al_2O_3, SiO_2, NaCl, and Na_2SO_4 were mixed in a mole ratio of $3 : 3 : 6 : 2(1 - x) : x$, and the mixture was ball-milled for 10–20 hr. This was followed by a 3-hr prefiring at 800°-850°C in a covered platinum crucible. The partially sintered material was broken up with a mortar in an agate bowl and then milled for 3–5 hr. This material was fired again. The milling-firing cycles were repeated several times before the final firing at 1000°C for 1 hr in air. Firing temperatures, firing period, and milling-firing cycles are interrelated in their effects on the coloration and bleaching properties of final products, and the optimum conditions must be found experimentally. The products were identified by x-ray powder diffraction. The diffraction spectra sometimes showed a small trace of another phase apart from sodalite, especially in the bromo-sodalite containing sulfate.

Experimental Methods

Contrast ratio measurements were performed in two ways: reflectance and transmission measurements.

For reflectance measurements, powder specimens with a particle size of 10-20 μm were deposited on an aluminum foil in a thickness of 40-50 μm by use of an applicator blade, and were colored in a demountable cathode-ray tube. As many as eight different samples were mounted at one time and measured under the same conditions. A reference light beam irradiated the surface of the sodalite screen. The brightness was low enough so that its effect on the decay of coloration could be ignored. The ratio of reflection intensities before and after electron beam irradiation then were calculated. Thus, the coloration is expressed by the constant ratio $C_{ref.} = R_0/R$, where R_0 and R are initial and final diffuse reflectances. In this way, a wide variety of prepared samples were surveyed and this was followed by measurements on a few excellent samples in the transmission mode.

Contrast ratio measurements in the transmission mode were performed in an actual cathode-ray tube with the sodalite screen instead of the usual phosphor screen. The screen density was 3 mg/cm^2 and the particle size was 1-3 μm. A transparent, conductive SnO_2 film was provided for the inner surface of the faceplate and funnel part of the glass bulb. The usual aluminum backing and graphite coating were omitted to facilitate back-screen illumination by both the measuring light and the erasing light (18). Thus, the contrast ratio, $C_{tran.} = I_0/I$, was obtained where I_0 and I are the intensities of transmitted light before and after electron beam irradiation.

A narrow band pass filter with the central wavelength equal to the peak wavelength of the induced absorption spectrum was used in all measurements.

Cathodochromic Properties

Halogen sites in sodalite can be replaced by SO_4^{2-} radicals, partially or fully. That is, the solid solution of sodalite and noselite can be synthesized in a form $Na_6Al_6Si_6O_{24}\cdot 2(1 - x)NaX\cdot xNa_2SO_4$ (X = halogen) in any value of x between 0 and 1. Although a small trace of second phase apart from sodalite is occasionally detected by an x-ray diffractometer and although the evaporation of NaX and Na_2SO_4 in the course of firing might not be negligible, the synthesized specimen is denoted by its starting formula in the following.

The cubic lattice parameter, a_0, increases monotonically with x and the peak wavelength λ of the induced absorption spectrum moves towards longer wavelengths. Figure 2 shows a plot of peak wavelength against lattice parameter. It is desirable that λ is matched to the peak wavelength, 555 nm, of the sensitivity curve for the human eye. Thus, the composition with $x \sim 0.4$ in the solid solution of sodalite and noselite or the pure bromo-sodalite is most suitable. The induced absorption spectrum is shown for $Na_6Al_6Si_6O_{24}\cdot 1.2NaCl\cdot 0.4Na_2SO_4$ ($x = 0.4$) in Fig. 3. The line width becomes broader with x and is 180-200 nm in this composition. This width is about 2 times broader than that of pure chloro-sodalite.

The contrast ratio $C_{ref.}$ *vs.* x is plotted in Fig. 4. The accelerating voltage was 15 kV, beam diameter was about 8 mm, and charge density was 100 μcou-

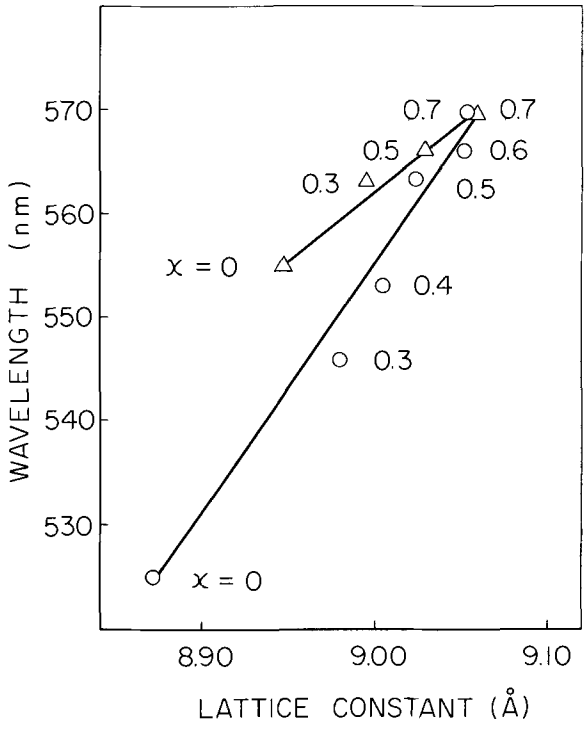

Fig. 2. The dependence of the peak wavelength of the absorption spectrum on the cubic lattice parameter in the composition $Na_6Al_6Si_6O_{24}\cdot 2(1 - x)NaX\cdot xNa_2SO_4$. Circles and triangles correspond to X = Cl and X = Br, respectively.

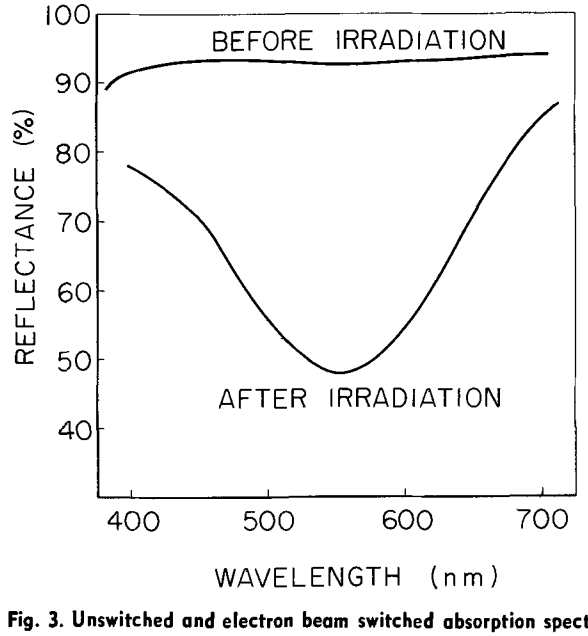

Fig. 3. Unswitched and electron beam switched absorption spectra of $Na_6Al_6Si_6O_{24}\cdot 1.2NaCl\cdot 0.4Na_2SO_4$.

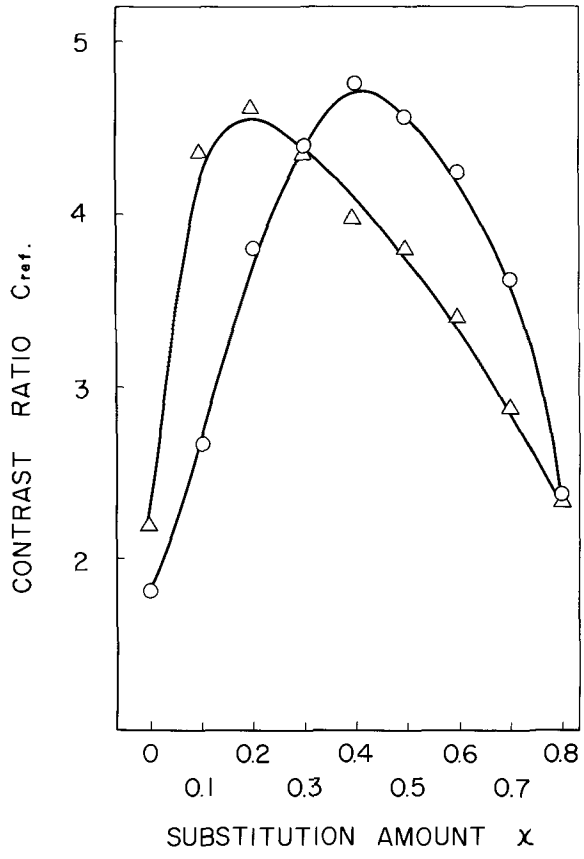

Fig. 4. Relationship between contrast ratio, $C_{ref.}$, and x in $Na_6Al_6Si_6O_{24}\cdot 2(1-x)NaX\cdot xNa_2SO_4$. Circles and triangles correspond to X = Cl and X = Br, respectively. Accelerating voltage is 15 kV and charge density is 100 μcoulombs/cm².

lombs/cm². The current density was 5 μA/cm². As is seen from this figure, $C_{ref.}$ increases with x, reaches a maximum, and decreases again with further increase of x. In the chloro-sodalite and noselite system, the maximum contrast ratio 4.7 is obtained at $x = 0.4$. At $x = 0$, *i.e.*, pure chloro-sodalite, $C_{ref.}$ is only about 2.0. However, when the latter was treated in a hydrogen atmosphere at 800°C for 30 min, $C_{ref.}$ increased to about 3.5. The treated material also showed the weak photochromism as reported by Medved (1). In the products with x higher than 0.3, this treatment did not cause an increase of $C_{ref.}$, but sometimes caused a decrease of $C_{ref.}$ and an increase of residual coloration (residual coloration is described later).

In the bromo-sodalite and noselite system, the maximum contrast ratio is obtained in the composition with $x \sim 0.2$. This value of x is smaller than that in the chloro-sodalite and noselite system. One plausible reason for this difference is that the evaporation of NaBr occurs more actively, and thus the deviation of final Br/SO_4 ratio from the initial one is more significant in the $Br\text{-}SO_4$ system than in the $Cl\text{-}SO_4$ system. The maximum $C_{ref.}$ is 4.5 and comparable with 4.7 in the $Cl\text{-}SO_4$ system.

Bleaching properties also change depending on composition. In Fig. 5 some thermal decay curves at room temperature are shown. The decay rate becomes larger with x. At the composition with $x = 0.4$, a contrast ratio fell to half of its initial value in 30 min. At a typical room environment (200 lux), it takes about 2 min to reach the same situation.

In general, a charge density exceeding a certain threshold value gives rise to a residual coloration after optical bleaching is attempted. Figure 6 shows the relation between the contrast ratio $C_{res.}$ of residual coloration and the substitution amount x. Here,

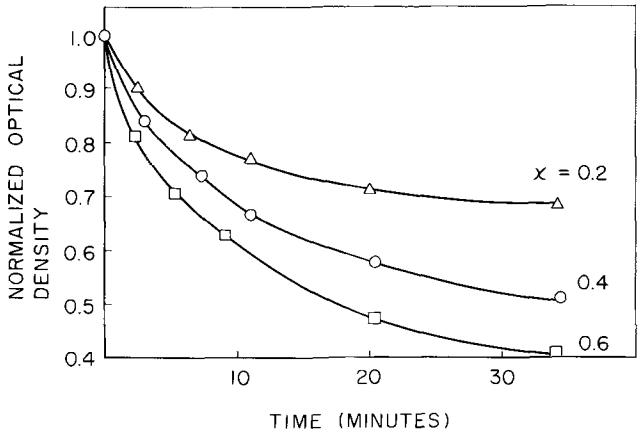

Fig. 5. Thermal decay of induced coloration in $Na_6Al_6Si_6O_{24}\cdot 2(1-x)NaCl\cdot xNa_2SO_4$.

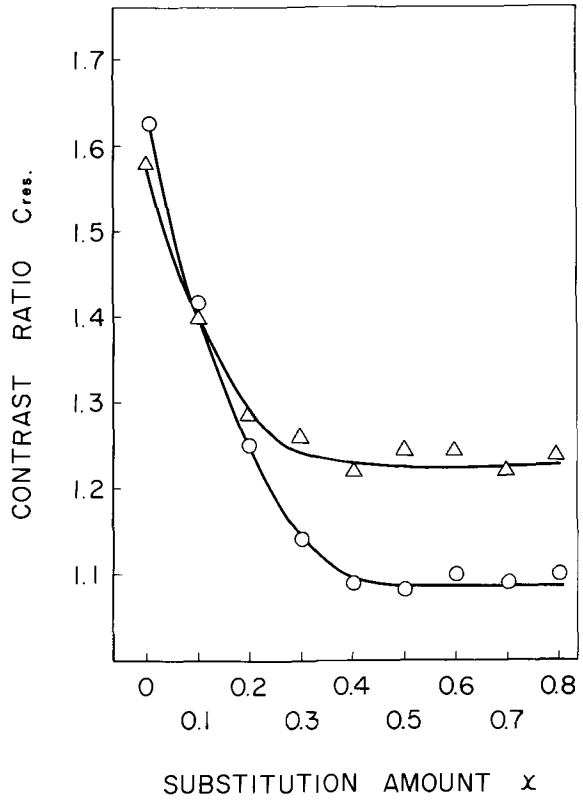

Fig. 6. Relationship between contrast ratio, $C_{res.}$, of residual coloration and x in $Na_6Al_6Si_6O_{24}\cdot 2(1-x)NaX\cdot xNa_2SO_4$. Circles and triangles correspond to X = Cl and X = Br, respectively. Induced coloration was bleached by a tungsten lamp for 1 min.

the coloration induced at 15 kV and 100 μcoulombs/cm² was erased by light from a 300W tungsten lamp positioned at a distance of 40 cm from the sample for 1 min. As shown in this figure, $C_{res.}$ decreases with the increase of x. For instance, in the $Cl\text{-}SO_4$ system, when $x = 0$, $C_{res.} = 1.62$, and when $x = 0.4$, $C_{res.} = 1.09$. When x exceeds 0.4, $C_{res.}$ becomes nearly constant. The color (absorption spectrum) of residual coloration also varies with composition. At $x = 0$, it is the same as for that of the initially developed coloration, that is, magenta. With increasing x, the residual coloration gradually becomes yellowish brown, whereas the electron beam initially develops a purple color. The persistence of this yellowish brown coloration is still a function of the bleaching light. That is, the residual coloration in this case involves both the optical- and thermal-erase mode components. The residual coloration in the composi-

tion with $x = 0.4$ is completely bleached in several hours by the light in a room environment, whereas in the dark it is maintained over 1 day or so. On the other hand, the magenta residual coloration at $x = 0$ is hardly affected by light and it is maintained over 1 week even in a room environment. The thermal-erase mode coloration dominates the residual coloration in this case.

In the Br-SO_4 system, $C_{res.}$ becomes nearly constant for x higher than 0.3. However, the lowest $C_{res.}$ is only 1.22 (optical density 0.09) and higher than the 1.09 (optical density 0.04) obtained in the Cl-SO_4 system. This undesirable result in the Br-SO_4 system might again have a relation with the active evaporation of NaBr during firing. Our attempt to synthesize the solid solution of iodo-sodalite and noselite was unsuccessful, since the evaporation loss of NaI was quite serious. The sintered products exhibited low $C_{ref.}$ and high $C_{res.}$ although the effect of SO_4^{2-} was still observed. It is a future subject to find out the best firing condition for the Br-SO_4 or I-SO_4 system.

The $C_{ref.}$ and $C_{res.}$ *vs.* charge density are shown in Fig. 7 for $x = 0.2$ and 0.4 in the Cl-SO_4 system. An increase in sensitivity by a factor of 2-3 can be achieved in the initially induced coloration by going from $x = 0.2$ to $x = 0.4$. On the other hand, the sensitivity of residual coloration for $x = 0.4$ is about one order of magnitude lower than that for $x = 0.2$. The threshold charge density for the occurrence of residual coloration is below 1 μcoulombs/cm^2 for $x = 0.2$ and about 5 μcoulombs/cm^2 for $x = 0.4$ in the present condition. When the charge density exceeds several hundred μcoulombs/cm^2, the residual coloration at $x = 0.4$ also becomes purple rather than yellowish brown, and the dependence on bleaching light becomes weak.

In the present sample series, the composition $Na_6Al_6Si_6O_{24}\cdot 1.2NaCl\cdot 0.4Na_2SO_4$ shows the best compromise between $C_{ref.}$ and $C_{res.}$. This compromise in the above composition is also somewhat better than that in iodo-sodalite which has been reported to be most suitable for optically reversible applications (6). The thermal decay time of optically reversible coloration is about one order of magnitude longer than that in iodo-sodalite.

The contrast ratio, $C_{tran.}$, measured in the transmission mode (18) showed a higher value than that in the reflection mode, as pointed out by Faughnan *et al.* (15). The result for the composition $Na_6Al_6Si_6O_{24}\cdot 1.2NaCl\cdot 0.4Na_2SO_4$ is shown in Fig. 8. As expected, higher accelerating voltages produce higher contrast ratios. To obtain $C_{tran.} = 2$, a charge density of 0.5 μcoulombs/cm^2 at 20 kV is required.

From this result, the number of F centers created per incident electron can be roughly estimated by use of the Smakula equation (19). This can be written

$$Nf = 0.87 \times 10^{17} \frac{n}{(n^2 + 2)^2} k_{max} W_{1/2} \quad [1]$$

where N = number of F centers per cm^3, f = oscillator strength, n = refractive index of the material, k_{max} = absorption coefficient, in cm^{-1}, at the peak of the absorption band, and $W_{1/2}$ = full width, in eV, of the absorption band at half intensity. To produce an optical density, D, in a penetration depth, t, it is necessary that

$$Nt = 6.5 \times 10^{15} D \quad [2]$$

centers per cm^2 switch. The reasonable values $f = 0.5$, $n = 1.5$, and $W_{1/2} = 0.8$ eV are adopted. From Eq. [2], $C_{tran.} = 2$ ($D = 0.3$) yields $Nt \approx 2 \times 10^{15}$ cm^{-2}. The charge density 0.5 μcoulombs/cm^2 corresponds to 3.1×10^{12} incident electrons per cm^2. This means that one incident electron with a voltage of 20 kV creates $\sim$ 650 F centers. Since it takes at least three bandgaps of energy [$\sim$ 18 eV (11)] to create one electron-hole pair (20), the efficiency is about 45%. The efficiency falls with increasing charge density, and it becomes 8% at 10 μcoulombs/cm^2.

In the composition $Na_6Al_6Si_6O_{24}\cdot 1.2NaCl\cdot 0.4Na_2SO_4$, 20% of the halogen sites are empty and this corresponds to a possible vacancy density of 4.4×10^{17} cm^{-2} within a penetration depth [4 μm at 20 kV (21)]. Maximum contrast ratio 7.7 at 20 kV ($D = 0.86$) yields 5.6×10^{15} F centers cm^{-2}. This amount is two orders of magnitude smaller than that of existing vacancies.

Consideration of the Role of Sulfate

The optically reversible cathodochromic switching will be the result of a charge-transfer process (8). A number of electron-hole pairs are created by the incident electrons. The released electrons are then captured in "already existing" halogen ion vacancies to form F centers giving rise to the coloration. The holes also should be captured by some centers to make the coloration stable. These hole-trapping centers are not yet known with certainty. Sodium ion vacancies, or impurity O^{2-} ions on the halogen sites, have been proposed to be such centers. The trapped electrons and/or holes are released again by erasing light and they recombine to result in the initial uncolored state.

The optically irreversible coloration, that is, the thermal-erase mode coloration, has been assumed to have an intimate relation with the ionic displacement

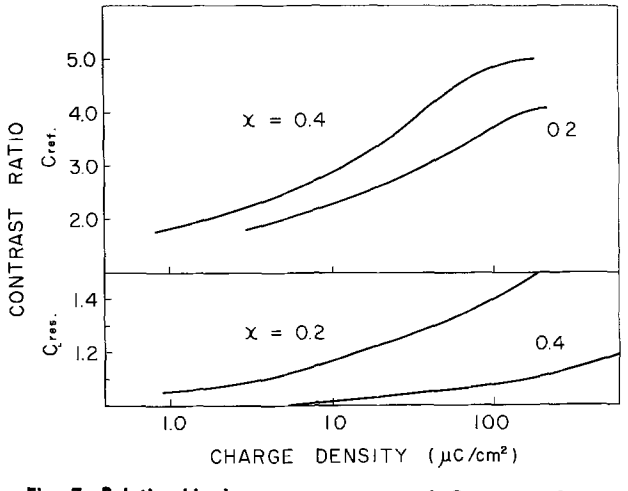

Fig. 7. Relationship between exposure and $C_{ref.}$ and $C_{res.}$ in $Na_6Al_6Si_6O_{24}\cdot 2(1 - x)NaCl\cdot xNa_2SO_4$.

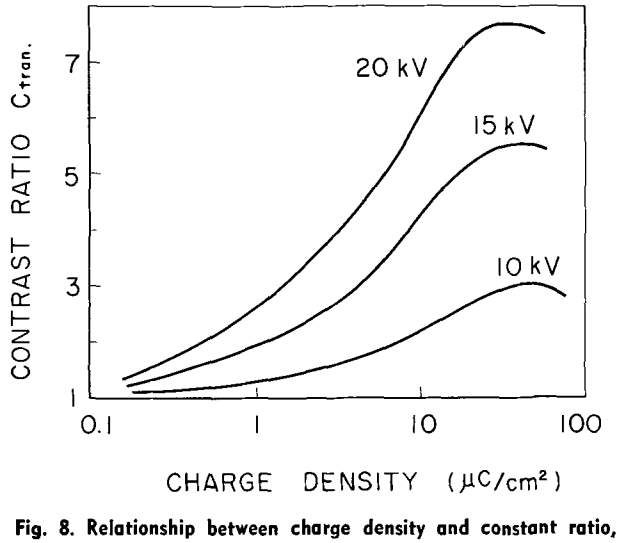

Fig. 8. Relationship between charge density and constant ratio, $C_{tran.}$, at different accelerating voltages, measured in transmission mode in $Na_6Al_6Si_6O_{24}\cdot 1.2NaCl\cdot 0.4Na_2SO_4$.

(15) or motion (11) as the result of radiation damage. Bolwijn *et al.* (11) emphasized the motion of O^{2-} ions incorporated occasionally on the halogen sites. As a result, halogen vacancies are "newly" created and this was followed by the change of nature of hole-trapping centers. The holes trapped by these modified centers are conjectured to have a negligible probability of recombining with electrons until these centers are converted to the initial ones by heating the material.

Cathodochromic sodalites thus far reported contain a halogen deficit of 10-30% (9, 15). This creation of halogen vacancies is usually accompanied by the creation of sodium vacancies and/or the incorporation of oxygen ions on halogen sites, both of which might make the occurrence of thermal-erase mode coloration easy.

The role of SO_4^{2-} radicals can be threefold. First, they could create halogen vacancies without being accompanied by sodium ion vacancies and/or contamination by oxygen. This will improve the sensitivity of optical-erase mode coloration and reduce the sensitivity of the thermal mode. Secondly, the existence of relatively large and immobile SO_4^{2-} radicals in the lattice will block the motion of other ions (22). This also suppresses the occurrence of thermal-erase mode coloration. Thirdly, SO_4^{2-} radicals might act as hole-trapping centers by themselves. The reaction will be written as $SO_4^{2-} + \text{hole} \rightarrow SO_4^{1-}$. This possibility will be confirmed by the fact that the presence of SO_4^{1-} in sodalite was detected by electron spin resonance measurements (23). By these roles of sulfate, the optically reversible coloration can be stabilized. In contrast to S-doped sodalites, SO_4-doped sodalites were found not to be photochromic at 254 nm, and the energy levels of SO_4^{2-} were assigned to be within 1 eV from the valance band (10).

The occurrence of thermal-erase mode coloration in sodalites containing sulfate will be mainly ascribed to the dissociation of sulfate radicals by the electron bombardment. The possible existence of O^{2-} ions may still play an important role. A method for a further reduction of the thermal-erase mode coloration is now under study. The result will be reported elsewhere.

Acknowledgments

The authors acknowledge their thanks to F. Muramatsu for assistance in preparing sodalite materials and to Y. Uno and members of his group for manufacturing the sodalite cathode-ray tubes and evaluating their characteristics. Acknowledgments are extended to Y. Tsujimoto and Y. Fukuda, of the Central Research Laboratory of Matsushita Electric Industrial Company, Limited, for the use of their demountable apparatus.

Manuscript submitted Dec. 26, 1972; revised manuscript received April 27, 1973. This was Paper 40 presented at the Chicago, Illinois, Meeting of the Society, May 13-18, 1973.

Any discussion of this paper will appear in a Discussion Section to be published in the June 1974 JOURNAL.

REFERENCES

1. D. B. Medved, *Am. Mineralogist*, **39**, 615 (1954).
2. R. D. Kirk. *This Journal*, **101**, 461 (1954).
3. W. G. Hodgson, J. S. Brinen, and E. F. Williams, *J. Chem. Phys.*, **47**, 3719 (1967).
4. E. F. Williams, W. G. Hodgson, and J. S. Brinen, *J. Am. Ceram. Soc.*, **52**, 139 (1969).
5. D. W. G. Ballentyne and K. L. Bye, *J. Phys. D. Appl. Phys.*, **3**, 1438 (1970).
6. W. Phillips, *This Journal*, **117**, 1557 (1970).
7. S. D. McLaughlan and D. J. Marshall, *J. Phys. Chem.*, **74**, 1359 (1970).
8. R. C. Duncan, B. W. Faughnan, and W. Phillips, *Appl. Opt.*, **9**, 2236 (1970).
9. D. J. Schipper, C. Z. van Doorn, and P. T. Bolwijn, *J. Am. Ceram. Soc.*, **55**, 256 (1972).
10. C. Z. van Doorn, D. J. Schipper, and P. T. Bolwijn, *This Journal*, **119**, 85 (1972).
11. P. T. Bolwijn, D. J. Schipper, and C. Z. van Doorn, *J. Appl. Phys.*, **43**, 132 (1972).
12. P. M. Heyman, I. Gorog, and B. Faughnan, *IEEE Trans. Electron Devices*, **ED-18**, 685 (1971).
13. M. J. Taylor, D. J. Marshall, P. A. Forrester, and S. D. McLaughlan, *Radio Eng. Electron.*, **40**, 17 (1970).
14. W. Phillips and Z. J. Kiss, *Proc. IEEE (Letters)*, **56**, 2072 (1968).
15. B. W. Faughnan and I. Shidlovsky, *RCA Rev.*, **33**, 273 (1972).
16. P. G. R. King, *J. Inst. Elec. Engrs., (London)*, **93**, 171 (1946).
17. W. Pauling, *Z. Krist.*, **74**, 213 (1930).
18. Y. Uno and H. Maeda, 1972 SID Symposium, Digest of Technical Papers, p. 76.
19. J. H. Schulman and W. D. Compton, "Color Centers in Solids," Pergamon Press, Oxford, England (1963).
20. J. D. Kingsley and G. W. Ludwig, *This Journal*, **117**, 353 (1970).
21. A. E. Grun, *Z. Naturforsch.*, **12a**, 89 (1957).
22. R. M. Barrer, *Proc. Chem. Soc.*, 99 (1958).
23. L. V. Bershov, V. O. Martirosyan, A. N. Platonov, and A. N. Tarashchan, *Neorganish Mater.*, **5**, 1780 (1969).

Properties of Epitaxial Gallium Arsenide from Trimethylgallium and Arsine

Susumu Ito, Tsuneo Shinohara, and Yasuo Seki

Central Research Laboratories, Nippon Electric Company, Shimonumabe, Kawasaki, Japan

ABSTRACT

Electrical and optical properties of epitaxial GaAs layers grown from trimethylgallium and arsine were studied by Hall and photoluminescence measurements. The conduction type of the layers grown on GaAs substrates was changed from p- to n-type with increase of [As]/[Ga], the mole ratio of arsine to trimethylgallium introduced, without intentional doping. An emission (P_2) at 1.488 eV due to shallow acceptors was observed on most of the samples.

Correlations between the carrier concentration and the intensity of the P_2 emission with [As]/[Ga] suggest that the main acceptor impurities in the epitaxial layer are amphoteric ones on As sites, such as carbon and silicon contained in the trimethylgallium source. Results of the mass-spectrographic analysis of the layers are consistent with the above suggestion.

Many GaAs epitaxial growth techniques have been proposed and performed. Among them, the use of trimethylgallium and arsine, as demonstrated by Manasevit *et al.* (1, 2), has many attractive points, such as (*i*) simplicity in apparatus because of a single temperature zone, (*ii*) independent regulation of gaseous components of gallium and arsenic, (*iii*) no gaseous etchants and less autodoping, (*iv*) low growth temperatures ($\geqq$ 600°C), and (*v*) easiness of heteroepitaxial growth on insulating substrates.

Some reports (1-6) have been made on the deposition procedures and on the surface morphology of the epitaxial layers grown on various substrates. Few reports, however, have been presented on the properties of the layer grown on the GaAs substrate, although electrical properties of the heteroepitaxial layers on Al_2O_3 have been reported (7).

This paper presents some electrical and optical properties of the epitaxial layers grown on GaAs substrates from trimethylgallium and arsine in connection with deposition conditions.

Experimental

Apparatus.—The apparatus used here is similar to that used by Manasevit *et al.* (2), as shown in Fig. 1. It consists of a vertical quartz reactor, a SiC-coated graphite pedestal which can be inductively heated, a quartz bubbler containing trimethylgallium (TMG), appropriate flow meters for monitoring carrier gases, TMG, and arsine, and pertinent stainless-steel piping and joints.

All "deposition temperatures" reported here are the readings of a thermocouple inserted into the pedestal. No preparations were made to prevent the rf field from affecting the readings of the thermocouple except for the insertion of a large inductance in the emf measurement circuit. The readings agreed well with those of an infrared radiation thermometer through the quartz reactor.

Substrates.—Although many kinds of materials have been used as the substrate (1, 2, 5), {100} GaAs wafers were used in this experiment to exclude influences of defects that frequently originate at the interface between the substrate and the epitaxial layer in heteroepitaxy. GaAs wafers were mechanically polished and then etched in a $3H_2SO_4$-H_2O_2-H_2O solution. No further treatments, such as gas etching, were made on the substrate preparation.

Key words: chemical vapor deposition, organic gallium source, GaAs substrate, impurity.

Trimethylgallium (TMG).—The TMG was obtained from several commercial sources and was used without further purification.[1] The nominal purity, according to the makers, is better than 99.5%. The bubbler containing this material is kept at 0°C during deposition.

Arsine.—AsH_3 diluted to 1% with argon was used.[2] The AsH_3 flow rate was adjusted by a pressure regulator and a needle valve.

Deposition procedures.—Gallium and arsenic contents in the reaction atmosphere were adjusted by regulating the flow rate of the gases, *i.e.*, hydrogen through the TMG bubbler and 1% AsH_3. Flow rates of TMG and AsH_3 were in the ranges from 1.1×10^{-5} to 1.1×10^{-4} mole/min and from 2.2×10^{-4} to 8.8×10^{-4} mole/min, respectively. An additional hydrogen gas flow was introduced to keep the total gas flow rate constant (2500 cm³/min).

The deposition temperatures were varied from 550° to 850°C. The AsH_3 flow started when the pedestal temperature reached 500°C, prior to introduction of TMG into the reactor, in order to prevent substrate decomposition. After the deposition is completed, the AsH_3 flow is also continued until the temperature has dropped to 500°C.

[1] Three TMG sources, A, B and C, used in this experiment were purchased from Alfa-Inorganics, Incorporated, U.S.A., K & K Laboratories, Incorporated, U.S.A., and Kojundo Kagaku Kenkyujo Japan, respectively.

[2] The diluted AsH_3 tanks (Electronic Grade) were purchased from Nihonsanso, Incorporated, Japan.

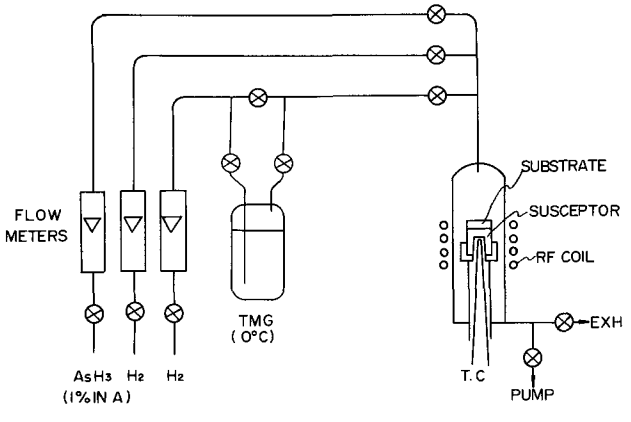

Fig. 1. Deposition apparatus

Evaluation procedures.—Conventional d-c Hall measurements were carried out on a bridge-shaped sample etched in the epitaxial layer grown on the Cr-doped semi-insulating substrate. Contacts of indium for the electrical measurement were alloyed at about 350°C in a hydrogen atmosphere. The magnetic field used in the Hall measurement was 6000 Gauss. The Hall measurements and the C-V measurements, with a palladium Schottky barrier used, gave similar carrier concentrations, and the latter showed flat profiles, independent of the film thickness (2.0 ~ 20μ).

Photoluminescence of the epitaxial layers was measured at 90°K by the same method as reported by Iwasaki and Sugibuchi (8).

Results and Discussion

Effect of deposition parameters and starting materials.—Growth rate of the GaAs epitaxial layers was found to be proportional to the TMG concentration and nearly independent of the deposition temperature in the range from 600° to about 800°C, as reported by Manasevit and Simpson (2). The carrier concentration was not affected by the growth rate in the range from 0.07 to 0.27 μm/min at a fixed temperature when a constant mole ratio of AsH_3 to TMG was used. Increase of the deposition temperature brought a slight increase in the electron concentration.

Electrical properties of the undoped layers were found to effectively depend on the TMG source used and on the mole ratio of AsH_3 to TMG introduced into the reactor. The AsH_3 sources used here had little effect on electrical and optical properties of the layers.

The electron concentrations obtained from three different TMG sources (Sources A, B, and C) used were $(2 \sim 5) \times 10^{16}$ cm^{-3}, $(1 \sim 5) \times 10^{16}$ cm^{-3}, and $(1 \sim 4) \times 10^{17}$ cm^{-3}, respectively, under the same growth conditions (deposition temperature = 600°C, growth rate = 0.2 μm/min, flow rates of TMG and AsH_3 = 5.7×10^{-5} mole/min and 7.2×10^{-4} mole/min, respectively).

Both n- and p-type epitaxial layers were grown on the GaAs substrates by changing the mole ratio of AsH_3 to TMG. Figure 2 shows the variation of the carrier concentration plotted against the mole ratio of AsH_3 to TMG, [As]/[Ga], introduced into the reactor. The variation implies some contributions of vacancies to the carrier concentrations of the layers. Detailed discussions on the variation will be made in the next section.

Optical properties.—Figure 3 shows a typical photoluminescence spectrum of the epitaxial layer. Three peaks, at 1.503 (P_1), 1.488 (P_2), and 1.2 (P_4) eV, were commonly observed in all cases. The weak peak (P_3) at 1.38 eV, which may be due to copper (9, 10), was sometimes observed. The copper atoms may come from residuals on the substrate surface or may be diffused from the substrate into the epitaxial layer. The P_1 emission at 1.503 eV is the near bandgap emission, and the P_4 emission at 1.2 eV may be the self-activated luminescence by gallium vacancy-donor complexes (11).

The P_2 emission at 1.488 eV should be noted. This emission has not been observed so intensively in undoped epitaxial layers prepared by the Ga-$AsCl_3$ system or by the liquid regrowth. A close correlation between the P_2 emission and the carrier concentration in the epitaxial layers can be seen in Fig. 4 for p- and n-type layers, where I_1 and I_2 are the peak intensities of P_1 and P_2, and I_2/I_1 is taken as a measure for simplicity instead of each integrated intensity of the P_2 emission. A main difference in the experimental conditions between the p- and n-type series is on the mole ratio of AsH_3 to TMG, [As]/[Ga], introduced. Both series imply that I_2/I_1 increases with increase of the acceptor concentration in the epitaxial layers. It may be concluded that the P_2 emission is due to shallow acceptors with an energy level of

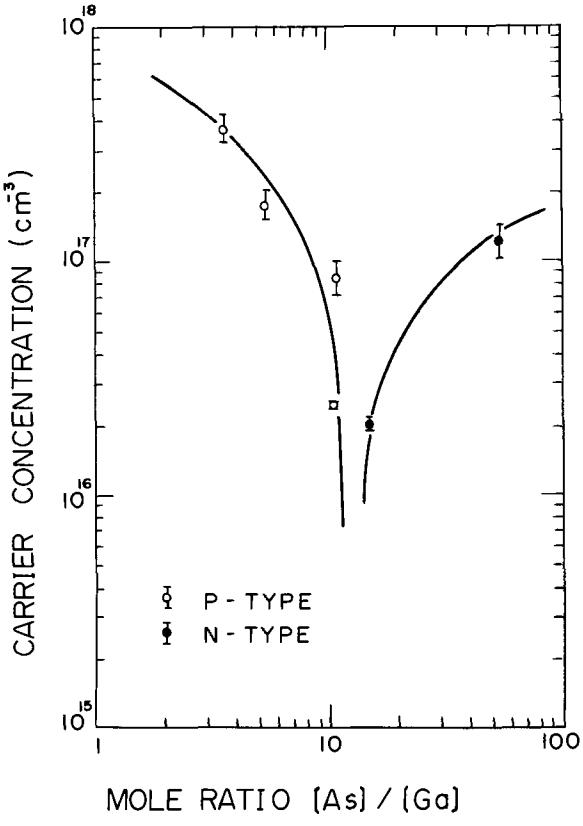

Fig. 2. Carrier concentration vs. introduced gas ratio of AsH_3 to TMG ([As]/[Ga]).

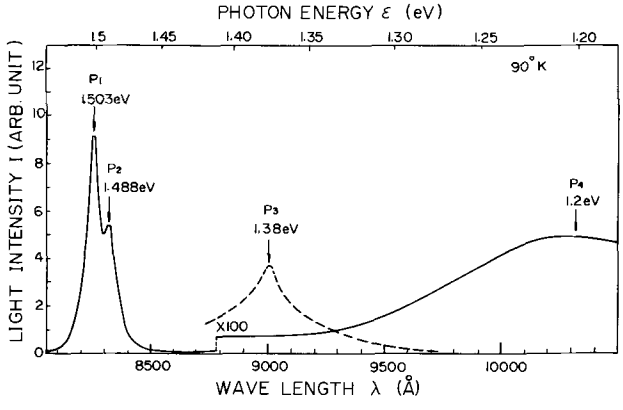

Fig. 3. Typical photoluminescence spectrum of an epitaxial GaAs layer grown by the TMG-AsH_3 system at 90°K.

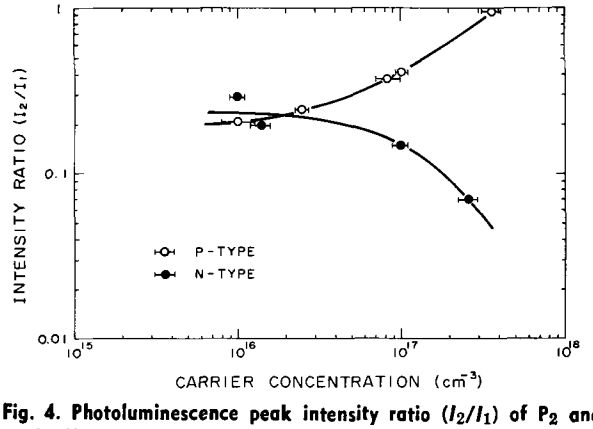

Fig. 4. Photoluminescence peak intensity ratio (I_2/I_1) of P_2 and P_1 at 90°K vs. carrier concentration.

about 20 meV above the top of the valency band and related to the main acceptors in the epitaxial layers.

Some of the group II and IV elements, such as zinc, magnesium, cadmium (12-14), germanium, silicon, and carbon (10, 12, 13, 15), are known to have a similar acceptor level. It seems that Fig. 2 shows a reaction between the impurities and the arsenic or gallium vacancies on the crystal surface during the deposition. Considerations of the vacancies will give a suggestion on the origin of the P_2 emission. If we can represent the deposition process as follows

$$Ga(CH_3)_3(g) + \frac{3}{2}H_2(g) \rightleftarrows Ga(l) + 3CH_4(g) \quad [1]$$

$$AsH_3(g) \rightleftarrows \frac{1-x}{2}As_2(g) + \frac{x}{4}As_4(g) + \frac{3}{2}H_2(g) \quad [2]$$

$$Ga(l) + V_{Ga} \underset{\text{decomposition}}{\overset{\text{deposition}}{\rightleftarrows}} Ga(s) \quad [3]$$

$$\text{and } \frac{1-x}{2}As_2(g) + \frac{x}{4}As_4(g) + V_{As} \underset{\text{decomposition}}{\overset{\text{deposition}}{\rightleftarrows}} As(s) \quad [4]$$

then, by the law of mass action, we have

$$\frac{[V_{Ga}]}{[V_{As}]} = \alpha(T) \cdot \left(\frac{P_{CH_4}}{P_{H_2}}\right)^3 \cdot \frac{P_{AsH_3}}{P_{TMG}} \quad [5]$$

where x indicates the fraction of As_4 to the total arsenic molecules; (s), (l), and (g) indicate the material states (crystalline solid, liquid, and gas states, respectively); V and $[V]$ indicate a vacancy and its concentration; P_i indicates the partial pressure of material i; α indicates the proportional constant of the reactions; and T is the absolute temperature. Here it was assumed that $\frac{1-x}{2}$ and $\frac{x}{4}$ molecules of As_2 and As_4 attack and occupy an As site. It is reasonable to assume that P_{AsH_3}/P_{TMG} in the equilibrium is proportional to [As]/[Ga], the introduced gas ratio, and that the concentrations of the Ga and As vacancies vary according to Eq. [5]. The high [As]/[Ga] value in the deposition atmosphere will suppress the formation of the As vacancy and will enhance the formation of the Ga vacancy in the layer, so that the impurities substitute in Ga sites will increase. The group II elements on Ga sites act as acceptors, whereas the group IV elements are amphoteric and are acceptors on As sites and donors on Ga sites. The layers grown under the different values of [As]/[Ga] will show different features in the photoluminescence spectrum and in the conduction type depending on the origin of the acceptors.

Figure 5 shows the experimental results obtained according to the above suggestion, where the variations of I_2/I_1 are seen as a function of [As]/[Ga]. The points near the upper line are on p-type samples, except for the lowest point of an n-type one, formed in successive runs of a reaction series where source A TMG was used. Those near the lower one are on n-type samples formed in another series where source B TMG was used. In both series, I_2/I_1 increases with decrease of [As]/[Ga], with increase of the As vacancy concentration, and with decrease of the Ga vacancy concentration. These lines suggest that the P_2 emission is related to the group IV elements and not to the group II elements.

Further discussions can be made from the standpoint of the chemical equilibrium and the law of mass action, when the group IV elements are the origin of the P_2 emission. Reactions between one of the group

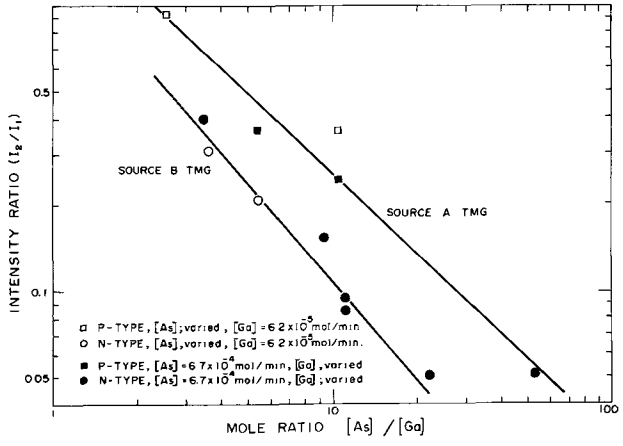

Fig. 5. Photoluminescence peak intensity ratio (I_2/I_1) of P_2 and P_1 of p- and n-type samples grown from source A and B at 90°K vs. introduced gas ratio of AsH_3 to TMG ([As]/[Ga]).

IV elements, M_i, and the vacancies, V_{Ga} and V_{As}, can be written as follows

$$V_{Ga} + M_i(g) \rightleftarrows M_i(\text{Ga site}) \quad [6]$$

and

$$V_{As} + M_i(g) \rightleftarrows M_i(\text{As site}) \quad [7]$$

If the donor and acceptor concentrations, N_D and N_A, in the epitaxial layer are mainly due to the group IV elements, then we have

$$N_D - N_A \cong \sum_i \{[M_i(\text{Ga site})] - [M_i(\text{As site})]\}$$

$$\cong \sum_i P_{M_i} \left\{ \alpha'_i(T) \cdot \frac{P_{CH_4}^3}{P_{H_2}^{3/2}} \cdot \frac{1}{P_{TMG}} - \alpha''_i(T) \cdot P_{H_2}^{3/2} \cdot \frac{1}{P_{AsH_3}} \right\} \quad [8]$$

where i, P_{M_i}, and M_i denote one of the group IV elements, its partial pressure, and concentration in GaAs, respectively; $\alpha'_i(T)$ and $\alpha''_i(T)$ are the proportional constants. It can be expected from Eq. [8] that $N_D - N_A$ may be varied by changing the mixing ratio of the source materials. Figure 2 shows this situation clearly. If the group II elements, instead of the group IV elements, were the main acceptor impurity source, $N_D - N_A$ should increase with increase of [As]/[Ga], contrary to the experiments.

The peak intensity of the P_2 emission also varies with the deposition temperature, T, as shown in Fig. 6. Increase of I_2/I_1 with increase of the deposition temperature may be explained that many more As

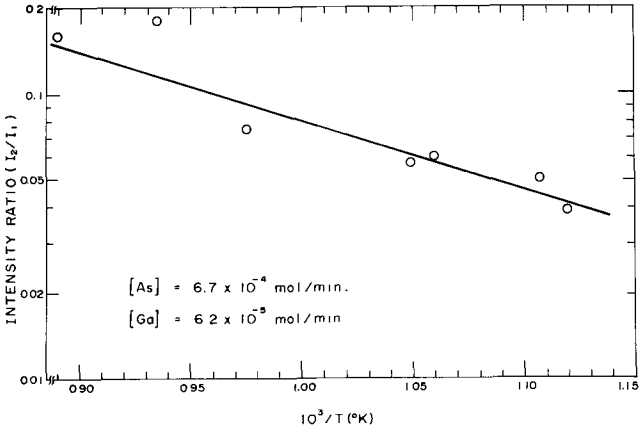

Fig. 6. Photoluminescence peak intensity ratio (I_2/I_1) of P_2 and P_1 of n-type samples at 90°K vs. deposition temperature (T).

vacancies than Ga vacancies are formed at these temperatures (16, 17).

Further evidence on the origin of the P_2 emission or of the main acceptor impurities in the epitaxial layer may be seen in Table I, in which the impurity contents in the layer examined by the mass-spectrographic analysis are tabulated. In the table, the upper data are Rai-Choudhury's (4), and the lower are the data obtained in the present experiment. Both show that the major impurities are carbon and silicon and that the minor ones are magnesium and zinc (oxygen and chlorine are also seen at high contents, but they seem to be not so electrically active in GaAs). These data support the model wherein the group IV elements are the main impurities and mainly contribute to the P_2 emission in the epitaxial layers.

When the growth rate was varied from 0.07 to 0.27 μm/min, there was little change in I_2/I_1 and the carrier concentrations of the epitaxial layers provided a constant value of [As]/[Ga]. This may be explained in the following way. If the group IV elements, *i.e.*, carbon and silicon, come from the TMG source, Eq. [8] can be rewritten

$$N_D - N_A \cong \sum_i \frac{P_{Mi}}{P_{TMG}} \left\{ \alpha'_i(T) \cdot \frac{P_{CH_4}{}^3}{P_{H_2}{}^{3/2}} - \alpha''_i(T) \cdot P_{H_2}{}^{3/2} \cdot \frac{P_{TMG}}{P_{AsH_3}} \right\} \quad [9]$$

and

$$N_D - N_A \propto \sum_i \frac{P_{Mi}}{P_{TMG}} \; (= \text{constant}) \quad [10]$$

when P_{AsH_3}/P_{TMG} = constant or [As]/[Ga] = constant at a fixed deposition temperature. A similar result might be deduced from Eq. [9] if these carbon and silicon atoms come from the AsH_3 source and the TMG container. The amounts of impurities from the AsH_3 source or the TMG container are, however, negligible since no appreciable changes are observed in the carrier concentration and in the photoluminescence spectrum when different AsH_3 sources or different TMG containers, such as quartz, glass, and stainless-steel ones, are used. The fact that the carrier concentrations of the epitaxial layers were changed when different TMG sources were used and that the main metallic impurities in the TMG sources used here were silicon (25 ~ 40 ppm), rather than magnesium (1 ppm) and zinc (not detectable), is another confirmation of the model wherein the main acceptor impurities are silicon and carbon that come from the TMG sources. One of possible sources of carbon may be organic compounds contained in the TMG sources. [The carbon contamination by the decomposition of the methyl radicals of TMG is thought to be small in the light of the chemical equilibrium (4).] It has been reported that carbon contamination of the order of 10^{18} cm^{-3} is observed in the high purity GaAs by the Ga-$AsCl_3$ system (18). The carbon atoms seem not to be the main contributors to the acceptor densities or to the P_2 emission, although the behavior of carbon in GaAs is still uncertain.

An emission at 1.40 eV associated with silicon has been reported (8) in the epitaxial layers by the Ga-$AsCl_3$ system. This emission was, however, not observed in the present experiments. Relatively low concentrations of silicon may be the reason for no appearance of the emission because it could be observed at higher concentrations ($> 10^{17}$ cm^{-3}) (19).

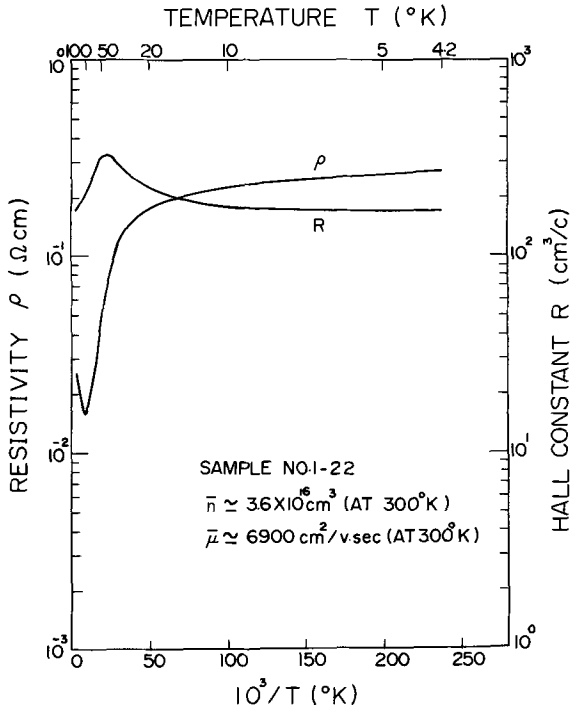

Fig. 7. Hall constant (R) and resistivity (ρ) of a typical epitaxial layer vs. temperature (T).

Electrical properties.—Epitaxial layers with $n < 10^{16}$ cm^{-3} and $\mu > 5000$ cm^2/V · sec at room temperature are desired for GaAs devices such as Gunn effect devices, FET's, Schottky barrier devices, and so on. The Hall constants and resistivities of some samples (2.0 ~ 20.0 μm in thickness) with n and μ near the above values were measured at temperatures from 4.2° to 300°K.

Figure 7 is a typical example of the Hall measurements, where the Hall constant, R, and resistivity, ρ, are shown as a function of the temperature, T. The impurity conduction (20, 21) can be seen as like the other samples examined, that is, the Hall constant has a maximum value at a low temperature. The impact ionization of electrons from the "donor band" to the conduction band at an external field, 12 V/cm, were observed as drastic changes of R and ρ at 4.2°K. This field is quite similar to that (10 V/cm) observed in the epitaxial GaAs layer by the Ga-$AsCl_3$ system (22).

Effective carrier concentrations ($\bar{n}$) and mobilities ($\bar{\mu}$) of this sample at 300° and 77°K are tabulated in Table II, together with some other similar ones, where

$$\bar{n} = -\frac{1}{qR} = \frac{(n_c + bn_d)^2}{n_c + b^2 n_d}, \quad b = \frac{\mu_d}{\mu_c} \quad [11]$$

and

$$\bar{\mu} = -\frac{R}{\rho} = \frac{n_c\mu_c{}^2 + n_d\mu_d{}^2}{n_c\mu_c + n_d\mu_d} \quad [12]$$

where q is the electronic charge; n_c, n_d, and μ_c, μ_d are the electron concentrations and the mobilities of the conduction band and the donor band, respectively; and the scattering factors of the carriers are taken to be unity for simplicity.

Table I. Impurity concentrations in GaAs grown by the TMG-AsH_3 system in parts per million

	C	N	O	Si	S	Fe	Cu	Zn	Mg	Cl
Rai-Choudhury (4)	238.4	1.78	220.4	4.46	1.47	1.60	2.24	0.89	—	—
Present experiment	25	—	5	1 ~ 5	0.1 ~ 3	<0.3	<0.1	0.2 ~ 0.3	0.1 ~ 0.6	1 ~ 28

Table II. Effective carrier concentration ($\bar{n}$), mobility ($\bar{\mu}$), estimated values of impurity concentration (N_A and N_D), compensation ratio ($K = N_A/N_D$), and donor level ($E_C - E_D$) of typical epitaxial layers

Sample No.	Thickness t (μm)	300°K $\bar{n}$ (cm⁻³)	300°K $\bar{\mu}$ (cm²/V·sec)	77°K $\bar{n}$ (cm⁻³)	77°K $\bar{\mu}$ (cm²/V·sec)	Estimated values K (= N_A/N_D)	N_D (cm⁻³)	N_A (cm⁻³)	$E_C - E_D$ (meV)
1-22	2.4	3.6×10^{16}	6,900	2.5×10^{16}	12,500	0.49	7.1×10^{16}	3.5×10^{16}	2.2
1-29	18.0	1.1×10^{16}	6,000	8.5×10^{15}	15,400	0.70	3.6×10^{16}	2.5×10^{16}	2.0
2-5	8.0	7.0×10^{15}	5,100	4.9×10^{15}	12,400	0.79	3.3×10^{16}	2.6×10^{16}	2.4
11-4	7.8	13×10^{16}	5,500	7.8×10^{15}	11,700	0.59	3.2×10^{16}	1.9×10^{16}	5.5

The growth conditions of these samples are as follows: (*i*) deposition temperature = 650° ~ 670°C; (*ii*) [As]/[Ga] = 9 ~ 11; (*iii*) samples 1-22, 1-29, and 2-5 were grown from the source A TMG; and (*iv*) sample 11-4 was grown from the source B TMG. The relatively low mobilities at 77°K suggest that all samples are compensated with acceptor impurities. Donor and acceptor concentrations (N_D and N_A) and μ_c were estimated by the Brooks-Herring's formula (23) where μ_c was calculated by the following equations

$$\mu_c = \frac{2}{1 + b\bar{\mu}} \quad [13]$$

$$b = \left(\frac{2R_{max}}{R_{4.2°K}} - 1\right) - 2\sqrt{\frac{R_{max}}{R_{4.2°K}}\left(\frac{R_{max}}{R_{4.2°K}} - 1\right)} \quad [14]$$

at the temperature when R is maximum. The donor levels ($E_C - E_D$) were also estimated using these N_D and N_A and the following relation (24)

$$\frac{n_c\,(n_c + N_A)}{N_D - N_A - n_c} = \frac{N_c}{g}\exp\left\{-\frac{E_C - E_D}{kT}\right\} \quad [15]$$

In Eq. [15], N_C is the effective density of states of the conduction band and g is the degeneracy of the donor level, where $g = 2$. Table II shows these estimated values together with the compensation ratio ($K = N_A/N_D$). The estimated values of the donor level are quite similar to that observed in GaAs prepared by other epitaxial methods (18). Somewhat greater values of the donor level than that reported before may be in part due to the experimental errors of about 20% in total. Large values of the compensation ratio explain the relatively low electron mobilities at 77°K and agree well with the results of the photoluminescence measurements, in which the 1.488 eV emission due to the shallow acceptors is observed with a relatively high intensity; they also agree with the mass-spectrographic analysis.

Conclusions

Epitaxial GaAs has been grown on GaAs substrates by the pyrolysis of TMG and AsH_3. Both n- and p-type layers were obtained by changing the mole ratio of TMG to AsH_3 introduced into the reactor without intentional doping. Epitaxial layers with a relatively good quality ($n \sim 10^{16}$ cm^{-3}, $\mu \sim 6000$ cm^2/V·sec at room temperature) were grown by use of a suitable TMG source and a suitable flow rate of TMG and AsH_3. Hall measurements indicate that these layers show the impurity conduction at low temperatures, and are heavily compensated with acceptor impurities. Donor levels are estimated to be 2.0 ~ 5.5 meV by the Hall measurements.

Photoluminescence measurements suggest that the main acceptor impurities in the epitaxial layer correspond to an emission with a peak at 1.488 eV beside the near bandgap emission at 1.503 eV. The origin of the acceptor impurities is thought to be carbon, silicon, or both from the TMG source.

Acknowledgments

The authors would like to acknowledge the many helpful discussions of Dr. S. Asanabe, Dr. K. Sugibuchi, and H. Iwasaki.

Manuscript submitted Dec. 11, 1972; revised manuscript received April 9, 1973. This was Paper 178 presented at the Cleveland, Ohio, Meeting of the Society, Oct. 3-7, 1971.

Any discussion of this paper will appear in a Discussion Section to be published in the June 1974 JOURNAL.

REFERENCES

1. H. M. Manasevit, *Appl. Phys. Letters*, **12**, 156 (1968).
2. H. M. Manasevit and W. I. Simpson, *This Journal*, **116**, 1725 (1969).
3. H. M. Manasevit and W. I. Simpson, Abstract No 63, page 154, Electrochem. Soc. Extended Abstracts, Spring Meeting, Boston, Massachusetts, May 5-9, 1968.
4. P. Rai-Choudhury, *This Journal*, **116**, 1745 (1969).
5. H. M. Manasevit and A. C. Thorsen, *Met. Trans.*, **1**, 623 (1970).
6. K. Lindeke, W. Sack, and J. J. Nickl, *This Journal*, **117**, 1316 (1970).
7. A. C. Thorsen and H. M. Manasevit, *J. Appl. Phys.*, **42**, 2519 (1971).
8. H. Iwasaki and K. Sugibuchi, *Appl. Phys. Letters*, **18**, 420 (1971).
9. T. N. Morgan, M. Pilkuhm, and H. Rupprecht, *Phys. Rev.*, **138**, A1551 (1965).
10. H. J. Queisser and C. S. Fuller, *J. Appl. Phys.*, **37**, 4895 (1966).
11. E. W. Williams, *Phys. Rev.*, **168**, 922 (1968).
12. D. E. Hill, *ibid.*, **133**, A866 (1964).
13. E. W. Williams and H. B. Bebb, *J. Phys. Chem. Solids*, **30**, 1289 (1968).
14. H. Kressel and F. Z. Hawrylo, *J. Appl. Phys.*, **41**, 1865 (1970).
15. H. Kressel, J. U. Dunse, H. Nelson, and F. Z. Hawrylo, *ibid.*, **39**, 2006 (1968).
16. H. R. Potts and G. L. Pearson, *ibid.*, **37**, 2098 (1966).
17. E. Munoz, W. L. Snyder, and J. L. Moll, *Appl. Phys. Letters*, **16**, 262 (1970).
18. C. M. Wolfe and G. E. Stillman, "Proceedings of the 3rd International Symposium on Gallium Arsenide and Related Compounds," p. 3, Aachen, Germany (1970).
19. K. Sugibuchi, Private communication.
20. C. S. Hung, *Phys. Rev.*, **79**, 727 (1950).
21. C. S. Hung and J. R. Gliessman, *ibid.*, **79**, 726 (1950).
22. S. Asai, T. Toyabe, and M. Hirao, "Proceedings of the 10th International Conference on Physics of Semiconductors," p. 578, Cambridge, England (1970).
23. H. Brooks, in "Advances in Electronics and Electron Physics," L. Marton, Editor, Vol. 7, p. 158, Academic Press, Inc., New York (1955).
24. G. L. Pearson and J. Bardeen, *Phys. Rev.*, **75**, 865 (1949).

Reproducible High-Efficiency GaP Green-Emitting Diodes Grown by Overcompensation

O. G. Lorimor, W. H. Hackett, Jr., and R. Z. Bachrach

Bell Laboratories, Murray Hill, New Jersey 07974

ABSTRACT

High-efficiency GaP green light-emitting p-n junctions have been reproducibly grown employing an overcompensation technique in a vertical dipping LPE system. In this technique both the n- and p-type layers are grown in a single LPE crystal growth run, eliminating potential interface problems at the junction. For junction material grown at an initial temperature of 900°C the EL quantum efficiencies of encapsulated mesa diodes ranged from 0.08 to 0.14% and averaged 0.10% at 5 mA (~5-10 A/cm²). Minority carrier diffusion lengths (L_e,L_h) and relative cathode-luminescence efficiency (CL) were measured in a scanning electron microscope. At excitation levels equivalent to current densities of ~1-10 A/cm² in a p-n junction, both L_e and L_h range from 3 to 5μ with maximum measured values of $L_h = 7.2\mu$ and $L_e = 5.6\mu$ for material grown from 900°C. At the same excitation level the CL efficiency of the p-layers was typically found to be approximately 2-3 times that of the n-layers. Typical values for L_e, L_h, CL, and the EL efficiencies were found to be larger by ~50% for material grown from 900°C compared to similarly grown material from 1000°C. The major assets of the overcompensation technique are the high degree of reproducibility in obtaining high efficiencies and that only a single growth process is necessary to form the p-n junction.

GaP p-n junction material used in the fabrication of both red and green LED's is customarily grown in two separate LPE grown runs (1). With this double LPE procedure, the surface of the first grown layer may become oxidized, contaminated, and possibly damaged during the handling and preparation of the crystal prior to the growth of the second layer. Such defects could degrade diode performance by increasing the deep-state space charge recombination, resulting in nonreproducible electroluminescent efficiencies.

There is some direct evidence of nonreproducible junction characteristics in GaP electroluminescent diodes made from material grown by the usual techniques. For example, recent measurements of the charge storage time of GaP green LED's have been made by abruptly switching a forward biased diode into reverse bias (2). These measurements indicate that, for material with similar electroluminescent decay times, the storage time can be a sensitive measure of injection efficiency. Specifically, in cases where the storage time is shortest at 1-10 A/cm², the space charge current is largest resulting in low injection efficiencies and low electroluminescent efficiencies. Variations in the space charge current were found in diodes from the same slice as well as from different slices. Consequently, it appeared that additional measures are required to provide reproducible, "high-quality" space charge regions necessary for consistently high-efficiency GaP green LED's.

In an attempt to achieve reproducibly small space charge currents, a different junction fabrication technique was investigated in which both LPE layers are grown in a single crystal growth run. Since the seed need not be removed from the growth system between LPE layer growths, interface contamination or damage should be eliminated. An overcompensation technique similar to that described by Shih *et al.* (3) was incorporated into our growth system. After growth of the n-layer, sufficient Zn is added to overcompensate the melt, and the p-layer is subsequently grown. This technique reduces the time and effort required for LPE growth by about a factor of two.

Experimental

The LPE layers were grown in an open-flow dipping system similar to that described by Dawson and Whelan (4) for GaAs and presently used for the growth of GaP. Two modified versions of this system were used to grow the overcompensated material. The first was a small-scale system capable of growing on one seed up to ½ × ½ in. in size. Figure 1 shows a schematic of this system. The seed holder is hollow so that Zn can be dropped through the seed holder tube into the melt from the Zn drop tube during a run. The GaP source piece is used to complete the saturation of the melt with P so that no undissolved GaP remains on the melt to serve as competing growth centers (4). In this system the crucible and seed holders are fabri-

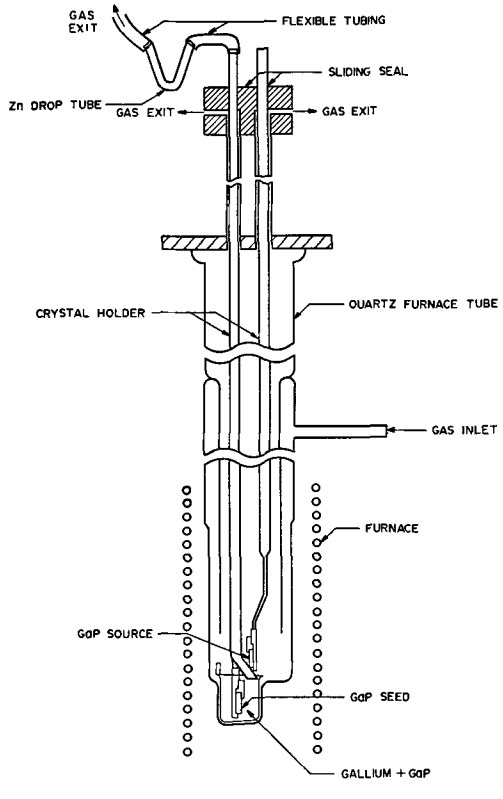

Fig. 1. Vertical dipping system as used for the small, single slice overcompensation technique.

Key words: crystal growth, minority carrier diffusion lengths, material characterization, scanning electron microscope.

cated from quartz. A 15g melt is used. The gas ambient is H_2 flowing at $\sim$ 100 cm^3/min.

The second system for the growth of the overcompensated material is nearly identical to the first except for a larger crucible and modified seed holder, as shown in Fig. 2. Growth is simultaneous on two full wafers up to 0.9-in. diameter. The seeds are mounted back-to-back on the seed holder plate. Again the Zn used to overcompensate the melt is dropped into the melt through the seed holder tube. Both the seed holders and crucible are fabricated from quartz. A 60g melt is used.

In the second system a stirring mechanism is used to produce an $\sim$ 30° oscillatory motion of the seeds about the vertical axis of the seed holder at a rate of four cycles per minute. The purpose of the stirrer is to promote the uniform dopant distribution in the melt and provide more uniform growth of the LPE layers. In previously grown double LPE material it had been found that the stirring increased the uniformity of the EL efficiency within a slice.

The overcompensation system is prepared for crystal growth by placing a Ga melt, slightly undersaturated with GaP, containing $\sim 5 \times 10^{-4}$ m/o (mole per cent) Te in the crucible. A new melt is used for each growth run. An n-type LEC crystal(s) is placed on the seed holder, as is shown in Fig. 1 and 2. The Zn ($\sim$ 0.15 m/o), which is used for overcompensating the melt to dope the p-layer, is placed in the Zn drop tube. The simultaneous N-doping is accomplished by the addition of $\sim 10^{-3}$ atm NH_3 to the H_2 gas stream. This ammonia partial pressure results in a N-concentration in the LPE layer of $\sim 8 \pm 2 \times 10^{+18}$ cm^{-3} at both 900° and 1000°C as determined by optical absorption measurements (5). After the melt is equilibrated at the initial growth temperature, saturation is completed by dipping the GaP source piece into the melt. Prior to dipping the seed, it is removed from the melt and rotated out of the way.

The n-layer is grown by cooling the melt 10° or 20°C from 900°C in 1 hr. Immediately after completion of the n-layer growth, with the seed left in the melt and the furnace held at constant temperature, the Zn is dropped into the melt through the hollow seed holder tube. After waiting 30 min for the Zn to thoroughly dissolve and distribute uniformly in the melt, the p-layer is grown by further cooling over intervals ranging from 10° to 30°C in times varying from 1 to 2 hr. Growth is terminated by removing the seed from the melt. This growth schedule results in both n- and p-layers which range in thickness from $\sim$10 to $\sim$30μ. When the larger cooling intervals are used, both layers are commonly 20 to 30μ thick. One should note that with this technique, only the p-layer is overcompensated.

For comparison purposes some double LPE crystals are also discussed where each LPE layer has been grown in a separate crystal growth run. This has been the standard process prior to the overcompensation technique. Table I compares some of the growth parameters of the double LPE material with the overcompensated material. Note that the differences in material growth are: (a) the standard n-layer is grown from 1000°C, whereas the n-layer in the overcompensated material is grown from 900°C, (b) in addition to Zn and N, the overcompensated p-layer also contains Te, and (c) the crystal was removed from the growth system between layer growths in the double LPE material but was not removed in the overcompensated material. Other growth parameters, for example, ambients, cooling rates, and crucible materials, are the same for both the overcompensated and double LPE material. The growth rates and temperatures given in Table I are those predominantly used. A few crystal growth runs were made where both layers were grown from 1000°C to study the effects of growth temperature. In cases where growth was from 1000°C, the dopant additions were adjusted to keep the net donor or acceptor concentration in each layer the same as when growth was from 900°C.

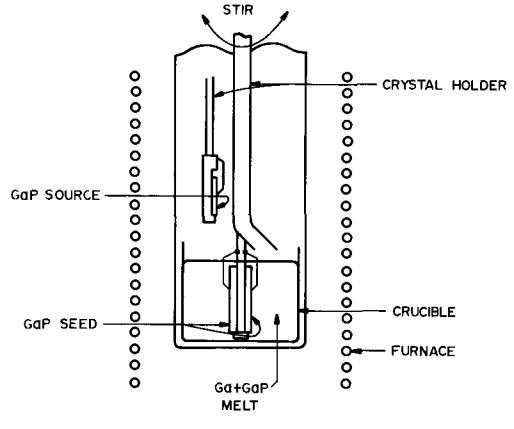

Fig. 2. Modified crucible and seed holder to grow simultaneously on two full-wafer seeds using the overcompensation technique.

Most of the quantum efficiencies were measured on mesa diodes. In the remaining cases, uncontacted diced diodes or contacted diced diodes were used. The mesa structures were formed by masking with 0.015 in. diameter gold balls and sandblasting. After wire bonding for electrical connections, the diodes were mounted on an alumina chip on a TO-18 header. This structure was domed with Maraset epoxy. The diced diodes (6) were 0.015 × 0.015 in. slurry cut dice. Prior to dicing both faces of the slice were polished, after which a SiO_2 layer was deposited onto the LPE layer side. Evaporated and alloyed contacts were formed through a metal mask on the substrate face and through holes etched in the SiO_2 layer on the LPE layer face. The dice were mounted p-side down directly on a TO-18 header. The uncontacted dice were mounted on modified TO-18 headers employing a spring-loaded wire as a pressure contact.

The efficiencies were measured in a close-coupled cavity designed by Ralston (7). Mesa diodes were measured at 5 and 50 mA which correspond to current densities of $\sim$5 and $\sim$50 A/cm^2, respectively. The efficiencies of the diced diodes were measured at twice the current as that used for the mesas to obtain data at equivalent current densities. Unencapsulated contacted diced diode data are multiplied by a factor of two for typical increases in optical coupling achieved by encapsulation (8), which results in efficiencies within ±20-30% of mesa diode efficiencies. The efficiencies of the uncontacted dice were measured only at 10 mA. These efficiencies were multiplied by an empirically determined factor of 1.6 for typical increases in optical coupling achieved by encapsulation, which also results in efficiencies within ±20-30% of mesa diode efficiencies.

The cathodoluminescence (CL) and diffusion length measurements were performed in a Cambridge

Table I. Comparison of growth parameters of double LPE and overcompensated techniques

	Over-compensated	Double LPE
Structure	p/n/LEC	p/n/LEC
n-Layer		
Dopants	Te,N	Te,N, or S,N
Typical N_d-N_a	1-2 × 10^{17}	1-2 × 10^{17}
Initial growth temperature, °C	900	1000
LPE growth run	First	First
p-Layer		
Dopants	Zn,Te,N	Zn,N
Typical N_a-N_d	5-8 × 10^{17}	5-8 × 10^{17}
Initial growth temperature, °C	880-890	900
Equilibration time	½ hr	½ hr
LPE growth run	Same run as n-layer	Second

"Stereoscan" scanning electron microscope (9). The measurements are generally made by scanning a focused electron beam across a polished surface perpendicular to the junction on a 15 × 15 mil die. A photomultiplier detection system is used to measure the cathodoluminescence emitted by the sample due to the electron beam excitation. The diffusion lengths are determined by measuring the induced junction current as a function of scan distance across the junction (9). The electron beam excitation levels are equivalent to diffusion current densities of ~ 1-10 A/cm² through a p-n junction. The low current EL efficiencies were measured at current densities of ~ 5-10 A/cm².

Results

Overcompensation.—A typical doping profile (10), $|N_d - N_a|$ as a function of depth, of the overcompensated material is shown in Fig. 3. Doping levels close to these are currently felt to be optimum for high-efficiency green LED's (11), and are essentially identical to those measured on crystals grown in the double LPE manner. The decrease in $N_a - N_d$ of the p-layer toward the surface is attributed to Zn loss during the crystal growth run, since it far exceeds the decrease expected from the temperature dependence of the Zn distribution coefficient (12, 13). This loss is also seen in the profiles from the double LPE material.

Figures 4 and 5 show the efficiencies measured at low (~ 5 A/cm²) and high (~ 50 A/cm²) current densities, respectively, for test diodes fabricated from nine successive crystal growth runs which were specifically made to obtain high efficiency material. These efficiencies are comparable to those of better diodes fabricated from material grown in the standard manner. In addition, the reproducibility in achieving the efficiencies is very high. Essentially every growth

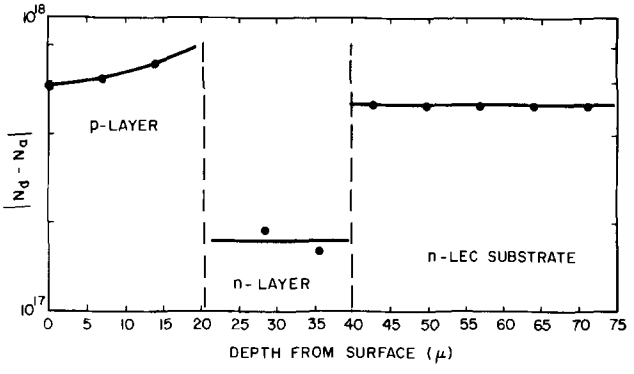

Fig. 3. Typical doping profile of the overcompensated material used for the fabrication of high-efficiency green LED's.

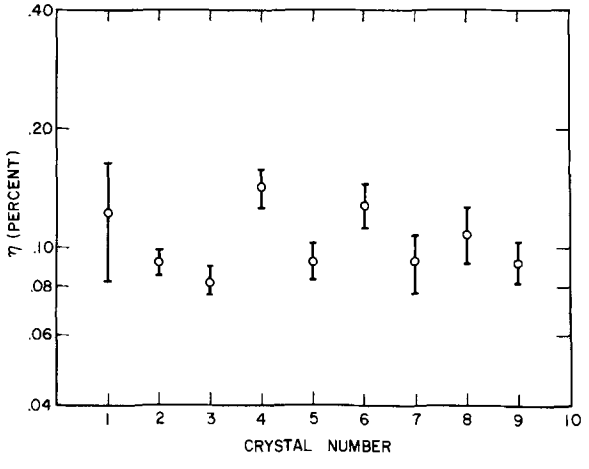

Fig. 4. Quantum efficiencies of encapsulated mesa diodes at 5 mA (~5 A/cm²) for nine successive overcompensation crystal growth runs.

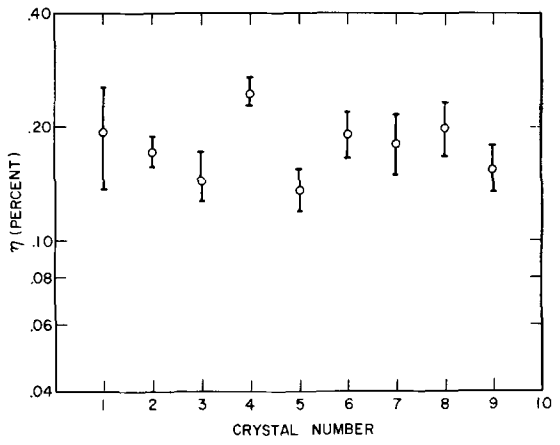

Fig. 5. Quantum efficiencies of encapsulated mesa diodes at 50 mA (~ 50 A/cm²) for nine successive overcompensation crystal growth runs.

which was made with the overcompensation procedure yielded efficiencies as high as those shown in Fig. 4 and 5. This reproducibility is to be compared with that obtained with the standard double LPE procedure where the efficiencies varied from ~0.04 to over 0.2% at 50 A/cm². Approximately half the standard growths resulted in efficiencies less than 0.1% at 50 A/cm². The average efficiency of the overcompensated crystals was 0.10% with the individual slices varying from 0.08-0.14%, at 5 A/cm² and nearly a factor of two higher at 50 A/cm². Thus, the important material improvement realized through overcompensation is reproducibility in achieving high efficiencies. Although equally high efficiencies were achieved with the standard process, the reproducibility was so poor that the average efficiency was approximately half that achieved with overcompensation.

To check whether the improved reproducibility of the overcompensated diodes is due to a uniform reduction of the space charge current, the current through the diodes at a forward bias of 1.4V was measured. At this voltage the current is typically dominated by deep-state space charge current (6). The current through the overcompensated and both good and poor standard diodes was typically $\lesssim 7 \times 10^{-5}$ A/cm². Larger currents were not observed in the overcompensated diodes, while occasionally a larger current was measured in a standard diode which correlated with a low EL efficiency (2). Thus, the overcompensation technique did not result in an obvious reduction of space charge current as was anticipated, but did eliminate anomalously high values. Thus it appears that there were often other problems with the standard technique, such as varying minority carrier lifetimes.

During the half-hour equilibration period and p-growth, one might expect that Zn diffuses into the n-layer and displaces the p-n junction from the metallurgical junction which might have a high concentration of defects. However, this effect does not appear to be important. Zn diffusion data indicates that the junction movement would be small, $\lesssim 1\mu$ (14), for the times and temperatures used in LPE growth. The standard procedure also included a similar half-hour equilibration period which should result in essentially equal Zn diffusions for both growth procedures. These conclusions are corroborated in the SEM, where there is no evidence of an interface of nonradiative recombination centers in the p-layer near the junction using high magnification CL scans. A significant concentration of such recombination centers at a metallurgical interface displaced from the p-n junction would have resulted in a localized decrease in CL.

To investigate whether the overcompensated p-layers were degraded by the presence of Te, measurements

of the minority carrier diffusion lengths, L_e, were made and compared to those for standard p-layers which are not overcompensated. These diffusion lengths are compared in Table II. In both techniques $3\mu \lesssim L_e \lesssim 5\mu$ with no noticeable difference between the two techniques. Thus it is concluded that for these doping levels, overcompensation does not degrade the p-layers.

Effects of growth temperature.—Extensive growth of GaP green LED material has been performed from two temperatures, 1000° and 900°C. Table III presents a summary of the average efficiency of the material grown from these temperatures by both the double LPE and overcompensation techniques. The average efficiency of the 900°C overcompensated growths was 0.104% measured on encapsulated mesa diodes at 5 A/cm². It is felt that this technique and temperature will give reproducible 5 A/cm² efficiencies of ~0.10%. All other combinations of growth techniques and temperatures used to date and listed in Table III result in average efficiencies lower by $\gtrsim$ 50%. We feel that the higher average efficiency of the overcompensated material grown from 900°C is primarily due to the lower growth temperature which in turn results in higher reproducibility.

Table IV presents a summary of the minority carrier diffusion lengths, relative CL intensities, and EL efficiencies for a few specific samples grown from these temperatures both by the double LPE and overcompensation techniques. The minority carrier diffusion lengths presented in this table are generally as long if not longer than those previously reported for LPE grown Zn-doped and Te-doped GaP (9, 15). When growth is from 900°C, the range generally found is $3\mu \lesssim L_h \lesssim 5\mu$ with a maximum of 7.2μ in the n-layers, and in the p-layers also $3\mu \lesssim L_e \lesssim 5\mu$ with a maximum of 5.6μ. When growth is from 1000°C in quartz, the diffusion lengths are reduced, $1.5\mu \lesssim L_{h,e} \lesssim 2.5\mu$ with a maximum of 3.7μ in both the n- and p-layers. In addition, both the n- and p-layers grown from 900°C have approximately a 50% greater CL intensity than similar layers grown from 1000°C. When both layers are grown from the same temperature, the CL efficiency of the

Table II. Minority electron diffusion lengths in the p-layers of both double LPE and overcompensated diodes as measured with an SEM

Crystal*	Growth technique	p-Layer N_a-N_d (cm^{-3})	p-Layer L_e (μ)
—	Overcompensated	8.8×10^{17}	3.5
2	Overcompensated	6.2×10^{17}	3.7-4.5
9	Overcompensated	7.0×10^{17}	4.8-5.6
A	Double LPE	4.3×10^{17}	3.5
B	Double LPE	5.3×10^{17}	2.5-3.2
C	Double LPE	$\sim 6 \times 10^{17}$	4.5

* The numbered samples correspond to the crystal numbers in Fig. 4 and 5.

Table III. Average efficiencies of diodes grown by double LPE and overcompensated techniques

Growth procedure	Growth temperature, °C p-Layer	Growth temperature, °C n-Layer	Average efficiency ~5 A/cm²	Average efficiency ~50 A/cm²
Overcompensated	900	900	0.104	0.180
Overcompensated	1000	1000	0.051	—
Double LPE	900	1000	0.048	0.094
Double LPE[a]	1000	1000	0.042	0.092

[a] The N concentration of these crystals is low by less than a factor of two. Since the efficiency should vary with the N concentration, these efficiencies are in effect comparable to those from the material growth by overcompensation entirely from 1000°C.

Table IV. Minority carrier diffusion lengths, relative CL intensities, and EL efficiencies for both double LPE and overcompensated material grown from both 1000° and 900°C

Note that in the overcompensation scheme only the p-layer, and not the n-layer is overcompensated. The numbered samples correspond to the crystal numbers in Fig. 4 and 5.

Crystal	Growth technique	Growth temp (°C)	N_d-N_a (cm^{-3})	Relative CL intensity	L_h (μ)	Growth temp (°C)	N_a-N_d (cm^{-3})	Relative CL intensity	L_e (μ)	$\frac{CL_p}{CL_n}$	Avg ~5 A/cm² η_{EL} (%)	Avg ~50 A/cm² η_{EL} (%)	Relative† efficiency
*	Overcompensated	900	1.0×10^{17}	—	5.0-7.2	900	8.8×10^{17}	—	3.5	—	0.111‡	—	Above average
2**	Overcompensated	900	9.2×10^{16}	—	3.5-4.5	900	6.2×10^{17}	—	3.7-4.5	3-4	0.117	0.195	Above average
4**	Overcompensated	900	1.0×10^{17}	30	3.8-4.5	900	6.5×10^{17}	85	4.7-4.9	2.8	0.143	0.258	Good
9	Overcompensated	900	1.9×10^{17}	22	3.1-3.6	900	7.0×10^{17}	77	4.8-5.6	3.5	0.093	0.158	Average
A	Double LPE	1000	1.5×10^{17}	—	1.75	900	4.3×10^{17}	—	3.5	13-16	0.117	0.234	Good
B	Double LPE	1000	1.6×10^{17}	—	1.4-2.1	900	5.3×10^{17}	—	2.5-3.2	7-9	0.042	0.057	Average
C	Double LPE	1000	2×10^{17}	—	1.65	900	6×10^{17}	—	4.5	18-22	0.044	0.091	Average
I***	Double LPE	1000	2.3×10^{17}	6	2.15-2.55	1000	8.4×10^{17}	17	2.25-2.55	3.0	0.044	0.103	Average
II***	Overcompensated	1000	1.7×10^{17}	4	1.35-1.9	1000	1.2×10^{18}	16	2.1-2.6	4.0	0.039	0.085	Below average
III	Overcompensated	1000	1.6×10^{17}	15	3.7	1000	7.0×10^{17}	38	3.7	2.6	0.070‡	—	Above average (best)

* This sample has an additional n-type LPE layer between the substrate and the n-LPE layer discussed here.
† Relative efficiency of the sample compared to the average of those shown in Table III grown in the same manner.
‡ Quantum efficiency extrapolated from a point contact measurement.
** The layers varied by a factor of two in thickness across this sample. These measurements were made where the layers were the thickest. The CL, L_e, L_h, and η all decreased with decreasing layer thickness.
*** N concentration low by ~ a factor of 2. However, the low N concentration should reduce only the CL and EL efficiencies and not the diffusion lengths.

p-layer is generally two to three times that of the n-layer. Consequently, since all other growth conditions were unchanged, we conclude that the increase in minority carrier diffusion lengths and CL for 900°C growth in quartz compared to 1000°C is entirely due to the temperature difference. However, one should note that the longest diffusion length measured in layers grown at 1000° (3.7μ) is comparable to that measured in many similar layers grown from 900°C. Also, as can be seen from Table IV, there are considerable differences in diffusion lengths for supposedly similar layers grown at the same temperature. It is felt that unknown interactions during LPE growth, which are more severe when growth is from 1000°C rather than 900°C, are both limiting the diffusion lengths to the present values and causing these variations. An experimental program is in progress to define these variations and interactions in an effort to increase the electroluminescent efficiencies in GaP green-emitting diodes.

Conclusions

An overcompensation technique has been successfully used for the growth of GaP LPE layers used in the fabrication of green LED's. In this technique both LPE layers are grown in a single crystal growth run which avoids potential oxidation, contamination and/or damage at the p-n junction interface. An additional advantage of this technique is that only one LPE growth is necessary to form the p-n junction. With an initial growth temperature of 900°C, material with average efficiencies of 0.10% at 5 A/cm^2 for encapsulated mesa diodes with adequately thick layers ($\gtrsim 20\mu$) was grown routinely and reproducibly. Because of the high degree of reproducibility in the efficiencies and the use of a single LPE growth step, this technique is an attractive approach for fabrication of GaP green-emitting junctions.

The EL efficiencies, relative CL, and minority carrier diffusion lengths have been measured and compared for the overcompensated material grown in quartz from both 900° and 1000°C and double LPE 900°C p-layers on 1000°C n-layers. The average EL efficiencies for the 900°C overcompensated material were larger by at least 50% than the efficiencies for the material grown entirely from 1000°C. These results correlate with the fact that the CL and the diffusion lengths in both n- and p-layers grown from 900°C were larger by ~ 50% than that in a corresponding layer grown from 1000°C. The CL of the p-layers was found to be typically two to three times that of the n-layers when both were grown from the same temperature. In material grown from 900°C, the minority carrier diffusion lengths L_e and L_h were both typically found to range between 3 and 5μ with values as large as $L_h = 7.2\mu$ and $L_e = 5.6\mu$. It appears clear that low-temperature crystal growth results in important improvements in material quality.

Acknowledgments

The invaluable technical assistance of Mrs. J. Armstrong, D. D. Roccasecca, and T. E. McGahan is gratefully acknowledged. The assistance of G. W. Kammlott and S. E. Haszko with the SEM measurements is also acknowledged.

Manuscript submitted Jan. 16, 1973; revised manuscript received May 1, 1973.

Any discussion of this paper will appear in a Discussion Section to be published in the June 1974 JOURNAL.

REFERENCES

1. See, for example, H. C. Casey, Jr. and F. A. Trumbore, *Mat. Sci. Eng.*, **6** (1970).
2. P. D. Dapkus, To be published.
3. K. K. Shih, J. M. Woodall, S. E. Blum, and L. M. Foster, *J. Appl. Phys.*, **39**, 2962 (1968).
4. L. R. Dawson, "Progress in Solid State Chemistry," Vol. 7, H. Reiss and J. O. McCaldin, Editors, p. 117, Pergamon Press (1972).
5. D. G. Thomas and J. J. Hopfield, *Phys. Rev.*, **150**, 680 (1966).
6. N. E. Schumaker and G. A. Rozgonyi, *This Journal*, **119**, 1233 (1972)
7. J. M. Ralston, *Rev. Sci. Instr.*, **43**, 876 (1972).
8. R. Z. Bachrach, R. W. Dixon, and O. G. Lorimor, *Solid-State Electron.*, **16**, 1037 (1973).
9. W. H. Hackett, Jr., R. H. Saul, R. W. Dixon, and G. W. Kammlott, *J. Appl. Phys.*, **43**, 2857 (1972).
10. T. E. McGahan and W. H. Hackett, Jr., *Rev. Sci. Instr.*, **41**, 1182 (1970).
11. R. A. Logan, H. G. White, and W. Weigman, *Solid State Electron.*, **14**, 55 (1972).
12. A. S. Jordan, *This Journal*, **118**, 781 (1971).
13. R. H. Saul and W. H. Hackett, Jr., *ibid.*, **117**, 921 (1970).
14. L. C. Luther and K. B. Wolfstirn, *J. Electronic Materials*, To be published.
15. B. L. Smith and M. Abbott, *Solid-State Electron.*, **15**, 361 (1972).

Etching Studies of Diffusion Source Boron Glass

Lillian Rankel Plauger

Bell Telephone Laboratories, Incorporated, Murray Hill, New Jersey 07974

ABSTRACT

For selective boron doping of silicon, a SiO_2 diffusion mask is used. In many cases, it is advantageous to retain the same SiO_2 mask on the silicon slice after diffusion and remove the boron diffusion source glass. To accomplish retention of the SiO_2 mask while dissolving boron diffusion source glass, a selective etch is required that favors dissolution of boron-doped glass. Etching solutions that fulfill this need have been found.

When selectively doping silicon with boron, a borosilicate glass is deposited on a SiO_2 diffusion masked substrate (see Fig. 1). This boron diffusion source glass is subsequently removed, and in many instances the SiO_2 diffusion mask must be left in place. In cases such as this, an etching solution must be found that favors the dissolution of borosilicate glass over SiO_2.

It is known that "P" etch [15 parts HF (49%), 10 parts HNO_3 (70%), and 300 parts H_2O] dissolves various types of glass and mixed oxide layers more rap-

Key words: borosilicates, diborate, diffusion sources, etching borosilicates.

p-layer is generally two to three times that of the n-layer. Consequently, since all other growth conditions were unchanged, we conclude that the increase in minority carrier diffusion lengths and CL for 900°C growth in quartz compared to 1000°C is entirely due to the temperature difference. However, one should note that the longest diffusion length measured in layers grown at 1000° (3.7μ) is comparable to that measured in many similar layers grown from 900°C. Also, as can be seen from Table IV, there are considerable differences in diffusion lengths for supposedly similar layers grown at the same temperature. It is felt that unknown interactions during LPE growth, which are more severe when growth is from 1000°C rather than 900°C, are both limiting the diffusion lengths to the present values and causing these variations. An experimental program is in progress to define these variations and interactions in an effort to increase the electroluminescent efficiencies in GaP green-emitting diodes.

Conclusions

An overcompensation technique has been successfully used for the growth of GaP LPE layers used in the fabrication of green LED's. In this technique both LPE layers are grown in a single crystal growth run which avoids potential oxidation, contamination and/or damage at the p-n junction interface. An additional advantage of this technique is that only one LPE growth is necessary to form the p-n junction. With an initial growth temperature of 900°C, material with average efficiencies of 0.10% at 5 A/cm^2 for encapsulated mesa diodes with adequately thick layers ($\gtrsim 20\mu$) was grown routinely and reproducibly. Because of the high degree of reproducibility in the efficiencies and the use of a single LPE growth step, this technique is an attractive approach for fabrication of GaP green-emitting junctions.

The EL efficiencies, relative CL, and minority carrier diffusion lengths have been measured and compared for the overcompensated material grown in quartz from both 900° and 1000°C and double LPE 900°C p-layers on 1000°C n-layers. The average EL efficiencies for the 900°C overcompensated material were larger by at least 50% than the efficiencies for the material grown entirely from 1000°C. These results correlate with the fact that the CL and the diffusion lengths in both n- and p-layers grown from 900°C were larger by ~ 50% than that in a corresponding layer grown from 1000°C. The CL of the p-layers was found to be typically two to three times that of the n-layers when both were grown from the same temperature. In material grown from 900°C, the minority carrier diffusion lengths L_e and L_h were both typically found to range between 3 and 5μ with values as large as $L_h = 7.2\mu$ and $L_e = 5.6\mu$. It appears clear that low-temperature crystal growth results in important improvements in material quality.

Acknowledgments

The invaluable technical assistance of Mrs. J. Armstrong, D. D. Roccasecca, and T. E. McGahan is gratefully acknowledged. The assistance of G. W. Kammlott and S. E. Haszko with the SEM measurements is also acknowledged.

Manuscript submitted Jan. 16, 1973; revised manuscript received May 1, 1973.

Any discussion of this paper will appear in a Discussion Section to be published in the June 1974 JOURNAL.

REFERENCES

1. See, for example, H. C. Casey, Jr. and F. A. Trumbore, *Mat. Sci. Eng.*, **6** (1970).
2. P. D. Dapkus, To be published.
3. K. K. Shih, J. M. Woodall, S. E. Blum, and L. M. Foster, *J. Appl. Phys.*, **39**, 2962 (1968).
4. L. R. Dawson, "Progress in Solid State Chemistry," Vol. 7, H. Reiss and J. O. McCaldin, Editors, p. 117, Pergamon Press (1972).
5. D. G. Thomas and J. J. Hopfield, *Phys. Rev.*, **150**, 680 (1966).
6. N. E. Schumaker and G. A. Rozgonyi, *This Journal*, **119**, 1233 (1972)
7. J. M. Ralston, *Rev. Sci. Instr.*, **43**, 876 (1972).
8. R. Z. Bachrach, R. W. Dixon, and O. G. Lorimor, *Solid-State Electron.*, **16**, 1037 (1973).
9. W. H. Hackett, Jr., R. H. Saul, R. W. Dixon, and G. W. Kammlott, *J. Appl. Phys.*, **43**, 2857 (1972).
10. T. E. McGahan and W. H. Hackett, Jr., *Rev. Sci. Instr.*, **41**, 1182 (1970).
11. R. A. Logan, H. G. White, and W. Weigman, *Solid State Electron.*, **14**, 55 (1972).
12. A. S. Jordan, *This Journal*, **118**, 781 (1971).
13. R. H. Saul and W. H. Hackett, Jr., *ibid.*, **117**, 921 (1970).
14. L. C. Luther and K. B. Wolfstirn, *J. Electronic Materials*, To be published.
15. B. L. Smith and M. Abbott, *Solid-State Electron.*, **15**, 361 (1972).

Etching Studies of Diffusion Source Boron Glass

Lillian Rankel Plauger

Bell Telephone Laboratories, Incorporated, Murray Hill, New Jersey 07974

ABSTRACT

For selective boron doping of silicon, a SiO_2 diffusion mask is used. In many cases, it is advantageous to retain the same SiO_2 mask on the silicon slice after diffusion and remove the boron diffusion source glass. To accomplish retention of the SiO_2 mask while dissolving boron diffusion source glass, a selective etch is required that favors dissolution of boron-doped glass. Etching solutions that fulfill this need have been found.

When selectively doping silicon with boron, a borosilicate glass is deposited on a SiO_2 diffusion masked substrate (see Fig. 1). This boron diffusion source glass is subsequently removed, and in many instances the SiO_2 diffusion mask must be left in place. In cases such as this, an etching solution must be found that favors the dissolution of borosilicate glass over SiO_2.

It is known that "P" etch [15 parts HF (49%), 10 parts HNO_3 (70%), and 300 parts H_2O] dissolves various types of glass and mixed oxide layers more rap-

Key words: borosilicates, diborate, diffusion sources, etching borosilicates.

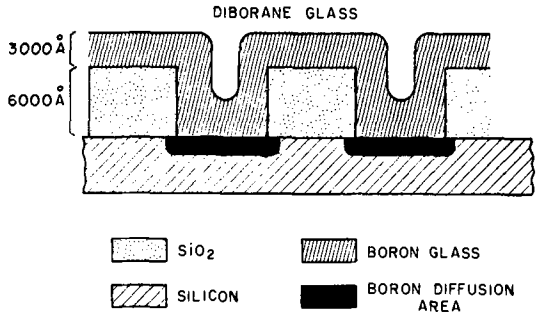

Fig. 1. Doping of silicon with boron diffusion source glass

idly than it dissolves silicon dioxide (1-4). Since "P" etch contains HNO_3, it was decided to investigate etching solutions with a relatively high concentration of oxidizing agents. These etching solutions were evaluated on borosilicate glass formed by low-temperature gaseous diborane with high-temperature anneal of deposited film. Etch rate of each glass was correlated with boron concentration. The etching characteristics of solutions formulated during this study are compared to well known standard solutions such as buffered HF and "P" etch.

Experimental

Silicon slices 3.2-cm in diameter were prepared according to Table I. The diborane glass depositions were done in a bell jar vertical reactor. A resistance-heated platform 8 in. in diameter provided the heat.

Table I. Glass deposition conditions

Gas flow rates and composition

	B_2H_6,* cm³/min	m/o B_2H_6	m/o B_2O_3, *IR*
Low B*	40	1.96	4.5
Medium B*	100	4.76	6.5
High B*	200	9.09	9.0

Weight per cent boron

	Microprobe % B	*IR*	B atoms/ cm³†
Low B	1.6	1.6	6×10^{18}
Medium B	2.6	2.4	5×10^{19}
High B	3.7	3.3	1.3×10^{20}

* Metered gas flow of 1% SiH_4 and 0.1% B_2H_6 molar per cent $B_2H_6 = [(B_2H_6)/(B_2H_6 + SiH_4)] \times 100$.
† Concentration of B in silicon after 1100°C diffusion for ½ hr in N_2 atmosphere.

Table II. Composition of etching solutions, HF(49%) HNO_3(70%)

1.	Buffered HF	113g NH_4F 170 ml H_2O 28 ml HF
2.	"P" etch	15 ml HF 10 ml HNO_3 300 ml H_2O
3.	HNO_3-HF "R" etch	100 ml HNO_3 100 ml H_2O 1 ml HF
4.	HNO_3-HF "S" etch	100 ml HNO_3 100 ml H_2O 4.4 ml HF

SiH_4 was diluted to 1% in N_2 and B_2H_6 was diluted 0.1% in N_2. Nitrogen was the buffer gas with a total flow rate of 3000 cm³/min; SiH_4 flowed at 200 cm³/min and O_2 at 50 cm³/min. The diborane-doped SiO_2 deposition was allowed to proceed until 5700Å of glass had formed. This thick glass deposit allowed more data points for the etching study. However, in device processing, 1500-3500Å is the typical thickness for diffusion source diborane deposited glass. After borosilicate or SiO_2 deposition, the slices used for the etching study were photoresisted with AZ-111. For each etching experiment, a small area of photoresist was developed and the glass underneath etched. With this method, the etching behavior of all solutions could be evaluated on material prepared in an identical manner. Also, this photoresist technique was chosen because cutting or breaking a silicon slice covered with an oxide layer causes stress which changes the etch rate (5). With diborane-deposited glass, the boron concentration could be controlled by gas concentrations in the reaction chamber (6).

Oxide thicknesses 1500Å or less were measured on a Gaertner Model L119 ellipsometer. Film thicknesses greater than 1500Å were measured on a Perkin Elmer 402 uv-visible spectrophotometer with a specular reflectance accessory using the interference fringe technique in the 200-800μ range (7).

The molecular per cent B_2O_3 in the SiO_2 film of the diborane-deposited borosilicate glass was determined by measuring the infrared absorption of 5000-10,000Å films on a Perkin Elmer 457 grating spectrophotometer using procedures previously described (4, 7-9). *IR* measurements were made immediately after deposition. These results were confirmed with measurements of boron concentration made on a Material Analysis Company 400 microprobe analysis instrument (agreement within ~10%).

The four etching solutions and their compositions are listed in Table II. All solutions were allowed to stand for one day in stoppered bottles after preparation and before use since freshly prepared solutions did not give reproducible results. All etching solutions were maintained at 25°C in a Colora Model NB temperature bath, and agitation of the solution was used during etching. Oxide thickness measurements were made before and after 1-min etching intervals. Five data points were taken and the slope of the best straight line through the data points is a measurement of the etch rate (in angstroms per minute).

When the HNO_3-HF-H_2O solutions system is in certain concentration ranges (high concentrated hydrofluoric and nitric) silicon etching can be quite significant (10). Thus, silicon etching was measured in "R," "S," and "P" etch by converting weight loss to thickness loss. Silicon slices with four different boron concentrations were evaluated (see Table III). Silicon etching was also detected by sheet resistance measurements. Increased sheet resistance indicates silicon etching.

Results and Discussion

Annealed diborane deposited glass etches faster than SiO_2 (steam oxidized at 1050°C) with all etching solutions except buffered HF (see Table IV). From Fig. 2 it can be noted that etch rate is linearly concentration dependent upon HF. High concentrations of HNO_3 in

Table III. Etching boron-doped silicon

Boron conc, B-atoms/ cm³	Resistivity, ohm-cm	Orientation	"P" etch: 15 ml HF, 10 ml HNO_3, 300 ml H_2O, μ/min	"R" etch: 1 ml HF, 100 ml HNO_3, 100 ml H_2O, μ/min	"S" etch: 4.4 ml HF 100 ml HNO_3, 100 ml H_2O, μ/min
5×10^{14}	4-15	100	0	0	0
5×10^{18}	0.03-0.04	100	0	0	0.2
1×10^{19}	0.01-0.02	111	0	0	0.4
5×10^{20}	0.0006-0.0009	100	0	0.08	0.5

Table IV. Diborane formed borosilicate

	Low B, Å/min	Medium B, Å/min	High B, Å/min	Steam oxidized
Buffered HF	450	325	275	900
"P" etch	250 (1.9)*	300 (2.3)	425 (3.3)	128
"R" etch	140 (2.8)	200 (4.0)	300 (6.0)	50
"S" etch	400 (3.0)	600 (4.4)	750 (5.6)	135

* Favorable etch rate differential:

$$\text{etch rate differential} = \frac{\text{borosilicate glass etch rate}}{\text{SiO}_2 \text{ etch rate}}.$$

etching solutions greatly favor the boron glass dissolution as compared to undoped SiO_2 with a favorable etch rate ratio (see Table IV).

When choosing an etching solution, silicon etching must be considered. As boron concentration increases in silicon, the boron-doped silicon becomes less resistant to etching in higher concentrations of HF (see Table III). Below a critical concentration of HF in the etches in Fig. 2, silicon does not dissolve. In the HF concentration range in "R" etch (100 ml HNO_3, 100 ml H_2O, 1 ml HF), silicon does not etch at all until we reach the very highly boron (VHB) doped silicon of 5×10^{20} atoms/cm^3. This silicon (isolation-type diffusion) etches at 0.08 μ/min. When one considers that an isolation-type diffusion is 2-4μ deep, this amount of silicon etching can be tolerated.

When choosing an etching solution for a specific application, etch rate, relative silicon etch rate, and favorable differential oxide etch rate must be taken into account. Of all the etches investigated here, "R" etch (see Table IV and Fig. 2) seems to be the most useful since it offers a favorable etch rate ratio (see Table IV).

Conclusions

From this study, etching solutions have been found that dissolve diffusion source diborane formed glass (350°C deposition and 1100°C anneal) from 2.8 to 6.0 times faster than 1050°C steam oxide grown SiO_2 diffusion masking. With an etch rate differential such as this, the diborane diffusion source glass can be dissolved while allowing the SiO_2 to remain in place. This can eliminate the photoresist protection of SiO_2 diffusion source masking during etching.

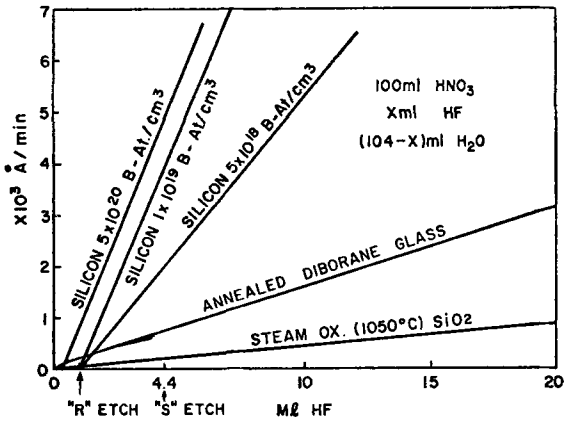

Fig. 2. Etch rates of borosilicate glass (3.7% B) and silicon as a function of HF concentration containing: 100 ml HNO_3, x ml HF, (104 − x) ml H_2O, where when HF = x = 1 ml = "R" etch; x = 4.4 ml = "S" etch.

Acknowledgments

The author wishes to acknowledge V. E. Hauser for presentation of this problem and guidance throughout this study. The helpful comments of P. J. Boddy and D. R. Turner concerning this work and manuscript are appreciated.

Manuscript submitted March 16, 1972; revised manuscript received Dec. 19, 1972. This was Paper 173 presented at the Cleveland, Ohio, Meeting of the Society, Oct. 3-7, 1971.

Any discussion of this paper will appear in a Discussion Section to be published in the June 1974 JOURNAL.

REFERENCES

1. W. A. Pliskin and R. P. Gnall, *This Journal*, **111**, 872 (1964).
2. A. H. El-Hoshy, *ibid.*, **117**, 1583 (1970).
3. J. Dey, M. Lundgren, and S. Harrell, *Kodak Photoresist Seminar Proc.*, **2**, 4 (1968 ed.).
4. W. A. Pliskin, "Measurement Techniques for Thin Films," p. 280, B. Schwartz and N. Schwartz, Editors, The Electrochemical Society Softbound Symposium Series, New York (1967).
5. L. Hall, *This Journal*, **118**, 1506 (1971).
6. A. W. Fisher and J. A. Amick, *RCA Rev.*, 549 (1968).
7. F. Reizman and W. Van Gelder, *Solid-State Electron.*, **10**, 625 (1967).
8. R. O. Schwenker, *This Journal*, **118**, 313 (1971).
9. E. A. Taft, *ibid.*, **118**, 1985 (1971).
10. H. Robbins and B. Schwartz, *ibid.*, **106**, 505 (1959).

Solid-State Ionics: High-Conductivity Solid Copper Ion Conductors: N-Alkyl (or Hydro)-hexamethylenetetramine Halide-Copper(I) Halide Double Salts

Takehiko Takahashi,* Osamu Yamamoto, and Shoichiro Ikeda

Department of Applied Chemistry, Faculty of Engineering, Nagoya University, Nagoya, Japan

ABSTRACT

Copper ion conductivity has been found in the system N-alkyl (or hydro)-hexamethylenetetramine halide-copper(I) halide in the solid state. At 20°C, in the system N-methyl-hexamethylenetetramine bromide-copper(I) bromide, the highest conductivity of 0.017 $(ohm\text{-}cm)^{-1}$ was found at 87.5 mole per cent CuBr, which was essentially ionic. The conductivities are discussed also for a number of similar double salts.

In recent years, in order to find high ionic conductivity solids, Ag_3SI (1, 2), $RbAg_4I_5$ (3, 4), KAg_4I_4CN (5), $Ag_{19}I_{15}P_2O_7$ (6), double salts composed of silver iodide and some organic compounds (7-9), and β-Al_2O_3 (10) have been examined and several promising results have been achieved. The charge carrier in these compounds is the silver or alkali ion, and no other ion conductors which exhibit high ionic conductivity at ambient temperature have been reported. From a view point of the application of solid electrolytes, the silver-containing compounds are considered to be expensive, therefore it is of interest to look for other ionic conductors of low price, for example, copper ion conductors. The present paper reports the copper ion conductivity of the system copper(I) halides and N-alkyl (or hydro)-hexamethylenetetramine halides.

Experimental

Copper(I) iodide, which was purified by recrystallizing in hydroiodic acid, was washed repeatedly with acetic acid before being dried in vacuo on P_2O_5. Copper(I) bromide and copper(I) chloride were purified by the same method using hydrobromic acid and hydrochloric acid, respectively. N-methyl-hexamethylenetetramine iodide ($C_6H_{12}N_4CH_3I$) was prepared by the method described in the literature (11), the melting point of which was 189°C, which agreed well with the reported value (190°C), and the iodine content in it coincided with the calculated value ($C_6H_{12}N_4CH_3I$, found: I, 44.7%, calcd.: I, 45.0%). By the same method, the other six kinds of N-alkyl (or hydro)-hexamethylenetetramine halide were prepared, namely, N-hydro-hexamethylenetetramine iodide ($C_6H_{12}N_4HI$, found: I, 47.6%, calcd.: I, 47.4%). N-ethyl-hexamethylenetetramine iodide ($C_6H_{12}N_4C_2H_5I$, found: I, 42.8%, calcd.: I, 42.9%), N-hydro-hexamethylenetetramine bromide ($C_6H_{12}N_4HBr$, found: Br, 36.0%, calcd.: Br, 36.2%), N-methyl-hexamethylenetetramine bromide ($C_6H_{12}N_4CH_3$ Br, found: Br, 33.2%, calcd.: Br, 34.0%), N-ethyl-hexamethylenetetramine bromide ($C_6H_{12}N_4C_2H_5Br$, found: Br, 31.7%, calcd.: Br, 32.1%), and N-hydro-hexamethylenetetramine chloride ($C_6H_{12}N_4HCl$, found: Cl, 20.7%, calcd.: Cl, 20.1%). The appropriate quantities of copper(I) halide and N-alkyl (or hydro)-hexamethylenetetramine halide were mixed with a small amount of ethyl alcohol and dried completely at about 80°C before being pressed by a hand press to form a pellet under 4000 kg/cm², and then heated in a sealed evacuated Pyrex vessel for 10 hr at 100°C for the systems $C_6H_{12}N_4HI$-CuI, $C_6H_{12}N_4C_2H_5I$-CuI, and $C_6H_{12}N_4C_2H_5Br$-CuBr, at 120°-100°C for the systems $C_6H_{12}N_4HBr$-CuBr and $C_6H_{12}N_4HCl$-CuCl, and at 150°-130°C for the systems $C_6H_{12}N_4CH_3I$-CuI and $C_6H_{12}N_4CH_3Br$-CuBr. These reaction temperatures were chosen below the decomposition temperatures of the reaction products, which were determined by thermogravimetric analysis.

The total electrical conductivity was measured with a 1000 Hz conductance bridge, as the frequency dependence of the conductivity was not observed for all the samples investigated. In order to reduce the contact resistance, a mixture of powdered copper (325 mesh) and the sample (2:1 weight ratio) was used for electrodes. The sample of about 1g was stacked between two electrodes, and pressed into a pellet of 13 mm diameter. The conductivity measurements were carried out in nitrogen gas.

Electronic conductivity was measured by Wagner's polarization method (12). To cell (I) with a copper anode and a graphite cathode, d.c. was applied at a voltage less than the decomposition voltage

Cu/sample/graphite [I]

The sample was formed in the shape of pellet, about 2 mm thick and 13 mm in diameter, by pressing at a pressure of about 4000 kg/cm². A constant current supplier was used and the resulting voltage was measured with a recorder preconnected with a high impedance electrometer.

X-ray diffraction patterns of the powdered samples were obtained with a diffractometer using CuKα radiation. The scanning speed was 1°/min.

Results and Discussion

Total electrical conductivity.—The sample composition of the N-alkyl (or hydro)-hexamethylenetetramine halide-copper(I) halide system was between 66.7 and 97.5 m/o (mole per cent) copper(I) halide. The sample pellet with copper electrodes was annealed for several hours at 100°-150°C in nitrogen gas flow before being slowly cooled to room temperature in the oven to measure the conductivity. The conductivities of seven kinds of the N-alkyl (or hydro)-hexamethylenetetramine halide-copper(I) halide system are shown in Table I. For comparison, the conductivities of CuI, CuBr, and CuCl, which were measured by the same method, are also shown in the table. In the systems $C_6H_{12}N_4HI$-CuI and $C_6H_{12}N_4C_2H_5I$-CuI, no high conductivity solid material is obtained at room temperature. The conductivities of these materials are comparable to or less than that of CuI. On the other hand, the high conductivity materials are found in the systems $C_6H_{12}N_4CH_3I$-CuI, $C_6H_{12}N_4HBr$-CuBr, $C_6H_{12}N_4CH_3Br$-CuBr,

* Electrochemical Society Active Member.

Key words: copper ion conductor, copper(I) halide, electronic conductivity, N-alkyl-hexamethylenetetramine halide.

Table I. Total electrical conductivity of the N-alkyl (or hydro)-hexamethylenetetramine halide-copper(I) halide system at 20°C

CuX (X = I,Br,Cl) m/o	Total electrical conductivity (ohm-cm)$^{-1}$						
	[H]HI-CuI[a]	[H]CH_3I-CuI	[H]C_2H_5I-CuI	[H]HBr-CuBr	[H]CH_3Br-CuBr	[H]C_2H_5Br-CuBr	[H]HCl-CuCl
100	$\sim 7 \times 10^{-7}$	$\sim 7 \times 10^{-7}$	$\sim 7 \times 10^{-7}$	$\sim 10^{-7}$	$\sim 10^{-7}$	$\sim 10^{-7}$	$\sim 2 \times 10^{-7}$
95		4.6×10^{-4}		4.2×10^{-4}	2.3×10^{-3}	3.0×10^{-5}	
90		6.7×10^{-4}			9.0×10^{-3}	2.7×10^{-4}	1.9×10^{-3}
87.5		8.4×10^{-4}		6.0×10^{-3}	1.7×10^{-2}	3.2×10^{-4}	4.3×10^{-3}
85	5×10^{-7}	1.1×10^{-3}	5×10^{-7}	4.6×10^{-3}		3.0×10^{-4}	3.2×10^{-3}
80		2.8×10^{-4}		8.2×10^{-4}	4.0×10^{-3}	5.2×10^{-5}	7.0×10^{-4}
66.7		5.0×10^{-6}		1.0×10^{-6}	10^{-7}		

[a] [H] = $C_6H_{12}N_4$.

$C_6H_{12}N_4C_2H_5Br$-CuBr, and $C_6H_{12}N_4HCl$-CuCl. In the plot of conductivity *vs.* mole per cent copper(I) halide, the total conductivities pass through a maximum at 85 m/o CuI for the $C_6H_{12}N_4CH_3I$-CuI system, at 87.5 m/o CuBr for the systems $C_6H_{12}N_4HBr$-CuBr, $C_6H_{12}N_4CH_3Br$-CuBr, and $C_6H_{12}N_4C_2H_5Br$-CuBr, and at 87.5 m/o CuCl for the $C_6H_{12}N_4HCl$-CuCl system as shown in Fig. 1. The highest conductivity was found in the system $C_6H_{12}N_4CH_3Br$-CuBr to be 0.017 (ohm-cm)$^{-1}$ at 20°C at the composition of 7CuBr·$C_6H_{12}N_4CH_3Br$, the value of which is five orders of magnitude larger than that of CuBr. These results suggest that the intermediate compounds with high electrical conductivity exist in these systems. The conductivities of these high conductivity materials remained constant for about half a year or more at room temperature, which indicated that decomposition did not occur during storage under ambient conditions.

The temperature dependence of the conductivity was determined for 17CuI·3$C_6H_{12}N_4CH_3I$, 7CuBr·$C_6H_{12}N_4HBr$, 7CuBr·$C_6H_{12}N_4CH_3Br$, and 7CuCl·$C_6H_{12}N_4HCl$. The results in the several temperature cycles are shown in Fig. 2. The conductivity *vs.* the reciprocal of the absolute temperature curves indicate that the phase transition and the decomposition do not occur up to the temperatures investigated. The decomposition temperatures of the samples measured by thermogravimetric analysis were 159°C for 17CuI·3$C_6H_{12}N_4CH_3I$, 106°C for 7CuBr·$C_6H_{12}N_4HBr$, 167°C for 7CuBr·$C_6H_{12}N_4CH_3Br$, and 124°C for 7CuCl·$C_6H_{12}N_4HCl$. Above these decomposition temperatures, the conductivities decreased with time. From the curves shown in Fig. 2, the activation energies can be calculated as 6.1 kcal/mole for 17CuI·3$C_6H_{12}N_4CH_3I$, 4.1 kcal/mole for 7CuBr·$C_6H_{12}N_4HBr$, 4.1 kcal/mole for 7 CuBr·$C_6H_{12}N_4CH_3Br$, and 6.2 kcal/mole for 7CuCl·$C_6H_{12}N_4HCl$. The values of the activation energy correspond to that for the high ionic conductivity solids known so far (2-4 kcal/mole) (6) and suggest that these new compounds have the structural defects similar to those of silver ion conductors (1, 13-15).

Electronic conductivity.—According to Wagner's theoretical analysis (16), the current density J in cell (I) is given by

$$J = I/A = (RT/LF)\,[\sigma_e\{1 - \exp(-EF/RT)\} + \sigma_h\{\exp(EF/RT) - 1\}] \quad [1]$$

where I is the current, A the cross-sectional area, L the thickness of the sample, E the applied voltage, and F the Faraday constant. σ_e and σ_h are the excess

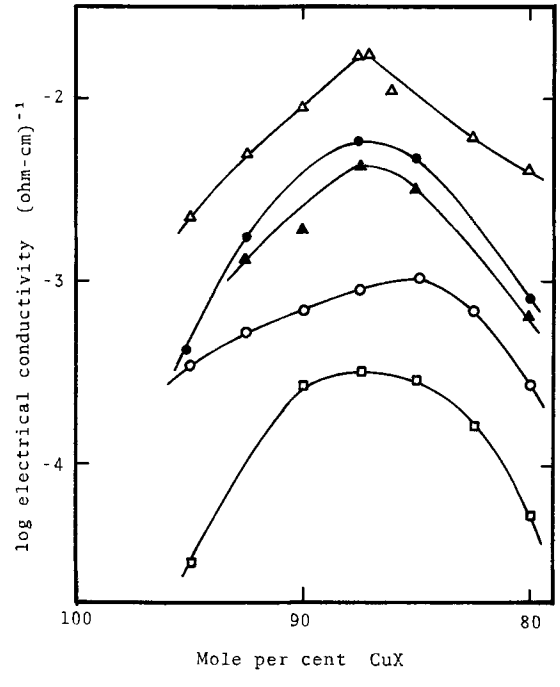

Fig. 1. Composition dependence of the total electrical conductivities of the systems $C_6H_{12}N_4RX$-CuX (X = I, Br, Cl; R = H, CH_3, C_2H_5) at 20°C. ○, $C_6H_{12}N_4CH_3I$-CuI; ●, $C_6H_{12}N_4HBr$-CuBr; △, $C_6H_{12}N_4CH_3Br$-CuBr; □, $C_6H_{12}N_4C_2H_5Br$-CuBr; ▲, $C_6H_{12}N_4HCl$-CuCl.

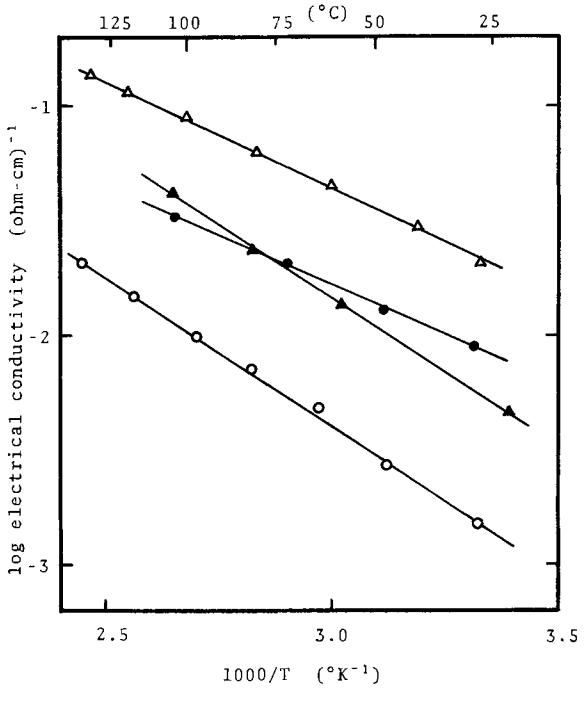

Fig. 2. Temperature dependence of the total electrical conductivities of 17CuI·3$C_6H_{12}N_4CH_3I$ (○), 7CuBr·$C_6H_{12}N_4HBr$ (●), 7CuBr·$C_6H_{12}N_4CH_3Br$ (△), and 7CuCl·$C_6H_{12}N_4HCl$ (▲).

electron and hole conductivities of the sample which is in equilibrium with metallic copper, and the other symbols have their usual meanings. Typical *I vs. E* curves for $37CuBr \cdot 3C_6H_{12}N_4CH_3Br$ at various temperatures are shown in Fig. 3. These curves show a quasi-exponential increase of *I*. Since the excess electron conduction is negligible, Eq. [1] may be written as

$$\log I = \log(\sigma_h ART/LF) + EF/2.30\,RT \qquad [2]$$

if $EF/RT >> 1$. The plots of log *I vs. E* shown in Fig. 3 give virtually straight lines whose slopes are close to the value of $F/2.30\,RT$. The values of σ_h were then calculated from Eq. [2]. Figure 4 shows the values of σ_h for the $C_6H_{12}N_4CH_3I$-CuI, $C_6H_{12}N_4HBr$-CuBr, $C_6H_{12}N_4CH_3Br$-CuBr, and $C_6H_{12}N_4HCl$-CuCl systems as a function of the composition of copper(I) halide at 100°C. For comparison, the electronic conductivities of CuBr and CuCl were measured at 100°C to be about 3×10^{-9} (ohm-cm)$^{-1}$ and 8×10^{-12} (ohm-cm)$^{-1}$, respectively, which were obtained by extrapolating the data at 160°-200°C, because the reproducible current-voltage curve was difficult to obtain at low temperature. The electronic conductivity of CuI at 100°C, obtained by extrapolating the data at 130°-350°C, is about 3×10^{-6} (ohm-cm)$^{-1}$ (17). The electronic conductivity in each system decreases with decreasing copper(I) halide content; this conductivity of the highest conductivity solid is less than 10^{-11} (ohm-cm)$^{-1}$ at 100°C. Thus, it is concluded that the conduction in the new compounds prepared in the N-alkyl (or hydro)-hexamethylenetetramine halide-copper(I) halide systems is essentially ionic. The temperature dependence of the electronic conductivities of $17CuI \cdot 3C_6H_{12}N_4CH_3I$ and $7CuBr \cdot C_6H_{12}N_4CH_3Br$ is shown in Fig. 5. At room temperature, these conductivities were too small to measure by this method. Thus, the transport number of ions in these compounds are considered to be nearly unity.

X-ray diffraction analysis.—Analysis was carried out at room temperature for the samples containing various compositions of copper(I) halide in the N-alkyl (or hydro)-hexamethylenetetramine halide-copper(I) halide system. The results obtained are summarized in Table II. For the samples in the $C_6H_{12}N_4HI$-CuI and $C_6H_{12}N_4C_2H_5I$-CuI systems, only the peaks due to the starting materials were observed, which indicated that no intermediate compounds were obtained in both systems. In the $C_6H_{12}N_4CH_3I$-CuI system, the sample containing 15 m/o CuI gave a single-phase pattern, which was named phase 1. In the composition range of 33.3-60 m/o CuI the patterns of three phases corresponding to CuI, $C_6H_{12}N_4CH_3I$, and an intermediate compound, which was named phase 2, were observed. According to the results of the electrical conductivity measurements, phase 1 has the high ionic conductivity and phase 2 is a poor conductor at room temperature.

The x-ray results for the $C_6H_{12}N_4HBr$-CuBr system showed that only an intermediate compound, phase 3, existed at the composition near 87.5 m/o CuBr. It has high ionic conductivity at room temperature. In the system $C_6H_{12}N_4CH_3Br$-CuBr, three intermediate compounds at the composition of 87.5 m/o CuBr, phase 4, 50 m/o CuBr, phase 5, and 33.3 m/o CuBr, phase 6, were found. Phase 4 has high ionic conductivity and

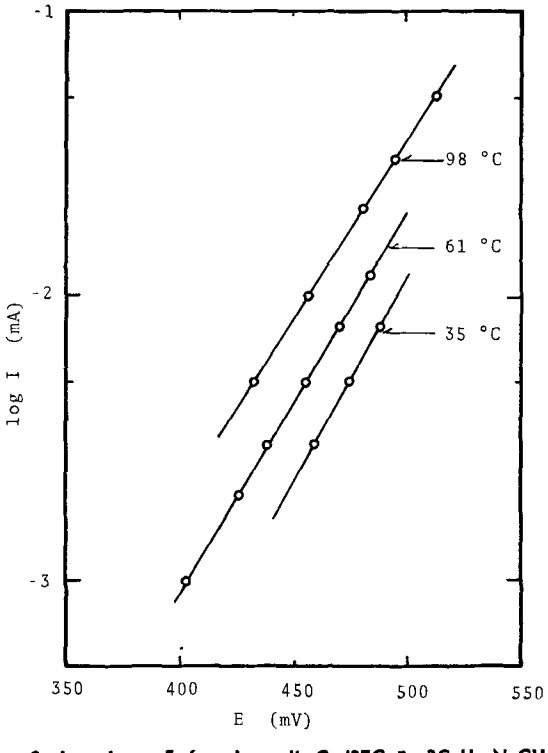

Fig. 3. Log *I* vs. *E* for the cell Cu/$37CuBr \cdot 3C_6H_{12}N_4CH_3Br$/graphite.

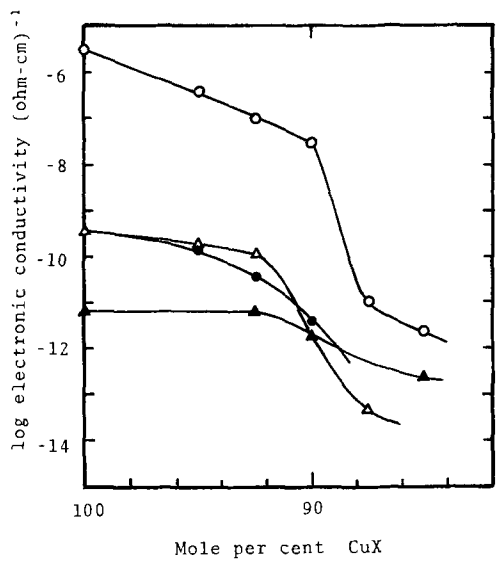

Fig. 4. Composition dependence of the electronic conductivities, σ_h, of the systems $C_6H_{12}N_4RX$-CuX (X = I, Br, Cl; R = H, CH_3) at 100°C. ○, $C_6H_{12}N_4CH_3I$-CuI; ●, $C_6H_{12}N_4HBr$-CuBr; △, $C_6H_{12}N_4CH_3Br$-CuBr; ▲, $C_6H_{12}N_4HCl$-CuCl.

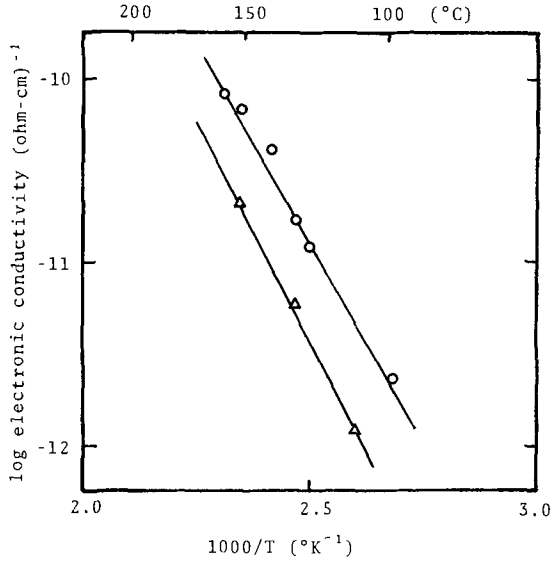

Fig. 5. Temperature dependence of the electronic conductivities, σ_h, of $17CuI \cdot 3C_6H_{12}N_4CH_3I$(○) and $7CuBr \cdot C_6H_{12}N_4CH_3Br$ (△).

Table II. Results of x-ray investigation

System	Mole per cent CuX (X = I,Br,Cl)	Phase observed at room temperature
$C_6H_{12}N_4HI$-CuI	90	$C_6H_{12}N_4HI$, CuI
	80	$C_6H_{12}N_4HI$, CuI
$C_6H_{12}N_4CH_3I$-CuI	90	CuI, phase 1
	85	Phase 1
	66.7	Phase 2, CuI, $C_6H_{12}N_4CH_3I$
	50	Phase 2, CuI, $C_6H_{12}N_4CH_3I$
	33.3	Phase 2, $C_6H_{12}N_4CH_3$
$C_6H_{12}N_4C_2H_5I$-CuI	90	CuI, $C_6H_{12}N_4C_2H_5I$
	85	CuI, $C_6H_{12}N_4C_2H_5I$
$C_6H_{12}N_4HBr$-CuBr	90	CuBr, phase 3
	87.5	Phase 3
	66.7	Phase 3, CuBr, $C_6H_{12}N_4HBr$
	50	Phase 3, CuBr, $C_6H_{12}N_4HBr$
	33.3	CuBr, $C_6H_{12}N_4HBr$
$C_6H_{12}N_4CH_3Br$-CuBr	90	CuBr, phase 4
	87.5	Phase 4
	80	Phase 4, phase 5
	66.7	Phase 5
	50	Phase 6
	33.3	Phase 6, $C_6H_{12}N_4CH_3Br$
$C_6H_{12}N_4C_2H_5Br$-CuBr	90	CuBr, phase 7
	87.5	CuBr, phase 7
	80	CuBr, phase 7
$C_6H_{12}N_4HCl$-CuCl	7.5	CuCl, phase 8
	12.5	CuCl, phase 8
	15	Phase 8
	17.5	Phase 8

phases 5 and 6 are poor conductors at room temperature. The x-ray pattern of phase 4 showed a strong resemblance to that of phase 3.

All samples in the system $C_6H_{12}N_4C_2H_5Br$-CuBr were prepared at 100°C. Their diffraction patterns showed almost the same peaks as those of CuBr and small peaks which were different from those of the starting materials. Electrical conductivity measurement suggested that an intermediate compound may exist at the composition near 87.5 m/o CuBr, and, therefore, the small peaks may be due to a new compound, phase 7. In the system $C_6H_{12}N_4HCl$-CuCl, an intermediate compound, phase 8, was found at the composition near 15 m/o CuCl.

Conclusion

High copper ion conductivity solids are found in the systems $C_6H_{12}N_4CH_3I$-CuI, $C_6H_{12}N_4HBr$-CuBr, $C_6H_{12}N_4CH_3Br$-CuBr, $C_6H_{12}N_4C_2H_5Br$-CuBr, and $C_6H_{12}N_4HCl$-CuCl. The highest conductivities in each system are found at the composition $17CuI \cdot 3C_6H_{12}N_4CH_3I$, $7CuBr \cdot C_6H_{12}N_4HBr$, $7CuBr \cdot C_6H_{12}N_4CH_3Br$, $7CuBr \cdot C_6H_{12}N_4C_2H_5Br$, and $7CuCl \cdot C_6H_{12}N_4HCl$. The conduction in these materials is essentially ionic.

Manuscript submitted Jan. 29, 1973; revised manuscript received May 8, 1973.

Any discussion of this paper will appear in a Discussion Section to be published in the June 1974 JOURNAL.

REFERENCES

1. B. Reuter and K. Hardel, *Naturwissenschaften*, **48**, 161 (1961).
2. T. Takahashi and O. Yamamoto, *Electrochim. Acta*, **11**, 779 (1966).
3. J. N. Bradley and P. D. Greene, *Trans. Faraday Soc.*, **63**, 424 (1967).
4. B. B. Owens and G. R. Argue, *Science*, **157**, 308 (1967).
5. G. W. Mellors and D. V. Louzos, *This Journal*, **118**, 846 (1971).
6. T. Takahashi, S. Ikeda, and O. Yamamoto, *ibid.*, **119**, 477 (1972).
7. B. B. Owens, *ibid.*, **117**, 1536 (1970).
8. M. L. Beradelli, C. Biondi, M. De Rossi, G. Fonseca, and M. Giomini, *ibid.*, **119**, 114 (1972).
9. B. B. Owens, J. H. Christie, and G. T. Tiedeman, *ibid.*, **118**, 1144 (1971).
10. Y. Y. Yao and J. T. Kummer, *J. Inorg. Nucl. Chem.*, **29**, 2453 (1967).
11. A. Wohl, *Ber.*, **19**, 1840 (1886).
12. J. B. Wagner and C. Wagner, *J. Chem. Phys.*, **26**, 1597 (1957).
13. S. Geller, *Science*, **157**, 310 (1967).
14. S. Geller and M. D. Lind, *J. Chem. Phys.*, **52**, 5854 (1970).
15. S. Geller and B. B. Owens, *J. Phys. Chem. Solids*, **13**, 1241 (1972).
16. C. Wagner, Proc. 7th Meeting C.I.T.C.E., Lindau, 1955, p. 361, Butterworths, London (1957).
17. T. Takahashi and O. Yamamoto, *Denki Kagaku*, **31**, 42 (1963).

Technical Notes

A Technique for Anodizing IC Aluminum Layers

K. V. Heber

Laboratoire d'Electronique et de Traitement de l'Information, Centre d'Etudes Nucleaires de Grenoble, Grenoble-Gare, Cedex, France

In electrolysis experiments, the properties of the electrical contact with the sample are of prime importance. The main difficulty arises from the fact that this contact must be electrically isolated from and chemically protected against the liquid to prevent its corrosion as well as the formation of a current path which bypasses the sample. For simplicity, contact is generally made to the backside of the sample. In the anodic oxidation of integrated circuit (IC) interconnection Al layers, however, contact to the frontside of the samples, *i.e.*, to the Al layer itself instead of to the supporting wafer, is to be preferred. We have found a technique to produce suitable electrodes having the required qualities without taking up much of the sample's area.

Key words: anodization contacts, noncorroding contacts.

Electrode Description

The idea of the electrode is to protect the contact wire by a suction pad. Figure 1 gives a schematic view. The mechanical problem of how to make a suction pad of small diameter, housing a contact wire, and fitting tight into the holder has been solved by the use of polymerizing silicone rubber, which was molded in the holder around the wire. The suction pad's surface is simply the surface of the meniscus which forms on the surface of any liquid contained within walls, in this case of the fluid rubber. The pad will be set free after

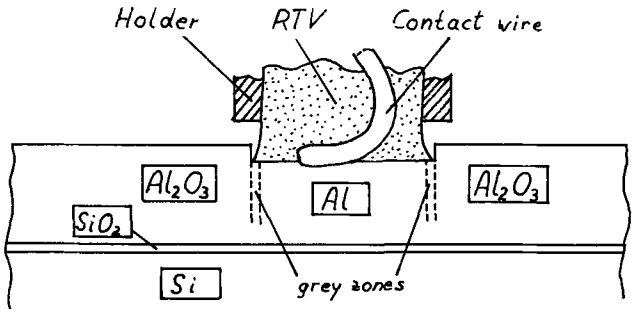

Fig. 1. Schematic cross section of sample and contact electrode after anodization.

hardening of the rubber in order to give the arrangement of Fig. 1.

In the present execution, electrodes have been fabricated with suction pads of 5 and 3 mm diameter. Contact is made by a gold wire, 0.5 mm diameter. Holder material is PVC (polyvinyl-chloride); silicone rubber quality is RTV 501 (Rhone Poulenc). Anodizations are done in 10% H_2SO_4. Three such electrodes are set up for one 1½ in. diameter IC wafer. With this system, the sample has only to be pressed against the electrode. The end of the wire, lying flat on the surface of the suction pad, will establish a good electrical contact to the sample, and the pad will adhere to the sample surface and form a tight barrier against penetration of the liquid.

Results

As an illustration of the effectiveness of the suction pad, Fig. 2 represents the picture of a dot left by the suction pad during the anodization of an aluminum layer evaporated on top of an oxidized silicon IC wafer. The dot, reflecting, appears in white, whereas the formed Al_2O_3 is transparent and thus shows the black color of the silicon underneath. Note the neat metal surface which has not been attacked at all, proving the efficiency of the suction pad as a penetration barrier.

Figure 2 also represents a Talystep reading the border profile. The step results from the thickness differences between the Al and the Al_2O_3 layers. Step width is 20 μm, indicating the good mechanical resolution of the system. It is interesting to note that the gray bordering zone, which appears on the picture of the dot, does not appear in the profile reading. It might represent a region of more or less complete transformation of Al into Al_2O_3 without difference in thickness of the metal layer. This transition zone has been indicated in the schematic picture of Fig. 1. Another interesting detail illustrated in Fig. 2 is the print, on the right-hand side, left by the contact wire as it dug into the aluminum, scratching away any superficial oxide layer. This print makes evident the good mechanical quality of the contact.

The resistivity of the electrode depends much on the PVC used and on the quality of fabrication. The mentioned silicone rubber has specified resistivities of 10^{14} ohm-cm.

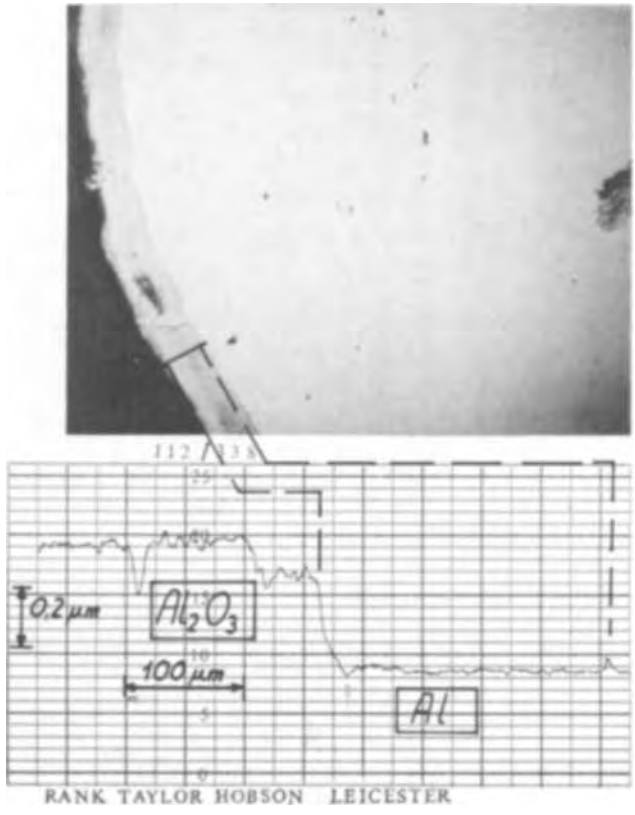

Fig. 2. (top) Picture of anodized IC wafer with part of a contact dot. Magnification 28X. Black tone, Al_2O_3; gray tone, transition zone; white tone, Al. (bottom) Talystep profile reading along line in picture, across dot border.

Protection by a suction pad is thus a good means to prevent corrosion of a contact. The system described gave good electrical and mechanical performances and offers full protection of the contact. It is versatile, can be easily fabricated, and has a purely mechanical action, without need of a thermal or chemical treatment of the sample. This feature opens another protection application: a suction pad might replace protection by resist layers, waxes, or other masking substances which are polluting in themselves or by their cleaning solutions, methods which are often used, *e.g.*, in step etching or other monitoring procedures of IC technology.

Acknowledgment

The author is indebted to M. Valignat for valuable suggestions and to the LETI Microelectronics group for helpful discussions.

Manuscript submitted Jan. 2, 1973; revised manuscript received April 23, 1973.

Any discussion of this paper will appear in a Discussion Section to be published in the June 1974 JOURNAL.

Electrical Characteristics of MOS Structures on <111> and <100> Oriented N-Type Silicon as Influenced by Use of Hydrogen Chloride during Thermal Oxidation

G. Baccarani and M. Severi

Istituto di Elettronica, Facoltà di Ingegneria, Università di Bologna, Bologna, Italy

and G. Soncini

C.N.R.—Laboratorio LAMEL, Bologna, Italy

It is well known that the electrical properties of the SiO_2-Si interface are strongly affected by the semiconductor crystallographic orientation (1-4). In particular, the high and low-frequency C-V characteristics of MOS capacitors, obtained by thermal oxidation of <111> oriented n-type Si slices, show, with respect to simultaneously processed <100> oriented slices of the same resistivity: (*i*) a higher value of the flatband voltage, V_{FB}; (*ii*) a higher ratio of the high-frequency capacitance value measured in strong inversion, C_{min}, to the value measured in strong accumulation, C_{ox} (4); and (*iii*) stronger deviations from ideal MOS characteristics. In particular the low-frequency C-V curve for the <111> orientation exhibits a plateau in the inversion region, and the minimum in this region is expanded along the voltage axis (4).

Observation (*i*) could be explained by assuming that <111> oriented MOS structures are characterized, with respect to <100> oriented ones, by a larger amount of oxide charge, Q_{ox},[1] and by a smaller acceptor-type or a larger donor-type interface-state charge.

Observation (*ii*) could be accounted for by a more efficient doping redistribution process during thermal oxidation due, possibly, to the higher oxide growth rate for the <111> oriented slices (5) and by the presence of donor-type defect centers within the <111> oriented Si, which would result in an apparent increase in doping concentration (4).

Finally observation (*iii*) could be due to a higher interface-state density (6), to the presence of defect centers within the Si, giving localized energy levels in the lower half of the semiconductor bandgap (4), or to larger surface potential fluctuations, which would explain the broadening of the low-frequency minimum. These fluctuations, however, cannot account for the plateau in the low-frequency curve (4).

The purpose of this note is to discuss the above hypotheses on the basis of new experimental results obtained by adding small amounts of high-purity gaseous HCl to the oxygen gas stream during thermal oxidation of Si. The addition of HCl to the oxidizing atmosphere is known to affect the SiO_2-Si interface by strongly reducing the apparent interface-state density (7, 8)[2] and by increasing the generation lifetime (9). Furthermore, it will be shown that the (HCl) oxidation step, followed by a standard low-temperature annealing treatment after Al evaporation, allows us to obtain, in a very convenient way, nearly ideal MOS C-V characteristics for both <111> and <100> oriented structures, which differ only in the value of the flatband voltage. These experimental results may possibly help to a better understanding of the physical nature of the interface states, and their correlation with processing parameters.

Key words: (HCl) SiO_2, MOS structures, crystallographic orientation.

[1] We define Q_{ox} as the charge per unit area (located either within the oxide or at the interface) which does not depend upon bias at room temperature.

[2] By "apparent interface-state density" we mean the density obtained on the basis of the analysis suggested by Berglund (10), which has been shown (11) to be affected by errors when effects such as deep defect centers in the semiconductor space charge region or surface potential fluctuations influence the low-frequency C-V characteristic.

Sample Preparation and Experimental Results

To ensure meaningful comparisons, 1 ohm-cm, n-type <111> and <100> oriented Si slices were simultaneously processed to form MOS capacitors. Thermal oxidation was performed in a dry oxygen gas stream to which small amounts of high-purity gaseous HCl could be added. In our experiments an HCl content of 0.3% was used, since the best electrical properties of the Si-SiO_2 interface were obtained under these conditions (8). Oxidation time (2 hr 18 min) and temperature (1100°C) were kept constant. After thermal oxidation, Al dots were evaporated on the front oxide through a metal mask. Back contacts were obtained by the usual back oxide etching and subsequent Al evaporation on the bare Si surface.

Typical high and low-frequency C-V characteristics for <100> and <111> oriented MOS capacitors subject to four different processing procedures are shown in Fig. 1 and 2, and their most relevant parameters are listed in Table I. Figure 1 refers to capacitors whose

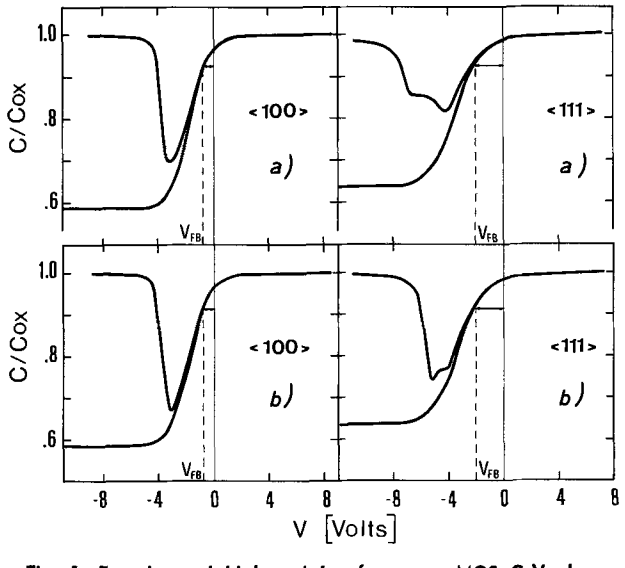

Fig. 1. Experimental high and low-frequency MOS C-V characteristics for <100> and <111> oriented standard MOS capacitors. The low-frequency curves are those which exhibit a minimum under negative bias voltage. Curves a, oxide grown in dry oxygen at 1100°C; curves b, oxide grown in dry oxygen at 1100°C, sample annealed at 525°C after Al evaporation.

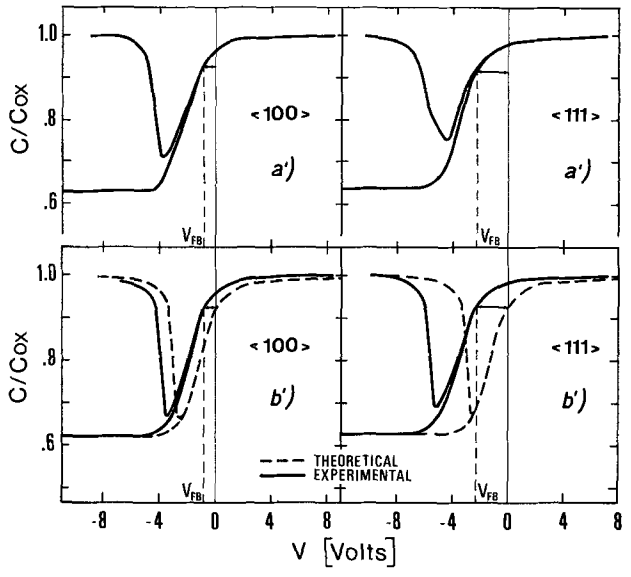

Fig. 2. Experimental high and low-frequency MOS (C-V) characteristics for <100> and <111> oriented MOS capacitors with oxide grown in the presence of HCl. The low-frequency curves are those which exhibit a minimum under negative bias voltage. Curve a', oxide grown in dry oxygen mixed with 0.3% HCl by volume; curves b', oxide grown in O_2-HCl mixture, sample annealed at 525°C after Al evaporation.

oxide was grown in a dry oxygen gas stream. Figure 2 refers to capacitors whose oxide was grown in a dry oxygen stream to which 0.3% by volume of gaseous HCl was added, all the other processing steps being the same as in Fig. 1. Cases a and a' (see Fig. 1 and 2) refer to capacitors without any low-temperature heat-treatment, while cases b and b' refer to capacitors that were processed together with those of cases a and a' but were further subjected to a 525°C annealing for 10 min in a dry N_2 ambient after Al evaporation.

The high-frequency C-V characteristics were measured at 1 MHz with a Boonton 71 AR capacitance meter, while the low-frequency C-V curves were obtained by the voltage ramp technique (12). In the low-frequency measurements, care was taken to ensure quasi-equilibrium conditions by using very low ramp speeds (13). For samples with oxide grown in the presence of HCl a ramp speed of less than 20 mV/sec was usually necessary, due to the high generation lifetimes. During the measurements the samples were kept in the dark, at room temperature, in a dry N_2 ambient.

The apparent interface-state density, N_{ss}, (Table I gives only the mid-gap value) was obtained by comparing the theoretical with the experimental low-frequency characteristics (10); the semiconductor doping concentration, N_{sp}, used in these calculations was determined from the ratio C_{min}/C_{ox}. This procedure is known to minimize errors due to doping redistribution (14).

Generation lifetime τ was measured by simultaneously displaying the capacitance and current transients due to the application of a voltage step at the metallic gate (15). This method does not require any knowledge of doping concentration, and it avoids the uncertainty of the graphical differentiation of the capacitance *vs.* time curve which is necessary to obtain the Zerbst plot (16). Finally, oxide thickness was measured by a Talystep.

The C-V characteristics of the MOS structures obtained by thermal oxidation in a dry O_2 ambient (Fig. 1, case a) show the typical features outlined in the opening paragraphs of this paper. In particular the <111> oriented capacitor exhibits, with respect to the <100> oriented one, a larger flatband voltage, V_{FB}, and a larger relative value of the high-frequency capacitance minimum, C_{min}. In addition the low-frequency <111> characteristic shows a plateau in the inversion region, and the minimum is much broader than in the corresponding <100> characteristic. After the low-temperature annealing treatment (Fig. 1, case b) the low-frequency <111> characteristic still exhibits stronger deviations with respect to the ideal one, even though the broadening is reduced in comparison with case a. No changes in flatband voltage, V_{FB}, or high-frequency capacitance minimum, C_{min}, are observed.

When HCl is added to the oxidizing atmosphere (Fig. 2) the <111> low-frequency C-V curve for case a' is much less distorted than for case a of Fig. 1. The equivalent surface charge, $Q_{eq} = C_{ox} V_{FB}$, is practically unaffected, while for the <111> oriented structure the doping concentration, N_{sp} (determined from C_{min}/C_{ox}), decreases considerably. Finally, after the annealing treatment (Fig. 2, case b') the shapes of the experimental characteristics become practically the same for the <100> and <111> oriented structures, and very similar to the theoretical ones. However V_{FB} and Q_{eq} remain essentially unchanged, as is clear from Table I.

A large increase in generation lifetime is observed for samples with oxide grown in the presence of HCl, while the 525°C (Al) sintering does not seem to affect this parameter (see Table I).

Discussion

The experimental results obtained by the four processing procedures described above will be used to evaluate the consistency of the hypotheses proposed in the opening paragraphs of this paper to account for the different properties of MOS capacitors prepared on <100> and <111> oriented Si by oxidation in dry oxygen.

With reference to the two possible explanations concerning observation (*i*), we note that the shapes of the C-V characteristics become practically ideal for both orientations in case b'. Correspondingly the apparent interface-state density, N_{ss}, becomes $\simeq 0.7 \times 10^{10}$ cm^{-2} eV^{-1} at midgap (see Table I). Since the real surface states are surely less than the apparent ones, we may conclude that in case b', Q_{eq} is primarily due to the oxide charge, Q_{ox}, rather than the interface-state

Table I. Device parameters of MOS capacitors

Sample preparation	Orientation	Thickness (Å)	V_{FB} (V)	Q_{eq}/q (10^{10} cm^{-2})	C_{min}/C_{ox}	N_{sp} (10^{15} cm^{-3})	N (10^{15} cm^{-3})	N_{ss} (10^{10} cm^{-2} eV^{-1})	τ (μsec)
a, dry O_2, 1100°C	<111>	2000	1.9	20.0	0.64	8.2	5.5	80.0	0.5
	<100>	1900	0.5	5.6	0.59	5.0	5.5	20.0	0.5
b, dry O_2; N_2 annealing after metalization, 525°C	<111>	2000	1.9	20.0	0.64	8.2	5.5	15.0	0.5
	<100>	1900	0.5	5.6	0.59	5.0	5.5	4.0	0.5
a', dry O_2 + 0.3% HCl, 1100°C	<111>	2300	2.2	20.0	0.64	5.8	5.5	5.0	50-100
	<100>	2200	0.6	5.7	0.63	5.0	5.5	3.0	50-100
b', dry O_2 + 0.3% HCl, 1100°C; N_2 annealing after metalization, 525°C	<111>	2300	2.1	19.0	0.63	5.5	5.5	0.7	50-100
	<100>	2200	0.6	5.7	0.62	5.0	5.5	0.7	50-100

The flatband voltage, V_{FB}, is corrected for metal-semiconductor work function difference. N_{sp} represents the doping concentration determined from C_{min}/C_{ox}. N represents the doping concentration determined from resistivity measurements. The interface-state density N_{ss} is reported at midgap. Due to the scatter of data, the range of generation lifetime (τ) values is given for cases a' and b'.

charge, Q_{ss}. In the other cases the constancy of Q_{eq} suggests, as a reasonable hypothesis, that Q_{ox} is always larger than Q_{ss}; otherwise an eventual change of Q_{ss} should be exactly balanced by an equal (and opposite) change of Q_{ox}. This seems to support the assumption that the difference in flatband voltage observed between the two orientations is due to a different amount of oxide charge and not to a difference in interface-state charge.

Regarding observation (*ii*) we may exclude the possibility that doping redistribution plays an essential role in increasing the value of N_{sp} (determined from C_{min}/C_{ox}) for the <111> orientation in cases a and b. In fact, the addition of HCl enhances the oxidation rate and should consequently enhance the redistribution; but Table I, case b', shows that N_{sp} assumes in these conditions the expected value, not only for the <100> orientation but also for the <111> orientation. It is worthwhile to observe that the presence of the plateau in the inversion region of the <111> low-frequency C-V curve (cases a and b) occurs together with the higher values of N_{sp}, and that when the plateau is strongly reduced (case a') or totally disappears (case b'), N_{sp} decreases toward its expected value. This suggests a common origin for the two effects, and seems to support the model proposed by Castagne and Vapaille (4) which is based on a defect within the <111> oriented Si. This defect should behave like a donor-type center to account for the apparent increase in doping concentration, and its energy level should be localized in the lower half of the semiconductor band-gap to justify the position of the plateau in the low-frequency curve. Our experimental results show that this defect is definitely related to the oxidation step since its concentration can be strongly reduced by performing the oxidation of <111> oriented Si in the presence of HCl.

The fact that the semiconductor generation lifetime is practically the same for the <100> and <111> standard MOS structures (Table I, cases a and b) demonstrates that the proposed defect in <111> oriented Si does not act as an efficient generation-recombination center. This is consistent with the energy level of these defects in case a [$\simeq$0.2 eV below the intrinsic Fermi level, in agreement with Ref. (4)]. The low-temperature annealing treatment (case b) seems to shift this level closer to the semiconductor midgap, without sensibly altering the generation lifetime. This result could possibly be interpreted by assuming for these centers a very small capture cross section.

With regard to observation (*iii*), it is well known from MOS conductance measurements that <111> oriented SiO_2-Si interfaces are characterized by a higher density of real interface states than <100> oriented ones (6). However we emphasize that the stronger deviations from ideal MOS characteristics of the <111> low-frequency C-V curve cannot be caused only by a higher interface-state density. In discussing observation (*ii*) the presence of defect centers within the <111> oriented Si has emerged as the most probable hypothesis to account for the apparent increase in doping concentration, and it is well known that such defects are responsible for deviations in the theoretical high and low-frequency C-V curves (17, 4).

Finally, we cannot specify the role of the surface potential statistical fluctuations in altering the MOS C-V characteristics, since from our experiments it is not possible to separate the effect of the real interface states from that of the fluctuations.

Summary

The influence of sample orientation on the electrical properties of the standard SiO_2-Si interface has been critically discussed on the basis of new experimental results obtained by performing the oxidation of n-type Si slices in the presence of HCl. It has further been shown that the (HCl) oxidation, followed by a 525°C annealing treatment, gives <100> and <111> MOS structures with high generation lifetimes practically no interface states, and nearly ideal high and low-frequency C-V characteristics.

Manuscript submitted Oct. 4, 1972; revised manuscript received March 20, 1973.

Any discussion of this paper will appear in a Discussion Section to be published in the June 1974 JOURNAL.

REFERENCES

1. P. Balk, P. J. Burkhardt, and L. V. Gregor, *Proc. IEEE*, **53**, 2133 (1965).
2. B. Deal, M. Sklar, A. S. Grove, and E. H. Snow, *This Journal*, **114**, 266 (1967).
3. G. Abowitz, E. Arnold, and J. Ladell, *Phys. Rev. Letters*, **18**, 543 (1967).
4. R. Castagne and A. Vapaille, *Solid State Commun.*, **9**, 1347 (1971).
5. A. S. Grove, O. Leistiko, and C. T. Sah, *J. Appl. Phys.*, **35**, 2695 (1964).
6. E. H. Nicollian and A. Goetzberger, *Bell. System Tech. J.*, **46**, 1055 (1967).
7. R. J. Kriegler, Y. C. Cheng, and D. R. Colton, *This Journal*, **119**, 388 (1972).
8. M. Severi and G. Soncini, *Electron. Letters*, **8**, 402 (1972).
9. P. H. Robinson and F. P. Heiman, *This Journal*, **118**, 141 (1971).
10. C. N. Berglund, *IEEE Trans. Electron Devices*, **ED-13**, 701 (1966).
11. R. Castagne and A. Vapaille, *Surface Sci.*, **28**, 157 (1971).
12. M. Kuhn, *Solid-State Electron.*, **13**, 873 (1970).
13. M. Kuhn and E. H. Nicollian, *This Journal*, **118**, 370 (1971).
14. G. Baccarani, S. Solmi, and G. Soncini, *Alta Frequenza* (English issue), **40**, 674 (1971).
15. P. U. Calzolari, S. Graffi, A. Mazzone, and C. Morandi, Paper F7.3A presented at the 2nd European Solid-State Device Research Conference, University of Lancaster, England, September 1972.
16. M. Zerbst, *Z. Angew. Phys.*, **30**, 1 (1966).
17. C. T. Sah, Solid-State Electronics Laboratory Technical Report No. 1, Electrical Engineering Research Laboratory, University of Illinois, 1964.

Low Temperature Chemical Vapor Deposition of Boron Doped Silicon Films

Lou H. Hall* and K. M. Koliwad

Texas Instruments Incorporated, Dallas, Texas 75222

Chemical deposition of polycrystalline silicon is finding increasing application in the fabrication of integrated circuits, such as silicon-gate MOS devices (1), dielectric isolations (2), and two-phase CCD's (3). Polycrystalline silicon is also used in photomask fabrication. Doping of silicon films can occur during an *in situ* codeposition or during a subsequent high tem-

* Electrochemical Society Active Member.
Key words: silane, diborane, catalysis, thin films, activation energy.

perature source-drain diffusion. Many workers have reported on doped and undoped polycrystalline films (4-8).

Eversteyn and Put (8) have reported the effect of the addition of arsine, phosphine, and diborane in growing doped silicon films in the temperature region of 600°-900°C. We report here the use of diborane to grow boron doped silicon films in the region of 300°-550°C. The effect of deposition temperature and gas stream dopant concentration on the growth rate and apparent activation energies are discussed.

The catalytic effect of diborane on the decomposition of silane was studied by measuring the deposition rate of silicon as a function of substrate temperature and gas stream dopant concentration. The silane concentration was kept constant at 0.44% (20 cc/min) of the total flow, 4.5 liters/min. Nitrogen was used as a carrier and diluent gas. Diborane, 1.0% in ultrahigh purity argon, was used as the dopant source. Silicon wafers with approximately 5000Å thermal oxide were used as substrates. The gas stream boron/silicon atom ratio was varied from 6×10^{-3} to 24×10^{-3}. Semiconductor grade silane from Matheson was used without additional purification.

The reactor used was a horizontal 2 in. I.D. quartz tube heated by rf loading into a 5½ in. × 1¾ in. × ⅜ in. carbide-coated graphite susceptor. The temperature was measured by use of an infrared radiation pyrometer. Emissivity and absorption corrections were made for the substrates and quartz tube. The temperature range studied was from 300°-550°C with the uncertainty ±5°C or less.

The thicknesses of boron doped silicon films were obtained by partial masking of the film and removin' the unmasked portion with an HF, HNO_3, and acetic acid solution. The thicknesses were mechanically measured by use of the Talystep I; accuracy is ±2% for films in a 1,000-20,000Å thickness range. The majority of the films had thicknesses of approximately 5,000-10,000Å. Thickness variation across a slice was less than 10%, while variation in deposition rate over several depositions was ±10% or less.

At temperatures below 500°C the growth rate of undoped silicon films becomes negligibly small. Yasuda *et al.* (9) have reported an activation energy of 1.1 eV for the reaction above 500°C. The addition of diborane significantly lowers the film growth temperature. Figure 1 shows the deposition rate as a function of gas stream dopant concentration at deposition temperatures T = 300°, 375°, and 550°C. At the higher boron/silicon ratio in the gas stream the film growth is less sensitive to additional dopant increase.

The decomposition rate of silane as measured by the film growth rate exhibits two distinct regions of temperature dependence. The Arrhenius plot of deposition rate is shown in Fig 2. In the deposition temperature range 350°-550°C the apparent activation energy is 0.18 eV; while, at temperatures below 350°C the film growth is governed by a higher apparent activation energy, 0.54 eV. Eversteyn and Put (8) have reported an activation energy of 0.30 eV for the boron doped silicon deposition below 620°C. While we show two distinct activation energy regions, it is interesting to note that the value of 0.30 eV is closed to the average of our observed values. Taking the high temperature work of Eversteyn and Put (8) into account, the growth of boron doped silicon films exhibits three regions of temperature dependence: 0.87 eV at T = 620°-900°C, 0.18 eV at T = 350°-550°C, and 0.54 eV at T = 300°-350°C. The activation energies obtained from this study were at a boron/silicon gas stream ratio of 6×10^{-3}.

In addition to a temperature dependence on growth rate, there is also a dopant concentration dependence. This dependence manifests itself in a decrease in apparent activation energy with increasing diborane concentration.

The growth of boron doped silicon films can be considered to be a sum of two growth rates; an uncatalyzed rate and a diborane catalyzed rate. The diborane catalysis of silane may be very similar to the use of diborane and hydrogen to produce other higher boranes by complex, reversible reactions at temperatures in the region of 100°-250°C (10). It is believed that borine, BH_3, is an intermediate in these borane syntheses. The effect of hydrogen as compared to inert gas ambients on the decomposition of silane has been previously reported by Yasuda (9) and Richman (11).

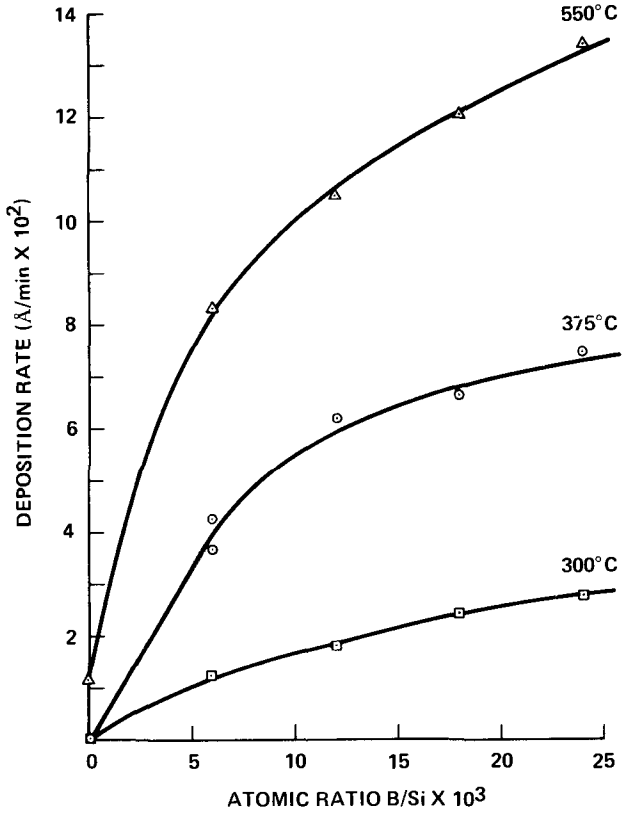

Fig. 1. Deposition rate (Å/min) vs. gas stream dopant concentration at deposition temperature T = 550°, 375°, and 300°C.

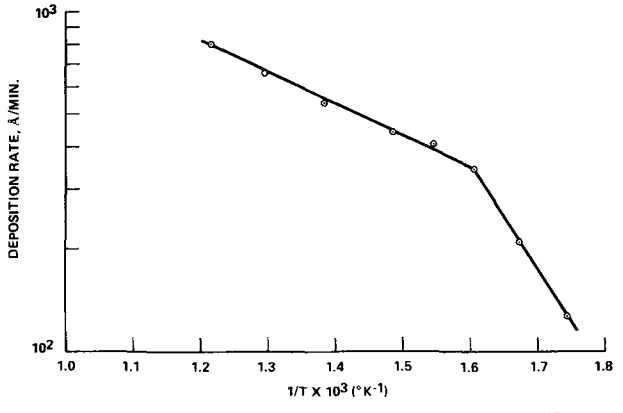

Fig. 2. Growth rate dependence on temperature at B/Si atom ratio 6×10^{-3} in the gas stream.

Below 350°C the activation energy of the diborane catalyzed decomposition of silane is 0.54 eV (12.5 kcal/mole). Between 350° and 550°C the activation energy is low, <0.20 eV (4.5 kcal/mole). While the rate controlling mechanism is not established, the low-temperature catalysis mechanism may be the formation of borine or similar boron active species.

Whatever the catalysis mechanism, diborane can be used to lower the growth temperature of silicon films several hundred degrees below the temperature needed to grow undoped silicon films.

In conclusion, we observed that both the diborane concentration and substrate temperature affect the

growth of boron doped silicon films in a temperature region 300°-550°C. Two distinct activation regions were observed: 350°-550°C and below 350°C; apparent activation energies were 0.18 eV and 0.54 for the two regions.

Acknowledgments

We want to thank Imogene Killen for technical assistance and Dr. Dale DeVries for helpful discussions.

Manuscript submitted Feb. 14, 1973; revised manuscript received May 4, 1973.

Any discussion of this paper will appear in a Discussion Section to be published in the June 1974 JOURNAL.

REFERENCES

1. F. Faggin and T. Klein, *Solid-State Electron.*, **13,** 1125 (1970).
2. K. E. Bean, H. P. Hentzschel, and D. Colman, *J. Appl. Phys.*, **40,** 2358 (1969).
3. W. F. Kosonocky and J. E. Carnes, *IEEE J. Solid State Circuits*, **SC-6,** 314 (1971).
4. T. I. Kamins, J. Manolin, and R. N. Tucker, *J. Appl. Phys.*, **43,** 83 (1972).
5. T. I. Kamins, *ibid.*, **22,** 4357 (1971).
6. R. C. Chittick, J. H. Alexander, and H. F. Sterling, *This Journal*, **116,** 77 (1969).
7. A. L. Fripp and L. H. Slack, *ibid.*, **120,** 145 (1973).
8. F. C. Eversteyn and B. H. Put, *ibid.*, **120,** 106 (1973).
9. Y. Yasuda, M. Yamanaka, T. Moriya, and T. Yoshii, Paper 23 presented at Electrochem. Soc. Meeting, Houston, Texas, May 7-11, 1972.
10. F. A. Cotton and G. Wilkinson, Editors, "Advanced Inorganic Chemistry," Interscience-Wiley, New York (1966), Section on Boron Hydrides and Related Compounds, p. 272.
11. D. Richman, Y. S. Chiang, and P. H. Robinson, *RCA Rev.*, **31,** 613 (1970).

JOURNAL OF THE ELECTROCHEMICAL SOCIETY

ELECTROCHEMICAL SCIENCE
AND TECHNOLOGY

NOVEMBER
1973

Solid Electrolyte Properties and Crystal Forms of Lead Fluoride

John H. Kennedy,* Ronald Miles,* and James Hunter*

Department of Chemistry, University of California, Santa Barbara, California 93106

ABSTRACT

Electrolyte properties of α-PbF_2 and β-PbF_2 were studied using single crystals, pressed pellets, and thin films. Ionic conductivity and heat of movement of mobile species were determined for both forms of lead fluoride. In addition, the electronic conductivity and transport number for the cubic β-PbF_2 were determined. Converison of α-PbF_2 to β-PbF_2 was studied by differential thermal analysis, with an observed transition temperature in the range 334°-344°C. Partial reconversion of β-PbF_2 back to α-PbF_2 was effected by pressing the material at pressures above 30,000 psi. A voltage of 1.7 mV (α-PbF_2 positive) generated between pellets of α-PbF_2 and β-PbF_2 separated by a salt bridge implied that the β-PbF_2 is the more stable form at room temperature and atmospheric pressure.

Some of the solid electrolyte properties of lead fluoride have been known since the early work of Tubandt (1) who reported a value of 1.0 for the transport number for the fluoride ion. However, it was not clear which of the two crystal forms of lead fluoride was being measured in these early studies. One form of lead fluoride is α-PbF_2, with orthorhombic symmetry and a density of 8.445 (2). This is the predominant form in commercial lead fluoride powder. The other form is β-PbF_2, with cubic symmetry and a density of 7.750 (2). The orthorhombic form can be converted to the cubic form by heating to about 315°C (2). After cooling, the material remains in the cubic form. This situation bears some resemblance to the silver iodide and lithium sulfate systems, where a low-conductivity, low-temperature, stable form converts at a specific temperature to a higher conductivity cubic form (3). However, in these cases the material reverts to the low-conductivity form on cooling, while the lead fluoride remains in the cubic form. One might expect to find that the orthorhombic, high-density lead fluoride would have lower conductivity than the lower density cubic form.

There is some uncertainty about the nature of the transition between the two forms of lead fluoride, and about which form is the more stable at room temperature. Values for the transition temperature between the two phases vary from 200° to 400°C (2). It might be assumed that the orthorhombic form is more stable at room temperature and that the cubic form is more stable at higher temperatures, and much of the literature follows this assumption. However, there is evidence to the contrary. Sauka (2) found that rapid precipitation of PbF_2 from solutions of $Pb(NO_3)_2$ and NH_4F gave mostly the orthorhombic form, while very slow precipitation gave predominantly the cubic form, thus implying that the cubic form is the more stable at room temperature.

* Electrochemical Society Active Member.

Key words: differential thermal analysis, lead fluoride, ionic conductivity, solid electrolyte, thin film.

The alkaline earth fluorides, which have the same crystal structure as cubic lead fluoride, have been studied in great detail (4-6). Similarly, the other lead halides, which have the same structure as orthorhombic lead fluoride, have also been extensively investigated (7-9). Lead fluoride however, with crystal modifications common to both of these groups, has received little attention since Tubandt's work. We report here the results of a more extensive study of the electrolyte properties of both forms of lead fluoride.

Experimental

Lead fluoride synthesis.—Orthorhombic α-PbF_2 (ROC/RIC 99.9% pure) was used without further purification. Powder x-ray results confirmed its orthorhombic nature and showed no lines due to impurities. Cubic β-PbF_2 was made from the α-form by heating to over 400°C under a nitrogen atmosphere. Only a short time period was necessary to ensure that all of the sample had converted. The β-PbF_2 may be quenched by removing it quickly from the oven, or it may be allowed to cool slowly. No conversion to the α-form was noted either way. DTA studies of the α to β conversion showed an endothermic phase change at about 342°C. Neither x-ray nor DTA could detect a phase change on cooling. The β-PbF_2 was slightly gray whereas the α-form was white. This might have been due to some small decomposition, although no lead was detected in the powder pattern.

Thin films.—Thin films of PbF_2 were prepared by vacuum evaporation from resistance sources. Initial attempts to evaporate PbF_2 from tungsten or molybdenum boats gave durable, clear films, but were brown in color, indicating possible decomposition of the PbF_2. Evaporation from alumina-coated molybdenum boats gave much clearer, although much more brittle films. The PbF_2 was evaporated onto glass microscope slides approximately 6 in. above the source. Evaporation was monitored with a Sloan Omni-II and 5-MHz quartz crystal oscillator. The films were deposited at about

5000 Å/min, with thicknesses ranging from 6000 to 84,000Å. Pb and Au films for electrodes were vacuum evaporated from Ta and W boats, respectively.

Two types of cells were constructed; one type consisted of successive layers of electrode material, electrolyte, and electrode material (Fig. 1a), while the other type had thin fingers of electrode material covered by a layer of electrolyte (Fig. 1b). In the first type of cell, the current moved vertically between the electrodes through the thin layer of electrolyte. The electrodes were either both lead, or one lead and one gold. In the second type of cell, the current traveled horizontally between the electrodes. In these cells, the electrodes were lead.

Thin films of PbF_2 for x-ray study were made concurrently with many of the conductivity cells by using a second substrate holder. On these slides, half of the slide was protected for the initial deposit of lead. Then PbF_2 was deposited over the entire slide. In this way the crystal form and orientation of PbF_2 films over glass and lead substrates were observed.

Blocking electrode cells.—A Harrison 6203-B power supply was used to vary the voltage across Wagner-type polarization cells (13-16), and the current measured by reading the voltage drop across a series resistor with a Hewlett Packard 412A VTVM.

X-ray diffraction patterns.—A Philips Electronics x-ray diffraction unit No. 12045, with No. 52572 scintillation counter, was used with CuK_α x-rays (1.54178Å) at 40 kV for powder and thin-film studies. The powder was ground with a Crescent Dental "Wig-L-Bug" Model 5A amalgamator using a stainless steel vial. Powder x-ray spectra of samples less than 100 mg could be taken by sprinkling the powder on a glass slide that had a uniform smooth film of silicone grease smeared on it. X-ray spectra of thin-film cells, which were deposited on glass microscope slides, were recorded directly after the slides were cut to fit the holder.

Pellet preparation.—Pellets were pressed with a Perkin-Elmer evacuable die, 13 mm diameter. Graphite electrodes were painted on with colloid graphite suspension (d.a.g. 154) and dried at 100°C for 12 hr. Gold and lead electrodes were either pressed on or applied by vacuum deposition. In the transport number experiments, a layer of mixed Pb and PbF_2 was pressed at the interface to lower polarization.

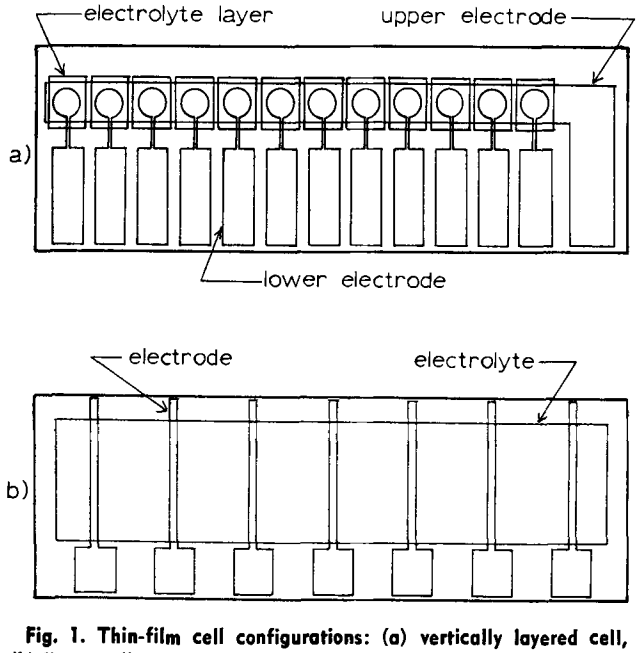

Fig. 1. Thin-film cell configurations: (a) vertically layered cell, (b) linear cell.

Conductivity measurements.—A GRC 1650-A impedance bridge linked to a Wavetek VCG III frequency source was used to measure a-c resistances, and parallel and series capacitances. The d-c resistances were measured with a Keithley 602 electrometer. The thin films or pressed pellets were heated from 25° to 150°C in an Associated Testing Laboratories environmental chamber and to 250°C in a Blue M oven.

For a-c measurements the bridge voltages used were well below the electrolyte decomposition potential. At each temperature, there was a strong frequency dependence. A cell can be represented by the following equivalent circuit:

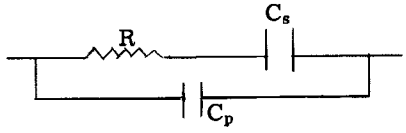

where R is the actual resistance and C_s and C_p are series and parallel capacitances.

The impedance of a capacitor is $X_c = 1/\omega c$ where $\omega = 2\pi f$. The measured cell resistance (R_m) when C_s is large satisfies $1/R_m = \omega C_p + 1/R$. For pressed pellets from 25° to 200°C, plots of $1/R_m$ *vs.* f gave straight lines whose zero frequency intercepts were $1/R$. Above 200°C, straight lines were obtained from $R_m = k\omega^{-1/2} + R$. This semi-empirical equation allows for concentration polarization. The square root of the frequency dependence comes from the random walk aspect of the current being limited by the diffusion of the current carrying species to the electrode (10).

Transport number of β-PbF_2.—The Hittorf method of weighing the electrodes after the passage of a current was used. A Keithley 261 picoampere source was used to provide a constant current of 3 μA. The current was integrated with a Bissett-Berman E-cell coulometer. The voltage drop across the cell was about one volt. The cell was maintained at 150°C in air. At that temperature, Pb electrodes developed an oxide coating. To avoid this, cathodes were made of vacuum-deposited gold on PbF_2, and they alone, not the anodes were weighed. Middle sections of PbF_2 were also weighed to ensure no weight change.

Differential thermal analysis.—DTA measurements were made on the α- to β-phase transition of PbF_2. A Fisher Model 260P Differential Thermalyzer with platinel thermocouples was used. The samples were placed in quartz crucibles, and the temperature difference noted *vs.* the α-Al_2O_3 standard. Experimental temperatures were calibrated with the AgI phase transition at 147°C.

Single-crystal synthesis.—A single crystal was grown by Stockbarger's technique as described by Jones (11). Graphite electrodes were applied by painting on d.a.g. 154, and thin-film electrodes of lead by vacuum deposition. High internal resistance made a-c measurements possible only at high temperatures. However, d-c measurements with lead electrodes gave Arrhenius plots as low as room temperature.

Results and Discussion

Relative stability.—As we stated earlier, the stability relation between the α- and β-form of PbF_2 is still uncertain. Differential thermal analysis was carried out to observe the transition temperature and how it varied with heating and cooling rates. For a rapidly occurring phase change, DTA patterns up or down do not vary appreciably with the heating or cooling rate. But, if the energy barrier for interconversion is sufficiently high, this is not true, and the transition temperature can be passed with little observed conversion to the now more stable form. The true transition temperature may have to be far exceeded before the rate of interconversion becomes rapid. In this case, the rate of interconversion will be highly temperature de-

pendent, and the observed "transition temperatures" will depend on how fast the material is heated and how long it is at a given temperature. It appears that this is the case with lead fluoride, for which transition temperatures have been reported from 200° to 400°C. Our studies showed no DTA peaks on cooling cycles. As further evidence, it was found that even over a small range of heating rates of 5°-25°C/min, there was a noticeable change in the observed transition temperature, as shown in Fig. 2. As a check, a series of DTA's of AgI at different heating rates gave no variation from the single 147°C transition temperature. This evidence strongly implies that the observed phase change of α-lead fluoride to β-lead fluoride in the temperature range of 335°-345°C was from a metastable to a stable state and was rate controlled.

Sauka's precipitation work is evidence that the cubic β-PbF_2 is more stable even at room temperature. As further evidence, a cell of the type: Pb/β-PbF_2// KF(aq)//α-PbF_2/Pb was constructed by slipping filter paper saturated with KF solution between two pellets. After several hours, an equilibrium cell potential of +1.7 mV was reached. With the following half-cell reactions

Left half-cell: $Pb + 2F^- \rightarrow \beta\text{-}PbF_2 + 2e^-$

Right half-cell: $\alpha\text{-}PbF_2 + 2e^- \rightarrow Pb + 2F^-$

Cell reaction: $\alpha\text{-}PbF_2 \rightarrow \beta\text{-}PbF_2$

the positive 1.7 mV observed indicates that the β-PbF_2 form is the more stable at room temperature, with a free energy difference between the two forms of 78 cal/mole.

α-PbF_2 has a higher density (8.75) than β-PbF_2 (7.68). By pressing pellets of β-PbF_2 at different pressures, the β-phase was converted to the α-phase (Fig. 3). This indicated that α-PbF_2 was the stable form at room temperature at high pressure. All pressed pellets of β-PbF_2 used in this work showed some reconversion. Pellets of α-PbF_2 could be converted to pure β-PbF_2 by heating, but there was a marked increase in size which caused them to be brittle, and they often crumbled.

Conductivity of polycrystalline PbF_2.—The d-c resistances, and the frequency-independent resistances obtained from the a-c measurements, were the sum of the bulk resistance and the electrode contact resistance. When the resistances of cells of various thicknesses were plotted *vs.* thickness, the slope times the contact area was equal to the contact independent resistivity.

The intercept values (contact resistance) were not reproducible indicating that the contact resistance varied appreciably from sample to sample. One series of pellets was prepared by cleaning the surfaces by glow-discharge followed by vacuum deposition of gold electrodes. In this case the zero thickness intercept was well defined and equal to 1700 ohms at 200°C as an example. Resistivity values for the lead fluoride were the same as those found for the other pellets.

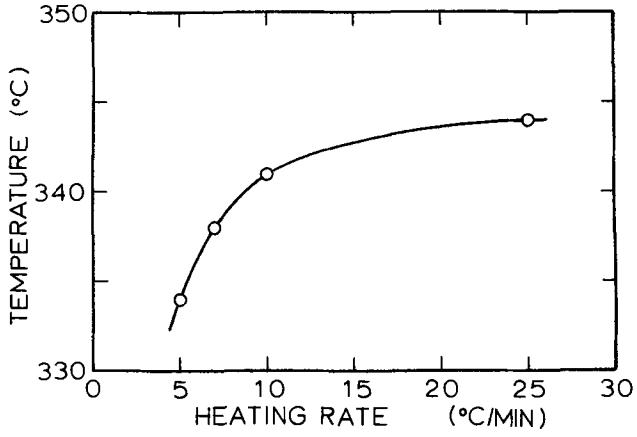

Fig. 2. Conversion temperature of α-PbF_2 to β-PbF_2 as a function of DTA heating rate.

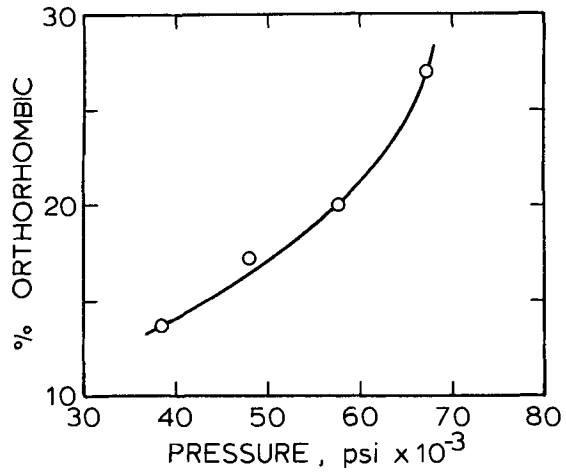

Fig. 3. Conversion of β-PbF_2 to α-PbF_2 as a function of pressure at room temperature.

Arrhenius plots of the conductivities are shown in Fig. 4 and 5. Log σ was used instead of the more exact log σT because the temperature change was not large enough to cause appreciable deviation from linearity. All of the Arrhenius plots gave only one slope over the temperature range 25°-250°C. If the effect were due to defects present in a fixed concentration, this slope would be related to ΔH_m, the heat of movement. On the other hand, if the concentration of defects were varying with T, the slope would contain contributions from ΔH_m and ΔH_f, the heat of formation. It is probable that the first situation pertains, *i.e.*, the PbF_2 was not sufficiently pure to exhibit intrinsic conductivity at temperatures below 250°C. The ΔH values are given in Table I and are in line with ΔH_m values for other crystals (Table II). Both forms of PbF_2 exhibited the same heat of movement. Also, ΔH_m for polycrystalline PbF_2 followed the halogen trend toward higher energy for lower atomic numbers and fell between the reported values for CdF_2 and CaF_2 which are thought to be fluoride ion vacancy conductors.

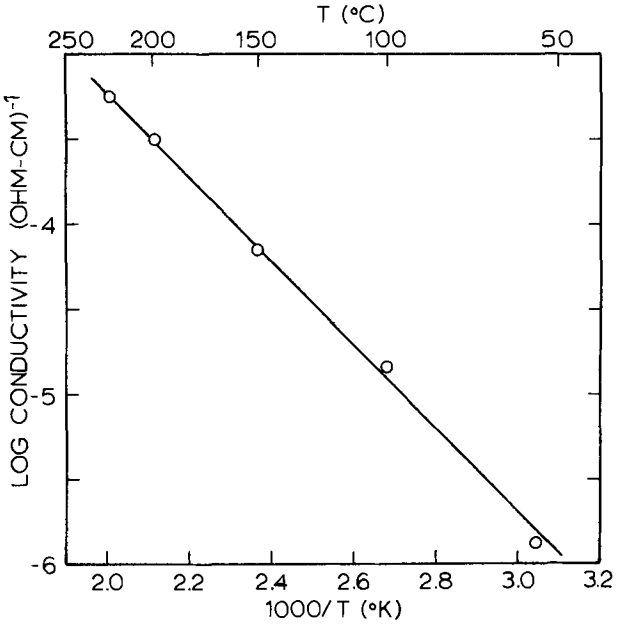

Fig. 4. Ionic conductivity of Au/β-PbF_2/Au pressed pellet cell vs. temperature measured by a-c technique.

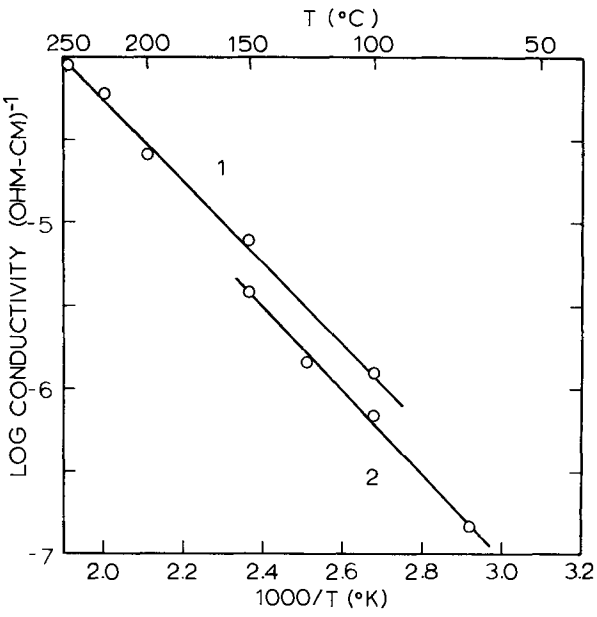

Fig. 5. Ionic conductivity of α-PbF_2 pressed pellet cells *vs.* temperature. Curve 1, Au/α-PbF_2/Au a-c technique; curve 2, Pb/α-PbF_2/Pb d-c technique.

There was some variation in ΔH_m measured for various cells. ΔH_m appeared to depend more on the type of cell than on the crystal modification of PbF_2 used in the cell. All values were about 0.5 eV, but the pressed pellet and thin-film cells of both α- and β-PbF_2 with lead electrodes gave slightly higher values for ΔH. Single-crystal PbF_2 exhibited the highest observed activation energies which may indicate that the lower values for polycrystalline samples reflected some grain boundary conduction. A-C measurements with the lead electrode cells gave the same results as d-c measurements.

The conductivity depended on the phase of the lead fluoride and its history. Aging was noted for all cells, thin films being the most notable. In general, the β-PbF_2 was about an order of magnitude more conductive than the α-form.

Single-crystal conductivity.—Resistance measurements were made on a β-PbF_2 crystal using both a-c and d-c techniques. For the a-c measurements, d.a.g. electrodes were used, and for d-c measurements vacuum-evaporated lead was used.

Room temperature conductivity could not be reliably determined by the a-c technique as the conductivity was too low at room temperature. However the d-c technique with an electrometer worked satisfactorily, and the conductivity measured was 2.0×10^{-8} $(ohm\text{-}cm)^{-1}$. At 150°C, the conductivity measured by the a-c method was 4.1×10^{-5} $(ohm\text{-}cm)^{-1}$ and by the d-c method was 6.0×10^{-5} $(ohm\text{-}cm)^{-1}$. As the d-c study was run after the a-c study, the difference could be attributed to aging effects, which were observed to occur even during a single run when the crystal was left for several hours at elevated temperatures. These conductivity values agree reasonably well with the values for pressed pellets of β-PbF_2.

Arrhenius plots of σ *vs.* $1/T$ gave ΔH as 0.60 eV by the a-c technique and 0.65 eV by the d-c technique. These values are somewhat larger than those obtained from the pressed pellets, but reasonable, since a grain boundary conduction mechanism with a somewhat lower ΔH_m may be contributing to polycrystalline conductivity.

Conductivity of thin films.—Conductivity measurements on thin-film cells were made using both a-c and d-c techniques. The PbF_2 studied in this case was found by x-ray analysis to be (within the accuracy of the x-ray equipment) exclusively the cubic form. Also, the x-ray data indicated that there was considerable preference of orientation of PbF_2 films in the (100) plane, when deposited over either glass or lead.

A-C resistance measurements were made on several vertical type cells (Fig. 1a). Interpretation of these measurements was made difficult because of a large frequency dependence of the resistances. In these cells the electrolyte thickness was very small, thus the resistance due to the electrolyte may not be large compared to the resistances due to the electrode interfaces, and these contact resistances can tend to mask the electrolyte resistance. Ignoring the contact resistance, and calculating the conductivity from a-c resistance values at 1000 Hz, gave conductivity values at 25°C from 0.9×10^{-6} to 5.8×10^{-6} $(ohm\text{-}cm)^{-1}$, for various cells. By plotting resistance *vs.* electrolyte thickness one should be able to subtract out the contact resistance, as was done with the pressed pellets, and find the true conductivity. However, difficulties were encountered in getting consistency from one cell to another, and thus this method of finding the conductivity was not effective.

In order to avoid the above-mentioned problems, cells of the linear type (Fig. 1b) were constructed. In these cells the current path through the electrolyte was much longer, the effective electrode area much smaller, and thus, the resistance much higher than in the vertical cells. The problem of interpreting frequency dependence of a-c resistance was avoided by using d-c resistance instead, measured with an electrometer. Because of the linear geometry, it was also possible to plot resistance *vs.* conduction path distance through the electrolyte for each cell, and subtract out any contact effects. Figure 6 shows the resistance *vs.* conduction path distance for a typical linear cell. The contact resistance is seen to be very small in relation to the electrolyte resistance, and the slope of the line gave a conductivity value of 5.4×10^{-6} $(ohm\text{-}cm)^{-1}$ at room temperature. Other cells gave conductivity values from 5.5 to 6.6×10^{-6} $(ohm\text{-}cm)^{-1}$ at room temperature. These are the values initially after the cells were made. Upon standing the cells aged, and the conductivity dropped. This aging was accelerated by heating, with the conductivity dropping to 1×10^{-6} $(ohm\text{-}cm)^{-1}$ or less (see Table I).

An Arrhenius plot of log σ *vs.* $1/T$ for a typical cell is shown in Fig. 7. The cell was heated, cooled, and then reheated. Upon initial heating, log σ *vs.* $1/T$ was linear with a slope corresponding to a ΔH of 0.53 eV.

Table I. Conductivity and activation energy for lead fluoride samples

	$-\Delta H_m$, eV	Conductivity, 25°C $(ohm\text{-}cm)^{-1}$	Conductivity, 150°C $(ohm\text{-}cm)^{-1}$
Pressed pellets			
C/α-PbF_2/C	0.51	—	3.9×10^{-6}
C/β-PbF_2/C	0.50	—	3.2×10^{-5}
Au/α-PbF_2/Au	0.48	—	5.3×10^{-6}
Au/β-PbF_2/Au	0.48	—	6.3×10^{-5}
Au/β-PbF_2/Au (pressed gold)	0.47	—	6.6×10^{-5}
Pb/α-PbF_2/Pb	0.56	—	3.1×10^{-6}
Single crystal			
C/β-PbF_2/C	0.60	—	4.1×10^{-5}
Pb/β-PbF_2/Pb	0.65	2.0×10^{-8}	6.0×10^{-5}
Thin films			
Pb/β-PbF_2/Pb average of fresh films	0.54	5.7×10^{-6}	—
Pb/β-PbF_2/Pb aged film	0.55	9.6×10^{-7}	4.5×10^{-4}

Table II. Heats of activation

Material	ΔH_m, eV	ΔH_f, eV	Species	Ref.
CaF_2	0.55	—	$V_F^{\cdot}$	4
CdF_2	0.45	2.19	$V_F^{\cdot}$	5
$PbBr_2$	0.25	1.71	$V_{Br}^{\cdot}$	9
$PbCl_2$	0.30	1.65	$V_{Cl}^{\cdot}$	8
PbF_2	0.5	—	$V_F^{\cdot}$	This work

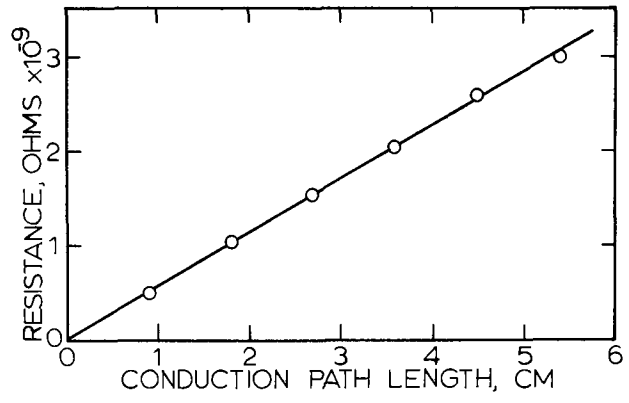

Fig. 6. Resistance of linear thin-film cell as a function of conduction path distance.

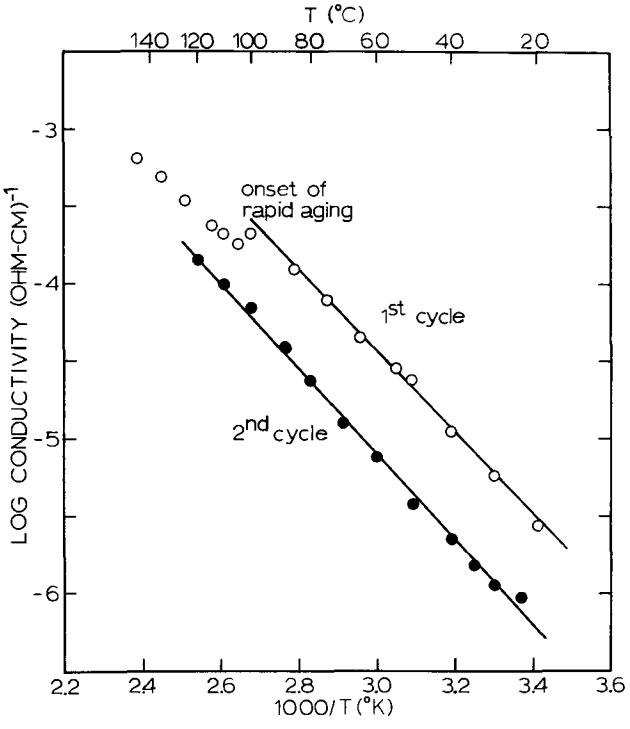

Fig. 7. Ionic conductivity of thin-film β-PbF_2 vs. temperature, measured by d-c technique.

At about 100°C however it appeared that the aging process in the film accelerated, and the resistance increased rapidly, changing the apparent slope of the graph. Upon cooling it was observed that there was some crazing of the PbF_2 film. However the cell was still operable, with a room temperature conductivity of about 1×10^{-6}. Data for a second heating cycle are also shown in Fig. 7. For this second heating cycle the slope yielded a ΔH of 0.55 eV, essentially the same as for the initial section of the first heating cycle. The ΔH values for all the linear cells ranged from 0.53 to 0.57 eV. These values are in good agreement with the results from the pressed pellets, but somewhat lower than those from the single crystal. However, the conductivity values were not at all in agreement with either the single crystal or pressed pellet measurements, rather they tended to be an order of magnitude larger (see Table I). One possible explanation is that the calculations for the thin films were erroneous because of the unusual geometry of the cell. However, a similar cell reported in a previous paper (12), using $RbAg_4I_5$, gave results entirely consistent with those from pressed pellets. Another possibility is that the films contained large amounts of impurities, possibly from decomposition during evaporation, or even from the evaporation source, so that the material was effectively doped, whereas the pressed pellets were as pure as the original PbF_2 powder.

Electronic conductivity.—Electronic conduction in solid electrolytes which are primarily ionic conductors can be studied by direct current polarization (13-16). Excessive electronic conduction, either by electrons or electron holes, would hinder the use of PbF_2 in a galvanic cell. Cells of the type Pb/β-PbF_2/Au were fabricated and polarized with the gold electrode positive. The lead and gold electrodes were vacuum deposited on the β-PbF_2 pressed pellets.

Electronic current which flows after steady state is reached is the sum of the currents due to electrons and holes

$$i = i_e + i_h = RT/LF\,[\sigma^o_e\,(1 - \exp(-EF/RT)) + \sigma^o_h\,(\exp(EF/RT) - 1)]$$

where L = cell constant (thickness/area), E = applied potential, and σ^o_e and σ^o_h = specific conductivities for electrons and holes in PbF_2 in contact with Pb.

For a polarization cell of the type M/MX/Blocking electrode, a plateau current will be observed with increasing potential for conduction by electrons, but an exponentially increasing current shows conduction by electron holes.

The graph of current *vs.* potential for β-PbF_2 was exponential (Fig. 8), and the plot of LF/RT log i *vs.* potential was linear (Fig. 9). If we assume only electron hole current, the equation for the current reduces to

$$i = RT/LF\,\sigma^o_h\,[\exp(EF/RT) - 1]$$

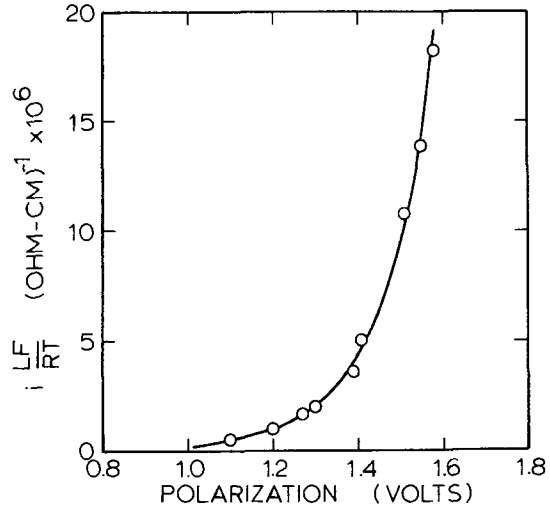

Fig. 8. Electronic current of β-PbF_2 pressed pellet cell vs. applied voltage at 150°C.

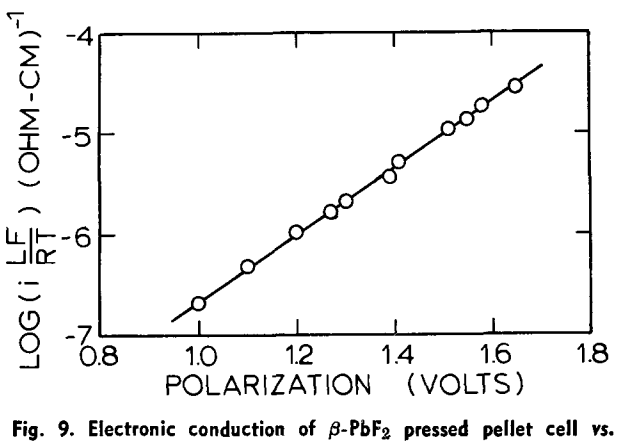

Fig. 9. Electronic conduction of β-PbF_2 pressed pellet cell vs. applied voltage at 150°C.

The slope of Fig. 9 should be $F/2.3\ RT$, or 11.9 $(V)^{-1}$. Data from two cells gave slopes of 3.36 and 3.41 $(V)^{-1}$. The slopes were, therefore, about three times smaller than theoretical. Wagner and Wagner also noted slopes about four times smaller than expected for $PbCl_2$ and $PbBr_2$ (17).

A value for the apparent hole conductivity can be calculated from the intercept of Fig. 9. Table III compares the calculated σ^0_h for β-PbF_2 with other lead halides.

Schoonman reported PbO formation at the cathode interface (18). Tetragonal lead oxide is an oxygen ion vacancy conductor, and the following analogous reaction could be postulated for PbF_2

$$\tfrac{1}{2}\,O_2 + 2PbF_2 \rightarrow PbF_4 + PbO$$

The cell voltage calculated from free energies of formation is -1.59V. In Fig. 8, the observed voltage at which the current dramatically increased was very near this potential. Therefore, if this were the case, all faradaic processes were not blocked, and the observed current still contained an ionic contribution. Therefore, the current due to electron holes then would be even lower than that observed. From this we see that electronic conductivity can represent at most only 10^{-4}% of the total conductivity at 150°C.

Transport number.—The transport numbers for Pb^{2+} and F^- in β-PbF_2 were measured using the cell

$$Pb/\beta\text{-}PbF_2//\beta\text{-}PbF_2//\beta\text{-}PbF_2/Au$$

The cell consisted of three pellets held together under pressure. The gold electrode was then cathodically polarized at 150°C. The blocking electrode study showed that only a minute fraction of the total conductivity could possibly be electronic. Therefore, the weight change could be attributed to the migration of fluoride ions away from the cathode and lead ions into the cathode section.

The observed weight change at the cathode was used to calculate the fluoride ion transport number. The weight change per coulomb of charge is $+1.075$ mg/coulomb for lead and -0.197 mg/coulomb for fluoride. A total of 4.90 coulombs was passed through the cell at about one volt. There was a weight loss of -0.51 mg in the cathode section (the middle β-PbF_2 section showed no weight change within experimental error). The fluoride ion transport number was then calculated

$$-t_- \text{ (0.197 mg/coulomb)} + (1 - t_-)\text{ (1.075 mg/coloumb)} = -0.51 \text{ mg/4.90 coulomb}$$

$$t_- = 0.93 \pm 0.02$$

Therefore, the lead ion transport number was 0.07 $\pm$ 0.02. This showed the conduction mechanism to be predominantly fluoride ion. Tubandt measured t_- for PbF_2 (crystal form unspecified) at 200°C and found it to be 1.0 (1).

Table III. Electron hole conductivities in lead halides

Compound	σ^0_h (ohm^{-1} cm^{-1})	Temperature °C	Ref.
$PbCl_2$	1.2×10^{-4}	300	17
$PbBr_2$*	$9 \times 10^{3} \exp[-2.34(F/RT)]$	150	18
	1.179×10^{-4}		
$PbBr_2$†	$1.6 \exp[-0.8(F/RT)]$	150	18
	5.0×10^{-10}		
$PbBr_2$‡	$1.2 \exp[-0.74(F/RT)]$	150	18
	1.8×10^{-9}		
β-PbF_2 (cell No. 1)	$1.14 \exp[-0.86(F/RT)]$	150	This work
	5.6×10^{-11}		
β-PbF_2 (cell No. 2)	$1.04 \exp[-0.93(F/RT)]$	150	This work
	9.2×10^{-12}		

* From thermodynamic data.
† Blocking electrode experiment.
‡ Conductivity experiment on $PbBr_2$ in Br_2 atmosphere.

Summary

The evidence presented supports the conclusion that the β-form of PbF_2 is the more stable form at atmospheric pressure and all temperatures from room temperature to melting. The high density α-form is the stable form at high pressure.

Cubic PbF_2, like many other cubic-structured compounds, is more conductive than the orthorhombic. However, a similar heat of movement of about 0.5 eV for both forms indicates that they conduct by the same mechanism. Transport number measurements show that the mechanism is predominantly fluoride ion and analogy to other compounds suggests that the fluoride ion vacancy is the mobile species. Furthermore other cubic fluorides form Frenkel defects while orthorhombic lead halides exhibit Schottky defects. This, too supports the hypothesis that lead fluoride conducts by fluoride ion vacancy since this alone is common to the two defect mechanisms.

A doping study with aliovalent cations will be necessary to prove the fluoride ion vacancy conduction mechanism. Also, high purity PbF_2 samples might yield information on the energy needed to form the defects needed for conduction.

Acknowledgment

The authors acknowledge partial financial support of this project by the National Science Foundation, Grant No. GH-37144. The authors also thank Mr. Neil Nighman for growing the single crystal of lead fluoride.

Manuscript submitted Feb. 1, 1973; revised manuscript received April 30, 1973.

Any discussion of this paper will appear in a Discussion Section to be published in the June 1974 JOURNAL.

REFERENCES

1. C. Tubandt, *Z. Anorg. Chem.*, **115**, 105 (1921).
2. Ya. Sauka, *J. Gen. Chem.*, **19**, 1453 (1949).
3. A. Kvist, "Physics of Electrolytes," Vol. 1, p. 340, 343, J. Hladic, Editor, Academic Press, New York (1972).
4. R. W. Ure, *J. Chem. Phys.*, **26**, 1363 (1957).
5. Y. T. Tan and D. Kramp, *ibid.*, **53**, 3691 (1970).
6. E. Barsis and A. Taylor, *ibid.*, **45**, 1154 (1966).
7. G. Simkovich, *J. Phys. Chem. Solids*, **24**, 213 (1963).
8. K. J. DeVries and J. H. Van Santen, *Physica*, **29**, 482 (1963).
9. J. Schoonman, *J. Solid State Chem.*, **4**, 466 (1972).
10. J. Braunstein and G. D. Robbins, *J. Chem. Ed.*, **48**, 52 (1971).
11. D. A. Jones, *Proc. Phys. Soc.*, **65B**, 165 (1955).
12. J. H. Kennedy, F. Chen, and J. Hunter, *This Journal*, **120**, 454 (1973).
13. C. Wagner, *Z. Elecktrochem.*, **60**, 4 (1956).
14. J. B. Wagner and C. Wagner, *J. Chem. Phys.*, **26**, 1597 (1957).
15. D. O. Raleigh, *Progress in Solid State Chem.*, **3**, 83 (1966).
16. A. V. Joshi and J. B. Wagner, *J. Phys. Chem. Solids*, **33**, 205 (1972).
17. J. B. Wagner and C. Wagner, *This Journal*, **104**, 509 (1957).
18. J. Schoonman and A. J. H. Macke, *J. Solid State Chem.*, **5**, 105 (1972).

Controlled Porosity and Pore Size Substrates for Nickel-Cadmium Cells

D. J. Gordy, E. Luksha,* and C. J. Menard*

Gould Inc., Gould Laboratories, Energy Technology, Mendota Heights, Minnesota 55118

ABSTRACT

A novel process for the preparation of improved cadmium electrode plaques with precisely controlled pore size and porosity is described. The requirements for these plaques include far better uniformity, reproducibility, and life than is currently available with conventional materials. The key features of the work were preparation of plaques via a powder metallurgical technique which consisted of isostatically compacting a blend of a nickel powder with a fugitive pore-former and subsequently sintering the "green" compact. Cadmium electrodes were prepared from these materials and cycle tested in negative-limited cells using an accelerated, torturous test regime. Results were obtained which showed the new structures yielded electrodes that were superior to the conventional structures in mechanical properties and performance. BET surface areas, SEM photomicrographs, and mechanical strengths using a three-point bend test were used to help in the thorough characterization of the electrodes and the components prepared.

There is currently a need for very long-lived, highly reliable secondary batteries. Nickel-cadmium batteries of the sealed type are uniquely suited for such applications mainly because of their long lives if suitably constructed and if employed under the proper set of operating conditions, *e.g.*, partial discharges, low temperatures, and low rates of charge and discharge. Under torturous conditions the utility of nickel-cadmium batteries becomes severely limited because cells can fail due to any number of factors, a very common one being cell failure due to excessive gassing on overcharge. This can be a result of aging effects on both electrodes and especially degradation of the cadmium electrode.

Such failures can be blamed on lack of uniformity and reproducibility of the battery components. This is resonable, for if components are not uniform and reproducible, it is not possible to effectively account for them in the design of the system.

Past efforts to produce uniform materials have been concerned with bulk or macroscopic uniformity, that is, special attention was given to produce, for example, plaques and electrodes of thickness, loading, porosity, etc. within tighter limits (1). In spite of this, electrodes that were apparently uniform on a bulk basis have shown widely differing aging characteristics indicating that perhaps not all key variables have been considered.

Rather than concentrating on macroscopic uniformity, in the work discussed herein the uniformity on the microscopic scale was controlled, and its role on the life and aging characteristics were evaluated by testing highly porous plaques of very closely controlled porosity, pore size, and pore-size distribution.

To this end, powder metallurgical techniques were chosen to prepare uniform plaques because these are the most versatile and direct processes for the fabrication of porous materials suitable for practical electrode components. A pore-former type process was selected as the most promising. With the use of a pore-former, one can precisely control both induced and interstitial porosity to make a structure to meet a specific application. Interstitial porosity is the naturally occurring void volume between neighboring particles in a more or less close-packed aggregate. Induced porosity, on the other hand, is formed by the addition of a fugitive pore-former to the unconsolidated powder. An interconnected void volume is subsequently formed by the removal of the added powder (2).

* Electrochemical Society Active Member.

Key words: electrode substrates, nickel plaques, nickel-cadmium cells.

To prepare an induced-pore electrode plaque, a nickel powder was first screened to yield an average particle diameter of the desired size. Then a powdered pore-former of the proper particle size to form pores of the necessary diameter was blended with the nickel powder. The blended powder mixture was then compacted to cold-sinter the nickel particles. The pore-former was removed from the compact leaving a structure that was subsequently sintered at the desired times and temperatures.

Pressure was applied to the powder blend isostatically in a flexible mold in a pressurized fluid. Because a powder does not behave in an ideal hydrodynamic manner under pressure, a consequence of interparticle and die wall friction, die pressing usually results in variations in microstructure throughout the compact. Uniform microstructures can best be achieved by isostatic pressing.

The isostatic compaction process used in this work was the so-called wet-bag process. Parts were compacted, via pressurized liquid against rubber diaphragms from two directions. A detailed description of the process is given in the Experimental section.

Experimental

The experimental work involved pore-former preparation, nickel powder preparation, blending of the two powders, compaction of the powder blend, removal of the pore-former, sintering of the "green" plaque, and electrode fabrication, and testing. The following is a brief outline of these procedures.

Plaque preparation.—Figure 1 illustrates the process flow of the various operations required in the fabrication of the plaques. Each operation is described in some detail in the paragraphs that follow.

Pore-former.—$(NH_4)_2CO_3$ was used as a pore-former. It was prepared by grinding Fisher purified grade powder in a porcelain ball mill. The powder was sieved and when a sufficient fraction of -37μ powder was obtained, it was sieved again in a 3-in. micro mesh sieve stack (44μ, 30μ, 20μ, 10μ). The various fractions were then stored until needed. All operations on the pore-formers (grinding, sieving, etc) were performed in a dry room (R.H. 3-5%).

Nickel powder.—Inco Type 287 powder was used in the work except where otherwise stated. It was treated by heating in a vacuum oven for 1 hr at 210°C, and then cooled in a dry room. The powder was sieved and the -37μ fraction was stored in the dry room and the remaining fractions discarded.

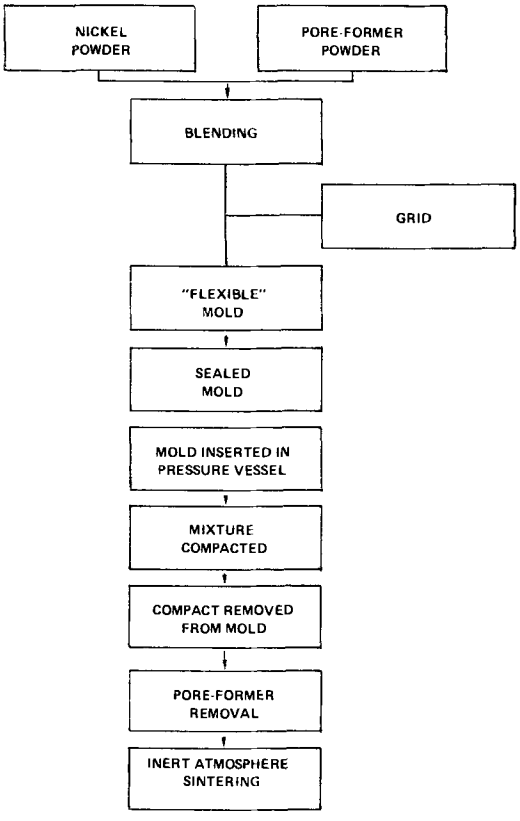

Fig. 1. Process flow chart, plaque fabrication

Powder blending.—To prepare a blend for an 80% porous structure, for example, the nickel and $(NH_4)_2CO_3$ were weighed out to obtain Ni: $(NH_4)_2CO_3$ ratio of 1.5:1, the ratio required to yield an 80% plaque. The normal working weight was 200g. This was used to aid in handling and to avoid changes in composition due to storage. The powders were then mixed and brushed through a sieve. The blend was placed in a Patterson-Kelley twin-shell dry blender and allowed to mix for 30 min. After mixing, the material was again brushed through a sieve and then stored in the dry room. All the above operations were carried out in a dry room. The blend for a 60% porous structure was prepared in a similar manner except that the Ni: $(NH_4)_2CO_3$ ratio was 9:1, the value required to prepare a plaque of 60% porosity.

Powder compaction.—The blend was then loaded into the cavity of a flexible mold (Fig. 2) which already contained an annealed 20-mesh, 7-mil wire, woven screen, by brushing through an appropriate size sieve. For the -37μ size pore-former, a 45μ sieve was used. The essential feature of this mold was the two flexible ends which permitted compaction, via the rubber parts, from both sides of the specimen. This mold allowed the preparation of a part 3 in. in diameter. All excess material was struck off, and the mold closed and inserted into an Autoclave Engineers 4-in. isostatic press and compacted at a pressure of 7000 psi for 1 min.

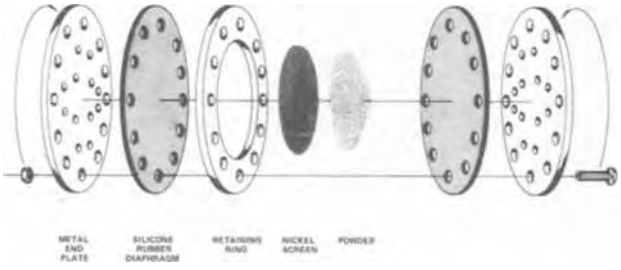

Fig. 2. Exploded view of flexible mold used to isostatically compact powders.

Pore-former removal.—After compaction, the "green" sintered specimen was removed from the mold and the $(NH_4)_2CO_3$ pore-former was removed by placing the sample in a vacuum oven and decomposing under vacuum at 210°C for 20 min.

Green plaque sintering.—The "green" plaques were then removed from the decomposition oven and immediately placed into a vacuum oven where they were sintered in a TM Vacuum Products oven at a pressure of less than 50μ at 870°C for 10 min. Helium was used as a back fill and cooling media.

Plaque characterization.—Mechanical testing.—Mechanical strengths were measured for representative specimens on an Instron Tensile Tester by a three-point bend method.

Photomicrographs.—Scanning electron photomicrographs of selected specimens were taken and measurements made on them to determine induced pore size and ratio of induced to interstitial porosity. Examination of photomicrographs was also used as a criteria for microscopic uniformity, along with such items as $Cd(OH)_2$ crystal size and distribution, in virgin and cycled electrodes.

BET surface area.—Surface areas of selected sintered plaques were determined with a Numinco-Orr Surface Area Pore-Volume Analyzer, Model 2100, using krypton as the adsorbate. Surface areas were utilized for comparison with other properties.

Cadmium electrode processing.—The structures prepared as described above were impregnated by a thermal process (3) in a manner that minimized plaque damage. All electrodes in this study were loaded to 2.452 ± 0.053g CdO/cm^3 of plaque (0.0706 ± 0.0048 A/cm^2 $Cd(OH)_2$ loading). It was felt that a constant loading per cubic inch of free space would yield electrodes far too low in energy density.

The electrodes were then placed in 30% KOH (prepared from mercury cell grade 45% KOH) and charged against nickel dummies to a minimum of 50% overcharge (based on the calculated theoretical capacity) during a 16-hr charge cycle. They were then discharged to 0.0V *vs.* a nickel oxide reference electrode at a current of 200 mA, washed free of KOH in hot deionized water, and air dried at 70°C for 1 hr.

Electrochemical testing.—Cadmium electrodes thusly prepared were cycled in 2.35×1.62 in. sizes in specially constructed prismatic hardware in a nickel-cadmium sandwich configuration, using nickel electrodes of sufficient capacity to assure negative-limited performance under all test conditions. These cells were cycled on fully automatic equipment to 100% depth (0.00V) using the regime shown in Table I.

All the charge and discharge data were recorded on a L&N Speedomax Type G multipoint recorder and a statistically significant sample size was tested for each type of electrode prepared.

The use of negative-limited cells assured that these electrodes will receive more torturous treatment than they would receive in a practical cell. In this way, performance differences and aging characteristics between different type electrodes would show themselves with the expenditure of a minimum amount of test effort.

Table I. Charge and discharge data

Cycle No.	Charge rate	Discharge rate, A
1-3	150 mA for 16 hr	0.24
4	150 mA for 16 hr	1.20
5	150 mA for 16 hr	2.40
6	150 mA for 16 hr	4.80
7-end	1.20 A for 1 hr	1.20

Results

Mechanical strengths of isostatically compacted plaques.—The mechanical strengths of cadmium electrode substrates are important properties to consider when one is preparing electrodes that are expected to be long lived. Furthermore, mechanical strengths are useful tools for general characterization of electrodes and plaques.

Flexural yield strengths were evaluated with an Instron three-point bend test jig; the results are shown as the square of the powder content, $(1 - P)$, where P is the fraction porosity in Fig. 3.

The values of the flexural yield strengths varied between 900 and about 8000 psi between porosities of 80 and 60%. The relationship between mechanical strength and porosity was, $(1 - P)^2 = 2 \times 10^{-5}S$ where S is the flexural yield strength in units of psi.

Especially noteworthy was the exceptionally high values of mechanical strength of the 60% plaques, in the 8000 psi range. Conventional, gravity-sintered plaques sintered under the same conditions had mechanical strengths of 643 psi for a 79.2% porous plaque.

BET surface areas of substrates.—Surface areas of special specimens were determined using a modified BET method with krypton as the adsorbate. The surface areas were in the range of 0.11 to 0.17 m^2/g of powder content in the plaque. The contribution of the screen weight to the total plaque weight was subtracted for the sake of this discussion. The specimens whose surface area was measured did have support screens however. The specific surface areas in terms of powder weights are shown as a function of total porosity including screen in Fig. 4. The specific surface area is seen to be a linear function of porosity in this range for the two different pore sizes. The reduction in surface area with decreasing porosity is a reflection of the packing of the nickel powder. With the low porosity materials, a particle has more neighbors to bond with during pressing and to form necks with during sintering. There is, therefore, a marked decrease in powder surface area with decreasing porosity.

The surface areas of the compacted plaques also show some dependence on induced pore size. This effect is rather small however. One may easily visualize changes in the number of interparticle bonds and, therefore, surface area when the size and quantity of pore-former particles are varied. The use of larger pore-former particles with the same quantity of metal powder results in a plaque with a thicker pore wall. As a result, each particle will have a different number of neighbors to form necks with during sintering, depending on the size of the pore-former. The surface area will, therefore, exhibit small differences.

Figure 4 shows the two lines intersecting. On the basis of the above discussion, one would not expect this to happen. In reality, different ratios of pore-former to nickel powder were required to prepare plaques of differing porosity irrespective of the pore size.

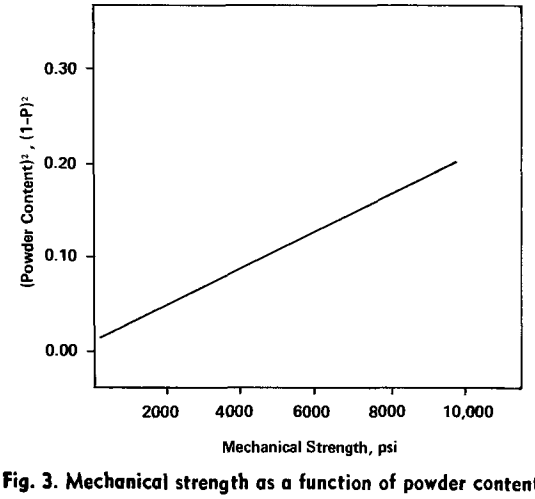

Fig. 3. Mechanical strength as a function of powder content

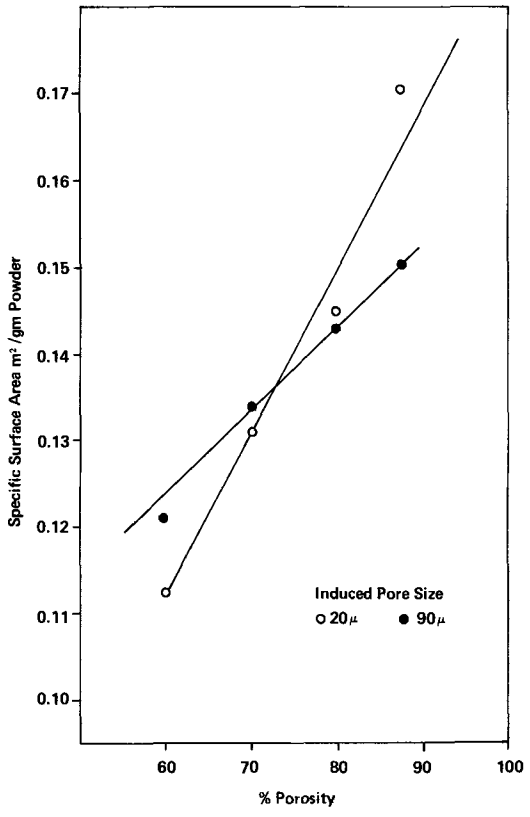

Fig. 4. Specific surface area as a function of plaque porosity

Results of cycle testing.—Accelerated testing of the cadmium electrodes prepared was performed in specially constructed negative-limited cells at high charge and discharge rates. This was an extremely punishing regime for cadmium electrodes. It was employed in an effort to minimize the amount of experimental time in evaluating the differences between various electrodes. The results are therefore not necessarily typical of cadmium electrodes in conventional positive-limited systems in which they are never discharged to 100% depth. The results are therefore best used only for comparative study of this type. Eighty per cent porosity plaques at the 90, 50, 25, and 15μ inducted pore-size levels were tested. Also, performance of state-of-the-art electrodes (gravity-sintered plaques) were evaluated for the purpose of comparison. In addition, a blended powder, Inco Type 287 with Sherritt-Gordon 1μ powder, was evaluated.

A summary of the test results of the accelerated cycle data obtained is given in Table II. The degradation of capacity rates was determined via a linear regression analysis of the test data, using the seventh to the last cycle. A straight line was found to fit the data well. Since the differences in the test data were small, a numerical summary made it easier to compare the isostatically compacted electrodes and conventional electrodes prepared from gravity-sintered plaques from the point of view of efficiency and degradation rates. As far as degradation rates were concerned, there were no statistically significant differences, with one exception, between all the electrodes tested. The electrodes prepared from the 60% 25μ plaques inexplicably had higher degradation rates than all the other electrodes. Therefore, it seemed that the degradation rate under the test conditions employed were independent of the plaque properties and were not used as a criterion for cell life. Some real differences were observed in electrode efficiencies. The 80% structures

Table II. Summary of cycle test data

Least squares fit to Y = A + BX
Y = efficiency, X = cycle number

Electrodes	%P_{ind}*	A†	B‡	Smoothed efficiency at cycle 50
State-of-the art (thermal)	0	37.33	−0.100 ± 0.058	32.3 ± 2.4
From 60% 15μ plaques	40	22.22	−0.0694 ± 0.054	18.7 ± 2.3
From 60% 25μ plaques	40	33.20	−0.182 ± 0.052	24.1 ± 2.2
From 60% 50μ plaques	40	21.98	−0.064 ± 0.086	18.8 ± 3.6
From 60% 90μ plaques	40	23.22	−0.085 ± 0.082	19.0 ± 3.5
From 80% 15μ plaques	91	40.28	−0.120 ± 0.076	34.3 ± 3.2
From 80% 25μ plaques	91	41.51	−0.0873 ± 0.092	37.1 ± 3.9
From 80% 25μ plaques (blended powders)	91	41.64	−0.140 ± 0.079	34.6 ± 3.3
From 80% 50μ plaques	91	32.54	+0.048 ± 0.048	34.9 ± 2.0
From 80% 90μ plaques	91	38.00	−0.086 ± 0.031	33.7 ± 1.3

* Per cent porosity induced, calculated.
† Electrode efficiency at the zero cycle, if it is possible to extrapolate through the first seven cycles, ± average 95% confidence limit.
‡ Rate of degradation of the electrode efficiency per cycle ± 95% confidence limit.

with pore sizes 25μ or less had efficiencies higher than conventional electrodes.

The electrodes prepared from the higher induced porosities, 91% *vs.* 40%, had considerably higher efficiences at the end of 50 torturous cycles. We could not account for this difference on the basis of increased loading per unit volume of the free space of the 60% electrodes. (Recall that all electrodes had the same loading per unit total volume.) On the basis of their loadings alone, we expected 60 and 80% porous electrodes to have essentially the same efficiencies. The low efficiencies of the 60% electrodes were perhaps related to their low induced porosity. Further work will be required if this phenomenon is to be clarified.

Scanning electron microscopy of isostatically compacted plaques and cadmium electrodes.—The SEM was used as a tool for judging the extent of microscopic uniformity.

Figure 5 shows representative SEM photomicrographs, 60 and 80% 25μ, of isostatically compacted structures and are qualitatively quite revealing as far as microscopic uniformity is concerned. The micrographs at approximately 70X magnification show the nature of the induced porosity, rather large pores uniformly distributed throughout the plaque. The 80% porosity material apparently is a little bit more uniform in this respect. The actual size of the induced pores was less than the size of the pore-former particles. The reduction in size was probably due for the most part to shrinkage during sintering.

Small interstitial pores well under 10μ are evident which no doubt contribute substantially to the total porosity and performance of the electrode. No very extensive agglomerates of material are visible, that is, all the porosity is seemingly interconnected.

These observations are contrasted with the details also shown in Fig. 5 for a state-of-the-art gravity sintered plaque prepared under identical conditions of sintering time and temperature. Very large irregular pores not uniformly distributed are evident. Also present in the gravity-sintered structure are islands of large agglomerates of nickel metal.

Routinely at the end of the accelerated test program, SEM photomicrographs of selected specimens of the cycled cadmium electrodes were taken in an effort to find morphological changes that may have occurred during the cycle testing. Typical examples are shown in Fig. 6 for electrodes made from 60% 25μ and 80% 15μ plaques. The $Cd(OH)_2$ crystal size variation with the plaque structure is important because the crystal

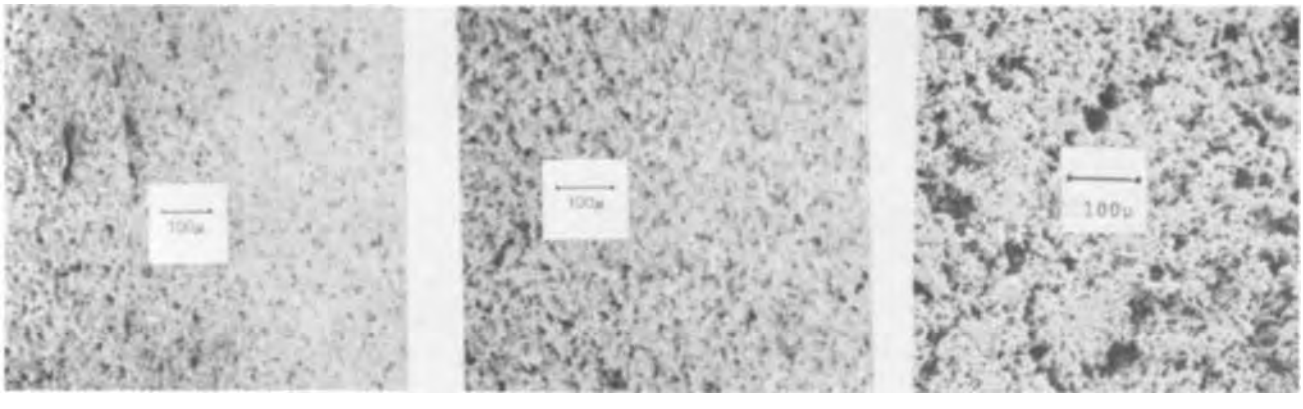

Fig. 5. Scanning electron micrographs of isostatically compacted plaques and a gravity-sintered material. (Left), 60% porosity, 25μ pore-former; (center), 80% porosity, 25μ pore-former; (right), state-of-the-art gravity-sintered plaque.

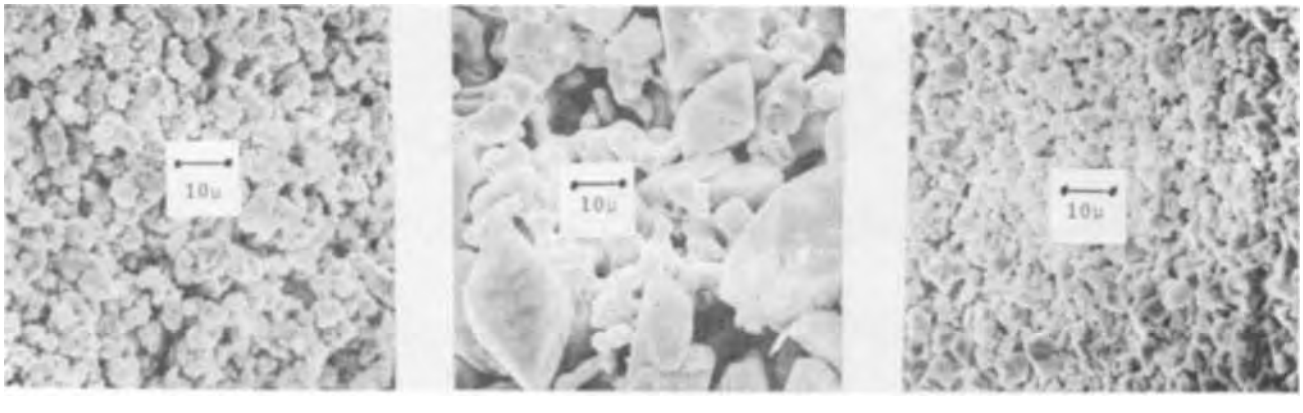

Fig. 6. SEM photomicrographs of cadmium electrodes. (Left), cycled electrode prepared from 60%, 25μ pore-former, isotatically compacted plaque; (center), cycled electrode prepared from 80%, 15μ pore-former, isostatically compacted; (right), formed but not cycled electrode prepared from 60% 50μ pore-former, isostatically compacted plaque.

size is perhaps a key property governing the performance degradation of cadmium electrodes during cycling.

Of interest in the micrographs is the appearance of the nickel substrate. A typical example of a formed but not cycled electrode is also given in Fig. 6. Note that the plaque substructure is completely covered with $Cd(OH)_2$ crystals. With cycling, morphological changes occurred in which cadmium active mass migrated from the nickel surfaces onto other cadmium hydroxide particles. Also prominent in the micrographs is the evidence of corrosion of the nickel substrate. This was due either to the electrode processing or to the cycling.

The $Cd(OH)_2$ crystal sizes, $\bar{d}$, were determined in this way for all the electrodes prepared in this program and are given in Table III along with the smoothed 50th cycle efficiency.

The $Cd(OH)_2$ crystal size was dependent on the substrate porosity, the 60% porous substrates have crystal sizes in the 0-2μ range and the 80% porous substrates have crystal sizes of about 7-10μ. This difference in crystal sizes is evident in Fig. 6. However, the crystal size was perhaps confounded with the depth of discharge and perhaps porosity, of the two different groups of electrodes. Intuitively one would generally expect higher discharge efficiencies for electrodes with the smaller crystal sizes, yet the opposite was observed.

No definite relationship between crystal size and electrode efficiency was observed. A trend of decreasing crystal size with increasing induced pore size was evident however.

As an additional point of interest, the formed but uncycled electrodes had average crystal sizes of 3.0μ, so that upon cycling, crystal sizes of the electrodes with the 60% porous substrates decreased while those with the 80% porous substrates increased.

It thus appears that the $Cd(OH)_2$ crystal size in these electrodes at the loading levels studied is dependent on both the plaque pore size and porosity.

Conclusions

Cadmium electrode substrates with precisely controlled microstructures were prepared having 60% and 80% porosities, each at 15, 25, 50, and 90μ induced pore-size levels. Cadmium electrodes were prepared from these materials and tested using an accelerated regime. The results reveal that cadmium electrodes prepared from 60% porosity 25μ induced pore-size plaques had efficiencies only 5-10 percentage points lower than state-of-the-art electrodes judging from the results of an accelerated test regime. These plaques had vastly superior mechanical properties, about 8000 psi as compared to 645 psi for the conventional gravity-sintered material in use today. This added strength was observed to eliminate cracking and physical degradation of the electrodes during processing and cycling. The electrical performance of these electrodes was poorer than state-of-the-art electrodes.

Table III. $Cd(OH)_2$ crystal size after cycling

Electrode type	Smoothed 50th cycle efficiency	$\bar{d}$ (μ)
60% 15μ	18.7	2.3
60% 25μ	24.1	1.4
60% 50μ	18.8	1.0
60% 90μ	19.0	0-1.0
80% 15μ	34.3	9.8
80% 25μ	37.1	6.8
80% 50μ	34.9	7.3
80% 90μ	33.7	4.7

Cadmium electrodes prepared from 80% porous 25μ induced pore-size plaques, under the torturous test regime employed, proved to be the best electrodes made during the course of this program from the point of view of highest efficiency. They were superior to state-of-the-art electrodes in this respect, in addition to having somewhat superior mechanical strengths and better uniformity.

It was also observed that the plaque pore size and porosity were contributing factors to $Cd(OH)_2$ crystal size. No relation between crystal size and efficiency was found however.

The induced porosity was observed to be a factor in electrode performance. Higher induced porosity apparently yielded better electrodes. This property was confounded with loading, however. The best performance at both the 60% and 80% porosities was observed with the 25μ induced pore sizes.

Morphological changes of $Cd(OH)_2$, determined from SEM photomicrographs, were identified after the cycling procedure. With the 60% structures, the crystals apparently decreased in size with cycling, while with the 80% porosity structures the crystals increased in size.

Some small degree of corrosion of the plaques was evident from photomicrographs. The corrosion was due either to processing or cycling.

BET surface areas were measured and varied between 0.11 and 0.17 m^2/g depending on plaque pore size and porosity.

Three-point bend tests were performed on selected specimens and varied between about 900 and 8000 psi between porosities of 80% and 60%. As a point of comparison, a 79% sintered material had a bend strength of 643 psi.

Acknowledgments

This work was performed under Contract NAS 5-21097 with the Goddard Space Flight Center, Greenbelt, Maryland, to develop improved components for use in aerospace nickel-cadmium cells.

Manuscript received March 22, 1973.

Any discussion of this paper will appear in a Discussion Section to be published in the June 1974 JOURNAL.

REFERENCES

1. A. L. Essex *et al.*, "Development of Uniform and Predictable Battery Materials for Nickel-Cadmium Aerospace Cells," NASA Report, N69-16974. Has a good review of work up to 1968 on preparing nickel plaques for use in battery plates.
2. P. Schwarzhopf and D. A. Pearson, "Fabrication of Polyporosity Microstructures," U.S. Pat. 3,362,818 (1968).
3. A. M. Heuninckx, "Process for Making Sintered Type Cadmium Electrodes," U.S. Pat. 2,952,570 (1960).

Anion Effects on the Dissolution of Steel in ECM Binary Electrolyte Systems

James P. Hoare* and Kao-Wen Mao*

Electrochemistry Department, Research Laboratories, General Motors Corporation, Warren, Michigan 48090

ABSTRACT

Steady-state potentiostatic polarization, galvanostatic stripping, and current efficiency measurements were carried out on mild steel (Type 1020) anodes in O_2-stirred solutions of Na_2SO_4 to which increasing amounts of NaCl were added. A salt layer is formed at steel anodes in Na_2SO_4 solutions. A precipitate is deposited from this salt layer onto the anode surface and is converted to a protective anodic film at sufficiently anodic potentials. In the presence of Cl^- ions, the salt layer becomes more soluble and the protectiveness of the anodic film is lessened. With increasing Cl^- ion concentration, a family of curves with increasing current in the passive region is obtained. If the anodic film is formed by the direct oxidation of the anode surface (as in $NaNO_3$/NaCl mixtures), a different family of curves is obtained. For the case where a noncomplexing, film-dissolving anion, such as ClO_4^-, is present (Na_2SO_4/$NaClO_4$ or $NaNO_3$/$NaClO_4$), a third family of curves is found. This behavior is related to the interaction between the type of film-dissolving anion present in solution, and the type of anodic film formed on the electrode surface.

The number of electrolytes composed of water solutions of a single salt suitable for the electrochemical machining (ECM) of steel is limited to only a few systems including NaCl, $NaClO_3$, $NaClO_4$, and $NaNO_3$. If one considers mixtures of salts, the number of suitable electrolytes is greatly increased.

Since the ECM process takes place at potentials corresponding to the transpassive region of the anodic polarization curve obtained on steel in the given electrolyte (1-3), it is necessary to determine the kind of anodic films formed on steel in this electrolyte and how anions present in the solution interact with these films (4). Such ECM parameters as control of dimensions and geometry, tapering, out-of-roundness, and surface roughness depend on the presence of a potential-dependent, protective, anodic film (4-6).

This report describes some experiments which were carried out on steel anodes in electrolytes composed of solutions of Na_2SO_4 and NaCl and designed to shed light on the nature of the interaction of the anions present in solution with the anodic film on the steel surface as a function of potential and electrolyte composition.

Experimental

As described earlier (1, 4), anodes were prepared from mild steel (Type 1020) wires and mounted in triplicate in a two-compartmented Teflon cell. To a 1M solution of Na_2SO_4, the required amount of 0.1M NaCl was added to give the desired mixed electrolyte composition (see Table I). Steady-state, anodic polarization measurements and galvanostatic film-stripping data were obtained in O_2 stirred (~300 cm^3/min) solutions according to procedures presented previously (1, 4). Current efficiency determinations were carried out in the closed-cell system of the laboratory ECM test rig by using methods detailed in the literature (7). The anodes in this case were mild steel tubes.

Results

The results of the steady-state polarization studies obtained on mild steel anodes in O_2 stirred solutions of 1M Na_2SO_4 and 1M Na_2SO_4 containing from 3×10^{-3} to 1M NaCl are presented in Fig. 1a as the average data of three complete runs on three different anodes. It requires the presence of only a relatively small amount of Cl^- ions to cause considerable changes in the polarization curve obtained on steel anodes in 1M Na_2SO_4 solutions. As the Cl^- ion content of the electrolyte increases, the passivation current increases rapidly so that in the 1M Na_2SO_4 + 1M NaCl solution, the behavior is the same as in $SO_4^=$-free NaCl solution. Results similar to these were reported by Condit (8) for the anodic polarization of Fe-Ni alloys in 1*N* H_2SO_4 solutions containing Cl^- ions.

Shown in Fig. 1b is the total charge, Q, associated with the anodic film formed on the steel surface as a function of potential. In the presence of small amounts of Cl^- ions, Q is much larger for steel in Na_2SO_4 mixed electrolytes than in Cl^--free Na_2SO_4 solution. A considerable portion of the large values determined for the charge in Fig. 1b may be due to a large increase in the anode area caused by the severe pitting which takes place in the low Cl^- content Na_2SO_4 solutions as noted in Fig. 2a. In such cases, the roughness factor used in the calculation of Q is larger than 10 which is the value used in determining the data in Fig. 1b. It is interesting to note that a large increase in Q occurs at a potential (1.2V *vs.* SCE) where O_2 evolution begins.

The film on steel in Cl^--free Na_2SO_4 solution is precipitated on the anode surface from a salt layer because the active-passive transition of the polarization curve is shifted with stirring as noted in rotating-disk studies (9). At a threshold anodic potential, this fluffy, nonprotective precipitate is converted to a more compact, protective, oxide film.

This transition from the fluffy precipitate to the compact film can be observed on the series of traces in Fig. 3 obtained from the stripping pulses applied to the steel anode which had been held in the Na_2SO_4 solution containing 3×10^{-3}M NaCl at a given potential. For the electrode potentiostated at 0V (*vs.*

Table I. Threshold potential for formation of compact film on steel in Na_2SO_4 solution containing Cl^- ions

Solution composition	Threshold potential (V)
1M Na_2SO_4	~0.1
1M Na_2SO_4 + 3×10^{-3}M NaCl	~0.7
1M Na_2SO_4 + 6×10^{-3}M NaCl	~1.0
1M Na_2SO_4 + 1×10^{-2}M NaCl	+1.4
1M Na_2SO_4 + 1M NaCl	—
4.5M NaCl	—

* Electrochemical Society Active Member.

Key words: transpassive corrosion, mixed electrolytes, electrochemical machining.

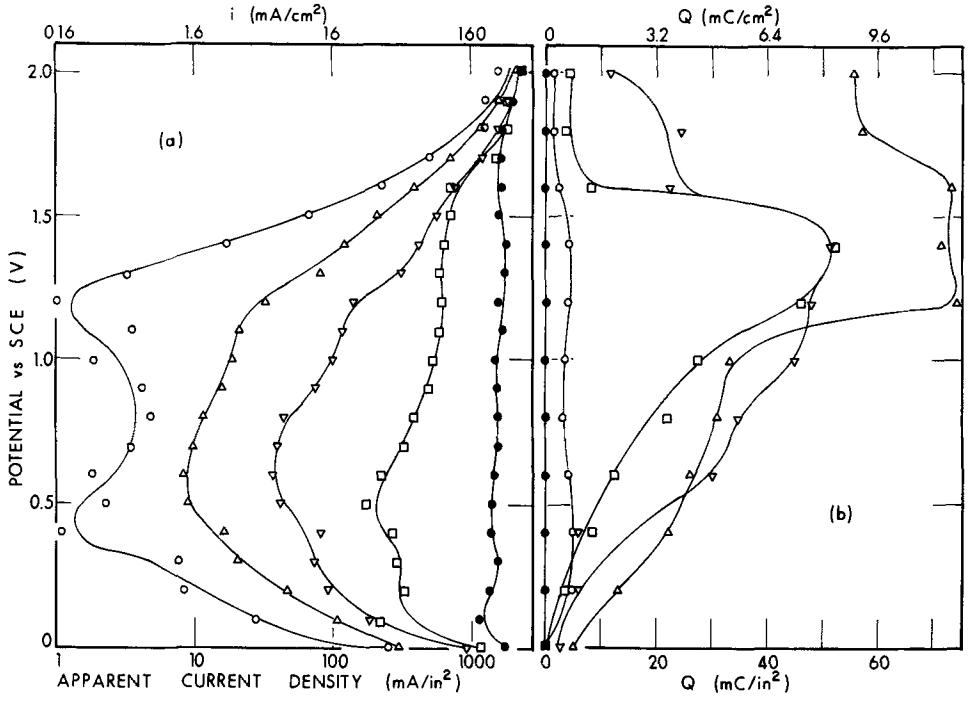

Fig. 1. a, Steady-state polarization curves obtained on mild steel anodes in O_2 stirred solutions of 1M Na_2SO_4 (○), 1M Na_2SO_4 + 3 x 10^{-3}M NaCl (△), 1M Na_2SO_4 + 6 x 10^{-3}M NaCl (▽), 1M Na_2SO_4 + 1 x 10^{-2}M NaCl (□), and 1M Na_2SO_4 + 1M NaCl (●). b, A plot of the total charge, Q, associated with the anodic film present on mild steel anodes as a function of potential in same solutions studied in Fig. 1a. A roughness factor of 10 was assumed in calculating Q.

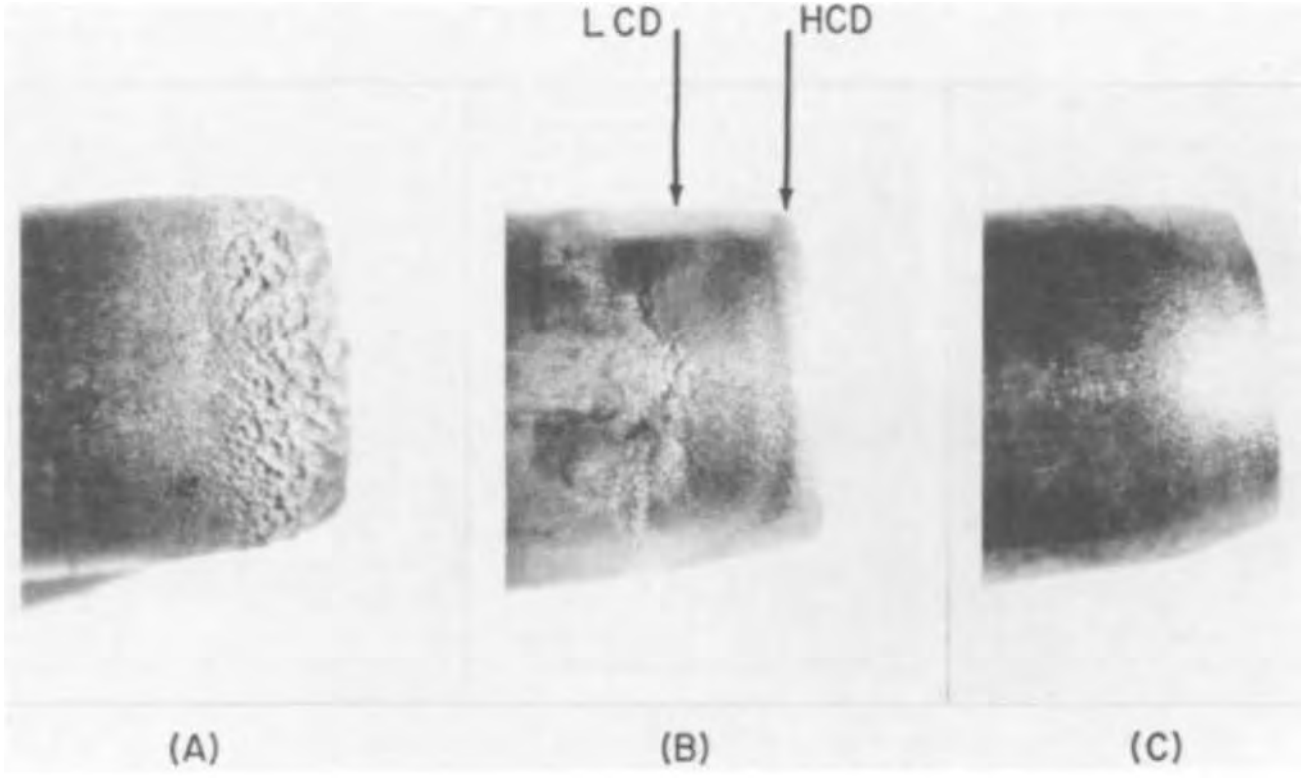

Fig. 2. Photomicrographs of the ends of mild steel tubes machined in the ECM test rig at 240 A/in.² in (A) 1M Na_2SO_4 + 5 x 10^{-3}M NaCl, (B) 1M Na_2SO_4 + 1M NaCl, and (C) 4.5M NaCl.

SCE), Fig. 3a, only one arrest appears on the trace which grows in length with increasing potential (see Fig. 3b at 0.6V). Above 0.6V, a second arrest appears on the trace as in Fig. 3c (electrode held at 1V) at higher overvoltage values. This lower arrest grows at the expense of the upper arrest in Fig. 3d (at 1.2V) and Fig. 3e (at 1.6V) until only the lower arrest remains (Fig. 3f at 2.0V). We believe that the upper arrest corresponds to the fluffy, nonprotecting precipitate which is more easily reduced, and hence, appears at a low overvoltage; whereas, the lower arrest corresponds to the compact, protective, oxide layer which, being more difficult to reduce, appears at the higher overvoltage.

Above a threshold potential (~0.7V) in the case of Fig. 3, the fluffy precipitate is converted to a protective oxide layer which grows with increasing potential at the expense of the fluffy precipitate as shown in the plots of Q associated with the fluffy precipitate (open symbols) and that with the compact layer (closed symbols) in Fig. 4. As noted in Fig. 4 and in Table I, the threshold potential is shifted to more noble values with increasing Cl^--ion content until the appearance of the compact film is no longer detected at potentials below 2V (*vs.* SCE).

The results of current efficiency measurements at mild steel anodes in Na_2SO_4/NaCl mixed electrolytes are recorded in Table II. For Cl^--free 1M Na_2SO_4 solu-

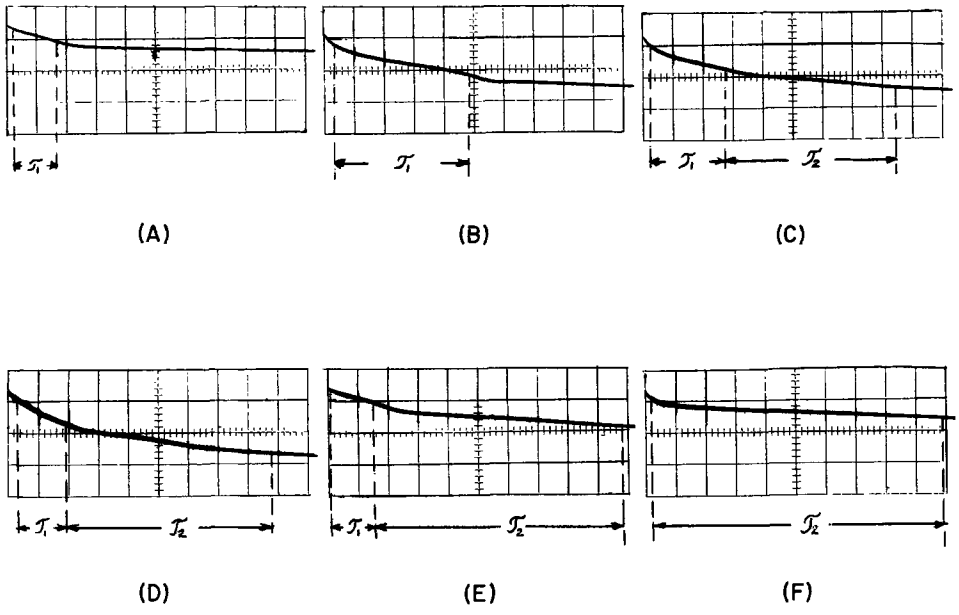

Fig. 3. Recorded traces of galvanostatic cathodic stripping pulses applied to mild steel anodes in 1M Na_2SO_4 + 3 x 10^{-3}M NaCl solution which had been potentiostated at (A) 0V (vs. SCE), (B) 0.6V, (C) 1.0V, (D) 1.2V, (E) 1.6V, and (F) 2.0V; x-axis is (A) 50 msec/cm, (B and C) 100 msec/cm, (D-F) 200 msec/cm; y-axis is 0.35 V/cm; apparent i is 0.4 A/in.^{2} Transition times for fluffy precipitate (τ_1) and for compact oxide (τ_2) are shown. For the sake of clarity, the tangents from which τ was determined (20) are not shown.

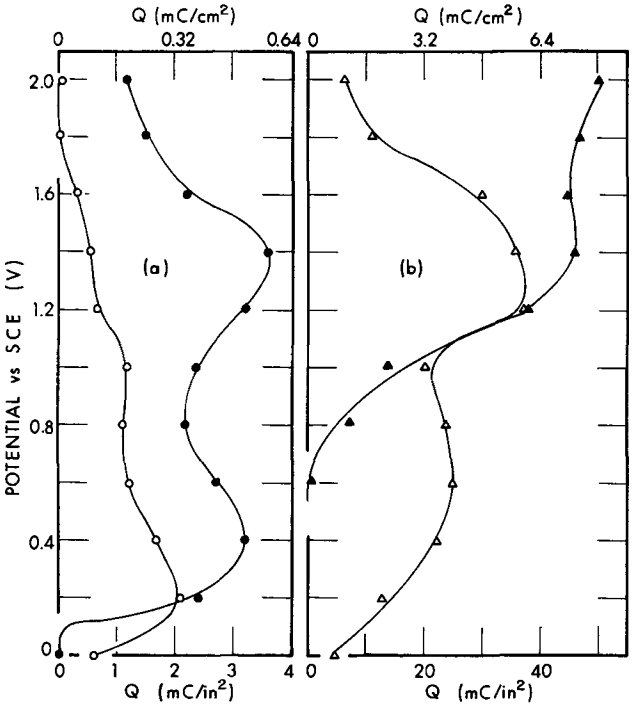

Fig. 4. Plots of the charge Q associated with the fluffy, nonprotecting precipitate deposited on the anode surface (open symbols) and with the compact, protective, anodic film (closed symbols) as a function of potential in 1M Na_2SO_4 (a) and 1M Na_2SO_4 + 3 x 10^{-3}M NaCl (b) solutions.

tion, the compact protective film is quickly formed on the metal surface, and because nearly all of the current is consumed in O_2 evolution, this film must possess a high degree of electronic conductivity. Virtually no attack of the anode is observed on steel in 1M Na_2SO_4. When Cl^- ions are present in small amounts, they can cause local breakdown of the protective film producing the severe pitting observed in Fig. 2a. Still, more than half the current goes into O_2 evolution (Table II) and many sites are covered by the protective film (triangles in Fig. 1b) on steel anodes in 1M Na_2SO_4 solutions containing about 10^{-3}M NaCl. When the Cl^- content reaches 1M, the protective film is absent and virtually all current is consumed in the uniform removal of metal through the porous, fluffy precipitate as noted in Fig. 2b. The metal removal in this case is similar to that found in $SO_4^=$-free NaCl solution (see Fig. 2c and Table II).

Table II. Current-efficiency data on mild steel anodes

Electrolyte composition	Current (A/in.^{2})	Current efficiency for metal removal (%)	Current efficiency for O_2 evolution (%)
1M Na_2SO_4	300	5.5	90
1M Na_2SO_4 + 5 x 10^{-3}M NaCl	240	40.0	54
1M Na_2SO_4 + 1M NaCl	240	95.0	0
4.5M NaCl	240	96.0	0

Discussion

These data along with other similar investigations (4, 10, 11) indicate that the interaction of anions with the anodic film present produce definite patterns in the shape of the anodic polarization curve. Consequently, the analysis of these patterns in the polarization curves along with current efficiency studies can provide hints as to the nature of the anodic films present at the anode surface in a given electrolyte.

In Fig. 5, three idealized patterns of anodic behavior are sketched from polarization data obtained on steel anodes in various mixed electrolytes as a function of the electrolyte composition. Figure 5a describes the case where the passivating current is shifted to the right towards increasing current density. For the case where the active-passive transition is shifted upwards towards more noble potentials, the pattern in Fig. 5b is applicable. Finally, the third case is represented by the pattern in Fig. 5c where the

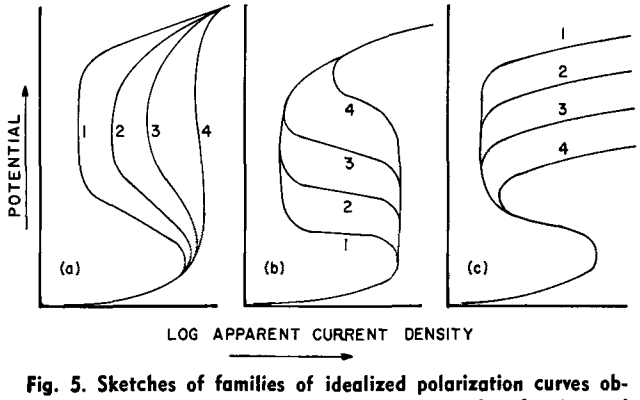

Fig. 5. Sketches of families of idealized polarization curves obtained on mild steel anodes in mixed solutions of a film-forming and a film-dissolving anion numbered in the direction of solutions with increasing concentration of the film-dissolving anion.

transpassive region is lowered towards less noble potentials.

The Cl^- ion is known to form highly soluble complexes with iron and to be a highly efficient agent for the dissolution of anodic films on iron (12-16). In this case, concentrated salt layers are formed at the iron surface but a protective film is not produced at any potential. Both $SO_4^=$ ions and ClO_4^- ions form concentrated salt layers at iron anodes from which porous, nonprotective precipitates are deposited on the iron surface as noted by the stirring dependency of the active-passive transition in such solutions (9). Above a threshold potential, these precipitates are converted to protective anodic films. A compact, protective film is formed by the direct oxidation of the metal surface on iron anodes in solutions of NO_3^- or ClO_3^- ions since the shape of the polarization curve is independent of stirring. These protective films possess a high degree of electronic conductivity (7).

In a solution of Na_2SO_4, the protective film forms from the salt layer at relatively low potentials on steel anodes (Fig. 4a), but when Cl^- ions are added, the salt layer is made more soluble, the precipitate is deposited at higher potentials, and the protective film appears at more noble potentials as noted by the data of Table I. Since the presence of Cl^- ions lowers the protective qualities of the anodic film on steel in $SO_4^=/Cl^-$ mixed electrolytes, the current in the passive region increases with increasing Cl^- content, and the family of polarization curves at various Cl^- ion concentrations follow the pattern of Fig. 5a.

If the protective anodic film is formed by the oxidation of the electrode surface (such as steel in $NaNO_3$ solution), the addition of Cl^- ions to the $NaNO_3$ solution lowers the oxidizing power of the electrolyte by providing competition with NO_3^- ions for adsorption sites on the electrode surface. Consequently, a more anodic potential must be reached before the protective film can be formed on the steel surface. Once this film is formed, however, the steel surface is strongly protected so the current in the passive region does not increase. Instead, the active-passive transition is shifted to more noble potentials (11), and the family of polarization curves for increasing Cl^- content of the NO_3^-/Cl^- mixed electrolyte produces the pattern shown in Fig. 5b.

In the transpassive region, it appears from the data in Fig. 1b and 2a that the Cl^- ion does not remove the passive film uniformly. The film is dissolved at weak points (such as inclusion or dislocation sites) in the film producing localized attack without complete removal of the film. Severe pitting and uneven metal removal takes place. This behavior was also observed (11) for the NO^3-/Cl^- case.

Another good agent for the dissolution of passive films on iron is the ClO_4^- ion (17). Since ClO_4^- ions do not form complexes with iron, and since they are not as strongly adsorbed on the electrode surface as Cl^- ions are, the presence of ClO_4^- ions in a solution of $NaNO_3$ has little effect on the formation of the passive film on a steel anode. However, ClO_4^- ions remove the passive film in the transpassive region uniformly and completely by a suggested ion-exchange mechanism (4) after a threshold concentration of adsorbed ClO_4^- ions on the surface of the film is reached. As the ClO_4^- ion concentration added to a solution of $NaNO_3$ is increased, the threshold concentration of adsorbed ClO_4^- ions for film dissolution is attained at less noble potentials, thus shifting the transition from the passive to the transpassive region on steel anodes in NO_3^-/ClO_4^- mixed electrolytes to less anodic potentials (4). As a result, a family of polarization curves for various ClO_4^- concentrations follows the pattern pictured in Fig. 5c. A similar family of curves was reported by Leckie and Uhlig (18) on 18-8 stainless-steel anodes in $Na_2SO_4/NaCl$ mixed electrolytes.

When ClO_4^- ions are added to a Na_2SO_4 solution, the transpassive region of the curve is also lowered towards less noble potentials on steel anodes in the SO_4^-/ClO_4^- mixed electrolytes (10) according to the pattern of Fig. 5c. However, since perchlorate salts are generally more soluble than sulfates (19), the salt layer becomes more soluble in the presence of ClO_4^- ions and the protective film is formed on the steel surface at slightly more anodic potentials in the mixed electrolyte than in the ClO_4^--free Na_2SO_4 solution. In the case of $NaClO_3$ solutions, where the protective anodic film is formed by the oxidation of the steel surface, the addition of $NaClO_4$ has virtually no effect on the active and passive regions of the polarization curves (10). For the anodic polarization of steel in ClO_3^-/ClO_4^- mixed electrolytes, the transpassive region is shifted to less noble values, as in Fig. 5c, with the addition of ClO_4^- ions to the $NaClO_3$ solution (10).

In general, because Cl^- ions are strongly adsorbed and complex with iron, their presence in mixed electrolyte systems affect the formation and protectiveness of the anodic film. Therefore, the Cl^- content of the electrolyte greatly affects the position of the active and passive regions of the polarization curves in the low concentration range. Since Cl^- ions dissolve anodic films unevenly in the transpassive region by local attack, their presence causes virtually no effect on the position of the transpassive region. These systems are exemplified by Fig. 5a and 5b. The ECM process takes place in the transpassive region. So the uneven, localized dissolution of the anodic film causes severe pitting and nonuniform metal removal in both the low current density (lcd) and the high current density (hcd) region of the machined surface (11) (see also Fig. 2a).

On the other hand, ClO_4^- ions are weakly adsorbed and do not complex with iron. Consequently, they have little or no effect on the active or passive regions of polarization curves obtained on steel anodes in the $NaClO_4$ mixed electrolytes studied. In the transpassive region, ClO_4^- ions remove the film uniformly by an ion-exchange mechanism, and their presence greatly affects the shape and position of the transpassive region of the polarization curve. This behavior results in the pattern of Fig. 5c. Since the passive film is uniformly thinned by the presence of ClO_4^- ions, the surface of the electrochemically machined steel in such mixed electrolytes is electropolished in the hcd region (4, 10), although in some cases, some pitting is found in the lcd region (10).

Figure 6 summarizes the results found for the polarization of mild steel anodes in binary mixed electrolytes containing both a film-forming and a film-dissolving anion as a function of the composition of

	NaCl	$NaClO_4$	Na_2SO_4	$NaNO_3$	$NaClO_3$
$NaClO_3$	Fig. 5b*	Fig. 5c	-	-	C
$NaNO_3$	Fig. 5b	Fig. 5c	-	C	
Na_2SO_4	Fig. 5a	Fig. 5c	B		
$NaClO_4$	Fig. 5a*	B			
NaCl	A				

Fig. 6. Summary of passivation behavior of mild steel anodes in various mixed electrolytes. A, Only salt layers are formed which are not protective; B, precipitate deposited from salt layer and converted to protective anodic film; C, protective film formed by direct oxidation of anode surface. Asterisk (*) denotes that these systems were not studied, but the results are predicted from the results of the systems studied.

the electrolyte. Those systems such as $NaNO_3/NaClO_3$ which do not contain a film-dissolving anion are of no interest to this investigation. Also included in Fig. 6 along the diagonal is the type of film formed in the single electrolyte indicated.

From data obtained on the ECM of high strength alloys (21), it was concluded that no universal electrolyte exists for the machining of all metals. Consequently, one must tailor the electrolyte to the metal to be machined. The use of mixed electrolytes as shown here greatly increases the number of electrolytes available for ECM application; and by proper choice of the components of the solution and their relative concentrations, the tailoring of the electrolyte becomes more feasible. Such data as that obtained from polarization, film stripping, and current-efficiency studies are invaluable as aids in determining the proper choice of electrolyte.

Manuscript submitted March 12, 1973; revised manuscript received May 29, 1973.

Any discussion of this paper will appear in a Discussion Section to be published in the June 1974 JOURNAL.

REFERENCES

1. J. P. Hoare, *This Journal*, **117**, 142 (1970); *Nature*, **219**, 1034 (1968).
2. J. P. Hoare, M. A. LaBoda, M. L. McMillan, and A. J. Wallace, *This Journal*, **116**, 199 (1969).
3. K. Chikamori and S. Ito, *Denki Kagaku Oyobi Butsuri Kagaku*, **37**, 602 (1969).
4. K-W Mao, M. A. LaBoda, and J. P. Hoare, *This Journal*, **119**, 419 (1972).
5. M. A. LaBoda and J. P. Hoare, in "Fundamentals of Electrochemical Machining," C. L. Faust, Editor, p. 227, The Electrochemical Society Softbound Symposium Series, Princeton, New Jersey (1971).
6. J. P. Hoare, K-W Mao, and A. J. Wallace, *Corrosion*, **27**, 211 (1971).
7. K-W Mao, *This Journal*, **118**, 1870 (1971); *ibid.*, **118**, 1876 (1971).
8. D. O. Condit, *Corrosion*, **28**, 95 (1972).
9. D-T Chin, *This Journal*, **119**, 1043 (1972).
10. J. P. Hoare and K-W Mao, *Corrosion*, **29**, 143 (1973).
11. K-W Mao and J. P. Hoare, *Corrosion Sci.*, In press.
12. K. Schwabe, *This Journal*, **110**, 663 (1963).
13. N. D. Stolica, *Corrosion Sci.*, **9**, 205 (1969).
14. V. Ashworth, P. J. Boden, J. S. L. Leach, and A. Y. Nehru, *ibid.*, **10**, 481 (1970).
15. J. M. Kolotyrkin, G. V. Golovina, and G. M. Florianovich, *Dokl. Akad. Nauk SSSR*, **148**, 1160 (1963).
16. C. M. Shepherd and S. Schuldiner, *This Journal*, **119**, 572 (1972).
17. T. P. Hoar, *Trans. Faraday Soc.*, **45**, 683 (1949).
18. H. P. Leckie and H. H. Uhlig, *This Journal*, **113**, 1262 (1966).
19. N. V. Sidwich, "The Chemical Elements and Their Compounds," p. 1232, Oxford Press, London (1950).
20. R. Thacker and J. P. Hoare, *J. Electroanal. Chem.*, **30**, 1 (1971).
21. J. P. Hoare, A. J. Chartrand, and M. A. LaBoda, *This Journal*, **120**, 1071 (1973).

The Behavior of Resistive Layers in the Localized Corrosion of Stainless Steel

H. S. Isaacs*,[1]

Brookhaven National Laboratory, Upton, New York 11973

ABSTRACT

The dissolution of austenitic stainless steels in artificial crevices has been studied as a function of potential and chloride ion activity. Impedance measurements have shown the presence of a resistive layer on the steel which limited the rate of the electrode reaction in the localized corrosion of stainless steels. The potential across the layer, equal to the product of the direct current and layer resistance, varied linearly with the electrode potential indicating ohmic ionic conduction across the layer. The growth of the layer was limited by its solubility and the diffusion of metal cations in the aqueous phase in the cavity. The layer had the properties of a metal chloride with a given solubility product. Increased chloride activity decreased the saturation concentration of the metal cation, its concentration gradient, and gave decreased dissolution rates or currents.

Austenitic stainless steels are highly susceptible to various forms of localized corrosion including crevice corrosion (1-3), pitting (1, 3-15), and stress corrosion cracking (16, 17). The dissolution kinetics within the localized cells would be expected to differ from that of a surface in direct contact with the bulk solution as the concentration of species within the localized area of corrosion are highly concentrated in dissolved cations, hydrogen ions, and chlorides (5-9). The differences in kinetics have been considered to involve the formation of surface layers or films on the anode (10-13), chloride salts (7), and hydrogen bubbles (5). The present investigation is a limited study of dissolution and interfacial characteristics of austenitic stainless steels within artificial crevices or occluded cells (18), where the solution within the crevices was restricted from mixing with the bulk solution.

* Electrochemical Society Active Member.
[1] Present address: Metals and Ceramics Division, Oak Ridge National Laboratory, Oak Ridge, Tennessee, 37830.
Key words: diffusion controlled dissolution, impedance measurements, chloride activity, simulated crevices.

Experimental

With all forms of localized corrosion the anode is in contact with a volume of solution restricted from mixing with, and markedly different in composition from, the bulk solution. Two anode systems simulated these conditions. The first system (3) was modeled on a covered pit (19, 20) as shown in Fig. 1, similar to that used by Suzuki and Kitamura. A hemispherical hole 3.2 mm in diameter was drilled into a plate of Type 304 stainless steel to which an electrical lead was spot welded. The surface of the steel, except for the hemisphere, was coated with a thin layer of silicone rubber to act as a bond, and an aperture in a clear plastic was placed centrally over the hemisphere as in Fig. 1. This aperture was 1.0 mm in diameter and about 0.3 mm deep. The saturated calomel reference electrode (SCE)

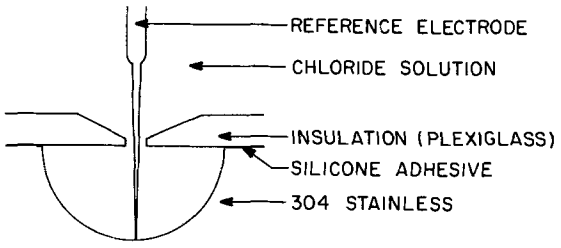

Fig. 1. Schematic of hemispherical cavity

probe with a diameter of about 0.2 mm passed through the aperture and was positioned just above the surface of the hemisphere. The hemispherical cavity had the advantage that the reference electrode was close to the steel surface and would reduce any ohmic potential drops due to solution resistance or precipitation of salts within the cavity (7).

The second anode system which consisted of a wire imbedded into an axial hole drilled in a 25 mm diameter polytetrafluoroethylene cylinder also has been used to simulate pits (4-7). The wires, 0.75 ± 0.03 mm in diameter, were of Types 308 and 321 stainless steels. The face of the cylinder and the cross section of the wire were dry abraded down to 600-grade emery. The cylinder was then inserted into a glass tube with the abraded surface forming the bottom of a container, and the wire protruding from the bottom of the cylinder acted as the electrical lead.

The impedance apparatus employed a constant magnitude square wave current excitation and was similar to that described previously (21). The current wave was superimposed on the direct current from a potentiostat, which controlled the d-c potential of the specimen. The time constant of the potentiostat was sufficiently large to prevent compensation for the potential response to the current wave. The potential responses were less than 10 mV and were displayed on an oscilloscope after amplification and could also be compared or balanced with the response of a variable analog circuit of capacitor and resistor in parallel. Any series resistance could also be measured.

The nominal compositions of the steels are shown in Table I. The solutions used were made from analytical grade reagents and distilled water. All experiments were conducted at room temperature.

Results

The polarization behavior of the hemispherical cavity was found to be more dependent on time than potential once pitting had initiated. A polarization curve obtained in 1.0*N* NaCl is shown in Fig. 2. The potential was held initially at −0.2V (SCE), increased in steps of 0.1 to 1.0V and back for two cycles, and held at each decivolt for 2 min in this experiment. The initial currents were small (<10 μA/cm^3) until the potential was increased to 0.2V, where pitting initiated. The current variations to 0.5V were similar to that expected for a stainless steel surface exposed directly to the bulk solution (15). However, above 0.5V the current decreased, an effect not observed with freely exposed surfaces. The current continued to decrease for all subsequent measurements for the first cycle and was significantly lower on the second cycle at positive potentials. Observation of the hemisphere after polarization showed it was etched but with no deep pits,

Table I. Nominal composition of stainless steels

Type	Weight per cent Cr	Ni	Ti
304	18-20	8-10	—
308	17-19	10-13	—
321	17-19	9-12	0.4 max

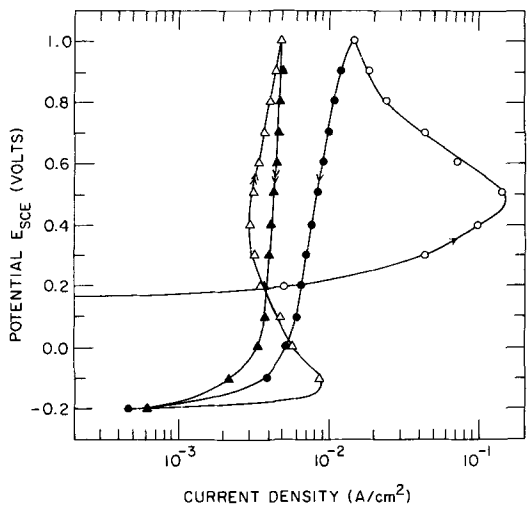

Fig. 2. Polarization behavior of hemispherical anode in 1.0*N* NaCl holding at each decivolt for 2 min. Arrows indicate the direction of potential change. First cycle ○ ●; second cycle △ ▲.

indicating the entire surface had been active in contrast to the localized pitting on freely exposed surfaces. The breakdown of the remaining passive surface was probably accelerated by the changes in composition within the cavity. Compositional changes could be seen after pitting initiated as the solution within the cavity changed to a light green and then to a very dark green.

The current-time behavior for a hemispherical cavity at a constant potential is shown in Fig. 3. The current initially increased to a maximum and then decreased with time, after the solution became dark green. Comparison of the shape of this curve with that in Fig. 2 on considering the potential axis in terms of the time of each measurement suggests that the current behavior was more dependent on time than on the potential. The over-all shapes of both the polarization and current-time curves in replicate experiments were always the same but their magnitudes and the position of the maximums varied. For example, when the current-time behavior was recorded, the time taken to reach the maximum was from 3 to 8 min at 0.3V, while at higher potentials the range of times to reach the maximum decreased. These variations are probably a result of the statistical variations in the number and growth of pits (14). The greater the number of pits or the current from them, the more rapid would be the compositional changes of the solution within the cavity and the shorter the time taken to reach the current maximum.

Changes in color of the solution were obviously due to change in concentration of the dissolving cations, but as chloride ion concentrations would also increase (9), the influence of chloride concentration in the bulk solution was studied. The polarization measurements are shown in Fig. 4 with 1.0*N* NaCl, 4.0*N* LiCl, and

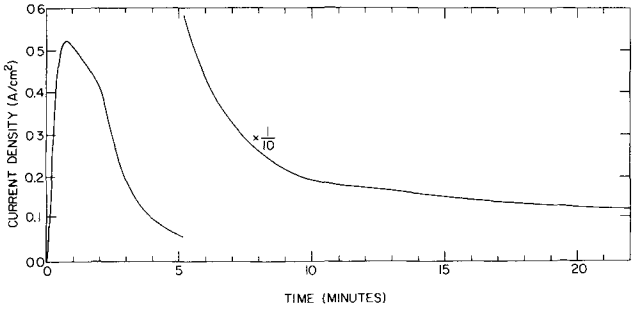

Fig. 3. Variation of the current with time for a hemispherical cavity held at E_{SCE} = 0.5V.

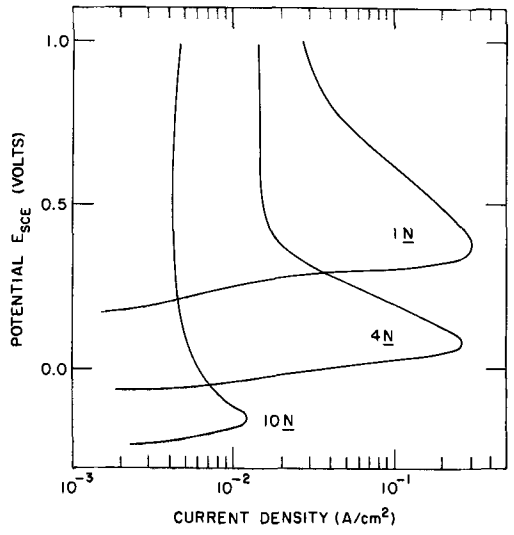

Fig. 4. Polarization behavior of hemispherical anodes in 1*N* NaCl, 4*N* LiCl, and 10*N* LiCl on increasing the potential and holding at each decivolt for 1 min.

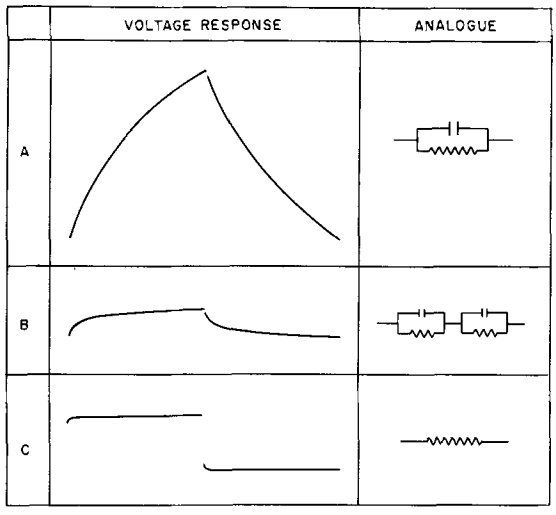

Fig. 5. Voltage responses and approximate electrical analogs of a hemispherical anode interface to a square wave current of constant magnitude. Cycle time: 10 msec. Voltage changes in A: approximately 6 mV.

10.0*N* LiCl solutions. As expected, the pitting potential decreased with increased chloride concentration (15) but the current then decreased more rapidly with potential, indicating higher chloride concentrations were more effective in inhibited dissolution. Measurements with dilute chloride solutions below one normal were unsuccessful probably as a result of this trend. For example, when 0.75*N* NaCl solution was used the current increased rapidly after pitting initiated but the higher currents lead to boiling of the liquid at the aperture and steam bubbles periodically broke the electrical circuit. The rapidity with which the bubble contracted and disappeared after the circuit was broken was inconsistent with the bubble being hydrogen as had been suggested (5).

The behavior of the hemispherical steel solution could, from the polarization measurements, be divided into three regions, viz. (A) the passive surface prior to pitting, (B) the surface when pitting initiates and the current increases (with time, Fig. 3; or potential, Fig. 2), and (C) the surface when the current decreases after the maximum is reached.

The impedance characteristics of the interface obtained using square wave current excitation, could also be defined in these three regions, A, B, and C. The shapes of the voltage responses to the current wave are shown in Fig. 5 for these regions with a repeat cycle of 10 msec. The shape in Fig. 5A was characteristic of the passive surface and was closely approximated by a capacitor and resistor in parallel. The values at −0.2V were close to 30 μF/cm² and 550 ohm-cm², and on increasing the potential the capacitance decreased and the resistance increased. This equivalent circuit was observed until pitting initiated and the current increased rapidly with time. The increased current at pitting sites is analogous to a leakage path across the interface or from an equivalent low resistance in parallel with the analog components of the passive surface. This low resistance would be expected to decrease as the current increases (22). The voltage response, Fig. 5B, observed after pit initiation only approximated this equivalent circuit, in that the magnitude of the response decreased as the current increased, but its shape was more complex and indicative of an equivalent circuit of more than one capacitor in series, each with a parallel resistor.

The shapes of the voltage responses in Fig. 5A and 5B are representative of those observed for a wide range of metals (21, 22) and show a time dependence for the period of each half-cycle. Any equivalent circuits of these responses must involve capacitors to give the potential changes with time. In contrast, a series resistance would only give an instantaneous potential change when the alternating current switches from one-half cycle to the next and then remain constant. The presence of a small series resistance of 0.8 ohm-cm² also accounts for the separation of the half-waves in responses A and B and was probably the result of solution resistance.

The response in Fig. 5C, observed after the current maximum was reached (in Fig. 2, 3, and 4) differs markedly from those of A and B, and from responses observed with a wide range of metal electrodes. This response is closely approximated by a series resistance. The departure from pure resistive behavior was due to some initial curvature indicating a time constant of less than 10^{-4} sec, but this detail was not studied. The magnitude of this response, or that of its analog series resistance, varied with time and potential and these changes were unambiguous.

The potential dependence of the measured series resistance, shown in Fig. 6, was measured with the same cavity and just prior to the currents given in Fig. 2. Above 0.5V (SCE) the resistance increased rapidly as the current decreased and the hysteresis of the resistance on the second cycle was the inverse of that

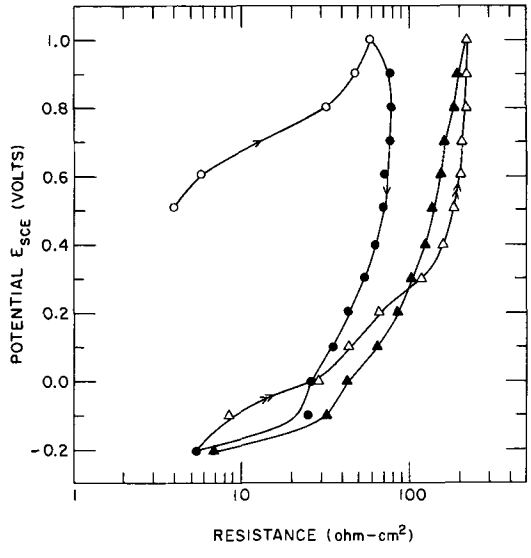

Fig. 6. Variations of the measured series resistance with potential during polarization measurements shown in Fig. 2.

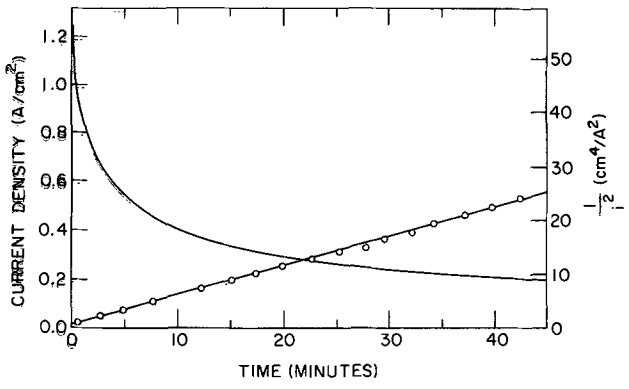

Fig. 7. Variations in current and the square of reciprocal current (○) with time for a wire type anode at E_{SCE} = 0.8V in 1.0*N* NaCl.

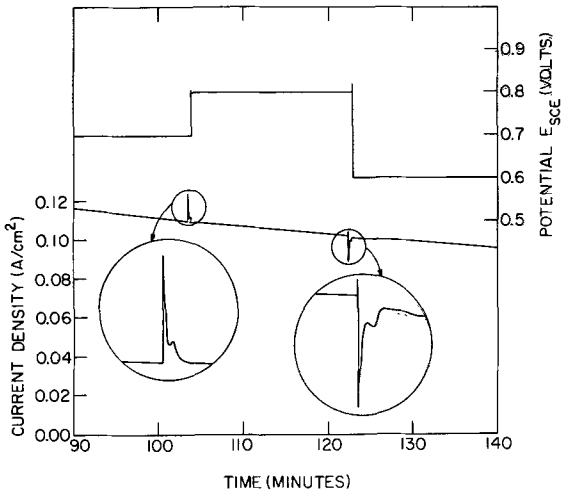

Fig. 8. Variations in current with potential changes for a wire-type anode in a mixed solution of 1.5*N* $MgCl_2$ plus 0.1*N* H_2SO_4 after being held at E_{SCE} = 0.7V for 105 min.

of the current, suggesting the series resistance and the direct polarization current were interrelated. Resistance measurements were also made with the hemispherical cavity in other chloride solutions and showed the same inverse relation to the current.

The experiments conducted on the wire-type electrode were similar to those of Novakovski and Sorokina (7). In general, the potential was held constant and the current-time curve was recorded. An example of the current variations with time is shown in Fig. 7 for a Type 308 stainless steel wire in 1.0*N* NaCl at 0.8V. The current decreases with time and the square of the reciprocal current was proportional to the time as plotted in Fig. 7. A series of measurements were conducted at different potentials in different chloride solutions and the resulting slopes (di^{-2}/dt) and the intercepts as the ordinate (i_o^{-2}) are given in Table II. In some cases breaks in the curves were observed and are noted in Table II.

In runs 1 to 4 with the mixed solution of 1.5*N* $MgCl_2$ and 0.1*N* H_2SO_4, the influence of the potential was not marked in the range 0.35–0.85V (SCE) nor were the breaks (or parallel shifts) of the curves after about 10 to 30 min. These results disagree with those of the previous investigators (7) who indicated a much greater potential dependence, with a stainless steel containing titanium. However, in Table II, for runs 3 and 4 or 6 and 7, the presence of titanium or changes in chromium and nickel concentrations did not influence the results significantly.

An example of the effect of changing the potential on current during a run is given in Fig. 8. Except for the perturbations following the potential change, these changes had no significant influence on the basic shape of the curve indicating that the major factors controlling the current were independent of the potential. The perturbations were complex and lasted for up to 5 min and consisted of a rapid change followed by further damped oscillations, but the current then approached its value prior to the change. The perturbations are enlarged in the insets in Fig. 8 and were found to be dependent on the potential change and its direction.

Utilizing the wire electrodes it was observed that the magnitude of the current decreased markedly with increased chloride concentrations above 4*N*. Once again this was an indication that the chloride ion inhibited the anodic current or dissolution of the steel. The slopes of the plots of the square of the reciprocal current are given in Table II for different lithium chloride concentrations in runs 9 to 14. Above 4*N* LiCl the position of the intercept at zero time also increased markedly with increased chloride ion concentration. This indicated that the currents observed were low soon after the experiments were initiated. In the case of the 10*N* solution marked perturbations were observed at the initiation of the tests other than those associated with the breakdown of passivity, and more akin in shape to those shown in Fig. 8.

The inhibition of the dissolution of the steel in the cavities was marked in the case of chloride ions, but a smaller dependence on the cation was also found. At 4*N* chloride concentration the lithium chloride and hydrochloric acid solutions gave smaller currents (or greater slopes, runs 8, 11, and 15 in Table II) than those in sodium chloride solutions.

Table II. Slopes, intercepts, and calculated additional diffusion paths obtained from the linear variations of the square of the reciprocal current with time for wire-type anodes

Run	Steel	Solution	Potential, V	i_o^{-2}, A^{-2} cm⁴	$\frac{di^{-2}}{dt}$, A^{-2} cm⁴ sec⁻¹	Δ, cm	Remarks
1	308	1.5*N* $MgCl_2$ + 0.1*N* H_2SO_4	0.35	1.87	0.011	0.064	Shift between 12-25 min
				6.97	0.011	0.125	
2	308		0.55	2.03	0.013	0.057	Shift between 7-20 min
				6.03	0.013	0.099	
3	308		0.70	1.00	0.013	0.040	Shift between 10-30 min
				6.03	0.013	0.099	
4	321		0.80	6.24	0.013	0.100	
5	308		0.85	3.64	0.013	0.025	
6	308	1*N* NaCl	0.8	0.73	0.010	0.045	
7	321	1*N* NaCl	0.8	0.31	0.010	0.029	
8	308	4*N* NaCl	0.8	1.77	0.013	0.053	
9	308	1*N* LiCl	0.5	0.83	0.011	0.043	
10	308	2.5*N* LiCl	0.5	1.14	0.014	0.040	
11	308	4.0*N* LiCl	0.8	0.94	0.017	0.030	
12	308	5.0*N* LiCl	0.5	4.26	0.041	0.026	Decreased slope after 10 min
				1.37	0.026	0.023	
13	308	7.5*N* LiCl	0.5	11.9	0.068	0.026	
14	308	10*N* LiCl	0.5	412	0.420	0.025	
15	308	4*N* HCl	0.8	4.48	0.016	0.069	

Discussion

The dissolution behavior of stainless steel in a cavity may be divided into three stages. During the first stage the steel surface is passive. The second stage involves the breakdown of passivity followed by rapid dissolution. The initiation of breakdown has been investigated in detail in pitting experiments (6, 14, 15), but there is little knowledge of the subsequent undermining of passivity as the composition of the solution changes within the cavity. The third stage which occurs when the surface is no longer passive will be considered here. The currents or dissolution rate of the steel are extremely high, but the surface during the third stage is not in the same "active" state as defined by potentials below the Flade potential.

The surface properties in the third stage are markedly different from those normally encountered. This is shown by the potential response of the interface to a square current wave that is approximated by a series resistance. A closer analogy would involve the presence of a capacitor in parallel with the resistor. The approximate value of the capacitance may be calculated from the time constant of the initial response of the potential as the time constant is the product of the capacitance and resistance. The observed time constant was about 10^{-4} sec and taking the resistance as 100 ohm-cm^2 gives a capacitance of about 1 μF/cm^2. This value is too low to be accounted for in terms of a metal-solution electrochemical double layer which usually has a value greater than about 20 μF/cm^2 (23) and indicates that no double layer plays a part in the major interfacial characteristics. In view of this it is unlikely that classical concentration polarization is involved as the impedance characteristics would be significantly different (22). Hydrogen bubbles (5) also would not account for the observed changes in shape of the potential response from one similar to that in Fig. 5B to that in Fig. 5C. If hydrogen increased the solution resistance, the effect would be one of a pure series resistance which would only influence the response when the current stepped from one half-cycle to the next. If hydrogen bubbles decreased the effective surface area the time constants (or curvature) of the interface would not be changed but the current density and hence the magnitude of the response would be increased and would not account for the shape observed in Fig. 5C.

The characteristics of the interfacial region are probably the result of a compact layer (10, 11) approximately 100Å thick (asuming a dielectric constant of 8) having a resistivity of about 10^8 ohm-cm. These values are calculable from the voltage response. In comparison, the thickness of passive layers on iron (24) and steels (25) can be up to 50Å, while for anodic oxide films on the "valve" metals the films may be approximately this value and considerably thicker (26, 27). In the case of the valve metals, however, the resistivity of the major part of the oxide is considerably greater than 10^{10} ohm-cm (27), and orders of magnitude greater than that of the resistive layer.

The potential (V) across the layer is given by the product of the polarization current (i) and the series resistance (R) at each electrode potential (E_{SCE}) and time at which they were measured. The relation between these potentials as shown in Fig. 9 is linear. The slope of the line closely approximating unity, indicates that Ohm's law is obeyed within experimental error. The ohmic behavior also leads to the conclusion that conduction occurs via a "low field" mechanism, or that current through the film is directly proportional to the field within the layer. If a "high field" conduction process was operative, the current could be expected to increase logarithmically (or possibly some other function) with the field in the oxide. For this reason and as a result of other probable complications

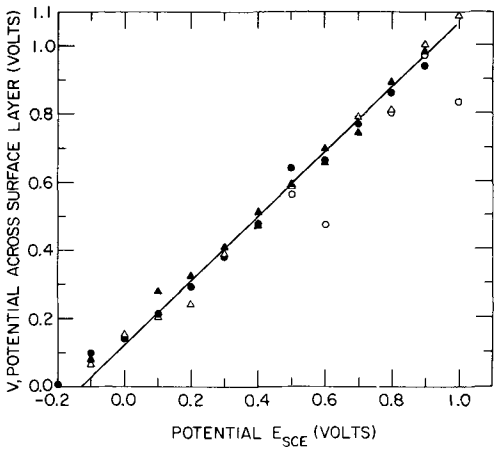

Fig. 9. Variations of potential across the surface layer with electrode potential. The potential across the layer was obtained from the product of the polarization current (Fig. 2) and series resistance (Fig. 3).

(28), the relation shown in Fig. 9 would not be obtained.

The results in Fig. 9 also show that when the electrode potential is changed the potential change occurs within the resistive layer. The current flowing is a function of the layer's resistance and the potential across the film which is given by

$$V = E_{SCE} + 0.125 \qquad [1]$$

This relation has also been obtained with solutions containing higher chloride concentrations, *e.g.*, 4.0*N* NaCl and 10.0*N* LiCl. The electrochemical reactions taking place at both the steel-layer and layer-solution interfaces were, therefore, not changed by the higher chloride concentrations. There is, nevertheless, a marked dependence of the current on chloride concentration and this dependence must result from other factors taking place in the highly concentrated solution.

Independent of the mode of ionic conduction within the layer it can be considered that the effective rate of arrival of metal ions at the solution-layer interface is equivalent to the current. The arriving ions may then either increase the thickness of the layer or enter the solution and diffuse away from the interface. One simplification will be considered; the rate of diffusion predominates and the contribution to the growth of the layer is negligibly small.

The diffusion processes are more easily considered in the wire-type cavity as opposed to the hemispherical cavities where the concentration gradients will depend on distance from the interface and could be complicated by convection processes within the cavity.

When the steel wire had dissolved to a depth equal to l, the rate of diffusion or the diffusion current will be given from Fick's first law as

$$i = \frac{n\mathbf{F}D(Cs - C)A}{l + \Delta} \qquad [2]$$

where n is the average valency of the diffusion ions, **F** the Faraday, D the diffusion coefficient of the ions, Cs the concentration at saturation in the solution at the solution-layer interface, C the concentration in the solution which, in the tests conducted, may be considered to be zero, and A is the cross-sectional area of the wire. The value of Δ may be considered as an additional diffusion path.

The depth to which the wire has dissolved, l, is a function of the total charge passed and is given by

$$l = \frac{M}{An\mathbf{F}\delta} \int_0^t idt \qquad [3]$$

where M is the average molecular weight of the steel of density δ and t is the time. Substitution of Eq. [3] for l in Eq. [2] and integrating between $i = i_0$ when $t = 0$ and $i = i$ when $t = t$ gives

$$\frac{1}{i^2} - \frac{1}{i_0^2} = \frac{2M}{A^2 D \delta n^2 \mathbf{F}^2 (Cs - C)} t \qquad [4]$$

When $t = 0$, $l = 0$ and the value of i_0 can be obtained from Eq. [2], giving

$$\frac{1}{i_0} = \frac{\Delta}{n\mathbf{F}D(Cs - C)A} \qquad [5]$$

According to Eq. [4] the reciprocal of the square of the current should be proportional to time. This is observed to be the case as shown in Fig. 7. Assuming the steel to have 19% chromium and 9% nickel and taking $M = 55.4$ g/mole, $n = 2.2$, $\delta = 8$ g/cm^3, $D = 0.5 \times 10^{-5}$ cm^2/sec (29), and $A = 1$ cm^2 the derivative of Eq. [4] gives

$$\frac{di^{-2}}{dt} = \frac{6.15 \times 10^{-5}}{Cs - C} \qquad [6]$$

The slope of the plot in Fig. 7 is $0.010 \mathrm{A}^{-2}$ cm^4 sec^{-1} (Table II) and on substitution in Eq. [6] with the bulk concentration (C) as zero gives a value of approximately $6 \cdot 10^{-3}$ moles/cm^3 or a 6 molar concentration. This calculated saturation concentration is close to that expected for the metal chlorides involved and indicates that a model based on simple diffusion and solubility of a chloride layer is in reasonable agreement with the experimental results for bulk concentrations from 1 to about 4N chloride ion. Increased chloride and different chloride salts influenced the slopes in Table II, which, in turn, would change the calculated saturation concentration. The slopes are a function of the activity of chlorides in the bulk solution. For example, the mean activity coefficients of lithium chloride and hydrochloric acid are approximately equal at a given concentration, while that of sodium chloride is significantly lower (30). Comparing the slopes for runs 11, 15, and 8 in Table II indicated the same dependence: lithium and the acid gave approximately the same slope, while that with sodium chloride was significantly lower. These results are interpretable in terms of a solubility model (Eq. [3]). The chloride layer formed on the anode surface can be considered as a compound with a given solubility product and any increase in chloride concentration or activity would lead to a decreased metal ion saturation concentration and an increased slope.

The variation of slope with lithium chloride concentration (runs 9-14) is complex. In concentrated solutions the mean activity coefficient of the salt increases with increased concentration rather than decreases as is well known for dilute solutions (30). These changes led to an increased slope which was marked above bulk concentrations of 4N. The rate of increase in slope was also more rapid than the square of the concentration but approximated the square of the activity calculated from the square of the product of the concentration and mean activity coefficients (30) of lithium chloride. At and below 4N concentrations the effect of bulk activity was small probably as a result of the significantly higher activities within the cavity.

The intercepts on the ordinate (i_0^{-2}) of the i^{-2} *vs.* t plots as shown in Table II depended on the solution and increased with increased concentration as has been observed previously (7). In the derivation of Eq. [4] and [5] the presence of this intercept has been attributed to an effective additional diffusion path Δ. This value may be obtained on dividing Eq. [5] by the derivative of Eq. [4] which gives

$$\Delta = \frac{n\mathbf{F}A\delta}{2M} \Big/ i_0 \frac{di^{-2}}{dt} \qquad [7]$$

The values of Δ have been determined and are also given in Table II and vary from 0.025 to 0.10 cm. The shift in the curves observed in the sulfate-containing solutions giving values of Δ of approximately 0.1 cm suggest that this is due to an increased diffusion path possibly as a result of a precipitate forming at the mouth of the pit. The lower values may either result from a "lid" although no "lid" could be seen after the experiments in 10N LiCl. The magnitude of Δ can also be accounted for in terms of a diffusion layer (31) in the increased density of solution (9) existing from the cavity. The high density solution could reduce the effects of convection currents that normally control the magnitude of the diffusion layer and give rise to an unusually large value.

The above discussion shows that the current is controlled by (*i*) the resistance of the resistive layer and the potential across it, and (*ii*) the diffusion of metal ions from the cavity. There is, however, no anomaly as the arrival of metal ions at the layer-solution interface at constant potential must be almost equal to the flux of metal ions diffusing from it. If the rate of arrival was greater than the diffusion flux the thickness of the resistive layer must increase as the excess would not enter the saturated solution. This, in turn, would increase the resistance of the layer and reduce the current until both fluxes are again equal. The system is thus self-regulating as concluded by other authors (7).

The potential would also not be expected to influence the currents because of the self-regulation of the system and this was found experimentally in runs 1 to 5 in Table II. If the potential was stepped during a run it would be expected that the perturbations in the current would be observed for a short period following the potential change. If the potential was increased the current across the layer would increase above that of the diffusion flux. The thickness of the layer would then increase until its resistance at the new potential reduced the current to a value equal to the diffusion flux. Similarly, when the potential is decreased the current would initially drop, the layer would dissolve and the current would then rise to the value once again equivalent to the diffusion flux. Figure 8 shows the experimental results. Following the potential change, the current does again approach a value equal to that prior to the change. However, the perturbations in the observed current (shown in insets in Fig. 8) are more complex than the above model would indicate. These perturbations are probably the result of the rapid changes in the current and the movement of the ions which led to changes in composition and complex chemistry of the solution within the cavity. These transient changes, in turn, could influence the solubility of the resistive layer, its thickness, and the flow of current.

Summary

1. High currents or corrosion rates are observed over a wide range of potential in localized corrosion.

2. A resistive layer forms on the surface of stainless steel anodes in concentrated chloride solutions containing high concentrations of metal ions present in restricted cavities.

3. The resistivity of the layer is approximately 10^8 ohm-cm and field-assisted migration across the layer is ohmic.

4. The thickness of the layer is a function of the electrode potential and the rate of diffusion of metal ions from the layer-solution interface.

5. The solubility of the metal ions and the current depends markedly on the chloride concentration and the complex chemistry within the cavity.

Acknowledgments

The author wishes to thank Dr. D. H. Gurinsky for his interest in this work, Drs. L. Newman and S. W. Feldberg for their many helpful discussions, and Mr.

G. Kissel for his assistance. This work was performed under the auspices of the United States Atomic Energy Commission.

Manuscript submitted Jan. 30, 1973; revised manuscript received June 12, 1973.

Any discussion of this paper will appear in a Discussion Section to be published in the June 1974 JOURNAL.

REFERENCES

1. International Conference on Localized Corrosion, Williamsburg, Va., Dec. 6-10, 1971, To be published NACE Houston.
2. I. L. Rosenfeld and I. K. Marshakov, *Corrosion*, **20**, 115t (1964).
3. T. Suzuki and Y. Kitamura, *ibid.*, **28**, 1 (1972).
4. N. D. Greene and M. G. Fontana, *ibid.*, **15**, 25t, 32t (1959).
5. R. P. Frankenthal and H. W. Pickering, *This Journal*, **119**, 1304 (1972).
6. B. E. Wilde and E. Williams, *Electrochim. Acta*, **16**, 1971 (1971).
7. V. M. Novakovski and A. N. Sorokina, *Corrosion Sci.*, **6**, 227 (1966).
8. M. Pourbaix, *J. Less Common Metals*, **28**, 51 (1972).
9. H. H. Uhlig, *Trans. AIME*, **140**, 411 (1940).
10. T. P. Hoar, in Ref. 1.
11. T. P. Hoar, D. C. Mears, and G. P. Rothwell, *Corrosion Sci.*, **5**, 279 (1965).
12. U. F. Frank, Proc. 1st Intern. Congress on Metallic Corrosion, London, 1961, p. 197, Butterworths, London (1962).
13. K. J. Vetter, in Ref. 1.
14. W. Schwenk, *Corrosion*, **20**, 129t (1964).
15. H. P. Leckie and H. H. Uhlig, *This Journal*, **113**, 1262 (1966).
16. R. W. Staehle, in "The Theory of Stress Corrosion Cracking in Alloys," p. 223, J. C. Scully, Editor, NATO, Brussels (1971).
17. H. J. Engells, in Ref. 16, p. 86.
18. B. F. Brown, *Corrosion*, **26**, 249 (1970).
19. I. L. Rosenfeld and I. S. Danilov, *Corrosion Sci.*, **7**, 129 (1967).
20. H. S. Isaacs and G. Kissel, *This Journal*, **119**, 1628 (1972).
21. H. S. Isaacs and J. S. Ll. Leach, *ibid.*, **110**, 680 (1963).
22. H. S. Isaacs and J. S. Ll. Leach, *ibid.*, **115**, 237 (1968).
23. P. Delahay, in "Double Layer and Electrode Kinetics," Interscience Publishers, Inc., New York (1965).
24. J. Kruger, *Corrosion*, **22**, 88 (1966).
25. K. N. Goswami and R. W. Staehle, *Electrochim. Acta*, **16**, 1895 (1971).
26. L. Young, in "Anodic Oxide Films," Academic Press, Inc., New York (1961).
27. J. W. A. Scholte and W. Ch. van Geel, *Philips Res. Rept.*, **8**, 47 (1953).
28. Ref. 26, p. 163.
29. T. R. Meuller, Ph.D. Thesis, Univ. Kansas, Lawrence, 1961.
30. H. H. Harned and B. B. Owen, "The Physical Chemistry of Electrolytic Solutions," Reinhold Publishing Corp., New York (1958).
31. V. G. Levich, "Physicochemical Hydrodynamics," Prentice Hall, Englewood Cliffs, N. J. (1962).

Initial Stages of Electromonocrystallization of Nickel on Copper-Film Substrates

Shohei Nakahara and Rolf Weil*

Department of Metallurgy, Stevens Institute of Technology, Hoboken, New Jersey 07030

ABSTRACT

The first stage of electromonocrystallization, the growth of single-crystal electrodeposits, in a number of instances is the development of three-dimensional, epitaxial crystallites (TEC). The absence or presence of TEC as well as their morphology is determined by the codeposited foreign species, either intentionally added or apparently resulting from a high pH in the solution adjacent to the cathode. When a complete deposit layer has formed, strains result from the difference between the lattice dimensions of the deposit and substrate as well as from the coalescence of TEC. Surface undulations are also related to the joining of TEC. Dislocations of the misfit type develop at certain deposit thicknesses; their spacing and straightness again are related to the presence of foreign substances. The coalescence of TEC and possibly of atom layers too thin to be visible also results in dislocation and twin formation.

Many recent fundamental studies of electrocrystallization have involved single-crystal substrates and deposits in order to avoid the complications of grain boundaries and the variation of the growth processes with orientation. In order to differentiate between the electrolytic growth processes within one single crystal and those in polycrystalline deposits, the term "electromonocrystallization" is introduced here. Many investigations of electromonocrystallization have been primarily concerned with describing the transition of an ion from the electrolyte to the metal structure. Other studies on a much larger than atomic scale have employed optical observations (1-6) or special x-ray-diffraction techniques (7-8). There have been only a few studies of electromonocrystallization processes which used electron microscopy. Of course, there have been many observations of electrodeposits using both transmission and scanning electron microscopy, but they have yielded very little information of how the structures developed. Unfortunately, it has not been possible to perform the *in-situ* experiments (9) which have been so valuable in studying the growth processes of vapor deposits. The electron microscopic examinations by Lawless (10-11) of the initial stages of electromonocrystallization of deposits while still attached to thin-film substrates have elucidated the growth mechanisms. However, Lawless did not systematically investigate the effects of the plating variables and foreign substances in the electrolyte which are known to alter the crystallization processes. This study is therefore primarily concerned with the effects of the pH, metal-ion concentration and buffering of the plating bath as well as the deliberate additions of three organic substances (coumarin, saccharin, and phenosafranine) on electromonocrystallization using essentially the same types of samples as Lawless.

* Electrochemical Society Active Member.
Key words: electrocrystallization, thin films, nickel.

Experimental Procedure

The substrates were produced by vapor depositing about 50 nm of copper onto cleaved and polished {001} faces of potassium-chloride crystals. During the evaporation in a vacuum of about 10^{-5} Torr, the KCl crystals were in contact with a heater, which maintained their surface temperature at 350°C. After evaporation, the samples were held at 400°C for several hours to anneal them. When the coated KCl crystals had cooled, they were removed from the vacuum chamber, cleaved into pieces 0.5 cm by 2 cm and stored in a desiccator.

Just before plating, the KCl was dissolved by floating the sample on the surface of distilled water. The copper films, which continued to float after the salt had dissolved, were rinsed several times by transferring them on a wet glass slide onto the surfaces of several water-filled dishes. The final dish contained a 10% H_2SO_4 aqueous solution to remove any oxide film. With one end touching a piece of copper foil for electrical contact, the film was floated in a dish containing the plating solution. A nickel anode lay on the bottom and had a platinum wire attached to it for electrical contact.

The compositions of the plating solutions are listed in Table I. Coumarin was chosen as an addition agent because it reduces macrostress in polycrystalline deposits (12). Saccharin results in compressive macrostress (12). Phenosafranine was selected as an additive because of the large size of its molecule, which was known to be included wholly in electrodeposits and because it increases tensile macrostresses (13). The structures of phenosafranine and coumarin are schematically represented in Fig. 1. The current density was 5 mA/cm² and the *p*H was either 1.5, 3, or 6 as also shown in Table I. The plating thicknesses were 1-200 nm. The temperature at the surface of the plating bath was maintained at 30°C. The current was preset using a constant-current source. The plating solutions were prepared with triple-distilled water (two distillations in the presence of oxidizing agents to remove organic impurities) and reagent grade chemicals. The electrolyte was purified by treatment with activated charcoal and by low-current-density electrolysis for at least 48 hr. The *p*H was adjusted either with sulfuric acid or nickel carbonate.

After plating and rinsing, the samples were cut into pieces about 0.3 cm², placed on 200-mesh electron-microscope sample grids and dried. In general, bicrystal films, *i.e.*, nickel deposits still attached to the copper substrates, were examined. Unplated samples of each lot of the copper-substrate material were also examined. In some instances the copper was dissolved in an aqueous solution composed of 50 g/liter H_2SO_4 and 500 g/liter CrO_3 so that only the thin nickel deposit could be studied. A few samples which were too thick for transmission electron microscopy were thinned by electropolishing (14a). Some surface replicas (14b) were also examined. In some instances, the nickel films on the copper substrates were shadowed (14b) to enhance the contrast due to surface features. Stereo electron microscopy of both replicas and the thin samples themselves was also employed. In order to see the location of codeposited molecules, phase-contrast electron microscopy (15) was used. A few nickel films still attached to the copper substrates were also annealed for 20 min at 200° and 400°C.

Table I. Composition and pH values of plating baths

Bath	Composition (moles/liter)	*p*H values
A	0.43 $NiSO_4$	1.5, 3
B	0.43 $NiSO_4$, 0.5 H_3BO_3	1.5, 3, 6
C	1.3 $NiSO_4$, 0.5 H_3BO_3	1.5
D	1.3 $NiSO_4$, 0.5 H_3BO_3, 0.14 nickel acetate	3
E	0.43 $NiSO_4$ 0.5 H_3BO_3, 10^{-3} coumarin	1.5, 3
F	1.3 $NiSO_4$, 0.5 H_3BO_3, 10^{-3} coumarin	1.5
G	0.43 $NiSO_4$, 0.5 H_3BO_3, 2×10^{-4} saccharin	1.5
H	0.43 $NiSO_4$, 0.5 H_3BO_3, 3×10^{-6} phenosafranine	1.5, 3
I	0.43 $NiSO_4$, 0.5 H_3BO_3, 2×10^{-4} saccharin, 3×10^{-6} phenosafranine	3

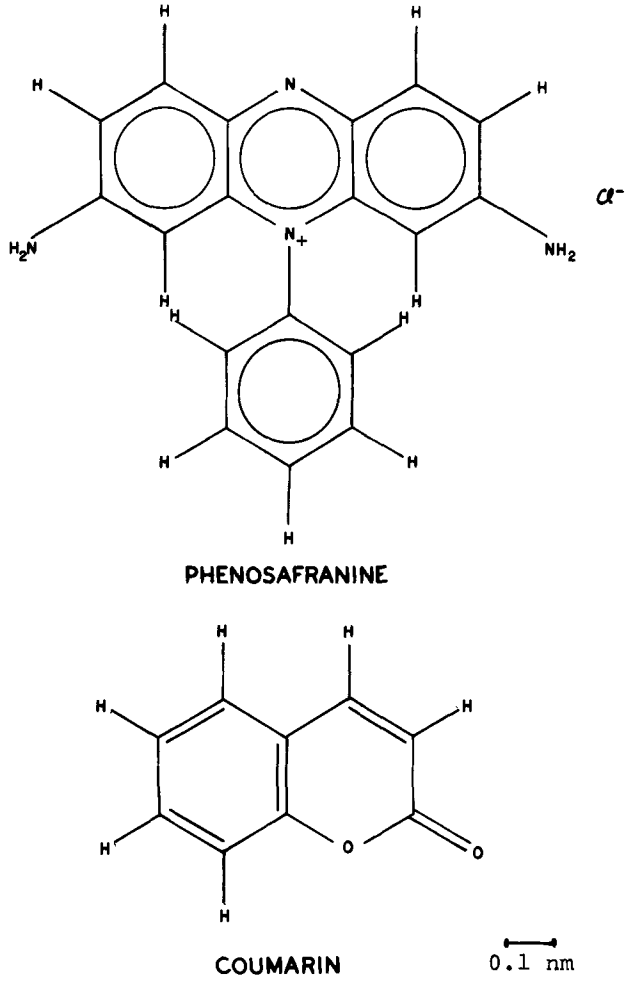

Fig. 1. Schematic representation of coumarin and phenosafranine molecules drawn approximately to scale.

Results

The {001}-oriented copper substrate films contained about 10^8 twin faults per square centimeter extending in both <110> directions. In addition, there were some vacancy clusters and a number of dislocations mostly with mixed Burgers vectors. As a result of contact with the sulfuric acid solutions, about 10^8 etch pits per square centimeter developed as manifested by stereo electron microscopy. Copper films when examined prior to the sulfuric acid treatment exhibited rectangularly shaped oxide particles.

The general results of the electron microscopic studies of the early stages of electromonocrystallization of nickel on copper-film substrates were that under a number of plating conditions, isolated, three-dimensional, epitaxial crystallites, hereafter called TEC, developed. In all samples, when a continuous deposit covered the substrate, elastic strains and surface undulations were observed. Subsequently, misfit and other dislocations and in some instances twins developed. The specific results for the several baths and *p*H values are listed in Table II and described below.

At *p*H 1.5 in deposits from the bath containing only nickel sulfate in the lower concentration (bath A) only a few, relatively large, rectangularly shaped TEC were observed. The average length of the edges, which were straight, was 130 nm. In addition to the TEC, some triangularly shaped crystallites were observed and identified as nickel hydroxide from their electron diffraction patterns. The addition of boric acid (bath B) resulted in a slight decrease in the size of the TEC in the plane parallel to the substrate as well as in the

Table II. Results

Bath	pH	TEC structure	Misfit dislocation structure: Estimated minimum deposit thickness of formation (nm)	Misfit dislocation structure: Type	Misfit dislocation structure: Spacing (nm)
A	1.5	Large, s.s.* (triangular hydroxide)	20	Straight	18
B	1.5	Large, s.s.	8	Straight	15
C	1.5	Large, s.s. (Fig. 2)	3	Straight	50
E	1.5	None	3	Straight	50
F	1.5	none	n.d.‡	Straight	50
G	1.5	Small, i.s.† (Fig. 3) (triangular hydroxide)	8	Irregular	30
H	1.5	Small, s.s. (Fig. 4)	6	Irregular	10
A	3	Large, i.s. (Fig. 5)	10	Irregular	10
B	3	None	5	Straight	10
D	3	None	5	Straight	50
E	3	Small, i.s.	n.d.	Irregular	n.d.
H	3	Small, i.s.	15	Irregular	30
I	3	Small, i.s.	5	Irregular	15
B	6	None	5	Straight	70

* Straight sided.
† Irregularly sided.
‡ Not determined.

perpendicular direction. Increasing the nickel-ion concentration and maintaining that of boric acid (bath C) resulted in a further decrease in the TEC size in the plane parallel to the substrate, but an increase in height, *i.e.*, in the perpendicular direction. Figure 2 shows TEC as grown in the higher nickel-ion-concentration electrolyte (bath C). The sides of TEC tend to be parallel to <110> directions. By means of replicas it was established that these TEC had a pyramidal shape.

The addition of coumarin to the baths of both nickel concentrations also containing boric acid (baths E and F) at *p*H 1.5 resulted in deposits in which TEC were not observed. Saccharin additions (bath G), on the other hand, caused a large increase in the number of TEC accompanied by a considerable decrease in their dimensions in the plane parallel to the substrate surface as seen in Fig. 3. The height of the TEC appears to be about the same as that of the ones in Fig. 2 as judged from their transparency to electrons. Another noteworthy feature of the TEC, which developed in the bath containing saccharin, is that the sides are no longer straight. Some triangular nickel hydroxide crystallites were also observed in samples produced in this bath. These crystallites developed, however, after the nickel deposit became continuous. The addition of

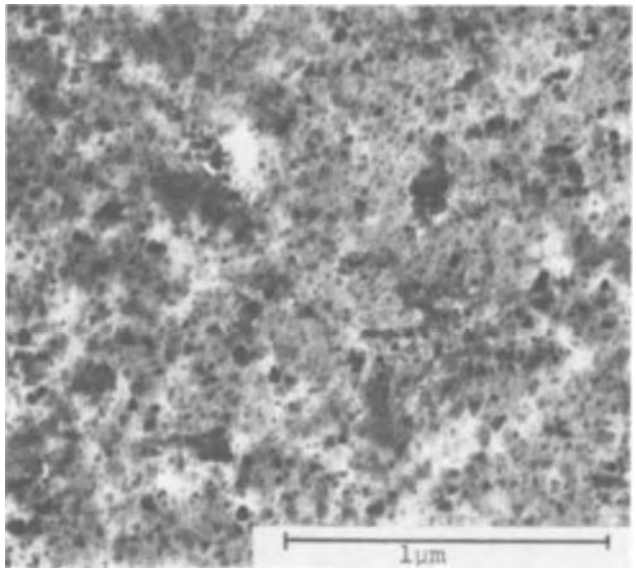

Fig. 3. Small, irregularly shaped TEC. Plated in bath G at *p*H 1.5

phenosafranine to the electrolyte (bath H) also resulted in a great increase in the number of TEC. However, as seen in Fig. 4 the sides of the TEC are straight. If the sample shown in Fig. 4 is examined under phase-contrast conditions, a number of small white dots are seen. The dots have been interpreted (15) as being the sites of incorporated molecules. A majority of the sites appeared to be at the edges of the TEC. The rest of the sites were found within the TEC.

At *p*H 3, in the bath with only nickel sulfate in the lower concentration (bath A) the formation of irregularly shaped TEC measuring about 80 nm parallel to the substrate-surface plane was observed. The TEC are shown in Fig. 5. In some samples plated for a slightly longer time, the size of the TEC increased up to 300 nm. These larger crystallites were no longer transparent to electrons. In addition to the TEC, the triangular nickel-hydroxide crystallites were observed again. No TEC were visible in deposits produced at *p*H 3 in the bath to which boric acid had been added (bath B). In one experiment, the current density was inadvertently raised to 15 mA/cm^2, *i.e.*, three times that used in all the other experiments. The deposits so produced showed irregularly shaped TEC. No TEC were seen in deposits produced in the bath (D) to

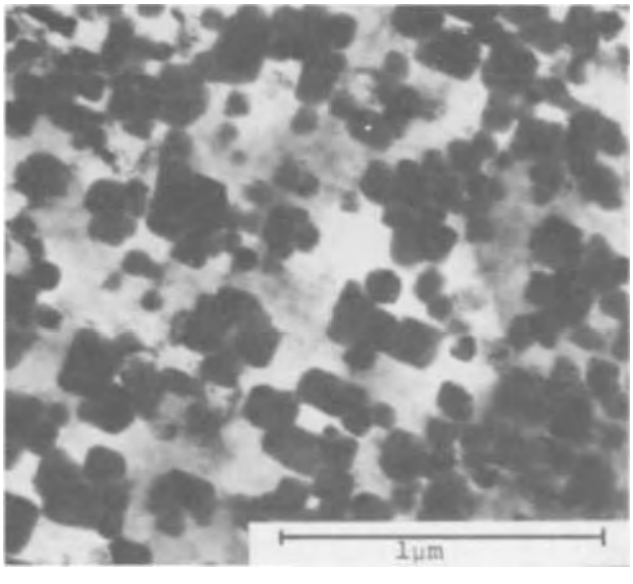

Fig. 2. Relatively large TEC with straight sides plated in bath C at *p*H 1.5.

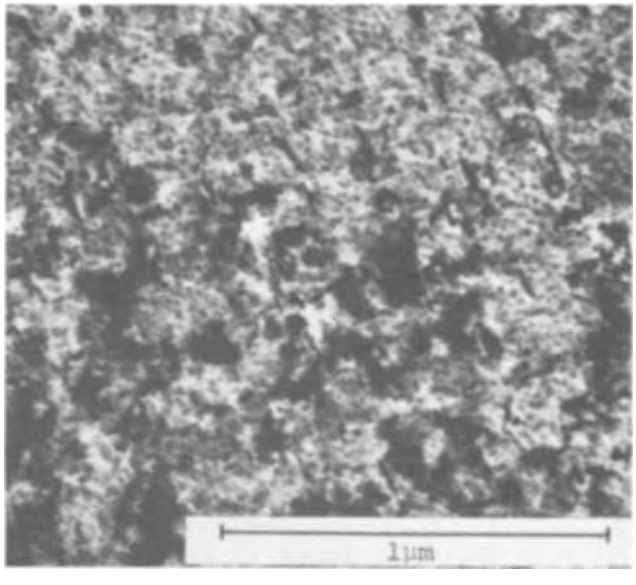

Fig. 4. Small, straight-sided TEC. Plated in bath H at *p*H 1.5

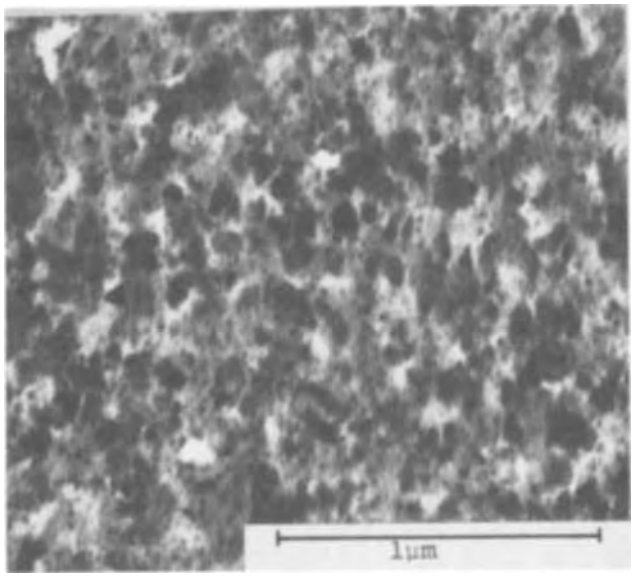

Fig. 5. Irregularly shaped TEC. Plated in bath A at pH 3

which a stronger buffering agent, nickel acetate, had been added.

At pH 3, the addition of coumarin to the low-nickel-concentration bath which also contained boric acid (bath E) resulted in the growth of small (about 35 nm) irregularly shaped TEC. It may be recalled that there were no observed TEC in bath E at pH 1.5. The addition of phenosafranine (bath H) resulted in structures essentially the same as those produced at the lower pH. Irregularly shaped TEC were observed in samples plated in a bath containing both phenosafranine and saccharin (bath I).

At pH 6, no visible TEC resulted from deposition in the bath with the lower nickel concentration and boric acid (bath B).

The structures which developed after the nickel deposit became continuous were similar in all samples. This structure is shown in Fig. 6. The thicknesses at which the deposits became continuous depended, of course, on the previous structure. When there were no TEC, the deposits became continuous essentially immediately. When there were TEC, the average thickness was estimated from the plating times to have been about 2-5 nm. The contrast in Fig. 6 is due to Moiré patterns, thickness variations, and strains. There were point-to-point thickness variations as determined by the use of replicas of the surfaces as well as by a contrast enhancement when the samples themselves were shadowed. In the electron diffraction patterns of the samples shown in Fig. 6, there was no recognizable separation of the spots due to copper and nickel also indicating that lattice-misfit strains were present.

There were some differences between the structure of samples which had exhibited straight and irregularly shaped TEC, respectively. The sample shown in Fig. 6 at an earlier stage of growth had exhibited regularly shaped TEC. Here the Moiré pattern consists of rather straight lines which are indicated by the arrow. These lines lie essentially parallel to <100> directions in this case. Figure 7 represents a sample which showed irregularly shaped TEC at the earlier growth stage. Here the lines are not straight. The electron diffraction patterns of samples such as are shown in Fig. 7 consisted of small arcs of circles instead of spots, indicating a tendency toward polycrystallinity. When the TEC stage was not visible, the structure of a continuous nickel film was similar to that of Fig. 6. The lines were again rather straight, however not as pronounced.

The relaxation of some of the elastic strains was indicated by the separation of the electron diffraction spots of copper and nickel as well as by a decrease in their size and was accompanied by the appearance of misfit dislocations. The Burgers vectors of these dislocations, which are indicated by an arrow in Fig. 8 were found to be of the ½ <110> type and to have an edge character. The fact that their images were not seen in nickel films separated from their substrates proved that the dislocations were located at the interface between the copper and nickel and therefore of the misfit variety. Rough estimates of the average deposit thicknesses at which misfit dislocations were first observed are listed in Table II.

The degree to which the misfit dislocations were straight also could be related to the TEC structure. In the samples in which TEC were not visible at the earlier stage of growth, well-defined, straight misfit dislocations such as seen in Fig. 8 were observed. Also when the TEC were large in the plane parallel to the substrate surface and had straight sides, such as in the baths without additives at pH 1.5, the dislocations were straight and well defined. In areas wherein dislocations had not formed, the lines that characterized the earlier stage of growth were still visible. Figure 9

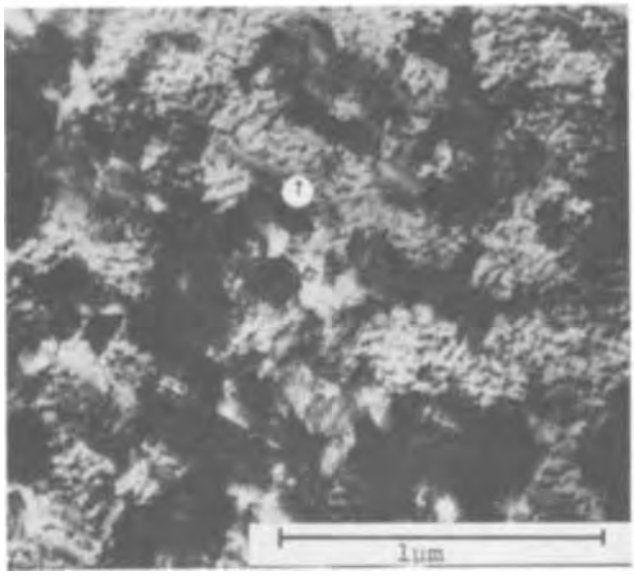

Fig. 6. Structure after nickel deposit was continuous. At earlier stage, TEC had straight sides.

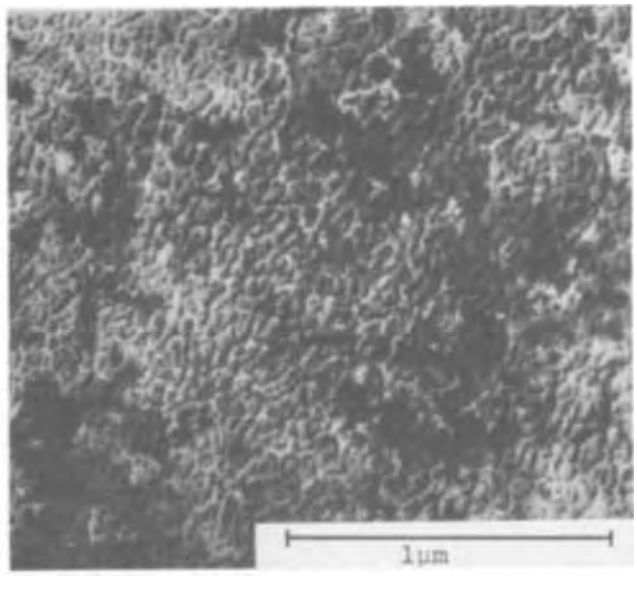

Fig. 7. Structure after nickel deposit was continuous. At earlier stage, TEC had irregularly shaped sides.

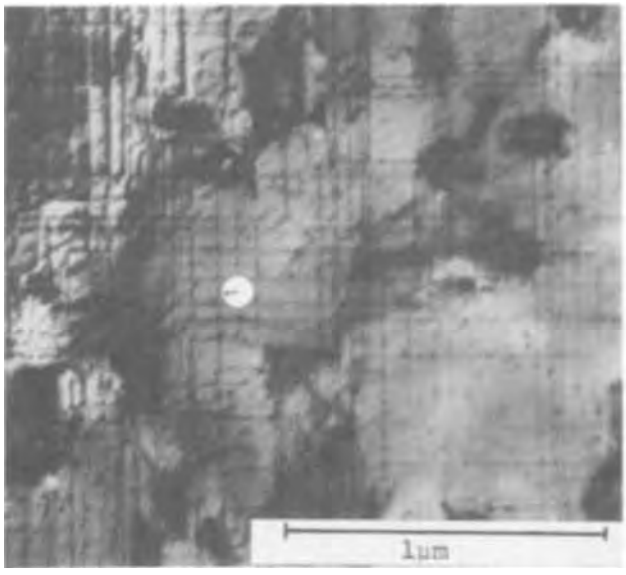

Fig. 8. Straight misfit dislocations. At earlier stage, sample showed no TEC.

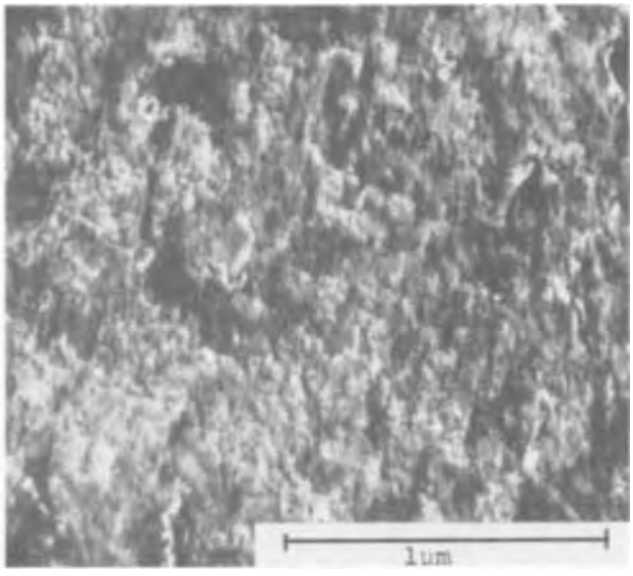

Fig. 10. Irregularly shaped dislocation structure. At earlier stage, TEC had irregularly shaped sides.

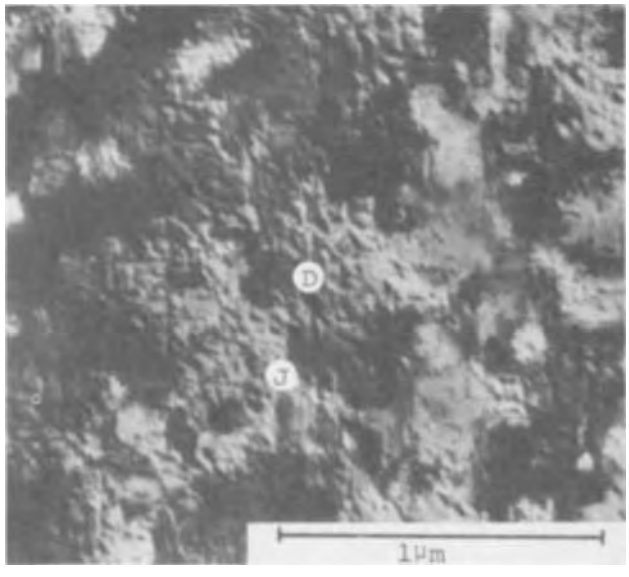

Fig. 9. Straight misfit dislocation at D and structure from continuous-deposit stage at J. At earlier stage, TEC were straight sided.

shows straight misfit dislocations, the orthogonal network of lines, one of which passes under "D." The structure which developed prior to the misfit-dislocation formation, which was shown in Fig. 6, is also still visible in Fig. 9 in regions such as the one marked "J." Samples plated under conditions which resulted in very small TEC or irregularly shaped, large ones exhibited dislocations which were not straight as shown in Fig. 10. After the copper substrates had been dissolved, the nickel deposits still contained a high dislocation density. These dislocations did not lie in the nickel-copper interface and were therefore not of the misfit variety, *i.e.*, caused by the difference in lattice dimensions between deposit and substrate. The electron diffraction patterns of samples which did not exhibit straight dislocations, consisted of rings or arcs which are indicative of some degree of polycrystallinity.

The average spacings of the misfit dislocations are listed in Table II. At *p*H 1.5, coumarin resulted in a wide spacing. Saccharin caused a smaller increase, while phenosafranine reduced the spacing. At *p*H 3, the stronger buffer, nickel acetate resulted in a large average distance between misfit dislocations. The greatest spacing occurred in samples plated at *p*H 6. In some samples, especially those with irregular, rather than straight misfit dislocations, it was difficult to determine the spacing accurately. This difficulty arose because the misfit dislocation could not be readily distinguished from those which resulted from other causes.

One sample which was plated in the bath containing phenosafranine at *p*H 3 to a thickness of approximately 500 nm on examination in a high-voltage (800 kV) electron microscope while still attached to the copper substrate exhibited essentially the same dislocation structure as one only 100 nm thick. The fact that the dislocation contrast did not change with a five-fold thickness increase suggests that the elastic relaxation due to their formation is limited to the immediate neighborhood of the interface. This short range of the misfit strains was further confirmed when the substrate was thinned by partial dissolution and the misfit dislocations remained. The samples plated in the bath with phenosafranine had a much higher twin density than the copper substrates.

The fine dislocation structure in a sample plated in the bath containing phenosafranine at *p*H 1.5 did not change upon annealing for 20 min at 300°C in vacuum. However, the number of twins decreased. The electron diffraction pattern confirmed the decrease in the twin density. Spots or arcs due to oxide which were present in the diffraction pattern before annealing, also disappeared. Annealing at 400°C for 20 min resulted in alloying between the deposit and substrate and the disappearance of misfit dislocations.

Discussion

The TEC stage of electromonocrystallization has been previously reported in deposits of platinum on gold (16), gold on silver (17) and on iron (18), and copper on nickel (10) and on copper (19). The development of TEC in evaporated films has been frequently observed (9). It had not been seen in nickel electrodeposits. In two studies nickel was plated on a thin copper substrate at *p*H 4 (10) and at *p*H 2.6 (20) in a Watts bath and the bicrystals examined by transmission electron microscopy; no TEC were observed. In this study, no TEC were seen either in the additive-free bath with boric acid (bath B) at *p*H 3. Evidently, whether TEC are formed depends not only on the type of metal plated and the substrate but also on the plat-

ing conditions and whether there are foreign substances present in the bath.

In order to explain the effects of addition agents, the pH and buffering of the bath, and the metal-ion concentrations, which were the variables of this study, it is necessary to consider how and why TEC form. Gradmann (21) postulated that a deposit should grow as monolayers if its surface energy is lower than that of the substrate. Actually, the surface energy of nickel is greater than that of copper (22). Therefore, it would be expected that the deposition of nickel on copper should occur by TEC formation. Of course, the relative values of the surface energies can be altered by absorbed foreign substances, other plating variables, and the crystallographic orientation.

It has been generally postulated that electromonocrystallization occurs by the first arriving atom of the deposit attaching itself to a kink site in the substrate. Subsequent atoms would join to fill the row. The mechanism of spiral growth from emerging screw dislocations has been invoked so that there would be no need for the nucleation of new rows or layers. However, under nonideal conditions, the dislocations in the substrate have not been observed to affect the structure of the deposits unless there were foreign substances associated with them (1, 2, 7, 8). The motion of layers in copper deposits from a perchlorate bath on {100} planes of the same metals was also interpreted (2) on the basis of the potential data as indicating that the atoms did not go to kink sites. It thus appears probable that there is two-dimensional nucleation (23) associated with foreign substances. In many instances it is likely that defects in the substrate also play a role in the nucleation. Sard and Weil (19) observed twins under most of the visible TEC in copper plated in acid-sulfate baths. However, in some samples of the present study, nucleation could not have occurred on defects in the substrate. For example, in Fig. 4, there are 10^{11} TEC per square centimeter, whereas the number of defects in the substrate was of the order of 10^8 cm^2. In the sample shown in Fig. 4, the phenosafranine molecules, the sites of which were found to occur within TEC, could have nucleated the growth. The nucleation by foreign substances has been postulated by Eichhorn, Schlitter, and Fischer (24), and it seems reasonable that it could occur if the molecule had the right shape and orientation with respect to the underlying crystal lattice. The three-dimensional epitaxial growth could occur by bunching (1). Here foreign substances would impede the spreading of layers. The observed sites of phenosafranine at the edges of TEC are suggested to be those of molecules which resulted in bunching.

On the basis of the growth mechanisms suggested above, it would appear that there was very little or no impediment to lateral layer spreading when no TEC were observed. When there were only a few large TEC, which had a small height-to-width ratio (*i.e.*, the dimension perpendicular and parallel to the substrate, respectively), the impediment to lateral growth was also small. Possibly, these TEC were nucleated at defects in the substrate. As expected, impediment to lateral growth was lowest in the additive-free baths as in deposits produced therein, either no TEC or the larger, but flatter ones were observed.

The effect of boric acid at pH 1.5 on the initial electrocrystallization phenomena appears to have been the prevention of the formation of the triangular, nickel-hydroxide crystallites. These hydroxide crystals were also observed in thin nickel deposits on copper by Ives, Edington, and Rothwell (20) and were said to require a high pH in the cathode films. The data of Knödler and Neugeboren (25) however indicate that at pH 1.5, the value used in this study, and 5 mA/cm^2, the acidity of the solution adjacent to the cathode should be the same as that in the bulk. At higher current densities, there is an increase in the pH of the cathode film over that of the bulk; the increase being much greater if boric acid is absent. However, the solutions studied by Knödler and Neugeboren (25) contained 1 mol/liter nickel ions, while the hydroxide crystallites developed in the 0.43 molar solutions (bath A). Equivalent hydrogen evolutions would be expected in a low nickel-ion-concentration solution at a low current density and in a more concentrated electrolyte at a high plating rate. Thus the conditions of this study would be equivalent to those under which Knödler and Neugeboren found the larger increase in pH in the absence of boric acid. Thus, it is possible to explain why the absence of boric acid caused the formation of the hydroxide crystallites even at relatively low current densities. The reason why no TEC or hydroxide crystallites were observed in deposits plated at the high pH may be that the type of hydroxide, which forms, depends on pH (20). Apparently the type which forms at pH 6 did not impede lateral growth so as to cause TEC to develop. The effect of the pH, the presence or absence of boric acid, and the nickel-ion concentrations on the formation of TEC and their sizes would be expected to depend on the hydroxide species which form, how they are adsorbed, and the amount which is present as crystallites.

The effect of coumarin on the development of TEC also can be explained on the basis of lateral-growth impediment. Rogers and Taylor (26) reported that several reaction products are present in nickel-plating baths containing coumarin. The amount of each product depends, among other factors, strongly on pH. At pH 4 (26, 27), melilotic acid was said to be the principal reaction product for coumarin concentrations in the order of 10^{-3} molar, *i.e.*, the amount used in baths E and F. At pH 1.5, o-hydroxyphenylpropanol and o-propyl phenol (28) are the principal products. These compounds are not as strongly adsorbed as melilotic acid. Thus at the pH 3 of this study, the formation of TEC was probably due to melilotic acid. At pH 1.5, with less adsorption of foreign material, lateral growth would not be impeded and no TEC would form.

The irregular shape of the TEC, which formed in the baths containing saccharin, at pH 3 in the presence of coumarin and at pH 3 in the additive-free without boric acid, was probably caused by the size and mode of adsorption and incorporation of foreign substances either from the bath additives or hydroxides. At this point, it is only possible to postulate a mechanism. The fact that the sites of codeposited products from coumarin were not observed by phase-contrast microscopy suggests that the small dimension of the molecules was essentially perpendicular to the electron beam, which, in turn, was perpendicular to the substrate surface. As the phenosafranine-molecule sites were visible by phase-contrast microscopy, it is suggested that this additive was adsorbed with the large dimensions perpendicular to the beam. The sketches of the coumarin and phenosafranine molecules in Fig. 1 are drawn approximately to scale. It has been found (28) that only sulfide ions from saccharin molecules are codeposited. Therefore the structure of saccharin is not shown in Fig. 1. The basic substances which resulted in the TEC formation in bath A at pH 3 could also have been small in size. Thus it may be postulated that if the size and orientation of the codeposited molecules are such that they could have stopped a whole row of atoms from growing parallel to the substrate surface as apparently in the case of phenosafranine, straight-edged TEC would develop. On the other hand, if the impediment is such that part of a row was stopped from growing and the rest could continue, irregularly shaped TEC would result. This type of growth impediment would be expected from small molecules or large ones which are oriented with their small dimensions facing the advancing row. Further studies of the way that molecules are adsorbed and interefere with growth are needed before the reasons for the shapes of the TEC can be confirmed.

The effect of the substrate on the development of TEC was not a variable in this study. It is known (16) that the shape of TEC changes with orientation of the substrate. Even slight deviations from the {100} orientation appear to have affected TEC formation. In another study (29) deposition of nickel from bath B at pH 3 resulted in visible TEC when cube-textured copper was the substrate, whereas on the more closely [100]-oriented vapor-deposited copper films grown on KCl, there were none. It is also possible that the difference in the defect densities and surface morphologies of the two types of copper substrates affected the development of TEC.

The strain contrast in Fig. 6 which was generally observed after a complete layer of the deposit had been laid down was undoubtedly due primarily to the difference in the lattice parameters of copper and nickel. Strains must have been present already in the TEC stage, but other contrast effects probably masked them. The fact that the separation of the diffraction spots was not the equilibrium distance was evidence of strain. As the thicknesses of the deposit and substrate was comparable, it is likely that both were in a state of stress of opposite signs.

The coalescence of TEC and even the meeting of layers too thin to be visible because of lack of thickness contrast was another probable source of strain. It is very likely that there were misorientations between the joining TEC and even the layers too thin tc be seen. The misorientations probably lead to strains as well as the introduction of defects which are discussed below. The requirement to minimize the surface energy would probably lead to coalescence before the regions between the structural components have been completely filled in and thus increase the strains. The coalescence of irregularly shaped TEC also must have resulted in their rotation, again probably because of surface-energy requirements or to lower the strains. The arcs of circles in the electron diffraction patterns of the samples which exhibited irregularly shaped TEC in the earlier stage of growth are indicative of rotation of the crystallites on joining. Rotation of TEC has been observed (9) during vapor-deposition experiments carried out in an electron microscope. The lines visible in Fig. 6 and 7 are probably Moiré patterns and partially due to strain contrast; the strain resulting from the coalescence of the structural components, *i.e.*, TEC and atom layers too thin to be seen by electron microscopy. The structure shown in Fig. 6 bears a strong resemblance to that observed by Matthews and Crawford (30) in vapor-deposited nickel-copper bicrystals and said to be a Moiré pattern. The thickness variations which also contributed to the contrast particularly if the TEC stage preceded the formation of a complete deposit layer, were also very likely due to coalescence. The fact that the lines in Fig. 6 and 7 were more pronounced when there was a TEC stage and the evidence from the replicas and shadowed bicrystals supports this conclusion. It can be readily seen why the region of coalescence of TEC would be thinner. Tanabe and Kowasaki (18) found it to be so also.

The coalescence of TEC as well as the meeting of layers one or more atoms high and slightly misoriented with respect to one another can lead to the formation of dislocations. If there are misorientations in the plane parallel as well as in that perpendicular to the substrate, the dislocations would have mixed Burgers vectors. The formation of dislocations due to the joining of slightly misoriented structural components is a well-known phenomenon. The formation of dislocations due to coalescence of TEC in vapor deposits has been seen (9). The joining of layers to form dislocations has also been observed in copper deposits (7). The dislocations which did not disappear when the substrate was dissolved probably formed from the joining of structural components. These dislocations had mixed Burgers vectors, in general. In addition to dislocations, the coalescence of TEC can also lead to twin formation. Matthews and Allison (31) have described a mechanism by which the smaller TEC rotates into a twin orientation if it is easier than attaining parallel alignment. The very large number of twins observed in deposits plated in the baths for which phenosafranine was the additive may have been due to the small size of the TEC which allowed them to rotate into a twin orientation. In order to form a twinning plane, it is obviously necessary that the TEC have straight sides bounded by {111} planes. The TEC produced in the phenosafranine bath probably conformed to this requirement. The necessity to align in a twin orientation rather than parallel may have been due to the large phenosafranine molecules at the edges of the TEC in the way suggested by Hinton, Schwartz, and Cohen (32). The possibility that mechanical twins are formed to relax high stresses should also not be discounted.

The development of dislocations to relieve the misfit strains between the crystal lattices of the deposit and substrate has been widely observed in vapor deposits. Misfit dislocations have also been previously observed in electrodeposited bicrystals (11, 33).

The deposit thicknesses at which misfit dislocations developed appear to have varied considerably with the plating conditions and bath compositions. This variation is probably real in spite of the inherent uncertainties involved in determining the values. The uncertainties arose because the experiments were not specifically designed to determine the critical deposit thicknesses. In general, the plating times were varied in a geometric progression. Thus, the deposit in which the misfit dislocations were observed was twice as thick as the one in which these defects were not present. Also the values listed in Table II were calculated from the plating times which at best yield an average thickness. The local thickness variations have already been discussed. The plating efficiency also was not known accurately. However, it appears that the thickness values in Table II are larger than the value of 1.46 nm which Matthews and Crawford (30) determined by a more accurate method in nickel vapor deposits on copper. The value, which Matthews and Crawford (30) found, is also close to the theoretical thickness which they calculated for the nickel-copper system. The reason for the greater critical thickness in Table II may be that codeposited foreign substances such as additive molecules or hydroxides interfered with the glide, which Matthews and Allison (31) said was necessary for misfit-dislocation formation.

The interference of codeposited foreign substances on dislocation glide may also have been responsible for the variation in the spacings listed in Table II. The misfit-dislocation spacing for nickel deposits on copper was calculated by Matthews and Crawford (30) to be about 8 nm. All values in Table II exceed this theoretical spacing. When the spacings of the misfit dislocations are greater than the theoretical value, the strains have obviously not been completely relieved. The misfit dislocations which were not straight probably experienced local pinning by codeposited, foreign substances.

The results of the annealing experiments are included for information only. There are not enough data to draw any significant conclusions.

Conclusions

1. The influence of addition agents, the pH, and buffering of the bath and the nickel-ion concentration on the formation and shape of TEC can be explained by the interference of codeposited, foreign substances on the lateral spreading of the deposit.

2. When a complete deposit layer has been formed, strains and surface undulations develop, which can be related to the presence and shape of TEC in the earlier growth stage.

3. The coalescence of TEC results in the formation of dislocations and probably in some instances, twins.

4. Misfit dislocations form in the deposit-substrate interface. Their spacing, configuration, and the deposit thickness at which they are first observed apparently depend on the presence of codeposited foreign substances.

Acknowledgments

The permission to publish this paper and the support of the American Electroplaters' Society, Inc. are gratefully acknowledged. The members of the Project Committee, Messrs. U. Bertocci, H. Brown, C. Cupp, D. Hardesty, R. Sard, and K. Willson provided many useful suggestions and discussion while the work upon which this paper is based, was in progress and reviewed this manuscript. The U. S. Steel Corporation Research Laboratories permitted us to examine several samples in the high-voltage electron microscope. The electron microscope used to examine most of the samples was obtained partially through a grant of the National Science Foundation.

Manuscript received April 11, 1973. This was Paper 132 presented at the Cleveland, Ohio, Meeting of the Society, Oct. 3-7, 1971.

Any discussion of this paper will appear in a Discussion Section to be published in the June 1974 JOURNAL.

REFERENCES

1. H. J. Pick, G. G. Storey, and T. B. Vaughn, *Electrochim. Acta*, **2**, 1965 (1960).
2. L. H. Jenkins, *This Journal*, **117**, 630 (1970).
3. L. H. Jenkins and R. B. Durham, *ibid.*, **117**, 1506 (1970).
4. A. Damjanovic, M. Paunovic, and J. O'M. Bockris, *J. Electroanal. Chem.*, **9**, 93 (1965); *Electrochim. Acta*, **10**, 111 (1965).
5. L. Peraldo Bicelli and G. Poli, *Electrochim. Acta*, **11**, 289 (1966).
6. E. Budevski, W. Bostanoff, T. Witanoff, Z. Stoinoff, A. Kotzewa, and R. Kaichew, *ibid.*, **11**, 1697 (1966).
7. U. Bertocci and C. Bertocci, *This Journal*, **118**, 1287 (1971).
8. P. E. Lighty, D. Shanefield, S. Weissmann, and A. Shrier, *J. Appl. Phys.*, **34**, 2233 (1963).
9. G. A. Basset, J. W. Menter, and D. W. Pashley, "Structures and Properties of Thin Films," C. A. Neugebauer, J. B. Newkirk, and D. A. Vermilyea, Editors, p. 12, John Wiley & Sons, Inc., New York (1959).
10. K. R. Lawless, *J. Vacuum Sci. Technol.*, **2**, 24 (1965).
11. E. R. Thompson and K. R. Lawless, *Electrochim. Acta*, **14**, 269 (1969).
12. S. A. Watson, *Trans. Inst. Metal Finishing*, **40**, 41 (1963).
13. H. R. Brown, Private communication.
14. G. Thomas, "Transmission Electron Microscopy of Metals," John Wiley & Sons, Inc., New York (1967); a, p. 150; b, p. 134.
15. M. L. Albert, R. Schneider, and H. Fischer, *Z. Naturforsch.*, **19**, 1120 (1964).
16. W. A. Jesser, J. W. Matthews, and D. Kuhlmann-Wilsdorf, *Appl. Phys. Letters*, **9**, 176 (Aug. 15, 1966).
17. E. W. Dickson, M. H. Jacobs, and D. W. Pashley, *Phil. Mag.*, **11**, 575 (1965).
18. Y. Tanabe and S. Kamasaki, *J. Metal Finishing Soc. Japan*, **22**, 54 (1971).
19. R. Sard and R. Weil, *Electrochim. Acta*, **15**, 1977 (1970).
20. A. G. Ives, J. W. Edington, and G. P. Rothwell, *ibid.*, **15**, 1797 (1970).
21. U. Gradmann, *Phys. Kondes. Materie*, **3**, 91 (1964).
22. B. E. Sundquist, *Acta Met.*, **12**, 67 (1964).
23. G. Eichkorn, H. Fischer, and F. W. Schlitter, *Colloq. Intern. Centre Nat. Rech. Sci.*, **152**, 341 (1965).
24. G. Eichkorn, F. W. Schlitter, and H. Fischer, *Z. Physik. Chem., Neue Folge*, **62**, 1 (1968).
25. A. Knödler and K. W. Neugeboren, *Metalloberfläche*, **24**, 78 (1970).
26. G. T. Rogers and K. J. Taylor, *Trans. Inst. Metal Finishing*, **43**, 75 (1965).
27. J. Edwards and M. J. Levett, *ibid.*, **45**, 12 (1967).
28. G. T. Rogers and K. J. Taylor, *Electrochim. Acta*, **13**, 109 (1968).
29. R. Weil and J. B. C. Wu, *Plating*, **60**, 622 (1973).
30. J. W. Matthews and J. L. Crawford, *Thin Solid Films*, **5**, 187 (1970).
31. J. W. Matthews and D. L. Allison, *Phil. Mag.*, **8**, 1283 (1963).
32. R. W. Hinton, L. H. Schwartz, and J. B. Cohen, *This Journal*, **110**, 103 (1963).
33. E. R. Thompson and K. R. Lawless, *Appl. Phys. Letters*, **9**, 138 (Aug. 15, 1966).

Sensitizer Aging Effects on Metalization and Imaging in the Photoselective Metal Deposition (PSMD) Process

J. F. D'Amico* and M. A. DeAngelo

Western Electric Company, Engineering Research Center, Princeton, New Jersey 08540

ABSTRACT

The PSMD imaging system employs aqueous $SnCl_2$ sensitizer solutions to generate electroless metal photopatterns on dielectric substrates. We have measured how aging in several typical sensitizer solutions affects their ability to generate electroless copper photopatterns on polyimide H film (DuPont Kapton®). Specimens, consecutively sensitized as the solution aged, have been characterized with respect to (*i*) tin deposition (by x-ray fluorescence), (*ii*) catalytic activity for metalization (by optical density determination of the deposited electroless copper), and (*iii*) imageability (by image contrast measurements of the developed copper patterns). The system imageability is found highly dependent on the sensitizer solution age, while the capability for blanket metalization was relatively unaffected.

Photoselective metal deposition (PSMD), a process for metal patterning dielectric substrates by uv light exposure and electroless (chemical) plating, has been the subject of several recent papers (1-4). These have reported a general outline of this system and its applications (1, 2), an analysis of the sensitization mechanism by Mössbauer spectroscopy (3), and a description of the optical response in a typical imaging system (4). In this paper, we shall elaborate on still another aspect, that of sensitizer aging in normal room am-

* Electrochemical Society Active Member.

Key words: sensitizer, sensitizer aging, electroless plating, electroless patterning, photoimaging.

bient, and shall describe how this phenomenon affects both metalization and imaging in a typical PSMD system.

The process of electroless metalization is, of course, a subject of broader technological interest than that of electroless metal imaging, and as such has been studied extensively for many years (5). Among very recent papers on this topic, those by Cohen and West (6), Feldstein and Weiner (7, 8), and Feldstein, Weiner, and Schnable (9) are of particular relevance to the subject covered in this paper.

Photoselective metal deposition combines electroless plating with a step involving uv light exposure through a mask to develop an image. The electroless metalization process requires that surfaces to be covered be made "catalytic," so that the plating reaction may be initiated. The most common catalyst is palladium, which can be conveniently microdeposited by the sequence:[1] (*i*) sensitization [immersion in $SnCl_2$; deposits Sn(II) species] and (*ii*) activation (immersion in $PdCl_2$; deposits Pd).[2] For imaging, a uv light exposure after step (*i*) eliminates Sn(II) by photooxidation, thus pre-empting Pd deposition and thereby making the exposed regions "noncatalytic." Thus PSMD imaging is positive working, since it generates a replica of the photomask.

Photoreactive deposits in the PSMD process are formed on substrates which are briefly immersed in an aqueous sensitized solution containing a Sn(II) salt. The work reported here deals exclusively with sensitizers of a specific chemical composition, namely, dilute stannous chloride dihydrate ($SnCl_2 \cdot 2H_2O$) acidified with HCl. In terms of chemical ingredients, this is our least complex solution and accordingly is a good starting point for sensitizer research.

In aqueous $SnCl_2$-HCl solutions, the Sn(II) is present in a variety of forms (10-12), *i.e.*, a soluble aquo complex as well as soluble complexes of chlorides, oxychlorides, hydroxides, and hydroxy-chlorides. In addition, insoluble oxides (these may or may not be readily visible) are also present. On standing in the laboratory, the soluble species undergo a continuous hydrolysis and polymerization to become irreversibly converted into the insoluble oxides. The insoluble oxides combine to form a colloid or sol which has been observed to play an important role in the sensitization process (1-4, 6, 7). In this paper we give a general description of colloid formation in typical sensitizer solutions. We also relate the observed solution and colloid properties to their effects on the sensitization and metalization of the substrate.

An important factor affecting sensitization is the extent of "wetting" of the substrate by the solution (7, 9, 13). In "wetting," the liquid containing soluble tin complexes forms a film on the substrate. During the subsequent water rinse, the *p*H in this film is rapidly raised to the point where the soluble complexes are hydrolyzed to the insoluble oxide which then deposits on the substrate and contributes to the sensitization.

In attempting to understand sensitizer film formation, it is clear that we must look not only at the deposit on the substrate but also at the condition of the solution at the time of sensitization. The ultimate objective of a detailed study of the mechanism and kinetics of sensitization is to provide a basis for tailoring formulations and process procedures to optimize the imaging characteristics on a wide variety of useful substrates.

[1] A one-step tin-palladium solution is also widely used to generate electroless deposits. This sensitizator/activator, however, cannot be used for PSMD image generation.

[2] There is some disagreement in the literature as to the state of the deposited Pd. In ref. (3), the results of Mössbauer analysis for $SnCl_2$/HCl sensitized Kapton are interpreted in terms of a Sn(II)-Pd(II) redox. In ref. (8), radio tracer results for $SnCl_2$/HCl sensitization of Teflon are explained in terms of a substrate-adsorbed ionic Pd complex.

Experimental

Solutions of varying initial tin concentrations were prepared and allowed to stand in the laboratory ambient. At selected times, coupons of polyimide film were sensitized in these solutions. The coupons were then divided into three parts, each measured as follows:

Part I: X-ray fluorescence analysis to determine the total weight of tin deposited.

Part II: Metalization of the specimen with electroless copper to correlate the extent of metalization with the tin deposited on the substrate. The extent of metalization was determined by measuring the optical density of the copper layer deposited after a fixed time in the electroless bath. A greater value of optical density indicates a substrate more highly catalytic to the metalization. This technique is detailed in ref. (4).

Part III: Exposure to ultraviolet radiation, then repeat the metalization as in Part II. This step evaluates the imaging sensitivity of the specimen.

Preparation of solutions.—The sensitizer solutions were prepared by dissolving[3] 0.15, 0.30, and 3.0g of $SnCl_2 \cdot 2H_2O$ in 300 ml of deionized water, then immediately adding 3 ml conc HCl to all solutions. The order of addition of ingredients and the time before acidification of the solution affects the rate of colloid formation and must be standardized if reproducible results are to be obtained.[4] The solutions described have nominal initial tin concentrations[5] of 0.0022, 0.0044, and 0.044M and are designated as solutions C, B, and A, respectively. Nominal *p*H value in these solutions was 1.0. (The measured *p*H's varied from 0.95 to 1.05 due to stannous chloride hydrolysis, the more concentrated solutions becoming the slightly more acidic.) Also prepared was a solution containing 4.7g of $SnCl_4 \cdot 5H_2O$ and 3 ml conc HCl in 300 ml of deionized water. This solution, 0.0044M in Sn(IV), is the stannic counterpart of solution B.

Ambient conditions for solution aging.—Standard ambient.—Solution aging was carried out in the laboratory ambient under normal fluorescent lighting. Sensitizer solution volumes of 300 ml were placed in 500 ml polypropylene beakers and left undisturbed on the laboratory bench. When not in use, the beakers were covered (but not sealed tightly) with waxed cardboard tops to prevent particulate contamination.

Aging in bubbled nitrogen or air.—Exceptions to the above procedures were made in order to discover how solution aging was affected by the elimination or the enhancement of oxygen in the solutions. A 200 ml volume of solution A was placed in a stoppered 500 ml Erlenmeyer flask through which N_2 was gently bubbled. Nitrogen escape was through a side arm plugged to a very small opening to prevent back diffusion of air. A duplicate setup bubbling air at the same rate was also run along with a control solution (unstirred A in beaker). Observations to detect colloid formation and the presence of Sn(II) (by indicator paper) were made at selected times in the aging cycle.

Preparation and metalization of substrates.—Standard process.—Test specimens were 3 × 2½-in. coupons of 2 mil polyimide H-film (DuPont Kapton®) which were prepared by the following process:

a. Etch 5 min in room temperature 10*N* NaOH, then rinse 5 min in a gently flowing cascade washer with 22°-24°C deionized water. (Water resistivity exceeded 2 megohm-cm).

b. Sensitize by a 3-min immersion in the unstirred sensitizer solution, 300 ml in a 500 ml polypropylene beaker. Rinse for 1 min as in *a.*

[3] The initial solids readily dissolve but the solutions formed contain a cloudy white suspension which clears on addition of the acid.

[4] Addition of the $SnCl_2 \cdot 2H_2O$ to the acid followed by water dilution slightly inhibits the colloid formation while a delay of 15 min in acidification of the solution slightly enhances the colloid formation. These conclusions are based on visual observations of the rate of haze formation of the solutions on standing.

[5] Some of the initial salt may be in the stannic state due to air oxidation of the reagent. The reagent is also hygroscopic.

c. Dry in N_2 jet and remove a ¾ × 2½-in. section for tin analysis.

d. Immerse remaining section for 30 sec in activator solution, 0.5g reagent $PdCl_2$ and 5 ml conc HCl diluted to one liter. Then rinse for 2 min as in *a*.

e. Dry in N_2 jet, then divide specimen. Expose one part to uv radiation, the other remaining unexposed.

f. Metalize both parts by a 1.5-min immersion in a 300-ml bath of Enthone 400 electroless copper at room ambient temperature (23° ± 1°C). The Enthone bath was prepared fresh each day with dilution as recommended by the supplier.

Alternative process using an acid tin rinse.—For several specimens, a modified procedure employing an acid tin rinse in place of the water rinse, step b above, was used. Specimens were immersed for 30 sec into a beaker containing 300 ml of 0.1M HCl, then given a 30-sec rinse in the cascade washer. The normal process sequence was then continued at step c.

Detection of stannous species in solution.—Detection of stannous in the sensitizer solutions was made using an indicator paper prepared by depositing ammonium phosphomolybdate on filter paper (14). The prepared paper has a bright yellow color which is reduced by stannous to a deep "molybdenum" blue. The intensity of the blue color gives a semiquantitative indication of the concentration of stannous tin present in the solution.

Stannous detection was made at specified times, a few drops of solution being withdrawn and deposited onto the filter paper. The stated limits of detection for this test are 1.5 mg/liter, which corresponds to a stannous concentration about 0.3% of the initial value in our most dilute solution. Experimentally, we were able to verify detection down to 10 mg/liter of Sn(II). We assume this higher value is due to the presence of dissolved oxygen in our initial solutions, since no attempt was made to purge this species. [The equilibrium solubility (15) of oxygen in 0.1M HCl at 25°C, 1 atm is about 0.00025M. This quantity of oxygen should react 28 mg/liter of stannous species.]

Determination of total tin deposit.—Tin deposits on the substrates were determined by x-ray fluorescence using a General Electric XRD-6VS vacuum spectrometer. Calibration was made using tin oxide/polyimide standards determined by atomic absorption analysis of tin after removal from the substrates. The precision of this method for total tin analysis is estimated to be about 5%, the absolute accuracy of the calibration 25%.

Specimen preparation for x-ray fluorescence measurements of the tin deposit required removing the sensitizer deposit from the "back" side of the specimen. This was accomplished by a local etch with 10*N* NaOH.

Exposure of sensitized specimens.—The polyimide specimens were sensitized in solution A (10 g/liter initial $SnCl_2 \cdot 2H_2O$) at various times during the solution aging, then exposed to 250 nm radiation. Exposure was made by passing the output from a 900W high-pressure xenon arc through a Bausch & Lomb high intensity monochromator, the specimen being placed at the monochromator exit slit. The monochromator grating dispersion was 3.2 nm/mm, and thus the wavelength spread in the 1.5 mm slit image was 4.8 nm. The light intensity incident on the sensitizer was 0.77 ± 0.02 mW/cm², as determined by an Eppley thermopile placed at the same position as the exposed specimen.

After exposure, specimens were metalized with copper to develop a positive slit image, *i.e.*, the slit outline was non- or partially metalized, while elsewhere blanket metalization occurred. The procedure for the metalization was as described in the section on Preparation and metalization of substrates. The exposure technique and related apparatus were discussed in an earlier paper (4).

Following metalization, optical densities, *D*, of the copper deposits in both exposed and unexposed regions were measured at 670 nm using a Cary 14 spectrophotometer. This instrument was used in the double beam mode with a blank polyimide substrate in the reference beam. The results for *D* thus refer only to the copper deposit.

Results

Tin deposit vs. solution age.—In Fig. 1, tin deposits produced by solutions A-C in the standard ambient are plotted as a function of solution age at the time of the sensitization.

Repeat measurements on adjacent portions of the same specimen showed a reproducibility of 0.04 μg/cm², average deviation. The observed scatter is due to processing variations from specimen-to-specimen.

The curves in Fig. 1 are indexed to correlate the deposition with visual observations of the solutions. The index key and observations are presented in Table I.

Tin deposition from stannic solution.—In Fig. 2 we have plotted tin deposition results in the standard ambient for the 0.0044M Sn(IV) solution. The deposition curve for solution B, replotted from Fig. 1, is also shown for comparison. At the earliest times, deposits from the stannic solution are comparable to those obtained only after the stannous solution is well aged. Precipitation and settling are seen to occur at earlier times in the stannic solution. The results in Fig. 2 are consistent with a sensitization model in which the rate of colloid formation (and the subsequent tin deposition) are controlled by the Sn(II) oxidation to Sn(IV), as was suggested earlier by Cohen, D'Amico, and West (3). This limitation is not present in the stannic solution and thus the tin deposition rate, rather than build slowly, begins at its highest value.

Detection of stannous in solution: mean solution activity.—The observed times when negative tests for stannous first occurred are indicated in Fig. 1 by the stars. At the times indicated, the solutions are estimated to contain less than 1.5 mg/liter (or 6.6 μM) of Sn(II), a value based on the detection limit stated in ref. (14).

The approximate lifetimes of the solutions are given in Table II. The mean rate of conversion of the initial stannous into the stannic form is also given in this table.

In addition to testing the solutions for the presence of stannous, substrates were also continuously sensitized in the solutions to observe whether or not they continued to catalyze metalization. When stannous detection was positive, uniform metalization also occurred. When the stannous test became negative, metalization became marginal (*i.e.*, spotty) or nonexistent.

Solution aging in bubbled nitrogen and air.—Solution A, aged in bubbled N_2 for up to 600 hr, showed no signs

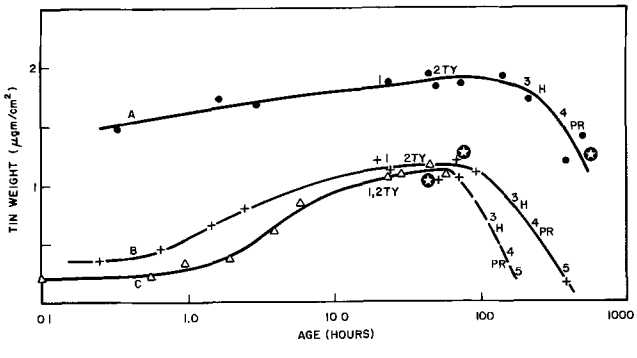

Fig. 1. Tin deposition vs. sensitizer solution age. ● Solution A, + solution B, and △ solution C containing initial $SnCl_2 \cdot 2H_2O$ weights of 10, 1, and 0.5 g/liter, respectively. Visual observations made during aging are also indicated. (Key, see Table I.)

Table I. Visual observation of solution aging

Solution age (hr)	A (10 g/l)	B (1 g/l)	C (0.5 g/l)
0	Clear, no TY	Clear, no TY	Clear, no TY
6.5	Clear, no TY	Clear, no TY	Clear, no TY
22.5	Slight yellow (1), very slight TY	Slight yellow (1), slight TY	Slight yellow (1), (2), definite TY
30	Slight yellow, slight TY	Slight yellow, definite TY (2)	Slight yellow, definite TY
46.5	Slight yellow (2), definite TY	Yellow, definite TY	Slight yellow, definite TY
54	Yellow, definite TY	Yellow, definite TY	Fading yellow, strong TY
71	Deep yellow, definite TY	Deep yellow, definite TY	Very slight yellow, strong TY
78	Very deep yellow, strong TY	Deep yellow, definite TY	Very slight yellow, strong TY
102	Very deep yellow, strong TY	Yellow, strong TY	Colorless, very strong TY
144	Very deep yellow, strong TY	Colorless, very strong TY	Colorless, haze in solution (3)
167	Very deep yellow, very strong TY	Colorless (3), haze in solution	Colorless (4), haze in solution precipitation
181	Very deep yellow, very strong TY	Colorless, increased haze	Colorless, clear solution (5), precipitate settled
205	Very deep yellow haze (3)	Colorless haze (4), start of precipitation	—
229	Deep yellow, strong haze	Colorless haze precipitation	—
316	Pale yellow, very dense haze	Colorless, clear solution (5) precipitate settled	—
340	Pale yellow, very dense haze	—	—
362	Pale yellow, strong haze (4), precipitate settling	—	—
620	Pale yellow, strong haze, precipitate settled	—	—

Observation key, Fig. 1 and Table I:
(1) First observable yellowing.
(2) TY Tyndall effect prominent.
(3) H Solution haze prominent.
(4) PR Onset of colloid precipitation.
(5) Precipitation completed; solution clear and colorless.
✪ First negative test for Sn(II) by indicator paper.

of colloid formation, *i.e.*, no Tyndall effect, hazing, precipitation or yellowing. Furthermore, phosphymolybdate tests for Sn(II) showed no noticeable depletion of Sn(II), as evidenced by the depth of the blue color on the indicator paper.

The solution aged in bubbled air, on the other hand, showed an enhanced rate of colloid formation and Sn(II) depletion. Solution yellowing and a Tyndall effect were observed within an hour, and the indicator paper test for Sn(II) became negative at 40 hr. For control solution A, this point in the aging cycle was reached at times greater than 533 hr.

Electroless copper deposits vs. solution age.—Results of the 1.5-min metalization are shown in Fig. 3 where we have plotted optical density D of the copper film *vs.* the solution age at the time of sensitization. Maximum error limits based on repeated determinations under "identical" conditions are also shown in the figure. (These values are calculated to be ± 0.03.)

Table II. Duration of Sn(II) detection in the sensitizer solutions

Solution	Initial conc of $SnCl_2 \cdot 2H_2O$ (g/liter)	Range of solution active life* (hr)	Mean rate of $SnCl_2 \cdot 2H_2O$ conversion (g/liter/hr)
A	10	533-700	0.014-0.019
B	1	69-79	0.013-0.015
C	0.5	42-54	0.009-0.012

* Last positive detection on left, first negative detection on right.

Table III. Tin deposition and copper optical density D for acid vs. water tin rinses

Solution	Age (hr)	Tin deposit ($\mu g/cm^2$) Water rinsed	Tin deposit ($\mu g/cm^2$) Acid rinsed	Copper optical density D Water rinsed	Copper optical density D Acid rinsed
A	0.25	1.35	0.34	—	—
	3.0	—	—	0.72	0.41
	20	1.61	1.19	—	—
	100	—	—	0.70	0.60
B	0.25	0.32	0.02	—	—
	22	0.98	0.61	—	—

Tin and copper deposition for acid rinsed sensitizer.—Specimens sensitized using the acid tin rinse showed tin and copper depositions as presented in Table III. For fresh solution B, 94% of the normal tin deposit is removed by the acid rinse while in fresh solution A, 75% is removed. As aging occurs, the acid soluble contribution to the sensitization decreases in both solutions.

The copper deposition results for solution A show a decrease in the metalization, indicating a decrease in the surface concentration of palladium, presumably from a decrease in surface concentration of Sn(II) resulting from the acid rinse. This removal is clearly not complete, since the metal deposition has not been reduced to zero.

Imaging sensitivity vs. solution age.—Specimens sensitized in solution A at various ages were exposed to 250 nm radiation then metalized with copper. Measurements of the 670 nm optical density D *vs.* solution age, with exposure time at constant light intensity as a parameter are presented in Fig. 4. Similar measurements for the unexposed regions are also shown in this figure. Increased exposures, we observe, are required to maintain image contrast as the sensitizer solutions age.

Discussion

Tin deposit vs. solution age.—In Fig. 1 we observe that the tin weights increase with solution age but at long times this trend is reversed. If sufficient time is allowed, the tin deposits approach zero. In reviewing Fig. 1 and Table I, we observe that the general increase in deposit weight follows the colloid development in

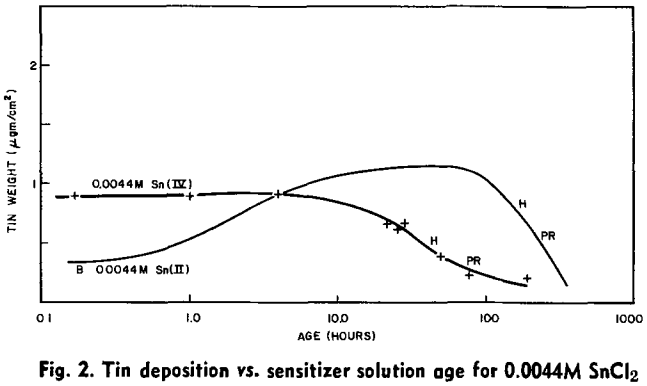

Fig. 2. Tin deposition *vs.* sensitizer solution age for 0.0044M $SnCl_2$ and $SnCl_4$ solutions, both at pH ~1.

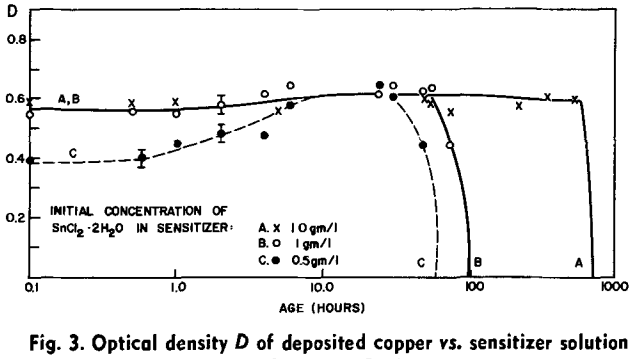

Fig. 3. Optical density D of deposited copper *vs.* sensitizer solution age. Electroless plating time fixed at 1.5 min.

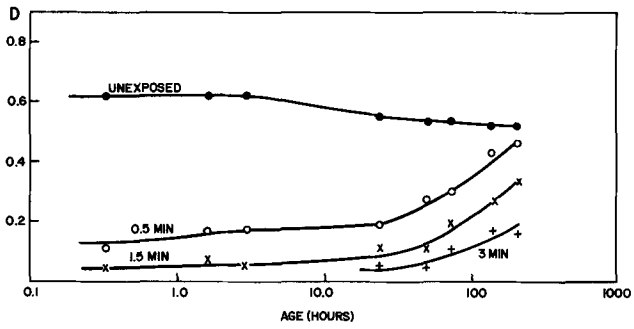

Fig. 4. Obtainable image contrast vs. age of sensitizer solution A. Exposure time to 250 nm radiation as a parameter. Light intensity constant at 0.77 mW/cm².

solution. However, when the colloid particles become quite large, as evidenced by the presence of a strong haze and then a settling precipitate, the amount of deposit begins to fall and the solution clears. The clear solution no longer sensitizes the substrate, although it can still produce a non-negligible deposit. This deposit is presumed to contain only Sn(IV) species, a conclusion supported by the Mössbauer results in ref. (3).

We envision the sensitization to occur by a combination of two processes: (*i*) formation on the substrate of an adsorbed liquid film containing soluble aquo, chloro, and hydroxy-chloro tin complexes (during subsequent rinsing, these complexes are immediately hydrolyzed to form insoluble oxides and hydroxides, some of which adhere to the substrate) and (*ii*) formation of the colloid in solution, with adsorption of colloid particles onto the substrate during immersion in the solution.

In general, we expect both processes to be operative in the buildup of the sensitizer layer although the relative contribution of each may not be readily identifiable. We could reason, however, that (*i*) should be favored when colloid formation is minimal, *e.g.*, very fresh solutions (the colloid needs time to form), or highly acidic solutions (where hydrolysis is suppressed). When extensive colloid formation has occurred, (*ii*) should play an appreciable role.

Our division of sensitization into two processes was made to identify the participating mechanisms and is not meant to imply that (*i*) and (*ii*) are necessarily independent of each other. In fact, it is likely that the deposit via (*ii*) has a strong influence on the solution wetting of the substrate and thus affects the amount of adsorbed liquid which participates in process (*i*). This interaction makes it difficult, with our present knowledge, to give a clear-cut interpretation of experimental results.

At this point one might legitimately question whether process (*ii*) does, in fact, contribute an appreciable tin deposit to the sensitizer layer formation under any circumstances. One could, as an alternative, view process (*ii*) not as a layer building step, but as one which regulates the liquid layer thickness by control of the wetting. This regulation could presumably be accomplished by a deposit insignificant compared to that made later when the liquid layer undergoes hydrolysis. The validity of this view is tested in the acid rinse experiments described above. In Table III we observe an appreciable tin fraction deposited after acid rinse (except for fresh B solution). Thus we have demonstrated that the colloid process (*ii*) does in fact contribute appreciably to the sensitizer layer formation.

At very long times the colloid formation culminates in the precipitation and settling of the insoluble oxide. In solutions B and C this precipitate is apparently all stannic since no stannous species was detectable at the time of precipitation. In solution A, precipitation occurs prior to the complete depletion of the stannous species, so that from this data alone it is not evident what the chemical state of the precipitate may be. Precipitates from A, in fact, are pale yellow, while those from B and C are white. This implies the presence of stannous in the A precipitate.

Relation between the tin oxidation and the colloid formation.—It is clear from the results presented that the tin oxidation in solution plays a dominant role in the colloid formation. The slowly increasing tin depositions with solution age can be explained as due to the gradual buildup of colloid (presumably a form of SnO_2) as the oxidation process proceeds. This buildup and the other signs of aging, solution yellowing and the depletion of Sn(II), stopped completely when oxygen was removed from the system by N_2 bubbling. The aging process, on the other hand, was markedly accelerated when air bubbling was used.

As suggested earlier (3), the colloid may be principally a stannic oxide or hydroxide form, produced by generation of stannic species in excess of their equilibrium concentration by the air oxidation. The solubility products for tin oxides, reported as $Sn(OH)_2$ and $Sn(OH)_4$ by Latimer and Hildebrand (16), are 5×10^{-26} and 1×10^{-56} M/liter, respectively. For solutions of $pH = 1$, the equilibrium concentrations of uncomplexed stannous and stannic species are calculated to be 5M and 10^{-4}M, respectively. Thus the solubility of stannous oxide in our solutions is appreciable while that of the stannic oxide would be quite small, its exact value depending on the equilibrium concentrations of the complexes, mostly chlorides, which are formed.

If the colloid is entirely stannic, then sensitizer deposits due only to process (*ii*) should be incapable of metalizing the substrate[6] and the required stannous species must be provided by process (*i*). This aspect of the model can be tested by comparing the metalization results for the water and acid tin rinses. With the acid rinse, the soluble tin complexes in the liquid film would be washed off the substrate rather than deposited, leaving only the colloid deposit from process (*ii*). In Table III, a 43% reduction in the copper absorbance is noted for the 3-hr acid rinsed specimen, as compared to its water-rinsed counterpart. A 14% reduction is noted for the 100-hr solution.

The metalization differences noted in Table III cannot be immediately translated into a fractional depletion in stannous species on the substrate, since the relation between D and [Sn(II)] is not yet known. However, we feel safe to assume that even when acid rinsed, the colloid deposit still contains a non-negligible component of Sn(II) since it continues to deposit electroless copper. This Sn(II) component is very likely the result of entrainment during the colloid formation, or possibly adsorption at the colloid particle surface. This entrainment/adsorption apparently increases as the colloid system becomes more developed, since the older of the solutions produced lesser changes in D after the acid rinse.

Detection of stannous in solution: lifetime of solution activity.—The ability of the sensitizer to promote metalization was found to coincide with a positive test for stannous in solution; the failure of metalization likewise coincided with a negative test result. These results are consistent with our basic assumption (1-4) that the imaging reaction is, in fact, a Sn(II) to Sn(IV) photo-oxidation.

In Table II we estimated the mean rate of conversion of the initial stannous chloride dihydrate, based on the duration of stannous detection in solution. These values should be considerd as order estimates since the reaction end point was semiquantitative. In Table II we note that the mean $SnCl_2 \cdot 2H_2O$ conversion

[6] The authors have sensitized polyimide substrates using solutions made with $SnCl_4 \cdot 5H_2O$ in place of $SnCl_2 \cdot 2H_2O$. While appreciable tin deposits were found (Fig. 2, this paper) no metalization was produced.

rates are not too different in each of the solutions, but it would not be correct to conclude from this data that the oxidation reaction is necessarily zero order in [Sn(II)], *i.e.*, independent of the concentration of reactant.

The auto-oxidation of stannous tin solutions has received considerable attention in the literature (17-22). The reported results deal mainly with the kinetics of stannous chloride and oxygen in HCl solutions, with vigorous stirring or shaking of the solutions to insure that the measurements were not limited by the diffusion rates in the solution. There is poor agreement in the published work. In ref. (17) and (19), the reaction rate was found first order in stannous chloride concentration for dilute solutions, but independent of the stannous chloride concentration (*i.e.*, zero order) at higher concentrations. In ref. (20) and (22), the reaction was found half order in the analytical concentration of stannous chloride and, in ref (20), first order with respect to the dissolved oxygen. The reaction rate was also found to be strongly dependent on the HCl content of the solutions (17, 18, 22) although again the published results are not in quantitative agreement.

We have already presented results which prove that agitation produces an appreciable acceleration of aging in our solutions. In the published work, Filson and Walton (18) describe experiments which demonstrate that the solution aging can be appreciably altered by the extent of agitation with an air jet in solution.

Thus it is apparent that diffusion effects play an important role in determining the reaction rates, at least in poorly stirred solutions. One might assume that the rate limitation must be due to oxygen diffusion from the ambient into solution. The diffusivity of gases in dilute electrolytes, however, is characteristically quite large (23), which implies the replenishment of the dissolved, reacted oxygen should be rapid enough to maintain the equilibrium solubility of oxygen in the solution. This conclusion was also reached by Filson and Walton (18). The final resolution of this problem awaits an actual measurement of the oxygen and stannous concentration profile in the solutions.

Electroless copper deposits vs. solution age.—In Fig. 3 we observe that solutions A and B produce nearly identical copper films over a wide range of solution ages, although the B solution becomes spent earlier, as we have already discussed. Solution C by contrast produces an initially thinner deposit which becomes comparable to the others after about 5 hr. (The error bars in the figure indicate to what extent we can differentiate the behavior of the various solutions.)

In Fig. 1 a significant difference in the tin deposit from solution A compared to that from B was observed, yet the copper deposits were essentially identical. For solution C, copper deposits in the first several hours were slightly less than the others; the tin deposit from C was simultaneously reduced.

The copper weight deposited should depend on the amount and distribution of the palladium metal, which in turn is presumed to depend on the amount and distribution of stannous in the sensitizer layer. The stannous in the sensitizer has not yet been quantitatively determined. It is present in very minute amounts and in air is spontaneously converted to the stannic state, both factors leading to difficulty in the determination.

In qualitative terms, we expect that the stannous to total tin ratio in solution decreases with age. A similar (but probably not identical) decrease should also occur in the sensitizer layer. In solution the mean colloid particle size appears to increase with age, so the observed increase in tin deposit might well be due to coverage of the substrate by larger particles, with or without a change in the fraction of the surface covered.

In viewing Fig. 1 it seems reasonable to conclude that the sensitizer deposits from solutions A, B, and C must be differently formed, at least for times less than 10 hr. Yet A and B produce nearly identical copper deposits over their entire active lifetimes while C produces an equal deposit after about 6 hr. Thus, the metalization process as carried out here is not highly dependent on the sensitizer structure. These results are consistent with a model for the metalization in which the deposits are initially enhanced by increased sensitizer (and thus palladium) but after some minimum deposit of palladium, no further enhancement of the metalization occurs. Applying this model here, we conclude (Fig. 3) that the Pd deposits generated from solutions A and B exceed this "minimum" from the earliest measured times, but that those from C do not attain the "minimum" until the solution ages for about 6 hr.

Imaging sensitivity vs. solution age.—As indicated in Fig. 4, image contrast is reduced as the A solution ages and thus greater incident light energy is required to produce images. We have already noted that the solutions, up to a point, deposit steadily increasing amounts of tin so that the loss in imaging sensitivity could be the result of having to react a greater amount of sensitizer to produce the nonmetalized portions of the images. This explanation, however, has some serious problems:

1. The continuous oxidation of stannous in solution should produce a decrease in stannous on the sensitizer and thus improve the sensitivity by making it easier to inhibit the metalization. Recall that the unexposed substrate retains its metalizing capability (Fig. 3) for nearly the entire solution active lifetime.

2. We reported earlier (4) that the sensitizer deposits are quite uv transparent ($D \sim 0.05$ at 250 nm) so that only a small per cent of the incident light is absorbed, the major part of the light energy being absorbed or transmitted through the substrate. Thus, any increase in the sensitizer deposit should merely absorb more of the incident light, with the result that the image contrast would remain unaltered. To explain the image contrast reduction we could, as an alternative, assume that the form of the deposit changes with age, producing a film of reduced optical density and/or reduced quantum efficiency for the oxidation reaction. Experimental verification of such an explanation for sensitizers on the polyimide substrate is not possible at present, since this substrate is not uv transparent.

Conclusions

1. Tin sensitization depends on solution variables such as the initial stannous tin concentration, pH, and the solution age. The oxidation of tin in solution generates a colloid system, principally stannic oxide or hydroxide species, whose state and presence play a dominant role in the sensitization process.

2. The substrate metalization was found relatively insensitive to the weight of sensitizer deposit or its stannous content. This, however, was not the case for imaging sensitivity, which was markedly reduced as heavier, more stannic deposits were produced by solution aging. The use of the solutions must evidently be terminated prior to the time when metalization stops, in order to avoid the need for excessive light exposures.

3. Sensitizer solutions stored/used in a nonoxidizing ambient or nitrogen bubbled could be used for much longer periods and should maintain relatively constant imaging characteristics. The usefulness of this approach in terms of cost factors will depend on the specific application.

4. The general hypothesis that stannous-based PSMD imaging is a photoinduced oxidation was further supported by our observations that the metalization capability on the substrate is coincident with the positive detection of stannous species in solution, and the converse.

Acknowledgments

The authors gratefully acknowledge critical reviews of our manuscript by J. T. Kenney and F. A. Litt.

Manuscript submitted Feb. 5, 1973; revised manuscript received June 13, 1973. This was Paper 217 presented at the Miami Beach, Florida, Meeting of the Society, Oct. 8-13, 1972.

Any discussion of this paper will appear in a Discussion Section to be published in the June 1974 JOURNAL.

REFERENCES

1. D. J. Sharp, *Plating*, **58**, 786 (1971).
2. J. F. D'Amico, M. A. DeAngelo, J. F. Henrickson, J. T. Kenney, and D. J. Sharp, *This Journal*, **118**, 1695 (1971).
3. R. L. Cohen, J. F. D'Amico, and K. West, *ibid.*, **118**, 2042 (1971).
4. J. F. D'Amico, F. A. Litt, and M. A. DeAngelo, *ibid.*, **119**, 956 (1972).
5. W. Goldie, "Metallic Coating of Plastics," Vol. I and II, Electrochemical Publications Ltd., Middlesex, England (1968).
6. R. L. Cohen and K. West, *This Journal*, **119**, 433 (1972).
7. N. Feldstein and J. A. Weiner, *ibid.*, **119**, 668 (1972).
8. N. Feldstein and J. A. Weiner, *ibid.*, **120**, 475 (1973).
9. N. Feldstein, J. A. Weiner, and G. L. Schnable, *ibid.*, **119**, 1486 (1972).
10. R. S. Tobias, *Acta Chem. Scand.*, **12**, 198 (1958).
11. J. D. Donaldson, *Prog. Inorg. Chem.*, **8**, 287 (1967).
12. H. B. Weiser, in "Inorganic Colloid Chemistry," Vol. II, The Hydrous Oxides, John Wiley & Sons, Inc., New York (1938).
13. J. T. Kenney, W. P. Townsend, and J. A. Emerson, *J. Colloid Interface Sci.*, **42**, 589 (1973).
14. F. Feigl, "Spot Tests in Inorganic Analysis," 5th ed., p. 108, Elsevier, New York (1958).
15. "International Critical Tables," 1st ed., Vol. III, p. 271, E. W. Washburn, Editor, McGraw-Hill Book Co., New York (1928).
16. W. M. Latimer and J. H. Hildebrand, "Reference Book of Inorganic Chemistry," 3rd ed., p. 562, Macmillan Co., New York (1951).
17. S. Mirjamoto, *Bull. Chem. Soc. Japan*, **2**, 259 (1927).
18. G. W. Filson and J. H. Walton, *J. Phys. Chem.*, **36**, 740 (1932).
19. R. Haring and J. Walton, *ibid.*, **37**, 133 (1933).
20. S. Lachman and F. Tompkins, *Trans. Faraday Soc.*, **40**, 130 (1944).
21. E. Baker, *J. Appl. Chem.*, **3**, 323 (1953).
22. E. A. Kutner and B. P. Matseevskii, *Latvijas PSR Zinatnu Akad. Vestis, Kim. ser.*, **6**, 666 (1967).
23. See, for example, R. C. Reid and T. K. Sherwood, "The Properties of Gases and Liquids," chap. 8, McGraw-Hill Book Co., New York (1958).

A Study of Transient Processes Preceding the Electrodeposition of Cr on Pt

J. C. Saiddington and G. R. Hoey*

Corrosion Section, Extractive Metallurgy Division, Mines Branch, Department of Energy, Mines and Resources, Ottawa, Ontario, Canada

ABSTRACT

Galvanostatic polarization data with simultaneous microscopic observations of a Pt cathode surface were obtained in conventional chromium plating baths. The results show that the deposition of chromium on bright activated platinum is preceded by heavy evolution of hydrogen and a prolonged shift of potential during which the formation of a chromic oxide film may be observed at the cathode surface at higher current densities. The final shift of potential just prior to the establishment of metal deposition was found to be associated with a distinct decline of gas evolution regardless of the presence or absence of the chromic oxide film which, when formed, was observed to disintegrate before steady-state conditions of Cr deposition were reached. These observations are compared with those made earlier with Fe electrodes and the results are discussed in the light of possible processes involved in bringing about the shift of the potential to the value of Cr deposition.

An earlier investigation (1) of the deposition of Cr on Fe electrodes has shown that, under reproducible galvanostatic experimental conditions, certain transient phenomena occur at the cathode surface prior to the commencement of the chromium plating processes. These results were discussed in detail in the previous work but are here simplified by dividing the whole transition period into two transient regions, I and II.

Transient region I was found with Fe electrodes to be characterized by heavy gas evolution and by a gradual shift of the potential from the initial hydrogen evolution to a level at which formation of a chromic oxide film could be observed under the microscope. Transient region II coincided with the disintegration of the chromic oxide film with an accelerated shift of potential to the value of chromium deposition, and with a change in the pattern of gas evolution.

Transient region I was attributed to electrode reactions that can proceed without bringing about the deposition of chromium. Transient region II, on the other hand, was attributed to processes that are associated with the establishment of the reduction of hexavalent chromium to metal. These processes, it was concluded on the basis of microscopic observations, involve changes in the consistency of the liquid layer adjoining the cathode surface resulting in the formation of a transparent viscous film.

The term "viscous film" was chosen arbitrarily to differentiate between the solid chromic oxide film that forms during potential region I and the liquid film that comes into existence during potential region II.

Vagramyan and Solov'eva (2) call the liquid film a "phase film," a term perhaps more appropriate since the viscous conditions in the liquid layer have never been determined. However, this term is also not completely satisfactory even though it is meant to indicate phase transformations in the $Cr(OH)_3$-CrO_3 system as a possible cause of the film formation. The processes involved are apparently more complex since they are potential dependent, they do not occur in the absence

* Electrochemical Society Active Member.

Key words: hydrogen evolution, microscopic observations, cathodic films.

of $SO_4^=$, and, as is shown in the present paper, they affect the evolution of gaseous hydrogen.

Solov'eva, Petrova, Klimasenko, and Vagramyan (3) investigated the composition of the liquid film present at the cathode surface during chromium plating. They found that the concentration of Cr^{3+} and of $SO_4^=$ ions in the film is higher than in the bulk of the electrolyte, while that of Cr^{6+} is lower.

Weiner and Schiele (4) have shown that the chromic oxide film that forms in potential region I contains only Cr_2O_3 with some traces of the cathode metal.

Okada and Yamamoto (5) assumed that the increase in thickness of the chromic oxide film is the cause of the increase of hydrogen overpotential on Pt in region II. Their explanation was at variance with our inferences made on the basis of the investigation with Fe electrodes (1). Since the above authors did not observe potential region I during polarization of steel and we did not study the formation of chromic oxide on Pt, some corroborating work with Pt cathodes was in order.

The experimental results of the present investigation show that the whole transition period with Pt electrodes can also be divided, as in the case of Fe, into two distinctly different regions of polarization. The first region, corresponding to region I on Fe electrodes, is characterized by a continuous heavy gas evolution and by a gradual and very protracted shift of potential toward more negative values with time. This region may or may not terminate with the formation of a visible chromic oxide film, which depends on the current density. The second region of polarization, corresponding to II on Fe, is associated with distinct inhibition of visible gas evolution, with disintegration of the chromc oxide film whenever such film is observed to form at region I, and with the establishment of the Cr deposition process. This second region is concomitant with some transformations within the liquid layer adjoining the cathode surface. The transformations may lead to the formation of an adsorbed cathode film. The chromic oxide film that forms in region I disintegrates prior to the commencement of chromium deposition and this evidence contradicts the hypothesis of Okada and Yamamoto (5) about its role in the increase of hydrogen overvoltage values during region II.

Experimental

The experimental technique employed in this study was similar to the one used in the investigation of chromium deposition on iron (1) except that smaller Pt cathodes were employed.

High-purity (99.9%) platinum wire 2 mm in diameter, was mounted, cross sectioned, and metallographically polished, producing a geometric section area of 0.03145 cm^2. To obtain reproducible potentials of initial hydrogen evolution it was necessary to activate the polished surface by dipping it into hot (80°-90°C) chromic acid (750 g/liter of CrO_3) for 1 min, to double-rinse with distilled water, and to dry, as recommended by Breiter (6). Dry electrodes were then placed into the plating cell and were allowed to soak for 1 min in the plating bath to acquire the solution temperature which in all instances was 50°C. The potential-time curves were obtained by running the potentiometric recorder at a predetermined speed while the electrode was immersed in the bath with the current off. After 1-min period the current was then switched on. The initial transient from the potential of rest to the inflection was a straight line at all current densities investigated. The inflection coincided with the beginning of visible hydrogen evolution.

All electrolyses were performed in conventional plating solutions containing 250 g/liter of CrO_3 and 2.5 g/liter of H_2SO_4 using galvanostatic current control. Simultaneous microscopic observations were recorded photomicrographically and were subsequently correlated with the polarization data.

Results and Discussion

Preliminary investigations.—To control the reproducibility of initial Pt surface conditions a brief activation treatment (6) was necessary. In the absence of such a treatment neither the potential of rest nor the potential of initial hydrogen evolution was reproducible.

Table I shows electrode potentials at various surface conditions. With specimens not subjected to the activation treatment (experiments 1 and 2) both, the rest potential and the initial evolution of hydrogen, varied considerably. After activation treatment these potentials were rigorously reproducible (experiments 3 and 4). Under these conditions the potential of initial hydrogen evolution corresponded closely to the calculated potential of hydrogen evolution on Pt, as is shown later on.

The initial evolution of hydrogen and the rest potentials were considerably different when a previously activated and polarized electrode were reused without again reactivating it (experiments 5, 6, 7, and 8, Table I). The rest potentials were then more active and so was the potential of initial hydrogen evolution presumably due to the adsorption at the cathode surface of the products of electrolysis and of impurities from the plating bath. Reactivation would restore the reproducible potentials.

The requirements of Pt activation for electrochemical measurements were studied by a number of workers (7-9). The theories of activation were reviewed by James (10). His study indicates that the removal of adsorbed impurities is by far the most important result of a brief activation treatment. An oxygen layer that forms on the surface during chromic acid treatment (6) apparently protects the electrode until cathodic current is applied. When the electrolysis is started, the oxygen layer is first removed but the active surface soon becomes inactive, probably due to the adsorption of the products of the electrochemical or of secondary chemical reactions.

When electrolysis was continued uninterrupted, the conditions at the surface continued to change with time. Such changes were indicated by the shift of the potential to more negative values, a phenomenon reflecting higher activation energy requirements for the over-all current carrying processes.

Although some workers (11, 12) expressed an opinion that hydrogen evolution is the only reaction taking place at higher current densities, at more negative potentials prior to the deposition of chromium, other work suggests (13-15) that partial reduction of chromic acid ($Cr^{6+} \rightarrow Cr^{3+}$) is also in progress but to a much smaller degree, leading to the formation of chromic oxide films (4). These films are assumed to be porous (16) or semiconductive (17), thus allowing the

Table I. Potential of Pt electrode in conventional Cr plating bath at various surface treatments

Exp. No.	Surface treatment	Volts vs. SCE: Rest potential	Volts vs. SCE: Initial H_2 evolution*
1	Polishing, rinse (no activation)	+0.67	−0.25
2	Polishing, rinse (no activation)	+0.98	−0.20
3	Polishing, rinse, activation**	+0.95	−0.36
4	Polishing, rinse, activation	+0.95	−0.36
5	Polishing, rinse, activation, electrolysis,† rinse	+0.69	−0.55
6	Polishing, rinse, activation, electrolysis, rinse, dry	+0.60	−0.57
7	Polishing, rinse, activation, electrolysis, soak,‡ 10 min	+0.26	−0.55
8	Polishing, rinse, activation, electrolysis, soak 30 min	+0.27	−0.65

* Constant current 0.440 A/cm^2 at 50°C.
** 1 min dip in hot (80°-90°C) chromic acid (750 g/liter CrO_3) and double rinse [ref. (6)].
† Electrolysis at 0.440 A/cm^2 at 50°C, 5 min.
‡ Left in the bath with current off before switching it on again.

discharge of hydrogen ion to proceed. Since the structure and the rate of formation of such films does depend on the current density and the method of the surface preparation (14) so will the inhibition of hydrogen evolution.

To examine the reproducibility of polarization under the experimental conditions adopted, a series of potential-time curves was obtained with activated electrodes, after first subjecting them to a number of polarizing cycles in the conventional plating bath at the same C.D. of 0.440 A/cm^2 and a temperature of 50°C. Each polarization was carried out from the potential of rest to the potential of chromium deposition which in some instances (*e.g.*, curve 3) would be delayed for up to 2 hr. Usually in such situations there was still a significant shift of potential toward more negative value after about 30 min of polarization. If after 30 min the shift of potential was not significant the electrolysis would be terminated after 45 min for experimental expediency because it was found, in separate extended runs, that under such conditions no further shift of potential occurred and no chromium deposition resulted after several hours of electrolysis. When chromium did deposit at reasonable short periods of time, it was stripped with hydrochloric acid and the electrode was then thoroughly rinsed and reactivated but not repolished, before the next sequence. The curves obtained in this manner are shown in Fig. 1a.

Curve 1 represents surface conditions after about ten polarizing sequences. Under these conditions the electrode could not be polarized to the potential of chromium deposition at the C.D. of 0.440 A/cm^2 at any reasonable period of time. After about 30 min the shift of potential would level off at approximately −0.7V and additional polarization would have no further marked effect. The curve was then considered experimentally reproducible.

Curve 2 is similar to curve 1 and was obtained with a smaller number of polarizing cycles (eight cycles). This curve runs at slightly more negative potentials and like curve 1 would begin to level off after about 30 min of electrolysis.

Curve 3 terminated with the deposition of Cr after approximately 2 hr of electrolysis. It was obtained after six to seven polarizing sequences and could not be exactly reproduced.

Curve 4 represents polished and activated surface without previous polarization history. All other surface conditions (curves 1-3 and 5-7) would revert to curve 4 after repolishing and reactivation.

Curves 5, 6, and 7 were obtained with an intermediate number of polarizing cycles (two to five cycles) and could not be reproduced in duplicate experiments. Their shape could not be correlated with the number of previous polarizations nor with their duration. Thus, for instance, curve 5 was obtained after five polarizations, curve 6 after two, and curve 7 after three cycles.

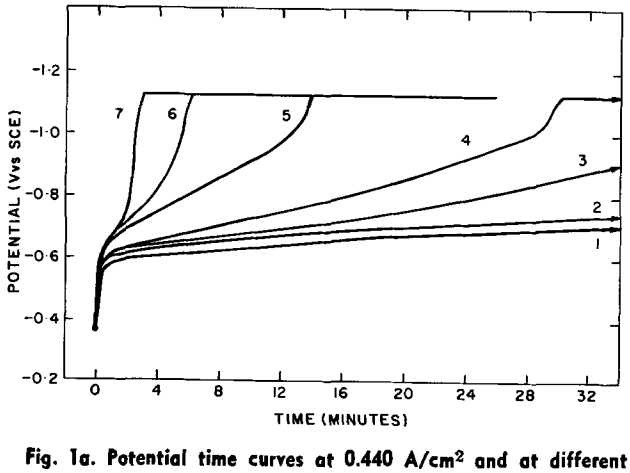

Fig. 1a. Potential time curves at 0.440 A/cm^2 and at different polarization histories of the electrodes.

The phenomenon of the variation of the shift of potential with the polarization history is of a certain fundamental interest. One can speculate that each polarization affects platinum electrode in depth just underneath the surface since repolishing restores the original conditions. The initial evolution of hydrogen, however, appears not to be affected by previous polarization history and can always be reproduced by reactivation of the surface. Full explanation of this phenomenon would require a separate detailed study which could not be considered within the scope of this work.

For the purpose of the present investigation surface conditions resulting from polishing and activation but without previous polarization history were found most appropriate. They were associated with curve 4 shown in Fig. 1a and provided reproducible transitions within the potential ranges I and II. In addition such surface conditions appeared to be similar to those used by Reinkowski and Knorr (11) and were, therefore, employed in the present work.

Potential vs. time curves at various current densities. —The preliminary experimental work summarized in Table I and Fig. 1a shows that activation treatment was essential to obtain the reproducible inflection that coincided with the initial evolution of hydrogen.

The transients from the potential of rest to the initial evolution of hydrogen were investigated by Okada, Nakamura, and Ishida (18), who studied potential-charge curves in this region by oscillographic technique.

They found that four inflection points are observed in the conventional plating bath when a C.D. of 0.200 A/cm^2 is used. The first two points were attributed to the reduction of oxides present on the surface. The third inflection was assumed to be associated with the formation of a chromic-chromate film, while the fourth corresponded to the initial evolution of hydrogen at −0.412V *vs.* SCE at 20°C. At lower current densities (0.05 and 0.005 A/cm^2) current carrying reactions were detected and they were considered to be the result of the partial reduction of chromic acid ($Cr^{6+} \rightarrow Cr^{3+}$). In pure chromic acid (absence of $SO_4^=$), in which hydrogen evolution proceeds with practically 100% current efficiency (17), potential-charge curves were the same at all current densities as those obtained in the plating bath (presence of $SO_4^=$) at 0.200 A/cm^2.

This observation shows that the partial reduction of chromic acid contributes little to the over-all current carrying processes at 0.200 A/cm^2 and that these processes can be considered as being mainly due to the discharge of hydrogen ion.

In the present investigation, which was performed with the same equipment as the earlier work (1), potential-time curves were recorded using a potentiometric recorder wth a one-half second response time over a 9-in. grid. Under these conditions it was not possible to resolve the three intermediate inflection points, and the trace was a straight vertical line until the evolution of hydrogen began at measurable rates. This point corresponded to the inflection 4 on the charging curves recorded by Okada, Nakamura, and Ishida (18). This point is accepted as a start of the potential-time transients in the present work.

Reproducible potential-time curves at four current densities of 0.220, 0.440, 0.660, and 1.320 A/cm^2 are shown in Fig. 1b. The initial evolution of hydrogen at the C.D. of 0.220 A/cm^2 was observed to take place at −0.300V *vs.* SCE (at 50°C). At higher current densities this potential was progressively more negative as indicated by the starting point on all four curves.

To check the potential of hydrogen evolution on bright smooth platinum at 0.220 A/cm^2 calculation of the overpotential was made using the following Tafel equation (19)

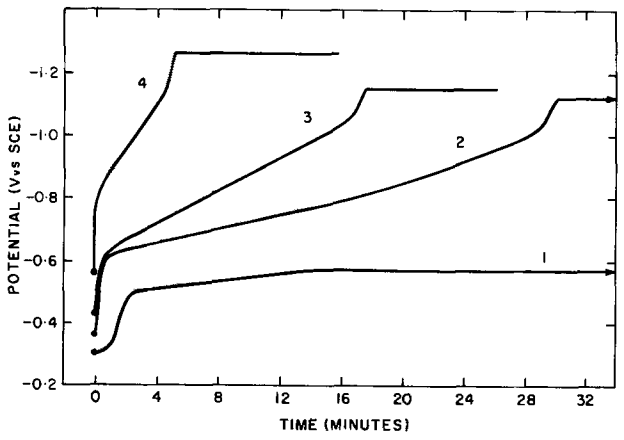

Fig. 1b. Potential time curves at the following current densities: C.D. A/cm²: curve 1, 0.220; curve 2, 0.440; curve 3, 0.660; curve 4, 1.320.

$$\eta = \frac{RT}{\alpha F} \ln \frac{i_o}{i}$$

where α (transfer coefficient) = 2 and i_o (exchange current density) = 10^{-3} A/cm² (20). At 0.220 A/cm², η was found to be −0.075V at 50°C. Using the reversible potential of +0.0134V *vs.* NHE, calculated for a solution containing 250 g/liter of CrO_3 ($pH = -0.212$), the potential of hydrogen evolution was found to be −0.303V *vs.* SCE. Applying the temperature correction to the overvoltage value in the manner recommended by Latimer (21), that is 2.5 mV increase for each 1°C decrease of temperature, the overvoltage at 20°C would be about −0.150V and the potential of hydrogen evolution about −0.38V *vs.* SCE which is fairly close to the value observed by Okada, Nakamura, and Ishida (−0.41V), particularly if one considers that no surface roughness corrections were made.

Schuldiner (22) found experimentally that the current-overvoltage relationship for hydrogen evolution on bright platinum in 0.1*N* H_2SO_4 solution fits the equation $\eta = a - b \log i$ where $a = -0.26$, $b = 0.12$, and i is the true current density corrected by the roughness factor 2.16 (determined experimentally). The equation is applicable to the relatively low current density range 0.015-0.050 A/cm² (nominal C.D. approximately 0.03-0.100 A/cm²). If the nominal C.D. is extrapolated to 0.220 A/cm², the overvoltage η = −0.14V *vs.* 25°C. After correcting to 50°C the potential of hydrogen evolution becomes −0.305V *vs.* SCE which is in good agreement with the first calculation and with our experimental observations (−0.300V *vs.* SCE).

Since the above equation applies only to lower current densities and the surface roughness of platinum used in the present work was not determined, more accurate calculations cannot be made. However, even these approximate values show that the potential of initial hydrogen evolution was within the range generally observed by other investigators, thus, at an acceptable level of reproducibility.

Continued polarization at 0.220 A/cm² resulted in a shift of potential to −0.57V *vs.* SCE at which hydrogen evolution proceeded for over 50 min without deposition of Cr.

The difficulty of polarizing platinum to the potential of chromium deposition at the same range of C.D. and potentials (at equivalent temperatures) was also observed by Reinkowski and Knorr (11). They had to increase the current to 0.300 A/cm² to bring about the shift of potential to the level of chromium deposition.

Chromium deposition is easily brought about at the 0.220 A/cm² current density on Fe cathodes as was shown in earlier work (1). The reason is higher hydrogen overvoltage characteristics of Fe associated with shorter transients in potential region I.

To effect the deposition of Cr on Pt under the reproducible surface conditions, three current densities (0.440, 0.660, and 1.320 A/cm²) were used in the present work. At each current density two transient regions could easily be detected. Transient region I characterized by heavy evolution of hydrogen extended over protracted periods of time even at the highest current density investigated. This region as is shown in Fig. 1a was significantly affected by previous polarization history of the platinum electrode. Although the cause and effect of this phenomenon was not established, it is reasonable to assume that surface changes that occur during each polarization affect the inhibition of hydrogen ion discharge which is the main current carrying reaction in this region. Whether diffusion of the discharged hydrogen into the bulk of the metal is involved it is not known. Weiner (23) has shown that current-voltage curves on platinum are shifted to more negative values if the metal is saturated with hydrogen. Hoare and Schuldiner (24) found, however, that the permeation of Pt with hydrogen is detectable only in the presence of catalytic poisons. This observation was confirmed by Gileadi, Fullenwider, and Bockris (25). Thus in order to accept the concept of hydrogen diffusion into platinum and associated changes of overpotential with time one would have to assume in the present work that chromic acid or some products of its decomposition act as catalytic poison, an assumption that, thus far, has not been verified experimentally.

The second transient II observed with curves 2, 3, and 4, (Fig. 1b) was characterized by an accelerated shift of potential to the level of chromium deposition in a manner similar as in the case of Fe cathodes (1). This shift of potential was not affected by the previous polarization history of the electrode and by the duration of transient region I. When region I was very short (curves 6 and 7, Fig. 1a) it would merge in transition with region II thus obliterating the distinct step observed with curves 3, 4, 5 (Fig. 1a) and curves 2, 3, 4 (Fig. 1b). A short region I is indicative of processes that suppress the low overvoltage characteristics of Pt. It is perhaps noteworthy to emphasize that regardless of the progress of polarization during region I transient region II would always start at about −1.02V and terminate at the same potential of −1.12V *vs.* SCE at which the deposition of Cr would begin at the C.D. of 0.440 A/cm².

This final shift of potential in region II was attributed by Okada and Yamamoto (5) to the increase of hydrogen overpotential as a result of the thickening of the chromic oxide film that forms in region I. Microscopic observations correlated with curves 2 and 3 (Fig. 1b) show, in the next section, that the transient region II is associated with the decline of the evolution of gaseous hydrogen regardless of whether the chromic oxide forms on the surface or not.

Transient region II does not occur in the absence of $SO_4^=$ (1, 5), thus indicating the involvement of such an anion in the electrochemical processes that contribute to the inhibition of visible hydrogen evolution.

Correlation of microscopic observations with potential-time curves.—Microscopic observations made during experiment 1, Fig. 1b (C.D. 0.220 A/cm²) are illustrated by a series of photomicrographs in Fig. 2. The individual photomicrographs show (a) the appearance of the surface immersed in the plating bath before commencement of the electrolysis, (b) very few hydrogen bubbles observed in the first 10 sec, (c) continued low gassing at the 20th second, (d) similar low gassing after 1 min of electrolysis, (e) increase of gassing coinciding with the shift of potential to −0.57V, and (f) the same intensity of hydrogen gas evolution after additional 53 min of electrolysis.

The above microscopic observations correlate well with the changes of the potential with time. The initial range of potential (−0.300 to −0.302V) coincided with

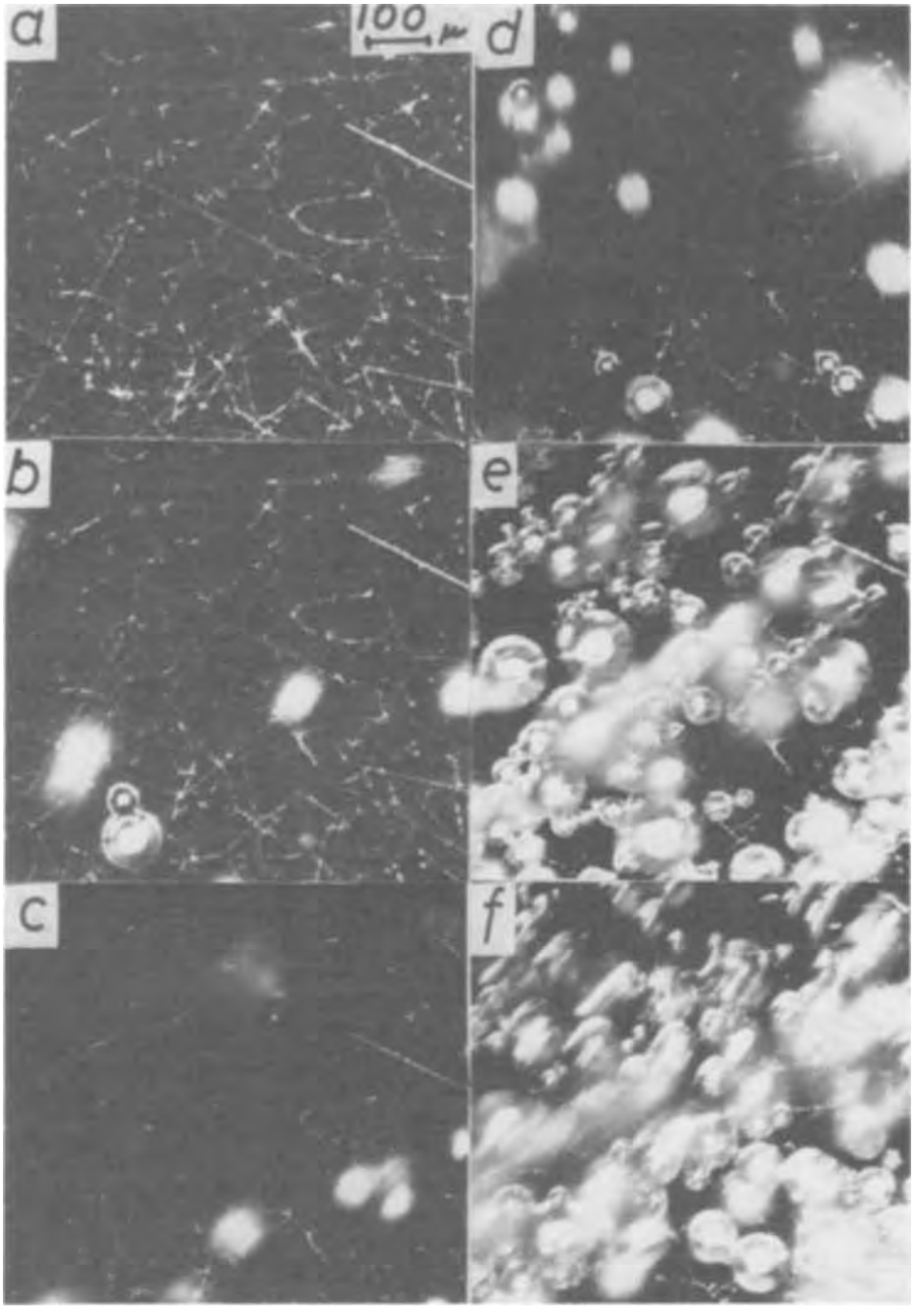

Fig. 2. Photomicrographs of the cathode surface polarized with a constant C.D. of 0.220 A/cm². Original magnification X100. Dark field illumination. Exposures 1/125 sec. a, Immersion before electrolysis, time 0. Rest potential vs. SCE + 0.950V. b, 10 sec; c.p. −0.300V. c, 20 sec; c.p. −0.305V. d, 1 min; c.p. −0.320V. e, 2 min; c.p. −0.470V. f, 54 min 45 sec; c.p. −0.570V.

low level of gassing. This probably means that the concentration of dissolved molecular hydrogen in the diffusion liquid layer was still below saturation (26).

The sharp increase of gas evolution coincided with the shift of the potential to −0.57V as is evident from comparison of curve 1 with Fig. 2e. Apparently upon saturation of the diffusion layer, the process of gas bubble formation reached steady-state conditions and continued unaltered for over 53 min.

To bring about the deposition of chromium the current density was increased to 0.440 A/cm² (Fig. 1b, curve 2). At this value, the potential of about −0.6V was reached rather rapidly, but from then on up to about −1.00V the potential shifted gradually over a period of about 26 min and this shift was accompanied by changes in the gassing pattern as is illustrated in Fig. 3A. The individual photomicrographs show (a) Pt surface immersed in the solution before electrolysis, (b) hydrogen evolution approximately 1 sec after the current was turned on, (c) hydrogen evolution in the fourth minute of the electrolysis, (d) hydrogen evolution in the 18th minute, (e) gassing pattern at −1.01V just before the final shift of the potential to the chromium deposition level, and (f) the beginning of the decrease of gassing coinciding with the potential shift from −1.01 to −1.08V.

The beginning of the decline of gassing observed in photomicrograph (f) was recorded before the steady-state potential of chromium deposition was reached.

A plausible explanation of this phenomenon would be to assume that some chromium is deposited on platinum at potentials less negative than the steady-state value (−1.12V *vs.* SCE at 0.440 A/cm²) and, that because of higher hydrogen overpotential on Cr, the discharge of hydrogen ion ceases when a thin layer of chromium is established. The undisputable evidence is, however, that hydrogen evolution on chromium begins vigorously as soon as $SO_4^=$ is removed from the bath as was shown in the previous work (1). This observation demonstrates, thus, that the decline of gassing is not due to higher overvoltages associated with chromium and that the key factor is the

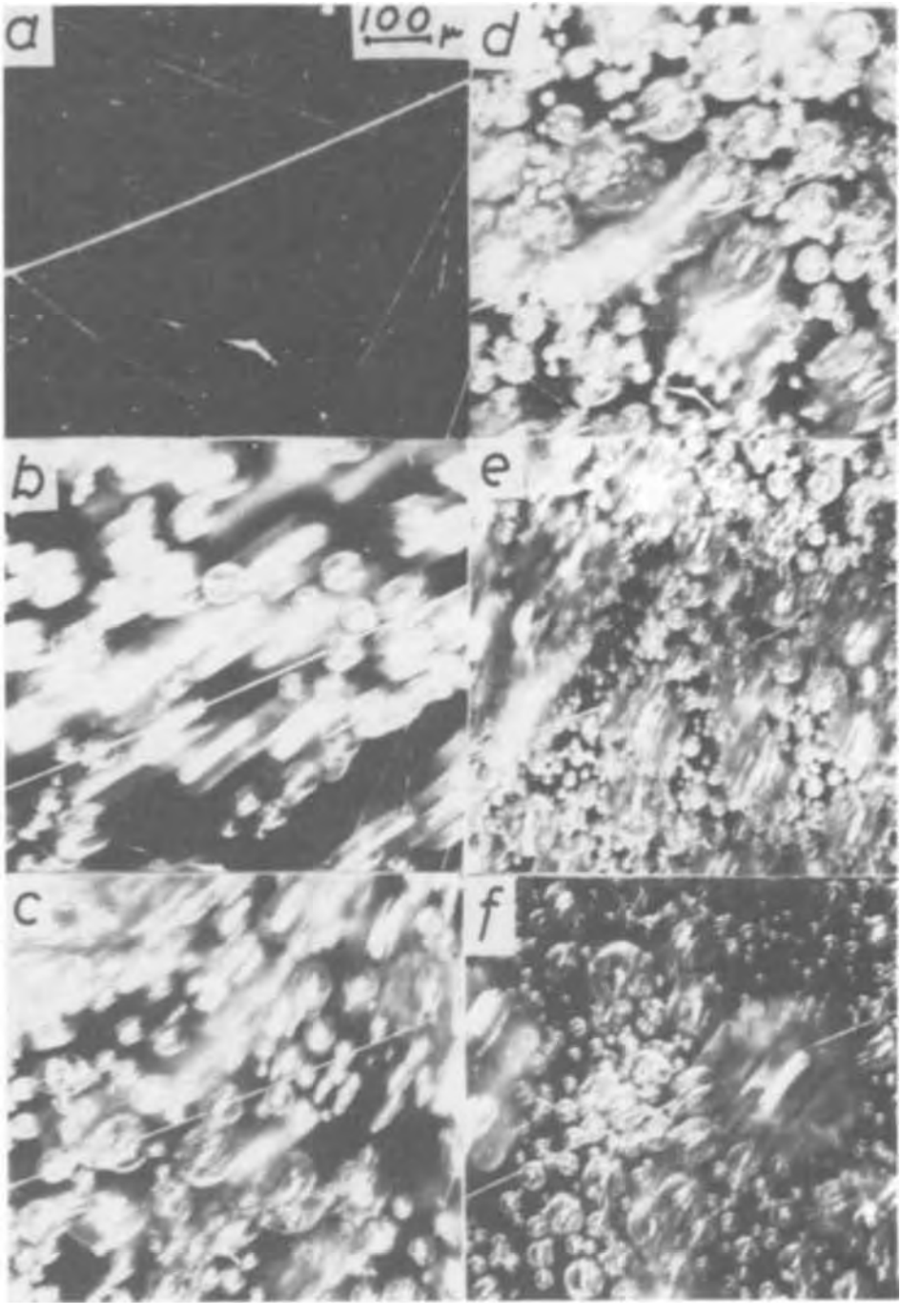

Fig. 3A. Photomicrographs of the cathode surface polarized with a constant C.D. of 0.440 A/cm^2. Original magnification X100. Dark field illumination. Exposures a-c 1/125 sec, d-f 1/250 sec. a, Immersion before electrolysis, time 0. Rest potential +0.950V vs. SCE. b, 1 sec; c.p. —0.360V. c, 4 min; c.p. —0.650V. d, 18 min; c.p. —0.820V. e, 29 min 10 sec; c.p. —1.010V. f, 29 min 45 sec; c.p. —1.080V.

presence of $SO_4^=$. The $SO_4^=$ ion itself does not inhibit the evolution of hydrogen and for this reason solutions of sulfuric acid are used extensively in investigations of hydrogen overvoltages on various metals (19). The presence of $SO_4^=$ in the plating bath must, therefore, induce some potential dependent conditions that are not associated with permanent changes of the surface characteristics. These conditions inhibit reversibly the visible evolution of hydrogen.

The decline of visible evolution of hydrogen observed in (f) became quite distinct 10 sec later on and is illustrated in photomicrograph (g) in Fig. 3B which is a continuation of Fig. 3A. The photomicrographs in Fig. 3B show (g) the decline in the number of gas bubbles and the increase of their size as the potential approaches the value of —1.09V, (h) continuation of the same phenomenon 10 sec later on, (i) further decrease of gassing as the deposition of chromium begins at —1.12V, (j) visual evidence of chromium deposition 15 sec later on, (k) complete cessation of gassing (white streaks are reflections of light from gas bubbles in movement), and (l) a burst of gassing along an initial crack formed in the deposit after 2 min 45 sec of plating.

The above experimental evidence demonstrates that the establishment of the chromium deposition processes is concomitant with the inhibition of gaseous hydrogen evolution. The decline of gas evolution precedes the deposition of chromium and the cause of the decline is open to speculation.

The diffusion of molecular hydrogen into the bulk of platinum is a possible cause but it seems unlikely that such a process would begin suddenly after the previous prolonged gassing during the shift of the potential from —0.6 to —1.0V. The phenomenon, which is potential dependent, is more likely to be caused by the commencement of certain electrochemical reactions that either contribute to the blocking of the bubble generating processes or change the conditions in the liquid layer adjoining the cathode surface. The discharge of hydrogen ion over the entire cathode during chromium deposition is not considered impeded because it

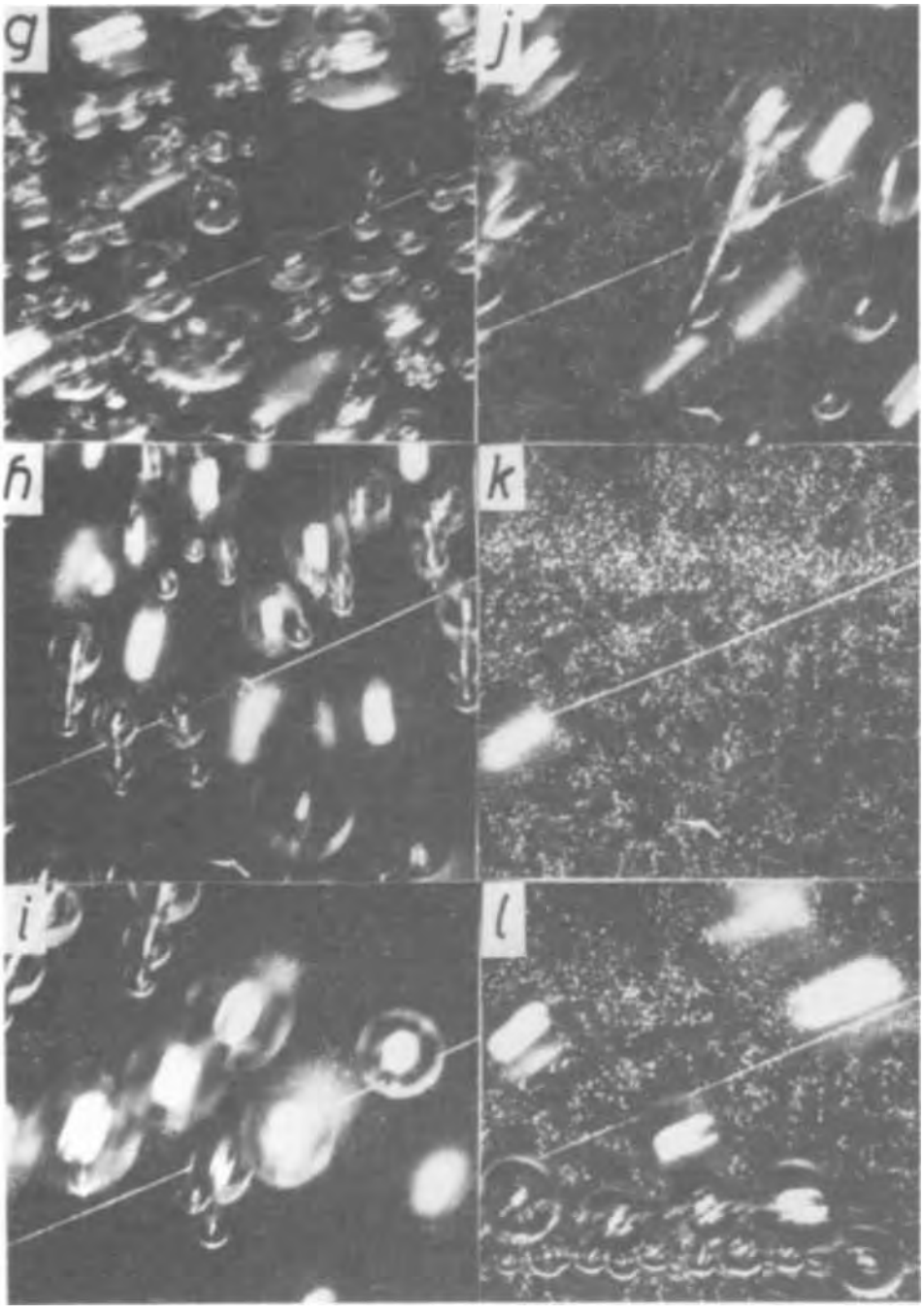

Fig. 3B. Continuation of Fig. 3A. Exposure 1/250 sec. g, 29 min 55 sec; c.p. —1.090V. h, 30 min 5 sec; c.p. —1.100V. i, 30 min 15 sec; c.p. —1.120V j, 30 min 30 sec; c.p. —1.120V. k, 32 min; c.p. —1.120V. l, 33 min; c.p. —1.120V.

was shown by many investigators (27-29) that Cr plating is only 15-20% efficient owing to the evolution of hydrogen.

A detailed study of cumulative current efficiencies by Griffin (29) has shown that in a conventional plating bath at 45°C and at a C.D. of 200 mA/cm^2 the current efficiency distribution for the processes $2H^+ \rightarrow H_2$, $Cr^{6+} \rightarrow Cr^3$, and $Cr^{6+} \rightarrow Cr^0$ is about 60, 30, and 10%, respectively. In similar studies by Solov'eva and Petrova (28) at 40°C and at a nominal C.D. of 250 mA/cm^2 the current distribution for the above reactions was found 65, 15, and 20%, respectively. In the absence of $SO_4^=$, virtually all the current was consumed for the liberation of hydrogen at about 100% current efficiency. When $SO_4^=$ was added gradually up to the concentration level of the conventional plating bath, the reactions $Cr^{6+} \rightarrow Cr^{3+}$ and $Cr^{6+} \rightarrow Cr^0$ gradually increased in terms of the current consumption while $2H^+ \rightarrow H_2$ dropped steeply to the level quoted above.

It must be pointed out that in the above investigations large cathode areas were used for prolonged periods of electrolysis, thus providing average data.

Jones and Saiddington (30) have shown that practically all visible hydrogen evolution occurs at cracks which do not form continuously but in a periodic manner in a small restricted area of about 1 mm diameter. The crack formation is preceded by a period of quiescence. The period of quiescence, it is shown in the present work, precedes the formation of the first crack and begins at potentials associated with the end of the region I and with the beginning of the region II.

Photomicrograph (k) in Fig. 3B shows that the deposition of chromium is associated with the complete absence of gas evolution at the site under observation. The question arises, therefore, as to what processes are in progress when there is no visible gas evolution.

If we assume that hydrogen ion discharge and chromium deposition occur simultaneously at this site some of the reduced hydrogen will probably be incorporated

into the growing deposit, perhaps as hydride, thus, giving rise to high stresses which are eventually relieved by cracking. Some of it may be adsorbed in the deposit or in the cathode film, in the molecular form, until the formation of cracks begins when it is released as gas bubbles.

Alternatively one would have to assume that either no hydrogen ion discharge is taking place or that part or all of the discharged hydrogen is used up for the reduction of chromic acid to metal and to trivalent chromium. In the absence of more direct evidence all explanations on the cessation of gas evolution must necessarily remain speculative, although the first alternative is here considered more probable than the others.

The formation of a crack is a macro event that disrupts locally the progress of the electrochemical processes. The molecular hydrogen is released along the exposed ridges (see Fig. 3B), until the crack is bridged over (30). The evolution of hydrogen along the crack lines induces higher pH values and, hence, more favorable conditions for the precipitation of hydrated chromic oxide which is trapped inside the cracks as they are bridged over (31). The existence of the chromic oxide inside the cracks was demonstrated by Cohen (32) who stripped electrolytically the deposited chromium and analyzed the remaining network of isolated inclusions.

Higher current densities are expected to produce higher pH conditions at the cathode surface and, thus, a more favorable environment for the formation of the chromic oxide film. This contention has been borne out experimentally at a current density of 0.660 A/cm^2 as is evident from the photographic record in Fig. 4 that corresponds to curve 3, Fig. 1b. The individual photomicrographs in Fig. 4 show (a) the appearance of the surface immersed in the bath before electrolysis, (b) gassing in the 30th second at −0.61V, (c) hydrogen evolution in the 15th minute at −1.00V, (d) heavy gassing associated with the formation of a chromic oxide film at −1.01V, (e) the presence of a visible solid chromic oxide film at −1.035V, (f) transient gas-

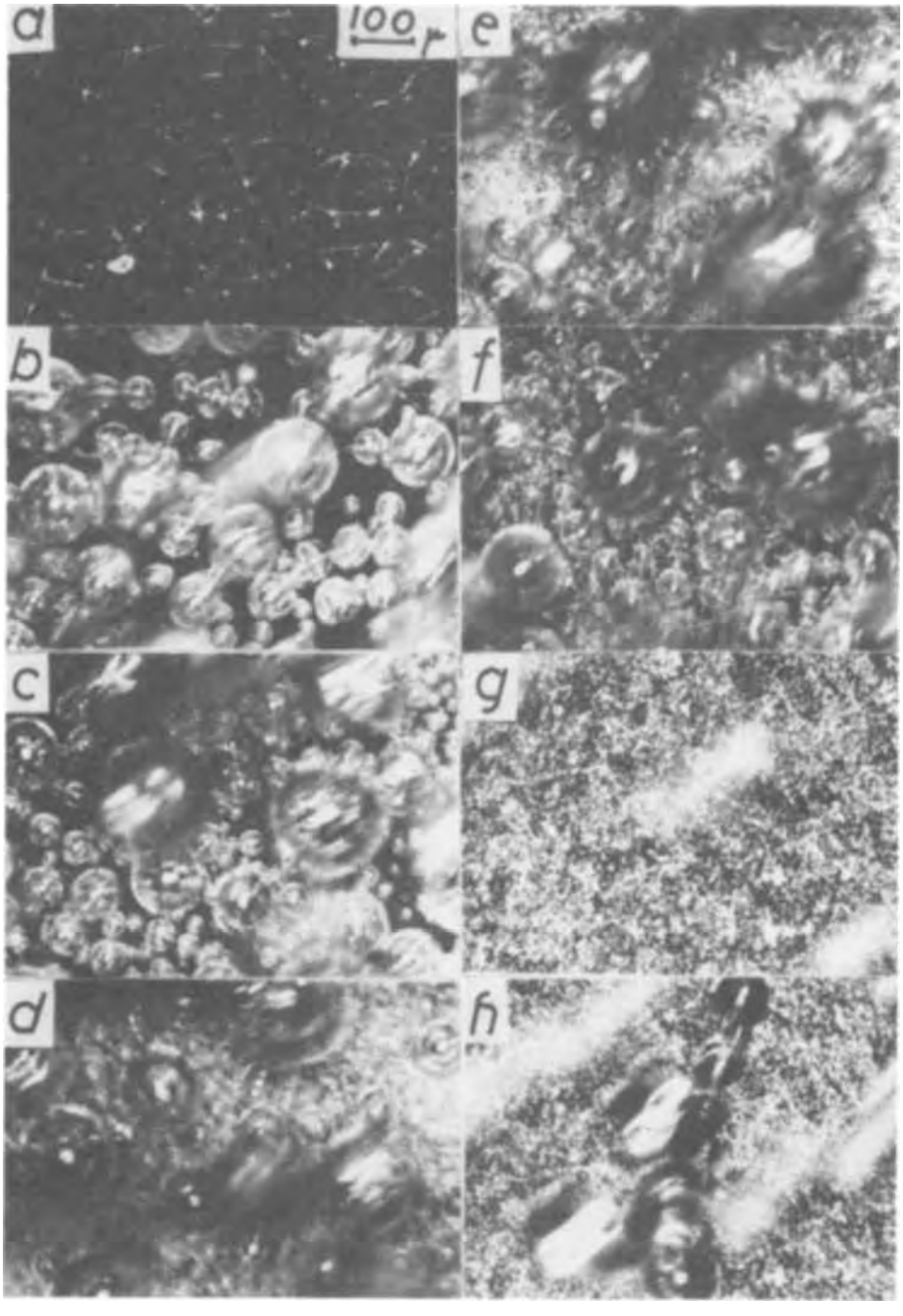

Fig. 4. Photomicrographs of the cathodes surface polarized with a constant C.D. of 0.660 A/cm^2. Original magnifications X100. Dark field illumination. Exposures 1/125 sec. a, Immersion before electrolysis, time 0. Rest potential +0.950V vs. SCE. b, 30 sec; c.p. −0.610V. c, 14 min 55 sec; c.p. −1.00V. d, 15 min 55 sec; c.p. −1.010V. e, 16 min 20 sec; c.p. −1.035V. f, 16 min 50 sec; c.p. −1.065V. g, 17 min 25 sec; c.p. −1.150V. h, 18 min 30 sec; c.p. −1.150V.

sing after the break-up of the chromic oxide film during potential shift from −1.035 to −1.065V, (g) complete absence of surface gassing during chromium plating at −1.150V, and (h) formation of a first crack and the accompanying gas evolution.

Photomicrographs (b) to (d) show an increase of gassing with the increase of potential in region I. This gassing appears more intense than the one observed in Fig. 3A, a phenomenon not unexpected in view of the higher current density employed. The peak of gas evolution is seen in photomicrograph (d). From this level onward, the gassing continued to decline as the potential shifted to more negative values (region II). This decrease of gassing permitted one to observe quite clearly the presence of a solid chromic oxide film in (e). The chromic oxide film might have formed earlier but its presence cannot be detected in (d) because of the intense gas evolution. With the shift of the potential from −1.035 to −1.065V the chromic oxide film disintegrated rapidly and its absence is self-evident in (f). Residual gassing eventually ceased completely by the time chromium deposition potential of −1.15V was reached when photomicrograph (g) was taken. The first crack [Fig. 4 (h)] formed after about 1½ min of chromium plating at steady-state conditions.

The formation of a visible chromic oxide film was observed only at higher current densities. Hence the effect of higher pH and perhaps higher Cr^{3+} concentration in the diffusion layer on such a process is indicated. Susumu Igawa (33) who investigated the composition of such films with various techniques came to a conclusion that a general formula of the chromic oxide film is (CrO_3) $(Cr_2O_3) \cdot 10H_2O$ representing a hydrated chromic oxide with adsorbed chromic anhydride.

It should be noted that the formation of the chromic oxide film had no apparent effect on the progress of gassing decline during region II, on chromium deposition at steady-state conditions, and on the initiation of crack formation. This attests to the incidental nature of such a film and to its irrelevance in the transient processes that lead to the establishment of chromium plating processes.

The disintegration of the chromic oxide film occurred before commencement of chromium deposition as is evident in Fig. 4. The hypothesis of Okada and Yamamoto (5) about thickening of the film during transition in region II is thus contradicted.

The formation and break-up of the chromic oxide film was also observed visually at the highest current density examined (1.320 A/cm²). Turbulent conditions of electrolysis did not permit, however, successful photomicrography and detailed analysis of the visual observations could not be made.

Summary

The experimental results show that the transient processes in region I associated with the evolution of hydrogen prior to the deposition of chromium on platinum are extensively protracted in comparison with those on an Fe substrate. The observation can be explained plausibly by low overvoltage characteristics of Pt. The actual shift of potential with time during region I depends on the progress of processes that inhibit the evolution of hydrogen, which is the main current carrying reaction. These processes are affected by the conditions of the cathode surface and are accelerated at higher current densities.

The chromic oxide film that forms on Pt in region I disintegrates before the deposition of chromium begins just as it does on Fe. This evidence confirms the earlier findings made with Fe cathodes and contradicts the hypothesis of Okada and Yamamoto (5) about the increase of hydrogen overvoltage with the thickening of the chromic oxide film during potential shift in region II.

The transient processes associated with the shift of the potential in region II do not appear to be significantly affected by the conditions of the cathode surface nor by the overvoltage characteristics of the metal substrate.

The shift of potential in region II is unambiguously associated with a rapid decline of gas evolution prior to the commencement of chromium deposition. The decline of gas evolution and the simultaneous increase of the polarization are not affected by the prior formation of a solid chromic oxide film; they are assumed to be caused by some not yet determined transformations in the liquid layer adjoining the cathode surface that apparently involve the formation of a liquid cathode film.

Microscopic observations show that the initial deposition of chromium is accompanied by a complete cessation of the visible gas evolution in the area under examination. No conclusions can be made on the basis of this observation whether the discharge of the hydrogen ion ceases at this stage of electrolysis. Other evidence indicates that hydrogen enters the deposit and the substrate from which it can be expelled on heating (34). The current efficiency studies (28, 29) made with large cathodes during prolonged periods of electrolysis give average data that do not necessarily apply to the small areas examined in the present work. These average data show that up to 65% of the total current is consumed for hydrogen gas evolution. Such a high rate strongly suggests that the discharge of hydrogen ion is in progress throughout the electrolysis and that only the local gas evolution process is temporarily affected. Final conclusions cannot be reached, however, until detailed determinations of current efficiencies in the small surface areas affected are made.

Manuscript submitted Oct. 30, 1972; revised manuscript received June 19, 1973. This was Paper 197 presented at the Miami Beach, Florida, Meeting of the Society, Oct. 8-13, 1972.

Any discussion of this paper will appear in a Discussion Section to be published in the June 1974 JOURNAL.

REFERENCES

1. J. C. Saiddington and G. R. Hoey, *This Journal*, **117**, 1011 (1970).
2. A. T. Vagramyan and Z. A. Solov'eva, Article on the Theory of Chromium Electrodeposition, Translation of "Itogi Nanki: Khimiya" (1966). Dept of Commerce and the Natl. Science Foundation, Washington, D.C., p. 123.
3. Z. A. Solov'eva, Yu. S. Petrova, N. L. Klimasenko, and A. T. Vagramyan, *Zh. Priklad. Khim.*, **35**, 1806 (1962).
4. R. Weiner and C. Schiele, *Z. Physik. Chem. N.F.*, **26**, 248 (1960).
5. H. Okada and K. Yamamoto, *Electrochem. Technol.*, **6**, 389 (1968).
6. M. W. Breiter, *J. Electroanal. Chem.*, **8**, 230 (1964).
7. M. Breiter, C. A. Knorr, and W. Völkl, *Z. Elektrochem.*, **59**, 681 (1955).
8. M. W. Breiter, *Electrochim. Acta*, **11**, 905 (1966).
9. A. C. Makrides and M. T. Colthorp, *This Journal*, **107**, 472 (1960).
10. S. D. James, *ibid.*, **114**, 1113 (1967).
11. D. Reinkowski and C. A. Knorr, *Z. Elektrochem.*, **58**, 709 (1954).
12. E. Müller, *ibid.*, **43**, 361 (1937).
13. E. Liebreich, *ibid.*, **27**, 94 (1921); **29**, 208 (1923).
14. R. Weiner, *Metalloberfläche*, **14**, 7, 69, 357 (1960).
15. M. A. Shluger and V. A. Kazakov, *Zh. Priklad. Khim.*, **33**, 644 (1960).
16. E. Müller, *Z. Elektrochem.*, **50**, 172 (1944).
17. M. Käppel and H. Gerischer, *ibid.*, **64**, 235 (1960).
18. H. Okada, K. Nakamura, and I. Ishida, *Nature*, **185**, 377 (1960).
19. B. E. Conway, "Electrochemical Data," p. 335, Elsevier Publishing Co., New York (1952).
20. G. Milazzo, "Electrochemistry," p. 230, Elsevier Publishing Co., New York (1963).
21. W. M. Latimer, "Oxidation Potentials," 2nd ed., p. 33, Prentice Hall, New York (1952).
22. S. Schuldiner, *This Journal*, **99**, 488 (1952).

23. R. Weiner, *Z. Electrochem.*, **42**, 377 (1936).
24. J. P. Hoare and S. Schuldiner, *This Journal*, **103**, 237 (1956).
25. E. Gileadi, M. A. Fullenwider, and J. O'M. Bockris, *ibid.*, **113**, 926 (1966).
26. J. P. Glass and J. W. Westwater, *Intern. J. Heat Mass Transfer*, **7**, 1427 (1964).
27. R. Bilfinger, *Metallwaren-Ind. Galvano-Tech.*, **43**, 3 (1945).
28. Z. A. Solov'eva and Yu. S. Petrova, *Zh. Priklad. Khim.*, **34**, 1752 (1961).
29. J. L. Griffin, *Plating*, **53**, 196 (1966).
30. M. H. Jones and J. C. Saiddington, *Tech. Proc. Am. Electroplaters' Soc.*, **48**, 32 (1961).
31. M. H. Jones, M. G. Kenez, and J. C. Saiddington, *Plating*, **52**, 39 (1965).
32. J. B. Cohen, *Trans. Electrochem. Soc.*, **86**, 441 (1944).
33. Susumu Igawa, *Kinzoku Hyomen Gijutsu*, **22**, (3) 117 (1971); *C.A.* **75**, 93893e (1971).
34. C. Levy and G. A. Consolazio, *This Journal*, **103**, 624 (1956).

A Study of Contamination on Electroplated Gold, Copper, Platinum, and Palladium

D. L. Malm and M. J. Vasile

Bell Laboratories, Murray Hill, New Jersey 07974

ABSTRACT

Electroplated gold, copper, palladium, and platinum have been examined for surface and bulk impurities using spark source mass spectrometry and ion scattering spectrometry. Electroplated metals were found to have more contamination on their surfaces than cast metals after the same cleaning procedures. Methods such as rinsing in distilled, deionized water or ultrasonic cleaning in trichloroethylene did little to remove surface impurities from electroplates. A mild etch followed by a distilled, deionized water rinse was found to be the most effective method for cleaning the surfaces, with the exception of the platinum electroplate. Bulk impurities indicative of plating bath contamination were found in many instances.

The use of electroplated metals as connector and contact surfaces within the electronics and communications industries is extensive. Little information is available concerning the nature or extent of the impurities on the surfaces of electroplates and the effectiveness of cleaning procedures used to remove them. A variety of techniques has been applied to the determination of the bulk impurities codeposited with hard gold electroplates (1-4) and their effects on vacuum arcs (5). During the course of the mass-spectrometric study on electroplated gold (5), it became apparent that electroplated surfaces were considerably more contaminated than other surfaces of corresponding cast specimens, even though in one case (soft electroplated gold) the bulk purity level was comparable to that of cast gold. This study was undertaken to extend the spark source mass spectrometric determinations to the detection of surface impurities on electroplated copper, platinum, and palladium. Each of these materials was also examined for bulk impurities.

The spark source mass spectrometer can be used to examine the surface impurities present on a given sample (6) with a high degree of sensitivity. However, its sampling depth resolution is only about 6000Å (5). To obtain a more detailed picture, ion scattering spectrometry (7) was also used in this study to investigate the changes in impurity concentrations with depth in some of the systems.

Experimental

A commercially available[1] RF spark source mass spectrometer with photoplate detection was used. The electroplates were deposited on 0.125 cm diameter OFHC copper rods. The rods were tapered with rounded ends to minimize shielding of the ions from the first accelerating plate of the mass spectrometer. The arc conditions were chosen such that each spectrum was obtained without over exposing any of the lines on the photoplate. Total ion exposure measured with the beam monitor was of the order of 10^{-11} coulombs.

The sampling procedure used for surface analysis was to record spectra from at least ten points on the electrodes. The electrodes were manipulated so that a fresh area on each of the members was subjected to the arc. Bulk analyses were performed by presparking a given area (5) and following this with five successive arcing events on the presparked region. The arithmetic means and standard deviations of the ion intensities were computed for all the ions recorded in the surface and bulk analyses. No corrections were applied for line width, ionization efficiency, or relative volatility of the ions observed; however, the response of the photoplate was corrected for the masses of the singly charged ions and the kinetic energies of the doubly charged ions. The results are expressed as ion per cent by first computing the total exposure for all ions and then taking the percentage of the total for each ionic species in the spectrum (5).

Ion scattering studies were performed on a commercially available ion scattering spectrometer.[2] Singly charged helium ions, accelerated to 1.5 kV were used as a primary beam. The ion beam profile was measured and found to be 0.7 mm, full width at half maximum intensity and 1.4 mm, full width at 10% maximum intensity. The corresponding current densities are 23 $\mu A/cm^2$ and 6.5 $\mu A/cm^2$, respectively. Ion scattering analyses were confined to gold- and platinum-plated specimens on planar substrates.

Electroplating of the substrate was done in a manner that maximized the plating efficiency of each of the systems. The electroplates were deposited to a thickness of approximately 0.0025 cm. A thin deposit of soft gold was plated on the copper rods prior to plating from acidic baths. Clean glass cells and platinum anodes were used in each plating operation. The plated samples were rinsed with distilled water after plating,

Key words: electroplating, surface contamination, ion scattering spectrometry, spark source mass spectrometry.

[1] MS-7, manufactured by AEI Ltd., Manchester, United Kingdom.

[2] ISS Model 520, 3M Company, St. Paul, Minnesota.

dried, and kept in glass containers prior to analysis. No special precautions were taken to purify or modify the plating baths, since one of the objects of this study was to determine the impurities that remain on the electroplated surfaces under normal circumstances. The compositions of the plating baths are given in Table I. (The exact compositions of some of these baths are proprietary to their manufacturers, so only information relevant to this study is given.)

To determine if cleaning methods have any effect on the type and amount of surface impurities, three different treatment were used: (*i*) ultrasonic cleaning in trichloroethylene, (*ii*) 10 min rinsing in deionized, distilled water, and (*iii*) etching in an appropriate acid for about 15 sec, followed by a rinse in distilled deionized water.

Etchants used for each system are given in Table I. The samples were dried by infrared heating in a laminar flow hood and mounted in the mass spectrometer ion source for analysis. High-purity control specimens of the same metal in cast form were treated and analyzed under identical conditions.

Results and Discussion

Surface analyses by spark source mass spectrometry sample only a small fraction of the total surface area. Surface contamination is frequently nonuniformly distributed; hence, a particular impurity may show a weak response at one location and a very much more intense response at another. As a consequence, the standard deviation of the ion percentage of a surface impurity is usually large. The ratio of the standard deviation to the ion percentage for many surface impurities ranges between about 0.75 and 1.5, while for bulk impurities, this ratio rarely exceeds 0.3. Bulk impurities usually exhibit no change in response between surface and bulk sampling.

Tables II through VI contain the results of the mass spectrometric analyses of electroplates and cast specimens. The water wash and bulk analyses for cast specimens are not listed, since the water-wash results do not differ significantly from those of solvent cleaning, and the bulk analyses showed no impurities.

The surface analyses of electroplated and cast (OFHC) copper are given in Table II. Cleaning the surface by water rinsing or ultrasonic solvent treatment had very little effect in removing surface impurities. Etching the surface removed all the surface impurities except carbon and oxygen, which result from adsorbed hydrocarbons and oxygen or water. It is of interest to note that the carbon concentration dropped by a factor of two with the etch treatment,

Table I. Electroplate bath descriptions and etchants for cleaning

Copper
Copper cyanide, potassium cyanide, potassium carbonate, potassium sodium tartrate.
pH 12.2-12.8.
Temperature 55°-66°C.
Dilute nitric acid, room temperature.

Palladium
Palladium diamino dinitrite, ammonium sulfate, ammonium hydroxide.
pH 7.5-8.5.
Temperature 27°-33°C.
Aqua regia, room temperature.

Platinum
Platinum ammonium chloride, hydrochloric acid.
pH 0.5-1.5.
Temperature 49°-60°C.
Aqua regia, room temperature.

Hard gold
Potassium gold cyanide, potassium citrate, cobalt citrate.
pH 3.3-3.9.
Temperature, ambient.
Aqua regia, room temperature.

Soft gold
Potassium gold cyanide, ammonium citrate.
pH 5.0-5.5.
Temperature 60°-65°C.
Aqua regia, room temperature.

Table II. Copper

(Relative ion per cent by SSMS)

	Electroplate				Cast (OFHC)	
	Water	Solvent	Etch	Bulk	Solvent	Etch
Cu	75.5	73.3	87.1	100	79.0	98.2
Cl	2.2	3.3	—	—	—	—
S	2.6	2.5	—	—	—	—
K	0.7	—	—	—	—	—
Si	0.7	0.4	—	—	—	—
Al	0.4	0.2	—	—	—	—
Mg	—	0.2	—	—	—	—
Na	—	0.4	—	—	—	—
O	5.4	6.4	7.3	—	7.8	0.7
N	0.6	0.6	—	—	1.0	—
C	12.0	12.7	5.6	—	11.7	1.2

while the oxygen concentration remained unchanged within the precision of the measurements. Some of the surface impurities such as Al, Mg, Cl, and S cannot be correlated with the nominal composition of the plating bath (see Table I). The distilled, deionized water treatment cannot be responsible for these impurities since it is also the last step in the etch treatment, and in that case they were absent. Plating bath contamination, airborne contamination, and sample handling are the most obvious sources of these contaminants. The bulk purity of copper electroplates was found to be quite high, with no measured impurity levels in the mass spectrum at as much as 0.1 ion per cent, which corresponds to an estimated purity of 1 part in 10^4 in the plate. The specimen of OFHC copper showed impurities due to adsorbed atmospheric gases and organics after solvent cleaning. Etching this sample reduced the concentrations of carbon and oxygen by an order of magnitude, and the surface analysis for the etched OFHC sample is probably indicative of the contamination level that can be expected from the adsorption of residual gases in the mass spectrometer.

Palladium electroplate (Table III) showed somewhat cleaner surfaces than copper, with only chlorine and copper as surface impurities which do not correlate with the bath composition. The water washing was somewhat more efficient at removing surface impurities from Pd than solvent cleaning. A mild etching of the surface removed all but atmospheric gases. The presence of nitrogen and oxygen in the bulk of the electroplate at effectively the same levels as the surface is a strong indication that some of the diamino dinitrite complex is being codeposited with palladium. If these were surface impurities, a considerable decrease in their intensity would be expected upon presparking. There was a small response for carbon in the bulk which is an order of magnitude less intense than on the surface. This could arise from the vaporization of surface adsorbed species at the periphery of the arc, but this effect would not account for the constant response for oxygen and nitrogen in surface and bulk sampling. The ratio of the standard deviations for the oxygen and nitrogen responses to the average responses for each of these elements was small (0.13-0.23), which is a further indication that they are bulk impurities. The analysis of cast palladium showed a considerably cleaner surface than its electroplated counterparts, with the most significant reduction occurring in the response for carbon.

Table III. Palladium

(Relative ion per cent by SSMS)

	Electroplate				Cast	
	Water	Solvent	Etch	Bulk	Solvent	Etch
Pb	85.7	86.0	87.7	95.8	97.2	97.2
Cu	—	1.1	—	—	—	—
Cl	—	0.8	—	—	—	—
S	1.4	4.1	—	—	—	0.9
O	2.9	3.0	1.8	1.3	0.6	0.6
N	2.8	2.4	1.5	2.2	0.3	—
C	7.2	6.9	9.1	0.7	1.5	1.3

Platinum electroplate (Table IV) exhibited a wide variety of surface impurities, none of which could be removed by the cleaning treatments used. The 15 sec etch did not yield any improvement over the solvent wash and only a small improvement over the water washing. Extending the duration of the etching to 30 and 60 sec again resulted in no significant improvement. Etching the specimen in aqua regia could have contaminated the surface with copper from the attack of the unplated end of the rod, and some chlorine might also well have remained on the surface.

At least four of the surface contaminants remaining after the etch treatments (viz., Fe, O, N, and C) persisted as bulk impurities in each of the tests. Sporadic low level responses were found for sulfur and aluminum in the bulk probing, and it is likely that the presence of the former is due to peripheral surface contributions. There are apparently two sources of contamination of the platinum electroplate: the plating bath and the etching procedure itself. The latter possibility produces a paradox, since the same procedure on a bulk platinum specimen yielded an extremely clean surface.

Table V contains the data obtained for surface analyses of cobalt-hardened gold, which is known to be heavily contaminated in the bulk with a polymeric material containing carbon, hydrogen, and nitrogen. This polymer is believed to be nonuniformly dispersed (8) below the surface of the electroplate, so etching or presparking should not reduce the response for carbon and nitrogen. Solvent cleaning produced the best results for the hard gold electroplates, but the contribution from bulk impurities is so extensive that comparisons of the cleaning procedures cannot be made.

Surface contamination of soft gold electroplates was also examined, since in this case it is known that the bulk impurity level is very low (3). Table VI shows that both solvent cleaned and etched soft gold surfaces are heavily contaminated with organic material and/or atmospheric gases. Comparison of the soft gold electroplate surface contamination with that of copper electroplates which has high bulk purity shows that the gold surface is more heavily contaminated. Similarly, the surface of the cast gold specimen was more contaminated than the surfaces of cast copper, platinum, or palladium. A high degree of very tenaciously held organic contamination on gold surfaces is in accord with the results of Schrader (9) and Bernett and Zisman (10). These authors found that a gold surface could be wet (zero contact angle) only if extreme precautions were taken to eliminate the possibility of organic contamination.

Ion scattering studies on hard gold electroplate indicated that the carbon-containing impurities are not uniformly dispersed either over the surface or in the bulk of the electroplate. The results of ^4He scattering from the surface of a cobalt-hardened gold are shown in Fig. 1. The diffuse scattering between relative energies of 0.3 and 0.5, which can be adequately explained by sequential double scattering from carbon and hydrogen atoms (11), dropped rapidly as about 20 monolayers were removed with a corresponding increase in the count rate for ions scattered from gold. The number of monolayers removed was computed using an average sputtering rate of 30 monolayers per hour (12) and is only an approximation. The results shown in Fig. 1 also indicate that in this particular instance, the organic surface impurity is not related to the codeposited bulk polymer, since it was removed rather easily by ion bombardment. In contrast to the removal of surface hydrocarbons, Fig. 2 shows that the ion scattering response for cobalt and potassium increased with depth of sampling. The mass spectrometric work also showed that potassium was a bulk impurity in most types of hard gold electroplates.

A sample of nickel-hardened gold electroplate gave opposite results, in that at one location the diffuse

Table IV. Platinum

(Relative ion per cent by SSMS)

	Electroplate				Cast	
	Water	Solvent	Etch	Bulk	Solvent	Etch
Pt	60.5	79.0	73.4	80.4	80.3	98.1
Cu	2.3	2.3	4.0	—	—	—
Fe	2.2	2.6	1.8	5.8	—	—
Cl	1.3	1.7	1.3	—	0.8	—
Si	1.4	0.6	2.0	—	0.4	—
S	5.2	2.5	1.7	0.6	0.9	—
Al	—	—	—	1.9	2.0	—
O	9.3	3.6	4.7	5.6	3.9	0.6
N	4.7	1.9	2.4	2.2	1.2	—
C	15.9	5.9	8.7	3.5	10.6	1.3

Table V. Gold

(Relative ion per cent by SSMS)

	Hard electroplate				Cast	
	Water	Solvent	Etch	Bulk	Solvent	Etch
Au	29.7	61.5	35.0	48.4	68.5	88.4
Co	4.2	3.6	4.0	6.1	2.5	—
K	7.1	4.1	12.0	5.9	0.6	—
Cl	1.2	—	—	—	3.8	—
S	2.9	—	4.4	—	0.3	—
O	1.9	2.3	2.2	1.7	5.0	1.8
N	11.1	7.6	13.8	14.0	2.3	—
C	41.8	21.0	28.6	23.5	16.9	8.2

Table VI. Gold

(Relative ion per cent by SSMS)

	Soft electroplate		
	Solvent	Etch	Bulk
Au	50.6	69.5	100
K	3.2	—	—
O	12.2	5.2	—
N	3.6	2.6	—
C	30.7	22.5	—

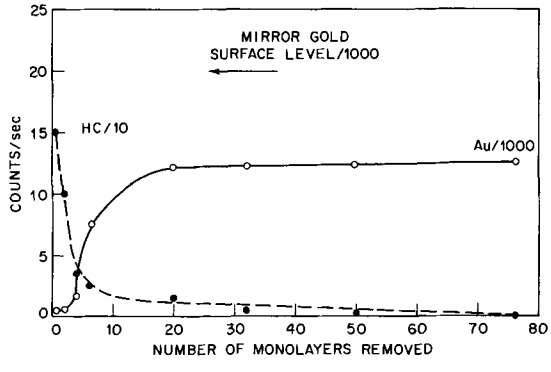

Fig. 1. ^4He ion scattering from hydrocarbons and gold on a cobalt-hardened gold electroplate as a function of the number of monolayers removed.

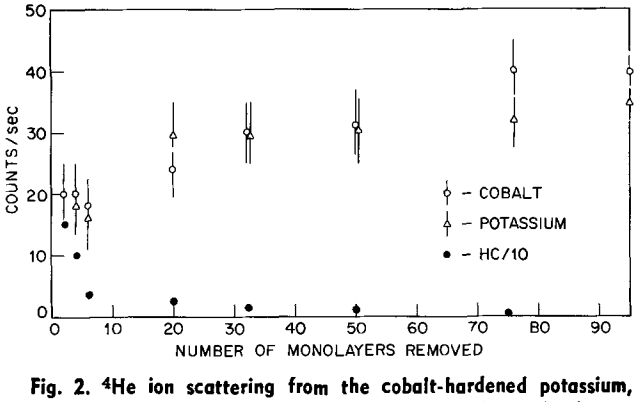

Fig. 2. ^4He ion scattering from the cobalt-hardened potassium, and surface hydrocarbons (cobalt-hardened gold electroplate).

scattering due to organic impurities intensified and then remained constant with sampling depth. At a different location on the same sample, no hydrocarbon response could be obtained after penetration to a depth of about 400 monolayers.

A sample of electroplated platinum was also examined by ion scattering, since the mass spectrometer consistently showed iron and the light elements carbon, nitrogen, and oxygen as bulk impurities. The presence of the light elements was confirmed to at least 120 monolayers, as can be seen in Fig. 3. The signal from ions scattered by platinum steadily decreased, while that due to scattering from oxygen increased. The diffuse scattering attributed to the carbon-containing species also increased with sampling depth. Iron in the bulk or on the surface of this sample could not be detected by ion scattering.

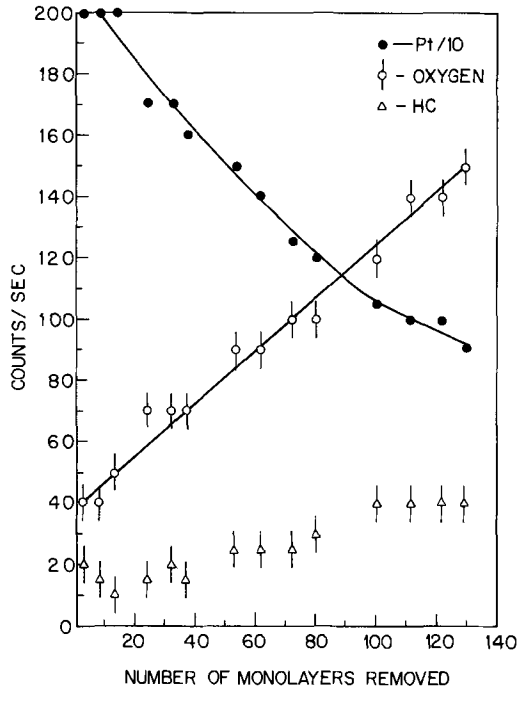

Fig. 3. ^4He ion scattering signals from platinum electroplate as a function of the number of monolayers removed.

The results presented in this study are indicative of the types of impurities that are present on the surface and in the bulk of electroplates. The plating was carried out under laboratory conditions, but the prior uses of the plating baths are not documented. One consistent result that appears in each of the systems studied is the higher level of surface contamination of electroplates relative to cast specimens. This may be due to a higher surface free energy of the electroplate coupled with an immediate supply of adsorbants. The incorporation of bulk impurities is also apparently not limited to hard gold plates.

It is unfortunate that quantitative data on surface coverage cannot be obtained from either of the techniques employed in his study without extensive calibration. It is appropriate to menion, however, that ions of elements with low ionization potentials will appear in the mass spectra at relative concentrations very much higher than their atomic ratios in the matrix would predict.

Acknowledgment

The authors would like to thank Mrs. I. D. Payne for reducing the mass spectrometric data and Mr. T. A. Palumbo for the electroplating of the specimens.

Manuscript submitted April 17, 1973; revised manuscript received June 19, 1973.

Any discussion of this paper will appear in a Discussion Section to be published in the June 1974 JOURNAL.

REFERENCES

1. G. B. Munier, *Plating*, **56**, 1151 (1969).
2. T. F. Egan, *Microchem. J.*, **13**, 646 (1968).
3. C. K. Kim and M. J. Vasile, *Anal. Chim. Acta*, **56**, 339 (1971).
4. L. Holt and J. Stanyer, *Trans. Inst. Metal Finishing*, **50**, 24 (1972).
5. M. J. Vasile and D. L. Malm, *Anal. Chem.*, **44**, 650 (1972).
6. D. L. Malm, "Physical Measurements and Analysis of Thin Films," E. M. Hurt and W. G. Guldner, Editors, Plenum Press, New York (1969).
7. R. F. Goff and D. P. Smith, *J. Vacuum Sci. Technol.*, **7**, 72 (1970).
8. M. Antler, Private communication.
9. M. E. Schrader, *J. Phys. Chem.*, **74**, 2313 (1970).
10. M. K. Bernett and W. A. Zisman, *ibid.*, **74**, 2309 (1970).
11. R. Honig, Private communication.
12. R. F. Goff, Private communication.

Anodic Current Efficiency and Dimensional Control in Electrochemical Machining

Der-Tau Chin* and Augustine J. Wallace, Jr.

Electrochemistry Department, Research Laboratories, General Motors Corporation, Warren, Michigan 48090

ABSTRACT

An experimental study has been made to examine the relationship between dissolution current efficiency and dimensional control during the electrochemical machining (ECM) of steel in NaCl, $NaClO_3$, and $NaNO_3$ electrolytes. The current efficiency for iron dissolution was measured in a flow cell under controlled anodic current densities ranging from 1 to 100 A/cm^2. The laboratory results were then compared to those obtained under actual ECM conditions. It is shown that the current efficiency *vs.* current density curve is a useful tool to determine optimal ECM operating conditions for achieving the best possible combination of dimensional control and surface finish.

The high quality of electrochemical machining (ECM) dimensional control obtained with $NaClO_3$ and with $NaNO_3$ has generally been attributed to the ability of these electrolytes to form a passive film on the anode. According to a polarization hypothesis (1), metal is removed most heavily from the high current

* Electrochemical Society Active Member.
Key words: electrochemical machining, transpassive dissolution, throwing power.

density region of the anode where the distance to the cathode is small and where the dissolution takes place at a potential corresponding to the transpassive state on the anodic polarization curve. On more remote areas of the anode, away from the cutting area, the distance to the cathode is larger, and the anodic process takes place at a potential corresponding to the passive state on the polarization curve. Consequently, in the latter areas, there forms a passive film which prevents further passage of the current resulting in little or no metal removal at these places. This hypothesis appears to give a logical basis for the fact that ECM dimensional control can be more easily achieved in a passivating electrolyte than in a nonpassivating electrolyte.

Recently, Landolt (2) pointed out the importance of current efficiency in ECM dimensional control. His results indicate that good dimensional control can be achieved with an ECM electrolyte if the current efficiency for metal removal is an increasing function of anodic current density. This concept can be illustrated more clearly if we consider two points on the anode surface: one point is in the high current density (hcd) region, and the other point is away from the hcd region, *i.e.*, in the low current density (lcd) region. The current density on the anode is assumed to be the highest in the hcd region directly facing the cathode, and then to decrease asymptotically to zero with increasing distance from the hcd region. If we denote i_H and i_L as the hcd and lcd anodic current densities, respectively; d_H and d_L as the distances from the cathode; ϕ_H and ϕ_L as the sums of the anodic and the cathodic overpotentials; and η_H and η_L as the current efficiencies for metal removal at the hcd and the lcd points, then

$$\begin{pmatrix}\text{rate of metal removal}\\ \text{at the hcd point}\end{pmatrix} = \frac{i_H\,\eta_H}{n\mathbf{F}} = \frac{k\,(E-\phi_H)\,\eta_H}{n\mathbf{F}\,d_H} \quad [1]$$

$$\begin{pmatrix}\text{rate of metal removal}\\ \text{at the lcd point}\end{pmatrix} = \frac{i_L\,\eta_L}{n\mathbf{F}} = \frac{k\,(E-\phi_L)\,\eta_L}{n\mathbf{F}\,d_L} \quad [2]$$

Here E is the applied cell voltage; k, the conductivity of the electrolyte; $\mathbf{F}$, the Faraday constant; and n, the number of electrons transferred for the metal dissolution reaction. The metal removal ratio can be obtained by dividing Eq. [1] by Eq. [2]. It has been shown that during ECM, the cell voltage is much larger than the sum of the overpotentials on the electrodes (2, 3). Thus as a first approximation, we may assume $E - \phi_H \simeq E - \phi_L$. This leads to

$$\text{(metal removal ratio)} = \frac{\begin{bmatrix}\text{rate of metal removal}\\ \text{at the hcd point}\end{bmatrix}}{\begin{bmatrix}\text{rate of metal removal}\\ \text{at the lcd point}\end{bmatrix}} \simeq \frac{d_L\,\eta_H}{d_H\,\eta_L} \quad [3]$$

The higher the metal removal ratio, the better is the ECM dimensional control. Therefore, Eq. [3] implies that good dimensional control can be obtained by (*i*) operating at the smallest possible electrode gap, d_H, and (*ii*) choosing an electrolyte and a current density for the hcd region which give high current efficiency ratios (η_H/η_L) over the entire anode surface.

The fact that the smaller the electrode gap the better the ECM dimensional control has been known for some time (4). The purpose of the present study was to quantitatively verify Eq. [3] with regard to the current efficiency dependence on the metal removal ratio.

The current efficiencies of the dissolution of a mild steel in NaCl, $NaClO_3$, and $NaNO_3$ electrolytes were measured in a flow cell under controlled anodic current densities ranging from 1 to 100 A/cm^2. The results were then used to predict the ECM performance of the electrolytes, and the predictions were compared with results obtained in a practical ECM test apparatus. This paper summarizes the details of these studies.

Experimental

Current efficiency measurement.—The flow cell used for the current efficiency measurements is shown schematically in Fig. 1. It consisted of two acrylic semicylindrical cell blocks, each 5.25 cm in diameter and 13.34 cm long. The first block contained a replaceable anode and a reference capillary at its center; the second block contained a copper cathode and a shallow groove which was 0.635 cm wide by 5.7 cm long. During the run, the two cell blocks were held tightly together with two toggle clamps to form a rectangular channel for electrolyte flow whose depth could be varied by inserting stainless steel spacers of various thicknesses between the blocks. In this way, the anode and the cathode were facing each other across an electrolyte gap of controlled geometry. A 0.318 cm diameter mild steel rod[1] inserted through a hole of the same diameter in block 1 was used as the anode. The cylindrical surface of the rod was insulated by the block; only the rod end with a surface area of 0.0792 cm^2 was exposed to the electrolyte. The cathode was square in shape and had a larger surface area of 0.4 cm^2 exposed to the electrolyte. A 2-liter acrylic tank equipped with a cooling coil was used as a solution reservoir. The electrolyte was circulated between the reservoir and the flow cell with a variable speed micropump. A rotameter was used to measure the rate of electrolyte flow.

For each run, the end of the mild steel rod was polished with grinding paper, rinsed in water, and dried with hot air. The electrode was weighed and installed in the flow cell. A constant current supplied by a Magna 4700 potentiostat was then applied to the cell. An Eagle Signal Flexopulse was used to control the dissolution time which varied from 120 sec at low

[1] Composition of the mild steel rod: Fe, 98.5%; C, 0.08%; S, 0.26%; P, 0.021%; Mn, 1.06%; Si, 0.004%.

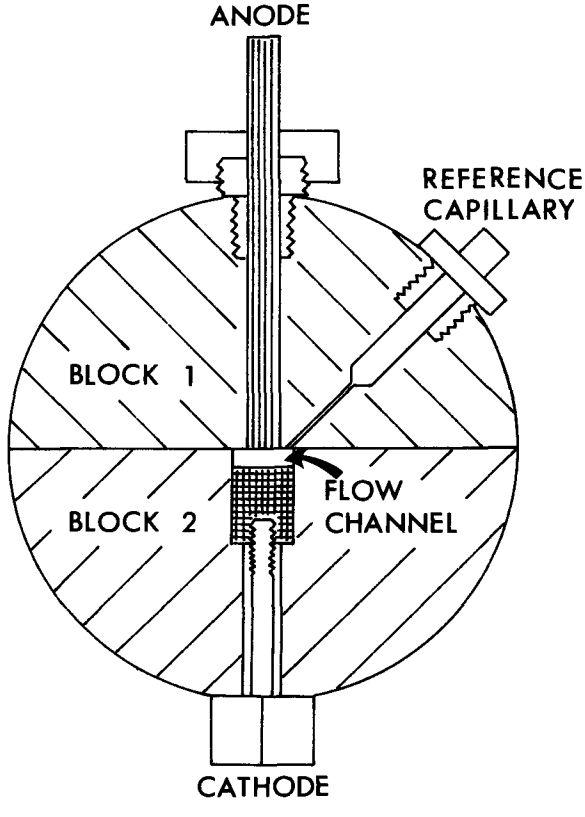

Fig. 1. Flow cell in which the direction of electrolyte flow is perpendicular to the plane of the figure.

current densities to 5 sec at 100 A/cm². After dissolution, the rod was rinsed, dried, and weighed again to determine the amount of metal removal. The current efficiency was then calculated on the basis of Fe going into the electrolyte as Fe^{++} ions. The electrolytes used were 4M NaCl, 4M $NaClO_3$, and 4M $NaNO_3$. An electrode spacing of 0.04-0.08 cm at the beginning of the run was used for the tests. The temperature of the electrolytes was maintained at 21° ± 1°C for all the runs.

ECM tests.—Two ECM tests were used to demonstrate the quality of dimensional control obtained with 4M solutions of NaCl, $NaClO_3$, and $NaNO_3$ at a temperature of 21°-25°C.

The first test was made in the same flow cell used for the current efficiency measurement with positions of the anode and the cathode reversed. The cathode was now a 0.159 cm diameter copper rod mounted in block 1, and the anode was a piece of mild steel having a much larger surface area mounted in block 2 (see Fig. 1). The ECM was carried out at a cathodic current density of 25 A/cm² with an initial electrode spacing of 0.02 cm. The rate of electrolyte flow was kept at a Reynolds number of 8000.

The second ECM test was made in an impinging jet-flow cell similar to that described in earlier studies (1, 5). The cathode was a circular copper tube, 0.440 cm ID and 0.627 cm OD with its outer cylindrical surface insulated by a vinyl coating. The anode was a flat 1008 steel panel, 7.5 cm wide × 2.5 cm long × 0.0625 cm thick, held horizontally above the tip of the cathode tube with an initial spacing of 0.05 cm. The electrolyte was introduced through the cathode tube to produce a vertical jet which impinged on the anode panel at a rate of 1.5 liter/min. In this way, the steel panel was electrochemically machined at current densities of 25 and 100 A/cm² based upon the annular cathode area. For each electrolyte, the running time was adjusted between 1 and 12 min in order to obtain 100 mg of metal removal. After ECM, the surface of the anode was examined with a topographic microscope (6) to determine the cutting profile.

Results and Discussion

Figure 2 gives the results of the current efficiency measurements in NaCl for two different electrolyte flow rates. The accompanying photomicrographs in the figure show the mild steel surface after dissolution at the various current densities. The indicated Reynolds numbers (Re) are calculated based on the equivalent diameter of the flow channel. Since the laminar flow region terminates at a Reynolds number of approximately 2000, these flow rates should both be turbulent. It is seen that the mild steel dissolves in NaCl with 100% current efficiency, independent of current density, until a critical current density is reached, whereupon the current efficiency decreases with increasing current density and then levels off at a constant value of 80%. The surface after dissolution is rough in the low current density region; however, some polishing seems to take place when the efficiency begins to drop to the lower level. Finally, at the lower constant efficiency of 80%, the surface appears to be highly polished. At this point, the surface is marked with flow streaks caused by recession of the tip of the mild steel rod into the channel wall during the dissolution process. These flow streaks imply a flow dependence for the surface finish obtained at high current densities. The effect of reducing the flow rate is to decrease the critical current density where the efficiency begins to drop, and thus to extend the current density region where polishing of the surface can be achieved.

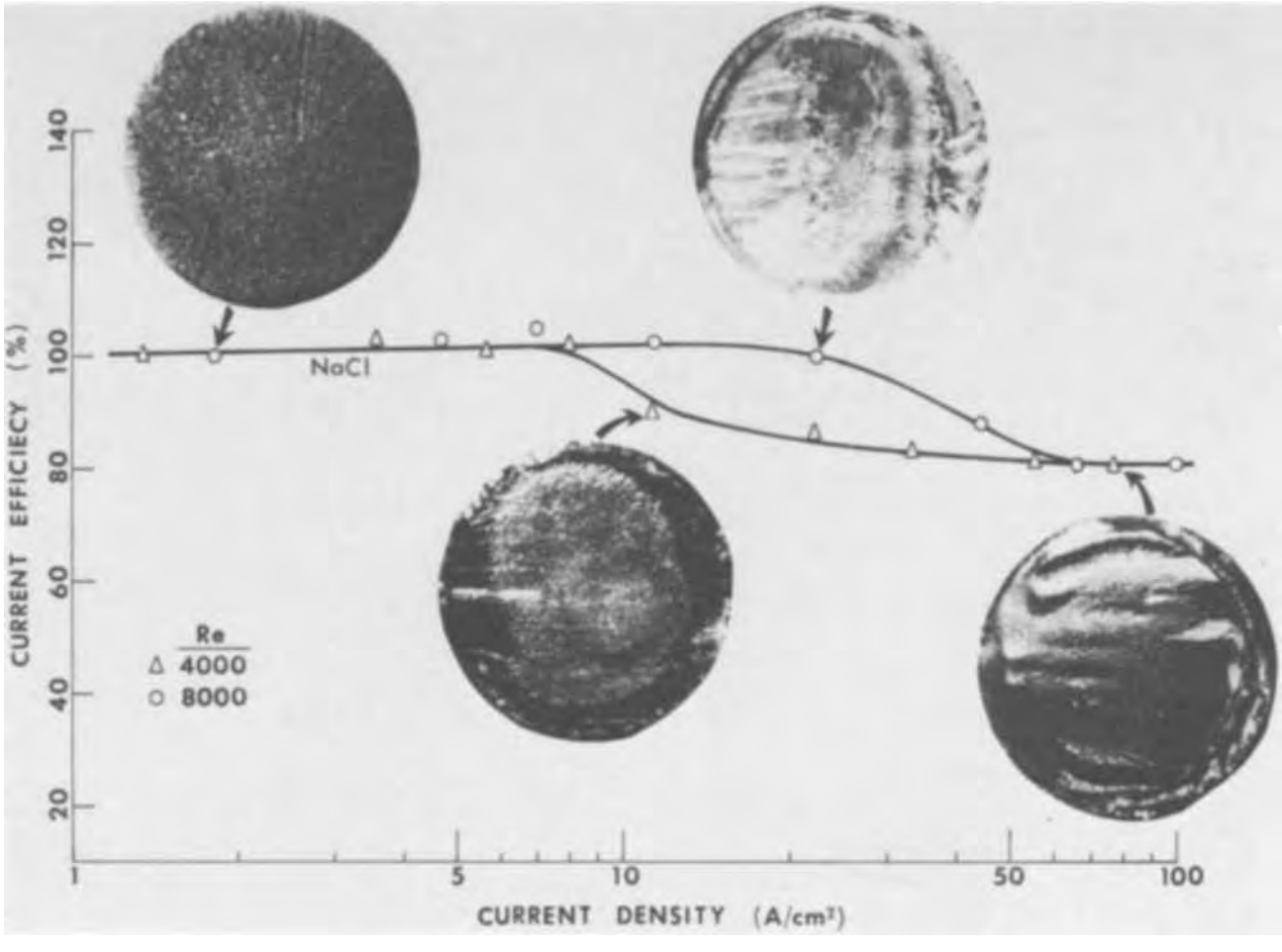

Fig. 2. Results of current efficiency measurements in NaCl electrolyte

The results of current efficiency measurements obtained in $NaClO_3$ and $NaNO_3$ electrolytes are given in Fig. 3 for two different flow rates. It is seen that both curves are an increasing function of anodic current density. In the low current density region (current densities less than 2 A/cm² for chlorate and less than 3 A/cm² for nitrate), the current efficiency is zero, and the current is presumably consumed in the generation of oxygen on the anode (7). Metal dissolution does not take place until the current density reaches a threshold value, whereupon the dissolution efficiency increases with increasing current density. The curve for $NaClO_3$ starts to level off at approximately 10 A/cm², beyond which the current efficiency becomes higher than 100%. The surface, after dissolution in $NaClO_3$, is rough for efficiencies less than 100% and polished for efficiencies of 100% or higher. Again, in the polished region, flow streaks are observed on the surface indicating the dependence of electropolishing on local flow rates over the anode. The curve for $NaNO_3$ starts to level off at a higher current density of 25 A/cm²; it never reaches 100% current efficiency within the current density region investigated. The surface obtained from $NaNO_3$ is rough throughout the entire range of 3-100 A/cm². Changes in the rate of electrolyte flow have apparently no effect on the current efficiency for current densities below the choking limit. Choking is causd by excessive gas evolution in the electrode gap resulting in the gap being filled with gas bubbles. At this point, the current efficiency drops sharply and finally, at a sufficiently high current density, electric sparking occurs across the gap resulting in excessive damage to both anode and cathode. The mechanism of choking and sparking has been studied elsewhere (8, 9) and will not be discussed further here.

The polishing phenomena observed in this study can be explained by Hoar's theory (10) that brightening of the surface is due to the presence of an ionically conductive film on the anode. The flow streaks on the polished surface suggest that, during the ECM of steel, this film is a salt layer resulting from the precipitation of anodic products on the anode surface (11). The salt layer formation requires supersaturation of the anodic products in the immediate neighborhood of the anode; it is obvious that the higher the electrolyte flow rate, the faster the products are flushed away and the lower is the possibility that the products will precipitate out on the anode surface. This notion agrees with the results shown in Fig. 2, namely, that the critical current density for electropolishing in NaCl increases with increasing flow rate. Since no oxygen was detected during the ECM of steel in NaCl (7), the drop in the current efficiency in the polishing region is probably caused by consumption of part of the current in the oxidation of a ferrous compound to a ferric compound at the metal/salt layer interface. Brightening of the mild steel surface in $NaClO_3$ can only be achieved in the current density region where the current efficiency is 100% or higher. The surface, after the dissolution, is always rough in the low current density region where there is oxygen evolution on the anode. The oxygen bubbles provide vigorous agitation in the immediate neighborhood of the anode; the anodic products, therefore, do not have a chance to form a salt layer on the anode surface. This explains why no polishing could be obtained in $NaNO_3$ electro-

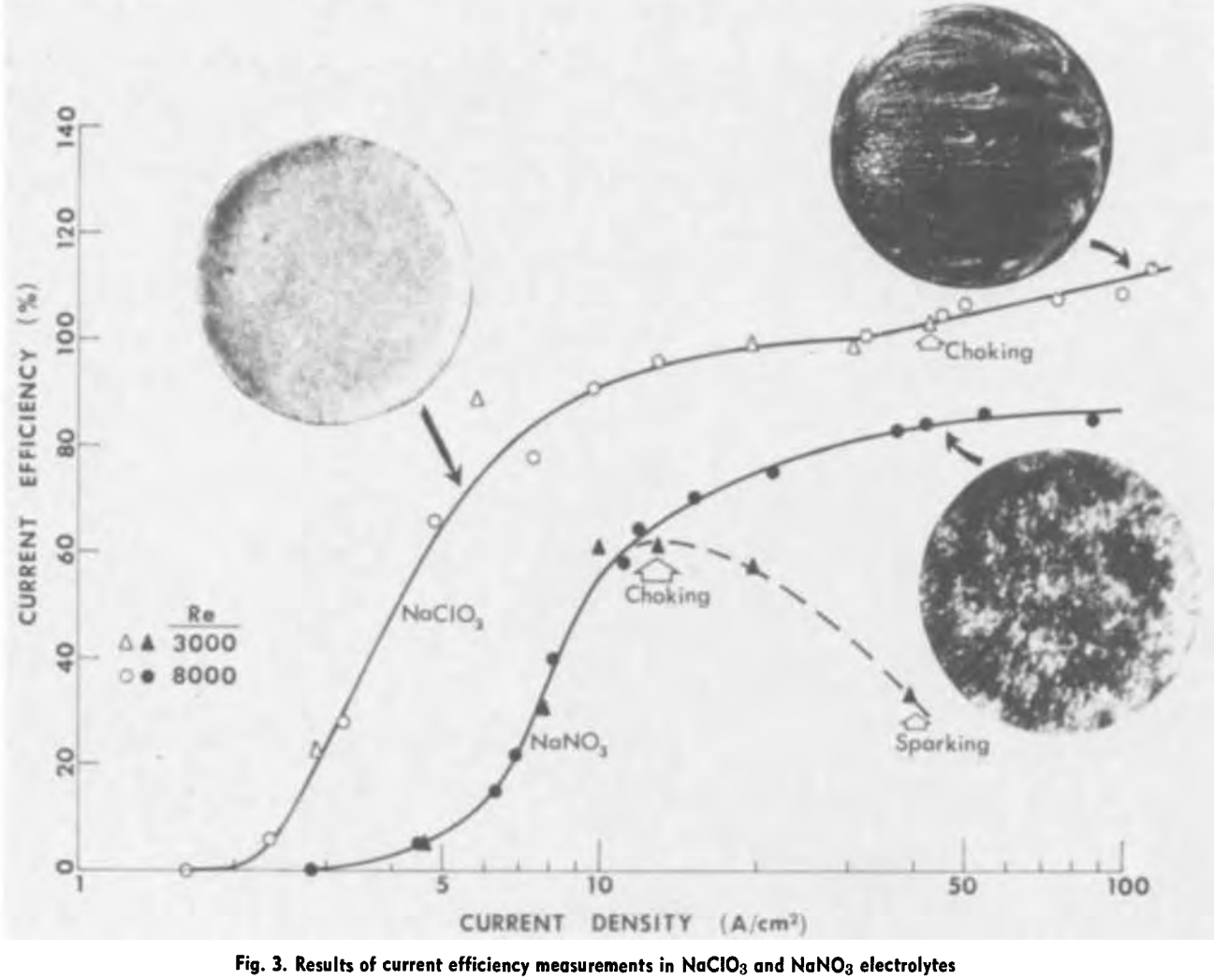

Fig. 3. Results of current efficiency measurements in $NaClO_3$ and $NaNO_3$ electrolytes

lyte, because oxygen was always generated on the anode within the current density range investigated. It is not known at the present time why the current efficiency in $NaClO_3$ continues to increase with current density after reaching the 100% level. Further study is necessary to resolve this particular issue.

Current efficiency and ECM dimensional control.— Since the current efficiency curve for NaCl is rather flat, it would be expected that the current efficiency ratio, η_L/η_H in Eq. [3] be approximately equal to unity at every point on the anode surface, and that the dimensional control be determined solely by the distance ratios, d_L/d_H. For $NaClO_3$ and $NaNO_3$, the S-shaped curves in Fig. 3 suggest that the current efficiency ratios are a dominant factor in obtaining successful dimensional control. They further suggest that an optimum current density can be chosen for the hcd region such that a high current efficiency ratio can be obtained throughout the lcd region on the anode surface. This optimum current density is about 10 A/cm² for $NaClO_3$ and 25 A/cm² for $NaNO_3$. If ECM is operated at current densities below the optimum value, the metal removal rate is too slow although the current efficiency ratio in Eq. [3] is large enough to provide good dimensional control. On the other hand, if ECM is operated above the optimum current density, then the leveling off of the current efficiency curve leads to a decrease in the efficiency ratio, and poor dimensional control is obtained. This suggests a two-stage operation for the average ECM process: the first stage is to cut the metal at the optimum current density in order to achieve the best possible dimensional control; and the second stage is to finish the surface at very high current densities with only a few seconds of running time.

In order to compare the qualities of dimensional control among the three electrolytes, we arbitrarily chose a current density of 25 A/cm² for the hcd region. Figure 4 shows the relationship between the ratio of the rate of the metal removal in the lcd region to that in the hcd region, $i_L\eta_L/i_H\eta_H$, and the current density ratio, i_L/i_H. These curves are calculated from the current efficiency curves (Re = 8000) given in Fig. 2 and 3, assuming i_H = 25 A/cm². Since the current density in the lcd region decreases with increasing surface distance from the hcd area, the ratio, i_L/i_H, should be equal to 1 at the edge of the hcd region, decreasing asymptotically to zero with increasing surface distance. The curve for NaCl is seen to fall on the diagonal line, indicating that metal removal is taking place even at locations remote from the hcd area. The curves for $NaClO_3$ and $NaNO_3$ are below the diagonal line, indicating that the actual metal removal rate in the lcd region is less than would be expected from the current density ratios. Since metal removal stops taking place at i_L/i_H = 0.2 for nitrate and at 0.1 for chlo-

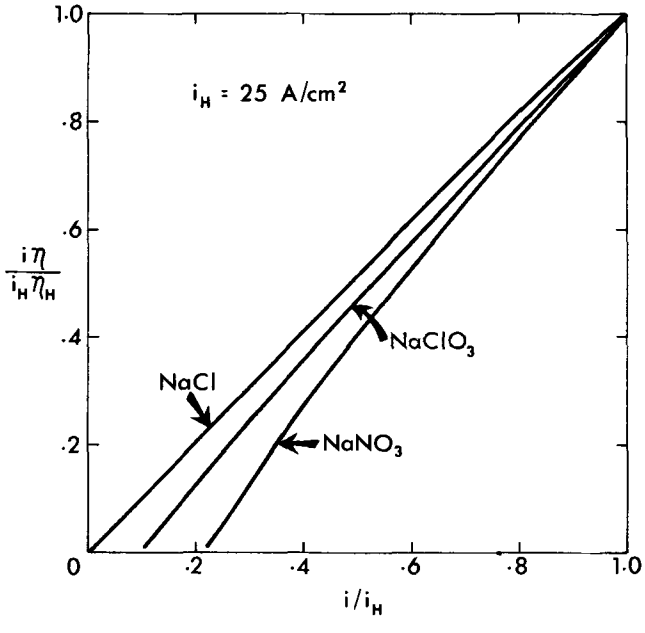

Fig. 4. Comparison of ECM dimensional control obtained at 25 A/cm² for NaCl, $NaClO_3$ and $NaNO_3$ electrolytes. The photomicrographs show the size of cutting areas after 4 mg metal removal in the first ECM test. The diameters of the cuts are: A, 0.236 cm; B, 0.223 cm; and C, 0.209 cm.

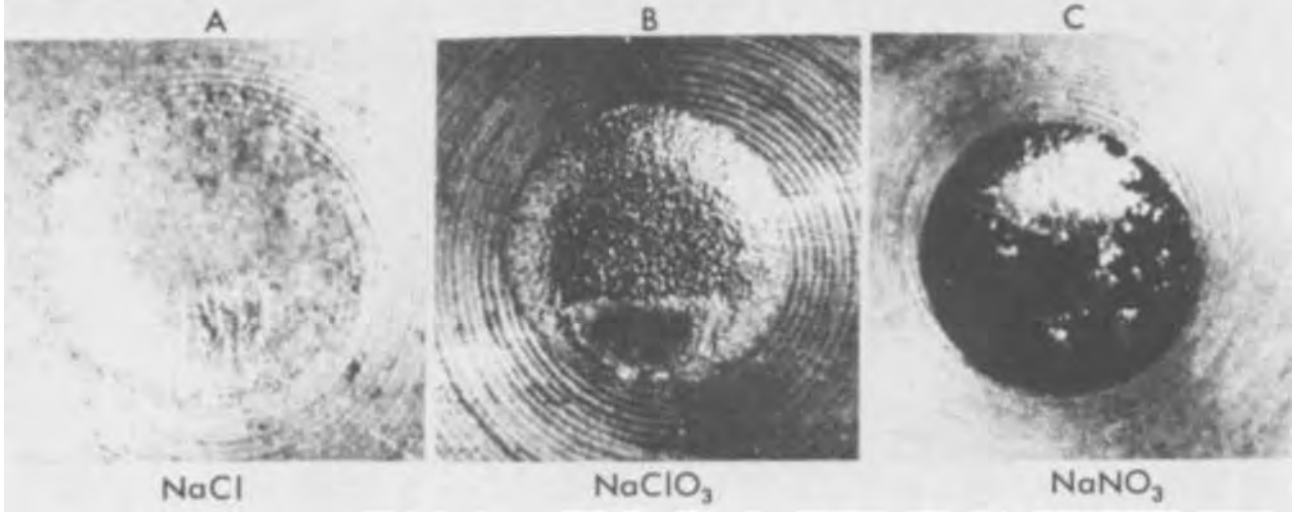

rate, it is expected that the quality of the dimensional control obtained from these electrolytes follows the order $NaNO_3 > NaClO_3 > NaCl$.

That this prediction agrees well with the ECM results is shown by the photomicrographs given in the same figure. These photomicrographs show the size of the cutting area after 4 mg of metal removal in each electrolyte at a cathodic current density of 25 A/cm², obtained in the first ECM test. The diameters of the cutting areas are 0.236 cm for NaCl, 0.223 cm for $NaClO_3$, and 0.209 cm for $NaNO_3$ as compared to the cathode diameter of 0.159 cm. Since the smaller the cutting hole, the better is the dimensional control, these results clearly verify the current efficiency dependence given in Eq. [3]. Also, the cutting edge for NaCl is not as sharp as the edges obtained with $NaClO_3$ and $NaNO_3$; this is in agreement with the measurement in NaCl metal removal of 100% efficiency even at very low current densities.

The results obtained from the second ECM test are given in Fig. 5 for two different cathodic current densities. The black horizontal line in each photomicrograph represents the surface profile after 100 mg metal removal. It is seen that at 100 A/cm², the best dimensional control is still achieved by $NaNO_3$ (Fig. 5D): the cutting edge is sharp with no metal removal in the area facing the center of the cathode tube (0.440 cm ID × 0.627 cm OD); the depth of penetration and the diameter of the cutting area are 0.042 and 0.787 cm, respectively, as compared to 0.036 and 0.863 cm for $NaClO_3$ (Fig. 5C). Again, the worst result is obtained with NaCl; Fig. 5A shows that not only is the edge

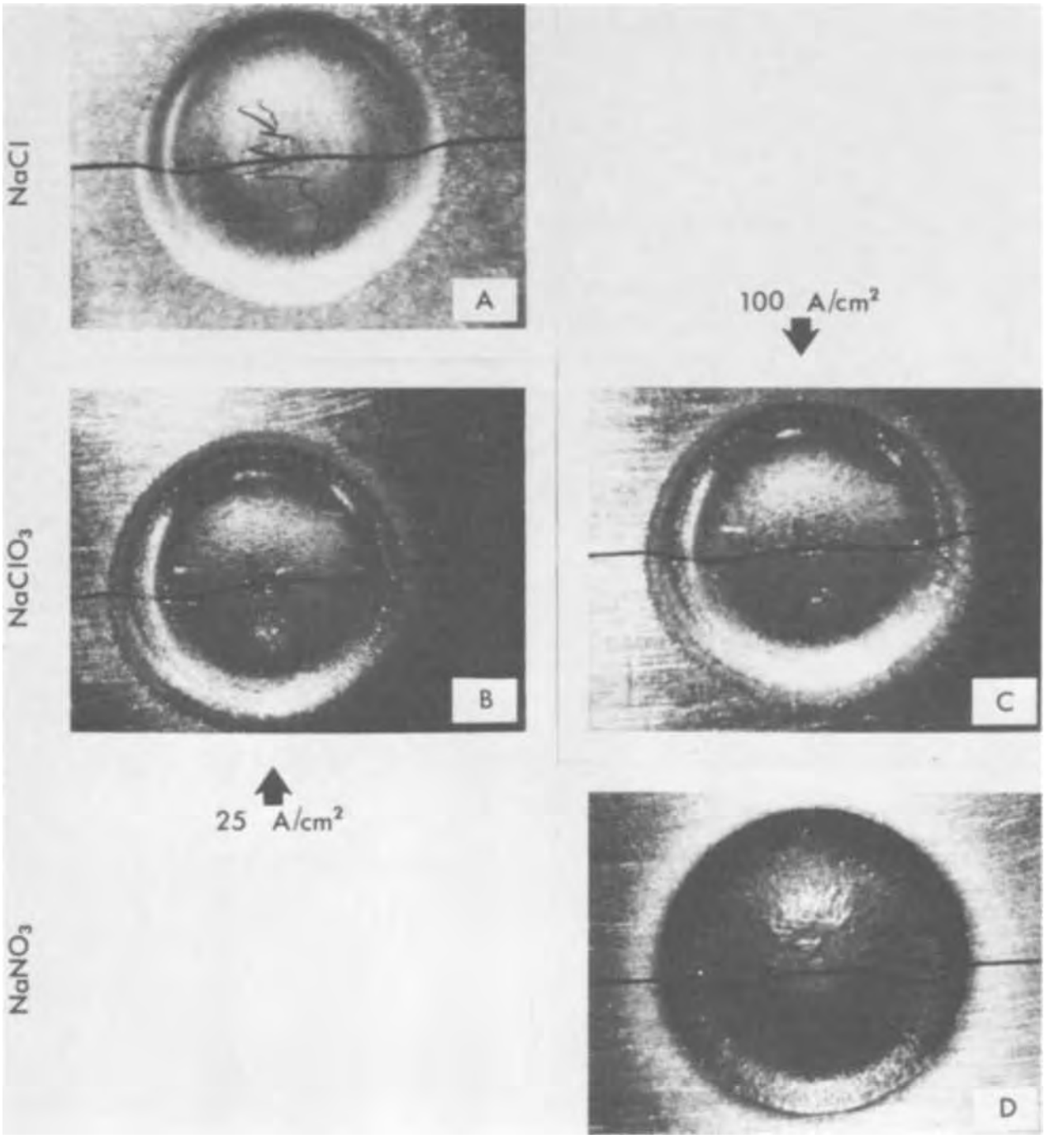

Fig. 5. Results of the second ECM test. The black horizontal line in each topographic photomicrograph illustrates the surface profile after 100 mg metal removal in each electrolyte. The numbers in the following parentheses denote diameter of the cutting area, depth of penetration in the area facing the tubular wall of the cathode, and depth of metal removal in the area facing the center of the cathode tube, respectively: A, (0.774, 0.037, and 0.019 cm); B, (0.762, 0.038, and 0.019 cm); C, (0.863, 0.036, and 0.018 cm); D, (0.787, 0.042, and 0 cm).

of the cutting area not sharp, but that there is metal removal taking place over the entire anode surface exposed to the electrolyte. At 25 A/cm^2, the depth and the diameter of the cut in NaCl are 0.037 and 0.774 cm, respectively, whereas the corresponding values in $NaClO_3$ (Fig. 5B) at the same current density are 0.038 and 0.762 cm. Figures 5B and 5C demonstrate that the quality of dimensional control in a passivating electrolyte becomes worse with increasing current density if the ECM is operated above the optimum current density (a cut 0.038 cm deep × 0.762 cm diameter in Fig. 5B as against a cut 0.036 cm deep × 0.863 cm diameter in Fig. 5C). Apparently this is due to the fact that, in the neighborhood of 100 A/cm^2, the current efficiency curve is flatter (Fig. 3), and the current efficiency ratio in the lcd region is correspondingly smaller than is the case at 25 A/cm^2.

Conclusions

The relation between the dissolution current efficiency and dimensional control has been demonstrated experimentally for the ECM of steel in NaCl, $NaClO_3$, and $NaNO_3$ electrolytes. The results indicate that the current efficiency measurement under controlled anodic current densities and electrolyte flow rates is a simple and useful method to determine the optimum operating conditions for achieving the best possible dimensional control and surface finish.

Manuscript submitted April 16, 1973; revised manuscript received June 8, 1973.

Any discussion of this paper will appear in a Discussion Section to be published in the June 1974 JOURNAL.

REFERENCES

1. J. P. Hoare, M. A. LaBoda, M. L. McMillan, and A. J. Wallace, Jr., *This Journal*, **116**, 199 (1969).
2. D. Landolt, *ibid.*, **119**, 708 (1972).
3. D. Landolt, R. H. Muller, and C. W. Tobias, *ibid.*, **118**, 40 (1971).
4. A. E. DeBarr and D. A. Oliver, "Electrochemical Machining," American Elsevier Publishing Co., New York (1968).
5. D-T. Chin and A. J. Wallace, *This Journal*, **118**, 831 (1971).
6. R. L. Saur, *Rev. Sci. Instr.*, **29**, 1023 (1958).
7. K-W. Mao, *This Journal*, **118**, 1870 (1971); *ibid.*, **118**, 1876 (1971).
8. J. F. Thorpe and R. D. Zerkle, in "Fundamentals of Electrochemical Machining," C. L. Faust, Editor, pp. 1-39, The Electrochemical Society Softbound Symposium Series, Princeton, New Jersey (1971).
9. R. A. Mirzoev, N. K. Svechkopal, and A. G. Lukina, Cited in *Chem. Abs.*, **77**, 12990a (1972).
10. T. P. Hoar, D. C. Mears, and G. P. Rothwell, *Corrosion Sci.*, **5**, 279 (1965).
11. D-T. Chin, *This Journal*, **118**, 174 (1971).

Electrosynthesis of Dialkyltin Derivatives

Harris E. Ulery

Organic Chemicals Department, E. I. Du Pont De Nemours and Company, Incorporated, Wilmington, Delaware 19899

ABSTRACT

Reduction of alkyl halides at a Sn cathode in TEAX/MeCN results in mixed degrees of alkylation of this metal. Primary products include RSn, R_2Sn, and/or reactive polytins containing these units. Final products depend on environment and tend to be complicated mixtures. A direct synthesis with good yields of dibutyltin oxide and dioctyltin oxide results from aerating the catholyte. A mixture of alkyltin halides is formed in an undivided cell by the interaction of anode and cathode products; other products include the tetraethylammonium alkylhalostannates. Factors governing the course of cathodic alkylation are discussed.

Previously (1) we reported that the reduction of organic bromides at a tin cathode results in an efficient alkylation of this metal. Typically, the degree of alkylation and the complexity of product mixtures vary with the nature of the alkyl source and the conditions of electrolysis. In $Et_4N^+Br^-$/MeCN, methyl bromide has been shown to give Me_4Sn and other organotins with essentially quantitative use of metal and with high electrical efficiency (1). Looking to cheaper alkyl sources we have found that alkyl chlorides are also readily reduced to mixtures of organotins.

Of particular interest would be a direct alkylation route to materials of commercial importance. Butyl derivatives of tin represent the largest group of industrially used organotins (2). They are employed chiefly as stabilizers for polyvinyl chloride, and the U.S. market for these materials is expected to exceed $15 million by 1975. Some dioctyltin derivatives have received official sanction in the U.S. and in Europe as stabilizers of PVC used for food packaging. In this report we disclose a promising electrosynthetic approach to this class of compounds.

Key words: electroreduction, sacrificial electrode, tin cathode, cathodic alkylation mechanism, dialkyltin, dialkyltin halides, dialkyltin oxides, dibutyltin, dibutyltin oxide, dioctyltin oxide, tetraethylammonium alkylhalostannates.

Experimental

Equipment.—The apparatus used in this work has been described previously (1). Modifications consisted of a settling tank in the catholyte circulation stream which was provided with an air inlet tube. To prevent loss of alkyl halide, the air stream was exhausted through a high efficiency condenser which was cooled with dry-ice acetone.

To allow reaction of anolyte and catholyte products, a mixing valve was employed between the independently circulated streams, or the separating membrane was removed.

Chemicals.—Reagents were Eastman White Label grade or the equivalent. The commercial grade acetonitrile contained *ca.* 0.5% water as determined spectroscopically. Tetraalkylammonium halides were used as received and are referred to by their acronyms (*e.g.*, TEAB, TEAC).

Tetraalkylammonium alkylhalostannates.—Frequently, insoluble by-product salts were formed which were identified as 2:1 complexes between TEAX and an alkyl tin halide. The preparation of many of these tetraalkylammonium alkylhalostannates has been reported by Seyferth (3). Elemental analyses for new

Table I. Elemental analyses for some complexes between a tetraalkylammonium halide and various tin halides

Compound*	% C		% H		% N		% Sn		% Halogen	
	Fd	Calc	Fd	Calc	Fd	Calc	Fd	Calc	Fd	Calc
2TEAC/$SnCl_4$	32.9	32.4	6.9	6.8	4.7	4.7	20.3	20.5	36.2	35.9
2TEAB/$SnCl_4$	28.7	28.2	6.0	5.9	3.9	4.1	16.6	17.4	44.8	44.4
2TPrAB/$SnCl_4$	36.1	36.8	7.1	7.2	3.4	3.5	15.0	15.2	37.4	37.2
2TBAB/$SnCl_4$	43.4	42.5	7.9	8.0	3.0	3.1	12.5	13.1	33.2	33.5
2TEAB/$SnBr_4$	22.5	22.4	4.6	4.7	3.3	3.3	13.7	13.8	54.9	55.8
2TEAC/$BuSnCl_3$	40.4	39.8	8.2	8.2	4.7	4.6	18.1	19.7	28.6	27.7
2TMAC/Bu_2SnCl_2	—	—	—	—	—	—	23.0	22.3	26.8	27.2
2TEAB/Me_2SnBr_2	29.7	29.6	6.4	6.4	4.0	3.8	16.6	16.3	44.2	43.9
2TBAB/Bu_2SnCl_2	50.4	50.7	9.7	9.6	3.2	3.0	11.9	12.5	24.8	24.3
1TEAC/$SnCl_2$	27.2	27.0	5.7	5.6	3.7	3.9	33.2	33.5	28.9	29.8

* The alkyl groups are: methyl (M), ethyl (E), n-propyl (Pr), n-butyl (B), n-pentyl (Pe), n-hexyl (Hx), n-heptyl (Hp).

complexes prepared during these investigations are given in Table I. These were obtained by refluxing 2:1 molar mixtures of the tetraalkylammonium halide and the tin halide in MeCN. Since many of these salts do not have well-defined melting points, it was convenient to characterize them by differential thermal analysis (DTA) and gravimetric thermal analysis (GTA). The thermal characteristics of these complexes are given in Table II. In the second block of Table II, thermal data are given for the parent tetraalkylammonium salts.

Results

Electrolysis of n-BuCl (divided cell).—The reduction of n-BuCl in TEAC/MeCN approximates a 2**F** process. Under various conditions of temperature, catholyte composition, and current density, the average electrical requirement was 2.28 e^-/Sn atom consumed (Table III).

The catholyte becomes yellow to brown as electrolysis proceeds, and a solid product forms. The following observations indicate this is most probably a composition approaching that of polydibutyltin (5, 6a): (*i*) Initially formed, the composition is a filterable, flocculent, brown solid. (*ii*) When the solvent is removed from freshly isolated material, it undergoes a reaction in air, occasionally igniting the filter paper. (*iii*) Material collected under N_2 was analyzed and found to contain *ca.* 49% Sn *vs.* 51% expected for $(C_8H_{18}Sn)_x$. (*iv*) Fresh material suspended in MeCN and aerated was converted, apparently quantitatively, to dibutyltin oxide (6b). (*v*) The original wet solid darkens after several hours, forming a gum which reacts only slightly with air, but in the presence of chlorine dissolves to give a mixture of butyltin halides.

Table II. Transition temperatures (°C) of several tetraalkylammonium compounds

Compound*	DTA			GTA	MP
	1st	2nd	3rd		
2TMAC/$SnCl_4$	259	355		385	
2TEAC/$SnCl_4$	315			330	
2TEAB/$SnCl_4$	300			330	
2$Et_3NHBr/SnCl_4$	113	260		285	113
2TPrAB/$SnCl_4$	115	157	256	250-275	256
2TBAB/$SnCl_4$	59	122	226	250	226
2TEAB/$SnBr_4$	77			305	
1TEAC/$SnCl_2$	98			300	
2TEAC/$BuSnCl_3$	166	187	231	200	187
2TMAC/Bu_2SnCl_2	125			240	
2TEAC/Bu_2SnCl_2	59	95	184	200	
2TBAB/Bu_2SnCl_2	190	267		150	195-200
TMAC	122	177	258	300	d >230
TEAC	95	110	283	250	>300
Et_3NHBr	205	238		250	248
$TEAClO_4$	93	345		335	>300
TEA_2SO_4	107	185	325	300	182-7
TMAB	345			340	
TEAB	164	255		265	>300
TPrAB	97	250		245	295d
TBAB	88	108	217	150-200	237
TMAI	368			330	
TEAI	161	290		270	>300
TPrAI	134	266		255	>300
TBAI	110	137	224	150-200	144
TPeAI	117	203	234	200	137
THxAI	62	93	275	215	103
THpAI	75	111	292	195	121

* The alkyl groups are: methyl (M), ethyl (E), n-propyl (Pr), n-butyl (B), n-pentyl (Pe), n-hexyl (Hx), n-heptyl (Hp).

Table III. Electroreduction of n-butyl chloride in divided cell[a]

Conditions		Observations				
				% total Sn loss recovered as		
C.D.[c] (A/cm²)	Temp. (°C)	Sn loss (g)	Elect. use (e⁻/Sn)	$(Bu_2Sn)_x$ and/or Bu_2SnO	Bu_3SnCl	Bu_4Sn
0.10	35	43.1	2.18	79[f]	[b]	[b]
0.05	35	23.6	1.95	—[f]	[b]	[b]
0.05	30	20.3	2.18	80[g]	1	4
0.041	35	21.6	2.16	66[h]	5	24
0.035	15	10.4	2.02	24[g]	[b]	[b]
0.025	33	12.8	2.44	29[h]	[b]	[b]
0.025	35	13.9	2.45	33[h,i]	[b]	[b]
0.025	32	13.5	2.39	(30)[d,g]	[b]	[b]
0.025	35	11.6	2.50	(20-40)[d,h,i]	[b]	[b]
0.017	25	3.3	2.55	(45)[d,e,h,i]	[b]	[b]

[a] Circulating catholyte with initial composition = 10% TEAC, 30% n-BuCl, 60% MeCN.
[b] Identified in catholyte by G.C.
[c] Constant current; voltage varied over 6-35V.
[d] Estimated from crude product.
[e] Catholyte contained only 15% n-BuCl.
[f] Catholyte not aerated.
[g] Catholyte aerated during electrolysis.
[h] Catholyte aerated after electrolysis.
[i] Catholyte purged with argon prior to electrolysis.

Below 0.1 A/cm² the formation of metal fines was negligible, the remaining cathode loss being represented by soluble Sn products. Material balances were not generally attempted due to the complicated nature of the product composition. Gas chromatography (G.C.) analyses invariably indicated major amounts of Bu_4Sn and lesser amounts of Bu_3SnCl. In some cases Bu_2SnCl_2 was detected. Product catholytes gradually produced Sn containing solids, which on the basis of their *IR* spectra were mixtures of the butyltin chloride/TEAC complexes. The amber tones of the catholytes are indicative of mixtures of soluble branched chain polytins (6a).

If oxygen is not carefully excluded, Bu_2SnO is invariably observed as a side product. When air is bubbled into the circulating catholyte, the brown $(Bu_2Sn)_x$ is converted to the solid oxide (white). The oxidation proceeds via a rapidly formed yellow intermediate, possibly a peroxide; this in turn is more slowly converted to Bu_2SnO. The oxygen does not appreciably lower the electrical efficiency. In semicontinuous operation the oxide tended to clog the cell. The oxidation rate was somewhat slower than the rate at which solids had to be removed. Alternatively, the heavy flocculent mass of $(Bu_2Sn)_x$ was readily removed from the circulating stream by bleeding the bottom of the catholyte reservoir. The concentrate could be aerated *ad libitum*, and the solution quantities to be filtered were much reduced.

Higher alkyl chlorides also enter into a sacrificial reaction with Sn. In one example, a 30/10/60 weight per cent (w/o) solution of n-octyl chloride/TEAC/MeCN was reduced at 0.025 A/cm². Postaeration gave

28% of the consumed Sn (10.7g) as dioctyltin oxide, which was identified by comparison of its *IR* spectrum with that of a known standard. The electrical requirement was 2.42 e^-/Sn.

Using a 10/10/20/60 w/o solution of n-octadecyl chloride/TEAC/PhCN[1]/MeCN, a similar run at 0.028 A/cm² resulted in a Sn loss of 15.6g. The sacrificial reaction required only 1.76 e^-/Sn. The dark alkyl polytin semisolid could not be isolated during the run. Attempts to aerate it subsequently showed it to be far less reactive than $(Bu_2Sn)_x$ or $(Oc_2Sn)_x$. The aeration product was inhomogeneous and was not identified.

Electrolysis of n-BuCl (undivided cell).—Using a range of electrolyte compositions, the electrolysis of n-BuCl was conducted at 0.1 A/cm², but without a separator. The electrical consumption varied over 2.0–3.4 e^-/Sn (Table IV). Only a small amount of dark polymeric material somewhat resembling $(Bu_2Sn)_x$ was formed during a run. It contained *ca.* 45% Sn and some chlorine. Most of the tin loss appeared as a complex mixture of the butyltin chlorides and their complexes with TEAC. The final electrolyte contained excess chlorine.

Aeration of the electrolyte during a run prevented the formation of the dark polymer. The white solids produced were a mixture of Bu_2SnO (less than 10% of Sn loss) and $(Et_4N)_2SnCl_6$ (up to 20%) which was identified by comparison with material prepared independently. Lesser amounts of the butyltin chloride/TEAC complexes formed more slowly. Bu_3SnCl was the major volatile tin produce identified by G.C. Aeration also reduced the average electrical consumption to less than 2 e^-/Sn (Table IV).

Similar results were obtained in a divided cell when anolyte was bled into the catholyte. On the basis of two runs at 0.025 A/cm², up to 68% of the tin converted appeared as Bu_3SnCl (48%) and $(Et_4N)_2SnCl_6$ + Bu_2SnO (9-19%).

[1] Benzonitrile was necessary to solubilize the alkyl chloride.

Table IV. Electroreduction of n-BuCl (undivided cell)

Electrolyte composition[a]		Conditions			Observations	
% BuCl	% TEAC	Aeration	C.D. (A/cm²)	Temp.[b] (°C)	Sn loss[c] (g)	El. consumed (e^-/Sn)
30	5	No	0.1	45	12.9	3.42
30	1	No	0.1	60	32.8	2.01
30	1	No	0.1	20	25.6	2.58
10	10	No	0.1	36	14.6	2.28
30	5	Yes[d]	0.1	—	23.5	2.82
30	5	Yes	0.05	—	10.9	3.03
10	10	Yes	0.1	40	51.7	1.29
10	15	Yes	0.1	38	20.0	1.66
10	20	Yes	0.1	38	17.6	1.75
10	25	Yes	0.1	36	22.4	1.49

[a] Electrolyte also contained 1% MeOH.
[b] Average values.
[c] 60-90% of the tin loss appeared as butyltin chlorides and complexes with TEAC.
[d] Less than 10% Bu_2SnO was formed.

Electrolysis of EtCl (undivided cell).—A 30/1/69 w/o mixture of EtCl/TEAC/MeCN electrolyzed at 0.1 A/cm² yielded a dark, pyrophoric precipitate containing 15% Cl and 60% Sn [$(Et_2Sn)_x$ requires 67% Sn]. The electrical consumption was 2.37 e^-/Sn.

Electrolysis of MeBr (undivided cell).—In the absence of a separator, MeBr/TEAB/MeCN electrolytes rapidly developed a bright orange color indicative of polybromide. Eventually a yellow solid begins to precipitate. This was identified as tetraethylammonium dimethyltetrabromostannate, a 2:1 complex between TEAB and Me_2SnBr_2, by comparison with independently prepared material (Tables I and II). Of the consumed Sn, 10-40% appeared in this form. The principal volatile product was Me_3SnBr with lesser amounts of Me_4Sn and Me_2SnBr_2, all of which were identified by G.C. The product electrolytes were quite unstable at room temperature and continued to produce additional solid complexes on standing.

The observed electrical requirements for this system are summarized in Table V. These are inflated by a gas forming reaction due to hydroxylic inhibitor.

Discussion of Results

Divided cell.—For a variety of alkyl sources, the cathodic alkylation of Sn conforms to the general equation

$$n\,RX + M_x + ne^- \rightarrow R_nM_x + nX^- \qquad [1]$$

With n-BuCl, the observed dialkylation products and electrical efficiencies (Table III) indicate a major reaction which requires that $n = 2x$; the value of x depends on whether dibutyltin leaves the electrode as a monomeric species ($x = 1$) on a higher consolidated form ($x > 1$) retaining some Sn-Sn bonds. Results with other alkyl chlorides indicate that dialkylation is generally favored.

Other degrees of alkylation are also indicated. Nearly all alkyl halides studies (1, 12) have yielded products with significant amounts of R_4Sn. The alkyl chlorides typically required more than $2e^-$/Sn but less than $4e^-$/Sn. Since known (1) nonsacrificial reactions (R-X dimerization and reduction of H^+ and Et_4N^+) were unimportant below 0.05 A/cm², electrical requirements exceeding $2e^-$/Sn may be attributed to higher alkylation processes ($n > 2x$) or side reactions involving earlier formed reducibles (*e.g.*, R_3SnCl). The possibility of monoalkylation is indicated when the electrical consumption falls below $2e^-$/Sn. This was observed for both butyl (Table III) and octadecyl chloride.

Low current densities correlate with a higher degree of alkylation. This is seen in Table III as a decrease in the dialkylation product and an increase in the electrical requirement for Sn consumption. Our failure to obtain a higher degree of alkylation with certain alkyl bromides (1) may be due to the relatively high C.D. employed (0.1 A/cm²).

The primary source of Bu_3SnCl is probably the following known (8) reaction

Table V. Electrolysis of MeBr (undivided cell)

Electrolyte[a]			Conditions		Observations		
% MeBr	% TEAB	% Inhibitor	C.D. (A/cm²)	Temp.[b] (°C)	Sn loss (g)	El. consumed (e^-/Sn)	% elect yield[c]
30	8	1 W	0.1	39	12.1	5.46	73
30	4	1 W	0.1	40	13.6	4.85	83
30	2	1 W	0.1	41	15.3	4.32	93
30	1	1 W	0.1	49	15.5	4.26	94
25	10	3 M	0.1	37	7.5	8.80	45
25	3	3 M	0.1	43	9.9	6.58	61
25	3	3 M/G	0.1	39	14.1	4.68	85
25	3	3 G	0.1	38	15.9	4.15	96
25	3	3 P	0.1	38	13.7	4.82	83
25	3	3 P	0.1	39	12.1	5.46	73

[a] W = Water, M = Methanol, G = Glycerol, P = Polyethylene glycol-300.
[b] Average values.
[c] Assuming 4 e^-/Sn.

$$[Bu_2Sn] + BuCl \rightarrow Bu_3SnCl \quad [2]$$

Our polymeric form of dibutyltin reacts only slowly and incompletely with BuCl (8). At the same time, reaction [2] may contribute to the dramatic decrease in dialkyltin products with decreasing C.D. Low electrolysis rates imply higher concentrations of reactant and lower concentration of primary products at the electrode surface. If the primary product is monomeric Bu_2Sn, its polymerization will be disfavored relative to reaction [2]. Similarly, aeration during electrolysis would scavenge Bu_2Sn, thereby minimizing reaction [2].

Undivided cell. Eliminating the cell divider allows the anodically produced halogen to react with both the cathode and the cathode products. The electrical consumption during the electrolysis of n-BuCl is no greater in the undivided cell than found in the divided cell. This indicates cathodic reduction of the polychloride is minimal. Some reduction may occur since polychloride effectively inhibits the formation of metal fines at 0.1 A/cm^2. Sloughing of the cathode is a consequence of the reduction of Et_4N^+ (1). In the presence of the polyhalide, the potential of this cation would never be reached. Had this been recognized earlier, the inhibitors used with MeBr (Table V) could have been omitted.

In all cases, the polyhalide was not consumed as fast as it was produced. This attests to the more selective behavior of polyhalide oxidizing agents (7) and may be a result of steric hinderance in the polytins.

With both EtCl and n-BuCl the formation of solid alkyltin polymers was not completely suppressed by the presence of polychloride. By contrast, no solid polymer was ever observed during reduction of MeBr. If polymer is formed by a subsequent reaction of a primary species (*e.g.*, R_2Sn), then polymerization is competitive with scavenging by polyhalide (*e.g.*, Eq. [3])

$$R_2Sn + X_3^- \rightarrow R_2SnX_2 + X^- \quad [3]$$

The failure to observe a polymer with MeBr may simply reflect a high rate of Sn-Sn cleavage by polyhalide when the alkyl group is quite small. While Me_2SnBr_2 (as its complex with TEAB) is the major product in an undivided cell, the high electrical consumptions (Table V) leave it unclear whether this results from Eq. [3] or halogenolysis of higher degree alkylation products.

Alternatively some alkyl polytin may form as a primary cathode product (Eq. [1], $x > 1$). This possibility is consistent with the range of electrical efficiencies based on Sn loss.

In combination but not separately, chlorine and oxygen appear to have changed the half-cell chemistry of the cathode. As a consequence of aeration, the current requirement for the electrolysis of n-BuCl at 0.1 A/cm^2 was reduced to average less than $2e^-$/Sn. Either chemical dissolution of tin occurs or there is competition from a 1**F** process. The appearance of $(Et_4N)_2SnCl_6$ in this case may be evidence that a viable monoalkylation species, [BuSn] (5) was formed (Eq. [4]-[7])

$$[BuSn] + 3/2\ Cl_3^- \rightarrow BuSnCl_3 + 3/2\ Cl^- \quad [4]$$

$$2BuSnCl_3 \rightleftarrows Bu_2SnCl_2 + SnCl_4 \quad [5]$$

$$BuSnCl_3 + Bu_2SnCl_2 \rightleftarrows Bu_3SnCl + SnCl_4 \quad [6]$$

$$2Et_4NCl + SnCl_4 \rightarrow (Et_4N)_2\,SnCl_6\downarrow \quad [7]$$

Removal of the hexachlorostannate operates to increase the degree of alkylation of tin remaining in solution. The build-up of tributyltin chloride in solution is dictated by this as well as the fact that alkyltin halides become progressively slower in their reactions with TEAC as the degree of alkylation increases.

A chemical source of free radicals might also increase the Sn loss/**F** (9). Bromination of R_4Sn has been described by an ionic mechanism (10). Under the influence of light, however, a radical chain process is established (10b), in which R· is an intermediate. Perhaps oxygen and chlorine interact to generate radicals independent of electron transfer at the cathode.[2]

Mechanistic considerations.—While we tend to refer to Eq. [1] as an "n-electron" reaction, the reduction undoubtedly involves a succession of one-electron transfers which result in the stepwise alkylation of the metal. We envision the alkylation as proceeding with metal-carbon bond formation being essentially synchronous with carbon-halogen bond rupture (4). Since the environment differs for each succeeding step, the rate of transfer and mechanistic details will vary in some discrete way.

Electronic considerations anticipate a discontinuity in the alkylation sequence after the second group is attached. At each step intermetallic bonding is necessarily reduced. Pauling (11) estimates the metallic valence of tin to be 2.64. A similar calculation gives a corresponding value of 2.76 for lead. In each case the introduction of two alkyl groups would reduce the valence to less than unity. Consequently, no further alkylation should be possible without freeing orbitals used for metallic bonding. Electron pairing order may also be a factor since the valence shells of tin and lead contain two *s* and two *p* electrons.

Variation in geometric details may not be critical during the first two alkylation steps. Photomicrographs (1) of tin cathodes sacrificed to MeBr give strong evidence that metal removal in this case is an orderly progression along lattice planes. Initiation of alkylation at an edge position is favored by the higher potential which develops here (15). Also, an edge provides greater exposure of the metal atom for a second alkylation step. From this point on, however, steric factors should be relatively more important in determining product distributions.

With modest thermal activation a weakly attached di- or trialkyl metal moiety may be free to diffuse[3] over the crystalline surface. Depending on the location of the metal atom, this mobility may be necessary to reduce steric interference to further alkylation. This situation is depicted schematically in Fig. 1.

If alkylation is fast compared to surface diffusion (*e.g.*, at high C.D.) reaction would shift to adjacent metal atoms. The larger this organometal aggregate, the larger will be its thermal energy compared to the residual metallic bonding; hence, the more likely its dissociation from the surface. Adjacent metal atoms become the most likely centers for further reaction: their free valence number has increased as a consequence of the reduced metallic bonding to an alkylated neighbor. With tin, this is consonant with the formation of stable polytin products.

Several factors could facilitate surface mobility and thereby promote the sacrificial reaction:

1. Weak intermetallic bonding. The lower melting point of tin (232°C) compared to lead (327°C) reflects less internal bonding in this metal. We expect greater mobility with tin. Conversely, metals with strong internal bonding would be expected to passivate after further alkylation becomes sterically impossible. Some confirmation of this derives from the observation that it is the "soft" or relatively low melting metals which are most receptive to cathodic alkylation (12) and alkyl radical scavenging (9).

2. Small alkyl group size. Diffusion rates decrease with increasing size of the diffusing group. Electron micrographs of tin (1) and lead cathodes used with MeBr are unique in that they reveal an exceptionally clean removal of metal along latttice planes. This suggests that metal removal was sufficiently rapid to maintain a fresh edge with a selectively higher potential. With higher alkyls, the reaction locus appears to "wander" so that lattice planes are no longer pre-

[2] Several chlorine oxides capable of radical dissociation are known (16), which are potential anode products.
[3] Via desorption-resorption equilibria.

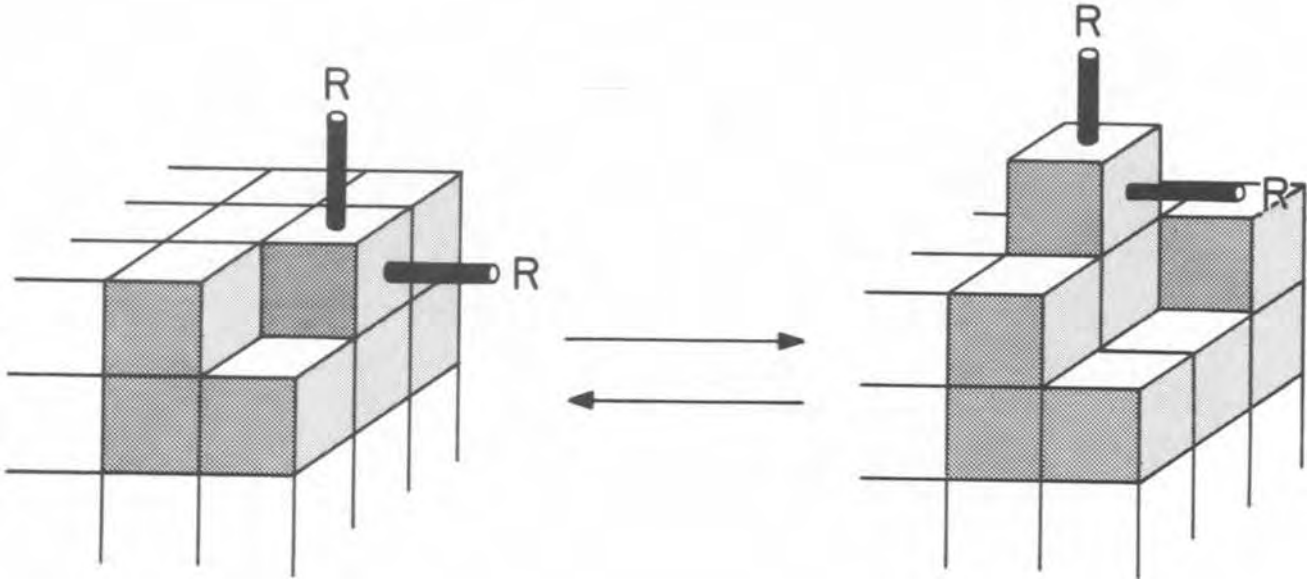

Figure 1

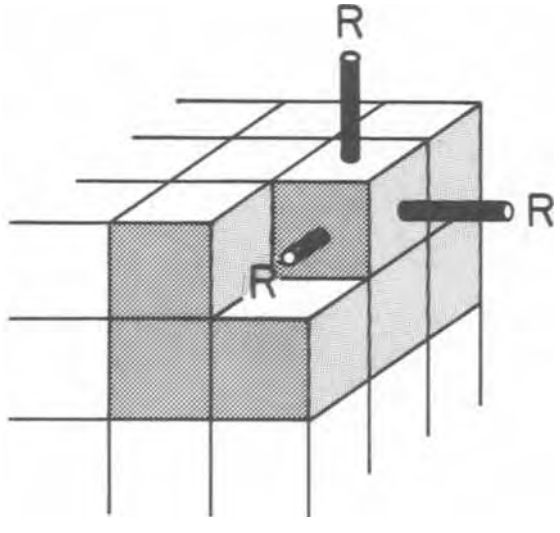

Figure 2

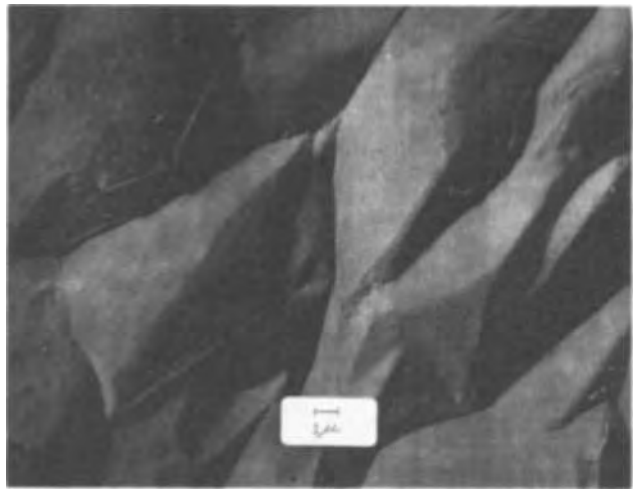

Fig. 3. Surface detail of tin cathode after electrolysis of n-BuCl. The cathode was: 30% n-BuCl, 10% TEAC, 60% MeCN (no aeration).

served (Fig. 3). This would be expected if alkylation centers on an edge remain in place long enough to force alkylation to move to nonedge positions. The methyl group is probably small enough to allow the rapid formation of three carbon-metal bonds before reorganization of the surface is required for further alkylation (Fig. 2).

With minimal bonding to other metal atoms as a restraint, the R_3M-group might reorient rapidly, permitting tetraalkylation at a higher C.D. Alternatively, facile trialkylation would enhance termination of polytin chains formed on the surface, thus favoring lower MW products. Alkyl group size may be particularly important for Pb in view of its higher metallic bonding: MeBr (1,4) can be quantitatively reduced at Pb according to Eq. [1] ($n = 4, x = 1$). While tetraethylation of Pb is also observed, a triethylation process (Eq. [1]; $n = 6, x = 2$) has been identified (13) as a principal side reaction. Dialkylation ($n = 2x$) may occur during the reductions of i-PrBr and PhBr (4), but the relatively unstable dialkyl lead was not isolated.

3. Strong C-M bonds. Enhanced bonding of the metal to the organic group as for example through a π-bond, would weaken intermetallic bonds, *i.e.*

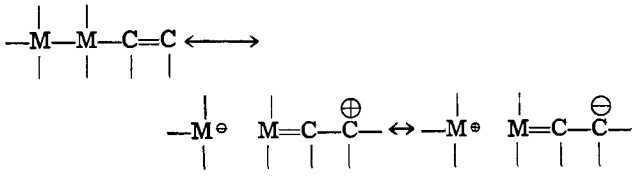

The efficient formation of tetraallyltin, tetraallyllead and tetraphenyltin (1) in spite of the size of the organic group may be evidence of the influence of carbon-metal bond strength in favoring surface diffusion.

4. Low current densities. Surface diffusion can be important only at current densities low enough to result in partial alkylation of the electrode surface. Higher current densities eliminate the surface concentration gradient essential for diffusion and imply that nonpassivating products are formed.

5. Low electrolyte adsorption. Cation adsorption leads to high effective current densities, and hence, high alkylation rates by decreasing the active area of the electrode (14). Higher yields of Me_4Sn and Me_4Pb were obtained with TEAB than with TBAB. While several factors may be involved, adsorption of the latter electrolyte appears to be the greater. This would favor a lower degree of alkylation.

Conclusions.—There now appears to be a significant difference in the sacrificial behavior of Sn and Pb cathodes toward alkyl halides in TEAX/MeCN media. The reluctance of Pb to react with higher alkyl halides is pronounced. Reaction with alkyl chlorides in particular is generally disfavored by the high reduction potentials of the C-Cl bond on Pb. In contrast, the scope of the cathodic sacrifice of Sn encompasses not only the alkyl chlorides, but is far less restricted by alkyl group size. It is suggested that this contrasting behavior results largely from differences in the chemical stabilities of partially alkylated metal atoms at the cathode surface. This in turn may be related to the concatenation behavior of the metal.

While the Sn cathode is more readily sacrificed, the reduction is immensely complicated by the variety of stable lower alkylation products. Nonetheless, as illustrated by the formation of R_2SnO, useful products in good yields are possible by a suitable choice of conditions.

Acknowledgments

I am indebted to T. Tessmer for his considerable contribution as my laboratory assistant. Electronmicrographs were obtained by W. Kay. In particular I would mention J. D. Sterling, his critical comments and enduring encouragement are the backbone of this report.

This is contribution No. 471, Jackson Laboratory, Organic Chemicals Department, E. I. Du Pont De Nemours & Co., Inc., Wilmington, Delaware 19899.

Manuscript submitted Feb. 22, 1973; revised manuscript received April 9, 1973.

Any discussion of this paper will appear in a Discussion Section to be published in the June 1974 JOURNAL.

REFERENCES

1. H. E. Ulery, *This Journal*, **119**, 1474 (1972).
2. International Technical Surveys, Inc., *Organotin Market Survey*, **2**, 70 (1965).
3. D. Seyferth, U.S. Pat. 3,070,615 (1962).
4. H. E. Ulery, *This Journal*, **116**, 1201 (1969).
5a. H. C. Kuivila and O. F. Beumel, Jr., *J. Am. Chem. Soc.*, **83**, 1246 (1961).
b. H. Shinkawa, *Kobunshi Kagaku*, **25**, 666 (1968); *Chem. Abstr.*, **70**, 48077C (1969).
c. D. Blake, G. E. Coates, and J. M. Tate, *J. Chem. Soc.*, **1961**, 618.
d. W. P. Neumann, *Angew. Chem.*, **75**, 225 (1963).
e. W. P. Neumann, *Ann Chem.*, **672**, 34 (1964); *ibid.*, **677**, 1 (1964).
6a. W. P. Neumann, "The Organochemistry of Tin," pp. 128ff, Interscience Pub., New York (1970).
b. *Ibid.*, p. 111.
7. L. F. Fieser and M. Fieser, "Reagents for Organic Synthesis," pp. 966ff, John Wiley and Sons, Inc., New York (1967).
8a. V. T. Bychkov and N. S. Vyazankin, *Zh. Obshch. Khim.*, **35**, 687 (1965).
b. K. Sisido, S. Kozima, and Isibasi, *J. Organometallic Chem.*, **10**, 439 (1967).
c. K. Sisido, T. Miyanisi, K. Nabika, and S. Kozima, *ibid.*, **11**, 281 (1968).
9a. F. A. Paneth and W. Hofeditz, *Ber.*, **62**, 1335 (1929).
b. W. A. Waters, "The Chemistry of Free Radicals," Oxford University Press, New York (1946).
10. S. Boué, M. Gielen, and J. Nasielski, *J. Organometallic Chem.*, **9**, 443, 461, 481 (1967).
11. L. Pauling, "Nature of the Chemical Bond," 3rd ed., pp. 400ff, Cornell University Press, Ithaca New York (1960).
12. E. F. Silversmith and W. J. Sloan, U.S. Pat. 3,197,392 (1965).
13. M. Schuler, Unpublished results.
14. M. Bonnemay, E. Levart, and E. P. d'A. d'Orsay, *Compt. Rend.*, **260**, 2493 (1965).
15. C. Kasper, *Trans. Electrochem. Soc.*, **77**, 353, 365 (1940).
16. C. C. Addison, "Mellor's Comprehensive Treatise on Inorganic and Theoretical Chemistry," Suppl. II, Part 1, pp. 514ff, Longmans, Green, and Co., New York (1956).

An ESR and Electrochemical Study of the Tetrasulfurtetranitride Anion Radical

J. D. Williford, R. E. VanReet, M. P. Eastman, and K. B. Prater*

Department of Chemistry, University of Texas at El Paso, El Paso, Texas 79968

ABSTRACT

The tetrasulfurtetranitride anion radical has been produced by constant potential electrolytic reduction and its ESR spectrum conclusively identified. The decay of the anion radical was followed by ESR and electrochemical methods and found to obey a first-order rate law. It is suggested that the anion radical decays by intramolecular bond rupture.

Tetrasulfurtetranitride (S_4N_4) is a molecule about which there has been discussion concerning its structure (1-3) and bonding (4, 5). In order to answer some of the questions raised in the above studies, several attempts have been made to generate the anion radical of S_4N_4 ($S_4N_4^-$) and to interpret its electron spin resonance (ESR) spectrum.

Chapman and Massey (6) reacted S_4N_4 with potassium in dimethoxyethane at room temperature. They first observed a claret-red solution which appeared to be diamagnetic. Later, the solution turned green and yielded a spectrum consisting of nine narrow lines with $a_N = 3.22G$. The spectrum is characteristic of a radical with four equivalent nitrogen atoms, suggesting delocalization of the unpaired electron. Further reaction with potassium caused an increase in the intensity, followed by a decrease almost to zero, followed by a second increase in intensity. The second strong spectrum was said to be identical to the first. The authors suggested that these observations might be explained by the formation of $S_4N_4^{-2}$, $S_4N_4^{-3}$, etc., some of which would be diamagnetic.

Meinzer, Pratt, and Myers (7) obtained a spectrum consisting of nine relatively broad lines with $a_N = 1.185G$ by the constant current electrolytic reduction of S_4N_4 in tetrahydrofuran (THF) at −25°C. They observed that this radical decomposed rapidly at higher temperatures and was difficult to detect above

* Electrochemical Society Active Member.
Key words: tetrasulfurtetranitride, anion radical, ESR, cyclic voltammetry.

0°C. They also observed the same radical from the reduction of S_4N_4 with potassium at about −25°C. Further reduction with potassium yielded other spectra. They argued, based on a consideration of the g-value for the radical, the hyperfine splitting, and the line broadening effect produced by neutral S_4N_4, that the nine line spectrum which they had obtained at low temperature was the spectrum of $S_4N_4^-$, and that $S_4N_4^-$ had a structure similar to that of S_4N_4. However, no detailed electrochemical studies were carried out to confirm that the observed radical was produced by one electron reduction of S_4N_4.

In this paper we present the results of ESR and electrochemical studies of the kinetics of the disappearance of $S_4N_4^-$ and a confirmation of the assignment by Meinzer, Pratt, and Myers of the low temperature spectrum to $S_4N_4^-$.

Experimental

The S_4N_4 was prepared by the method of Jolly (8). All experiments were carried out in acetonitrile (MeCN) which had been slurried over CaH_2, triply distilled from P_4O_{10}, and bubbled with dry nitrogen. The supporting electrolyte was tetraethylammonium perchlorate (TEAP). A Wenking 66TS 10 potentiostat and a Hewlett Packard 7004 A X-Y recorder were used in all experiments.

The cyclic voltammetry study utilized a Beckman platinum button working electrode and a Ag/0.01*M* Ag^+ reference half cell. The low temperature cyclic voltammetry was carried out in a methanol constant temperature bath which was cooled with cold dry nitrogen passing through immersed copper coils. This cooling was bucked by a heating element in the methanol which was feedback controlled using a thermistor as a detector. The bath was continuously stirred and was found to hold the temperature constant to ±0.3°C. Temperatures were measured with a copper-constantan thermocouple and a Keithley Model 160 Digital Multimeter.

The *in situ* constant potential electrolytic reduction of S_4N_4 for the ESR studies was carried out in a 3 mm soft glass tube with a platinum wire sealed in the bottom. This wire was run up the outside of the tube and served either as the working electrode or as a contact for a mercury pool working electrode. The auxiliary electrode was a platinum coil at the top of the tube about 10 cm from the working electrode and well out of the ESR cavity. The reference electrode was a silver wire placed between the working and auxiliary electrodes.

The ESR measurements were made on a Varian V-4500-10 spectrometer employing a V-3900 12 in. magnet and 100 kHz field modulation. Temperature was controlled by means of a Varian V-4557 variable temperature controller. Measurements of the relative radical concentration as a function of time were made in the following manner. First, the magnetic field was set at that point at which the maximum in the first derivative of the center line occurred. Second, the electrolysis was terminated by disconnecting the working electrode and the decay of the ESR signal was measured as a function of time. Because of the broad lines (about 0.6G), small drifts in the magnetic field introduced a negligible error. In the work reported here, no change in the first derivative line width or line shape was noted with radical concentration; thus, the radical concentration can be considered to be proportional to the intensity of the ESR signal.

Results and Discussion

Cyclic voltammograms of S_4N_4 at room temperature and at −25°C are shown in Fig. 1. At −25°C, the peak currents and peak separation are consistent with a one-electron reduction as found coulometrically by Brown (9), although some charge transfer irreversibility is indicated. An additional reduction process is

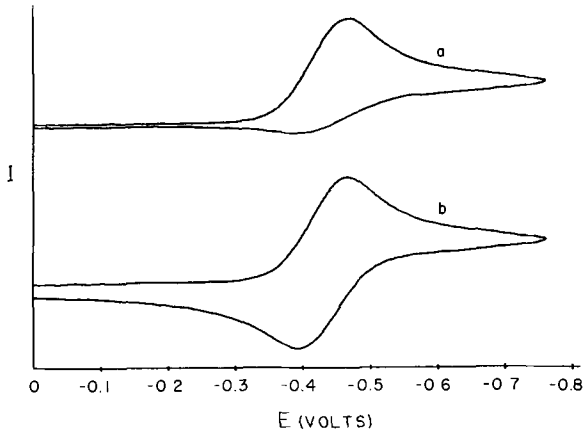

Fig. 1. Cyclic voltammograms of 1 mM S_4N_4 in acetonitrile/0.1M TEAP at a scan rate of 11.4 V/min. Potentials are vs. Ag/0.01M Ag^+. a, 25°C; b, −25°C.

observed at more negative potentials in the form of an ill-defined and totally irreversible wave. This process may be the production of the S_4N_4 dianion which Gleiter (4) has predicted to have a structure different from that of S_4N_4. At room temperature, the radical anion is quite unstable and gives rise to several products which are oxidizable at more positive potentials. There was no indication of any decomposition product being reducible at potentials more positive than the S_4N_4 reduction process.

In situ constant potential electrolytic reduction of S_4N_4 at the peak potential for the one-electron process gave rise to a strong nine-line ESR spectrum at −25°C as shown in Fig. 2. Computer simulation of this spectrum using nine overlapping Lorentzian lines of equal width yields a best fit for $a_N = 1.17 \pm 0.2$G. This value agrees, within experimental error, with the value of 1.185G reported by Meinzer, Pratt, and Myers (7) for the low temperature radical in THF. [The greater precision of the measurement in THF (7) results from their use of a digital technique in recording and analyzing the spectrum.]

The decay of this radical was followed as described above. The decay curves, such as the one shown in Fig. 3, were found to obey a first-order rate law over the temperature range −25° to +3°C and over the concentration range of S_4N_4 from 3 to 5 mM. Similar results were obtained from saturated solutions which were about 7 m*M*. The ESR signals obtained from 1m*M* solutions were too weak for kinetic measurements. The rate constants obtained by this method are presented in Fig. 4 in the form of an Arrhenius activation energy plot. This treatment yields a value of 11.2 ± 0.9 kcal/mole for the activation energy of the first-order decay reaction of the radical.

While the fact that this radical was detected after the constant potential electrolytic reduction of S_4N_4 at

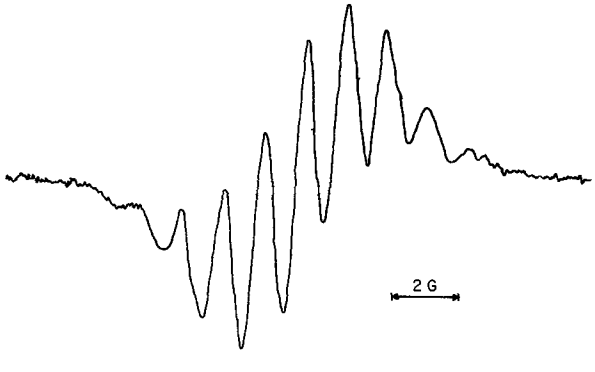

Fig. 2. ESR spectrum of $S_4N_4^-$ generated by *in situ* constant potential reduction of S_4N_4 in MeCN at −20°C.

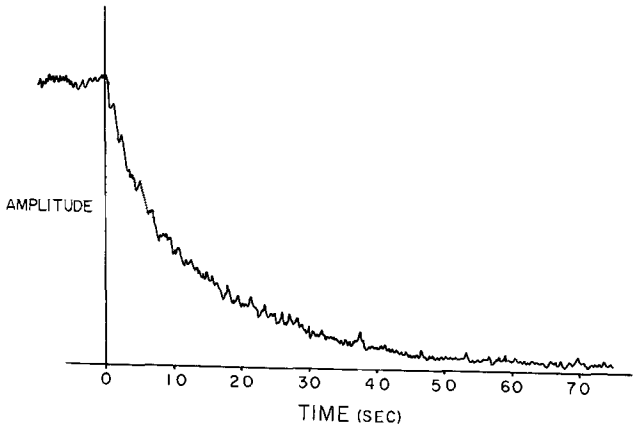

Fig. 3. ESR signal amplitude decay curve for $S_4N_4^{-}$ at −30°C

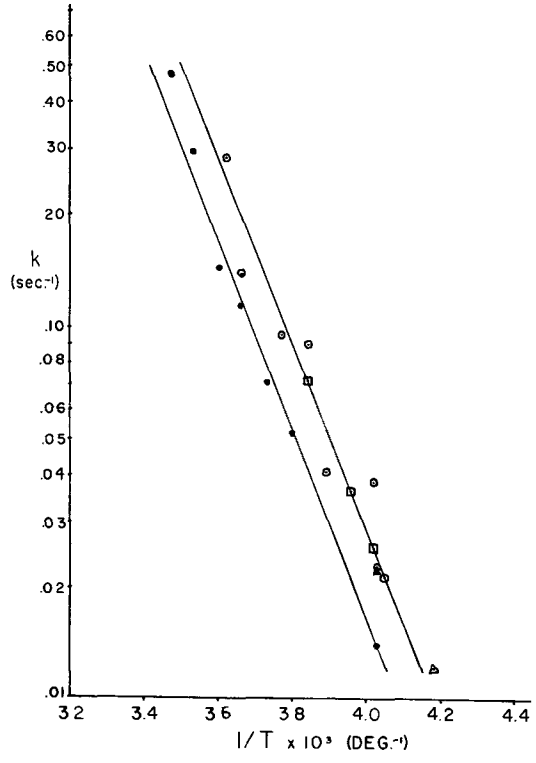

Fig. 4. Semilog plot of the observed first-order rate constants vs. 1/T. ● Electrochemical, 0.99 x 10^{-3}M S_4N_4, 0.1M TEAP; ⊙ ESR, 5 x 10^{-3}M S_4N_4, 0.1M TEAP; □ ESR, 3 x 10^{-3}M S_4N_4, 0.1M TEAP; △ ESR, 5 x 10^{-3}M S_4N_4, 0.2M TEAP.

the peak potential for the one-electron process would strongly suggest that this radical is $S_4N_4^{-}$, it is not impossible that the nine-line spectrum could be due to some decomposition product of $S_4N_4^{-}$. To eliminate this possibility, the kinetics of the disappearance of $S_4N_4^{-}$ (that is, the product of the one-electron reduction of S_4N_4), were measured electrochemically by monitoring the ratio of the anodic to cathodic peak currents obtained from cyclic voltammetry as a function of voltage scan rate and utilizing the first-order EC working curve of Nicholson and Shain (10). The results of such a study on 0.99 × $10^{-3}M$ S_4N_4 solutions are shown in Fig. 5. It is clear that the measured rate constants are functions of scan rate at a given temperature. It is felt that this scan rate dependence is due largely to charge transfer irreversibility. Thus, the measured rate constants were extrapolated linearly to zero scan rate. The extrapolated rate constants are presented in Fig. 4. The value of the activation energy obtained from the extrapolated electrochemical data is 11.1 ± 0.5 kcal/mole.

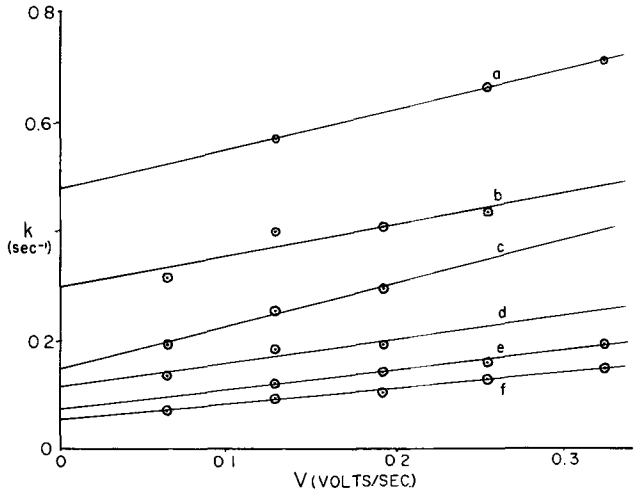

Fig. 5. Electrochemical first-order rate constants plotted vs. voltage scan rate. a, 15°C; b, 10°C; c, 5°C; d, 0°C; e, −5°C; f, −10°C.

The activation energy for the decay of the radical with the nine-line spectrum as measured by ESR and the activation energy for the decay of $S_4N_4^{-}$ as measured electrochemically are identical within experimental error. The values of the rate constants obtained in the two experiments are not identical, however, within the apparent experimental error of each set of results. It is seen that the rate constants obtained from the ESR experiment are larger and more scattered than those obtained from the electrochemical experiment. One could use this discrepancy to argue that the two decaying species were not the same. However, the agreement of the activation energies and all the other circumstantial evidence suggests that the radical with the nine-line spectrum is $S_4N_4^{-}$ and that some other explanation for the discrepancy in the rate constants must be sought.

Two possible sources of this disagreement have been considered. It is possible that the linear extrapolation of the electrochemical data to zero scan rate in order to eliminate the effects of charge transfer irreversibility yielded erroneous values for the rate constants. Admittedly, the choice of a linear extrapolation of the data was arbitrary; but assuming no anomalous behavior between 3.8 V/min and zero, any other type of regression would have yielded similar results. As soon as our rotating ring-disk electrode (RRDE) apparatus is modified to permit work at low temperatures, a RRDE study of S_4N_4 will be undertaken. Charge transfer irreversibility will not be a factor in this study.

The second source of error results from the fact that, since the ESR experiment was carried out in a tube of small cross-sectional area, in a fairly high resistance medium and with the auxiliary electrode some 10 cm from the working electrode, significant Joule heating of the solution in the cavity is probable. To test this hypothesis, a thermocouple was taped to the outside of the tube and the tube was then insulated. An electrolysis under conditions similar to those of the ESR experiment was then carried out. After about 2 min of electrolysis, a temperature rise of approximately 0.5°C was detected on the outside of the glass tube. Considering the poor thermal conductivity of glass, it seems reasonable to suppose that the temperature of the solution within the tube may have risen by as much as 3°-4°C. Such a temperature difference would be sufficient to cause the deviations which were observed. Joule heating would also explain the scatter in the ESR data as the electrolysis time before the kinetic measurement was made varied.

It is felt by the authors that, in view of the above arguments, one can safely conclude that the nine-line spectrum presented here as well as that presented by

Meinzer, Pratt, and Myers (7) is the ESR spectrum of $S_4N_4^{-\cdot}$. We can now consider some of the properties of $S_4N_4^{-\cdot}$ as indicated by this study.

It has previously been shown that orbitally degenerate hydrocarbon-free radicals exhibit anomalously broad ESR lines (11-14). For example, the benzene anion radical, which has a degenerate ground state, exhibits a line width of about 0.3G (12), while the nondegenerate anthracene anion radical exhibits a line width of 0.025G (15). Studies of bonding in S_4N_4 show that an added electron would be placed in a degenerate orbital (4, 5). Meinzer, Pratt, and Myers report the line width of $S_4N_4^{-\cdot}$ to be 0.461G in THF (7) while a value of 0.6G was observed in MeCN in this study. These line width values suggest that $S_4N_4^{-\cdot}$ should be regarded as an orbitally degenerate anion radical.

An analysis of the line widths in MeCN showed little temperature and no field dependence. Similar observations were made in THF (7). In addition, the spectra obtained from MeCN solutions showed no evidence of a statistical variation in line widths like that observed in situations where electron transfer and/or Heisenberg spin exchange are significant (16). The above indicates that exchange reactions and/or slow rotation (17) contribute only slightly if at all to the over-all line width, and that the difference in line widths for $S_4N_4^{-\cdot}$ in THF and in MeCN represents the effect of solvent on the relaxation times for this orbitally degenerate radical. Clearly, detailed studies of T_1 and T_2 for the $S_4N_4^{-\cdot}$ system would provide interesting information which could be compared with that previously obtained for hydrocarbon radicals (11-14).

The facts that $S_4N_4^{-\cdot}$ disappears by a process which is first order in $S_4N_4^{-\cdot}$ and zero order in S_4N_4 and that the activation energy for this process is on the order of a vibrational transition suggest that $S_4N_4^{-\cdot}$ decays by an intramolecular bond rupture. This further suggests that S_4N_4 fragments such as S_2N_2 and others which are known are likely products of the decay of $S_4N_4^{-\cdot}$. These possibilities will be considered in the RRDE study.

Finally, many colors have been observed in reduced solutions of S_4N_4. In none of our experiments in scrupulously dry and deoxygenated solutions could we detect a change in the already yellow solution upon production of $S_4N_4^{-\cdot}$. We conclude, therefore, that $S_4N_4^{-\cdot}$ is probably also yellow. In our early experiments, in which oxygen was not completely removed from the solutions, a fairly intense red color was observed upon reduction. This red substance was later found to result from a reaction between hydroxide ion, produced from the reduction of oxygen, and neutral S_4N_4. Identical uv-VIS spectra were obtained when the red substance was produced electrolytically and by direct reaction between S_4N_4 and NaOH in MeCN. Attempts to isolate the red substance failed. The final product which was isolated from either experiment was found to contain Na_2SO_4. Similar results have been obtained for the reaction between S_4N_4 and hydroxide in aqueous media (18).

Summary

The assignment by Meinzer, Pratt, and Myers of the low-temperature, nine-line ESR spectrum to $S_4N_4^{-\cdot}$ has been substantiated by the determination of the rate of decay of the ESR spectrum and by the electrochemical measurement of the rate of decay of $S_4N_4^{-\cdot}$. The anion radical was found to decay by a first-order process suggesting an intramolecular bond rupture.

Acknowledgments

Acknowledgment is made by K. B. Prater to the donors of the Petroleum Research Fund, administered by the American Chemical Society, and to the Robert A. Welch Foundation for partial support of this research. Acknowledgment is made by M. P. Eastman to the Research Corporation for partial support of this research.

Manuscript submitted April 27, 1973; revised manuscript received May 30, 1973.

Any discussion of this paper will appear in a Discussion Section to be published in the June 1974 JOURNAL.

REFERENCES

1. G. S. Lu and J. Donohue, *J. Am. Chem. Soc.*, **66**, 818 (1944).
2. D. Clark, *J. Chem. Soc.*, **1952**, 1615.
3. B. D. Sharma and J. Donohue, *Acta Cryst.*, **16**, 891 (1963).
4. A. G. Turner and F. Mortimer, *Inorg. Chem.*, **5**, 906 (1966).
5. R. Gleiter, *J. Chem. Soc. (A)*, **1970**, 3174.
6. D. Chapman and A. G. Massey, *Trans. Faraday Soc.*, **58**, 1291 (1962).
7. R. A. Meinzer, D. W. Pratt, and R. J. Myers, *J. Am. Chem. Soc.*, **91**, 6623 (1969).
8. W. L. Jolly, "Inorganic Syntheses," Vol. IX, McGraw-Hill Book Co., New York (1967).
9. O. R. Brown, *J. Electroanal. Chem.*, **34**, 419 (1972).
10. R. S. Nicholson and I. Shain, *Anal. Chem.*, **36**, 706 (1964).
11. M. G. Townsend and S. I. Weissman, *J. Chem. Phys.*, **32**, 309 (1960).
12. R. G. Kooser, Ph.D. Thesis, Cornell University, 1968.
13. R. G. Kooser, V. W. Volland, and J. H. Freed, *J. Chem. Phys.*, **50**, 5243 (1969).
14. M. R. Das, S. B. Wagner, and J. H. Freed, *ibid.*, **52**, 5404 (1970).
15. J. R. Bolton and G. K. Fraenkel, *ibid.*, **40**, 3307 (1964).
16. M. P. Eastman, R. G. Kooser, M. R. Das, and J. H. Freed, *ibid.*, **51**, 2690 (1969).
17. J. E. Wertz and B. R. Bolton, "Electron Spin Resonance Elementary Theory and Practical Applications," McGraw Hill Book Co., New York (1972).
18. C. G. R. Nair and A. R. V. Murthy, *J. Inorg. Nucl. Chem.*, **25**, 453 (1963).

Polarography of Some 1,1-Dithiolates and Their Mercury Complexes in Acetone

A. M. Bond,* A. T. Casey, and J. R. Thackeray

Inorganic Chemistry Department, Melbourne University, Parkville, Victoria 3052, Australia

ABSTRACT

Dialkyldithiophosphate and dimethyldithioarsinate anions (L^-) have been found to interact with the DME in acetone via the processes $6L^- + 2Hg^\circ \rightleftharpoons 2Hg^{II}(L)_3^- + 4e$ and $2Hg^{II}(L)_3^- + Hg^\circ \rightleftharpoons 3Hg^{II}(L)_2 + 2e$. The mercury complexes resulting from these steps have also been investigated polarographically, although many could not be isolated, and the over-all mechanism has been compared to those exhibited by other 1,1-dithiolate anions. No reduction steps were observed for any of the dithiolates studied.

Recent electrochemical studies on 1,1-dithiolate anions in nonaqueous solvents have shown that they can oxidize mercury at a DME to yield mercury dithiochelate complexes (1, 2). Interestingly, the closely related dialkyldithiocarbamates, (I), and O-alkylxanthates, (II), were found to react via completely different intermediates, although at sufficiently positive potentials both produced mercury(II) complexes of the formulation $Hg^{II}L_2$ (where L = dialkyldithiocarbamate or alkylxanthate).

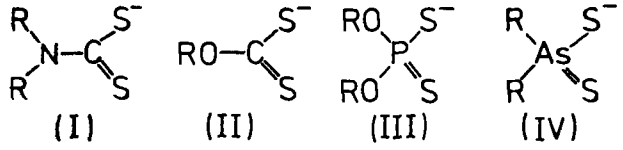

(I) (II) (III) (IV)

(R represents an alkyl group)

In view of the considerably different polarographic behavior caused by simply changing an $-NR_2$ group (attached to $-CS_2^-$) for an $-OR$ group, it was thought that comparative studies on the distinctly different O,O'-dialkyldithiophosphate, (III), and dimethyldithioarsinate, (IV), anions would be of interest. Moreover, if these potential ligands do interact with the DME, then identification of the resulting products should provide an insight into the chemistry of their mercury complexes.

Apart from interaction with the mercury electrode, a number of alternative electrochemical oxidation and reduction processes can be envisaged for all of these entities. They could undergo a two-electron oxidation to yield the corresponding disulfides (*e.g.*, thiuram disulfides from dithiocarbamates and dixanthogens from xanthates), and in fact the formation of dixanthogens has been extensively studied at a number of electrodes because of their application to flotation technology (3-5). Isolated thionyl groups can also be reduced, and in this regard comparative studies have been made between thiones and ketones (6). Possible reduction pathways are therefore also of interest.

The behavior of uncoordinated 1,1-dithiolate anions also has direct application to the electrochemistry of transition metal complexes incorporating these ligands. Indeed, knowledge of the ligand behavior has already facilitated the interpretation of complicated electrode processes undergone by some vanadium(IV) dithiochelates at the DME (1,7). Thus the electrochemistry of 1,1-dithiolates is of interest to a number of fields, and it is envisaged that the work presented here will prove of value to other electrochemical investigations involving transition metal dithiochelates.

* Electrochemical Society Active Member.
Key words: polarography, dialkyldithiophosphate, dimethyldithioarsinate, mercury complexes.

Abbreviations

The following abbreviations have been used in the text: dadtp, O,O'-dialkyldithiophosphate; dpdtp, O,O'-diisopropyldithiophosphate; dtcac, dimethyldithioarsinate (or dithiocacodylate); Et, ethyl; dedtp, O,O'-diethyldithiophosphate.

Experimental

Preparations.—Ammonium O,O'-dialkyldithiophosphates.—The stoichiometric amount of P_4S_{10} was added to the appropriate alcohol in benzene to produce a solution of the corresponding dialkyldithiophosphoric acid. Ammonia was then bubbled through the solution until the ammonium dialkyldithiophosphate precipitated.

Bis(dialkyldithiophosphato)mercury(II) complexes.—The stoichiometric amount of the required ammonium dialkyldithiophosphate was mixed with $Hg(NO_3)_2$ in water. The resulting white solid was well washed with water and finally recrystallized from ethanol. This compound has been reported previously (8).

Sodium dimethyldithioarsinate.—This compound was prepared by the method of Casey *et al.* (9)

Attempts to prepare bis(dimethyldithioarsinato)mercury(II).—When the stoichiometric amount of sodium dimethyldithioarsinate was mixed with $Hg(NO_3)_2$, a yellow solid deposited. This product immediately turned brown in the atmosphere and further attempts to isolate a pure sample under argon failed.

Materials.—Sodium dialkyldithiophosphates were used as received from Cyanamid, Wayne, New Jersey. Their solubility in acetone was not as great as the ammonium salts and so they were only used for specific experiments as indicated in the text. "Pronalys" acetone was employed for all polarographic measurements and was used as received from May and Baker.

Instrumentation.—Conventional d-c polarograms were recorded in acetone with a Metrohm Polarecord (E261) using 0.1M tetraethylammonium perchlorate as supporting electrolyte. A three-electrode, *iR* compensated system using a Metrohm *iR* compensator (E446) was employed for all conventional d-c measurements. The reference electrode was a Metrohm Ag/AgCl EA425 electrode (0.1*M* LiCl, acetone). The auxiliary (or third) electrode was either a tungsten or platinum wire electrode, or a Ag/AgCl electrode identical to the reference. Controlled drop-time and current sampled polarograms were recorded with a Princeton Applied Research Corporation (PAR) Electrochemical System, Model 170. A Metrohm Polarographie Stand (E354) was utilized to obtain short, controlled drop times between 0.16 and 0.32 sec. The PAR Model 172 Drop Timer was used with a drop time close to 2 sec to record current sampled polarograms

Table I. Dependence of half-wave potentials ($E_{1/2}$) and wave heights (i_d) on concentration for ammonium O,O'-diethyldithiophosphate

Concentration, M	$E_{1/2}$ (wave 2) (V vs. Ag/AgCl)	$(E_{1/4} - E_{3/4})$ (V)	i_d (μA)	$E_{1/2}$ (wave 1) (V vs. Ag/AgCl)	$(E_{1/4} - E_{3/4})$ (V)	i_d (μA)	$E_{1/2}$ (wave 4) (V)	i_L (μA)
10^{-2}	+0.185	0.076	13.6	−0.164	0.072	33.0	−0.380	1.8
5×10^{-3}	+0.171	0.072	6.8	−0.153	0.062	17.3	−0.368	0.8
10^{-3}	+0.140	0.072	1.34	−0.142	0.056	3.35	−0.335	0.2
5×10^{-4}	+0.135	0.069	0.62	−0.121	0.056	1.74	−0.335	0.08

The Metrohm Polarecord (E261) was used in conjunction with the Metrohm AC Modulator (E393) and the Metrohm *iR* Compensator (E446) to provide a three-electrode a-c polarograph as described elsewhere (10). With this instrumentation, the total alternating current was recorded using an applied alternating potential of 10 mV rms at a frequency of 50 Hz. Cyclic and linear sweep voltammetry were achieved with the PAR Electrochemical System using a J-tube mercury electrode as the working electrode.

All test solutions were thoroughly degassed with acetone-saturated argon and a continuous stream of argon was passed over solutions while measurements were being taken. Solutions were thermostated to 20.0° ± 0.1°C in a water-jacketed cell.

Results and Discussion

Polarographic behavior of ammonium O,O'-dialkyldithiophosphates.—O,O'-dialkyldithiophosphate anions show three characteristic oxidation waves (see Fig. 1). No reduction waves other than those attributable to the sodium or ammonium cations were observed up to the solvent limit of −2.2V *vs.* Ag/AgCl. Oxidation waves 1 and 2 were investigated over the concentration range 5×10^{-4} to 10^{-2}M; however, wave 3 occurred close to the positive potential limit (~ + 0.8V *vs.* Ag/AgCl) and therefore was not characterized. Typical results of studies at different concentrations are given in Table I.

The heights of waves 1 and 2 were both linearly proportional to $\sqrt{h}$ (where h is the height of the mercury column head) and to concentration over the range 5×10^{-4} to 10^{-2}M. With increasing concentration the half-wave potential of wave 1 became more negative and that of wave 2 more positive. A-C polarograms of waves 1 and 2 showed that they were asymmetric (see Fig. 2), but the current per unit concentration was large in both cases and characteristic of fast electrode processes. Cyclic voltammetry at a J-tube mercury electrode also confirmed the presence of two rapid and separate charge transfer steps.

In addition to the two main waves, a small wave was found at slightly more negative potentials than wave 1 (see Fig. 1 and 2). This wave (wave 4) was particularly evident in a-c polarograms and may arise from an adsorption/desorption process, since it occurs close to the electrocapillary maximum (see Fig. 3). The marked decrease in drop time of the DME in the potential range of waves 1 and 2 indicates that the compound(s) and/or product(s) of the anodic reaction is strongly adsorbed. Thus although both waves 1 and 2 arise from rapid charge transfer processes, their behavior is likely to be complicated by adsorption phenomena.

The ratio of the limiting current of wave 1 to that of wave 2 was approximately 1:2.2 ± 0.1 as measured

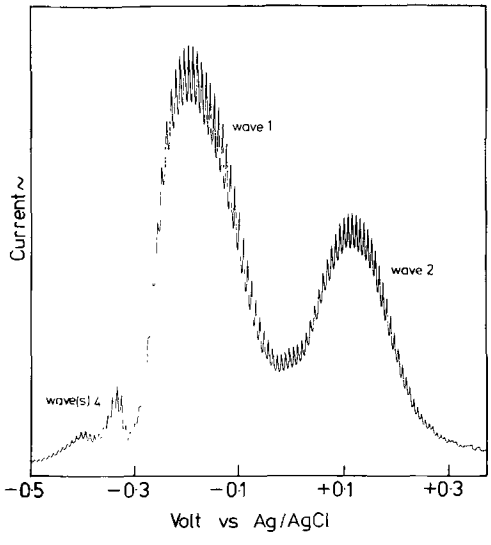

Fig. 2. The a-c polarogram of 10^{-2}M ammonium diethyldithiophosphate.

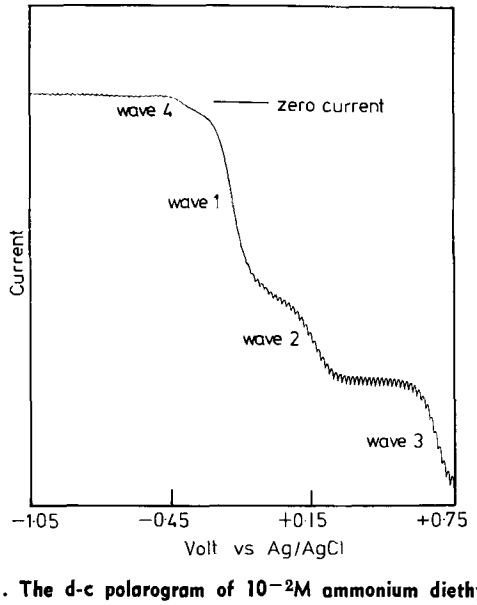

Fig. 1. The d-c polarogram of 10^{-2}M ammonium diethyldithiophosphate.

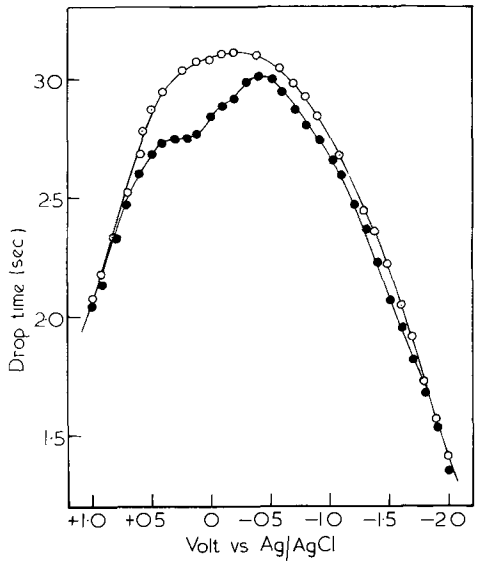

Fig. 3. The electrocapillary curves (DME at h = 74 cm) of (a) 0.1M Et_4NClO_4 (⊙), and (b) solution (a) plus 10^{-3}M ammonium diethyldithiophosphate (●).

from controlled drop-time polarograms, and the total height of waves 1 plus 2 was close to the height of the wave from the one-electron reduction of the sodium ion (from controlled, drop-time polarograms of sodium dialkyldithiophosphates).

Similar polarographic behavior was obtained from potassium O-alkylxanthates in acetone (2). For these ligands the following processes were found consistent with the observed polarographic behavior at the DME

$$2Hg^{\circ} + 6ROCS_2^- \rightleftharpoons 2Hg^{II}(ROCS_2)_3^- + 4e \quad [1]$$

$$2Hg^{II}(ROCS_2)_3^- + Hg^{\circ} \rightleftharpoons 3Hg^{II}(ROCS_2)_2 + 2e \quad [2]$$

where process [1] gave rise to wave 1 and process [2] to wave 2. Since the total height of waves 1 and 2 for dithiophosphates is close to that from the corresponding xanthate waves, it is likely that both ligand systems initiate the same processes at the DME. If the dithiophosphates undergo the above mechanism, and both electrode processes are reversible, then the potential at the DME for wave 1 ($E^{(1)}$) should be given by

$$E^{(1)} = C_1 + \frac{RT}{2F} \ln \left[\frac{[Hg(dadtp)_3^-]_0}{[dadtp^-]_0^3} \right] \quad [3]$$

and for wave 2 by

$$E^{(2)} = C_2 + \frac{RT}{2F} \ln \left[\frac{[Hg(dadtp)_2]_0^3}{[Hg(dadtp)_3^-]_0^2} \right] \quad [4]$$

where C_1 and C_2 are constants, and the subscript zero denotes concentrations at the surface of the DME. The equations for the two waves may be written

$$E^{(1)} = C_1' + \frac{RT}{2F} \ln \left[\frac{i}{(i_d - i)^3} \right] \quad [5]$$

$$E^{(2)} = C_2' + \frac{RT}{2F} \ln \left[\frac{i^3}{(i_d - i)^2} \right] \quad [6]$$

and the half-wave potentials of these waves should change with i_d (or concentration of $dadtp^-$) according to

$$E^{(1)}{}_{1/2} = C_1'' - \frac{RT}{F} \ln [dadtp^-] \quad [7]$$

$$E^{(2)}{}_{1/2} = C_2'' + \frac{RT}{2F} \ln [dadtp^-] \quad [8]$$

A plot of potential *vs.* $\log \left[\frac{i}{(i_d - i)^3} \right]$ for wave 1 from a 10^{-2}M solution of NH_4dedtp is shown in Fig. 4. The relationship was linear except for the negative potential extreme of the wave and the slope was 33 mV (cf. thoretically predicted value of 29 mV). These slight deviations from theory probably result from adsorption phenomena or incomplete reversibility. Figure 5 shows plots of potential against $\log \left[\frac{i^3}{(i_d - i)^2} \right]$ for wave 2. Slopes were again slightly higher than predicted and deviations from linearity were obtained from the negative potential side of the wave. The slope and deviation from linearity increased with increasing concentration, indicating that adsorption is the most likely explanation for these departures from theory.

The $(E_{1/4} - E_{3/4})$ values given in Table I may also be used as criteria for the proposed mechanism. From Eq. [5] and [6] it follows that $(E_{1/4} - E_{3/4})$ should be 56 mV for wave 1 and 69 mV for wave 2. The values agree with those theoretically predicted at low concentrations, but as the concentration is increased they become progressively higher.

The half-wave potentials of the waves vary with concentration in the directions predicted by Eq. [7] and [8]; however the magnitudes of the changes are not exactly those expected from theory. The ratio of the two wave heights is in close agreement with the 1:2 value required by the reaction mechanism.

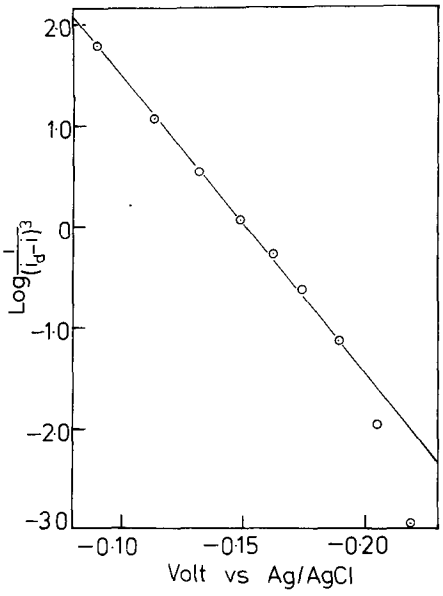

Fig. 4. A plot of potential *vs.* $\log \left[\frac{i}{(i_d-i)^3} \right]$ for wave 1, (from a 10^{-2}M solution of ammonium diethyldithiophosphate).

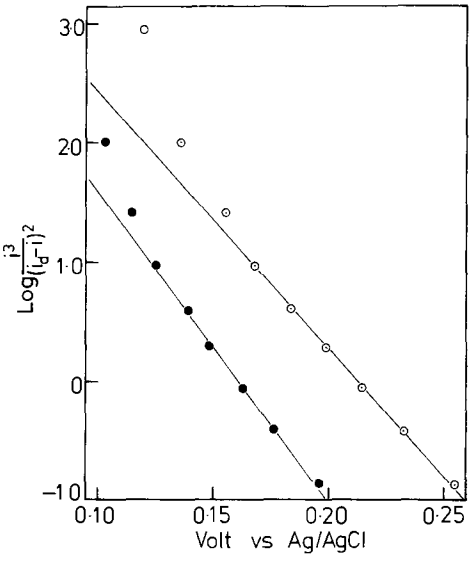

Fig. 5. A plot of potential *vs.* $\log \left[\frac{i^3}{(i_d-i)^2} \right]$ for wave 2, [from a 10^{-2}M solution of ammonium diethyldithiophosphate (⊙) and a 10^{-3}M solution (●)].

In summary, the proposed mechanism provides at least an adequate qualitative description of the system and departures from theoretically predicted behavior are most likely associated with adsorption phenomena. To test the validity of the mechanism further, studies were undertaken on mercury(II) dialkyldithiophosphates.

Polarographic behavior of mercury(II) dialkyldithiophosphates.—The polarogram of bis(dipropyldithiophosphato)mercury(II) was similar to that of the free ligand except that waves 1 and 2 were now cathodic, as expected from the proposed mechanism (see Fig. 6A). However, it was noted that wave 2 from the mercury compounds was somewhat more drawn out than the corresponding oxidation wave from the ligand anions, and the two cathodic waves were not as well separated as the anodic waves from the ammonium salt. Figure 6B illustrates the complexity of wave 2 further, since it is even more drawn out when both

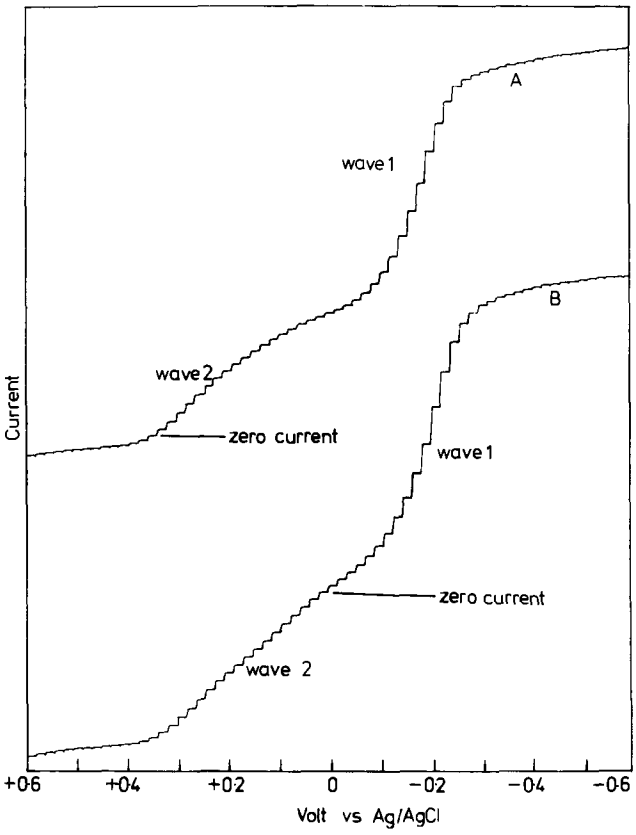

Fig. 6. (A) A current-sampled d-c polarogram of $Hg^{II}(dpdtp)_2$ ($\sim 10^{-3}$M). (B) A current-sampled polarogram of $Hg^{II}(dpdtp)_2$ plus one mole equivalent of dpdtp anions.

$Hg(dpdtp)_2$ and $dpdtp^-$ are present in solution. This indicates partial irreversibility, greater adsorption of mercury species, or that other additional complexities are associated with the $2Hg(dadtp)_3^- + Hg^\circ \rightleftharpoons 3Hg(dadtp)_2 + 2e$ process. Dakternieks and Graddon (8) have shown that $Hg(dadtp)_2$ complexes associate slightly to dimers in solution and it may be this phenomenon that causes the slight difference in behavior. The mechanism also requires the existence of $Hg(dadtp)_3^-$ species. Unfortunately attempts to isolate such entities as tetraethylammonium salts resulted in failure. Similar results to that illustrated in Fig. 6 were obtained by adding two and three mole equivalents of $dpdtp^-$ anions to a $Hg(NO_3)_2$ solution. Interestingly, the current height after adding one mole equivalent of $dpdtp^-$ anions was close to that after the addition of equimolar amounts. Furthermore, no cathodic current due to the reduction of solvated Hg^{2+} ions was seen. This suggests that $Hg(dadtp)^+$ species are viable entities in addition to $Hg(dadtp)_2$ and $Hg(dadtp)_3^-$. Prior to this work only the $Hg(dadtp)_2$ species has been reported (8).

Polarographic behavior of sodium dimethyldithioarsinate.—Polarograms from this ligand were qualitatively similar to those of the dithiophosphates except that oxidation waves 1 and 2 were much closer, making individual characterization of the waves difficult (see Fig. 7). Again no ligand reduction waves were found. At 10^{-3}M wave 1 had a half-wave potential of −0.378V, and wave 2 occurred at $E_{1/2} = -0.208$V. The limiting current of wave 1 was estimated as 34 μA and wave 2 as 17 μA. At higher concentrations wave 2 exhibited a severe maximum. The waves were too close to assess the individual dependencies of their limiting currents on the mercury column height; however the total limiting current of both waves was proportional to $\sqrt{h}$ and to concentration. The total limiting current was also close to that obtained from the one-electron reduction of the sodium ion introduced into solution as the counterion for the ligand.

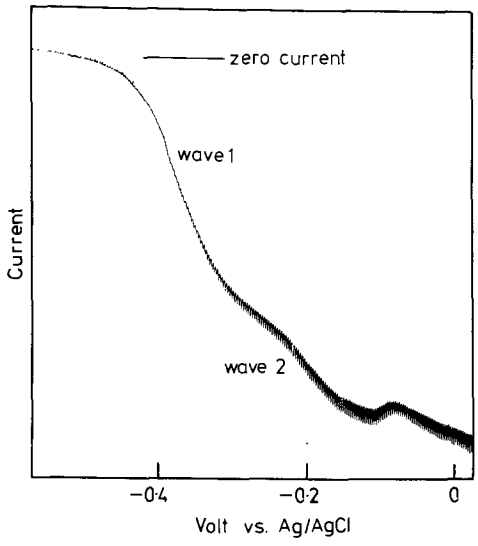

Fig. 7. The d-c polarogram of 10^{-3}M sodium dimethyldithioarsinate.

Polarographic behavior of mercury(II) dimethyldithioarsinate species.—Attempts to isolate a pure sample of bis(dimethyldithioarsinato)mercury(II) resulted in failure (see Experimental section); however the polarographic behavior of mercury(II) complexes with this ligand was investigated by preparing the complexes in the polarographic cell under argon, using stoichiometric amounts of mercuric nitrate and the ligand anion. Although polarograms were not as definitive as those of the mercury(II) dithiophosphate species (because of the close proximity of the two waves and the nature of the experiment), they strongly suggest that the dimethyldithioarsinate ligand interacts with the DME in a similar manner to the dithiophosphate ligands. Both waves 1 and 2 were cathodic after the addition of two mole equivalents of free ligand, and wave 2 became anodic after three mole equivalents had been added. A cloudy solution was observed when one mole equivalent of ligand had been added, probably due to the low solubility of ionic $[Hg(C_2H_6AsS_2)]^\oplus(ClO_4^-)$ in acetone. The solution cleared when a further mole equivalent of ligand was present owing to the greater solubility of the neutral bis complex; no precipitation of $[Et_4N]^\oplus[Hg(C_2H_6AsS_2)_3]^-$ occurred. As for the corresponding dithiophosphato complexes, the $Hg(dtcac)^+$, $Hg(dtcac)_2$, and $Hg(dtcac)_3^-$ species all appear to be viable entities and very strong evidence for the existence of hitherto unreported mercury(II) complexes of this ligand has therefore been obtained.

Discussion

Whereas alkylxanthate, dialkyldithiophosphate, and dimethyldithioarsinate anions interact with the DME via the processes outlined in Eq. [1] and [2], the behavior of dialkyldithiocarbamate anions (1) is fundamentally different and may be described by Eq. [9] and [10]

$$2Hg^\circ + 2R_2NCS_2^- \rightleftharpoons 2Hg^I(S_2CNR_2) + 2e \quad [9]$$

$$2Hg^I(S_2CNR_2) \overset{\text{rapid}}{\rightleftharpoons} Hg^{II}(S_2CNR_2)_2 + Hg^\circ \quad [10]$$

This difference in mechanism must be related to the stability of the various tris(1,1-dithio)mercury(II) complex anions, and possibly also to that of the mercury(I) species. Kemula *et al.* (11) have determined the following stability constants for diethyldithiocarbamatomercury(II) complexes from potentiometric studies in water

$$Hg^{2+} + {}^-S_2CNEt_2 \rightleftharpoons Hg(S_2CNEt_2)^+ \qquad K_1 = 2.1 \times 10^{22}$$

$$Hg(S_2CNEt_2)^+ + {}^-S_2CNEt_2 \rightleftharpoons Hg(S_2CNEt_2)_2$$

$$K_2 = 5.7 \times 10^{15}$$

$$Hg(S_2CNEt_2)_2 + {}^-S_2CNEt_2 \rightleftharpoons Hg(S_2CNEt_2)_3^-$$

$$K_3 = 1.7 \times 10^1$$

Thus the formation of the anionic tris dithiocarbamate complexes is strongly discriminated against in favor of the bis and $Hg(S_2CNEt_2)^+$ species (even with a large excess of ligand). The same conclusion was reached from polarographic studies in acetone (1).

The above observations are consistent with studies on transition metal complexes with these ligands. For example, NiL_2 complexes readily form base adducts when L is an alkylxanthate (12) or dialkyldithiophosphate (13, 14), but not when L is a dialkyldithiocarbamate (12).

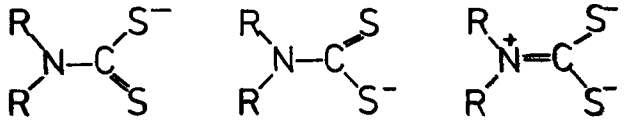

(a) (b) (c)

It is believed that canonical form (c) contributes greatly to the structure of dialkyldithiocarbamate complexes, whereas the corresponding form for the other ligands is of much less significance. Since form (c) results in a larger charge transfer from ligand to metal, the capacity for further coordination to the metal is lowered.

The greater ligand to metal charge donation for dithiocarbamates is also reflected by the relative $E_{1/2}$ values from the HgL_2 reduction waves. For diethyldithiocarbamate the reduction (see Eq. [9] and [10]) occurred at -0.505V (10^{-3}M). Comparable half-wave potentials for the mercury complexes with the other ligands may be calculated from the $E_{1/2}$ values of waves 1 and 2, since the processes given in Eq. [1] and [2] are over-all thermodynamically equivalent to the process $HgL_2 + 2e \rightleftharpoons Hg + 2L^-$. Half-wave potentials calculated for this reaction at concentrations of 10^{-3}M were -0.212V (L = ethylxanthate), -0.048V (L = diethyldithiophosphate), and -0.274V (L = dimethyldithioarsinate). The stability of the mercury(II) complexes is obviously greatest for the dithiocarbamate complex. The actual determination of stability constants was prohibited by the extremely complex nonreversible nature of the mercury(II) nitrate reduction and no data is available on the $E°$ value for the $Hg^{2+}|Hg(o)$ couple in acetone.

The polarographic behavior of 1,1 dithio acids is markedly different to that of the free 1,1 dithio ligands and obviously involves the hydrogen ion. Experiments on xanthate anions showed that the height of wave 1 diminished upon the addition of hydrogen ions whereas that of wave 2 increased. The equilibrium $L^- + H^+ \rightleftharpoons LH$ apparently must be considered in the presence of protons. Presumably the formation of tris species is inhibited for the dithio acids and the height of wave 1 probably reflects the equilibrium concentration of free ligand anions. The half-wave potential of wave 2 became more positive as the hydrogen ion concentration was increased, indicating a change in the electrode process and the need to incorporate terms involving protons in any description of the mechanism. Joris *et al.* (15) observed a similar shift toward more positive potentials with increasing hydrogen ion concentration for the oxidation wave from dithiocarbamate anions. They showed that the behavior was consistent with that predicted from the equilibrium existing between protonated and unprotonated forms of the dithiolate.

It is interesting to note that Bond *et al.* (16) observed an oxidation wave at $E_{1/2} = +0.226$V for O-ethylthioacetothioacetate, (V)

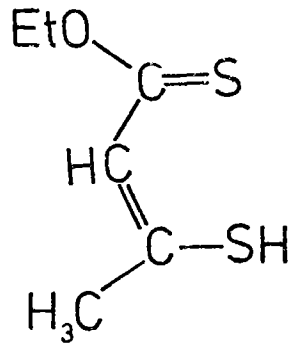

(V)

and a reduction wave at $E_{1/2} = -0.41$V for the bis-(O-ethylthioacetothioacetato)mercury(II) complex. In light of our observations it is likely that the behavior of the mercury(II) complex reflects the behavior of the free ligand anion, the sodium salt of which has not been isolated in a pure state. The difference in the electrode processes undergone by the mercury complex and the protonated ligand may be attributed in part to the presence of the hydrogen atom.

The lack of any reduction waves up to the solvent limit of -2.2V *vs.* Ag/AgCl is surprising considering the possible pathways mentioned at the beginning of this paper. This observation is of considerable significance in studies on transition metal dithiochelates since there is often difficulty in deciding upon the nature of any reduction waves obtained. The results of this work indicate that any reduction waves seen in metal complexes incorporating ligands (I)-(V) cannot be attributed to dissociated ligand. Furthermore, reduction pathways of the type observed for thioketones (6) must occur at extremely negative potentials, be markedly inhibited in aprotic solvents such as acetone, or be inapplicable to 1,1 dithiolates.

Acknowledgment

J.R.T. thanks the Commonwealth of Australia for a CPRA.

Manuscript submitted March 26, 1973; revised manuscript received June 13, 1973.

Any discussion of this paper will appear in a Discussion Section to be published in the June 1974 JOURNAL.

REFERENCES

1. A. M. Bond, A. T. Casey, and J. R. Thackeray, *Inorg. Chem.*, **12**, 887 (1973).
2. A. M. Bond, A. T. Casey, and J. R. Thackeray, *J. Electroanal. Chem.*, In press.
3. S. G. Salamy and J. C. Nixon, "Recent Developments in Mineral Dressing," p. 503 and references therein, Institute of Mining and Metallurgy, London (1953).
4. R. Woods, *J. Phys. Chem.*, **75**, 354 (1971), and references therein.
5. R. Woods, *Australian J. Chem.*, **25**, 2329 (1972).
6. R. M. Elofson, F. F. Gadallah, and L. A. Gadallah, *Can. J. Chem.*, **47**, 3979 (1969), and references therein.
7. A. M. Bond, A. T. Casey, and J. R. Thackeray, Submitted to *J. Chem Soc.*
8. D. R. Dakternieks and D. P. Graddon, *Australian J. Chem.*, **24**, 2077 (1971).
9. A. T. Casey, N. S. Ham, D. J. Mackey, and R. L. Martin, *ibid.*, **23**, 1117 (1970).
10. A. M. Bond and J. R. Thackeray, *Chem. Instrument.*, **4**, 299 (1973).
11. W. Kemula, A. Hulanicki, and W. Nawrot, *Roczniki Chem.*, **36**, 1717 (1962); **38**, 1065 (1964).
12. D. Coucouvanis, *Prog. Inorg. Chem.*, **11**, 342 (1970), and references therein.
13. S. Ooi and Q. Fernando, *Inorg. Chem.*, **6**, 1558 (1967).
14. S. E. Livingston and A. E. Mihkelson, *ibid.*, **9**, 2545 (1970).
15. S. J. Joris, K. I. Aspila, and C. L. Chakrabarti, *Anal. Chem.*, **41**, 1441 (1969).
16. A. M. Bond, A. R. Hendrickson, and R. L. Martin, *This Journal*, **119**, 1325 (1972).

The Current Distribution Within Tubular Electrodes under Laminar Flow

Richard Alkire* and Ali Asghar Mirarefi**

Department of Chemical Engineering, University of Illinois, Urbana, Illinois 61801

ABSTRACT

A computational method has been developed for calculating the current density distribution within tubular electrodes under laminar flow. Calculations have been carried out for operating conditions which are intermediate between the secondary current distribution and the limiting current distribution. The potential distribution within the tube was determined from Laplace's equation while the reactant concentration along the electrode surface was found from the convective diffusion equation. The two equations were strongly coupled so that they needed to be solved simultaneously. Although central emphasis has been placed on details of the computational method, several salient features of behavior are discussed. The results illustrate how the current distribution within tubular electrodes depends on counterelectrode placement as well as the geometric, charge transfer, mass transfer, and ohmic parameters of the system.

Determining the current and potential distributions within electrolysis cells is important both for the analysis of experimental data obtained at individual electrodes, and for the design and scale-up of useful overall cell configurations. Accordingly, a variety of calculational methods have been developed. The purpose of these calculations has been to elucidate how the current and potential distributions depend on the characteristic nature of a cell including, for instance, its electrolyte conductivity, cell and electrode geometry, charge transfer characteristics, fluid flow patterns, solution concentrations, and electrode resistances. Owing to the large number of variables, the nature of the problem is very complex indeed. However, several situations of limited validity can be analyzed with comparative ease. For example, when the electrode reaction proceeds at low rates, the potential distribution may be determined on the basis of the Laplace equation. When the potential distribution depends solely on the cell geometry, the distributions are referred to as "primary" current and potential distributions. If the electrode reaction is sluggish, the potential distribution depends not only on cell geometry, but also on the solution conductivity and the electrode reaction overpotential; such results are called "secondary" distributions. On the other hand, at very high reaction rates, the rate of mass transfer to the electrode surface becomes the central phenomenon of interest. In the limiting situation where only mass transfer restrictions are important (*i.e.*, at the limiting current) then the current distribution along an individual electrode may be obtained from the laws of convective diffusion.

Electrochemical cells, however, are often operated under conditions which do not conform to either of the limiting situations described above. In order to gain an understanding of behavior in these more complex situations, it is necessary to take account simultaneously of the several phenomena which influence the current distribution (1). Owing to the complexity of the problem, only a few examples are available. These include treatments of natural convection in a cell with vertical electrodes (2), laminar forced convection in a two-dimensional slot (3, 4), and rotating disk electrodes (5). In the investigation reported below, an analysis has been conducted on a class of tubular electrodes operated under laminar flow.

* Electrochemical Society Active Member.
** Electrochemical Society Student Associate.
Key words: current distribution, tubular electrode, mathematical model.

Theoretical Formulation

The system under investigation is shown in Fig. 1. The tubular electrode of length l is positioned between two long pipe sections made of insulator material. Electrolytic solution flows through the assembly in fully developed laminar flow and thereby supplies reactive solute species to the electrode surface where electrochemical reaction occurs. As indicated in Fig. 1, two coordinate systems find use: one is based on the pipe axis (x,r) and the other is based along the electrode surface, beginning at the upstream edge (z,y). The counterelectrode may take one of two positions with respect to the tubular electrode: upstream ($x = 0$) as in Fig 1B, or downstream ($x = l_1 + l + l_2$) as in Fig. 1A. Other than its position far upstream or far downstream, the detailed nature of the counterelectrode is not of interest in the present study.

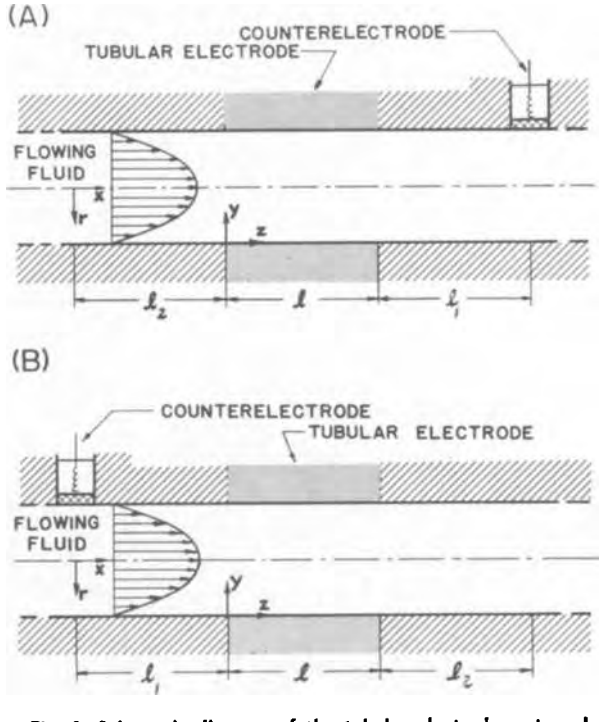

Fig. 1. Schematic diagram of the tubular electrode system. Laminar flow is from left to right. (A) The counterelectrode is on the right; (B) the counterelectrode is on the left.

The electrochemical phenomena which occur in the model tubular electrode system can be complex. Several simple aspects have been selected for study in accord with the following assumptions: (*i*) Electrolysis proceeds under steady-state conditions with fully developed laminar flow in the tubular electrode. (*ii*) The reactive solution species are present in dilute concentrations; owing to the presence of supporting electrolyte, the reactive species do not migrate in the electric field. (*iii*) Concentration differences in the electrolyte, caused by reaction, are confined to a thin shell near the tube periphery; the dimensionless Péclet number, $2R_o<v_z>/D_i$ is large.

Because concentration differences are confined near the electrode surface, two distinct regions may be identified within the electrolyte flowing through the electrode: (*a*) the diffusion layer region, near the electrode surface, within which the concentration of reactive solute varies, and (b) the bulk region, which fills the remainder of the volume within the tubular electrode. Separate equations will be developed for the two regions which share a common boundary at the outer edge of the diffusion layer.

Dimensional equations.—The potential applied between the tubular electrode and the nonpolarized counterelectrode, ϕ_A, is consumed by various irreversible phenomena occurring within the cell. These include ohmic losses in the electrolytic phase, surface overpotential owing to charge-transfer, and concentration overpotential within the thin mass transfer region

$$\phi_A = \phi^o + \eta_s + \eta_c \qquad [1]$$

The concentration overpotential, η_c, depends on the solute concentration at the electrode surface and thus varies with axial position along the electrode

$$\eta_c = \frac{R_gT}{n\mathbf{F}} \ln \frac{c_s}{c_\infty} \qquad [2]$$

Likewise, the surface overpotential depends on position since it is influenced both by the local solute concentration and by the local reaction rate. The rate expression chosen for study is

$$j = i_o \left(\frac{c_s}{c_\infty}\right)^\gamma \left[e^{\frac{\alpha n\mathbf{F}}{R_gT}\eta_s} - e^{-\frac{\beta n\mathbf{F}}{R_gT}\eta_s} \right] \qquad [3]$$

Additional equations are needed in order to determine the concentration distribution within the diffusion layer and the potential distribution in the bulk region. As mentioned previously, these two regions share a common boundary along the outer edge of the thin diffusion layer. It is convenient to denote the potential along this boundary by ϕ_o

$$\phi_o = \phi_A - \phi^o = \eta_s + \eta_c \qquad [4]$$

Diffusion Layer Region

In accord with the assumption that the Péclet number is large, the steady-state equation of laminar convective diffusion in the tube is

$$v_x \frac{\partial c_i}{\partial x} = D_i \left[\frac{\partial^2 c_i}{\partial r^2} + \frac{1}{r}\frac{\partial c_i}{\partial r} \right] \qquad [5]$$

Since the diffusion layer is very thin, the velocity distribution is approximately linear with distance from the wall; in addition, the second term in the brackets of Eq. [5] becomes negligible with respect to the first term. By changing the coordinates of Eq. [5] to the (z,y) system, and by inserting the approximations stated above, one obtains

$$\left(\frac{2v_{max}}{R_o}\right) y \frac{\partial c_i}{\partial z} = D_i \frac{\partial^2 c_i}{\partial y^2} \qquad [6]$$

wherein the velocity distribution in the diffusion layer is approximated by the relation $v_z = (2v_{max}/R_o)y$. Equation [6] corresponds to the Lévêque solution which is a good approximation provided that $(zD_i/2<v_z>R_o^2) << 0.01$. At the limiting current condition, the boundary conditions on Eq. [6] would be

$$\begin{aligned} &c_i = 0 \quad \text{at} \quad y = 0, \quad z > 0 \\ &c_i = c_\infty \quad \text{at} \quad y = \infty, \quad z > 0 \\ &c_i = c_\infty \quad \text{at} \quad z \leq 0 \end{aligned} \qquad [7]$$

By using the combination of variables approach, the solution for this limiting case of behavior is (6)

$$\frac{c_i}{c_\infty} = \frac{1}{\Gamma(4/3)} \int_o^\eta e^{-\eta^3} d\eta \qquad [8]$$

where

$$\eta = \left(\frac{2v_{max}}{9R_oD_iz}\right)^{1/3} y \qquad [9]$$

The limiting current distribution is therefore found to be

$$j_{lim} = \frac{n\mathbf{F}D_i}{s_i}\frac{\partial c_i}{\partial y}\bigg|_{y=0} = \frac{n\mathbf{F}D_ic_\infty}{s_i\Gamma(4/3)}\left(\frac{2v_{max}}{9R_oD_iz}\right)^{1/3} \qquad [10]$$

For currents below the limiting current, the surface concentration of solute is not zero and the boundary conditions of Eq. [7] do not apply. However, one may nevertheless obtain a relation between the surface concentration distribution and the current distribution by applying Duhamel's theorem (7) to Eq. [10]

$$j = \frac{n\mathbf{F}D_i}{s_i\Gamma(4/3)}\left(\frac{2v_{max}}{9R_oD_i}\right)^{1/3} \int_o^z \frac{dc_s(z')}{dz'}\frac{dz'}{(z-z')^{1/3}} \qquad [11]$$

Equation [11] will be used in the subsequent analysis.

Bulk Region

The potential distribution in the bulk region may be taken into account in two ways, the second of which is approximate but nevertheless useful in initiating calculations. The general solution corresponds to the solution of the Laplace equation in circular cylindrical coordinates

$$\frac{1}{r}\frac{\partial}{\partial r}\left(r\frac{\partial \phi}{\partial r}\right) + \frac{\partial^2 \phi}{\partial x^2} = 0 \qquad [12]$$

With reference to Fig. 1A, the boundary conditions are

$$\begin{aligned} &\frac{\partial \phi}{\partial x} = 0 && x = 0, \quad 0 \leq r \leq R_o \\ &\phi = \phi_A && x = l_1 + l + l_2, \quad 0 \leq r \leq R_o \\ &\frac{\partial \phi}{\partial r} = 0 && 0 \leq x < l_2, \quad r = R_o \\ &\frac{\partial \phi}{\partial r} = -\frac{j}{\kappa} && l_2 \leq x \leq l_2 + l, \quad r = R_o \\ &\frac{\partial \phi}{\partial r} = 0 && l_2 + l < x \leq l_2 + l + l_1, \quad r = R_o \end{aligned} \qquad [13]$$

These boundary conditions indicate that the current distribution along the electrode surface must be known before the potential distribution in the bulk region can be determined. In order to obtain a preliminary estimation of the current distribution, an approximate method is used as described in the next paragraph. The approximate method is accurate when the tubular electrode is very long in comparison with its diameter.

Outside the diffusion layer, the concentrations are uniform. Thus one may, by differentiating Ohm's law, obtain an equation for the conservation of charge

$$\nabla \cdot i = -\kappa \nabla^2 \phi \qquad [14]$$

For long thin tubes, the potential in the solution is nearly uniform across the cross section. An approximation to the potential field, commonly invoked in the analysis of porous electrodes (8), is that the potential is one-dimensional. The local reaction thus appears as a pseudohomogeneous source term in the charge balance equation

$$\frac{d^2\phi}{dx^2} = \frac{2}{R_o\kappa} j \qquad [15]$$

Since reaction proceeds only on the electrode surface, one has

$$j = 0 \qquad 0 \leq x < l_2$$
$$j = 0 \qquad l_2 + l < x \leq l_2 + l + l_1 \qquad [16]$$

By combining Eq. [3] and [15] one obtains

$$\frac{d^2\phi}{dx^2} = \frac{2i_o}{R_o\kappa}\left(\frac{c_s}{c_\infty}\right)^\gamma \left[e^{\frac{\alpha n\mathbf{F}}{R_gT}\eta_s} - e^{-\frac{\beta n\mathbf{F}}{R_gT}\eta_s} \right] \qquad [17]$$

with the boundary conditions

$$\phi = \phi_A, \qquad x = l_2 + l + l_1$$
$$\frac{d\phi}{dx} = 0, \qquad x = l_2 \qquad [18]$$

Equation [17], with its boundary conditions, can be used as an approximation to Eq. [12]. In some situations, the approximation is a very good one; in other situations, it is merely necessary in order to proceed with an iterative solution of the more generally valid Eq. [12].

The equations listed above are sufficient in number to determine the behavior of tubular electrodes over a wide range of applied potentials. Before conducting the calculations, it is convenient to transform the equations into dimensionless form and thereby reduce the number of independent parameters.

Dimensionless model equations.—The following dimensionless ratios will find use

$$X = \frac{x}{l}, \qquad Z = \frac{z}{l}, \qquad \rho = \frac{r}{R_o},$$
$$\gamma_o = \frac{R_o}{l}, \qquad \gamma_1 = \frac{l_1}{l}, \qquad \gamma_2 = \frac{l_2}{l},$$
$$\Phi^* = \frac{n\mathbf{F}}{R_gT}\phi, \qquad \Phi_A{}^* = \frac{n\mathbf{F}}{R_gT}\phi_A,$$
$$\Phi_o{}^* = \frac{n\mathbf{F}}{R_gT}\phi_o, \qquad j^* = \frac{2n\mathbf{F}l^2}{R_gTR_o\kappa} j$$
$$\eta_s{}^* = \frac{n\mathbf{F}}{R_gT}\eta_s, \qquad \eta_c{}^* = \frac{n\mathbf{F}}{R_gT}\eta_c, \qquad C = \frac{c_s}{c_\infty}$$

The equations which define the model are therefore

$$\Phi_o{}^* = \eta_s{}^* + \eta_c{}^* \qquad [19]$$
$$\eta_c{}^* = \ln C \qquad [20]$$
$$j^* = \xi C^\gamma [e^{\alpha\eta_s{}^*} - e^{-\beta\eta_s{}^*}] \qquad [21]$$
$$j^* = \frac{2}{3} N \int_o^Z \frac{dC(Z')}{dZ'} \frac{dZ'}{(Z - Z')^{1/3}} \qquad [22]$$

and

$$\frac{1}{\rho}\frac{\partial}{\partial\rho}\left(\rho\frac{\partial\Phi^*}{\partial\rho}\right) + \gamma_o{}^2\frac{\partial^2\Phi^*}{\partial X^2} = 0 \qquad [23]$$

with boundary conditions

$$\frac{\partial\Phi^*}{\partial X} = 0 \qquad X = 0, \quad 0 \leq \rho \leq 1$$
$$\Phi^* = \Phi_A \qquad X = \gamma_2 + 1 + \gamma_1, \quad 0 \leq \rho \leq 1$$
$$\frac{\partial\Phi^*}{\partial\rho} = 0 \qquad 0 \leq X < \gamma_2, \quad \rho = 1$$
$$\frac{\partial\Phi^*}{\partial\rho} = -\frac{\gamma_o{}^2}{2} j^* \qquad \gamma_2 \leq X \leq \gamma_2 + 1, \quad \rho = 1$$
$$\frac{\partial\Phi^*}{\partial\rho} = 0 \qquad \gamma_2 + 1 < X \leq \gamma_2 + 1 + \gamma_1, \quad \rho = 1 \qquad [24]$$

An approximate potential distribution can be found from

$$\frac{d^2\Phi^*}{dX^2} = \xi\sigma[C^{\gamma-\alpha}e^{\alpha\Phi^*} - C^{\gamma+\beta}e^{-\beta\Phi^*}] \qquad [25]$$

with

$$\Phi^* = \Phi_A{}^* \quad \text{at } X = \gamma_2 + 1 + \gamma_1$$
$$\frac{d\Phi^*}{dX} = 0 \quad \text{at } X = \gamma_2$$
$$\sigma = \begin{cases} 0 & \text{for } 0 \leq X < \gamma_2 \text{ and } \gamma_2 + 1 < X \leq \gamma_2 + 1 + \gamma_1 \\ 1 & \text{for } \gamma_2 \leq X \leq \gamma_2 + 1 \end{cases} \qquad [26]$$

Two important dimensionless parameters appear in the foregoing equations of the model

$$N = \frac{3n^2\mathbf{F}^2l^2D_ic_\infty}{s_iR_gTR_o\kappa\Gamma(4/3)}\left(\frac{2v_{max}}{9D_iR_ol}\right)^{1/3} \qquad [27]$$

$$\xi = \frac{2n\mathbf{F}l^2}{R_gTR_o\kappa} i_o \qquad [28]$$

It seems worthwhile to comment briefly on how these important parameters are qualitatively related to the relative importance of ϕ^o, η_s, and η_c, which sum to the applied potential in accord with Eq. [1]. The parameter N contains the ratio D_ic_∞/κ and can thereby be thought of as the ratio of the importance of concentration overpotential to ohmic (IR) potential losses in the electrolyte phase. N may also be considered to be a dimensionless limiting current density averaged over the electrode surface since it contains j_{lim} as given by Eq. [10]. A large value of N therefore implies that the mass transfer process proceeds with relative ease in comparison with passage of current through the electrolytic solution. Consequently, large values of N may be expected to cause the concentration overpotential to be small with respect to the applied potential. For small values of N, the mass transfer process tends to be rate limiting so that one approaches the limiting current behavior. That is, with small values of N, the quantity η_c tends to be the dominant term on the right side of Eq. [1]. The parameter ξ contains the ratio i_o/κ and thereby indicates approximately the ratio of ohmic (IR) potential losses to charge-transfer overpotential by surface reaction. A large value of ξ corresponds to a situation where the current distribution tends to be highly nonuniform owing to the low solution conductivity and "reversible" electrode reaction. On the other hand, a small value of ξ suggests that the current distribution will tend to be uniform. The applied potential will then tend to be consumed more by the surface overpotential than by the (geometry-dependent) ohmic resistance.

Two additional quantities find use

$$\beta_a = \int_{\gamma_2}^{\gamma_2+1} j^* dX = \int_o^1 j^* dZ \qquad [29]$$

$$J = \frac{j^*}{\beta_a} \qquad [30]$$

The quantity β_a is the dimensionless average current density flowing to the tubular electrode and is obtained by integrating the current distribution over the entire electrode. The quantity J is the dimensionless current

distribution which has been normalized by the total current density. That is,

$$\int_{\gamma_2}^{\gamma_2+1} J dX = 1 \qquad [31]$$

Method of Solution

The equations which describe the theoretical model consist of three algebraic relations (Eq. [19]-[21]), one integral equation [22], and a differential equation (either Eq. [23] or [25]). The five equations must be solved simultaneously in order to determine the five unknown quantities: concentration overpotential, surface overpotential, current distribution, surface concentration distribution, and potential distribution. The procedure for solving the equations is complex because the equations are strongly coupled. An iterative procedure was developed whereby two groups of equations were solved alternately, with successive correction, until convergence was achieved. The calculations, outlined below, were carried out on an IBM 360 digital computer.

In the bulk region of electrolyte, the solution of Eq. [23] provides the potential distribution along the tube wall. The solution of Eq. [23] was obtained with use of Green's function (9, 10)

$$\Phi_o^* = \Phi_A^* + \sum_{n=1}^{\infty} \cos(\lambda_n X) \left[\frac{-\gamma_o I_o(\gamma_o \lambda_n) \int_{\gamma_2}^{\gamma_2+1} j^* \cos(\lambda_n X) dX}{(2n-1)\frac{\pi}{2} I_1(\gamma_o \lambda_n)} \right] \qquad [32]$$

The Appendix contains details of this step. From Eq. [32] it may be recognized that the potential distribution along the surface, Φ_o^*, may be calculated provided that the current distribution along the surface, $j^*(X)$, is known.

Within the mass transfer layer, the remaining equations [19]-[22] are solved simultaneously in order to obtain the reaction rate and the surface concentration distributions. The integral in Eq. [22] is evaluated by the method of Acrivos and Chambré (11). In order to obtain the solution, the potential distribution along the electrode surface must be known. However, in the preceding paragraph it was already mentioned that the potential distribution could be determined only if the current distribution was known.

During the iterative procedure outlined below, the first trial distribution was found to be crucial in determining the number of iterations and, in many cases, in determining the successful convergence of subsequent trials. In order to obtain reasonable initial trial values, the one-dimensional model for the potential field in the tube was employed. The solution of this approximate situation has been reported in other studies on porous and resistive electrodes (12, 13). The following iterative procedure has been found successful:

1. Obtain a trial potential distribution (one-dimensional) with uniform solute concentration ($C = 1.0$) by solving Eq. [25] with its boundary conditions.
2. With the trial potential distribution in hand, proceed to solve Eq. [19] through [22] simultaneously to obtain a trial distribution of current and surface concentration.
3. Integrate the trial current distribution twice, in accord with Eq. [15], to provide a new guess for the potential distribution along the electrode surface.
4. Repeat steps 2 and 3 above until two successive distributions agree within a specified convergence criterion. A trial solution is now available which obeys the one-dimensional potential distribution approximation.
5. Substitute the current distribution obtained from step 4 into Eq. [32] and obtain a trial distribution of the potential along the tube wall.
6. Proceed to solve Eq. [19] through [22] simultaneously to obtain a trial distribution of current and concentration.
7. With the trial current distribution in hand, employ Eq. [32] to generate a new trial potential distribution.
8. Repeat steps 6 and 7 above until convergence is achieved. The solution so obtained obeys the two-dimensional potential equation.

In most cases it was found necessary to average new and previous distributions in order to achieve convergence.

The over-all procedure outlined above involves a number of detailed calculations which deserve further comment. Step 1 was carried out by linearizing the nonlinear terms about a trial solution and then placing them in finite difference form. The resulting tridiagonal matrix was inverted easily, and the procedure repeated until convergence upon the nonlinear equation was achieved. Steps 2 and 6, which involve the simultaneous solution of Eq. [19] through [22], were accomplished by first substituting Eq. [19] and [20] into [21] with the result

$$j^* = \xi[C^{\gamma-\alpha} e^{\alpha\Phi_o^*} - C^{\gamma+\beta} e^{-\beta\Phi_o^*}] \qquad [33]$$

Now subtract Eq. [22] from [33] to eliminate j^*, and denote the difference by the function $f(C)$. With a trial potential distribution in hand, it is recognized that the simultaneous solution of [22] and [33] is now equivalent to finding the concentration distribution such that $f(C) = 0$ at every point along the electrode surface. In order to find the solution, one begins at the upstream edge where $C = 1$. The surface concentration at the first incremental step downstream is then found by trial and error following Newton's method of convergence

$$C_{i+1} = C_i + \frac{f(C_i)}{\frac{df}{dC}} \qquad [34]$$

where C_i represents a guess of the correct surface concentration and C_{i+1} represents an improved guess. The derivative df/dC is evaluated analytically, that is, by differentiating the function $f(C)$ and determining the value of the derivative. The integral expression which Eq. [22] contributes to the function $f(C)$ is evaluated by a numerical method (11). By this procedure, one proceeds downstream step by step, taking the first guess of C_i to be that of the preceding interval, and then solving [22] and [33] at each incremental step. The potential and concentration distributions obtained in this manner are then substituted into Eq. [33] in order to compute the trial current distribution. One may then continue with either step 3 or 7 in the over-all iteration sequence outlined previously.

Results and Discussion

Calculations based on the preceding theoretical model have been conducted in order to test the calculational method and to illuminate several characteristic features of tubular electrode behavior. All calculations have been conducted for cathodic deposition with use of a symmetric transfer coefficient ($\alpha = \beta = 0.5$). The dimensionless parameters employed in the following analysis should permit application of the results to a wide variety of actual systems.

First consider behavior when the reaction rate is sufficiently low that mass transfer limitations are absent. It may be realized that the current distribution depends on both γ_o (radius/length ratio) and ξ (ohmic/charge-transfer overpotential ratio). The most reactive portion of the tubular electrode will tend to be that

portion most accessible to the counterelectrode. Figure 2 illustrates the current distribution in a long tube of twenty-five radii in length ($\gamma_o = 0.04$). The counterelectrode is positioned on the right side of the cell. From Fig. 2 the current distribution is seen to depend on the parameter ξ which denotes the ratio of potential loss in the electrolyte to surface overpotential. For very small values of ξ, the current distribution is very uniform since the cell potential is consumed by surface overpotential which does not depend on distance from the counterelectrode. For large values of ξ, the resistance of the electrolytic solution is important so that the electrode regions nearest the counterelectrode are highly reactive. When the tubular electrode is very long with respect to its diameter, as in Fig. 2, the potential distribution in the solution tends to be one dimensional so that results are similar to those available in the literature on porous electrodes (14).

Continuing discussion in the complete absence of mass transfer, Fig. 3 shows how the tubular electrode radius/length ratio influences the current distribution for one particular value of ξ. For very long narrow tubes (small γ_o) the reaction rate is highest near the counterelectrode; the current does not penetrate into the tube owing to the high solution resistance. As the radius of the tube is increased relative to its length, however, the portion of the tube furthest from the counterelectrode becomes increasingly reactive. Regions in the middle of the tube become the least reactive. For large values of γ_o, the current distribution would become symmetric about the middle of the tube, in which case the counterelectrode position is immaterial. From these considerations it is recognized that the parameter γ_o determines to what extent the tube restricts current from flowing to the edge far from the counterelectrode, while the parameter ξ influences the uniformity of the reaction distribution. Results for $\xi = \infty$ would correspond to the "primary" current distribution in which case the current density at each edge of the electrode would tend toward infinity. The foregoing results have been obtained in the complete absence of mass transfer limitations and are thereby independent of the direction or nature of electrolyte flow in the tube.

In contrast to the previous paragraph, consider now the behavior encountered at the limiting current.

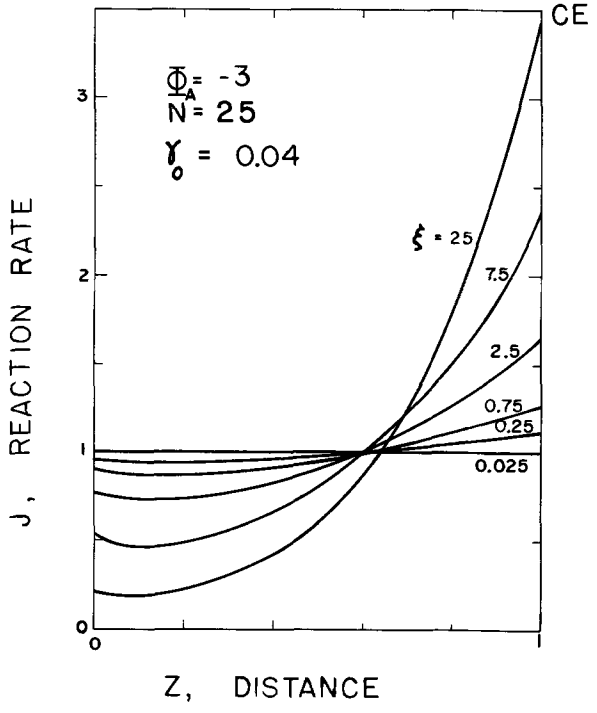

Fig. 2. Dependence of the secondary current distribution on the parameter ξ. The counterelectrode is on the right.

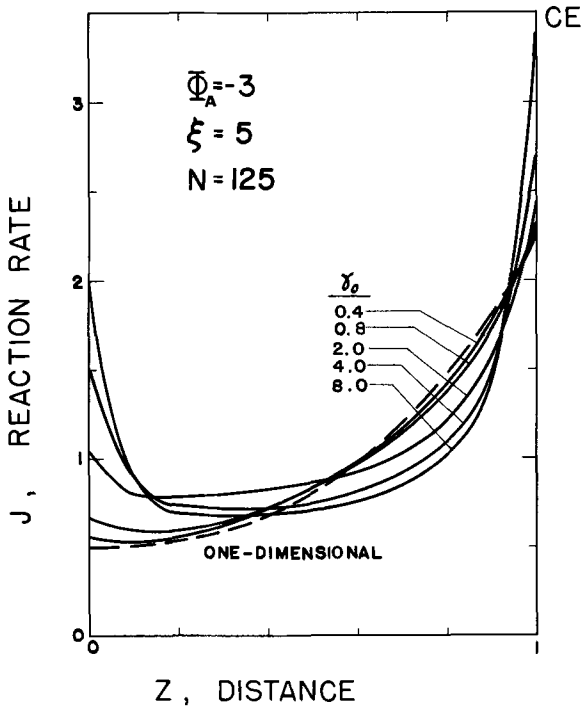

Fig. 3. Dependence of the secondary current distribution on the parameter γ_o. The counterelectrode is on the right.

As indicated in both parts of Fig. 1, electrolyte flows through the cell from left to right. Therefore the limiting current distribution, shown in Fig. 4, is highest at the left-hand (upstream) edge of the electrode and decreases with distance downstream owing to depletion of reactive species near the electrode surface. The limiting current distribution is given by Eq. [10] which in dimensionless notation is

$$j^*_{\lim} = \frac{2}{3} N \left(\frac{1}{Z}\right)^{1/3} \qquad [35]$$

Equation [35] indicates that the limiting current is infinitely large at the upstream edge of the electrode ($Z = 0$) since the mass transfer diffusion layer is of zero thickness. The limiting current distribution is independent of the parameters γ_o and ξ and, in addition, is independent of whether the counterelectrode is

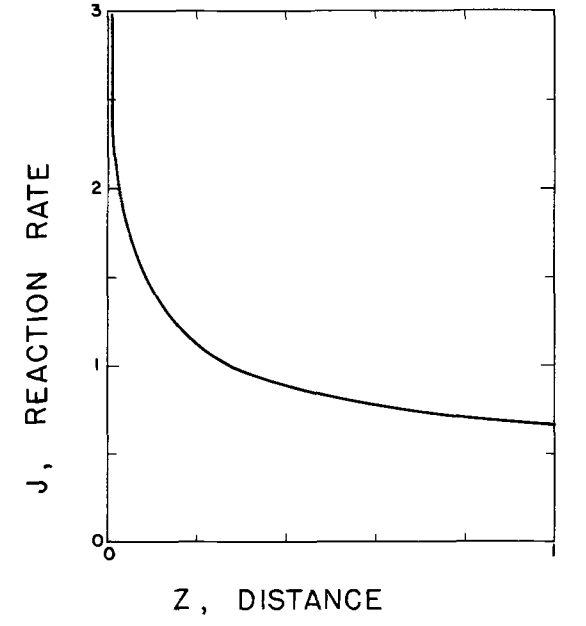

Fig. 4. The limiting current distribution. Electrolyte flow is from left to right.

placed upstream or downstream from the tubular electrode. Comparison of Fig. 4 with either of Fig. 2 and 3 indicates clearly that the limiting current distribution can be exceedingly different from the secondary current distribution, especially when the counterelectrode is placed downstream. By integrating Eq. [35] in accord with the definition of β_a, Eq. [29], one finds at the limiting current

$$\beta_{alim} = N \qquad [36]$$

Now let us turn to several examples of more complex behavior at intermediate currents. In view of the large number of system parameters, it would be cumbersome to report detailed parameter studies for every possible case. Only a few features, which seem to be of special interest, have been chosen for discussion at this time.

Consider first the behavior of long tubes where the counterelectrode is downstream with respect to the fluid flow, as in Fig. 1A. For one set of conditions ($\Phi_A^* = -3$, $\gamma_0 = 0.04$), Fig. 5 shows how the parameter N influences the current distribution. When the average limiting current density is very high (large N), mass transfer processes are inconsequential; the reaction rate along the tube is therefore highest near the counterelectrode (downstream region) owing to the high solution resistance and small tube radius. When the average limiting current density is very low (small N), then mass transfer processes predominate and the upstream region of the electrode is most reactive. At intermediate current levels, both ends of the electrode are more reactive than the center: the upstream region because it is accessible to reactive species, and the downstream region because it is accessible to the counterelectrode.

The concentration of reactive species adjacent to the electrode surface varies with distance along the electrode. Figure 6 illustrates how N influences the surface concentration distribution in a long tube ($\gamma_0 = 0.04$) with a reversible reaction ($\xi = 25$). The counterelectrode is downstream. When N has large values, concentration overpotential effects are relatively minor; depletion occurs primarily in downstream regions where the electrode is most reactive. As the average limiting current density (N) is decreased, lower surface concentrations are encountered. The surface concentration decreases more rapidly in upstream regions, where the diffusion layer is thin. At the limiting current, the concentration is uniform along the entire

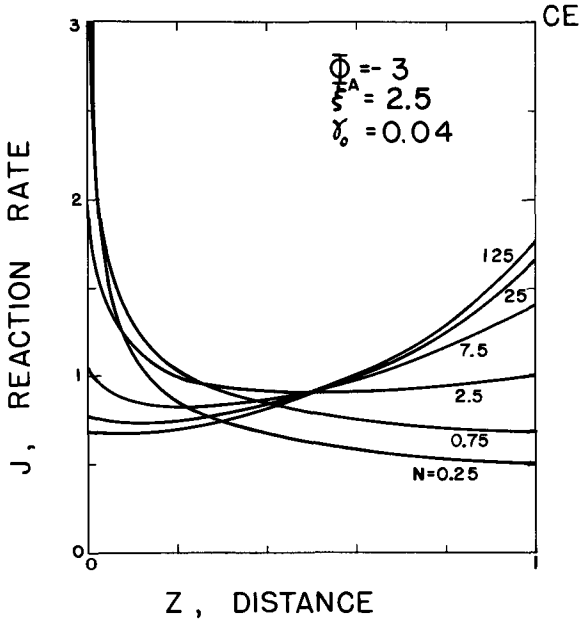

Fig. 5. Dependence of the current distribution on parameter N. Flow is from left to right; the counterelectrode is on the right.

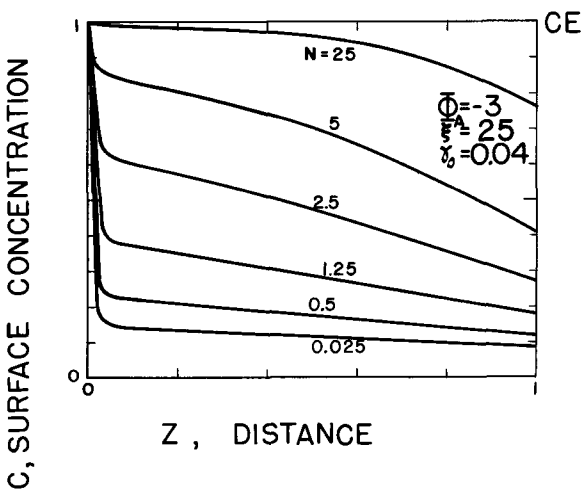

Fig. 6. Concentration distribution along electrode surface near the limiting current condition. Flow is from left to right; counterelectrode is on the right.

electrode surface and, in accord with Eq. [20], has the value

$$C = e^{\Phi_A^*} \qquad [37]$$

The concentration distribution along the electrode surface also depends upon ξ. For long tubes ($\gamma_0 = 0.04$) near the limiting current ($N = 0.5$), the results of Fig. 7 are typical. Flow of electrolyte is from left to right, and the counterelectrode is downstream on the right. For low values of ξ, the charge-transfer resistance predominates behavior so that the reaction distribution is uniform and the extent of concentration depletion is minor since the product (ξN) is small. As ξ is increased, charge-transfer becomes subordinate to mass transfer resistances; the surface concentration then decreases strongly over upstream portions of the electrode where reactivity is highest. For still larger values of ξ, the ohmic resistance of the electrolyte begins to influence behavior by rendering the upstream regions (far from the counterelectrode) less reactive owing to the resistance of electrolyte within the tube; therefore the concentration overpotential decreases.

In the concluding example, consider the behavior of a long tube where the counterelectrode is placed upstream with respect to the fluid flow, as indicated in Fig. 1B. The dependence of the current distribution on the level of the current is provided in Fig. 8. As in the discussion of Fig. 4, the limiting current distribution is encountered when N is small, and the secondary distribution is encountered when N is large. Based on the preceding discussion, it is recognized that the

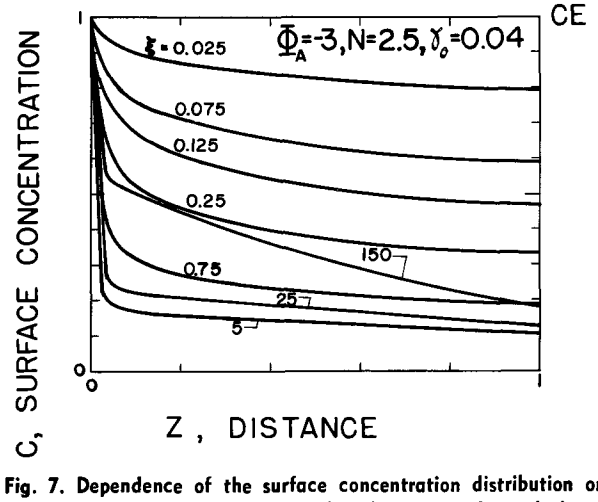

Fig. 7. Dependence of the surface concentration distribution on parameter ξ. Flow is from left to right; the counterelectrode is on the right.

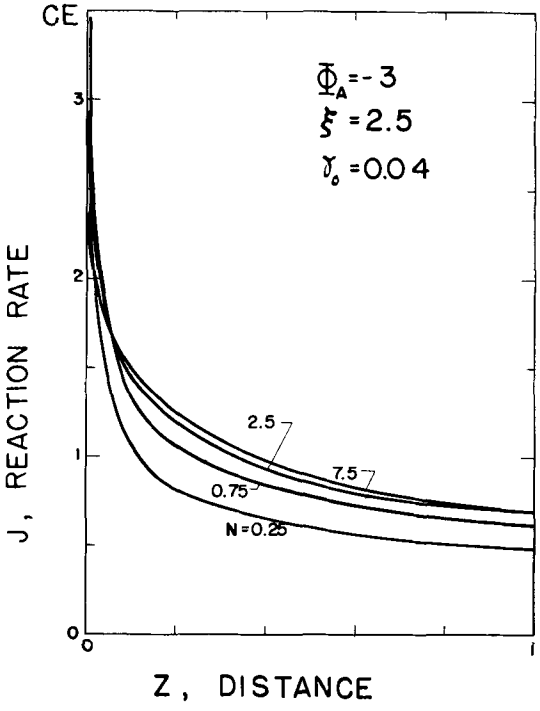

Fig. 8. Dependence of the current distribution on parameter N. Flow is from left to right; the counterelectrode is on the left.

secondary current distribution will be uniform to an extent which depends on the parameter ξ. For a situation somewhat near the limiting current, Fig. 9 illustrates how the reactant concentration varies with distance along the electrode surface for various values of ξ. For small values of ξ, the charge-transfer overpotential is of major importance and the concentration depletion is of minor extent. At intermediate values of ξ, concentration overpotential becomes predominant and the surface concentration takes on very low values. At still higher values of ξ, the ohmic resistance of the electrolyte renders downstream portions essentially inert with the consequence that the diffusion layer becomes replenished with reactant species which diffuse in from the bulk region. A minimum in the surface concentration distribution is thereby observed.

Conclusions

The computational method developed in this study provides a nonintuitive method for predicting electrochemical behavior over a wide range of current densities. The calculations provide a unified treatment of the dependence of two-dimensional tubular electrode behavior on charge-transfer, mass transport, ohmic and geometric parameters of the system as well as counterelectrode positions. The method of calculation is general in nature and may be applied to other geometries and other convective flow situations. The Green's function and the Lighthill transformation methods provide powerful routes for solving the potential distribution and the laminar convective transport aspects of the problem. The crucial assumptions are that the fluid moves in steady laminar flow (Re $<$ 2100), the reacting species do not migrate (small transference number), and the diffusion layer is thin with respect to the tube radius ($zD_i/2<v_z>R^2_o < 0.01$). The Lévêque approximation, invoked in this study to gain Eq. [6], could be improved upon by including higher order terms (15). Other assumptions are also made along the route, but these may be easily modified to suit special circumstances, for example, the choice of reaction rate expression. In order to extend the method to account for turbulent convection or the homogeneous chemical reactions which accompany electrochemical reaction, the Lighthill transformation method would have to be discarded in favor of an alternative method.

The treatment given above has emphasized details of the computational method and has discussed a few general features of the results; additional calculations would be profitable. For example the behavior of flow-through porous electrodes, although exceedingly complex from a physical point of view, has been mathematically modeled by one-dimensional equations of charge- and species-transport. The present study provides a method for assessing conditions under which these crucial assumptions are valid.

In a series of publications Blaedel *et al.* (16), investigated the utility of flow-through tubular platinum electrodes for use in electroanalytical studies. The principal advantages of the method were that it permitted steady-state measurements and thereby avoided fast-response electronic circuitry, and that it enjoyed a high sensitivity owing to the high rate of mass transfer. However the highly nonuniform potential field within the tubular electrode was found to cause deviations from behavior predicted for the limiting current condition. Attempts to modify the measurement circuit to account for the uncompensated resistance were unsuccessful. As a result it had been concluded that the method was restricted to low current densities for which ohmic resistance effects were negligible. The present theoretical formulation provides a sound basis for taking into account the uncompensated resistance phenomena which limited the analysis of Blaedel's experimental data at high current densities.

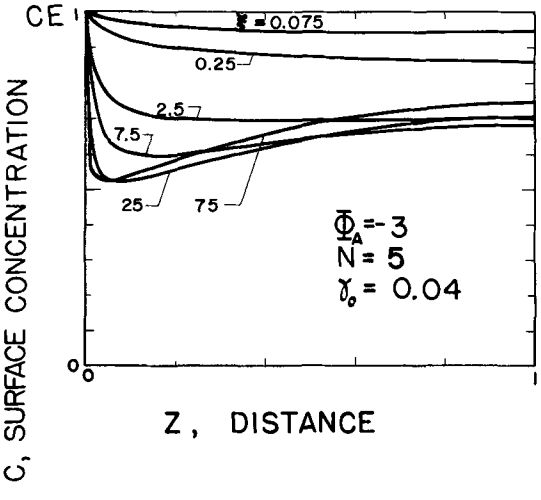

Fig. 9. Dependence of surface concentration distribution on parameter ξ. Flow is from left to right; counterelectrode is on the left.

Acknowledgments

Portions of this study constituted partial fulfillment of requirements for a Master of Science degree in the Department of Chemical Engineering, University of Illinois, Urbana-Champaign. The authors acknowledge with appreciation the receipt of a DuPont Grant-in-Aid during the conduct of this investigation. The computer costs associated with the study were funded by the University of Illinois Research Board. Professor Robert L. Sani generously assisted by suggesting the Green's function method for solving the potential distribution problem.

Manuscript submitted March 16, 1973; revised manuscript received June 11, 1973. This was Paper 235 presented at the Chicago, Illinois, Meeting of the Society, May 13-18, 1973.

Any discussion of this paper will appear in a Discussion Section to be published in the June 1974 JOURNAL.

APPENDIX

It is convenient to change the variable in Eq. [23] and the boundary conditions [24] by introducing

$$\Psi = \Phi^* - \Phi_A^* \qquad [A\text{-}1]$$

Thus one obtains the equation

$$\frac{1}{\rho}\frac{\partial}{\partial\rho}\left(\rho\frac{\partial\Psi}{\partial\rho}\right) + \gamma_o^2\frac{\partial^2\Psi}{\partial X^2} = 0 \qquad [A\text{-}2]$$

with the boundary conditions

$$\frac{\partial\Psi}{\partial X} = 0 \qquad X = 0, \qquad 0 \leq \rho \leq 1$$

$$\Psi = 0 \qquad X = \gamma_2 + 1 + \gamma_1, \qquad 0 \leq \rho \leq 1$$

$$n \cdot \nabla\Psi = 0 \qquad 0 \leq X < \gamma_2, \qquad \rho = 1$$

$$n \cdot \nabla\Psi = -\frac{1}{2}\gamma_o^2 j^* \qquad \gamma_2 \leq X \leq \gamma_2 + 1, \qquad \rho = 1$$

$$n \cdot \nabla\Psi = 0 \qquad \gamma_2 + 1 < X \leq \gamma_2 + 1 + \gamma_1, \qquad \rho = 1 \qquad [A\text{-}3]$$

Equation [A-2] will now be integrated with use of the Green function, $G(\eta,\zeta;\rho,X)$ which is to be found such that it satisfies the relation

$$\frac{1}{\eta}\frac{\partial}{\partial\eta}\left(\eta\frac{\partial G}{\partial\eta}\right) + \gamma_o^2\frac{\partial^2 G}{\partial\zeta^2} = \frac{1}{2\pi\eta}\delta(\eta-\rho)\delta(\zeta - X) \qquad [A\text{-}4]$$

with the side conditions

$$\frac{\partial G}{\partial\zeta}(\eta,0;\rho,X) = 0$$

$$G(\eta,\gamma_2 + 1 + \gamma_1;\rho,X) = 0$$

$$n \cdot \nabla G(1,\zeta;\rho,X) = 0 \qquad [A\text{-}5]$$

Consider first the homogeneous portion of Eq. [A-4]

$$\frac{1}{\eta}\frac{\partial}{\partial\eta}\left(\eta\frac{\partial G}{\partial\eta}\right) + \gamma_o^2\frac{\partial^2 G}{\partial\zeta^2} = 0 \qquad [A\text{-}6]$$

One may postulate a solution of the homogeneous equation by separation of variables

$$G = x(\zeta)R(\eta) \qquad [A\text{-}7]$$

Substituting Eq. [A-7] into Eq. [A-6] generates an ordinary differential equation for determining the eigenfunctions

$$x_n(\zeta) = \sqrt{2}\cos(\lambda_n\zeta) \qquad [A\text{-}8]$$

where

$$\lambda_n = \frac{(2n-1)\pi}{2(1+\gamma_2+\gamma_1)}, \quad n = 1, 2, 3, \ldots$$

The quantity $\delta(\zeta - X)$ may now be expanded in terms of the eigenfunctions x_n. With use of the orthogonality property of the eigenfunctions, one thereby gains

$$\delta(\zeta - X) = \sum_{n=1}^{\infty}\frac{x_n(X)}{1+\gamma_2+\gamma_1}x_n(\zeta) \qquad [A\text{-}9]$$

Now we are prepared to postulate a solution of the inhomogeneous equation having the form

$$G(\eta,\zeta;\rho,X) = \sum_{n=1}^{\infty} x_n(\zeta)R_n(\eta) \qquad [A\text{-}10]$$

from which one obtains

$$R_n(\eta) = \begin{cases} \dfrac{-x_n(X)\left[I_o(\gamma_o\lambda_n\rho)K_1(\gamma_o\lambda_n) + I_1(\gamma_o\lambda_n)K_o(\gamma_o\lambda_n\rho)\right]}{2\pi K(\rho)I_1(\gamma_o\lambda_n)} & I_o(\gamma_o\lambda_n\eta), \quad \eta < \rho \\ \dfrac{-x_n(X)\left[I_o(\gamma_o\lambda_n\eta)K_1(\gamma_o\lambda_n) + I_1(\gamma_o\lambda_n)K_o(\gamma_o\lambda_n\eta)\right]}{2\pi K(\rho)I_1(\gamma_o\lambda_n)} & I_o(\gamma_o\lambda_n\rho), \quad \eta > \rho \end{cases} \qquad [A\text{-}11]$$

wherein

$$K(\rho) = \gamma_o\lambda_n\rho(1+\gamma_1+\gamma_2)\left[K_1(\gamma_o\lambda_n\rho)I_o(\gamma_o\lambda_n\rho) + K_o(\gamma_o\lambda_n\rho)I_1(\gamma_o\lambda_n\rho)\right] \qquad [A\text{-}12]$$

and I_o, K_o, I_1, and K_1 are modified Bessel functions. We are now ready to invoke Green's theorem

$$\int_v (G\nabla^2\Psi - \Psi\nabla^2 G)\,dV = \int_s (Gn\cdot\nabla\Psi - \Psi n\cdot\nabla G)\,dS \qquad [A\text{-}13]$$

in order to gain the preliminary result

$$\Psi(\rho,X) = \sum_{n=1}^{\infty}\frac{2\cos(\lambda_n X)I_o(\gamma_o\lambda_n\rho)\left[I_o(\gamma_o\lambda_n)K_1(\gamma_o\lambda_n) + I_1(\gamma_o\lambda_n)K_o(\gamma_o\lambda_n)\right]}{K(\rho)I_1(\gamma_o\lambda_n)}\int_{\gamma_2}^{\gamma_2+1}\left(-\frac{\gamma_o^2}{2}\right)\cos(\lambda_n\zeta)j^*\,d\zeta \qquad [A\text{-}14]$$

In accord with Eq. [A-1], the potential in the electrolyte just outside the diffusion layer is

$$\Phi_o^* = \Phi^*(1,X) = \Phi_A^* + \Psi(1,X) \qquad [A\text{-}15]$$

or

$$\Phi_o^* = \Phi_A^* + \sum_{n=1}^{\infty}\cos(\lambda_n X)\left[\frac{-\gamma_o I_o(\gamma_o\lambda_n)\int_{\gamma_2}^{\gamma_2+1} j^*\cos(\lambda_n X)\,dX}{(2n-1)\frac{\pi}{2}I_1(\gamma_o\lambda_n)}\right] \qquad [A\text{-}16]$$

SYMBOLS

C	c_s/c_∞, surface concentration, dimensionless
c_i	concentration of species i, g-mole/cm^3
c_s	reactant concentration at electrode surface, g-mole/cm^3
c_∞	reactant concentration in bulk region, g-mole/cm^3
D_i	diffusion coefficient of species i, cm^2/sec
$\mathbf{F}$	Faraday's constant, 96,500 coulombs/g-equivalent
i_o	exchange current density of electrode reaction, A/cm^2
j	local reaction rate, A/cm^2
j^*	$2n\mathbf{F}l^2j/R_gTR_o\kappa$, local reaction rate, dimensionless
J	j^*/β_a, normalized local reaction rate, dimensionless
l	length of tubular electrode, cm
l_1	distance from counterelectrode to edge of tubular electrode, cm
l_2	distance from rear edge of tubular electrode to rear plane of equipotential, cm
n	number of electrons taking part in electrode reaction
N	$\dfrac{3n^2\mathbf{F}^2l^2D_iC_\infty}{s_iR_gTR_o\kappa\Gamma(4/3)}\left(\dfrac{2v_{max}}{9D_iR_ol}\right)^{1/3}$, average limiting current density, dimensionless
r	spatial variable in radial direction, cm
R_o	radius of tubular electrode, cm
R_g	gas constant, 8.31 joules/g-mole deg
s_i	stoichiometric coefficient of the reacting species
v_{max}	fluid velocity along tube axis, cm/sec
$\langle v_x\rangle$	mass average fluid velocity, cm/sec
x	spatial variable in axial direction, cm
X	x/l, spatial variable in axial direction, dimensionless
y	spatial variable normal to electrode surface, cm
z	spatial variable along electrode surface parallel to direction of fluid flow, cm

Z	z/l, spatial variable along electrode surface, dimensionless
α	parameter in reaction rate expression
β	parameter in reaction rate expression
β_a	average current density, Eq. [29], dimensionless
γ	parameter in reaction rate expression
γ_0	R_0/l, geometric aspect ratio, dimensionless
γ_1	l_1/l, geometric ratio, dimensionless
γ_2	l_2/l, geometric ratio, dimensionless
$\Gamma(4/3)$	gamma function
η_c	concentration overpotential, V
η_c^*	$(nF/R_gT)\eta_c$, concentration overpotential, dimensionless
η_s	charge-transfer overpotential, V
η_s^*	$(nF/R_gT)\eta_s$, charge-transfer overpotential, dimensionless
κ	electrolyte conductivity, (ohm-cm)$^{-1}$
λ_n	eigenvalues of the Green function solution, Eq. [32]
ξ	$\frac{2nFl^2}{R_gTR_0\kappa} i_0$, reaction velocity parameter, dimensionless
ϕ	potential in electrolyte phase, V
Φ^*	$(nF/R_gT)\phi$, potential in electrolyte phase, dimensionless
ϕ_A	potential applied across cell, V
Φ_A^*	$(nF/R_gT)\phi_A$, applied potential, dimensionless
ϕ^o	ohmic potential loss in electrolyte, V
ϕ_0	potential at outer edge of diffusion layer, V
Φ_0^*	$(nF/R_gT)\phi_0$, potential at outer edge of diffusion layer, dimensionless

REFERENCES

1. J. Newman, "Electrochemical Systems," chap. 31, Prentice-Hall, Englewood Cliffs, N. J. (1973).
2. K. Asada, F. Hine, S. Yoshizawa, and S. Okada, *This Journal*, **107**, 242 (1960).
3. J. Newman, *Intern. J. Heat Mass Transfer*, **10**, 983 (1967).
4. W. R. Parrish and J. Newman, *This Journal*, **116**, 169 (1969); **117**, 43 (1970).
5. J. Newman, *ibid.*, **113**, 1235 (1966); **114**, 239 (1967).
6. R. B. Bird, W. E. Stewart, and E. N. Lightfoot, "Transport Phenomena," p. 551, John Wiley & Sons, Inc., New York (1960).
7. W. H. Smyrl and J. Newman, *This Journal*, **119**, 212 (1972).
8. R. de Levie, in "Advances in Electrochemistry," vol. 6, P. Delahay, Editor, Interscience (Wiley), New York (1967).
9. M. D. Greenberg, "Applications of Green's Functions in Science and Engineering," Prentice-Hall, Englewood Cliffs, N. J. (1971).
10. B. S. Baker, D. Gidaspow, and D. Wasan, in "Advances in Electrochemistry and Electrochemical Engineering," Vol. 8, P. Delahay and C. Tobias, Editors, Interscience (Wiley), New York (1971).
11. A. Acrivos and P. L. Chambre, *Ind. Eng. Chem.*, **49**, 1025 (1957).
12. R. C. Alkire, *This Journal*, **118**, 1935 (1971).
13. R. C. Alkire and A. Tvarusko, *ibid.*, **119**, 340 (1972).
14. R. Alkire and B. Place, *ibid.*, **119**, 1687 (1972).
15. J. Newman, *J. Heat Transfer*, **91C**, 177 (1969).
16. W. J. Blaedel *et al.*, *Anal. Chem.*, **35**, 2100 (1963); **38**, 879 (1966); **39**, 1065 (1967); **40**, 512 (1968); **43**, 1538 (1971).

Technical Notes

The Hydrogen-Loss Concept of Battery Failure: The PbO_2 Electrode

S. M. Caulder,* J. S. Murday, and A. C. Simon*

Naval Research Laboratory, Washington, D.C. 20375

A problem common to all secondary batteries is the gradual loss of capacity during cycling. The cause of this degradation in performance has been attributed to loss of active material (PbO_2), rearrangement of the microstructure of the active material into a less porous configuration, loss of contact between individual particles of the active material, or of the contact between active material and the current-conducting grid. Recent preliminary pulsed nuclear magnetic resonance (NMR) investigations revealed a new factor, the presence of a hydrogen species in the electrochemically prepared PbO_2 structure, which appears to be related to the loss of capacity of the lead-acid batteries, and may be present in other battery systems as well (1).

Several observations made recently at this laboratory on lead dioxide electrodes are as follows. (*i*) X-ray analyses have shown the loss in capacity with charge-discharge cycling was not accompanied by a corresponding increase in lead sulfate on the charged positive plate, as would be the case if active particles were becoming insulated from the matrix. (*ii*) A difference in chemical and thermal reactivity was observed between chemically prepared lead dioxide samples and those prepared by electrochemical means. (*iii*) Differential thermal analysis (DTA) showed distinct differences in the thermal degradation mechanisms (2) of these two materials, although x-ray analysis failed to show any structural differences. DTA also indicated that, after long periods of cycling, the lead dioxide in the cycled plates gave a thermal decomposition path resembling that of the chemically prepared PbO_2, rather than that of the electrochemical form. (*iv*) Differential scanning calorimetry, established that the electrochemically prepared form of lead dioxide gave an exothermic peak at 180°C. (*v*) High temperature mass spectroscopy at 10^{-6} mm showed this peak to be associated with water evolution. No exothermic peak or water evolution was observed at 180°C with chemically prepared PbO_2. However, mass spectroscopy did show some adsorbed water to be evolved from both the chemical and electrochemical lead dioxide when the samples were subjected to a 10^{-6} mm vacuum and heated to 100°C. Previous investigations (3, 4) have also shown that upon heating PbO_2 gives off water of an undetermined origin.

* Electrochemical Society Active Member.

Key words: lead dioxide, lead dioxide electrode, pulsed nuclear magnetic resonance, hydrogen species, capacity loss.

These investigations did not show, however, whether the H_2O was present as a water molecule, as OH^- and H^+ ions, or as oxygen and hydrogen constituents in some unknown structure. To further illuminate this point, a pulsed NMR (5, 6) study of the hydrogen nuclear relaxation times was made of the two compounds. It is evident from the relative magnitudes of the hydrogen signals (Fig. 1) that the electrochemical form has more hydrogen. The nonexponential character of its relaxation time indicates that the electrochemically prepared samples of lead dioxide has hydrogen present in at least two different configurations. The chemically prepared samples showed uniform hydrogen behavior as evidenced by a single exponential relaxation time.

If one decomposes the relaxation data for the electrochemical PbO_2 into an exponential (long-time behavior) and a gaussian (short-time behavior) the long-time behavior (upper solid line in Fig. 1) is similar to that found in the chemical sample. The chemical nature of the slow relaxing hydrogen is not yet clear. The relaxation time of the fast component does not change appreciably with temperature in the range $3.0 < 10^3/T\ °K < 10$; this behavior coupled with the gaussian decay implies that hydrogen nuclei motion is so slow ($\gamma_j < 5 \times 10^4$ jumps/sec) that no motional narrowing of the NMR line occurs in this temperature range (the rigid lattice condition of NMR). From the magnitude of the relaxation time one can calculate a hydrogen-hydrogen separation of slightly greater than 2Å. This means the hydrogen species corresponding to the fast relaxation component are not present in the form of water molecules which have a separation of 1.6Å. Thus, it has now been established that another species other than water is associated with the electrochemically prepared PbO_2.

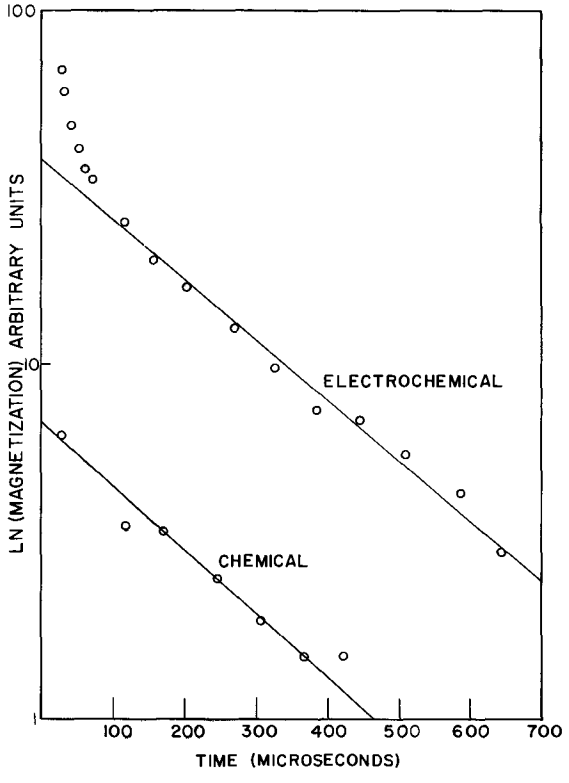

Fig. 1. Typical hydrogen signal of chemical and electrochemical PbO_2. Solid lines indicate slow relaxation component of the hydrogen signal. The fast relaxation component of the electrochemical PbO_2 is shown by the nonconnected circles.

The other interesting part of this investigation is that as the number of charge-discharge cycles increases the concentration of fast relaxing hydrogen species decreases. This observation seems to indicate that the reactive electrochemical form of lead dioxide changes upon extended cycling, perhaps reverting to the relatively inert chemical form.

The results of the NMR investigation suggest that the loss of hydrogen from the lead dioxide structure is connected with loss of reactivity and, consequently, capacity. The mechanism involved is not yet clear. It seems that the lead dioxide in its less reactive (chemically prepared) form cannot be reduced to lead sulfate. This suggests that the hydrogen species present in the electrochemical form are in some manner necessary for this reduction. It is possible that these hydrogen species may either catalyze the reduction or form a necessary chemical step in the reduction of lead dioxide. These and other possibilities will be investigated.

Acknowledgment

We wish to thank the Naval Research Laboratory for the support of this joint investigation and for permission to publish this work. Appreciation is also expressed to the International Lead-Zinc Research Organization, Incorporated, which has assisted in this and other investigations by maintaining the position of Research Associate at the Naval Research Laboratory for one of the authors (S.M.C.)

Manuscript submitted Feb. 16, 1973; revised manuscript received June 18, 1973.

Any discussion of this paper will appear in a Discussion Section to be published in the June 1974 JOURNAL.

REFERENCES

1. A. Tvarusko, *This Journal*, **111**, 125 (1964).
2. S. M. Caulder and A. C. Simon, Abstract No. 53, p. 131, Electrochem. Soc. Extended Abstracts, Fall Meeting, Atlantic City, New Jersey, Oct. 4-8, 1970.
3. M. I. Gillibrand and B. Halliwell, in "Power Sources", D. H. Collins, Editor, p. 179, Pergamon Press, London (1967).
4. N. E. Bagshaw, R. L. Clarke, and B. Halliwell, *J. Appl. Chem.*, **16**, 180 (1966).
5. E. R. Andrew, "Nuclear Magnetic Resonance," Cambridge University Press, Cambridge (1955).
6. A. Abragam, "The Principles of Nuclear Magnetism," Oxford University Press, Oxford (1961).

Nondestructive Monitoring by Mössbauer Spectroscopy of the Rate of Corrosion of Coated Metal at the Metal-Polymer Interface

Henry Leidheiser, Jr.,* G. W. Simmons, and Elsie Kellerman

Center for Surface and Coatings Research, Lehigh University, Bethlehem, Pennsylvania 18015

Food containers, metals exposed to the atmosphere, and structural metals exposed to corrosive environments are often protected by polymeric coatings, simple or complex in formulation. The rate of corrosion at the metal-polymer interface in the earliest stages is difficult to determine, particularly when the coating

* Electrochemical Society Active Member.
Key words: Mössbauer spectroscopy, corrosion, cobalt, coatings, polybutadiene.

is opaque. The purpose of this communication is to describe, by means of an example, a method based on Mössbauer spectroscopy whereby the extent of corrosion in such systems can be followed. The example method is directly applicable to cobalt substrates and depends for its operation on having Co-57 at the interface, measuring the resonance absorption of the 14.4 keV gamma ray produced in one stage of the transition of Co-57 to the ground state of Fe-57, and determining from the resulting spectra the extent of conversion of elemental metal to a metal compound. Extension of the method to substrates containing tin and antimony is readily accomplished. It remains to be shown that the method can characterize the quality of protection offered by coatings to steel substrates.

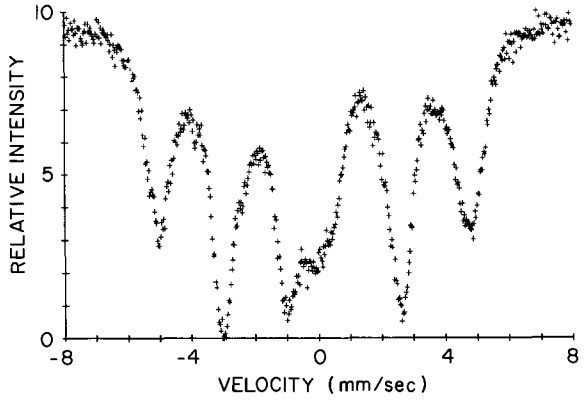

Fig. 1. Mössbauer spectrum obtained from a 50Å thick electrodeposit of cobalt containing Co-57.

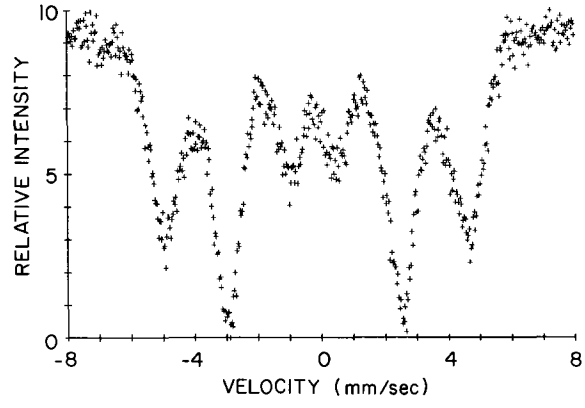

Fig. 2. Mössbauer spectrum of the Co-57 electrodeposit subjected to cathodic treatment in sodium hydroxide. Spectrum was taken *in situ* during cathodic treatment.

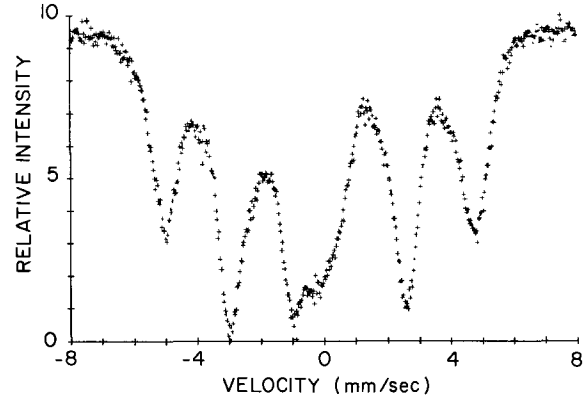

Fig. 3. Mössbauer spectrum after coating sample with polybutadiene to a thickness of 0.001 cm and curing in air at 200°C for 30 min. Ionic cobalt at the metal-polymer interface has increased in amount over that for uncoated sample.

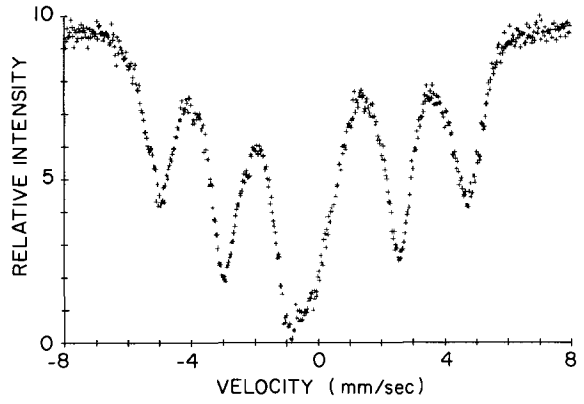

Fig. 4. Mössbauer spectrum of coated sample after exposure to 3% NaCl solution for 84 hr. Note that center peaks characteristic of cobalt oxide have increased in intensity relative to those in Fig. 3.

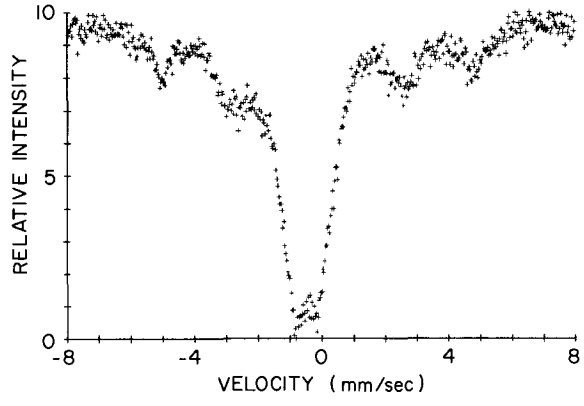

Fig. 5. Mössbauer spectrum of an uncoated sample exposed to 3% NaCl for 1 hr. Spectrum before exposure to NaCl was similar to that shown in Fig. 1.

Cobalt doped with Co-57 was electrodeposited on cobalt from a saturated ammonium oxalate solution. The mass deposited was equivalent to a uniform coating 50Å in thickness. The Mössbauer emission spectrum of such a sample using an enriched stainless-steel absorber is given in Fig. 1. The six-line spectrum (clearly shown in Fig. 2) is characteristic of elemental metal while the central peak (clearly shown in Fig. 5) is characteristic of ionic cobalt. Computer analysis of the spectrum of Fig. 1 leads to the result that 61% of the electrodeposit consists of elemental cobalt and 39% of the deposit consists of cobalt oxide. The oxide presumably forms after removal from the plating bath since *in situ* determination of the Mössbauer spectrum during cathodic treatment yields the six-line spectrum

Table I*

Sample description	Composition of 50Å thick cobalt at the interface: Per cent elemental cobalt	Per cent ionic cobalt
Starting sample with 50Å thick electrodeposit	61	39
Sample coated with polybutadiene to a thickness of 0.001 cm	61	39
Sample cured at 200°C for 30 min	52	48
Coated sample exposed to 3% NaCl for 84 hr	43	57
Uncoated reference sample exposed to 3% NaCl for 60 min	26	63 + 11 lost to solution

* The numbers in the table are computer determinations of the relative areas of the spectrum due to elemental metal and of the spectrum due to the compound. To a first approximation the numbers represent the relative amounts of the two species since it is reasonable to expect that the recoil-free fraction in both the metal and the compound will be approximately the same.

shown in Fig. 2 characteristic of elemental metal. It is estimated that the air-formed oxide is approximately 20Å thick.

The sample was coated to a thickness of 0.001 cm with a proprietary polybutadiene. The emission spectrum did not differ significantly from that of the uncoated sample. The coating was cured at 200°C in air for 30 min and the spectrum shown in Fig. 3 was obtained. The coated sample was then exposed to air-saturated, 3% sodium chloride for 48 and 84 hr. The spectrum of the sample exposed for 84 hr is given in Fig. 4 where it will be noted that the center peak characteristic of cobalt oxide has increased in relative intensity.

A companion uncoated sample, yielding an initial spectrum similar to that of Fig. 1, was exposed to the sodium chloride solution for 60 min. Approximately 26% of the electrodeposit remained as elemental cobalt after this time, as determined from the spectrum in Fig. 5 and the gain in radioactivity of the solution.

In the coated sample there was no loss of cobalt to the solution as indicated by the negligible radioactivity of the solution and the absence of any measurable change in the radioactivity of the solid. The uncoated sample lost approximately 11% in activity during the 60 min exposure to NaCl. A summary of the data obtained in this demonstration experiment is given in Table I.

Acknowledgment

Partial support of this research by Army Research Office, Durham, is gratefully acknowledged.

Manuscript submitted April 9, 1973; revised manuscript received June 21, 1973.

Any discussion of this paper will appear in a Discussion section to be published in the June 1974 JOURNAL.

Etching of High Alumina Ceramics to Promote Copper Adhesion

J. G. Ameen, D. G. McBride, and G. C. Phillips

IBM Corporation, System Products Division, Endicott, New York 13760

The electronic packaging industry is constantly trying to miniaturize all levels of circuit packaging to improve performance and to reduce the size of their machines. The first level of packaging, beneath the chip, is the module. For the size of this level of packaging to be decreased, circuit density must be increased so that more chips can be placed on the module. Increased circuit density requires reduced circuit-line widths.

For various reasons, such as dimensional stability, rigidity, and heat transfer, ceramic is used as a module material. Because thick film screening is limited to 0.005 in. wide lines, it is desirable to use copper metalization, photolithographic, and etching techniques to achieve the required fine-line circuitry. However, the adhesion of copper to ceramic is inherently low and becomes worse with thermal cycling (the result of mismatched coefficients of thermal expansion).

Elmore and Hershberger (1) have reported that fused[1] NaOH etches ceramic with resultant improved adhesion of copper to ceramic.

This pretreatment study was initiated to investigate other methods (2) of ceramic etching to increase surface roughness. The assumption was that of the two possible bonding mechanisms (chemical and mechanical), mechanical keying played the predominant role. Therefore, the hypothesis was that increased surface roughness would yield improved adhesion of copper to ceramic.

Experimental

Analytical Techniques

The analytical techniques (3) used for evaluation of the selected pretreatments were as follows.

Metallography.—The metallograph was used to observe opaque cross sections for internal structure analysis, depth of attack of the various pretreatments, and the nature of the copper/ceramic interface. The edge retention of cross-section samples was maintained by using a hard nickel plate over an electroless copper plate, and polishing was done in a unidirectional motion. The surface profile was highlighted by using oblique and polarized lighting techniques. The degree of polishing has an effect on the observable microstructure. Relatively coarse polishing reveals the alumina grain, whereas fine polishing eliminates the appearance of the alumina grain boundaries and exposes the glass and porosity phases.

SEM (scanning electron microscope).—For the ceramic surface morphology to be observed after pretreatments, it was necessary to vapor deposit between 200 and 350Å of gold on the surface for electrical continuity. Investigation of the range of magnification revealed that 2400× magnification was best for comparisons.

Surface finish by Proficorder.—Samples of all substrates characterized were submitted for surface-finish measurements by the Proficorder. Measurements included a plot of the peaks and valleys in addition to a cumulative plot of center-line averages (CLA) in microinches.

Surface area.—Surface area determinations were made by an outside vendor using the BET method, a krypton-gas absorption technique. The amount of absorption is proportional to surface area.

Flexural strength.—Because there was some concern that the pretreatments used to prepare the ceramic surfaces would be detrimental to the flexural strength (5) of the substrates, a three-point load flexural strength test was performed on selected pretreated samples.

Dot-bend test.—This adhesion test involves soldering a 185 mil diameter brass stud over a 150 mil etched Cu dot on the ceramic substrate. Care is taken to center the stud over the dot, forming a cantilever beam. The brass stud is then pulled at a 90° angle to the stud.

All of the preceding measurements are reproducible within experimental limits. See the text for specific details.

Pretreatments

The following is a summary of the various pretreatments considered; commercially available ceramic substrates (96% alumina) were placed into the solutions at various conditions of concentration, time, and temperature:

Key words: Cu plating, ceramic, adhesion, characterization, etching.

[1] There is an arbitrary distinction between the terms "fused NaOH" and "molten NaOH." The fused process refers to the technique of soaking a piece of ceramic in aqueous NaOH solution to coat it with a layer of NaOH, followed by a subsequent high-temperature bake. The molten NaOH process refers to treating ceramic substrates in hot (400°-500°C) liquid (nonaqueous) NaOH.

Treatment	Concentration	Temperature	Time (min)
HNO_3	70.6%	Boiling	30
HF	48%	120°F	30
H_2SO_4	95.7%	550°F	30
H_3PO_4	86%	Boiling	30
NaOH (aqueous)	25M	375°F	30
$HF:HNO_3$	2:1	Room temp.	30
NaOH	Molten	425°C	15
HBF_4	48-50%	Room temp.	30
HF (ultrasonic)	48%	120°F	15
TaF_5	100%	100°C	15
Vapor blast	—	—	5
$NH_4F \cdot HF$	(30% NH_5F_2, 50% H_2SO_4, 20% H_2O) by weight	120°F	10
No pretreatment	—	—	—

Metalization

Following pretreatment, the ceramic substrates were sensitized and activated using standard $SnCl_2$ and $PdCl_2$, respectively. The $SnCl_2$ and $PdCl_2$ concentrations and the length of time of soak in these were held constant to hold sensitizer and activator effects constant (6). The ceramic was then plated in a proprietary IBM electroless Cu plating bath and subsequently in a standard electrolytic pyrophosphate Cu bath. After the ceramic underwent standard photolithographic techniques, the desired patterns were etched.

Results and Discussion

Of the surface treatments investigated, many had no observable effect on dot-bend values; these were dropped from further study. The ones showing some effect were submitted for further testing.

Figure 1 shows a cross section of a substrate with no pretreatment. Fluoride type etchants (2HF : HNO_3, HBF_4, and HF with ultrasonic vibration) revealed a significant depth of attack but to various degrees. Figure 2 shows the results of the ultrasonic HF treatment which had the greatest depth of attack. The gray area (below the top) represents the depth of attack. With this treatment, the glassy phases between the grains were removed; the alumina grains pulled away from the surface during polishing. On the other hand, the NaOH (molten) vigorously attacked the surface of the ceramic (Fig. 3), but no depth of attack was observed. The etching appears to be a surface effect only. Figures 4 and 5 show substrates etched with HF (concentrated) and NaOH (molten), respectively, after copper plating. It is significant to note that although there is a greater depth with the HF treatment the Cu plating did not penetrate to that depth. In fact, in both cases, the copper is plated only onto the surface. None of the other pretreatments showed any observable effect.

Fig. 1. Cross section of substrate with no pretreatment (48X)

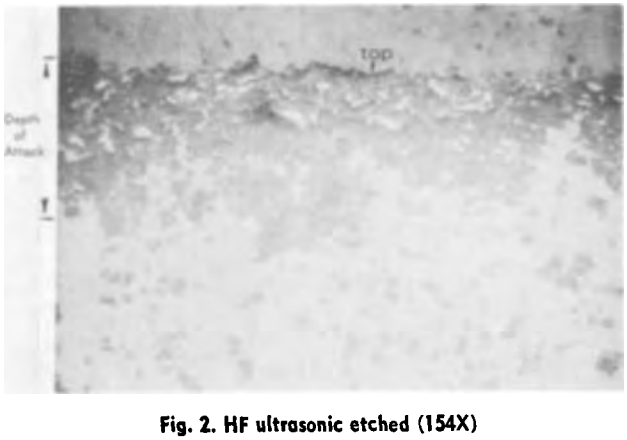

Fig. 2. HF ultrasonic etched (154X)

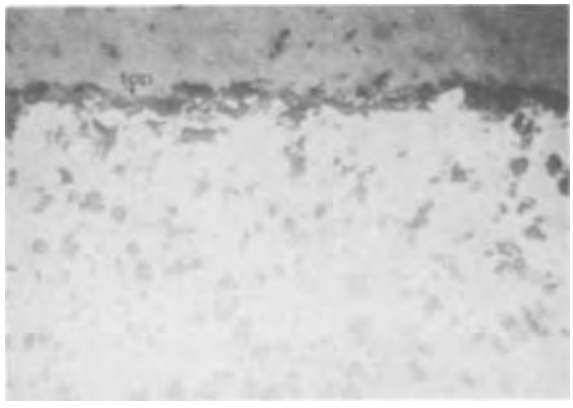

Fig. 3. NaOH (molten), etched (168X)

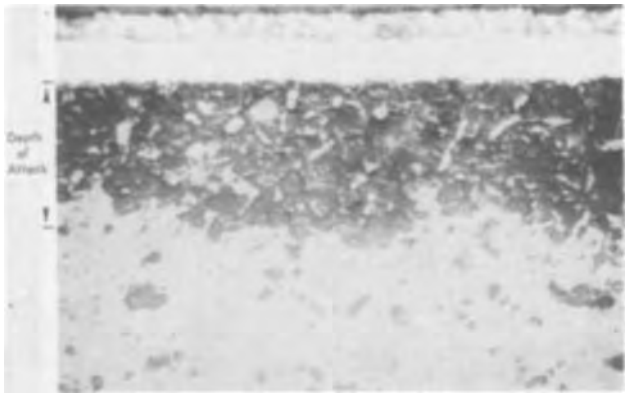

Fig. 4. HF etched, Cu plated (154X)

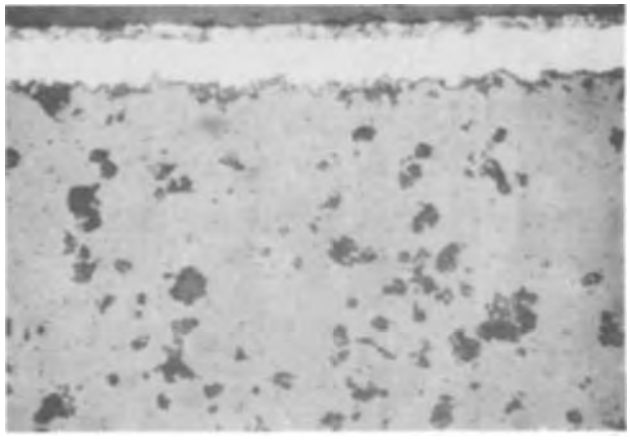

Fig. 5. NaOH (molten) etched, Cu plated (168X)

(SEM) Scanning Electron Microscope

Scanning electron microphotographs of the treated surfaces revealed definite differences between the pretreatments that were found to attack the ceramic.

Figure 6 is an SEM of a substrate with no pretreatment. After etching with HF (Fig. 7) (or any of the other fluoride systems), the alumina grains are more distinct because of the removal of the glassy phase. Figure 8 shows the effects of the NaOH (aqueous) pretreatment. The glassy phases were etched away first, followed by the preferential etch of the alumina grains along crystallographic directions producing a

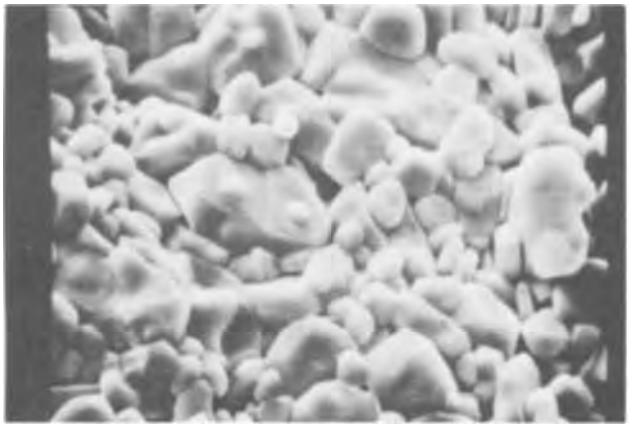

Fig. 6. SEM of substrate with no pretreatment (1152X)

Fig. 9. SEM NaOH (molten), etched (1152X)

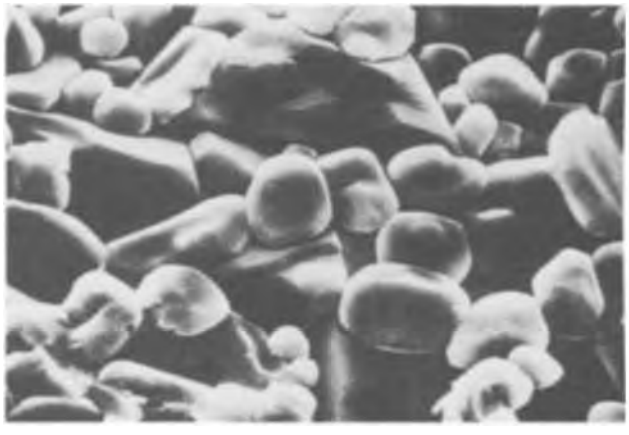

Fig. 7. SEM HF ultrasonic, etched (1152X)

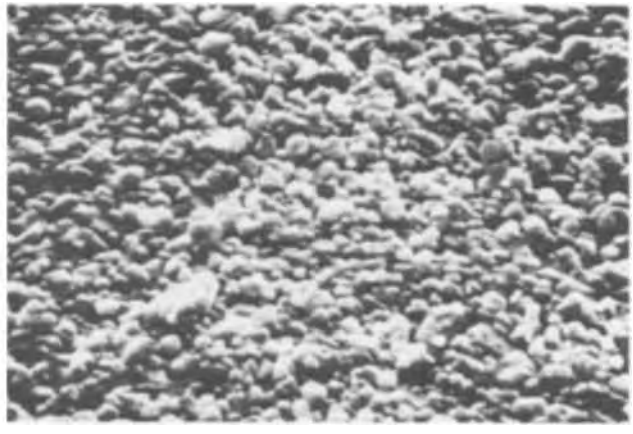

Fig. 10. SEM, activated alumina, with no pretreatment (1152X)

Fig. 8. SEM NaOH (aqueous), etched (1152X)

Fig. 11. SEM, activated alumina, NaOH (molten), etched (1152X)

well-defined grain structure. NaOH (molten) had the most aggressive attack (Fig. 9). The glassy phases are etched rapidly first and then the individual grains are etched at a constant rate.

Commercially available activated alumina (fine grain) was similarly etched in NaOH (molten). Since all the magnifications are the same, the smaller particle size for these substrates as compared to all previous substrates investigated are obvious. Figures 10 and 11 show the ceramic with no pretreatment and after etching in NaOH (molten), respectively. This surface also demonstrated the considerable microroughness characteristic of this process. The remaining treatments showed no difference in their SEM's from the as-received surface.

Dot-Bend Surface Finish

The proof of the hypothesis that mechanical interlocking played the key role in the adhesion promotion mechanism and that increased surface roughness would yield increased copper-to-ceramic adhesion was substantiated with the dot-bend and degree-of-roughness data. Figure 12 shows the plot of surface roughness (CLA) *vs.* dot-bend values. Substrates with no pretreatment yielded a dot bend $\bar{x}$ of 3.2 lb ($\sigma = 0.29$ lb) and a roughness of approximately 21 μin. (CLA). Substrates treated in boiling HNO_3 had a dot bend $\bar{x}$ of 2.6 lb ($\sigma = 0.23$ lb) with a surface roughness of approximately 16 μin. (CLA). The nitric acid slightly smoothed the surface, reducing adhesion. HF (ultra-

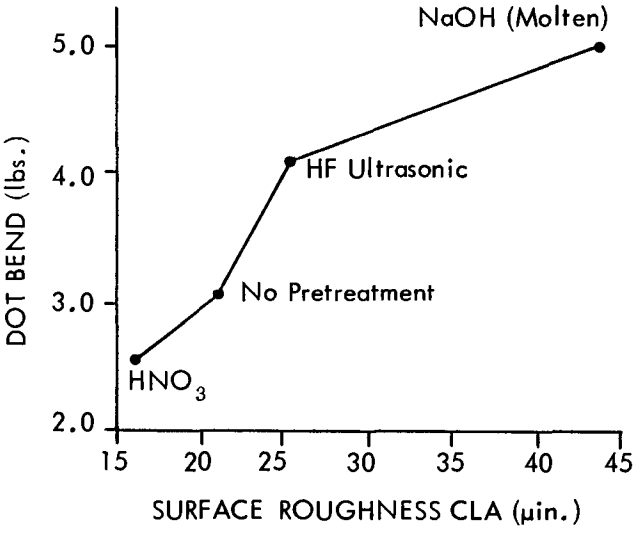

Fig. 12. Dot bend vs. surface roughness

sonic) etching resulted in a dot bend $\bar{x}$ = 4.2 lb (σ = 0.54 lb) with a surface roughness of 25 μin. (CLA). NaOH (molten) etching promoted the greatest copper-to-ceramic adhesion with a dot bend $\bar{x}$ = 5.0 lb (σ = 0.45 lb) and a surface roughness of approximately 44 μin. (CLA). The $\bar{x}$'s are at a 95% confidence level.

The other treatments gave dot bends and CLA's comparable to the no-pretreatment substrates and will not be mentioned further. The other fluoride treatments behaved similarly to HF (ultrasonic) but the effects were not quite as pronounced.

Surface Area

With the BET method of krypton absorption, surface area determinations were performed by Micromeritics Instrument Corporation, Norcross, Georgia, on substrates treated with the various etchants found to attack ceramic (Table I). Substrates having no pretreatment yielded a small surface area. A mild $NH_4F \cdot HF$ pretreatment approximately tripled the surface area; concentrated HF further increased the surface area to approximately 30 times; and HF (ultrasonic) drastically increased the surface area by two orders of magnitude. NaOH (molten) increased the surface area to three times that of the no-pretreatment case, but was many times less than that obtained wih HF. This information confirmed the depth of attacks observed by the metallograph. The HF etch produced a large depth of attack, producing a large surface area, while the NaOH (molten) roughened up the surface but with no appreciable depth of attack.

Flexural Strength

Flexural strength measurements (4) were made on substrates treated with the etchants found to attack ceramic (Table I). The NaOH (molten) process does not decrease flexural strength although there is a reduction in those substrates etched in $NH_4F \cdot HF$. This reduction is probably a result of the increased depth of attack characteristic of fluoride ceramic etchants.

Adhesion Optimization

Because the best copper-to-ceramic adhesion was obtained with NaOH (molten), experiments were run to optimize the adhesion, as measured by dot bend, with respect to time and temperature in the molten NaOH. Figure 13 demonstrates the characteristic effect on adhesion as a function of time of soak at a specific temperature. (The dot-bend values are statistical averages with a 10-15% variation.) Figure 14 displays the effect of the temperature of the molten NaOH on adhesion. These two studies show that the best adhesion was found to be at 420°C for 10 min of soak. The cyclic variance of the dot-bend values with time and temperature is believed to be due to the structure of the ceramic. In the first few seconds the glassy phases and surface debris are removed promoting adhesion; further etching attacks the alumina grains, resulting in a further increase in adhesion. Still further etching weakens the ceramic surface, resulting in the removal

Table I. Surface area and flexural strength vs. pretreatment

Pretreatment	$m^2/gm \times 10^{-4}$	Flexural strength (psi)
As-received	9.5	21,000
$NH_4F \cdot HF$	24.7	19,500
NaOH (fused)	34.9	21,000
NaOH (molten)	32.2	21,000
HF	341.4	—
HF (ultrasonic)	895.0	—

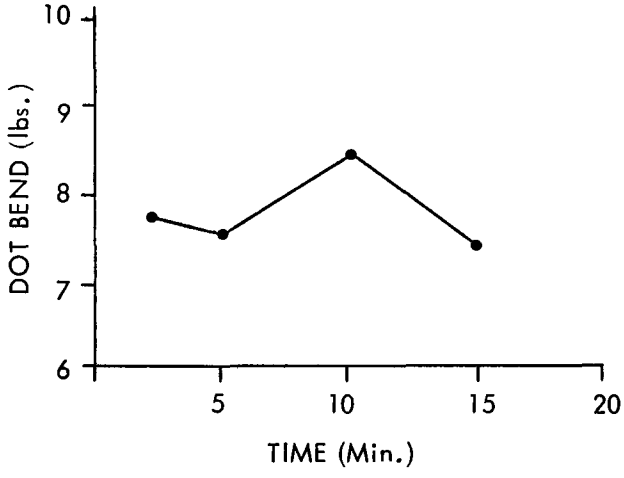

Fig. 13. Time vs. dot bend at constant temperature (420°C)

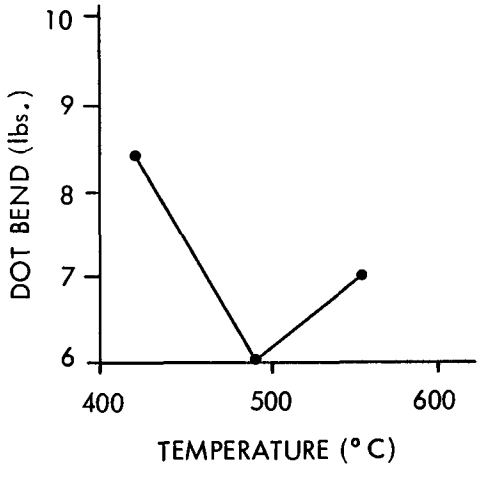

Fig. 14. Temperature vs. dot bend at constant time (10 min)

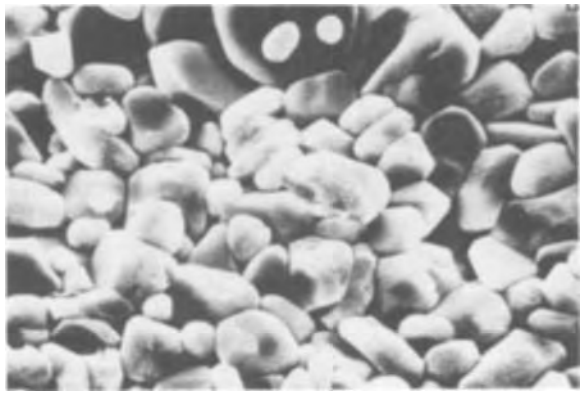

Fig. 15. SEM, 10 sec, NaOH (molten), etched (1152X)

of individual grains and, hence, a decrease in adhesion. Even further etching causes new grains to be exposed with a resultant improved adhesion. (See Fig. 15-18)

Summary

Twelve pretreatments on ceramic substrates were evaluated with a view toward increasing surface roughness and thereby increasing copper-to-ceramic adhesion.

NaOH (molten) yielded a microroughened surface with greatly improved copper-to-ceramic adhesion and no reduction in flexural strength.

Fig. 16. SEM, 30 sec, NaOH (molten), etched (1152X)

Fig. 17. SEM, 60 sec, NaOH (molten) etched (1152X)

Fig. 18. SEM, 3 min, NaOH (molten), etched (1152X)

NaOH (aqueous) slightly roughened the ceramic with only slightly improved adhesion over substrates with no pretreatment. Individual grains were preferentially etched along crystallographic directions.

HNO_3 smoothed the ceramic with a slight reduction in adhesion.

Various concentrations of HF roughened the ceramic surface. HF (concentrated) and HF (ultrasonic) roughened the surface moderately, but attacked to a considerable depth, thus reducing flexural strength with a moderate improvement in copper-to-ceramic adhesion.

Manuscript submitted Dec. 7, 1972; revised manuscript rceived June 11, 1973. This was Paper 226 presented at the Miami Beach, Florida, Meeting of the Society, Oct. 8-13, 1972.

Any discussion of this paper will appear in a Discussion Section to be published in the June 1974 JOURNAL.

REFERENCES

1. G. V. Elmore and R. F. Hershberger, Paper 213, presented at Electrochemical Soc. Meeting, Miami Beach, Florida, Oct. 8-13, 1972, To be published.
2. S. G. Stalnecker, Jr., US Pat. No. 3,296,012.
3. N. A. Gjostein, H. P. Bonzel, and N. G. Chavka, Res. Devel., **000**, 24 (1970).
4. R. F. Gruszka, R. E. Mistler, and R. B. Runk, *Ceram. Bull.*, **49**, 575 (1970).
5. H. P. Kirchner, W. R. Buessem, R. M. Gruver, D. R. Platts, and R. E. Walker, Ceramic Finishing Company Report for the Department of the Navy, Contract No. N000 19-70-C-0418, Dec. 6, 1970.
6. J. P. Melka, Jr., *Plating*, 1085, (1971).

JOURNAL OF THE ELECTROCHEMICAL SOCIETY

SOLID-STATE SCIENCE
—AND TECHNOLOGY

NOVEMBER
1973

Influence of Oxide Structure on the Oxidation Rate of Nickel Single Crystals

M. J. Graham, R. J. Hussey, and M. Cohen*

Division of Chemistry, National Research Council of Canada, Ottawa, Ontario, Canada K1A OR9

ABSTRACT

The influence of metal orientation and the prior oxide film on the oxidation rate of nickel single crystals has been investigated at 600°C in 5×10^{-3} Torr oxygen using a manometric technique and the specimens examined before and after oxidation by electron diffraction, x-ray emission analysis, and electron microscopy. For nickel electropolished in sulfuric acid, the order of decreasing oxidation rate is found to be (100), (111), and (112). This anisotropy together with changes in oxidation rate with surface pretreatment can be explained by modification in the structure of the prior oxide; when a single orientation prior oxide persists the oxidation rate is low; when the oxide contains twin orientations or becomes polycrystalline, the oxidation rate is increased. The results may be interpreted in terms of a variation in the number of easy diffusion paths in the oxide; the higher the density of these paths the greater is the oxidation rate.

Recent investigations in this laboratory on the oxidation of polycrystalline nickel have emphasized the influence of surface preparation on the oxidation rate (1-4). Cold-worked nickel was considered to oxidize faster than annealed nickel because the oxide formed on cold-worked metal was finer grained and, therefore, contained more grain boundaries to act as easy paths for nickel diffusion (3, 4). Various pretreatments of annealed surfaces, e.g., electropolishing, etching, or hydrogen reduction also resulted in markedly different oxidation kinetics (2). The observed different rates of oxidation were explained in terms of a varying density of easy diffusion paths: hydrogen-reduced nickel oxidized most rapidly because the oxide produced contained the highest density of leakage paths, whereas electropolished or etched nickel oxidized more slowly because on some metal grains a single-crystal type of overgrowth, low in leakage paths, was produced. The role of leakage paths in governing oxidation anisotropy has been considered in the past by many groups, including Lawless and Gwathmey, Cathcart, Smeltzer and co-workers (5-12).

Preliminary experiments on a single-crystal spherical segment illustrated the variation of oxide thickness with nickel orientation; by visual observation the order of decreasing oxidation rate on electropolished nickel of the major crystallographic planes was determined as (100), (110), (111), and (112). This study deals with the chemical and structural analysis of the surface oxide before and after oxidation and examines the influence of the prior oxide film in determining subsequent oxidation behavior of these low index faces.

Experimental

Specimen preparation.—Nickel single-crystal disks (0.05-0.15 cm thick) with (100), (111), or (112) surfaces were spark machined from 1.2 cm diameter cylindrical rods supplied by Materials Research Corporation.[1] After an extensive chemical polish (1) to eliminate contamination and damage from cutting (~100 μm Ni removed), specimens were mechanically polished through 0.1 μm diamond, electropolished in a 4:3 (by volume) sulfuric acid solution and then annealed in vacuum at 700°C for 2½ hr. Prior to oxidation specimens were either electropolished in sulfuric acid or electropolished and then etched in 0.8*N* nitric acid for 30 sec. Electropolishing removed ~8 μm Ni and etching ~200Å Ni.

Procedure.—The prepared specimens were oxidized in a manometric apparatus (1). A "furnace-raised" starting procedure (2) was normally used in which the electropolished or etched disk was heated to the oxidation temperature of 600°C in 5×10^{-3} Torr oxygen. The specimen reached 600°C in about 3 min. Some runs were terminated once the specimen had reached 600°C, but most were continued for oxidation times up to 1 hr. In some experiments the oxide film remaining after a decarburizing anneal at 700°C (1) was reduced in hydrogen at 600°C, the specimen cooled, and oxygen admitted at room temperature. A furnace-raised oxidation at 600°C was then performed.

Surface and oxide examination.—Surfaces before and after oxidation were analyzed by an electron-excited x-ray emission technique (13) and were structurally characterized by reflection electron diffraction and electron microscopic examination of two-stage Formvar platinum-carbon replicas. Oxide films were stripped from the metal by immersing in 30% hydrochloric acid and examined by transmission electron microscopy.

Results

Oxidation curves.—Figure 1 illustrates the differing rates of oxidation of the (100), (111), and (112) electropolished surfaces at 600°C and 5×10^{-3} Torr oxy-

* Electrochemical Society Active Member.
Key words: nickel oxidation, kinetics, oxidation anisotropy.

[1] Total impurities <0.005% by weight as determined by spark source mass spectrometry; typical analysis has been given previously (1).

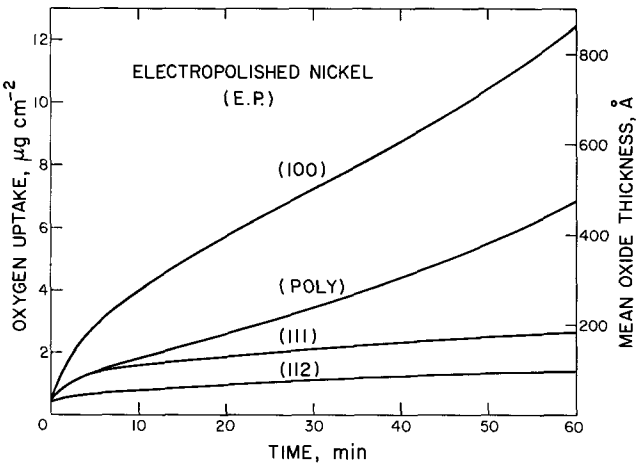

Fig. 1. Oxidation curves at 600°C in 5 × 10^{-3} Torr oxygen for nickel crystals electropolished in sulfuric acid.

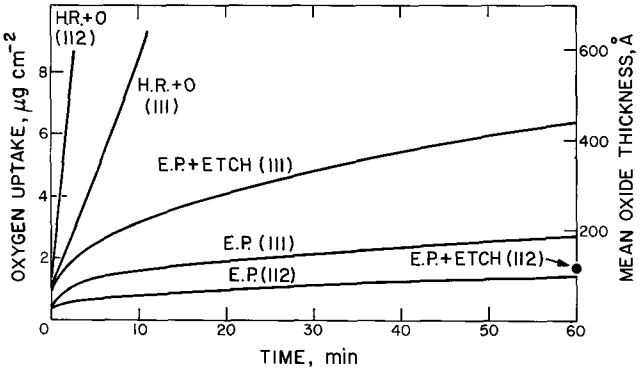

Fig. 2. Oxidation curves at 600°C in 5 × 10^{-3} Torr oxygen for (111) and (112) nickel after electropolishing in sulfuric acid (EP), after electropolishing and then etching in nitric acid (EP + etch), or after hydrogen reduction at 600° followed by oxygen exposure at room temperature (HR + O).

gen. Also included is the curve for polycrystalline nickel which oxidizes more slowly than (100) but more quickly than (111) and (112) surfaces. The oxidation curves for both polycrystalline and (100) nickel show an increase in rate after about 30 min of oxidation.

Figure 2 shows a comparison between the rates of oxidation of the (112) and (111) nickel disks at 600°C after different surface pretreatments. As was the case for electropolished specimens (EP), (112) nickel subsequently etched in nitric acid (EP + etch) oxidizes more slowly than etched (111) nickel. A much more rapid rate is found at 600°C if oxygen is first admitted at room temperature to a hydrogen-reduced surface (HR + O) and then the specimen heated to 600°C in 5 × 10^{-3} Torr oxygen. After this treatment the (112) surface oxidizes more rapidly than the corresponding (111) surface.

In calculating oxide thickness a surface roughness factor of unity has been assumed. This, together with a bulk density of nickel oxide of 6.75 leads to a calculated thickness of 69.2Å for an oxygen uptake of 1 μg cm^{-2}.

Surface analysis.—Table I shows the determination by x-ray emission of the C, O, and N content of prior oxide films on prepared nickel surfaces. The C content of the films after electropolishing or etching was relatively large (2-3 monolayers) and of the same order as oxygen. Nitrogen was found after the nitric acid etch; S was not detected following the sulfuric acid electropolish. Also included in the table are analyses of thin oxides formed during the heat-up period to 600°C of furnace-raised oxidations in 5 × 10^{-3} Torr oxygen: N and C are removed from the film during this period.

Structure.—Reflection electron diffraction patterns typical of nickel single-crystal surfaces before and after oxidation are presented in Fig. 3 and 4. Epitaxial relationships between the oxide and metal for both the prior oxides and those grown for different times at 600°C are given in Table II.

Figure 3a, c, and f show patterns from (112), (111), and (100) electropolished nickel. Strong elongated reflections from the nickel substrate and more diffuse streaks and spots from the oxide are observed. The pattern from the (112) surface is interpreted as (111) oxide growing on the (111) atomic steps which constitute the (112) macrosurface. The (111) oxide on (112) metal is oriented in a direction antiparallel with respect to the (111) steps. On (111) nickel the parallel orientation oxide was also sometimes observed. On (100) nickel the oxide formed from electropolishing has a preferred fiber axis, again with (111) oxide parallel.

After oxidation at 600°C, structural differences in the oxide are apparent. On (112) nickel a highly epitaxed mosaic oxide is produced (Fig. 3b). On (111) nickel a mosaic containing both parallel and antiparallel oriented oxide is formed (Fig. 3e). Two sets of these twin-related orientations are present on (100) nickel after 5 min oxidation (Fig. 3g); after 1 hr, the outer oxide is polycrystalline (Fig. 3h). (Twin-related oxide orientations will subsequently be referred to simply as twins or twinned oxide.)

The diffraction patterns from (112) and (111) surfaces after etching or hydrogen reduction both before and after oxidation at 600°C are given in Fig. 4. After etching, reflections from (111) nickel appear broader than from the (112) surface (Fig. 4a and c); the oxide reflections appear sharper and elongated for the (111) as compared to the (112) surface. In both cases only the antiparallel orientation of oxide is present. On heating the etched (111) surface to 600°C the nickel

Table I. Analysis of prior oxide and thin oxide films

Surface preparation	Ni orientation	Concentration, μg cm^{-2}					
		Prior to oxidation			After oxidation to 600°C		
		O[a]	C[b]	N[c]	O[a]	C[b]	N[c]
H_2SO_4 electropolish (EP)	(112)	0.06 ± 0.02[d]	0.07 ± 0.02	—			
	(111)	0.09 ± 0.01	0.08 ± 0.03	—	0.32	0.00	—
	(100)	0.07	0.07	—			
	Polycrystalline	0.07	0.07	—			
HNO_3 etch after H_2SO_4 electropolish (EP + etch)	(111)	0.10 ± 0.03	0.07 ± 0.03	0.02 ± 0.01	0.25	0.02	0.00
Oxidized 25°C after H_2 reduction at 600°C (HR + O)	(112)	0.13	0.00	—	1.30	0.00	—
	(111)	0.11	≤0.03	—	0.49	0.00	

[a] 1 monolayer ≡ 0.043 μg cm^{-2} (1μg cm^{-2} ≡ 69.2Å NiO).
[b] 1 monolayer ≡ 0.032 μg cm^{-2}.
[c] 1 monolayer ≡ 0.038 μg cm^{-2}.
[d] Variation determined from duplicate experiments.

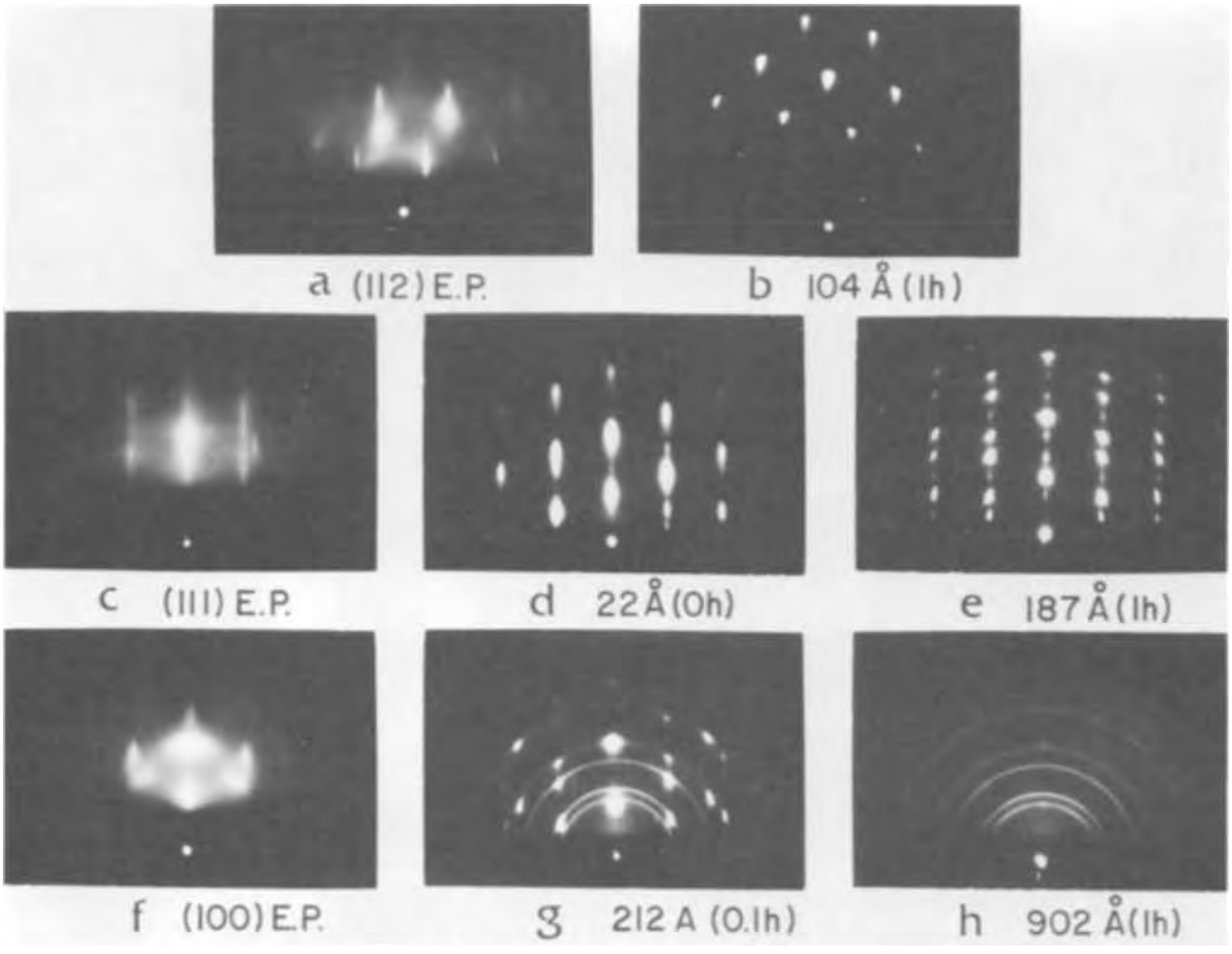

Fig. 3. Reflection diffraction patterns from (112), (111), and (100) nickel after electropolishing in sulfuric acid (a, c, and f) and after oxidation at 600°C in 5×10^{-3} Torr oxygen (b, d, e, g, and h). Oxide thicknesses and oxidation times are indicated; see Fig. 1 and Table II for kinetics and oxide structure. Electron beam parallel to $[0\bar{1}1]$ azimuth.

Table II. Oxide Structure

Surface preparation	Prior oxide: Planes (hkl)Ni//(hkl)NiO		Prior oxide: Directions [hkl]Ni//[hkl]NiO		Oxidation time, hr	After oxidation at 600°C: Planes (hkl)Ni//(hkl)NiO		After oxidation at 600°C: Directions [hkl]Ni//[hkl]NiO	
H_2SO_4 electropolish (EP)	(112)	*	$[0\bar{1}1]$	$[01\bar{1}]$	1	(112)	*	$[0\bar{1}1]$	$[01\bar{1}]$
	(111)	(111)	$[0\bar{1}1]$	$[01\bar{1}]$	1	(111)	(111)	$[0\bar{1}1]$	$[01\bar{1}]$
			$[0\bar{1}1]$	$[0\bar{1}1]$**				$[0\bar{1}1]$	$[0\bar{1}1]$
	(100)	(111)	Fiber		0.1	(100)	(111)	$[0\bar{1}1]$	$[01\bar{1}]$
								$[0\bar{1}1]$	$[01\bar{1}]$
								$[011]$	$[01\bar{1}]$
								$[011]$	$[0\bar{1}1]$
					1	(100)	Polycrystalline		
HNO_3 etch after H_2SO_4 electropolish (EP + etch)	(112)	*	$[0\bar{1}1]$	$[01\bar{1}]$	1	(112)	*	$[0\bar{1}1]$	$[01\bar{1}]$
								$[0\bar{1}1]$	$[01\bar{1}]$
	(111)	(111)	$[0\bar{1}1]$	$[01\bar{1}]$	1	(111)	(111)	$[0\bar{1}1]$	$[01\bar{1}]$
								$[0\bar{1}1]$	$[01\bar{1}]$
Oxidized 25°C after H_2 reduction at 600°C (HR + O)	(112)	*	$[0\bar{1}1]$	$[01\bar{1}]$	0†	(112)	*	$[0\bar{1}1]$	$[01\bar{1}]$
								$[0\bar{1}1]$	$[0\bar{1}1]$‡
					0.05	(112)	Polycrystalline		
	(111)	(111)	$[0\bar{1}1]$	$[01\bar{1}]$	0†	(111)	(111)	$[0\bar{1}1]$	$[01\bar{1}]$
			$[0\bar{1}1]$	$[0\bar{1}1]$				$[0\bar{1}1]$	$[01\bar{1}]$
								$[\bar{2}11]$	$[01\bar{1}]$
								$[\bar{2}11]$	$[0\bar{1}1]$
					0.17	(111)	Polycrystalline		

* (111) antiparallel oxide on (111) steps of (112) macrosurface.
† Formed during heat-up period to 600°C.
** Sometimes observed,
‡ $[0\bar{1}1]$ oxide also parallel to $[01\bar{1}]$ oxide.

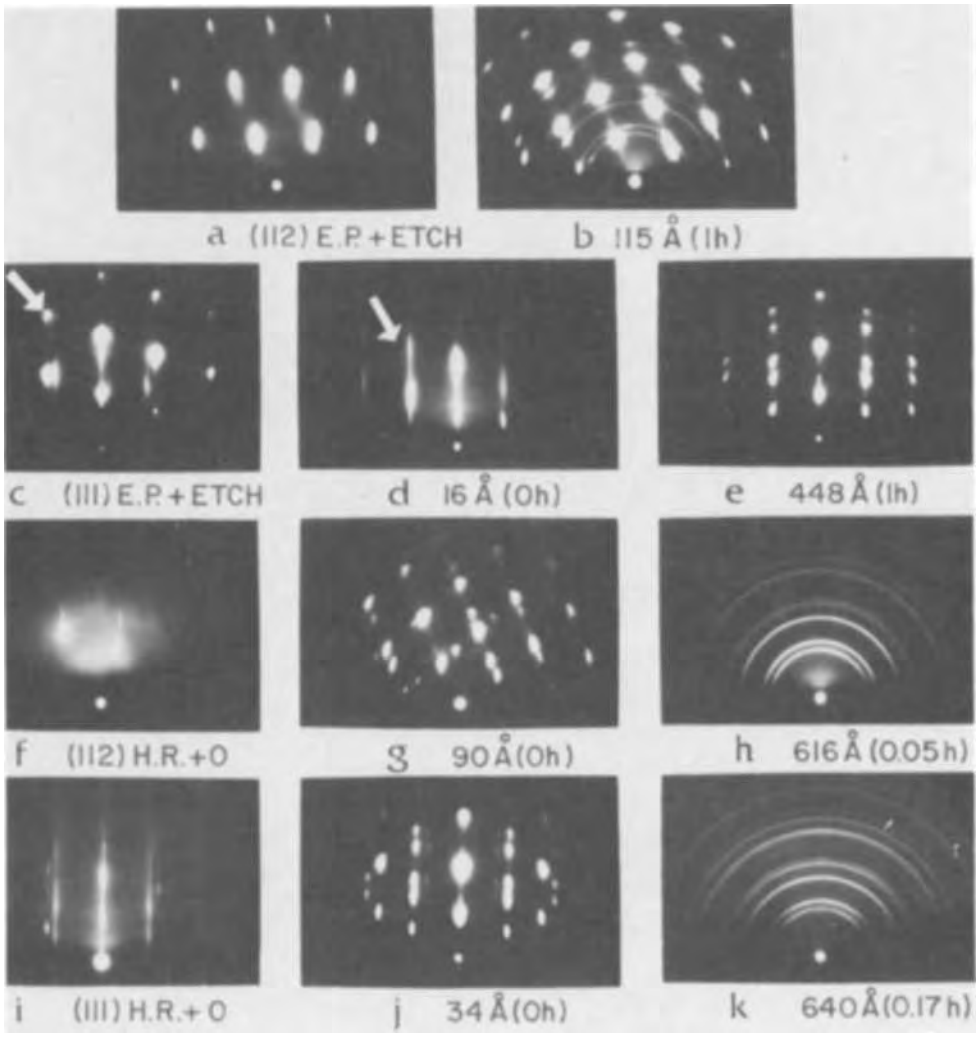

Fig. 4. Reflection diffraction patterns from (112) and (111) nickel: (a and c) after electropolishing and then etching in nitric acid (EP + etch); (f and i) after hydrogen reduction at 600°C followed by oxygen exposure at room temperature (HR + O); (b, d, e, g, h, j, and k) after oxidation at 600°C in 5 × 10^{-3} Torr oxygen. Oxide thicknesses and oxidation times are indicated; see Fig. 2 and Table II for kinetics and oxide structure. Electron beam parallel to [$0\bar{1}1$] azimuth.

spots sharpen (arrows indicate pertinent reflections in Fig. 4c and d), and the oxide spots broaden. After an hour of oxidation at 600°C a twinned oxide is formed both (112) and (111) surfaces (Fig. 4b and e) with the antiparallel twin predominant in the former case. In both instances a little polycrystalline oxide is present. A twinned oxide is produced at room temperature on (111) nickel previously subjected to a carbon burnout anneal (1) and hydrogen reduction at 600°C (Fig. 4i).[2] In contrast the oxide on the corresponding (112) surface (Fig. 4f) exists in the antiparallel orientation only. On heating to 600°C in oxygen two additional twins are observed, one parallel with respect to the substrate and the other parallel to the original antiparallel oxide (Fig. 4g). On oxidizing the (111) specimen an oxide comprising two sets of twins is observed (Fig. 4j). On further oxidation a polycrystalline oxide is formed on both (112) and (111) nickel (Fig. 4h and k).

Replicas of (111) and (112) nickel surfaces prior to oxidation are shown in Fig. 5a and b. Smooth featureless surfaces such as that shown in Fig. 5a for (111) nickel are observed after electropolishing. Some roughening is produced on etching (112) (Fig. 5b); etched (111) after heating in oxygen to 600°C is shown in Fig. 5c where large etch pits, some 200Å deep, are observed. A smoother surface is produced after the hydrogen reduction treatment; Fig. 5d shows a (111) surface subsequently exposed to oxygen at room temperature and then oxidized to 600°C.

[2] Twinned metal is sometimes observed. On annealing at 900°C after hydrogen reduction at 600°C the singly oriented (111) metal surface is restored; on exposure to oxygen at room temperature, a twinned oxide is still produced. Thus, twinned oxide results after HR + O treatment whether the metal is twinned or untwinned.

Surface replicas of oxides produced at 600°C are shown in Fig. 6. On slowly oxidizing (112) nickel, the ~100Å thick single-crystal oxide formed after 1 hr has maintained a fairly smooth surface (Fig. 6a). A rougher oxide is produced on etched (111) nickel (Fig. 6c). Thicker oxides on electropolished (100) and hydrogen-reduced (111) nickel (Fig. 6b and d, respectively) show a greater degree of roughening with increased oxide thickness.

Discussion

Although all the surface preparations produce initial oxide films on all nickel single crystals which are highly oriented, the subsequent oxidation behavior appears to depend on both minor differences in the initial oxide film and on the orientation of the underlying metal. With some orientations and pretreatments an initial single-crystal type of film is preserved for long periods of time, while with others the oxide becomes twinned or polycrystalline. The resulting oxidation rate is a function of the number and type of crystallite boundaries which act as easy diffusion paths in the oxidation process. As pointed out below, the oxide crystallite size and distribution appears to be independent of small differences in chemical composition of the initial oxide film.

Surface analysis.—X-ray emission analyses of the oxide films (Table I) showed that roughly equal quantities (2-3 monolayers) of oxygen and carbon are present in films on different single crystals after electropolishing or etching. The room temperature film on hydrogen-reduced nickel contains a similar amount of oxygen but much less C. The probable source of this

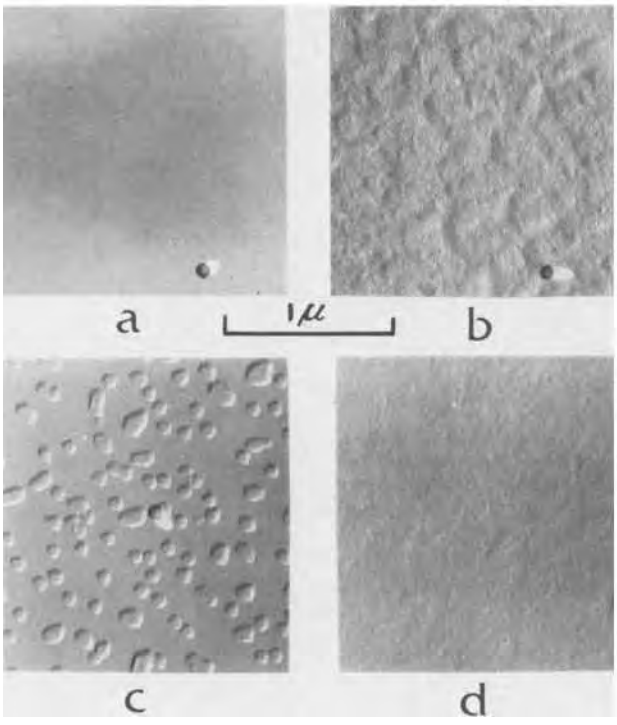

Fig. 5. Electron micrographs of replicas of (111) and (112) nickel surfaces. a, (111) after electropolishing; b, (112) after electropolishing and etching (340Å Ni removed during etch); c, (111) after electropolishing and etching (125Å Ni removed during etch) and heating to 600°C in 5×10^{-3} Torr oxygen; d, (111) after room temperature oxidation of a hydrogen-reduced surface followed by heating to 600°C in 5×10^{-3} Torr oxygen. All ×30,000.

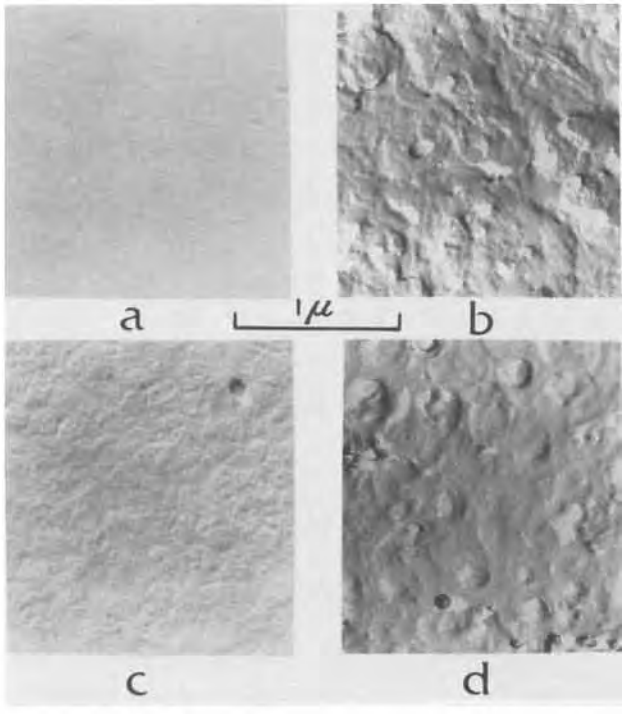

Fig. 6. Electron micrographs of replicas of surfaces of nickel oxides formed at 600°C in 5×10^{-3} Torr oxygen. a, on electropolished (112), 104Å thick oxide; b, on electropolished (100), 900Å; c, on electropolished and etched (111), 448Å; d, on (111) after hydrogen reduction at 600°C followed by oxygen exposure at room temperature, 640Å. All ×30,000.

latter C is CO in the vacuum system which "cracks" on the nickel surface on cooling from 600°C to room temperature. The large C content after electropolishing or etching is more difficult to account for. The source could be residual impurity in the nickel which concentrates at the surface during polishing or, more likely, results from the absorption of atmospheric CO_2 or organic contaminants either during polishing or on subsequent air exposure. As seen in Table I, on heating to 600°C the oxide thickens and C and N are removed from the film. (Nitrogen is observed after a nitric acid etch.) Different single crystals with similar surface C levels are found to oxidize at quite different rates [cf. electropolished (100) and (112) in Fig. 1], and it is considered that the C content of the film is not a major factor in determining the observed oxidation anisotropy. Physical rather than chemical differences account for the variation in oxidation rate.

Oxidation rate anisotropy of electropolished nickel.— Electropolished (112) nickel oxidizes at the slowest rate (Fig. 1) because the single orientation prior oxide is maintained during oxidation at 600°C (Fig. 3a and b). We observed on oxidizing an electropolished spherical segment that orientations in the region of (112), *e.g.*, (113), (115), also oxidize at the low rate. Perhaps the growth stress in the oxide can be better accommodated when growing on such stepped surfaces and the original, unique epitaxy of oxide is retained.

As seen in Fig. 1, electropolished (111) nickel oxidizes faster than (112). While (111) oxide is formed on both (112) and (111) faces of nickel, in the latter case it is twinned. Two types of twin boundaries may be defined: a twin boundary that coincides with the (111) twinning plane is called a coherent twin boundary (14), whereas twin boundaries that do not coincide with the twinning plane are termed noncoherent twin boundaries (15). Coherent twin boundaries in the present case lie parallel to the film surface. Boundaries normal to the film surface would be noncoherent and as proposed by Cathcart *et al.* (8) could constitute paths of easy diffusion. The interfacial free energy of noncoherent twin boundaries approaches that of a high angle grain boundary (15) and so these boundaries have good potential as easy diffusion paths. The presence of these paths in the oxide on (111) nickel could account for the faster oxidation rate of this face compared with that of (112) nickel.

Electropolished (100) oxidizes much faster still. The prior oxide has a fiber texture (Fig. 3f), and on oxidation at 600°C the two sets of oxide twins (Fig. 3g) could provide a greater density of incoherent boundaries and hence more rapid nickel transport leading to a greater oxidation rate. The increase in oxidation rate after about 30 min for both (100) and polycrystalline nickel suggests recrystallization of the oxide, probably to relieve stress due to epitaxial strain, resulting in the production of mismatch boundaries which provide a greater outward nickel flux. The outer oxide as seen in Fig. 3g and h, eventually becomes polycrystalline. Polycrystalline oxide crystallites were observed in the early stages of oxidation of (100) nickel at 500°C in a recent study by Homma *et al.* (16).

Dark field electron microscopy gave some indication of oxide crystallite size. It showed the 104Å thick oxide growing on electropolished (112) nickel to have a large particle size, ~2000Å in diameter (Fig. 7). This large block mosaic shows angular misorientation with a maximum of about 5° as evidenced by the increase in half width of reflections with increasing order (Fig. 3b). Elongation of reflections toward the shadow edge is due to refraction by the flat surface facets of the mosaic blocks. Kikuchi lines were also observed from this oxide. The 179Å thick oxide on electropolished (111) is shown to contain triangular-shaped crystallites (bright field inset of Fig. 8). Between these grains, as revealed by dark field in Fig. 8, is a much finer grained mosaic; some crystallites are as small as 100Å in diameter. The line broadening in reflection diffraction (Fig. 3e) is due to this small mean particle size and small angular misorientation. As seen in Fig. 3e

Fig. 7. Dark field electron micrograph [from (200) reflection] of 104Å oxide formed at 600°C in 5×10^{-3} Torr oxygen on electropolished (112) nickel. ×16,000.

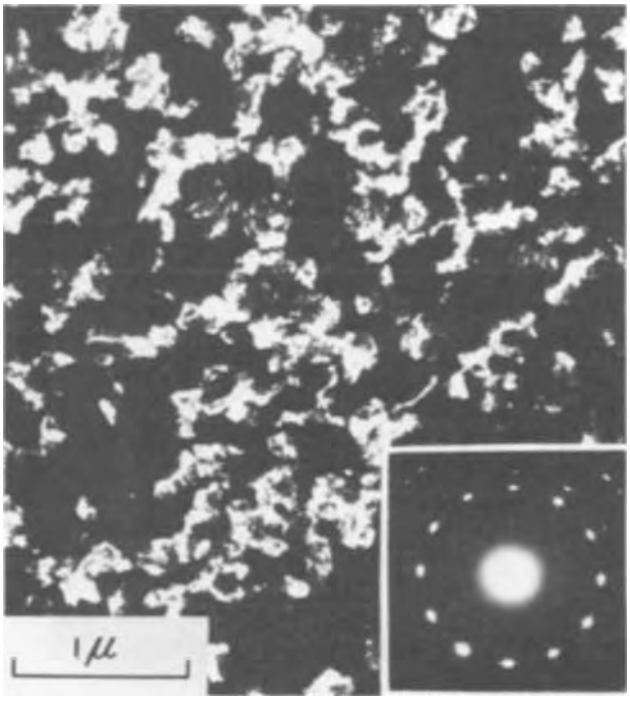

Fig. 8. Dark field micrograph [from (220) reflection] and selected area diffraction pattern from 179Å oxide formed at 600°C in 5×10^{-3} Torr oxygen on electropolished (111) nickel. Top inset: bright field micrograph showing triangular crystallites. ×30,000.

no significant increase in spot broadening is apparent with higher orders of reflection. The low angle boundaries between crystallites comprising the epitaxed mosaics are considered to be ineffective as easy diffusion paths and the oxide on the slower oxidizing (112) is growing at a rate essentially governed by diffusion of nickel through the oxide lattice (2).

Oxide grains, ~1000Å in diameter, are evident in dark field examination of the 212Å thick oxide stripped from (100) nickel (Fig. 9). The oxide grains are less well oriented and the oxide as seen by reflection diffraction shows some polycrystallinity (Fig. 3g). The high angle boundaries between crystallites of different orientations are considered to be very effective leakage paths for nickel transport. Hence, the oxidation rate of electropolished (100) is much faster than either (111) and (112).

Effect of oxide structure on the oxidation of (111) and (112) nickel.—Oxidation anisotropy of electropolished nickel arises from the effect of the underlying orientation on both the initial and final oxide structures. Differences in prior oxide structure and thus changes in oxidation rate of a given orientation were achieved by varying the surface preparation.

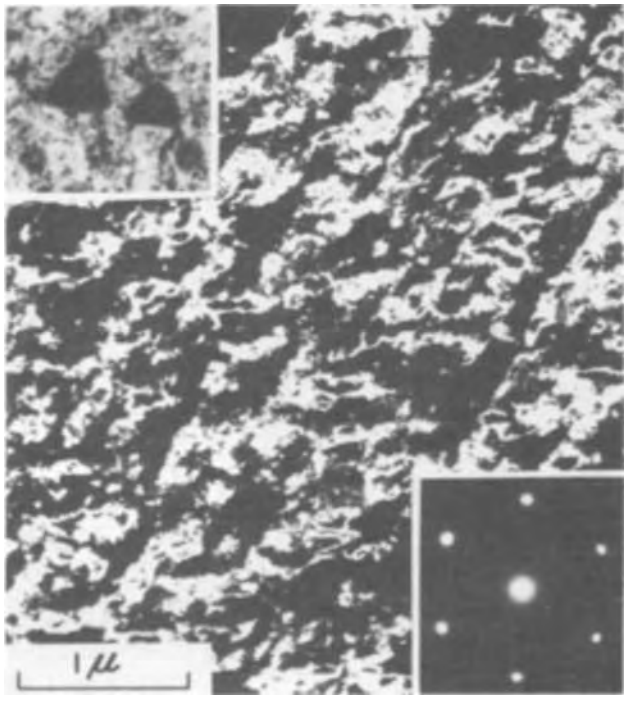

Fig. 9. Dark field micrograph [from (220) reflection] and selected area diffraction pattern from 212Å oxide formed at 600°C in 5×10^{-3} Torr oxygen on electropolished (100) nickel. ×30,000.

Previous work on nickel has shown that the particular order of oxidation of single-crystal faces depends very much on the surface treatment. Herchl *et al.* (12) found that vacuum-annealed (100) oxidized faster than (110) or (111). The hydrogen-annealed specimens of Cathcart *et al.* (8) oxidized at decreasing rates in the order (110), (100), (111) at 500° and 600°C; the oxide on the fastest oxidizing plane was found to be polycrystalline. In "hot-bare" oxidation (1) at 600°C of a hydrogen-reduced, single-crystal, spherical segment, (112) nickel oxidized at the fastest rate, quite the opposite of what is found after electropolishing. The change in oxidation rate occurs because the hot-bare procedure produces oxide with the highest density of easy diffusion paths (2), probably because the oxide is formed from an extremely large number of nuclei.

The increased oxidation rate of etched over electropolished (111) nickel (Fig. 2) is too large to be explained by a greater surface roughness. A twinned oxide is produced in both cases (Fig. 4e and 3e) but the ratio of each twin may be different. Cathcart *et al.* (8) have observed by an x-ray method different proportions of each oxide twin after different surface treatments, and find that the oxidation rate is greater the more equal is the amount of each twin. In the present case one twin orientation may be more predominant in oxides growing on electropolished (111) nickel giving the possibility of fewer incoherent twin boundary leakage paths than on etched (111) nickel where a more equal ratio could provide a larger number of incoherent boundaries and thus a greater oxidation rate. [A low density of leakage paths is also consistent with the observation that electropolished (111) nickel oxidizes only a little faster than the corresponding (112) surface (Fig. 1).] In support of this view, one oxide orientation did appear predominant in the 179Å thick oxide formed on electropolished nickel. Bright field electron microscopy revealed triangular-shaped crystallites [Fig. 8 (top insert)], most of which were oriented in the same direction. No evidence for twin-related orientations was apparent in micrographs of the oxide formed at 600°C on etched (111).

The antiparallel oxide twin predominates on the etched (112) sample after oxidation (Fig. 4b), and

the number of incoherent boundaries may be even less than those present in oxide on electropolished (111) (Fig. 3e). The small difference between the oxidation rates of etched and electropolished (112) (Fig. 2) suggests that the parallel oriented oxide together with the random oriented oxide observed in the etched case (Fig. 4b) are probably superficial and thus do not affect the rate-controlling process. The variation in rates could be within experimental reproducibility, or reflect the difference in initial surface roughness. [Cf. *e.g.*, Fig. 5a with Fig. 5b.]

In the present study, the fastest rates observed are on (112) and (111) nickel after an initial room temperature oxidation of a hydrogen-reduced surface (HR + O, Fig. 2). The room temperature oxide on (112) is of a single orientation while that on (111) is twinned (Fig. 4f and i). During oxidation at 600°C the oxide on (112) soon becomes twinned (Fig. 4g) and, as for the (111), becomes polycrystalline on further heating (Fig. 4h and k). Presumably, during oxide growth stress relief results in the production of arrays of leakage paths and a mismatched oxide after a short time (Fig. 4g and j). The number of crystallite boundaries in the polycrystalline oxide is high and so, consequently, is the oxidation rate. Hot-bare oxidation (1), *i.e.*, where oxygen is admitted at 600°C to an oxide-free surface, would be faster still since the propensity is for polycrystalline oxide to form at a very early stage (2). Thus, the density of high angle leakage path boundaries is very high initially and the oxidation rate would approach a maximum.

Summary

Consistent with the views of Cathcart and others, oxidation rate anisotropy may be explained by differences in population of leakage paths in the oxide. Structurally different prior oxides are produced by various surface pretreatments: where a single-orientation prior oxide is produced and maintained during growth, the oxidation rate is very low; if a singly oriented oxide becomes twinned, comprising one or two sets of twin-related orientations, the oxidation rate is increased; if, in the extreme case, the oxide becomes polycrystalline, then the oxidation rate is very high. Thus, correlation is observed between the density and type of easy diffusion path in the oxide and the oxidation rate.

Acknowledgments

The authors thank Mr. G. I. Sproule for his skillful assistance in the electron microscopy, and Drs. D. F. Mitchell and P. B. Sewell for valuable discussions on the interpretation of electron diffraction data. The work reported in this paper was NRCC No. 13068.

Manuscript submitted March 23, 1973; revised manuscript received May 22, 1973. This was Paper 103 presented at the Boston, Massachusetts, Meeting of the Society, Oct. 7-11, 1973.

Any discussion of this paper will appear in a Discussion Section to be published in the June 1974 JOURNAL.

REFERENCES

1. M. J. Graham and M. Cohen, *This Journal*, **119**, 879 (1972).
2. M. J. Graham, G. I. Sproule, D. Caplan, and M. Cohen, *ibid.*, **119**, 883 (1972).
3. D. Caplan, M. J. Graham, and M. Cohen, *ibid.*, **119**, 1205 (1972).
4. M. J. Graham, D. Caplan, and M. Cohen, *ibid.*, **119**, 1265 (1972).
5. K. R. Lawless and A. T. Gwathmey, *Acta Met.*, **4**, 153 (1956).
6. F. W. Young, Jr., J. V. Cathcart, and A. T. Gwathmey, *ibid.*, **4**, 145 (1956).
7. J. V. Cathcart, G. F. Petersen, and C. J. Sparks, Jr., Proc. Sagamore Conference on Physical and Chemical Characteristics of Surfaces and Interfaces, Univ. of Syracuse Press, Syracuse, N. Y. (1967).
8. J. V. Cathcart, G. F. Petersen, and C. J. Sparks, Jr., *This Journal*, **116**, 664 (1969).
9. W. W. Smeltzer, R. R. Haering, and J. S. Kirkaldy, *Acta Met.*, **9**, 880 (1961).
10. J. M. Perrow, W. W. Smeltzer, and R. K. Ham, *ibid.*, **15**, 577 (1967).
11. J. M. Perrow, W. W. Smeltzer, and J. D. Embury, *ibid.*, **16**, 1209 (1968).
12. R. Herchl, N. N. Khoi, T. Homma, and W. W. Smeltzer, *Oxid. of Metals*, **4**, 35 (1972).
13. P. B. Sewell, D. F. Mitchell, and M. Cohen, *Develop. Appl. Spectr.*, **7A**, 61 (1969).
14. R. L. Fullman, *J. Appl. Phys.*, **22**, 448 (1951).
15. R. L. Fullman, *ibid.*, **22**, 456 (1951).
16. T. Homma, N. N. Khoi, W. W. Smeltzer, and J. D. Embury, *Oxid. of Metals*, **3**, 463 (1971).

The Anodization of Si in an RF Plasma

D. L. Pulfrey, F. G. M. Hathorn, and L. Young*

Electrical Engineering Department, University of British Columbia, Vancouver 8, British Columbia, Canada

ABSTRACT

The anodization of Si in a 1 MHz oxygen plasma is described. *In-situ* film thickness measurements were made using a single angle "s" light reflectance technique and this data, coupled with information on the variation of sample voltage with thickness, was used to determine the dependence of ionic current on oxide field strength. The data for a given oxide thickness could be described by an equation of the form given by the theory of ionic conduction by a thermally activated, field-assisted process. However, the ionic current and, in particular, the oxide field strength were dependent on oxide thickness. MOS C-V measurements on oxides of different thickness indicated a change in flatband voltage that could be attributed to a progressive build-up of positive charge within the oxide. This space charge could be reduced by a low temperature annealing treatment. The oxides were found to be slightly absorbing optically, to have a relative permittivity in the range 3.5-3.9, and to possess good insulation properties as long as the oxide thickness did not exceed about 2500Å.

The formation of a thin film of SiO_2 on Si is a key step in modern integrated circuit technology and, although the oxidation of Si by thermal means is well-established there would appear to be a need for a low temperature oxidation process that is compatible with other steps in the device-processing sequence. Plasma anodization would seem to satisfy these requirements and the technique applied to silicon has already re-

* Electrochemical Society Active Member.
Key words: anodization, silicon, rf plasma.

ceived some attention (1-4). Several methods of producing the oxygen plasma have been tried: (*i*) A high frequency (2450 MHz) discharge (1, 2); this method with sample temperatures around 400°C, enabled reasonable quality oxide films to be grown at high rates (6000Å in 2 hr). (*ii*) A d-c arc hot-cathode plasma (4); high quality SiO_2 films have been produced by this method at fast rates (900Å in 10 min) using a sample temperature of 225°C. (*iii*) A d-c cold cathode discharge (3); in this case no data on oxide properties was given. The average oxide growth rate was very slow (1000Å in 4-5 hr) at the temperatures used (32°-55°C) and depended on the sample position in the discharge, with the positive column being the most productive region.

For the d-c cold cathode plasma (3) no detailed oxide growth mechanism was proposed although, following the work of O'Hanlon and Pennebaker (5), it was suggested that the growth process relied in some way on the presence of negative oxygen ions in the plasma. Recent work on this topic (6, 7) suggests that in d-c cold cathode discharges the plasma negative ions do not play an important part in film growth by plasma anodization. This conclusion is shared by Ligenza and Kuhn (4) in discussing the growth mechanism involved in film formation in a d-c arc hot cathode plasma. In this instance a low field diffusion process of negative ions, formed by electron attachment to positive or neutral oxygen mildly implanted in the oxide, is postulated. However, in the work using high frequency plasmas (1, 2) it has been suggested that the oxide growth mechanism involves a diffusion of negative oxygen ions which enter into the oxide from the plasma. The oxide growth rate dD/dt could be expressed as

$$dD/dt = K/D \qquad [1]$$

where K is a parabolic rate constant. This relationship differs from that presented in all other published work on plasma anodization in which a quantitative measure of growth rate dependence on oxide and plasma properties has been considered. These latter works (8-11) have all pertained to the anodization of Ta or Nb and have utilized rf (6.7 MHz) or cold cathode d-c plasmas. In both cases a thermally activated, high field-assisted, ionic conduction process, similar to that existing in the solution-anodization of many elements (12), has been suggested, *i.e.*

$$dD/dt = K_0 \exp \beta E/kT \qquad [2]$$

where K_0 is a temperature-dependent constant, β is a term relating to the charge on the mobile ion and the distance this ion moves between potential wells in the oxide, E is the field in the oxide, k is Boltzmann's constant, and T is the sample temperature.

Whether the difference in the growth mechanisms represented by Eq. [1] and [2] is due to the nature of the plasmas used, or to the differences in materials anodized, cannot be ascertained as no quantitative data on the growth mechanism for the anodization of Si in d-c or rf plasmas is available. It was the aim of this work to provide such information. The plasma source chosen was an externally coupled rf (1 MHz) voltage and this was preferred to a cold cathode discharge because an electrodeless system is desirable to minimize sample contamination and because oxide growth rates would appear to be higher in rf plasmas [*e.g.*, for Ta at 350°K, dD/dt is of the order of 3 Å/min in a d-c plasma (11), whereas a value of about 150 Å/min in a rf plasma (9) has been quoted].

Experimental Procedure

The discharge was maintained in a 5 cm diameter, 1m long quartz tube by a Philips (PH102-02-10-20 Model) 12 kW, 0.5-1.0 MHz generator. The rf power was coupled to the discharge by a two-turn coil and under normal operating conditions (oxygen pressure 30 mTorr) the generator output power was 3 kW. The discharge tube was supported by stainless steel end caps which were rigidly mounted to an optical bench. Seals were effected by Viton O rings. The system was sorption pumped through one end cap, to which a 1-cm diameter Al rod was attached to serve as the cathode for the anodization circuit. The other end cap allowed gas and sample holder entry. The sample holder was of fused quartz and is shown in Fig. 1. Gas (compressed air) or liquid (water) could be circulated through the sample holder and thermal contact between the sample and holder was achieved by the action of the tungsten wires, W, on the quartz sleeve, Q, which served to press the sample, S, onto the aluminum foil disks, A. The sample temperature could be estimated by the Chromel-Alumel thermocouple, T. A 6-mm diameter circular area on the face of the sample was defined by the mica washer, M. The mica mask was necessary to prevent film breakdown (13) which otherwise rapidly occurred at the edges of the film adjacent to the quartz shield, Q. The sample was situated about 30 cm away from the cathode. The exciting coil enclosed a region about 10 cm away from the sample and at the discharge pressure and power levels used the sample was just engulfed in the outer region of the visible plasma.

Typically oxygen pressure during anodization was 30 mTorr and this was maintained by manual adjustment of a leak valve in the gas supply line. The system was continuously pumped during anodization. Prior to anodization the system was evacuated to the limit of the sorption pump (about 4 mTorr) and then back filled to about 1 Torr with oxygen.

Silicon, p-type (10^{16} atoms/cm^3), of (111) orientation was used, and the substrates were about 1.5-mm thick and were cut into roughly circular pieces of about 1.5-cm diameter. The Si substrates were received with one face polished and the only further treatment given to the surface to be anodized was a 30-sec rinse in distilled water and 48% HF (ratio by volume 1:1), followed by drying in a stream of N_2 gas. Al was deposited by vacuum evaporation onto a circular (about 0.8-cm diameter) region on the back face of each substrate and alloyed in, at 580°C for 5 min in an atmosphere of H_2, to form an ohmic contact.

The optical properties of the thin anodic films were determined from *in-situ* measurements of the intensity of linearly polarized light after reflection by the sample (14). A schematic of the optical arrangement is shown in Fig. 2. The light source was a 0.5 mW He-Ne

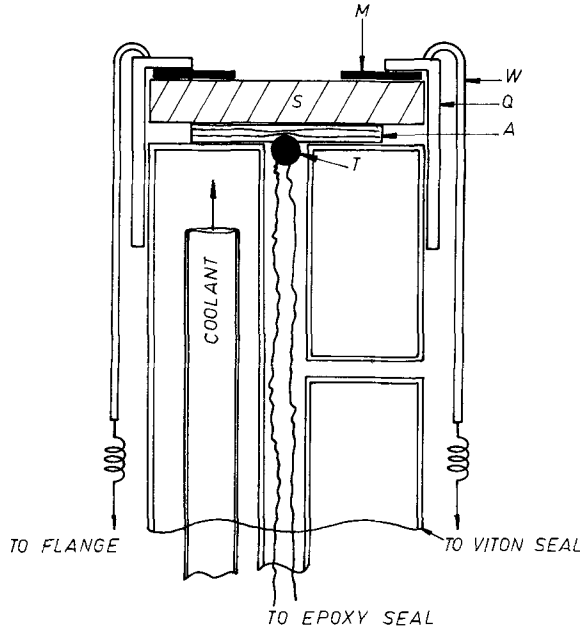

Fig. 1. Schematic cross-sectional view of the quartz sample holder. See text for description.

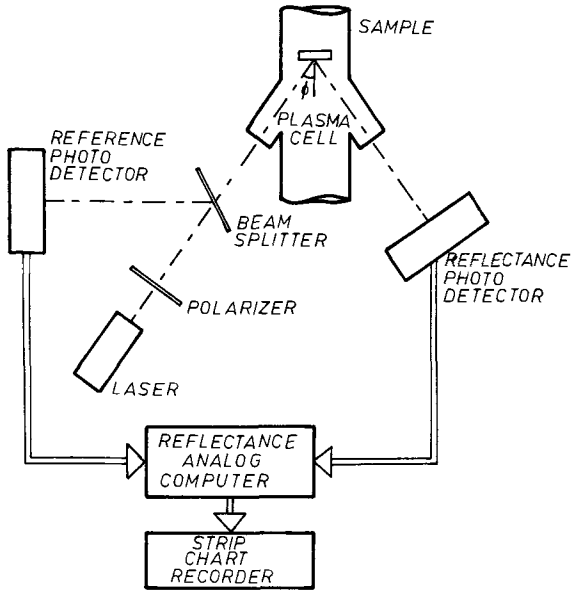

Fig. 2. Schematic of the optical system

(6328Å) laser and linearly polarized light (E vector perpendicular to the plane of incidence) was obtained by rotating the polarizer ("Polaroid" sheet) until a maximum output was obtained on the detectors. "S" light was employed in this investigation rather than "p"-light in order to obtain a larger sample reflectance at the angle of incidence (35°-37°) used. The angle of incidence was adjusted so that the laser beam entered and left the quartz windows of the cell at as close as possible to normal incidence. Bandpass filters (100Å) were placed in front of each detector to allow measurements to be made with the laboratory well-lighted and the sample immersed in the oxygen plasma. At the outset of the work RCA 7102 photomultipliers were used as detectors and a measure of the intensity of the reflected light as a fraction of the intensity of the reference beam was achieved by feeding the photomultiplier output signals through separate decade potential dividers and adjusting the values of the said dividers to obtain a null signal on an oscilloscope used with a differential input channel. At a later stage, the system was automated to provide a continuous record of the sample reflectance. Photodiode detectors were used in this case and the output signals were fed into a reflectance analog computer that has been described in detail elsewhere (15).

Electrical contact between the sample and the constant current source that was used as the anodizing power supply was provided via the thermocouple leads. Constant anodizing currents in the range 0.5-4.0 mA were used: the lower limit being set by the slow growth rate and the upper limit being determined by the onset of instabilities in the anodization circuit. Ionic current densities were obtained by taking the ionic current density producing a growth rate dD/dt for an oxide A_xO_y as given by

$$J_{ion} = \frac{\rho 2y\mathbf{F}}{M} \cdot \frac{dD}{dt}$$

where $\mathbf{F}$ is 9.65×10^4 coulombs, M the gram molecular weight, and ρ the density. For SiO_2, ρ was taken as 2.2 g/cm³ (16).

To obtain a measure of the oxide field strength, the sample voltages with respect to a fine Pt wire probe and also with respect to the cathode (grounded) were recorded on a strip chart recorder. The unshielded tip of the Pt probe was initially situated about 3 cm away from the sample surface, *i.e.*, directly under the exciting coil. Such a position of the probe seemed advantageous, as regards heating it to keep it clean during anodization (17), but ultimately the probe was withdrawn from the plasma because of system and sample contamination from vaporized or sputtered probe material. The voltage data reported here, therefore, all refer to potentials measured with respect to the cathode. To obtain reproducible data it was found necessary to clean the cathode after about 20 hr of exposure to the plasma. Calculations of both the integral field strength (V/D) and the differential field strength (dV/dD) in the oxide were made.

Table I. Comparison of oxide refractive index and thickness values as calculated by the reflectance technique and by ellipsometry

Sample No.	Oxide thickness, A: From reflectance	Oxide thickness, A: From ellipsometry	Refractive: From reflectance n_1	Refractive: From reflectance k_1	Refractive: From ellipsometry n_1	Refractive: From ellipsometry k_1
2	2965	3005	1.354	0.013	1.356	0.026
4	4000	4035	1.387	0.034	1.385	0.007

Results and Discussion

Refractive index of the oxide.—The refractive index ($N_1 = n_1 - ik_1$) of the oxide was calculated from a comparison of the observed and theoretical variations of sample reflectance with oxide thickness (14). The method is sensitive to the presence of optical absorption in the films and some absorption was detected in the plasma-anodized films of SiO_2. The values of n_1 for the various samples covered the range 1.35-1.42, while values of k_1 fell within the bounds of 0.014-0.034. Specific values for two samples are shown in Table I, along with results calculated from two-zone ellipsometer readings taken on the completed oxides. The refractive index was evaluated from the ellipsometer data by computing the value of N_1 that would give an oxide thickness close to that indicated from the reflectance data. The thickness agreement between the two methods, as shown in Table I, seems very reasonable in view of the fact that the ellipsometer laser beam was smaller (by an areal factor of 2) than the laser beam used in the reflectance measurements, and some nonuniformity in oxide thickness is to be expected on account of perturbation of the plasma by the sample holder. Because of this no attempt was made to obtain an exact match in oxide thickness, even though this may have resulted in better agreement between the values of k_1 as calculated by the two methods. In any event, the ellipsometer computations confirm that the oxides were somewhat absorbing and that the real part of the refractive index is similar to that previously reported (16) for the growth of thin film SiO_2 by various methods. No attempt was made to investigate the cause of the absorption in the films.

Oxide growth rate and current efficiency.—The current efficiency, η, of the oxide growth process was very low and for the range of anodizing currents and temperature used, see Fig. 3, never exceeded 0.5%. A low

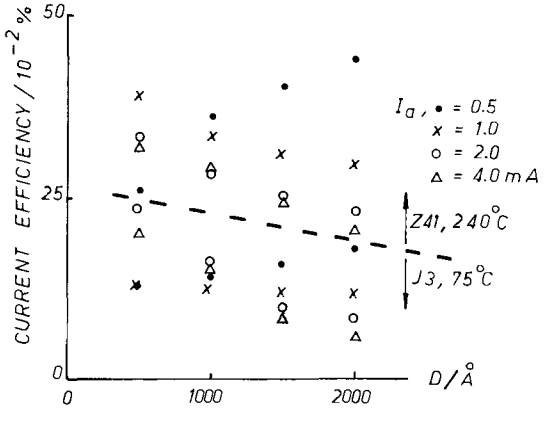

Fig. 3. Variation of current efficiency with oxide thickness

current efficiency seems to be a feature of plasma anodization (18) and presumably arises because of the availability of a copious supply of high energy electrons in the plasma which can readily enter the oxide. Thus even with materials such as Ta_2O_5 and Nb_2O_5, which can be grown anodically in aqueous solution at current efficiencies of 100%, current efficiencies of around 1% are realized in plasma anodization (11). The anodization of Si in solution (19, 20) however, proceeds at a current efficiency of about 1% and thus the low value reported here for plasma anodization is less unexpected. The behavior shown in Fig. 3 is typical of most samples anodized and the salient features are: (*i*) a decrease in η with film thickness, D, for anodizing currents of 2.0 and 4.0 mA, (*ii*) an independence (or sometimes an increase) of η with D for anodizing currents of 0.5 and 1.0 mA. The fall of η with D may indicate a deterioration in oxide insulating properties as growth proceeds. Alternatively, following Fritzsche's (20) idea of the growth mechanism being an impact ionization process in which Si ions are created at sites of collision between lattice atoms and high energy electrons, it would be expected that more ionizing collisions per electron would occur as D increases, *i.e.*, the electronic current would increase, and this would lead to a reduction in η if the oxide contained trapping sites for the Si ions (see section below on MOS measurements). Observation (*ii*) would then suggest a field dependence of the trapping mechanism.

Although current efficiencies were low, a value of 0.5% for $I_a = 4.0$ mA (sample area = 0.3 cm^2) corresponds to an oxide growth rate of 30 Å/min. Such growth rates are common in the thermal oxidation of Si in dry oxygen (16).

Oxide field strength (21).—The field, E, in the oxide was estimated in two ways, namely: the integral method in which E at a thickness D was taken as V_{ox}/D where V_{ox} represents the voltage drop across the film; and the differential method in which E at a thickness D was given by $\Delta V_{ox}/\Delta D$, where ΔV_{ox} is the change in voltage drop across the film in increasing the thickness by ΔD about the median value D. In the differential method, for a change in oxide thickness ΔD, the measured change in voltage (between sample and cathode) ΔV is likely to be a good approximation to ΔV_{ox}, providing the conditions in the plasma do not change during the time required to grow ΔD of oxide. The measured voltage (between sample and cathode) V will only approximate to V_{ox} if the voltage drop in the rest of the anodizing circuit is small and, furthermore, measurements of integral field, for a given anodizing current, taken at different oxide thicknesses will only be comparable if the plasma conditions do not change in the interim period. To get meaningful kinetics data (see below) this period will be much larger than that required to form ΔD as mentioned in the differential measurement. However in this investigation it was found that more reproducible data could be obtained using the integral method. Large errors in $\Delta V_{ox}/\Delta D$ are perhaps to be expected when both the voltage change and thickness change are small (ΔD was typically 100Å), and furthermore a measure of ΔV, (and ΔD) would seem to be relevant only when V (and D) was varying linearly with time. Whereas dD/dt was usually constant during a formation dV/dt was not. Even disregarding the voltage transient on switching anodizing currents the value of dV/dt invariably changed over any appreciable period of growth, *i.e.*, the field in the oxide was a function of D. Figure 4 compares integral and differential field measurements for a sample anodized at 240°C. In the integral field calculations, an attempt was made to allow for the voltage drop across the nonoxide components of the anodizing circuit by extrapolating the V *vs.* D curves to zero thickness and then taking E as given by $(V - V_0)/D$ where V_0 is the voltage intercept at the $D = 0$ axis, see Fig. 5. From Fig. 4 it can be seen that for low

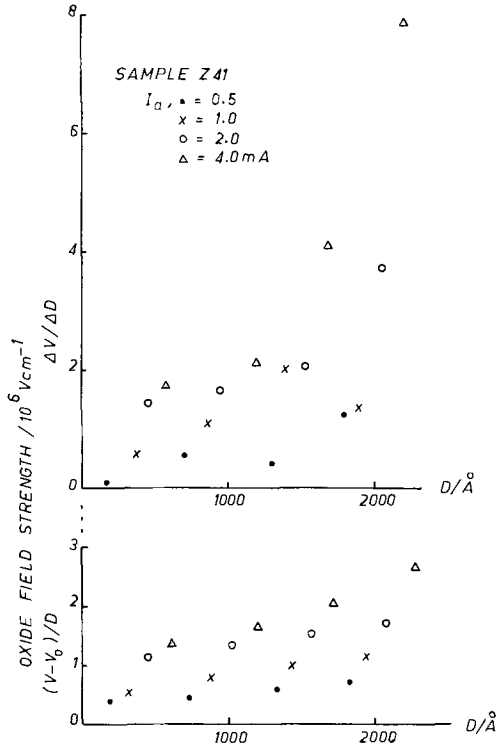

Fig. 4. Variation of oxide field strength with oxide thickness, using both "integral" and "differential" methods to estimate E.

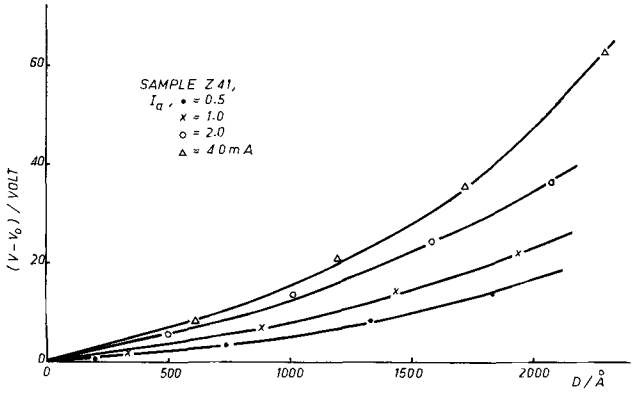

Fig. 5. Variation of estimated voltage drop across the oxide with oxide thickness.

(0.5, 1.0 mA) anodizing currents the integral field is slightly lower than the differential field; this is also the case for high (2.0, 4.0 mA) anodizing currents up to about $D = 1500$Å, after which the differential field values rapidly increase. This latter behavior can be anticipated from Fig. 5 and its explanation may be related to the field-enhanced trapping mechanism suggested earlier. Figure 4 indicates the reduced scatter in the integral field measurements and this was even more apparent at lower temperatures where the voltage transients on switching anodizing currents were longer, leading to large uncertainties in the $\Delta V/\Delta D$ calculations. For this reason the integral field method was used to estimate E.

Dependence of ionic current on oxide field strength.—Because of the thickness dependence of both E and J_{ion} the relationship between J_{ion} and E can be meaningfully derived only by using data at a particular value of thickness. Accordingly, for each anodization, plots of J_{ion} *vs.* D and E *vs.* D (see lower plot of Fig. 4) were made and, for each anodizing current, J_{ion} and E values were read off at thicknesses of 500, 1000, 1500, and 2000Å. The results are shown in Fig. 6, from which it appears that log J_{ion} is linearly related to E, with a

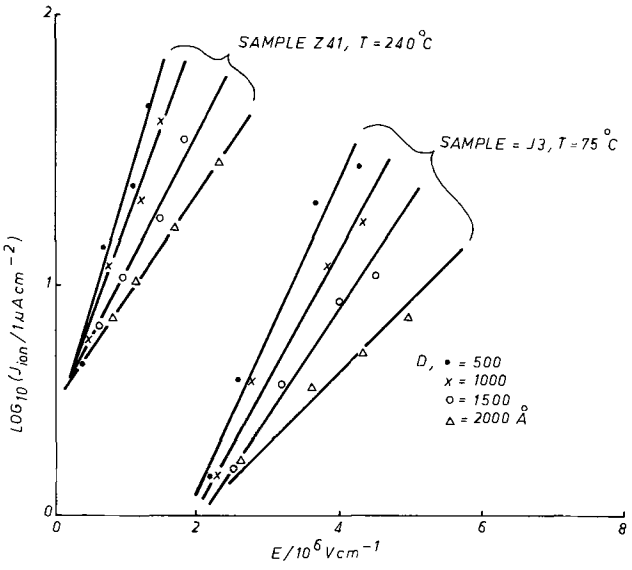

Fig. 6. Variation of ionic current density with oxide field strength

slope that is a function of film thickness. For a given thickness then, a field-assisted, thermally activated, high field ionic conduction mechanism, characterized by the following equation

$$J_{\text{ion}} = J_0 \exp \frac{(\beta E - W)}{kT} \qquad [3]$$

describes the data; J_0 and β are constants and W is the zero field activation energy. However, Eq. [3] would have to be modified by the inclusion of thickness dependent terms for J_{ion} and E, if the equation is to describe the oxide growth mechanism at all thicknesses. It is perhaps noteworthy that the "Tafel plots" of Fig. 6 can, for a given temperature, be made to coincide by plotting E *vs.* $(1 + D/D_0) \cdot \log J_{\text{ion}}$ where D_0 is a constant. The results of this operation performed on the two samples referred to in Fig. 6 are shown in Fig. 7, where D_0 has been taken as 2000Å for sample Z41 and 750Å for sample J3, thus suggesting that D_0 is temperature dependent. The implied equation for the ionic current relationship with field is thus

$$J_{\text{ion}} = J_0 \exp\left(-\frac{W}{kT}\right) \exp\left\{\left(\frac{D_0(T)}{D_0(T) + D}\right) \cdot \frac{\beta E}{kT}\right\} \qquad [4]$$

A particular growth process that can be described by Eq. [4] is not obviously apparent.

An alternative approach to explaining the variation of the log J_{ion} *vs.* E data with thickness would be to disregard the variation of J_{ion} with D and consider only the thickness dependence of E. This seems reasonable in view of the relative magnitudes of the two effects (see *e.g.* Fig. 3 and 4) and also because of the variation in the thickness dependence of J_{ion} from sample to sample. While in all samples anodized at 0.5, 1.0, 2.0, and 4.0 mA, J_{ion} at the two higher values of I_a decreased with D, a number of samples anodized solely at 2.0 mA showed a constant value of J_{ion}. Possibly the high current (4.0 mA) formations produced inferior oxide due to increased disturbances in the plasma. Thus, whereas the variation of J_{ion} with D may not be an intrinsic feature of the growth process, the variation of E with D would appear to be so as the samples anodized solely at 2.0 mA showed an increase of E with D similar to that recorded during anodizations using the four previously mentioned anodizing currents.

An increase in E with D could be caused by the progressive build up of positive space charge in the oxide such that the measured field in the oxide could be expressed as

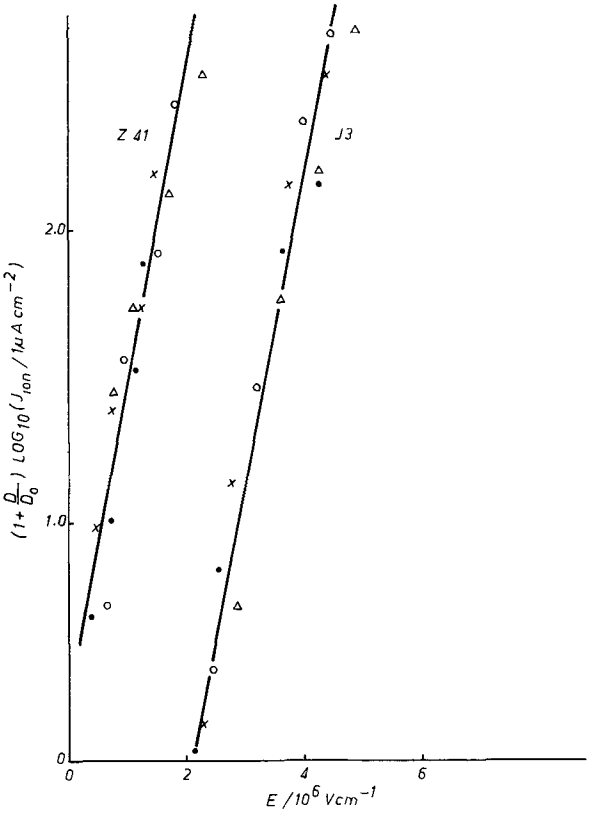

Fig. 7. Variation of $(1 + D/D_0)$ log J_{ion} with oxide field strength where D_0 = 2000Å for sample Z41 and 750Å for sample J3.

$$E = E_{J\text{ion}} + A(D) \qquad [5]$$

where $E_{J\text{ion}}$ is the field in the charge-free oxide required to drive an ionic current J_{ion} through the oxide and $A(D)$ is the component of field in the oxide due to the space charge. Using Eq. [5] in Eq. [3] it is possible to see in principle how the data of Fig. 6 could indeed be compatible with a high field ionic conduction mechanism. The simplest form of $A(D)$ would be that of a uniform distribution, ρ, of positive charge in which case

$$A(D) = \frac{\rho D}{2\,\epsilon_{\text{ox}}} \qquad [6]$$

where ϵ_{ox} is the permittivity of the oxide. However in practice, the distribution given by Eq. [6] would not allow the data of Fig. 6 to be completely described by a simple equation such as Eq. [3], as the slope of the log J_{ion} *vs.* E plots varies with thickness. Apparently the space charge term must also show a dependence on J_{ion} or I_a, say $B(D, I)$, with the effect being smaller at low total or ionic currents. A model involving the field-enhanced trapping of positive charge (holes or ions) could presumably produce the required general form of B. Evidence that the oxides did indeed contain a net positive charge density is furnished by the MOS C-V measurements described below.

MOS measurements.—MOS capacitors were fabricated from samples of various oxide thickness by evaporation of Al gate electrodes (diameter 76 × 10^{-3} cm) through a beryllium-copper mask. All the samples were anodized (separately) at I_a = 2.0 mA and T = 240°C. C-V measurements at 1 MHz were made using a Boonton capacitance meter; also C-V and G-V measurements were made at 500 kHz using a Boonton 75-C bridge.

An interesting point of the C-V measurements would seem to be the variation of flatband voltage V_{FB} with D; see Fig. 8. The increase in V_{FB} with D could be attributed to a progressive build up of positive charge within the oxide, and this apparently continues until

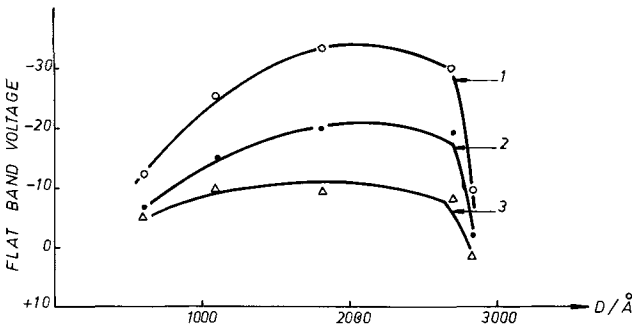

Fig. 8. Variation of flatband voltage with oxide thickness for Al/plasma-grown SiO_2 capacitors. ○ = unannealed samples; △ = samples annealed with Al gate electrode; ● = samples annealed without Al gate electrode.

around 2200Å whereafter V_{FB} falls, slowly at first to about 2700Å and then very rapidly. The decrease in V_{FB} presumably indicates a discharge or neutralization of the space charge. Supporting evidence for this suggestion may be inferred from the *G-V* relationships; namely, the sample of oxide thickness 2840Å (see Fig. 8) did not exhibit a peak in *G*, as shown by the samples of *D* equal to 1100, 1810, and 2695Å and consistent with the presence of surface states at the silicon/oxide interface, but rather displayed a conductance that increased rapidly with negative bias leading to oxide breakdown. The thinnest oxide tested, 590Å, also showed this behavior. Presumably in the case of these latter two samples the oxide conductivity is high and dominates the measured *G*. In the case of the thicker sample, where positive charge has been postulated to be present in the oxide, the increased conductivity of the oxide could be expected to result in neutralization of the trapped charge. Oxides thicker than about 2500Å exhibited small (3×10^{-5}m diameter) "blistered" regions and these are probably related to the suggested conductivity increase.

A positive space charge in the oxide can be thought of as either trapped holes or trapped Si ions. The distinction would appear to be that holes would be formed by ionizing radiation (or electrons) from the plasma, whereas the trapped Si ions could be a proportion of those released from the semiconductor in the normal course of supplying ions for the high field ionic conduction process. In either event, neutralization of this space charge would be expected on annealing the samples, *i.e.*, thermally injecting electrons into the oxide, and this is confirmed by the data shown in Fig. 8; curve 1 is the variation of V_{FB} with *D* for the unannealed samples and curves 2 and 3 show the effect of annealing for 1 hr in dry nitrogen at 350°C; curve 3 related to *C-V* measurements taken on capacitors where the Al gate electrode was evaporated prior to annealing, while curve 2 is for the case of post-anneal Al gate evaporation.

Fritzsche (20) has proposed that Si ions are involved in the anodic growth process and are created by ionizing collisions between lattice atoms and electrons accelerated to high velocities by the high field within the oxide. The oxide field strengths in the plasma anodization process reported here are an order of magnitude less than those recorded in solution anodization by Fritzsche (20), and Young and Zobel (19), so presumably ion formation would be much reduced in the plasma case. However, the fact that the current efficiencies for oxide growth appear to be similar for plasma and solution anodization suggests that growth-supporting Si ions are not produced in this manner. Furthermore, taking the ionization energy for SiO_2 to be 11 eV (20), at oxide field strengths of 2×10^6 V/cm an electron would need a mean free path of 550Å to gain sufficient energy to cause ionization. Such a path length seems improbable.

For the classical high field ionic conduction mechanism to be responsible for ion movement within the oxide the mobile Si ions, assuming these to be the sole ionic charge carriers during plasma anodization as is reputedly the case in solution anodization (22), would originate at the semiconductor/oxide interface. The region of densest trapped charge would thus perhaps be expected to be close to this interface, forming a charge region similar to that designated Q_{ss} in literature (23) on MOS structures with conventional, thermally grown, oxide. In this case, writing the oxide capacitance per unit area as C_{ox}, we have

$$V_{FB} = -\frac{Q_{ss}}{C_{ox}} = -\frac{Q_{ss}}{\epsilon_{ox}} D$$

and thus V_{FB} would be expected to increase with oxide thickness even if Q_{ss} was constant. By drawing a straight line through the data points up to $D = 2000$Å on curve 1 of Fig. 8, a value of Q_{ss}/ϵ_{ox} of 2×10^6 V/cm is obtained. The oxide permittivity can be estimated from measurements of the MOS capacitance in strong accumulation, see Fig. 9, and a value of $3.5\epsilon_0$ yields a Q_{ss} of 4×10^{12} charges/cm^2. Such a magnitude of charge is not unreasonable but, even though the space charge field is of the order of those measured during anodization, it is independent of oxide thickness and thus does not have the form required by Eq. [5]. A progressive build up of space charge throughout the oxide thus seems a more likely explanation of the flatband and oxide field dependencies on oxide thickness. The space charge could be due to trapped holes but if so these are not likely to be produced by Fritzsche's mechanism because the required mean free path of electrons in the oxide is comparable with the film thickness. Injection of holes from the substrate is also unlikely, Alternatively, positive space charge could be due to silicon (entering from the substrate) or to vacant oxygen sites. Whatever the mechanism it appears that trapping is field dependent and leads to a decrease in slope of the "Tafel plots" with increasing oxide thickness.

Acknowledgment

The authors would like to thank Mr. F. Scholz for experimental assistance during the early part of this work and Mr. J. J. H. Reche for many helpful discussions and for constructing the reflectance analog computer. Grateful acknowledgment for financial assist-

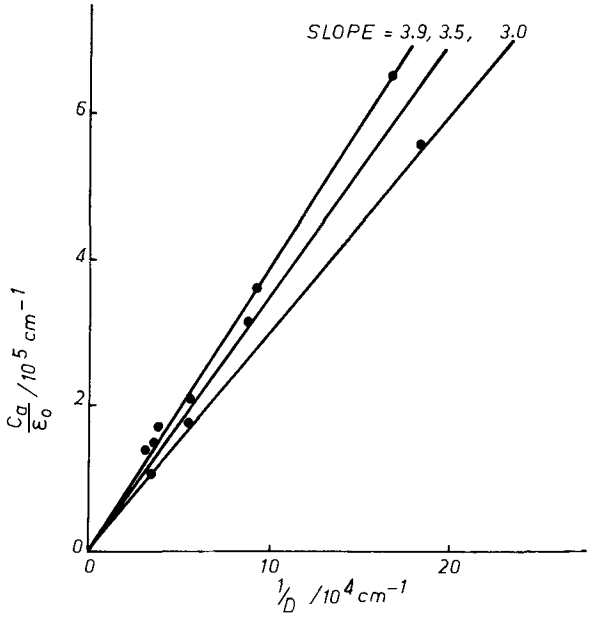

Fig. 9. Estimation of the relative permittivity of plasma-grown SiO_2. C_a = MOS capacitance/unit area in strong accumulation.

ance is given to the National Research Council of Canada and the United States Air Force, Avionics Laboratory, Wright-Patterson Air Force Base (contracts F33615-68-C-1704, F33615-70-C-1225, and F33615-71-C-1886).

Manuscript submitted Jan. 3, 1973; revised manuscript received June 11, 1973.

Any discussion of this paper will appear in a Discussion Section to be published in the June 1974 JOURNAL.

REFERENCES

1. J. R. Ligenza, *J. Appl. Phys.*, **36**, 2703 (1965).
2. J. Kraitchman, *ibid.*, **38**, 4323 (1967).
3. M. A. Copeland and R. Pappu, *Appl. Phys. Letters*, **19**, 199 (1971).
4. J. R. Ligenza and M. Kuhn, *Solid State Technol.*, **Dec.**, 33 (1970).
5. J. F. O'Hanlon and W. B. Pennebaker, *Appl. Phys. Letters*, **18**, 554 (1971).
6. G. Olive, D. L. Pulfrey, and L. Young, *Thin Solid Films*, **12**, 527 (1972).
7. J. F. O'Hanlon, Private communication: J. F. O'Hanlon and M. Sampogna, *J. Vacuum Sci. Technol.*, In press.
8. V. S. Mikhalkin and L. L. Odynets, *Elektrokhimiya*, **6**, 359 (1970).
9. V. S. Mikhalkin and L. L. Odynets, *ibid.*, **7**, 848 (1971).
10. E. V. Makara, V. S. Mikhalkin, and L. L. Odynets, *ibid.*, **7**, 1096 (1971).
11. W. L. Lee, G. Olive, D. L. Pulfrey, and L. Young, *This Journal*, **117**, 1172 (1970).
12. L. Young, "Anodic Oxide Films," Academic Press, New York (1961).
13. N. Ramasubramanian, *This Journal*, **117**, 947 (1970).
14. D. L. Pulfrey and J. J. H. Reche, *Appl. Optics*, **12**, 1577 (1973).
15. J. J. H. Reche and D. L. Pulfrey, *Rev. Sci. Instr.*, **44**, 914 (1973).
16. R. M. Burger and R. P. Donovan, Editors, "Fundamentals of Silicon Integrated Device Technology," Vol. 1, Prentice Hall, Englewood Cliffs, N. J. (1967).
17. J. A. Nilson, Ext. Abstr. 163, Electrochem. Soc. Meeting, Washington D.C., 1971.
18. C. J. Dell'Oca, D. L. Pulfrey, and L. Young, *Phys. Thin Films*, **6**, 1 (1971).
19. L. Young and F. G. R. Zobel, *This Journal*, **113**, 277 (1966).
20. C. R. Fritzsche, *J. Phys. Chem. Solids*, **30**, 1885 (1969).
21. G. Olive, D. L. Pulfrey, and L. Young, *This Journal*, **117**, 945 (1970).
22. P. F. Schmidt and A. E. Owen, *ibid.*, **111**, 682 (1964).
23. A. S. Grove, "Physics and Technology of Semiconductor Devices," John Wiley & Sons, Inc., New York (1967).

Physical Properties of Thick Sputter-Deposited Glass Films

D. M. Mattox and G. J. Kominiak

Sandia Laboratories, Division 5332, Albuquerque, New Mexico 87115

ABSTRACT

The coefficient of thermal expansion (CTE) of 5μ thick rf sputter-deposited Corning 1720 glass films was measured using a cantilever beam technique. The films were rf-bias sputtered in an argon (Ar films) and an argon-5% oxygen (Ar/O_2 films) gas mixture. The Ar films deposited with a low substrate bias (+30, 0, and −50V) exhibited an erratic CTE on initial heating but were well behaved after a 600°C air anneal. High bias (−100, −200V) Ar films and Ar/O_2 films showed no erratic behavior on initial heating. Chemical analysis indicated no significant change in the minor constituents of the sputtered glass, but neutron activation analysis showed a progressively greater oxygen depletion with increasing negative bias for both the Ar and Ar/O_2 films. Etch rates were shown to increase with increasing negative bias. It is suggested that the structural changes that occur in some glass films at temperatures far below the strain point of the bulk glass (670°C) are due to a combination of intrinsic stress and a high concentration of defects. Surface coverage by the sputter-deposited glass films is discussed.

The use of sputtered films of any type has several potential problem areas: (*i*) The films may contain high concentrations of defects and be highly stressed. This may be reflected in unusual physical behavior such as the room temperature structural changes noted in high-rate sputter-deposited copper (1). (*ii*) For complex materials such as glasses, alloys, and compounds, there may be compositional changes during deposition (2) which can affect the properties of the material. For SiO_2, oxygen depletion is a commonly observed compositional change (3). (*iii*) Sometimes there are unusual structural and crystalline modifications found in sputter-deposited films which may give properties differing from those of the bulk material (4). It is the exception rather than the rule when deposited films have bulk properties.

Generally, the physical properties of thin sputter-deposited glass films are not of great concern; however, as the film thickness increases, the properties may become important in specific applications. In this investigation, the coefficient of thermal expansion (CTE) of 5μ thick rf sputter-deposited glass films was investigated as a function of substrate bias during deposition and as a function of sputtering gas composition. It was found that after annealing, the sputter-deposited films had a CTE close to that of the bulk glass. Before annealing, films deposited under some conditions showed an erratic behavior of the CTE.

The ability of the deposited films to cover surface topography was also studied. Generally, it has been found that films deposited by some type of negative substrate bias deposition technique show a better ability to cover surface discontinuities than do films deposited with no bias (5).

Key words: sputtered glass films, bias, strain point, surface coverage, composition, coefficient of thermal expansion.

Experimental

An axially symmetric sputtering system with a planar diode design was used to rf sputter deposit the glass films (6). The substrates were clamped to an electrically isolated, water-cooled holder which was an integral part of the top plate of the vacuum system. This "sputter-up" design was used to minimize the problem of dust and debris falling on the substrate and causing pinholes. The 0.6 cm thick Corning 1720

glass (an alumino-silicate glass) plate used as a sputtering target was laid on a water-cooled copper block. A problem was encountered in nonuniform heating of the glass plate during sputtering, causing cracking. The edges of the cracks then showed increased sputtering rates. Copper was also found to migrate along nonseparated cracks, giving contamination in the deposited film. This problem was alleviated by the insertion of a 0.3 cm thick fused quartz plate between the 1720 glass sputtering target and the copper cooling block.

The rf sputtering supply was a commercial MRC Model 3007 unit capacitively coupled to the target and substrate holder by conventional "L" tuning networks. Power input and rf peak voltage were held constant during deposition and the reflected power was minimized. Substrate biases were obtained either by tuning the substrate with respect to ground (7) to obtain low positive (+30V), zero, and low negative (−50V) biases, or by utilizing the rf splitting network on the power supply to obtain higher negative biases (−100 and −200V).

A shutter which could be rotated in a plane parallel to the electrodes and moved vertically was used in the system. This shutter allowed sputter cleaning of the substrates and presputtering of the target without cross contamination. It also allowed slow target warm-up and a stable sputtering condition to be established before beginning sputter deposition on the substrates.

A target-substrate distance of 7 cm was used throughout the investigation. A 50 oersted axial magnetic field was used for all depositions except for the high negative bias conditions where the magnetic field prevented the establishing of a stable discharge.

Commercial pure argon (Ar) gas and an argon-5% oxygen (Ar/O_2) gas mixture was used for sputtering. Flow rates were controlled using a variable leak while the gas pressure was monitored using a Schultz-Phelps high pressure ionization gauge. Vacuum system throughput was controlled by throttling the gate valve. The gas inlet was in the top of the chamber, and gas was removed through the baseplate.

For measurement of physical properties, glass films deposited in pure argon (Ar films) were deposited on 1 × 7 cm tungsten beams 0.1 mm thick. When using Ar/O_2, plasma oxidation of the tungsten was excessive and the glass films (Ar/O_2 films) were deposited on 0.2 mm thick alumina beams. Films for chemical analysis were deposited on carbon, high resistivity low oxygen silicon slices, and low gas content platinum. The substrates were clamped to the water-cooled substrate block using no contacting material.

In order to cover steps and defects, film thicknesses of 5-10μ were desired. With the sputtering conditions used, the deposition rate was about 1 μ/hr (4 $\mu g/cm^2$/min). The sputtering rate in Ar varied from 5 $\mu g/cm^2$/min at 2 kV target potential and +30V bias to 3 $\mu g/cm^2$/min at −200V bias. Rates in Ar/O_2 showed the same variation with bias and about a 20% decrease in deposition rate at a given bias as compared to argon sputtering. This decrease of sputtering rate with the addition of oxygen is appreciably less than that reported in the literature for sputtering SiO_2 films (8).

The substrates were solvent cleaned before being mounted in the vacuum system. The vacuum system was pumped to 5×10^{-6} Torr, after which the gas inlet was opened and gas flow regulated to give 1μ indicated pressure in the chamber. The gate valve of the vacuum system was then throttled to give a final pressure of 10μ in the chamber. The pressure was monitored throughout the deposition.

The substrates were sputter cleaned at 1 kV rf for about 30 min with the shutter covering the sputtering target. The shutter was then moved to cover the substrates and the target was presputtered. The presputtering of the target was done by slowly increasing the input power so as to allow gradual heating of the target to prevent shattering from thermal shock. The target voltage was raised to 2 kV peak-to-peak rf which required a power level of about 1000W to the 15 cm diameter target.

After steady state was established, the shutter was opened and the deposition was made for a predetermined time to give the desired film thickness. After the deposition was complete, the system was allowed to cool under vacuum before the films were removed. In order to form pinhole-free films, it was found necessary to deposit the film using two to three depositions. Between depositions the substrates were removed and the surface rubbed with acetone on a lint-free cloth. This procedure apparently moved or removed particulate contamination to the extent necessary to prevent pinholes from propagating through the several glass layers. The layers were lightly sputter cleaned between depositions.

After deposition the coated beam was mounted in a muffle furnace having an optical window in such a way that the deflection on heating was perpendicular to the gravitational field to eliminate gravitational deflection. The cantilevered beam was then heated in 100°C increments and the deflection of the free end was measured using an optical cathetometer.

The radius of curvature ρ of the beam was then determined using the equation

$$\frac{1}{\rho} \approx \frac{2\delta}{L^2}$$

where δ = the deflection of the end of the beam and L = the beam length.

The coefficient of thermal expansion (CTE) was calculated using the equation (9, 10)

$$\frac{1}{\rho} = 6(\alpha_f - \alpha_s)\Delta T(1+m)^2/h \left\{ 3(1+m)^2 + (1+mn)\left(m^2 + \frac{1}{mn}\right) \right\}$$

where ρ = radius of curvature, α_f = expansion coefficient of film, α_s = expansion coefficient of substrate, ΔT = temperature increment, m = thickness of substrate/thickness of film, and h = total thickness. Bulk modulus values were used for the glass film.

Results

Figure 1 shows the normalized beam deflection of an Ar +30 film (argon gas, +30V bias) as a function of temperature. On initial heating, the deflection is seen to vary erratically and actually change sign. Other Ar low bias films showed the same behavior on initial heating, though not as radically as did the Ar +30 films. The Ar/O_2 films did not show this erratic behavior with the exception of the Ar/O_2 −50 films, in

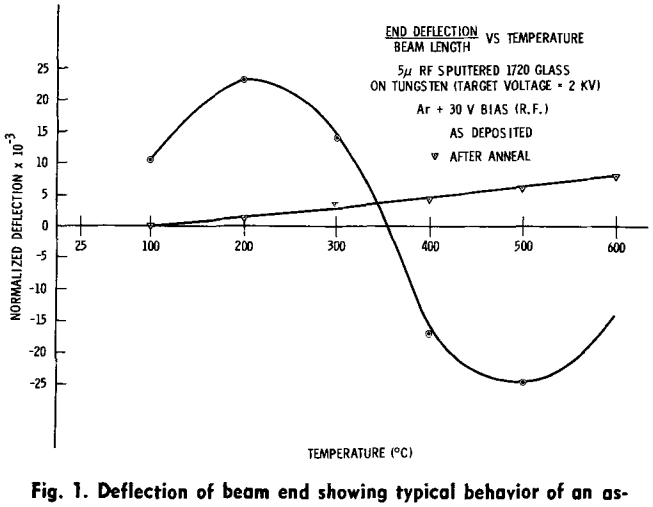

Fig. 1. Deflection of beam end showing typical behavior of an as-deposited film and an annealed film (extreme examples).

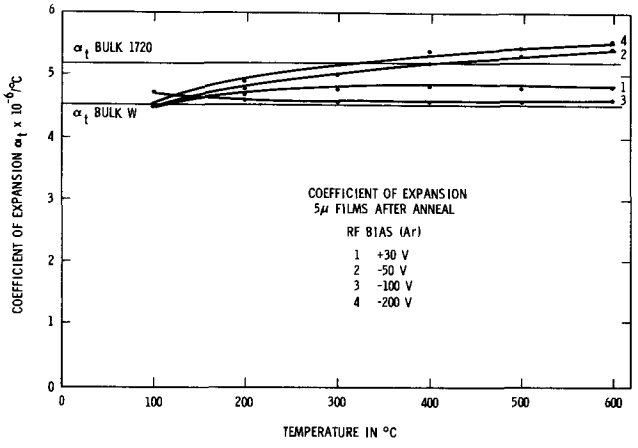

Fig. 2. Coefficient of thermal expansion of 5μ thick glass films after annealing as a function of rf bias on the substrate during deposition. Values accurate to ± 10%.

which it occurred to a slight extent. Initial deflection of the beam at room temperature showed that the Ar +30 as-deposited films had a high compressive stress.

After annealing to 600°C in air for less than 1 hr, all beams showed the type of deflection shown by the straight line in Fig. 1. Figure 2 shows the CTE of Ar films prepared with various biases after annealing compared with the literature values of bulk tungsten and bulk Corning 1720 glass in the 0°-600°C temperature range. The values compare very well. The CTE of the Ar/O_2 films was very close to that of the annealed Ar films. The initial erratic behavior of the Ar films was the source of some concern since stress during initial heating might cause failure in service.

The deposited glass films were analyzed by emission spectroscopy for the minor constituents which normally control the CTE. There was no appreciable change in the minor constituents of the sputter-deposited Ar glass films compared with those of the bulk glass. Neutron activation analysis of the silicon-oxygen ratio was made on the glass films using bulk 1720 glass as a standard. Table I shows that the oxygen depletion is greatest in the high negative bias Ar and Ar/O_2 films. Low bias Ar/O_2 films and the Ar +30 films show the least oxygen depletion. Some oxygen was recovered on annealing the high bias Ar films in air at 600°C, but little oxygen change was noted in the Ar/O_2 films on annealing. The oxygen depletion was also evident in the color; near stoichiometric films were clear and nearly colorless while the oxygen-deficient films had a brown coloration.

The *IR* transmission of thin films (5000Å) deposited on high purity, low oxygen silicon was studied. The +30V films show a broad absorption peak in the range 1100-900 cm^{-1}. The −200V films show a definite Si-O stretching band at about 1100 cm^{-1}. In the Ar +30V film a definite shift of 25 cm^{-1} toward shorter wavelengths was found on annealing, suggesting a bond length change due to stress relief (11, 12) or change in composition. The low bias Ar films also showed appreciable moisture pickup at room temperature, as evidenced by the absorption peak at 3333 cm^{-1} in the as-deposited films. The high bias Ar and Ar/O_2 films showed no such water pickup.

Table I. Oxygen content of glass films as a function of deposition conditions and subsequent anneal. Values obtained by neutron activation analysis using bulk glass as a standard

As deposited Gas	Bias	% (±5) depletion	After 600°C in air % (±5) depletion
Ar	+30	3	4
Ar	0	13	13
Ar	−50	17	15
Ar	−100	16	6
Ar	−200	20	8
Ar/O_2	+30	0	0
Ar/O_2	0	6	7
Ar/O_2	−50	13	12
Ar/O_2	−200	18	15

Thick films (~100μ) were deposited for etch rate studies. A region was masked using acid stopoff and the films were etched in "P-etch" (13)[1] for a period of time sufficient to give about a 25μ step in the glass. After etching, the acid stopoff was removed and the step height was measured using a Talysurf profilometer. Figure 3 shows the etch rates for Ar and Ar/O_2 as-deposited films. The etch rates increased with negative bias and even in the best films, exceed the rate of bulk 1720 by a factor of 2. The high bias films showed bubbling on etching while the low bias films showed no bubbling. After annealing to 600°C in air, the films became fragile, the etch rates approached that of the bulk, and no bubbling was observed on etching. Fusion analysis shows several weight per cent (w/o) argon in the −200V Ar and Ar/O_2 films before annealing and zero (0.01 w/o detection limit) to several tenths of a weight per cent in the zero bias films.

The ability of the sputter-deposited glass films to cover surface discontinuities was found to be very dependent on the type of discontinuity. As shown in Fig. 4, a 5μ glass film covered a 5μ step very well but did not bridge over a void in the surface. Very thick films can fill a void to some extent, as shown in Fig. 5, but the geometrical shadowing of void walls tend to leave a "pipe" of unfilled void. If the void geometry is such that the bottom and walls are out of the line of sight from the target, such as shown in Fig. 6, incomplete sealing of the void can result. This is also the case if the depth of the defect is large compared to the width.

It was found that a high negative rf bias on the substrates during deposition caused appreciable changes in the film morphology when the films were deposited on a surface having severe topological features. Figure 7 shows a fracture cross section of thick glass films deposited on a grainy carbon surface with a +30 and −200V bias. The low bias films show a columnar structure similar to that observed in thick metal films (4). The bias-deposited films show no such structure. The columnar structure is attributed to geometrical shadowing effects as the film is deposited over the rough surface. Ion bombardment of the bias-deposited film during deposition causes resputtering which tends to erode peaks and fill valleys, thus preventing the development of the columnar structure (4).

[1] P-etch = 15 parts hydrofluoric acid, 10 parts nitric acid, and 300 parts water.

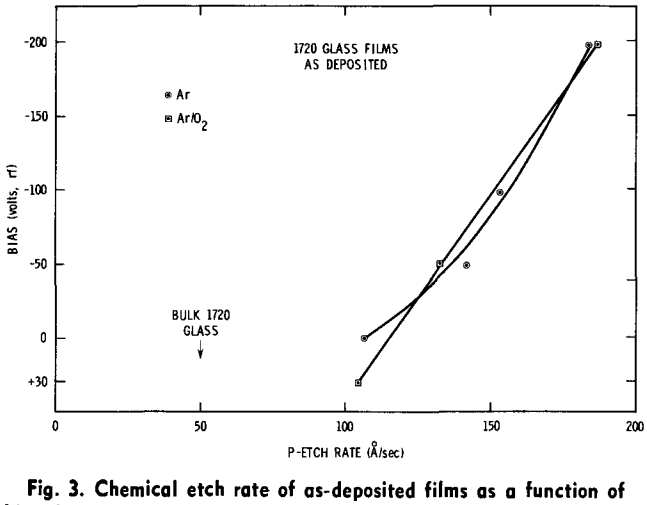

Fig. 3. Chemical etch rate of as-deposited films as a function of bias during deposition (P-etch is 15 parts HF, 10 parts HNO_3, and 300 parts H_2O).

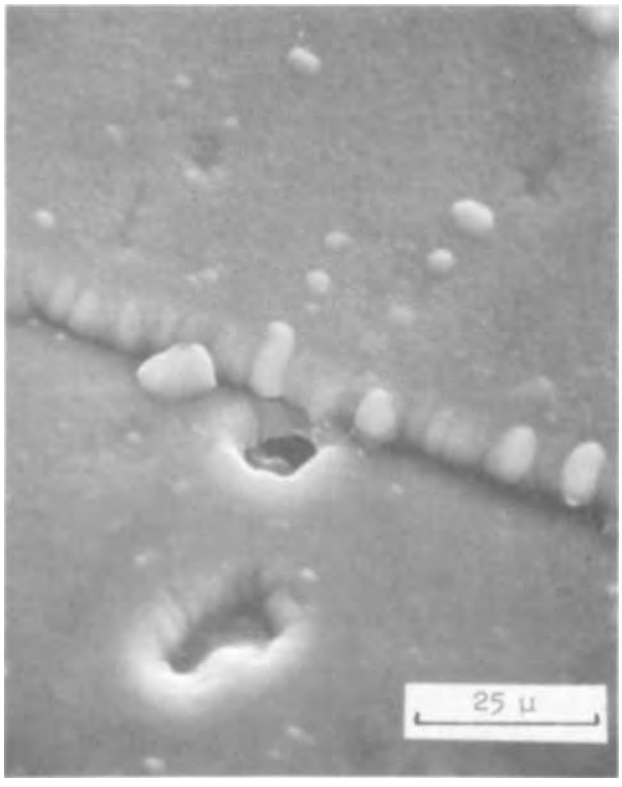

Fig. 4. A 5μ thick tungsten step on a porous surface coated with 5μ of glass. Note that the glass layers did not bridge over the pore in the substrate [scanning electron microscope (SEM)].

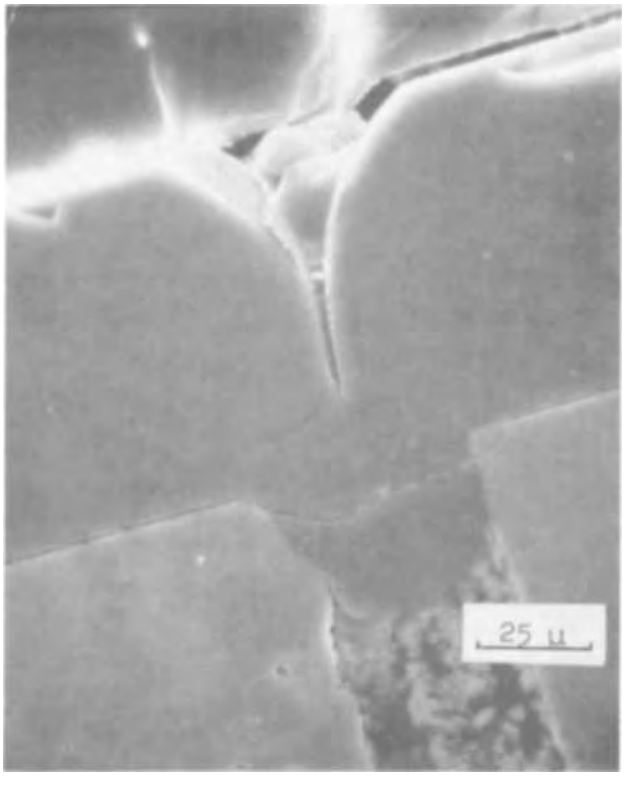

Fig. 5. Very thick glass film deposited over large defect between glass bonded plates. Note the "pipe" of unfilled void caused by geometrical shadowing (SEM fracture cross section).

Discussion and Conclusions

These data indicate that the sputter-deposited 1720 glass films may show structural changes, as evidenced by the CTE behavior, at temperatures as low as 300°C,

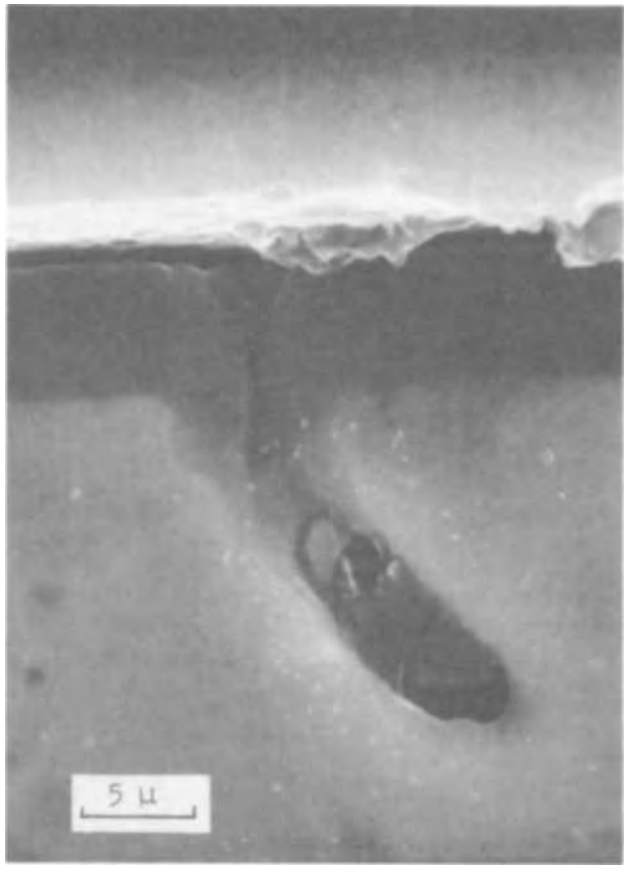

Fig. 6. Small pore in which the bottom is uncoated because of the inability of the depositing glass to reach the bottom either by migration or resputtering (—50V bias) (SEM fracture cross section).

which is far below the strain point of the bulk glass (670°C). The effect is particularly pronounced in films sputtered in pure argon with a low bias on the substrate during deposition. The effect is less pronounced with high substrate biases, probably due to heating during deposition. The effect is also less pronounced when the films are sputter deposited using an Ar-5% O_2 gas mixture for the sputtering gas. After annealing, all films showed a well-behaved CTE and have values close to that of the bulk glass.

All films deposited using pure argon as the sputtering gas showed oxygen depletion. The oxygen depletion increases with negative bias for both Ar and Ar/O_2 films. The oxygen depletion did not seem to drastically affect the CTE of annealed films.

Optical analysis data are not definitive because of the lack of sharply defined adsorption peaks. These data indicate some shift in the Si-O absorption peak in the low bias Ar films with annealing due either to stress relief or compositional change.

The etch rate data seem to be inconsistent with the other data if compared to similar data for SiO_2 films (13). In deposited SiO_2 films, oxygen depletion leads to decreased etch rate while stress and radiation damage give an increased etch rate. In this study the increased etch rate with the substrate bias may be due to appreciable argon incorporated in the deposited films at the high negative biases (14, 15) as well as the ion bombardment damage introduced during the deposition.

It seems that the most stable stoichiometric films are produced by sputtering in Ar/O_2 with a zero or slightly positive (+30V) bias. Films having stable CTE's can be deposited by applying a negative rf substrate bias during deposition, though this leads to an oxygen deficiency. The bombardment during deposition probably causes heating, which anneals the film. A similar effect could probably be obtained by

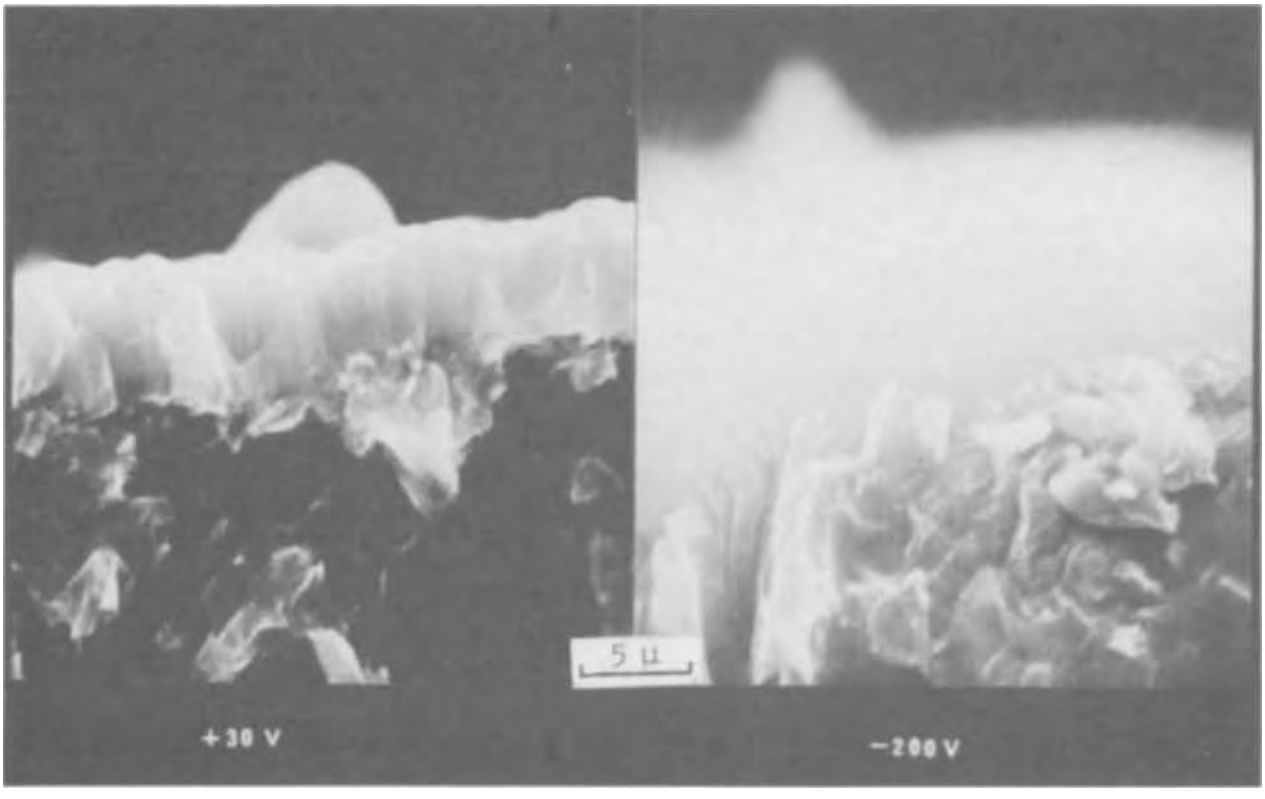

Fig. 7. Fracture cross section of glass films deposited on grainy carbon surfaces with and without a negative substrate bias during deposition. Note the isotropic morphology of the deposit made with a negative substrate bias (SEM).

heating the films to 300°-400°C during deposition. The ion bombardment during deposition could have the undesirable effect of incorporating appreciable amounts of inert gas into the film which could be released during subsequent heating.

The origin of the initial erratic CTE behavior of some films does not appear to be directly related to oxygen deficiency since the most erratic films (+30 Ar) show little oxygen deficiency. It is suggested that a combination of high intrinsic film stress and a high concentration of point defects is the origin of the initial behavior of the CTE. This is consistent with the findings for neutron and x-ray irradiated glasses where low temperature annealing of such defects is noted in their optical behavior (16).

Though the bias deposition of the glass films did significantly change the structure of the films and improve the defect-covering ability, it was still unable to cause complete coating of some defects.

Acknowledgment

The authors would like to acknowledge the analytical work performed by other members of this organization: Emission spectroscopy, D. E. Wanner; neutron activation analysis, B. T. Kenna and P. E. Harrison; scanning electron microscopy, J. K. Maruin; fusion analysis, W. J. Kass and W. J. Andrezejewski.

This work was sponsored by the U. S. Atomic Energy Commission.

Manuscript submitted Dec. 12, 1972; revised manuscript received *ca.* April 27, 1973. This was Paper 172 presented at the Miami Beach, Florida, Meeting of the Society, Oct. 8-13, 1972.

Any discussion of this paper will appear in a Discussion Section to be published in the June 1974 JOURNAL.

REFERENCES

1. J. W. Patten, E. D. McClanahan, and J. W. Johnston, *J. Appl. Phys.*, **42**, 4371 (1971).
2. R. C. Krutenat, R. F. Wielonski, and F. M. Lawrence in "1968 Transactions of the International Vacuum Metallurgy Conference," R. B. Barrow and A. Simkovich Editors, p. 235, American Vacuum Society, New York (1968).
3. T. W. Hickmott, *J. Appl. Phys.*, **42**, 2543 (1971).
4. D. M. Mattox and G. J. Kominiak, *J. Vac. Sci. Technol.*, **9**, 528 (1972).
5. J. L. Vossen, *ibid.*, **8**, S12 (1971).
6. Leon Maissel, in "Handbook of Thin Film Technology," Leon I. Maissel and Reinhard Glang, Editors, Chap. 4, McGraw Hill Book Company, New York (1970).
7. J. S. Logan, *IBM J. Res. Develop.*, **14**, 172 (1970).
8. R. E. Jones, H. F. Winters, and L. I. Maissel, *J. Vac. Sci. Technol.*, **5**, 84 (1968).
9. Abner Brenner and Seymour Senderoff, *J. Res. Nat. Bur. Std.*, **42**, 105 (1949).
10. S. Timoshenko, *J. Opt. Soc. Am. and Rev. Sci. Instr.*, **11**, 233 (1925).
11. Takehiko Kubota and Mototaka Kamoshida, *Japan. J. Appl. Phys.*, **11**, 15 (1972).
12. R. Bruckner, *J. Non-Cryst. Solids*, **5**, 123 (1970).
13. W. A. Pliskin, in "Physical Measurements and Analysis of Thin Films," Edward M. Murt and William G. Guldner, Editors, Chap. 8, Plenum Press, New York (1969).
14. G. C. Schwartz and R. E. Jones, *IBM J. Res. Develop.*, **14**, 52 (1970).
15. S. P. Faile and Della M. Roy, *J. Am. Ceram. Soc.*, **49**, 638 (1966).
16. E. Lell, N. J. Kreidl, and J. R. Hensler, in "Progress in Ceramic Science," J. Burke, Editor, Vol. 4, p. 3, Pergamon Press, New York (1966).

Microstructural Analysis of Evaporated and Pyrolytic Silicon Thin Films

R. M. Anderson

IBM System Products Division, East Fishkill Development Center, Hopewell Junction, New York 12533

ABSTRACT

Transmission electron microscopy, scanning electron microscopy, and x-ray analysis are used to study the structure of evaporated and pyrolytic silicon films (less than 1μ thick) deposited at or heat-treated in the temperature range of 500°-1040°C. It is established that the thin silicon film subjects of this investigation can have three different morphologies: pseudoamorphous, equiaxed grains, or dendritic. These are attributed to be functions of deposition temperature for pyrolytic films and heat-treatment temperature for evaporated films. The nucleation phenomena of pyrolytic silicon thin films as a function of time spent in N_2 prior to silicon deposition is investigated. Also the analysis of possible silicon film impurities is performed.

The use of polycrystalline silicon thin films has lately become of interest in the fabrication of monolithic integrated circuits (1, 2). Several processes can be used to deposit silicon. These include sputtering, evaporation, and chemical vapor deposition. The microstructural analysis of the resulting silicon films has been limited to films deposited on Si_3N_4 or SiO_2 at temperatures over 800°C, and/or films from 10 to 50μ thick (3-5). DeLuca (6) examined pyrolytic thin silicon films deposited on fused silica with deposition temperatures in the range of 700°-1000°C. He employed x-ray diffraction techniques, reflection electron diffraction, and replication electron microscopy to determine the crystallinity, preferred orientations, and surface roughness of the films.

In this paper the internal structure of thin evaporated and pyrolytic polycrystalline silicon films, as revealed by transmission electron microscopy, is of prime interest. Specifically, knowledge of the internal structure of the polycrystalline silicon as a function of the heat-treatment for evaporated silicon films and the effect of deposition temperature for pyrolytic silicon films is studied. The effect of substrate and substrate cleanliness on the structure of pyrolytic silicon thin films, including the sensitivity of the silicon nucleation process as a function of time at temperature in the reactor, is also considered. Transmission electron microscopic results are correlated with scanning electron microscopy of the silicon film surfaces and x-ray analysis of the bulk. Structural data are correlated with sheet resistances of the films. The extension of the temperatures of interest down to 500°C is prompted for reasons of compatibility with the processing of shallow-junction semiconductor devices and the smooth polycrystalline silicon films we find produced at low temperatures.

Key words: semiconductor silicon, electron microscopy, FET (field effect transistor), thin films.

Experimental

Evaporated silicon film sample preparation.—The silicon film evaporations were performed in a Temescal CV-10 four-pocket 180° E-gun system at a pressure of 1×10^{-6} Torr. The rotary hearth substrate temperature was maintained at 300°C. The deposition source was 0.001 ohm-cm boron-doped silicon and the substrates consisted of 3700Å of steam grown SiO_2 on <100> p-type silicon wafers. The deposition rate was 3000 Å/min and the films thickness was 9000Å. The films were heat-treated in flowing nitrogen in an open tube furnace. Four-point probe sheet resistances were measured and are included in Table I.

Pyrolytic silicon film sample preparation.—An Applied Materials Nitrox system modified for high purity FET (field effect transistor) applications was used for all pyrolytic polycrystalline silicon depositions. The samples to be studied for effect-of-deposition temperature were deposited on Si_3N_4 (300Å) on a <100> 1 ohm-cm n-type silicon wafer. The carrier gas was N_2 at a flow rate of 72 liters/min and a SiH_4[1] flow of 55 cm^3/min. Samples were prepared at deposition temperature increments of 25°C from 500°-900°C. Deposition parameters and some relevant electrical measurements from selected samples are tabulated in Table II. To investigate the influence of the substrate on the growth of the films, samples were deposited at 725°C, an N_2 flow of 60 liters/min, and a SiH_4 flow of 30 cm^3/min. The substrates were: (*i*) thermal SiO_2 (500Å), (*ii*) pyrolytic Si_3N_4 (300Å) on pyrolytic SiO_2 (300Å), and (*iii*) pyrolytic Al_2O_3 (900Å) on pyrolytic SiO_2 (300Å). All wafers were <100> 1 ohm-cm n-type silicon. The wafers were fractured in half. Both halves were then chemically cleaned using standard procedures, and then one half was given an additional 160°C, 5-min H_2SO_4 cleaning step.

[1] Matheson Corporation, 100% SiH_4, semiconductor grade.

Table I. Evaporated silicon film data

Sample No.	Heat-treatment temperature, °C (60 min in N_2)	Sheet resistance (ohm-cm)	Twin probability	N.R.F. stress (psi)	Low angle Laue crystallite size	Orientation
1	As-deposited	1.13×10^4	—	—	Noncrystalline	—
2	450	1.13×10^4	—	—	Noncrystalline	—
3	650	1.13×10^4	0.0153	—	Insensitive region*	[110]**
4	650	1.13×10^4	0.0173	—	Insensitive region	[110]
5	850	5.9	0.0038	42,000	Insensitive region	Random
6	850	6.17	0.0060	39,000	Insensitive region	Random
7	1040	2.38	0.0048	4,000	Insensitive region	Random
8	1040	3.45	0.0133	18,000	Insensitive region	Random

* X-ray insensitive region 1500-8000Å.
** Only (220) reflection observed.

Table II. Selected pyrolytic silicon thin film parameters

Dep. temp, °C	Dep. rate, Å/min	Thickness, μ	Resistivity, ohm-cm	Breakdown voltage across 1750Å deposited SiO_2, V
500	33	0.12	—*	—*
600	210	2.0	3.6×10^6	>140
700	760	2.3	3.5×10^6	>140
800	820	2.1	1.4×10^6	46.7
900	600	1.7	1.2×10^6	3.2 and 53.6**

* Not measured.
** V_{BD} for 900°C samples exhibited two gaussian peaks.

Nucleation experiments were made on samples deposited at 710°C, the N_2 flow was 60 liters/min and SiH_4 flow equaled 55 cm^3/min. The substrates were Si_3N_4 (300Å) on pyrolytic SiO_2 (300Å).

Specimen Preparation

The samples were first examined by x-ray diffractometry and low-angle Laue techniques and then fractured into small rectangular pieces to fit in the JEOLCO JEM-200 electron microscope specimen holder. The electron microscope specimens were inverted on a glass microscope slide and masked with wax, leaving the silicon exposed at the center of the back of the specimen. The silicon substrate was etched through the wax mask with a mixture of HF-HNO_3-CH_3COOH (1:2:3) down to the insulator film. All subsequent removal of insulator films and polycrystalline silicon thinning was performed in a Commonwealth ion milling machine. Final Si film thicknesses varied from 1000-7000Å.

Results

Evaporated polycrystalline silicon films.—The morphology of the as-deposited evaporated polycrystalline silicon is pseudoamorphous, *i.e.*, a very small nondiscernible microstructure with just enough order to produce broad diffuse rings centered on major reflections in the electron diffraction patterns. The polycrystalline silicon is unchanged after heat-treating at 450°C for 60 min in N_2.

After the 650°C, 60-min heat-treatment, silicon dendrite structures were observed, indicating that the nucleation of crystalline silicon occurs at a temperature $\leq$ 650°C. Several dendrites are seen in Fig. 1 nucleated in the pseudoamorphous silicon film. The dendrite at A in Fig. 1 is seen in the dark-field electron micrograph. Figure 2 was taken with the $(1\bar{1}1)$ spot as the operating reflection. The selected area electron diffraction pattern is shown as an insert in Fig. 2. Selected area electron diffraction patterns of the individual dendrites were all similar to the Fig. 2 insert which is indexed as the silicon [011] zone. When the directions in the selected area diffraction patterns are rotated to coincide with the directions in the corresponding micrographs, it is noted that the $[01\bar{1}]$ is parallel to long, central arms of the dendrites indicating that the growth direction of the dendrite is in the close-packed $[01\bar{1}]$ as expected. Further, the fine radial structures on the dendrite central arms are normal to the [111] directions in the micrographs. The angle that new dendritic arms make with the central arm is 107°, which is close to the angle (109.5°) that separates the traces of the $(\bar{1}11)$ and the (111) planes in a cubic [011] stereographic projection. The parallel lines and gray spots on the amorphous film are artifactual thickness variations produced during ion-milling of the specimen.

X-ray diffractometry of the 650°C heat-treated sample produced only a weak silicon (220) peak, after the silicon single-crystal substrate reflections were rotated off the Ewald sphere (7). This confirms the highly oriented early stages of the film's crystallization.

Fig. 1. Dendritic silicon nucleating in amorphous evaporated silicon film. Parallel lines and gray spots on amorphous film are ion-milling specimen preparation artifacts.

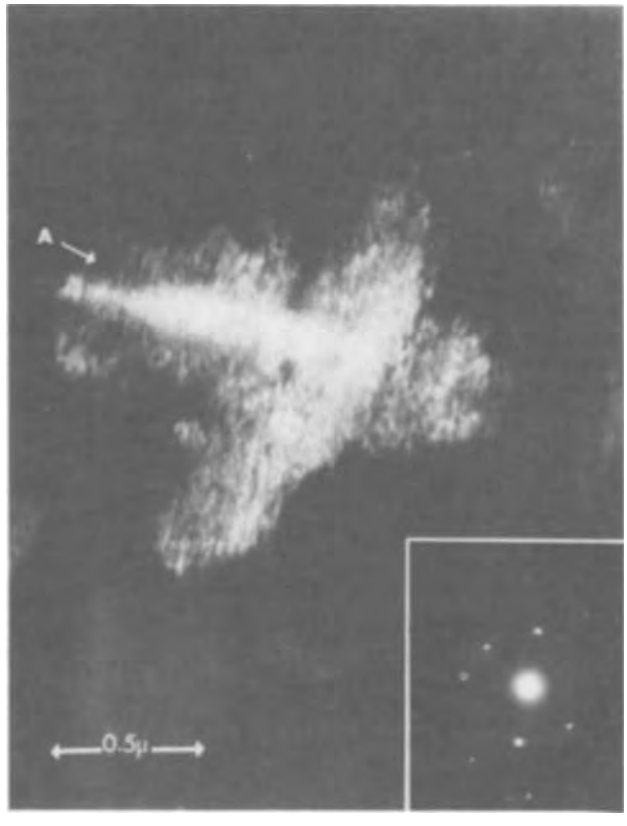

Fig. 2. Dark-field photograph of the dendrite at A in Fig. 1. Insert is selected area electron diffraction pattern from dendrite. The $(1\bar{1}1)$ reflection at 12 o'clock was the operating reflection for the dark-field photograph.

The microstructures of the films heat-treated at 850°C for 60 min indicated that these films went through a dendritic nucleation process as dendrite remnants are observed in the microstructure of the film. Figure 3 depicts several silicon dendrite remnants separated by equiaxed polycrystalline silicon grains. The density of dendrite remnants is lower than the density of dendrites observed in the 650°C film. The polycrystalline silicon grain structure is obscured by a combination of a thin amorphous film on the surface and by occasional crystalline inclusions within the film. The thin amorphous film can be successfully removed by ion-milling and reflections from the crystalline inclusions observed, as shown in the electron diffraction pattern insert in Fig. 3. There are too few unique reflections to make a positive identification of the crystalline inclusions; however, the indexed reflections we noted correspond to the strong reflections reported for Si_2ON, SiO_2 (tridymite), and/or the low temperature modification of Si_3N_4. The normal mean grain size of the equiaxed grains in the 850°C, 60-min film samples is 6400Å with a standard deviation of 1300Å. Now that the polycrystalline silicon film has fully crystallized we see a dramatic decrease in sheet resistance as tabulated in Table I.

After the 1040°C, 60-min heat-treatment the polycrystalline silicon film had a microstructure consisting solely of equiaxed silicon grains (Fig. 4). No dendrite remnants were observed. The film had a lower number of defects but grain boundaries were still unclear. The normal mean grain size for this film is 2050Å with a standard deviation of 230Å. Confirmation of the decreased grain size compared with the 850°C, 60-min sample is seen in the diffraction pattern inserts in Fig. 3 and 4, taken with the same selector aperture, where the polycrystalline silicon rings are observed to be more nearly continuous for the higher temperature. The same nonpolycrystalline silicon reflections mentioned above were occasionally observed in the diffraction pattern of this sample.

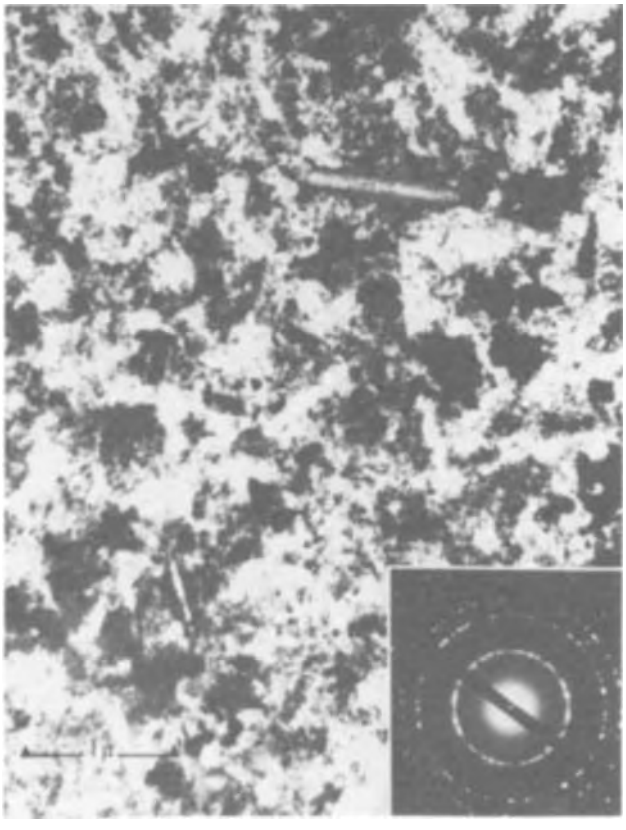

Fig. 3. Microstructure and diffraction pattern of evaporated film after 850°C heat-treatment; dendrite remnants are seen at D.

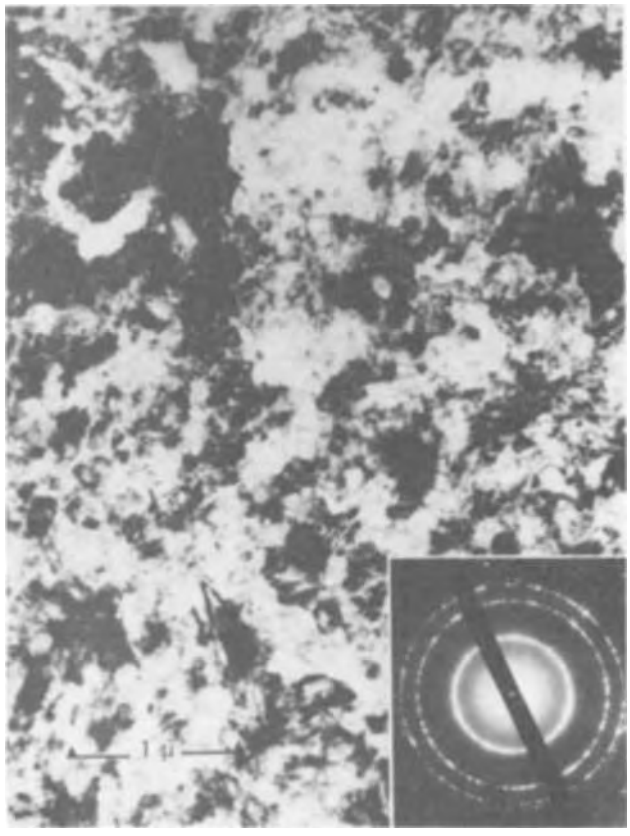

Fig. 4. Microstructure and diffraction pattern of evaporated film heat-treated at 1040°C.

X-ray diffractometry of the 850° and 1040°C heat-treated samples produced a sufficient number of diffraction peaks for a Nelson-Riley function plot, which in turn yielded stress data for the films (7). The higher order peaks in the back-reflection region were too weak, due to sample thinness, to yield a stacking fault calculation or two-exposure stress analysis. Table I shows that all films have a high faulting density, which is listed as twin probability. This probability decreases with increasing heat-treatment temperature which correlates with the lower number of defects observed in the 1040°C samples. Of significance is the observation from Table I that the stress determined from the Nelson-Riley function plots is reduced with increasing heat-treatment temperature, halving from 850° to 1040°C.

Pyrolytic polycrystalline silicon films.—Pyrolytic silicon films deposited at temperatures up to 650°C have pseudoamorphous structures. Typical diffraction patterns show broad diffuse rings. The first ring corresponds to the silicon (111) diffraction radius and the second ring spans the radii of the (220) and (311) silicon rings. SEM micrographs of the films show smooth featureless surfaces for deposition temperatures to 650°C.

The sample deposited at 675°C exhibited a small equiaxed polycrystalline-silicon grain structure, indicating that the transition between a pseudoamorphous silicon film and a crystalline silicon film occurs between the 650° and the 675°C deposition temperatures. This transition point is confirmed by x-ray, low-angle Laue photographs and the change in appearance of the surface as seen by the SEM. The samples retained an equiaxed grain structure from 675° through 875°C depositions, exhibiting only grain growth. All of the samples observed in this lot in the deposition temperature range from 675° to 875°C had a vertical duplex grain structure consisting of small discontinuous 200-300Å grains at the film-substrate interface, and con-

tinuous large grains[2] through the balance of the film's thickness. This morphology is seen in Fig. 5 taken through an entire 1μ thick film; the large grains (~1 cm in the photo) have small (~1 mm) grains superimposed on them. A sample was prepared by ion-milling the polycrystalline silicon from the surface side down to the substrate interface, as seen in Fig. 6. Some areas are etched completely through the large grains (at E) revealing the small slower etching grains at the interface clearly. Figure 7 is a montage of a diffraction pattern from the small silicon grains contrasted with a diffraction pattern from large silicon grains. As seen in Fig. 7, the small-grain silicon diffraction pattern contains extra silicon rings which arise from silicon reflections which are normally disallowed due to crystal structure factor reasons.

To gain a better understanding of the formation of the small grain silicon layer at the oxide interface, we prepared a set of samples with increasing thicknesses of polycrystalline silicon; 130, 270, 400, 800, and 1600Å thick films were examined. The 130Å thick film was discontinuous and the remainder of the films were continuous with the grain sizes reported in Table III. Interestingly, the small grain layer did not nucleate under the thin samples. Selected area diffraction patterns of the thinnest (130Å thick) sample exhibited the normal complement of silicon reflections, which eliminated one reason for the forbidden reflections as being due to the relaxation of the diamond cubic structure factor rules as a result of extreme sample thinness.

A TEM sample prepared using the center of the thick, polycrystalline silicon specimen instead of the interface (Fig. 8) shows a normal polycrystalline silicon microstructure consisting of uniform equiaxed grains which contain numerous twin lamella. The microstructure in Fig. 8 is also seen throughout the thickness of the thin nucleation layer specimens and

[2] Grain size data is tabulated in Table III.

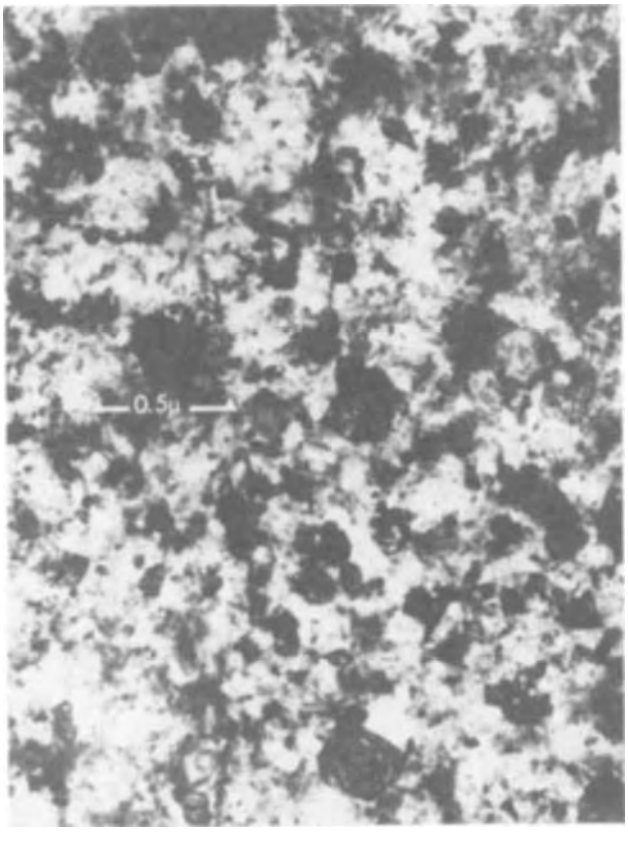

Fig. 5. Microstructure of pyrolytic silicon film deposited at 700°C. Superposition of large grains in bulk of film and small anomalous grains at the substrate interface.

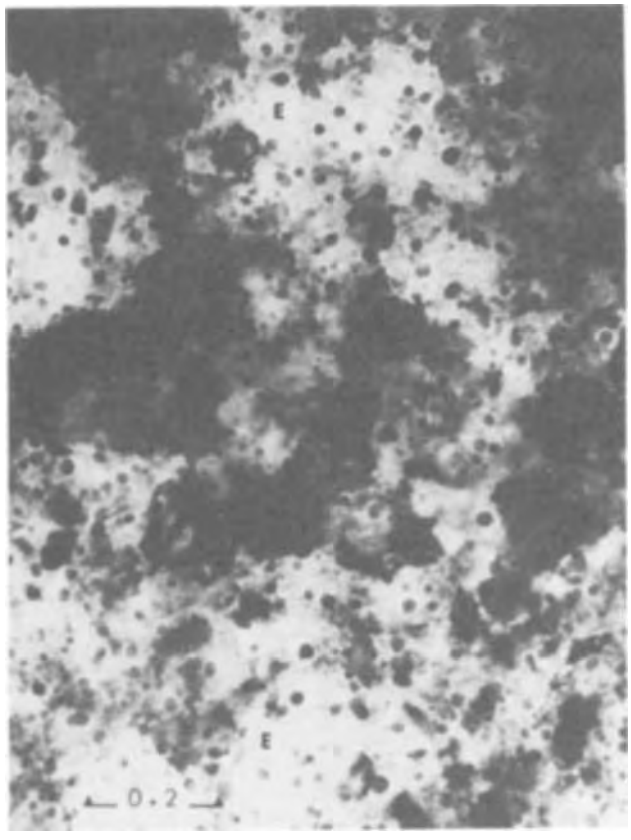

Fig. 6. Silicon film from Fig. 5 after ion-milling down to ~500Å from film substrate interface. Discontinuous anomalous silicon grains are clearly visible.

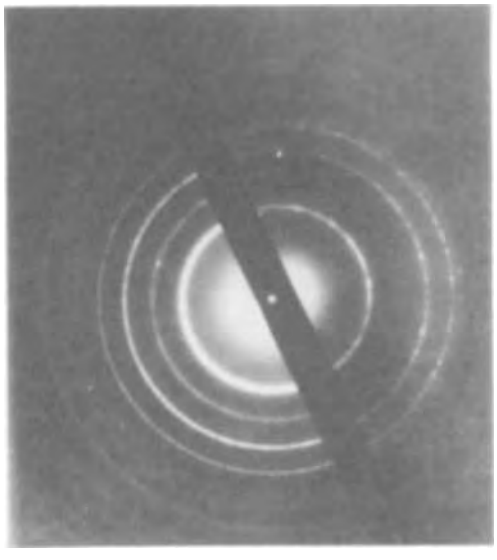

Fig. 7. A montage of selected area electron diffraction patterns from normal polycrystalline silicon grains, left, and anomalous grains, right.

is typical of virtually all of the polycrystalline evaporated and pyrolytic silicon samples observed in this study.

X-ray, low-angle Laue photographs of the 1μ thick 700° and 800°C deposited samples show a randomly oriented polycrystalline silicon film with a crystallite size in the 1500-8000Å x-ray insensitive region.

The 1μ thick films have a very low stress (3000 psi) and a moderately high lattice parameter shift due to solid solution effects.

SEM photos of the 700° and 800°C samples (Fig. 9) show a typical polycrystalline surface: the bumps are about 1000Å high.

Table III. Grain size data for pyrolytic silicon thin films

1. Effect of deposition temperature samples

Dep. temp, °C	Normal mean grain size, Å	Standard deviation, Å	Grain boundary area per unit volume,*** mm^2/mm^3
<675	—*	—*	*
700	1470	50	4.1×10^5
800	1870	90	3.3×10^5
900	—**	**	5.2×10^5

* Films are amorphous.
** Film has dendritic structure consisting of 1.5μ dendrites and ~500Å equiaxed grains.
*** Calculated using appropriate grain shape factors.

2. Effect of substrate and substrate cleanliness

Substrate,	Dep. temp, °C	H_2SO_4 step?	Normal mean grain size, Å	Standard deviation, Å
SiO_2	725	No	2419	100
Si_3N_4	725	No	2590	130
Al_2O_3	725	No	2680	100
SiO_2	725	Yes	2410	140
Si_3N_4	725	Yes	2340	120
Al_2O_3	725	Yes	2590	120

3. Thin nucleation layer experiment

Dep. temp, °C	Dep. time, sec	Film thickness, Å	Normal mean grain size, Å	Standard deviation, Å
715	10	130	210	10
715	20	270	290	10
715	30	400	380	20
715	60	800	560	40
715	120	1600	800	70

* Film not continuous.

Polycrystalline silicon samples deposited at and above 900°C exhibit a dendritic structure. A typical morphology is seen in Fig. 10. The dendrites "D" bear the same crystallographic relationships to the substrate and internally as the dendrites observed in evaporated films. The spaces between the dendrite arms are filled with small, equiaxed polycrystalline silicon grains approximately 500Å in size. X-ray diffractometry confirms the {110} sheet texture.

SEM photographs (Fig. 11) of the 900°C deposited sample show that dendrite arms stick up from the surface to heights of up to 2μ. We measured the density of dendrites taller than 1μ as one per $10\mu^2$ and the density of smaller sharp dendrites at about ten times the density of the larger ones. The sharpest point observed on a tall dendrite had a tip radius of 500Å; most of the tall dendrites have tip radii of 2000-3000Å. A subsequent oxidation and HF strip of the film removed the large dendritic spikes.

As seen in the grain size data in Table III, there is very little difference between the films deposited on SiO_2, Si_3N_4, and Al_2O_3. In all cases the films were morphologically similar and the thin layer of anomalous silicon grains was noted at the substrate interfaces. The films were also insensitive to the different cleaning procedures performed on the substrates prior to deposition.

Selected wafer samples from the effect-of-deposition temperature lot were divided in half: one half for microstructural analysis and the other half for a thermal SiO_2 deposition 1750Å thick. Breakdown voltage measurements were made of the SiO_2 and are tabulated in Table II. Breakdown voltage is seen to correlate with the surface morphology of the film; the double peak on the 900°C samples probably is due to random samples either containing or not containing dendritic spikes.

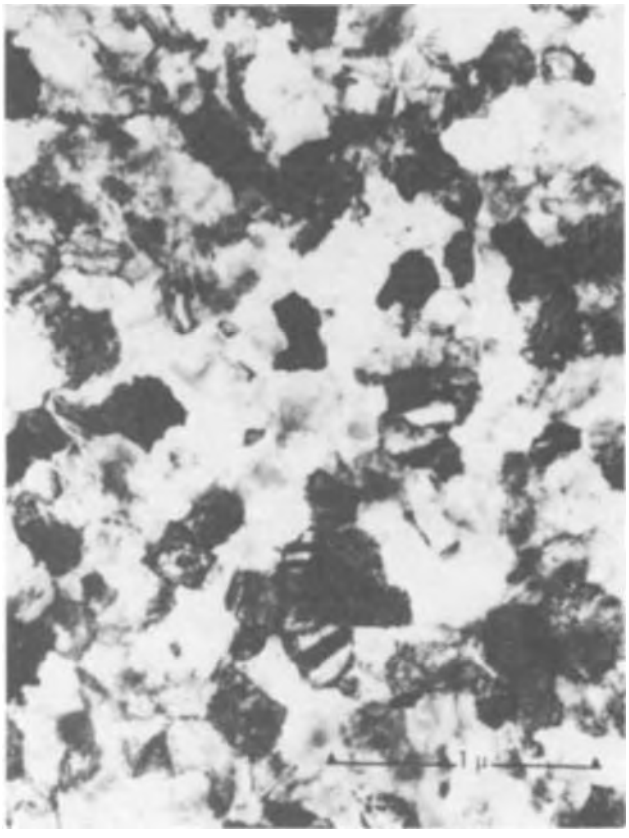

Fig. 8. Microstructure of normal polycrystalline pyrolytic silicon grains, 800°C sample.

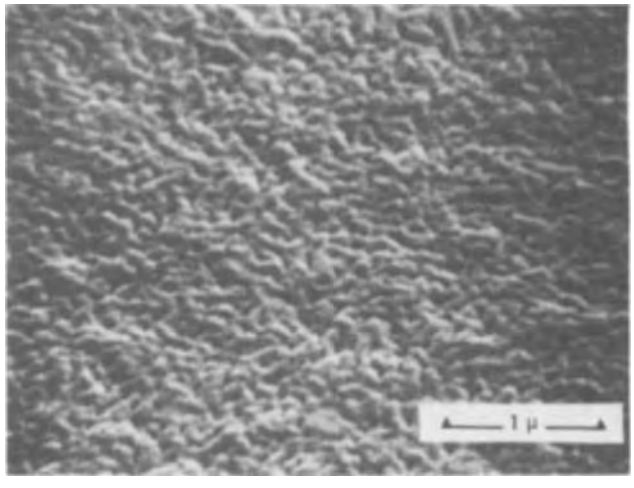

Fig. 9. Scanning electron micrograph of surface of 800°C polycrystalline silicon surface.

Analysis of silicon film impurities.—Reference has been made in the text to the observation of impurities, viz., amorphous surface films, crystalline inclusions in the films, defects within the silicon grains, and anomalous small silicon grains at the substrate interface of certain pyrolytic silicon films. The possibility exists that some of the results obtained may be due to impurities in the films. The silicon films that are the subject of this investigation were fabricated in carefully controlled laboratory apparatus used for FET applications, and only the highest quality materials obtainable were used. Electrical resistivity and Hall effect measurements could not detect any trace of impurities in the films. X-ray diffractometry and low-angle Laue analysis revealed no gross crystalline impurities.

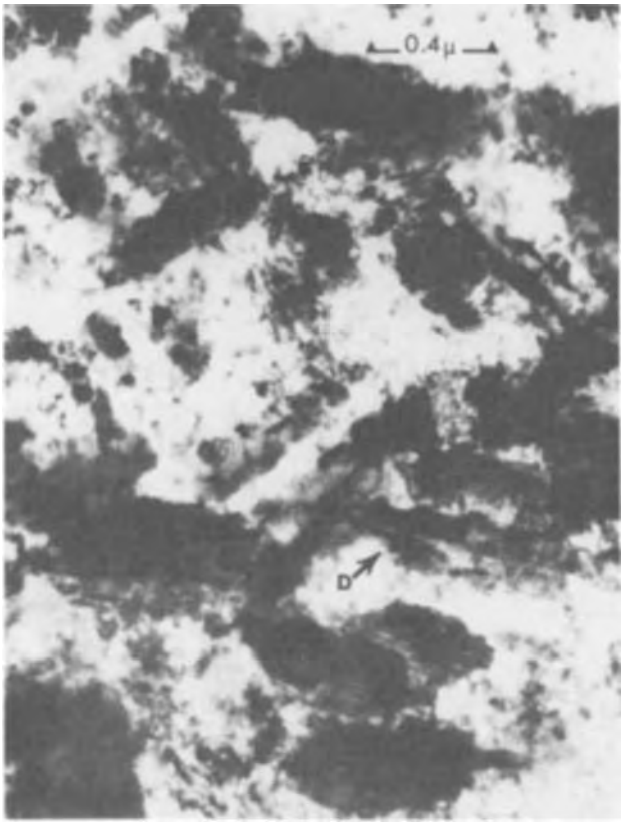

Fig. 10. Transmission electron micrograph of mixed silicon dendrites and equiaxed silicon grains between dendrites on 900°C pyrolytic sample.

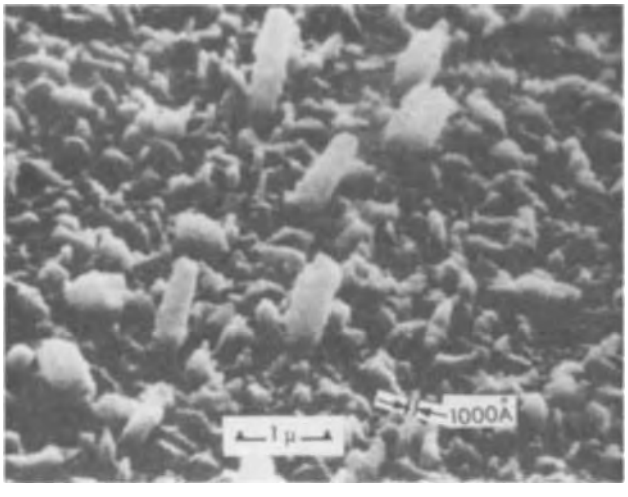

Fig. 11. Scanning electron micrograph of surface of dendritic 900°C sample.

Selected area electron diffraction techniques were able to obtain nonsilicon reflections from the occasional crystalline inclusions observed in the films and, as discussed above, tentatively identified the inclusions as silicon-oxy-nitride compounds. No silicon carbide reflections were observed.

X-ray microprobe analysis of the films was performed. Using the microprobe's energy dispersive analyzer (variable fraction-of-a-per cent sensitivity for elements with atomic numbers of eleven and above), no impurities were detected. Three specimens representing amorphous, polycrystalline, and dendritic morphologies, from both the evaporated and sputtered lots of specimens, were chosen on the basis of maximum TEM observable impurity content. The six specimens were examined by the microprobe's wavelength dispersive analyzer for carbon, oxygen, and nitrogen content with calibration against graphite, SiO_2, and BN standards. The microprobe's electron beam accelerating potential was varied to obtain a rough distribution of the above elements with depth. The microprobe's sensitivity for nitrogen may be as poor as 1% due to a high background signal arising from scattering from multiple orders of silicon. The microprobe detected a thin oxide film on the surface of all of the samples, but no nitrogen or carbon impurity was observed.

Next, the ESCA technique was used to examine the surfaces of virgin pieces of the samples examined by the x-ray microprobe wavelength dispersive analyzer. Essentially, the technique consists of bombarding the sample with monoenergetic x-rays and measuring the kinetic energy distribution of the ejected electrons. Since the ejected photoelectrons have kinetic energies of approximately 1 keV or less, the mean free paths of these electrons are short and the total sampling depth is within the first 100Å. Each element has a characteristic photoelectron spectrum which allows for the analysis of elements above helium in the periodic chart. A major feature of information provided by the ESCA technique is that a shift in kinetic energy of the photoelectron for an individual element is related to its chemical bonding in a molecule. The surface spectra from all of the samples were essentially identical. Silicon, oxygen, carbon, and SiO_2 were detected. Comparison of the peak height and area of the silicon and SiO_2 peaks, with appropriate standards, established that the surface SiO_2 films are 20-50Å thick. The significance of the observed carbon peak is questionable in that a small carbon peak is artifactually produced in the oil-diffusion pumped ESCA apparatus.

Another set of four virgin samples was examined in a Cameca secondary ion mass analyzer. The samples examined were the worst-case pyrolytic dendritic, polycrystalline, and amorphous samples and a polycrystalline evaporated sample. An ion spectra was obtained as the analyzer sputtered into the silicon film. The mass numbers detected corresponded to various orders of silicon, oxygen, silicon oxides, carbon, and argon. Ionized argon was used used as the primary ion species. The analyzer cannot detect nitrogen in the presence of doubly ionized ^{28}Si, due to interference from the silicon half mass. Otherwise the sensitivity of the ion analyzer is 1-10 ppm. Next, an analysis in depth for silicon, oxygen, and carbon was made. The argon ion beam of the analyzer is swept in a square raster on the sample eroding through the film and insulator and into the substrate. The mass spectrometer is set to detect a particular mass number, $^{30}Si^+$ for example, and the detector current is plotted *vs.* time as the argon beam moves into the sample. The substrate silicon and its oxygen and carbon content are assumed to be standards and the ratio of detector currents for silicon, oxygen, and carbon in the film is compared with the silicon, oxygen, and carbon in the substrate silicon. Table IV lists the ratios of detector currents for the species indicated. When the experimental error for this procedure is considered, ratios of

Table IV. Ion mass analyzer data

Sample	Spectrometer detector current ratio $I_{film}/I_{substrate}$		
Mass:	^{30}Si	^{16}O	^{12}C
Pyrolytic			
Amorphous	1.0	1.3	1.6
Polycrystalline	1.0	2.1	6.1
Dendritic	1.0	1.5	6.0 → 2.0*
Evaporated			
Polycrystalline	1.0	2.3 → 1.4*	1.7

* These current ratios started at the high value at the surface of the film and decayed exponentially to the lower value at the substrate interface.

two or less may be discounted for planar samples. Increasing surface topography induces surface effects which increases the yield of sample ions, decreasing the significance of higher detector current ratios. In addition, for the dendritic case, the angle of impingement of the primary beam is such that enhanced sputtering yield may be obtained. In the light of these arguments it is concluded that there is very little real difference in the carbon and oxygen contents of the films compared to their substrates, with the exception of the effects of the surface native oxide film.

Discussion

Evaporated polycrystalline silicon film.—When the silicon crystallite nucleates in the thin amorphous silicon film at 650°C, the associated volume contraction and orientation change sets up stresses in the amorphous silicon. This stress, when combined with the residual stress present in the amorphous film, apparently provides the driving force for dendritic growth.

At 850°C the nucleation is initiated as a dendritic process in competition with the nucleation of equiaxed grains resulting in a relatively low density of dendrites in a matrix of equiaxed polycrystalline silicon grains. At 1040°C the nucleation of low-mobility equiaxed polycrystalline silicon grains is dominant, and the large number of crystallites nucleated limits the initial grain size when the nuclei coalesce. Further, the silicon-oxy-nitride compounds may have a greater role in limiting the silicon grain size as they undergo nucleation and growth.

Pyrolytic polycrystalline silicon film.—The observation of the small-grained layer of polycrystalline silicon at the substrate interface of the initial effects-of-deposition temperature samples, with the attendant anomalous diffraction pattern and the absence of the small-grain layer in the nucleation study, may be explained as follows. The silicon wafers in the pyrolytic reactor are sitting at an elevated temperature in a nitrogen atmosphere prior to the silicon deposition, causing the surface monolayer to be composed almost entirely of adsorbed nitrogen atoms. The nucleation samples had their silicon depositions started immediately after they came to temperature; whereas the effect-of-temperature samples sat at temperature for roughly 20-40 min prior to silicon deposition. We, therefore, speculate that the initial small-grain silicon layer is nucleated on an altered surface, most likely a gaseous nitrogen saturated surface which produces anomalous small silicon grains. There will be large amounts of interstitial nitrogen in the lattice leading to distortion of the lattice. When the silicon film builds up to a thickness that reduces the effect of nitrogen at the interface, through long diffusion distances, then the silicon renucleates a normal silicon lattice with large grains. The presence of interstitial impurities distorting cubic lattices and giving forbidden reflections in electron diffraction patterns is well known (8). Additional evidence for this explanation of the small grain layer is the high, lattice-parameter shift due to solid solution effects, noted by x-ray diffractometry, and the absence of any differences in the grain size of thick films as functions of substrate cleanliness.

Impurity effects.—The role that impurities play in the nucleation of the three morphologies is limited. Without a doubt, the effect of prolonged heating in nitrogen prior to the deposition of polycrystalline pyrolytic silicon is important in that it induces the formation of a small-grain silicon layer at the interface. Having established the necessity of starting the silicon deposition immediately on reaching temperature in nitrogen, we have never again observed the small grain silicon layer on comparable subsequent samples. More significantly, no variation in the temperature of transformation from amorphous to polycrystalline silicon morphologies was detected in samples with or without the small grained layer of silicon.

The author feels that the 20-50Å thick SiO_2 layer on all samples is inescapable and is of no consequence to the nucleation of the three morphologies. Likewise, the unproven possibility of carbon contamination in pyrolytic samples deposited at temperatures in excess of 900°C would presumably come from the graphite susceptor under the specimens and is only seen after the dendrites are nucleated. This is evidenced by the decay of the questionable ion analyzer carbon ratio from high values at the surface to low values at the nucleation interface.

This leaves the occasional TEM observed silicon-oxy-nitride compounds. They are certainly real and except for their possible role of inhibiting grain growth they would appear to have no effect on the nucleation of the three morphologies. Support for this statement comes from subsequent work with silicon films wherein the transformation temperatures between morphologies was constant despite a near total absence of silicon-oxy-nitride compounds.

Conclusion

We have established that the thin polycrystalline silicon film subject of this investigation can have three different morphologies: pseudoamorphous, equiaxed grains, or dendritic, as functions of deposition temperature for pyrolytic films and heat-treatment temperature for evaporated films. We note that the pseudoamorphous films are smooth and uniform and should perform best in semiconductor applications. We further note that polycrystalline silicon has a slightly rougher surface and has a morphology which is apparently sensitive to the time spent at temperature in nitrogen prior to silicon deposition for pyrolytic silicon. The dendritic polycrystalline silicon has the least satisfactory surface morphology due to the presence of large dendritic spikes.

Acknowledgment

The author wishes to thank R. Gdula, J. Gardiner, and H. Demsky for preparing the silicon films, N. O'Neil for transmission electron microscopy specimen preparation, C. Goldsmith for x-ray analyses, F. Ordonez for performing scanning electron microscopy, S. Cvikevich for x-ray microprobe analysis, R. Flitsch for ESCA analysis, and P. Kuehner for ion analyzer work. The author is indebted to G. Das and G. Walker for helpful discussions. Constructive suggestions made by the Journal's reviewer are gratefully acknowledged.

Manuscript submitted March 5, 1973; revised manuscript received June 6, 1973.

Any discussion of this paper will appear in a Discussion Section to be published in the June 1974 JOURNAL.

REFERENCES

1. J. C. Sarace, R. E. Kerwin, D. C. Klein, and R. Edwards, *Solid State Electron.*, **11**, 553 (1968).
2. L. L. Vadaz, A. S. Grove, T. A. Rowe, and G. E. Moore, *IEEE Spectrum*, **6**, 28 (1969).
3. M. Maekawa, *Japan. J. Appl. Phys.*, **11**, 1251 (1972).
4. C. C. Mai, T. S. Whitehouse, R. C. Thomas, and D. R. Goldstein, *This Journal*, **118**, 331 (1971).
5. T. I. Kamins, J. Manoliu, and R. N. Tucker, *J. Appl. Phys.*, **43**, 83 (1972).
6. R. D. DeLuca, in "Semiconductor Silicon," Rolf R. Haberecht and Edward L. Kern, Editors, pp. 299-315, The Electrochemical Society, Inc., Softbound Symposium Series, New York (1969).
7. G. A. Walker and C. C. Goldsmith, *J. Vacuum Sci. Technol.*, **7**, 6 (1970).
8. G. Das, *Thin Solid Films*, **12**, 305 (1972).

An Interstitial Model for the Dielectric Relaxation of ZnF_2 Doped with Lithium

Thomas A. Roth

Department of Industrial Engineering, Kansas State University, Manhattan, Kansas 66506

ABSTRACT

The thermally activated release of the dielectric polarization, obtained by the ionic thermoconductivity method, of ZnF_2 doped with lithium is examined in terms of an interstitial model. Single crystals of lithium-doped ZnF_2 are studied in the range of temperature from that of liquid nitrogen to 275°K. Crystals cleaved such that the electrostatic potential can be applied in the [001], [100], and [110] directions are used. Of the three crystallographic orientations studied, only when the polarizing electrostatic potential is applied in the [001] direction is a strong discharge current observed. Peaks, several orders of magnitude smaller than those found in [001] oriented crystals, are found when the potential is applied in the other two directions. The dipolar imperfections in ZnF_2 doped with lithium give a discharge current peak at $T_m = 236.5° \pm 5.0°K$ for all three crystal orientations following polarization at 285° ± 2.5°K for 3 min. The activation energy for the dipolar relaxation for the [001] orientation is 0.320 ± 0.002 eV and the observed relaxation times are given by

$$\tau(T) = 1.70 \times 10^{-13} \exp(0.32/kT)$$

The number of dipoles is found to be 1.40×10^{18} cm^{-3}. Agreement between the number of dipolar defects experimentally determined and the number calculated from doping level information is good. It is proposed that the dielectric relaxation of ZnF_2 doped with lithium is due to the $(Li_I^{\cdot} - Li_{Zn}')$ dipole and that rotation of the dipole is accomplished by interstitial lithium ion movements parallel to the c-axis of the crystal.

The dielectric relaxation of ZnF_2 doped with lithium was examined in a previous paper (1) in terms of possible vacancy movements. The presence of the relatively small and mobile lithium ion suggests re-examination of the relaxation process in terms of possible interstitial movements. It is the intent of this paper to propose an interstitial model for the relaxation process in order to provide the basis for comparison of the two mechanisms and to attempt to resolve which is responsible for the dielectric relaxation of ZnF_2:LiF.

Zinc fluoride has the tetragonal rutile, TiO_2, type crystal structure (2, 3). Each zinc ion is surrounded by six fluorine ions approximately at the corners of a regular octahedron, and each fluorine ion is surrounded by three zinc ions approximately at the corners of an equilateral triangle.

Electric dipoles may be formed in ZnF_2 when it is doped with lithium, as illustrated in Fig. 1. One monovalent lithium ion is proposed to replace the divalent zinc ion in the normal cation lattice position. To maintain charge neutrality in the crystal, for the case under consideration, a second monovalent lithium ion is considered to accompany the substitutional Li^+ and is expected to occupy an interstitial position between the fluorine ions in the immediate neighborhood of the substitutional Li^+. The interstitial Li^+ and the substitutional Li^+ can form a $(Li_I^{\cdot} - Li_{Zn}')$ dipole.[1] The substitutional Li^+ is expected to be relatively immobile and remain in the normal lattice position in the presence of an external field. Rotation of the dipole due to application of the external field is accomplished by movement of the relatively mobile interstitial Li^+ cation from one interstitial position to another. The most probable interstitial sites are taken to be the same as those reported for the rutile crystal (5).

Key words: dielectric relaxation, dielectric loss, zinc fluoride, crystal defects.

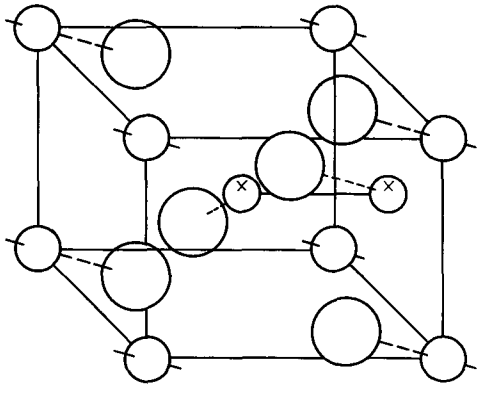

Fig. 1. Tetragonal crystal structure of ZnF_2 in which one Zn^{++} has been replaced by a substitutional Li^+ and an interstitial Li^+ resulting in a $(Li_I^{\cdot} - Li_{Zn}')$ dipole. The zinc ions are represented by the smaller circles; the fluorine ions, by the larger circles; and the lithium ions, by the circles marked with an x.

The orientation of the $(Li_I^{\cdot} - Li_{Zn}')$ dipoles is random and variable in the absence of fields since the interstitial cation can occupy a number of equivalent sites around the substitutional Li^+. Application of an electric field results in movement of the interstitial cations with dielectric relaxation occurring when the field is removed due to the redistribution of the interstitial cations among the possible lattice sites. The activation energy in the low temperature range is expected to be the motion energy for the interstitials.

The dielectric relaxation of ZnF_2 single crystals doped with lithium has been studied in the present work using the ionic thermoconductivity method of Bucci *et al.* (6-9). Since the dielectric relaxation of doped materials is expected to be dependent on movement of defects in the crystal, as proposed above, the occurrence of strong, thermally activated current discharges observed in the ionic thermoconductivity method are expected to be dependent on the crystallo-

[1] The dipoles described here are written in terms of Kröger's notation (4) in which the major symbol is the ion or vacancy in the lattice position normally occupied by the subscripted symbol. A subscripted I indicates that the ion is in an interstitial position. The superscripted symbol indicates the effective charge on the ion or vacancy with ·, x and, ' indicating positive, neutral, and negative, respectively.

graphic orientation of the single crystals. ZnF_2:LiF single crystals cleaved such that polarization and discharge may be studied in three different crystallographic orientations have been used in order to determine the orientation dependence of the discharge current.

As outlined by Bucci and Fieschi (6), the ionic thermoconductivity method for the study of dielectric relaxation consists of the following three basic steps: (*i*) The sample is polarized in a static field F_p, for a time t, at a temperature T_p. (*ii*) The sample is cooled to a temperature $T_o << T_p$, where any ionic motion is completely hindered, and the external field is taken off. (*iii*) The sample is subsequently warmed at a constant rate $b = dT/dt$, and the discharge current is registered as a function of temperature.

The dipoles, initially, are randomly oriented in the absence of an external electric field. The dipoles will be distributed in a random way among the possible orientations, so that the total polarization will be zero. The application of the field F_p causes the dipoles to become polarized, *i.e.*, assume a preferred orientation. The preferred orientation of the dipoles is preserved by reducing the temperature to a value low enough to hinder the relaxation, *i.e.*, rerandomization, of the dipoles. The lowering of the temperature insures a long relaxation time for the rerandomization process. When the sample is warmed at a constant rate b, the relaxation time is gradually shortened, the dipoles lose their preferred orientation and a depolarization, or discharge, current $i(T)$ is observed. The discharge current is characterized by an initial exponential rise as the temperature increases, peaking, and a falling off to zero.

When the discharge current is due to the relaxation of dipoles, the peak of the current corresponds to the particular type of dipolar imperfection in the sample and can be used to obtain information on the relaxation time and number of dipoles in the sample (6). If several types of dipolar imperfections are present in the sample, several peaks are to be expected, each peak corresponding to a particular type of dipolar imperfection in the sample.

When only one kind of dipolar defect is assumed to be present in the material, the following parameters can be obtained from the ionic thermoconductivity data (6-9):

(*i*) The activation energy for the dipole orientation, E, can be obtained from the initial slope (the low temperature side) of the curve obtained by plotting $\ln i(T)$ *vs.* $1/T$ and from the equation

$$\ln i(T) = -E/kT + \ln (P_o/\tau_o) \qquad [1]$$

where P_o is the induced polarization per unit volume and τ_o is the relaxation time at 0°K.

(*ii*) When E is known, τ can be obtained from

$$kT_m^2 = bE\tau(T_m) = bE\tau_o \exp(E/kT_m) \qquad [2]$$

where T_m is the temperature corresponding to the peak, $i(T_m)$, in the ionic thermoconductivity curve and b is the warming rate, dT/dt.

(*iii*) The number of dipolar defects, N_d, is obtained from

$$N_d = P_o kT_p/\alpha p^2 F_p A \qquad [3]$$

where T_p is the polarizing temperature, α is a geometrical factor depending on the possible dipolar orientation, p is the electrical moment of the dipole, F_p is the polarizing electrical field, and A is the sample area.

Experimental Procedure

Single crystals of ZnF_2 doped with lithium, in the amount of 2.9×10^{18} atoms of Li per cm^3, were grown in the crystal growth facilities of the Center for Materials Research at Stanford University. The concentration of the lithium was originally determined in the melt based on the assumption that the content of the solid would be the same. No evidence of segregation was apparent in the single-crystal boule. Inference of the lithium content from atomic absorption measurements on the lithium-doped ZnF_2 crystals indicated the assumption to be valid. The crystals were cleaved into right rectangular parallelepiped samples on the order of $4 \times 4 \times 1$ mm in size. The crystallographic orientation of the cleaved crystals was such that the electrostatic potential could be applied in the [001], [100], and [110] directions of the ZnF_2:LiF crystal. Conductive silver lacquer was used to provide electrical contacts on the crystals.

Polarization of the samples was done at 285.0° ± 2.5°K under vacuum followed by a liquid nitrogen quench. Heated high-purity nitrogen, at a flow rate of 3.5 liters/min, was used to warm the samples at a warming rate of approximately 0.1°K/sec. The temperature was measured by means of a copper-constantan thermocouple attached to the sample holder in contact with one of the electrodes. Current measurements were made using a Cary 401 vibrating-reed electrometer with a current sensitivity of 10^{-17} A. The current and temperature were recorded simultaneously on strip-chart recorders from liquid nitrogen temperature to approximately 275°K in most tests with an occasional sample being heated to about 300°K. Reproducibility of ionic thermoconductivity measurements made on different samples was on the order of magnitude of 7.5%. Measurements on the same sample gave a reproducibility on the order of 2.5%. These errors arose mainly from a translation of the scale of the current and therefore are not expected to affect the values of E and τ_o.

Prior to placement in the sample holder for the ionic thermoconductivity studies, the crystals were heated in a high-purity helium gas atmosphere at about 475°K for one-half hour and then quenched to room temperature with high-purity helium gas. The purpose of the heat-treatment was to dissolve clusters of dipoles thereby increasing the intensity of the dielectric relaxation (8). In samples that had not been given the above treatment prior to testing, only relatively weak discharge currents were observed.

Results and Discussion

Only when the polarizing electrostatic potential is applied in the [001] direction, of the three crystallographic orientations studied, is a strong discharge current observed. Figure 2 illustrates a typical ionic thermoconductivity discharge of the [001] direction oriented crystals during heating from liquid nitrogen temperature to near room temperature. Also shown in Fig. 2 are the weaker discharges observed for the [100] and [110] oriented crystals. The curves of the figure have been smoothed and do not exhibit the

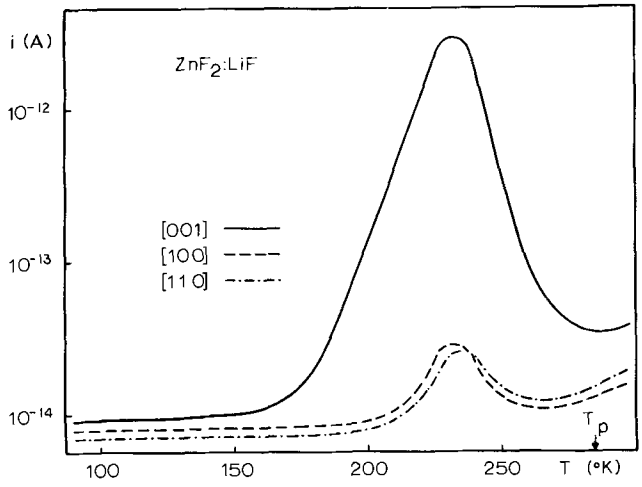

Fig. 2. Typical ionic thermoconductivity discharge currents in ZnF_2:LiF for the three crystallographic orientations of this work.

discontinuities resulting from the translation of the current range actually experienced in the tests. As seen in Fig. 2, peaks, several orders of magnitude smaller than those found in [001] oriented crystals, are found when the potential is applied in the [100] and [110] directions.

The dipolar imperfections in ZnF_2 give a discharge current, $i(T_m)$, at $T_m = 236.5° \pm 5.0°K$ for all three crystal orientations following polarization at $T_p = 285.0° \pm 2.5°K$ for 3.00 ± 0.25 min.[2] The activation energy for the dipolar relaxation obtained from the slope of the [001] orientation, as shown in Fig. 3, is $E = 0.320 \pm 0.002$ eV[3] and the observed relaxation times are given by

$$\tau(T) = 1.70 \times 10^{-13} \exp(0.32/kT) \quad [4]$$

By putting $p = 1.5 \times 10^{-17}$ esu, $\alpha = 2/3$, and $T_p = 285°K$, the number of dipoles is found to be 1.40×10^{18} cm^{-3} from Eq. [3].

As indicated above, the temperature T_m corresponding to the maximum current in all cases, regardless of crystal orientation, is similar, $236.5° \pm 5.0°K$. Since all samples were given the same treatment prior to and during the study, the apparent reason for the strong discharge current peaks only for [001] oriented crystals is that the rotation of the dipoles due to movement of the defects is easier in this orientation than in the other two directions.

In the previously proposed vacancy model for the dielectric relaxation of ZnF_2 doped with lithium (1), ($V_F{\cdot} - Li_{Zn}'$) dipoles were discussed. When only one monovalent lithium ion replaced the divalent zinc ion, an anion vacancy was proposed to maintain charge neutrality. Rotation of the dipole during relaxation was considered to be due to fluorine ions moving between adjacent lattice sites as made possible by the existence of the relatively mobile vacancies created by the addition of the relatively immobile lithium ions to the crystal. The vacancy has six possible equivalent positions around the lithium ion and the orientation of the dipole can change by an anion moving to the vacant site. Possible movements of the adjacent fluorine ions into the vacant site are given in Fig. 4. From Fig. 4, it is apparent that movement of the fluorine ions and vacancies, with the resulting rotation of the dipoles, should be as easily accomplished when polarization and relaxation are studied in the [100] direction as when studied in the [001] direction. Figure 4 and inspection of scale size solid models of the ($V_F{\cdot} - Li_{Zn}'$) dipole in ZnF_2 suggest that ion and vacancy movement, when polarization and depolarization are studied in the [110] direction, may be slightly more difficult due to the coordination of the fluorine ions in the crystal structure. Nowick and Heller (5), however, indicate that the relaxation behavior for the [100] and [110] directions should be similar.

Dielectric relaxation of ZnF_2 resulting from rotation of dipoles due to the presence of vacancies was observed in some early tests of the crystals. Prior to placement in the sample holder for the ionic thermoconductivity studies, the crystals were heated in a high-purity helium gas atmosphere at about 475°K for one-half hour, then quenched to room temperature with high-purity helium gas, as noted above. In the early stages of the investigation, the quench was attempted in air. The air-quench however resulted in oxidation of the crystals, as evidenced by discoloration of the originally colorless crystals. Crystals thus exposed to an air cooling gave discharge currents as shown in Fig. 5 for a [110] oriented crystal. Two discharge current peaks were observed for air-cooled ZnF_2:LiF crystals. The initial peak, T_{m1}, corresponds to the peak shown in Fig. 2 for the helium-cooled crystal. The peak at T_{m1} in Fig. 5 and the peak in Fig. 2 for the [110] orientation both are found at 236.5°K. The higher temperature peak, T_{m2}, of Fig. 5 was observed in both lithium-doped ZnF_2 and undoped ZnF_2 crystals which were heat-treated together and equally exposed to the atmosphere during the air-quench. The current peaked at 265°K in each case when the second discharge was observed. No second discharge was observed when the doped or undoped crystals were quenched in the high-purity helium gas. The second current discharge was therefore attributed to ($V_F{\cdot} - O_F'$) dipoles formed during the oxidation of the air-cooled crystals. The anion vacancy of the ($V_F{\cdot} - O_F'$) dipole would be expected to be more mobile than the substitutional oxygen with rotation of the dipole during relaxation occurring via a vacancy movement mechanism. The activation energy for dipole orientation for the second discharge was found to be 0.46

[2] For all numerical values reported in this paper in the form $A \pm B$, B is the standard deviation.

[3] The value of the activation energy previously published (1), 0.641 eV, was incorrectly reported and found to be in error by a factor of 2.

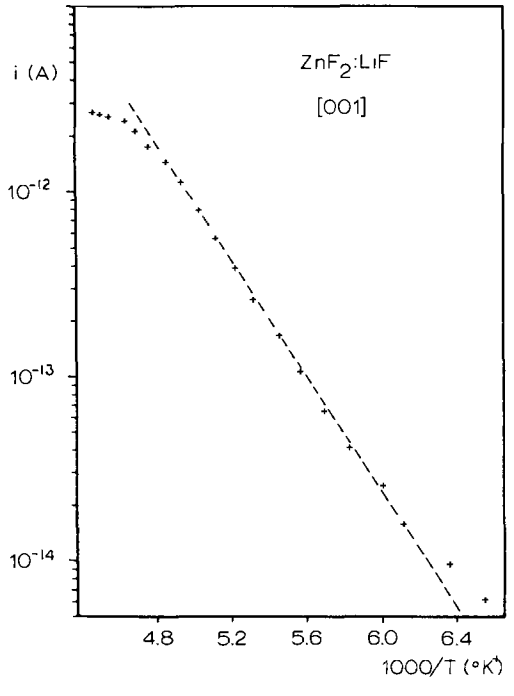

Fig. 3. The $\log_{10} i$ as a function of $1000/T$ for the low-temperature side of the current discharge for lithium-doped ZnF_2 in the [001] orientation. The activation energy is determined from this plot.

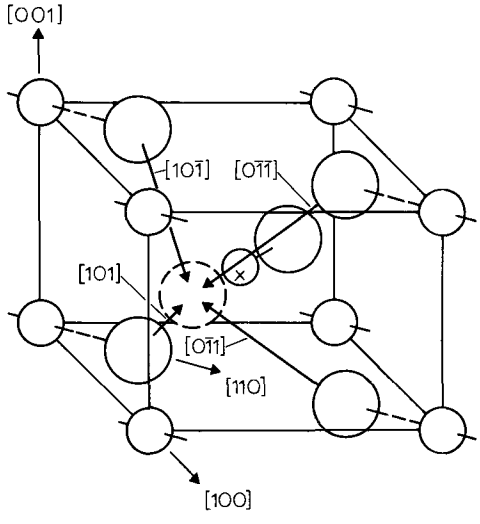

Fig. 4. Crystal structure of ZnF_2 in which one ZnF_2 has been replaced by one LiF resulting in a ($V_F{\cdot} - Li_{Zn}'$) dipole. The crystallographic directions possible for changes in the vacancy position, as represented by replacement of the vacant lattice site by a neighboring fluorine ion, are indicated.

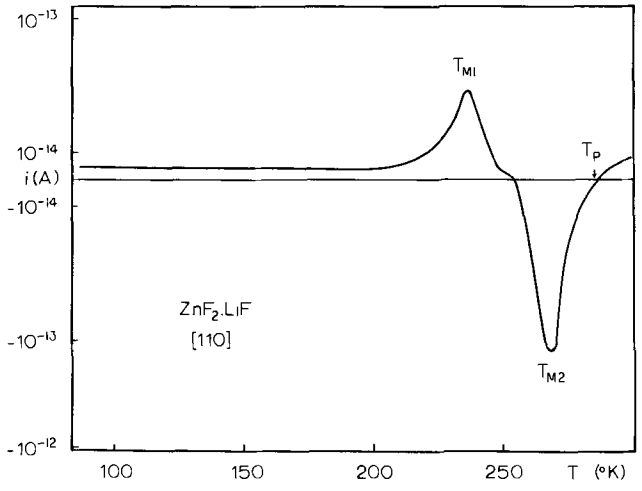

Fig. 5. Typical ionic thermoconductivity discharge current in lithium-doped ZnF_2 after air-cooling from the annealing temperature.

eV which is similar to the 0.42 eV value Rossing and Coble (10) found for the dipole in CaF_2. The crystal structure of lithium-doped ZnF_2 containing both ($Li_I^{\cdot}$ — Li_{Zn}') and ($V_F^{\cdot}$ — O_F') dipoles is illustrated in Fig. 6.

The magnitude of the second discharge peak was similar, *i.e.*, the same order of magnitude, for each of the three orientations studied implying that the movement of vacancies in each of the three directions occurred with equal ease. Referring back to the current discharge peaks observed at 236.5°K in Fig. 2 and 5, should this relaxation result from a vacancy movement mechanism involving the ($V_F^{\cdot}$ — Li_{Zn}') dipole, the magnitude of the current discharge peak for each of the three orientations should be similar.

The higher temperature discharge, T_{m2}, of Fig. 5 is noted to exhibit a change in the sign of the current discharge. The change in sign of the current was observed for all the oxidized ZnF_2 crystals, doped and undoped. A change in the sign of the current may be achieved by inverting the crystal with respect to the electrodes between the polarizing and depolarizing stages of the test. However, no such inversion was performed to obtain these results. Until further study of the occurrence of the change in the sign of the current discharge can be undertaken, the phenomenon remains unexplained.

The number of dipolar defects determined using Eq. [3] provides additional verification that an interstitial mechanism is responsible for the current discharge peak at 236.5°K. Bucci *et al*, (8), in testing samples with different concentrations of impurity atoms, found that as the concentration of impurity atoms in the melt increased, a relatively smaller fraction of them entered into the crystal. For the relatively low concentration of lithium added to the ZnF_2, the number of dipoles should be directly proportional, and quite similar, to the number of added impurity atoms should the ($V_F^{\cdot}$ — Li_{Zn}') dipole be responsible for the relaxation since one F^- vacancy is proposed to be created for every Li^+ substituted for a Zn^{++}. Formation of the ($Li_I^{\cdot}$ — Li_{Zn}') dipole requires two Li^+ ions for each Zn^{++} replaced. The experimentally determined number of dipolar defects for the interstitial model would thus be on the order of half the number of Li^+ ions originally added to the ZnF_2. The number of dipolar defects calculated using Eq. [3] is slightly less than one-half the number of lithium ions added in the doping process, thereby, supporting the interstitial model.

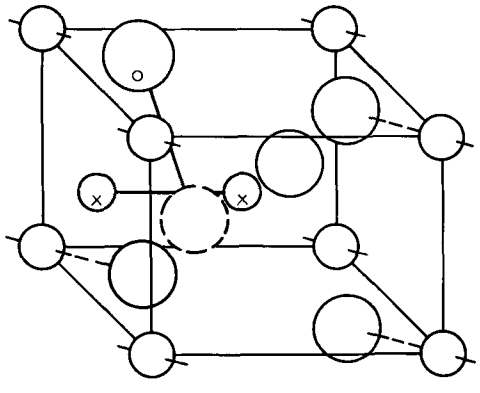

Fig. 6. Crystal structure of ZnF_2 containing both ($Li_I^{\cdot}$ — Li_{Zn}') and ($V_F^{\cdot}$ — O_F') dipoles. The larger circle, marked with an o, represents the oxygen.

In a study of the diffusion of lithium in rutile, Johnson has found the movement of the interstitial lithium ion to be extremely anisotropic (11). Diffusion was found to be several orders of magnitude faster parallel to the c-axis, *i.e.*, in the [001] direction, than diffusion perpendicular to the c-axis. Similar results would be expected for the movement of lithium in ZnF_2 with the same crystal structure and similarly sized interstices as TiO_2. Similar results were indeed found; the [001] direction in the ZnF_2 crystals was the only direction studied which gave appreciable dielectric relaxation currents, thus, strongly suggesting that the currents were the result of movement of the interstitial lithium ions.

Although the dielectric relaxation of ZnF_2:LiF as associated with interstitial ion movement has been compared to the diffusion of lithium in rutile, the comparison must be limited. The polarization of the dielectric and subsequent relaxation is due to the orientation of the dipoles uniformly distributed in the volume of the crystal. The components making up the dipole are assumed to be near neighbors and to remain associated during the polarization and relaxation processes, as indicated by the low activation energies observed for dielectric relaxation involving interstitial ions. The movement of defects considered here is limited to smaller distances than would be the case for dissociation of the dipoles and diffusion of the defects.

Manuscript submitted July 19, 1972; revised manuscript received June 4, 1973. This was Paper 94 presented at the Miami Beach, Florida, Meeting of the Society, Oct. 8-13, 1972.

Any discussion of this paper will appear in a Discussion Section to be published in the June 1974 JOURNAL.

REFERENCES

1. T. A. Roth, *J. Appl. Phys.*, **42**, 246 (1971).
2. W. L. Bragg, "Atomic Structure of Minerals," p. 103, Cornell University Press, Ithaca, N. Y. (1937).
3. N. N. Greenwood, "Ionic Crystals, Lattice Defects and Nonstoichiometry," p. 56, Butterworths, London (1968).
4. F. A. Kröger, "The Chemistry of Imperfect Crystals," p. 196, North-Holland Publishing Co., Amsterdam (1964).
5. A. S. Nowick and W. R. Heller, *Adv. in Phys.*, **14**, 101 (1965).
6. C. Bucci and R. Fieschi, *Phys. Rev. Letters*, **12**, 16 (1964).
7. C. Bucci, R. Cappelletti, R. Fieschi, G. Guidi, and L. Pirola, *Nuova Cimento* (Suppl.), **4**, 608 (1966).
8. C. Bucci, R. Fieschi, and G. Guidi, *Phys. Rev.*, **148**, 816 (1966).
9. C. Bucci and S. Riva, *J. Phys. Chem. Solids*, **26**, 363 (1965).
10. B. R. Rossing and R. L. Coble, Presented at the Annual Meeting, American Ceramic Society (1967).
11. O. W. Johnson, *Phys. Rev.*, **A 136**, 284 (1964).

Surface Oxide on Etched Aluminum

Alan W. Smith

The Boeing Company, Seattle, Washington 98124

ABSTRACT

The formation and properties of the surface oxide formed on aluminum etched in a sulfuric acid-sodium dichromate solution have been investigated using electrical impedance, electron microscopy, and contact angle measurements. The frequency dependence of the impedance measurements is shown to follow the theory of Gevers and DuPré for amorphous dielectrics. By anodizing in neutral solutions, known oxide layers are added. From this and literature data, the dielectric constant at any frequency, the roughness factor, and the thickness of the oxide layer can be estimated. From the roughness factor, a porous cell structure is derived which is confirmed by electron micrographs. From the effects of drying the oxide, the presence of a hydrous layer which has a high dielectric loss and poor wettability is indicated. Upon heating to high temperatures, the loss decreases and the surface becomes more wettable. It is shown that this hydrous layer occurs, except when the surface is polarized anodically during eching. When the surface is polarized anodically, the anodic cell structure is prominent and little or no hydrous layer forms. The addition of copper ion to the etch causes a surface layer to form as under anodic polarization.

The surface of etched aluminum displays a variability with respect to adhesive bonding and a high sensitivity to slight changes in etching conditions. In order to help explain the causes of this sensitivity, the formation and properties of the surface oxide were examined. Electrical impedance measurements as a function of frequency give one of the few ways of characterizing such thin layers. This was the principal technique used, but electron microscopy was also used to confirm certain conclusions and contact angle measurements were used to amplify the characterization of the surface.

Experimental

Unless otherwise noted, the samples examined consisted of 99.99% aluminum etched in a 300 g/liter sulfuric acid, 30 g/liter sodium dichromate solution at 65°C.

The electrical impedance was measured with a Hewlett-Packard vector impedance meter, Model 2800A. High accuracy was obtained by monitoring the output with a recording potentiometer and calibrating the meter at each frequency with precision capacitors and resistors. The low applied voltage of this instrument, 3 mV for most measurements, helped avoid errors due to electrode reactions.

Three different electrolytic cells were used. The one with the best geometry consisted of two 0.32 cm diameter aluminum wires covered with varnish except at the ends. The wires were bent so that the two ends nearly touched forming a parallel plate cell. In another cell two flat aluminum samples were separated by an O-ring filed with solution. The area of each sample exposed to the solution was 0.40 cm^2 and the samples were 0.2 cm apart. In both cases, the impedance is twice that of a single oxide layer. A one aluminum plate cell used the same O-ring which was connected to a reservoir containing a large platinum electrode. This cell was used for anodization. Concentrated solutions of potassium sulfate and potassium dichromate (adjusted to $pH = 6$) were used with little difference in results.

The results for the three cells showed only minor differences. Corrections for series resistance of the solution were substantial for the two O-ring cells but negligible for the wire cell except at the highest frequencies. This correction was made by subtracting from the measured impedance the infinite frequency extrapolated equivalent series resistance. The impedance values in the platinum electrode cell increase for a time, amounting to a small anodization of the aluminum.

Key words: aluminum, impedance, etching, wettability, oxide.

Measurements of impedance were also made by evaporating a layer of aluminum on top of the oxide layer as previously discussed (1).

The topology of the surface was examined by use of replicas. The replicas were obtained by pressing an acetone-softened, acetate-based film on the surface and peeling it off when hardened. The replica was shadowed with germanium at 45°, covered with carbon and then the acetate film was dissolved away. The carbon-germanium films were then examined in a JEM-6A electron microscope.

To make comparative measurements of wettability, contact angles of liquid drops have been used. Because of the variability of results from sample to sample (or even across some samples), simple techniques were used. A Gaertner goniometer was used to measure the contact angles of water and of 1-Bromonapthalene. Liquid drops were touched to the surface and measured immediately. On mechanically polished surfaces the results found for 1-Bromonapthalene were similar to those reported in the literature (2).

Contamination is an important consideration. It has been stated that clean metal oxides should give a zero contact angle with water (2, 3). However, it was possible here to obtain high contact angles as well as low, depending only on the etching conditions, immediately after evaporation of the rinse water. These angles did not change after hours in a clean desiccator or oven at 60°C.

Results and Discussion

Frequency dependence of electrical impedance.—The inverse specific capacitance, A/C, is given by

$$\frac{A}{C} = \frac{4\pi}{\epsilon' r} d \qquad [1]$$

where A is the apparent surface area, C is the measured capacitance, ϵ' is the dielectric constant, r is the roughness factor (ratio of true to apparent surface area), and d is the thickness of the dielectric.

Although both ϵ' and r do vary, the term $4\pi/\epsilon'$ is of the order of one and, when r is not too different from one, A/C is thus of the order of the layer thickness.

For thin surface oxide layers on aluminum, the log of the inverse specific capacitance is linear in the log of the measuring frequency. This is shown in Fig. 1. The various treatments shown in Fig. 1 will not be

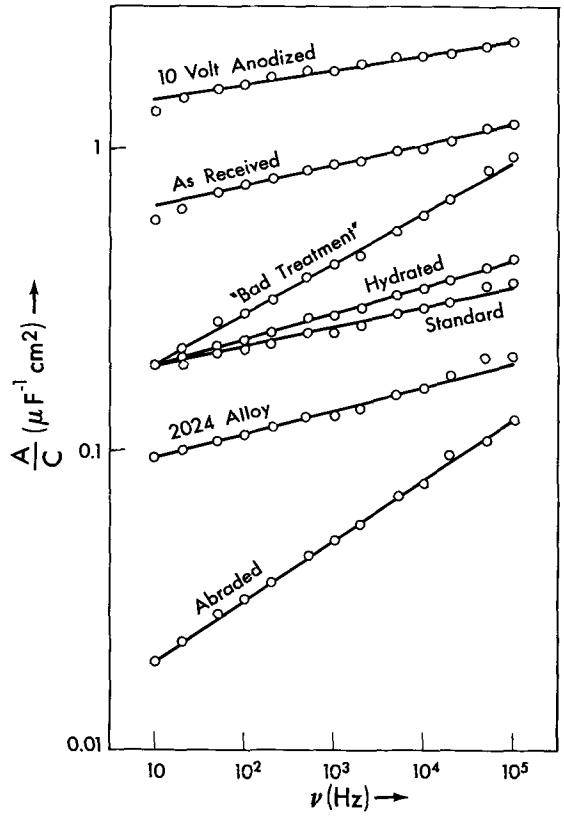

Fig. 1. Log inverse specific capacitance vs. log frequency. Two plate cell, "bad treatment" is contaminated standard etch. Hydrated is exposed to steam for 1 min.

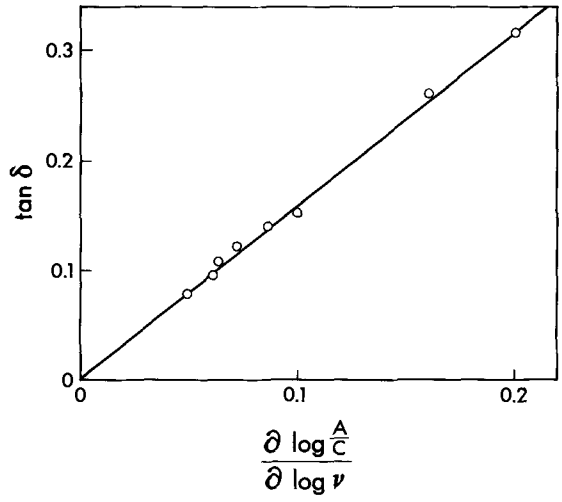

Fig. 2. Loss tangent vs. slopes of lines in Fig. 1

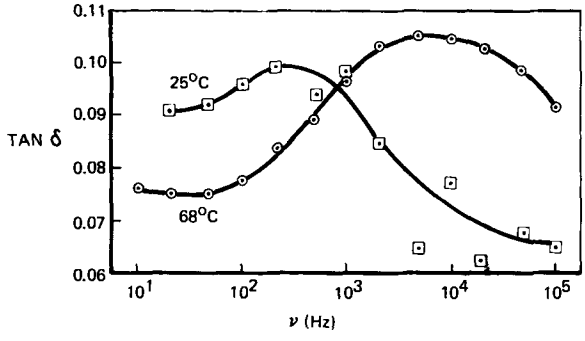

Fig. 3. Loss tangent vs. frequency, wire cell

pursued further. They are included here to show the generality of this linear relation.

The frequency dependence of the capacitance of thicker anodic films has been attributed either to a resistivity varying across the layer or to relaxation processes with a variable activation energy (4). The latter explanation is preferred here because of the good fit with a theory which is less arbitrary in nature.

Gevers and DuPré have developed expressions for the electrical impedance of amorphous dielectrics assuming relaxation processes with a broad distribution of activation energies (5). The oxide produced on aluminum at low temperatures has been held to be truly amorphous (6). Gevers and DuPré give the relationship between the dielectric constant, ϵ', and the angular frequency, ω, as

$$\frac{\partial \log \epsilon'}{\partial \log \omega} = -\frac{2}{\pi} \tan \delta \qquad [2]$$

where δ is the loss angle. In the treatment for thicker anodic layers, Eq. [2] was developed by setting ϵ'', the imaginary part of the dielectric constant, to be independent of frequency (4). The relationship shown in Fig. 1 is obtained by setting the loss tangent independent of frequency. Since the capacitance is proportional to the dielectric constant, Eq. [2] may be transformed to

$$\frac{\partial \log A/C}{\partial \log \nu} = \frac{2}{\pi} \tan \delta \qquad [3]$$

where ν is the frequency. This is precisely what is seen in Fig. 1. Figure 2 is a plot of the slopes from Fig. 1 *vs.* the loss tangent. The solid line is drawn from Eq. [3] and is a good fit to the data. The loss tangent is, in fact, fairly independent of frequency for our data whereas ϵ'' is not.

Figure 3 shows data taken with the two wire cell with care taken to get the highest accuracy. It seems that, although the loss tangent is fairly constant with frequency, there is a peak. The shift in peak with temperature is similar to previous observations on thicker layers, and is what would be expected from a relaxation process (1).

Figure 4 shows the inverse capacitance from the same set of measurements. The modest variation in loss tangent is hardly reflected in the inverse capacitance-frequency dependence. Gevers and DuPré obtained the relation

$$\frac{\partial \log \epsilon'}{\partial T} = a \tan \delta \qquad [4]$$

and also obtain a value of a from 0.04 to 0.06, nearly independent of the frequency and of the type of dielectric. The data shown in Fig. 4 gives $a = 0.05$.

It should be noted that the agreement of these results with the relations of Gevers and DuPré indicates that a variation in resistivity across the layer is not necessary. Such a variation is not precluded, however.

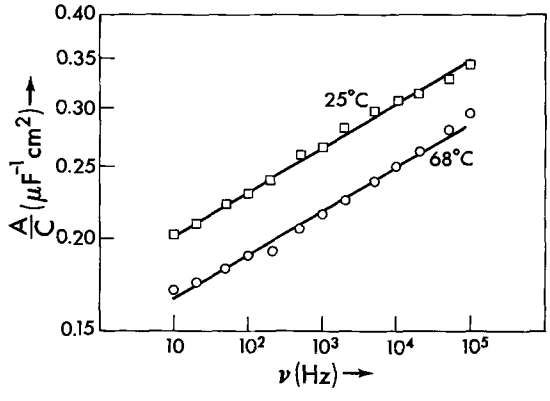

Fig. 4. Log inverse specific capacitance vs. log frequency, wire cell.

Effect of barrier layer addition.—From the large variation in dielectric constant with frequency noted above, it may be concluded that the thickness of the oxide layer cannot be learned from impedance measurements. However, more information may be obtained by adding further oxide thickness by anodization.

It has been shown that the oxide layer on the surface can be thickened to a limited amount by anodizing in nearly neutral solutions of sodium sulfate or sodium dichromate (7, 8). This thickening has been shown to be due to growth in barrier layer without the formation of porous layer seen in acidic solutions (7). If the increase in inverse capacitance with increase in voltage of anodization on a flat surface is known, then anodization on a rough surface can be used to obtain the roughness factor (9). Results in the literature on anodizing aluminum in near neutral electrolytes indicate that the oxide layer has a dielectric constant of about 9.0 and that the oxide layer thickness increases by about 12.7 Å/V of anodization potential (10-12).

For thick barrier layers the loss tangent is less than 0.01 (1, 4). It is interesting to observe the change in loss tangent as the thin etch-produced oxide is thickened. Figure 5 shows such results for two samples which differed in initial loss tangent. The inverse of the loss tangent is linear in anodization voltage and goes to zero in both cases at about −3V. The samples were anodized *vs.* a platinized platinum electrode which has been seen in some tests to approximate a hydrogen electrode when acting as a cathode. The above inverse relation has been seen in data on thicker anodic oxides (13).

If one assumes that centers of dielectric loss are formed during etching and that anodization causes little increase in their number, then the loss tangent which is averaged over the thickness will be inversely proportional to thickness. This implies that samples with zero applied voltage already have about 3V across the barrier layer. This agrees well with the work of Videm who found a value of −3.15V for the point of zero oxide thickness (14).

Since the loss tangent decreases steadily with anodization, we might expect the slope of log A/C *vs.* log ν to decrease steadily. In Fig. 6 we have divided A/C by $V + 3$ where V is the anodizing voltage. This normalizes the inverse capacitance with respect to thickness. Not only does the slope decrease with anodizing voltage but the lines converge at about 10^7 Hz. It can be assumed that the relaxation processes cease to be important at some high frequency. Here the inverse capacitance would become frequency independent. Not knowing the inverse capacitance curve at all frequencies until it becomes flat, one could not calculate the dielectric constant at lower frequencies. However,

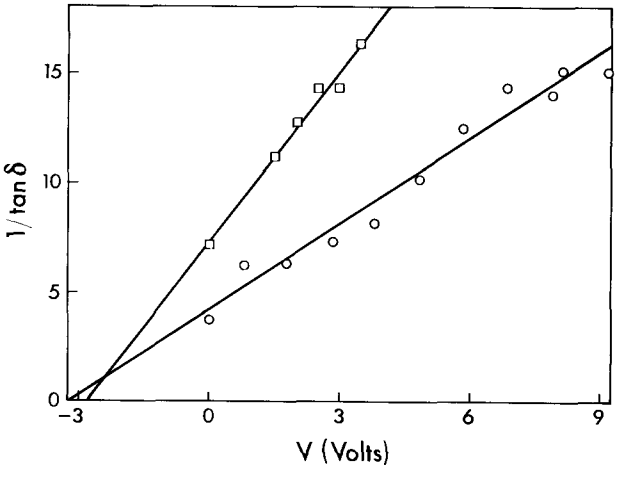

Fig. 5. Inverse loss tangent *vs.* anodizing voltage. ○, 10% $Na_2Cr_2O_7$ (*p*H-6); □, 5% K_2SO_4.

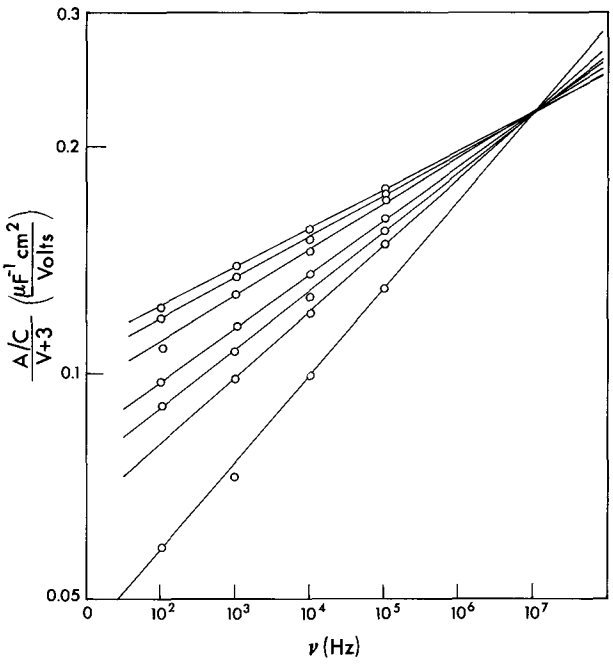

Fig. 6. Log inverse specific capacitance divided by anodizing voltage plus three volts *vs.* log frequency. The lines (going from bottom to top) refer to anodization voltages of: 0, 0.8, 1.8, 2.8, 4.8, 6.9, and 9.2V respectively.

if the shape of the curves of all samples is the same except for relative slope they must flatten out to reach a value equal to that given by the extrapolated line at 10^7 Hz. We may assume this value to be the value of 9 obtained for low loss anodic oxides. Equation [2] may be solved, for example at 1 kHz, to give

$$\log_{10}(\epsilon'_{1kHz}/9) = \frac{8}{\pi}\tan\delta \qquad [5]$$

Knowing the dielectric constant and using $\Delta d = 12.7$ Å/V one may obtain a roughness factor. This has been done for the data shown in Fig. 6 and a roughness factor of 0.74 obtained. Although these surfaces are rather flat, a roughness of less than one is impossible. However, the results are real, the low value of r coming from the fact that this etch produces a porous oxide like a porous anodic treatment would. Anodizing in a neutral electrolyte merely increases the thickness of the oxide at the base of the pores. If the oxide between the pores is considerably thicker, the area obtained from the anodization experiment will be simply that of the pores. When the oxide was removed by a one minute dip in cold 10% HNO_3 + 10% HF (by volume) only a thin barrier layer oxide remained. After anodizing this surface and making the same calculations, a roughness factor of 1.1 was obtained. Electron micrographs showing the presence of a porous cell structure will be given later.

The thickness that is obtained by impedance measurements can only refer to the thickness of the oxide at the pore bottoms. The fact that the samples with zero applied volage to a platinum electrode have about 3V across the oxide layer gives a thickness of about 38Å. Freshly etched samples have somewhat thinner layers.

Effect of drying.—The thickness of the oxide obtained by impedance measurements varied from sample to sample and more so if the samples were allowed to dry before impedance measurements. Figure 7 shows inverse capacitance of samples before and after drying. Not only is there an increase in inverse capacitance on drying but also an increase in loss tangent except at low frequencies. The curvature of the line for the undried sample at low frequencies indicates some leakage

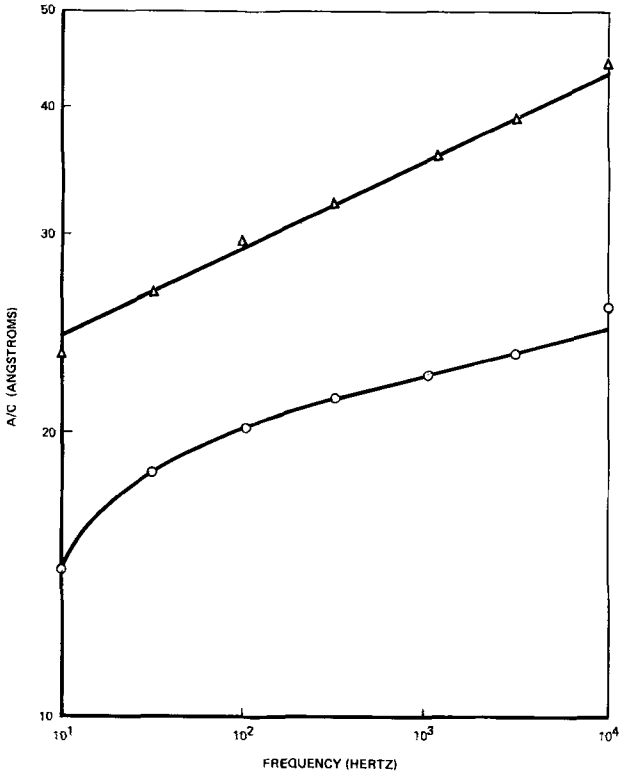

Fig. 7. Inverse specific capacitance vs. frequency. ○, sample not dried; △, sample dried overnight.

across the barrier layer. The imperfections causing this disappear after drying, giving the nearly straight line as is usually observed.

The increase in specific capacitance on drying is not held to be due to oxidation of the surface at this temperature. Rather it is held to be due to changes in an outer layer rendering it less permeable to the solution. A highly permeable oxide layer would not be noticed by impedance measurements.

A further means of probing the total thickness of the oxide is to evaporate aluminum on the surface and to measure the impedance of this capacitor. Initial attempts gave low resistive impedances. Concluding that aluminum was evaporating into pores or cracks, an evaporation angle of 45° was chosen. Low loss samples were obtained in most cases. Eight values of A/C scattered between 340 and 1300 Å were obtained.

Thus the total thickness of these oxides are more than an order of magnitude thicker than the barrier layer observed in electrolytic solutions and they are quite variable in thickness. This will be discussed more later.

When samples dried in air were heated, the loss tangent decreased. This is shown in Fig. 8. This decrease is believed to be due to the loss of moisture which is the source of much, if not all, the dielectric loss. Figure 9 shows how the inverse capacitance changes with drying at elevated temperatures. In concurrence with the results for anodic layers, there is a convergence at about 10^7 Hz for the lower temperatures. These results are interpreted to indicate that the oxide dried out but did not grow in thickness up to 262°C, but that a thickening did occur at 325°C.

Another measurement that was made during the drying studies was the contact angle of liquids on the surface. Figure 10 shows the effect of drying to higher temperatures. The same treatment which caused the loss tangent to decrease also causes the wettability to increase, giving lower contact angles for water. Great care was taken in these samples to avoid contamination.

Effect of potential during etch.—One of the most likely sources of variability in an etch is the potential

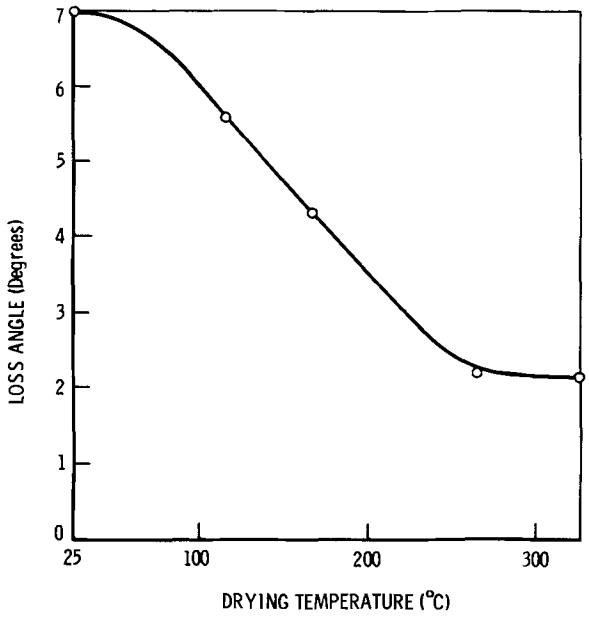

Fig. 8. Dielectric loss angle vs. drying temperature (22 hr at temperature).

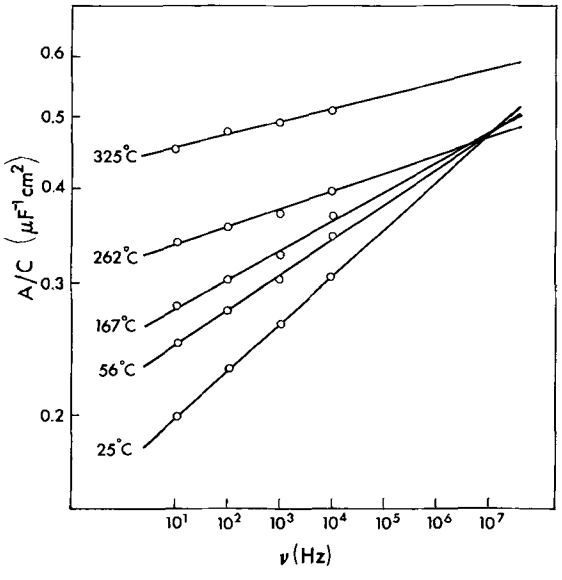

Fig. 9. Log inverse specific capacitance vs. frequency, samples heated one day to temperatures indicated.

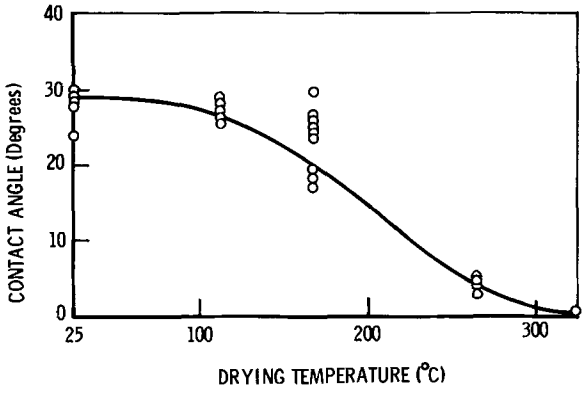

Fig. 10. Contact angles for water on samples etched in "used" solution vs. drying time (22 hr at temperature).

of the surface. When the potential is not controlled, the surface will reach a potential where the cathodic and anodic reactions have equal rates. On any specific

area, due to small chemical differences in the solution or in the metal, either the anodic or cathodic reactions may predominate. In an anodic area, the solution becomes more acidic and positive ions are drawn away from the surface. In a cathodic area, the opposite is true. For these reasons, it should be interesting to etch the surface under controlled potential.

Figure 11 shows the increase in inverse capacitance on drying as a function of the potential applied during etching. It seems clear that the layer noticeable after drying occurs when the surface becomes cathodic, rather than anodic. On a surface with more cathodic than anodic reaction, the aluminum ions formed tend to be held near the surface and because of the increased pH caused by the cathodic reaction, have more tendency to precipitate as a hydroxide or hydrous oxide. Note that this outer hydrous layer is still being formed when the net reaction is neither cathodic or anodic. The inverse capacitance of one anodic sample, measured using the evaporated electrode technique was 210Å, which was smaller than any nonanodic sample.

Contact angle measurements show the same trend. Figure 12 shows that the contact angle is low when the surface is anodic and high when it is cathodic. This was confirmed by a strong adhesion of electron microscope replica films to the anodic sample but not to the neutral or cathodic sample.

The above discussions can be clarified by actual examination of the surface by electron microscopy. Figures 13-15 show the appearance of the surface etched under different applied potentials. The porous

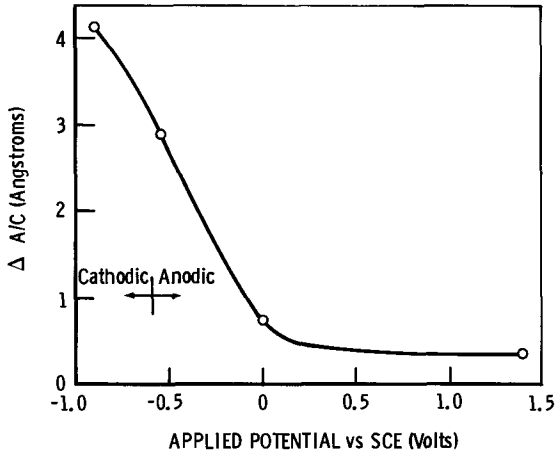

Fig. 11. Change in inverse specific capacitance (at 3.16 kHz) of samples dried in oven at 60° vs. potential applied to sample during etching.

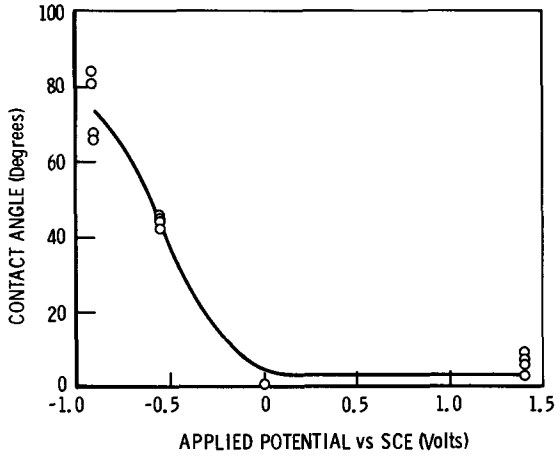

Fig. 12. Contact angles for water on samples dried in oven at 60°C vs. potential applied during etching.

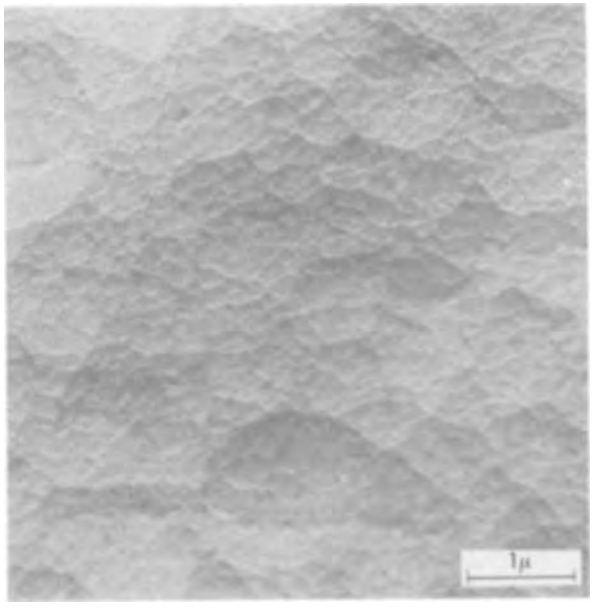

Fig. 13. Electron micrograph of surface etched with no applied potential.

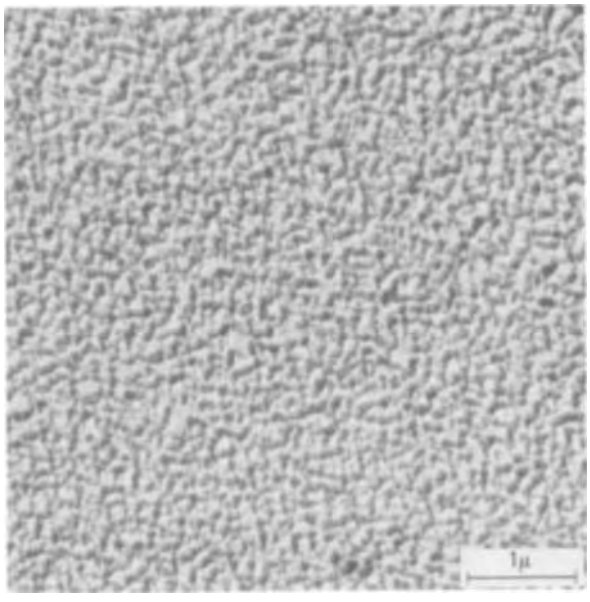

Fig. 14. Electron micrograph of surface etched with + 1.9V vs. SCE applied.

cell structure postulated in the first section of this paper is clearly evident with an anodic polarization during etching. When there is no applied potential, the cell structure is absent. It is presumed to be hidden by the hydrous layer. There is some structure present which appears similar to that characterized as a pseudo subgrain structure (15). This structure is absent in the anodic polarization which is actually a mild electropolish, the anodic surface being noticeably shinier than the others.

The cathodic surface shows some pores or pits which differ from the anodic cell structure. It is possible that these are due to the release of hydrogen from the surface. Although the normal cathodic reaction is the reduction of dichromate ion, hydrogen bubbling is seen on cathodic surfaces and when the oxide layer is thick.

Effect of copper.—An effect that has been shown earlier but not discussed, is the effect of impurity ions. It has long been known by practical etchers that a solution is apt to give unreliable surfaces until it has been used for a while. Copper ion was chosen for the

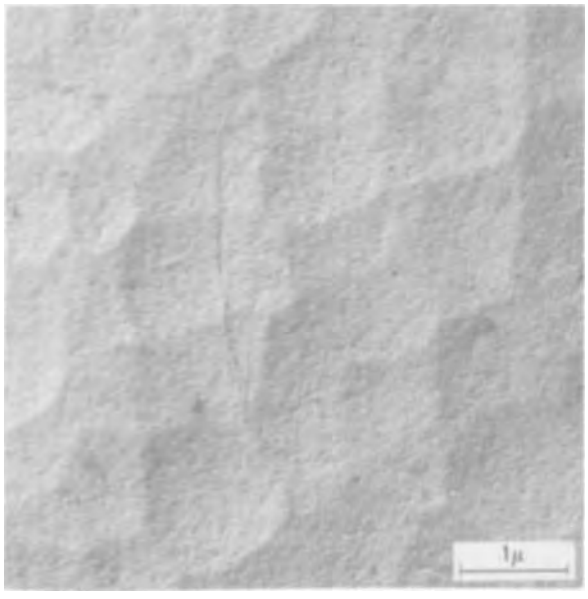

Fig. 15. Electron micrograph of surface etched with —1.0V vs. SCE applied.

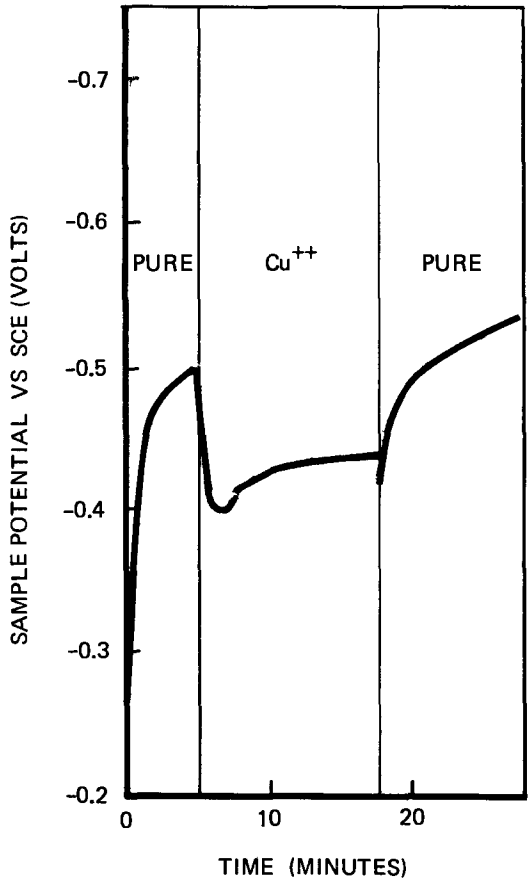

Fig 16. Sample potential vs. time in FPL etch with addition of 1.6×10^{-2}M cupric sulfate.

present study since it is an easily reducible ion which might be expected to catalyze the cathodic reaction. Copper ions increase the etch rate by a factor of 2 for 1.6×10^{-2}M copper sulfate. The anodic reaction, metal dissolution, is limited by the rate of the cathodic reaction. Figure 16 shows that the surface potential becomes more positive when copper is added to the solution.

Figure 17 shows how the inverse capacitance changes as a function of copper ion concentration. Both the

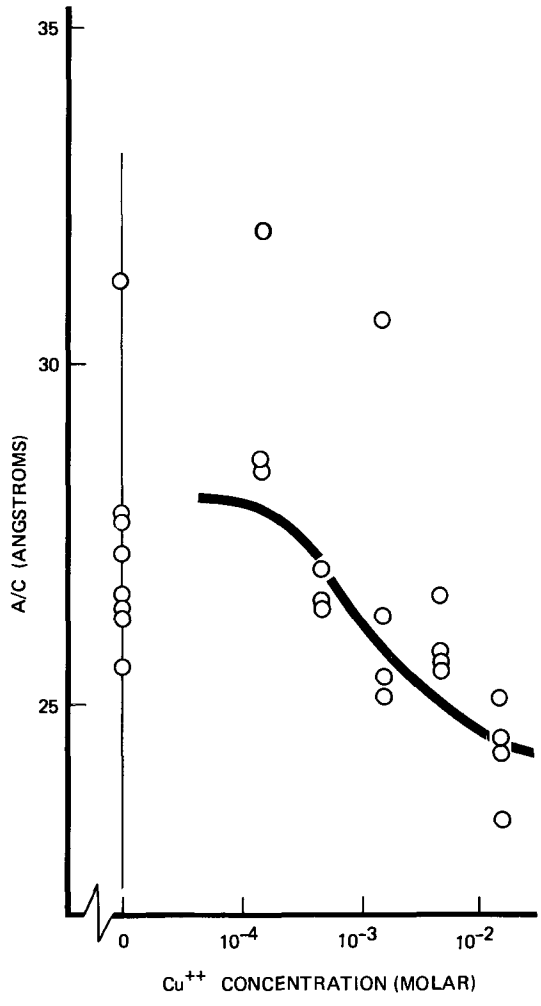

Fig. 17. Inverse specific capacitance (at 3.16 kHz) of samples dried in oven at 60°C vs. concentration of cupric ions in etchant.

average value of the inverse capacitance and the spread in the values decreases as the copper ion concentration is increased.

The increase in inverse capacitance shown by drying is more marked if the sample is heated in water vapor which tends to seal the oxide. Figure 18 shows the results of a study of rinse time using this sealing technique. There was no effect of rinsing within these limits. However, the high, variable values of the inverse capacitance obtained with a pure etchant are in sharp contrast to the low, nearly constant values obtained with a copper containing etchant.

In other regards, the addition of copper ions gives the same effects as anodic polarization. Figure 19 is an electron micrograph of a surface etched in a copper containing solution. The porous cell structure is quite obvious.

Figure 20 shows the effect of copper ion concentration on the contact angle. This is again similar to an anodic potential.

It is believed that copper ion actually deposits out on the surface providing local copper cathodes while the rest of the surface becomes anodic. At copper concentrations above that used here, a definite copper hue is given to parts of the surface by the etchant treatment. The surface examined in Fig. 19 looked uniform under the electron microscope but only a tiny fraction of the surface was examined. Alloys' surfaces have been examined which showed areas with and areas without the porous cell structure.

Manuscript submitted Dec. 11, 1972; revised manuscript received April 16, 1973.

Any discussion of this paper will appear in a Discussion Section to be published in the June 1974 JOURNAL.

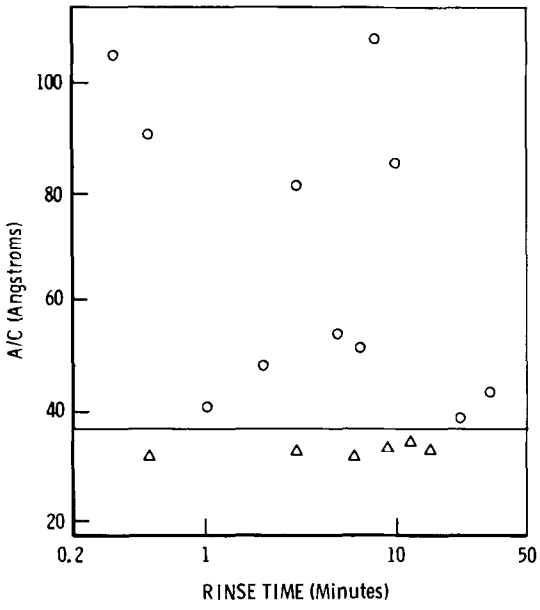

Fig. 18. Inverse specific capacitance (at 3.16 kHz) of samples exposed to saturated water vapor at 60°C for 20 min vs. time of rinse after etch. ○, pure etchant; △, etchant containing 8 x 10^{-3}M cupric sulfate.

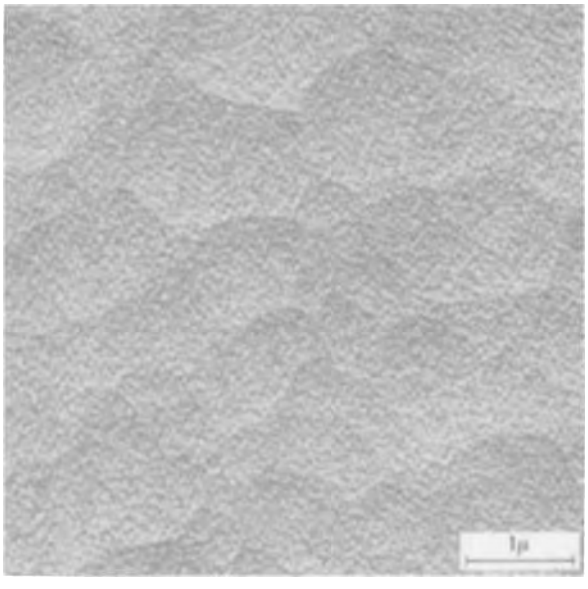

Fig. 19. Electron micrograph of surface etched in solution containing 8 x 10^{-2}M cupric sulfate.

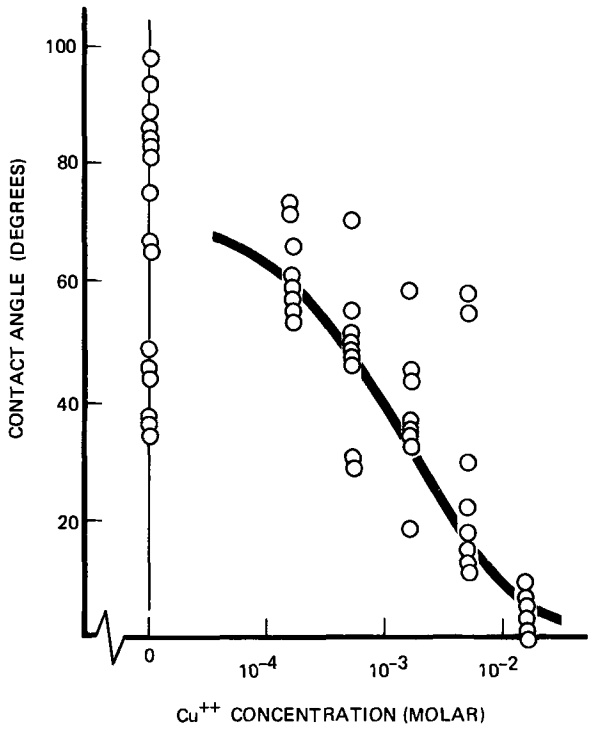

Fig. 20. Contact angle for water on samples dried in oven at 60°C vs. concentration of cupric ions in solution.

REFERENCES

1. S. H. A. Begemann and A. W. Smith, *This Journal*, **117**, 1440 (1970).
2. M. K. Bennett and W. A. Zisman, "Effect of Adsorbed Water on the Critical Surface Tension on Metal Surfaces," Naval Research Lab., Report 6727, June 1968, AD 673396.
3. R. E. Johnson and R. Dettre, in "Surface and Colloid Science," Vol. II, p. 85, Wiley-Interscience, New York (1969).
4. Young, "Anodic Oxide Films," Academic Press, New York (1961).
5. M. Gevers and F. K. DuPré, *Trans. Faraday, Soc.*, **42**, 47 (1946).
6. F. P. Fehlner and N. F. Mott, *Oxidation of Metals*, **2**, 59 (1970).
7. G. C. Wood and J. P. O'Sullivan, *Electrochim. Acta.*, **15**, 1865 (1970).
8. M. A. Heine and M. J. Pryor, *This Journal*, **114**, 1001 (1967).
9. R. C. Plumb, *ibid.*, **105**, 509 (1958).
10. A. C. Harkness and L. Young, *Can. J. Chem.*, **44**, 2409 (1966).
11. W. J. Bernard and J. W. Cook, *This Journal*, **106**, 643 (1959).
12. W. Ch. Van. Geel and B. J. J. Shelen, *Philips Res. Rept.*, **12**, 240 (1957).
13. W. Ch. Van. Geel and J. W. A. Scholte, *ibid.*, **6**, 54 (1951).
14. K. Videm, "Proc. Third Intern. Cong. on Met. Corr.," Vol. 1, p. 521, MIR, Moscow (1969).
15. M. Gy. Hollo, in "First Annual Congress on Metallic Corrosion," p. 45, Butterworths, London (1962).

Growth of GaP Layers from Thin Aliquot Melts: Liquid Phase Epitaxy as a Commercial Process

A. A. Bergh, R. H. Saul, and C. R. Paola

Bell Laboratories, Murray Hill, New Jersey 07974

ABSTRACT

The highest electroluminescent device performance in most III-V semiconductor materials was obtained on thin layers grown by liquid phase epitaxy (LPE). LPE has not been developed, however, as a commercial process. From a comparison of the factors affecting layer quality and process economy, it is concluded that a commercial LPE process favors the use of thin melts (possibly discarded after deposition), should provide substrate protection prior to deposition, and should be able to terminate LPE growth. A system has been designed in which a large volume of a saturated melt is sectioned into many small but equal thin melts (aliquot) for each substrate. The key to forming aliquots is wetting the substrate by the large volume of the melt in an apparatus constructed of nonwetted materials. The application of the above concepts to a multislice operation is described. Gallium phosphide LPE layers were grown in a single slice aliquot system from melts of 0.5-12 mm in thickness at cooling rates of 0.6°-6°C/min. Constitutional supercooling had no effect on the surface quality of the grown layers. The layers were degraded, however, if the substrates were thermally etched prior to deposition. High deposition efficiency and excellent thickness control were obtained for layers grown from thin melts. The deposition efficiency for layers grown from thick melts is limited by diffusion controlled mass transport in the melt. The diffusion coefficient of P in Ga has been evaluated at ~1000°C and no spontaneous nucleation was observed in melts supercooled by less than approximately 15°C.

The first commercial application of liquid phase epitaxy (LPE) in the semiconductor industry was the manufacture of germanium alloy junction transistors (1). Since this process required the LPE growth on each individual device, it could not compete economically with gas phase epitaxy or diffusion used in batch processing over the entire semiconductor wafer. The interest in LPE was revived with the successful utilization of this process for III-V semiconductors. Some high performance devices could be achieved only through the application of this method. Two outstanding examples are GaP LED's (2, 3) and heterostructure GaAs, GaAlAs lasers (4). Other device applications are discussed in a recent review article (5).

The quest for improved device performance, increased yield, and the requirements for batch processing have placed increased demands on the LPE technology. Higher quality material is demanded at lower cost. The purpose of this paper is to show, using GaP LED material as an example, that both requirements can be met simultaneously.

Requirements for GaP LED Material

To produce p-n junctions in GaP with high electroluminescent efficiency, two consecutive LPE layers must be grown, each approximately 25μ thick. Layer growth is accomplished by the depletion of a saturated Ga melt; the dopants are introduced into the melt prior to deposition.

High-quality devices impose the following material requirements: (*i*) uniform distribution of dopants in the plane of the junction with only a limited variation in the doping level perpendicular to the junction; (*ii*) precise thickness control and junction planarity over large-area substrates (usually over an inch in diameter); and (*iii*) smooth surface morphology to meet the requirements of subsequent device processing.

Economic considerations of a commercial LPE technology, on the other hand, ask for (*i*) small quantities of starting materials, (*ii*) short throughput time, *i.e.*, large production capacity, and (*iii*) reproducibility to achieve high production yields.

Key words: crystal growth, light emitting diodes, gallium phosphide.

Doping Uniformity

The uniform distribution of dopants in the plane of the junction requires that the dopants are evenly distributed in the melt. The distribution of dopants perpendicular to the junction plane is affected by the change in distribution coefficients with decreasing temperature during LPE growth (6), and by the loss of volatile dopants. The temperature dependence of the distribution coefficients of two commonly used dopants, Zn (p-type) (7) and Te (n-type) (8) have been determined. The solid solubility of Zn decreases, while that of Te increases as LPE growth proceeds. Combining this information with the Ga-GaP liquidus data (9), the variation of the net carrier concentration is obtained in the growth direction, as shown in Fig. 1. Following a relatively small change over the first two thirds of deposition, the Zn concentration drops sharply, while the concentration of Te rises abruptly at the end of deposition. This affects the concentration

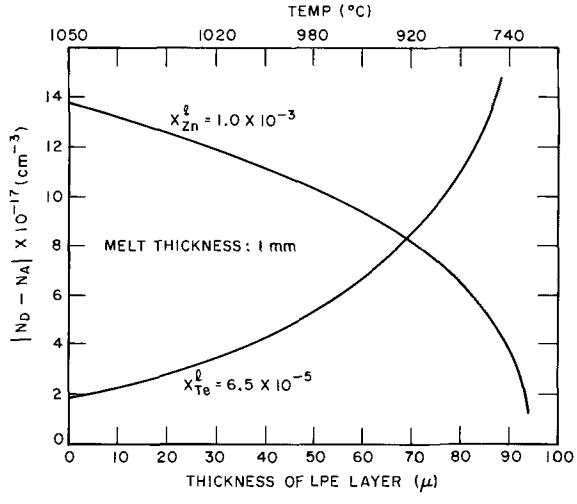

Fig. 1. Variation of the net carrier concentration perpendicular to the plane of the p-n junction in GaP layers grown from Zn- or Te-doped melts assuming 100% deposition efficiency.

of dopants at the p-n junction and/or at the surface where ohmic contacts are applied. Large changes in doping level can have a deleterious effect on both the efficiency of the junctions and on the properties of the ohmic contacts. This condition therefore must be avoided by terminating the LPE deposition after the depletion of approximately 50-75% of the melt or it must be corrected by removing part of the LPE layers after deposition. To avoid extra processing steps and the inherent risk of introducing damage and contamination during the material removal steps, it is desirable to design the LPE apparatus to terminate the growth.

Thickness Control and Planarity: Quality of LPE Layers

Although the Ga-GaP liquidus curve is well known, the fraction of the supersaturated GaP which deposits on the substrate during LPE is usually unpredictable. The uncertainty in the deposition efficiency, ζ, can be attributed to the slow transport of phosphorous atoms to the substrate and the loss of phosphorous atoms from the melt due to spontaneous nucleation and growth from the melt resulting from constitutional supercooling. (Deposition efficiency, ζ, is defined as the ratio of GaP deposited onto the substrate to the amount computed from the Ga-GaP liquidus curve.) To consider the transport of phosphorous atoms to the substrate, it is assumed that the cross-sectional area of the melt is equal to that of the area of the substrate exposed to the melt. It is also assumed that no convection occurs in the melt during LPE growth.

Two types of transport phenomena may in general be considered (10) for deposition: the transfer of heat away from the melt, and the diffusion of phosphorous atoms from the melt to the substrate. The relative transport rates can be assessed by comparing the values of thermal diffusivity of Ga ($\alpha \sim 10^{-1}$ cm^2/sec) and diffusion coefficient of P in Ga ($D \sim 10^{-5}$ cm^2/sec). The value of thermal diffusivity is higher by approximately four orders of magnitude, and hence mass transport and not heat flow limits the rate of LPE deposition under most LPE growth conditions. As a first approximation, we assume that the melt is isothermal and that the temperature is abruptly lowered from the initial to the final value. Rode has given an analytical treatment of the P concentration gradient for arbitrary cooling rates and a temperature-dependent P diffusion coefficient in the absence of convection (11). The concentration gradient in the melt for abrupt cooling can be described by the following equation (12)

$$\frac{C}{C_o} = \frac{4}{\pi} \sum_{n=0}^{\infty} \frac{1}{(2n+1)} \exp\left[-D(2n+1)^2\pi^2 t/w^2\right] \sin\frac{(2n+1)\pi x}{w} \quad [1]$$

where C is the concentration of phosphorous atoms at distance x from the substrate toward the melt in excess of the equilibrium value. The initial concentration of excess phosphorus in the isothermal melt of thickness w is C_o, and the LPE deposition proceeds over time t. Some numerical values for this problem are given in Ref. (12) and are reproduced in Fig. 2. The substrate is at $x/w = 0$ and parallel to the ordinate. The numbers on the plotted curves are the values of Dt/w^2. Taking $D = 2.6 \times 10^{-5}$ cm^2 sec^{-1} for P in molten Ga, a value which fits best our experimental data (see section on Deposition Efficiency), the distribution of phosphorous atoms in the melt after 30 min of deposition is given by curves 1.5, 0.3, 0.1, and 0.03 for melt thicknesses of 1.8, 3.9, 6.8, and 12.5 mm, respectively. While over 90% of the 1.8-mm melt is depleted, only approximately 20% of the phosphorus is depleted from the 12.5-mm thick melt. Increasing the deposition time to 3 hr ($Dt/w^2 = 0.18$) still results only in approximately 50% deposition efficiency.

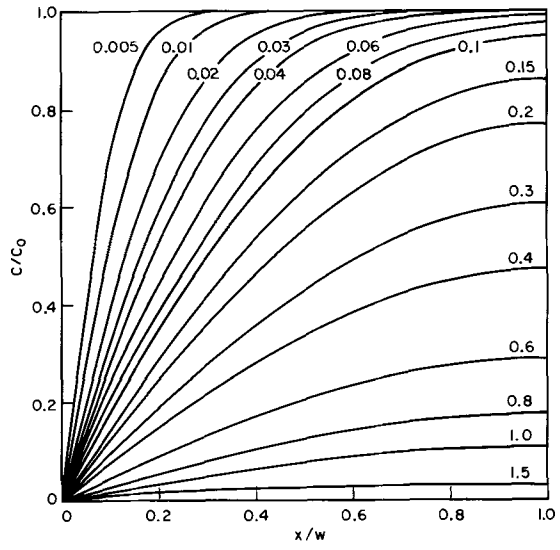

Fig. 2. Computed values of phosphorous concentration in the melt during LPE deposition assuming an instantaneous temperature drop in the near isothermal melt and the absence of spontaneous nucleation in the melt. The numbers on the curves are the values of Dt/w^2.

Although the above calculations give optimistic values for some practical LPE conditions (the available phosphorous atoms are reduced by spurious nucleation in the supersaturated melt and cooling is accomplished over a finite time, reducing the effective value of C_o in Eq. [1]), they clearly point out the importance of using thin melts to obtain high deposition efficiency.

Tiller and Kang (13) and later Minden (14) mathematically treated the effect of cooling rate and melt thickness on the minimum temperature gradient perpendicular to the substrate required to avoid constitutional supercooling. Table I shows the minimum temperature gradients calculated for typical GaP LPE conditions from Eq. [26c] of Minden's paper (14). It is assumed that a 20μ thick LPE layer is to be grown in 30 min. Cooling rates and temperature ranges for deposition (ΔT) are adjusted accordingly. In terms of the required temperature drop across the melt, the 0.5-mm melt is the most favorable. In fact, for layer thicknesses exceeding 4 mm, the required temperature drop across the melt is greater than the total cooling interval, indicating that supercooling cannot be avoided in LPE runs using thick melts and fast cooling. Since the degree of supercooling and hence the onset of spontaneous nucleation in the melt can be expected to change with the experimental conditions, a high degree of thickness control can be expected only for layers grown from thin melts if the melt is to be substantially depleted.

Economic Considerations

Economic considerations also favor thin melts. One of the major expenses in a conventional LPE process

Table I. Minimum temperature gradient (dT/dx) required across the melt of thickness w at the end of deposition to avoid constitutional supercooling. Computed from Eq. [26c], Ref. (10)

Total cooling time = 30 min
LPE layer thickness = 20μ
Initial temperature, T_i = 1040°C
Temperature range, $\Delta T = T - T_f$
(T_f = temperature of substrate at the end of deposition)

w, mm	ΔT, °C	Depletion of melt, %	Cooling rate, °C/min	dT/dx, °C/mm
0.5	108	67	3.6	6.0
1	40	33	1.3	4.5
2	18	17	0.6	4.1
4	8	8	0.3	2.9
12	3	3	0.1	1.1

is the large amount of starting materials. This expense can be recovered by the extensive reuse of the melt, placing stringent requirements, however, on the apparatus and ultraclean operating conditions. The reduction of the melt thickness, on the other hand, greatly reduces the cost of the starting material, and hence both layer quality and process economy favor the use of thin melts.

LPE Apparatus

The use of thin melts to grow III-V semiconductor layers has been suggested before. Donahue and Minden (15) proposed, for example, a limited volume boat, as shown in Fig. 3. Since the spacing between the substrate holder and the crucible wall was not wetted by Ga during the rotation of the boat, the minimum melt thickness obtainable was ~3 mm. We have achieved much smaller melt thicknesses by using surfaces wetted by Ga. Since the formation of very small volumes of melt is not practical, a large volume of saturated melt is divided into small but equal fractions (aliquot) using two sliders. The thin melt can be discarded after the LPE growth.

The parts of the apparatus are shown in Fig. 4. A melt reservoir is held in the frame with cover plates to seal the top of the frame. Two sliders are positioned into the frame, moving underneath the reservoir and cover plate from left to right. Slider 2 contains the substrate and the dump well used in the removal of the aliquot from the substrate when the growth is terminated. Slider 1 has an opening slightly larger than the substrate and is used to form the aliquot. Both sliders are aligned under the reservoir and simultaneously translated from left to right to form the aliquot.

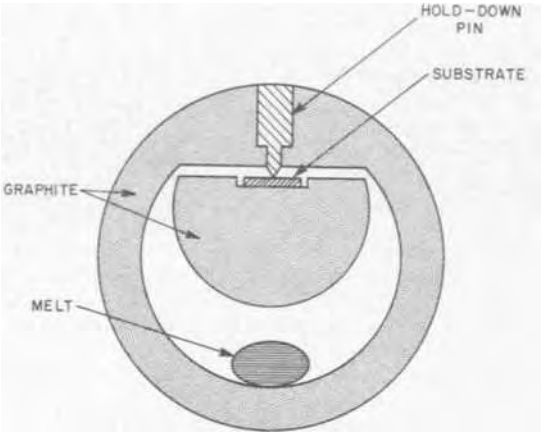

Fig. 3. Transverse cross section of a limited volume boat proposed by Donahue and Minden (15).

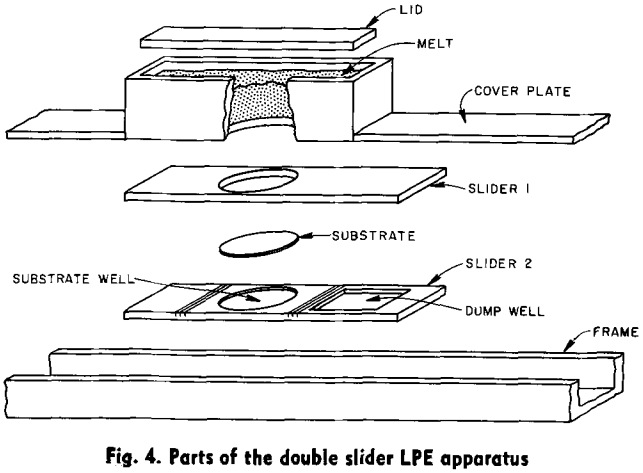

Fig. 4. Parts of the double slider LPE apparatus

Table II. Effect of the gaseous ambient on the contact angle (degrees) of gallium on various surfaces at two temperatures (750°/1000°C)

Surface	Ambient: Hydrogen	Ambient: Nitrogen (containing 5 ppm O_2)
GaP	110/60	100/60
Graphite	130/120	98/50
Quartz-smooth	125/100	90/90
Quartz-rough	110/100	98/60

Formation of Aliquot and Termination of LPE Growth

In order to form a thin aliquot, the liquid must be in contact with a surface which is wetted by the liquid. On the other hand, the removal of the melt must be accomplished with a surface which is not wetted, to avoid the formation of a film between two wetted surfaces. The wetting of GaP and various structural materials by molten gallium were determined from linear cross sections of Ga droplets (16). The contact angles are listed in Table II for two temperatures, 750° and 1000°C. The gaseous ambient in the furnace was changed from reducing (hydrogen) to slightly oxidizing (nitrogen + 5 ppm O_2). The GaP surfaces were wetted ($\theta < 90°$) at the higher temperatures in both ambients. None of the structural materials was wetted in the reducing ambient; however, the contact angles decreased in the oxidizing ambient, especially for graphite. This change in wetting is probably caused by the formation of Ga_2O_3 on the liquid which is then deposited over the adjacent surfaces. It can be expected, therefore, that a reducing ambient facilitates the termination of the deposition.

The essential features of aliquot formation are shown in Fig. 5. First the substrate is lined up with the saturated melt in the reservoir, (a). Note that the GaP is wetted by the liquid gallium, while the other parts of the apparatus are not.

The aliquot is formed by the simultaneous movement of the two sliders past the reservoir, (b). Since the liquid wets the entire GaP surface, melts of 0.5 mm can be formed reproducibly. After the deposition of the LPE layer, the growth is terminated by wiping the melt into the dump well, as shown in Fig. 5(c). Since the graphite is not wetted by the melt (in reducing ambients), complete wiping can be obtained with a clearance of less than 75μ between the grown LPE layer and the bottom of slider 1.

Multislice LPE Operation

The essential features of the system described so far are: (i) the formation of aliquots for each sub-

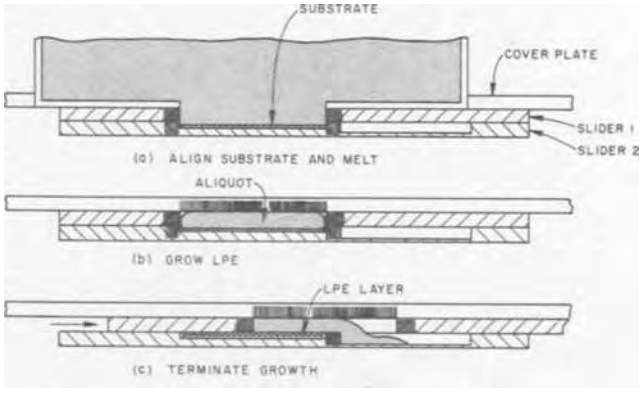

Fig. 5. The substrate is exposed to the saturated melt (a). A small but equal fraction (aliquot) is confined over the substrate during LPE growth (b). The melt is wiped off to terminate LPE growth by the relative movement of the sliders (c).

strate using the wetting of GaP by molten Ga, (*ii*) LPE deposition from thin, confined melts (aliquots), and (*iii*) the ability to terminate LPE growth. There are many ways to incorporate the above principles into a production system. Aliquots can be formed sequentially or simultaneously. LPE deposition can be carried out in a single temperature zone which is cycled or in a lower temperature zone of the same furnace in which the saturated melt is formed. In principle, a variety of forces (mechanical, gravitational, pneumatic, or centrifugal) can be applied to remove the aliquot melts upon the termination of growth.

Figure 6 demonstrates the operational steps for a multislice LPE deposition. Each slider pair contains one substrate and one dump well. After the saturated melt is formed (a), the slider pairs are moved along to sequentially form the desired number of aliquots (b) and (c). After LPE deposition is accomplished, the sliders on the top are moved to wipe off the aliquots, thereby terminating the growth (d). LPE deposition can be carried out simultaneously in a single zone furnace or sequentially in a multizone furnace.

The experiments described in the following sections were carried out with only one pair of sliders using quartz or graphite apparatus. A conventional diffusion furnace with a 24-in. flat zone was modified to provide constant cooling rates. This was accomplished by inserting a Eurotherm variable emf ramp generator in series with the primary thermocouple. Only one aliquot was formed from a saturated melt at 1030°C. In a typical run, the furnace temperature was lowered by 10°-100°C, the LPE growth was terminated, and the substrate was removed from the furnace. After inserting a new substrate, the furnace again was equilibrated at 1030°C and the growth sequence repeated. The layers were grown on the P{111}-face of chemically polished GaP substrates grown by the liquid encapsulation Czochralski method (17). The cross-sectional areas of the substrates and aliquot melts were approximately 6 cm^2.

Deposition Efficiency

The control of layer thickness requires tight control over the precipitation of GaP from the melt. Two factors will influence the effective deposition efficiency: (*i*) the degree of supersaturation in the melt, and (*ii*) precipitation at places other than the substrate. Under normal growth conditions, spontaneous nucleation is expected to reduce the concentration of phosphorous atoms in the melt, and hence the effect of cooling rate on layer thickness will be smaller than anticipated.

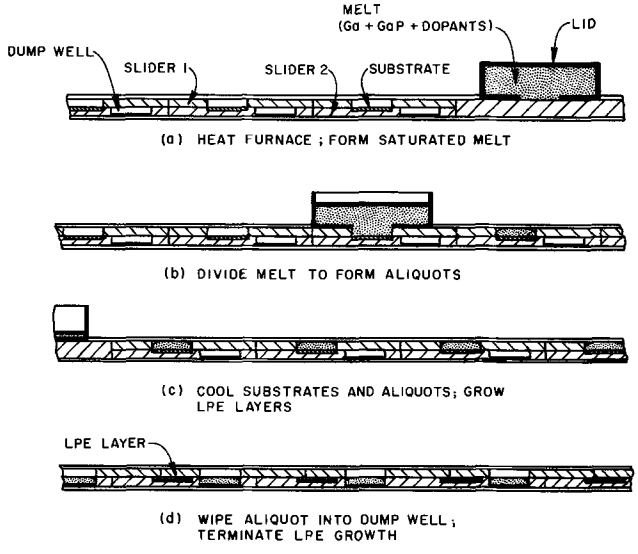

Fig. 6. Multislice LPE deposition in a double slider aliquot LPE apparatus. (a) A large volume of the saturated melt is prepared at the initial growth temperature. (b) Small fractions of the melt (aliquots) are formed over each substrate. (c) LPE layers are deposited by cooling to a lower temperature. (d) LPE growth is terminated by wiping off the aliquots.

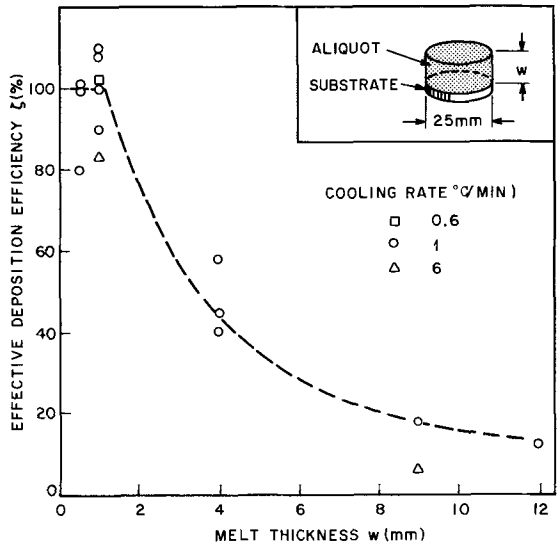

Fig. 7. The effective deposition efficiency as a function of melt thickness and cooling rate.

To evaluate the effect of melt thickness, w, on the effective deposition efficiency, ζ, a series of layers were grown, varying the thickness of slider 1 to obtain the desired values of w. Figure 7 schematically depicts the geometry of the melt and substrate used in the experiments as well as the determined values of ζ as a function of w. Each data point represents a separate run. The initial temperature was 1030°C and the temperature increments for growth were selected (see Table III) to produce layer thicknesses in the range compatible with effective wipeoff. The data in Fig. 7 show that close to 100% effective deposition efficiency is obtained for $w \leq 1$ mm. The efficiency falls off roughly as w^{-1} for increasing values of w. For a given temperature interval of growth, the thickness of the grown LPE layer is proportional to the melt thickness, w, for $w \leq 1$ mm. The decrease in efficiency with melt thickness for $w > 1$ mm results in the following paradox. Since ζ falls off as w^{-1} for thicker melts, the thickness of the grown layer is approximately independent of the melt thickness. As a consequence, the growth of thick LPE layers requires growth over wide temperature ranges or material transport from a source piece to the substrate in a thermal gradient. The values in Fig. 7 agree reasonably with the results of other LPE systems, such as tipping ($w \sim 5$ mm) (18) or dipping ($w \sim 15$ mm) (19).

Diffusion limited deposition efficiency for abruptly cooled melts can be expressed from Eq. [1] as follows

$$\zeta = 1 - \int_{x=0}^{w} \frac{C}{C_o}\, dx \qquad [2]$$

The variation of ζ as a function of the dimensionless parameter Dt/w^2 is given in Fig. 8. The experimental data in Fig. 7 are transposed into Fig. 8 by selecting a value of $D = 2.6 \times 10^{-5}$ cm^2 sec^{-1} and defining t as the cooling interval, ΔT, divided by the cooling rate. The value of D was selected to obtain best fit for the

Table III. Cooling increments used for LPE growth

Melt thickness, w (mm)	Cooling increment, ΔT (°C)
0.5	75
1.0	75
4	18
9	12
12	12

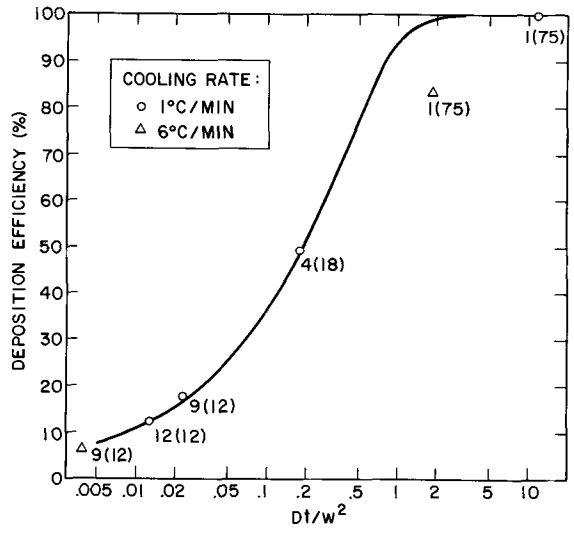

Fig. 8. Deposition efficiency as a function of the dimensionless parameter Dt/w^2. The solid curve is calculated from Eq. [2] assuming $D = 2.6 \times 10^{-5}$ cm^2 sec^{-1} and the data points are transferred from Fig. 7 as discussed in the text. The numbers adjacent to the data points denote the melt thickness in millimeters and the cooling increment in degrees centigrade, respectively.

calculated universal curve. Exact calculations of Ref. (11) for each data point indicate a time value of $D = 5.7 \times 10^{-5}$ cm^2 sec^{-1}. The numbers next to the data point indicate the respective melt thickness, w, and cooling increments, ΔT. For cooling intervals of $T \leq 12$°C, good agreement can be obtained between the experimental and calculated values by the proper selection of the diffusion constant, D, even for large values of w. The agreement is also quite good for large temperature increments ($\Delta T = 75$°C) and slow cooling. The deviation from the theoretical curve for the large ΔT and fast cooling is attributed to spontaneous nucleation in the melt. Supercooling in this experiment exceeds 15°C.

Quality and Surface Morphology of Grown Layers

Under our experimental conditions, melt thickness and cooling rate had little effect on the uniformity of the thickness of the grown layers. However, the largest taper and the only nonplanar junction was observed with the extreme conditions of thick melt ($w = 9$ mm) and high cooling rate (6°C/min). For all other cases, the variation in layer thickness was less than ±10%, reaching values as low as ±3% across the 2.5-cm substrate diameter. Constitutional supercooling, present in the thick melts, had been shown to have little effect on the surface morphology (20), contrary to previous observations (21). However, two factors were found to influence the surface quality of the grown layer: (*i*) the condition of the substrate surface prior to deposition, and (*ii*) formation of a second phase in heavily doped melts. Thermal decomposition of the substrate exposed to a large volume of the apparatus results in rough substrate surfaces (22). This leads to perturbed internal boundaries (junctions) and Ga occlusions, as shown in Fig. 9. Occlusions of this type point to the importance of the protection of the substrate prior to LPE growth, as provided by the cover plate in Fig. 4. Although rough surfaces can be substantially corrected by melting a part of the substrate in a slightly undersaturated melt, the over-all surface planarity cannot be fully restored. In fact, nonuniform meltback itself can lead to an irregular growth interface with subsequent Ga entrapment (23). It has been reported that the formation of a second phase leads to similar surface degradation in layers heavily doped by oxygen (24) or nitrogen (25). We have observed similar effects in tellurium-doped layers with net carrier concentrations in excess of 5×10^{18} cm^{-3}, presumably due to the formation of gallium telluride.

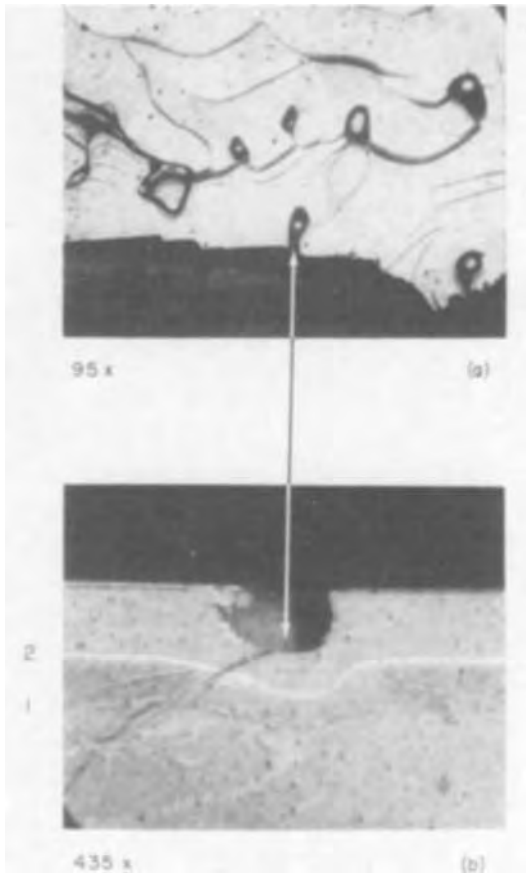

Fig. 9. Gallium occlusions in a 70μ thick LPE layer on a vapor etched substrate. Topview of a 70μ thick LPE grown on a vapor etched substrate showing gallium occlusions (a) and the cross-sectional view of an occlusion from which the gallium is removed (b). The depression at the substrate-LPE layer interface denoted 1 on (b) resulted from the vapor etching. The interface denoted 2 was introduced by an abrupt increase in the cooling rate and it amplifies the depression in the substrate leading to the gallium occlusion.

Summary

It is shown that a commercial LPE system for GaP LED material where the dopants are added to the melt can be optimized by using thin melts and by the termination of the LPE growth. An LPE system is proposed which forms thin melts by sectioning off small but equal parts of a saturated solution (aliquot) taking advantage of the fact that GaP is wetted by molten Ga. The performance of a prototype system has been evaluated, and conceptual modifications for mass production techniques are enumerated. Close to 100% deposition efficiency and hence excellent control over layer thickness and uniformity is obtained with aliquot melts of less than 1 mm. The deposition efficiencies obtained with larger melt thicknesses are in good agreement with calculated values assuming diffusion limited material transport and a low value of the diffusion constant, $D = 2.6 \times 10^{-5}$ cm^2 sec^{-1}. Exact calculations (11) yield $D = 5.7 \times 10^{-5}$ cm^2 sec^{-1} for P in Ga. The deviation from the calculated values for large temperature increment and high cooling rate is attributed to spontaneous nucleation in the melt when supercooling exceeds ~15°C. The thickness of the grown layer is roughly independent of the thickness of the melt for melt thicknesses in excess of 1 mm. The utility of the grown layer is affected by the quality of the substrate and the amount of dopants in the melt and not by the degree of constitutional supercooling.

Acknowledgment

The authors would like to acknowledge helpful discussions with D. L. Rode on mass transport during

LPE deposition and the exact value of the diffusion constant of P in Ga as well as access to his unpublished work. D. L. Rode has also provided the numerical solutions given in Table I. O. G. Lorimor assisted in the preparation of Fig. 1. D. D. Roccasecca assisted in the crystal growth and in the evaluation of LPE layers. We have also benefited from helpful discussions with F. A. Trumbore, L. R. Dawson, and O. G. Lorimor.

Manuscript submitted Feb. 12, 1973; revised manuscript received *ca.* June 1, 1973.

Any discussion of this paper will appear in a Discussion Section to be published in the June 1974 JOURNAL.

REFERENCES

1. "Transistor Technology," F. J. Biondi, Editor, Vol. III, p. 175, D. Van Nostrand Co., Inc., Princeton, N. J. (1958).
2. R. H. Saul, J. Armstrong, and W. H. Hackett, Jr., *Appl. Phys. Letters*, **15**, 229 (1969).
3. R. A. Logan, H. G. White, and W. Weigmann, *ibid.*, **13**, 139 (1968).
4. I. Hayashi, M. B. Panish, P. W. Foy, and S. Sumski, *ibid.*, **17**, 109 (1970).
5. L. R. Dawson, in "Progress in Solid State Chemistry," Vol. VII, p. 117, H. Reiss and J. O. McCaldin, Editors, Pergamon Press, Oxford (1972).
6. R. H. Saul and W. H. Hackett, Jr., *This Journal*, **117**, 921 (1970).
7. A. S. Jordan, *ibid.*, **118**, 781 (1971).
8. R. H. Saul and W. H. Hackett, Jr., *J. Appl. Phys.*, **41**, 3554 (1970).
9. C. D. Thurmond, *J. Phys. Chem. Solids*, **26**, 785 (1965).
10. W. A. Tiller, *J. Crystal Growth*, **2**, 69 (1968).
11. D. L. Rode, To be published.
12. H. S. Carslaw and J. C. Jaeger, "Conduction of Heat in Solids," p. 96, Oxford University Press (1959).
13. W. A. Tiller and C. Kang, *J. Crystal Growth*, **2**, 345 (1968).
14. H. T. Minden, *ibid.*, **6**, 228 (1970).
15. J. A. Donahue and H. T. Minden, *ibid.*, **7**, 221 (1970).
16. D. Baker, *Proc. Inst. Elec. Engrs. (London,)* **106**, 442 (1959).
17. S. F. Nygren, C. M. Ringel, and H. W. Verleur, *This Journal*, **118**, 306 (1971).
18. R. H. Saul, Unpublished.
19. O. G. Lorimor, Unpublished.
20. R. H. Saul and D. D. Roccasecca, *J. Appl. Phys.*, **44**, 1983 (1973).
21. See, for example, W. A. Tiller, in "The Art and Science of Growing Crystals," p. 276, J. J. Gilman, Editor, John Wiley & Sons, Inc., New York (1963).
22. G. A. Rozgonyi and R. H. Saul, *J. Appl. Phys.*, **43**, 1186 (1972).
23. M. R. Lorenz and M. Pilkuhn, *ibid.*, **37**, 4094 (1966).
24. M. Kowalchik, A. S. Jordan, and M. H. Read, *This Journal*, **117**, 407C (1970).
25. R. A. Logan, H. G. White, and W. Weigmann, *Solid State Electron.*, **14**, 55 (1971).

Thin Silicon Film on Insulating Substrate

Greg L. Kuhn and C. John Rhee

Motorola Incorporated, Semiconductor Research and Development Laboratories, Semiconductor Products Division, Phoenix, Arizona 85008

ABSTRACT

Experimental results on a new technique for making a thin silicon epitaxial layer on an insulating substrate are presented. The technique utilizes the anisotropy of the etch rate of silicon in the aqueous potassium hydroxide-isopropyl alcohol system. The silicon film can be either n- or p-type with a thickness in the low micron range (under 3 μm). The thickness variation can be controlled to ± 0.5 μm across a 2 in. diameter wafer.

The great interest in silicon-on-insulator can be readily understood if one considers its potential application in device technology, especially in JFET's, fast MOST logic/memory circuits, and in radiation resistant devices.

Work is being done in the field of silicon-on-insulator by utilizing silicon-on-sapphire (1), silicon-on-spinel (2), and silicon-on-polycrystalline silicon (3). Mechanical polishing and electrochemical and electrolytic thinning (4-6) are the most commonly used techniques in fabricating silicon-on-polycrystalline silicon.

This paper describes another possible technique for making a thin silicon epitaxial layer on an insulating material by utilizing a self-regulating silicon etching step to precisely control the layer thickness. This layer can be n- or p-type with a thickness in the low micron range (under 3 μm) and with uniformity of control of ± 0.5 μm across a 2 in. diameter wafer.

There is one basic chemical etching process, called the KOH etch stop, which makes this SOIS (silicon-on-insulating-substrate) technique fundamentally different from dielectric isolation techniques. The etch stop consists of a highly boron-doped silicon layer. Figure 1 shows the etch rate of <100> oriented silicon as a function of boron doping concentration. An etch rate differential of as high as 50:1 is observed.

Key words: silicon-on-insulated-substrate (SOIS), anisotropic etch, polycrystalline silicon, P+ etch stop.

Experimental

Steps 1 through 7 of Fig. 2 depict the basic processes of the SOIS technique. One begins with a planarized, polished N or P^- silicon substrate. Boron is diffused into the substrate to obtain the etch stop buffer layer (step 1). Depositing a boron doped epitaxial layer is

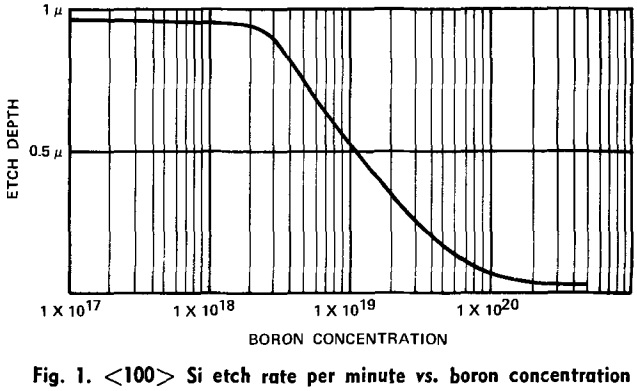

Fig. 1. <100> Si etch rate per minute vs. boron concentration in KOH-H_2O-isopropyl alcohol system at 80°C.

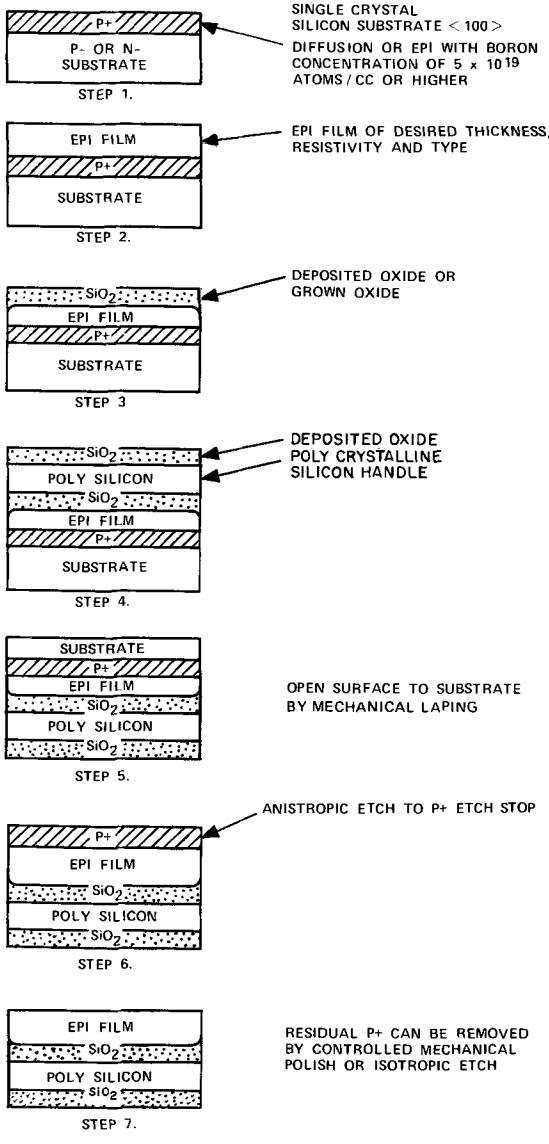

Fig. 2. Fabrication steps for thin single crystal silicon on SiO_2

an alternate method of obtaining this P^+ film. A thin single crystalline film of desired thickness and resistivity, in which the active devices will be fabricated, is epitaxially deposited on the P^+ layer (step 2). At the end of the epi cycle an insulator is deposited. The insulator can be SiO_2, Si_3N_4, or others, or any combination thereof (step 3). Polycrystalline silicon is then deposited directly on the insulator and is capped with another layer of insulator (step 4). The wafer is then mechanically backlapped to within 7.5×10^{-3} cm (3 mils) of the P^+ buffer layer. An additional 5×10^{-3} cm (2 mils) are removed by isotropic etching (step 5).

The remaining substrate is removed using the anisotropic KOH etch solution (step 6). The P^+ buffer layer acts as an etch stop when it is exposed to the solution. This allows one to remove the remaining portion of the substrate which may be left across the wafer due to any error introduced by the mechanical backlapping. The large etch rate differential allows one to obtain a uniform silicon layer at this point. The P^+ etch stop is now removed using an isotropic silicon etch and the SOIS material fabrication is complete (step 7).

Results and Discussion

In this section the material fabrication steps are discussed in detail and the experimental results are presented. The initial substrate in our experiment was a 2 in. diameter <100> silicon wafer that was 5-6 ohm-cm n-type. An n-type wafer was chosen to enable one to easily test when the P^+ etch stop was reached. The testing was done using a standard hot-point probe and visual inspection. During the boron diffusion into the starting substrate prior to epi deposition the highest possible P^+ concentration is needed to obtain the maximum etch rate differential. However, deposition of a high quality epi layer on the heavily doped substrate is a difficult task. Both epi deposition on a diffused P^+ layer and on a doped P^+ epi layer are under investigation. For our experiment the P^+ diffused layer had a surface concentration of 2.5×10^{20} atoms/cm^3 with a junction depth of 2 μm, and the initial n-type epi thickness was 5 μm. Then 1 μm of SiO_2 was deposited directly on the epi. The thickness and type of this insulator are dictated by the subsequent devices and circuits to be fabricated on the finished wafer.

In order to minimize the boron out-diffusion into the epi and original n-type substrate during the polycrystalline silicon deposition cycle, the poly should be deposited at the lowest possible temperature with a maximum deposition rate. The buried layer diffusion profile for our work is shown in Fig. 3(a). The P^+ diffusion curve, before epi and polycrystalline cycles, was calculated as the complementary error function with boundary conditions of surface concentration and diffusion depth. The P^+ diffusion curve after epi and polycrystalline silicon cycles was calculated as a Gaussian redistribution also using surface concentration and diffusion depth as boundary conditions. The boron redistribution was predominantly a function of the polycrystalline silicon deposition cycle. For our experiment we deposited 3.5×10^{-2} cm (14 mils) of polycrystalline at 1000°C using a SiH_4 (silane) source. The calculated and experimental redistribution data match well as can be seen by comparing Fig. 3(a) and 3(b).

A wafer warpage problem was encountered for polycrystalline silicon deposition at temperatures $\leq$1000°C. This problem was somewhat alleviated by using a thicker starting substrate, which was 5×10^{-2} cm (20 mils) for our experiment. At present, several sources, deposition temperatures, and rates are being investigated to solve the problems of warpage and out-diffusion during the polycrystalline silicon deposition cycle.

After polycrystalline deposition, the original <100> substrate is removed to within 25 μm of the P^+ etch stop by standard backlapping and back etching. The remaining 25 μm of starting substrate are removed at the rate of 0.9 μm/min in the aqueous KOH-isopropyl alcohol anisotropic etch. The surface appearance becomes shiny as the P^+ layer becomes exposed because of the surface leveling with respect to the boron diffusion profile.

The control in thickness uniformity by the use of the etch stop can be illustrated by the use of an example. Assume that there is a 25 μm (1 mil) taper across a 2 in. diameter wafer. Further assume that the P^+ etch stop is just becoming exposed in certain portions while there are other areas that still have 25 μm substrate material remaining (see Fig. 4). By the time this 25 μm thick portion etches out (about 25 min) the portion where the P^+ etch stop was first exposed is only etched by 0.5 μm. Thus it can be seen that the 25 μm taper has been reduced to a 0.5 μm taper across a 2 in. diameter wafer. However, it should be mentioned that there is a change in etch-rate differential due to boron redistribution, and thus the uniformity control degrades accordingly. Figure 5 shows a typical wafer with P^+ etch stop exposed across an entire wafer.

The wafer now has a P^+ layer, epi and insulator on supporting polycrystalline silicon as shown in Fig. 6. What remains before achieving a finished substrate is the removal of the P^+ etch stop. This is accomplished using an isotropic silicon etch. Among several silicon etches that were investigated the HNO_3:CH_3COOH:HF silicon etch, as reported by Sumitomo (9), was found to be most reliable. He reported an etch rate

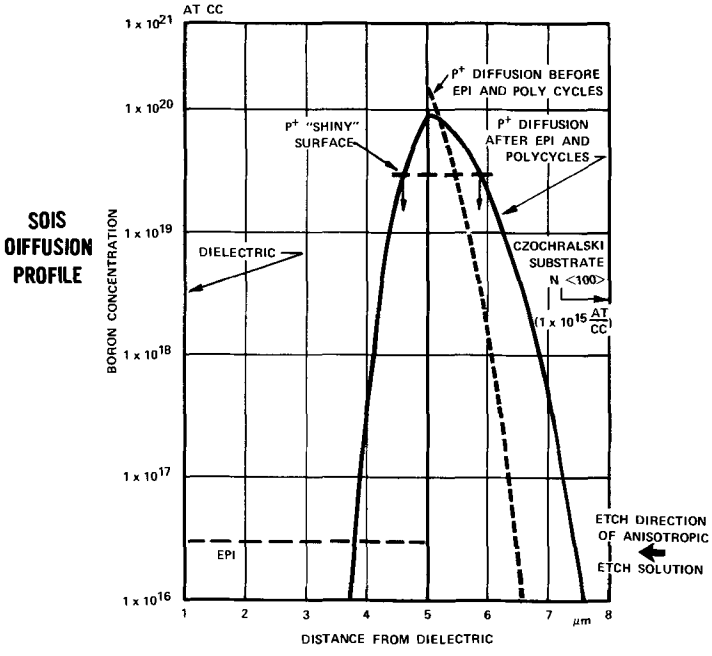

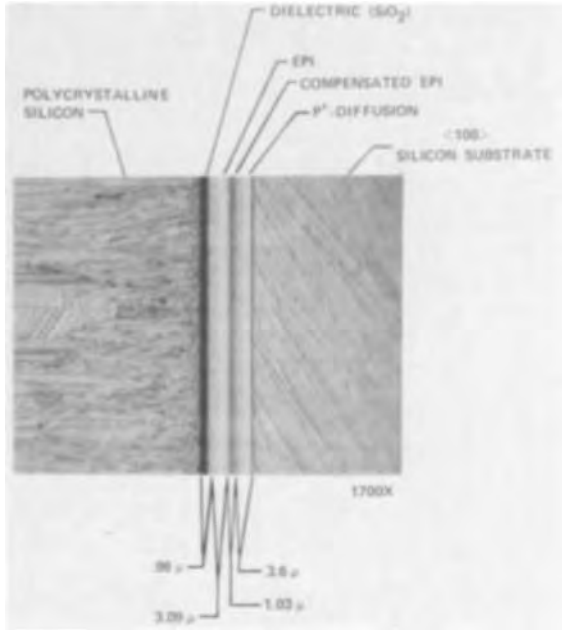

Fig. 3. P+ etch stop doping profile. (a) Theoretical, (b) experimental

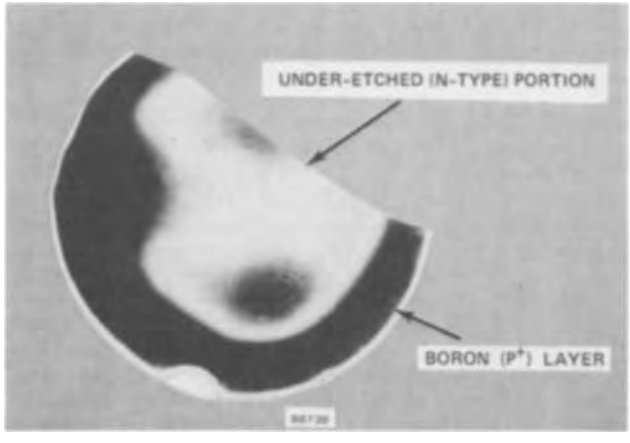

Fig. 4. A wafer with underetched portion (n-type)

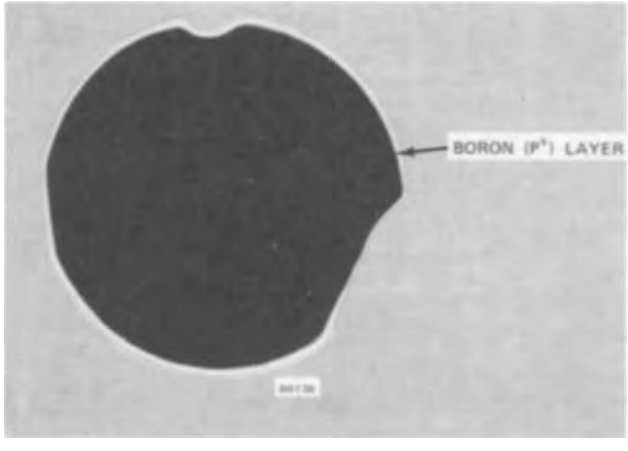

Fig. 5. A wafer with P+ etch stop exposed on entire surface

differential of approximately 70:1 between 5.8×10^{-3} and 3×10^{-1} ohm-cm p- or n-type material. This etch rate differential provides an adequate etch stop at the interface between the P+ buffer layer and n-type epi.

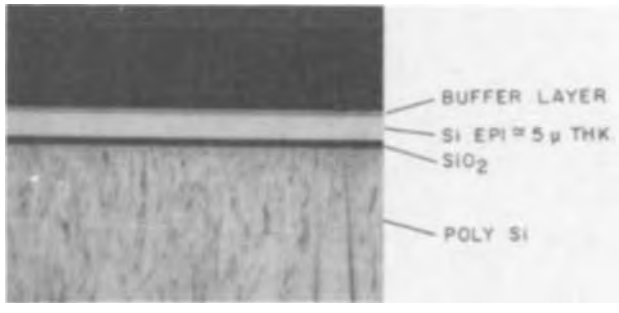

Fig. 6. Thin silicon film on SiO_2 with P+ etch stop (P+ buffer-layer thickness varied from 1.6 to 2.2 μm across 2 in. diameter wafer).

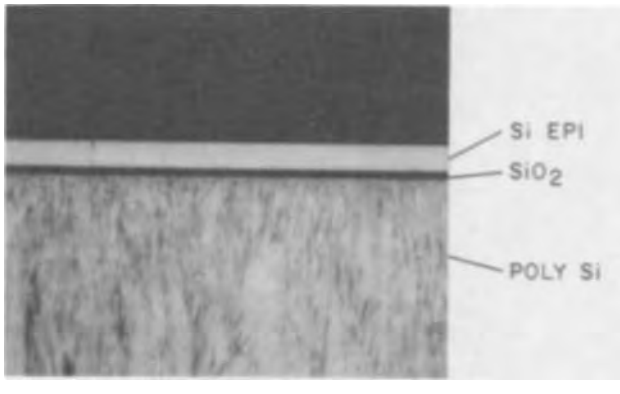

Fig. 7. Thin silicon film on SiO_2 with P+ etch stop removed

Figure 7 shows a cross-sectional view of a finished wafer.

Conclusion

In conclusion, it has been shown that a thin single crystal silicon film with an epi uniformity of ±0.5 μm across a 2 in. diameter wafer can be produced on an insulating substrate. This is attained by the use of two etch stops. The first etch stop is the P+ buffer layer and the second etch stop is the relatively high resistivity epi layer. Further refinement in the poly-

crystalline silicon deposition cycle, and limitation of the extent of boron out-diffusion, will determine the feasibility of this technology as applied to batch processing.

Acknowledgments

Acknowledgment is made to the Air Force Cambridge Research Laboratories which supported portions of this work under contract F19628-72-C-0308.

Manuscript submitted March 2, 1973; revised manuscript received May 21, 1973. This was Paper 239 presented at the Miami Beach, Florida, Meeting of the Society, Oct. 8-13, 1972.

Any discussion of this paper will appear in a Discussion Section to be published in the June 1974 JOURNAL.

REFERENCES

1. J. F. Allison *et al.*, *Proc. IEEE*, **57**, 1490 (1969).
2. P. Robinson and D. Dumin, *This Journal*, **115**, 75 (1958).
3. M. J. J. Themnissen, J. A. Appels, and V. Verkuylen, *ibid.*, **117**, 959 (1970).
4. H. J. van Dijk and J. deJonge, *ibid.*, **117**, 553 (1970).
5. T. I. Kamins, *Proc. IEEE*, **60**, 915 (1972).
6. C. Wen and K. Weller, *This Journal*, **119**, 547 (1972).
7. J. B. Price, Abstract No. 236, page 584, Electrochem. Soc. Extended Abstracts, Fall Meeting, Miami Beach, Florida, Oct. 8-13, 1972.
8. U.S. Pat. No. 3,721,588.
9. Y. Sumitomo, T. Yasui, H. Nakatsuka, T. Oohashi, H. Tsutsumi, and H. Muraoka, Abstract No. 25, page 74, Electrochem. Soc. Extended Abstracts, Spring Meeting, Houston, Texas, May 7-11, 1972.

Etch Rate Characterization of Boron-Implanted Thermally Grown SiO_2

F. N. Schwettmann,* R. J. Dexter, and D. F. Cole*

Texas Instruments Inc., Dallas, Texas 75222

ABSTRACT

The effect of boron implantation on the etch rate of thermally grown SiO_2 has been studied for a wide range of energies, doses, and anneal conditions. For unannealed oxides, a significant increase in etch rate is observed with increasing dose. The depth of maximum damage as determined by the peak in the etch rate profile occurs at approximately 60% of the ion range as predicted by LSS theory. When annealing is carried out in nitrogen, high temperatures (~1200°C) are required to remove all measurable damage created by high dose implants. When an oxygen or steam ambient is used, considerably lower temperatures achieve the same result. Although the ion profile as determined from the etch rates can be approximated by LSS theory, skewing of the profile towards the surface indicates that higher moments are required in the distribution calculation.

In the fabrication of silicon semiconductor devices using ion implantation, thermally grown SiO_2 is frequently used as a mask to define the area which is to be implanted. The nature of the damage and the ion distribution in the oxide mask before and after annealing can affect both the subsequent processing steps and the final device characteristics. A recent study by Dalton and Pickar (1) provides a measure of the damage caused by the implantation process. They found a significant increase in the oxide etch rate when a boron dose of 1×10^{15} ions/cm^2 is implanted through a 2000Å thick layer at 150 keV. It was also indicated that anneal temperatures as high as 1050°C are required to remove any measurable damage. At the high energy used in their study, most of the energy dissipation of the implanted ions will be due to electronic interactions. This will result in considerably less damage than will occur in the case of a masking oxide where nuclear interactions become significant as the ions come to rest within the oxide.

At the present time there is little information concerning the ion distribution in the oxide. Volod'ko *et al.* (2) have reported that the range for boron implanted in thermally grown SiO_2 is in good agreement with LSS theory (3). On the other hand, they report a range straggling that is greater than theory predicts. Their experimental technique involved the measurement of the surface resistivity of the annealed underlying silicon after implanting through various thickness oxide films. This technique, as indicated by the authors, suffers from two deficiencies. One is the use of an average value of mobility, thereby neglecting its variation with concentration. Also, the SiO_2-Si interface is assumed to have no influence on the distribution of the impurity atoms in the oxide.

The purpose of this paper is to determine by an etch rate characterization study the following: (*i*) the damage distribution in the oxide caused by the implantation; (*ii*) the effect of anneal temperature, time, and ambient on this damage; and (*iii*) the ion distribution in the oxide so that the minimum oxide thickness for masking can be determined.

Experimental

Czochralski grown silicon slices of (111) orientation with a resistivity of 5-10 ohm-cm were oxidized at 1100°C in steam to an oxide thickness of about 1 μm. The implantation was carried out with B^{11} ions obtained from an rf source using BF_3 as the source gas. The ion beam was accelerated, focused, mass analyzed, and electrostatically scanned over the target surface. The dose was varied from 1×10^{12} to 1×10^{16} ions/cm^2 at energies of 30 to 150 keV. The dose rate was approximately 0.1 μA/cm^2. After implantation, the slices were cleaned in an rf glow discharge at room temperature with an oxygen ambient followed by a 20 min soak in a solution of 7 parts sulfuric acid and 3 parts hydrogen peroxide (30-35%) at 60°-80°C. The slices were then rinsed for 20 min in deionized water and spun dry.

Etch rate profiles were obtained on both annealed and unannealed slices. Annealing was carried out at 900°-1250°C in a fused quartz tube and unless otherwise indicated, in a nitrogen atmosphere. Other ambients considered were oxygen and steam. Two differ-

* Electrochemical Society Active Member.

Key words: ion implantation, silicon dioxide, boron, etch rates, annealing.

ent etch solutions were used in order to separate the damage and the boron profiles. It has been shown (4) that when P-etch[1] is used as etchant, the etch rate for boron doped SiO_2 is greater than for an undoped oxide. The opposite is true for a buffered HF solution, *i.e.*, the etch rate for boron-doped SiO_2 is slower than for the undoped oxide. For this study a buffered HF, referred to hereafter as C-etch, of the following composition was used: 40 parts HF (49%), 325 parts NH_4F (40%), and 10 parts H_2O. Etching was carried out at 25°C for 15-180 sec depending on the implanted dose and anneal conditions.

Two different techniques were used to determine the oxide thickness for the etch rate calculation. For well-annealed slices, ellipsometry was used. Since the refractive index of boron-doped oxides has been shown to be the same as for undoped thermal oxides (5), interpretation of the measurement is straightforward. For slices which were implanted at high doses and not annealed, an increase in the refractive index has been reported (6). For these samples a different technique was used to determine the oxide thickness. Prior to the implantation the slice was coated with photoresist and a pattern formed. The oxide defined by the photoresist was then implanted, the resist removed, and the slice cleaned as described earlier. The step difference between the implanted and unimplanted region formed during etching was measured by a Taylor-Hobson Talystep.[2]

Results and Discussion

Etch sensitivity.—The sensitivity of P-etch and C-etch to the boron concentration and extent of damage was determined by measuring the etch rates for a wide range of boron doses. A summary of these results for implants made at 82 keV is shown in Table I. Considering the P-etch data first, a relatively high dose of 1×10^{16} ions/cm^2 annealed at 1200°C for 30 min in N_2 gives, within experimental error, an etch rate comparable to unimplanted oxide. Since both the damage and boron should cause an increase in the etch rate, it is apparent that the etch is not sensitive enough to detect boron at this concentration level [theoretical peak value based on LSS theory (3) = 7×10^{20}/cm^3]. Therefore, any enhancement in the etch rate for lower doses and anneal conditions can be attributed to residual damage in the oxide. This result also shows that no residual damage can be detected using P-etch for a sample annealed at 1200°C.

The sensitivity of P-etch to damage is shown by the low dose results in Table I. For a dose of 1×10^{12} ions/cm^2, an unannealed oxide has an etch rate that is only slightly greater than that of unimplanted SiO_2. When the dose is increased to 1×10^{13} ions/cm^2, the damage becomes more apparent as the relative etch rate increases to 1.06. At a dose of 1×10^{14} ions/cm^2, this increases to 1.49 and at 1×10^{15} ions/cm^2 to 3.82. These results are the average values for the top 4000Å of oxide, hence larger values are to be expected at the peak damage depth. A similar result is also shown for C-etch at a dose of 1×10^{15} ions/cm^2. In this case, the relative etch rate is less, 1.89 compared to 3.82 for P-etch.

[1] 15 parts HF (49%), 10 parts NHO_3 (70%), and 300 parts H_2O.
[2] Rank Precision Industries, Limited, Leicester, England.

Table I. Sensitivity of etch rate to boron concentration and damage

Dose (ions/cm^2)	Anneal conditions: Temp. (°C)	Anneal conditions: Time (min)	Etch	Relative etch rate
1×10^{16}	1200	60	P	1.02
1×10^{13}	None		P	1.03
1×10^{13}	None		P	1.06
1×10^{14}	None		P	1.49
1×10^{15}	None		P	3.82
1×10^{15}	None		C	1.89
1×10^{13}	1200	30	C	0.99
1×10^{15}	1200	30	C	0.99
1×10^{16}	1200	30	C	0.79

The last three rows in Table I illustrate the effect of dose on the relative etch rate for well-annealed samples using C-etch. At low doses the etch rate is identical to unimplanted oxide, while at 1×10^{16} ions/cm^2 a reduced rate is observed. At this dose level, the boron concentration is sufficiently high that the expected decrease in etch rate is easily detected.

The calculated relative etch rates are based on comparison with an unimplanted sample etched at the same time. The average etch rate for unimplanted oxide is 2.4 Å/sec using P-etch and 16.8 Å/sec with C-etch. The observed maximum variation in the absolute etch rate was ± 10% while the variation in the relative etch rate was usually better than ± 2%.

Unannealed profiles.—Typical etch rate profiles obtained with P-etch for unannealed implants of 82 keV B^{11} at 1×10^{14} and 1×10^{15} ions/cm^2 are shown in Fig. 1. At the lower dose, the maximum etch rate is twice that of the unimplanted oxide, while at 1×10^{15} ions/cm^2 the peak rate is about 5.5 times greater. These peak values are observed at a depth of 1900 ± 100Å. A similar result was observed with C-etch, except that the peak value in the etch rate was lower. It should be noted that for the higher dose, the etch rate shows a higher value for the initial surface layer. This was found in almost all the high dose samples investigated. The depth of the peak value is approximately 60% of the ion range as predicted by LSS theory (3). This value is typical of the damage/ion depth ratios observed when various ions are implanted in silicon (8).

Effect of anneal variables.—The effect of anneal temperature on the average relative etch rate using P-etch is shown in Fig. 2. As expected, higher anneal temperatures are required to remove the damage formed by heavier doses. However, a significant fraction of the damage is annealed out at all of the temperatures indicated. For example, at 1×10^{15} ions/cm^2, the average relative etch rate of the unannealed oxide is 3.82. At 900°C after 60 min, the relative etch rate is down to 1.25. Increasing the anneal temperature to 1000°C results in a small decrease in the relative etch rate to 1.15. A similarly small decrease is observed at 1100°C.

If the curves shown in Fig. 2 are extrapolated to a relative etch rate of 1.0, the dose at which all the measurable damage is removed can be determined. A plot of this dose *vs.* anneal temperature is shown in Fig. 3. For a given dose and anneal temperature, this figure indicates whether residual damage will be present in

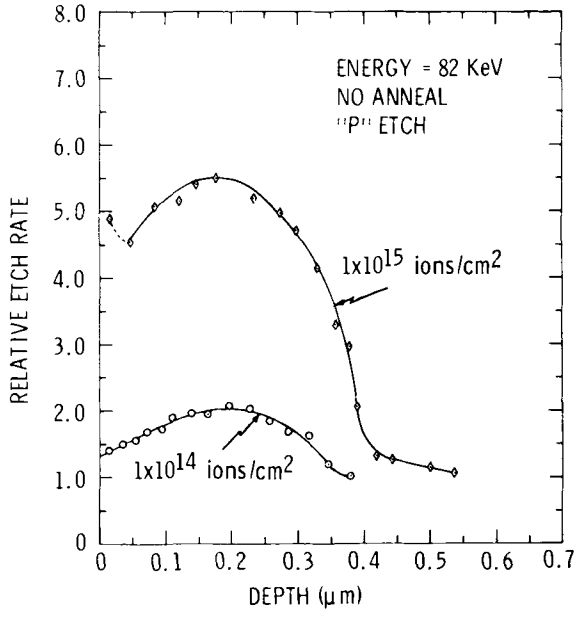

Fig. 1. Effect of dose on the etch rate profile for unannealed oxide.

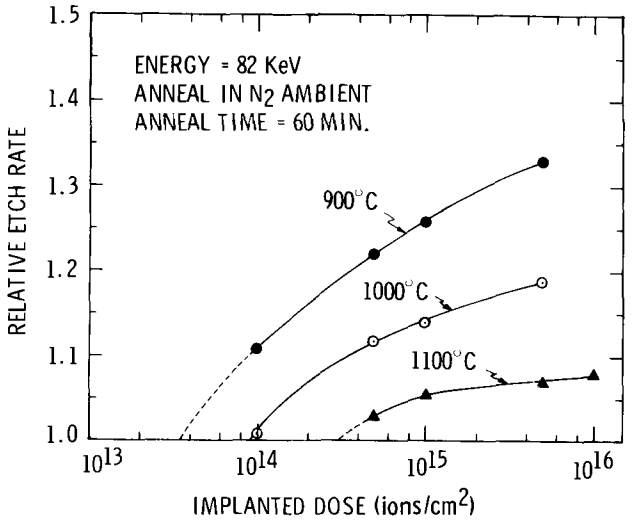

Fig. 2. Effect of dose and anneal temperature on the relative etch rate.

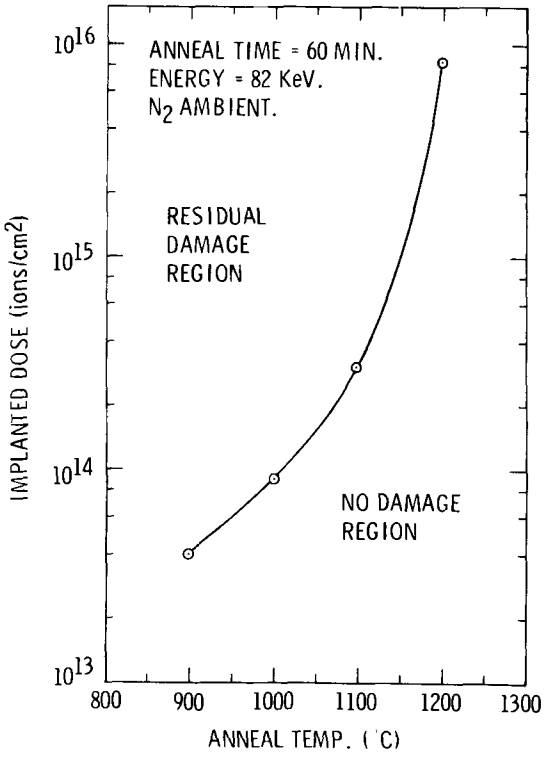

Fig. 3. Implanted dose-anneal temperature correlation defining regions of damage and no-damage.

the oxide. The area to the right of the curve is the "damage free" region while to the left residual damage will be observed.

The effect of anneal time and ambient are shown in Table II. At 1×10^{14} ions/cm², increasing the anneal time from 30 to 120 min at 900°C results in a small decrease in the relative etch rate, 1.12-1.06. Annealing in an oxygen ambient also results in a small decrease in the etch rate. The most dramatic change is observed for annealing in steam. As indicated in Table II, the damage resulting from a dose of 1×10^{16} ions/cm², can be completely removed by annealing at 900°C in steam. In a nitrogen ambient, a comparable result requires a temperature of 1200°C. This is not surprising since it has been shown (9) that steam is more effective than a dry atmosphere in densifying oxides deposited at low temperatures (300°-400°C).

The etch rate technique is a relative measure of a number of oxide properties such as density, stoichiometry, and bond strain. The initial rapid decrease in etch rate at all anneal temperatures and ambients is believed to be due to densification as vacancy clusters anneal out. In the second stage where the etch rate decreases slowly with time and temperature, recombination of oxygen with immoble silicon atoms having unsaturated bonds is suggested. The migrating oxygen can be either that present initially in the oxide and displaced during implantation or from trace quantities in the nitrogen ambient. Since oxygen diffuses slowly in the oxide (10), particularly at 900°C, the recombination process restoring the stoichiometry of the oxide will be slow as observed. In the case of steam, both the solubility and diffusivity are considerably larger (10), giving rise to the more rapid annealing.

Table II. Effect of anneal time and ambient on the relative etch rate using "C"-etch

Dose (ions/cm²)	Temp. (°C)	Time (min)	Ambient	Relative etch rate
1×10^{14}	900	30	N_2	1.12
1×10^{14}	900	60	N_2	1.10
1×10^{14}	900	120	N_2	1.06
5×10^{14}	1000	30	N_2	1.26
5×10^{14}	1000	30	O_2	1.15
5×10^{14}	900	60	N_2	1.22
5×10^{14}	900	60	Steam	0.98
1×10^{15}	900	60	N_2	1.26
1×10^{15}	900	60	Steam	1.02
1×10^{16}	900	60	N_2	1.35
1×10^{16}	900	30	Steam	1.03

Annealed profiles.—The variation of relative etch rate with depth for a dose of 1×10^{16} ions/cm² annealed at 1200°C is shown in Fig. 4. As expected from the results shown in Table I, the relative etch rate decreases with the increase in boron concentration. The two lower energy curves, 55 and 82 keV, are nearly symmetrical about the minimum, while at the higher energy the curve is skewed towards the surface. A plot of the minimum etch rate depth as a function of energy is shown in Fig. 5. The solid curve is the projected range values taken from Johnson and Gibbons (7) and corrected for the difference in density of quartz (2.66 g/cm³) used in their calculations and that of thermally grown SiO_2 (2.26 g/cm³) used here. This correction gives a projected range that is about 18% greater (2.66/2.26 = 1.18) than the tabulated values (7). The etch rate minimum is seen to be in good agreement

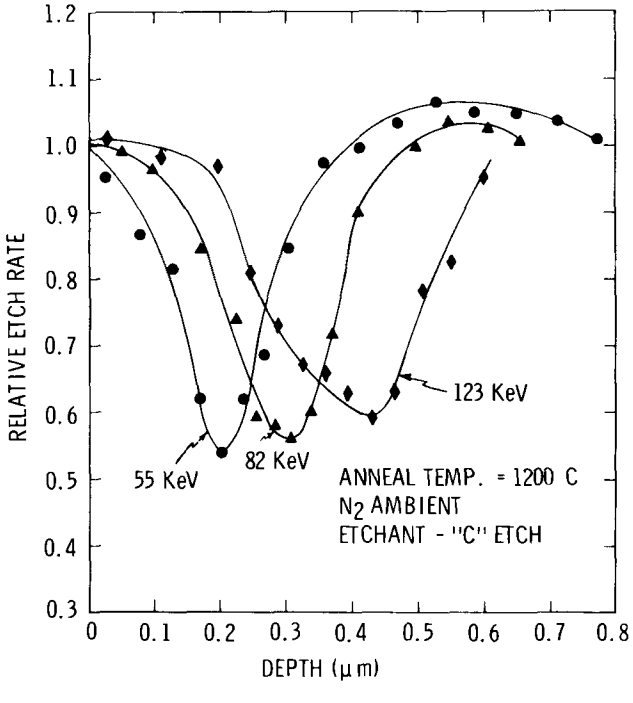

Fig. 4. Variation of the etch rate profile with implant energy

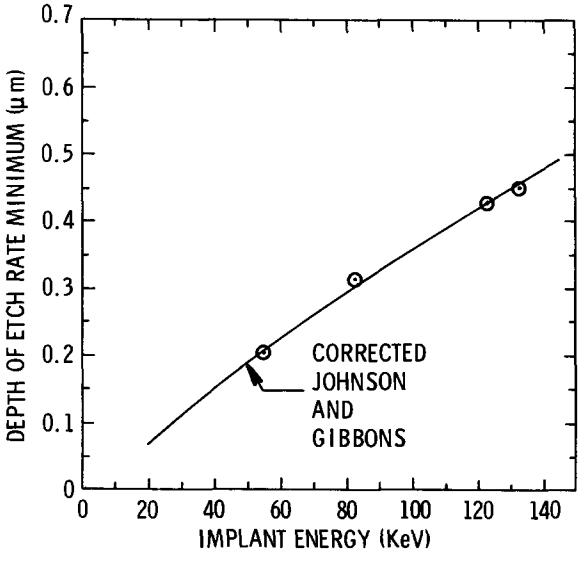

Fig. 5. Comparison of experimental and calculated projected range.

with the calculated projected range values. These values also agree well with the results of Volod'ko *et al.* (2).

A direct measure of the range straggling cannot be obtained from Fig. 4 since a relation between the etch rate and boron concentration is not available. In order to generate an approximate calibration curve, the etch rate profiles for a wide range of implant energies and doses was obtained. It was assumed that the minimum value in the profile corresponded to the peak boron concentration calculated using the range straggling values given by Johnson and Gibbons (7). The results are shown in Fig. 6. The minimum concentration which can be detected by the C-etch is approximately 10^{19}/cm^3. Using this data and the etch rate profiles in Fig. 4, the concentration profiles shown in Fig. 7 were generated. The solid curves shown were calculated using the experimental range value in Fig. 5 and the range straggling of Johnson and Gibbons (7). For the two lower energies, the experimental results agree quite well with the calculated values except at the low concentrations where the error in the calibration curve is greatest. In each case, agreement is better at depths beyond the peak concentrations. The region closer to the surface shows a greater departure from Gaussian, particularly at the higher energies. The range straggling agreement is in contrast to the results of Volod'ko *et al.* (2) who found that the range straggling was 2 to 3 times the LSS value.

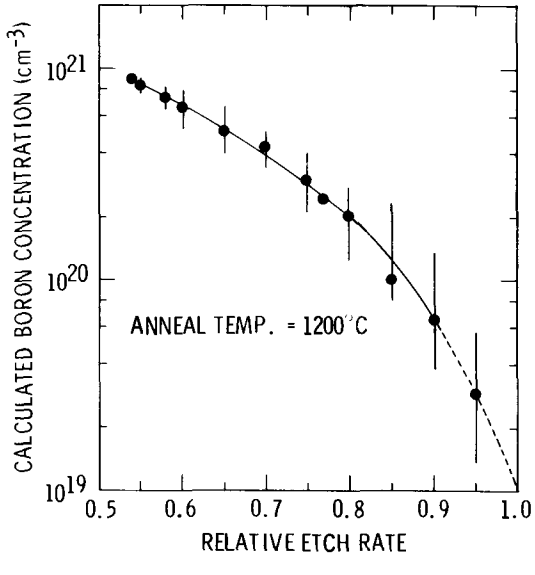

Fig. 6. Calibration curve relating the etch rate to the calculated boron concentration.

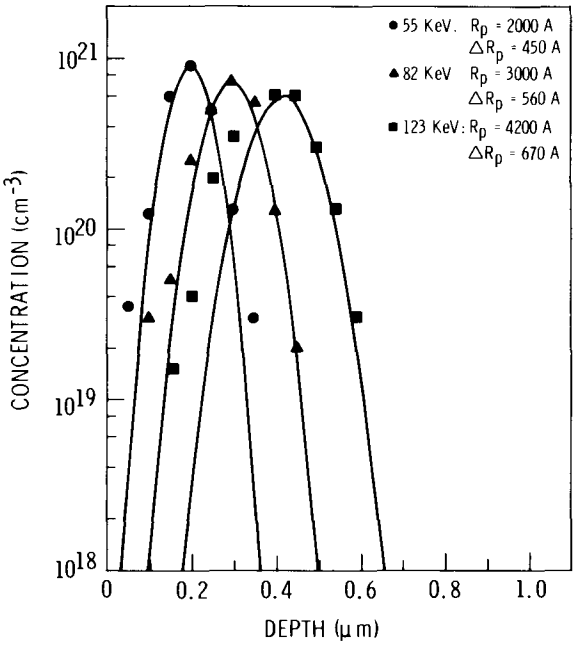

Fig. 7. Comparison of the calculated and experimentally derived boron concentration profiles. The curves were calculated using the indicated projected range and projected range straggling values.

In making a comparison between the experimental and theoretical predictions, several factors need to be kept in mind. First, since an assumption concerning the shape of the ion distribution was made in generating the calibration curve, some degree of circular reasoning is involved in generating the ion profiles. The final result then, is more of a check for consistency than an absolute determination. Second, the etch rate profiles were determined after the samples had been annealed at 1200°C. Possible broadening of the distribution could have occurred as a result of thermal diffusion. Preliminary measurements obtained by ion microanalysis (12), however, indicate that the 1200°C anneal for 30 min does not cause any measurable change in the boron profile. These data also show that the range straggling used in generating the calibration curve (Fig. 6) are reasonably close to the measured values on the deeper side of the distribution.

An important observation in the data of Fig. 7 and also in the initial ion microanalysis results is that the boron profiles are not symmetrical about the range value but are skewed towards the surface. If the amount of enhanced diffusion towards the more heavily damaged surface layer during implantation is assumed to be small, then higher moments need to be considered in calculating the ion distribution. Gibbons (13) has shown that for boron implanted in silicon, a profile that is skewed towards the surface is expected when higher order terms are included. At higher energies the effect should be even more pronounced. Similar results are expected for boron implanted in SiO_2 (13). The need for higher order moments makes comparison with tabulated values where only the first two moments are considered, invalid. However, for most practical applications, a reasonable approximation can be obtained by using the range values shown in Fig. 5 and the range straggling given by Johnson and Gibbons (13).

Minimum oxide thickness for masking.—The data shown in Fig. 7 were used to determine the minimum oxide thickness required to prevent boron from penetrating into the underlying silicon. The minimum thickness was chosen as the depth at which the concentration of boron was 10^{14}/cm^2. The results for the dose

range 1×10^{14} to 1×10^{16} ions/cm^2 are shown in Fig. 8.

In order to confirm that the boron did not penetrate through the oxide at the values given in Fig. 8, a number of samples were implanted with 1×10^{16} ions/cm^2 at the energy corresponding to the minimum thickness and standard MOS C-V measurements (14) made to determine the average surface concentration. Half of each slice was unimplanted as a standard for comparison. For the six energies investigated, the surface concentration on the implanted side was found to be identical within experimental error, to the unimplanted side.

Conclusions

Determination of the etch rates of boron-implanted SiO_2 using P-etch and a buffered HF solution provides a simple technique for evaluating both the damage and boron distributions. The maximum etch rate in the damage profile is located at a depth that is approximately 60% of the ion range as predicted by LSS theory (3). High anneal temperatures are required to remove all measurable damage when annealing is carried out in nitrogen. Considerably lower temperatures can be used when annealing in a steam ambient. While the boron distribution can be approximated by a Gaussian, the skewing of the measured profiles indicates that higher moments are required in the determination of the distribution.

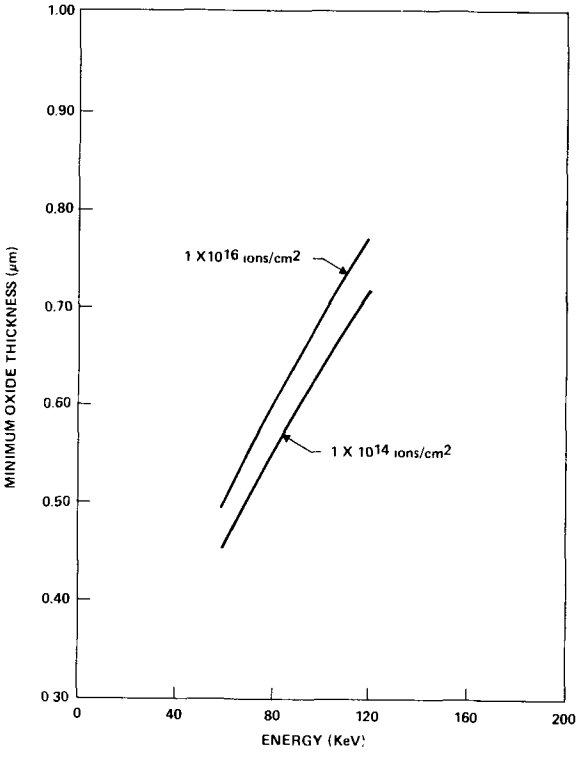

Fig. 8. Minimum oxide thickness required to mask a boron implant

Acknowledgments

The authors wish to thank R. Nevels for the implantation, Z. Zetty for the annealing, and A. Guffey for the etching and ellipsometer measurements. Thanks are also due to J. Aiken for his continued encouragement and support. We are also most grateful for the reviewer's comments, particularly regarding the density correction for the tabulated projected range values.

Manuscript submitted March 7, 1973; revised manuscript received April 27, 1973. This was Paper 251 presented at the Miami Beach, Florida, Meeting of the Society, Oct. 8-13, 1972.

Any discussion of this paper will appear in a Discussion Section to be published in the June 1974 JOURNAL.

REFERENCES

1. J. V. Dalton and K. A. Pickar, 196 RNP presented at Electrochem. Soc. Meeting, Washington, D.C., May 9-13, 1971.
2. V. G. Volod'ko, E. I. Zorin, P. V. Pavlov, and D. I. Tetel'baum, *Soviet Phys.-Solid State*, **10**, 828 (1968).
3. J. Lindhard, M. Scharff, and H. E. Schiott, *Klg. Danske Videnskab, Mat. Fys. Medd.*, **33**, No. 14 (1963).
4. W. A. Pliskin in "Measurement Techniques for Thin Films," B. Schwartz and N. Schwartz, Editors, p. 280, The Electrochemical Society Softbound Symposium Series, New York (1967).
5. R. O. Schwenker, *This Journal*, **118**, 313 (1971).
6. A. R. Bayly and P. D. Townsend, "Proc. Europ. Conf. Ion Implantation," Reading 1970, p. 120, Peregrinis Ltd., Stevenage, England.
7. W. S. Johnson and J. F. Gibbons, "LSS Projected Range Statistics in Semiconductors," Stanford University Bookstore, Stanford, California (1970).
8. B. L. Crowder and R. S. Title, in "Ion Implantation," F. H. Eisen and L. T. Chadderton, Editors, p. 87, Gordon and Breach, London, England (1971).
9. W. A. Pliskin and H. S. Lehman, *This Journal*, **112**, 1013 (1963).
10. B. E. Deal and A. S. Grove, *J. Appl. Phys.*, **36**, 3770 (1965).
11. J. H. Ormrod and H. E. Duckworth, *Can. J. Phys.*, **41**, 1424 (1963).
12. R. B. Dobrott, Private communication.
13. J. F. Gibbons, Private communication.
14. C. Jund and R. Poirier, *Solid-State Electron.*, **9**, 315 (1966).

Liquid-Phase Epitaxy Growth of Gallium Phosphide by a Centrifugal Tipping Technique

S. Y. Lien and J. L. Bestel

Engineering Research Center, Western Electric Company, Princeton, New Jersey 08540

ABSTRACT

A new growth technique for GaP single crystal material based on the liquid-phase epitaxial growth method is presented. This technique relies on centrifugal force to bring the saturated growth solution in contact with the substrate. The apparatus, referred to as the "centrifugal tipper," is described and its principles of operation are explained. Epitaxial layers, both n- and p-type, up to 100 μm thick, have been grown over a temperature range of 950°-1050°C. These layers exhibit good surface quality and variations in thickness of less than ± 1 μm. A p-type material with photoluminescence efficiency of 1.5% was produced. This new technique has demonstrated multi-slice capability for the growth of GaP light-emitting diode material.

Liquid-phase epitaxial (LPE) growth has been, to the present time, the most successful method for producing high quality GaP light-emitting diode material (1). This report describes a growth technique based on LPE growth which produces luminescent epitaxial material with good surface and thickness uniformity. The apparatus used in this growth technique is referred to as the "centrifugal tipper" since it relies on centrifugal force to "tip" the growth solution over the substrate.

The centrifugal tipper and its fundamental principles are described, and the properties of the epitaxial layers grown by this method are presented.

Apparatus

Description of the apparatus.—For the purpose of discussion, the centrifugal tipper (Fig. 1) can be divided into three major subsystems: the crucible assembly, the drive assembly, and the heating unit.

The crucible assembly, which is made of ultrapure graphite is depicted in Fig. 2 and consists of four major parts: the outer crucible which contains the growth solution, the inner core which holds the substrate, the middle core which protects the substrate, and the nut which holds the inner and middle crucibles fastened together. The crucible used on the centrifugal tipper was designed to accommodate eight 25 mm diameter substrates.

The drive assembly consists of a motor-driven shaft which passes through the crucible and is guided above and below by two sets of bearings. Two sets of chevron seals are placed next to the bearings toward the crucible in order to seal the tipping chamber from the outside atmosphere. These seals also prevent the bearing lubricant from being pumped out during evacuation of the chamber. The drive shaft serves another very important function besides rotating the crucible assembly. It is used to remove the heat from the crucible during cooling by a flow of water in the shaft (this water cooling also protects the bearing and seals from overheating).

The heating unit consists of an rf generator and coil. The coil was designed in such a way that the spacing between its loops can be varied. The loops can thus be kept close together where more heat is needed and farther apart where less heat is needed.

Principles of operation of the centrifugal tipper.—The principle of operation of the centrifugal tipper is to spread the saturated GaP in Ga solution over the substrate by centrifugal force. When the crucible is spun the solution is forced outwards by the centrifugal force and flows through the canals which connect the solution cavity to the growth cells. When the cavity is filled with the solution, the temperature of the crucible is lowered thus promoting the growth of an epitaxial layer on the substrate. At the end of the growth process, the rotation of the crucible is stopped and the solution returns to the solution cavity via the connecting canals.

Effect of the centrifugal force on the liquid solution.—In choosing a suitable rotation rate to fill the growth cavity with the liquid solution, a cylindrical crucible without internal structural restrictions rotating on a vertical axis was assumed. The free surface of the liquid under the centrifugal force is then paraboloidal, and the relationship between the height of the paraboloid from the vertex (h), the radius of the cylinder (r), and the rotation rate (N) is given by

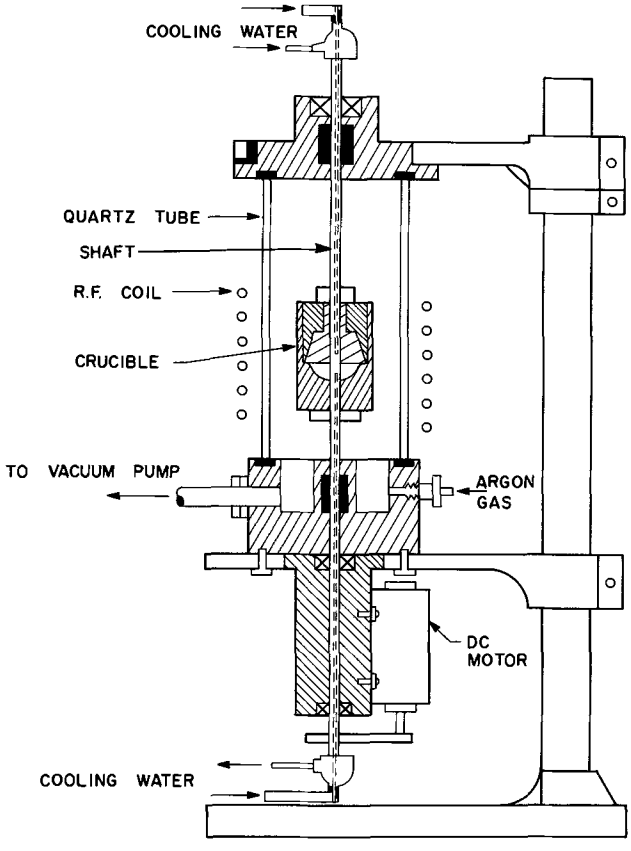

Fig. 1. Apparatus for centrifugal tipping. The cross-sectional view of the centrifugal tipper is shown.

Key words: crystal growth, liquid-phase epitaxy growth, gallium phosphide, centrifugal tipping.

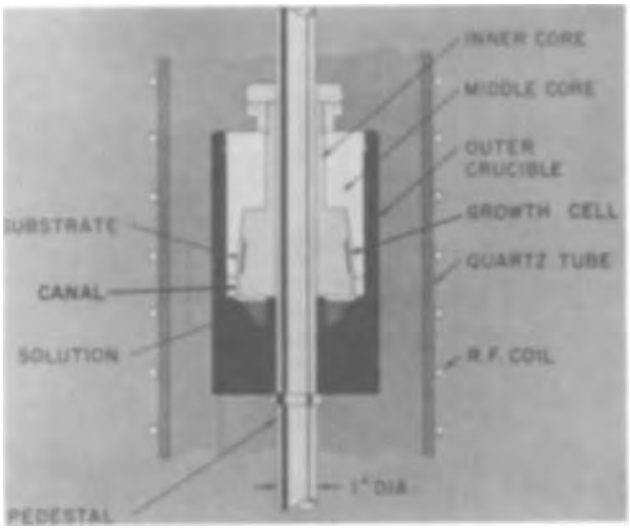

Fig. 2. Crucible assembly. The cross-sectional view of the crucible assembly is shown.

$$h = r^2\omega^2/2g$$

or

$$h = 2\pi^2N^2r^2/g \qquad [1]$$

where ω is the angular velocity and g is the gravitational constant. For a growth cavity situated 25 mm from the rotation axis and about 50 mm from the bottom of the crucible, a rotation rate of 500 rpm or more is needed to completely fill the cavity.

Effect of the buoyancy forces on the substrate.—There is a radial pressure gradient inside the growth cavity due to the centrifugal force field since the pressure is proportional to the square of the radius. When a substrate is immersed in the solution under a centrifugal force field, it experiences two buoyancy forces: the first one is in a vertical direction and is due to the earth's gravitational field; the second is in a radial direction and is due to the centrifugal field. At 500 rpm the magnitude of the centrifugal force ($\sim 10g$) is much larger than that of the gravitational force and the latter can be neglected. The force acting on the solid is therefore

$$f = \omega^2(r_2^2 - r_1^2)(d_s - d_l)A/2 \qquad [2]$$

Where r_1 is the radial distance from the axis of rotation to the inner surface of the solid, r_2 the radial distance from the same axis to the outer surface of the solid, d_s the density of the solid, d_l the density of the liquid, and A the cross-section area of the solid in a tangential plane. If the density of the liquid is greater than that of the solid, the latter will be pushed toward the axis of rotation and vice versa. In the case of a GaP substrate in a GaP-Ga solution, the density of the solid GaP is 4.13 g/cm^3 (2), and the density of the solution is about 5.91 g/cm^3 (since the concentration is so low that we are assuming its density to be equal to the density of pure Ga). As a consequence, the GaP substrate will be pushed toward the axis of rotation when the growth cavity is filled with the growth solution.

Effects of adverse temperature gradients in the liquid.—Bénard (3) experimentally demonstrated that a layer of liquid will display a cell pattern through thermal convections. Rayleigh (4) gave a theoretical interpretation of the Bénard cell formation. He showed that the formation of cells under a temperature gradient depends on the numerical value of a nondimensional parameter, R. This parameter is now referred to as the Rayleigh number and is given by

$$R = g\cdot\alpha\cdot\beta\cdot d^4/k\cdot\nu \qquad [3]$$

where g is the gravitational constant, d the thickness of the liquid layer, β the temperature gradient across the liquid layer, and α, k, and ν the coefficient of volume expansion, thermometric conductivity, and kinematic viscosity, respectively. Rayleigh showed that cell formation will occur when the parameter R exceeds a certain critical value R_c.

Chandrasekhar (5) has calculated R_c values for different boundary conditions. In the case of a layer of liquid lying between two rigid surfaces, $R_s = 1708$. The centrifugal tipping apparatus was therefore designed in such a way as to keep the Rayleigh number below 1708. If this precaution were not taken, Bénard cells would arise in the growth solution which would lead to uneven epitaxial surfaces.

Two types of temperature gradients can occur in the centrifugal tipper: those which lie in a direction parallel to the substrate, and those which lie in a direction perpendicular to the substrate. These two types of gradients will give rise to two types of Bénard cells. The first type of temperature gradient can and should be eliminated by proper spacing of the coils. The second type of gradient, however, is desirable to prevent constitutional supercooling. The growth cavity must therefore be designed around this temperature gradient. According to Eq. [3], R varies as d^4 and therefore R can be drastically reduced by decreasing the thickness of the solution layer (or growth cavity thickness).

From Eq. [3] the growth cavity thickness was estimated, again assuming the solution was pure Ga; the data for liquid Ga were taken from the "Liquid Metals Handbook."[1] For a temperature drop across the layer of 5°C and a centrifugal field of $10g$ (corresponding to about 500 rpm) it was found that the cavity thickness should be less than 3 mm.

Operation.—In the growth of an epitaxial layer, the first step is to place the Ga-GaP and dopants (25g Ga, 0.06 mole fraction of GaP, 0.0005 mole fraction of pure Zn, 0.0035 mole fraction of Ga_2O_3 for p-type, and a 0.00015 mole fraction of Te for n-type) in the outer crucible and the substrate with (111) orientation in the growth cell of the inner crucible. The middle crucible is then placed over the inner one, tightened in position with a nut, and placed inside the outer crucible. The crucible assembly is then placed on the shaft and enclosed in an argon atmosphere. The whole unit is heated with the rf generator to the growth temperature (about 1050°C) at the rate of 50°C/min. The temperature is monitored by a fixed thermocouple placed near the top of the crucible. When the growth temperature is reached, the crucible assembly is allowed to equilibrate and is then spun at a rate sufficiently high (500-1000 rpm) to force the solution into the growth cell. The temperature is then lowered at a 100°C/min cooling rate to 950°C by reducing the rf power until the end of the growth operation is reached at which point the rotation of the crucible assembly is stopped. The temperature at the end of the growth operation has been determined experimentally in such a way as to allow for the growth of an epitaxial layer of about 100 μm thickness. This thickness can be reduced by narrowing the temperature range over which epitaxial growth occurs. After cooling to room temperature, the crucible assembly is dismounted and the substrate removed.

Results

The object of these experiments was to demonstrate the growth of LPE layers of uniform thickness, high surface quality, and luminescence uniformity using the centrifugal tipper.

The surface roughness of the epitaxial layers was measured on a Taly-Surf machine and was found to be low. A typical value for the center line average is about 1 μm. The surface irregularities were found to consist of steps (Fig. 3a and b) which occurred only in one direction on a given substrate. This direction was found to be unrelated to the position of the sub-

[1] "Liquid Metals Handbook," second edition, published by Atomic Energy Commission, June 1952.

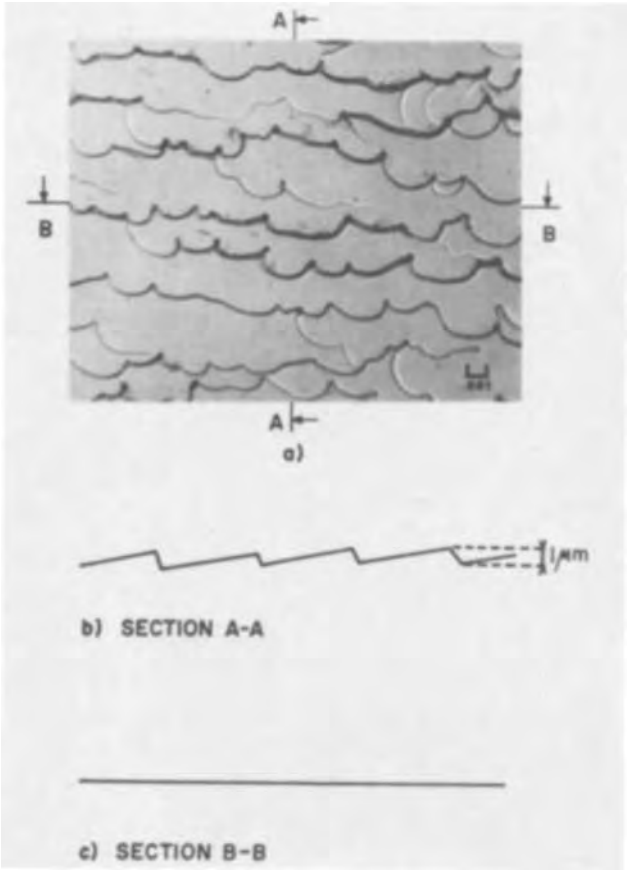

Fig. 3. Surface morphology of the grown p-layer. The surface of the grown p-layer has directional steps which are not related to the substrate position in the crucible, and is thought to be related to the crystal orientation.

strate in the crucible and therefore is thought to be related to the substrate orientation.

The centrifugal tipper has yielded epitaxial layers of extremely good thickness uniformity. No taper was apparent upon examination under the microscope (200X) of several 25 mm long cleaved layers.

Preliminary results indicate that material with a photoluminescence efficiency of about 1.5% can be grown. Photoluminescence scanning of the layers indicates that the efficiency is uniform across the samples (Fig. 4, the ripples in the photograph are due to interference effects inherent to the scanner). The carrier concentration for the n-type material was found to be around 10^{18} cm^{-3} near the outer surface of the layer and to decrease to 5×10^{17} cm^{-3} at a depth of 100 μm.

Conclusion

The centrifugal tipper technique described in this paper demonstrated its potential as a production method for the fabrication of GaP LED material. Its use could also be extended to the fabrication of other devices requiring the growth of epitaxial layers.

Fig. 4. Photoluminescence scan of the surface of a grown p-layer. Light area corresponds to 1.45% photoluminescence efficiency.

Acknowledgments

The authors wish to thank M. S. Gervasio for his valuable technical assistance.

Manuscript submitted Oct. 25, 1972; revised manuscript received May 25, 1973. This was Paper 50 presented at the Houston, Texas, Meeting of the Society, May 7-11, 1973.

Any discussion of this paper will appear in a Discussion Section to be published in the June 1974 JOURNAL.

REFERENCES

1. R. H. Saul, J. Armstrong, and W. H. Hackett, Jr., *Appl. Phys. Letters*, **15**, 229 (1969).
2. H. H. Wieder, *J. Vacuum Sci. Technol.*, **8**, 210 (1971).
3. H. Bénard, *Rev. Gen. Sci. Pures Appl.*, **II**, 1261 (1900).
4. Lord Raleigh, *Phil. Mag.*, **32**, 529 (1916).
5. S. Chandrasekhar, "Hydrodynamic and Hydromagnetic Stability," p. 43, Oxford University Press, England (1961).

Growth and Characterization of InP-InGaAsP Lattice-Matched Heterojunctions

G. A. Antypas* and R. L. Moon*

Corporate Research Laboratories, Varian Associates, Palo Alto, California 94303

ABSTRACT

Liquid phase epitaxy has been employed for the growth of InP-InGaAsP lattice-matched heterojunctions. The epitaxial layers were grown at 650°-625°C on (100), (111)A, and (111)B oriented InP substrates from In-rich liquid solutions. The layers were characterized by x-ray diffraction, photoluminescence, and electron microprobe measurements for the determination of lattice constant, bandgap energy, and composition. Quaternary layers lattice matched to InP substrates were grown having bandgap energies between 1.12-1.41 eV. Mirror-smooth layers have been routinely grown over 100% of the substrate with absolutely no solution droplets remaining on the surface following growth. We experimentally determined a number of liquidus isotherms in the In-rich region of the quaternary system. In the concentration range and temperature investigated the distribution coefficient of G, $K_{Ga} = 25$ while that of As varies between 9.7 and 13.4 for X^s_{Ga} of 0.055 and 0, respectively.

Semiconductor heterojunctions are necessary for the efficient operation of a number of electronic devices, *i.e.*, heterojunction lasers, light emitting diodes, photoemitters, heterojunction transistors, etc. The solid solution properties of III-V ternary alloys injected new interest in the fabrication of these devices. With the exception of Ga-Al-V ternary alloys, however, all other III-V ternary systems are faced with severe lattice-mismatch problems which are detrimental to the growth as well as the electrical and optical properties of these alloys. The one-to-one dependence of bandgap on lattice constant can be relaxed by the addition of a fourth component to the solid, introducing an extra degree of freedom and permitting the independent variation of lattice constant and bandgap. The first system to demonstrate the lattice-matching properties of quaternary alloys was GaAlAsP-GaAsP (1) in which the substitution of Al for Ga results in a bandgap increase while the constant ratio of As/P across the heterojunction maintains lattice matching. This system was used for the fabrication of heterostructure lasers that were operated pulsed at room temperature. Lattice-matched heterojunctions operating at lower energies than GaAs can be fabricated using the lattice-matching properties of InP-InGaAsP which makes possible the growth of low defect density heterojunctions between 0.7 and 1.35 eV. The ease of fabrication of heterojunctions in this system exceeds that of the AlGaAs-GaAs for a number of reasons: (*i*) low growth temperatures (~650°C), (*ii*) heterostructure lasers operating in the infrared can be fabricated by the growth of only two layers, (*iii*) ease of electrical contact to InP compared to AlGaAs, and (*iv*) absence of the formation of tenacious oxides such as Al_2O_3 requiring special boat design. Figure 1 shows the variation of the bandgap as a function of lattice constant. The area bounded by the four ternaries represents the quaternary region with bandgap variations between 0.35 and 2.23 eV. In this system neither the substitution of Ga for In nor As for P, or vice versa, results in lattice matching, therefore, to obtain lattice matching, a simultaneous variation of Ga/In and As/P is necessary. In this system two readily available substrates can be used in obtaining lattice-matched heterojunctions. The GaAs-GaInAsP system can cover the energy range of 1.425-2.23 eV, while the InP-InGaAsP covers the range of 0.7-1.35 eV. The former will result in heterojunctions covering an almost identical range to that covered by the GaAs-GaAlAs heterojunctions; therefore its utility could be considered rather limited. The latter, however, is the only system for which lattice matching can be obtained for energies lower than 1.35 eV. Lattice-matched heterojunctions such as InGaAs-InGaP can, in principle, be fabricated in a manner similar to that used in the preparation of GaAs-InGaP (2,3). No information has been reported as yet on the preparation or properties of such heterojunctions.

Materials Growth and Characterization

The important property of III-V quaternary alloys is that lattice matching can be achieved over a wide energy range. Considering the large number of quaternaries, lattice-matched heterojunctions can be prepared (at least theoretically) over the energy range of 0.3-2.45 eV. In the absence of any available thermodynamic data on any quaternary system, our investigations consisted of trial-and-error procedures for determining the growth properties of such systems. Thus, we have investigated the InGaAsP (4), GaAlAsSb (4), and InGaAsSb (5) systems, along with the GaAlAsP sys-

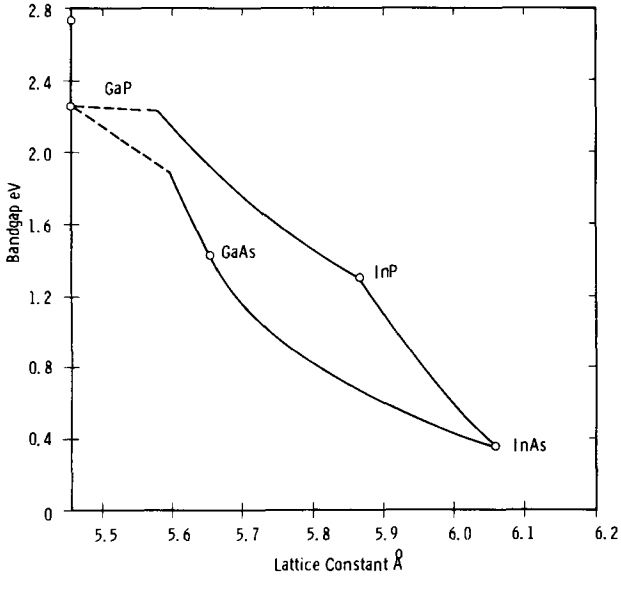

Fig. 1. Bandgap vs. lattice constant for the InGaAsP quaternary system. ——— Direct bandgap, - - - - - indirect bandgap.

* Electrochemical Society Active Member.

Key words: LPE, III-V semiconductors, quaternary, lattice-matching, heterojunctions.

tem reported by Burnham *et al.* (6), representing a series of systems covering practically the whole energy range of III-V semiconductors. We present here some experimental data on the growth properties of the InGaAsP system. The epitaxial layers were grown by liquid phase epitaxy on InP substrates. Although layers have been grown on both (100) and (111)A substrates, the results reported here are from layers exclusively grown on (111)B substrates. A horizontal growth system was employed, with a graphite boat similar in design to that reported by Rosztoczy *et al.* (7), in a palladium purified hydrogen environment. Epitaxial layers have been grown at temperatures as high as 750°C and as low as 580°C. These are considered practical limits due to the decomposition of the InP substrate at 750°C and the low solubility of P at 580°C. The layers for this study were grown in the interval of 650°-625°C. A variety of cooling rates have been tried varying between 0.1 and 2°C/min. The surfaces of the grown layers were mirror-smooth, with no apparent dependance of the cooling rate on the as-grown surface. Figure 2 is a photograph of the as-grown surface of a quaternary layer lattice matched to InP; layers of this quality can be routinely grown over 100% of the substrate with no liquid droplets remaining on the substrate following removal of the melt. This is certainly a very important feature since a portion of the solution remaining in contact with the substrate during cooldown to room temperature will result in local growth of material of different composition than that of the rest of the epitaxial layer. An interference photomicrograph is shown in Fig. 3 indicating the absence of gross growth features. The thickness variations of the epitaxial layer grown on ¾ in. diameter substrates are less than 10% across the diameter of the layers. Figure 4 shows a (110) cleave of the epitaxial layers having a bandgap of 1.17 eV and is lattice matched to InP. Figure 1 shows the quaternary region of the InGaAsP system bounded by the four ternary systems. The variation of the bandgap *vs.* lattice constant for a series of quaternary layers is shown in Fig. 5. In this figure the epitaxial layers were grown on a (111)B InP substrate in the 650°-625°C range under a cooling rate of 0.5°C/min. The melts were prepared with In, Ga, As (InAs was the As source, the As was always below the solubility limit) and were saturated with P from an InP substrate. The lattice constant was determined by x-ray diffraction of the Cu-Kα radiation, and the bandgap was determined by photoluminescence measurements at 77°K using a 0.5W argon ion laser with a dry-ice-cooled S-1 photomultiplier as the detector. The concentration in the solid was determined by microprobe measurements. Table I shows in detail solid and liquid concentrations, lattice constant, and bandgap. In this figure we can see that the increase in Ga in the liquid solu-

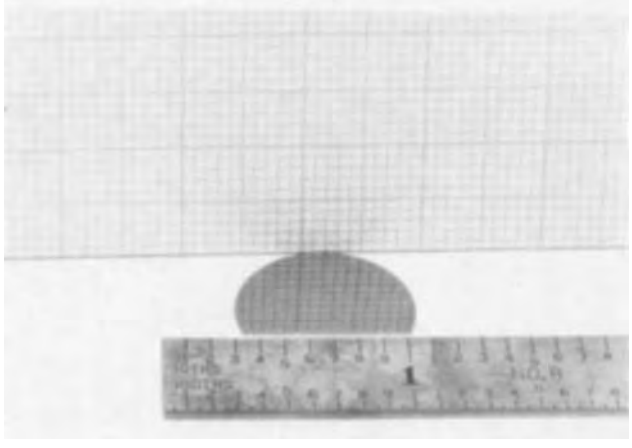

Fig. 2. Typical as grown surface of liquid phase epitaxial InGaAsP layer lattice matched to InP (scale in inches).

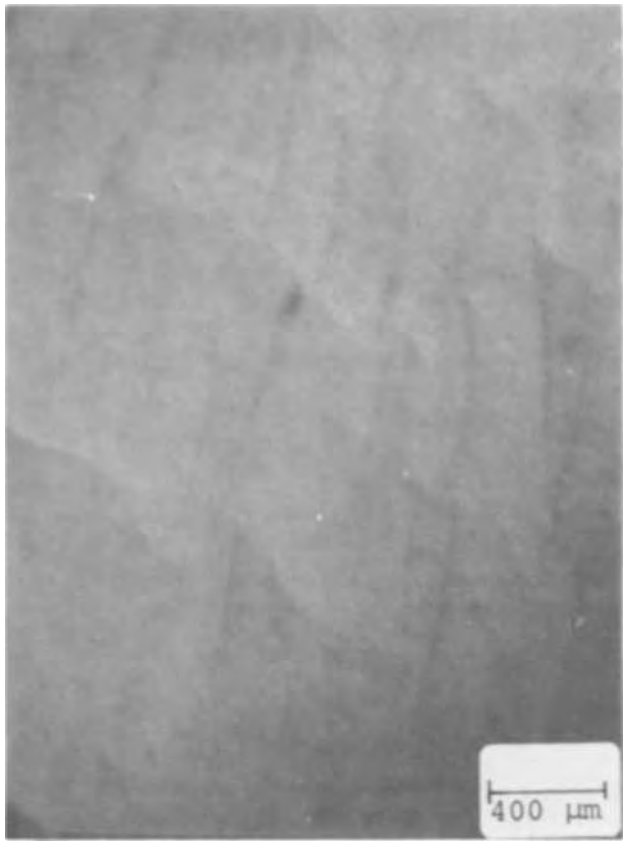

Fig. 3. Interferometer photomicrograph of the wafer shown on Fig. 2.

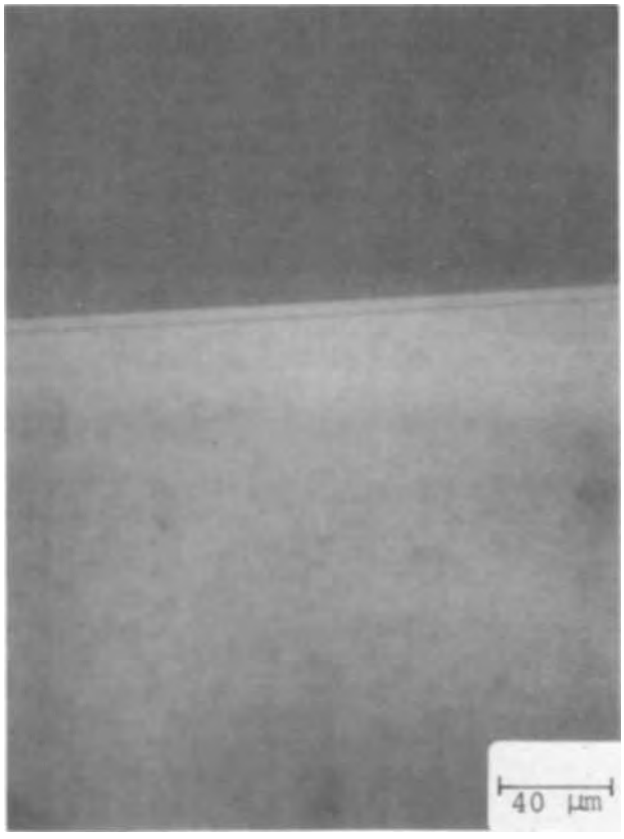

Fig. 4. Interferometer photomicrograph of the (110) cleavage plane of the wafer shown on Fig 2.

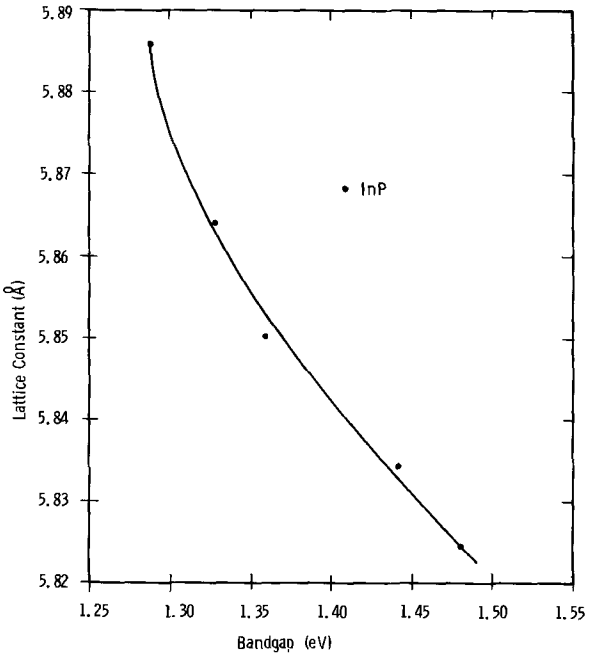

Fig. 5. Dependence of the 77°C bandgap energies on lattice constant for a number of InGaAsP epitaxial layers (details shown on Table I).

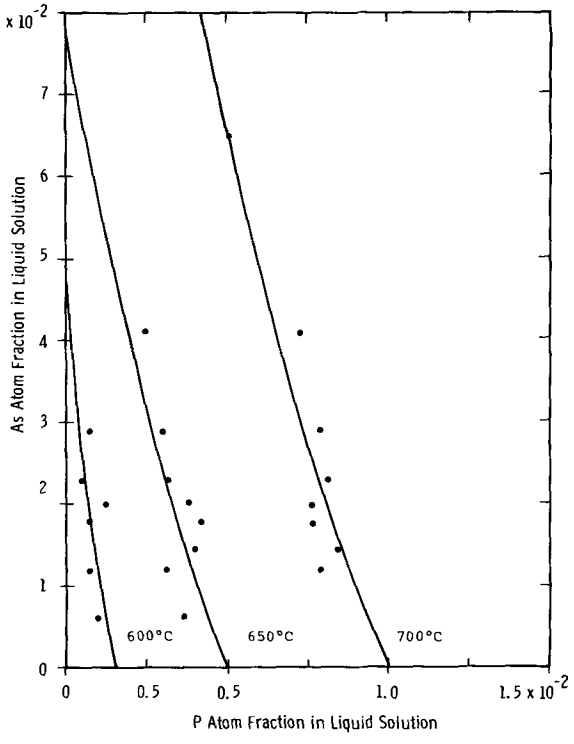

Fig. 6. Solubility of P as a function of As in liquid quarternary solutions for $X^{l}_{Ga}/X^{l}_{In} = 4.2 \times 10^{-3}$ at 600°, 650°, and 700°C. Curves are drawn through our experimental points.

tion is accompanied by a decrease in the lattice constant and an increase in bandgap energy. A number of series of runs as those shown on this figure were made in increasing As concentrations. In each series the first layer grown was with zero Ga to establish the InAsP boundary. In Fig. 5 we also show the InP point. The layer grown from solution No. 2 in Table I had a lattice constant of 5.864Å and a bandgap of 1.33 eV. InP, on the other hand, has a lattice constant of 5.868Å and a bandgap of 1.41 eV. Although no attempt was made to perfectly lattice match any layer to InP substrates during this series of runs, the lattice mismatch between epitaxial layer and substrate is 0.068% with a heterojunction barrier of 0.080 eV. In a similar manner, lattice matching has been achieved for layers having bandgap variation between 1.12 and 1.41 eV. No attempt has been made as yet to lattice match quaternary layers of lower bandgaps to InP, although no serious problems are anticipated.

Phase Diagram Investigations

The technique used in determining solubility parameters consists of preparing a liquid solution of In-Ga-As (InAs was used as the As source). The As concentration in the solution was always below the solubility limit determined by the X^{l}_{Ga} to X^{l}_{In} ratio in the solution. Solubility curves were determined at 600°, 650°, and 700°C by equilibrating the solution at the saturation temperature prior to contact with a single crystalline, chemically polished InP substrate. Following contact, the solution and InP substrate were kept at temperature for 2 hr which was experimentally determined to be of sufficient time for complete saturation. Subsequently the melt was separated from the InP substrate, and the substrate weight loss established the solubility limit of P. Figure 6 showed the solubility curves at 600°, 650°, and 700°C for a solution with a ratio X^{l}_{Ga} to X^{l}_{In} of 0.42×10^{-2}. The solid lines are drawn through the points and intersect the ordinate and abscissa at points coinciding with the extrapolated data of Antypas (8), Wu and Pearson (9) for the InGaAs system, and McVittie (10) for the InGaP system. A second series of solubility experiments was to investigate the dependence of P solubility on Ga, at constant As concentration. The results at 600° and 700°C are shown in Fig. 7. A comparison between Fig. 6 and 7 indicate that the solubility of P is decreased appreciably by the addition of Ga, while the presence of As has a less pronounced effect. This is very similar to the solubility of P in ternary solutions of InGaP and InAsP.

Since all the epitaxial layers grown were in the InP-rich corner of the quaternary region, the distribution of the solute Ga and As is certainly of primary interest. Figure 8 shows the distribution of Ga in layers grown in the temperature range of 650°-625°C from solution listed in Table I. In the region of X^{s}_{Ga} of zero to 0.055 the distribution coefficient K_{Ga} remains practically constant at 25. The distribution of As as a function of Ga in the solid solution, however, varies between 13.4 for zero Ga to 9.7 for 0.225% of Ga in the liquid solution. This variation is shown in Fig. 9, and it is obvious that such dependance will make the growth of a quaternary

Table I. Growth and characterization parameters for InGaAsP layers prepared by LPE at 650°-625°C

Run No.	Melt composition in grams* In	InAs	Ga	Solid composition in atomic per cent X^{s}_{Ga}	X^{s}_{As}	Lattice constant, A	Bandgap, eV (77°K)
1	2.086	0.020	0	0	7.59	5.886	1.29
2	2.086	0.020	0.0010	2.27	6.18	5.864	1.33
3	2.086	0.020	0.0020	4.27	5.57	5.850	1.36
4	2.086	0.020	0.0029	5.36	5.48	5.834	1.44
5	2.086	0.020	0.0037	6.3†	5.4†	5.824	1.48

* Solution was saturated in P from an InP source at 650°C.
† Estimated from Fig. 8 and 9.

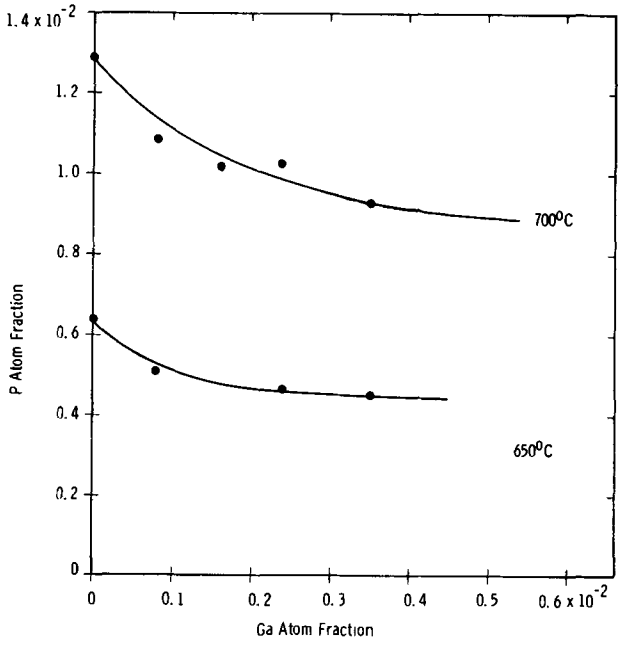

Fig. 7. Solubility of P as a function of Ga in quaternary liquid solutions for constant $X^l_{As} = 0.0145$ at 650° and 700°C. Curves are drawn through our experimental points.

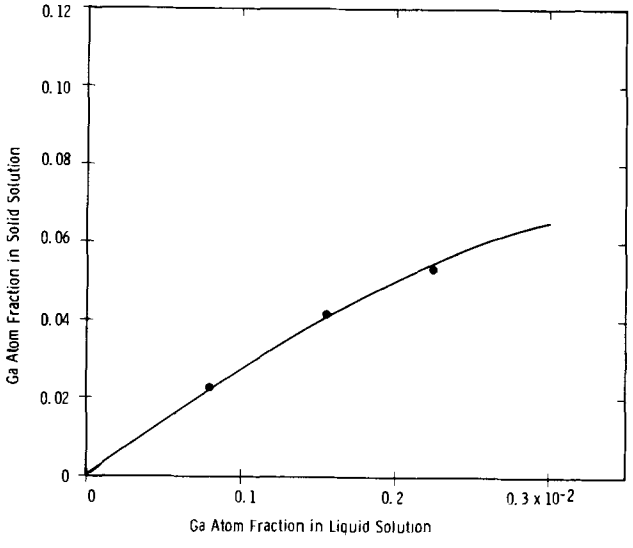

Fig. 8. Distribution of Ga in quaternary solid solutions grown from liquid solution with $X^l_{As} = 5.65 \times 10^{-3}$. Curve drawn through our experimental data.

InGaAsP of a given lattice and bandgap dependent on trial-and-error procedure to determine the distribution coefficients of Ga and As.

Summary

Heterojunctions are useful for devices requiring either electrical confinement or a change in optical properties from one layer to another. Both requirements must be satisfied for efficient operation of electro-optical devices. In such devices dislocations at the junction between two nonlattice-matched materials may introduce nonradiative recombination centers which degrade device performance. We have reported here the preparation of lattice matched heterojunctions in the InGaAsP-InP system. Lattice matching has been achieved in the bandgap energy range of 1.12-1.41 eV, although this range can be extended between 0.8-1.41 eV. The photoemission properties of the quaternary layers were investigated resulting in the highest 1.06 micron quantum efficiency known. James *et al.* (11) have reported on the photoemission properties of a number of quaternary alloys. Investigation on the heterojunction properties of lattice-matched InGaAsP-InP structures based on photodiode measurements reported by Antypas *et al.* (4) indicates that low defect density heterojunctions can be fabricated in this system.

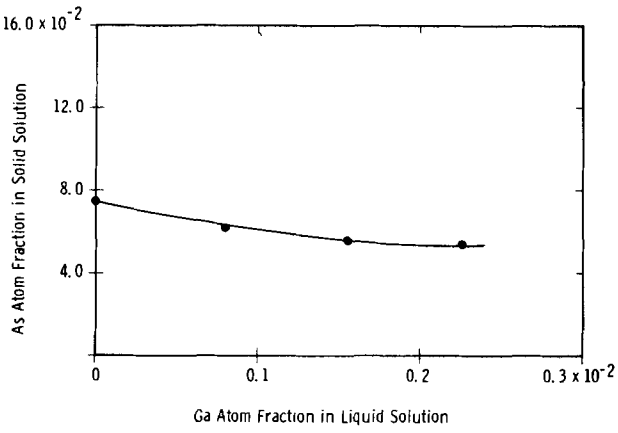

Fig. 9. Distribution of As as a function of Ga in layers grown from liquid solutions with constant As concentration $X^l_{As} = 5.65 \times 10^{-3}$. Curve drawn through our experimental data.

Acknowledgments

The technical assistance of L. Garbini, J. von Szeremy, and B. Oxley is gratefully appreciated.

This work was supported by the U. S. Army Night Vision Laboratory, Fort Belvoir, Virginia.

Manuscript submitted March 2, 1973; revised manuscript received June 11, 1973.

Any discussion of this paper will appear in a Discussion Section to be published in the June 1974 JOURNAL.

REFERENCES

1. R. D. Burnham, N. Holonyak, Jr., and D. R. Scifres, *Appl. Phys. Letters*, **17**, 445 (1970).
2. C. J. Nuese, D. Richman, and R. B. Clough, *Trans. Met. Soc. AIME*, **2**, 789 (1971).
3. G. B. Stringfellow, *J. Appl. Phys.*, **43**, 3455 (1972).
4. G. A. Antypas, R. L. Moon, L. W. James, J. Edgecumbe, and R. L. Bell in "Gallium Arsenide and Related Compounds, 1972," p. 48, Conf. Series #17, IPPS, London (1973).
5. G. A. Antypas, Unpublished.
6. R. D. Burnham, N. Holonyak, Jr., H. W. Korb, H. M. Nacksey, D. R. Scifres, J. B. Woodhouse, and Zh. I. Alferov, *Soviet Phys.-Semiconductors*, **6**, 77 (1972).
7. F. E. Rosztoczy, J. F. Caldwell, J. Kinoshita, and M. Omori, *Appl. Phys. Letters*, To be published.
8. G. A. Antypas, *This Journal*, **117**, 1393 (1970).
9. T. Y. Wu and G. L. Pearson, *J. Phys. Chem. Solids*, **33**, 409 (1972).
10. J. P. McVittie, PhD. dissertation, Stanford University, 1972.
11. L. W. James, G. A. Antypas, R. L. Moon, J. Edgecumbe, and R. L. Bell, *Appl. Phys. Letters*, **22**, 270 (1973).

Minority Carrier Generation Studies in MOS Capacitors on N-Type Silicon

D. R. Young and C. M. Osburn*

IBM Thomas J. Watson Research Center, Yorktown Heights, New York 10598

ABSTRACT

The pulsed capacitance technique was utilized to determine minority carrier generation rates in MOS capacitors. The addition of HCl, Cl_2, CCl_4, or C_2HCl_3 to oxygen during thermal oxidation was effective in gettering trapping centers in the silicon and resulted in lifetimes greater than 150 μsec. Higher halide concentrations and high oxidation temperatures improve the gettering process. The capacitance-time plot showed that the generation rate in long-lifetime structures was proportional to the volume of carrier-depleted silicon and that the generation of carriers on the surface was very small, *e.g.*, $S \approx 10^{-2}$ cm/sec.

Minority carrier current in the depletion regions of semiconductor devices leads to various undesirable device characteristics such as high leakage currents in p-n junctions, excessive dark currents in photodetectors, and reduction of switching threshold in charge-coupled FET devices.

The theoretical or ideal generation rate of minority carriers in silicon is very small at room temperature. Hence, the much larger rates typically observed in most samples studied to date have been attributed to anomalous effects, the predominant process being carrier generation at impurity sites located in the depletion region (1,2). It can be shown that those sites (acceptor or donor) with levels close to the center of the gap are the most prolific in electron-hole generation; consequently, the temperature dependence of the generation rate indicates a thermal activation energy between 0.5 and 0.6 eV (3) or about half the bandgap of silicon.

In practice, it is found that large sample-to-sample variations exist in the minority carrier generation rate. The work reported here is part of a long-range program to gain added insights concerning the mechanisms responsible for minority carrier generation and to develop material technologies that will result in a significant reduction in the minority carrier generation rate as well as a decrease in its variability. The pulsed capacitance technique was chosen for measuring the minority carrier density and has been described earlier by Zerbst (4).

The gettering of metallic impurities from silicon is one technique previously used for reducing both minority carrier generation rates and diode leakage current (1, 5-12). Copper, iron, manganese, and gold have been shown (1, 2) to introduce recombination-generation centers in the forbidden energy gap of silicon and thereby reduce the lifetime of excess minority carriers. Actual gettering has been accomplished by KCN (1); P_2O_5 (1, 7, 9, 10, 12); B_2O_5 (1, 12); V_2O_5 (12); Ni (7); boron diffusion; and phosphorous diffusion (1, 5). Furthermore, reduced minority carrier generation has been obtained by Cl_2 annealing (5), precleaning oxidation tubes with HCl (13), and oxidation in Cl_2 (9, 11) or HCl (8, 9, 11).

In addition to improving the minority carrier lifetime, treatments have recently been shown to reduce mobile charge densities in SiO_2 (14-18), improve its breakdown strength (15, 16, 19), and enhance dielectric integrity under accelerated bias-temperature stress (20). Because of their simplicity of application and consequent technological advantages, HCl, Cl_2, CCl_4, and C_2HCl_3 oxidation processes were selected for this study.

Experimental Procedure

Metal-oxide-semiconductor capacitors were fabricated on 2 ohm-cm, p- and n-type <100>-oriented silicon wafers. Most measurements were made on n-type wafers to avoid surface inversion due to the positive space charge in the SiO_2. The wafers were ultrasonically cleaned using NH_4OH-H_2O_2, HCl-H_2O_2, and HF solutions. Oxides from 200 to 1000Å thick were grown in dry oxygen at 1000°C, using additions of 1-6% HCl (99.995% pure) or Cl_2 (99.99%) to the oxygen ambient; additions up to 3% CCl_4, 6% C_2HCl_3, or 9% HBr were also tested. By using reasonable precautions to insure pure SiO_2 films, mobile Na^+ ion concentrations in the SiO_2 were kept very low [$\approx 5 \times 10^{10}$/cm^2, as determined using the flatband voltage shift technique (21)]. One hundred aluminum electrode dots (10-50 mil diameter) were electron-gun evaporated through metal masks onto each wafer in a clean evaporation system; the samples were then given a 5 min anneal at 500°C in dry nitrogen to remove radiation damage.

Results

Processing.—The influence of processing on minority carrier generation was best determined from statistical measurements of inversion times of a large number of MOS capacitors, where the inversion time is defined as the time required for the capacitance to go from deep depletion to equilibrium inversion. In the absence of large surface generation Schroder and Guldberg (22) showed that these inversion times are directly proportional to the lifetime. Inversion times from less than 1 msec to over 1000 sec were observed, giving a wide range of measurable characteristics.

Dramatic improvements in inversion times are obtained with HCl or Cl_2 oxidations and are illustrated in Fig. 1, where statistical distributions of inversion

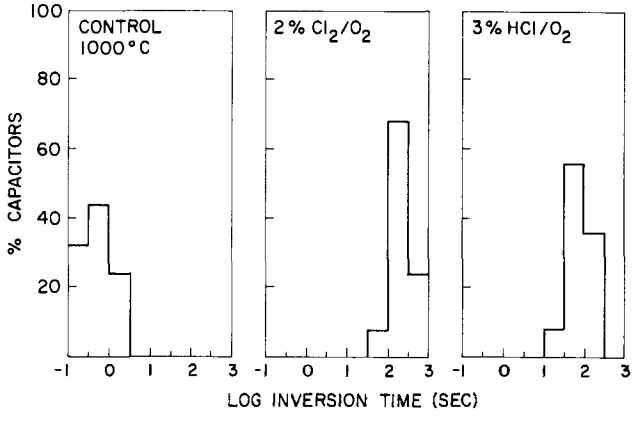

Fig. 1. Statistical distributions of inversion times for control; Cl_2-grown, and HCl-grown oxides.

* Electrochemical Society Active Member.

Key words: minority carrier generation, impurity gettering, metal oxide semiconductor (MOS), halogen oxidation.

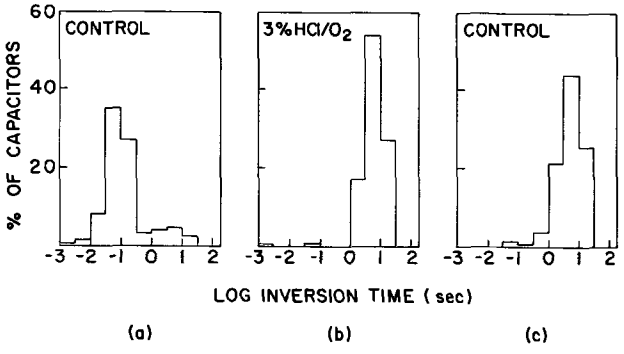

Fig. 2. Effect of sequential oxidation, after oxide stripping, on inversion time showing permanence of HCl gettering. (a) Initial control oxide; (b) after oxide strip and HCl oxidation; and (c) after strip of HCl oxide and regrown in control furnace.

times of halide-grown oxide capacitors are compared to normally grown ones. The halide oxidation not only improves the average time but also reduces the statistical variation. Increases up to two or three orders of magnitude in the inversion time were seen with the HCl treatment. Figure 2 shows the permanence of the HCl oxidation after additional processing; (a) is a histograph of the inversion times for a standard- or control-grown oxide structure; (b) indicates the characteristics when the control oxide is removed and then regrown in 3% HCl-97% O_2; and, (c) indicates the characteristics after the HCl oxide is stripped and regrown in the control furnace with no HCl present. A comparison of (a) and (b) shows the effectiveness of HCl while (b) and (c) are almost identical, indicating that once the impurities have been gettered from the silicon, they are not reintroduced by a later oxidation under very clean conditions. Merely growing an oxide by stripping and reoxidizing does not improve the lifetime and shows that the gettering effect is independent of a layer of silicon surface being oxidized away during preoxidation.

Both the oxidation temperature and the concentration were varied for the different halide additions in order to optimize the process. As seen in Table I, raising the temperature from 850°-1150°C for HCl oxides results in longer inversion times. Likewise, higher HCl concentrations (from 1 to 6%) yield improved properties. In practice, a lower HCl concentration is desirable in order to maintain close control over the oxidation rate and to prevent droplet formation and silicon pitting (8). Increasing the HCl/O_2 gas velocity during oxidation from 0.37 to 3.3 cm/sec did not improve the inversion time. Apparently the gettering process is dependent only on the HCl concentration and not on the flow rate. Measurements (23) of the silicon doping profile showing no enhanced phosphorus pile up at the surface confirmed that the longer inversion times were a result of the gettering and not because of additional dopant segregation. Both CCl_4 and C_2HCl were also seen to improve lifetime whereas HBr gave shorter storage times (Table I).

Table I. Effect of halide addition and oxidation conditions on average time for pulsed capacitance to reach equilibrium inversion (sec)

Halide	Oxidation temperature (°C)	Halide concentration 0%	½%	1%	3%	6%	9%
HCl	1000	3.75	—	68	77.2	79.7	—
HCl	850	—	—	—	16.4	—	—
HCl	1150	—	—	—	205.1	—	—
HCl	1150	8.0	—	—	97.2	—	84.9
Cl_2	1000	6.8	—	246	6.6	1.8	—
CCl_4	1000	7.2	4.1	50	46.1	—	—
C_2HCl_3	1000	4.6	—	61.2	118.6	99.4	—
HBr	1000	3.30	—	0.72	1.04	1.36	0.85

Additional processing variations were tested in order to evaluate more fully means for improving lifetimes. Some results are shown in Fig. 3. Figure 3c shows that a 30 min 1000°C HCl/N_2 anneal following oxide growth is detrimental to the quality of the capacitors since the inversion times after the anneal are considerably shorter than those for the control-grown oxide. An HCl/N_2 anneal at 1000°C before growth results in a very nonuniform attack or pitting on the surface of the Si wafer, and is therefore quite unacceptable. Surprisingly enough, the growth of 250Å HCl oxide after growth of a 250Å control oxide was found to be similar to oxides grown entirely in HCl (Fig. 3d). Apparently, the 250Å thick SiO_2 film is not sufficient to block the gettering action.

Attempts to optimize the chlorine oxidation conditions were not as successful as those with HCl. Wafer corrosion and nonuniform oxides often occurred when Cl_2/O_2 was used. Growth of a thin oxide before adding Cl_2 was helpful but not entirely effective in eliminating this etching. At 1000°C the Cl_2 concentration had to be kept below 2-3%; at higher temperatures even these concentrations gave poor results. Increasing the chlorine concentration from 1 to 6% during 1000°C oxidation resulted in an increased number of oxide shorts and shorter inversion times. This same effect was seen at the high concentrations of CCl_4 and C_2HCl_3 (Table I).

The postmetallization anneal (5 min at 500°C in N_2) given after the electron-gun evaporation of aluminum to reduce surface states and radiation damage was found to increase the inversion time. In some capacitors the inversion time increased by more than a factor of 100, and the average improvement was a factor of three. Apparently the surface-state generation component of the total generation can be dominant, at least in unannealed samples.

Electrode area.—In the course of the measurements a wide range (over six orders of magnitude) of inversion times was seen. In order to understand better the wide variation of results, inversion times were measured as a function of capacitor electrode area. Quite surprisingly, the fraction of capacitors having short inversion times was less for 32 mil diameter electrodes than for either 10 or 50 mil diameter ones. This

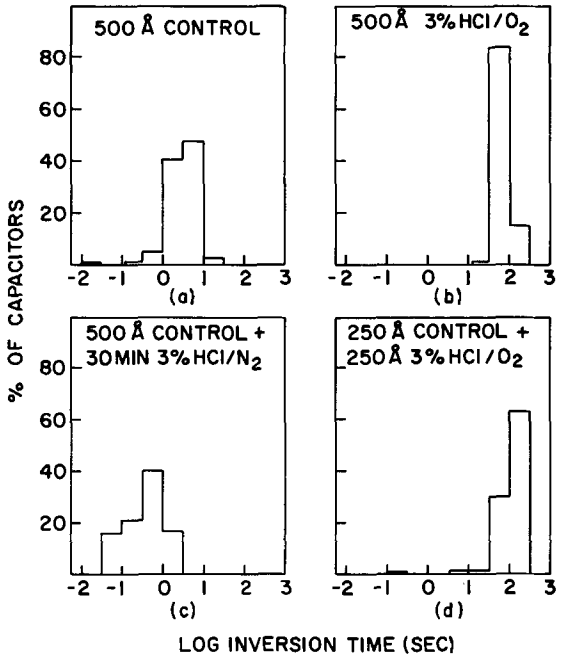

Fig. 3. Effect of processing variations on inversion time for (a) control oxidation; (b) normal 3% HCl/O_2 oxidation; (c) annealed in 3% HCl in N_2 at 1000°C following oxidation; and (d) 250Å of HCl grown after 250Å of control oxide was grown.

is in contrast to the behavior seen in dielectric breakdown in SiO_2 films on Si, for example, where the fraction of low electric field breakdown events is directly proportional to the electrode area (19, 24, 25). Apparently the capacitor area dependence of minority carrier generation is more complex than that of dielectric breakdown. Several different processes having different area dependencies that shorten inversion times can be considered:

(*i*) Generation centers. Since even the smallest capacitor covers many centers, the effect of these centers should be independent of electrode size.

(*ii*) Perimeter generation. If minority carriers were generated at the edge or surface of a capacitor dot, then the inversion time would be expected to vary directly as the electrode diameter.

(*iii*) Localized defects. If random defects are present, the generation rate would be proportional to the number of defects that a capacitor dot covered. In the case of defects under the electrode, this number varies as the capacitor area; for edge defects, this number varies as the diameter. In the case of a single defect, the inversion time should be proportional to the electrode diameter squared since the charge required for full inversion should vary with the area. Nevertheless, no one of these three mechanisms explains the phenomena we have observed.

Generation process.—A linear Zerbst (4) plot (Fig. 4) of a better sample signifies a generation rate proportional to the depletion volume. The intercept with $C_\infty/C = 1$ gave a surface generation velocity 1.06×10^{-2} cm/sec which was lower than the value of 1 cm/sec reported by Schroder (10) in phosphorous-gettered silicon. Minority carrier lifetime, using the technique of Heiman (26), was 168 μsec. This might be compared with a lifetime of 0.2 μsec quoted by Zerbst and 7.6 μsec, as reported by Heiman. Robinson and Heiman (8), also using an HCl treated oxide, obtained a lifetime of 100 μsec. Dumin and Henry (9) and later Schroder (10) reported lifetimes of nearly 1000 μsec in silicon gettered with $POCl_3$.

The temperature dependence of the generation rate has also been studied and the effect of the HCl treatment is readily apparent (*c.f.*, Fig. 5). It is observed that the old process resulted in an activation energy of 0.57 eV for the temperature range covered by the measurement (18°-120°C) whereas the HCl sample had an activation energy of 0.69 eV up to 55°C and 0.9 eV for higher temperatures. This is similar to the diode leakage studies discussed by Grove (3) and can be explained as follows. Impurity site generation ($d\sigma/dt$) is given by

$$\left(\frac{d\sigma}{dt}\right)_{\text{impurities}} = \frac{-\sigma_i U_{th} N_t N_i}{2\cosh\left(\frac{E_i - E_t}{kT}\right)} \qquad [1]$$

where σ_i is the cross section, U_{th} is the thermal velocity, N_t is the impurity concentration, N_i is the intrinsic carrier concentration, and $E_i - E_t$ is the position of the impurity level with respect to the intrinsic level. The temperature dependence is that of N_i with an activation energy approximately equal to one half the gap width if $E_i \simeq E_t$. The generation rate due to diffusion is given by

$$\left(\frac{d\sigma}{dt}\right)_{\text{diff}} = \frac{D}{NL} N_i^2 \qquad [2]$$

where D and L are the diffusion constant and diffusion length, respectively, for the minority carriers and N is the doping concentration. The temperature dependence of this goes as N_i^2 which has an activation energy of the full gap or 1.1 eV.

As a result, it can be seen that impurity generation is important at lower temperatures, and that diffusion becomes important at higher temperatures as seen by

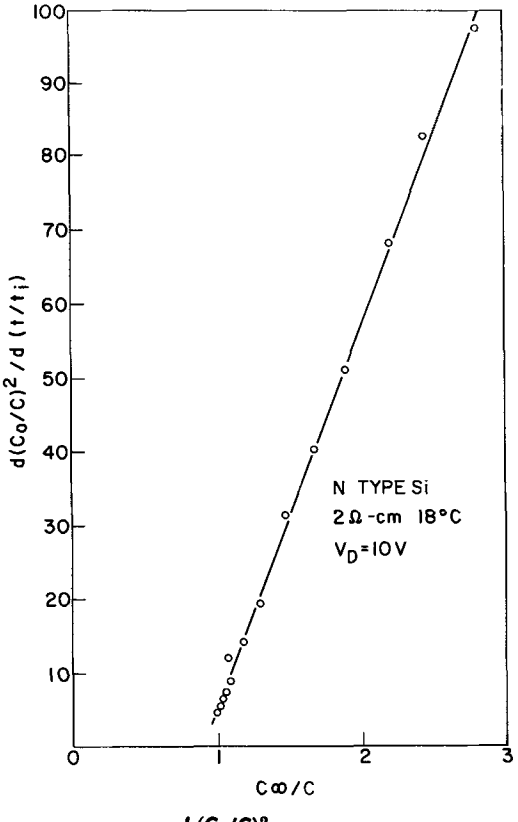

Fig. 4. Linear plot of $\frac{d\,(C_0/C)^2}{d\,(t/t_i)}$ vs. C_∞/C signifying a generation rate proportional to the depletion volume. The intercept at $C_\infty/C = 1$ gives the surface generation. t_i = time for full inversion.

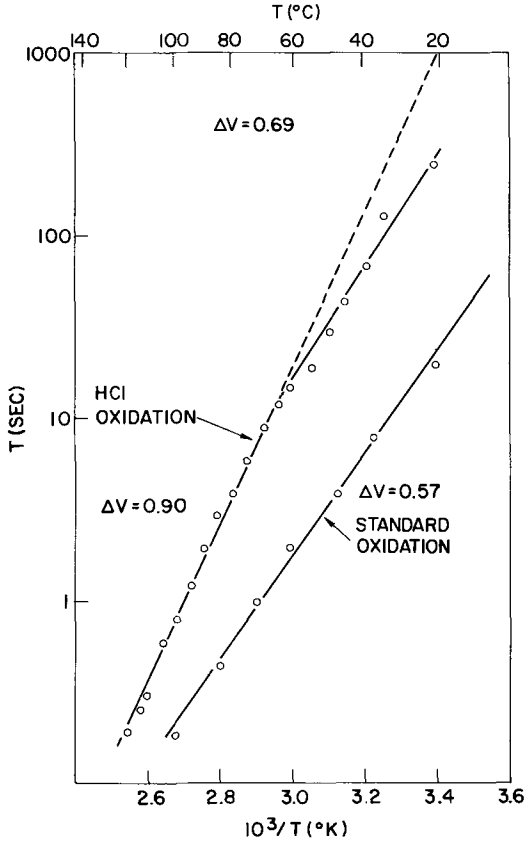

Fig. 5. Temperature dependence of inversion time of standard and HCl oxidized capacitors.

the data of Fig. 5. As the impurity concentration decreases, the onset of diffusion can be seen at lower temperatures.

Summary

The measurement of the capacitance buildup in an MOS capacitor following application of a depletion voltage was found to be a straightforward method to determine the surface generation rate. This technique avoids the problems associated with the measurement of low level leakage currents in diodes to obtain the generation rate.

The use of HCl, Cl_2, CCl_4, or C_2HCl_3 gas additions to oxygen during thermal oxidation of silicon was found to result in a very significant (up to two to three orders of magnitude) decrease in the generation rate; HBr slightly increased generation. Increasing HCl concentration from 0 to 6% and increasing oxidation temperature from 850° to 1150°C were seen to give improved properties. Experiments have confirmed that once HCl oxidation has occurred, subsequent oxide stripping and standard processing can also result in superior capacitors. The thermal activation energy for generation in standard capacitors was 0.57 eV or about half the silicon bandgap, while HCl oxidized ones had a 0.90 eV activation. Apparently the chlorine oxidation was effective in removing impurities such as Cu and Au that have states near the center of the silicon bandgap. The HCl gettering process was not diminished by the presence of a 250Å residual oxide on the silicon; however, the use of HCl/N_2 mixtures either before or after oxide growth resulted in either silicon pitting or a large number of shorted capacitors. The use of chlorine gettering was restricted because of substrate attack.

The variation of the inversion time with capacitor area suggests that several processes are important in addition to carrier generation at impurity centers. Evidence was also seen for localized defects and perimeter generation. Additional work is planned to describe these mechanisms.

Detailed analysis of the generation process in good capacitors shows that the generation rate is proportional to the depletion volume. A very small surface generation, $S = 1.06 \times 10^{-2}$ cm/sec, is observed along with a long lifetime of 168 μsec.

Acknowledgments

The authors would like to acknowledge many stimulating discussions with A. Berman and D. Kerr. The skillful measurements and sample preparation of E. Alley and D. Ormond are gratefully appreciated. W. P. Dumke contributed to the theoretical interpretation of the results.

Manuscript submitted Nov. 13, 1972; revised manuscript received June 5, 1973.

Any discussion of this paper will appear in a Discussion Section to be published in the June 1974 JOURNAL.

REFERENCES

1. R. N. Hall and J. H. Racette, *J. Appl. Phys.*, **35**, 379 (1964).
2. A. Goetzberger and W. S. Shockley, *ibid.*, **31**, 1821 (1960).
3. A. S. Grove, "Physics and Technology of Semiconductors," p. 172, John Wiley & Sons Inc., New York (1967).
4. M. Zerbst, *Z. Angew. Phys.*, **22**, 30 (1966).
5. B. M. Waldner and L. Sivo, *This Journal*, **107**, 298 (1960).
6. E. J. Mets, *ibid.*, **112**, 420 (1965).
7. J. E. Lawrence, *Trans. AIME*, **242**, 484 (1968).
8. P. H. Robinson and F. P. Heiman, *This Journal*, **118**, 141 (1971).
9. D. J. Dumin and W. N. Henry, *Met. Trans.*, **2**, 677 (1971).
10. D. K. Schroder, *IEEE Trans. Electron. Devices*, **ED-19**, 1018 (1972).
11. R. S. Ronen and P. H. Robinson, *This Journal*, **119**, 747 (1972).
12. S. W. Ing, Jr., R. E. Morrison, L. L. Alt, and R. W. Aldrich, *ibid.*, **110**, 533 (1963).
13. A. Berman, D. A. Kerr, and J. R. Petrak, Private communication.
14. R. J. Kriegler, Y. C. Cheng, and D. R. Colton, *This Journal*, **119**, 388 (1972).
15. E. Terner, Private communication.
16. R. A. Gdula, Private communication.
17. R. J. Kriegler, *Appl. Phys. Letters*, **20**, 449 (1972).
18. R. J. Kriegler, in "Semiconductor Silicon," Howard R. Huff and Ronald R. Burgess, Editors, p. 363, The Electrochemical Society Softbound Symposium Series, Princeton, New Jersey (1973).
19. C. M. Osburn and D. W. Ormond, *This Journal*, **119**, 597 (1972).
20. C. M. Osburn and N. J. Chou, *ibid.*, **120**, 1377 (1973).
21. E. H. Snow, A. S. Grove, B. E. Deal, and C. T. Sah, *J. Appl. Phys.*, **36**, 1664 (1965).
22. D. K. Schroder and J. Guldberg, *Solid-State Electron.*, **14**, 1285 (1971).
23. Y. J. van der Meulen and C. M. Osburn, To be published.
24. C. Fritzsche, *Z. Angew. Phys.*, **24**, 43 (1967).
25. N. Chou and J. Eldridge, *This Journal*, **117**, 1287 (1970).
26. F. P. Heiman, *IEEE Trans. Electron. Devices*, **ED-14** (11), 781 (1967).

Electrical Conduction at Elevated Temperatures in Thermally Grown Silicon Dioxide Films

T. G. Mills*[1]

TRW Semiconductor Division, Lawndale, California 90260

and F. A. Kroger*

Department of Material Science, University of Southern California, Los Angeles, California 90007

ABSTRACT

In order to study electrical conduction at elevated temperatures in high purity, amorphous silicon dioxide films, emf and conductance measurements have been made on solid-state electrochemical cells incorporating films grown by thermal oxidation of phosphorus- or boron-doped silicon substrates in a double-wall fused silica furnace. No mobile ions were detected by capacitance-voltage measurements on MOS structures stressed at 150°C. Values of the ionic transport number, the ratio of ionic current to total current, were obtained as a function of temperature, oxygen partial pressure, and substrate doping by comparing the open circuit voltages measured for the cells with theoretical values calculated from the free energy of formation. On the basis of the experimental results and a theoretical model, it is proposed that the species primarily responsible for ionc conduction at elevated temperatures is a native defect, specifically, a doubly charged oxygen interstitial.

Electrical conduction in amorphous silicon dioxide films has been investigated at elevated temperatures by various workers. Either predominantly electronic or ionic conduction has been reported in most cases studied (1, 2); however, mixed conduction was reported by Jorgensen (3). The only well-established mechanism for conduction in SiO_2 films is the drift of mobile alkali ions as demonstrated by MOS measurements and chemical analysis (4, 5). In the absence of alkali ions, either electronic or ionic conduction occurs, depending upon the mechanism for creating electronic or native ionic defects.

Jorgensen (3) studied electrical conductance in SiO_2 films by observing the effects of an electric field on the growth of such films. He found that the growth could be stopped by applying a sufficiently high electrical potential, E_{stop}. The emf measured on a cell, Pt, Si/SiO_2/$_{Pt}O_2$ is related to E_{stop} by the expression

$$\bar{t}_i = E/E_{stop} \qquad [1]$$

$\bar{t}_i$ is the average ionic transference number, defined as the ratio of the ionic conductance to the total conductance. Jorgensen used this expression to obtain values of $\bar{t}_i$ from the measured values of E and E_{stop}. By this method, he determined that at 1000°-1152°K, SiO_2 was a mixed conductor with $\bar{t}_i = 0.4$, and that the ionic conduction was due to a doubly charged species.

Similar results have been obtained by a different technique in our work. Transport number values were determined by open-circuit emf measurements on solid-state electrolytic cells incorporating SiO_2 films on Si substrates. The dependence of the emf and current-voltage characteristics of these cells on temperature, oxygen pressure, and substrate doping was interpreted in terms of a theoretical defect model in order to investigate the conductance mechanism and the identity of the conducting species.

Experimental Procedure

Three types of electrochemical cells, as shown schematically in Fig. 1, were fabricated to study conduction in amorphous SiO_2 films: Type I (symmetrical, for current-voltage measurements), Pt, Si/SiO_2/Si,Pt; Type II (asymmetrical, for emf measurements), Pt,Si/SiO_2/(Ge,Si),Pt; and Type III (asymmetrical, for emf measurements), $_{Pt}^{O_2}$/Si/SiO_2/$_{Pt}^{O_2}$.

Type I and II cells had a fixed oxygen and Si activity at a given temperature. For Type I, the O_2 activity is established by the free energy of formation of SiO_2, while for Type II the Si activity is established

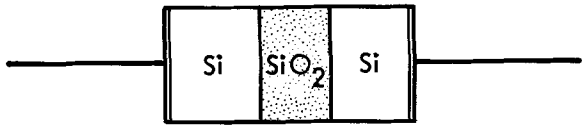

TYPE I. SYMMETRICAL CELL (LOW O_2 PARTIAL PRESSURES)

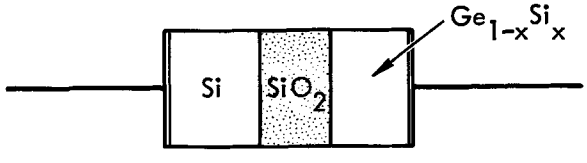

TYPE II. ACTIVITY CELL FOR EMF AT LOW OXYGEN PARTIAL PRESSURE

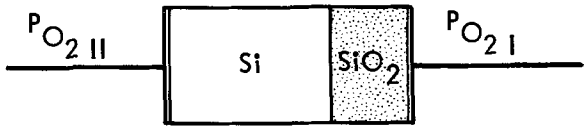

TYPE III. O_2 CELL FOR EMF AT VARIABLE OXYGEN PARTIAL PRESSURE

Fig. 1. Schematic diagrams of electrochemical cells used for investigating conduction in amorphous SiO_2 films.

* Electrochemical Society Active Member.
[1] Present address: TRW Systems, One Space Park, Redondo Beach, California 90278.
Key words: emf measurements, ionic conduction, insulating films.

by the concentration of the Si at the (Ge,Si)/SiO_2 electrode. The oxygen activity at the Pt,O_2/SiO_2 electrode of the Type III cells is varied by changing the oxygen partial pressure, P_{O_2}. An electrochemical stabilized zirconia pump is used to establish P_{O_2} while the pressure is monitored with the aid of a stabilized zirconia electrochemical pressure gauge. Details of the pump and gauge will be given later.

Oxide films 3000Å thick were formed on 1.5 in. Si wafers by thermal oxidation at 1453°K using dry 99.999% oxygen in a clean double-wall furnace. The Si wafers, which were syton polished and chemically cleaned prior to oxidation, were doped with B or P at concentrations ranging from 10^{13} to 10^{16} atoms/cm^3.

Type I cells were formed by pressing two oxidized Si wafers together at 1100°C, while Type II cells were formed by pressing one oxidized Si wafer and a Ge-Si alloy wafer together at 900°C. The wafers were pressed at 1000 psi between pyrolytic graphite plates in a dry nitrogen ambient.

The Si-Ge alloys for Type II cells were formed by mixing the desired proportions of Si and Ge in a carbon crucible and heating to approximately 1100°C in argon, then permitting the melt to cool slowly. The Si and Ge in the alloy were virtually undoped, with impurity concentrations of the order of 10^{12} atoms/cm^3 and 10^{13} atoms/cm^3, respectively. The concentration of silicon in the alloy was determined by electron microprobe analysis. These concentrations were used to determine activities according to Hiskes and Tiller (6). This may be compared to the work of Thurmond and Struthers (7) where an ideal solution is assumed at low concentrations. (See Table I).

The oxide films were investigated for mobile alkali ions by using the techniques described by Deal *et al.* (4). Aluminum dots were deposited on the Si wafers through a metal mask, the contacts were annealed at 450°C for five minutes and C-V measurements made on an impedance comparator, employing a sweep voltage from a function generator. The data were plotted automatically on an x-y recorder.

Electrical contacts were made to the cells by sputtering −1000Å of platinum on each side of the thermally pressed wafer. The wafer was then diced into 1.0 × 0.5 cm segments for electrical measurements. Platinum leads were attached using a pressure contact.

The high-temperature electrical measurements were all made in a double-wall fused quartz furnace. The conductance and emf measurements were made on the Type I and II cells under dry N_2 ambient, while Type III cells were measured under various O_2 partial pressures. The emf was measured on a high impedance Cary voltmeter, as the open circuit potential across the cell. The emf was measured as a function of temperature and O_2 partial pressure. For the temperature dependence measurements, data were taken both with temperatures decreasing and increasing in increments of 50°C.

In the case of Type I and Type II cells, a fixed O_2 partial pressure is established at each half cell by the temperature and the free energy of formation of SiO_2, hence 30 min was allowed for stabilization at each temperature. (This will be discussed later.)

The O_2 partial pressure for the Type III cells was controlled and measured over the range of 10^{-3}-10^{-20} atm by using a pump and detector fabricated from stabilized zirconia (8). The pump was a ZrO_2 tube open at both ends with Pt electrodes formed inside and on the outside of the tube by using Pt paste and Pt foil. This tube was inserted in line with the gas flow as indicated in Fig. 2. Potentials of up to 3V, giving currents up to 13 mA, were applied across the Pt/ZrO_2/Pt pump cell. The O_2 partial pressures obtained were determined from the open circuit voltage E_a measured across the detector cell

$$\ln P_{O_2} = \frac{4F}{RT} E_a + \ln [P_{O_2}]_{ref} \quad [2]$$

The detector cell was a ZrO_2 tube closed on one end, with Pt electrodes formed on both the inside and outside of the tube. The closed end of the pump was inserted and sealed into the vacuum-tight, sampling furnace in close proximity with the cells to be measured. The open end of the tube was exposed to the room ambient. For the detector, the reference P_{O_2} was that of the room ambient, with the temperature of the detector cell being that of the sample. For efficiency in the O_2 pump, the pump was maintained at a constant temperature, 600°C, with a separate furnace.

Table I. Ge-Si alloy concentrations

Before alloying atom fraction Si	After solidification: Atom fraction Si (electron microprobe)	After solidification: Si activity (Hiskes and Tiller)[a]
0.200	0.204	0.306
0.010	0.0088	0.00968
0.001	0.0012	0.0012

[a] Ref. (6).

Results

Figure 3 shows current density as a function of voltage for typical Type I cells, containing SiO_2 grown on P-doped Si. Approximately ohmic behavior is shown up to 3V; at higher voltages the current density is proportional to V^n, with $n \simeq 2$, which is characteristic of carrier injection.

Figure 4 shows values of log σT as a function of $(1/T)$ for SiO_2 grown on B- and P-doped Si as mea-

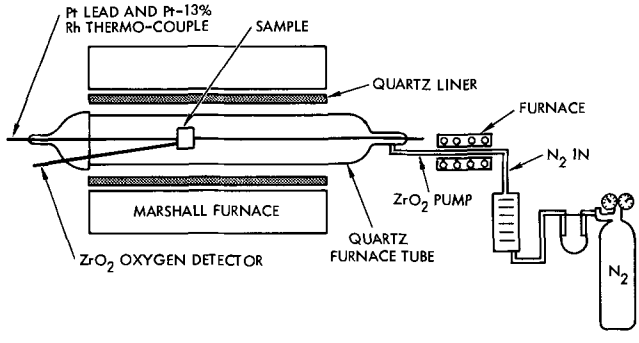

Fig. 2. EMF and conductance measurement apparatus

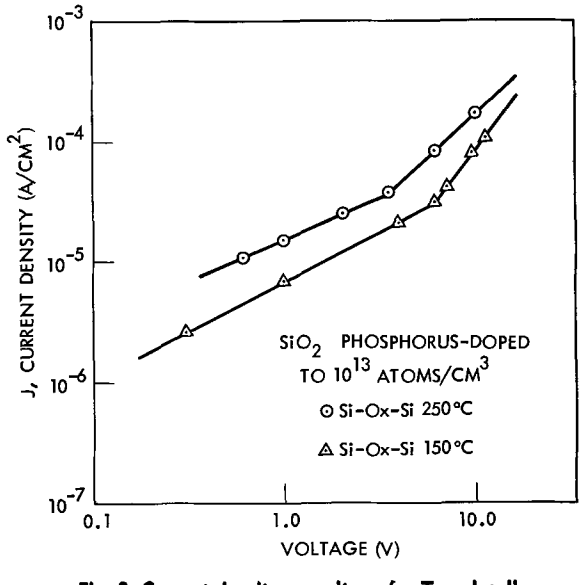

Fig. 3. Current density vs. voltage for Type I cells

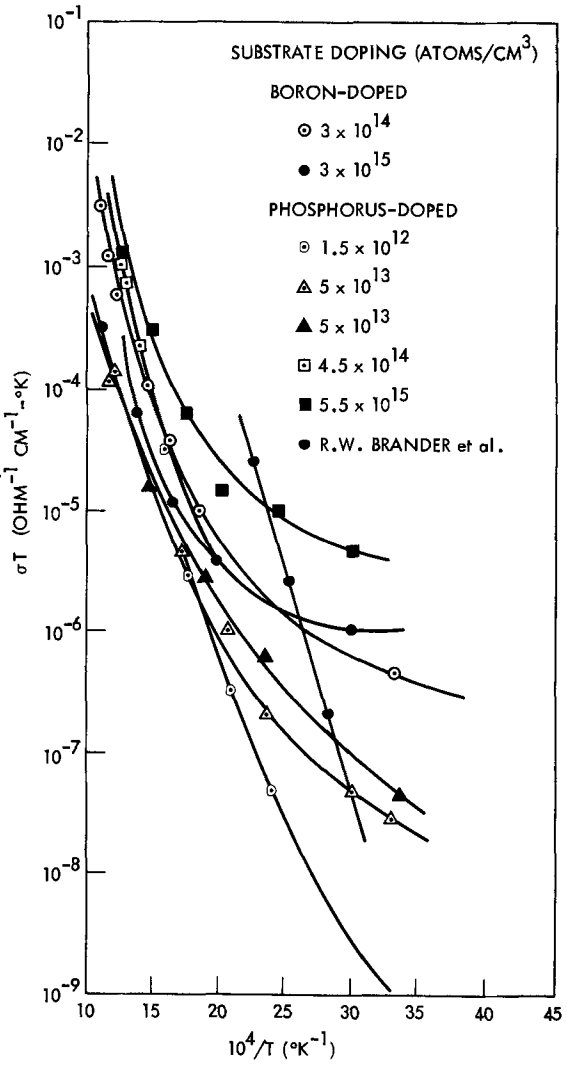

Fig. 4. Log σT vs. reciprocal temperature for Type I cells

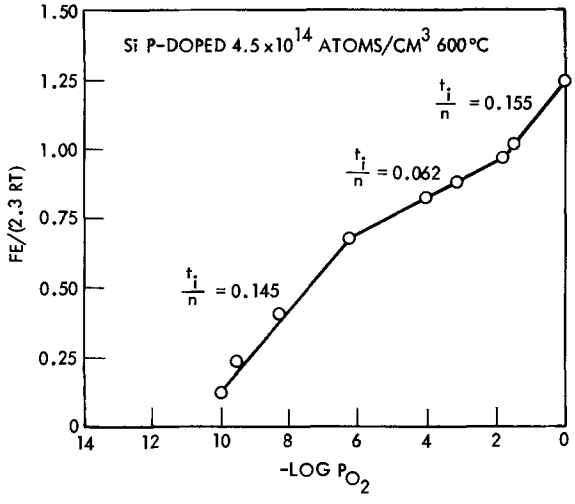

Fig. 5. EMF vs. log O_2 partial pressure for a Type III cell with P-doped substrates.

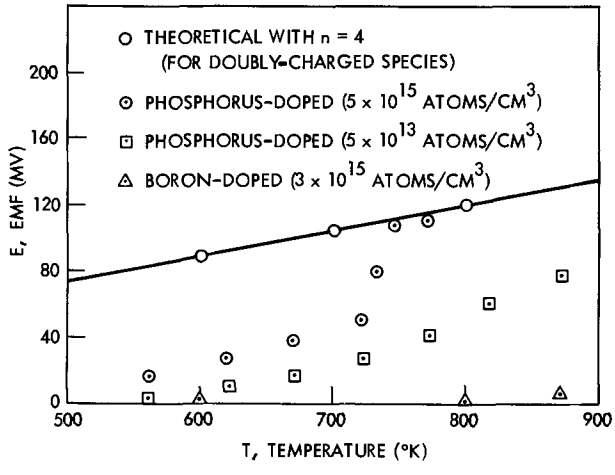

Fig. 6. EMF of Type II cells vs. temperature

sured in Type I cells. The conductivity σ is defined as $\sigma = IL/AV$, where A is the area and L is the thickness of the oxide. Typical values of A were 0.5 and 1.0 cm^2 and typical values of L were 3000-6000Å. The measurements were made at voltages in the range where the behavior is nearly ohmic. Data reported by Brander *et al.* (1) on cells with Al electrodes are shown for comparison with our Type III cells with Pt/SiO_2 electrodes. Brander's oxides were on B-doped substrates with 3 × 10^{15} atoms/cm^3.

The results of emf measurements at 600°C on cells containing SiO_2 films grown on P-doped Si with variable O_2 activities are shown in Fig. 5. It is assumed throughout this paper that the concentration of dopant in the SiO_2, both P and B, is proportional to the dopant concentration in the Si on which the oxide film is grown. The points at low P_{O_2} were obtained for Type II cells with (Ge-Si) alloys of various compositions. The points at higher P_{O_2} were measured on Type III cells.

Figure 6 shows emf as a function of T for Type II cells containing SiO_2 films grown on P- and B-doped Si. The method of deriving theoretical values of the emf will be described in the Discussion section.

Discussion

In this section, the emf data for Type II and III cells are used to obtain values for the ionic transference number (t_i), the ratio of the ionic conductance to the total conductance. These values are then used, together with the data for total conductance obtained for Type I cells, to provide evidence concerning the identity of the species primarily responsible for the ionic conductance.

For a cell with a gradient in the chemical potential of oxygen or a corresponding but opposite gradient in the chemical potential of Si between the electrodes on the right and the left sides of the cell, the emf is given by

$$E = \frac{1}{\mathbf{F}}\int_{I}^{II} (t_i/n)\, d\mu_{O_2} \qquad [3]$$

$$= \frac{RT}{\mathbf{F}}\int_{I}^{II} (t_i/n)\, d \ln P_{O_2} \qquad [4]$$

$$= \frac{RT}{\mathbf{F}}\int_{II}^{I} (t_i/n)\, d \ln a_{Si} \qquad [5]$$

Here t_i is the local value of the ionic transference number and n is the number of equivalents transported for a reaction involving one g-mole of O_2; $n = 4$ corresponds to transport by ions or ionic defects with conventional charges. Lower values of n correspond to abnormal charges (9). From Fig. 1, we see that Eq. [4] is applied to Type III cells and Eq. [5] to Type II cells.

Using Eq. [4] and [5], if we neglect the possible variation of t_i/n with P_{O_2} or a_{Si}, we can take this quantity out of the integral, replacing it by its average value, leaving only the integral of ln P_{O_2} or ln a_{Si}. For Type II cells of Si^I/SiO_2Si^{II}-Ge with $a_{Si^I} = 1$, we have

$$RT\int_{II}^{I} d\ln a_{Si} = RT\int_{I}^{II} d\ln P_{O_2} = -\Delta G^\circ \quad [6]$$

where ΔG° is the standard Gibbs Free Energy of the reaction

$$Si(s) + O_2(g) \rightleftarrows SiO_2(s) \quad [7]$$

Combining Eq. [6] with Eq. [4] and [5] gives the expression

$$E = t_i \Delta G^\circ / n\mathbf{F}_e \quad [8]$$

Theoretical values for the emf of a cell involving a completely ionic conductor with doubly charged ions have been obtained by using Eq. [8] and assuming $t = 1$, $n = 4$, and the literature values of ΔG° for the formation of crystalline SiO_2.

The theoretical emf values are plotted against temperature in Fig. 6.

It is seen in Fig. 6 that the experimental emf values for the higher P concentration at the highest temperatures are in good agreement with the theoretical values. This indicates that the conducting ionic species is doubly charged.

Based on an assumption that the ions are doubly charged, $\bar{t}_i$ for a Type II cell is given by the ratio E_{obs}/E_{the}.

Evaluation of this ratio for the data in Fig. 6 shows that the oxides grown on B-doped substrates exhibit predominately electronic conduction, while those grown on P-doped substrates are mixed conductors, with the ionic component increasing with increasing temperature and increasing P concentration in the substrate.

If the variable t_i/n is kept under the integral in Eq. 4 $\mathbf{F}E/RT$ can be differentiated with respect to P_{O_2} at side II to give the value of t_i/n at P_{O_2}II. The slope of a plot of $\mathbf{F}E/RT$ *vs.* ln P_{O_2} gives t_i/n over a given pressure range as shown in Fig. 5, where t_i/n varies from 0.145 at low P_{O_2} to 0.062 at medium P_{O_2} and 0.155 at high P_{O_2}. The values of t_i for the respective P_{O_2} ranges, assuming $n = 4$, may be compared with the $\bar{t}_i$ value of 0.4 measured by Jorgensen (3).

In an attempt to identify the species primarily responsible for ionic conductivity in oxides grown on P-doped substrates, the ionic conductance was calculated from

$$\sigma_i = t_i \sigma_t \quad [9]$$

where σ_t is the total measured conductance and t_i, the value obtained in Fig. 5. The activation energy for ionic conduction was then determined from the slope of a plot of $\sigma_i T$ *vs.* T^{-1}, as shown in Fig. 7. It can be compared with self-diffusion data by using the Nernst-Einstein relation. Since no measurable self-diffusion of Si in SiO_2 has been observed, the only data available for comparison are those for oxygen in SiO_2 (11). The activation energy of 1.2 eV derived from the high temperature region (673°-873°K) in Fig. 7 is close to the value of 1.3 eV derived from the oxygen self-diffusion data.

This agreement is consistent with the identification of oxygen as the major conducting ionic species in P-doped SiO_2. However, the activation energy data do not indicate whether the conducting species is an oxygen vacancy or interstitial. This may be investigated by comparing the observed dependence of the ionic transference ratio t_i/n on P_{O_2} and doping concentration with the dependence of the electronic and ionic defects on these parameters as predicted by a theoretical defect model.

Defect chemistry theory predicts that doping SiO_2 with foreign donors would cause an increase in O''_i and a decrease in $h^\cdot$, while it would cause a decrease in $V^{\cdot\cdot}_O$ and an increase in e'. Doping with foreign acceptors would have the opposite effect.

The defect notation is that of Kroger and Vink (12) where the species $h^\cdot$, e', $V^{\cdot\cdot}_O$, and O''_i refer to ionized holes, electrons, vacancies, and oxygen interstitials. The

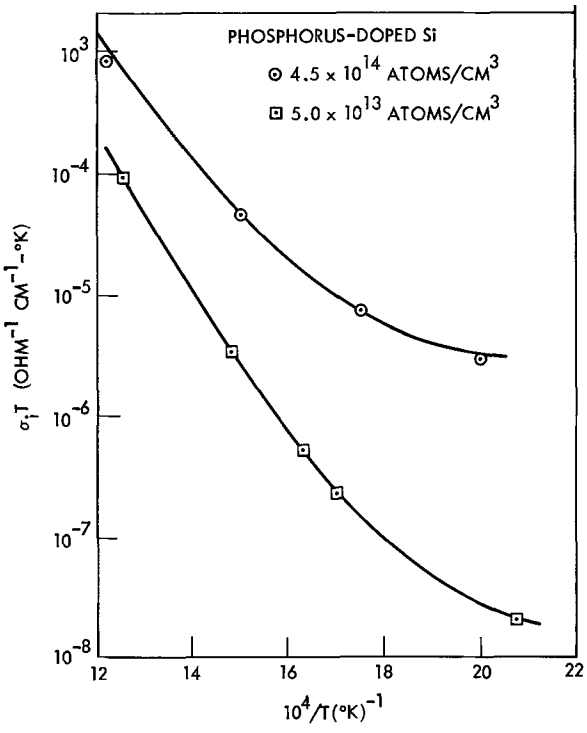

Fig. 7. Log $\sigma_i T$ vs. reciprocal temperature

superscript refers to the effective charge, with a dot positive and dash negative, while the subscript refers to the site; thus $V^{\cdot\cdot}_O$ is an oxygen vacancy with a net effective charge of +2.

It is observed (Fig. 6) that t_i/n is larger for SiO_2 grown on P-doped substrates than for SiO_2 grown on B-doped substrates.

Since it is assumed that P is a donor and B an acceptor in SiO_2, then the observed dependence of t_i/n on doping is consistent with O''_i, not $V^{\cdot\cdot}_O$, as the major conducting species.

If it is assumed that there is a mixture of abnormal and normal charges, the transference ratio (from Fig. 5) when plotted as a function of P_{O_2} gives the results as shown in Fig. 8. The trend of a decrease in t_i/n with increase in P_{O_2} follows the theory, while the magnitude of t_i/n favors a mixed charge model. The increase in t_i/n at high P_{O_2} is not explained by the theoretical defect chemistry model.

In summary, from this work we see an agreement of the measured emf with the theoretical emf if we assume normal charges. A correlation of the activation

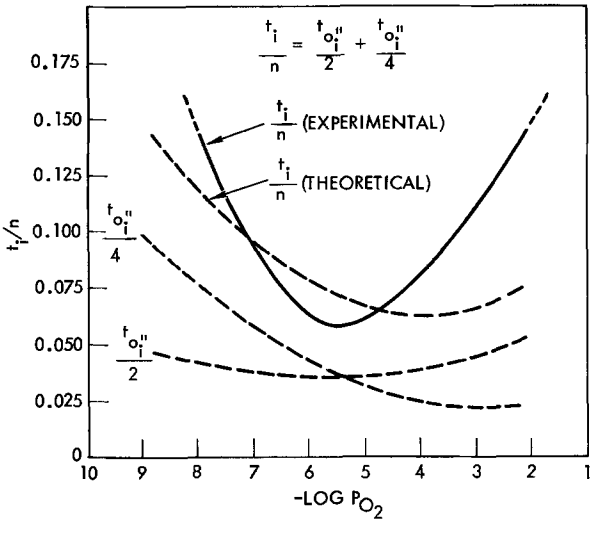

Fig. 8. Ionic transport ratio vs. $-\log P_{O_2}$

energy of the conducting species with the activation energy of self-diffusion of O_2 in SiO_2 is also shown. The agreement in the behavior of the t_i/n value as a function of P_{O_2} and of the P and B concentrations with that predicted for O''_i and $h^{\cdot}$ suggests the species to be a doubly charged oxygen interstitial. A more conclusive identification would require additional experimentation, including numerical calculation of the dopant and defect concentrations. The possibility of alkali ions as the conducting species was eliminated, in that the MOS C-V curves showed less than 0.1V shift on 1000Å test oxides stressed typically at 150°C but sometimes even as high as 300°C.

Manuscript submitted July 17, 1972; revised manuscript received June 6, 1973.

Any discussion of this paper will appear in a Discussion Section to be published in the June 1974 JOURNAL.

REFERENCES

1. R. W. Brander, D. R. Lamb, and R. C. Rundle, *Brit. J. Appl. Phys.*, **18**, 23 (1967).
2. J. R. Ligenza and W. G. Spitzer, *J. Phys. Chem. Solids*, **14**, 131 (1960).
3. P. J. Jorgensen, *J. Chem. Phys.*, **37**, 874 (1962).
4. B. E. Deal, M. Sklar, A. S. Grove, and E. H. Snow, *This Journal*, **114**, 266 (1967).
5. E. Yon, W. H. Ku and A. B. Kuper, *IEEE Trans Electron Devices*, **13**, 276 (1966).
6. O. R. Hiskes and W. A. Tiller, *Mater. Sci. Eng.*, **4**, 169 (9169).
7. C. D. Thurmond and J. D. Struthers, *J. Phys. Chem.*, **57**, 827 (1963).
8. D. Yuan and F. A. Kroger, *This Journal*, **116**, 594 (1969).
9. F. A. Kroger, *Proc. Brit. Ceramic Soc.*, **1**, 187 (1964).
10. R. A. Swalin, "Thermodynamics of Solids," John Wiley & Sons, New York, (1962).
11. F. J. Norton, *Nature*, **181**, 701 (1961).
12. F. A. Kroger and H. J. Vink, *Philips Res. Rept.*, **14**, 557 (1959).

Growth of Polycrystalline Silicon Films: Grain Size

A. Emmanuel and H. M.-Pollock

Department of Physics, University of Lancaster, Lancaster, England

ABSTRACT

Transmission electron microscopy has been used to study the structure of polycrystalline films grown on silicon nitride and silicon dioxide substrates by chemical vapor deposition from silane gas. The effects of substrate temperature, type of carrier gas (nitrogen or hydrogen), and gas flow rate were examined. For substrate temperatures of 720°C (993°K) and above, the films were polycrystalline, and under certain conditions a uniform grain size of *ca.* 30 nm was obtained. At the highest temperatures (*ca.* 1040°-1100°K), the films were discontinuous and showed also a type of secondary structure. Results obtained by field emission microscopy have been used to show how incident flux and surface diffusion coefficient may affect grain size in polycrystalline films: it is likely that the observed noncrystalline/polycrystalline transition is affected by recrystallization, decrease in density of preferred sites for nucleation, and change in critical nucleus size.

Polycrystalline silicon films have recently become important in silicon device technology (1). The effect of the presence of grain boundaries is to enhance the diffusion coefficient of dopants, to reduce the active carrier concentration, and to lower the hole mobility. This paper describes research whose objects were as follows: to grow polycrystalline silicon films with a small, uniform grain size on silicon dioxide and silicon nitride substrates by chemical vapor deposition from silane gas; to use transmission electron microscopy to study the effect of substrate temperature, silane-to-carrier gas molar ratio, and type of carrier gas, on the structure of the deposit; and to relate the measurements of surface diffusion coefficients described elsewhere (2) to the observed grain sizes of the films. Preparation of the films was carried out at Ferranti Electronics Ltd., Wythenshawe, Manchester, in collaboration with Mr. R. Nuttall and Mr. J. R. Sowerby.

Polycrystalline silicon may be grown by chemical vapor deposition on the silicon dioxide or silicon nitride surface, using thermal decomposition of silane (3) in the approximate temperature range 920°-1300°K. As described below, we find that at temperatures below the lower limit the deposited silicon becomes noncrystalline; the upper limit, which depends on the particular carrier gas used, is marked by the onset of homogeneous decomposition (for gas pressures within the viscous range).

Key words: chemical vapor deposition, surface diffusion, nucleation, coalescence, amorphous-polycrystalline transition.

Experimental

It was considered important that the films to be examined should be grown under conditions similar to those prevailing during normal device fabrication.

Deposition apparatus.—A horizontal quartz tube with RF generator for substrate heating was used, the susceptor material being silicon carbide-coated graphite on a tilted quartz jig. The carrier gases used were nitrogen and hydrogen and their flow rates were respectively 26 and 30 liters/min (8.7-10.0 cm/sec). Silane, in the form of 3% silane in either hydrogen or nitrogen, was introduced at flow rates ranging from 5 to 210 cm^3/min. Facilities were included for the deposition of silicon nitride through the reaction between ammonia and silane at 1190°K (4).

Preparation of samples.—(111)-oriented 0.01 ohm-cm n-type silicon substrates were cleaned according to a schedule involving degreasing with toluene, a sulfuric acid-hydrogen peroxide dip, a deionized water wash, a hydrofluoric acid dip, a deionized water wash, and a hydrogen chloride gas etch. A 0.5 μm thickness of silicon dioxide was then grown by conventional thermal oxidation; 0.1 μm of silicon nitride was deposited with a substrate temperature of 1090°K, except in the ex-

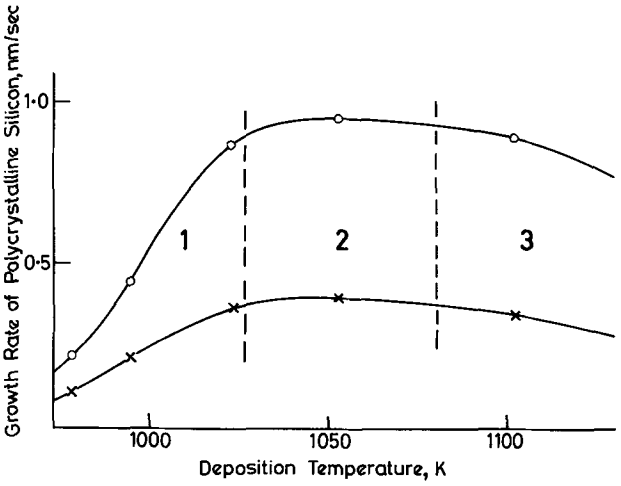

Fig. 1. Growth rate of polycrystalline silicon as a function of temperature, with acknowledgments to J. R. Sowerby and R. Nuttall [quoted in ref. (5)]. Carrier: nitrogen; ×, "low" deposition rate (molar ratio 4.2 x 10^{-5}); ○, "high" deposition rate (molar ratio 2.1 x 10^{-4}); 1, "steeply rising" region; 2,"leveling-off" region; 3, "falling" region.

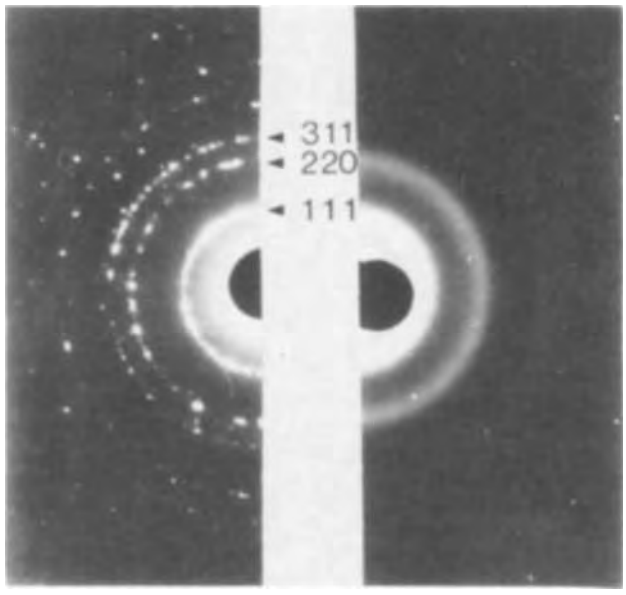

Fig. 2. Electron diffraction patterns: polycrystalline silicon (e.g., from film shown in Fig. 5, left) and noncrystalline silicon (e.g., from film shown in Fig. 3, right).

periments for which the silicon was to be grown directly onto silicon dioxide. The substrates thus pretreated were then introduced into the experimental chamber and the polycrystalline silicon layer was then deposited to a thickness of between 85 and 100 nm onto the substrate at the required temperature, at one of two different rates corresponding to molar ratios of silane to carrier gas of 2.1×10^{-4} and 4.2×10^{-5} (which will be referred to as "high" and "low" deposition rates, although the absolute rate does, of course, depend strongly on the substrate temperature, as shown in Fig. 1). The approximate layer thicknesses were estimated by means of the color of the interference fringes seen by reflected light, calibrated by "Talystep" measurements at intervals. A further 0.1 μm of silicon nitride was then deposited through the reaction between silane and ammonia, after which the slices were removed from the reaction chamber and introduced into another deposition system where a final 1.0 μm of silicon dioxide was deposited by oxidation of silane at a substrate temperature of 720°K. After removal from the deposition apparatus, the sample was glued face downward to a glass slide by means of a heat-resistant wax. The silicon substrate was then removed by an etch in a solution containing 11 parts nitric acid, 5 parts acetic acid, and 2 parts hydrofluoric acid (C.P. 4 etch), and the slide then dipped into hot toluene to dissolve the wax. The composite film then floated off and was further washed in toluene. A 40% hydrofluoric acid bath was then used to dissolve the silicon dioxide and nitride layers, leaving small pieces of polycrystalline silicon film which were washed and allowed to dry on electron microscope specimen grids.

Results

The effects of the film deposition parameters on the film grain size are summarized in Table I. Growth rates are approximate only, being estimated from the deposition time and the film thickness as judged from interference colors as described above. The following points were noted:

1. The films are always polycrystalline, as indicated by selected-area diffraction patterns (Fig. 2), except when deposited at temperatures as low as 923°K, in which case they were found to be noncrystalline, *i.e.*, with a grain size of less than 1 nm (see Fig. 2 and 3).

Table I. Effects of film deposition parameters on film grain size

Substrate	Temp, °K	Region* and molar ratio of silane	Average grain size/nm	Type (grain size)	Growth rate/ (nm·sec^{-1})	$\log_{10} J$ (J in atoms m^{-2} sec^{-1})	Calculated $\log_{10} D_{max}$ (D in m^2 sec^{-1})	$\log_{10}\left(\frac{J}{D}\right)_{min}$
Si_3N_4††	898, 923	1, low	<1	Noncrystalline	*ca.* 0.1	*ca.* 18.7	−19.1	*ca.* 38
Si_3N_4††	898, 923	1, high	<1	Noncrystalline	*ca.* 0.1	*ca.* 18.7	−19.1	*ca.* 38
Si_3N_4	993	1, high	30	Small	0.42	19.32	−18.5	37.8
Si_3N_4	1013	1, high	30	Small	0.75	19.57	−18.2	37.8
Si_3N_4	993	1, low	30	Small	0.20	19.00	−18.5	37.5
Si_3N_4	1043	2, high	30** + *ca.* 100	Mostly small	0.96	19.68	−17.8	37.5
SiO_2	1043	2, high	50	Larger	0.96	19.68	−17.8†	37.5†
Si_3N_4	1013	1, low	30	Small	0.32	19.20	−18.2	37.4
Si_3N_4	1043	2, low	30** + *ca.* 100	Mostly small	0.40	19.30	−17.8	37.1
Si_3N_4	1103	3, high	30** + *ca.* 100	Mostly small	0.87	19.63	−17.1	36.7
SiO_2	1103	3, high	50	Larger	0.87	19.63	−17.1†	36.7†
Si_3N_4	1043	(Hydrogen carrier)	30	Small	0.17	18.85	−17.8	36.6
SiO_2	1043	(Hydrogen carrier)	220	Very large	0.17	18.85	−17.8†	36.6†
Si_3N_4	1103	3, low	30** + *ca.* 100	Mostly small	0.34	19.23	−17.1	36.3
Si_3N_4	1043	(Hydrogen carrier)	50	Larger	0.033	18.21	−17.8	36.0

* Region (see text and Fig. 1): 1, steeply rising; 2, leveling off; 3, falling.
** Discontinuous film, with some "secondary structure."
† Assuming D has a similar value for Si on SiO_2 as for Si on Si_3N_4.
†† Dr. B. E. Watts and Dr. D. G. Barlow (6) have informed us that they observe the noncrystalline structure (for silicon growth under similar conditions at 650°C) on silicon dioxide substrates also.

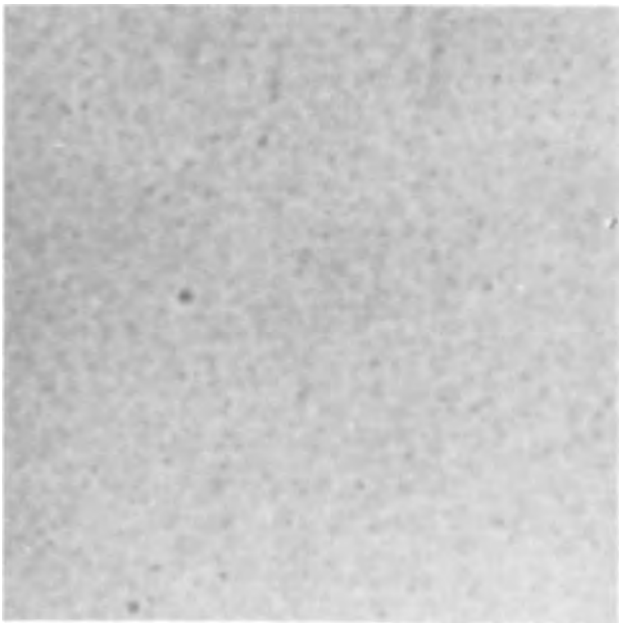

Fig. 3. Noncrystalline silicon film grown under conditions similar to those described for Fig. 5, but with the silicon nitride substrate at 898°K.

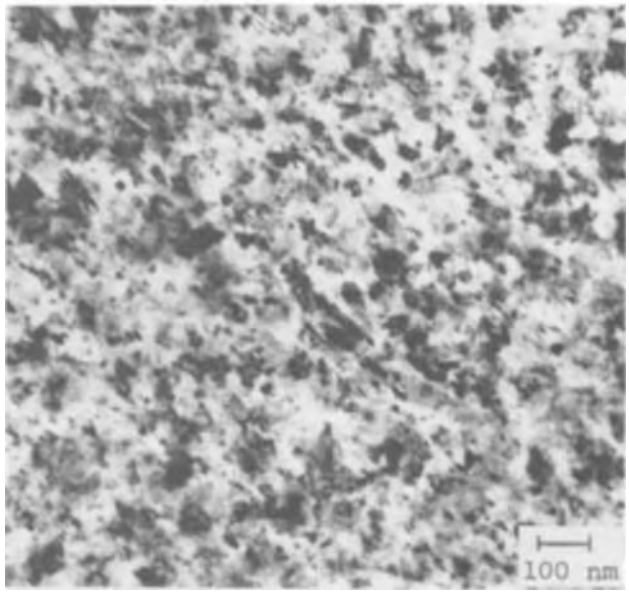

Fig. 4. Polycrystalline silicon film (thickness *ca.* 100 nm) originally deposited onto silicon nitride at 993°K (low molar ratio of silane, nitrogen carrier). The grain size is uniform and small (*ca.* 30 nm).

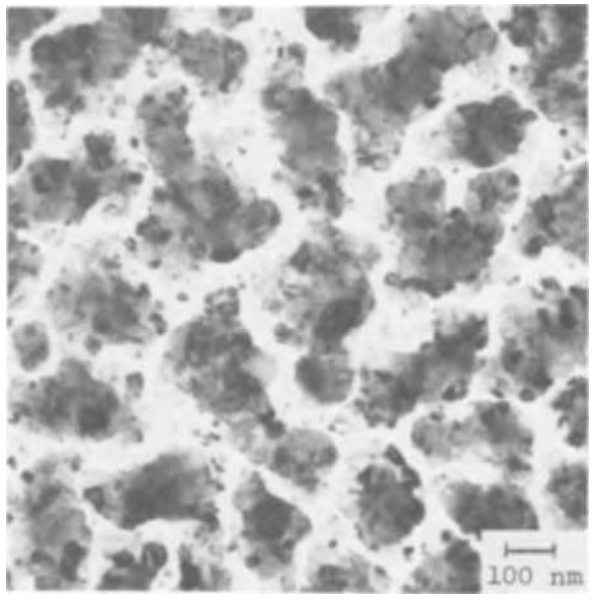

Fig. 5. Discontinuous film, with some "secondary structure" (thickness *ca.* 100 nm, high molar ratio, nitrogen carrier, silicon nitride substrate at 1103°K).

2. Curves for growth rates of silicon films as a function of substrate temperature may be divided into different regions of silane decomposition including a "steeply rising" region within which the rate increases rapidly with temperature, and "leveling-off" and "falling" regions within which the growth rate either increases slowly or decreases as the substrate temperature is raised (see, for example, Fig. 1). Provided that the deposition took place within the "steeply rising" region, and provided that the substrate was silicon nitride at 990°K or above, a typical small size of grain (up to 30 nm diameter) was obtained, the deposition being reasonably uniform over the full extent of the substrate. This type of film appears similar in structure to those grown by Cowher and Sedgwick (7) from SiH_4-H_2 and $SiBr_4$-H_2 mixtures. To the eye, the film presented a uniform reflecting surface (except that when a hydrogen carrier gas was used, the deposit was less uniform, the film causing certain areas of the substrate to show up in relief, such a cleaning residues or surface irregularities). Figure 4 shows a typical deposit of the uniform small-grained type. A phosphine-doped deposit [0.1% phosphine in hydrogen at a flow rate of 50 cc/min introduced into the reacting gas flow, the silicon nitride substrate temperature being 1043°K, the carrier nitrogen (26 liters/min), and the molar ratio 2.1×10^{-4}] also showed this typical small grain size.

3. At the two highest substrate temperatures used (1043° or 1103°K), the film was discontinuous (see Fig. 5 and 6). The micrographs suggest that in addition to the normal polycrystalline structure there is also an additional or "secondary" structure, although a dark-field image (Fig. 6) shows that most of the grains have the same size as before. To the naked eye these films presented a slight powdery appearance.

4. Some large grains were seen in films deposited onto silicon dioxide substrates or grown at a very low rate (0.033 nm/sec). These films presented a marked powdery appearance to the eye.

Discussion

The most striking feature of the structure of the polycrystalline silicon films is the abrupt change from the noncrystalline type of film to a structure with a grain size of *ca.* 30 nm as the substrate temperature is raised. It is possible that rapid crystallization would be aided by heat released during a true amorphous-crystalline transition such as that observed by Matthews and Mader (8) in their studies of certain two-metal systems. Although Brodsky *et al.* (9) state that amorphous silicon films, once deposited, crystallize on annealing at temperatures within the range 720°-920°K, Chopra (10) sets an upper limit of *ca.* 420°K for the amorphous-crystalline transition in silicon, considerably lower than the substrate temperatures used in this study. De Luca (11) has discussed the relation between deposition parameters and observed preferred orientations of silicon grown on fused silica substrates. In any case other deposition parameters besides temperature would be expected to affect the grain size in the film. Sloope and Tiller (12), in a discussion of their observations of an "amorphous"-crystalline transition for germanium films grown on calcium fluoride substrates, assume that the film becomes crystalline when the time for one atomic layer to form exceeds the mean time between jumps made by an adatom. In this discussion we attempt to see how the deposition param-

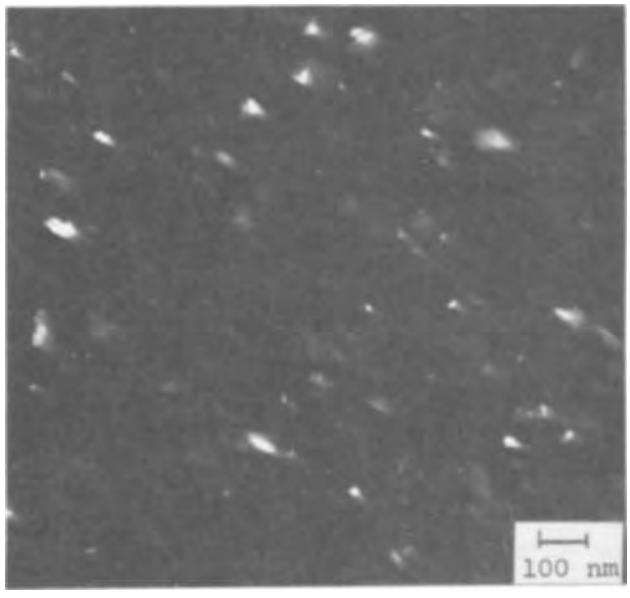

Fig. 6. Dark-field image of the film shown in Fig. 5

eters could affect the film structure, according to theories of nucleation kinetics and thin film growth as described by Stowell *et al.* (13-16) and to what extent the surface diffusion measurements described in ref. (2) are relevant to the observed grain sizes.

Since substrate temperature affects both the film deposition rate and the surface diffusion coefficient of silicon, it seemed appropriate to list the observed grain sizes in order of decreasing J/D, where J is the flux of silicon atoms/square meter/second condensed (calculated from the film thickness and deposition time, and provisionally assuming complete condensation of silicon atoms) and D is an upper limit for the surface diffusion coefficient of silicon on silicon nitride [estimated from the results of experiments described in ref. (2)]. Complete condensation has not been proved to apply, but it may be noted that Joyce *et al.* (3) justify the same assumption for their experiments with silicon substrates in which the substrate temperatures were higher than in the present study. In general, grain size could be expected to increase with decreasing J and increasing D, and Table I tends to confirm this expectation.

In analyses of the growth of silicon films on silicon substrates (5, 17, 18), the value of E_d has been unknown *a priori*, although Joyce *et al.* (3) and Henderson and Helm (17) deduced values of this quantity from their analyses. It can be more useful, however, to know absolute values of the diffusion coefficient D as well as its activation energy, since the pre-exponential D_o in the expression $D = D_o \exp(-E_d/kT)$ can vary over many orders of magnitude (19).

In this analysis, the quoted upper limits of D for diffusion of silicon on silicon nitride were calculated as follows: from the micrographs showing diffusion of silicon on tungsten emitters of known tip radius, the characteristic distance, x, for migration in the field emission microscopy experiments described in ref. (2) was estimated to be 300 nm. Since both the temperatures at which diffusion was measured, and the temperatures at which the flat films were grown, were lower than the minimum temperature for detectable evaporation of silicon (2), we assume that the diffusion equation

$$D = \overline{x^2}/(4t) = D_o \exp(-E_d/kT)$$

is valid: if we substitute the above value of x in this equation, using the observed values of t and E_d for silicon on tungsten, we obtain a pre-exponential, D_o, equal to 5.10^{-4} m^2 sec^{-1}. This is larger than the expected value of 3×10^{-6} as calculated from the expression νa^2, where ν is a typical atomic vibration frequency and a is the expected jump distance on the surface. The discrepancy may be due to a positive entropy factor, as observed in other work (19). The higher of the two values is preferred in this estimate of an upper limit for D. For each temperature, the diffusion coefficient for silicon on tungsten was that obtained from the expression $D = \overline{x^2}/(4t)$, using the values of t shown in Fig. 3 of ref. (2). The upper limit for D for silicon on silicon nitride was then taken as one tenth of this value, since the diffusion times were always at least ten times as long at a given temperature within the relevant temperature range.

We first see whether the observed numbers of grains per unit area N_g are explicable on the assumption that N_g is equal to N_s, the saturation nucleus density during initial nucleation of the film, *i.e.*, that each grain grows from one nucleus until the substrate is covered, after which the grain size is maintained throughout subsequent film growth. Grain growth through subsequent recrystallization is neglected on this assumption. It is shown in Appendix A that this assumption can possibly be justified for the noncrystalline films (with nucleation at normal sites on the silicon nitride lattice), but that even if we include the possibility of nucleation at surface defects or other preferred sites, the observed noncrystalline/polycrystalline transition cannot be explained.

It is therefore necessary to include the possibility of grain growth through coalescence and recrystallization. It is shown in Appendix B that crystallization or recrystallization can be expected over the whole range of conditions, as judged by a criterion involving J/D, and described by Stowell (16). We propose that the films deposited onto silicon nitride substrates grow as follows: at the largest values of J/D, nuclei form very close together ($\lesssim 1$ nm) on the silicon nitride substrate, at preferred sites with $i = 0$ and at normal sites with $i = 1$. (E_i is the binding energy of a critical nucleus containing i atoms, one less than the number of atoms in the smallest stable cluster.) The "preferred sites" formula (Table III) predicts that a lower density of nuclei is required at saturation under these conditions than does the "normal sites" formula (Table II), so that nucleation at preferred sites is probably predominant. After the substrate is covered, subsequent nucleation of silicon on silicon takes the same form so that a noncrystalline structure is obtained throughout the film. If J/D is lowered, there will be a tendency for the initial noncrystalline layer to crystallize as the gap between J/D and a critical value, $(J/D)_s$, widens (see Appendix B). Under these conditions, crystallites of silicon may appear upon which subsequent layers may nucleate, finding a much lower density of preferred sites (N_{do}) than was offered by the noncrystalline silicon nitride substrate. This decrease in N_{do} for the "preferred sites" nucleation will lead[1] to a decrease in N_s (Table III), again producing a larger crystallite size. If, moreover, the "preferred sites" nucleation rate is sufficiently reduced, it may, at the lower values of J/D, become swamped by "normal sites" nucleation with $i = 1$ (for which the calculated values[1] of N_s are not far from those predicted by the preferred sites formula even with sites separated by as little as 1 nm). This increase in the number of atoms in the critical nucleus will help to improve the crystallinity of subsequent layers. If, on the other hand, nucleation at preferred sites such as grain boundaries continues to predominate, recrystallization will not give a grain size larger than 30 nm owing to the reduction in the critical value $(J/D)_s$. As discussed earlier, a Mader-type of amorphous crystalline transition might be expected, at lower temperatures. Quite apart from this, it is possible that the abrupt onset of polycrystallinity observed here arises from the three co-operative

[1] An increase in the value of D appropriate to diffusion of silicon on silicon instead of on silicon nitride does not invalidate this statement.

effects, namely, recrystallization, decrease in density of preferred sites, and change in critical nucleus size. The calculations show that as the temperature increases, the increase in surface diffusion coefficient outweighs the increase in flux produced by the higher silane decomposition rate.

There is not enough evidence to say whether the larger grain sizes seen in films deposited at the lowest fluxes and on silicon dioxide substrates are produced by changes in J, D, or N_{dO}, or by other factors such as change in carrier gas. It is interesting to note that Cowher and Sedgwick (7), describing the structure of silicon grown on silicon dioxide, find that the particle size increases to up to 300 nm as the boron doping is increased to 10^{25} m^{-3}. The secondary structure seen in films deposited at the highest temperatures and in the "leveling-off" or "falling" regions of silane decomposition could be associated with silicon produced by homogeneous decomposition of silane in the gas phase, some distance from the substrate surface. The explanation of grain size given here is, of course, subject to the uncertainties underlying the theory of nucleation and growth. These include the assumptions that complete condensation of the arriving silicon atoms applies and that recrystallization occurs only before the film becomes continuous. If condensation is not complete, the values of J used in Table I will be affected as well as the nucleation process. Lewis (20) has suggested that a transition from complete to incomplete condensation, which would sharply reduce nucleation rate and density, may contribute toward the onset of polycrystallinity, although in this case an abrupt decrease in film growth rate as a function of substrate temperature would be expected, contrary to observation (5). In addition, as described in ref. (2) it is probable that the values of diffusion coefficient employed do not correspond to true surface diffusion of silicon atoms on a silicon nitride surface. However, in view of the similar deposition conditions used for the preparation of samples for the electron microscope and field emission studies, we are justified in using the numerical values to show how flux and diffusion coefficient may affect grain size in polycrystalline films.

Conclusions

1. Conditions have been established for the growth of polycrystalline silicon films with a small, uniform grain size on silicon nitride substrates.

2. Measurements of surface diffusion coefficients made by field emission microscopy can be used in support of a mechanism put forward to explain the observed transition from a noncrystalline to a polycrystalline structure.

Acknowledgments

We are grateful to Ferranti Electronics Ltd. (Mr. R. Nuttall and Mr. J. R. Sowerby) for the provision of experimental facilities and of Fig. 1, and to Dr. M. J. Stowell, Dr. B. E. Watts, and Dr. B. Lewis for valuable criticism.

Manuscript submitted Jan. 2, 1973; revised manuscript received May 24, 1973.

Any discussion of this paper will appear in a Discussion Section to be published in the June 1974 JOURNAL.

APPENDIX A

Assumption of One Grain per Nucleus ($N_g = N_s$)

Nucleation at normal lattice sites.—We first see whether nucleation at normal lattice sites on the silicon nitride substrate can explain the observed grain sizes, using the expression

$$N_s = C(i)\,(J/D)^{2i/(2i+5)} \exp|2/(2i+5)\cdot E_i/kT|$$

with $i \geq 1$, $C(1) = 10^{7.2}$, $C(2) = 10^{1.2}$, $C(3) = 10^{-2.6}$, as derived by Routledge and Stowell (13) for all but extreme cases of incomplete condensation (21), modified by Stowell and Hutchinson (14), and converted to SI units with a silicon nitride surface site density of 10^{19}. Here E_i is the binding energy of a critical nucleus containing i atoms (one less than the number of atoms in the smallest stable cluster), and N_s is the saturation nucleus density. We make the same assumptions as the authors of these papers. Table II shows the calculated minimum values of $\log_{10}N_s$: for the polycrystalline films, the calculated minimum values of grain density exceed the observed values by a factor of at least 400 and, even allowing for the fact that the above expression is inaccurate for coverages of greater than 10%, the assumption of $N_g = N_s$ must be rejected. For the noncrystalline films only we have a straightforward explanation; it is, however, more likely that here $i = 0$ and that even in this case nucleation is not occurring at normal lattice sites, since at substrate temperatures so low that even a cluster consisting of $0+1 = 1$ atom must be stable, the same type of noncrystalline structure is obtained.

Nucleation at preferred sites.—The predicted values of N_s and nucleation rate for nucleation at normal substrate sites with $i = 1$ are so large that nucleation solely at surface defects or other preferred sites on the silicon nitride substrate can be neglected, unless we postulate $i = 0$. The appropriate expressions for "preferred sites" nucleation are then

$$N_s/N_{dO} = 0.1B \qquad \text{for } B \leq 10$$

or

$$N_s/N_{dO} = 1 \qquad \text{for } B \geq 10$$

with

$$B = \left\{ \sigma_i(i + 5/2) \left[\frac{N_0}{N_{dO}} \right]^{i+3/2} \exp\left[\frac{E_i + \Delta E_i}{kT} \right] \left[\frac{J}{DN_0^2} \right]^i \right\}^{1/(i+5/2)}$$

where $\sigma_0 = \sigma_1 = 1$, $\sigma_2 = 1.25$, N_0 is the density of all substrate sites (normal and preferred), N_{dO} is the density of preferred sites, ΔE_i is the additional binding energy of an i-sized cluster to a preferred site, and the other parameters have the same meaning as before. These expressions have been derived by Stowell and Hutchinson with certain assumptions (14) for the condition of complete condensation. Table III lists values of $\log_{10}N_s$ calculated for various possible values of N_{dO}, and for $i = 1$ and 2 as well as 0 for the sake of completeness. It shows that for the experimental conditions used, the value of B is very high (>40) and that saturation therefore occurs, with the calculated value of N_s equal to the assumed density of preferred sites N_{dO}, for all except very large values of N_{dO}. If we take a distance of 30 nm between preferred sites, formation of the polycrystalline films of grain size *ca.* 30 nm is explained on the original assumption that N_g becomes equal to N_s; but if the nuclei are always this far apart, then under the conditions for which a noncrystalline structure was observed, we would have $N_g > N_s$, *i.e.*, more than one grain per nucleus. If we assume a smaller distance (*e.g.*, *ca.* 1 nm) between preferred sites, a noncrystalline structure will be predicted throughout the range of experimental conditions; in any case we probably cannot neglect nucleation at normal sites which has already predicted a distance of this magnitude between nuclei at saturation (Table

Table II. Minimum values of $\log_{10}N_s$ assuming nucleation at normal lattice sites (N_s in m^{-2})

The calculation employs values of T, J, and D corresponding to conditions for the preparation of films with the different observed grain sizes.

Observed grain size →	Noncrystalline (~1 nm)	30 nm	50 nm	220 nm
$i = 1$	$\log N_s = 18.2$	17.7 to 18.1	17.6 to 18.0	17.8
$i = 2$	$18.3 + 1.2\,E_2$	—	$17.4 + 1.0\,E_2$ to $18.2 + 1.1\,E_2$	—
$i = 3$	$18.4 + 1.1\,E_3$	—	$17.2 + 0.8\,E_3$ to $18.3 + 1.0\,E_3$	—
$\log N_g$ (log of observed grain density)	*ca.* 18	15.1	14.7	13.4

Table III. Minimum values of $\log_{10}N_s$ assuming nucleation at preferred sites (N_s in m^{-2}), and calculated according to various postulated values of preferred sites density N_{dO}

Assumed distance between preferred sites →		1 nm	3 nm	10 nm	30 nm
	log N_{dO}	18.1	17.1	16.1	15.1
$i = 0$	log B	0.6	1.3	1.8	2.4
	log N_s	17.7	= log N_{dO}	= log N_{dO}	= log N_{dO}
$i = 1$	log B	0.2 + 1.3 ΔE_1 to* 0.7 + 1.4 ΔE_1	0.8 + 1.3 ΔE_1 to* 1.3 + 1.4 ΔE_1	1.6 + 1.3 ΔE_1 to* 2.1 + 1.4 ΔE_1	2.3 + 1.3 ΔE_1 to* 2.8 + 1.4 ΔE_1
	log N_s	$\gtrsim$ 17.3	$\gtrsim$ 16.9	= log N_{dO}	= log N_{dO}
$i = 2$	log B				2.3 + 1.1 (E_2 + ΔE_2) to* 3.1 + 1.2 (E_2 + ΔE_2)
	log N_s				= log N_{dO} 15.1
Nearest value of log N_g (log of observed grain density)		*ca.* 18 (noncrystalline)			

* The ranges listed here correspond to the variation in T, J, and D for the different experimental conditions.

II). We must then seek some other explanation of polycrystalline film growth when observed.

APPENDIX B

Assumption of <1 or >1 Grain per Nucleus; Effects of Recrystallization and Coalescence

In order to explain the sharp transition from a noncrystalline to a polycrystalline structure, it is therefore necessary to include the possibility of grain growth through coalescence and recrystallization. Lewis (22) has given a general account of the relative importance of nucleation density and coalescence. It is interesting to compare the values of J/D for the condensing silicon atoms with the critical value, $(J/D)_s$, for which recrystallization is impossible before the growing film becomes continuous: $(J/D)_s$ may be estimated on the assumption that surface diffusion dominates over volume diffusion during any coalescence, from Stowell's formula (16)

$$(J/D)_s = 6\cdot10^6\,\gamma\,\Omega^{1/3}\,N_{sd}{}^{3/2}/(kT)$$

where γ is the surface energy of silicon and Ω is the atomic volume. If $J/D > (J/D)_s$, the initial nucleation density and orientation structure will be frozen into the film: if $J/D < (J/D)_s$, recrystallization may or may not be possible. It is important to note that this formula applies to the coalescence of crystalline islands only. Using a value of 1 Jm^{-2} for γ, we have the values of $(J/D)_s$ shown in Table IV. Thus we see that if the still discontinuous film were being formed from monocrystalline nuclei 30 nm apart, recrystallization would not be possible but that for the higher values of N_s predicted by nucleation theory, we would expect at least some recrystallization during the growth stage.

We have mentioned also the possibility that the initial nuclei are widely separated (*e.g.*, by *ca.* 30 nm), but that under conditions of high J/D the adatoms joining them do not assume crystalline packing, so that $N_g > N_s$. Although Table IV indicates that a film forming from nuclei 30 nm apart should not recrystallize under the experimental conditions used, this conclusion does not apply to noncrystalline nuclei. Thus crystallization or recrystallization can be expected over the whole range of conditions: there is, however, no need to assume an initial nucleation at widely separated preferred sites if we adopt the growth mechanism described in the discussion.

Table IV. Critical values of $\log(J/D)_s$ above which recrystallization should be impossible

Nuclei 1 nm apart at saturation	40.0	
Nuclei 10 nm apart at saturation	37.0	
Nuclei 30 nm apart at saturation	35.5	
Minimum values of $\log(J/D)$ employed	*ca.* 38 for noncrystalline films	36.0 to 37.8 for polycrystalline films

REFERENCES

1. C. C. Mai, T. S. Whitehouse, R. C. Thomas, and D. R. Goldstein, *This Journal*, **118**, 331 (1971).
2. A. Emmanuel, R. H. Smallwood, and H. M.-Pollock, Submitted for publication.
3. B. A. Joyce, R. R. Bradley, and G. R. Booker, *Phil. Mag.*, **15**, 1167 (1967).
4. M. T. Duffy and W. Kern, *RCA Rev.*, **31**, 742 (1970).
5. A. Emmanuel, M.Sc. Thesis, University of Lancaster, England (1972).
6. B. E. Watts and D. G. Barlow (Plessey Co., Ltd., Allen Clark Research Centre), Unpublished.
7. M. E. Cowher and T. O. Sedgwick, *This Journal*, **119**, 1565 (1972).
8. J. W. Matthews and S. Mader, *J. App. Phys.*, **41**, 3800 (1970).
9. M. H. Brodsky, R. S. Title, K. Weiser, and G. D. Pettit, *Phys. Rev.*, **B1**, 2632 (1970).
10. K. L. Chopra, "Thin Film Phenomena," McGraw-Hill Book Co., New York (1969).
11. R. D. De Luca, in "Semiconductor Silicon," R. R. Haberecht and E. L. Kern, Editors, The Electrochemical Society (1969).
12. B. W. Sloope and C. O. Tiller, *J. App. Phys.*, **36**, 3174 (1965).
13. K. J. Routledge and M. J. Stowell, *Thin Solid Films*, **6**, 407 (1970).
14. M. J. Stowell and T. E. Hutchinson, *Thin Solid Films*, **8**, 41 (1971).
15. M. J. Stowell, *Phil Mag.*, **26**, 361 (1972).
16. M. J. Stowell, *Thin Solid Films*, **1**, 55 (1968).
17. R. C. Henderson and R. F. Helm, *Surface Sci.*, **30**, 310 (1972).
18. R. F. C. Farrow and J. D. Filby, *This Journal*, **110**, 149 (1971); *R. R. E. Research Rev. No. 10*, 15/1 (1971).
19. J. P. Jones, *Proc. Roy. Soc.*, **A284**, 469 (1965).
20. B. Lewis, Private communication.
21. B. Lewis and D. S. Campbell, *J. Vac. Sci. Tech.*, **4**, 209 (1967).
22. B. Lewis, *Thin Solid Films*, **7**, 179 (1971).

Correlation of Dielectric Dispersions with Electronic and Ionic Conduction Mechanisms in Glass

Mary Splann Mizzoni

Corning Glass Works, Research and Development Laboratory, Corning, New York 14830

ABSTRACT

Three iron oxide-containing glasses of different network formers, namely, a phosphate, a borate, and a silicate, were compared to an alkali-lime-silicate glass. Tests by the Tubandt method established the main conduction mechanism, whether electrons or ions, in each glass. The conductivity data and loss factor and dielectric constant data from frequencies of 10^{-2}-10^{5} Hz were measured as a function of temperature. As dielectric theory predicts, dispersions of the dielectric constant with associated relaxation peaks in the loss factor were observed in the four glasses. An analysis of these properties revealed that the same mechanism was responsible for the a-c and the d-c conductivity in each glass. The shape of the dielectric constant curves below the dispersion frequencies varied with the conduction mechanism. Interpretation of these data showed only the silicate glass to have mixed ionic-electronic conductivity.

The earliest papers written on the electrical conductivity of electronically conducting glasses were concerned with proving that the conduction mechanism was electronic (1-3). Mazurin *et al.* (4) employed the Tubandt method to show electronic conductivity in iron-containing silicate glasses. Several electrical properties were related in both vanadium and tungsten phosphate glasses by Ioffe *et al.* (5). Electrical resistivity and thermoelectric power on iron phosphate glasses were reported by Hansen (6). Later, Hansen and Splann (7) published the dielectric properties of these same glasses with 55% FeO_x-45% P_2O_5 and varying Fe^{3+}/Fe_{total} ratios. From the relaxation peaks in the loss factor, the activation energy of the a-c conduction mechanism was found to be equal to that of the d-c conduction mechanism. The "hopping" mechanism (8) was proposed for these related mechanisms. It was also observed that a measurable static dielectric constant, independent of temperature and frequency, was obtained well below the dispersion frequencies. To the author's knowledge, this phenomenon had not been reported previously for glasses. This was indicative of electronic conductivity only. The dispersion of the dielectric constant data gave support to the validity of the relaxation peaks.

Kinser (9) reported on this same glass system, relating dielectric relaxations to crystal formations in the glass. He was able to do this as he observed relaxation peaks only in samples with finely dispersed crystals (10). This work has been extended recently (11).

The dielectric behavior of vanadium phosphate glasses was published by Mansingh *et al.* (12) from frequencies of 10^{2}-10^{9} Hz and from temperatures of 80°-350°K. Isard (13) has shown, using published data, the similarity in the dispersion of conductivity of electronic and ionic dielectrics with random structures.

Because of the random structures of glass, theory (14) predicts that all glasses will have a dispersion in the a-c conductivity from which relaxation spectra are obtained. In many glasses, the peak in the relaxation is masked by the contribution of d-c conductivity to the measured a-c losses. Careful measurements over a suitably wide frequency and/or temperature range are required to locate them (15).

It is the purpose of this paper to show that low frequency dielectric relaxations are found in several glasses of diverse compositions. The relaxation peaks are associated with the dispersions in the dielectric constant. The behavior of three electronically conducting glasses, a phosphate, a borate, and a silicate, is compared to that of a common alkali-lime-silicate glass. Each of the electronically conducting glasses contains iron oxide, which is believed to be responsible for this conductivity. Tests by the Tubandt method substantiate the conduction mechanisms. From the activation energy data, it is shown that the same conduction mechanism is responsible for a-c and d-c conductivity in each glass.

Key words: dielectrics, glass, conductivity, dispersion, relaxation.

Experimental Procedure

The glasses were melted in 400-600g batches in fused silica crucibles at 1300°, 1250°, and 1400°C for the phosphate (glass A), the borate (glass B), and the silicate (glass C) iron containing glasses. They were poured on steel or graphite molds and annealed. The alkali-lime-silicate glass, Corning Code 0080 (glass D), was obtained from a production melt. The compositions of the glasses are given in Table I.

X-ray diffraction patterns and transmission micrographs showed no evidence of crystalline phases down to 30Å in glasses A, B, and D. Widely scattered crystals, about a micron in diameter, were observed in glass C.

Tests by the Tubandt method (16) were performed on each of these glasses. This precise method for determining the conduction mechanism is based on weight transfer during electrification. No weight is transferred if the conduction mechanism is electronic. The weight transfer can be calculated if no more than two species are involved in ionic or ionic-electronic conduction (17). Gold electrodes were evaporated on one face of each of two disks of each composition. The disks were 1½ in. in diameter and polished to a thickness of 2.00 mm. For some of the tests, a third disk was

Table I. Glass compositions in mole per cent

	FeO_x	P_2O_5			
Phosphate glass A	55	45			
	FeO_x	Ce_2O_3	B_2O_3		
Borate* glass B	4.3	25.5	70		
	FeO_x	PbO	ZrO_2	SiO_2	
Silicate glass C	9.7	29.1	2.9	58.4	
	Na_2O	K_2O	CaO	MgO	SiO_2
Alkali-lime-silicate glass D	15.3	0.3	5.5	5.3	72.9

* Ref. (21). In varying compositions in this system, the iron oxide is believed to be the main contributor to electronic conductivity because (i) in decreasing the Ce_2O_3 and increasing FeO_x, the resistivity decreases; and (ii) in increasing the Ce_2O_3 and keeping the FeO_x constant, the resistivity is unchanged.

inserted between the electroded ones. The disks and combinations of disks were carefully weighed before and after testing to ±0.0005g. The disks were stacked between gold-plated stainless-steel electrodes, raised in temperature in a measurement furnace and the voltage applied. A known current was passed for a known period of time. Weight changes were calculated, assuming ionic conductivity by Na^+, by the equation

$$M = \frac{kIAt}{N} \qquad [1]$$

where M = weight change, g'; k = 6.281 × 10^{18}, charges/A sec; I = current, A; A = atomic weight of conducting ion; t = duration of electrification, sec; and N = Avogardo's number, 6 × 10^{23} molecules/mole.

Measurements of electrical properties, d-c and a-c, were made on similar samples. Three-terminal gold electrodes were evaporated on glasses A, B, and C. Hanovia Liquid Gold Bright electrodes were fired on glass D in the same configuration. The experimental procedures and theory were described previously (7). Briefly, the d-c conductivity γ_{dc} was obtained (18) with a potential of 20V with a Beckman electrometer. Two bridges were used to measure the a-c properties: a low-frequency bridge from 10^{-2} to 10^3 Hz, designed by Weingarten (19) [and used by Heroux (20)] and General Radio Type 1615A from 10^2 to 10^5 Hz.

The total conductivity γ_T was calculated from the following equations

$$\gamma_T = \frac{1}{R} \times \frac{t}{A} \text{ mho/cm} \qquad [2a]$$

where R = resistance (d-c or a-c), ohms; t = thickness of specimen, cm; and A = eff. area of electrodes, cm^2 and

$$\gamma_T = \frac{\tan \delta_T \times K' \times f}{1.8 \times 10^{12}}$$

$$= \frac{K''_T \times f}{1.8 \times 10^{12}} \text{ mho/cm} \qquad [2b]$$

where K' = relative dielectric constant = C × t/0.0885A; C = capacitance, pF; f = frequency, Hz; and K''_T = loss factor.

The total conductivity is the sum of a-c and d-c contributions. To obtain the relaxation peaks, the d-c contributions were subtracted, as

$$\gamma_{ac} = \gamma_T - \gamma_{dc} \qquad [3]$$

From this, the loss $factor_{ac}$ was calculated

$$K''_{ac} = \frac{\gamma_{ac} \times 1.8 \times 10^{12}}{f} \qquad [4]$$

Results and Discussion

Data from tests by the Tubandt method are tabulated in Table II. The temperature, current, voltage, and time of electrification are listed for each glass. The measured weights of each disk and combinations of them are listed before and after testing. A calculated weight transfer, based on ionic conductivity by sodium ions, is shown. For glasses A, B, and C there is no significant weight change. This indicates that most or all of the current was carried by electrons. Little adjustment of the voltage was required to maintain a constant current over a prolonged period of time. This lack of build-up of space-charge polarization further indicates electronic conductivity.

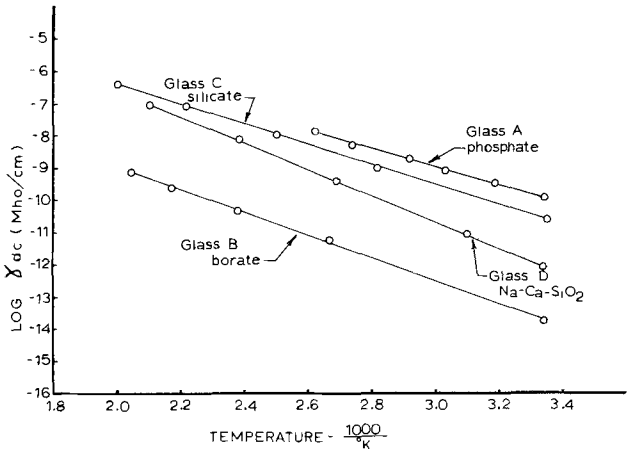

Fig. 1. D-C conductivity vs. temperature for glasses A, B, C, and D.

For glass D, the alkali-lime-silicate, the results were different. The Tubandt test was performed three times, each with essentially the same results. To prevent fusion to the contacting electrodes, weighed gold foil was placed between the electroded surface and the contacting electrode. The results of the last test are listed. The anode disk lost the amount of weight that was calculated. The middle disk did not change in weight. The cathode disk weighed more than the anode disk lost and continued to gain weight, as the additional active Na^+ in the cathode disk picked up water from the atmosphere. Because this glass is an ionic conductor, build-up of the space-charge polarization increased the resistance greatly. A constant current could not be maintained for 8 hr. The weight transfer calculation was dependent on four current levels, as the voltage and temperature were raised during the test.

From these tests it is shown that glasses A, B, and C are electronically conducting and that glass D is ionically conducting. With this difference established, the electrical behavior of the glasses will be compared.

Figure 1 shows the log of the d-c conductivity *vs.* 10^3/°K for each glass. In the temperature range shown,

Table II. Tubandt test results

Glass No.	Test temp, °C	No. of disks	Current, A	Voltage, V	Time, sec	Measured weight, g: Before	Disk	After	Calculated weight transfer, g*
A	256	2	0.4 × 10^{-3}	125-85	1.87 × 10^5	2.9470	c**	2.9464	
						2.9954	a	2.9950	0.018
						5.9419	c+a	5.9417	
B	517	2	0.4 × 10^{-3}	217-250	1.01 × 10^5	2.0548	c	2.0546	
						3.4585	a	3.4581	0.0097
						5.5131	c+a	5.5130	
C	404	3	0.2 × 10^{-3}	35-40	2.59 × 10^5	5.5848	c	Fused	
						5.5601	M	Together	
						5.5974	a	5.5984	0.012
						11.1461	c+M	11.1471	
			0.9 × 10^{-3}		1.88 × 10^4	4.6442	c	4.6624 ↑	
			0.65 × 10^{-3}		3.60 × 10^3				
			0.4 × 10^{-3}		3.60 × 10^3				
D	473-513	3	0.3 × 10^{-3}	70-250	3.60 × 10^3	4.6663	M	4.6663	
						4.6669	a	4.6617	0.0051
						13.9857	c+M+a	13.9887	

* Calculated weight transfer is based on ionic conductivity by sodium ions.
** c = cathode sample, a = anode sample, and M = sample between cathode and anode samples.

Table III. Activation energy

	dc (eV)	ac (eV)
Phosphate (glass A)	0.54	0.57
Borate (glass B)	0.72	0.70
Silicate (glass C)	0.61	0.64
Alkali-lime-silicate (glass D)	0.84	0.89

the data establish straight lines. As the conductivity is represented by

$$\gamma_{dc} = \gamma_0 e^{-E/kT} \quad [5]$$

where E is the activation energy and γ_0 is a constant, the activation energies were obtained from the slopes of the lines. These are listed in Table III.

Figures 2-5 show the dispersion in the dielectric constant K' and the relaxation peaks in the loss factor K''_{ac} *vs.* log f for each glass. Data for typical curves are given at two temperatures.

Figure 2 is for glass A, the phosphate glass. These data were previously published, as glass 1 (7). The loss factor peaks at the same frequency that the midpoint of the dispersion of the dielectric constant curve occurs. The following relationship is observed

$$K''_{ac} < \tfrac{1}{2}(K'_s - K'_\infty) \quad [6]$$

which indicates a distribution of relaxation times. This is common for glasses because of their random structure. Both the dispersion of the dielectric constant and the relaxation peaks shift to higher frequencies with increasing temperature.

The dispersion of the dielectric constant, which is unaltered data, confirms the peak in the relaxation data. In this glass, unlike most glasses, the dielectric constant levels off below the dispersion frequencies and is independent of temperature, within experimental error. This static dielectric constant is also indicative of electronic conductivity. Heroux (20), in a study of lithium borosilicate glasses, showed that the interfacial polarization of ionic conductivity caused a rapid increase in the dielectric constant at frequencies below the dispersion.

Figure 3 gives similar data for glass B. Because this is a lower conductivity glass, the static dielectric constant was observed over a wider temperature and frequency range. For example, the dielectric constant is constant at 1 Hz, below the dispersion frequencies, over a span of 100°C.

Figure 4 gives comparable data for glass C. Again, a relaxation peak is seen at the frequency of the midpoint of the dispersion of the dielectric constant. However, no static dielectric constant is observed for this glass. This is interpreted as the effect of a mixed ionic-electronic conductivity. As gold electrodes were used for this test, it is assumed that this ionic conductivity is associated with tramp alkali in the glass. This slight ionic conductivity is possibly noted in the results of the Tubandt test. While the weight changes were insignificant, three disks were required for the test and two of them fused together. The behavior of the dielectric constant gives positive support to the interpretation of ionic as well as electronic conductivity in this glass. Similar behavior of the dielectric constant curves were previously reported for the iron phosphate glasses, using silver electrodes (7).

Curves for the ionically conducting glass D are shown in Fig. 5. They show a close resemblance to the electronically conducting glasses. Again, the peaks of the relaxation curves occur at the frequencies of the midpoints of the dielectric constant dispersions. However, the dielectric constant rises rapidly below the relaxation frequencies as a result of a build-up of the space-charge polarization. This is typical for ionically conducting glasses (20).

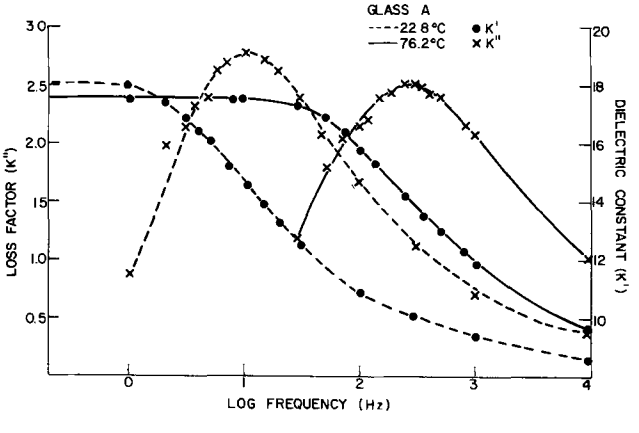

Fig. 2. Glass A, loss factor and dielectric constant vs. frequency

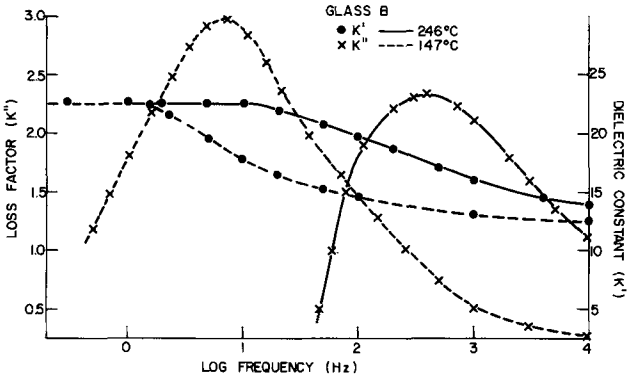

Fig. 3. Glass B, loss factor and dielectric constant vs. frequency

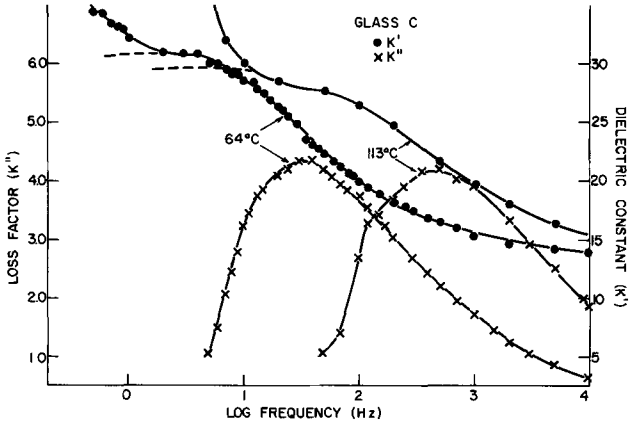

Fig. 4. Glass C, loss factor and dielectric constant vs. frequency

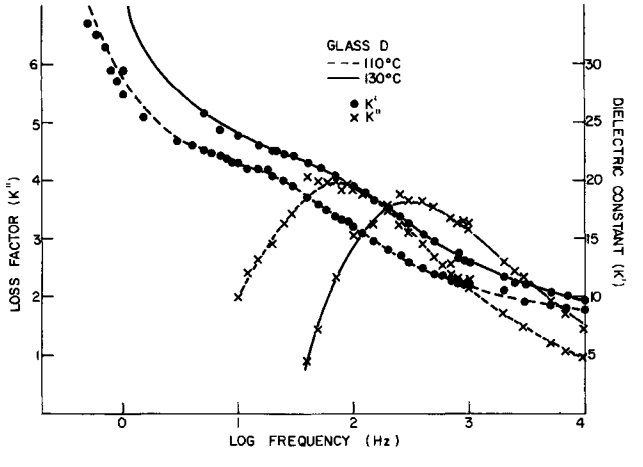

Fig. 5. Glass D, loss factor and dielectric constant vs. frequency

From the loss factor data on glasses A, B, C, and D, the activation energies of the a-c conduction mechanisms are obtained. A plot of the log of the frequency at which this maximum loss factor occurs *vs.* 1000/°K is shown in Fig. 6 for each glass. As the relaxation time $\tau = \tau_0 e^{E/kT}$, where $\tau = 2\pi f$, E is the activation energy, and τ_0 is a constant, the activation energies are obtained from the slopes of the curves. These are tabulated in Table III. The activation energies for each glass for the d-c and a-c conductivities agree well. This indicates that the same mechanism of conduction is responsible for d-c and a-c conductivity.

Conclusions

1. Based on the results of the Tubandt tests, the main conduction mechanism is electronic in glasses A, B, and C and ionic in glass D.
2. The loss factor$_{ac}$, for each glass, peaks in the frequency range in which the midpoint of the dispersion of the unaltered dielectric constant occurs.
3. From the slopes of the dielectric constant curves below the relaxation frequencies and the results of the Tubandt tests, it is deduced that the conduction mechanism is only electronic for glasses A and B, mixed ionic-electronic for glass C, and only ionic for glass D.
4. The agreement in the activation energy data indicates that the main conduction mechanism is the same for a-c and d-c conduction in each glass.

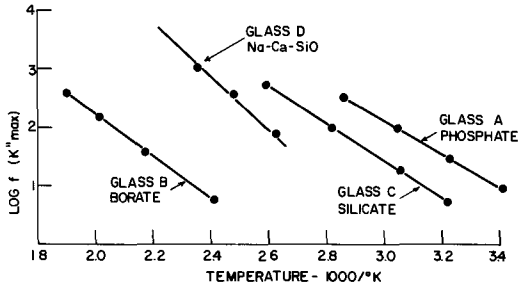

Fig. 6. Frequency of loss factor maximum vs. temperature for glasses A, B, C, and D.

Acknowledgments

The author wishes to thank Drs. Hansen, G. B. Hares, A. M. Filbert, and P. C. Schultz for supplying the glass samples, Mr. G. B. Carrier for the crystal analyses, Mr. W. H. Barney for his helpful discussions of this paper, and Mrs. M. B. Bentley for her experimental assistance.

Manuscript submitted March 20, 1972; revised manuscript received June 6, 1973.

Any discussion of this paper will appear in a Discussion Section to be published in the June 1974 JOURNAL.

REFERENCES

1. M. Munakata, *Solid State Electron.*, **1**, 159 (1960).
2. J. D. Mackenzie, *Modern Aspects of Vitreous State*, **3**, 126 (1964).
3. A. E. Owen, *Glass Ind.*, **48**, 637 (1967).
4. O. V. Mazurin, G. A. Pavlova, E. Ia Lev, and E. K. Leko, *Soviet Phys., Tech. Phys.*, **2**, 2511 (1957).
5. V. A. Ioffe, I. B. Patrina, and I. S. Poberovskaya, *Soviet Phys., Solid State*, **2**, 609 (1960).
6. K. W. Hansen, *This Journal*, **112**, 994 (1965).
7. K. W. Hansen and M. T. Splann, *ibid.*, **113**, 895 (1966).
8. I. G. Austin and N. F. Mott, *Advance Phys.*, **18**, 41 (1969).
9. D. L. Kinser, *This Journal*, **117**, 546 (1970).
10. M. S. Mizzoni and D. L. Kinser, *ibid.*, **117**, 1586 (1970).
11. A. W. Dozier, L. K. Wilson, E. J. Friebele, and D. L. Kinser, *J. Am. Ceram. Soc.*, **55**, 373 (1972).
12. A. Mansingh, J. M. Reyes, and M. Sayer, *J. Non-Crystalline Solids*, **7**, 12 (1972).
13. J. O. Iszard, *ibid.*, **4**, 357 (1970).
14. H. E. Taylor, *J. Soc. Glass Technol.*, **41**, 353T (1957).
15. A. E. Owen, *Prog. Ceram. Sci.*, **3**, 171 (1963).
16. C. Tubandt and S. Eggert, *Z. Anorg. Chem.*, **110**, 196 (1920).
17. K. Hughes and J. O. Isard, *Phys. and Chem. Glasses*, **9**, 40 (1968).
18. A.S.T.M. Standard C657-70T and Standard D-150.
19. I. R. Weingarten, National Research Council Publication 396, Annual Report of Conf. on Elec. Insulation, National Academy of Science, USA, 1955.
20. L. Heroux, *J. Appl. Phys.*, **29**, 1639 (1958).
21. A. M. Filbert and G. B. Hares, Private communication, 1972.

Kinetics of Thermal Growth of HCl-O_2 Oxides on Silicon

K. Hirabayashi and J. Iwamura

Toshiba Research and Development Center, Tokyo Shibaura Electric Company, Ltd., Kawasaki, 210, Japan

ABSTRACT

Growth kinetics at 1100°C are investigated as a function of HCl/O_2 mole ratio below 10% for (111), (100), (311), and (110) oriented wafers. It is concluded that the considerable increase of the oxidation rate in the presence of HCl is caused by three reasons: The first is enhanced diffusion of O_2 and H_2O molecules in the HCl oxide. The second is enhanced reactions at the Si-SiO_2 interface, resulting from a catalytic action of HCl. The third is the contribution of H_2O to the oxidation, which is formed by the reaction, $2HCl + \frac{1}{2} O_2 \rightleftarrows H_2O + Cl_2$. The diffusivity of O_2 and H_2O molecules in the HCl oxide was measured by a technique which is based on dry or wet oxidation after an initial HCl growth. Infrared spectroscopy of the output gas from the furnace and the observation of the Si-SiO_2 interface through a microscope and secondary electron microscope revealed the nature of the enhanced reactions, which are closely related to HCl gaseous etching of Si.

Recently it has been reported that clean SiO_2 films for MOS devices can be obtained by the addition of HCl to dry O_2 during the high temperature oxidation of silicon (1-6). The use of HCl reduces the number of Na^+ ions and surface states at the Si-SiO_2 interface. No significant change between standard and HCl oxide is observed in oxide charge, dielectric strength, dielectric constant, and index of refraction, but the oxidation rate and the diffusivity of Na^+ ions in the oxide are considerably increased in the presence of HCl. It has been suggested that a Si-O-Cl complex is formed

Key words: silicon dioxide, oxidation, HCl-O_2.

during the high temperature oxidation in the presence of HCl and that the actual position of chlorine is substitutional for oxygen, resulting in a nonbridging bond (4).

The increase of the oxidation rate cannot be explained only by the presence of H_2O molecules, formed by the reaction, $2HCl + \frac{1}{2}O_2 \rightleftarrows H_2O + Cl_2$. It is reasonable to suspect that the structure difference between standard and HCl oxide may explain the enhanced oxidation rate. In this paper we investigate the oxidation kinetics at 1100°C as a function of HCl/O_2 mole ratio below 10% for (111), (100), (311), and (110) oriented wafers. By the use of a kinetic model, the effect of diffusion of oxidizing species is separated from that of chemical reactions at the $Si-SiO_2$ interface. The diffusivity of O_2 and H_2O molecules in the HCl oxide is measured by a technique which is based on dry or wet oxidation after an initial HCl growth.

First in the analysis, we neglect the presence of H_2O. Assuming that the equilibrium concentration of O_2 molecules in the oxide and the number of O_2 molecules incorporated into a unit volume of oxide are not changed in the presence of HCl, it is concluded that the enhancement of the oxidation rate is induced not only by enhanced diffusion of O_2 molecules in the oxide but also by enhanced reactions at the $Si-SiO_2$ interface, resulting from a catalytic action of HCl. Second, the effect of H_2O is taken into account, and then the theory explains the experiment fairly well.

In order to clarify the nature of the reactions, infrared spectroscopy is applied to the output gas from the furnace. The structure of the $Si-SiO_2$ interface is observed through a microscope and secondary electron microscope. The roughening of $Si-SiO_2$ interface in the case of large HCl/O_2 mole ratio and large oxide thickness is discussed in relation to the HCl gaseous etching of silicon.

Kinetic Model

Consider a growing film of thickness X (Fig. 1). In the figure, F_1 is the flux of a oxidizing species across the oxide and f_1 is the HCl flux. The oxidizing species are O_2 and H_2O, formed by the reaction, $2HCl + \frac{1}{2}O_2 \rightleftarrows H_2O + Cl_2$. At equilibrium, the reaction for a 1:10 mixture of HCl and O_2 results in the O_2 partial pressure of 0.89 atm and the H_2O partial pressure of 0.016 atm at the total pressure of 1 atm and 1100°C (7). For such a small content of H_2O we may apply the concept of perturbation, and first we neglect the presence of H_2O.

The flux across the oxide is derived from Fick's first law

$$F_1 = D\frac{C_0 - C_i}{X} \quad [1]$$

$$f_1 = \delta\frac{\gamma_0 - \gamma_i}{X} \quad [2]$$

where C_0 and γ_0 are the concentration of O_2 and HCl, respectively, at the outer surface of the oxide. C_i and γ_i are the concentration at the oxide-silicon interface. D and δ are the diffusivity of O_2 and HCl, respectively.

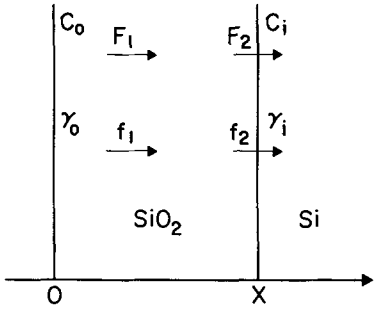

Fig. 1. Schematic representation of the growing film

As we see later the diffusivity, D, increases with the HCl/O_2 mole ratio, and at the $Si-SiO_2$ interface the reaction, $Si + O_2 \rightarrow SiO_2$, is apparently accelerated by the presence of HCl. The HCl molecule behaves like a catalyst. Then, for small concentration of HCl, the reaction constant, k, can be written in the first order approximation

$$k = k_0 + k'\gamma_i \quad [3]$$

where k_0 is the reaction constant for the dry oxygen.

The flux at the SiO_2-Si interface is given by

$$F_2 = kC_i \quad [4]$$

$$f_2 = \kappa\gamma_i \quad [5]$$

where κ is the reaction constant for HCl. The reaction relevant to HCl will be discussed later in relation to the HCl gaseous etching of Si. In a quasi-stationary state we obtain

$$F_1 = F_2 \quad [6]$$

$$f_1 = f_2 \quad [7]$$

The growth rate of the oxide film is then

$$\frac{dX}{dt} = \frac{k}{N}C_i \quad [8]$$

where N is the number of oxygen molecules incorporated into a unit volume of oxide. From Eq. [1]-[8] we get

$$\frac{dX}{dt} = \frac{DC_0/N}{X + \frac{D}{k_0} - \frac{Dk'\gamma_0/k_0^2}{\kappa X/\delta + 1 + k'\gamma_0/k_0}} \quad [9]$$

If we assume that both C_0 and γ_0 are independent of X, the integration of Eq. [9] with the initial condition, $X = 0$ at $t = 0$, leads to

$$2\frac{DC_0}{N}t = X^2 + \frac{2D}{k_0}X - \frac{2Dk'\gamma_0}{k_0^2}\frac{\delta}{\kappa}\log\frac{\kappa X/\delta + 1 + k'\gamma_0/k_0}{1 + k'\gamma_0/k_0} \quad [10]$$

This assumption is justified if the gas-phase mass-transfer coefficients of O_2 and HCl are large enough compared with the corresponding reaction coefficients (8). It is also assumed in Eq. [9] that D and δ are independent of X.

If X is small enough to be

$$\frac{\kappa}{\delta}X << 1 + \frac{k'\gamma_0}{k_0} \quad [11]$$

the growth law can be cast into the following linear-parabolic relationship

$$Bt = X^2 + AX \quad [12]$$

where

$$B = 2DC_0/N \quad [13]$$

$$A = 2D/(k_0 + k'\gamma_0) \quad [14]$$

This relation is readily obtained if the reaction constant is changed to be

$$k = k_0 + k'\gamma_0 \quad [15]$$

instead of Eq. [3].

Second, if we take into account the presence of H_2O, the same approximation as used in Eq. [A-10] of Appendix I leads to

$$(B_1 + B_2)\,t = X^2 + \frac{A_1B_1 + A_2B_2}{B_1 + B_2}X \quad [16]$$

that is

$$Bt = X^2 + AX$$

$$B = B_1 + B_2 \quad [17]$$

$$A = \frac{A_1B_1 + A_2B_2}{B_1 + B_2} \quad [18]$$

where B_1, B_2, A_1, and A_2 are defined as in Eq. [A-5]-[A-8] of Appendix I. The reaction constants, k_1 and k_2, in Eq. [A-7] and [A-8] increase with the concentration of HCl in the same way as Eq. [15] in the present case.

In the following section, we show the change of A and B for the (111), (100), (311), and (110) orientations when the HCl/O_2 mole ratio is varied from 0 to 10%.

Change of A and B

N-type 10 ohm-cm Si slices were used. All slices were cleaned immediately prior to oxidation. Slices were oxidized at 1100°C in various mixtures of HCl and dry O_2. Oxide thicknesses were determined using multiple-beam interferometric techniques. Accuracy of the measurement was ±25Å. For the case of HCl/O_2 mole ratios of 0 and 10%, the graphs of the oxide thickness *vs.* the oxidation time are shown in Fig. 2 and 3, respectively. It should be noted that for the dry oxygen, the growth rate of the (111) orientation is larger than that of the (100) orientation, whereas for the 1:10 mixture of HCl and O_2, they are in the reverse order. The inversion occurs between 2 and 3% of HCl mole ratios.

The oxide thickness as a function of oxidation time was fitted to Eq. [12] by the least square method in order to determine A and B. The values of A and B are summed up in Table I. In Fig. 4 and 5, B and B/A are plotted *vs.* HCl/O_2 mole ratio. The apparent orientation dependence of B may be explained by the inaccuracy in the determination of the oxide thickness. It may be concluded from Fig. 4, and Eq. [17], [18], [A-5]-[A-8] that the orientation dependence of the growth rate is owing to the orientation dependence of the effective reaction constant. The negative values of A, found in

Table I. Change of A and B

HCl/O_2 mole ratio (%)	$B(10^{-4}\ \mu^2/min)$ $A(10^{-2}\ \mu)$	(111)	(100)	(311)	(110)
0	B	4.2	3.9	3.9	3.8
0	A	8.6	7.4	6.2	4.5
0.3	B	5.3	5.2	5.1	5.7
0.3	A	7.8	8.2	5.9	6.5
2	B	6.1	5.9	6.0	6.5
2	A	5.5	5.5	3.0	2.2
3	B	6.8	6.4	5.6	7.2
3	A	6.1	4.1	−1.4	1.8
5	B	6.3	6.7	6.5	6.5
5	A	2.9	3.2	1.1	−1.9
7	B	7.2	6.9	6.6	7.3
7	A	4.8	2.2	−0.04	−0.11
10	B	7.2	7.4	7.1	7.1
10	A	5.2	3.6	1.3	−3.0

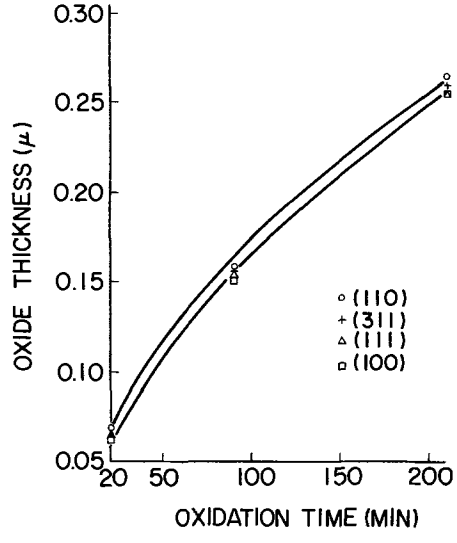

Fig. 2. Oxide thickness vs. oxidation time for the dry oxygen. The fitted curves by the least square method are also shown for (111) and (110).

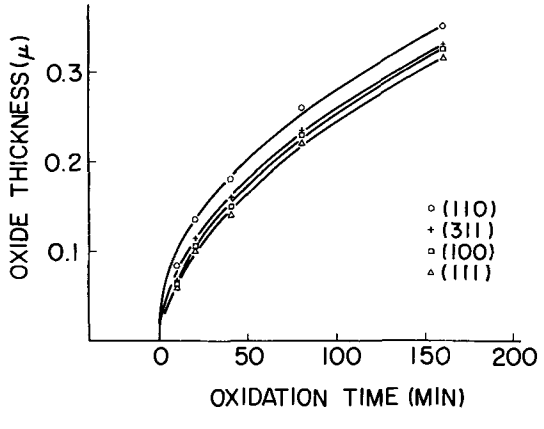

Fig. 3. Oxide thickness vs. oxidation time for the HCl/O_2 mole ratio of 10%. The fitted curves by the least square method are also shown.

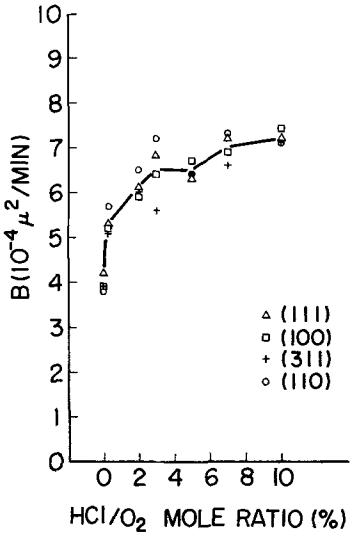

Fig. 4. B vs. HCl/O_2 mole ratio. The arithmetic mean value is shown by the solid line.

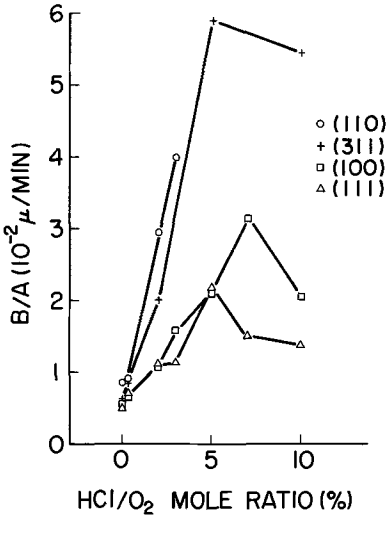

Fig. 5. B/A vs. HCl/O_2 mole ratio

Table I, cannot be expected from Eq. [18]. The growth as a function of time was found hardly to obey the linear-parabolic relationship for HCl/O_2 mole ratios beyond 10%. The approximations used to derive Eq. [12] are considered to be applicable only to smaller mole ratios. The occurrence of negative values of A could be avoided if the experimental data were fitted to Eq. [10] instead of Eq. [12]. For further investigation, higher degree of accuracy in the determination of oxide thickness is required especially for oxides thinner than 0.1μ, to which the values of A are sensitive.

The increase of B with the HCl/O_2 mole ratio may be attributed to the increase of the diffusivity of O_2 and H_2O in the HCl oxide if we assume that for both O_2 and H_2O, the equilibrium concentration in the oxide and the number of molecules incorporated into a unit volume of the oxide are equal to those of the standard oxide (see Eq. [17], [A-5], and [A-6]).

Diffusion of O_2 and H_2O in the HCl Oxide

In this section we determine the diffusivity of O_2 and H_2O in the HCl oxide grown at 1100°C in the 1:10 mixture of HCl and O_2, using a technique which is based on the dry or wet oxidation after the initial HCl growth. Wafers of the (100) orientation were used.

Theoretical relationship between the oxide thickness, X, and the oxidation time, t, in the dry or wet oxygen is expressed as

$$Bt = (X - X_0)(X + X_0 + A') \qquad [19]$$

where

$$A' = A + 2\left(\frac{D}{D_0} - 1\right)X_0 \qquad [20]$$

(see Appendix II). A and B are determined independently by the oxidation of bare silicon wafers. X_0 is the thickness of the initial HCl oxide. D and D_0 are the diffusivity of the oxidizing molecules in the growing oxide and the HCl oxide, respectively.

Diffusion of O_2 in the HCl oxide.—Values of X and t are shown in Table II. X_0 is 0.21μ. According to Table I, A and B are determined as $A = 7.4 \times 10^{-2}\mu$ and $B = 3.9 \times 10^{-4}\ \mu^2$/min. The values of D/D_0 obtained from Eq. [19] and [20] are also shown in Table II. Thus the diffusivity of O_2 in the HCl oxide is approximately 1.6 times larger than that in the dry oxide.

Diffusion of H_2O in the HCl oxide.—As the wet oxygen, where the bubbler temperature is 90°C, is used here instead of pure steam, the analysis is rather complicated. In this case, the oxidation in a mixture of H_2O and O_2 should be considered as in Appendixes I and II. Bare silicon wafers were oxidized in the wet oxygen, and then the oxide thickness as a function of time was fitted to Eq. [A-10], leading to $B^* = 0.47 \times 10^{-2}\ \mu^2$/min. If we take into account that for pure steam, $B = 0.917 \times 10^{-2}\ \mu^2$/min (9) and for dry oxygen, $B = 3.9 \times 10^{-4}\ \mu^2$/min, the value of B^* shows that the wet oxygen is a 1:1 mixture of O_2 and H_2O.

The oxide thickness, X, as a function of the oxidation time, t, after the initial oxidation of $X_0 = 0.21\mu$, is shown in Table III. Using the values, $A_1 = 0.074\mu$, $A_2 = 0.157\mu$ (9), $B_1 = 0.5 \times 3.9 \times 10^{-4}\ \mu^2$/min, $B_2 = 0.5 \times 0.917 \times 10^{-2}\ \mu^2$/min, $D_1/D_{01} = 0.64$ (assuming that the diffusivity of O_2 in the wet oxide is the same as in the dry oxide), and Eq. [A-21]-[A-23], we can determine the values of D_2/D_{02}, which are shown in Table III. The results are not strongly dependent on the value of D_1/D_{01}. Thus the diffusivity of H_2O in the HCl oxide is approximately 2.6 times larger than that in the wet oxide.

Next we compare the diffusivity of H_2O in the wet oxide with that in the dry oxide. Instead of the initial HCl oxide used in the above experiment, the dry oxide of $X_0 = 0.18\mu$ was used. The oxide thickness, X, as a function of the oxidation time, t, in the wet oxygen is shown in Table IV. Using Eq. [A-21]-[A-23] and assuming that the diffusivity of O_2 in the wet oxide is the same as in the dry oxide, we can determine the values of D_2/D_{02}, which are shown in Table IV. The results are not strongly dependent on the value of D_1/D_{01}. The gradual increase of D_2/D_{02} with the oxidation time suggests that the H_2O molecules are gradually incorporated into the network of the dry oxide in some form and the structure of the dry oxide is getting near to that of the wet oxide.

The diffusivity of H_2O in the dry oxide is approximately 1.5 times larger than that in the wet oxide, and thus the diffusivity of H_2O in the HCl oxide is approximately 1.7 times larger than that in the dry oxide.

Contribution of H_2O in the HCl oxidation.—The ratio of B for the HCl/O_2 mole ratio of 10% and for the dry oxygen is 7.4/3.9 = 1.9, which is larger than the ratio of the corresponding diffusivity of O_2 (= 1.6). The difference may be attributed to the presence of H_2O. In the reaction, $2HCl + \frac{1}{2}O_2 \rightleftarrows H_2O + Cl_2$, at equilibrium, the O_2 partial pressure is 0.89 atm and the H_2O partial pressure is 0.016 atm at the total pressure of 1 atm and 1100°C. Then, from Eq. [17], [A-5], and [A-6], we obtain by taking into account the increase in the diffusivity

$$B_1 = 0.89 \times 1.6 \times 3.9 \times 10^{-4}\ \mu^2/\text{min}$$

$$B_2 = 0.016 \times 2.6 \times 0.917 \times 10^{-2}\ \mu^2/\text{min}$$

$$B_1 + B_2 = 9.3 \times 10^{-4}\ \mu^2/\text{min}$$

which is too large compared with the actual value, $B = 7.4 \times 10^{-4}\ \mu^2$/min. Here we assumed that the diffusivity of H_2O in the steam oxide is the same as that in the wet oxide.

It may be doubted whether the H_2O partial pressure is lower than the equilibrium value, 0.016 atm. The initial O_2 pressure is 0.91 atm, which is little different from the equilibrium value, 0.89 atm. Let us denote the H_2O partial pressure as P_{H_2O} and use a tentative value, 0.9 atm, for the O_2 partial pressure. In order to explain the actual value of B, we should choose as $P_{H_2O} = 0.0075$ atm, which is approximately half of the equilibrium value.

As the final example, we show in Table V the results of the HCl oxidation after the initial dry oxidation of $X_0 = 0.21\mu$. The calculated thickness in Table V was obtained by assuming the O_2 partial pressure of

Table II. HCl oxidation followed by dry oxidation

t (min)	X (μ)	D/D_0
60	0.27	0.61
120	0.32	0.59
180	0.35	0.68

Table III. HCl oxidation followed by wet oxidation

t (min)	X (μ)	D_2/D_{02}
20	0.40	0.35
40	0.51	0.41
60	0.60	0.42

Table IV. Dry oxidation followed by wet oxidation

t (min)	X (μ)	D_2/D_{02}
20	0.355	0.57
40	0.46	0.66
60	0.545	0.72

Table V. Dry oxidation followed by HCl oxidation

t (min)	X (μ)	Calculated thickness (μ)
50	0.255	0.259
90	0.295	0.294

0.9 atm, the H_2O partial pressure of 0.0075 atm, and $A_1 = A_2 = 0.036\mu$ in Eq. [A-22] and [A-23] (see Table I), and using Eq. [A-21]. The results are not strongly dependent on the values of A_1 and A_2.

Chemical Reactions at the Si-SiO_2 Interface

From Eq. [17] and [18], we obtain

$$\frac{B}{A} = \frac{(B_1 + B_2)^2}{A_1B_1 + A_2B_2} \qquad [21]$$

If the HCl/O_2 mole ratio is sufficiently small, B_2 becomes negligibly small. Then we get

$$\frac{B}{A} = \frac{B_1}{A_1} = \frac{C_0}{N}(k_0 + k'\gamma_0) \qquad [22]$$

where C_0, N, k_0, k' are for O_2 (see Eq. [13] and [14]). As C_0 is considered to be constant in the above range of the HCl/O_2 mole ratio and γ_0 is approximately proportional to the HCl/O_2 mole ratio, it is concluded that B/A is a linear function of the HCl/O_2 mole ratio. Actually, it is the case for the HCl/O_2 mole ratio below 5%, as we see in Fig. 5. The values of k' are dependent on the orientation

$$k'(111) \simeq k'(100) < k'(311) < k'(110) \qquad [23]$$

Thermodynamic analyses of an equilibrium Si-H-Cl system for the Cl/H ratio of 1 at 1100°C were made in the same approximation as used in the work of Lever (10). The result of the analyses indicates that H_2, HCl, $SiHCl_3$, $SiCl_2$, $SiCl_4$, and SiH_2Cl_2 need be considered. By the addition of O_2, $SiHCl_3$, $SiCl_2$, $SiCl_4$, and SiH_2Cl_2 are changed into SiO_2 and HCl. Silicon dioxide is hardly attacked by HCl as is shown later. If the rate of the two-step reactions mentioned above is larger than the rate of the direct oxidation

$$Si + O_2 \rightarrow SiO_2$$

the hydrogen chloride may be considered as a catalyst.

The reactions in the absence of O_2 are no other than those of the HCl gaseous etching of silicon. Then, we expect some parallelism between k' and the gaseous etch rate which is considered to be proportional to κ of Eq. [5]. The gaseous etch rate at 1100°C for the HCl/H_2 mole ratio of 5% is 0.5 μ/min for (111), 0.8 μ/min for (100), and 0.9 μ/min for the (110) orientation (11), and thus

$$\kappa(111) < \kappa(100) < \kappa(110)$$

In relation [23], $k'(111)$ is nearly equal to $k'(100)$. However, if we notice that for the dry oxygen, the growth rate of the (111) orientation is larger than that of the (100) orientation, whereas for the HCl/O_2 mole ratio larger than 2%, they are in the reverse order, we may conclude that $k'(111) < k'(100)$ and $k_0(111) > k_0(100)$. Then, the parallelism between k' and κ is complete. It should be noted that the orientation dependence of k_0 is different from that of k'

$$k_0(100) < k_0(111) < k_0(311) < k_0(110)$$

$$k'(111) < k'(100) < k'(311) < k'(110)$$

In the presence of H_2O, Si_2OCl_6 is produced in addition to SiO_2 (12). In order to verify the above reactions at the Si-SiO_2 interface, we exposed silicon wafers covered with the HCl oxide of 0.4μ thickness, to the HCl gas at 1100°C. The output gas from the furnace was introduced into a cell with KBr windows. The infrared absorption spectra of the output gas was measured by a Beckman's infrared spectrometer *IR* 10, in double beam operation. As shown in Fig. 6, H_2O, HCl, Si_2OCl_6, SiH_2Cl_2, $SiHCl_3$, and $SiCl_4$ were detected. For the HCl/O_2 mole ratio of 720, the same gaseous species were detected, but not for the HCl/O_2 mole ratios below 180.

The observation of the wafers through a microscope revealed triangle-shaped etch pits for (111), square-shaped pits for (100), and line-shaped pits for the (110) orientation. The shape of the etch pits is reasonable since the etch rate is largest in the <110> directions. Interference color was observed at the pits, which indicates that only Si is etched off at the pits and not SiO_2.

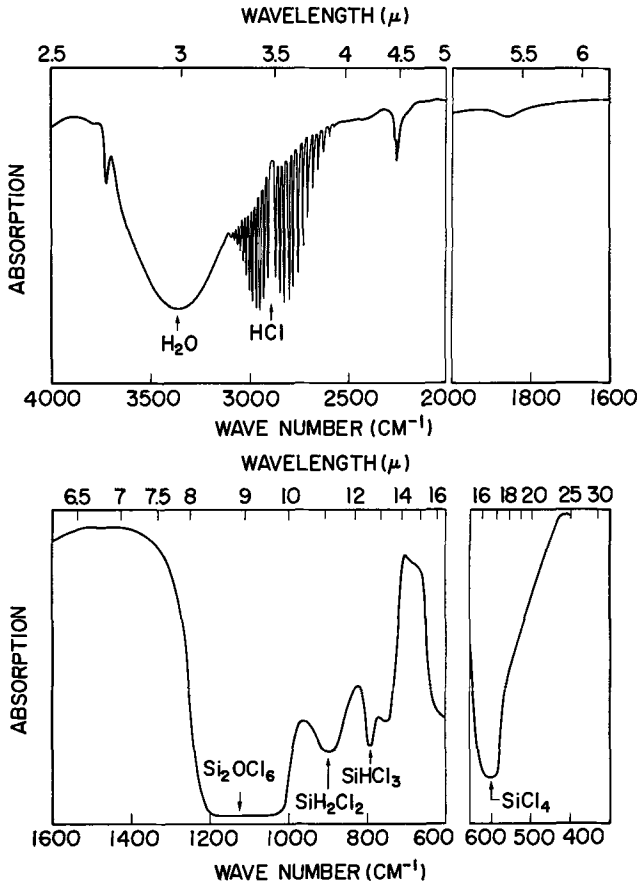

Fig. 6. Infrared absorption spectra of the output gas from the furnace. See the text.

Roughening of the Si-SiO_2 Interface

Especially in the case of large HCl/O_2 mole ratio and large oxide thickness, the color of oxide-covered silicon wafers becomes dirty. The observation through a scanning electron microscope indicates that this is because of the roughening of the Si-SiO_2 interface. Figure 7 is the SEM photograph of a (110) silicon wafer covered with the HCl oxide of 0.25μ thickness grown in a 7:100 mixture of HCl and O_2. The upper part in the figure is coated with an Al film of 300Å thickness. As the Al film prevents the penetration of electrons, the pattern in the Al-coated part is of the Al film itself and thus of the oxide. It is evident from the figure that many holes are at the Si-SiO_2 interface and the oxide film is curved along the wall of the hole. It should be noted, though not evident from Fig. 7, that there are no pinholes in the oxide over the silicon holes at the interface. This is also shown by the measurement of the dielectric strength (1). Figure 8 is the SEM photograph of the same wafer after the oxide film is removed. Line-shaped etch pits are observed in the figure. Figure 9 shows how large values of HCl/O_2 mole ratio and oxide thickness induce the roughening of the Si-SiO_2 interface for the (111), (100), (311), and (110) orientations.

From Eq. [1], [2], [4]-[7], and [15], we obtain for the concentrations of O_2 and HCl at the Si-SiO_2 interface

$$C_i = \frac{C_0}{1 + \frac{k}{D}X} \qquad [24]$$

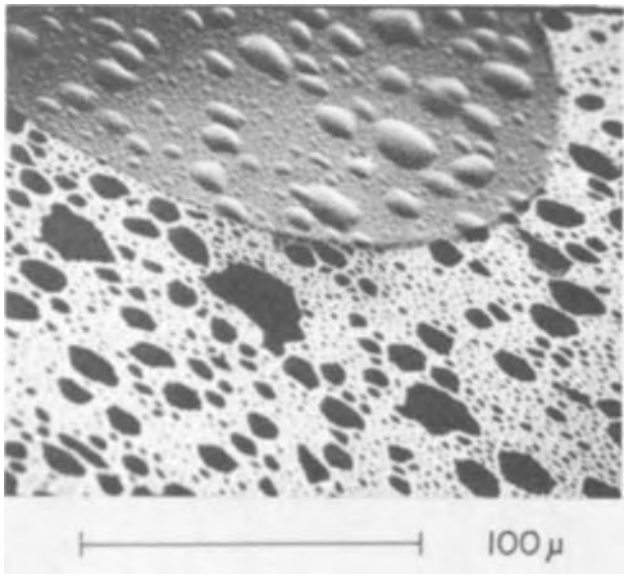

Fig. 7. SEM photograph of a (110) silicon wafer covered with the HCl oxide of 0.25μ thickness grown in a 7:100 mixture of HCl and O_2. The upper part in the figure is coated with an Al film of 300Å thickness.

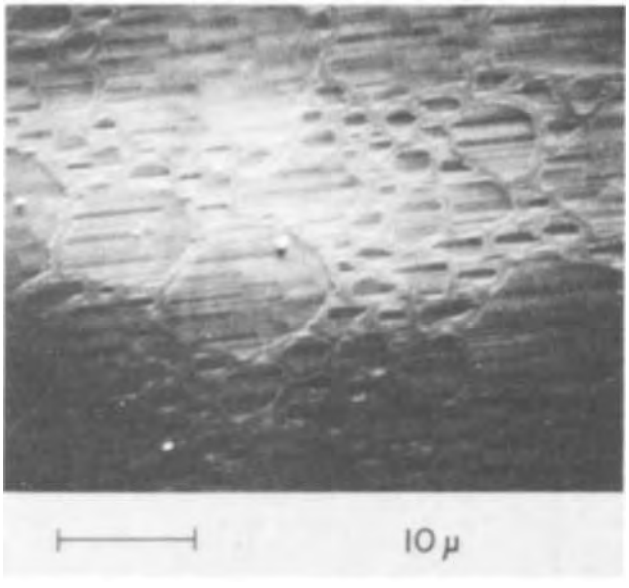

Fig. 8. SEM photograph of the same wafer as in Fig. 7 after the oxide film is removed.

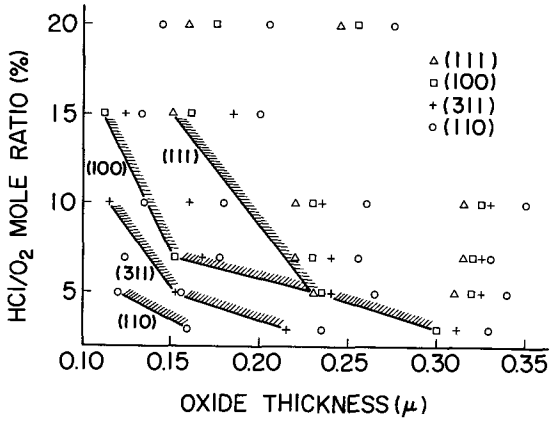

Fig. 9. Observed roughening of the Si-SiO_2 interface for various values of HCl/O_2 mole ratio and oxide thickness. Approximate boundaries between roughened and not roughened regions are shown by the hatched lines.

and

$$\gamma_i = \frac{\gamma_0}{1 + \frac{\kappa}{\delta} X} \qquad [25]$$

Then, if the relation

$$\kappa/\delta < k/D = (k_0 + k'\gamma_0)/D \qquad [26]$$

holds, γ_i/C_i becomes much larger than γ_0/C_0 for large values of X. Thus, for large thickness of the oxide, the deficiency of the oxygen may possibly occur in the oxidation of the intermediate products, $SiHCl_3$, etc., leading to the etching of the interface. This explanation is justified only when the relation [26] is verified. Another explanation is that the oxidation of the intermediate products are not always complete and the etching of the interface occurs slowly with increasing the oxidation time.

Conclusion

The considerable increase of the oxidation rate in the presence of HCl is caused by three reasons. The first is the enhanced diffusion of O_2 and H_2O molecules in the HCl oxide. This is consistent with the Kriegler's suggestion that the HCl oxide includes larger amount of nonbridging bounds than the dry oxide, which induces the enhanced diffusion of Na^+ ions.

The second is the enhanced reaction at the Si-SiO_2 interface, resulting from the catalytic action of HCl. The intermediate products of the reaction are the same as those for the HCl gaseous etching of silicon. The third is the contribution of H_2O molecules, formed by the reaction, $2HCl + \frac{1}{2} O_2 \rightleftarrows H_2O + Cl_2$. The effect of the H_2O molecule is thought to be minor for the HCl/O_2 mole ratio below 5%.

The roughening of the Si-SiO_2 interface is not desirable for device fabrications. It is probable that the roughening leads to the gradual increase of the surface state density observed in the case of (100) orientation for the HCl/O_2 mole ratio above 8% (1). The roughening is severer for the (100) orientation than for the (111) orientation.

Acknowledgments

We wish to thank Dr. Y. Takeishi for encouragement during the course of this work, Dr. Y. Nishi for helpful discussions concerning the HCl gaseous etching and the infrared spectroscopy, and Mr. H. Hara for suggestions on the effect of H_2O.

APPENDIX I.

Oxidation in Two Kinds of Oxidizing Species

Let us define relevant parameters as in Table A-I. For the sake of simplicity we assume that the concentration of oxidizing molecules at the outer surface of the oxide is equal to the equilibrium concentration in the oxide, which is proportional to the partial pressure of the oxidizing species. The flux of O_2 reaching the Si-SiO_2 interface across the oxide of thickness, X, is given by

$$D_1 \frac{C_{01} - C_{11}}{X} = k_1 C_{11} \qquad [A\text{-}1]$$

and the flux of H_2O is

$$D_2 \frac{C_{02} - C_{12}}{X} = k_2 C_{12} \qquad [A\text{-}2]$$

Table A-I. Relevant parameters in the oxidation in two kinds of oxidizing species

Oxidizing species	Reaction constant	Number of oxidizing molecules/unit volume	Concentration at the Si-SiO_2 interface	Concentration at the outer surface of the oxide	Diffusivity
O_2	k_1	N_1	C_{11}	C_{01}	D_1
H_2O	k_2	N_2	C_{12}	C_{02}	D_2

The growth rate of the oxide film is then

$$\frac{dX}{dt} = \frac{k_1}{N_1} C_{i1} + \frac{k_2}{N_2} C_{i2} \qquad [A-3]$$

From Eq. [A-1]-[A-3] we obtain

$$\frac{dX}{dt} = \frac{B_1}{2X + A_1} + \frac{B_2}{2X + A_2} \qquad [A-4]$$

where

$$B_1 = 2D_1C_{01}/N_1 \qquad [A-5]$$

$$B_2 = 2D_2C_{02}/N_2 \qquad [A-6]$$

$$A_1 = 2D_1/k_1 \qquad [A-7]$$

$$A_2 = 2D_2/k_2 \qquad [A-8]$$

Integrating Eq. [A-4] with the initial condition, $X = 0$ at $t = 0$, we get

$$(B_1 + B_2)t = X^2 + \frac{A_1B_1 + A_2B_2}{B_1 + B_2} X - \frac{B_1B_2(A_1 - A_2)^2}{2(B_1 + B_2)^2} \log\left[\frac{2(B_1 + B_2)X + B_1A_2 + B_2A_1}{B_1A_2 + B_2A_1} \right] \qquad [A-9]$$

When the condition, $A_1 \simeq A_2$, is satisfied, the last term can be neglected, and the linear-parabolic relationship is obtained

$$B^*t = X^2 + A^*t \qquad [A-10]$$

where

$$B^* = B_1 + B_2 \qquad [A-11]$$

$$A^* = \frac{A_1B_1 + A_2B_2}{B_1 + B_2} \qquad [A-12]$$

The condition, $A_1 \simeq A_2$, seems to be satisfied at 1100°C. For instance, the observed values are

$$A_1 = 0.086\mu \text{ and } A_2 = 0.083\mu \quad (9)$$

for the (111) orientation, and $A_1 = 0.074\mu$ and $A_2 = 0.157\mu$ (9) for the (100) orientation.

APPENDIX II

Diffusion in Double Layered Oxide

Consider the oxidation in the system schematically represented in Fig. A-1. The system is realized, for instance, when silicon wafers are oxidized in the dry or wet oxygen after the initial HCl oxidation.

The flux, F_0, of the oxidizing species across the initial oxide is

$$F_0 = D_0 \frac{C_0 - C_1}{X_0} \qquad [A-13]$$

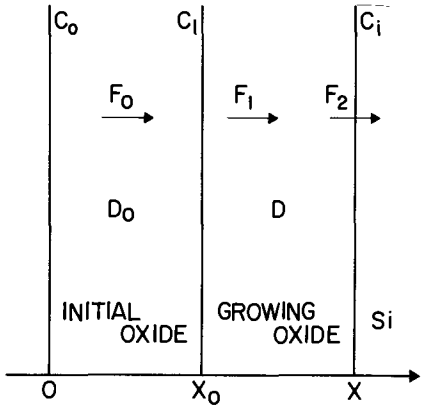

Fig. A-1. Schematic representation of the oxidation of silicon covered with a film of thickness X_0.

where D_0 is the diffusivity of the oxidizing species in the initial oxide, C_0 the concentration of the oxidizing molecules at the outer surface of the initial oxide, and C_1 is the concentration at the interface of the initial oxide and the growing oxide. The flux, F_1 across the growing oxide is

$$F_1 = D \frac{C_1 - C_i}{X - X_0} \qquad [A-14]$$

where C_i is the concentration at the Si-SiO_2 interface. In a quasi-stationary state we have

$$F_0 = F_1 = F_2 = kC_i \qquad [A-15]$$

where k is the reaction constant. The growth rate of the oxide film is then

$$\frac{dX}{dt} = \frac{k}{N} C_i \qquad [A-16]$$

where N is the number of oxidizing molecules incorporated into a unit volume of the growing oxide. Solving Eq. [A-13]-[A-16] with the initial condition, $X = X_0$ at $t = 0$, we obtain

$$Bt = (X - X_0)(X + X_0 + A') \qquad [A-17]$$

where

$$B = 2DC_0/N \qquad [A-18]$$

$$A' = A + 2\left(\frac{D}{D_0} - 1\right) X_0 \qquad [A-19]$$

and

$$A = \frac{2D}{k} \qquad [A-20]$$

As A and B are determined independently by the oxidation of bare silicon wafers, we can estimate the value of D/D_0 from Eq. [A-17] and [A-19].

When the oxidizing species are O_2 and H_2O, the same approximation as Eq. [A-10] leads to

$$(B_1 + B_2)t = (X - X_0)\left(X + X_0 + \frac{A'_1B_1 + A'_2B_2}{B_1 + B_2} \right) \qquad [A-21]$$

where

$$A'_1 = A_1 + 2\left(\frac{D_1}{D_{01}} - 1\right) X_0 \qquad [A-22]$$

$$A'_2 = A_2 + 2\left(\frac{D_2}{D_{02}} - 1\right) X_0 \qquad [A-23]$$

D_1 and D_{01} are the diffusivity of O_2 in the growing oxide and the initial oxide, respectively. Similarly, D_2 and D_{02} are for H_2O.

Manuscript submitted April 13, 1973; revised manuscript received June 25, 1973

Any discussion of this paper will appear in a Discussion Section to be published in the June 1974 JOURNAL.

REFERENCES

1. R. J. Kriegler, Y. C. Cheng, and D. R. Colton, *This Journal*, **119**, 388 (1972).
2. R. J. Kriegler, *Appl. Phys. Letters*, **20**, 449 (1972).
3. R. J. Kriegler, J. D. Morris, and D. R. Colton, Paper 280 presented at Electrochem. Soc. Meeting, Miami Beach, Florida, Oct. 8-13, 1972.
4. R. J. Kriegler, *Thin Solid Films*, **13**, 11 (1972).
5. P. H. Robinson and F. P. Heimann, *This Journal* **118**, 141 (1971).
6. R. S. Ronen and P. H. Robinson, *ibid.*, **119**, 747 (1972).
7. H. Hara, Private communication.
8. A. S. Grove, "Physics and Technology of Semiconductor Devices," John Wiley & Sons, Inc., New York (1967).
9. W. A. Pliskin, *IBM J. Res. Dev.*, **10**, 198 (1966).
10. R. F. Lever, *ibid.*, **8**, 460 (1964).
11. Y. Nishi, Private communication.
12. M. J. Rand, *Anal. Chem.*, **35**, 2126 (1963).

Technical Notes

Preparation of Ohmic Contacts to n-Ge by Diffusion from As-Doped SiO_2

James W. Holm-Kennedy and Tony P. C. Ku

Electrical Sciences and Engineering Department, University of California at Los Angeles, Los Angeles, California 90024

This note describes a rather simple and convenient procedure for fabricating ohmic contacts to lightly doped n-type Ge. The contacts are found to be ohmic at low electric fields over the range of temperature investigated (77°-300°K). They are noninjecting up to high fields at 77° and 195°K. At 300°K they begin to inject at fields above approximately 25 V/cm, presumably because the n-Ge used is nearly intrinsic at this temperature.

Previously reported techniques for fabricating ohmic contacts to n-Ge have included the use of indium amalgam (1) and alloying (2). It is not clear that the In amalgam contacts will remain noninjecting at moderate electric fields. These contacts are often on a surface previously damaged by sand blasting or lapping in order to achieve ohmicity. Damaged surfaces serve to kill lifetime and frequently will suppress injection at low applied voltages by simply causing rapid minority carrier recombination at the contact. Surface-damaged contacts, however, often inject at higher applied voltages. Further, it is difficult to define contacts to precise dimensions with In amalgam because the amalgam is liquid at room temperature. Contacts of Sb alloyed to n-Ge were investigated but these were found to be lightly injecting. Alloying with Sb-doped Au (0.1% Sb) has been reported to give a low-field ohmic contact to n-Ge (2).

We report here an alternative technique which employs an As-doped SiO_2 diffusion source to create an n^+ region. We chose to use As as the impurity because it supplies a shallow donor state (3) and has a relatively high saturation solubility at moderate temperatures (4). Sb or P might be expected to serve equally well. However, alloying of Sb dots and diffusion of Sb from an Sb-doped SiO_2 source did not provide high-electric-field ohmic contacts in the present case. This is presumably because Sb has a much lower saturation solubility in Ge than As (4). P was not tested but is expected to give results comparable to those obtained with As.

Doping with As can be achieved by heating a Ge wafer that has been sealed together with elemental As in an evacuated closed quartz tube. This closed-tube diffusion technique is awkward, however, because As oxidizes rapidly in air and has a vapor pressure considerably above 1 atm at the diffusion temperatures of interest. To prevent explosions, it is necessary to keep the weight of the As charge below maximum value determined by the volume of the quartz tube. These properties, coupled with the hazards of handling elemental As, make its use undesirable. We have circumvented the problem by using doped SiO_2 as an impurity source, a standard method used in Si technology (5).

Key words: semiconductor contacts, doped oxide, planar diffusion.

The following contacting procedure was used. A 22 ohm-cm (donor concentration $\sim 10^{14}$/cc) n-Ge wafer was lapped with No. 600 grit Al_2O_3, ultrasonically cleaned with Rustlick 660J detergent (Rustlick, Incorporated, Boston, Massachusetts), and thoroughly rinsed with deionized water (DI). The lapped surface was etched until shiny in CP4A (3:3:5:: conc glacial acetic acid: conc HF: conc HNO_3, by volume), dipped in methanol, rinsed in DI and dried with a dry nitrogen jet. Arsenosilica film (Emulsitone, Livingston, New Jersey) was applied to the surface of the wafer by spinning at 3000 rpm for 15 sec. After the film was cured at 200°C in air for 15 min or longer, the wafer was ready for shallow diffusion. The diffusion was performed in an open quartz tube at 650°C for 7 min in flowing forming gas (10% H_2, 90% N_2). (Diffusion temperatures to 850°C and times up to 30 min also produced good ohmic contacts.) The wafer was then slowly removed from the furnace to avoid the introduction of strain caused by thermal quenching. The arsenosilica film was etched away using HF acid leaving the wafer with an exposed n^+ surface having an estimated surface concentration (6) greater than $\sim 10^{20}/cm^3$ in an n^+ layer of less than 0.1 μm estimated thickness.

Metallization was accomplished by electroless Ni plating. A photoresist technique was then used to selectively mask the Ni. KMER photoresist (Eastman Kodak Company, Rochester, New York) was spun onto the n^+ side of the Ni-plated wafer at 1000 rpm for 10 sec. The wafer was dried in air at room temperature for an hour or longer and then cured in air at 100°-200°C for 15 min. The contact areas were then defined using standard planar techniques by exposing the KMER to ultraviolet light for 10 sec and developing the KMER in isopropyl alcohol. This was followed by a post bake in air at 120°C for 15 min to dry the remaining KMER. The unprotected Ni was removed with a Ni etch (1:1:1:: conc HNO_3: conc HCl: acetone, by volume). The exposed portion of the n^+ layer was removed by a quick dip in CP4A (mesa technique). Finally, the hardened photoresist was removed with J100 solution (IRCL, Richardson, Texas) leaving well-defined ohmic contacts under the Ni contacting pads.

Contacts made to lightly doped n-Ge (22 ohm-cm) following the above procedure were of low resistance, $< 5 \times 10^{-4}$ ohm-cm^2 at 300°K and $< 5 \times 10^{-5}$ ohm-cm^2 at 77°K (the lower limit which we could conveniently determine for our sample geometry using a Tektronix curve tracer.

The contacts proved to be non-injecting at 77°, 195° and 300°K. They maintained their ohmic integrity at

77° and 195°K to electric fields in excess of 1500 V/cm, the upper limit of the high voltage system used. The contacts did, however, inject minority carriers (holes) at 300°K for fields in excess of about 25 V/cm, probably because the Ge was so lightly doped that at room temperature a significant number of thermally generated holes were present. The contacting technique is expected to provide contacts which do not inject holes at 300°K even at high electric fields if the n-Ge is made sufficiently extrinsic.

Since the difficulty of obtaining ohmic contacts generally decreases with increasing extrinsic carrier concentration and increasing operating temperature, on the basis of our results for lightly doped samples we believe that the procedure described above is a simple, effective method for fabricating ohmic contacts to n-type Ge. The method should also provide a convenient planar diffusion technique for reliable n-type diffusion in Ge.

Acknowledgment

This work was supported by the National Science Foundation.

Manuscript submitted Dec. 4, 1972; revised manuscript received June 20, 1973.

Any discussion of this paper will appear in a Discussion Section to be published in the June 1974 JOURNAL.

REFERENCES

1. R. Hill, D. Richardson, and S. Wilson, *J. Phys. D: Appl. Phys.*, **5**, 185 (1972).
2. S. M. Sze, "Physics of Semiconductor Devices," p. 416, Wiley-Interscience, New York (1969).
3. S. M. Sze, "Physics of Semiconductor Devices," p. 30, Wiley-Interscience, New York (1969).
4. F. A. Trumbore, *Bell Syst. Tech. J.*, **39**, 205 (1960).
5. K. Reindl, *Solid-State Electron.*, **16**, 181 (1973).
6. S. M. Sze, "Physics of Semiconductor Devices," p. 31, Wiley-Interscience, New York (1969).

Thermal Oxidation of Silicon after Ion Implantation

C. R. Fritzsche* and W. Rothemund

Institut für Angewandte Festkörperphysik der Fraunhofer-Gesellschaft D-78 Freiburg, West-Germany

In semiconductor device technology ion implantation is applied to generate n- and p-type regions or special donor and acceptor profiles. It appears likely that ion implantation can also be used to influence technological processes, as for instance, thermal oxidation. This opens the possibility of selective oxidation and of the production of stress-free protective films. Normally selective oxidation is achieved using silicon nitride layers for masking during thermal oxidation, while stress-free films have been made with oxinitrides (1). Since the nitride as well as the oxide can be formed by implantation of nitrogen or oxygen ions, respectively, into silicon (2,3), we expected that these ions would influence the oxide growth. This paper reports on the growth of oxides after implantation of nitrogen, which was found to influence the oxidation strongly. Some information will also be given concerning the effect of implanted oxygen and carbon.

Experimental

Ions were implanted into polished (111) surfaces of 20 ohm-cm p-type silicon. The beam current depended upon the ion species and did not exceed 16 μA, which according to our beam sweep corresponds to a maximum current density of 5 $\mu A/cm^2$. The crystal axes were tilted by 7° to the beam axis. The distribution of ions is assumed to be close to the profiles calculated from LSS theory (4) at least at lower fluences and in the neighborhood of the concentration peak. The implanted species were N_2^+, O^+, and C^+. From the mass spectra obtained with N_2 or CO_2 in the ion source we conclude that about 5% CO^+ was contained in the beam used for N_2^+ implantations. We are sure that our results with N_2^+ are not due to CO^+ since the effects of C and O were investigated separately and found to be small.

During implantation, half of the sample was covered with an impermeable 0.1 mm steel sheet so that comparison of implanted and unimplanted material with otherwise identical processing was possible. The conditions of oxidation are given in the figures and tables. Three types of thickness measurements were made: Interferometric measurements of the surface step between the oxide layers grown on the implanted and the unimplanted part of the wafer, interference measurements of the oxide thicknesses after step etching with HF, and ellipsometric measurements.

* Electrochemical Society Active Member.

Key words: silicon dioxide, oxinitrides, ion implantation, oxidation rate, planar technology.

Results

If 4×10^{15} N_2^+ ions per cm^2 are implanted with 30 kV, the oxidation proceeds as shown in Fig. 1 and 2. Consider first the results of oxidations at 1140°C in dry oxygen shown in Fig. 1. The unimplanted silicon shows the well-known square root relation between oxide thickness and time. However, only a very thin film with high refractive index is found on the implanted surface for up to 26 min of oxidation. Longer oxidation results in a substantial growth of films with a refractive index close to that of common thermally grown SiO_2, for which 1.46 is a typical value. With lower temperatures of oxidation, higher thickness differences can be achieved. Figure 2 shows the results of oxidations at 1010°C in dry oxygen. At this low temperature ex-

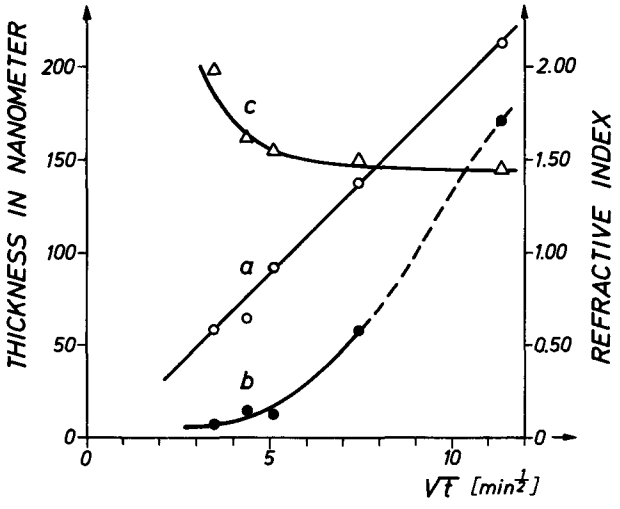

Fig. 1. Time dependence of oxide growth. Dry oxygen, 1140°C. N_2^+-implantation 30 kV, 4 x 10^{15} ions/cm^2. Ellipsometric measurements. (a) Thickness unimplanted, (b) thickness implanted, (c) refractive index implanted.

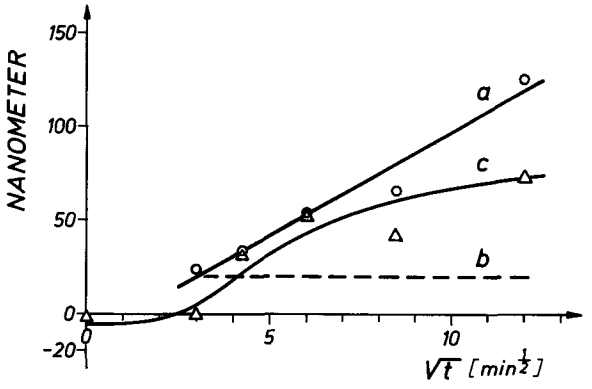

Fig. 2. Time dependence of oxide growth. Dry oxygen, 1010°C. N_2^+-implantation 30 kV, 4 x 10^{15} ions/cm^2. (a) Thickness unimplanted, ellipsometric measurements; (b) thickness implanted, upper limit of interferometric measurements; (c) surface step interferometric.

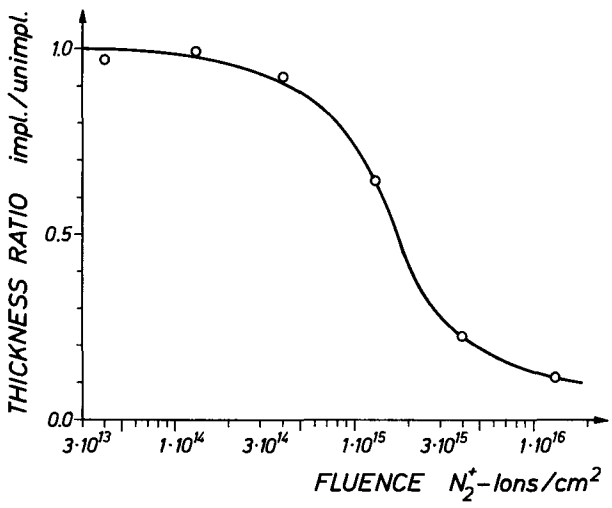

Fig. 3. Dependence of oxide growth upon fluence of 30 keV N_2^+-ions. Dry oxidation 18 min at 1140°C.

tremely thin films result on the implanted side, and we are not able to interpret the ellipsometric measurements in this case. If we assume a well-defined interface below a homogeneous surface layer on normal silicon, the measurements indicate initial layer thicknesses between 50 and 70 nm decreasing with oxidation times longer than 36 min. Apparently, these values are due to an implanted layer but not to a thermally grown layer. However, the suppositions for this evaluation are not adequately fulfilled. Therefore, we have plotted in Fig. 2 the surface step between the oxides on the implanted and the unimplanted side, which gives a lower limit for the difference in the thicknesses of the grown layers. The sign of the step is taken positive if the unimplanted surface is higher than the implanted surface. The negative value immediately after implantation is believed to be real, because we know from many other experiments that for silicon targets and energies higher than 20 keV lattice expansion is more pronounced than sputtering. Between 16 and 36 min of oxidation the surface step is only slightly smaller than the oxide thickness on the unimplanted side. Visually the implanted surface appears metallic for oxidation times up to 114 min. Practically no oxide growth was observed on this side.

Figure 3 shows the dependence of the oxide thickness ratio implanted to unimplanted upon the fluence of N_2^+ ions. On the unimplanted side the oxide thickness is 74.1 nm. The implantations have a distinct effect at 4×10^{14} N_2^+ ions/cm^2, but even at the lower fluences we always found thickness ratios smaller than 1. The impeding influence of implanted nitrogen was also observed after wet oxidation. This can be seen from Table I, sample 13c. Because of the larger thicknesses, higher ion energies and higher doses are necessary.

Table I also shows the effect of carbon and oxygen. Since in both cases the effect is weak, it is noteworthy that fluctuations of thickness within one single layer are mostly smaller than 1.0 nm and the accuracy of the ellipsometric measurement itself is still higher. Carbon implantation impedes the oxidation. Although somewhat higher thickness differences have been achieved with thinner layers, sample 1 was chosen for the table, because N_{max} and the thickness on the unimplanted side allow comparison with sample 3 and 42. The effect of oxygen depends even qualitatively upon dose and oxidation conditions. When the peak concentration was high, we observed an enhancement of oxide growth at 1140°C in dry oxygen (samples 2c and 42 in Table I). In other experiments, we implanted twice, first with 45 kV, 1.5×10^{16} ions/cm^2, and second with 30 kV, 1.0×10^{16} ions/cm^2, so that in spite of the high total fluence the maximum concentration was moderate. There, we observed an impeded oxide growth at 1010°C in dry oxygen (samples 22 and 24). The infrared absorption of sample 22 was recorded immediately after implantation and the experiment was repeated with sample 23. If absorbing Si-O oscillators are formed by the implantations, their number is limited by the total fluence, which is 2.5×10^{16} cm^{-2}. The number of oxygen atoms per cm^2 of a thermally grown layer with the same thickness as indicated in Table I for sample 22 unimplanted is 3.3×10^{17}. Thus, only very small bands can be expected after implantation. The result is shown in Fig. 4. Absorption bands sufficiently high above the background occur in both samples at 968 cm^{-1} and 888 to 895 cm^{-1}. A possible interpretation is given at the end of the next section.

Discussion

The effect of nitrogen implantation on oxide growth is pronounced even at fairly low concentrations. Let us assume that within the first impacts all the N_2^+ ions are split into two parts of equal mass with half the initial energy each. Then, from LSS theory [see Ref. (4)] a projected range $R_p = 41.0$ nm, a standard deviation $\Delta R_p = 18.1$ nm, and a peak concentration $N_{max} = 1.8 \times 10^{21}$ nitrogen atoms per cm^3 result for 30 kV implantations of 4×10^{15} N_2^+ ions per cm^2. To form a continuous layer of Si_3N_4 a concentration of 4.8×10^{22}

Table I. Dependence of oxide thickness on experimental conditions

Nr.	Ion	kV	Fluence [ions · cm^{-2}]	Oxidation	Thickness [nm] unimpl.	Thickness [nm] impl.	R_p [nm]	N_{max} [cm^{-3}]
13c	N_2^+	80	3.0×10^{16}	1140°C wet	295.7	164.4	111.6	6.0×10^{21}
3	N_2^+	80	1.3×10^{16}	1140°C dry	88.4	6.6	111.6	2.6×10^{21}
1	C^+	35	4.6×10^{16}	1140°C dry	89.0	84.6	115.0	4.4×10^{21}
42	O^+	45	3.0×10^{16}	1140°C dry	73.5	81.2	108.8	3.2×10^{21}
2c	O^+	45	3.0×10^{16}	1140°C dry	69.7	73.9	108.8	3.2×10^{21}
47	O^+	45	8.0×10^{15}	1140°C dry	79.5	80.5	108.8	8.5×10^{20}
2b	O^+	45	1.0×10^{14}	1140°C dry	69.7	69.4	108.8	1.1×10^{19}
22	O^+	45 + 30	$1.5 + 1.0 \times 10^{16}$	1010°C dry	76.0	62.0	—	2.4×10^{21}
24	O^+	45 + 30	$1.5 + 1.0 \times 10^{16}$	1010°C dry	59.0	54.5	—	2.4×10^{21}

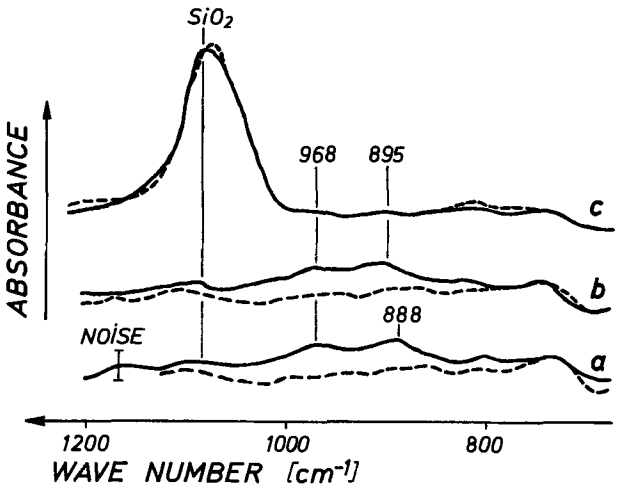

Fig. 4. Infrared spectra. Curves (a) and (b) samples 22 and 23 before oxidation. Curve (c) sample 22 after oxidation. Solid lines: implanted, dashed lines: not implanted.

is necessary. Although the calculated N_{max} of our implantations is more than an order of magnitude lower, the oxide growth is strongly impeded as shown in the figures. For the interpretation of our results it is important, whether the distribution of the implanted nitrogen remains constant inside the silicon during oxidation. If it remains, the concentration at the oxide silicon interface can be calculated from the oxide thickness, because the implantation profile is known from theory and the thickness of the silicon layer consumed by the oxidation is determined by the condition that the oxide contains as many silicon atoms as were contained in the silicon layer. We have performed this calculation from the data of Fig. 3, and found that at low fluences the interface concentration increases with increasing fluence and suddenly approaches the constant value of 3.2×10^{20} nitrogen atoms per cm^3 for fluences above 2×10^{15} N_2^+ per cm^2. From investigations of the solid solubility of nitrogen in silicon (5) and in silicon dioxide (1) it seems likely that during the oxidation the implanted nitrogen precipitates as Si_3N_4, but the growing surface film is truly an oxinitride polymer and not a mixture of SiO_2 and Si_3N_4. Qualitatively the refractive index indicated in Fig. 1 is consistent with this assumption, since after Tombs *et al.* (6) it varies continuously in oxinitrides and increases up to 2.2 with increasing nitrogen content. However, the high values obtained by short oxidations are inconsistent with the calculated interface concentrations. Perhaps, the precipitation does not take place inside the silicon. Since, according to the assumed Gaussian profile, 84% of the implanted atoms are located within the small distance of $R_p + \Delta R_p = 59$ nm from the surface, and are embedded in a lattice damaged heavily by the implantation, most of the nitrogen may be pushed out during recrystallization, which is known to take place within some minutes at about 600°C or less depending upon ion species and fluence (7). At the same time, the surface begins to cover with oxide which, after Tombs *et al.* (6), can form a continuous series of solid solutions with silicon nitride. A film, which impedes the oxidation substantially, should have a high nitrogen content and a thickness of at least a few interatomic distances. The Si-N distance in Si_3N_4 is 1.4 to 1.75×10^{-8} cm. Assume that after recrystallization most of the implanted nitrogen is contained in a 5×10^{-8} cm surface layer. Then, the fluence necessary to form Si_3N_4 is 1.2×10^{15} N_2^+ ions per cm^2, and this is just the value at which the curve of Fig. 3 falls most rapidly. We have no direct evidence that the nitrogen is pushed to the surface during heating, but the strong influence of low doses on the oxide growth becomes more plausible by this assumption. The time dependence of thickness and surface step in Fig. 1 and 2 is not only determined by the growth rate but includes contraction or expansion of the implanted as well as the growing layer. These effects have not yet been studied in sufficient detail.

The enhancement of oxide growth by implantation of high doses of oxygen is not surprising, since not all the oxygen needed for oxidation has to diffuse through the oxide in this case, and production of SiO_2 by implantation and annealing in inert gas is known to be possible (2, 3). More difficult to understand is the observation that a relatively slight change of the oxidation conditions results in an impeded oxide growth on the implanted area. In this connection, it is interesting that the absorption spectrum shown in Fig. 4 does not exhibit the band at about 1030 cm^{-1}, which was observed in our work on SiO_2 produced by ion implantation (3). The small band at 968 is very close to that reported by Ritter (8) at 980 cm^{-1} for SiO. Ritter also reports an Si_2O_3 band at 870 cm^{-1}, but in contrast to our band at 884 to 895 cm^{-1}, it was accompanied by a stronger band at 1050 cm^{-1}. The possible frequencies of the Si-O bond cover almost the full range between 800 and 1100 cm^{-1} and depend upon the sequence of silicon and oxygen atoms as well as the type of linkage between these groups (8-10). The arrangement will not be well-defined immediately after implantation, particularly as long as the fluence does not suffice to surround every silicon atom by four oxygen atoms. Therefore, we assume that under the conditions of implantation used in this work the oxygen atoms do not assemble to form the well known SiO_4 tetrahedrons of SiO_2, but remain distributed in the damaged silicon and form a mixture of lower oxides. Normally oxygen dissolved in silicon is indicated by a band at 1090 cm^{-1}, and it is likely that the implanted material can be converted to this solution when the sample is heated for oxidation. Should the lower oxides be volatile, and should they evaporate in noticeable amounts before conversion, this could indeed have a negative influence on the growth rate of SiO_2 layers.

Acknowledgments

We are indebted to K. Eisele for his suggestions concerning the manuscript and to R. Junghanns, J. Schaub, and K. Fruh for their assistance in the experimental work.

Manuscript submitted April 16, 1973; revised manuscript received July 10, 1973.

Any discussion of this paper will appear in a Discussion Section to be published in the June 1974 JOURNAL.

REFERENCES

1. C. M. Drum and M. J. Rand, *J. Appl. Physics*, **39**, 4458 (1968).
2. J. A. Borders and W. Beezhold, in "II Intern. Conf. Ion Implantation in Semiconductors," I. Ruge and J. Graul, Editors, p. 241, Springer, Berlin, Heidelberg, New York (1971).
3. C. R. Fritzsche, and W. Rothemund, *This Journal*, **119**, 1243 (1972).
4. W. S. Johnson and J. F. Gibbons, "Projected Range Statistics in Semiconductors" distributed by Stanford University Bookstore (1969).
5. W. Kaiser and C. D. Thurmond, *J. Appl. Physics*, **30**, 427 (1959).
6. N. C. Tombs, F. A. Sewell, and J. J. Comer, *This Journal*, **116**, 862 (1969).
7. J. W. Mayer, L. Eriksson, and J. A. Davies, "Ion Implantation in Semiconductors," Academic Press, New York and London (1970).
8. E. Ritter, *Optica Acta*, **9**, 197 (1962).
9. A. Faessler and H. Krämer, *Ann. Physik VII*, **4**, 263 (1959).
10. F. Matossi, *J. Chem. Phys.*, **17**, 679 (1949).

JOURNAL OF THE ELECTROCHEMICAL SOCIETY

ELECTROCHEMICAL SCIENCE AND TECHNOLOGY

DECEMBER 1973

Solid-State Ionics: Studies on the Solid Electrolytes in the System Ag_2X-AgI-HgI_2

Takehiko Takahashi,* Katsumi Kuwabara, and Osamu Yamamoto

Department of Applied Chemistry, Faculty of Engineering, Nagoya University, Nagoya, Japan

ABSTRACT

Compositions exhibiting high ionic conductivity in the solid state at ambient temperature were determined in the system Ag_2X-AgI-HgI_2 (X = S, Se, or Te) to be $Ag_{2.0}Hg_{0.25}S_{0.5}I_{1.5}$ (N-1), $Ag_{1.85}Hg_{0.40}Te_{0.65}I_{1.35}$ (N-2), $Ag_{1.80}Hg_{0.45}Se_{0.70}I_{1.30}$ (N-3), or $Ag_{2.0}Hg_{0.5}Se_{1.0}I_{1.0}$ (N-4). The electrical conductivities of these compounds were measured by means of the 1000 Hz a-c bridge and the values obtained at 25°C were 1.47×10^{-1}, 9.40×10^{-2}, 1.00×10^{-1}, and 4.30×10^{-2} $(ohm\text{-}cm)^{-1}$ for N-1, N-2, N-3, and N-4, respectively. The activation energies for conduction were calculated from the conductivity curves to be 2.95, 3.24, 3.34, and 3.58 kcal/mole for the above four compounds. In order to interpret the high ionic conductivities and the low activation energies for conduction of these compounds, the crystal structure was analyzed in detail by means of powder x-ray diffraction, and it was found that N-1 had the same structure as that of α-AgI. The cations in N-1 were statistically distributed over forty-two sites of 6(b), 12(d), and 24(h) of the space group Im3m and the anions were randomly distributed at the corner and the center of the cell. N-2, N-3, and N-4 had somewhat different structures from that of N-1. The cations in N-2, N-3, and N-4 were statistically distributed over thirty sites of 6(b) and 24(h), and the anions were distributed in the same manner as N-1. The proposed crystal structures of the four solids were verified by comparing the calculated values of the relative intensities of the x-ray diffraction lines with the experimental values. The distribution factors were defined and were discussed together with the activation energies for conduction.

Studies on solid electrolyte devices have been made from various viewpoints. One of the most typical examples is solid electrolyte galvanic cells (1-3), and the other devices such as memory elements with variable resistance (4, 5) and solid electrolyte coulometers (6, 7) have also been studied.

Solid electrolytes used in these fields are required to have high ionic conductivity at room temperature. As the solids satisfying such a requirement, β-Ag_3SI and $RbAg_4I_5$ have been recommended for example (8-10).

β-Ag_3SI has a silver ion conductivity of 1.0×10^{-2} $(ohm\text{-}cm)^{-1}$ at 25°C and its activation energy for conduction is very small (4.0 kcal/mole) (8). This material has a so-called average structure, in which three silver ions are distributed statistically over twelve sites in the {100} plane of the cube (11). $RbAg_4I_5$ has a silver ion conductivity of 2.1×10^{-1} $(ohm\text{-}cm)^{-1}$ at 25°C and its activation energy for conduction is 1.7 kcal/mole (10). This electrolyte has an average structure like that of β-Ag_3SI: sixteen silver ions are statistically distributed over seventy-two sites in its unit cell (12, 13).

It is most significant in the above-mentioned fields to find various solid electrolytes which exhibit high ionic conductivities at ambient temperature and to consider a relation between crystal structures and electrical conductivities and activation energies for conduction.

In recent years, several materials possessing high ionic conductivities were found in the systems Ag_2X-AgI-HgI_2 (X = S,Se,Te) in the authors' laboratory (14-17). It is the purpose of this paper to determine their compositions, to analyze their crystal structures, and to make clear the relations between the crystal structures and the electrical conductivities.

Experimental

Preparation of the samples.—The starting materials were obtained as follows: Ag_2S was precipitated by passing hydrogen sulfide gas through a solution of silver nitrate; Ag_2Se was prepared by means of heating the mixture of silver powder (99.9%) and selenium powder (99.99%) in vacuo at 400°C for 36 hr; Ag_2Te was prepared by means of heating the mixture of silver powder (99.9%) and tellurium powder (99.99%) at 420°C for 24 hr in an evacuated sealed glass tube; AgI was precipitated by the addition of KI(aq) into $AgNO_3$(aq); HgI_2 was the powder of the guaranteed grade reagent.

In the Ag_2S-AgI-HgI_2 system, Ag_2S, AgI, and HgI_2 were precisely weighed, fully mixed, vacuum-sealed in a Pyrex glass tube, and heated in an electric furnace. Various conditions were examined beforehand and the reaction temperature and time were fixed at 400°C and 20 hr. As the reaction products had a tendency to be decomposed by moisture and light, they were kept in a dark desiccator.

The systems Ag_2Te-AgI-HgI_2, Ag_2Se-AgI-HgI_2, and Ag_2Se-HgI_2 were treated like the above system; the

* Electrochemical Society Active Member.

Key words: solid electrolyte, ionic conductivity, silver ion conductor.

reaction temperatures and times chosen were 300°C for 40 hr, 300°C for 20 hr, and 200°C for 48 hr, respectively.

Conductivity measurement.—The electrode was made of a mixture of the silver powder and the sample in order to reduce the contact resistance at the electrode-electrolyte interface (18). The composition was selected to obtain a high performance. A silver plate was used as an electronic collector of silver electrode. Samples were pressed by 4 tons/cm^2 pressure to form pellets 13 mm diameter and about 2 mm thick. A set of the pellet, the mixed electrode, and the collector was compressed by a stainless-steel frame with spring. This set was put in an electric furnace, the temperature of which was regulated within ±0.5°C by a thermistor-type automatic controller between 20° and 100°C.

The electrical conductivities were measured by the use of an a-c bridge using an oscilloscope as a zero-indicator. The frequency was fixed to 1000 Hz.

Measurement of transport number.—Transport numbers of ionic conductivity solids are measured by the methods proposed by Tubandt (19), Wagner (20), and Mitoff (21). In this paper, the Mitoff emf method was employed in which the theoretical emf was calculated from the free enthalpy change of the reaction $Ag(s) + \frac{1}{2} I_2(g) = AgI(s)$ (22). As shown in the previous work (23), the mercury ion conduction was not found.

X-ray diffraction.—A copper anode tube was operated at 15 mA and 35 kV. The goniometer scan speed was selected to 1°/min or ¼°/min. Powdered silicon was used as an inner standard material to correct diffraction angles. The observed diffraction intensities discussed later are the mean values of the diffraction lines obtained from a large number of samples.

Density measurement.—Density was measured to calculate the number of molecules contained in a unit cell. Toluene was used as a solvent since the samples had a tendency to be decomposed by a common alcoholic solvent such as n-butanol. The measurements were made using 5.00 cm^3 picnometer at 25°C.

Results and Discussion

Ag_2S-AgI-HgI_2 System

Total conductivity.—It was found in this system that a mixture of 33.3 m/o (mole per cent) Ag_2S, 44.4 m/o AgI, and 22.3 m/o HgI_2 showed a comparatively high conductivity (15, 24). The isoconductivity curves were drawn in the three component diagram, and it was recognized that a hill was formed near the composition of 30 m/o Ag_2S, 55 m/o AgI, and 15 m/o HgI_2. It was suggested that there was a new compound with a composition of about $(Ag_2S)_{0.30}(AgI)_{0.55}(HgI_2)_{0.15}$ in the Ag_2S-AgI-HgI_2 system.

X-ray diffraction and determination of composition.—X-ray diffraction patterns of the high conductivity sample showed simple lines corresponding to a body-centered cubic lattice. The composition range with the single phase of body-centered cubic structure was as follows; (number of sulfur atom)/(number of iodine atom) = 0.33-0.42 and (number of mercury atom)/(number of silver atom) = 0.12-0.19. In these ranges, the ratio of the number of the component atoms was determined on the basis of the total number of anions in a unit cell being integral as described in the latter section. This ratio was Ag:Hg:S:I = 8:1:2:6. The mole composition of Ag_2S:AgI:HgI_2 was calculated from the atomic ratio to be 28.6:57.1:14.3. This compound is designated N-1.

Ionic conductivity.—The Arrhenius plot of the total conductivity of N-1 is shown in Fig. 1. The value at 25°C is 1.47×10^{-1} (ohm-cm)$^{-1}$; this is higher than that of β-Ag_3SI by one order of magnitude and is comparable to that of $RbAg_4I_5$. The conductivity curve has a good linearity, and the activation energy for conduction is calculated from the slope to be 2.95 kcal/mole which is smaller than that of β-Ag_3SI. The open-circuit voltage of the galvanic cell Ag|sample (N-1)|I_2 was 680 mV at 25°C which was nearly equal to the theoretical value of 687 mV for Ag|AgI|I_2. It might be said from this that the contribution of electron to the total conductivity was very poor.

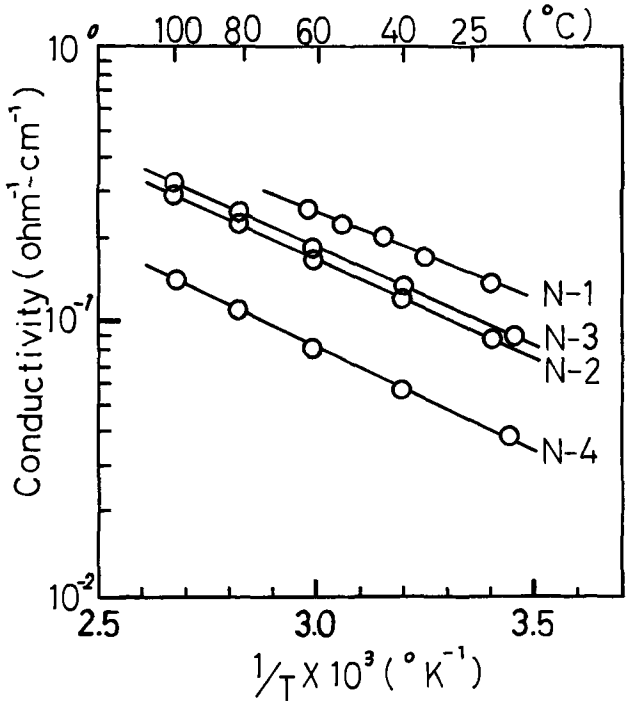

Fig. 1. Conductivity curves of the four compounds. N-1: $Ag_{2.0}Hg_{0.25}S_{0.5}I_{1.5}$. N-2: $Ag_{1.85}Hg_{0.40}Te_{0.65}I_{1.35}$. N-3: $Ag_{1.80}Hg_{0.45}Se_{0.70}I_{1.30}$. N-4: $Ag_{2.0}Hg_{0.5}Se_{1.0}I_{1.0}$.

Unit cell.—It was found from x-ray diffraction that the sample N-1 had a body-centered cubic lattice and that the lattice constant was 4.969Å. The interplanar spacings of N-1 were calculated by the use of the lattice constant. They are given together with the observed intensities in Table I. The observed density of N-1 was 6.5 and the x-ray density was 6.70.

The number of molecules in the unit cell was evaluated using the lattice constant and the density. With respect to N-1, one unit of $Ag_2Hg_{0.25}S_{0.5}I_{1.5}$ was contained in a unit cell. It should be noticed that the sum of the numbers of the anion is 2.00 and that of the cation is 2.25. It is a well-known fact that some compounds, such as silver chalcogenides, are nonstoichiometric and have electronic conductivity. The compound N-1 is, however, not nonstoichiometric and has high ionic conductivity. These facts might not be easily accepted by strict crystallographic theory but would be understood through the following information.

Rahlfs examined the distribution of x-ray intensity for α-Ag_2S and concluded that silver ions construct an average structure like α-AgI (25). This was confirmed by Boettcher *et al.* (26). According to them, α-Ag_2S

Table I. Indices, calculated interplanar spacings, and the observed intensities of x-ray diffraction of $Ag_{2.0}Hg_{0.25}S_{0.5}I_{1.5}$

No.	hkl	d_{cal} (A)	I_{obs}*
1	110	3.513	S
2	200	2.485	S
3	211	2.026	VS
4	220	1.756	MS
5	310	1.571	W
6	222	1.434	VW
7	321	1.327	MS
8	400	1.242	VW

* S, strong; VS, very strong; MS, medium strong; W, weak; VW, very weak.

has a unit cell which contains two molecules; two anions occupy the sites of body-centered cubic lattice and four silver ions are statistically distributed over forty-two sites. On the other hand, Reuter and Hardel studied the structure of α-Ag_3SI and reported as follows (11): one sulfur and one iodine are statistically distributed at the corner and the center of the elemental cell, whereas three silver ions are also randomly arranged over forty-two sites. Their conclusion was that the structure of α-Ag_3SI was a disordered mix-phase of α-AgI and α-Ag_2S.

These average structures are generally characterized by the fact that the ions in a crystal can occupy many more lattice sites than their numbers and that they are statistically distributed over those sites. From this viewpoint, it might be proposed that the number of cations in a unit cell is not necessarily an integer.

As mentioned above, the sample N-1 has high ionic conductivity and low activation energy for conduction and the crystal system is body-centered cubic. It was suggested from these experimental results that the crystal structure of the sample N-1 was an average one.

Location of ions.—The space group Im3m was chosen among ten groups which were in a cubic system in the translation group I. Location of ions was assumed to be analogous to α-AgI; cations in the sample N-1 are statistically distributed over the sets of 6(b), 12(d), and 24(h) of the space group, as shown in Fig. 6, whereas sulfur and iodine ions are also randomly distributed at the corner and the center of the cube.

The intensities of the diffraction lines were calculated by the usual formula

$$I = A \cdot \frac{1 + \cos^2 2\theta}{\sin^2 \theta \cdot \cos \theta} \cdot P \cdot F^2 \qquad [1]$$

where the fractional term contains Lorentz, polarization, and geometrical factors, P is the multiplicity term, and A is an absorption term which has been assumed to be proportional to θ (27). The structure factor term F includes arbitrary isotropic temperature factors. The temperature factor was neglected for α-AgI by Strock (28) and for α-Ag_2S by Rahlfs (25), but it was computed for α-AgI using the Debye factor $B = 8.0$ by Hoshino (29). Recently, the structure of MAg_4I_5 was analyzed by Bradley *et al.* (9); according to them, Debye factors for the anion and the cation were chosen to be 2.5 and 5.0, respectively. Referring to these data, the average Debye factor B was chosen to be 3.0 for the anions and 5.0 for the cations in the present calculation.

The calculated and the observed intensities are given for each diffraction line of N-1 in Fig. 2, which shows good agreement. The degree of agreement between the calculated and the observed intensities is quantitatively judged from the discrepancy factor

$$R = \frac{\Sigma||F_o| - |F_c||}{\Sigma|F_o|} \qquad [2]$$

where F_o and F_c are the observed and the calculated structure factors, respectively.

The factor obtained is listed in Table II. It might be said on the basis of the small value that the agreement is good and that the previous assumption with respect to the average structure is reasonable.

In the third column of the table, the distribution factor of cations is defined as a ratio of the real number of cations in a unit cell to the number of the available cation sites in the same cell (for example, in the sample N-1 the former is 2.25 and the latter is 42, so the ratio is equal to $2.25/42 = 0.054$). It might be said that the number of vacant sites of cations increases with the decrease of the distribution factor of cations and that the disturbance effect of divalent anions on the migration of cations increases with the increase of the number of divalent anions in a unit cell.

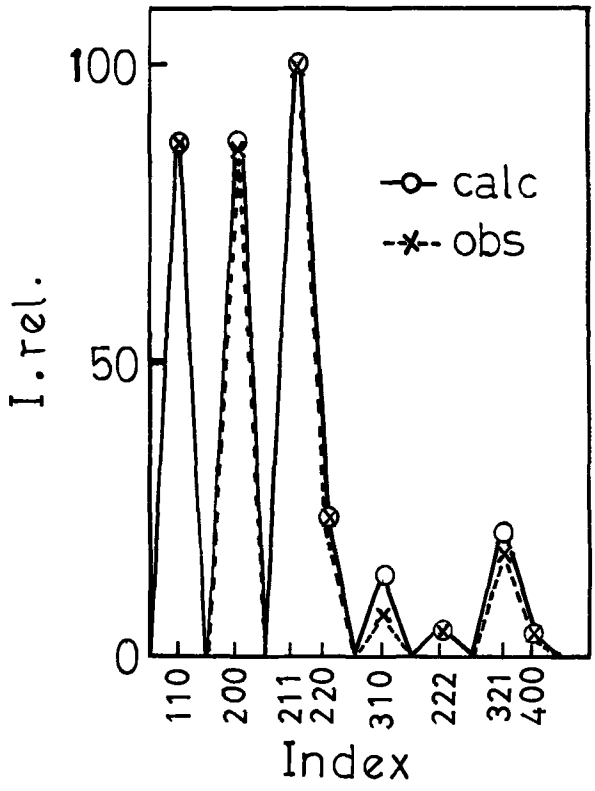

Fig. 2. Comparison of the calculated and the observed relative diffraction intensities of $Ag_{2.0}Hg_{0.25}S_{0.5}I_{1.5}$.

These tendencies correspond to the magnitude of the activation energy for conduction. For example, the activation energy for silver ion in AgBr (140°-250°C) is 16 kcal/mole which is larger than that of N-1 (30). The distribution factor of silver ion in AgBr is 1.0 which is also markedly larger than that of N-1. AgBr has a face-centered cubic lattice with rock-salt type. It has been interpreted that the activation energy for conduction in such a solid is equal to the sum of the energy for the production of the Frenkel defect and the energy for their migration. In contrast to AgBr, the compound N-1 has many structural defects. It can therefore be presumed from these data that N-1 has a negligibly small energy for the production of cation vacancies and that the activation energy for conduction consists of the energy for cation migration predominantly.

Ag_2Te-AgI-HgI_2 System

Total conductivity.—The electrical conductivities were measured with 5-10 m/o intervals and the isoconductivity curves were drawn in the three component diagram in a manner similar to the Ag_2S-AgI-HgI_2 system. It was observed that the curves made a hill near the composition of 40 m/o Ag_2Te, 35 m/o AgI, and 25 m/o HgI_2.

X-ray diffraction.—X-ray diffraction of the samples in the vicinity of $(Ag_2Te)_{0.40}(AgI)_{0.35}(HgI_2)_{0.25}$ showed a simple phase pattern which consisted of the lines corresponding to a body-centered cubic lattice. As in the case of the Ag_2S-AgI-HgI_2 system, the composition range with the body-centered cubic lattice in the

Table II. Discrepancy factors and distribution factors of cation in several compounds

Compound	Discrepancy factor	Distribution factor of cations
N-1	0.0706	0.054
N-2	0.0522	0.075
N-3	0.0692	0.075
N-4	0.0681	0.083

reaction products was examined and the ratio of the number of the component atoms in the above-stated sample was determined strictly and the mole composition of Ag_2Te:AgI:HgI_2 was evaluated from the atomic ratio to be 40.6:34.4:25.0. This compound is named N-2.

Ionic conductivity.—The total conductivity curve of N-2 is shown in Fig. 1. The value is 9.40×10^{-2} (ohm-cm)$^{-1}$ at 25°C. The conductivity curve has a good linearity and the activation energy for conduction is calculated from the slope to be 3.24 kcal/mole. The open-circuit voltage of the galvanic cell with N-2 as the electrolyte was 675 mV which suggested that N-2 had an ionic transport number of about unity.

Unit cell.—The compound N-2 had a body-centered cubic structure and the lattice constant was 5.081Å. Table III shows the interplanar spacings of N-2 together with the observed intensities. The observed and the x-ray densities were 6.6 and 6.76, respectively. The number of molecules in the unit cell was calculated by the use of the lattice constant and the density to be one unit of $Ag_{1.85}Hg_{0.40}Te_{0.65}I_{1.35}$. As in the compound N-1, the sum of the number of anions was 2.00 and that of the cations was 2.25.

Location of ions.—The space group Im3m was selected from the translation group I. A primarily assumed structure which was identical with that of α-AgI failed in agreement between the calculated and the observed intensities. It is therefore supposed that cations in the compound N-2 are statistically distributed in the sets of 6(b) and 24(h) of the space group as shown in Fig. 6 and that anions are distributed at the corner and the center of the cubic lattice. The calculated results are shown together with the observed intensities in Fig. 3, where good consistency is recognized between them. The discrepancy factor obtained by means of Eq. [2] is shown in Table II. The small value indicates that the above-mentioned assumption relating to the average structure is appropriate. The distribution factor of the cation is also given in Table II. It is larger than that of N-1 and corresponds to the relation in the activation energy.

Ag_2Se-AgI-HgI_2 System

Ionic conductivity.—The mole composition of Ag_2Se:AgI:HgI_2 in the highest conductivity compound was determined by the method used in the cases of N-1 and N-2. This single-phase compound, $(Ag_2Se)_{0.452}(AgI)_{0.258}(HgI_2)_{0.290}$ is designated N-3.

The total conductivity curve of N-3 is shown in Fig. 1 indicating a good linearity. The conductivity is 1.00×10^{-1} (ohm-cm)$^{-1}$ at 25°C and the activation energy is calculated to be 3.34 kcal/mole. The emf of the cell Ag|sample (N-3)|I_2 was 677 mV at 25°C which indicated that the ionic transport number was nearly equal to unity.

Unit cell.—The lattice constant of N-3 was 4.995Å. The calculated interplanar spacings are given in Table IV together with the observed intensities. The observed and the x-ray densities were 6.5 and 6.72, respectively. It was found by calculation of the number of molecules that one unit of $Ag_{1.80}Hg_{0.45}Se_{0.70}I_{1.30}$ was included in a unit cell.

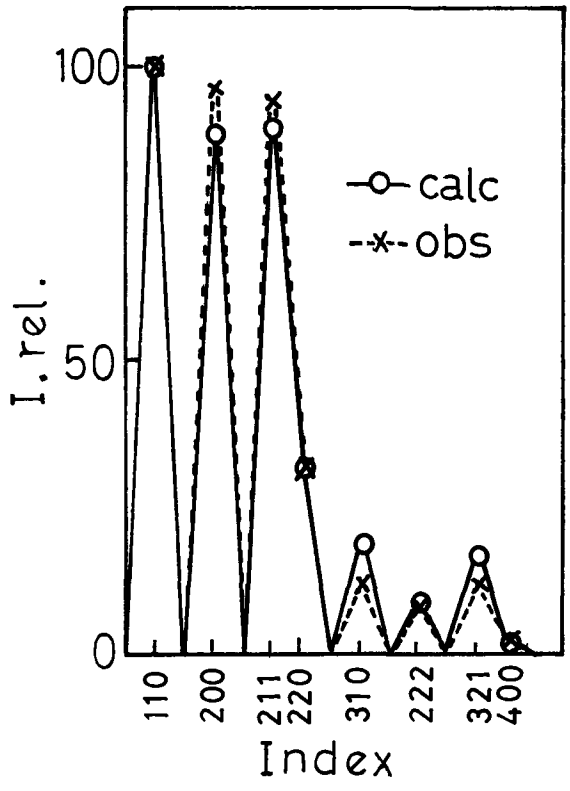

Fig. 3. Comparison of the calculated and the observed relative diffraction intensities of $Ag_{1.85}Hg_{0.40}Te_{0.65}I_{1.35}$.

Location of ions.—When the cations in N-3 are assumed to be statistically distributed as in α-AgI, the discrepancy factor is large which contradicts the above assumption.

In order to minimize the discrepancy factor, a second assumption was made as follows; cations and anions in N-3 were also randomly distributed in the same sites as N-2. The observed and the calculated intensities of the diffraction lines are shown in Fig. 4; they are consistent with each other. The discrepancy factor of 0.0692 given in Table II suggests that the proposed average structure is reasonable. The distribution factor of N-3 is shown in Table II; the factor of the cation is equal to that of N-2.

Ag_2Se-HgI_2 System

Ionic conductivity.—It was found by means of conductivity measurements and x-ray diffraction that another compound in the Ag_2Se-AgI-HgI_2 system was obtained. The single-phase compound was $(Ag_2Se)_{0.667}(HgI_2)_{0.333}$ which was named N-4. The total conductivity curve of N-4 is shown in Fig. 1. The activation energy for conduction is 3.58 kcal/mole and the emf of the cell Ag|sample (N-4)|I_2 was 675 mV at 25°C, comparable to the theoretical value of 687 mV for Ag|AgI|I_2.

Table III. Indices, calculated interplanar spacings, and the observed intensities of x-ray diffraction of $Ag_{1.85}Hg_{0.40}Te_{0.65}I_{1.35}$

No.	hkl	d_{cal} (A)	I_{obs}*
1	110	3.593	VS
2	200	2.540	S
3	211	2.075	S
4	220	1.797	MS
5	310	1.607	W
6	222	1.467	W
7	321	1.358	W
8	400	1.270	VW

* S, strong; VS, very strong; MS, medium strong; W, weak; VW, very weak.

Table IV. Indices, calculated interplanar spacings, and the observed intensities of x-ray diffraction of $Ag_{1.80}Hg_{0.45}Se_{0.70}I_{1.30}$

No.	hkl	d_{cal} (A)	I_{obs}*
1	110	3.533	S
2	200	2.498	VS
3	211	2.040	S
4	220	1.766	MS
5	310	1.580	W
6	222	1.442	W
7	321	1.334	W
8	400	1.249	VW

* S, strong; VS, very strong; MS, medium strong; W, weak; VW, very weak.

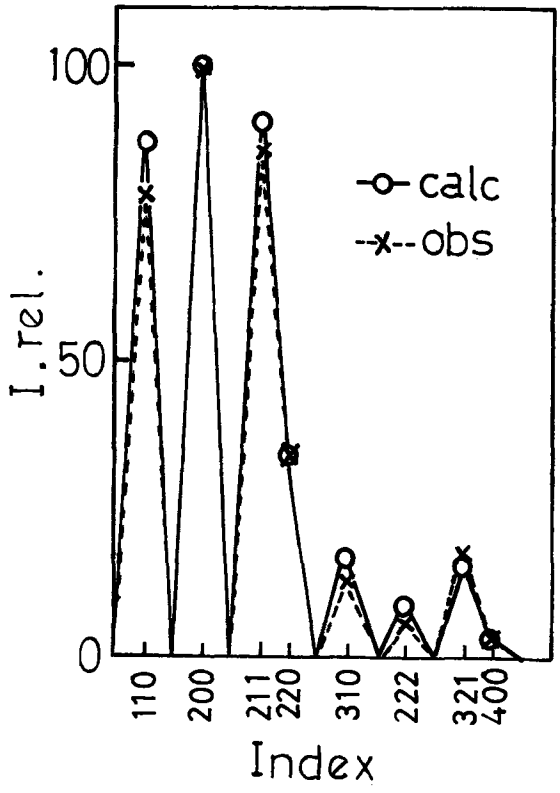

Fig. 4. Comparison of the calculated and the observed relative diffraction intensities of $Ag_{1.80}Hg_{0.40}Se_{0.70}I_{1.30}$.

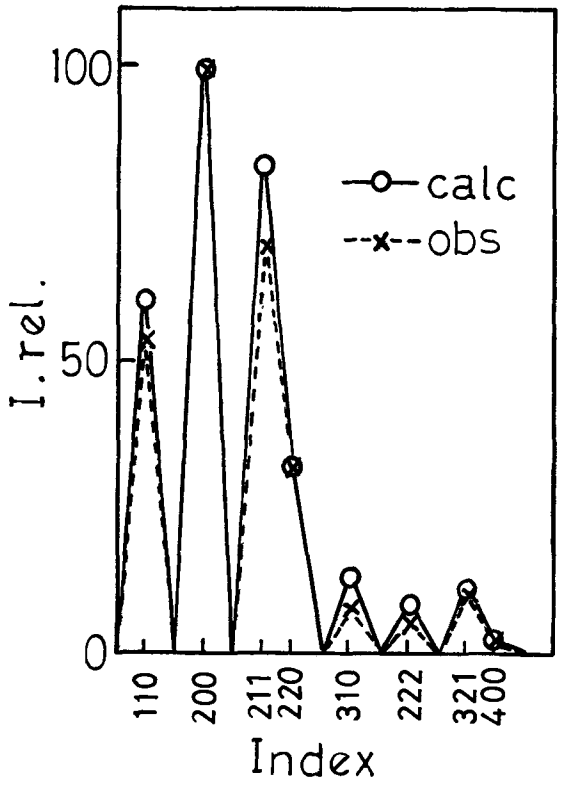

Fig. 5. Comparison of the calculated and the observed relative diffraction intensities of $Ag_{2.0}Hg_{0.5}Se_{1.0}I_{1.0}$.

Unit cell.—The compound N-4 had a body-centered cubic structure whose lattice constant was 5.000Å. Table V shows the interplanar spacings of N-4 together with the observed intensities. The observed and x-ray densities were 6.8 and 7.07, respectively. It was found that one unit of $Ag_{2.0}Hg_{0.5}Se_{1.0}I_{1.0}$ was contained in a unit cell.

Location of ions.—It was supposed that the cations of N-4 were statistically distributed over the sets of 6(b) and 24(h) of the space group Im3m and the anions were distributed at the corner and the center of the cube. The calculated intensities are shown together with the observed intensities in Table II. The small value of 0.0681 suggests that the supposed average structure is reasonable. The observed and calculated intensities of the diffraction intensities are shown in Fig. 5. The distribution factor of N-4 is given in Table II; it is the largest of four compounds.

Conclusion

The compounds described in this paper have high ionic conductivities at room temperature and have the average structures belonging to the space group Im3m. A typical compound which belongs to the space group Im3m and has the average structure is the high temperature phase of silver iodide, that is α-AgI. From various data the above-mentioned compounds have been seen to have modified structures of α-AgI. That is to say, these compounds have structures in which a part of the silver sites of α-AgI is substituted by mercuric ion and a part of the iodine sites of α-AgI is substituted by chalcogen ions.

The ionic radii and the electrical charges of the component elements have to be considered in these substitutions. Mercuric ion has nearly an equal size to the silver ion and both selenium and tellurium ions have approximately the same sizes as that of iodine, but the radius of the sulfur ion is considerably smaller than that of the iodine ion. N-2, N-3, and N-4 have, however, thirty sites with (b) and (h) of Im3m for cation distribution and only N-1 has a structure identical with that of α-AgI which contains forty-two cation sites with (b), (d), and (h).

When the lattice constant of the body-centered cube shown in Fig. 6 is a_o, the distances of (b), (d), and (h) from anion sites are 1/2a, $2\sqrt{5}/8a$, and $3\sqrt{2}/8a_o$, re-

Table V. Indices, calculated interplanar spacings, and the observed intensities of x-ray diffraction of $Ag_{2.0}Hg_{0.5}Se_{1.0}I_{1.0}$

No.	hkl	d_{cal} (Å)	I_{obs}*
1	110	3.536	S
2	200	2.500	VS
3	211	2.041	S
4	220	1.768	MS
5	310	1.581	W
6	222	1.443	W
7	321	1.338	W
8	400	1.250	VW

* S, strong; VS, very strong; MS, medium strong; W, weak; VW, very weak.

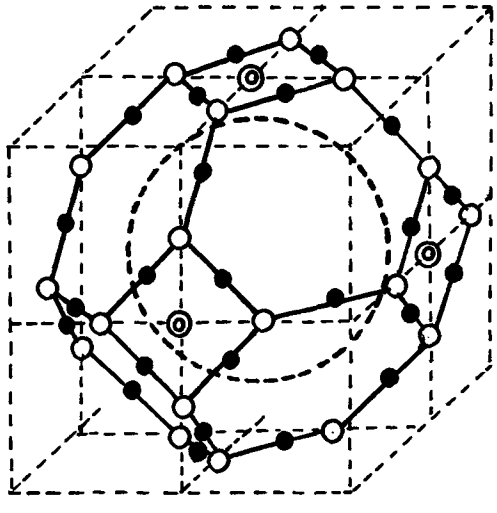

Fig. 6. Distribution of cations in space group Im3m. Large dotted circles and small circles are anion sites and cation sites, respectively ⊙, 6(b); ○, 12(d); and ●, 24(h).

Table VI. Interionic distances

Compound	Anion-Anion	Anion-Cation
$Ag_{2.0}Hg_{0.25}S_{0.5}I_{1.5}$	4.31	2.48-2.78
$Ag_{1.85}Hg_{0.40}Te_{0.65}I_{1.35}$	4.40	2.54-2.69
$Ag_{1.80}Hg_{0.45}Se_{0.70}I_{1.30}$	4.32	2.50-2.65
$Ag_{2.0}Hg_{0.5}Se_{1.0}I_{1.0}$	4.33	2.50-2.65
α-AgI	4.37	2.52-2.86
α-Ag_2S	4.23	2.44-2.74
α-Ag_2Se	4.33	2.50-2.79
α-Ag_2Te	4.38	2.52-2.82
β-Ag_6SI	4.24	2.51 (Ag-S) 3.11 (Ag-I)
$RbAg_4I_5$	4.56	2.83-2.88 (Ag-I) 3.63 (Rb-I)

spectively. The (d) site is farthest from the anion site and its appearance will be influenced by the size and the charge effect of the anion.

Table VI shows the interionic distances of these compounds together with those of other compounds possessing average structures. The distances of the anion-anion in these compounds correspond to the sum of Pauling's ionic radii, while those of the anion-cation are larger than the sum of their ionic radii. The latter indicates the partial covalency of the compounds. On the other hand, a simple correlation is found between the activation energy for conduction and the distribution factors of the cations and the number of divalent anions. From these facts, the compounds investigated in this paper are verified to have a modified crystal structure of α-AgI, which gives an important index to the study on solid electrolyte.

Manuscript submitted April 25, 1973; revised manuscript received July 2, 1973.

Any discussion of this paper will appear in a Discussion Section to be published in the June 1974 JOURNAL.

REFERENCES

1. D. O. Raleigh, in "Progress in Solid State Chemistry," Vol. 3, pp. 83-134, H. Reiss, Editor, Pergamon Press, New York (1966).
2. T. Takahashi and O. Yamamoto, *Electrochim. Acta*, **11**, 779 (1966).
3. G. R. Argue, B. B. Owens, and I. J. Groces, *Proc. Ann. Power Sources Conf.*, **22**, 103 (1968).
4. B. Widrow, Stanford Univ., Stanford, Calif., Solid State Electronics Lab. Tech. Report No. 1553-2, Oct. 1960.
5. T. Takahashi, O. Yamamoto, and K. Kuwabara, Extended Abstracts C.I.T.C.E., **17**, 397 (1966).
6. O. Yamamoto and T. Takahashi, *Denki-Kagaku*, **36**, 894 (1968).
7. J. H. Kennedy and F. Chen, *This Journal*, **116**, 207 (1969).
8. T. Takahashi and O. Yamamoto, *Denki-Kagaku*, **32**, 610 (1964).
9. J. N. Bradley and P. D. Greene, *Trans. Faraday Soc.*, **63**, 424 (1967).
10. B. B. Owens and G. R. Argue, *Science*, **157**, 308 (1967).
11. B. Reuter and K. Hardel, *Z. Anorg. Allgem. Chem.*, **340**, 168 (1965).
12. J. N. Bradley and P. D. Greene, *Trans. Faraday Soc.*, **65**, 2516 (1967).
13. S. Geller, *Science*, **157**, 310 (1967).
14. T. Takahashi, O. Yamamoto, and K. Kuwabara, *Denki-Kagaku*, **35**, 264 (1967).
15. T. Takahashi and O. Yamamoto, *ibid.*, **35**, 651 (1967).
16. T. Takahashi, O. Yamamoto, and K. Kuwabara, *ibid.*, **35**, 682 (1967).
17. T. Takahashi, O. Yamamoto, and K. Kuwabara, *ibid.*, **36**, 530 (1968).
18. B. B. Owens and G. R. Argue, *This Journal*, **117**, 898 (1970).
19. C. Tubandt, "Handbuch der Experimental Physik," p. 381, Akademische Verlagsges, Leipzig (1932).
20. C. Wagner, C.I.T.C.E. 7th, p. 361 (1955), Lindau.
21. S. P. Mitoff, *J. Chem. Phys.*, **36**, 1383 (1962).
22. T. Takahashi and O. Yamamoto, *Electrochim. Acta*, **11**, 779 (1966).
23. T. Takahashi, O. Yamamoto, and K. Kuwabara, *Denki-Kagaku*, **36**, 530 (1968).
24. T. Takahashi and O. Yamamoto, *ibid.*, **33**, 733 (1965).
25. P. Rahlfs, *Z. Phys. Chem.*, **B31**, 157 (1936).
26. A. Boettcher *et al.*, *Z. Angew. Phys.*, **7**, 478 (1955).
27. J. M. Bijvoct, N. H. Kolkmeyer, and C. H. MacGillavry, "X-ray Analysis of Crystals," Butterworths, London (1951).
28. L. W. Strock, *Z. Phys. Chem.*, **B25**, 411 (1934).
29. S. Hoshino, *J. Phys. Soc. Japan*, **12**, 315 (1957).
30. R. J. Friauf, *Phys. Rev.*, **105**, 843 (1957).

Lithium Anode Cells Operating at Room Temperature in Inorganic Electrolytic Solutions

James J. Auborn,* Kenneth W. French, Sheldon I. Lieberman, Vinod K. Shah, and Adam Heller

GTE Laboratories Incorporated, Waltham, Massachusetts 02154

ABSTRACT

Lithium anode electrochemical cells have been operated at room temperature using electrolytic solutions of lithium salts in inorganic solvents such as phosphorus oxychloride, thionyl chloride, and sulfuryl chloride. Lithium metal can be electrodeposited from these solutions accompanied, in the case of chlorine-containing electrolytes, by the simultaneous electrogeneration of chlorine at the positive electrode. The resulting lithium/chlorine electrochemical cells have open-circuit potentials of 4.0-4.3V, depending on the presence of excess Lewis acid in the electrolyte. The solvents are compatible with both lithium metal and with strong oxidants including chlorine (Cl_2), cupric fluoride (CuF_2), polycarbon monofluoride $(CF)_n$, and tungsten trioxide (WO_3) which can be used as cathode materials. The solvents themselves, while difficult to oxidize, can be electrochemically reduced at various catalytic surfaces (such as carbon black and metals) and act as cathode depolarizers. This catalytic solvent reduction process leads to cells with exceptionally stable voltages and energy densities in excess of 500 W-hr/kg.

We describe in this study a family of inorganic solvents with which room temperature lithium anode cells are made. The solvents, liquid oxyhalides of phosphorus and sulfur, are thermodynamically stable relative to their constituent elements, differing in this respect from organic solvents. Some of our solvents resemble fused salts in their stability to chlorine and other strong oxidants, the use of which (as depolarizers) becomes possible. Because of this stability toward oxidation, the solvents do not irreversibly decompose when the cells are charged at substantial overpotentials. Although lithium metal is stable in these electrolytic solutions, the solvents can be electrochemically reduced at catalytic surfaces and act as cathode depolarizers.

Experimental

Materials.—Phosphorus oxychloride ($POCl_3$) was purchased from Baker and Adamson. Commercial phosphorus oxychloride is purified by stirring over lithium metal in a dry nitrogen or argon atmosphere for 24 hr followed by distillation of purified phosphorus oxychloride from this mixture. The distillate contains <1 ppm moisture. Sulfuryl chloride (SO_2Cl_2) and thionyl chloride ($SOCl_2$) were purchased from Research Organic/Inorganic Chemical Corporation and purified by the same procedure. Lithium hexafluorophosphate ($LiPF_6$), lithium tetrafluoroborate ($LiBF_4$), fluorographite-A $[(CF)_n]$, and fluorographite-B $[(C_4F)_n]$ were purchased from Ozark-Mahoning Company; and aluminum chloride ($AlCl_3$), from Rocky Mountain Research, Inc. Other anhydrous materials used in these studies were purchased from their manufacturers and used without further purification. Southwestern Graphite Company Grade 1651 Microcrystalline Graphite and Ashland Chemicals Company XC-6310-4 Carbon Black were used as conductive additives to cathode materials not having sufficient electronic conductivity of their own. Shawinigan 100% Compressed Acetylene Black was used in catalytic cathodes containing carbon alone. Teflon 7C molding powder and Teflon 42 emulsion used as cathode binders were obtained from du Pont.

Electrolytic solutions.—The electrolytic solutions were prepared either *in situ* by adding lithium halide to stoichiometric quantities of $AlCl_3$, $SbCl_5$, $TiCl_4$, $ZrCl_4$, SO_3, $AlBr_3$, BCl_3, and BF_3 to make $LiAlCl_4$, $LiSbCl_6$, Li_2TiCl_6, Li_2ZrCl_6, $LiSO_3Cl$, $LiAlBr_4$, $LiBCl_4$, and $LiBF_4$, respectively, or by dissolving anhydrous salts such as $LiPF_6$ or $LiAsF_6$ in the purified solvents. All operations were conducted inside a fiberglass glove box flushed with argon.

Cell construction.—Cathodes were constructed by pressing a blend of active material (typically 80-90%) with a conducting additive (usually carbon or graphite) and binder (Teflon or polyethylene) onto an expanded copper or nickel screen in a heated square die 3.75 cm on each side at 2000 psig for 3 min. These cathodes were then heat sealed in a nonwoven polypropylene envelope and dried in a vacuum oven before being transferred to the argon glove box for assembly into a cell. The anodes were prepared in the argon glove box by pressing expanded nickel screen onto lithium foil, purchased from Foote Mineral Company. The anodes were folded to envelop the cathode on both sides. Later, carbon cathodes were prepared in a 4 × 8 cm configuration, enveloped with glass mat separator and lithium foil and folded in half. The electrodes were placed in polyethylene or Teflon rectangular jars of various sizes to contain from 8 to 25 ml of electrolyte. Open-circuit voltages and discharge characteristics were obtained with the cells in the argon glove box since they were not sealed but only covered with a tight fitting cap.

Results

Anodes: stability of lithium to phosphorus and sulfur oxyhalides.—Lithium metal appears visibly stable to attack by phosphorus oxychloride at 25°C. $POCl_3$ forms a brown layer on the surface of the metal upon boiling for several hours. Lithium is more stable to attack by thionyl chloride and sulfuryl chloride. The metal does not form an observable coating upon boiling for two weeks in either of these solvents.

Passage of current through phosphorus oxychloride solutions of $LiBCl_4$, $LiAlCl_4$, or Li_2ZrCl_6 results in simultaneous electrodeposition of metallic lithium and electrogeneration of chlorine at carbon, nickel, or platinum electrodes. The resulting Li/Cl_2 electrochemical cells have open-circuit potentials from 4.0 to 4.3V at 25°C, being higher when an aprotic Lewis acid (BCl_3, $AlCl_3$, or $ZrCl_4$) is present in excess. Prior to this observation Li/Cl_2 cells required the use of fused salt electrolytes.

* Electrochemical Society Active Member.

Key words: lithium anode cells, phosphorus oxychloride, thionyl chloride, inorganic electrolytes.

Table I. Physical properties of inorganic covalent oxyhalides

Property	$POCl_3$	$SOCl_2$	SO_2Cl_2
Molecular weight	153.4	119	135
Melting point, °C	+1.25[a]	−104.5[d]	+54.1[e]
Boiling point, °C	+105.8[a]	+77[d]	+69.4[e]
Density at 25°C, g/cm³	1.645[a]	1.629[d]	1.657[e]
Surface tension at 25°C, dynes/cm	31.6[a]	30.8[d]	28.4[e]
Viscosity at 25°C, centipoise	1.065[a]	0.603[d]	0.674[e]
Dielectric constant	13.7 (25°)[a]	9.05 (22°)[d]	9.15 (22°)[e]
Conductivity, ohm^{-1} cm^{-1}	2×10^{-8} (10°)[b]	3×10^{-9} (20°)[b]	2×10^{-8} (20°)[b]
Cryoscopic constant, deg/mole solute	7.68[a,c]		
Ebullioscopic constant, deg/mole solute	5.47[a]		

[a] Reference (1).
[b] Reference (2).
[c] The cryoscopic constant is incorrectly reported as 76.8 deg/mole solute by Ref. (3) and (4). The value shown in the table has been verified in our labortary.
[d] Reference (5).
[e] Reference (6).

Lithium is also electrodeposited upon passage of current through solutions of lithium salts in any of the other phosphorus and sulfur oxyhalides. The character of the deposits, although not dendritic, is soft and spongy.

Physical properties of the solvents.—The inorganic oxychlorides considered in this study are colorless liquids, some physical properties of which are listed in Table I. Phosphorus oxychloride, thionyl chloride, and sulfuryl chloride are miscible in all proportions. Phosphorus oxychloride is the stronger Lewis base and is a better solvent for many electrolytes. The melting point of this solvent (1.25°C) is higher than desired for many battery applications. A 1:1 mixture of phosphorus oxychloride and thionyl chloride, however, remains liquid to −40°C.

Electrolytes: solubilities and conductivities of solutions of lithium salts in phosphorus and sulfur oxyhalides.—Adequate solubilities of lithium salts in the covalent oxyhalides are reached only in salts with large anions. The solubility of LiCl in $POCl_3$ is only 0.005 g/liter (1). We find that the conductivity of the saturated LiCl solution is 2.4×10^{-6} ohm^{-1} cm^{-1} at 25°C. Lewis acids are usually soluble in covalent oxyhalides. Seidell (7) and Gutmann (2) list about 30 Lewis acids which dissolve at high (>1M) concentrations. In spite of these solubilities, the acid solutions are poor ionic conductors in sharp contrast with protic acids. We find that the conductivities of the Lewis acid solutions are in the 10^{-5} to 10^{-4} ohm^{-1} cm^{-1} range. (For example, the conductivity at 25°C of a 0.3M solution of $ZrCl_4$ in $POCl_3$ is 2.41×10^{-5} ohm^{-1} cm^{-1} and that of a 2M $AlCl_3$ solution in $SOCl_2$ is 1.74×10^{-4} ohm^{-1} cm^{-1}). While LiCl, a base in the solvent systems under consideration, is relatively insoluble in the pure solvents, it does dissolve in the acid solutions (Eq. [1] and [2])

$$POCl_3 + AlCl_3 \rightleftarrows POCl_3{:}AlCl_3 \rightleftarrows POCl_2^+ + AlCl_4^- \quad [1]$$

$$POCl_2^+ + LiCl \rightleftarrows Li^+ + POCl_3 \quad [2]$$

and the resulting neutral solutions are conductive. The concentration and conductivities of some of these solutions are shown in Table II. $LiBCl_4$ and $LiAlCl_4$ yield the most conductive solutions in $POCl_3$. $LiBF_4$, although more soluble in $POCl_3$ than either $LiBCl_4$ or $LiAlCl_4$, seems to be less dissociated. The most conductive inorganic oxyhalide systems are obtained with $LiAlCl_4$ solutions in $SOCl_2$ where the conductivity reaches 2.04×10^{-2} ohm^{-1} cm^{-1} at 1.73M. The conductivities of $LiAlCl_4$ solutions in $SOCl_2$ are shown as a function of electrolyte concentration in Fig. 1.

Some of the electrolytes which dissolve in $POCl_3$ are practically insoluble in $SOCl_2$. $LiBF_4$ and $LiPF_6$ are not satisfactory electrolytes in $SOCl_2$. BCl_3 solutions in $SOCl_2$ do not dissolve LiCl, showing that the equilibria analogous to Eq. [1] and/or [2] are displaced to the left. A 1.2M solution of $LiBCl_4$ can be prepared in 1:1 volume mixture of $POCl_3$ and $SOCl_2$, and the conductivity of the solution is only slightly below that of $LiBCl_4$ in $POCl_3$ itself.

Table II. Conductivities of solutions of lithium salts in phosphorus and sulfur oxyhalides at 25°C

Solvent	Electrolyte	Concentration (M)	Conductivity $\times 10^3$, ohm^{-1} cm^{-1}
$POCl_3$	$LiPF_6$	0.4	3.7
$POCl_3$	$LiAsF_6$	0.7	5.8
$POCl_3$	$LiAlCl_4$	0.9	7.8
$POCl_3$	$LiSbCl_6$	1.0	2.2
$POCl_3$	Li_2TiCl_6	1.0	5.7
$POCl_3$	Li_2SnCl_6	1.0	6.1
$POCl_3$	$LiSO_3Cl$	1.0	2.8
$POCl_3$	$LiAlBr_4$	1.0	6.3
$POCl_3$	$LiBCl_4$	1.2	8.7
$POCl_3$	$LiBF_4$	1.5	1.1
$SOCl_2$	$LiAlCl_4$	1.0	14.6
$SOCl_2$	$LiAlCl_4$	2.0	20.4
$SOCl_2$	$LiSbCl_6$	1.0	12.5
SO_2Cl_2	$LiAlCl_4$	1.0	7.4
$POCl_3$:$SOCl_2$ (1:1)	$LiBCl_4$	1.2	6.0

Cathodes and depolarizers.—A group of halogen/platinum, halogen/graphite, 38 nonmetallic solids. Sixteen metallic systems, and carbon were investigated. The nonmetallic solids included sulfur, selenium, metal oxides, metal sulfides, metal halides, and carbon fluorides. The insulators in the group were studied in mixtures with a conductive additive, usually carbon. The metals included mercury, titanium, platinum, palladium, nickel, cobalt, iron, 304 stainless steel, molyb-

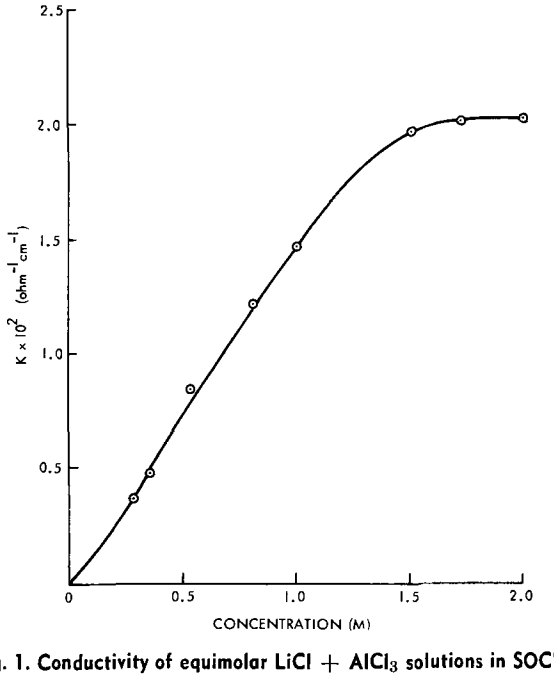

Fig. 1. Conductivity of equimolar LiCl + $AlCl_3$ solutions in $SOCl_2$

denum, tungsten, lead, niobium, tantalum, manganese, silver, and gold. Graphite and carbon black cathodes were also investigated.

Chlorine dissolves in phosphorus oxychloride to form a 10% solution (by weight) at 25°C and atmospheric pressure. Bromine is miscible with phosphorus oxychloride (at 25°C) in all proportions. The solubility of iodine was not determined but was found to exceed 10% (by weight).

Relatively few of the nonmetallic solids screened were stable to and insoluble in phosphorus oxychloride for the 60 day period of our tests, which were conducted at ambient temperature. Rapid reaction with the solvent followed by partial or complete dissolution was observed in SbF_3, BiF_3, CrO_3, V_2O_3, V_2O_5, and MnO_2. Pb_3O_4, PbO_2, Ni_2O_3, NiO_2, CuO, and CoF_3 reacted slowly and dissolved. NiF_2 and $PbCl_2$ reacted with the solvent. Chloranil and fluoranil dissolved. Nb_2O_5, AgI, CuCl, MoO_3, Bi_2O_3, HgO, $NiCl_2$, $CuCl_2$, CuF_2, and Ag_2S showed evidence of possible reaction or slight solubility. There was no conclusive evidence for instability or solubility of CuS, NiS, Ag_2O, AgBr, polycarbon monofluoride $(CF)_n$, or polytetracarbon monofluoride $(C_4F)_n$. HgS, $HgCl_2$, Hg_2Cl_2, S, and WO_3 were stable to attack and insoluble in phosphorus oxychloride.

Cell characteristics.—Li/Cl_2 cells.—The characteristics of the Li/Cl_2 system were investigated in a series of cells of varying configurations, having platinum, nickel, or carbon electrodes. Some of these utilized chlorine dissolved in the electrolytic solutions, while others operated like fuel cells using externally supplied chlorine.

The Li/$POCl_3$:$LiBCl_4$/Cl_2 cell appears to be reversible, as indicated by the electrodeposition of lithium and the electrogeneration of chlorine on platinum electrodes at potentials exceeding only slightly the open-circuit potential. The observed emf of the cell and the emf estimated from thermodynamic data are similar. In a typical experiment, a cell with platinum electrodes (1 cm^2 each, separated by 0.64 cm), filled with 1.8M $LiBCl_4$ (having an internal resistance of 84 ohms) was repeatedly charged and discharged. A 10 mA/cm^2 charging rate required a 5.35V external potential. Upon termination of the charging process the open-circuit potential of the unstirred cell was 4.30V, dropping to 4.186V in 5 min and remaining steady. The drop in potential could be associated with chlorine concentration differences, the chlorine forming a supersaturated solution on the cathode immediately following charging. The 4.186V potential could be reproduced in $LiAlCl_4$-saturated $POCl_3$ solution upon replacement of the electrogenerated solution in the cathode compartment by a chlorine-saturated solution.

Discharge of the Li/Cl_2 cells through varying external resistances shows a linear relationship between the cell polarization and the current density. This polarization is due predominantly to electrolyte (and separator) resistance. Similar results were obtained with a lithium foil and chlorine gas supplied through a cylindrical porous graphite cathode. Lithium/chlorine cells were also made with the other electrolytic solutions listed in Table II.

Li/Br_2 cells.—Cells similar to the Li/Cl_2 cells were made with bromides and bromine. Thus by charging a $LiAlBr_4$ solution in $POCl_3$, a Li/$LiAlBr_4$:$POCl_3$/Br_2 cell was made. At 25°C the open-circuit potential of the cell, which appears to be reversible, is 3.73V.

Cells with metallic cathodes.—The open-circuit potentials of Li/$POCl_3$:$LiAlCl_4$/Me cells with saturated $LiAlCl_4$ solutions at 25°C range from 2.05 to 2.92V. The values are: Pb, 2.05V; Ta, 2.30V; Ti, 2.50V; W, 2.50V; Nb, 2.60V; Pd, 2.70V; Ag, 2.70V; Fe, 2.70V; Mn, 2.70V; Mo, 2.75V; Co, 2.75V; 304 stainless steel, 2.80V; Ni, 2.80V; Pt, 2.90V; Hg, 2.90V; and Au, 2.92V. Current densities at 50% polarization based on geometric areas range from 0.053 mA/cm^2 (Ti) to 0.357 mA/cm^2 (Au). The current density for Hg is 0.175 mA/cm^2 at 50% polarization.

Lithium cells with solid nonmetallic cathodes.—The open-circuit potentials of the Li/CuF_2 cells in phosphorus oxychloride ranged from 3.7 to 4.0V, depending on the electrolyte. The potential was 4.0V with $LiPF_6$, 3.78V with $LiBF_4$, 3.63V with $LiBCl_4$, and 3.66V with $LiAlCl_4$. The discharge curves of these four cells are shown in Fig. 2. Current densities at 50% polarization reach 19 mA/cm^2. Cathode utilization efficiencies are moderate to high and depend on the electrolyte used. The efficiency in the Li/$POCl_3$:$LiBCl_4$/CuF_2 cell reaches 61%. Two voltage plateaus are observed in the discharge curve. A Li/$POCl_3$:$LiBCl_4$/$(CF)_n$ cell discharged at 1 mA/cm^2 exhibits a single, flat voltage plateau at 1.2V. The open-circuit potential of this cell is 2.86V. The utilization efficiency of the $(CF)_n$ cathode is 57%.

The open-circuit potential of the Li/$POCl_3$:$LiBCl_4$/WO_3 cell is 2.58V. The cathode utilization efficiency at 1 mA/cm^2 is 120% if reduction to WO_2 is assumed, an obviously wrong assumption. The current density at 50% polarization is 12 mA/cm^2. The discharge characteristics of this cell at 1 mA/cm^2 are characterized by a single voltage plateau at 2.3V.

The open-circuit potential of the Li/$POCl_3$:$LiBCl_4$/S cell is 3.3V with a sulfur-carbon cathode, and 3.1V with a sulfur-silver cathode. The cathode utilization efficiency is low (14%). Discharge characteristics of these cells are characterized by voltage plateaus at 2.3V for the carbon and 1.4V for the silver additive.

The open-circuit potentials of Li/$(C_4F)_n$ cells in $POCl_3$ range from 3.11 to 3.70V and depend on the electrolyte used. Their cathode utilization efficiency, assuming reduction of the cathode to carbon, substantially exceeds 100%, reaching 470% at 1 mA/cm^2 in $LiBCl_4$ in the experiment shown in Fig. 3. Typical current densities at 50% polarization are 4 mA/cm^2. The polytetracarbon monofluoride cathodes become inactive when discharged against lithium. They cannot be used over again with fresh lithium and electrolytic solution. Expended cathodes "swell" to about twice

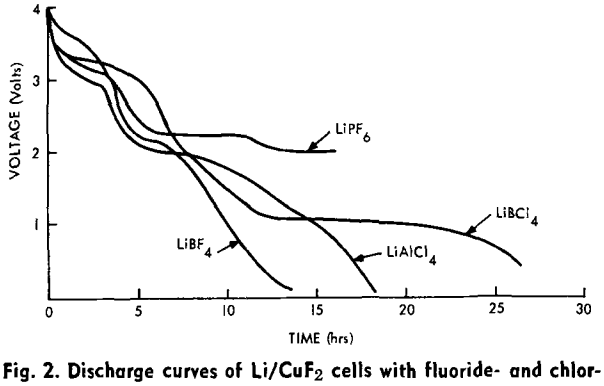

Fig. 2. Discharge curves of Li/CuF_2 cells with fluoride- and chloride-based saturated electrolytes. Solutions in $POCl_3$ at 25°C.

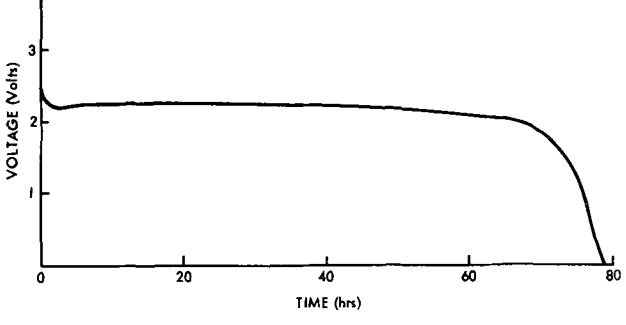

Fig. 3. Discharge curve of a Li/$POCl_3$:$LiBCl_4$/$(C_4F)_n$ cell at 1 mA/cm^2 (28 mA) rate.

their original thickness. Atomic absorption spectroscopic analysis shows that they pick up phosphorus and lithium. In ~1M $LiBCl_4$:$POCl_3$ solutions no boron from the electrolyte is detected in the spent cathodes.

Li/$(C_4F)_n$ cells made with a 1:1 $POCl_3$:$SOCl_2$ solvent and an acidic electrolyte consisting of 1M BCl_3 and 0.8M LiCl (0.8M $LiBCl_4$ plus 0.2M BCl_3) have open-circuit potentials from 3.90 to 4.05V. Current densities at 50% polarization (2V) range between 3-4 mA/cm². The cells exhibit flat voltage plateaus at 2.8-3.1V for 70-90% of their life when discharged at 1 mA/cm² (28 mA). A discharge curve typical to these cells is shown in Fig. 4. Energy densities of the cells range from 194-225 W-hr/kg, the weight including all cell components other than the case. Coulombic capacities of the cells exceed those expected from reduction of $(C_4F)_n$ to carbon by factors from 2.75 to 3.34.

Li/$SOCl_2$:$LiAlCl_4$/$(C_4F)_n$ cells, with 1-2M $LiAlCl_4$ solutions in thionyl chloride by itself exhibit flat discharge characteristics, high energy densities, and moderate power densities. The open-circuit potential of a Li/$SOCl_2$:$LiAlCl_4$/$(C_4F)_n$ cell with 1M $LiAlCl_4$ is 3.62V. The cell potential at a 1 mA/cm² discharge rate is 3.30V. The potential remains constant through the discharge of the cell and drops abruptly when the cell is exhausted. Ninety-six per cent (96%) of the cell's energy capacity can be obtained at a 1 mA/cm² rate above 3.0V. The discharge curve of this cell is shown in Fig. 5.

Substitution of high surface area graphite or carbon black for $(C_4F)_n$ in the thionyl chloride cells produces similar, and in some cases better, results. Voltage-current characteristics for 50% discharged $(C_4F)_n$ and acetylene black cathodes are shown in Fig. 6. The acetylene black cathode is capable of handling over five times the current density of $(C_4F)_n$ in this instance. Discharge curves of Li/$SOCl_2$:1.8M $LiAlCl_4$/C cells with folded 4 × 8 cm cathodes surrounded on both sides with lithium foil in 8 ml cases are shown in Fig. 7 at 1 mA/cm² (64 mA) and in Fig. 8 at 10 mA/cm² (640 mA). These particular cells exhibit energy densities of 578 and 408 W-hr/kg, respectively. These energy densities, like all reported here, include the mass of all cell components except the case.

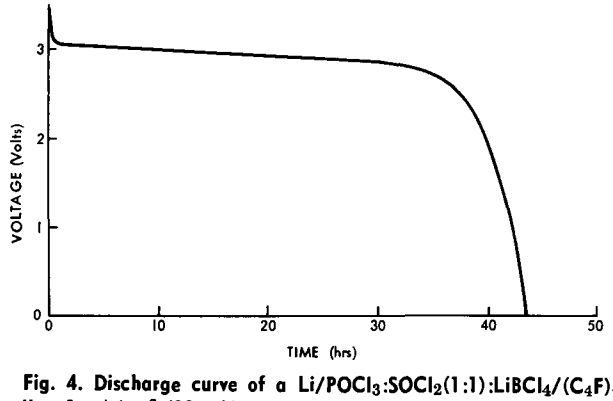

Fig. 4. Discharge curve of a Li/$POCl_3$:$SOCl_2$(1:1):$LiBCl_4$/$(C_4F)_n$ cell at 1 mA/cm² (28 mA) rate.

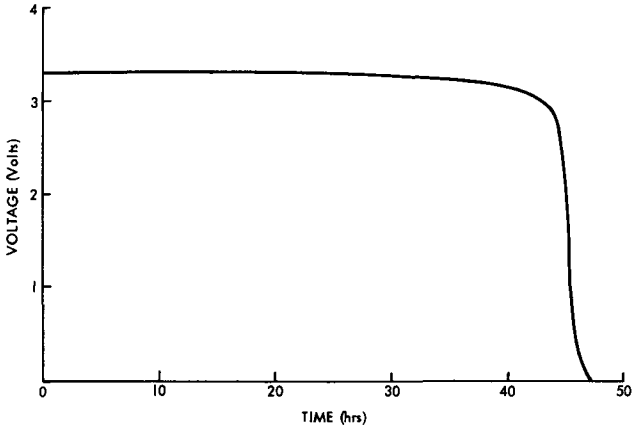

Fig. 5. Discharge curve of 242 W-hr/kg Li/$SOCl_2$:$LiAlCl_4$/$(C_4F)_n$ cell at 1 mA/cm² (28 mA) rate.

Discussion

Stability of lithium in phosphorus oxychloride and in thionyl chloride.—It is evident from the Results section that the rate of reaction of lithium with the inorganic oxyhalides considered is very slow. Since lithium is sufficiently electropositive to be able to reduce any of the solvents, we conclude that upon contact with the oxyhalides a passivating layer is formed

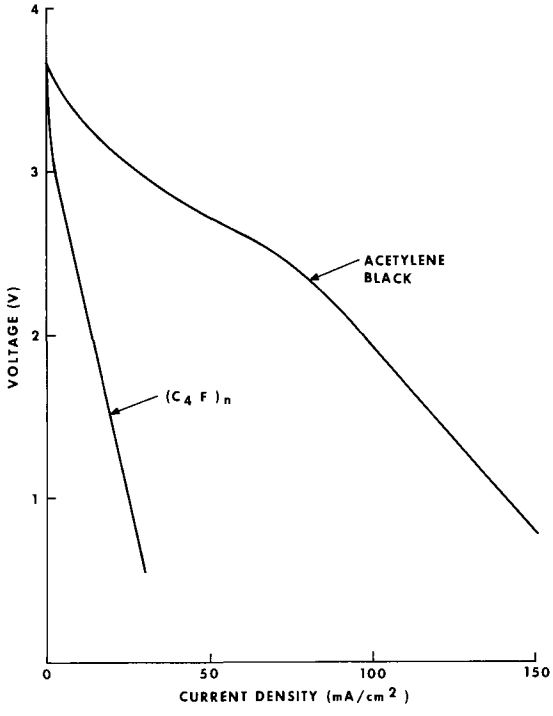

Fig. 6. Polarization characteristics of $(C_4F)_n$ and C cathodes vs. Li in 1.8M $LiAlCl_4$ thionyl chloride solution.

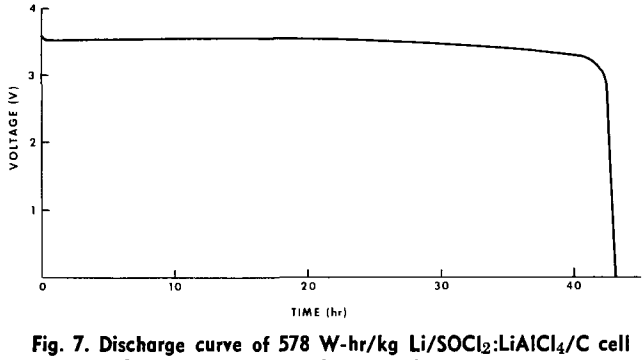

Fig. 7. Discharge curve of 578 W-hr/kg Li/$SOCl_2$:$LiAlCl_4$/C cell at 1 mA/cm² (64 mA) rate with folded cathode.

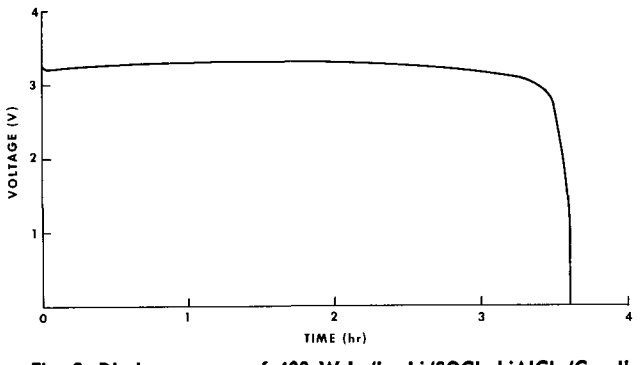

Fig. 8. Discharge curve of 408 W-hr/kg Li/$SOCl_2$:$LiAlCl_4$/C cell at 10 mA/cm² (640 mA) rate with folded cathode.

on the surface of the metal. The nature and the stability of this passivating layer vary with the solvent and with the electrolyte. While lithium appears to be stable at room temperature for at least two weeks in any of the oxyhalides discussed, $POCl_3$ reacts with the metal at its boiling point to form a thick brown coating. Thionyl chloride is superior in its stability to reduction by lithium. Two weeks of boiling with this solvent has no visible effect on lithium, the metal retaining its metallic appearance. The addition of thionyl chloride to the phosphorus oxyhalides also improves the stability of the latter.

Lewis acids, such as BCl_3 or $AlCl_3$, exhibit a corrosive effect on lithium in boiling $POCl_3$ or $SOCl_2$. This suggests that the passivating coating is basic, possibly the lithium salt of a reduced oxyacid. Indeed both thionyl chloride and phosphorus oxychloride can be active as cathode depolarizers, being reduced in electrolytic processes.

Solvent stability.—The most significant difference between the present and the previously reported ambient temperature lithium cells in which organic solvents were used is in the stability of the solvents. The solvents described in the results are thermodynamically stable. All organic solvents used in lithium batteries are metastable in the thermodynamic sense. Because of this, when the systems are perturbed by application of a substantial overpotential or by intense local heating the change is irreversible in organic electrolyte solutions, but is reversible in the inorganic solutions. In phosphorus oxychloride, for example, charging overpotentials result in the formation of trivalent phosphorus compounds and dissolved chlorine. These recombine to regenerate the solvent.

Solubilities and conductivities.—The dielectric constants of the inorganic solvents under consideration are too low to be adequate to overcome the electrostatic lattice energies of salts consisting of small ions. However, if the solvents are sufficiently strong coordinating agents (electron pair donors), large solvated lithium ions can be formed. If the anions are also large the electrostatic attraction is sufficiently reduced for the lithium salts to dissolve, in spite of the low dielectric constants. In all of the presently considered systems the solubilities and conductivities depend on the sizes of the anions and on the donor strengths of the solvents.

The linear increase in the conductivity of $LiAlCl_4$ in $SOCl_2$ with electrolyte concentration (Fig. 1) shows that even in this solvent, having a dielectric constant of 9.05 (at 22°C), the ions are substantially dissociated. The addition of Lewis acids by themselves to the oxyhalide solvents leads only to conductivities of 10^{-4}-10^{-5} ohm^{-1} cm^{-1}, two orders of magnitude below the 10^{-2}-10^{-3} ohm^{-1} cm^{-1} conductivities of the lithium salt solutions. We explain this difference in dissociation by the ionic size, the acid cations $POCl_2^+$ or $SOCl^+$ being smaller than the solvated lithium ions $[Li(POCl_3)_n]^+$ and $[Li(SOCl_2)_n]^+$. As a result, the acid solutions consist predominantly of associated ion pairs (Eq. [3]). Neutralization of the acids by lithium salts leads to conductive solutions of dissociated ions (Eq. [4])

$$POCl_3 + AlCl_3 \rightarrow POCl_3{:}AlCl_3 \rightleftarrows POCl_2^+ + AlCl_4^- \quad [3]$$

$$LiCl + POCl_3{:}AlCl_3 + (n-1)\,POCl_3 \rightleftarrows [Li(POCl_3)_n]^+ + AlCl_4^- \quad [4]$$

The number of solvent molecules solvating the lithium cations is less than six and probably less than five as evidenced by the attainment of 2M $LiAlCl_4$ solutions in $SOCl_2$ and by the attainment of 1.8M $LiBCl_4$ solutions in $POCl_3$ (the ratio of solvent molecules to lithium cations is about 6:1 in the first and about 5:1 in the second). This value of n is consistent with the measurements of the stability constants for hydrated lithium ions in propylene carbonate (8), which show that the number of solvating molecules is three or more.

Thionyl chloride has a lower viscosity than the other oxyhalides (0.6 cp at 25°C) and is also substantially less viscous than water. The low viscosity and the dissociation of ion pairs account for the fact that the conductivity of 1.73M $LiAlCl_4$ solutions reaches 2.04×10^{-2} ohm^{-1} cm^{-1}.

Cathode and cell characteristics.—Li/Cl_2 cells.—Phosphorus oxychloride is stable to oxidation and is compatible with chlorine, bromine, and iodine. The observed open-circuit potentials of cells with differing electrolytes and varying Lewis acid concentrations range from 4.0 to 4.3V at 25°C. These values are in reasonable agreement with the available thermochemical data. The free energy of formation ($\Delta G°_f$) of LiCl at 25°C is −91.79 kcal/mole (9). The free energy of dissolution of chlorine in $POCl_3$ has not been reported; however, for carbon tetrachloride the value is +1.09 kcal/mole (10). Assuming a similar value for $POCl_3$ the calculated emf for a neutral solution, for the simple reversible reaction shown by Eq. [5], is 4.00V

$$Li(s) + \tfrac{1}{2}Cl_2(POCl_3) \rightleftarrows LiCl(s) \quad [5]$$

When an excess of a Lewis acid, such as $AlCl_3$ is present in the solution (and when the solution is saturated in the $LiAlCl_4$ electrolyte), the cell reaction is that shown by Eq. [6]

$$Li(s) + \tfrac{1}{2}Cl_2(POCl_3) + AlCl_3(POCl_3) \rightleftarrows LiAlCl_4(s) \quad [6]$$

Since the free energy of solvation of $AlCl_3$ and the free energy of formation of $LiAlCl_4$ are not available, we cannot calculate the emf. However, since the free energy of formation of $NaAlCl_4(s)$ from NaCl(s) and $AlCl_3(s)$ is −6.86 kcal/mole (11), an increase in the emf of our acidic cells by 0.30V to a maximum of 4.30V is not surprising.

The rates of electrode reactions at both the Li anode and the Cl_2(Pt) or Cl_2(C) cathodes are fast (>20 mA/cm^2), as expected for simple electron transfer reactions. Polarization of these cells is due to resistance of the electrolytic solution. At 50% polarization the cells deliver ~40 mW/cm^2.

Lithium cells with metallic cathodes.—The origin of the emf of our Li/$POCl_3$:$LiAlCl_4$/metal cells (with the cathode metal being any of the 16 listed in the Results section) can be either in electrochemical alloying or in catalytic reduction of the solvent at the cathode surfaces. However, the measured potentials of 2.05-2.92V are much above the potentials that have been determined for electrochemical alloying or in catalytic reduction of the solvent at the cathode surfaces. Lewis and Keyes determined the potential for the amalgamation reaction of lithium in propylamine in 1913 and found it to be 0.9457V (12), in agreement with the 1968 value of 0.947V of Cogley and Butler (13) who used a different solvent. Since the 2.90V of the Li/$POCl_3$:$LiAlCl_4$/Hg cell cannot be explained by formation of an amalgam, we conclude that the reduction of the solvent takes place at the cathode metal surface. This reduction leads to the formation of the observed LiCl precipitate and to the formation of soluble trivalent phosphorus compounds.

Li/CuF_2 cells.—Assuming that the reported free energies of formation for CuF_2 and CuF (−119.28 and −41.04 kcal/mole, respectively) (14) are correct, CuF_2 should be reduced directly to metallic copper, and only one voltage plateau should be observed in the discharge curve of the cell. The reversible emf for the reaction shown in Eq. [7] is calculated to be 3.46V as the free energy of formation of LiF at 25°C is −139.5 kcal/mole (9)

$$Li(s) + \tfrac{1}{2}CuF_2(s) \rightleftarrows LiF(s) + Cu(s) \quad [7]$$

However, the measured open-circuit potentials are higher, ranging from 3.63 to 4.00V depending on the electrolyte. The higher than theoretical open-circuit potentials suggest that reaction [7] is not the only cell reaction. A reaction which explains the observed cell potentials is the electrolytic reduction of solvent, catalyzed by the fresh porous copper surface formed upon reduction of the CuF_2.

The discharge curve of the $Li/POCl_3:LiBCl_4/CuF_2$ cell as well as the discharge curves of cells with the other electrolytes do not show a stable voltage plateau. The lack of such a plateau can be explained by the presence of at least two processes, solvent reduction and the reduction of cupric fluoride.

Li/S cells.—The open-circuit potentials of $Li/POCl_3:LiBCl_4/S$ cells are well above the 2.6V emf for reaction [8] (15)

$$Li + \tfrac{1}{2}S \rightleftarrows 1/2\,Li_2S \qquad [8]$$

Since our cathodes contained carbon or silver, reduction of the solvent at the metal surfaces could be a cause for the higher potentials. A reaction in which lithium chloride and thiopyrophosphoryl chloride are produced according to Eq. [9]

$$2Li + S + 2POCl_3 \rightleftarrows 2LiCl + P_2O_2SCl_4 \qquad [9]$$

may also explain the high emf. (Reaction [9] seems plausible in view of the known reaction of hydrogen sulfide with phosphorus oxychloride to form hydrogen chloride and thiopyrophosphoryl chloride (3).) We note that cells with selenium and metal oxide cathodes also have higher than expected open-circuit potentials probably for related reasons. Indeed, the formation of lithium chloride is observed in all of these cells.

$Li/(C_4F)_n$ and Li/C cells.—The $LiPOCl_3:LiBCl_4/(C_4F)_n$ cells as well as the $Li/POCl_3:LiBCl_4/WO_3$ cells exhibit greater coulombic capacities upon discharge than can be explained by reactions [10] and [11]

$$\frac{1}{n}(C_4F)_n + e^- \rightarrow 4C + F^- \qquad [10]$$

$$WO_3 + 2POCl_3 + 2e^- \rightarrow WO_2 + P_2O_3Cl_4 + 2Cl^- \qquad [11]$$

These cells also exhibit flat voltage plateaus at 2.2V in $POCl_3$ when discharged at 1 mA/cm^2. In some cells more than 5 faradays are passed per gram atom fluorine present in the $(C_4F)_n$. The only component present in our cells which can account for the added cathode capacity is the solvent itself. The reduction of the solvent is indicated by our experiments to be by at least a two-electron process. It is possible that the particular open graphite-like structure of $(C_4F)_n$ might act as a surface upon which the $POCl_3$ or $Cl_3PO:BCl_3$ adduct can be electrochemically reduced. A similar process occurred with $SOCl_2$ and SO_2Cl_2. $(C_4F)_n$ has a planar structure like graphite, but the distance between the planes of hexagonally arranged carbon atoms is 5.4Å (compared with 3.35Å in graphite) and the carbon planes are in identical positions one above each other (instead of offset as in graphite) (16, 17). Decomposition of $(C_4F)_n$ results in the formation of amorphous carbon; analysis of partially discharged $(C_4F)_n$ cathodes by x-ray crystallography revealed no structure, the cathodes behaving essentially like amorphous carbon. Substitution of carbon black for $(C_4F)_n$ in lithium anode cells operating in $LiAlCl_4$ solutions of $POCl_3$, $SOCl_2$, and SO_2Cl_2 confirmed our hypothesis for catalytic reduction of the solvents. The open-circuit voltages were similar to those observed with $(C_4F)_n$ and the discharge charcteristics improved, especially at the high rates, because of the increased electronic conductivity and surface area of the carbon electrodes. Solvent reduction explains the observed open-circuit potentials, as well as the exceptional voltage stability seen in the discharge curves (Fig. 3-5, 7, 8). Obviously the common mechanism that accounts for the increasing internal resistance or decreasing potential of conventional cells, the inbound movement of the reactive cathode layer, is inoperative in a cell in which the solvent is the depolarizer and the cathode is fixed.

The open-circuit potential of cells containing $SOCl_2$ (neutral solution) is 3.6-3.7V whether $(C_4F)_n$ or C catalytic cathodes are used. This potential increases to 3.9-4.0V in $SOCl_2$ solutions containing excess Lewis acid ($AlCl_3$ or BCl_3). The observed reaction products in discharged cells include lithium chloride, sulfite, and sulfur. These products as well as the observed emf of the cells suggest that the cell reaction is that shown in Eq. [12] for neutral solution

$$8Li + 3SOCl_2 \rightleftarrows 6LiCl + Li_2SO_3 + 2S \qquad [12]$$

The calculated emf for the reaction of Eq. [12] is 3.61V. The reactions in acid solution are similar except that $LiAlCl_4$ or $LiBCl_4$ rather than LiCl is formed.

Conclusion

Inorganic phosphorus and sulfur oxyhalides which are liquid at room temperature are useful solvents and depolarizers in lithium cells. Conductivities of lithium salts in these solutions reach 2.04×10^{-2} ohm^{-1} cm^{-1}. A broad range of cathodes is compatible with the solvents, including strongly oxidizing ones such as Cl_2(C) and sulfur. However, the best cathode electrodes are conductive materials, such as polytetracarbon monofluoride and carbon, which aparently aid the reduction of the solvent. With these electrodes, the solvent becomes the depolarizer. Unlike conventional solid cathodes the distance between the reactive zones of the electrodes remains constant upon discharge and the cells exhibit exceptional voltage stability. Since the electrolytic solution is also the depolarizer, the weight of the cathode does not burden the cell and energy densities of 570 W-hr/kg to 90% of the initial voltage are realized in simple cells. Furthermore, the problem of limitation of the shelf life by transport of the cathode depolarizer is altogether eliminated.

Acknowledgments

This work was supported in part by the United States Navy Office of Naval Research and more recently by the United States Army Electronics Command.

Manuscript submitted Nov. 6, 1972; revised manuscript received June 14, 1973.

Any discussion of this paper will appear in a Discussion Section to be published in the June 1974 JOURNAL.

REFERENCES

1. J. R. Van Wazer, "Phosphorus and Its Compounds," Vol. 1, Interscience Publishers, Inc., New York (1958).
2. V. Gutmann, "Halogen Chemistry," Vol. 2, Chap. 5, Academic Press, New York (1967).
3. P. Pascal, "Nouveau Traite de Chimie Minerale," Vol. 10, Masson, Paris (1961).
4. International Critical Tables, Vol. 4, 214-5, McGraw-Hill Book Co., New York (1928).
5. Gmelin, "Handbook of Inorganic Chemistry," Vol. 9, p. 1791, Verlag Chemie (1965).
6. Gmelin, *ibid.*, p. 1802.
7. A. Seidell and W. F. Linke, "Solubilities of Inorganic and Metal Organic Compounds," 4th ed., American Chemical Society, Washington, D. C. (1965).
8. D. R. Cogley, J. N. Butler, and E. Grunwald, *J. Phys. Chem.*, **75**, 1477 (1971).
9. "JANAF Thermochemical Data," Vol. 3, Dow Chemical Co., Midland, Mich. (1965).
10. D. D. Wagman *et al.*, "Selected Values of Chemical Thermodynamic Properties," NBS Tech. Note 270-4 (1969).
11. D. D. Wagman *et al. ibid.*, Note 270-3.
12. G. N. Lewis and F. G. Keyes, *J. Am. Chem. Soc.*, **35**, 340 (1913).

13. D. R. Cogley and J. N. Butler, *J. Phys. Chem.*, 72, 4568 (1968).
14. "JANAF Thermochemical Data," Addendum II, Dow Chemical Co., Midland, Mich. (1966).
15. J. R. Coleman and M. W. Bates, "Power Sources," Vol. 2, p. 289, D. H. Collins, Editor, Pergamon Press, New York (1968).
16. W. Rudorff, "Advances in Inorganic Chemistry and Radiochemistry," Vol. 1, pp. 223-266, H. J. Emelus and A. G. Sharpe, Editors, Academic Press, Inc., New York (1959).
17. G. R. Hennig, "Progress in Inorganic Chemistry," Vol. 1, pp. 125-205, F. A. Cotton, Editor, Interscience Publishers, Inc., New York (1959).

Lithium Inorganic Electrolyte Cells Utilizing Solvent Reduction

Wishvender K. Behl,* John A. Christopulos,* Maria Ramirez, and Sol Gilman*

Power Sources Technical Area, United States Army Electronics Technology and Devices Laboratory (ECOM), Fort Monmouth, New Jersey 07703

ABSTRACT

This paper describes a study of room temperature lithium cells employing solutions of $LiBCl_4$ in $POCl_3$ and $LiAlCl_4$ in $SOCl_2$ as electrolytes and polytetrafluoroethylene (Teflon)-bonded carbon black electrodes as cathodes. A novel feature of these cells is that during discharge the solvents, *i.e.*, $POCl_3$ and $SOCl_2$, are electrochemically reduced and behave as soluble cathodes. Sealed prototype cells were fabricated using a polyethylene-polyester laminated bag container. Based on total cell weight, a prototype cell yielded an experimental energy density of 244 W-hr/lb for a 57-hr discharge rate (20 mA constant current; 1 mA/cm^2 current density). The performance of these cells is also compared with the performance of prototype lithium-organic electrolyte-graphite monofluoride and lithium-inorganic electrolyte-tetracarbon monofluoride cells.

Recently, solutions of lithium-inorganic salts (*e.g.*, $LiBCl_4$, $LiAlCl_4$, etc.) in phosphorous oxychloride ($POCl_3$) and thionyl chloride ($SOCl_2$) have been reported (1) as electrolytes for room temperature lithium-chlorine cells. Attempts also have been made to use cathodes other than chlorine gas, *e.g.*, graphite fluorides (CF and C_4F), metal halides, metal oxides, etc. (2, 3). Among the various cathode materials studied (2, 3), cells with tetracarbon monofluoride (C_4F) cathodes yielded the highest energy densities. It was also reported that during discharge C_4F also catalyzes (3) the reduction of the solvents, *i.e.*, $POCl_3$ and $SOCl_2$, so that coulombic efficiencies far in excess of theoretical were obtained. In the present studies, it is demonstrated that both $POCl_3$ and $SOCl_2$ can be electrochemically reduced at an adequate rate on uncatalyzed carbon black electrodes and behave as soluble cathodes. Results are presented for prototype room temperature lithium-inorganic electrolyte cells using polytetrafluoroethylene (Teflon)-bonded carbon black electrodes as cathodes. Some new data on the performance of room temperature lithium-inorganic electrolyte-C_4F and lithium-organic electrolyte-CF cells at current densities of 1-10 mA/cm^2 are also presented by way of comparison with the newer systems.

Experimental Procedure

Chemicals.—The chemicals used in the experiments were purified as described. Reagent grade phosphorous oxychloride (Fisher Scientific Company) and analytical grade thionyl chloride (Matheson, Coleman and Bell Company) were refluxed over lithium metal for a period of 24 hr and then distilled. Propylene carbonate (Eastman Kodak Company, T_B = 121°-123°C at 17 mm pressure) was dried with 5A molecular sieves and submitted to vacuum fractionation at 7 mm Hg. The first fraction of 300 mliters was discarded. Reagent grade methyl acetate (Fisher Scientific Company) was used as received.

* Electrochemical Society Active Member.

Key words: carbon black cathodes, inorganic electrolytes, lithium anodes, lithium cells, phosphorous oxychloride, thionyl chloride, solvent reduction.

Reagent grade lithium chloride (Fisher Scientific Company) was further purified by heating at 100°-120°C for a period of 16-20 hr under a flowing atmosphere of hydrogen chloride (HCl) gas in a closed Vycor vessel. The temperature was then increased to 50° above the melting point of lithium chloride (610°C) and the bubbling of hydrogen chloride gas continued for another 4-5 hr. This was followed by bubbling chlorine gas for another 2-3 hr. The latter treatment with chlorine gas helped to remove the black organic impurities usually found after treatment with HCl gas. The excess of hydrogen chloride gas and chlorine gas was removed by bubbling argon gas and the temperature was gradually lowered to room temperature. The anhydrous lithium chloride, so obtained, was stored in Pyrex tubes in an inert atmosphere of argon gas. Anhydrous lithium tetrachloroaluminate ($LiAlCl_4$) was prepared by mixing weighed amounts [50:50 m/o (mole per cent)] of reagent grade lithium chloride with iron and water-free Fluka aluminum chloride (Columbia Organic Chemical Company) and then treated with hydrogen chloride gas and chlorine gas according to the prescribed procedure for the purification of lithium chloride.

Reagent grade lithium perchlorate (K&K Laboratories, Inc.) was vacuum dried and lithium hexafluoroarsenate (U. S. Steel Corporation) was used as received.

Preparation of electrolytes.—A 1M solution of lithium tetrachloroborate ($LiBCl_4$) in phosphorous oxychloride ($POCl_3$) was prepared by adding 21.196g of purified lithium chloride into distilled 200-300 ml of phosphorous oxychloride. Boron trichloride gas (Research Organic Inorganic Chemical Corporation) was then bubbled into the solution until the weight of the dissolved boron trichloride gas reached 117.17g. Lithium chloride is sparingly soluble in phosphorous oxychloride but as the requisite amount of boron trichloride gas is added, all of the lithium chloride dissolves and results in a clear solution. The volume of the resulting solution was increased to 500 ml by adding distilled $POCl_3$ to yield a 1M solution. It was found that

the addition of boron trichloride can be accomplished more easily by first liquefying the boron trichloride gas with an acetone-dry ice mixture so that it drips into the phosphorous oxychloride.

A 1.5M solution of lithium tetrachloroaluminate in thionyl chloride, 0.75M solution of lithium hexafluoroarsenate in methyl acetate, and 1M solution of lithium perchlorate in propylene carbonate were simply prepared by addition of requisite amounts of solutes into the solvents inside a Dry-Train, Dry-Lab (Vacuum Atmospheres Corporation) in pure dried argon atmosphere.

Preparation of electrodes.—Carbon black cathodes.—These electrodes were prepared by making a paste of 81 w/o (weight per cent) carbon black (XC-6310-4, Ashland Chemical Company) and 19 w/o Teflon binder (TFE-fluorocarbon resin dispersion No. 30, du Pont) in a small amount of water (5 mliters/g of carbon black-Teflon binder mixture). A 0.29-0.45g of the paste was then spread on two sides of a nickel grid (Exmet 3/0, 1.25 × 1.25 in.) which had a previously spot welded nickel wire lead. The electrode was sandwiched between two Whatman No. 42 filter papers and pressed between two stainless steel plates at a pressure of 8000 psi using a hydraulic press. The electrode was then removed and vacuum dried at 110°-120°C for a period of 24 hr.

Graphite fluoride cathodes.—Graphite fluorides were obtained from Ozark-Mahoning Company. The C_4F cathodes were prepared by making a paste of 72.53 w/o C_4F, 16.77 w/o carbon black, and 10.69 w/o Teflon binder in a small amount of water (2.5 mliters/g of cathode mixture). A 0.47-0.77g sample of the paste was spread on two sides of the nickel grid and pressed and dried as described above. The CF cathodes were prepared either by dry or wet processes. In the dry process method, a 1-1.47g sample of the cathode mixture (80 w/o CF, 15 w/o graphite, and 5 w/o Teflon powder) was put on two sides of copper foam metal (1.25 × 1.25 in.; 0.1 in. thick), having a previously spot welded copper wire lead, in a die and pressed between two stainless steel plates using a hydraulic press at a pressure of 10,000 psi. The CF cathodes in the wet process were prepared according to the procedure described by Watanabe and Fukuda (4). The electrodes so prepared, were dried at 120°C under vacuum for a period of 24 hr.

Lithium anodes.—The lithium anodes were prepared from commercial lithium ribbon (0.015 in. thick; Foote Mineral Company) stored in decahydronaphthalene. A 1.25 × 1.25 in. sample of this ribbon was pressed at 460 psi onto a nickel screen (Exmet 3/0; 1.25 × 1.25 in.), having a previously spot welded nickel wire lead, between two stainless steel plates greased with petroleum jelly (Snow White, USP, Fisher Scientific Company). The finished anodes were thoroughly washed with carbon tetrachloride before use.

Preparation of cells.—The cells were prepared by sandwiching the cathode between two Viskon nonwoven rayon separators and placing a lithium anode on the outside of each separator. The electrode assembly was then placed inside a polyethylene-polyester laminated bag (2.5 × 2.8 in.) containing 2-3 mliters of the electrolyte. The bag was then heat sealed so that approximately 2-3 in. of the electrode leads protruded out. All these steps were completed inside a Dry-Train, Dry-Lab (Vacuum Atmospheres Corporation).

Instrumentation.—The cells were discharged at constant currents up to 100 mA using a precision current source (North Hills Electronics, Inc., Model CS-11). For higher constant currents, a Kepco Power Supply (Model CK8-5M) was used in the current mode. For this purpose, the Kepco Power Supply was modified by placing a variable resistor in series to obtain the desired currents. The voltage-time curves were recorded on a Moseley Strip Chart Recorder (Model 7100B). The currents were read on a Weston Milliammeter (Model 901) placed in series with the cell.

Results and Discussion

Lithium-inorganic electrolyte cells.—The following lithium-inorganic electrolyte cells were investigated

Li | $LiBCl_4$-$POCl_3$ (1 molar) | Carbon black [I]

Li | $LiAlCl_4$-$SOCl_2$ (1.5 molar) | Carbon black [II]

Li | $LiAlCl_4$-$SOCl_2$ (1.5 molar) | C_4F [III]

Typical discharge curves for these cells at different current densities are presented in Fig. 1-4. The current densities are based on the geometric area of the cathode (including both sides) which in most cases was

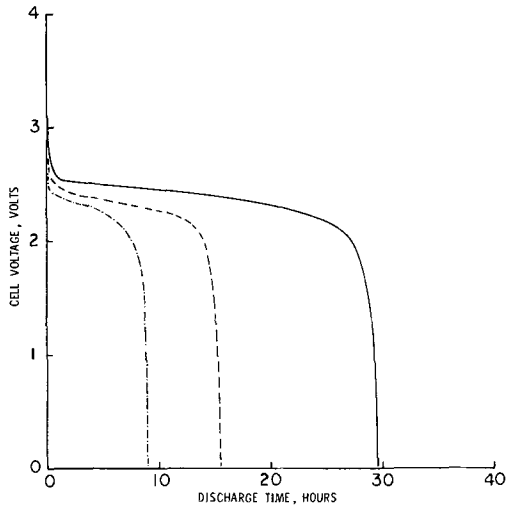

Fig. 1. Discharge curves for the cell: Li/$LiBCl_4$-$POCl_3$ (1M)/carbon black; ——— C.D. 1 mA/cm² (20 mA discharge current); - - - - C.D. 2 mA/cm² (40 mA discharge current); —·—·—·— C.D. 3 mA/cm² (61 mA discharge current).

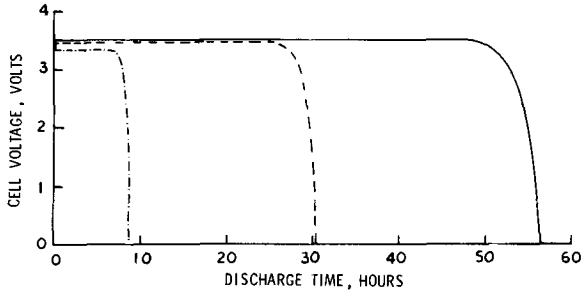

Fig. 2. Discharge curves for the cell: Li/$LiAlCl_4$-$SOCl_2$ (1.5M)/carbon black; ——— C.D. 1 mA/cm² (20 mA discharge current); - - - - C.D. 2 mA/cm² (36 mA discharge current); —·—·—·— C.D. 5 mA/cm² (100 mA discharge current).

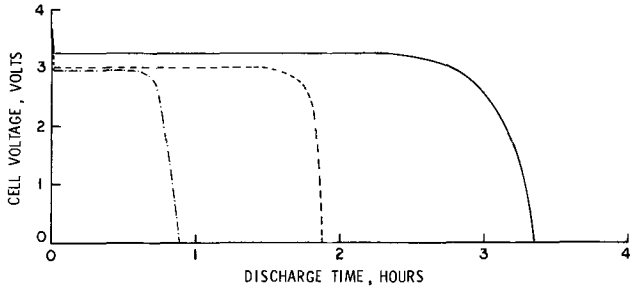

Fig. 3. Discharge curves for the cell: Li/$LiAlCl_4$-$SOCl_2$ (1.5M)/carbon black; ——— C.D. 10 mA/cm² (195 mA discharge current); - - - - C.D. 15 mA/cm² (300 mA discharge current); —·—·—·— C.D. 20 mA/cm² (430 mA discharge current).

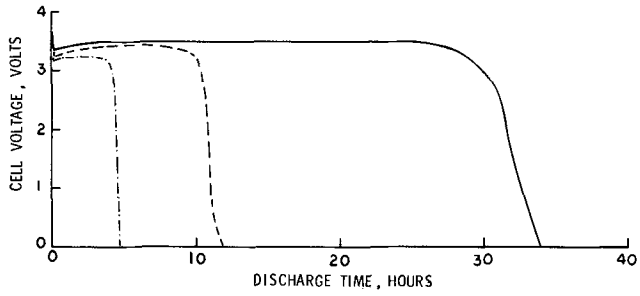

Fig. 4. Discharge curves for the cell: Li/LiAlCl$_4$-SOCl$_2$ (1.5M)/C$_4$F; ——— C.D. 1 mA/cm^2 (20 mA discharge current); – – – C.D. 2 mA/cm^2 (39 mA discharge current); —·—·—·— C.D. 5 mA/cm^2 (118 mA discharge current).

20 cm^2. The open-circuit voltages for cells I, II, and III were 3.1, 3.65, and 3.65V, respectively, and showed a variation of less than ± 0.05V in a number of experiments. Upon discharge, cell I showed a large initial drop in voltage and exhibited a slightly sloping discharge plateau. In contrast to cell I, cells II and III showed only a small initial drop in voltage and exhibited exceptionally flat discharge plateaus. Toward the end of cell life, cell voltages for cells I, II, and III declined sharply to zero volt. The discharge curves for cells I-III were recorded at successively increasing current densities until either the cell voltage plateau fell below 2V or the 1-hr rate was reached. For cell I, the cell voltage plateau fell below 2V at current densities greater than 3 mA/cm^2 and thus no discharge curves are reported for higher current densities. For cells II and III, the 1-hr rate was reached at current densities of 20 and 10 mA/cm^2, respectively.

The electrochemical reduction of solvents, in solutions of triethylammonium chloride in phosphorous oxychloride and thionyl chloride, at platinum electrodes was first reported by Spandau, Beyer, and Preugschat (5). The cathodic product in the case of $POCl_3$ was found to have the stoichiometric formula PO and is believed to be polymeric. The cathodic products in case of $SOCl_2$ were found to be temperature dependent and, at temperatures above 0°C, predominantly consisted of SO_2, Cl_2, and S_2Cl_2.

The voltammetric reduction of the solvents in solutions of $LiBCl_4$ in $POCl_3$ and $LiAlCl_4$ in $SOCl_2$ at platinum, pyrolytic graphite and porous carbon electrodes was confirmed (6) in this laboratory using the techniques of cyclic and rotating ring-disk voltammetry. Assuming the cathodic reaction products to be the same as postulated by Spandau *et al.* (5), the net cell reaction in cell I may be given by the following equation

$$3Li + POCl_3 \rightarrow PO + 3LiCl \qquad [1]$$

Since SO_2 is known (7) to undergo further reduction in anhydrous nonaqueous solvents to dithionate ($S_2O_4^{--}$) and Cl_2 to chloride (Cl^-) (6) ions, the net cell reaction in cell II may be given by the following equation

$$8Li + 4SOCl_2 \rightarrow Li_2S_2O_4 + 6LiCl + S_2Cl_2 \qquad [2]$$

Assuming the net cell reactions given by Eq. [1] and [2] to be correct for cells I and II, respectively, the approximate free energy changes for reactions [1] and [2] are calculated from the open-circuit voltages to be, respectively, −214 kcal/mole of $POCl_3$ and −168 kcal/mole of $SOCl_2$. From these free energy of reactions, it would be expected that lithium metal would react spontaneously with both phosphorous oxychloride and thionyl chloride. However, in practice, lithium metal is extremely stable in solutions of $LiBCl_4$ in $POCl_3$ and $LiAlCl_4$ in $SOCl_2$. Lithium-inorganic electrolyte cells with these solutions have been stored for over two weeks without any appreciable loss of performance. The stability of lithium metal in $POCl_3$ and $SOCl_2$ solutions may be due to the formation of a passivating layer of the reaction products which protects it from any further chemical reaction.

The end of cell life in cells I and II is caused by the passivation of the carbon black cathodes by the accumulation of reaction products. Thus, attempts to regenerate the cells at the end of cell life by addition of more electrolyte were not successful. The energy densities and power densities for cells I and II were determined by discharging the cells to zero volt and the data are summarized in Table I. The amount of the solvent reduced at the carbon black cathodes was also determined from the total discharge time by use of Faraday's law and assuming the cell reactions given by Eq. [1] and [2] to be correct. From a knowledge of the initial amount of the solvent, the per cent solvent utilization was also calculated at various current densities. These data are also summarized in Table I.

In cell III, if C_4F is considered the active cathodic material, the electrode reactions would be given by the following equations

$$\text{Anode:} \quad Li \rightarrow Li^+ + e \qquad [3]$$

$$\text{Cathode:} \quad C_4F + e \rightarrow 4C + F^- \qquad [4]$$

$$\text{Net cell reaction:} \quad Li + C_4F \rightarrow 4C + LiF \qquad [5]$$

Table I. Summary of performance data for lithium-inorganic electrolyte cells

Cell	Discharge current (mA)	Current density (mA/cm^2)*	Weight of carbon or C$_4$F (g)	Weight of electrolyte (g)	Weight of solvent† (g)	Per cent solvent utilization‡	Total cell weight (g)	Energy density‡ (W-hr/lb)	Power density‡ (W/lb)
I	20	1**	0.296	3.482	3.161	35.71	6.45	95	3.2
	40	2**	0.283	3.732	3.388	34.67	6.55	93	6.2
	61	3**	0.265	3.063	2.780	37.66	6.12	87	10.2
II	20	1**	0.365	4.540	3.832	66.02	7.531	230	4.1
	20	1	0.223	3.280	2.769	78.55	6.136	244	5.0
	36	2**	0.274	5.200	4.389	54.72	8.285	199	6.6
	40	2	0.258	3.199	2.700	58.52	6.152	170	9.5
	100	5**	0.244	5.000	4.221	46.27	7.986	156	22.9
	100	5	0.213	3.800	3.208	51.89	6.662	160	21.3
	195	10**	0.325	4.350	3.672	39.13	7.362	124	37.6
	215	11	0.232	3.350	2.828	38.81	6.269	97	42.2
	300	15**	0.288	5.000	4.221	29.18	8.041	85	45.9
	300	15	0.321	3.173	2.678	27.34	6.249	69	62.7
	430	20**	0.328	4.660	3.934	22.25	7.788	58	72.5
	400	20	0.221	2.730	2.304	23.11	5.604	47	78.3
III	20	1**	0.411	3.124	2.637	55.59	6.369	150	4.5
	39	2**	0.349	3.272	2.762	35.42	6.226	104	9.3
	118	5	0.414	2.870	2.422	32.43	6.149	71	23.7
	100	5**	0.561	5.610	4.736	17.43	9.015	58	15.6
	186	10	0.342	2.701	2.280	11.46	5.816	23	36.5
	200	10	0.537	4.957	4.184	9.55	8.365	28	31.1

* Current densities are based on the geometric area, including both sides, of the cathode.
† Densities of electrolytes: 1M $LiBCl_4$-$POCl_3$ = ~1.73 g/cm^3; 1.5M $LiAlCl_4$-$SOCl_2$ ~ =1.69 g/cm^3.
‡ Per cent solvent utilization, energy density, and power density determined by discharging cells to zero volt.
** The discharge curves for these current densities are plotted in Fig. 1-4. Cell I: Li|$LiBCl_4$-$POCl_3$ (1M)|Carbon black; cell II: Li|$LiAlCl_4$-$SOCl_2$ (1.5M)|Carbon black; cell III: Li|$LiAlCl_4$-$SOCl_2$ (1.5M)|C_4F.

Table II. Performance of various carbons as cathodic materials in Li | $LiAlCl_4$-$SOCl_2$ (1.5M) | carbon cells

Carbon source	Bulk density (g/cm^3)	Weight of carbon (g)	Current density* (mA/cm^2)	Weight of electrolyte (g)	Weight of solvent† (g)	Per cent solvent utilization‡	Total cell weight (g)	Energy density‡ (W-hr/lb)	Power density‡ (W/lb)
Carbon black	0.06	0.365	1	4.54	3.832	66.0	7.531	230	4.1
(Ashland Chemical Co.)	0.06	0.274	2	5.20	4.389	54.7	8.285	199	6.6
Shawinigan Black	0.068	0.327	1	5.21	4.395	67.9	8.160	258	4.3
(Shawinigan Chemicals Ltd.)	0.068	0.353	2	4.94	4.168	55.3	7.941	197	8.9
Darco Carbon G-60	0.286	0.897	1	5.29	4.464	65.1	9.120	188	2.9
(Atlas Chemical Ind.)	0.286	1.066	2	4.99	4.207	35.0	8.922	99	6.0
Charcoal Activated, N.F.	0.290	0.694	1	5.14	4.338	49.9	8.831	136	3.2
(S. B. Penick & Co.)	0.290	0.685	2	5.25	4.433	32.0	8.922	81	5.2

* Current densities are based on the geometric area, including both sides, of the cathode.
† Density of electrolyte: 1.5M $LiAlCl_4$-$SOCl_2$ = ~1.69 g/cm^3.
‡ Per cent solvent utilization, energy density, and power density determined by discharging cells to zero volt.

Considering the net cell reaction for cell III to be given by Eq. [5], the amount of C_4F reduced was determined from the total discharge time by use of Faraday's law. Knowing the initial amount of C_4F used, the per cent cathodic efficiencies at current densities of 1, 2, and 5 mA/cm^2 were calculated to be of the order of 402, 316, and 214%, respectively. Such high cathodic efficiencies indicate that even at C_4F cathodes, the main cathodic reaction is probably the reduction of the solvent. Taking the net cell reaction to be given by Eq. [2], the per cent solvent utilization at C_4F cathodes at various current densities was determined as described above. The energy densities and power densities for cell III were also determined. These data are also summarized in Table I.

From the data presented in Table I, it is seen that lithium-inorganic electrolyte cells employing $SOCl_2$ as the solvent yield higher energy densities as well as power densities as compared to the cells employing $POCl_3$ as the solvent. For cells based on $SOCl_2$, higher per cent solvent utilization as well as energy densities and power densities are obtained by using carbon black instead of C_4F as the cathodic material. Further, for cell II, 90% or more of the total cell capacities are delivered at cell voltages of 3V or higher at lower current drains (1-10 mA/cm^2).

Since the lithium-inorganic electrolyte cells discussed above are based solely on the reduction of the inorganic oxychloride solvent, *i.e.*, $POCl_3$ and $SOCl_2$, these cells do not require the use of any additional active cathode material. The reduction of the inorganic oxychloride solvent can presumably be achieved at other inert cathode materials. However, the highly developed surfaces of the cathodes used in this study are required for practical performances. The results reported in Table I were obtained by using carbon black (Ashland Chemical Company) as the cathodic material. However, several other types of carbon obtained from different sources were also used as cathodic materials in the Li/$LiAlCl_4$-$SOCl_2$ (1.5M)/C type cells. The preparative techniques for these cathodes were the same as those already described for carbon black cathodes. Due to the higher bulk density of some of these carbon powders, the weight of the carbon in the cathodes was 2-3 times higher than the weight of carbon black in cathodes of approximately identical size and thickness. The comparative performance of the various carbons was studied at discharge current densities of 1 and 2 mA/cm^2. The data are summarized in Table II.

It is clear from the data presented in Table II that the highest per cent solvent utilization as well as energy densities and power densities are obtained with carbon black cathodes (Ashland Chemical Company and Shawinigan Chemicals Ltd.). The reasons for the superior behavior of carbon black as the cathodic material as compared to other types of carbon are not yet understood in detail but probably involve such physical properties as porosity, wettability, and solvent absorption.

In the study of lithium-inorganic electrolyte cells discussed above, no attempt was made to optimize the weights of carbon black in the cathodes or the amount of electrolyte in the cells. The data presented in Table I, therefore, only demonstrate the feasibility of lithium-inorganic electrolyte cells as a viable power source and show the relative energy densities, power densities, and current carrying capabilities that can be achieved from these systems. It is believed that even higher per cent solvent utilization as well as energy densities and power densities can be achieved by a careful optimization of the weights of carbon black vis-a-vis the weights of the electrolyte in each of the cells studied.

Lithium-organic electrolyte cells.—The following typical lithium-organic cells were investigated to provide a direct comparison of their performance with the lithium-inorganic electrolyte cells under identical experimental conditions

Li | $LiClO_4$ — Propylene carbonate (1 molar) | CF [IV]

Li | $LiAsF_6$ — Methyl acetate (0.75 molar) | CF [V]

The electrode reactions in cells IV and V may be represented as

$$\text{Anode:} \quad Li \rightarrow Li^+ + e \qquad [6]$$

$$\text{Cathode:} \quad CF + e \rightarrow C + F^- \qquad [7]$$

$$\text{Net cell reaction:} \quad Li + CF \rightarrow C + LiF \qquad [8]$$

Typical discharge curves for cells IV and V at various current densities are presented in Fig. 5 and 6, respectively. Both cells showed an open-circuit potential of

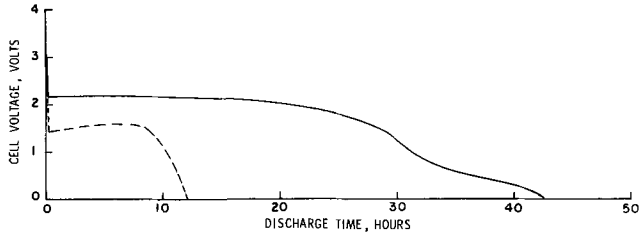

Fig. 5. Discharge curves for the cell: Li/$LiClO_4$-propylene carbonate (1M)/CF; ——— C.D. 1 mA/cm^2 (20 mA discharge current); – – – – C.D. 2 mA/cm^2 (50 mA discharge current).

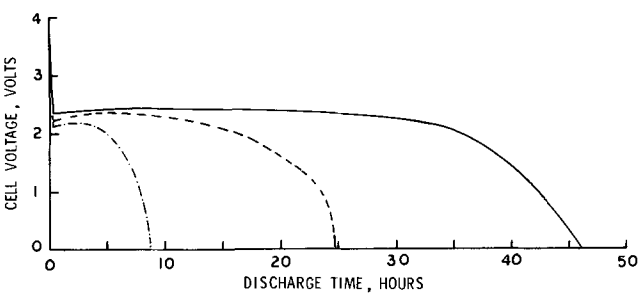

Fig. 6. Discharge curves for the cell: Li/$LiAsF_6$-methyl acetate (0.75M)/CF; ——— C.D. 1 mA/cm^2 (20 mA discharge current); – – – – C.D. 2 mA/cm^2 (40 mA discharge current); —·—·—·— C.D. 5 mA/cm^2 (100 mA discharge current).

Table III. Summary of performance data for lithium-organic electrolyte cells

Cell	Discharge current (mA)	Current density† (mA/cm²)	Weight of CF (g))	Cathodic efficiency‡ (%)	Total cell weight (g)	Energy density‡ (W-hr/lb)	Power density‡ (W/lb)
IV	20	1*	0.804	124.5	7.647	80	1.9
	50	2*	1.117	135.5	7.835	45	3.8
V	20	1*	1.142	86.1	7.351	119	2.6
	40	2*	1.110	101.1	7.432	118	4.8
	60	3	1.177	104.4	7.672	118	6.7
	100	5*	1.100	90.5	7.186	98	11.4
	176	10	0.915	111.3	7.612	79	15.8
	293	15	1.037	94.8	7.444	—	—

† Current densities are based on the geometric areas, including both sides, of the cathode.
‡ Cathodic efficiency, energy density, and power density determined by discharging cells to zero volt.
* The discharge curves for these current densities are plotted in Fig. 5-6. Cell IV: Li|$LiClO_4$-Propylene carbonate (1M)|CF; cell V: Li|$LiAsF_6$-Methyl acetate (0.75M)|CF.

3.45V and exhibited somewhat flat discharge plateaus. At current densities higher than 1 mA/cm², discharge plateaus for cell IV fell well below 2V whereas cell V could be discharged at cell voltages of 2V or higher, up to current densities of 10 mA/cm². The cathodic efficiencies, energy densities, and power densities for cells IV and V were calculated from the experimental data by discharging the cells to zero volt. The results are summarized in Table III. The cathodic efficiencies in cell V were close to 100% but were of the order of 124-135% in cell IV. The higher cathodic efficiencies in cell IV have been attributed (8) to a slight reduction (9) of propylene carbonate following the reduction of graphite fluoride. However, unlike the lithium-inorganic electrolyte cells I-III, the electrochemical reduction of the solvent, *i.e.*, propylene carbonate, in cell IV occurs (9) at a voltage of less than 1V and thus does not contribute significantly to the over-all energy densities.

From a comparison of the energy density and power density data presented in Tables I and III, it is seen that the lithium-inorganic electrolyte cells based on $SOCl_2$ yield higher energy densities as well as power densities and current carrying capabilities than those obtained from lithium-organic electrolyte cells.

Summary and Conclusions

The lithium-inorganic electrolyte cells were investigated and shown to possess higher energy densities and power densities as well as better current carrying capabilities as compared to the lithium-organic electrolyte cells studied. The lithium-inorganic electrolyte cells consist of a lithium anode, solutions of $LiBCl_4$ in $POCl_3$ or $LiAlCl_4$ in $SOCl_2$ as electrolytes, and polytetrafluoroethylene(Teflon)-bonded carbon black cathodes. It was also shown that the lithium-inorganic electrolyte cells are solely based on the electrochemical reduction of the solvents, *i.e.*, $POCl_3$ or $SOCl_2$, and thus do not require the use of any active cathode materials. The lithium-inorganic electrolyte cell, Li/$LiAlCl_4$-$SOCl_2$ (1.5M)/carbon black was found to be superior in performance to other lithium cells studied and yielded an experimental energy density of the order of 244 W-hr/lb for a 57-hr discharge rate (20 mA constant current; 1 mA/cm² current density).

Acknowledgment

The authors wish to thank Miss Rose V. Rinaldi of this Laboratory for her many helpful suggestions.

Manuscript submitted March 28, 1973; revised manuscript received June 15, 1973. This was Paper 59 presented at the Boston, Massachusetts, Meeting of the Society, Oct. 7-11, 1973.

Any discussion of this paper will appear in a Discussion Section to be published in the June 1974 JOURNAL.

REFERENCES

1. J. J. Auborn, A. Heller, and K. W. French, *Proc. 25th Power Sources Symp.*, **25**, 6 (1972).
2. J. J. Auborn, K. French, and A. Heller, Quarterly Report ECOM-0060-1, Contract No. DAAB07-72-0060 (ECOM), GTE Laboratories, Inc., April 1972.
3. J. J. Auborn, K. French, A. Heller, S. Lieberman, and V. Shah, Quarterly Report ECOM-0060-2, Contract No. DAAB07-72-C-0060 (ECOM), GTE Laboratories, Inc., July 1972.
4. N. Watanabe and M. Fukuda, U.S. Pat. 3,536,532, (Oct. 27, 1970).
5. H. Spandau, A. Beyer, and F. Preugschat, *Z. Anorg. Allgem. Chem.*, **306**, 13 (1960).
6. W. K. Behl and J. A. Christopulos, To be published.
7. R. P. Martin and D. T. Sawyer, *Inorg. Chem.*, **11**, 2644 (1972).
8. H. F. Hunger and G. Heymach, *This Journal*, **120**, 1161 (1973).
9. A. N. Dey and B. P. Sullivan, *This Journal*, **117**, 222 (1970).

Chemical and Electrochemical Behavior of Lithium Electrodes in Dimethyl Sulfite, Electrolytic Solutions

William H. Tiedemann*,[1] and Douglas N. Bennion*

Energy and Kinetics Department, School of Engineering and Applied Science, University of California, Los Angeles, California 90024

ABSTRACT

Lithium has been shown to be chemically stable in dry $LiClO_4$-dimethyl sulfite solutions. If water is present above 20 ppm, the lithium reacts with the solution to form hydrogen gas and Li_2SO_3. Lithium electrodes are shown to exhibit two levels of electrochemical activity in $LiClO_4$-dimethyl sulfite solutions. The lower exchange current densities are attributed to film formation on the lithium due to trace water concentrations. For water concentrations below 500 ppm, the film can be removed by a 20 sec, 20 mA/cm^2 anodic pulse. The exchange current density, i_o, on a film free surface is 15 mA/cm^2 for a 1.12M $LiClO_4$ solution. The transfer coefficient, α, is 0.49.

Lithium metal is an attractive choice as a battery negative because of its low equivalent weight and its chemical behavior as a strong reducing agent. Beginning in the 1960's, studies were undertaken to find solvent-electrolyte systems in which lithium was stable and behaved electrochemically in a reversible manner (1, 2).

Studies in 1M $LiClO_4$-propylene carbonate (PC) by Burrows and Jasinski (3) indicate that the Li/Li^+ electrode behaves as a suitable reference electrode. Cogley and Butler (4) have shown lithium amalgam electrodes to be reversible in lithium chloride-dimethyl sulfoxide (DMSO) solutions. Butler *et al.* (5) have shown that in $LiClO_4$-PC solutions the exchange current density for the Li/Li^+ electrode decreases with increasing water content. They also observed that for constant water content the exchange current density decreased with time following a current pulse. These experiments did not allow a distinction between the effects of recrystallization of the cold-worked surface or film formation on the surface. Early studies of the effects of water in nonaqueous electrolytic solutions (6) dealt mainly with cathodic deposition of lithium.

Burrows and Kirkland (7) showed that strong complexing between Li^+ and water present in quantities below 500 ppm decreased the activity coefficient of the water. They also detected a film on the lithium surface which was postulated to be LiOH. Dey (8), working in $LiClO_4$-PC solutions, also observed a film on the lithium surface which could be removed by anodic polarization. Dey reports the film composition may be Li_2CO_3 and that the lithium ion has a transference number of one in the film. Scarr (9), also working in $LiClO_4$-PC solutions, has shown that, depending on pretreatment, lithium electrodes exhibit two levels of electrochemical activity. The observed behavior was believed due to a film which can be removed at high current densities and whose formation is sensitive to water concentration. Jackson and Blomgren (10) have also considered the effects of possible film formation on lithium electrode behavior.

Meibuhr (11, 12) examined the kinetics of the solid lithium electrode in $LiClO_4$-PC as a function of temperature. For the range of current densities, temperature, and $LiClO_4$ concentrations studied, the anodic and cathodic polarization data were symmetrical. No mention of film formation or dual activity was made.

The possible existence of a protecting film on the lithium surface suggests two types of stability. The film can protect the lithium from chemical reaction with the solvent during inactive times. However, electrochemical stability or lack of corrosion reactions during cathodic or anodic operation of a lithium electrode must be considered separately. The existence of this electrochemical stability might be demonstrated by (*i*) reversible or Nernst-type response to changes in lithium ion concentration, (*ii*) extended anodic and cathodic polarization tests in which no decomposition products can be detected, and (*iii*) cyclic tests which yield high coulombic efficiency for anodic dissolution and cathodic deposition.

It has been demonstrated (13-16) that dimethyl sulfite (DMSU) is a potentially useful, nonaqueous battery solvent. In the present study, two aspects of the behavior of lithium in electrolytic solutions in dimethyl sulfite have been investigated. The chemical stability of lithium in DMSU-$LiClO_4$ and DMSU-$LiCF_3SO$ solutions containing controlled amounts of water below 3000 ppm has been measured including analysis of reaction products. The electrochemical stability has been measured with special emphasis on the effects of trace amounts of water, the exchange current density, and characterization of film formation on lithium electrodes.

Experimental Equipment and Procedure

All experiments were performed in a VAC dry box equipped with oxygen, nitrogen, and water removal trains in an argon recirculating atmosphere. The temperature of the dry box was maintained at 28° ± 1°C with an auxiliary heater and controller. The chemical stability tests were run on six systems: (*i*) DMSU-lithium, (*ii*) DMSU-lithium-$LiClO_4$, (*iii*) DMSU-lithium-$LiCF_3SO_3$, (*iv*) DMSU-lithium-$LiCF_3SO_3$-H_2O, (*v*) DMSU-lithium-$LiClO_4$-H_2O, and (*vi*) DMSU-lithium-H_2O. The first three systems had water contents of about 50 ppm as determined by Karl Fischer titration (13, 17-19). Known amounts of water were added to the solutions and titration procedures standardized. The last three systems contained less than 3000 ppm water. Two types of cells and procedures were used to determine chemical stability. The first was a glass vessel from which liquid samples could be withdrawn periodically by inserting a syringe through a rubber port. The solution did not contact the rubber directly. No degradation of the rubber was observed. Water content of the samples was measured and recorded as a function of time. The second cell was also a glass vessel arranged so that gas evolution from the system could be monitored quantitatively with time. The gas was collected by displacement of vacuum pump oil in an inverted burette. The gas samples were analyzed using a mass spectrometer. The white precipitate which formed was analyzed as summarized in the Results section. The cells contained approximately 100 ml

* Electrochemical Society Active Member.
[1] Present address: Globe-Union, Inc., Milwaukee, Wisconsin 53201.
Key words: batteries, lithium, dimethyl sulfite, nonaqueous electrolytic solutions.

of solution to which 2g of freshly cut lithium rod, diced to ⅛-in. cubes, were added.

The electrochemical polarization tests were made using a lithium wire as the reference electrode. Data of Burrows and Jasinski (3) and Meibuhr (11) indicated that lithium behaves as a suitable reference electrode in $LiClO_4$-PC solutions. It was also found to work well in DMSU solutions as shown in the Results section.

Lithium electrodes were prepared by inserting a freshly cut lithium disk into a heavy wall glass tube of about 1 cm ID. The tube containing the lithium disk was placed on a clean, polished, flat nickel plate. While the tube was firmly held against the plate, a rod was inserted from the top of the tube and pressed against the lithium disk. The pressure caused the lithium to flow to meet the wall of the tube providing a liquid tight seal and a flat lithium surface of well-defined surface area. The electrode was stored in a vacuum container inside the dry box until the experiments were run.

Some experiments were run by dipping the electrode holder directly into the electrolytic solution. However, nonuniform current distribution and difficulties in correcting for resistance losses in the solution arise for this geometry (20). In order to realize uniform current density and a negligible resistance loss, a special cell was built to hold the electrode as shown in Fig. 1. This cell is similar to one described by Kahan *et al.* (21). The reference electrode was in side compartment D. The liquid junction contact between the main compartment and the reference electrode compartment was in the plane of the test electrode along ledge F. In order to eliminate concentration polarization, pulse currents were applied. The pulses were long compared to double layer charging times and short compared to the time needed for significant concentration changes to occur at the test electrode face.

Lithium is known to attack glass at elevated temperatures. However, for the duration of these experiments at room temperature, no attack of the glass was noted.

Continuous polarization experiments were performed in a cell filled with 100 ml of solution containing previously measured concentrations of water and electrolyte. The solution was stirred with a coated, magnetic stirring bar. No significant temperature variations (less than ± 1°C) were observed when a thermometer was placed next to the cell. A Luggin capillary tube containing a lithium reference electrode was placed at the edge of the disk in the plane of the disk. The working electrode was pulsed with an anodic current of 20 mA/cm² for 10 sec to remove any film. The counter-electrode was a 0.5 × 0.065 in. lithium ribbon cylinder (Foote Mineral Company) at the bottom of the cell.

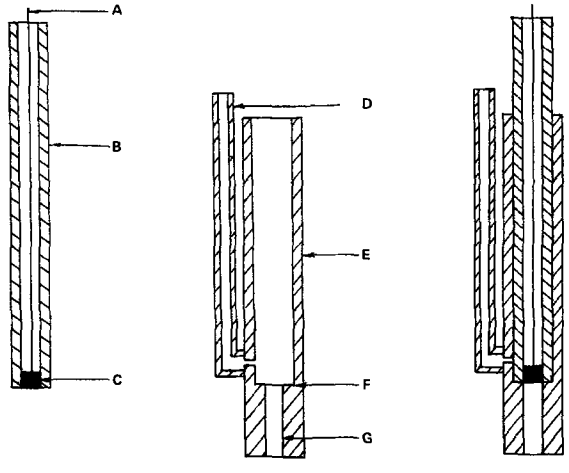

Fig. 1. Cell design for uniform current distribution and iR-free polarization measurements. A = electrode contact wire, B = electrode holder, C = electrode specimen, D = reference electrode, E = positioning tube, F = precision ground ledge, G = same diameter as specimen.

Current was increased anodically or cathodically and then decreased back to zero. Less than 30 sec were needed to establish steady state for each reading. Ohmic potential corrections were made as described elsewhere (20).

Micropolarization current pulse experiments were performed using the complete cell assembly shown in Fig. 1 dipped into a container holding about 100 mliters of solution. Galvanostatic pulses of 1-10 msec with a rise time of 5 μsec were applied. The potential between the reference and working electrode was observed on an oscilloscope. Clear separation between double layer charging and the beginning of concentration overpotential was obtained. No mass transfer effects were observed until times greater than 20 msec at 2 mA/cm². Prior to the test pulses, an anodic pulse of 20 mA/cm² was generally applied for 20 sec to remove any film unless behavior in the presence of a film was being examined.

Further details of the experimental equipment and materials are available elsewhere (22).

Results

The chemical stability of lithium in a 1.2M $LiClO_4$ solution in DMSU containing 1000 ppm water is characterized by the gas evolution rate following lithium addition to the solutions. The initially shiny lithium surface began to turn dull 2-8 hr after lithium was added, depending on initial water content, and a white precipitate began to form. After five days, the rate of gas evolution was too slow to detect. Freshly cut lithium was added to the solution at the end of 200 hr. No further reaction could be detected. The $LiClO_4$ solutions were colorless. Similar experiments with $LiCF_3SO_3$ produced solutions which were light yellow. A mass spectrometer analysis of the gas showed it to contain 80% hydrogen, trace quantities of ethane or a molecule which behaves similarly to ethane in a mass spectrometer, and the rest argon. The rate of gas evolution depends on stirring rate, suggesting a liquid phase diffusion step is rate limiting.

The quantity of gas collected as a function of the water initially present in the solution is shown in Table I. The nearly constant ratio of 22.4 liters of gas per mole of water indicates that one mole of water was producing one mole of hydrogen in the reaction which was being observed.

In separate experiments, the water content was measured as a function of time as shown in Fig. 2. After five days the water content was below the detection limit of 10-20 ppm.

A series of tests were run to determine the composition of the white precipitate. The results are summarized in Table II. In each case the test was specific for Li_2SO_3. It may be that the lithium sulfite was hydrated, the tests were not specific enough to determine water associated with the salt.

Solutions 1, 2, and 3 which initially contained less than 50 ppm water showed no observable reaction with the lithium except for a very light precipitate. One solution has been under observation for two years. No observable change has taken place; the lithium appears dull but metallic. For similar long-term tests with

Table I. Volume of gas collected for different H_2O and $LiClO_4$ concentrations

Concentration of $LiClO_4$, M	Weight of solution tested, g	H_2O concentration of solution, ppm	Volume of gas collected at 28°C, liters	Moles of H_2O in solution	Ratio of volume of gas collected to moles of H_2O, liters/mole
2.9	71.44	2900	0.242	0.0115	21.0
2.4	40.5	3900	0.180	0.0088	20.4
1.2	35.0	1000	0.044	0.00195	22.6
0.0	60.0	1000	0.072	0.0330	21.8
2.92	70.7	2950	0.280	0.0116	24.1

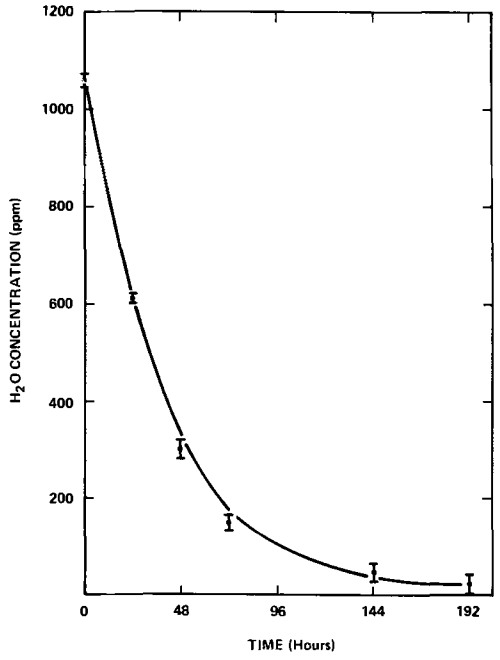

Fig. 2. H_2O content in 127g of a 1M $LiClO_4$ solution contacted with approximately 2g of lithium chips as a function of time. T = 28°C, solution volume = 100 ml.

$LiCF_3SO_3$ as the electrolyte, the solution turned a yellow-brown after a few weeks.

In a separate test, LiOH was added to pure dimethyl sulfite and stirred. Over a three week observation period, no gas evolution was observed, and Li_2SO_3 was subsequently identified in the precipitate.

Results of pulse, micropolarization tests for anodic current pulses at various concentrations are shown in Fig. 3; similar results for cathodic pulses are shown in Fig. 4. Results for the steady polarization of the plane electrode in a stirred solution are not shown. The large correction factor (20) made these results less accurate. However, to within the accuracy of those measurements, the results are in agreement with the more accurate results shown in Fig. 3 and 4.

Figures 3 and 4 are clearly within the linear polarization-current region

$$i = i_o \frac{\mathbf{F}}{RT} \eta \qquad [1]$$

The slopes of the curves in Fig. 3 and 4 as well as the plane disk electrode results were used to determine i_o as a function of concentration. The results are shown in Fig. 5 on a log-log plot. The importance in making a correction for nonuniform current distribution (20) is shown by comparison of the two triangular shaped points. The fact that the results for the electrode stored for ten days (the square point) falls within the error limits of the data taken with freshly prepared samples

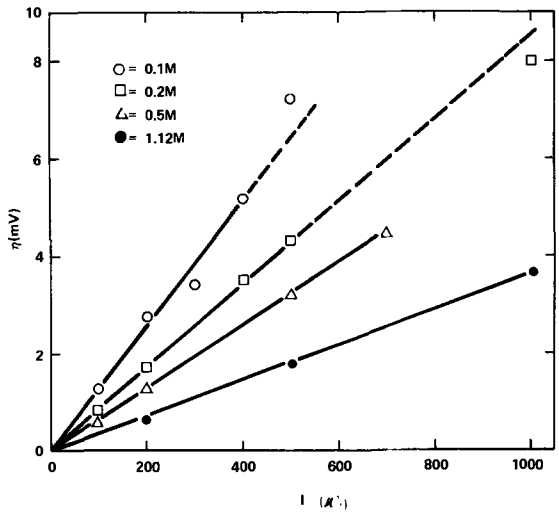

Fig. 3. Pulse, anodic, linear polarization for various concentrations of $LiClO_4$-$(CH_3O)_2SO$. Area = 0.486 cm^2, H_2O content < 20 ppm, T = 28°C.

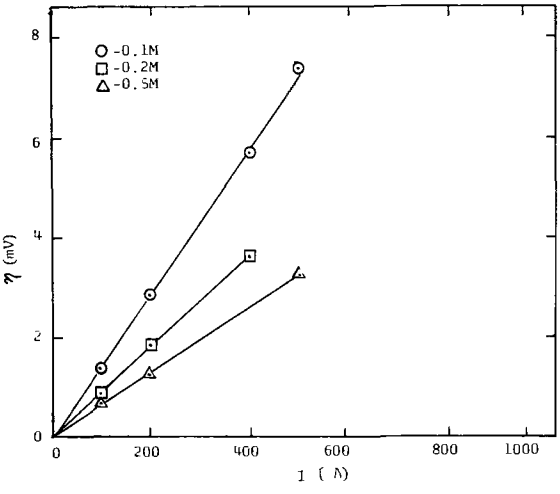

Fig. 4. Cathodic pulse polarization for various concentrations of $LiClO_4$-$(CH_3)_2SO$, area = 0.486 cm^2, H_2O content < 20 ppm, T = 28°C.

indicates that effects of surface strain could not be detected.

If the reaction is a simple, one-electron transfer with the charge transfer step rate controlling, it can be shown (22, 23) that the transfer current density is related to concentration as follows

$$i_o = k_a^{(1-\alpha)} k_c^{\alpha} c^{\alpha}$$

where k_a and k_c are the kinetic rate constants for the anodic and cathodic rates, respectively, c is the concen-

Table II. Comparison of tests of precipitates with $Li_2SO_3 \cdot H_2O$

	$Li_2SO_3 \cdot H_2O$	Precipitates of			Precipitates of Sol. 5	
		Solution 4	Solution 5	Solution 6	1000 ppm H_2O	3000 ppm H_2O
Color	White	White	White	White	White	White
Solubility in organic solvents	Insoluble	Insoluble	Insoluble	Insoluble	Insoluble	Insoluble
Solubility in H_2O	Very soluble	Very soluble	Very soluble	Very soluble	Very soluble	Very soluble
pH of aqueous liquid weights	8.6	8.4	8.8	8.6	8.7	9.0
Temperature of H_2O dehydration	140°C	145°C	140°C	145°C	140°C	145°C
Temperature at which salt decomposes	~450°C	~455°C	460°C	450°C	450°C	455°C
Per cent of lithium in precipitate*	14.8 (2 samples tested)	14.9 (6 samples tested)	14.8 (8 samples tested)	14.7 (5 samples tested)	14.9 (3 samples tested)	14.9 (6 samples tested)
Presence of Cl^-	$<10^{-5}$M	$<10^{-5}$M	$<10^{-5}$M	$<10^{-5}$M	$<10^{-5}$M	$<10^{-5}$M
Solubility in $AgClO_4$ solutions	Slightly soluble	Slightly soluble	Slightly soluble	Slightly soluble	Slightly soluble	Slightly soluble
Solubility in $Ba(ClO_4)_2$ solutions	**	**	**	**	**	**

* Contacted with MeOH for 24 hr then vacuum dried at 160°C for 24 hr.
** Forms a large, white precipitate which dissolves in dilute HCl with SO_2 gas evolved.

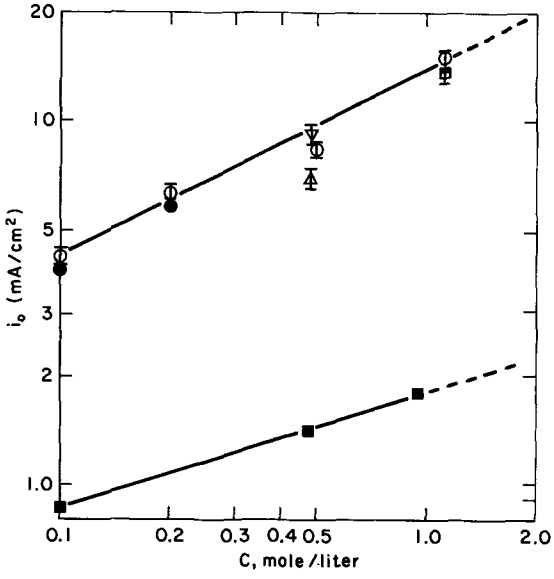

Fig. 5. Plot of i_0 for various experimental conditions, $T = 28°C$. ○ = Uniform current distribution (iR-free) anodic; ● = uniform current distribution (iR-free) cathodic; △ = disk electrode (iR-free); ▽ = disk electrode (iR-free plus correction for nonuniform current distribution); □ = electrode stored for 10 days before testing (uniform current distribution); ■ = H_2O content of 500 ppm.

tration of the lithium ion, and α is the transfer coefficient. From the least squares slope of the upper curve in Fig. 5, the transfer coefficient is found to be 0.49.

All of the electrochemical polarization data discussed above was taken in solutions with below 50 ppm water and using a 20 mA anodic, prepolarization pulse. In solutions with higher water content, comparing data taken with and without a prepolarization pulse, the apparent exchange current density increases when the prepolarization is omitted as shown in Fig. 6. In Fig. 7 is shown the variation of the overpotential with time for constant current pulses following a prepolarization pulse. Above 500 ppm water content a prepolarization pulse will no longer yield the higher exchange current density current-voltage behavior. A log-log plot of the apparent exchange current as a function of $LiClO_4$ concentration for a wet solution (500 ppm water) is shown as the lower curve in Fig. 5.

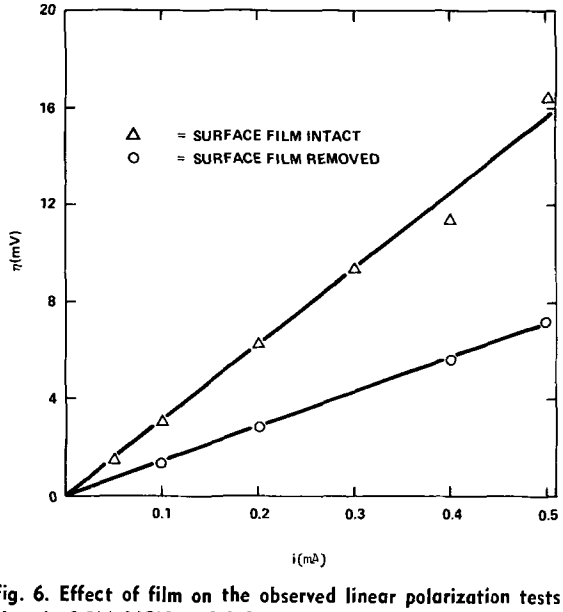

Fig. 6. Effect of film on the observed linear polarization tests on lithium in 0.1M $LiClO_4/(CH_3O)_2SO$, area = 0.468 cm², H_2O content = 100 ppm, $T = 28°C$.

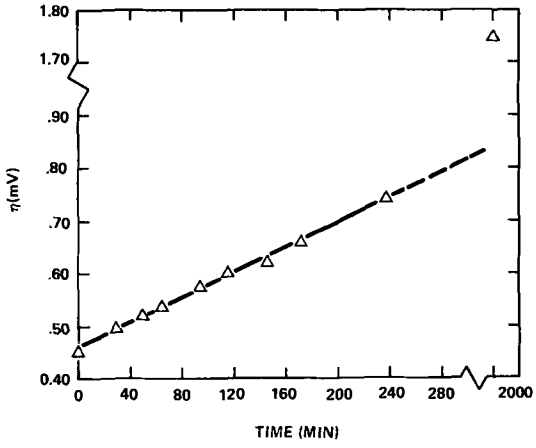

Fig. 7. Observed overpotential variation with time for a constant current pulse. $I = 50$ μA, area = 0.468 cm², C = 0.2M, H_2O = 200 ppm, $T = 28°C$.

Discussion

The results of the chemical stability tests suggest that $LiClO_4$-DMSU solutions are stable with lithium or at least that reaction rates are not observable, except for a thin film formation or dulling of the surface, for up to two years provided the water content is below about 20 ppm. It appears that dry $LiCF_3SO_3$-DMSU solutions react slowly with lithium. Results of other workers (24-27) also suggest that such a conclusion is at least reasonable.

The chemical behavior of the aliphatic sulfides and the effects of water, various electrolytes, and alkali metals have been studied by numerous workers (28, 39). Cottrell and Mann (31) found that when perchlorates were present Cl^-, CO, and $NaCH_3SO_3$ were slowly formed. In our experiments, no Cl^- was detected in the precipitate and H_2 was evolved, not CO, indicating that the perchlorate was not involved in the reaction which we observed. Cottrell and Mann also observed different reaction products depending on water concentration. In the present study, the reaction product composition was independent of the water present, and the same product was observed in the absence of perchlorate ions implying that the perchlorate was not involved. Possibly the differences between this work and that of Cottrell and Mann are due to inherent greater stability of the sulfur bonds in dimethyl sulfite toward reaction with lithium compared to the compounds studied by Cottrell and Mann. Such variations in sulfur bond stability have been observed previously in this laboratory (40).

O'Connor and Lyness (36) observed that sodium and potassium appear to attack DMSO directly forming salts of methanesulfenate and methylsulfinyl carbanion along with methane and dimethyl sulfide. This type of attack does not appear to occur between lithium and dimethyl sulfite. The formation of hydrogen and subsequent decrease in water concentration indicates that it is the water which reacts directly with lithium to form hydrogen. Since no significant quantities of OH^- ions were found in the precipitate, it is reasonable to assume LiOH or Li_2O are at best intermediate species. It has been shown (29, 30) that the addition of dimethyl sulfite to aqueous KOH solutions results in the formation of K_2SO_3 (the reaction is complete). Our test of adding LiOH to dimethyl sulfite solutions yielded Li_2SO_3. From these results it is concluded that lithium first reacts with water, and an intermediate, possibly LiOH or Li_2O, reacts with dimethyl sulfite to form Li_2SO_3. This implies that in dry dimethyl sulfite solutions lithium is chemically stable, and such systems can be considered for secondary battery applications.

Film formation on lithium electrodes in $LiClO_4$-PC solutions has been considered by Dey (8), Scarr (9), Burrows and Kirkland (7), and Cogley and Butler

(4). Originally the composition of the film was considered to be LiOH (11). However, Dey (8) has suggested that in $LiClO_4$-PC solutions the film composition is more likely Li_2CO_3. The results of the present study indicate that a film formed in $LiClO_4$-DMSU solutions is probably Li_2SO_3.

Scarr (9) observed two levels of lithium activity in $LiClO_4$-PC solutions which were explained by the presence or absence of a surface film on the lithium. An anodic pulse of 3-5 mA/cm^2 or greater appears to remove the film. The lithium has a higher exchange current density with the film removed. Once removed, the film re-forms. These results in PC compare well with our observations for DMSU. The rate of film formation is implied in Fig. 7. The value of the exchange coefficient, α, of 0.55 in PC compares favorably with our observations of 0.49 in DMSU solutions. Scarr reports the higher value of the exchange current density, i_o, to be 1.22 mA/cm^2 in a 0.5M $LiClO_4$-PC solution. Our study in DMSU gives an i_o of 9.7 mA/cm^2 at 0.5M $LiClO_4$ (see Fig. 5). Scarr chose to locate his reference electrode near the edge and in the same plane as the working electrode. As shown by Tiedemann *et al.* (20), the observed overpotential for such a geometry can be four times as high as is characteristic of the average current density. If one attempts to correct Scarr's results for the nonuniform current density, reference electrode placement, and concentration polarization (22), a value of i_o equal to about 7 mA/cm^2 at a $LiClO_4$ concentration of 0.5M is obtained.

Butler *et al.* (5) performed experiments in $LiClO_4$-PC solutions on freshly cut lithium surfaces and obtained an i_o of 8 mA/cm^2 in a 0.257M solution. This value compares well with the results in DMSU (see Fig. 5). Butler *et al.* were concerned about possible recrystallization effects following slicing of the lithium. In our study, effects of recrystallization could not be detected; note the square point in Fig. 5. Comparing results of these experiments implies that recrystallization of fresh lithium slices occurs in a matter of seconds as is the case for lead and tin (41).

Acknowledgment

Financial support for this work was provided in part by Naval Air Systems Command on Contract No. N00019-71-C-0342.

Manuscript submitted Feb. 26, 1973; revised manuscript received July 5, 1973. This was Paper 44 presented at the Cleveland, Ohio, Meeting of the Society, Oct. 3-7, 1971.

Any discussion of this paper will appear in a Discussion Section to be published in the June 1974 JOURNAL.

REFERENCES

1. R. Jasinski, *J. Electroanal. Chem.*, **15**, 89 (1967).
2. R. Jasinski, *Electrochem. Technol.*, **6**, 28 (1968).
3. B. Burrows and R. Jasinski, *This Journal*, **115**, 365 (1968).
4. D. R. Cogley and J. N. Butler, *ibid.*, **113**, 1074 (1966).
5. J. N. Butler, D. R. Cogley, and J. C. Synnott, *J. Phys. Chem.*, **13**, 4026 (1969).
6. A. S. Meyer, Jr. and C. M. Boyd, *Anal. Chem.*, **31**, 215 (1950).
7. B. Burrows and S. Kirkland, *This Journal*, **115**, 1164 (1968).
8. A. N. Dey, Abstract 62, p. 154, Electrochem. Soc. Extended Abstracts, Fall Meeting, Atlantic City, N. J., Oct. 4-8, 1970.
9. R. F. Scarr, *This Journal*, **117**, 295 (1970).
10. G. W. Jackson and C. E. Blomgren, *ibid.*, **116**, 1483 (1969).
11. S. G. Meibuhr, *ibid.*, **117**, 56 (1970).
12. S. G. Meibuhr, General Motors Corp. Research Pub., GMR-1005 (1970).
13. N. P. Yao, E. D'Orsay, and D. N. Bennion, *This Journal*, **115**, 999 (1968).
14. J. S. Dunning, W. H. Tiedemann, and D. N. Bennion, *ibid.*, **118**, 1886 (1971).
15. W. H. Tiedemann and D. N. Bennion, *J. Chem. Eng. Data*, **16**, 368 (1971).
16. Z. I. Mirza, M. S. Thesis, University of California, Los Angeles, June 1970.
17. E. E. Archer and H. W. Jeater, *Analyst*, **90**, 351 (1965).
18. A. S. Meyer, Jr. and C. M. Boyd, *Anal. Chem.*, **31**, 215 (1959).
19. J. Mitchell, Jr., *ibid.*, **23**, 1069 (1951).
20. W. H. Tiedemann, J. Newman, and D. N. Bennion, *This Journal*, **120**, 256 (1973).
21. B. D. Cahan, Z. Nagy, and M. A. Genshaw, *ibid.*, **119**, 64 (1972).
22. W. H. Tiedemann, Ph.D. Dissertation, University of California, Los Angeles, January 1972. Also issued as UCLA-ENG-7228 Final Report to U.S. Navy on Contract N00019-71-C-0342, April 1972.
23. John Newman, "Electrochemical Systems," pp. 171-178, Prentice Hall, Inc., Englewood Cliffs, N. J. (1973).
24. P. L. Allen and A. Hickling, *Trans. Faraday Soc.*, **53**, 1626 (1957).
25. A. Arbusow, *Chemisches Zentralblat*, **1909II**, 684 (1909).
26. W. E. Bissinger, F. E. Krug, and C. W. Hamilton, *J. Am. Chem. Soc.*, **70**, 3940 (1948).
27. R. D. Brooks, R. A. Durie, and H. Silberman, *Australian J. Chem.*, **17**, 55 (1964).
28. D. R. Cogley and J. N. Butler, Final Report, to U.S. Air Force, Contract AF19(628)5525, 1968.
29. von L. Carius, *Annalen der Chemie und Pharmacie*, **110**, 209 (1859).
30. von L. Carius, *ibid.*, **111**, 93 (1859).
31. P. T. Cottrell and C. K. Mann, *This Journal*, **116**, 1499 (1969).
32. D. J. Cram, *J. Am. Chem. Soc.*, **15**, 332 (1953).
33. E. E. Gilbert, "Sulformation and Related Reactions," Interscience Publishers, Inc., New York (1965).
34. E. C. E. Hunter and J. R. Partington, *J. Chem. Soc., London*, **1933**, 309.
35. R. C. Passerini, "Ultraviolet Absorption Spectra of Organic Sulfur Compounds," N. Khavasch, Editor, "Organic Sulfur Compounds," *Vol. 1*, Chap. 7, Pergamon Press, New York (1961).
36. D. E. O'Connor and W. I. Lyness, *J. Org. Chem.*, **30**, 1620 (1965).
37. J. P. Reinheimer, W. F. Kieffer, S. W. Frey, J. C. Cochran, and E. W. Barr, *J. Am. Chem. Soc.*, **80**, 164 (1958).
38. C. M. Suter, "The Organic Chemistry of Sulfur Tetracovalent Sulfur Compounds," John Wiley & Sons, Inc., New York (1944).
39. S. Winstein and G. C. Robinson, *J. Am. Chem. Soc.*, **80**, 169 (1958).
40. D. N. Bennion, N. P. Yao, and E. D'Orsay, Interim Report No. 2 to U.S. Army, Contract No. DA-44-009-AML-1661(T), September 1967.
41. A. Phillips and R. M. Brick, "Structure and Properties of Alloys," 2nd ed., p. 111, McGraw-Hill Book Co., New York (1942).

Stress Corrosion Cracking Behavior of Precracked 18-8 Stainless Steel

R. T. Newberg* and H. H. Uhlig†

Department of Metallurgy and Materials Science, Massachusetts Institute of Technology, Cambridge, Massachusetts 02139

ABSTRACT

The critical potential is measured below which cracks in 18-8 exposed to $MgCl_2$, 130°C, no longer propagate. Some inhibiting ions, effective for crack initiation, are also evaluated with respect to crack growth. A surface oxide film is found to slowly form on stainless steels exposed to $MgCl_2$ solution; its role both in crack initiation and in crack growth is evaluated.

The importance of using precracked specimens to evaluate the stress corrosion cracking (SCC) behavior of titanium alloys in NaCl solutions at room temperature was first pointed out by Brown (1). He showed that cracks did not initiate in smooth stressed specimens, whereas cracks continued to propagate in specimens partially precracked by fatigue. The effect is usually ascribed to the stable passive film on titanium alloys which under normal exposure conditions in aerated neutral chloride solutions is not broken down, whereas, with continuing plastic flow, fresh metal is exposed. Furthermore, within a crevice, both low oxygen concentration caused by continuing uniform corrosion of metal, and acid anodic corrosion products induce breakdown of the passive film or prevent its reformation, and hence the crack process continues. It is of interest to learn whether similar conditions affect initiation and propagation of stress corrosion cracks in the stainless steels which also show pronounced passive behavior.

Results have shown that cracks in austenitic (2, 3) and ferritic stainless steels (4) initiate only above a well-defined critical potential. Pertinent questions are: does a critical potential also exist below which a crack stops propagating? Is such a potential the same as for crack initiation? Do inhibitors, effective for preventing initiation of SCC, also inhibit crack growth?

Experimental

Materials used for test specimens consisted of commercial Type 304 stainless steel of the following composition: 18.8% Cr, 9.2% Ni, 1.5% Mn, 0.06% C, 0.05% N, or Type 310 stainless steel of the composition: 24.8% Cr, 19.5% Ni, 1.7% Mn, 0.03% C, 0.05% N. The sheets originally 1/16-in. thick were cold rolled to 40-42 mil (0.102-0.107 cm) thick strip, and sheared to specimens measuring 1 3/4 × 3/16 in. (4.5 × 0.5 cm). After pickling in 15 v/o (volume per cent) HNO_3, 5 v/o HF at 90°C for 5 min, these were then tested as cold rolled or as heated in argon to 1050°C for 30 min and water quenched. They were stressed beyond the elastic limit to the shape of a C having a final span of 1 7/16 in. (3.7 cm), and held by porcelain insulators at constant flow stress by spring loading. Failure times were recorded by an electric clock. Electrical connection was made by means of a stainless steel wire of the same composition as the specimen, spot-welded to one end, and enclosed by closely fitting Teflon tubing.

The usual test solution was $MgCl_2$ solution boiling at 130°C, or LiCl solution boiling at 145°C. The electrolyte was contained in a Pyrex flask connected by means of a ground glass joint to a water-cooled condenser. Three side arms, separated from the main flask by glass frit separators, were filled with the same or more dilute electrolyte solution; two accommodated auxiliary electrodes and one a saturated calomel reference electrode, the latter being located near the surface of maximum stress in the test specimen. The detailed design of the apparatus was depicted in a previous publication (3). In general, failure times of stressed specimens were noted for a variety of fixed potential differences between the specimen and the saturated calomel electrode, the potential during the test being controlled by a potentiostat. The potential, determined within ± 3 mV, at or below which failure by SCC did not initiate for at least 100 hr was defined as the critical potential. It is reported on the standard hydrogen scale, neglecting small liquid junction and thermal gradient potentials. The applied potential required to stop crack growth was assessed by precracking a specimen for a fraction of an hour slightly above the critical potential, then polarizing the specimen up to 100 hr at various potentials below the critical value, followed by polarizing again to a potential slightly above the critical value until total failure occurred.

Results

Critical potential for crack initiation and crack propagation.—The critical potentials for crack initiation in smooth quenched 18-8 stainless steel exposed to $MgCl_2$ boiling at 130° and at 154°C are shown in Fig. 1. The value, −0.128 ±0.003V (SHE), is the same for the two concentrations of $MgCl_2$ within experimental variations of the test.

No cracks were found to initiate in stressed specimens polarized in $MgCl_2$ at 130°C for as long as 100 hr at or below the critical potential; for comparison the normal failure time of specimens not polarized is

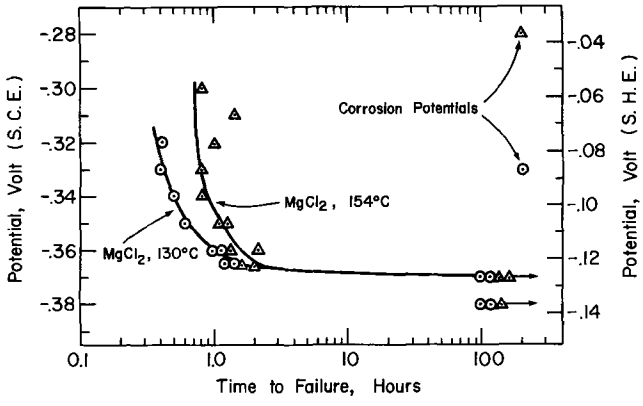

Fig. 1. Effect of applied potential on time to failure of 18-8 stainless steel, water quenched from 1050°C, in $MgCl_2$ at 130° and 154°C.

* Electrochemical Society Student Associate.
† Electrochemical Society Active Member.
Key words: oxide films on stainless steels, inhibitors of stress corrosion cracking, stress-sorption cracking, critical potentials for stress corrosion cracking.

1.4 ± 0.2 hr (3 specimens). Of importance is the observation that precracked specimens also polarized 5 mV below the critical potential do not fail within the maximum time of test equal to 100 hr. The specimens were precracked to a depth of 0.005-0.010 in. (0.013-0.025 cm) (as determined microscopically) by immersion for 0.2 or 0.3 hr in $MgCl_2$ at 130°C at a potential of −0.118V, which is 10 mV above (noble to) the critical potential (Fig. 2). This result means that even though visible shallow cracks have initiated, they will not propagate at applied potentials below the critical potential for crack initiation. Hence the critical potential for crack propagation is approximately the same as that for crack initiation.

It was observed that when smooth stressed specimens are prepolarized for several hours at 5 mV below the critical potential, the subsequent time to failure at a potential 10 mV above the critical value results in failure times that are longer than for specimens not prepolarized. The longer the time of prepolarization below the critical potential, the longer is the subsequent time to failure above the critical potential. The longer failure time following prepolarization is apparently the result of a prolonged induction time for crack initiation caused by slow build-up of a surface oxide (or basic chloride) film on exposure of stainless steels to the $MgCl_2$ solution. This explanation was supported by experiments in which specimens were pickled in the 15 v/o HNO_3, 5 v/o HF mixture at 90°C for 1 min after polarizing below the critical potential (without removing the specimen from the test apparatus) and noting the same short failure times as are observed for specimens not prepolarized.

The surface oxide film, which on long exposure times becomes thick enough to exhibit interference colors, also temporarily delays crack growth of precracked specimens, although not to the same extent as it delays crack initiation. The deeper the crack, the longer is the delay time caused by accumulation of oxide. But again, pickling the precracked specimens after polarization below the critical potential eliminated the observed delay in crack growth. Leckie (5) found similarly that prolonged cathodic polarization of a precracked Ti alloy in 3% NaCl increased subsequent failure time because of an accumulated surface oxide. The effects on 18-8 stainless steel are summarized in Table I.

Induction time for crack initiation.—Although an artificially produced thick surface film, as described, can appreciably slow down time for crack initiation or for resumption of crack growth, any thin oxide film formed on 18-8 or 25-20 stainless steel for a short time under normal exposure conditions at the corrosion potential has less effect. One of the properties of a growing surface oxide film resulting from normal exposure of stainless steels to $MgCl_2$ solution, as Lee and Uhlig showed (3), is to slowly shift the corrosion potential in the noble direction. At such time as the corrosion potential becomes equal to or noble to the critical potential, a crack is able to initiate. The time for the slow drift plus the additional time for crack initiation after critical and corrosion potentials coincide is the normal induction time.

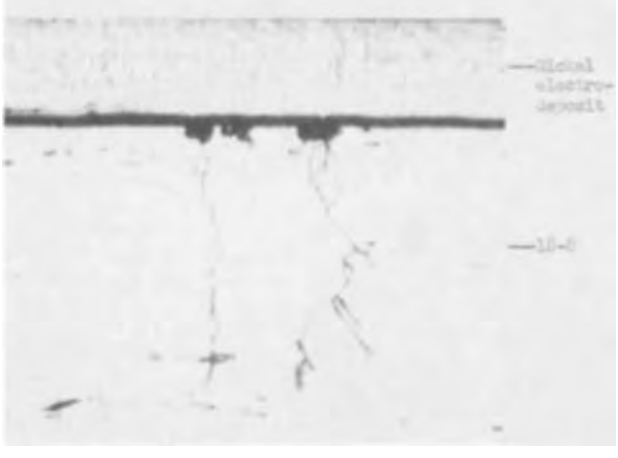

Fig. 2. Precracked 18-8 stainless steel specimen, water quenched from 1050°C, 18 min at −0.118V (SHE). ×300.

Table I. Effect of applied potential on crack propagation in 18-8 stainless steel, $MgCl_2$ 130°C*

Initial polariz. at −0.118V (above crit. pot.), hr	Subsequent polariz. at −0.133V (below crit. pot.), hr	Failure time after polariz. again at −0.118V, hr	Total failure time at −0.118V, hr
0	20	9.9	9.9
0	20	6.5	6.5
0	100	32.4	32.4
0	100	37.4	37.4
0.2	20	0.2	0.4
0.2	20	1.0	1.2
0.3	20	4.0	4.3
0.3	20	3.5	3.8
Following specimens were pickled briefly after polarization at −0.133V (below critical potential)			
0	20	0.5	0.5
0	20	0.5	0.5
0	100	0.5	0.5
0	100	0.5	0.5
0	100	0.7	0.7
0.2	100	0.2	0.4
0.2	100	0.3	0.5
0.3	100	0.2	0.5
0.3	100	0.2	0.5

* Critical potential for crack initiation = −0.128V (SHE).

For 18-8 stainless steel in $MgCl_2$ at 130°C, the initial corrosion potential and the critical potential are not far apart so that the induction time for cracks to initiate is short and in the order of 5 to 10 min. But for the same alloy exposed to LiCl at 145°C, the corrosion potential and the critical potential are farther apart and the induction time is longer. In absence of a thick surface oxide, but at a favorable potential, a crack initiates rapidly, as was shown by immediately polarizing pickled test specimens upon immersion in LiCl solution to a value either 5 or 45 mV above the critical potential and noting visible initiation of cracks within less than 2 min. The same situation applies to Type 310 stainless steel in $MgCl_2$ at 154°C which has an observed induction time for crack initiation of about 1 hr. The data are summarized in Table II.

Effect of inhibiting ions.—An inhibiting effect of nitrate ions on SCC of austenitic stainless steels in chloride solutions was reported by Phillips and Singley (6) and by several others (7-9). Uhlig and Cook (2) reported inhibiting effects of NO_3^-, acetate, I^-, and benzoate ions added to boiling $MgCl_2$ solution at 130°C. In accord with the latter results it was found in present measurements that 4% NaI added to $MgCl_2$ boiling at 130°C extends failure time of 18-8 to >200 hr. For the same concentration of $MgCl_2$ (approximately 36.5%) boiling at 130°C, but maintained at a lower temperature of 100°C, only 1.9% NaI was needed to extend failure time to >200 hr. The effect of I^- and other inhibiting ions is one of raising the critical potential for SCC to more noble values. In the case of I^-, the corrosion potential is simultaneously shifted in the active direction so that when the corrosion poten-

Table II. Induction time for initiation of cracks

Alloy (water quenched)	Test solution	Crit. pot. (SHE), V	Time of first cracks to appear. Not polarized	Polarized above critical potential, min
18-8	$MgCl_2$, 130°C	−0.128	5-10 min	<2
18-8	LiCl, 145°C	−0.153	3 hr	<2
25-20	$MgCl_2$, 154°C	−0.103	1 hr	<5

Table III. Effect of NaI additions to $MgCl_2$ 130°C on failure times of precracked 18-8 stainless steel

NaI added, w/o	Average failure time (hr)
0.19	7.6 (2 specimens)
3.8	32.0 (2 specimens)
7.5	44.0 (1 specimen)

tial becomes active to the critical potential no cracks are observed to initiate. In the context of the present paper, it is also important to know the effect of inhibiting anions on propagation of cracks already initiated. Cracks about 0.005 in. (0.013 cm) deep were initiated in stressed 18-8 specimens by first immersing them (unpolarized) for 20 min in $MgCl_2$ boiling at 130°C, then transferring the specimens without removal from the test apparatus to a similar $MgCl_2$ solution at 130°C containing the NaI addition. It was found that up to 7.5% NaI very much slowed down but did not prevent failure of precracked specimens, whereas 4% NaI had effectively prevented crack initiation. Data are summarized in Table III.

Because of the lower transference number of I^- (slightly lower diffusion rate)[1] compared to Cl^-, it follows that within the narrow confines of a growing crack, the diffusing Cl^- ions always precede I^- ions to the crack tip which the inhibiting ions must reach in order to be effective. Although this situation has no influence on crack initiation, it makes I^- less effective as an inhibitor of crack growth. The question is: What would the situation be for a more rapidly moving inhibiting ion such as OH^- having a higher transference number than Cl^-? Such an experiment is not readily accomplished in $MgCl_2$ solution because of the limited solubility of $Mg(OH)_2$. In LiCl solution, however, the higher solubility of LiOH is more favorable. Normal failure time of 18-8 specimens in LiCl (saturated at room temperature) boiling at 145°C is 9.5 ± 2.3 hr (4 specimens) and 0.4% LiOH inhibits crack initiation. It was found that an addition of 0.8% LiOH to this solution was required to limit propagation of cracks 0.005-0.010 in. deep in precracked specimens assuring absence of failure for a period of at least 200 hr. Hence the faster moving OH^- ion is an effective inhibitor of crack propagation, but with more being needed for this purpose than to inhibit crack initiation.

The action of OH^- in LiCl solution, as for inhibiting anions in $MgCl_2$ solution, is to shift the critical potential in the noble direction. For example, 0.4% LiOH added to the above LiCl solution raises the critical potential of 18-8 by 15 mV from −0.153V (SHE) to −0.138V.

Discussion

The same approximate measured critical potential above which, but not below, cracks rapidly initiate in smooth specimens and propagate in precracked specimens indicates that the stress intensity factor is not a sensitive parameter governing the initiation of failure of 18-8 stainless steels by stress corrosion cracking. The results imply that either smooth or superficially precracked test specimens lead to the same results, and that notches or irregularities in the metal surface are not important. Since smooth and precracked specimens behave similarly it is also evident that fracture or breakdown of a passive film on stainless steels, unlike the situation for Ti alloys, is not an essential step in either crack initiation or crack propagation. Instead, the oxide film that slowly builds up in $MgCl_2$ solution, and which is obviously not the original passive film,[2] serves to delay both crack initiation and the continued growth of cracks that have already initiated only after it has attained appreciable thickness. The fact that the responsible oxide film forms visibly either below or above the critical potential for SCC can be taken as evidence that the critical potential is not that value necessary to inhibit corrosive attack, as in the usual cathodic protection of metals against corrosion. This fact is difficult to harmonize with any theory of SCC dependent on metal dissolution at the metal surface or at the base of a notch or crack. Similarly an initial corrosion potential that is active to the critical potential is inconsistent with the electrochemical model, interpreting the critical potential, in accord with the theory of cathodic protection, as the open-circuit anode potential of a corrosion cell. Instead, the critical potential, as has been discussed before (2-4), is better interpreted as the value above which damaging anions (*e.g.*, Cl^-) adsorb on appropriate defect sites causing disruption of metal bonds, and below which such anions desorb (stress-sorption cracking). On this model the action of inhibiting anions is to displace the damaging anions at the metal surface, making it necessary to polarize the specimen to a more noble value in order for damaging anions to reach the critical concentration necessary for crack initiation and growth.

The present results as reported for precracked specimens are valid only for cracks that are not deep. The limited throwing power of current in deep cracks or the limited surface diffusion of anions along deep crack surfaces alters the situation. Furthermore, differential aeration and analogous cells may appreciably change the composition and pH of electrolyte within a deep crack, thereby modifying the environmental factors acting to cause crack growth. These changes are less pronounced in shallow cracks of the order that are presently studied.

The effect of cold working a metal is to produce more defect sites on which damaging anions can adsorb, thereby making it easier for adsorption to occur, followed by a lowering of the critical potential to a more active value. This explains the more active critical potential for cold-worked 18-8 stainless steel (35% reduction of thickness) equal to −0.145V (SHE) as reported by Uhlig and Cook (2), compared to the value presently reported for the water-quenched alloy equal to −0.128V. Similarly, the critical potential for cold-rolled Type 310 stainless steel (35% reduction of thickness) (−0.123V) in $MgCl_2$ at 130°C is 10 mV more active than the value for the water-quenched alloy (−0.113V). This same trend of critical potential with cold work is also found for various nickel-bearing ferritic stainless steels, except for the 5% Ni, 18% Cr-Fe stainless steel which, because of its two-phase structure, is a special case (4).

The present interpretation of the induction time for crack initiation as being due to the time for the corrosion potential to reach the critical potential accompanying build-up of an oxide film and subsequent penetration of the oxide film, suggests a supplementary interpretation of the earlier results of Uhlig and Sava (11). They drew the conclusion that any oxide or so-called passive film on Type 310 (25-20) stainless steel in $MgCl_2$ solution at 154°C has no effect on failure times. This was based on tests of stressed cold-rolled specimens pickled at various times after previous immersion in $MgCl_2$ (0.5, 0.75, 1.25, and 1.5 hr) and then reimmersed in the same $MgCl_2$ solution. Their data showed that the failure times after pickling decreased linearly with time of previous immersion in the $MgCl_2$ solution, but that total failure times (including preimmersion times) for all specimens remained at 4.5 hr. The linear decrease is caused by metallurgical changes resulting from short-time heat-treatment at 154°C, as was further shown by tests on intentionally heat-treated specimens (in air). If we now take into account that the critical potential is unaffected by preimmersion (Table I), and, as subsequent measurements have shown, that the induction time for crack initiation (as observed microscopically) remains at about 1 hr for any of the pickled specimens whether preimmersed or not, the decrease in failure time with preimmersion time is then a measure of the rate of crack growth. In

[1] t_{I^-} for 0.05M ZnI_2 at 25°C = 0.618; t_{Cl^-} for 0.05M $ZnCl_2$ at 25°C = 0.635 (10).

[2] Anodic polarization curves of Type 304 stainless steel in $MgCl_2$ at 130°C show no passive region (2).

other words, the data of Uhlig and Sava show that heating of Type 310 stainless steel at 154°C for t_{Ht} in hours decreases the crack propagation time, t_{prop}, in accord with the equation

$$t_{Ht} = -0.96t_{prop} + 3.4$$

Since the total time to failure equals $t_{Ht} + t_{induction} + t_{prop}$ and taking $t_{induction} = 1$ hr, then substituting the equivalent of t_{prop} from the above equation $[3.4 - t_{Ht}]/0.96$, it is clear that within 4% experimental variation, total failure time for any of the intermediate pickled specimens preimmersed up to 1 hr is 4.55 hr. This value is close to what was observed.

It can be concluded, therefore, that a surface oxide film slowly forms on 25-20 stainless steel in $MgCl_2$ solution at 154°C, as it does on 18-8 stainless steel, and that its effect on the induction time is consistent with that described earlier in this paper.

The shift of corrosion potential of 18-8, and perhaps other stainless steels as well, with growth of an oxide film accompanies a gradually decreasing uniform corrosion rate in $MgCl_2$ solution (12). Lee and Uhlig (3) showed by weight loss measurements of a 19% Cr, 21% Ni stainless steel exposed 190 hr to $MgCl_2$ solution at 130°C and analysis of the solution for metal ions, that the surface oxide film is rich in iron (least soluble hydroxide) and is deficient in nickel.

The increased rate of crack propagation in stressed 25-20 stainless steel specimens following their heat-treatment at 154°C for 0.5-1.25 hr is presumably brought about by the favorable diffusion of impurities (*e.g.*, N atoms) to dislocations and similar imperfection sites taking part in the crack growth mechanism. Without sufficient alloyed nitrogen or similar specific impurities, the alloy is known to resist failure by SCC (13-16). An analogous effect of heat-treatment on crack propagation rates would be expected at 130°C.

Conclusions

1. The critical potential for crack propagation is approximately the same as that for crack initiation in 18-8 stainless steel. Hence the stress intensity factor, relating to an irregular, notched or precracked stainless steel surface, is not a sensitive factor in its stress corrosion cracking behavior.

2. The induction time for crack initiation consists in part of the time required for the corrosion potential to achieve the more noble value of the critical potential. For stainless steels exposed to $MgCl_2$ solution, the drift of potential accompanies slow build-up of a surface oxide film. A supplementary delay results from the time needed to penetrate the surface oxide.

3. Iodide ions in concentrations effective for inhibiting crack initiation, slow down but do not stop crack growth in 18-8 stainless steels in $MgCl_2$ solution. Hydroxyl ions, having a higher transference number than Cl^-, when added to LiCl solution more effectively inhibit crack growth as well as crack initiation.

Acknowledgment

Winston Liang carried out several supplementary experiments. The research was supported by the Office of Saline Water, United States Department of the Interior, to whom the authors express their appreciation.

Manuscript submitted Feb. 2, 1973; revised manuscript received June 11, 1973. This was Paper 110 presented at the Boston, Massachusetts, Meeting of the Society, Oct. 7-11, 1973.

Any discussion of this paper will appear in a Discussion Section to be published in the June 1974 JOURNAL.

REFERENCES

1. B. F. Brown, *Mater. Res. Stand.*, **6** (3), 129 (1966); (*et al.*) NRL Memo. Report 1574, 2nd Interim Report of Prog., U.S. Naval Res. Lab., Washington, D.C. (1964).
2. H. Uhlig and E. Cook, *This Journal*, **116**, 173 (1969).
3. H. Lee and H. Uhlig, *ibid.*, **117**, 18 (1970).
4. R. Newberg and H. Uhlig, *ibid.*, **119**, 981 (1972).
5. H. Leckie, *Corrosion*, **23**, 187 (1967).
6. J. Phillips and W. Singley, *ibid.*, **15**, 450t (1959).
7. S. Rideout and R. Mittleberg, U.S. AEC Report CONF 778-3 (1964).
8. A. Couper, *Mater. Protect.*, **8** (10), 17 (1969).
9. R. Bryant and J. Greer, *ibid.*, **9** (11), 19 (1970).
10. B. Conway, "Electrochemical Data," p. 167, Elsevier Publishing Co., New York (1952).
11. H. Uhlig and J. Sava, *Corrosion Sci.*, **5**, 291 (1965).
12. H. Uhlig and J. Lincoln, Jr., *This Journal*, **105**, 325 (1958).
13. H. Uhlig, R. White, and J. Lincoln, Jr., *Acta Met.*, **5**, 473 (1957).
14. H. Uhlig and R. White, *Trans. Am. Soc. Metals*, **52**, 830 (1960).
15. H. Uhlig, "Corrosion and Corrosion Control," p. 318, 2nd ed., John Wiley & Sons, Inc., New York (1971).
16. F. S. Lang, *Corrosion*, **18**, 378t (1962).

Thermal and Mechanical Effects on the Corrosion Behavior of Ti-6Al-4V Alloy

D. L. Dull* and L. Raymond

Metallurgy Department, The Aerospace Corporation, Los Angeles, California 90045

ABSTRACT

Anodic and cathodic polarization behavior of Ti-6Al-4V alloy were determined by potentiostatic and galvanostatic techniques in deaerated 1, 5, and 10*N* sulfuric acid solutions. In the active region, metallurgical processing, which included cold rolling and thermal treatment, had no effect on the corrosion behavior. It is suggested that a titanium hydride film exists on the titanium alloy surface. In the passive region, plastic deformation, due to cold rolling, did increase the passive current density; whereas crystallographic texturing, did not have an effect. The introduction of an α'-phase due to thermal treatment produced an additional peak in the passive region.

Titanium alloys have found wide usage in commercial applications because of their high specific strengths and excellent corrosion resistance in aqueous solutions containing chloride ions. Most research studies have been directed at anodic and cathodic behavior of titanium alloyed with noble elements (1-4). Of the commercially used titanium alloys, relatively little data

* Electrochemical Society Active Member.
Key words: material processing, titanium alloy, metal working, polarization.

are available discussing cathodic and anodic behavior. Levy (5) has studied the anodic behavior of Ti-6Al-6V-2Sn alloy (heat-treated to three strength levels), Ti-75A (annealed), and Ti-13V-11Cr-3Al alloy (annealed) in H_2SO_4 at various temperatures. Later research by Levy and Sklover (6) extended the study of anodic behavior to HCl solutions and included Ti-8Al-1Mo-1V alloy (single and duplex annealed) and Ti-6Al-4V alloy (annealed). Peters and Myers (7), again on the anodic behavior, have studied Ti-75A (annealed), Ti-6Al-2.5Sn (annealed), Ti-6Al-4V alloy (annealed), Ti-8Al-1Mo-1V alloy (duplex annealed), and Ti-13V-11Cr-3Al alloy (solution treated and aged) in H_2SO_4 solutions. It can be concluded that these titanium alloys do exhibit a typical active-to-passive transition in H_2SO_4 and HCl solutions in the concentration ranges studied. Increases in test temperature increased both the critical current density for passivity and the passive current density.

Tomashov and Ivanov (8) studied the effects of cold rolling and annealing on the corrosion of titanium in H_2SO_4 and HCl solutions. They identified effects of crystallographic texture and plastic deformation due to cold rolling. Their results showed that the effects of increasing the amount of cold rolling is to decrease the corrosion rate. This is contrary to corrosion studies of nontitanium-base materials where, generally, plastic deformation has an opposite effect or no effect; representative examples are summarized by France (9).

Heat-treatment of titanium alloys affects the microstructure and is expected to affect the anodic behavior. Levy (5) shows that the aging temperature of a solution-treated Ti-6Al-6V-2Sn alloy will change the critical current density for passivation. He postulates that this is due to the different α-phase-to-β-phase ratio resulting from the aging heat-treatment.

This study will determine the effects of cold rolling and thermal treatment on both the anodic and cathodic behavior of a Ti-6Al-4V alloy in 1, 5, and 10*N* H_2SO_4 solutions. Thermal treatments include annealed, and solution-treated and aged (STA) conditions. Cold rolling is used to bring about crystallographic texturing and an increased dislocation density.

Experimental Procedure

Characterization of material processing.—The starting material was 0.380-cm thick Ti-6Al-4V alloy sheet in the mill annealed (MA) condition (760°C, air cooled). Sheet stock material was processed by cold cross rolling to about 0.190-cm. The cold rolling was done in 20 passes, with initial reduction of 0.05 cm and the final reduction of 0.003 cm. An additional annealing treatment (700°C for 2 hr) was given to one section and another section was STA conditioned (940°C, water quench, 540°C for 4 hr, air cooled). A portion of the STA section was further cold cross rolled to 0.127-cm thickness. A list of the five processing sequences and the average Knoop hardness numbers are presented in Table I. The applied load of the Knoop Hardness Tester was parallel to the sheet normal. Metallographic examination of the processed material (Fig. 1) shows the annealed material contains a primary α-phase with an intergranular β-phase. The STA material contains primary α-phase in an α'-matrix.

Table I. List of material processes

Processing	Symbol	Knoop hardness number	Metallurgical phases present
Mill annealed[a]	MA	285	Primary α and β
Mill annealed[a] and 50% cold cross rolled	MAX	338	
Mill annealed,[a] 50% cold cross rolled, and annealed[b]	MAXA	328	
Solution treated and aged[c]	STA	335	Primary α and α'
Solution treated and aged and 30% cold cross rolled	STAX	351	

[a] 760°C, air cooled.
[b] 700°C for 2 hr.
[c] 940°C, water quench, 540°C for 4 hr, air cooled.

The sheet textures for the MA, MAX, and STA conditions that are represented by the (0002) basal quarter pole figures were determined with a General Electric Model 4968C autointegrating pole figure goniometer and are shown in Fig. 2. The details of the experimental procedure were reported in a previous work (10).

For the MA condition, the basal poles are primarily contained in the transverse direction with a small concentration in the rolling direction (RD). In the case of the MAX, the basal poles formed an annular concentration about the sheet normal with an absence of basal poles in the periphery. The rolling operation has caused the basal poles to rotate from the transverse and rolling directions to near alignment with the sheet normal. This allows one to compare the corrosion characteristics between the basal planes and the prismatic planes; *i.e.*, type I prism $(10\bar{1}0)$ and type II prism $(11\bar{2}0)$. In this study, an attempt was not made to resolve the more prominent prismatic plane. For the STA condition, a strong concentration of basal poles were found in the rolling and transverse directions. In addition, there was a strong concentration of basal poles at an angle of 40° from both the sheet normal and the transverse directions.

Electrochemical polarization.—Specimens (1.27-cm OD) were machined from the processed sheet, and each was mounted to a 1.27-cm-OD aluminum rod with silver epoxy paint. The specimen was then sealed with shrinkable Teflon tubing that encased the two materials and exposed only the titanium flat sheet surface to the solution. The electrochemical test cell basic design was from Greene (11). The following modifications were included: (*i*) a flat surface specimen holder was added, (*ii*) a saturated calomel electrode with a Luggin capillary probe replaced the salt bridge, and (*iii*) an enclosed platinum sheet electrode was used to eliminate oxygen in the test solution due to the oxygen evolution reaction.

An Anotrol potentiostat (Model 4700 M) was used for anodic polarization, and a Sorensen d-c power supply was used for cathodic polarization using galvanostatic techniques. A Keithley electrometer (Model 610B) was used to measure the potential *vs.* SCE. The H_2SO_4 solutions were prepared from reagent grade concentrated H_2SO_4 diluted with demineralized-distilled water ($>10^6$ ohm-cm). The solution was deaerated with 99.99% purity N_2 for at least 24 hr before a specimen was inserted into the test cell. Activation of the Ti-6Al-4V alloy specimen was performed by immersing in a 1:1:3 HF, HNO_3, lactic acid solution and rinsing with distilled water before inserting into the test cell.

Cathodic polarization was begun after a minimum incubation period of 24 hr for the 5 and 10*N* solutions and 48 hr for the 1*N* solution. During this incubation period, the corrosion potential increased in the noble direction. Reproducibility of cathodic data was not obtained unless these minimum immersion times were used. A steady-state potential was obtained within a 3-min interval with each incremental current increase. Anodic polarization was performed after cathodic polarization by increasing the potential in 20 mV increments and taking a reading after 3 min. In the passive region, larger incremental millivolt readings were taken.

Results

Cathodic polarization.—Cathodic polarization curves of the MA and STA materials in 1, 5, and 10*N* H_2SO_4 solutions are presented in Fig. 3 and 4. The cathodic polarization curves of the other processes can be readily superimposed on these curves (*i.e.*, MAX and MAXA on MA, and STAX on STA). Tafel regions were 1-2 decades in 1*N* H_2SO_4 solution. Corrosion currents were determined by extrapolating the Tafel slope to the measured corrosion potential. To obtain the corrosion

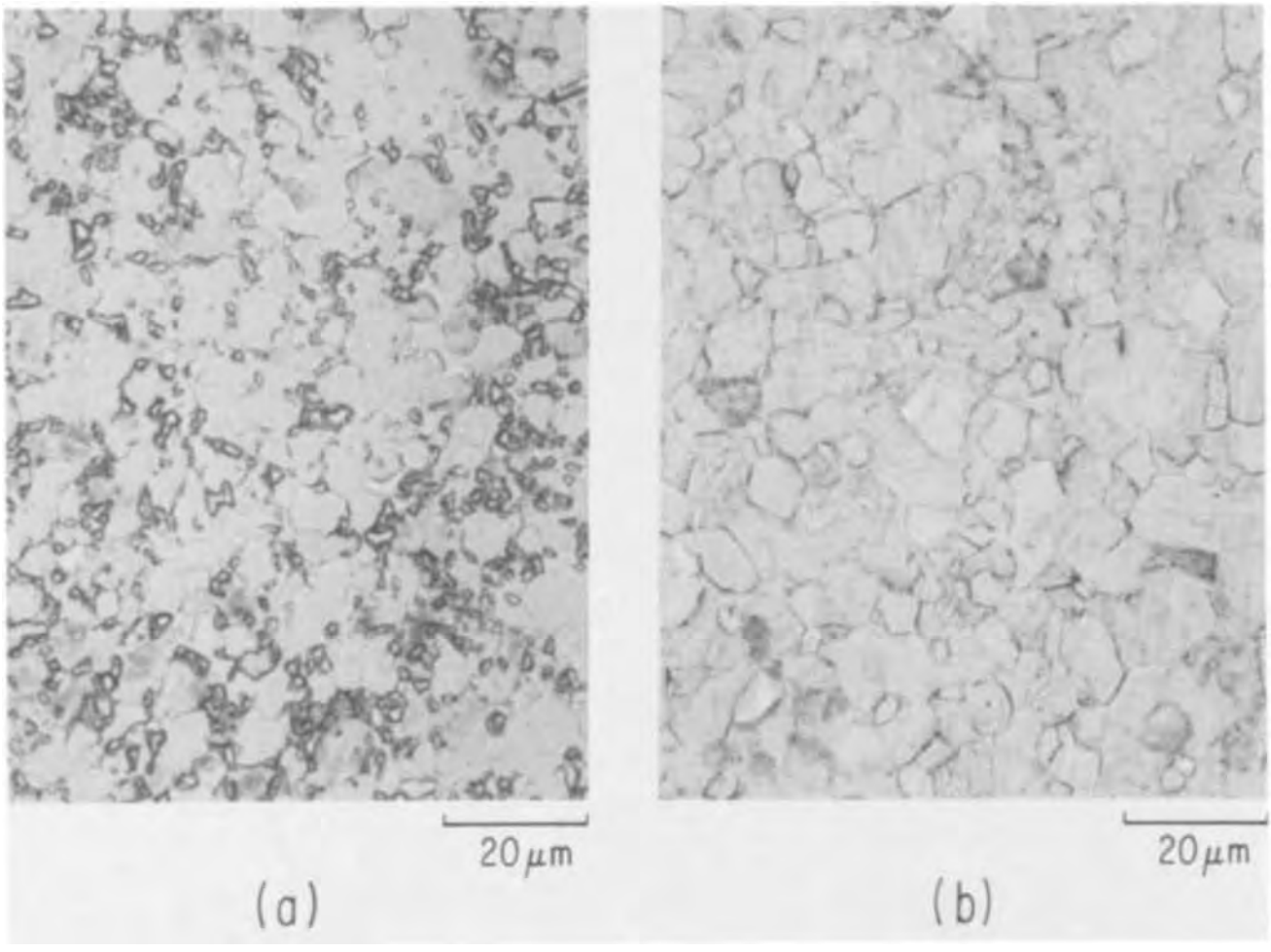

Fig. 1. Results from metallographic examination of Ti-6Al-4V alloy. (a) MA material: primary α-phase with an intergranular β-phase. (b) STA material: primary α in an α' matrix.

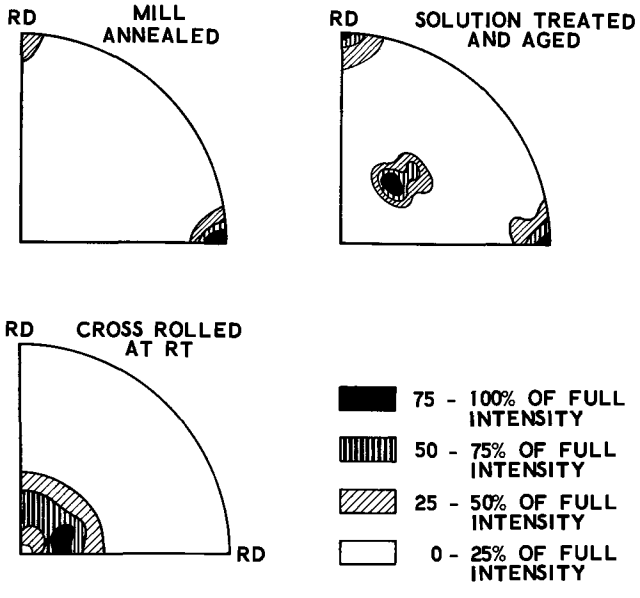

Fig. 2. The (0002) basal pole figures of Ti-6Al-4V alloy processed by various methods.

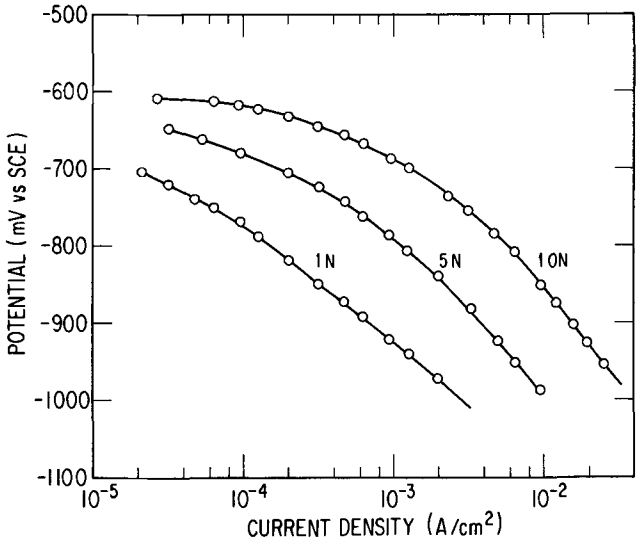

Fig. 3. Results from cathodic polarization of MA Ti-6Al-4V alloy in H_2SO_4.

current density for the 5 and 10N solutions, the Tafel slope determined for the 1N solution was drawn tangent to the polarization curves of the 5 and 10N solutions and extrapolated to the corrosion potential. A summary of the cathodic polarization data is presented in Table II. From these results, there appears to be no effect on the electrode kinetics of the hydrogen evolution reaction due to either cold rolling or thermal treatment.

Anodic polarization.—Anodic polarization curves of MA, MAX, and STA material in 1, 5, and 10N H_2SO_4 solutions are presented in Fig. 5-7. The MAXA and STAX curves were similar in shape to the MA and STA anodic curves, respectively. Each material is shown to exhibit active to passive behavior. The annealed materials show a single active to passive be-

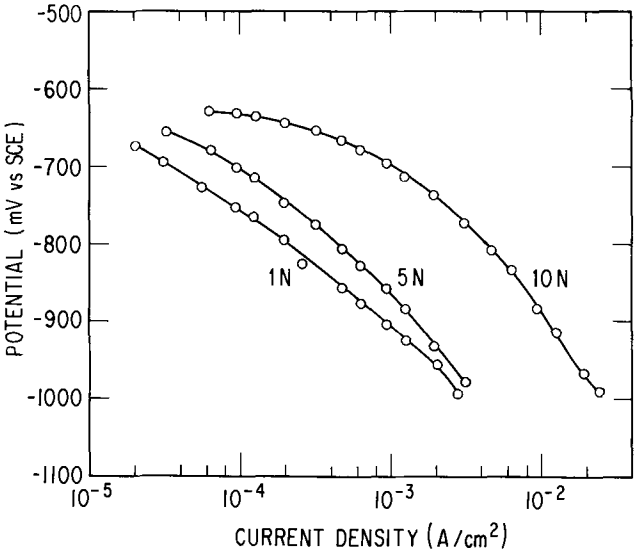

Fig. 4. Results from cathodic polarization of STA Ti-6Al-4V alloy in H_2SO_4.

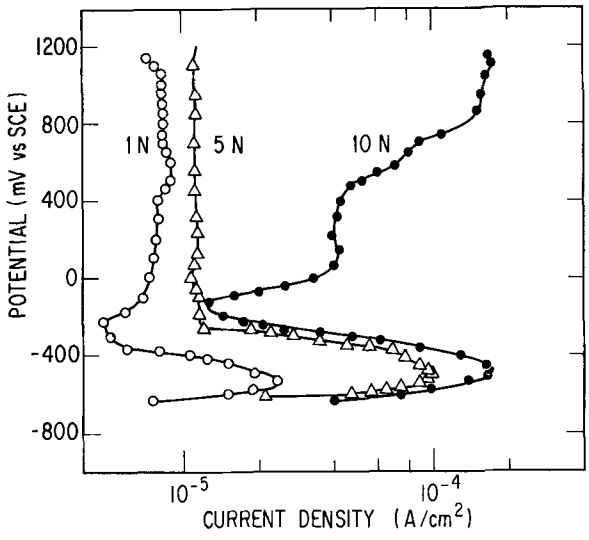

Fig. 5. Results from anodic polarization of MA Ti-6Al-4V alloy in H_2SO_4

havior, whereas the heat-treated material exhibits an additional peak in the passive region. The effect of cold rolling can be shown by comparison of Fig. 5 and 6. In the 1 and 5*N* H_2SO_4 solutions, the passive current density for the MAX is shown to increase with increases in noble potential, whereas it remains constant for the MA condition. A summary of anodic polarization data is presented in Table III. There appears to be no effect on the primary passivation characteristics due to either cold rolling or thermal treatment.

Discussion

Anodic and cathodic polarization.—The results from anodic polarization of the MA material are in good agreement with Peters and Myers (7) with the exception that in the 10*N* solution the passive film exhibits a form of breakdown.

Although data about cathodic polarization of commercial titanium alloy in H_2SO_4 is not readily available in the literature, a good comparison can be made with the work of Thomas and Nobe (12) on pure titanium. The observed Tafel slopes in our study ranged from 153-168 mV and agrees quite well with the reported value of 150 mV for pure titanium. The corrosion current density of the Ti-6Al-4V alloy, which contains two phases, are found to be slightly higher than those reported for pure titanium. The corrosion potentials of Ti-6Al-4V alloy measured in H_2SO_4 agree with Peters and Myers (7).

Effect of mechanical cold rolling and thermal treatment on cathodic polarization.—The processing methods used showed no significant effect on the corrosion potential, corrosion rate, or Tafel slope for the hydrogen evolution reaction (HER). Electrode kinetic studies have found that a film exists on the material surface in the active region. Thomas and Nobe (12) have studied the kinetics of the HER on titanium in the pH range of 0.25-2.25. To explain their experimental results, they assumed that a thin incipient film formed on the material surface. It was then possible to propose a mechanism for the HER based on the Temkin adsorption

Table II. Summary of cathodic polarization data

Process symbol	Corrosion potential (mV *vs.* SCE) 1*N*	5*N*	10*N*	Corrosion current density (μA/cm²) 1*N*	5*N*	10*N*	Tafel slope (mV/decade) 1*N*
MA	−655	−630	−600	18	89	300	153
MAX	−640	−615	−600	16	125	270	158
MAXA	−665	−620	−630	19	102	300	168
STA	−650	−630	−620	25	35	330	155
STAX	−660	−655	−615	23	36	200	153

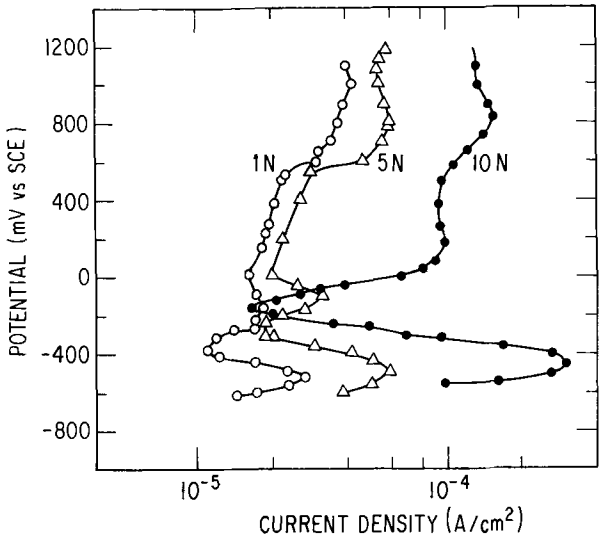

Fig. 6. Results from anodic polarization of MAX Ti-6Al-4V alloy in H_2SO_4.

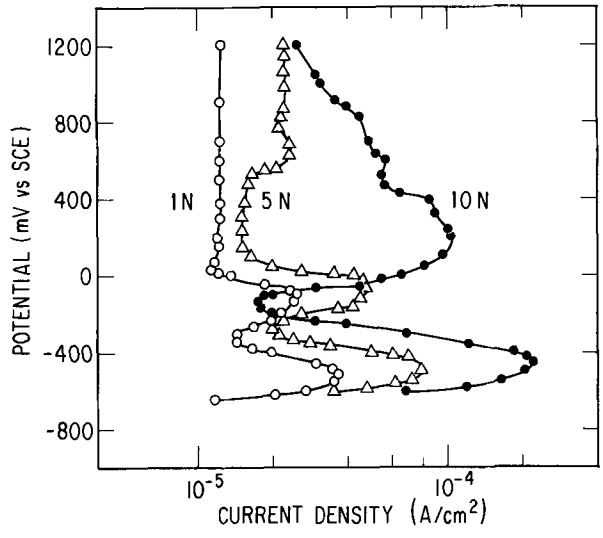

Fig. 7. Results from anodic polarization of STA Ti-6Al-4V alloy in H_2SO_4.

isotherm. Owen *et al.* (13) used a scanning electron microscope to observe surface morphology in their studies of titanium hydride formation on Ti-6Al-4V alloy in 5*N* HCl solution at the active corrosion poten-

Table III. Summary of anodic polarization data

Process symbol	Primary passivation potential (mV vs. SCE) 1N	5N	10N	Critical current density (μA/cm²) 1N	5N	10N
MA	−520	−480	−460	24	98	163
MAX	−520	−480	−440	27	62	296
MAXA	−520	−480	−460	24	88	215
STA	−520	−500	−460	36	80	218
STAX	−540	−500	−460	34	94	175
	Peak in passive region					
STA	−140	−80	200	25	47	100
STAX	−180	−100	20	18	64	105

tial and under cathodic polarization conditions. They showed that when the passive film is not stable, *e.g.*, in 5*N* HCl solution, a titanium hydride film will readily form. In a study of the electrochemical corrosion of titanium, Tomashov *et al.* (14) showed that the anodic polarization behavior of titanium is affected by prior cathodic polarization in a sulfuric acid solution. They demonstrated that after a forward-reverse anodic polarization run, the active corrosion potential became more active by approximately 0.1V. This effect was attributed to a titanium hydride film on the surface, which was produced by a prior cathodic polarization, that undergoes dissolution during the forward anodic polarization run.

In another study of anodic dissolution of titanium in sulfuric acid, Armstrong *et al.* (15) observed that after some time at a constant cathodic overpotential, the rate of hydrogen evolution increased and the metal dissolution decreased. This observed lowering of the hydrogen overpotential was attributed to the formation of a titanium hydride on the surface.

In a passivity study, Sukhotin and Tungusova (16) compared the anodic polarization of titanium and titanium hydride and found them to be similar in their transition from the active to passive state in a sulfuric acid solution. It was postulated that the passivation of titanium is due to the appearance of a passivating oxide on an already covered hydride surface. They further calculated the standard potential for the reaction, $Ti + 2H^+ + 2e \rightleftharpoons TiH_2$, to be 0.21V *vs.* SCE based on the free energy of formation being −20.9 kcal/mole to thermodynamically support the presence of titanium hydride layer on the titanium surface. The free energy of formation of TiH_2 has also been reported to be −25.13 kcal/mole by another source (17).

It is thus suggested from the literature, that in the active region where the titanium has been exposed to either concentrated acid solutions or cathodic polarization that the film which forms on the titanium surface is most likely a titanium hydride. This formation of a titanium hydride film on the Ti-6Al-4V alloy surface can explain why thermal treatment and cold rolling have no observable effects on the corrosion behavior. Further, it explains why an incubation period was required before the cathodic polarization data became reproducible. If a titanium hydride was not present, definite effects on corrosion behavior would be expected since the HER is markedly influenced by metallurgical variables (18). The various processing methods of the Ti-6Al-4V alloy in this study have considerably changed the metallurgical variables. These changes include: (*i*) crystallographic orientation, (*ii*) increased dislocation density due to plastic deformation, and (*iii*) metallurgical phases present (intergranular β in a primary α-matrix or primary α in an α'-matrix). However, since these effects did not change the corrosion behavior, either the various processing methods have no effect or the presence of a titanium hydride film on the surface in the active region conceals any influence of the various processing methods. The latter explanation is believed more reasonable. This titanium hydride film formation would also explain the differences between the results of our study and those of Tomashov and Ivanov (8) where they used weight loss techniques.

Effect of cold rolling and thermal treatment on anodic polarization.—Cold rolling and thermal treatment have been shown to have little effect on the active-to-passive transition. The effect of the metallurgical variables is apparently diminished by the presence of the titanium hydride film during the transition. It may be that the passive oxide film is forming directly on the titanium hydride film as suggested by Sukhotin and Tungusova (16).

Cold rolling and thermal treatment show significant effects in the passive region. The effects of cold rolling, in particular, rotation of the basal plane about the rolling direction and increased dislocation density, are shown in Fig. 8. The MA anodic polarization curve represents a material whose basal poles lie primarily in the transverse direction with a small concentration in the rolling direction (see Fig. 2). The dislocation density in MA material is considered minimal. The MAX curve represents a cold-rolled material in which the basal poles are rotated to form an annular concentration about the sheet normal with an absence of basal poles in the periphery. In addition, the dislocation density has been increased. The effect of cold rolling increased the passive current density at a given potential. To determine which of the cold rolling effects was more influential, the material was given the additional annealing treatment that produced a recrystallized structure without a loss of the crystallographic texture obtained from cold rolling. This caused the material to behave as the MA material. The MAXA represents this material. It can be deduced that crystallographic texturing is not as significant an influence as the dislocation density. Foroulis and Uhlig (19) during their study of the effect of cold work on iron and steel corrosion concluded that crystallographic orientation should have a more significant effect on corrosion behavior than dislocation density. However, our observations are being made on material that is in the passive region. It appears that the effect of the increased dislocation density is to increase the available active dissolution sites in the passive film. The crystallographic orientation does not play a dominant role because the corrosion of titanium in the passive region is limited by diffusion of the titanium ion through the passive film. When the material is given an annealing treatment, the dislocation density is decreased. This reduces the active dissolution sites and results in a decrease of the passive current density. This same behavior was also observed in the 5*N* H_2SO_4 solution; however, it was not observed in the 10*N* solution because the passive film exhibited a form of breakdown.

The effect of thermal treatment in the passive region is shown in Fig. 7. The introduction of the α'-phase appears to produce an additional peak in the passive

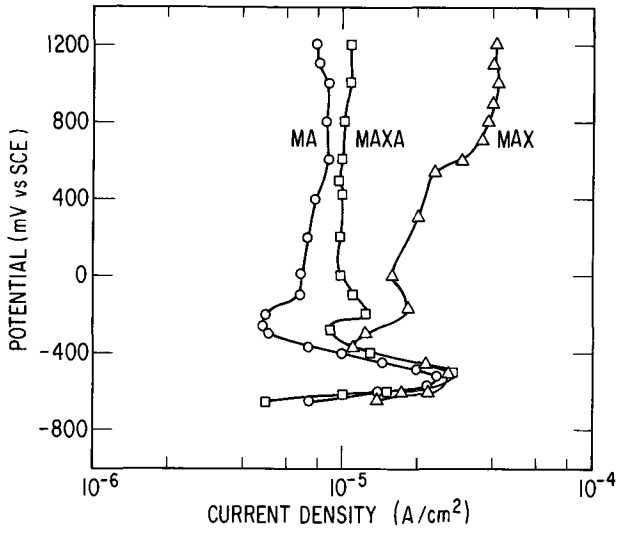

Fig. 8. Effects of cold rolling on Ti-6Al-4V alloy in 1*N* H_2SO_4; see text.

region. This additional peak has not been reported in the titanium alloy literature because most of the titanium alloys studied have been in the annealed condition. Levy (5) studied the effect of strength level on a Ti-6Al-6V-2Sn alloy and did not observe an additional peak although his microstructure is similar to ours for his highest strength material. The discrepancy is apparently due to the activation procedure and cathodic polarization testing conducted in our study prior to the anodic polarization. Cold rolling had no significant effect on the shape of the anodic polarization behavior of the STA material.

Conclusion

The metallurgical variables have shown no effect on the corrosion behavior of Ti-6Al-4V alloy in the active region. Neither of the effects of cold rolling, increased dislocation density and rotation of the basal pole from the transverse direction to a direction parallel to the sheet normal, influenced the corrosion current density or corrosion potential. The thermal treatment that changed the microstructure of the annealed condition from β-phase in a primary α-matrix to primary α-phase in an α'-matrix, *i.e.*, the STA condition, also showed no effects. It is thus suggested that a titanium hydride film exists on the titanium alloy surface.

The metallurgical variables do have an effect on the passive region. Cold rolling increased the passive current density of Ti-6Al-4V alloy consisting of β-phase in a primary α-matrix. This increase is attributed to an increase in the dislocation density and not to crystallographic texturing. Increased dislocation density is believed to increase the active dissolution sites in the passive film. Since the titanium ion transport through the passive film is rate determining, effects of crystallographic orientation are not observed. The thermally treated material, which consisted of primary α in an α'-matrix, exhibited an additional peak in the passive region. This peak is attributed to the introduction of the α'-phase. The cold rolling showed no significant effect on thermally treated material.

Manuscript submitted Feb. 12, 1973; revised manuscript received July 18, 1973. This was Paper 76 presented at the Miami Beach, Florida, Meeting of the Society, Oct. 8-13, 1972.

Any discussion of this paper will appear in a Discussion Section to be published in the June 1974 JOURNAL.

REFERENCES

1. A. J. Sedriks, J. A. S. Green, and D. L. Novak, *Corrosion*, **28**, 137 (1972).
2. J. C. Griess, Jr., *ibid.*, **24**, 96 (1968).
3. N. D. Tomashov, R. M. Altovsky, and G. P. Chernova, *This Journal*, **108**, 113 (1961).
4. M. Stern and H. Wissenberg, *ibid.*, **106**, 759 (1959).
5. M. Levy, *Corrosion*, **23**, 236 (1967).
6. M. Levy and G. N. Sklover, *This Journal*, **116**, 323 (1969).
7. J. M. Peters and J. R. Myers, *Corrosion*, **23**, 326 (1967).
8. N. D. Tomashov and Y. M. Ivanov, *Zashchita Metal.*, **1**, 36 (1965).
9. W. D. France, *Corrosion*, **26**, 189 (1970).
10. D. L. Dull and M. F. Amateau, TR-0066(5250-10)-15, The Aerospace Corp., El Segundo, Calif. (February 1970).
11. N. D. Greene, "Experimental Electrode Kinetics," Rensselaer Polytechnic Institute, New York (1965).
12. N. T. Thomas and K. Nobe, *This Journal*, **117**, 622 (1970).
13. E. L. Owen, R. C. May, F. H. Beck, and M. G. Fontana, *Corrosion*, **28**, 292 (1972).
14. N. D. Tomashov, G. P. Chernova, and F. M. Altovskii, *Russ. J. Phys. Chem.*, **35**, 523 (1961).
15. R. D. Armstrong, J. A. Harrison, H. R. Thirsk, and R. Whitfield, *This Journal*, **117**, 1003 (1970).
16. A. M. Sukhotin and L. I. Tungusova, *Zashchita Metal.*, **4**, 8 (Jan.-Feb. 1968).
17. JANAF Thermochemical Data, The Dow Chemical Co., Midland, Mich. (June 30, 1963).
18. M. Stern, *This Journal*, **102**, 663 (1955).
19. Z. A. Foroulis and H. H. Uhlig, *ibid.*, **111**, 522 (1964).

The Transient Behavior of Passivated Iron under Cathodic Potential Pulsing

Kotaro Ogura[*,1] **and Norman Hackerman**[†]

Department of Chemistry, Rice University, Houston, Texas 77001

ABSTRACT

Electrochemically reduced iron was first anodized in a basic solution at potentials in the passive region. The steady-state passivated iron then was subjected to a single cathodic potential pulse and then was cathodically reduced. In the initial stage of pulsing, the log of response current was linearly related with time at various preanodizing potentials. This relationship held at each temperature, but the slope depended on the solution temperature and the preanodizing potential. The shape of the cathodic reduction curve and the amount of charge needed for reduction were approximately the same whether or not the cathodic potential pulse was applied before cathodic reduction. Experimental results support the premise that cathodic potential pulsing does not influence the so-called bulk oxide but only the surface of passivated iron. In particular, the adsorbed oxygen on passive iron is influenced by the pulsing. The response current is explained by the cathodic reduction of adsorbed oxygen. Various kinetic parameters for the reduction reaction of adsorbed oxygen under cathodic pulsing were estimated from the experimental results, and it was found that appreciable coverage on passive iron by adsorbed oxygen appeared only at potentials far more noble than those in the Flade region.

It has been reported (1-5) that the electrode potential of passivated iron is controlled simply by the thickness of the surface oxide. However, it is questionable (6) whether a surface oxide such as γ-Fe_2O_3, which has to be assumed to be a good electronic conductor, can control the electrode potential. There is no agreement as to where the potential drop appears.

Recently it was reported that the potential of passivated iron is not a linear function of the film thickness (7) but is controlled by a small amount of electric charge accumulating in or on the surface film (8). Work from this laboratory (9-11) has emphasized that interface conditions between metal and solution are very important for producing or maintaining passivity and that the solid part of this interface cannot be treated simply as the bulk oxide-covered or clean surface metal (12, 13).

Experimental

Materials.—Zone-refined iron was supplied by Battelle Memorial Institute and had the following impurities: carbon, 10 ppm; oxygen, 23-28 ppm; nitrogen, 2 ppm; hydrogen, 0.1 ppm. The samples were 4-mm diameter rods which were inserted into a cylindrical Teflon plug, leaving one flat edge exposed. The plug was mounted in a glass support with a brass center rod screwed through the Teflon plug and into the iron rod to provide good electrical contact. After abrading with 4/0 emery paper, the specimens were electropolished in a mixture of glacial acetic acid and 70% perchloric acid at a current density of 0.45 A/cm^2 (14). The electropolishing was performed before each anodization, and the roughness factor was assumed to be approximately 1.0. All solutions used were 0.01M [0.5 w/o (weight per cent)] in $Na_2B_4O_7$ and pH of 9.20. According to Dulat (15), the specific conductivity of solution of borax in water at 20°C is: 1.72×10^{-3} mho/cm for 0.5 w/o borax; 3.17×10^{-3} mho/cm for 1 w/o borax; 5.79×10^{-3} mho/cm for 2 w/o borax. Solutions were prepared from analytical reagent grade borax and water redistilled from an alkaline permanganate solution. The solution was deaerated with nitrogen which had been passed through a column of active copper heated at 200°C, and the final solution was pre-electrolyzed for 48 hr at a current density of 80 μA/cm^2.

Cell.—The electrolytic cell was constructed of Pyrex and consisted of three compartments. The test cell was connected to the counterelectrode cell through a fine frit and to the reference electrode cell through a solution-lubricated glass stopcock. All three partitions contained the same solution. Potentials were measured with respect to the reversible hydrogen electrode (RHE). Both the counterelectrode and the reference electrode were of platinum. The three compartments were water-jacketed and temperature was maintained to ±0.5°C.

Electrical apparatus and procedure.—The passivation of iron was carried out potentiostatically at various anodizing potentials controlled by a Wenking fast-rise potentiostat. Potentials were measured on a Model 610B Keithley electrometer. Current was recorded as the ohmic drop across a standard resistance of 100 ohms on a Tektronix 535A oscilloscope equipped with a Type B calibrated preamplifier. The electrode was anodized for 20 min unless otherwise noted and then a single cathodic potential pulse of 5 msec was applied. The pulse generator was a Tektronix 160-series instrument and was triggered by an initiating pulse derived from the oscilloscope. After a single cathodic potential pulse was applied and the response current recorded photographically on the oscilloscope, the electrical circuit was quickly changed to a constant current circuit in order to reduce the passive film. Cathodic reduction was carried out at a current density of 20.9 μA/cm^2. The change in potential was followed by an X-Y recorder (Moseley Company, Model 2DR2) equipped with a Model 610B Keithley electrometer with gain of unity and an input impedance of 10^{13} ohms. In order to obtain the Q-values, the area of current *vs.* time curve was determined by a graphical integration using a planimeter.

Results

Current-time curves.—The cathodic potential pulse was applied to the steady-state passive electrode which had been preanodized at various potentials from 20 to 1690 mV (RHE). Typical response currents are plotted against time in Fig. 1 at pulse amplitudes of 50,

* Electrochemical Society Student Associate.
† Electrochemical Society Active Member.
[1] Present address: Department of Applied Chemistry, Yamaguchi University, Ube, Yamaguchi-Ken, Japan.
Key words: pulsing, passivated iron, cathodic reduction.

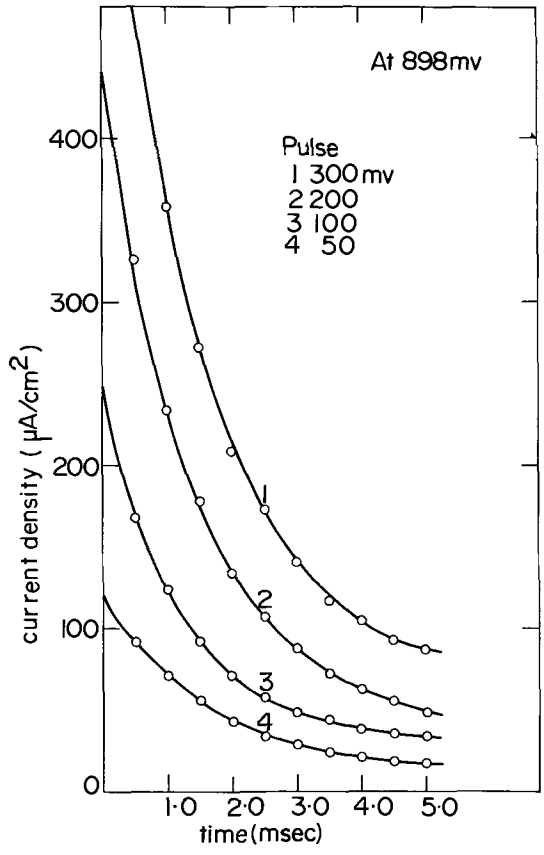

Fig. 1. Response current density of various cathodic potential pulses during preanodizing at 898 mV.

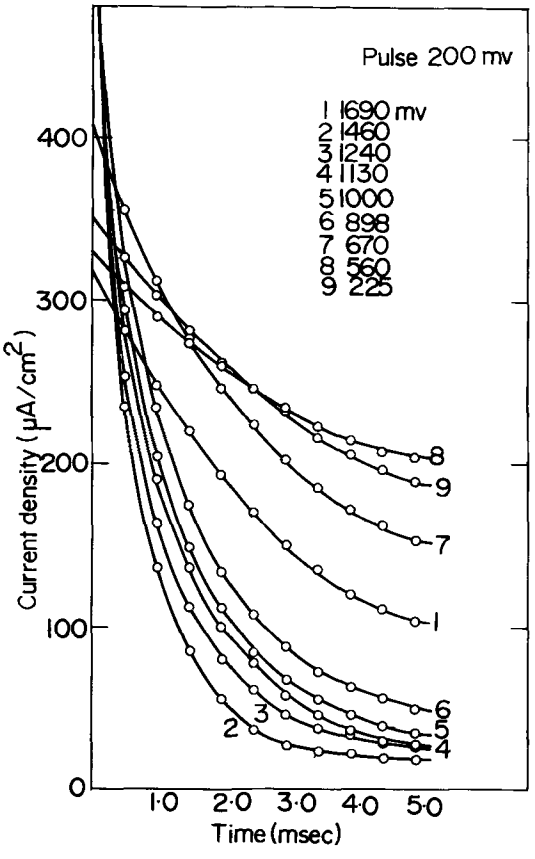

Fig. 2. Response current density of cathodic 200 mV pulse during various preanodizing potentials.

100, 200, and 300 mV. Response currents depended on preanodizing potentials and pulse amplitude. The drop of current with time was smaller in the less noble potentials than in the more noble potentials. Current density was significantly affected by the potential pulse amplitude, increasing with increasing pulse amplitude, especially at the less noble potentials.

Figure 2 shows the current-time relationship for various preanodizing potentials at a constant pulse amplitude of 200 mV. As preanodizing potentials were increased, current densities decreased except at 1690 and 225 mV. This can be also seen in Fig. 3.

Current-potential curves.—In Fig. 3, current densities at a pulse duration of 5.0 msec are plotted *vs.* preanodizing potentials. Except for the potential region more negative than 300 mV and more positive than 1600 mV, response current generally decreased as preanodizing potential, at each pulse amplitude, was increased. The potential regions more negative than 300

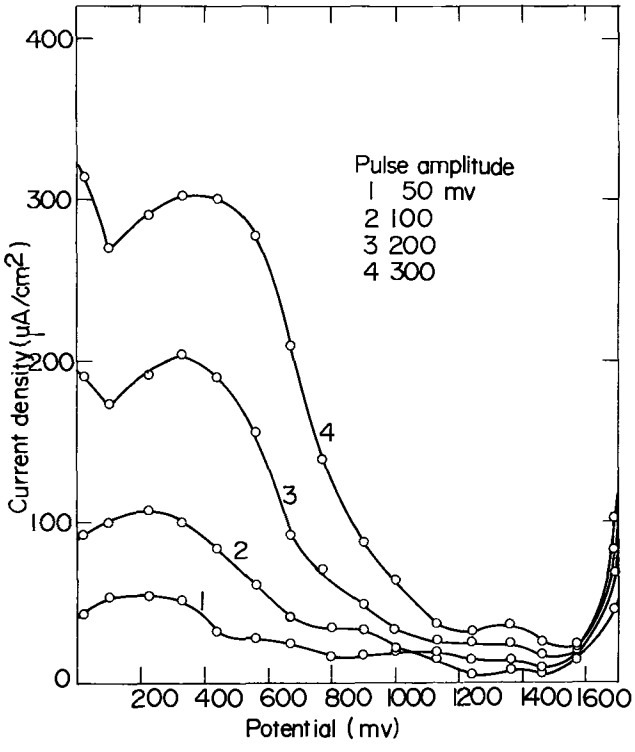

Fig. 3. Response current density at pulse duration of 5.0 msec vs. preanodizing potential.

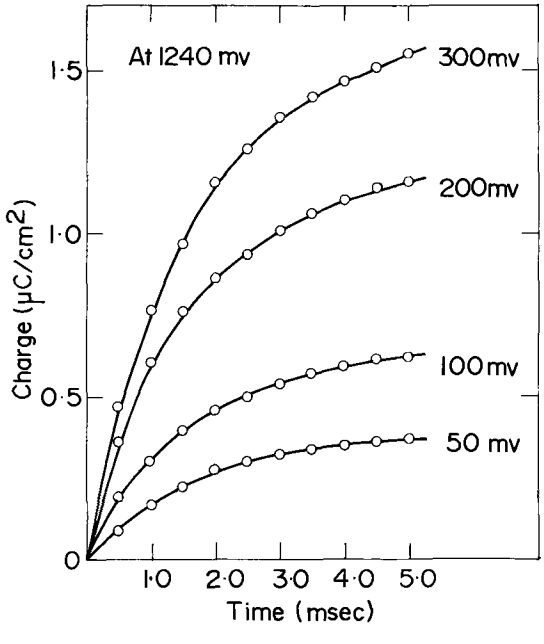

Fig. 4. Amount of charge passed under cathodic pulsing at various pulses vs. time.

mV and more positive than 1600 mV are discussed in a later section in greater detail.

Amount of charge passed under cathodic pulsing.—In Fig. 4, the amount of charge passed during cathodic pulsing is plotted against time at the constant preanodizing potential of 1240 mV. The amount of charge was calculated from the original current-time curves. Even at a pulse amplitude of 300 mV, the amount of charge passed during 5.0 msec was only 1.55 μcoulombs/cm^2. This value is small compared with that measured from the current after the potential was changed abruptly to the anodic side (about 1 mcoulomb/cm^2). This is in agreement with the data reported by Sato (7) and Cartledge (8).

Logarithmic current-time curves.—The logarithmic response currents of various pulses at various preanodizing potentials are shown in Fig. 5-8. In the initial stage of pulsing, the log of current is linearly related with time. This relationship held at each temperature, but the slope depended on the solution temperature and the preanodizing potential.

Cathodic reduction.—After the specimen was subjected to a cathodic potential pulse, the electrode was cathodically reduced. A typical chronopotentiogram is shown in the upper part of Fig. 9. The first arrest occurs at about +250 mV, the second at about −130 mV, and the third at about −200 mV. Q_A and Q_B are the amount of charge for the complete reduction and for the first wave, respectively. In Fig. 9, Q_A and Q_B are plotted *vs.* preanodizing potential for cases with and without cathodic potential pulsing before cathodic reduction. The plot of the amount of charge *vs.* the anodizing potential has been reported before (16). The amount of charge was approximately the same in both cases with and without potential pulsing before reduction. As shown in Fig. 10, the amounts of charge, Q_A and Q_B, are independent both of the length of preanodizing time and of potential pulsing, after 20 min anodization. Cathodic reduction of passivated iron is therefore independent of a previously applied cathodic pulse.

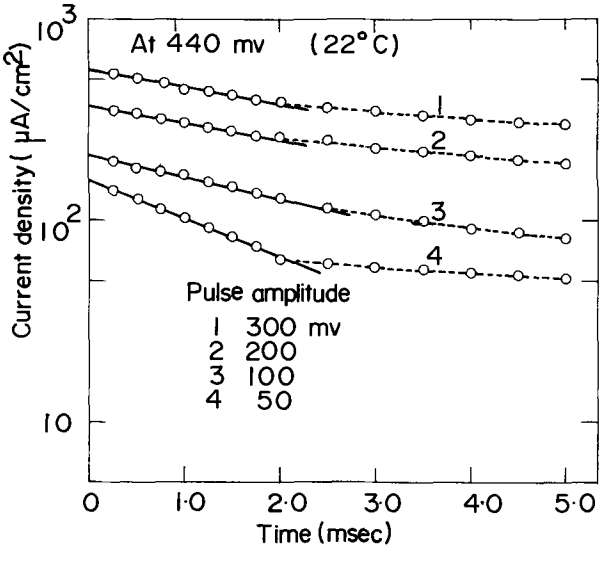

Fig. 5. Logarithmic dependence of response current on time during preanodizing at 440 mV in a 22°C solution.

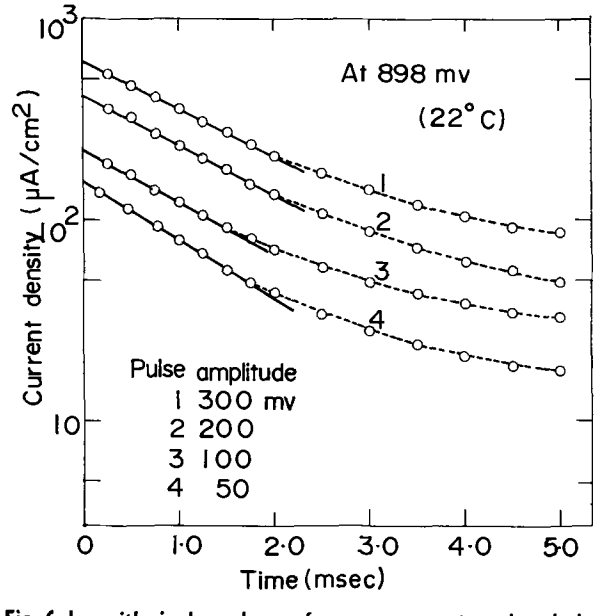

Fig. 6. Logarithmic dependence of response current on time during preanodizing at 898 mV in a 22°C solution.

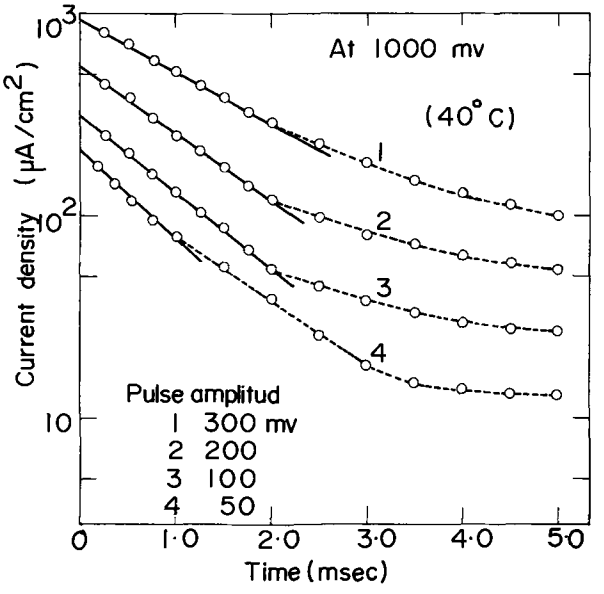

Fig. 7. Logarithmic dependence of response current on time during preanodizing at 1000 mV in a 40°C solution.

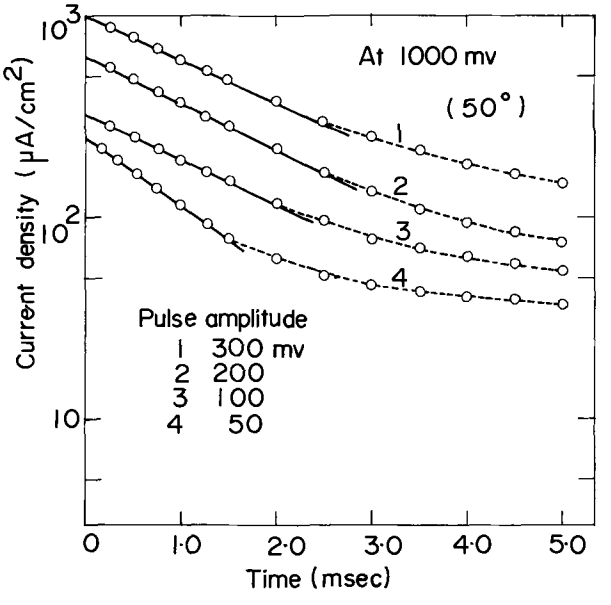

Fig. 8. Logarithmic dependence of response current on time during preanodizing at 1000 mV in a 50°C solution.

Discussion

In an alkaline solution, water molecules in the Helmholtz double layer at a passive iron surface tend to be oriented with the oxygen atom toward the passive film (17, 18). The water zone contributes to

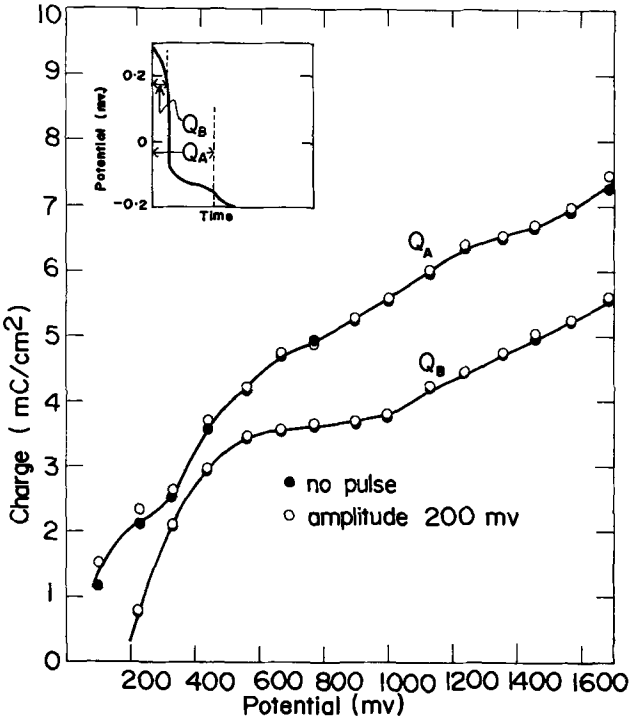

Fig. 9. Amount of charge needed for cathodic reduction vs. preanodizing potential.

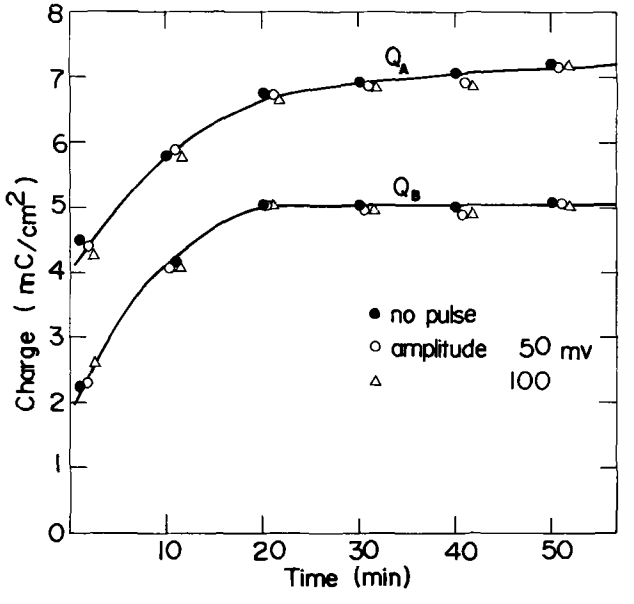

Fig. 10. Amount of charge needed for cathodic reduction vs. preanodizing time.

the anodic inhibition of iron or to the growth of a passive film. According to Bloom and Goldenberg (19) or Nagayama and Cohen (16), the outermost γ-Fe_2O_3 layer of the passive film may have a defect structure which involves cation vacancies or adsorbed oxygens.

As shown in Fig. 9 and 10, the amount of charge required for the reduction of the passive film was approximately the same whether or not a cathodic potential pulse had been applied before reduction. This means that the constitution of the passive film was not influenced by the potential pulse applied previously. Therefore, cathodic pulsing does not appear to control the so-called bulk oxide but only the surface on passivated iron. Further, with the fast-rise potentiostat, the electrical double layer capacity should be charged within microsecond order, whereas the current density was followed by an oscilloscope in millisecond order. Thus, the current density due to double layer charging or discharging could be considered to be zero.

This behavior appears to be explainable only by the cathodic reduction of adsorbed oxygen during the cathodic pulsing, since the transient current due to discharging the electric double layer can be neglected in a potentiostatic experiment using a high response potentiostat. The following reaction can be considered to occur under cathodic pulsing

$$Me_xO_y - O + H_2O + 2e \rightarrow Me_xO_y + 2\,OH^- \qquad [a]$$

where Me_xO_y is the passive film and $-O$ is the adsorbed oxygen on passive film. In other words, the response current of the potential pulse is due to the reduction of adsorbed oxygen and is represented by the following equation

$$i = n\mathbf{F}C_0k_0 \exp\left(-\frac{\alpha n\mathbf{F}V}{RT}\right) \qquad [1]$$

where C_0 is the surface concentration of adsorbed oxygen, and the other symbols have their usual significance. V is the electrode potential which was measured with respect to the reversible hydrogen electrode (RHE). The reverse reaction was neglected because of the large amplitude of the cathodic pulse.

If the response current is due only to the reduction of adsorbed oxygen, the rate of decrease of adsorbed oxygen can be expressed by Eq. [2]

$$-\frac{dC_0}{dt} = \frac{i}{n\mathbf{F}} \qquad [2]$$

From Eq. [1] and [2]

$$C_0 = C_0^* \exp\left(-k_0t\, e^{-\alpha n\mathbf{F}V/RT}\right) \qquad [3]$$

where C_0^* is the initial concentration of adsorbed oxygen. The time is calculated from the instant of applying the pulse. By substituting Eq. [3] into Eq. [1]

$$i = n\mathbf{F}k_0C_0^* \exp\left(-k_0t\, e^{-\alpha n\mathbf{F}V/RT} - \frac{\alpha n\mathbf{F}V}{RT}\right) \qquad [4]$$

Equation [4] is the expression for the response current under cathodic potential pulsing.

Transient behavior at room temperature.—Figures 5 and 6 show the logarithmic current *vs.* time plot. The logarithm of current is linearly related with time in the initial stage of pulsing. This relationship can be explained by Eq. [4]; that is, by differentiating the logarithm of Eq. [4] with time

$$\left(\frac{\partial \log i}{\partial t}\right) = -\frac{k_0}{2.303} \exp\left(-\frac{\alpha n\mathbf{F}V}{RT}\right) \qquad [5]$$

The initial slopes in Fig. 5 and 6 correspond to the right-hand side of Eq. [5]. The equation states that the plot of log i *vs.* time yields a straight line. The deviation from the line observed under the condition of long time as shown in Fig. 5 and 6 must be due to the contribution of the reduction of bulk oxide. Note that k_0 can be estimated from these experimental results and is discussed later.

Figure 3 shows the response current density at the pulse duration of 5.0 msec *vs.* preanodizing potential. Except for the potential region more negative than 300 mV and more positive than 1600 mV, response currents generally decreased as preanodizing potential was increased. The concentration of adsorbed oxygen in reaction [a] must be a function of the preanodizing potential, because the chemical force between the passive film and the adsorbed oxygen depends on the electrode potential. The shift of the preanodizing potential in the positive direction means an increase of the adsorbed oxygen concentration, and causes the initial potential of reaction [a] to become more noble. Here, the concentration of adsorbed oxygen can be con-

trolled only by the electrode potential since the pH of the solution was always constant. In Fig. 3, various potential pulses were applied to the electrode preanodized at a constant potential. In other words, the concentration of adsorbed oxygen was always constant before applying various pulses. The increase of the response current density with decreasing preanodizing potentials in the region between about 1600 mV and about 300 mV can be explained by the cathodic polarization of reaction [a].

When there is onset of oxygen evolution in the noble preanodizing potential, however, there will be the reduction of the molecules dissolved during preanodization

$$O_2 + 4H^+ + 4e \rightarrow 2H_2O \qquad [b]$$

This may be the reason why the current density in Fig. 3 increased at potentials more noble than about 1600 mV. On the other hand, the decrease of current density at potentials less noble than about 300 mV, as shown in Fig. 3, may be due to the dissolution of bare iron. If the electrode potential passes through the Flade region by the applied potential pulse, the passivated iron would become active, and there should be dissolution of iron. The response current (which is negative) of the cathodic potential pulse will be reduced by the current for this reaction since it is anodic.

The amount of charge passed under cathodic pulsing shown in Fig. 4 corresponds to the decreased amount of adsorbed oxygen according to reaction [a]. For the 200 mV pulse amplitude, the amount of charge is about 1.6 μcoulombs/cm² at 5.0 msec at the preanodizing potential of 1240 mV. This corresponds to 9.9×10^{12} adsorbed oxygen atoms/cm², while for the 50 mV pulse amplitude, 2.2×10^{12} adsorbed oxygen atoms/cm² are obtained.

In Fig. 11, the logarithm of the current density at zero time in Fig. 5 and 6 is plotted *vs.* the electrode potential which was obtained by subtracting the pulse amplitude from the preanodizing potential. At each preanodizing potential, the logarithmic current density is linearly related with the electrode potential

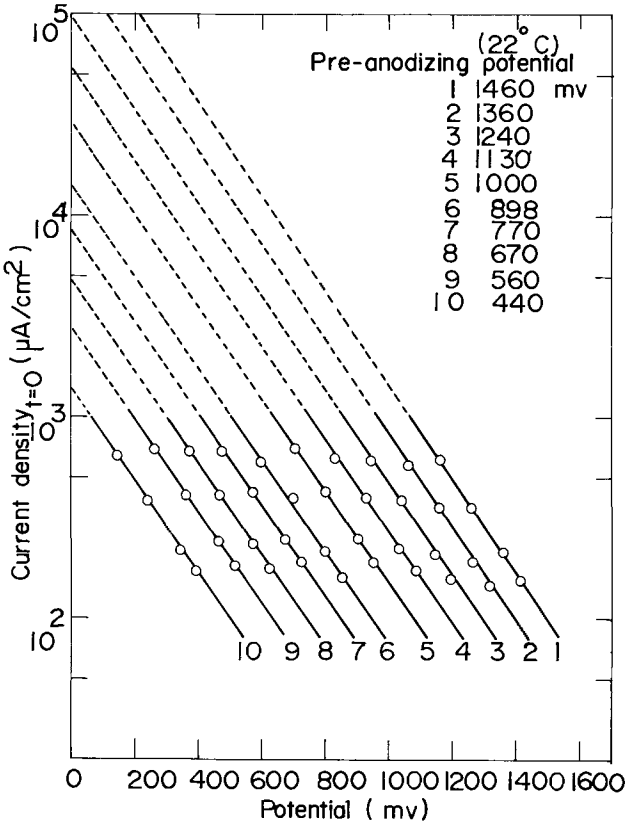

Fig. 11. Response current at the time of zero *vs.* electrode potential for specimen preanodized at various potentials.

Table I. Concentration of adsorbed oxygen on passivated iron before applying cathodic potential pulse at various preanodizing potentials

Preanodizing potential (mV)	i_o^* (mA/cm²)	C_o^* (10^{-10} mol/cm²)
1460	540	10.6
1360	180	3.52
1130	55	1.07
1000	29	0.56
898	14	0.27
770	8.5	0.17
670	4.8	0.09
560	2.8	0.05
440	1.4	0.03

(RHE), and the slope is always 2.27×10^{-3} (mV^{-1}).

If the logarithmic current of Eq. [4] is differentiated by V at zero time, Eq. [6] is obtained

$$\left(\frac{\partial \log i}{\partial V}\right)_{t=0} = -\frac{\alpha n \mathbf{F}}{2.303RT} \qquad [6]$$

The slope in Fig. 11 corresponds to the left-hand side of Eq. [6]. In the equation, α is an unknown parameter, and n is 2 according to reaction [a]. From the experimental results, α was estimated to be 0.1. The intercept of the line at electrode potential zero yields the logarithm of current density at zero time. From Eq. [4], the current density on this condition can be represented by Eq. [7]

$$i^*_{\substack{t=0 \\ V=0}} = n\mathbf{F}k_oC_o^* \qquad [7]$$

The value of i^* for each preanodizing potential is tabulated in Table I. If the value of k_o is known, the concentration of adsorbed oxygen at the preanodizing potential can be estimated from Fig. 11 and Eq. [7].

k_o was calculated by the following method. If the logarithm of the left-hand side of Eq. [5] is plotted against the electrode potential, the intercept at the potential of zero should give (k_o/2.303). Such a plot is shown in Fig. 12 and the intercept is 1.15×10^2 (1/sec). From this value, k_o was estimated to be 2.65×10^2 (1/sec).

The concentration of adsorbed oxygen on passivated iron at various preanodizing potentials was calculated by using k_o, and the results are shown in Table I.

Figure 13 shows the surface coverage θ of adsorbed oxygen which was obtained by assuming that the coverage at 1360 mV is 1.0. Appreciable coverage appears at about 300 mV, and increases abruptly at about

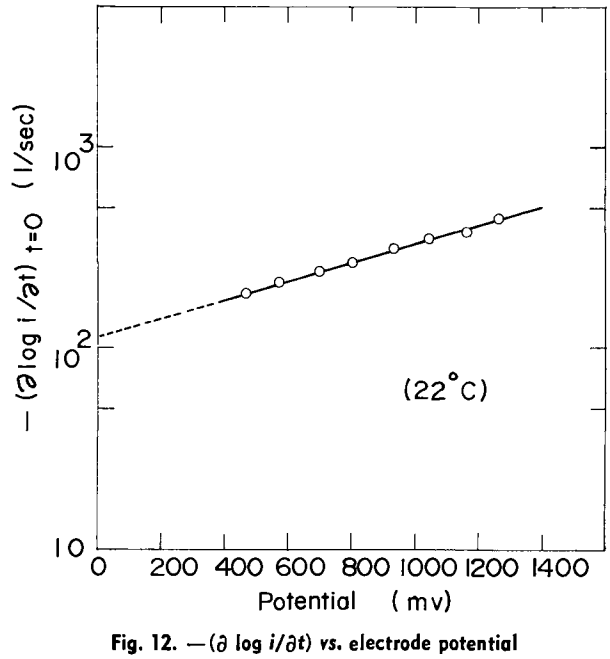

Fig. 12. $-(\partial \log i/\partial t)$ *vs.* electrode potential

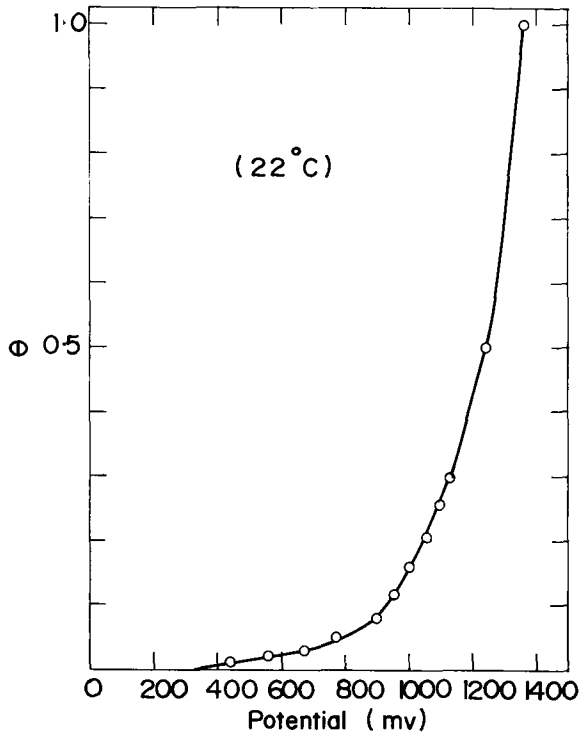

Fig. 13. Coverage vs. preanodizing potential

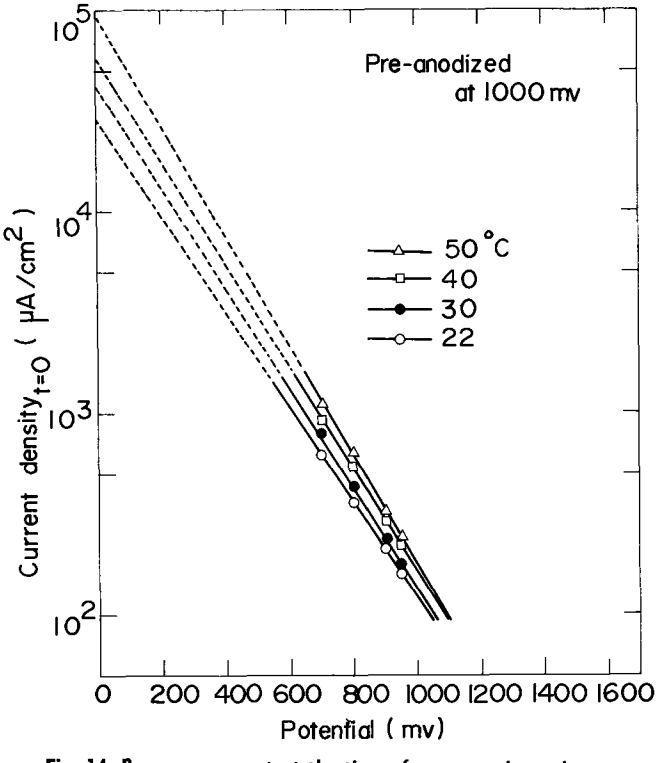

Fig. 14. Response current at the time of zero vs. electrode potential in various solutions. All specimens were preanodized at 1000 mV.

900 mV. It may be concluded that the adsorption of oxygen atom on passive film appeared only at potentials more noble than the Flade region, and that oxygen evolved effectively at more noble potentials than 1360 mV. In another experiment (20), a passive film was produced and the cathodic potential pulse was applied in a solution containing chelating agents. Reduction of the adsorbed oxygen by the cathodic pulse was depressed, presumably because adsorbed oxygen was replaced by the chelating agent.

Temperature dependence of the transient behavior.— In Fig. 7 and 8, the logarithmic current density is

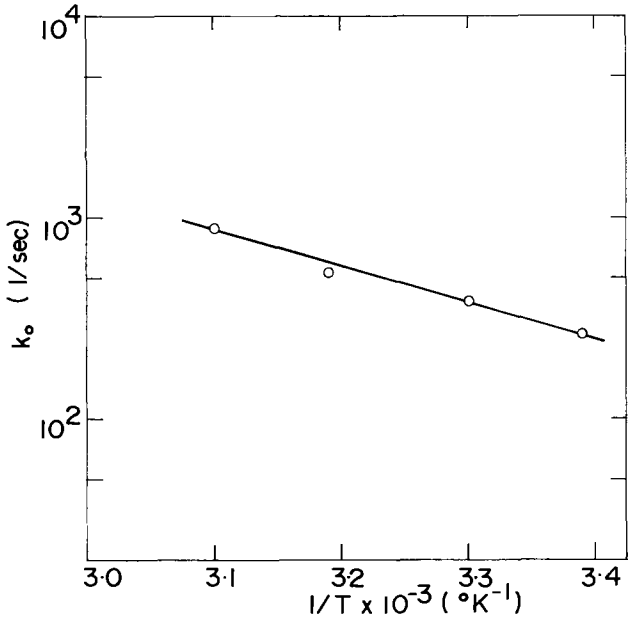

Fig. 15. Arrhenius plot of k_o

shown *vs.* time at the temperatures 40° and 50°C. The logarithm of the current density at zero time is plotted against the electrode potential in Fig. 14 according to the same procedure as that in Fig. 11. The intercept at the electrode potential of zero is $i^*_{\substack{t=0\\V=0}}$ of Eq. [7], and depends on the solution temperature. If the value of k_o is known, C_o^* can be evaluated. k_o was estimated by the same method as that employed above, and the result is shown in Fig. 15. Using these values and $i^*_{\substack{t=0\\V=0}}$ in Fig. 14, C_o^* was calculated according to Eq [7]. C_o^* was not influenced significantly by the change in the solution temperature, and was about 0.6×10^{-10} mole/cm^2 at the preanodizing potential of 1000 mV. However, a dependence of k_o on temperature was observed, and the logarithmic k_o is plotted against $1/T$ in Fig. 15. From this Arrhenius plot, the activation energy of reaction [*a*] was found to be 8.24 kcal/mole. Although there are no data in the literature for comparison, it should be noted that 8 kcal/mole is close to the activation energy often quoted (21) for an electrochemical reaction on metal.

Acknowledgments

The financial support by the Robert A. Welch Foundation of Houston, Texas, is gratefully acknowledged. The authors are also indebted to the Battelle Memorial Institute of Columbus, Ohio, for the zone-refined iron. They thank Dr. Shiro Haruyama of Tokyo Institute of Technology for helpful discussions.

Manuscript submitted Feb. 26, 1973; revised manuscript received July 2, 1973.

Any discussion of this paper will appear in a Discussion Section to be published in the June 1974 JOURNAL.

REFERENCES

1. K. F. Vetter, *Z. Elektrochem.*, **58**, 230 (1954).
2. K. G. Weil, *ibid.*, **59**, 711 (1955).
3. H. Wroblowa, V. Brusic, and J. O'M. Bockris, *J. Phys.*, **75**, 2823 (1971).
4. J. L. Ord and J. H. Bartlett, *This Journal*, **112**, 160 (1965).
5. J. L. Ord, *ibid.*, **113**, 213 (1966).
6. J. Kruger and J. P. Calvert, *ibid.*, **114**, 43 (1967).
7. N. Sato, *Electrochem. Acta*, **12**, 1135 (1967).
8. G. H. Cartledge, *Chimica*, **23**, 450 (1969).
9. N. Hackerman, *Z. Elektrochem.*, **62**, 632 (1958).
10. E. S. Snavely and N. Hackerman, *Can. J. Chem.*, **37**, 268 (1959).

11. G. M. Schmid and N. Hackerman, *This Journal*, **109**, 1096 (1962).
12. P. V. Popat and N. Hackerman, *J. Phys. Chem.*, **65**, 1201 (1961).
13. N. W. Wisdom and N. Hackerman, *This Journal*, **110**, 319 (1963).
14. P. W. Sewell, C. D. Stockbridge, and M. Cohen, *Can. J. Chem.*, **37**, 1813 (1959).
15. J. Dulat, *Proc. Intern. Congr. Metall. Corrosion, 2nd*, New York (1963), p. 135.
16. M. Nagayama and M. Cohen, *This Journal*, **109**, 781 (1962).
17. U. R. Evans, *Corrosion Sci.*, **9**, 813 (1969).
18. J. M. West, "Electrodeposition and Corrosion Process," p. 70, D. Van Nostrand Co., London (1969).
19. M. C. Bloom and L. Goldenberg, *Corrosion Sci.*, **5**, 623 (1965).
20. K. Ogura and N. Hackerman, To be submitted.
21. N. Tanaka and R. Tamamushi, *Electrochem. Acta*, **9**, 963 (1964).

The Nucleation with $SnCl_2$-$PdCl_2$ Solutions of Glass Before Electroless Plating

C. H. de Minjer* and P. F. J. v.d. Boom

Philips Research Laboratories, Eindhoven, Netherlands

ABSTRACT

It has been generally accepted that metallic palladium nuclei are formed by the nucleation procedure of nonconducting substrates with stannous chloride and palladium chloride solutions. However, results of experiments on glass using radioactive tracers and ellipsometry have shown that no metallic palladium is present after the nucleation procedure. The results indicate that presumably a tin-palladium complex, containing one palladium atom per two tin atoms is formed and that this initiates the nickel-phosphorus deposition from a suitable electroless plating solution.

Before a nonconductive substrate can be plated by an electroless process, it is necessary to nucleate the substrate. A widely used procedure for this nucleation involves "sensitization" and "activation" in a stannous chloride and a palladium chloride solution, respectively. The explanation widely accepted for this procedure [see for example Ref. (1) to (5)] is that the stannous ions reduce the palladium ions to finely divided metallic palladium nuclei on the surface of the substrate according to the equation

$$Sn^{2+} + Pd^{2+} \rightarrow Sn^{4+} + Pd \qquad [1]$$

The palladium nuclei should then initiate the autocatalytic plating process.

Recently some doubt has been raised against this simple explanation. Goldie (6) concludes in a literature survey of the nucleation and activation process that the detailed mechanism is somewhat obscure. Chow and co-workers (7)[1] mention that Eq. [1] presumably leads to the formation of a Pd-layer on the substrate. However, irradiation of the sensitized and activated substrate with uv light inhibits the deposition of nickel or cobalt. The authors believe that this can be explained by a change in the crystalline structure of the Pd nuclei, but they also state that more information concerning the detailed chemistry is desirable. Tsukahara *et al.* (8)[1] conclude that the nuclei formed by the sensitization and activation probably consist of negatively charged $Sn^{II}Pd^{II}$ colloidal particles which by an intramolecular redox reaction may slowly decompose into palladium metal and Sn^{IV}.

On the other hand, Cohen and co-workers (9, 10) found, using Mössbauer spectroscopy, that on a sensitized Kapton substrate more Sn^{2+} ions and less Sn^{4+} ions are present than on a sensitized + activated substrate. They consider this as support for the reaction given by Eq [1]. A disadvantage of their technique is that the measurements were carried out in vacuum and therefore the sample had to be dried. This may have led to changes in the composition of the films.

A recent survey of the nucleation process is given by Feldstein (11).[1]

An argument against the likelihood of the reaction given by Eq. [1] is that in a solution containing $SnCl_2$ and $PdCl_2$ no palladium precipitates. It is known (12-15) that in this case complexes are formed. Khattak and Magee (14) suggest the following formula

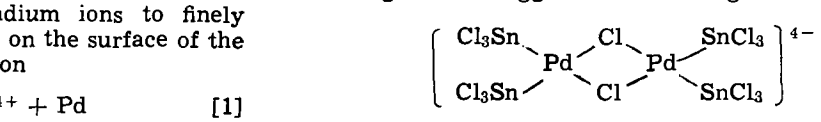

with palladium in the univalent and tin in the bivalent state. Tsukahara (8) gives the formula $[Pd^{II}Sn^{II}{}_mCl_x]^{n-}$ with $m = 2$ or 6.

A commercial solution,[2] which is claimed to be a combination of sensitizer and activator, contains a palladium complex as well. This solution shows no Tyndall effect.[3]

During an investigation to achieve optimum conditions of the nucleation procedure we also studied the mechanism of this procedure, using radioactive tracer techniques and ellipsometry.

We obtained a very homogeneous nucleation by introducing an immersion of the substrate in a silver nitrate solution between the stannous chloride and the palladium chloride steps. In accordance with reaction [1] we expected the following reactions to occur

$$Sn^{2+} + 2Ag^{+} \rightarrow Sn^{4+} + 2Ag \qquad [2]$$

and

$$2Ag + Pd^{2+} \rightarrow 2Ag^{+} + Pd \qquad [3]$$

Due to the complication of the silver nitrate step our investigations into the mechanism of the nucleation procedure were performed with and without this step.

* Electrochemical Society Active Member.

Key words: electroless deposition, nucleation, sensitization.

[1] Published between first and revised edition of this paper.

[2] Shipley catalyst 6F.

[3] After revision of this manuscript two papers dealing with $PdCl_2$-$SnCl_2$ solutions were published. Cohen and West (21), using Mössbauer technique, found that in concentrated acid solutions first a complex is formed and that this gradually decomposes whereby SnPd alloys could be detected. Rantell and Holtzman (22) found an indication that the active component of catalyst F6 is a complex chloride of Sn^{II} and Pd^{II} and that no colloidal particles could be detected larger than 5-10 nm.

Experimental Procedures and Results

Substrate.—Sheets of soda lime glass were used, 50 × 50 × 1 mm for examination with the electron microscope, 30 × 30 × 1 mm for the radioactive tracer techniques, and 100 × 25 × 1 mm for ellipsometry.

The sheets were carefully cleaned, first with trichloroethylene, followed by an immersion in a CrO_3-H_2SO_4 solution for several hours and an immersion in a 65 w/o (weight per cent) HNO_3 solution for at least 15 min. In this way the sodium ions are removed from the glass surface layer. Finally the glass sheets were rubbed with a slurry of $CaCO_3$ and MgO in water and dipped in a 16 w/o HNO_3 solution for 1 min.

Nucleation procedure.—As mentioned above two procedures were followed, one with and one without a $AgNO_3$ step.

With a $AgNO_3$ step.—The glass sheets were successively dipped in the solutions given in Table I. Freshly prepared $SnCl_2$ solutions were used. Between each step the samples were rinsed in running deionized water for 1 min.

During immersion in the silver nitrate solution the substrate darkens somewhat. This darkening disappears on immersion of the substrate in the palladium chloride solution.

Without a $AgNO_3$ step.—The same as the above, except that step b (Table I) was omitted.

Nickel plating.—Only electroless nickel plating was used in this investigation. The plating solution contained per liter: 30g $NiCl_2 \cdot 6H_2O$, 10g $NaH_2PO_2 \cdot H_2O$, 30g aminoacetic acid, pH 3.8 (measured at room temperature), temperature 95°C, and duration variable.

All chemicals used were of A.R. quality.

Checking of the homogeneity of the nucleation.—A homogeneous nucleation was very important for the interpretation of the results obtained from radioactive tracer and ellipsometric measurements. Therefore the homogeneity was checked by making a transmission micrograph of an approximately 80Å thick layer of nickel-phosphorus. This layer was deposited on a nucleated glass sheet and after evaporating a thin carbon film on it, the carbon + nickel layer was detached from the glass using hydrogen fluoride. The carbon layer acted as a support for the nickel-phosphorus film for examination with the electron microscope.

Figures 1 and 2 give the results, Fig. 1 of a layer obtained when a $AgNO_3$ solution was included in the nucleation process, Fig. 2 of a layer obtained without the $AgNO_3$ step. Figure 1 shows a regular pattern of small particles with sizes of 100-150Å. The pattern in Fig. 2 shows particles of the same size, but it is less dense; the number of particles is only about one half of that in Fig. 1. We were of the opinion that the nucleation was homogeneous enough to justify a quantitative analysis.

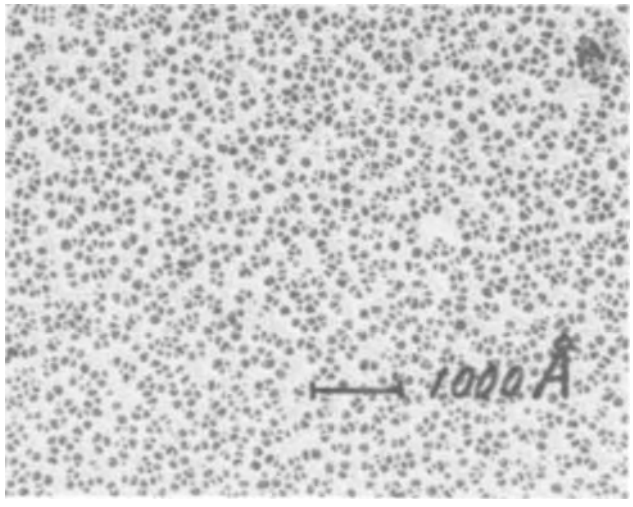

Fig. 1. Transmission electron micrograph of a NiP layer, about 80Å thick, nucleated with a $AgNO_3$ step included.

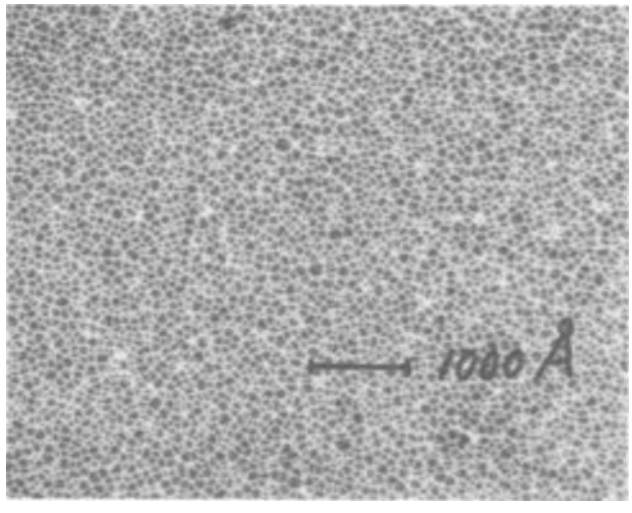

Fig. 2. Transmission electron micrograph of a NiP layer, about 80Å thick, nucleated without a $AgNO_3$ step.

Also, before and after each step of the nucleation procedure, replicas of the surface were made and examined in the electron microscope. They all showed the same appearance thus indicating that the nucleation process was homogeneous. No agglomerated clumps were found. Transmission micrographs of thin silicon oxide layers dipped in the $SnCl_2$ solution showed no clumps either. This is in contrast to the results of Sard (3). The high $SnCl_2$ concentration, used by Sard, may be responsible for this difference in results.

Analysis with radioactive tracers—The amounts of tin, silver, palladium, and chlorine left on the substrate after each step followed by rinsing, were determined by using radioactive isotopes of these elements. Some properties of the isotopes used are shown in Table II.

Table I. Solutions and conditions of nucleation procedure with a $AgNO_3$ step included

Step	Solution composition per liter		Temperature	Duration
a	$SnCl_2 \cdot 2H_2O$	100 mg	Room	1 min
	HCl sp. gr. 1.19	0.1 ml		
b	$AgNO_3$	1g	Room	1 min
c	$PdCl_2$	100 mg	~4°C	1 min
	HCl sp. gr. 1.19	3.5 ml		
d	Water, deionized		95°C	At least 15 sec

Table II. Isotopes used for analysis with radioactive tracers

Element	Isotope	Half life	Delivered as	Active conc. mg/ml	Active conc. mCi/ml	Peak measured, keV
Tin	Sn^{113}	115 days	Sn^*Cl_4 in 6M HCl	0.072 Sn*	1.0	393 (In^{113m})
Silver	Ag^{110m}	253 days	Ag^*NO_3 in 0.1M HNO_3	0.64 Ag*	1.0	658
Palladium	Pd^{109}	13.5 hr	Pd^*Cl_2 in 0.042M HCl	0.0605 Pd*	10^{-3}	88
Chlorine	Cl^{36}	3.1×10^5 years	HCl* in 0.38M HCl	10-12 Cl*	44×10^{-3}	—

The activities of Sn^{113}, Ag^{110m}, and Pd^{109}, all γ-emitters, were measured by means of a NaI(Tl) well-type scintillation detector and a single-channel spectrometer. The radiation of Cl^{36}, a β-emitter, was measured with a Philips Liquid Scintillation Analyser, using both the liquid scintillation and the Čerenkov method. The efficiency of the liquid scintillation method is about a factor of 20 higher than that of the Čerenkov method but the latter is less sensitive to "quenching." With each of the isotopes a solution was prepared, such that the same total concentrations of all components as given in Table I were maintained as far as possible. The final solution had to have a specific activity high enough to allow determination of the amount of the element on the glass substrate with a reasonable accuracy. This means that only small amounts of the radioactive Sn and Ag isotope solutions had to be added to the corresponding non-active solutions, whereas relatively high amounts of the radioactive Pd and Cl solutions were necessary. The accuracy of the method for Sn, Ag, and Pd is 10% (2s) or better, for Cl 30% (2s).

Radioactive tin was added in the stannic form.[4] Prerequisites for using this as radioactive tracer in our case are that the small amount of stannic ions added has no effect on the nucleation procedure and that there is a fast exchange between the isotopes of Sn^{2+} and Sn^{4+} ions. The first effect is negligible, because a small amount of stannic ions is always formed in a $SnCl_2$ solution by oxidation with air. We checked that an amount of Sn^{4+} ions up to a ratio of $Sn^{4+}:Sn^{2+}$ of at least 1:100 has no noticeable effect on the nucleation process, whereas the ratio of active Sn^{4+} to nonactive Sn^{2+} in the solution was approximately $1:25 \times 10^3$.

According to Haïssinsky's Handbook (16) Sn^{2+} and Sn^{4+} in a 9M HCl solution exchange their isotopes within several minutes. Though our solution contains only about 0.001M HCl, the extremely low concentration of Sn^{4+} ions causes a fast exchange. We checked this by varying the $*Sn^{4+}$ concentration and the time elapsed between adding the radioactive solution and immersion of a glass sheet. Within 15 to 20 min a constant amount of tin was found on the glass independent of the $*Sn^{4+}$ concentration, assuming a complete exchange.

Only the total amount of tin left on the glass could be measured.

The quantity of tin was determined by measuring the 393 keV peak of the daughter In^{113m} (half life 1.66 hr). The measurements were made the day after performing the experiments because an equilibrium had to be reached.

The radioactive silver was delivered as a $AgNO_3$ solution containing 0.1 mol HNO_3. Normally we use a solution of only $AgNO_3$. The ratio of active Ag* to nonactive Ag in the final solution was approximately $1:10^3$, therefore the concentration of HNO_3 in the final solution was only 10^{-4}M. This did not noticeably affect the nucleation procedure.

The radioactive palladium was obtained by irradiation of 10.1 mg $PdCl_2$ in a reactor in a flux of 3×10^{11} $nsec^{-1}$ cm^{-2} for 110 min. The activated product was dissolved in 3.5 mliters 1.2M HCl and this solution was diluted to 100 mliters. The experiments were carried out within a few hours after irradiation because of the short half life of Pd^{109}. The results were corrected for its decay. The Cl^{38} formed during irradiation of $PdCl_2$ has a half life of 37 min, much shorter than that of Pd^{109} and should not have affected our results.

The radioactive chlorine was delivered as a solution of HCl^{36} with a small amount of inactive HCl. The analysis of chlorine was less accurate than that of the other elements, due to the low specific activity of Cl^{36} as a consequence of its long half life and to the limited amount of HCl* that could be added to the $SnCl_2$ and $PdCl_2$ solutions to maintain the concentrations at their usual values. From earlier experiments we knew that a high concentration of HCl in the $SnCl_2$ solution results in a poor nucleation. After we found that only traces of chlorine were left on the glass after the treatment in the $SnCl_2$ solution, in both solutions the concentration of active chlorine was made as high as possible. The ratio of active Cl* to nonactive Cl in the $SnCl_2$ solution was about 1:1 and in the $PdCl_2$ solution about 1:0.23.

After a solution with one of the active elements had been prepared, a new glass sheet was used for each following step included. As an example, to determine the amount of tin left on the surface, a glass sheet was immersed in the $SnCl_2$ solution containing active Sn*, rinsed, and kept in water until the activity could be measured. Another glass sheet was also immersed in the same solution, rinsed, immersed in the $AgNO_3$ solution, rinsed, and kept in water until measuring, and so on.

Duplicate experiments were performed using the same solution and for most elements all the analyses were repeated with freshly made solutions.

Instead of rinsing with running deionized water three beakers with fresh deionized water for each glass sheet were used. The test specimen was immersed in each beaker for 20 sec. This rinsing was sufficient, because in the third beaker no activity was found and rinsing six times instead of three times did not change the amount left on the surface.

The results are collected in Table III.

The amount of tin is strikingly constant during the whole procedure. Also the same amount of tin is present on the surface with and without an intermediate $AgNO_3$ step. The average of all the values, obtained with the $AgNO_3$ step included, is 0.109 μg Sn per cm^2. Assuming a homogeneous film, this corresponds to 1 atom Sn on approximately 18Å^2 or 1 atom per 4.2Å in a square arrangement, which is close to a monomolecular layer of a tin compound.[5] Only traces of Cl are left on the surface after immersion in the $SnCl_2$ solution. Sharp (1) assumes that a hydrated stannous complex is adsorbed on the surface. We suggest a chemical reaction between the stannous ions and the OH-groups present on the glass surface.

For simplicity we shall first consider the case of silica glass, characterized by a random network of interlinked SiO_4-tetrahedra. If this silica glass is brought into contact with an aqueous solution, each Si atom at the surface may be bonded to one, two, or even three OH-groups by chemisorption. Figure 3 gives an example.

Several reactions with stannous ions can be assumed. Examples are

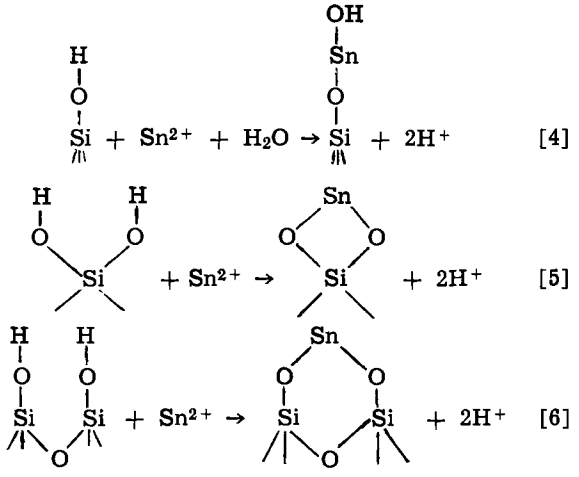

[4] The Radiochemical Centre Amersham in England was unable to deliver Sn in the stannous form and we did not succeed in finding a simple method to reduce the $*Sn^{4+}$ to $*Sn^{2+}$ without contaminating the solution. In a paper published after revision of this manuscript Feldstein and Weiner (23) give results of a study using $*Sn^{2+}$ as well as $*Sn^{4+}$.

[5] Feldstein and Weiner (23), using aged combined $SnCl_2$ and $SnCl_4$ solutions on a hydrophobic substrate (Teflon), found values approximately a factor 20 to 30 higher.

Table III. Amounts of Sn, Ag, Pd, and Cl left on a glass substrate after the subsequent steps of the nucleation process

$SnCl_2$ + rinsing	$AgNO_3$ + rinsing	$PdCl_2$ + rinsing	Warm water	Ni bath + rinsing	Amounts in $\mu g/cm^2$					
					Sn	Ag	Pd	Cl[a] LSC[c]	Cl[b] LSC[c]	Cl[b] Čerenkov
+	–	–	–	–	0.106	—	—	~0.001	—	—
					0.125			~0.004		
+	+	–	–	–	0.126	0.152	—	0.003	—	—
					0.126	0.169		0.002		
+	+	+	–	–	0.104	0.135	0.068	—	0.46	1.40
					0.121	0.140	0.050		0.20	0.54
						0.163				
						0.165				
+	+	+	+	–	0.097	0.068	0.057	—	0.06	0.06
					0.094	0.090	0.041		0.05	0.03
+	+	+	+	+	0.112	0.071	0.044	—	—	—
					0.100	0.082	0.041			
					0.101	0.072				
					0.096	0.076				
+	–	+	–	–	N.D.[d]	—	0.041	—	0.04	0.13
							0.041		0.07	0.18
+	–	+	+	–	N.D.	—	0.040	—	0.07	0.04
							0.040		0.06	0.01
+	–	+	+	+	0.094	—	0.040	—	—	—
					0.112		0.040			

[a] With activated Cl* in $SnCl_2$ solution.
[b] With activated Cl* in $PdCl_2$ solution.
[c] Liquid scintillation method.
[d] Not determined.

The Sn atoms on the surface will be surrounded by H_2O molecules. In silica glass the distance between 2 Si atoms in the Si-O-Si bridges is 3.02Å (17). However, the distance between Si atoms of neighboring $Si-O_4$ units not linked by oxygen atoms will be somewhat larger. According to Eq. [4]-[6] one Sn atom will be bonded to one or two Si atoms. Therefore the distance between the Sn atoms on silica glass may be expected to vary between 3 and 6Å.

The network of soda lime glass, in which about 15% of the oxygen ions are nonbridging, after extracting the metal ions from the surface, will be somewhat looser than that of silica glass. Thus the average distance between the Si atoms will definitely be somewhat greater than 3Å. Therefore, as a consequence of the calculated average distance of 4.2Å between the Sn atoms, the occupation of the Sn atoms might be close to one Sn atom per Si atom on the glass surface.

The amount of silver left on the surface after immersion in the $AgNO_3$ solution is *ca.* 0.16 $\mu g/cm^2$. This corresponds to 1.6 atom Ag per atom Sn.

During a subsequent immersion in the $PdCl_2$ solution no silver is removed. This contradicts reaction [3] according to which silver should be replaced by palladium.

After a dip in warm water the amount of silver is decreased to about half of its value and this reduced amount is maintained after nickel plating. We repeated these experiments with and without the step in warm water and also varied the duration of this step. Table IV gives the results. In all cases the amount of silver left after nickel plating is considerably lower than that after immersion in the $PdCl_2$ solution. However, without a dip in warm water the amount of silver left is higher than with this dip. A dip of 15 sec or 3 min in warm water makes hardly any difference. We know from earlier experiments that in our procedure a dip in warm water is essential for a homogeneous nucleation. Here again 15 sec or 3 min in water at 95°C gave the same results.

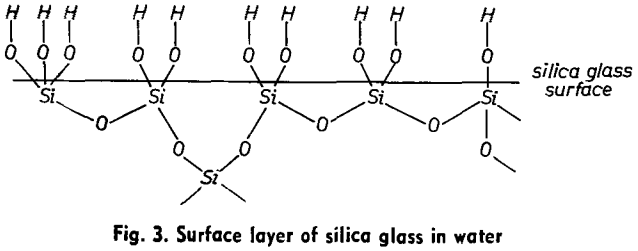

Fig. 3. Surface layer of silica glass in water

Table IV. Effect of rinsing in warm water before Ni-plating on the amount of Ag left on the substrate

Warm water	Steps after immersion in $SnCl_2$, $AgNO_3$, and $PdCl_2$ solutions: Ni bath + rinsing	μg Ag per cm^2
—	–	0.163
		0.165
—	+	0.090
		0.092
10 sec	+	0.072
		0.076
3 min	+	0.069
		0.069

The amount of palladium left on the surface after immersion in the $PdCl_2$ solution is 0.04-0.05 $\mu g/cm^2$, independent of whether a preceding step in a $AgNO_3$ solution is included or not.

No change of the amount of palladium occurs during dipping in warm water or during nickel plating.

The amount of chlorine left after the $SnCl_2$ step is negligible, as stated above. After immersion in the $PdCl_2$ solution, a relatively high amount of Cl is left on the surface, especially if a preceding step in a $AgNO_3$ solution is included. This amount is not reproducible. We repeated the experiments several times. The extreme values found were 0.2 and 1.4 $\mu g/cm^2$, corresponding to 6 and 40 Cl atoms per Sn atom, respectively. Although the chlorine analysis is less accurate than the analyses of the other elements, the spread in the chlorine values is much greater than can be attributed to the accuracy.

The large amount of Cl left on the surface makes it unlikely that Eq. [1] or [2] + [3] is representative for the mechanism of the nucleation process. The formation of a complex compound is more probable.

We found in the case of an intermediate $AgNO_3$ step

$$Sn : Pd : Ag : Cl = 1 : (0.4\text{-}0.5) : 1.6 : (6\text{-}40)$$

and without a $AgNO_3$ step

$$Sn : Pd : Cl = 1 : 0.4 : (1\text{-}5.5)$$

The ratio Sn : Pd is (2 to 2.5): 1. This is approximately the same as in the complex given by Khattak (14) and in the complex with $m = 2$ mentioned by Tsukahari (8).

After the dip in warm water the amount of chlorine on the surface is decreased to approximately 1 Cl atom per Sn atom, whether or not a preceding $AgNO_3$ step

is included. We assume that the Cl removed is replaced by OH groups. This hydrolysis might also occur at temperatures lower than 95°C but at a slower rate and might be an explanation for the poor reproducibility of the amount of Cl found after the immersion in the $PdCl_2$ solution.

Whether the chlorine left after the dip in warm water stays on the surface during nickel plating has not been determined.

Ellipsometry.—To obtain more evidence that no metallic palladium or silver is formed during the nucleation process, some experiments were performed using an ellipsometer.

Ellipsometry measures the change in the state of polarization of polarized light upon reflection from a surface. It yields two parameters, designated Δ and ψ, from which the optical constants, viz., refractive index and extinction coefficient of a film-free substrate, can be calculated. Formation of a layer on the substrate generally leads to changes in the ellipsometric parameters, and these changes give information concerning the thickness and the optical constants of this layer. The method is capable of detecting even small fractions of a monomolecular layer in many cases (18).

A layer which is optically nonabsorbing (low extinction coefficient) will give mainly a change in Δ and have only a negligible effect on ψ. Optically absorbing layers (high extinction coefficient), however, will show a significant change both in Δ and in ψ. The method therefore is well suited to an investigation of whether the films formed during the nucleation procedure are metallic or nonmetallic. As has been shown recently by Smith (19) a metallic film in submonolayer quantities still has metal-optical properties.

From the measurements with radioactive isotopes we know that *ca.* 0.16 $\mu g/cm^2$ silver and *ca.* 0.05 $\mu g/cm^2$ palladium are left on the surface. Assuming a homogeneous distribution these amounts correspond roughly with a monolayer of silver and 0.3 of a monolayer of palladium, or with *ca.* a 3Å thick layer of silver and a 1Å thick layer of palladium. We expect these values to be high enough to decide by ellipsometric measurements whether these elements are in the metallic or in the nonmetallic state.

The ellipsometer used was built in this laboratory. The sensitivity was ± 0.005 degree. A block diagram of the arrangement is shown in Fig. 4.

A He-Ne laser beam with a wavelength of 6328Å was used. The light of this beam is linearly polarized. The ¼ λ plate before the polarizer serves to obtain circularly polarized light, otherwise the intensity after the polarizer is dependent on the position of the polarizer. The value of Δ for a glass sheet immersed in water is somewhat temperature dependent. Δ changed by approximately +0.1 degree for an increase in temperature of 1°C. ψ showed no noticeable change.

Therefore the experiments were carried out at a constant temperature in a cell surrounded by a water

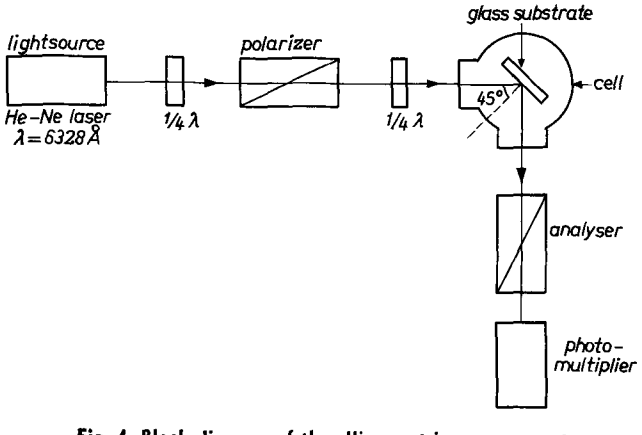

Fig. 4. Block diagram of the ellipsometric arrangement

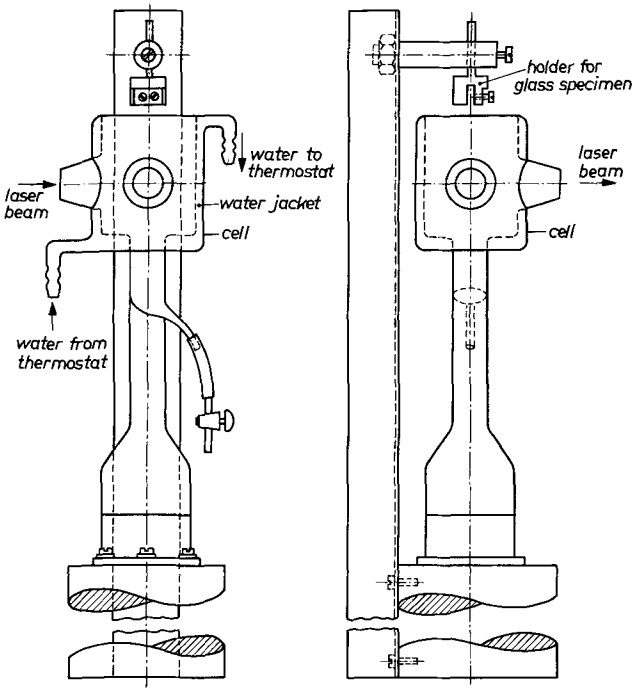

Fig. 5. Cell used for ellipsometric measurements

jacket except at the cell windows (see Fig. 5). Through this jacket water from a thermostat could be circulated to keep the temperature in the cell constant within 0.1°C. The temperature of the thermostat was chosen to be close to room temperature. All the solutions and rinsing water were kept in the thermostat before use, except those to be used at temperatures differing from room temperature, viz., the $PdCl_2$ solution (*ca.* 4°C), hot water (95°C), and the Ni solution (95°C).

Both the test specimen and the cell had to be rigidly mounted.

After cleaning the glass sheet, it was placed in the cell, which had previously been filled with deionized water and the ellipsometer was adjusted. For each test series the stabilities of the cell and the test specimen were checked by pouring hot and cold water into the cell; after the temperature was constant again, the readings of the ellipsometer had to be the same. Then the nucleation procedure was started by emptying the cell, pouring the $SnCl_2$ solution into it, removing the $SnCl_2$ solution after 1 min, and rinsing both glass sheet and cell by pouring deionized water into the cell for 1 min, after which Δ and ψ were read. Then the $AgNO_3$ solution was poured into the cell, and so on. If a solution at a low or a high temperature was used, the cell was rinsed until the temperature in it was again close to that of the thermostat before readings were made.

Several series were performed. Table V gives a summary of the results. All the values of $\delta\Delta$ and $\delta\psi$ are deviations from the initial values before immersion in the $SnCl_2$ solution, hence not per step.

As can be seen from Table IV, Δ has changed somewhat after each step, always in the same direction. The change in ψ is much smaller. For comparison a few calculated values of $\delta\Delta$ and $\delta\psi$ both for homogeneous films with high and low extinction coefficients are given in Table VI.

The values of the refractive indices (n) and extinction coefficients (K) are more or less arbitrarily chosen. The thickness has been varied to a maximum of 5Å for the strongly absorbing (metallic) and to a maximum of 25Å for the slightly absorbing films (nonmetallic). These values are more or less representative for monolayers of a metal and a metal-ion complex, respectively.

The small experimental values of $\delta\Delta$ and $\delta\psi$ (Table V) can only be interpreted in terms of nonmetallic

Table V. Changes in ellipsometric parameters Δ and ψ during the nucleation procedure on a glass substrate

Nucleation steps				Number	$\delta\Delta$ in degrees			$\delta\psi$ in degrees		
$SnCl_2$ + rinsing	$AgNO_3$ + rinsing	$PdCl_2$ + rinsing	Warm water	of experiments	Min.	Max	Avg	Min.	Max	Avg
+	−	−	−	5	−0.15	0.00	−0.08	0.000	+0.005	+0.000
+	+	−	−	3	−0.38	−0.30	−0.35	0.000	+0.025	+0.015
+	+	+	−	3	−0.52	−0.50	−0.51	+0.015	+0.030	+0.025
+	+	+	+	3	−0.57	−0.48	−0.52	+0.025	+0.045	+0.035
+	−	+	−	2	−0.32	−0.22	−0.27	0.000	+0.015	+0.005
+	−	+	+	2	−0.34	−0.29	−0.32	+0.015	+0.015	+0.015

Table VI. Calculated values for $\delta\Delta$ and $\delta\psi$ with $n_{water} = 1.3330$, $n_{glass} = 1.5200$ and $\lambda = 6328$Å. Angle of incidence = 45.0°

Thickness in Å	n	K	$\delta\Delta$	$\delta\psi$
		Strongly absorbing layers (metallic)		
1	1.4000	1.40	−3.34	+0.30
3			−8.85	+0.94
5			−13.11	+1.61
1	1.4000	2.10	−5.27	+0.56
3			−12.71	+1.78
5			−17.40	+3.02
1	1.4000	2.80	−7.54	+0.82
3			−16.59	+2.66
5			−21.10	+4.48
1	1.4000	3.50	−10.22	+1.11
3			−20.42	+3.66
5			−24.22	+6.08
		Slightly absorbing layers (nonmetallic)		
5	1.4700	0.030	−0.13	+0.01
15			−0.39	+0.02
25			−0.64	+0.03
5	1.4700	0.045	−0.15	+0.01
15			−0.44	+0.02
25			−0.72	+0.04
5	1.4900	0.030	−0.09	+0.01
15			−0.28	+0.02
25			−0.46	+0.04
5	1.4900	0.045	−0.11	+0.01
15			−0.33	+0.03
25			−0.54	+0.05

films. The thickness of the films (for thin films $\delta\Delta$ changes linearly with the thickness) increases with each following step, except after the warm water treatment.

ψ changes rapidly immediately after filling the cell with the electroless Ni solution.

A sodium hypophosphite solution, either warm or cold, added to the cell after the nucleation procedure had been completed, caused no significant change in Δ or in ψ. This indicates that if a Sn-Pd complex is present on the surface, this is not reduced by hypophosphite to metallic palladium.

Our conclusion that no metallic Ag or Pd is formed during nucleation is further supported by recent ellipsometric measurements of Kelly (20), who followed the reduction of $PdCl_2$ on TiO_2 by illumination. He found changes in Δ and ψ, which indicated a metallic film. This could be proved for thicker films by reflection high-energy electron diffraction. The sensitivity of the ellipsometric measurements was high enough to detect 0.1 of a metallic Pd monolayer.

Experiments with mixed solutions of $SnCl_2$ and $PdCl_2$.—We also did some qualitative experiments by mixing various volumes of the solutions of $SnCl_2$ and $PdCl_2$, given in Table I. Yellow colored solutions were obtained. No palladium was formed. Heating gave in most cases a flocculent, nonmetallic precipitate.

If to the mixed solutions a sodium hypophosphite solution is added, no metallic palladium is formed. Upon heating a precipitate arises, which contains metallic palladium only if the ratio Sn^{2+} : Pd^{2+} in the mixed solution is low. This is in agreement with our finding that a nucleated substrate in a NaH_2PO_2 solution shows no light absorbing film in the ellipsometer.

By mixing solutions of $SnCl_2$ and $PdCl_2$ at higher pH's and with a small excess of chloride, dark colored solutions may occur. In such solutions a black precipitate is formed by oxidation with air. This precipitate is nonmetallic and consists of a palladium hydroxide or perhaps a basic palladium salt. If air is excluded the solutions are stable. This result might be in agreement with the opinion of Khattak (14) that a complex with univalent palladium is formed.

Discussion and Conclusions

The foregoing results can be summarized as follows. After immersion in a $SnCl_2$ solution a very reproducible amount of tin is left on the surface as a chlorine-free compound. This amount, corresponding closely to a monolayer, is maintained during all the subsequent steps, including the nickel plating. We suggest that the tin is chemically bonded to the Si-O groups of the pretreated glass surface.

The amount of palladium left after the immersion in a $PdCl_2$ solution, both with and without an intermediate dip in a $AgNO_3$ solution, is also reproducible and the same amount is also maintained during the subsequent steps. The ratio of Sn:Pd is approximately 2:1. After the $PdCl_2$ step a large amount of chlorine is found. This makes it unlikely that palladium metal is formed. The amount of Cl is not very reproducible, it varies from 6 to 40 Cl atoms per Sn atom when a $AgNO_3$ step is included and from 1 to 6 without a $AgNO_3$ step. A dip in warm water removes much of the Cl, but an amount is left corresponding approximately to 1 Cl atom per Sn atom. We expect that the Cl atoms removed are replaced by OH groups, consistent with the fact that the ellipsometric parameters change very little.

The amount of silver left after a dip in a $AgNO_3$ solution does not change during the following dip in a $PdCl_2$ solution. Thus, no exchange of Ag and Pd takes place. This gives evidence that the silver is not present in the metallic state either. The silver ions will be taken up by the Sn containing film in another way than the palladium ions, because the amount of palladium left on the surface is not affected by a previous dip in a $AgNO_3$ solution. An adsorption of the silver ions and a complex forming of the Pd ions is a very speculative assumption and has to be verified by further experiments.

Nearly half of the silver is removed by a dip in warm water. This indicates that the silver ions occupy two different sites on the surface presumably on Sn and on Si positions.

Ellipsometric measurements show clearly that no strongly light absorbing film is formed. This makes it very likely that the silver and palladium present on the surface are not in the metallic state.

Finally, a further support for the fact that no metallic palladium is formed, is that palladium either as bulk metal or as sputtered film is only a poor catalyst for electroless nickel deposition. It shows a long initiation period, much longer than a surface nucleated with a $SnCl_2$-$PdCl_2$ solution. The behavior of palladium metal as catalyst depends very much on its pretreatment, in many cases no nickel deposits at all.

The main conclusion from our results is therefore that during the $SnCl_2$-$PdCl_2$ nucleation process on glass, either with or without an intermediate $AgNO_3$ step, no metallic film could be detected. The formation of a Sn-Pd complex is more likely. The structure and

composition of such a complex cannot be deduced from our results. We only know that the Sn:Pd ratio is about 2:1 and that an excess of Cl is present before heating in water. Whether the Pd occurs in a univalent or a bivalent state is not known.

No suggestion can be made about the mechanism of initiation of the nickel deposition of the nucleated glass surface. We could not detect a metallic film after a treatment with a hypophosphite solution. Possibly the Sn-Pd complex reduces the nickel-ions. Further study is necessary to solve this problem.

Acknowledgment

The authors wish to thank J. R. M. Gijsbers and H. B. Haanstra, G. P. H. Peskens and M. L. Verheijke, E. E. de Kluizenaar, C. J. Loyen, and Dr. F. Meyer for their help with the electron microscopy investigations, the radioactive tracer techniques, and the ellipsometric measurements, respectively.

Manuscript submitted July 10, 1972; revised manuscript received June 24, 1973.

Any discussion of this paper will appear in a Discussion Section to be published in the June 1974 JOURNAL.

REFERENCES

1. D. J. Sharp, *Plating*, **58**, 786 (1971).
2. D. McBride and G. P. Vlasak, *This Journal*, **118**, 2055 (1971).
3. R. Sard, *ibid.*, **117**, 864 (1970).
4. G. Müller, "Galvanisieren von Kunststoffen," p. 64, E. G. Leuze Verlag, Saulgau/Wittenberg, Germany (1966).
5. "Printed Circuit Group of the Institute of Metal Finishing," p. 222, R. Drapes Ltd., Teddington, Middlesex, England (1969).
6. W. Goldie, "Metallic Coating of Plastics," Vol. 1, p. 39, Electrochem. Publ. Ltd., Hatch End, Middlesex, England (1968).
7. S. L. Chow, N. E. Hedgecock, M. Schlesinger, and J. Rezek, *This Journal*, **119**, 1013 (1972).
8. M. Tsukahara, *J. Metal Finishing Soc. Japan*, **23**, 83 (1972); Ref. *Metalloberflaeche*, **26**, 355 (1972).
9. R. L. Cohen, J. F. D. Amico, and K. W. West, *This Journal*, **118**, 2042 (1971).
10. R. L. Cohen and K. W. West, *ibid.*, **119**, 433 (1972).
11. N. Feldstein, To be published, presented at AES symposium "Plating in the Electronic Industry," January 1973.
12. W. B. Pollard, *Analyst*, **67**, 184 (1942).
13. G. H. Ayres and J. H. Alsop, *Anal. Chem.*, **31**, 1135 (1959).
14. M. A. Khattak and R. J. Magee, *Chem. Commun.*, 400 (1965).
15. G. E. Batley and J. C. Bailar, *Inorg. Nucl. Chem. Letters*, **4**, 577 (1968).
16. M. Haissinsky, "Nuclear Chemistry and its Application," p. 567, Addison-Wesley Publishing Co., Reading, Mass. (1964).
17. W. Eitel, "Silicate Science," Vol. 1, p. 11, Academic Press, New York (1964).
18. G. A. Bootsma and F. Meyer, *Surface Sci.*, **14**, 52 (1969).
19. T. Smith, *J. Opt. Soc. Am.*, **62**, 291 (1972).
20. J. Kelly, To be published.
21. R. L. Cohen and K. W. West, *This Journal*, **120**, 503 (1973).
22. A. Rantell and A. Holtzman, *Trans. Inst. Metal Finishing*, **51**, 62 (1973).
23. N. Feldstein and J. A. Weiner, *This Journal*, **120**, 475 (1973).

Dimethylamine Borane as the Reducing Agent in Electroless Plating Systems

Mark Lelental

Research Laboratories, Eastman Kodak Company, Rochester, New York 14650

ABSTRACT

The interaction of dimethylamine borane (DMAB) with evaporated metal nuclei that exhibit catalytic and noncatalytic behavior towards nickel electroless plating baths has been studied. The adsorption of DMAB, followed by its catalytic decomposition, was found to be the initial step of nickel electroless plating. Elemental boron, deposited on the surface of the catalyst, was identified as a product of the latter reaction. The process of nickel deposition was shown to require a larger metal aggregate for catalysis than that necessary for the DMAB decomposition reaction. A mechanism for this reaction is proposed and possible sources of inefficiencies in the electroless-plating pathway are discussed.

Amine boranes are useful reducing agents for many types of electroless plating solutions. An advantage such systems have over solutions that use sodium hypophosphite as a reducing agent is the production of a relatively pure metal deposit and the ability to be catalyzed by a wide range of materials (1, 2). A properly formulated solution is thermodynamically unstable but kinetically stable, its decomposition being accelerated by the presence of a catalyst that leads to the deposition of metal. The mechanism of electroless deposition usually presupposes adsorption of the reducing agent onto the catalytic surface, followed by autocatalytic metal deposition. Metallic palladium is the catalyst most commonly used for the initiation of electroless plating. For some practical applications of this process, the minimum number of atoms (or critical size) of a given material able to form catalytically active centers is taken as a measure of its catalytic activity. Hamilton and Logel (3) have studied such catalyst-size effects in electroless plating deposition. This paper presents the details of a study of the interaction of an amine borane type of reducing agent with the surface of a catalyst.

Key words: amine, boranes, electroless, plating, palladium.

The interactions of dimethylamine borane (DMAB) solutions with vacuum-deposited Pd, Ni, and Bi films were studied by analytical techniques that monitored boron content on the metal surface. In the case of Pd, for which there is a considerable interaction with DMAB, the kinetics of this surface reaction were also studied as a function of DMAB concentration, temperature, and Pd coverage. On the basis of these studies, a mechanism of the catalytic decomposition of DMAB on palladium is proposed. A similar investigation of the interaction of hypophosphite and nickel ions on evaporated metal films has been carried out using radiotracer techniques and will be the subject of a later report (4).

Experimental

The palladium catalyst was prepared as a thin metallic film deposited on double-coated tape (3M Company, No. 665) by the vacuum-deposition technique of Hamilton and Logel (5). The Pd coverage was varied over the range 1.6-0.05 mg/ft^2. These values span the range of sizes and coverages above and below the critical size. This method of preparing the catalyst film allows the coverage of Pd film to be related to the size of the metal nuclei. Therefore, critical coverage represents a film of Pd nuclei of a critical size for catalysis in the appropriate electroless plating solution.

The electroless plating was carried out at room temperature and solution employed in these studies had the following composition:

$NiCl_2 \cdot 6H_2O$ (Baker and Adamson, reagent grade)	0.1M
Gluconic acid (Eastman Organic Chemicals, technical grade)	0.65M
NH_4OH	to pH = 9.0
DMAB (Callery Chemical Co.)	1%

A spectrophotometric method based on the formation of a boron-curcumin complex was used for the determination of boron (6). The complex is very stable and its high extinction coefficient makes it highly suitable for boron analysis. However, protonated curcumin in the acidic solution forms a strongly interfering complex, which must be destroyed before any measurement can be made. This was accomplished as proposed by Grinstead (7) by neutralization of the solution with ammonium acetate. For our studies, the determination of boron was carried out by modification of the procedures of Hughes and Metcalfe (8), and of Grinstead (7):

1. Introduce a dry sample containing 0.05–3.5 μg of boron into 125-ml polyethylene bottle.
2. Add 3 ml of curcumin (Eastman Organic Chemicals) reagent (0.125g of curcumin in 100 ml of glacial acetic acid).
3. Add 3 ml of acid reagent (equal volumes of 96% sulfuric acid and glacial acetic acid).
4. Mix and let stand for 2 hr.
5. Neutralize using 15.0 ml of ammonium acetate–acetic acid reagent (250g of ammonium acetate plus 300 ml of glacial acetic acid in sufficient water to make 1 liter).
6. Measure the absorbance at 555 nm in 1-cm cells against a boron-free blank.

For levels below 2 μg of boron, replacement of all glassware by polyethylene equipment was necessary to obtain reproducible results and low blanks.

The calibration curve was determined by placing 25, 50, and 100 microliters of solutions (containing 80 μg/ml and 10 μg/ml of boron as boric acid) on 0.5 in.^{2} of the double-coated tape mounted on a microscope slide. After drying, the tape was removed from the slide and placed in a polyethylene vial. The relationship between absorbance and boron content was determined (Fig. 1). For the studies of the interaction between catalyst and DMAB, the samples (metal nuclei-tape-glass slide) were immersed in aqueous DMAB solutions for the given period of time and then washed with water to remove excess DMAB. Then either 0.5 in.^{2} or 0.25 in.^{2} of the dried tape was analyzed by the same procedure as used for the standards. Four independent samples were analyzed for each boron determination. All determinations of absorbance were carried out using a Beckman DK-2A ratio recording spectrophotometer. The absorbance was calculated as follows

$$A = A_M - A_B$$

where A_M is the absorbance for a sample containing metal nuclei on tape (expressed as absorbance/0.5 in.^{2} of tape) and A_B is the blank absorbance for tape alone (expressed as absorbance/0.5 in.^{2} of tape). The amount of boron was read from the calibration curve.

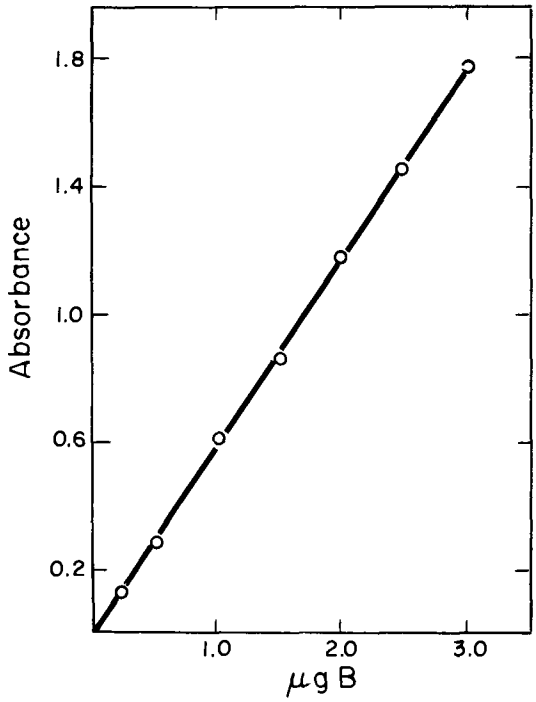

Fig. 1. Calibration curve for colorimetric determination of boron

Results and Discussion

Catalytic Nuclei (Pd)

Pd–DMAB interaction as a function of palladium coverage.—The films were immersed for 10 min in a 1% aqueous DMAB solution. The amount of "adsorbed" DMAB, as measured by the boron content, is shown in Fig. 2.

The results indicate that there is a much greater amount of boron on the palladium surface than would be expected assuming monolayer adsorption of the DMAB. For example, for Pd coverage of 0.5 mg/ft^2, the specific adsorption (Γ = number of moles of adsorbate/number of moles of adsorbent) is 9.83. This indicates that the mechanism of the interaction of

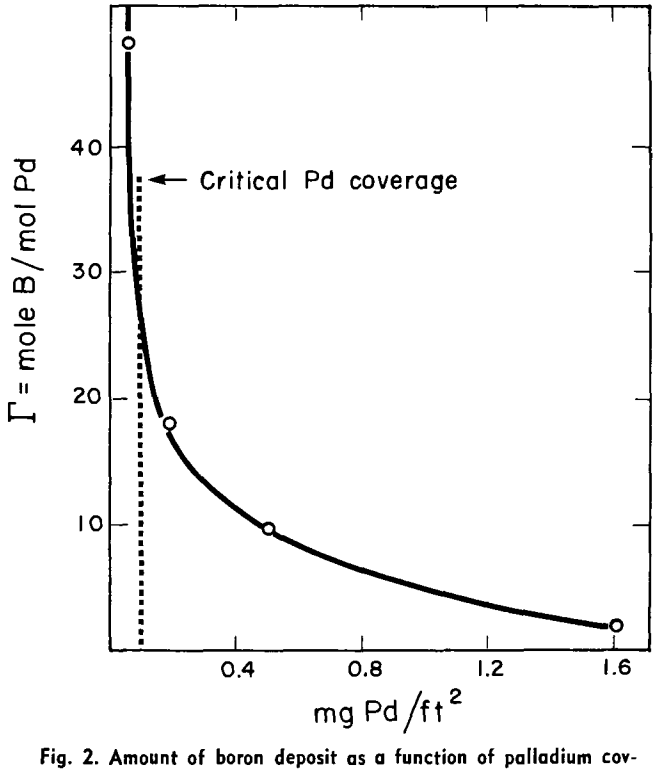

Fig. 2. Amount of boron deposit as a function of palladium coverage.

DMAB with the catalytic surface is different from that previously found for the hypophosphite system in which a monolayer adsorption was found (4). The results also show that even in the case of Pd coverages that are subcritical for nickel deposition, there is appreciable Pd–DMAB interaction. For example, a Pd coverage of 0.05 mg/ft² gives $\Gamma = 48.3$. The failure of the surface reaction between DMAB and Pd to terminate at subcritical Pd coverages indicates that another effect is responsible for the lack of nickel deposition in this region. A similar conclusion resulted from studies of adsorption of hypophosphite ions, where again no discontinuity of adsorption on Pd was observed below critical size.

Kinetics of the surface reaction between DMAB and Pd.—The results described above indicated that Pd-DMAB interaction is not a simple monolayer adsorption. To further elucidate this interaction it was studied as a function of time, concentration of DMAB, and temperature. Figure 3 illustrates the relationship between time and the amount of boron-containing species resulting from the surface reaction. Excess DMAB was used to keep the DMAB concentration essentially constant throughout the run.

The results indicate that the boron-containing product of this surface reaction is itself a catalyst for further reaction. This reaction is thus autocatalytic. The decrease of the rate of metal deposition with time is often observed in the electroless plating process for which autocatalytic behavior is well-established. This effect might be due to the accumulation in the solution of products of the reactions involved in electroless plating or to changes in the morphology of a metal deposit. The decrease of the rate of boron deposition with time might be due to the similar factors. Another possibility that must be taken into account is diffusion of palladium through the boron layer. Application of methods of surface examination, such as ESCA or Auger spectroscopy, could definitely establish the validity of this hypothesis. Such studies are in progress in these Laboratories. Studies of the rate of Pd-DMAB surface reaction as a function of DMAB concentration were carried out at two Pd coverages, one supercritical (0.5 mg Pd/ft²), and the other subcritical (0.04 mg Pd/ft²). Figure 4 illustrates the results of these studies.

A linear relationship exists between the amount of boron deposited as a result of surface reaction and DMAB concentration for the Pd coverages in both cases. The observation that even in the advanced stage of the process the rate varies significantly for the two Pd coverages indicates that in spite of the assumed coverage of the Pd nuclei by the boron-containing reaction product, the nature of the original Pd deposit still influences the course of the reaction.

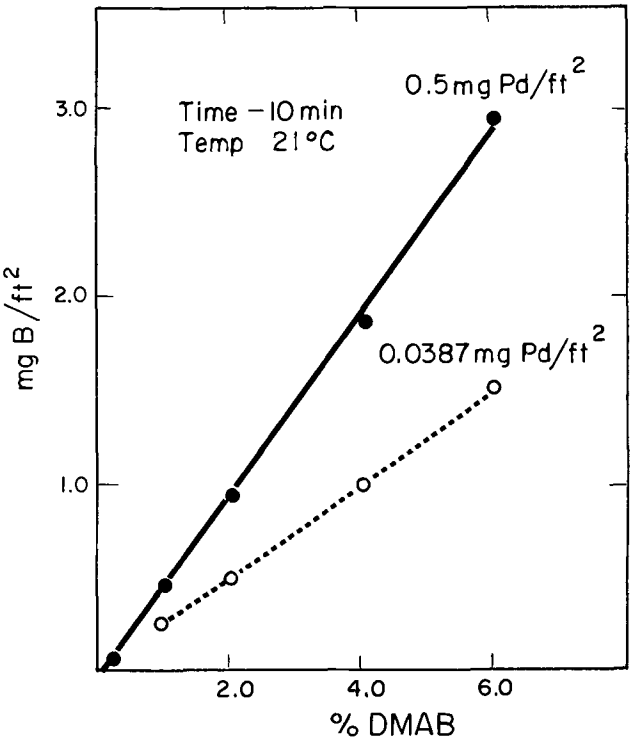

Fig. 4. Effect of DMAB concentration on boron deposition

The effect of temperature on the rate of boron deposition is shown in Fig. 5.

The increased rate of the surface reaction with increasing temperature is further evidence that the DMAB–Pd interaction is not a simple adsorption process. The activation energy of the over-all process in the temperature range 21°-32°C was estimated from

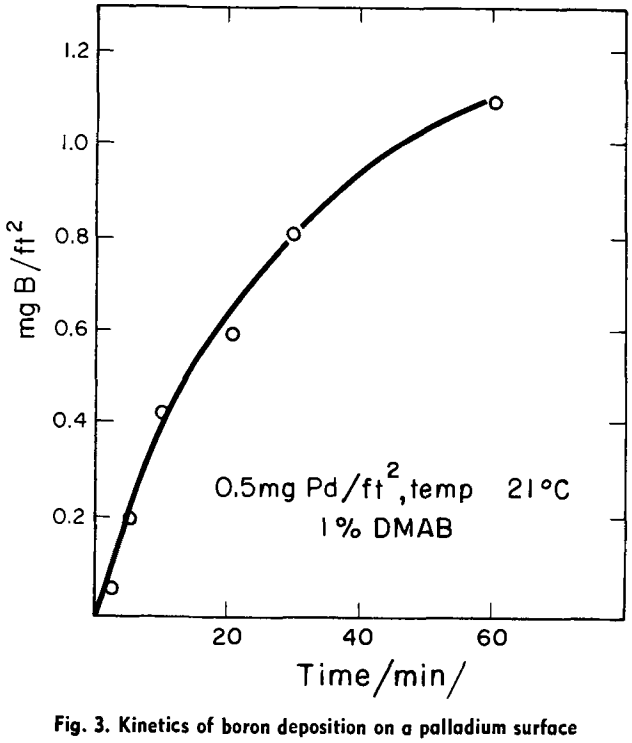

Fig. 3. Kinetics of boron deposition on a palladium surface

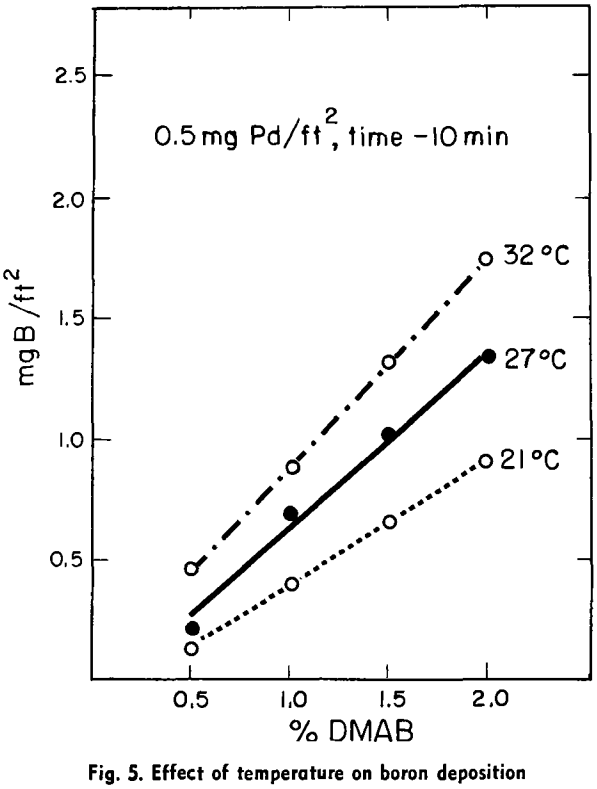

Fig. 5. Effect of temperature on boron deposition

the log k *vs.* $1/T$ relationship to be 12.2 kcal/mole. This applies to the reaction in the early (10 min) stage.

Products of the catalytic decomposition of DMAB on surface of palladium films.—Analysis by attenuated total reflectance (ATR) infrared spectroscopy of a Pd surface that had been treated with aqueous DMAB solution failed to detect the presence of any B-H-containing species on the Pd surface ($\nu_{B\text{-}H}$ = 1800-2400 cm^{-1}). Laser Raman spectroscopy also failed to detect the presence of any B-H-containing material on the Pd surface. The boron deposit was also investigated by x-ray diffraction methods.

A sample consisting of Ag foil on which Pd had been deposited by vacuum deposition was immersed into DMAB solution, washed, dried, and subsequently studied by the Debye-Scherrer method and diffractometry. Several successive scans were made under the conditions 45 kV, 24 mA, 3° tube Soller slit, 0.3° defining slit, 6° take-off angle, and a 3.5×10^{-6}-in.-thick beta filter in order to obtain the highest possible x-ray flux. The resulting diffraction patterns showed several low maxima between 3.5 and 7.5Å, which is the region of greatest diffracted intensity for both rhombohedral and tetrahedral boron. On the basis of these results, the presence of at least one crystallographic form of elemental boron on the palladium surface appears rather likely.

Nickel deposited from Ni–amine borane electroless plating bath always contains boron. It is possible that the boron in both cases (DMAB alone and electroless Ni) comes from the same mechanism of decomposition of amine borane.

Mechanism of the catalytic decomposition of DMAB on palladium.—In addition to elemental boron, the decomposition products of DMAB on metallic palladium are hydrogen, boric acid, and dimethylamine (9). On the basis of these products, the following mechanism is proposed

$$(CH_3)_2\overset{H}{\underset{|}{N}}\text{—}BH_3 + Pd^\circ \rightarrow \{[(CH_3)_2HN\text{—}BH_3]Pd\} \quad [1]$$

$$(CH_3)_2\overset{H}{\underset{|}{N}}\text{—}BH_3 \rightarrow Pd\cdots(BH_3) + (CH_3)_2NH \quad [2]$$
$$\vdots$$
$$Pd$$

$$Pd\cdots BH_3 \xrightarrow{3H_2O} \begin{cases} Pd\cdots B + 3/2H_2 \\ Pd + H_3BO_3 + 3H_2 \end{cases} \quad [3]$$

The cleavage of the B-N bond and formation of an adsorbed complex involving the borine radical [*i.e.*, $Pd\cdots(BH_3)$] could be facilitated by the initial adsorption of DMAB on the Pd surface. Borine is a powerful Lewis acid and would be hydrolyzed rapidly to produce boric acid and H_2. A competitive reaction is the reduction to elemental boron with the evolution of hydrogen. The suggestion of an adsorbed borine intermediate is consistent with electrochemical and chemical data for similar systems. Elder and Hickling (10) proposed the formation of a $Pt\cdots BH_3$ complex during the oxidation of aqueous $NaBH_4$ at a platinum electrode. Jones (11) has suggested that the reduction of organic carbonyl functions by trimethylamine borane proceeds by the formation of a $R_2\overset{+}{C}\text{-}O\text{-}BH_3$ species. Brown and co-workers (12) have proposed that diborane reduction of ketones most likely proceeds by an initial complexation of the BH_3 moiety with carbonyl oxygen followed by the intermolecular hydride shift. Kelly and Marchelli (13) postulated that the general acid-catalyzed hydrolysis of BH_3 adducts of a series of alkyl, aryl, and heterocyclic amines proceeded by a rate-determining electrophilic replacement of BH_3 from the nitrogen by the proton of the acid, followed by the rapid hydrolysis of the borane fragment. Formation of elemental boron by catalytic decomposition of BH_3 appears likely in view of the mechanism proposed by Machalov and co-workers (14) for the decomposition of $NaBH_4$ in $NiCl_2$ solution. The BH_3 formed as an intermediate can decompose, Eq. [4], or hydrolyze, Eq. [5]

$$BH_3 \xrightarrow{k_1} B + 3/2H_2 \quad [4]$$

$$BH_3 + 3H_2O \xrightarrow{k_2} H_3BO_3 + 3H_2 \quad [5]$$

The ratio of the two rate constants depends on the conditions under which the process is carried out, specifically, the composition of the electroless plating bath, pH, and temperature. Variations of these parameters lead to different boron contents in the deposited nickel.

Boron deposition on Pd surface and catalytic activity of Pd nuclei.—Pd metallic films were prepared by stepped vacuum evaporation using the method developed by Hamilton and Logel (5). The samples were divided into six sections varying only in Pd coverage. In the following experiments the Pd coverages varied in a geometrical progression so that each step differed from the preceding by a factor of ½.

The number of developable steps is related to the activity of a particular electroless plating solution. Such stepped deposits also allow the evaluation of a critical Pd coverage necessary for catalytic nickel deposition. Pd samples prepared by stepped evaporation were immersed in 1% aqueous DMAB solution for 10 min during which time 15–25 monolayers of boron were deposited on them, and were subsequently placed in the nickel–gluconic acid-DMAB electroless plating bath. The same number of active steps were observed for samples treated by the above procedure as in the case of identical samples that were immersed without pretreatment into an aqueous solution of DMAB. This indicates that the deposition of elemental boron, which is a product of DMAB decomposition on palladium, does not alter the catalytic activity of palladium towards nickel deposition.

Noncatalytic Nuclei

Nickel and bismuth metal nuclei prepared by vacuum deposition do not catalyze metal deposition from nickel–DMAB solutions. The interaction of DMAB with Ni and Bi metal nuclei was studied using the same technique as described for Pd. Table I contains results of these experiments. The level of sensitivity of the curcumin spectrophotometric boron determination does not allow us to conclude that DMAB is not adsorbed on the surface of Ni and Bi metal nuclei. But the analytical results indicate that if any adsorption of DMAB does take place it is not followed by catalytic decomposition of the adsorbed species. The fact that Ni and Bi metal nuclei do not catalyze the decomposition of DMAB (during our time scale) might be the main reason why these nuclei are not catalytically active towards nickel deposition. It is rather surprising that nickel nuclei prepared by vacuum deposition do not catalyze the initiation of nickel electroless plating, but chemically deposited nickel is catalytically active for the continuation of this process. However, it is often observed that the activity of catalysts varies depending

Table I. DMAB-Ni, Bi interaction

Metal nuclei	Coverage, mg/ft²	Deposited boron, mg/ft² (10 min)	$\Gamma = \frac{\text{mole of B}}{\text{mole of metal}}$
Ni	1.9	0.0006	below 0.06
Bi	2.0	0.0003	below 0.22
Pd	1.6	0.5356	3.10

upon the method of their preparation. The fact that nickel films prepared by vacuum deposition are not able to initiate the nickel electroless plating process might be caused by the presence of an oxide film. Nevertheless, other possibilities, such as impurities in chemically deposited nickel, as well as the presence of structural defects, also have to be taken into account.

Conclusions

These studies of the interaction of DMAB with palladium nuclei indicate that decomposition of DMAB takes place giving elementary boron in addition to the products previously reported: boric acid, hydrogen, and dimethylamine (9). The deposition of elemental boron on palladium in this reaction neither inhibits the reaction nor does it lead to a change of the critical Pd coverage necessary for subsequent nickel deposition. Since the DMAB decomposition occurs even in the cases of Pd coverages that were subcritical for nickel deposition, one must consider two different kinds of critical coverages: (*i*) critical coverage towards catalytic oxidation of reducing agent; and (*ii*) critical coverage towards the over-all nickel deposition process.

Hamilton and Logel (3) have found that two-atom Pd nuclei catalyze the decomposition of aqueous DMAB solution with the deposition of boron but larger Pd particles (4-20 atoms) are required for nickel deposition.

This leads to the conclusion that nickel deposition is dependent on processes complementary to the adsorption and decomposition of the reducing agent on the catalyst surface. Such processes may involve a catalyzed ligand dissociation reaction of the Ni^{+2} complex or electron transfer from the catalyst surface to some activated Ni^{+2} species. The actual electron-transfer reaction could involve Pd-H^-, Pd-H_2, or a Pd electrode mechanism. Proposed mechanisms of nickel deposition are based on these processes (15-21). It is also possible that adsorption of a complexing agent on the surface of the catalyst competes with adsorption of reducing agent. That might explain why the value of critical Pd coverage towards nickel deposition is highly dependent on the kind of complexing agent used in the formulation of the nickel physical developer. The fact that Ni and Bi metal nuclei are not able to catalyze the decomposition of DMAB might be the reason that they do not catalyze nickel deposition.

On the basis that cleavage of the N-B bond of the adsorbed amine borane occurs in the first stage of the process, we conclude that the energy of this bond and the ability of a catalyst to facilitate its cleavage are the critical parameters of the process.

Acknowledgments

I wish to thank Mr. Samuel Donley for x-ray diffraction examinations, and Drs. Joseph Yudelson and Henry Gysling for many helpful comments and suggestions.

Manuscript submitted May 14, 1973; revised manuscript received July 2, 1973.

Any discussion of this paper will appear in a Discussion Section to be published in the June 1974 JOURNAL.

REFERENCES

1. N. Feldstein, *RCA Rev.*, **317** (1970).
2. M. Lelental, To be submitted for publication.
3. J. F. Hamilton and P. C. Logel, *J. Catal.*, In press.
4. M. Lelental and J. S. Yudelson, To be submitted for publication.
5. J. F. Hamilton and P. C. Logel, *Thin Solid Films*, In press.
6. H. S. Roth and B. Miller, *Arch. Pharm.*, **297**, 660 (1964).
7. R. R. Grinstead and S. Snider, *Analyst*, **92**, 532 (1967).
8. M. R. Hughes and J. Metcalfe, *ibid.*, **87**, 956 (1962).
9. G. O. Mallory, *Plating*, **58**, 319 (1971).
10. J. P. Elder and A. Hickling, *Trans. Faraday Soc.*, **58**, 1852 (1962).
11. W. M. Jones, *J. Am. Chem. Soc.*, **82**, 2528 (1960).
12. H. C. Brown, H. I. Schlesinger, and A. B. Berg, *J. Org. Chem.*, **61**, 673 (1939).
13. H. C. Kelly and F. R. Marchelli, *Inorg. Chem.*, **3**, 431 (1964).
14. K. N. Machalov, N. V. Tremasov, and Kh. V. Shifrin, *Tr. Kazansk. Chim.-Technol. Inst.*, **30**, 95 (1964).
15. G. Gutzeit, *Plating*, **46**, 1158, 1275, 1377 (1959).
16. G. Gutzeit, *ibid.*, **47**, 63 (1960).
17. R. M. Lukes, *ibid.*, **51**, 969 (1964).
18. A. Brenner and G. E. Riddel, *Proc. Am. Electroplaters' Soc.*, **34**, 156 (1947).
19. N. Feldstein and P. R. Amodio, *Plating*, **56**, 1246 (1969).
20. N. Feldstein and P. R. Amodio, *This Journal*, **117**, 1110 (1970).
21. G. Salvago and P. L. Cavallotti, *Plating*, **59**, 665 (1972).

Fabrication of Semitransparent Masks

N. Feldstein*,[1] and J. A. Weiner

RCA Corporation, David Sarnoff Research Center, Princeton, New Jersey 08540

ABSTRACT

A chemical plating technique has been devised for the preparation of semitransparent photomasks. The deposited thin film meets the optical requirement of being opaque in the ultraviolet range and transparent enough in the visible range for see-through applications. Suitable etchants are available to provide good edge definition of photolithographically delineated semitransparent films without deteriorating common resist compositions. Analytical characterization of the deposited films revealed that they are primarily composed of cuprous oxide. The major advantage of the present approach is the low cost. Masks made by the present system are more durable (harder) than emulsion-type masks, but less durable than iron oxide semitransparent masks.

In the manufacturing of electronic parts, photomasks are widely used in defining images on photosensitive materials. In the manufacturing of semiconductor devices, two main types of photomasks are used: (*a*) photographic emulsion on glass (silver in gelatin), and (*b*) chromium film on glass.

In both cases, the opaque regions absorb the incident light, allowing only selective areas of the photosensi-

* Electrochemical Society Active Member.
[1] Present address: Surface Technology, Incorporated, Princeton, New Jersey 08540.
Key words: semitransparent mask, chemical plating, cuprous oxide.

tive material to interact with the light. Both masks have certain advantages and certain limitations, all stemming from the basic characteristics of such materials.

The following are some of the limitations encountered with the silver emulsion masks: (*i*) These masks are soft and hence are easily scratched. (*ii*) Dimensional changes take place due to moisture absorption by the gelatin. (*iii*) Due to the fogginess of the gelatin material, there is a significant optical density gradient at the edges. This gradient is due to the tapering of silver concentration. (*iv*) A limitation is encountered due to the excessive thickness of the emulsion mask (4μ thickness) for fine-line definition.

Although chromium masks overcome some of the above limitations, they too possess certain limitations: (*i*) Due to an aging phenomenon, the etch time varies even though the samples may have been prepared in the same batch. (*ii*) Due to the high reflectivity, multiple reflections can occur, resulting in a poor edge definition. (*iii*) Lack of resilience with growth spikes from epitaxial silicon layers.

Due to their opaqueness at the sodium D line (589 nm), registration of opaque masks with existing patterns is a difficult task, especially whenever positive photoresists are used. In meeting this difficulty, it has been recognized that the availability of semitransparent masks would overcome this registration problem. A typical semitransparent mask should have the following characteristics: (*a*) The film should have virtually zero transmission in the region below 450 nm. This region corresponds to the spectral range in which most commercial resists are sensitive (Fig. 1). (*b*) For the purpose of alignment, the film should be at least 30% transmitting in the 589 nm region. (c) The deposited film should be readily etchable in solvents which are compatible with commercial photoresists. (*d*) The deposited film should be abrasion resistant to ensure faithful transfer of the image on a repeated basis.

In recent publications, several materials and deposition techniques have been described for fabrication of semitransparent masks. Sinclair, *et al.* (1) have studied the spectral behavior and etch characteristics of various oxide films deposited by d-c reactive sputtering. They demonstrated that films of iron oxide, vanadium oxide, nickel oxide, iron oxide-vanadium oxide, and iron oxide-nickel oxide met the optical requirements. The iron oxide-vanadium oxide was best in view of its good etch properties in both acids and alkalis. Moreover, several oxides, including copper oxide, were found to be inferior because of their spectral absorption properties, and thus were eliminated as potential candidates. The copper oxide films were formed by the sputtering of copper in 100% O_2.

MacChesney *et al.* (2) characterized iron oxide films prepared by chemical vapor deposition using iron pentacarbonyl. Much of their investigation was focused on the deposition parameters and the etchability of the iron oxide films. Peters *et al.* (3) have devised a sputtering technique for iron oxide deposition; in CO-CO_2 mixtures resulting films could be properly delineated in 6M HCl solution. In the published work (3), data related to the scratch resistance values for the iron oxide films were found to be superior over those obtained using evaporated chromium films. More recently, a further comparison (4) of the merits of iron oxide *vs.* chromium film is available. More recently Janus (5) has presented a critical review of iron oxide masks in comparison to other systems. Taylor *et al.* (6) have studied the potential use of polycrystalline hexaferrite films for semitransparent masks. Although the films met the optical requirements to obtain pinhole-free films, a thickness greater than 2000Å was required. Loprest *et al.* (7) have also described the overall characteristics of the GAF Microline high resolution plates. These plates consist of a thin coating of a positive-working resist with a diazo dye as the sensitizer. By contrast to all other mask systems, the image development for this system is carried out using ammonia vapor at atmospheric pressure. The thickness of the light-sensitive layer is about 3.3μ and a line resolution of 2000 lines/mm was reported. Using a wide variety of photographic dyes, a method for the fabrication of see-through masks was described (8). Ables (9) has devised a process in which Lippman emulsions are exposed to light and, after conventional development, the black image is intensified according to the reaction

$$Ag^{o} + HgBr_2 \rightarrow (AgBr)(HgBr)$$

The product of the reaction is a white or bleached image which is then redeveloped in a saturated sodium sulfite solution. The resulting silver-mercury-sulfite image is sepia in color. In a slight variation, Drouge (10) redevelops the (AgBr)(HgBr) image in conventional developers or ammonia solution followed by a treatment in a dilute potassium dichromate-sulfuric acid solution. The resulting images are orange. Blome and Fok (11) have devised a selective process by which evaporated silicon oxide was deposited, providing hard and semitransparent silicon monoxide films. Diem (12) has also described a process for silicon semitransparent masks. Kiba (13) has described a process suitable for transparent masks. In his process copper is deposited by vapor plating and is subsequently oxidized at elevated temperatures. In a subsequent modification (14), a patterned film of aluminum is deposited prior to the copper deposition. With heat-treatment, oxidation and diffusion of the copper take place selectively. Unwanted aluminum and copper are subsequently etched. A commercial product (15) prepared by sputtering deposition was examined by x-ray diffraction and was shown to be primarily cuprous oxide.

In this paper, a chemical plating process for fabrication of semitransparent masks is described. The deposited films are based on a copper-containing compound which is readily deposited from aqueous solutions on heterogeneous interfaces, and provides the proper optical characteristics required for see-through mask application.

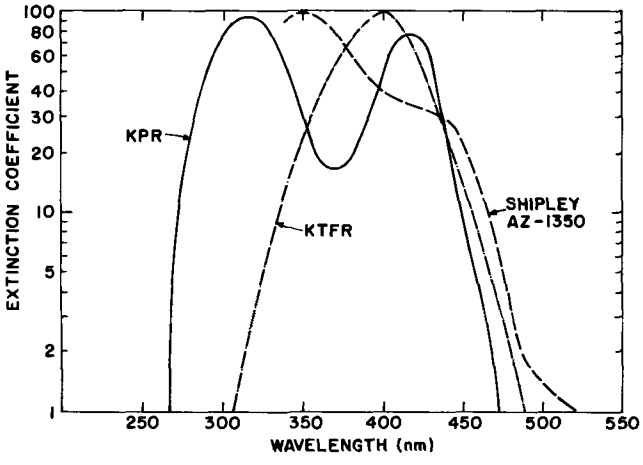

Fig. 1. Spectral sensitivities of commonly used resists

Experimental Procedures

In the current work, the glass substrates were pretreated in a fashion similar to the pretreatment of dielectrics prior to chemical (electroless) plating (16). Following an adequate cleaning procedure, the substrates were immersed in a sensitizer solution ($SnCl_2$/HCl) followed by an immersion in an activator solution ($PdCl_2$/HCl). Typical compositions used for the sensitizer and activator were as follows: sensitizer solution, $SnCl_2 \cdot 2H_2O$ 10 g/liter and HCl (conc) 30 ml/liter; activator solution, $PdCl_2$ 1 g/liter and HCl (conc) 1 ml/liter.

Due to a reaction (17) taking place between the adsorbed tin(II) and palladium(II), adsorbed palladium nuclei are present on the surface after the activation step. It is the presence of such nuclei that provides

Table I. Electroless copper plating bath

$CuSO_4$	0.06M
Sodium salt of ethylenediamine-tetraacetic acid (Na_4·EDTA)	0.1M
NaOH	1.0M
NaH_2PO_2	1.5M
Temperature, °C	65
Immersion time, min	1

the catalytic sites required for the initiation of the autocatalytic plating process (16-18).

The "electroless copper" bath given in Table I is of typical composition which was used in the current process. In addition to sodium hypophosphite, other reducing agents were also found effective in producing the semitransparent films. Specifically, hydrazine sulfate $[(NH_2)_2SO_4H_2]$ and sodium hydrosulfite $(Na_2S_2O_4)$ provided films similar to those obtained when using hypophosphite. Following the plating cycle, a thin, adherent yellow film was present on the surface. The durability of the films was evaluated using a Tukon Microhardness Tester. In each case, the end point was defined as the required load to produce a break in the film.

Results and Discussion

Figure 2 shows the spectral characteristics of the current films in the visible and uv ranges. In a typical deposition cycle, the film thickness was found to be approximately 600Å. As seen, the deposited film shows a high degree of transmission in the visible range, with a substantial transmission decrease in the spectral region below 450 nm. As mentioned earlier, it is this optical property which is essential for see-through photomasks. The low transmission level in the spectral range below 450 nm provides good light absorption for the actinic light used to expose typical commercial resists.

In an attempt to characterize the deposited film, an x-ray diffraction technique was employed. Results show a diffuse pattern which closely resembles published diffraction patterns of cuprous oxide (Cu_2O). Furthermore, the visual appearance of the deposits (Cu_2O) is in agreement with reported observations. As reported previously (19, 20), cuprous oxide may range from yellow to red in color depending on the particle size. Wet chemical analysis of the deposited films showed a copper content of 82% by weight; the theoretical value of copper present in cuprous oxide is 89%. Using an attenuated total reflection method, the infrared spectra was found to be similar to a previously reported spectra (21) of cuprous oxide.

Figure 3 shows the variations in deposit weight as

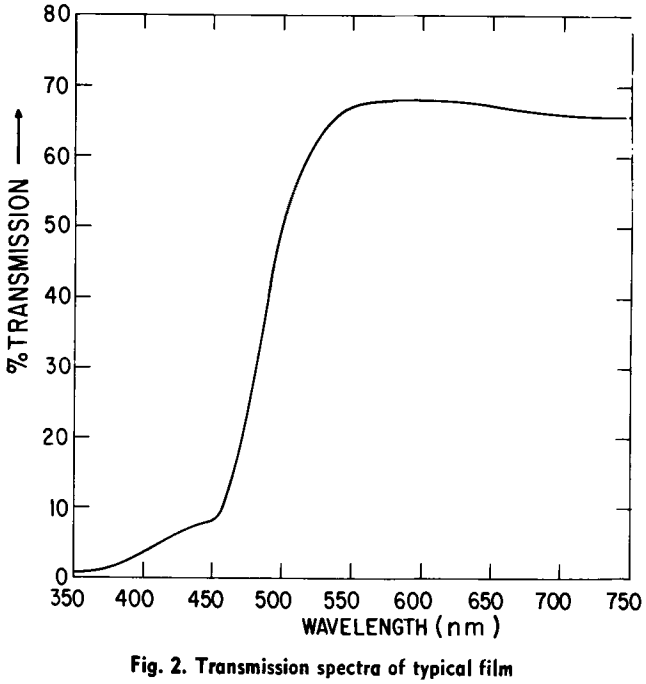

Fig. 2. Transmission spectra of typical film

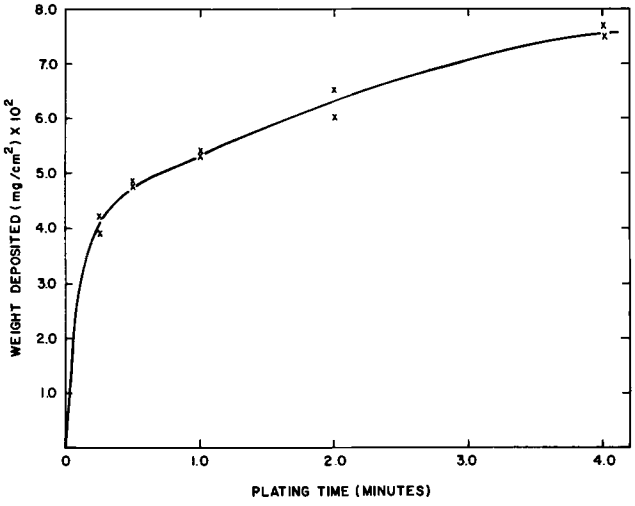

Fig. 3. Weight gain vs. immersion time

plating time was varied. As seen, the deposition phenomenon shows a leveling effect with deposition time, suggesting that the process is not a true autocatalytic plating process. In general, it was observed that prolonged deposition cycles (> 2 min) resulted in inferior uniformity. To account for the mechanism of deposition, Table II is provided. Although reactions [1] and [2] are similar to those proposed in electroless nickel plating (21, 23), the reduction of divalent copper is carried out to the monovalent ion. Due to the extreme insolubility of cuprous oxide in alkaline media, a heterogeneous precipitation takes place. The deposited cuprous oxide, however, does not provide sufficient catalytic activity for the continuation of the plating process, hence, cessation takes place with time. The disproportionation of copper(I) (reaction [4]) is generally prevented by the presence of strong complexing agents for copper(I).

In order to evaluate the efficiency of the copper reduction, a typical solution was thermally decomposed by boiling for about 30 min. The depletion in hypophosphite concentration was determined by an iodine/thiosulfate titration, and the precipitated Cu_2O was dissolved in ammonium hydroxide and analyzed for copper content. The molar ratio of the consumed hypophosphite to copper(I) formed was then calculated. Results based on several repeated runs showed a $Cu^+/H_2PO_2^-$ ratio of 1.95 ± 0.15. The value of 2.00 would be anticipated (see Table II) if only Cu^{+2} is reduced and no other specie(s) was reacting with the adsorbed hydride. Based on these results, it is believed that reaction [4] of Table II does not take place to any appreciable extent.

For the purpose of pattern delineation, it was found that alkali metal hydroxide solutions have virtually no effect, and this is consistent with the low solubility of cuprous oxide in such media. However, good edge definition has resulted with dilute hydrochloric acid, dilute ammonium hydroxide, or ammonium persulfate. In dilute solutions (5-10% by volume) of concentrated ammonium hydroxide (58% NH_4OH) an etch time of about 1 min was established. Figure 4 shows a typical test pattern of the current see-through mask as well as a developed resist pattern prepared from the see-through mask.

As mentioned previously, it is desirable to achieve films which are highly scratch resistant. Having this property, faithful replication can be carried out over many printings. The films deposited by the current method were found to be soft when compared to iron

Table II. Basic reactions in the Cu_2O deposition

[1]	$Pd + H_2PO_2^- + OH^-$	→	$[Pd\text{-}H]^- + PO_2^- + H_2O$
[2]	$PO_2^- + OH^-$	→	HPO_3^{-2}
[3]	$2Cu^{+2} + 2[Pd\text{-}H]^-$	→	$2Cu^+ + H_2 + 2Pd$
[4]	$2Cu^+$	→	$Cu + Cu^{+2}$
[5]	$2Cu^+ + 2\ OH^-$	→	Cu_2O(ppt) $+ H_2O$

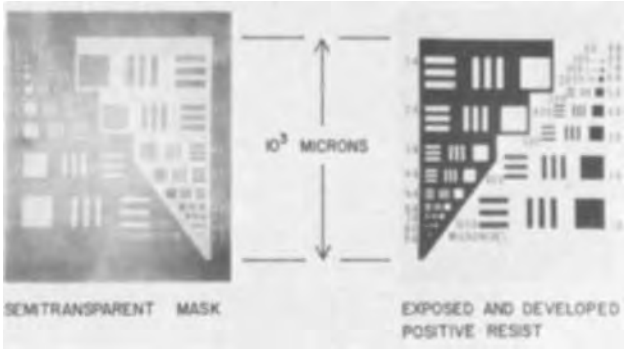

Fig. 4. Unit pattern of Qualitron test mask

oxide masks. Two approaches were undertaken to improve this limitation. In the first method, it was found that a baking for about 30 min at about 200°C provided increased durability for the film. In fact, it was found that this modification resulted in scratch resistant values better than those obtained for conventional silver-halide emulsion masks, however, not as good as the iron oxide. Alternatively, it was found that special commercial protective films (22) may be deposited on the copper oxide films. Typical materials used successfully were Scotch-Clad Strip Coating No. 2253, product of 3M Company, and Maskguard, product of Atomel Corporation, Mill Valley, California. These films do not affect the optical characteristics of the masks and they provide a "buffer zone" for abrasion. These films are conveniently deposited and removed, if necessary.

Conclusions

A process for the fabrication of semitransparent photomasks has been developed. The developed process utilizes chemical plating techniques for depositing thin cuprous oxide films. These films provide the necessary optical requirements and they can be readily delineated with common etchants. Using dilute ammonium hydroxide as a typical etchant, good edge definition was obtained. The heat-treated copper oxide film was found to be of greater durability when compared to emulsion masks, but of lower durability in comparison to iron oxide masks.

In comparing the current process with those reported on the same subject, it is apparent that the present technique is especially useful in the ease of preparation of both small- and large-size masks. Moreover, the present process does not require elaborate capital equipment. Hence, it is believed that the present approach may provide photomasks at reduced costs.

Acknowledgments

The authors wish to thank R. Paff for his assistance with the x-ray diffraction, P. J. Zanzucchi for his assistance with the IR analysis, and G. L. Schnable for useful discussions and the reviewing of this paper.

Manuscript submitted Feb. 12, 1973; revised manuscript received April 18, 1973.

Any discussion of this paper will appear in a Discussion Section to be published in the June 1974 JOURNAL.

REFERENCES

1. W. R. Sinclair, M. V. Sullivan, and R. A. Fastnacht, *This Journal*, **118**, 341 (1971).
2. J. B. MacChesney, P. B. O'Connor, and M. V. Sullivan, *ibid.*, **118**, 776 (1971).
3. F. G. Peters, W. R. Sinclair, and M. V. Sullivan, *ibid.*, **119**, 305 (1972).
4. Staff editor, *Circuits Manufacturing*, **12**, p. 32 (October 1972).
5. A. R. Janus, *Solid State Technol.*, **16**, 33 (1973).
6. R. C. Taylor and V. Sadagopan, *This Journal*, **119**, 788 (1972).
7. F. J. Loprest and D. E. Barr, *Solid State Technol.*, **14**, No. 6, 6 (1971).
8. H. V. Parsonage and M. I. Kruger, U.S. Pat. 3,592,-649, July 13, 1971.
9. D. D. Abies, *Photographic Sci. Eng.*, **10**, 229 (1966).
10. L. J. Drouge and R. J. Weidner, *Solid State Technol.*, **15**, No. 6, 59 (1972).
11. E. R. Blome and S. S. M. Fok, U.S. Pat. 3,625,728, Dec. 7, 1971.
12. A. R. Diem, U.S. Pat. 3,721,584 (1973).
13. W. M. Kiba, U.S. Pat. 3,561,963, Feb. 9, 1971.
14. W. M. Kiba, U.S. Pat. 3,620,797, Nov. 16, 1971.
15. Telic Corporation, Santa Monica, Calif.
16. W. Goldie, "Metallic Coating of Plastics," Vol. 1, chap. 5, Electrochemical Publication Limited, Middlesex, England (1968).
17. N. Feldstein and J. A. Weiner, *This Journal*, **120**, 475 (1973).
18. J. P. Morton and M. Schlesinger, *ibid.*, **115**, 16 (1968).
19. J. W. Mellor, "Comprehensive Treatise on Inorganic and Theoretical Chemistry," Vol. 3, pp. 117-131, Longmans Green & Co., New York (1927).
20. H. Lal, *J. Sci. Ind. Research (India)*, **12B**, 424 (1953).
21. M. O'Keeffe, *J. Chem. Physics*, **39**, 1789 (1963).
22. R. M. Lukes, *Plating*, **51**, 523 (1969).
23. N. Feldstein and T. S. Lancsek, *This Journal*, **118**, 869 (1971).
24. D. J. Holthaus, "Proceeding of the Second Kodak Seminar on Microminiaturization," p. 12 (1966).

Activities of Organic Compounds in Aqueous Electrolyte Solutions

D. M. Mohilner,* L. M. Bowman,[1] S. J. Freeland, and H. Nakadomari

Colorado State University, Department of Chemistry, Fort Collins, Colorado 80521

ABSTRACT

A gas chromatographic method is described which permits the direct measurement of the activities of neutral organic compounds in aqueous electrolyte solutions. This method has a relative precision of about 0.5%; it is convenient and fairly rapid, and the apparatus required is relatively inexpensive. The significance of such activity measurements to electrosorption studies of organic compounds on electrodes is discussed. The method is equally applicable to organic compounds which are either liquid or solid in the pure state at the temperature of the electrosorption studies. It may also be used to determine the complete activity-composition phase diagrams of two component mixtures of the organic compound and water.

Determination of the isotherms for electrosorption of neutral organic compounds at electrodes from aqueous electrolyte solutions is always based in principle on the following fundamental equation derived from the thermodynamic theory of electrocapillarity (1)

$$\Gamma_{ow} = -(1/RT)\,(\partial\gamma/\partial \ln a_o)_{T,p,E,a_s} \qquad [1]$$

In Eq. [1], Γ_{ow} is the relative surface excess of the organic compound (with water as the reference component), R is the gas constant, T is the absolute temperature, γ is the interfacial tension of the electrode, a_o is the activity of the organic compound in the bulk electrolyte solution, and the subscripts T, p, E, and a_s indicate that the differentiation is carried out at constant temperature, pressure, electrode potential, and activities of all other solutes. In practice, however, although it is the thermodynamically correct relationship, Eq. [1] has almost never been used (2) because the activities of organic compounds in aqueous electrolyte solutions have not been generally available (3), and the measurement of these activities appeared too difficult. Instead, the following approximate equation has served as the basis of almost all published studies of electrosorption of organic compounds

$$\Gamma_{ow} = -(1/RT)\,(\partial\gamma/\partial \ln c_o)_{T,p,E,c_s} \qquad [2]$$

Equation [2] differs from Eq. [1] in two important ways. First, the differentiation is carried out at constant concentration, c_s, of the electrolyte. This means that the tacit assumption has been made that the activity of the electrolyte in the solution is unaffected by the presence of the organic compound. Recent work in this laboratory (4) has shown that this assumption is definitely false. Second, it is assumed that the differentiation may safely be carried out with respect to the concentration, c_o, instead of the activity, a_o, of the organic compound in the bulk solution. For a fixed activity of the electrolyte, this assumption would be valid if the activity coefficient of the organic compound were constant over the range of concentrations studied, *i.e.*, if the organic compound obeyed Henry's law over the entire concentration range. It will be shown below that this assumption is not generally valid. For comparison of adsorption data for the same organic compound from solutions of different electrolytes or from solutions of the same electrolyte at different electrolyte activities, the assumption that the concentration of the organic compound may be safely substituted for the activity is always very seriously wrong as was first shown by Frumkin (5) as early as 1919. Recently Bauer (6) has discussed this problem and has indicated a method of introducing activity corrections as the ratio of the solubility of the organic compound in the electrolyte solution to the solubility in pure water. Such a correction, however, is valid only if the organic compound obeys Henry's law in both the electrolyte and in pure water up to saturation, which is not generally true. Therefore it is apparent that from the standpoint of electrosorption studies there is a need for a convenient and precise method for determining the activities of organic compounds in aqueous electrolyte solutions.

This paper describes such a method. It is based on the use of a gas chromatograph equipped with a gas-sampling valve and a flame ionization detector. The apparatus required is relatively inexpensive.

Related prior work utilizing gas chromatography to measure the equilibrium vapor pressure of pure organic liquids at different temperatures for determination of heats of vaporization via the Clausius-Clapeyron equation was published by Mackle and co-workers (7-8), who gave a design for a gas-sampling valve. Wichterle and co-workers (9-10) described a gas chromatographic method for measuring equilibrium partial vapor pressures for two-component nonelectrolyte solutions such as hexane-toluene, and they also gave a design for a gas-sampling valve. Related measurements using a gas-tight syringe instead of a gas-sampling valve were reported by Klopstock and Rogozinski (11). Pollak and Cave (12) described a gas chromatographic method using a gas-sampling valve for measuring the activity coefficients of methanol and of ethanol in benzene. Maffiolo and Vidal (13) described a gas chromatographic method for measuring the equilibrium partial vapor pressures for two- and three-component nonelectrolyte mixtures such as acetone-hexane and aniline-benzene-hexane. None of this prior work was concerned with the measurement of the activities of organic compounds in aqueous solutions or in the presence of electrolytes, and in all cases a thermal conductivity detector was used, although Pollak and Cave (12) did refer to the enhanced sensitivity which would be expected with a flame ionization detector. The method described in the present paper is specifically designed to yield activities of organic compounds in three-component, aqueous electrolyte solutions, and it takes special advantage of the fact that a flame ionization detector does not respond to water.

Theoretical

The principle of the method is the measurement of the equilibrium partial vapor pressure, p_o, of the organic compound in the solution. The activity may then be calculated as the ratio of p_o to the vapor pressure, p_o^*, of the pure liquid organic compound at the same temperature as the solution. This means the standard state chosen is the pure liquid compound (14). The advantage of this choice of the standard state over that of a hypothetical solution obeying Henry's law is that it facilitates comparison of electrosorption data ob-

* Electrochemical Society Active Member.
[1] Present address: Department of Chemistry, University of Utah, Salt Lake City, Utah 84100.
Key words: activity coefficients, gas chromatography, electrosorption, phase diagram.

tained from different electrolytes or from solutions with different activities of the same electrolyte (15). Vapor pressure may safely be used in the calculation in place of fugacities because at the low values of the pressures encountered the vapors behave nearly ideally, and, moreover, any slight deviation of the vapors from ideality tend to cancel in taking the ratio (14). Thus the activity of the organic compound in a given electrolyte solution will be taken as

$$a_o = p_o/p_o^* \quad [3]$$

In fact, the quantities actually measured are not p_o and p_o^* but rather the integrals of gas chromatograms produced by equal-volume gas samples of the vapor in equilibrium with solution or the pure liquid organic compound. These integrals, I_o, and I_o^*, respectively, are each directly proportional (with the same proportionality constant) to the corresponding vapor pressures. Thus the activity of the organic compound in the electrolyte solution will be given by

$$a_o = I_o/I_o^* \quad [4]$$

Experimental

General description of the apparatus.—A block diagram of the apparatus is shown in Fig. 1. Samples either of the solution or of the pure liquid organic compound are placed in glass tubes A and B. The bottom of each tube is a fine porosity glass frit which serves the dual purpose of holding the liquid sample in the tube and of dispersing the nitrogen gas which is passed through the liquids into very fine bubbles. Each of the tubes is provided with a jacket through which water from a thermostat is pumped. Prepurified nitrogen gas from a tank is bubbled at a rate of 3-6 cm³/min through the two tubes which are connected in tandem by glass tube C using stainless steel Swagelok unions with Teflon ferrules. The purpose of tube A is simply to presaturate the nitrogen with water and/or organic vapor. The gas bubbling through tube B then becomes saturated with water vapor and/or organic vapor at the equilibrium partial pressures corresponding to the thermostat temperature (25°C in the experiments described below). This means that each unit volume of gas passing out of tube B contains a quantity of water and/or a quantity of the organic compound which is directly proportional to the corresponding equilibrium partial vapor pressure. The thermostated portions of tubes A and B are 1/2 in. OD and are about 3 ft long. The tubes are filled only about 1/3 full to prevent the carrying over of spray. Tube B is connected to the gas-sampling valve by glass tube D. Tube D is wrapped over its entire length with a spiral of Chromel wire which is heated by passing an electric current from a variable transformer. It is very important that tube D be heated. Otherwise condensation could occur on its walls which would invalidate the measurements.

The gas chromatograph used is a Hewlett-Packard Model 700 equipped with a flame ionization detector.

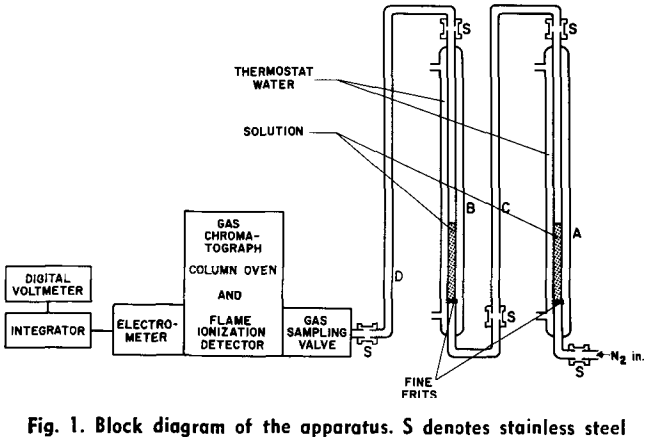

Fig. 1. Block diagram of the apparatus. S denotes stainless steel Swagelok union with Teflon ferrules.

The main reason a flame ionization detector was chosen is that it does not respond to water (or N_2). This insures that there is no interference from the water peak which for aqueous solutions is much larger than the organic peak. The enhanced sensitivity of a flame ionization over a thermal conductivity detector is a secondary reason for the choice. For the experiments described below which involved the determination of the activities of aliphatic alcohols, the chromatographic column was a 6 ft length of ⅛ in. OD stainless steel tubing packed with Porapak-Q,[2] 80-100 mesh. For other type compounds, column packings can be chosen as appropriate (16). For the experiments described in this paper the column oven was controlled at 220°C while the detector and injector port were controlled at 300° and 190°C, respectively.

The gas-sampling valve used was a Hewlett Packard Model 19021A heated dual-loop gas sampling valve whose temperature was maintained at 145°C by a Hewlett-Packard Model 19045A temperature controller. It is necessary to use a heated gas-sampling valve; otherwise errors due to adsorption or condensation in the sample loops will invalidate the measurements. The 1/16 in. OD stainless steel tube connecting the gas-sampling valve to the injection port of the chromatograph was also heated by wrapping it with a heating tape controlled by a variable transformer.

The Model 19021A gas-sampling valve contains two sample loops (5 cm³ in the experiments described here). Depending on the position of the control knob, one loop is connected to the helium carrier gas stream, and its contents are swept into the injection port and thence into the column. The other loop is connected to tube D (Fig. 1) and is thus being filled with vapor from the solution (or pure compound) in tube B. When the control knob is turned, the sample loop which was being filled is connected to the carrier gas stream, and its contents are swept into the column. At the same time the first loop is connected back to tube D, and it is refilled with a new sample of vapor.[3] The dual sample loops thus permit repetitions of measurements to be made at a maximum rate. In the experiments described in this paper the measurements could be made about every 4 min.

The entire organic sample eluted from the chromatographic column is burned in the hydrogen-air flame of the detector, and the resulting tiny electric current produced in the detector is transduced by the electrometer (Hewlett-Packard Model 5771A) into an analog voltage signal which is directly proportional to the instantaneous amount of organic sample being burned. Hence the time integral of this analog voltage is directly proportional to the total amount of the organic compound in the gas sample and therefore also to the partial pressure of the organic compound in the vapor phase in tube B which is in equilibrium with the liquid phase in the tube at the thermostat temperature (25°C).[4] The analog voltage signal from the electrometer is fed into an integrator circuit (Fig. 1), and the output of the integrator is read out on a digital voltmeter (Fluke Model 8300A).

Integrator and control circuit.—Figure 2 shows a typical chromatogram for an aliphatic alcohol (2-butanol) on the Porapak-Q column. The chromatogram is asymmetric and exhibits a considerable degree of "tailing." Integration of a peak with such tailing is troublesome because the integrator tends to drift slowly for a long period. This leads to irreproducibility in the results because one cannot be sure when to

[2] Manufactured by Waters Associates, Inc., Framingham, Massachusetts.

[3] The sample loop which is being filled with vapor from tube D exhausts to the atmosphere. Thus the total pressure in the sample loop and hence on the liquid in tube B is the ambient barometric pressure. However, the results of the activity measurements are independent of fluxuations in the barometric pressure because of the negligibly small influence which the total pressure on the liquid exerts on the vapor pressure (14).

[4] It is important to realize that this proportionality is exact in spite of the fact that tube C and the gas-sampling valve are at different temperatures from tube B. In fact, the temperature of tube C is immaterial. The only requirement is that the temperature of the gas-sampling valve be kept constant.

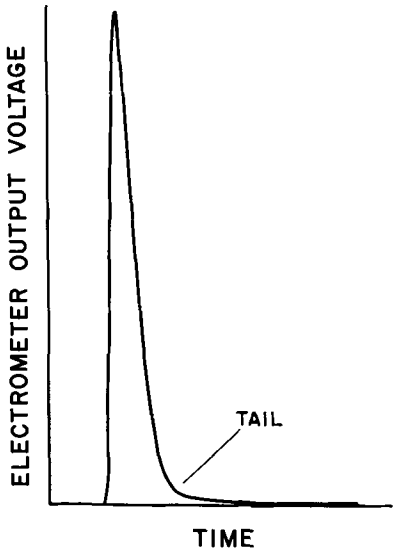

Fig. 2. Typical gas chromatogram of aliphatic alcohol on Porapak-Q.

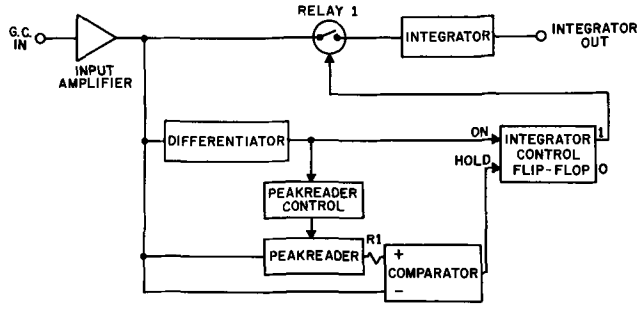

Fig. 3. Block diagram of integrator control circuit

stop the integration. It was found that a satisfactory solution to this problem was to stop the integration when the analog voltage from the electrometer had dropped to some preselected fraction of the peak voltage. For this purpose the circuit shown in block diagram in Fig. 3 and in detail in Fig. 4 was designed. This circuit automatically turns on the integrator when the chromatogram begins and then automatically stops the integration and causes the integrator to hold its voltage when the analog voltage output of the electrometer has dropped to the preselected fraction of the peak value (0.5% in the experiments described below). The actual value of this fraction is determined by the value of resistor R1 in Fig. 3 and 4.

The principle of operation of this circuit can be understood with reference to Fig. 3. The analog voltage signal from the electrometer (G.C. IN) is fed into an input amplifier which serves primarily for impedance matching. The output of this amplifier is then fed into a differentiator. When the derivative goes from zero on the base line to positive when the chromatogram begins, the integrator control flip-flop is switched to the "1" state. This causes mercury wetted relay 1 to close thereby connecting the integrator input to the output of the input amplifier. Simultaneously the positive going derivative causes the peak reader control which operates mercury wetted relay 2 (Fig. 4) to connect the peak reader amplifier, which then starts following the chromatogram. When the peak of the chromatogram occurs the derivative passes through zero. This causes the peak reader to hold the value of the peak voltage. The output of the peak reader is fed through resistor R1 into one input of a comparator, *i.e.*, the preset fraction of the peak voltage is fed into this input of the comparator. Simultaneously, the

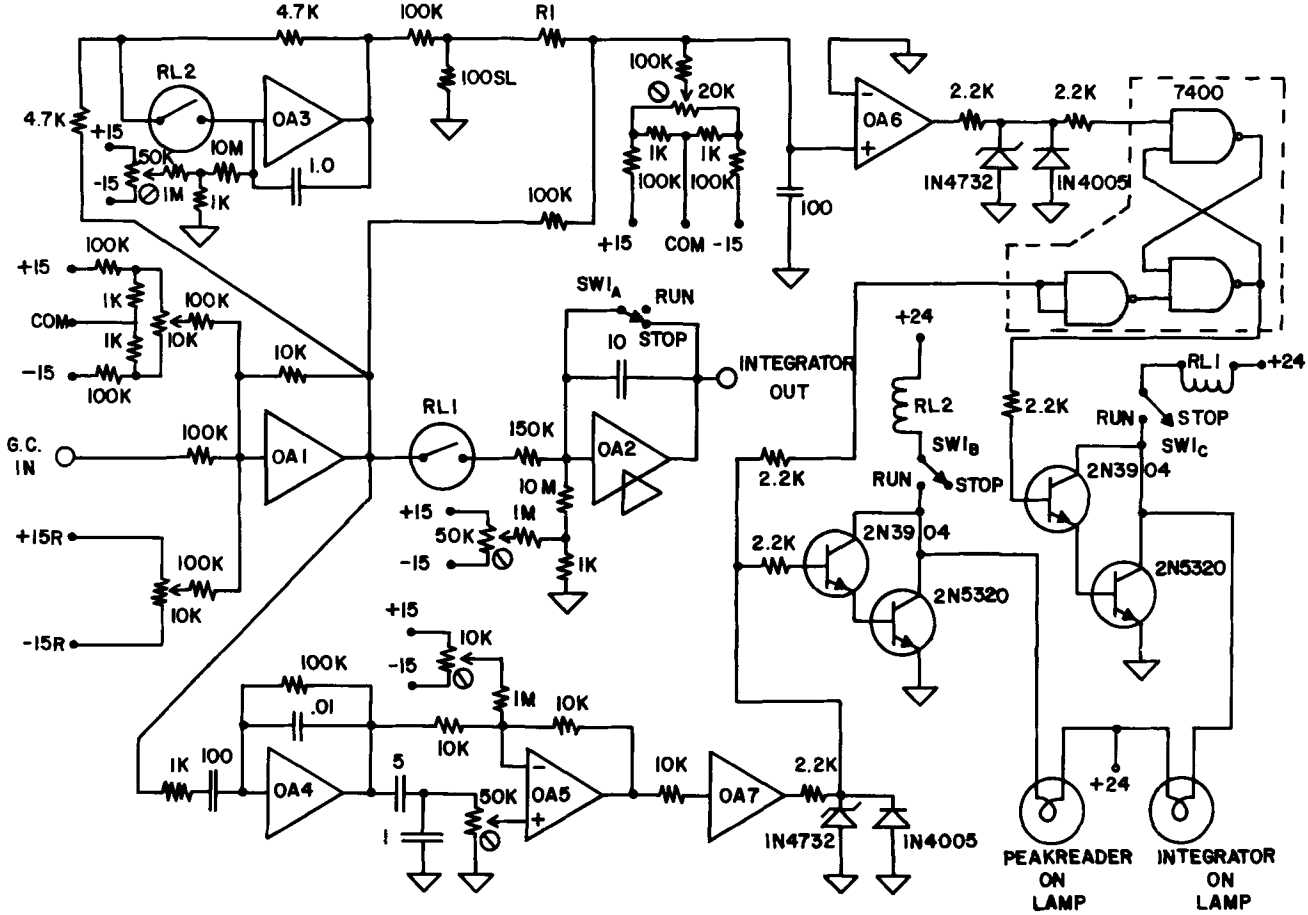

Fig. 4. Circuit diagram of integrator control circuit. The operational amplifiers used are: OA1, Philbrick 1020; OA2, Philbrick 1700, chopper stabilized; OA3, Philbrick 1023; OA4 and OA5, Philbrick SQ10A; OA6 and OA7, Model 741.

input amplifier which is following the chromatogram feeds into the other input of the comparator. When the voltage at this second input of the comparator drops to the value of the preset fraction of the peak voltage, the comparator changes state which in turn causes the integrator control flip-flop to switch to the "O" state. This action opens relay 1, and the integrator holds the integral of the chromatogram which is then read by the digital voltmeter. This circuit can be built for a very small fraction of the cost of a commercial gas chromatographic integrator. We have found it to be quite reliable, and it is convenient to use.

Operating Procedure.—In order to make precise measurements of the activity of an organic compound in a series of solutions, the following procedure has been found to be most effective. Two identical sets of tubes (Fig. 1) A, B, C, D, and A', B', C', and D' are used. The first pair of tubes, A and B, is filled with the pure compound. The first solution in the series is put in tubes A' and B'. Separate nitrogen tanks provide the flow of prepurified nitrogen into each of the two pairs of tubes. Tube D for the pure compound is connected to the gas-sampling valve. Successive samples of vapor from the pure compound are passed through the gas chromatograph, and the sensitivity of the flame ionization detector is adjusted until a suitably large integral is obtained (typically, 6.0-7.0V). The sensitivity of the flame ionization detector may be varied most easily by changing the output pressure at the air tank, keeping the output pressure at the hydrogen tank constant.[5] When the detector sensitivity has been set, a series of at least five samples of vapor from the pure organic compound are sent through each sample loop and the average value of the integral I_0^* for each loop is determined. Typical relative standard deviations of about 0.5% are obtained. Tube D is then disconnected and tube D' from the pair of tubes containing the solution is connected to the gas-sampling valve. Several samples of vapor are sent through each sample loop and the average value of the integral I_0 is obtained.[6] Then, in order to insure that the sensitivity of the detector has not drifted, tube D' is disconnected and tube D is reconnected to the gas-sampling valve, and several samples of vapor from the pure organic compound are again chromatographed. If the value of I_0^* now obtained lies within the confidence limits of the previous determination it may be assumed that the detector sensitivity was the same when the solution was chromatographed as it was when the value of I_0^* was first determined. If the detector has drifted, it must be reset so that the original value of I_0^* is obtained, and then the vapor from the solution is again chromatographed. This procedure is followed for each solution sample. It insures that the solution chromatograms are integrated at the same detector sensitivity as the pure compound and thus that the activities determined are valid.[7]

Results and Discussion

The quality of activity data which can be obtained with this apparatus using the procedure described above is illustrated by Fig. 5. This is a plot of the activity of 2-butanol at 25°C *vs.* its mole fraction in aqueous solutions of sodium sulfate in which the mean ionic activity, $a_\pm$, is held constant[8] at a value of 0.07087. The relative probable error in the activity was calculated not to exceed 0.5% for each of the seven concentrations (0.5, 0.6, 0.7, 0.84, 1.0, 1.2, and 1.4M) of the 2-butanol at which the activity was measured. The points for the three lowest concentrations fit quite accurately on a straight line passing through the origin. This means that for concentrations of 2-butanol up to 0.7M Henry's law is obeyed, and the activity coefficient of 2-butanol is constant. However, for concentrations of 2-butanol greater than 0.7M the true activity deviates negatively from the Henry's law line, and these deviations become quite serious in the high concentration region. For example, in the range of concentrations between 1.2 and 1.4M, it can be shown that the value of the relative surface excess Γ_{ow} calculated by Eq. [1] from the true activities is nearly twice as high as the Γ_{ow} values which would be calculated assuming Henry's law was still valid in this range. This result illustrates the fact that the assumption of a constant activity coefficient for the organic compound can produce very serious errors in the interpretation of electrosorption data.

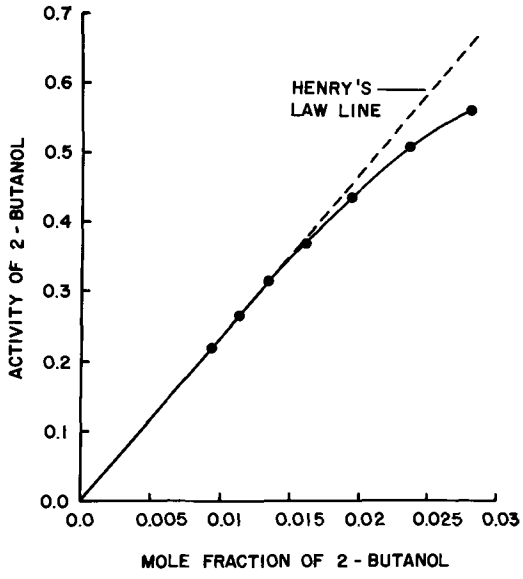

Fig. 5. Activity of 2-butanol in aqueous solutions of Na_2SO_4 in which the mean ionic activity, $a_\pm = 0.07087$.

It is strongly recommended that in future studies of the electrosorption of organic compounds on electrodes from aqueous electrolyte solutions two preliminary experimental steps not previously employed should always be taken. First, a preliminary study should be made to determine what concentration of the electrolyte is required for each concentration of the organic compound to yield a constant mean ionic activity (4) in the series of solutions to be used in the electrosorption studies.[9] After the recipe for preparation of the series of solutions has been thus established, the activity of the organic compound in each of the solutions should be determined by the method described above. Of course, it will not be necessary to make an actual measurement of the activity for every solution in the electrosorption study. It is only necessary to establish the activity-composition curve (such as Fig. 5) for the system. In most cases six to eight actual measurements will probably be sufficient to establish this curve.

It should be pointed out that a slight modification in the method described above will permit its extension to organic compounds which are solids in the pure

[5] It is very important for this purpose to use two-stage reduction valves such as the Matheson Model 8. Single-stage reduction valves do not permit a sufficiently sensitive pressure adjustment.

[6] The two sample loops have the same nominal volume, but their actual volumes may typically differ from each other by several per cent. It is therefore important when calculating the activity to divide the I_0 value by the I_0^* value for the same sample loop.

[7] An alternative procedure would be to use nitrogen which contains a suitable concentration of another gas which can serve as an internal standard. Besides the obvious requirement that the internal standard be detectable by flame ionization, it would have to possess the following three properties: (*i*) It would need a retention time which was sufficiently longer than that of the compound which was being studied that there would be time to take the integral of that compound, reset the integrator, and then take the integral of the chromatogram of the internal standard. (*ii*) It would have to be essentially totally insoluble in water. (*iii*) It would have to be essentially totally insoluble in the pure organic compound whose activity is being measured. Properties (*ii*) and (*iii*) seem very difficult to obtain with a single substance.

[8] This is the value of the mean ionic activity of a 0.1M (0.10045*M*) solution of sodium sulfate in pure water (17). In order to maintain $a_\pm$ constant in the presence of the organic compound the concentration of the Na_2SO_4 must be adjusted for each solution (4). For example, when the concentration of 2-butanol is 1.0M, the concentration of the Na_2SO_4 required to make $a_\pm = 0.07087$ is 0.0498M.

[9] The only time this step is unnecessary is when the solutions are to be saturated with a solid salt, in which case the mean ionic activity is automatically constant.

state at the temperature of the electrosorption experiments. The only change needed is to fill tubes A and B (cf. section on Operating Procedure) with a saturated solution of the solid organic compound in pure water. In the saturated solution, the fugacity of the organic compound in the solution, and therefore also of the compound in the vapor phase in equilibrium with the solution, will be equal to the fugacity of the pure solid compound. Therefore, the ratio of the integral of the chromatogram of the vapor sample from the electrolyte solution, I_o, to the integral, I_o^*, of the chromatogram of the vapor sample from the saturated solution of the compound in pure water will yield the activity of the organic compound in the electrolyte solution. In this case, however, the standard state will be the pure solid organic compound at the temperature of the electrosorption studies.

This same method can also be applied to the problem of determining the complete activity-composition phase diagram for two component mixtures of an organic compound and water. This application of the method is illustrated in Fig. 6. Here we have measured the activity of 2-butanol in two component mixtures with water over the mole fraction range of zero to unity for both components. This system exhibits phase separation into a water-rich and an alcohol-rich phase when the concentration of the 2-butanol reaches a value of 1.8M. The activity of the 2-butanol in each of the two saturated solutions should be the same. The measurements verified this fact. In addition it can be seen from Fig. 6 that the activity of the alcohol approaches the Raoult's law line as the mole fraction approaches unity, as it should. The very large deviations of the alcohol activity from the Henry's law line as the concentration of 2-butanol approaches that of saturation shows clearly that activity corrections based on solubility measurements assuming Henry's law is valid up to saturation will be seriously in error. The activity-composition curve for the water in this system could easily be obtained from the data in Fig. 6 by integration of the Gibbs-Duhem equation (14).

Conclusions

A gas chromatographic method for the measurement of the activities of neutral organic compounds in aqueous electrolyte solutions has been developed, and the importance of application of this method to electrosorption studies has been indicated. The measurements with the apparatus described are convenient and quite precise, and the apparatus is relatively inexpensive. The method may be applied to organic compounds which are either liquid or solid in the pure state at the temperature of the electrosorption experiments. In addition, the same apparatus can be used to determine the complete activity-composition phase diagram of two-component mixtures of the organic compound and water.

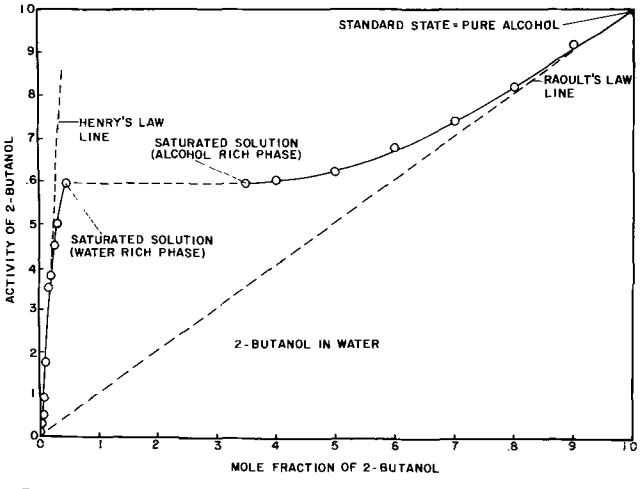

Fig. 6. Activity of 2-butanol in two component mixtures with water

Acknowledgment

This work was supported by the United States Air Force Office of Scientific Research under Grant No. AF-AFOSR-70-1887.

Manuscript submitted June 5, 1973; revised manuscript received July 30, 1973.

Any discussion of this paper will appear in a Discussion Section to be published in the June 1974 JOURNAL.

REFERENCES

1. For a review, *cf.*, D. M. Mohilner, in "Electroanalytical Chemistry," Vol. 1, pp. 241-409, A. J. Bard, Editor, Marcel Dekker, New York (1966).
2. For recent review, *cf.*, B. B. Damaskin, O. A. Petrii, and V. V. Batrakov, "Adsorption of Organic Compounds on Electrodes," Plenum Press, New York (1971); R. Payne, *J. Electroanal. Chem.*, **41,** 277 (1973).
3. F. A. Long and W. F. McDevit, *Chem. Rev.*, **51,** 119 (1952).
4. D. M. Mohilner and H. Nakadomari, *J. Phys. Chem.*, **77,** 1594 (1973).
5. A. N. Frumkin, "Elektrokapilyarnye Yavlenie i Elektrodyne Potentsialy," Odessa, 1919; *cf.*, A. N. Frumkin and B. B. Damaskin, in "Modern Aspects of Electrochemistry," No. 3, p. 151, J. O'M. Bockris and B. E. Conway, Editors, Butterworths, Washington, D.C. (1964).
6. H. H. Bauer, H. R. Campbell, and A. K. Shallal, *J. Electroanal. Chem.*, **21,** 45 (1969).
7. H. Mackle, R. G. Mayrick, and J. J. Rooney, *Trans. Faraday Soc.*, **56,** 115 (1960).
8. H. Mackle and R. T. B. McClean, *ibid.*, **60,** 817 (1964).
9. I. Wichterle and E. Hala, *Ind. Eng. Chem. Fundamentals*, **2,** 155 (1963).
10. I. Wichterle and L. Boublikova, *ibid.*, **8,** 585 (1969).
11. J. Klopstock and M. Rogozinski, *J. Chromatog.*, **50,** 504 (1970).
12. P. Pollak and R. T. B. Cave, *Can. J. Chem.*, **45,** 3089 (1967).
13. G. Maffiolo and J. Vidal, *Bull. Soc. Chim. France*, **1970,** 2810.
14. I. Klotz, "Chemical Thermodynamics," Revised ed., W. A. Benjamin, New York (1964).
15. *Cf.* J. H. Hildebrand and R. L. Scott, "The Solubility of Nonelectrolytes," 3rd ed., Dover Publications, Inc., New York (1964).
16. H. M. McNair and W. R. Supina, "Column Selection in Gas Chromatography," American Chemical Society (1970).
17. H. S. Harned and B. B. Owen, "The Physical Chemistry of Electrolytic Solutions," 3rd ed., p. 553, Reinhold Publishing Corp., New York (1958).

Electromotive Force Measurements on Cells Involving Beta-Alumina Solid Electrolyte

Nabendu S. Choudhury*[1]

National Aeronautics and Space Administration, Lewis Research Center, Cleveland, Ohio 44135

ABSTRACT

Open-circuit emf measurements have been made to demonstrate that a two-phase, polycrystalline mixture of β-alumina and α-alumina could be used as a solid electrolyte in galvanic cells with reversible electrodes fixing oxygen or aluminum chemical potentials. These masurements indicate that such a two-phase solid electrolyte may be used to monitor oxygen chemical potentials as low as that corresponding to Al, Al_2O_3 coexistence ($P_{O_2} \approx 10^{-47}$ atm at 1000°K). The activity of Na_2O in β-alumina in coexistence with α-alumina was also determined by emf measurements.

Normally available polycrystalline beta-alumina (nominal composition $Na_2O \cdot 11Al_2O_3$) has been shown (1-4) to be really a two-phase mixture of beta-alumina (approximate composition $Na_2O \cdot 9Al_2O_3$) and alpha-alumina (Al_2O_3 with negligible or no doped sodium oxide). The three component, two-phase system has three degrees of freedom ($F = C - P + 2$; where F is the number of degrees of freedom, C the number of components, and P the number of phases) and at a particular temperature and pressure (which is nominally fixed at 1 atm), this is reduced to only one. Thus the thermodynamic state of the system at a particular temperature and pressure is completely defined if the chemical potential of any one of the components, *viz.* Na, O, or Al, is fixed.

The above considerations do not include electronic defects. However, if electronic defects are also considered, the local electroneutrality condition (together with the various chemical equilibria between electrons, ions, and neutral species) must also be taken into account in effect providing an additional constraint. Moreover, beta-alumina is known to be a good Na^+ ion conductor with negligible or no electronic conduction (5, 6) and alpha-alumina is an excellent insulator. Therefore, the measured open-circuit emf's, in an electrochemical cell with beta-alumina solid electrolyte, do not depart significantly from the thermodynamic emf's (6). These results were also confirmed by recent experiments conducted in this laboratory (7).

In all previous investigations (6-8), involving open-circuit emf measurements with beta-alumina solid electrolyte, the Na chemical potential has been controlled at both electrodes. The purpose of the present investigation is to determine if meaningful open-circuit emf's may be measured with electrodes fixing O or Al chemical potentials. If the phase rule applies as described above, fixing O or Al chemical potential is equivalent to fixing the Na chemical potential.

Experimental Technique

The beta-alumina solid electrolyte disks were prepared in this laboratory from beta-alumina powder (<325 mesh) supplied by Aluminum Corporation of America. The powder was pressed into ¾ in. diameter, ⅛ in. thick disks at 55,000 psi and sintered with β-alumina powder in dry air at 1690°C for 1 hr. The resulting material had 60-65% theoretical density and was kindly supplied by Dr. W. L. Fielder of this laboratory.

The cell for measuring emf's consisted of solid reversible electrodes and a beta-alumina solid electrolyte disk. The electrodes were held in contact with the beta-alumina disk by spring pressure applied through α-alumina tubes, which constituted the cell assembly. The design was similar to that described by Skelton and Patterson (9). Platinum lead wires were connected to the electrodes. The tip of a Pt-Pt, 13% Rh thermocouple, insulated by α-alumina tubes, was positioned close to the cell. The cell assembly enclosed in a closed-end α-alumina furnace tube formed a gas-tight system. Insulated feed-throughs were used to provide electrical connections external to the system. The heating system consisted of a wire (Kanthal) wound tube furnace with a controller to maintain the cell temperature to within ±1°C. The α-alumina furnace tube was shielded by a grounded stainless steel tube to minimize electrical noise. All electrical connections external to the furnace were made with shielded cables, with the shields appropriately grounded.

The cell emf's were monitored with an electrometer (input impedance 10^{14} ohms) or a digital voltmeter (input impedance 10^9 ohms). The temperature was monitored with a potentiometer in conjunction with a null detector. An electronic cold junction compensator was used to provide compensation for the cold junction temperature of the thermocouple.

At the beginning of each run, the system was evacuated to 10^{-2} Torr, flushed with helium and evacuated again. This procedure was repeated several times. The helium was purified by passing it through copper turnings held at 400°C and a liquid nitrogen cold trap before entering the system. Subsequent to the flushing and evacuation procedure the system was filled with helium and a slow and steady flow of helium was maintained through the system. The furnace was then brought to the measuring temperatures. The emf's were recorded after waiting for at least ½ hr at each temperature. The attainment of equilibration was indicated by reproducibility of the recorded emf's on cycling the cell temperature within the range of measurements.

Results and Discussion

Electrodes fixing oxygen chemical potential.—Stable and reproducible open-circuit emf's were obtained from the following cells with electrodes fixing oxygen partial pressures

$$\text{Fe,FeO}/\beta\text{-alumina/Ni,NiO} \qquad [\text{I}]$$

and

$$\text{Ni,NiO}/\beta\text{-alumina/Cu,Cu}_2\text{O} \qquad [\text{II}]$$

Figure 1 illustrates the data obtained from 689° to 990°C for cell [I]. Kiukkola and Wagner's (10) data for the cell $Fe,FeO/CaO,ZrO_2/Ni$, NiO are indicated in Fig. 1 as the solid line. The data for cell [II] are shown in Fig. 2 along with Lasker and Rapp's (11) estimated

* Electrochemical Society Active Member.

[1] Present address: Metallurgy and Ceramics Research Laboratory, Aerospace Research Laboratories, Wright-Patterson AFB, Ohio 45433.

Key words: β-alumina, solid electrolyte, open-circuit emf, free energy, Po_2 gauge.

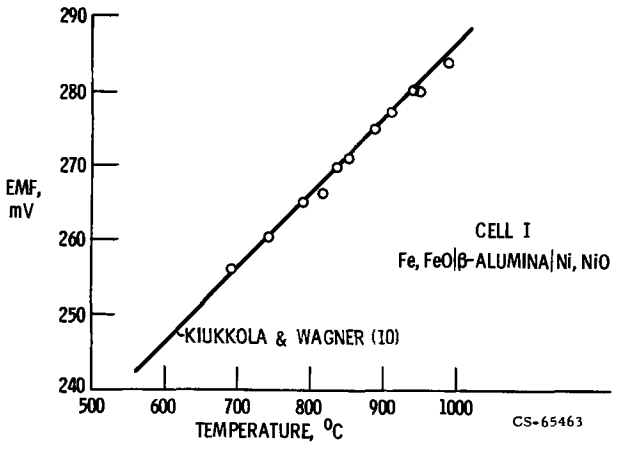

Fig. 1. Open-circuit emf against temperature for the cell Fe, FeO/β-alumina/Ni, NiO.

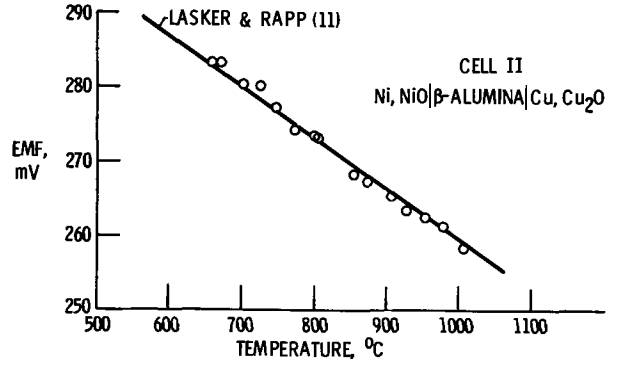

Fig. 2. Open-circuit emf against temperature for the cell Ni, NiO/β-alumina/Cu, Cu_2O.

thermodynamic emf for the cell. It is apparent that the open-circuit emf's observed with beta-alumina are in good agreement with the previously measured (with oxygen ion conducting solid electrolyte) and calculated thermodynamic emf's. It should be noted that the rate of equilibration at lower temperatures was progressively sluggish. For example, at 650°C cell [II] attained equilibrium only after waiting for 12 hr. In a few of the runs with Cu,Cu_2O electrodes, a considerable amount of Cu penetration was visually observed in the beta-alumina disks.

Determination of the Na_2O activity in beta-alumina.— Consider the reaction

$$Na_2O + xAl_2O_3 = Na_2O \cdot xAl_2O_3 \qquad [1]$$

where $Na_2O \cdot xAl_2O_3$ is the composition of β-alumina in coexistence with α-alumina. Because both β-alumina and α-alumina coexist in the standard state in the solid electrolyte, the standard free energy change for the above reaction is given by $RT \ln a_{Na_2O}$, where a_{Na_2O} is the activity of Na_2O in β-alumina in coexistence with α-alumina. This may be determined with a cell of the type M,MX_2,NaX/β-alumina/M', M'O provided M, MX_2 and NaX coexist in the standard state. The open-circuit emf for the above cell is given by

$$E = -\frac{RT}{F} \ln \frac{a_{Na}(R)}{a_{Na}(L)} \qquad [2]$$

The Na activities in the left- and right-hand sides of the cell are given by

$$RT \ln a_{Na}(L) = \Delta G^\circ_{NaX} - \frac{1}{2}\Delta G^\circ_{MX_2} \qquad [3]$$

$$RT \ln a_{Na}(R) = \frac{1}{2} RT \ln a_{Na_2O}$$

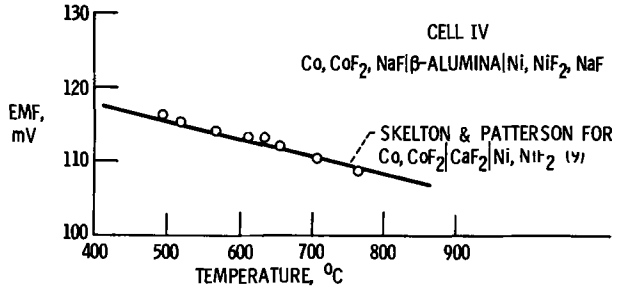

Fig. 3. Open-circuit emf against temperature for the cell Co, CoF_2, NaF/β-alumina/NaF, NiF_2, Ni.

$$+ \frac{1}{2}\Delta G^\circ_{Na_2O} - \frac{1}{2} 2\Delta G^\circ_{M'O} \qquad [4]$$

Combining Eq. [2], [3], and [4]

$$RT \ln a_{Na_2O} = -2EF + 2\Delta G^\circ_{NaX} - \Delta G^\circ_{MX_2} + \Delta G^\circ_{M'O} - \Delta G^\circ_{Na_2O} \qquad [5]$$

Ni,NiF_2,NaF/β-alumina/Cu,Cu_2O [III]

was the cell investigated in the present study. That Ni,NiF_2, and NaF coexist in the standard state at least up to 760°C was confirmed by measuring the open-circuit emf of the cell

Co,CoF_2,NaF/β-alumina/Ni,NiF_2,NaF [IV]

The observed emf's of cell [IV] between 490° and 764°C were in good agreement (Fig. 3) with those measured by Skelton and Patterson (9) with the cell Co,CoF_2/CaF_2/Ni,NiF_2. The solid line in Fig. 3 represents the least-square best fit of Skelton and Patterson's (9) data. It should be noted that NaF and NiF_2 form a eutectic at around 790°C (12), and this limits the use of Ni,NiF_2, NaF electrode to below this temperature.

Reproducible emf's were obtained for the cell Ni,NiF_2,NaF/β-alumina/Cu,Cu_2O between 576° and 725°C. The emf data for the above cell [III] is given in Table I and also illustrated in Fig. 4.

The least-square best fit of the data between 576° and 725°C is given by

$$E(\text{III})\ \text{mV} = (646.5 - 0.190T) \pm 1 \qquad [6]$$

where T is in °K. Above 725°C the emf's were low and irreproducible; presumably because of excessive evaporation of NaF affecting the Cu,Cu_2O electrode.

The standard free energies of formation of NiF_2 and NaF may be obtained from publications of Skelton and Patterson (9) and Steinmetz and Roth (13). The $\Delta G^\circ_{Na_2O}$ and $\Delta G^\circ_{Cu_2O}$ values may be obtained from JANAF tables (14). Using these values, the activity of Na_2O in β-alumina may be calculated from Eq. [4] and [5]. For example, at 1000°K $RT \ln a_{Na_2O} = -77.0$ kcal/mole, at 900°K $RT \ln a_{Na_2O} = -77.8$ kcal/mole, and at 800°K $RT \ln a_{Na_2O} = -78.7$ kcal/mole; the corresponding a_{Na_2O} values at 1000°, 900°, and 800°K are $10^{-16.83}$, $10^{-18.89}$, and $10^{-21.50}$, respectively.

In a review article on β-alumina electrolytes, Kummer (15) reported the thermodynamic data on β-alu-

Table I. Emf of cell [III]

Ni,NiF_2,NaF/β-alumina/Cu,Cu_2O

Temperature (°C)	Emf (mV)
576	484
606	480
631	475
633	474
657	469
659	470
679	465
705	460
706	461
725	456

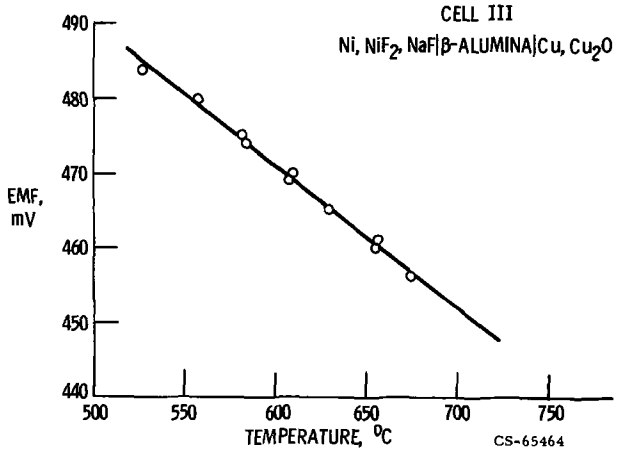

Fig. 4. Open-circuit emf against temperature for the cell Ni, NiF_2 NaF/β-alumina/Cu, Cu_2O.

mina obtained from emf measurements. The cell is schematically represented by $P_{O_2},Al_2O_3/\beta$-alumina (single phase)/$NaAlO_2,P_{O_2}$. In this work β-alumina was assumed to be a line compound in the analysis of the emf data. From the observed emf's between 1000° and 1600°C the standard free energy change per mole of β-alumina for the reaction

$$2NaAlO_2 + 10Al_2O_3 = Na_2O \cdot 11Al_2O_3$$

was calculated as −9.0 kcal at 1000°C and ≈0 at 140°C. $Na_2O \cdot 11Al_2O_3$ was the assumed stoichiometric formula for β-alumina; however, the observed emf's as well as the standard free energy change per mole of β-alumina is independent of the stoichiometry.

Beta-alumina is represented as $Na_2O \cdot xAl_2O_3$ instead of $Na_2O \cdot 11Al_2O_3$ in the following analysis. From the data reported by Kummer (15), the interpolated value of the standard free energy change per mole of β-alumina, at 1000°K, for the reaction

$$2NaAlO_2 + (x-1)Al_2O_3 = Na_2O \cdot xAl_2O_3 \quad [7]$$

is given by −6.14 kcal. The tabulated (14) free energies of formation of Na_2O, Al_2O_3, and $NaAlO_2$ may be combined to give the standard free energy change of −44.34 kcal, at 1000°K, for the reaction

$$Na_2O + Al_2O_3 = 2NaAlO_2 \quad [8]$$

Combining reactions [7] and [8] the standard free energy change at 1000°K for the reaction

$$Na_2O + xAl_2O_3 = Na_2O \cdot xAl_2O_3 \quad [1]$$

is given by −50.48 kcal.

However, as mentioned earlier the present work indicates a standard free energy change of −77.0 kcal, at 1000°K for reaction [1].

An attempt was made to resolve the apparent inconsistency by taking into account that β-alumina does in fact have a range of stoichiometry, from 1 to 4, rather than being a line compound. The cell reported in the review article (15) may then be represented as $P_{O_2},Al_2O_3/\beta(1),\beta(2)/NaAlO_2,P_{O_2}$, where β(1) is β-alumina ($Na_2O \cdot xAl_2O_3$) in equilibrium with Al_2O_3 and β(2) is β-alumina ($Na_2O \cdot yAl_2O_3$) in equilibrium with $NaAlO_2$. Thus the standard free energy change of −6.14 kcal at 1000°K corresponds to $RT \ln a_{Na_2O}(L)/a_{Na_2O}(R)$ where $a_{Na_2O}(L)$ is the Na_2O activity fixed by β-alumina ($Na_2O \cdot xAl_2O_3$) and Al_2O_3 coexistence and $a_{Na_2O}(R)$ is the Na_2O activity fixed by β-alumina ($Na_2O \cdot yAl_2O_3$) and $NaAlO_2$ coexistence. The value of $RT \ln a_{Na_2O}(L)$, at 1000°K, is given by −77.0 kcal/mole according to the present investigation. Therefore, combination of the previously reported results (15) with those of the present investigation yields $RT \ln a_{Na_2O}(R) = -70.86$ kcal/mole at 1000°K.

The thermodynamic stabilities of β(1) and β(2) toward decomposition into $NaAlO_2$ and Al_2O_3 are examined below. Reactions [1] and [8] may be combined to yield

$$Na_2O \cdot xAl_2O_3 = 2NaAlO_2 + (x-1)Al_2O_3 \quad [9]$$

Using the values of −77.0 kcal for reaction [1] and −44.34 kcal for reaction [8], the standard free energy change for reaction [9] is given by 32.66 kcal; which means that β(1) ($Na_2O \cdot xAl_2O_3$) is stable toward above mentioned decomposition at 1000°K.

Consider the reaction

$$Na_2O \cdot yAl_2O_3 + (y-1)Na_2O = 2yNaAlO_2 \quad [10]$$

The standard free energy change for the above reaction is given by $(y-1)RT \ln a_{Na_2O}(R)$ where $a_{Na_2O}(R)$ is the activity of Na_2O in a coexistent mixture of β-alumina ($Na_2O \cdot yAl_2O_3$) and $NaAlO_2$. Reactions [8] and [10] may be combined to yield

$$Na_2O \cdot yAl_2O_3 = 2NaAlO_2 + (y-1)Al_2O_3 \quad [11]$$

The standard free energy change for reaction [11] is given by

$$\begin{aligned}\Delta G^\circ_{11} &= (y-1)(RT \ln a_{Na_2O}(R) - \Delta G^\circ_8) \\ &= (y-1)(-70.86 + 44.34) \\ &= -26.52(y-1)\,\text{kcal} \qquad \text{at } 1000^\circ\text{K}\end{aligned} \quad [12]$$

Thus β(2) ($Na_2O \cdot yAl_2O_3$) is unstable toward decomposition into $NaAlO_2$ and Al_2O_3.

The apparent paradox of β(1) being stable and β(2) unstable toward decomposition may be resolved if an intermediate stable phase between β-alumina and $NaAlO_2$ in the Na_2O-Al_2O_3 system exists. Such a phase (*viz.* β″-alumina) is known to exist in the Na_2O-Al_2O_3 system (2, 4). Thus the coexistence of $NaAlO_2$ and β-alumina, as employed in the cell reported in the review article (15), must correspond to a thermodynamically metastable situation.

Electrodes fixing aluminum chemical potential.—Metallic aluminum was used as anodes fixing aluminum chemical potential in the following cells

$$Al/\beta\text{-alumina}/AlF_3,NiF_2,Ni \quad [V]$$

and

$$Al/\beta\text{-alumina}/NaF,NiF_2,Ni \quad [VI]$$

Emf measurements with compacted aluminum powder electrodes were not successful. However, reasonably stable emf's were obtained with Al electrodes in the form of a foil (1/16 in. thick). These cells had relatively short lives. It was further observed that the cell life could be prolonged when operated under vacuum instead of flowing helium. It is believed that rapid oxidation of aluminum at elevated temperatures is the cause of poor cell lives. However, under vacuum the cells lasted for 8 to 12 hr, during which the open-circuit emf data could be recorded.

The open-circuit emf of cell [V] is given by $E_V = -\frac{1}{3F} RT \ln a_{Al}$ where a_{Al} is the activity of aluminum at the cathode. Therefore, the emf E_V is also given by

$$E_V = -\frac{1}{3F}\left(\Delta G^\circ_{AlF_3} - \frac{3}{2}\Delta G^\circ_{NiF_2}\right) \quad [13]$$

Skelton and Patterson (9) have measured the open-circuit emf of the cell $Al,AlF_3/CaF_2/Ni,NiF_2$, which is also given by Eq. [13]. The data for cell [V] are plotted in Fig. 5, which also shows the least-square best fit line of Skelton and Patterson's (9) data. The agreement seems to be satisfactory at temperatures above 540°C. At temperatures below 540°C the observed open-circuit emf's of cell [V] fall significantly below

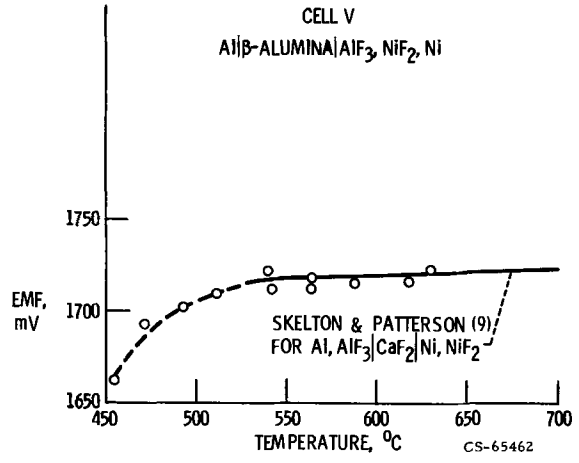

Fig. 5. Open-circuit emf against temperature for the cell Al/β-alumina/AlF_3, NiF_2, Ni.

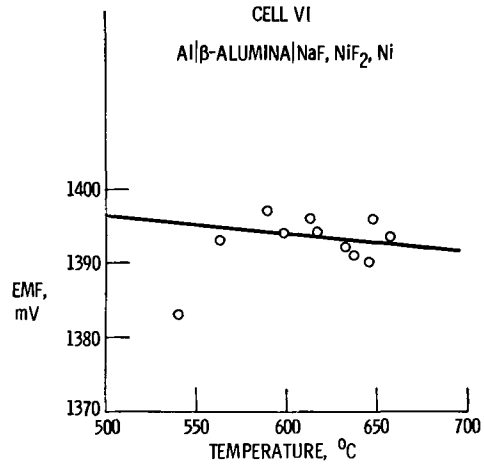

Fig. 6. Open-circuit emf against temperature for the cell Al/β-alumina/NaF, NiF_2, Ni.

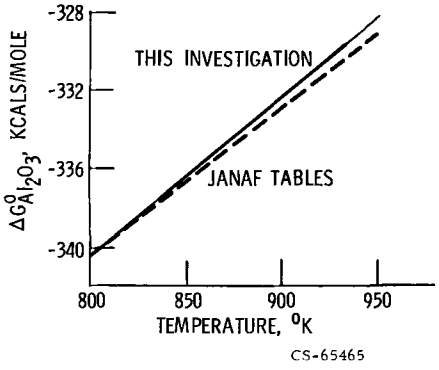

Fig. 7. Free energy of formation of Al_2O_3 against temperature plot comparing the values estimated in the present investigation with those tabulated in JANAF tables.

those observed by Skelton and Patterson (9). This may be due to sluggish electrode equilibration and/or departure from the proposed α-alumina, β-alumina equilibrium in the electrolyte.

Open-circuit emf data for cell [VI] are given in Table II and plotted in Fig. 6. The least-square best fit of the data from 563° to 656°C is given by

$$E(\text{VI})\,\text{mV} = (1414 - 0.023T) \pm 3 \qquad [14]$$

The departure of the observed emf at 540°C from the linear relationship is similar to that observed with cell [V] and may be accounted for in the same way.

Equations [6] and [14] may be combined to obtain the open-circuit emf between Al, Al_2O_3, and Cu,Cu_2O electrodes. Attempts were not successful to directly measure the open-circuit emf of such a cell below the melting point of aluminum (660°C). This is presumably because of the inability of the Cu,Cu_2O electrode to achieve equilibration in a relatively short time (8-12 hr) at these temperatures. Though not pursued in the present investigation, such measurements may be feasible at higher temperatures with different cell geometries. For example, the β-alumina solid electrolyte may be in the form of a flat bottomed cup with molten aluminum inside and the Cu,Cu_2O electrode contacting the outer flat surface of the electrolyte.

The free energy of formation of Al_2O_3 was calculated from Eq. [6] and [14] and the $\Delta G^\circ_{Cu_2O}$ (14) values. This is given by Eq. [15] below for the limited temperature range of 560°-660°C

$$\Delta G^\circ_{Al_2O_3} = (-404.8 + 0.081\,T) \pm 0.6\ \text{kcal/mole} \qquad [15]$$

Figure 7 compares the $\Delta G^\circ_{Al_2O_3}$ values, according to Eq. [15] with those given in JANAF tables (14). The agreement seems to be quite satisfactory in view of the scatter in the data of cell [VI] and the different methods of estimation.

The reaction between sodium and alumina.—Consider the reaction

$$6Na + Al_2O_3 = 3Na_2O + 2Al \qquad [16]$$

Table II. Emf of cell [VI]

Al/β-alumina/NaF,NiF_2,Ni	
Temperature (°C)	Emf (mV)
540	1383
563	1393
588	1397
598	1394
612	1396
616	1394
632	1392
636	1391
645	1390
646	1396
656	1394

The standard free energy change for the above reaction is given by

$$(3\Delta G^\circ_{Na_2O} - \Delta G^\circ_{Al_2O_3})$$

It has been discussed above that the standard free energy change of the reaction

$$Na_2O + xAl_2O_3 = Na_2O\cdot xAl_2O_3 \qquad [1]$$

is given by $RT \ln a_{Na_2O}$, where a_{Na_2O} is the activity of Na_2O in β-alumina in coexistence with α-alumina.

Combining Eq. [1] and [16] the standard free energy change for the reaction

$$6Na + (3x + 1)Al_2O_3 = 3(Na_2O\cdot xAl_2O_3 + 2Al \qquad [17]$$

is given by

$$\Delta G^\circ = 3\Delta G^\circ_{Na_2O} - \Delta G^\circ_{Al_2O_3} + 3RT \ln a_{Na_2O} \qquad [18]$$

Using the data from JANAF tables (14) for $\Delta G^\circ_{Na_2O}$ and $\Delta G^\circ_{Al_2O_3}$ and $RT \ln a_{Na_2O}$ value of −77.0 kcal/mole (see above), the estimated ΔG° for reaction [17] at 1000°K is −106.8 kcal. The value of ΔG° at 573°K is −129.3 kcal. The negative value of the ΔG° indicates that polycrystalline two-phase β-alumina (*i.e.*, a mixture of α-alumina and β-alumina) in equilibrium with Na is able to liberate free aluminum at the interface. This may have some implications concerning the development of electronic conductivity and blackening of β-alumina in prolonged contact with liquid sodium at 573°K observed Miles and Wynn Jones (16).

Beta-alumina and β″-alumina solid electrolytes are being actively considered for development of commercial Na-S rechargeable battery systems (15). These materials must be resistant to metallic sodium attack for such applications. Therefore, the thermodynamics of the reaction with Na need to be considered. The par-

ticular case of Al_2O_3 reacting with Na to form aluminum and the next Na_2O-rich compound (*viz.* β-alumina) in the Na_2O-Al_2O_3 system may be generalized to examine the criterion for the stability of any phase $Na_2O \cdot aAl_2O_3$ to attack by metallic sodium to form the next soda-rich phase $Na_2O \cdot bAl_2O_3$ and aluminum. The over-all reaction may be represented by

$$6(a-b)\mathrm{Na} + (1+3b)(Na_2O \cdot aAl_2O_3) = (1+3a)(Na_2O \cdot bAl_2O_3) + 2(a+b)\mathrm{Al} \quad [19]$$

The standard free energy change for the above reaction is given by

$$\Delta G^\circ_{19} = (a-b)[3(\Delta G^\circ_{Na_2O} + RT \ln a_{Na_2O}) - (\Delta G^\circ_{Al_2O_3} + RT \ln a_{Al_2O_3})] \quad [20]$$

where a_{Na_2O} and $a_{Al_2O_3}$ are the activities of Na_2O and Al_2O_3 in $Na_2O \cdot aAl_2O_3$ and $Na_2O \cdot bAl_2O_3$ coexistence. ΔG°_{19} may also be represented by

$$\Delta G^\circ_{19} = (a-b)\left[-\frac{1}{b}\Delta G^\circ_{Na_2O \cdot bAl_2O_3} + \left(3+\frac{1}{b}\right)RT \ln a_{Na_2O} + 3\Delta G^\circ_{Na_2O} - \Delta G^\circ_{Al_2O_3}\right] \quad [21]$$

where $\Delta G^\circ_{Na_2O \cdot bAl_2O_3}$ is the standard free energy change for the reaction

$$Na_2O + bAl_2O_3 = Na_2O \cdot bAl_2O_3 \quad [22]$$

For $Na_2O \cdot aAl_2O_3$ to be resistant to attack by metallic sodium ΔG°_{19} must be positive. ΔG°_{19} may be evaluated for any pair of coexistent intermediate phases with the help of Eq. [20] or Eq. [21] and [22]; but the relevant thermodynamic data are not completely available for the Na_2O-Al_2O_3 system. However, let us examine the case when $b = 1$, *i.e.*, $Na_2O \cdot bAl_2O_3 = 2NaAlO_2$. At 1000°K $\Delta G^\circ_{Na_2O \cdot Al_2O_3}$ for the reaction

$$Na_2O + Al_2O_3 = 2NaAlO_2 \quad [8]$$

is given by −44.34 kcal. Using the tabulated values (14) for $\Delta G^\circ_{Na_2O}$ and $\Delta G^\circ_{Al_2O_3}$ together with $\Delta G^\circ_{Na_2O \cdot Al_2O_3}$ at 1000°K in Eq. [21], ΔG°_{19} may be written as

$$\Delta G^\circ_{19} = (a-1)(4RT \ln a_{Na_2O} + 168.46)\ \text{kcal} \quad [23]$$

The phase diagram (2,4) for the Na_2O-Al_2O_3 system indicates that the alumina-rich phase next to $NaAlO_2$ is most likely β''-alumina. Thus for β''-alumina to be stable in contact with metallic sodium at 1000°K $RT \ln a_{Na_2O}$ should be ≥ -42.025 kcal/mole, according to Eq. [23]; where a_{Na_2O} is the activity of Na_2O in a coexistent mixture of $NaAlO_2$ and β''-alumina. The critical value of a_{Na_2O} may also be evaluated at other temperatures of interest and then compared with the actual value, if available.

Possible use of two-phase polycrystalline β-alumina in solid electrolyte P_{O_2} gauges.—The fact that β-alumina behaves as a solid electrolyte at the extremely low oxygen partial pressure of Al, Al_2O_3 coexistence ($P_{O_2} \approx 10^{-47}$ atm at 1000°K) suggests that it may be used to monitor very low oxygen chemical potentials. The commonly known oxygen ion conducting solid electrolyte P_{O_2} gauges are limited by the onset of electronic conduction to oxygen partial pressures of around 10^{-37} atm at 1000°K (17). Although the upper P_{O_2} limit in this investigation corresponded to Cu,Cu_2O equilibrium, it is probable that β-alumina may be used as a solid electrolyte at higher oxygen partial pressures without significant hole conduction. The low temperature limit for sufficiently fast equilibration in β-alumina for use as an oxygen monitor seems to be around 550°C. This temperature is lower than the operating temperatures of known oxygen ion conducting solid electrolytes in which the limiting factor is poor ionic conductivity. β-alumina being a much better conductor, by some three orders of magnitude, suggests the possibility of reducing the operating temperature below 550°C with better material and cell design. Thus P_{O_2} gauges constructed with β-alumina solid electrolyte may offer the advantages of lower operating temperature and wider response (especially at extremely low P_{O_2}) and may find applications in semiconductor and metallurgical industries.

Acknowledgment

This research was conducted while the author held an NRC-NASA Resident Research Associateship.

Manuscript submitted April 23, 1973; revised manuscript received June 25, 1973. This was Paper 274 presented at the Chicago, Illinois, Meeting of the Society, May 13-18, 1973.

Any discussion of this paper will appear in a Discussion Section to be published in the June 1974 JOURNAL.

REFERENCES

1. M. Harata, *Mater. Res. Bull.*, **6**, 461 (1971).
2. R. C. DeVries and W. L. Roth, *J. Am. Ceram. Soc.*, **52**, 364 (1969).
3. Y. LeCars, J. Théry, and R. Collongues, *Compt Rend Acad. Sci., Paris, Series C*, **274**, 4 (1972).
4. N. Weber and A. Venero, Paper 5-J1-70, 72nd Annual Meeting of Am. Ceram. Soc. (May 1970).
5. Y. F. Y. Yao and J. T. Kummer, *J. Inorg. Nucl. Chem.*, **29**, 2453 (1967).
6. L. Hsueh and D. N. Bennion, *This Journal*, **118**, 1128 (1971).
7. W. L. Fielder, Private communication.
8. N. K. Gupta and R. P. Tischer, *This Journal*, **119**, 1033 (1972).
9. W. H. Skelton and J. W. Patterson, *J. Less-Common Metals*, **31**, No. 1, 47 (1973).
10. K. Kiukkola and C. Wagner, *This Journal*, **104**, 379 (1957).
11. M. F. Lasker and R. A. Rapp, *Z. Physik. Chem. N. F.*, **49**, 198 (1966).
12. E. M. Levin, C. R. Robbins, and H. R. McMurdie, "Phase Diagram for Ceramists," The American Ceramic Society, Ohio (1964).
13. E. Steinmetz and H. Roth, *J. Less-Common Metals*, **16**, 295 (1968).
14. JANAF Thermochemical Tables, prepared by the Dow Chemical Company, Thermal Research Laboratory, Midland, Michigan, last supplements June 30, 1971.
15. J. T. Kummer, *Prog. Solid State Chem.*, **7**, 141 (1972).
16. L. J. Miles and I. Wynn Jones, *Proc. Brit. Ceram. Soc.*, **19**, 179 (1971).
17. J. W. Patterson, *This Journal*, **118**, 1033 (1971).

A Solid-State Electrode for Reducible Gases

B. C. LaRoy, A. C. Lilly, and C. O. Tiller

Philip Morris Research Center, Richmond, Virginia 23261

ABSTRACT

The electrical properties of solid-state electrochemical cells using thin-film lanthanum fluoride electrolyte have been investigated as a function of the ambient atmosphere. The conductivity of the cells has been found to increase with the concentration of the reducible gases O_2, CO_2, SO_2, NO_2, and NO. Sensitivity to a given gas is observed when the cell's terminal voltage exceeds a "characteristic potential" which correlates with the electron affinity of the gas. With suitable choice of anode material a galvanic cell is formed which may be used as a "self-energized" O_2 electrode or as a low current battery or O_2 fuel cell.

Lanthanum fluoride has an unusually high anionic conductivity and polarizability at room temperature (1-3). Its Debye temperature is only ~360°K (4) although it melts at 1766°K. Thus the room temperature Schottky defect density is high. The lowest activation energy for F^- diffusion is ~0.4 eV in both single crystals (1) and thin films (5). Single crystals have a d-c electrical resistivity of 10^7 ohm-cm and a static dielectric constant of 10^6 at room temperature (2). Thin evaporated films of LaF_3 have higher resistivities (~10^{12} ohm-cm) and lower dielectric constants (~10^3) (5). But thin films are still good anion conducting electrolytes at ambient temperatures. The fact that thin-film LaF_3 is a good F^- anion conductor with low electronic conductivity made it reasonable to investigate it as an electrolyte for other anions.

Cell Description

The films were deposited by evaporation of 99.999% pure materials in an ion pumped ultrahigh vacuum system at pressures below 10^{-7} Torr. They were evaporated from W or Ta boats and deposited on glazed alumina substrates at substrate temperatures of 200°-300°C. A layered configuration was used. Cr metal was first deposited to promote adhesion. The anode metal was deposited next, followed by an electrolyte layer 0.2-1.2 μm thick and then by the cathode metal. To promote access of gas to the cathode-electrolyte interface, an open gridlike structure was used. (Figure 1 illustrates cell structure schematically.)

LaF_3 electrolyte was used for most investigations, but CeF_3, NdF_3, and PrF_3 gave similar results. Au and Ag cathodes and Bi, Al, La, Pr, and Au anodes have been used. All layers were deposited during one evacuation of the vacuum system by use of a mask changing arrangement. Twenty such cells were deposited on a 5 by 5 cm substrate. Each individual cell was about 5 mm square with an anode area of 0.14 cm^2 and a cathode area of 0.04 cm^2.

Other configurations, including coplanar, have been used with qualitatively the same results as are reported here. Linear dimensions have been made as small as 0.25 mm.

Key words: solid electrolyte, lanthanum fluoride, gas electrode.

Electrical Measurements

The cells were removed from the vacuum deposition system and placed in a hermetically sealed brass chamber. Tank gases were passed through $CaSO_4$ dryers, flow meters, appropriate valves, and into the chamber which was kept at a slight positive pressure (<2.5 cm of water).

Chamber response was determined for N_2 to O_2 transitions by using a Westinghouse Model 211 Pulmonary Function Monitor. Transition time to 90% of a mixture change was about 4 sec. Oxygen content in the chamber could be reduced to less than 3 ppm. The compositions of gas mixtures were determined from the ratio of flow rates of the gases entering the chamber.

The electrical circuit used for all measurements is shown in Fig. 2. The power supply furnished either regulated d.c. or a voltage ramp of variable rise rate. Terminal potentials were monitored with a Keithley 603 electrometer millivoltmeter having an input resistance of 10^{14} ohms. Currents were measured by a Keithley 417 high-speed picoammeter or (when a well-known shunt resistance was desired) by a Cary 31 vibrating-reed electrometer in parallel with an appropriate shunt resistor. System accuracy was ± 10% or better as determined by measuring known resistors in the 10^8-10^{12} ohm range. Current changes of ± 10^{13}A

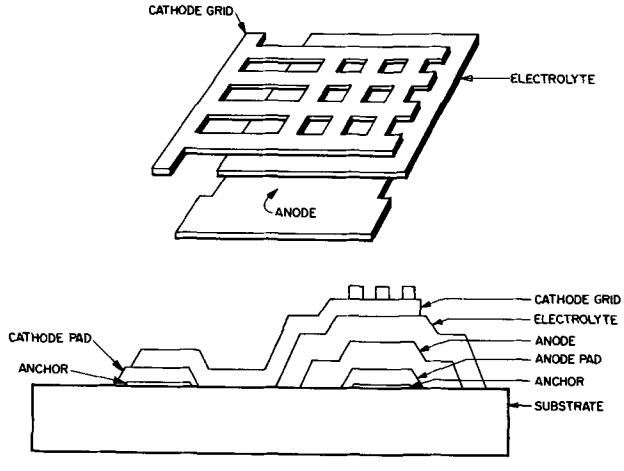

Fig. 1. Schematic of cell construction

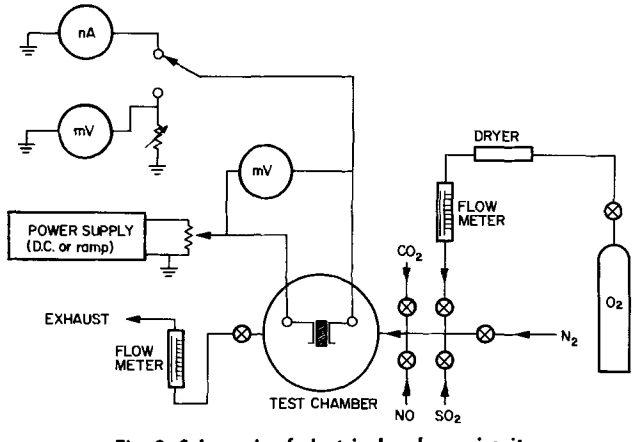

Fig. 2. Schematic of electrical and gas circuits

were easily resolved. By our convention "positive current" signifies anion transport from cathode to anode within the electrolyte.

Polarization and Initial Response

In 1 atm of nitrogen gas, typical cells exhibit d-c dielectric constants between 360 and 1100 and steady-state resistivities between 10^{12} and 10^{13} ohm-cm. The temperature coefficient of resistivity ($\Delta R/R/\Delta T$) is typically 0.1/°C below 100°C (5). Above 100°C conductivity increases strongly with temperature. When shunted by a small external resistance and biased to a fixed terminal potential, the initial current surge decays to a stable background current over a period of about 1 hr.

Upon exposure to a reducible gas the resistivity of a virgin cell decreases by two orders of magnitude or more. Then, during a "break-in" period in the reducible gas, the initial sensitivity decays in an exponential-like fashion, reaching a constant rate ($100\Delta I/I$/time ~0.1-0.5/hr) after about 2 hr. Figure 3 illustrates this initial period for a Cu(anode)/LaF_3(electrolyte/Au(cathode) cell which has been polarized with 0.3V for some time before the initial oxygen application at $t = 0$.

Changes in the electrode-electrolyte interfaces undoubtedly contribute to the initial decrease in sensitivity. However, another significant factor is the neutralization of a net positive charge (F^- deficiency) within the virgin cells. Fine gold probes deposited within the electrolyte layer at varying distances from the electrodes allowed the determination of internal potential profiles and, hence, the relative charge distributions. Upon the application of oxygen, the net internal charge became negative and the profile was indicative of injection and transport of negative carriers. When the O_2 atmosphere was removed after the break-in period, the net internal charge approached neutrality, but never again became positive. ...

Exposure of a broken-in cell to a different reducible gas requires an additional "break-in" treatment. In this case, the sensitivity changes much less than during the initial break-in period. Polarization by the reduced species or buildup of reaction products seems the most probable cause of this behavior. Background current is somewhat reduced during break in, again probably due to polarization, or reaction product buildup at the electrodes.

The current increase of a typical broken-in cell upon exposure to oxygen is characterized by two parts: an initial "fast" part where 25% of maximum amplitude is reached within 4 sec, followed by a "slow" part during which current rises to 90% of maximum in about 4 min. Upon removal of oxygen the current decrease has a similar "fast" part followed by a return to 90% of the baseline, in 5-10 min.

Equilibrium Response to Oxygen

When cells with copper or bismuth anodes are polarized and broken in as previously described, cell current becomes a relatively stable function of terminal potential and of the concentration of oxygen in the ambient atmosphere.

Figure 4 shows current *vs.* terminal potential for a Bi/LaF_3/Au cell in 1 atm of nitrogen and in 1 atm of oxygen. Each data point was recorded after allowing several hours for polarization. All data for nitrogen were taken first, followed by all oxygen data. As terminal potential is increased a particular potential, V_c, is noted below which the cells are rather insensitive to oxygen, but above which sensitivity increases strongly with V.

No classical half-wave potential is observed. Therefore, we conclude that diffusion is not a mobility limiting factor in these cells.

In the absence of a half-wave potential, V_c has been used as a characteristic potential. Since the cells have finite electrode potentials, V_c has been defined as the difference between the terminal potential giving zero current in oxygen and the terminal potential where the oxygen current begins its rapid increase (see Fig. 4). Defined in this way, V_c is largely independent of anode material. Static data from cells with Cu and Bi anodes yield $V_c = 230 \pm 30$ mV as characteristic for oxygen.

At a constant terminal potential above V_c cell current varies as the sum of linear and logarithmic terms in oxygen concentration. The variation is quite linear at concentrations above 20% of O_2 in mixtures of O_2 and N_2. Below 20% the logarithmic term causes significant curvature.

Figure 5 shows current sensitivity $(I - I_0)/I_0$ *vs.* per cent oxygen for cells having Bi, Cu, and Au anodes. Current (I) was monitored as the oxygen concentration was varied. I_0 is the background current in the absence of oxygen.

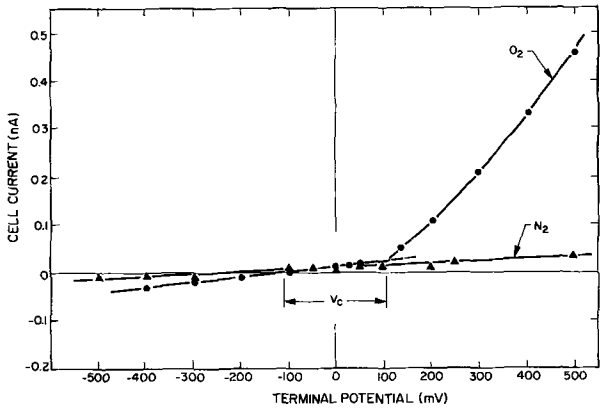

Fig. 4. Typical static current-potential relationship for a Bi/LaF_3/Au cell in 1 atm of O_2 and 1 atm of N_2.

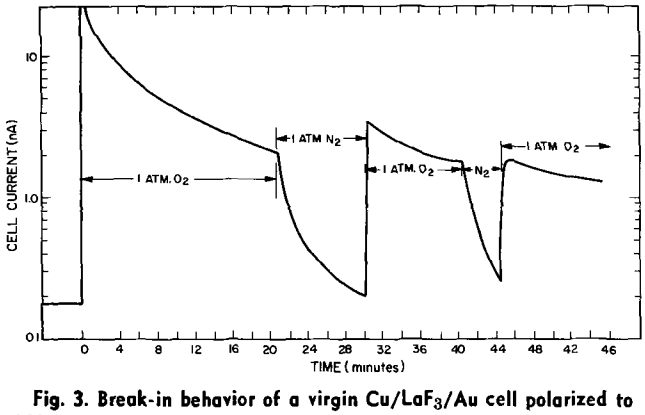

Fig. 3. Break-in behavior of a virgin Cu/LaF_3/Au cell polarized to 300 mV.

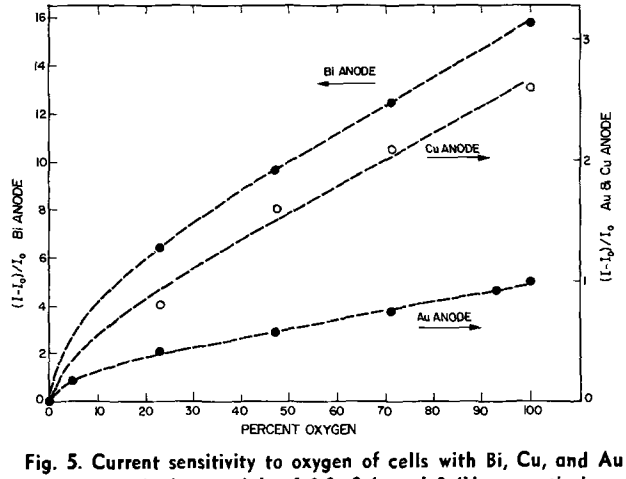

Fig. 5. Current sensitivity to oxygen of cells with Bi, Cu, and Au anodes at terminal potentials of 0.0, 0.4, and 0.4V, respectively.

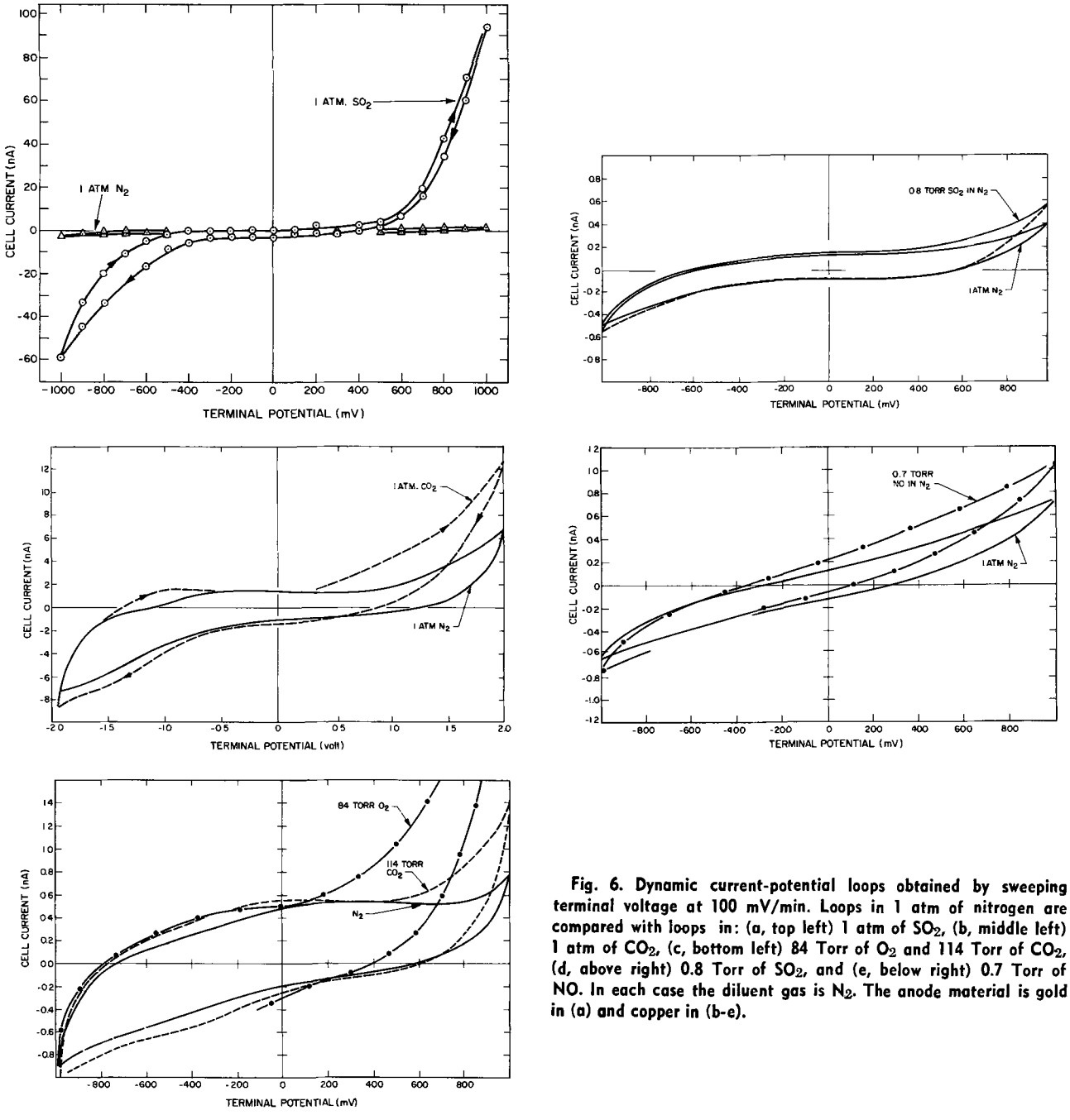

Fig. 6. Dynamic current-potential loops obtained by sweeping terminal voltage at 100 mV/min. Loops in 1 atm of nitrogen are compared with loops in: (a, top left) 1 atm of SO_2, (b, middle left) 1 atm of CO_2, (c, bottom left) 84 Torr of O_2 and 114 Torr of CO_2, (d, above right) 0.8 Torr of SO_2, and (e, below right) 0.7 Torr of NO. In each case the diluent gas is N_2. The anode material is gold in (a) and copper in (b-e).

Cells with Bi anodes are the most sensitive and have the greatest low concentration nonlinearity. Cells with blocking gold anodes respond more linearly. Probably, the logarithmic term arises from interfacial phenomena at the anode.

Cells made early in the program had higher background currents than cells produced recently. In the early cells, current variation was nearly linear with oxygen concentration (6). Evidently, the oxygen conductivity of these cells was shunted by a comparable oxygen independent conductivity. Thus, sensitivity to low oxygen concentrations was preferentially reduced.

Potential Sweep Data—Other Reducible Gases

By sweeping the terminal potential at a constant rate of 100 mV/min, data showing cell sensitivity to several additional reducible gases were obtained. The dynamic current-potential traces form loops due to the high polarizability of LaF_3. Even in this nonequilibrium situation, greater currents are observed (for a given potential magnitude) when anion flow is toward a reactive anode. However, "dynamic" sensitivity is also observed with a blocking anode material (*e.g.*, gold). Figures 6 (a and b) illustrates the current-potential data in 1 atm of SO_2 and CO_2. Figure 6 (a, d, and e) shows similar data for lower partial pressures of O_2, CO_2, SO_2, and NO.

For the dynamic curves we have taken $V_c = 1/2\,[V_+ - V_-]$ where V_+ and V_- are the forward and reverse bias terminal potentials at which the first significant sensitivity was observed. This procedure, which was necessitated by small gas-to-gas and cell-to-cell differences in curve characteristics, led to fairly large uncertainties in V_c. Still, the characteristic potentials were found to be indicative of the gas species (Table I).

Table I. Characteristic potentials and electron affinities of various gases

Gas	V_c (mV)	E_A (eV)	Reference
NO	<50	$0.024\ ^{+0.010}_{-0.005}$	(7)
O_2	230 ± 30	0.440 ± 0.008	(8)
CO_2	500 ± 50	1.2 ± 0.3	(10)
SO_2	400 ± 100	0.5-1.0	(9)
NO_2	<100	>2.04	(12)

In the case of nitrogen oxides, the dynamic current-potential curves show no region of insensitivity (Fig. 6e). Also, we were unable to locate a region of static bias where the cells were insensitive to NO or NO_2. Therefore, V_c is near zero. Table I shows upper limits set by the resolution achievable in the experiment.

$Au/LaF_3/Au$ cells were used to determine the approximate current-concentration curves for SO_2, CO_2, NO, and NO_2. For each gas the cells were polarized to a static potential above V_c and broken in until the time-rate of sensitivity decrease was small. All data were then taken within a few minutes.

Due to the blocking nature of the gold anodes, sensitivities were small. However, relative sensitivities could be obtained with less regard for electrode reactions.

Figure 7 shows current variation with the concentration of CO_2, SO_2, and NO. N_2 was the diluent gas in these cases. In the case of NO_2, current increased exponentially with concentration. Figure 8 shows data when a refrigerant gas of similar density (Genetron 12) was used as the diluent. Similar behavior was noted when the diluent was N_2, but noise was increased. This exponential sensitivity may be due to dissociation of NO_2 on the cathode (or on the specimen chamber walls) yielding NO.

In many cases, the solid-state cells have a shelf life of several months and maintain useful calibration for several days of use. However, the factors affecting lifetime are very complicated (*e.g.*, use lifetime depends on the rate of change of the oxygen current as well as on its magnitude) and are still under investigation.

Cells with like, gold, electrodes degraded by use or storage are easily "rejuvenated" by heating to 300°C in high vacuum for several hours.

Galvanic Cells

Cells with reactive anodes develop open-circuit potentials which presumably arise from the oxidation of the anode by F^- and the reduced species. These potentials range from 200 mV for Cu to about 1.5V for La.

Finite currents may be drawn from such a cell. Figure 9 plots current against the terminal potentials obtained at three oxygen concentrations by shunting a $Bi/LaF_3/Au$ cell with varying load resistors. As the load increases, current becomes increasingly sensitive to oxygen pressure, yielding a "self-energized" oxygen

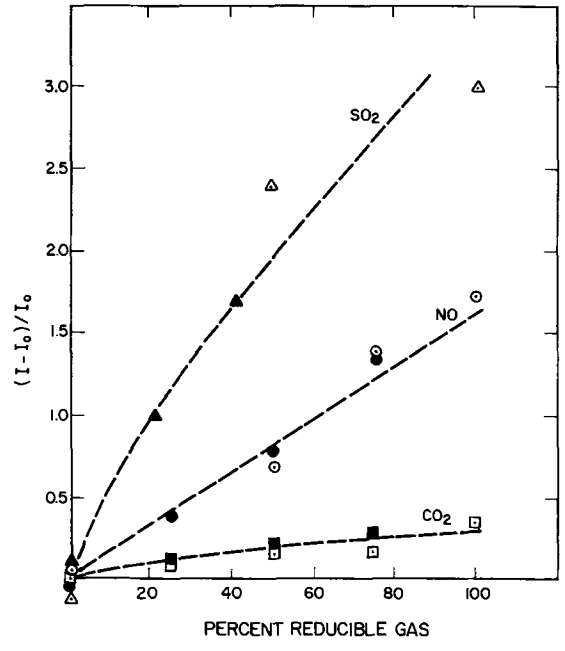

Fig. 7. Current sensitivity of $Au/LaF_3/Au$ cells to CO_2 at 1.1V bias, NO at 1V bias, and SO_2 at 1.6V bias. Open data points, concentration increasing; closed data points, concentration decreasing.

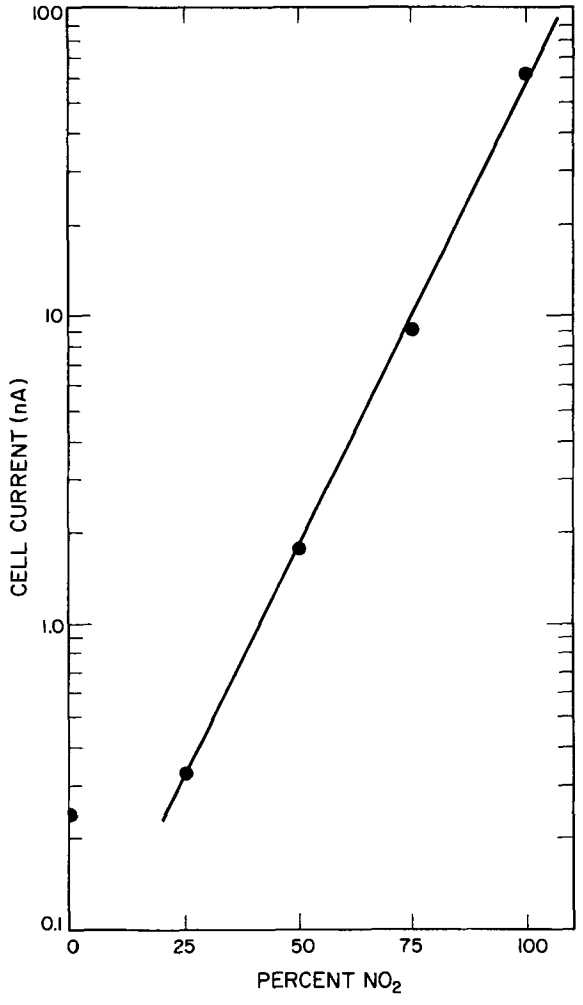

Fig. 8. Current variation with NO_2 concentration for a $Au/LaF_3/Au$ cell biased at 300 mV.

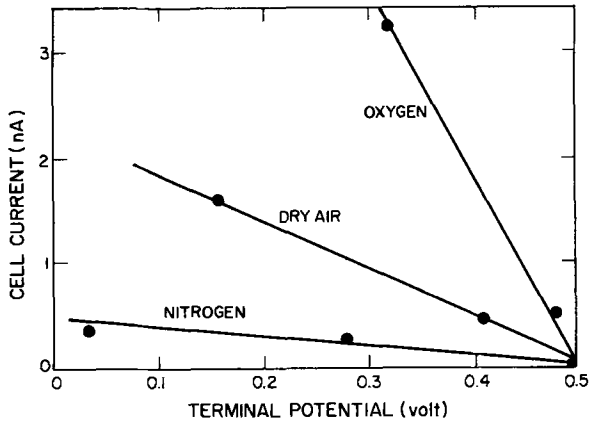

Fig. 9. Load characteristics of a galvanic $Bi/LaF_3/Au$ cell

electrode. Maximum oxygen sensitivity is obtained at zero terminal volts when the cell is short circuited and nearly the entire emf generated by the anode reaction is impressed at the cathode-electrolyte interface.

Although current is limited by cell resistivity, power densities of 1-10 Whr/kg have been estimated from discharge curves. This may indicate some utility for such cells as low discharge batteries.

Mechanisms

The observed behavior is consistent with a model constituted by (*i*) reduction of a gas at the ca hode-electrolyte interface, (*ii*) nondiffusion limited transport through the electrolyte, and (*iii*) oxidation of

the gas at the anode. That is, the cell constitutes a solid-state analog to the liquid reducible gas electrode.

Reduction.—Our potential probe measurements have shown strongly polarized layers less than 0.2 μm thick at the cell electrodes. Nearly the entire terminal potential appears across these polarization layers, giving ample electric field for reduction of a gas. In agreement with this, we observe little difference between the polarization and sensitivity of cells which have electrolyte thicknesses between 0.5 and 2.0 μm.

In Fig. 10 we have plotted literature values for electron affinity against V_c for the various gases. The electron affinities quoted for NO (7), O_2 (8), and SO_2 (9) are for the addition of a single electron to the entire molecule. The "electron affinity" of CO_2 is the same as that of O (10), probably due to dissociation on metallic surfaces (10, 11) ($CO_2 \rightarrow CO + O$).

The monotonic increase of characteristic potential (V_c) with the electron affinity of the incident gas (Fig. 10) indicates that the rate limiting reactions are

$$NO + e^- \rightarrow NO^-$$

$$SO_2 + e^- \rightarrow SO_2^-$$

$$O_2 + e^- \rightarrow O_2^-$$

$$O + e^- \rightarrow O^- \text{ (for } CO_2\text{)}$$

The electron affinity of NO_2 is uncertain, but it is greater than 2 eV (12) which is inconsistent with our V_c of <100 mV. This supports our previous speculation that NO_2 dissociates to yield NO which has a very low electron affinity.

Two gases, CO and N_2O, which do not form stable molecular anions did not alter cell conductivity.

Transport.—The apparent mobility of other ionic species in a solid fluorine ion electrolyte is surprising. We offer two possible models of the mechanism. The first depends on the high grain boundary area of the polycrystalline films (crystallite dimensions are 20-200Å). Large ions might carry significant current through defects at such boundaries.

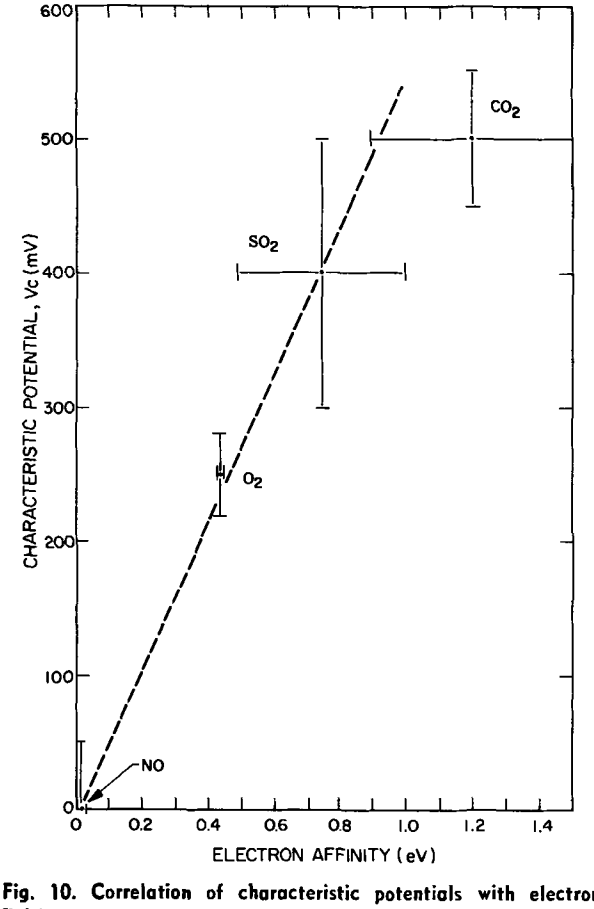

Fig. 10. Correlation of characteristic potentials with electron affinities.

The second possibility is mobility of other than fluorine ions through Schottky defects in the LaF_3 lattice. Fluorine in LaF_3 exists in three magnetically nonequivalent sites. Covalent bonding predominates in two of the sites. In the third site, the fluorines make up a layered array with approximately 60% ionic bonding and about 40% π-bonding (13). The high polarizability and conductivity of LaF_3 at room temperature is primarily due to motion through the latter sites.

From x-ray Debye-Waller factors, Zalkin *et al.* (14) find that the mean square displacement of the ionically bound fluorines is 1.7Å[2]. Therefore ions of widely varying size might substitute into F^- defects. Although large ions such as NO^-, SO_2^-, or O_2^- might not "fit" these defects, O^- with a radius of 1.76Å should substitute for the 1.33Å F^- (15) without significantly straining the lattice.[1] The proportions of π-bonding will be larger for O^- than for F^-, but ionic bonding should still predominate and lead to high O^- mobility. As previously noted, O^- is the probable product of the "reduction" of CO_2 (10, 11). We speculate below on the evolution of O^- in the cases of other gases.

In the case of oxygen, the creation of O_2^- is consistent with the observed characteristic potential. This O_2^- is probably created in an excited state which has a lifetime of 10^{-13} sec (17). In a solid a stabilizing collision within this time is probable. However, stabilization in the large fields at the polarized interface might also be accomplished through a reaction such as

$$O_2^- \text{ (excited)} \rightarrow O + O^-$$

Similar processes of varying efficiency might cause evolution of O^- in the cases of SO_2 and NO. Thus there are plausible sources of a species which should be mobile in the LaF_3 lattice. Experiments with films of varying grain size or designed to monitor the species arriving at the anode-electrolyte interface would do much to clarify the picture.

Anode.—A chemically reactive anode material is necessary to obtain appreciable steady-state sensitivity to oxygen. In light of the previous discussion we believe that the reduced species combine chemically with the anode material, thus diminishing further polarization of the interface and allowing continuing charge transfer.

Summary

Thin-film metal/rare earth fluoride/metal cells were found to constitute solid-state electrodes for reducible gases at ambient temperatures. Cell conductivity increases with gas concentration when the cell is biased above a characteristic potential which corresponds with the electron affinity of the gas.

The observed behavior fits a model where reduction and oxidation of the gas species occurs at the cathode and anode interface, respectively. Charge is transported through the electrolyte. Several different models for the mechanism are still considered possible.

We believe that the small size, sturdiness, and projected low cost of fabrication of these cells makes them potentially useful multigas selective electrodes for a variety of applications.

Acknowledgments

We are grateful to Mr. E. M. Gentry for his work in cell fabrication, to Mr. L. C. Bartlam for electrical measurement, and to Drs. D. A. Lowitz and D. T. Sawyer for many helpful consultations.

[1] One of the reviewers of this paper has pointed out that $O^=$ has almost exactly the same radius of F^-. Indeed $O^=$ should have good mobility in LaF_3. However, the attachment of the second electron would require the addition of an energy of 5.8 eV [the one electron affinity of O is +1.45 eV; the two electron affinity is −7.3 eV (16)] which could only be supplied by a very high surface polarization energy. We cannot rule out the existence of $O^=$ in the lattice, but the formation of O^- is a lower energy and more straightforward process.

Manuscript submitted March 8, 1973; revised manuscript received June 29, 1973. This was Paper 167 presented at the Houston, Texas, Meeting of the Society, May 7-11, 1972.

Any discussion of this paper will appear in a Discussion Section to be published in the June 1974 JOURNAL.

REFERENCES

1. A. Sher, R. Solomon, K. Lee, and M. W. Muller, *Phys. Rev.*, **144**, 593 (1966).
2. R. Solomon, A. Sher, and M. W. Muller, *J. Appl. Phys.*, **37**, 3427 (1966).
3. W. L. Fielder, "Ionic Conductivity in Lanthanum Fluoride," NASA publication (1969) (available from National Technical Information Service, Springfield, Va., Access No. N69-40056).
4. W. M. Yen, W. C. Scott, and A. L. Shawlow, *Phys. Rev.*, **136**, 271 (1964).
5. C. O. Tiller, A. C. Lilly, and B. C. LaRoy, To be published, *Phys. Rev.*
6. B. C. LaRoy, A. C. Lilly, and C. O. Tiller, Abstract No. 168, page 430, Electrochem. Soc. Extended Abstracts, Spring Meeting, Houston, Texas, May 7-11, 1972.
7. M. W. Siegel, R. J. Celotta, J. L. Hall, J. Levine, and R. A. Bennett, *Phys. Rev.*, **A6**, 607 (1972).
8. R. J. Celotta, R. A. Bennett, J. L. Hall, M. W. Siegel, and J. Levine, *Phys. Rev.*, **A6**, 631 (1972).
9. D. Feldmann, *Z. Naturforsch.*, **25A**, 621 (1970).
10. J. D. Craggs and B. A. Tozer, *Proc. Roy. Soc. (London), Ser. A*, **A254**, 229 (1960).
11. L. R. Clavenna and L. D. Schmidt, *Surface Sci.*, **33**, 11 (1972).
12. J. Berkowitz and W. A. Chupka, *J. Chem. Phys.*, **55**, 2733 (1971).
13. A. G. Lundin, S. P. Gabuda, and A. I. Lifshits, *Soviet Phys-Solid State*, **9**, 273 (1967).
14. A. Zalkin, D. H. Templeton, and T. E. Hopkins, *Inorg. Chem.*, **5**, 1466 (1966).
15. "Handbook of Chemistry and Physics," 51st ed., The Chemical Rubber Co., Cleveland, Ohio (1970).
16. V. I. Vadeneyev, L. V. Gurvich, V. N. Kondrat'yev, V. A. Medvedev, and Ye. L. Frankevich, "Bond Energies Ionization Potentials and Electron Affinities," St. Mantin's Press, New York (1966).
17. A. Herzenberg, *J. Chem. Phys.*, **51**, 4942 (1969).

Transport Properties of LaF_3 Thin Films

A. C. Lilly, Jr., B. C. LaRoy, C. O. Tiller, and Bruce Whiting[1]

Philip Morris Research Center, Richmond, Virginia 23261

ABSTRACT

Pulsed current-voltage measurements have been carried out on thin films of LaF_3 varying in thickness from 1000 to 10,000Å. The *I-V* data fit a relationship of the form $I = I_0 \sinh \alpha V$ normally associated with ionic conduction. If it is assumed that the internal field is equal to the externally applied field, the derived ionic jump distance is of the order of 20Å. However, potential probe measurements show a strong concentration of positive space charge near the cathode. When the effect of the space charge on the internal electric field is accounted for, a smaller value is obtained for the ionic jump distance, which is more in agreement with the crystal structure of LaF_3.

Lanthanum fluoride is a material that exhibits somewhat unusual electrical transport properties. Previous workers (1-3) have concluded that the electric current in LaF_3 single crystals is carried almost exclusively by F^- ions with negligible electronic conduction. As shown by Sher *et al.* (1) LaF_3 crystals are good ionic conductors at room temperature probably because of their low activation energy for formation of Schottky defects. Because of their good anionic conduction properties, we have used thin films of LaF_3 in chemical sensing devices. Since thin films in general have different properties than the bulk materials, we have examined the transport properties of ions in thin films of LaF_3 ranging in thickness from 1000 to 10,000Å.

Experimental Procedures

Since LaF_3 single crystals exhibit a large amount of polarization (2), it is important to measure currents a short time after a voltage has been applied to the films if transport properties free of interfacial effects are to be studied. In this work we have taken the high frequency model for the electrodes and the LaF_3 film as a parallel resistance and capacitance network. To measure the components of the network, we compared the current through a variable r-c parallel network connected to one channel of an oscilloscope. The resistance and capacitance of the network was then matched to that of the sample. This matching was determined by the coincidency of the current-time curves on a Tektronix 502 oscilloscope after a 200-500 μsec voltage pulse was applied. Steady-state current values were measured with a Keithley 417 picoammeter.

The thin films were evaporated in an ion-pumped ultrahigh vacuum system using 99.999% pure materials. They were thin-film sandwich structures consisting of an alumina substrate with LaF_3 between metallic electrodes (Al-Al or Au-Au). The evaporated films of LaF_3 are polycrystalline with crystallite sizes ranging from 20 to 200Å. The density of the films was not measured. Also the exact stoichiometry of the film is not known. Batsanova (4) reports the principal component of the gas phase over boiling LaF_3 at 2600°K to be LaF_3. However, mass spectrometer measurements also show ionic species La^+, LaF^+, and LaF_2^+ formed from dissociation of gaseous LaF_3. Undoubtably some fluorine is lost in the evaporation process as evidenced by the net positive change inside the films; however, all films are made under the same conditions and the electrical properties are reproducible.

A series of special samples was processed in order to establish a potential profile in the LaF_3 films. These samples had the normal Au top (cathode) and bottom (anode) electrodes, but also had a third Au probe inserted in the LaF_3 layer at various distances from the cathode. This probe was inserted by stopping the LaF_3 deposit during deposition, depositing the probe, and then completing the LaF_3 deposition.

In all potential probe experiments a constant potential difference of 300 mV was applied between the cathode and anode. The cathode was held at −300 mV

[1] Present address: Department of Physics, Carnegie-Mellon University, Pittsburgh, Pennsylvania 15200.

Key words: transport properties, lanthanum fluoride, solid electrolyte.

and the anode maintained at essentially ground potential. The potential difference between one of the electrodes and the probe was measured with a Cary 31V vibrating reed electrometer.

Experimental Results

If the thin film of LaF_3 is an ionic conductor then the current-voltage (I-V) characteristics should follow a relationship of the form (5)

$$I = A \sinh (aq\ E/kT) \qquad [1]$$

where E is the electric field, a is one-half the ionic jump distance, q is the ionic charge, T is the absolute temperature, and A is a constant. A careful examination of the pulsed I-V data on several different samples disclosed that Eq. [1] gives the best fit to the data. For instance, in Fig. 1 and 2 are shown plots of the experimental points and the best fit $I = A \sinh (aq\ E/kT)$ curve obtained by fitting a and A. The fit is quite good over the entire range of the data. The calculated ionic jump distances from the data shown in Fig. 1 and 2, and in other cases, range from 15 to 25Å. However, it must be realized that this assumes that the internal field is the same as the applied field. In reality there are space-charge effects leading to an enhancement of the field near the cathode.

Even though scatter in the data was evident from sample to sample, the general trends of the potential profile measurements were clearly indicated and are shown in Fig. 3. The data in Fig. 3 show a potential profile as it occurs after a 30 min polarization in an N_2 or O_2 atmosphere. The samples were in the gas shown prior to charging and such profiles were obtained as a function of time. As charging time increased, the internal potentials became more positive with the major change having taken place after 30 min. Clearly the potential profiles are indicative of a large change in potential relative to ground at a distance of 1000Å from the cathode. The potential profile in O_2 shows a build-up of negative charge near the anode which is thought to be due to the reduction of O_2 molecules at the cathode and the subsequent movement of these oxygen anions into the LaF_3 film (6). Taking the modification of the internal field by charge accumulation into account when applying Eq. [1], the derived jump distance is approximately 4-5Å, or smaller, which is more in agreement with the 2-3Å expected from the trigonal crystal structure of LaF_3.

The experimental I-V results are independent of the electrodes used, in this case gold and aluminum. Solomon *et al.* (3) found the same electrode independence. In Fig. 4 a plot is shown of steady-state resistance *vs.* applied voltage in a 2400Å LaF_3 film. Note that the curve is of an ohmic character up to 1.6V, and is very nonlinear at higher voltage. In Fig. 5 the nonohmic

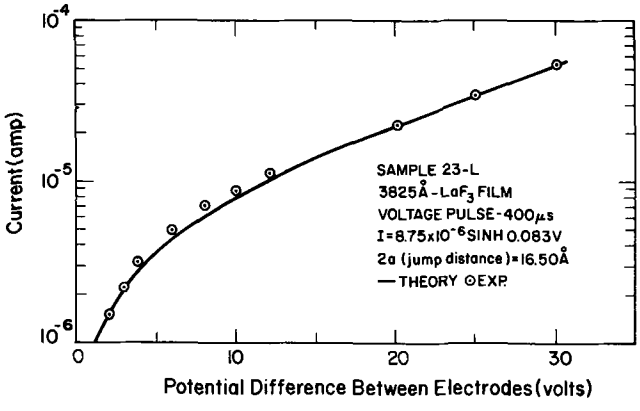

Fig. 1. Pulsed I-V characteristic for LaF_3 film of thickness 3825Å. The voltage pulse was of 400 μsec duration. The data has been fitted to an equation of the form $I = 8.75 \times 10^{-6}$ sinh (0.083V) and an ionic jump distance of 8.25Å.

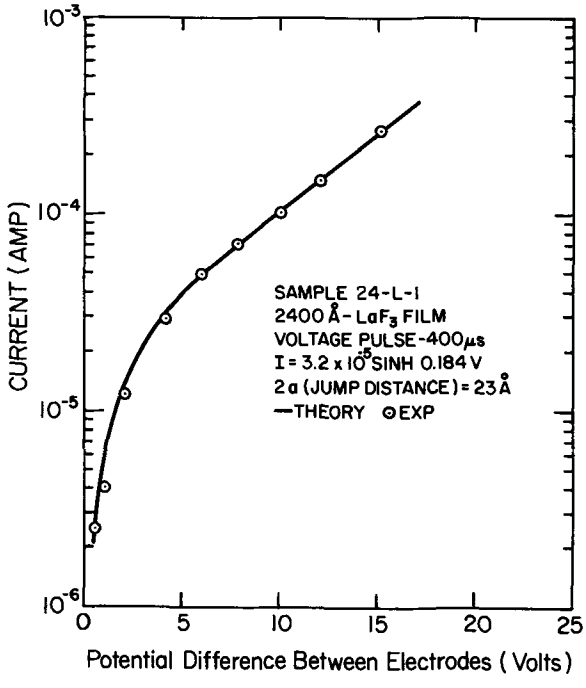

Fig. 2. Pulsed I-V characteristic for LaF_3 film of thickness 2400Å. The voltage pulse was of 400 μsec duration. The data has been fitted to an equation of the form $I = 3.2 \times 10^{-5}$ sinh (0.184V) and an ionic jump distance of 11.5Å.

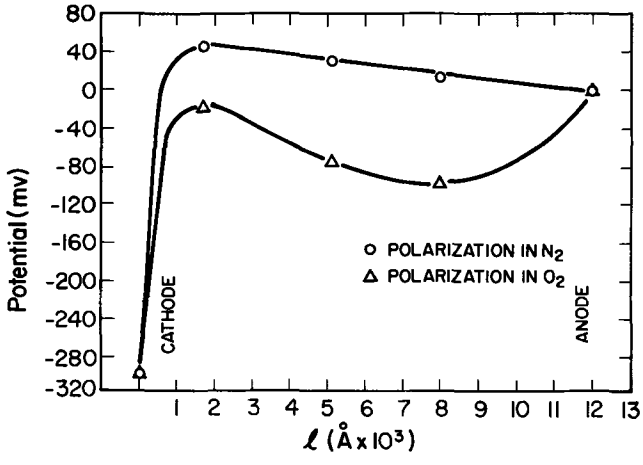

Fig. 3. Potential profile in the interior of LaF_3 films after 30 min charging in N_2 or O_2. The bias voltage is −300 mV applied to the cathode.

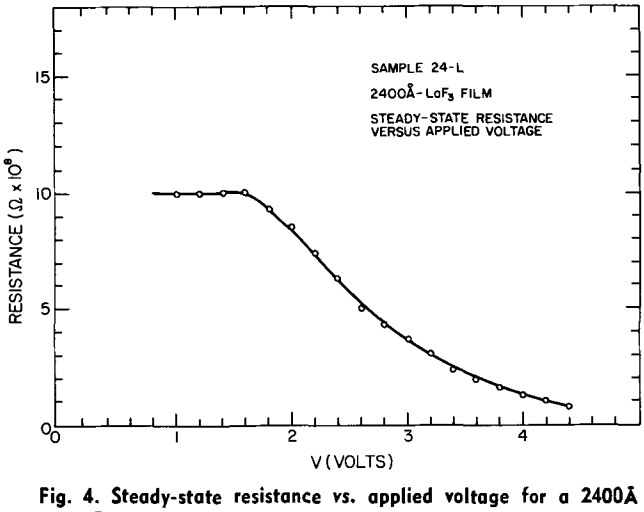

Fig. 4. Steady-state resistance *vs.* applied voltage for a 2400Å thick LaF_3 film.

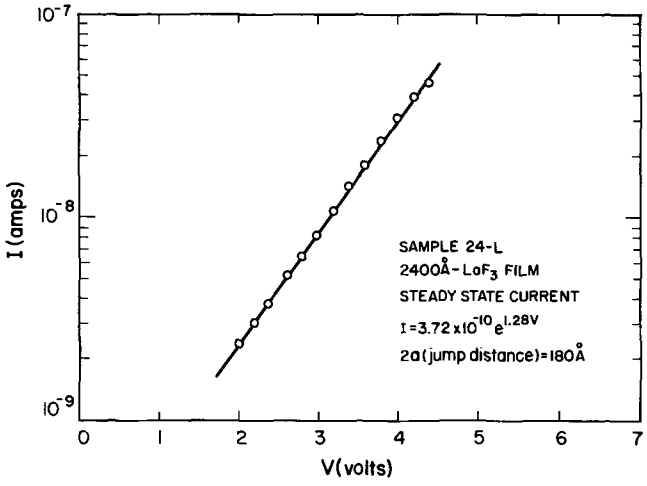

Fig. 5. Log I vs. applied voltage for a 2400Å thick LaF_3 film. Data is fitted to an equation of the form $I = 3.72 \times 10^{-10}$ exp (1.28V) which gives an apparent jump distance of 180Å.

portion of the I-V curve for the same sample is shown to fit Eq. [2]

$$I = 3.72 \times 10^{-10} e^{1.28V} \qquad [2]$$

which is another form of Eq. [1] with V, the potential difference between the electrodes, expressed explicitly. If we interpret the parameters as before, then a jump distance of 180Å can be derived. This value appears unrealistic and simply means that with the longer polarization time involved, the space charge layer has further enhanced the internal electric field near the cathode. In Table I a compilation is given of the pulse and steady-state electrical parameters, as a function of thickness of the LaF_3 film. The capacitance values for the pulse measurements are fairly constant with changing sample thickness indicating that the apparent dielectric constant is independent of inter-electrode distance. This indicates that the high polarization effect in LaF_3 is primarily an electrode effect. This is consistent with the potential probe data. The steady-state resistivity, is greater than the pulse resistivity by 10^2, and indicates the large effect of the interfacial polarization on the steady-state charge transport.

Discussion of Results

Single crystals of LaF_3 have previously been reported to have unusual electrical properties. For instance a small activation energy (0.069 eV) for Schottky defect formation has been measured and the defects are believed to be formed neutral (molecular holes). The interaction of LaF_3 in the crystal with a molecular hole to produce LaF_2^+ and F^- with a dissociation energy of approximately 0.40 eV (1) is thought to be the mechanism of carrier generation. Conductivity measurements by Sher *et al.* (1) and NMR experiments by Lee (7), Lundin *et al.* (8), and Goldman and Sher (9) all suggest that the electrical conductivity is due to ionic motion (F^-) with little electronic contribution. Solomon *et al.* (2) observed a large persistent polarization in LaF_3. They suggest the existence of a permanent double layer at the surface of the LaF_3 crystals, and potential probe measurements confirm this.

The results of thin films have many of the same features as the single crystal results. The measurements in this work certainly indicate a space-charge region near the electrodes plays a large role in the transport properties. The potential probe measurements given in Fig. 3 are similar to those obtained by Solomon *et al.* (2) on single crystals. Also, recent conductivity work on thin films of LaF_3 by Tiller *et al.* (10) agrees in the value of the conduction energy (0.43 eV) with conductivity (1-3) and NMR data (6-8) on single crystals of LaF_3.

The pulse resistivity of the LaF_3 thin films is of the order of 10^9 ohm-cm, or two orders of magnitude greater than the resistivity of the single crystal. However, the polycrystalline nature of the thin film and possible changes in stoichiometry could account for this difference. Lancaster (11) has observed that on heating CeF_3 films to 400°C in an ultrahigh vacuum system, fluorine gas was detected above the film. The I-V characteristics fit very well the $I \sim$ sine αV relationship that is indicative of ionic conduction over energy barriers controlled by the electric field. However, because of the strong positive space-charge region near the cathode, the internal electric field is different from the applied electric field. When this difference is accounted for, the ionic jump distances derived are more consistent with the values that would be expected in the LaF_3 structure.

The capacitance of the LaF_3 films is largely independent of the thickness, the I-V curves seem to be independent of the electrode material, and the potential probe measurements show a concentration of space charge near the surface. All of this evidence points to some form of persistent surface polarization in LaF_3 thin films. The same evidence exists for LaF_3 single crystals. The evaporation process probably leads to some degree of stoichiometry change if Lancaster's loss (11) of F_2 in CeF_3 can be assumed to happen in LaF_3 also. This plus the polycrystalline nature of the thin films must account for the two order of magnitude lower resistivity in the films.

Frenkel (12) has pointed out that a permanent double layer might exist in ionic crystals containing Schottky defects if there is a difference in activation energy for formation of vacancies between cations and anions. Frenkel's model predicts a charged layer of the ions that have the smaller activation energy. The evidence indicates that this phenomenon is active in both single crystals and thin films of LaF_3.

Conclusions

LaF_3 thin films exhibit the $I \propto \sinh \alpha V$ behavior characteristic of ionic conductors. The dominant charge carrier is thought to be an F^- ion hopping in vacancies created by the formation of Schottky defects. Because of the evaporation process there is probably a net loss of fluorine leaving a strong net positive space charge in the deposited LaF_3 with charge neutrality maintained by excess charge on the metal electrodes. An applied field enhances the positive space-charge layer in the vicinity of the cathode. The transport data

Table I. Electrical characteristics of LaF_3 thin films as a function of thickness

Sample	Thickness (Å)	Pulse time (400 μsec)			Steady-state	
		Resistance (ohms)	Capacitance (μF)	Resistivity (ohm-cm)	Resistance (ohms)	Resistivity (ohm-cm)
22-L	5800	2.2×10^6	0.04	2.3×10^9	1.5×10^9	1.5×10^{12}
23-L	3825	1.5×10^6	0.02	2.3×10^9	1×10^{10}	1.6×10^{12}
24-L	2400	1.5×10^6	0.02	3.7×10^9	1×10^{10}	2.5×10^{12}
26-L	1200	4.7×10^6	0.01	2.3×10^9	1.5×10^9	7.5×10^{12}
27-L	1015	1.5×10^6	0.03	8.9×10^9	4×10^8	2.4×10^{13}
28-L	740	2.2×10^6	0.03	1.8×10^{10}	7.7×10^7	0.6×10^{12}

Applied voltage: 1V.

are consistent with the existence of persistent surface polarization in thin films. This permanent polarization has also been observed in single crystal experiments by other workers.

Acknowledgments

The authors wish to thank Dr. David A. Lowitz and Dr. John C. Schug for helpful discussion involving this work. Also we thank Mr. E. M. Gentry and Mr. Branch Crooks for aid in the experimental work.

Manuscript submitted March 8, 1973; revised manuscript received June 29, 1973. This was Paper 168 presented at the Houston, Texas, Meeting of the Society, May 7-11, 1973.

Any discussion of this paper will appear in a Discussion Section to be published in the June 1974 JOURNAL.

REFERENCES

1. A. Sher, R. Solomon, K. Lee, and M. W. Muller, *Phys. Rev.*, **144**, 593 (1966).
2. R. Solomon, A. Sher, and M. W. Muller, *J. Appl. Phys.*, **37**, 3427 (1966).
3. W. L. Fielder, NASA publication (1969) (Available from National Technical Information Service, Springfield, Va., Access No. N69-40056).
4. L. R. Batsanova, *Russ. Chem. Rev.*, **40**, 465 (1971).
5. N. F. Mott and P. W. Gurney, "Electronic Processes in Ionic Crystals," p. 40, Oxford University Press, New York (1940).
6. B. C. LaRoy, A. C. Lilly, and C. O. Tiller, To be published, *This Journal*.
7. K. Lee and A. Sher, *Phys. Rev. Letters*, **14**, 1027 (1965).
8. A. G. Lundin, S. P. Gabuda, and A. I. Lifshits, *Soviet Phys.-Solid State*, **9**, 273 (1967).
9. M. Goldman and L. Sher, *Phys. Rev.*, **144**, 321 (1966).
10. C. O. Tiller, A. C. Lilly, and B. C. LaRoy, To be published, *ibid.*
11. N. C. Lancaster, *J. Phys. D: Appl. Phys.*, **5**, 1133 (1972).
12. J. Frenkel, "Kinetic Theory of Liquids," p. 36, Oxford University Press, New York (1946).

The Electro-Oxidation of Acetylene on Heterogeneous Au-Pt Alloys

J. W. Johnson,* C. K. Wu, and W. J. James*

Departments of Chemical Engineering and Chemistry and The Graduate Center for Materials Research, University of Missouri-Rolla, Rolla, Missouri

ABSTRACT

The anodic oxidation of acetylene was studied in aqueous solutions (pH = 0.3-12.6) at 80°C on heterogeneous Au-Pt alloy electrodes. The results were interpreted in terms of parallel reactions occurring separately on the Au-rich and Pt-rich phases. The polarization behavior on the separate phases was very similar to that of the corresponding pure metals.

The electro-oxidation of acetylene has previously been studied on platinized Pt and Au (1, 2). On platinized Pt, CO_2 was produced with high coulombic efficiency. A suggested reaction mechanism was

$$C_2H_2 = C_2H_2(ads) \quad [1]$$

$$H_2O = OH(ads) + H^+ + e \quad [2a]$$

or

$$OH^- = OH(ads) + e \quad [2b]$$

$$C_2H_2(ads) + OH(ads) \xrightarrow{\text{r.d.s.}} \ldots \rightarrow CO_2, H^+, e \quad [3]$$

On Au, the CO_2 coulombic efficiency varied from 3-80%, depending on pH and acetylene partial pressure. Discontinuities in the Tafel curves were interpreted in terms of a "transition region," on either side of which different reaction sequences were operative. The mechanism below the transition region (b.t.r.) was proposed to be the same as that for Pt except for a change in the rate determining step (r.d.s.) and the appearance of a resinous by-product

$$C_2H_2 = C_2H_2(ads) \quad [4]$$

$$H_2O \xrightarrow{\text{r.d.s.}} OH(ads) + H^+ + e \quad [5a]$$

or

$$OH^- \xrightarrow{\text{r.d.s.}} OH(ads) + e \quad [5b]$$

$$C_2H_2(ads) + OH(ads) \rightarrow \ldots \rightarrow CO_2, H^+, e, \text{resin} \quad [6]$$

Above the transition region (a.t.r.), the sequence proposed was

$$C_2H_2 = C_2H_2(ads) \quad [7]$$

$$C_2H_2(ads) + H_2O \xrightarrow{\text{r.d.s.}} C_2H_2OH(ads) + H^+ + e \quad [8a]$$

or

$$C_2H_2(ads) + OH^- \xrightarrow{\text{r.d.s.}} C_2H_2OH(ads) + e \quad [8b]$$

$$C_2H_2OH(ads) \rightarrow \ldots \rightarrow CO_2, H^+, e, \text{resin} \quad [9]$$

The differences in these reaction sequences have been attributed to differing properties of the metals for hydrocarbon adsorption ,water discharge, and oxide formation. The pure metals differ greatly in these respects. On Pt it is believed that the unsaturated hydrocarbons absorb by the breaking of one C-C bond and the forming of covalent bonds between the organic radical and metal atoms The unpaired electrons of the radical and d-band vacancies of Pt apparently participate in this bonding. Pt has *ca.* 0.55 such vacancies, thus 4 adjacent atoms (sites) are required for acetylene adsorption (3). The equilibrium constant (K_p) for this case (Eq. [1]) has been estimated to be 10^4-10^6 atm^{-1}. The anodic discharge of water also appears to occur readily on Pt which leads to appreciable coverages of oxygen-containing species. In fact, the coverage of these latter species becomes so extensive that they prevent acetylene adsorption and stop its oxidation at potentials well below those required for oxygen evolution.

Au has no d-band vacancies available for covalent bonding. However, it does possess a uniquely small

* Electrochemical Society Active Member.

Key words: acetylene, oxidation, Au-Pt alloys.

energy for d-s promotion so that d-vacancies can be created rather easily to allow adsorption (4). Thus, 2 adjacent sites are needed to accommodate bonding with acetylene, but spacial and other mechanistic requirements may increase the number to 4 or more. Values of $n = 5$, $K_p = 10^4$ and $n = 8$, $K_p = 2.5$ were successful in correlating the kinetic data for acidic and basic electrolytes, respectively. No passivation region at the higher potentials was found on Au comparable to Pt.

A recent study of the anodic oxidation of ethylene on heterogeneous Au-Pt alloys (5) indicated qualitatively that the total current could be attributed to separate (parallel) reactions occurring on the Au-rich (α_2) and Pt-rich (α_1) phases.[1]

Therefore

$$I = I_{\alpha 1} + I_{\alpha 2} \qquad [10]$$

and in terms of current densities[2]

$$i = \beta_1 i_{\alpha 1} + \beta_2 i_{\alpha 2} \qquad [11]$$

Poor reproducibility of the experimental current-potential data prevented quantitative comparison. As very good reproducibility of data had been obtained earlier with acetylene oxidation on the pure metals, this study using the alloy electrodes was carried out hoping that a more meaningful test of the parallel reaction postulation could be made.

Experimental

The electrolytic cell, apparatus, reference electrodes, etc. have been described previously (1, 2, 5, 7). The studies were made potentiostatically and at 80°C except as noted. The gas flow rate (acetylene or acetylene-nitrogen mixtures) was kept constant to provide uniform stirring. The anion normality of the electrolyte was held constant at unity to insure good conductance.

Reagents.—Sulfuric acid, potassium sulfate, potassium carbonate, and potassium hydroxide, "Fisher Certified" reagents; acetylene, Matheson purified (>99.6% purity); nitrogen, Matheson prepurified (>99.997% purity); and conductivity water.

Anodes.—The anodes were prepared from the same Au-Pt alloy foils and wires as described previously (5). They were rectangular with geometric areas of 15.1 cm^2. Before each experiment they were cleaned by a brief immersion in boiling 1*N* KOH to dissolve any polymer film that may have formed during the previous run. They were subsequently activated by a cathodic polarization as also described previously. Repetitive runs showed the activity of the anodes to remain constant (within experimental error) during the course of the study.

Results

Rest potentials.—The open-circuit (rest) potentials in the presence of acetylene are shown in Table I. There is no consistent trend in the values, although for several *p*H's, they are intermediate to the values for Au and Pt. There was no noticeable effect of acetylene partial pressure.

Polarization behavior.—The current-potential relations are shown in Fig. 1-4. Individual points on the curves are steady-state values and could be reproduced within 5-10%. The curves for 80Au-20Pt and 20Au-80Pt are quite similar to those for pure Au and Pt, respectively. The other two alloys, 60Au-40Pt and 40Au-60Pt, have some regions of behavior similar to the pure metals and others with an intermediate behavior. Distinct discontinuities in the curves are observed as compared with a transition region (inflection point) for pure Au and the 80Au-20Pt alloy. The Tafel slopes and *p*H effects[3] are also tabulated in Table I.

With all the alloy anodes, the acidic anolytes became limpid amber in color and a brown resinous film formed on the anode surface after several hours of polarization. Basic anolytes became colored similarly, but no film was formed on the anode surface, apparently due to its solubility in these media.

Temperature effect.—The effect of temperature on the current at constant potential was determined for all the alloys in 1*N* H_2SO_4 and 1*N* KOH. Arrhenius plots are shown in Fig. 6 for the 60Au-40Pt anode and are typical of the others. The corresponding activation energies are summarized in Table II. In general, the latter are consistent with the observed Tafel slopes.

Pressure effect.—Studies with reduced acetylene partial pressures were also made in 1*N* H_2SO_4 and 1*N* KOH. The reduced pressures were obtained by mixing acetylene and nitrogen with a calibrated gas pro-

[1] A similar behavior has also been reported by Breiter [Ref. (6)] for Pt-Au alloys for oxygen-layer formation and reduction.

[2] β_1, β_2 = fractions of α_1 and α_2 phases in the alloys, respectively. Ratios of β_1/β_2 are shown in Table I.

[3] The effect of pH on current for the 60Au-40Pt alloy is shown in Fig. 5 and is typical of the relationships for the other alloys.

Table I. Rest potentials, Tafel slopes, and pH effects for anodic oxidation of acetylene on Au-Pt electrodes at 80°C

Electrolyte pH	Parameter	Electrode: Au[a]	80Au-20Pt[b]	60Au-40Pt[b]	40Au-60Pt[b]	20Au-80Pt[b]	Pt[c]
—	β_2/β_1[d]	—	98/2	75/25	33/67	18/82	—
0.3	*RP*	0.28	0.19	0.10	0.13	0.13	0.26
	TS	140	140	100	70	70	70
2.1	*RP*	0.28[e]	0.13	0.03	0.08	0.10	0.19[f]
	TS	140[e]	140	100	80	70	70[f]
3.8	*RP*	—	0.03	−0.08	0.03	0.09	—
	TS	—	140	100	80	70	—
9.8	*RP*	0.03[g]	−0.02	−0.29	−0.19	−0.30	−0.36[h]
	TS	140[g]	120	90	100	70	70[h]
		140[g]	140	140			
11.2	*RP*	−0.20[i]	−0.19	−0.37	−0.35	−0.38	−0.45[j]
	TS	140[i,k]	100[k]	70[k]	70[k]	70	70[j]
		140[i,m]	140[m]	160[m]	100[m]		
12.6	*RP*	−0.34	−0.42	−0.42	−0.42	−0.44	−0.58
	TS	140[k]	120[k]	70[k]	70	70	70
		140[m]	140[m]	120[m]			
Acidic	*PE*	*ca.* 0	*ca.* 0	*ca.* 0.1	*ca.* 0.2	*ca.* 1	*ca.* 1
Basic	*PE*	*ca.* 1[k]	*ca.* 0.8[k]	*ca.* 1[k]	*ca.* 1	*ca.* 1	*ca.* 1
		ca. 1[m]	*ca.* 0.8[m]	*ca.* 0.7[m]			

RP, rest potential, V(SHE); *TS*, Tafel Slope, mV/decade; *PE*, pH effect ($\partial \log i/\partial$pH).
[a] From Johnson, Reed, and James (2).
[b] Atomic ratio.
[c] From Johnson, Wroblowa, and Bockris (1).
[d] Ratio of Au-rich (α_2) to Pt-rich (α_1) phase determined by x-ray analysis.
[e] pH = 1.45.
[f] pH = 1.2.
[g] pH = 8.6.
[h] pH = 8.7.
[i] pH = 11.6.
[j] pH = 11.9.
[k] Below transition region.
[m] Above transition region.

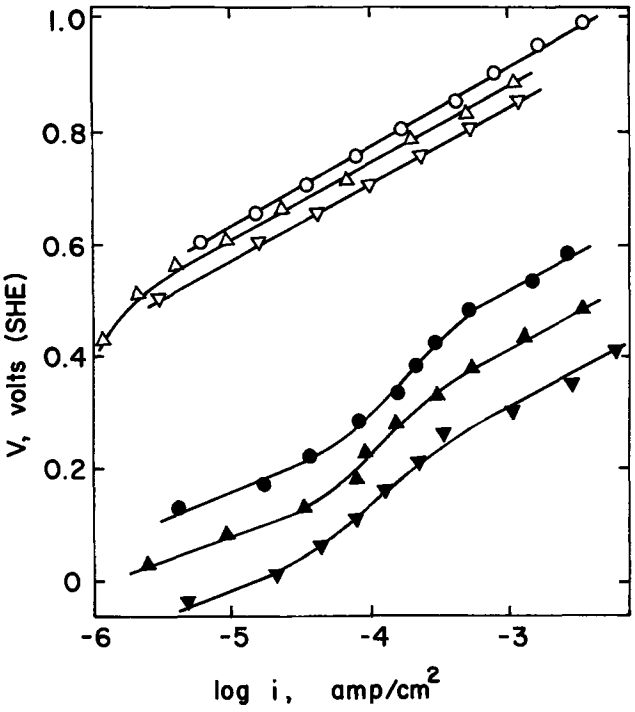

Fig. 1. Polarization curves for the anodic oxidation of acetylene on 80Au-20Pt alloy at 80°C (P_A = 1 atm). ○, pH = 0.3; △, 2.1; ▽, 3.8; ●, 9.8; ▲, 11.2; ▼, 12.6.

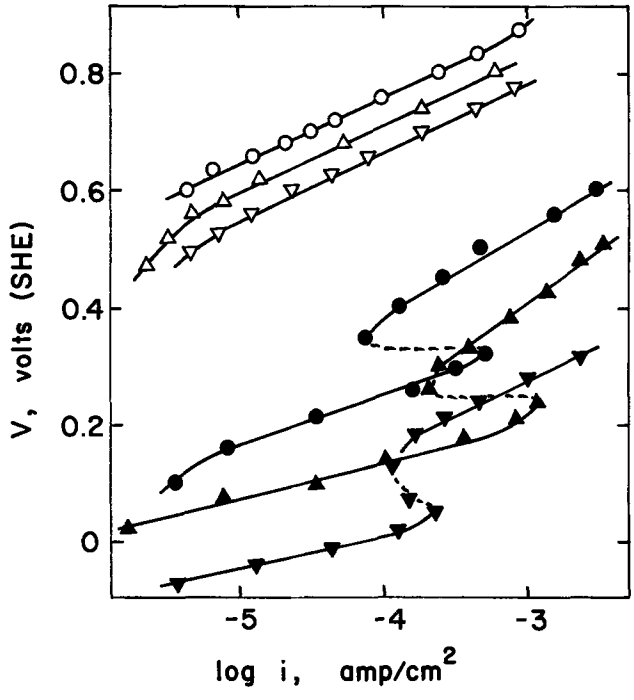

Fig. 2. Polarization curves for the anodic oxidation of acetylene on 60Au-40Pt alloy at 80°C (P_A = 1 atm). (Symbols same as Fig. 1.)

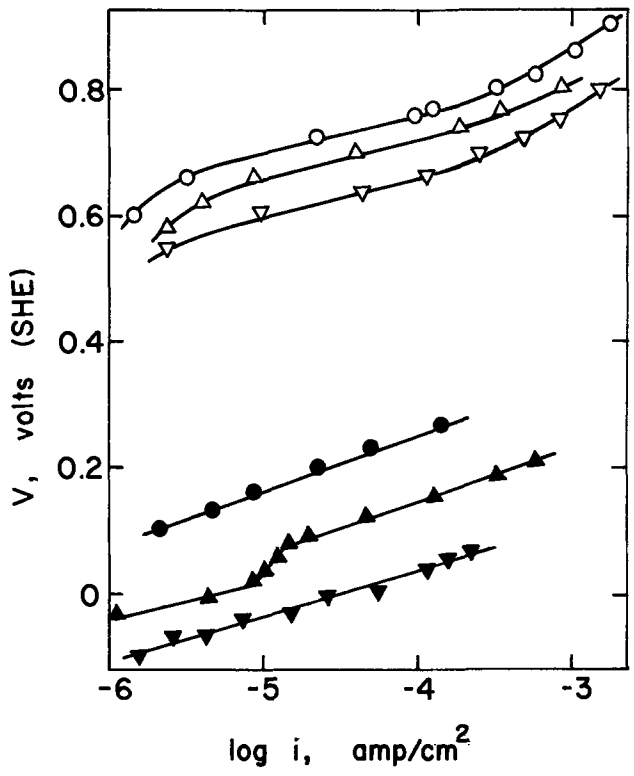

Fig. 3. Polarization curves for the anodic oxidation of acetylene on 40Au-60Pt alloy at 80°C (P_A = 1 atm). (Symbols same as Fig. 1.)

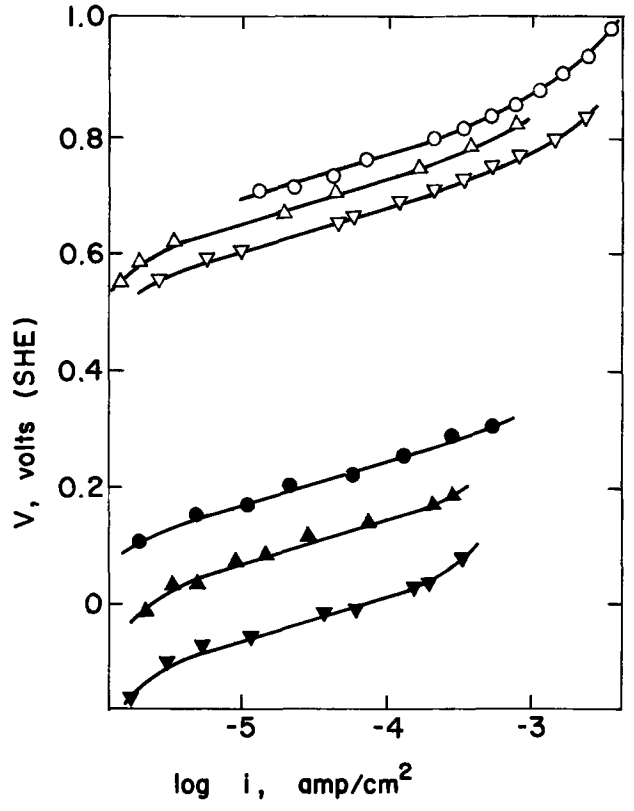

Fig. 4. Polarization curves for the anodic oxidation of acetylene on 20Au-80Pt alloy at 80°C (P_A = 1 atm). (Symbols same as Fig. 1.)

portioner. Figure 7 shows the results for the 60Au-40Pt alloy which are typical of the others. The pressure effects for all the alloys have been summarized in Table II.

Reaction products.—Faradaic efficiency studies for CO_2 production were carried out and the results are shown in Table III. The resinous films mentioned above appeared similar to those reported previously for Au (2). They were not soluble in ether, carbon tetrachloride, hexane, or benzene, but dissolved appreciably in warm 1*N* KOH. The anolytes were also extracted with the above solvents, but only ether showed any evidence of extraction by flame-ionization gas chromatographic analyses. Qualitative tests of the anolytes were negative for aldehyde and ketone groups. Infrared reflectance spectra of the films on the anodes indicated the presence of C—C and C=C bonds, but not O—H as reported previously for Au (2). *IR* analyses of extracts from the amber-colored basic

anolytes gave positive results for all three groups, C—C, C=C, and O—H. It thus appears that the OH group may have been introduced by the dissolution in basic media and that the film produced during polarization most likely has a polyacetylene-type structure.

Discussion

An examination of the experimental results[4] indicates that the Au-Pt alloys can be classified into three categories: (*i*) the high Au content alloy (80Au-20Pt) which behaves similarly to Au; (*ii*) the intermediate compositions (60Au-40Pt and 40Au-60Pt) which have distinct behaviors; and (*iii*) the high Pt content alloy (20Au-80Pt) which behaves similarly to Pt. As the Au-rich and Pt-rich phases are predominant at the opposite ends of the concentration range, this allows one to infer that the α_2 and α_1 phases have kinetic characteristics similar to the pure metals, Au and Pt. Thus the reaction sequence for the α_2 phase below the transition region should (*i*) involve species in addition to acetylene or its derivatives since $\partial i/\partial P < 0$; (*ii*) exhibit no *p*H dependence in acidic solutions and a unit dependence in basic solutions; and (*iii*) have a r.d.s. associated with the first electron transfer since the Tafel slope is $2(2.3\ RT/\mathbf{F})$.[5] Equations [4]-[6] satisfy these criteria and lead to the rate expression (2)

$$(i_{\alpha 2})_{\text{b.t.r.}} = n\mathbf{F}(k_{5a}a_{H_2O} + k_{5b}a_{OH^-})(1 - \theta_A) \exp(\alpha \mathbf{F}V/RT) \quad [12]$$

Above the transition region on the α_2-phase, the reaction sequence should (*i*) involve acetylene or species derived therefrom since $\partial i/\partial P > 0$; (*ii*) have a *p*H dependence approaching unity in basic solutions; and (*iii*) again have a r.d.s. associated with the first electron transfer since the Tafel slope is $2(2.3\ RT/\mathbf{F})$.[5] Equations [7]-[9] satisfy these criteria and lead to the rate expression (2)

[4] No mechanistic significance was attached to the rest potentials. In general they are 0.2-0.4V more positive than the corresponding reversible values for complete oxidation to CO_2. The lack of specific knowledge of by-products does not allow an exact calculation of the reversible values. This together with the absence of an acetylene partial pressure effect and the apparent low exchange current densities led to the rest potentials not being given further consideration. With such conditions they are often "mixed" values or possibly only remotely related to the reaction under consideration. The observations of this study are similar to several others involving hydrocarbons. Piersma (8) has summarized several interpretations of these potentials.

[5] Assuming Langmuir-type adsorption and low coverages of reaction intermediates.

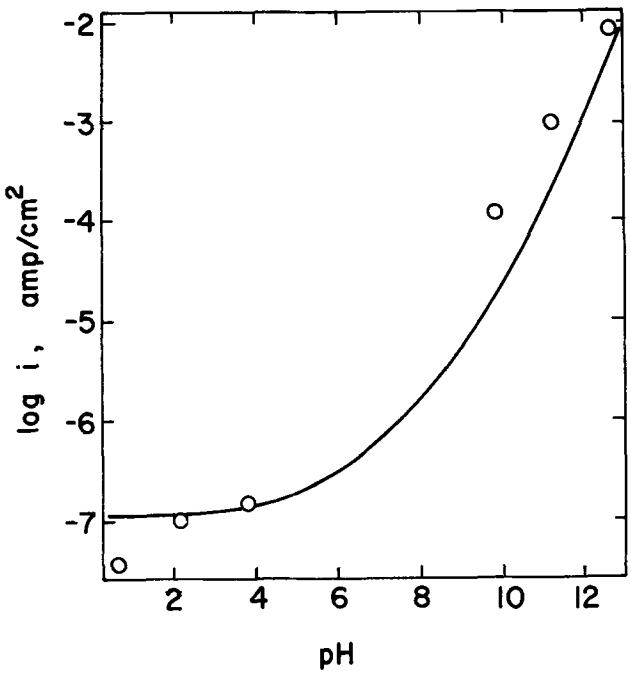

Fig. 5. Comparison of experimental and calculated effect of *p*H on current density for the anodic oxidation of acetylene on 60Au-40Pt alloy at 80°C ($P_A = 1$ atm, $V = 0.40$V). ○, experimental data points; ———, Eq. [11], [13], and [14] using constants evaluated for Pt and the 80Au-20Pt alloy.

$$(i_{\alpha 2})_{\text{a.t.r.}} = n\mathbf{F}(k_{8a}a_{H_2O} + k_{8b}a_{OH^-})\theta_A \exp(\alpha \mathbf{F}V/RT) \quad [13]$$

Similarly, the reaction sequence for the α_1-phase should (*i*) involve species in addition to acetylene or derivatives since $\partial i/\partial p < 0$; (*ii*) exhibit a *p*H effect of *ca.* unity; and (*iii*) have a r.d.s. involving a chemical reaction following the first charge transfer since the Tafel slope is 2.3 $RT/\mathbf{F}$.[5] Equations [1]-[3] satisfy these criteria and give the rate expression

$$i_{\alpha 1} = n\mathbf{F}k_3(K_{2a}a_{H_2O}/a_{H^+} + K_{2b}a_{OH^-})\theta_A(1 - \theta_A) \exp(\mathbf{F}V/RT)$$
$$= n\mathbf{F}k_3K_2a_{H^+}{}^{-1}\theta_A(1 - \theta_A) \exp(\mathbf{F}V/RT) \quad [14]$$

Table II. Apparent activation energies and pressure effects for the anodic oxidation of acetylene on Au-Pt electrodes

Electrode	Solution	Temperature effect: Potential [V(SHE)]	Temperature effect: E'_a (kcal)	Pressure effect*: Potential [V(SHE)]	Pressure effect*: $\partial i/\partial P_A$** A/cm² atm
Au[a]	1*N* H_2SO_4	0.73	19.9	0.68	neg
		0.83	18.8	0.73	pos → neg***
	1*N* NaOH	−0.03[k]	19.3	0.02[k]	pos → neg***
		0.02[k]	18.7	0.07[k]	pos → neg***
		0.32[m]	13.2	0.17[m]	pos
		0.37[m]	12.6	0.22[m]	pos
80Au-20Pt	1*N* H_2SO_4	0.75	18.8	0.70	pos → neg
		0.80	18.3	0.75	pos → neg
	1*N* KOH	0.01[k]	20.3	0.01[k]	pos
		0.06[k]	19.9	0.06[k]	pos
		0.31[m]	12.0	0.26[m]	pos
		0.36[m]	11.4	0.29[m]	pos
60Au-40Pt	1*N* H_2SO_4	0.75	22.5	0.70	neg
		0.80	21.4	0.75	neg
	1*N* KOH	−0.03[k]	19.3	−0.05[k]	pos → neg
		0.02[k]	18.3	0.01[k]	pos → neg
		0.21[m]	12.3	—	—
		0.26[m]	11.2	0.26[m]	pos
40Au-60Pt	1*N* H_2SO_4	0.76	22.8	0.70	neg
		0.86	20.4	0.75	neg
	1*N* KOH	0.06	23.3	−0.04	neg
		0.11	22.0	0.01	neg
20Au-80Pt	1*N* H_2SO_4	0.74	20.6	0.70	neg
		0.84	18.4	0.80	neg
	1*N* KOH	−0.02	22.8	−0.04	neg
		0.08	20.6	0.01	neg
Pt[c]	1*N* H_2SO_4	0.74	22.4	0.72	neg
		0.79	21.2	0.70	neg
	1*N* NaOH	−0.055	26.7	−0.055	neg
		−0.005	25.4	−0.005	neg

* At 80°C, $10^{-2} \leq P_A \leq 1$ atm.
** Slope of $i - P_A$ plots (steady-state C.D.'s) at constant potential.
*** Sign of slope ($\partial i/\partial P_A$) changes from plus to minus with increasing pressure.
[a-m] See Table I.

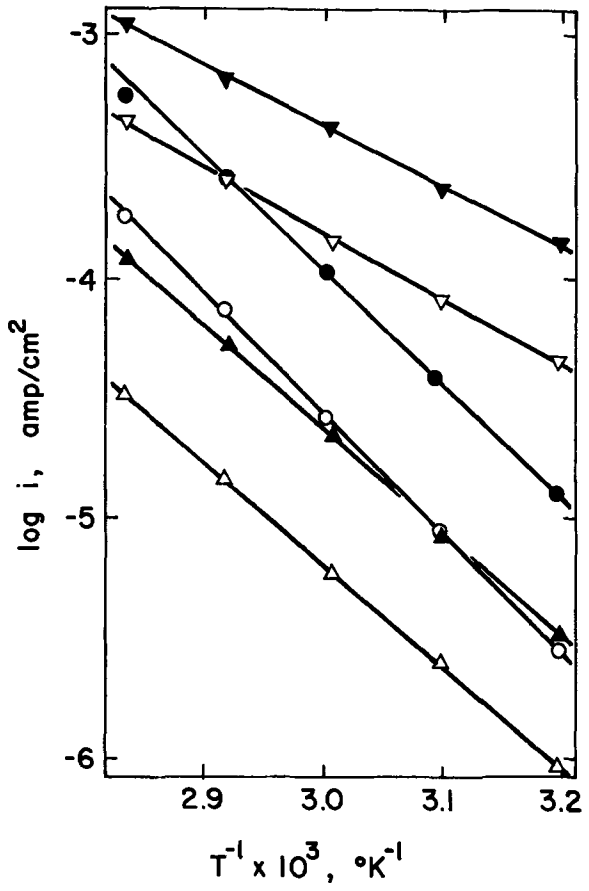

Fig. 6. Effect of temperature on the anodic oxidation of acetylene on 60Au-40Pt alloy (P_A = 1 atm). 1N H_2SO_4: ○, 0.75V; ●, 0.80V, 1N KOH: △, −0.03V; ▲, 0.02V; ▽, 0.21V; ▼, 0.26V.

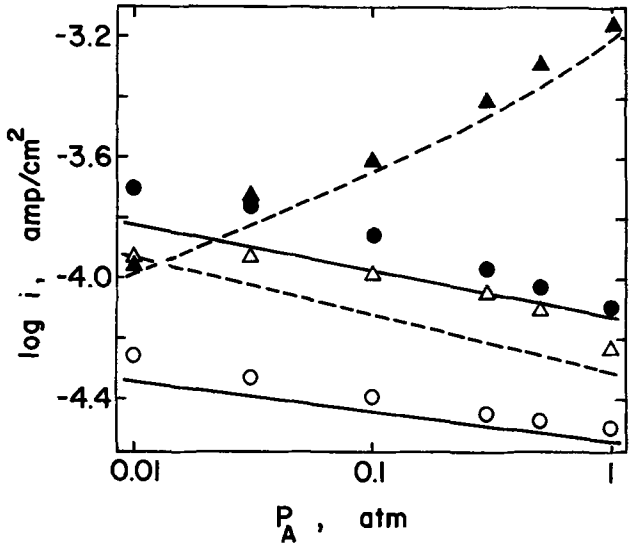

Fig. 7. Comparison of experimental and calculated effect of partial pressure on current density for the anodic oxidation of acetylene on 60Au-40Pt alloy at 80°C. Experimental data: ○, 0.70V, 1N H_2SO_4; ●, 0.75V, 1N H_2SO_4; △, 0.01V, 1N KOH; ▲, 0.26V, 1N KOH. Equation [11] using C.D. values for Pt and the 80Au-20Pt alloy: ———, 1N H_2SO_4; — — —, 1N KOH.

The 80Au-20Pt alloy was found to consist almost entirely of the α_2-phase (see Table I). Thus the C.D.'s for this electrode are the same as those indicated in Eq. [12] and [13] and can be used directly in Eq. [11]. The composition of the α_1 phase corresponding to the above α_2 composition is *ca.* 95% Pt (9). No alloy was available whose composition corresponded to this value, so the C.D.'s for smooth Pt have been substituted for those of the α_1 phase of Eq. [14] for use in Eq. [11]. There is some justification for this substitution in that the polarization characteristics of Pt and the Pt-rich alloy are similar and, of the electrodes available, the Pt composition of pure Pt is more nearly the same as that of the α_1 phase than any of the others. Equations [12]-[14] can now appropriately be combined with Eq. [11] to represent the polarization behavior of heterogeneous Au-Pt alloy electrodes for acetylene oxidation. In particular Eq. [12] and [14] substituted into Eq. [11] will represent current densities on Au, Au-rich (b.t.r.), Pt-rich, and Pt anodes. Equations [13] and [14] substituted into Eq. [11] will represent C.D.'s on Au-rich (a.t.r.) anodes. It is important to keep in mind that the α_1-phase will passivate (as also will Pt) when the potential becomes sufficiently positive, thus eliminating its contribution to the C.D. This is apparently responsible for the discontinuity region (d.r.) seen most markedly in basic solutions for the 60Au-40Pt alloys.[6] At potentials below the d.r., both the α_1 and α_2 phases are contributing to the current. Relatively speaking, the larger portion is contributed by the α_1 phase. As the potential is increased, the α_1 phase passivates, and further potential increases are necessary before the α_2 phase will contribute appreciable currents. The Tafel slope for either of the above cases reduces to the form

$$\partial V/\partial \log i = (2.3\,RT/\mathbf{F})\,i/(\beta_1 i_{\alpha 1} + \alpha\beta_2 i_{\alpha 2}) \qquad [15]$$

A comparison of the slopes calculated from Eq. [15] with the experimental values is shown in Table IV. Figure 8 shows the polarization curves for the two-phase alloys in 1N H_2SO_4 and 1N KOH as calculated using Eq. [11] and the experimental i-V data for the 80Au-20Pt alloy and smooth Pt. The curves correspond very closely to the experimental points as shown in the figure. The effects of electrolyte pH and acetylene partial pressure calculated in the same manner are shown in Fig. 5 and 7, respectively, for the 60Au-40Pt alloy. The experimental values are also shown for comparison. The agreement is fair and typical of that for the other alloys.

The resulting equation for the apparent activation energies for the two-phase alloy electrodes using the combined equations (Eq. [11]-[14]) is

$$E'_a = \beta_1(E_{\alpha 1} - \mathbf{F}V)\,(i_{\alpha 1}/i) + \beta_2(E_{\alpha 2} - \alpha\mathbf{F}V)\,(i_{\alpha 2}/i) \qquad [16]$$

The effect of potential on the activation energy is

$$\partial E'_a/\partial V = -\mathbf{F}(\beta_1 i_{\alpha 1} + \alpha\beta_2 i_{\alpha 2})/i \qquad [17]$$

Values for Eq. [17] are also shown in Table IV along

Table III. Coulombic efficiency of CO_2 production for the anodic oxidation of acetylene on Au-Pt electrodes at 80°C

Electrode	1N H_2SO_4 Current density (A/cm² × 10³)	1N H_2SO_4 CO_2 efficiency (%)	1N KOH Current density (A/cm² × 10³)	1N KOH CO_2 efficiency (%)
Au[a]	0.80	59	1.67*	80
80Au-20Pt	0.67	87	0.33	81
60Au-40Pt	0.67	69	0.33	78
40Au-60Pt	0.67	73	0.20	82
20Au-80Pt	0.33	75	0.20	60
20Au-80Pt	0.33	77	0.20	82
Pt[c]	0.20	100	0.10*	95

* For 1N NaOH.
a,c See Table I.

[6] These discontinuities should be distinguished from the inflections (transition regions) which occur with the α_2 phase and Au. This latter behavior has been attributed to potential-dependent acetylene adsorption (2).

Table IV. Comparison of calculated* and experimental kinetic parameters for the anodic oxidation of acetylene on Au-Pt electrodes

Electrode		α_2-α_1 comp		Tafel slope		$-\partial E'_a/\partial V$		
Au (%)	Pt (%)	β_2 (%)	β_1 (%)	Calc[a] (mV)	Expt (mV)	Calc[b] (kcal/V)	Expt (kcal/V)	Remarks[c]
100	0				140		12	a.e., b.e., b.t.r., a.t.r.
80	20	98	2	133-139	140	12	11	a.e.
				133-139	100-120	12	9	b.e., b.t.r.
				140	140	12	12	b.e., a.t.r
60	40	75	25	94-126	120	13-17	22	a.e.
				96-122	70-100	13-17	20	b.e., b.t.r.
				140	120-160	12	22	b.e., a.t.r
40	60	33	67	75-98	70-80	17-21	28	a.e.
				76-93	70-90	17-21	26	b.e., b.t.r.
				140	100	—	—	b.e., a.t.r.
20	80	18	82	73-86	70	19-22	22	a.e., b.e.
0	100				70		24	a.e.
					70		26	b.e.

* Calculated for the experimentally determined limits of $0.3 \leq i_{a_1}/i_{a_2} \leq 3$ over the corresponding linear Tafel regions for smooth Pt and the 80Au-20Pt alloy.
[a] From Eq. [15].
[b] From Eq. [17].
[c] Symbols for remarks: a.e., acidic electrolyte; b.e., basic electrolyte; b.t.r., below transition region; a.t.r., above transition region.

with the corresponding experimental values for comparison.

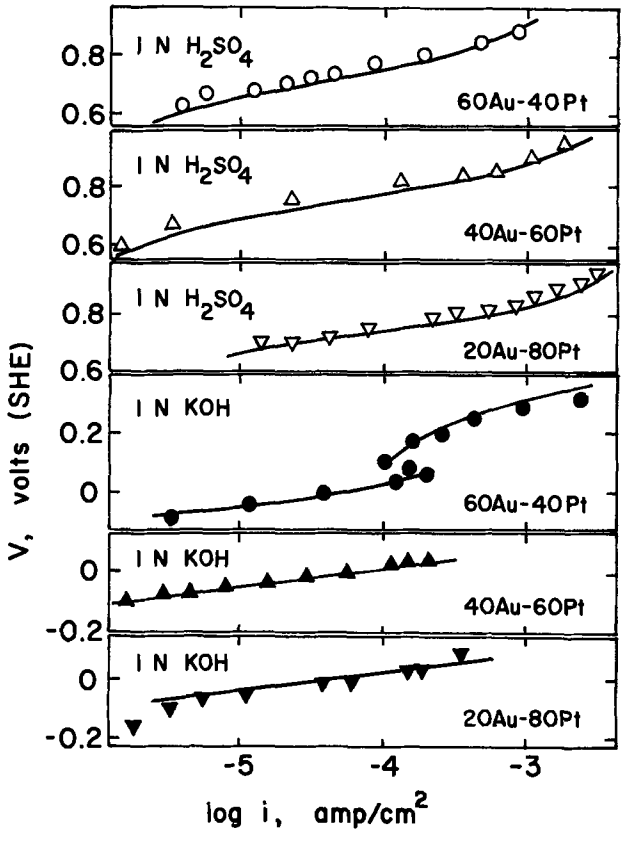

Fig. 8. Comparison of experimental and calculated polarization curves for the anodic oxidation of acetylene on heterogeneous Au-Pt alloys at 80°C (P_A = 1 atm). Experimental data symbols: ○, ●, △, ▲, ▽, ▼; Eq. [11], using C.D. values for Pt and the 80Au-20Pt alloy: ————.

It thus appears from an examination of Fig. 5 and 7 and Table IV that the behavior of the heterogeneous Au-Pt alloy anodes for the anodic oxidation of acetylene can be satisfactorily explained in terms of parallel electrochemical reactions occurring separately on the Au-rich and Pt-rich phases. It is also indicated that one phase can passivate while the other remains active.

Acknowledgments

This paper is based on a dissertation presented by one of us (C. K. W.) in partial fulfillment of the Ph.D. degree in Chemical Engineering at the University of Missouri-Rolla. It is contribution No. 130 from the Graduate Center for Materials Research.

Manuscript submitted July 13, 1971; revised manuscript received June 15, 1973.

Any discussion of this paper will appear in a Discussion Section to be published in the June 1974 JOURNAL.

REFERENCES

1. J. W. Johnson, H. Wroblowa, and J. O'M. Bockris, *This Journal*, **111**, 863 (1964).
2. J. W. Johnson, J. L. Reed, and W. J. James, *ibid.*, **114**, 572 (1967).
3. H. Dahms and J. O'M. Bockris, *ibid.*, **111**, 728 (1964).
4. D. O. Hayward and B. M. W. Trapnell, "Chemisorption," p. 232, Butterworths, London (1964).
5. J. W. Johnson, S. C. Lai, and W. J. James, *Electrochim. Acta*, **16**, 1763 (1971).
6. M. W. Breiter, *ibid.*, **10**, 543 (1965).
7. W. Wroblowa, B. J. Piersma, and J. O'M. Bockris, *J. Electroanal. Chem.*, **6**, 401 (1963).
8. B. J. Piersma, Ph.D. Thesis, University of Pennsylvania, pp. 270-271, University Microfilms, Inc., Ann Arbor, Michigan, Mic. 65-13,370 (1965).
9. A. S. Darling, R. A. Mintern, and J. C. Chaston, *J. Inst. Metals*, **81**, 1424 (1952-1953).

Corrosion of an Iron Rotating Disk

Nader Vahdat and John Newman*

Inorganic Materials Research Division, Lawrence Berkeley Laboratory and Department of Chemical Engineering, University of California, Berkeley, California 94720

ABSTRACT

The corrosion rate of iron rotating disks is studied by calculating the current and potential distribution on the surface of the disk. The results show that for rotation speeds high enough to create turbulent flow on the outer portion the rate of corrosion may be nonuniform. The surface toward the center of the disk can corrode with a maximum rate, while the edge of the disk remains almost unattacked. The effect of different parameters on the corrosion behavior of the rotating disk is studied.

LaQue (1) has conducted some corrosion experiments with copper and iron disks rotating in seawater. The copper disks corroded most rapidly at the periphery and remained almost unattacked at the center. But it is remarkable that the greatest attack on the iron disks occurred toward the center on the more slowly moving surfaces. LaQue's iron disks were 3, 4, and 5 in. in diameter and were rotated at 120 radian/sec (about 1146 rpm) in seawater at 15°C. The maximum corrosion rate might correspond to a local current density of 0.19 mA/cm^2. Under ideal hydrodynamic conditions, the flow would be expected to become turbulent at a radial position of about 5 cm or 2 in. at this rotation speed.

This particular corrosion system is attractive for analysis because the hydrodynamic flow (2, 3) is well known near a rotating disk, and one can calculate the current and potential distribution for this geometry. Levich (4) has found the limiting rate of mass transfer, and Newman (5) has given the current distribution below the limiting current.

In practice, usually the anodic and cathodic reactions occur on different parts of the same surface (or on two different surfaces which are in contact) and cause localized corrosion. The rotating disk seems to be an ideal case for studying localized corrosion because it is the simplest model that can be used to study this complicated situation (6).

It should be noted that velocity does not have a direct effect on the rate of corrosion; its only role is that it usually (but not always) increases the rate of transfer of corrosive species to the metal, and consequently it may increase the corrosion rate. In the case of a rotating disk in the laminar region, the limiting rate of mass transfer to the disk is not a function of linear velocity. Consequently, the disk should be corroded uniformly in spite of the fact that there is a velocity gradient on its surface.

The results for the copper disks can be explained by the fact that the surfaces towards the periphery of the disk move with a higher velocity (being in the turbulent region) and that the amount of oxygen that reaches them is higher. Consequently, the corrosion rate would be higher too. For the iron disks, the results can be explained when it is noted that iron is an active-passive metal and when a high oxygen concentration tends to produce a protective oxide coating on such metals. The surfaces towards the periphery of the disk are passivated because of the greater amount of oxygen that reaches them.

As stated in the Conclusions, the nonuniform rate of corrosion is not always achieved. For example, a very small or a very large disk could give a uniform corrosion rate. By the same token, the corrosive medium is also an important factor in determining the corrosion pattern.

* Electrochemical Society Active Member.

Key words: passivation, localized corrosion, potential and current distribution.

In the case of an iron rotating disk, the outer region of the disk, which is exposed to a higher oxygen concentration, acts as a cathode to the central portion. The reaction taking place on these cathodic areas would be the reduction of oxygen

$$O_2 + 4H^+ + 4e^- \rightarrow 2H_2O$$

and the anodic reaction (taking place on the inner region of the disk) would be the dissolution of iron

$$Fe \rightarrow Fe^{++} + 2e^-$$

These local anodes and cathodes form a corrosion cell and a current will pass through the solution. As there is no external current to the rotating disk, the total net current on the disk should be zero, *i.e.*

$$I_{net} = I_{Fe} + I_{O_2} = 0 \qquad [1]$$

Development of the Model

The current and potential distribution on the surface of a rotating disk are (5)

$$\Phi_0 = \frac{RT}{\mathbf{F}} \sum_{n=0}^{\infty} B_n P_{2n}(\eta) \qquad [2]$$

$$i(\eta) = -\frac{\kappa_\infty}{r_0 \eta} \frac{RT}{\mathbf{F}} \sum_{n=0}^{\infty} B_n P_{2n}(\eta)\, M'_{2n}(0) \qquad [3]$$

where Φ_0 is the ohmic potential, R is the gas constant, T is absolute temperature, $\mathbf{F}$ is Faraday's number, B_n is a constant, $P_{2n}(\eta)$ is the Legendre polynomial of order $2n$, $i(\eta)$ is the current density, κ_∞ is the conductivity of the solution, η is the rotational elliptic coordinate, and $M'_{2n}(0)$ is a known constant [see Ref. (5)].

In the case of corrosion of the rotating disk, the current density, $i(\eta)$, in Eq. [2] would be the net current density which is the sum of anodic and cathodic current densities at each point on the disk, *i.e.*

$$i(\eta) = i_{Fe}(\eta) + i_{O_2}(\eta) \qquad [4]$$

If the relations between the iron and oxygen current densities and the potential are known, one is in a position to solve Eq. [1]-[4] to determine the current and potential distribution on the disk, and consequently find the corrosion behavior of the disk. The polarization curve of iron, which gives the relation between iron current density and potential, is a function of several parameters such as the ferrous ion concentration, the chloride ion concentration, and the *p*H of the solution. To simplify the problem, these composition effects have been neglected here. In most practical cases, the corrosive medium is neutral. Pourbaix (7) has given a set of iron polarization curves for the whole range of pH. From these results, the passivation current has the value 1.5 mA/cm^2 at

a pH of 7. Thus, we can construct the following equation to describe the kinetics of iron in a neutral solution

$$i_{Fe} = 1.5 \times 10^{-3} \exp[-5 \times 10^3 (V - \Phi_o + 0.2)^2] + 10^{-7} \quad [5]$$

for $V - \Phi_o > -0.25$ where $V - \Phi_o$ is the potential of the electrode relative to a hydrogen electrode close to its surface. (It should be noted that the concentration overpotential of iron has been neglected.) This equation shows a maximum current density centered at an electrode potential of -0.2V. At more cathodic potentials, the current density increases with electrode potential as is customary for anodic dissolution. At more anodic potentials, the electrode begins to passivate, and the current density decreases toward a value of 10^{-7} A/cm^2 in the passive region.

In the case of oxygen, one should consider both the concentration and surface overpotentials because both are important. The limiting rate of mass transfer to a rotating disk in laminar flow was calculated by Levich (4) and is given by the following equation

$$Nu_{lam} = C_1 Re^{1/2}_{loc} Sc^{1/3} \quad [6]$$

where Nu_{lam} is the local Nusselt number, Re_{loc} is the local Reynolds number, Sc is the Schmidt number, and C_1 is a function of the Schmidt number (8) approaching 0.6205 for large Schmidt numbers.

For the turbulent region there are some experimental correlations in the literature. Ellison (9, 10) has given the following expression for the rate of mass transfer to a rotating disk in the turbulent region for Reynolds numbers between 8.9×10^5 and 1.18×10^7 and for Schmidt numbers between 35 and 1350

$$\overline{Nu_t} = 1.17 \times 10^{-2} Re^{0.896} Sc^{0.249} \quad [7]$$

where $\overline{Nu_t}$ is the average Nusselt number and Re is the over-all Reynolds number. Equation [7] can be used to find the local rate of mass transfer to the disk in the turbulent region. By definition

$$\overline{N_i} \pi r^2 = \int_0^r 2\pi r N_i dr \quad [8]$$

where $\overline{N_i}$ is the average rate of mass transfer to the disk. Differentiation of this equation with respect to r and substitution of Re_{loc}, $\overline{Nu_t}$, and Nu_t (from their definitions) yield

$$\frac{d}{dRe^{1/2}_{loc}} (\overline{Nu_t} Re^{1/2}_{loc}) = 2Nu_t \quad [9]$$

From Ellison's correlation one can then get

$$Nu_t = 1.6332 \times 10^{-2} Re^{0.896}_{loc} Sc^{0.249} \quad [10]$$

where Nu_t is the local Nusselt number in the turbulent region.

Equations [6] and [10] yield the following expressions for the limiting current density on the surface of the rotating disk

$$i_{lim} = nFDc_\infty C_1 \sqrt{\frac{\Omega}{\nu}} Sc^{1/3} \text{ for laminar region} \quad [11]$$

$$i_{lim} = nFDc_\infty C_2 \sqrt{\frac{\Omega}{\nu}} \left(\frac{r^2\Omega}{\nu}\right)^{0.396} Sc^{0.249}$$

for turbulent region [12]

where Ω is the rotation speed (radians/sec), ν is the kinematic viscosity, and $C_2 = 1.6332 \times 10^{-2}$.

The kinetics of the oxygen reaction will be described by the following equation

$$i_{O_2} = i_o(c_o) \left[\exp\left(\frac{\alpha_a F}{RT}\eta_s\right) - \exp\left(\frac{-\alpha_c F}{RT}\eta_s\right) \right] \quad [13]$$

where η_s is the surface overpotential, α_a and α_c are the transfer coefficients, and $i_o(c_o)$ is the exchange current density. For the reduction of oxygen, the first term in Eq. [13] can be neglected (this is a good approximation for the potentials far removed from the equilibrium potential of oxygen). The concentration overpotential can be written as

$$\eta_c = -\frac{RT}{nF} \ln \frac{c_o}{c_\infty} \quad [14]$$

and the total potential is

$$V = \eta_s + \eta_c + \Phi_o + U \quad [15]$$

where U is the equilibrium potential of oxygen relative to a normal hydrogen electrode (about 1.229V).

The exchange current density depends on the concentration of reactants and products on the surface of the electrode. If the concentration variations of OH^- and H_2O are neglected, one can write the following equation for the oxygen exchange current density

$$i_o(c_o) = i_o(c_\infty) \left(\frac{c_o}{c_\infty}\right)^{1+\alpha_c/n} \quad [16]$$

where $i_o(c_\infty)$ is the oxygen exchange current density evaluated at the bulk concentration, c_∞. And the ratio of oxygen concentration on the surface to that in the bulk solution can be expressed as

$$\frac{c_o}{c_\infty} = 1 - \frac{i_{O_2}}{i_{lim}} \quad [17]$$

Substitution of Eq. [14], [15], [16], and [17] into Eq. [13] yields

$$i_{O_2} = -i_o(c_\infty) \left(1 - \frac{i_{O_2}}{i_{lim}}\right) \exp\left[-\frac{\alpha_c F}{RT}(V - \Phi_o - U)\right] \quad [18]$$

where $i_o(c_\infty)$ can be found from the polarization curve of oxygen reduction on iron. The kinetics of oxygen reduction on iron depends on the oxygen concentration and the pH of the solution, but unfortunately there are not adequate data in the literature to show the effects of these parameters. Delahay (11) has given a polarization curve for oxygen reduction on iron at pH = 7. From this result the following value is found for $i_o(c_\infty)$

$$i_o(c_\infty) \exp\left(\frac{\alpha_c F}{RT} U\right) = 7.4 \times 10^{-4} \text{ A/cm}^2 \text{ for } c_\infty = 10^{-7} \frac{\text{mole}}{\text{cm}^3}$$

To show the effect of oxygen concentration on the corrosion rate, the following value is assumed for $i_o(c_\infty)$ at $c_\infty = 5 \times 10^{-7}$ mole/cm^3

$$i_o(c_\infty) \exp\left(\frac{\alpha_c F}{RT} U\right) = 16.0 \times 10^{-4} \text{ A/cm}^2 \text{ for } c_\infty = 5 \times 10^{-7} \frac{\text{mole}}{\text{cm}^3}$$

Equations [5] and [18] give the desired relations that can be used in parallel with Eq. [1]-[4] to find the current and potential distribution on the disk. It should be noted that there are six equations with six unknowns, namely i_{Fe}, i_{O_2}, $i(\eta)$, Φ_o, B_n, and V. These

simultaneous equations are highly nonlinear and should be solved by numerical methods. The following iterative procedure is used to solve the equations. (*i*) A net current distribution is assumed for the disk. (*ii*) Equation [3] is used to find the coefficients, B_n. (*iii*) The ohmic potential, Φ_o, is calculated from Eq. [2]. (*iv*) A value is assumed for the potential, V, of the disk. (*v*) Iron and oxygen current densities are calculated from Eq. [5] and [18], respectively. (*vi*) The current densities found in step (*v*) should satisfy Eq. [1]; if they do not, another value is assumed for V, and the step (*v*) is repeated. (*vii*) The sum of iron and oxygen current densities should be equal to the net current assumed in step (*i*) at each point on the disk; if it is not, using a multidimensional Newton-Raphson method, another value is found for the net current, and the calculations enumerated in steps (*ii*) through (*vi*) are repeated until no significant changes occurred in the net current.

Limitation of the Model

The iron current density is a function of Fe^{++} concentration, chloride ion concentration, and *p*H of the solution, as well as potential. In general one can write

$$i_{Fe} = i_{Fe}(V - \Phi_o, c_{Fe^{++}}, c_{Cl^-}, pH)$$

In the case of corrosion of the rotating disk, the outer portion of the disk acts as the aerated cathode where oxygen is being reduced to water and/or hydrogen peroxide with an increase of *p*H, while the central portion of the disk, which is active, is the less well aerated anode where the metal undergoes corrosion and hydrolysis with decrease of pH. Thus, the *p*H does not remain uniform on the surface of the disk.

The concentration of iron ions and chloride ions are likewise not uniform on the surface of the disk. Fe^{++} is higher at the center and decreases towards the periphery. Migration may increase the concentration of the chloride ion on the central portion of the disk.

It should be noted that the variations of $c_{Fe^{++}}$, c_{Cl^-}, and *p*H are not large, and they are neglected in this work. They may, however, be crucial to the stability of a situation where part of the disk is active and part is passive.

Results and Discussion

The corrosion rate of the rotating disk depends principally on oxygen concentration, rotation speed, conductivity of the solution, radius of the disk, and a factor that takes into account the relation between the rates of oxygen and iron reactions on the surface of the disk. For the last variable, one can use the ratio of oxygen and iron current densities at a potential corresponding to the maximum of the iron polarization curve and for a high rate of oxygen transfer to the disk ($\Omega \to \infty$). That is

$$A = \left| \frac{i_{O_2}}{i_{Fe}} \right|_{\substack{\max i_{Fe} \\ \Omega \to \infty}} \qquad [19]$$

would be the last variable. This quantity is indicated in the graphical representation of the results.

Figure 1 shows the iron current density (which is proportional to the rate of corrosion), oxygen current density, and the ohmic potential on the surface of the rotating disk. The iron current density curve shows that the corrosion rate is high at the center, increases slowly with radial position, passes through a weak maximum, and then drops rapidly to a very low value at the periphery. This is in agreement with the experimental results (1). The curve for the oxygen current density has a flat part which is related to the laminar region of the disk, and a sharp increase of the current, that shows the transition from laminar to turbulent region. The ohmic potential is

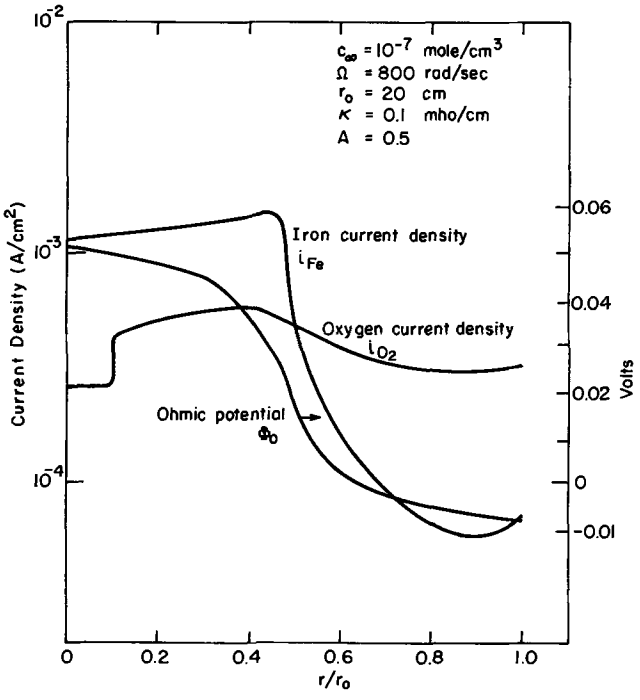

Fig. 1. Iron and oxygen current densities and ohmic potential distribution on the surface of an iron rotating disk.

high and positive at the center and decreases to negative values at the periphery. The net current would also be positive at the center and negative at the edge of the disk. This shows that in the central portion of the disk, anodic current has the larger contribution to the net current and that the cathodic reaction dominates on the outer portion.

The effect of rotation speed on the corrosion rate of the rotating disk is shown in Fig. 2 and 3. As it was mentioned earlier, the only effect of velocity is to increase the rate of transfer of oxygen to the disk (in the turbulent region). Thus, increasing the rotation speed has much the same effect on the corrosion as increasing the oxygen concentration. One

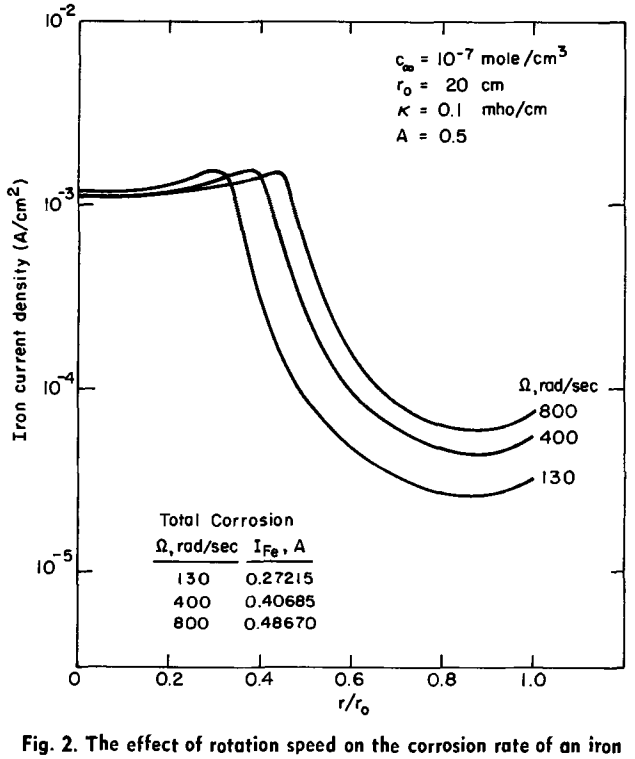

Fig. 2. The effect of rotation speed on the corrosion rate of an iron rotating disk.

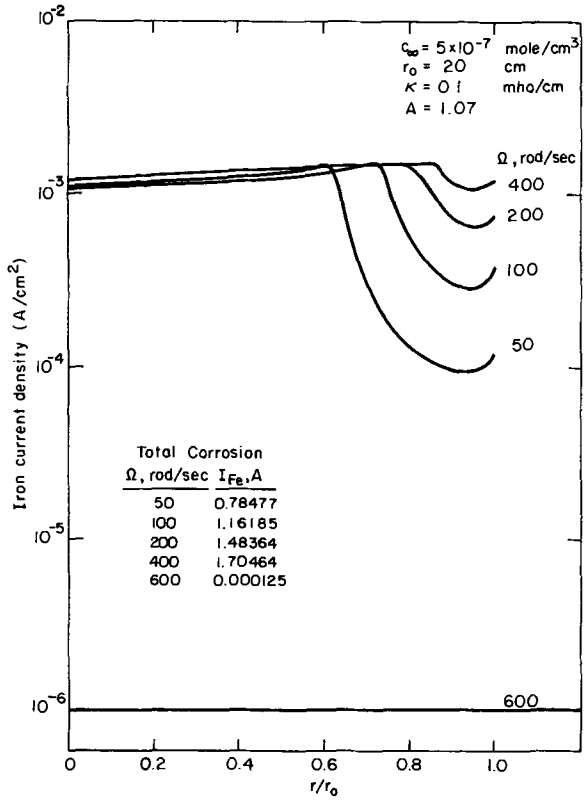

Fig. 3. The effect of rotation speed on the corrosion rate of an iron rotating disk.

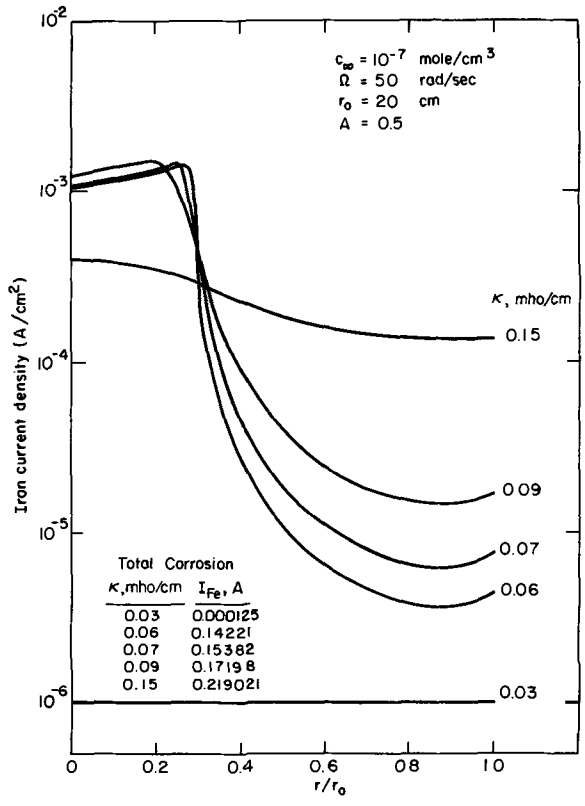

Fig. 4. The effect of conductivity of the solution on the corrosion rate of an iron rotating disk.

should, of course, note that changing the oxygen concentration will change $i_0(c_\infty)$. As the rotation speed is increased, the point of maximum corrosion on the disk moves toward the periphery, and the total corrosion of the disk increases. But if the rotation speed is increased to higher values, provided there is no limitation as far as the electrode kinetics of oxygen is concerned ($A > 1$), there will be a sudden change in the shape of the corrosion distribution, and the whole disk is passivated.

Figure 4 shows the corrosion behavior of the rotating disk when the conductivity of the bulk solution is a parameter. As the conductivity increases, the corrosion rate becomes more uniform. For the solutions with low conductivity, the nonuniformity in the corrosion rate increases, and the central region of the disk will have the maximum rate of corrosion, while passivation occurs at the edge. As the conductivity decreases, a larger area of the disk is passivated, and for very low conductivities, the whole disk would be in the passive region. It can be understood from Fig. 4 that for large values of conductivities, total passivity can also be achieved provided that rotation speed is high enough. Also, there will be no limitation for the electrode kinetics of oxygen.

The effect of the size of the rotating disk on the corrosion rate is given in Fig. 5. It shows that increasing the radius of the disk has a tendency to increase the nonuniformity of the corrosion rate, and for very large disks, the whole disk is passivated. For small disks, the whole area of the disk would be in the laminar region, and, consequently, the corrosion rate would be uniform, as is shown in Fig. 5. It should be noted that the size of the disk is an important factor in the corrosion rate, because it is not only a variable as far as the ohmic potential is concerned but also a factor that determines the limiting rate of oxygen transfer to the disk.

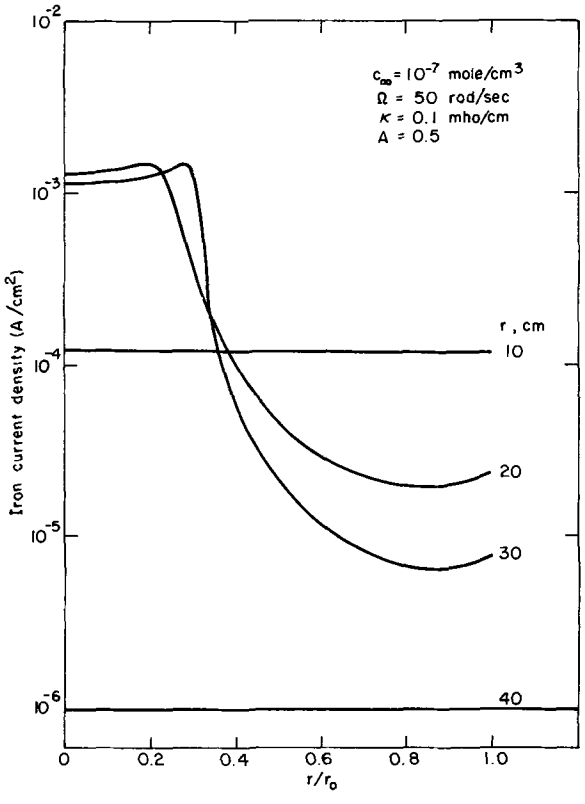

Fig. 5. The effect of the size of the disk on the corrosion rate of an iron rotating disk.

Conclusions

The development described in the preceding sections shows that the main reason for the peculiar corrosion behavior of an iron rotating disk is the passivation that occurs at the edge of the disk. Besides that, in order to have such a nonuniform corrosion rate on the surface of the rotating disk, the outer region of the disk has to be in the turbulent region. That is, if the size of the disk is small and/or the rotation speed is low so that the whole disk is in laminar region, one would get a uniform corrosion rate. The results also show that by changing the different parameters of

the system, one can get total passivity. It should be noted that in a system where the rate of transfer of corrosive species to the metal is high, the relation between the anodic and cathodic reaction rates is very important, because it is usually the electrode kinetics that limits the corrosion rate.

Because of the peculiar shape of the iron polarization curve, for a given condition of the system, it is possible to get three different schemes for the corrosion behavior of the rotating disk from the model developed above. Thus one would wonder which one of these solutions is physically meaningful. It should be noted that in the corrosion experiments of active-passive metals such as iron, one usually expects to obtain a hysteresis. That is, the corrosion rate of the metal at a given condition depends on the way the system approaches that specific condition. Thus, in the case of an iron rotating disk, one would also expect to get a hysteresis by increasing and decreasing the rotation speed, and the actual corrosion scheme of the disk would be one of the three solutions obtained from the calculations depending upon the way we approach a given condition.

Acknowledgment

This work was supported by the United States Atomic Energy Commission.

Manuscript submitted July 11, 1972; revised manuscript received June 22, 1973.

Any discussion of this paper will appear in a Discussion Section to be published in the June 1974 JOURNAL.

LIST OF SYMBOLS

B_n	coefficients in series for potential
c_0	concentration at electrode surface, mole/cm^3
c_∞	bulk concentration, mole/cm^3
D	diffusion coefficient of oxygen, cm^2/sec
$\mathbf{F}$	Faraday's constant, coulomb/equivalent
i	net current density at electrode surface, A/cm^2
i_{Fe}	iron current density, A/cm^2
i_{lim}	limiting current density, A/cm^2
i_{O_2}	oxygen current density, A/cm^2
i_o	exchange current density, A/cm^2
I	total net current on the disk, A
I_{Fe}	total iron current on the disk, A
I_{O_2}	total oxygen current on the disk, A
M_{2n}	a Legendre function
n	number of electrons produced when one oxygen molecule reacts (−4)
N_i	flux of species i, mole/cm^2-sec
Nu	$N_i r/D(c_\infty - c_0)$, local Nusselt number
$\overline{\text{Nu}}$	$N_i r_0/D(c_\infty - c_0)$, average Nusselt number
P_n	Legendre polynomial of order n
r	radial coordinate, cm
r_0	radius of disk, cm
R	universal gas constant
Re	$= r_0^2\,\Omega/\nu$, over-all Reynolds number
Re_{loc}	$= r^2\,\Omega/\nu$, local Reynolds number
Sc	ν/D, Schmidt number
T	absolute temperature, °K
U	equilibrium potential of oxygen, V (~1.229 NHE)
V	potential of metal disk electrode, V
α_a, α_c	transfer coefficients
η	elliptic coordinate
η_c	concentration overpotential, V
η_s	surface overpotential, V
κ_∞	conductivity of bulk solution, ohm^{-1} cm^{-1}
Φ_0	external potential extrapolated to electrode surface, V
Ω	rotation speed, radians/sec

REFERENCES

1. F. L. LaQue, *Corrosion*, **13**, 303t (1957).
2. Th. v. Karman, *Z. Angew. Math. Mechanik*, **1**, 233 (1921).
3. W. G. Cochran, *Proc. Cambridge Phil. Soc.*, **30**, 365 (1934).
4. B. Levich, *Acta Physicochimica U.R.S.S.*, **17**, 257 (1942).
5. John Newman, *This Journal*, **113**, 1235 (1966).
6. John Newman, Presented before National Association of Corrosion Engineers, Williamsburg, Virginia, December, 1971.
7. Marcel Pourbaix, *Corrosion*, **6**, 395 (1950).
8. John Newman, *J. Phys. Chem.*, **70**, 1327 (1966).
9. Bart Trousdale Ellison, Dissertation, University of California, Berkeley, California (1969).
10. B. T. Ellison and I. Cornet, *This Journal*, **118**, 68 (1971).
11. Paul Delahay, *ibid.*, **97**, 205 (1950).

Technical Notes

Studies of $LiAlCl_4$ Solutions in Aprotic Solvents

M. Eisenberg,* K. Wong, and K-C Tsai*

Electrochimica Corporation, Mountain View, California 94040

Solutions of the Lewis acid, $AlCl_3$, coordinated with lithium chloride in nonaqueous aprotic solvents have been widely used in the lithium battery development work in recent years (1). The purpose of this study was to obtain basic information on the electrochemical stability of the LiCl-$AlCl_3$ solutions in aprotic solvents such as propylene carbonate, nitromethane, and their mixtures and to elucidate the mechanism of various redox processes pertaining to such electrolytes.

* Electrochemical Society Active Member.

Key words: nonaqueous electrolytes, lithium chloroaluminate, cyclic voltametry, propylene carbonate.

Cyclic voltametry was employed for the present study. This technique, involving a procedure of linear potential sweeps, is well established in electroanalysis for determination of reaction mechanisms in the oxidation and reduction of soluble species (2-6).

Experimental Procedure

Materials and electrolyte preparation.—Lithium chloride (LiCl) was vacuum dried at 150°C for 48 hr and the aluminum chloride ($AlCl_3$) was purified by sublimation just prior to its use. The solvents used were doubly distilled under partial vacuum (approx.

Table I. Compositions of the electrolytes employed in the cyclic voltametric studies

Electrolyte No.	Solutes, moles/liter		Solvents, %	
	LiCl	$AlCl_3$	Propylene carbonate	Nitromethane
1	0.8	0.8	100	—
2	0.8	0.8	—	100
3	0.8	0.8	50	50
4	0.4	0.8	100	—
5	0.4	0.8	0	100
6	0.4	0.8	50	50
7	—	0.8	50	50

50 mm Hg) and treated with a molecular sieve. All solutions were prepared in ground glass flasks inside a dry argon glove box. Karl Fischer titrations for water impurities gave a range of 20-50 ppm.

Seven solutions of varying concentrations of solutes and solvents were investigated. The compositions of these solutions are given in Table I.

Electrochemical cell and instrumentation.—The electrochemical studies were carried out in a typical three-electrode glass cell. A bright platinum rod with an exposed apparent surface area of 1 cm^2 was used as the working electrode. A concentric cylindrical platinum gauze (1 in. ID) with an exposed area much greater than the area of the working electrode was used as the counterelectrode. The reference electrode was Ag-AgCl(s) (immersed in the same nonaqueous electrolyte as under study) placed in a separate compartment with a Luggin capillary located about 3 mm away from the working platinum electrode. It was used to measure the potential between working and reference electrodes at both open-circuit voltage and under load conditions.

A Heath polarography Module EUA-19-2 with moderate sweep rates (0.05-2.00 V/min) was employed for all studies. The cyclic polarograms were recorded on a Houston Instruments HR-96T X-Y Recorder. The rest potential (at open-circuit voltage) was measured with a Keithley 621 Electrometer.

Two sets of experiments were conducted for the studies: (*i*) effects of solution compostiions on cyclic polarogram at a fixed slow scan rate of 2.0 V/min; (*ii*) effect of scan rate (0.2-2.0 V/min) on peak potentials.

Results and Discussion

All of the electrolytes tested yielded similar cyclic polarograms with the exception of electrolyte No. 7 containing no lithium chloride. The polarograms for the first six electrolytes were all similar to the two given in Fig. 1 for electrolyte No. 1 and No. 4. Figure 2 shows the polarogram for electrolyte No. 7.

In Fig. 1, the cyclic polarograms indicate an irreversible process for the oxidation and reduction reaction since there are no anodic current peaks corresponding to the observed cathodic current peaks $E_{pc(1)}$ and $E_{pc(2)}$.

Judging from the studies of Cauquis and Serve (2) and from the present results, it is very unlikely that the neutral organic solvents participate in the redox processes within the potential range studied. Therefore, we might assume the following.

(*i*) The anodic potential limit, E_{pa} (+1.6-1.7V) at the platinum electrode was caused by either the oxidation of Cl^- or of $AlCl_4^-$. The presence of $AlCl_4^-$ is due to the chemical equilibrium in this solvent system (1).

$$LiCl + AlCl_3 \rightleftharpoons Li^+ + AlCl_4^- \qquad [1]$$

(*ii*) The cathodic potential limit $E_{pc(3)}$ (−3.0 to −3.4V) was caused by the reduction of either Li^+ or Al^{+++} or the complex ion of aluminum, *i.e.*, $(AlCl_2 \cdot 2X)^+$ (1), where X = molecule of solvent.

The two-step reduction processes, namely $E_{pc(1)}$ at +1.1V and $E_{pc(2)}$ at −0.45V in Fig. 1 appear to involve an oxidized species which was produced previously at peak, E_{pa}. This was confirmed in separate experiments in which the range of potential scanning was limited to only ±1.5V. As shown in Fig. 3 (illustrated for solution No. 4) in this potential range the oxidation peak E_{pa} does not appear and neither do the cathodic (reduction) peaks $E_{pc(1)}$ and $E_{pc(2)}$.

(*iii*) Changes in solvents and their mixtures did not alter the curve shape of the cyclic polarogram. In other words, only the dissolved salts, LiCl-$AlCl_3$, participated in the observed redox processes.

(*iv*) In Fig. 2, the polarogram for electrolyte No. 7 with $AlCl_3$ as the only solute, indicates only a single peak, E_{pc} (−0.45V), in the cathodic polarization following the oxidation process at E_{pa} (+1.70V). The redox mechanism would presumably be

Chlorine formation:

$$AlCl_3 \rightleftharpoons \tfrac{1}{2}Cl_2 + AlCl_2^+ + e^- \text{ at } E_{pa} \qquad [2]$$

Chlorine reduction:

$$\left.\begin{aligned} \tfrac{1}{2}Cl_2 &\rightleftharpoons Cl^- - e^- \\ Cl^- + AlCl_2^+ &= AlCl_3 \end{aligned}\right\} \text{ at } E_{pc} \qquad [3]$$

The broad peak at E_{pc} could be explained by mass transfer effects due to the diffusion of dissolved Cl_2 away from the working platinum electrode. This was also the phenomenon observed in Fig. 1 for the second

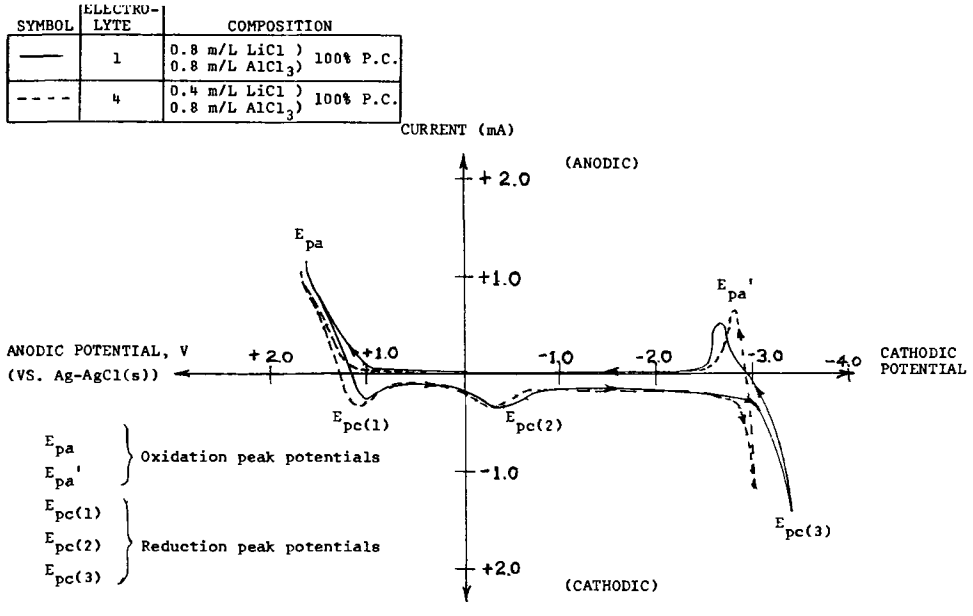

Fig. 1. Cyclic polarograms for electrolytes No. 1 and 4 at platinum electrode. A = 1 cm^2; scan rate = 2 V/min.

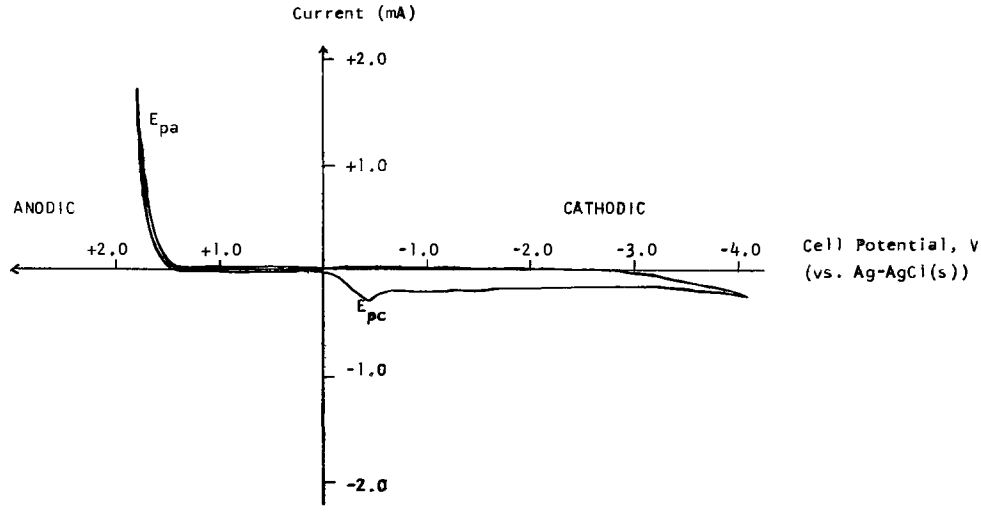

Fig. 2. Cyclic polarogram for the electrolyte No. 7 (no LiCl) at Pt electrode. $A = 1$ cm^2; scan rate = 2 V/min.

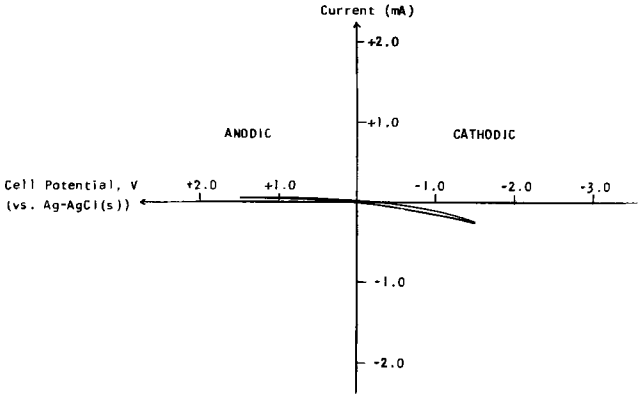

Fig. 3. Control cyclic polarogram for solution No. 4 at Pt electrode in the potential range +1.5 to −1.5V. $A = 1$ cm^2; scan rate = 2 V/min.

reduction peak at $E_{pc(2)}$ at lower scan rates. Figure 2 also points out that cathodic reduction of aluminum ions or its complex ions does not occur even up to potentials of −4V. By comparing results of Fig. 1 and 2, we conclude for solutions containing both LiCl and $AlCl_3$ that the anodic oxidation at E_{pa} (Fig. 1) is most likely due to $AlCl_4^-$, not Cl^-, and that the cathodic reduction of $E_{pc(3)}$, a reversible reaction, is due to Li^+, not Al^{+++} or $(AlCl_2 \cdot 2X)^+$.

(v) Scan rate studies on electrolyte No. 3 (0.8 moles/liter LiCl-$AlCl_3$ in 50% propylene carbonate and 50% nitromethane) shown in Fig. 4 revealed that the peak potentials corresponded to two-step reduction processes (involving the species generated at the same electrode at the previous anodic sweep in which $AlCl_4^- \rightarrow (AlCl_2^+) + Cl_2 + 2e^-$).

The two reduction steps are postulated as

$$(\text{at } E_{pc(1)}) \qquad AlCl_2^+ + e^- \rightleftharpoons (AlCl_2\cdot) \qquad [4]$$

$$(\text{at } E_{pc(2)}) \qquad (AlCl_2\cdot) + Cl_2 + e^- \rightleftharpoons AlCl_4^- \qquad [5]$$

The peak potentials corresponding to each of these two reduction steps were studied as a function of scan rate as shown in Fig. 4.

The apparent number of charge transfers corresponding to $E_{pc(1)}$ and $E_{pc(2)}$ were calculated by the equation for a totally irreversible process (3)

$$[E_{pc(1)}]_2 - [E_{pc(1)}]_1 = \frac{RT}{F} \cdot \frac{1}{\alpha n_1} \ln \left[\frac{v_1}{v_2} \right]^{1/2} \qquad [6]$$

where n_1 is the number of charge transfers, α is the transfer coefficient, and v_1, v_2 are scan rates. It was found that both reducing processes correspond to one charge transfer only.

Scan rate studies also indicated a possible ECE (electrochemical-chemical-electrochemical) mechanism (4-6). The kinetics of this mechanism are

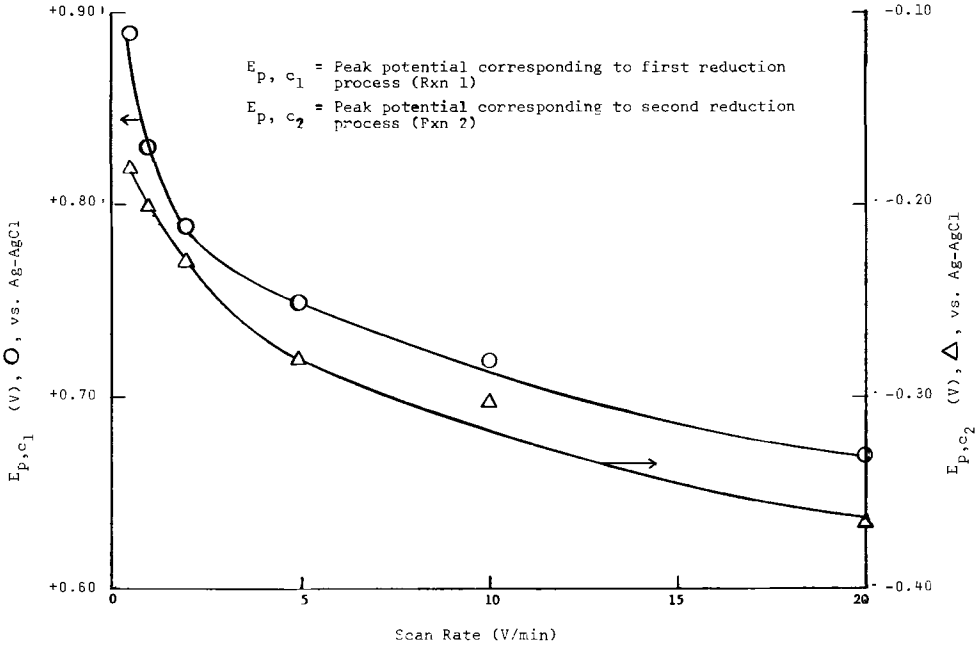

Fig. 4. Reduction peak potentials vs. scan rates for electrolyte No. 3.

$$0 \overset{ne^-}{\rightleftharpoons} R_1 \underset{k_b}{\overset{k_f}{\rightleftharpoons}} R' \overset{ne^-}{\rightleftharpoons} R_2 \quad [7]$$

i.e.

$$AlCl_2^+ \overset{e^-}{\rightleftharpoons} (AlCl_2\cdot) + Cl_2 \underset{K_b}{\overset{K_f}{\rightleftharpoons}} (AlCl_4\cdot) \overset{e^-}{\rightleftharpoons} AlCl_4^- \quad [8]$$

since, at lower scan rates, the peak corrsponding to the second reduction, Eq. [5], was significantly broadened. This indicates strongly that the diffusion of chlorine molecules away from the platinum working electrode significantly affects this process as would be expected for the chemical step in Eq. [8].

Conclusions

From the results of these studies, we propose the following as the most likely mechanisms for the redox processes involving aprotic solvent electrolytes containing both $AlCl_3$ and LiCl.

Oxidation: one step reaction

$$AlCl_4^- \rightleftharpoons AlCl_2^+ + Cl_2 + 2e^- \qquad \text{at } E_{pa}$$

Reduction: two step reactions

$$AlCl_2^+ + e^- \rightleftharpoons AlCl_2\cdot \qquad \text{at } E_{pc(1)} \quad [4]$$

and

$$AlCl_2\cdot + Cl_2 + e^- \rightleftharpoons AlCl_4^- \qquad \text{at } E_{pc(2)} \quad [5]$$

ECE mechanism:

$$AlCl_2^+ \overset{e^-}{\rightleftharpoons} AlCl_2\cdot + Cl_2 \underset{k_b}{\overset{k_f}{\rightleftharpoons}} AlCl_4\cdot \overset{e^-}{\rightleftharpoons} AlCl_4^- \quad [8]$$

Acknowledgment

The support of the U.S. Naval Ordnance Systems Command is gratefully acknowledged.

Manuscript submitted Oct. 24, 1972; revised manuscript received July 16, 1973. This was Paper 3 presented at the Miami Beach, Florida, Meeting of the Society, Oct. 8-13, 1972.

Any discussion of this paper will appear in a Discussion Section to be published in the June 1974 JOURNAL.

REFERENCES

1. F. W. Breivogel and M. Eisenberg, *Electrochim. Acta*, **14**, 459 (1969).
2. G. Cauquis and D. Serve, *Bull. Soc. Chim. France*, **1966**, 302.
3. R. S. Nicholson and I. Shain, *Anal. Chem.*, **36**, 706 (1964).
4. D. H. Geske and A. H. Maki, *J. Am. Chem. Soc.*, **82**, 2671 (1960).
5. A. C. Testa and W. H. Reinmuth, *Anal. Chem.*, **33**, 1320 (1961).
6. D. H. Geske, J. L. Ragle, M. A. Mambenek, and A. L. Balch, *J. Am. Chem. Soc.*, **86**, 987 (1964).

Optical Evidence Concerning the Discharge of MnO_2 in Acid and Alkaline Electrolytes

Chin-Ho Lee,*[1] Boris Cahan,* and Ernest Yeager*

Chemistry Department, Case Western Reserve University, Cleveland, Ohio 44106

Optical transmission measurements have been made *in situ* on γ-MnO_2 during discharge in acid and alkaline solutions. The γ-MnO_2 was electrodeposited on a conducting tin oxide coated quartz flat. The optical data are compatible with disproportionation in acid media [MnIV $\overset{+e}{\longrightarrow}$ MnIII; 2MnIII $\rightarrow$ MnIV + MnII] and the stepwise reduction in basic media [MnIV $\overset{+e}{\longrightarrow}$ MnIII $\overset{+e}{\longrightarrow}$ MnII].

Yoshizawa and Vosburg (1) propose that the discharge of MnO_2 proceeds through a disproportionation reaction in acid media, *i.e.*

$$\text{MnIV} \overset{+e}{\longrightarrow} \text{MnIII}$$

$$2\text{MnIII} \rightarrow \text{MnIV} + \text{MnII}$$

For alkaline solutions, Kozawa and Yeager (2) have proposed the stepwise discharge mechanism; *i.e.*

$$\text{MnIV} \overset{+e}{\longrightarrow} \text{MnIII} \overset{+e}{\longrightarrow} \text{MnII}$$

According to these mechanisms, MnIV should be present in the oxide until virtually complete discharge in acid media. In alkaline media MnIV should no longer be present after ~50% discharge provided the first reduction step proceeds more readily than the second at the potentials of this electrode under polarization. Optical transmission measurements provide a means for verifying these predictions. The results of such studies are reported herein.

* Electrochemical Society Active Member.

[1] Present address: Gould Laboratories, Cleveland, Ohio 44108.

Key words: manganese dioxide, batteries, electrode behavior, optical absorption.

Experimental

Electrolytic γ-MnO_2 has been electrodeposited on a quartz plate which is optically flat and coated[2] with a conductive layer of SnO_2 with a resistance of ~40 ohm/□. Electronic contact was made to the SnO_2 transparent region by means of an insulated gold contact (Fig. 1). This arrangement minimized the nonuniformity of the current distribution arising from *IR* drop in the SnO_2 film. The niobium and gold layers in the opaque region of the electrode mount were laid down by sputtering and vapor deposition, respectively, and subsequently coated with a thin layer of polystyrene as an insulator. The thin niobium layer was required to obtain good adhesion of the gold. The MnO_2 was electrodeposited on the transparent SnO_2 region from 0.5*M* $MnSO_4$ + 0.5*M* H_2SO_4 solution at 90°C for 2 min at an apparent current density of 1 mA/cm^2, yielding a layer of ~0.1μ and of very uniform ap-

[2] The SnO_2 coated optical flats were prepared by Liberty Mirror, a subsidiary of Libby-Owen Ford Glass Company, Brackenridge, Pennsylvania.

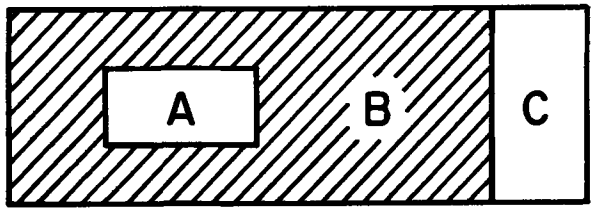

Fig. 1. Transparent electrode arrangement on quartz optical flat. A, transparent region: SnO_2/electrolytic γ-MnO_2, 2 cm^2 area; B, opaque region (insulated from electrolyte): SnO_2/Nb/Au/polystyrene; C, electrical contact area: SnO_2/Nb/Au.

pearance. Gamma-MnO_2 should be formed under these conditions (3).

The optical transmission measurements were carried out in a quartz electrochemical cell. The discharge was under galvanostatic control with a gold counterelectrode and a reference electrode consisting of a small bead of α-HPd, positioned close (1 mm) to the MnO_2 electrode just outside of the optical beam. The electrolytes used for the discharge were 0.1*M* H_2SO_4 + 0.9*M* Na_2SO_4 and 1*M* NaOH, prepared from reagent grade chemicals without further purification. The solutions were saturated with helium (purified with heated copper turnings and molecular sieves) and an atmosphere of helium maintained within the cell to eliminate O_2 from the solution.

The *in situ* optical transmission measurements were made using the tungsten source and monochromator of a Beckman Model DU spectrophotometer (single beam) in which the sample compartment was replaced with an assembly accommodating the electro-optical cell. The output of a 1P28 photomultiplier used as a detector was displayed on an x-y plotter. Some additional not *in situ*, absorption measurements were also carried out with MnO_2 electrodes using the Cary Model 15 spectrophotometer.

The potentials of the MnO_2 electrodes were measured relative to the reference α-HPd electrode with a Keithley electrometer, Model 610B. The optical-electrochemical measurements were made by following the change of the absorbance with charge; *i.e.*, $(1/I)dI/dQ = d\ln(I/I_0)/dQ = -(2.30)dA/dQ$. The first data points for a freshly prepared MnO_2 electrode were obtained by discharging at constant current (25 μA/cm^2) for 10 sec and recording the optical intensity change, followed by reversing the current and recording the change in intensity during 10 sec of charging at the same current. From these, data dA/dA with dQ corresponding to both charging and discharging were determined; both values of dA/dQ were always the same within a few per cent. The electrode was then discharged for a fixed time (4 to 8 min) at a constant current of 25 μA/cm^2 and then allowed to remain under open-circuit conditions until the voltage stabilized. This required typically a few minutes in acid solution and up to 20 min in alkaline solution. The 10 sec discharging and charging procedure was then repeated to obtain dA/dQ. This procedure of continuous discharge followed by evaluation of dA/dQ after voltage stabilization was repeated until the optical and potential measurements indicated complete discharge. The dependence of the absorbance on the state of charge was subsequently calculated by integrating the dA/dQ data.

This procedure minimizes problems of optical instability which might be encountered in continuous recording of the optical intensity with discharge. Furthermore, progressive changes in the electrode other than just the electrochemical reduction (*e.g.*, surface roughening and electrode nonhomogeneity) can seriously interfere with the use of the directly recorded optical intensity *vs.* time or total charge data to calculate dA/dQ. The derivative method used in the present work should be much less subject to this type of error. The values of dA/dQ evaluated by this procedure correspond to those of the electrode after reequilibration and not while on discharge. Thus the integral curves calculated from the derivative data dA/dQ correspond essentially to equilibrium conditions at each state of discharge.

Results

In Fig. 2 and 3 are plotted the open- and closed-circuit potentials, the open-circuit dA/dQ, and the integrated relative absorbance curves, the latter calculated from the dA/dQ data. The open-circuit potentials correspond to equilibrium values at designated states of discharge. The closed-circuit values are those at the end of 4 or 8 min intervals, just before the interruption of the current. In acid media, the potential and optical absorption data rather clearly indicate the

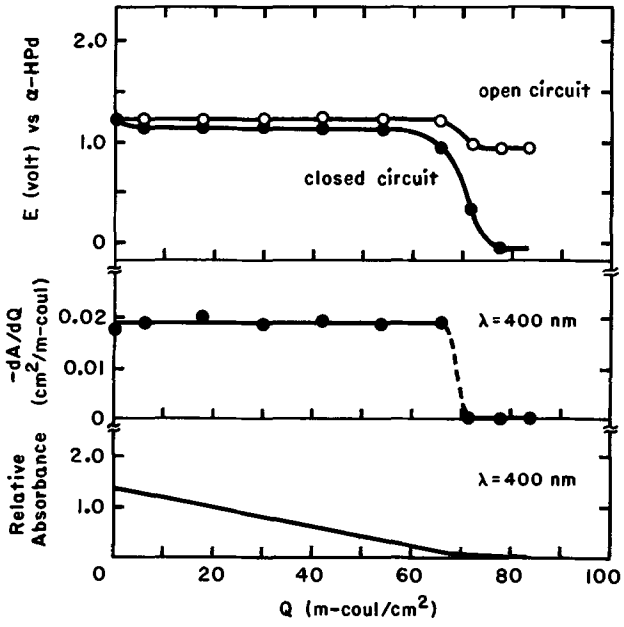

Fig. 2. Galvanostatic discharge of transparent γ-MnO_2 electrode (120 mcoulombs/cm^2, 0.1μ) in helium saturated 0.1*M* H_2SO_4 + 0.9*M* Na_2SO_4 solution at ~25°C. Discharge current density = 25 μA/cm^2.

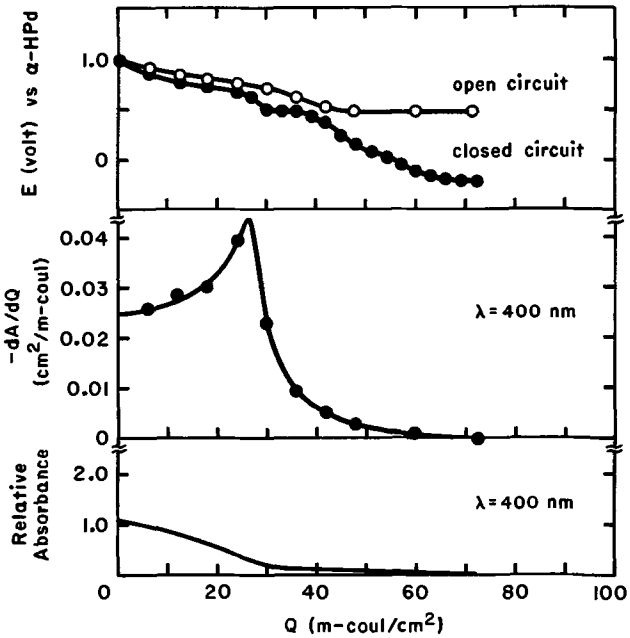

Fig. 3. Galvanostatic discharge of transparent γ-MnO_2 electrode (120 mcoulombs/cm^2, 0.1μ) in helium saturated 1*M* NaOH solution at ~25°C. Discharge current density = 25 μA/cm^2.

discharge to be effectively complete at ~70 mcoulombs/cm^2 as compared with 120 mcoulombs/cm^2 involved in the electrodeposition of the γ-MnO_2. This difference occurs principally because of the physical loss of material from the electrode surface during discharge and to some lesser extent because of coulombic inefficiency during the initial electrodeposition. In alkaline solution, the potential and absorbance data do not as clearly indicate the point of complete discharge but it still is ~70 mcoulombs/cm^2.

The potential curves shown in Fig. 2 and 3 exhibit the same charge dependence as reported by Yoshizawa and Vosburg (1) and Kozawa and Yeager (2). The relatively constant open-circuit potential found for the acid electrolyte has been interpreted by these authors as evidence for a disproportionation reaction involving two phases: an MnIV rich phase and MnII rich phase,

each of relative constant activity with respect to these ions. The more complex potential-charge curves for alkaline solution have been shown by Kozawa and Yeager (2) to be compatible with the stepwise discharge, the first portion of which involves a single solid phase with changing activities of MnIV and MnIII and the second two phases involving MnIII and MnII of relatively constant activities with respect to these ions.

The absorbance *vs.* charge data in Fig. 2 and 3 were measured at $\lambda = 400$ nm. This wavelength was chosen because it corresponds to a maximum value in the visible for dA/dQ. Only relative absorbance values were obtained from the integration of dA/dQ *vs.* Q and the final values of A in the discharge state were arbitrarily taken as zero. The electrodes used in both the acid and alkaline solutions had approximately the same initial thickness and initial apparent optical adsorbance. At the completion of discharge in the alkaline solution, the apparent absorbance of the electrode was still significantly greater than that of the transparent substrate, because of the presence of MnII oxide. In the acid solution all of the MnII entered the solution and the apparent absorbance of the electrode was essentially that of the electrode substrate. The decrease in absorbance is more rapid for the alkaline electrolyte and becomes essentially constant at approximately one-half of the complete discharge, in contrast to the acid electrolyte where the absorbance decreases linearly with discharge until discharge is complete.

The interpretation of the optical-electrochemical data is contingent on the absorption characteristics of MnO_2 and MnIV relative to the lower oxides and MnIII and MnII. The absorption spectrum of the electrolytically formed γ-MnO_2 was determined not *in situ* with the Cary spectrophotometer and is shown in Fig. 4 together with the corresponding spectrum for β-MnO_2 formed on the same SnO_2/quartz substrate by thermal decomposition of concentrated $Mn(NO_3)_2$. Spectral data for MnO_2 is lacking in the literature. Geschwind *et al.* (4), however, have examined the spectra of MnIV in an α-Al_2O_3 matrix (insert in Fig. 4). The Mn-O-Mn and Mn-Mn interactions in the pure oxides would be expected to modify very substantially the spectra compared to that for a dilute MnIV system. Nonetheless, there is some evidence of the absorption peak at ~480 nm in the MnIV-α-Al_2O_3 also in the spectrum for β-MnO_2. The specific absorptivity ($\epsilon = A$/thickness) of the γ-MnO_2 is much higher than that of the β-MnO_2 at $\lambda < 500$ nm, and the absorption edge is displaced to higher wavelengths.

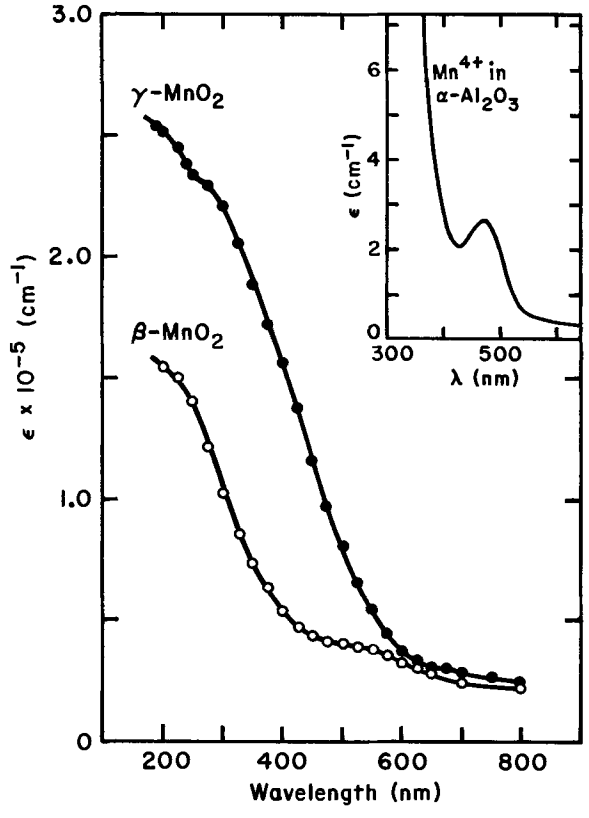

Fig. 4. Optical absorption spectra specific absorptivity of γ- and β-MnO_2 deposited on transparent substrate (present work). Insert figure: Mn^{4+} in α-Al_2O_3 matrix ($Mn^{4+} < 0.08$ w/o) reported by Geschwind *et al.* (4).

The absorption of the MnO_2 is much higher than that of the lower oxide. From Fig. 4, the molar absorptivity a_M based on the concentration in moles/liter of MnIV in the γ-MnO_2 is $a_M = A/bc \cong 10^3$ liter-cm^{-1} mole^{-1} where c is the concentration in moles/liter and b the thickness in centimeters. The concentration of MnIV in the α-Al_2O_3 matrix in the work of Geschwind *et al.* (4) was only known to fall in the range 10^{-3}-10^{-1} weight per cent (w/o). From their spectra, this would correspond to $a_M = 3 \times 10^1$ to 3×10^3 liter-cm^{-1} mole^{-1} at 400 nm. These values are to be compared with $a_M = 20$-100 for MnIII in various solid matrices at $\lambda = 476$-625 nm (5) and $a_M = 10^{-2}$-10^{-1} liter-cm^{-1} mole^{-1} for octahedrally coordinated MnII and 1-10 liter-cm^{-1} mole^{-1} for tetrahedrally coordinated MnII at comparable wavelengths (5). Thus, the decrease in absorbance of the γ-MnO_2 electrodes appears to be virtually entirely a consequence of the decrease in the concentration of MnIV in the electrode.

After discharge in acid solution, some pink color characteristic of Mn^{2+} was evident in the solution. The Mn^{2+} in the solution, however, does not contribute appreciably to the observed changes in adsorbance because of the low molar absorptivity of Mn^{2+} compared to the MnIV of the electrode phase. Loss of Mn^{2+} into the bulk of the solution, does result in the lack of rechargeability in acid solution.

The molar absorptivity, a_M, and hence dA/dQ, is not expected to be constant as the MnIV concentration in a particular oxide phase is reduced because of differences in the various Mn-O-Mn and Mn-Mn interactions involving MnIV and lower valency states. This explains the lack of consistency for dA/dQ in Fig. 3 for the alkaline solution where only one phase is believed to be present until the discharge is approximately one-half complete (2, 3). In acid media, two separate phases of invariant composition are proposed to be present over almost all of the discharge (1) and hence dA/dQ is essentially constant.

On the basis of this interpretation, the optical data for the acid electrolyte indicates the presence of MnIV until the discharge is virtually complete. In alkaline electrolyte, the MnIV is no longer evident after one-half discharge. These observations agree with predictions based on the disproportionation and stepwise reduction mechanisms in acid and alkaline solutions, respectively. They, however, should not be considered as confirming these mechanisms, but rather just as verification of thermodynamic expectation under open-circuit conditions at various states of discharge. In acid solution, the composition of the MnIV containing a solid phase must be constant on the base of the constancy of dA/dQ. Therefore, any appreciable amount of MnIII, if formed, would be expected to be in a separate solid phase. At pH < 3, however, pure Mn_2O_3 is not stable thermodynamically in contact with MnO_2 (6). Consequently, it would be very unlikely to find any significant amount of MnIII in the electrode in contact with acid solution. The reduction, as examined under essentially equilibrium conditions, should then proceed from MnIV to MnII with negligible build-up of MnIII. At pH > 3, Mn_2O_3 is thermodynamically stable in equilibrium with MnO_2 as well as $Mn(OH)_2$. Thus, under open-circuit conditions, MnIII would be expected to exist in the electrode at various stages of discharge. The large variation in dA/dQ during the first half of the discharge argues that the MnIV

and MnIII are probably in the same solid phase in contact with the alkaline solution.

Acknowledgments

This research has been supported by the Consumer Products Division of the Union Carbide Corporation, and the Office of Naval Research. The authors are pleased to acknowledge their helpful discussions with Dr. A. Kozawa and other scientists at the Union Carbide Technical Center in Parma, Ohio.

Manuscript submitted May 4, 1973; revised manuscript received July 2, 1973.

Any discussion of this paper will appear in a Discussion Section to be published in the June 1974 JOURNAL.

REFERENCES

1. S. Yoshizawa and W. C. Vosburgh, *This Journal*, **104**, 399 (1957).
2. A. Kozawa and J. F. Yeager, *ibid.*, **112**, 959 (1965).
3. See for example, D. Boden, C. J. Venuto, D. Wisler, and R. B. Wylie, *ibid.*, **114**, 415 (1967).
4. S. Geschwind, P. Kislink, M. P. Klein, J. P. Remeika, and D. L. Wood, *Phys. Rev.*, **126**, 1684 (1962).
5. A. B. P. Lever, "Inorganic Electronic Spectroscopy," pp. 290-297, American Elsevier Publishing Co., Inc., New York (1968).
6. Marcel Pourbaix, "Atlas of Electrochemical Equilibria," p. 290, (English Edition) Pergamon Press, Oxford, England (1966).

Deposition of Silver on Platinum in Lithium Chloride-Potassium Chloride Eutectic

Wishvender K. Behl*

Power Sources Technical Area, U. S. Army Electronics Technology and Devices Laboratory (ECOM), Fort Monmouth, New Jersey 07703

Recently, Hills and co-workers (1) reported a study of monolayer formation as well as metal deposition processes for Ni(II) and Ag(I) on platinum electrodes in lithium chloride-potassium chloride eutectic at 400°C using the chronopotentiometric, cyclic voltammetric, and potential step techniques. Cyclic voltammograms for the reduction of Ni(II) at fast scan rates ($\geq$8 V/sec) showed a prepeak corresponding to the monolayer formation at potentials ~0.5V positive to the main cathodic peak. Similarly, on the reverse scans at these scan rates, the main anodic peak due to the dissolution of the deposited nickel metal was followed by a small anodic peak due to the removal of the monolayer. At slow scan rates (<8 V/sec), only one cathodic peak and one anodic peak were observed due to the deposition and dissolution of nickel metal, respectively. The deposition of silver, on the other hand, was complicated by the presence of a prepeak at potentials ~0.1V positive to the main cathodic peak at all scan rates resulting in drawn out voltammograms. Further, on the reverse scans, only one anodic peak due to the dissolution of the deposited silver metal was observed at all scan rates.

The deposition of silver at platinum electrodes in lithium chloride-potassium chloride eutectic at 450°C was also studied in this laboratory employing the technique of cyclic voltammetry. Except for the temperature of 450°C [400°C in case of Hills *et al.* (1)], these studies were carried out at about similar Ag(I) concentrates as well as voltage scan rates. At slow scan rates (<2 V/sec), unlike Hills *et al.* (1), only one cathodic and one anodic peak were observed due to the deposition and dissolution of silver metal, respectively. At fast scan rates (>2 V/sec), a prepeak at potentials ~0.5V positive to the main cathodic peak was observed due to the monolayer formation. The deposition of silver in our studies was found to be similar to the deposition of nickel as reported by Hills and co-workers (1). This note summarizes our results and also examines in detail the applicability of theory of linear sweep voltammetry (2, 3) to the reduction of Ag(I) in lithium chloride-potassium chloride eutectic at 450°C.

Experimental

The cell assembly, the experimental details for the preparation and purification of the lithium chloride-potassium chloride eutectic, and the instrumentation have been described earlier (4). The eutectic solvent was compartmented by use of Pyrex tubes (10 mm diameter) with fritted-glass bottoms. A three-electrode system was used for all measurements. The Pt/Pt(II) system was used as the reference electrode and a graphite rod as the counterelectrode. The indicator electrode consisted of a 0.5 mm diameter platinum wire sealed into a 6 mm diameter Pyrex or soda-lead glass (Corning 0120) tubing so that a 5 mm length of the wire protruded from the seal. The exact length of the exposed wire was measured by optical micrometry. The Pt(II) concentration (0.02M) in the reference compartment and Ag(I) concentration in the indicator compartment were generated by anodic dissolution of high purity platinum foil and silver rod, respectively, at a current density of 2-3 mA/cm^2. The exact metal ion concentration was determined at the end of the experiment by weighing the eutectic in each compartment and was expressed in moles/liter. The density value (5) of 1.648 g/ml at 450°C for the lithium chloride-potassium chloride eutectic was used.

Results and Discussion

Cyclic voltammograms for Ag(I) concentrations of 7.44, 11.90, 14.88, and 18.60 mM were recorded at scan rates of 0.033-100 V/sec. Typical voltammograms for 11.90 mM solutions of Ag(I) at scan rates of 0.05 and 20 V/sec are shown in Fig. 1. The scans were started in the cathodic direction at the working electrode potential of −0.2V *vs.* Pt/Pt(II) reference, and the direction of polarization reversed at the working electrode potential of −1.2V *vs.* Pt/Pt(II) reference. At the end of each scan, the potential of the working electrode was held at −0.2V *vs.* Pt/Pt(II) reference for a few minutes and the solution stirred before taking the next voltammogram.

At scan rates of 0.033-2.0 V/sec, only one cathodic and one anodic peak were observed due to the deposition and dissolution of silver metal, respectively. Hills and co-workers (1) reported a prepeak at potentials ~0.1V positive to the main cathodic peak at similar scan rates and Ag(I) concentrations. In our experiments, no such prepeak was observed at scan rates less than 2V/sec. However, a small prepeak at potentials ~0.5V positive to the main reduction peak was observed at higher scan rates (>2 V/sec). The deposition of silver is thus similar to the deposition of nickel reported by Hills and co-workers (1), and the prepeak

* Electrochemical Society Active Member.

Key words: cyclic voltammetry, electrodeposition, lithium chloride-potassium chloride eutectic, monolayer, silver.

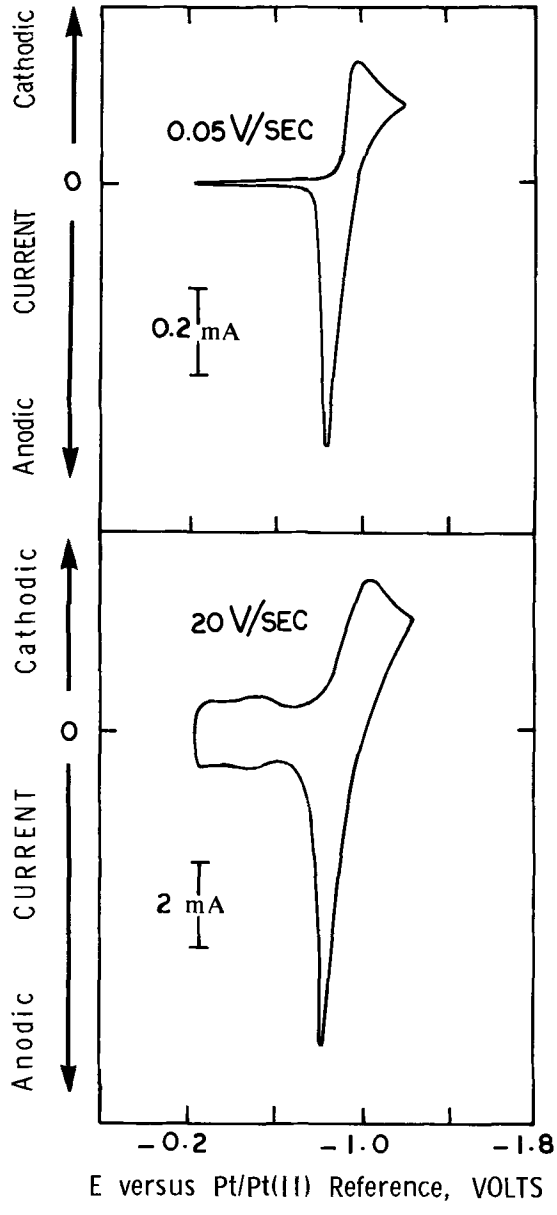

Fig. 1. Cyclic voltammograms for the reduction of 11.9 mM solutions of silver chloride at scan rates of 0.05 and 20 V/sec.

at fast scan rates may be regarded as due to the monolayer formation. Thus, analogous to the behavior of nickel (1), by reversing the direction of polarization after the main reduction peak, the main anodic peak due to the dissolution of deposited silver metal is followed by a small peak due to the removal of the monolayer. No such anodic peak for the removal of the monolayer was observed by Hills *et al.* (1) in the case of silver at all scan rates.

The peak currents for the reversible deposition of an insoluble substance at 450°C are given by the equation (2, 6)

$$i_p = 236n^{3/2}ACV^{1/2}D^{1/2} \qquad [1]$$

where i_p is the peak current (amperes), n is the number of electrons in the charge transfer step, A is the area of the electrode (cm^2), C is the concentration (moles/liter), V is the voltage scan rate (V/sec), and D is the diffusion coefficient (cm^2/sec).

Assuming that the activity of the deposited silver metal remains constant and equal to unity, the peak potential (E_p) (2, 6) and half-peak potential ($E_{p1/2}$) (7) are related to Ag(I) concentration and to each other by the following equations

$$E_p = E^\circ + \frac{RT}{n\mathbf{F}} \ln fC - \frac{0.854\,RT}{n\mathbf{F}} \qquad [2]$$

$$E_{p1/2} = E^\circ + \frac{RT}{n\mathbf{F}} \ln fC - \frac{0.0815\,RT}{n\mathbf{F}} \qquad [3]$$

$$\Delta E = E_p - E_{p1/2} = -\frac{0.7725\,RT}{n\mathbf{F}} \qquad [4]$$

where E° is the standard electrode potential, f is the activity coefficient of silver chloride in solution, and R, T, and $\mathbf{F}$ have their usual thermodynamic significance. Thus, the peak and half-peak potentials (E_p and $E_{p1/2}$) are dependent on Ag(I) concentration and shift to more anodic values as the concentration is increased. The difference between the peak and half-peak potentials (ΔE), on the other hand, is independent of the concentration. For a reversible process, E_p, $E_{p1/2}$, and ΔE are all independent of the voltage scan rate.

The reduction of Ag(I) leads to the deposition of solid silver metal and is thus similar to the deposition of an insoluble substance. The peak currents would, therefore, be given by Eq. [1]. The peak currents were determined by extrapolating the residual part of the voltammograms to the peak potential and measuring the height between this base line and the peak of the voltammograms. As predicted by Eq. [1], the plots of peak currents (i_p) *vs.* the square root of voltage scan rate ($V^{1/2}$) resulted in straight lines passing through the origin (Fig. 2). This linear relation was observed up to a scan rate of 0.5 V/sec. At higher scan rates, the peak currents tended to be lower than those predicted by Eq. [1]. Although Hills *et al.* (1) also observed straight line i_p *vs.* $V^{1/2}$ plots for the reduction of Ag(I), their plots did not pass through the origin.

The anodic dissolution of silver metal is unlikely (1, 8) to be diffusion controlled and thus the anodic current increases until all the deposited metal is stripped. The anodic peak is, therefore, very sharp and the anodic peak height is much greater than the cathodic peak height. However, from an integration of the current under the main cathodic and anodic peaks, it was found that the coulombs of charge deposited during the cathodic process were completely recovered during the anodic process.

The peak and half-peak potentials of Ag(I) reduction voltammograms were measured at all concentrations and scan rates and the data for one concentration are summarized in Table I.

The difference, ΔE, between the peak and half-peak potentials was found to be of the order of 45-50 mV up to a scan rate of 0.5 V/sec as compared to the theoretical value of 48 mV predicted by Eq. [4] for the reversible deposition of an insoluble substance at the electrode surface involving a one-electron change at

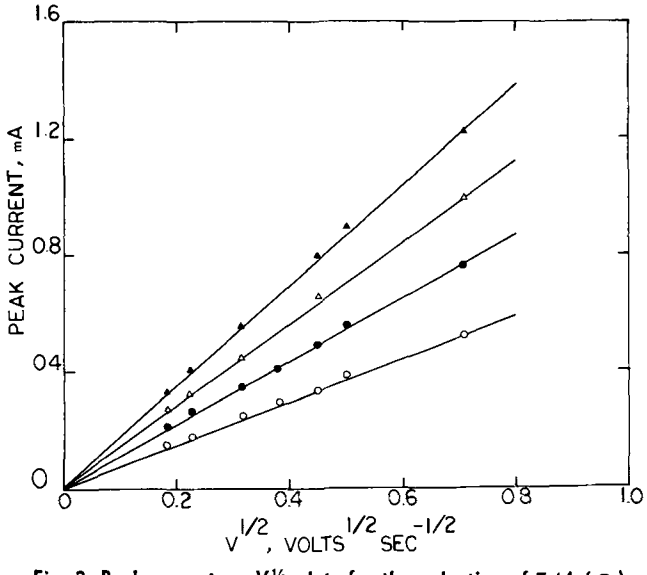

Fig. 2. Peak current *vs.* $V^{1/2}$ plots for the reduction of 7.44 (○), 11.9 (●), 14.88 (△), and 18.6 (▲) mM solutions of silver chloride.

Table I. Peak and half-peak potential data for the reduction of Ag (I) in lithium chloride-potassium chloride eutectic at 450°C

Concentration (mM/liter)	Scan rate (V/sec)	E_p (V)	$E_{p1/2}$ (V)	$(E_p - E_{p1/2})$ (V)
11.90	0.03	−0.975	−0.925	−0.050
	0.05	−0.975	−0.930	−0.045
	0.10	−0.975	−0.925	−0.050
	0.14	−0.975	−0.925	−0.050
	0.20	−0.975	−0.925	−0.050
	0.25	−0.970	−0.920	−0.050
	0.50	−0.980	−0.930	−0.050
	1.0	−0.980	−0.925	−0.055
	2.0	−0.985	−0.920	−0.065
	5.0	−1.000	−0.920	−0.080
	10	−1.020	−0.910	−0.110
	20	−1.030	−0.885	−0.145

450°C. Further, up to a scan rate of 0.5 V/sec, E_p, $E_{p1/2}$, and ΔE were all found to be independent of the voltage scan rate. The peak and half-peak potentials shifted to more positive values with increase in Ag(I) concentration and a plot of $E_{p1/2}$ *vs.* log *C* (Fig. 3) resulted in a straight line with theoretical slope as predicted by Eq. [3]. The plot of $E_{p1/2}$ *vs.* log *C* shown in Fig. 3 was extrapolated to 1M concentration of Ag(I) and the $E_{p1/2}$ value so obtained was substituted in Eq. [3] to obtain the E° value for the Ag(I)-Ag(O) couple *vs.* the 0.02M platinum reference. It was assumed that the activity coefficient of silver chloride remains constant over the concentration range studied and the activity coefficient term in Eq. [3] is included as a constant in the E° value. The E° value so obtained was then converted to 1.0M platinum reference using the Nernst equation. The standard electrode potential, E°, for the Ag(I)-Ag(O) couple was found to be −0.771V *vs.* 1.0M platinum reference and is in fairly good agreement with the value of −0.743V obtained by Laitinen and Liu (9) from the equilibrium emf measurements.

From the results presented above, it can be concluded that the reduction of Ag(I) in molten lithium chloride-potassium chloride eutectic occurs reversibly up to a voltage scan rate of 0.5 V/sec. At higher scan rates, the voltammograms tend to be more drawn out so that the difference between the peak and half-peak potentials is larger than that predicted by Eq. [4]. Also, the peak currents tend to be lower than those predicted by Eq. [1]. At lower scan rates, Eq. [1] can be used to calculate the diffusion coefficient of Ag(I) in this solvent. For this purpose, the $i_p/V^{1/2}$ values were obtained from the linear i_p *vs.* $V^{1/2}$ plots and substituted in Eq. [1] to calculate the peak current constants ($K_p = i_p/V^{1/2}AC$) as well as diffusion coefficients (D) at various Ag(I) concentrations in the eutectic. These results are summarized in Table II. The constancy of the K_p values presented in Table II clearly demonstrates the linear dependence of peak currents on the Ag(I) concentration as predicted by Eq. [1]. The average peak current constant and diffusion coefficient were found to be 1.16($10^3 A$ $sec^{1/2}$ $V^{-1/2}$ cm/mole) and 2.39 × 10^{-5} (cm^2/sec), respectively. The value of the diffusion coefficient obtained in our study is in good agreement with the previously reported values of 2.5 × 10^{-5} (cm^2/sec) at 400°C (1), 2.6 × 10^{-5} (cm^2/sec) (10), and 3.2 × 10^{-5} (cm^2/sec) (11, 12) at 450°C.

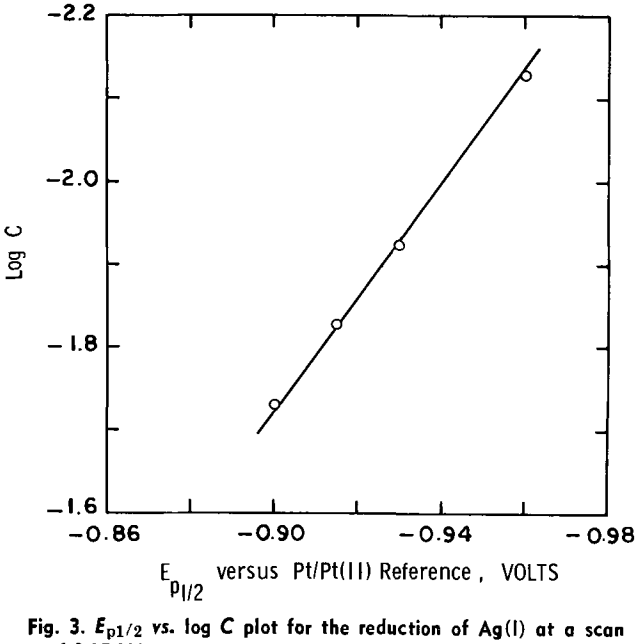

Fig. 3. $E_{p1/2}$ *vs.* log *C* plot for the reduction of Ag(I) at a scan rate of 0.05 V/sec

Table II. Peak current constants and diffusion coefficients of Ag(I) in lithium chloride-potassium chloride eutectic at 450°C[a]

Concentration × 10^3 (moles/liter)	10^3 × $i_p/V^{1/2}$ ($AV^{-1/2}$ $sec^{1/2}$)	Peak current constant $K_p = i_p/V^{1/2}AC$ (10^3 A $sec^{1/2}$ $V^{-1/2}$ cm/mole)	Diffusion coefficient × 10^5 (cm^2/sec)
7.44	0.73	1.20	2.57
11.90	1.09	1.12	2.24
14.88	1.41	1.16	2.40
18.60	1.74	1.14	2.34
		Average = 1.16	Average = 2.39
		Avg. dev. = ±0.025	Avg. dev. = ±0.10
		Std. dev. = ±0.035	Std. dev. = ±0.14

[a] Area of the electrode: 0.082 cm^2.

Summary and Conclusions

The deposition of silver on platinum in lithium chloride-potassium chloride eutectic was studied at 450°C employing the technique of cyclic voltammetry. It was shown that at low scan rates (0.033-0.5 V/sec), the reduction of Ag(I) occurs reversibly and obeys the equations for the reversible deposition of an insoluble substance. The diffusion coefficient of Ag(I) in lithium chloride-potassium chloride eutectic was determined from the experimental data and found to be 2.39 × 10^{-5} cm^2/sec. At higher scan rates (>2 V/sec), a prepeak due to the monolayer formation was observed at potentials about 0.5V positive to the main reduction peak. On reversing the direction of polarizations after the main cathodic peak at scan rates of >2 V/sec, the sharp anodic peak due to the dissolution of the deposited silver metal was followed by a relatively smaller peak due to the removal of the monolayer. At scan rates below 2 V/sec, no peaks were observed for the formation or removal of the monolayer.

Manuscript submitted May 4, 1973; revised manuscript received July 19, 1973.

Any discussion of this paper will appear in a Discussion Section to be published in the June 1974 JOURNAL.

REFERENCES

1. G. J. Hills, D. J. Schiffrin, and J. Thompson, *This Journal*, **120**, 157 (1973).
2. P. Delahay, "New Instrumental Methods in Electrochemistry," pp. 122-125, Interscience Publishers, Inc., New York (1965).
3. R. S. Nicholson and I. Shain, *Anal. Chem.*, **36**, 706 (1964).
4. W. K. Behl, *This Journal*, **118**, 889 (1971).
5. E. R. VanArtsdalen and I. S. Yaffe, *J. Phys. Chem.*, **59**, 118 (1955).
6. T. Berzins and P. Delahay, *J. Am. Chem. Soc.*, **75**, 555 (1953).
7. G. Mamantov, D. L. Manning, and J. M. Dale, *J. Electroanal. Chem.*, **9**, 253 (1965).
8. M. M. Nicholson, *J. Am. Chem. Soc.*, **79**, 7 (1957).
9. H. A. Laitinen and C. H. Liu, *ibid.*, **80**, 1015 (1958).
10. H. A. Laitinen and W. S. Ferguson, *Anal. Chim. Acta.*, **18**, 1 (1958).
11. C. E. Thalmayer, S. Bruckenstein, and D. M. Gruen, *J. Inorg. Nucl. Chem.*, **26**, 347 (1964).
12. I. I. Naryshkin, V. P. Yurkinskii, and P. T. Stangrit, *Elektrokhimiya*, **5**, 1476 (1969).

Electrogenerative Bromination

Alan D. Miller and Stanley H. Langer*

Department of Chemical Engineering, University of Wisconsin, Madison, Wisconsin 53706

As part of a program to identify and develop techniques for operating feasible electrogenerative processes (1-3), we describe here electrogenerative bromination in which bromine and an olefin are reacted with the aid of suitable electrodes and electrolyte to give dibromoethane and bromohydrin. (We define "electrogenerative processes" as those in which two or more materials react at electrodes so that favorable thermodynamic factors drive the reaction to give a useful chemical product with the generation of by-product electricity.) Bromine is reduced at the cathode to bromide ions which are transported through the electrolyte to the anode where they combine with olefin, while electrons are conducted through an external circuit to the cathode. Bromine vapor in a nitrogen gas stream and the olefin are introduced to cathode and anode chambers, respectively. The chambers are bounded by gas-permeable, liquid-impermeable electrodes separated by a free electrolyte phase. In contrast to earlier work on other electrogenerative systems (1-3), a diaphragm was needed to separate catholyte and anolyte. This limited the transport of free bromine, probably as Br_3^- and Br_5^- (4-6), which would give some direct chemical halogenation of olefin at the anode. Both electrodes operate at positive potentials relative to the standard hydrogen electrode. The rate of bromination and the potential of the cell are controlled by the electrical resistance of the external circuit.

Electrode reactions, based on product analyses, with bromide electrolyte appear to be

Cathode

$$Br_2 + 2e^- \rightarrow 2Br^- \qquad [1]$$

Anode

$$RCH{=}CHR' + 2Br^- \rightarrow \underset{\displaystyle Br}{\overset{\displaystyle |}{RCH}}\!\!-\!\!\underset{\displaystyle Br}{\overset{\displaystyle |}{CHR'}} + 2e^- \qquad [2]$$

or

$$RCH{=}CHR' + 2Br^- + H_2O \rightarrow \underset{\displaystyle Br}{\overset{\displaystyle |}{RCH}}\!\!-\!\!\underset{\displaystyle OH}{\overset{\displaystyle |}{CHR'}} + HBr + 2e^- \qquad [3]$$

No significant amount of glycol is formed in the electrolyte. Electrogenerative bromination requires no external power source.

Furthermore, we have also used chlorine gas instead of bromine vapor at the cathode where reaction is

$$Cl_2 + 2e^- \rightarrow 2Cl^- \qquad [4]$$

accompanied by

$$Cl_{2(aqueous)} + 2Br^- \rightarrow Br_{2(aqueous)} + 2Cl^- \qquad [5]$$

and

$$Br_{2(aqueous)} + 2e^- \rightarrow 2Br^- \qquad [6]$$

Chlorine gas sometimes can be used advantageously at the cathode because of ease of handling and convenience.

Experimental

A free electrolyte cell similar to that of Landi *et al.* (7) was used for all runs. It typically can be represented as

$$\underset{\text{Anode}}{\text{Olefin} \mid Br^-(aq.) \mid \text{Membrane} \mid Br^-(aq.) \mid Br_2}_{\text{Cathode}}$$

where the total free electrolyte chamber thickness varied from 0.25-0.5 in. The cell was constructed so that only the anode, Kel-F, and Teflon came in contact with the olefin. The free electrolyte chamber could be subdivided with diaphragms into two or three compartments. Kel-F inserts were used in the electrolyte chamber to thicken it and were sometimes fitted with inlet and outlet ports to permit electrolyte flow during operation.

The electrodes used were gas-permeable, liquid-impermeable commercial American Cyanamid Type LAA-1 (7). They have a platinum black loading of 9 mg/cm^2 on a 50 mesh tantalum screen and are wet proofed with Teflon. In later experiments, carbon-tetrafluoroethylene film electrodes (8), American Cyanamid LSE, were used on the halogen side of the cell. These electrodes were 95% graphitic carbon, 0.02 in. in thickness, had 45% porosity, and were supported on an open tantalum screen. All electrodes had an exposed area of 5.1 cm^2.

The electrolyte used in this study was generally 2 or occasionally 3M aqueous potassium bromide. A cell with electrolyte chamber ¼ in. thick and 2M KBr had an internal resistance of about 0.7 ohm in our cell configuration without a separator.

Diaphragms when used were either an AMFion Product anion with ion exchanger A60 (American Machine and Foundry Company) or an American Cyanamid TA-1 etched polytetrafluoroethylene flock. The former added considerably to cell resistance. For instance, a ¼ in. cell with 2M KBr electrolyte and membrane had a cell resistance of about 4 ohms. The (American Cyanamid) TA-1 membrane consisted of 95% polytetrafluoroethylene, 5% carbon. It is 0.63 mm in thickness and has an 80% porosity when wet with most pores having a diameter of 10 μm or less. A ¼ in. free electrolyte cell with 2M KBr electrolyte and a single TA-1 membrane gave an internal resistance of about 1.3 ohm. The A60 AMF ion exchange membrane was used as a separator, together with 3M KBr electrolyte, when electrode potentials were measured to minimize interference of molecular bromine or complexed bromide at the anode. This scheme is not desirable for ordinary cell polarization work because of the high internal resistance of the cell.

Cells were operated with continuous flow of reactive gases through anode and cathode compartments. Product analysis was by gas chromatography. Off gas from the anode compartment during operation at steady state was injected and the coulometric yield of 1,2 dibromoalkane was calculated from the chromatogram. The bromohydrin formed remained in the cell electrolyte because of its solubility in this aqueous phase. To close the material balance, a sample of electrolyte was converted to trimethylsilyl ethers and hexamethyldisiloxane (from water) with hexamethyldisilazane (9, 10). Conversion was effected by the refluxing of a 0.3 cm^3 sample of electrolyte with 5 cm^3 (50% excess) of hexamethyldisilazane for 13 hr. The reaction mixture was protected from the atmosphere with a drying tube attached to the reflux condenser. Ammonium salt that formed sublimed into the condenser. Acid is formed in the cell electrolyte during operation. When knowns for comparison were converted, a catalytic amount of acid, a few cubic centimeters of HCl vapor, was added to the reaction mixture.

The converted mixture was analyzed by means of gas chromatography (on silicone d.c. 550; chromosorb, W) to determine the yield of bromohydrin. Because electrolyte sometimes contained complexed bromine, it

* Electrochemical Society Active Member.

Key words: platinum electrodes, polarization, dibromoethane, bromohydrin.

was allowed to stand overnight to release this bromine before analysis was attempted. Closures of the material balance of 90% or generally better were obtained. This balance is important because it permits comparison of total product formed with coulombs generated by the electrogenerative cell. This permits identification of chemical reaction and of transport of molecular bromine from cathode to anode, probably complexed with bromide ion (4-6). Under conditions where bromine could be transported as a complex with bromide ion (in the absence of a diaphragm), product analyses indicated that such transport resulted in formation of dibromoethane.

Potentials of individual electrodes were measured on an operating ethylene-bromine cell with LAA-1 electrodes by referring the anode to a mercurous bromide (11, 12) electrode with a Luggin capillary. Other experimental details are given in our earlier description of electrogenerative chlorination (3).

Results and Discussion

Bromine-ethylene cells were operated with both an LAA-1 platinum electrode and an LSE carbon electrode at the cathode. The anode was always a platinum black electrode. When electrode potential measurements were made on an operating cell, the open-circuit potential for the cell was *ca.* 0.6V. This potential is reproducible with new cells but apparently is affected by the formation of Br_3^- ions and is not attained again after some operation of the cell. The bromine electrode was operated with nitrogen-saturated bromine (vapor pressure about 200 mm at 24°C). The potential of the bromine-bromide electrode under our operating conditions was 1.04V, in good agreement (within 0.002V) after conversion to standard-state conditions with the standard potential of 1.065V. The olefin electrode had a potential of 0.45-47V relative to the standard hydrogen electrode based on a mercury-mercurous bromide standard potential of 0.139V (11, 12).

The polarization curve for an ethylene-bromine cell with 2M KBr free electrolyte (5/16 in. thick) and a TA-1 membrane separator is shown in Fig. 1. This cell used an LSE carbon electrode as the cathode. An LSE carbon electrode was also operated as a bromide electrode with varying current, referenced to a mercurous bromide electrode, in a concentration cell arrangement

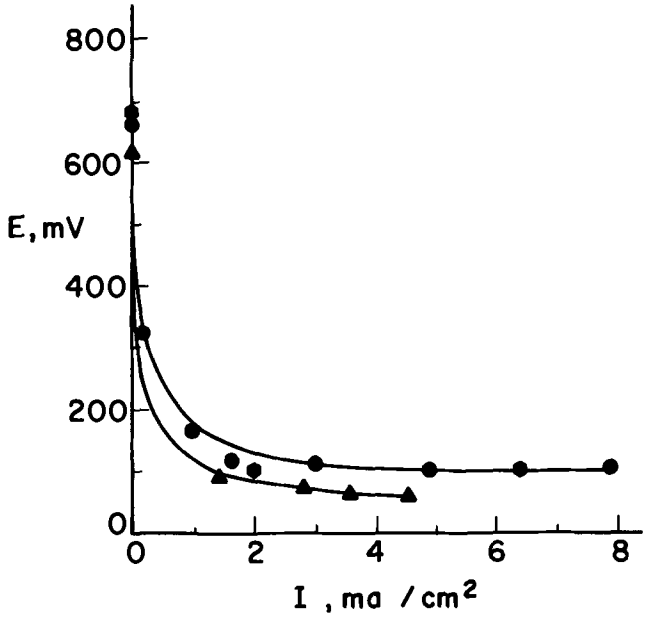

Fig. 1. Current density-cell voltage, E, curves (*IR* corrected), LAA-1 (platinum black) anodes, LSE (carbon) cathodes, TA-1 diaphram; 2M KBr aqueous electrolyte. ●, C_2H_4/KBr(2M)//KBr (2M)/Cl_2; ▲, C_2H_4/KBr(2M)//KBr (2M)/Br_2; ⬢, C_3H_6/KBr(2M)// KBr (2M)/Cl_2.

with an LAA-1 platinum counterelectrode and 2M KBr electrolyte. The carbon-bromine electrode showed polarization of less than 0.01V at currents up to 15 mA/cm². Considering this study, as well as results from the cell with LAA-1 electrodes, it is apparent that practically all polarization occurs at the anode or ethylene electrode.

Because of the ease of handling chlorine at room temperature and the fact that it is commercially significantly less expensive than bromine, we tested cells that incorporated a chlorine cathode, a 2M potassium bromide electrolyte, a separator, and an ethylene anode. These cells generally were operated either with flow or for a short enough period so that chloride ion was not discharged. The polarization curve for such a static cell run for a period of time of less than 1 hr is included in Fig. 1. The change in cell operating potential essentially is due to a shift in potential at the cathode. Under our conditions the cathode operated at a potential range of 1.09-1.11V relative to a standard hydrogen electrode. This potential rises with time toward the chlorine-chloride electrode potential, of course.

With the use of flowing electrolyte cells, it was possible to study, over a limited range, the effect of potential on reaction at the anode. In the potential region of 0.8-1.05V at the anode, and current densities of 0.2-10 mA/cm², dibromoethane was found to represent 20 ± 2% of the electrogenerated current. Both two-compartment and three-compartment cells were used in flow experiments which involved sweeping the center or cathode compartment with electrolyte so that the 2M KBr electrolyte was changed every 15 min. The remainder of the generated current resulted in the formation of ethylene bromohydrin. This was ascertained by collection of the electrolyte from a static cell run for a period of time less than 1 hr. Under these conditions, only bromohydrin was found in the electrolyte (*i.e.*, no chlorohydrin or glycol was detected), suggesting that the reaction proceeds through a $BrCH_2CH_{2Adsorbed}$ species.

With a mixed chloride-bromide electrolyte, dibromo-, bromo-chloro-, and some small amount of dichloro-compounds (after periods of operation greater than 2 hr) were observed in the off gas. The relative amounts of chloro-compounds could be controlled to some degree by variation of the ratio of chloride to bromide in the electrolyte. Under these conditions, as might be expected from the ethylene electrode operating potential, bromo-compounds tend to predominate. For instance, in a crude experiment with 1M KBr-1M KCl electrolyte, dihaloalkanes were separated in the ratio dibromoethane-2, chlorobromoethane-1, at a potential of 0.3V and 2 mA/cm².

Polarization data for a propylene-chlorine cell with 2M potassium bromide electrolyte and a TA-1 membrane are also represented in Fig. 1. This cell was somewhat more difficult to study because of the relatively low vapor pressure of dibromopropane. In order to insure vaporization of this compound, the propylene flow rate through the anode compartment was increased to the point where only 2% conversion took place. At 0.91V *vs.* S.H.E. and 10 mA/cm², 21% of the calculated amount of dibromopropane was recovered based on generated current. Within the accuracy of our material balance, the remaining corrected propylene apparently formed propylene bromohydrin. Some propylene glycol, of the order of 5%, was detected but this appears to stem from chemical hydrolysis of propylene bromohydrins during conversion to trimethylsilyl ethers; we found this glycol at the same concentration when analyzing a known commercial sample of propylene bromohydrin.

We are continuing work in this area with the objective of controlling the reaction product at the anode. Nevertheless, the high yield and facile formation of bromohydrin (of the order of 80%) is of interest since these materials are prospective intermediates for formation of olefin oxides (13). The selective formation of

alkyl bromides relative to chlorides suggests potential utilization of electrode reactions similar to those reported here as a means of selectively recovering bromide ion from mixed salts.

Acknowledgment

We thank the University of Wisconsin Alumni Research Foundation, the Continental Oil Company, and the Union Carbide Corporation for support of this work.

Manuscript submitted March 9, 1973; revised manuscript received July 9, 1973.

Any discussion of this paper will appear in a Discussion Section to be published in the June 1974 JOURNAL.

REFERENCES

1. S. H. Langer, and H. P. Landi, *J. Am. Chem. Soc.*, **86**, 4694 (1964).
2. S. H. Langer, I. Feiz, and C. P. Quinn, *ibid.*, **93**, 1092 (1971).
3. S. H. Langer, and S. Yurchak, *This Journal*, **117**, 510 (1970).
4. A. I. Popov, "Halogen Chemistry," Vol. 1, Academic Press, London (1967).
5. D. B. Scaife, and H. J. V. Tyrrell, *J. Chem. Soc.*, **1958**, 386.
6. T. Iwasita, and M. C. Giordano, *Electrochim. Acta*, **14**, 1045 (1969).
7. H. P. Landi, U. S. Pat. 3,407,096 (1968).
8. H. P. Landi, J. D. Voorhies, and W. A. Barber, in "Fuel Cell Systems II," Advances in Chemistry Series 90, American Chemical Society, Washington, D. C. (1969).
9. S. H. Langer, S. Connell, and I. Wender, *J. Org. Chem.*, **23**, 50 (1958).
10. S. H. Langer, R. A. Friedel, I. Wender, and A. G. Sharkey, Jr., *Anal. Chem.*, **30**, 1353 (1958).
11. W. R. Crowell, R. W. Mertes, and S. S. Burke, *J. Am. Chem. Soc.*, **64**, 3021 (1942).
12. W. D. Larson, *ibid.*, **62**, 764 (1940).
13. N. Ibl and A. Selvig, *Chem.-Ing. Tech.*, **42**, 180 (1970).

The Thermal Decomposition of Potassium Oxalate in Fused Nitrates

A. G. Keenan and Carlos G. Fernandez

Department of Chemistry, University of Miami, Coral Gables, Florida 33124

Electrochemical studies of oxide ion and of various oxide electrodes in fused salts have been of considerable interest for some time. Numerous methods for adding oxide ion to nitrate melts have appeared in the literature (1-3). Swofford and McCormick (4, 5) recommend potassium oxalate because of the purity and ease of weighing the chemical. In sodium potassium nitrate eutectic above 280° they give, for the decomposition, the equation

$$C_2O_4^{2-} \rightarrow CO_2 + CO + O^{2-} \quad [1]$$

Other workers (6-8), however, have given quite a different equation for the reaction, namely

$$C_2O_4^{2-} + NO_3^- \rightarrow CO_3^{2-} + CO_2 + NO_2^- \quad [2]$$

Carbonate ion is a product instead of oxide, and a second electroactive species, nitrite, is produced in addition.

A careful examination of the above references shows that in no case was an unequivocal quantitative confirmation of the respective stoichiometries carried out despite statements implying the contrary.

In the course of continuing our previous electrochemical studies in nitrate melts (9-11), we have now shown that reaction [2] is the correct one in potassium nitrate at 350°C. This stoichiometry is maintained for reaction times varying from 1 to 12 hr.

Experimental

All chemicals used were reagent grade and were oven-dried at 110°C at least 24 hr before being used. KNO_3 was vacuum-dried at 130° for 24 hr and then kept in oven at 110° until needed.

Carbonate determination.—To a test tube containing 5g KNO_3, which had been kept molten for 12 hr at 350°, a weighed pellet of $K_2C_2O_4$ was added and allowed to react for various times. The melt was then frozen, dissolved in boiled distilled water, and titrated with standard HCl, using phenolphthalein and methyl red as indicators.

The typical weak-base titration curve obtained with two distinct end points leaves no doubt that carbonate was the base present. The volume of titrant required for neutralization to the first end point was identical within experimental error to the volume from the first to the second end points. This shows that the only base was carbonate. In a series of four replicate experiments the mole ratio of carbonate obtained to oxalate added was 1:1 within 0.2%.

Nitrite determination.—A stock solution of $K_2C_2O_4$ in molten KNO_3 was prepared. After different reaction times, a sample was withdrawn, frozen, weighed, and dissolved in 50 ml of distilled water. This solution was then analyzed for nitrite, using the method of Wetters and Uglum (12). This consists of the determination of the absorbance of a solution of nitrite and nitrate at 355 nm. At this wavelength nitrate does not interfere with the nitrite absorbance. The molar absorptivity of nitrite is 23.3. A Cary Model 17 spectrometer was used.

Again, in a series of five replicate experiments, it was found that 1 mole of nitrite was produced per mole of oxalate added. The error of the analysis was shown to be about 3% using known mixtures of nitrite and nitrate.

Carbon dioxide determination.—KNO_3 melts containing known amounts of oxalate were allowed to decompose in an evacuated apparatus and the gas produced was expanded into a 10 cm *IR* cell. Qualitative analysis with a Beckman IR 10 spectrometer showed a strong CO_2 peak but no trace of CO. For a more sensitive test, samples of the gas were also run on a Consolidated Electrodynamics Corporation Type 21-103C mass spectrometer.

No trace of CO was found within the sensitivity of the spectrometer which is about 0.1%.

Carbon dioxide was determined quantitatively by expanding the product gas into a volumetric apparatus and measuring the temperature and pressure. Using standard gas laws, the 1:1 stoichiometry was checked within the experimental accuracy of about 8%.

Acknowledgment

This work was supported by a contract from the Office of Naval Research, Material Sciences Division, Power Program.

Manuscript received May 21, 1973.

Key words: oxide electrode, fused nitrates, oxalate decomposition, oxide, carbonate.

Any discussion of this paper will appear in a Discussion Section to be published in the June 1974 JOURNAL.

REFERENCES

1. R. N. Kust, *Inorg. Chem.*, **3**, 1035 (1964).
2. R. M. Novik and Yu S. Lyalikov, *Zh. Anal. Khim*, **13**, 691 (1958).
3. A. M. Shams El Din, *Electrochim. Acta*, **9**, 613 (1964).
4. H. S. Swofford and P. G. McCormick, *Anal. Chem.*, **37**, 970 (1965).
5. P. G. McCormick and H. S. Swofford, *ibid.*, **41**, 146 (1969).
6. A. M. Shams El Din, *Electrochim. Acta*, **13**, 135 (1968).
7. E. A. El Hosary and A. M. Shams El Din, *J. Electroanal. Chem.*, **30**, 33 (1971).
8. J. M. Schlegel and C. A. Pitak, *J. Inorg. Nucl. Chem.*, **32**, 2088 (1970).
9. K. Notz and A. G. Keenan, *J. Phys. Chem.*, **70**, 662 (1966).
10. A. G. Keenan, K. Notz, and F. L. Wilcox, *ibid.*, **72**, 1085 (1968).
11. A. G. Keenan and W. H. Duewer, *ibid.*, **73**, 212 (1969).
12. J. M. Wetters and K. L. Uglum, *Anal. Chem.*, **42**, 335 (1970).

DISCUSSION SECTION

This Discussion Section includes discussion of papers appearing in the *Journal of The Electrochemical Society*, Vol. 119, No. 7, 8, and 12; July, August, and December 1972; Vol. 120, No. 2 and 6; February and June 1973.

Corrosion Kinetics of Iron in Acid Sulfate Solutions. Effects of Impurities in the Metal

S. Barnartt (pp. 812-817, Vol. 119, No. 7)

W. J. Lorenz and A. A. El Miligy:[1] In the paper under discussion, Barnartt's investigations using nonsteady-state galvanostatic pulse measurements in the case of the anodic dissolution of pure zone refined iron and iron containing impurities are important, because they deal with the problem of superpolarization. It is well known that pure iron, with a low density of crystal imperfections, dissolves in oxygen-free acid solutions containing no surface active substances in accordance with the noncatalyzed (Bockris-) mechanism as described in the literature.[2,3] The appearance of anodic superpolarization in such a case of consecutive reaction mechanism was explained by (*i*) the diffusion of protons into the bulk of the solutions, which protons are formed in the first step of the noncatalyzed mechanism, which has a relatively high exchange current density;[4] (*ii*) the time-dependent formation of an intermediate in the case of a consecutive charge transfer-mechanism;[3,5-9] and (*iii*) crystallization steps, *e.g.*, formation of negative nuclei, kinks, or adatoms and the surface diffusion of adatoms.[10,11]

However, our investigations[12] using rotating-disk electrodes showed that the first explanation cannot be taken into consideration. Heusler arrived also to the same conclusion.[13] Also, the second possibility is not valid in the case of pure iron dissolution. We have found that the appearance of a steady-state anodic Tafel slope of $b_+ = +40$ mV implies that $i_{0,1} >> i_{0,2}$. Following the theory of the consecutive charge-transfer mechanism, anodic superpolarization cannot occur below a certain critical overpotential value.[3,5-9] This would contradict experimental results. Therefore the last explanation is the most probable one.

We think it is necessary to make some remarks regarding Barnartt's results as well as his conclusions in the paper being discussed.

(*i*) The considerable increase of the corrosion potential and the corrosion current density during the first 20 hr was not confirmed by our investigations in the systems of pure iron (various types)/H_2SO_4 or $HClO_4$. The steady-state corrosion current density agrees, however, with the reported data for pure iron. Therefore, it is possible that the pretreatment of the electrode in Barnartt's investigation produces some surface coverages with oxygen and/or anions.

(*ii*) Barnartt states that the superpolarization value $\Delta\epsilon_m$ is always greater than that corresponding to the open-circuit value $\Delta\epsilon_{oc}$. We have studied systematically the anodic superpolarization and open-circuit phenomena on iron in relation to pulse duration and pulse height. From this it has been found that Barnartt's statement is right for his applied pulse durations and current densities. However, Fig. 1 shows that the inverse relationship occurs for shorter pulse durations. These values were measured in the system pure ommet-iron (total impurities $\leq$ 300 ppm)/0.5M H_2SO_4 at 298°K using a multichannel pulse galvanostat (MEGA-PHYSIK, Rastatt, Germany) with a rise time of 10^{-7} sec. The charging of the double layer was completed and the maximum superpolarization value was reached in a time which is always smaller than the first point in each $\Delta\epsilon_{oc}$ curve of Fig. 1. The ohmic drop was always separately eliminated in these measurements.

(*iii*) The time necessary for reaching the maximum superpolarization value decreases with increasing pulse height. Whereas in the case of the open-circuit measurements, the time necessary to reach the minimum potential is longer and practically independent of the pulse height and pulse duration, *i.e.*, 50 ± 20 msec. An example is given in Fig. 2. The difference between this minimum potential and the steady-state corrosion potential increases with increasing pulse height and pulse duration. The slow attainment of the corrosion potential will be mainly due to surface diffusion processes of adatoms and diffusion of Fe^{2+} ions into the bulk of the electrolyte.

(*iv*) Barnartt's anodic Tafel slopes of $b_+ = +65 \ldots +69$ mV obtained from open-circuit measurements are

[1] Institut für Physikalische Chemie und Elektrochemie der Universität Karlsruhe, Germany.

[2] F. Hilbert, Y. Miyoshi, G. Eichkorn, and W. J. Lorenz, *This Journal*, **118**, 1919 (1971).

[3] H. Rosswag, G. Eichkorn, and W. J. Lorenz, Submitted to *Z. Physik. Chem. NF.*

[4] J. O'M. Bockris and H. Kita, *This Journal*, **108**, 676 (1961).

[5] I. H. Plonski, *ibid.*, **116**, 944 (1969); *ibid.*, **116**, 1688 (1969).

[6] I. H. Plonski, *ibid.*, **117**, 1048 (1970).

[7] I. H. Plonski, *Rev. Roumaine Phys.*, **16**, 449 (1971); *ibid.*, **16**, 467 (1971); *ibid.*, **16**, 875 (1971); *ibid.*, **16**, 979 (1971); *ibid.*, **16**, 989 (1971).

[8] H. C. Albaya and W. J. Lorenz, *Z. Physik. Chem. NF.*, **82**, 277 (1972).

[9] J R. Vilche, H. C. Albaya, F. Hilbert, and W. J. Lorenz, *ibid.*, **82**, 277 (1972).

[10] J. O'M. Bockris and G. A. Razumney, "Fundamental Aspects of Electrocrystallization," p. 39, Plenum Press, New York (1967).

[11] H. R. Thirsk and J. A. Harrison, "A Guide to the Study of Electrode Kinetics," p. 115, Academic Press, London and New York (1972).

[12] W. J. Lorenz, Unpublished results.

[13] K. E. Heusler, "Elektrochemische Auflösung und Abscheidung von Metallen der Eisengruppe," Habilitationsschrift TH, Stuttgart (1966).

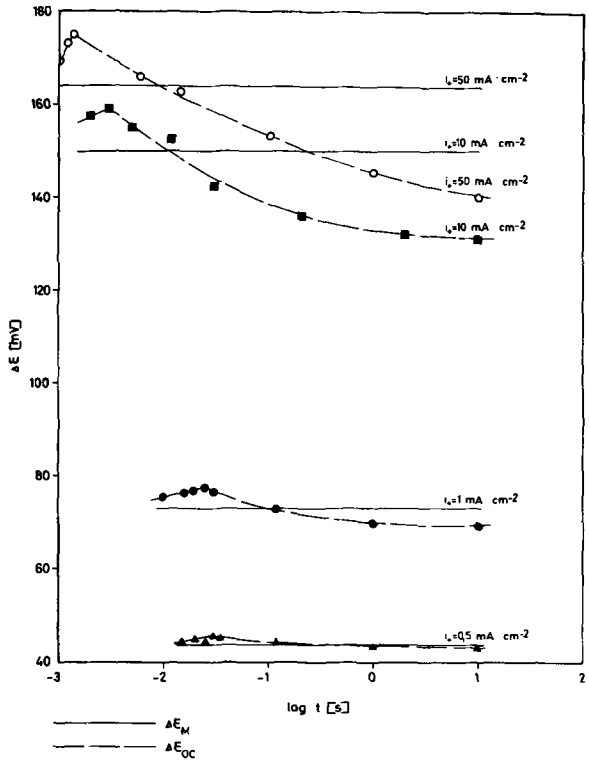

Fig. 1. Potential values of superpolarization maximum, $\Delta\epsilon_M$, and open-circuit minimum, $\Delta\epsilon_{OC}$, as a function of galvanostatic pulse height and pulse duration. System: Fe/0.5M H_2SO_4; $T = 298°K$.

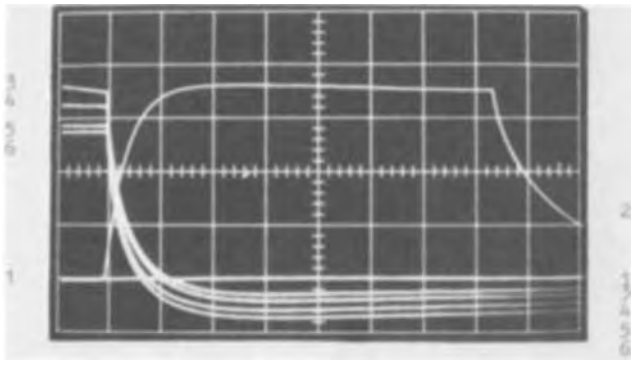

Fig. 2. Potential time dependence for galvanostatic pulse measurements with a pulse height of $i_+ = 1$ mA/cm^{-2} and various pulse durations. System: Fe/0.5M H_2SO_4; $T = 298°K$. 1, Steady-state corrosion potential ϵ_{corr}; 2, determination of $\Delta\epsilon_M$, $t = 37$ msec, ordinate is 20 mV/cm^{-1}, abscissa is 5 msec/cm^{-1}; 3, $t = 30$ msec, ordinate is 20 mV/cm^{-1}, abscissa is 20 msec/cm^{-1}; 4, $t = 120$ msec, ordinate and abscissa as in 3; 5, $t = 1020$ msec, ordinate and abscissa as in 3; 6, $t = 10{,}020$ msec, ordinate and abscissa as in 3.

typical of nonsteady-state values, which agrees with earlier results based on $\Delta\epsilon_m$ values.[2] This is due to relatively small variations between $\Delta\epsilon_m$ and $\Delta\epsilon_{oc}$ in the range of applied current density and pulse duration. If the pulse height and the pulse duration are relatively high, Fig. 1 shows that these variations would increase. In this case

$$b_{+,\,\text{steady-state}} < b_{+,\,\Delta\epsilon_{oc}} < b_{+,\,\Delta\epsilon_m}$$

However, in the case of shorter pulse durations the following sequence results

$$b_{+,\,\text{steady-state}} < b_{+,\,\Delta\epsilon_m} < b_{+,\,\Delta\epsilon_{oc}}$$

Therefore one must be careful in interpretations of results only based on galvanostatic, open-circuit measurements.

(*v*) The open-circuit technique and the interpretation of $\Delta\epsilon_{oc}$ implies that the reference state is of certain surface activity which corresponds to the charging conditions. Consequently for different charging conditions the reference point varies. Usually the surface activity of a metal electrode at the corrosion potential in the steady state is taken as the reference point. Under this condition the nonsteady-state $\Delta\epsilon_m$ values are related to a nearly constant reference point.

(*vi*) The roughness of the electrode surface is another factor which influences the reference state and the interpretation of the $\Delta\epsilon_{oc}$ values. Capacity measurement with rapidly galvanostatic pulses in the microsecond range can be used as an indication of the roughness of the electrode surface before and after anodic polarization at a certain potential. This has been carried out at the steady-state corrosion potential and after anodic polarization in the minimum potential value of the open-circuit measurement, whereby the pulse height and its duration were varied. The results show an increase of about 10-15%, *e.g.*, from 35 up to 40 μF/cm^{-2}. In other words, the electrode surface in the two mentioned states is not the same, but the differences are not very high. On the other hand, during anodic polarization the electrode capacity increases due to its dependence on the electrode potential.[14,15]

The conclusions from these remarks are that definite interpretations of $\Delta\epsilon_{oc}$ measurements are difficult as long as quantitative explanation of the observed superpolarization phenomena based on crystallization processes does not exist.

S. Barnartt: Studies of anodic pulses at relatively high current densities, such as the data in Fig. 1 of Lorenz and El Miligy's discussion above, are very helpful. Further studies at high current densities are necessary before a mechanistic interpretation of superpolarization, of the maximum potential change $\Delta\epsilon_m$, and of apparent steady-state potentials can be established.

In the paper under discussion a constant $\Delta\epsilon_{oc}$, independent of pulse length, was obtained up to $\Delta\epsilon_{oc} = 60$ mV. I observed also that at higher potentials $\Delta\epsilon_{oc}$ decreased with increasing pulse time, in agreement with Fig. 1 above of Lorenz and El Miligy. An important feature of such high current density pulses is that the corrosion potential ϵ^* drifts markedly with succeeding pulses, so that an anodic Tafel line corresponding to a fixed surface activity is unattainable.

Good agreement between $\Delta\epsilon_{oc}$ and $\Delta\epsilon_m$, as shown by Lorenz and El Miligy in the above discussion at $\Delta\epsilon \simeq 45$ mV, was found in my work only in the case of Ferrovac E iron, Fig. 2 of the paper under discussion. High-purity iron showed much poorer agreement at all times. It should be emphasized that $\Delta\epsilon_m$ cannot be a true measure of charge-transfer polarization, for $\Delta\epsilon_m$ data do not give consistent Tafel slopes when analyzed by the three-point method, a method which may be used as a stringent test for charge-transfer controlled corrosion.

I agree with Lorenz and El Miligy that the electrode pretreatment used possibly produced oxygen and/or anions tightly bound to the iron surface. The gradual increase in corrosion current density is probably caused primarily by removal of such surface films, and only secondarily by dissolution of the metal to produce a faceted surface of greater area. This view was supported by experiments in which the iron was corroded to a faceted surface and the specimen was removed; the original acid pretreatment was then repeated and the specimen replaced in the cell: the second corrosion period yielded essentially the same slow rise in i^* as was found in the first corrosion period.

[14] W. J. Lorenz and H. Fischer, *Electrochim. Acta*, 11, 1597 (1966).
[15] W. J. Lorenz, K. Sarropoulos, and H. Fischer, ibid., 14, 179 (1969).

Electrochemical Reactions with Consecutive Charge-Transfer Steps: Steady-State and Time-Dependent Behavior under Charge-Transfer and Diffusion Control

K. J. Bachmann (pp. 1021-1027, Vol. 119, No. 8)

V. V. Losev:[16] If an electrode process with consecutive charge-transfer steps is accompanied by formation of appreciable concentrations of low-valency intermediates, then the diffusion rate of these intermediates cannot be neglected in comparison with the rate of their further electrochemical reactions, and the elucidation of the mechanism and derivation of kinetic parameters on the basis of steady-state current density potential curves becomes a complicated problem. This conclusion has been clearly demonstrated in the paper under discussion. Bachmann has shown in his paper that at comparable values of the limiting current of intermediate diffusion and of the smaller exchange current even at intermediate concentrations, which are 2-3 orders of magnitude lower than the concentrations of initial substance and final product, the effect of intermediate diffusion should give rise to a noticeable distortion of the slopes of Tafel lines. In spite of this difficulty there exists, in our opinion, even under such conditions, some possibility of using steady-state curdent density potential curves for the elucidation of the mechanism and derivation of kinetic parameters of stepwise electrode processes.

First of all it should be noted that in the presence of appreciable intermediate concentrations a steady state can be realized under different conditions. Bachmann, in the paper under discussion, has derived the equation of the steady-state current density potential curve under the usual conditions; upon polarization, the concentrations of all reacting species at the electrode surface (including intermediates) differ from their equilibrium values existing prior to the flow of an external current, whereas in the bulk of the solution the initial equilibrium concentrations are maintained. This condition can be easily realized, particularly in the case of electrodes with a small ratio of electrode surface, S, to the cell volume, V (disk electrode, dropping mercury electrode), when the change of intermediate concentration in the bulk of the solution during the polarization measurements (*e.g.*, their accumulation under anodic polarization at $i_{01} > i_{02}$) is negligible.

But one can assume also a different steady-state condition, namely, that at any polarization, the bulk concentration of intermediates practically coincides with their concentration at the interface (as shown below this assumption can be easily realized under certain experimental conditions). Under such steady-state conditions, even at an appreciable intermediate concentration, the rate of their diffusion from the electrode (for the case mentioned above) should be negligible as compared with the rate of their further electrochemical oxidation on the electrode. Then the steady-state condition mentioned in Bachmann's paper

$$i_\nu = i_{\nu+1} \qquad [1]$$

will be satisfied and the results of polarization measurements can be described by the usual equation of the steady-state polarization curve for a stepwise process derived by Vetter. Of course, upon changing to a new polarization value during the measurement of a current density potential curve, when the new intermediate concentration at the interface is rapidly reached, and while their bulk concentration still corresponds to the previous value of polarization, a considerable gradient of intermediate concentrations arises between the interface and the bulk of the solution. But as the intermediates are accumulated in the bulk of the solution, this gradient will gradually decrease, and therefore the diffusion rate of intermediates from the electrode will decrease as well until the above-mentioned steady state is practically reached and the condition of Eq. [1] is satisfied. By choosing appropriate experimental conditions (a large ratio S/V) one can reach the steady state during a reasonable time interval.[17-19]

Finally, the steady state can also set in when the intermediate concentration in the bulk of the solution practically remains always equal to zero.[17] It is necessary to use such a steady-state condition, *e.g.*, in the important case where the intermediates are unstable and enter into a chemical reaction.

If the steady-state current density potential curve is obtained under conditions where an appreciable gradient of intermediate concentration exists, and their diffusion rate from the electrode is comparable with the rate of their further oxidation on the electrode (in the case of anodic polarization and $i_{01} > i_{02}$), then the results of polarization measurements can be corrected as follows: from the over-all current there can be singled out the fraction corresponding to the formation of such intermediate particles which do not enter into subsequent electrochemical reactions but diffuse into the bulk of the solution. The remaining current is distributed in equal parts between all electrochemical steps which makes it possible to apply Eq. [1] to this remaining current.[21] An equation of the current density potential curve including such a correction and expressed in terms of the experimental measurable value of effective valency, n_i,[23] enables us to use the results of polarization measurements for the elucidation of the mechanism and derivation of kinetic parameters of stepwise electrode processes.[21] This equation is applicable in the case of diffusion transport of intermediates between the interface and the bulk of the solution, as considered in the paper under discussion, as well as in the more general case when the intermediates are unstable and enter also into chemical reactions, *e.g.*, are partly oxidized to the stable final product by solution components.[21]

K. J. Bachmann: In Vetter's papers[28,29] concerning the steady-state current density overvoltage characteristics for the case of electrochemical reactions involving two consecutive charge-transfer steps, the assumption was made that at equilibrium, the concentration of the intermediate reaction product is small compared to the concentrations of both the most reduced and the most oxidized substance entering into the electrode reaction. When a current is passed through such an electrode, the concentration of the intermediate substance is assumed to remain small so that its diffusion flux from the interface into the bulk of the solution or

[16] Karpov Institute of Physical Chemistry, Moscow, USSR.

[17] A. I. Molodov, G. N. Markosyan, and V. V. Losev, *Electrochim. Acta*, 17, 701 (1972).

[18] A. I. Molodov, V. I. Barmashenko, and V. V. Losev, *Elektrokhimia*, 7, 18 (1971).

[19] The described steady-state condition has been briefly mentioned in a footnote to our paper[20] to which Bachmann refers in the paper under discussion. Apparently because of some misunderstanding, Bachmann attributes to us the statement that "the continuity condition $i_\nu = i_{\nu+1}$ is always satisfied even at high concentrations of the intermediate products." Meanwhile, as it follows explicitly from the said footnote to the paper,[20] as well as from our subsequent papers,[17,18,21,22] we stated that the condition of Eq. [1] is satisfied not always but only when, due to the gradual intermediate accumulation (*e.g.*, during anodic polarization at a constant potential), their bulk concentration becomes practically equal to their concentration at the electrode surface and hence their diffusion rate from the electrode becomes negligible.

[20] V. V. Losev and V. V. Gorodetsky, *Elektrokhimia*, 3, 1061 (1967).

[21] A. I. Molodov and V. V. Losev, *ibid.*, 7, 812 (1971).

[22] V. V. Losev, in "Modern Aspects of Electrochemistry," B. E. Conway and J. O'M. Bockris, Editors, Vol. 7, p. 319, Plenum Press, New York (1972).

[23] The effective valency n_i (or the value $\nu = 1/n_i$ used by Wagner in his analysis of a stepwise electrode process, accompanied by formation of appreciable concentration of intermediates[24]) can be found, for example, by radiotracer measurements[18,25-27] or by means of the rotating ring-disk electrode.

[24] C. Wagner, *Electrochim. Acta*, 14, 971 (1969).

[25] A. I. Molodov, G. N. Markosyan, and V. V. Losev, *Elektrokhimia*, 5, 918 (1969).

[26] A. I. Molodov, *ibid.*, 6, 365 (1970).

[27] V. V. Losev, *Electrochim. Acta*, 15, 1095 (1970).

[28] K. J. Vetter, *Z. Naturforsch.*, 7a, 328 (1952); *ibid.*, 8a, 832 (1953).

[29] K. J. Vetter, "Elektrochemische Kinetik," Springer-Verlag, New York (1961).

vice versa may be neglected with respect to the rate at which the intermediate substance is produced and consumed in the two consecutive charge-transfer reaction steps. Under steady-state conditions, the continuity condition

$$i_1 \approx i_2 \qquad [1]$$

is established, where i_1 and i_2 are the C.D.'s carried by the two consecutive charge-transfer reactions. If there exists no other sources or sinks for the intermediate reaction products but consecutive charge-transfer reactions at the electrode interface, then this steady-state continuity condition is applicable to electrochemical reactions involving an arbitrary number of n consecutive charge-transfer steps, *i.e.*

$$i_\nu = i_{\nu+1} \qquad [2]$$

where $\nu = 1, 2, \ldots, n-1$. This case has been considered by Hurd.[30]

Referring to the work of Vetter,[28,29] Losev and Gorodetskii[20] have pointed out that the condition of small intermediate concentration is unnecessary. As I expressed in the paper under discussion my reservations concerning this point of view, I was indeed under the impression that Losev and Gorodetskii meant their comment to be true for the general case considered by Vetter. Losev's discussion of my paper and his recent publications[17,18,21,22] are most welcome. They give the special conditions, which Losev *et al.* assume to be adequate for using Eq. [2] above as a reliable basis for analyzing the current density overvoltage characteristics even at relatively high intermediate concentrations. These conditions are:

(*i*) The ratio of the electrode surface to the electrolyte volume is so large that during an electrolysis at constant potential rapid accumulation of the products of the electrochemical reaction in the bulk of the solution decreases any transient concentration gradients for the intermediate reaction products at the electrode surface within a reasonably short period of time to zero.

(*ii*) The intermediate concentrations in the bulk of the solution "remain always equal to zero," which may be the case when the intermediate products are unstable and enter into chemical reactions.

Knowing now the specific steady-state conditions considered by Losev, I still doubt that Eq. [2] above *i.e.*, the formalism derived elsewhere[20,28-30] provides a reliable basis for analyzing the current density overvoltage characteristics unless the intermediate concentrations are small compared to the concentrations of the most reduced substance (S_1) and most oxidized substances (S_{n+1}) entering into the consecutive charge-transfer mechanism

$$S_\nu \overset{i_\nu}{\rightleftharpoons} S_{\nu+1} + z_\nu e^-, \quad \nu = 1, 2, \ldots, n \qquad [3]$$

If condition (*i*) is satisfied, then the change in bulk concentration of all intermediate products must be generated in an anodic reaction from S_1 and in a cathodic reaction from S_{n+1}. Furthermore, not only the intermediate products are accumulated, but the concentration of S_1 decreases and the concentration of S_{n+1} increases in an anodic reaction (vice versa in the cathodic case) so that the equilibrium electrode potential rapidly approaches the externally imposed value, in which case the total C.D. approaches zero, *i.e.*, there is no true steady state under Losev's experimental condition.[28] A "quasi steady state" could be postulated if S_1 and S_{n+1} are available in much larger concentration than the intermediate products. In my opinion, the best and only way of characterizing the reliability of such an analysis of the current density overvoltage characteristics is to provide an error analysis for the deduced kinetic parameters.

Condition (*ii*) considered by Losev is not in conflict with what I have said in the paper under discussion, since I never objected to utilizing Vetter's analysis if the relative concentrations of the intermediate products are sufficiently small. I would like to point, however, to the fact that a finite equilibrium concentration of the intermediate products at the interface is required to establish an equilibrium potential characteristic of reaction [3] and to define the exchange C.D.'s of the various reaction steps. Since chemical reactions involving the intermediate products lead to branching in the equivalent mass flow at the interface, I do not believe that the interaction of consecutive charge-transfer reactions with chemical reactions is covered by the simple analysis given elsewhere.[20,28-30] In the general case, where the electrochemical reaction is controlled by charge-transfer, diffusion, and chemical reactions, the steady-state continuity condition Eq. [2] has to be replaced by

$$i_\nu = i_{\nu+1} + i^{D}_{\nu+1} + i^{R}_{\nu+1} \qquad \nu = 0, 1, 2, \ldots, n \qquad [4]$$
$$i_0 = i_{n+1} = 0$$

where $i^{D}_{\nu+1}$ and $i^{R}_{\nu+1}$ denote the equivalent C.D.'s with which the substance $S_{\nu+1}$ is consumed or produced at the interface via chemical reactions or by exchange with the bulk via diffusion. Note that no charge is carried across the interface by $i^{D}_{\nu+1}$ and $i^{R}_{\nu+1}$. I have treated in the paper under discussion the case of n consecutive charge-transfer reactions, when

$$i^{R}_{\nu+1} = 0$$

and

$$i^{D}_{\nu+1} = -FD_{\nu+1}\,(\partial c_{\nu+1}/\partial x) \qquad [5]$$

If $i^{R}_{\nu+1} \neq 0$, then not only the diffusion of $S_{\nu+1}$ but also the diffusion of the reaction products has to be taken into account. The relation between the concentration of $S_{\nu+1}$ and the rate of the chemical reaction depends on the specific nature of the reaction. In general, the current densities carried by the various charge-transfer reaction steps will not be equal in this case, *i.e.*

$$i_\nu \neq i_{\nu+1} \qquad [6]$$

except for the very special condition

$$i^{D}_{\nu+1} = -\,i^{R}_{\nu+1}$$

I agree with Losev that, in the absence of chemical reactions, the interpretation of the steady-state c.d. overvoltage curve is considerably simplified if the diffusion currents of all intermediates are known from an independent set of experiments.

[30] R. M. Hurd, *This Journal*, 109, 327 (1962).

The Kinetics of the p-Toluquinhydrone Electrode

F. Kornfeil (pp. 1674-1679, Vol. 119, No. 12)

J. C. Reeve:[31] The following comments may be of interest not only to those considering Dr. Kornfeil's valuable results in the paper under discussion concerning consecutive charge-transfer reactions, but to those interested in such reactions in general.

The term "pseudo-Tafel region" was introduced by Hurd[30] to describe what seemed, from a point by point calculation, to be a linear region of the Tafel diagram between two limiting anodic situations (where the steps are separately "rate-determining," rather than simultaneously "rate-determining" as in the transition region). This was unfortunate, since there is in fact no such special region,[32] and any apparent pseudo-Tafel behavior in such cases simply arises from experimental or graphical lack of precision. Vetter, in his classic works cited by Dr. Kornfeil in the paper under discussion, made no claim for such a region. In the paper being discussed an additional complication is introduced in that its Eq. [8] is said to have "pseudo-Tafel form." In fact, this not only has normal Tafel form (as usual ignoring small possible changes in α_2 with

[31] Chemistry Department A, Technical University of Denmark, Lyngby, Denmark.

[32] J. C. Reeve, *Coll. Czech. Chem. Comm.* (in English), 36, 757 (1971).

vice versa may be neglected with respect to the rate at which the intermediate substance is produced and consumed in the two consecutive charge-transfer reaction steps. Under steady-state conditions, the continuity condition

$$i_1 \approx i_2 \qquad [1]$$

is established, where i_1 and i_2 are the C.D.'s carried by the two consecutive charge-transfer reactions. If there exists no other sources or sinks for the intermediate reaction products but consecutive charge-transfer reactions at the electrode interface, then this steady-state continuity condition is applicable to electrochemical reactions involving an arbitrary number of n consecutive charge-transfer steps, *i.e.*

$$i_\nu = i_{\nu+1} \qquad [2]$$

where $\nu = 1, 2, \ldots, n-1$. This case has been considered by Hurd.[30]

Referring to the work of Vetter,[28,29] Losev and Gorodetskii[20] have pointed out that the condition of small intermediate concentration is unnecessary. As I expressed in the paper under discussion my reservations concerning this point of view, I was indeed under the impression that Losev and Gorodetskii meant their comment to be true for the general case considered by Vetter. Losev's discussion of my paper and his recent publications[17,18,21,22] are most welcome. They give the special conditions, which Losev *et al.* assume to be adequate for using Eq. [2] above as a reliable basis for analyzing the current density overvoltage characteristics even at relatively high intermediate concentrations. These conditions are:

(*i*) The ratio of the electrode surface to the electrolyte volume is so large that during an electrolysis at constant potential rapid accumulation of the products of the electrochemical reaction in the bulk of the solution decreases any transient concentration gradients for the intermediate reaction products at the electrode surface within a reasonably short period of time to zero.

(*ii*) The intermediate concentrations in the bulk of the solution "remain always equal to zero," which may be the case when the intermediate products are unstable and enter into chemical reactions.

Knowing now the specific steady-state conditions considered by Losev, I still doubt that Eq. [2] above *i.e.*, the formalism derived elsewhere[20,28-30] provides a reliable basis for analyzing the current density overvoltage characteristics unless the intermediate concentrations are small compared to the concentrations of the most reduced substance (S_1) and most oxidized substances (S_{n+1}) entering into the consecutive charge-transfer mechanism

$$S_\nu \overset{i_\nu}{\rightleftharpoons} S_{\nu+1} + z_\nu e^-, \quad \nu = 1, 2, \ldots, n \qquad [3]$$

If condition (*i*) is satisfied, then the change in bulk concentration of all intermediate products must be generated in an anodic reaction from S_1 and in a cathodic reaction from S_{n+1}. Furthermore, not only the intermediate products are accumulated, but the concentration of S_1 decreases and the concentration of S_{n+1} increases in an anodic reaction (vice versa in the cathodic case) so that the equilibrium electrode potential rapidly approaches the externally imposed value, in which case the total C.D. approaches zero, *i.e.*, there is no true steady state under Losev's experimental condition.[28] A "quasi steady state" could be postulated if S_1 and S_{n+1} are available in much larger concentration than the intermediate products. In my opinion, the best and only way of characterizing the reliability of such an analysis of the current density overvoltage characteristics is to provide an error analysis for the deduced kinetic parameters.

Condition (*ii*) considered by Losev is not in conflict with what I have said in the paper under discussion, since I never objected to utilizing Vetter's analysis if the relative concentrations of the intermediate products are sufficiently small. I would like to point, however, to the fact that a finite equilibrium concentration of the intermediate products at the interface is required to establish an equilibrium potential characteristic of reaction [3] and to define the exchange C.D.'s of the various reaction steps. Since chemical reactions involving the intermediate products lead to branching in the equivalent mass flow at the interface, I do not believe that the interaction of consecutive charge-transfer reactions with chemical reactions is covered by the simple analysis given elsewhere.[20,28-30] In the general case, where the electrochemical reaction is controlled by charge-transfer, diffusion, and chemical reactions, the steady-state continuity condition Eq. [2] has to be replaced by

$$i_\nu = i_{\nu+1} + i^{D}_{\nu+1} + i^{R}_{\nu+1} \qquad \nu = 0, 1, 2, \ldots, n \qquad [4]$$
$$i_0 = i_{n+1} = 0$$

where $i^{D}_{\nu+1}$ and $i^{R}_{\nu+1}$ denote the equivalent C.D.'s with which the substance $S_{\nu+1}$ is consumed or produced at the interface via chemical reactions or by exchange with the bulk via diffusion. Note that no charge is carried across the interface by $i^{D}_{\nu+1}$ and $i^{R}_{\nu+1}$. I have treated in the paper under discussion the case of n consecutive charge-transfer reactions, when

$$i^{R}_{\nu+1} = 0$$

and

$$i^{D}_{\nu+1} = -FD_{\nu+1}\,(\partial c_{\nu+1}/\partial x) \qquad [5]$$

If $i^{R}_{\nu+1} \neq 0$, then not only the diffusion of $S_{\nu+1}$ but also the diffusion of the reaction products has to be taken into account. The relation between the concentration of $S_{\nu+1}$ and the rate of the chemical reaction depends on the specific nature of the reaction. In general, the current densities carried by the various charge-transfer reaction steps will not be equal in this case, *i.e.*

$$i_\nu \neq i_{\nu+1} \qquad [6]$$

except for the very special condition

$$i^{D}_{\nu+1} = -\,i^{R}_{\nu+1}$$

I agree with Losev that, in the absence of chemical reactions, the interpretation of the steady-state c.d. overvoltage curve is considerably simplified if the diffusion currents of all intermediates are known from an independent set of experiments.

[30] R. M. Hurd, *This Journal*, 109, 327 (1962).

The Kinetics of the p-Toluquinhydrone Electrode

F. Kornfeil (pp. 1674-1679, Vol. 119, No. 12)

J. C. Reeve:[31] The following comments may be of interest not only to those considering Dr. Kornfeil's valuable results in the paper under discussion concerning consecutive charge-transfer reactions, but to those interested in such reactions in general.

The term "pseudo-Tafel region" was introduced by Hurd[30] to describe what seemed, from a point by point calculation, to be a linear region of the Tafel diagram between two limiting anodic situations (where the steps are separately "rate-determining," rather than simultaneously "rate-determining" as in the transition region). This was unfortunate, since there is in fact no such special region,[32] and any apparent pseudo-Tafel behavior in such cases simply arises from experimental or graphical lack of precision. Vetter, in his classic works cited by Dr. Kornfeil in the paper under discussion, made no claim for such a region. In the paper being discussed an additional complication is introduced in that its Eq. [8] is said to have "pseudo-Tafel form." In fact, this not only has normal Tafel form (as usual ignoring small possible changes in α_2 with

[31] Chemistry Department A, Technical University of Denmark, Lyngby, Denmark.

[32] J. C. Reeve, *Coll. Czech. Chem. Comm.* (in English), 36, 757 (1971).

potential) but represents the normal anodic behavior complementary to the cathodic behavior indicated (the step $S_m \rightleftarrows S_o$ is "rate-determining" throughout). This behavior is marked as the "pseudo-Tafel region" in Fig. 4 of the paper under discussion but the short line shown at higher anodic overpotentials (where there has been a change of "rate-determining step") is very misleadingly called "the true Tafel line." Hurd[30] also called this region "the true Tafel-region," but only as opposed to the transition region, where there was supposed (incorrectly) to be an unexpected Tafelian behavior.

It is clear that terms such as "pseudo-Tafel behavior" and especially the term "pseudo-Tafel region" should be used with greater caution than hitherto.

Regarding the attainment of the steady state ($\gamma = 0.5$), it is said that (diffusion polarizations are to be supposed eliminated) "the stationary concentration of S_m can differ only slightly from its thermodynamic equilibrium concentration" for the given potential. In this statement it is not made clear between which solution species and S_m equilibrium is considered. In the here so-called pseudo-Tafel region, S_m will be in equilibrium with S_r. However, in the here so-called Tafel region, S_m can be in equilibrium with S_o at lower overpotentials and actually fall with increasing potential, but be nearly zero or again increasing at higher overpotentials (as in the present examples) depending on how closely α_1 approximates to α_2.[33]

It is possibly noteworthy that results, such as those used in Fig. 8 and 9 of the paper under discussion, can be used to determine i_o and both the sum and the difference of the reciprocal component current Tafel laws at $\eta \sim 0$ without making further suppositions.[34,35]

F. Kornfeil: I am grateful to the author of the above discussion for his interest and comments. I hope that the following arguments will help to remove at least the major part of any misunderstandings that may still exist.

First, and most importantly, it should be noted that, as a consequence of the experimental techniques used in the potential measurements, the transfer overpotential is the only component of the overpotential appearing in the experimentally determined values of the electrode potential. Since $\gamma \approx 0.5$, this means that all polarization curves presented are identical with the curves one would obtain from measurements in the steady state, if the diffusion coefficients of all reacting species and the rate constants of all chemical reactions involved in the reaction sequence were infinite. Therefore, the two charge-transfer steps clearly must proceed at equal rates over the entire range of overpotentials, irrespective of the sometimes very large difference between the individual exchange current densities $i_{0,1}$ and $i_{0,2}$.

Second, Dr. Reeve in the above discussion, is mistaken in his view that the phenomenon of the pseudo-Tafel lines is due to a lack of experimental or graphical precision. Inspection of Eq. [6] and [6a] of my paper under discussion reveals that, assuming $\gamma = 0.5$, at sufficiently large values of η, Eq. [6] simplifies to

$$i = 2i_{0,1} \exp\left(\frac{\alpha_1 \mathbf{F}}{RT}\eta\right)$$

with the intercept $2i_{0,1}$ in perfect analogy to the extrapolation of the Tafel line in a one-electron process. However, at intermediate values of η and the condition $i_{0,1} >> i_{0,2}$ the denominator of Eq. [6a] in the paper under discussion becomes unity and the numerator approximates $\exp(2\mathbf{F}\eta/RT)$ resulting, as pointed out by Vetter,[29] in another linear relationship between log i and η, namely

$$i = i_{0,2} \exp\left(\frac{1 + \alpha_2}{RT}\mathbf{F}\eta\right)$$

the pseudo-Tafel region, with the "wrong" intercept $2i_{0,2}$ (identical with the cathodic intercept), thereby raising the possibility of confusing an electrode reaction consisting of two consecutive charge-transfer steps with a single-step transfer of two electrons. What actually constitutes "sufficiently large" and "intermediate" values of the overpotential in this context depends on the kinetic parameters and their interrelations and has been clarified in Hurd's excellent analysis of this problem.[30]

If one remains faithful to the convention of referring to the linear portions as Tafel lines, then Hurd's terminology calling the straight line at the highest overpotentials the "true" Tafel line and the linear part of the polarization curve occurring at lower overpotentials the "pseudo"-Tafel line seems a most appropriate and logical choice. In view of the arguments presented above, it is, therefore, difficult to understand, both from the scientific and etymological points of view, why Dr. Reeve should find the term pseudo-Tafel region misleading. In fact, I fail to see any valid reason why electrochemists should, or the Ancient Greeks would, object to its continued use.

In regard to the last part of Dr. Reeve's discussion, the statement as to the small difference between the equilibrium and the steady-state concentrations of the intermediate should, in retrospect, have been presented in a more quantitative fashion. At any rate, a clear distinction should be made here between the steady-state concentration and the equilibrium concentration, a thermodynamic quantity governed by the equilibria existing among the quinone, meriquinone, semiquinone, and hydroquinone molecules. The assertion of the small concentration difference is based on considerations, via Faraday's laws, of the very small quantity of charge required for the observed rapid attainment of the steady-state condition.

[33] I. H. Plonski, *This Journal*, 116, 944 (1969).
[34] J. C. Reeve and G. Bech-Nielsen *Corr. Sci.*, 13, 351 (1973).
[35] K. B. Oldham and F. Mansfeld, *ibid.*, In press.

The Kinetics of Chlorine Evolution and Reduction on Titanium-Supported Metal Oxides Especially RuO_2 and IrO_2

A. T. Kuhn and C. J. Mortimer (pp. 231-236, Vol. 120, No. 2)

G. Faita and G. Fiori:[36] Kuhn and Mortimer ascribe, in the paper under discussion, the differences existing between their data and those of our work[37] mainly to experimental procedures.

The first objection concerns the method used for obtaining the necessary ohmic drop correction.

Kuhn and Mortimer in their paper describe the method used by us[37] as "short-circuiting the working electrode to the counterelectrode." This procedure would be obviously incorrect and as a matter of fact was not applied. The actual experimental arrangement is sketched in Fig. 1.

The transistor-driven mercury switch is placed across the cell terminals: but the cell is electrically isolated

[36] Institute of Electrochemistry and Metallurgy, The University of Milan, 20133 Milan, Italy.
[37] G. Faita and G. Fiori, *J. Appl. Electrochem.*, 2, 31 (1972).

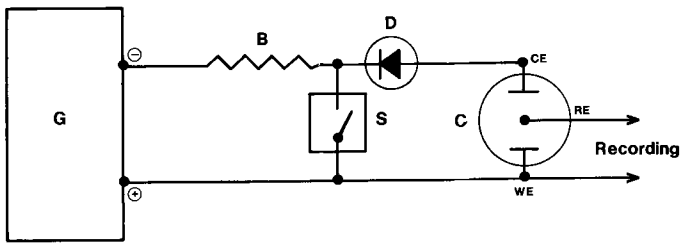

Fig. 1. Block diagram of the experimental apparatus used for ohmic drop correction. G, galvanostat; B, buffer resistor; D, diode; C, cell; S, mercury switch.

by a fast low-leakage silicon diode (*e.g.*, SGS EC-401 or BAY 73 with a 1 nA reverse current and a 8 pF capacitance). In view of this experimental arrangement the above mentioned criticism seems to be rather immaterial.

The second objection concerns the fact that in our work[37] the cell was purged with a slow nitrogen flow passing over the NaCl solutions. Kuhn and Mortimer in the paper under discussion suggest that the solution was not saturated with chlorine and consequently concentration polarization at the electrode surface may arise.

As a matter of fact, the potential values which is recorded just after switching off the current is given by the following equation

$$E = E_{rev} + \eta_1 + \eta_2$$

where E_{rev} is given by $E^\circ + RT/\mathbf{F} \cdot \ln (a_{Cl_2})$ sol/a_{Cl^-}; η_1 is the concentration polarization ($RT/2\mathbf{F} \cdot \ln (a_{Cl_2})$ surface/(a_{Cl_2}) sol; and η_2 is the activation polarization.

Now, (a_{Cl_2}) surface increases as the anodic current density increases and its upper limit is represented by the chlorine saturation solubility in the brine. This limit is probably reached, with the rotating disk equipment used by us,[37] in the 10 mA/cm^2 range, above which the chlorine activity at the electrode surface remains constant together with the concentration polarization.

The consequence is that the total overpotential is given by the sum η_1(constant) + η_2; hence our data at high current densities should be decreased by a constant value whose magnitude depends on the ratio (a_{Cl_2}) surface/(a_{Cl_2}) sol. (This will be a few millivolts in the operating conditions used in our work.[37])

The correct data (which were reported in Fig. 1 in our paper[37]) are independent of the chlorine concentration in the solution. In addition, it is important to stress that the Tafel *b* coefficient does not change for current densities above 10 mA/cm^2 and remains 32 mV/ decade of current in 4M NaCl at 20°C and *p*H = 2, up to 2 A/cm^2.

As far as the data below 10 mA/cm^2 are concerned, they are almost unaffected by the concentration polarization effects just opposed to what has been suggested.

That the situation is as above described is futhermore substantiated by Fig. 10 of the paper under discussion which shows that the anodic polarization curves for two different chlorine pressures (1 and 0.05 atm) are virtually identical above about 1 mA/cm^2.

Having stated this the most obvious conclusion is that the electrodes described in the paper under discussion of Kuhn and Mortimer behave in a different way with respect to those described in our paper[37] simply because they are different and not because of experimental procedures.

In fact the following points should have been taken into account:

(*i*) The coating tested in the paper being discussed is a solid solution of TiO_2, RuO_2, IrO_2 as has been demonstrated spectroscopically.

(*ii*) The coating tested in the paper under discussion has a (Ru-Ir) to Ti molar ratio of 0.1. An electrode with such a content of precious metal described in Kuhn's and Mortimer's paper (Fig. 7, curves e and f) is characterized by an overpotential of 0.6V at 1 A/cm^2 which seems to be too high for economic industrial operations. On the other hand, the coating prepared according to our work[37] (U. S. Patent 3,616,445, Appl. 690,407) exhibits an overpotential of only 125 mV; this value is confirmed by experimental measurements on actual chlor-alkali cells equipped with DSA (this is the commercial name for the anodes obtained by using the coating described in the above-mentioned U.S. patent).

An interesting feature of the RuO_2-TiO_2 electrodes obtained by Kuhn and Mortimer in their paper is represented in Fig. 2; the necessary data have been obtained from Fig. 7 of the paper under discussion and represent the limiting cathodic current densities ($\eta = -0.6$V). The relationship between current and Ru/Ti molar ratio is described by a straight line; a possible explanation of this linear dependence is that the chlorine discharge takes place only on Ru sites or RuO_2 islands (TiO_2 has a very low electrocatalytic effect).

If this mechanism holds, the high anodic overpotentials for the coatings with the lower Ru percentages can be readily explained; the observed apparent current density corresponds to quite larger actual current densities on the electrocatalytic centers.

S. Trasatti:[38] We have been working on RuO_2 film electrodes in this laboratory since early 1968 with particular regard to the intrinsic properties of such films to try to gain some insight into the rationale behind their undoubtedly peculiar behavior. Although, we have so far just published a preliminary note,[39] a number of papers is in preparation, and all of the aspects touched by the authors of the paper under discussion will be examined in detail there. We feel, however, that some discussion should be made here to clarify some points in the paper under discussion where the authors refer to results from this laboratory.

Roughness factor.—Although optical inspection gives evidence for compactness and microscopical homogeneity, recent BET measurements[40] in this laboratory give for the specific area of the films a value of about 14 m^2-g^{-1}. Since 2μ thick films were used (1.4 mg RuO_2 cm^{-2}), the roughness factor is as a result of the order of 200. This is in fairly good agreement with the value of 240 reported by Kuhn and Mortimer in the paper being discussed. Although this roughness factor should influence the charge associated with surface transformations, it is doubtful whether it could affect the value of reaction rates at potentials removed from the equilibrium value, due to the fact that sites available to rare gas in BET measurements are probably difficult to reach by particles in solution by diffusion. However, assuming for the roughness factor the possible value of 200, we will show that this cannot account for the charge measured by us[39] to change the potential of RuO_2 from oxygen evolution to about 0.4V.[41] Since 1 cm^2 of a 2μ thick RuO_2 film contains

[38] Laboratory of Electrochemistry, The University of Milan, 20133 Milan, Italy.

[39] S. Trasatti and G. Buzzanca, *J. Electroanal. Chem.*, 29, App. 1 (1971).

[40] S. Pizzini, G. Buzzanca, C. Mari, L. Rossi, and S. Torchio, *Mat. Res. Bull.*, 7, 499 (1972).

[41] Charges in Table I in our paper[39] are from integration of *i/E* voltammetric curves and not from charging curves.

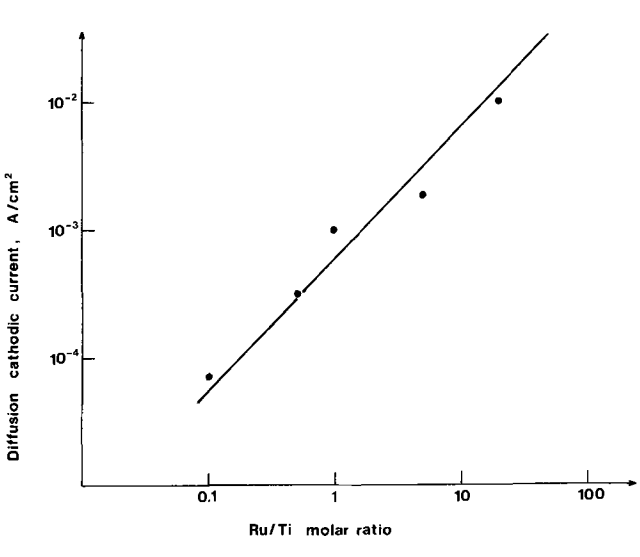

Fig. 2. Relationship between diffusion cathodic currents and Ru/Ti molar ratio (%).

6.3×10^{18} Ru atoms, the charge associated with a one-electron exchange reaction over all the film thickness would be about 1 coulomb/cm^{-2}. With reference to the (100) face of RuO_2, the number of surface Ru atoms is 0.5×10^{15} per cm^2.[42] With a roughness factor as above, the charge associated to a one-electron exchange surface reaction would be $80 \times 200 = 16$ mcoulombs/cm^{-2}.[43] Since the experimental charge[39] is about 70 mcoulombs/cm^{-2}, there are still 54 mcoulombs/cm^{-2} which cannot be accounted for by surface modifications. Thus, only about 5.4% of the Ru atoms in the bulk appear to exchange electrons during changes in potential. However, the problem is more complicated than it would appear at first sight. In fact, it should be reasonable to assume constancy in the roughness factor with change in film thickness. However, we measured[39] a charge of 17 mcoulombs/cm^{-2} for a ½μ thick RuO_2 film. In this case, all the charge could be accounted for by surface reactions, if the above roughness factor is adopted. Undoubtedly, the two results are contrasting and could be understood only if: (*i*) the BET surface area is not the electrochemical surface area; (*ii*) atoms in the surface are also reduced and oxidized in small fractions; and (*iii*) the roughness factor decreases with decreasing thickness of the film. Which of these models holds in practice cannot be established at the moment. We would like to emphasize here that chemical analysis[40] has given for the nonstoichiometry of RuO_2 the same order of magnitude and the same direction of change as those suggested in Table I of our paper.[39]

Electrical properties of RuO_2 films.—It is not completely clear which model is proposed by Kuhn and Mortimer in the paper under discussion as regards the nature of conduction in RuO_2 films. The authors seem prone to consider RuO_2 films as n-type semiconductors due to the low value of conductivity. This is, in principle, not really a correct argument since Bi is known to exhibit low conductivity while it is a metallic conductor. Further, reference to the dependence of conductivity on the firing temperature to support the above view does not appear to be relevant. In fact, measurements carried out by Pizzini's group[40] in this laboratory on RuO_2 films on silica show conductivity increases with increasing firing temperature. Opposite behavior would be expected if the semiconducting nature were related to the composition of the film, as Kuhn and Mortimer seem prone to think in the paper under discussion. In other words, a lower firing temperature would result in a higher nonstoichiometry which in turn would be responsible for a higher conductivity due to an increasing number of electrons. Results show that this is not the case. The positive temperature coefficient of conductivity[40] for temperatures higher than about 700°C is to be related to evolution of the structure towards the crystalline state rather than to semiconducting properties. Since the crystal has a higher conductivity, an increasing number of small crystals in the film as the temperature is increased accounts for the increase in conductivity. On the contrary, for T below 700°C the temperature coefficient of conductivity is practically zero which suggests rather a metallic behavior. On the other hand, if the number of electrons is reasonably high, a material could behave electrochemically as a metal even though it were rigorously a semiconductor. In fact, if the rate of the electron movement is higher than the rate of any step in the electrochemical reaction, the resulting whole process is not limited by the semiconducting nature. This may be the case of RuO_2 films. Our results with the Fe^{2+}/Fe^{3+} redox couple show that the activation energy is about 5 kcal-mol^{-1} for all types of films, which coincides with the value found for all metals investigated.[44] From this point of view, RuO_2 films can be defined with certainty as metallic in nature. Ti-Ru mixed oxides are more likely to be effectively n-type ionic semiconductors where Ru atoms should act as donors at least for Ru content below 20%.

Kinetics of Cl_2 evolution on RuO_2.—Kuhn and Mortimer in the paper being discussed observe that their results are in disagreement with those obtained by Faita and Fiori.[37] These authors give a detailed defense above in this Discussion Section. However, with reference to results obtained by us, the explanation given by Kuhn and Mortimer in their paper, in terms of different atmospheres above the solution during measurements, appears to us to be quite reasonable. In fact, we have carried out measurements in solutions saturated with Cl_2 and N_2, alternatively. The curve in N_2-saturated solutions is similar to that of Faita and Fiori with a Tafel slope of about 35 mV dec^{-1}, whereas the curve in Cl_2-saturated solutions exhibits a lower overvoltage at low current density (a few millivolts at 1 mA/cm^{-2}). The exchange current measured from linear i/η plots has been found to be about 5 mA/cm^{-2} in very good agreement with the value of Kuhn and Mortimer in the paper under discussion. However, in Cl_2-saturated solutions the i/E curve loses in definition and no definite Tafel line can be identified. In the paper being discussed the authors worked with stationary electrodes, whereas Faita and Fiori worked with rotating-disk electrodes. We are not of the opinion, as it appears in the paper under discussion, that the use of either type of electrode is irrelevant. In fact, in N_2-saturated solutions we obtained a quite definite Tafel line for current density up to 10 mA/cm^{-2} working with stationary electrodes. At higher currents, the overvoltage started to increase more rapidly in spite of vigorous stirring, whereas Faita and Fiori with the rotating-disk electrode were able to obtain a definite Tafel line at currents higher than 1 A/cm^{-2}.

A. T. Kuhn and C. J. Mortimer: The comments from Drs. Trasatti, Faita, and Fiori are, perhaps, best considered and replied to jointly, and their points fall into four categories: (*i*) problems relating to the removal of ohmic drops; (*ii*) the effect of Cl_2 concentration on the anodic i-V data; (*iii*) the catalytic activity of the anodes; and (*iv*) the nature of their electrical conductivity.

(*i*) Considering now the information (not originally proffered) that their circuit included a diode, and taking into account the other data now published, we are entirely satisfied as to the validity of the ohmic drop corrections of Faita *et al.*

(*ii*) Regarding the effect of dissolved Cl_2 concentration on the i-V data, we still have reservations regarding the explanation given by Faita *et al.* above in their discussion, since differences between N_2 and Cl_2 purged runs would be expected to disappear at high C.D.'s (as they do for N_2 and H_2 purged h.e.r. measurements) when plotted as E *vs.* log i (Fig. 10 in the paper under discussion). Indeed, the use of η/log i plots as seen in Faita *et al.'s* paper leaves quite open the question of what value of E_{rev} their η was based on. In an N_2 purged cell it may be suspected that the Cl_2 concentration increased (certainly in the diffusion layer) as the amount of electrogenerated Cl_2 increased from zero to the high C.D.'s used. In this context, Faita *et al.* will doubtless be considering the comments of Trasatti above. Taking Trasatti's reservations as to our statement that the use of rotating-disk electrode made no difference to the shape of the current-voltage plots, it should be borne in mind that our statement applied only under the conditions we reported in the paper being discussed (*e.g.*, Cl_2 saturated).

(*iii*) We agree with Faita *et al.* that our electrodes with 10% precious metal appear to show less activity than their samples, but the comments of Trasatti regarding differences in N_2 and Cl_2 purged data should here be borne in mind. If, this factor having been

[42] J. T. Sommerfeld and G. Parravano, *J. Phys. Chem.*, 69, 102 (1965).
[43] S. Trasatti, *Electrochim. Metal.*, 2, 12 (1967).
[44] D. Galizzioli and S. Trasatti, *J. Electroanal. Chem.*, In press.

6.3×10^{18} Ru atoms, the charge associated with a one-electron exchange reaction over all the film thickness would be about 1 coulomb/cm^{-2}. With reference to the (100) face of RuO_2, the number of surface Ru atoms is 0.5×10^{15} per cm^2.[42] With a roughness factor as above, the charge associated to a one-electron exchange surface reaction would be $80 \times 200 = 16$ mcoulombs/cm^{-2}.[43] Since the experimental charge[39] is about 70 mcoulombs/cm^{-2}, there are still 54 mcoulombs/cm^{-2} which cannot be accounted for by surface modifications. Thus, only about 5.4% of the Ru atoms in the bulk appear to exchange electrons during changes in potential. However, the problem is more complicated than it would appear at first sight. In fact, it should be reasonable to assume constancy in the roughness factor with change in film thickness. However, we measured[39] a charge of 17 mcoulombs/cm^{-2} for a ½μ thick RuO_2 film. In this case, all the charge could be accounted for by surface reactions, if the above roughness factor is adopted. Undoubtedly, the two results are contrasting and could be understood only if: (*i*) the BET surface area is not the electrochemical surface area; (*ii*) atoms in the surface are also reduced and oxidized in small fractions; and (*iii*) the roughness factor decreases with decreasing thickness of the film. Which of these models holds in practice cannot be established at the moment. We would like to emphasize here that chemical analysis[40] has given for the nonstoichiometry of RuO_2 the same order of magnitude and the same direction of change as those suggested in Table I of our paper.[39]

Electrical properties of RuO_2 films.—It is not completely clear which model is proposed by Kuhn and Mortimer in the paper under discussion as regards the nature of conduction in RuO_2 films. The authors seem prone to consider RuO_2 films as n-type semiconductors due to the low value of conductivity. This is, in principle, not really a correct argument since Bi is known to exhibit low conductivity while it is a metallic conductor. Further, reference to the dependence of conductivity on the firing temperature to support the above view does not appear to be relevant. In fact, measurements carried out by Pizzini's group[40] in this laboratory on RuO_2 films on silica show conductivity increases with increasing firing temperature. Opposite behavior would be expected if the semiconducting nature were related to the composition of the film, as Kuhn and Mortimer seem prone to think in the paper under discussion. In other words, a lower firing temperature would result in a higher nonstoichiometry which in turn would be responsible for a higher conductivity due to an increasing number of electrons. Results show that this is not the case. The positive temperature coefficient of conductivity[40] for temperatures higher than about 700°C is to be related to evolution of the structure towards the crystalline state rather than to semiconducting properties. Since the crystal has a higher conductivity, an increasing number of small crystals in the film as the temperature is increased accounts for the increase in conductivity. On the contrary, for T below 700°C the temperature coefficient of conductivity is practically zero which suggests rather a metallic behavior. On the other hand, if the number of electrons is reasonably high, a material could behave electrochemically as a metal even though it were rigorously a semiconductor. In fact, if the rate of the electron movement is higher than the rate of any step in the electrochemical reaction, the resulting whole process is not limited by the semiconducting nature. This may be the case of RuO_2 films. Our results with the Fe^{2+}/Fe^{3+} redox couple show that the activation energy is about 5 kcal-mol^{-1} for all types of films, which coincides with the value found for all metals investigated.[44] From this point of view, RuO_2 films can be defined with certainty as metallic in nature. Ti-Ru mixed oxides are more likely to be effectively n-type ionic semiconductors where Ru atoms should act as donors at least for Ru content below 20%.

Kinetics of Cl_2 evolution on RuO_2.—Kuhn and Mortimer in the paper being discussed observe that their results are in disagreement with those obtained by Faita and Fiori.[37] These authors give a detailed defense above in this Discussion Section. However, with reference to results obtained by us, the explanation given by Kuhn and Mortimer in their paper, in terms of different atmospheres above the solution during measurements, appears to us to be quite reasonable. In fact, we have carried out measurements in solutions saturated with Cl_2 and N_2, alternatively. The curve in N_2-saturated solutions is similar to that of Faita and Fiori with a Tafel slope of about 35 mV dec^{-1}, whereas the curve in Cl_2-saturated solutions exhibits a lower overvoltage at low current density (a few millivolts at 1 mA/cm^{-2}). The exchange current measured from linear i/η plots has been found to be about 5 mA/cm^{-2} in very good agreement with the value of Kuhn and Mortimer in the paper under discussion. However, in Cl_2-saturated solutions the i/E curve loses in definition and no definite Tafel line can be identified. In the paper being discussed the authors worked with stationary electrodes, whereas Faita and Fiori worked with rotating-disk electrodes. We are not of the opinion, as it appears in the paper under discussion, that the use of either type of electrode is irrelevant. In fact, in N_2-saturated solutions we obtained a quite definite Tafel line for current density up to 10 mA/cm^{-2} working with stationary electrodes. At higher currents, the overvoltage started to increase more rapidly in spite of vigorous stirring, whereas Faita and Fiori with the rotating-disk electrode were able to obtain a definite Tafel line at currents higher than 1 A/cm^{-2}.

A. T. Kuhn and C. J. Mortimer: The comments from Drs. Trasatti, Faita, and Fiori are, perhaps, best considered and replied to jointly, and their points fall into four categories: (*i*) problems relating to the removal of ohmic drops; (*ii*) the effect of Cl_2 concentration on the anodic i-V data; (*iii*) the catalytic activity of the anodes; and (*iv*) the nature of their electrical conductivity.

(*i*) Considering now the information (not originally proffered) that their circuit included a diode, and taking into account the other data now published, we are entirely satisfied as to the validity of the ohmic drop corrections of Faita *et al.*

(*ii*) Regarding the effect of dissolved Cl_2 concentration on the i-V data, we still have reservations regarding the explanation given by Faita *et al.* above in their discussion, since differences between N_2 and Cl_2 purged runs would be expected to disappear at high C.D.'s (as they do for N_2 and H_2 purged h.e.r. measurements) when plotted as E *vs.* log i (Fig. 10 in the paper under discussion). Indeed, the use of η/log i plots as seen in Faita *et al.'s* paper leaves quite open the question of what value of E_{rev} their η was based on. In an N_2 purged cell it may be suspected that the Cl_2 concentration increased (certainly in the diffusion layer) as the amount of electrogenerated Cl_2 increased from zero to the high C.D.'s used. In this context, Faita *et al.* will doubtless be considering the comments of Trasatti above. Taking Trasatti's reservations as to our statement that the use of rotating-disk electrode made no difference to the shape of the current-voltage plots, it should be borne in mind that our statement applied only under the conditions we reported in the paper being discussed (*e.g.*, Cl_2 saturated).

(*iii*) We agree with Faita *et al.* that our electrodes with 10% precious metal appear to show less activity than their samples, but the comments of Trasatti regarding differences in N_2 and Cl_2 purged data should here be borne in mind. If, this factor having been

[42] J. T. Sommerfeld and G. Parravano, *J. Phys. Chem.*, 69, 102 (1965).
[43] S. Trasatti, *Electrochim. Metal.*, 2, 12 (1967).
[44] D. Galizzioli and S. Trasatti, *J. Electroanal. Chem.*, In press.

eliminated, the difference persisted, it might indicate some merit in having a mixed precious metal system, or otherwise it could be a reflection simply on their and our preparative techniques. Further consideration of the activities of electrodes containing differing ratios of Ru:Ti have brought us to the same conclusion in the anodic sense, as Faita *et al.* have demonstrated on the cathodic side. We would not, however, refer to the cathodic limiting current as a diffusion limited one.

(*iv*) With regard to the type of conductivity shown by the oxide films, a-c impedance measurements on these films[45] in Cl_2 saturated brines at E_{rev} failed to show the behavior characteristic of a semiconductor, and reminding Trasatti that our suggestion of "η" type conductivity was clearly labeled as tentative, we would now agree with him.

The Thermal Power of the Solid Electrolyte Ag_4MI_5 and of Molten Mixtures of the Same Composition

K. E. Johnson, S. J. Sime, and J. Dudley
(pp. 703-707, Vol. 120, No. 6)

S. Chandra:[46] In the paper under discussion the authors have reported some very interesting studies on solid and molten $Ag+MI_5$ (M = K, Rb). Their values of the thermal power, θ, is lower than our values reported earlier[47] by a factor of three. Our measurements were made using massive silver electrodes which may not be reversible with the system as pointed out by the above authors in the paper under discussion. It is now well realized that obtaining a reversible electrode for such systems is very tricky. A value lower than our value is also expected on the basis of a recent theory given by Rice and Roth.[48] However, it has been our experience that the conductivity of Ag_4KI_5 depends upon the quenching rate, and a rapid quenching rate usually gives a higher conductivity sample. This is probably due to a higher degree of cationic disorder which sets in the lattice for rapid quenching rates. In obtaining their compounds, the above authors of the paper being discussed solidify the molten mixture by cooling it below the eutectic temperature without going through a rapid quenching sequence. Even though the thermopower reported by the above authors corresponds with the theory[48] better than our values,[47] it may be fortuitous. In my opinion a more confirmed value of thermopower would be obtained by using our system for pellets or single crystals but using better reversible electrodes. Two such electrodes may be: (*i*) silver electrode amalgamated with mercury and (*ii*) a pellet of powdered silver plus compound Ag_4KI_5.

K. E. Johnson, S. J. Sime, and J. Dudley: Chandra *et al.* made measurements only of the thermopower of solid Ag_4MI_5. Alhough silver electrodes could be reversible to these compounds in the solid state, we doubt if brass ones would be; the formation of a silver layer on the brass by a solid-state reaction

$$Ag^+ + Zn/Cu \rightarrow Ag + \tfrac{1}{2}Zn^{2+}/Cu^+$$

would be necessary to have a chance of creating a reversible system and other ions would be generated. A silver amalgam electrode may lead to better contact between electrode and compound but we would be reluctant to introduce mercury into the system for fear of mercury ion contamination of the compound when microcurrents flow. A pellet of powdered Ag + Ag_4MI_5 for an electrode does not seem to help either as one would still need to make a connection to it.

Since the values of thermal power obtained by us in the paper under discussion showed no sharp rise on going from liquid where contact is easy, to solid, we conclude that Chandra *et al.* had poor electrode/compound contact and measured some temperature-sensitive function of this. Rapid quenching would tend to preserve the level of disorder appropriate to high temperatures so we might expect their values for the solids to correspond more to ours for liquids which are even lower. As stated in the paper being discussed, the nonlinearity of the results of Chandra *et al.* also makes them suspect. Thermal power values of 300-700 $\mu V\ K^{-1}$ seem to be common for silver salts in the liquid state.

[45] C. J. Mortimer, To be published.
[46] Physics Department, Ravishankar University, Raipur (M.P.), India.
[47] S. Chandra, H. B. Lal, and K. Shahi, *J. Phys. D.*, 5, 443 (1972).
[48] M. J. Rice and W. L. Roth, *J. Solid State Chem.*, 4, 294 (1972).

Hydrogen Overpotential on Zinc Containing Small Impurities in Concentrated Alkaline Solutions

T. S. Lee
(pp. 707-709, Vol. 120, No. 6)

F. Mansfeld:[49] The conclusion of the paper under discussion that "one can visualize that almost all the impurities, including mercury in the zinc, will make zinc more readily corroded in the alkaline medium" is in contradiction to many published results. Earlier studies of Vondracek and Jzak-Krisko[50] showed that alloying of zinc with Al, Pb, and Hg decreased corrosion rates (r_{H_2}) in 0.5*N* H_2SO_4, while Cd, As, Sn, Sb, Fe, and Cu increased r_{H_2}. Krug and Borchers[51] found that alloying with Fe (up to 310 ppm) increased r_{H_2}, but alloying with Pb up to 1% reduced this increase. Mansfeld and Gilman[52] prepared Zn-Pb and Zn-Al alloys [up to 1 weight per cent (w/o) Pb or Al] and showed that r_{H_2} values in 6*N* KOH were lower for these alloys than for pure zinc (99.999%). I found in addition that very pure zinc (99.999%) corroded faster in 6*N* KOH than zinc of lesser purity (99.95% and 99.9%) and attributed this to lead impurities, since similar r_{H_2} values were found for 99.5% Zn and a Zn-0.8 w/o Pb alloys prepared from high purity materials.[53]

T. S. Lee's conclusion in the paper under discussion is, therefore, not substantiated by experimental facts. In addition, it is well known that corrosion rates are determined by the interaction of oxidation and reduction reactions. An increase of the rate of the hydrogen evolution due to alloying might still not lead to an increase of corrosion rates because a still larger decrease of the rate of the metal oxidation reaction has resulted from alloying. For the case of zinc in KOH, the experimental evidence suggests, however, that alloying elements affect mainly the rate of the hydrogen evolution reaction.[51,53] More recent detailed investigations by Borchers and Krug[54] have shown that Cd and Pb accumulate on the surface of Zn during the initial corrosion period and then inhibit corrosion due to their higher hydrogen overpotential. Similarly from my results[53] it can be seen that the corrosion rate of pure Zn (99.999%) was constant over 160 hr after an initial decrease for 40 hr, while less pure zinc showed a longer period of decreasing corrosion rates. These results[53,54] also suggest that the beneficial effect of alloying elements can be entirely missed in short time experiments as it was apparently in the paper under discussion.

T. S. Lee: First of all, the main purpose of the paper under discussion was to present hydrogen overpotential data in concentrated KOH solution with uniformly prepared samples in clean environment. Mansfeld's comment above seems to have missed this point completely.

Second, the remarks the author made in the paper under discussion and quoted by Mansfeld were only intended to refer to the few impurities mentioned in the paper, *i.e.*, Cd, Fe, Ca, Mn, and Hg; this was not

[49] Science Center, Rockwell International, Thousand Oaks, California 91360.
[50] R. Vondracek and I. I. Jzak-Krisko, *Rec. Trav. Chim.*, 44, 376 (1925).
[51] H. Krug and H. Borchers, *Electrochim. Acta*, 13, 2203 (1968).
[52] F. Mansfeld and S. Gilman, *This Journal*, 117, 1328 (1970).
[53] F. Mansfeld, *Corrosion Sci.*, 11, 557 (1971).
[54] H. Borchers and H. Krug, *Metall*, 24, 952 (1970).

a general statement. It was also implied in the statement that impurities were present in the concentration range of 200-500 ppm and were uniformly distributed within the samples. It is general knowledge in electrochemistry that if sample A has a higher hydrogen overpotential than sample B, then sample A shows less corrosion than sample B in the same environment. The remarks in the paper under discussion were made following this kind of reasoning after comparing the hydrogen overpotential data. Mansfeld's comment above might be the result of misreading the paper.

Finally, the corrosion rate measurement by immersing a piece of the sample in the solution and letting the corrosion products accumulate on the surface of the sample with time is quite different from the hydrogen overpotential measurement. In the latter case, the surface of the sample at the beginning and the end of the experiment is, or is nearly, the same, while in the corrosion rate experiment, as mentioned by Mansfeld in his discussion, the surface of the sample at the beginning and the end of the experiment is quite different due to the corrosion reaction. The interpretation of data obtained from the same surface within a few hours is more easily or meaningfully obtained than from a different surface after 160 hr reaction. Besides, after certain lengths of time, the very minute amount of impurities in the solution may be readsorbed on the electrode surface which will effect the measurement.

As to the accuracy of correlating hydrogen overpotential data with those of corrosion rate measurements, there is a very nice correlation in our laboratory between my hydrogen overpotential measurements and J. C. Cessna's[55] corrosion rate measurements. In general, zinc containing Pb or Hg (in amounts greater than those discussed in the paper) has a higher hydrogen overpotential in concentrated KOH solution than pure zinc. In the corrosion rate measurement, it shows a lower corrosion rate which is completely agreeable with the published results. However, the result of the Zn-Al alloy in the work of Mansfeld *et al.* is quite different from the work obtained in this laboratory. Since it belongs in another subject of discussion, it will not be discussed here.

[55] J. C. Cessna, Private communication.

Erratum

In the paper "Electrogenerated Chemiluminescence. XI. Electrochemistry and Electrogenerated Chemiluminescence in Scintillator Dye Melts" by Csaba P. Keszthelyi and Allen J. Bard which appeared on pp. 241-246 in the February 1973 JOURNAL, Vol. 120, No. 2, the cathodic limit on the righthand side of Fig. 4 should read -1.60 not -1.90.

JOURNAL OF THE ELECTROCHEMICAL SOCIETY

SOLID-STATE SCIENCE AND TECHNOLOGY

DECEMBER 1973

Effects of Postdeposition Annealing Treatments on Charge Trapping in CVD Al_2O_3 Films on Si

D. A. Mehta

Western Electric Company, Allentown, Pennsylvania 18103

and S. R. Butler and F. J. Feigl

Lehigh University, Bethlehem, Pennsylvania 18015

ABSTRACT

Al_2O_3 films, 200 nm thick, were chemically vapor deposited on (100) silicon substrates by hydrolysis of $AlCl_3$ at 900°C in a H_2-rich atmosphere of H_2 and CO_2. Heat-treatment in H_2 atmosphere produces no change in the charge state of the oxide. Heat-treatment in O_2, N_2, or Ar atmospheres produces only a redistribution of the negative charge grown in during deposition. Heat-treatment in H_2 subsequent to that in O_2, N_2, or Ar restores the original charge distribution. The flatband voltage characterizing these shifts approached a constant value with time (10V). The temperature dependence of the rate of approach to saturation is consistent with first-order kinetics and an activation energy of 1.42 eV. These results and the effects of annealing on optically active charge trapping centers are interpreted in terms of a simple phenomenological model. It is suggested that the charge trapping centers are due to a hydrogen-related species formed during film deposition.

A recent paper described an investigation of electronic charge trapping in chemically vapor-deposited thin films of Al_2O_3 on silicon (1). That investigation was carried out on evaporated metal-Al_2O_3 insulator-silicon MIS structures. The techniques used to study trapping phenomena were photoinjection-photodepopulation measurements (2) and high-frequency capacitance-voltage (C-V) measurements (3). The results of these measurements were interpreted in terms of two distributions of trapped negative charges within the insulator.

Electrons photoemitted into the insulator and trapped within the insulator accounted for most of the insulator charge.[1] This negative charge was distributed rather uniformly throughout the insulator. It was also determined to be a bounded distribution as a function of energy within the forbidden gap of the insulator, beginning approximately 2 eV below the conduction band edge. Some of this photoinjected trapped charge could thus be released by photons of energy 2.5 eV and removed from the insulator. In addition, a smaller negative charge distribution was incorporated into the Al_2O_3 films during deposition. This charge was concentrated near the metal electrode.

The present paper presents and discusses a program of postdeposition heat-treatments carried out on chemically vapor-deposited thin films of Al_2O_3 and their effect on the electronic trapping behavior of such films.

Key words: MIS structure, thin dielectric films, photoconduction in insulators, C-V measurements, chemical vapor deposition.

[1] The charging of insulator films by photoemission of charge carriers and subsequent capture into localized defect states is referred to as photoinjection. It was previously demonstrated that negative charging of alumina films could be achieved by photoinjection of electrons from both the silicon and metal electrodes [see Ref. (1)].

These measurements were undertaken to obtain some insight as to the nature and origin of the trapping centers responsible for capture of photoinjected electrons (4). Results have been interpreted in terms of a phenomenological model of hydrogen-related defects.

Experimental Procedure

Sample preparation.—All MIS specimens used in this investigation were prepared as previously described (1), with the insulator consisting of 200 nm of Al_2O_3. This thickness was selected on the basis of practical technological significance and on the basis of having thick enough film to obtain large measurable currents during photodepopulation measurements. Al_2O_3 was deposited by hydrolysis of $AlCl_3$ at 900°C in a hydrogen-rich mixture of H_2 and CO_2 (5). The volume fraction of gases entering the reaction zone were 0.02 CO_2, 0.005 $AlCl_3$, and the remainder H_2. Transmission electron diffraction on these films indicated a structure similar to bulk κ Al_2O_3 (6), with a grain size of 10-30 nm.

Measurement techniques.—The principal measurement techniques used were photoinjection-photodepopulation (2) and high frequency C-V measurements (3). The equipment and procedures used have been described in detail in the previous publication in this series (1). A brief technical description of the first technique is given in the Appendix to the present paper. The photoinjection-photodepopulation and C-V measurements were made in separate experimental facilities.

In general, flatband voltages, V_{FB}, as determined by C-V measurements (7, 8), are used to determine the

product $\bar{x}\,Q$, where $\bar{x}$ is the first moment (the centroid) of the charge distribution within the insulator and Q is the total charge within this distribution

$$\bar{x} = \frac{1}{Q}\int_0^L x\,\rho(x)\,dx,\quad Q = \int_0^L \rho(x)\,dx \qquad [1]$$

In these expressions $\rho(x)$ is the charge density within the insulator at some distance x from the metal electrode interface (L = insulator thickness, see Table I). As discussed in the section on Results and Discussion these measurements were performed at any desired stage of the fabrication and annealing processes on the insulator films. Also, these measurements have been made both before and after photoinjection of electronic carriers into the insulator (1).[1] In this case, the associated differences in V_{FB} were interpreted in terms of electrons captured in trapping states during transport across the insulator film.

The insulator charge was also investigated by electrometric measurements of trapped charge released by optical photons below the photoinjection threshold.[2] The measurement of primary interest was total released charge *vs.* applied voltage (Q-V), measured with fixed optical wavelength [480 nm in the present case, this being slightly below the silicon-Al_2O_3 photoinjection threshold (9)]. As discussed previously (1), these experiments were analyzed in terms of optically accessible trapped charge (*i.e.*, that fraction of the total insulator charge which can be optically excited into the Al_2O_3 conduction band by 480 nm light) and "fixed" insulator charge (*i.e.*, that fraction of the insulator charge which cannot be photoexcited to conducting states by 480 nm light). In these experiments, the centroid $\bar{x}$ and the total charge Q within the insulator charge distribution $\rho(x)$ can be separated (2).

The Q-V measurements, as the C-V measurements, can be performed at any desired stage of the oxide deposition-heat-treatment cycle. Also, C-V measurements were made before and after photodepopulation to determine the internal consistency of the basic experimental interpretation just described.

Heat-treatments.—All heat-treatments were carried out in a diffusion furnace and/or a closed reactor (the same unit used for film deposition) at temperatures at or below the deposition temperature. Transmission electron microscopy and diffraction data obtained on samples subjected to the most severe heat-treatments showed no measurable change in crystal structure or morphology from as-deposited samples. Thus, all specimens measured in the present program were structurally the same as polycrystalline bulk κ-alumina.

The following annealing sequences on Si/Al_2O_3 specimens were studied: (*i*) a series of heat-treatments was carried out in nitrogen atmosphere (3 lpm flow rate) as a function of temperature (450°-900°C) and time (0.25-48 hr); (*ii*) a series of annealing treatments was carried out at 900°C for 2 hr in N_2, Ar, O_2, and H_2 atmospheres; and (*iii*) a series of annealing treatments was carried out at 900°C for 2 hr in various mixtures of H_2 and N_2, in order to determine the effect of variations of the partial pressure of H_2 (p_{H_2}). High frequency C-V measurements were performed on specimens after each step in the sequences just described. On selected specimens, C-V measurements were also performed after photoinjection and after subsequent photodepopulation at 480 nm. Photodepopulation Q-V measurements were also performed at selected steps in the several annealing sequences.

Each of the measured data points to be described in the next section represents an average of at least six samples. Variations from sample to sample are shown by error bars or ranges wherever such variations were measurable. In the cases where these are not shown, the variations were within the experimental accuracy (better than ± 10%) of the particular measurement.

[2] Optical excitation of trapped charge carriers into mobile states and removal of the released charge from the insulator is referred to as photodepopulation.

Table I. Definitions of terms

MOS capacitor characteristics
- A = area of the metal electrode (0.1 ± 0.02 cm²)
- L = thickness of the dielectric (2.0 ± 0.1 × 10^{-5} cm)
- C = capacitance per unit area
- ϵ = dielectric permittivity of Al_2O_3 = 8.42 × 10^{-13} F/cm
- e = electronic charge (coulomb)
- N = charge density in the insulator (cm^{-3})

CV measurements
- V_{FB1} = flatband voltage of as-deposited sample (V)
- V_{FB2} = flatband voltage after photoinjection in as-deposited sample (V)
- V_{FB3} = flatband voltage after photodepopulation in as-deposited sample (V)
- V'_{FB1} = saturation flatband voltage value reached during heat-treatment in nitrogen (V)
- V'_{FB2} = flatband voltage after photoinjection in heat-treated samples (V)
- V'_{FB3} = flatband voltage after photodepopulation in heat-treated samples (V)

Q-V measurements (see Fig. 3a, 3b)
- q = total releasable charge = $q_+ - q_-$ (coulomb)
- $\bar{x}_1$ = distance of the centroid of the released charge from the metal-insulator interface = $\dfrac{q^+}{q_+ - q_-}$ (cm)
- Q_{f1} = part of the fixed charges having centroid $\bar{x}_1 = AC\dfrac{V_+ - V_0}{V_+ - V_-}$
- Q_{f2} = remaining part of the fixed charges (coulomb)
- $\bar{x}_2$ = distance of the centroid of Q_{f2} from the metal-insulator interface (cm)

Corresponding quantities in heat-treated specimens are designated by primed variable (*e.g.*, q', x', etc.)

Results and Discussion

In this section, the results of various experiments are presented and described. These results are analyzed in terms of a phenomenological model of hydrogen-related electron trapping defects in Al_2O_3 in the section on Model for Electron Trapping in Al_2O_3. The notation and terminology used to describe the experimental results and the analysis are listed in Table I. These notations are consistent with Ref. (1) and (7). Further simplification is made by using the centroid and the total charge to characterize the spatial distribution of the charges in the insulator (*i.e.*, $\bar{x}$ and Q as described in Eq. [1]). These are preferred to the integral expressions in Eq. [1], since this is the extent to which charge distributions can be specified using the present techniques.

As-deposited samples.—The photoinjection-photodepopulation and C-V measurements on as-deposited samples were described in the first paper in this series (1). A summary of the results of these measurements is given in Table II, since the measurements on heat-treated samples (described below) are to be compared with the results on as-deposited samples. It was shown in (1) that the thin films of chemically vapor-deposited Al_2O_3 on silicon have "grown-in" negative charges (denoted by N_{f2}) localized near the metal electrode interface. The centroid was found to be $0.14L$ measured from the metal-Al_2O_3 interface (4). These charges give rise to the initial flatband voltage, V_{FB1}, observed on the as-deposited samples. During photoinjection, additional charges N_T are trapped in the insulator, with centroid $\bar{x}_1 = 0.7L$. This increases the flatband shift to V_{FB2}. During photodepopulation, electronic charge of number density n_T is removed from the insulator, leaving behind a "fixed" negative charge N_{f1}. Thus, only a partial recovery in the flatband voltage occurs ($V_{FB3} > V_{FB1}$).

Heat-treated samples.—The heat-treatments were carried out on Al_2O_3 deposited on silicon, with time, temperature, and atmosphere as parameters, as described in the section on Experimental Procedure.

Figure 1 shows the results of flatband voltage measurements as a function of time and temperature of heat-treatment. These heat-treatments were carried out in an N_2 atmosphere. The curves are computer-plotted least squares best fit to the experimental data

Table II. Summary of results on as-deposited samples

Flatband voltage shifts (see Table I)

$V_{FB1} = 2.0 \pm 1.0V$ $V_{FB2} = 38.5 \pm 2.0V$ $V_{FB3} = 29.0 \pm 2.0V$

Equivalent charge densities (see Table I)
The numbers quoted are volume-average equivalent charge densities, related to net charge or voltage data from C-V or Q-V experiments by the defining relations

$$eLN = \frac{Q}{A} = CV$$

1. Fixed charges in as-deposited samples
$\bar{x}_2 N_{f2} = \frac{C}{e}(V_{FB1})$: $N_{f2} = 2.1 \times 10^{17}$ cm^{-3}, $\bar{x}_2 = 0.14L$
2. Trapped charges introduced by photoinjection
$\bar{x}_1 N_T = \frac{C}{e}(V_{FB2} - V_{FB1})$: $N_T = 6.4 \times 10^{17}$ cm^{-3}, $\bar{x}_1 = 0.70L$
$\bar{x}_1 N_{f1} = \frac{C}{e}(V_{FB3} - V_{FB1})$: $N_{f1} = (4.9 \pm 0.2) \times 10^{17}$ cm^{-3}, $\bar{x}_1 = 0.70L$
3. Trapped charges removed by photodepopulation
$\bar{x}_1 n_T = \frac{C}{e}(V_{FB2} - V_{FB3})$: $n_T = (1.5 \pm 0.2) \times 10^{17}$ cm^{-3}, $\bar{x}_1 = 0.70L$

From Q-V measurements:

$$n_T = \frac{q}{eLA} = \frac{q_+ - q_-}{eLA}$$

$$N_{f1} = \frac{Q_{f1}}{eLA} = \frac{C(V_+ - V_-)}{eL}$$

$$\frac{\bar{x}_1}{L} = \frac{V_+ - V_o}{V_+ - V_-} = \frac{q_+}{q_+ - q_-}$$

and the parameters are given in the figure caption. The following observations can be made from the results: (a) the flatband voltage as a function of time reaches a saturation value, V'_{FB1}; (b) V'_{FB1} is approximately independent of temperature; and (c) the rate at which V'_{FB1} is reached is determined by

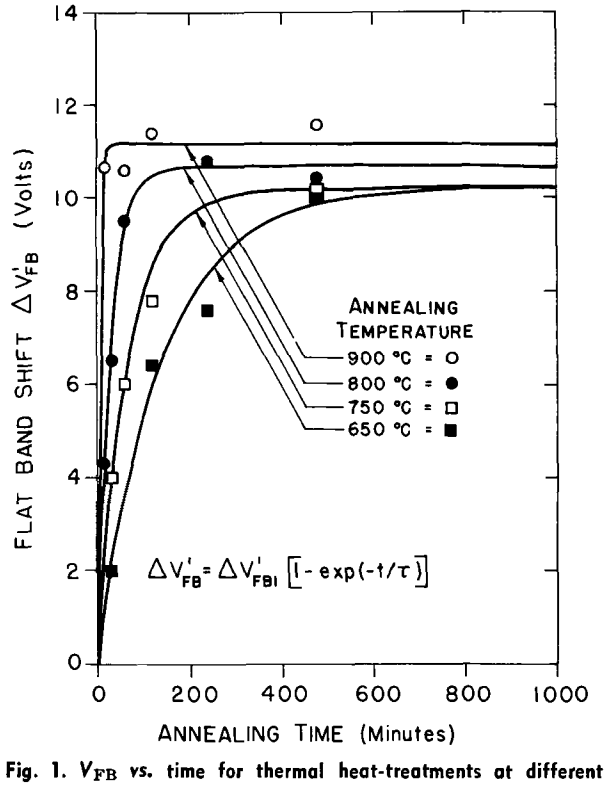

Fig. 1. V_{FB} vs. time for thermal heat-treatments at different annealing temperatures T. The solid curves represent least squares best fits of the data to the two-parameter exponential function indicated in the drawing. The root mean square deviation for the several curves range from 0.192 (800°C) to 0.419 (650°C). The average value of $V'_{FB1} = V_{FB1} + \Delta V'_{FB1}$ for the several curves is 12.5V. A 48-hr anneal at 600°C resulted in $V'_{FB} = 12.3V$, consistent with the data shown. A 48-hr anneal at 450°C produced no significant flatband shift [see Ref. (4)].

Table III. Results of heat-treatments in various atmospheres (900°C, 2 hr)

Atmosphere of heat-treatment	Flatband voltage V_{FB} after heat-treatment,* V
N_2	12.4 ± 2.0
A	10.0 ± 2.0
O_2	12.7 ± 2.0
H_2	2.9 ± 1.0
N_2 followed by H_2	2.9 ± 1.0

* Flatband voltage in as-deposited condition was 2.0 ± 1.0V.

$$\Delta V'_{FB} = \Delta V'_{FB1}(1 - \exp -t/\tau) \quad [2]$$

where

$$\Delta V'_{FB} = V'_{FB}(t) - V_{FB1}$$

$$\Delta V'_{FB1} = V'_{FB1} - V_{FB1}$$

and where the reaction time τ is a decreasing function of temperature.

In order to determine the effect of ambient atmosphere on V'_{FB1}, heat-treatments were carried out at 900°C for 2 hr in various atmospheres as previously described. The results are listed in Table III. There is essentially no change in V_{FB} produced by hydrogen annealing treatments. However, in all other atmospheres, the shift in V_{FB} after heat-treatment is the same. Therefore, the effect observed in these heat-treatments appears to be caused by a change in some hydrogen-related species rather than some oxidation-reduction process. Further, as indicated in Table III, samples which had been heat-treated in N_2 and subsequently heat-treated in H_2 at 900°C exhibited flatband shifts essentially the same as those observed in as-deposited specimens. Thus, the effect of heat-treatment in nitrogen is reversible by subsequent heat-treatment in hydrogen.

Assuming that a change in some hydrogen-related species was responsible for the observed shift in the flatband voltage, a dependence on H_2 partial pressure in the annealing ambient was anticipated. A limited number of heat-treatments were carried out in various mixtures of H_2 and N_2 at 900°C for 2 hr, and the results of these experiments are shown in Fig. 2. These data

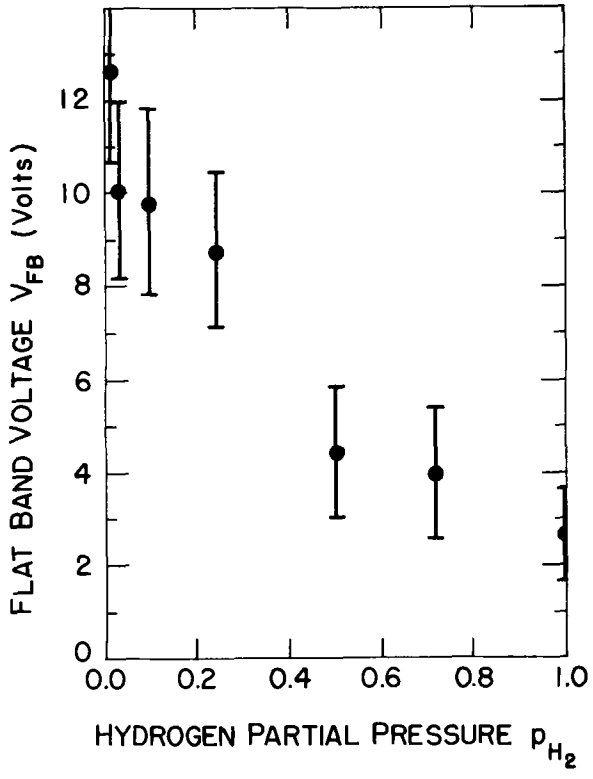

Fig. 2. V'_{FB} vs. p_{H_2}, for a 2-hr annealing treatment at 900°C. The indicated errors represent extreme values for the several specimens measured.

Table IV. Results of C-V measurements on heat-treated samples

Condition of sample (See Table I)	Flatband voltage, V
After heat-treatment, V'_{FB1}	12.0 ± 2.0
After photoinjection, V'_{FB2}	40.3 ± 3.0
After photodepopulation, V'_{FB3}	33.7 ± 2.0

are V'_{FB1} *vs.* p_{H_2}, the partial pressure of H_2 during the annealing treatment. It can be seen that V'_{FB1} increases monotonically as p_{H_2} is reduced.

In all of these measurements the observed flatband shifts are proportional to $\overline{xQ}$, as defined in Eq. [1]. Thus, an increasing V_{FB} may be caused by an increase in net negative charge Q during annealing, a shift in centroid of the initially existing charges in the as-deposited samples toward the Si/Al_2O_3 interface (*i.e.*, an increase in $\bar{x}$), or both. As described later, the results of C-V measurements after photoinjection on heat-treated samples showed that no charge had been added to the insulator during the heat-treatment. Therefore, the centroid of the as-deposited negative charges must have shifted toward the Si/Al_2O_3 interface.

Photoelectrical measurements.—On some samples which had been heat-treated to saturation (*i.e.*, to attainment of V'_{FB1}), the photoinjection and photodepopulation measurements were carried out, as described in Ref. (1) and in the section on Experimental Procedure. Table IV lists the results of C-V measurements after heat-treatment, after photoinjection, and after subsequent photodepopulation. It can be seen from these results that the flatband voltage after photoinjection on heat-treated samples, V'_{FB2}, is essentially the same as V_{FB2}, the flatband voltage after photoinjection on as-deposited samples (see Table II). Also, the recovery resulting from photodepopulation, $\Delta V'_{FB} = V'_{FB2} - V'_{FB3}$, is apparently less than the corresponding ΔV_{FB} on as-deposited samples.

Figure 3 shows the results of Q-V measurement on as-deposited and on heat-treated samples. From this data, the parameters $n't$, N'_{f1}, N'_T, $\bar{x}'_1$, etc., were calculated and the results are summarized in Table V. These results indicated: (*i*) the centroid of both fixed and optically released charges in heat-treated samples is essentially the same as the centroid of photoinjected charges in as-deposited samples, (*ii*) the density of the optically released charge is less in heat-treated samples than in as-deposited samples, and (*iii*) there are no charges in the heat-treated samples which correspond to the grown-in charges N_{f2} located near the metal-Al_2O_3 interface in the as-deposited samples (see Table II). It should be noted that the locations of the centroids were quite reproducible from sample to sample and, therefore, they may be related to the deposition process.

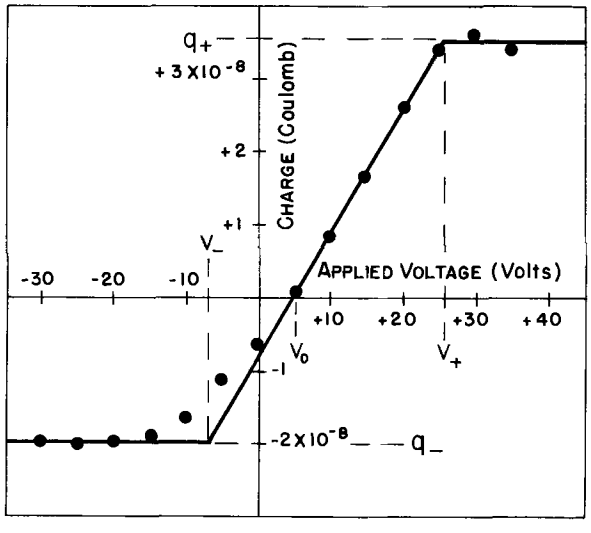

Fig. 3a. Photodepopulation Q-V data (solid circles) from as-deposited MIS specimen. The important quantities $q'_\pm$, $V'_\pm$, and V'_0 are indicated by dash lines on the diagram (see Tables I and II). The solid lines represent the idealized response expected from the distributions n'_T and N'_{f1} [see Tables I and II, Fig. 4(B-D), and Ref. (1)]. Deviations from this idealized curve are associated with the interfacial grown-in negative charge distribution N_{f2} [see Tables I and II and Ref. (1)].

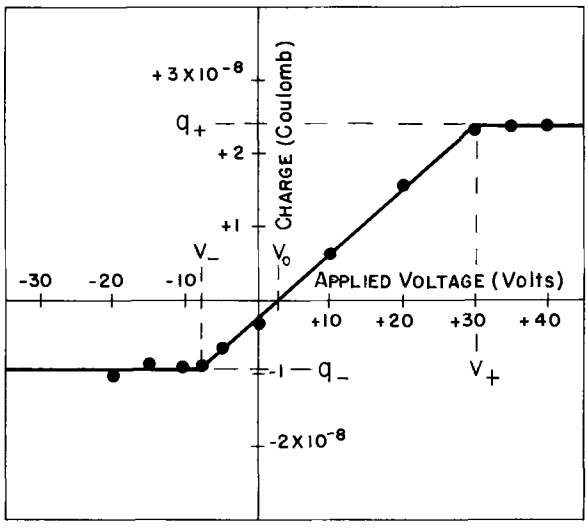

Fig. 3b. Photodepopulation Q-V data (solid circles) from MIS specimen heat-treated in nitrogen. The annealing time was sufficient to produce a saturated flatband shift V'_{FB1} (see Fig. 1). The important quantities $q'_\pm$, $V'_\pm$, and V'_0 are indicated by dash lines on the diagram (see Tables I and V). The solid lines represent the idealized response expected from the distributions n'_T and $N'_f = N'_{f1} + N'_{f2}$ [see Tables I and V and Fig. 4(E-H)]. The absence of significant deviation from the idealized response indicates that no interfacial distribution exists (*i.e.*, no charges corresponding to Q_{f2} or N_{f2} in as-deposited samples).

Model for Electron Trapping in Al_2O_3

The observed shift in the flatband voltage was apparently caused by a change in some hydrogen-related species in the Al_2O_3 films (see Table III). Incorporation of hydrogen in these films is consistent with deposition conditions, since hydrolysis of $AlCl_3$ is accomplished in nominally 98% by volume hydrogen atmosphere. The over-all deposition reaction, suggested by Tung and Caffrey (5), is

$$2AlCl_3 + 3H_2 + 3CO_2 = Al_2O_3 + 6HCl + 3CO \quad [3]$$

It can be shown that the thermodynamics of this reaction are favorable for formation of the stable phase α-Al_2O_3 (10). However, the deposit is a metastable phase, κ-Al_2O_3. In bulk materials, κ-Al_2O_3 is produced as one of the metastable products resulting from dehydration of AlO-OH (11). These metastable phases

Table V. Results of Q-V measurements on heat-treated samples (see Fig. 3b)

Numbers quoted are volume-average equivalent charge densities, defined in Table II.

Density of optically releasable charges, n'_T	(1.0 ± 0.1) × 10^{17} cm^{-3}
Density of fixed charges, N'_f	(5.7 ± 0.2) × 10^{17} cm^{-3}
Density of total charges, $N'_f + n'_T$	6.7 × 10^{17} cm^{-3}
Centroid of n'_T and N'_f, $\bar{x}'_1$	(0.75 ± 0.10) L

$$n'_T = \frac{q'}{eLA} = \frac{q'_+ - q'_-}{eLA} \qquad N'_f = \frac{Q'_{f1}}{eLA} = \frac{C(V'_+ - V'_-)}{eL}$$

$$\frac{\bar{x}'_1}{L} = \frac{V'_+ - V'_0}{V'_+ - V'_-} = \frac{q'_+}{q'_+ - q'_-}$$

As indicated in Fig. 3b, Q'_{f2} is zero in heat-treated specimens (see Table I). Thus, the interfacial charge distribution observed in as-deposited films (N_{f2}) is not observed in heat-treated films.

are reported to be nearly, but not completely, anhydrous. They retain some of the crystal structural characteristics of the parent phase (12). Thus, it is reasonable to expect some form of hydrogen-related "defect" species in these Al_2O_3 films.

The proposed model is summarized in Fig. 4 which shows a one-dimensional schematic representation of the spatial distribution of charge in Al_2O_3. It also demonstrates the variation of these distributions with specimen heat-treatment, and/or photoinjection and photodepopulation. Note that the distributions are represented by $\overline{x}Q$, *i.e.*, by total charge located at the distribution centroids. It is proposed that both negative charges near the metal electrode interface (N_{f2}, see Table II) and hydrogen-related defect centers exist in the as-deposited films, Fig. 4A, B, and E. The hydrogen species are presumed to be neutral (when unoccupied) trapping centers. During heat-treatment some of the neutral centers thermally decompose, consuming the initially existing negative charge from the N_{f2} distribution, Fig. 4F. One possible mode in which this process can occur is that the decomposition of the defect center releases an H^+ ion. This H^+ ion then diffuses toward the outer surface, combines with a negative charge, and escapes as part of a neutral H_2 molecule. The extent of this process would thus depend on the hydrogen content of the ambient. It should be emphasized that it is not necessary to postulate a detailed process such as described above for analysis of any result except the dependence of the flatband voltage on partial pressure of hydrogen. The over-all process may be described by a reaction

(Neutral defect) + (Negative charge from N_{f2})

= (Negatively charged defect) [4]

It is further suggested that the neutral hydrogen defect centers can also be converted to negatively charged defects by trapping electrons during the photoinjection process (Fig. 4C). The concentration of these centers is given by $N_T(x)$ (with centroid $\overline{x_1}$). At any given stage of the annealing cycle:

$N_d(x)$ = concentration of decomposed centers at x

$N_u(x)$ = concentration of undecomposed centers at x

where,

$$N_T(x) = N_d(x) + N_u(x) \quad [5]$$

If is is assumed that the total number of centers that will decompose at any position x, at saturation, is proportional to the total concentration of these centers at x, *i.e.*

$$N_d(x) = AN_T(x), \qquad A = \text{constant}$$

then

$$N_u(x) = N_T(x)(1 - A) \quad [6]$$

Therefore, $N_u(x)$, $N_d(x)$, and $N_T(x)$ will all have the same centroid $\overline{x_1}$, Fig. 4F. Although there is no prior justification for this last assumption, it is reasonable since the decomposition events should be thermally activated in a random manner. It is also consistent with the observed results of Q-V measurements on as-deposited as well as heat-treated samples, since the centroid of the charges N_T and N'_T and N'_{f2} is the same (see Tables II and V and Fig. 4B and G).

The maximum number of neutral grown-in centers that can decompose is limited by N_{f2} according to Eq. [4]. Thus, after heat-treatment, the saturation flatband voltage, V'_{FB1}, is given by

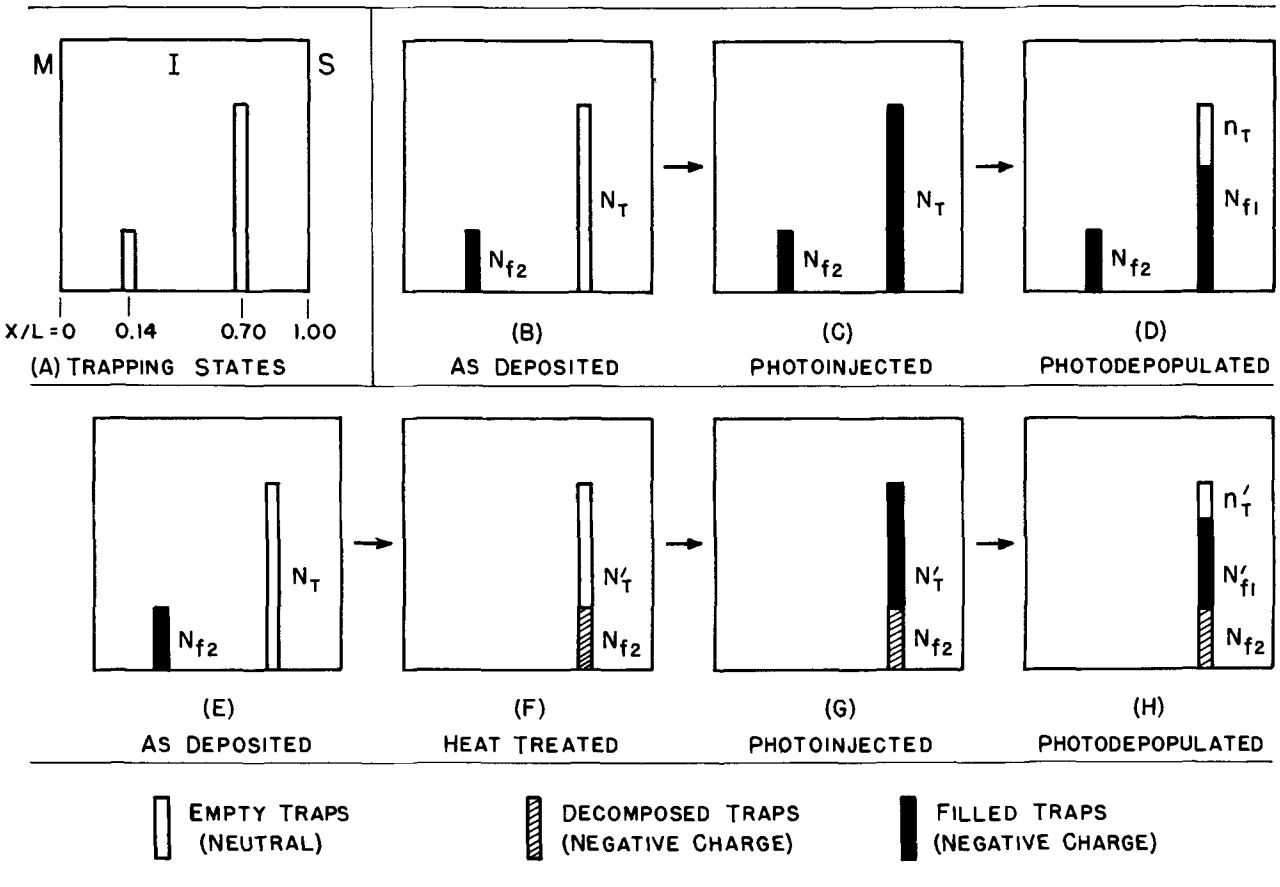

Fig. 4. Schematic representation of spatial charge distributions in MIS specimens incorporating CVD-alumina dielectrics. (A) Over-all geometry and equivalent negative charge distributions, represented by volume-average number densities N and centroids $\overline{x}/L$. (B-D) Photoinjection-photodepopulation sequence on as-deposited Al_2O_3 films [see Table II and Ref. (1)]. (E-H) Proposed heat-treatment-photoinjection-photodepopulation sequence on CVD Al_2O_3 films (see Tables III-V).

$$V'_{FB1} = \frac{\overline{x}}{L} BN_{dmax} = \frac{\overline{x_2}}{L} BN'_{f2} \frac{\overline{x}}{\overline{x_2}} = V_{FB1} \frac{\overline{x}}{\overline{x_2}}, \quad B = \frac{eL^2}{\epsilon} \qquad [7]$$

where $N_{dmax} = N'_{f2}$ the maximum concentration of decomposed centers and $V_{FB1} = \frac{\overline{x_2}}{L} BN_{f2}$ is the as-deposited flatband shift. Note that, as in Ref. (1), the work-function term and the surface-state term in the expression of the flatband voltage (7) are neglected since their contribution was shown to be within the range of reproducibility of the C-V measurements. Using the values of $V_{FB1} = 2.0$V, $\overline{x}_1 = 0.7L$, and $\overline{x}_2 = 0.14L$ for the as-deposited samples, the predicted value of V'_{FB1} is 10V. This value agrees with the observed value of $V'_{FB1} = (12 \pm 2)$ V (see Tables II and IV).

Time dependence of the flatband voltage during heat-treatment.— If N_d = concentration of centers decomposed at time t then $(N_{dmax} - N_d)$ equals the concentration of centers that remain to be decomposed, and if first-order kinetics are assumed

$$\frac{d(N_{dmax} - N_d)}{dt} \propto (N_{dmax} - N_d) \qquad [8]$$

and therefore

$$\frac{N_{dmax} - N_d}{N_{dmax}} = \exp(-t/\tau) \qquad [9]$$

where τ is a characteristic decay time for the decomposition reaction, Eq. [4]. The concentration of defect centers may be converted to flatband voltage, and the result is given by Eq. [2] and is fit to the data in Fig. 1.

A plot of $1/\tau$ *vs.* $1000/T$, T = absolute temperature, is shown in Fig. 5. From the slope of this plot, an activation energy E was determined from the decomposition reaction [4], $E = 33 \pm 1$(kcal/mole). According to the suggested mechansim of the decomposition process this energy can be related to either the decomposition of the center or the diffusion of the hydrogen ion. Diffusion data on hydrogen-related species in alumina are not available and, therefore, it is not possible at the present time to isolate the rate limiting process. We suggest that the kinetics of the postulated decomposition reaction, Eq. [4], are limited by diffusion of hydrogen.

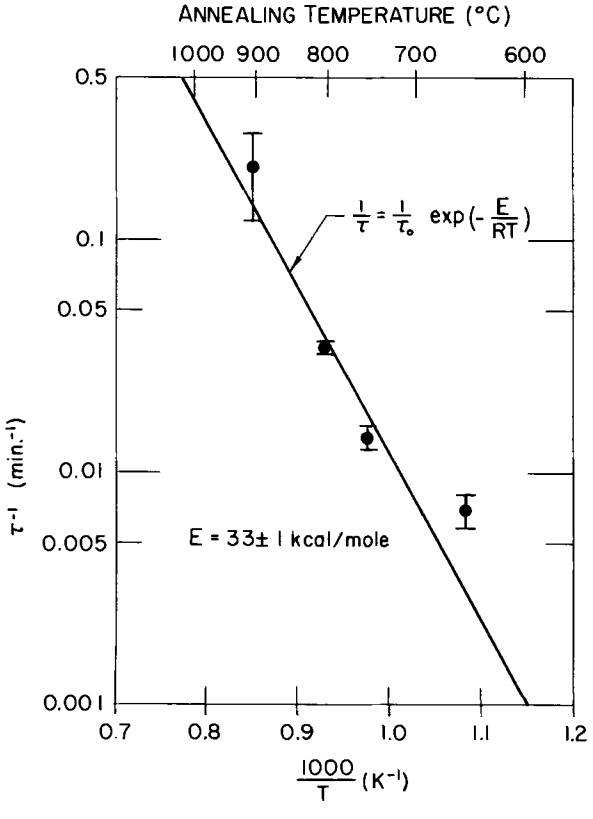

Fig. 5. $1/\tau$ *vs.* $1000/T$, where $1/\tau$ = statistically fit parameter from isothermal annealing data (Fig. 1) and T = annealing temperature. The error estimates on individual data points (solid circles) are obtained from the statistical fit of Fig. 1. The solid line is a statistically weighted least square fit of the data to the two-parameter exponential function indicated on the drawing. R is the gas constant. The quoted error on the resultant activotion energy represents the rms error of the weighted fit.

Photoinjection-photodepopulation in heat-treated samples.—The basic thesis, depicted in Fig. 4E and F, is that heat-treatment results in a reaction between some of the centers N_T and the charges denoted as Q_{f2}. These decomposed centers are negatively charged and cannot trap electrons during photoinjection. Thus, the maximum number of centers that can trap electrons in samples heat-treated to saturation is $N'_T = N_T - N_{f2}$ (Fig. 4F).

If it is further assumed that the distribution in energy of available trapping states (1) is diminished uniformly during decomposition (*i.e.*, the density of sites is diminished without altering the distributions in space and energy) it follows that

$$\frac{n'_T}{N'_T} = \frac{n_T}{N_T} \qquad [10]$$

Using the values of N_T, N_{f1}, N_{f2}, and n_T obtained for as-deposited samples (Table II), the predicted value of $n'_T = 1.0 \times 10^{17}$ cm^{-3}. This value is in excellent agreement with the observed value of $n'_T = 1.0 \times 10^{17}$ cm^{-3}. Similar calculations can be performed to predict the value of various measured parameters from both C-V and Q-V experiments, based on the proposed model of trapping defects and on the equivalent trapping state densities obtained for as-deposited films. Such predicted values are compared with the measured values of the important parameters in Table VI. It is clearly demonstrated that the proposed model is entirely consistent with the experimental results of this research.

Flatband shifts from heat-treatments in H_2/N_2 gas mixtures.—A brief series of heat-treatments in H_2/N_2 atmospheres was described in the section on Results and Discussion. The data show a monotonic increase in the saturation flatband shift with decreasing hydrogen partial pressure. This would be expected if the decomposition of these centers requires hydrogen to be removed from the film. Attempts have been made to develop an analytical expression for the functional dependence of the flatband voltage on p_{H_2} based on the thermodynamics of the reaction represented by Eq. [4] and are presented elsewhere (4). The reversibility of the charge redistribution resulting from subsequent hydrogen heat-treatments implies that no significant structural relaxation occurs upon decomposition. In view of the small "atom" fraction that these hydrogens constitute this seems reasonable. In this respect it should be noted that the very small grain size of these films (~20 nm) implies a rather large number of grain boundary related sites. Thus, the sites which decompose because the hydrogen can get away from them may be related to grain boundaries.

Table VI. Comparison of observed and predicted values of various parameters based on the proposed phenomenological model

	Observed value	Predicted value
n'	1.0×10^{17} cm^{-3}	1.0×10^{17} cm^{-3}
N'_t	5.7×10^{17} cm^{-3}	5.4×10^{17} cm^{-3}
Charges corresponding to N_{f2}	0	0
V'_{FB1}	12.0V	10.0V
V'_{FB2}	36.5V	40.3V
$\Delta V'_{FB}$ (= $V'_{FB2} - V'_{FB1}$)	6.3V	6.5V

Summary and Conclusions

The present experiments indicate that postdeposition annealing treatments in Ar, O_2, and N_2 atmospheres result only in a redistribution of the negative charge grown into chemically vapor-deposited films of Al_2O_3 on silicon. The flatband voltage shift after heat-treatment, which is a measure of this redistribution, reaches a saturation value of approximately 10V. This saturation value is independent of annealing temperature in the range of 600°-900°C. No flatband shift (and hence no charge redistribution) is observed after annealing in H_2 atmospheres. Also, the effect of heat-treatment in Ar, N_2, and O_2 is reversible by subsequent heat-treatment in hydrogen. The temperature dependence of the rate of approach to saturation is consistent with a first-order kinetic process with an activation energy of approximately 33.0 kcal/mole.

The total insulator charge after ultraviolet photoinjection of electrons into the Al_2O_3 films was the same in heat-treated specimens (for all annealing atmospheres) as in as-deposited specimens. The average number density of total negative charges was approximately 6×10^{17} cm^{-3}. The fraction of insulator charge which could be photodepopulated by 2.5 eV photons was approximately 25% in as-deposited films and 17% in films annealed in Ar, N_2, or O_2. In both as-deposited and annealed specimens, photoinjected electronic charge was distributed rather uniformly throughout the insulator film, with a distribution centroid located approximately $0.7L$ from the metal electrode (L = insulator thickness). Fixed charges which incorporated into the as-deposited specimens near the metal-Al_2O_3 interface (average density 2×10^{17} cm^{-3}) were not observed in specimens annealed in Ar, N_2, or O_2.

The experiments were interpreted in terms of a phenomenological model of hydrogen-related trapping centers in Al_2O_3. During the annealing treatments these centers decompose. This decomposition consumes the negative interfacial charges grown into the Al_2O_3 MIS specimens during initial deposition. Thus, the number of centers decomposing during subsequent heat-treatment is limited by the number of grown-in charges. The hydrogen-related defect, which is electrically neutral in the as-deposited sample, can also be negatively charged by trapping conduction electrons, and these centers are responsible for electron capture during photoinjection.

Acknowledgment

We should like to acknowledge many enlightening discussions with Dr. J. J. Curry of Bell Telephone Laboratories, Allentown, Pennsylvania. We also wish to express appreciation for Mr. V. Kapoor of Lehigh University for his help with computer analysis of some of the data. Partial support for S. R. Butler was provided by National Science Foundation.

Manuscript submitted Jan. 8, 1973; revised manuscript received July 5, 1973.

Any discussion of this paper will appear in a Discussion Section to be published in the June 1974 JOURNAL.

APPENDIX

The investigation of charge trapping behavior described in this work involved photoinjection-photodepopulation measurements. The technique of photoinjection-photodepopulation, and the equipment used in these measurements, are described in detail in previous papers (1, 2, 4). An outline of the principles involved in these measurements is presented here.

Figure 6(a) shows a schematic energy band diagram of a metal/insulator/silicon system. It also shows a discrete trap level in the forbidden energy gap of the insulator. Figure 6(b) represents the first step of the measurement cycle, *i.e.*, photoinjection. During photoinjection, electrons are excited out of the valence band of silicon (or, alternatively, from the metal) into states in the conduction band of the insulator by means of photons of energy $h\nu_1$. In simplest approximation this requires that $h\nu_1 > |E_{c\,ins} - E_{v\,Si}|$. If an external field is applied across the insulator, a large photocurrent can be observed in the external circuit. While this photocurrent is flowing through the insulator, some of the charges are captured into localized states with energies lying in the forbidden energy gap of the insulator. The fraction of available trapping states filled during the photoinjection step will be a function of the detailed balance between the capture of electrons in the traps and the re-emission of the trapped electrons due to simultaneous photoexcitation.

Photodepopulation is carried out subsequent to photoinjection. During photodepopulation, electrons are excited out of the traps into the conduction band of the insulator by photons of energy $h\nu_2$. This requires that $h\nu_2 > |E_{c\,ins} - E_T|$ (however, to avoid photoinjection, $h\nu_2 < |E_{c\,ins} - E_{c\,Si}|$). By applying the proper bias voltage, these charges can be collected in the external circuit. These charges are measured by high precision electrometry. The photodepopulation step is represented by Fig. 6(c).

The photodepopulation measurements can be used to determine the energy and spatial distribution of trapping states in the insulator by judicious choice of measurement variables (2). Most of the work described in this paper deals with the parameters representing the spatial distribution. These parameters are obtained

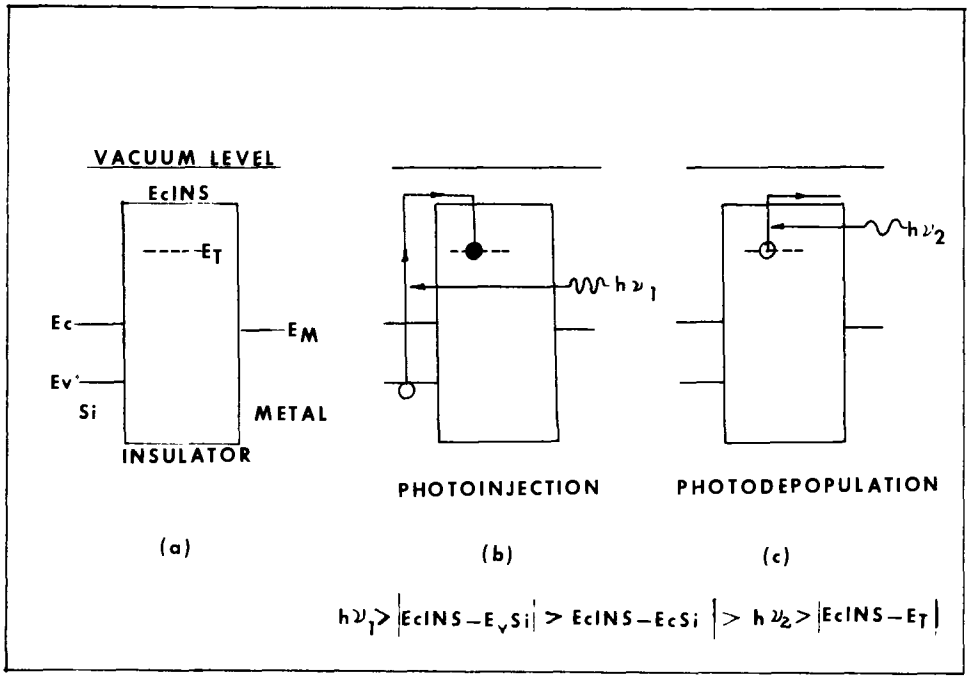

Fig. 6. Schematic representation of photoinjection and photodepopulation processes in MIS structures: (a) hypothetical energy band diagram, (b) photoinjection process, and (c) photodepopulation process.

from determination of the total charge transported through the external (electrometer) circuit during photodepopulation with fixed optical wavelength and fixed applied voltage (Q-V measurement). The wavelength used throughout this series of measurements was 480 nm, slightly longer than the wavelength threshold for photoinjection of electrons from silicon into Al_2O_3 at the applied voltages used (9). The released charge was measured for a time sufficient to reach a steady-state condition, *i.e.*, until the photodepopulation current stabilized at dark current value. The photodepopulation measurements were carried out on the same sample at various voltages while keeping the wavelength of the depopulation light source the same and populating the traps each time by photoinjection with uv light as previously described. The released charge, Q, in each case, was plotted as a function of applied voltage, V. The spatial distribution parameters were obtained from the analysis of these Q-V measurements (4).

REFERENCES

1. D. A. Mehta, S. R. Butler, and F. J. Feigl, *J. Appl. Phys.*, **43**, 4631 (1972).
2. J. H. Thomas and F. J. Feigl, *J. Phys. Chem. Solids*, **33**, (1972).
3. L. M. Terman, *Solid State Electron.*, **5**, 285 (1962).
4. D. A. Mehta, Unpublished dissertation, Lehigh University, 1972.
5. S. K. Tung and R. Caffrey, *Trans. Met. Soc.*, AIME, **233**, 572 (1965).
6. H. C. Stumpf, A. S. Russell, J. W. Newsome, and C. M. Tucker, *Ind. Eng. Chem.*, **42**, 1398 (1950).
7. S. M. Sze, "Physics of Semiconductor Devices," Chap. 9, p. 425, John Wiley & Sons, Inc., New York (1969).
8. K. Lehovec, *Solid State Electron.*, **11**, 135 (1968).
9. N. Szydlo and R. Poirier, *J. Appl. Phys.*, **42**, 4880 (1971).
10. O. Kubaschewski and E. L. Evans, "Metallurgical Thermochemistry," Pergamon Press, New York (1958).
11. J. F. Brown, D. Clark, and W. Elliott, *J. Chem. Soc.*, (1953); also, G. Erwin, *Acta Cryst.*, **5**, 103 (1952).
12. W. H. Gitzen, "Alumina as a Ceramic Material," The American Ceramic Society, Columbus, Ohio (1970).

New High Sensitive Electron Resist Materials

G. Paal,[1] U. D. Strähle, and G. Kielhorn

AEG-Telefunken, Research Institute Ulm, Germany

ABSTRACT

New negative-working electron resist materials have been synthesized, their sensitivities and technological properties were investigated and compared with the data of materials known from the literature.

Several electron-optical methods for the production of exposure masks and the exposure of wafers have become known in semiconductor technology recently, in addition to the customary light-optical procedures.

Basically, common photoresists may be used for exposure by electron beam, too. Their electron resist sensitivities, defined as the amount of charge per electron resist surface necessary for optimum exposure, are, however, insufficient for obtaining acceptable exposure times. At a maximum sensitivity of 10^{-5} coulombs/cm^2, for instance, a value often reported in the literature (see Table II), exposure times for various electron beam diameters result as listed in Table I, with beam current densities between 1 and 1000 A/cm^2 being possible today. If structure-writing is performed the exposure times quoted may be reduced by selection of advantageous electron beam paths, but they are still too high for commercial application. Therefore, the necessity arises for the synthesis of new materials which, while fulfilling the technical requirements, possess an increased sensitivity for electron beam exposure.

[1] Present address: IBM Laboratories, 703 Böblingen, Germany.

Key words: cross-linking, cross-linkable polymers, polymers, imaging, imaging on polymers, electron beam exposure.

Copolymer	R'	R''
M1	CH_3	CH_3
MG1	CH_3	CH_3 and $-CH_2-\underset{\diagdown\,\diagup\ O}{CH}-CH_2$
C1	H	CH_3
C2	H	CH_3

The newly developed materials described here are copolymers of methacrylate and acrylate esters, containing polymerizable double bonds.

These copolymers accord with the following schematic structure

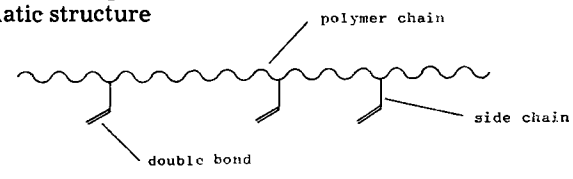

They are obtained by modification of suitable copolymers containing either isocyanate or hydroxy functions, with reactive vinyl monomers like 2-hydroxyethylmethacrylate, 2-isocyanatoethylmethacrylate, or isopropenylisocyanate.

The following materials were synthesized and investigated:

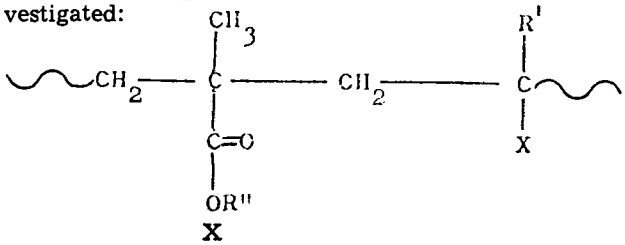

X

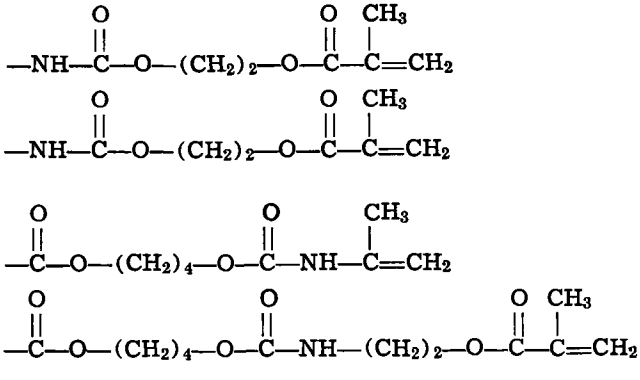

Table I. Wafer exposure times for an electron resist sensitivity of 10^{-5} coulombs/cm²

(The listed exposure times are valid for an exposure of the entire area of the wafer with a focused electron beam with scan-type deflection and an electron beam acceleration voltage of approximately 10 kV, without consideration of the attainable data flux of the data transmission and the speed of beam deflection through the deflection system)

Electron beam diameter (μm)	Exposure time per unit area at an electron beam density of 1 A/cm² (sec/cm²)	1000 A/cm² (sec/cm²)
0.01	10^7	10^4
0.1	10^5	10^2
1	10^3	1

At electron beam exposure of films of these materials the exposed areas become insoluble; the unexposed areas retain their solubility and can be removed.

Experimental

Preparation and exposure of the films.—Thin films 0.1 μm thick of the photoresists KAR-3, KTFR, KOR (Kodak), AZ 1350, and the copolymers M1, MG1, C1, and C2 are produced by centrifuging the filtered solutions onto Cr-plated glass substrates. As thinners or solvents, respectively, the original thinners were used for the photoresists, and acetic acid ethyl ester for the copolymers M1, MG1, C1, and C2. The films were dried in air for 10 min, then heated at 60°C for another 10 min. The development of the films exposed by the electron beam was performed with the original developers for commercial photoresists and with trichloroethylene for the copolymers M1, MG1, C1, and C2.

Several 1 × 1 mm² sections on a substrate were exposed in a scanning electron microscope (Cambridge Stereoscan). The line spacing amounted to 2 μm and the line width to about 0.5-0.7 μm at a 500-line scan.

The electron beam acceleration voltage of 20 kV and the exposure time of 20 sec per section was kept constant throughout the experiments. In order to obtain a step-function of the exposure the electron beam current was controlled from section to section within the range from 10^{-11} to 10^{-8}A. The sample current was conducted off through a chromium layer below the substrate, its amperage was measured for the calculation of the electron resist sensitivity. After exposure and development of the substrates the line structure was microscopically evaluated. From the data of the individual sections showing optimum exposure the sensitivity of the electron resist films was then calculated.

Results of the Measurements and Discussion

The values of electron resist sensitivities that were measured are listed in Table II and compared with literature values. It is seen from the table that sensitivity figures reported in the literature check with our measurements within the order of magnitude. These sensitivity values may be taken for a calibration of the measuring apparatus. The highest electron resist sensitivity of the materials measured was found in the newly developed copolymers M1, MG1, and C2 (negative working) with 4 × 10^{-7}, 2 × 10^{-7}, and 1 × 10^{-7} coulombs/cm². They possess, at the same time, good technological properties. For the (negative working) copolymer C1, a poor sensitivity was measured with 2 × 10^{-6} coulombs/cm². The cross-linking of these materials is initiated by a free radical symbolized by R· which is generated during the electron beam exposure. It is known that through the interaction of high energy radiation with organic polymers free radicals may be formed (6). A free radical is a chemically reactive species having an unpaired valence electron, and can react with the double bond of a polymer chain as shown in Eq. [1]

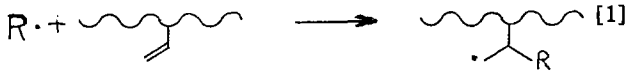

[1]

The product of this step is another free macro radical which in turn can react with a third molecule according to Eq. [2]

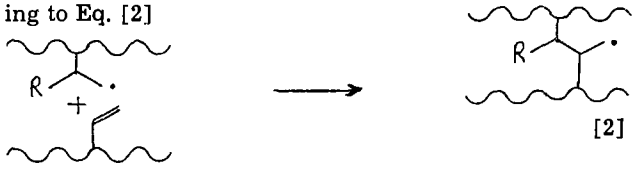

[2]

Again, the product is a free macro radical which continues to react in the same manner, thus producing a polymer network. We think that the high sensitivity of the novel materials can be explained by this chain mechanism of cross-linking.

Synthesis of the Polymers

Copolymer M1.—To 10g of dichloromethane, 5g methacrylic acid-methyl ester (freshly distilled), 5g isopropenylisocyanate, and 10g benzene are added. The dichloromethane is then distilled off in order to remove water traces. Now 20 mg α,α-azoisobutyronitrile is added and polymerized in nitrogen atmosphere for 24 hr at 50°C. Precipitation with petroleum ether and repeated re-precipitation from $CHCl_3$/petroleum ether

Table II. Electron beam sensitivity of macromolecular organic materials

Type	Material	Film thickness, μm	Acceleration voltage, kV	Electron resist sensitivity: Measured values, 10^{-8} coulombs/cm²	Electron resist sensitivity: Literature values, 10^{-8} coulombs/cm²	Literature reference[a]	Remarks
Positive resists	Cellulose acetate	0.5	10	—	50,000	3	Poor chemical resistance
	Poly ( ) methylstyrene	0.5	10	—	10,000	3	Not resistant in H_2F_2
	Polymethylmethacrylate	0.5	10	—	5,000	4, 3	Good chemical resistance
	Polyisobutylene	0.5	10	—	5,000	3	—
	KAR-3	0.3	20	>50,000	—	—	Sensitivity too low
	AZ-1350	0.36	30	—	8,000	2	Good resolution, not resistant in alkalies
	AZ-1350	—	10	—	3,000	2	—
	AZ-1350	0.08-0.12	20	1,000-3,000	—	—	—
Negative resists	Polystyrene	0.5	10	—	10,000	4	—
	Polyvinylchloride	0.5	10	—	3,000	4	Good chemical resistance
	KTFR	0.15-0.25	14	—	300	1, 2	Good resolution, good chemical resistance
	KTFR	0.08-0.12	20	800-2,400	—	—	—
	KOR	0.15-0.25	14	—	100-300	1	Formation of bubbles, uneven surface structure
	KOR	0.08-0.12	20	200-600	—	—	—
	Epoxydized polyisopyrene	0.3-1.0	15	—	5	5	Good chemical resistance
	Epoxydized polybutadiene	0.3-1.0	15	—	2	5	—
	Copolymer M1	0.08-0.12	20	40-120	—	x	Good chemical resistance
	Copolymer GM1	0.08-0.12	20	20-60	—	x	Good chemical resistance
	Copolymer C1	0.08-0.12	20	200-600	—	x	Swelling during development
	Copolymer C2	0.08-0.12	20	10-30	—	x	Good chemical resistance

[a] x is newly developed materials.

yields 2.6g of copolymer M. Then 2.6g copolymer M is dissolved in 30 ml dry dimethylformamide (DMF) and modified by reaction with 8.5g 2-hydroxy ethylmethacrylate at 50°C for 16 hr. After precipitation, dissolving in $CHCl_3$, drying with Na_2SO_4, precipitating with petroleum ether, and repeated re-precipitation, the copolymer M1 thus obtained is dried in vacuum.

Copolymer MG1.—To 10g of dichloromethane, 2.5g methacrylic acid methyl ester (freshly distilled), 2.5g methacrylic acid glycidyl ester (freshly distilled), 5.0g isopropenyl isocyanate, and 10g benzene are added. The dichloromethane is distilled off in order to remove water traces. After its removal from the mixture, 20 mg α,α-azoisobutyronitrile are added and copolymerized in nitrogen at 50°-55°C for 24 hr. After precipitation in petroleum ether, repeated re-precipitation from chloroform/petroleum ether and drying, 5.2g of copolymer MG are obtained.

The copolymer MG is modified by reaction with 16g of 2-hydroxyethylmethacrylate in dry DMF at 50°-55°C for 16 hr. After cooling off it is precipitated with water, dissolved in chloroform, dried with Na_2SO_4, and precipitated with petroleum ether. The copolymer MG1 is obtained after re-precipitation from chloroform/petroleum ether and drying in vacuum.

Copolymer C1.—4.4g copolymer C [composition 25 m/o (mole per cent) butanediolmonoacrylate and 75 m/o methacrylic acid methyl ester], 0.3g dibutyl-tin-diacetate, 0.1g hydroquinone, and 1.7g isopropenylisocyanate are dissolved in 20 ml dry DMF and heated in nitrogen atmosphere at 60°C for 14 hr. Precipitation is now performed with H_2O, the gluey sediment is dissolved in $CHCl_3$, dried with Na_2SO_4, precipitated in petroleum ether. The copolymer C1 is obtained after repeated re-precipitation from $CHCl_3$/petroleum ether and drying in vacuum.

Copolymer C2.—4.4g copolymer C (composition 25 m/o butanediolmonoacrylate and 75 m/o methacrylic acid methyl ester), 0.3g dibutyl-tin-diacetate, 0.1g hydroquinone, and 3.2g 2-isocyanatoethylmethacrylate are dissolved in 20 ml dry DMF and heated in nitrogen atmosphere at 60°C for 14 hr. Then it is precipitated with H_2O, dissolved in $CHCl_3$, dried with Na_2SO_4, and precipitated in petroleum ether. The copolymer C2 is obtained after repeated re-precipitation from $CHCl_3$/petroleum ether and drying in vacuum.

Acknowledgment

We gratefully acknowledge the support of this work by the Department of Education and Science of the German Federal Government. We thank Dr. Ricker and Dr. Hersener for their assistance with the electron beam exposure of the specimens.

Manuscript submitted Feb. 16, 1973; revised manuscript received July 20, 1973.

Any discussion of this paper will appear in a Discussion Section to be published in the June 1974 JOURNAL.

REFERENCES

1. R. F. M. Thornley and T. Sun, *This Journal*, **112**, 1151 (1965).
2. K. D. Perkins and R. Bennett, *Kodak Photoresist Seminar Proc.*, 2, 39 (1968).
3. I. Haller, M. Hatzakis, and R. Srinivasan, *IBM J. Res. Develop.*, **12**, 251 (1968).
4. H. Y. Ku and L. C. Scala, *This Journal*, **116**, 980 (1969).
5. T. Hirai, Y. Hatano, and S. Nonogaki, *ibid.*, **118**, 669 (1971).
6. R. W. Lenz, "Organic Chemistry of Synthetic High Polymers," Interscience Publishers, Inc., New York (1968).

The Preparation and Properties of a Polysiloxane Electron Resist

E. D. Roberts

Mullard Research Laboratories, Redhill, Surrey, England

ABSTRACT

The preparation of polymethylcyclosiloxane (PMCS) is described. PMCS may be used as a resist in which siliceous film patterns may be formed by irradiation with an electron beam. These siliceous patterns are readily developed and may be used directly in semiconductor technology as diffusion barriers or as etch-resistant layers, and after suitable heat-treatment they may be used also as passivating layers. Transistors have been made using PMCS film patterns defined by electron beams as diffusion barriers and as passivating layers. The sensitivity of PMCS to irradiation may be increased by controlled condensation to give a higher molecular weight polymer, or by introducing vinyl groups to replace some of the methyl groups in the polymer. The chemical changes which occur in PMCS upon irradiation by electrons have been investigated and it is shown that at doses normally used in making film patterns of use in semiconductor technology, cross-linking occurs mainly through the hydroxyl groups present in the polymer. Subsequent treatment (thermal or radiation) can eliminate organic residues to produce a film which is identical to thermally grown silica.

In recent years, electron beam techniques have been studied extensively with a view to making solid-state electronic devices having geometrical features with dimensions less than about 2 μm. At these dimensions, normal photolithographic techniques for defining patterns become unreliable and yields of working devices rapidly diminish with the dimensions. It is believed that electron beam techniques will enable improved yields of devices with features down to 1 μm or less to be obtained.

Much work on electron beam technology has used otherwise conventional techniques, the electron beam merely replacing the ultraviolet lamp and mask normally used to obtain the desired film patterns. Conventional photoresists have been used (1-3) followed by chemical etching steps to produce patterns in silica

Key words: siliceous films, electron irradiation, diffusion barriers, passivating layers.

films, for example, though special resists appropriate particularly to electron beam technology have also been developed (3-8). Generally these electron resists are not photosensitive and do not require to be used in special lighting conditions.

In our application of electron beams to semiconductor technology, it was felt that in order to obtain the full advantage of the potentially high resolution which the method offers, steps involving chemical etching should be avoided so that film patterns produced by the electron beam should not be degraded by the undercutting which always accompanies chemical etching. The beam would be used to produce directly film patterns of any material required. Silica films are used extensively in silicon planar technology as diffusion barriers and as insulating and passivating layers, and the ability to define silica film patterns directly by an electron beam should be a useful process.

Earlier publications (5, 9) described our work on the preparation of siliceous films from various silicon compounds by electron beams, and it was concluded that the most satisfactory materials for this purpose were a range of solid siloxane polymers. These polymers are normally soluble, but become cross-linked and therefore insoluble when irradiated by electrons. Solutions of the polymers were applied to a substrate (usually silicon) which was spun rapidly to produce a film of polymer on the substrate. The spun films were irradiated by an electron beam, usually scanned to trace out the required pattern at a rate which produced sufficient cross-linking to render the polymer insoluble. Upon rinsing the film in a solvent, only the unirradiated polymer dissolved, leaving a pattern of cross-linked siliceous film upon the substrate. Subsequent treatment enables the film to be converted to silica, which may be used as a diffusion barrier (5), a passivating layer, or an etch-resistant mask.

This paper describes the preparation and use in electron beam technology of one of these electron resists—polymethylcyclosiloxane (PMCS)—and discusses the chemical reactions which occur during irradiation. Typically, films of this substance shrink in thickness by up to 8-9% during an exposure of 150 $\mu C/cm^2$ by 10-15 keV electrons. At exposures greater than about 140 $\mu C/cm^2$, no further loss in film thickness occurs during the solvent development process. Subsequent heat-treatment, including densification, results in further shrinkage, the silica film ultimately produced being about 60-65% of the thickness of the PMCS film originally applied to the substrate. Lateral shrinkage during these processes is negligible. PMCS required at least 140 $\mu C/cm^2$ to form a fully exposed image, and this exposure is rather high. Methods of making more sensitive resists of similar type are therefore also considered.

Preparation of Polymethylcyclosiloxane

It was shown by Wagner et *al.* (10) that some organotrichlorosilanes could be hydrolyzed to give soluble solid polymers if suitable precautions were taken to minimize the time of contact between the hydrolysate and the hydrochloric acid produced by the reaction. We have found that the procedure may be applied also to methyltrichlorosilane, though the risk of producing insoluble three-dimensionally cross-linked polymer is greater with this than with other organotrichlorosilanes, and some product is always lost by this side reaction.

Polymethylcyclosiloxane was prepared by hydrolyzing methyltrichlorosilane in a medium of diethyl ether and ice using a procedure similar to that described by Wagner et *al.* (10). Any insoluble gel which formed during the preparation was rejected. The resulting solution of methylsiloxane polymer in ether was evaporated to dryness, yielding a solid residue. The solid product can condense spontaneously through the hydroxyl groups present in it to an insoluble cross-linked form. It was, therefore, stored and used as a 25% w/w (weight in weight) solution in methyl isobutyl ketone, which remains stable for at least 9 months.

The polymer was found to contain no elements except silicon, carbon, hydrogen, and oxygen and no functional groups except hydroxyl. It is probable that each silicon atom has a methyl substituent group, for it is unlikely that during hydrolysis the silicon-methyl bond would be broken. The average molecular weights of the polymers (determined cryoscopically in acetic acid or in 1,4-dioxan) usually lie within the range 500-700, though it has been shown that fractions having molecular weights between 280 and 1200 are present. It seems likely that the polymer is a mixture of chains of cyclic methylsiloxanes (probably mainly cyclotetrasiloxanes) containing some silanol groups. It contains 40% by weight of silicon.

Irradiation of PMCS by Electrons

The apparatus in which PMCS films were exposed to electrons to produce patterns of siliceous film have been described elsewhere (5,9). Figure 1 shows the variation with exposure of the thickness of exposed and developed siliceous film on a silicon substrate. The thicknesses have been normalized to that of the unexposed PMCS film applied initially. The exposures were made in a machine (9) in which a focused beam of electrons of energy 15 kV and nominally 0.25 μm in diameter was scanned with overlapping lines in a TV-type raster to expose uniformly a 100 μm square area of the resist. The current was measured with a sensitive ammeter in series with the substrate to correspond with our practical application of this technique. No corrections for the effects of secondary electrons have been made. The exposure was calculated from the measured current, exposed area, and total exposure time and was varied by changing the scanning speed. The film thicknesses were measured with a Talystep 1 instrument, the interference colors observed in the films corresponding closely with those expected at the measured thicknesses.

Figure 1 shows that the film shrinks in thickness by about 8% when adequately exposed (140 $\mu C/cm^2$). This shrinkage occurs during irradiation and no material appears to be leached out during development. A film initially 4800Å thick was 4400Å thick after irradiation, and remained 4400Å thick after development in acetone.

Chemical Changes during Electron Irradiation

The changes occurring in PMCS films during electron irradiation and during subsequent heat-treatments have been studied by infrared spectroscopy. For this purpose, PMCS films on silicon substrates which had been polished on both sides were irradiated by an

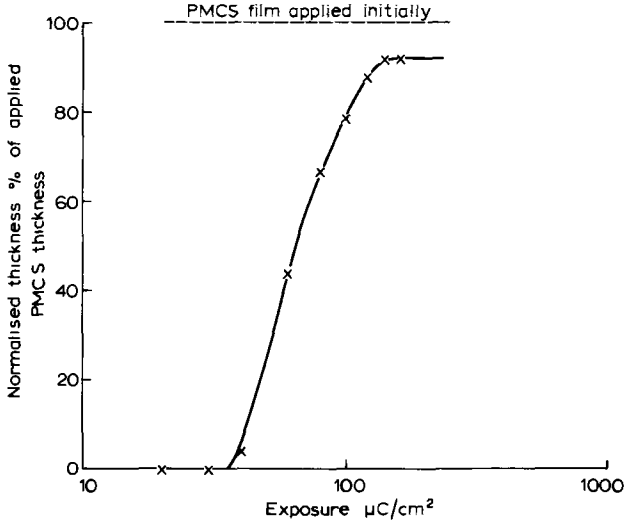

Fig. 1. Variation in thickness of irradiated developed PMCS patterns with exposure.

electron beam 1 cm in diameter (5), the exposed circular pattern being developed in acetone. The maximum electron energy available in this machine (5) is 10 keV. The exposure characteristics at this energy appear to be identical with those at 15 keV shown in Fig. 1, so the large area films for infrared spectroscopy were irradiated with 10 keV electrons. The exposure was determined by a purpose-built charge integrating instrument, which may be preset to deliver the desired exposure to the specimen. Although the current density in the large area flood beam (5) is less by a factor about 10^6 than that in the finely focused scanned beam described earlier (9), we have been unable to detect any difference in its effect on the resist when the average exposure is the same in each.

The infrared absorption spectrum of a film of PMCS is given in Fig. 2, together with assignments for the absorption bands (11). The band between 1000 and 1100 cm^{-1} is of most interest. The maximum absorption occurs at 1090 cm^{-1}, corresponding with the presence of tetrasiloxane rings. The changes which occur upon irradiation and subsequent heat-treatment of PMCS films may be seen in Fig. 3-5.

Figure 3 shows the effect of increasing exposure to the electron beam. The exposures used lie near the ends of the working range which is considered to be satisfactory for defining patterns of fine geometry in the resist (85-300 $\mu C/cm^2$).

The most noticeable change is the almost complete elimination of the absorptions at 3200-3300 cm^{-1} and at 900 cm^{-1}, which are due to the Si-OH group in PMCS. The peaks due to the Si-Me groups are also reduced and the shape of the broad band centered around 1090 cm^{-1} in PMCS is altered, the maximum absorption having shifted to about 1020 cm^{-1}. During irradiation at these exposures, PMCS becomes insoluble in solvents and infusible which means that cross-links are produced between molecules, and this process is accompanied by a reduction in thickness of the film by about 10%. The spectra suggest that cross-linking occurs extensively through hydroxyl groups, and to a lesser extent at these exposures through methyl groups, the over-all reactions probably being:

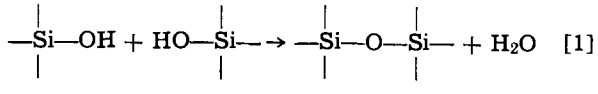

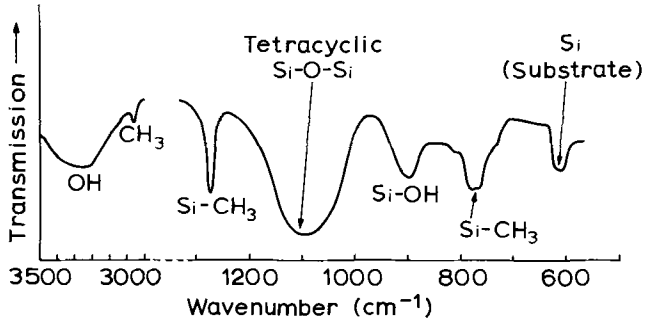

Fig. 2. Infrared absorption spectrum of PMCS film on silicon

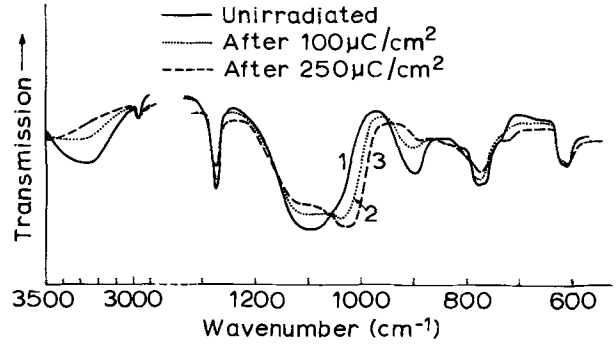

Fig. 3. Effect of electron irradiation on infrared absorption of PMCS.

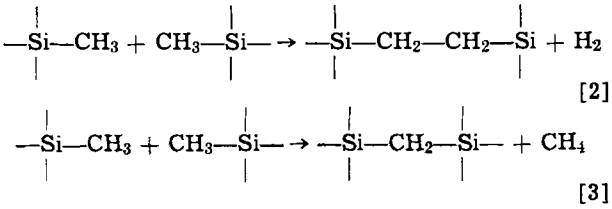

Although the absorption peaks which correspond to the siloxane and alkylene bridges produced all appear in the region 1000-1150 cm^{-1} where there is already a broad intense band, a small superimposed peak appears in Fig. 3 (curve 3) and Fig. 4 (curves 1 and 2) at about 1060 cm^{-1}, which could be indicative of the formation of alkylene bridges (11). It is noteworthy that this peak disappears again after subsequent treatment during which the organic residues are reduced markedly [Fig. 4 (curve 3)].

The broad band at 1000-1150 cm^{-1} shows a double absorption in the irradiated films which is not unlike that observed in both long chain and higher cyclic siloxane polymers (12). Cross-linking of PMCS molecules could be regarded as producing some large rings or long highly branched chains within a cross-linked network.

Figure 4 shows the effects of still higher exposures. The samples were prepared by irradiating PMCS films on silicon at 250 $\mu C/cm^2$ and developing the exposed pattern in acetone. The developed patterns were then re-exposed as shown in the figure. Direct irradiation with the total required exposure would result in loss of resolution of patterns, and if it were desired to give a large exposure to patterns in practice, it would be done in two stages, as was done with these samples. Continuation of the same trends as were observed with lower doses occurs, the absorption due to residual organic groups being markedly reduced, especially when the exposure has reached 2750 $\mu C/cm^2$. This must imply scission of many of the silicon-alkyl bonds within the film, the organic groups being eliminated as volatile fragments. The broad peak centered on 1020 cm^{-1} is tending to move back towards higher wave numbers at these higher exposures and the whole spectrum is approaching that shown by amorphous silica (13). It appears that the effect of very high exposures is to convert the siliceous film to a form resembling closely the thermal silica films commonly used in semiconductor technology.

Figure 5 is the spectrum of a film exposed at 250 $\mu C/cm^2$ which after development, has been heated in wet oxygen (saturated with water vapor at 95°C) at 650°C for 8 min. This treatment seems to eliminate all hydroxyl groups and virtually all organic residues and the spectrum is almost identical with that of amorphous silica (13). It has also been found that PMCS films defined by the electron beam and heat-treated in this way have after densification in nitrogen at 1000°C, the same refractive index and etch rate in hydrofluoric acid as amorphous silica has. The process is therefore a convenient method of converting PMCS film patterns to silica.

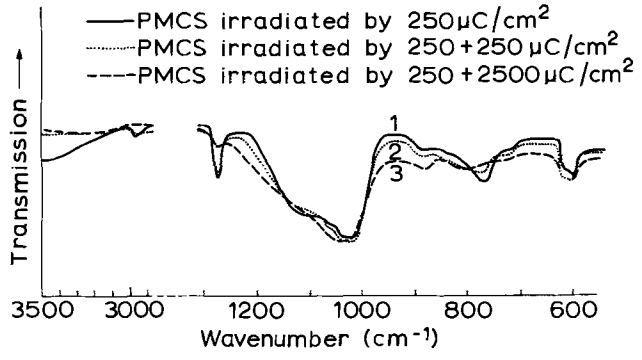

Fig. 4. Effect of second exposure to electrons on infrared spectrum of PMCS.

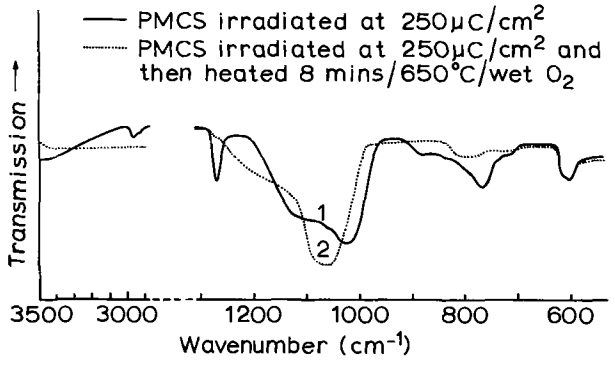

Fig. 5. Effect on infrared spectrum of heating electron beam defined film of PMCS in oxidizing atmosphere.

Preparation of PMCS of Higher Sensitivity

It was shown by Wagner (10) that silanol condensation in vinylcyclosiloxane polymers occurred in the presence of ammonia to produce higher polymers.

It was observed with a few early batches of PMCS that freshly prepared material required an exposure around 150 $\mu C/cm^2$ to produce a satisfactory image, while after a few weeks' storage an exposure around 30-40 $\mu C/cm^2$ only was required. It was found that the average molecular weights of the polymers had increased during storage from 500-700 to 700-1100, and that the polymer solutions contained ammonia equivalent to about 1 ppm by weight on the polymer. Until this was discovered, the ether extract of polymer had been washed during the preparation only until the washings were neutral to phenolphthalein, In subsequent preparations, a procedure using Nessler's reagent was introduced. It is estimated that after testing the washings in this way, the residual ammonia is less than 0.02 ppm on the polymer, and indeed the solutions have remained stable for periods up to 9 months.

The increase in sensitivity observed suggested that more sensitive PMCS might be made if the ammonia-catalyzed silanol condensation could be conducted in a controlled manner.

Methyltrichlorosilane was therefore hydrolyzed and was washed until free from hydrogen chloride (10). The ether extract was treated with dilute ammonia solution for various lengths of time, after which the ammonia was washed out as described above, and the polymer worked up to prepare a working solution (25% w/w in methyl isobutyl ketone). The ammonia concentration was calculated according to an equation, the derivation of which is given in the Appendix.

The results obtained on polymer treated with 0.2% by weight of ammonia are shown in Fig. 6. The increase in molecular weight of the polymer is accompanied by a decrease in the hydroxyl content as shown in Fig. 7. Clearly the ammonia treatment has caused further condensation of the polymer molecules through their hydroxyl groups. The expected increase in sensitivity has also occurred in the early stages (up to 3½ hr treatment) (Fig. 6). Continued treatment, however, produced an unexpected fall in molecular weight accompanied by a decrease in sensitivity to electrons. This must imply chain scission, but the end result cannot be due to simple hydrolytic fission of the chains, for this would produce an increase in the hydroxyl content of the polymer, which is contrary to observation (Fig. 7).

It is easy to understand that the larger molecules present after condensation would require a smaller number of cross-links to render them insoluble than would the smaller molecules originally present, resulting in the observed increase in sensitivity to electrons of the material of increased molecular weight.

The variation of residual film thickness with exposure for condensed PMCS of this type is shown in Fig. 8 (curve 1), together with curves for the two cyclo-

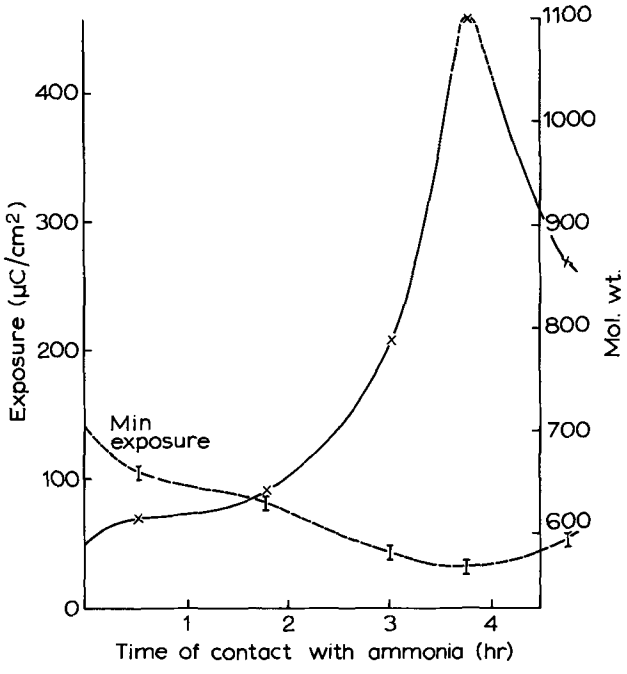

Fig. 6. Effect on properties of PMCS of ammonia-catalyzed condensation (0.2% NH_3 on PMCS).

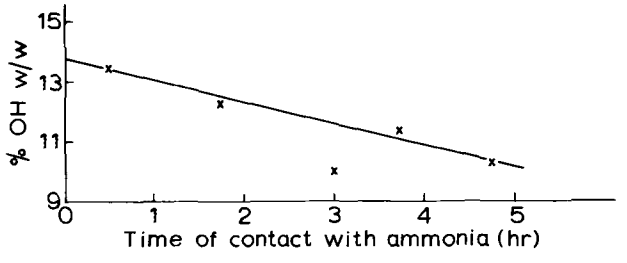

Fig. 7. Change in hydroxyl content of PMCS during ammonia-catalyzed condensation (0.2% NH_3 on PMCS).

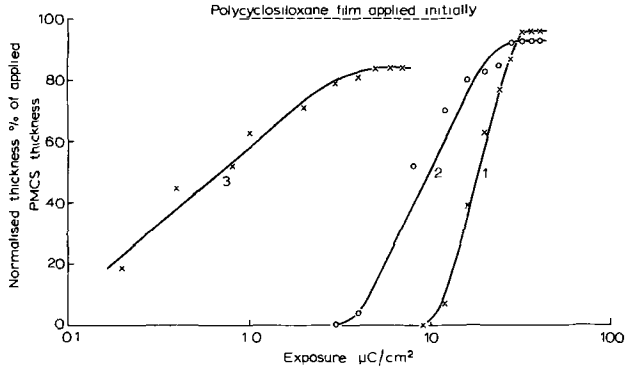

Fig. 8. Variation in thickness of irradiated developed polysiloxane patterns with exposure. Curve 1, PMCS after condensation with 0.2% ammonia, curve 2, methyl/vinyl siloxane copolymer; curve 3, polyvinyl cyclosiloxane.

siloxane polymers containing vinyl groups which are described below.

Other methods of increasing the electron sensitivity.—We have shown earlier (5) that a polymer made by hydrolysis of vinyltrichlorosilane has much higher sensitivity to electrons than PMCS does. Indeed the sensitivity appears to depend markedly upon the nature of the organic group present, as is shown by the values given in Table I. The great sensitivity of the vinyl polymer is almost certainly due to a chain reaction occurring through the vinyl group and initiated by the electron beam. Similar large increases in sensitivity have been observed in other systems when a vinyl group is introduced (14).

Table I. Variation of sensitivity of polycyclosiloxane electron resists with nature of organic group attached to silicon atom

Organic group attached to silicon	Minimum exposure required to form satisfactory image ($\mu C/cm^2$)
vinyl	4
methyl	130
ethyl	250
phenyl	800

Conversely, the low sensitivity of the phenyl compound is probably due to steric hindrance (shielding) of the hydroxyl group by the bulky phenyl group coupled with the known resistance of the phenyl group itself to the effects of ionizing radiation.

We have not investigated polyvinylcyclosiloxane extensively, but we have shown that fine geometrical patterns can be defined in it (detail <1 μm) and that it can be used as a diffusion barrier (5). It needs however, to be applied initially as a thicker film than PMCS to have the same ability to prevent diffusion of dopants into silicon. This may be the result of the larger amount of organic residues which could result in the film being rather more porous than PMCS films. This is one of the reasons why we have not favored it, believing that the more closely the structure of the polymer approached that of silica (*i.e.*, the smaller the organic radicals present) the better the system was likely to perform. We have found, however, that methyl-vinyl copolymers can be made which should enable the advantages of both materials to be brought together in one compound. Cohydrolysis of a mixture of 5 moles methyltrichlorosilane with 1 mole of vinyltrichlorosilane yields a polymer not very different in composition from PMCS but which enables patterns to be formed within the exposure range 10-80 $\mu C/cm^2$. Exposure curves for the two polymers containing vinyl groups are given in Fig. 8 (curves 2 and 3).

Use of PMCS in Semiconductor Technology

We have used film patterns defined in the resist PMCS by electron beams as a barrier against the diffusion of arsenic, boron, and phosphorus and satisfactory results have been obtained even in processes involving high doping levels such as those for emitter regions. In this method, the diffusion barrier pattern is formed by applying a film of PMCS to the silicon substrate, exposing it to an electron beam to produce the required pattern [generally using a scanned electron beam (9)] which is developed by rinsing the silicon slice in acetone for a few seconds. During development all the unirradiated PMCS is dissolved away leaving a pattern of siliceous film corresponding to the electron irradiation pattern. The siliceous pattern so produced may be used directly as a diffusion barrier, though it is beneficial whenever possible to densify the film before the diffusion process by heating in nitrogen at temperatures up to 1250°C (5). After diffusion, the siliceous diffusion barrier is completely removed from the substrate by treatment with hydrofluoric acid, and a fresh PMCS film is applied to provide a new pattern for the next diffusion stage. Thus in this method, none of the silicon substrate is used to provide the oxide diffusion masks.

We have also used PMCS film patterns defined in the same way by the electron beam as passivating layers in making bipolar transistors. For this purpose, it was found beneficial to heat the developed patterns for 10 min in wet oxygen at 680°C followed by densification in dry nitrogen for 30 min at 900°C. The heat-treatment in wet oxygen has been shown to eliminate almost completely any organic residues in the film (Fig. 5).

n-p-n Bipolar transistors with diffusion barriers and passivating layers defined by electron beams in PMCS have been made. Figure 9 is a photomicrograph of such a transistor before metalization showing the passivating layer produced by electron irradiation of PMCS. The outlines of the diffused base and emitter regions may be seen clearly, these areas having also been defined in PMCS films (which were subsequently removed) by the beam.

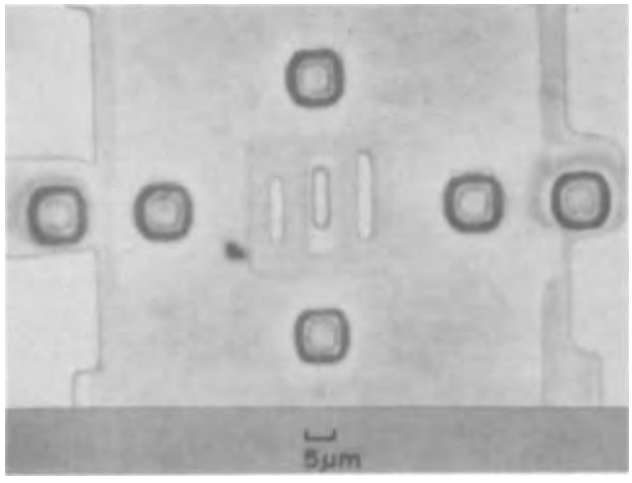

Fig. 9. Electron beam defined passivating layer on n-p-n bipolar transistor.

The preparation of transistors using PMCS will be described in more detail in a separate paper (15). We have yet made only transistors with emitters 5 μm wide, and these have had gains up to 100, but some have shown rather high leakage currents, sometimes being as high as 10 μA. The transistors had no phosphosilicate glass layers over the passivating layer, however, as in their method of fabrication any phosphosilicate glass which forms during the last diffusion is removed before applying the passivating layer. This is in contrast to some conventional processing. It is known that conventionally made transistors also can show high leakage currents if there is no phosphosilicate glass layer over the passivating layer. A method whereby phosphosilicate glass patterns can be formed by electron beam techniques over passivating layers similarly defined has been described recently, together with test results on the composite films (14). Tests of MOS capacitors having a dielectric of silica with a thin layer of phosphosilicate glass upon it, both layers being defined by electron beams in PMCS type resists, have shown that capacitance-voltage characteristics of the capacitors do not change when the capacitors are subjected to temperature-voltage stress, though there is a large change under these conditions if the phosphosilicate glass is not present. By analogy with conventional processing, it is expected that the application of an

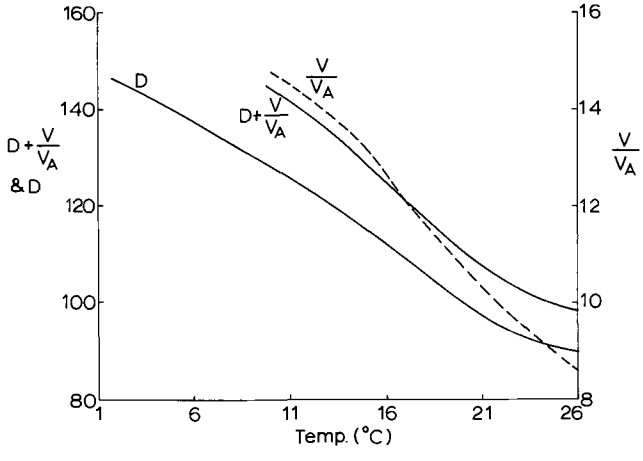

Fig. 10. Variation with temperature of terms required in calculating ammonia concentration during catalyzed condensation of PMCS.

electron beam defined phosphosilicate glass layer (14) to a passivating layer prepared from PMCS should stabilize the transistors, and the leakage current should then decrease to normally encountered values. This has yet to be confirmed experimentally, however.

PMCS film patterns have also been used as etch-resistant films, particularly for etching silicon with hydrofluoric acid/nitric acid mixture, and we have used them for etching patterns in metal films. The difficulty of removing the exposed PMCS film makes it less attractive for the latter application, however, unless the system is such that hydrofluoric acid may be used for removing the PMCS etch resist.

Summary and Conclusions

A method of preparing a polymethylcyclosiloxane has been described. It has been shown that upon irradiation by electrons, cross-linking between molecules occurs initially through silanol groups, while at higher exposures, this probably occurs also through methyl groups. At very high exposures or upon subsequent heat-treatment, organic residues are almost completely eliminated leaving a film with properties almost identical to amorphous silica.

A method whereby the average molecular weight of the polymer may be increased is described, and this leads to polymers having greater sensitivity to the effects of electron irradiation. Still further increases in sensitivity may be achieved by introducing vinyl groups into the polymer molecules.

Siliceous films may be produced in any desired pattern by irradiating films of the siloxane polymers described with electron beams which are masked or scanned to produce the desired pattern and then subjecting the irradiated films to a suitable development process. The siliceous films may be used in semiconductor technology as diffusion barriers, etch resistant layers, and, after suitable heat-treatment, as passivating layers.

Acknowledgments

The author thanks the directors of Mullard Research Laboratories for permission to publish this paper. He also acknowledges the contributions of Messrs. R. C. Barclay and B. F. Martin who have assisted with some of the experimental work, Miss A.M. Cole who determined the infrared spectra, Mr. P. Gould who carried out the transistor processing and evaluation, and Dr. P. J. Daniel, Mr. H. N. G. King, and Mr. J. M. S. Schofield with whom helpful discussions took place.

This paper incorporates work carried out partly under a CVD contract and is published by permission of the Ministry of Defence (Procurement Executive).

Manuscript submitted Jan. 3, 1973; revised manuscript received July 2, 1973.

Any discussion of this paper will appear in a Discussion Section to be published in the June 1974 JOURNAL.

APPENDIX

Calculation of Ammonia Concentration during Catalyzed Condensation of Cyclosilanols

Let W = wt of polymer used, V = volume of ether used, A_p = per cent by weight of ammonia on polymer in ether layer at equilibrium, A_w = per cent by weight of ammonia in ammonia solution used, V_a = volume of ammonia solution used, S_w = solubility of water in ether, g/100 ml, S_e = solubility of ether in water, g/100 ml, Δ_e = specific gravity of ether, and D = distribution coefficient of ammonia between water and ether.

At equilibrium

Net volume of ether layer =
$$V - S_eV_a/100\Delta_e + S_wV/100 = V_e$$
Net volume of water layer =
$$V_a - S_wV/100 + S_eV_a/100\Delta_e = V_w$$
Concentration of ammonia in ether layer =
$$WA_p/100V_e$$
Concentration of ammonia in water layer =
$$(A_wV_a - WA_p)/100V_w$$

$$\therefore \quad (A_wV_a/WA_p - 1)V_e/V_w = D$$

If $S_eV_a/100\Delta_e = S_wV/100$

then $V_e = V$ and $V_w = V_a$

$$A_wV/WA_p = D + V/V_a$$
$$V/V_a = S_e/S_w\Delta_e$$

The terms on the right of the last two equations are temperature-dependent, and Fig. 10 shows this dependency. The value of $D + V/V_a$ may be obtained by measuring the temperature of the solution and reading its value from the graph. V and W are predetermined, and A_w or A_p may be obtained by fixing the value of one of them.

In this work, A_p was specified and the value of A_w required to give this value was calculated. The ammonia concentration was adjusted to this value and V_a was calculated from the value of V/V_a appropriate to the temperature of the solution.

REFERENCES

1. B. Broyde, *This Journal*, **116**, 1241 (1969).
2. B. Broyde, *ibid.*, **117**, 1555 (1970).
3. N. Atoda and K. Kanaya, *Bull. Electrotech. Lab.*, **33**, 1297 (1969).
4. I. Haller, M. Hatzakis, and R. Srinivasan, *IBM J. Res. and Develop.*, **12**, 251 (1968).
5. E. D. Roberts, Electron and Ion Beam Science and Technology, Third International Conference, Robert A. Bakish, Editor, p. 571, Electrochemical Society Softbound Symposium Series, New York (1968).
6. H. Y. Ku and L. C. Scala, *This Journal*, **116**, 980 (1969).
7. Y. Yatsui, T. Nakata, and K. Umehara, *ibid.* **116**, 94 (1969).
8. A. Maekawa, C. Munakata, C. Hirano, O. Morita, T. Kozawa, K. Isoda, and S. Nonogaki, Electron and Ion Beam Science and Technology, Fourth International Conference, Robert Bakish, Editor, p. 503, Electrochemical Society Softbound Symposium Series, New York (1970).
9. J. M. S. Schofield, H. N. G. King, and R. A. Ford, Electron and Ion Beam Science and Technology, Third International Conference, Robert A. Bakish, Editor, p. 561, Electrochemical Society Softbound Symposium Series, New York (1968).
10. G. H. Wagner, D. L. Bailey, A. N. Pines, M. L. Dunham, and D. B. McIntire, *Ind. Eng. Chem.*, **45**, 367 (1953).
11. A. Lee Smith, *Spectrochim. Acta*, **16**, 87 (1960).
12. N. Wright and M. J. Hunter, *J.A.C.S.*, **69**, 803 (1947).
13. G. Hass and C. D. Salzberg, *J. Opt. Soc. Am.*, **44**, 181 (1954).
14. E. D. Roberts, Electron and Ion Beam Science and Technology, Fifth International Conference, Robert Bakish, Editor, p. 102, Electrochemical Society Softbound Symposium Series, Princeton, N. J. (1972).
15. J. M. S. Schofield, To be published.

A New Family of Positive Electron Beam Resists—Poly(Olefin Sulfones)

L. F. Thompson and M. J. Bowden

Bell Laboratories, Murray Hill, New Jersey 07974

ABSTRACT

Poly(olefin sulfones) have been shown to represent a new class of positive electron beam resists exhibiting sensitivities in the region of 1-3 $\times$ 10^{-6} coulombs cm^{-2}. Processing variables have been evaluated and exposure characteristics determined. These materials can be used in two development modes, (*i*) as a conventional solvent-developed system and (*ii*) as a system which self develops during e-beam irradiation by depolymerization followed by vaporization. Limitations of this "vapor development" process are discussed.

Recent trends in microelectronic fabrication are towards reducing the size of large scale integrated circuits. Standard photolithographic techniques can be used to generate detail on a scale of ~3-5μ in both thin film conductor and dielectric materials. Structures with a 1-3μ resolution limit can only be fabricated with great difficulty using optical techniques. In contrast it has been shown (1) that electron beam lithography is capable of producing high resolution (<1μ) patterns with high yields.

Two primary competing reactions occur when a polymer is irradiated with a 1-30 kV electron beam, cross-linking, and chain scission. A polymer behaves as a positive resist if the rate of chain scission is substantially greater than the rate of cross-linking. Chain scission reduces the average molecular weight and increases the solubility of the polymer. When cross-linking is the predominant reaction, the converse is true and the polymer is termed a negative resist. A second reaction can occur to amplify the scission process, namely chain depropagation. This results when two polymer radicals, formed by chain scission, spontaneously split off monomer units. The extent of chain depropagation depends on the rate of radical termination and the rate of depropagation. If the polymer chain completely depolymerizes, the film will be totally removed thereby eliminating a solvent development step. We have termed this process vapor development.

The general use of electron beam fabrication techniques will require new classes of polymeric resist materials which have been designed for this process and optimized with respect to resolution, sensitivity, and etch resistance. The use of photoresists in e-beam lithography is not desirable since these systems are unnecessarily complex. Electron resists can be pure polymer systems offering significant advantages. Both positive and negative resists are desirable for a versatile lithographic system. However, most polymeric systems cross-link under irradiation and of the few which do degrade (notably polymethyl methacrylate), none have sensitivities high enough for economic fabrication of devices.

Poly(olefin sulfones) constitute a family of alternating copolymers of sulfur dioxide and an olefin. They have been reported to degrade rapidly under γ-irradiation (2), with a G(scission) of 10-12, far higher than any other existing positive resist. We have recently shown that they can be readily degraded in an electron beam and serve as good positive electron beam resists (3). These materials can be used in two development modes—firstly, as a conventional solvent-developed system and secondly, under proper conditions, as a solvent-free, vapor-developed system. The use of polysulfones as positive resists in both modes is described in this paper. The resists have been evaluated as chemical etching masks for silicon dioxide and tungsten and as a lift-off[1] mask for gold and aluminum.

Key words: electron resist, electron beam technology, electron photoresist, positive electron beam resist, aliphatic polysulfones.

Experimental

The preparation of the polysulfones has been described elsewhere (3). Table I lists the materials evaluated in this study and their pertinent properties and constants. The polymers were spin coated (4) onto either silicon dioxide or tungsten substrates from the solvents given in Table I. Silicon dioxide used in this study was thermally grown from steam to a thickness of 200-600 nm. The tungsten (6) was deposited on a SiO_2/Si substrate by a chemical vapor deposition technique and was nominally ~100-200 nm thick.

Resist films of 300-500 nm thickness were found to give optimum results for solvent-developed systems. Films of 100-200 nm were optimum for a vapor-developed system. All films were prebaked at 110°C for 0.1-1.5 hr. It should be noted that data in Table I were obtained in the course of a preliminary evaluation of a large number of materials, and hence some values may be less than optimum.

The polymers were subsequently exposed using a Cambridge Stereoscan Mark II scanning electron microscope (SEM) equipped with a beam blanker. The beam could be externally modulated to produce test patterns consisting of evenly spaced bars and spaces. The smallest structure that could be obtained using this system was ~1μ widths on 2μ centers. However, for smaller test patterns, the beam could be used in a single sweep mode which permitted structures of <0.4μ to be written. After exposure the sample was spray-developed (for solvent mode development) for ~15 sec using the developer given in Table I and postbaked for 0.5 hr at 110°C.

Two alternative processing steps may be used after the postbake. Firstly, the polymer resist pattern may be used as an etching mask. In this mode, buffered HF was used for etching the SiO_2 and a buffered $K_3Fe(CN)_6$/KOH solution was used to etch the W. In the second mode the positive resist image may be used as an evaporation mask in the lift-off or parting-layer technique described by Hatzakis (5).

The following method was adopted to evaluate the sensitivity of the positive resists. The electron beam was carefully adjusted to a known voltage and current. A resist film was prepared as previously described on 200 nm of SiO_2. Pads of known area (usually ~1 mm^2) were exposed for varying times at constant current. The exposed sample was developed and postbaked as described and then etched with buffered HF (2 min for 200 nm of SiO_2). The resist was stripped and the etched sample examined with the SEM. The critical dose was taken as the lowest dose which still allowed complete and clean etching of the SiO_2. This method was found to give reproducible critical dose values with good accuracy.

[1] A description of this technique is given in Ref. (5).

Table I. Evaluation parameters of polysulfone electron beam resists

All materials were prebaked and postbaked at ≥ 110°C for ≥ 0.5 hr.

Resist	Code number	T_c (°C) $[M][SO_2] = 27$ mol^2 l^{-2}	Solvent	Developer*	Sensitivity* coulomb cm^{-2}	Comments
Poly(propylene sulfone)	PPrS-M1	90	DMSO			Does not spin a film from DMSO at room temperature. Polymer is insoluble in all other solvents.
Poly(butene-1 sulfone)	PBS-M2	64	MEK	60% MEK 40% 2-PrOH	$1\text{-}2 \times 10^{-6}$	Spins excellent films although preferably from less volatile solvents than MEK. Behaves as an excellent etch mask when prebaked at ≥100°C. Does not readily depolymerize, *i.e.*, very little evidence of vapor development below 10^{-5} coulomb cm^{-2}. Similar in this regard to PMMA.
	PBS-M20	64	MEK 60% Cyclohexanone 40%	85% MEK 15% 2-PrOH	$1\text{-}2 \times 10^{-6}$	
Poly(pentene-1 sulfone)	PPS-M1	63	MEK	50% MEK 50% 2-PrOH	$1\text{-}2 \times 10^{-6}$	Similar to PBS.
Poly(hexene-1 sulfone)	PHS-M4	60	MEK	35% Xylene 65% 2-PrOH	$1\text{-}2 \times 10^{-6}$	Xylene preferred spinning solvent. Partially vapor-develops at these doses. Erosion of the resist during etching was sometimes observed.
	PHS-M14	60	Xylene	35% Xylene 65% 2-PrOH	$1\text{-}2 \times 10^{-6}$	
Poly(octene-1 sulfone)	POS-M1		MEK	60% Heptane 40% 2-PrOH	$1\text{-}2 \times 10^{-6}$	Poor etch mask. Partially vapor-develops.
Poly(cis butene-2 sulfone)	Pc-B-2S-M1	46	Dioxane	60% Dioxane 40% 2-PrOH	$2\text{-}4 \times 10^{-6}$	The 2-butenes do not spin good films from dioxane.
Poly(trans butene-2 sulfone)	Pt-B-2S-M1	38	Dioxane	60% Dioxane 40% 2-PrOH	$2\text{-}4 \times 10^{-6}$	
Poly(butene-2 sulfone)	PB-2S-M1		Dioxane	60% Dioxane 40% 2-PrOH	$2\text{-}4 \times 10^{-6}$	
Poly(hexene-2 sulfone)	PH-2S-M1		MEK	50% MEK 50% 2-PrOH	$1\text{-}2 \times 10^{-6}$	Poor etch mask when film thickness is <200 nm. Can be completely vapor-developed at $2\text{-}4 \times 10^{-6}$ coulomb cm^{-2} for film thickness <150 nm.
Poly(heptene-2 sulfone)	PHp-2S-M1	−39	MEK	20% Xylene 80% 2-PrOH	$1\text{-}2 \times 10^{-6}$	Poor etch mask. Completely vapor-develops at $1\text{-}2 \times 10^{-6}$ coulomb cm^{-2} for film thickness <150 nm.
Poly(cyclopentene sulfone)	PcycloPS-M1	102.5	Dioxane	60% Dioxane 40% 2-PrOH	$2\text{-}3 \times 10^{-6}$	No evidence of depolymerization at exposures $<10^{-5}$ coulomb cm^{-2}. Does not spin good films from dioxane. Improved by spinning from dioxane/chlorobenzene. Poor etch mask.
Poly(cyclohexene sulfone)	PcycloHS-M1	24	Dioxane	60% Dioxane 40% 2-PrOH	$1\text{-}2 \times 10^{-6}$	Chlorobenzene preferred spinning solvent. Partially vapor-develops at these doses. Completely vapor-develops at 5×10^{-6} coulomb cm^{-2} for film thickness <150 nm. Good etch mask.
	PcycloHS-M1	24	Chlorobenzene	60% Dioxane 40% 2-PrOH	$1\text{-}2 \times 10^{-6}$	
Poly(2-methyl pentene-1 sulfone)	PMPS-M3	−34	Xylene	15% Xylene 85% 2-PrOH	$1\text{-}2 \times 10^{-6}$	Excellent etch mask. Can be completely vapor-developed at film thickness <150 nm with sensitivities of 5×10^{-7}-1×10^{-6} coulomb cm^{-2}.
Poly(2-methyl butene-1 sulfone)	PMBS-M1		MEK Dioxane			Material spins poor films from both solvents.

* The polysulfones exhibit very sharp contrast which requires careful adjustment of the developer for each polysulfone in order to maximize sensitivity. The developer solutions listed represent the average of several samples.

The effect of accelerating voltage on sensitivity and resolution on poly(butene-1 sulfone) (PBS) was evaluated. The sensitivity of PBS was determined at 5, 10, 20, and 30 kV. The resolution as a function of beam potential was evaluated by exposing a 400 nm film of PBS on 200 nm of SiO_2 with a 100 nm diameter electron beam operating in the single sweep mode. Providing care was exercised not to overexpose the resist, this mode gave the highest resolution attainable with a given set of operating conditions. The resist was then processed and the SiO_2 etched.

The width of the etched grooves was determined and taken to be the resolution for a particular exposure. The effect of overexposure was determined with a similar technique at 5 kV, by varying the sweep time between 0.4 and 0.02 sec; 0.04 sec being the correct time to expose the resist to its critical dose.

Results and Discussion

Solution development.—The sensitivity of all of the polysulfones, using optimum conditions and developer, was found to be ~1-3 × 10^{-6} coulomb cm^{-2}. There is a direct correlation between sensitivity and the magnitude of G(scission), the number of main chain bonds broken per 100 eV absorbed, as seen in Table II. This similarity in the sensitivities of the polysulfones indicates that they all have similar G(scission) values. This is in agreement with the results of Brown and O'Donnell (2) who reported similar G(scission) values (as determined from molecular weight measurements on γ-irradiated samples) for PBS and poly(hexene-1 sulfone). It is clear from these data that sensitivity will not be of major importance in the choice of a polysulfone as an electron beam resist.

From Table I several of the polymers can be eliminated because of poor film properties[2] and adhesion.

[2] *i.e.*, The film does not serve as an impermeable etching mask.

Table II. Sensitivity and G(scission) for several positive resists

Polymer	G(scission)	Sensitivity (coulombs cm^{-2})
Poly(α methyl styrene)	0.3	1×10^{-4} (4)
Poly(methyl methacrylate)	1.7	5×10^{-5} (4)
Poly(isobutylene)*	4.0	5×10^{-5} (4)
Poly(butene-1 sulfone)	11	2×10^{-6}

* We have obtained sensitivities of $2\text{-}3 \times 10^{-5}$ for this resist using the developing solutions quoted in Ref. (4).

This may well be a function of spinning solvent, the choice of which is limited by the individual solubility characteristics of the polymers. Of the remaining polysulfones, PBS, poly(pentene-1 sulfone) (PPS), poly(2-methylpentene-1 sulfone) (PMPS), and poly(cyclohexene sulfone) (PcyloHS) have adequate properties to be useful as positive resists. It was found that the polysulfones vapor-develop at rates dependent on the nature of the olefin, as discussed in detail later. When this process occurs, organic vapor and SO_2 are released into the column of the SEM, resulting in marked contamination after several exposures. Hence it is desirable that the rate of vapor development be a minimum in order to reduce contamination of the electron column. When the solvent development mode is being employed, PBS and PPS are the best choices for a solvent-developed positive resist system.

Detailed evaluation of PBS.—PBS was found to serve as a good electron beam resist with a sensitivity of 2×10^{-6} coulomb cm^{-2} (at 5 kV) when used as described.

Figure 1 shows the patterns obtained by etching SiO_2 and W through PBS delineated with an electron beam as described above. Figure 2 shows micrographs of Al/Au patterns evaporated through a PBS mask. The resolution is <800 nm with edge acuity of ±100 nm.

Effect of voltage and overexposure.—The sensitivity of PBS was found to increase with decreasing voltage as shown in Fig. 3. This is in agreement with previous findings for negative resists (7). For a 400-500 nm film of polymer resist, the most efficient energy absorption and hence the highest sensitivity occurs at ~5 kV. For negative resists, transverse electron scattering (coupled with backscattered electron) will increase the line width, with increased exposure, to approximately twice the diffusion range at any accelerating voltage (7, 8). Figure 4 is a plot of maximum line width as a function of accelerating voltage for epoxidized polybutadiene negative resist and PBS positive resist. The effect of voltage on resolution is more pronounced with a negative resist. The sulfone positive resists vapor-develop when overexposed and their scattering density decreases, minimizing line broadening.

Although somewhat material dependent, the best resolution has been obtained using a 5-15 kV electron beam with both positive and negative resists.

Vapor development.—The term vapor development refers here to the process of polymer removal during exposure—a process which eliminates the need for solution development. All the polysulfones investigated vapor-developed, but unlike solution development, the dose required was a function of olefin structure, *e.g.*, 10^{-4} coulomb cm^{-2} for 150 nm of PBS compared with 5×10^{-7} coulomb cm^{-2} for 150 nm of PMPS. Thermodynamic considerations lead one to predict that during irradiation *in vacuo* with product gases being continually removed, all positive resists should completely vapor-develop. The process is, however, complicated by several factors, *e.g.*, radical termination which can markedly decrease vapor-developed sensitivity (3).

When ~150 nm films are used, very high resolution patterns (<400 nm) with good edge acuity (±30 nm)

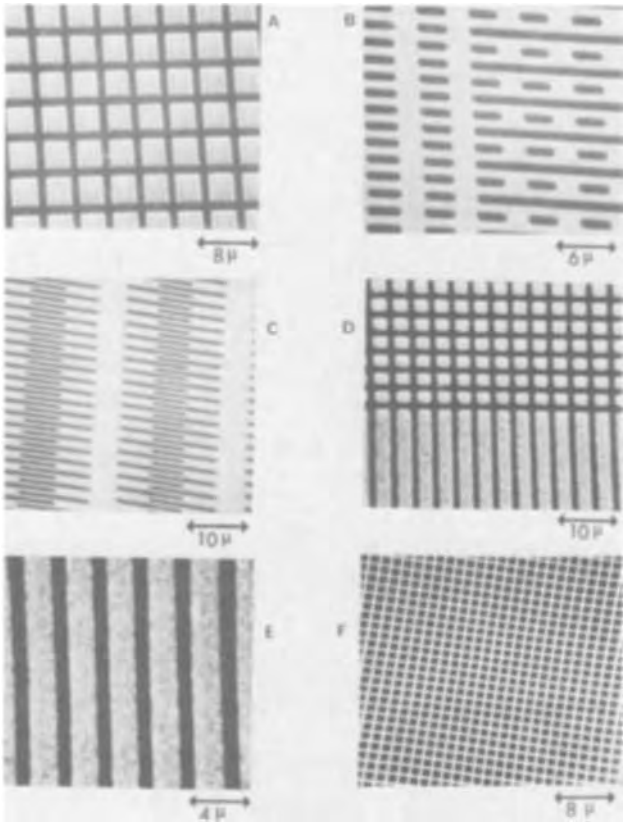

Fig. 1. Typical patterns etched through PBS masks in SiO_2 and W. Exposure 2×10^{-6} coulomb cm^{-2} at 5 kV. (A) and (B) etched in 200 nm SiO_2; (C) etched in 600 nm SiO_2; (D), (E), and (F) etched in 100 nm W.

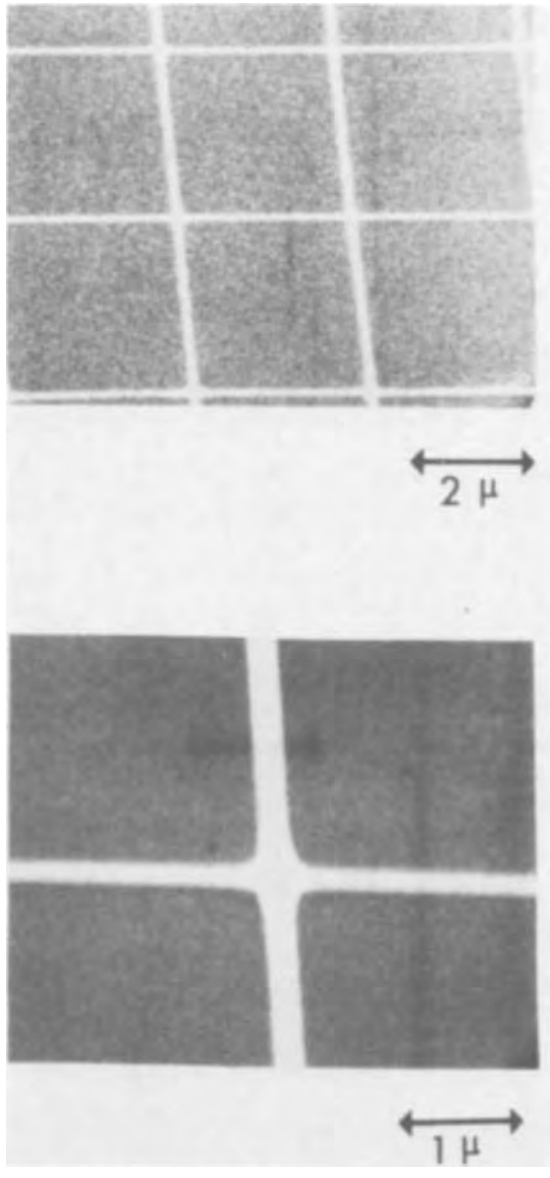

Fig. 2. Electron micrographs of Al/Au patterns evaporated through a PBS mask. Exposure 2×10^{-6} coulomb cm^{-2} at 5 kV.

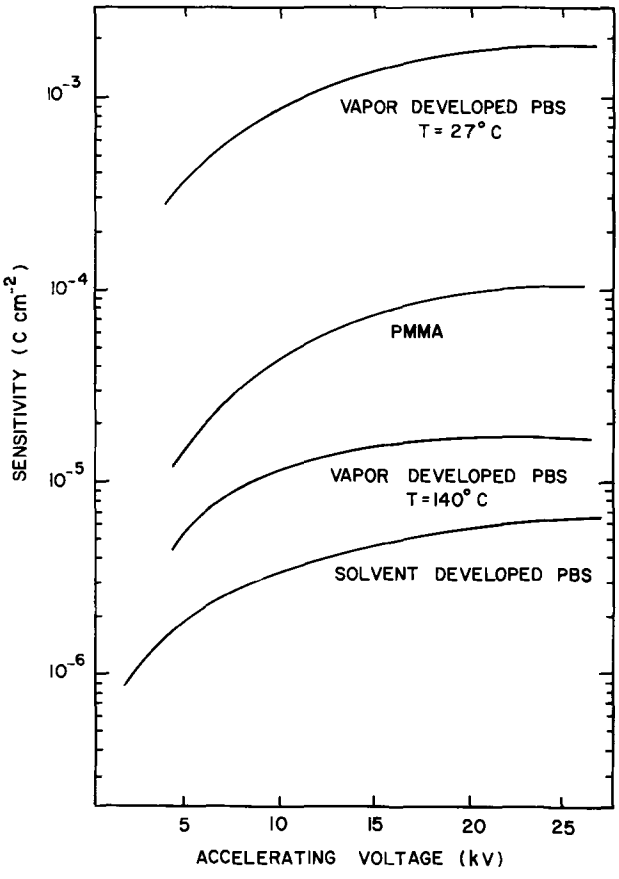

Fig. 3. Variation of sensitivity with accelerating voltage for various electron beam resists.

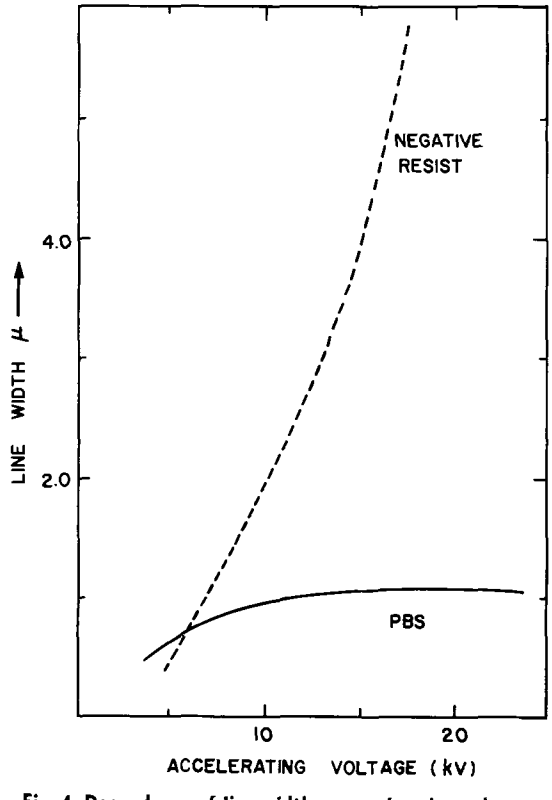

Fig. 4. Dependence of line width on accelerating voltage.

can be made. Figure 6 shows several patterns etched in 200 nm SiO_2 through vapor-developed resists.

The vapor-developed sensitivity depends markedly on several other parameters, *e.g.*, film thickness and temperature, and will be described in detail at a later date.

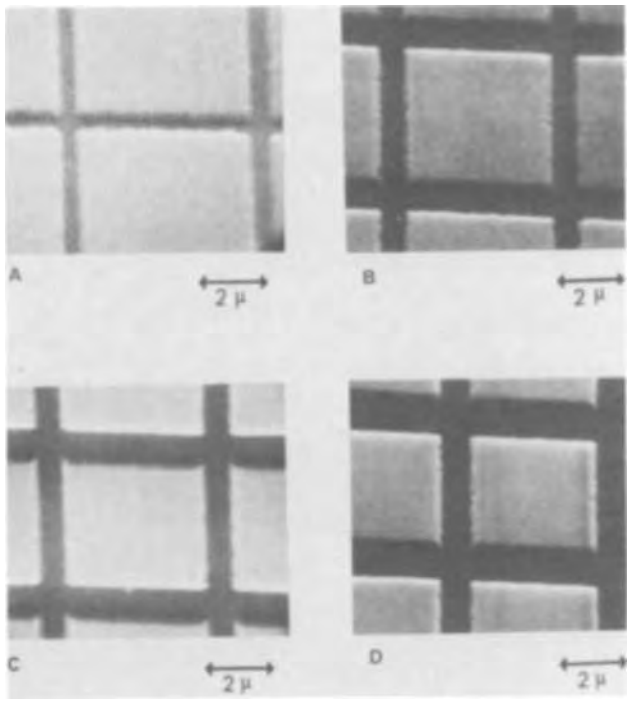

Fig. 5. Electron micrograph showing variations of resolution with dose (scan time at constant current) illustrating the effect of overexposure (A) 0.04 sec scan, (B) 0.1 sec scan, (C) 0.2 sec scan, and (D) 0.4 sec scan.

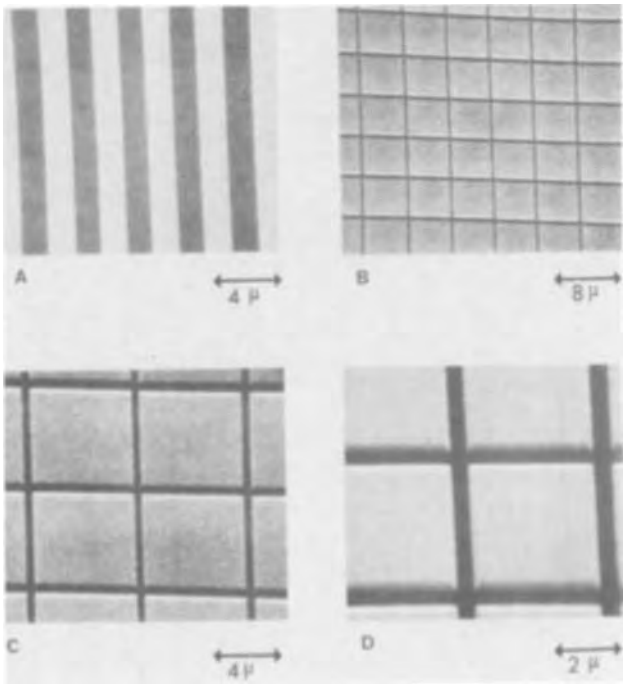

Fig. 6. Electron micrograph of typical patterns etched in SiO_2 through a vapor-developed PBS mask.

Conclusions

1. The family of poly(olefin sulfones) all undergo chain scission at about the same rate and can all serve as positive electron beam resists.
2. Poly(butene-1 sulfone) was found to exhibit best over-all resist properties.
3. All the polysulfones studied can be used in two development modes, *viz.*, solvent and vapor.
4. The optimum accelerating voltage to use is 5 kV for a 400-500 nm resist film.

Acknowledgment

The authors would like to recognize R. D. Heidenreich and E. D. Feit for helpful discussions and C. M. Melliar-Smith for supplying the tungsten substrate.

Manuscript submitted March 8, 1973; revised manuscript received July 25, 1973.

Any discussion of this paper will appear in a Discussion Section to be published in the June 1974 JOURNAL.

REFERENCES

1. S. Magdo, M. Hatzakis, and Ch. Ting, *IBM J. Res. Develop.*, **15**, 446 (1970).
2. J. R. Brown and J. H. O'Donnell, *Macromolecules*, **5**, 109 (1972).
3. M. J. Bowden and L. F. Thompson, *J. Appl. Polymer Sci.*, In press.
4. R. Glang and L. V. Gregor, in "Handbook of Thin Film Technology," L. I. Maissel and R. Glang, Editors, Chap. 7, McGraw-Hill, Book Company, New York (1970).
5. M. Hatzakis, *This Journal*, **116**, 1033 (1971).
6. J. M. Shaw and J. A. Amick, *RCA Rev.*, **31**, 306 (1970).
7. L. F. Thompson, E. D. Feit, C. M. Melliar-Smith, and R. D. Heidenreich, *J. Appl. Phys.*, In press.
8. R. D. Heidenreich, E. D. Feit, L. F. Thompson, and C. M. Melliar-Smith, *ibid.*, In press.

Triboluminescence and Triboelectrification by the Motion of Mercury Over Glass Coated with Scintillator Dyes

Csaba P. Keszthelyi* and Allen J. Bard**

Department of Chemistry, The University of Texas at Austin, Austin, Texas 78712

ABSTRACT

The conversion of mechanical energy into electrical energy and light (triboelectrification and triboluminescence) by the movement of mercury over glass surfaces coated with scintillator compounds was investigated. The motion of mercury over the coated glass involves the build-up of potential differences in excess of 20V; the nature of these triboelectric potentials differs significantly from those observed in the absence of scintillator coating. Twelve scintillator compounds were investigated with the observed luminescence being characteristic of the coating material.

Interfacial processes can generate potentials of varying magnitude, and from a fundamental aspect, these voltage-producing interfacial processes involve energy conversion. Scintillator compounds are characterized by a relatively efficient conversion of one form of energy into another; that is, in the usual experimental situation, the kinetic energy of high energy particles is converted into light energy. The study was concerned with the electrification, *i.e.* the separation of electrical charges, which occurs upon rubbing together dissimilar materials, a process termed "triboelectrification" or sometimes "static electrification." The related optical phenomenon is called triboluminescence (1), the emission of light when certain materials are rubbed or certain crystals are crushed. It has been known for a long time that triboelectrification and triboluminescence occurs when mercury moves over a glass surface in the presence of inert gases. For example, Picard (2) in 1675 observed a "whitish glow" in a Torricelli barometer. He attributed this to some "phosphors" ostensibly present as impurities. The explanation that is in general agreement with present thinking, namely, that a static electric charge builds up, was first put forth by Huksbee (2) in 1705. Recent workers in this field have observed chemical reactions in a triboelectric discharge (3, 4) and have studied the spectra of light generated by the relative motion of contiguous surfaces of mercury and glass (5-7). In related experiments, contact electrification potentials as high as 100V have been measured (8). While many details of the basic mechanism remain obscure, the process involves charge separation at the mercury-glass interface with the subsequent charge recombination reaction being energetic enough (>20 eV) to produce excited states of the inert gases, mercury and even of the silicon and boron of the glass, and to cause decomposition of such molecules as methane. We report here that coating the glass surface with a scintillator compound results in intense luminescence that is color-specific to the coating during movement of mercury over the surface and that this light emission is localized at the scintillator coating and does not extend into the interior volume as has been reported when only mercury and glass are involved (6). Other significant differences that can be attributed to the scintillator coating and potential difference measurements are also discussed.

Experimental

The structures and fluorescence maxima of the scintillator compounds that we used as coating with positive results are shown in Fig. 1. In our previous work involving scintillator compounds (9) we found that the commercially available samples are of a high quality and required no further purification. The FTD, ATD, APD, and BTD samples were sent to us by Prof. Richard L. Taber, Colorado College, who reported them to be extensively purified by column chromatography; these were used as received. The purity of the other compounds that were used as coatings (rubrene, phthalocyanine, $\alpha,\beta,\gamma,\delta$-tetraphenylporphin) was ascertained as described previously (9).

The glass surface to be coated was always cleaned first by rinsing with reagent CH_2Cl_2, hydrochloric acid, distilled water, ethanol, and methylene chloride (spectroscopy grade) several times. The last CH_2Cl_2 rinse was checked using an Aminco-Bowman spectrophotofluorometer and a quartz cuvette to make sure that no traces of luminescent impurities, especially those from a previous coating, were still evident. The glass was almost always coated by contacting it with a

* Electrochemical Society Student Member.
** Electrochemical Society Active Member.
Key words: luminescence, static electrification, scintillator compounds.

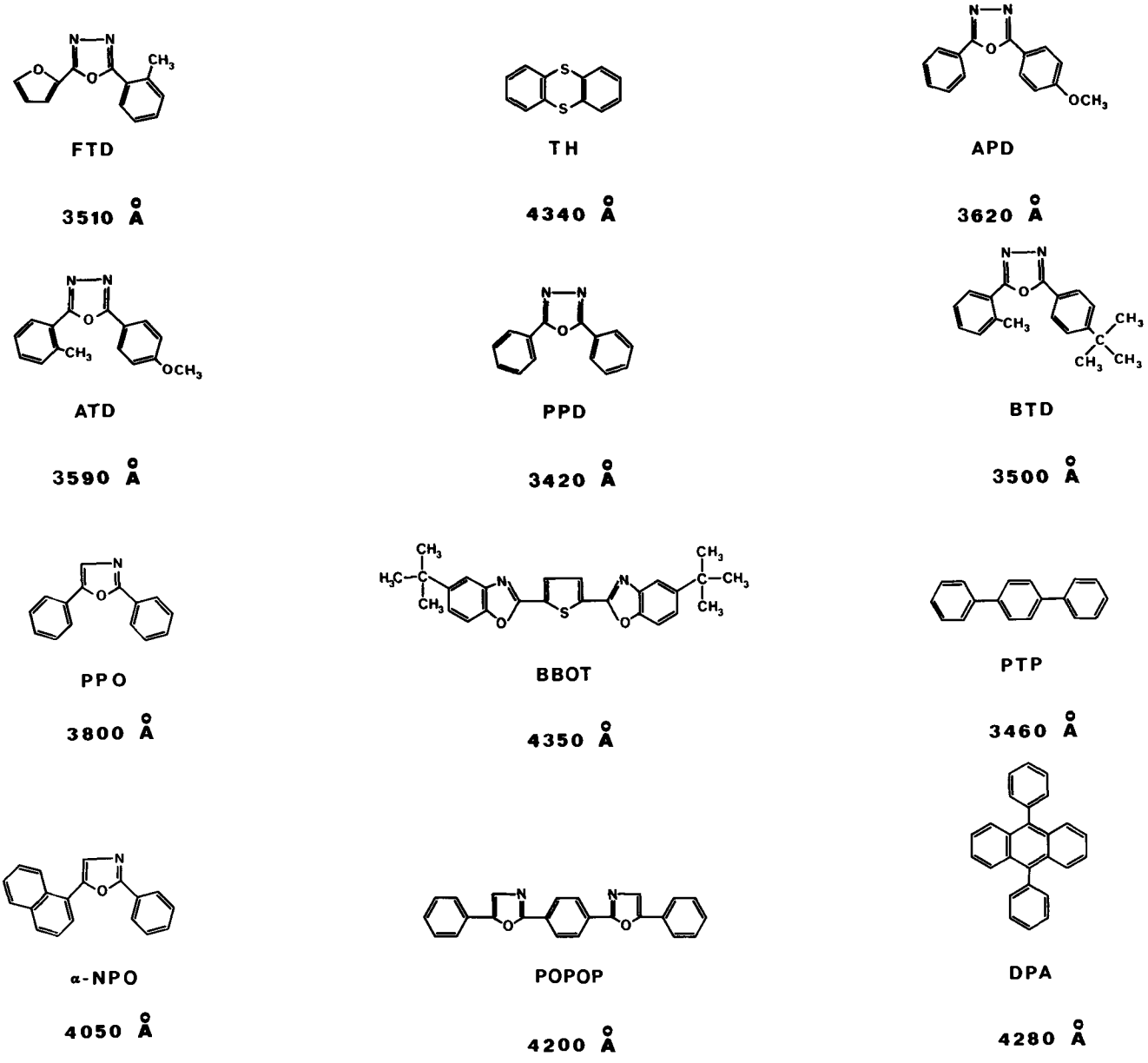

Fig. 1. Structures of the scintillator compounds that were used as coating. [Principal fluorescence or scintillation emission is indicated by λ (Å)].

CH_2Cl_2 solution saturated with the compound being investigated; using approximately 0.5 ml solution for the length of the tube indicated in Fig. 3; the liquid was slowly rocked back and forth in the horizontally held tube that was slowly rotated until all the CH_2Cl_2 had evaporated. Vapor deposition was also employed as a coating technique. By use of a "heat gun," it was possible to make the coating more homogeneous, melting the coating at either specific spots or along the entire surface. The observations were made either in hermetically sealed cells (Fig. 2) or in a detachable vacuum-line type arrangement using "Swagelock" couplings.

Potentials were measured in an arrangement resembling Debeu's (8) by using either an electrometer (General Radio Company, Type 1230-A) or a solid state operational amplifier (Philbrick-Nexus) in a voltage follower arrangement yielding an input resistance $>10^{12}$ ohms. A Moseley 7005-A XY recorder was used to obtain the potential-time plots shown in Fig. 4 and 5. The electrometer could measure voltages up to 10V, the Philbrick operation amplifier limits ~20V.

The rate of the rise and fall of the distilled Hg column could be controlled by the arrangement shown on the top of Fig. 3, whereby the vacuum pump or a noble gas source was alternately connected to the main coated tube. It was found impossible to achieve a steady rate of rise under our experimental setup, and recorded measurements were confined to the falling Hg column. The He, Ne, and Ar were a high purity, commercially available, grade, used as received. The imbedded electrodes (cf. Fig. 3) were of platinum wire.

Results and Discussion

For a preliminary investigation of the triboluminescence, the hermetically sealed cell arrangements shown in Fig. 2 were employed. These were coated tubes containing a small amount of mercury sealed under vacuum which produced light emission upon moving or shaking the mercury. Such closed cells functioned essentially without change over a period of several months when used intermittently. For a continuous test, a glass wheel, scintillator coated, and containing mercury, was rotated by connection to a motor revolving at 0.5-5 rpm; emission was observed for 48 hr in this arrangement before the test was terminated. In these cells, even the slightest movement of the Hg in the coated tube produced the characteristic luminescence.

We have made quantitative measurements of the triboelectric potentials generated at the scintillator interface by the movement of the mercury using the arrangement indicated in Fig. 3. In this apparatus,

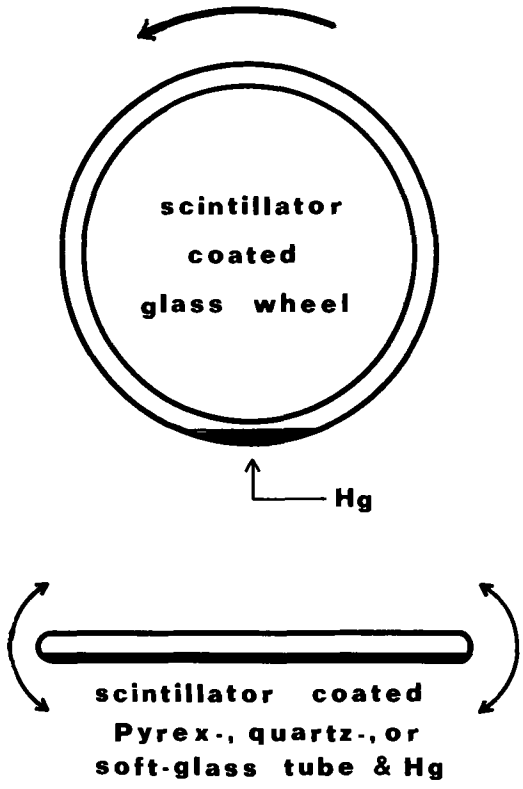

Fig. 2. Triboluminescence could be observed for prolonged periods of time in these hermetically sealed cells; the 9 in. diameter evacuated hollow wheel could be rotated by using an electric stirrer motor equipped with speed control.

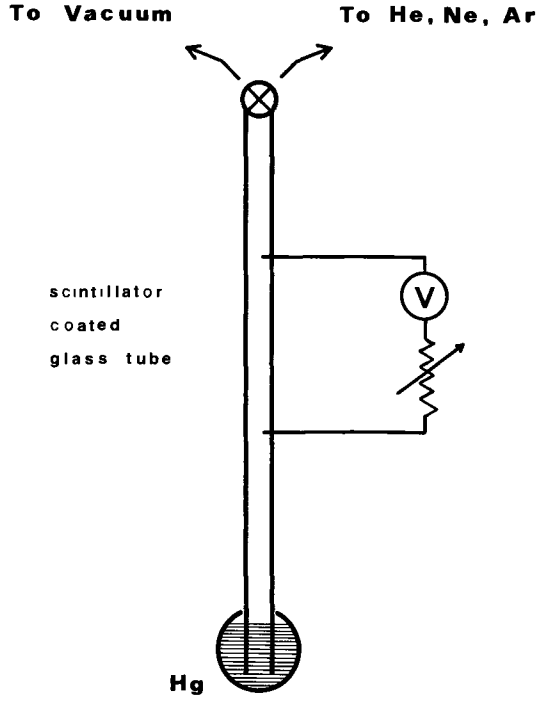

Fig. 3. Triboelectric potentials were measured accordingly (total length of the 6 mm OD tube was 34 in., separation of the imbedded electrodes was 10 in.).

which resembles an ordinary mercury-in-glass barometer except that here the glass has been coated with scintillator compound, the mercury in the reservoir can be made to rise and fall at a given rate in the tube by applying either vacuum or inert gas pressure at the inlet. The potential between the mercury and the glass can be measured by means of the two platinum wires sealed into the tube. In a typical experiment the mercury column, formed by applying a vacuum to the inlet, is allowed to fall by slow addition of inert gas. Flashes of light are observed at the mercury-coated glass interface. The potential-time behavior (termed here a "potentiogram") between the platinum contacts taken at various ohmic resistance settings of the electrometer is shown in Fig. 4. While the two electrodes remain shorted by the descending Hg column, the reading on the electrometer (or from the operational amplifier in the voltage follower arrangement) is, naturally, zero. There is a sudden increase in potential as the Hg level moves below the top platinum lead (with the lead contacting the mercury positive with respect to the upper glass lead); subsequent variations and the detailed shape of the potentiogram are highly reproducible for a given coating, but vary from coating to coating. This allows "finger-printing" a coating surface, and also checking for any bald spots, striations, etc. The maximum voltage generated by the triboelectrification process could not be determined in these experiments, but we did find it to be in excess of the amplifier limiting voltage of about 20V when the high impedance solid-state operational amplifier was substituted in place of the electrometer in Fig. 4. With the electrometer, the highest resistance setting corresponding to the vacuum tube impedance of the electrometer itself could not be applied for fear of damaging the instrument. Debeu (8) measured maximum voltages in excess of 100V on contact electrification using nickel as the stationary phase, and NaCl or quartz particles as the moving phase; our maximum voltages may well be in the same range.

The rate at which the mercury column was falling had an effect on the generated voltage; lower voltage readings occur at the slower flow rates probably because of leakage of the built-up charge, lateral migration processes inside the scintillator coating, etc. Tentative evidence of such losses is found in the generally declining shape of potentiograms as the Hg column moves farther away from the upper platinum electrode, making the effective scintillator column length being monitored by the electrometer increasingly longer.

The light pulses are quite irregular in their time distribution, and no correlation could be observed between certain positions on the coated tube and light emission either. The typical pulse length was between 0.2 and 0.5 sec; the rise time and decay characteristics have not been measured. By comparison to calibrated light sources with the aid of the photodiode we used in electrogenerated chemiluminescence quantum efficiency measurements (10) the number of photons emitted per cm^2 in these experiments is estimated to be certainly greater than 10^{15} in a pulse.

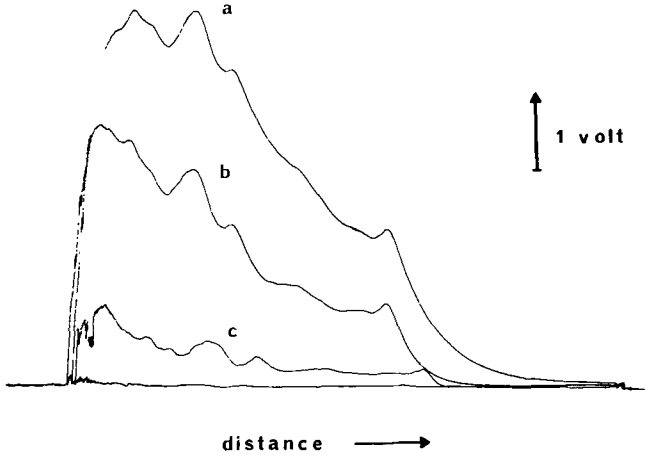

Fig. 4. Potentiogram of the triboelectrically generated voltages with apparatus of Fig. 3; constant recorder sensitivity is indicated by the "1 volt" scaler. The resistance settings of the electrometer were (a) 10^{11}, (b) 10^{10}, (c) 10^9 ohms. The rate of fall of the Hg column was 3 in./min.

Significantly different results are obtained in the same cells under similar conditions when the scintillator coating is removed. As Fig. 5 shows, now complete discharges occur, involving breakdown of the gas in the bulk volume. When a large number of potentiograms are examined, it is unmistakable that the voltage build-up and discharge pattern is quite random, in sharp contrast with the potentiograms taken in the presence of a scintillator coating, where the potentiograms are highly reproducible and also "fingerprint" minute details of the coating surface. In all the experiments when the type of glass varied, we found no specific or obvious differences in behavior. On the other hand, when other fluorescent (nonscintillator) compounds, such as rubrene, TPP, or PC were used as coatings, no intense orange or red triboluminescence resulted.

While a detailed mechanism of the phenomenon can obviously not be presented on the basis of the experiments here, these results combined with previous studies of static electrification and solid-state luminescent processes allow some possible schemes to be presented. The process of contacting mercury with glass causes the mercury to become positively charged and the glass negatively charged as a result of electrons from the mercury moving into unfilled surface states of the glass (6). The separation of the mercury and glass surfaces initiates a discharge, and based on the fact that emission from He has been observed under these conditions as well as decomposition methane and other hydrocarbons, the excitation energy produced by this discharge is greater than 20 eV (7). Thus, one mechanism for the luminescence of the scintillator would involve energy transfer from excited state species of the mercury or inert gas to the scintillator coating. However, the lack of luminescence of certain fluorescent dyes and the relative independence of the emission on the type or pressure of inert gas makes other mechanisms worth considering. The discharge process could lead to highly energetic electrons; the interaction of these "soft β-rays" with the scintillator could produce emission. Yet a third mechanism is suggested by experiments on charge injection into aromatic crystals (11, 12). In these experiments, the direct injection of electrons and holes into crystals, or injection via insulator crystal electrodes and solutions, leads to electron-hole combination in the crystal and light emission. The charge separation across the scintillator coating could lead to this kind of process in these experiments.

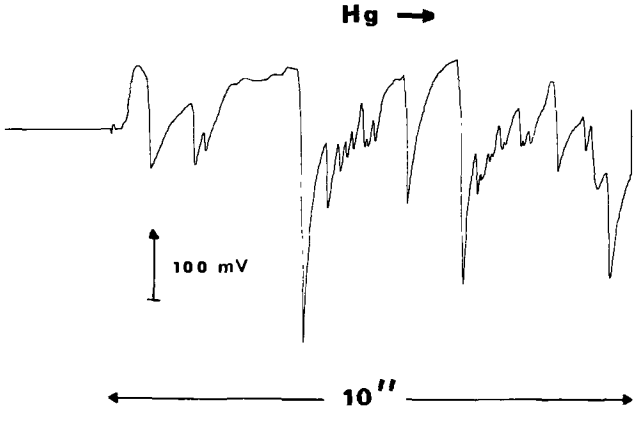

Fig. 5. Potentiogram of triboelectrically generated voltages under the same conditions as Fig. 4, except that the scintillator coat was completely removed; the resistance setting of the electrometer was 10^{11} ohms.

Acknowledgment

This work was supported in part by the U.S. Army Research Office-Durham, and by the 1972 Joseph W. Richards Fellowship of The Society. This was Paper 48 presented at the 28th Southwest Regional Meeting of the American Chemical Society, December 6-8, 1972, Baton Rouge, La. We are grateful to Professor Richard L. Taber for the substituted oxadiazole samples.

This paper was submitted to the faculty of the University of Texas at Austin in partial fulfillment of the requirements for the degree of Doctor of Philosophy.

Manuscript received June 13, 1973.

Any discussion of this paper will appear in a Discussion Section to be published in the June 1974 JOURNAL.

REFERENCES

1. L. B. Loeb, *Science*, **102**, 573 (1945); L. B. Loeb, "Static Electrification," Springer-Verlag, Berlin (1958).
2. Recorded in "A History of Science, Technology, and Philosophy in the Eighteenth Century," by A. Wolf, p. 213, MacMillan, New York (1939).
3. J. H. Johnson, R. H. Knipe, and A. S. Gordon, *Can. J. Chem.*, **48**, 3604 (1970).
4. W. G. Alcock, E. J. Hayward, B. Mile, and B. Ward, *ibid.*, **50**, 3813 (1972).
5. K. Ikenoue and Y. Sasada, *Mem. Defense Acad., Math., Phys. Chem. Eng. (Yokosuka, Japan)*, **2**, 49 (1972).
6. G. L. Dybwad and C. E. Mandeville, *Phys. Rev.*, **161**, 527 (1967).
7. S. De Paoli and O. P. Strausz, *Can. J. Chem.*, **48**, 3756 (1970).
8. D. E. Debeu, *Phys. Rev.*, **66**, 9 (1944).
9. C. P. Keszthelyi and A. J. Bard, *This Journal*, **120**, 241 (1973).
10. A. J. Bard, C. P. Keszthelyi, H. Tachikawa, and N. E. Tokel, "Chemiluminescence and Bioluminescence—Proceedings of the 1972 International Conference," M. J. Cormier, D. M. Hercules, and J. Lee, Editors, p. 193, Plenum Press, New York (1973).
11. W. Helfrich and W. G. Schneider, *J. Chem. Phys.*, **44**, 2902 (1966).
12. H. P. Schwob and D. F. Williams, *ibid.*, **58**, 1542 (1973).

A Technique for Measuring the Saturation of Phosphors at High Current Densities

E. F. Gibbons, R. G. DeLosh, T. Y. Tien, and H. L. Stadler*

Scientific Research Staff, Ford Motor Company, Dearborn, Michigan 48121

ABSTRACT

A technique is described which allows for the measurement of the saturation of luminous intensity of phosphors up to high current densities. The actual light intensity profile of the spot is measured and is related to the current density profile across the spot, the latter being obtained from measurements on a nonsaturating phosphor. This technique thus uses a point-by-point measurement of relative efficiency *vs.* beam current density, and therefore no assumptions concerning the beam current profile have to be made, and no averaging of beam current over spot diameter is required. Typical data are presented from several classes of materials. For the samples reported, La_2O_2S:Tb showed the least degree of saturation, (Zn, Cd)S:Ag the greatest degree, and Zn_2SiO_4:Mn was intermediate to these two.

Most phosphors, when excited by an electron beam, show a less than linear increase in brightness with increasing beam current density. This phenomenon is known as saturation and is indicated schematically in Fig. 1 where both intensity and efficiency are displayed as a function of beam current density. This effect can be particularly troublesome in multicolored cathode ray tubes using high current densities, *e.g.*, post deflection focusing (PDF) type color television tubes.

* Electrochemical Society Active Member.
Key words: luminescence, phosphors, saturation.

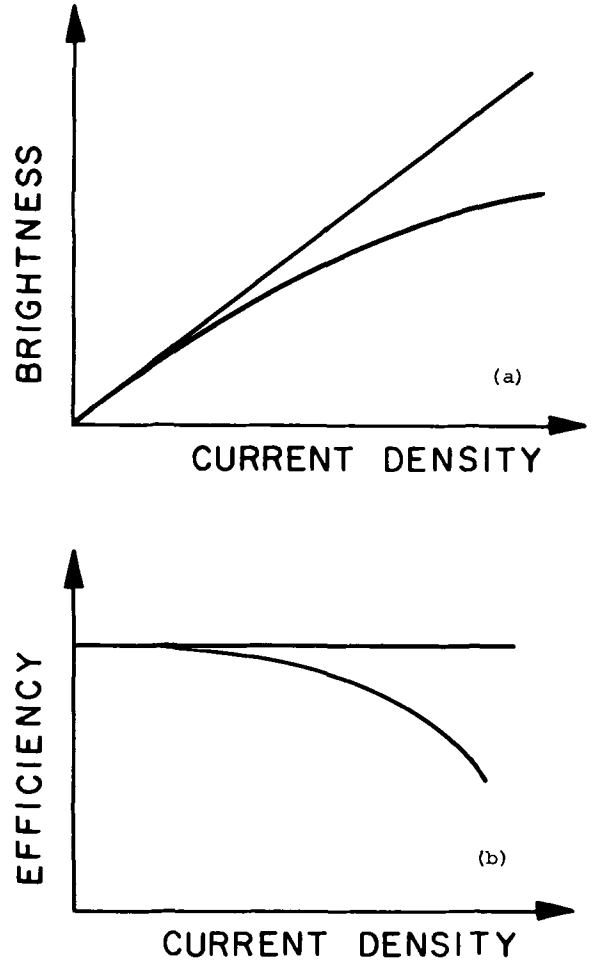

Fig. 1. Effect of current density on: a) brightness or b) efficiency of a nonlinear phosphor.

Two disadvantages will accrue if the phosphors chosen for this type of tube exhibit saturation in the current density range used by the tube: (*i*) the anticipated brightness increase will not be achieved, and (*ii*) the color balance and white field produced by color mixings will vary with beam current density. For these reasons, the intensity *vs.* beam current density data is an important factor in choosing the appropriate phosphors for these types of applications.

Measurement of the saturation of various phosphors has been reported by a number of authors (1-6), with the work of Meyer and Palilla (6) being most directly concerned with television tube application. In these previous works, some assumption was made about the current density profile across the electron beam and a calculated average current density was used in the saturation plots. The technique reported in this article determines the actual current density profile of the spot, and so provides a point by point measurement of intensity *vs.* beam current density.

Apparatus

Phosphors used in this experiment were either obtained commercially (so designated in the appropriate figures) or prepared in the laboratory. Samples were settled onto 2.5 × 7.5 cm microscope slides using a potassium silicate-barium acetate settling method. After lacquering, the slides were aluminized in a vacuum evaporator. Aluminum deposition was regulated by a quartz crystal thickness monitor such that all samples measured had an aluminum backing of 1000 ± 50Å. Saturation measurements were made in a demountable electron beam gun system shown in Fig. 2. The electron beam gun was a Raytheon Type QV-359 operated at 23 kV and with peak beam currents of 8 mA. The vacuum system was an oil-free system, using a sorption pump for roughing and an ion pump for high vacuum pump down. When samples were being changed, the electron beam gun could be isolated from the sample chamber by means of a gate valve. This allowed the gun to always remain under high vacuum after cathode break-in had been performed, and thus extending gun life indefinitely.

At the high beam currents used in these experiments, the coils located at the gun neck were not sufficient to prevent self-defocusing of the beam by the time it reached the sample plane. It was therefore necessary to provide auxiliary focusing coils closer to the sample plane and separate deflection coils just before the sample plane. A typical spot size for these measurements was 0.025 in. diameter at the 10% maximum intensity point. All these coils were operated from highly regulated constant current supplies.

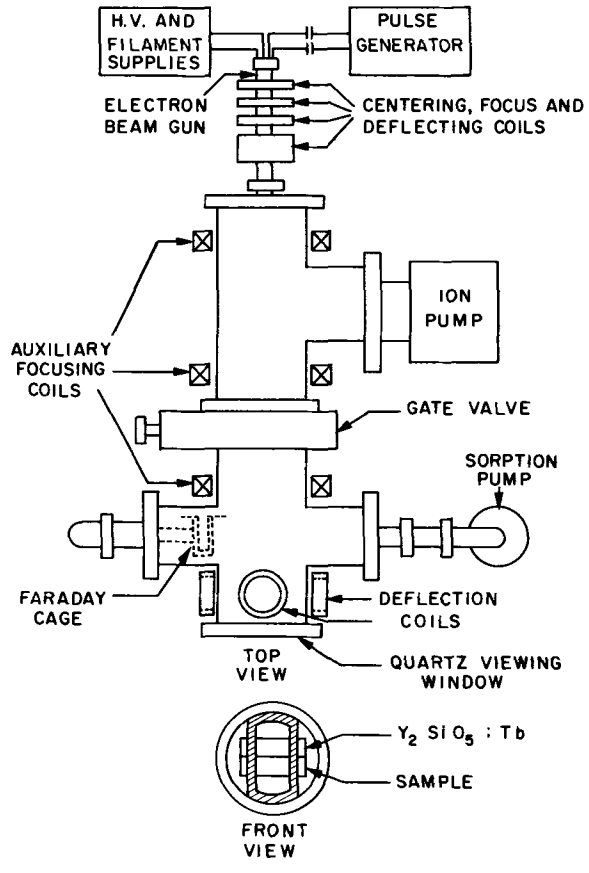

Fig. 2. Demountable electron beam gun system

The sample light spot intensity was measured using a photometer which observed a 0.002 in. diameter area of the spot. During the course of the measurement, the photometer remained focused on one spot and the electron beam was slowly scanned across it. The beam was swept horizontally by changing the current through the horizontal deflection coils. This was done by using a 1/6 revolution per hour motor to drive a ten turn potentiometer. The voltage across the horizontal deflection coil was then used as the signal for the x-amplifier on an x-y recorder. The signal from the photometer's photomultiplier was applied to the y-amplifier of the recorder. For each set of excitation conditions, a suitable neutral density filter was used so that the photomultiplier response was linear over the light intensities encountered. The resulting intensity profile of a nonsaturating phosphor is shown in Fig. 3.

The system was also provided with a Faraday cage mounted on a linear motion feedthrough for measurement of total beam current. The Faraday cage could be moved to the axis of the system for current measurement, and then withdrawn during the saturation measurements.

Current pulses were obtained by biasing the electron beam gun into cutoff, and turning it on by applying positive voltage pulses, obtained from a Hg-reed relay, delay line generator, to the grid. By this means the current pulse could be controlled from 0 to 8 mA and from 6 nsec to any desired duration. A typical current pulse is shown in Fig. 4.

Determination of the Current Density Distribution

Principle.—For a nonsaturating phosphor, the intensity is directly proportional to the current density. Therefore, the intensity profile shown in Fig. 3 is the same as the current density profile across the light spot. Hence, if the area under the current density curve and the total current are known, the current density at any point in the profile can be calculated. In this calculation the light intensity profile of the Y_2SiO_5:Tb is approximated by a series of annular steps, the ith step being of height h_i and radius r_i. The steps are taken at a uniform spacing of Δr. Since h_i is directly proportional to the current density at that point, J_i, for a nonsaturating phosphor

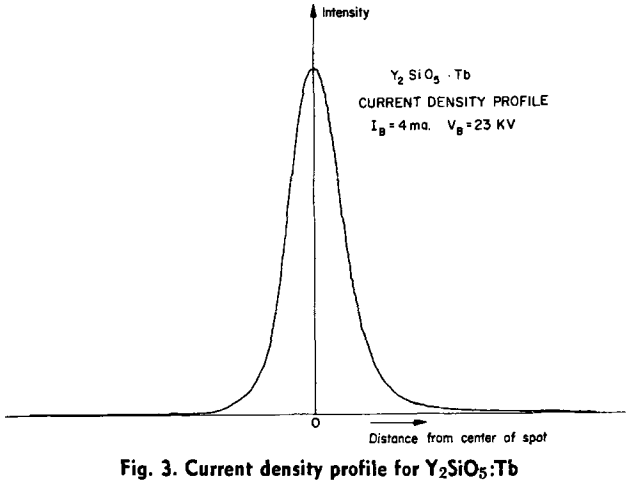

Fig. 3. Current density profile for Y_2SiO_5:Tb

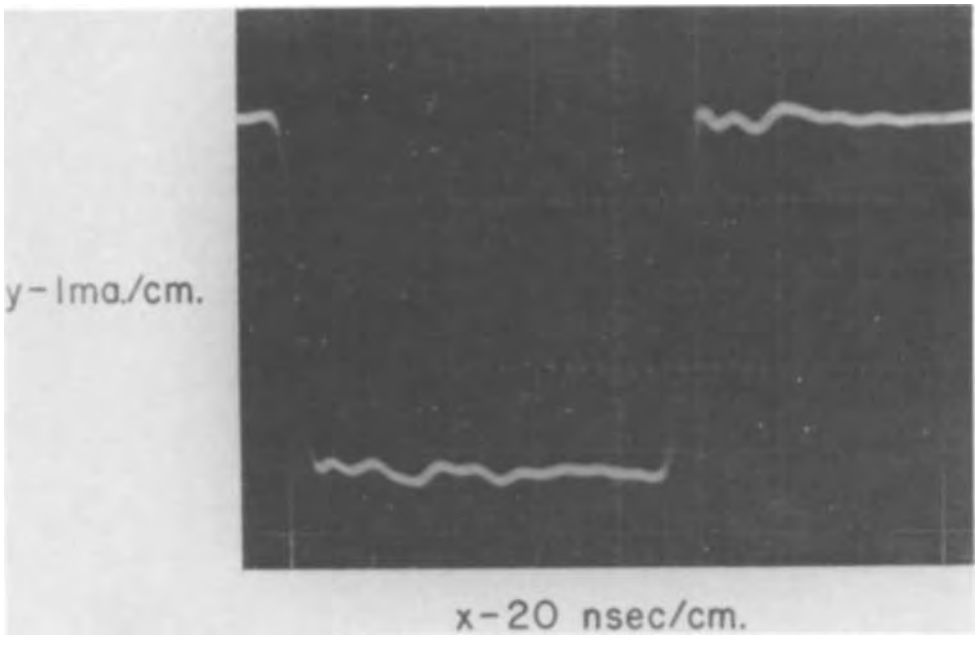

Fig. 4. Current pulse into the Faraday cage.

$$h_i = \alpha J_i \quad [1]$$

where α is a proportionality constant. Denoting the total current into the ith annular region as I_i,

$$I_i = (2\pi r_i \Delta r) J_i \quad [2]$$

Therefore, using [2] in [1] and solving for I_i

$$I_i = \frac{h_i}{\alpha} (2\pi r_i \Delta r) \quad [3]$$

The total current into the light spot is I

$$I = \sum_i I_i \quad [4]$$

or, using [3] in [4]

$$I = \frac{2\pi\Delta r}{\alpha} \sum_i h_i r_i \quad [5]$$

Therefore, the proportionality constant between light spot intensity and current density for Y_2SiO_5:Tb, α, is given by

$$\alpha = \frac{2\pi\Delta r}{I} \sum_i h_i r_i \text{ cm}^2/\text{A} \quad [6]$$

The intensity profile was approximated by using 20 steps. It was found that doubling this number provided no significant increase in accuracy.

It is therefore only necessary to measure the total current in the beam and to relate the dimensions of the x-y plot to the actual dimensions of the light spot to convert the intensity profile to a current density profile.

Technique.—The measurement of the total beam current is easily accomplished by means of the traveling Faraday cage. A 100 msec wide current pulse as recorded on a Tektronix 551 oscilloscope is shown in Fig. 4.

To relate dimensions on the x-y plot to actual dimensions of the light spot, advantage is taken of the optical system of the photometer. The spot photometer is constructed such that a lens system focuses the light from the sample plane onto the cathode of a photomultiplier tube. A mirror, with a precision aperture, intercepts the light beam and reflects all but the light passing through the aperture to an eye piece. The size of the aperture determines the cross-sectional area of the sample plane that is actually observed by the photomultiplier. A camera placed at the eyepiece will then photograph the light received from the sample plane, less that transmitted through the aperture. If the light spot is then positioned such that the photometer indicates an intensity of 10% of maximum, a photograph taken through the eyepiece will show a dark area at some distance from the center of the light spot. The diameter of the area will be determined by the diameter of the aperture chosen, thus the actual dimensions of the light spot can be determined. Also, since it is known that the dark area in the photograph is at the 10% intensity point, the dimensions of the light spot can then be correlated to the dimensions of the x-y plot. In practice, the negative of such a photograph is used and a microdensitometer trace is made from the negative. Such a trace is shown in Fig. 5 where a 0.006 in. aperture has been used for emphasis. A 0.002 in. aperture was used for the actual measurements. This would be an exact measurement in the limit where the ratio of photometer aperture to spot diameter is zero; with the 0.002 in. aperture, a 0.025 in. spot size, and assuming a Gaussian distribution of intensity, the error incurred in determining the 10% radius in this manner is about 2%.

The slope observed at the edges of the aperture spot is caused by the rounding of the mirror at the aperture opening. Microdensitometer traces were made through several different cross sections of the light spot to ensure that the beam was actually symmetric.

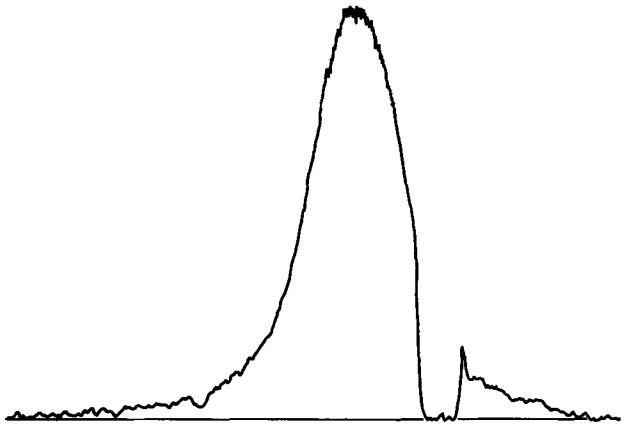

Fig. 5. Typical microdensitometer trace

Measurement of Saturation Characteristics

The procedure involved in measuring the saturation characteristics of a given phosphor is to mount a settled slide of this phosphor, along with a slide of a nonsaturating phosphor, in the demountable system. For a given set of excitation conditions—beam current, pulse width, and repetition rate—a light intensity profile is recorded for the nonsaturating phosphor. This is then converted to a current density profile as just described. The beam is then moved to the test slide and the same beam conditions are used to obtain a light intensity profile for the sample phosphor. Assuming that the same current density distribution pertains to the saturating phosphor as was determined for the Y_2SiO_5:Tb slide, an intensity (or efficiency) *vs.* current density plot can be derived.

The assumption that the electron beam did not change its shape when it was moved from the Y_2SiO_5:Tb reference slide to the test slide was checked by substituting a second slide of Y_2SiO_5:Tb for the test sample. The current density distribution for the second Y_2SiO_5:Tb slide was taken to be identical with that of the reference slide, as was done for measurements on saturating phosphors. If there were no change in the current density profile in moving the spot from one slide to the other, the relative efficiency *vs.* current density plot for the second Y_2SiO_5:Tb slide should be a straight line with zero slope. The results of several measurements are shown in Fig. 6. This shows a measurement error of less than ±5% except at the lowest current densities. These measurements were made periodically throughout the course of the experiment. Another check on the equality of the two current distributions was made by applying very small beam currents to the reference slide and a saturating sample. The current density at all points in the spot was below

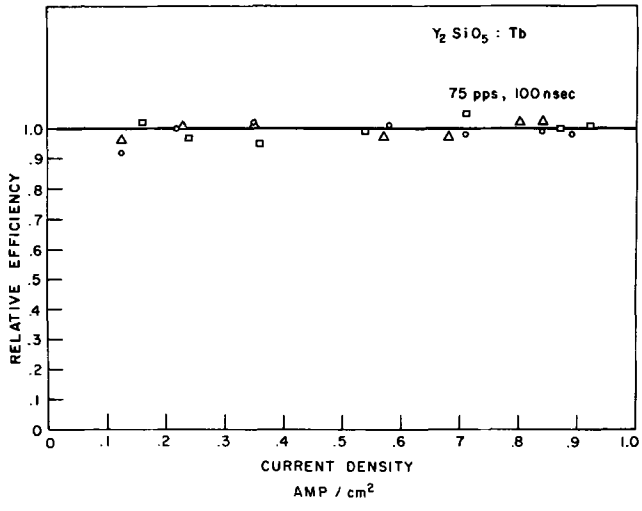

Fig. 6. Estimate of measurement error using an Y_2SiO_5:Tb sample

the level where saturation is noticeable. It was found that the two intensity profiles were proportional, thereby indicating equality of the two current distributions. Finally, the use of a grounded aluminum film on the back of the samples largely eliminates the importance of the electronic properties of the various materials.

The superposition of the light intensity profile of a saturating (Zn,Cd)S:Ag, and a nonsaturating, Y_2SiO_5:Tb, phosphor is shown in Fig. 7. The (Zn,Cd)S:Ag was a commercially obtained green television phosphor. From this plot it is evident that the (Zn,Cd)S:Ag is considerably brighter at the lower current densities, but at the highest current densities its relative brightness has fallen off considerably.

For a nonsaturating phosphor, Y_2SiO_5:Tb was chosen since it had been reported by Meyer and Palilla to have a luminous efficiency that was independent of current density. This was verified by measuring the total brightness from a defocused spot and then focusing the beam, producing current densities of several A/cm^2 in the center. Since no change in brightness was observed, it can be inferred that there was no change in luminous efficiency. There were conditions of sufficiently high beam current density where even the Y_2SiO_5:Tb showed saturation. This limited the useful range of current densities to approximately 3 A/cm^2 maximum current density.

The relative efficiency at any current density was obtained by taking the ratio of the intensity of the sample at that point to the intensity of the Y_2SiO_5:Tb and comparing it to the same ratio at low current density. The low current density ratio was obtained by using a raster scan and low beam current. A point-by-point comparison across a low current density spot could also be used to obtain the low current density ratio, and this technique gives the same results as the raster scan measurement, however, the raster scan measurement was much faster and easier to make.

Results

Relative efficiency *vs.* beam current density data are shown for several different phosphors in Fig. 8-10. In Fig. 8, the data for La_2O_2S:Tb, it is seen that although

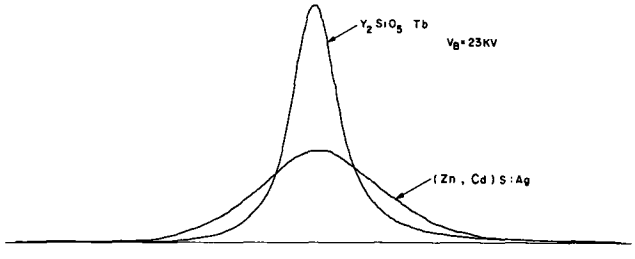

Fig. 7. The light intensity profiles of a saturating (Zn,Cd):Ag, and nonsaturating, Y_2SiO_5:Tb phosphor.

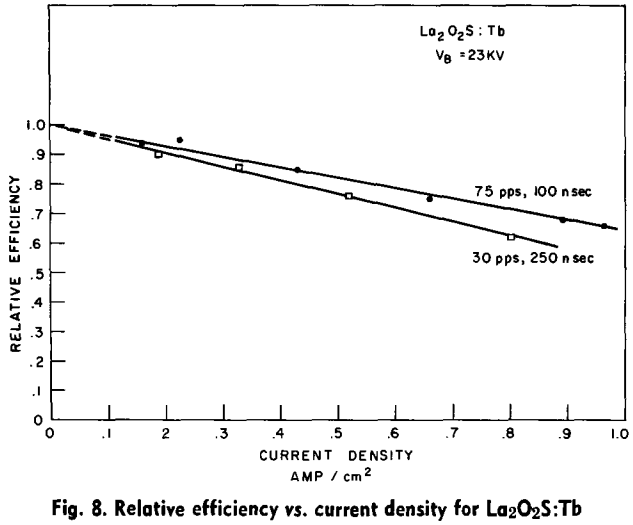

Fig. 8. Relative efficiency *vs.* current density for La_2O_2S:Tb

the two excitation conditions produce the same excitation time per second, the longer width pulse causes greater saturation. Also, this material shows the least saturation of the three samples shown. This is consistent with the results of Ref. (6) which showed that the rare earth doped oxides showed the least degree of saturation of the phosphors reported. ZnS:Ag and (Zn,Cd)S:Ag showed the greatest loss in relative efficiencies. Figure 9 shows the results for (Zn,Cd)S:Ag out to a current density of 3.2 A/cm^2. It is apparent that this phosphor loses efficiency very rapidly, even at low current densities, and at high current densities has less than 10% of its maximum efficiency. Therefore, even at moderate current densities a number of other phosphors would be brighter than (Zn,Cd)S:Ag.

Figure 10 shows the data for willemite which shows a degree of saturation intermediate to the rare earth activated phosphors and the sulfide phosphors. Also, the data show an increased effect for increasing pulse width. It should be pointed out that other authors (1, 2) have shown that the loss of relative efficiency for Zn_2SiO_4:Mn is very strongly dependent on manganese concentration, so the data of Fig. 10 should only be applied to the particular material studied, NBS standard phosphor 1021.

These data all show a greater saturation effect for a given current density than has been reported previously (6). We attribute this difference to the use of an average current density for the previous data. Because of the nonlinear relationship between light intensity and current density, the inner region of the light spot contributes far less, per unit current density, to the total spot brightness than do the outer regions. Hence,

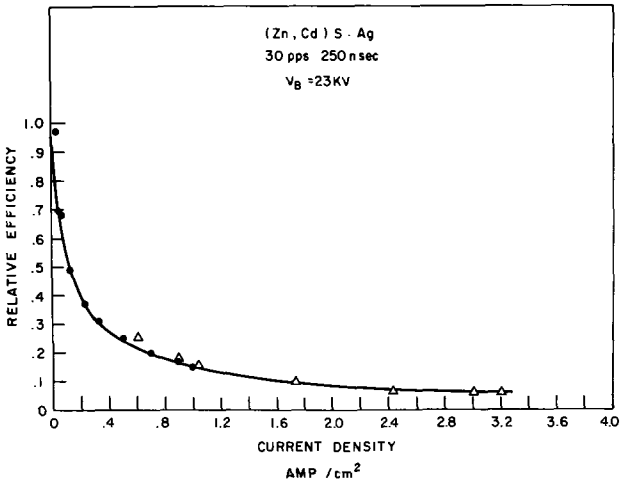

Fig. 9. Relative efficiency *vs.* current density for (Zn,Cd)S:Ag (sample obtained commercially).

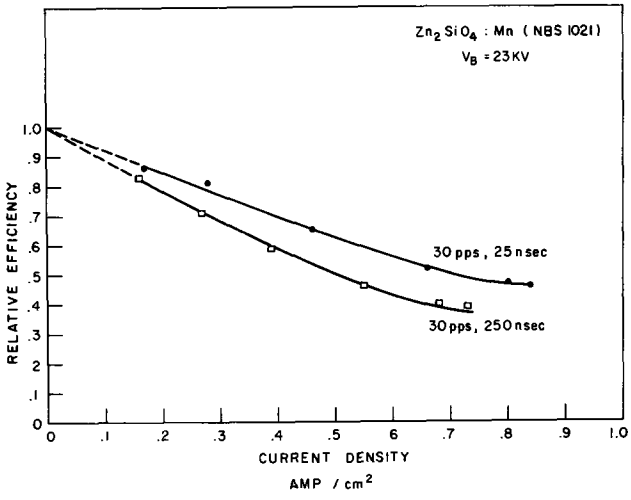

Fig. 10. Relative efficiency *vs.* current density for Zn_2SiO_4:Mn (sample obtained from NBS).

the low current density regions of the spot contribute a disproportionate fraction of the spot light, and the over-all saturation effect is apparently less. The difference between the average current density method and the point by point technique reported here is about a factor of two for high current densities.

Manuscript submitted April 12, 1973; revised manuscript received July 20, 1973.

Any discussion of this paper will appear in a Discussion Section to be published in the June 1974 JOURNAL.

REFERENCES

1. A. Bril, *Physica*, **15**, 361 (1949).
2. A. Bril and F. A. Kröger, *Philips Tech. Rev.*, **12**, 120 (1950).
3. P. H. Dowling and J. R. Sewell, *This Journal*, **100**, 22 (1953).
4. G. F. J. Garlick, *Proc. I.R.E.*, **43**, 1907 (1955).
5. P. A. Einstein, *Brit. J. Appl. Phys.*, **8**, 190 (1957).
6. V. D. Meyer and F. C. Palilla, *This Journal*, **116**, 535 (1969).

Effects of Comminution on the Luminescence of Phosphors

S. Kuboniwa, T. Hoshina, T. Narahara, and M. Kanamaru

SONY Corporation Research Center, 174 Fujitsukacho, Hodogaya-ku, Yokohama, Japan

ABSTRACT

Luminescent properties of ball-milled $Zn_{0.97}Cd_{0.03}S$:Cu,Al and ZnS:Ag,Al phosphors have been measured. Particle size reduction, or the increase in the surface area, by comminution leads to a large luminescent loss of phosphors due to nonradiative recombination of the free carriers at the crystal surface. The milling condition adopted in this study does not have an appreciable effect on the surface or the bulk properties relevant to luminescence. The average width of the dead layer of the phosphors is estimated to be of the order of 0.1μ. The penetration range of the electron beams into the phosphor layers decreases with decreasing particle size. Particle-size effects on the parameters that determine luminescence are discussed.

Comminution of phosphor particles by means of milling or crushing leads to luminescent loss. Size reduction and lattice defects in the comminution process are caused by pressure, impact, or attrition, or by a combination of these. Size reduction of the phosphor particles leads to an increase in the surface area relative to the whole volume. The crystal lattice is strongly perturbed at and near the surface, and the dangling bonds formed can bind atoms from the ambient. As a result, energy levels of high density are formed in the forbidden gap near the surface. They act as nonradiative recombination centers for the free carriers. The size reduction due to comminution, therefore, increases the fraction of the less-luminescent parts of the phosphors. This is one of the possible causes for luminescent degradation and is regarded as a major cause in this report. Damaging of phosphor crystals in the comminution process can also produce recombination centers in the lattice. The increase in multiple reflection of fluorescent light at crystal surfaces may cause a loss of externally emitted light.

In this report, particle size effects on cathodo- and photoluminescent properties of $Zn_{0.97}Cd_{0.03}S$:Cu,Al and ZnS:Ag,Al phosphors are investigated. These phosphors are used as the green and blue primaries for color picture tubes.

Experimental Procedures

$Zn_{0.97}Cd_{0.03}S$:Cu,Al and ZnS:Ag,Al phosphors were ball-milled for up to 10 hr. The slurry consisted of phosphors (42g), methanol (50 mliters), and water (95 mliters) and was milled in a 500-mliter polyethylene pot with glass balls of 10 mm diameter at the rotation rate of 100 rpm. This milling condition is not so hard as to cause a large crystallographic change of the phosphors. The widths of the x-ray diffraction lines and the estimated lattice constants have shown only a small change caused by the ball milling. Nevertheless, the luminescent intensity is greatly reduced. The crystallographic investigation of the ball-milled phosphors and the study of the comminution mechanism will be reported in another paper (1). Some of the results are given in Table I.

Key words: phosphors; luminescence; (Zn,Cd)S:Cu,Al; ZnS:Ag,Al; comminution; ball milling.

For cathodoluminescent measurements, phosphors were packed in metal trays or sedimented on aluminum plates. The samples were placed in a demountable cathode-ray excitation apparatus. Luminescence was measured from the bombarded side. The current density of the electron beam incident on a sample was determined from the luminescent area measured by a cathetometer and from the beam current detected by a picoammeter, which was inserted between an electron-gun power supply and a pre-accelerating-voltage generator as shown in Fig. 1. The luminescence was detected by HTV-R376 photomultiplier tube through a SPEX-1700-II monochromator. The pressure was lower than 2×10^{-6} Torr.

Table I. Some properties of the samples used

	(Zn,Cd)S:Cu,Al		ZnS:Ag,Al	
Type of the crystal structure	Wurtzite, Zn:Cd = 0.971:0.029		Zinc blende	
Concentrations[a] of				
Cu	$1.1\ 10^{-4}$			
Ag			$2.3\ 10^{-4}$	
Al	$8.5\ 10^{-4}$		$2.7\ 10^{-3}$	
Silica as the coating material	0.26 wt %		0.23 wt %	
Milling time (hr)	Mean diameters[b] (μm)	Specific surface area[c] (m^2/g)	Mean diameters[b] (μm)	Specific surface area[c] (m^2/g)
0	11.6	1.20	7.8	0.45
0.5	10.1	1.35	7.3	0.53
2	7.2	1.63	6.6	0.73
4	5.6	2.00	5.9	0.80
6	4.9	2.20	5.1	1.05
10	4.1	2.65	4.4	1.32

[a] Atomic ratios to the total cations.
[b] Average values over the weight-size distributions. Measured by sedimentation method.
[c] Measured by BET method.

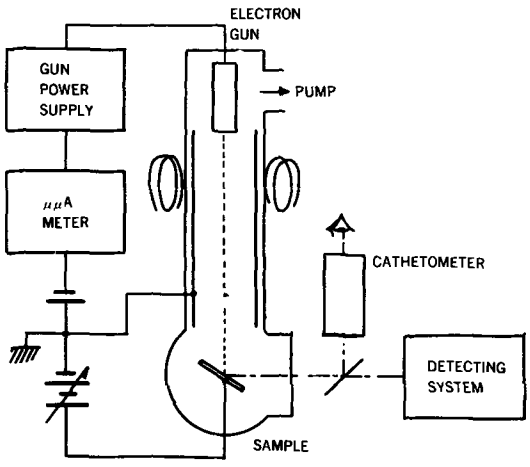

Fig. 1. Schematic diagram for the method of cathodoluminescent measurement.

The beam voltage dependence of the luminescent efficiency for steady excitation by the electron beam of 0.5 $\mu A/cm^2$ was measured. The beam current and the luminescent area were adjusted at each measuring voltage to maintain a constant current density. The measurements were made for the samples sedimented on aluminum plates. Comparison of the luminescent intensity of the sample phosphors was made for thickly packed samples at several voltages to eliminate the difference in reflectivity of the aluminum plates.

Decay-time measurements were carried out using the stroboscopic method (2). Phosphors sedimented on aluminum plates were excited by electron beam pulses of a 5-μsec duration at a frequency of 30 Hz. The time-averaged current density was 0.2 $\mu A/cm^2$, which was identical with the pulse height of 1.3 mA/cm^2. The triggering pulse from a pulse generator was delayed and supplied to a high voltage pulse generator which fed the gating pulses (−1.5 to −2 kV) to an HTV-R566 (S-20) photomultiplier. The gating-pulse width was varied from 0.1 to 10 μsec for initial and later stages of luminescent decay.

Excitation spectra were measured at room- and liquid-nitrogen temperatures. Exciting monochromatic light was obtained using a 150W Xe-lamp and a SPEX 1700-II monochromator equipped with a grating blazed at 3000Å. Phosphor particles were sedimented on a quartz plate to form an elementary layer of thickness equivalent to the surface mean diameter. The coating densities are given in the captions of Fig. 7 and 8. The quartz plate coated with the phosphors was placed on a black-coated holder to prevent the scattering of the emitted light. The samples were held in a vacuum for the room temperature measurements or directly immersed in liquid nitrogen. The exciting monochromatic light was swept from the shorter wavelength region at the rate of 50 Å/min.

Diffuse reflection spectra were measured for thickly packed samples using a double monochromator. The absolute reflectivity was determined by comparison with that of MgO and its published data (3). The measuring light was swept from the shorter wavelength region at the rate of 250 Å/min.

Experimental Results

The fluorescent spectra of the green- and the blue-emitting phosphors are shown in Fig. 2. The ball milling did not cause any appreciable change in the fluorescent spectra.

Figure 3 shows the dependence of the luminescent intensity on milling time for excitation by the 10 kV electron beam (0.5 $\mu A/cm^2$) and the above-bandgap radiation of 335 nm. The degree of the luminescent degradation is larger for $Zn_{0.97}Cd_{0.03}S$:Cu,Al than for

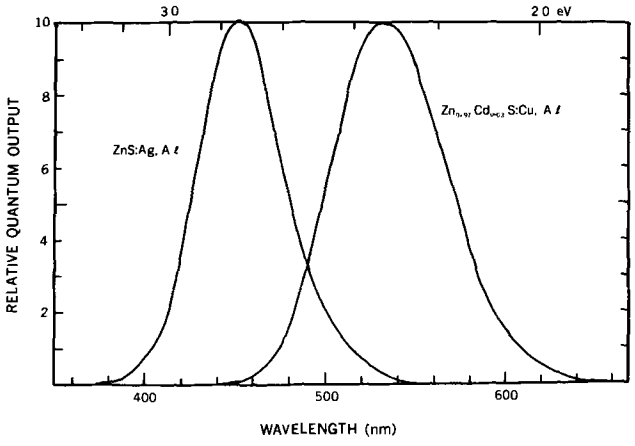

Fig. 2. Luminescent spectra of $Zn_{0.97}Cd_{0.03}S$:Cu,Al and ZnS:Ag,Al.

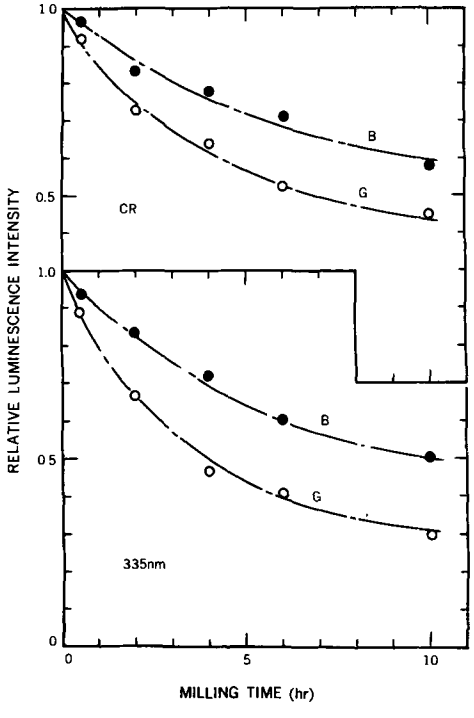

Fig. 3. Milling-time dependences of the luminescent intensities of $Zn_{0.97}Cd_{0.03}S$:Cu,Al (G, green) and ZnS:Ag,Al (B, blue) under the excitation of the 10 kV electron beam and the 335 nm light.

ZnS:Ag,Al, and larger for the uv excitation than for the cathode-ray excitation.

Figures 4 and 5 show the variations of the beam-voltage dependence of the luminescent efficiency of the green and the blue phosphors with milling time. The fluorescent efficiencies increase with the applied voltage and show a tendency to reach the limiting values. The solid curves are the theoretical ones calculated using Eq. [6] and the parameters in Tables II and III. The curves for the ball-milled phosphors are approximately scaled-down versions of that of the nonmilled phosphors except in the region of very low voltages.

Figure 6 shows the luminescent decay curves for the nonmilled and the 10-hr-milled phosphors. The decay curves are normalized for the intensity at the end of the 5 μsec-exciting pulse to be unity. The change of the decay curves is not so large as to make a contribution to the luminescent degradation. The fact that the short-term time decays are slower for 3 kV than for 10 kV excitation, in spite of the larger generation rate of electron hole pairs per unit volume for the former, is evidence of the large loss of the generated free carriers in the near-surface region. The short-term time decay for 20 kV was also slower than that

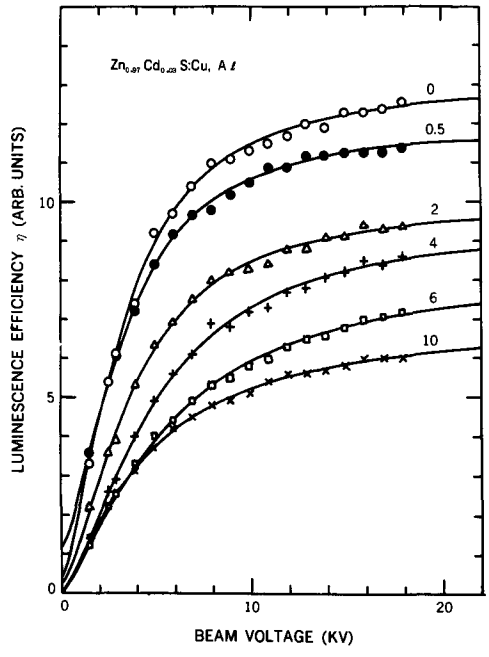

Fig. 4. Voltage dependences of the cathodoluminescent efficiencies of $Zn_{0.97}Cd_{0.03}S$:Cu,Al ball-milled for 0, 0.5, 2, 4, 6, and 10 hr.

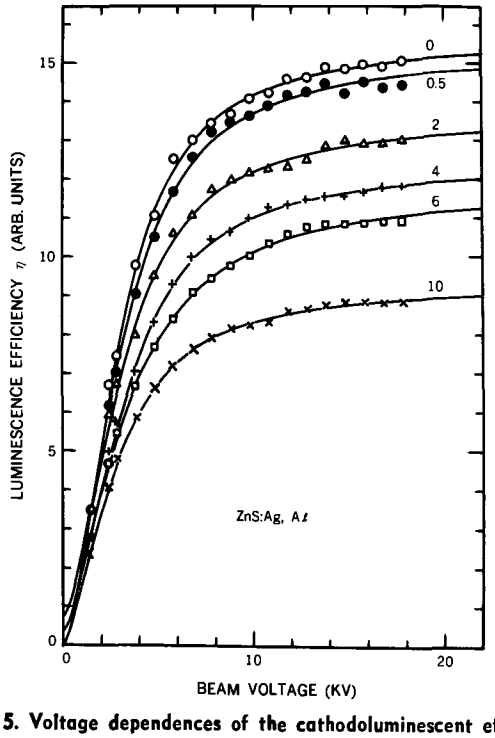

Fig. 5. Voltage dependences of the cathodoluminescent efficiencies of ZnS:Cu,Al ball-milled for 0, 0.5, 2, 4, 6, and 10 hr.

for 10 kV, which was caused by the decrease in the electron-hole pair generation rate per unit volume (see the next section).

Figures 7 and 8 show the excitation spectra at room and liquid nitrogen temperatures. The spectra are normalized with respect to their maxima. The spectra show no appreciable and no systematic change due to the milling in the region of the wavelength shorter than the bandgap light. The decrease in maxima with milling time is due to the decrease in the layer thickness, or the coating density of the phosphor. The layer thickness does not affect the shape of the excitation spectra in the region of the above-bandgap radiation, since the absorption coefficient is of the order of 10^5 cm^{-1}.

Figure 9 shows the diffuse reflection spectra. Little change in the reflection by the ball milling is observed

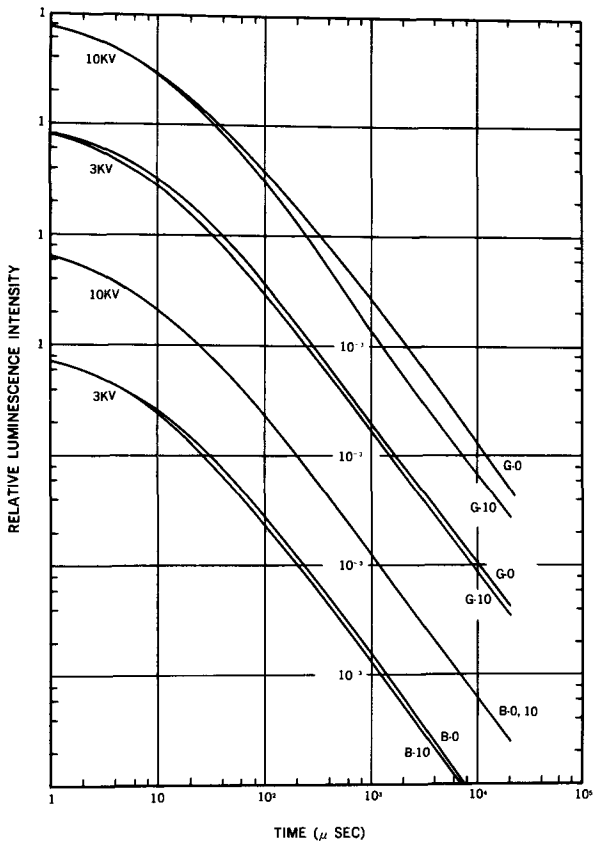

Fig. 6. Decay curves for the green (G) and the blue (B) emitting phosphors ball-milled for 0 and 10 hr at room temperature. The exciting electron beam pulse is of 5μ-sec duration with 30 Hz. The time-averaged current density is 0.2 μA/cm².

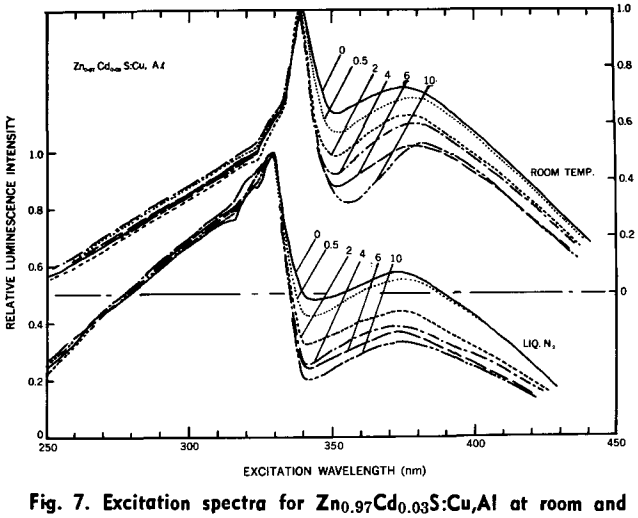

Fig. 7. Excitation spectra for $Zn_{0.97}Cd_{0.03}S$:Cu,Al at room and liquid nitrogen temperatures. The coating densities of the phosphor are 4.3, 3.6, 2.4, 1.8, 1.5, and 1.3 mg/cm² for 0, 0.5, 2, 4, 6, and 10-hr-milled samples, respectively.

in the region of the above-bandgap light and of the fluorescent light. In the region of the impurity absorption band for $Zn_{0.97}Cd_{0.03}S$:Cu,Al, the reflection increases with milling time due to the particle-size reduction.

Luminescence of Phosphor Particle Layers

In this section we shall follow the treatment of Gergely (4, 5) for phosphor luminescence and extend it to the case of phosphor particle layers, in which effects of particle size on luminescence are taken into account.

Donor-acceptor pair recombination causes green and blue luminescence in ZnS:Cu,Al and ZnS:Ag,Al

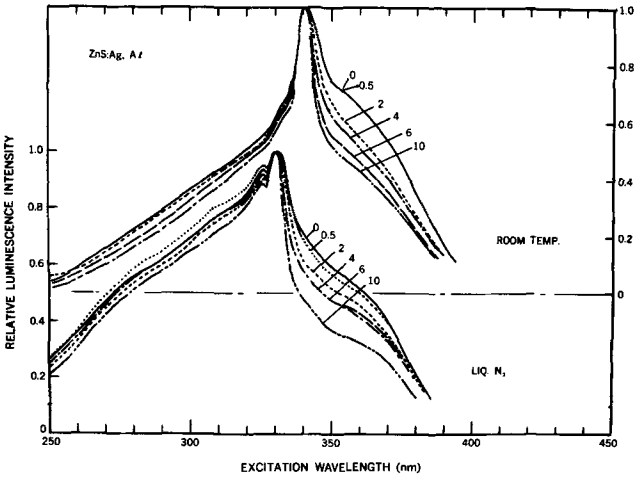

Fig. 8. Excitation spectra for ZnS:Ag,Al at room and liquid nitrogen temperatures. The coating densities of the samples are 2.5, 2.3, 2.1, 1.8, 1.6, and 1.3 mg/cm^2.

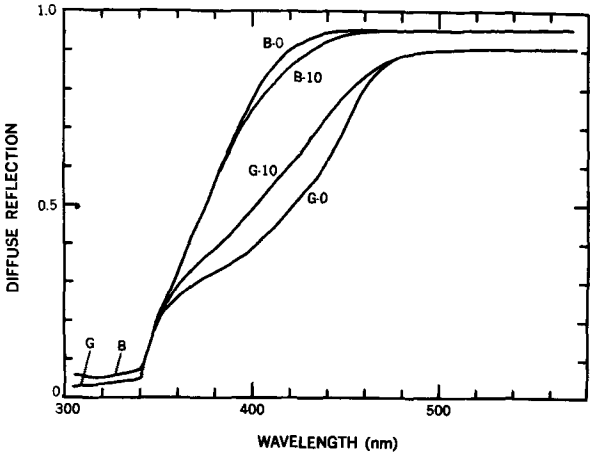

Fig. 9. Diffuse reflection spectra for the nonmilled and 10-hr milled green and blue phosphors.

(6), respectively. The acceptors with captured holes form energy levels high above the top of the valence band. The thermal activation of trapped holes occurs with negligibly small probability at room temperature and below compared with the recombination probability with electrons trapped at the donor sites. Under steady excitation, therefore, the rate for free holes to be captured per unit time by ionized acceptors is balanced with that for captured holes to recombine with electrons trapped at donors (see Fig. 10). The trapping rate for free holes is given by p/τ_p, where p is the density of free holes and $1/\tau_p$ is the probability for a free hole to be trapped by an ionized acceptor. Then the luminescent intensity, I, can be expressed in terms of the hole density p in the form

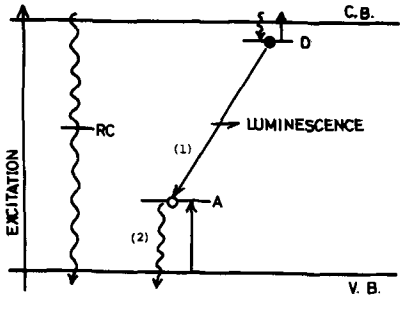

Fig. 10. Band diagram for ZnS phosphors. Arrows indicate electron transitions; the waved ones nonradiative. D, A, and RC indicate donor, acceptor, and nonradiative recombination centers, respectively. At equilibrium, the process (1) and (2) are balanced; thermal ionization of holes from the acceptor is neglected in the text.

$$I = \int_{V_c} \left\langle \frac{p}{\tau_p} E_r \right\rangle_{avg} dv \qquad [1]$$

where the average should be performed over all donor-acceptor pairs, E_r is the energy of the electronic transition in the pair of interest, and V_c the volume of the luminescent region.

The differential equation governing the generation and recombination kinetics of free holes under steady excitation is given by

$$g - \frac{p}{\tau} + D\Delta p = 0 \qquad [2]$$

where g is the generation rate of free holes by the excitation per unit time per unit volume, τ the lifetime of free holes, and D the diffusion constant of holes.

For electron beam excitation, g is assumed to be proportional to the energy dissipation rate of the electron beam in crystals. A simple model for the energy dissipation which is based on the observation by Young (7) was fairly successfully used to explain the secondary electron emission of solids by Lye and Dekker (8). It states that a constant amount of energy is dissipated per unit time per unit path length as an electron beam penetrates into solids until the electron beam consumes its entire energy in the effective penetration depth, R, which is called the range of electron penetration. Gergely also used this model, and g is given by

$$g = \frac{iV}{kR}, \quad 0 \leq x \leq R$$
$$= 0, \quad x > R \qquad [3]$$

where x is the distance in the solid from the bombarded surface, and k is the average energy consumed per generated low-energy electron-hole pair [about 10 eV for ZnS being estimated from the bandgap dependence of the radiation ionization energy which was measured for various semiconductors (9)], i the current density, and V the accelerating voltage.

Gergely has obtained the solution $p(x)$ of Eq. [2] using Eq. [3] for a semi-infinite crystal whose surface is bombarded uniformly by an electron beam (4). Substituting the solution into Eq. [1] gives the cathodoluminescent efficiency η in the form

$$\eta = \frac{I}{iV} = K\left(1 - Q\frac{1 - e^{-\beta R}}{\beta R}\right) \qquad [4]$$

where

$$K = \frac{C}{k}\left\langle \frac{\tau}{\tau_p} E_r \right\rangle_{avg}$$

$$Q = \frac{S}{D\beta + S}$$

$$\beta = \frac{1}{\sqrt{D\tau}}$$

C is the external efficiency of the luminescent light, and S is the nonradiative recombination velocity of free holes at the crystal surface.

Now, let us extend the above single-crystal treatment to the case of phosphor particle layers. Phosphor layers consist of particles of different sizes and irregular shapes. It is not advantageous to make a microscopic consideration on such particle layers. It seems better to regard the particle layers as a single crystal as a whole. Then Eq. [4] may still be used for phosphor layers. However, the parameters must necessarily have meanings or expressions different from those for a single crystal.

K is the ultimate efficiency at the high voltage limit. Luminescent loss increases with increasing surface area of phosphor, because of the high density of non-

radiative recombination centers for free carriers in the surface region of the particles. Therefore, the ultimate efficiency K is reduced by a factor of $(1 - S_A\rho l)$, going from the semi-infinite crystal to particle layers, where S_A is the specific surface area of the phosphor, ρ the specific gravity, and l a proportional constant. We consider the case where the particle size is not so extremely fine as the factor $(1 - S_A\rho l)$ and may be approximated by $\exp(- S_A\rho l)$. $S_A\rho$ can be also expressed as $6/d_m$, d_m being the average diameter, if the particles are spherical. Accordingly, K may be written as follows

$$K = \frac{C}{k}\left\langle\frac{\tau}{\tau_p}E_r\right\rangle_{avg}\exp(-S_A\rho l)$$

$$\frac{C}{k}\left\langle\frac{\tau}{\tau_p}E_r\right\rangle_{avg}\exp(-6l/d_m)$$

$S_A\rho$ and $6/d_m$ are usually connected by a shape factor due to irregular shapes of particles. The constant l takes different values for the above two expressions. It may be regarded as the average width of the "dead surface layer" of particles.

The hole lifetime τ in the case of particle layers should be considered as the one averaged over the whole volume of particles. Particle size reduction or increase in the surface area of the phosphors reduces the average lifetime of free holes because of the large contribution of the surface region of short lifetime to the average. The surface recombination velocity of holes S is not a function of the particle size but of the surface properties.

The electron range R should be considered also particle-size dependent for the following reason. R is related to the accelerating voltage V by the empirical formula

$$R = bV^n \qquad [5]$$

where b and n are experimental parameters characteristic of solids. Young's model states that the electron beam energy almost linearly decreases going into a solid and becomes zero at the distance R from the solid surface, as shown in Fig. 11a. The average slope is $-iV/R$ which is larger for larger V because $n > 1$. When the crystal is cracked into two parts, for example, at the distance $R/2$, the distance-energy line is deflected at the interface as shown in Fig. 11b. The resultant penetration depth R_1 is easily calculated as

$$R_1 = R\left(\frac{1}{2} + \frac{1}{2^n}\right) < R$$

Although this is a very simplified model, the probability that an electron beam, or part of it, experiences the second or the third surface increases as the particle size decreases, because electrons can penetrate through fine particles and also through the edge region of even larger particles. This tendency may be enhanced as the particle shape becomes complex. As a result, the average electron range decreases with decreasing particle size. In addition, the simple range energy relation of Eq. [5] may not hold for particle layers. We proceed, however, in this simple treatment on the assumption that the relation of Eq. [5] still holds for particle layers, but b and n are different from those for single crystal and are particle-size dependent.

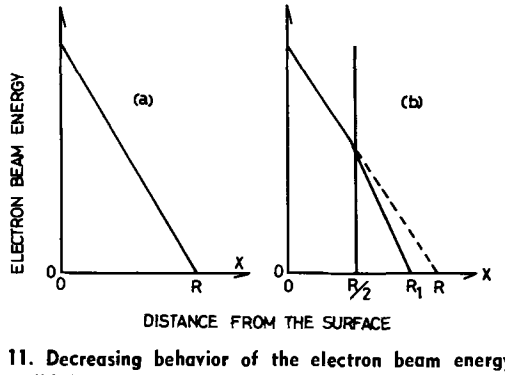

Fig. 11. Decreasing behavior of the electron beam energy in a perfect solid (a) and in a solid cracked into two parts at $R/2$ (b). x indicates the distance in the solid from the surface. R is the electron range.

In the case of excitation by above-bandgap light, the generation rate of electron hole pairs, $g(x)$, per unit time per unit path length is given by

$$g(x) = N_\lambda\,(1 - R_\lambda)\,\alpha_\lambda \exp(-\alpha_\lambda x)$$

where N_λ is the flux of the exciting light, R_λ the reflectance, and α_λ the absorption coefficient. Gergely has obtained an expression of luminescent intensity for such cases (5). A little modification of his expression [Eq. [14] of Ref. (5)] as we have done for cathodoluminescence leads to the following formula for photoluminescent intensity I_p

$$I_p = K_p\,N_\lambda\,(1 - N_\lambda)\left(1 - Q\frac{\alpha_\lambda}{\beta + \alpha_\lambda}\right)$$

where $K_p = kK$, and K and Q are formally the same as those in Eq. [4]. K_p does not have the meaning of the ultimate efficiency as K has in the case of cathodoluminescence. Considerations are to be confined within the region invaded by the exciting light, the depth of which is of the order of 0.1μ (inverse of α_λ). The ratio of the surface area to the volume in such a region is necessarily larger than that of the entire phosphor. Accordingly, K_p for bandgap excitation has a stronger dependence on the measured specific surface area S_A or on the mean diameter d_m than that of cathodoluminescence, as seen later (Fig. 12 and 13).

Let us summarize the formulas obtained for convenience of later discussion:
for cathodoluminescent efficiency η

$$\eta = K\left(1 - Q\frac{1 - e^{-\alpha V^n}}{\alpha V^n}\right) \qquad [6]$$

and for photoluminescent intensity I_p under bandgap excitation

$$I_p = K_p\,N_\lambda\,(1 - R_\lambda)\left(1 - Q\frac{\alpha_\lambda}{\beta + \alpha_\lambda}\right) \qquad [7]$$

where

$$K = \begin{cases} \dfrac{C}{k}\left\langle\dfrac{\tau}{\tau_p}E_r\right\rangle_{avg}\exp(-S_A\rho l) \\ \dfrac{C}{k}\left\langle\dfrac{\tau}{\tau_p}E_r\right\rangle_{avg}\exp(-6l/d_m) \end{cases} \qquad [8]$$

$$K_p = kK \qquad [9]$$

$$Q = \frac{S}{D\beta + S} \qquad [10]$$

$$\beta = \frac{1}{\sqrt{D\tau}} \qquad [11]$$

$$\alpha = b\beta \qquad [12]$$

The notations used are given at the end of the paper.

Discussion

Cathodoluminescence.—The values of the parameters K, α, n, and Q in Eq. [6] have been determined by the method of least squares, which minimizes the sum of the squared differences between the observed and the calculated efficiencies. They are given in Tables II and III, together with the resultant root mean square deviations.

The ultimate efficiency K at the high voltage limit should vary exponentially with the specific surface area S_A or with the inverse of the average diameter

Table II. Experimentally determined values of the parameters for $Zn_{0.97}Cd_{0.03}S$:Cu,Al

Milling time (hr)	0	0.5	2	4	6	10
K (arb. units[a])	13.2	12.1	10.1	9.56	8.35	7.04
α (kV^{-n})	0.313	0.298	0.258	0.199	0.204	0.308
n	1.37	1.39	1.37	1.32	1.21	1.09
Q	0.973	0.901	0.977	1.0	1.0	1.0
rmsd (arb. units[a])	0.15	0.09	0.11	0.11	0.09	0.07

[a] The same units as η in Fig. 4.

Table III. Experimentally determined values of the parameters for ZnS:Ag,Al

Milling time (hr)	0	0.5	2	4	6	10
K (arb. units[a])	15.7	15.4	13.7	12.5	12.0	9.39
α (kV^{-n})	0.288	0.280	0.280	0.267	0.340	0.367
n	1.56	1.50	1.49	1.48	1.28	1.38
Q	1.0	0.912	0.949	0.973	1.0	1.0
rmsd (arb. units[a])	0.12	0.14	0.14	0.08	0.08	0.05

[a] The same units as η in Fig. 5.

$1/d_m$, as seen from Eq. [8], if the luminescent degradation is caused only by particle size. The variation of the factor $\left\langle \frac{\tau}{\tau_p} E_r \right\rangle_{avg}$ in K is not changed by the milling performed, since it little affects the luminescent spectra and the decay curves. The external radiation efficiency C may be considered to vary little because of the ball milling, since the luminescence is observed from the bombarded side and the diffuse reflectance in the luminescent region is affected little by the milling (Fig. 9). In such selected conditions of ball milling a linear relation is reasonably expected when log K is plotted against S_A or $1/d_m$, which is demonstrated in Fig. 12 and 13.

The value of l can be estimated from the slopes of the lines log K-S_A and $-1/d_m$. Silica applied to the phosphors as the coating makes a large contribution to the measured specific surface area in spite of its small quantity relative to the phosphor (Table I). However, the silica coating does not affect the slopes, since the surface area of silica does not change because of the ball milling according to our subsidiary measurement. A reasonable value of l as the dead layer width is obtained from the slope of log K-S_A but not

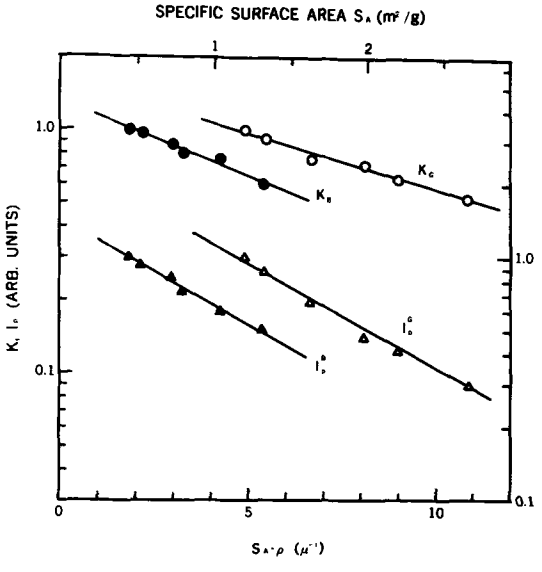

Fig. 12. Variations with the specific surface area S_A of the ultimate efficiency K for cathodoluminescent and of the photoluminescent intensity I_p under the 335 nm excitation.

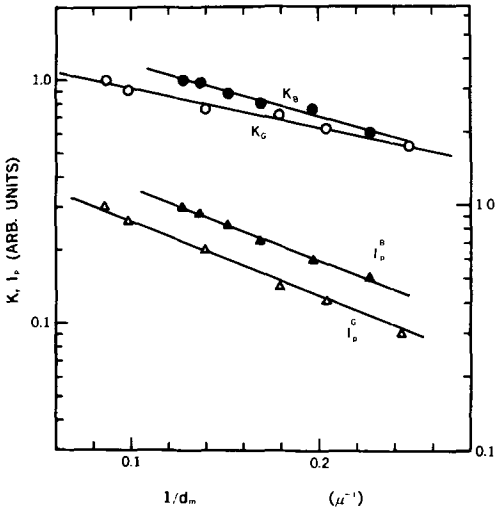

Fig. 13. Variations with the inverse of the mean diameter $1/d_m$ of K for cathodoluminescent and of the photoluminescent intensity I_p under the 335 nm excitation.

from log K-$1/d_m$, since the mean diameter is only a measure of the particle size without the irregularity of the particle shapes being taken into account. The values of l obtained are 0.10 and 0.14μ for the green and the blue phosphors, respectively. It should not be implied that each particle is covered by a dead layer of the width l, since l has only the meaning of the average over a whole particle group, which may include nonluminescent fine particles or particles less luminescent due to inhomogenous distribution of activators.

The variation of the exponent n of the range-energy relation with the mean diameter is shown in Fig. 14. The value of n for the nonmilled samples are approximately in agreement with those obtained by Ludwig and Kingsley (10). The exponent n decreases as the mean diameter decreases, especially rapidly below about 6μ. As described in the previous section, such tendency of n is caused by the decrease in the electron range R with decreasing particle size. Feldman (11) obtained $n = 2.4$ for transparent thin films of ZnS.

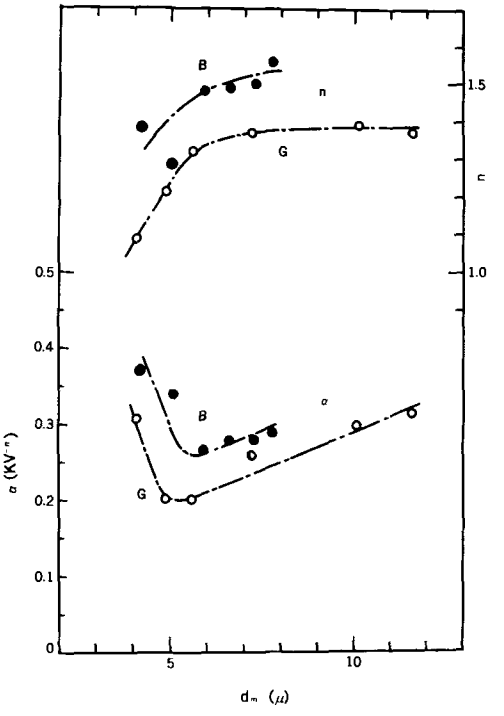

Fig. 14. Particle size dependences of n and α ($= b\beta$). d_m is the mean diameter. The approximate dependences are indicated by chained curves.

This large value of n compared with that obtained here may be considered to have been caused by the fact that the material he used was transparent without interface.

The value of α which is equal to $b\beta$ decreases with decreasing mean diameter and it rapidly increases also from near 6μ as shown in Fig. 14. β should increase with decreasing particle size, as discussed in the previous section, since the average hole lifetime decreases. The first decrease of α with decreasing mean diameter, therefore, indicates that b decreases much faster than β increases in this region. Such decrease of n and b with decreasing particle size is qualitatively consistent with the discussion in the previous section that the electron range R should decrease with decreasing particle size.

The "range" R used in this study may be different from the so-called range of electron penetration. The electron range R here means the range within which free holes and electrons are generated as the electron beam goes through into the phosphor. Generation and annihilation processes of elementary excitations such as plasmons, phonons, and excitons would affect the processes of electron-hole pair generation. Therefore, the electron range here is dependent on the properties of crystal structure, impurities, defects, and of the constituent atoms of the crystal, as well as particle size. In addition, it should be questioned for more rigorous treatment if the simple proportionality between the electron-hole pair generation rate and the energy dissipation rate of the electron beam holds in the wide range of the beam energy. Mayer has observed deviations from monotonic dependence of luminescent intensity on landing energy at x-ray levels of the constituent atoms for various phosphors (12). Young's model for energy dissipation of electrons is also questionable (13). However, it is convenient and not unreasonable in the simplified and semiquantitative treatment to see the gross features of the problem.

Photoluminescence.—The variation of the photoluminescent intensity under the excitation of the 335 nm light can be explained by Eq. [7]. The reflectance R_λ is not changed appreciably by ball milling as seen from Fig. 9. The parameter Q for cathodoluminescence takes values near unity almost independently of the milling time (Tables II and III). This fact means that the surface recombination velocity is much larger than $D\beta$ and that the variation of β does not much affect Q. Therefore, Q for photoluminescence must also have small milling-time dependences and take values near unity. The average lifetime of holes τ is considered extremely short because the bandgap light produces holes only in the surface region of high densities of recombination centers. Accordingly, it is reasonable to consider that $1/\beta$, or the average diffusion length of holes in the surface region, is much smaller than the penetration depth of the exciting light, or $1/\alpha_\lambda \cong 0.1\mu$. Thus, the variation of the photoluminescent intensity is ascribed to the variation of K_p. The plot of log I_p *vs.* S_A and $1/d_m$ shows linear relations as seen in Fig. 12 and 13, and the slopes are steeper than those of log K *vs.* S_A and $1/d_m$ for the cathodoluminescence. This steeper slope is, as discussed in the previous section, due to the fact that the ratio of the surface area to the volume in the region invaded by the exciting light is larger than that of the entire phosphor. Kremheller *et al.* (14) have also observed a linear dependence of the logarithm of photoluminescent intensity on measured surface area. They ascribed, however, the luminescent loss to the creation of trapping levels due to the exposure of internal surface chloride.

The voltage dependence of the cathodoluminescent efficiency has been found the most helpful in understanding the luminescent degradation in this study. The other measurements, decay curves, excitation and diffuse reflection spectra are complementary. Let us explain some of their meanings.

The short-term time decays of the luminescence for the ball-milled phosphors are little faster than those of the nonmilled ones. This may result from the higher densities of excited donor-acceptor pairs for milled phosphors than those for nonmilled ones. The decrease in the effective electron range R results in the increase in the average generation rate of free carriers per unit path length of the electron beam.

The average rate of generation of electron-hole pair per unit path length is larger for the smaller beam voltage according to Eq. [3], since $n > 1$. The slower initial decay for 3 kV in spite of the larger generation rate than for 10 kV is evidence of the large surface recombination loss of free carriers.

The excitation spectra in the region of wavelength shorter than the bandgap light do not show appreciable and systematic variation with milling time, in contrast to the spectra observed by Gergely *et al.* (15); their spectra for the ground samples show large decreases compared with the unground samples as the excitation wavelength becomes shorter. This is because the surface recombination loss is enhanced in the region of high absorption coefficient. Accordingly, the invariance of our spectra indicates that the particle surface is not seriously damaged by the ball milling adopted in this study.

Conclusions

1. The luminescent degradation of the $Zn_{0.97}Cd_{0.03}S$:Cu,Al and ZnS:Ag,Al phosphors by our ball milling is caused mainly by the particle size reduction, which increases the less-luminescent surface region relative to the whole volume of the phosphor. Bulk and surface properties relevant to luminescence are little changed by the ball milling adopted. The conclusion is mainly based on the fact that the linear dependences of log K and log I_p on S_A and $1/d_m$ are found. Other experiments also support this conclusion.

2. The average width of the dead layer of the phosphors is estimated to be of the order of 0.1μ.

3. The electron range in phosphor layers, or the average range of generation of electron-hole pairs, decreases with decreasing particle size.

4. Supplementary remarks: Effects of ball milling on phosphors depend on its condition, namely, sizes and materials of milling pot and balls, quantities of phosphors and balls, dispersion media and milling time. Under some conditions of ball milling, induced lattice defects may make a large contribution to luminescent loss. The authors have found that the linear dependence of log K on S_A is not obtained in such cases. Milling stability of phosphors also depends on the condition of synthesizing.

Acknowledgments

The authors are indebted to Mrs. T. Moriya and Mr. T. Abe for help with the sample preparation and measurements. They also express their thanks to Drs. S. Shima and T. Mitsuma for their encouragement throughout the course of this work.

Manuscript submitted Sept. 11, 1972; revised manuscript received *ca.* March 6, 1973.

Any discussion of this paper will appear in a Discussion Section to be published in the June 1974 JOURNAL.

LIST OF SYMBOLS

τ	average lifetime of free holes
$1/\tau_p$	probability for a free hole to be captured by an ionized acceptor
E_r	radiative transition energy
k	average energy consumed per generated electron-hole pair
C	external radiation efficiency of luminescent light
S	surface recombination velocity of free holes
D	diffusion constant for free holes
S_A	specific surface area of phosphor

ρ	specific gravity of phosphor
d_m	average diameter of phosphor particles
l	average width of dead layer
V	accelerating voltage of the electron beam
b, n	parameters that determine the electron range as $R = bV^n$
N_λ	exciting light flux
R_λ	reflectance of the phosphor layer
α_λ	absorption coefficient of the exciting light

REFERENCES

1. T. Narahara, M. Kanamaru, S. Kuboniwa, and T. Hoshina, In preparation.
2. C. F. Hendee and W. B. Brown, *Philips Tech. Rev.*, **19**, 50 (1957).
3. W. K. Middleton and C. I. Sandars, *J. Opt. Soc. Am.*, **41**, 419 (1951).
4. Gy. Gergely, *Acta Phys. Hung.*, **12**, 221 (1960); *J. Phys. Chem. Solids*, **17**, 112 (1960).
5. Gy. Gergely, *J. Phys. Chem. Solids*, **24**, 681 (1963).
6. S. Shionoya, "1967 International Conference on II-VI Semiconducting Compounds", p. 1, D. G. Thomas, Editor, W. A. Benjamin, New York (1967); A. Suzuki and S. Shionoya, *J. Phys. Soc. Japan*, **31**, 1455 (1971).
7. J. R. Young, *J. Appl. Phys.*, **28**, 524 (1957).
8. R. G. Lye and A. J. Dekker, *Phys. Rev.*, **107**, 977 (1957).
9. C. A. Klein, *J. Appl. Phys.*, **39**, 2029 (1968).
10. G. W. Ludwig and J. D. Kingsley, *This Journal*, **117**, 348 (1970).
11. C. Feldman, *Phys. Rev.*, **117**, 455 (1960).
12. V. D. Meyer, *This Journal*, **119**, 920 (1972).
13. J. D. Kingsley and J. S. Prenner, *J. Appl. Phys.*, **43**, 3073 (1972).
14. A. K. Kremheller, S. Faria, and A. K. Levine, *This Journal*, **107**, 753 (1960).
15. Gy. Gergely, J. Adams, and Gy. T. Bauer, *J. Phys. Chem. Solids*, **24**, 687 (1963).

Indium Phosphide

I. A Photoluminescence Materials Study

E. W. Williams, W. Elder, M. G. Astles,[1] M. Webb, J. B. Mullin, B. Straughan, and P. J. Tufton

Royal Radar Establishment, Malvern, Worcestershire, England

ABSTRACT

Solution-, vapor-, and melt-grown InP have been analyzed with photoluminescence measurements over the temperature range 5°-300°K. Although undoped material is discussed, the main emphasis is on doped InP grown from an indium solution for use as LED material. Optical activation energies were determined for hydrogenic donors, 7-10 meV; simple acceptors, zinc −50 meV, cadmium −58 meV, and mercury −98 meV; the isoelectronic trap bismuth, −31 meV; transition metal acceptors, copper −60-73 meV and manganese −270 meV.

Indium phosphide lived in the shadow of gallium arsenide during the sixties and there was little interest in it. In 1970 it finally "arrived" on the semiconductor scene when the three level microwave oscillator was invented by Hilsum and Rees (1). The place of indium phosphide in semiconductor history was strengthened by the observation of Blom and Woodall (2) that the narrow line width of the spectra of indium phosphide light emitting diodes made them very efficient pumps for multiphoton phosphors so that brighter visible light output in a variety of colors was possible.

Light emitting diodes were the main motivation for the work described in this trilogy of papers on indium phosphide. The first paper is a review of some of the photoluminescence measurements made on indium phosphide prepared at this laboratory. Photoluminescence was used to analyze the material produced by solution growth (3), vapor growth (4), and by liquid encapsulation melt growth (5). The emphasis will be on solution-grown material since this was used for the preparation of the light emitting diodes. The technique of solution growth will be discussed in detail in the second paper. In the third, the subject will be double epitaxy light emitting diodes with efficiencies of 1.3% at room temperatures.

Earlier studies on indium phosphide photoluminescence concentrated on the study of undoped material. Two lines near 1.41 and 1.37-1.38 eV at 4.2°K were associated with excitons and with band to acceptor recombination (6-8). The 1.41 eV line consisted of several components at helium temperatures and these have now been more clearly resolved at 1.8°K to show free exciton, excitons bound to ionized and neutral donors, and excitons bound to neutral acceptors (9). Two-hole and two-electron transitions were also observed at this low temperature (9).

The present paper describes measurements made in the temperature range 5°-300°K and will stress the measurements made on the doped indium phosphide used in the light emitting diodes.

Studies of the half width and the peak position of the luminescence lines as a function of doping have proved particularly useful in understanding the mechanisms involved in heavily doped InP. The measurements of Roder *et al.* (10) on solution-grown InP doped with zinc and tellurium are compared with the present work and the tellurium results are reinterpreted. The optical activation energies of the dopants have been estimated and it is shown that for the group II elements, the acceptor activation energy increases with atomic size for the series zinc, cadmium, and mercury. The transition metals copper and manganese are also briefly mentioned.

Experimental Technique

The experimental setup was similar to the one described previously (11). A d-c 150W Atlas tungsten iodide lamp was used for excitation instead of a mercury lamp and a 230 Hz miniature Bulova tuning fork chopper replaced the old mechanical chopper.

The samples were glued with rubber solution onto the sample holder of a continuous flow helium cryostat (12) capable of giving temperatures from 5°K upwards. This cryostat worked simply by an immersion heater in the bottom of a 15 liter helium Dewar boiling off helium gas which flowed over the sample and cooled it. The faster the boil off, the colder the sample became.

The spectra were all corrected for the photomultiplier and optical system response.

[1] Present address: Services Electronics Research Laboratory, Baldock Hertfordshire, England.

Key words: photoluminescence, indium phosphide.

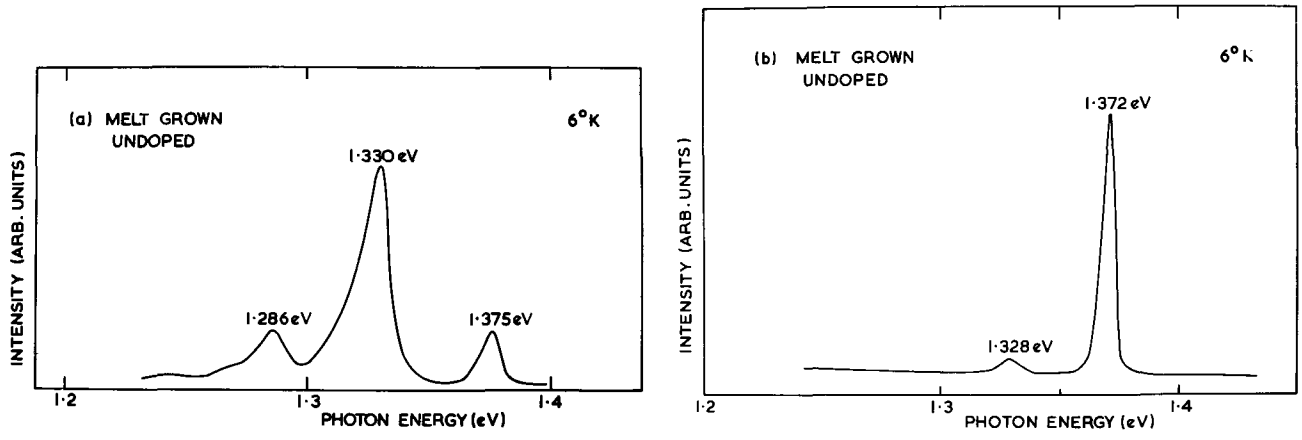

Fig. 1. Photoluminescence at 6°K of undoped melt-grown InP (a) grown from mercury contaminated feed material and (b) a recent crystal grown from an uncontaminated InP feed.

Comparison of Growth Techniques for Undoped InP

Melt-grown material.—The InP crystals were grown in a pressure puller using boric oxide as a liquid encapsulant (5). The high temperature of growth (1050°C) means that more impurities and lattice defects can be incorporated into the material than when lower growth temperatures are used as in the case of epitaxially grown material. As was mentioned in a previous publication, when measurements were made at 77°K as many as six lines were observed in the photoluminescence spectrum of the bulk undoped material (13). Two lines at 1.41 and 1.37 eV were always observed but in addition two other lines at 1.32 and 1.16 eV were often observed, and less frequently, lines at 1.35 and 1.28 eV were seen.

The near band edge peak at 1.41 eV contains a large number of components (9) all of which were unresolved even when the temperature was lowered to 5°K. Most of these components are due to recombination associated with excitons bound to acceptors and donors. Mass spectrographic analysis (14) indicates that silicon is present, so silicon may be partly responsible for this line. But the role of other donors, sulfur and perhaps oxygen, for which this analysis is insensitive may perhaps be more important.

The peak near 1.37 eV was thought to be associated with zinc acceptors because of the zinc doping experiments with solution-grown material mentioned below, and the low temperature studies of zinc doped vapor-grown material (15) indicate that zinc acceptors produce a line at about 1.373 eV. Furthermore, mass spectrographic analysis (14) also clearly indicates the presence of zinc in the undoped pulled material.

Mercury is the likely cause of the 1.32-1.33 eV line. It was first suspected when it was found that the InP starting material was being treated with mercury. A typical spectrum of the highest purity crystals grown from this mercury-treated starting material is shown in Fig. 1(a). Notice the strong 1.33 eV line. These crystals were frequently p-type. The carrier concentration $N_A - N_D$ of the p-type sample shown in Fig. 1(a) was 3×10^{16} cm^3.

New crystals pulled from acid-treated starting material with no mercury present show very little emission at 1.33 eV as shown in Fig. 1(b). The small peak at 1.33 eV may be mainly caused by the first LO phonon replica of the 1.37 eV zinc acceptor-unknown donor pair line as the ratio of its size to the zero phonon line at 1.37 eV is similar to the phonon associated with the line seen in zinc doped samples. The carrier concentration of this second n-type sample was $N_D - N_A = 5.13 \times 10^{15}$/cm^3. All of the crystals grown from acid-treated material were n-type. Hence the above results imply that mercury produces a deep acceptor level which gives an emission line at 1.33 eV. This implication has been confirmed by (*i*) mercury diffusion into an epitaxial layer and (*ii*) mercury doping of the bulk material. The mercury diffusion will be discussed below but the doping experiments will be described elsewhere since they are not yet completed.

Lines at 1.35 and 1.28 eV have been observed in the 77°K spectra of undoped melt-grown indium phosphide and they were particularly strong in the less pure crystals. The 1.35 eV line is known to be associated with copper (see below), but the 1.28 eV line is of unknown origin.

A broad emission line at 1.16 eV was frequently observed and this has been discussed previously (13). It was always enhanced by the presence of excess indium so it was thought to be associated with phosphorus vacancies.

Vapor-grown undoped InP.—Over fifty samples grown by the PCl_3 technique (4) were run at 6°K. No deep level emission associated with the 1.16, 1.28, 1.33, or 1.35 eV lines was ever observed. This is probably because of the higher purity of vapor-grown material which normally has a much higher mobility than the bulk material. Mobilities as high as 60,000 cm^2/V-sec at 77°K were measured (4). The line at 1.37 eV was much sharper than with the melt-grown material and this enabled three other lines to be seen near to the 1.37 eV line. Two of these lines occurring at about 1.38 and 1.39 eV are shown in Fig. 2. This sample had a net carrier concentration of 2.4×10^{15} and a mobility of 23,000 cm^2/V-sec at 77°K. The third line occurs close to 1.36 eV but was never clearly resolved and just appeared as a weak shoulder. The LO phonon replica of the 1.37 line (Ac + LO) was also observed at 1.33 eV. The 1.39 eV line increased in intensity when the samples were heat-treated at 500°C in hydrogen for only 5 min; it also increased as the epitaxial layer was gradually etched off, and was very strong as the epi-

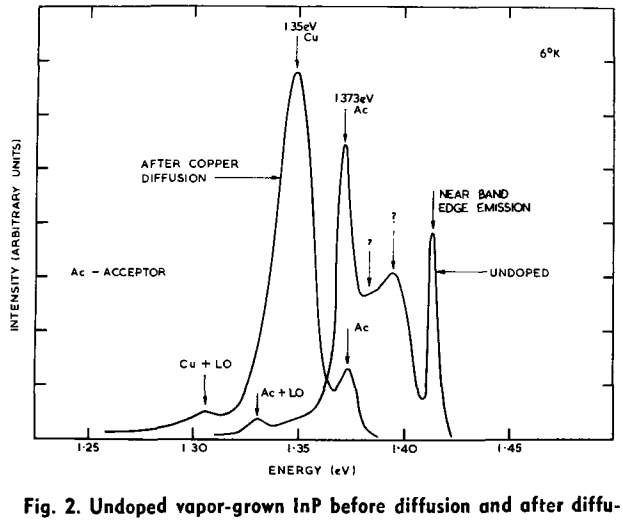

Fig. 2. Undoped vapor-grown InP before diffusion and after diffusion with copper for 5½ hr at 750°C. Photoluminescence spectra at 6°K.

taxial substrate interface was approached (16). Further work needs to be done before the origin of the 1.39 eV line can be ascertained and it would be pointless to speculate upon its nature at this stage of the work.

The ratio of the intensity of the two main lines at 6°K varied in a random manner for consecutively vapor-grown layers as did the carrier concentration and mobility.

At 77°K, however, the highest mobility samples all showed a very strong 1.41 eV line and an extremely weak 1.37 eV line, as has been mentioned previously by Joyce and Williams (4). The variation of the half width of the 1.41 eV line at 77°K as a function of $N_D - N_A$ which was reported in this paper is compared with doped samples grown by solution and by melt growth in Fig 3. This half-width variation can be used in place of Hall measurements as a measure of the carrier concentration. This is useful for epitaxial layer evaluation because the carrier concentration can be measured regardless of whether the substrate is semi-insulating or highly conducting and additionally it is a nondestructive technique. This was particularly useful for selecting good microwave device material for undoped layers grown on tin doped substrates. If the substrate quality was poor or had a doping level above $7 \times 10^{17}/cm^3$, impurities could be incorporated into the epitaxial layer during the growth. Gaseous interaction with the back of the substrate during growth was eliminated as a possible effect because layers grown on semi-insulating Cr doped substrates during the same run were uncontaminated by the substrate.

Finally, it should be mentioned that it was found that the presence of a strong 1.37 eV peak at 77°K correlated with strong compensation in the material and poor microwave device characteristics.

Solution-grown undoped InP.—Only a few photoluminescence measurements were made on undoped InP grown from indium solutions using phosphine saturation and a modified Nelson technique (3) because the main emphasis was on doped layers for light emitting diode studies. A series of six undoped layers grown sequentially and using the same growth conditions were all n-type and had carrier concentrations in the range 3×10^{15} to $2 \times 10^{16}/cm^3$ and mobilities at 77°K of between 12,000 and 19,000 cm^2/V-sec. The luminescence properties were very similar to the vapor-grown layers. The widths of the 1.37 and 1.41 eV lines were almost the same as for the vapor-grown material and the ratio of the intensities of the two lines varied in an arbitrary fashion from run to run. The 1.41 eV line was very slightly wider than for the best vapor-grown sample indicating a higher donor doping level. The 1.37 eV line was generally stronger and was once again believed to be due to contamination of zinc. None of the three extra lines sometimes seen in vapor growth were observed.

The first undoped layers were grown from indium solutions saturated with undoped single crystalline InP under a purified hydrogen flow and these also gave emission at 1.41 and 1.37 eV at helium temperatures but there was also a very strong 1.16 eV line. The electrical properties were much more variable and varied from 8×10^{15} to $4 \times 10^{17}/cm^3$. All the undoped samples were n-type and the highest mobility was 28,000 cm^2/V-sec for a carrier concentration of 8×10^{15} at 77°K.

Doping Studies

Group II impurities.—The addition of zinc, cadmium, and mercury to indium phosphide renders it p-type. Zinc and cadmium always gave p-type behavior but in the case of mercury the doping was much more difficult and p-type behavior is not always obtained due to the lower solubility of mercury in indium phosphide. The luminescence spectra at 50°K of these three group II acceptors is shown in Fig. 4. The zinc and cadmium samples were solution grown with doping levels of 1.2×10^{16} and 7.4×10^{16} holes/cm^3 at 300°K. The mercury doped sample was n-type with $N_D - N_A = 3 \times 10^{16}/cm^3$ at 300°K. The mercury doping was thought to be in the region of $2 \times 10^{16}/cm^3$ from a calculation of N_A from Hall measurements at 77° and 300°K. The temperature of 50°K was chosen for recording the spectra for two reasons. First, conduction band to acceptor recombination dominates at this temperature and second, the band to acceptor lines are clearly resolved from the near band edge peak at 1.40-1.41 eV. In the case of the zinc spectrum the peak occurs at 1.373 eV and this coincides with the peak most commonly observed in undoped solution-, vapor-, and melt-grown crystals. Cadmium on the other hand shows a peak at 1.362 eV and mercury shows a line at 1.324 eV. LO phonon coupling is observed for all three lines and the first phonon replica appears to be of equal relative strength for all three acceptors. However, in the case of cadmium and zinc, the phonon replica is unresolved from another impurity line. This was concluded from studies of the cadmium and the zinc line as a function of doping and as

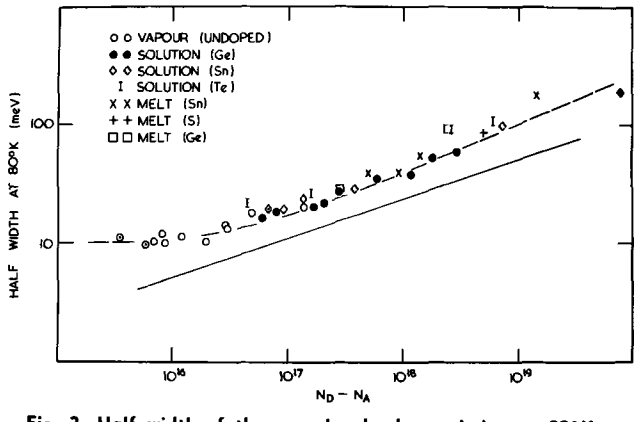

Fig. 3. Half width of the near band edge emission at 80°K *vs.* $N_D - N_A$ for n-type undoped vapor-grown and doped solution and melt-grown InP.

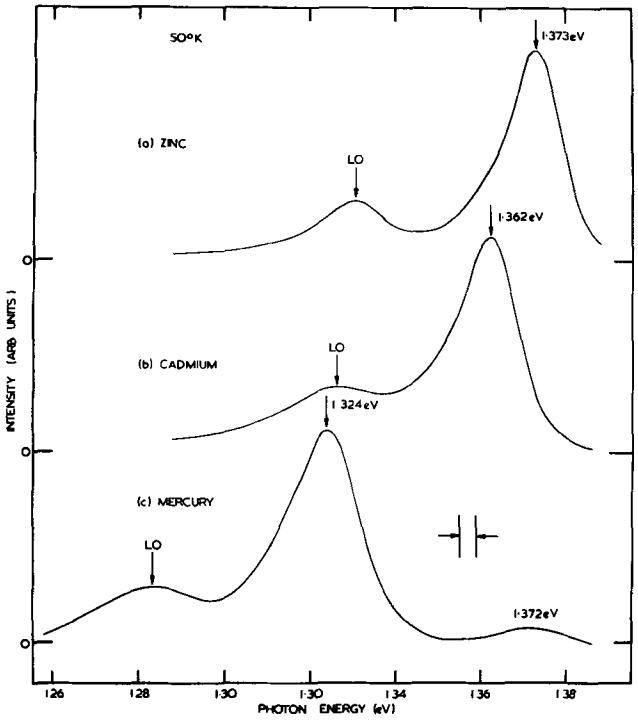

Fig. 4. Comparison of (a) zinc $N_A - N_D = 12 \times 10^{16}/cm^3$, (b) cadmium $N_A - N_D = 7.4 \times 10^{16}/cm^3$, and (c) mercury $N_A - N_D = 3 \times 10^{16}$ doping. Photoluminescence at 50°K. (a) and (b) are solution grown, (c) is melt grown.

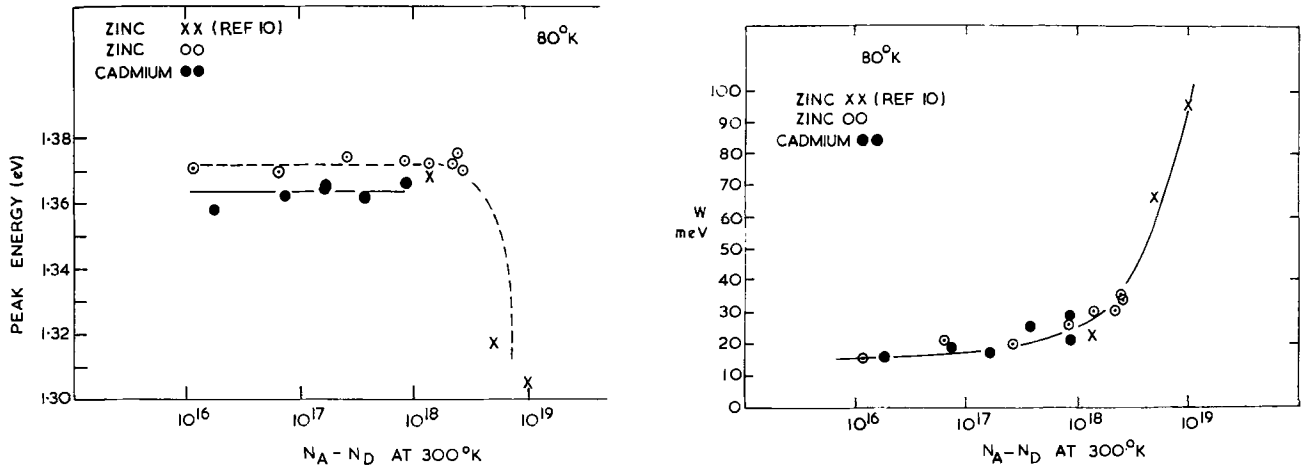

Fig. 5. (a, left) Variation of the peak energy of the band to acceptor luminescence line at 77°K with $N_A - N_D$ at 300°K for zinc and cadmium doped InP. (b, right) Half width of the band to acceptor luminescence line at 77°K vs. net hole concentration at 300°K for zinc and cadmium doping.

a function of temperature. The possibility of this extra impurity line being mercury is obvious from Fig. 4 since the mercury line almost coincides with the phonon replica of the zinc and cadmium.

The energy of the peak at 80°K of the zinc and cadmium lines as a function of doping is shown in Fig. 5(a). The results of Roder *et al.* (10) on heavily zinc doped solution-grown material are also plotted on the figure to show the expected shift of the peak as the impurity level broadens into a band as the doping increases. The half width of the emission is plotted in Fig. 5(b) for those samples shown in 5(a).

From the constant value of the peak at lower doping levels, the activation energy can be calculated by subtracting the peak energy from the bandgap. The activation energies are tabulated in Table I. They were corrected by $\frac{1}{2}kT$ to take account of the distribution of electrons in the conduction band. They compare very closely with those determined from measurements made on vapor-grown InP at 2°K on excitons bound to zinc and cadmium (15).

The activation energy was also found from temperature studies of the quenching of the luminescence. The activation energy is given by the equation

$$I = I_0 \exp(\Delta E/kT)$$

where I_0 is the intensity at 0°K and ΔE is the activation energy. Table I shows that the quenching activation energy for zinc and mercury was in reasonably close agreement with that found from the peak energy positions. An extensive study of the temperature quenching was not carried out because the peak position of the luminescence gave a more accurate determination of the activation energy.

The temperature variation of the position of peak energy of the luminescence for all three acceptors is shown in Fig. 6 and compared to the bandgap variation of Turner *et al.* (17). The zinc sample had a doping level of 6×10^{16} compared to 7×10^{16} for the one of the cadmium samples (Fig. 6, open circles) and 2×10^{16} for the second cadmium specimen (Fig. 6, shaded circles). The zinc and cadmium samples showed an increase in "optical" activation energy as the temperature was reduced from 80° to 6°K of about 7 meV. Here "optical" activation energy is the difference between the peak energy and the bandgap at a fixed temperature. The increase in "optical" energy was observed for all samples of zinc and cadmium doped samples in the doping range 1×10^{16} to $4 \times 10^{17}/cm^3$. The shift is accounted for by the change in electron recombination mechanism from conduction band to acceptor level at 80°K to donor to acceptor recombination at 6°K. The 7 meV shift is then reasonable because this is close to hydrogenic donor binding energy in InP which is 7 meV (using an effective mass of 0.078m) (18). The two mechanisms were not resolved as two separate peaks presumably because the doping level was too high.

The mercury doped sample had a doping level of about $2 \times 10^{16}/cm^3$ and followed the bandgap quite

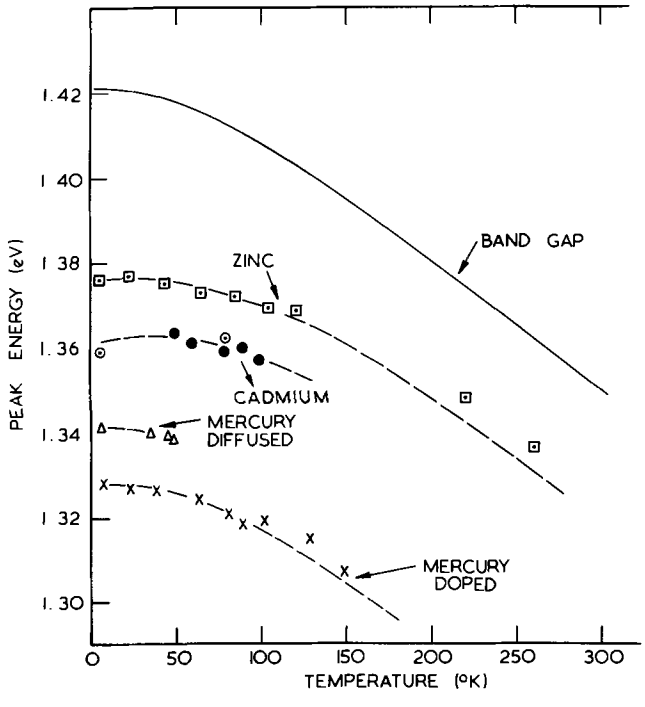

Fig. 6. Temperature dependence of the peak of the emission for zinc ($N_A - N_D = 1 \times 10^{18}/cm^3$), cadmium (open circles, $N_A - N_D = 1.8 \times 10^{16}/cm^3$; closed circles, $N_A - N_D = 7.4 \times 10^{16}/cm^3$, mercury diffused ($N_A$ unknown), and mercury doped ($N_A - N_D = 3 \times -0^{16}/cm^3$). The bandgap was obtained from absorption data (17).

Table I. Activation energy for group II acceptors in indium phosphide

Impurity	Photoluminescence at 50°K[a] (meV)	1.8°K exciton data (Ref. 15)	Intensity quenching (meV)
Zinc	50 ± 2	47.3	35 ± 5
Cadmium	58 ± 2	56.3	—
Mercury	98 ± 2	——	90 ± 5

[a] The bandgap used to calculate the optical activation energy was 1.420 eV at 50°K. This is 2 meV greater than the bandgap measured by Turner *et al.* (17). This 2 meV error in the Turner *et al.* bandgap was estimated from the position of the free exciton at 1.8°K (9).

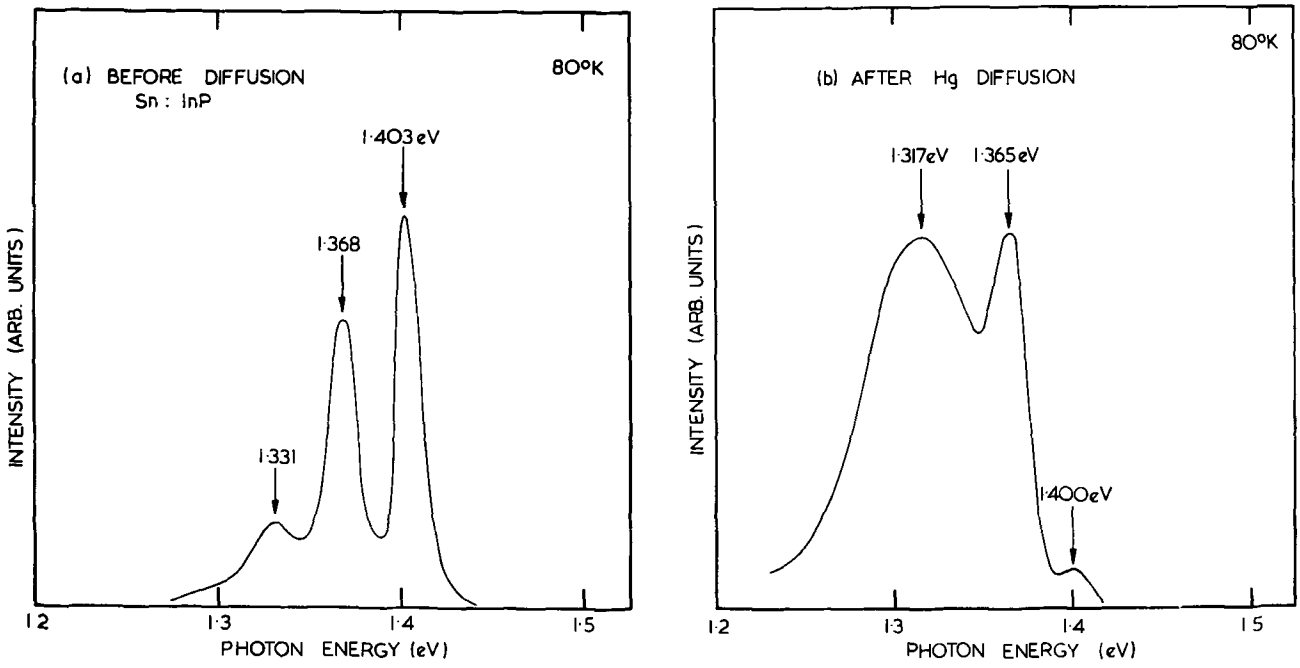

Fig. 7. Photoluminescence spectrum at 77°K. (a) A tin doped solution-grown layer ($N_D - N_A = 1 \times 10^{17}/cm^3$). (b) After diffusion of mercury into the tin doped layer at 750°C for 24 hr.

closely in the range 100°-6°K. In this case there appeared to be no change in mechanism.

The mercury diffused sample shown in Fig. 7 was prepared by mercury diffusion for 24 hr at 750°C into a tin doped epitaxial layer with a carrier concentration of 1×10^{17} electrons/cm³. A tin doped layer in preference to an undoped layer was used in an attempt to avoid the 1.37 line which was always present in the undoped samples. However the 1.37 eV always occurred at 80°K as is shown in Fig. 7 and it was very difficult to resolve the mercury line from the "zinc" line. This zinc contamination occurred even though the sample and the mercury were enclosed in a tantalum box within the quartz ampoule during the diffusion. At 6°K only one line was observed in the mercury diffused samples at 1.342 eV and its half width was just slightly larger than the mercury doped sample shown in Fig. 8 at the same temperature. The mercury diffused sample showed large changes in linewidth and peak position with changes in the exciting light intensity whereas the mercury doped sample showed none. For example, on reducing the magnitude of the intensity by two decades, the peak shifted from 1.342 to 1.334 eV and the half width changed from 23 to 35 meV. This change could possibly be interpreted as due to donor-acceptor pair recombination but such large shifts have never been observed in a direct gap III-V compound before. The shift observed for InP for the 1.37 eV line in undoped material is about 1 meV per decade of intensity change (6). It is therefore more likely that doping inhomogeneity may be causing the large peak shift for the diffused sample.

Group III isoelectronic impurities.—Boron doping of melt-grown crystals did not affect the electrical or the luminescence properties of the material. Local mode absorption studies of the boron doped crystal showed two absorption bands due to B^{10} and B^{11} and the concentration of boron was estimated to be about 10^{17} boron atoms/cm³ (19). The luminescence spectrum at 6°K of the same samples as used for the local mode studies was identical to the undoped spectrum shown in Fig. 1(a). From this it was concluded that boron did not produce any luminescence lines in the energy region 1.42-1.10 eV.

Preliminary results on an aluminum doped crystal indicate that aluminum produces a line close to the 1.32 eV line and further studies are in progress (14).

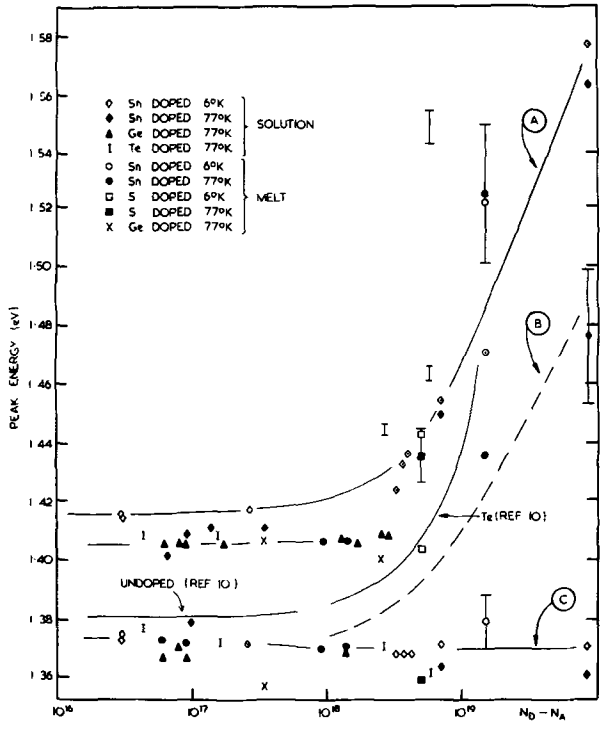

Fig. 8. Variation of the peak energy with doping of three lines seen in n-type indium phosphide grown from indium solutions and from the melt.

Group IV.—It is well known that silicon is an amphoteric impurity in GaAs and that the highest efficiency light emitting diodes have been made from silicon doped solution-grown GaAs (20). Consequently, it has been hoped that one of the group IV elements would also be strongly amphoteric in InP and that this characteristic could again be used for making efficient light emitting diodes. The many variations in the liquid epitaxial growth technique that were applied in an attempt to prepare p-type material with group IV elements were all unsuccessful (3). All the three elements attempted, *i.e.*, silicon, germanium, and tin, showed normal n-type behavior just like the group VI elements. The photoluminescence measurements on sili-

con, germanium, tin, and lead doping in melt-grown crystals have been reported previously (13) and will only be summarized briefly.

Silicon.—In the silicon solution-growth experiments, heavily doped n-type material was produced in contrast to the melt-grown crystals where no silicon was incorporated. However, the results were difficult to reproduce and the doping varied from 10^{16} to 10^{19} over the same epitaxial layer. The photoluminescence spectra of this inhomogeneous material is shown in the accompanying paper on materials growth (3). Although the 1.37 eV line associated with acceptors was observed in the lightly doped (less than $1 \times 10^{17}/cm^3$) samples it varied in a random manner and could not be correlated with silicon acceptors and could well have been due to zinc impurities.

Germanium.—In the solution-grown germanium doped samples, the 1.37 eV line was only observed when the doping level was below 1.5×10^{18} and above this up to carrier concentrations of 3×10^{18} only the 1.41 eV line was observed. The small variation of the peak energy of these two lines with doping is shown in Fig. 8 and the half width of the 1.41 eV line is plotted in Fig. 3. A typical spectrum at 80°K of a more lightly doped sample is shown in Fig. 9. The doping level was 6×10^{16} carriers/cm^3. Note the large 1.13 eV peak. A large 1.1-1.2 eV peak was observed in all the germanium doped samples both solution and melt grown. No correlation was observed between the intensity of the 1.37 and the 1.1 eV lines and the germanium doping level.

Tin.—The photoluminescence spectra of the tin doped solution-grown samples were similar to those of germanium in that the 1.41 and 1.37 eV lines were observed at 77°K over the same carrier concentration range (1×10^{16} to 3×10^{18}) that was studied for germanium. The 1.1 to 1.2 eV line was either very small or not observed in the solution-grown material and this was also typical of the melt-grown tin doped material.

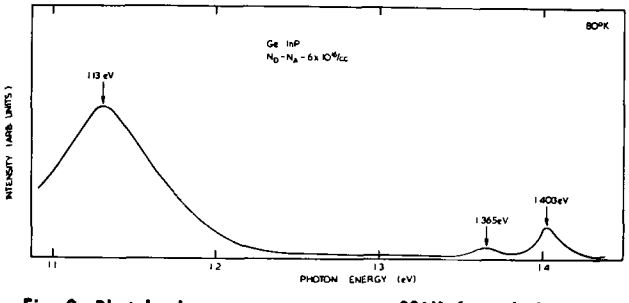

Fig. 9. Photoluminescence spectrum at 80°K for solution-grown germanium doped InP ($N_D - N_A = 6 \times 10^{16}/cm^3$).

The peak energies for the 1.37 and 1.41 eV lines as a function of doping are plotted in Fig. 8 for measurements made at 80° and 6°K. The half width of the 1.41 eV line at 80°K is plotted in Fig. 3. The change of approximately 10 meV in the position of the 1.41 eV line between these two temperatures is equal to the bandgap change. At carrier concentrations above 3×10^{18} the near band edge peak shifted to higher energies. This shift is a Burstein-Moss type shift and is due to the overlap of the donor impurity band within the conduction band and the consequent filling up of the (000) minima in the conduction band. This type of shift has also been observed for tellurium doped solution-grown InP and the results are summarized by the curve in Fig. 8 and they will be discussed below. The exact nature of the shift for the tin doped samples with concentrations above 1×10^{19} was complicated by the appearance of an extra luminescence peak above the intrinsic bandgap. Figure 10 compares two solution-grown samples. Figure 10(a) shows only one peak above the intrinsic bandgap E_G and the doping level of this sample was 7.1×10^{18}; in Fig. 10(b) however, with a doping level of 8.5×10^{19}, two peaks are observed above E_G. Two peaks were also observed in a melt-grown InP crystal which had a doping level of between 1 and 2×10^{19} electrons/cm^3. Figure 11 shows a plot of the spectrum obtained from the melt-grown crystal at five temperatures. The arrow under each curve indicates the bandgap at the temperature of measurements. The three peaks observed in the heavily tin doped spectra in Fig. 10 and 11 have been labeled A, B, and C and they have been plotted on Fig. 8. In the authors' opinion the mechanisms responsible for the three lines at 80°K are: A, band-to-band recombination (the tin donor states are merged with the conduction band); B, band-to-acceptor Ac1, where the concentration of Ac1 is less than 1×10^{18} carriers/cm^3 so that no acceptor band is formed; and C, band-to-acceptor Ac2 where the concentration of Ac2 is greater than 1×10^{18} carriers/cm^3 and increases proportionally to the tin doping. The variations with tin doping are consistent with this model and the curves on Fig. 8 have been labeled A, B, and C accordingly. The increase in half width of C for the solution-grown samples as a function of doping is clearly shown in Fig. 10 and this was observed for all solution-grown samples. From Fig. 5b it can be seen that the acceptor states begin to form a band at a carrier concentration of 1×10^{18} and Fig. 5(a) shows how the peak of the emission decreases in energy because most of the electron recombination occurs near to the top of acceptor band which is moving deeper into the forbidden gap. This decrease in energy is counteracted by the shift of the electron fermi level higher into the conduction band, hence there is little change in energy of line C. Line B, however, will follow line A because the concentration

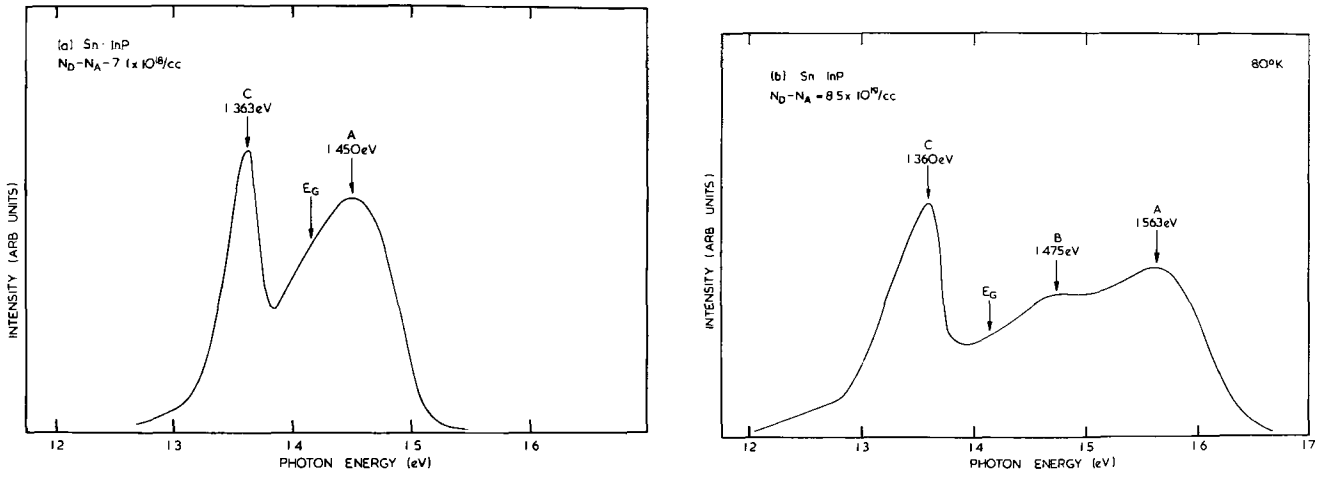

Fig. 10. Photoluminescence of heavily tin doped solution-grown InP at 80°K. (a) $N_D - N_A = 7.1 \times 10^{18}/cm^3$; (b) $N_D - N_A = 8.5 \times 10^{19}/cm^3$.

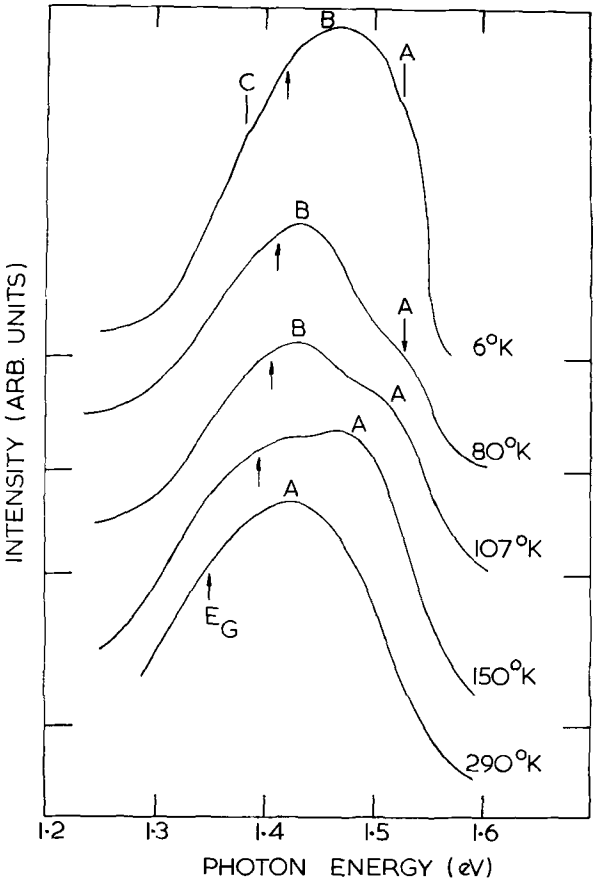

Fig. 11. Photoluminescence of heavily tin doped melt-grown InP, $N_D - N_A = 1.5 \times 10^{19}/cm^3$, as a function of temperature.

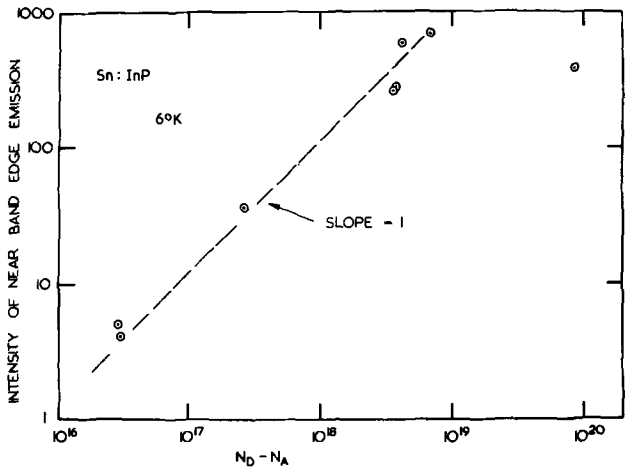

Fig. 12. Intensity of near band edge emission for solution-grown InP as a function of the tin donor concentration. The dotted line has a slope of 1.

of acceptor Ac1 is small in comparison to the donor concentration. The origins of Ac1 and Ac2 are unknown. Ac2 may be due to tin acceptors but one cannot be certain of this because a similar C line was observed for S and Te doped InP.

The temperature studies shown in Fig. 11 indicate that, assuming the proposed model is correct, band-to-acceptor recombination dominates at helium temperatures and that band-to-band recombination becomes dominant as the temperature is raised to 300°K. This behavior was also observed for the solution-grown samples. This is consistent with experimental observations for GaAs where donor-acceptor recombination often dominates at low temperatures.

The fact that the peak positions and half widths for these heavily doped (10^{19} to 10^{20}) samples do not lie exactly on the curves in Fig. 8 and Fig. 3 indicates that the carrier concentrations made by Hall measurements may be in error to some extent. This is hardly surprising since the Hall voltage is very small for these doping levels.

Of these three lines, A, B, and C, only the intensity of A which is thought to be associated with band-to-band recombination could be correlated with tin doping. This was expected because the half width of the A line was found to be proportional to the donor concentration (see Fig. 3). Figure 12 shows the intensity plot for line A at 6°K as a function of doping for solution-grown material. This shows that up to carrier concentrations of 5 to 7 $\times$ 10^{18} the intensity increase is directly proportional to the increase in the tin donor concentration and the accompanying paper (3) shows that this donor concentration is proportional to the quantity of tin going into the indium melt. This means that a large majority of the tin atoms which are electrically active act as donors and that there are extremely few acceptors present. This is confirmed by the Hall measurements which are summarized elsewhere (3). This also implies that the acceptor Ac2 proposed in the above model is not associated with tin.

A falloff at concentrations above 10^{19} is to be expected because carrier concentration quenching should set in. The mechanisms involved in the quenching cannot be discussed until more data have been assembled to derive the exact shape of the falloff in intensity.

Group V isoelectronic impurities.—Bismuth doping of solution-grown InP produces a luminescence line at 1.392 eV at 6°K whose intensity is proportional to the bismuth concentration. The luminescence line and its associated phonon replicas have been reported elsewhere (21). High concentrations of bismuth were required in order to produce 10-100 ppm of bismuth in the layers. As expected, bismuth did not show any electrical activity.

Group VI impurities.—The group VI impurities S, Se, and Te, all act as conventional donors in InP just as they do in GaAs.

The luminescence properties of four solution-grown layers doped with tellurium are summarized in Fig. 3 and 8. The half width at 80°K of the 1.41 eV line, or the A line at heavy doping levels, is plotted in Fig. 3. In each case the tellurium points appear to lie above the dotted line. Whether there is any significance in this larger half width is not known and further samples need to be studied before it is confirmed. In Fig. 8 the peak energy is plotted as a function of donor doping. For lower doping levels, below 2 $\times$ 10^{17} donors/cm^3, the tellurium points are close to those of the Group IV. At heavier doping levels there is some disagreement in that the peak positions of the two tellurium doped samples, with doping levels of 2.4 $\times$ 10^{18} and 5.8 $\times$ 10^{18} electron/cm^3 both lie appreciably above the A line for the tin doped samples. The reason for this is not understood and more samples need to be evaluated to see if this difference is confirmed. It is tempting to speculate that for some reason, perhaps because of heavy compensation, the Hall measurements always give a low reading for the carrier concentration. This would also explain the "apparent" larger half width seen in Fig. 3.

However, this still does not explain one result; in the heaviest doped sample with 5.8 $\times$ 10^{18} electrons/cm^3, an extra line is observed above line A at 1.55 eV. A spectrum of this sample at 80°K is shown in Fig. 13. The A line and the C line are observed as with the tin sample shown in Fig. 10 but in addition there is a shoulder centering at approximately 1.55 eV.

The tellurium doped solution-grown samples of Roder *et al.* (10) at 20°K are also summarized by the curve shown in Fig. 8. For doping levels up to 4 $\times$ 10^{18} they show a constant displacement from the estimated B line but they then move towards the A line at heavier doping levels. This could be explained by a gradual change in the mechanism from band-to-acceptor to band-to-band recombination at very high

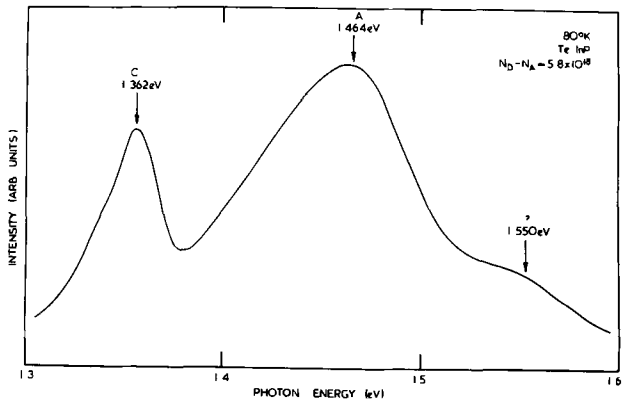

Fig. 13. Photoluminescence at 80°K of heavily doped solution-grown tellurium doped InP with $N_D - N_A = 5.8 \times 10^{18}/cm^3$.

doping levels. This is in disagreement with the interpretation of Roder *et al.* since they proposed that band-to-acceptor recombination dominated for all the tellurium doped samples because they were unable to resolve a band-to-band line at high doping levels.

Only one sulfur doped sample was evaluated and this was melt grown. The doping level was 5×10^{18} electrons/cm^3. Peaks A and C were observed, but B was not resolved. The peak energy is plotted for both 77° and 6°K in Fig. 8 and the half width is shown in Fig. 3. In both cases the agreement with the group IV elements is quite good.

Transition metals.—Copper.—Copper was evaporated onto the surface of an undoped vapor-grown layer of InP and it was diffused for 5½ hr at 750°C. The photoluminescence spectrum at 6°K of this layer both before and after copper diffusion is shown in Fig. 2 and the electrical properties are summarized in Table II. A new line is seen at 1.348 eV and this line does not occur if the heat-treatment takes place without copper. This disagrees slightly with the first results for copper diffused samples reported elsewhere by the authors when the spectrum at 80°K was shown and the copper line was at 1.355 eV (13). The first phonon replica of the copper line is clearly observed at 6°K in Fig. 1. The Hall measurements for the copper diffused sample are given in Table II. They clearly show that copper is an acceptor in indium phosphide. Inhomogeneities in the copper doping level are suspected because of the abnormally high mobility.

Whether the new copper luminescence level is due to a singly or doubly ionized copper acceptor or to a copper acceptor-donor complex is not known. Temperature studies indicate that more than one line may be present. Figure 14 shows the temperature dependence of the peak energy of the copper. At 80°K the luminescence was quenched and this was in contrast to earlier results in which the copper line was observed at 1.355 eV at 80°K on the first diffused samples. The difference between the two copper diffusion results is very confusing and indicates that more than one copper line is involved. It should be noted that the copper diffusions reported here were carried out on much better vapor-grown layers with a lower background doping than those used in the previous study.

Table II. Electrical properties of transition metal doped indium phosphide

Sample	Type	Temperature (°K)	Mobility (cm²/V-sec)	N/cm³
Undoped layer (used for copper diffused layer below)	n	300 77	3,204 22,800	7.2×10^{15} 2.4×10^{15}
Copper diffusion	p	300	707*	5.3×10^{15}
	p	77	1,435*	7.3×10^{15}
Manganese doped 32 mm	p	300	867	1.6×10^{16}
Manganese doped 58 mm	p	300	888	6.9×10^{16}

* Inhomogeneities in copper doping level suspected because of this abnormally high mobility.

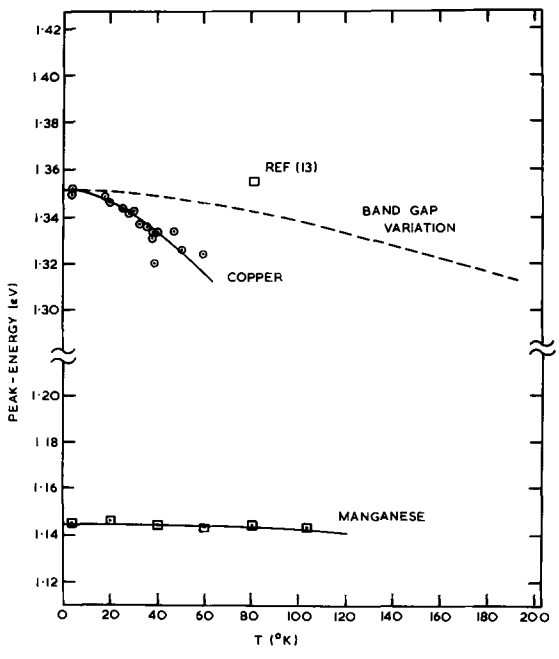

Fig. 14. Temperature variation of the peak of the emission associated with copper and manganese acceptors in InP compared to the bandgap (19)

Manganese.—The samples used in the photoluminescence measurements were cut from an InP crystal grown from a manganese doped InP melt. They were p-type and their electrical properties are summarized in Table II. The 58 mm sample was nearer the bottom of the crystal and had a concentration of manganese of $6.9 \times 10^{16}/cm^3$. The photoluminescence intensity was very weak for this sample and it could only be observed at helium temperatures. The spectrum is shown in Fig. 15. For the more lightly doped sample the

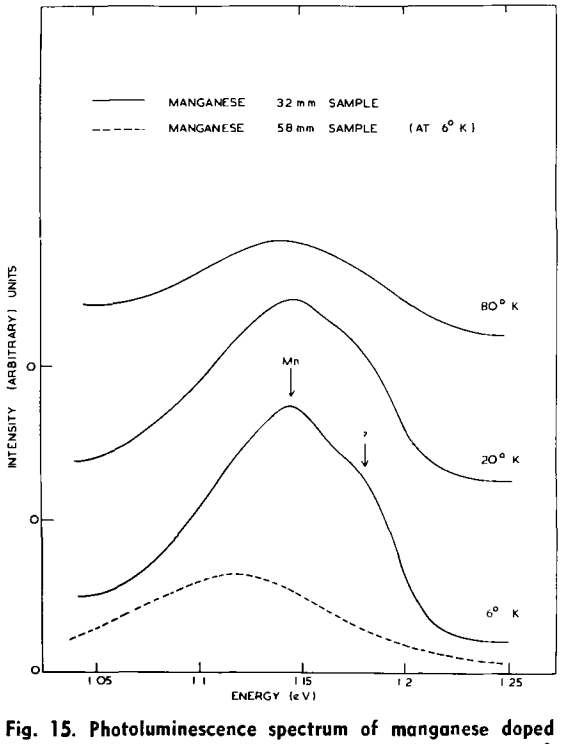

Fig. 15. Photoluminescence spectrum of manganese doped InP. Solid line, 32 mm sample, with $N_A - N_D = 1.6 \times 10^{16}/cm^3$; dotted line, 58 mm sample, with $N_A - N_D = 6.9 \times 10^{16}/cm^3$.

luminescence intensity was higher and it was studied as a function of temperature. Unfortunately, another line at about 1.18 eV is unresolved from the manganese line and this may have lowered the position of the manganese line. The spectrum for this sample with a doping level of 1.6×10^{16} is shown in Fig. 15 for three temperatures: 6°, 20°, and 80°K. The extra line is not associated with manganese since it was not present in the more heavily doped sample. The extra line appeared to be quenched at higher temperatures and only one line was observed at 80°K at approximately 1.14 eV. The peak position of the manganese line varied little with temperature as is shown in Fig. 14.

One attempt at manganese diffusion into an undoped vapor-grown layer of indium phosphide produced a line at 1.15 eV at 80°K of about half the width of the line observed at 80°K from the lightly doped manganese sample shown in Fig. 15. The manganese was diffused in at 650°C for 17 hr. The smaller half width indicated that the doping level was lower than 2×10^{16} but Hall measurements were not possible because of the nonuniform nature of the diffusion.

Conclusion

Zinc is the most common acceptor impurity in undoped melt-, vapor-, and solution-grown indium phosphide. This was confirmed by a comparison of the peak energy at 80°K and the temperature dependence of the zinc line in zinc doped solution-grown and undoped material. The temperature studies of the group II acceptors cadmium and zinc show a change in mechanism as a function of temperature from band to acceptor recombination at helium temperatures to band to band recombination at 50°K and above. Mercury, on the other hand, shows no change in mechanism. The optical activation energies at 50°K of zinc, cadmium, and mercury are summarized in Table I and Fig. 16. The optical activation energy was calculated by subtracting the peak energy from the bandgap at 50°K.

The optical activation energies for all the dopants studied are shown in Fig. 16. The exciton lines due to hydrogenic donors could not be resolved at 6°K which was the lowest measurement temperature used. The isoelectronic trap bismuth was reported previously (21) and is included for completeness. Copper was briefly reported in an earlier publication (13) and the spread in optical activation energy from 60 to 73 meV shown in Fig. 16 represents the difference between the present copper diffusion studies and those reported previously. The difference is indicative of copper forming more than one level, and the peculiar temperature results which show a large deviation from the bandgap temperature dependence is more typical of a copper complex than of a single copper substitutional acceptor behavior. The manganese luminescence line, on the other hand, follows the bandgap and indicates that manganese is a substitutional acceptor and is not forming complexes. The broad luminescence level in the region 1.1-1.2 eV is not shown on Fig. 16 because there is no strong evidence as to its nature. There is no doubt that it is always strongly enhanced in the presence of excess indium and this has led to the proposal that it may be associated with phosphorus vacancies. For some unknown reason it is enhanced by germanium doping but not with tin doping.

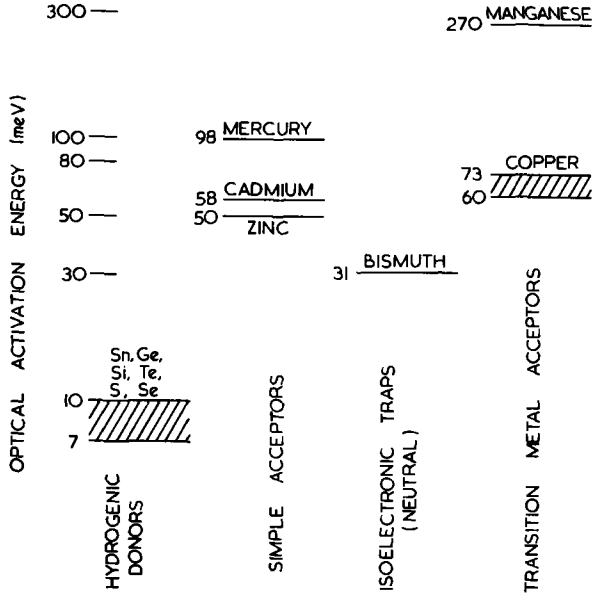

Fig. 16. Summary of optical activation energies of donors, simple acceptors, the isoelectronic trap bismuth, and transition metal acceptors [simple acceptors, see definition in Ref. (22)].

Acknowledgments

The authors are grateful to P. J. Dean, A. M. White, H. J. Queisser, J. W. Allen, and M. H. Pilkuhn for many helpful comments.

Experimental assistance was provided by P. Porteous, A. Ashford, and A. Royle. A. J. White contributed some very useful ideas in the early stages of this work.

Manuscript submitted Dec. 4, 1972; revised manuscript received May 29, 1973.

Any discussion of this paper will appear in a Discussion Section to be published in the June 1974 JOURNAL.

REFERENCES

1. C. Hilsum and H. D. Rees, *Electron. Letters*, **6**, 277 (1970).
2. G. M. Blom and J. M. Woodall, *Appl. Phys. Letters*, **17**, 373 (1970).
3. M. G. Astles, F. G. H. Smith, and E. W. Williams, *This Journal*, **120**, 1750 (1973).
4. B. D. Joyce and E. W. Williams, "Symposium on GaAs and Related Compounds," p. 61, Institute of Physics, Aachen, Germany (1970).
5. J. B. Mullin, R. J. Heritage, C. H. Holliday, and B. W. Straughan, *J. Crystal Growth*, **3**, 281 (1968).
6. R. C. C. Leite, *Phys. Rev.*, **157**, 672 (1967).
7. U. Heim, O. Roder, H. J. Queisser, and M. Pilkuhn, *J. Luminescence*, **1**, 542 (1970).
8. V. Heim, *Solid State Commun.*, **7**, 445 (1969).
9. A. M. White, P. J. Dean, L. L. Taylor, R. C. Clarke, D. J. Ashen, J. B. Mullin, and P. D. Greene, *J. Phys. C*, **5**, 1727 (1972).
10. O. Roder, U. Heim, and M. H. Pilkuhn, *J. Phys. Chem. Solids*, **31**, 2625 (1970).
11. E. W. Williams and R. A. Chapman, *J. Appl. Phys.*, **38**, 2547 (1967).
12. K. Maeda, *J. Phys. Chem. Solids*, **26**, 595 (1965).
13. J. B. Mullin, A. Royle, B. W. Straughan, P. J. Tufton, and E. W. Williams, *J. Crystal Growth*, **13**, 640 (1972).
14. J. B. Mullin, A. Royle, B. W. Straughan, P. J. Tufton, and E. W. Williams, Symposium on GaAs and Related Compounds, p. 118, Institute of Physics, Colorado (1973).
15. A. M. White and P. J. Dean, To be published.
16. A. Ashford, Private communication.
17. W. J. Turner, W. E. Reese, and G. D. Pittit, *Phys. Rev.*, **136**, 1467 (1964).
18. L. Eaves, R. A. Stradling, S. Askenayz, J. Leotin, J. C. Portal, and J. P. Ulmet, *J. Phys. C.*, **L42**, (1970).
19. R. C. Newman, F. Thompson, J. B. Mullin, and B. W. Straughan, *Phys. Letters*, **33A**, 113 (1970).
20. I. Ladany, *J. Appl. Phys.*, **42**, 654 (1971).
21. P. J. Dean, A. M. White, E. W. Williams, and M. G. Astles, *Solid State Commun.* **9**, 1555 (1971).
22. E. W. Williams and H. B. Bebb, "Semiconductors and Semimetals," Vol. 8, p. 327, Academic Press, New York (1972).

Indium Phosphide

II. Liquid Epitaxial Growth

M. G. Astles,[1] F. G. H. Smith, and E. W. Williams

Royal Radar Establishment, Malvern, Worcestershire, England

ABSTRACT

An improved technique is described for the growth of InP by liquid-phase epitaxy. The use of gold-plated reflector tubes in the furnace design has improved the control of layer quality, and background doping levels have been consistently reduced to $3 \times 10^{15}/cm^3$ by replacing polycrystalline InP by $PH_3(g)$ as a source of phosphorus. The behavior of the dopants Sn, Ge, Si, Te, Zn, Cd, and Bi in InP are discussed and the distribution coefficients "k" are found to be

$$k_{Sn} = 0.0019,\ k_{Ge} \triangleq 0.005,\ k_{Si} \triangleq 4,\ k_{Te} = 0.27,$$

$$k_{Zn} = 1.14,\ k_{Cd} \simeq 0.002,\ k_{Bi} \triangleq 0.002 \text{ to } 0.0002$$

The dopants Sn and Zn were found to be the most suitable for n and p doping for LED fabrication. The Group IV elements yielded n-type material only, although the mobility measurements indicated possible amphoteric behavior for Ge. The Hall mobilities at room temperature for the n-type samples show good agreement with theory.

In this paper, we describe improved techniques for the growth of InP by liquid-phase epitaxy (LPE), and the behavior of the dopants Sn, Ge, Si, Te, Cd, Zn, and Bi in InP.

We were particularly interested in the behavior of the Group IVB dopants because of the possibility of a similar amphoteric doping to that which has been found for Ge (1, 2) and Si (3) in GaAs.

The technique used throughout is the Nelson horizontal tipping method which was chosen for its simplicity of operation and ease of control (4). Also, at the normal growth temperatures for InP (600° → 700°C), loss of phosphorus from the substrate surface during the pregrowth stages is not a serious problem.

We had previously established that for flat, uniform interfaces between substrate and grown-layer, a controlled amount of etch-back before growth was necessary in addition to careful substrate preparation. It is also obviously important to be able to tip off the solution cleanly at the end of the growth cycle. The desired control could not be obtained in the type of furnace then used. This was a standard helically wound resistance furnace with concentric stainless steel radiation shields, with asbestolite outer casing and silica wool insulation. The visibility in such a furnace was very poor, which made proper equilibration of the solution before growth very difficult. The temperature profiles were also poor, having temperature plateaus much shorter than the length of the boats used, and often changed considerably with use.

In order to improve control, the furnace system was redesigned using gold-plated reflector tubes. The design is illustrated in Fig. 1. The golded tube reflects 95% of the incident *IR*, while allowing visible light in the green region to pass through. This enables the solution to be observed easily during the run. A longer temperature plateau is also obtained and this ensures that the temperature is constant to within ±2°C over the length of the boat (8 cm), and this profile can be maintained by cutting helical grooves in the silica former to hold the KANTHAL windings in place. All gas lines and fittings were of PTFE or stainless steel.

[1] Present address: Services Electronics Research Laboratory, Baldock, Hertfordshire, England.

Key words: indium phosphide, liquid epitaxy.

Materials

The growth solutions were prepared using 6 9's indium supplied in ingots under argon gas by Johnson-Matthey Chemicals. The indium was etched in 50% HNO_3 aq before use. Originally, polycrystalline InP was used as a phosphorus source but this was thought to be responsible for the large variations in the background doping levels in the epitaxial layers between 8×10^{15} and 1×10^{17} cm^{-3} n-type. So this was replaced by phosphine (PH_3) supplied as a 5% V/V mixture in high-purity hydrogen. Phosphine dissociates at temperatures above about 150°C as follows

$$4\,PH_3 \rightleftarrows P_4 + 6\,H_2$$
$$\uparrow\downarrow$$
$$P_2$$

The phosphorus then reacts with the molten indium until the solution is saturated with phosphorus and InP crystals start to form round the edges of the solution. A slight increase in temperature will then dissolve these crystals. Not only did the use of PH_3 bring down the background doping level to 3×10^{15} to 2×10^{16} cm^{-3}, but it also simplified the growth procedure. The presence of phosphorus vapor in the ambient during the pregrowth stages also helped to offset any loss of

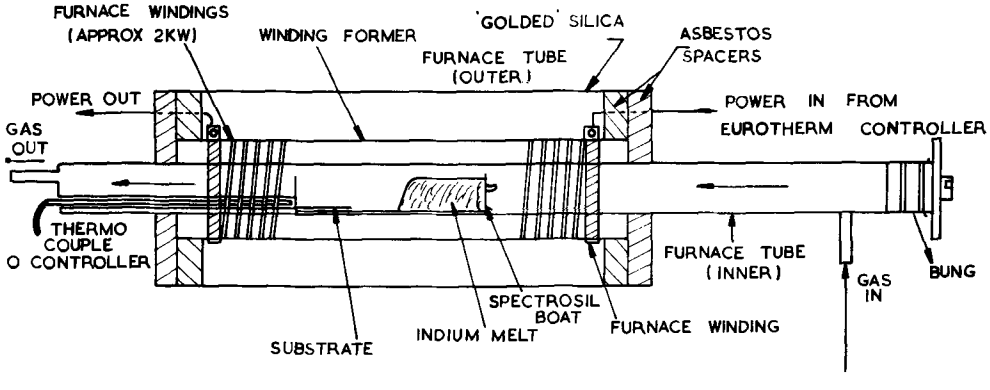

Fig. 1. Cross section of furnace, showing the position of the substrate and solution before tipping.

phosphorus from the substrate. With the earlier growth system, small indium inclusions could often be seen at the interface between substrate and layer when runs were done at 645°C or above. Since using the new system, this behavior has not been found. The dopants Bi, Sn, and Cd were used as 6 9's shot supplied by Cominco. The dopants Ge and Si were used as polycrystalline device grade. The dopants Te and Zn were used as 1% W/W alloys in indium metal (6 9's).

The InP substrates were grown by the liquid-encapsulation Czochralski method at RRE (5), and were used either on the (100) or (111) orientations. The substrates were chemi-mechanically polished with 2% bromine/methanol solution, followed by cleaning in a Soxhlet containing Propan-2-ol. For Hall measurements, the layer is grown on Cr-doped semi-insulating substrates.

Growth Procedure

When the materials have been loaded into the "Spectrosil" silica boat, this is placed in the furnace such that it is within the temperature plateau region. Having flushed the system with O_2-free N_2 gas for 15 min and Pd-diffused H_2 gas for 15 min, the furnace is brought up to the desired growth temperature. Above 600°C, any residual indium oxide on the solution surface is removed by reaction with the hydrogen gas. After passing the PH_3 at a rate of about 50 ml/min until saturation has occurred, the temperature is raised 1°C at a time, with gentle agitation of the solution, until residual InP crystals on the surface of the solution have dissolved. The temperature is then raised by a further 0.5° to 1°C to allow for etch-back before growth. This etch-back, which was estimated to be about 5 μm must be enough to remove any surface roughness from the substrate, but not enough to significantly back-dope the solution. The solution is gently tipped over the substrate, and the cool down commenced. After cooling at $\simeq$ 1°C/min for typically 20-30 min, the solution is tipped off, and this can usually be done without leaving any of the solution in contact with the substrate. When the furnace has cooled to room temperature, the sample is removed from the boat and any indium adhering to the slice is removed by ultrasonic treatment in a solution of mercuric chloride in dimethyl formamide. In most cases, however, the indium tipped off cleanly leaving a reasonably flat mirror finish surface.

Examination of Epitaxial Layers

Having cleaved the sample and stained with warm potassium ferricyanide/potassium hydroxide solution, the grown layer can be discerned under the microscope. The interfaces are usually straight and sharp, although with some dopants, particularly Zn and Cd, diffuse junctions can occur due to diffusion during growth. Having measured the layer thickness, Hall specimens are fabricated using indium dots for n-type and Pb/Cd dots for p-type material. Measurements were carried out at room and liquid-N_2 temperatures using the Van der Pauw technique.

Unfortunately, it is not yet possible to make reproducible impurity profile measurements by Schottky-barrier methods as is possible with GaP and GaAs (6). However from electron microprobe analysis on Sn-doped layers it appears that there are no significant doping gradients through the grown layers. This is not surprising as the rates of growth are quite low (0.5 to 1 μm/min), and the cooling range is quite small ($\simeq$20° to 30°C).

For the dopants Sn, Ge, Si, and Zn, growth on the (111)A, (111)B, and (100) faces was compared and found to yield very similarly doped material whatever the orientation. An exhaustive study as a function of growth temperature and cooling rate was not carried out. A solubility limit was seen for only one of the dopants examined. This will be discussed later.

Background Doping Levels

It is obviously necessary before commencing a series of controlled doping experiments, to ascertain that the background level is fairly low and repeatable. As mentioned above, the change to PH_3 as a phosphorus source gave a great improvement, the level being consistently in the range 1-2 $\times$ 10^{16} cm^{-3} (n) for a starting temperature of 650°C, using (111)B orientation and without baking the indium beforehand.

The possible sources of this residual impurity concentration were thought to be: (*i*) impurities in the indium starting material, (*ii*) contamination from the silica boat, (*iii*) leaks in the apparatus, e.g., through PTFE tubing and seals, (*iv*) impurities introduced with the PH_3 gas which could not be purified by normal means, and (*v*) impurities from the substrate introduced during the "etch-back" stage. It was found that baking the indium for 1 hr at 670°C after saturating with PH_3 gas at 650°C improved the background doping level from 1.8 $\times$ 10^{16} cm^{-3} to 8 $\times$ 10^{15} cm^{-3} (n). However, similar baking before passing the PH_3 had no effect on the background level. This suggests that the PH_3 gas is a source of impurities, although the nature of these impurities is not known. The extent of contamination from the boat was difficult to ascertain. After a few runs in a silica boat, a discoloration could be seen on the walls where the solution had been in contact, and after considerable use slight devitrification was found. But the rate of attack was very slow and was not thought to be a significant source of impurities at these low temperatures. Growth in vitreous carbon boats was found to have no significant effect on background doping.

It was hoped to overcome the problem of leaks in the apparatus by working at a pressure slightly above atmospheric. However, since the PTFE tubing used on the gas inlet was known to be slightly porous to oxygen, it was replaced by flexible 1/16 in. stainless steel tubing and a very slight improvement in background level was obtained.

The effect of introduction of impurities into the solution during the back-etching of the substrate is calculated to be negligible for a 5μ etch-back of the substrates used.

A marked temperature dependence of background-doping level was found, as illustrated in Fig. 2. An undoped run at 660° → 640°C produced n-type material with a doping level of 2 $\times$ 10^{16} cm^{-3}, whereas a run in the same furnace using a cooling range of 580° → 500°C produced a doping level of 2 $\times$ 10^{17} cm^{-3}. The Hall measurements implied that shallow donor impurities were involved and this was confirmed by photoluminescence studies (7).

The highest purity n-type material was obtained with growth temperatures in the range 780°-660°C. The carrier concentration was in the range 3 to 5 $\times$ 10^{15}/cm^3 and the mobility was 20,000 to 27,000 cm^2/V-sec at liquid nitrogen temperatures.

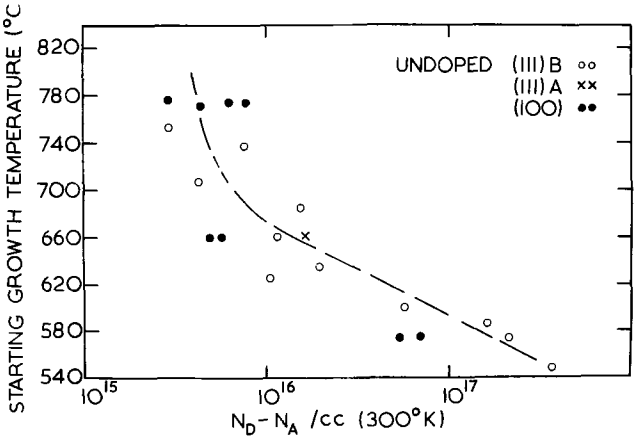

Fig. 2. Plot of starting growth temperature against (N_d — N_a) at room temperature.

Doping Experiments

Tin-doping.—We have done most work on tin doping, as it emerged as an easily controllable n-type dopant. There was also the possibility that Sn might behave amphoterically in InP. A wide range of dopings and growth temperatures was studied, and in all cases, only n-type material was obtained. Figure 3(a) shows a plot of log ($N_d - N_a$) against log (atomic per cent Sn in solution). The starting growth temperature was 650°C. The figures have been corrected for background doping levels. The gradient of the line in Fig. 3(a) is approximately 1. If the data is plotted linearly as ($N_d - N_a$) *vs.* weight per cent tin in solution, then the gradient can be used to calculate the distribution coefficient "k" under these growth conditions:

Since k is defined as $k_{Sn} = \dfrac{[\text{Sn in solid}]}{[\text{Sn in liquid phase}]}$

where the [ ] brackets denote concentration in gram atoms of tin per gram of solid or liquid, then this can be written as

$$k_{Sn} \simeq \frac{(N_d - N_a)}{W_{Sn}} \times \frac{AW_{Sn} \times 100}{N \times \rho_{InP}}$$

where W_{Sn} = weight per cent of tin in the growth solution, AW_{Sn} = atomic weight of tin, ($N_d - N_a$) = net donor concentration assumed equal to the concentration of tin atoms in the solid (cm^{-3}), ρ_{InP} = density of InP = 4.80 g cm^{-3} (8), and N = Avogadro's number. The value of k_{Sn} calculated in this way is 0.0019.

There is no significant orientation effect at these temperatures, the data for (111)A, (111)B, and (100) all lying very much on the same straight line shown in Fig. 3(a).

Germanium doping.—Work on Ge doping in GaAs has shown Ge to be capable of amphoteric doping. Rosztoczy *et al.* (1) have prepared p-type Ge-doped GaAs while Whelan *et al.* (2) prepared n-type material by melt growth. We have grown Ge doped InP using a wide range of doping concentrations and as wide a range of temperatures as possible. All material was n-type. The results are shown in Fig. 3(b). The gradient of this line is $\simeq$ 0.71. This contrasts with all the other dopants studied, (with the possible exception of Si) where the gradient was $\simeq$ 1. Whether this is due to a compensation of Ge donors by Ge acceptor centers which increases with increasing Ge concentration, due to a complex center or some other mechanism is not yet clear.

The value of the distribution coefficient calculated at low germanium concentrations was $\simeq$ 0.005.

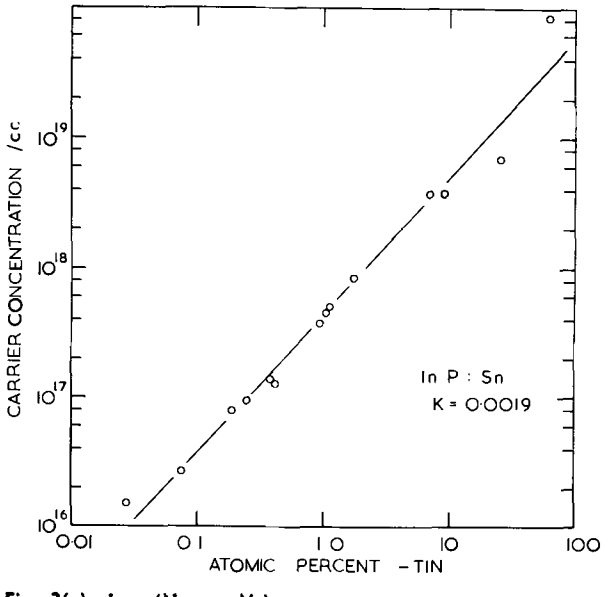

Fig. 3(a). Log ($N_d - N_a$) at room temperature against log (atomic per cent Sn in solution).

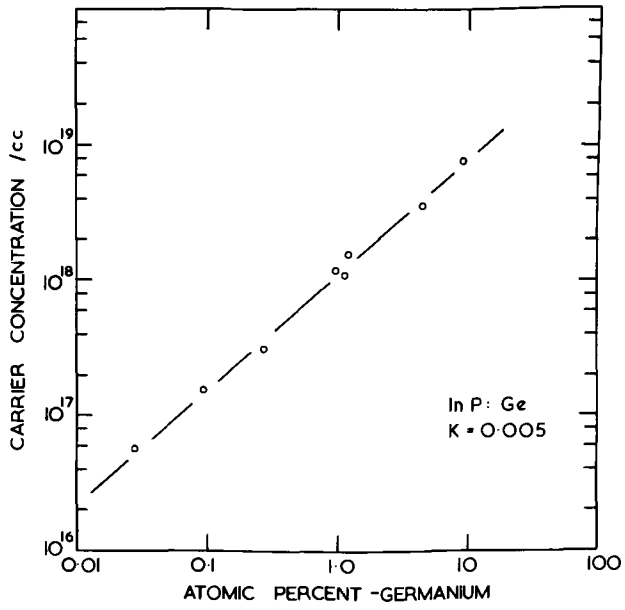

Fig. 3(b). Log ($N_d - N_a$) at room temperature against log (atomic per cent Ge in solution).

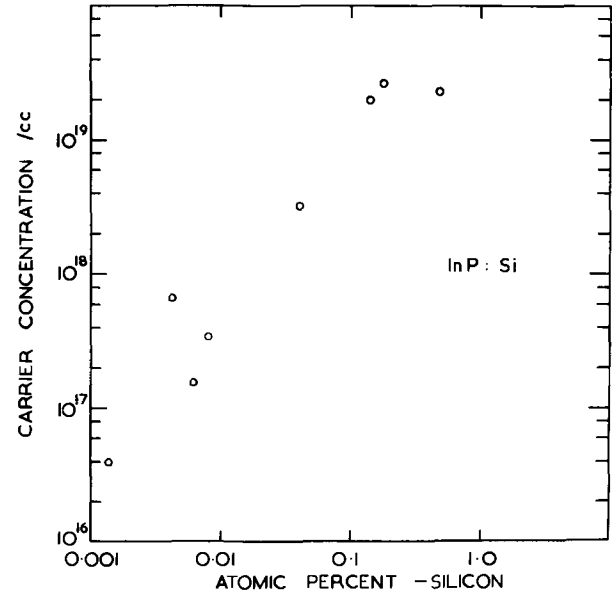

Fig. 3(c). Log ($N_d - N_a$) at room temperature against log (atomic per cent Si in solution).

Silicon doping.—We have investigated Si-doping in InP under a wide range of growth conditions. There are several practical difficulties involved. The main one is the rather low solubility of silicon in indium in the operating temperature range, for example, 0.1 atomic per cent (a/o) at 700°C and only 0.03 a/o at 610°C. Also great care must be taken to ensure that the indium solvent is entirely free of any residual oxygen before allowing the silicon dopant to come into contact with the solution otherwise small white flakes of SiO_2 form on the surface of the solution and remain there throughout the run. Rather erratic results were obtained as is shown in Fig. 3(c) where the carrier concentration ($N_d - N_a$) is plotted against log (atomic per cent of silicon in the indium solution), but the following points emerged. In spite of the scatter the distribution coefficient is obviously quite high but it was not estimated in view of the inhomogeneity of some of the samples (see below). Doping concentrations in the solution above 0.1 a/o yield n-type material with $N_d - N_a$ = 2 to 3 $\times$ 10^{19} cm^{-3} when grown at about 680°-640°C. This could represent either the solubility limit of Si in InP or correspond to the solubility limit of silicon in the indium solvent. Local mode absorption

studies on some of these heavily silicon-doped samples confirmed that the concentration of silicon donors, Si_{In}, was in the region of 10^{19} but there was no evidence for silicon acceptors Si_p, or for nearest neighbor Si_{In}-Si_p pairs (9). It should be pointed out however, that Si_p is more difficult to detect by local-mode absorption than Si_{In}.

Ahn *et al.* have recently shown that the transition temperature from n- to p-type in silicon-doped solution grown GaAs can be increased by over 100°C by changing from (111)B substrates to (111)A substrates (10). This gave rise to the hope that p-type material might be produced in InP if the right orientation of substrate were used. Several attempts with (111)A and (100) substrates at growth temperatures in the region 600°-700°C were all unsuccessful in that n-type material was always produced and the results were not too different from those for (111)B substrates.

On cleaving and staining the layers distinct subinterfaces, SI, running parallel to the surface across the whole layer were observed as shown in Fig. 4. That these interfaces are due to sudden changes in silicon doping was shown by electron microprobe analysis. A scan of Si counts across the layer is also shown in Fig. 4. It can be seen that there are two distinct zones of concentration, the transition point coinciding almost exactly with the visible boundary seen in the photomicrograph of the cleave. The microprobe analysis also showed the presence of silicon-rich precipitates in the grown layers. From the results of microprobe analysis on one of the homogeneous Si-doped samples, we have estimated k to be $\simeq 4$.

The photoluminescence spectra from the heavily doped silicon layers also indicated that there were inhomogeneities present. Figure 5 shows a comparison of a heavily doped silicon layer (full line) with a doping level of 1.1×10^{19} and a lightly doped layer (dashed line) with $N_d - N_a = 2 \times 10^{16}$ cm^{-3}. The lightly doped layer shows no emission above the bandgap E_G at 6°K (1.423 eV). The heavily doped layer however shows a broad line well above the bandgap and a sharp cutoff of the luminescence in the region of the bandgap. Both of these features are also observed at nitrogen temperatures but in this case it is seen from Fig. 5 that the cutoff has shifted to lower energies by an amount which is the same order as the change in bandgap. With the prior knowledge that the microprobe results on the same heavily doped sample show doping fluctuating from 10^{19} to 10^{17}, it appears possible that these fluctuations could cause the cutoff. The low carrier concentration regions would absorb some of the emission and produce the distorted luminescence curve that is observed. These inhomogeneities also explain why no similar sharp cutoff was observed for the heavily doped Sn and Te samples of InP; the spectra for Sn and Te were shown in a previous paper (7).

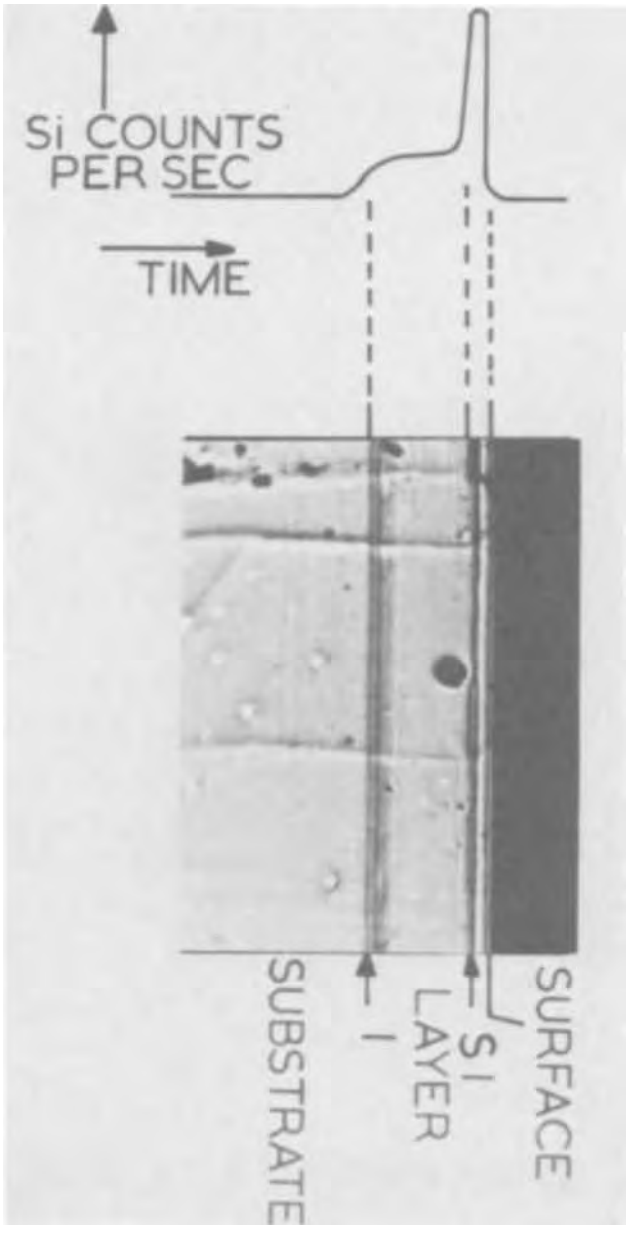

Fig. 4. An electron microprobe scan of a cleaved silicon doped layer compared to a photomicrograph of the same layer. The subinterface (SI) which is 4 μm from the surface separates a low doping region from a high doping region which is revealed by a large increase in the number of silicon counts/sec on the microprobe. The layer was 18 μm thick and on close examination it appears to be full of striations.

Tellurium doping.—Tellurium is a familiar n-type dopant in III/V compounds. In InP, we have been able to dope up to 1×10^{19} cm^{-3} using tellurium. It is a convenient dopant in that it substitutes exclusively on P-sites, dissolves readily in the indium solvent and is nonvolatile at our growth temperatures. It has however a fairly high distribution coefficient, and we found it necessary to use a 1% tellurium in indium alloy as the dopant source in order to weigh the desired amounts accurately. The results of Hall measurements on Te-doped layers grown on Cr-doped substrates are shown in Fig. 6. The results have again been corrected for background doping. The gradient of the plot is again approximately 1. The value of "k" is calculated to be 0.27.

Cadmium doping.—Cadmium was investigated as a possible alternative to zinc as a p-type dopant in InP, as the latter has a rather high distribution coefficient and is hence difficult to control. Although p-type material was grown using Cd-doping, the high vapor pressure of Cd at the growth temperatures (100 mm Hg at 611°C) led to rapid loss of Cd from the solution. The use of lower growth temperatures to overcome this difficulty led in several cases to n-type material. This is thought to be due to contamination with shallow donor impurities from the phosphine since we have already mentioned that growth at low temperatures yields higher background n-type doping levels. These background levels were thought to be high enough to overcompensate the cadmium doping. The plot of log $(N_a - N_d)$/log (atomic per cent Cd) is shown in Fig. 7(a). Again the gradient is approximately 1. From the gradient of the plot of weight per cent Cd against $(N_a - N_d)$, the value of "k" is calculated to be $\simeq 0.002$.

Zinc-doping.—In order to accurately weigh out the required weights of zinc over the range of doping studied, a 1% alloy of zinc in 6 9's indium was used. None of the problems encountered above with cadmium doping were found here. The results are shown in Fig. 7(b). It can be seen that above about 3×10^{18}

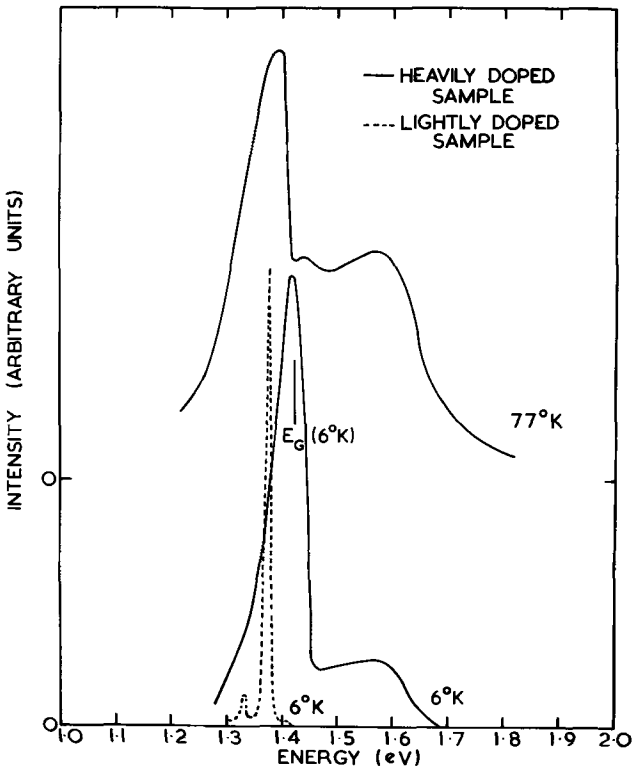

Fig. 5. Photoluminescence spectrum (full line) at 77° and 6°K of the heavily silicon doped sample shown in Fig. 5 compared to a lightly n-type silicon doped sample (dotted line) with a carrier concentration of 2×10^{16}/cc.

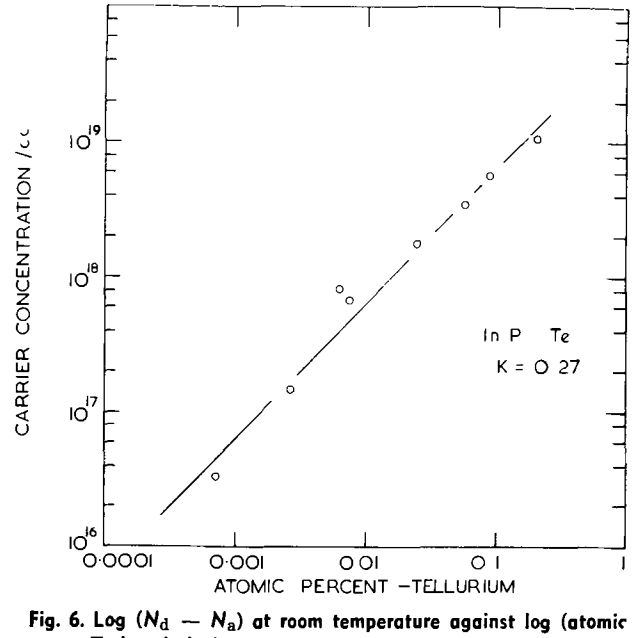

Fig. 6. Log (N_d — N_a) at room temperature against log (atomic per cent Te in solution).

cm^{-3}, the carrier concentration levels off. It is possible that this represents the solubility limit of zinc in indium phosphide at these temperatures. The gradient of the plot of weight per cent zinc/(N_a — N_d) yields a value of "k" of 1.14.

Bismuth doping.—Several Bi-doped epitaxial layers were grown to investigate the behavior of iso-electronic impurities in InP. The results of this work have been recently reported (11). Since bismuth is electrically neutral in InP, it is impossible to deduce the bismuth concentration from electrical measurements. However, it was estimated from x-ray fluorescence measurements that the bismuth was present in concentrations of between 10-100 ppm when the atomic per cent of bismuth in the solution was ≏ 3%. This information gives limits of "k" between ≏ 2×10^{-3} to 2×10^{-4}.

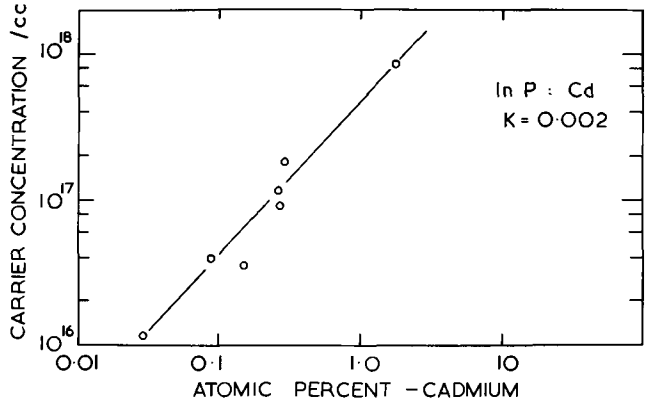

Fig. 7(a). Log (N_a — N_d) at room temperature against log (atomic per cent Cd in solution).

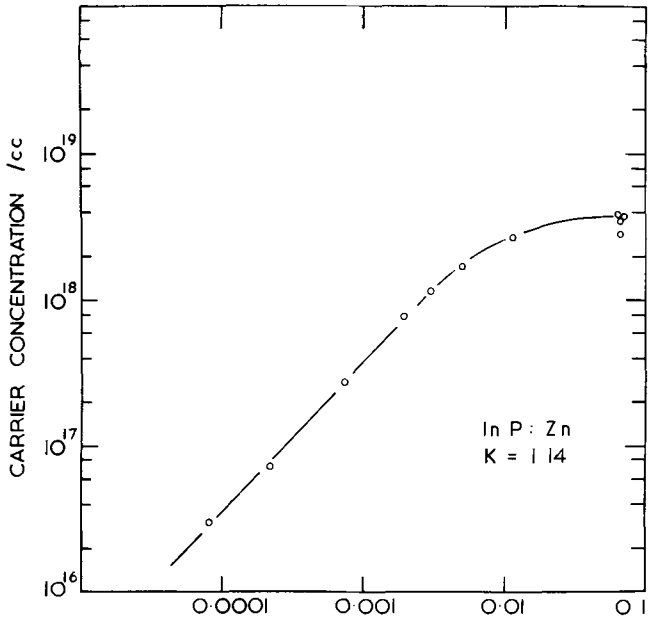

Fig. 7(b). Log (N_a — N_d) at room temperature against log (atomic per cent Zn in solution).

General Properties of the Epitaxial Layer

Surface features.—One surface feature which was found on all layers grown on (111) oriented substrates was the "overlapping scales" or "sea-shore ripples" effect illustrated in Fig. 8. The ripples are less than 0.5 μm in height.

The ripple density can be reduced by careful optical orientation of the substrates to make sure they are exactly (111). Figure 8 shows a zinc-doped layer grown on a substrate which was optically aligned over part of its area. A large flat region was obtained on this optically oriented section and all the ripples appear to be originating from it. The ripples on the optically oriented section are much more widely spaced than those on the section that was not optically oriented.

The (111) surface quality was generally superior to the (100) surfaces and optically oriented slices gave near "mirror" layer quality with very few features. The (100) surface varied from run to run and from dopant to dopant in a seemingly arbitrary fashion. The surfaces were sometimes pitted with holes up to 1 μm in depth. Figure 9 shows three of the different types of (100) surfaces obtained for (a) zinc, (b) tellurium, and (c) silicon doping.

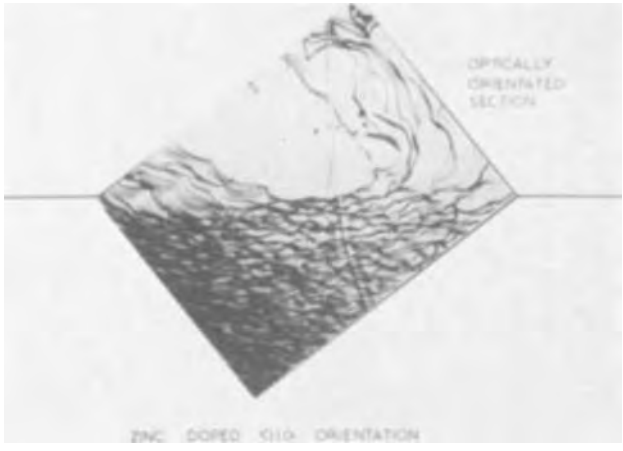

Fig. 8. Photomicrograph of a layer grown on a (111) partly optically orientated substrate.

The importance of etch-back.—It has been mentioned earlier that it is vital to ensure a controlled etch-back of the substrate surface before growth commences. Figures 10(a) and 10(b) show how the amount of etch-back affects the appearance of the interface between substrate and layer. In Fig. 10(a) it can be seen how irregularities at the interface produced by insufficient etch-back cause holes and poor quality layers. In Fig. 10 (b), the etch-back has produced a good interface and the layer quality is much superior. The thickness of the interface shown in Fig. 10(b) is estimated to be about 0.5 μm.

Layer thickness.—As well as controlling the layer and surface quality, the thickness must be carefully controlled for most device applications. The technique used here is not suitable for the growth of very thin layers of less than 2 μm in which case the Rupprecht dip system (12) or the sliding pot system are more suitable. However for LED devices where layers between 3 and 30 μm are required, our method is quite suitable since reasonably flat layers can be grown in this region.

The growth cycle can be considered as 3 stages: (*i*) etch-back phase, (*ii*) growth before nucleation in the solution takes place, and (*iii*) growth after nucleation in solution has occurred until tip off. As mentioned earlier, we intentionally imposed approximately 1°C of undersaturation and in addition there was possibly unintentional etch-back due to temperature fluctuations in the furnace. So, cooling at 1°C/min, the etch-back phase could last for 1 to 2 min.

In most runs in the temperature range 630° → 660°C, it was observed that after cooling about 15°C from the starting temperature small crystals would start to appear round the walls of the boat which would then grow until the end of the run. It is quite likely therefore that the rate of deposition on the substrate is greater in phase (*ii*) than in phase (*iii*) due to "competition" from crystal growth in the solution. Thus when measuring the growth rate, an average over these three phases is being taken, and it is difficult to draw any conclusions about the effects of substrate orientation and dopant concentration on the growth rate because of the scatter of the data. In Fig. 11, we have plotted the measured growth rates (μm/min) against median growth temperature $\left(\frac{\text{Tstart} + \text{Tfinish}}{2}\right)$ for several dopants on (111)B material. At the temperature of 640°C where most layers were grown, the spread of growth rate is from about 0.45 to 0.75 μm/min. The main trend evident is the increase in growth rate as a function of increasing temperature corresponding to the increase of solubility with increasing temperature.

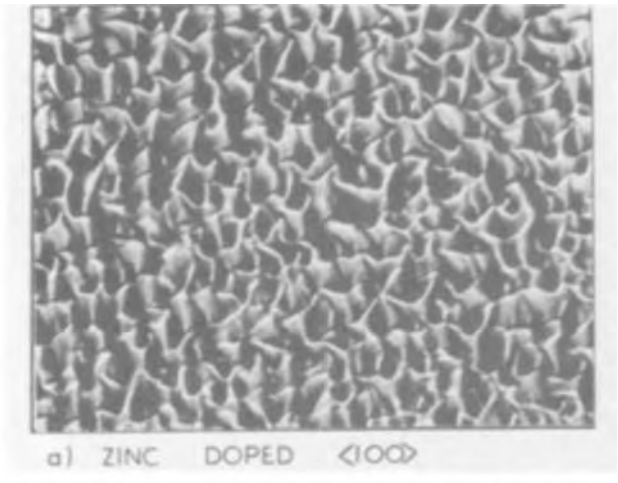

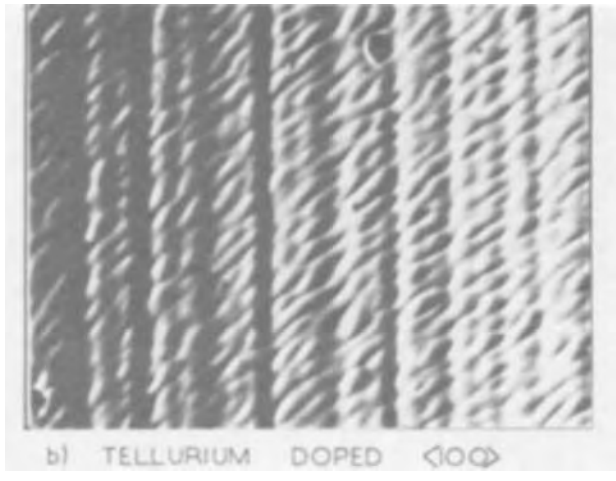

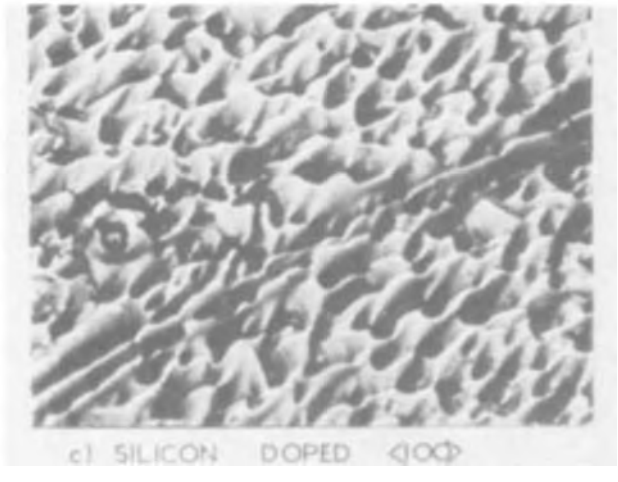

Fig. 9. Layers grown on (100) orientated substrate. (a) Zinc doped, (b) tellurium doped, (c) silicon doped (Magnification 90×).

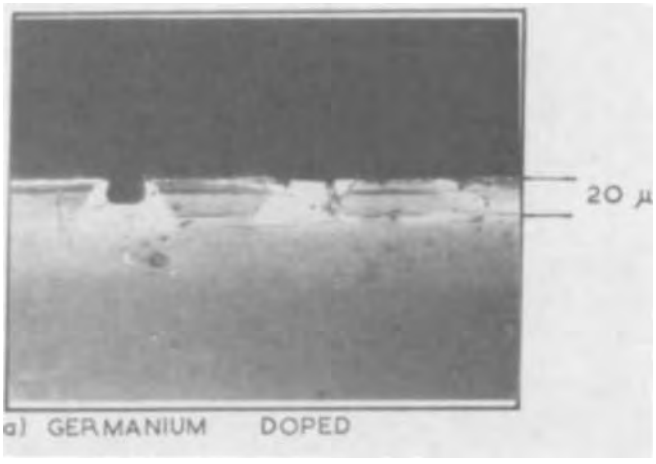

Fig. 10(a). A cleave of an epitaxial layer with insufficient etch-back of the substrate. (Magnification 400×).

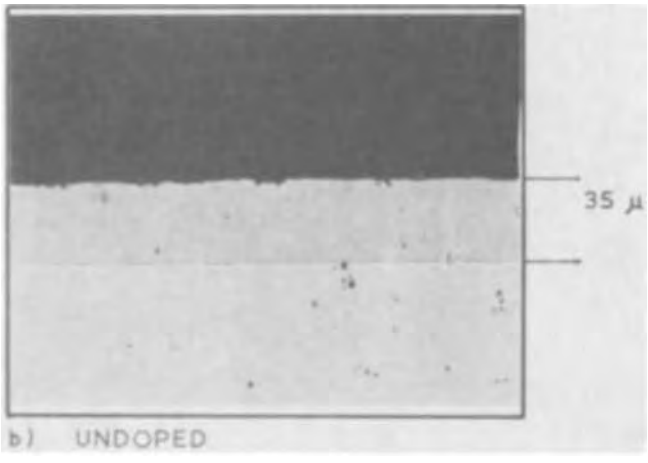

Fig. 10(b). A cleave of an epitaxial layer with the correct amount of etch-back of the substrate. (Magnification 400×).

For growth on other orientations, it was generally found that growth rates on (100) orientation were similar to those on (111)B, while (111)A growth rates

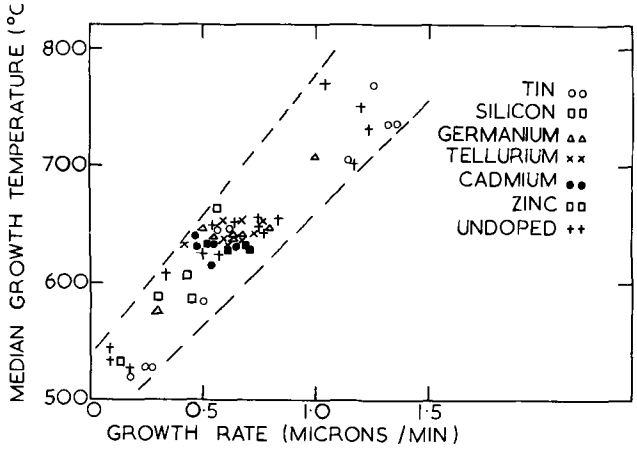

Fig. 11. The variation of the growth rate of epitaxial indium phosphide with the median growth temperature.

in the few cases we studied were significantly higher.

Fluctuations in growth rate much higher than normal were found for Zn-doped layers which were mainly grown on (100) orientation. This is possibly due to diffusion of zinc into the substrate during growth. In fact there was evidence in some runs that zinc was diffusing into the substrate before the growth cycle via the vapor phase.

Mobilities.—The Hall mobilities at room temperature of n-type samples are plotted against $(N_d - N_a)$ in Fig. 12. The theoretical curve due to Moore (13) for ionized impurity scattering is plotted on the figure assuming Ehrenreich's value of 4700 cm^2/V sec for the limiting mobility due to lattice scattering (14). It can be seen that the fit is quite good at low doping levels but deteriorates at higher doping levels. The divergence from Moore's curve is greater for the heavily doped Group IV doped samples (Si,Ge) than for the tellurium-doped samples, which is possibly an indication of compensation occurring with the Group IV elements, particularly Ge. Although the scatter of the mobilities at 77°K was greater, a similar trend was seen at high doping levels in that the Group IV doped samples have much lower mobilities than the Te-doped samples with similar values of the carrier concentration.

Conclusions

The distribution coefficients, k, for all the dopants studied are summarized in Table I and compared to the

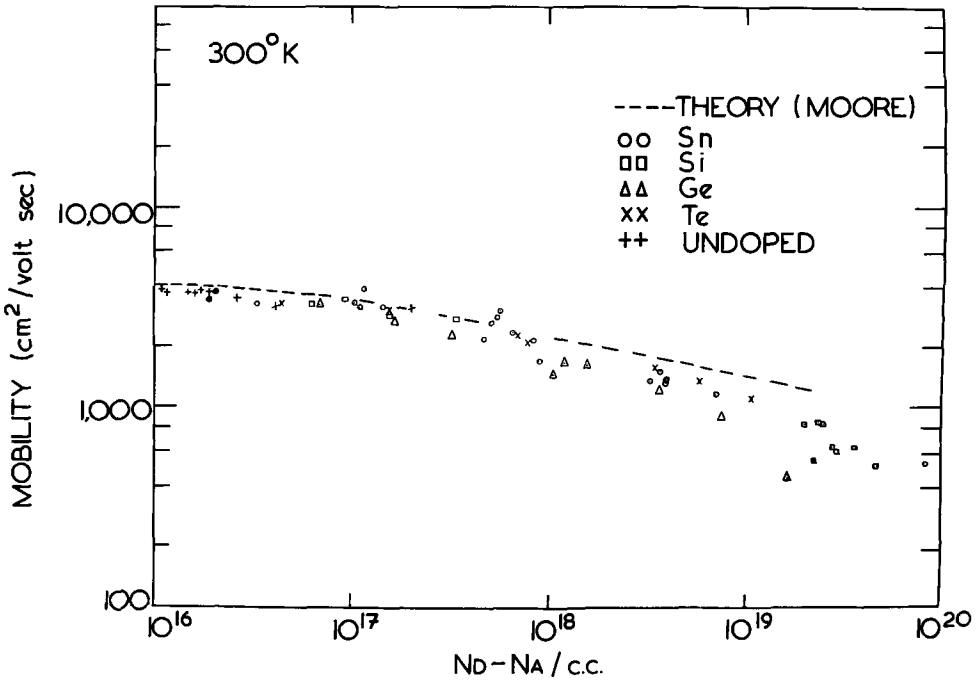

Fig. 12. The Hall mobilities of n-type samples compared to theory [Ref. (14)].

Table I. InP distribution coefficients

Dopant	Solution		Melt	
	k	k [Ref. (16)]	k [Ref. (17)]	k [Ref. (18)]
Tin	0.0019	0.0022	0.021	0.03
Germanium	0.005	0.011	0.024	—
Silicon	Approx: 4	—	—	—
Tellurium	0.27	0.4	—	0.05
Sulfur	—	—	—	0.5
Selenium	—	—	—	0.4
Zinc	1.14	—	—	0.008
Cadmium	Approx: 0.002	—	—	—
Bismuth	0.002 to 0.0002	—	—	—

results of Rosztoczy *et al.* (15). Rosztoczy used similar growth temperatures to ours but his indium solutions were saturated with polycrystalline InP feed material and not with phosphine. The tin values agree very closely but the germanium and tellurium results differ by a factor of two. These latter differences are probably due to differing degrees of electrical compensation in the material, since the assumption is made that the concentration of donor impurity, N_d, is approximately equal to $(N_d - N_a)$.

As expected, the melt growth values (16, 17) of the impurity distribution coefficients which are shown in Table I differ from the solution growth values because of the large difference in growth temperature. In the case of zinc there is an enormous difference and this can be explained as a large loss of zinc from the melt in the melt growth process since the vapor pressure of zinc is so high at the melting point of InP.

The vapor pressure of cadmium is higher than zinc and this makes its use as a p-type dopant in solution grown InP more difficult. Hence zinc was chosen as the most suitable p-type dopant for LED material since none of the Group IV elements appeared to form p-type material. The high distribution coefficient of zinc makes it necessary to dilute the zinc with indium before adding it to the indium solution.

Tin and germanium were both useful n-type dopants and could be added directly to the melt without dilution because of their low distribution coefficients. Tin was used in preference to germanium for LED material because of the higher photoluminescence efficiency of the layers.

Finally, the modified Nelson technique using phosphine and a gold-plated reactor was very suitable for LED double epitaxy for the following reasons:

(*i*) Good interfaces can be obtained provided there was sufficient etch-back. (*ii*) High quality flat layer surfaces were obtained with (111) optically oriented substrates. (*iii*) Reproducibility from run to run was much better than with the old reactor system using polycrystalline InP. (*iv*) The photoluminescence efficiency of the layers was good for both tin and zinc doping. (*v*) 1.3% power efficiency at 300°K was achieved with several double epitaxy diodes.

Acknowledgments

The authors are particularly grateful to P. J. Dean for his many constructive comments. Experimental assistance was provided by P. Porteous, Mrs. M. Webb, and W. H. E. Wilgoss. Substrates were grown by B. W. Straughan and P. J. Tufton. The microprobe measurements were made at Harwell by D. M. Poole under contract.

Manuscript submitted Dec. 4, 1972; revised manuscript received May 29, 1973.

Any discussion of this paper will appear in a Discussion Section to be published in the June 1974 JOURNAL.

REFERENCES

1. F. E. Rosztoczy, F. Ermanis, I. Hayashi, and B. Schwartz, *J. Appl. Phys.*, **41**, 264 (1970).
2. J. M. Whelan, J. D. Struthers, and J. A. Ditzenberger, in "Properties of Elemental and Compound Semiconductors," H. C. Gatos, Editor, p. 141, Interscience Publishers, Inc., New York (1960).
3. H. Rupprecht, J. M. Woodall, K. Konnerth, and D. G. Pettit, *Appl. Phys. Letters*, **9**, 221 (1966).
4. H. Nelson, *RCA Rev.*, **24**, 603 (1963).
5. J. B. Mullin, R. J. Heritage, C. H. Holliday, and B. W. Straughan, *J. Crystal Growth*, **3, 4**, 281 (1968).
6. D. Colliver, Private communication.
7. E. W. Williams, W. Elder, M. G. Astles, M. Webb, J. B. Mullin, B. Straughan, and P. J. Tufton, *This Journal*, **120**, 1741 (1973).
8. N. N. Sirota, "Semiconductors and Semimetals," Vol. 4, Chap. 2, Academic Press, New York (1968).
9. F. Thompson and R. C. Newman, To be published.
10. B. H. Ahn, R. R. Shurtz, and C. W. Trussell, *Appl. Phys.*, **42**, 4512 (1971).
11. P. J. Dean, A. M. White, E. W. Williams, and M. G. Astles, *Solid State Commun.*, **9**, 1555 (1971).
12. H. Rupprecht, Symp. on GaAs, Reading, (Institute of Physics) p. 57 (1966).
13. E. J. Moore, *Phys. Rev.*, **160**, 618 (1967).
14. H. Ehrenreich, *J. Phys. Chem. Solids*, **12**, 97 (1959).
15. F. E. Rosztoczy, G. A. Antypas, and C. J. Casau, Symp on GaAs, Aachen, (Institute of Physics) p. 86 (1970).
16. J. B. Mullin, A. Royle, B. W. Straughan, P. J. Tufton, and E. W. Williams, *J. Crystal Growth*, **13, 14**, 640 (1972).
17. A. G. Thompson and J. W. Wagner, *J. Phys. Chem. Solids*, **32**, 2613 (1971).

Indium Phosphide

III. Double Epitaxy Light Emitting Diodes with 1.5% Efficiency at 300°K

E. W. Williams, P. Porteous, M. G. Astles,[1] and P. J. Dean

Royal Radar Establishment, Malvern, Worcestershire, England

ABSTRACT

Indium phosphide double epitaxy light emitting diodes with a 1.5% quantum efficiency and 1.3% power efficiency at 300°K are reported. The emission spectrum half width is 50% of the amphoterically doped GaAs diode spectrum and this makes the diodes four times more efficient as infrared pumps for the two-photon phosphor green emitting diodes. The peak of the diode emission varies from 1.29 to 1.30 eV at 300°K.

Indium phosphide infrared light emitting diodes can be made into green lamps by coating them with two photon phosphors (1). These green lamps are potentially more attractive than gallium phosphide nitrogen doped diodes because the peak of their emission at 5500Å coincides with the maximum of the eye response

[1] Present address: Services Electronics Research Laboratory, Baldock Hertfordshire, England.

Key words: indium phosphide, light emitting diode.

Table 1. Properties of double epitaxy diodes[a]

(Tin-doped (III) B substrates — $n = 1 \times 10^{18}/cm^3$)

Diode	Growth temperature range (°C)	Thickness (microns) Tin	Thickness (microns) Zinc	Carrier concentration/cm³ Tin	Carrier concentration/cm³ Zinc	Efficiency % (300°K)
A6	667-626	36	16	6×10^{16}	3×10^{18}	1.25
A7	667-626	36	16	6×10^{16}	3×10^{18}	1.25
A18	667-626	36	16	6×10^{16}	3×10^{18}	0.24
C1	659-614	7	13	6×10^{16}	4×10^{18}	0.75
G3	659-614	7	13	6×10^{16}	4×10^{18}	0.65
T1[b]	673-642	5	11	6×10^{16}	4×10^{18}	1.3
T2[b]	673-642	5	11	6×10^{16}	4×10^{18}	1.1
T3	673-642	5	11	6×10^{16}	4×10^{18}	0.3

[a] All grown with either Method II or III.
[b] n side up.

curve giving a pure green color. The gallium phosphide lamps appear yellowy green because their maximum intensity is at 5650Å, and they have a broad spectral distribution. However, by filtering the emission can be narrowed a little and made to look greener.

The three requirements for an infrared light emitting diode that would be best suited to the two-photon phosphor made from lanthanum trifluoride (2) doped with Yb and Er are: (*i*) a narrow emission spectrum, (*ii*) output peaking at 1.271 eV, and (*iii*) a high efficiency. The first is fitted by InP and not by GaAs, whereas for the third GaAs leads the way since efficiencies of 32% have been realized at room temperature (3).

The highest efficiency so far reported for InP diodes is 0.75% at room temperature (1). These diodes were prepared with a vertical dip solution growth system. The solution was saturated with solid indium phosphide at 750°C in a reactor flushed with forming gas. A cool rate of 0.22°C/min was used to grow, first, a tin-doped layer, then a zinc-doped layer.

Blom and Woodall (1) tried no other dopants, but their choice of tin and zinc was fortuitous since these appear to be the best dopants, as has already been explained in previous papers. Using tin- and zinc-doped double epitaxy diodes prepared in the manner described below a 1.5% quantum efficiency with 1.3% power efficiency has been achieved. In this paper we briefly discuss the electrical and optical properties of these double epitaxy diodes and compare them with gallium arsenide silicon-doped diodes.

Materials Preparation

The horizontal liquid-epitaxial growth technique for single layers was described in previous papers. For double-layer growth, three different methods were used.

Method I. The n-type Sn-doped layer was grown on the Sn-doped substrate, and then in a separate run, a zinc-doped p-type layer was grown on this to form a p/n junction.

Method II. Having grown the Sn-doped layer, the solution is tipped off, and an amount of 1% zinc/indium alloy is dropped into the solution from a quartz spoon, sufficient to overcome the n-type behavior of the Sn in the solution. The solution is brought back to the saturation point with approximately 0.5°C added on to allow for a small amount of etch-back before growth. A compensated p-type (Sn + Zn)-doped layer was then grown.

Method III. The procedure is similar to Method II, except that after the growth of the Sn-doped layer, the temperature rundown is stopped (no tip-off of solution) and the zinc/indium is added as above. After 5 min the rundown is recommenced.

Cooling rates were always 1°C/min over a range 675°-610°C. Table I gives specific examples of the growth conditions under which some of the best double layers were grown. It should be noted that the material grown by Methods II and III (with compensated p-layers) gave consistently higher diode efficiencies. Figure 1 shows a photograph of a stained, cleaved cross section of two of the layers. Figure 1(a) shows a double layer grown on a (111) tin-doped substrate. The interface between the tin and zinc epitaxial layers is flat and the layer thickness was constant across the slice. The tin doping level was $6 \times 10^{16}/cm^3$ and the zinc doping was $4 \times 10^{18}/cm^3$. The junction is about 1 μm wide. The wide junction is almost certainly due to the indiffusion of zinc into the tin layer during the growth of the zinc layer. In Fig 1(b) for the double-layer grown on a (100) tin-doped substrate the interface is not perfectly flat, and this is because of insufficient etch-back prior to the growth of the second layer. The stain used to reveal the junction for 1(b) was an iron and nitric stain, and this gives a large color difference between n- and p-type layers. The more n-type the layer is, the darker is the stain. The p-type zinc layer has a doping level of $4 \times 10^{18}/cm^3$. The tin substrate which has a doping level of $1 \times 10^{18}/cm^3$ shows up darker than the tin epitaxial layer which has a doping level of $6 \times 10^{16}/cm^3$. The striations in the substrate are thought to be caused by doping fluctuations since they appeared most frequently on the heavily doped substrate where solubility problems occur.

Diode Properties

The first double epitaxy diodes were made with alloyed contacts, using tin for the n-type substrate and tin-2% zinc alloy for the p-type layer. These diodes were generally soft and leaky but nevertheless effi-

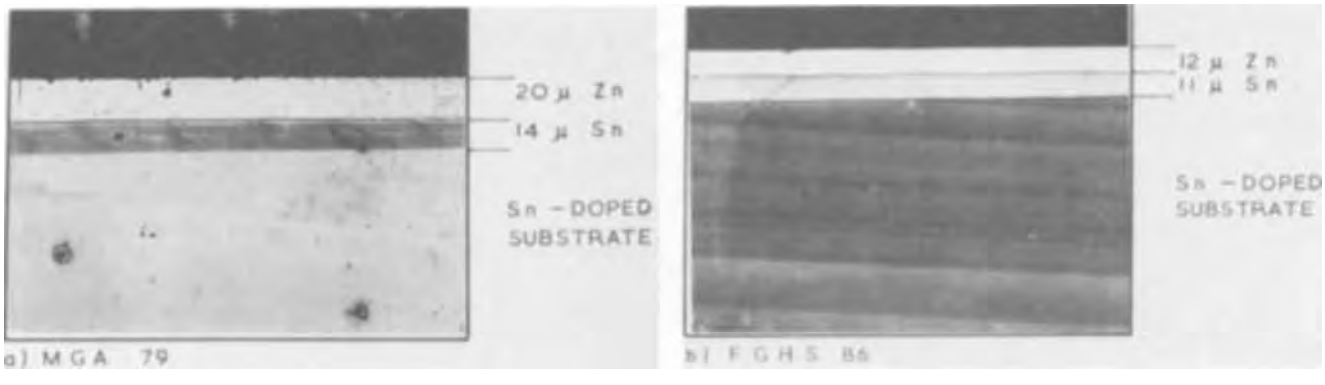

Fig. 1. Photomicrographs of a cleave of two double epitaxy growths on InP. Tin is the dopant for the first layer and zinc for the second. In (b) the etch-back after the growth of the first layer was not sufficient so the interface between the layers is not flat. (Magnification 440×).

ciencies up to 1.0% were realized on some of the diodes. However, diodes made from one slice often varied in efficiency by as much as ten times.

More recently evaporated contact diodes have been used with gold-germanium for the n-type substrate and gold-zinc for the p layer. These diodes generally gave much better I-V characteristics, and the leakage current in the reverse direction was often two or three orders of magnitude less than for the alloyed contact diodes. Diodes made from the same slice sometimes showed identical efficiencies but more usually they varied by up to a factor of three or four. Two characteristics are shown in Fig. 2 for diodes T2 and T3 shown in Table I. The upper curve (a) is for T3 with the p layer uppermost and the n-type substrate mounted on the header. The lower curve is for T2 which was a "flip chip" diode made from the same double layer as T3 with the n-type substrate uppermost and the p layer next to the header. The reverse breakdown is slightly better for (a) but the forward characteristics for (b) show a much sharper knee. The better forward characteristics are typical of the highest efficiency diodes. In this case T2 has a 1% efficiency at 300°K compared to 0.3% for T3. The large difference in efficiency is thought to be the result of the difference in absorption in the two cases. Due to the wide difference in doping of the two layers, $6 \times 10^{16}/cm^3$ for the tin layer and $4 \times 10^{18}/cm^3$ for the zinc layer, the light emission would be expected to be on the n side of the junction and with the much lower doping level on the n side the light transmission through the n layer will be much higher than through the p region, as has been shown from recent absorption studies (4). This is borne out not only by the efficiency difference but also by the uniform emission of light that is observed under an infrared microscope from the "flip-chip" diode.

Figure 3 shows a typical detailed forward characteristic for diode T2. Over seven orders of magnitude of the current the slope is constant and from the diode equation

$$I = I_0 \exp (V/nkT)$$

n is calculated to be 2.3. This value of n indicates that the majority of the recombination occurs in the space charge region of the diode.

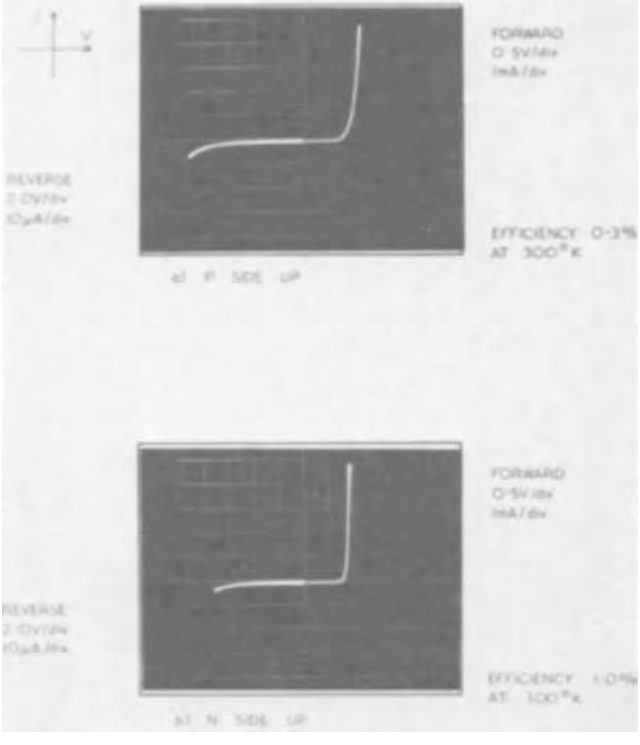

Fig. 2. I-V characteristics for the double epitaxy diodes (a) p side up, (b) "flip-chip" or n side up.

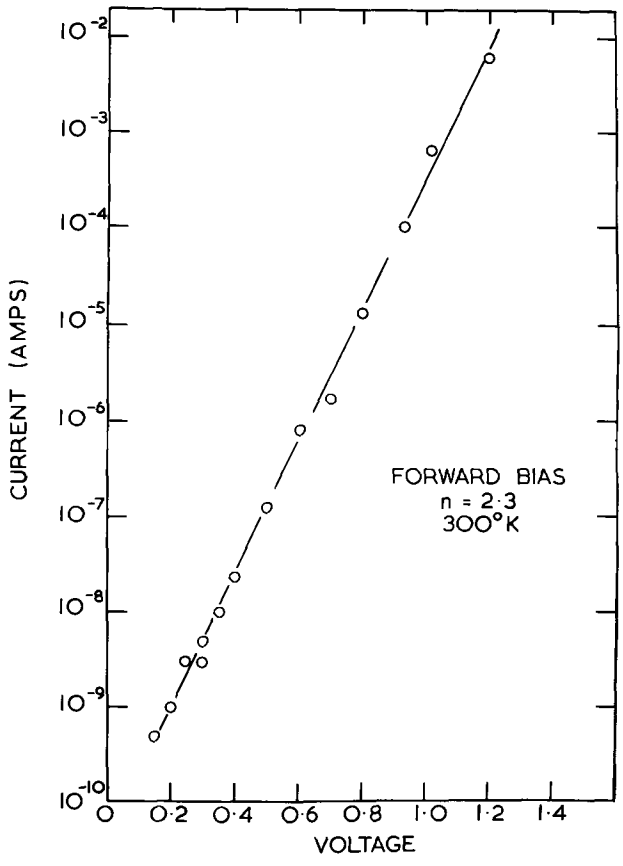

Fig. 3. A detailed forward characteristic for a "flip-chip" diode plotted as log I against V. From the equation $I = I_0 \exp V/nkT$, the slope of the graph gives $n = 2.3$.

Figure 4 illustrates the power efficiency, the quantum efficiency, and the diode integrated emission intensity as a function of current for the "flip-chip" diode T2. The power efficiency for the best diodes generally peaked at about 100 to 150 mA (current density 40-60 A/cm^2). The highest power efficiency was 1.3% at 300°K with a quantum efficiency of 1.5%. As expected the intensity was proportional to the current and only saturated at very high currents.

The room temperature spectral emission of the two types of diodes whose characteristics were shown in Fig. 2 are shown in Fig. 5. As expected, because of the smaller absorption the diode with the n side up, or the "flip-chip" diode, has a narrower emission line. The narrower spectrum is about half the width of a GaAs:Si diode spectrum, as is shown in Fig. 5.

Conclusion

The InP diodes described here and the GaAs:Si diodes were both required to match the peak of the excitation curve of the two-photon LaF_3:Yb;Er phosphor which is shown by the arrow at 1.271 eV on Fig. 5. This clearly indicates that neither diode gives a perfect match to the phosphor. The GaAs:Si spectrum can be made to peak at 1.271 eV by increasing the silicon doping (3). Unfortunately, this also increases the half width so that net gain is very small since it can easily be shown that the infrared to visible conversion efficiency is inversely proportional to the half width. The smaller half width of the spectrum of the indium phosphide diodes and the fact that the visible light output from the phosphor is proportional to the square of the infrared diode power that is absorbed, means that the green phosphor coated diodes are four times better than gallium arsenide coated diodes when the two diodes have the same infrared power efficiencies.

Consequently the InP cleaved diodes with a 1.5% efficiency described here are almost equivalent to the

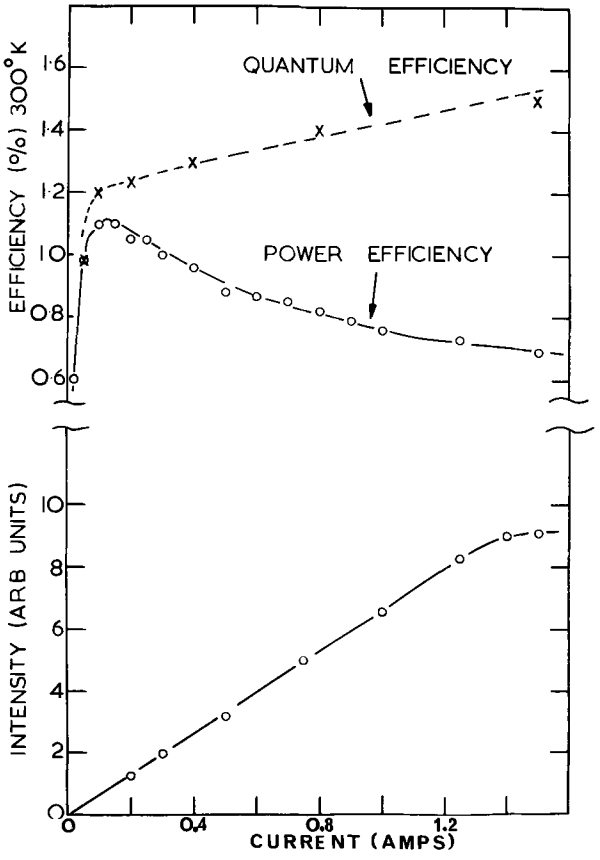

Fig. 4. The power efficiency, quantum efficiency, and diode integrated emission intensity ot 300°K as a function of current for a "flip-chip" diode.

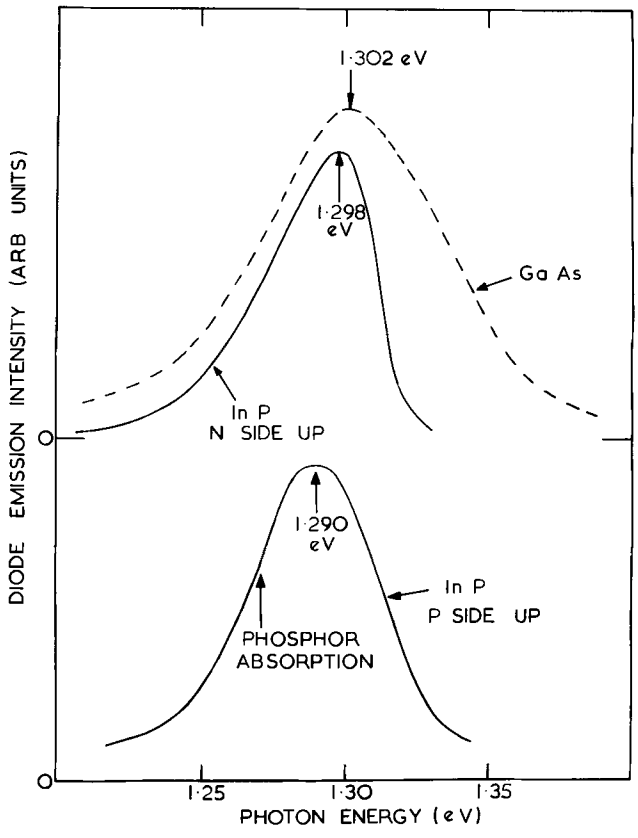

Fig. 5. The room temperature spectral emission of the two types of diode shown in Fig. 2. The "flip-chip" diode spectrum is compared to a GaAs:Si diode. The arrow at 1.271 eV indicates the peak of the excitation curve of the LaF_3:Yb;Er two-photon phosphor.

best GaAs:Si cleaved diodes with efficiencies in the range 6% to 10%, and the InP doping levels were not optimized.

Since amphoterically doped diodes of InP could not be fabricated (5) the obvious next step is to try doming or coating with high refractive index glass domes so that the efficiencies can be increased. Provided efficiencies of 10% or greater can be achieved with InP then the narrower half width of the emission will mean that InP would be preferred to GaAs for the two photon phosphor diode.

Acknowledgments

The authors are particularly grateful to Dr. R. Hall and to Mr. K. Brown of the Thorn Lighting Company for many helpful discussions and for the fabrication of some diodes from our epitaxial layers. Technical support was provided by Mr. F. G. H. Smith and Mrs. M. Webb. Dr. A. M. White and Mr. W. Elder provided many useful comments and helped with the first efficiency measurements. This series of three papers on indium phosphide are published with the permission of the Director of RRE.

Manuscript submitted Dec. 4, 1972; revised manuscript received May 29, 1973.

Any discussion of this paper will appear in a Discussion Section to be published in the June 1974 JOURNAL.

REFERENCES

1. G. M. Blom and J. M. Woodall, *Appl. Phys. Letters*, 17, 373 (1970).
2. S. V. Galginaitis, G. E. Report No. 70-C-298, September 1970; J. D. Kingsley, G. E. Fenner, and S. V. Galginaitis, *Appl. Phys. Letters*, **15**, 115, (1969).
3. I. Ladany, *J. Appl. Phys.*, **42**, 654 (1971).
4. R. Hall, K. E. Brown, J. R. Fitzpatrick, E. W. Williams, P. Porteous, and M. G. Astles, Colorado Conference on GaAs and Related Compounds, September 1972, p. 177, Proceeding published by the Institute of Physics.
5. M. G. Astles, F. G. H. Smith and E. W. Williams, *This Journal*, **120**, 1750 (1973).

Growth and Characterization of Polycrystalline Silicon

P. Rai-Choudhury* and P. L. Hower

Westinghouse Research Laboratories, Pittsburgh, Pennsylvania 15235

ABSTRACT

Polycrystalline silicon is deposited by pyrolysis of silane in an rf heated epitaxial reactor. The grains exhibit a fibrous microstructure having an <110> preferred orientation in the growth direction. Growth is inhibited in the presence of excess arsine and accelerated in the presence of diborane. The results are explained in terms of catalysis and poisoning of surface adsorption sites responsible for reaction. A simple model for current conduction in polycrystalline silicon is described based on grain size, grain doping, and effective barrier height due to the grain boundary. This model satisfactorily explains the observed temperature dependence of the resistivity of undoped films and also the large values of resistivity which are observed for dopant concentrations $\lesssim 10^{15}$ cm^{-3}.

Polycrystalline silicon is finding increasing applications in dielectrically isolated structures for high speed and radiation hardened circuitry, silicon gate MOS technology, and field plate structures (1, 2). In addition, some potential applications as solar energy collectors in the harnessing of solar energy are being proposed (3). Therefore, a better understanding of the processing technology, as well as the electrical and optical properties of polycrystalline silicon, is needed.

By controlling the parameters of the deposition process, polycrystalline silicon having a wide range of properties can be produced. The properties of the silicon can be tailored to make it behave as a dielectric, a resistive, or a semiconductive film. However, no satisfactory model exists which predicts the resistivities of these films as the grain size or the doping level is varied. Phenomenologically, the carrier mobility in polycrystalline silicon may be represented by four contributions; namely, the lattice, impurities, dislocations, and the grain boundary effects (4). Optical properties can also be affected significantly by grain size and doping.

Cowher and Sedgwick (5) have recently grown polycrystalline silicon from pyrolysis of SiH_4 as well as from the $SiBr_4$-H_2 system. They have observed a slight deterioration of surface quality of the films deposited from SiH_4 with increasing dopant concentration at 650°C. The mobility of carriers in their films is lower than the single-crystal bulk value by a factor of about 2 to 3. The acceptor concentration in their boron-doped films seems to increase very rapidly to the mid 10^{18} cm^{-3} region with only a slight increase of the B_2H_6 concentration in the gas phase. Ford *et al.* (6) have also reported that the acceptor concentration of the boron-doped layers was always high ($\geq 2 \times 10^{19}$ cm^{-3}) and suggested the possibility of grain boundaries acting as acceptor centers. Their films were grown on an oxidized silicon surface at about 300 Å/min at 600°C. Recently, oxidation characteristics of polycrystalline silicon were studied by Kamins and MacKenna (7). The oxidation rate in the reaction-rate-limiting region is found to be between those of (100) and (111) single-crystal silicon. The orientation dependence, of course, becomes unimportant when high temperature ($\sim$ 1200°C) is used or thicker oxide is grown.

In this study the effects of dopant concentration in the gas phase on the film resistivity, growth rate, and grain size are examined. Also a simple model for current conduction is described which explains the observed temperature dependence of the resistivity of undoped films as well as the consequences of doping.

* Electrochemical Society Active Member.

Key words: grains, grain boundaries, doping, currents, transport.

Experimental Procedure

Substrates used were (111) silicon, oxidized silicon, silicon nitride coated silicon, and ($1\bar{1}02$) sapphire. One of the reasons for selecting these different substrates was to find out the importance of the substrate orientation in establishing the microstructure of the deposit at low growth temperatures. Silicon was deposited by pyrolysis of SiH_4 in hydrogen carrier gas, and the layer doped to the desired level by controlled injection of AsH_3 or B_2H_6. The reactor used was a horizontal rf heated system having a silicon-coated graphite susceptor. The doping results at low temperature (680°C) from SiH_4 pyrolysis were compared with those at high temperature (1200°C) from H_2 reduction of $SiCl_4$.

The resistivity and thickness of the doped films were determined by measuring the spreading resistance along a beveled surface (8). The undoped film resistivities were determined by measuring the resistance for a known geometry. Using the same geometry the temperature dependence of the conductivity was also measured. The concentrations of the dopants were measured using a spark source mass spectrometer. The microstructure and the orientation of the films were determined using transmission electron microscopy and reflection electron diffraction.

Results

The results are presented in three sections dealing with the microstructure of the films, effects of doping on growth rate, and the electrical properties of the films. However, it must be emphasized that the results from these three sections are interrelated in a rather complex manner. An effort is made to present the relevant data in each section without unduly complicating the text through use of descriptive figure captions and cross-referring wherever it seems necessary. Discussion of experimental data in all three sections are, at best, semiquantitative. The energetics and kinetics of the growth and microstructure of films, the nature of absorption sites and its dependence on impurities (*e.g.*, catalysis and catalyst poisoning), and the charge carrier transport through various crystal defects, are all subjects difficult to treat analytically.

Microstructure of the films.—Films were normally grown at temperatures between 650°-680°C at a silane partial pressure of 5.4×10^{-3} atm. Simultaneous growth on different substrates indicates that the microstructure and the orientation of the films are essentially dictated by the growth conditions, rather than the substrate orientation. Figure 1 shows the reflection electron diffraction patterns of silicon grown at 680°C on different substrates. The <110> preferred

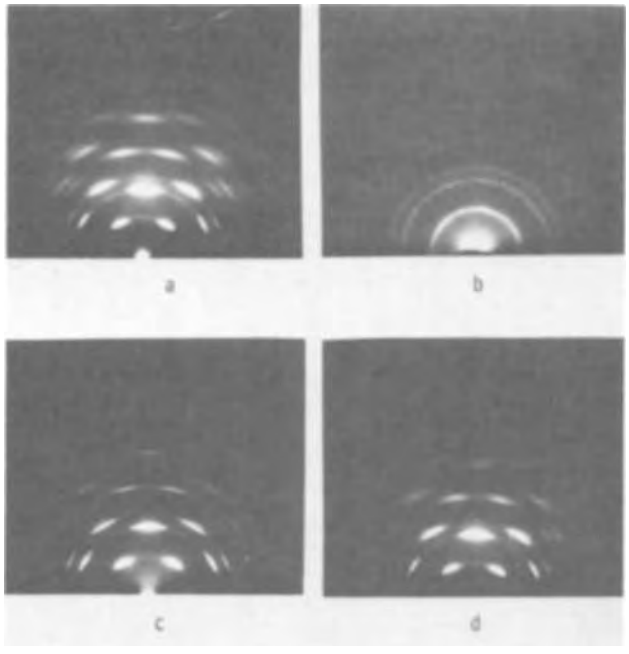

Fig. 1. Reflection electron diffraction of deposited silicon on different surfaces. (a) Si/Si, (b) Si/Al_2O_3, (c) $Si/SiO_2/Si$, (d) $Si/Si_3N_4/Si$.

orientation, seen in films grown on (111) silicon is also present in films grown on SiO_2 as well as Si_3N_4-coated silicon substrates. The films grown on $(1\bar{1}02)$ sapphire, on the other hand, show only random orientation. Since the layers on (111) silicon did not follow the substrate orientation, the initial nucleation as well as the growth of these films are essentially independent of substrate orientation (9). These results can be explained by considering the ease of nucleation on {110} and the energetics of growth in <110> direction, and are discussed in more detail later. The growth habit of the silicon films on sapphire substrates is complicated by the presence of mechanical damage, interfacial strain, and by unknown factors that results in the heteroepitaxial growth of silicon on sapphire (10).

In layers several micrometers thick, the grain size is a function of temperature, doping level in the film, and the substrate surface preparation. At and below about 850°C the grain size of films deposited on oxidized silicon is comparable to those on bare silicon substrates, and has only a slight temperature dependence. In the temperature range of 650°-750°C the grains of the undoped films, grown on both oxidized and bare silicon substrates, may be described as fibrous, having an <110> preferred orientation and grain size of the order of 0.2 μm. The grains also tend to grow in preferred directions in the plane of the wafer. At about 950°C, while the grains in the films on oxidized silicon are still comparable to those grown at lower temperatures, the films on bare silicon consist of very large grains showing evidence of epitaxy. It should be mentioned that when submicron thick layers are grown, the grains are of the order of 0.02 μm. In thicker films ($\geq$ 1 μm) the grain size seems to have stabilized at about 0.2-0.5 μm. Further work is required to establish the thickness dependence of the grain size. The larger grains in thicker films usually consist of several crystallites. The boundaries between these crystallites also probably form effective barriers to current transport. Thus, a mere increase in the observed grain size does not necessarily decrease the resistance to current flow.

At a given growth temperature, the grain size is affected only at high doping levels (for both boron and arsenic), and the films show a strong preferred orientation in the growth direction at high growth rate. Figure 2 shows the effect of arsenic doping on the microstructure. The films remain fibrous until the arsenic concentration in the solid exceeds about 10^{19} atoms/cm^3. At higher doping levels the fiber-type grains change to rods and platelets and the deposition rate decreases rapidly.

The results of boron doping are somewhat different. At high boron doping ($>10^{19}$ atoms/cm^3) the grains tend to lose the fiber-like texture as shown in Fig. 3 without losing the <110> preferred orientation. At very high B_2H_6 partial pressures ($\geqq 10^{-5}$ atm) the growth rate increases significantly and the films exhibit a strong <110> orientation in the growth direction. However, the orientation of the grains is quite random in the plane of the (111) wafer. Note again that the films do not follow the orientation of the substrate. Figure 4 shows a comparison of the reflection electron diffraction patterns of undoped films, heavily boron-doped films grown rapidly, and heavily arsenic-doped films grown slowly (see also Table I). Arsenic doping tends to weaken the preferred orientation which is present in the undoped films, whereas, boron doping enhances the preferred orientation.

Effects of doping on growth.—The presence of dopant atoms in the gas phase above a certain level influences the nucleation and growth behavior of the deposits. In this regard boron and arsenic behave in striking contrast. The effects of dopant partial pressure in the gas phase on the growth rate of the polycrystalline silicon is shown in Fig. 5. As may be expected, at low dopant partial pressures the growth rate is independent of the amount of dopants present in the system. Presence of AsH_3 above a certain partial pressure causes a significant decrease in the growth rate of silicon, whereas, the reverse is the case with B_2H_6. Considering the effects of AsH_3: substituting SiH_4 by $SiCl_4$ and using a higher temperature (1200°C) for single crystal growth also produces similar effects as shown in Fig. 6. A significant decrease in the growth rate of silicon is observed above about 0.1% AsH_3. In order to maintain high enough arsenic concentrations on the silicon surface (as adsorbed species) so that growth inhibition is effective, it is necessary to increase the AsH_3 partial pressure with increasing temperature. Recently Farrow and Filby (11) have also observed similar effects using a molecular beam growth system. These results may be explained using the concept of catalyst poisoning by Group VB elements which is a common occurrence in systems containing metal catalysts (12). Poisoning occurs be-

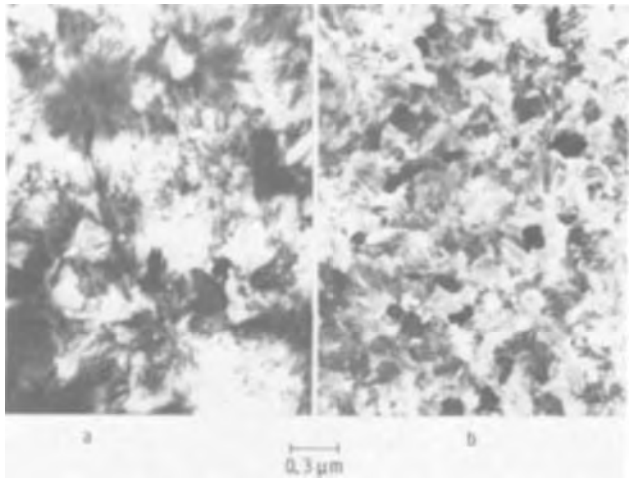

Fig. 2. Micrographs showing the effect of AsH_3 partial pressure on the microstructure of the films grown at 680°C. (a) $P_{AsH_3} = 9.6 \times 10^{-8}$ atm, $N_{As} = 2.5 \times 10^{19}$ atoms/cm^3; (b) $P_{AsH_3} = 9.6 \times 10^{-6}$ atm, $N_{As} = 1.6 \times 10^{20}$ atoms/cm^3.

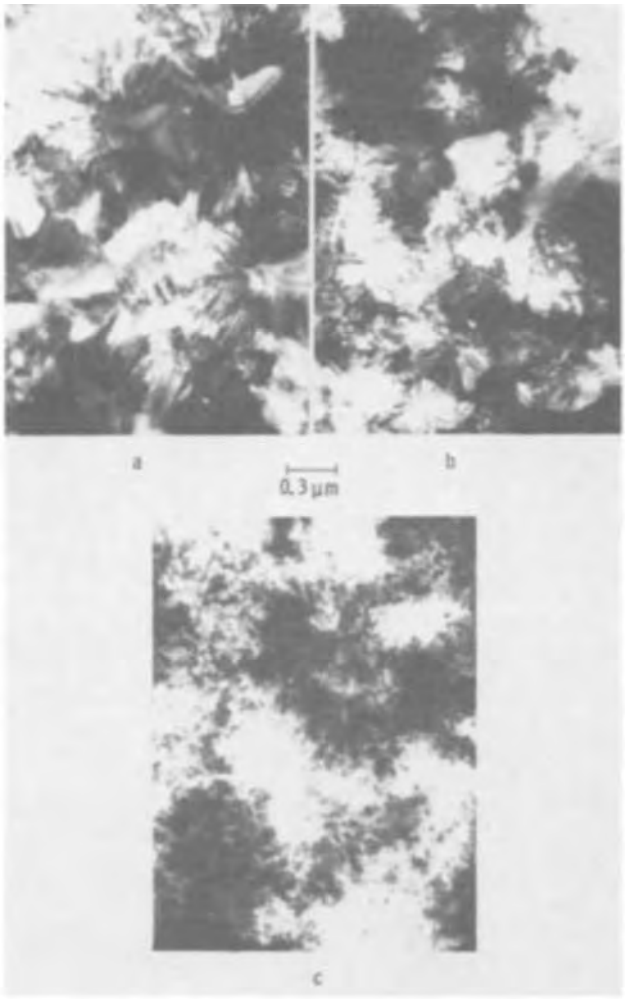

Fig. 3. Micrographs showing the effect of B_2H_6 partial pressure on the microstructure of the films grown at 680°C. (a) $P_{B_2H_6} = 0$ atm, $N_B = 5 \times 10^{13}$ atoms/cm^3; (b) $P_{B_2H_6} = 1.1 \times 10^{-6}$ atm, $N_B = 2.0 \times 10^{19}$ atoms/cm^3; (c) $P_{B_2H_6} = 1.1 \times 10^{-5}$ atm, $N_B = 2.0 \times 10^{20}$ atoms/cm^3.

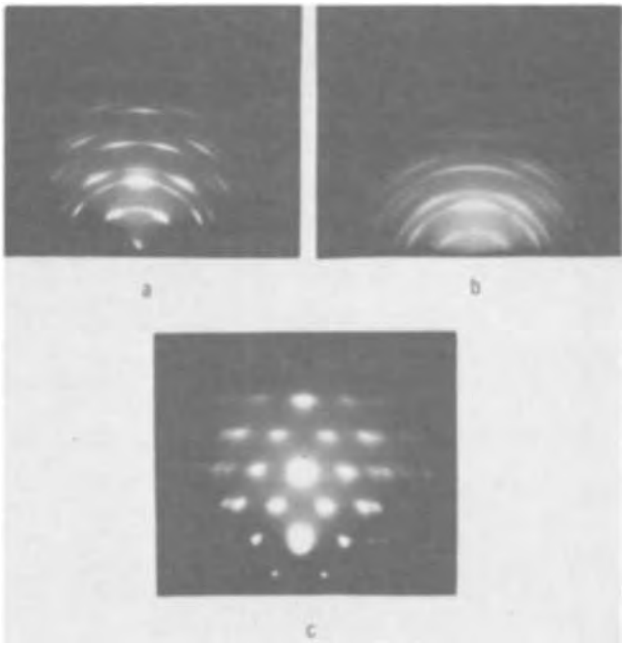

Fig. 4. Reflection electron diffraction patterns of silicon films deposited at 680°C showing preferred orientation. (a) Undoped film, growth rate = 0.13 μm/min; (b) heavily arsenic-doped film, growth rate = 0.018 μm/min; (c) heavily boron-doped film, growth rate = 0.4 μm/min.

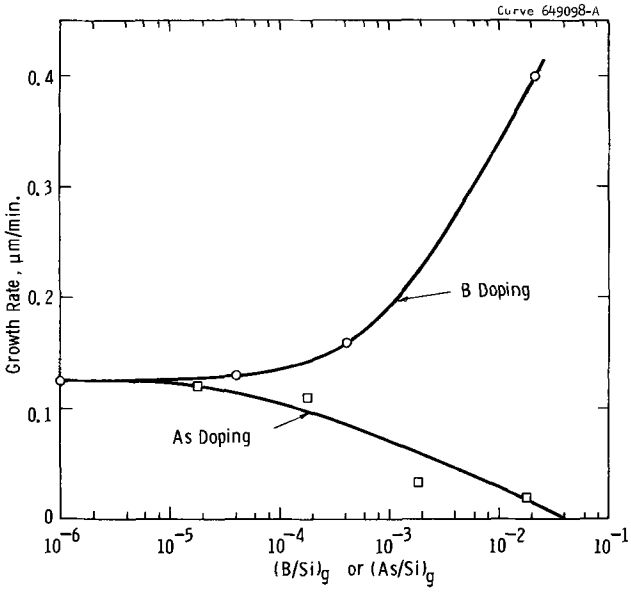

Fig. 5. Effect of dopant concentration in the gas phase on the growth rate of silicon at 680°C; $P_{SiH_4} = 5.4 \times 10^{-3}$ atm.

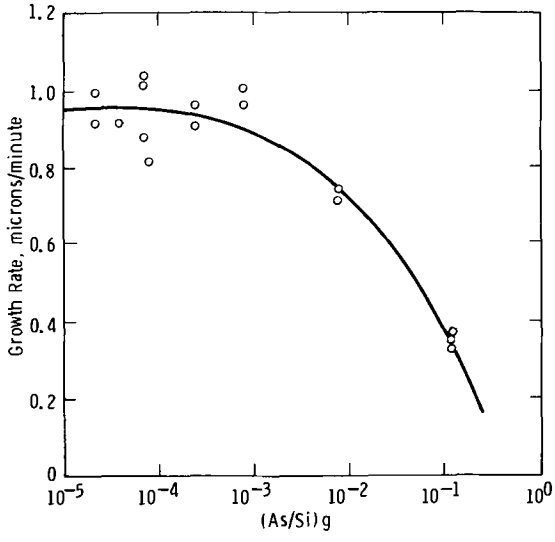

Fig. 6. Effect of arsenic to silicon ratio in the gas phase on the deposition rate of silicon from $SiCl_4$-H_2 system at 1200°C.

cause of a strong adsorptive bond between catalyst and poison. On the basis of their results, Farrow and Filby postulated that arsenic atoms become strongly bound to certain surface sites which are active in inducing silane pyrolysis. In spite of the fact that the SiH_4 pyrolysis is energetically more favorable (*i.e.*, having a large negative free energy change) compared to the H_2 reduction of $SiCl_4$, the arsenic poisoning is equally effective in both cases. This is due to the fact that at low temperature the SiH_4 pyrolysis is essentially a surface reaction and the growth rate is limited by the number of available adsorption sites.

The presence of B_2H_6, on the other hand, results in increased adsorption of SiH_4, and probably decreases the size and increases the number of stable nuclei. This would, of course, increase the growth rate with increasing B_2H_6 partial pressure (see Fig. 5) as long as pyrolysis of SiH_4 is not a limiting factor. Similar increase in the growth rate of the borosilicate films from SiH_4-O_2-B_2H_6 system were observed with increase in the B_2H_6 partial pressure (13). The increase in the growth rate is more than that which could be accounted for by a simple linear combination of SiO_2 and B_2O_3 deposition rates. Another example is found in the growth of II-VI compounds (14); addition of Group III elements enhances the growth whereas Group V elements poison the growth.

Electrical properties of the films.—Although boron can be trapped in the growing films in excess of its solid solubility limit, it is considerably more difficult to incorporate excess arsenic (15). Moreover, at doping levels above 10^{19} atoms/cm^3 the resistivity of the films and the number of dopant atoms in the silicon matrix do not bear a simple relationship, especially in polycrystalline silicon. Heavy doping tends to decrease the grain size (see Fig. 2 and 3), which in turn, effects the resistivity. Thus in examining the dependence of the film resistivity on the impurity concentration it is difficult to hold the grain size constant at high doping levels.

The resistivity of undoped films grown on oxidized silicon substrates was comparable to that on bare silicon substrates at growth temperatures up to about 850°C. At 950°C the films on oxidized substrates were still of very high resistivity. Table I shows some of the doping data for both n- and p-type films deposited on silicon substrates at 680°C along with the corresponding deposition rates. Control of the film resistivity was difficult above about 0.2 ohm-cm for both boron- and arsenic-doped layers. These results are explained using the barrier conduction model, a detailed discussion of which appears in the next section.

Discussion

Development of a preferred orientation.—The development of <110> preferred orientation in the direction of the film growth on differently prepared silicon substrates (see Fig. 1) clearly indicates the absence of any influence of the substrate orientation (under the present experimental conditions). Thus nucleation of {110} islands is kinetically favored. This is not unexpected when the ease of nucleation on various planes is considered. Atoms in {110} surfaces are arranged in planar zigzag chains, each atom being bonded to two nearest neighbors in the chain with the remaining two bonds extending diagonally out on each side. If the first depositing atom makes only one bond to the existing surface then three dangling bonds are created. Once the first atom is in place, other atoms can deposit adjacent to it without change in the number of unsatisfied bonds, and consequently, without any increase in the energy barrier. In the case of oxidized silicon wafers heating in hydrogen tends to reduce the surface oxides and the depositing silicon atoms will attach themselves to surface silicon atoms with minimum steric hindrance (16). {110} planes, once nucleated, might be difficult to extinguish by the slow growing {111} faces, since four of the six {111} are at right angles to a growing (110) plane while the other two {111} are at 35·36°. Since the surface energy of the (110) plane (1510 ergs/cm^2) is relatively high (17, 18) the crystallites tend to grow in the [110] direction rather than in the (110) plane.

The other possible preferred orientation in the film growth direction is the development of <100>. This is less likely since a depositing atom needs to bond to two adjacent surface atoms. Moreover, the four bonding {111} faces are at 54·74° from the (100) and will extinguish the (100) face easily (18).

Table I. Doping results of polycrystalline silicon

Doping compound	Dopant partial pressure, atm	Film growth rate, μm/min	Film type	Film resistivity, ohm-cm	Dopant concentration in films by mass spectroscopy, atoms/cm^3
None	0	0.13	p	6.5×10^6	5×10^{18} boron
B_2H_6	9×10^{-9}	0.13	p	4.5	—
B_2H_6	1×10^{-7}	0.13	p	0.12	1.8×10^{18} boron
B_2H_6	1×10^{-6}	0.16	p	0.018	2.0×10^{19} boron
B_2H_6	1×10^{-5}	0.18	p	0.0055	2.0×10^{20} boron
B_2H_6	6×10^{-5}	0.40	p	0.005	9.5×10^{20} boron
AsH_3	1×10^{-8}	0.13	n	$\sim 10^7$	—
AsH_3	1×10^{-7}	0.12	n	0.22	2.5×10^{19} arsenic
AsH_3	1×10^{-5}	0.033	n	0.023	1.6×10^{20} arsenic
AsH_3	1×10^{-4}	0.018	n	0.045	8.5×10^{19} arsenic

$P_{SiH_4} = 5.4 \times 10^{-3}$ atm. $T = 680$°C, $V = 30$ cm/sec.

Barrier model for conduction in polycrystalline silicon.—The major electrical characteristics of polycrystalline silicon films can be described in terms of three film parameters; namely, grain size l_g, grain doping N_D or N_A, and an effective barrier height ϕ_B due to the interface state density at the boundary. A one-dimensional band diagram similar to that considered by Kamins (19) is shown in Fig. 7. It is assumed that $\phi_B > \phi_n$, and therefore there will be a depletion region of positive space charge over the distance l_2. It is also assumed that current transport across the depletion regions is similar to that of two Schottky barrier diodes connected as shown in the figure. These diodes appear in series with a resistor, which is due to the neutral portion of the grain.

When an external voltage is applied to the sample, a current density J will flow and the voltage will divide among the grains. Within each grain there will be a component V_1 across the neutral region and a component V_2 across the depletion region. Since $V_2 << kT/q$, we can write the film resistivity ρ as

$$\rho = \frac{1}{l_g}\frac{V_1 + 2V_2}{J} = \left(\rho_1 l_1 + \frac{2kT/q}{J_o}\right)\Big/ l_g \quad [1]$$

$$= \rho_{bulk} + \rho_{barrier}$$

where J_o is a factor which is exponentially dependdent on ϕ_B and also the built-in field, as we shall describe further.

From Eq. [1] we can see that bulk resistivity values can be approached either by growing very large grains or by increasing J_o. The latter can be accomplished by reducing ϕ_B or by increasing the built-in field to the point where the barrier tunneling probability is significant. For the latter case we can adapt Yu's analysis (20) for the contact resistance R_c of metal-Si junctions. The barrier resistivity is then

$$\rho_{barrier} = 2R_c/l_g \quad [2]$$

where R_c has dimensions of ohm-square centimeters and is a function of ϕ_B and N_D that behaves as $\exp(\phi_B/\sqrt{N_D})$ for large N_D.

If we consider the case of decreasing N_D, with ϕ_B and l_g fixed, there will be a value of N_D for which tunneling is no longer significant (20). This defines the lower limit of the heavily doped range. For smaller N_D, barrier transmission is due entirely to thermionic emission and the barrier resistivity is given by

$$\rho_{barrier} = \frac{2k/q}{l_g A^* f_p T}\exp(q\phi_B/kT) \quad [3]$$

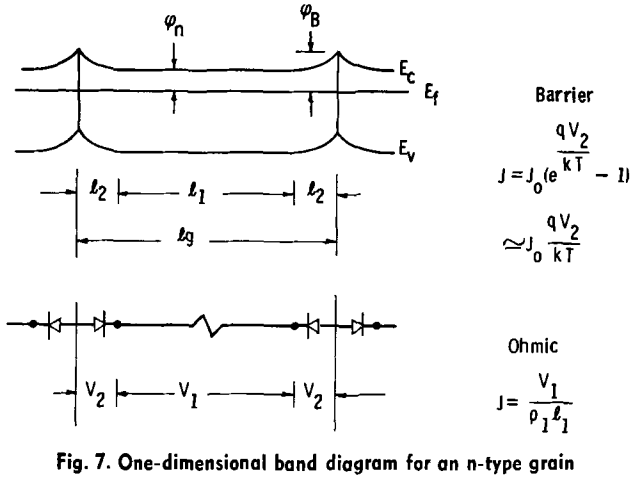

Fig. 7. One-dimensional band diagram for an n-type grain

where A^* is the effective value of the Richardson constant and f_p is the probability that an electron will be emitted over the potential energy maximum associated with the barrier. As the built-in field is reduced, f_p will decrease due to the increasing probability that an electron will be backscattered due to an electron, optical-phonon collision (21).

For the middle range of doping, Eq. [3] applies with $f_p \cong 1$. In this range, $\rho_{barrier}$ is independent of N_D and changes only with ϕ_B and l_g. Equation [3] indicates that $\rho_{barrier}$ (as a function of T) should show an "activation energy" $= q\phi_B$, if we ignore the slight temperature dependence due to the terms preceding the exponential term. This fact is used later in the experimental check of the model.

As N_D continues to decrease, the depletion layers will widen and eventually they will fully deplete the grain. For further decreases in N_D, the built-in field decreases rapidly and can lead to large increases in barrier resistivity. The third or "lightly doped" range is defined by

$$N_D < 8 \frac{\epsilon}{q} \frac{\phi_B - \phi_n}{l_g^2} \qquad [4]$$

In this range f_p can be approximated by (21)

$$f_p = \exp\left[1/(2\lambda\sqrt{2\pi N_D l_g})\right] \qquad [5]$$

where $\lambda (\cong 60\text{Å})$ is the mean-free-path for electron, optical-phonon collisions. In this range $\rho_{barrier}$ is again dependent on N_D, and because of the exponential dependence introduced by [5], resistivity will increase rapidly with decreasing N_D.

Applicability of Hall data.—To check the model against experiment we wish to compare measured resistivities against those predicted by the model. It might appear that Hall sample data would also provide a check, and while Hall data has been shown to be in qualitative agreement with the barrier model (19), the data require some interpretation. In particular the Hall coefficient is largely determined by the neutral portion of the grain (22) for the case where the resistivity is dominated by the barrier. Combining resistivity and Hall coefficient measurements in the usual manner then gives a Hall mobility and a Hall concentration that is not directly interpretable in terms of the model parameters. For this reason, and also because Hall measurements are difficult on high resistivity samples, we have elected to check the model using ρ *vs.* concentration and ρ *vs.* temperature data.

Comparison with experiment.—The solid curves of Fig. 8 are theoretical plots of resistivity *vs.* concentration with l_g fixed at 0.2 μm and ϕ_B as the parameter. As noted earlier, resistivity for the experimental points was determined from spreading resistance profiles and also by fabricating resistors using an aluminum surface electrode pattern. Concentrations were obtained from mass spectrometer measurements of boron and arsenic.

The dotted curve is a plot of measured resistivity *vs.* concentration of n- and p-type polycrystalline Si/SO_2 films as reported by Fripp and Slack (23). Their data is in close agreement with that of Kamins (19), which was obtained over a smaller doping range. These workers obtained concentration values from simultaneously grown epitaxial films on single-crystal substrates. The discrepancy between our data and that of Ref. (19) and (23) may be due to the different methods of determining the concentration. In either case the value obtained can only be regarded as an estimate to the electrically active grain doping.

If we ignore this discrepancy for the moment, the data suggests that ϕ_B is not constant, but is dependent on impurity concentration and decreases to small values at large doping values. This is in agreement with

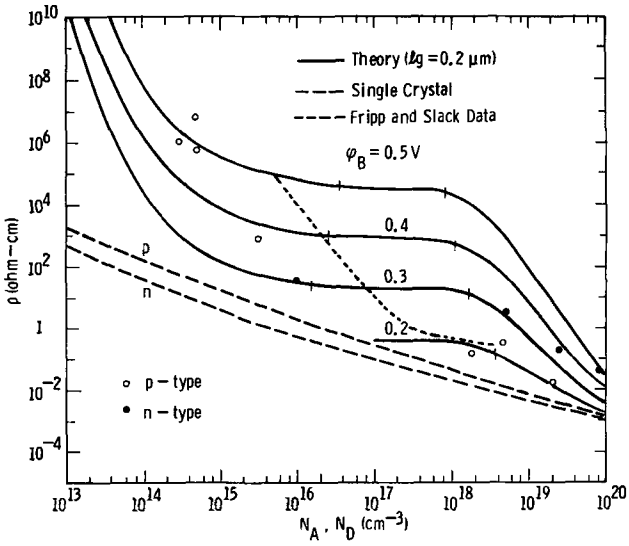

Fig. 8. Resistivity vs. concentration with ϕ_B as the parameter. The vertical bars indicate the three doping ranges of the model.

Kamin's observation that ϕ_B may decrease due to a "saturation" of the interface states as doping increases. The relatively large resistivity values of the heavily doped ($N_D > 10^{19}$ cm^{-3}) n-type films are attributed to a significant reduction in l_g from the typical 0.2 μm value.

We have measured ρ *vs.* T for a p-type film ($N_A = 2 \times 10^{18}$ cm^{-3}) and in comparing the data with the model, we find $\phi_B \cong 0.1$V, which is in agreement with Fig. 8. Data was also taken for a lightly doped sample ($N_A = 5 \times 10^{14}$ cm^{-3}) and is shown in Fig. 9. From Fig. 8, the model predicts that $\phi_B = 0.5$V which is good agreement with the observed value of 0.55V.

At low temperatures ϕ_B is observed to have a second, smaller value, $\phi_B = 0.126$V. Approximately the same value has been reported for amorphous films which were annealed at temperatures in the range 550°-750°C, and are therefore likely to have many properties in common with polycrystalline films (24). We have no explanation for this smaller value of ϕ_B

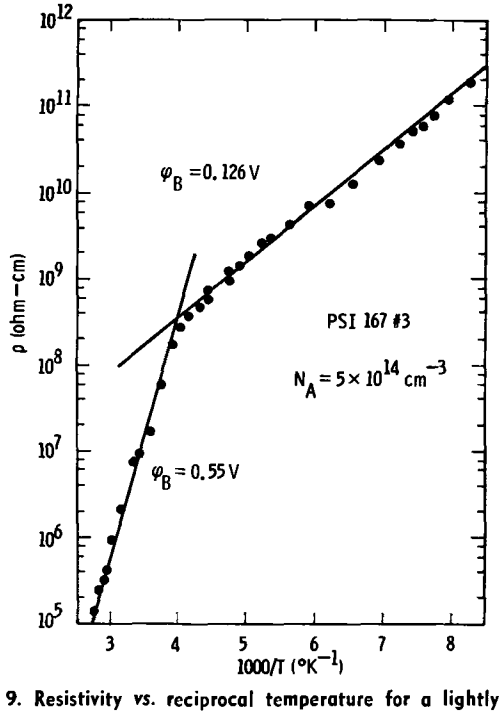

Fig. 9. Resistivity vs. reciprocal temperature for a lightly doped film.

except to ascribe it to the temperature behavior of the interface states.

The decreasing of ϕ_B with concentration does suggest that the density of interface states is less than that of a free silicon surface, for which ϕ_B is very nearly independent of concentration. In addition the similarity of ρ *vs.* concentration data for p- and n-type polycrystalline films suggests that interface donor and acceptor states have energy density profiles which are reflected with respect to the center of the band, which is also in contrast to a free silicon surface; however, this is somewhat speculative and additional work is required to elucidate the detailed behavior of the interface states.

Summary

At temperatures of 850°C or below, polycrystalline silicon films grown on differently prepared silicon substrates have comparable grain size. The microstructure is fibrous with grains growing in preferred <110> as well as some preferred directions in the plane of the substrate. Initial nucleation and growth of thin films are essentially independent of substrate orientation. The preferred orientation is enhanced in heavily boron-doped films accompanied by an increase in the deposition rate. In heavily arsenic-doped layers the preferred orientation tends to disappear along with a sharp decrease in the deposition rate.

A simple model has been described which can be used to estimate film resistivity as a function of grain size, grain doping, barrier height, and temperature. Comparison of the model with experimental ρ *vs.* concentration data indicates that the barrier height increases as doping decreases, with ϕ_B reaching a level near mid-gap for lightly doped films. Resistivity *vs.* temperature measurements on lightly and heavily doped films confirm this behavior of ϕ_B and provide a self-consistent check of the model.

Acknowledgment

The authors would like to thank W. Cifone, R. F. Yut, and J. H. Rieger for assistance with the experimental work.

Manuscript submitted Oct 5, 1972; revised manuscript received June 5, 1973. This was Paper 240 presented at the Miami Beach, Florida, Meeting of the Society, Oct. 8-13, 1972.

Any discussion of this paper will appear in a Discussion Section to be published in the June 1974 JOURNAL.

REFERENCES

1. F. Fagin and T. Klein, *Solid-State Electron.*, **13,** 1125 (1970).
2. G. Spadea and P. L. Hower, Paper No. 20.5, 1971 IEDM, Washington, D. C.
3. A. B. Meinel and M. P. Meinel, *Physics Today,* **25,** (2), 44 (1972).
4. R. L. Ramey and W. D. McLennan, *J. Appl. Phys.,* **38,** 3491 (1967).
5. M. E. Cowher and T. O. Sedgwick, Paper 58, presented at Washington, D. C., Meeting of the Society, May 9-13, 1971.
6. K. D. Ford, R. Thomas, and S. J. Laverty, Paper 172 presented at the Cleveland, Ohio, Meeting of the Society, Oct. 3-7, 1971.
7. T. I. Kamins and E. L. MacKenna, *Trans. AIME,* **2,** 2292 (1971).
8. R. G. Mazur and D. H. Dickey, *This Journal,* **113,** 225 (1966).
9. E. Bauer, "Single Crystal Films," p. 43, Pergamon Press, Inc., New York (1964).
10. A. J. Hugh, Presented at the AACG-II, Princeton, 1972.
11. R. F. C. Farrow and J. D. Filby, *This Journal,* **118,** 149 (1971).
12. E. M. Maxted, "Advances in Catalysis," Vol. III, p. 129, Academic Press, Inc., New York (1951).
13. D. M. Brown and P. R. Kennicott, *This Journal,* **118,** 293 (1971).
14. A. G. Fischer, Unpublished work.
15. P. Rai-Choudhury and E. I. Salkovitz, *J. Crystal Growth,* **7,** 361 (1970).
16. B. A. Joyce, R. J. Bennett, R. W. Bicknell, and P. J. Etter, *Trans. AIME,* **233,** 556 (1965).
17. R. J. Jaccodine, *This Journal,* **110,** 524 (1963).
18. P. Rai-Choudhury and D. K. Schroder, *ibid.,* **120,** 664 (1973).
19. T. I. Kamins, *J. Appl. Phys.,* **42,** 4357 (1971).
20. A. Y. C. Yu, *Solid-State Electron.,* **13,** 239 (1970).
21. S. M. Sze, "Physics of Semiconductor Devices," p. 386, Wiley-Interscience, New York (1969).
22. J. Volger, *Phys. Rev.,* **79,** 1023 (1950).
23. A. L. Fripp and L. H. Slack, *This Journal,* **120,** 145, (1973).
24. M. H. Brodsky, R. S. Title, K. Weiser, and G. D. Petit, *Phys. Rev.,* **B, 1,** 2632 (1970).

Electrical Characteristics and Thermal Stability of Platinum Silicide-to-Silicon Ohmic Contacts Metalized with Tungsten

A. K. Sinha*

Bell Laboratories, Murray Hill, New Jersey 07974

ABSTRACT

The present work was undertaken in order to determine the effect of various thermal treatments up to 800°C and of CVD Si_3N_4 encapsulation on the electrical characteristics of PtSi-to-Si contacts containing an overlay of W-metalization. Ohmic PtSi contacts were made to four sets of p-type Si samples doped in the 10^{18}-10^{20} cm^{-3} range and three sets of n-type Si samples doped in the 10^{19}-10^{20} cm^{-3} range. The measured contact resistivities, $\rho_{c,s}$, contain large spreading resistance contributions, but they establish useful upper limits to effective impedance at contact areas having dimensions of the order of 20 × 20 μm. The measured $\rho_{c,s}$ values range from 1.1×10^{-6} to 7.1×10^{-5} ohm-cm^2 for p-type Si samples and from 9.4×10^{-7} to 8.4×10^{-6} ohm-cm^2 for n-type Si samples. No significant degradation of contacts was observed at 600° or 700°C, or upon 680°C Si_3N_4 deposition. At 800°C (½-hr anneal) an excessive amount of WSi_2 is formed in the contact areas. Its effects may range from no change in contact resistance to an electrical "open." A large disagreement exists between the measured contact resistivities and those predicted by calculations based on one-dimensional electron tunneling through a potential barrier at the metal-semiconductor interface. A major part of the discrepancy results from extending the theory to very small (<150Å) depletion widths for alloyed interfaces that are physically not sharp. A three-dimensional micromodel that includes effects of nonuniform current flow and mobility differences between n- and p-type Si may be more appropriate.

The importance of ohmic contacts to diffused (doped) silicon layers is generally recognized in integrated circuit technology. In recent years, much interest has centered on PtSi-to-Si contacts, and there have been several reports of experimental (1-5) and theoretical (4, 6, 7) investigations. However, the exact situation does not appear to be clear yet. Most of the measured contact resistance values (1-3, 5) differ significantly from those predicted by the usual theoretical model, namely, tunneling of electrons through a potential barrier at the metal-semiconductor interface.

Also, since the original proposal of PtSi as the ohmic contact material in beam-lead technology (8), which utilizes Ti/Pt (or Pd)/Au metalization, there have been several investigations concerning the use of single-layer refractory metalizations such as W (9-11) for Si integrated circuits. Tungsten is potentially better able to withstand high-temperature processing steps such as chemical vapor deposition (CVD) of dielectrics (12) in the large scale integration (LSI) and multilevel metalization technologies.

The present study was made in order to provide new contact resistance data on ohmic PtSi/Si contacts metalized with W, and, in particular, to evaluate the electrical and metallurgical stability of these contacts as a function of various thermal treatments, including CVD Si_3N_4 encapsulation, in the range 600°-800°C. Some earlier results on high-temperature metallurgical stability of PtSi thin films were described in Ref. (13).

Experimental Procedure

Contact fabrication.—Bulk-doped n- and p-type Si samples, (100)-oriented and 0.25 mm thick, were used. The dopant was either As or B, and the dopant concentrations, $N_{D,A}$, were deduced from the supplied resistivity data, ρ_{Si}, by using published ρ_{Si} *vs.* $N_{D,A}$ plots (14). The Si wafers were cleaned and then steam-oxidized at 1050°C to give 3000Å thick SiO_2. Contact windows, having dimensions of 20 × 20 μm at 2.5 mm spacing, were etched through the oxide on one-half of the slice by standard photolithographic techniques. The oxide was completely removed from the other half. A layer of PtSi, 900Å thick, was formed on the exposed Si areas by backsputter cleaning the Si, sputtering 450Å of Pt, and then sintering *in-situ* at 700°C for 10 min (13). The unreacted Pt over SiO_2 was removed by etching in hot aqua regia. It was possible to ascertain the effectiveness of PtSi sintering by microscopic observation, supplemented by x-ray diffraction, on the control-half of the slice. The PtSi/Si samples were then metalized with an approximately 3000Å thick W film by low-voltage rf-diode sputtering (15) or by electron-beam evaporation (11) at about 300°C substrate temperature. Isolation pads were etched around the contact windows, and W was left unetched over the PtSi in the control-half of the slice. Various contact samples were annealed in H_2 or vacuum at 600°C (1 hr), 700°C (1 hr), or 800°C (½ hr). To evaluate the effect of Si_3N_4 encapsulation step on the W/PtSi/Si contact, approximately 1200Å of CVD Si_3N_4 (16) was deposited at 680°C and then etched away in a constant boiling (160°C) aqueous solution of H_3PO_4. Finally, contacts were made to the back side of the Si slices by first removing any residual oxide with dilute HF and then evaporating 5000Å of Al over the entire area.

Four sets of p-type Si samples and three sets of n-type Si samples were processed in this manner. Each set, with a given doping level, consisted of five to eight wafers.

Measurements.—Contact resistance measurements were made with an Electroglas Auto Probe Model 190 tester. Figure 1 illustrates the measurement procedure. The sample current was maintained a 1 mA. The probe was positioned on the contact area so that the voltage drop V_{xz} from X to the aluminized back Z was minimum. This was done in order to minimize contributions to the measured V_{xz} from the sheet resistance of the W film. Next, the probe was moved to a point Y in the middle of the control-half, which has an area of ~3.5 cm^2, approximately 10^6 times that of the contact area. The voltage drop V_{yz} contains mainly contributions from the "probe resistances" as Y and Z as well as any wire resistances in the measurement circuit. The area is too

* Electrochemical Society Active Member.

Key words: thin films, metal-semiconductor contact, heat-treatment, device fabrication.

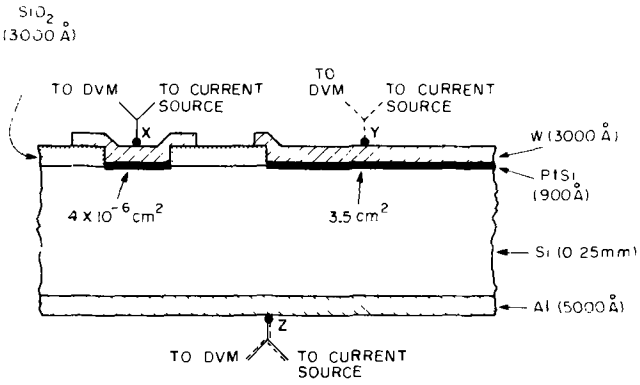

Fig. 1. Schematic of ohmic contact resistance measurement procedure.

large for any appreciable contribution from spreading or ohmic contact resistance. V_{yz} was always found to be less than 1 mV (for 1 mA current) and stayed constant within 5% for several scans of the probe from X to Y to X′ to Y′ to X″ to Y″, etc. indicating a reproducible "probe resistance."

It is important here to emphasize the distinction between the apparent contact resistance, $R_{c,s}$ (ohms), which was directly measured, and the apparent contact resistivity, $\rho_{c,s}$ (ohm-cm^2), which was derived from it. These quantities are defined as follows

$$R_{c,s} = I^{-1}(V_{xz} - V_{yz}) \quad [1]$$

$$\rho_{c,s} = AR_{c,s} \quad [2]$$

where I is the sample current and A is the area of the contact, which in the present case was equal to 4×10^{-6} cm^2. The subscript c,s means that the quantity includes both contact and spreading resistance contributions. Thus, the true contact resistance and the true contact resistivity will be represented by R_c and ρ_c, respectively. The ohmic nature of contact was verified by determining the I-V profile with a Tektronix Type 576 curve tracer, as shown in Fig. 2. Here, line A represents the resistance XZ and line B represents the resistance YZ so that the difference between their slopes is a measure of $R_{c,s}$. At least 20 contacts were measured on each wafer and then a logarithmic distribution plot was made (Fig. 3). As might be expected, samples with smaller $R_{c,s}$, which were obtained by subtracting two numbers (V_{yz} and V_{xz}) of comparable magnitude, tended to show a greater variation than those with larger $R_{c,s}$.

For diagnostic studies, the as-prepared or heat-treated samples were examined using optical microscopy, scanning electron microscopy, and x-ray diffraction on the control-half of the sample.

Experimental Results

Table I summarizes the median values of the apparent contact resistance, $R_{c,s}$, as a function of Si doping level and thermal treatment. Also listed for comparison (see Discussion section) are the expected values for the spreading resistance contributions, R_s, which were estimated using the formula (17)

$$R_s \approx \rho_{Si}/4r \quad [3]$$

where ρ_{Si} is the resistivity of the Si sample and r is the effective contact radius, assumed in the present case to be equal to 10 μm. Values of R_s obtained using the above formula are known to differ from the true spreading resistances by factors which may range from 0.8 to 3 (18). These, however, were not determined in the present case.

It may be seen in Table I and Fig. 4 that annealing at 600° or 700°C or Si_3N_4 deposition at 680°C did not cause any significant change in the $R_{c,s}$ values. This is reflected in cosmetically clean appearance of contact areas after, *e.g.*, 600°C anneal (Fig. 5a) or after a typical Si_3N_4 deposition and subsequent Si_3N_4 etch (Fig. 5b). Some roughness in the surface of W in Fig. 5b was caused by a slight attack on W by the H_3PO_4 etch used

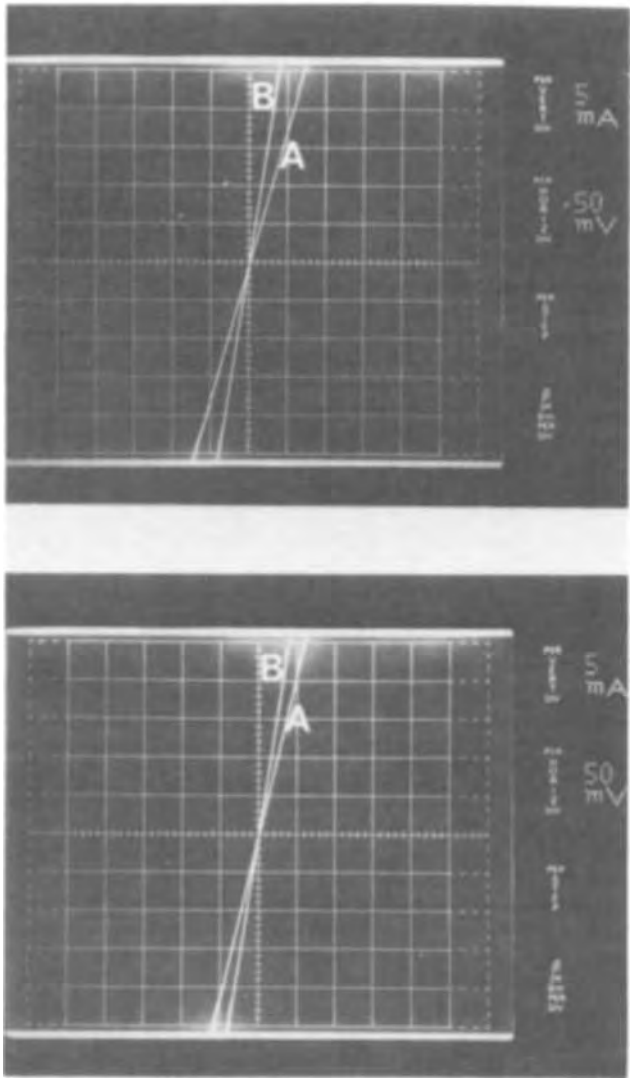

Fig. 2. Current-voltage profile for W-metalized PtSi/Si contacts with Al on the back side of Si. A, *I-V* trace across a small area contact (4×10^{-6} cm^2) and B, *I-V* trace across a large area contact (~3.5 cm^2). (a, upper), PtSi/n-Si (1.6×10^{19} cm^{-3}) and (b, lower), PtSi/p-Si (3.3×10^{19} cm^{-3}).

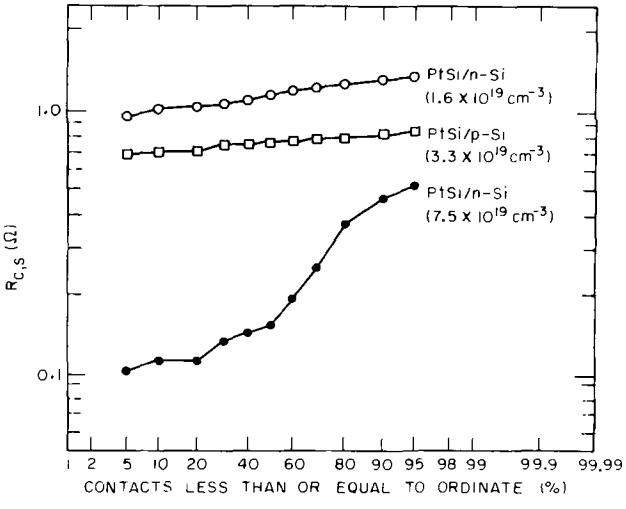

Fig. 3. Distribution plots of measured contact resistance data $R_{c,s}$ on three different slices. Twenty measurements were made on each slice.

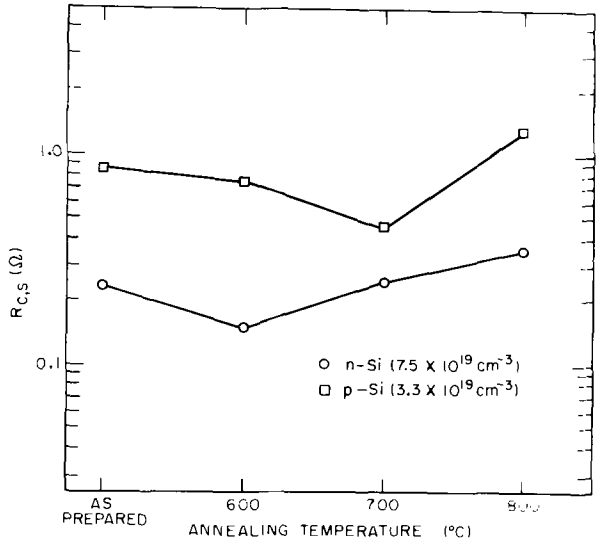

Fig. 4. Effect of thermal treatments on contact resistance $R_{c,s}$. Annealing times were 1 hr at 600° and 700°C, and ½ hr at 800°C.

for Si_3N_4. In one Si_3N_4 deposition run, however, there was partial formation of WSi_2 at the edges of the contact window (Fig. 5c). This was probably due to an inadvertent and momentary rise in temperature during Si_3N_4 deposition. Such partial WSi_2 formation does not cause any significant increase in the contact resistance.

Annealing at 800°C (1/2 hr) results in unpredictable behavior. The contacts on various slices ranged from those with essentially unchanged $R_{c,s}$ to those which had become highly resistive and nonohmic or were electrically open (Table I). Such variability in contact resistance correlates with excessive WSi_2 formation illustrated in Fig. 6. WSi_2 possesses a rough texture, and the higher diffusivity of Si at the walls of the contact windows results in an apparent "spill-over" of WSi_2 outside the contact window. Although WSi_2 has several desirable properties, *e.g.*, metallic conductivity and oxidation resistance in air at 900°C, its formation in contact areas is clearly undesirable. It can be concluded from lattice parameter data (19) on WSi_2 (tetragonal, 6 atoms/cell, a = 3.211Å, c = 7.868Å) that its formation involves a 27% decrease in volume with respect to the components W and Si. This can cause development of large internal stresses especially near edges of contact windows, and can thereby lead to microcracks and electrical "opens." Therefore, it appears likely that the observed increases in contact resistance upon 800°C anneal primarily involve poorly reproducible mechanical/metallurgical effects and not the creation of any additional potential barrier between WSi_2 and PtSi.

Figure 7 shows the variation of median contact resistivity $\rho_{c,s}$ as a function of doping level of n- and p-type Si substrates. Also shown are two sets of previously published theoretical curves for ρ_c which have considered tunneling and tunneling/thermionic emission (7) processes.

Discussion

An examination of Table I shows that the spreading resistance contributions, R_s, are large and comparable in magnitude to the measured contact resistances, $R_{c,s}$. Therefore, the true contact resistances, R_c, are much smaller than the measured $R_{c,s}$ values. However, since all small area ohmic contacts to Si layers are associated with some spreading resistance, $R_{c,s}$ does provide a useful estimate of the effective impedance at contact areas having dimensions of the order of 20 × 20 μm. Contact resistance data reported by most of the previous investigators (1-5) also contain relatively large spreading contributions, but these were obtained on contacts having different sizes and shapes. Since the spreading resistance decreases as the first power of the

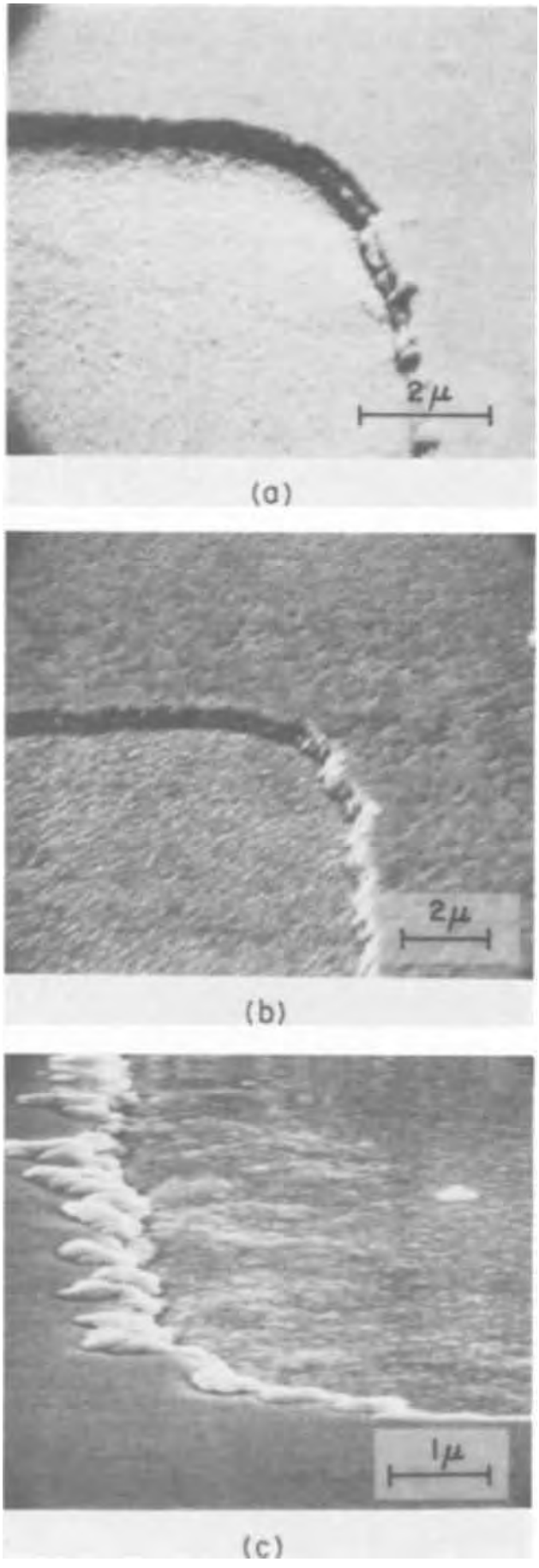

Fig. 5. Microstructures of W-metalized PtSi/Si contact areas: (a) after 600°C anneal, (b) after 680°C Si_3N_4 deposition and subsequent H_3PO_4 etch to remove Si_3N_4, and (c) after Si_3N_4 deposition with probably an inadvertent temperature rise during deposition.

Table I. Ohmic contact resistance of PtSi-to-Si contacts (area = 4×10^{-6} cm^2) metalized with tungsten (data include spreading resistance)

Silicon type, $N_{D,A}$ (cm^{-3})	Apparent contact resistance, $R_{c,s}$ (ohms)					Spreading resistance, R_s (ohms)
		Thermal treatment			Si_3N_4 dep.	
	As prepared	600°C 1 hr	700°C 1 hr	800°C ½ hr	(680°C, ~½ hr)	
n = 7.5 × 10^{19}	0.24	0.15	0.25	0.35	0.19	0.28
n = 1.6 × 10^{19}	1.17	1.80	2.50	•	0.85	1.12
n = 9.5 × 10^{18}	2.00	1.55	3.00	•	1.90	1.63
p = 1.7 × 10^{20}	0.52	0.11	0.16	•	0.32	0.20
p = 3.3 × 10^{19}	0.87	0.75	0.45	1.30	1.70	1.00
p = 1.8 × 10^{19}	3.75	3.25	1.60	•	4.00	1.75
p = 1.2 × 10^{18}	17.00	19.00	19.50	•	15.00	15.00

• Nonohmic or "open" contacts.

contact radius (Eq. [3]) whereas the true contact resistance decreases as the square of the radius, comparisons between $\rho_{c,s}$ values obtained by different investigators are not meaningful unless the measurements are made on contacts of very nearly the same size and shape. There is, however, enough qualitative agreement between the present results and those of most previous investigators (1-3, 5) so that several of the conclusions (see below) reached on the basis of comparison of presently obtained data with predictions of the tunneling model are applicable to a wide range (with respect to sizes and shapes) of alloyed PtSi contacts in silicon integrated circuits (SIC's).

Since theoretical analysis of the contact resistance problem yields only ρ_c values (in ohm-cm^2), in order to compare the experimental results with theoretical ones (Fig. 7) it is necessary to obtain values of $\rho_{c,s}$ by multiplying the measured values of $R_{c,s}$ by the contact area. It should again be emphasized that the very large spreading resistance contributions make the values of $\rho_{c,s}$ obtained in this way only upper limits to the values of ρ_c. Therefore, it is significant that the experimental values of $\rho_{c,s}$ for n-type samples are much smaller than the theoretical values, since correcting for the spreading resistance would make the discrepancies even larger, However, no definite conclusion can be drawn from the comparison between the experimental $\rho_{c,s}$ values for p-type samples and the theoretical ρ_c values of Chang, Fang, and Sze (7); since the latter are lower than the former, the discrepancies would be reduced by correcting for the spreading resistance.

In view of the large disagreement between the experimental data and the contact resistivities predicted by the tunneling model (6, 7) especially for n-Si, it is important to examine the possible reasons for the inapplicability of this model to the PtSi/Si contacts studied in the present investigation. The tunneling theory predicts the resistance of a potential barrier, at the metal-semiconductor interface, as a function of the depletion width. Simple calculations show that the depletion width for the PtSi/Si interface is less than 150Å for doping levels (n- or p-type) exceeding the mid-10^{18} cm^{-3} range. The fact that the depletion widths for Si samples used in the present work are so

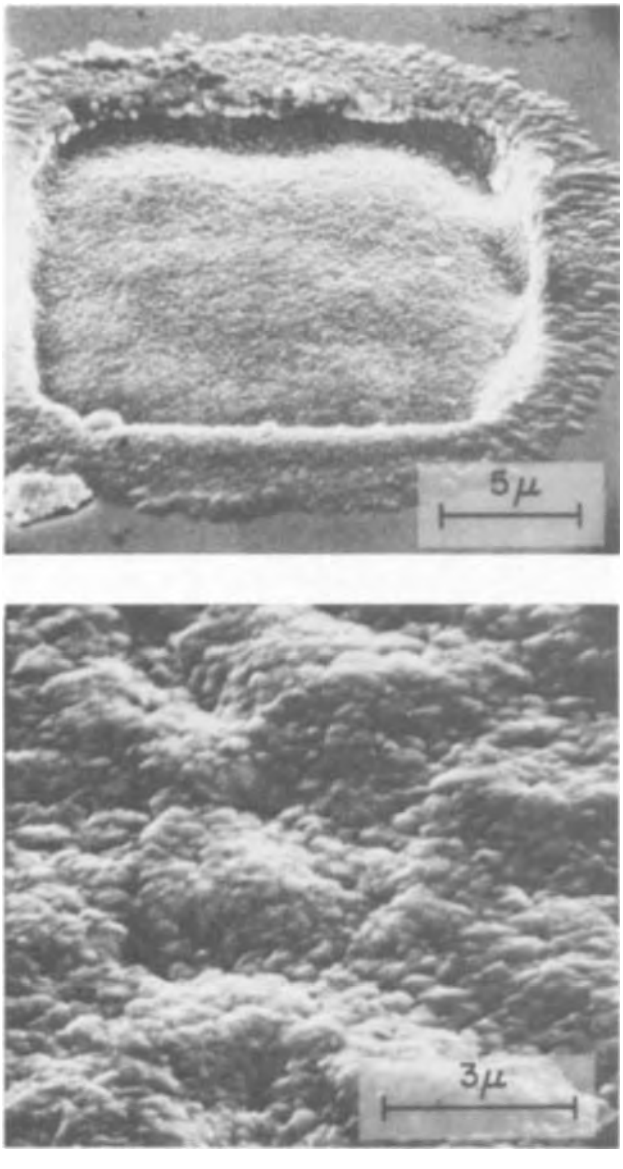

Fig. 6. Microstructure of contact samples annealed at 800°C. (a, upper) WSi_2 formation and "spill-over" outside the contact areas and (b, lower) surface texture of WSi_2 on PtSi on Si.

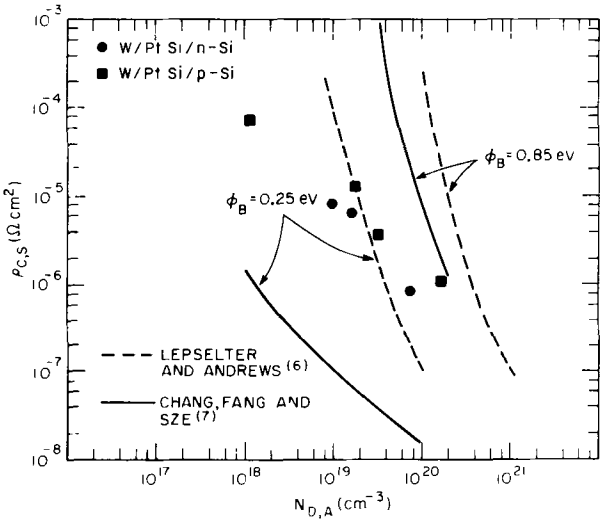

Fig. 7. Measured contact resistivity, $\rho_{c,s}$, vs. dopant concentration, $N_{D,A}$. Also shown are theoretically calculated curves for n- and p-type Si with PtSi/Si barrier heights of 0.85 and 0.25V, respectively.

small is very significant. It has been previously shown (13) that our as-prepared PtSi films contain surface irregularities of the order of a few hundred angstroms, distances which are greater than the estimated depletion widths. In addition to the roughness at the interface, there is a lattice mismatch between the diamond cubic Si and orthorhombic PtSi, and it is probable that the distribution coefficients of As and B between PtSi and Si are not exactly equal to unity. These factors, which are present in most alloyed ohmic contacts, preclude the possibility of any ideally sharp metal-silicon interface. Under such conditions, then, the idealized one-dimensional tunneling model (6-7) loses its validity. A three-dimensional micromodel that includes the effects of nonuniform current flow and mobility differences between n- and p-type Si may be more appropriate in the case of alloy-type ohmic contacts to semiconductors.

Summary and Conclusions

1. PtSi ohmic contacts were made to four sets of p-type Si ($N_A = 10^{18}$-10^{20} cm^{-3}) and three sets of n-type Si ($N_D = 10^{19}$-10^{20} cm^{-3}) samples. Each set consisted of five to eight different wafers, and at least 20 measurements were made on each wafer.

2. Measured contact resistances, $R_{c,s}$, for 20 × 20 μm contacts include large spreading resistance contributions.

3. Annealing at 600° or 700°C (1 hr) or Si_3N_4 deposition at 680°C does not cause any degradation of the ohmic contact or any significant metallurgical interaction.

4. At 800°C (1/2 hr), WSi_2 forms in the contact areas. Its effects may range from no change in contact resistance to an electrical "open."

5. Wide disagreement exists between the presently measured ohmic contact resistances and theoretical values based on a model of one-dimensional electron tunneling through a potential barrier. It is questionable whether such an idealized one-dimensional tunneling model is applicable to metal/highly doped semiconductor contacts containing irregular interfaces.

Acknowledgments

Appreciation is extended to R. S. Wagner, H. J. Levinstein, and B. Chawla for valuable discussions and to T. E. Smith for experimental assistance.

Manuscript submitted Jan. 8, 1973; revised manuscript received June 29, 1973. This was Paper 69 presented at the Chicago, Illinois, Meeting of the Society, May 13-18, 1973.

Any discussion of this paper will appear in a Discussion Section to be published in the June 1974 JOURNAL.

REFERENCES

1. D. Shinoda, in "Ohmic Contacts to Semiconductors," p. 200, B. Schwartz, Editor, The Electrochemical Society, Softbound Symposium Series, New York (1969).
2. H. Sello, *ibid.*, p. 277.
3. L. E. Terry and R. W. Wilson, *Proc. IEEE*, **57**, 1580 (1969).
4. A. Y. C. Yu, *Solid-State Electron.*, **13**, 239 (1970).
5. C. Y. Ting and C. Y. Chen, *ibid.*, **14**, 433 (1971).
6. M. P. Lepselter and J. M. Andrews, in "Ohmic Contacts to Semiconductors," B. Schwartz, Editor, p. 159, The Electrochemical Society, Softbound Symposium Series, New York (1969).
7. C. Y. Chang, Y. K. Fang, and S. M. Sze, *Solid-State Electron.*, **14**, 541 (1971).
8. M. P. Lepselter, *Bell System Tech. J.*, **40**, 233 (1966).
9. D. M. Brown, W. E. Engeler, M. Garfinkel, and P. V. Gray, *Solid-State Electron.*, **11**, 1105 (1968).
10. J. M. Shaw and J. A. Amick, *Solid-State Technol.*, **14**, 53 (1971).
11. A. K. Sinha, T. E. Smith, T. T. Sheng, and N. N. Axelrod, *J. Vacuum Sci. Technol.*, **10**, 436 (1973).
12. M. T. Duffy and W. Kern, *RCA Rev.*, **31**, 742 (1970).
13. A. K. Sinha, R. B. Marcus, T. T. Sheng, and S. E. Haszko, *J. Appl. Phys.*, **43**, 3637 (1972).
14. J. C. Irvin, *Bell System Tech. J.*, **41**, 387 (1962).
15. R. S. Wagner, A. K. Sinha, T. T. Sheng, H. J. Levinstein, and F. B. Alexander, To be published.
16. D. Ady and R. Curran, Unpublished work.
17. G. F. Foxhall and J. A. Lewis, *Bell System Tech. J.*, **43**, 1609 (1964).
18. R. G. Mazur and D. H. Dickey, *This Journal*, **113**, 255 (1966).
19. W. B. Pearson, "Handbook of Lattice Spacings and Structures of Metals and Alloys," Vol. II, p. 393, Pergamon Press, Inc., New York (1965).

The Etch Rate of Gadolinium Gallium Garnet in Concentrated Phosphoric Acid of Varying Composition

D. C. Miller

Bell Laboratories, Murray Hill, New Jersey 07974

ABSTRACT

The etch rate of $Gd_3Ga_5O_{12}$ in concentrated phosphoric acid between 140° and 180°C was found to vary directly with the square of the H_3PO_4 concentration when dilution of the H_3PO_4 with higher acids of the type $H_{n+2}P_nO_{3n+1}$ ($n = 2,3,4\ldots$) occurs as a result of dehydration. When the H_3PO_4 concentration is reduced by dilution with water, however, the etch rate continues to increase reaching a maximum value at a dilution of approximately 50 mole per cent (m/o) H_2O at 140°C. For any given acid composition the etch rate varies exponentially with temperature.

Phosphoric acid above 250°C has been used to chemically polish a number of oxide single crystals (1-4), and between 160° and 170°C to reveal defects (5) in nonmagnetic garnet substrates (6, 7) and magnetic garnet epitaxial layers (8-10) used in bubble domain devices (11, 12). When heated, phosphoric acid dehydrates resulting in changes in the etching properties of the acid. These changes are especially deleterious at polishing temperatures but can be overcome by stabilizing the water content of the acid by bubbling steam through the bath (4). In the 140°-180°C range the selectivity of the acid is not affected by dehydration (5) but the etch rate is. Hence, precision etching of epitaxial garnet layers for thinning and circuit delineation, and the process-related etching of substrates for cleaning and defect analysis, requires that the etching properties of the acid be understood and controlled.

Key words: garnets, etching, phosphoric acid.

The changes which occur in the chemistry of phosphoric acid upon heating and the effect these changes have on the etch rate of $Gd_3Ga_5O_{12}$ are presented below.

Chemistry of Concentrated Phosphoric Acid

Commercial 85% phosphoric acid consists of orthophosphoric acid (H_3PO_4) and H_2O. Upon heating, the acid loses the excess water by boiling which commences at about 170°C and continues until the temperature reaches about 250°C. Upon further heating, dehydration will continue until essentially P_2O_5 remains at around 1000°C (13). However, as a result of dehydration, different acids form having the general formula $H_{n+2}P_nO_{3n+1}$ where $n = 2, 3 \ldots$, each representing an increase in the P_2O_5/H_2O ratio (14, 15). The equivalent concentration of P_2O_5 governs the ratios of the different phosphoric acids present and is related to the density, d, of the solution by the following empirical relationship (15)

$$d = 0.0167 \text{ (weight per cent } P_2O_5) + 0.66 \quad [1]$$

The per cent of the total P_2O_5 present in the solution in the form of each of the polyphosphoric acids has been determined for mixtures having P_2O_5 concentrations between 68.8 and 86.3 weight per cent (w/o) (16). These results and Eq. [1] have been used to calculate the mole per cent (m/o) H_3PO_4 present in the solution as a function of the density and this is shown graphically in Fig. 1. The maximum H_3PO_4 concentration attained is less than 100% (17, 18) at the stoichiometric composition (72.44 w/o P_2O_5). This solution has a density of 1.87 g/cm³ and contains a few per cent of equal amounts of water and pyrophosphoric acid ($H_4P_2O_7$).

The decreasing concentration to the left in the figure represents dilution with water and to the right dilution with acids having higher P_2O_5/H_2O ratios. Dehydration and the accompanying compositional changes are reversible, though re-establishment of the equilibrium composition after dehydration may take weeks. The equilibrium composition (density) depends upon the temperature and partial pressure of water in the ambient and is about 1.90 g/cm³ at 160°C in an open system, for example. If kept sealed, the composition characteristic of the conditions prevailing before sealing will be maintained upon heating or cooling (15, 17).

Experimental

Commercial 85% orthophosphoric acid with an mitial density of about 1.68 g/cm³ was used for all of the etching experiments reported here. The acid was contained in platinum beakers. However, below about 200°C Teflon and Pyrex (which dissolve at the rate of approximately 0.05 μm/min at 150°C) may also be used. Specimens were held with Teflon forceps.

Samples were dipped directly into the acid at the etching temperature for 1-15 min. Following etching, the samples were quenched in vacuum pump oil at 75°C to stop the etching action yet minimize the chances of thermal cracking. Then the samples were cleaned in consecutive hot Alconox solutions, the first containing 15 w/o KOH to aid in neutralizing any acid remaining on the specimens. The specimens were then rinsed in distilled water and blown dry.

The etch rates were determined in two ways. For short etching times (1-4 min), regions of the substrates were masked with SiO_2 deposited by electron beam evaporation. Then, after phosphoric acid etching, the SiO_2 was removed with dilute HF and the resulting steps measured with the Tally-Step machine. For long eching times (1-2 hr) when 50 μm or more was removed from both sides of the substrate, the over-all thickness change was measured with a micrometer. Results obtained using both techniques on the same specimen were in close agreement. The acid bath temperature was monitored with either a platinum-platinum 10% rhodium or a platinum encased chromel-alumel thermocouple immersed in the bath.

The water content or composition of the acid was determined by measuring its density for which volumetric flasks and hygrometers were used before and after etching at 25°C, the temperature to which all of the densities reported here have been normalized. In order to avoid error caused by either the gain or loss of moisture by the acid between the time of etching and measurement, the density was also determined during etching by a weight loss method. The method consists of first measuring the density of the fresh acid at 25°C in a volumetric flask or by use of a hygrometer. This was normally found to be between 1.625 and 1.685 g/cm³. The fresh acid is then weighed in the etching beaker at 25°C and again weighed during etching. Then, by assuming all weight loss is due to loss of H_2O ($\simeq$ 1 g/cm³ at 25°C) and that the density of the acid is the result of a simple mixing of H_2O and acid, the density of the acid during etching corrected to room temperature is given by

$$\frac{w_f}{\frac{w_I}{\rho_I} - (w_I - w_f)/\rho_{H_2O}} \cong d \quad [2]$$

where w_I is the initial acid weight, w_f is the acid weight during etching, ρ_I is the initial density of the acid, and ρ_{H_2O} is the density of water at 25°C. This approximation was found to be inadequate for precise measurement of the density and thus a calibration curve was determined that relates the density measured using this relationship to the "true" density. The true density was measured by overfilling volumetric flasks with the hot acid, sealing them until cooled to the measurement temperature, and then releveling them by removing excess acid. The calibration curve is shown in Fig. 2.

The surfaces of the specimens were polished with diamond followed by Syton,[1] which leaves the surfaces damage free. This is important because damaged surfaces etch faster than perfect surfaces and over-all

[1] Product of Monsanto Chemical Corporation.

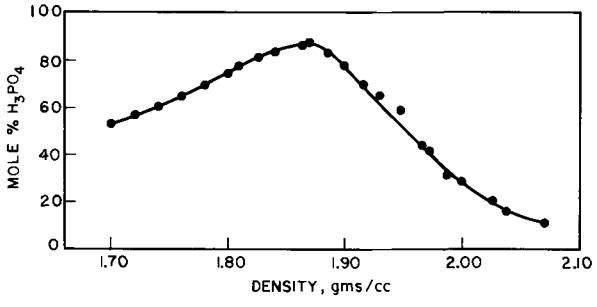

Fig. 1. Concentration of H_3PO_4 in mole per cent vs. the density of phosphoric acid.

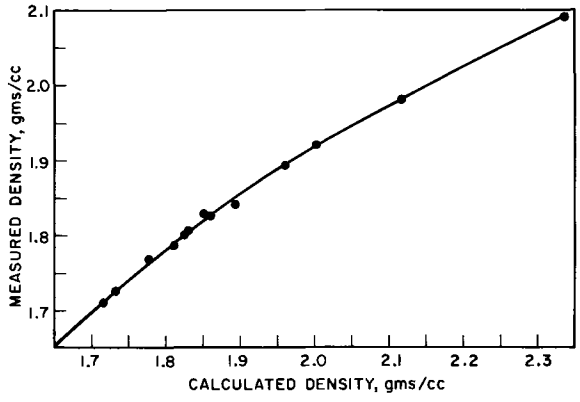

Fig. 2. Density of phosphoric acid measured using volumetric flasks and hygrometers vs. that calculated using the weight loss method.

falsely high etch rates would have been measured had as-sawn or rough polished substrates been used. Furthermore, the etch rate of garnet in the 140°-180°C temperature range is affected by small changes in composition (5). In order to minimize the possibility that small differences in stoichiometry and impurity concentration could introduce a source of error in the measurements, one (111) slice of $Gd_3Ga_5O_{12}$ was cut into 50 pieces and used in determining all of the data reported here.

Results

The etch rate of $Gd_3Ga_5O_{12}$ in the <111> direction as a function of acid density for four different temperatures is shown in Fig. 3. Every point on the curves is the average of at least three determinations at the specified temperature and density, and can be relied upon to ± 5%. Note that the etch rate continues to increase linearly as the acid is diluted with water until about 50% dilution is reached at 140°C (~ 1.70 g/cm³) whereupon the rate decreases.

This behavior cannot be readily related to the chemistry of the acid. Even though there is some disagreement about the maximum H_3PO_4 concentration attainable (18), it is unlikely that the reported H_3PO_4 concentrations (17) are enough in error to account solely for the observed behavior. It is most likely that dissociation of the acid must occur before etching can proceed and the concentration of the dissociated species reaches a maximum at some level of dilution (50% at 140°C, for example). Unfortunately, knowledge of the dissociation equilibria of concentrated phosphoric acid is limited to lower temperatures (18, 19) and more dilute solutions (20). Because of the large deviations from ideality present, neither Raoult's nor Henry's law can be applied or sensible extrapolations made of existing data.

Using the results of Huhti and Gartaganis (17) and Eq. [2] the etch rate data for solutions diluted with higher acids can be replotted as a function of H_3PO_4 concentration and this is shown in Fig. 4 for 150° and 170°C. If indeed the etch rate is a function of the ionized species present, then in view of the small etch rate

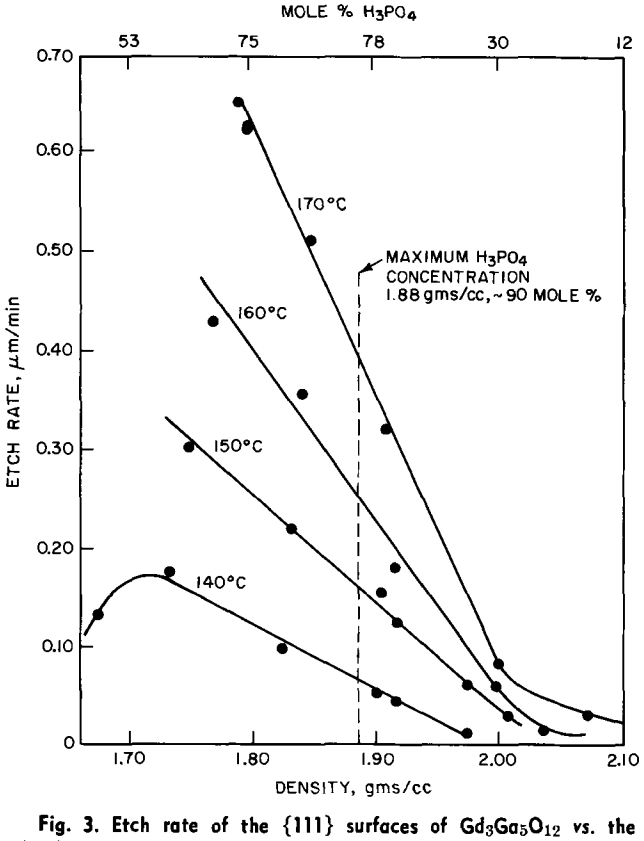

Fig. 3. Etch rate of the {111} surfaces of $Gd_3Ga_5O_{12}$ vs. the density of phosphoric acid.

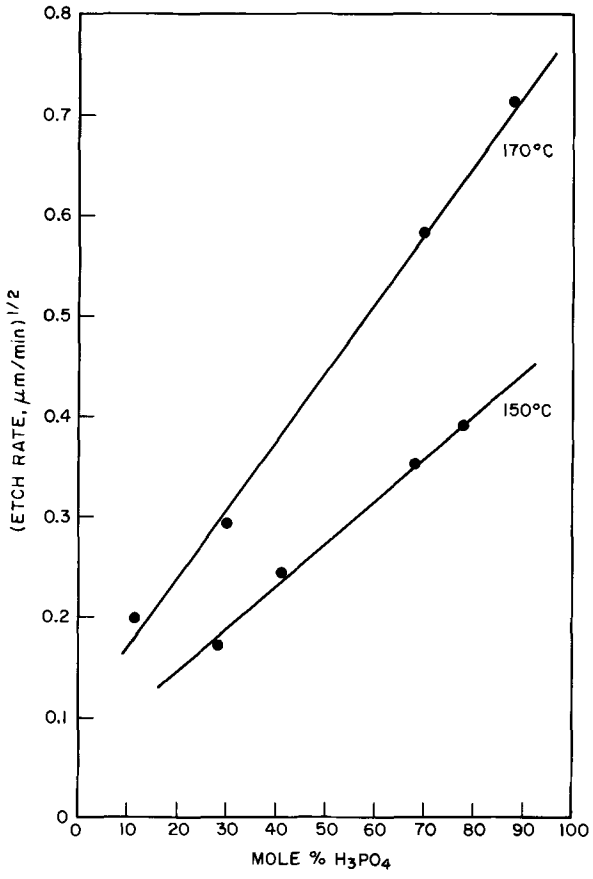

Fig. 4. Square root of the etch rate of the {111} surfaces of $Gd_3Ga_5O_{12}$ vs. mole per cent H_3PO_4 in phosphoric acid at 170° and 150°C.

indicated at 0% H_3PO_4, it is probable that the higher acids are only slightly dissociated and therefore serve to dilute the partially dissociated H_3PO_4. The square law dependence of the etch rate on concentration may indicate that the ionized species is formed by a reaction, such as

$$2H_3PO_4 \leftrightarrow H_2PO_4^- + H_4PO_4^+$$

and

$$\text{etch rate} \propto [H_4PO_4^+] = K'[H_3PO_4]^2$$

The variation of the etch rate as a function of temperature for the different densities is shown in Fig. 5. The variation is exponential with an activation energy of 25.5 kcal/mole for all three compositions. This suggests that the same component of the acid etches the garnet independent of the over-all acid composition. The negative deviation from exponential behavior at 140°C, which is largest at 1.980 g/cm³, probably arises from the development of a diffusion boundary layer at the crystal surface. The boundary layer thickness, and hence the etch rate, is controlled by the viscosity of the acid, which increases rapidly with decreasing temperature and increasing density.

It is also important to note that all of these data were taken from the same 0.030 in. thick by 0.8 in. diameter <111> slice of $Gd_3Ga_5O_{12}$ sectioned into many pieces. When attempts were made to measure etch rates on samples having different orientations that were cut from other $Gd_3Ga_5O_{12}$ boules, and (111) samples from these different boules were etched in order to correlate the data with that of Fig. 4 and 5, not only were they found to have considerably different absolute etch rates but large differences in activation energy as well (as high as 42.1 kcal/mole in one case). In addition, etch rate variations of an order of magnitude were observed to occur with magnetic garnet films of different compositions. Therefore, it must be concluded that etch rates are extremely sensitive to small variations in stoichiometry and impurity concen-

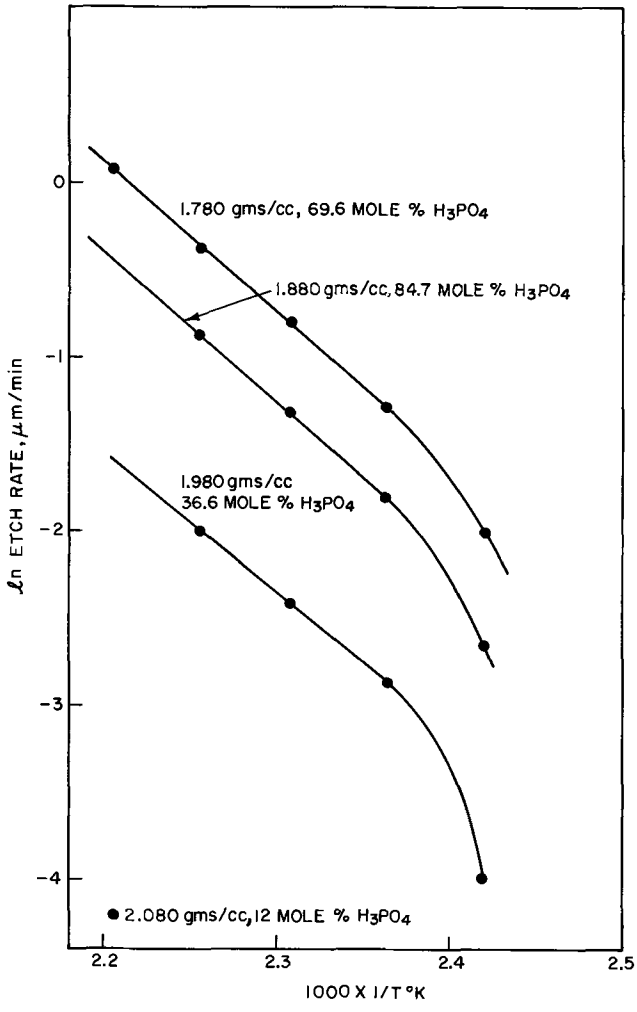

Fig. 5. Ln of the etch rate of the {111} surfaces of $Gd_3Ga_5O_{12}$ vs. inverse temperature at different densities.

tration. Such variations in the composition of $Gd_3Ga_5O_{12}$ can be caused by Ga_2O_3 evaporation during growth, growth atmosphere composition, starting material purity, and other variables (7). In view of this sensitivity, it may also be concluded that the etch rates will be extremely anisotropic. This was observed here qualitatively and is suggested by other results (21).

The great selectivity of the acid can be very useful in a variety of applications in addition to defect studies. For example, the steps produced by the SiO_2 mask were quite sharp, with no undercutting. This can be used to good advantage, since steps, grooves, and other configurations with possible circuit applications can be easily delineated. Despite the large differences observed in the absolute etch rates of the various garnets studied, the functional dependence of the etch rates on the phosphoric acid composition appeared to be the same as that of $Gd_3Ga_5O_{12}$.

Conclusions

The etch rate of $Gd_3Ga_5O_{12}$ in concentrated phosphoric acid varies directly with the square of the H_3PO_4 concentration when the H_3PO_4 is diluted with higher acids of the type $H_{n+2}P_nO_{3n+1}$ ($n = 2, 3, 4 \ldots$) formed as a result of dehydration. When the H_3PO_4 is diluted with water the etch rate continues to increase, reaching a maximum at a dilution of 50% H_2O at 140°C. The activation energy for etching is independent of acid composition but extremely dependent on the stoichiometry and impurity concentration of the $Gd_3Ga_5O_{12}$.

Acknowledgments

The author wishes to thank C. D. Brandle for growing the $Gd_3Ga_5O_{12}$, B. J. Roman for the SiO_2 depositions, D. DeSantis for technical assistance, and J. W. Nielsen for helpful discussions.

Manuscript submitted Oct. 17, 1972; revised manuscript received June 1, 1973.

Any discussion of this paper will appear in a Discussion Section to be published in the June 1974 JOURNAL.

REFERENCES

1. B. Cockayne and D. S. Robertson, *Brit. J. Appl. Phys.*, **15**, 643 (1964).
2. J. Basterfield, *ibid.*, (*J. Phys. D.*), **2**, 1169 (1969).
3. L. K. Shick, *This Journal*, **118**, 179 (1971).
4. D. C. Miller, *J. Electron. Mater.*, **1**, 499 (1972).
5. D. C. Miller, *This Journal*, **120**, 678 (1973).
6. C. D. Brandle and A. J. Valentino, *J. Crystal Growth*, **12**, 3 (1972).
7. C. D. Brandle, D. C. Miller, and J. W. Nielsen, *ibid.*, **12**, 195 (1972).
8. R. C. Linares, *ibid.*, **3**, 443 (1968).
9. H. J. Levinstein, S. Licht, R. W. Landorf, and S. L. Blank, *Appl. Phys. Letters*, **19**, 486 (1971).
10. S. L. Blank and J. W. Nielsen, *J. Crystal Growth*, **17**, 302 (1972).
11. A. H. Bobeck, *Bell Syst. Tech. J.*, **46**, 1901 (1967).
12. A. H. Bobeck, *IEEE Trans. Magnetics*, **MAG-6**, 445 (1970).
13. J. R. Van Wazer, *Encyclopedia Chem. Tech.*, **10**, 412 (1953).
14. D. Balarett, *Z. Anorg. Chem.*, **67**, 234 (1910); *ibid.*, **69**, 215 (1911).
15. R. N. Bell, *Ind. Eng. Chem.*, **40**, 1464 (1958).
16. L. V. Kubasova, *Russ. Chem. Rev.*, **40**, 1 (1971).
17. A. L. Huhti and P. A. Gartaganis, *Can. J. Chem.*, **34**, 785 (1956).
18. R. A. Munson, *J. Phys. Chem.*, **68**, 3374 (1964).
19. C. J. Peacock and G. Nickless, *Z. Naturforsch.*, **24(2)**, 245 (1969).
20. I. K. Karpov and S. A. Kashik, *Zh. Fiz. Khim*, **43(1)**, 233 (1969).
21. A. Reisman, M. Berkenblit, J. Cuomo, and S. A. Chan, *This Journal*, **118**, 1653 (1971).

Silicide Formation in Tungsten and Other Refractory Metalizations on PtSi on Silicon

A. K. Sinha,* Mildred H. Read, and T. E. Smith

Bell Laboratories, Murray Hill, New Jersey 07974

ABSTRACT

We have evaluated the alloying behavior of W and other refractory metal films on PtSi on Si at temperatures ranging from 700° to 900°C. Nearly complete WSi_2 formation is observed in the case of W/PtSi/Si samples annealed above 750°C (1 hr). Si appears to be the diffusing species, and PtSi provides an unpassivated interface between W and PtSi/Si. WSi_2 is a metallic conductor with a resistivity of ~54 μohm-cm. Unlike W, WSi_2 does not oxidize upon heating in air up to 900°C. Its formation in the ohmic contact areas is, however, undesirable because of the volume changes accompanying its formation. In the case of other refractory metalization systems, M/PtSi/Si where M is Ti, V, Cr, Ni, NiCr, Mo, and Ta, PtSi also offers little resistance to M-silicide formation at high temperatures (800°-900°C).

Information on the high-temperature metallurgical compatibility of various thin-film materials systems is of considerable importance in the design of certain LSI (large scale integration) processing schemes. It becomes a critical factor when postmetalization steps such as Si_3N_4 encapsulation by CVD (chemical vapor deposition) (1) are involved. A refractory metal metalization such as tungsten on SiO_2 is generally able to withstand temperatures in excess of 900°C. However, a potential problem area lies in the ohmic contact regions of the LSI circuits. Here the reliability and performance of the device would depend rather critically on the metallurgical interactions involved.

In the present work, we have studied the alloying behavior of thin W-films over the ohmic contact material PtSi (2, 3) at temperatures ranging from 700° to 900°C. In addition, the nature of intermetallics formed during high-temperature annealing of other thin-film metalizations of type Si/PtSi/M (where M is Ti, V, Cr, Ni, NiCr, Mo, and Ta) and Si/PtSi/M/W has been also determined.

Experimental

PtSi was deposited (3) on n-type Si having (100) orientation and doped with As to 7-14 ohm-cm resistivity. Some of the Si wafers were steam oxidized at 1050°C to 5000Å thick SiO_2 and then an array of circular windows 20 mils in diameter was etched through the oxide. PtSi was produced within the windows, as well as on Si blanks by first backsputter cleaning the Si surface and then sputtering 450Å of Pt followed by *in situ* sintering at 700°C for 10 min. The unreacted Pt outside the windows was etched away with hot aqua regia.

Thin films of W were deposited on the above samples in an oil-free vacuum station using a Varian 6 kW e-gun (4). The source material consisted of MRC Marzgrade tungsten slugs and the background pressure during evaporation was kept at or below $\sim 3 \times 10^{-7}$ Torr. The thickness was monitored using a quartz crystal rate monitor. Deposition rates were typically at 300 Å/min, and the thickness of W deposits varied from 2500 to 3500Å. In addition to e-gun evaporation, some W-films were also deposited by low-voltage rf-diode sputtering (5). The deposition of Ti, V, Cr, Ni, and NiCr films, 1000-2000Å thick, was accomplished with filament evaporation in a conventional diffusion-pumped bell-jar system. Molybdenum was evaporated using an e-gun in a separate vacuum station from that used for W evaporation. The β-Ta (1000Å thick) was produced by d-c sputtering.

Following the metalization, the samples were annealed at various temperatures ranging from 700° to 900°C for ½ to 1 hr periods in a vacuum better than 2×10^{-6} Torr. The metallurgical interactions following the high-temperature anneal were studied using optical microscopy, x-ray diffraction [with a glancing angle wide-film Debye Scherrer camera (6)], sheet resistance measurements, and Talystep step-height measurements across the windows.

Results

Figures 1(a) through (d) show the effect of a 900°C, 1-hr vacuum anneal on the microstructure and topography of various contact windows on oxidized silicon wafers. Figures 1(a) and (b) show PtSi (900Å) in the contact windows before and after the 900°C thermal treatment. In the latter state, the PtSi has assumed a rough surface; this process, which is always accompanied by grain growth, was recently shown to involve partial agglomeration of the PtSi film (3). Figure 1(c) shows the microstructure in the as-deposited state of a PtSi contact sample coated with 3000Å of W. Upon annealing this sample at 900°C (1 hr), it may be seen from Fig. 1(d) that the tungsten within the PtSi contact windows undergoes a profuse reaction. The reaction product, which was subsequently identified as WSi_2, has a very rough texture. Judging from the Talystep trace, there appears to be an unusual increase in the volume of the material within the windows as a result of WSi_2 formation. In particular, there is a "pile-up" of WSi_2 at the edge of the windows. It was possible to etch away the unreacted W (over SiO_2) outside the windows using a ferricyanide-ethylene diamine etch, leaving sharply delineated WSi_2 over the PtSi dots. No evidence was observed of any appreciable lateral diffusion of either Pt or Si (as WSi_2); this is attributed to the relatively large thickness of the SiO_2 walls.

With a view to identifying the reaction product observed in Fig. 1(d), approximately 3500Å of W was e-gun evaporated on a 1¼ in. Si blank previously coated with 1400Å of sintered PtSi. After annealing this sample at 900°C for 1 hr in vacuum, its x-ray diffraction pattern showed a large number of strong lines which were identified as being due to WSi_2. In addition, several lines from the underlying PtSi which possessed a preferred (020) orientation parallel to the substrate were present. Positive phase identification was made by comparing the observed x-ray diffraction lines and their intensities along with those calculated for WSi_2 ($MoSi_2$, C11b type) and PtSi (FeP, B31 type). For computing the diffraction patterns of these compounds, the atomic positional parameters compiled

* Electrochemical Society Active Member.

Key words: platinum silicide contacts, thin films, tungsten metalization.

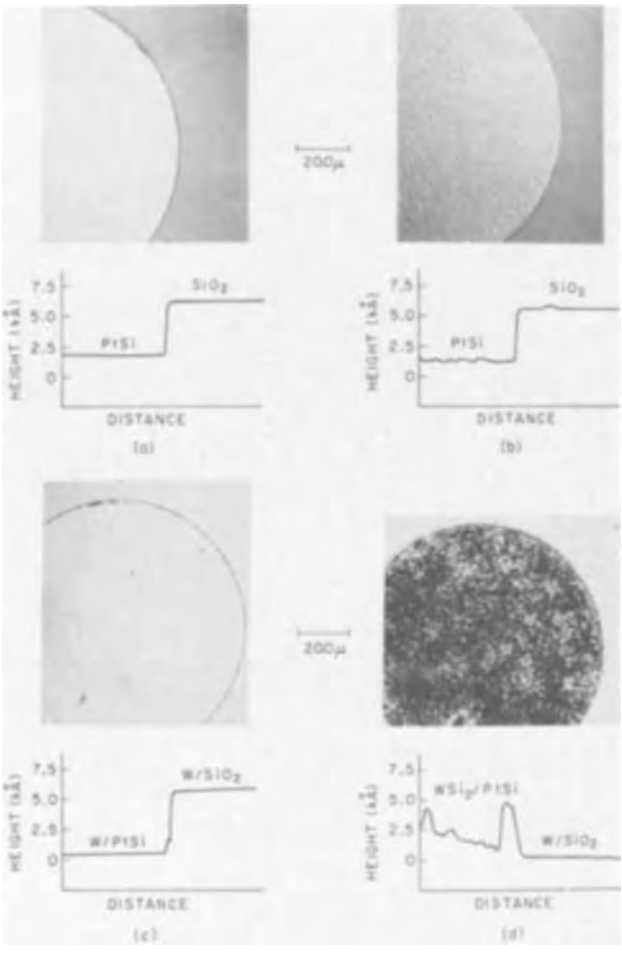

Fig. 1. Microstructure and topography of contact windows on an oxidized silicon wafer: (a) as-deposited PtSi, (b) PtSi annealed at 900°C, 1 hr, (c) as-deposited W/PtSi, and (d) W/PtSi annealed at 900°C, 1 hr.

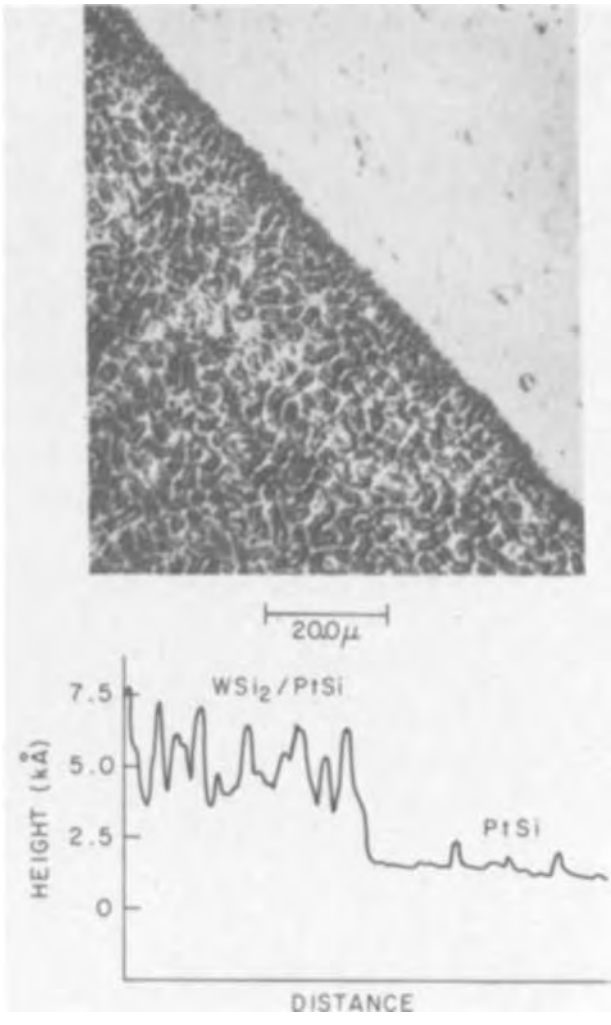

Fig. 2. Microstructure and topography of an annealed (900°C, 1 hr) sample of PtSi on Si partially coated with W (dark area).

by Pearson (7), and the program written by Yvon, Jeitschko, and Parthe (8) were used. There is a satisfactory agreement between the observed and calculated x-ray patterns for WSi_2. Almost complete (> 90%) WSi_2 formation was also observed in the case of W/PtSi/Si samples annealed for 1 hr at 850°, 800°, and 750°C, but not at 700°C. Heating the PtSi films in air at 500°C for 3 hr, or at 800°C in vacuum for 1 hr, prior to W deposition, did not affect the rate of WSi_2 formation upon subsequent annealing.

Figure 2 shows the microstructure of the annealed (900°C, 1 hr, vacuum) W/PtSi/Si sample which has reacted to form WSi_2 as well as a Talystep scan across WSi_2 to PtSi which had been shielded during the W deposition. The average step height of 3750Å is approximately the same as the thickness of W (approximately 3500Å) originally deposited on the PtSi/Si blank. This would suggest that in the W/PtSi/Si blank, the WSi_2 formation upon annealing is due to diffusion of Si through PtSi. Accordingly, both the WSi_2/Pt interface and the PtSi/Si interface sink down into Si. The sheet resistance of the annealed WSi_2/PtSi/Si combination was measured as 0.51 ohm/□. Assuming 3500Å of W in the unannealed W/PtSi/Si sample to give rise to 8750Å WSi_2 and taking into account the contribution of 1400Å of annealed PtSi ($\rho = 40$ μohm-cm), we estimate the resistivity of WSi_2 film to be ~54.5 μohm-cm. The WSi_2 film over PtSi has a matte surface, and unlike W which can be readily anodized (in, *e.g.*, aqueous citric acid solution) WSi_2 does not form anodic films to any appreciable extent, nor can it be oxidized upon heating in air up to 900°C (15 min). Its adhesion to PtSi, judging from the scotch tape peel test, is considered as being good.

The observation [Fig. 1(d)] that the growth of WSi_2 over PtSi largely occurs outward from Si would suggest the possibility of lateral spread of WSi_2 if the SiO_2 thickness at the contact windows were small enough. This was confirmed in an experiment with a charge-coupled device structure where the oxide thickness was approximately 2000Å. Figure 3(a) shows that the formation of WSi_2 (at 900°C, 1 hr, vacuum anneal) from 3000Å of W over PtSi in the contact windows results in a considerable "spill-over" of the WSi_2. Figure 3(b) shows the effect of an identical heat-treat-

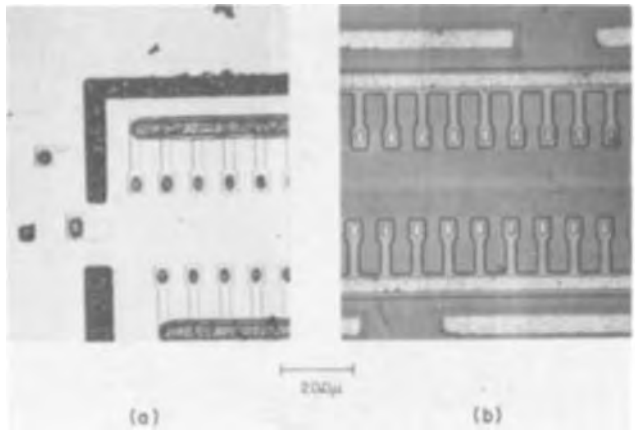

Fig. 3. Effect of a 900°C, 1-hr anneal on a CCD test structure containing (a) PtSi in the contact windows and metalized with W and (b) PtSi in the contact windows but no W overlay.

ment on the PtSi contact pads without W metalization over them. In this case, except for a coarsening effect, the PtSi contact areas remain well-defined.

The lateral spread as well as the spiky morphology of WSi_2 over PtSi may result in shorts both at the level of the W metalization and at levels above it, if WSi_2 penetrates an overlying dielectric film. With a view to prevent or retard such WSi_2 formation, the possibility of a barrier metal between PtSi and W was investigated. Inasmuch as the barrier metals themselves should possess good adhesion to the PtSi contacts, the present investigation was limited to Ti, V, Cr, Ni, NiCr, Mo, and β-Ta (1000-2000Å of each).

In the case of Si/PtSi/M type of systems V, Cr, and Ta reacted to form their disilicides which have the hexagonal $CrSi_2$ type of crystal structure. Upon annealing Ni-film on PtSi on Si, it was found that a quasi-binary (Ni,Pt) Si alloy had formed. This alloy has the same crystal structure as PtSi, but its lattice constants were 3-5% smaller than that of PtSi. Nichrome behaved similarly in that Ni was incorporated into the quasi-binary silicide (Ni,Pt) Si. In addition, a small quantity of fcc Ni(Cr) was also detected. The diffraction pattern of annealed Si/PtSi/Ti sample could not be associated with any of the previously reported silicides (7) of Ti. In the case of thin-film systems of type Si/PtSi/M/W, annealing in the range 800°-900°C always resulted in the formation of WSi_2 in addition to the previously mentioned silicides of the metal M. Chromium was found to be somewhat exceptional in this regard; in the case of Si/PtSi/Cr/W films, only localized formation of WSi_2 was observed in the optical microscope. The x-ray diffraction pattern contained reflections from both WSi_2 and W, with approximately equal intensities. The retarding effect of Cr may be due to its ability to form a passivating oxide layer on its surface.

Discussion

The present results clearly show that PtSi thin-films offer little resistance to high-temperature migration of Si across them into W and other refractory metalizations. This migration does not appear to be related to the phenomenon of agglomeration which was observed in PtSi thin-films at 900°C (3). We have observed profuse WSi_2 formation in Si/PtSi/W films at temperatures (750°-800°C) at which no agglomeration of PtSi thin films takes place. It appears, however, almost certain that PtSi provides an unpassivated (oxide-free) interface between W and PtSi/Si and that PtSi also provides rapid diffusion paths for Si atoms thereby permitting rapid W-Si interaction. This view is supported by results of $^4He^+$ ion Rutherford backscattering experiments which indicate that the surface of PtSi stays remarkably free of excess Si or oxygen even after annealing in air up to 600°C (9).

The crystallographic data on WSi_2 suggest that strong W-Si bonds may be present in this intermetallic: (*i*) In the WSi_2 structure (C11b, $MoSi_2$ type), shown in Fig. 4, each W atom is surrounded by a shell of 10 near-neighbors all of which are Si atoms. There is, thus, a larger number of W-Si bonds in WSi_2 (10 *vs.* 6.7) than that expected on the basis of simple alloy composition considerations. (*ii*) The volume of WSi_2 unit cell (80.6 Å^3, 6 atoms per unit cell) represents a contraction of 27% over the volumes of the component W (15.8 Å^3/atom) and Si (20 Å^3/atom) atoms. In a discussion of $MoSi_2$-type structures, Laves (10) pointed out that if both A-A and A-B contacts are assumed to be present, the geometry of C11b structure would require an ideal radius ratio R_A/R_B of unity. A tendency to meet such geometrical requirements is generally present in the case of most intermetallics. This may result in considerable adjustments in the volumes of the component atoms. In particular, Si has been known to undergo large volume contractions of up to 48%, and an associated decrease in the covalent nature

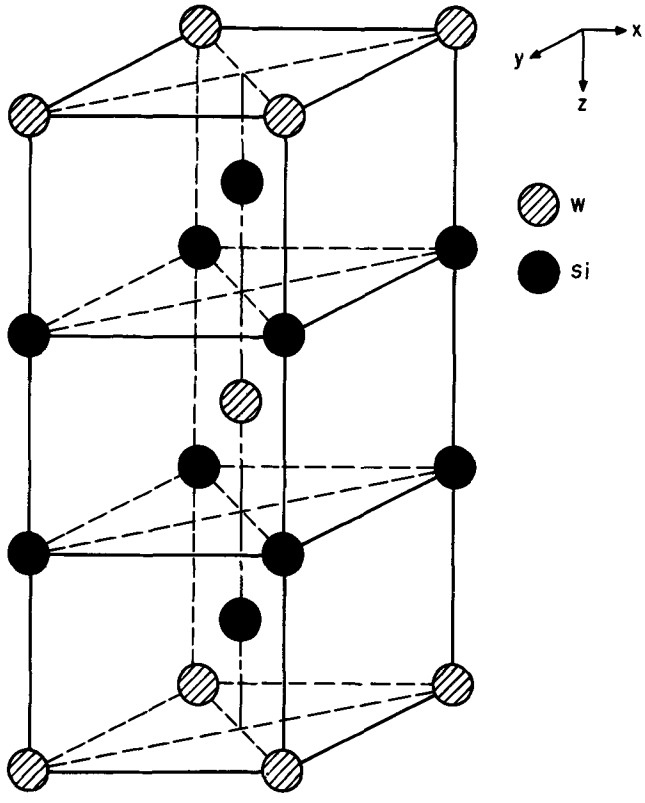

Fig. 4. Atomic arrangement in the tetragonal unit cell of WSi_2

of its bonds (11). A contraction of the order of 33% in the volume of Si atoms would be needed in order to satisfy the geometrical requirements of WSi_2 structure.

The increase in the metallic character of Si bonds which accompanies WSi_2 formation (and contraction of Si atoms) is perhaps partly responsible for the relatively low electrical resistivity of WSi_2, a compound rich in a semimetal. The presently observed increase in the volume of metalization upon WSi_2 formation correlates with the large volume (40.3Å^3) of WSi_2 per W atom which is greater than the atomic volume of elemental W by a factor of 2.5.

It is of interest to comment briefly on the possible diffusion processes leading to WSi_2 formation in W/PtSi/Si structures. Since PtSi stays untransformed during the heat-treatment of W/PtSi/Si films, it effectively acts as a marker. Thus, if W were to diffuse across PtSi into the Si, the PtSi layer would move up and its x-ray reflections would get stronger as WSi_2 formation proceeds. On the other hand, if Si were diffusing across PtSi, the PtSi layer would move down into the Si. The latter appears to be the case in the present experiments in which "PtSi-reflections" definitely did not increase in intensity upon W-silicide formation.

There are several possible ways in which Si may diffuse through PtSi into an overlying metal film. Among the simpler modes, we may cite migration of Si atoms along the grain boundaries of PtSi or, along the two sets of chains of Si atoms which are present in the crystal structure of PtSi (3). Searcy *et al.* (12) have estimated the thermodynamic bond energies of various transition metal-silicon (M-Si) bonds. According to their data, the M-Si bond energies (in electron volts/atom) for the metals studied in the present work increase in the order

Cr (4.81) → Ni (4.98) → Pt (5.38) → V (5.41)

→ Ti (5.45) → Mo(6.10) → Ta (6.75) → W (6.92)

It is significant that Cr forms one of the weakest bonds with Si whereas most of the other transition metals

studied form bonds with Si that are stronger than the Pt-Si bond. Interestingly, Cr was the only metal among the various metals tested that offered some promise as a barrier to WSi_2 formation in thin-film systems of type W/M/PtSi/Si. The fact that the bond energy for the W-Si bond is much larger than that for the Pt-Si bond raises the possibility of a reactive W/PtSi interface. A recent kinetic study (13) of WSi_2 formation in the system W/PtSi/Si indicated that the simple diffusion model [*e.g.*, square root of time dependence observed earlier in the W-Si system (14)] is not applicable to the present case. The thermal activation energy is unusually high at ~4.4 eV/mole. It was suggested that the W/PtSi interface may very well be a reactive one especially during the nucleation stage of WSi_2 formation. Such a complex, but thermodynamically possible nucleation process would then involve the creation of W-Si bonds at the expense of Pt-Si bonds at the W/PtSi interface and the nearly simultaneous restoration of the Pt-Si bonds by the out-diffusing Si atoms. The net effect is again the migration of Si atoms through PtSi into the W-film.

Migration of Si atoms through PtSi would also explain why there was little change in the average thickness of W metalization over PtSi/Si blanks even after WSi_2 formation (Fig. 2). However, when W is present over PtSi in the contact windows, the constraint at the SiO_2 walls may cause considerable buckling of the WSi_2. The "spill-over" of WSi_2 is probably due to an enhanced diffusion of Si at the SiO_2/W interface which is present along the windows. The spiky morphology of WSi_2 suggests that fingers of WSi_2/PtSi may protrude into Si, thereby providing additional channels for easy diffusion of Si.

Conclusions

(*i*) W on PtSi on Si reacts to form WSi_2 at temperatures above 750°C (1-hr anneals). Si is the diffusing species and PtSi provides an unpassivated interface between W and PtSi/Si. (*ii*) WSi_2 is a metallic conductor with a resistivity of approximately 54 μohm-cm. However, excessive WSi_2 formation in contact windows is undesirable because WSi_2 possesses a rough texture and it can extend outside the contact windows. (*iii*) Various transition metal silicides are also formed upon annealing (at 800°-900°C) other refractory metalization M on PtSi on Si, where M is Ti, V, Cr, Ta, Mo, Ni, and NiCr. (*iv*) Upon high-temperature annealing of thin-film systems of type W/M/PtSi/Si, WSi_2 is formed in all cases except that of Cr where about 50% of W stays untransformed at 900°C (1-hr anneal).

Acknowledgments

The authors would like to thank H. J. Levinstein, R. S. Wagner, and C. D. Thurmond for their interest and valuable discussions.

Manuscript submitted Jan. 24, 1973; revised manuscript received June 25, 1973.

Any discussion of this paper will appear in a Discussion Section to be published in the June 1974 JOURNAL.

REFERENCES

1. See, *e.g.*, M. T. Duffy and W. Kern, *RCA Rev.*, **31**, 742 (1970).
2. M. P. Lepselter, *Bell System Tech. J.*, **40**, 233 (1966).
3. A. K. Sinha, R. B. Marcus, T. T. Sheng, and S. E. Haszko, *J. Appl. Phys.*, **43**, 3637 (1972).
4. A. K. Sinha, T. E. Smith, T. T. Sheng, and N. N. Axelrod, *J. Vacuum Sci. Technol.*, **10**, 436 (1973).
5. R. S. Wagner, A. K. Sinha, T. T. Sheng, and F. B. Alexander, *ibid.*, To be published.
6. M. H. Read and D. H. Hensler, *Thin Solid Films*, **10**, 123 (1972).
7. W. B. Pearson, "A Handbook of Lattice Spacings and Structures of Metals and Alloys," Vol. II, Pergamon Press, Inc., New York (1967).
8. K. Yvon, W. Jeitschko, and E. Parthe, Report of the Laboratory for Research on the Structure of Matter, University of Pennsylvania, Philadelphia, Pa., 1969.
9. A. Hiraki, M. A. Nicolet, and J. W. Mayer, *Appl. Phys. Letters*, **18**, 178 (1971).
10. F. Laves, in "Theory of Alloy Phases," American Society for Metals, Cleveland (1956).
11. T. Yoshioka and P. A. Beck, *Trans. AIME*, **233**, 1788 (1965).
12. A. W. Searcy and L. N. Finnie, *J. Am. Ceram. Soc.*, **45**, 268 (1962).
13. A. K. Sinha and T. E. Smith, *J. Appl. Phys.*, **44**, 3465 (1973).
14. P. R. Gage and R. W. Bartlett, *Trans. AIME*, **233**, 832 (1965).

Technical Notes

Symmetry of Luminescing $(WO_4)^{-2}$ Groups in $CaWO_4$

R. J. R. S. B. Bhalla*

Lamp Division, Westinghouse Electric Corporation, Bloomfield, New Jersey 07003

Calcium tungstate represents an important class of self-activated luminescent materials (1). It has also been used as host material for rare earth activated lasers (2). Polarized emission of some rare earth activated $CaWO_4$ single crystals has been studied by photoluminescence and valuable information obtained about the symmetry of the activator sites (2). However, no information is available about the symmetry of the fluorescing $(WO_4)^{-2}$ groups in the self-activated $CaWO_4$ or any other tungstate phosphor. Polarized emission from appropriately oriented single crystals can be used to determine the symmetry of fluorescing $(WO_4)^{-2}$ groups in $CaWO_4$.

In the present communication, results of a cathodoluminescence study on the single crystals of $CaWO_4$ are reported. Polarization of the emission is observed and interpreted for the first time. Complete cathodoluminescence analyses including the emission spectrum, polarization of emission, and the rise and decay characteristics, were carried out using an electron microprobe analyzer, suitably modified for such studies

* Electrochemical Society Active Member.
Key words: $CaWO_4$, cathodoluminescence, $(WO_4)^{-2}$ groups, polarized emission.

(3-5). This arrangement allows measurements to be made on very small single crystals (of the order of 0.001 and up to 1 cm).

Samples were prepared as polished thin sections so as to facilitate orientation determination under a polarizing light microscope. Selected single crystal chips were crushed and set in Lakeside 70 by melting the thermoplastic in an oven at 90°C. Finally, the sample surface was polished successively with 6, 3, 1, and ¼μ diamond pastes and coated with a thin layer of carbon (200-400Å) by vacuum evaporation to provide a conducting path for the electrons. This method of preparation yielded grains with many different crystallographic orientations.

The cathodoluminescence in the electron microprobe was observed through the light microscope (magnification 280X) which enabled observations to be made on the electron beam side of the sample surface. This is an advantage over the conventional cathodoluminescence apparatus when intrinsic anisotropy of the emission is to be examined. In the conventional cathode ray tube type of arrangement, the emitted radiation is examined on the opposite side of the screen; therefore, the radiation has to travel through the crystal thickness before reaching the detector. Such measurements may simply reflect the basic symmetry of the crystal rather than site symmetry of the luminescence centers.

Cathodoluminescence spectra were obtained using an interference-type spectrometer described by Greer and White (6). $CaWO_4$ emitted a characteristic bright-blue luminescence, and the emission spectrum consisted of a single broad and fairly symmetric band with a peak around 4400Å, in agreement with the published literature (7). The most important observation, however, was that the emission was found to be polarized. The grains oriented such that the c-axis was in the crystal plane, showed maximum polarization, while the grains oriented with the c-axis perpendicular to the crystal plane showed no polarization. Intermediate orientations showed intermediate degrees of polarization. The electric vector of the emitted luminescence was in a direction along the c-axis. The degree of polarization, measured as $p = \frac{(I' - I'')}{(I' + I'')}$, where I' and I'' are maximum and minimum intensities observed as the analyzer is rotated around its axis, was found to be 0.3. Spectra of emission were also examined in the two polarization directions; however, no significant change in the position or the shape of the band was found. The rise and decay traces of the luminescence were also obtained by pulsing the electron beam (4, 5). No detailed analysis was carried out but no differences were found in the decay times, measured through the monochromator at different wavelengths of the emission band (4200–6400Å). For the crystals oriented such that the c-axis was in the surface, the rise and decay times were measured with the analyzer parallel and perpendicular to the c-axis; however, no significant differences were found. Typical decay time at 25 keV potential and 50 $\mu A/cm^2$ current density (absorbed electrons), measured as the time required for the luminescence intensity to decay to $1/e$ of the maximum intensity, was of the order of 20 μsec. It may be pointed out here that cathodoluminescence rise and decay times can be dependent upon the primary beam energy and the current density, this dependence is more pronounced for the single crystals in comparison with the powders (4, 8). In the present study, no attempt was made to investigate the primary beam energy and current density dependence of the rise and decay characteristics.

Relatively little theoretical work has been done on the problem of luminescence in pure (unactivated) crystals such as $CaWO_4$. Recently Walter and Butler (9) carried out semiempirical LCAO-MO (linear combination of atomic orbitals-molecular orbital) calculations on the $(WO_4)^{-2}$ and isoelectronic $(VO_4)^{-3}$ complexes, assuming them to have tetrahedral symmetry, and explained the photoluminescence and excitation spectra of $CaWO_4$ and YVO_4 powders. In this communication an attempt is made to explain the polarization of emission considering the energy level scheme as calculated by Walter and Butler (9). The selection rules were calculated considering the effect of various lower symmetries on the emitting level of $(WO_4)^{-2}$ complex.

According to Walter and Butler (9) the emission transition is $2e \rightarrow t_1$. The configuration of the ground state would be $(t_1)^6$ and the first excited state would have the configuration $(t_1)^5$ $(2e)$. When the effect of electrostatic repulsion of the electrons is also taken into account the configuration $(t_1)^6$ $(2e)$ yields multiplets $^1T_1$, $^1T_2$, $^3T_1$, and $^3T_2$, whereas the configuration $(t_1)^6$ results in a singlet term $^1A_1$. Symmetry considerations show that for perfect T_d symmetry the only electric dipole allowed transition to the ground level would be from the levels with T_2 symmetry. The transitions from T_1 levels are forbidden. However, any lowering of symmetry would split the triply degenerate T_1 levels and the transition could then become allowed. Walter and Butler assign $^3T_1$ as the lowest lying excited state level. Since the ground state is a singlet, a transition from the triplet state is allowed only to the extent that there is spin-orbit coupling. The $(WO_4)^{-2}$ tetrahedron in the $CaWO_4$ is slightly distorted and has D_{2d} symmetry (10), being slightly contracted along the z-axis. The lowering of the symmetry has no effect on the ground state level, A_1, but the excited state level, T_1, would split up into two levels with the symmetries E and A_2, respectively. The selection rules under D_{2d} symmetry are given in Table I. Only the transition $E \rightarrow A_1$ is allowed in a direction perpendicular to the z-axis (c-axis of $CaWO_4$). Thus if the symmetry of emitting $(WO_4)^{-2}$ groups is the same as that obtained by crystallographic considerations then the crystals oriented such that the c-axis in the surface should show polarization with the electric vector of the emitted radiation in a direction perpendicular to the c-axis. This is, however, contrary to the experimental observation where it was found that the major electric vector of the partially polarized emission is in a direction along the c-axis. This means that the symmetry of the emitting $(WO_4)^{-2}$ groups is not the same as that deduced from the crystallographic considerations. Various theoretically possible symmetries which a tetrahedral molecule can assume are D_{2d}, C_{3v}, S_4, D_2, C_{2v}, C_3, C_2, and C_s. The triply degenerate level T_1 would split into either two or three levels under the influence of the lower symmetries, and the polarization under the reduced symmetry can be calculated using group theoretical arguments. These considerations show that polarization can be explained satisfactorily if the pseudo-symmetry of the molecule is taken as C_s. Complete selection rules for various possible symmetries are given elsewhere (4, 11). Under the field of symmetry C_s, the level T_1 would split up into three levels. Two of these levels would have a A'' symmetry and the third A'. The two transitions from the A'' levels, $A'' \rightarrow A'$, are allowed in the z direction (c-crystallographic axis) and the transition $A' \rightarrow A'$ is allowed in the (x,y) direction (perpendicular to the c-axis). Thus a partial polarization of the emitted radiation with the major electric vector along the c-axis would be expected as observed.

Table I. Electric-dipole selection rules under the D_{2d} symmetry for the emission transition $T_1 \rightarrow A_1$ (tetrahedral).

Transition	Polarization of emitted radiation	
	(x,y)	z
$E \rightarrow A_1$	Allowed	Forbidden
$A_2 \rightarrow A_1$	Forbidden	Forbidden

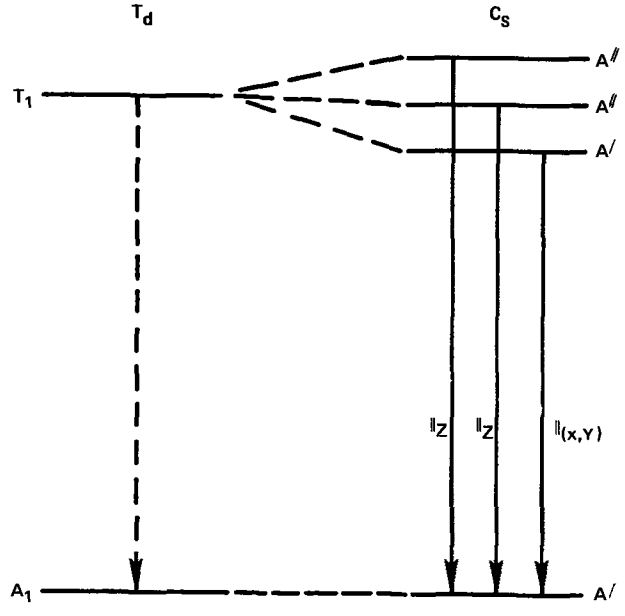

Fig. 1. Selection rules under the reduced symmetry. The T_d transition $T_1 \rightarrow A_1$ is forbidden, however, under the reduced symmetry C_s, the level T_1 splits into three levels, two with the symmetry A'' and one A'. The transitions $A'' \rightarrow A'$ are allowed along the c-axis, and the transition $A' \rightarrow A'$ is allowed perpendicular to the c-axis.

The energy level diagram and the polarization under C_s symmetry is shown in Fig. 1. Under C_s symmetry the calculated value of polarization, p, is 0.33 (assuming equal transition probability from each level). This compares fairly well with the observed value of 0.3.

It may be pointed out here that only electric dipole type transitions were considered to explain the observed polarization. Also, if the first excited level is $^3T_1$, the transitions to the ground state ($^1A_1$) are allowed only to the extent that there is spin-orbit coupling. Walter and Butler (9) place $^3T_1$ as the lowest excited state level immediately followed by a $^1T_1$ level. The selection rules remain unchanged irrespective of whether the lowest lying excited level is $^3T_1$ or $^1T_1$.

It is not clear at present what causes this reduction of the symmetry of the luminescing $(WO_4)^{2-}$ groups from D_{2d} to C_s. It must be remembered that the symmetry of the bulk of the $(WO_4)^{2-}$ groups is the same as determined by the crystallographic consideration, and it is only the symmetry of luminescing groups which deviates from that determined by the crystal structure analysis. The luminescing $(WO_4)^{2-}$ groups with C_s symmetry can be expected to be present in the crystals in only trace activator quantities to avoid concentration quenching.

It may be speculated that because of the degenerate nature of the first excited state level T_1 the symmetry is spontaneously lowered because of the Jahn-Teller effect. However if such were the case then it is not clear why this happens only to the fraction of the groups which are responsible for the luminescence emission. Another possibility is that the equilibrium lattice defects produced during the high temperature synthesis are located in such a way that they cause the neighboring $(WO_4)^{2-}$ groups to deform to the C_s symmetry and these deformed groups then act as luminescence centers.

Acknowledgments

The author would like to thank Professors E. W. White, W. B. White, Rustum Roy, H. K. Henisch, and other members of the luminescence group at the Materials Research Laboratory, The Pennsylvania State University for many helpful discussions. Part of this work was supported by the Advanced Research Project Agency. The major part of this work was performed at the Materials Research Laboratory, The Pennsylvania State University.

Manuscript submitted June 3, 1973; revised manuscript received Aug. 27, 1973. This was Paper 32 presented at the Chicago, Illinois, Meeting of the Society, May 13-18, 1973.

Any discussion of this paper will appear in a Discussion Section to be published in the June 1974 JOURNAL.

REFERENCES

1. J. L. Ouweltjes, "Modern Materials," Vol. 5, Academic Press, New York (1965).
2. L. G. VanUitert, in "Luminescence of Inorganic Solids," P. Goldberg, Editor, p. 465, Academic Press, New York (1966).
3. R. J. R. S. B. Bhalla and E. W. White, *This Journal*, **119**, 740 (1972).
4. R. J. R. S. B. Bhalla, Ph.D. Thesis, Materials Research Laboratory. The Pennsylvania State University (September 1970).
5. J. Lebiedzik, E. W. White, and R. J. R. S. B. Bhalla, Unpublished.
6. R. T. Greer and E. W. White, Trans. 2nd Conf. Electron Microprobe Analysis, Paper 51 (1967).
7. M. A. Aia, *This Journal*, **114**, 367 (1967).
8. G. F. J. Garlik, in "Luminescence of Inorganic Solids," P. Goldberg, Editor, p. 685, Academic Press, New York (1966).
9. W. Walter and R. H. Butler, *This Journal*, **116**, 1245 (1969).
10. See for example W. L. Bragg and G. F. Claringbull, "Crystal Structure of Minerals," Cornell University Press, Ithaca, New York (1965).
11. R. J. R. S. B. Bhalla and E. W. White, *J. Luminescence*, **4**, 194 (1971).

A Simplification of Kämper's Striation Etch for Silicon

K. R. Mayer

Siemens AG, B GE 1, Munich 46, Germany

Kämper (1) proposed a method for revealing striations in dislocation-free silicon crystals working on a wide resistivity range of 0.001 up to 3000 ohm-cm. Previous methods, such as Vieweg-Gutberlet's (2) simple CrO_3/HF etch, are suitable for silicon of relatively low resistivity ($\rho < 1$ ohm-cm) only.

Kämper's method essentially consists of chemical polishing, two pretreatment procedures ("passivation," "activation"), and of the striation etching itself (see Table II) under illumination of the sample. Reaction time is about 15-20 min. Finally, the coating formed during the etching is removed by KOH.

Kämper's method has been criticized because it is complicated and difficult to be performed (3). As an alternative, it was observed that striations can be revealed in silicon of high resistivity (up to 1500 ohm-cm) by a simple CrO_3/HF etch after annealing the sample (3, 4) (annealing temperature $T = 1000°$-$1250°C$). It must be taken into account, however, that annealing

Key words: etching, silicon, striations.

might result in a change of material properties thus leading to a loss of both sharpness and fine structure of the chemically etched striations.

Therefore we tried to simplify Kämper's method. Our essential results are as follows (see also Table II). First, in order to obtain spotless surfaces, the wafer must be kept under liquid throughout the entire procedure. This is to prevent the wafer's surface from being exposed to air. In addition the chemical polishing step has to be stopped by HNO_3 (65%), not by water. In this way the formation of an adverse coating can be avoided [Archer, (5)]. Under these conditions Kämper's pretreatment steps 2 and 3 are not necessary.

Our striation etch consists of HF (48%), $NaNO_2$ (200-1000 mg/100 ml HF, depending on the sample resistivity), and a few drops of a usual acid wetting agent. The dangerous addition of acetic anhydride (which is proposed by Kämper to lower the surface tension) to the HF giving a strongly exothermic reaction can thus be avoided.

When HNO_3 is used as an oxidant, it must be taken into account that the reaction with silicon starts very slowly. This can lead to an uneven etch attack on the surface. Therefore we used $NaNO_2$ instead of HNO_3. $NaNO_2$ decomposes immediately in the acid solution to yield various nitrogen oxides [*e.g.*, NO_2, N_2O_4, HNO_2, see (6)] which give a faster reaction with silicon.

The illumination of the sample is effectuated by a 100W lamp. At least for silicon of very high resistivity ($\rho > 100$ ohm-cm) it is favorable to use the infrared part of radiation only by inserting a suitable filter ($\lambda > 650$ nm, as usually applied in *IR* photography). We found that illumination with shorter wavelengths often gives more hazy surfaces. The reason for this has not been well understood as yet.

The following procedure is proposed. Use thoroughly cleaned Teflon beakers and a particular sample holder (Fig. 1). The surface of the wafer must be lapped (grain size, 20 μm or less).

Polish the clean, lapped wafer chemically in a mixture of HNO_3 (65%), HF (40%), and acetic acid (100%) (8:5:5 parts by volume) for 10 min. Take 5 ml of etchant for each cm² of area to be etched. Stop by adding the same quantity of HNO_3 (65%). Immerse the sample together with the holder into water and thereafter into acetic acid. Make sure that the wafer remains entirely covered by the liquid. With chemically-mechanically polished wafers we often obtained bad results.

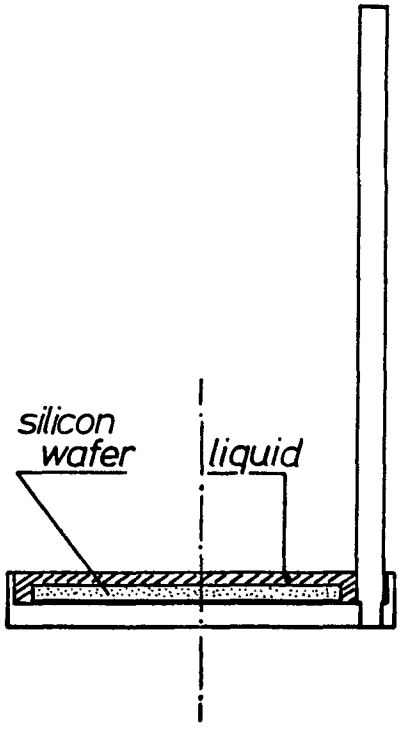

Fig. 1. Teflon sample holder

Table I.

Resistivity (ohm-cm)	Type	$NaNO_2$ (mg/100 ml HF)
<50	n	200
50-200	n	400
>200	n	1000
1-1000	p	1000

Add 2-5 drops of a slightly acid wetting agent [e.g., "Mirasol" (trade name of TETENAL, Photowerk, Hamburg, Germany), pH = 4-5].

Prepare about 5 ml striation etchant per cm² of area to be etched by dissolving the necessary amount of $NaNO_2$ in HF (48%) as given in Table I.

Switch on illumination. The sample together with the sample holder is taken out of the acetic acid. Let the acetic acid run off in such a way that a thin acid film remains on the wafer in order to protect the surface against contact with air. Immerse the sample together with the holder into the striation etch. Shake carefully. A completely uniform and colored coating develops. Etching is finished after 15-20 min. During the etching the solution may become opaque which does not affect the surface quality.

Immerse the sample into water. Finally dissolve the coating in a 10% KOH-solution (1-2 min). Rinse with water.

With wafers cut perpendicular to the growth axis it may be of some advantage to leave the colored coating on the surface in order to improve the visibility of the striation pattern and to get satisfactory photographs. The coating stays stable for several days. Obviously, the visibility of the striation pattern on cross-sectioned wafers also depends on the curvature of the striations with respect to a plane parallel to the growth axis (Fig. 2).

The experiments were mainly carried out with as grown n-type silicon crystals (phosphorus doped). Even with highly boron doped p-type silicon the striations do not appear as sharp as in n-type silicon. This is likely to be caused by a smaller periodic variation of the dopant concentration (the segregation coefficient of boron is nearly unity).

The described method can be applied to both floating-zone and crucible-grown silicon.

Table II gives a comparison of Kämper's original method with our simplified striation etching.

Figure 3 shows striation patterns of crystals of high resistivity (n- and p-type, respectively) as revealed by the simplified striation etching. There is little knowledge about the reaction mechanism of the striation etching. Undoubtedly, the etch rate only depends on the oxidation rate because the etchant contains a strong excess of HF (6).

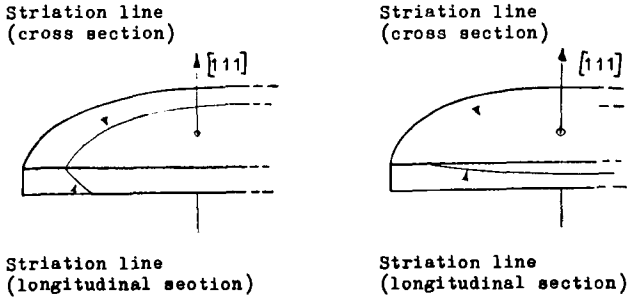

Fig. 2. Visibility of striations on a cross-sectioned wafer depending on the curvature of the striations on a longitudinal section (schematic). (a, left) Strong curvature (sharp striation line on the cross section) and (b, right) weak curvature (blurred striation line).

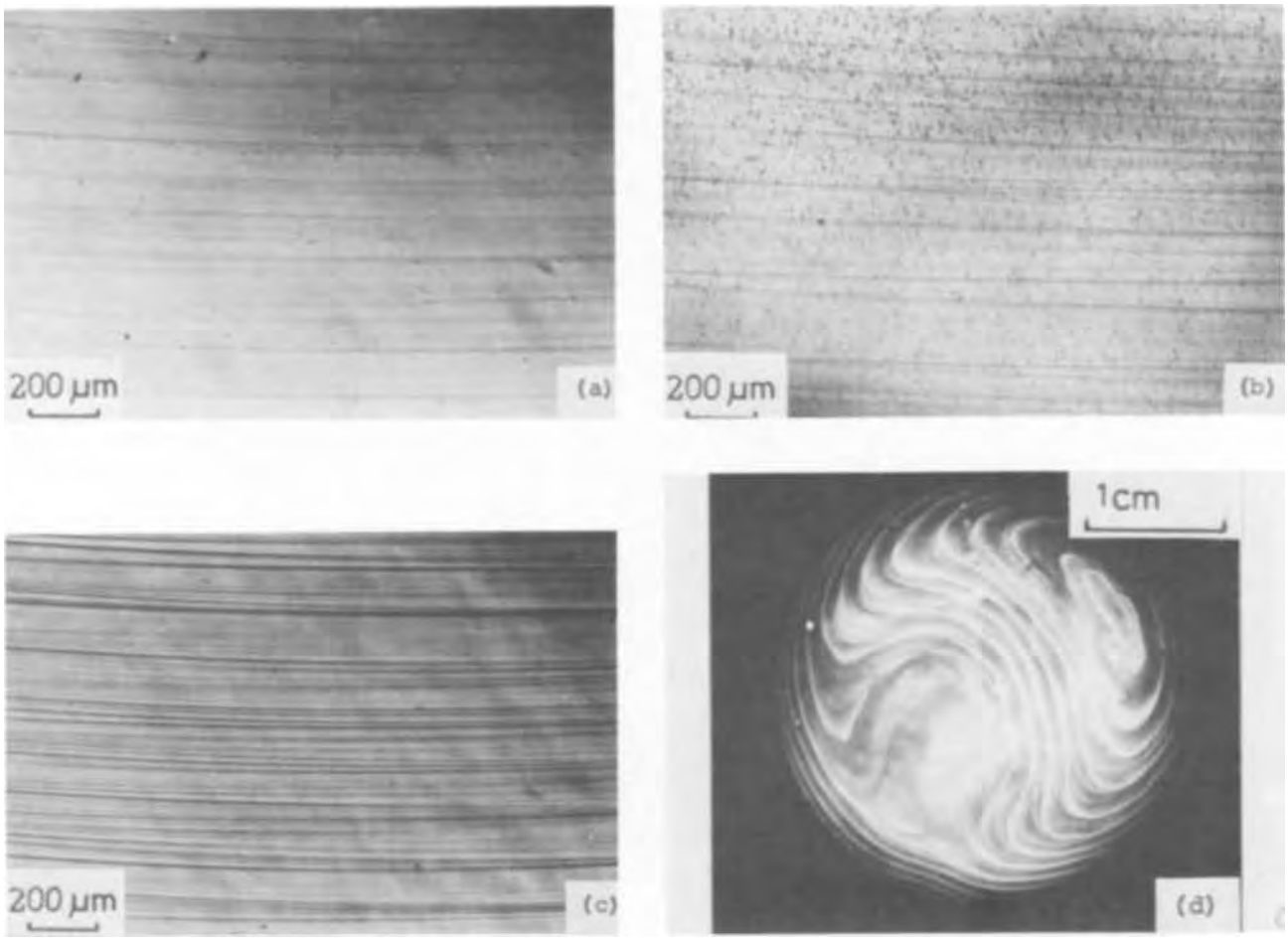

Fig. 3. Striations revealed by the simplified etch. (a) 1000 ohm-cm, n-doped; (b) 500 ohm-cm, p-doped; (c) 5 ohm-cm, n-doped; (a-c) are longitudinal sections; and (d) 30 ohm-cm, n-doped, cross section.

The oxidation itself can schematically be represented by an electron transition process from silicon to the oxidant depending on the electron density in the conduction band of the crystal. Therefore, a local periodic variation of the electron density (which is thought to be essentially caused by a variation of the dopant concentration) results in a periodically varying etch attack thus giving the striated pattern.

As to the necessary illumination of the sample during the etching, it seems that the average electron density of high-resistivity silicon (*i.e.*, $\rho > 1$ ohm-cm) must be increased in order to obtain a satisfactory reaction. This, however, leads to a decrease of the relative variation of the electron density in comparison with the original, not illuminated sample. With samples of lower resistivity the illumination is not always necessary.

On the other hand, some—as yet unknown—recombination centers may be present, the concentration of which varying in a similar way as the dopant concentration does. This would result in a periodic variation of the electron density generated by illumination. It is not clear whether or not this effect plays an important role.

Additionally, in the presence of relatively high concentrations of nondoping impurities (*e.g.*, oxygen or carbon), a completely different reaction mechanism may become predominant. As an example, striations caused by fluctuations of a high carbon concentration can simply be revealed by the common Sirtl etch (7).

Table II.

Steps	After Kämper	Simplified
1	Chemical polishing	Chemical polishing
2	Passivation (HNO_3/acetic acid)	—
3	Activation (KOH)	—
4	Striation etching (HF, acetic anhydride, HNO_3, $NiSO_4$)	Striation etching (HF, $NaNO_2$, wetting agent)
5	Final treatment (KOH)	Final treatment (KOH)

Acknowledgments

The author would like to thank Mr. H. Benda for stimulating discussions and Mr. A. Steidel and Mr. M. Süss for performing the experiments.

This work has been supported by the technological program of the Federal Department of Research and Technology of the FRG. The author alone is responsible for the content.

Manuscript submitted March 13, 1973; revised manuscript received July 9, 1973.

Any discussion of this paper will appear in a Discussion Section to be published in the June 1974 JOURNAL.

REFERENCES

1. M. Kämper, *This Journal*, **117**, 261 (1970).
2. F. Vieweg-Gutberlet, *Solid-State Electron.*, **12**, 731 (1969).
3. A. J. R. de Kock and P. G. T. Boonen, *This Journal*, **119**, 1241 (1972).
4. F. Dannhäuser, J. Krausse, and K. Mayer, *Solid-State Electron.*, **15**, 1383 (1972).
5. R. J. Archer, *J. Phys. Chem. Solids*, **14**, 104 (1960).
6. H. Robbins and B. Schwartz, *This Journal*, **106**, 505 (1959).
7. T. Abe, Y. Abe, and J. I. Chikawa, "Semiconductor Silicon 1973," R. Huff and R. R. Burgess, Editors, p. 95, The Electrochemical Society Softbound Symposium Series, Princeton, N. J. (1973).

Vapor Phase Epitaxial Growth of GaN on GaAs, GaP, Si, and Sapphire Substrates from $GaBr_3$ and NH_3

Yasuo Morimoto, Kosuke Uchiho, and Shintaro Ushio

Research Laboratory, OKI Electric Industry Company, Ltd., 550-5, Higashi-asakawa, Hachioji, Tokyo 192, Japan

GaN is a III-V compound with wurzite-type crystal structure to which serious attention is now paid because of the potentiality for the application to optoelectronic devices. Various methods for the preparation of GaN crystals have been investigated (1). Recently application of the reaction between $GaBr_3$ and NH_3 has been proposed (2), which involves the reaction below

$$GaBr_3 + NH_3 \rightarrow GaN + 3HBr \quad [1]$$

Beside the above reaction, there should be a reaction described as

$$HBr + NH_3 \rightarrow NH_4Br \quad [2]$$

because NH_4Br was found to be included in GaN films grown on GaAs substrates as mentioned in the section below. This reaction [1] proceeds at fairly low temperature below 600°C, probably due to the weak binding force between Ga and Br (2), and so the growth of GaN is possible at low temperature. Since only Si and SiC were used as substrates in Ref. (2), the growth behavior of GaN was investigated in detail using substrates other than Si such as GaAs, GaP, and sapphire. The substrate surfaces used were (111) for GaAs, GaP, and Si, and (0001) for sapphire. The reactor arrangement and the typical temperature distribution in the reactor are shown in Fig. 1. The source $GaBr_3$ which presents as a complex $GaBr_3 \cdot 4NH_3$ (2) absorbing NH_3 is carried by NH_3 to the reaction zone and GaN is formed. The source ($GaBr_3 \cdot 4NH_3$) temperature and the flow rate of the carrier gas (NH_3) were kept constant at 240°C and at 1 liter/min, respectively. In this note growth behavior of GaN on GaAs, GaP, Si, and sapphire substrates are investigated in detail as a function of the growth temperature. And the quality of GaN films prepared is examined by x-ray diffraction and microphotographic observation. Preliminary measurements are also made on electrical properties of GaN films and on the changes of it due to the annealing.

Key words: GaN, heteroepitaxy.

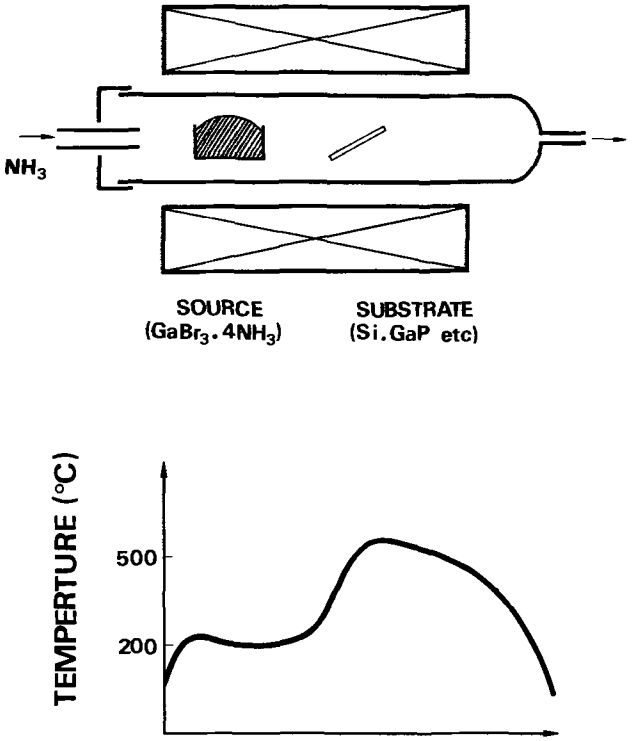

Fig. 1. Reactor arrangement for the vapor phase epitaxial growth of GaN. The typical temperature distribution in the reactor is also represented.

Results and Discussions

Yellow powder of GaN was deposited on the quartz reaction tube between 400° and 600°C. Below 400°C no deposition occurred, and above 600°C, black films were obtained which is due to the formation of Ga metal. From x-ray diffraction it was found that these deposits were GaN crystal with lattice constant of $a = 3.186$Å and $c = 5.178$Å.

The general tendency of the epitaxial growth of GaN on a substrate was described by four characteristic temperatures, T_1, T_2, T_3, and T_4. No deposition occurred below T_1 and black films were obtained above T_4. The films grew but the surface was gray and rough between T_1 and T_4. Yellow and transparent GaN films were formed between T_2 and T_4. The films obtained in the higher temperature side ($T_3 \sim T_4$) completely fell off from the substrates after the growth run or fell off by weak thermal or mechanical stimulus. The GaN films grown in the lower temperature region ($T_2 \sim T_3$) were adherent. This can be attributed to the difference of thermal dilation coefficient between GaN and substrates that the temperature range ($T_2 \sim T_4$) is separated into two parts, $T_2 \sim T_3$ and $T_3 \sim T_4$. Different values of T_1, T_2, T_3, and T_4 were obtained for different substrates. These values and also the scheme of the general tendency of the growth behavior are given in Table I. The temperature range, $T_2 \sim T_3$, is assigned to be the most suitable growth condition. The temperature gradient at the substrates did not act as an important factor in the range, $T_2 \sim T_3$, since GaN films were formed similarly in up- and down-temperature gradient regions.

Films of 3 to 6 μm in thickness were obtained in the growth run of 6 hr.

The quality of GaN films deposited on each substrate between T_2 and T_3 are discussed below.

1. GaAs substrate specification: Te-doped N-type, $n = 1.5 \times 10^{18}$ cm^{-3}; (111) A and B plane. The surface of the films deposited was very rough, on which many cracks were observed even with a naked eye. And the films were of very poor adhesion. This may be due to the large mismatch of lattice constants between GaN and GaAs (about 25%). Typical x-ray diffraction pattern is given in Fig. 2. The most intense line (0002) and weak line ($10\bar{1}1$) of powder pattern of GaN were observed, which indicates the GaN on GaAs substrates to be polycrystalline though the growing plane was oriented to (0001). An interesting fact was that very intense reflections from NH_4Br were observed. NH_4Br may be produced by reaction [2]. The inclusion of NH_4Br to GaN epitaxial layer was not observed by x-ray diffraction for other substrates, however, there can be a possibility of NH_4Br included in semiconductor grade of NH_4Br into GaN layer grown on GaP, Si or semiconductor grade sapphire substrates.

Table I. The growth behavior of GaN and the values of T_1, T_2, T_3, and T_4

Temperature	T_1	T_2	T_3	T_4
Form of the deposit	No deposit	Gray deposit with rough surface	Yellow, transparent and adherent deposit	Yellow and transparent but nonadherent deposit	Black deposit

	Temperature (°C)			
Substrate	T_1	T_2	T_3	T_4
GaAs	400	450	470	600
GaP	400	450	550	600
Si	400	430	540	600
Sapphire	380	420	570	650

2. GaP substrate specification: Undoped N-type, $n = 10^{16}$ cm^{-3}; (111) A and B plane. Although cracks were not observed with a naked eye, the film surface was fairly rough by the microphotographic observation. X-ray diffraction showed the deposit to be single crystalline, however very weak reflection from (1011) was observed, indicating the presence of a small amount of polycrystal and so the nonuniform growth of GaN crystals.

3. Si substrate specification: Sb-doped N-type, $n = 10^{19}$ cm^{-3}, $\rho = 0.01$ ohm-cm; P-doped N-type, $n = 10^{15}$ cm^{-3}, $\rho = 18$ ohm-cm; B-doped N-type, $n = 10^{19}$ cm^{-3}, $\rho = 0.01$ ohm-cm; B-doped N-type, $n = 10^{15}$ cm^{-3}, $\rho = 30$ ohm-cm; (111) plane. The GaN films deposited similarly on Si substrates irrespective of the conduction type (N- or P-type) or the carrier concentration of the substrates. The microphotograph of the film surface is shown in Fig. 3. Though there are many defects, the surface was very smooth compared with that of GaN grown on GaAs or GaP substrates. The conduction type of the substrates was found to have a remarkable effect on the adhesion property of the films to substrates, that is, the films were not adherent on P-type Si, while fairly adherent on N-type Si. On the other hand, the carrier concentration had little effect on the adhesion property of the films. The intense and weak reflection line from (0002) and (0004), respectively, were only observed by x-ray diffraction, which shows a uniform growth of single crystalline GaN over the substrates.

4. Sapphire substrate specification: (0001) plane. Sapphire was found to be the best substrate among all the substrates mentioned above, on which GaN single crystal films with mirror-like surface were readily formed. Any defects could not be observed on the surface even by the microphotographic observation, the formation of which could not be avoided on the surface of GaN films grown on GaP or Si substrates as shown in Fig. 3. A satisfactory adhesion to sapphire was also achieved.

Preliminary measurements on the electrical properties of GaN were also done which were performed mainly on GaN films grown on sapphire substrates because of the good quality of the films. The ohmic

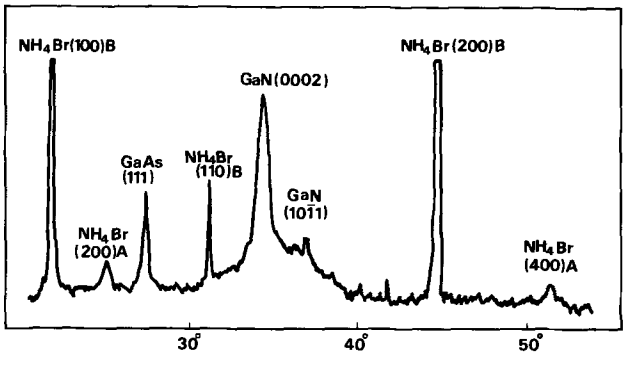

Fig. 2. Typical x-ray diffraction pattern from GaN films deposited on GaAs substrates. The most intense line for powder specimen is (10$\bar{1}$1) which is observed weakly. The line A and B show peaks from NH_4Br of high and low temperature phase, respectively. The reflections from GaAs are thought to arise from substrates, GaAs where GaAs is bare for cracks of GaN films.

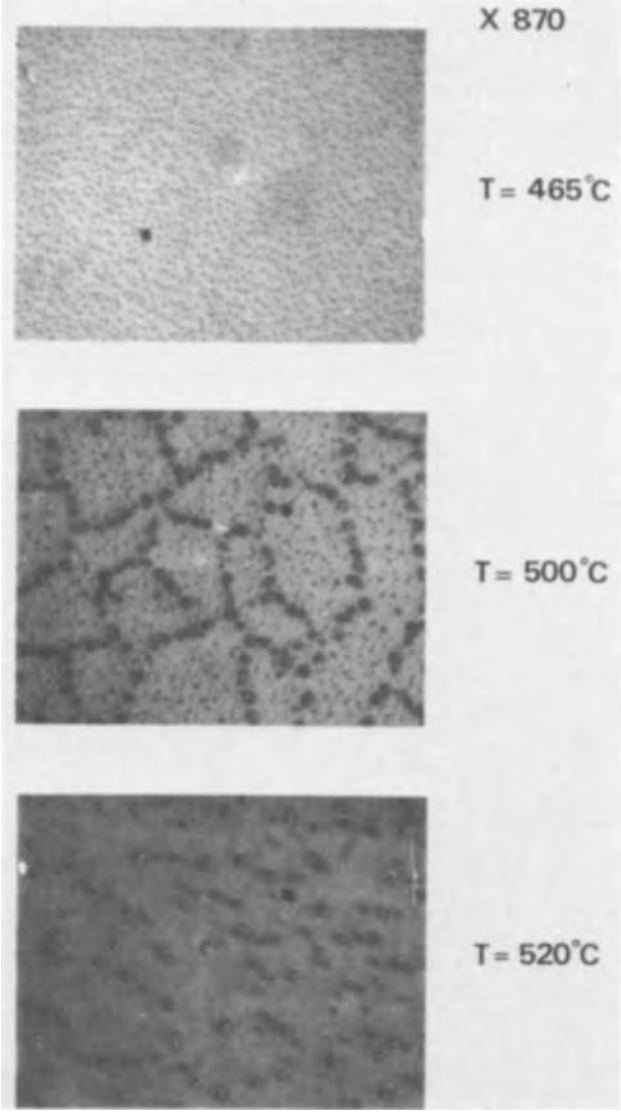

Fig. 3. The microphotograph of the GaN film surface grown on Si substrates. The temperatures shown indicate the growth temperature. The defects observed in this figure could not be recognized with a naked eye. The magnification of the microscope was ×870.

contact was achieved with Al or In by evaporation. The alloying of In to GaN was unsuccessful below 550°C. Above 550°C the films fell off from the substrates and seemed to decompose thermally because the color of the films changed into black. The atmosphere during this heat-treatment was nitrogen. Thus the alloying of In was not at all successful. The current *vs.* voltage characteristics of as-grown GaN crystals was similar to Fig. 6 in Ref. (2). Ohmic characteristics were observed in the small current region. Resistivity measured at room temperature by van der Pauw's method was of the order of 10^4 to 10^6 ohm-cm. The space charge limited current was observed in the large current region. Resistivity decreased two or three orders of magnitude when GaN films were annealed at above 400°C for 6 hr in vacuum or nitrogen atmosphere. This can be attributed to the generation of nitrogen vacancies formed by the thermal decomposition of GaN though clear evidence of it is not obtained. The temperature dependence of the resistivity of annealed GaN is given in Fig. 4. Since Hall effect could not be detected (high carrier concentration ?) the type of conduction was not determined clearly. However both as-grown and annealed GaN (both undoped) were thought to be N-type because ohmic character appeared for In-GaN-Si(N-type)-Au structure, on the other hand rectification behavior appeared for In-GaN-Si(P-type)-Au structure where forward direction appeared when In electrode was biased negative.

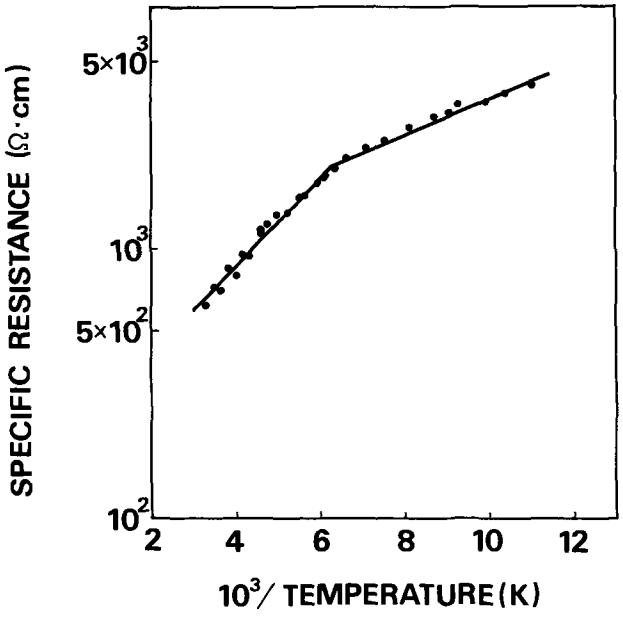

Fig. 4. Temperature dependence of resistivity of GaN annealed at about 500°C in vacuum for 6 hr. This Arrhenius plot gives two activation energies of 31 and 13 meV for high and low temperature region between 77° and 300°K.

Acknowledgment

The authors express their sincere thanks to K. Taniguchi, M. Sano, and M. Kizawa in the Reliability Engineering Center for their serious efforts on x-ray diffraction measurements. They are also indebted to Mr. H. Okamoto in the Reliability Engineering Center for reading the manuscript.

Manuscript submitted May 14, 1973; revised manuscript received July 26, 1973.

Any discussion of this paper will appear in a Discussion Section to be published in the June 1974 JOURNAL.

REFERENCES

1. H. P. Maruska and J. J. Tietjen, *Appl. Phys. Letters*, **15**, 327 (1969); B. B. Kociski and D. Kahng, *J. Vacuum Sci. Technol.*, **6**, 593 (1969); M. R. Lorenz and B. B. Binkowsky, *This Journal*, **109**, 24 (1962); R. A. Logan and C. D. Thurmond, *ibid.*, **119**, 1727 (1972).
2. T. L. Chu, *This Journal*, **118**, 1200 (1971).

Graphical Technique to Determine the Density of Surface States at the Si-SiO_2 Interface of MOS Devices Using the Quasistatic C-V Method

R. Van Overstraeten, G. Declerck, and G. Broux

Fysika en Elektronica van de Halfgeleiders, Departement Elektrotechniek, Katholieke Universiteit Leuven, B-3030 Heverlee, Belgium

The low-frequency C-V technique of Berglund (1) is a well-known technique to study surface states at the silicon-silicon dioxide interface. Problems arising at the low measurement frequencies are avoided by using the quasistatic C-V method of Kuhn (2) and Castagné (3). The current response of the MOS capacitor on a linear voltage ramp is measured with an operational amplifier to plot the C-V curve directly.

The relation between the surface potential ϕ_s and the gate voltage V_g is calculated with the Berglund integration

$$\phi_s(V_g) = \int_{V_{G1}}^{V_G} \left(1 - \frac{C_{LF}}{C_{ox}}\right) dV_g + \Delta_B \qquad [1]$$

In this formula C_{LF} is the experimental low-frequency MOS capacitance; C_{ox} is the oxide capacitance, found in strong accumulation; and Δ_B is the integration constant of Berglund. From expression [1] it can be seen that Δ_B is the surface potential at V_{G1}. As explained by Kuhn (2), Δ_B is obtained by fitting theoretical and experimental $C_{LF} - \phi_s$ curves in accumulation and strong inversion and by taking V_{G1} in accumulation where ϕ_s is well known.

The surface-state capacitance C_{ss} is derived from the experimental low-frequency MOS capacitance by

$$q N_{ss} = C_{ss} = \frac{C_{LF}}{1 - \dfrac{C_{LF}}{C_{ox}}} - C_{si} \qquad [2]$$

N_{ss} is the density of surface states in cm^{-2} eV^{-1} and C_{si} is the semiconductor capacitance which can be calculated as soon as the $\phi_s - V_G$ relation is determined. In practice the $N_{ss} - \phi_s$ curve is calculated using a computer. The inputs of the computer program are the measured value of the impurity doping, the oxide thickness, and the plotted C-V curve. The Berglund

Key words: method, density of surface states.

integration is performed according to Eq. [1] and N_{ss} *vs.* ϕ_s is calculated according to Eq. [2].

Accuracy of the Low-Frequency C-V Method

Before coming to the new graphical technique it is necessary to discuss the accuracy obtainable with the low-frequency method.

Influence of measuring inaccuracies.—As this effect has already been discussed in detail by Kuhn (2) only a numerical example will be given. The experimental data are: $N_D = 1.45 \times 10^{15}$ cm^{-3}; $C_{LF} = 1.17 \times 10^{-8}$F cm^{-2} at the minimum of the C-V curve ($\phi_s = -500$ mV); $d_{ox} = 1345$Å; and $C_{ox} = 2.50 \times 10^{-8}$F cm^{-2}. C_{si} calculated at $\phi_s = -500$ mV is 1.62×10^{-8}F cm^{-2}. Equation [2] gives

$$qN_{ss} = C_{ss} = 22.1 \times 10^{-9} - 16.2 \times 10^{-9}$$

$$= 5.9 \times 10^{-9}\text{F cm}^{-2}$$

or $N_{ss} = 3.7 \times 10^{10}$ cm^{-2} eV^{-1}. This N_{ss} value can still easily be detected whereas a density of 1.0×10^{10} cm^{-2} eV^{-1} would lead to

$$qN_{ss} = C_{ss} = 17.8 \times 10^{-9} - 16.2 \times 10^{-9}$$

$$= 1.6 \times 10^{-9}\text{F cm}^{-2}$$

From this last example it may be seen that $C_{LF} \cdot (1 - C_{LF}/C_{ox})^{-1}$ and C_{si} are of the same order of magnitude and that the difference C_{ss} is one order of magnitude smaller. A small error on these two terms thus gives a larger error on C_{ss}.

In general it may be stated that the measuring errors of C_{ox} and C_{LF} are of the order of a few per cent, as is the error of the theoretical value of C_{si} because of the uncertainties of the impurity concentration and of the integration constant Δ_B (Eq. [1]).

For a surface-state density of 1.0×10^9 cm^{-2} eV^{-1} the two right hand terms of Eq. [2] are two orders of magnitude larger than C_{ss}. Due to the measuring errors, the differences C_{ss} is totally inaccurate.

It may thus be concluded that it is very difficult to determine the density N_{ss} with an accuracy better than 1.0×10^{10} cm^{-2} eV^{-1}. The accuracy is best at the minimum of the low-frequency C-V curve as the two terms in Eq. [2] become smallest at that point. This conclusion will be used to set up the graphical technique.

Influence of the inaccuracies of Δ_B on the $N_{ss} - \phi_s$ curve.—Figure 1 shows the computer results for N_{ss} *vs.* ϕ_s for several Δ_B values. From this figure it may be derived that:

(*i*) Inaccuracies in the integration constant Δ_B strongly affect the N_{ss} curve in accumulation and strong inversion. The surface-state density is almost independent of Δ_B at a surface potential ϕ_s near −500 mV. This potential lies in the range where the low-frequency capacitance reaches the minimum value of the C-V curve.

(*ii*) Figure 1 also presents the N_{ss} values found on the same MOS structure by means of the conductance technique of Nicollian-Goetzberger (4, 5). The agreement between these results and those found at −500 mV by the quasistatic technique is quite good.

Influence of the oxide charge fluctuations on the $N_{ss} - \phi_s$ curve.—Figure 2 (5) shows the apparent surface-state density N^*_{ss} caused by surface potential fluctuations (3). The parameter to describe the surface potential fluctuations is the standard deviation σ_q of the oxide charge distribution. The results of Fig. 2 are obtained by theoretical calculations based on experimental values of the standard deviation σ_s of the surface potential fluctuations. As a complete discussion is given in Ref. (5), one only has to remark here that: (*i*) small deviations of the integration constant Δ_B clearly affect the $N^*_{ss} - \phi_s$ curve in accumulation and strong inversion; (*ii*) at midgap the influence of the oxide charge fluctuations is smaller than 1.0×10^{10} cm^{-2} eV^{-1}; and (*iii*) a peak density can be found at $\phi_s = 2\phi_F$.

Summary.—From the previous discussion it may be concluded that the low-frequency C-V method allows an accurate determination only at a bias corresponding to the minimum of the C-V curve. Even at that point it is difficult to determine N_{ss} within an accuracy better than 1.0×10^{10} cm^{-2} eV^{-1}.

Our graphical technique is based on the measurement of the low-frequency minimum capacitance. It is no limitation that N_{ss} will be determined only at one ϕ_s value, since it has been shown earlier (5) that N_{ss} is nearly constant in depletion and weak inversion.

Graphical Technique

For quality control purposes Fogels and Salama (6) already suggested a similar method to obtain an approximate surface-state density near midgap. However it is possible to base an easier graphical technique for Eq. [2] by rewriting the equation as

$$\frac{qN_{ss}}{C_{ox}} = \frac{\left(\frac{C_{LF}}{C_{ox}}\right)_{min}}{1 - \left(\frac{C_{LF}}{C_{ox}}\right)_{min}} - \left(\frac{C_{si}}{C_{ox}}\right)_{min} \qquad [3]$$

In this formula $(C_{LF}/C_{ox})_{min}$ is the experimental low-frequency minimum capacitance ratio, and $(C_{si}/C_{ox})_{min}$

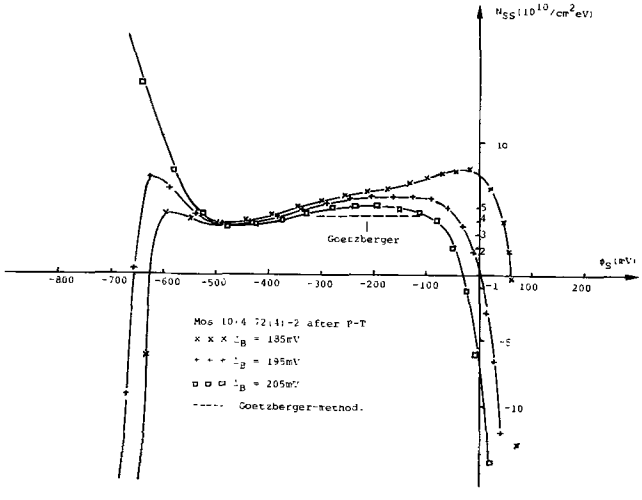

Fig. 1. Experimental results of the Berglund-Kuhn technique. The doping concentration $N_D = 1.45 \times 10^{15}$ cm^{-3} and the oxide thickness is 1345Å. The influence of different Δ_B values is shown. A comparison is made with the Goetzberger method.

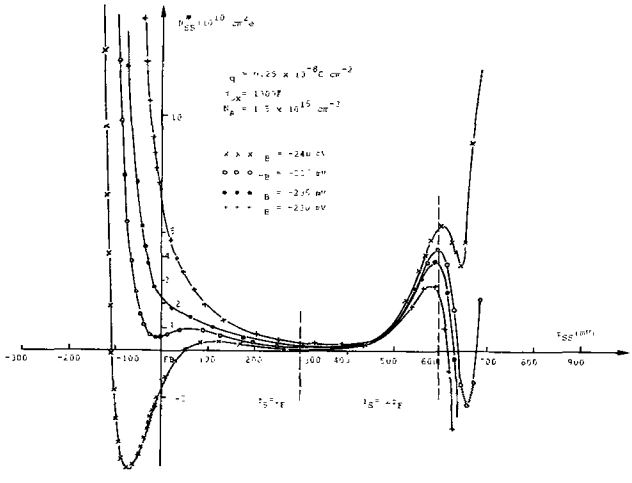

Fig. 2. Apparent surface-states density N^*_{ss} caused by surface potential fluctuations. The standard deviation σ_Q of the oxide charge fluctuation is 2.5×10^{-9} coulomb cm^{-2}.

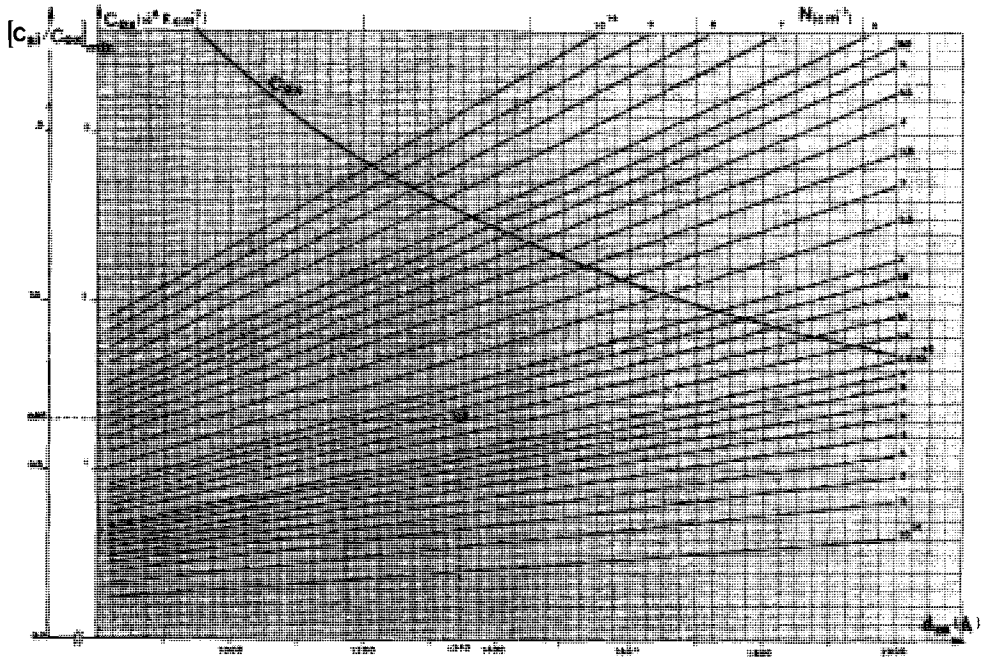

Fig. 3. $(C_{si}/C_{ox})_{min}$ is found as a function of measured N and d_{ox} values. The oxide capacitance C_{ox} is also presented.

is the theoretical low-frequency semiconductor capacitance, divided by the oxide capacitance. $(C_{si}/C_{ox})_{min}$ is calculated from the oxide capacitance and the doping concentration. A good value for the concentration can be found by measuring the minimum of the high-frequency C-V curve.

The graphical technique is presented in Fig. 3 and 4. Figure 3 shows $(C_{si}/C_{ox})_{min}$ as a function of the measured N and d_{ox} values. The oxide capacitance C_{ox} is also shown. Figure 4 shows qN_{ss}/C_{ox} as a function of $(C_{si}/C_{ox})_{min}$ for several values of $(C_{LF}/C_{ox})_{min}$ (Eq. [3]).

The technique is illustrated with the same example as given in Fig. 1. The experimental data are: $N_D = 1.45 \times 10^{15}$ cm^{-3}; $(C_{LF}/C_{ox})_{min} = 0.47$; $d_{ox} = 1345$Å;

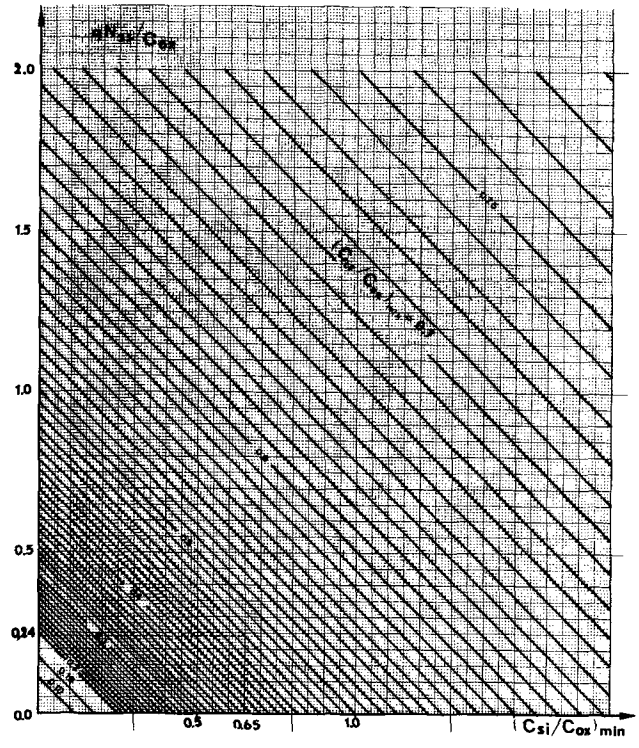

Fig. 4. Determination of qN_{ss}/C_{ox} as a function of experimental $(C_{LF}/C_{ox})_{min}$ and of the $(C_{si}/C_{ox})_{min}$ found in Fig. 3.

and $C_{ox} = 2.50 \times 10^{-8}$F cm^{-2} ($C_{ox} = \epsilon_{ox}/d_{ox}$ with $\epsilon_{ox} = 3.38 \times 10^{-13}$ F/cm).

From Fig. 3 the theoretical $(C_{si}/C_{ox})_{min}$ can be determined using the measured values of N_D and d_{ox}, giving for our numerical example $(C_{si}/C_{ox})_{min} = 0.65$.

Then Fig. 4 directly leads to $qN_{ss}/C_{ox} = 0.24$ as $(C_{si}/C_{ox})_{min}$ and $(C_{LF}/C_{ox})_{min}$ are known. Finally the density N_{ss} of surface states is found as 3.8×10^{10} cm^{-2} eV^{-1}, in very good agreement with the results of Fig. 1 at $\phi_s = -500$ mV.

Conclusion

A fast graphical technique is presented to evaluate the quality of MOS samples and to obtain an accurate value for the surface-state density at the minimum of the low-frequency C-V curves. Figures 3 and 4 can be extended to thicker oxide layers or to other substrate dopings when necessary. As for the normal low-frequency C-V method, the accuracy of this graphical technique is limited by measurement errors in the C-V characteristic and by errors on the substrate doping and on the oxide thickness. An accuracy of 1.0×10^{10} cm^{-2} eV^{-1} can be achieved.

Acknowledgments

The authors thank the Computer Center of the University for running the programs. G. Declerck is indebted to the Nationaal Fonds voor Wetenschappelijk Onderzoek for his Fellowship, and G. Broux to the Instituut tot Aanmoediging van het Wetenschappelijk Onderzoek in Nijverheid en Landbouw also for his Fellowship.

Manuscript submitted Jan. 23, 1973; revised manuscript received July 5, 1973.

Any discussion of this paper will appear in a Discussion Section to be published in the June 1974 JOURNAL.

REFERENCES

1. C. N. Berglund, *I.E.E.E. Trans. Electron Devices*, **ED-13**, 701 (1966).
2. M. Kuhn, *Solid-State Electron.*, **13**, 873 (1970).
3. R. Castagné and A. Vapaille, *Surface Sci.*, **28**, 157 (1971).
4. E. H. Nicollian and A. Goetzberger, *Bell System Tech. J.*, **46**, 1055 (1967).
5. G. Declerck, R. Van Overstraeten, and G. Broux, *Solid-State Electron.*, To be published.
6. E. A. Fogels and C. A. T. Salama, *This Journal*, **118**, 2002 (1971).

DISCUSSION SECTION

This Discussion Section includes discussion of papers appearing in the *Journal of The Electrochemical Society*, Vol. 119, No. 7, 8, and 11; July, August, and November 1972; Vol. 120, No. 4 and 6; April and June 1973.

On the Mechanism of Low-Temperature Oxidation (23°-450°C) of Polycrystalline Nickel

M. J. Graham and M. Cohen (pp. 879-882, Vol. 119, No. 7)

P. J. Zimmer:[1] Regarding the saturation of the wall of the system with oxygen to minimize the subsequent absorption of oxygen during the oxidation of the metal in the paper under discussion, it would seem that this has no effect on the final result, because, in step (*iii*) of the above-mentioned paper, the subsequent reduction of the sample with hydrogen would remove the oxygen absorbed, if not by reaction to form H_2O, then by replacement, leaving the walls in the same state as if the oxygen were not used.

M. J. Graham and M. Cohen: The walls of the metal UHV system remain saturated with oxygen following the hydrogen reduction procedure [step (*iii*) in the paper under discussion], because only the specimen and the quartz tube are at the reduction temperature of 600°C. The rest of the system is at room temperature and oxygen is not removed from these cold walls which constitute the major internal surface area. Thus, the blank adsorption correction in a subsequent oxidation experiment is minimized when the walls are presaturated.

A Limitation of the Pulsed Capacitance Technique of Measuring Impurity Profiles

A. R. LeBlanc, D. D. Kleppinger, and J. P. Walsh (pp. 1068-1071, Vol. 119, No. 8)

J. Olenski:[2] Messrs. LeBlanc, Kleppinger, and Walsh have given in the paper under discussion the expression for an apparent impurity concentration obtained from real capacitance-voltage characteristics of an MOS structure

$$N(W) = \frac{-C^3}{q\epsilon_s\left(\frac{C_o}{C_o+C_s}\right)^2\frac{\beta\epsilon_s}{L_D F^2}\frac{\left\{F\left(e^{-\beta\psi_s}+\frac{n_{po}}{p_{po}}e^{\beta\psi_s}\right)-\frac{1}{2F}\left[1-e^{-\beta\psi_s}+\frac{n_{po}}{p_{po}}(e^{\beta\psi_s}-1)\right]^2\right\}}{1+\frac{\epsilon_s}{L_D C_o F}\left[1-e^{-\beta\psi_s}+\frac{n_{po}}{p_{po}}(e^{\beta\psi_s}-1)\right]}} \quad [1]$$

This can be transformed into

$$N(W) = p_{po}\frac{\left[1-e^{-\beta\psi_s}+\frac{n_{po}}{p_{po}}(e^{\beta\psi_s}-1)\right]^3}{\left[1-e^{-\beta\psi_s}+\frac{n_{po}}{p_{po}}(e^{\beta\psi_s}-1)\right]^2-2F^2\left(e^{-\beta\psi_s}+\frac{n_{po}}{p_{po}}e^{\beta\psi_s}\right)} \quad [2]$$

or in another form

$$N(W) = p_{po}\frac{\left(\frac{dB}{du_s}\right)^3}{\left(\frac{dB}{du_s}\right)^2-2B\frac{d^2B}{du_s^2}} \quad [3]$$

where $B = F^2$ and $u_s = \beta\psi_s$.

We can assume for small surface potentials $\beta\psi_s$ that a charge of minority carriers in a surface charge layer is negligible as compared to a charge of majority carriers and ionized impurity atoms. It means in our considerations that

$$e^{-\beta\psi_s} >> \frac{n_{po}}{p_{po}}e^{\beta\psi_s} \quad [4]$$

Then we can omit all components multiplied by $\frac{n_{po}}{p_{po}}$ and Eq. [2] simplifies to

$$N(W) \cong p_{po}\frac{(1-e^{-\beta\psi_s})^3}{[1-e^{-\beta\psi_s}]^2-2e^{-\beta\psi_s}(e^{-\beta\psi_s}+\beta\psi_s-1)} = p_{po}\frac{(1-e^{-\beta\psi_s})^3}{1-e^{-\beta\psi_s}(e^{-\beta\psi_s}+2\beta\psi_s)} \quad [5]$$

As can be seen from Eq. [5] the apparent impurity concentration normalized to the real acceptor concentration N_A given by

$$\frac{N(W)}{N_A} \cong \frac{(1-e^{-\beta\psi_s})^3}{1-e^{-\beta\psi_s}(e^{-\beta\psi_s}+2\beta\psi_s)} \quad [6]$$

depends on temperature and not on acceptor concentration. The dependence on concentration is important only when condition [4] is not valid. But for typical silicon substrates and epitaxial layers the maximum depth calculated from surface potential defined by that condition is beyond the region where the apparent concentration increase is observable. Assuming that $e^{-\beta\psi_s} = 100\frac{n_{po}}{p_{po}}e^{\beta\psi_s}$, $\beta = 38.7V^{-1}$, and $N_A = 2.10^{15}$ cm^{-3}, we obtain the surface potential value $\psi_{se} = 0.245V$ while $\frac{N(\psi_{se})-N_A}{N_A} = 0.1\%$ as calculated from Eq. [6]. This difference becomes smaller when N_A is increased. Thus the curves $N(W) = f(\psi_s)$ presented in the paper under discussion for different impurity concentrations can be transformed into one plot $\frac{N(W)}{N_A}$ which does not depend on N_A. That plot is shown in Fig. 1. On the other hand we can, *a priori*, neglect the charge of minority carriers when the

[1] Chemistry Department, Villanova University, Villanova, Pennsylvania 19085.
[2] Institute of Electron Technology, Warsaw, Poland.

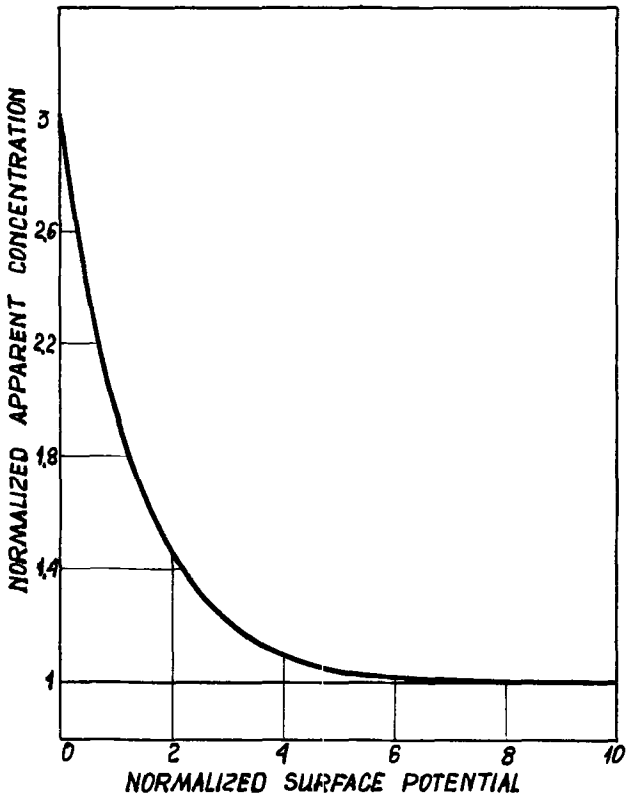

Fig. 1. Apparent impurity concentration normalized to real concentration N_A vs. normalized surface potential $u_s = \beta\psi_s$ calculated from Eq. [6].

structure is pulse biased from accumulation in the inversion direction. The minority carrier concentration for deep depletion is established by a d-c bias and does not vary when the pulse is short enough. Then we can always use Eq. [6] instead of Eq. [2].

Oxidation State of Anodic Tantalum Oxide after Heat-Treatment. I. Galvanostatic Method as Applied after Heating in Vacuum

Gerhart P. Klein (pp. 1551-1560, Vol. 119, No. 11)

E. Günzel:[3] Recently we carried out similar experiments to those of Klein in the paper under discussion with vacuum annealed anodic Ta_2O_5-films. Our specimens were powder pellets sintered at 2000°C and 10^{-5} Torr. The charge of the pellets was $CV_A = 1100$ μF·V (V_A = anodizing voltage), and they were anodized with a current density of 20 mA/pellet at 60°C in various electrolyte solutions. Heat-treatment conditions were 450°C, 10^{-5} Torr for 10 min. Reanodization was performed with 0.5 mA/pellet in the anodizing solution. Figure 1 shows the loss of oxygen as number of electrons/cm^3 *vs.* reanodization voltage. With this configuration the curves in the paper under discussion can be compared directly with our curves.

Pure stoichiometric Ta_2O_5-films are obtained by anodization in aqueous solutions of chromic acid. This was found by radiotracer experiments.[4] After heat-treatment the distribution of the defect concentration in these films exhibits nearly a uniform gradient independent of the electrolyte concentration (0.05 and 2M, curve A). One must conclude that deviations from the shape of curve A are caused by the incorporation of foreign ions. In oxide films containing phosphorous there is a maximum of deficiency concentration at $V/V_A = 0.4 \ldots 0.5$ (curves B-D) which was also found by the author in the paper under discussion for

[3] Siemens AG, Grundlagenentwicklung für Bauelemente, Munich 80, Germany.
[4] H. Wörl, W. D. Münz, and E. Günzel, *Metall*, To be published.

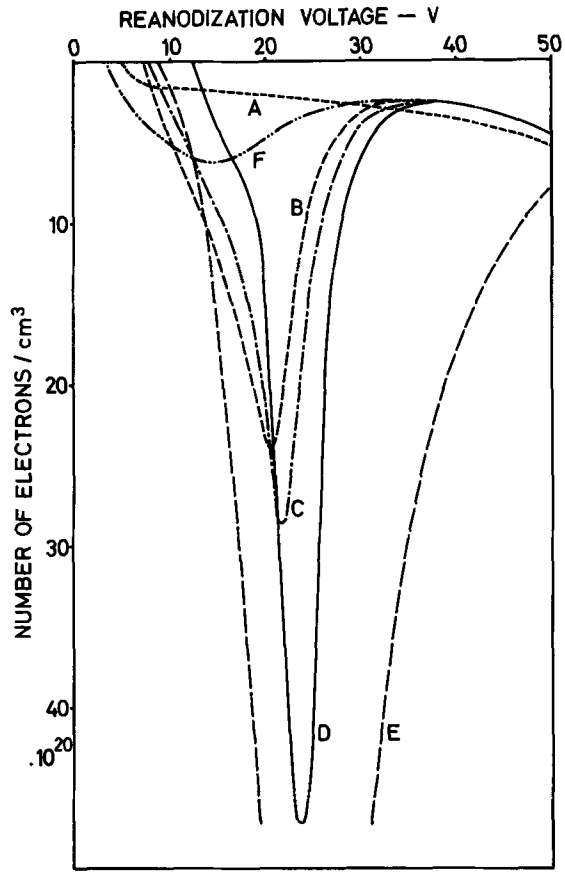

Fig. 1. Oxygen loss vs. reanodization voltage. Anodization voltage, 50V. Curve A, 0.05 and 2M chromic acid electrolyte; curve B, 0.002M phosphoric acid electrolyte; curve C, 0.1M phosphoric acid electrolyte; curve D, 5.0M phosphoric acid electrolyte; curve E, 5.0M sulfuric acid electrolyte; curve F, 0.2M citric acid electrolyte.

short times of heating. This maximum becomes sharper with increasing electrolyte concentration.

During anodization in sulfuric acid solutions there will be an incorporation of sulfur which markedly depends on the acid concentration (compare works of Footnotes 5 and 6). In contrast to dilute solutions (0.1M) we found a considerable effect with concentrated solutions (curve E: 5M). This curve suggests that sulfur is incorporated not only in the outward part of the oxide layer (like phosphorous) but in the entire oxide.

Curve F was obtained for an oxide film which was formed in 0.2M citric acid, *i.e.*, that even components of organic electrolytes can be incorporated into oxide films on tantalum and that this foreign matter can influence the oxygen distribution after heat-treatment.

It is demonstrated by such experiments that the maximum amount of oxygen loss after vacuum heat-treatment, and the oxygen diffusion, are increased by the presence of certain foreign ions. This result is in apparent contradiction to former investigations[7,8] in which anodic Ta oxide layers were heat-treated in air. It was found that in this case the oxygen diffusion is hindered by incorporated phosphorous. It can be assumed, however, that during heat-treatment in air at least the oxygen atoms in the outer part of the layer diffuse via interstitial sites whereas during heat-treatment *in vacuo* diffusion via vacancies takes place. Both kinds of diffusion can be affected by incorporated foreign ions in different ways.

[5] J. J. Randall, W. J. Bernard, and R. R. Wilkinson, *Electrochim. Acta*, **10**, 183 (1965).
[6] G. Amsel, C. Cherki, G. Feuillade, and J. P. Nadai, *J. Phys. Chem. Solids*, **30**, 2117 (1969).
[7] D. M. Smyth, T. B. Tripp, and G. A. Shirn, *This Journal*, **113**, 100 (1966).
[8] R. E. Pawel, *ibid.*, **114**, 1222 (1967).

Electrically Active Stacking Faults in Silicon

K. V. Ravi, C. J. Varker, and C. E. Volk
(pp. 533-541, Vol. 120, No. 4)

H. F. Mataré:[9] The electronic effects of process-induced defects (stacking faults) in silicon are of major importance to the device manufacturer. The authors of the paper under discussion are to be commended for their careful study of fundamental features of these defects, using modern tools.

They clearly demonstrate the two distinct regions around a defect zone, the reverse and forward biased regions, and the resulting contrast due to enhanced carrier generation within the depleted area. Similar SEB pictures on grown-in defects under lateral fields have been published before.[10]

Precipitates like SiO_2 and B, which are supposed to be present near the stacking faults, cannot however account for the differences in their electrical behavior as the independence of junction reverse current from the number of faults shows, and as the noncorrelation of fault length and reverse leakage and the correlation of fault length and "threshold-voltage" show. These properties of the stacking faults can be understood when one applies the known electronic model of defect line charges. The authors' opinion in the paper under discussion that impurity decoration will alter and perturb the behavior of dislocations or faults is correct but insulator inclusions (like SiO_2) in particular, will not eliminate the strong electronic effects of the non-closed lattice (dangling bonds). With the assumption that one sees here the SEM replica (EBIC mode) of the npn- or pnp-dislocation junctions, one can explain that:

(*i*) Space charge reversal occurs at transition from the self-biasing mode ($VR = OV$) to a biased mode.[10]

(*ii*) Current enhancement occurs due to a hook effect at the npnp-structures.

(*iii*) Longer faults have a higher transfer resistance and are less lossy for the main junction, as their bond overlap is incomplete.

(*iv*) Dislocation orientation is crucial with respect to the effect on the external junction field. Strongest effects on leakage current should be expected when the electric field vector is parallel to the Burgers vector of the partial dislocation, as in this case the dislocation shunts the external field.

The above conclusions are in line with the degenerate, high conductivity of dislocation cores and numerous scanning electron-beam studies on dislocations in silicon and germanium-mono- and bicrystals, subjected to lateral surface fields.[11]

K. V. Ravi, C. J. Varker, and C. E. Volk: We would like to thank Dr. Mataré for his comments on our paper.

A good agreement between theory and experiment is the fond hope of all investigators. However, most experiments have to contend with numerous uncontrolled or uncontrollable parameters which generally preclude an exact or, often, even an approximate verification of an idealized theory. We believe the case of crystallographic defects in semiconductors and their electrical ramifications is a good example of the situation wherein the theoretically expected behavior of the defects have not been verified by experiment. It is flattering that Dr. Mataré believes that our work has perhaps bridged this gap between theory and experiment. However, we believe that this is not the case.

A detailed atomistic model of structural defects cannot be derived from the electron-beam induced current (EBIC) display alone. A thorough analysis using transmission electron microscopy and detailed electrical measurements are also required.

The correct interpretation of contrast effects using the EBIC mode is of utmost importance and considerable effort has been expended by us to prevent misinterpretation of these effects. A detailed analysis of the I-V characteristics of a given diode always preceeds the EBIC analysis. This permits a direct correlation between the EBIC technique and the resulting I-V characteristics of the diode.

The zone of contrast surrounding the decorated stacking fault results directly from minority carrier recombination in a low lifetime region surrounding the stacking fault. When this zone extends into the space charge region, as in the case of electrically active stacking faults, the generation zone is easily observed with the EBIC technique.

The concentration of minority carriers in the space charge region of p-n junctions can be altered between a depletion of minority carriers when the reverse voltage is greater than kT/q to an excess of minority carriers when the forward voltage is greater than kT/q. Consequently, when the applied voltage V is in the range $-100 \text{ meV} < V < +100 \text{ meV}$ the magnitude of the recombination contrast can be enhanced or suppressed by altering the voltage across the p-n junction. However, the resulting display includes the effects of the video amplifier and the coupling circuit between the device and the amplifier chain. In our technique, a-c coupling is used to prevent the reverse current instabilities associated with high leakage junctions under voltage bias from degrading the quality of the display during the scan. When these factors are considered, the observed contrast effects can be understood in more conventional terms.

With regard to the mechanism(s) of recombination and generation of charge carriers at the stacking fault it seems to us that an analysis based upon the so-called "defect line charge" model of dislocations ignores the obvious perturbations resulting from impurity precipitation at the defects. Indeed if Fig. 5 and 8 of the paper under discussion are compared there is a direct correlation between the fault length and reverse leakage. The fault length in turn is related to the degree of decoration of the fault. As has been shown, boron is very likely to be a major constituent of the precipitates at the faults and it has also been determined subsequently that fast diffusing metallic impurities are also involved in the precipitates.[12] Consequently, the theoretically expected electronic effects of dangling bonds will be overshadowed by the effects of precipitates, their strain fields, and by a local increased concentration of impurities in solid solution around the faults. To make the assumption that "one sees the SEM replica of the npn- or pnp-dislocation junctions" is not valid and is not supported by any evidence. Regarding the four points raised by Dr. Mataré the following rebuttals are deemed to be in order:

(*i*) EBIC signals do not exhibit a polarity reversal under biased conditions as suggested in the above discussion. The pseudo-contrast reversal at low voltages results directly from the differentiating effect of capacitive coupling.

(*ii*) Current enhancement coincides with a voltage-power law relationship in the I-V characteristics of the diode.[12] There is no experimental evidence for a hook transistor effect, but considerable experimental evidence exists that an impurity atmosphere and/or strain field surrounds the fault which can introduce a generation-recombination zone around the fault.

(*iii*) The relationship between fault length and threshold voltage can be explained in terms of the position of the stacking fault and the associated pre-

[9] International Rectifier Corporation, Semiconductor Division, Los Angeles, California 90245.

[10] H. F. Mataré and C. W. Laakso, *J. Appl. Phys.*, 40, 476 (1969).

[11] H. F. Mataré, "Defect Electronics in Semiconductors," pp. 194-210, 261-282, 448-455, John Wiley & Sons, Inc., New York (1971).

[12] C. J. Varker and K. V. Ravi, *J. Appl. Phys*, In press.

cipitates with respect to the depletion region of the p-n junction.

(iv) Dislocation orientation is perhaps important if one considers a "clean" undecorated dislocation. Since the fault and the bounding dislocation are profusely decorated the more important factor is the strain/impurity atmosphere surrounding the fault. It has been found that both the strain field as well as the g-r zone surrounding the defect are roughly symmetrical with respect to the defect.

The Kinetics of Thin Oxide Film Formation on Iron Using Proton-Impact-Excited X-Ray Analysis

P. B. Needham, Jr., H. W. Leavenworth, Jr., and T. J. Driscoll
(pp. 778-783 Vol. 120, No. 6)

B. Chattopadhyay:[13] The authors in the paper under discussion have discussed the oxidation kinetics in terms of Uhlig's theory for logarithmic oxidation[14] which has been criticized[15-17] for neglecting the effect of surface-state charge. We[16,17] have modified Uhlig's model for p-type oxide formation by using Bardeen's concept on the rectifier theory of the metal/semiconductor junction.[18] This modified theory has been justified by estimating successfully certain critical parameters from the oxidation data of metals,[17] such as copper,[14] nickel,[19] and cobalt.[20] We would like to apply the theory to the present case of iron.

Our theory[16,17] applies to the oxide containing a uniform density space charge layer, *i.e.*, the so-called first stage of oxidation.[14] The energy drop due to surface-state charge, eV_s is estimated to be 2.34 eV, using the work function of iron as 4.7 eV[21] and the activation energy of oxidation as 3.58 kcal (0.155 eV)/mole. The surface-state charge density, n_s, is next estimated to be $6 \times 10^{14}/cm^2$ using the dielectric constant of ferrous oxide[22] as 14. This value of n_s, which is higher than $10^{13}/cm^2$, indicates the ineffectiveness of the metal property on the double layer[18] (of surface-state charge and space charge). The space charge density, on the other hand, is calculated as $7.5 \times 10^{19}/cm^3$ which is a reasonable figure for the density of trapping centers in the oxide.[16,17] Results at the highest temperature, namely 350°C, are used for present calculations. The energy increase due to space charge, eV_p, is finally estimated as 0.146 eV (using the maximum thickness in the first stage of oxidation, *viz.* 50Å). The results obviously show that $eV_s >> eV_p$, and thus indicate the importance and predominant contribution of surface-state charge over the space charge to the potential across the oxide. Therefore, it would be perhaps more justifiable to adopt the modified[16,17] rather than the original theory[14] to explain the direct logarithmic oxidation kinetics.

P. B. Needham, Jr., H. W. Leavenworth, Jr., and T. J. Driscoll: In the paper under discussion our experimental oxidation results were discussed in terms of Uhlig's theory of logarithmic oxidation for two reasons: (i) Uhlig's theory[14] predicts kinetics involving a transition to a higher logarithmic rate constant at some oxide thickness and (ii) the oxide thicknesses where we found such a transition to occur agreed well with values predicted using our experimental parameters (rate constants, time constants, and activation energy) with equations based on Uhlig's theory.[23] In the paper being discussed we stated that this agreement may have been fortuitous since there were unanswered questions concerning the effects of initial surface impurities (particularly sulfur), the stoichiometry of the oxide films, and the crystallographic orientation of the large substrate grains. Considering Fromhold's criticism[15,24] of Uhlig's theory because of Uhlig's use of boundary conditions which result in nonconservation of electrical charge during oxide film growth, it is welcome to find a proposed[17] alternate mechanism which might provide results similar to Uhlig's (which offer the best apparent interpretation of much experimental data, including the dependence of oxidation rate on the substrate crystal orientation, lattice transformation, and Curie temperature) without violating the conservation of electrical charge. We feel that the introduction of surface states at the metal-oxide interface seems reasonable and that such states could be important in describing oxidation data where electronic transfer is the rate-limiting step. However, there are, we feel, two problem areas in Chattopadhyay's development of the surface-state charge model[17] and the equations with which he has calculated (or estimated) the values of eV_s and eV_p using our experimental results.

(i) Chattopadhyay has stated[17] that the "negative space charge will induce a surface-state charge of opposite sign on the localized electronic states associated with the surface lying in the forbidden energy region between the conduction and valence bands of the semiconducting oxide." This seems to indicate that the positive surface charge which Chattopadhyay introduces must be equal in magnitude to the space charge in the semiconductor (Fe_3O_4) during oxide growth. Since the trapped charge in the space charge region initially increases with increasing oxide thickness, the concentration of charged surface states, n_s, and the resulting potential, V_s, must also increase (at least initially) with increasing oxide thickness, y. Chattopadhyay, however, has made the surface state potential V_s independent of the oxide film thickness y. The closest case to a thickness-dependent surface charge in the literature is Fromhold's[24] consideration of positive charge at the metal-oxide interface (located on the metal, and not on the oxide as in Chattopadhyay's case) which compensates negative charge trapped in the space charge region. He guarantees over-all charge neutrality by including it as a boundary condition to Poisson's equation, and obtains logarithmic oxidation kinetics for the case where the oxide thickness is much larger than the maximum electron tunneling distance in the oxide. Fromhold finds a much smaller effect on the transfer of electrons into oxide from charge in the interfacial and space charge regions due to, among other reasons, the necessity of reducing the positive charge at the metal-oxide interface (compared to Uhlig's) to guarantee over-all charge neutrality. In Chattopadhyay's model, however, it is not clear exactly what kind of charge balance is implied by the boundary conditions.

(ii) To obtain logarithmic rate law oxidation kinetics of the form $y = K_0 \ln (1 + t/\beta)$,[17] Chattopadhyay has used, in addition to the before-mentioned surface-state potential, V_s, a space charge potential V_p derived using Poisson's equation in which, we feel, an incorrect approximation was used in the final equation describing the potential V_p at the metal-oxide interface due to the space charge layer

$$V_p = 4\pi n_v e [\gamma y + (1/2)y^2]/\epsilon$$

Here $n_v e$ is the space charge density, γ is an interfacial layer in the semiconductor equivalent to the average length of the individual surface dipole (about 3Å), y is the oxide thickness beyond γ, and ϵ is the dielectric

[13] Department of Metallurgy and Materials, City of London Polytechnic, London E1 7PF, England.
[14] H. H. Uhlig, *Acta Met.*, 4, 541 (1956).
[15] A. T. Fromhold, *This Journal*, 115, 882 (1968).
[16] B. Chattopadhyay, Ph.D. Thesis, London University (1967).
[17] B. Chattopadhyay, *Thin Solid Films*, 16, 117 (1973).
[18] J. Bardeen, *Phys. Rev.*, 71, 717 (1947).
[19] H. H. Uhlig, J. Pickett, and J. MacNairn, *Acta Met.*, 7, 111 (1959).
[20] B. Chattopadhyay and J. C. Measor, *J. Mater. Sci.*, 4, 456 (1969).
[21] A. B. Cardwell, *Phys. Rev.*, 92, 554 (1953).
[22] "Handbook of Chemistry and Physics," 49th ed., Chemical Rubber Co., Cleveland, Ohio (1968-69).
[23] V. O. Nwoko and H. H. Uhlig, *This Journal*, 112, 1181 (1965).
[24] A. T. Fromhold, Jr., *Nature*, 200, 1309 (1963).

constant of the oxide. He has dropped the term containing y^2 as an approximation for thin films. This would seem to us to neglect the scale of the constant γ, the thickness of the dipole layer region (*i.e.*, the surface-state charge region). At oxide thicknesses greater than $y = 6$Å, this deleted term will be larger than the γy term, and with the term y^2 in the exponential of the growth rate equation, $dy/dt = A \exp(-py^2 - \alpha y)$, where A, p, and α contain various constants, a direct-logarithmic rate law will not be obtained.

Errata

In the paper "The General Problem of Rediffusion in Semiconductor Devices" by Malcolm Fullenwider which appeared on pp. 1134-1135 in the August 1973 JOURNAL, Vol. 120, No. 8, the argument of the third term on the right-hand side of Eq. [3] should be:

$$\frac{(2n+1)L+x}{2(Dt)^{1/2}}$$

so that Eq. [3] reads:

$$C(x,t) = C_o - C_o \sum_{n=0}^{\infty} (-1)^n \operatorname{erfc} \frac{(2n+1)L+x}{2(Dt)^{1/2}} - C_o \sum_{n=0}^{\infty} (-1)^n \operatorname{erfc} \frac{(2n+1)L+x}{2(Dt)^{1/2}} \quad [3]$$

The purpose of this communication is to present a corrected version of Fig. 3 which appeared in the paper "The Electrolytic Behavior of CaF_2 Crystals under Reducing Conditions," by J. W. Hinze and J. W. Patterson which appeared on pp. 96-99 in the January 1973 JOURNAL, Vol. 120, No. 1. The corrected version, shown below, differs from the original only in that emf *vs.* temperature line "predicted from Wagner's analysis" (1) is shifted upwards, significantly closer to the observed data for the cell $Ca|CaF_2|Th, ThF_4$ and to the emf *vs.* temperature line "predicted from thermodynamic data." The error was detected as the result of a private communication on the matter from C. Wagner (March 9, 1973).

The main conclusion that "... the usefulness of CaF_2 as a solid electrolyte extends down to its stability limit ..." remains unaffected; however, the original version of Fig. 3 constitutes a misrepresentation of Wagner's analysis because the line so predicted should not have been that far removed from the overlying thermodynamic emf line.

The source of this excessive discrepancy was traced to the inconsistent use of ΔG^o_f data for CaF_2 by Hinze and Patterson in their paper. Whereas the thermodynamic emf line was calculated on the basis of JANAF data (2) for CaF_2 formation, the other line was calculated from equivalent emf data given by Hamer *et al.* (3). The corrected figure shown in this erratum uses the JANAF values for both lines and thus brings them closer together.

REFERENCES

1. C. Wagner, *This Journal*, **115**, 933 (1968).
2. "JANAF Thermochemical Data," Dow Corning Co., Midland, Michigan (June 30, 1971).
3. W. J. Hamer, M. S. Malmberg, and B. Rubin, *This Journal*, **112**, 750 (1965).

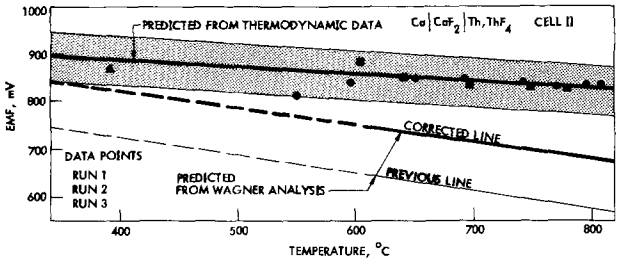

Fig. 3. Open-circuit emf *vs.* temperature for the cell Ca | CaF_2 | Th, ThF_4.

JOURNAL OF THE ELECTROCHEMICAL SOCIETY

REVIEWS AND NEWS

OCTOBER 1973

Energy Options[1]

Arthur M. Bueche

General Electric Research and Development Center, Schenectady, New York 12301

Under the heading of "energy options," as you might guess, it is my intention this morning to discuss some of the technical options available as we seek solutions to the "energy crisis."

The "energy crisis," of course, is a phrase that came into public prominence only during the past year. It presently runs a mere second among current items of interest to the daily press, the weekly news magazines, and other news media, but, in time, we can expect it to be back in "the number one spot." And this is appropriate because the "energy crisis" is a very real one, deserving the full attention of all of us.

Among the technical options, I will spend a little extra time this morning on one of particular interest to electrochemists, the so-called "hydrogen economy," although it is apparent as one reviews the list of other energy options that electrochemical technology of one kind or another is involved in nearly all of them.

However, we should also remember that when one speaks of "energy options," there are those who look well beyond just technology. Indeed, some people even try to claim that the energy crisis is not really a technical problem at all. Depending on how you look at it, it is a geopolitical problem, involving massive shifts in the world's balance of power based on ownership of oil reserves. Or it is a strictly domestic political problem, dependent on decisions with regard to natural gas prices, depletion allowances, and off-shore drilling regulations. Or it is strictly an economic problem, meaning that consumers are finally going to have to start paying a fair price for the incredible energy bargains they have been getting in the past. Or it is an environmental problem, which is really just a communications problem, educating people to understand the trade-offs required in matching their needs and desires for energy with their ecological hopes and dreams. Or it is a sociological and psychological problem, where the actual habits and wishes of people must be changed in the direction of using less energy; meaning, as a result, that their lives will be less easy, less pleasant, and less productive.

On the other hand, in spite of all of these alternatives, the energy crisis may just have to be a technological problem.

I say this because it has been proved over and over again in the past that it is easier to invent something new than it is to change people's habits; that it is easier to get a new technical idea than it is to alter the attitudes of different countries and cultures toward each other; that it is easier to do research than it is to improve the ability of people (even in the same family) to communicate with each other; that getting patents and putting them to use is easier to accomplish than upsetting the built-in political and economic status quo. For all these reasons, in the long run, the most likely, only source of workable answers to the energy crisis can realistically be expected to come from new technology.

[1] The Electrochemical Society Lecture delivered at the Chicago, Illinois, Meeting of the Society, May 14, 1973.

Let me qualify what I mean when I say "in the long run." Certainly, we are now exploiting many of the benefits of recent and current research and development to alleviate the energy crisis: nuclear plants of improved effectiveness are going on line; combined-cycle steam and gas generating stations are on the market and will very soon be in operation; more sophisticated and integrated systems-control methods are being introduced to improve the reliability of electric power. And there are other examples. These things are helping alleviate the present problems, although admittedly not rapidly enough or on a large enough scale, to provide the major solutions we must eventually have. That is what I mean about "in the long run," because it is an inescapable fact that many of the technological advances that can, hopefully, make additional major contributions to the solution of the energy crisis are several years, and in some cases, several decades, in the future.

To put this whole matter in perspective, let us take a quick look at where our present energy comes from, where it is used, and where some experts believe changes in these patterns will occur during the next 15 or so years.

Figure 1 shows the sources of our energy at the beginning of this decade. Oil, at 42%, is, of course, the area of greatest present concern, especially with its potential effect on the U.S. balance of payments and the resultant possible impact on the balance of power between nations. Natural gas supplies are being rapidly depleted. The greatest challenges to the technologists are in the areas of coal, where our reserves are extremely bountiful, and in nuclear energy, where the potential for electric power is so great. Water (hydro) is not considered a major new source of energy; we have pretty much already put to use our best opportunities for hydro-plants in the United States.

Who uses all this energy? Figure 2 shows the percentages. Surprisingly, the electric utility industry is not the overwhelming user of energy that many people have been led to believe. Rationing of electric energy

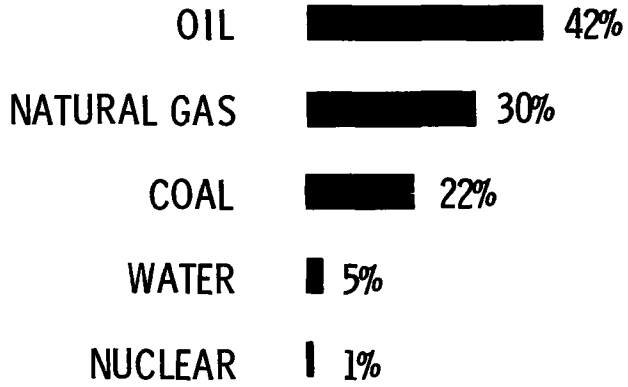

Fig. 1. Sources, energy use, 1970

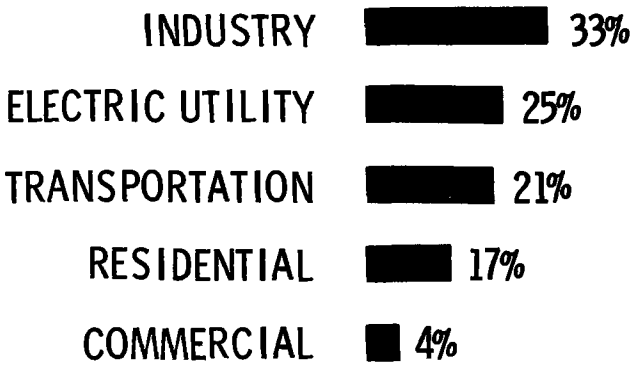

Fig. 2. Markets, energy use, 1970

seems self-defeating in view of its relative advantages, cleanliness, and efficiencies.

Indeed, all the most respected analysts of future trends (see Fig. 3) insist that the electric utility industry will have to grow substantially during the next 15 years, from about 25% of the total to some 37%. This is a tremendous challenge to R&D people in the electrical industry to make sure that this necessary increase in their services is accomplished with optimum effectiveness. Actually, in terms of per capita consumption, the changes in energy use during the next 15 years will be more in terms of the "type" of energy used rather than the "total."

Now let us look at the electric utility industry itself (Fig. 4). In 1970, nearly one half of its fuel was coal. Oil, surprisingly, was only 11% (although it has since increased because of ecological pressures), which means that changes in national and international oil policies would have rather less over-all effect on the utility industry than on other segments of our economy and society. Or conversely, rationing electricity would probably result in only minor savings of oil.

The future prognostications here are another great challenge to those performing R and D for the electrical business (Fig. 5). Because of the question marks related to the future of natural gas and oil supplies, and the generally accepted fact of rather limited op-

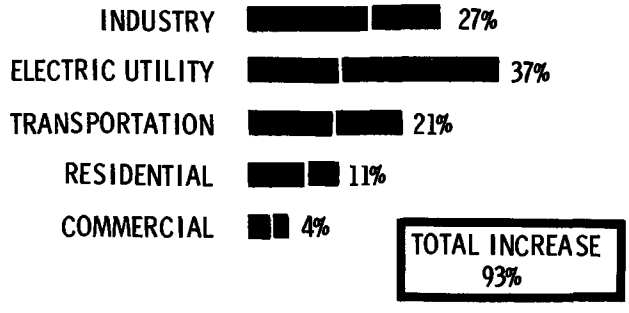

Fig. 3. Markets, energy use, 1970-1985

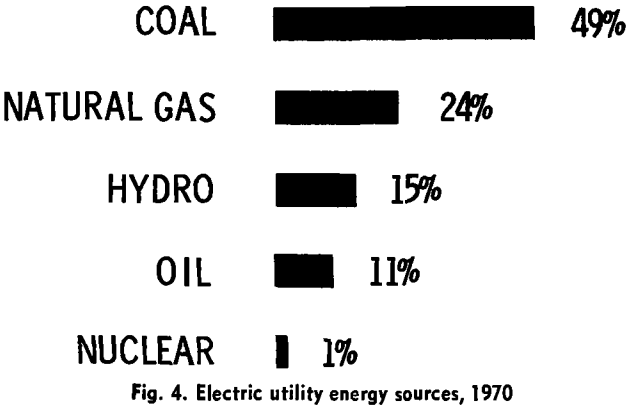

Fig. 4. Electric utility energy sources, 1970

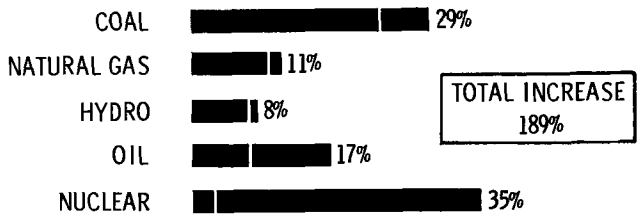

Fig. 5. Electric utility energy sources, 1970-1985

portunities for more hydro-power, we must do our utmost to find ways to increase the anticipated use of coal. This can be done by finding better ways to mine it, clean it, and, most likely, gasify it. At the same time, we might well turn our creative attention to the apparently vast reserves of shale oil. Similarly, we are challenged to make sure the estimated increase in nuclear power meets, and hopefully exceeds, the estimates of the experts who prepared these prognostications.

All of these challenges, all of these long-term responsibilities for finding real solutions to the energy crisis, put a substantial burden on the technologist.

Actually, potential technological solutions to the energy crisis fall into rather simple sounding options:

(*i*) Find new kinds of fuel, new basic energy sources, not now being used, such as fusion power and solar energy.

(*ii*) Find enlarged sources of present fuels; improve ways to locate and secure oil, gas, and uranium.

(*iii*) Improve on presently available fuels to produce cleaner oil and gas; especially cleaner coal, perhaps by gasifying it and scrubbing it in the process; and learn more effective means of enriching uranium.

(*iv*) Improve energy conversion techniques for higher efficiency, less waste, less left-over heat, and fewer environmental side effects.

(*v*) Improve transmission and power delivery systems for efficiency, safety, and environmental reasons, perhaps even going to the "hydrogen economy" that I have mentioned.

(*vi*) Improve the efficiency of the "end-use" of our available energy; *i.e.*, better engines, more efficient lamps and appliances, better insulation to reduce energy requirements for both heat and air conditioning, more effective use of waste heat now being thrown away, and so on.

Let me try to describe some of the electric industry technology that is being, and will be, conducted in a search for solutions in one or more of these six areas.

Actually, electric power research and development in the United States is in a state of rapid growth and considerable ferment. This situation arises because of the "energy crisis" we have discussed and from the additional fact that, as I have just listed, there are such vast technological options and opportunities for finding solutions.

Let us look briefly at the present national commitment to electric power R&D (Fig. 6). Federal Government funding now totals about $280 million per year, with 90% of this coming from the Atomic Energy Commission (AEC). However, it can be anticipated that an increasing share of the Federal Government's R&D support in this area will come from sources other than the AEC.

The electrical manufacturers are the second largest factor in electric power R&D. The utility industry itself has traditionally had relatively low direct R&D expenditures; instead they have relied heavily on the manufacturers to do the R&D, who then recover their R&D costs through the prices of their products.

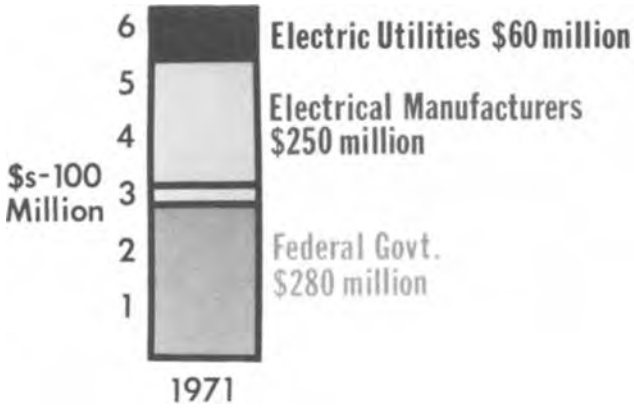

Fig. 6. Electric power R&D funding, 1971

This whole situation has the potential for explosive change, although actual change to date has not been radical.

Here is how we believe the situation will develop over the next five years (Fig. 7). The Federal Government, whose electric power R&D expenditures have been rising at 15-20% annually, will still remain the dominant factor. The electrical manufacturers will remain a strong number two.

Based on initiatives presently under way, the electric utilities are aiming to become a much more significant factor in R&D. Their share of the national total will likely increase from something under 10% in 1971 to over 20%, as shown here.

Now, I should hedge this prediction by reminding you that I referred to "utility industry initiatives presently under way." The prediction could be completely changed, however, if some proposed legislation is passed and implemented. For example, Senator Jackson has introduced a bill that would establish a $2 billion per year federal program in energy R&D. No one is sure who would provide and spend what under this proposal, but it would surely send the totals "right off the chart" (Fig. 8).

Well, I count myself among the world's staunchest advocates of increased R&D in this area, but I must admit to having some misgivings about how we could suddenly find the good people, the facilities, the potentially workable ideas, and the intelligent management needed to make proper and effective use of such vast amounts of money. In spite of some claims to the contrary, the job of solving the energy crisis is not really directly comparable to putting a man on the moon.

We in the manufacturing part of the electrical business readily recognize the more immediate, short-range

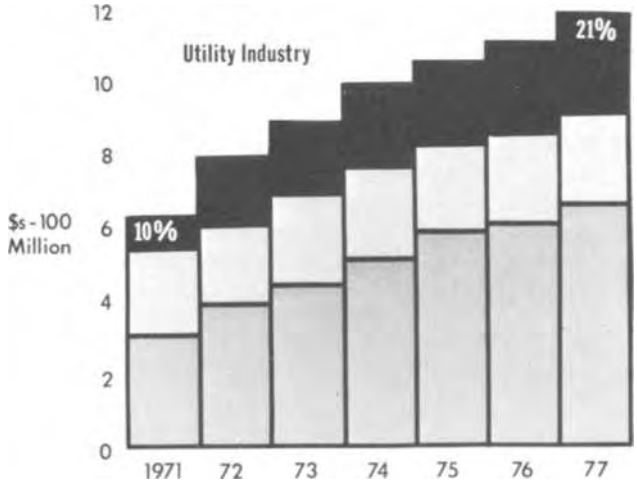

Fig. 7. Electric power R and D funding, 1971-1977

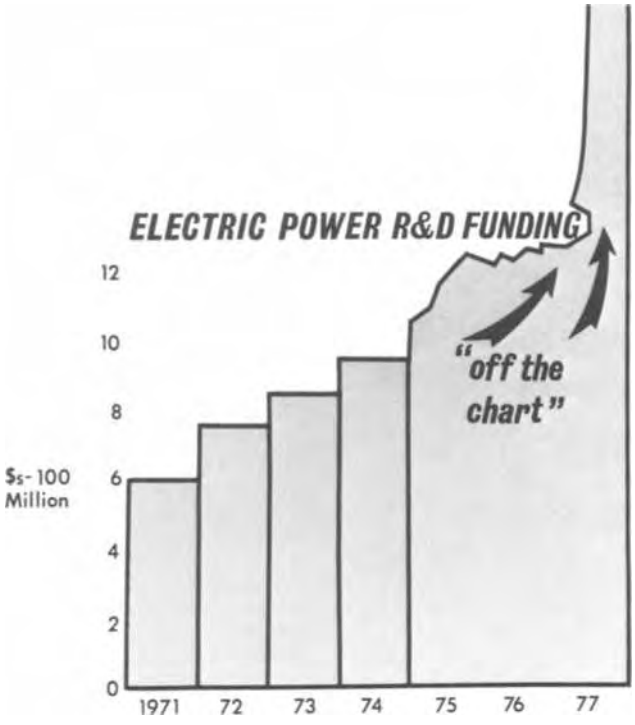

Fig. 8. Electric power R&D funding proposed for 1971-1977

problems we should be solving: improving generation efficiency through combination steam and gas cycles and by developing turbines that will operate at higher temperatures; assuring the life of nuclear fuel and the reliability of nuclear plants; exploring new methods for transmitting larger blocks of power over longer distances; trying to find answers to the ever-increasing problems of power-plant siting (a particular concern for the electric utility industry itself); continuing the constant search for higher reliability throughout the entire electric power systems of our country.

These, and many other areas I will not take time to mention, are some of the short-range challenges for the manufacturers and to the new cooperative R&D efforts of the electric utility industry. At the same time, we have some very exciting long-range options.

So let me conclude by spending a few minutes examining some of the more "far-out" energy technologies that have been touted as "the" answer that will solve our energy, economic, political, and environmental problems in one fell swoop, if only "those crazy scientists who could so easily put a man on the moon would just buckle down and put their minds to it."

There are more than a dozen such future hopes—*e.g.*, fusion, MHD, solar power, cryogenic transmission, the hydrogen economy, and so on—that have received enough public attention to convince many people that they are nearer, and easier, and cheaper, and cleaner, and safer than the facts, as we now know them, warrant.

But it remains that some of these are very real hopes for helping solve future energy crises before the end of this millenium.

Let me review several areas in which we in General Electric are deeply involved, from an R&D standpoint, and give you some candid views about their prospects.

First, in the basic area of energy sources—that is, fuel—the (perhaps) ultimate source for this planet is controlled thermonuclear fusion.

Hydrogen fusion, of course, is essentially the process of getting energy from the same source as the sun, from the joining of lightweight atoms. It is the hydrogen-bomb reaction—controlled.

Starting some 16 years ago, and for nearly a decade, General Electric was in the unique position of investing several million dollars of its own money to support fully its own research program on Controlled Nuclear Fusion. We knew from the beginning that it was a long shot, and it turned out that our first effort was premature.

We explored all the best ideas that we, or anyone else, had at the time and finally concluded, a half dozen years ago, that practical fusion power was just too far in the future to justify a continued commercial investment, at least until a better idea came along.

Now, in the past year or so, a new idea has come along: laser-ignited fusion. So we are involved again in fusion research. Along with EXXON, Northeast Utilities, the Empire State Electric Energy Research Corporation, and the New York State Atomic and Space Development Agency, we will be investing substantial sums of money over the next 3 years, plus the talents of some of our top scientists, in the laser-ignited fusion program being led at the University of Rochester in New York by Professor Moshe Lubin.

The most optimistic of realistic guesses about fusion is that it will not be ready for a major role in the energy picture until at least the turn of the century, by which time the evolution of other technologies and factors may vastly affect its economic viability. There are those who believe that fusion's ultimate role will be providing, from isolated locations, nuclear fuel for more conventional nuclear generating plants. Meanwhile, it is too big an idea basically to ignore. So, we are not ignoring it. But we believe it should be approached as an area of research, not as a large-scale development effort at this point in time.

Another obvious area for fuel research is to make better use of our most abundant fossil fuel: coal. At Schenectady we are substantially enlarging our R&D program in coal gasification. We have unique ideas that may make it possible to use even the dirtiest "caking" coals. Also, based on a tradition of research with membranes of various kinds, we have good ideas for taking the pollutants out of gasified coal before it is burned, which has obvious advantages over today's method in which one tries to take the SO_2 and other crud out of stack gases after combustion.

Coal gasification is not a long shot like fusion, for example. But making the process attractive enough to offset the economic, ecological, and social problems of expanding the coal mining industry will take substantial time. However, a commercial gasification process is available right now; and we have recently announced a joint program in this area with Lurgi, a German engineering firm with long experience in coal gasification.

I will mention four unique approaches to energy conversion in which we are currently making R&D investments.

Our investment in magnetohydrodynamics (MHD) is being made in the hope that we can get generating efficiencies of above 50%. (This, of course, is also the aim of our work on combined cycles and other approaches to more conventional power generation.)

The basic concept of MHD is that a very hot ionized gas, a plasma at temperatures in the range of 3100°-4900°F, replaces the metal conductor that moves through a magnetic field to create a current in a conventional generator. In past years, we invested heavily in this tempting idea and built some large test equipment. But the purely technical problems of gas conductivity and noncorroding electrode materials were formidable. More recently, people in our space business have made progress in developing a closed-cycle MHD system, as contrasted with the more frequently promoted open-cycle method, which shows sufficient scientific promise to justify continuing investigations.

The superconducting generator is another "long-term" prospect on my list. Our people, and others, have already demonstrated that superconductivity offers the possibility of decreasing by a factor of nearly three the size of generators for a given rating.

Another idea for improved energy conversion efficiency is the so-called "potassium topping" cycle. We recently proposed to the Office of Coal Research a program in which potassium (or cesium) would be used instead of boiling water in a coal-fired furnace boiler. In the potassium vapor turbine, the potassium would leave the boiler at a temperature of up to 1500°F, drive a turbo-generator, and then the potassium vapor leaving the topping-turbine would condense on the outside of condenser tubes, producing boiling water inside the tubes at 1050°F to run a conventional power plant. Addition of the "potassium topping" cycle offers the potential of total plant efficiencies in the range of 50-60%.

In the past years, General Electric has invested very heavily in fuel cell research.

Our invention of the ion-exchange fuel cell led to the first actual "practical application" of a fuel cell: the Gemini spacecraft unit that provided reliable onboard electricity without exceeding extremely stringent weight limits.

Currently, we are concentrating on fuel cells for the space shuttle and for some specialty marine applications. Fuel cells can be reliable, environmentally attractive power plants, but we believe that problems of cost of materials and their availability, of life, and of specialized fuel requirements are such that they must be regarded as still in the research phase.

We are also making substantial long-range investments in energy handling with regard to storage and delivery.

Three specific items might be mentioned briefly.

(*i*) One of our calculated-risk investments is in new types of batteries that may be useful for bulk energy storage as a possible substitute, perhaps underground, for the pumped hydro-plants that are frequent targets of the environmentalists. Success here might well influence our decision making with regard to the trade-off between base load and peaking capability of our power generation methods and will influence the development of system interties.

(*ii*) We are now in the second phase of an Edison Electric Institute (and Government) supported R&D program on cryogenic cable; *i.e.*, taking advantage of the vastly improved conductivity of metals at liquid nitrogen temperatures. Our first 40 ft test cable performed very well; the current phase is one of scale-up and refinement. But the day is still some years off before all of Chicago can be supplied with power through a few underground, supercold cables.

(*iii*) High voltage d-c power equipment is already a reality. The big "future" here, I believe, is that we have barely begun to tap the potential for using new solid-state technology for power conditioning on a very large scale.

For example, we can expect to see solid-state devices replacing a wide variety of electromechanical ones in applications such as voltage regulators and similar equipment that must stand up to many, many switchings. Solid-state science can profoundly affect the power delivery industry just as surely as it has already revolutionized the communications and information handling industries. For example, it can give us new options for transmitting large blocks of power through d-c interties, which will result in still more stable and versatile power systems.

Well, all of the long-range items I have mentioned so far are ones in which we are performing "at the bench" R&D programs, many of them on a very substantial scale. Perhaps I should also mention one intriguing area where we have carried out extensive techno-economic studies and have more recently begun experimental research.

This is in the area loosely referred to as the "hydrogen economy." The interest in hydrogen stems from

three major facts. First, hydrogen can be burned in a completely compatible manner from an ecological viewpoint.

Now, it is well known that if you burn hydrogen directly in air, you reach very high flame temperatures that not only cause basic problems with the materials in the combustor, but also produce a disturbing quantity of oxides of nitrogen.

However, if you dilute the combustion with steam you can reach manageable temperatures of 3000°F. We have already operated gas turbine stages 200°F above that, so we know that this is possible. At 3000°F there is a theoretical Carnot efficiency above 80% and a practical efficiency above 50%, an attractive prospect, and oxides of nitrogen can be kept well within reasonable bounds. (Of course, another possible alternative is to recover the oxygen as well as the hydrogen from any process based on the thermal decomposition of water, which I shall discuss in a moment, and delivering them side-by-side. The recombining combustion process then can become completely "clean," or, shall we say, as clean as water can be.)

Second, hydrogen affords much flexibility in designing utility systems. We can envision distributed generation (gas turbine and even perhaps fuel cell plants of about 100 MW) near the load.

Third, and most significant, hydrogen can be inexpensive to transmit. Overhead electric transmission costs 6-18 cents per million BTU per 100 miles; underground transmission may cost 5-10 times as much. By contrast, hydrogen gas may be transported by pipeline for less than 2 cents per million BTU per 100 miles.

Of course, hydrogen is more expensive than other fuels. However, as the cost of other fuels rises, and we will all be noticing this in our home heating and gasoline bills in the days ahead, hydrogen becomes, on a percentage basis, less of a premium fuel. Right now most hydrogen is produced by natural gas reforming; before we run out of natural gas, we must consider making hydrogen from our abundant coal resources. Our own scientists recently have devised a method to achieve this, using the cracking of steam with molten tin and the reduction of the tin oxide with coal.

Even more attractive is the possibility of producing hydrogen and oxygen using only heat and water. Of course, to do this directly requires temperatures above 5000°F, and it would be extremely difficult to separate the gases. However, using a series of chemical reactions, it should be possible to devise processes that operate at 1000°F, or lower, which might ultimately be attainable from a high temperature nuclear reactor. Our people in Schenectady have devised a series of such processes, and since the first was conceived during Hurricane Agnes in 1972, we have given the subsequent ideas girls' names. "Beulah" is a copper-magnesium-chlorine process. "Catherine" is a very intriguing lady I will tell you about at some later time.

We have, of course, also looked at straight electrochemical production of hydrogen. Even though we have devised a highly efficient cell (above 80% efficiency at 100 A/ft^2) using ion exchange membrane electrolytes, we do not presently see how to make hydrogen electrolytically for less than $3 per million BTU, and there is a speculative chance of making it thermochemically for about half of that cost. Whether the latter is any bargain will depend tremendously on the future availability, and thus price, of conventional fuels.

We believe hydrogen could be distributed and used safely although some public education will be required. I can assure you that we are working hard in this area, but at the same time, don't hold your breath. We need several more years of research before we can make any meaningful judgment on the ultimate value of this technology.

During our discussion period I will be glad to give you our viewpoint about a variety of other energy sources, conversion, and distribution schemes in which we are not, not now at least, investing much if any effort. I refer to such things as thermionic converters, thermoelectricity, solar energy, outer space solar energy collectors with microwave transmission to earth, geothermal power, and so on.

Geothermal power, at the most optimistic, I believe, could provide only a very small percentage of our total power needs, and that only in limited geographical areas. In any case, the mention of geothermal power reminds me of a TV network broadcast I heard a few weeks ago in which the commentator's concluding comment had an interesting message for all of us.

This TV newscast included a couple of minutes explaining the idea of geothermal power. With background views of Yellowstone Park geysers and hot springs, the possibility of using heat from the bowels of the earth to run turbine generators was outlined. Then the announcer finished, "The enviromentalists don't see geothermal power as a threat yet because they don't think there's much hope it will work." Well, one man's hope is another man's threat.

But there is something in what the TV man said. In looking at these long-term solutions for future energy crises, it is easy for we technologists to be concerned only with the fantastic basic technical problems confronting us—trying to show they will work!

But let us not forget:

(*i*) If fusion succeeds, there will be all sorts of worries about centralization of huge energy sources.

(*ii*) MHD temperatures mean more oxides of nitrogen, and, along with topping cycle possibilities, elements like potassium could easily be added to the vocabulary of ecologically dirty words.

(*iii*) Unless new metals for fuel cells can be found, their broad use could be a big drain on our balance of payments.

(*iv*) We have already heard about the "Hindenburg syndrome" which might slow down acceptance of the "hydrogen-economy."

(*v*) Solar energy would require terribly wasteful use of land, and I hesitate to even ponder the environmentalists' response to those microwave beams bringing power from outer space.

(*vi*) Some of the best new high-density batteries are based on (heaven forbid!) sodium and sulfur.

(*vii*) Coal gasification does not necessarily do away with either the hazards of deep mining or the problems of strip mining.

Now, some of these "negative-scare" items I have just listed are secondary technological problems which we must not overlook. Others are economical and political matters. Through them all runs an undercurrent of a need I mentioned earlier, the need to help people continue to understand that the high energy society they demand will itself inevitably demand certain trade-offs.

But you will recall that I started this morning with the basic thesis that, in the long run, it is easier to generate new technology than it is to change the habits, *mores*, prejudices, and desires of people and their long-established institutions.

So, we technologists will have to take responsibility for solving some of those secondary as well as the basic technical barriers as these new ideas for solving the energy crisis come along.

All things considered, I think technology has been remarkably responsive to the needs and wants of the people in the past. I am confident that creative technical people will keep coming along at an ever-increasing rate and that they will, indeed, help give us the kind of world we want for ourselves and our children in the future.

JOURNAL OF THE ELECTROCHEMICAL SOCIETY

REVIEWS AND NEWS

NOVEMBER 1973

Humphry Davy, Innovator in Electrochemistry

Samuel Ruben*

Ruben Laboratories, New Rochelle, New York 10801

The early developments of the sciences, particularly electrochemistry, in England were initiated by self-motivated men with imaginative minds and an inherent sense of direction. They engaged in self-motivated experimental work to fulfill their bold dreams and complemented this by practical applications of their scientific results. A natural driving curiosity was a distinctive characteristic of the personalities of these men. In order to make their efforts more fruitful, they required means of disseminating their accumulated knowledge; they found these means in lectures, discussions, and publications, such as the ones provided by the Royal Institution.

The Royal Institution of London enjoys a special place in the history of science. Its role in the scientific community seems to reflect the personality of Count Rumford, its adventurous founder. He was endowed with a creative mind and a desire to combine scientific discoveries and advances with the dissemination of this new knowledge for purposes of improving the arts and industries.

Humphry Davy and his successor, Michael Faraday, were two outstanding and dedicated individuals who had the ability to educate themselves to the highest levels in the sciences. The Royal Institution provided both men with the opportunity to fulfill their dreams; each made major contributions to the development of chemistry and electrochemistry.

Humphry Davy was born in Penzance, Cornwall, on December 17, 1778, the eldest child of a middle-class family. He was endowed with a quick, imaginative mind and the ability to learn rapidly from books. These books served not only as a means of instruction, but also as a source of inspiration to him.

He attended a local grammar school where, among other subjects, he was taught Latin and Greek. At fourteen years of age he was enrolled in a better school at Truro where he acquired a knowledge of the classics. Being somewhat of a romanticist, he retained this knowledge and in the many lectures which he gave he frequently delighted his audiences by quoting related passages from the Greek philosophers. These illuminated his lectures and made them more than briefs on science and, thus helped to establish his reputation as a fascinating lecturer and natural philosopher.

After Truro, Davy spent a year applying his imaginative mind to literary fields, particularly poetry. He also engaged in fishing and hunting, activities for which he retained a love, which accompanied an appreciation for the beauty of nature throughout his life. His ability for composing poetry in later years received encouragement from Coleridge and Southey, and some of his poems were even published in Southey's "Annual Anthology" of 1799 and 1800. At this time he had only a speculative interest in the sciences.

When his father died, the family was left with an estate diminished by unwise investments. This situation made it imperative that he acquire a training so that he could assist in the support of the family. He decided that he would like to follow the medical profession. Therefore, on February 10, 1795, he applied for an apprenticeship with Dr. J. Borlaise, a surgeon and apothecary, and was accepted. He enjoyed his duties as an assistant to Dr. Borlaise and planned to meet the requirements for practicing medicine by completing his apprenticeship and the necessary studies and by taking the examinations given by Edinburgh University. He kept an excellent record of his experiences with Borlaise, including personal thoughts relative to his work. During his two years of experience with Borlaise, he became interested in the chemistry of blood and the problems involving the chemistry of respiration. He would later make some original contributions in these areas.

At this stage of his life he was fortunate to meet people who recognized and encouraged his creative thinking, assisting him in the process of self-education and encouraging his interest in the science of chemistry. He had become a good friend of Gregory Watt, a son of the famous inventor, James Watt, who had been educated in the sciences at Glasgow and who admired Davy's keen mind. Watt introduced him to Davies Giddy, a member of the Royal Society, who had a profound influence on the course of Davy's intellectual life. Besides encouraging his creative thinking, Giddy allowed Davy full use of his excellent library, a privilege which was of inestimable value as a motivating factor. In later years, he helped him by introducing his work to his friends, Dr. Beddoes and Count Rumford. Giddy changed his name to Gilbert in 1808 and was known by this name in the various offices he occupied in the Royal Society.

By 1797 Davy's interests were principally in the study and understanding of the growing science of chemistry. He was fortunate to become interested in it at a time when it was no longer under the influence of the phlogiston theory. Work of men in various countries of Europe had changed thinking from the qualitative phlogiston theory with its variable unknown "phlogiston" element to a quantitative scientific approach based on measurable changes in weights and volume. This approach was stressed particularly by Lavoisier, the father of modern chemistry, whose measurements with a chemical balance became the true arbiters for determining chemical compositions, reactions, and analyses. The greatest motivating force in 1797 which excited Davy's interest in the study of chemistry was Lavoisier's *Traité Élémentaire de Chimie*, which gave him a comprehensive picture of the science of chemistry as it was then understood. It contributed to his involvement in a vigorous study of chemistry and experimental work. Lavoisier had the subject of compounds arranged under a system of nomenclature which indicated their compositions, and to some extent, their derivations. While studying Lavoisier's book, Davy made and collected apparatus to learn the facts of chemistry through practical experience derived from experimental work. There were

* Electrochemical Society Active Member.
Key words: Davy, self-motivation, Royal Institution of London.

some items in the book which he could not logically accept and he began gathering the information required to disprove them. Ten years later he was able to prove the fallacy of Lavoisier's description of muriatic acid as "oxymuriatic" acid. He published a paper in which he proved that oxygen was not the essential component of muriatic acid, but that the acid was essentially composed of an aqueous solution of a compound of hydrogen and an element which he identified as chlorine.

One man who assisted Davy by helping him develop a better understanding of the rudiments of science and laboratory equipment was Robert Dunkin. Dunkin was an instrument maker who was as well versed in mathematics, electricity, and magnetism as anyone of his time. He constructed a number of instruments and demonstrated their operations to Davy, thus teaching him some of the rudiments of laboratory science. Davy's highly imaginative, although still undisciplined mind caused him to express unproven, speculative thoughts as facts in these early stages of his self-education and experimental work. However, bitter experience taught him how readily one could stray from the truth and his critical faculties eventually developed, enabling him to engage in meaningful research and to make outstanding contributions to the growing science of chemistry.

Davy quickly recognized the importance of publishing one's work. Each paper published was like the rung of a ladder—a step toward recognition by one's peers. A faulty rung not based on proven results would cause a halt in progress until it was replaced by one which could withstand the tests of scientific criticism.

Davy's two-year apprenticeship to Borlaise had inspired an interest in the chemistry of physiology, and particularly in the chemistry of respiration in a wide range of living organisms. As a consequence of his studies in these areas, he was able to prove that the carbon cycle operated in the sea as well as on land. He was fascinated by a book written in 1795 by Dr. Mitchell entitled "Remarks on the Gaseous Oxyde of Azote and Its Effects," and in 1798, became critical of Dr. Mitchell's statement that nitrous oxide gas was an agency for spreading contagious diseases, producing ill effects when it was breathed in or came in contact with the skin. Davy set up a simple assembly of apparatus necessary to produce nitrous oxide. He then tested the effects of the nitrous oxide gas on animals by having them breathe it or by allowing skin contact. He found that the animals experienced no ill effects. He experimented with it on himself and found some very interesting results unrelated to the statements published in Dr. Mitchell's book.

Since he needed larger quantities of nitrous oxide gas to continue his research on its physiological effects, he wrote to Dr. Beddoes at Bristol about his experiments. Dr. Beddoes knew of Davy through their mutual friend, Davies Giddy, and on October 2, 1798, he offered Davy the position of chemical assistant at the Medical Pneumatic Institute. This institute, founded by Dr. Beddoes, was dedicated to the study and application of the therapeutic value of various gases. Davy was asked to complete an account of his initial work on nitrous oxide and this was published in 1799. A year later he published an intensive study on the effects of nitrous oxide gas on humans in a separate volume entitled "Researches, Chemical and Philosophical, Chiefly Concerning Nitrous Oxide." He reported pleasurable effects upon breathing the gas and found it was nontoxic. Also, he found that it had an analgesic effect in small quantities, relieving him of a toothache which returned when the gas was discontinued. He discovered that it had an anesthetic action when taken in large quantities. Thus began the history of what in dental practice has been referred to as "laughing gas." Davy found that some of the gas was absorbed in the bloodstream, but that it did not combine chemically with the blood and could be freely eliminated without having a toxic effect. Further studies of the physiological effects of other gases, such as nitric oxide and a mixture of carbon monoxide and hydrogen, nearly proved fatal to him. In his work on gases he had determined the residual capacity of the lung. The publication of his work in 1800 created great interest and was a true rung in his ladder toward professional recognition and fame.

In January 1800, he learned of a great discovery: chemically produced electricity. This discovery would play an important part in his rise to fame since it helped to make possible his notable contributions to electrochemistry. He recognized the importance of Alessandro Volta's announcement of the electric pile which had been described in a communication to the Royal Society. Volta's electric pile, composed of dissimilar metals separated by an absorbent spacer saturated with an aqueous conductive solution, for the first time made possible the generation of a continuous flow of electric current. Before this time experiments with electricity were limited to intermittent discharges of short duration provided by an electrostatic generator and stored in a "Leyden jar." Now, electrical effects could be studied with a continuous controllable flow of current which was more readily measurable with regard to intensity and quantity. Utilizing the electricity from voltaic cells, Davy duplicated the work of Nicolson and Carlyle who had reported the fact that when an electric current was passed through water, hydrogen and oxygen were liberated at their respective poles. Cavendish had demonstrated that the gases liberated and combined to form water when subjected to an electric spark.

Davy was evidently acquainted with the higher capacity cell of Cruickshank, who had changed the structure of the voltaic cell by inserting large plates of zinc and copper alternatingly in a resin-lined, grooved wooden box. After assembly of the plates in their respective grooves, Cruickshank added a conductive aqueous solution in the space between them. With these larger plates, he obtained a sufficiently strong current to decompose several compounds electrolytically in solution, and he electrodeposited several metals. Davy believed there was much to be learned about the fundamentals of voltaic generation of electric currents. He duplicated the higher capacity cell of Cruickshank and became involved in a study of the controlling chemical factors. When he constructed a voltaic cell using zinc and silver electrode elements separated by a porous spacer containing muriatic acid, he obtained greater electrical force than with electrodes separated by spacers impregnated with saline solutions. He reported that cells having spacers containing nitrous acid were also capable of increased electric output. With this work he proved that the generation of electric current was dependent upon the oxidation of its zinc element and that the total force generated included the result of the chemical activity of the solution in contact with the positive electrode. He investigated many other compositions of solutions in contact with dissimilar metal electrodes and related their composition to voltaic cell characteristics. In his work on various active solutions, he made dual-electrolyte cells with the more highly oxidizing electrolyte in contact with the positive electrode. Davy found that carbon derived from charcoal could be combined with zinc to form a spaced couple which would generate an electric current. This finding was not considered to be of great importance because Volta had experimented with graphite electrodes, but years later in the development of commercial electric batteries such as the LeClanché cell and its progeny, the dry cell, carbon became the electrode material for contacting the negative reactant or depolarizer such as manganese dioxide.

In September 1800, his first paper on galvanism was published in Nicolson's Journal. A second paper followed three weeks later. In 1801 Count Rumford, who was acquainted with Davy's work on galvanism, invited him for an interview. This led to a recommendation to the Board of Managers of the Royal Institution

that Davy be appointed assistant lecturer in chemistry. On February 16, 1801, the Board concurred, adding other duties such as assistant editor of the Journal of the Institution.

Davy continued his work on galvanism after his employment at the Royal Institution, and six weeks later gave his first lecture on this subject. This lecture, on April 25, 1801, was attended by Count Rumford, Sir Joseph Banks, and other distinguished philosophers. It was a brilliant success and was reported in the *Philosophical Magazine*. Five months later he was promoted to lecturer in chemistry.

In January 1802, his unique personality was expressed when he gave his first course in chemistry. His highly imaginative mind aided him in expressing his ideas concerning chemistry and relating chemistry to all the sciences. His audience was fascinated by the breadth of his vision in relating chemistry to mineralogy, biology, zoology, physiology, and medicine. He philosophized on the opportunities presented to those engaged in the related disciplines by a better understanding of chemistry. These lectures indicated the thorough knowledge of the sciences he had acquired from the literature, through discussions, and by keen observations of his experimental work.

Count Rumford had originally intended that the Royal Institution orient its studies toward industrial problems and in order to increase its financial support, it began to do so. The important English industries, dyeing and tanning, felt a great need for better processes, and Davy was asked to cease his laboratory work on galvanism to study these needs. After two months of study and visits to tanneries, Davy returned to his laboratory to investigate new and old substances useful for tanning and a method of depilating skins with alkaline materials. His observations and comments on the processes of tanning were published in the *Journal of the Royal Institution*. The over-all results of his work were published as a tanner's guidebook which was used by the industry for many years. In 1805 he was awarded the Copley medal by the Royal Society for his work on the chemistry of tanning.

The success of Davy's lectures, largely due to his humanistic approach to the interpretation of the sciences, had a secondary effect of materially helping the Royal Institution in a period of financial stress. This was appreciated by the Board of Managers and on May 21, 1802, they conferred upon him the title of Professor of Chemistry. On November 17, 1803, he was elected Fellow of the Royal Society. The Board of Managers also extended his duties by requesting him to plan and give a course on agricultural chemistry to the members of the Agriculture Board. These lectures were based on the results of many experiments, discussions with farmers, and extensive study of the available literature on the subject of agricultural chemistry. In 1804 he was elected a Fellow Commoner of Jesus College, Cambridge. In 1805 he was asked to collect minerals in Cornwall, the lakes in Wales and in Ireland, and to study the geology of these regions. He made an analytical study of what he observed and cast it in a comprehensive report. Later, he gave a lecture on this subject. Continuous study and laboratory work accompanied by creative thinking helped establish his reputation as one of the outstanding philosophers of chemistry.

Davy was now allowed to resume his experimental work on the studies of galvanism. He showed that the relation of electricity to chemical affinity was basic to the understanding of electrochemical action. Using the electricity from voltaic cells, he was able to prove that one could change the material state of substances and their residual chemical properties. In his first Bakerian lecture of November 20, 1806, Davy predicted the value of electricity in discovering the true elements of materials. He proved this later by his isolation of metallic potassium and sodium from their hydroxide compounds.

One of his important contributions toward the establishment of the fundamentals of electrochemistry was his generalization on the study of migration of materials in solution caused by the application of an electrical current. He stated that,

> Hydrogen, the alkaline substances of metals and certain metallic oxides are attracted by negatively electrified metallic surfaces and repelled by positively electrified metallic surfaces and contrawise, oxygen and acid substances are attracted by positively electrified surfaces; and these attractive and repulsive forces are sufficiently energetic to destroy or suspend the usual operation of chemical affinity. It is very natural to suppose that these excellent and attractive energies are communicated from one particle to another particle of the same kind so as to establish a conducting chain in the liquid and that the locomotion takes place in consequence (3, 6).

Considering the state of the art at this period, Davy's explanation of chemical and electrical affinities was an instructive guide for work in the developing science of electrochemistry. His imaginative mind foresaw the industrial possibilities of using electricity to decompose neutral materials and, thus, to produce alkaline or acidic compounds on a large scale. His lecture, "On Some Chemical Agencies of Electricity," created much interest for it brought a new concept to the minds of chemists. In 1807, he was awarded the medal and prize from the French Institute for the best experimental work of the year on galvanism. Napoleon had established this medal when he was First Consul, and it was awarded to Davy despite the fact that England and France were at war.

Davy's work on the electrochemical decomposition of fixed alkalies led to his most famous discovery on October 6, 1807—the isolation of the metals, potassium and sodium. He accomplished this by the electrochemical decomposition of molten potash which produced metallic potassium for the first time. The same technique was later used to produce metallic sodium. He initially named the metals "potagen" and "sodagen," but later changed them to "potassium" and "sodium." He not only discovered these metals in a pure state, but also determined their physical and chemical properties. At a later time he applied the same methods to produce the alkaline-earth metals, but was not successful. This failure was due to the fact that hydroxide compounds of the alkaline-earth metals are not electrolytically conductive or fluid enough when heated. By using the method reported by Berzelius, namely, that of using a mercury electrode to form amalgams, he was able to produce some of the alkaline-earth metals. He also produced alkaline-earth metals and boron by reduction of their oxides with the alkali metals. His work verified Lavoisier's belief that oxygen was a component of the basic alkaline compounds, and his discoveries supported his own theories concerning the electrical nature of chemical affinity—a fundamental concept of electrochemistry.

He published two important books, "Elements of Chemical Philosophy" in 1812, and "Elements of Agricultural Chemistry," a year later. His "Elements of Chemical Philosophy," noted for its excellent presentation of contemporary chemical science included a sketch of the history of chemistry. Davy's wide reading enabled him to relate the work of the alchemists and the chemists of Lavoisier's period to the development of the science of chemistry. He stressed his thoughts on the laws governing chemical combinations and proportions by which elements combine. The imaginative thinking of Davy can be noted from the statements in the following paragraph,

> . . . whether matter consists of individual corpuscles or physical points endowed with attraction and repulsion, still the same conclusion may be formed concerning the powers by which they act and the quantities which they combine and these

> powers seem capable of being measured by their electrical relations and the quantities on which they act being expressed by numbers. The laws of crystallization of different proportions and the electrical polarities of bodies seem to be intimately related and completely illustrative of their connection and probably will constitute the mature age of chemistry (3, 6).

Many years later the prophetic meaning of these sentences was appreciated.

He returned to the laboratory to continue his experimental work and investigated the properties of a compound of nitrogen and chlorine discovered by Dulong in Paris which had aroused his interest. While performing experiments to determine the compound's characteristics, a vial exploded and wounded him by blasting small splinters of glass into his face. He concluded that the compound was nitrogen chloride and presented a paper on its properties to the Royal Society.

During Davy's last four lectures on chemistry at the Royal Institution, there was a young man in the audience who was enthralled with the lectures and wrote a meticulous set of notes. Michael Faraday had been invited to the lectures by Mr. Dance, a member of the Institution and an admirer of Faraday's keen mind and serious dedication to studies of the chemical sciences. Faraday sent Davy a plea for a position as a chemical assistant at the Royal Institution and included the notes he had made of Davy's lectures. Davy recognized the unique qualities of Faraday's mind, but was unable to employ him as his chemical assistant at that time. He promised to communicate with him if such an opportunity occurred. He did give him a few days work as his temporary secretary while his eyes were recovering from the effect of the nitrogen chloride explosion. Three months later Davy discharged his laboratory assistant for misconduct and recommended to the Board of Managers that Faraday be engaged as his chemical assistant. They concurred on March 1, 1813. This appointment proved to be of tremendous benefit both to the Royal Institution and to Faraday. The Royal Institution benefited from Faraday's skill in measurements, his patience, and his unerring intuition; Faraday benefited from a close association with the outstanding chemical philosopher, Humphry Davy.

Davy and Faraday had certain qualities and interests in common. Both had creative minds and were compulsive readers of scientific literature. They both educated themselves to be experts in their subjects. It has been written that of the many outstanding contributions Davy made to the Royal Institution and to science, his recognition of Faraday's abilities was one of his greatest.

Davy asked Faraday to accompany him as his assistant on a trip to the Continent in October, 1813, about six months after Faraday had become his chemical assistant. Lady Davy was to accompany them as well. There they would meet prominent scientists such as Ampère, Laplace, Gay-Lussac, Chevreul, Berthollet, Guyton de Morveau, Humboldt, De La Rive, and Volta for discussions and exchange of information. They would also study the volcanoes of France and Italy. They received passports and *laissez-faire* from France even though England and France were still at war. They carried portable chemical apparatus in their private coach which they used in demonstrating chemical experiments.

In November 1813, while in Paris, they met Clement and Desmorne who showed them a new elemental material considered to be a complex form of chlorine which had been discovered only two years before by M. Courtois, a salt peter manufacturer. This subject became a matter of investigation and Davy identified it as the element, iodine. In Genoa at the home of a chemist, the pair observed experiments with electric fish (torpedoes). In a paper given some years later, Davy reported his investigations showing that this new source of electricity was developed by nerves. In Florence they were delighted to see the first telescope built by Galileo who had used it for discovering the satellites of Jupiter. At the Accademia del Cimento they borrowed a large optical lens for producing an intense localized area of heat. With this lens they investigated the combustion of diamonds. In March 1814, they identified the combustion product as pure carbon dioxide and established the fact that diamonds were a crystalline form of pure carbon. While in Milan they had a visit from Alessandro Volta, the man who had discovered the means of generating a continuous flow of electric current by chemical reaction. Volta's great discovery was an important step for the significant developments in electrochemistry later made by both Davy and Faraday.

Shortly after his return from the trip to the Continent, Davy devoted study time to the problem that had plagued the coal mining industry: the recurrent explosions in coal mines caused by the ignition of coal gas and air. Many lives had been lost over the years in all countries by miners caught in these explosions which were ignited by their illuminating equipment. His studies on combustion and heat transmission through confined areas led to his invention in October 1815, of the mine safety lamp in which the flame was enclosed by copper gauze. This lamp could, therefore, be used in atmospheres containing explosive quantities of the coal gas without igniting them. It also gave a qualitative indication of the presence of explosive concentrations of combustible gas by increases in the intensity of the flame. A flame of decreased intensity was an indication that the oxygen content in the atmosphere was less than 18%. While records show that others had worked on a mine safety lamp, it was Davy's systematic experiments on utilizing the heat conductivity of surrounding wire gauze cylinders for the prevention of an ignition path from the flame of the wick to the external atmosphere that made his lamp the first effective and practical mine safety lamp.

Davy believed that the duty of men of science was to contribute their discoveries to the benefit of mankind. He refused to patent his lamp and dedicated its use to the mining industry. In October 1818, he received the Rumford gold and silver medals from the Royal Society for his development of the safety lamp. He was also presented a service of silver plates by the Newcastle mining industry. In his will he requested that these be used for the establishment of the annual Davy medal for outstanding discoveries in chemistry.

In 1818 Davy was named a baronet. He went again to Italy with a plan to devise a method of unrolling the papyri documents discovered at Herculeum. On November 30, 1820, he succeeded Sir Joseph Banks as President of the Royal Society, a position he held until 1827.

Davy became interested in electrical and related magnetic effects. He had been impressed by the announcement of Oersted's discovery of the magnetic properties of a conductor carrying a current. In investigating the magnetic effects surrounding an electrically heated platinum wire, he found these effects to be independent of the wire's temperature. He reported experiments in which steel needles placed transversely to conductors became magnetized. In basic observations on the conductivity of different metallic conductors, he showed that the melting point limited the quantity of electricity that could be transmitted through the conductor and that its conductivity was increased if cooled, and the converse occurred when it was heated.

In January, 1824, he invented a method for galvanic protection of the copper sheathing of the hulls of naval vessels by electrically connecting a mass of more oxidizable metals such as iron, tin, or zinc to it. This method which had worked in the laboratory, failed when tried in actual seawater. This was not because of incorrect reasoning, but because of the rapid overlaying accumulation of organic materials such as weeds

and barnacles which obscured the galvanic protective action. A century later this process of galvanic protection was to prove invaluable in the protection of oxidizable metal structures.

His last Bakerian lecture of October, 1824, on the relation of electrical and chemical changes, contained his last published thoughts on electrochemistry and earned him the Royal Society Medal. The minutes of the Board of Managers of the Royal Institution of February 4, 1825, include the following item:

> It appears that Sir Humphry Davy, having stated that he considered the talents and services of Mr. Faraday, assistant in the laboratory, entitled to some mark of approbation from the managers, and these sentiments met the cordial concurrence of the board; Resolved, that Mr. Faraday he appointed director of the laboratory.

Thus, Michael Faraday, the man whom Davy had served as mentor and whose career had taken on significance as Davy's laboratory assistant, now, twelve years later, became the director of the laboratory. That Faraday in the ensuing years fulfilled his sponsor's expectations was evidenced by his many discoveries. He was the first scientist to place electrochemistry on a quantitative basis and the first to generate an electric current flow in a conductor by induction from a magnetic field.

Davy was elected President of the Royal Society for the seventh time in 1826. But in that year he suffered a stroke and resigned from the Society. His health was failing rapidly and he decided to leave England and settle in Rome. In 1828, having to forego scientific work and field sports, he devoted his time to writing a book on fishing, "Salmonia," which he illustrated with his own drawings. Although partially paralyzed from several strokes, he spent his last month in Italy writing a series of dialogues which were posthumously published under the titles "Consolations in Travel" and "The Last Days of a Philosopher." He suffered another stroke and was soon joined in Rome by his wife and brother, John. His recovery was slow, and he insisted on moving to Geneva where he died during the night of his arrival, May 29, 1829, at the age of fifty.

In generalizing on the self-motivation of Sir Humphry Davy, a characteristic which helped to produce one of the outstanding scientists of his era, the following may be cited: his love and respect for books; his imaginative mind which gave expression to new concepts and translated them into reality; the inspiration and encouragement derived from people with whom he shared common interests; public interest; and, finally, the encouragement given by his peers to the establishment of electrochemistry as a science.

He was torn in spirit between two loves—creative science and poetic expression. His friend, Wordsworth, the renowned poet, commented on Davy's integration of the study of chemistry with aesthetic satisfaction in his "Lyrical Ballads" (1802) when in the preface he wrote:

> Poetry is the first and last of all knowledge—it is as immortal as the heart of man. If the labours of Men of Science should ever create any material revolution, direct or indirect, in our condition and in the impressions which we habitually receive, the poet will sleep then no more than at present, but he will be ready to follow the steps of the Man of Science. The remotest discoveries of the chemist, the botanist, the mineralogist will be a proper object of the poet's art upon which it can be employed (13).

Manuscript submitted Oct. 12, 1972; revised manuscript received May 22, 1973.

Any discussion of this paper will appear in a Discussion Section to be published in the June 1974 JOURNAL.

REFERENCES

1. Antoine L. Lavoisier, "Traité Elémentaire de Chimie," Imprimerie Impériale, Paris (1789).
2. Humphry Davy "Researches Chemical and Philosophical Concerning Nitrous Oxide," J. Johnson & Co., Bristol (1800).
3. Humphry Davy, "Elements of Chemical Philosophy," J. Johnson & Co., London (1812).
4. Humphry Davy, "Elements of Agricultural Chemistry," Longman & Co., London (1813).
5. R. Hunter, "Humphry Davy on the Safety Lamp for Coal Mines with some Researches on Flame" (1818).
6. Humphry Davy, Six Discourses Delivered Before the Royal Society (Murray) (1829).
7. J. A. Paris, "The Life of Sir Humphry Davy," Colburn & Bentley (1831).
8. John Davy, "Memoirs of the Life of Sir Humphry Davy," Longmans (1836).
9. Humphry Davy, "Collected Works," John Davy, Editor, Murray (1839).
10. Bence Jones, "Life and Letters of Faraday," Longmans (1870).
11. T. E. Thorpe, "Humphry Davy, Poet and Philosopher," Cassell (1896).
12. J. P. Kendall, "Humphry Davy, Pilot of Penzance," Faber (1954).
13. H. Hartley, "Humphry Davy," Nelson, London (1966).
14. J. Z. Fullmer, "Sir Humphry Davy's Published Works," Harvard University Press, Cambridge (1969).
15. Sir Harold Hartley, "Studies in the History of Chemistry," pp. 92-133, Clarendon Press, Oxford (1971).

Report of the Electrolytic Industries for the Year 1972[1]

A. T. Emery*

Hooker Chemical Corporation, Subsidiary of Occidental Petroleum Corporation, Niagara Falls, New York 14302

and J. Parker*

Electrode Corporation, Chardon, Ohio 44024

Chlorine—Caustic Soda

I. Production.—U.S. production of chlorine reached a record level of 9,800,000 tons in 1972, an increase of 6.3% over 1971, and 1% over 1970, the previous record year. Canadian production was 922,120 tons, up 7.3% from the preceding year (1).

Production rates increased significantly in the second half of 1972. U.S. operations rose from a low of 86.7% of capacity in January to 93.7% in November and 95% by the end of the year. In Canada, production rates increased from 82.8% of capacity in January to 97.5% of capacity in December.

During 1972, there were start-ups of new or expanded chlorine facilities at four locations and the

[1] This report is sponsored by the Industrial Electrolytic Division of The Electrochemical Society. While it is primarily a summary of production and developments in the chlor-alkali industry, reports of other electrolytic industries are included.
The material presented herein has been gathered from many sources, as noted in the References, and does not necessarily represent the opinions of the authors.

* Electrochemical Society Active Member.

shutdown of operations at two others. Eighteen plants converted their cells to coated metal anodes. In Canada there was one expansion, one shutdown, and two conversions to metal anodes. Total U.S. capacity in 1972 was 28,600 tons/day, slightly lower than in 1971 due primarily to the closing of one major production plant. In Canada, capacity increased by just over 3% to 2,814 tons/day (1-4).

Supplies of caustic continued tight. Most major producers were eliminating discounts on both caustic and chlorine. Suppliers announced price increases on chlorine of $6/ton in May. Caustic prices were similarly increased by the major producers in September to $81/ton for standard grade (5-7, 10). A further increase of $7/ton in the price of chlorine was announced by major producers in November and December. All companies concerned point out that the chlorine price increases are aimed at cutting back discounts and do not lift the selling price over the current $75 list (13). With the probability of tight supplies of both caustic and chlorine continuing, there seems little possibility of price erosion from current levels (6).

Only marginal capacity increases in the chlor-alkali industry are expected during 1973. These will be due largely to modernization of existing facilities. The year for substantial capacity increases will be 1974 when several plants in the 800-1500 tons/day range will come on stream. All of these plants will use diaphragm cells. Most companies are steering clear of mercury cells, at least for the time being (1, 8, 9). The Chlorine Institute estimates that by the end of 1974, expansion now announced will boost U.S. chlorine capacity of 28,600 tons/day by more than 6500 tons; an increase of over 24% (1). In 1972, 72.4% of U.S. chlorine production was from diaphragm cells and 24.2% from mercury cells; miscellaneous production from all other sources accounted for 3.4% (3).

The turnaround in the chlorine industry is being helped by the booming demand for vinyl chloride. New chlorine plants are needed to keep pace with this demand to avoid chlorine shortages in the 1974-1975 period. PVC expansions at eight locations amounting to 1.4 billion lb/yr additional production have been announced. Vinyl is the biggest single consumer of chlorine, accounting for 17% of all U.S. chlorine consumption (10, 11).

Chlorinated solvent demand, which fell off during 1971, is expected to aid chlorine growth with a 5-6% increase in solvents output during the next five years (9).

Caustic is continuing in short supply because of the continuing heavy demand of the paper and glass industries and year end improvement in the aluminum industry. With soda ash also in short supply, caustic users will be unable to switch until producers are able to bring in new trona capacity. PPG postponed a scheduled shutdown of its Barberton, Ohio soda ash unit to aid the supply of caustic products (12).

Although chlorine plant operating rates are about 95% and could climb higher during 1973, chlorine producers are concerned over the future impact of new technology on their markets. The N.L. Industries magnesium plant at Rowley, Utah will produce by-product chlorine. Du Pont is building a 500 tons/day chlorine plant at Corpus Christi, Texas to recover chlorine from by-product hydrogen chloride via Kellogg's Kelchlor process. Mobay is using Uhde electrolytic cells to recover chlorine from by-product muriatic acid (9).

The energy crisis with the attendant threat of power shortages and the probability of higher power rates adds to the concern of electrolytic chlorine producers

PPG's announced 1,500 tons/day plant at Lake Charles, Louisiana has been postponed for about a year because power is not available despite a firm contract for natural gas (9).

The Chlorine Institute in its February, 1973 meeting took note of the stringent environmental and Occupational Safety and Health Act (OSHA) standards and their impact on chlorine plant design. One industry spokesman estimated that capital costs for a new chlorine plant could increase 2.5-4.5% to pay for additional facilities to comply with regulations governing safety and plant effluents (20).

II—Current Changes in Chlorine Operations (2-4, 14-17, 19, 23)

Company and location	Type of cell	Total expanded capacity tons/day	Completion date
A. Production Started			
Linden Chloride Products Linden, N. J.	Start-up of existing Krebs mercury cell plant	460	½ in 1972 ½ in 1974
Vicksburg Chemical Co. Vicksburg, Miss.	Start-up of existing nonelectrolytic potassium nitrate-chlorine plant	90	September 1972
Pennwalt Corp. Portland, Ore.	Diamond diaphragm Expansion and conversion of existing plant to DSA®	330	December 1972
Vulcan Materials Co. Wichita, Kans.	Hooker diaphragm converted to DSA®	275	1972
Stauffer Chemical Co. St. Gabriel, La.	Uhde mercury cells	520	1972
Mobay Chemical Co. Baytown, Texas	Uhde HCl cells	200	1972
Canadian Occidental Petroleum Ltd. North Vancouver, B.C.	Added Hooker HC-60 cells with DSA®	395	1972
Hooker Chemical Corp. Montague, Mich.	Hooker S-3 conversion to DSA®	220	1972
Pennwalt Corp. Wyandotte, Mich.	Diamond cells converted to DSA®	260	1972
Velsicol Chemical Corp. Memphis, Tenn.	Added 8 Hooker S-4 cells with DSA®	150	1972
BASF Wyandotte Geismar, La.	Diamond cells converted to DSA®	410	1972
BASF Wyandotte Geismar, La.	Hooker S-4 cells converted to DSA®	400	1972
B. Plant Shutdowns Scheduled			
AMAX Vicksburg, Miss.		90	
Dow Chemical of Canada, Ltd. Sarnia, Ontario	Mercury	700	1973
BASF Wyandotte Geismar, La.	Uhde mercury	150	December 1973
Olin Corp. Saltville, Va.	Mercury	300	March 1, 1972
Sobin Chlor-Alkali Inc. Niagara Falls, N. Y.	All chlorine production diaphragm cells	50	February 1, 1972
Stauffer Chemicals Co. Niagara Falls, N. Y.	All chlorine production diaphragm cells	175	December 31, 1972
Domtar Pulp & Kraft Paper Ltd. Cornwall, Ontario	Vorce cells		August 1972
Canadian Industries Ltd. Hamilton, Ontario	All chlorine production mercury cells		End of 1974
Hooker Chemical Corp. Niagara Falls, N. Y.	Vorce cells		1974
Pennwalt Corp. Portland, Ore.	Gibbs cells		1972
Dow Chemical of Canada Ltd. Thunder Bay, Ontario	Mercury cells		1973

DSA® is a registered trademark of the Electronor Corporation.

III—New or Expanded Plants Planned or Under Construction (2-4, 23)

Plant and Location	Type of cell	Capacity	Completion date
Diamond-Shamrock Houston, Texas	Diamond diaphragm cells	1,200 tons/day	1974
Georgia-Pacific Plaquemine, La.	Hooker H-4 diaphragm cells	800 tons/day	Late 1974
Hooker Chemical Corp. Niagara Falls, N. Y.	Hooker H-4 diaphragm cells	1,000 tons/day	1973-1976 Modernization
Hooker Chemical Corp. Taft, La.	Hooker H-4 diaphragm cells	900 tons/day	1974
PPG Industries Lake Charles, La.	PPG-DeNora diaphragm cells	1,500 tons/day	Not announced
Canadian Industries Ltd. Becancour, Quebec	Diaphragm cells	390 tons/day	1974
Du Pont Corpus Christi, Texas	Kellogg process —nonelectrolytic	500 tons/day	1st Quarter 1974
Shell Chemical Co. Houston, Texas	Hooker S-4 converted to DSA®	Expand to 375 tons/day	1973
Olin Corp. Charleston, Tenn.	Mathieson mercury cells	Double capacity	1973
BASF Wyandotte Geismar, La.	Diamond diaphragm cells Hooker diaphragm cells converted to DSA®		1972-1973
American Magnesium Co. Snyder, Texas	Restart magnesium cells	20,000 tons/yr	1973
Dow Chemical Co. Freeport, Texas	Dow diaphragm cells		2nd Quarter 1974
Dow Chemical Co. Midland, Mich.	Dow diaphragm cells		1st Quarter 1973
Dow Chemical Co. Pittsburgh, Calif.	Dow diaphragm cells		Middle 1973
Dow Chemical of Canada Ltd. Sarnia, Ontario	Replacement of mercury cells with Dow diaphragm cells		Mid-1973
N.L. Industries Grantsville, Utah	BASF—magnesium cells	225 tons/day	1972
Dow Chemical Co. Dallasport Washington	Magnesium cells	50,000 tons/yr	Not announced
Diamond-Shamrock Deerpark, Texas	Addition and conversion of diamond cells to DSA®	810 tons/day	1st Quarter 1973
Hooker Chemical Corp. Taft, La.	Conversion of existing S-4 cells to DSA® Conversion of existing C-60 cells to DSA® With increased load	700 tons/day	1973

DSA® is a registered trademark of the Electronor Corporation.

IV. Developments.—A. Metal anodes.—The North American chlor-alkali industry has continued its program of converting chlor-alkali cells to coated titanium anodes. More than 30 cellrooms are now completely converted from graphite and an additional 12 plants have signed contracts and are in various stages of change over.

These metal anodes are producing more than 7000 tons of chlorine each day and with the additional contracted capacity, more than one-third of the total North American market will be producing chlorine from the titanium-based anodes.

The actual capacity of several plants has been expanded by either running at higher current density or adding additional cells to run on the same electrical circuit. The first plant to be completely converted to DSA® has been in operation for over 3 yr, while many cells have now completed 5 yr operation using these anodes.

In a number of ways the titanium based anodes have played their part in minimizing pollution, particularly in relation to the diaphragm-type cells. An interesting statistic is the fact that during 1972, 1 billion kWhr of electrical energy has been saved by using these anodes rather than graphite.

The development of the application of metal anodes in processes other than chlor-alkali continues. Chlorate, hypochlorite, and metalwinning cells are successfully operating with titanium based anodes (23).

Olin-Mathieson who in early 1972 announced a new titanium anode jointly developed with ICI's Imperial Metal Industries Limited (34), is continuing to convert their Augusta, Georgia mercury cell plant to the new metal anode system.

Chemnor, Panama City, Panama, has received what it considers to be the second basic U.S. patent on dimensionally stable anodes. It has been granted U.S. Pat. 3,711,385 on the use of a platinum group metal oxide in the coatings for metal anodes used in electrolytic chlorine production. Its first key U.S. Patent, 3,632,498, was issued January 4, 1972 (35).

B. New chlorine process developments.—Hooker Chemical Corporation announced that it will use a 150,000A diaphragm cell using metal anodes and designated as the H-4 in new Hooker plants located at Niagara Falls, New York and Taft, Louisiana (25). Hooker also reports that the cell has been licensed to a major chlorine producer (4).

Diamond-Shamrock is offering for licensing, a diaphragm cell equipped with metal anodes for operations up to 150,000A (21).

A number of U.S. companies have announced designs of sodium hypochlorite cells for on-site treating of municipal sewage; Pacific Engineering's Pepchlor unit using lead dioxide electrodes; also Diamond's Sanilec cell and Engelhard's Chloropac cell, both using noble metal or oxide coatings on titanium. A unit is also available from Ionics, Incorporated of Watertown, Massachusetts which features a TFE ion exchange membrane developed by du Pont. The membrane keeps hydrogen from mixing with chlorine during production of sodium hypochlorite from salt. Ionics, Incorporated which designed the system has installed a unit in a Boston waste treatment plant (26, 27).

Asahi Chemical Industry Company of Japan announced a chlorine cell based on a special ion exchange membrane that produces caustic of mercury cell grade without the danger of mercury pollution. Asahi states that the costs are no higher than for caustic produced by orthodox methods (28). A $1.7 million 4400 metric ton/yr chlorine-caustic pilot unit will be erected at Asahi's Nobeoka Works on Kyushu Island (29).

Kellogg announced that it plans to install its Kelchlor process for converting large quantities of by-product or waste hydrogen chloride into chlorine at a cost under $20/ton including investment. The process is a variation of the Deacon process using homogeneous catalysis (oxides of nitrogen). The process will be installed in a du Pont fluorocarbon plant at Corpus Christi, Texas (18, 22).

Two companies have methods for deriving chlorine directly from seawater using electrolysis methods. Kyushu Electric Power Company of Japan with Kyushu University developed the method to keep shellfish and other marine life off seawater cooled coastal plant converters and piping instead of using liquid chlorine (30).

Naikai Engyo Company of Okayama, Japan is using an Asahi Glass process for concentrating seawater by means of electrodialysis using membranes. Salt is recovered by crystallization. The process is said to require less labor and far less space than solar basins. The plant will produce 150,000 tons/yr of salt (33).

DeNora announced a similar electrolyzer equipped with metal anodes designed by DeNora. Using seawater as the raw material a final active chlorine concentration of 1-2 gal/liter can be obtained. The unit is expected to find applications in sewage treatment as well as control of organisms in seawater cooling systems (31).

The chemical division of PPG Industries announced the development of a system for purifying disphragm cell caustic. The system, which is available for licensing, will upgrade standard grade caustic for some

critical applications by removing small but unacceptable amounts of sodium chloride, sodium chlorate, and metal impurities. Purity and clarity of product is much higher than achievable with PPG's ammonia extraction (DH) process. The system has been in commercial use by PPG for three years (32).

C. Mercury cells.—The closing or conversion of mercury cell plants that began with the publicity given the health hazards associated with mercury continued into 1972. However, much of the alarm that buffeted the industry two years ago has subsided. Production statistics from the Chlorine Institute indicate that in 1972 four more plants in the U.S. and Canada either shut down or announced conversion to diaphragm cells. Only two mercury cell plants started up in 1972 and virtually all future expansion plans announced for the 1973-1975 period are with diaphragm cells (1-3).

A number of companies have made available equipment and processes for controlling mercury emissions. Several that were announced during 1972 are:

Union Carbide	Molecular sieve process (Purasiv System) for removing mercury from hydrogen (36)
Sobin Chemical	A process using sodium borohydrate for mercury reduction (37)
Showa Denka	A process for recovering mercury from hydrogen (38)
FMC	New patented mercury recovery process available for licensing (39)
Monsanto	Removal of mercury from hydrogen and air streams with Brinks mist eliminator (40)

U.S. consumption of mercury during 1972 was estimated at 52,000 flasks, slightly lower than 1971. Mercury used as make-up in the production of chlorine declined by about 10%. U.S. production in 1972 was 6300 flasks, the lowest since 1950. About 20 mines were active during the year compared to 55 in 1971. At year's end there were less than 6 producing mines (24). Producing states are California 81%, Idaho 3%, with small amounts from Alaska, Nevada, and Texas (24). The average New York price of mercury during 1972 was $218/flask compared to $295 in 1971 and $408 in 1970. The price continued its downward trend, hitting $145/flask in May. Beginning about midyear, prices were strengthened by news of a cutback in Canadian production and the withholding of mercury from North America by Italy and Spain and the conservative selling policy of the GSA for its surplus mercury. By year end the price had recovered to about $280/flask. Only 500 flasks were sold by the GSA during 1972 (24).

Imports of mercury during 1972 amounted to 30,000 flasks compared to 27,000 flasks in 1971. Imports were from Canada (43%) Mexico (20%) Algeria (12%); Peru, Spain, and Yugoslavia combined (19%) (24).

Other Alkalis and Electrolytic Processes

Caustic Potash.—Caustic potash production in 1972 was 176,950 tons, down 10% from the 198,192 tons produced in 1971. A total of 13 plants reported caustic potash production during 1971 (41).

Diamond-Shamrock Chemical Company announced completion of a dry caustic potash plant at Delaware City, Delaware. The company stated that this was the first new plant to come on stream in over 10 years. The facility will produce dry caustic potash in flake and crystal form (42).

Sobin shut down its 23,000 tons/yr caustic potash plant at Niagara Falls, New York in February 1972. However, the company will continue to manufacture caustic potash at Hooker Chemical's mercury cell plant at Niagara Falls under terms of an agreement between Hooker Chemical Corporation and Sobin announced last year. The Hooker facility has a 36,000 tons/yr capacity (3, 43).

In early November, Sobin Chemical announced elimination of discounts on caustic potash and potassium carbonate to take effect January 1, 1973. The current list price for 45% liquid caustic potash in bulk shipments is $4.25 per hundred weight and $7.00 per hundred weight for 50% liquid caustic potash from west coast terminals (44).

Soda Ash.—Total production of soda ash for the year was 7.46 million tons, an increase of 5% over 1971. Of this total 3.23 million tons were natural soda ash, an increase of over 12.5% over 1971, and 4.23 million tons of synthetic soda ash, about the same tonnage as for 1971 (45, 46). Trona Mines of Wyoming supplied the major portion of the natural soda ash with the remainder coming from dry lake beds in California (48). The synthetic production was comprised of 1,867,000 tons light ash and 1,960,000 tons dense ash (46).

Demand for soda ash was quite strong this year and is expected to carry through 1973. Production was suppressed somewhat by gas shortages and problems with salt suppliers (47).

Forty-seven per cent of the total sodium carbonate produced in the U.S. goes into manufacture of glass, 25% into manufacture of other chemicals, 7% into pulp and paper, 6% into alkali cleaners, 3% into water treatment, 6% exported, and 6% for others. A tight caustic soda market in 1972 helped sodium carbonate to maintain its glass market (47).

Year end soda ash prices were quoted at $2.475/100 lb for light and dense soda ash. Bulk soda ash in car lots at the works was quoted at $1.775/100 lb for the light and dense soda ash (48).

A number of expansions by natural soda ash producers are under way in the west.

Hooker Chemical Corporation's plant at Searles Lake, California is based on evaporation of saline brine and will produce 150,000 tons a year of soda ash and other related chemicals. Completion of the facility is expected late in 1973.

Stauffer Chemical Company completed its 500,000 ton expansion at its Green River, Wyoming plant to bring the company's over-all capacity at this site to 1,500,000 tons/yr (49).

Kerr-McGee Chemical Corporation intends to increase the capacity of its 150,000 tons/yr plant at Trona, California to 1,050,000 tons annually. Completion is expected in 1974 (50).

Allied Chemical is currently doubling its capacity at Green River, Wyoming to 1.1 million tons annually. The expanded facilities are scheduled for completion early in 1973. Recently Allied announced another expansion phase which when completed in 1974 will give the Green River, Wyoming plant a capacity of 2.2 million tons of soda ash per year (50).

FMC is reported to have made a 500,000 ton expansion at its Green River, Wyoming plant to bring the plant's capacity to 1,750,000 annual tons. Another expansion of 750,000 tons at this facility is planned for completion by 1975 (51).

PPG's planned shutdown of its 600,000 tons/yr synthetic soda ash plant at Barberton, Ohio slated for the end of 1972 is being delayed until the end of March, 1973. Operations are being maintained as long as possible to help prevent a critical shortage of soda ash while new capacity is coming on stream by western producers. Shutdown of this plant is forced by pollution problems (52).

A modification in the Solvay system producing soda ash with HCl instead of calcium chloride as a by-product was unveiled at a recent annual American Institute of Chemical Engineers meeting. The proposed modification substitutes the use of reactive magnesia in place of limestone to causterize ammonium chloride. The pollution-free method for production of the synthetic soda ash is not given much chance of success in the U.S. because of the current trend toward natural soda ash. However, in industrial countries lacking natural soda ash the process might find a market (53).

Sodium Chlorate.—Preliminary data from the U.S. Department of Commerce indicates that U.S. produc-

tion of sodium chlorate in 1972 was 182,500 tons, a decrease of about 6% from 1971 production of 193,752 tons (54).

Sodium chlorate production facilities in the U.S. and their 1972 listed capacities are as follows (55):

Company	Capacity (tons/yr)
Brunswick Chemical Co. Brunswick, Ga.	7,000
Georgia-Pacific Corp. Bellingham, Wash.	3,500
Hooker Chemical Corp. Columbus, Miss.	62,500
Hooker Chemical Corp. Niagara Falls, N. Y.	15,500
Huron Chemicals Co. Butler, Ala.	4,000
Huron Chemicals Co. Riegelwood, N. C.	7,000
Kerr-McGee Hamilton, Miss.	32,500
Kerr-McGee Henderson, Nev.	30,000
Pacific Engineering and Production Co. Henderson, Nev.	6,000
Penn-Olin Corp. Calvert City, Ky.	31,000
Pennwalt Corp. Portland, Ore.	16,500
PPG Industries, Inc. Lake Charles, La.	15,000
Total	230,500

Paper bleaching accounts for about 70% of the U.S. sodium chlorate consumption followed by the production of other chlorates at 16% and herbicides at 7% (55).

Sodium chlorate stocks which reached a historical high of over 20,000 tons at the close of 1971 were reduced during 1972 to about 7000 tons by year's end (55).

Hooker Chemical will start up its $5 million 45,000 ton/yr sodium chlorate plant at Taft, Louisiana at the end of the first quarter in 1973. The plant will use a new cell design embodying metal anodes with precious metal coatings supplied from England by Marston Excelsior Limited, an affiliate of Imperial Metal Associates. This plant was originally scheduled to come on-stream in the first quarter of 1972 but construction was held off because of the slowdown in the southern pulp and paper industry, the prime outlet for chlorate (56, 57).

Kerr-McGee has just completed incremental expansions of 10% at both its Hamilton, Mississippi and Henderson, Nevada production sites. Capacity of each plant is now 33,000 tons yearly (59).

Brunswick Chemical Company is considering an expansion that could add 1000 tons/yr capacity in 1973 (55).

During 1972, Electric Reduction Company of Canada, which supplies over 60% of that country's needs, announced expansion at both its North Vancouver and Buckingham, Quebec plants. The present capacity at North Vancouver is 45,000 tons per year. The 20% expansion planned for Buckingham will increase annual capacity of that site to about 35,000 tons (58).

Squamish Chemicals Limited, a subsidiary of GOW Enterprises, announced that a 12,000 tons/yr sodium chlorate plant had begun production at Squamish, B.C. Most of its output will be sold to the MacMillan, Bloedel Mill at Harmac, British Columbia and the Cariboo Pulp and Paper Mill at Quesnel, British Columbia (60).

A further market for sodium chlorate could develop if plans to use solid propellant boosters for the space shuttle program materializes. This program, scheduled for the 1980's may require up to 100 million lb/yr propellant. The propellant used will most likely be a synthetic rubber mixed with ammonium perchlorate (63).

The list price for pulp and paper grade sodium chlorate remained at $134.50/ton for most of the year. Late in 1972, as stocks were diminished, major producers announced price increases of $6/ton. This action eliminated discounts and raised the list price to $135/ton (61, 62).

Sodium.—Metallic sodium production in 1972 totaled 159,886 short tons, an increase of 4.5% from the 153,075 tons in 1971 (64). Behind this increase in sodium production was a strong domestic and export demand for lead antiknock compounds. U.S. production of lead antiknock compound was up by 8% in 1972. With crude oil supplies tight and refiners straining to squeeze all the gasoline they could out of the barrel, refiners were using all the antiknock compounds they could get to improve the octane rating of their product. U.S. exports also filled the gap caused by a strike at Octell, Limited, the United Kingdom's only antiknock producer.

However, with low lead and no lead regulations still very much a factor, decline in sodium production is expected to reoccur around late 1973 (65).

About 83% of the sodium goes into tetraethyl and tetramethyl lead manufacture, 4% metal reduction, and 13% miscellaneous (67).

Lockheed Missiles and Space Company has developed to the prototype stage, fuel cells that use alkali metals such as sodium and lithium. The company has an undisclosed way to control the reaction; it is being used not only in a straightforward "static power cell" but also a dynamic cell that directly converts the electrochemical energy to rotational shaft energy without the need for a conventional electric motor (66).

Prices for sodium remained fairly constant during the year. Regular fused material in drums was quoted as 26.5-27.5¢/lb and the 12 pound brick at 30¢/lb (68).

Aluminum.—The U.S. aluminum industry increased production of primary metal by 4% to about 4,075,000 short tons, according to the Bureau of Mines, U.S. Department of the Interior. The relatively small increase in production in 1972, despite the estimated 11% gain in consumption resulted in a nearly balanced supply-demand position at the close of the year, compared with a severe oversupply situation at the end of 1971 (69).

Although demand grew markedly during 1972, prices remained low. Major producers adjusted the price for primary metal to 25¢/lb in May. This was below current list prices, but 1¢/lb above market levels (70). Prices on a broad range of aluminum products were firming by years end. Discounts of 1.5-3¢/lb on commodity sheet and foil products were eliminated (71).

With inventories reduced, smelters which operated at 84% of rated capacity during 1971, gradually increased output to a 93% operating level by the end of 1972 (72).

Major producers announced restarting of pot lines to meet the growing demand. In early 1972, Alcoa restarted a 20,000 tons/yr capacity line at its Warrick, Indiana smelter (73). Later in the year, Reynolds restarted two 25,000 tons/yr lines at Troutdale, Oregon; Kaiser started a 40,000 tons/yr line at Ravenwood, West Virginia; and Alcoa a 30,000 tons/yr line at its Rockdale, Texas smelter (74, 75).

Reynolds also plans to have two additional pot lines with a capacity of 35,000 tons/yr in operation at its Listerhill reduction plant in Sheffield, Alabama (73).

Olin Corporation announced in late November, 1972 that it planned to dispose of its unprofitable aluminum business. This would include partial ownership along with Revere Copper and Brass of a primary aluminum reduction complex, as well as a sheet and plate mill, four extrusion plants, and an architectural aluminum products operation (76).

The aluminum market growth is expected to be ahead of the economy as a whole as well as ahead of the rest of the base metals list. The average growth rate for the 1969-1980 period is expected to be 4.8% compared to 4.0% for copper, 3.4% for iron and steel, and 3.8% for the GNP for the same period. Rapid growth for aluminum is expected in industries supplying machinery, computers, and related equipment, electrical machinery and equipment, metal containers, and transport equipment (77).

Alcoa announced a new electrolytic process for aluminum that will cut pollution and reduce power re-

quirements. It plans a 15,000 tons/yr prototype for the process which should be operating in 1975. The new process starts with alumina which is treated with chlorine to form aluminum chloride. The chloride is reduced electrolytically providing chlorine for recycle. The approach eliminates emissions of fluorides and could cut electrical power consumption by 30% (78, 79).

Another process, called the Toth process, announced by the Applied Aluminum Research Corporation (AARC) of New Orleans, begins with a chlorination step that can use many types of alumina including some low grade minerals. Impurities are separated by fractional condensation. Aluminum chloride is then reacted with manganese metal to produce aluminum metal and manganese chloride (80).

The reaction proceeds quickly and at moderate temperatures, as low as 500°F. By-product manganese chloride from this process is converted to the oxide and the chlorine recycled. The manganese oxide is reduced carbothermally. Operating costs of the Toth process could be 20-45% less than for the conventional Bayer-Hall process (80).

Both Reynolds Metals and Kaiser Aluminum are licensing a USSR developed technique for ingot casting. The ingots are free of the undesirable "skin" that must be trimmed off those produced conventionally. In the Soviet method, skin formation is forestalled because the casting molds use an electromagnetic field that prevents the aluminum from touching the mold walls (82).

Officials of the Georgia Department of Industry and Trade were trying to get funding to build a pilot plant that would produce 5 tons/day alumina from kaolin clay via a nitric acid extraction process. The alumina content of kaolin averages 35-39%. Georgia has a 5 billion ton deposit of kaolin in the middle of the state. Costs for extraction would be roughly the same as from bauxite. It would have the advantage of being a fully domestic raw material whereas much of the bauxite consumed in the U.S. is imported (81).

Alcoa, as a hedge against future shortages of bauxite, announced purchase of a large deposit of anorthosite, a rock composed almost entirely of feldspar from which alumina can be recovered (83).

Magnesium.—Magnesium production hit a record 125,000 tons in 1972 due to a substantial increase in the fourth quarter. Fourth quarter output was approximately 34,500 tons compared to 29,000 tons for the previous quarter and 31,101 tons for the final quarter of 1971. The total output for 1971 was 123,485 tons (84).

U.S. consumption of primary magnesium metal in 1972 was 105,000 tons leaving an excess of 20,000 tons (85). Based on ten-month figures, the U.S. was a net exporter; 15,454 tons exported to 4,108 tons imported (84).

In plant operations and proposals, American Magnesium Company expects to have its 20,000 tons/yr plant in Snyder, Texas back into operation around the end of 1973 and plans to eventually increase production to design capacity of 30,000 tons/yr (85).

In Utah, N.L. Industries' magnesium and chlorine plant at Rowley, on the Great Salt Lake, started limited production with some trial shipments of 5,000-10,000 pound lots. Their December price list quoted 36.5¢/lb for solid ingot (86).

The proposed Alcoa plant at Addy, Washington will apparently use the Frech Magnatherm Process to extract magnesium and silicon from dolomite limestone in the area, Alcoa having received license for its use from Pechiney Ugine Kuhlmann. Construction on the $50 million, 40,000 tons/yr, facility is slated to begin in April, 1973 with start-up proposed for March, 1975 (87, 88).

Elsewhere in magnesium, Dow Chemical Company, which produced most of the 125,000 tons output last year, upped its prices by 1¢/lb in January, 1973. The new prices are 99.8% pig, 38.25¢/lb; AZ91B die casting, 33.75¢/lb; notched ingot, 39¢/lb. Dow also increased prices of magnesium oxide by $10/ton bulk (89).

Battelle's Magnesium Research Center in Columbus, Ohio is investigating a method of fluxless melting and casting of magnesium. This involves using SF_6 gas as an oxidation inhibitor in concentrations of 9.1% instead of flux. They look for a savings in price of 4¢/lb as well as a decreased risk of air pollution, less by-product sludge, and other benefits (90).

In Detroit, enthusiasm was rising due to new casting methods, the Frech process, as well as the fluxless melting technique. The Frech process is a hot casting method used in Europe which allows for increased automation as well as greater production speed (91). The enthusiasm for magnesium is due to a desire for less weighty engine elements for new automobiles which have more components to meet safety requirements. American Magnesium is known to be evaluating one or more large (119,000A) electrolyzers of Russian design (85).

Manganese.—There was no actual production of manganese ore containing 35% or more manganese in the United States in 1972 according to the Bureau of Mines, U.S. Department of the Interior.

Production of manganiferous ore, in Minnesota and New Mexico, was at a reduced rate from that of the previous year. Imports of ferromanganese were at an appreciably higher rate than in 1971, with the Republic of South Africa and France the principal sources. General imports of manganese ore containing 35% or more manganese were expected to be down to 1,800,000 tons with Gabon and Brazil continuing to be the two largest suppliers.

Domestic consumption of manganese was again expected to decrease from that of the previous year; a figure of 2,050,000 short tons is indicated. Consumption of ferromanganese and silicomanganese appeared to be little changed from 1971. Problems of pollution control, power availability, and imports, continued to face the producers of manganese ferro alloys (92).

In March, the American Metal Market dropped its price quotation for manganese ore containing 46-48% manganese from 59-63¢ nominal to 58-61¢ nominal per long ton unit. The producer's price for standard high carbon ferromanganese having a minimum manganese content of 78% continued at $190/long ton, FOB producer plant. American Metal Market's quote for the 78% alloy was $178-$180/long ton. Standard electrolytic manganese metal remained priced at 33.25¢/lb FOB producer plant for shipments of 30,000 lb or more (92).

South Africa's Electrolytic Metals Corporation is planning to boost electrolytic manganese production from 12,000 to 17,500 tons/yr. The added tonnage will be available by July, 1973 since only increased cell and auxiliary capacity is needed (93).

Delta Manganese, a subsidiary of London based Delta Metal Company Limited, is in the process of building an electrolytic manganese metal plant at Nelspruit, Eastern Transvaal, Republic of South Africa. Plans call for production to start by 1974 with initial capacity of 16,000 tons/yr to be achieved within two years (92).

The world's first commercial pellet plant for manganese ore, that of Industria e Comercio de Minerios S.A. at Santana, Amapa Territory, Brazil produced its first pellets in May (92).

The General Services Administration continued to offer surplus metallurgical grade manganese ore for sale on a negotiated basis with deliveries limited to 30,000 tons/fiscal yr. The offers met with little response (92). Interest was shown in manganese catalysts for the control of automotive emissions, with indications of cost and technical advantages over platinum. Bell Laboratories reported on its work with rare earth oxides of manganese. In Japan, Mitsui Mining and Smelting Company was prepared to market a newly developed manganese catalyst afterburner (92).

The Ethyl Corporation announced a manganese-based fuel additive package for use with lead free gasoline. According to Ethyl, the additive would bridge the gap between leaded and unleaded gasolines and will not poison platinum catalysts used in automobile exhaust systems (95).

The use of manganese additives to gasoline to improve their octane rating and to fuel oil to reduce pollutants and smoke from stack gases and exhaust from turbines has been criticized because of the neurological effects associated with long-term inhalations of high concentrations. An industry spokesman pointed out that the increase of manganese in the air from fuel was extremely small and posed no health problems. Manganese in the air of all major cities has been under observation by the Environmental Protection Agency and the U.S. Public Health Service for a number of years. Concentration ranges up to 14 μg manganese/m^3 have been noted. However, the average is much lower and none of it comes from fuel use. Apparently there are no neurological effects below 5000 μg/m^3 (94).

Hughes Tool Company launched a giant barge for a project in the Pacific involving the deep sea mining of manganese nodules from the ocean floor at depths up to 12,000 feet (96).

Beryllium.—Domestic consumption of beryllium ore decreased somewhat in 1972 from that for 1971. Imports declined again in 1972 to 3900 tons, down 7.2% from the preceding year. At mid-year the government stockpiles contained 229 tons of beryllium metal and 7,387 tons of beryllium-copper master alloy, both unchanged from 1971. Stockpiles also contained 20,296 tons of beryl ore (11% beryllium oxide equivalent), 712 tons less than the 1971 figure. U.S. production, approximately equal to last year, was almost entirely from Brush-Wellman's Utah mine (97).

Of the total beryllium demand, two-thirds of the metal went to alloys which are coming into increased use in electrical components. Because of beryllium-copper's high strength, electrical conductivity, and fatigue resistance, the alloy is being sought for electrical connectors in areas which require high reliability such as business machines, aircraft, communications, etc. (98).

A beryllium-titanium combination was found to improve qualities which allows fabrication of turbine blades of better aerodynamic shape, capable of higher speeds with superior resistance to both fatigue and to foreign objects striking the blades (99).

In May, Brush-Wellman was awarded a $13.5 million contract by the Navy to supply beryllium components for the Poseidon missile program (100).

During 1972 the price of the pure metal remained constant at $30-35/STU though some price reductions were posted for selected beryllium copper products (101).

Chromium.—Mining of chromite ore in the United States ceased in 1961; however the United States in 1972 continued to be one of the world's largest consumers according to the Bureau of Mines, U.S. Department of the Interior. Domestic consumption of chromite increased about 5% compared with 1971. The refractory industry accounted for most of the increased usage (102).

Total consumption of chromite during 1972 was 1,138,000 tons, an increase of 4.2% over 1971's 1,092,967 ton consumption (103).

Imports of chromite were lower than domestic consumption, but shipments of chromite from government stockpiles, sold in prior years, helped to reduce drawdown of the consuming industries stocks. Imports of chromium alloys reached a new yearly record high in August and were expected to reach 140,000-150,000 tons for the year (102).

A total of 12,556 tons of chemical grade chromite and 13,620 tons of refractory grade chromite were sold under these programs (102).

Published prices of chromite in 1972 per long ton FOB cars Atlantic ports, were as follows: South African (Transvaal) 44% chromium oxide, no ratio $24-27; Turkish 48% chromium oxide, 3 to 1 chromium to iron ratio $55-56 and Russian, 48% chromium oxide, 4 to 1 ratio, $45-46.50/metric ton loading point. This compares with the 1971 published price of $55-56 on the same pricing basis (102).

Some chrome ore was brought into the U.S from Rhodesia after March. Importation was legalized by the Byrd Amendment to the Military Authorization Act of 1971 which lifted the embargo on Rhodesia chrome. Without Rhodesian chrome domestic producers would be largely dependent on the Soviet Union for their requirements. Russian chrome increased from $25/ton to over $70 at one point in 1971, since the economic sanctions against Rhodesia went into effect in 1966. With the lifting of the embargo, prices have declined to their present levels (104, 105, 107).

Although chromium finds its largest market in the metallurgical refractories and chemical industries, the use of chrome-plated plastics by the automotive industry is growing at a rapid rate. Techniques are now available and in commercial use for applying chrome plate onto a variety of plastic surfaces. At the present time about 90% of the plastic currently being plated is ABS. The big gainers in the trend to plated plastics are plastics and suppliers of processes for treatment and plating. The main losers are the zinc producers and the zinc die casters (106).

Chrome producers are also looking to a substantial new market for chrome alloys which is expected to develop as the automotive industry adopts antipollution devices in new model cars. This could account for a total annual consumption of 40,000 tons of contained chrome on all new model cars after 1974.

Titanium.—The general titanium metal picture in 1972 showed improvement over 1971. Sponge consumption and ingot production were 7.5 and 10% higher, respectively, consumption of scrap and ingot increased 27% and 14% respectively, and stocks of sponge were reduced 300 tons during the ten month period (108).

	Metal production (short tons)			Metal consumption (109)		
Type	1971	1972	% Change	1971	1972	% Change
Sponge				12,145	13,068	7.5
Ingot	18,387	20,267	10	17,058	19,498	14
Scrap				6,149	7,801	27

Estimated industry capacity is 85 million lb for ingot and 47 million lb for sponge (110). Titanium Metals Corporation of America (TMCA) and Reactive Metals Incorporated (RMI) Companies, having reduced their inventories, reopened their sponge producing plants in February and April respectively to meet current orders. On June 28, GSA announced contracts for these companies. Each firm will deliver 6.5 million lb of sponge over a 2 yr term. These purchases by GSA will bring the stockpile holding up to 67 million lb (108).

Negotiations with Oregon Metallurgical Corporation for similar sponge deliveries have not been concluded. Importation of titanium sponge mostly from Japan totaled 4,000 short tons, an increase of 45% from 1971. Exports of mill products were one million pounds, an increase of 25% over 1971 (110).

The following chart shows the shifting pattern for titanium mill products (111):

	1961	1971
Commercial aircraft		
Airframe	4%	15%
Engine	10%	31%
Military aircraft		
Airframe	26%	10%
Engine	37%	20%
Missiles and space	16%	7%
Helicopter and ordnance	2%	1%
Industrial	5%	16%

Three general applications for titanium have formed the basis for the most recent growth in the industrial

category; the expanding use of titanium as a substrate for anodes used in the production of chlorine and related products, use of cathode structures in metal electrowinning processes and the evolution of low-cost welded tube product for containing brine or chlorine solution during heating or cooling processes and also for power plant surface condensers (111).

Domestic prices for titanium sponge (99.3% purity) at $1.32/lb remained unchanged for the second year while the same grade Japanese and United Kingdom sponge remained at the 1970 level of 1.20 to 1.25 U.S. dollars per pound. The price of rutile pigment at year end was 26 to 27¢/lb.

The titanium pigment industry found itself in tight supply throughout most of 1972. Domestic consumption of titanium dioxide was 780,000 tons, up about 42,000 tons from 1971. This was met by domestic production which was virtually the same as last year at 680,000 tons with the difference coming from imports.

Du Pont is reported going totally to the chloride route to produce titanium dioxide. The sulfate process plant in Baltimore, Maryland was closed and its production switched to Edge Moor, Delaware where the chloride process is used. In addition, Du Pont is doubling the capacity at New Johnsonville, Tennessee to 228,000 tons. Kerr-McGee, which has a 37,000 ton unit at Hamilton, Mississippi, is expanding the rated capacity of that plant in excess of 46,000 tons after the first quarter of this year (112).

Rutile production was reported for the first time in the United States since 1967 with the start-up of Titanium Enterprises' mine located at Green Cove Spring, Clay County, Florida. Planned production rate for total heavy mineral concentrate is 140,000 tons annually.

Benilite Corporation of America has licensed its process for converting ilmenite to rutile to Taiwan Alkali Company; production is expected late in 1973.

For the first time reconstituted rutile made from ilmenite became a factor in the market; imports were mainly from Australia and Japan.

Du Pont concluded an agreement with Allied Minerals NZ for joint operations of the heavy sand deposit at Eneabba, Western Australia. A pilot plant facility is to be operated first to study the full-scale production feasibility (108).

Lithium.—Production and consumption of lithium compounds during 1972 was at a record high according to the Bureau of Mines, U.S. Department of the Interior. Lithium carbonate produced from brines in California and Nevada accounted for much of the increase.

As a result of trade sanctions, domestic imports from Southern Rhodesia were nil for the fourth consecutive year. Previously they were over 90% of domestic imports. Although domestic exports were strong, Russian exports continued to penetrate the foreign market (113).

Foote Mineral Company mined spodumene at Kings Mountain, North Carolina and recovered lithium carbonate from brines at Silver Peak, Nevada. Lithium carbonate was recovered from brines at Trona, California by American Potash and Chemical Corporation. Lithium Corporation of America mined and milled spodumene at Bessemer City, North Carolina. Great Salt Lake Minerals and Chemical Corporation formed by Lithium Corporation of America and Salzdetfurth A.G., West Germany, harvested salts from the Great Salt Lake in Utah.

Processors of lithium raw materials to lithium primary products were Foote Mineral Company, American Potash and Chemical Corporation, and Lithium Corporation of America. Production data are not available for publication (113).

Industrial domestic uses were in ceramics and glass, greases, welding and brazing fluxes, air-conditioning equipment, rubber and pharmaceuticals.

Important developing markets for lithium were the large-scale use of lithium carbonate by the aluminum industry and the increased use of lithium hypochlorite for bleaches and as a sanitizing agent for swimming pools (113).

Much of the new research in lithium has been directed towards the development of light weight, high energy batteries. The AEC is working on a lithium-sulfur battery to power an automobile. The battery can deliver more than 100 Whr/lb, or five times more than the power of lead-acid batteries (114). Foote Mineral continues to support an active development program on lithium batteries for military uses (115). Lockheed announced development of a light alkali metal battery fueled with water and either sodium or lithium. According to Lockheed the battery will produce 10-100 times more electricity than a lead-acid battery when compared on a pound for pound basis (116). Other companies reportedly working on primary lithium batteries for consumer use are GTE Laboratories, ESB Incorporated, and P. R. Mallory (114).

In another field of research, the National Institute of Mental Health reported that the daily use of lithium carbonate may be effective in preventing broad swings in mood in people who suffer from manic-depressive state (117).

The price of 99.9% pure lithium metal at year end was $8.18/lb in 1000 lb lots; lithium carbonate was 52.5¢/lb in carload lots (118).

Copper.—During 1972 copper production from U.S. mines started relatively low and fluctuated greatly during the year, from 130,000 tons in January to a high of 147,000 tons in March to a low of 115,000 in July. Total mine production of recoverable copper was 1.64 million tons, an increase of 9% over last year's figures. Smelter output from domestic ores increased by 12% over 1971, to a figure of 1.67 million tons. Refinery production from primary materials was estimated to increase 13%, to a record high of 1.8 million tons. Production of refined from secondary materials was 420,000 tons, 5% greater than in 1971 (119).

Consumption of copper during 1972 was up 7% over the 1971 figures, to 2.22 million tons. U.S. imports of unmanufactured copper totaled 415,618 tons, up 15% from 1971. U.S. exports of refined and scrap copper was 200,000 tons, down 3% from 1971. Fabricator stocks of copper in all forms trended erratically downward from 511,000 tons at the start of the year to 471,000 by the end of October.

Over-all prices in 1972 on the domestic scene decreased 0.6¢/lb for electrolytic wirebar copper to 51.44¢/lb, while on the LME wirebar copper was quoted at an average of 48.53¢/lb, an increase of 0.04¢/lb (119). Prices were highest in March, 53.75¢/lb, and lowest in November, 47.00¢/lb, for copper in the domestic outside merchant market (120).

In the areas of plant proposals and announcements, Anaconda Company has started construction of a $22 million plant at Anaconda, Montana which is expected to produce 36,000 tons/yr of copper. The method of production uses ammoniacal hydrometallurgy to convert sulfide ore to copper metal. The process utilizes only chemical and electrical techniques eliminating the roasting and smelting steps that cause fumes, dust, and sulfur dioxide pollution. In this process, devised by research personnel at the Anaconda Primary Metals Division, Tucson, Arizona, copper concentrates are leached with ammonia at low temperature and pressure. The copper is extracted from this using an organic solvent and then an acid electrolyte, and finally, the metal is recovered by electrowinning. The main advantages of the process are that the equipment and plant costs may be reduced to one-tenth and one-half, respectively, that of conventional plants with the added bonus of being pollution free (121).

Also in copper production in January of 1972, Phelps Dodge Corporation disclosed that it had discovered a mineral zone in the Northwestern area of the Cape Province of the Republic of South Africa. The mineral zone is reportedly rich in lead and copper with minor zinc and silver values. Results from test drillings and

assays place the copper content at 0.8% and lead at 1.5%. The deposit is estimated to be 130 ft thick and 3000 ft long (122).

In Pinto Valley, Arizona, Cities Service Company started site preparation work on a 40,000 tons/day mine and mill complex. Two and one-half years will be needed to bring the ore body into production including an open pit mine which is expected to produce 125 million lb/yr of recoverable copper and molybdenum. The ore will be processed at the Inspiration Consolidated Copper Company facilities located nearby (123).

American Smelting and Refining Company has plans for a new copper mine near Casa Grande, Arizona, and a plant at Tucson for chemically recovering the copper. The plant and mine should be ready for operation by 1974 (124).

Phelps Dodge anticipates a mid-1974 starting date for operations at its Metcalf copper mine near Morenci, Arizona. The mine is expected to produce 50,000 tons/yr of ore (124).

A new pollution-free process to produce copper, elemental sulfur, and high grade iron from copper concentrates is being studied for commercial feasibility at a plant built and operated by Cyprus Metallurgical Process Corporation near Tucson, Arizona (125).

In a move which angered Chile's President Salvador Allende, a French court issued an injunction blocking distribution of Chilean copper in France in October. The court action was requested by Kennecott Copper on the grounds that despite the nationalization of its El Teniente mine it still retains its rights to the copper from the mine. Kennecott officials said they were prepared to take action throughout Europe if the court case was lost in France (126).

Still occupying a place in the limelight is the environmental part of copper production. Stringent limits on sulfur dioxide emissions have been declared and must be met by 1975. Various methods are being tried to achieve these limits using scrubbing or concentrating techniques, hydrometallurgical processes, and other methods to keep the gases from polluting the atmosphere. No matter which method is used, however, it appears certain that to meet standards in time great amounts of money will be needed and this will, no doubt, influence the copper market greatly in years to come (127). Capital investment costs to meet pollution controls through 1976 are estimated to range from 300 to 690 million dollars. Depending upon costs and foreign competition, it was estimated that U.S. supplies may be reduced 3.5-14% and U.S. prices increased by as much as 8% (128).

Development of precious metal anodes in conventional solvent extraction electrowinning facilities will permit electrorefined quality copper to be produced and could in itself prove to be a major factor in determining an acceptable solution to the pollution control problem (129).

Nickel.—Data published by the U.S. Department of the Interior indicate that the level of activity in the domestic nickel industry in 1972 was changed little from that in 1971. Domestic mines produced approximately 17,000 tons of nickel from laterite ore, from which the processing plant recovered about 13,000 tons of nickel in ferro nickel. By-product plants recovered about 2500 tons of nickel in various forms. Primary nickel consumption was approximately 165,000 tons, up 18% from 1971 (130).

A worldwide surplus of nickel supply over demand continued for the second full year. However, depressed demand, which was partially responsible for the surplus was alleviated in the U.S. by increased industrial activity in the last three quarters of the year (130).

Congress authorized disposal of all the nickel held in the national stockpile. Reportedly it will be sold to the Treasury Department for use by the mint (130).

Increasing imports of ferro nickel for consumption in the U.S. marked a substantial change in the pattern of nickel usage. Imports of ferro nickel from Japan, the Dominican Republic, New Caledonia, and Greece were reported (130, 133).

With nickel inventories near record highs at the start of 1972 major producers such as International Nickel Company and Falconbridge Nickel Mines announced cutbacks in production of 30% and 5% respectively (131).

Amax Nickel Refining Company announced that the metal refinery at Port Nickel, Louisiana purchased from Freeport Minerals, would be expanded and reactivated. The plant, originally built to handle nickel and cobalt concentrates from Moa Bay, Cuba, will start up in early 1974 with a capacity of 80 million lb/yr of nickel. Initial feed will be 54,000 tons of nickel-copper matte from Bamangwato Concessions Limited (Africa) (132).

By the end of 1972 the nickel business appeared to be improving slowly. However, primary metal producers indicated it might be a year or more before consumption gets fairly close to capacity. There appears to be optimism in the outlook for more growth in nickel plating, automobiles, housing, and accessories for auto catalytic units and the coming Wankel engine (133).

A high-yield hydrometallurgical process for recovering nickel from laterite and sulfide ores has been developed by Republic Steel. A 92% recovery is claimed. The system can handle grades of ore over a wide range, including low-grade sulfide concentrates, and it does not emit sulfur oxide gases (134).

Prices for primary nickel increased by 20¢/lb to $1.53 on the first of September, 1972.

Zinc.—U.S. mine production of zinc continued its decline through 1972 to 491,000 tons, down 2% from 1971 (135). The number of states reporting mine production in 1972 dropped to 17, two less than 1971. Ten states showed decreases, seven registered increases, and no production changes were reported from Montana or Nevada (136).

Smelter production from ore declined 150,000 tons. The decline resulted from lower mine production and a drop in imports of zinc concentrates. General imports of zinc in concentrates decreased 24% below that of 1971 to approximately 260,000 tons which is less than half the tonnage received in 1970 before the smelter closures (137). U.S. zinc metal production decreased by 62,000 tons to 774,500 tons. Japan in 1972 became the world's largest producer of zinc metal with 883,500 tons (138).

Imports of zinc metal increased to 525,000 tons, a 64% increase over 1971. Canada accounted for over half of the 200,000 ton increase in imports for 1971 (136).

Authority was given in April to dispose of 515,200 tons of zinc from the national stockpile for domestic use. Of this quantity of zinc, 171,375 tons had been disposed of by November, 1972.

If this rate of disposal continues, the surplus of zinc in the stockpile will be used up in two more years instead of nine as originally planned (136).

U.S. consumption of zinc in 1972 is indicated below (139):

Bases: Recoverable zinc content	Tons 1971	Tons 1972	% Change
Zinc slab	1,254,059	1,428,632	+14.0
Ores	119,258	140,400	+18.0
Zinc base scrap Copper base scrap Al-Mg base scrap	277,272	300,000	+8.2
Totals	1,650,589	1,869,032	+13.2

Consumption of zinc in the United States rose 13% to slightly over 1.87 million tons for an all time high. Increases were recorded for all but one of the broad use categories for 1972 as compared with 1971; galvanizing up 6%, brass and bronze up 38%, zinc-base alloys up 15%, rolled zinc up 40% and zinc oxide up 21%. The decline of 8% for other uses included wet batteries, zinc dust, light metal alloys, and desilverizing lead (136).

The cost-price squeeze was a major factor in the closures of five mines and two electrolytic smelters. The closure of the two smelters accounted for a capacity reduction of 252,000 tons and removed Anaconda from the zinc business. Two horizontal retort plants are scheduled to close in December, 1973, reportedly because it is uneconomical to install required air-pollution control equipment (137). Industry wide an estimated 62 million dollars will be required for the zinc industry to meet the 1976 pollution control standards. This will accelerate the trend towards the demise of high-cost producers (140). However, on the positive side a new zinc-copper mine was brought into production early in October by Kerramerican Incorporated at Bluehill, Maine (136). Asarco is planning to expand its 108,000 tons/yr electrolytic plant at Corpus Christi and in addition is planning a new electrolytic plant to go into operation by 1975 at another location (141).

With regard to technological improvements, the jarosite process in use at Texas Gulf Incorporated's new 120,000 tons/yr electrolytic zinc plant near Timmins, Ontario is reported to increase over-all zinc yield from 88 to 93%. The 5% boost in production is obtained by preventing zinc losses as zinc ferrite in the leaching operation (142). A process in use at Bunker Hill's Kellogg, Idaho electrolytic zinc plant is purported to reduce the mercury content of acid obtained from ore roasting at the plant from 100 ppm to less than 1 ppm (143).

The price of domestic zinc (prime western) was frozen at 18¢/lb by the Cost of Living Council, but the price of foreign zinc for sale in the U.S. increased three times during the year and in December reached 19.5, 20.00, and 20.25¢/lb depending on the source, country, and company (137). A new grade of foreign zinc was introduced in December, continuous galvanizing zinc (CGG), and was priced at the 20.25¢/lb (144). A number of requests to the Cost of Living Council have been made to declare zinc an international commodity and free from price control but have been rejected. There is some feeling that reconsideration is being contemplated, and some favorable action may be forthcoming.

Electrical Energy

U.S. power generation.—The following tables summarize the production and consumption of electrical energy for the twelve-month period January through December, 1972.

Production of Electrical Energy (Billion-kWhr)

	1971*	1972* (157)	Change (157)
Production by electric utilities			
Coal fired plants	714.8	770.6	+7.8
Gas fired plants	375.9	375.7	0.0
Oil fired plants	218.2	272.5	+24.9
Nuclear plants	37.9	54.0	+42.5
Total fuel burning	1,347.6	1,472.8	+9.3
Hydroelectric	266.3	272.7	+2.4
Total	1,613.9	1.745.5	+8.2
Private industry, self-generated	103.5	106.1	+2.5
Total U.S. power consumption	1,717.5	1,851.6	+7.8

* Both 1971 and 1972 figures are preliminary.

Installed Generating Capacity (Million-kW)

	1971	1972 (157)
Public owned capacity		
Steam	42.8	46.6
Hydro	36.8	37.3
Nuclear	0.9	0.9
Total	80.5	84.8
Investor owned capacity		
Steam	260.0	281.1
Hydro	19.1	19.3
Nuclear	7.8	14.4
Total	286.9	314.8
Total electrical utility industry capacity*	367.4	399.6

* Not including privately owned capacity.

Fuel Consumption—Electric Utility (12 months ending Dec. 31, 1972)

	1971	1972 (157)	Change (157)
Coal—millions of tons	327.93	351.0	+7.0
Gas—billions of cu ft	3992.98	3978.7	−0.3
Oil—millions of barrels	396.24	493.9	+24.6
Coal and coal equivalent—millions of tons	618.16	646.3	+4.5

Sales to Ultimate Consumers (12 months ending Dec. 31, 1972) Total industry (billion kWhr)

	1971	1972	Change
Residential	479.1	511.4	+6.8
Commercial	333.7	361.8	+8.4
Industrial	592.7	639.5	+7.9
Other	60.9	64.9	+6.5
Total	1466.4	1577.7	+7.5

Studies by various private and government organizations indicate that the United States is facing an energy crisis which is likely to remain critical over the next ten to twenty years. After that it is felt that new technology should start making its presence felt in a big way (145, 146).

Total energy requirements are expected to increase from 74 quadrillion BTU's in 1972 to a range of 112 to 130 quadrillion BTU's by 1985. Consumption of primary energy by the electrical utility industry is expected to grow from 19 quadrillion BTU's in 1972 to 44 quadrillion BTU's in 1985. This represents an increase in share of the total energy from 25% in 1972 to 36% in 1985 (147).

It is anticipated that the bulk of electrical power produced in the 1970's will be from fossil plants; in the 1980's from light water nuclear plants; and by the end of the 1990's from fast breeder nuclear plants.

The cost of electricity to large industrial customers is expected to double in the next 30 years. The following projection has been made of the average industrial rate for electrical power in the Detroit Edison system (148):

Year	Cost
1940-1970	1.0 to 1.2¢/kWhr
1980	1.4¢/kWhr
2000	2.0¢/kWhr

Nuclear power.—Only 4% of our present electrical energy requirements are provided by nuclear power, up from 2.2% in 1971. The National Petroleum Council (NPC) projects 300,000 MW of installed nuclear capacity by 1985. This would supply 48% of the total requirement for electricity (149).

During 1972, the Atomic Energy Commission (AEC) issued full power operating licenses for 7 nuclear power reactors, partial-power licenses for 2 others and construction permits for an additional 8 units. New applications during the year for construction of 6 new units, brought the number of nuclear power plant facilities licensed for operation and construction, or under AEC review for construction to 116 at year end. The partial-power licenses and several voluntary restrictions on power-generating levels were brought about by a fuel rod densification problem that was discovered during the spring at the Ginna Nuclear Power Plant (150).

At the end of 1972, the status of nuclear power plants in the U.S. was as follows (151):

29 Operable plants	14,683 Mwe
55 Being built	47,775 Mwe
76 Ordered	80,000 Mwe
160	142,458 Mwe

Of the plants ordered, 43 totaling some 45,500 Mwe (1 Mwe = 1,000 kW) in capacity are not yet under AEC licensing review.

The average time now for processing a construction permit application has risen from 12 months (1968) to 22 months. A combination of technological and environmental problems has disrupted the nuclear power program. The schedule called for 65 nuclear generators to be placed in operation between 1970 and 1975, but 23 have been delayed for periods ranging from a few months to years. In general, the program is two to three years behind the original timetable (149, 150).

The annual growth of nuclear power since 1957, when the first commercial plant (Shippingport, Pennsylvania) went into operation has been (151):

Year	Nuclear units ordered	Installed capacity (Mwe)
1972	35	37,929
1971	20	19,921
1970	14	14,305
1969	7	7,203
1968	14	12,872
1967	30	25,427
1966	20	16,345
Thru 1965	20*	8,456
Total	160*	142,458

* Excludes 7 small prototype plants no longer in operation.

Demand for nuclear fuel.—The table below commutes the forecasted growth of nuclear power to the requirements for uranium:

Year	Generating capacity GWE	U_3O_8 requirements short tons
1972	12	9,200
1975	59	18,200
1980	150	37,000
1985	300	66,600

The AEC estimates that there are sufficient recoverable reserves available to be mined at costs under $10/lb in the U.S. to meet domestic U_3O_8 requirements through 1985. However, unless mine exploration and development drillings are increased and new ore processing mills built or present ones expanded, the AEC predicts a shortage of uranium concentrate by 1980 (152).

Facilities for enrichment to uranium 235 appear, after completion of current improvement and upgrading programs, sufficient to meet needs until the early 1980's. To meet enrichment needs of the early 1980's and beyond, the AEC is encouraging private industry to develop plans directed toward the construction and operation of new commercial uranium enriching facilities (151).

AEC has a pilot plant facility under construction at Oak Ridge, Tennessee to demonstrate the operation of a uranium isotope separation cascade using the gas centrifuge process. This facility will be used to better define the economics of the centrifuge process as compared to the gaseous diffusion process for meeting the increased separative work requirements for enrichment of uranium in the post-1980 period. The facility is expected to be in operation by mid-1976 (151).

Nuclear authorities have calculated that with the expected growth in nuclear power and using only light-water reactors, the low cost uranium resources will be used up in less than 30 years. The AEC is working towards providing a cure with the fast breeder reactor. The light-water reactors are only able to recover less than 2% of the energy potentially available in natural uranium. The fast breeder, on the other hand, is able to recover some 70% of the energy potentially available in natural uranium (153).

Russia is reported to have started up the world's first commercial-scale nuclear breeder reactor this year (154). The U.S. is committed to successfully demonstrate a commercial size plant by 1980 (151).

New developments.—Superconductive materials are now being employed in electrical generators. The key feature of the generator is the windings of niobium titanium wire. When refrigerated to cryogenic temperatures, these windings can carry about 50 times more electricity than conventional generator windings, producing a magnetic field three to four times greater than normal. Because of such performance, superconducting generators are expected to occupy 10-30% the volume of conventional generators and to lose much less energy through dissipation as heat. By the late 1970's, this type of generator is expected to be commercial for ships, aircrafts, and central power stations (155).

A British firm is studying a concept whereby high-temperature gas cooled nuclear reactors will heat gases to high temperature reducing levels for production of iron and furnish electricity for downstream steel-making operation (156).

A new type of battery now under development at the Argonne National Laboratories shows promise of economically storing electrical energy produced during nighttime hours for use during peak-load periods. Design calculations show the lithium/sulfur battery is potentially capable of storing 11,000 kWhr of electric energy in a unit weighing 5-8 tons. The design goal is a battery costing only $15/kWhr of storage capacity (150).

Research in thermonuclear power continues to build up but there has as yet been no demonstration of technological feasibility. Commercial application of this source of power is still predicted after the year 2000.

Manuscript received July 23, 1973. This report was presented at the Industrial Electrolytic Luncheon at the Chicago, Illinois, Meeting of the Society, May 13-18, 1973.

Any discussion of this report will appear in a Discussion Section to be published in the June 1974 JOURNAL.

REFERENCES

1. H. W. Schultze, Chlorine Institute, Feb. 7, 1973.
2. R. Mitchell, Chlorine Institute.
3. Chlorine Institute Bulletin 10 Jan. 1973.
4. J. E. Currey, Hooker Chemical Corporation.
5. *Chemical Week*, p. 29, June 7, 1972.
6. *Chemical Marketing Reporter*, p. 22, June 5, 1972.
7. *Chemical Week*, p. 25, Sept. 13, 1972.
8. *Chemical Marketing Reporter*, p. 32, Jan. 1, 1973.
9. *Chemical Week*, p. 27, Feb. 28, 1973.
10. *ibid.*, p. 37, June 28, 1972.
11. *ibid.*, p. 13, Jan. 31, 1973.
12. *ibid.*, p. 31, Jan. 10, 1973.
13. *Chemical Marketing Reporter*, p. 34, Dec. 11, 1972.
14. *ibid.*, p. 3, Feb. 14, 1972.
15. *Ibid.*, July 31, 1972.
16. *ibid.*, June 26, 1972.
17. *ibid.*, Dec. 11, 1972.
18. *Chemical Week*, p. 43, April 12, 1972.
19. *ibid.*, p. 16, Aug. 2, 1972.
20. *ibid.*, p. 23, Feb. 14, 1973.
21. Diamond-Shamrock 1973 Cell Brochure.
22. *Chemical Week*, p. 43, April 26, 1972.
23. H. Stuart Holden, Electrode Corporation.
24. Mineral Industry Surveys, U.S. Dept of the Interior, Bureau of Mines, Annual Preliminary, "Mercury in 1972."
25. *Chemical Marketing Reporter*, p. 3, Dec. 11, 1972.
26. *Chemical Week*, p. 39, March 15, 1972.
27. *ibid.*, p. 47, Dec. 13, 1972.
28. *Chemical Marketing Reporter*, p. 4, July 24, 1972.
29. *Chemical Week*, p. 39, June 14, 1972.
30. *Chemical Marketing Reporter*, p. 32, Sept. 11, 1972.
31. *European Chemical News*, Sept. 1, 1972.
32. *Chemical Marketing Reporter*, p. 19, Oct. 23, 1972.
33. *Chemical Engineering*, p. 129, July 24, 1972.
34. *Chemical Marketing Reporter*, p. 17, Jan. 17, 1972.
35. *Chemical Week*, p. 40, March 14, 1973.
36. *ibid.*, p. 43, April 12, 1972.
37. *European Chemical News*, p. 28, April 14, 1972.
38. *Chemical Week*, p. 43, Oct. 25, 1972.
39. FMC, Company News Release.
40. *European Chemical News*, p. 29, Jan. 21, 1972.
41. Inorganic Chemicals, U.S. Dept. of Commerce, 1972.
42. *Chemical Marketing Reporter*, p. 3, Aug. 21, 1972.
43. *ibid.*, p. 28, Nov. 6, 1972.

44. *ibid.*, p. 12, Nov. 15, 1971.
45. *Engineering and Mining Journal*, p. 73, March, 1973.
46. Inorganic Chemicals, U.S. Dept. of Commerce, 1972.
47. *Chemical Marketing Reporter*, Nov. 13, 1972.
48. Mineral Industry Surveys, U.S. Dept. of the Interior, Bureau of Mines, Annual Preliminary, "Sodium Compounds in 1972."
49. *Chemical Marketing Reporter*, April 24, 1972.
50. *ibid.*, May 1, 1972.
51. *Chemical Week*, p. 28, March 14, 1973.
52. *ibid.*, p. 18, Feb. 14, 1973.
53. *Chemical Marketing Reporter*, December 11, 1972.
54. Inorganic Chemicals, U.S. Dept. of Commerce, January-December, 1972.
55. *Chemical Marketing Reporter*, p. 9, Dec. 25, 1972.
56. *Chemical Week*, p. 17, May 3, 1972.
57. *Chemical Marketing Reporter*, p. 19, Nov. 7, 1972.
58. *ibid.*, p. 29, Dec. 4, 1972.
59. *ibid.*, p. 5, Feb. 19, 1972.
60. *Paper Trade Journal*, April 2, 1973.
61. *Chemical Marketing Reporter*, p. 19, Nov. 27, 1972.
62. *ibid.*, p. 34, Dec. 11, 1972.
63. *Chemical Engineering*, p. 68, June 26, 1972.
64. Inorganic Chemicals, U.S. Dept. of Commerce, 1972.
65. *Chemical and Engineering News*, p. 6, Nov. 20, 1972.
66. *Chemical Engineering*, p. 51, March 20, 1972.
67. *Chemical Marketing Reporter*, June 5, 1972.
68. *ibid.*, Jan. 8, 1973.
69. Mineral Industry Surveys, U.S. Dept. of the Interior, Bureau of Mines, Annual Preliminary, "Aluminum and Bauxite in 1972."
70. *Chemical Marketing Reporter*, p. 22, May 8, 1972.
71. *Chemical Week*, p. 19, Jan 24, 1973.
72. *American Metals Market*, p. 8, December 15, 1972.
73. *Chemical Engineering*, p. 23, May 29, 1972.
74. *Chemical Week*, p. 24, Aug. 16, 1972.
75. *Chemical Marketing Reporter*, p. 4, Sept. 18, 1972.
76. *Chemical Week*, p. 12, Nov. 29, 1972.
77. *American Metals Market*, p. 10, Dec. 19, 1972.
78. *Business Week*, Jan. 11, 1973.
79. *Ibid.*, Jan. 20, 1973.
80. *Chemical and Engineering News*, Feb. 26, 1973.
81. *Chemical Engineering*, p. 17, Oct. 2, 1972.
82. *ibid.*, p. 71, Sept. 18, 1972.
83. *ibid.*, p. 73, July 24, 1972.
84. *American Metals Market*, Jan. 19, 1973.
85. *Engineering/Mining Journal*, March 9, 1973.
86. *Metals Week*, Jan. 8, 1973.
87. *Business Newsletter*, Jan. 24, 1973.
88. *Metals Week*, June 5, 1972.
89. *Chemical Marketing Reporter*, Dec. 18, 1972.
90. *Chemical Engineering*, Jan. 22, 1973.
91. *Chemical Week*, Jan. 17, 1973.
92. Mineral Industry Surveys, U.S. Dept. of the Interior, Bureau of Mines, Annual Preliminary, "Manganese in 1972."
93. *Metals Week*, p. 7, Nov. 27, 1972.
94. *Chemical Marketing Reporter*, p. 5, Sept. 18, 1972.
95. *American Metals Market*, p. 26, Nov. 29, 1972.
96. *Chemical Week*, p. 43, Jan. 26, 1972.
97. *Metals Week*, Jan. 8, 1973.
98. *American Metals Market*, Nov. 14, 1972.
99. Mineral Industry Surveys, U.S. Dept of the Interior, Bureau of Mines, Annual Preliminary, "Beryllium in 1972."
100. *Metals Week*, May 8, 1972.
101. *Ibid.*, Oct. 23, 1972.
102. Mineral Industry Surveys, U.S. Dept. of the Interior, Bureau of Mines, Annual Preliminary, "Chromium in 1972."
103. Mineral Industry Surveys, U.S. Dept. of the Interior, Bureau of Mines, "Chromium in December, 1972."
104. *Chemical Week*, p. 17, May 3, 1972.
105. *Ibid.*, p. 16, May 10, 1972.
106. *Business Week*, p. 58, Feb. 10, 1973.
107. *American Metals Market*, p. 1A, Oct. 18, 1972.
108. Mineral Industry Surveys, U.S. Dept. of the Interior, Bureau of Mines, Annual Preliminary, "Titanium in 1972."
109. Mineral Industry Surveys, U.S. Dept. of the Interior, Bureau of Mines, Titanium Quarterly, "Titanium in the Fourth Quarter 1972."
110. *Engineering and Mining Journal*, p. 124, March, 1973.
111. Application and Economics of Titanium 1972, Ward Minkler, Titanium Metals Corporation of America.
112. *Chemical and Engineering News*, p. 8, Feb. 19, 1973.
113. Mineral Industry Surveys, U.S. Dept. of the Interior, Bureau of Mines, Annual Preliminary, "Lithium in 1972."
114. *Chemical Week*, p. 55, May 24,1972.
115. *Chemical Marketing Reporter*, p. 5, May 8, 1972.
116. *Ibid.*, p. 7, Feb. 28, 1972.
117. *Chemical Week*, p. 41, March 8, 1972.
118. *American Metals Market*, Dec. 29, 1972.
119. Mineral Industry Surveys, U.S. Dept. of the Interior, Bureau of Mines, Annual Preliminary, "Copper in 1972."
120. *American Metals Market*, Jan. 4, 1973.
121. *Chemical Engineering*, Feb. 5, 1973.
122. *Chemical Marketing*, Jan. 31, 1972.
123. *Chemical Engineering*, p. 23, May 29, 1972.
124. *Chemical Week*, p. 21, May 17, 1972.
125. *Engineering and Mining Journal*, Dec., 1972.
126. *Chemical Week*, p. 17, Oct. 18, 1972.
127. *Mining Magazine*, pp. 279-285, April, 1972.
128. *Chemical Marketing Reporter*, March 20, 1972.
129. Howard I. Roe, Electrode Corporation.
130. Mineral Industry Surveys, U.S. Dept. of the Interior, Bureau of Mines, Annual Preliminary, "Nickel in 1972."
131. *Chemical Week*, p. 13, March 1, 1972.
132. *Ibid.*, p. 35, Jan. 17, 1973.
133. *American Metals Market*, p. 42, Dec. 11, 1972.
134. *Chemical Engineering*, p. 41, Dec. 11, 1972.
135. *Engineering and Mining Journal*, p. 73, March, 1973.
136. Mineral Industry Surveys, U.S. Dept. of the Interior, Bureau of Mines, Annual Preliminary, "Zinc in 1972."
137. *American Metals Market*, Jan. 4, 1973.
138. *Engineering and Mining Journal*, p. 131, March, 1973.
139. U.S. Dept. of the Interior, Bureau of Mines.
140. *Chemical Marketing Reporter*, March 20, 1973.
141. *Chemical Week*, p. 15, Aug. 30, 1972.
142. *Chemical Engineering*, p. 62, March 5, 1973.
143. *Chemical Week*, p. 47, Oct. 4, 1972.
144. *Metals Week*, p. 6, Dec. 12, 1972.
145. *Chemical Week*, p. 29, Sept. 20, 1972.
146. *Chemical and Engineering News*, p. 20, Nov. 13, 1972.
147. Guide to National Petroleum Council Report in United States Energy Outlook, Published by the National Petroleum Council—1972, p. 6.
148. *Chemical Engineering Progress*, p. 27, March, 1972.
149. *Chemical Week*, p. 35, Sept. 20, 1972.
150. 1972 Atomic Energy Programs, Regulatory Activities, p. 7.
151. 1972 Atomic Energy Programs, Operating and Developmental Functions.
152. *Engineering and Mining Journal*, p. 125, March, 1973.
153. *Chemical and Engineering News*, p. 35, Nov. 13, 1972.
154. *Chemical Engineering*, p. 18, Dec. 25, 1972.
155. *ibid.*, p. 70, Nov. 13, 1972.
156. *Ibid.*, p. 25, Feb. 5, 1973.
157. Robert Doelger, Edison Electric Institute.